




Bridge Maintenance, Safety, Management, Digitalization and Sustainability

Editors

Jens Sandager Jensen, Dan M. Frangopol and **Jacob Wittrup Schmidt**

IABMAS 25 CELEBRATING 25 YEARS

International Association for Bridge Maintenance and Safety

CRC Press
Taylor & Francis Group

BRIDGE MAINTENANCE, SAFETY, MANAGEMENT, DIGITALIZATION AND SUSTAINABILITY

Bridge Maintenance, Safety, Management, Digitalization and Sustainability collects the lectures and technical papers presented at the 12th International Conference on Bridge Maintenance, Safety and Management (IABMAS 2024, Copenhagen, Denmark, 24-28 June 2024). This Open Access book contains 480 contributions, including the T.Y. Lin Lecture, 9 Keynote Lectures, and 470 technical papers from 44 countries.

The contributions are presented bring together academic and technological developments in **Bridge Maintenance, Safety, Management, Digitalization and Sustainability**, to solve new and old problems with innovative solutions. Major topics include: advanced bridge design, construction and maintenance approaches, safety, reliability and risk evaluation, life-cycle management, life-cycle resilience, sustainability, standardization, analytical models, bridge management systems, service life prediction, structural health monitoring, non-destructive testing and field testing, robustness and redundancy, durability enhancement, repair and rehabilitation, fatigue and corrosion, extreme loads, needs of bridge owners, whole life costing and investment for the future, financial planning and application of information and computer technology, extensive data analysis and artificial intelligence for bridges, among others.

Bridge Maintenance, Safety, Management, Digitalization and Sustainability provides an up-to-date overview of the field of bridge engineering and significant contributions to making more rational decisions on bridge safety, maintenance, management, life-cycle, resilience, sustainability, and bridge innovations to enhance society's welfare. The Editors hope that this book will serve as a valuable reference to all concerned with bridge structure and infrastructure systems, including engineers, researchers, academics, and students from all areas of bridge engineering.


Taylor & Francis
Taylor & Francis Group
http://taylorandfrancis.com

PROCEEDINGS OF THE 12TH INTERNATIONAL CONFERENCE ON BRIDGE MAINTENANCE, SAFETY AND MANAGEMENT, 24-28 JUNE 2024, COPENHAGEN, DENMARK

Bridge Maintenance, Safety, Management, Digitalization and Sustainability

Edited by

Jens Sandager Jensen

COWI A/S, Lyngby, Denmark

Dan M. Frangopol

Lehigh University, Bethlehem, PA, USA

Jacob Wittrup Schmidt

University of Aalborg, Denmark



CRC Press
Taylor & Francis Group
Boca Raton London New York Leiden

CRC Press is an imprint of the
Taylor & Francis Group, an **informa** business

A BALKEMA BOOK

Designed cover images:

DJI_0003.JPG | Great Belt Bridge - FotoWeb (cowi.com) - Copyright © COWI 2024. All rights reserved.
06-07_BRIDGES_Great Belt Link_Knuth.jpg | Great Belt Link - FotoWeb (cowi.com) - Photo by Claus Knuth. Copyright © COWI 2024. All rights reserved.
01_Daniel Andersson_2002021115.jpg | Oeresund Bridge - FotoWeb (cowi.com) - Photo by Daniel Andresson. Copyright © COWI 2024. All rights reserved.
R_Hjortshoj - Koege Nord-142.jpg | Køge Nord Station - FotoWeb (cowi.com) - credited: 'Rasmus Hjortshøj - COAST'
R_Hjortshoj - Koege Nord Opening-16.jpg | Køge Nord Station - FotoWeb (cowi.com) - credited: 'Rasmus Hjortshøj - COAST'

First published 2024
by CRC Press/Balkema
4 Park Square, Milton Park, Abingdon, Oxon, OX14 4RN

and by CRC Press/Balkema
2385 NW Executive Center Drive, Suite 320, Boca Raton FL 33431

CRC Press/Balkema is an imprint of the Taylor & Francis Group, an informa business

© 2024 selection and editorial matter, Jens Sandager Jensen, Dan M. Frangopol and Jacob Wittrup Schmidt; individual chapters, the contributors

Typeset by Integra Software Services Pvt. Ltd., Pondicherry, India

The right of Jens Sandager Jensen, Dan M. Frangopol and Jacob Wittrup Schmidt to be identified as the authors of the editorial material, and of the authors for their individual chapters, has been asserted in accordance with sections 77 and 78 of the Copyright, Designs and Patents Act 1988.

The Open Access version of this book, available at www.taylorfrancis.com, has been made available under a Creative Commons Attribution-Non Commercial-No Derivatives (CC-BY-NC-ND) 4.0 license.

Although all care is taken to ensure integrity and the quality of this publication and the information herein, no responsibility is assumed by the publishers nor the author for any damage to the property or persons as a result of operation or use of this publication and/or the information contained herein.

British Library Cataloguing-in-Publication Data
A catalogue record for this book is available from the British Library

Library of Congress Cataloging-in-Publication Data
A catalog record has been requested for this book

ISBN: 978-1-032-77040-6 (hbk)
ISBN: 978-1-032-77560-9 (pbk)
ISBN: 978-1-003-48375-5 (ebk)
DOI: 10.1201/9781003483755

Bridge Maintenance, Safety, Management, Digitalization and Sustainability – Jensen, Frangopol & Schmidt (eds)
© 2024 The Editor(s), ISBN 978-1-032-77040-6
Open Access: www.taylorfrancis.com, CC BY-NC-ND 4.0 license

Table of contents

Preface xxxvii

Acknowledgements xxxix

Conference Organisation xli

IABMAS Executive Committee xlv

Sponsors xlvii

Editor Biographies li

T.Y. LIN LECTURE

Aesthetic value of bridges 3
M.-C. Tang

KEYNOTE LECTURES

Assessment of post-tensioned bridges in Norway 17
L. Bathen

Sustainability and digitalization in bridge management: How far we are? 27
J.R. Casas

Bridge management – past, present, and future 40
R.M. Ellis

Bridge engineering - Proving the sustainability case for refurbishment v replacement 50
D.K. MacKenzie

Thermo-mechanistic approach for evaluating service life of bridges and structural concrete 64
K. Maekawa & T. Ishida

From empirical and subjective O&M to statistical and objective asset management 77
S.C. Nørager

Innovations in building and bridge engineering associated with circular economy 85
L.M. Ottosen

AI support for bridge SHM and life cycle assessment 93
G. Marasco & S.N. Pakzad

Innovations in bridge management in Australia to rise to the challenges of today and the future 106
N.G. Powers

MINI-SYMPOSIA

MS01: Prediction and extension of the service duration of bridges
Organizers: A. Miyamoto, E. Brühwiler, R. Kiviluoma & A. Yabe

Field tests for remaining life prediction of aged bridges 119
A. Miyamoto

Behavior analysis of an integrated column by multiple steel pipes using monitoring measurement 132
S. Akamatsu, M. Hattori, Y. Taniguchi, M. Nishimura, Y. Aoki, S. Miyata & K. Sugiura

Prediction of bridge service duration for CBM by the indirect monitoring using vehicles 141
A. Yabe

Combining monitoring information and UHPFRC strengthening to extend bridge service duration 149
N. Bertola & E. Brühwiler

UHPFRC technology for the extension of the service duration of bridges 158
E. Brühwiler

Interpreting monitored responses of an orthotropic steel deck using FEM 167
S. Ye, R. Gibson, N. Yeung & S. Kite

Predicting time history response of bridges under vehicle load using CNN 175
H. Li & T. Wang

Behavior of CFST piers with compound concrete under cyclic lateral loading 184
J.-J. Wang, J.-L. Fu, S.-G. Cao, H. Hu & H. Tian

Extending the service duration of bridges by means of (R-)UHPFRC 192
S.D. Maria & D. Briccola

Optimization study on wet joints construction of steel plate composite beams 200
B. Wang & Z.Q. Liu

Analysis of the effect of hoop prestressed steel wire rope reinforcement on bridge piers and the loss of prestress 207
D.H. Sun, Z.Q. Liu & B. Huang

Development and application of anti-differential disturbance concrete for widening bridge 216
D.H. Chen, J. Song & C.Y. Zhu

Safety performance evaluation of suspension bridge tunnel anchor structure 226
W. Dou, Z.Q. Liu & J. Song

A review of the durability of concrete wet joints under the loading and corrosion 234
Y. Wang, Y. Shen & Y. Wang

PC-PINNs: Physics-informed neural networks for solving the phase-field model of pitting corrosion 244
N. Chen, R. Ma, A. Chen & C. Cui

Sensitivity analysis on the fatigue factors for fatigue reliability evaluation 253
M.Z. Mili, K. Sugiura, Y. Kitane & R. Matsumoto

Structural analysis of dapped-end beams through machine learning techniques 261
V. Picciano, G. Santarsiero, A. Masi & A. Digrisolo

Assessment of the efficiency of the base-isolation for a bridge structure 270
T. Zhelyazov, S. Ólafsson & R. Rupakhety

Fracture toughness of structural steel in Swedish bridges 278
M. Ablahad & H. Pétursson

MS02: Field testing of existing bridges
Organizers: E. Lantsoght, G. Sas & J. Schmidt

Collapse test of prestressed concrete slab-between-girder bridge 289
S.W.H. Ensink, E.O.L. Lantsoght & M.A.N. Hendriks

Bridge load testing: Recent advances in research, collaboration, and codes 297
E.O.L. Lantsoght, J.W. Schmidt & G. Sas

Reliability of I-girder PC bridges through proof load testing: Preliminary results 306
G. Addonizio, R. de Vries, E.O.L. Lantsoght & D. Losanno

Danish concrete bridge proof loading procedure and considerations 315
J.W. Schmidt, C.O. Christensen, R. Bang, C. von Scholten, P. Goltermann & S. Engelund

A comparative study of proof load configurations related to bridge classification 323
K.D.S. Damsgaard, S. Engelund, J.D. Sørensen, J.W. Schmidt, C.O. Christensen & C. von Scholten

Static and dynamic monitoring of bridges with contactless techniques 332
T. Moser, W. Lienhart & F. Schill

Shear stop criteria for reinforced concrete slab strips 341
G.I. Zarate Garnica, E.O.L. Lantsoght, Y. Yang & M.A.N. Hendriks

Development of a guideline for proof loading of bridges 350
S. Engelund, J.D. Sørensen, J.W. Schmidt, C. von Scholten & R. Bang

Load testing on existing prestressed concrete bridges to determine long-term effects on strain measurement 358
H. Burger, T. Tepho, O. Fischer & N. Schramm

Load testing and evaluation of inverted T-section slabs in road bridges 366
C.O. Christensen, J.W. Schmidt, R. Bang, C. von Scholten, P. Goltermann, K.D.S. Damsgaard & S. Engelund

Lessons learnt from load testing in the UK 375
D.P. Cousins

Long-term monitoring of ASR deteriorated bridges after reinforcement 383
M. Tsuda, S. Kagatani, S. Ura & K. Torii

The use of smart bridge bearings for railway bridge monitoring 391
P. Olaszek, A. Sakowski, N. Kur & M. Smoliński

Development of a proof loading method for railway bridges with masonry abutments 399
C. Wang, J. Gonzalez-Libreros, L. Elfgren, G. Sas, C. Daescu, O. Enoksson & T. Hojsten

Structural reliability updating using monitoring data from in-situ load testing and laboratory test results 409
R. de Vries, E.O.L. Lantsoght, R.D.J.M. Steenbergen, M.A.N. Hendriks & M. Naaktgeboren

Load testing of the first stress ribbon bridge in Slovenia 418
Đ. Đukić, D. Hekič, M. Kosič, R. Vezočnik, A. Anžlin, A. Štrukelj, M. Pipenbaher & T. Weingerl

Damage evaluation of a road bridge subjected to an avalanche 426
H. Naito, A. Uchida, K. Yoshinaga, A. Kamura & M. Kazama

In-situ, lab testing and FE simulations historical steel-concrete bridge decks 435
A. de Boer, B. Renckens & L. Ha

Practical experience with proof loading – examples from 3 bridges 444
J.H. Roldsgaard, J.K. Nørregaard, C. Pedersen, J. Vig & A. O'Connor

Integrated utilization of infrared and ultrasound technologies for bridges 453
I. Alqurashi, M. Debees, M. Matsumoto, A. Alqarfi & F. Necati Catbas

Determining load distribution in a riveted railway bridge through controlled field testing 460
B. Imam, S. Biswal, M.K. Chryssanthopoulos & P. Wildbore

Field assessment of a vibration-based damage identification procedure 469
J. Raedersdorff, A. Chateauneuf, D. Clair & A. Bouchaïr

Road overpasses with Gerber half-joints: Field tests and numerical models 477
D. De Domenico, M. Mazzeo, D. Messina & A. Recupero

MS03: Life-cycle performance assessment of existing bridges in an aggressive environment
Organizers: M. Akiyama, D.M. Frangopol & H. Matsuzaki

Self-healing performance of aged bacteria-based cementitious materials: An overview 487
N. Kim, S. Kim & H.K. Lee

Degradation prediction of FRP bars within concrete bridge decks in service 491
X.L. Zhao, Q. Zhao, I. Keitai, J.G. Dai & M.F. Kai

Load-bearing capacity assessment of RC beams using corrosion crack widths 497
T. Adachi, M. Akiyama, T. Yamada, S. Nakamura, Z. Xu & D.M. Frangopol

Probabilistic structural identification using time-dependent deflection of prestressed concrete bridges 503
S. Jia, M. Akiyama & D.M. Frangopol

Advanced framework for degradation modeling of operating structures 510
M.E.A. Ben Seghier, A. Jiménez Rios, J. Dai & V. Plevris

Modeling the deterioration of road bridges at the provincial level in Lao PDR 518
H. Silimanotham, A. Amir & M. Henry

Experimental investigation on shear behaviour of corroded and repaired prestressed concrete beams 525
B. Belletti, S. Ravasini, A. Sirico, J. Sanchez Montero, J. Torres, N. Rebolledo & P. Saura

Risk-based retrofit optimization of deteriorating reinforced concrete bridge columns subjected to corrosion and earthquakes 533
S. Kim, Y. Yang & D.M. Frangopol

Life-cycle assessment of riverine bridges under flood and corrosion 540
R.K. Arora, S. Banerjee & A. Kumar

Life-cycle cost-benefit analysis of an SMA-steel reinforced bridge under earthquakes 548
J. Qian, T. Guo, Y. Dong & Y. Zheng

Probabilistic assessment of corrosion initiation in RC structures under chloride attack 556
G.H. Vieira, L.C. Meneghetti, R.M. Teixeira & M.A. Silva

Why is maintenance and management of rails so important to railway bridges? 565
J. Wuorenjuuri

Retrofit of PRC bridges by external post-tension under different corrosion scenarios 571
G. Santarsiero, V. Picciano, A. Masi & G. Ventura

Life-cycle environmental impact assessment of bridge designs considering maintenance strategy 580
S.H. Lee, L.S. An & H.K. Kim

Damage assessment and expert system for the repair of ageing reinforced concrete components 586
F. Binder, U. Schneck & A. Strauss

MS04: Life-cycle redundancy, robustness and resilience of bridges and infrastructure networks under multiple hazards
Organizers: F. Biondini & D.M. Frangopol

Connectivity of road network with bridges and slopes under rainfall 597
Z. He, P.S. Firdaus, M. Akiyama, D.M. Frangopol & H. Matsuzaki

Measuring the extreme risk of coastal bridges under tropical cyclones 604
Y. Li, D. Zhu & Y. Dong

Resilience-based countermeasure strategy for bridges under multiple hazards 610
H. Ishibashi, M. Akiyama & S. Koshimura

Enhancing seismic resilience of aging highway bridges using FRP retrofit 617
V. Singh, S. Shekhar & N. Kotoky

Fragility curves for regular and irregular RC bridges via non-linear static analysis 626
H. Rezaei, E.M. Dehcheshmeh & Y. Tsompanakis

Connectivity of post-earthquake bridge networks under aging of isolators 634
H. Matsuzaki

Computational analysis of resilience in reinforced concrete railway bridge 642
A.L. Gamino, R.R. Santos, T.N. Bittencourt & M.M. Futai

Assessment of honeycomb cushion for enhancing bridge deck impact protection 650
H. Mraih, J. Hashemi, R. Kalfat, R. Al-Mahaidi & G. Lu

Multi-hazard resilience-based bridge prioritization for aging bridge networks in a changing climate 658
L. Jafari & F. Biondini

Probabilistic capacity model for concrete-filled steel tubes 666
A. Aloisio, A. Contento, J. Xue, G. Quaranta, P. Gardoni & B. Briseghella

MS06: AI and robotics for bridges: Monitoring, assessment, and maintenance
Organizers: Y. Dong, D.M. Frangopol, B. Wang & X. Lei

Bridge condition assessment with full-scale view and computer vision methods 679
X. Lei, Y. Dong & D.M. Frangopol

Data-driven prediction models for extreme wave impacts on coastal bridges 685
D. Zhu, J. Zhang & Y. Dong

Digital twin for intelligent maintenance towards sustainable bridges 693
J. Heng, L. Lai, Y. Dong, S. Kaewunruen & C. Baniotopoulos

Structural damage detection approach using input-output monitoring system and transfer learning 701
L. Ge, D. Dan & A. Sadhu

Data fusion in structural health monitoring: Integrating computer vision and strain gauges for enhanced inspection 709
K. Aminfar, M. Ghyabi, Y. Shen, D. Lattanzi, G. Ciaramella, M. Gherlone & C. Surace

A smart robotic system for autonomous inspection of large-scale concrete girder 717
Y. Cui, Y. Pan, D. Wang, M. Ji & S. Cao

LSTM-based structural pattern recognition for floating bridges 726
S. Ryu, S. Min, Y.J. Kang & S. Kim

Vision-based structural displacement measurements using deep learning and super-resolution 735
M.F. Abu Zouriq, D.G. Linzell & R. Nasimi

Multimodal data collection using mobile robotics for rapid structural assessment 742
F. Luleci, A. AlGadi & F. N. Catbas

MS08: Sustainable and efficient monitoring and digitization-based decision-making models
Organizers: A. Strauss & D.M. Frangopol

Human role in existing bridge digital twin frameworks, towards Industry 5.0 753
A. Jiménez Rios, V. Plevris & M. Nogal

Overview of assessment for bridges affected by HS2 tunnelling, UK 761
J. Tsekhanskiy, A. Bariyya, G. Ledsham-James, D. Shapley & Y. Li

Comparison of modal parametric and nonparametric vibration-based techniques 769
A. Dia & N. Makhoul

Limits of digital twin modelling 777
A. Beigel, A. Strauss, D.M. Frangopol & M. Cao

Vehicle impacts on reinforced concrete railway bridges 785
M. Reiterer, A. Strauss, B. Täubling & D.M. Frangopol

Advanced modelling methods of the Jauntal railway bridge 793
A. Strauss, B. Täubling-Fruleux, L. Novák, D. Novák, A. Oplustil, M. Kaulfus, H. Steiner, R. Zedlacher, A. Hüngsberg, G. Oberlerchner & D.M. Frangopol

Generation of digital twins for bridges of medium spans - Schwindegg Bridge pilot project 800
J. Wimmer & T. Braml

ANYTWIN – standardizing monitoring-based safety assessments of bridges and the integration into Digital Twins 808
A. Lazoglu, J.H. Bartels, R. Stein, M. Maibaum, L. Puttkamer & L. Ulbrich

Condition assessment of mechanical fasteners by use of smart bolts 817
M. Reiterer & R. Thukbatullin

MS09: Novel technologies and information fusion for structural health monitoring of bridges
Organizers: C.-W. Kim, V. Sarhosis, J. Li & Y. Zhang

Real-time scour depth estimation of a pier using vibration monitoring 827
D. Kawabe, C.W. Kim & V. Sarhosis

Structural integrity estimation of bridges based on acceleration measurement 835
H. Yu & C.W. Kim

Research on application of real-time dynamic safety monitoring system for medium and small span bridges 844
H. Hong, S.G. Cao, J.L. Fu & Y.K. Xu

Enhancing structural performance evaluation of PC girder bridges through Bayesian model updating 853
D.B. Chen & C.W. Kim

Framework of UAV bridge inspection with computer vision and deep learning 862
K. Yen & C.-M. Chang

Vision-based optimal sensor selection for full-field displacement reconstruction 870
Y.F. Weng, S.T. Quek, K.W. Yeoh & X.L. Lu

Domain adaptation for bridge health monitoring via physics-informed generative adversarial learning 878
L. Ge & A. Sadhu

Anomaly detection of bridges by Bayesian method with optimized sensor placement 887
C.W. Kim & Y. Hirate

Converting finite element models to irreducible element models for use in population-based SHM 896
C. O'Higgins, D.S. Brennan, C. Kent, D. Hester & S.E. Taylor

Impact factor of a seven span continuous cable-stayed bridge 904
S. Kimura, C.W. Kim, H. Sugiyama, M. Isa & K. Ono

Distributed fiber optic sensors for structural health monitoring of post-tensioned bridges 912
B. Piątek, T. Howiacki & T. Siwowski

Modeling temperature impact on sensor data in prestressed concrete bridges 921
V. Coric, C. Wang, J. Gonzalez-Libreros, L. Elfgren & G. Sas

Field testing of the longest Polish footbridge made of FRP composites using distributed fibre optic sensor system 929
M. Kulpa & T. Siwowski

Online noise parameters estimation for sigma-point Kalman filter using sequential importance resampling 937
W. Liu & F.-L. Zhang

MS10: MS Application of probabilistic techniques for the assessment and performance prediction of corroding concrete bridges
Organizers: R. Caspeele, W. Botte, R. Vrijdaghs, B. Belletti & J.R. Casas

Bayesian-updated POD of ultrasonic tomography in the inspection of PT bridges 947
I. Mazzatura, J.R. Casas, S. Caprili & W. Salvatore

Influence of repair interventions on the safety of a reinforced concrete road bridge subjected to chloride ingress 956
K. Van Den Hende, S. Helderweirt, W. Botte, S. Matthys, R. Caspeele & G. Lombaert

Probabilistic assessment of the moment-curvature response of PC beams with different corrosion scenarios 965
B. Belletti, S. Ravasini, S. Sandrini, R. Caspeele & W. Botte

A dynamic Bayesian network approach for multi-component fragility of aging bridges 974
F. Molaioni, C.P. Andriotis & Z. Rinaldi

Selection of NDT/PDT locations in a box culvert using value of information 983
S. Karmakar, S. Ghosh & S. Dauji

Assessment of a 60-year-old corroded concrete girder through finite-element analysis 992
L. Soto, M. Noël, B. Martín-Pérez & L. Sanchez

Analysis for the bridge fatigue failure and weight limit using the probabilistic machine learning method 1000
W. Yan

Stationary proposal importance sampling for structural reliability of aging RC bridges 1008
L. Capacci

MS11: Towards the realization of the submerged floating tunnels
Organizers: Y. Xiang, H.K. Lee, B. Faggiano, R. Landolfo & L. Martinelli

Coupled dynamic analysis method for wave action on a submerged floating tunnel 1019
B. Huang, W. Luo, X. Cui, S. Wang, H. Ding, K. Li & L. Cheng

Dynamic substructuring technique for submerged floating tunnels 1029
S. Corazza, F. Foti & L. Martinelli

Forming guidelines for software evaluation in bridge structural health monitoring systems 1037
T.A. Bayda, H.W. Shenton & M. Chajes

Nonlinear seismic-response time-history analysis of submerged floating tunnels 1044
Y.Q. Xiang, Y.G. Shen, C.F. Chao & L. Deng

Experimental investigation for dynamic behavior of the scaled segment model of submerged floating tunnels under waves 1054
H. Ding, L. Cheng, K. Li, D. Zhong & X. Hu

Numerical simulation of motion response of submerged floating tunnel under wave action 1063
H.B. Jiang, H.D. Zhao, W.D. Chen, P.Z. Lin & B. Ren

Modeling of two-dimensional water motion field during a seaquake 1071
V. Maugeri, L. Martinelli & F. Perotti

Analysis of hydroelastic response of a SFT based on the Discrete-Module-Beam method 1079
C. Ji, Y.Q. Chen, X.T. Zhang, X. Li, K. Li, D. Zhong & Zhou

Main issues of the structural analysis of SFT against environmental loads 1087
G. Iovane, F.M. Mazzolani, R. Landolfo, E. Begovic, E. Bilotta & B. Faggiano

MS12: Decision-making in bridge management - Gaps between research and practice and recommendations for the future
Organizers: P. Linneberg & A. Strauss

Current and future decision-making in Danish and Austrian bridge management 1099
P. Linneberg & A. Strauss

Comparison of ranking frameworks for specification of bridge scour monitoring systems using a case study database 1108
W. Yaqoobi, G. Gavriel, T. Tryfonas, P.J. Vardanega & M. Pregnolato

Next generation risks challenge bridge maintenance and management in Finland 1116
J. Wuorenjuuri

The effect of conceptualization on bridge maintenance prioritization 1122
K. Zangpo, A. Amir & M. Henry

Bridge condition index: A review of methodologies used in Bridge Management Systems 1130
A. Agredo Chávez, J. Gonzalez-Libreros, C. Wang & G. Sas

MS13: Bridge loading – measurement and modelling
Organizers: C. Caprani, A. Nowak, E. O'Brien & X. Ruan

Braking effects on vehicle-bridge interaction 1141
A. Aloisio, G. Quaranta, A. Contento & M.M. Rosso

Distributed fiber optic sensing during static and dynamic bridge loading 1148
L. Strasser & W. Lienhart

Structural load modelling of walking humans with gait cycle-dependent model parameters 1156
M.J.A. Fritzsche, S.R. Lorenzen, C. Hübler, A. Firus, M.A. Stasica & A. Seyfarth

CFD analyses for wind load assessment of the new Bomarsund arch bridge 1165
F. El Azrak, S. Sadrizadeh, J. Leander & R. Karoumi

Bridge damage evaluation model based on vehicle excitation and ML 1173
Z. Xiong, T. Cong, W. Zhang & Z. Liang

Experimental determination of trough bridges pressure distribution 1181
S. Sarmiento, J. González-Libreros, G. Sas, O. Enoksson & T. Höjsten

FE model and verification as digital twin of structural behavior for infrastructure management 1190
H. Shirahata, T. Kawai, M. Tai, T. Aoki & H. Hara

On the assessment of the vibrational response of highly-skewed high-speed railway bridges 1199
M.D. Martínez-Rodrigo, J.C. Sánchez-Quesada, E. Moliner, A. Romero & P. Galvín

Modal identification and soil-structure interaction analysis of a portal frame railway bridge 1207
J. Chordà-Monsonís, J.C. Sánchez-Quesada, E. Moliner, M.D. Martínez-Rodrigo, A. Romero & P. Galvín

Enhancing structural performance prediction through Bayesian updating with considering load and speed uncertainty 1215
F. Shaker & C. Caprani

Utilizing bWIM-data to calibrate new traffic load models on embankment 1224
H. Lilja, J. Qvisen & A. O'Connor

Torsion effects in Super-T girder grillage analysis 1232
J.W. Ngan, C.C. Caprani & M. Melhem

Reliability calibration of load factors for the Australian rail traffic load model 1239
C.C. Caprani & M. Shihabuddin Khan

Probabilistic updating of characteristic train load for the Little Belt Bridge anno 1935 1247
J.H. Roldsgaard, C. Pedersen, S.T. Nielsen, A. O'Connor & S.E. Gaardmand

Influence of the correlation of GVWs in the simulation of vehicle spatial distribution of extreme effects in long-span bridges 1255
X. Wang, X. Ruan, J.R. Casas & M. Zhang

PyBTLS: A Python package for traffic load simulation on short-to-medium bridges 1263
Z. Zhou & C. Caprani

SPECIAL SESSIONS

SS01: Short-span bridges and culverts: Analysis, evaluation, durability, and rehabilitation
Organizers: D. Beben, H. Sezen, J. Vaslestad & T. Maleska

Restoration of the Rochers Noirs Viaduct 1273
E. Combescure, S. Doussau, C. Lacipiere, N. Aubree & L. Pace

Load rating of cast-in-place reinforced concrete box culverts based on load testing 1281
A. Peiris, C. Hutchinson, I. Harik, A. Cole & E. Russell

Seismic finite element method simulation of a soil-steel bridge with a gravel-rubber mix 1288
T. Maleska, D. Beben, J. Nowacka, A. Fiamingo & M.R. Massimino

Long-term monitoring of earth pressure in a soil-steel composite railway tunnel 1296
T. Maleska, D. Beben & J. Vaslestad

Experimental tests of a soil-steel culvert with a shallow soil cover under static loading 1304
T. Maleska, D. Beben, P. Bobra & B. Jedraszak

Maximum shear strength of prestressed concrete deep beams 1312
X. Duanmu, D. Xu & K. Hu

Low carbon solution for short-span bridges: Soil-steel composite bridges versus concrete bridges 1320
G. Du & A. Czerepak

Soil-steel composite bridges, advantages – based on case studies 1329
B. Şentürk & M.N. Nonbo

The corrosion of reinforced concrete bridge structures and its influence 1336
G.-O. Shijir, D. Yagaanbuyant, K. Sambuu, M. Duinkherjav, S. Namsraijav, A. Gantulga, K. Tumur-Ochir & N. Bayasgalan

SS02: Bridge Weigh-in-Motion: Recent experiences, technology developments, and new applications
Organizer: D. Cantero

New feature based on influence lines for anomaly detection in bridge monitoring 1347
A. Döring, M. Vogelbacher, O. Schneider, J. Müller, S. Hinz & J. Matthes

Vehicle speed estimation in BWIM systems via convoluted reciprocity 1356
D. Cantero & C.W. Kim

Strain-based FEM-aided bridge health monitoring: A case study 1364
P. Rizzo, A. Enshaeian & A. Ghahremani

Actual bridge verification of monitoring technique using optical fiber sensors 1372
S. Aoki, T. Maeshima & I. Iwaki

Bridge Weigh-in-Motion applied to heritage iron truss bridges in France 1380
F.-B. Cartiaux, V.L. Corvec, J. Semiao & B. Jacob

Assessment of the accuracy of Bridge Weigh-In-Motion (B-WIM) system in Indonesia 1388
W. Nugraha, S. Ramadhani & G. Sukmara

Bridge weigh-in-motion event detection using wavelet scattering features and unsupervised learning 1397
V. Bokaeian, J. Bowmaster & K. Arjomandi

Machine-learning for analyzing bridge displacement using radar data 1405
M. Arnold & S. Keller

Accuracy of BWIM considering autocorrelation in bridge dynamic response 1413
K. Maruyama, I. Yoshida & H. Sekiya

Exploring Kriging metamodeling for applications in bridge Weigh-in-Motion prediction 1422
P. Agüero-Barrantes, S. Lobo-Aguilar, R.E. Christenson & A. Hain

Challenges of implementing bridge weigh-in-motion on a century-old steel-riveted railway bridge 1429
D. Hekič, M. Kosič, J. Kalin, A. Žnidarič & A. Anžlin

Radio-interferometry based continuous bridge deformation monitoring – a case study 1437
K. Leppänen, J. Salmi, M. Fattah, T. Heikkinen, M. Lehtinen, O. Leppänen, N. Väisänen, T. Tirkkonen & H. Raunio

A regression based B-WIM method for railway bridges 1445
S. Lachinger, J. Struhar & M. Ralbovsky

A deep learning-based BWIM system of a cable-stayed bridge 1452
B. Szinyéri, B. Kovari, I. Völgyi, D. Kollár & A.L. Joó

Load estimation precision for moving forces with position uncertainties through AKF 1460
C.Y. Zhou & C. Demartino

SS03: Estimating future preventive bridge interventions
Organizers: B.T. Adey, H. Mehranfar & S. Chuo

Improvements in providing overviews of future bridge interventions, their possession windows, and costs 1471
H. Mehranfar, B.T. Adey & S. Chuo

Connecting predictive algorithms to BIM to improve the planning process 1479
S. Chuo, H. Mehranfar, B.T. Adey & G. Elshani

Bridge deterioration modeling considering the climate change effects 1487
S. Moghtadernejad, Z. Lounis & J. Zhang

Application of open deep learning datasets for building vision-based bridge condition monitoring solutions 1496
K. Tomaszkiewicz & T. Owerko

Influence of the pavement conditions on the bridge response 1504
M.G. Mulas, M. Riso, A. Sgambati, F. Basone & M. Longo

SS04: Advances in machine learning and data-driven system identification techniques for structural health monitoring
Organizers: J. Diaz-Rozo, C. Bielza, C. Ocampo-Martinez & P. Larrañaga

Long-term performance evaluation of low-cost sensors using AI-driven tools 1515
F. Lozano-Galant, S. Emadi, S. Komarizadehasl, J. González-Arteaga, Y. Xia & J.A. Lozano-Galant

Fast bridge health monitoring deployment with transferable expertise 1523
R. Sojo-García, P. Larrañaga, C. Bielza & J. Díaz-Rozo

Anomaly detection with switching Kalman filter and imitation learning 1531
Z. Xin & J.-A. Goulet

Improving frequency-features by parametric study of data-driven SHM schemes 1539
C. Puerto-Santana, J. Diaz-Rozo & C. Ocampo-Martinez

Robust modal identification of a large-span bridge with the new SpCF technique 1547
S.D.R. Amador, L. Gaile, R. Brincker & C.E. Ventura

SS05: Underground and above-ground infrastructure resilience and sustainability
Organizers: M. Domaneschi, B. Chiaia, G.C. Marano, V. Villa & S. Argyroudis

Development of a novel bridge deck-to-pier connection for improved tsunami resilience 1559
R.K. Pagel, A. Palermo, I.N. Robertson & G.D. Francesco

The seismic response and resilience of nearby underground infrastructures 1567
M. Dalmasso, M. Civera & B. Chiaia

Blockchain technology conception in digital data collection for damage assessment and L.C.A. 1575
L. Gioberti, M. Domaneschi, V. Villa, B. Chiaia & N. Catbas

Analytical seismic resilience identifiers of bridges 1583
F. Soleimani & D. Hajializadeh

Dynamic measurements for assessing bridge response to foundation scour 1592
M. Aimar, M. Civera, B. Chiaia, S. Foti, A. Quattrone & D. Sabia

SS06: Forensic engineering and damaged structures. Critical cases studies and lesson learned of LATAM road bridges
Organizers: M.A. Valenzuela, M. Marquez, F. Cerda & G. Valdebenito

Seismic design modifications for damage prevention in skewed bridges 1603
T. Amaya & H. Santa María

Collapse of Cau Cau Bridge: Forensic engineering study 1611
M.A. Valenzuela & M. Márquez

Use of advanced non-destructive methods for the structural diagnosis of the Cau-Cau Bridge, Chile 1619
G. Valdebenito, M. Marquez, M. Valenzuela & J.L. Seguel

A study on machine learning for creating crack images of RC columns 1626
H. Yasukawa, H. Naito, H. Fujioka & S. Fujikura

SS07: Vehicle-based sensing solutions for indirect bridge condition monitoring
Organizers: R. Corbally, A. Malekjafarian, S.R. Lorenzen & C.-H. Kim

Mitigation of unwanted effects in drive-by acceleration data for bridge monitoring 1637
M. Casero, A. González & K. Feng

Smartphone-based monitoring: Improving the bridges braking force model 1646
M. Breveglieri & G. Feltrin

Bridge damage classification using multiple responses of vehicles and 1-D convolutional neural networks 1655
Z. Li, Y. Lan & W. Lin

Crowdsensing and indirect structural health monitoring in HE FUTURAL 1664
D. Garcia-Sanchez, D. Zamora, I. Arakistain & T. Katika

Fleet monitoring using a Bayesian approach to detect bridge bearing damage 1672
E.J. OBrien, Y. Ren, T.T.X. Tran, E. Ozer & V. Pakrashi

Indirect bridge condition monitoring using feature selection strategy 1679
R. Ghiasi, R. Corbally & A. Malekjafarian

Crowd-sensing drive-by monitoring for bridge frequency identification 1687
Y. Lan, Z. Li & W. Lin

Bridge low-frequency displacement estimation using bridge acceleration for a VBI system 1695
X. Lu, L. Sun, Y. Xia, C.W. Kim, K.C. Chang & Z. Han

Automated analysis of drive-by monitoring data 1704
J. Brötzmann, Y. Yang, U. Rüppel, M.M. Rupp & S.R. Lorenzen

OMA-driven structural assessment to prevent fatigue-induced failure in steel bridges 1712
G. Du, R. Brincker, S. Amador & U. Alibrandi

SHM for railway bridges: Real time analysis of the train transit and thermal data 1719
G. Ascari, A. Dalle Fratte, A. Terraneo & P. Scali

A deep-autoencoder-based drive-by methodology for high-speed railway bridge damage detection 1728
E.F. Souza, C. Bragança, T.N. Bittencourt, D. Ribeiro & H. Carvalho

Indirect continuous monitoring of bridge transitions using the CTM 2.0 1736
M.M. Rupp, S.R. Lorenzen, C. Hübler, K.U. Wolter, G. Grunert & R. Stein

Drive-by monitoring to assess railway bridge accelerations 1745
S.R. Lorenzen, M.M. Rupp & C. Hübler

Empirical study on smartphone-vehicle trip metadata and bridge modal property estimates 1754
T.J. Matarazzo, L. Cronin, G. Marasco, I. Dabbaghchian, S.N. Pakzad, S.S. Eshkevari, D. Sen, P. Santi & C. Ratti

SS08: Posttension analysis, design, and assessment in bridge construction
Organizers: U. Attanayake, H. Aktan, M. LaViolette & C. Rogers

Simplified stage construction and creep analysis of a segmental precast concrete bridge 1763
A. Guarnieri, F. Bontempi & F. Petrini

NDE for pre-stressing systems condition: Metrological validation 1772
S. Zorzi, F. Rossi, D. Tonelli, E. Tubaldi & D. Zonta

The impact of post-tension modeling techniques on calculated concrete member stresses 1780
K. Basnayake & U. Attanayake

Service life determination of post-tensioned hanger rods 1788
A.P. Ranasinghe & H.T. Al-Khateeb

The comparative analysis of post-tensioned tendons in ultra-high-performance box girders 1793
M. Tsas-Orgilmaa & H.S. Mook

Finite element analysis of over-height vehicle collisions on prestressed girder bridges 1801
A. Samadzad, S. Cathey, M. Whelan, N. Braxtan & S. Chen

Assessment of internal condition of a post-tensioned tie girder during construction 1809
U. Attanayake, H. Amunugama, K. Basnayake, H. Aktan & E. Niederleithinger

Reliability analysis of end cracking in continuous prestressed concrete girders 1817
A.M. Okeil & S. Ghimire

Selection of post-tensioned tie girders for the 2nd Avenue network tied arch bridge 1825
M. LaViolette, U. Attanayake & B. Wagner

Post-tensioning tendons under strand breakages: Modelling approach for bonded tendons 1834
B. Vecino, C.M.C. Renedo, J. Naranjo-Pérez, I.M. Díaz & J.H. García-Palacios

SS09: New Concepts and approaches in bridge management – BIM based bridge management, artificial intelligence, and other new concepts influencing future BMS
Organizers: R.M. Ellis, R. Hajdin & B. Baktas

Digital twin, BIM and asset management systems implementation 1845
E. Spallarossa & A. Bonicelli

Establishing data-driven life cycle benefits of bridge maintenance 1853
B. Bektaş

Sensitivity analysis of bridge structural vulnerability class based on Italian Guidelines 1861
S. Bianchi & L. Capacci

Automated construction of BIM models from point clouds to digitalise bridge assets 1869

R. Hajdin, L. Rakic, H. Diederich, R. Richter, J. Hildebrand, S. Schulz, J. Döllner & J. Bednorz

Leveraging digital twin tools for the Minnesota DOT Robert Street Bridge inspection 1877
S. Becher & B. Lovelace

SS10: Artificial Intelligence for uncertainty, risk, and reliability assessment of bridge infrastructure
Organizers: D. Choe & M. Roohi

A chain-based construction method for bridges monitored within one cluster 1887
K. Wang, X. Ma, Z. Jiang & Y. Liu

Deep learning of smart aggregate's impedance signal for damage monitoring 1894
Q.B. Ta, N.L. Pham, J.T. Kim & Q.Q. Pham

Neural network-based connectivity reliability analysis for bridge networks 1902
J. Wang & S. Li

Forward UQ based on Bayes-informed mixture distribution 1908
Y. Zhang, Y. Dong & R.W. Feng

Connectivity analysis of transportation networks incorporating bridges and pavements under uncertainty 1916
J. Xin, D.M. Frangopol, M. Akiyama & X. Han

U-Net model-based XCT images segmentation for steel corrosion in concrete 1922
M. Zhang & W. Wang

Fragility interval predictions in non-seismically designed bridges 1929
H. Neduri & J. Ghosh

Damage evaluation of steel columns using vibration testing and transfer learning 1937
K. Watanabe, H. Naito, T. Kimoto, M. Matsumura, N. Takeshima, S. Okada & K. Ono

Probabilistic modeling of bridge deterioration due to earthquakes 1946
L. Iannacone & P. Gardoni

A data-driven approach for quantifying reliability and resilience of transportation network 1955
S. Ghasemi, V. Aghaeidoost & M. Roohi

SS11: Approaches to bridge management/bridge management systems in response to today's challenges
Organizers: R.M. Ellis & R. Hajdin

Forecasting the condition of British railway bridges via a hindcast 1967
M.J. Hamer & G.S. Calvert

Vulnerability of network infrastructure due to potential extreme weather in PEI, Canada 1976
D.J. Evans & R.M. Ellis

Considerations for vulnerability and risk assessment of bridges and culverts including extreme weather events 1984
R.M. Ellis & Z. Kamranian

Province of New Brunswick Bridge Management System 1993
Z. Kamranian & R.M. Ellis

Bridge deterioration prediction models: A review of management systems in the world 2000
C.A.F. Souza, J.M.F. Carvalho, A.C.P. Martins, F.G. Bellon, M.S. Andrade, D.S. Oliveira, J.C.L. Ribeiro, K.M.L. Cesar, B.S. Borges & G.P. Teixeira

Developing a guideline for structural health monitoring of road bridges in Germany 2009
F. Hille, R. Herrmann, R. Schneider, S. Pitters, F. Wedel & I. Hindersmann

SS12: Realising the extension of BIM for existing bridges
Organizers: N. Powers, V. Samec & M.A. Valenzuela Saavedra

Overview of the use of BIM for bridges across Australia and New Zealand 2021
N.G. Powers

BIM-data of baseline digital twins for a new bridge maintenance system 2028
C.S. Shim, G.T. Roh, D.H. Kang & J.W. Park

Condition integration in BIM for existing bridges 2034
M. Köhncke & S. Keßler

Cloud-based asset management for image-based inspections of infrastructures 2040
G. Morgenthal & M. von Butler-Helmrich

Linking BrIM to BMS for bridges – validation of concepts 2048
V. Samec, K. Aas-Jakobsen, P. Hawryszków, I. Heise, M.A. Valenzuela & C. Shim

Strategies for effective bridge information management with OpenBIM 2057
C. Gragnaniello, G. Mariniello & D. Asprone

SS13: Design, construction and evaluation of steel/FRP & concrete composite bridge structures
Organizers: H. Xin, X. Xu, R. Liu & J. He

Cyclic behavior of replaceable LYP steel coupling beam with corrugated web 2067
J. He, S. Feng, Y. Ma, Q. Teng & W. Lin

Fatigue life extension for cracked OSDs using semi-rigid pavement layer 2076
B. Wang, R. Gong, D. Wang & A. Chen

Experimental and numerical study on static performance of steel cap beam 2083
S. Chong, S. Qingtian & L. Jinguo

Real-time multi-objective topology optimization method via deep learning 2090
C. Xiang, A. Chen, D. Wang & R. Ma

A method for stochastic modelling of fatigue stresses in orthotropic bridge decks subjected to local and global traffic loading 2098
A.G. Johansen, F.-I.G. Giske & M. Storheim

SS15: Steel bridge rehabilitation
Organizer: M. Sakano

Application of microwave vibrometry in bridge monitoring & dynamic analysis 2109
T. Bao & S. Bai

Maintenance of large expansion joint in Honshu-Shikoku Bridges 2115
M. Hongo, A. Moriyama, Y. Yano & Y. Yokoi

Fatigue behavior of steel plates subjected to marine environment 2122
A. Chang & Q.Q. Yu

Fatigue effect of welded gusset plate in steel-concrete composite bridge 2129
S.L. Yan, S.Y. Jia, S.W. Xu, J.N. Li & Y.Z. Wang

Evaluation of fatigue environment in welded parts of orthotropic steel deck 2137
K. Yoshida & H. Sekiya

A study of the effect of skew angle on natural frequencies of bridge girders 2144
M. Satomi, R. Handa, Y. Sugimoto & H. Onishi

The application of abrasive water-jet treatment on severely corroded weathering steel bridge 2153
Y. Toyota, S. Kainuma, S. Park, T. Ikeda & T. Arakawa

Analytical study on stress concentration zone of aseismic reinforced deck type arch bridge 2159
M.O. Ouchi, T.S. Suzuki & H.S. Shirahata

Rehabilitation methodology of a corroded steel-riveted highway bridge in an urban setting 2167
I. Netzer & A Kedar

Study on fatigue detection of weld toe in orthotropic steel deck 2175
R. Harashima, C. Hashizume, H. Sekiya, S. Morichika & M. Saeki

Fatigue crack detection in out-of-plane gussets using crack detection sensor 2183
K. Sunada, T. Kuroiwa, R. Kasakura & H. Sekiya

Fatigue crack monitoring by measuring strain without loading 2189
T. Ishikawa, N. Matsumoto & K. Komon

Mechanical properties of steel tube with partially bonded CFRP 2197
Y. Maeda, M. Mizutani & T. Ishikawa

Estimation of elastic buckling loads of defective steel plate repaired with CFRP 2206
M. Mizutani, E. Yo, T. Ishikawa, Y. Hidekuma & M. Dogaki

Fatigue retrofit using TRS for trough rib-to-crossbeam connections in orthotropic steel decks 2215
L.H. Ichinose, A. Tanabe, Y. Teranishi & M. Sakano

SS16: Redundancy in bridges: Design, fabrication and bridge maintenance
Organizer: A. Mosavi

Internal redundancy approach for built-up mechanically fastened steel tension members in the United States 2225
J.B. Lloyd

Development of the current AASHTO integrated fracture-control plan for steel bridges 2232
R.J. Connor

Fabrication aspects of redundancy 2238
R.D. Medlock

UHPC beam end encasement for the design of maintenance-free steel bridges 2245
B. Lassy, A. Hain & S. Motaref

Identifying system redundant members in a steel arch bridge through advanced finite element analyses 2253
A. Mosavi, H. Yuan, M. Tatarsky & M. Carter

SS17: Integrating digital twin with machine-learning techniques for structual damage identification
Organizers: J.F. Jiménez-Alonso, I. Duvnjak & I.M. Diaz

Bridge condition and performance monitoring: An engineering approach 2263
P.S. McCarten

Determination of precast concrete bridge slab connection stiffness by developing a digital twin 2271
S. Ereiz, I. Duvnjak, J. Pajan, M. Bartolac, J. Košćak & D. Damjanović

Damage detection of riveted truss bridge using ANN-aided AMS optimization method 2279
B. Šplíchal, D. Lehký & K. Lamperová

Evaluation of Low-cost Adaptable Reliable Accelerometer (LARA) technology 2287
E. Delgado, V. Torralba, S. Komarizadehasl, G. Ramos, J. Turmo & J.A. Lozano-Galant

Performance comparison between several SHM solutions: A viaduct of the Italian highway 2295
M. Ciano, M. Malavisi, D. Buggiani, L. Grottoli, D. Bolognini & F. Dacarro

Vibration-based NDT system for external tendons: Anomaly detection through machine learning classifiers 2303
J. Naranjo-Pérez, J. Jiménez-Alonso, I.M. Díaz, J.H. García-Palacios & C.M.C. Renedo

Machine learning-based clustering and regression for assessing temperature-induced variations on external tendon's natural frequencies 2311
L. Chillitupa-Palomino, C. Barrera-Vargas, J.H. García-Palacios, I.M. Díaz & J. Naranjo-Pérez

Integrating CWT and CNN for damage detection in high-speed railway bridges 2319
J.F. Jiménez-Alonso, J. Naranjo-Pérez, C.M.C. Renedo, J.H. García-Palacios & I.M. Díaz

Data-driven framework for damage detection in structural system 2327
R. Ghiasi, J.F. Jiménez-Alonso & A. Malekjafarian

Measurement and structural behavior of suspended swaying pedestrian bridge 2334
E.-S. Hwang, S.-H. Shin, T.R. Park & D. Hwang

SS18: Human-bridge managing interfaces through digital twinning
Organizers: R. Chacón, I. Stipanovic & J.R. Casas

A framework for an integrated & digitally-supported bridge management 2345
S. Moghtadernejad, Z. Lounis & J. Zhang

PONTI: An open WebGL-based tool in support to defect analysis and 3D visualisation of bridges 2353
R. Fascia, F. Barbieri, F. Gaspari, F. Ioli & L. Pinto

Advancing bridge asset management in Indonesia: Integrating scan-to-BIM for digital twin approach 2362
H.T. Saksena & R.P.P. Sastrawiria

Material characterization for HBIM data structures on a masonry arch bridge 2370
R. Chacón, C. Ramonell, H. Posada, L. Pelà, L. García-Ramonda, S. Gönen & A. Cabané

Integration of BIM and MIVES to automate the sustainability assessment of viaducts 2379
F. Lozano-Galant, J.C. Jurado, A. de la Fuente, J.A. Lozano-Galant & J. Turmo

SS20: Sensing technology and data processing algorithm towards bridge life-cycle maintenance and safety
Organizers: H. Qu, C. Guo & H. Zhang

A new multi-source data fusion method for seismic identification of bridge 2389
A. Chang & H. Qu

Defects detection of concrete bridge decks using UAV-based infrared thermography 2395
H.B. Zhang, Z. Zhou & G. Chen

Senmos: A user-centered approach to structural health monitoring with applications on Lillebæltsbroen af 1935 2401
K. Myrtue, S.D. Myrtue, J. Larsen & P.N.L. Sørensen

Investigation of the effect of surface condition variation on infrared imaging of concrete delamination 2409
C. Cheng, D. Chen, H. Cai, S. Wang, R. Wang & X. Cheng

Structural health monitoring of the 1915Çanakkale Bridge in Turkey, the largest monitoring system for the longest suspension bridge in the world 2417
S. Joye & M.D. Witt

SS22: Advancements in intelligent monitoring and maintenance of bridge infrastructure
Organizers: S. Setunge, A. Alani, G. Heravi, R. Dissanayake, T. Bui-Tien, M. Mahmoodian & A. Sidiq

Real-time structural integrity assessment of bridge infrastructure 2425
S.C. Jayasinghe, T.M. Nanayakkara, A. Alavi, M. Mahmoodian, A. Sidiq, Z. Sun, F. Shahrivar & S. Setunge

Optimal sensor placement applications for bridge structural health monitoring using the effective independence method 2433
Z. Sun, M.I. Manuel, M. Mahmoodian, A. Sidiq, R.W.K. Chan, S.C. Jayasinghe, F. Shahrivar & S. Setunge

Recent studies on the dynamic behaviour of various bridges in Spain 2441
J.A. López-Aragón & M.A. Astiz

Equivalent structural stress concentration factor for non-planar oblique butt joints 2450
X. Wei & Q.L. Jia

Electrochemical-chemical-mechanical phase field model for corrosion-induced cracking 2459
X. Fang, Z. Pan & A. Chen

Analysis of monitoring data on prestressed concrete bridges under construction 2466
T. Ohno, H. Sekiya, I. Yoshida, S. Morichika, A. Yasuda, M. Uno & N. Yoshiura

Piezo-Electric Dampers (PiDs) for energy harvesting purposes 2473
J.F. Martins, M. Francioli & F. Petrini

Infrastructure structural health monitoring of bridge with polarimetric radar sensor 2481
L. Zou & A.M. Alani

Precise 3D simulations in bridge deck inspections of ground penetrating radar survey 2490
D. Dai, Y. Zheng, H. Liu, L. Zou & A.M. Alani

New trends and possibilities of GPR in bridge inspection 2498
M. Solla, A. Elseicy & A. Alonso-Díaz

Øresund Bridge: Case study of a monitoring system for movement of bridge bearings 2507
A. Paciacconi & T. Richli

Thermal response prediction of the MX3D bridge's operational dataset 2511
T. Glashier, C. Buchanan & R. Kromanis

Identification of main cable shape of suspension bridge based on 3D point cloud 2520
R. Pan, D. Dan & Y. Li

A framework for bridge condition assessment using graph neural network 2528
G. Marasco, S. Sadeghi Eshkevari, I. Dabbaghchian, S.N. Pakzad & D. Sen

An innovative approach for a sustainable monitoring of large infrastructures networks 2536
M. Longo, S. Cirelli, D.L. Mazza, I. Alovisi, P. Darò, G. Mancini

Field monitoring of bridge link slab performance under long-term and live load effects 2544
A.M. Okeil & M. Canales

SS23: Structural health diagnosis under limited supervision for large bridges
Organizer: Y. Xu

Big model for bridge health diagnosis by cross-modal learning 2555
Y. Xu

Large vision model-based crack segmentation under limited supervision 2562
Y. Guo, S. Li & Y. Xu

Vibration-based fatigue assessment and damage detection in bridge cables 2567
B. Xu, J.R. Casas & Z.R. Wu

Monitoring to secure the Ile-de-Ré viaduct France 2576
S. Joye & M.D. Witt

SS25: Vulnerability assessment and retrofit of in-service bridges: Contributions and experiences
Organizers: M. Domaneschi, R. Cucuzza, G.A. Ferro, S. Mitoulis, M. Noori & V. Villa

Reliability of UT for the grouting inspection in PT bridges: A case study 2585
I. Mazzatura, J.R. Casas, S. Caprili & W. Salvatore

Resilience and sustainability assessment of a prestressed concrete viaduct 2594
M. Domaneschi, R. Cucuzza, R. Di Bari, S. Argyroudis, S. Mitoulis & N. Kopiika

Deterioration rate diagnosis to global climatic change: The case of Dnipro Dam in Ukraine 2603
N.S. Kopiika, J. Ninic, R. Cucuzza & S.A. Mitoulis

Model-driven strategy for bridge measurement-system design 2612
R. Galli & D. Briccola

Quality assurance of intervention in reinforced concrete bridges 2620
A.C.P. Martins, G.F.B. Milagres, J.M. Franco de Carvalho, C.A.F. Souza, F.G. Bellon, M.S. Andrade, D.S. Oliveira, K.M.L. César Jr & J.C.L. Ribeiro

Fatigue analysis and maintenance strategies for details in long-span bridge girders 2628
C. Deng, Y. Ren, X. Xu, Z. Fan, Q. Huang & Y. Li

A comparison of Italian and UK guidelines on the vulnerability assessment of bridges 2636
A. Lipari & P. Clemente

The knowledge process for the structural assessment of existing concrete bridges with post-tensioned cables: Application to a case study 2645
A. Natali, S. Celati, D. Gaudioso, W. Salvatore, D. Coletta & M. Malavisi

Sustainable repair of concrete structures in Denmark 2654
J.M. Frederiksen & C.M. Nielsen

Vulnerability assessment of timber piles by bending wave and dispersive wave testing methods 2662
W. Zatar & H. Nghiem

SS26: Risk-informed decision making and asset management of highway bridge portfolios
Organizers: A. Du, X. Wang & A. Shafieezadeh

Maintenance plan optimization system based on remaining life prediction 2673
A. Miyamoto

Risk-informed approach to determining optimal bridge inspection frequency for periodic replacement policies 2684
A.X.-X. Yuan & W. Chen

Fragility assessment of water-crossing bridge structures exposed to flood hazards 2693
J.M. Patel & J.E. Padgett

Combining condition deterioration and seismic risks for bridge asset management 2702
A. Ghavidel, A. Du & S. Kameshwar

A short-term hyperlocal meteorological forecast tool for mitigating bridge risks 2710
C.T. Georgakis, N. Lagaros, P. Tsakalis, I. Chamatidis & C. Demartino

SS27: Life-cycle performance safety, reliability, and risk of bridges and infrastructure systems under climate change
Organizers: F. Biondini, Z. Lounis & M. Ghosn

Remaining fatigue service life of the Hillsborough River Bridge in PEI, Canada 2721
C. MacAulay, G. MacDonald, A. MacDonald, R. Keefe & D. Evans

Climate change challenges: A study on bridge accessories and structural performance 2730
D. Greco, A. Moscatelli & D. Briccola

Fatigue life assessment of steel wires with multiple corrosion pits based on peridynamics 2738
Y. Yang, Q.W. Zhang, J.F. Liu, Y.F. Ji & Y.C. Ni

Fatigue life estimation for long span suspension bridges due to buffeting 2747
Z.Z. Banday, A. Fenerci, T.M. Lystad & O.A. Øiseth

Cellular automata damage models incorporating climate change effects for life-cycle assessment of concrete bridges 2755
G.V. Nava, A. D'Iorio & F. Biondini

SS28: Probability-based life-cycle design analysis of bridge engineering
Organizers: L. Wang, J. Peng, J. He, W. Lin & X. Zhou

Robustness evaluation of a twin I-girder bridge 2767
P. Acharya, R. Hao & W. Lin

Fatigue reliability analysis for welding details under traffic flow 2775
Q. Zheng, Z. Pan, X. Fang, R. Ma & B. Wang

Static and fatigue tests for hybrid welded-bolted demountable shear connectors 2783
J. He, Z. Wang, L. Wang, G. Vasdravellis & H. Xin

Optimization of maintenance program for bridge cable in service lifetime 2791
S. Liao, J. Peng, L. Wang & J. Zhang

Probabilistic inspection planning for the life cycle management of railway bridges 2797
I. Ames, T.N. Bittencourt, M.M. Futai, A.T. Beck & H. Carvalho

SS29: Risk-based assessment and prioritization of bridge stocks
Organizers: N. Scattarreggia & R. Monteiro

Management of earth retaining structures based on condition and criticality 2807
J.L. Amado, M.A. Pratas, B. Monteiro, A. Costa & M. Pinheiro

Automatic calibration of structural BIM models applied to bridges 2815
F. Lozano-Galant, E. Atencio, N. Tošić, J. González-Arteaga, Y. Xia & J.A. Lozano-Galant

Sustainable-centered approach for bridge management: A game-changer paradigm 2823
D. Duzzi & D. Briccola

Expediting the bridge management practice: A structural reliability-based method 2831
F. Brighenti, M.F. Bado, F. Poli, F. Romeo, D. Zonta, J.D. Rotilio & A. Ferman

Development of a bridge rating tool for optimised multi-hazard life-cycle-based maintenance 2840
M. Calò, N. Scattarreggia, G. Mucedero & R. Monteiro

Enhancing bridge monitoring through supervised anomaly classification 2848
I. Bayane, J. Leander & R. Karoumi

Reshaping bridge inspection with AI, 3D tools and BIM: Outcomes from an R&D initiative 2856
T. Mendonça, V. Brito, S. Costa, J. Matos & S. Fernandes

A quantitative methodology for risk-based priority ranking of deteriorated bridges: Application to a bridge stock 2865
S. Hamidpour, N. Scattarreggia, R. Nascimbene & R. Monteiro

An index-based method for risk assessment of existing bridges subjected to multiple hazard 2873
L.A. Grieco, N. Scattarreggia, R. Monterio & F. Parisi

The Italian guidelines for risk and safety evaluation of existing bridges: A case study 2882
P.P. Rossi, N. Spinella & A. Recupero

SS30: Virtual inspection
Organizers: P. Linneberg & S. Gjerding

Immersive visualization for enhanced operations and management of bridges 2893
B. Aryal & P. Linneberg

Digital transition in asset management – Virtual inspections of bridges 2901
N.L. Barnes & E.D. Hartwich

Norwegian coastal bridges 2909
T. Kvamstad, H.A. Moe & I.A. Lervik

Virtual supervision of the new Storstrøm Bridge: Status and potential with CVI 2917
T. Norsk

SS31: O&M of major bridges
Organizers: R. Percy & J.L. Jensen

Sustainability monitoring of cable systems 2927
J. Laigaard Jensen, J.F. Melén & I.F. Alcover

Tjörn bridge O&M challenges and mitigation 2935
J.L. Jensen, A. Larsen, A.H. Langager, S. Ussing, J.F. Melén & A. Maglica

Moisture monitoring in cable anchorages before and after dehumidification 2943
A. Parodi, J.L. Jensen, E. Stefansson, H. Sønderby, J.F. Melén & A. Maglica

Analysing ultrasonic testing data to optimise stay cable maintenance 2951
A. Boyez, R. Percy, J.L. Jensen & I.F. Alcover

The maintenance project of the special anti-seismic devices of the longest Italian bridge 2960
A. Greco & A. Lupoi

Experiences with repair of fatigue cracks in an orthotropic steel deck, New Little Belt Bridge, Denmark 2969
P.L. Sørensen, N. Bitsch & J. Præst

The organization, O&M operations and inspections of the 1915Çanakkale Bridge 2977
F. Aytekin & A.M. Kızılkaya

Traffic wind hazards on the Storebælt East Bridge and mitigation 2984
A. Larsen, L.F. Pedersen, N. Bitsch & F.R. Gottfredsen

Fatigue crack propagation simulation of Haibach hole for orthotropic steel bridge deck 2992
Z. Kang, J. Kang, L.W. Xu, P.Y. Li & C.S. Wang

Digital fatigue test of steel truss girders in long-span suspension bridge with double-deck 3001
Q.L. Wu, T.K. Zhang, J. Xu, S. Liu & C.S. Wang

SS32: Data-driven asset management
Organizers: I.F. Alcover, M. Saberi & J. Winkler

Change detection using Bayesian multivariate linear regression 3011
R.J. Hollamby & I.F. Alcover

Scoring system for technical evaluation of technologies for remote monitoring of bridges 3019
M. Saberi, K. McPherson, F. Zhang, A. Arvidsson, S. Fjendbo, C.V. Geem, M. Kreslin & A. Anžlin

Regional impacts of natural disasters on road bridges in the Philippines 3027
M.J. Adarne & M. Henry

Improved structural assessment of Newport Bridge using smartphone-based technologies 3035
J. Winkler, N. McKay & C. Hendy

Artificial intelligence to identify defects on bridges inspected by drone 3041
S. Flawinne

Improved structural health monitoring of the Lincent Bridge using innovative camera-based system 3049
L. Rivituso, S. Flawinne & J. Winkler

SS33: Sustainability in bridge design, operation and maintenance
Organizers: M.H. Faber & P. Linneberg

Life-cycle assessment of RC trough bridges in Sweden and Colombia: A comparative Study 3059
S.L. Leiva-Maldonado, J. Gonzalez-Libreros, C. Wang , G. Sas, P. Simonsson & D. Sas

Reducing the climate impact (GWP) from bridges in a Danish highway project 3067
J. Olesen, P.G. Pedersen & C.V. Scholten

Static behavior of steel-concrete bridge under pier girder consolidation 3075
W. Xie & Q. Su

On CO_2 efficiency and trade-offs between safety and sustainability in concrete bridge management 3084
M. Liu, J. Olesen, P. Linneberg, D.G. Lu & M.H. Faber

Fatigue design of continuous thermite-welded rail 3092
Y.C. Park & J.Y. Lee

SS37: Nordic Operation and maintenance strategies for bridges: Pioneering a sustainable future
Organizers: T. Bangsgaard, D. Honfi & B.T. Svendsen

Risk-based evaluation of fire protection on cable-supported bridges 3101
N.P. Høj, M. Bjelkerud & H. Matre

Maintenance strategies by the Swedish Transport Administration 3111
F. Olsson

Evaluation of post-tensioned bridges by state-of-the-art techniques 3117
G. Rapaport

Development and implementation of digital inspection notebook for bridges 3124
M. Tai, H. Shirahata, T. Kawai, T. Aoki, H. Hara & S. Takagi

Towards a service life extension of the Øresund Fixed Link 3133
I. Björnsson, S. Thöns, S. Celati & B. Hergart

SS39: Digital enabled asset management of major bridges
Organizers: T. Friis & I. Gualtero

Extending great belt bridge bearing service life using mobile computer vision 3145
J. Winkler, M.D. Havelykke & F. Bormlund

30 years' experience of optimizing the use of corrosion sensors 3152
P.H. Møller & S. Gjerding

Digital technologies for bridge damage detection: Drones and AI for remote inspections 3161
D. Buggiani, M. Malavisi & A. Baldacci

Service life strategies on hanger cables of the Great Belt Bridge 3169
P. Holmstrøm, D. Lang, T. Friis, M.N. Svendsen & M.D. Havelykke

Data-driven maintenance of Bogibeel Bridge - large scale structural health monitoring 3178
H. Gjelstrup, T. Bangsgaard & F. Houseini

Digital health monitoring of the Great Belt Suspension Bridge 3187
T. Friis, S.S. Christensen, S.T. Nielsen, M. Lollesgaard, T.B. Bangsgaard & M.D. Havelykke

Data-driven preventive maintenance and service life extension of the Sunshine Skyway Bridge – Tampa FL, USA 3196
I.A. Gualtero, A.H. Alvi, S.D. Womble, J.J. Jacobsen & V.S. Collie

Sustaining structural bearings – assessment of renovation design on Storebælt West Bridge 3205
A. Smyth, D. Lang, J. Fogh-Svensson, N. Grønkjær Rasmussen, M. Duus Havelykke & F. Raun Gottfredsen

SS41: Management and maintenance of urban bridges
Organizers: D. Honfi, L. Dunai & J. Vig

Cause identification for uplifting behavior of truss bridges 3215
K. Suzuki, Y. Nojima, K. Takeya, A. Akutsu, K.K. Vankayalapati, Y. Ito & E. Sasaki

Aerial-demolition method for bridges above intersections with heavy traffic 3223
R. Nakata, T. Oike, K. Fujiwara, S. Watanabe, K. Mori, Y. Ninomiya, T. Shimada, D. Fujimoto & I. Tada

Risk assessment of the K-bridge over the Danube 3231
B. Kövesdi, D. Kollár, L. Dunai & Z. Hodik

Development of the maintenance strategy for Västerbron 3240
J. Sandberg, L. Steen & J. Hedenström

Enhancing Dybbølsbro Bridge – Refurbishment and expansion without new substructure 3249
L. Thormann, C. Pedersen & J.F. Svensson

SS42: Community resilience and decision-support systems
Organizers: N. Makhoul, R. Kromanis, J. van de Lindt, A.R. Barbosa & F. Schmidt

Dynamic traffic simulation for transportation system resilience assessment 3259
X. Wang, P. Bocchini, P. Venkitasubramaniam & S. Xie

Adaptive transition of critical transport infrastructures 3267
D.V. Achillopoulou, N.K. Stamataki, N. Makhoul & R. Kromanis

Machine learning improving seismic infrastructure recovery time estimation 3276
N. Makhoul & B. Derras

Information entropy-driven recovery strategies for systems' resilience 3286
A. Tzioutziou & Y. Xenidis

Physics-based earthquake-tsunami fragility surfaces for risk and resilience analysis 3295
M. Harati & J.W van de Lindt

Bridge maintenance methodology accounting for climate change dependent parameters 3304
S.A. Keo & N. Makhoul

Enhancing urban resilience and sustainability under wind disasters with carbon emission as an indicator 3311
T.-Y. Wang & C.-Y. Lin

Identification of a suitable case study for the development of accessibility based vulnerability score for bridge maintenance decision making 3320
M. Lydon, A. Vega, E. Fitzpatrick, R. Higgins & A. Fenerich

SS43: Responding to structural emergencies: Post-event inspection to restoring the structure to full service
Organizers: S. Alampalli & M. Maqbool

A plan for assessing the damage to highway bridges after an earthquake 3329
J.S. O'Connor & S. Alampalli

Rapid response for ensuring safety following bridge hits 3337
M.A. Mohammed

Critical role of the bridges ensuring emergency services and disaster recovery in Turkey 3343
N. Memişoğlu Apaydin & R.B. Sikar

Human-centered post-disaster inspection of infrastructure using augmented reality 3352
F. Moreu, C.-M. Chang, Y.-T. Liu, K. Malek & A. Khorasani

Condition assessment and repair protocols for dynamically impacted bridge girders 3359
W. Zatar

SS44: AI and optimization methods for bridge management under uncertainty
Organizers: D.Y. Yang, C. Andriotis & K.G. Papakonstantinou

Data-derived train classification and monitoring of masonry bridge 3371
J. Cheng, A. Chen, M.J. DeJong & S. Cocking

Deep reinforcement learning-driven life-cycle management of bridge and pavement systems 3380
A. Bhattacharya, M. Saifullah & K.G. Papakonstantinou

Analyzing uncertainty in strain estimation framework for bridge condition assessment 3389
S.S. Eshkevari, I. Dabbaghchian, G. Marasco, S. Pakzad & D. Sen

Intelligent automatic operational modal analysis: Application to a suspension bridge 3397
M.M. Rosso, G.C. Marano, A. Aloisio & G. Quaranta

Managing aging bridges under seismic hazards through deep reinforcement learning 3405
Z. Metwally, C.P. Andriotis & F. Molaioni

Objective risk assessment for bridge management 3414
S.A. Moayyedi & D.Y. Yang

SS46: BRIDGITISE an EU network on the digitalization of bridge integrity management
Organizers: M.P. Limongelli, J.H. Roldsgaard, J. Jordan & M.H. Faber

Drone-based photogrammetric indoor inspection of box girder bridges 3425
J.C. Avendaño, J. Leander & R. Karoumi

Decision algorithms for the managing of steel railway bridges 3433
J. Garcia, F. Javier & C.R. Iván

Lightweight vehicles in indirect structural health monitoring: Current advances and future prospects 3441
P.F. Giordano, S. Quqa & M.P. Limongelli

Simultaneous WET and WIT with Q-learning for wireless bridge sensors network 3450
M.T. Mushtaq, V. Giuseppe, N. Cordeschi, A. Grieco & G. Boggia

Probabilistic digital twin for continuous bridge performance modelling 3457
P. Darò, D.L. Mazza, F. Basone, G. Mancini, M.P. Limongelli & M.H. Faber

SS47: Life-cycle of RC/PC bridges: Advances on experimental testing and computational methods from the BRIDGE|50 research project
Organizers: F. Biondini, F. Tondolo, S. Manto & C. Beltrami

Nonlinear structural analysis of 50-year-old PC bridge deck beams under load testing 3467
M. Anghileri & F. Biondini

Corrosion investigations on PC deck beams of a 50-year-old decommissioned viaduct 3476
M. Carsana, E. Redaelli & F. Biondini

Load tests on dismantled 50-year-old prestressed concrete bridge deck beams 3484
P. Savino, A. Quattrone, D. Sabia, B. Chiaia, F. Tondolo, M. Anghileri, F. Biondini & G. Rosati

Dynamic response of damaged precast bridge girders 3493
D. Sabia, A. Quattrone, F. Tondolo & P. Savino

Integrating BIM in experimental tests on bridge beams 3501
D.R. Polania, F. Tondolo, A. Osello, C. Trincianti & M. Chiara

GENERAL SESSIONS

GS01: BRIDGE MAINTENANCE - Application of new tools

Super-resolution enhanced vehicle recognition method for long-span bridge 3513
X. Shan, J. Zhang, Y. Pan, Y. Ma & D. Wang

Bayesian non-linear load estimation in long-span bridges via physics-informed Gaussian processes 3522
G.R. Tondo, I. Kavrakov & G. Morgenthal

A multi-task deep learning-based framework for structural details and corrosion detection in steel bridges 3530
M.Z. Esteghamati, M.H. Ahmed, S. Young & M. Halling

Tests of TIG welded lap joint between Fe-SMA and steel 3538
Z. Zhang, X. Qiang, X. Jiang & P. Jin

A decision method for ship-bridge collision pre-warning based on vision and radar data fusion 3546
H. Zhuang, D. Wang, Z. Gu, Y. Dong & J. Wang

GS05: BRIDGE MAINTENANCE - Inspection and diagnostic

Utilization of soundness assessment of medium and small span bridges based the ML models 3557
Arong, G.Z. Wang, M.X. Gao, Dongmei, S. Bai & Yiliguoqi

AI for bridge inspection with IBM Inspecto 3565
A.C.I. Malossi, R. Assaf, N. Avogaro, A. Bartezzaghi, B. Ebouky, T. Frick, I. Giurgiu, F.M. Janicki, P. Kluska, M. Rigotti, F. Scheidegger, A. Simeski, C. Skura, D. Caraballo, Y. Cinar, F. Bormlund & S. Gjerding

A review of recent research on visual inspection processes for bridges and the potential uses of AI 3573
P.J. Vardanega, T. Tryfonas, G. Gavriel, D.T. Nepomuceno, M. Pregnolato & J. Bennetts

Performance evaluation of TMDs for a continuous steel box girder 3581
G.L. Liu, X.H. Hu & R.J. Ma

Improvement of thickness estimation model on a steel member using local vibration mode based on data augmentation 3590
S. Kato, K. Hisazumi, T. Tominaga, Y. Yang & T. Nagayama

Crack detection method for RC beams with an automatic hammering device 3599
I. Uchiyama, H. Naito, K. Inada, Y. Kuriharam & K. Matsuhashi

An attempt to improve the accuracy of 3D point cloud considering bridge vibration effects 3608
A. Akutsu, J. Lin & E. Sasaki

Scour detection method of bridge foundation based on pier vibration mode under vehicle braking action 3617
Y. Li, Z.H. Zhang, Z.B. Sun & H. Sun

Field test study of bridge scour diagnostic method based on time-varying frequency 3625
Z.H. Zhang, Y. Li, C. Yang & H. Sun

Accuracy of the pulsed eddy current thickness measurement for a corroded steel pipe 3633
Y. Kitane, Y. Shichijo & Y. Itoh

GS07: BRIDGE MAINTENANCE - Non-destructive testing

Ground Penetrating Radar (GPR) for bridge inspection 3645
N. Roumia & C. Mazzotti

Advancements in bridges NDT: National Highways' "Structures Moonshot" – Paper No. 1 3653
C. Mundell, C. Hendy, T. Argyle & C. George

Advancements in Bridges NDT: National Highways' "Structures Moonshot" – Paper No. 2 3663
C. Mundell, C. Hendy, T. Argyle & C. George

Advancements in Structural Health Monitoring (SHM): Deformation Area Difference (DAD) method and model updating 3673
T. Čamo, E. Apostolidi & D. Waldmann-Diederich

A study on hammering inspection for unreinforced concrete based on wearable microphone measurement 3681
K. Takeya, S. Kobayashi, A. Akutsu, Y. Ito & E. Sasaki

GS17: BRIDGE SAFETY - Advanced computer simulation

Simulation of cylinder impact damage by peridynamics 3691
J.J. Zhang, Z.C. Pan & H.C. Chang

Analytical evaluation of DBTT in Charpy impact test for structural steels 3698
A. Jamil, H. Tamura, H. Katsuchi & C. He

Elastic-plastic bearing capacity simulation of steel-concrete composite bridge tower 3706
S.D. Sun, L.H. Yang, Y.W. Wang, K.Q. Cheng & C.S. Wang

Structural behavior of steel truss girder with thick concrete deck in cable-stayed bridge 3715
Y.Q. Li, Y.C. Feng, X. Hou, S.L. Yan, H.J. Liu & C.S. Wang

Reasonable degree of shear connection for thick concrete deck in cable-stayed bridge 3723
Y.Q. Li, Y.C. Feng, X. Hou, H.J. Liu & C.S. Wang

GS19: BRIDGE SAFETY - Assessment and evaluation

Development of a new abutment connection for rapid construction 3733
F. Sigurjónsson, R.S. Smárason, O.S. Haraldsson, B. Bessason & C.Y. Tsai

NDT for damage detection in FRP reinforced/strengthened concrete elements 3740
A.B. Mehrabi, S.S.K. Dolati, P. Malla, J.O. Polanco & A. Nanni

Calibration of constitutive model parameters of bridge steels using particle swarm optimization 3748
Y. Zhang, C. Li & H. Huo

Modal identification for rapid assessment of short span reinforced concrete bridges 3757
S.L. Leiva-Maldonado & F. Consuegra

Retroreflective sheeting materials as SHM passive strain sensors 3765
H.M. Power & H.W. Shenton III

Assessment method for arch bridges affected by HS2 tunnel settlement, UK 3773
A.S. Justo, A. Bariyya, C. Brown, R. Lee & M. Gilbert

Parametric evaluation and design of prestressed concrete beam bridges 3782
V.N. Moraes, T.E.T. Buttignol & L.M. Trautwein

Bridge deterioration estimation for small zones considering chemical attack 3790
F. Obunguta, K. Kaito, K. Sasai, K. Kobayashi, K. Matsushima & H. Bakamwesiga

Assessment of shear capacity of bridge beams with non-standard anchorage - an experimental study 3801
E. Nuti, A. Darby, M. Evernden, J. Bennetts, J.D. Shave & P. Valerio

Deep learning for evaluation of girder rotation during bridge deck construction 3809
L. Hui & R. Hindi

FEM-based dynamic analysis of noise barriers under train-induced aerodynamic load 3817
D. Liu, C. Wang, J. Gonzalez-Libreros, Y. Tu, L. Elfgren, G. Sas, O. Enoksson, T. Höjsten & Y. Tu

Analytical evaluation of Hybrid Deck Bulb Tee for superstructure replacement 3825
P. Agüero-Barrantes & A. Hain

PCA-based technique to assess the modal properties of the Itacaiúnas bridge during flooding 3832
R. Lopes, J. Weyl, V. Barros & T. Bittencourt

Recommendations for structural assessment of RC slabs using the finite element method 3838
M. Plos, M. Johansson, K. Zandi & J. Shu

Behaviour & management of pre-tensioned girder halving joints 3845
N. Stevens, T. Heldt, C. Lin & R. Sampaio

The behaviour and management of post-tensioned girder halving joints 3854
N. Stevens, R. Sampaio, T. Heldt & C. Lin

Fatigue behaviour of reinforced concrete inverted T headstock halving joints 3863
N. Stevens, C. Lin, T. Heldt & R. Sampaio

Enhancing safety on timber bridges: Feasibility and risk assessment of bridge barrier implementation 3871
E. Chaw, G. O'Connor, D. Milling, A.D. Silva, R. Daley & B. Wiggins

Design curves for masonry arch bridges over rivers in the UK 3880
J. Liu, G.D.D. Dieco, F.D.D. Dieco, F. Ragone & S.L. Nunn

Seismic performance of highway RC bridges with corroded piers 3889
D. Cardone, V. Possidente, G. Perrone, A. Spica, D. Bernardini, D. Ruta, A. Paolone, F. Braga, F. Buttarazzi & A. Rossi

Identification of governing structural safety criterion for existing bridges considering costs, occupancy and conditional fatality probability 3897
F. Liljefors & J. Köhler

A review of design and assessment methods for skew concrete slabs 3904
A. Lipari

Non-destructive testing of a post-tensioned concrete road bridge in Norway 3913
B. Täljsten, C. Popescu & M. Holmqvist

Comparison of partial factor methods for existing concrete structures: Application to a cable-stayed bridge 3922
L. Casti, F. Schmidt, F. Biondini, N. Makhoul & R. Pittet

GS25: BRIDGE SAFETY - Extreme loads

Seismic design of cable-stayed bridges in high intensity areas 3933
B. Li, Z. Zeng, Y. He & Y. Xu

A coupled thermal-mechanical-phase field model for concrete under fire 3941
K. Miao, Z. Pan, X. Fang & A. Chen

Modelling of thermo-mechanical behaviour of tunnels under fire conditions 3950
R.A.S. Díaz, E.O.L. Lantsoght & M.A.N. Hendriks

An unconventional barrier design 3958
Z. Kamranian, D. Penate, G. Norlander & F. Oudah

GS27: BRIDGE SAFETY - Repair and retrofitting strategy

Anchored response tailored prestressed CFRP strengthening – preliminary long-term and temperature investigations 3967
J.W. Schmidt, C.O. Christensen & P. Goltermann

Analytical study on the effects of flange size on the axial force introduced in the rivet 3976
K. Yamamoto & K. Nozaka

Novel Fe-SMA bonding method for repair of U-rib butt welds in OSDs 3985
Z.L. Lv, X. Jiang, X.H. Qiang, H.L. Wu & J.M. Ding

Experiment research on fatigue cracks at diaphragm cutouts reinforced employing Fe-SMA in steel bridge 3992
Y.P. Wu, X.H. Qiang, X. Jiang & Z.Y. Yang

Experimental study on seismic performance of different failure modes of RC shear keys 4001
H. Mei & A.X. Guo

Progressive failure analysis of strengthened masonry arch bridges 4010
T. Kamiński & C. Costa

Rapid repair of bridge beams and decks with prefabricated FRP panels 4019
M. Ehsani

Incremental repair method for corroded bolted connection 4027
E. Yamaguchi, N. Tamada, U. Agvaanluvsan, T. Takai & M. Wada

GS28: BRIDGE SAFETY - Safety and serviceability

A 2D TBI model to study lateral dynamics in ship impact event 4035
D. Riboldi, L. Bernardini & A. Collina

Energy absorption of bolted connection up to tensile ultimate state 4043
T. Takai, K. Tanii & S. Masudome

Effectiveness of geotechnical seismic isolation for post-tensioned rocking piers 4052
A. Contento, B. Briseghella, A. Di Egidio, A. Aloisio, H.-H. Tsang & P. Gardoni

Flexural behavior of concrete- steel composite girders with tubular flanges 4060
Y.R. Liu, B.Q. Gao, X.B. Qu, J.W. Zhang, Y.W. Wang & L. Duan

Flexural behavior of high strength steel-UHPFRC composite girders 4069
J.W. Zhang, F. Li, X.B. Qu, S.J. Li, W.T. Liu & C.S. Wang

Author index 4079


Taylor & Francis
Taylor & Francis Group
http://taylorandfrancis.com

Bridge Maintenance, Safety, Management, Digitalization and Sustainability – Jensen, Frangopol & Schmidt (eds)
© 2024 The Editor(s), ISBN 978-1-032-77040-6
Open Access: www.taylorfrancis.com, CC BY-NC-ND 4.0 license

Preface

The world economy is changing rapidly. On the one hand, issues like health and safety, quality, resilience, sustainability, climate change, social justice, and the environment are increasing their weight for decision-makers compared with traditional financial considerations. On the other hand, the advent of cheap, powerful computers, smartphones, and robots is changing society and economic interactions drastically.

However, one thing that seems stable in this turmoil is the importance given to maintenance and life-cycle evaluation in any infrastructure, making IABMAS (International Association for Bridge Maintenance and Safety) goals more and more relevant for the engineering community. In this context, academics and practitioners are rising to the challenge with research and practice focusing on innovative approaches to identify problems and implement solutions. IABMAS conferences bring together academic and technological developments in bridge safety, maintenance, management, life-cycle, resilience, and sustainability, among others, to solve new and old problems with innovative solutions. The most recent developments in the field are expected to be discussed at the 12th International Conference on Bridge Maintenance, Safety and Management (IABMAS 2024), held in Copenhagen, Denmark, on 24–28th of June 2024 (https://iabmas2024.dk/).

The First (IABMAS'02), Second (IABMAS'04), Third (IABMAS'06), Fourth (IABMAS'08), Fifth (IABMAS'10), Sixth (IABMAS'12), Seventh (IABMAS'14), Eighth (IABMAS'16), Ninth (IABMAS'18), Tenth (IABMAS'20) and Eleventh (IABMAS'22) International Conferences on Bridge Maintenance, Safety and Management were held in Barcelona, Spain, July 14–17, 2002, Kyoto, Japan, October 18–22, 2004, Porto, Portugal, July 16–19, 2006, Seoul, Korea, July 13–17, 2008, Philadelphia, USA, July 11–15, 2010, Stresa, Lake Maggiore, Italy, July 8–12, 2012, Shanghai, China, July 7–11, 2014, Foz do Iguaçu, Brazil, June 26–30, 2016, Melbourne, Australia, July 9–13, 2018, Sapporo, Hokkaido, Japan, April 11–15, 2021 (online) and Barcelona, Spain, July 11–15, 2022.

In this edition, the Conference will be in Copenhagen, Denmark, and IABMAS Denmark looks forward to celebrating the 12th edition and 25th anniversary of IABMAS. Again, face-to-face after some challenging years with COVID.

IABMAS 2024 is organized by IABMAS (https://iabmas.w.waseda.jp/) in collaboration with IABMAS Denmark (https://iabmas-danmark.dk). IABMAS encompasses all aspects of bridge maintenance, safety and management. Specifically, it deals with bridge repair and rehabilitation issues, bridge management systems, needs of bridge owners, financial planning, life costing and investment of the future, sustainability, bridge-related safety and risk issues, and economic and other implications.

The objective of the Association is to promote international cooperation in bridge maintenance, safety, risk, resilience, sustainability, and management to enhance society's welfare (www.iabmas.org). The interest of the international bridge community in the fields covered by IABMAS has been confirmed by the significant response to the IABMAS 2024 call for papers. The Conference Secretariat received 680 abstracts, 676 of which were selected for presentation at the Conference within mini-symposia (MS), special sessions (SS), and general sessions (GS). Finally, 480 papers were accepted for publication in this Open Access book. Contributions presented at IABMAS 2024 deal with the state-of-the-art and emerging

concepts and innovative applications related to the main aspects of safety, maintenance, management, life-cycle, resilience, sustainability, and technological innovations of bridges.

Significant topics include advanced bridge design, construction and maintenance approaches, safety, reliability and risk evaluation, life-cycle management, life-cycle resilience, sustainability, standardization, analytical models, bridge management systems, service life prediction, structural health monitoring, non-destructive testing and field testing, robustness and redundancy, durability enhancement, repair and rehabilitation, fatigue and corrosion, extreme loads, needs of bridge owners, whole life costing and investment for the future, financial planning and application of information and computer technology, extensive data analysis and artificial intelligence for bridges, among others.

Bridge Maintenance, Safety, Management, Digitalisation and Sustainability contains 480 contributions, including the T.Y. Lin Lecture, 9 Keynote Lectures, and 470 technical papers from 44 countries. This volume provides an up-to-date overview of the field of bridge engineering and significant contributions to making more rational decisions on bridge safety, maintenance, management, life-cycle, resilience, sustainability and bridge innovations to enhance the welfare of society. The Editors hope that this book will serve as a valuable reference to all concerned with bridge structure and infrastructure systems, including engineers, researchers, academics, and students from all areas of bridge engineering.

Jens Sandager Jensen and Dan M Frangopol,
Chairs of IABMAS 2024
&
Jacob Wittrup Schmidt
Chair of IABMAS 2024 Scientific Committee
June 2024

Bridge Maintenance, Safety, Management, Digitalization and Sustainability – Jensen, Frangopol & Schmidt (eds)
© 2024 The Editor(s), ISBN 978-1-032-77040-6
Open Access: www.taylorfrancis.com, CC BY-NC-ND 4.0 license

Acknowledgements

The Editors are extremely grateful to everyone who contributed to the scientific program and organization of the IABMAS 2024 Conference. The Editors would like to express their sincere thanks to all authors for their contributions, to the members of the International Scientific Committee and the Local Scientific Committee for their role in ensuring the highest scientific level of the Conference, and to the members of the Local Organizing Committee for their time and efforts dedicated to making IABMAS 2024 a successful event.

Moreover, the Editors thank all organizations, institutions, and authorities offering sponsorship and support. A special acknowledgement has to be given to the International Association for Bridge Maintenance and Safety (IABMAS) and IABMAS Denmark for endorsing and supporting the conference organization.

The conference organizers want to thank the following companies and institutions and their personnel sincerely: The Danish Road Directorate for a visit to the Nordhavnstunnel and the Storstrøms Bridge, Femern and Sund & Baelt for a visit to the Femarnbelt Tunnel, Storebaelt and Sund & Baelt for a visit to the Great Belt Bridge, Oeresundsbron for a visit to the Oresundsbridge, Copenhagen Municipality for a visit to Copenhagen Bridges, Rail Net Denmark and Bridge walking Lillebaelt for the visit to the Lillebaelt Bridge, By og Havn for a boat tour round Nordhavn and Lynetteholm and the Danish Technical University for a visit to the structural and materials testing facilities at the Technical University of Denmark (DTU).

The Editors are also highly thankful to Mitsuyoshi Akiyama, Sreenivas Alampalli, Nurdan Apaydin, Tulio Bittencourt, Eugen Brühwiler, Joan Ramon Casas, Necati Catbas, Airong Chen, Ranjith Dissanayake, Reed M. Ellis, Michel Ghosn, Pier Giorgio Malerba, Jens Sandager Jensen, Ho-Kyung Kim, David De León, Nigel G. Powers, and Matías A. Valenzuela co-chairs of the International Scientific Committee.

Finally, the Editors wish to express their sincerest appreciation to Helle Klestrup and the team at DIS Congress Service A/S, who professionally managed the Organizing Secretariat with outstanding expertise, patience, energy, and commitment, which have been very important for the successful organisation of this Conference.


Taylor & Francis
Taylor & Francis Group
http://taylorandfrancis.com

Bridge Maintenance, Safety, Management, Digitalization and Sustainability – Jensen, Frangopol & Schmidt (eds)
© 2024 The Editor(s), ISBN 978-1-032-77040-6
Open Access: www.taylorfrancis.com, CC BY-NC-ND 4.0 license

Conference Organisation

CONFERENCE CHAIRS

Jens Sandager Jensen	*COWI A/S, Denmark*
Dan M. Frangopol	*Lehigh University, Bethlehem, USA*

INTERNATIONAL SCIENTIFIC COMMITTEE

Chair

Jacob Wittrup Schmidt	*University of Aalborg, Denmark*

Co-Chairs

Mitsuyoshi Akiyama	*Waseda University, Japan*
Sreenivas Alampalli	*Stantec, USA*
Nurdan Apaydin	*General Directorate of State Highways, Turkey*
Tulio Bittencourt	*University of Sao Paulo, Brazil*
Eugen Brühwiler	*EPFL, Switzerland*
Joan Ramon Casas	*UPC - BarcelonaTech, Spain*
Necati Catbas	*University of Central Florida, USA*
Airong Chen	*Tongji University, China*
Ranjith Dissanayake	*University of Peradeniya, Sri Lanka*
Reed M. Ellis	*STANTEC, Canada*
Michel Ghosn	*The City College of New York/CUNY, USA*
Jens Sandager Jensen	*COWI A/S, Denmark*
Ho-Kyung Kim	*Seoul National University, Korea*
David De León	*Autonomous University of Mexico State, Mexico*
Nigel Powers	*ARRB, Australia*
Matías A. Valenzuela	*Pontificia Universidad Católica de Valparaíso, Chile*

Members

Riadh Al-Mahaidi	*Swinburne University of Technology, Australia*
João Amado	*Infraestruturas de Portugal, S.A., Portugal*
Andrej Anzlin	*ZAG, Slovenia*
Miguel Ángel Astiz	*Universidad Politécnica de Madrid, Spain*
Upul Attanayake	*Western Michigan University, USA*
Torben Bilgrav Bangsgaard	*Ramboll, Denmark*
Lise Bathen	*SVV, Norway*
Andre Beck	*University of Sao Paulo, Brazil*

Konrad Bergmeister	*University of Natural Resources and Life Sciences, Austria*
Fabio Biondini	*Politecnico di Milano, Italy*
Paolo Bocchini	*Lehigh University, USA*
Bruno Briseghella	*Fuzhou University, China*
Alp Caner	*Middle East Technical University, Turkey*
Colin Caprani	*Monash University, Australia*
Anders Carolin	*Trafikverket, Sweden*
Robby Caspeele	*Ghent University, Belgium*
Eleni Chatzi	*ETH Zurich, Switzerland*
Christian Overgaard Christensen	*University of Aalborg, Denmark*
Marios Chryssanthopoulos	*University of Surrey, UK*
Christian Cremona	*Bouygues Civil Works, France*
Paulo Cruz	*University of Minho, Portugal*
Alvaro Cunha	*University of Porto, Portugal*
Sofia Diniz	*Federal University of Minas Gerais, Brazil*
You Dong	*The Hong Kong Polytechnic University, China*
Lennart Elfgren	*Luleå University of Technology, Sweden*
Bruce Ellingwood	*Colorado State University, USA*
Allen Estes	*California Polytechnic State University, USA*
Dan M. Frangopol	*Lehigh University, USA*
Yozo Fujino	*Yokohama National University, Japan*
Hitoshi Furuta	*Kansai University and Osaka City University, Japan*
Paolo Gardoni	*University of Illinois at Urbana-Champaign, USA*
Kenneth Gavin	*Delft University of Technology, The Netherlands*
Jaroslaw Górecki	*UTP University of Science and Technology, Poland*
Guðmundur Valur Guðmundsson	*Icelandic Road and Coastal Administration (IRCA), Iceland*
Rade Hajdin	*University of Belgrade, Serbia*
Ólafur Sveinn Haraldsson	*Icelandic Road and Coastal Administration (IRCA), Iceland*
Jun He	*Changsha University of Science & Technology, China*
Santiago Hernández	*Universidade da Coruña, Spain*
Riyadh Hindi	*Saint Louis University, USA*
Ralph Holst	*German Federal Highway Research Institute, Germany*
Naeem Hussain	*ARUP, China*
Niels Peter Høj	*Hoj Consulting, Switzerland*
Kiyohiro Imai	*Honshu-Shikoku Bridge Authority, Japan*
Boulent Imam	*University of Surrey, England*
Ichiro Iwaki	*Nihon University, Japan*
Juan José Jorquera-Lucerga	*Universidad Politécnica de Cartagena, Spain*
Zahra Kamranian	*Stantec, USA*
Raid Karoumi	*KTH, Sweden*
Sunyong Kim	*Wonkwang University, South Korea*
Risto Kiviluoma	*WSP, Finland*
Seyedmilad Komarizadehasl	*Universitat Politècnica de Catalunya, Spain*
Eva Lantsoght	*Universidad San Francisco de Quito, Ecuador*
Chun-Qing Li	*RMIT University, Australia*
Huile Li	*Southeast University China*
Poul Linneberg	*COWI, Denmark*
Geert Lombaert	*KU Leuven, Belgium*

José Antonio Lozano-Galant	*Universidad de Castilla-La Mancha, Spain*
Wenliang Lu	*Beijing Jiaotong University, China*
Karin Lungren	*Chalmers University of Technology, Sweden*
Jerome Lynch	*Duke University, USA*
Haiying Ma	*Tongji University, China*
Adriano Maglica	*Trafikverket, Sweden*
Pier Giorgio Malerba	*Politecnico di Milano, Italy*
Barney T. Martin	*Modjeski and Masters Inc., USA*
Marcelo Márquez	*Ministerio de Obras Públicas, Chile*
José C. Matos	*Universidade do Minho, Portugal*
Hiroshi Matsuzaki	*National Defense Academy of Japan, Japan*
Stergios Mitoulis	*University of Birmingham, UK*
Luis Morán	*Universidad Nacional Mayor de San Marcos, Peru*
Fernando Moreu	*University of New Mexico, USA*
Guido Morgenthal	*Bauhaus University Weimar, Germany*
Ernst Niederleithinger	*BAM, Germany*
María Nogal	*Delft University of Technology, The Netherlands*
Eugene O'Brien	*University College Dublin, Ireland*
Jamie E Padgett	*Rice University, USA*
Shamim Pakzad	*Lehigh University, USA*
Hans Petursson	*Trafikverket, Sweden*
Lars Fuhr Pedersen	*COWI A/S, Denmark*
Carlo Pellegrino	*University of Padova, Italy*
Mario Plos	*Trafikverket, Sweden*
Cosmin Popescu	*Invator, Sweden*
Ignacio Pulido	*Ideam, Spain*
Gonzalo Ramos	*UPC - BarcelonaTech, Spain*
Joan Hee Roldsgaard	*Ramboll, Denmark*
Xin Ruan	*Tongji University, China*
Mehdi Saiid Saiidi	*University of California, Los Angeles (UCLA), USA*
Masahiro Sakano	*Kansai University, Japan*
Luís Santos	*Laboratório Nacional de Engenharia Civil, Portugal*
Gabriel Sas	*Luleå University of Technology, Sweden*
Richard Sause	*Lehigh University, USA*
Kristian Schellenberg	*Equi Bridges, Switzerland*
Álvaro Serrano	*MC2 Estudio de Ingeniería, Spain*
Erik Stoklund Larsen	*Danish Road Directorate, Denmark*
Alfred Strauss	*University of Natural Resources and Life Sciences, Austria*
Bjørn Thomas Svendsen	*Ramboll, Norway*
John Dalsgaard Sørensen	*University of Aalborg, Denmark*
Man-Chung Tang	*T. Y. Lin International, USA*
Jin-Guang Teng	*Hong Kong Polytechnic University, China*
Yiannis Tsompanakis	*Technical University of Crete, Greece*
José Turmo	*UPC - BarcelonaTech, Spain*
Björn Täljsten	*Invator, Sweden*
Dawid Wisniewski	*Equi Bridges, Poland*
Yiannis Xenidis	*Aristotle University of Thessaloniki, Greece*
You-Lin Xu	*The Hong Kong Polytechnic University, China*

Hiroshi Yokota	*Hokkaido University, Japan*
Eiki Yamaguchi	*Kyushu Institute of Technology, Japan*
Yuguang Yang	*TU Delft, The Netherlands*
David Y.Yang	*Portland State University, USA*
Victor Yepes	*Universitat Politècnica de València, Spain*
Mariano Angelo Zanini	*University of Padova, Italy*
Aleš Žnidaric	*Slovenian National Building and Civil Engineering Institute, Slovenia*

LOCAL ORGANISING COMMITTEE

Anders Bøwig Brøndum	*Rambøll A/S*
Christian Overgaard Christensen	*Aalborg University*
Martin Duus Havelykke	*Sund & Bælt Holding A/S*
Niels Christian Skov Nielsen (chair)	*Danish Road Directorate*
Mette Sloth	*COWI A/S*
Henrik Stang	*Technical University of Denmark*
Otto Bach Ulstrup	*Rail Net Denmark*

LOCAL SCIENTIFIC COMMITTEE

Sandro Diord Rescinho Amador	*Technical University of Denmark*
Paul Stig Andersen	*Rail Net Denmark*
Svend Gjerding	*Sund & Bælt Holding A/S*
Joan Hee Roldsgaard	*Rambøll A/S*
Lis Lassen	*The Danish Road Directorate*
Poul Linneberg	*COWI A/S*
Jacob Wittrup Schmidt (chair)	*University of Aalborg*

IABMAS 2024 SECRETARIAT

DIS Congress Service
Lautruphøj 1-3
2750 Ballerup
Denmark
Tel. + 45 4492 4492
Iabmas2024@discongress.com

CONFERENCE WEBSITE

https://iabmas2024.dk/

IABMAS WEBSITE

http://www.iabmas.org/

Bridge Maintenance, Safety, Management, Digitalization and Sustainability – Jensen, Frangopol & Schmidt (eds)
© 2024 The Editor(s), ISBN 978-1-032-77040-6
Open Access: www.taylorfrancis.com, CC BY-NC-ND 4.0 license

IABMAS Executive Committee

President of IABMAS

Dan M. Frangopol, *USA*

Vice-Presidents of IABMAS

Pier G. Malerba, *Italy*
Eiichi Watanabe, *Japan*

Members

Fabio Biondini, *Italy*
Tulio N. Bittencourt, *Brazil*
Eugen Brühwiler, *Switzerland*
Airong Chen, *China*
Paulo J. S. Cruz, *Portugal*
Yozo Fujino, *Japan*
Hitoshi Furuta, *Japan*
Jens S. Jensen, *Denmark*
Ho-Kyung Kim, *Korea*
Hyun-Moo Koh, *Korea*
Victor Popa, *Romania*
Man-Chung Tang, *USA*

Secretary General of IABMAS

Joan-R. Casas, *Spain*

Secretary of Executive Committee of IABMAS

Mitsuyoshi Akiyama, *Japan*


Taylor & Francis
Taylor & Francis Group
http://taylorandfrancis.com

Bridge Maintenance, Safety, Management, Digitalization and Sustainability – Jensen, Frangopol & Schmidt (eds)
© 2024 The Editor(s), ISBN 978-1-032-77040-6
Open Access: www.taylorfrancis.com, CC BY-NC-ND 4.0 license

Sponsors

ORGANISING ASSOCIATIONS

IABMAS, International Association for Bridge Maintenance and Safety

IABMAS Danmark

HOST ORGANISATIONS

COWI A/S

Danish Road Directorate

Rail Net Denmark

Rambøll

Sund og Bælt Holding A/S

GOLD SPONSOR



SILVER SPONSOR







EXHIBITORS















SUPPORTING ORGANISATIONS

ATLSS Engineering Research Center, Lehigh University, Bethlehem, PA, USA

IABSE

IALCCE, International Association for Life-Cycle Civil Engineering

RCEAS, P.C. Rossin College of Engineering and Applied Science, Lehigh University, Bethlehem, PA, USA

Transportation Research Board

IABMAS Australia Group

IABMAS Brazil Group

IABMAS Canada Group



IABMAS Chile Group



IABMAS China Group



IABMAS Italy Group



IABMAS Japan Group



IABMAS Korea Group



IABMAS Portugal Group (ASCP)



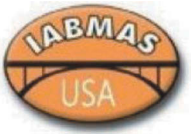
IABMAS Spain Group



IABMAS Sri Lanka Group



IABMAS Turkey Group



IABMAS USA Group

Bridge Maintenance, Safety, Management, Digitalization and Sustainability – Jensen, Frangopol & Schmidt (eds)
© 2024 The Editor(s), ISBN 978-1-032-77040-6
Open Access: www.taylorfrancis.com, CC BY-NC-ND 4.0 license

Editor Biographies

Mr. Jens Sandager Jensen is Project and Market Director in COWI's Transportation Division, which services the Danish market and provide O&M (Operation & Maintenance) specialist services in connection with Transportation projects in Scandinavia and Internationally.
Mr. Jens Sandager Jensen graduated from the Danish Engineering Academy in Denmark in 1982 with a BSc in Civil and Structural Engineering. Specialist knowledge areas are management, life cycle analysis, design of bridges and tunnels and asset management.

In 1982 he joined the Danish company Christiani & Nielsen working with design of marine and tunnel structures, before coming to COWI in 1988, where the first assignment was to be part of the design team for the Eastern Railway Tunnel under the Great Belt in Denmark.

Mr. Jens Sandager Jensen has been the project manager responsible for O&M activities on several major Danish infrastructure projects, amongst others the Eastern Railway Tunnel and the West Bridge of the Great Belt, the land works for the Øresund Bridge and the Copenhagen Metro. He has also worked as project manager to Rail Net Denmark with the responsibility of bridge maintenance in East Denmark.

During many years he has been responsible for Design Build projects for Contractors in the Scandinavian Infrastructure Market with high focus on time and cost savings for the Contractor Clients and at the same time fulfilling the requirements of the Public End Clients.

Mr. Jens Sandager Jensen has been involved in innovation and development within the field of O&M and has in COWI been responsible for major international research and development projects, amongst others the comprehensive EU projects "Sustainable Bridges; Assessment for future traffic demands and longer lives" and "MAINLINE – MAINtenance, renewal and Improvement of rail transport iNfrastructure to reduce Economic and environmental impacts".

Mr. Jens Sandager Jensen is furthermore active in IABSE and in IABMAS since 2002, including a member of The Executive Committee of IABMAS since 2016 and Chairman of IABMAS Denmark since inauguration in 2023. Finally since 2006 he has been a member of the organizing committee for yearly Danish Bridge Day and he has since 2011 been active in the Danish group responsible for defining the policies and regulations to be used in connection with transportation infrastructure structures and civil works.

Dan M Frangopol is the inaugural holder of the Fazlur R. Khan Endowed Chair of Structural Engineering and Architecture at Lehigh University. He is recognized as a pioneer in the field of life-cycle engineering of civil and marine structures under various types of hazards. Dr. Frangopol is the Founding President of the *International Association for Bridge Maintenance and Safety* (IABMAS) and the *International Association for Life-Cycle Civil Engineering* (IALCCE). He is the Founding Editor of *Structure and Infrastructure Engineering*. Dr. Frangopol is the recipient of several honors and awards from ASCE, IABSE, IASSAR, ISHMII, SAE and other professional organizations. He holds 4 honorary doctorates and 14 honorary professorships from major universities. In 2023 ASCE established the Dan M, Frangopol Medal for Life-Cycle Engineering of Civil Structures. Dr. Frangopol is an Elected Member of the US National Academy of Construction, and a foreign member of the Canadian, Japan and Mexican Academies of Engineering, Academia Europaea (London), Royal Academy of Belgium, Romanian Academy, Romanian Academy of Technical Sciences, and a Distinguished Member of ASCE.

Jacob Wittrup Schmidt is Associate professor at the University of Aalborg. His primary field of research concerns the assessment, upgrading, and service life extension of existing structures, focusing on bridges. In this regard, he has published significantly in the field of structural strengthening using Fiber Reinforced Polymer (FRP) materials and multidisciplinary approaches combining structural evaluations, probabilistic assessments, and testing in all scales. Jacob Wittrup Schmidt, a member of the IABMAS Technical Committee on bridge load testing, has performed several national in-situ bridge tests and pilot projects within his field of expertise and has authored an upcoming national proof loading guideline. In addition, he participates in national- and Eurocode standardization- and several international scientific committees.

T. Y. LIN LECTURE


Taylor & Francis
Taylor & Francis Group
http://taylorandfrancis.com

Bridge Maintenance, Safety, Management, Digitalization and Sustainability – Jensen, Frangopol & Schmidt (eds)
© 2024 The Author(s), ISBN 978-1-032-77040-6
Open Access: www.taylorfrancis.com, CC BY-NC-ND 4.0 license

Aesthetic value of bridges

Man-Chung Tang
T. Y. Lin International (China), Chongqing, China

ABSTRACT: In his book, *The Bridge and the Tower*, David Billington of Princeton University described bridge design as "structural art," which can be equated to architecture in buildings. However, in his opinion, bridge aesthetics should not be handled by architects but by engineers. He listed the three characteristics of a well-designed bridge as having "efficiency, economy, and elegance." He especially emphasized the virtue of efficiency. In Billington's opinion, an efficient structure would naturally look "better." This is in contrast with architecture, wherein decorative elements oftentimes have no practical purpose in and of themselves. Billington's criteria are certainly true for long-span bridges, which are situated far from a city and nowhere near any buildings. City bridges, however, are typically juxtaposed with many buildings or other types of structures. In such cases, being harmonious with the urban surroundings is just as important. Such a bridge can be less efficient and more expensive. Then the question becomes, "What should the acceptable added cost be for such a bridge?" This question can be applied to the maintenance of such bridges as well. Sadly, there are many beautiful bridges in disrepair.

1 INTRODUCTION

The objective of a bridge design is to produce a safe bridge that looks good and satisfies all functionality requirements at a cost acceptable to the owner. This means that a bridge must be safe, functional, economical, and beautiful. The safety of a bridge is guided by the applicable design specifications, while functionality is determined by the traffic requirements; they can be achieved by strictly following codes and specifications. There are no codes or specifications for economy and aesthetics. Whether a bridge is economical or not is typically measured by comparing it to other similar bridges. On the other hand, there are no specifications or rules to judge the aesthetics of a bridge. Then, how do we determine the aesthetic value of a bridge?

This is important because there are always various alternatives for any given bridge. Each alternative may have a different price tag. Should we choose the least expensive bridge concept, or should we build the more expensive one that people may find more beautiful?

2 STRUCTURAL ART

In his book, *The Bridge and the Tower* (Billington, 1983), David Billington of Princeton University described bridge design as "structural art," which can be equated to architecture in buildings. However, they are different! He listed the three characteristics of a well-designed bridge as having "efficiency, economy, and elegance." He especially emphasized the virtue of efficiency. Billington believed that an efficient structure would necessarily look better. This is in contrast with architecture, wherein decorative elements oftentimes have no practical purpose in and of themselves. Therefore, in his opinion, bridge aesthetics should not be handled by architects, but by engineers.

But, in the real world of bridge design, this assertion by Billington may not be true all the time. It is common that by emphasizing elegance, the bridge design may give up some

DOI: 10.1201/9781003483755-1

efficiency and/or to increase cost. Bridges are public facilities almost exclusively paid for by public funds where value must justify cost. But then, again, how do we determine the value of aesthetics?

Moreover, Billington's criteria are more suitable for long-span bridges, most of which are situated far from a city and not close to any buildings. City bridges, however, are typically juxtaposed with many buildings or other types of structures. In these cases, being harmonious with the urban surroundings is just as important. Such a bridge can be less efficient and more expensive in some cases. Then the question becomes, "What should the appropriate added cost to achieve beauty be for those bridges?"

There can be other factors that can be considered too, such as a city may want to build a bridge to commemorate a certain event or person, or to act as a signature of the city, etc.

Engineers like simple rules, such as the allowable tensile stress of high-strength steel used for cables is a certain percentage of its yield stress. Engineers would like to put the appropriate cost of aesthetics as a percentage of the construction cost. This kind of rule would make the choice simpler. But the problems with such a simple approach are twofold: first, this would necessitate that every bridge spend additional money just to show that the design has considered the aesthetics of the bridge. Otherwise, the designer may be criticized for not paying sufficient attention to bridge aesthetics. Obviously, richer localities are willing to pay more for aesthetics, while poorer localities may not. And secondly, how to calculate this percentage is a problem too. Nevertheless, without considering the value of aesthetics, we may end up with some really ugly bridges.

A bridge is a part of a city. An ugly bridge is equivalent to a pollution in the city. Once completed, it could be there for hundreds of years. We have no way to avoid seeing it. Therefore, people have attempted to introduce aesthetics as one of the design criteria. But, how?

3 EXAMPLES

Following are several examples of how people have put a value behind the aesthetics of bridges.

3.1 *Denny Creek Bridge, State of Washington, United States*

This bridge is near a ski resort area in the state of Washington, which is not far from Seattle. It is in a very scenic setting. The total length of the bridge is 1,203 m, with a regular span length of 57.3 m. The bridge, which was designed in 1978, was constrained by several severe restrictions in the design:

1. The bridge is in a high seismic zone and is located at the bottom of a hillside with relatively unstable rocks. Therefore, no blasting was allowed during construction. This means that the pier footings had to be hand dug with relatively small equipment;
2. The piers are 10 m to 49 m tall. They had to be able to resist possible rockslides;
3. After the piers were completed, falsework support was not allowed for the construction of the bridge girder; again, this avoided the danger of causing a rockslide;
4. The main reinforcement and all longitudinal prestressing steel were placed at least 20 cm below the girder surface to avoid corrosion due to salts being used to melt the snow and ice on the deck in winter;
5. Only trees that were in direct conflict with the bridge body were allowed to be cut; and
6. Aesthetics was one of the selection criteria. This is the first bridge in the US in which aesthetics was given a monetary value.

In the 1970s, this type of long viaduct in the US was built exclusively with precast I girders (Figure 1) or steel girders supporting a cast-in-place deck slab. The State of Washington even had standard precast girders named after the state. A citizen's group, after visiting some new bridges in Europe, requested that the state offer an alternative design that would be more aesthetically pleasing to match the beautiful surroundings of the area. DRC was one of the firms requested by the State to prepare a new design.

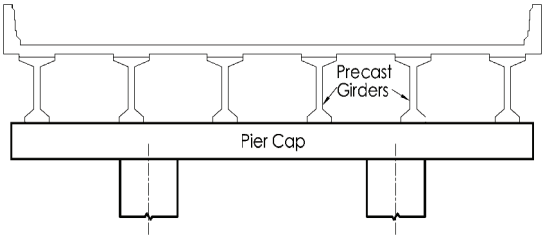


Figure 1. Bridge with precast girders.

Here is how we conceptualized our design to satisfy all requirements listed above and produced a beautiful bridge structure:

- First, to increase the resistance against a possible impact force from the rockslide, I used single-column piers instead of the double-column piers popular at the time. The stiffness (Moment of Inertia) of a single-column pier with the same quantity of material (cross sectional area) as two columns is about 6.36 times larger (Figure 2). Therefore, the safety against a possible rockslide is much higher.
- Second, I used a single-box cross section with tapered webs for the girder. This drastically reduced the chance of the bridge girder being hit by the rocks during a rockslide (Figure 3). Had we used the conventional precast beams, the bridge would have to be raised higher to avoid the sliding rocks.
- Third, the single-box cross section has much thicker webs, especially at the top portion, so prestressing tendons and reinforcement can be easily accommodated inside the webs and 12 cm below the deck surface (Figure 4).
- Fourth, because only trees that were in direct conflict with the bridge body could be cut, we proposed to build the bridge using the span-by-span method with a gantry so the construction did not touch the ground after the pier was built.
- Fifth, the box girder cross section with long cantilever overhangs looks very elegant along the valley full of trees. This was the first box girder in the US with such long cantilever slab overhangs (Figure 5, 6).

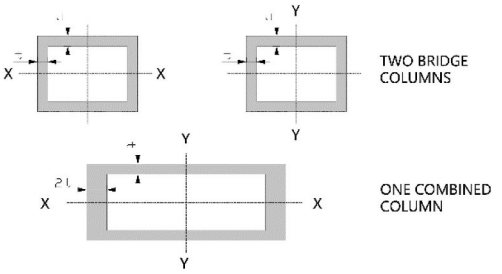


Figure 2. Single versus twin columns.

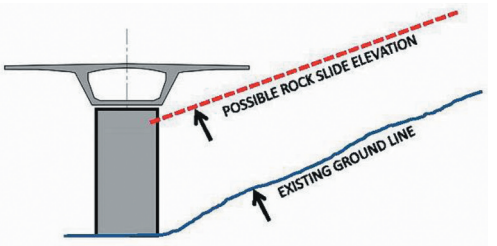


Figure 3. Rockslide protection.

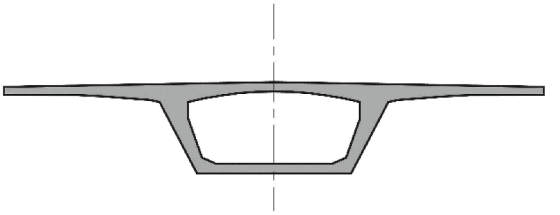


Figure 4. Girder cross section.



Figure 5. The Denny Creek Bridge – among trees.



Figure 6. The Denny Creek Bridge – trees under bridge protected.

People liked the aesthetics of this design so much that they offered a US$300,000 incentive for this bridge scheme, which was a first in the US. This was about 3% of the estimated construction cost. But it was not necessary. The bid price of this design was about 10% lower than the other two alternate schemes. This is a proof that a more beautiful bridge does not necessarily cost more.

The horizontal segmental method I developed for the construction of this bridge was one of the reasons why this alternative was so competitive. In the US, bridges are built by general contractors. For a general contractor, bridge building is only one part of their business. They also build roads, high rises, dams, or any other type structure they can contract to construct. This means that a general contractor may build a bridge only occasionally. Therefore, to save on costs, they will try to limit the use of any special equipment to a minimum because special equipment, such as gantries, or form-travelers, are usually scrapped after the project is finished.

Because we were not allowed to touch the ground anymore after the piers were done, we had to build the bridge girder from the top using a gantry that supports the entire span. Such a gantry would have been very heavy and expensive. Saving in the cost of the gantry was important.

Figures 7a and 7b present a schematic showing how the bridge was built. In Figure 7a, we divided the girder cross section into three parts and built the girder in three stages:

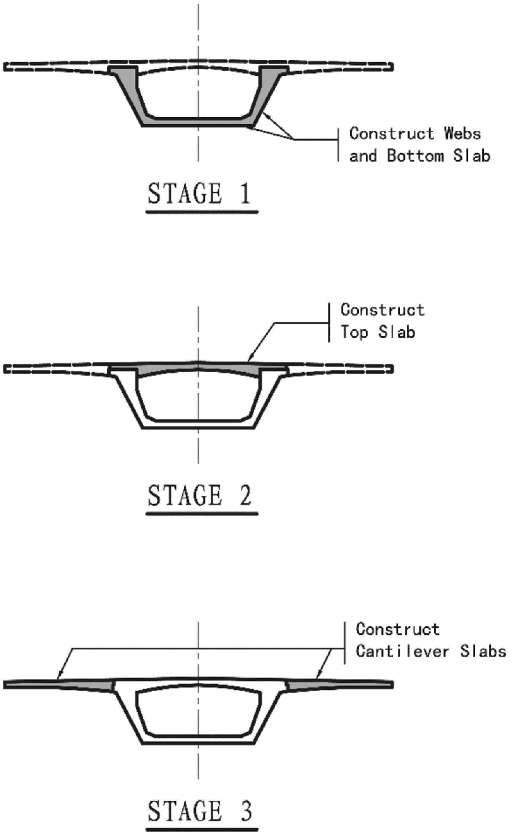


Figure 7a. Dividing the cross section into three parts.

The first stage consisted of the bottom slab and the webs. It was supported by the gantry during construction. The weight at this stage is about 1/3 of the total girder. That means that

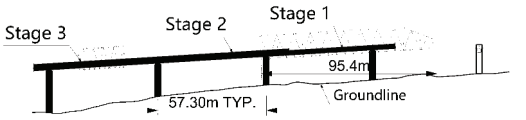


Figure 7b. The three stages of construction.

the gantry had to support only 1/3 of the total weight of the girder; therefore, it was less expensive. After the first stage was poured, stressed, and gained sufficient strength, the gantry was moved ahead for the construction of the next span.

The second stage consisted of the middle part of the top slab. The formwork for this portion of the top slab was supported directly by the completed U-shaped first stage of the girder. Its construction was very simple, and it was not on the critical path.

The third stage consisted of the two wing slabs. It was constructed using a simple formwork suspended from a steel frame running on top of the middle slab. Again, it was not on the critical path.

The advantage of this construction scheme is twofold: first, the main gantry for the first stage was very light because it only supported 1/3 of the weight of the girder; second, by dividing the girder into three sections, we provided three work areas, so it was easier to rotate the workers. This has to do with the US labor regulations: each worker belongs to a specific union; each union does only those type of work that is legally assigned to that union. For example, workers from Iron Workers Union are not allowed to do concrete work, which can only be done by Laborer's Union; the electricians are not allowed to do any steel work, etc. Having three work areas made the planning easier. The construction was very successful. The completed bridge is very well-liked by the citizens.

The design and construction of the Denny Creek Bridge was done specifically to meet the requirements of that project. Each bridge is unique. If the same bridge were built in another country today, without those labor union regulations and design requirements, it could be built differently.

In this case, we can assume that, from the owner's point of view, the aesthetic value of the bridge is at least $300,000.

3.2 *Eastern spans of the San Francisco-Oakland Bay Bridge, San Francisco, United States*

The replacement of the Eastern Spans of the San Francisco-Oakland Bay Bridge, or simply called the Bay Bridge, was a seismic safety project. For a seismic safety project, the government pays for whatever is necessary to sufficiently upgrade the structure to withstand the current design earthquake in the area. Anything beyond that will not be paid for by the government, which means, no money for aesthetics!

The old Eastern Spans of the San Francisco-Oakland Bay Bridge was opened to traffic in 1938. It was one of the world's most significant bridges at that time. "*This marks the physical beginning of the greatest bridge yet erected by the human race,"* said US President Herbert Hoover at the groundbreaking ceremony in 1933. But, the bridge was found to be incapable of withstanding earthquakes that could happen in this area, so it had to be upgraded. This is mainly because when this bridge was designed, the knowledge of earthquakes was still too primitive. Fortunately, no major earthquake had occurred in this area up to 1989; it had previously safely carried traffic up to that point. The Bay Bridge lies between the Hayward and the San Andreas faults, which can produce magnitude 7.5 and 8 earthquakes, respectively. The proposed bridge alignment is underlain by variable subsurface conditions. This is a location with the highest seismic activities and the worst soil conditions. The state of California's study found that a retrofit of the old bridge was not worthwhile, so they decided to build a new replacement bridge instead.

The total bridge is over 4 km long (Figure 8) and consists of four major sections, from left: (a) the Yerba Bueno Approach that transitions the girder configuration from a single two-

level girder in the tunnel to a two side-by-side deck configuration of the new bridge, (b) the self-anchored suspension bridge, or the main spans, (c) the Skyway, or the high-level viaduct, and (d) the Oakland approach. Even though the aesthetics of the entire bridge is important, the main spans are the most visible portion of this bridge.

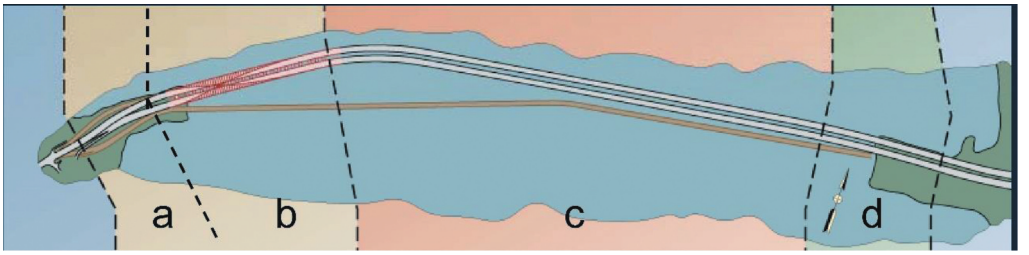


Figure 8. The New San Francisco-Oakland Bay Bridge eastern spans.

Bay Area residents were very concerned about the aesthetics of this bridge, especially the main spans. They did not like the scheme originally proposed by the California Department of Transportation (Caltrans). However, this was a seismic retrofit project for which no money could be spent for aesthetics. To make sure that the new bridge would be an aesthetically pleasing addition to the beautiful San Francisco Bay, Bay Area communities were willing to put up US$230 million to improve the aesthetics of the bridge. Representing the citizens of the area, the Metropolitan Transportation Committee established an Engineering and Design Advisory Panel (EDAP) to help select a signature bridge. EDAP had 34 members: approximately 1/3 were engineers, 1/3 were architects, and 1/3 were local San Francisco community stakeholders. EDAP established 17 rules for the design of the main spans, such as the bridge tower must be a vertical single tower not taller than 160 m and the deck girder must be separated into two 5-lane decks with a space of minimum 15 m in between. This formed part of the state Senate Bill authorizing the bridge replacement.

Caltrans selected the Joint Venture of T.Y. Lin International and Moffatt & Nichol from an international competition to design the bridge. Weidlinger Associates was a major subconsultant, and Donald MacDonald was the architect. I was the technical director of this joint venture and oversaw the conceptual design and preliminary design.

The very soft bay mud along the bridge alignment cannot resist large horizontal force, so both the earth-anchored suspension bridge and true arch bridge would not work. We proposed two alternative concepts: a cable-stayed bridge and a self-anchored suspension bridge.

These two bridge types do not need any anchorages in the ground. EDAP voted to select the single-tower self-anchored suspension bridge (Figure 9). The majority of the EDAP members felt that a suspension bridge would be more harmonious with the two existing suspension bridges already in the Bay—the Golden Gate Bridge and the Western Spans of the San Francisco-Oakland Bay Bridge. They also increased the main span of the bridge from 285 m to 385 m to make it more spectacular.

The bridge has been declared as part of the lifeline to transport first responders and emergency supplies in case of a seismic event. The design criteria specified that the bridge must provide the following:

1. Full service after a functional evaluation earthquake (450-year return period), showing only minor inelastic response, narrow cracking in concrete, and no apparent permanent damage; and
2. Be almost immediate serviceable after a safety evaluation earthquake (1,500-year return period), allowing only limited yielding of structural steel, some spalling of concrete, some yielding of steel reinforcement, and damage to expansion joints.

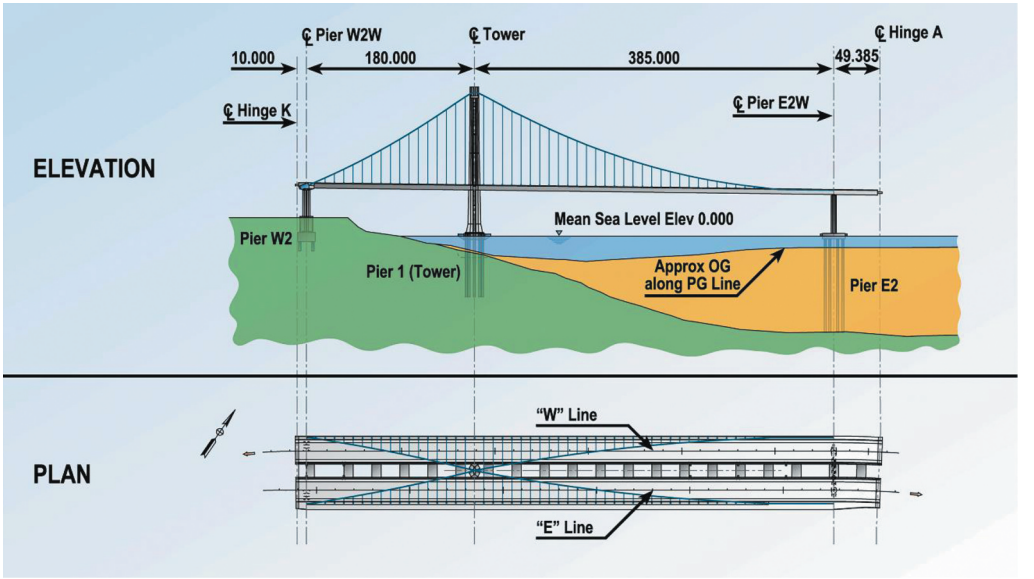
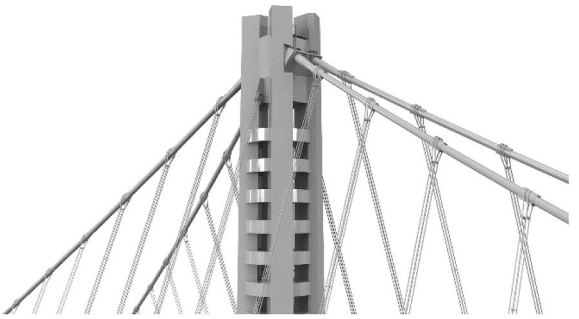
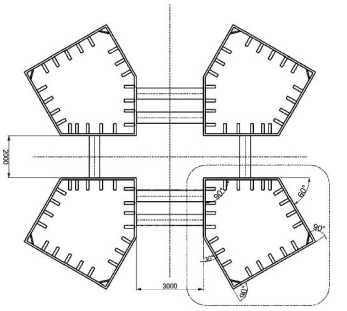


Figure 9. The San Francisco-Oakland Bay Bridge final selection – orange indicates young bay mud.

This is a very severe demand for a bridge located in an area with a thick layer of bay mud, especially for the design of the bridge tower. In addition, as most suspension bridges have a portal-shaped tower, the Bay Area residents preferred a single-pole tower. Because San Francisco is in a high seismic zone, a single-pole tower was deemed not allowable because it is not a non-redundant structure. But a single-pole tower really looks much better at this location. To solve this problem, we created a tower that consisted of four poles connected transversely by short shear struts (Figure 10a, 10b). Thus, under a severe earthquake, the shear struts may yield while keeping the vertical poles in elastic condition. The four poles are very close together, so they look like a single-pole tower.





Figures 10a and 10b. The tower configuration views.

Coming back to our question of aesthetic value: The Bay Area communities put up US$230 million to change the bridge from a design they did not like to a more beautiful design they preferred. Then we should be able to assume, at least for them, the aesthetic value of this bridge was US$230 million? Then, what percent of total cost does the $230 million represent?

The aesthetic improvement is mainly on the main spans, which cost US$2.1 billion. If we only count the main span, the $230 million amounts to 11% of the construction cost. But the bridge is actually very long. The construction cost of the entire bridge was US$4.1 billion; therefore, the $230 million is 5.6%. The official total cost of the bridge, including all other expenses such

as management, land acquisition, etc. as announced by Caltrans was about US$6.5 billion, so then the $230 million should be only 3.5%. Each of the three methods of expression can be justified: the 11% seems rational because the improvement was mainly on the main spans; the 5.6% seems rational also because this was one bridge, while the 3.5% also seems rational because from the Owner's point of view, that was the money it had paid for the bridge project.

The fact that the community was willing to put up $230 million to get a better-looking bridge is certainly a very special occurrence. But in San Francisco, just one of those tall buildings in the city may cost that much. If we had built a bridge in the Bay Area that people did not like, wouldn't that have been very regrettable?

If people are willing to pay so much money for the aesthetic of the bridge, then aesthetics must have a value!

3.3 *Sundial Bridge, Redding, California, USA*

The Sundial Bridge is located in the Turtle Bay Exploration Park in Redding County in northern California, about a four-hour drive north from San Francisco. Redding has a population of about 90,000. The bridge crosses the Sacramental River and connects the hiking trails on both sides of the river. At this location, the river is about 100 meters wide. In 1990, Redding County allocated US$3 million to build this bridge. In 1993, as I remember, the County asked two design firms, T.Y. Lin International and DRC Consultants, to submit a proposal for this bridge. The design requirements were as follows: (1) no pier in the river, (2) construction must not disturb or pollute the water, (3) aesthetics must be compatible with the local area, and (4) cost should be about US$3 million. TY Lin proposed a stress ribbon bridge and I, at DRC, proposed a deck arch. Both schemes would have fully met the requirements. They are both very low key and compatible with the tranquil surroundings.

The bridge is about 7 m wide and 210 m long, so the $3 million total cost would result in a per square meter price of about $2,040, which was quite reasonable for such a bridge at that time.

However, a local group, McConnell Foundation, which is a well-funded organization with affluent members such as lawyers and doctors, suggested that these two bridge schemes were not "outstanding enough." The Foundation preferred a spectacular bridge that could make Redding a global attraction so that many tourists would come to Redding, and in turn, help the local economy. In 1996, the Foundation hired Santiago Calatrava to design the bridge. They must have known that a spectacular design would definitely be more expensive. But they were willing to subsidize the project if it costed more than the US$3 million budget.

After Calatrava started to work on the bridge, the estimated cost of the project increased sharply as the design progressed. The call for tender was in 2000. The bridge was completed in 2004 (Figure 11). At the end of the project, the bridge had cost US$23.5 million, which is about eight times the original budget. The McConnell Foundation paid US$15.5 million for the overrun, while Redding County had to pay an additional US$5 million beyond the original budget of US$3 million. The unit price was US$15,220 per square meter.



Figure 11. The Sundial Bridge.

As a structural engineer, I can see why the bridge was so expensive. In order to create a unique form, practically every member of the bridge structure is eccentrically loaded. There are also curved surfaces that are very difficult to fabricate. For instance, it was said that *"More than 1,200 different plates each required 3-D calculations to determine the irregular polygon shape. Each plate edge had to be cut at a different angle to prepare for full penetration welds"* (Melnick, 2004).

The high cost caused a lot of discussions after the bridge was complete. Many criticized the high price, and many others lauded its beauty. One of the serious criticisms came from Professor David Billington. In a paper, "*Aesthetics and Economy in Pedestrian Bridge Design"* Woodruff & Billington (2007), authored by him and his graduate student Shawn Woodruff, Billington lamented: "Engineers have a duty to provide designs with a reasonable cost. The drive toward landmark pedestrian bridges or unique forms does not excuse us from the ethic of economy. Signature structures do not require extreme cost as proven by some of the examples of the national study. It is our duty to inform the public and to let them know other options exist."

On the other end of the criticism spectrum, the bridge was lauded as an engineering wonder. And it does attract more tourists to Redding as the McConnell Foundation had hoped for, even though no one had calculated whether the additional cost is economically worthwhile or not.

The bridge can also serve as a sundial. I do not know when the concept of the "Sundial" came to be used for this bridge. Sundials were used before clocks were available to find out the time of the day. The Sundial Bridge does look like a huge sundial, and it is lauded as the largest sundial in the world. Certainly, this proclamation attracts visitors too. Actually, this big sundial is accurate only one day a year, on the summer solstice, and only between 11:30 to 15:00. At all other times, people have to do some guessing!

4 SCULPTURING OR ENGINEERING

When people think of beauty, they will first think of "pure" art such as painting or sculptures. While sculpture is pure art, bridge engineering is also art, but it is applied art. The only purpose of a sculpture is to achieve beauty. The cost of the material of the sculpture itself is comparatively small and irrelevant. The sculptor can spend whatever time he wants to achieve perfection in a sculpture because a sculpture's sole purpose and value is in its aesthetics. The main purpose of a bridge is to carry traffic, so a bridge project must satisfy the safety and functional requirements at a predetermined cost within a predetermined time. Therefore, it could be catastrophic if an engineer treats his bridge project as a sculpture.

I visited the Sundial Bridge not long after it was completed. I recall seeing a plaque at the base of the tower stating that the bridge was "*sculpted by Santiago Calatrava*" and not the usual "*designed by Santiago Calatrava.*" Maybe this was the problem: Calatrava might have believed he was doing sculpture instead of designing a bridge! (Note: I understand this plaque was moved to a different place near the bridge).

Sculpture is pure art, which is priceless! Figure 12 shows a painting by the Dutch American Painter Willem de Kooning called "Interchange." (Burgess, 2023) It is one of the 10 most expensive painting in the world. In September 2015, collector Kenneth C. Griffin paid US$300 million to purchase it from the David Geffen Foundation. That is 12 times more than the total cost of the Sundial Bridge in Redding! Is this reasonable? Is this worthwhile? No one can say, because pure art is priceless!

Coming back to our discussion of the Sundial Bridge in Redding, the main point of contention is whether we should treat the bridge as a sculpture that *also* offers the function of a bridge or as a bridge that is artistic. As a bridge, the price is too high; as an art piece, price is irrelevant!



Figure 12. "Interchange" by Willem de Kooning.

It is also important to know about the McConnell Foundation. Its website states that *"Today, the Foundation's asset base is nearly $500 million"* (McConnell Foundation 2024).

Therefore, its payment of US$15.50 million for the Sundial Bridge was rather insignificant indeed!

Now the question becomes, *"If the party who pays the bill is happy with what it gets for the money, why are the bystanders complaining about the price?"*

Billington states that *"Engineers have a duty to provide designs with a reasonable cost."* Yes! But if the engineer is not only designing a bridge, but a monument, does he still have to be restricted by this rule?

5 OTHER EXAMPLES

Let us look at a few other expensive bridges:

The Sundial Bridge, at US$15,220 per square meter, was not the most expensive bridge in the world. Several bridges were more expensive (Figure 13). The first that comes to mind is the London Millennium Bridge. Its unit cost was US$32,600 per square meter of deck area (Note: cost figures may vary depending on exchange rate). The Peace Bridge in Calgary, Alberta, Canada, was US$20,000 per square meter. The Gateshead Millennium Bridge in Scotland, which cost about US$30,100 per square meter, is the champion! But the Gateshead Millennium Bridge is a moveable bridge that can be opened to allow ships to pass beneath, so its cost may not be comparable to the rest of the bridges.

It should be noted that almost all these expensive bridges were financed by some kind of foundation, just like the McConnell Foundation in the case of the Sundial Bridge. Usually, these foundations are quite wealthy, so paying for such a bridge is not a big deal for them. Compared to paying a huge sum for a painting that most people would never see, paying for a nice-looking bridge is by far a more meaningful thing to do.



Figure 13. Clockwise from top left: Gateshead, Grand Canal, Sun Dial, London Millennium, Peace (cross section), Peace (elevation).

By the same token, if a relatively wealthy community wants to build an artistic sculpture that can also serve as a bridge to make the area more attractive, is there anything wrong with that?

6 CONCLUDING REMARKS

What makes a bridge beautiful? I believe a beautiful bridge must be natural, simple, original, and harmonious with its surroundings. Looking at recent city bridges in the world, many of them may seem more suitable for Disneyland than in a working city—a phenomenon we may call the "Disneyfication" of cities. To attract attention, many bridges have such strange forms that they really do not look like or work like a bridge. Some of them, because of their unconventional shape, may even become a hindrance to pedestrians. As to the Sundial Bridge, besides being inefficient, does such a bridge really fit into the very tranquil surroundings of the Tuttle Bay area?

The main purpose of a bridge is to carry traffic and let people commute conveniently. They are not just decorations!

REFERENCES

Billington, David P. 1983. *The Tower and the Bridge*. New York: Basic Books.

Burgess, P. 2023. The 10 Most Expensive Paintings Ever Sold. https://insights.masterworks.com/art/history/the-10-most-expensive-paintings-ever-sold/. March 19, 2023.

Melnick Scott L. 2004. Sun Sculpture. *Modern Steel Construction*, October 2004.

McConnell Foundation. 2024. "Carl & Leah: How it all Started." The McConnell Foundation website. https://www.mcconnellfoundation.org/history/.

Woodruff, Shawn & Billington, David P. 2007. Aesthetics and Economy in Pedestrian Bridge Design. *International Journal of Space Structures*. March 1, 2007.

KEYNOTE LECTURES


Taylor & Francis
Taylor & Francis Group
http://taylorandfrancis.com

Bridge Maintenance, Safety, Management, Digitalization and Sustainability – Jensen, Frangopol & Schmidt (eds)
© 2024 The Author(s), ISBN 978-1-032-77040-6
Open Access: www.taylorfrancis.com, CC BY-NC-ND 4.0 license

Assessment of post-tensioned bridges in Norway

L. Bathen
Norwegian Public Roads Administration, NPRA, Norway

ABSTRACT: Norway has a high percentage of bridges compared to the total road length. Several bridges are exposed to extreme weather conditions. A considerable number of bridges was built in the period of 1960 – 1990 and among these, several bonded post-tensioned, which potentially had issues during execution. There were no explicit requirements for the inspection and assessment of post-tensioned components in bridges until 2021.

Post-tensioning concrete has been considered as a reliable and efficient construction method, demanding little maintenance in comparison to traditionally reinforced concrete. The awareness of the possibilities of severe damage on post-tensioned bridges built has increases considerably during the last years. The lack of systematic inspection routines was realized, and the Norwegian Public Roads Administration therefore initialed an activity on assessment and inspection of post-tensioned bridges The paper will present the results from the R&D projects and todays approach for assessing and inspection post-tensioned bridges in Norway.

1 NORWEGIAN POST-TENSIONED BRIDGES IN A HISTORICAL PERSPECTIVE

1.1 *Introduction*

It is essential to understand the historical development of construction methods for post-tensioned bridges and by that the potential risk of damage that may have resulted from them. Post-tensioned concrete bridges are susceptible to deterioration over time, and assessment to maintain their structural integrity and to prolong their service life is vital. Bridges need inspection and evaluation of corrosion of post-tensioned strands, wires, and bars, the remaining post-stressing forces, and eventually concrete deterioration. It is essential to understand the level of safety, reliability, and robustness. Errors during execution and construction are a significant reason why constructions are damaged at an unexpectedly young age. Correspondingly, insufficient maintenance is a contributing factor to accelerated damage development. This also applies to post-tensioned system. There are currently around 20.000 bridges and ferry quays in the national and county road network. Approximately 10% of bridges are prestressed (NPRA BRUTUS) (1). About 40 % of the prestressed bridges are post-tensioned, 800 -850 bridges in number. There are currently around 20.000 bridges and ferry quays in the national and county road network, of which over 2,000 bridges are built with prestressed concrete, both post- and pretensioned. The first post-tensioned bridges in Norway were built during the period 1958 -1960.

The building accelerated throughout the 1960s and reached a tentative peak in the early 1980s. A large proportion of the bridges are beginning to reach an age where extensive maintenance is expected:

- 22% of the bridge area is over 50 years old.
- 38% of the bridge area is between 30 and 50 years old.
- 40% of the bridge area is younger than 30 years.

DOI: 10.1201/9781003483755-2

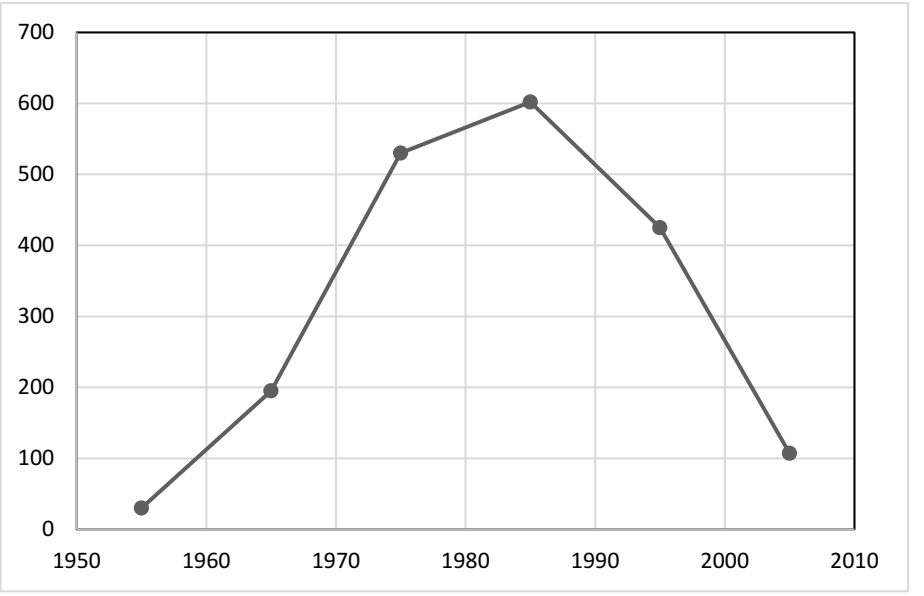


Figure 1. Prestressed bridges in Norway, year of building (NPRA, BRUTUS) (1).

Service life of post-tensioned structures is largely dependent on the service life of the post-tensioning components. It was a massive investment in roadbuilding and most needed bridges to districts and especially islands along the coastline in 1960-1990. This was a result of political and strategical decisions to connect small urban areas to the mainland and main road network. The industrial development and fishing industry needed transportation corridors to link to a market for their products. Also, it was a willingness to make it possible to live and flourish in districts of Norway. The necessity to guarantee a functional public transport infrastructure has led to the construction of many bridges, several of which are exposed to extreme weather conditions.

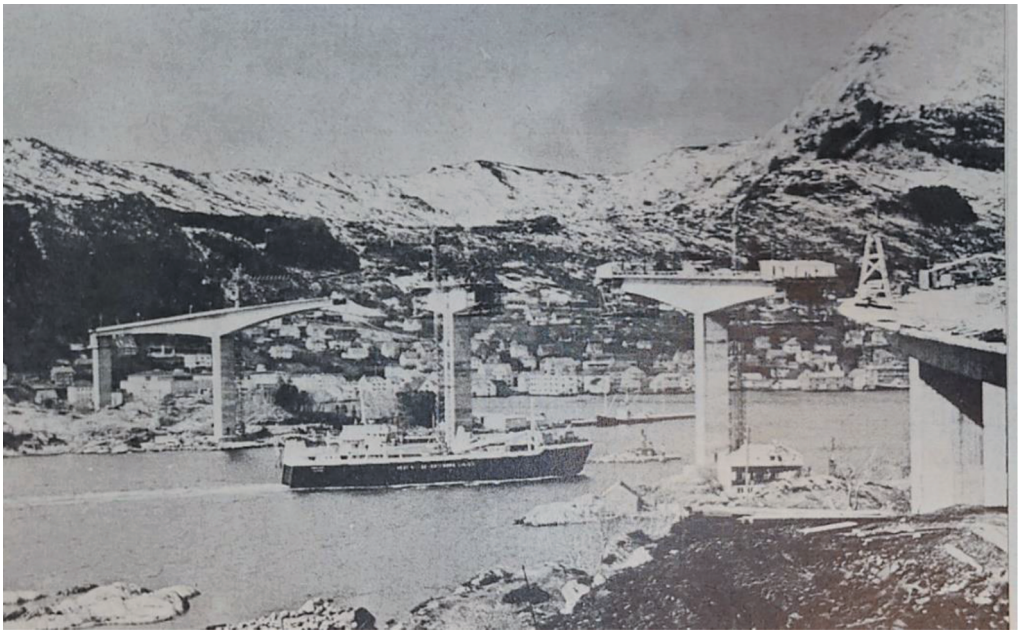


Figure 2. Måløy bridge during construction, 1973 (Photo; Byggeindustrien nr.1/1974).

Many bridges had been planned and fought for in many years before they came to realization. As an example, Måløy bridge was built during 1972–1973. The first plans for a bridge came as early as in 1918 (Ese) and the last decade before the building there was huge local engagement to raise financing. It was with its 1224 m, by the time of finalizing, the longest bridge in Norway and it is still one the biggest bridges in the country.

1.2 *PT- installation from the late 1950's until today*

Post-tensioning concrete has historically been considered as a reliable and efficient construction method, demanding little maintenance in comparison to traditionally reinforced concrete. Materials and methods for installation have changed over the years. When assessing any corrosion damage on post-tensioned components, it is important to establish the era in which the bridge was built. The constructions method has changed over the years with considerably more focus on execution and durability since the years between 1982–1986. In Norway we expect no damages due to corrosion on strands if requirements regulated by today's standards and regulations are followed. However, damages on post-tensioned bridges, especially those built prior to the revision of construction practice and standards, have been reported world-wide. In Norway damages are found occasionally as well, mainly coincidental during maintenance work.

The constructions method has changed over the years with considerably more focus on execution and durability since the years between 1982 - 1986. During these years the first regulation on grouting and properties of grout was introduced. Later the practice has developed, and both the quality of the grout and the grouting has improved significantly since the early 1980s. The first post-tensioned bridges in Norway were built during the period 1958 -1960, using prestressing bars. Later in the 1960s and 1970s, post-tensioning systems with wires were commonly used (widespread use of BBRV). During the 1970's post-tensioned bridges with high utilization of materials were executed. Prestressing strands gradually took over from wires in the early 80s. In Norway we can roughly divide practice for installation and grouting techniques in 4 periods based on the year of construction and thus which standards and common practice existed at the time. (Bathen & Nordbotten 2023) Table 1 shows the common practice and development for installation practice.

Table 1. Development of common installation practice in Norway.

Era	Common practice at the time
Late 1950s 1982.	A common practice during this era was that equipment for installation and grouting was sent to the construction site and the main contractor carried out the work. There is documentation from building periods of several bridges that there where issues with both installation and grouting practice.
1982–1997	NPRA changed its practice and introduced regulations. Post-tensioning companies had to execute prestressing and grouting on site instead of the main contractors. That changed focus a lot on installation of post-tensioning. Because of the high activity at the same time building condeeps for the North Sea it was considered a necessity to improve grouting practice in the industry. In 1982 and 1986 the Norwegian Concrete Association publishes NB13 Grouting (NCA 1982) (5) and NB14 Post-tensioning work (NCA 1986) (6) respectively. Procedures were improving, but there was still a risk of defective grouting. Standards for grouting and grout properties together with test-methods were developed in Great Britain 1992-1996. They became quickly adopted as Common European standards in 1997 and, also adopted in Norway. In Norway despite these standards there are some years where grouting had issues and can be deficient.
1997–2005	The industry began to adapt to NB14 (6) and the common European regulations. In the early 2000s, solutions for water management (joints, links, drains & pipes etc.) were improved.
2005–>.	It was introduced an additive, in 2005, which made the grout thixotropic, increased flow properties and made it easier to inject. That gave less chance of voids in ducts. There were no major changes in standards, regulations, or procedures. The era is considered as a relatively safe period in terms of cavities in the post-tensioned installations.

Figure 3 shows typical findings during maintenance work. Ducts are empty or partly filled with grout and the ducts in bridge decks get destroyed when using water chiseling. This is a typically result from the period between 1960 – 1980, maybe even some places until mid-1990´s.



Figure 3. Common finding during maintenance work, lack of grout inside ducts. (Photo; NPRA, BRUTUS) (1).

1.3 *Development of commonly used post-tensioning systems in past eras*

From the NPRA database BRUTUS (1) it has been possible to find what type of post-tensioning systems were commonly used in which era. In Table 2 it is listed what type of post-tensioning system that was commonly used in what era. There are three main groups that divides the practice; bridges prestressed whit single bars, a couple of years later tendons made of parallel wires and finally tendons made with multiple strands. The common use of multiple strands came first in the 80´s, but there are some bridges produced with that type of tendons from late 70's.

1.4 *Development of required cover thickness for bridges*

The required cover thickness for bridges has varied over the years since the first regulations in 1926. In the years from 1973 until 1988 it was at its lowest; 25 mm – 30 mm. Due to corrosion on rebars, the cover thickness for bridges changed in 1981, made stricter than common national standards. From 1997 the required cover thickness has been significantly more for bridges and ferry quays than common concrete structures in Norway. In 1994, rules for the provision of concrete cover were introduced. For reasons we don't fully understand today there was in 1973 an optimistic belief that required concrete quality combined with low concrete cover thickness gave enough durability and sustainability. The NPRA followed the national standards for concrete cover thickness more in general until 1988. Since 1988, requirements from NPRA for bridges have been stricter than for other structures. (Bathen & Nordbotten 2023). Table 3 gives an overview of the era for the required concrete cover thickness at the time. Table 4 gives an overview of the other national regulations, such as acceptable content of $CaCl_2$ in

Table 2. Commonly used PT-systems in Norway.

Era	Post-tensioning systems	Post-tensioned reinforcement type
~1955-1966	Dywidag	Single bars
Late 60's	Freyssinet (wedge cone system)	Tendons made of parallel wires.
Late 60's -middle of 80's	BBRV (button heads anchors)	
Late 70's		
	CCL	Tendons made of multiple strands.
80's →	VCL	
	Dywidag 6815	
	Dywidag 6812	
	Freysinnet	
	BBRV-656	

concrete mix and requirements for concrete quality, together with the required cover thickness for bridges. Through Table 4 it is possible to compare the development in NPRA and national regulations through the standardization body.

Table 3. Required concrete cover thickness in bridges, Norwegian Public Roads Administration.

Year of Requirement	Concrete cover thickness for bridges in Norway, mm
1926	50
1939	40
1963	30-50
1973	25
1981	30
1988	40
1994/1997	55/75/120

Table 4. National regulations in Norway versus NPRA requirements.

	1926	1939	1963	1973	1981	1988	1989	1994	1998	2003	2007	2008	2015/-18
National regulations													
$CaCl_2$ %			<2	<1	<1	<1	<1	<1	<1	0,4	0,4	0,4	0,4
Cover	50	40	30/50	25	25	25	40	40	40	40	40	60	60
NPRA													
$CaCl_{2\%}$			<2	<1	Only by perm	→		0.1	0.1	0.1	0.1	0.1	0.1
Cover	50	40	30/50	30	30	40	40	55/75/120		→			50/60/100
Quality				B350/C35		C45MA		SV40/ SV30		→			SV-standard
													SV-chemical SV-lowheat

1.5 *Development in design through standards and regulations*

Standards, national regulations, and inspection procedures regarding the construction of post-tensioned bridges are still under constant development. In 1969 and 1971, stricter requirements were introduced regarding design traffic loads compared to the regulations

from 1958. Concrete and reinforcement were more strongly utilized (NS 3473) and optimized regarding the use of materials. There are some bridges built in that era were material are strongly utilized. A significantly number of bridges has developed heavy corrosion on the ordinary reinforcement because of chloride ingress. Concrete and reinforcement were less utilized and changed in the revision of this standard a couple of times until the early 1990s. Comprehensive change in building practice was implemented from early 90´s. Since 2011, design loads from NS-EN 1991 have been used.

At the same time as the practice developed for grouting and tensioning of bridges, national rules and regulations have been developed under the auspices of The Norwegian Concrete Association. Publication no.14, post-tensioning work has since it was published in 1986 focusing on all parts of post-tensioning work at site. NCA, publications no. 13 (5) and no. 14 (6) have been important for the development of NS-EN 13670, Execution of concrete structures, in the sub-chapter on post-tensioning. Through NS-EN 13670, concrete contractors and contracting clients have been purposefully trained for post-tensioning work.

The use of waterproofing is difficult to track. In some places waterproofing was added when de-icing of roads was introduced locally. Waterproofing on post-tensioned concrete bridges has been a common practice since some time in the mid-1990s. Splicing tendons at the same cross-section was allowed until 1996. In the early 2000s, solutions for water management (joints, links, drains & pipes etc.) were improved. Before this, several unfortunate solutions were designed. From 1997 there was a requirement for waterproofing if de-icing of bridges and roads was frequent and AADT > 2000. The requirement was in force until 2015, when a requirement for waterproofing on all post-tensioned concrete bridges was introduced. On a significant number of existing bridges, the concrete wearing course has been replaced by waterproofing. Requirements related to details for waterproofing at bridge ends, along concrete edges, around drains and at joints were heavily revised in 2007 but took a few years to implement. It is highly likely that recommendations and requirements relating to details introduced in 1997 were not followed. Regulations that existed in the early 80s and up to 2005 prevented unfortunate execution, but there were still challenges when it came to grouting. On the contrary, it is interesting that we had to go all the way up to 2005 before we got a stable grout that is used without concerns about separation and lack of stability (Bathen & Nordbotten 2023). during the R&D-project Improved Bridge maintenance (2017-2022) (2, 3) which was later followed up by the R&D-project VESPA (2021-2024). The main goals for these projects have been to establish routines for systematical and periodical inspections of post-tensioned bridges. In addition, the projects aim on establishing routines for prioritizing order of inspections by a risk-rating tool adjusted to Norwegian conditions and traditions in building-technics. Also, the potential of repairs and strengthening are investigated. The methods developed within the projects are and will be implemented in the NPRA through regulations and guidelines, courses, and by practical training. Through these activities we are aiming to get a better overview of the condition of post-tensioned bridges in the road network and contribute to a forward-looking strategy for safe management of existing bridges.

2 THE R&D PROGRAM IMPROVED BRIDGE MAINTENANCE 2017-2021

2.1 *Introduction*

In 2017, the Road Directorate started the R&D program Improved bridge maintenance (2, 3). One of the activities in the program investigated damage of post-tensioned bridges.

Inspection of post-tensioned construction systems is difficult because tendons, anchorages and ducts are embedded in solid concrete. Indirect methods for locating voids in cable ducts are used to locate corrosion on tendons, because voids are locations where

corrosion can occur on tendons. In Improved bridge maintenance, among other things, inspection methods have been investigated to identify voids in tendons, possible corrosion mechanisms in non-grouted or poorly grouted ducts, and constructive consequences of damage to the post-tensioning. The activity was established due to well-founded suspicions of poor execution practices, especially in the 1970s and 1980s, before changes in practice in the industry from the late 1990s. Poor control and lack of quality at several points in the grouting process may have resulted in voids, poor adhesion, and corrosion. Corrosion of tendons results in a loss of load-bearing capacity.

The R&D program was carried out in the period 2017-2021. The program has consisted of the following 4 projects:

- Management tools for bridges,
- Reinforcement corrosion in concrete,
- Alkali-silica reactions in concrete and
- Rehabilitation of steel bridges.

The purpose of the program was to optimize the use of resources related to inspection, maintenance, and management of bridges, and to ensure that NPRA takes the right measures at the right time to ensure that the bridges are and remain safe. (Norwegian Public Roads Administration 2022) (2)

2.2 *Activity 2, reinforcement corrosion in concrete*

In 2018, NRPA, issued a request for a study of methods, possibilities, and restrictions for inspection of post tensioned concrete bridges as a part of the activity Reinforcement corrosion in concrete (NPRA 2022) (3). Various methods have been developed over many years to assess corrosion on ordinary reinforcement in concrete structures. Corrosion is a complicated mechanism affected by many factors. Surveying the extent of corrosion and its causes is challenging. Pre-tensioned reinforcement can be inspected to a large extent as ordinary reinforcement, but for constructions with post-tensioned reinforcement placed in ducts, corrosion measurements and assessments of the significance of this are more complicated. Tendons are placed within ordinary reinforcement in the concrete cross-section, and thus at a great depth from the surface. This makes it challenging to interpret results from non-destructive methods. (Karlsson et.al 2020)

Normally, the tendons are perceived as well protected against degradation as they are in grouted ducts, mounted with a good distance from exposed surfaces. The common opinion was that there are no issues considering post-tensioning as to severe damage and risk of failure. Experience has shown that corrosion occurs on post-tensioned tendons as well, and there are findings also in bridges in Norway. Post-tensioning components have to a small extent been inspected and examined for condition and function. Corrosion on these components is serious for two reasons:

- The damage develops hidden as the cables are inaccessible to visual inspection.
- Corrosion on tendons can in unfortunate situations lead to tendon failures with possible deformations and reduced load bearing capacity, without warning signs.

During repair work at the bridge in Herøysund in 2019, at the northern west coast of Norway, voids and severe corrosion were found inside the ducts. There were no outward signs of the damage to the post-tensioning. There were no chloride quantities in the grout that would indicate corrosion, and there was no damage to the concrete in the areas where we found severe damage to wires. NPRA experienced that damage can develop in post-tensioning systems and there is lack of obvious reasons why the damages have developed in such a scale. Figure 4 shows the condition inside a duct at Herøysund bridge. The finding was a result of a random opening along one of the tendons. This was the first time these types of severe damages were found in Norway, and it confirmed that it is a need for systematically inspections and a routine based assessment of post-tensioned components as well as other structural elements.



Figure 4. Severe corrosion on a tendon. Photo: Lise Bathen, NPRA.

Based on damages that was discovered, the ongoing activity in the R&D program was extended to investigate corrosion mechanisms in post-tensioned reinforcement, as well as to investigate the reason(s) for corrosion of the pre-stressed reinforcement. It has been investigated whether calculation models can be established for the constructive consequences of various types of breaks in the PT-system, and whether it is possible to establish a methodology on a general basis to investigate what the critical sections are for the individual bridge type. To be able to examine bridges with post-tensioned structures in a targeted manner, it is important to be able to examine the structures in the sections where tendon failure has the greatest impact. The results and findings in the R&D-program are reported and can be read at NPRA 2021 (2).

3 THE R&D PROGRAM VESPA

Experiences from Herøysund bridge and the knowledge from the R&D program Improved bridge maintenance (2, 3) are taken into the R&D program "VESPA" (maintenance of pre-stressed reinforcement), which is led by the Operation and Maintenance division, DoV. Through its activity, the R&D program VESPA will improve NPRA's overview of the condition of post-tensioned bridges and contribute to a forward-looking strategy for safe management of existing bridges. Post-tensioned concrete bridges form an important group of bridges, and they need assessment in a systematic way to ensure longevity and safety during the period of use. In VESPA, further development of research results from Improved Bridge Maintenance is being done. The objectives for VESPA are:

- To establish professional management by further developing of methods for inspecting post-tensioned concrete bridges, and by establishing routines for prioritizing inspection order of them.
- To contribute to a safe and secure assessment of damage of post-tensioned bridges, methods are developed to be able to make capacity and durability assessments for post-tensioned concrete bridges.
- To reduce the need for new construction and thereby contribute to the fulfillment of Norway's climate and environmental targets, tools and methods for remedial measures are developed when damage is found to the pretension system in existing bridges.

The purpose of VESPA has been to further develop inspection methods and maintenance strategies, as well as to implement the results in management routines and processes. Strategy

and methodology for inspections are developed. Routines for inspection are now implemented in NPRA´s inspection-program. VESPA is organized in four sub-projects:

- Inspection
- Case studies
- Mapping of consequences and remedial methodology
- Training of staff

Based on foreign experience and assessment-standards NPRA is developing a tool for prioritization of inspection order based on the knowledge of known issues in the era the bridges were built, reported issues during installation, the bridges importance in the road network and the possibilities or difficulties for driving detour if the bridge must be closed. These factors are the baseline for how to sort the order of inspections of our post-tensioned bridges. In addition, tools and methods for possible remedial measures will be mapped.

The R&D program will be finalized by the end of 2024. Routines and procedures for inspection of post-tensioned bridges are now implemented in NPRA regulations and results from ongoing investigations will be as well when it is finalized.

4 TODAY'S ASSESSING AND INSPECTION OF POST-TENSIONED BRIDGES

Inspection of post-tensioned reinforcement is carried out as needed, either as a routine based on vulnerability analysis, or in case of suspicion of poorly injected cable ducts and/or other damage to the post-tensioning. NPRA now recommends carrying out a special inspection of post-tensioned reinforcement before major maintenance is planned

Control of post-tensioned reinforcement is carried out with NDT methods, combined with some destructive, visual openings. Methods used in investigations will be selected based on local conditions. Current NDT methods are the use of cover meters, GPR, ultrasound and impact echo. The methods are used in combination with each other and provide information on cable location, extent of cavity and degree of grouting. Control of the degree of grouting with NDT, followed by visual inspection of individual tendons is therefore used to find voids in post-tensioning systems, which can give an indication of areas where corrosion may develop.

Choice of locations for control of tendons shall be based on preliminary investigations of documentation from the construction period, drawings, assessments, and visual observations. Suitable inspection areas can be high points of the duct-curvature, where ducts cross over supports, couplers and areas near anchorages. Critical areas for the bridge's carrying capacity shall be mapped. (NPRA 2023) (4).

There is a growing backlog on maintenance on bridges also in Norway. When it comes to post-tensioned structures it may not actually be a backlog since the common opinion up to today has been that there are no issues as to detoration of PT-systems. That has changed by the activity in the last couple of years in both Improved bridge maintenance and VESPA. The routines for doing inspections on the PT-system on a regular and systematic level will contribute to a well-functioning road network for the next generations.

ACKNOWLEDGEMENT

This is a presentation of work done and implementation of routines in NPRA from the two R&D programs "Improved Bridge Maintenance" and "VESPA" (maintenance of prestressed reinforcement) established by the NPRA respectively in 2017 and 2021. The work and findings presented are results of a cooperation work between the Operation and Maintenance and Legislation and Regulatory Authority departments of NPRA. I will especially acknowledge Karla Hornbostel, Magdalena Jadwiga Osmolska and Oliver James Hooper, for lifting assessment of prestressed systems to be a part of today's bridge management in Norway.

REFERENCES

Bathen L. & Nordbotten G. 2023 *fib Bulletin 110 Management of post-tensioned bridges 10-11* Contribution to the bulletin on Norwegian practice.

Byggeindustrien nr 1.1974

Ese K. Kulturhistorisk leksikon (fylkesarkivet.no) *Måløybrua - Noregs lengste bru i 1974*.

Karlsson A. & Holmqvist M. & Jilderda P. & Strand J. & Johansson B. Å. & Taljsten B. 2020 *Post-tensioned Concrete Bridges, Study of methods for inspection*.

Norwegian Public Roads Administration database of public bridges in Norway *BRUTUS*, https://brutus.atlas.vegvesen.no (1)

Norwegian Public Roads Administration 2021 *Improved bridge maintenance – R&D-program (2017-2021)* (2)

Norwegian Public Roads Administration 2022 *NPRA report 865 bruvedlikehold.pdf 38-45* (3)

Norwegian Public Roads Administration 2023 *N-V441 Bruinspeksjon* (4)

Norwegian Concrete Association 1982 *publication no. 13, Grouting of tendons* (5)

Norwegian Concrete Association 1986 *publication no. 14, Post-tensioning works* (6)

NS 3473 Concrete structures — Design and detailing rules (withdrawn 2010)NS-EN 13670 2009 *Execution of concrete structures*

NS-EN 1991 Eurocode 1 — Actions on structures

Bridge Maintenance, Safety, Management, Digitalization and Sustainability – Jensen, Frangopol & Schmidt (eds)
© 2024 The Author(s), ISBN 978-1-032-77040-6
Open Access: www.taylorfrancis.com, CC BY-NC-ND 4.0 license

Sustainability and digitalization in bridge management: How far we are?

J.R. Casas
Universitat Politècnica de Catalunya, UPC-BarcelonaTech, Barcelona, Spain

ABSTRACT: Sustainability and digitalization are two main topics in many research programs in Europe and worldwide. It seems that bridge managers can largely benefit from the current digital transformation where processes using digital technologies are able to create new or to enhance existing bridge management systems (BMS). The concepts of sustainability and digitalization are very different in essence and, therefore, the tools needed for their fully adoption in the bridge management environment have to be also different in their basis and formulation. For an optimal adoption and development of both topics, also the actual trends in the bridge management policies, as performance-based decision making and adaptive BMS should be considered. This paper analyzes the actual bridge management policies, trying to evaluate their actual level of sustainability and digitalization. It is shown that although in the technical aspects the final goals are not so far, the human factor (educational and organizational aspects) remains as the critical factor for a full and optimal implementation.

1 INTRODUCTION

Bridge management was born and has evolved in the last decades with the main objective of providing serviceability and safety to bridge users by allocating in an optimal way the limited allocated resources from the managing agencies. Using just two words, we can say that safety and economy have been the driven concepts for an important number of years. The concepts of sustainability and digitalization were never introduced with emphasis in the development of the management policies. However, although not explicitly mentioned, we should think whether those concepts were not implicitly hidden in most of the actual bridge management systems.

In developed countries, sustainability and digitalization have emerged with force and are nowadays overrunning all aspects of daily life. The first is acknowledged in the formulation of the United Nations Sustainability Development Goals (UNSDG) in 2015 (UN 2015, OECD 2016). Sustainability and digitalization are two main topics in many research and innovation programs in Europe and worldwide. It seems that bridge managers can largely benefit from the current digital transformation where processes using digital technologies are able to create new or to enhance existing bridge management systems (BMS). Being the budgets for bridge maintenance also scarce, sustainability is a must to be implemented in bridge management (BM) for a proper use of limited resources.

According to the UN mandate, sustainability must become a basic concept for efficient performance-based operation of any structure throughout its service life. Therefore, from the structural management point of view, sustainability is an objective, while digitalization is a tool/method/technique. Even more, some people think that digitalization is also a powerful tool to improve sustainability. Therefore, the approach of bridge management to these topics must be different: dealing with sustainability the correct question is: how to emphasize sustainability in actual bridge management objectives and optimization procedures? However,

DOI: 10.1201/9781003483755-3

dealing with digitalization a more appropriate question would be: how to introduce digitalization in actual bridge management tools to become more efficient?

This paper aims to analyze the actual bridge management policies, trying to evaluate their actual level of sustainability and digitalization and seeking to their level of accomplishment in relation to an optimal implementation (where to go and how far we are?), analyzing possible causes of the actual distance from that optimum and proposing possible actions to decrease it.

Both previous questions can not be answered independently one of the other as the proposed solutions (if available) have to be implemented is a common framework, which is the BMS itself. Also, some boundary conditions that are guiding the development of advanced BMS should be considered when seeking for an answer to the above stated questions, these are: the management of existing bridges based on performance-based criteria and the need for adaptive BMS. There is an agreement among the experts, that future and more advanced BMS should be based on performance-based criteria, being Key Performance Indicators (KPIs) and their evolution over time the basis for management decisions. Therefore, a performance-based approach seems to be the most appropriate way of advancing in the embedding of sustainable concepts and in providing digitized tools in actual and future BMS. Also, the concept of adaptive BMS, able to adapt to changing loads and environmental conditions as a result of the climate change, is emerging with force among the bridge community. Therefore, also this boundary should be considered when facing the sustainability and digitalization improvement of actual BMS.

2 BRIDGE MANAGEMENT SHOULD BE SUSTAINABLE: HOW ?

Being sustainability an objective of actual engineering policies, BM has to be sustainable. Sustainability of bridges has mostly been considered in design and construction stages, but less attention was given to sustainability of bridges during the in-service stage. Although sustainability in bridge management is also influenced by the design and construction decisions (for instance, the maintenance will be influenced by the type of material or bridge configuration chosen at the design (Balogun et al. (2018)) or by errors or mistakes during construction), the subject of this paper is focused on how to enhance the sustainability of the decisions taking during the bridge management itself.

Sustainability in the built environment is founded on 3 interdependent and interconnected sustainable pillars: economic, social and environmental (Hajek (2023)). Are these pillars found in the actual bridge management (BM) policies? Clearly, this happens with the economic one and to some extent to the social too. In addition, we should start from the basis that bridge management is sustainable by itself due to its definition and objectives. In fact, clear objectives of BM are:

- **Extension of service life of assets**: extending the life of existing bridges is a real direction towards sustainability
- **Optimal interventions**: The interventions should be decided with the objectives of minimizing cost and environmental impact and maximizing availability and safety (social pillar). And the tool to achieve this is the life-cycle assessment (including cost analysis).

In both objectives, we can find embedded performance indicators in relation to the 3 pillars of sustainability. The first objective is clearly in the direction of strengthening the economic (reduction of costs associated to failure, reduction of demolition and re-construction works), social (extending the life of landmark or heritage bridges) and environmental pillars (reduction of the use of natural resources and energy). The second one comprises all 3 pillars as well: economic (reduced costs of maintenance and interventions), social (guarantee safety, functionality, comfort and availability to the users) and environmental (reduction of gas emissions and energy).

BM is already based on Life-cycle assessment (LCA) principles. Therefore, the basics of sustainability are already there, but relevant applications are not yet available. In fact, BM has well adopted the economic and social aspects of sustainability. However, there is still a long

way to go regarding the environmental one. This requires adoption of a complete LCA and not just a life-cycle cost analysis (LCCA), although some environmental indicators could be also monetized to some extent.

Advanced BMS should be based on quality control specifications and performance-based criteria, being Key Performance Indicators (KPI) and their evolution over time the basis for management decisions. As concluded in the works carried out in the COST Action TU1406, KPI´s related to safety, serviceability, availability and cost have been clearly identified in most of the running BMS. But appropriate sustainability KPI´s are still missing and we are still far to achieve a satisfactory solution for them. Performance indicators related to more global KPIs should be observable, quantifiable and provide valuable information for decision making. Therefore, one existing gap is to identify which are the performance indicators most sensitive to the potential sustainability effects, the ones that provide most valuable information and those which are most observable. Failing to identify such relevant sustainability indicators, one cannot quantify a level of sustainability performance (and even less its evolution) within a decision-making process.

Therefore, the framework and architecture to emphasize sustainability in BM is already there: LCA. Life-cycle approaches offer bridge managers a practical predictive view of cost, safety, and condition, the goal being to limit economic and environmental impacts. But the input is still missing. It is necessary to establish the system boundaries and to collect appropriate data for the life-cycle environmental analysis. One can be the introduction of CO2 calculators in the BMS, but others have to be investigated (energy savings, re-use of materials in interventions,. . .).

BM is still a little far from the optimal situation. But the way to become closer has been identified. The future direction is to introduce better performance indicators for sustainability. In many cases, actually, LCA is mainly reduced to a life-cycle cost analysis. In some countries, life-cycle cost analysis has been used for decades, where discounted maintenance costs over a certain time period are compared for different intervention strategies. But LCA does not fit into normal asset management procedures as applied now by most of the stakeholders. Apart from finding the appropriate sustainability performance indicators, it is essential to give more weight to sustainable criteria in the life-cycle approach. In fact, recently, Strauss et al. (2023) published the results of a survey carried out on implemented decision-making models among 23 infrastructure managers from 20 countries worldwide. In the implemented survey, the importance of different KPIs in the scheduling of maintenance and repair of structures was queried. The interrogated stakeholders were given the chance to indicate a level of importance between 1 (not important) to 5 (very important) regarding the following criteria: reliability, availability, safety, economy, environment, special/extreme cases of loading or any other criteria to be described by the respondent. The results are shown in Figure 1.

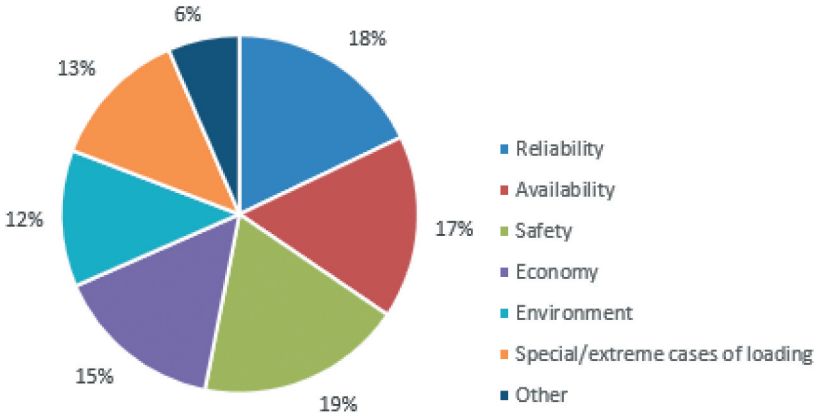


Figure 1. Importance of KPIs for scheduling of maintenance and repair of structures (Strauss et al. 2023).

The criterion given higher importance was safety, closely followed by reliability. In both cases, 15 out of 23 of the answers gave a ranking of 5 to these criteria. The third criterion considered most important was availability, followed by economy and special/extreme cases of loading. From the given choices, environment was considered the least important, although in two cases, stakeholders gave a ranking of 5 to this criterion. Another result from the same survey is that no one selected demands associated with climate change when asked about the incorporation of risk as a PI. Therefore, risk assessment incorporating climate change effects seems to be still in its infancy in practical BMS. For this reason, adaptive BMS has been hardly considered up to now.

Few, but some, realizations have been already done in this direction, however, still in the realm of academic research more than in practical applications. Xu and Guo 2022 have developed a condition-based maintenance approach for highway bridges, aiming to minimize the total carbon emissions of bridge networks subject to maintenance budget constraints. A two-dimensional Markov chain model is applied to predict the deterioration processes of bridges, and a Q-learning algorithm is proposed to determine the maintenance strategy for a single bridge. However, they are more interested on the environmental impacts of a bridge network than of a single bridge, which was the most analyzed until then. Contrary to the actual BMS, they propose a bridge deterioration model that contains the time factor to develop a sustainability-oriented maintenance management approach based on reinforcement learning with a target to minimize carbon emissions of bridge networks. The method is applied to the concrete bridges in New York state. The results of the study show the impacts of budget levels on maintenance plans and total carbon emissions. 10% drop in budget level results in 30 additional bridge repairs delayed as well as 39 tons extra annual carbon emissions.

3 BRIDGE MANAGEMENT SHOULD BENEFIT FROM DIGITALIZATION: HOW ?

To properly answer the question, we have to define what "digitalization" means. According to Callcut et al. (2021) "digitalization is the process of collecting information on physical assets and packaging them into a digital representation of these assets that can be processed automatically". According to this definition, we can understand that digitalization presents many opportunities to benefit BM, among them:

1. Improving and converting in more efficient the available methods and tools used in BM by digitalization: new data gathering techniques based on low-cost techniques, image processing, remote sensing, digitalization of visual inspection, automatization of the whole BM process.
2. Helping to move from "data" to "meaningful information". Probably, one of the main gaps identified by owners regarding inspection, non-destructive testing and SHM is that their main interest does not lie on gathering extensive amounts of data, but on how to use these data to assess the existing/remaining capacity of the bridges in their stock, which is generally not directly provided by just recording data from in-situ measurements. The question that defines the need for a full digitalization of the processes involved in BM is whether a full digitized approach will allow to transform the results from inspection and monitoring into information that can be used for optimal decision-making. The key point that a new tool as digitalization must help to solve is how to translate "data" into meaningful "information" and further into knowledge for appropriate decision-making. The definition and use of relevant Performance Indicators (PI) and Key Performance Indicators (KPI) is the right direction. Key performance indicators (KPIs) are used as metrics to monitor the performance of infrastructure and ensure the effectiveness maintenance and repair activities. Once the KPIs have been identified infrastructure, managers and asset owners can use data monitoring and condition assessment tools to collect the necessary data to measure and track these KPIs along time (Matos et al. (2016)). As an example, the paper by Stipanovic et al. (2023) presents PIs and KPIs for the assessment and monitoring of the following aspects: Productivity, Resource Efficiency, Cost, Health & Safety during

the operational life cycle stage. In the paper, quantifiable and measurable PIs and KPIs are proposed and applied on a highway bridge. Although digitalization by itself is not able to propose and define the most suitable PIs and KPIs, it can certainly help to automatize, facilitate and make more reliable the process of gathering the raw data, to extract and quantify the relevant PIs from it and predict their future evolution. Therefore, if correctly guided by engineering expertise, digitalization can be a useful tool to transform data into meaningful information through the use of KPIs.

In this sense, bridge managers can largely benefit from the current digital transformation where processes using digital technologies are able to create new, or to modify existing methodologies. Therefore, the integration of digitized structural health monitoring (SHM) systems, building information modelling (BIM) and other digitally-based tools into existing BMS is of interest. Being a tool more than an objective, digitalization can be seen more as a societal trend or an opportunity for better efficiency (in the same sense as performance-based decision making and adaptive BMS) than a requirement of future BMS. Digitalization with more or less intensity is already incorporated into actual bridge management. How far beyond the actual status of digitalization should BM move?

The maximum expression of asset digitalization is a Digital Twin (DT). Therefore, we can see DT as the most far away point we can go concerning digitalization. As a concept or idea, DT is something not completely new in structural and bridge engineering: All basics and elements of DT (data gathering, data analysis, model up-dating and prediction model) were already immersed to some extent into the so-called structural/system static or dynamic identification disciplines in application since many years ago, but, of course, dealt in a more primary way from the digital point of view: data gathering was achieved by analog sensors, rudimentary digital sensors and/or visual inspections, data analysis was carried out with limited digital tools, model up-dating was based on defining a numerical model (normally a FEM) that better reflected the recorded data. The up-dated model was afterwards used in the performance prediction. The only difference between this well-known procedure in bridge management and the actual DT paradigm is found on the level of digitalization and automatization of both approaches. The improvement in the automatization allows a faster prediction and intervention if needed.

Table 1. Comparison between BMS and DT frameworks.

BMS	**DT**
Inventory and data collection and management: based on drawings, sketches, pictures,..	Inventory: Based on BIM, image processing, remote sensing
	Artificial Intelligence and IoT technologies specifically tailored to bridges to process and share information (interoperability)
Diagnosis: Actual condition of the assets: mainly based on visual inspection (condition index) and limited NDT	Actual condition: based on Structural Health Monitoring
Fixed time for inspection intervals	Advanced analytics, driven by the integration of Geographic Information Systems (GIS) and
Condition-based diagnosis	Machine Learning (ML), allowing to optimize inspection schedules based on real-time traffic data, environmental conditions, historical bridge performance and risk
	low-cost and automatic technologies to collect bridge information
Prognosis: Performance prediction by proposed deterioration models based on deterministic or probabilistic approaches (Markov chain models).	Data analytics and predictive modeling.
	Model up-dating and damage detection
	Physical-based models
	Data-driven models
	Supervised and non-supervised machine learning
Optimal decision-making and intervention strategies: today still mainly periodic-based (fixed time interval)	Decision making: digital decision supported tools that allow preventive maintenance based on future performance, condition-based or risk-based

As noted, a clear analogy is seen between old structural identification techniques and modern DT. But this analogy is even more evident when comparing the framework of actual BMS and current DT, as presented in Table 1.

The tools (BMS and DT) are different, but the steps in both cases look very alike, comprising 4 main modules: data gathering, post-processing of data for performance up-dating, prediction of feasible future performance and consequent decision making.

Since actual BMS and DT present evident similarities, as shown in Table 1, and DT represents the higher level of digitalization, a relevant question to know how bridge management can benefit from digitalization is: **How far are actual BMS from DT?** In order to find an answer, let us look first to some general definitions:

A **Bridge Management System (BMS) is an** automatized tool that based on the identification of the bridges (**inventory**), their actual condition (**diagnosis**) and defined deterioration processes (**prognosis**) provides a decision-making framework to optimally allocate intervention operations to have safe bridges, preserve bridge capital and maintain their function (**optimal decision making**). The adopted decision shall ensure reliability, safety and functional, economic and environmental optimality.

A **Digital Twin (DT)** is a dynamic virtual representation of an object or physical system (**inventory**) throughout its lifecycle, that uses data in real-time to enable understanding, learning, and reasoning about the asset (**diagnosis**), allowing for a reduction in the total cost in bridge management processes, as it allows predictive and proactive maintenance (**prognosis**), avoiding unnecessary interventions and improving system availability (**optimal decision making**) (Bado et al. (2022), Massao et al. (2022)). Digital Twins require the use of scans, sensors, remote monitoring and automated computation models among others. Specific requirements of contact sensors, data images and remote sensing should be accomplished for an adequate connection between the physical and the digital assets (Casas et al. (2022)).

A main advantage on the use of a digital twin framework for existing bridges allows full interoperability: the integration of multiple simulation models and multiple data resources under a unified data structure to enable visualisation and prediction of bridge performance, something that is also done by BMS, but in a more rudimentary and slow way.

BMS and DT are not so far in some special cases. In fact, some long-span bridges are already digitally twinned to optimize their management and performance during service-life. However, this is not the case for the majority of bridges and we are still far in the case of standard bridges. How far? Several questions remain open: How to proceed with more standard bridges, how to digitalize their management? Is the methodology developed for landmark and iconic bridges valid for a huge number of standard bridges in a network? How to develop a network-based DT? Let us see if the answers can be obtained by analyzing one by one the steps involved in the DT paradigm.

-Inventory/BIM. 3D digital representations combined with BIM technologies are now widely used for new design and construction, but still need further development for existing assets. If available, digital models of existing bridges can be obtained from design drawings and quality control during construction. In their absence, digital-based techniques as photogrammetry, Lidar, terrestrial laser scanning (TLS) and others can be used to create a digital model of the bridge. However, requirements of accuracy, long-term reliability, format (an approach relying on big data implies to deal with both structured and unstructured data) are mandatory as the accuracy and relevance of data are crucial to ensure the validity of the datasets. Structured data is highly specific and is stored in a predefined format, where unstructured data is a conglomeration of many varied types of data that are stored in their native formats. This variety of structures is complemented by the variety of formats that can be found: text, image, audio, video, and also all sensor data. The use of digital twin tools can help improve the management of such heterogeneous information, storage (the increase in the number of structures requiring increased monitoring, coupled with increasingly numerous measurement devices on the structure, leads to new needs in terms of management and archiving of increasingly voluminous data), interoperability and data sharing.

BMS need to overpass the gap between static information, such as 2D drawings that often are incomplete and only reproduce the "as-design" version of the bridge, and a dynamic

digitized information represented by a BIM. Although the tools to evolve from actual bridge inventories to BIM models are already here, obtaining a BIM model for existing bridges in a standard format (usually Industry Foundation Classes (IFC)) is still particularly challenging due to their complex geometry. The final goal is the digitalization of the whole bridge inventory owners without the need to construct BIM models with a lot of manual effort. To reach this goal, there is still a way to go. However, initiatives are already in progress. The main difficulties in the field of scanning applied on bridge point clouds are encountered in how to obtain semantically meaningful bridge information models in an automated way. As an example, Hajdin et al. (2023) present a novel modular framework with procedures for the automated provision of BIM models from 3D point clouds for existing road bridges. The method is based on artificial neural networks (ANN). The work presented is a starting point for a comprehensive digitalization campaign of the whole bridge inventory in Germany.

-Data gathering/Monitoring. What distinguishes a DT from any other digital model or replica is its adequate real time connection to its physical counterpart. This is achieved by an appropriate monitoring system. Therefore, digitalizing the data gathering necessary for the management will highly improve its efficiency. This digitalization can be oriented in 2 main directions: the digitalization of the visual inspection and the incorporation of new digitized monitoring techniques. The first one is of paramount interest. In fact, visual inspection is still nowadays the most widely used technique to get required data to derive the condition state of existing bridges. The results of the survey presented by Strauss et al. (2023), show that all the respondents (23 infrastructure managers from 20 countries) to the questionnaire answered that they use condition rating based on visual inspection in their inspection and assessment procedure. Most of the limitations of visual inspection can be solved by the support of digitalization: use of un-maned aerial vehicles (UAV) equipped with cameras and videos, analysis of satellite images, virtual inspection using 3D models established by UAV and photogrammetry and other data-driven methodologies are on the way, avoiding costly access equipment, enhancing safety for workers and providing a basis for performance prediction.

A step forward towards digitalization is using inspection and monitoring tools that allow to reproduce the "as is" condition of the bridge and not the "as design" condition.

How far we are? The step forward requires proper instruments and expert inspectors. Moreover, the amount of information needed requires that several of these steps are made semi or completely automatically. Nevertheless, automated systems for bridge maintenance have always been of concern within a bridge management process, especially those that involve a large stock of older bridges where information is not easily available. Although following an appropriate monitoring policy should allow managers to get the best information about the maintenance and operation of their asset, the implementation of bridge monitoring systems in regular bridges remains a significant investment compared to the current inspection strategies. The use of high-tech monitoring constitutes a paradigm shift in surveillance strategies since it involves supplementing periodic (or non-periodic) visual inspections carried out by an operator, by some advanced monitoring frameworks. In practice, the use of long-term monitoring systems remains practically exclusive to major or landmark bridges or to special bridges. However, some pioneering experiences in short and medium-span bridges have already appeared recently. Hou et al. (2022) present a data-driven Load and Resistance Factor Rating (LRFR) framework that is empowered by a cyber-physical system (CPS) architecture that uses Internet connectivity to integrate measured bridge responses with truck weights measured by a weigh-in-motion (WIM) station. The CPS architecture uses computer vision of camera images to confirm trucks observed at a WIM station are identical to those observed at a bridge and correlates the monitored response and the load in the bridge.

This existing gap on SHM in the case of standard bridges can be closed by implementing digitalization in monitoring. How digitalization can help in this aspect? In several ways:

– By introducing cheaper sensors that allow to deploy permanent monitoring in a higher volume of bridges in the network (Komarizadehasl et al. (2022a,b)). Alternatively, the use of smartphones. Smartphones can provide crowd-sensing data. They may include several sensors as accelerometer, gyroscope, cameras, microphones, proximity sensors and GPS,

which could be used in the monitoring of different structural parameters (Mei & Gül (2019a), Morgenthal et al. (2018)). Several studies have shown that smartphones could be used as reliable sensors to collect acceleration data and apply them into indirect health monitoring techniques to assess structural condition (Feng et al. (2015)).

- By digitalizing the visual inspection: Using drones+images and remote sensing by satellite images. InSAR is a remote sensing technique that uses the phase information of radar signals emitted by Synthetic Aperture Radar (SAR) sensors mounted on satellites and backscattered by the Earth's surface to measure the displacement of reflective targets along the Line of Sight (LoS) of the satellites (Perisin (2018))
- By the use of the so-called drive-by bridge monitoring in which sensors are installed on vehicles and used to infer information about the condition of a bridge as they pass over it. A unique vehicle can inspect many bridges in a short period of time (Malekjafarian et al. 2022, Mei & Gül 2019b)
- By the implementation of Transfer Learning (TL) methodologies. These new methodologies will allow transfer of diagnostic information of one bridge across a population of similar bridges, augmenting SHM capability beyond that applicable to an individual element of the bridge network. TL is seen as a strategy enabling population-level bridge SHM. The training of an algorithm in the damaged situation of a fully monitored bridge can be extended to infer early-stage damage detection capabilities across a population of bridges with similar characteristics (Giglioni et al. (2023), Gardner et al. (2020,2022))

The reliability of the monitoring system and digitized data requires the implementation of cybersecurity solutions to ensure the integrity and confidentiality of the transmission of data and diagnostics. The requirements and needs that the gathered data should fulfill in order to be practically implemented in a DT are heterogeneous, some of them general and other case specific. A summary of a set of identified challenges and requirements for a seamless infusion of well-established SHM systems within DT platforms is available in Chacon et al. (2023). In addition, SHM-enabled DT must provide monitoring data in a way that can be integrated within data models that can guarantee interoperability (ability to effectively, accurately, and consistently communicate and exchange information, within different information technology systems) among digital systems

-Deterioration models/Model up-dating and prediction. Physical models need continuously up-dating for reliable prediction. Up-dating is carried out by the post-processing of the recorded data. This is probably the aspect where actual BMS and DT are more distant as the former are still far from what a DT uses for prediction of future performance. BMS perform prediction based on static or quasi-static deterioration models mainly based on Markov chains to deal with the inherent uncertainty. Up-dating of the transition matrices involved is not carried out automatically and on-line. However, in DT prediction is based either on physical models that can be automatically up-dated or data-driven algorithms that can react almost in real time thanks to the advantages of IoT. However, while UAVs provide detailed digitized visual data and monitoring acquires digitized sensor data almost continuously, interpreting this information requires expertise, emphasizing the importance of a harmonious blend of digital technology and human judgment. To digitize everything and provide capacity for on-line reaction does not mean that the problem is completely solved. Accurate and reliable post-processing of digital information is very important.

In this sense, it is worth mentioning the recent case of the Interstate-40 Mississippi River bridge in Arkansas. A visual inspection carried out in May 2021, detected the presence of a tie-beam fracture that forced and emergency shutdown of the bridge (Figure 2 left). Although state officials initially stated that the fracture in one of the 50-year-old bridge's two tied-arch truss navigation spans was not present during its most recent inspection in September 2020, a May 2019 drone video that was revisioned after the incident occurred, clearly shows the break already beginning to form (Figure 2 right). According to Arkansas DOT officials, the five-hour drone video was focused solely on assessing the 50-year-old structure's rods and connectors. Although the crack was already present in the video image, nobody took care to check for fatigue cracks in the main members, as this was not the basis of the inspection and the contract.

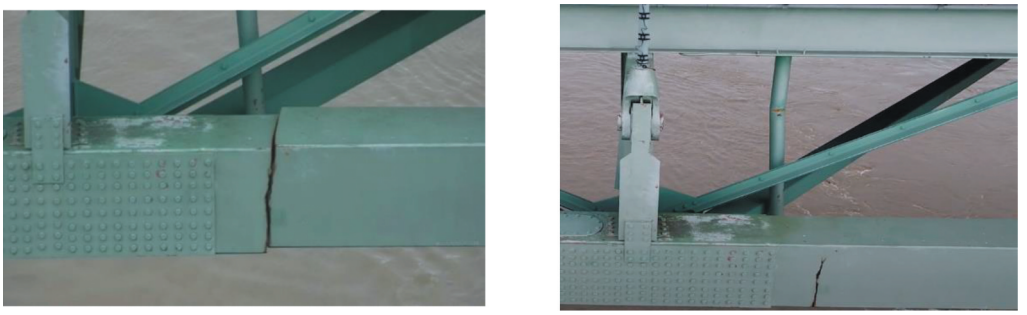


Figure 2. The crack as discovered in 2021 (left) and drone footage from 2019 showing the crack already existed (right). (Photo courtesy of Arkansas DOT via YouTube).

This example points the fact that SHM is not just deploying sensors or gathering images or cloud-points accurate enough to record the damage, but also the post-processing techniques should be as automatized and reliable as possible to proceed with a full analysis of the recorded data, something that relies on the availability of AI techniques and not only on human capacity.

-Decision making. Based on the interview with 9 infrastructure stakeholders from Europe and South America (Strauss et al. (In prep.)) is evident that the digital tools are seen by them **as decision-support** and not **decision-making tools**. Experienced engineers who have knowledge of the bridge stock make the decisions, supported by relevant evidence. The same interview revealed Strengths, Weaknesses, Opportunities and Threats (SWOT) related to digitalisation of decision-making in bridge management, summarised as follows:

Strengths:

- Consistency and traceability
- Enables working with complex contexts
- On demand evaluations based on the existing digital data
- Save time and increase objectivity and transparency
- Allows better control of assets and communication between stakeholders.
- Quality of data – completeness, structured, timeliness and accuracy
- Flexible to changing business needs
- Customization of the platform to operators and/or country specific needs
- Integration of data from various sources

Weaknesses:

- High investment requirements in software and operation, including IoT specialists. Sometime difficult to evaluate the gain of implementation
- Working with systems with automatic analytical capabilities requires data with a high accuracy
- Challenges related to data sharing, security, and standardization
- Employees who do not have a high affinity for digitization are difficult to get on board
- Inspection tools do not make you an inspector. Inspectors must have prior knowledge of bridges
- Integration with other IoT-infrastructure such as monitoring platforms and other platforms is needed
- Validation of data is an important task and a source of inconsistencies and errors

Opportunities:

- Recognize complex relationships based on a continuous data analysis
- Valuable as a tool to better use of resources and resource planning (budget and employees)
- Use of data analytics to get a better insight into a large variety of infrastructure problems

Threads/risks:

- Infrastructure managers become dependent on purchase of external services including but not limited to dependency of a particular software provider
- Different access to IoT and certification of the inspectors and professionals could lead to different response of damage index or base line, between regional and national level management
- Lack of expertise and inadequate use of software or other tools
- If change is not supported/anchored at executive board level, the implementation process becomes (too) complicated. A strong management mandate is needed.
- High costs
- Experts who may not be available on the job market are needed to meet future challenges

As presented in Table 1, as a concept/framework, digitalization is already within actual BMS and also in the next steps to follow in the thoughts and will of bridge managers. It seems that the future road to increasingly digitalization on the actual BMS is already paved. In fact, the results of a recent survey (Strauss et al. 2023) indicate that data-driven asset management is high on the agenda within owner/operator organizations. This comprises the application of BIM and AI, among others. However, as a tool, there is still a long way to go if the final goal is to incorporate all available digital technologies. However, at this point another questions arises apart from the original question **how far we are** from digitalization of BM, which is **how far we should go or we need to go?**

We know the actual trend, that is bridge management is evolving from reactive response to data-centered and performance-based predictive and preventative measures. This is partially due to costly consequences (societal and economical but also environmental) of un-planned maintenance, but also due to the new possibilities appeared by embracing new capabilities in value-generation through data exploitation. Then: a performance-based (condition-based, risk-based) maintenance requires a full DT or it is enough and better with less digitalization effort?

In fact, there are gaps in the actual bridge maintenance and management-related data collection, processing, analytics and simulations and is time to investigate the barriers to exploiting the value and potential offered by growing data and emerging technologies. One of these barriers is their lack of flexibility in fully digitized the systems to allow adaptability to change and account for human interaction. This needs to be considered on designing new management tools based on available digital technologies, by recognizing and anticipating components that may change in future and may difficult to establish a multifaceted (real-time, automated, secure, future-proof, resilient, precise) preventive and adaptive system for bridge decision support. For instance, climate change induces changes in load and environmental conditions, thus imposing adaptive strategies in existing bridge management tools. Digitalization can be a key component when facing future adaptive BMS. It becomes evident that digitalization should be the skeleton of future BMS, but the level of this digitalization should be decided according to specific needs. Probably a DT can be the answer for a manager taking care of a complex and extensive stock of bridges, but not for a medium or small stock. Different DT for different purposes and taking into account the size and complexity of the bridge stock, the feasible sources of data and other specific requirements can be the best solution to the need of adaptive BMS.

4 EDUCATIONAL AND ORGANIZATIONAL ASPECTS: THE HUMAN FACTOR

As mentioned before, one of the threads in relation to the introduction of digitalization in decision-making in bridge maintenance identified by the stakeholders is: “experts who may not be available on the job market are needed to meet future challenges”. There exist limitations in educational background of personnel with fundaments on civil and structural engineering know/how in regards with data acquisition, data processing and data analytics, i.e. in digitalization processes. This makes difficult to incorporate new techniques and tools developed in the research field to the standard management practice.

Therefore, a relevant issue, after responding where we want to go and how far we are from there, is to know **who** should lead the process. Is a bridge engineer the best suited for it? Is a bridge engineer with some complementary education the appropriate solution? Are actual academic CV in civil engineering bachelor and master programs appropriate for the implementation of sustainability and digitalization into the bridge management practice? Are there other best prepared professionals? According to the opinion of the stakeholders, presented as a weakness of the digitalization in BM: "Inspection tools do not make you an inspector. Inspectors must have prior knowledge of bridges".

Sustainability and digitalization offer significant advantages. However, their integration into routine bridge management practices presents important challenges. The implementation of the process of using digital technologies to optimize the management of bridges is not always straight-forward. Practical hurdles such as regulatory constraints, the requirement for skilled operators, and concerns over data privacy among others can impede widespread adoption. Additionally, while digitalization provides lots of raw data, interpreting this data and convert it into information requires expertise in the field of bridge engineering, again emphasizing the importance of a harmonious blend of the technology provided by the tool (digitalization) and human judgment provided by the education and expertise (professional background).

Practical implementation of research results achieved in both sustainability and digitalization fields, into bridge management practice is highly required. Which are the facts limiting the practical implementation? One of them is the different points of view and objectives between researchers and practitioners. For instance, in the case of digitalization one important advance emphasized by the new research developments (easier to carry out inspections, possibility to post-process results of inspections almost on-line, …) is the possibility of changing the schedule of basic inspections and move it from a periodical inspection schedule to a risk-based time inspection interval (Yang & Frangopol (2022)). As an example, in the case of USA, a gap between researchers and practitioners becomes evident in the field of bridge inspection planning. In fact, a 24-month inspection cycle is normally stated according to FHWA. However, some researchers argued against this fixed inspection interval showing that in some cases can derive in too-early or too-late inspections, compromising funds in one case or safety in the other (Nasrollahi & Washer, (2015); Washer et al. (2016)). According to this, FHWA now recognizes the possibility of risk-based interval inspection (FHWA (2019)). However, a recent survey carried out to twenty-six bridge personnel from state Departments of Transportation (DOTs) across the United States (Abdallah et al. (2023)) discovered that 24% of the participants agreed with the research proposal, while surprisingly 44% of participants supported the 24-month inspection cycle, and the remaining 32% stated that it has some advantages and some disadvantages. The main reason was that: "…. participants found that one of the main problems to apply a variable inspection planning framework is managing bridge inspectors, since a variable inspection schedule will lead to downsizing or hiring new inspectors, which is not an easy task in public organizations".

5 CONCLUSIONS

In the process of implementation of sustainability and digitalization into BM, two aspects are of importance: the technical and the human factor. Concerning the technical factor, full implementation is not so far. In fact, we have the tools (BIM, DT, VR,. …) and methods (performance/condition/risk-based maintenance) in one side, and the framework in the form of BMS in the other. Practitioners from bridge owners recognize that implementing novel methodologies or technologies often demands significant financial investment, be it in new equipment, training, or restructuring of existing frameworks. The main work is, therefore, to introduce these new tools and methods into the framework. However, the way to go looks longer in what concerns the human/organizational factor.

The literature review performed in Jiménez-Rios et al. (2023), examining a total of 76 relevant studies from 2017 up to 2022 shows "a consensus toward the future adoption of DT for bridge design, management, and operation among the scientific community and bridge practitioners. The main gaps identified are related to the lack of software interoperability, the

required improvement of the performance of anomaly detection algorithms, and the approach definition to be adopted for the integration of DT at the macro scale". The adaptation of data analytics methods and tools (software) is happening at a slow but regular pace. Particularly, there are limitations in training of personnel in regards to the digital aspects.

In summary, an adaptation rather than a revolution is needed. In any case, adaptation, as revolution, also requires leaders. The main findings of the work developed by Cortellazo et al (2019) show that: "leaders are key actors in the development of a digital culture: they need to create relationships with multiple and scattered stakeholders, and focus on enabling collaborative processes in complex settings, while attending to pressing ethical concerns"

In addition, adaption requires organizational changes, and these require enough resources and trained manpower to sustain these changes. Digitalization of the decision-making process has been identified as having many advantages, even by the practitioners. However, it has also been identified that employees from bridge owners who do not have a high affinity for digitalization are difficult to get on board

This is probably one of the main challenges that owners and DOTs face when incorporating digitized and sustainability-based planning approaches. Training is vital, ensuring that staff members are equipped with the necessary knowledge and skills to embrace new technologies or processes. Managing the workforce, and ensuring there is a sufficient number of skilled workers, is essential, as is securing adequate funding to support the implementation phase.

ACKNOWLEDGMENTS

The autor thanks the support given by Grant PID2021-126405OB-C31 funded by MCIN/AEI/10.13039/501100011033 and by "ERDF A way of making Europe".

REFERENCES

Abdallah A.M., Ozbek M.E.,Atadero R.A. 2023.Transferring Research Innovations in Bridge Inspection Planning to Bridge Inspection Practice: A Qualitative Study. *Infrastructures* 2023, 8, 164. DOI: 10.3390/infrastructures8110164

Bado M.F., Tonelli D., Poli F., Zonta D, Casas J.R. 2022. Digital Twin for Civil Engineering Systems: An Exploratory Review for Distributed Sensing Updating. *Sensors*, 22, 3168. DOI: 10.3390/s22093168

Balogun T., Tomor A., Lamond J., Gouda H., Booth C. 2018. Sustainability of bridge maintenance. *ICE Bridge Engineering* 172(1):1–27. DOI: 10.1680/jbren.15.00027

Callcut M, Cerceau Agliozzo J.P., Varga L., McMillan L. 2021. Digital twins in civil infrastructure systems. *Sustainability* 2021, 13, 11549. DOI: 10.3390/su132011549

Casas J.R., Stipanovic I., Chacon R. 2022. SHM digital twin requirements for residential, industrial buildings and bridges. Deliverable 5.1. ASHVIN H2020 Project (Assistants for Healthy, Safe, and Productive Virtual Construction Design, Operation & Maintenance using a Digital Twin). European Commission. Grant N. 958161

Chacon R., Casas J.R., Ramonell C., Posada H., Stipanovic I., Škarić S. 2023. Requirements and challenges for infusion of SHM systems within Digital Twin platforms. *Structure and Infrastructure Engineering*. DOI: 10.1080/15732479.2023.2225486

Cortellazzo L., Bruni E., Zampieri R. 2019. The role of leadership in a digitalized world: A review. *Frontiers in Psychology*, 10, 1938. DOI: 10.3389/fpsyg.2019.01938

COST TU1406: Quality specifications for roadway bridges, standardization at a European level (2015-2019). European Commission, Brussels.

Feng M., Fukuda Y., Mizuta M., Ozer E. 2015. Citizen sensors for SHM: Use of accelerometer data from smartphones. *Sensors*, 15, 2980–2998. DOI: 10.3390/s150202980

FHWA. 2019. Proposed Changes to the National Bridge Inspection Standards (NBIS). Federal Highway Administration. Washington D.C.

Gardner P., Liu X., Worden K. 2020. On the ap-plication of domain adaptation in structural health monitoring. *Mechanical Systems and Signal Processing* 138, 106550. DOI: 10.1016/j.ymssp.2019.106550

Gardner P., Bull P. L. A., Dervilis N., Worden K. 2022. On the application of kernelised Bayesian transfer learning to population-based structural health monitoring. *Mechanical Systems and Signal Processing* 167 (1):108519. DOI: 10.1016/j.ymssp.2021.108519

Giglioni V., Poole J., Venanzi I., Ubertini F., Worden K. 2023. On the use of domain adaptation techniques for bridge damage detection in a changing environment. Proceedings of EUROSTRUCT-2023, ce/papers 6, No. 5, 975–980

Hajdin R., Richter R., Rakic L., Diederich H., Hildebrand J., Schulz S., Döllner J., Bednorz J. 2023. Digitalization of bridge inventory via automated analysis of point clouds for generation of BIM models. Proceedings of EUROSTRUCT-2023, ce/papers 6, No. 5, 1189–1197.

Hajek P. 2023. Sustainability perspective in fib MC2020: Contribution of concrete structures to sustainability. *Structural Concrete*, 24:4352–4361. DOI: 10.1002/suco.202300022

Hou R., Jeong S., Lynch J.P., Ettouney M., Law K.H. 2022. Data-driven analytical load rating method of bridges using integrated bridge structural response and weigh-in-motion truck data. *Mechanical Systems and Signal Processing*, 163, 108128. DOI: 10.1016/j.ymssp.2021.108128

Jiménez Rios A., Plevris V., Nogal M. 2023. Bridge management through digital twin-based anomaly detection systems: A systematic review. *Front. Built Environ*. 9:1176621. DOI: 10.3389/fbuil.2023.1176621

Komarizadehasl S., Lozano F., Lozano-Galant, J.A., Ramos, G., Turmo, J. 2022a. Low-cost wireless structural health monitoring of bridges. *Sensors*, 22(15), 5725. DOI: 10.3390/s22155725

Komarizadehasl S., Huguenet P., Lozano F., Lozano-Galant J.A., Turmo, J. 2022b. Operational and analytical modal analysis of a bridge using low-cost wireless Arduino-based accelerometers. *Sensors*, 22(24), 9808. DOI: 10.3390/s22249808

Malekjafarian A., Corbally R., Gong W. 2022. A review of mobile sensing of bridges using moving vehicles: Progress to date, challenges and future trends. *Structures* 44, 1466–1489. DOI: 10.1016/j.istruc.2022.08.075

Massao M., Bittencourt T.N., Carvalho H., Ribeiro D. 2022. Challenges in the application of digital transformation to inspection and maintenance of bridges, *Structure and Infrastructure Engineering*, DOI: 10.1080/15732479.2022.2063908

Matos J., Casas J.R., Strauss A., Fernandes S. 2016. COST action TU1406: Quality specifications for roadway bridges, standardization at a European level(bridgespec) – performance indicators. Proceedings of FIB Symposium 2016. Cape Town.

Mei Q. & Gül M. 2019a. A crowdsourcing-based methodology using smartphones for bridge health monitoring. *Structural Health Monitoring*, 18 (5–6): 1602–1619. DOI: 10.1177/1475921718815457

Mei Q. & Gül M. 2019b. Indirect health monitoring of bridges using Mel-frequency cepstral coefficients and principal component analysis. *Mechanical Systems and Signal Processing* 119, 523–546. DOI:10.1016/j.ymssp.2018.10.006

Morgenthal G., Rau S., Taraben J., Abbas T. 2018. Determination of stay-cable forces using highly mobile vibration measurement devices. *J. Bridge Eng*. 23 (2), 04017136. DOI: 10.1061/(ASCE)BE.1943-5592.0001166

Nasrollahi M. & Washer G. 2015. Estimating inspection intervals for bridges based on statistical analysis of national bridge inventory data. *Journal of Bridge Engineering*, 20(9), 04014104. DOI: 10.1061/(ASCE)BE.1943-5592.0000710

OECD 2016. Better Policies for 2030 – An OECD Action Plan on the Sustainable Development Goals.

Perissin, D. 2018. Geometric Processing: Active Sensor Modeling and Calibration (SAR). In Comprehensive Remote Sensing; Elsevier: Amsterdam, The Netherlands, pp. 61–76.

Stipanovic I., Skaric S., Casas J.R., Chacón R., Ganic E. 2023. Inspection and maintenance KPIs to support decision making integrated into Digital Twin tool. Proceedings of EUROSTRUCT-2023. Vienna. DOI: 10.1002/cepa.2137

Strauss A., Orcesi A., Lampropoulos A., Briseghella B., Frangopol D., Sousa H., Casas J.R., Matos J., Schellenberg K., Valenzuela M., Akiyama M, Linneberg P., Hajdin R., Moser T. 2023. IABSE Survey of Implemented Decision-making Models used by Public and Private Owners/Operators of Road- and Railway Infrastructures, *Structural Engineering International*, DOI:10.1080/10168664.2022.2154731

Strauss A., Lampropoulos A., Frangopol D., Casas J.R., Matos J., Valenzuela M. Sánchez-Silva M., Linneberg P., Moser T., Ruan, X. In preparation. Bridge management - recent and new trends.

UN 2015. Resolution adopted by the General Assembly on 25 September 2015. RES 70/1 transforming our world: the 2030 agenda for sustainable development.

Washer G., Connor R., Nasrollahi M., Provines J. 2016. New framework for risk-based inspection of highway bridges. *Journal of Bridge Engineering*, 21(4), 04015077. DOI: 10.1061/(ASCE)BE.1943-5592.0000818

Xu G. & Guo F. 2022. Sustainability-oriented maintenance management of highway bridge networks based on Q-learning. *Sustainable Cities and Society* 81, 103855. DOI: 10.1016/j.scs.2022.103855

Yang D.Y. & Frangopol D.M. 2022. Risk-based inspection planning of deteriorating structures. *Structure and Infrastructure Engineering* 18(1), 109–128. DOI: 10.1080/15732479.2021.1907600

Bridge Maintenance, Safety, Management, Digitalization and Sustainability – Jensen, Frangopol & Schmidt (eds)
© 2024 The Author(s), ISBN 978-1-032-77040-6
Open Access: www.taylorfrancis.com, CC BY-NC-ND 4.0 license

Bridge management – past, present, and future

Reed M. Ellis, Ph.D., P.Eng.
Stantec Consulting Ltd., Edmonton, Canada

ABSTRACT: The history of bridge engineering is a story of human innovation. As long as humans have existed there has been a need to bridge gaps such as streams, gullies, canyons etc. The history of bridge management and bridge management systems (BMS) is also a story of innovation as bridge owners eventually began to be responsible for many structures, constructed using various materials, exposed to varying demands. BMS are powerful computer solutions that help bridge owners responsibly manage lifecycle costs, risk, determine optimized priority programs, report current and forecasted condition and other performance measures. Today BMS help sustainably maintain the inventory while considering a variety of socio-economic factors and are proving instrumental in helping owners manage the effects of climate change and extreme weather.

In this lecture, we will take a high level review of bridge management practices in the past, present, and postulate where bridge management might be heading in the future.

1 BRIDGE MANAGEMENT - PAST

As long as humans have existed there has been a need to bridge gaps such as streams, gullies, canyons etc. The first bridge was likely made by nature - as simple as a log fallen across a stream. Nature can even create beautiful natural stone arches, examples of which we can see today. The first bridge ever built by humans is lost to prehistory and has long disappeared and no records exist. The moment the first bridge was constructed humans probably from a tree, or a stone slab (Figure 1), was most likely the moment bridge engineering first began and knowledge about durability and maintenance thus followed, whether it was understood or not at the time. We learned about forms and materials originally from nature, and then from experimentation. Which materials lasted longer, which ideas worked better, how to build would naturally lead to innovation. It may be said that the history of bridge engineering is a story of human innovation.

Although we do not know for certain, it is said that the oldest constructed bridge still in use today is the Arkadiko Bridge in Greece, the construction of which dates from the Mycenaean period, around 1300 BC. It is a stone arch bridge constructed using stone blocks fitted together without mortar. It is part of a road linking the city-states of Mycenae, Argos and Tirynthos, with the port of Ancient Epidavros (Figure 2). There were undoubtedly many such structures in the ancient world that have not survived or no longer in use.

Already we can see that the ancient engineers were using the materials available to them in designs well-suited to the material. They had learned lessons on durable construction methods as well as something about which designs best survived earthquakes; basic logs as beam elements spanning streams, stones arranged to form an arch similar to those provided by nature. Maintenance would have been very basic, keeping the bridge clean, removing debris from streams, replacing worn out materials, whatever was necessary to keep the crossing in service.

Over time, and of course in all parts of the world, innovation continued with larger and more complex structures. Kingdoms and empires evolved and through the centuries road

DOI: 10.1201/9781003483755-4



Figure 1. Simple log bridge (left) and stone slab bridge (right).



Figure 2. Arkadiko bridge, Greece c.1300 BC (Wikipedia).

networks were developed that became essential to commerce as well as serving military purposes. Maintenance of these structures was considered a requirement and important enough that it was written in deeds and planned for in the original construction. There are both ancient and medieval records of this. In his excellent treatise entitled *The Bridges of Medieval England – Transport and Society 400 – 1800AD*, David Harrison investigates the excellent

design and construction of bridges from Roman, Anglo-Saxon, and medieval times to the Industrial Revolution including the immense efforts of construction of small and very large multi-span structures using large skilled workforce and the planned upkeep of these bridges by the state, church, bridge trusts, charitable donations and sometimes even using resident hermits. There are even records of bridge maintenance being considered a chivalrous activity. The overall situation was similar in other parts of Europe. But consider this, provide for the maintenance and preservation at the time of construction - there is a novel idea! Clearly, we can learn from those that came before us. Although maintenance was very much reactive in nature, it was considered important and planned for at the time of construction.

In the modern era, advances in materials, mathematics, engineering, and construction methods, led to larger and more complex structures. The great railway bridge building boom occurred in Europe the early 19th century and the latter half of the century in North America. In the 20th century, the great road network expansion in the 1950s, 60s and 70s saw a great number of bridges constructed and of course large innovations in design and construction. Owners/transport departments became responsible for large inventories of structures, constructed using various materials, various designs in different exposures carrying different loadings. Maintenance was mostly reactive and not treated in any sophisticated way. And for the recently expanded road networks, the structures were fairly new and not yet at the age when rehabilitation and replacements would be necessary. This would change drastically in the coming decades.

The first use of computerized systems for managing bridges and culverts appear in the 1970s when many departments developed inventory or inventory and inspection management systems on mainframe computers. Very primitive by today's standards, these tools helped to store and manage basic data which could be retrieved to inform management decisions. The growing inventories and required investments in transportation networks started to present challenges. In December 1967 in the USA, a tragedy occurred which would lead to innovation and significant advances in the management of bridges. On December 15, 1967, the Silver Bridge, which carried U.S. 35 over the Ohio River collapsed under the weight of rush-hour traffic, resulting in the deaths of 46 people. The cause was a brittle fracture of a single eye-bar in a suspension chain, due to a small 2.5 mm defect that was undetected (US Federal Highway Administration, FHWA 2021). The end results included the formation of the National Bridge Inspection Standards to "establish national bridge inspection standards in order to provide for the proper safety inspection of bridges." The standards would detail the methods by which inspections were to be conducted, the frequency of inspections, and the qualifications of bridge inspectors. Many countries followed suit during the 1970s and inspection programs were mandated, and funding was allocated to formalize processes to manage bridges.

During the next decade it became clear that the significant expansion of road networks that had occurred in various parts of the world had created challenges for maintenance, repair, rehabilitation (MR&R) and replacement of bridges in terms of needs identification, prioritising, funding, and having resources to manage these challenges. There was a need to have methodologies and tools to help with these tasks and research efforts began in various countries in the early 1980s. It wasn't until 1987 that term 'bridge management system' (BMS) was first used. Incidentally, in the transportation world, pavement management and pavement management systems had been a focus of research and development more than a decade earlier c. 1970 and the first concepts in bridge management evolved from these systems. The formative summary of pavement management systems (PMS) is given in the book entitled Pavement Management Systems (Haas, R. C. G., Hudson, W. R., 1978). Examples of the earliest bridge management system research projects include the NCHRP Project 12-28(2) (Hudson, et al.,1987) and FHWA Demonstration Project 71 (O'Connor, et al., 1989). These reports defined the essential components of bridge management systems and documented techniques which could be implemented for BMS development. These initial research projects provided the basis for further BMS development. The NCHRP research continued with the

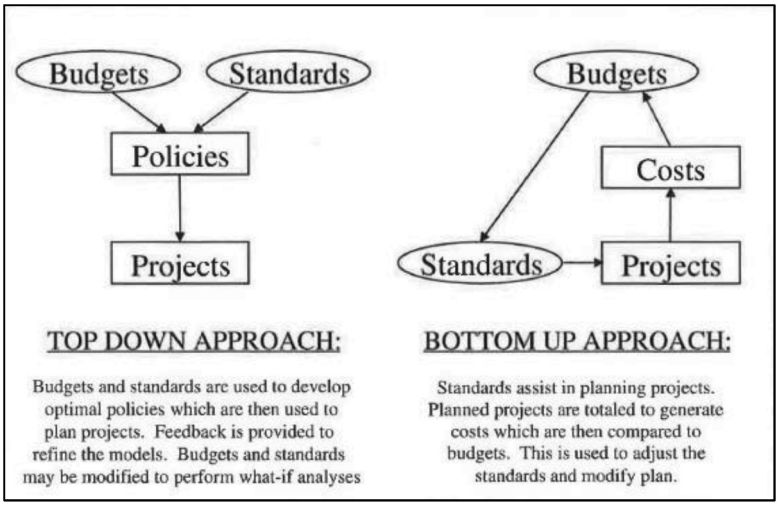


Figure 3. Alternative BMS development strategies (transportation research circular, 2000).

development of the BRIDGIT BMS. The FHWA project continued with the development of the Pontis bridge management system.

The BRIDGIT BMS was based on a bottom-up approach while the Pontis BMS was based on a top-down approach (Figure 3). A consensus was emerging on the required ingredients of bridge management systems (AASHTO, 1992) and these are still accepted today. Some of the key recommendations are that the BMS should help bridge managers manage the inventory data, the inspection program and all the data required, and ultimately make decisions about MR&R, improvements and replacements and do this within a financial framework that considers user costs, benefits, lifecycle cost analysis. Indeed, bridge management is defined in the 1992 AASHTO guideline as "*the process of combining management, condition assessment, engineering, and economic information in order to determine the best actions to take on bridges in a network over a specific time*". This requires a set of engineering and financial models such as cost, deterioration, user cost and safety models, and optimization algorithms. We will return to these requirements below, but it should be emphasized a BMS is more than an inspection and inventory database or repository.

Agencies and bridge managers continued to face challenges in managing large networks of aging and deteriorating bridges and require decision support tools for project and network level analysis that can help recommend MR&R strategies, improvement, or replacements under fiscal constraints (Transportation Research Circular 423, 1994). Research and development continued and not long after the early BMS, we see other systems developed in the early 1990s such as the Danish DANBRO, the Swiss Bridge Management System KUBA, and the Finnish Transport Agency SIHA. DANBRO originally focusing on inspection and routine maintenance and later added analysis modules. KUBA (Ludescher, H., & Hajdin, R., 1999) and SIHA (Finnish National Road Administration, 1991) were both originally based on many of the underlying concepts of the Pontis BMS but were adapted to suit local conditions. At the end of the 1990s we see the development of the next generation of BMS such as the new Ontario Bridge Management System (OBMS), Thompson et al, 1999. The OBMS followed a bottom-up approach as in the BRIDGIT system and expanded on many of the features from the other major systems listed above but had lifecycle cost and incremental benefit cost framework at three levels dependent on one another (element level treatments, project level strategies, and network level budgeting). The OBMS had a more detailed project-level capabilities than any existing system at the time (see Figure 4), and included a GIS

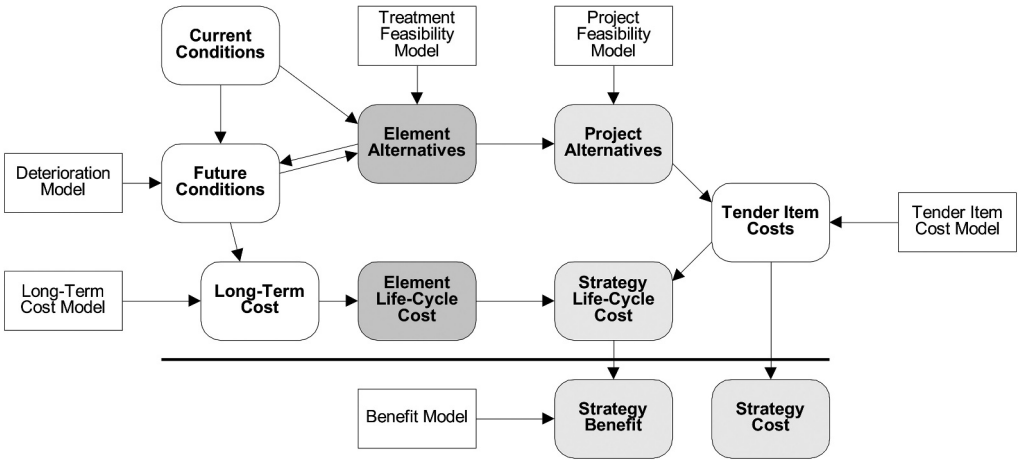


Figure 4. Project level models (Thompson et al, 1999).

interface that displayed bridge info on a GIS, together with image and document management capabilities (Thompson et al, 1999).

As with nearly all of the systems described above, in OBMS element level condition is expressed by recording the type, severity, and extent of deterioration of each major structural element. Condition is expressed as the percent or quantity of each element found to be in each of a number of condition states. As with most of the other systems described above, element level Markovian deterioration models were used. Various derivatives of this system are being used today by the majority of Transportation agencies in Canada (National Research Council of Canada, 2023).

In only a decade later, many other systems were under development in various parts of the world. Although each system has its own features, consensus was emerging on some common characteristics in these systems (Mirzaei et al, 2014):

a) The most common inspection and condition rating was element-level, condition state inspection recording severity and extent of defects.
b) The most common deterioration model being used was Markovian deterioration models applied to bridge and culvert elements.
c) Condition was the most common performance measure. Usually in some for of condition index.
d) The most common financial framework for decision making was minimum lifecycle cost analysis (LCCA), with benefit/cost (B/C) as ranking.

Bridges and Bridge Management came a long way from the earliest bridges to the modern era but it wasn't until the last few decades of the 20th century that bridge owners would have the technology to fully manage inventories of bridges and move from reactive maintenance to proactive maintenance. The age of BMS began roughly in the mid-1980s and the subsequent decades ended with systems that could help manage inventory and inspection information, perform analysis to calculate LCCA and B/C to develop prioritized MR&R activities, improvements, and replacements (Transportation Research Circular, Issue Number: 498, 2000). Bridge managers could now make informed decisions and create budgets and work programs along with forecasted condition depending on those budgets.

2 BRIDGE MANAGEMENT – PRESENT

With the framework in place for effective BMS, bridge management and BMS research and development continued throughout the first decades of the 21st century. Improvements in

bridge management/BMS have occurred in various countries. Today, in addition to the common characteristics described above, we can expect BMS to be able to perform risk analysis for risks associated with advanced deteriorated condition, vulnerability to scour, flooding, seismic, fatigue, and more (Mirzaei et al 2014, Sobanjo & Thompson 2013, Ellis et al 2012.). A few systems give the bridge manager the ability to consider multi-objective analysis (Patidar et al 2007). For example, BrM (AASHTOWare) includes an analysis that uses a utility function approach to allow the user to weight different objectives such as condition, lifecycle cost, and risk in the decision making process (Mirzaei et all, 2014).

The need for better performance measures for bridges led to research on best practices (e.g. NCHRP 2010) as to what should be reported and how performance measures can help understand effectiveness of design, construction, inspection, and preservation strategies thereby supporting good bridge management. Performance measures are being used such as condition (e.g. % bridge decks in Good or better condition by functional class, % of bridges posted weight restrictions). Vulnerability ratings for scour, flood, fatigue, fracture can be used as performance measures and many systems have this capability (Mirzaei et all, 2014). Also in the last decade, there has been increased emphasis on improving existing models such as deterioration models and treatment effectiveness. In many countries asset management practices began to place emphasis or requirements for industry accepted bridge management practices so agencies that have BMS are able to provide input into transportation asset management plans (TAMS).

Also during this time better field data collection tools such as field tablets etc. become available to improve the efficiency of inspection data collection. These tools are used on site but later synchronize the data collected with the BMS.

Building Information Modeling (BIM) has been widely applied in today's building construction industry for some time and the benefits of having a 3D model from conception, through design, construction and maintenance have been realized. In recent years we have seen BIM applied more commonly to bridges (BrIM). Linking BrIM to BMS is in the early stages but already seeing great possibilities to record inspection information such defects and maintenance issues on a 3D model. This will be particularly efficient when the models are created at the time of conception and used for the entire lifecycle including design and construction, inspection and maintenance.

Drones or Unmanned Aerial System (UAS) were first used in the last 10 years for bridge inspection purposes and the capabilities of these systems are continuing to improve with more automated flight capabilities, types of cameras, sensors etc.. Today we can use UAS to fly the bridge site in a pre-inspection to create a 3D model for BrIM and then superimpose inspection findings on the model which is then linked to a BMS. Examples of this are being presented in this conference (IABMAS '24 Special Session 9).

Increased awareness of the effects of climate change and extreme weather has emphasized the need for assessment of vulnerabilities to flood, scour, etc.. Various bridge management systems have this capability (Mirzaei et all, 2014). Recently an appraisal index, vulnerability rating and risk analysis is reported for wildfire (Ellis & Kamranian, 2023) and this is particularly of interest for the countries that were exposed to record wildfires in 2023 (Canada Natural Resources, 2023). The ways in which agencies can respond to the challenges of climate change vary for new design vs. existing infrastructure. In a recent survey and study commissioned by the National Research Council of Canada (NRC), it was determined that most of the advanced bridge owner agencies are aware of the challenges surrounding climate change and extreme weather (NRC, 2023). All Provincial government agencies responded that the effects of climate change and extreme weather events are being considered in the design of new structures. Most are using guidance from hydraulic studies, Environment Canada and other climatic data, and new Intensity-Duration-Frequency (IDF) curves to determine design flows and flood events, increases in scour potential, temperature range etc. In response to these challenges for new design, most have internal policies related to design requirements for increased freeboard, deck drainage, more stringent permafrost considerations, erosion and sediment control, river protection works, etc. The 2025 Canadian Highway Bridge Design Code will have specific climatic data to address the changing climate.

The situation is different for the assessment of existing structures when considering the impacts of climate change and extreme weather. Existing structures are generally designed to older standards. Most agencies surveyed indicated that they consider increased design storm events or temperature ranges obtained using updated climatic data. This generally translates into re-mediation such as increasing freeboard, river protection or training works, improved deck drainage etc.. Sometimes, hydraulic capacity can also be increased for example by constructing relief flow culverts beside existing structures.

Beyond the design parameters for mitigation of a particular vulnerability, the main challenge for agencies is to determine which structures should be prioritised and due to which vulnerability. Vulnerabilities and risks need to be identified and the need for remediation should be considered and prioritised over the transportation network, corridor, etc. Agencies identified that guidance would be useful in concepts such as:

a) what are the vulnerabilities to consider with respect to climate change and extreme weather? (e.g., types of extreme weather events, flooding, scour, seismic, wildfire, hurricane, tornados)
b) what analytical tools are needed to help determine and prioritise mitigation of these vulnerabilities?

These are areas of active and likely future work as agencies must manage risks and provide resilient transportation networks.

We have also seen increased use of non-destructive evaluation of bridges to determine for example crack detection and monitoring in steel bridges, or cracking, delamination and rebar corrosion in bridge decks. This information can feed level II decision making in bridge management although nearly all BMS continue to use visual inspection data. These tools continue to improve and there are robotic non-destructive evaluation and testing devices already in use. Artificial intelligence (AI) is being applied to damage detection using imaged-based methods and detection based on data from sensors and signals such as vibration or acoustic emission.

The use of sensors on bridges is far from new, having its origins along with structural health monitoring in the 1990s. Today sensors and instrumentation are miniaturized and inexpensive and easily installed for long-term monitoring of bridges or for load testing purposes. Bridge monitoring and bridge load testing can be very efficient and cost effective solutions for bridge owners. It is rare that these systems are directly linked to a BMS.

3 BRIDGE MANAGEMENT – FUTURE

Perhaps it is risky to try to predict the future, particularly when technology is involved, as it is in bridge engineering in general and specifically in bridge management/bridge management systems. Actually, prognosticators such as Shirole demonstrated impressive insights into the future that were remarkably accurate (TR Circular 423 Shirole, A.M., 1994). Writing in 1993, the author thought that the need for BMS development was great due to the increased demands, deteriorating structures, and shrinking budgets. It was suggested that improved decision support analysis would be needed, together with improved types of inspection data and collection of the data, significant improvements in computer power and storage, use of the new geographic information systems (GIS), and improved decision support for assessing vulnerability to flood, scour, fatigue and other hazards. These things would prove true within a decade. This author can only hope to do as well.

Looking to the future, is possible to foresee some emerging technologies and ways in which the challenges of effectively managing bridge inventories may be solved.

1. **Condition assessment and data collection.** We can expect to see improvements in condition assessment and data collection tools, and increased use of NDE. The promise of better data, collected in a more efficient way and populated into bridge management systems is ever appealing.

2. **Automated, Remote Inspection and Condition Assessment.** UAS technology has technology has improved incredibly in the last 5 years continued improvement in automated flight capabilities, payloads, types of cameras, sensors etc. will make this a regular part of the inspection program. Whether this is used for pre-inspection, on-site inspection, or live inspection to an off-site senior reviewer, this technology will move to mainstream, especially if linked to BrIM. AI plays a role in this area in the form of damage detection and model creation. Research is on-going in AI supported damage detection from images such as cracks, efflorescence and staining, exposed rebar, delamination, spalling, rust, repair areas and more. Research into acoustic sensors in combination with hammer sounding is showing promise in the ability to detect loose bolts and concrete delaminations. Once fully developed this will be truly revolutionary. Further improvements in efficiency will occur when these tools are linked directly to bridge management systems which can then provide decision support.
   The situation for robotic inspection and condition assessment is similar.
3. **3D models, BrIM, Digitization, Digital Twins and Extended Reality.** The use of bridge BIM or BrIM will continue to grow, not necessarily due to bridge inspection management needs, but because it makes the entire lifecycle management process more efficient including planning, design, construction, inspection and maintenance, and decommissioning. The growing trend towards digitization is driven by the improvement of technology including surveying, drone/UAS scanning, AI in processing, and computer and cloud hardware. AI will improve in the ability to detect structure elements from images (i.e. girders, bearings, cables, abutment walls etc.) and calculate quantities. Of course, big data, statistical analysis, and deep learning play a role in this, and these fields are evolving. Bridge managers will have real advantages as these tools are linked to BMS to provide informed decision support with the benefits of 3D visualization and reporting.
   We will see continuing research on, and increased application of digital twins in the bridge industry. A digital twin is a digital 3D replica of the physical bridge which models the behaviour of the real thing. The digital twin can connect to sensors and real time data from the physical structure. Before this is fully practical, we will have to solve the challenges associated with the immense amount of data to process.
   We will undoubtedly see increased development of extended reality (ER) tools in bridge inspection. These wearable displays will enable inspectors to interact visually and even physically (e.g. hammer sounding robot) with the physical bridge and maybe one day a digital twin. There are exciting possibilities in this area.
4. **Sensor, Structural Health Monitoring, Integration With Bridge Management Systems And Iot.** Inexpensive, miniaturized, low power sensors have been available for some time now, but improvements are likely to continue. The equipment and communication systems have become smaller and less costly, and we are finally seeing more application of sensors, structural health monitoring systems, live load testing, bridge weigh-in-motion (B-WIM). Personally, as an early adopter of some of these tools decades ago, it continues to surprise how slow general adoption and application of these tools has been. In future, I expect (and hope) wider use and direct integration with BMS and BrIM will become common. Sensors will one day be applied on most bridges. For example, perhaps every deck joint and large bridge bearing will be manufactured with sensors and all the owner has to do is connect them. Imagine if deck joint gaps and temperate were measured continuously and shared via the Internet of Things (IoT) directly to the BMS for monitoring and decision making, no longer requiring inspectors to take measurements in dangerous traffic situations. Imagine if bearings could share bridge bearing reactions continuously the same way thereby informing the bridge engineer of changes, potentially serious changes. In fact, deck joint gaps and bearing reactions can be an early indicator of issues before they become serious. It is an expectation and a hope that these things will become common in the future. As with all of these exciting technologies, it will reach full potential when bridge managers can access the information in their BMS in real time for decision support.

5. **Global positioning and satellite data.** Scientists have developed a technique for analyzing satellite data that can reveal subtle structural changes in bridges and other infrastructure. Using synthetic aperture radar (SAR) measurements from several different satellites and reference points, it is now possible to map relative displacement such as structural changes to a bridge. Using SAR and new processing, it has been possible to detect millimeter-sized changes to a bridge over time. A team from NASA, University of Bath, and the Italian Space Agency have successfully applied this technique to retroactively investigate the collapse of the Morandi Bridge, near Genoa, Italy in 2018. The researchers found there were subtle changes as early as 3 years before the collapse and significant increases in structural changes in the year prior to the collapse.

A new satellite NASA-ISRO SAR (NISAR) planned by NASA and the Indian Space Research Organization (ISRO) for 2024 is intended to greatly expand this coverage (Figure 5). This has promise in future to improve the safety of infrastructure globally.



Figure 5. Planned NASA-ISRO SAR (NISAR) (NASA, 2024).

5 SUMMARY

We have seen that bridge engineering, and the management of bridges has been linked to human innovation since the beginning of time, at least from the time of the first bridge. Through this journey, innovation has constantly occurred as the need arose that has enabled bridge managers to successfully manage this vital infrastructure whether this was a few bridges or the large complex inventories of today. The need drives the innovation and technology has contributed to the success. To the many bridge engineers out there have been privileged to have been part of this journey, you will have enjoyed the ride and no doubt feel confident about the future of bridge management. To those young aspiring bridge engineers, it's a great time to be a bridge engineer involved in design, inspection, preservation, and all the new technologies that comprise bridge management. Enjoy, you are in for an exciting ride!

REFERENCES

AASHTO, 1992. Guidelines for Bridge Management Systems.

AASHTOW are Bridge Management web page. https://www.aashtowarebridge.com/bridge-management

Canada Natural Resources, 2023. https://natural-resources.canada.ca/simply-science/canadas-record-breaking-wildfires-2023-fiery-wake-call/25303

Ellis, R.M., et al, 2012. Incorporating Risk and Criticality in Bridge Management Decision Making and Project Prioritization. 6th International Conference on Bridge Maintenance, Safety and Management, IABMAS 2012, Stresa, Lake Maggiore, Italy.

Ellis, R.M. & Kamranian, Z., 2023. Considerations for Vulnerability and Risk of Bridges Considering Extreme Weather Events, 12th International Conference on Bridge Maintenance, Safety and Management, IABMAS 2024. Copenhagen, Denmark.

FHWA 2021 History of National Bridge Inspection Standards https://www.fhwa.dot.gov/highwayhistory/national_bridge_inspection_standards.cfm

FINNRA (Finnish National Road Administration), 1991. Finland Bridge Management System, System Design Concept. Helsinki.

Haas, R. C. G., Hudson, W. R. 1978. Pavement Management Systems, McGraw-Hill.

Hudson, S.W., Carmichael, R.F., Moser, L.O., Hudson, W.R., and Wilkes, W.J., December 1987. "Bridge Management Systems." NCHRP Report 300, Project 12-28(2), Transportation Research Board, National Research Council, Washington, DC.

Ludescher, H., & Hajdin, R. (1999). Distinctive features of the Swiss road structures management system. Proceedings International Bridge Management Conference, Denver Colorado, United States.

Mirzaei, Z., Adey, B. T., Klatter, L., & Thompson, P. D., 2014. *The IABMAS Bridge Management Committee Overview of Existing Bridge Management Systems*. IABMAS.

NASA Jet Propulsion Laboratory NASA-ISRO SAR (NISAR) Mission. https://nisar.jpl.nasa.gov/news/14/new-method-can-spot-failing-infrastructure-from-space/#

National Research Council of Canada (2023). Review of State of Practice of Bridge Management in Canada and USA in a Changing Climate.

NCHRP 2010. Measuring Performance Among State DOTs, Sharing Best Practices Comparative Analysis of Bridge Condition - Final Report. NCHRP 20-24(37)E

O'Connor, D.S. and Hyman, W.A., October 1989. "Bridge Management Systems." Final Report, Report FHW A-DP-71-0lR, Demonstration Project 71, Demonstration Projects Division, Federal Highway Administration, Washington, DC.

Patidar, V., Labi, S., Sinha, K. C., and P. Thompson, 2007. NCHRP Report 590: Multiple-Objective Optimization for Bridge Management Systems.

Sobanjo, J.O & Thompson, P.D. 2013. Development of Risk Models for Florida's Bridge Management System, Prepared for the State Maintenance Office, Florida Department of Transportation

Thompson, P. D., Merlo, T., Kerr, B., Cheetham, A., Ellis, R. 1999. The New Ontario Bridge Management System. Proceedings 8th International Bridge Management Conference, Denver, CO.

The Bridges of Medieval England – Transport and Society 400 – 1800AD, David Harrison Oxford Press, 2004

Transportation Research Circular, Issue Number: 423, 1994, Shirole, A. M., Bridge Management to the Year 2000 and Beyond. Transportation Research Board.

Transportation Research Circular, Issue Number: 498, 2000, Current Status of Bridge Management System Implementation in the United States, Transportation Research Board. https://onlinepubs.trb.org/Onlinepubs/trcircular/498V1/498V1-001.pdf

Bridge Maintenance, Safety, Management, Digitalization and Sustainability – Jensen, Frangopol & Schmidt (eds)
© 2024 The Author(s), ISBN 978-1-032-77040-6
Open Access: www.taylorfrancis.com, CC BY-NC-ND 4.0 license

Bridge engineering - Proving the sustainability case for refurbishment v replacement

D.K. MacKenzie
COWI UK Limited

ABSTRACT: The demands on our existing transportation infrastructure are growing as our cities increase in size. We are constantly faced with the need of increasing the capacity of our existing networks. So do we rebuild or refurbish? We live in a world of finite resource and the idea of simply knocking something down and rebuilding it afresh is counter-intuitive to a society that seeks sustainable solutions. So how do we assess the sustainable benefit of refurbishing an existing structure?

There are several tools recently developed to measure the extent of embedded carbon in new projects that help us compare the sustainability of new construction and determine the most effective scheme. However, the same tools cannot be used to assess the relative sustainability of refurbishment versus replacement and yet decisions on this critical point are having to be met by bridge owners worldwide.

1 INTRODUCTION

We live in ever developing societies and with that comes the need to update our infrastructure. We have been faced with both increasing the volume of traffic flows and the weight of the vehicles using our bridge networks. In the past, with a few notable exceptions, we have tended to replace existing assets with new assets and justified them on purely commercial and operational bases. The view was very much "out with the old and in with the new" as we tended to take the view that it was easier to build new rather than refurbish the existing.

Our mindset has naturally been cost and programme driven, as we have striven to get the best return when seeking to increase the capacity of an existing structure. However, we are now facing a global climate emergency and, as engineers, we must be at the forefront of reducing the carbon content of our projects. We therefore need to place a greater emphasis on making better use on our existing assets and when the call comes to increase the capacity of our network, we must take a hard look at the value and benefit of retaining and strengthening of what is already there.

This view is not new. It has been explored by researchers evaluating the changes to the state of the art. Mizra (2006) carried out a qualitative review of Canadian infrastructure to review the effects of poor maintenance on structures and the consequential cost that arose. His conclusions were that the approach taken by bridge designers and subsequently by funders of infrastructure maintenance were that the construction industry only tends to consider "first cost" and not whole life costing. This work was driven by the huge cost of failing to maintain infrastructure; it will be seen from this paper that the additional impact on sustainability through embedded carbon and a failure to redevelop existing infrastructure also has significant consequences for global warming.

When we are faced with evaluating the basis for refurbishment against renewal, we are presented with a number of challenges. The obvious ones are that:

- the existing load bearing capacity is insufficient,
- the bridge needs to be widened,

DOI: 10.1201/9781003483755-5

- the structure is in very poor condition through insufficient maintenance or from damage, and
- the existing alignment does not suit the increased demands.

These are the basic structural requirements that are the immediate concerns of the bridge engineer, but there are many other factors of equal importance that also need consideration. These include as a minimum:

- the effects of construction on traffic flow during the refurbishment or replacement,
- the loss of amenity to users of the structure, which broadly align with the traffic effects,
- the effects on local businesses and residents nearby the structure where temporary access will be required to the site and will affect local traffic patterns on neighbouring roads,
- the environmental effects during construction due to noise, alternative access, lighting, and out of hours working,
- those environmental and biodiversity efforts created by increasing the capacity of the bridge,
- the effects of loss of heritage,
- the ease of future operation, and
- the maintainability of the scheme

All of these will drive up the carbon emissions on a project and impact its sustainability. Special consideration will need to be given to the long term environmental and biodiversity cases; this paper does not set down methodologies for this as they are generally better defined and are usually part of the statutory requirements for a project. However, they need to be added into the mix to ensure that the overall balance of sustainability is assessed.

It should be noted that at present, there are limited means for carrying out a complete comparison of the long term benefits between refurbishing/strengthening a structure and building from new. This paper therefore sets out the steps needed to develop this process into a more quantifiable basis so that there is an effective means for assessing the merit of preserving our existing heritage. We know that it is a "good thing" to preserve existing infrastructure and not just rip it up, but when does it become too much of a challenge and how do we legitimately justify new construction? A means for comparison is required.

2 WHAT IS REFURBISHMENT?

This paper considers how the case for refurbishment instead of replacement can be justified when the existing bridge capacity is insufficient. It is a clearly understood premise of modern bridge design that all bridges will have components where there is the need for regular refurbishment or replacement. The designer is required to assess the effects of replacement, be they items, for example, such as bearings or stay cables. This is planned refurbishment. This paper is concerned with major refurbishment or replacement of the entire structure, which is very rarely contemplated in the design of bridges. Some legislations require designers to consider safety in demolition of an asset (HSE 2015) but this is not linked to a whole life cost approach.

It is considered that there are two forms of major refurbishment. The first is when there is an increase in traffic volume and there are an insufficient number of lanes to carry the increased traffic volume across the bridge. Typically, this requires major intervention as there is a requirement to provide more space for traffic on the deck. However, it is not always necessary to widen the running surface as it may be possible to use narrower lanes and make other changes to the hard-shoulders and barriers to accommodate additional traffic lanes.

West Gate Bridge and Gade Valley Viaduct stand out as particular examples of successful widening schemes where better management of the available deck space obviated the need for construction of additional deck space. In both these projects, this ability to use the same traffic corridor to carry a greater volume meant that the works mainly comprised strengthening of the primary structure to carry the additional loads, but no change to the overall width of the deck. It should also be recognised that providing additional volume does not always result

in significant force increases as most design codes will have small additional loadings for the additional load when adding a seventh and eighth lane to a six lane bridge.



Figure 1. West Gate Bridge before widening.

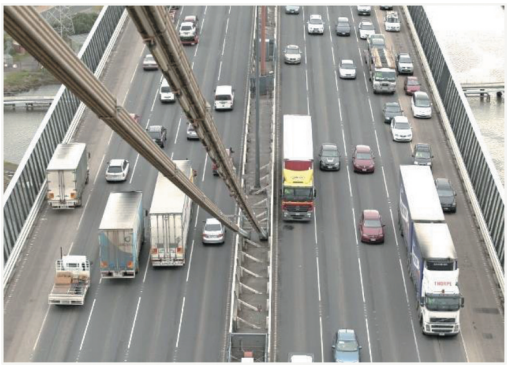


Figure 2. West Gate Bridge after widening.

The second form is when there is insufficient capacity to carry the traffic because either the traffic loads have gone up or the capacity has decreased due to deterioration. Here the refurbishment considerations will be driven by the ability to intervene to enhance the capacity of the deck. There have been some highly successful schemes where the bridge design engineers have demonstrated remarkable ingenuity to upgrade the structural capacity to the requisite level. These are presented in the case studies given throughout this paper.

There will of course be cases when the refurbishment needs to consider both a loss of capacity through deterioration as well as an increased demand for traffic flow and weight. Such cases are inevitable more challenging but, again, there have been some extremely impressive schemes (shown in the case studies) where the original structure has been enhanced with minimal interference and embedded carbon when compared with the alternative of complete refurbishment.

3 HOW DO WE MEASURE SUSTAINABILITY?

3.1 *Definition*

The starting point in any debate on sustainability is to set out some clear definitions of what we mean by sustainability. The United Nations (2021) offers "*Sustainable infrastructure systems are those that are planned, designed, constructed, operated and decommissioned in a manner that ensures economic and financial, social, environmental (including climate resilience), and institutional sustainability over the entire infrastructure life cycle*". The key message here is that sustainability is a whole life consideration and must consider all aspects of the lifecycle of a project. There are many definitions of sustainability that exist owing to the various nuances within the different types of infrastructure. The reader is referred to an overview carried out by Yanamandra (2020).

The challenge to the consideration of sustainability is that most bridges will have been designed on the basis of direct costs only with little or no direct calculation of whole life costs. Explicit consideration is required of the maintenance and depreciation of infrastructure over its service life. Such considerations will drive greater awareness at the design stage of potential limitations in bridges and their ability to accommodate changes in the future. It is appreciated that the foresight required to predict future change and to provide the means for upgrading capacity is not an easy subject. Some of the case studies considered in this paper show some remarkable foresight on the part of the bridge owners, which is to be commended, and should serve as a guide for all bridge engineers when considering the whole life value of either a new

or an existing structure. It is inevitable then that the sustainable design of bridges must be guided by overall socio-economic and environmental concerns which is inexorably linked to future use.

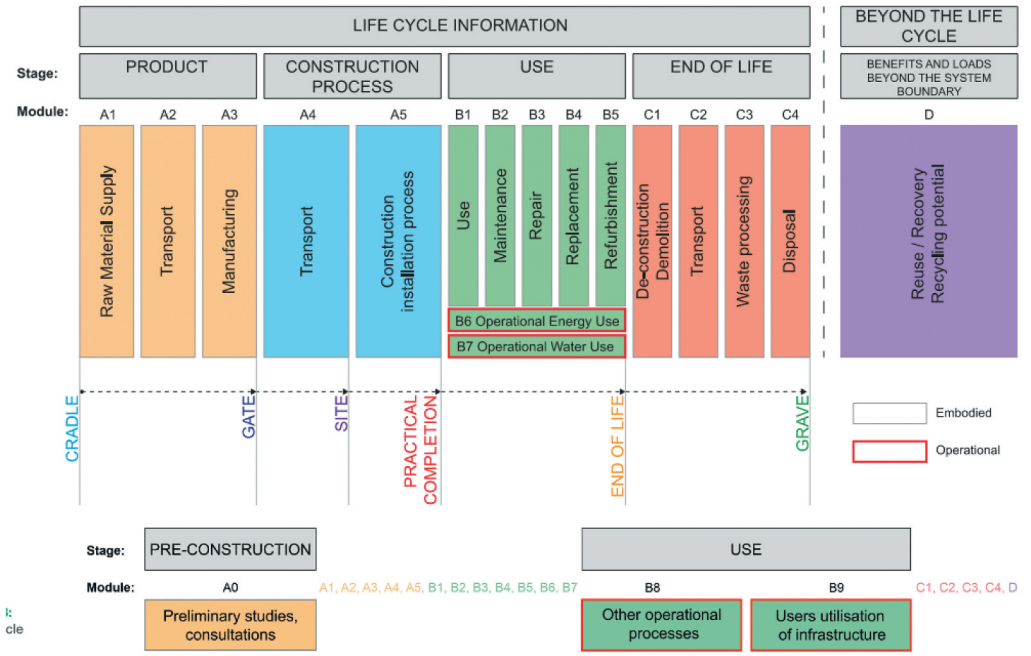


Figure 3. Lifecycle modules for construction projects.

Given the imperative to reduce carbon emissions, there has been widespread acceptance in the structural engineering community that the most appropriate role we can play is to reduce the embedded carbon in our structures and in the associated materials such as asphalt and barriers. The Institution of Structural Engineers has taken a particular lead here and through the work of Orr et al (2022) has set out a procedure for deriving the embodied carbon that is introduced into a structure over its life time. The process examines all stages of the structure which includes, importantly, the full operational and end of life stages of a project. These are necessary to assist in the comparative study of different schemes; if we simply limit comparisons to new build we cannot provide an accurate comparative assessment over the lifetime of a project and our comparison will fail.

Orr's work is used as the basic standard in the United Kingdom. He has developed a model to represent the full set of stages for the total lifecycle of a project. Figure 3 shows the stages for a typical construction project. Each stage broken down into a series of specific steps or modules which enables the means for assessing the embodied carbon at each stage of the lifecycle of an asset. It has been driven initially through the building sector but it is equally relevant to bridges.

It is worth also introducing some basic terminology around carbon. Figure 4 describes the various categories of carbon associated with an infrastructure project.

The emphasis on assessing embedded structural carbon was led initially in the building sector; further work carried out by Archer-Jones and Green (2021) and by Collings (2022) both provide the designer with some clear methodologies for the assessment of embedded carbon in bridges. They have been aided by the considerable work carried out by various contributors to develop databases for most construction materials and so the designer is well supported in the area.

Terminology

Carbon	=	Carbon dioxide equivalent emissions – a unit of global warming potential corresponding to 1kg of carbon dioxide ($kgCO_2e$)
CapCarb	=	Capital carbon associated with construction of the asset, the equivalent to upfront carbon for buildings (corresponding to lifecycle modules A1–A5). (Also referred to as embodied carbon)
OpCarb	=	Operational carbon associated with ongoing energy use, maintenance, refurbishment or replacement works (corresponding to lifecycle modules B1–B8)
UseCarb	=	In-use carbon associated with use of the asset by the public (corresponding to lifecycle module B9)

Figure 4. Carbon categories.

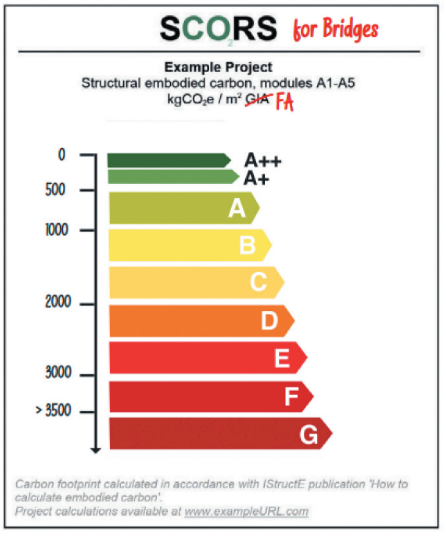


Figure 5. SCORBS ratings.

The work by Archer-Jones and Green is particularly useful as it extends the Structural Carbon Rating System Scheme (SCORS) for buildings with a similar system called Structural Carbon Rating System Scheme for Bridges or "SCORBS" (Figure 5). The rating is calibrated around the available deck areas as an appropriate comparative metric although the authors recognise that the form of bridge type does have an influence on the outputs. Nevertheless, the system provides designers with a clear relative scale for comparison of different schemes. Bridges can be rated against this scale with the intention that designs should seek the lowest possible rating.

3.2 *Calculating sustainability*

3.2.1 *Introduction*

The embedded carbon can be calculated for each module shown in Figure 3. The data that supports the calculations have been developed based on common industry databases. These are well developed for the Product and Construction Process modules but there is much less material available and increasingly less application of the modules as we move through the life cycles.

3.2.2 *Structurally embedded carbon*

Modules A1 to A5 relate to the embedded structural carbon and are the parameters that are most likely to be affected by decisions made by the design engineer. Many data sources are available Orr (2020) being an excellent starting point that provides guidance on the process. The process for calculating the specific embedded carbon content for modules A1 to A5, with advice on modules B, C and D has been set out by Archer-Jones (2023).

The embedded carbon for refurbishment can be calculated using the same processes as described in this document. It should be noted that the need for sophisticated temporary works is often a requirement for major bridge refurbishment. As such, special consideration is required to ensure that the embedded carbon employed in the manufacture and use and dismantling of the temporary works is included in the overall carbon accounting. Care must also be taken to use appropriate material indices such that any embedded carbon for the construction of those materials is not double counted.

3.2.3 *Carbon expended in use*

At present, the majority of the effort in calculating embedded carbon is in the Product and Construction Process Modules. However, for engineers considering the sustainability of existing bridges, the effort is required in the calculation of the operational modules, B1 through B9. There are considerably less data available for these assessments than for the A modules, where there has been, understandably, a greater drive to understand those design parameters which the design engineer can affect directly and thereby make the greatest initial contribution to reducing the amount of embedded carbon.

Wood and Archer-Jones (2023) have studied the B modules for the Clifton Suspension Bridge and set out a clear methodology for the assessment of the embedded carbon during operation. Their work has shown that the OppCarb (refer to Figure 4) for the operational phase (B1-B9) is relatively low per annum at 60 tCO2e. The key drivers here are operational energy costs and staff travel to the bridge to operate the bridge and the tolls. The cost of

Case Study – Clifton Suspension Bridge, UK



This heritage structure has been assessed for the operational carbon consumption which includes for major planned refurbishments such as deck replacement, resurfacing and painting. A notable outcome of this assessment is the was the disproportionate carbon cost of partial closures showing that maintaining traffic during refurbishment will have a significant effect on enhancing the sustainability of the works.

major maintenance over the years has be included based on the frequency of carrying out the works (such as painting, bearing replacement, resurfacing and deck replacement).

This annual carbon cost can be compared with an illustrative notional cost of a replacement structure of exactly the same form (but clearly not envisaged for this iconic structure designed by Brunel!) which would result an embedded carbon cost of 7800 tCO2e. This is a simplistic assessment as there are other parameters that need to be considered such as demolition costs of the old structure and the effects on traffic while the structures are changed. An outline assessment of this has been carried out and the cost of diverting traffic completely during a full bridge closure has been calculated at a carbon expenditure of 840 tCO2e so for an additional three-year closure of the bridge, the carbon costs would be of the order of 2500 tCO2e which needs to be added to the reconstruction and demolition costs. This needs to be assessed for all bridge refurbishments and replacements as part of the true carbon cost comparison.

The scope to reduce operational carbon is very much in the hands of the operator of the bridges. The work reported on Clifton shows the direct engagement of the bridge operator and owner, the Clifton Bridge Trust, and will enable it to set a proactive carbon policy in reviewing key items such as staff travel, the supply of electricity and better planning in the maintenance of components. This exercise is currently underway.

The Rochester Bridge Trust (2024) operates and owns two large crossings of the River Medway in south east England. In 2020 it carried out a major refurbishment of the bridges and calculated the carbon footprint of the project. It sought to offset the carbon through some direct tree planting in a new woodland plantation close to the site where it has direct control over the protection of this additional asset. Carbon offsetting has been used extensively in the past but is not generally considered to be genuinely sustainable as often the carbon creator has not control over the offset asset which means that the long term sustainability of the offset may not deliver the net carbon balance. This normally occurs long after a developer has taken the kudos for a net zero project! However, the Rochester Bridge Trust includes the management of the woodland as part of its total asset and so has protected the ensuing carbon savings.

The Trust has gone further in developing its net zero carbon approach by reviewing its maintenance strategy. Key findings from this are again the need to review all aspects of energy consumption. Staff travel and sequential planning of on-site bridge activities are key drivers here.

3.3 *Deferred carbon – the case of depreciation?*

There are several notable examples of bridges where the construction has been staged from the outset in recognition of the likely need for future expansion. Examples of this include the Auckland harbour bridge in New Zealand and the EJ Whitten bridge in Melbourne Australia. In both these cases the owners recognised that there would be future demand on the structures but that it was uneconomical to build the bridges with their full operational capacity from day one. As a consequence the designs were prepared in contemplation of the additional structure that might be required in the future but that the reduced plan area of the bridge was constructed initially. For both projects, the owners instructed the designers to include provision for the future works such that they could be incorporated with minimal intervention to what would become the existing structure. In both cases the period between the initial construction and that of the widened bridge was in excess of 10 years (over 20 in the case of E.J Whitten). Deferring the cost of building the full asset from day one meant that both bridges were affordable from the outset; in their full guise they were unaffordable. Naturally there is an additional initial construction cost for building in unused capacity from the outset, such as bigger foundations or stronger piers, but the costs for building these anew at a later stage will significantly increase the costs – this would be assessed using a net present value assessment to ensure it was value for money. Auckland Harbour Bridge was a major undertaking at the time of construction in 1960 so the foundations were built to provide additional capacity for a future deck that could be built at a later stage when funds were available. By making early provision in the foundations, the extensions required no costly new foundation work.

The question that arises is should we also discount future carbon against current carbon in the same way that we discount future costs? This question is currently under debate and is

Case Study – E.J Whitten Bridge, Australia



This refurbishment project was highly sustainable and showed a very strong client commitment to future proofing the structure. It was recognised that the major arterial route that crossed the bridge would promote reginal growth and so provision was made to build the foundations with sufficient capacity for additional loading. The site had poor access, so this extra commitment came at only a small incremental cost. Changes to design loadings meant that it was not feasible to construct the new deck from concrete and a lightweight steel box was inserted instead. The additional carbon cost of the new structure was considerably lower than would have arisen had the provisions not been made for future growth, justifying the effort and early commitment.

based around the premise that future construction will have to be more carbon efficient than at present having to general trends of decarbonization in the construction industry.

If we use E.J. Whitten as an example, the table below shows the cost of the original construction both with and without provision for adding an additional bridge deck to the foundations in the future. The carbon costs of the future works are then assessed, again on the basis that provision was or was not made at the time of initial construction.

Not surprisingly, the total carbon cost is significantly higher if provision is not made to incorporate the provision for future works at the time of original construction. However, if we were to achieve year on year savings of 4% in carbon efficiency then after twenty years it would appear that it is slightly more carbon efficient to defer the construction until later and it would be argued that no initial provision should be made or that it is entirely minimal. At 8% there is a large apparent saving in carbon if no provision is made.

This is a controversial point that is based on expectation that such improvement can and will be made if we are to achieve net zero targets by 2050 and so it leaves a conundrum that needs to be answered when we plan the development of new assets. Whether 8% is achievable

Table 1. Embedded Carbon in EJ Whitten with and without early provision.

	Embedded carbon (tCO_2e)		Total discounted carbon over 20 years		
	At first construction	At refurbishment	0%	4%	8%
Case 1: no early provision	6100	3000	9100	7426	6666
Case 2: early provision	7360	608	7968	7629	7475

or whether 4% to 5% is more likely, it is the author's firm opinion that the possibility of future expansion of all assets should be considered at the time of construction and a detailed review of how that would be achieved needs to be made. It should be emphasised here that the bridge was part of a much wider scheme and the alignment of the carriageways were arranged so that widening was into land that was reserved from the outset in between the carriageways. This means that the later works were much simpler and required no additional land take, resulting in significant overall project savings in embedded carbon. It was clear from this brief study that the information for the carbon assessments is not sufficiently mature for such a nuanced assessment and more data and research is required to assist in this important debate.

4 CHALLENGES TO REFURBISHMENT

4.1 *Heritage*

The consideration of the historical value of the structure will be an important feature in the decision on whether to replace or refurbish. These requirements will vary from country to country and depend on the strength of legislation that protects historical structures. In the United Kingdom, there is specific legislation to structures which have been "listed" and included on a register of historic monuments. Listed structures cannot be demolished without the direct approval of Historic England and such permission will only be granted for the higher level listed structures when all efforts to preserve the structure have been shown to be technically impossible by an independent body. Owners have a statuary duty to preserve and maintain such structures.

The justification for protecting historic structures is that the built environment contains a unique and dynamic record of human activity. The view espoused by English Heritage (2008) is that the built environment "has been shaped by people responding to the surroundings they inherit, and embodies the aspirations, skills and investment of successive generations. People value this historic environment as part of their cultural and natural heritage. It reflects the knowledge, beliefs and traditions of diverse communities. It gives distinctiveness, meaning and quality to the places in which we live, providing a sense of continuity and a source of identity. It is a social and economic asset and a resource for learning and enjoyment. Each generation should therefore shape and sustain the historic environment in ways that allow people to use, enjoy and benefit from it, without compromising the ability of future generations to do the same."

There are some very well known landmark structures in the UK that benefit from this protection. Structures such as Tower Bridge and Hammersmith Bridge in London are protected accordingly as national monuments. Hammersmith Bridge is presently closed to vehicular traffic due to defects in the pedestals and fatigue concerns over the deck. The owner has put in place strengthening schemes to restore the bridge back to an enhanced capacity while preserving as much of the original fabric as is possible. Where changes are required because they are life expired, sensitive treatment of the design of the new components is being applied to ensure that the structure is as little changed as possible while still delivering the required safety and durability. The process is still underway at the time of writing of this paper and the costs will be higher than replacing the bridge with a new structure.

Similar sentiments exist world-wide, albeit without the same level of protection. A notable case study is that of Lion's Gate Bridge where the challenge was to replace the deck of this aging suspension bridge.

4.2 *Traffic management*

Interruptions to the smooth operation of traffic across a network have a significant effect on the additional carbon produced. The case study with Clifton provides an interesting comparator of the cost of carbon from diverting traffic away from the bridge compared with the carbon embedded in the works.

It is self-evident that the most successful refurbishment works will be those where the traffic has minimal interruption. It will be difficult to avoid some delay to the traffic and therefore the cost of this impediment to free flow needs to be calculated and factored into the assessment of total carbon produced. The need to keep traffic flowing is likely to impact the programming of the works and so it will be necessary to establish the trade-off between a longer duration of limited interruption as opposed to the shorter duration of greater interruption. The need to apply intelligent engineering in developing innovative refurbishment schemes that do not restrict the traffic should be a worthy challenge for any talented engineer.

Case Study - Lion's Gate Bridge, Canada



This heritage structure opened in 1938 but with a deck design where the details were poorly configured that did not have the durability had the deck replaced and reconfigured to allow heavier vehicles to run on the new deck. The previous structure was life expired. Traffic disruptions were minimized by the innovative use of temporary works which also facilitated the replacement of the worn deck suspenders in a series of overnight operations where a complete section of deck was replaced. The structure is a landmark in Canada and this highly effective refurbishment allowed the preservation of the asset for minimal embedded carbon.

4.3 *Existing condition*

Much of our retrofit work is about keeping existing structures operating particularly where there has been absence of good maintenance or there have been poor design details that have led to a decrease in the capacity of the structure. The case for replacement of such structures can only be argued as being a last resort when there are no other means for enhancing the existing capacity.

The calculation for the embedded carbon in a refurbishment scheme can be determined using the data for modules A1 to A4. The data for A5 (construction installation processes)

may require some additional effort to piece together the enhanced construction activities. It is expected that there will be greater construction effort per tonne of material as the new material has to be fitted to the existing where there will be challenges of access, temporary loading and any reworking associated with unforeseen conditions in the original material. There is limited information on the impact of embedded carbon; it is proposed that in the absence of better information, rates should be increased by 50% to reflect the premium on handling and transport. This should not serve as being excessively penal – the example of Wye Bridge by Flint (1993) shows that the radical strengthening schemes of providing support from a new cable stay system reduced the internal deck stiffening to around 20% of what might otherwise have been achieved through deck stiffening alone.

4.4 *Increasing capacity*

The need for providing additional capacity will provide additional challenges owing to the need to either reconfigure the existing deck space or by adding additional decks alongside or above the existing running services. The expansion of the Gade Valley Viaduct and the West Gate Bridge were able to take advantage of the generous width of the existing structure. However, when there are significant increases in the capacity requirements, it is tempting to simply duplicate the crossing with a new structure alongside the existing. This becomes an expensive option in terms of cost and particularly of carbon because essentially a new independent structural system is being installed.

The primary cost in these instances is the addition of a new foundation. Depending on the form of deck this can add an additional 40% to the carbon cost of the structure and so it is

Case Study – Wye Bridge, UK



This first generation cable stayed bridge (and its grander neighbour, the Severn Bridge) had some serious shortcomings in its capacity, and was also subjected to significant increases in the demands on the structure. The application of some highly innovative engineering resulted in the doubling of the live load capacity for a very small fraction of additional steel tonnage. It was a highly sustainable refurbishment that allowed much heavier vehicles to use the bridge. Dramatic changes were made to the cable support of the bridge, which minimised the need for deck strengthening. Al of the works were carried out while the bridge remained open to traffic further contributing the overall sustainability of the project.

incumbent on the design engineer to examine the capacity of the existing foundations and to identify what additional capacity can be mobilised. The designer is of course helped here because of the observational data on the performance of the structure over its life to date and this, along with some enhanced site investigation, offers the opportunity for re use of the existing foundations. Even if some small additional capacity is required by means of local strengthening of the foundation, the overall carbon saving will be significant.

A particularly impressive example of how this works and can deliver a very carbon efficient refurbishment is the Huey P Long Bridge in the United States. Here there was a significant increase in the cross section of the bridge with minimal extension to the foundations. This was aided by a detailed investigation into the bearing strata of the bridge and a revaluation of the capacity.

4.5 *Programme and cost*

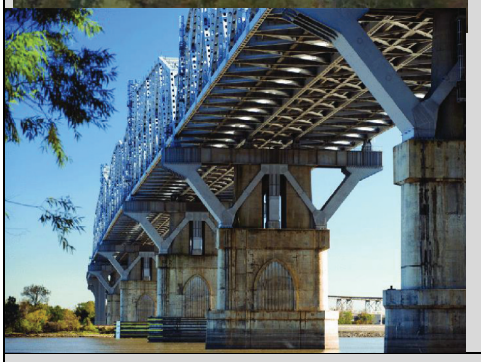
The design solutions for bridge construction are most usually determined on the basis of cost and time for construction. This becomes even more critical in a design and build project whether contractor is carrying the risk and will seek to develop the most efficient design from a cost perspective. Introducing some measure of carbon efficiency in terms of minimising embedded carbon should be an imperative on all projects. There is of course a fairly direct linkage between reduction in the use of materials and the reduction of embedded carbon. However on large structures the use of offsite fabrication at remote sites where construction costs are considerably lower means that this link between carbon and cost is broken. The construction industry and in particular its government funders is beginning to recognise that the reduction in embedded carbon needs to be a central part of the assessment of net value to society. At present in the United Kingdom, the National Highways, the government agency responsible for all major roads in England and Wales, is reviewing its procurement process is and will be including an assessment of social value which include an assessment of the embedded and operational carbon in all projects. At present it is proposed that 10% of the marks for the proposal assessment will be given to a social value rating which includes sustainability. It is the authors view that this proportion should be significantly increased.

This will greatly assist the fair assessment of refurbishment of existing structures. Refurbishment can be a complex operation and may take longer than, say, building a new bridge alongside the existing and then demolishing the existing. Such a replacement methodology can sometimes result in significant reductions in programme time and may not materially affect the traffic flow during the replacement period. However, it does represent a huge and unjustifiable increase in the overall carbon cost. In order to place a positive value of the reductions in embedded carbon, metrics such as those being considered by the National Highways will encourage the ascension of refurbishment over replacement.

There is a similar issue with encouraging private finance operations of bridge maintenance to also seek carbon reductions in the operation of traffic networks. The two examples described earlier in this paper of Clifton and Rochester show how bridge owners can make significant reductions in the net carbon emissions in the maintenance of bridges. To an extent, where the operator is also the owner of a publicly owned asset, there will be a much greater flexibility to drive down operational carbon emissions. However, many larger bridges are in the care of a dedicated asset manager who will be on a commercial setting where carbon optimisation is unlikely to have been a part of the original contractual set up. As willing as the concessionaire may be to make changes that cost slightly more, it is likely to be on a purely financially based reward system, thus a more nuanced approach will be required and it is likely to require some changes to the reward model for the concession.

Case Study - Huey P Long Bridge, USA





Case Study – Huey P Long Bridge was an existing mixed use bridge carrying road and rail. The demand for increased road traffic drove a major strengthening project which was complete in 2013. The designers reviewed the foundation capacity extensively and were able to determine that they could carry the additional weight of the new decks. Some additional strengthening was required of the piers to support the new decks. As a result, the cost and embedded carbon of the refurbishment was less than half that of a new crossing.

The decks were widened to provide three full size lanes each way with hard shoulders and to remove existing pinch points that seriously impeded traffic on the original road decks.

5 CONCLUSIONS

The construction industry is one of the greatest producers of greenhouse gases and it is incumbent on it to reduce this consumption at every opportunity. It is clear from the numerous examples of successful refurbishment of existing assets that need for greater capacity can be provided by some innovative engineering aided by forward planning at the time of construction. From society's perspective such projects will contribute to trying to achieve the goal of

net zero carbon industry. From the engineer's perspective such projects are uniquely challenging and offer some highly rewarding technical challenges.

The industry has developed some very good tools to assess embedded carbon but most of these are aimed at new construction and considerable work is required to ensure that we can use similar tools to justify the clear benefits of rehabilitation of structures. More work is required to collect information on operating processes and the cost of larger refurbishment projects. The work of client organisations such as the Rochester Bridge Trust is to be commended and encouraged.

It is the author's view, as expressed in this paper, that more needs to be done in the procurement process to ensure that embedded carbon is used as a metric for determining the overall efficiency of a project and as a basis for contract award. At present, most construction projects are effectively selected on a cost basis. A means for giving a much higher weighting to the embedded carbon in the development of options or in the development of tender submissions should be a direct requirement of every project.

ACKNOWLEDGEMENTS

The support of several leading industry specialist in sustainability is acknowledged. Particular support has been provided by Cameron Archer-Jones and Alistair Kean for proof reading this paper and for advising on the latest in current practice on achieving net zero bridges.

REFERENCES

Archer-Jones C. 2023. Carbon Calculation Guide for Bridges (in draft) v0.1. *Net Zero Bridges Group*,

Archer-Jones C. and Green, D.R. 2021. Carbon targets for bridges: a proposed SCORS-style rating scheme. *The Structural Engineer*, Volume 99, Issue 10.

Archer-Jones C. and Wood S. 2023. Carbon assessment - operation, maintenance and use of the Clifton Suspension Bridge. *The Structural Engineer*, p12–17 June 2023, Institution of Structural Engineers

Collings, D. 2022. The Carbon Footprint of Bridges *Structural Engineering International*, 32:4,

English Heritage 2008. Conservation Principles, policies and guidance for the sustainable management of the historic environment", www.historicengland.org.uk

Flint A.R. and Firth I.P.T. 1992. Strengthening of Wye Bridge. *Proc Ins. Civ. Engs*. Vol 92 issue 2

Health and Safety Executive 2015. The Construction (Design and Management) Regulations" www.legislation.gov.uk

Mizra S. 2006. Durability and sustainability of infrastructure – a state-of-the-art report, *Can. J. Civ. Eng. 33*: 639-649

Orr J.J. and Gibbons O.P. 2022. How to calculate embodied carbon (2nd edition), *Institution of Structural Engineers*

Orr J.J, Gibbons O.P., Arnold W. 2020. A brief guide to calculating embodied carbon. *The Structural Engineer 98(7)*:22-27

Rochester Bridge Trust 2024. Environment policy and Carbon Reduction targets" www.rbt.org.uk

United Nations Environment Programme 2021. International Good Practice Principles for Sustainable Infrastructure. Nairobi

Yanamandra, S. 2020. Sustainable Infrastructure: An Overview Placing infrastructure in the context of sustainable development. University of Cambridge Institute for Sustainability Leadership

Bridge Maintenance, Safety, Management, Digitalization and Sustainability – Jensen, Frangopol & Schmidt (eds)
© 2024 The Author(s), ISBN 978-1-032-77040-6
Open Access: www.taylorfrancis.com, CC BY-NC-ND 4.0 license

Thermo-mechanistic approach for evaluating service life of bridges and structural concrete

K. Maekawa
Yokohama National University, Yokohama, Japan, The University of Tokyo, Tokyo, Japan

T. Ishida
The University of Tokyo, Tokyo, Japan

ABSTRACT: To ensure the preventive maintenance of bridges, it is essential to assess both their current safety status and their remaining service life. To address this engineering challenge, a comprehensive approach that combines expertise in structural mechanics and thermodynamic materials science is proposed. This approach has been verified and validated across various scenarios as: (1) RC bridge decks under the high cycle traffic, (2) Long-term cracking and deflection in PC viaducts and pre-tensioned girders, (3) Remaining capacity of RC beams damaged by fire, (4) Ionic equilibrium and balance linked with steel corrosion, and (5) Remaining performance of rehabilitated bridges affected by significant earthquakes.

1 INTRODUCION

1.1 *Objective*

The assessment of the remaining lifespan of bridges in service is crucial for the effective management of road and highway infrastructures. This includes budget allocation, inspection programs, and technical training for engineers. There are two ways to meet the challenge. One approach involves a statistical analysis based on past records, data, and experiences from bridge inspection and monitoring, as well as the achieved serviceability and safety. Artificial intelligence technology (AI) is considered a promising tool for this purpose. Another method is behavioral simulation, which relies on the fundamentals of science and modeling of materials and structural members. This simulation begins with the current situation known from inspections. The first approach assumes that the future is an extension of the past, necessitating a substantial amount of reliable data. However, obtaining data related to the quality of construction is generally challenging, and the reliability of maintenance data cannot always be verified by AI.

On the other hand, the second approach relies on the soundness of the modeling and the use of appropriate indices to reflect the status. Through this method, we can assess the impact of construction quality, as it influences the current situations of bridges. Thus, the combination of these two approaches is considered to compensate for each other's strengths and weaknesses, and employing multiple methods may enhance overall reliability. Figure 1 illustrates the correlation between the first and second approaches across numerous bridges, including Tokyo Metropolis Highway Line #5 (Furukawa et al. 2019). Generally, the risk score, based on statistical survival analysis with maintenance data from the past 50 years, aligns with the remaining fatigue life of RC bridge decks computationally simulated with the current crack locations in concrete. This allows us to identify bridges that deviate from the correlation line. In the management of a vast amount of infrastructure, this approach can serve as a screening tool to identify problematic bridges that require careful examination and monitoring.

DOI: 10.1201/9781003483755-6

This paper presents the recent application of multi-scale, multi-chemo-physical, and mechanistic modeling of structural concrete to the life assessment of existing bridges in alignment with infrastructure management.

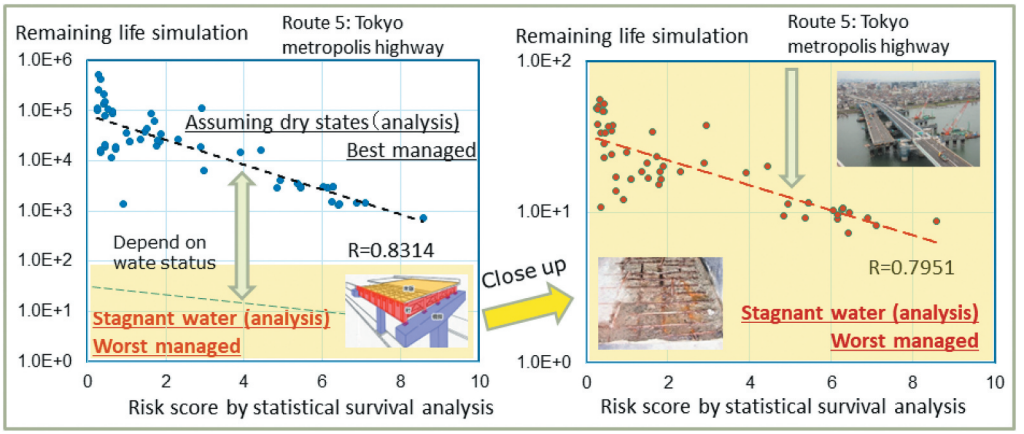


Figure 1. Combined statistical and scientific approaches to assess the remaining life of RC bridge decks in service under an estimated future large vehicle traffics.

1.2 *Electro-chemo-hygral and mechanistic multi-phase platform*

The evaluation of the service life of bridges requires a multifaceted understanding of 1) nonlinear structural mechanics, encompassing cracking and yielding of constituent materials; 2) the varying properties of solids, including erosion and aging; 3) the physical chemistry of substances and their transport and 4) the electric field within water in structural concrete. To address these complexities, referential volumes (REV) of different sizes are employed, each defining specific

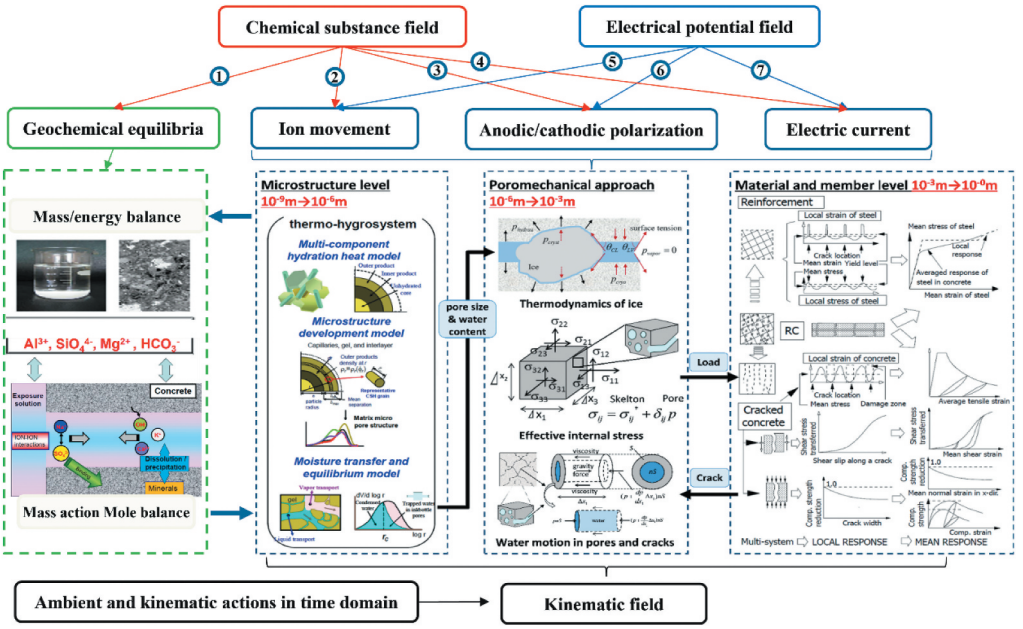


Figure 2. Electro-chemo-hygral and mechanistic multi-phase platform.

aspects of this multidisciplinary knowledge. For systematic utilization, a multi-scale view becomes essential for integration. The authors have developed a platform named *DuCOM-COM3* (dual concrete model) as a "dynamic library" of structural concrete (Maekawa et al. 2004,2008) applicable from the beginning of construction to the end of service life, as shown in Figure 2. Treating concrete cracking is crucial for evaluating the lifespan under ambient and mechanical actions. In reality, multi-directional cracking occurs due to ambient drying and wetting actions, as well as the complexity of applied loads during service, such as daily traffic and earthquakes as accidentals. The authors utilize REV with non-orthogonal multi-directional cracking, originally developed for the seismic analysis of reinforced concrete (RC), as shown in Figure 3.

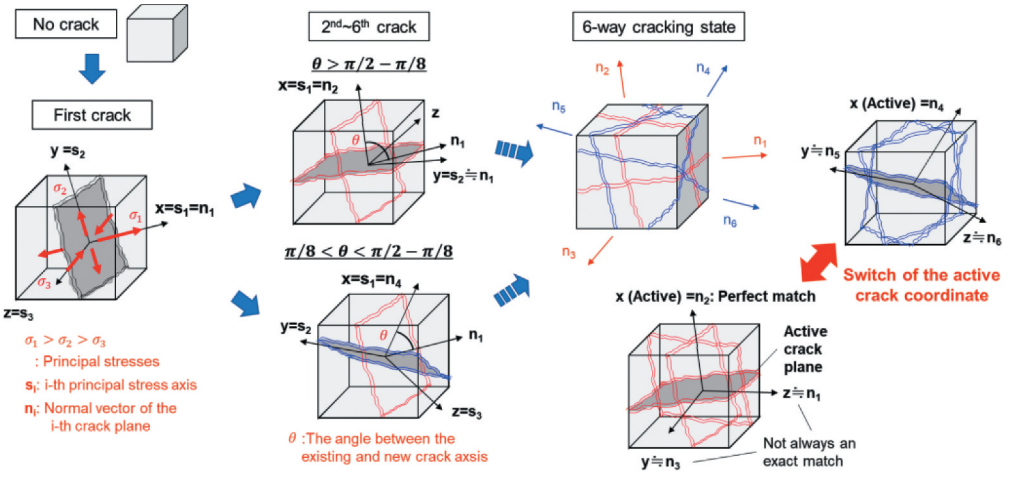


Figure 3. Referential volume of multi-directional cracking where stresses develop, and several substances are kept and in motion.

1.3 *Micro-meso-microscopic multi-scale platform*

As shown in Figure 4, substances related to durability may be contained in crack spaces, the orientations of which are described in Figure 3. These substances may be in motion under their partial pressure gradients. Within the multiphase platform, water with viscosity is present. Notably, the water pressure can rise when a crack rapidly closes, reaching the water in capillary pores. Additionally, alkali-silica reaction (ASR) and corrosion gels originating from aggregates, embedded steel, and reinforcing bars can be present. The crack space serves as a pathway for rapid migration and may influence the pressure, leading to further cracking.

This system has been successfully applied to pressurized gas and frozen ice (Gong et al. 2019) as well. The volume of crack spaces dynamically changes due to external forces, resulting in pressure that can contribute to the deterioration and aging of structural concrete with viods. Therefore, these meso-scale crack spaces play an extremely important role in integrating knowledge of structural mechanisms (macro-scale) and material sciences on the REV of micro-size (Maekawa et al. 2008, Wang et al. 2021 & 2022). The authors employ this meso-scale system for the evaluation of lifetime performance.

2 FATIGUE LIFE ASSESSMENT OF RC BRIDGE DECK

The direct stress-strain-path integral modeling has been commonly employed in the dynamic earthquake analysis of structural concrete, particularly under conditions of high nonlinearity but low cycles. Subsequently, this approach was extended to fatigue behavioral simulation,

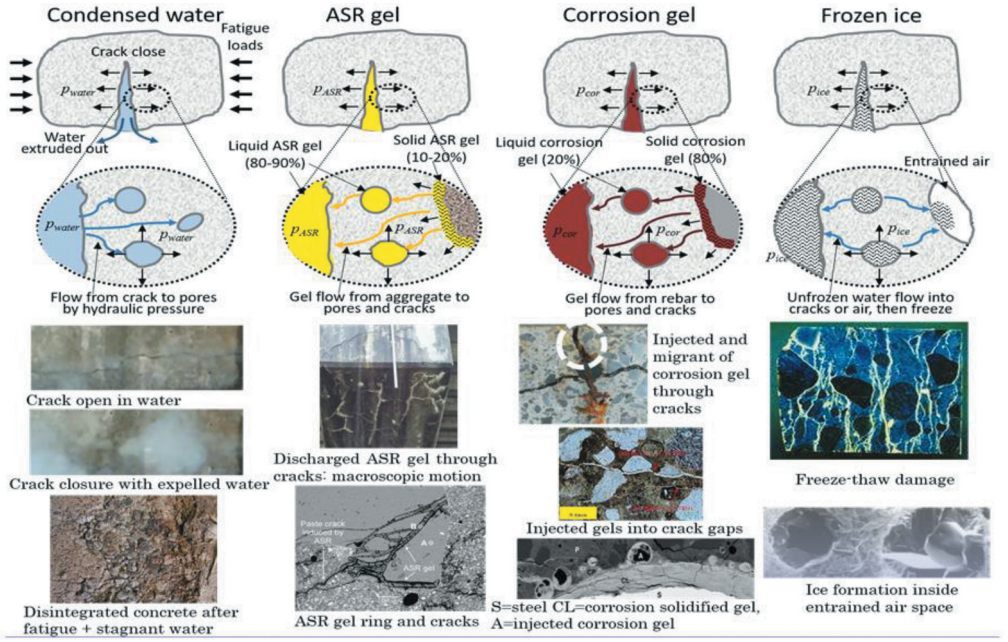


Figure 4. Meso-scale events related to durability and serviceability performance.

focusing on lower nonlinearity but higher cycles of loading, starting around the year of 2000. The extension became feasible through the enhancement of constitutive modeling, considering time-dependency and the accumulation of damages even under small amplitudes of stress and strains (Maekawa et al. 2006). Simultaneously, a high-speed computation algorithm was developed to address the highly cyclic repetition of loads, and successful experimental verification and validation were achieved. In particular, fatigue life simulation was examined using RC bridge deck slabs under moving wheel-type loading (Maeshima et al. 2014), as illustrated in Figure 5. Notably, moving traffic loads significantly deteriorate RC deck slabs due to the larger amplitude of shear along cracks and sections compared to fixed-point loading (Maekawa et al. 2006). This behavioral simulation was further extended to scenarios involving stagnant water (unsuccessful waterproofing) that may be set in motion by rising water pressure. The interaction of water kinetics with porous solids accelerates the damage to structural concrete, leading to a tremendously shortened service life. This mechanism is analogous to the liquefaction of saturated foundations.

This behavioral simulation was conducted using full-scale finite elements of a real bridge in service for about 50 years (see Figure 5), since the fatigue life of the deck slabs is also influenced by the boundary conditions with connected girders (Ishida et al. 2023). As mentioned earlier, the wet condition with stagnant water significantly impacts the fatigue life of slabs under moving loads. Hence, several ambient cases of wet and dry conditions were examined. For validation of the program *DuCOM-COM3*, inspection and monitoring data from the reference bridge were utilized as both ambient and structural boundary conditions, resulting in the evolution of damage, as illustrated in Figure 5. The computed loading cycles leading to deck failure were then converted to a service lifespan of 22 years, while the actual lifespan was 25 years, coinciding with the occurrence of bridge deck deterioration accompanied by graveling.

3 LONG-TERM SERVICEABILITY ASSESSMENT AT NORMAL TIMES

Although no corrosion of reinforcing bars or cracking/erosion by ASR is found, some bridges and viaducts exhibit excessive deflection compared to the design expectations over several decades (Wichukreangkrai et al. 2008). In such cases, it is crucial to assess

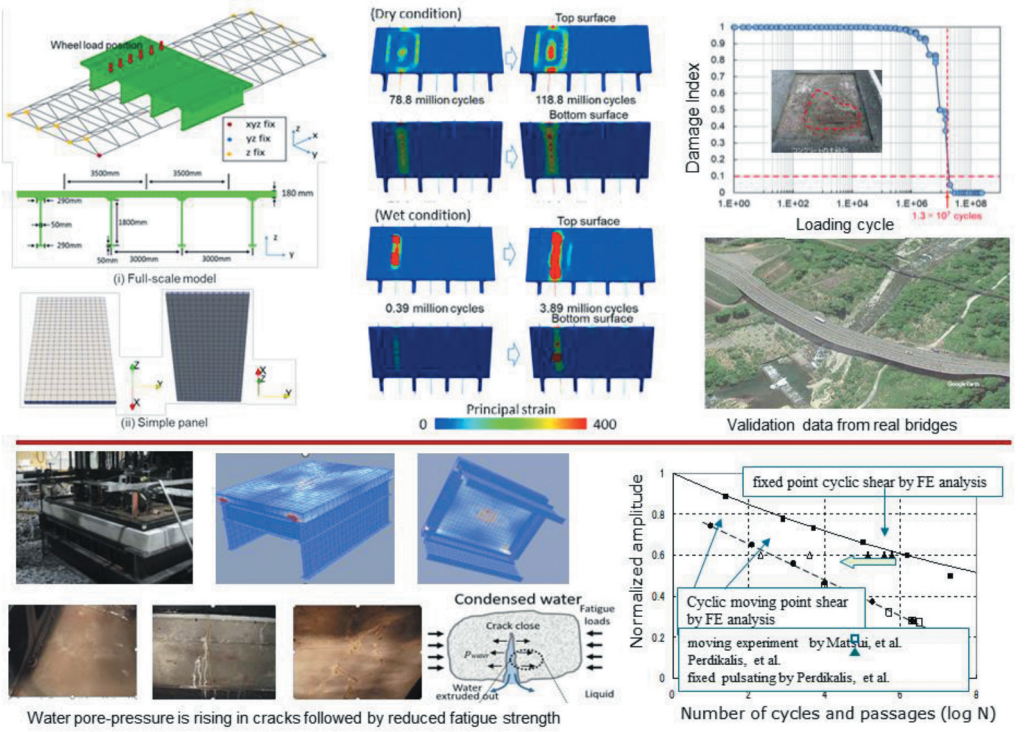


Figure 5. Fatigue life of RC bridge decks with and without stagnant water on the RC slabs.

the current safety level and consider possible future scenarios to prepare for potential risks. The multi-scale, multi-chemo-physics behavioral simulation was applied to long-span prestressed concrete hollow-type viaducts experiencing excessive deflection (Ohno et al. 2012), as shown in Figure 6.

Several years after the completion of these bridges, their deflections generally align with the estimates provided by design formulas. However, real deflections continue to increase and often surpass the initial design estimates. This excessive deflection, without noticeable damages to the concrete, is accurately reproduced in computational models and typically corresponds to the observed reality (Ohno et al. 2012). The substantial deflection over the service life is explained by locally different moisture contents within the structural concrete. The moisture state quickly equilibrates with ambient humidity if the thickness of webs and flanges is small, but it takes a longer time to achieve thermodynamic moisture equilibrium for larger-sized webs and flanges. This difference is closely tied to the size effect on deflection. The multi-scale platform can systematically handle these nonlinearities and provide a comprehensive understanding of future possible scenarios as an integrated knowledge of material sciences and structural mechanics.

We also observe excessive deflection in shorter span PC girders and viaducts, as illustrated in the bottom part of Figure 6 (Yoshino et al. 2023). Vertical gaps exist at the extreme edges of the bridges, between the pavement and the ground, as well as deflection at the span center. In computational models, both displacements at the center and edge are reproduced through the shrinkage of structural concrete. Deflections caused solely by ambient actions without loads and those induced by design loads alone are calculated. It is crucial to note that the deflection resulting from the combined influence of ambient and mechanical actions is greater than the simple summation of those caused by a sole action. This coupling nonlinearity is quite similar to the one of concrete material known as Pickett effect (1942). This is automatically considered without assuming the material parameters for creep and shrinkage.

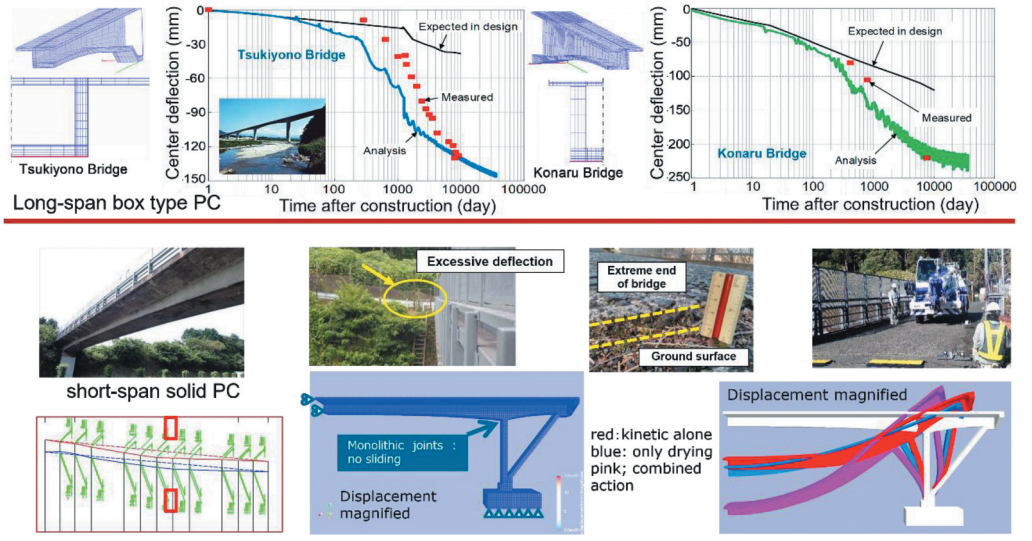


Figure 6. Excessive deflection of long and short span prestressed concrete viaducts.

The behavioral simulation was employed to investigate the cracking of pre-tensioning girders, as illustrated in Figure 7. It has been observed that cracking along the axis of pre-tensioning girders occurs long after production. Various potential causes, such as Alkali-Silica Reaction (ASR) and corrosion, were estimated, but the assessments were qualitative, lacking quantitative conclusions and waiting for the quantitative evaluation in order to evaluate the safety under the estimated scenario. The monitoring of emerging stresses in concrete computations indicates the possibility of cracking with the developed tensile strength of concrete (Tsuchiya et al. 2022). Similar to the case of long-span viaducts, local stresses around the surface of members and those at the core center vary repeatedly. The system records the accumulation of small damages estimated by

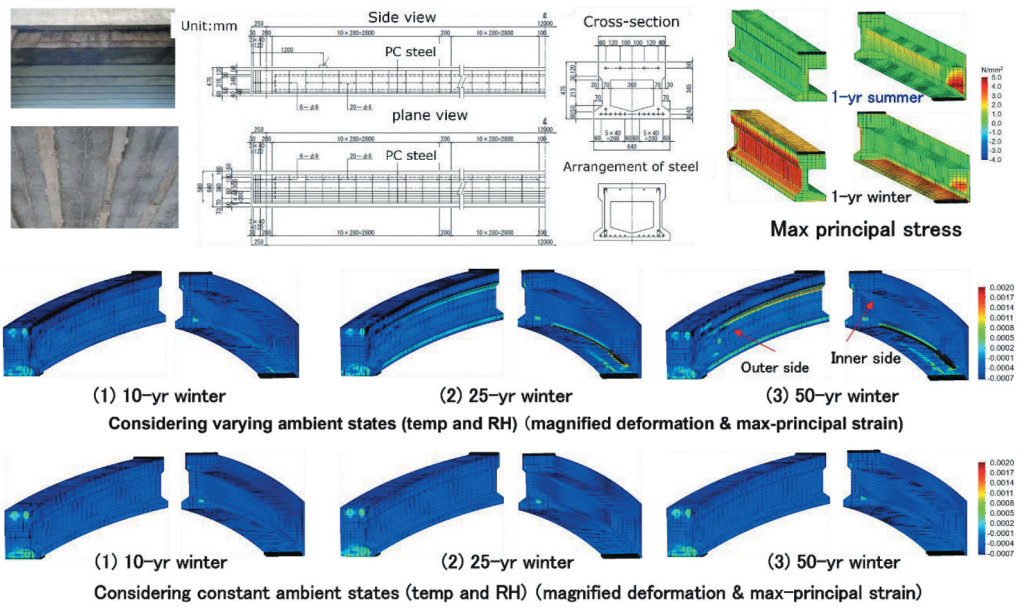


Figure 7. Cracking along the pre-tensioning girders long after construction.

the constitutive modeling (Maekawa et al. 2008). This new finding is reinforced by another trial simulation conducted under constant temperature and relative humidity. Under these fictitious ambient conditions, which do not promote cyclic stress paths, no cracking is reported. It can be inferred that varying ambient conditions are indispensable for long-term performance evaluation. Yearly averaged conditions alone may not capture the intricacies of the system effectively.

4 RESTORATION AND RESILIENCE AS EMERGENCY MANAGEMENT

4.1 *Damaged bridges after earthquake*

As for the crisis management of bridges, quick restoration of bridges and infrastructures damaged by earthquake is critical for resilience. Especially in urban areas, it is generally tough to have new reconstruction. For meeting the challenge at accidental events, we need a technology to trance and follow up collapsing processes beyond the design limit states on structural global safety.

Figure 8 illustrates an instance of damaged bridge abutments in railway infrastructures (Nishimura et al. 2024). This aging structure, designed over 45 years ago, had its seismic performance assessed as inadequate. Unfortunately, a major earthquake struck the abutment before the strengthening work could be carried out. One critical issue was the sinking of the column, leading to an excessive inclination of the rail track, as depicted in Figure 8. In fact, a significantly high compressive force was applied to the problematic column. To estimate the lift-up forces using hydraulic jacks and to examine the restored structure, it is imperative to computationally recreate the damage scenarios. This analytical aspect distinguishes the process from new construction, focusing solely on checking the limit states.

Figure 8 presents the actual lift-up force and its corresponding computational representation. At the onset of the lift-up operations, a notable stiffness was encountered and accurately replicated in the computation, despite the structural members already being damaged. It is crucial to note that even in the presence of pre-existing damage, structural members can still exhibit substantial tangential stiffness when the loading direction abruptly changes. This phenomenon is akin to pre-stressed cable trusses, where tensioned wires display high compressive tangential stiffness. The restoring force can be reasonably assessed to elevate the slabs to their original position. This assessment is critical to estimate how many jacks are needed for quick recovery. At the same time, some cracking and partial yielding may potentially occur. Thus, the evaluation of safety performance and serviceability after the crisis loads must consider the entire process of collapse beyond ultimate limit states and restoration.

Behavioral simulation of collapsing processes must account for extreme scenarios occurring at the meso-scale volume, where the cementing system linking sand and gravel particles is lost, as depicted in Figure 9. This situation cannot be accurately represented by reinforced concrete constitutive modeling, regardless of how many cracks are considered. Specifically, the strong anisotropy of cracked concrete is diminished to an isotropic granular assembly, wherein confinement critically keeps the remaining volumetric stiffness as well. In addressing this, we have applied the RC-graveling transition model (Yamanoi et al. 2020), which has been developed and successfully employed in the fatigue life evaluation of bridge slabs experiencing graveling in the presence of water (Maekawa et al. 2006). It is noteworthy that the shear resistance of graveling surpasses that of reinforced concrete under higher confinement. For bridge maintenance technology, confined disciplines may not exert a strong driving force.

4.2 *Damaged bridge after fire*

Road and railway bridges annually face fire incidents resulting from traffic accidents. In response, bridge managers must promptly formulate a restoration plan to facilitate the swift reopening of traffic. For both current and future evaluations of the performance of fire-damaged structural concrete, it is essential to consistently consider both microscopic and macroscopic events.

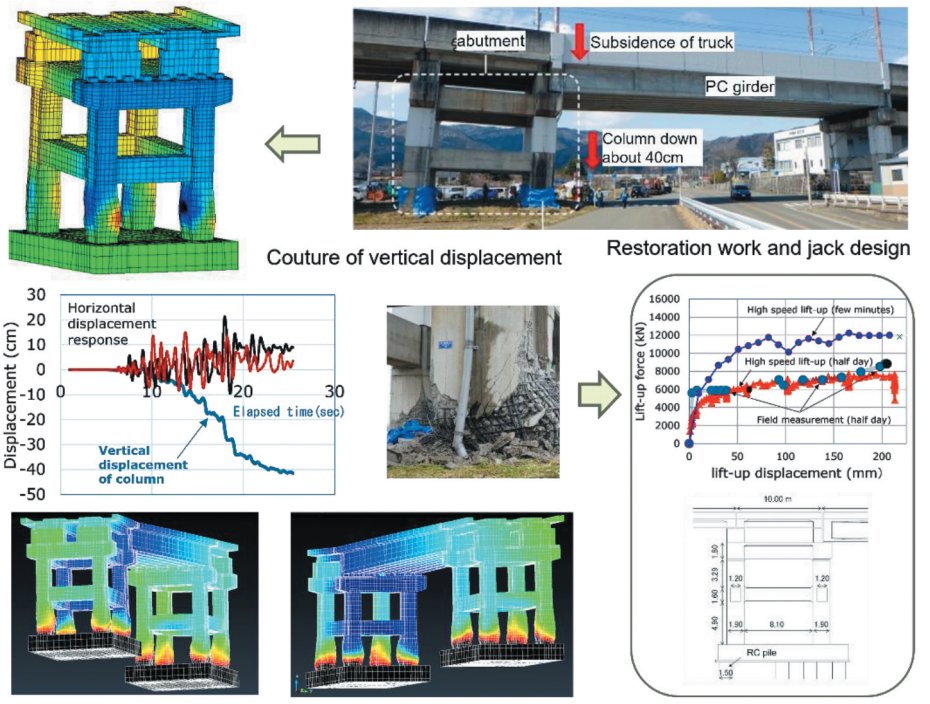


Figure 8. Restoration of railway bridges and abutments after great earthquake.

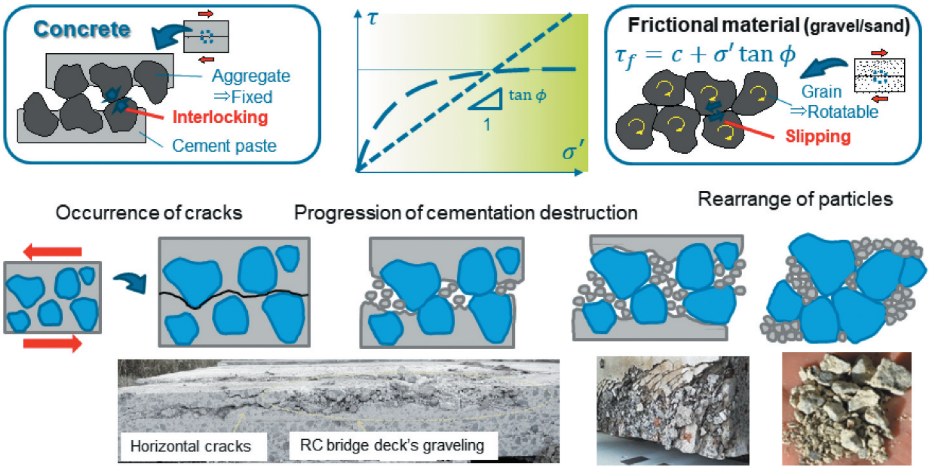


Figure 9. Graveling of concrete under large shear and erosion.

High temperatures can deteriorate crystallized solids, leading to changes in the micro-pore spaces lined with meso-scale mechanisms within the concrete composite. The elevated temperature can cause the release of chemically combined water in a gaseous phase, resulting in a rise in pore pressure. This phenomenon may occasionally lead to spalling of the surface concrete, followed by a deterioration in the axial capacity at the macro-scale.

Even after micro and macro-scale deterioration, a self-healing mechanism persists, wherein moisture and carbon dioxide in the air act as substances to fill up the void spaces, as illustrated in Figure 10. The recovery of the macroscopic performances and its scenario are welcome

especially for long-term performances even after fire accidents. Therefore, a multi-phase and multi-chemo-physics approach is deemed most suitable for this case (Iwama et al. 2020).

Figure 10 summarizes the chemical processes of non-organic substances with water and carbon dioxide under high-temperature conditions during a fire. Special attention is given to spalling in high-strength concrete concerning the risk assessment of macroscopic structural events. High-strength concrete, having fewer micro-pore spaces and lower permeability, can lead to vapor pressure confined inside the concrete. If this pressure exceeds the tensile strength, explosive spalling may occur. The interconnected events, evolving across varying sizes, are illustrated in Figure 1.

Figure 10 illustrates post-fired reinforced concrete beams in flexure and shear, clearly estimating the change in failure mode (Iwama et al. 2020). Fire action results in a loss of member capacity but an increase in ductility with higher fracture energy. In both reality and digital simulation, numerous smaller cracks near the surface of members are generated, interlinked with each other. Subsequently, discrete crack propagation is halted by the dispersed multi-directional cracking formed beforehand by fire. As a result, macroscopic performances are enhanced in terms of overall fracture energy.

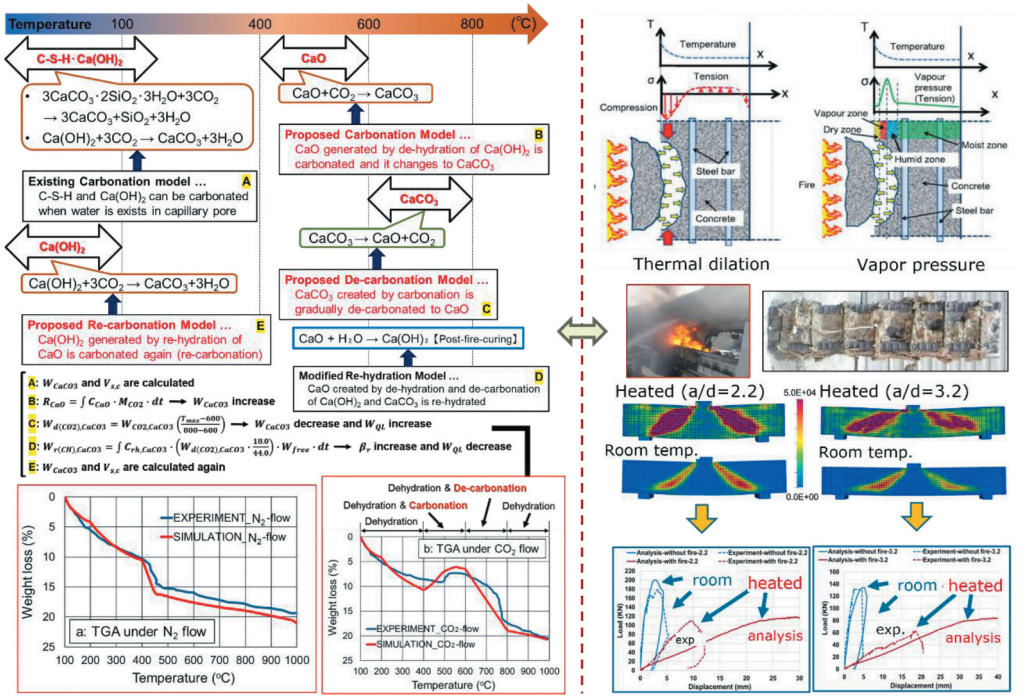


Figure 10. Micro and macroscopic modeling interlinked at high temperature of fire accident.

4.3 *Precast construction and joints*

The precast system facilitates both swift construction under normal circumstances and rapid restoration during emergencies, contributing to resilience. Figure 11 illustrates the reuse of existing structural members for newly constructed ones immediately following the 2011 earthquake in Tohoku, Japan. The intact members were severed from damaged bridges and transported to the new site to expedite transportation recovery. The overall bridges, comprising both old and new members, underwent examination in terms of the seismic performance and serviceability. Additionally, the precast system is currently underway for newly designed and constructed bridges as shown in Figure 11. The technical intricacies of precast systems stem from the evaluation of mechanical joint behaviors and their modeling within a computational framework. Figure 12 illustrates an example of RC joint through which reinforcing bars penetrate (Zewdie et al. 2022).

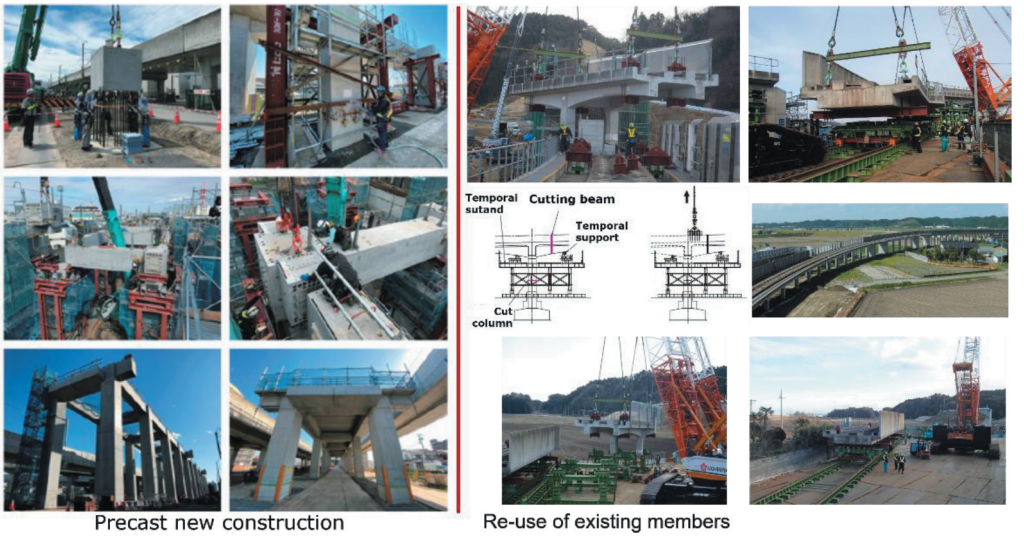


Figure 11. Precast construction: reuse of members after disaster.

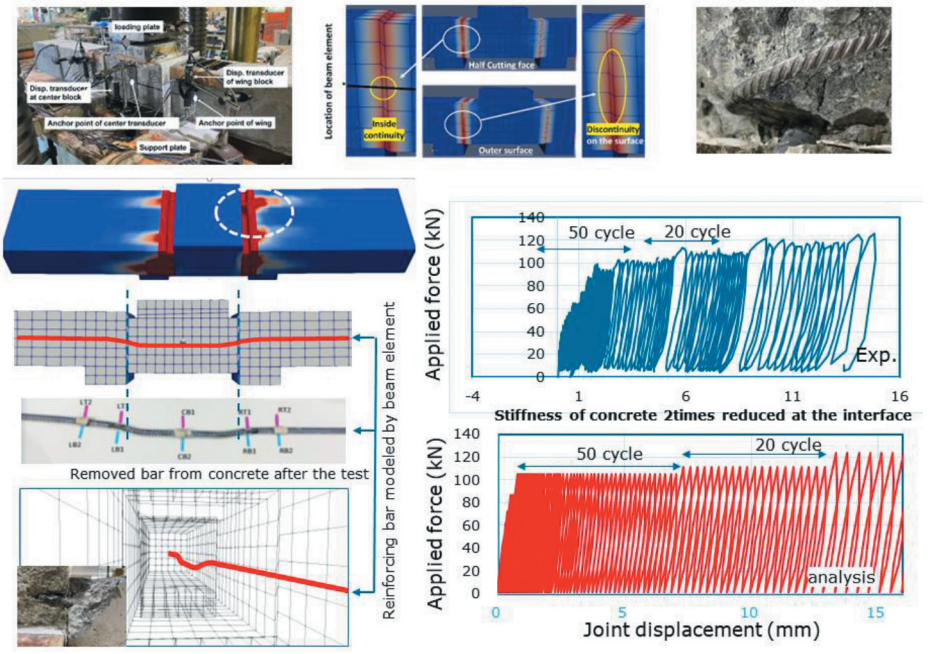


Figure 12. RC Joint kinetics along joint planes and the impact to surrounding structural members.

Joint dynamics have been represented by interface elements in FEM and placed at the junction planes of different members since 1980s. Generally, it fairly works if a pair of connected members are massive and/or well reinforced around the connection devices. In more general cases such as small concrete cover and lower confinement around the highly stressed areas, joint elements with finite volume becomes available with no reduced deformational field as shown in Figure 12. Especially, so called bond cracking along reinforcing bars can be reproduced in computation where the 3D stress field is reproduced by bearing force from the bent portion of reinforcing bars.

5 CORROSION RELATED MANAGEMENT

5.1 *Safety performance assessment of corroded members*

The upper part of Figure 13 displays the finite elements for RC with rebar corrosion. In this configuration, straight tensile rebars without end-hooks and with full anchorage of 90° hooks were positioned (Han et al. 2020 & 2022). Mass loss data from an accelerated corrosion test were utilized for validation (Maekawa et al. 2008). The load was applied at the midspan of the beam, considering uniform corrosion along reinforcing bars and incorporating a three-times volumetric expansion for corrosion products. A comparison between the tests and analyses is presented (Furukawa et al. 2019). As corrosion increases, stiffness and shear strength decrease due to splitting crack, accurately simulated. The FE model also captures the behavior of the corroded (NH) specimens, revealing an increased shear strength compared to no corrosion case. Beyond a corrosion degree of 3%, stiffness and shear strength gradually decrease, consistent with the prediction. The analysis highlights the formation of a diagonal compressive strut like arch similar to the past experiences.

The long-term shear behavior of RC members under sustained loads was examined. Since the impact of reinforcing bar corrosion is highly time-dependent, realistic timescales of the natural environment is applied. The bottom part of Figure 13 illustrates the model used for the long-term analysis, with a specific focus on the shear span-to-depth ratio. Three different current densities (15, 75, and 150 μA/cm^2) were considered for the corrosion simulations. The critical sustained load level causing delayed shear failure decreases as the shear span-to-depth ratio increases. Diagonal shear cracks are observed to initiate from flexural cracks. It is important to note that gradual corrosion does not lead to delayed shear failure. The critical time and corrosion degree at which shear failure takes place decreases with faster corrosion rates. Additionally, shear span-to-depth ratio amplifies the detrimental effects of corrosion on the long-term actions.

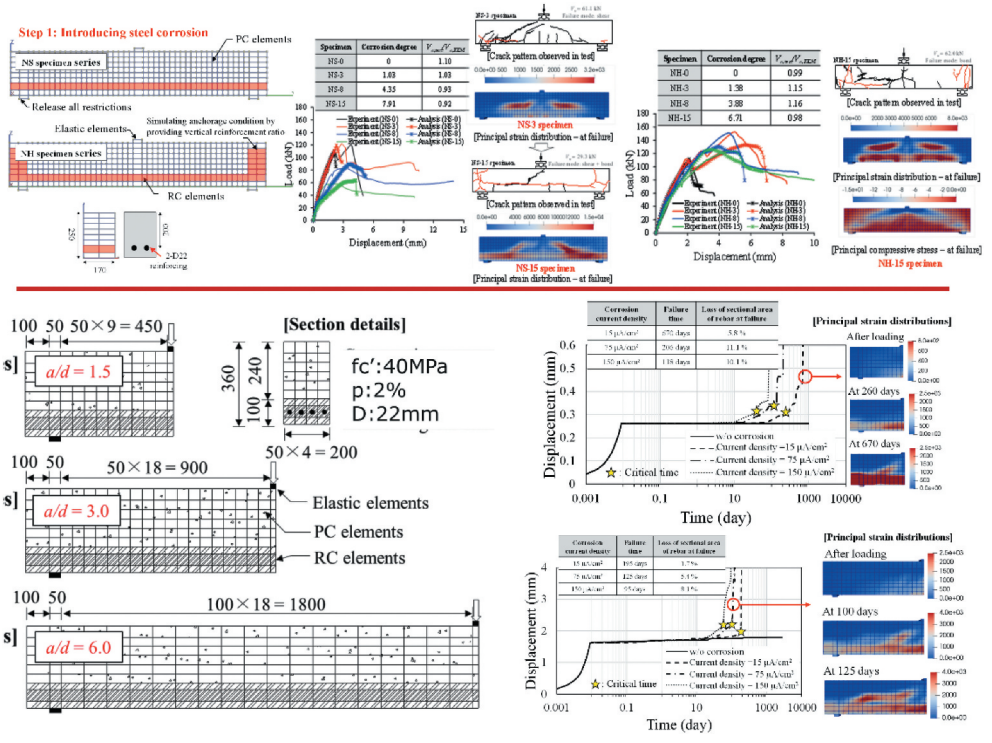


Figure 13. Corrosion impact to RC shear capacity under short and long-term loading.

5.2 *Electro-ionic kinetics for corrosion risk assessment*

Steel corrosion not only brings about varying macroscopic performances of structural concrete but also alters the ionic concentration in micro-pores and their equilibrium with solids of cement hydrates because steel corrosion is an electrochemical reaction. To assess long-term corrosion in conjunction with dynamic ionic equilibrium, the electric potential field must be integrated with the framework, as illustrated in Figure 2 and Figure 14 (Wang et al. 2022 & 2023). Here, the Nernst-Plank equations and polarization modeling for cathodic and anodic reactions are concurrently solved alongside the governing equation of solid mechanics. Consequently, reinforcing bars are conceptualized as smeared within the referential volume, enabling consistent utilization of smeared crack modeling.

With this scheme, ionic motions can be estimated and equilibrated minerals of cement hydrates are explicitly obtained. Figure 14 indicates dynamically varying ionic concentration of calcium accompanying the corrosion of reinforcing bars in tandem. At the anodic pole, much calcium ion is supplied by dissolution of portlandite which may cause erosion of concrete composites under CO_2 environment. This situation is produced when we apply the cathodic protection. Thus, the entire fields with mutual interaction will be the basis of long-term performance evaluation.

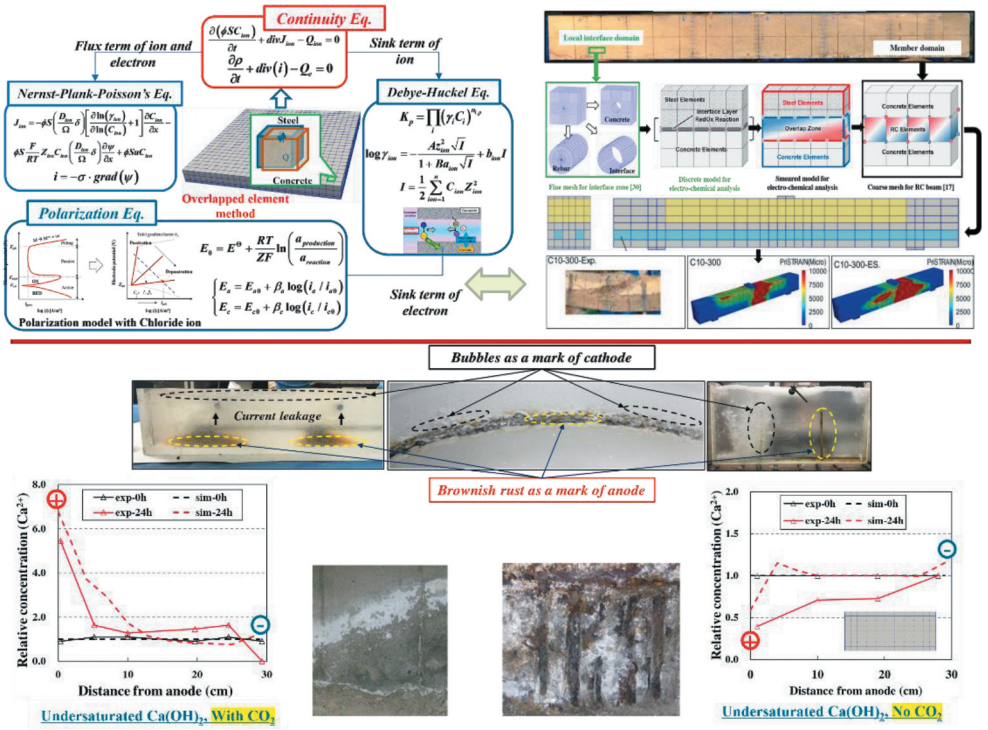


Figure 14. Electric potential field linked with chemo-physical and mechanical events in multi-scale referential volumes.

6 CONCLUSION

Chemo-physical and mechanical modeling on a multi-scale referential volume is presented for the evaluation of remaining lifespan of bridges within the framework of performance-based design and maintenance. Recent applications of the integrated system to the performance assessment of brides in service was presented for verification and validation. The risk of failure and modes of deformation of structural concrete are reasonably evaluated, but the integration of electric fields with thermodynamics of solids and multi-ions is just beginning. Upgrading

reliability is required and applicability ranges must be clarified. Thus, behavioral monitoring and inspection are indispensable. In other words, presented multi-scale modeling may serve engineers as a guide to seek for more appropriate parameters. Coupled deep experiences, practice and solid scientific knowledges are crucial for further progress.

REFERENCES

Furukawa, T. & Ishida, T. & Fathalla, E. & Fang, J. 2019. A proposal of data driven maintenance of RC decks focusing on deterioration mechanism. EASEC16: *Proceedings of The 16th East Asian-Pacific Conference on Structural Engineering and Construction.* Springer.

Gong,F. & Maekawa, K. 2019. Proposal of poro-mechanical coupling among ASR, corrosion and frost action for damage assessment of structural concrete with water. *Engineering Structures*. 188.

Han, S.J. & Lee, D. & Yi, S.T. & Kim, K.S. 2020. Experimental shear tests of reinforced concrete beams with corroded longitudinal reinforcement. *Structural Concrete*. 21(5). 1763–1776.

Han, S.J. & Ishida, T. & Tsuchiya, S. 2022. Multiscale numerical simulations of static shear and long-term behavior of RC members considering corrosion of reinforcing bars. *Journal of Advanced Concrete Technology*. 20(7). 492–506.

Ishida, T. & Kurihara, R. &, Takahashi, Sun, J.H. & Tsuchiya, Si. (2023). Advancing concrete structures design and maintenance through multi-scale and multi-physics modeling-based digital twin technology. *11th Int. Conf. on Fracture Mechanics of Concrete and Concrete Structures*.

Iwama, K. & Higuchi, K. & Maekawa, K. 2020. Thermo-mechanistic multi-scale modeling of structural concrete at high temperature. *J. of Advanced Concrete Technology.*18(5). 272–93.

Maekawa, K. & Fukuura, N. 2014. Nonlinear modeling of 3D structural reinforced concrete and seismic performance. *Infrastructure Systems for Nuclear Energy* John Wiley & Sons.

Maekawa, K. & Kishi, T. & Ishida, T. 2008. *Multiscale Modeling of Structural Concrete*. Taylor & Francis.

Maekawa, K. & Toongoenthong, K. & Gebreyouhannes, E. & Kishi, T. 2006. Direct path-integral scheme for fatigue simulation of reinforced concrete in shear. *Journal of Advanced Concrete Technology*. 4(1). 159–177.

Maekawa, K. & Pimanmas, A. & Okamura, H. 2004. *Nonlinear Mechanics of Reinforced Concrete*. Taylor & Francis.

Maeshima, T. & Koda, Y. & Tsuchiya, S. & Iwaki, I. 2014. Influenced of corrosion of rebars caused by chloride induced deterioration of fatigue resistance in RC road bridge deck. Journal of Japan Society of Civil Engineers. 70 (2).

Nishimura, S. & Onodera, S. & Tatsuki, S. & Maekawa, K. 2024. Damage analysis of RC railway abutment caused by Fukushima-Oki Earthquake. Proc. of Japan Concrete Institute, 46.

Ohno, M. & Chijiwa, N. & Suryanto, B. & Maekawa, K. 2012. An investigation into the long-term excessive deflection of PC viaducts by using 3D multi-scale integrated analysis, *Journal of Advanced Concrete Technology*. 10. 47–58.

Pickett, G. 1942. The effect of change in moisture-content on the creep of concrete under a sustained load, Journal of the ACI. 13 (4).

Tsuchiya, S. & Watanabe, T. & Saito, S. & Maki, T. & Ishida, T. 2022. Prediction of longitudinal cracks and evaluation of load carrying capacity for PC girders using multi-scale analysis. *Journal of Japan Society of Civil Engineers*. Ser. E2 (78)1.

Wang, Z. & Maekawa, K. & Gong, F. 2023. Space averaging of electric field accompanying corrosion of reinforcement and its verification by pseudo-concrete, *Journal of Advanced Concrete Technology*. 21(1). 25–41.

Wang, Z. & Maekawa, K. & Takeda, H. & Gong, F. 2022. Multi-ion kinetics in pseudo-concrete electrolyte associated with macro-cell corrosion, *Cement and Concrete Composites*. 133.104690.

Wang, Z. & Maekawa, K. 2021. Lifetime assessment of structural concrete: multi-scale integrated hygro-thermal-chemo-electrical-mechanistic approach and statistical evaluation. Structures and Infrastructure Engineering.

Wichukreangkrai, E. & Tsuchida, K. & Watanabe, Y. 2008. Long-term deflection monitoring of a cantilever prestresses concrete bridge with intermediate hinges over 25 years. *Creep, Shrinkage and Durability Mechanics of Concrete and Concrete Structures*. CRC Press.

Yoshino, M. & Kikuchi, S. & Wakatuki, K. & Chijiwa, N. 2023. Cause estimation and safety assessment of Tomei Expressway bridge with excessive deflection. *J. of Structural Eng*. 69A.

Yamanoi, Y. & Maekawa, K. 2020. Shear bifurcation and gravelization of low-strength concrete, *Journal of Advanced Concrete Technology*. 18(12). 767–777.

Zewdie, E. & Soltani, M. & Maekawa, K. 2022. Extended multi-directional crack model applied to the RC precast joint interface with shear dowel, *J.of Advanced Concrete Technology*. 20(8).

Bridge Maintenance, Safety, Management, Digitalization and Sustainability – Jensen, Frangopol & Schmidt (eds)
© 2024 The Author(s), ISBN 978-1-032-77040-6
Open Access: www.taylorfrancis.com, CC BY-NC-ND 4.0 license

From empirical and subjective O&M to statistical and objective asset management

S.C. Nørager
Danish Road Directorate, Copenhagen, Denmark

ABSTRACT: This paper delves into the Danish Road Directorate's (DRD) vision for a modernised asset management model. DRD manages the Danish national road network comprising 3800 km of road and 2400 structures and has over the past 40 years developed well-defined asset management process and solutions. Due to the technical debt in its IT-infrastructure, DRD is currently implementing new software solutions which have opened up for the development of a new asset management model. DRD's vision for the new asset management emphasises uniformity across assets and introduces functions like cross-asset optimisation and assessment of sub-optimum strategies. A governance framework ensures data quality and performance benchmarks, while automation plays a pivotal role in objective condition assessments and data collection. The implications of the new model on bridge assets are explored, with an evolving role for bridge engineers and the potential for enhanced understanding of asset behaviour through artificial intelligence (AI).

1 INTRODUCTION

Asset management plays a crucial role in maintaining infrastructure integrity and optimising resource allocation. For the Danish Road Directorate (DRD), this practice has evolved over the past 40 years, influenced by asset importance, characteristics, and the organisation's varying levels of expertise. DRD was established in 1949 to develop and manage the Danish national road network, which today consists of approximately 3800 km of road and approximately 2400 structures. The national road network represents only 5% of the entire road network in Denmark but caters for over half of the traffic. DRD manages directly the network and procures the contracting services required to carry out the different O&M activities.

In response to an aging IT-setup that requires an overhaul, DRD envisions a transformation in its practices. This paper delves into DRD's vision for a new asset management model, driven by the integration of digital solutions to enhance transparency, automation, and cost optimisation. The paper also explores the implications of this transition on bridge assets, emphasising the shift from subjective assessments to automated, data-driven condition evaluations and the promising role of artificial intelligence (AI) in revolutionising data collection and analysis.

2 DRD'S CURRENT PRACTICE OF ASSET MANAGEMENT

2.1 *General practice across assets*

DRD has 25 no. assets subdivided into approximately 105 no. elements managed in 21 different IT-system that cover activities like data collection, data registers, condition assessments, cost optimisation, job procurement, job management and financial control. The management of different assets has over time been developed into different models with different levels of

DOI: 10.1201/9781003483755-7

sophistication, partly reflecting the importance or value of the different asset classes (for example pavement and structures vs. street lighting), partly reflecting the idiosyncratic properties of different assets, and partly reflecting the different levels of knowledge within the company.

Using the terminology provided in Federal Highways handbook on management of ancillary (FHWA, 2019), adopted O&M strategies can be defined as 'condition-based', 'interval-based' and 'reactive'. Condition-based O&M is a proactive approach to asset management that includes predictive maintenance and continuous monitoring. Interval-based O&M follows a set schedule of activities, regardless of the asset's current condition. Reactive O&M is a strategy applied when asset failure doesn't severely impact its operation or when effective monitoring methods are lacking; it involves repairing assets after they fail and is commonly used when monitoring methods are ineffective or when there are no clear deterioration patterns.

DRD's pavements and structures are based on condition-based strategies (except winter road maintenance, which is a considerably different process and is not covered by this paper). The drainage system is a mix of different O&M strategies: Visible drainage infrastructure is condition-based, however interval-based cleaning and flushing of the entire drainage network is carried out to ensure function, and buried drainage infrastructure is reactive-based, as collecting routine condition data for these assets has proven to be prohibitive. ITS systems are interval-based, and most ancillary structures are reactive.

DRD's asset management process involves several key steps. Firstly, the responsible engineer gathers the necessary condition data for a specific asset. Subsequently, the engineer conducts a needs assessment, outlining the required O&M activity, associated costs, and scheduling considerations while striving to minimise the costs and to minimise the disruptions to road users.

The needs assessments for all assets are then consolidated by the O&M manager, who oversees the cross-asset coordination. This pivotal role involves two critical responsibilities: (1) Informing decision makers of the funding requirements and (2) prioritise O&M activities for the upcoming year based on the allocated budget approved by decision makers, thus finalising the production plan. As it takes one year to compile and agree the Danish national finance act (it is normally approved in parliament in November/December for the year starting in January), the funding requirements reported to decision makers is for two years ahead. The quality and precision of the forecasted funding requirements are therefore important for DRD. In addition, the prioritisation task by the O&M manager is to reconcile the needs and the allocated budget, as these may well have changed compared to the submitted funding requirements.

Finally, the responsible engineer executes the production plan, while the O&M manager oversees progress and financial aspects throughout the plan's implementation.

2.2 *Current practice for bridges*

DRD's current practice for bridges is documented in well-established project models and manuals published under the Danish Road Standards (Vejregler, 2018).

Bridge inspections are carried out at three levels of detail: Routine, principal and special inspections. Routine inspections are conducted regularly to ensure road safety and plan operation activities. The frequency of routine inspections depends on factors such as the nature, age, and condition of the structures, as well as traffic intensity and composition. They are also conducted in response to special events that might impact the infrastructure's integrity.

Principal inspections are carried out at regular intervals of up to 6 years to provide a comprehensive assessment of the structure's condition. These inspections involve a thorough examination of all structural elements and help determine the condition levels of individual components. They are crucial for identifying safety defects and prioritising major maintenance work.

Special inspections aim to provide more precise information than principal inspections, especially for prioritising significant repair work and ensuring safety compliance. These inspections are typically initiated based on findings from routine or principal inspections.

From the principal and special inspection a condition grade is assigned to structural elements and the overall structure based on damage, functionality, and impact assessments. The total condition grade ranges from 0 to 5, which can be summarised as:

Grade 0: No significant damage, similar to a newly constructed element.
Grade 1: Minor signs of degradation, repairs not needed, similar to a new element.
Grade 2: Minor damage or lower-level development, occasional improvement required.
Grade 3: Damage advanced, risk of lost function, remedial action needed within a few years.
Grade 4: Severe degradation, function close to termination, immediate remedial action required.
Grade 5: Complete degradation, immediate action essential.

If the condition is 0 to 3, there are automatic rules how to determine expected maintenance work and when they must be planned for based on standard life-time expectancies. If the condition is "3 with worsening development" to 5, the bridge engineer is responsible to determine the required maintenance works based on the condition assessment carried out and price it, plus activate a special inspection.

Based on the special inspection, the bridge engineer shall confirm the required maintenance work, the pricing and determine the optimum time to carry it out. This is done by estimating degradation curves and determining the point in time, where postponing the maintenance project by another year will increase the cost by over 4% above normal indexation. The 4% is set as a financial threshold which describes that an investment would be wiser somewhere else in society. The bridge engineer shall also consider possibilities to bundle maintenance works to reduce secondary costs such as contract mobilisation and traffic diversion. The maintenance works for the coming 12 years are then reported to the O&M manager in the needs assessment for the bridges. The process then follows the same general procedure.

2.3 *Strengths and weaknesses of current practices*

DRD's existing asset management practices have been thoroughly tested and have provided decision makers with clear guidance, ensuring a reliable road network for road users. These practices align with the current capabilities of the market.

However, many of DRD's in-house asset management software systems are reaching a point of technical debt, making it impossible to maintain them effectively. Consequently, DRD has procured a new asset management software that is currently in the implementation phase. The process of adopting this new software has presented DRD with opportunities to identify significant improvements to the current asset management model due to advancements in data collection, data storage capacity, and computational capabilities.

The current practices, in particular for bridges, rely heavily on subjective assessments, evaluations, and designs carried out by the engineers. While dependable, this reliance on subjective judgment results in higher deviations in outcomes. The evolving landscape of data computation opens the door to substantial enhancements in this regard, enabling more automated, data-driven, and objective decision-making, ultimately leading to improved maintenance strategies.

In the current practice for bridges, a substantial portion of condition data is stored in stagnant file formats, such as PDFs, with only key results transferred to the existing IT-systems. This approach, while adequate for planning necessary maintenance work, poses a significant barrier to analysing past performance and correlations to external factors. However, with the increased data capacity and text recognition technologies, it is now possible to extract, store, and analyse information, providing more objective insights into asset performance and more accurate estimations.

Another challenge is the reliance on different IT solutions across various assets, resulting in time-consuming data transfer, information compilation, and missed opportunities for cross-asset optimisation. This situation is particularly cumbersome for the O&M manager, who collects needs assessments from all assets. The current setup lacks flexibility, as it doesn't allow for a comprehensive evaluation of different scenarios when prioritising projects based on

condition assessments. Revising the system landscape will enable better support for this iterative process.

Furthermore, the use of different IT solutions for different assets limits opportunities for optimisation, such as reducing secondary costs, which are currently addressed on a per-asset basis. This prevents DRD from fully capitalising on the potential for optimisation across different asset categories.

Considering that assets have varying performance requirements and degradation curves, cross-asset optimisation has, until now, relied on manual intervention and subjective evaluations by the O&M manager. However, the evolution of data computation presents the opportunity for significant improvement, allowing for more automated, data-driven, and objective decision-making across asset classes.

In addition, given the technical debt associated with current IT solutions, accommodating technological advancements in data collection and computation is currently challenging.

3 DRD'S VISION FOR THE NEW ASSET MANAGEMENT MODEL

3.1 *The new asset management model*

DRD's ambition is to leverage the development of digital solutions into providing a more transparent and clearer decision-making process, which is more automated and better geared towards optimising costs. The ultimate goal is to be able to do cross-asset cost optimisation.

The functions of the cross-asset model can be defined as:

- Data collection
- Condition assessment
- Identification of O&M activities
- Cross-asset optimisation
- Assessment of sub-optimal strategies

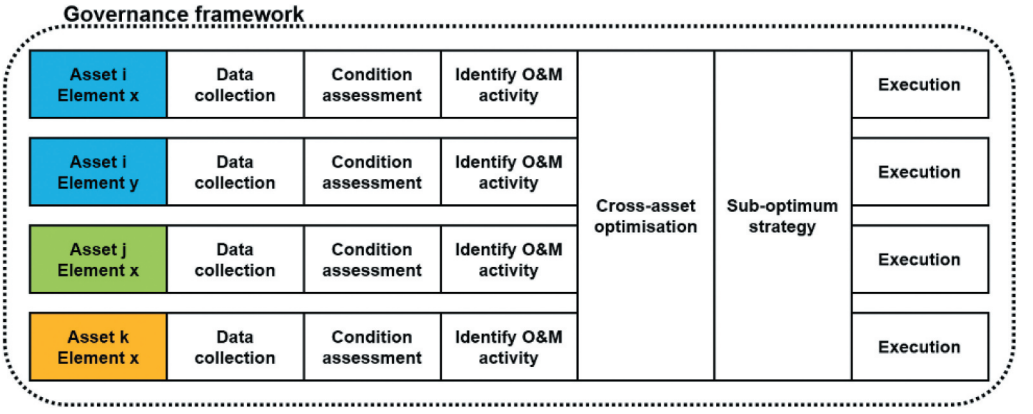


Figure 1. Overview of new asset management governance and functions.

To facilitate the cross-asset optimisation, it is imperative that uniform processes and assumptions underpin all assets. Consequently, a governance framework for the asset management model is being established, with the aim of providing precise guidance and coordination. This governance framework will define the model's structure, processes and essential constraints. For instance, the model will run at elemental level, which represents the primary asset subdivision. A standard bridge in DRD is defined in 15 elements, whereas streetlight could be divided into two elements: The post and the luminaire. Another example is the requirement that conditions on all elements must adhere to a uniform 1 to 5 scale, ensuring consistent and comparable reporting.

The governance framework delineates well-defined performance and service benchmarks for each element. It also establishes a clear and agreed hierarchy for these benchmarks in cases where budget constraints are encountered to ensure that elements that are required for uninterrupted traffic flow take precedence. The prioritisation process must take into account the traffic volumes to prevent a scenario where a bridge deck in a remote area is favoured over the pavement of a key motorway section. Different prioritisation models are under review.

Data is the core to the model and data quality is paramount when aiming at a high degree of automation. Data governance is therefore a key part of the governance framework. The data governance thoroughly defines the data type, data architecture, data ownership and what data sources shall be used. The utilisation of a single software solution to support the entire model is not envisaged. Instead, a modular approach within the IT landscape is advocated and in the process of being implemented. This approach allows for the flexibility to select the most suitable IT solution for each asset and provides the capacity to replace modules when more advanced solutions become available. For instance, the equipment and software employed for various data collection purposes may significantly differ among different assets.

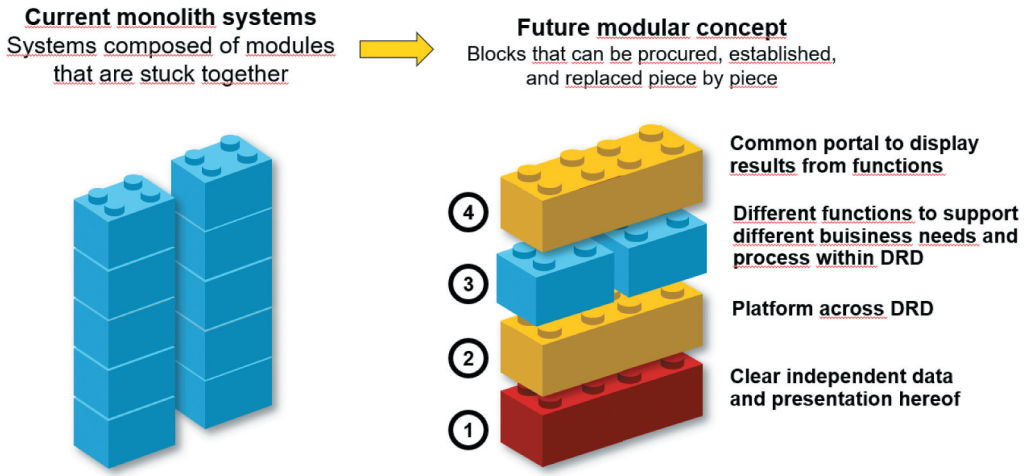


Figure 2. A modular IT-solution for the new asset management model.

The functions of data collection, condition assessment and identification of appropriate O&M activities based on defined maintenance strategies will in a broad sense stay same as current practice. The principal development introduced by the new model pertains to the automation of cross-asset optimisation and the ability to subsequently evaluate a sub-optimal strategy for a given financial constraint.

Cross-asset optimisation is designed to minimise costs by bundling O&M activities for various elements. For instance, it may involve anticipating the replacement of a waterproofing and wearing course on a bridge to coincide with the maintenance of an adjacent pavement section, thereby reducing the costs associated with mobilisation and traffic management. However, this economic advantage must be evaluated against the loss incurred by not fully utilising the lifespan of the bridge's waterproofing and wearing course. It's important to note that cross-asset optimisation operates without financial constraints and aims to establish the most favourable investment plan to achieve the agreed performance and service benchmarks. This fundamentally constitutes the needs assessment.

Sub-optimum strategy is carried out when allocated budgets differ from the needs. In this instance, the model will reverse the cross-asset optimisation and identify the preferred sub-optimal solution that ensures minimum monetary loss taking into account the prioritisation between asset elements (refer to description of performance/service levels). The loss is calculated as the loss from maintenance not being performed at the right time leading to increased

maintenance costs later; or the loss because maintenance is carried out too early resulting in the loss of the remaining lifespan of an asset. Basically, the loss will be the difference between the costs calculated under the sub-optimum strategy and the cross-asset optimisation. This will indicate the decision makers what the costs are for not meeting the needs, or in other words, what it costs to borrow in your assets when directing funds elsewhere.

It is obvious the model will only converge to results within certain boundaries. A scenario where a continuous major lack of funding takes place will not meet performance/service levels set. Asset owners that operate under these conditions, should consider a cross-asset optimisation model that maximises the benefits per euro spent. DRD's current pavement management system is an example for this latter type: The model runs an iterative process to find the best combination of maintenance strategies and pavement section that maximises the gains on 'road capital' given a certain budget (road capital is an effort to describe the financial value the pavement based on current costs and depreciation).

It is not expected that all assets will be able to enter the full model for different reasons. For instance, a maintenance building with no geographical relationship with the road network gains no benefit by having the O&M activities bundled with the rest of the network. Another example is that the cost of collecting data on individual signage may be too expensive to justify compared to a interval-based maintenance strategy that simply looks at replacing all signs along a 20km stretch. This however may well change with time, as data collection and condition assessment can be automated to an extent that costs are slashed and a condition-based approach, where only signs that do not meet performance requirements are replaced, is implemented. To ensure the flexibility that assets can change strategies and fall in and out of different functions of the model, it's imperative that all assets follow the overall governance framework.

The new asset management model shall also provide better overview of all the costs that go into the O&M, not only the execution of O&M activities. Risk allocation to cater for unexpected activities will be predicted based on past performance and the condition of the assets. In addition, a clear indication of the costs involved in data collection, engineering and overheads will allow a continuous evaluation of O&M strategies and opportunities.

3.2 *The resulting implications for bridge assets*

The new asset management model will necessitate adjustments to existing bridge-related practices. As an illustration, the role of the bridge engineer will evolve to encompass solely conducting investigations, condition assessments, and confirmation of maintenance strategies per element. However, the consolidation of activities will be automated, streamlining processes. The changes required for entering the new asset management model are modest.

Current technological development, however, will have a more profound change to the way we manage bridge assets: Data collection, data storage and data computation combined will allow a fundamental shift from subjective assessments by the bridge engineer to automated and objective condition assessment. It's imperative that the new model is futureproofed to accommodate these technological developments.

As mentioned previously, increased data storage and text recognition, allow the extraction of information from historic inspections and allow a better objective understanding of the behaviour of the assets. It will improve the investigation into the correlation between degradation of elements and external factors such as traffic, temperature, rainfall, salting and more. This in turn will result in an enhanced understanding of the performance of different solutions and allow for better future planning against increasing traffic volumes and changing weather patterns.

The significant advancements in data computation through AI are poised to revolutionise current practices. Currently, the assessment of conditions and the definition of O&M activities heavily depend on subjective evaluations of bridge engineers, given the inherent uniqueness of each structure. AI will transform these processes, automating them and yielding a substantial advantage in terms of objectivity and accuracy. Noteworthy research in this domain includes studies conducted by the university of Hartford (Fang et al., 2024) where deep neural networks are employed to predict bridge condition ratings.

AI will also play a crucial role for data collection. Recent years have witnessed significant advancements in various data collection methods, such as drones, photogrammetry, remote sensing, and structural health monitoring. However, incorporating this data into asset management models has posed challenges. DRD have over the past years run a series of different inspections with unmanned aerial vehicles (UAV) to follow the maturity of the technology and the related services. Although it represents substantial improvement on health and safety, and software capabilities to detect damages have improved drastically and have become more consistent, it still requires an engineer to review and interpret the inspection result to provide a condition rating and provide a needs assessment. As it is now, there is limited gains both on finances or time to roll out unmanned inspections on large scale. This difficulty is in part also attributed to the substantial investments required for model adjustments to accommodate new datasets. AI, on the other hand, has enormous potential to makes this type of inspection viable, but more importantly, will enhance the flexibility in the asset management model to introduce new datasets while phasing out old data acquisition methods. This will facilitate seamless transitions between different data acquisition approaches. Nevertheless, it is worth noting that a seamless transition will still necessitate a temporary coexistence of old and new data collection methods, which will lead to an increase in data collection costs over a period. An asset owner shall therefore carefully consider when new data collection methods are introduced.



Figure 3. Drone inspection of Møns Bridge with COWI VIRTUAL INSPECTION for the Danish Road Directorate (COWI, 2022).

REFERENCES

COWI 2022, Pilotprojekt afrapportering af eftersyn i CVI, Internal Danish Road Directorate report, Unpublished.

Fang, C., Jimenez Gil, D., Kazemzadeh, M., Xu, W. 2024, A Framework of Deep Neural Networks to Predict Bridge Condition Rating: Challenges and Opportunities, *TRB Annual Meeting* 2024.

Federal Highway Administration 2019, Handbook for including ancillary assets in transportation asset management programs, FHWA-H IF-19-068

Vejregler, 2019, Handbook on inspection of structures

Bridge Maintenance, Safety, Management, Digitalization and Sustainability – Jensen, Frangopol & Schmidt (eds)
© 2024 The Author(s), ISBN 978-1-032-77040-6
Open Access: www.taylorfrancis.com, CC BY-NC-ND 4.0 license

Innovations in building and bridge engineering associated with circular economy

L.M. Ottosen
DTU Sustain, Section for Construction Materials and Durability, Technical University of Denmark, Lyngby, Denmark

ABSTRACT: Circular economy is the central strategy in the EU chosen to decrease today's overconsumption of raw materials extracted from nature. Due to the vast amounts of raw materials used in the building and construction sector, it is pointed out as a key sector. At the end of life of structures, reuse of whole components is rated over recovery of materials for production of new components. The cases found in literature that relate bridge engineering and reuse are limited to a case on reuse of cut out concrete blocks in a pedestrian bridge. Related to buildings, there is more literature on reuse (though less than 100), so reuse is still very far from being mainstream. Learnings from reuse of the structural elements in buildings could inspire reuse in relation to bridges, however, there are no cases of reuse to the full strength potential. The barriers towards implementation of circular principles are several and can are categorized as: economic, sociological, political, organizational, technological, and environmental. The potential risks associated with structural safety when reusing elements need to be overcome by the development of methodologies for strength estimations and durability assessments.

1 INTRODUCTION

Our industrialized society is built on a linear use of resources. Mining activities from nature have supplied us with raw materials enabling us to develop the society we know today. Many resources are non-renewable. Still, we have a mainly linear use: extract - use - discard. This is not durable for future generation's supply of raw materials. In addition, the linear use of raw materials comes with environmental impacts. Waste needs to be handled and mining areas can mean environmental issues or even disasters.

The overconsumption of the earth's resources causes increasing concern worldwide, and to combat it, a strategy for circular economy has been developed in Europe (European Commission 2015, 2020). In "A new circular Economy Action Plan - For a cleaner and more competitive Europe, 2020" (European Commission 2020). In contrast to the linear economy, "take, made, dispose", the circular approach aims to prolong the lifespan of goods and reduce waste through efficient design and material use (Charef & Lu, 2021). The building and construction sector was pointed out as a key sector (European Commission 2020) in the transformation from a linear to a circular material use because this sector requires vast amounts of resources - it accounts for about 50% of all extracted materials. At the same time, the sector is responsible for over 35% of the EU's total waste generation. Also, greenhouse gas (GHG) emissions from material extraction, manufacturing of construction products, construction, and renovation of buildings are estimated to 11% of the total national GHG emissions (European Commission 2020). These are strong incitements for transforming the sector towards CE value chains as greater material efficiency could save about 80% of those emissions.

Incontestably, the circular economy requires non-trivial changes in terms of professional knowledge, stakeholder engagement, and their involvement in the asset lifecycle, material

DOI: 10.1201/9781003483755-8

circularity, procurement, policies, incentive schemes, and technologies (Charef & Lu, 2021). In a review, Anastasiades et al. (2020) concluded from a review that circularity relating to buildings was intensively studied in the scientific literature, but literature on circular economy in relation to bridge construction was not found. Due to this and because there are overall similarities (when dealing with the load carrying parts), it is interesting to outline current trends for circularity in the building sector, and this is exactly the aim of this paper. First, though, the general strategies and principles for circular economy are presented.

2 CIRCULAR ECONOMY – GENERAL STRATEGIES AND PRINCIPLES

2.1 *Definitions of circular economy and circular construction*

When discussing barriers to adopt circular economy in the construction industry, the need for a comprehensive understanding of the concept and its benefits is often raised (Ossio et al., 2023). The European Parliament (2023) explains a circular economy as a model of consumption and production where the life cycle of products is extended, primarily thanks to a better environmentally friendly design that makes it easier to repair, reuse and reproduce old products, an improved durability, better waste management, and new business models based on leasing, sharing, repair and recycling. However, critics claim that circular economy means many different things to different people. The review by Kirchherr et al. (2017) underlined this. They gathered 114 circular economy definitions.

Recognizing that there is a need for a commonly accepted definition of circular economy, the international standardization organization ISO published the standard "ISO/DIS 59004 Circular Economy – Terminology, Principles and Guidance for Implementation". In this standard, it is emphasized that the organization includes environment, social and economic systems based on the consideration that economic systems are embedded in the social systems which are in turn embedded in the environment. The standard defines the term "circular economy" as an economic system that uses a systemic approach to maintain a circular flow of resources through recycling, maintaining or increasing their value, and which contributes to sustainable development. The mentioned standard is one in a series, the ISO 59000 series, which is designed to harmonize the understanding of the circular economy and support the implementation of quantification.

The ISO 59000 series is not specific for any industry or sector, but it is generic. There is a need for standards which are sector specific for the building and construction industry, because of the special characteristics of this sector, such as the complexity of buildings and structures in e.g. the different lifetimes of components and not at least the often very long lifetime of the structural parts. In recognition of this, a number of European CEN standards are planned (Under CEN TC350), which will be developed specifically for Circular Construction. Danish Standards is in charge of this work. The first of the standards "Principles, terms and framework for implementation" will come out as a draft in the spring of 2024. The scoping of the next standards in the series are expected to be initiated in the same period.

2.2 *Principles of circular economy*

The circular economy is developed as a solution to the issue of resource depletion. As there have been and are different definitions on circular economy, there are different frameworks for implementation as well. The 2008 European Union Waste Framework Directive (European Commission, 2008) underlines that the waste hierarchy shall apply as a priority order in waste prevention and management legislation and policy: Prevention > preparing for reuse > recycling > other recovery (e.g. energy recovery) > disposal.

Another common way to express this is named the 4R framework: Reduce, reuse, recycle, recover. Many frameworks have extended the R categories, and, in the literature, a review found a total of 38 different R's (Reike et al. 2018). However, overall, they can be considered as undercategories to the 4Rs. One of the most used frameworks is the 9R framework developed by

Potting et al. (2017): Smarter product use and manufacture (refuse, reduce, rethink) > Extend lifespan of products and its parts (reuse, repair, refurbish, remanufacture, repurpose) > Useful application of materials (recycle, recover). A common ranking is that reuse is preferred over recycling.

2.3 *The development of circular economy as a concept*

Circular economy as a concept cannot be traced back to a single date or author. It has rather been formed through development over the years. As early as in the 1970s, some of the basic ideas were introduced. In literature, some key publications are often mentioned as specifically important milestones in this development (Stahel, 1982; Stahel & Reday, 1982; Pearce and Turner, 1989, and McDonough & Braungart 2002). A loop economy to describe industrial strategies for waste prevention, regional job creation, resource efficiency and dematerialization of the industrial economy was sketched in 1976 in a research report to the European Commission, and report was later published in 1982 as a book (Stahel & Reday, 1982). In the paper "The product-life-factor" (Stahel, 1982) formulated "extending the life of products optimizes the overall life of goods and reduces the depletion of natural resources and thus waste; it builds on and increases prosperity". The book by Pearce and Turner (1989) "Economics of natural resources and the environment" deals with the shift from the traditional linear or open economic system to the circular economic system, describing an economic system where waste in the extraction, production and consumption stages is transformed into inputs. They emphasize that economic efficiency is getting the most welfare possible out of a given resource. The concept of cradle-to-cradle as opposing the mainstream cradle-to-gate was formulated (McDonough & Braungart 2002).

Simultaneously to the theoretical development of the concept and thoughts they materialized. For example, in Denmark, the Kalundborg Symbiosis was formally established in 1972, when companies came together in the world's first industrial symbiosis, sharing streams of energy, materials and water. From 1989 it was named Kalundborg Symbiosis (Kalundborg Symbiosis, 2023).

Several countries have now set up plans in relation to the transformation to a circular economy (Charif & Lu, 2021). In 2000, the Japanese Government enacted the pioneering Law for Promotion of Efficient Utilization of Resources and a "comprehensive legal framework for moving towards a recycling-based society" (Su et al., 2013). In 2008, the Chinese Government introduced "the Law for the Promotion of the Circular Economy", to enable a shift towards the CE, followed by the "Circular Economy Development Strategies Action Plan" and more recently, "the 13th Five-Year Plan (2015–2020)" (Zhang et al., 2009).

The fact that the circular economy did not start as a movement with a clear starting point, but rather as initiatives that arose simultaneously, has added to the missing of a commonly recognized definition of "circular economy". It was, for example, emphasized in the literature study by (Kirchherr et al., 2017). Here, 114 definitions of circular economy were identified. The study concluded that the main objective of the circular economy is generally considered to be economic prosperity, followed by environmental quality; its impact on social equity and future generations is not mentioned in most studies.

The terms circular economy and sustainability are often used in academia, industry and by policy makers, but the similarities and differences between the two terms are not always clear. Geissdoerfer et al. (2017) concludes from a literature survey that the circular economy is often seen as a condition for sustainability, a beneficial relationship, or a trade-off.

3 CIRCULAR CONSTRUCTION AND LOAD-CARRYING ELEMENTS

The number of papers on circular construction has been increasing exponentially in the last few years, and by far most of the papers are from Europe (Ossio et al., 2023). There are very few studies with focus on circular construction principles related to bridges. Anastasiades et al (2020) performed a review and concluded that circularity in the construction sector generally

was discussed extensively in the current scientific literature, though nothing relating to bridge construction was found. Due to this and because there are overall similarities, this section outlines current trends for circularity in the building sector focusing on the strategies related to the materials (concrete, steel, and wood) in the structural components of a building.

The building sector is paying increased attention to circular strategies, but new buildings or renovation projects based on circular principles are still a niche and are generally in the stage of unique demonstration buildings (Ottosen et al. 2021, Eberhardt et al. 2022). There are still challenges to overcome in the implementation towards circular construction being mainstream. For example, the process of deconstruction is still based on cutting or breaking the structural members due to the monolithic nature of the connections (Selvaraj & Chan, 2024). This makes the reconstruction or reuse process more difficult as the structural member requires repair work. Further, the cutting and breaking work creates more waste and delays the process, eventually leading to higher costs. This indicates that the existing design for deconstruction technologies do not create a closed-loop system for resources (enabling reuse within the system), therefore, there is a need for new technology and design concepts to reuse the structural members (Selvaraj & Chan, 2024). Also, designing structures from reused elements is unlike conventional structural design because stock element availability is a design input. In other words, structures must be designed subject to availability of given element characteristics such as length and cross-section type, which have a major influence on the optimal structure layout and form. In this new paradigm structural form follows availability (Brütting et al. 2019). Topology and geometry optimization subject to stock availability allows to account for environmental considerations at early stages of the design process. Design through reuse of stock elements therefore opens new directions in structural form finding and optimization (Brütting et al. 2019). The potential of the different building design and construction strategies will most likely differ between different buildings, components, and materials. Thus, design and construction strategies should differentiate between the flow of different buildings, components, and material groups (Eberhardt et al. 2022).

Reused building components (bricks, beams, columns, truss, etc.) have far lower environmental impacts when compared with recycled materials (Geyer et al., 2002). It is primarily due to the significantly lower treatment and reprocessing required for building components reuse in comparison with recycling (Gorgolewski et al., 2008). Widespread reuse of building components can thus promote the circularity of materials in the building sector. However, the reuse of building components is not yet a mainstream practice (Rakhshan et al 2020). Recycling of construction materials will downgrade performance (Augiseau and Barles, 2017). The challenge then is to find different ways to meet the future demands for construction products by reusing existing products to reduce pressure on supplies and externalities (Hopkinson et al. 2019).

3.1 *Concrete*

Construction minerals account for the highest extraction rate of raw materials worldwide, and buildings present the largest material stock. Creating a circular economy requires an ability to couple closely the recovery and reuse of products from end-of-life buildings to stock replacement and maintenance (Hopkinson et al., 2019). Extracting pieces of concrete from obsolete buildings and reusing them, as is, in new assemblies is today rarely considered a strategy for improving the sustainability of the construction sector. By delaying the crushing of concrete into aggregates and avoiding the need for fresh cement in new buildings, the circular strategy is however expected to reduce greenhouse gas emissions and threats to natural ecosystems (Küpfer et al., 2023).

Küpfer et al. (2023) critically reviewed the state of practice and knowledge on the reuse of structural concrete components in new structures. Through a robust literature and case-study collection, the study builds a database of 77 case studies in Europe and the USA, (54 are built projects). They conclude among others that the practice has a long history. It has evolved since a pioneering period starting in 1967 (with a single case on reuse of floor slabs from a 6-story reinforced-concrete skeleton building for floor stabilization) and few cases in the

1990s, mostly in Northern Europe. Since 2011, the interest of concrete reuse has widened both in terms of type of reused components but also in terms of territories. Lately, the reuse of components extracted from cast-in-place concrete structures has gained interest. A large diversity of built projects has been identified, but the full potential remains unproven. Notably, applications involving reuse for equivalent or upcycled purpose related to reuse of components extracted from cast-in-place concrete structures are lacking.

An example of reuse of concrete in a footbridge is a study by (Devènes et al., 2022). Here cut out blocks of obsolete cast-in-place concrete walls were used for a new structural application: a 10 m-long post-tensioned segmented arch footbridge. With such a strategy, new and reliable concrete structures can be built with little to no cement inputs (Devènes et al., 2020).

Reuse is rated over recovery in a circular economy. However, in cases where reuse is not possible, recovery of secondary raw materials should be considered. Using recycled concrete aggregates (RCA) in new concrete can preserve the natural aggregate resources, reduce the need for landfill space and contribute to cost efficiency. However, due to characteristics of the RCAs, the short and long-term mechanical properties of the concrete are usually poorer than those of the natural aggregate concrete. Intense research is conducted to mitigate the negative effect, and due to the uncertainty and inferior properties of RCAs, they are generally utilized for non-structural applications such as pavement, filling material or gabion. However, the exploitation of RCA in structural is ongoing and constructions have been partly or fully built. Wang et al. (2021) recommended to improve environmentally friendly RCA treatments and hereby improve the load-carrying capacity of the concrete.

The global community is moving towards reducing CO_2 emissions resulting from the production and use of ordinary Portland cement while promoting the use of waste materials as alternatives and environmentally friendly construction materials (Oke et al. 2024). Research into de-carbonizing in construction using supplementary cementitious materials (SCMs) that are eco-friendly and, the utilization of the accelerated carbonation technique as a curing regime for developing green construction components are keys (Oke et al., 2024). The most extensively used SCMs in concrete production are derived from industrial by-products. Silica fume, ground granulated blast-furnace slag, and coal fly ash are the most popular SCMs used worldwide, however, the contribution of conventional SCMs in achieving mid- and long-term net-zero carbon goals has become controversial in recent years due to several constraints such as the limited supply, the associated transportation, and supply chain issues (Nehdi et al., 2024). Intensive research is ongoing worldwide on by-products and wastes from industrial, agricultural, and municipal processes as alternative SCMs, and these includes mine tailings and ashes from incineration of e.g. sewage sludge and wood.

3.2 *Steel*

Most research examining the second lifecycle of structural steel pertains to recycling rather than reuse, due to structural steel's especially robust recycling supply chain (Hopkinson et al 2019). There is a necessity to fundamentally change the material usage pattern to enable the circular economy in construction, which means the material recycling process (reproduction or remanufacturing) shall be changed to direct structural member reuse for a potential increase in productivity, profitability, and reduced material consumption in new construction, and steel has a major reuse potential (Selvaraj & Chan, 2024). Valen et al. (2023) investigated the technical feasibility, advantages, and disadvantages, when using the reclaimed steel members from decommissioned offshore platforms in a new onshore building and they concluded that the degree of practicality/feasibility of reuse of the decommissioned steel members was about 50%

3.3 *Wood*

In case a wooden bridge is chosen, the use of cutoffs of reclaimed wood is an option. An example related to reclaimed wood is (Browne et al., 2022) were prototypes of a beam and

load carrying wall were made from cutoffs of waste wood demonstrating a potential for waste wood to replace virgin material in typical structural functions, as well as offering new aesthetics, that maintain the waste stream's identity.

3.4 *Barriers and way forward*

Charef et al. (2021) assessed the barriers to circular economy in the construction sector and classified them into six categories: economic, sociological, political, organizational, technological, and environmental. The interrelation between the barriers from different categories was very common due to the holistic nature of the construction lifecycle. The barriers were also related to the diversity of stakeholders and the phases of the building process (Charef et al., 2021). Achieving the CE in construction is not only about people and technologies, but also requires regulations and policy knowledge (Charef & Lu, 2021). Integrated project procurement/delivery will reduce discontinuity, encouraging commitment from all stakeholders over a relatively long period. Incentive schemes should be developed to encourage material circularity not only during the design stage but also during the operation and end of life stages (Charef & Lu, 2021). Results indicate that addressing the economic, social, and regulatory barriers should be prioritized (Rakhshan et al., 2020).

A key challenge in choosing to reuse components today is the barrier constituted by the lack of standards, certification, and documentation systems for these materials. Such lack entails a significant documentation burden and risk for the owner when e.g. choosing to reuse components from another building. Rakhshan et al. (2020) state that although the impact of barriers under perception, risk, compliance, and market subcategories are very pronounced, the highest inter-dependency among the sub-categories is found between perception and risk. It suggests that the perception of the stakeholders about building components reuse is affected by the potential risks associated with this intervention (Rakhshan et al., 2020). This is in consistency with Krüger et al (2023) who state that limiting forces to a broader implementation of reuse of concrete in new structures include technical fears, project-management risks, and synchronization issues. This barrier must be overcome by the development of systems and methods that ensure equality in the choice between reused and new components, and this is exactly the aim of the StructuralReuse project (Ottosen & Gustafsson, 2024). The potential risks associated with structural safety when reusing elements must be overcome in order to use elements to the full strength potential. This includes both strength estimation and durability issues.

The digitalization of the construction industry, gaining momentum around the world, has already proven its worth in many activities and seems to be promising for the transition from linear to the circular economy. An overall improvement is reported, in terms of visualization, coordination, estimation and scheduling, whether during design or construction activities. It is also an excellent tool for strengthening the handover phase (Charef & Lu, 2021).

4 CONCLUSIONS

Papers dealing with aspects of circular economy and bridges are very sparce. The transition is more advanced related to buildings, though far from being mainstream. In a circular economy, reuse of whole elements rates over recovery of materials from demolished materials (such as e.g. recycled aggregates or steel for remelting). To adapt circular economy strategies, it is beneficial to include design for deconstruction principles, which can improve the possibility for reuse in the future. There is a need for implementation of methodologies enabling documenting the properties of the elements for reuse in order to overcome the risk related to using them.

ACKNOWLEDGEMENTS

This paper was prepared as part of the project StructuralReuse financially supported by The Industrial Fund Denmark and Realdania.

REFERENCES

Anastasiades, K., Blom, J., Buyle, M., Audenaert, A. (2020) Translating the circular economy to bridge construction: Lessons learnt from a critical literature review. Renewable and Sustainable Energy Reviews 117, 109522

Augiseau, V., Barles, S. (2017) Studying construction materials flows and stock: A review. Resources, Conservation and Recycling 123, 153–164

Browne, X., Larsen, O.P., Friis, N.C., Kühn, M.S. (2022) Material Value(s): Motivating the architectural application of waste wood. Architecture, Structures and Construction 2(4), 575–584

Brütting, J., Senatore, G., Fivet, C. (2019) Form follows availability - Designing structures through reuse. Journal of the International Association for Shell and Spatial Structures 60(4), 257–265

Charef, R., Lu, W. (2021) Factor dynamics to facilitate circular economy adoption in construction. Journal of Cleaner Production 319, 128639

Charef, R., Morel, J.-C.; Rakhshan, K. (2021) Barriers to Implementing the Circular Economy in the Construction Industry: A Critical Review. Sustainability 13, 12989

Devènes, J., Brütting, J., Küpfer, C., Bastien-Masse, M., Fivet, C. (2022) Re:Crete – Reuse of concrete blocks from cast-in-place building to arch footbridge Structures 43, 1854–1867

Eberhardt, L.C.M., Birkved, M., Birgisdottir, H. (2022) Building design and construction strategies for a circular economy. Architectural Engineering and Design Management 18(2), 93–113

European Commission (2008) Directive 2008/98/EC of the European Parliament and of the Council of 19 November 2008 on waste and repealing certain Directives

European Commission (2015) Closing the loop - An EU action plan for the Circular Economy.COM (2015) 614 final

European Commission (2020) A new Circular Economy Action Plan -For a cleaner and more competitive Europe. COM(2020) 98 final

Geissdoerfer, M., Savaget, P., Bocken, N.M.P., Hultink, E.J. (2017) The Circular Economy - A new sustainability paradigm? Journal of Cleaner Production 143, 757–768

Geyer R, Jackson T and Clift R (2002) Economic and environmental comparison between recycling and reuse of structural steel sections. In: International Iron and Steel Institute World Conference, Rome, Italy, 13–18

Gorgolewski M, Straka V, Edmonds J, et al. (2008) Designing buildings using reclaimed steel components. Journal of Green Building 3: 97–107

Hopkinson, P., Chen, H.M., Zhou, K., Wang, Y., Lam, D. (2019) Recovery and reuse of structural products from end-of-life buildings. Proceedings of the Institution of Civil Engineers – Engineering Sustainability 172(3): 119–128

Kalundborg Symbiosis (2023) https://www.symbiosis.dk/en/50-years-of-circular-production/ (assessed January 2024)

Kirchherr, J., Reike, D., Hekkert, M. (2017) Conceptualizing the circular economy: An analysis of 114 definitions. Resources, Conservation & Recycling 127 (2017) 221–232

Küpfer, C., Bastien-Masse, M., Fivet, C. (2023) Reuse of concrete components in new construction projects: Critical review of 77 circular precedents. Journal of Cleaner Production 383, 135235

Nehdi, M.L., Marani, A., Zhang, L. (2024) Is net-zero feasible: Systematic review of cement and concrete decarbonization technologies. Renewable and Sustainable Energy Reviews 191, 114169

McDonough, W. & Braungart, M. (2002) Cradle to Cradle: Remaking the Way We Make Things. North Point Press, New York

Oke, J.A., Abuel-Naga, H., Leong, E.-C. (2024) De-carbonizing in construction using supplementary cementitious materials and accelerated carbonation technique - a review. International Journal of Geotechnical Engineering 1–22

Ossio, F., Salinas, C., Hernandez, H. (2023) Circular economy in the built environment: A systematic literature review and definition of the circular construction concept. Journal of Cleaner Production 414, 137738

Ottosen, L.M., Gustafsson (2024) Enabling reuse of structural components through documentation of quality. In D.L. Vind (Ed.) Building A Circular Future - Insights from Interdisciplinary Research. BLOXHUB, 153–154

Ottosen, L.M.; Jensen, L.B., Astrup, T., McAloone, T.C., Rybert, M., Thuesen, C., Christiansen, S., Damø, A.J., Odgaard, M.H. (2021) Implementation stage for circular economy in the Danish building and construction sector. Detritus 16, 26–30

Pearce, D.W., Turner, R.K. (1989) Economics of natural resources and the environment. JHU Press

Potting, J., Hekkert, M., Worrell, E., Hanemaaijer, A. (2017) Circular economy: Measuring innovation in the Product chain. Policy Report. PBL Netherlands Environmental Assessment Agency, The Hague.

Rakhshan, K. Morel, J.-C., Alaka, H., Charef, R. (2020) Components reuse in the building sector – A systematic review. Waste Management & Research 38(4), 347–370
Reike, D., Vermeulen, W.J.V., Witjes, S. (2018) The circular economy: New or Refurbished as CE 3.0? - Exploring Controversies in the Conceptualization of the Circular Economy through a Focus on History and Resource Value Retention Options. Resources, Conservation and Recycling 135, 246–264
Selvaraj, S., Chan, T.-M. (2024) Recommendations for Implementing Circular Economy in Construction: Direct Reuse of Steel Structures. Journal of Constructional Steel Research 214, 108439
Stahel, W.R. (1982) The product-life-factor. In S.G. Orr (ed.) An inquiry into the nature of sustainable societies: The role of the private sector. Huston Area Research Center, 72–96
Stahel, W.R. & Ready, G. (1982) Jobs for Tomorrow, the Potential for Substituting Manpower for Energy
Su, B., Heshmati, A., Geng, Y., Yu, X., 2013. A review of the circular economy in China: moving from rhetoric to implementation. J. Clean. Prod. 42, 215–227
Valen, L.V., Siriwardane, S.C., Bjørheim, F., Røland, S. (2023) Reuse of decommissioned offshore steel components for new buildings: A case study. IOP Conf. Ser.: Mater. Sci. Eng. 1294 012027
Wang, B., Yan, L., Fu, Q., Kasal, B. (2021) A Comprehensive Review on Recycled Aggregate and Recycled Aggregate concrete. Resources, Conservation and Recycling 171, 105565
Zhang, H., Hara, K., Yabar, H., et al., 2009. Comparative analysis of socio-economic and environmental performances for Chinese EIPs: case studies in Baotou, Suzhou, and Shanghai. Sustain Sci 4, 263–279

Bridge Maintenance, Safety, Management, Digitalization and Sustainability – Jensen, Frangopol & Schmidt (eds)
© 2024 The Author(s), ISBN 978-1-032-77040-6
Open Access: www.taylorfrancis.com, CC BY-NC-ND 4.0 license

AI support for bridge SHM and life cycle assessment

G. Marasco & S.N. Pakzad
Lehigh University, Bethlehem, PA, USA

ABSTRACT: This paper focuses on opportunities that AI models bring to the monitoring and life cycle assessment of bridge structures. The paper examines different phases of data collection and generation and presents a holistic approach to curation of data. The paper then discusses various analytics that could be used to translate data to information that is useful in learning the fundamental characteristics of the structures and producing diagnostic measures for assessing the state of the structures. New classes of neural networks are developed to perform these analytical tasks accurately and in a scalable platform. These methods allow large volumes of data from various sources, including data from mobile sensors, to be utilized for assessment of critical structural systems.

1 INTRODUCTION

Structural systems are subjected to both gradual phenomena like aging, fatigue, and corrosion and shock phenomena such as earthquakes, flood, and tornadoes that can change their design properties. According to the latest annual report released by the American Road Transportation Builders Association (ARTBA), there is an urgent demand for maintenance across more than 222,000 spans, of which 76,600 bridges are identified for replacement. Among the bridges in need of attention, around 42,400 are rated as structurally deficient and in poor condition. These deficient bridges experience a daily traffic of 167 million motorists that make them highly prone to fatigue-related issues. Despite a decrease of 560 bridges in poor condition compared to 2022, the current rate of repairs suggests that it would take nearly 75 years to address all the identified issues. Hence, there is an urgent requirement for accurate, reliable, and scalable approaches to evaluate the structural conditions of the infrastructure asset. This is crucial not only for ensuring public safety but also for the correct allocation of financial resources toward repair and maintenance operations.

Over the past decades, significant strides have been taken to advance the Structural Health Monitoring (SHM) field (Farrar 2012). The continuous progress in three main thrusts — dynamic identification, damage diagnostics, and life cycle assessment — has proven crucial in translating research efforts into practical applications in the real world. SHM procedures significantly benefit from progress in two mutually connected domains: sensing technology and artificial intelligence (AI). Improvements in sensing technology are notably enhancing the temporal and spatial resolution of monitoring data. Meanwhile, AI is driving the evolution of more sophisticated data-driven approaches capable of managing big data volumes and physics-related information.

Different sources of data are used for this research. This includes conventional wired sensors, wireless sensors that are less expensive and more convenient to implement for short to medium term deployments, as well as mobile sensors that use data generated by phones inside cars that travel over bridges.

Among the significant advancements in sensing technology, smartphone sensors stand out as particularly noteworthy breakthroughs. Modern smartphones come equipped with dozens

DOI: 10.1201/9781003483755-9

of sensors including accelerometers, gyroscope, GPS, and high-resolution cameras (Sarmadi 2023). Thanks to the persistent focus on enhancing the accuracy and reliability of these sensors, they have become suitable for the SHM field. Their potentialities are exploited in mobile sensing approaches by overcoming limitations related to equipment cost and the restricted spatial and temporal resolution inherent in traditional sensor networks. Over time, we have been achieving significant advancements in methodologies for extracting bridge dynamic characteristics from mobile sensors. Ongoing progress is aimed at addressing challenges such as the complex interaction between vehicles and bridge dynamics. In the end, using mobile sensors is presenting the opportunity for a paradigm shift in scaling analysis of bridge structures to include all or a large part of the bridge assets across the nation.

The possibility to collect large volumes of data through cutting-edge sensing technologies brings SHM at big-data scale. This enables the effective training of advanced deep learning architectures. Convolutional Neural Networks (CNNs) (Rawat 2017), Vision Transformers (Rosso 2023), and Graph Neural Networks (GNNs) are examples of architectures used in SHM that require substantial datasets for successful implementation, showcasing valuable outcomes in tasks such as damage identification (Dang 2022) and life cycle assessment.

In both damage detection and life cycle assessment, the indispensable role of AI becomes evident in achieving precise, reliable, and real-time condition assessment procedures.

The creation of innovative neural network architectures has demonstrated significant potential in the realm of damage detection, particularly in image recognition (Maeda 2018). We proposed an optimized CNN to identify and localize damages in terms of cracks (Gulgec 2019).

The evolution of architectures capable of capturing nonlinear relationships among various signals across a structure proves effective in optimizing sensor networks, reducing equipment costs, and overcoming accessibility challenges in critical structural areas. Maes and Lombaert (Maes 2023) present a virtual sensing to monitor fatigue at structural elements not equipped with physical sensors. Virtual sensors relying on mathematical processing to generate the desired data are developed to circumvent the need for expensive and labor-intensive direct measurements. We proposed to use long short-term memory (LSTM) to build a data-driven model for life cycle assessment purposes (Gulgec 2020b), yielding excellent results in strain predictions. Furthermore, emerging architectures like Vision Transformers and GNNs show great promise in this field.

This paper provides a comprehensive review of the latest developments in sensing technologies and methodologies aimed at achieving efficient, accurate, robust, and real-time structural condition assessment solutions. A comprehensive strategy, based on sophisticated cloud-based storage solutions, is proposed to efficiently manage the large volumes of data collected or generated for the subsequent processing operations aim at extracting damage-sensitive features, detecting and localizing damage, quantifying its extent, and providing a prognosis about the structural remaining useful life. introduces novel approaches to transform data into information that is useful for structural condition assessment, advancing the dynamic identification, damage diagnostics, and fatigue life estimation. It provides methodologies for scalable infrastructure monitoring via mobile sensing in the civil engineering field, incorporating the interaction of vehicle suspension effects and vibrations caused by road roughness, enabling dynamic response extraction from vehicle data. Additionally, it presents techniques for bridge modal identification using asynchronous mobile data, a crucial step in integrating mobile sensing into system identification. In parallel, advanced deep learning architectures have been designed to efficiently detect and localize damage, such as cracks, utilizing long-term data availability. They excel in identifying abstract features and complex classifier boundaries for damage diagnosis, offering high accuracy and computational efficiency. Furthermore, cutting-edge AI algorithms, including Transformers, Convolutional Neural Networks, and Graph Neural Networks, are exploited to improve traditional bridge fatigue assessment. Deep neural network architectures are designed for indirectly sensing strain response from bridge acceleration data, overcoming equipment cost and accessibility limitations associated with critical structural areas. The outcomes demonstrate the feasibility and significant progress over existing methods.

The organization of this paper is as follow. Section 2 describes different sources of data into a cloud-based analytics perspective. Sections 3 illustrates the most recent analytics for dynamic identification, damage diagnostics, and fatigue life estimation. Section 4 provides the main conclusions and delineate potential future research directions.

2 SHM DATA SOURCES TOWARD ADVANCING IN SENSING TECHNOLOGIES

The methodologies employed in the initial phase of SHM processes, focused on data collection and generation, have undergone significant advancements in the last two decades. The progress of cyber-physical systems has sparked questions regarding the capture of data from physical infrastructure and its seamless integration into a connected information system. This Section delves into diverse data sources, highlighting their strengths and limitations in light of advancements in sensing technologies.

The structural condition of physical infrastructure can be measured directly or indirectly (Martin 2021). Despite direct measurements can be cost-intensive, prone to noise, and limited by technical challenges arising from spatial or environmental conditions, physical sensors are traditionally used to capture the structural response directly.

Wired networks using cables to send data to a central storage are the most common methods for collecting bridge data. Several studies show the implementation of wired sensing system to capture vibration data and estimate the dynamic characteristics of the structure (e.g., modal properties or parameterized function) (Maes 2021). However, the widespread use of wired networks is hindered by high maintenance and costs.

To overcome such limitations, wireless sensors networks (WSNs) are a valid alternative. Over the years, WSNs for SHM purposes have demonstrated their ability to offer precise and spatially dense ambient vibration data. We designed one of the largest WSN for SHM. It was developed, implemented, and validated on the 4200ft long span and the south tower of the Golden Gate Bridge (GGB). The network, composed by 64 nodes, recorded vibrations data at 1kHz, with a jitter below of 10 μs and an accuracy equal to 30 μG. Details are shown in (Kim 2007). Subsequently, we designed an integrated system, encompassing both hardware and

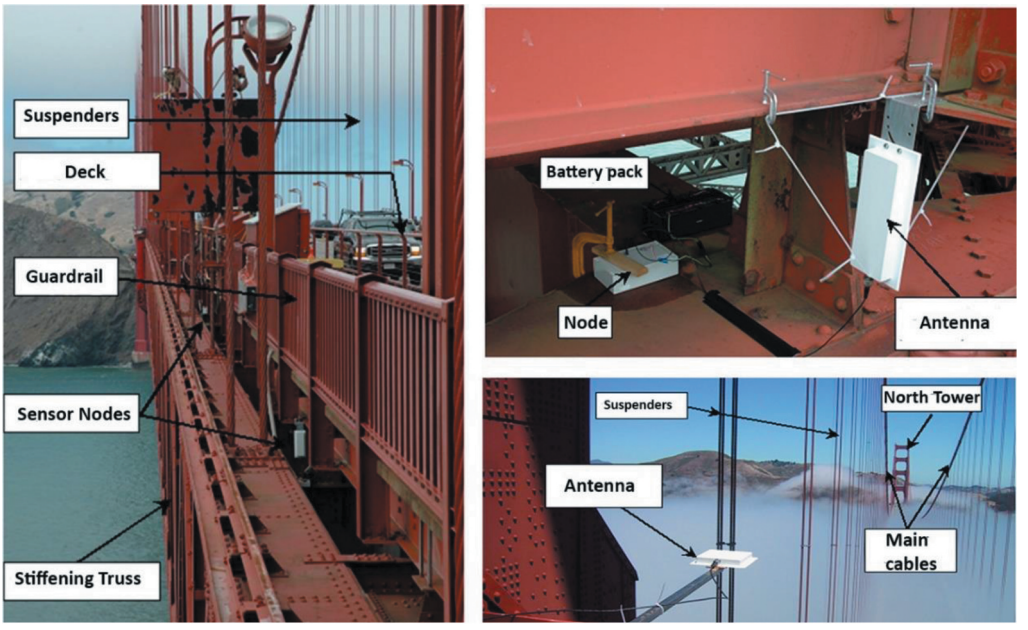


Figure 1. Views of the main-span and south tower of Golden Gate Bridge. Details about one WSN node with its battery pack and bi-directional antenna installed on the main-span.

software, for such scalable wireless sensor network, showing very accurate outcomes in identifying the bridge vibration modes.

Data obtained from the experimental setup were utilized to assess both the scalability of the network and the integrity of the data.

The performance remained robust and scalable, even in scenarios where a significant number of hops were necessary for communication. Deepening can be found in (Pakzad 2008).

Our later studies focusing on WSNs, the details of which are presented in (Pakzad 2009, Pakzad 2010), confirmed elevated resolution and confidence in detecting vibration modes. The errors in estimating vibration properties turned out to be minimal, with frequencies exhibiting the highest accuracy and damping ratios being the least accurate. Figure 1 shows a view of the WSN instrumentation deployed on the Golden Gate Bridge for the aforementioned investigations. It is worth nothing that a further benefit of WSNs lies in their efficiency in facilitating widespread sensor installations at a reduced cost. We demonstrated that this cost-effectiveness can be further enhanced through optimal sensor placement techniques, as illustrated in (Chang 2014). Yet, challenges persist concerning connectivity and power requirements.

Within the realm of direct measurements-based methodologies, the adoption of nondestructive techniques (NDT) that generate images/maps has become prominent. Examples include Digital Image Correlation (DIC) and Ground Penetrating Radar (GPR). The approaches associated with the automated analysis of these images are closely tied to classification challenges, and over the years, progressively sophisticated techniques rooted in AI have been devised. Recent breakthroughs have demonstrated remarkable outcomes, particularly with the utilization of Vision Transformer and CNNs. Deepening regarding the methodologies developed over time to analyze such data within the damage diagnostics area and the future research directions can be found in Section 3.2.

An additional direct methodology involves the utilization of mobile sensors, a strategy bolstered by the spread of smartphone devices and improvements in sensor accuracy. In a recent study (Matarazzo 2016), we highlighted the capacity of these sensors to capture structural vibration data during the transit of vehicles across the bridge. This ensures comprehensive spatial coverage with minimal sensor deployment. Details about the analytics methods developed over time to exploit this sensing approach in a dynamic identification perspective and the current challenges are provided in Section 3.1.

In addition to physical sensors, virtual sensors have emerged as a cost-effective alternative to make data acquisition more widespread and avoid labor-intensive direct measurements. The utilization of virtual sensors has been significantly enhanced by advancements in deep learning architectures. Virtual sensors, also referred to as soft sensors, act as substitutes for real ones, obtaining indirect measurements through mathematical processing (Wilson 1997). They have demonstrated remarkable effectiveness across diverse domains, including chemistry, computer science, and transportation systems, as illustrated in studies such as (Ankara 2004, Morgul 2014). The recent progress in deep learning has given rise to new classes of neural networks capable of understanding highly complex and nonlinear relationships within data. We have showcased the advantages of deploying such architectures in the SHM domain in a recent investigation (Gulgec 2020). The development of virtual sensors can generate data at numerous crucial structural points, starting from simpler and more cost-effective measurements. Section 3.3 provides insights into the advancements associated with this sensing approach for fatigue life estimation purposes.

3 METHODS

Processing operations within the SHM framework focus on three aims: to extract damage-sensitive features, to identify damage, and to provide with prognosis about the remaining useful life.

This section delves into recent advancements dynamic identification methods using smartphone-vehicle-trip (SVT) data, damage diagnostics methods based on image data, and fatigue

life estimation methods by means of virtual sensing. These advancements aim to effectively address the three aforementioned key aims.

3.1 *SVT data-based dynamic identification methods*

Vibration-based techniques for bridge monitoring have been developed over the past two decades for infrastructure dynamic characterization (Fritzen 2005). Conventionally, this involved setting up fixed spatially dense networks, wired or wireless, and employing system identification techniques to develop digital twins (Nicoletti 2023) and damage detection methods (Kostic 2017).

The main drawback associated with such networks is the high cost and the limited scalability of fixed sensors, hindering widespread adoption due to setup and maintenance expenses (Avci 2021). In this context, mobile sensing emerges as a promising solution.

This technique involves using sensors inside vehicles that travel across a bridge, measuring vibrations inside the cabin. Even though vibration signals include both bridge and vehicle dynamics, the aim is to predict the dynamic features of the bridge mitigating the impact of vehicle dynamic. Mobile sensors-based techniques have the capability to notably boost the speed and scale of infrastructure monitoring at unprecedented level, with low setup costs.

Compared to stationary sensing, the mobile one provides numerous advantages, offering better spatial resolution and requiring fewer sensors, as detailed in our recent studies (Matarazzo 2016a, Matarazzo 2016d). We demonstrated such advantages with laboratory tests and computer simulations in (Matarazzo 2018a).

Over the past decades, there has been a notable emphasis on addressing the challenge of estimating modal parameters such as frequency, damping, and mode shape using data collected from mobile sensor networks. Initially, the methods proposed focused on the estimation of individual modal parameters. For instance, Yang et al. (Yang 2004, Siringoringo 2012) presented methodologies for frequency estimation, while Gonzalez et al. (Gonzalez 2012) introduced techniques for damping estimation. In more recent times, we had substantial efforts in the development of Structural Identification (SID) techniques to produce a notable progression in the field, moving beyond the singular parameter focus of earlier methodologies. We firstly introduced structural identification formulas under the Expectation-Maximization framework, known as STRIDE. More details can be found in (Matarazzo 2016c, Matarazzo 2016b). Despite the high accuracy of the method in estimating modal parameters from datasets with incomplete observations, the STRIDE technique faced challenges related to scalability. To address this limitation, we presented an extension called STRIDEX, specifically designed for the truncated physical model (TPM); insights are included in (Matarazzo 2016b). This method offers comprehensiveness, convenience, adaptability, computational scalability, and is characterized by scalable information (Matarazzo 2018). In its initial implementation, STRIDEX demonstrated remarkable precision in generating a mode shape comprising 248 points using data from a pair of mobile sensors. Subsequent experimental tests highlighted its capability to successfully estimate higher modes and their associated mode shapes solely based on data collected from mobile sensors, as shown in (Matarazzo 2018b). Subsequently, in further studies we focused on the development of SID methods using matrix completion (MIMC) to obtain modal parameters from data recorded by a high number of mobile sensors (Eshkevari 2020).

To validated our proposed approaches, we presented studies where data from crowdsourced SVT are exploited to precisely identifying modal characteristics of real bridges. In (Matarazzo 2020) two case studies are showed. The first case study used smartphone data from "controlled" field experiments and "ridesourcing" datasets on a long-span suspension bridge in California, the Golden Gate Bridge. The second case study is applied to "partially-controlled" crowdsourced data recorded on a bridge in Ciampino, Italy. The methodology is developed to determine the most probable modal frequencies (MPMFs) via the synchrosqueezed wavelet transform and a data aggregation technique. In a further study, we showed the success of wavelet transforms in multiple real-world applications to identify modal frequencies and absolute mode shapes (AMS), namely mode shapes without the phase information, using highly

uncontrolled mobile sensing data. The study represents the most comprehensive real-world investigation into monitoring bridges using data from crowdsourced SVT, aiming to simulate the capabilities of detecting structural damage by means of AMS identification. The method examines more than 500 trip spanning four bridges (Golden Gate Bridge-USA, the Cadore Bridge-Italy, the Ciampino Bridge-Italy, and the Gene Hartzell Memorial Bridge-USA), with the main spans varying from 30 to 1300 meters in length. The presented approach offers three main advantages: (1) it relies solely on SVT data obtained from ordinary smartphones, eliminating the need for additional sensor data or GIS information, (2) given the continuous increase in smartphone usage, it facilitates regular and current estimations of AMS, and (3) it boasts a high spatial resolution in AMS. These functionalities can be integrated into a Software-as-a-Service (SaaS) system for automated collection, initial processing of data, and storage in the cloud. The system comes equipped with tools to facilitate the nearly real-time assessment of the structural conditions.

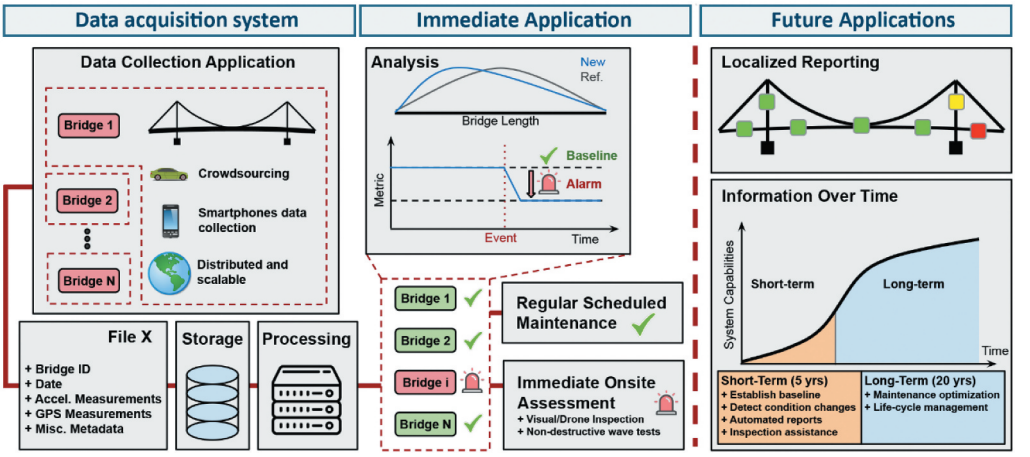


Figure 2. Scalable platform for system identification.

Figure 2 displays the flowchart outlining the envisioned scalable system identification platform. The smartphone app, equipped with bridge registries and user-defined geo-fences, automatically records vibration data upon entering these zones. The data is packaged and stored in the cloud. Periodically, a backend server processes the stored data, applies the algorithm to identify current AMS estimations for each bridge, and generates a time series of real-time dynamic features. This ongoing process enables continuous monitoring for anomalies indicative of structural changes, triggering automatic alerts for onsite inspections by bridge owners. More details can be found in (Eshkevari 2023).

Figure 3 illustrates the graphical representation of the procedure for identifying AMS.

After initial preprocessing, the synchrosqueezed wavelet transform is applied to shift each acceleration time series into the time-frequency domain, and then compute the instantaneous magnitudes. After that, the bridge is segmented with overlapping sections considering two parameters: the width (Δ) and the spatial stride (S). By calculating the average magnitudes within individual segment at the modal frequencies for each trip, a distribution of magnitudes is obtained for each location. The average of these distributions represents the AMS estimate. To enhance robustness on noisy datasets, a slight bandwidth (ε) encompassing the modal frequency is considered during the averaging step.

Our current research endeavors are centering around advancing SID techniques utilizing mobile sensors to obtain accurate frequencies, full-mode shapes (including phase information), and modal damping ratios of bridges. The uniqueness of this last our approach lies in estimating a dense spatial cross-spectrum. This is achieved by spatially averaging time-frequency cross-spectra obtained from pairs of mobile sensors at the same time on the bridge.

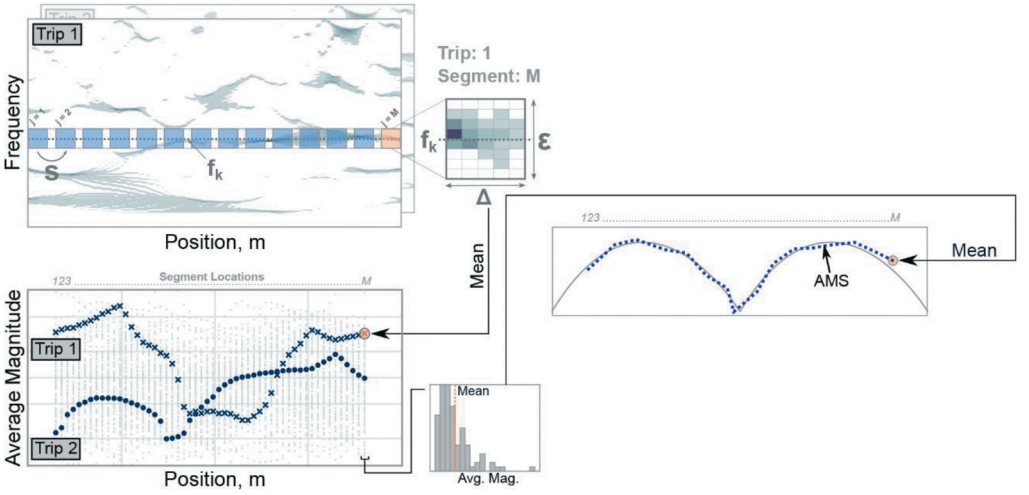


Figure 3. AMS identification methodology.

The averaging step involves computing mean values for both magnitude and phase within each spatially discretized cross-spectrum area. This effectively reduces the influence of vehicle dynamics on the results and numerical and laboratory experiments showed very promising outcomes.

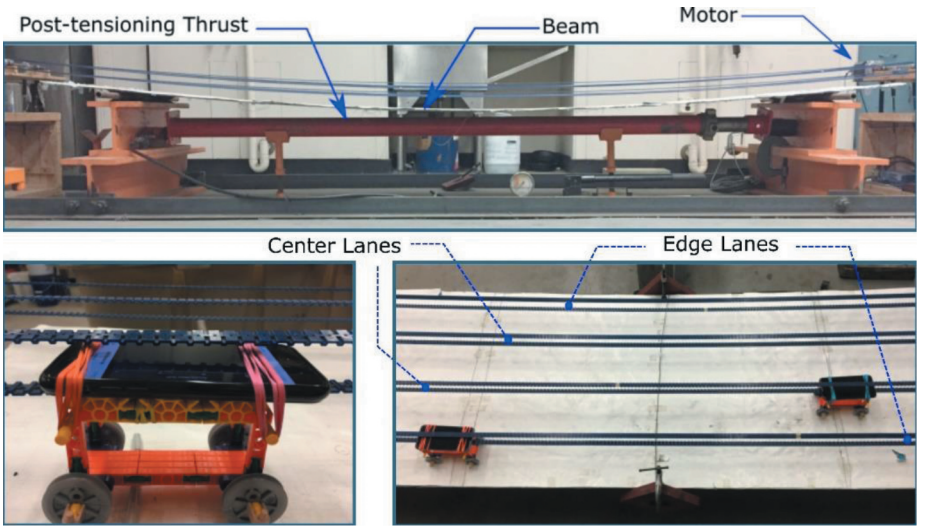


Figure 4. Layout of the test setup at Lehigh University.

The experimental mobile sensing platform depicted in Figure 4 illustrates the setup utilized at Lehigh University for validating the STRIDEX Structural Identification (SID) method and supporting the ongoing research endeavors.

3.2 *Image data-based damage diagnostics methods*

The assessment of structural integrity can be performed by means of a hierarchical approach to damage identification, as outlined by Farrar and Worden (Farrar 2012). This structured process encompasses five distinct levels: detection, localization, classification, assessment, and

prediction. Image recognition methodologies turn out to be critical for the acquisition of information for identifying, locating, and estimating the severity of structural damages.

The image recognition field has significantly benefited from the strides made in deep learning domain, which has become the backbone of support for structural assessment and damage identification techniques. Within this domain, one of the most pivotal contributions has stemmed from advancements in neural network architectures. Starting from the beginning of the 1990s, neural networks turned out to be an alternative to traditional techniques from statistical pattern recognition like the Bayesian discriminant and the Parzen windows. Foremost among these architectural advancements are CNNs. By exhibiting optimal performance when applied to the analysis of two-dimensional data formats, including images, videos, and similar visual data, the CNNs architectures are one of the most significant breakthroughs in image recognition. They eliminate the necessity for manually extracting features, possess the capability to recognize abstract and intricate classifier boundaries, and can discern diverse features of the problem. Moreover, thanks to the convolutional and pooling operations, they decrease the computational cost to address very complex tasks. Their demonstrated high precision, reliability, and computational performance across numerous studies establish them as a pillar in the realm of image recognition.

By leveraging image recognition techniques, the process aims to not only detect and pinpoint structural anomalies but also categorize them according to their nature and severity. This advanced approach aids both in identifying areas of concern and to facilitate a more comprehensive understanding of the structural condition.

We designed an optimized two-dimensional CNN specifically tailored for the accurate classification and localization of damage, present in the form of cracks within a gusset plate. The network is conceived to analyze strain fields in the form of tensors after an appropriate normalization process. Its design prioritizes efficiency in handling noisy data. To validate its performance, finite-element simulations of undamaged and damaged structural connections under different loading case, damage scenarios, and noise levels were initially conducted. Subsequently, the methodology has been validated using data obtained through DIC from laboratory testing. These tests involved inducing damaged conditions on the specimens, confirming the robustness of the proposed approach. In the proposed methodology, the initial layers of

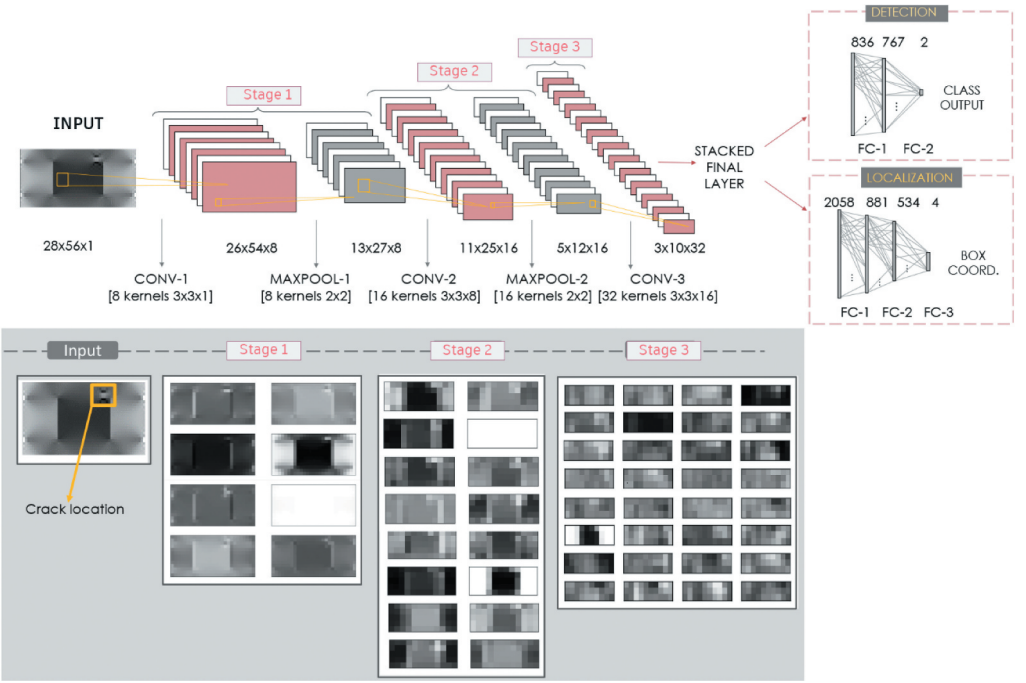


Figure 5. Proposed CNN architecture for crack identification.

a deep CNN are common for identification and localization. Subsequently, tailored back-end layers are formulated to address the specific requirements of each task. This design ensures a unified yet specialized architecture capable of effectively handling both identification and localization objectives. The features extracted in the initial layers of the network hold relevance for both tasks, thereby justifying the sharing of these network components. This deletes the necessity for maintaining two entirely distinct networks, resulting in a decrease in the overall training time and computational resource requirements. More details can be found in (Gulgec 2019, Gulgec 2020a).

Figure 5 illustrates the proposed CNN architecture. Despite the accurate outcomes obtained by the just presented approach, further research endeavors in this direction are essential for uncovering additional insights into the capabilities of CNNs, particularly in addressing more complex tasks related to damage detection.

3.3 *Virtual sensing-based fatigue life estimation methods*

Structural condition assessment can be performed not only by means of damage detection techniques but also estimating the structural remaining useful life. This is particularly important in steel bridges, where fatigue phenomena can cause important structural issues. Traditionally, it requires collecting strain (or stress) data at critical structural areas. While field measurements of strain signals contribute to reducing uncertainties compared to simulated ones, they are characterized by several shortcomings. These include elevated equipment costs, labor-intensive processes (Childers 2001), and challenges in accessing critical structural elements. By employing recorded stress or strain time histories, stress spectrums can be estimated to create rainflow diagrams. These diagrams are utilized to evaluate the remaining fatigue life of a structure through the counting of stress cycles, as outlined in (Fatemi 1998, Downing 1982).

The use of AI techniques to obtain strain signals with data-driven models has allowed to overcome such limitations. We showed the efficacy of LSTM to convert acceleration signals into strain signals. The methodology consists of training and testing steps. During training, the goal is to establish a connection between acceleration and strain for specific positions (R). A deep learning architecture is employed to minimize the error between predicted and actual strain signals. After the training, the model parameters are saved. In the testing step, the architecture uses acceleration data from specific locations to obtain strain data, accommodating cases where the number of requested locations exceeds R. The proposed approach undergoes a three-step training process to grasp extended time sequences. In each step, a randomly chosen sequence is divided into three parts: Part A, Part B, and Part C, which are subsequently employed in Step A, Step B, and Step C, respectively. During Step A, Part A, spanning from time i to $i+L$, is inputted into the first network (DNN 1). This sequence of length L is utilized for estimate abstract level features and serves as the initial state for Step B. This step functions as a nonlinear mapping of the input, capturing the sequence dynamics for enhanced learning performance and quicker convergence. In Step B, the second network (DNN 2), comprising LSTM memory cells, receives input from the sequence of length K and the initial state estimated in Step A. These memory cells act on the input sequence for further processing. The LSTM cell converts acceleration subsequences into strain ones, spanning from time $i+L+1$ to $i+L+K$, while simultaneously updating the internal and the hidden states. During Step C, the time series related to Part C is employed to enhance initial state estimations for DNN1 in subsequent iterations. The main objective of the proposed methodology is to simultaneously minimize the loss between the cell states from Steps B and C and the discrepancy between real and predicted strain signals. Figure 6 shows the flowchart of the general methodology. More details are shown in (Gulgec 2020). The method shows very good results but it is validated at a laboratory experiment scale with an unrealistic high loading. Moreover, advancements in machine learning field showed that LSTM is not the best architecture for such task.

Our recent research efforts have showcased the effectiveness of an advanced architecture that integrates Transformers and CNNs to convert acceleration signals to strain signals. This combination accurately estimate strain signals by using acceleration data collected from the Gene Hartzell Memorial Bridge in Easton, PA. As depicted in Figure 7, the deep neural

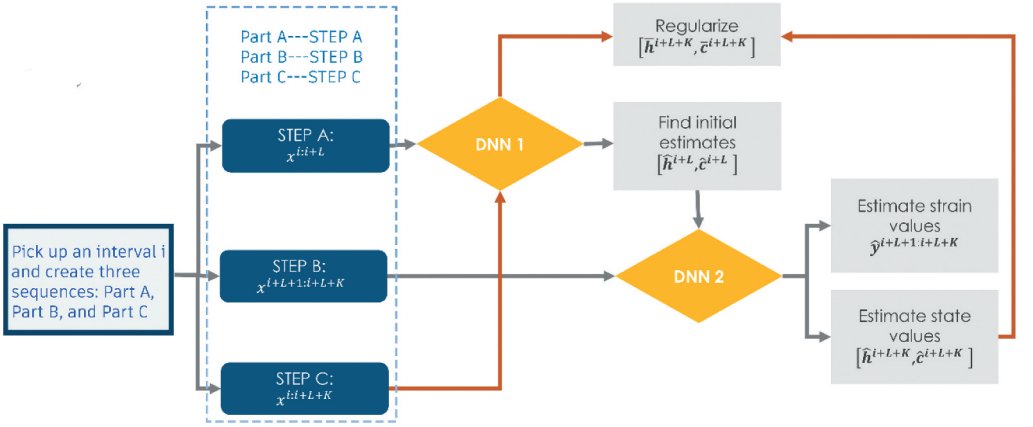


Figure 6. Proposed methodology based on a three-step training approach.

network makes predictions for two distinct versions of the strain signal: the pseudo-static and the dynamic version. The CNNs are adept at forecasting the pseudo-static component, while the Transformers excel in capturing the dynamic part.

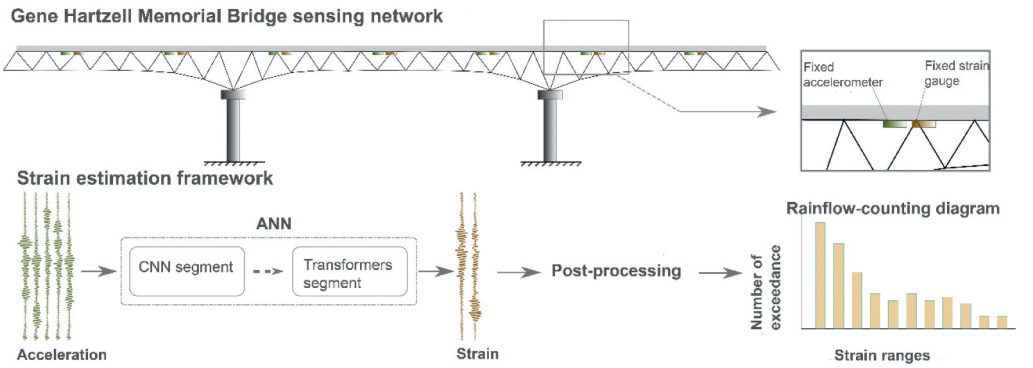


Figure 7. Strain estimation workflow.

In addition to CNNs and Transformers, GNNs emerge as potential architecture for the fatigue life estimation task. Most recent advancements in machine learning introduced the idea, already exploited in other fields like biology (Wang 2022), social networks (Ying 2018), and computer vision (Jiao 2022), that data can be organized on a graph structure. By considering the structural nodes, where sensors are positioned, as the graph's nodes, and the structural elements as its edges, information related to the mechanical connections among these nodes can be incorporated into the model. This integration is achieved through the utilization of the adjacency matrix characterizing the graph. Therefore, employing this architecture in the structural field enables the model to incorporate information concerning both spatial relationships and actual mechanical connections. This presents a promising avenue in civil engineering, and recent studies (Kim 2023) indicate the possibility to obtain further advantages by employing more advanced adjacency matrices. Despite up to this point the application of this architecture in civil engineering has primarily concentrated on areas such as damage classification (Dang 2022) and static structural response prediction problems (Whalen 2022), a recent study of ours has shown encouraging outcomes in the conversion of acceleration to strain signals for a numerical case study. For further details refer to (Marasco 2023). Ongoing efforts are dedicated to further developments in this domain.

4 CONCLUDING REMARKS

This paper introduces the most advanced sensing technologies as well as the most cutting-edge methods for converting raw data into meaningful information, specifically geared towards enhancing structural automatic condition assessment reliability and scalability. The focus is on advancing dynamic identification, improving damage diagnostics, and overcoming limitations of the current fatigue life estimation techniques. Firstly, it emphasizes the potential presented by mobile sensors in enhancing spatial resolution and reducing monitoring costs. The proposed techniques leverage asynchronous mobile data to successfully extract bridge dynamics in terms of modal parameters. Secondly, it underscores the contribution of advanced deep learning models to the improvement of damage diagnostics and fatigue life estimation techniques. A deep understanding of the state-of-the-art architectures, including CNNs, Transformers, and GNNs, enables the development of new architectures to address the current challenges in structural condition assessment. The proposed methodologies have undergone validation through both numerical simulations and real-world case studies, demonstrating significant promise in advancing the current state of the SHM field.

ACKNOWLEDGEMENT

This paper reflects research conducted by Thomas Matarazzo, Soheil Sadeghi Eshkevari, Nur Sila Gulgec, Debarshi Sen, Soheila Sadeghi Eshkevari, Liam Cronin, Iman Dabbaghchian, Giulia Marasco, and Shamim Pakzad at Lehigh University.

REFERENCES

Ankara, Z., Kammerer, T., Gramm, A. & Sch¨utze, A. 2004. Low power virtual sensor array based on a micromachined gas sensor for fast discrimination between H2, CO and relative humidity. *Sensors and Actuators B*: *Chemica*l. 100(1-2): 240–245.

Avci,O., Abdeljaber, O., Kiranyaz, S., Hussein, M., Gabbouj, M. & Inman, D.J. 2021. A review of vibration-based damage detection in civil structures: From traditional methods to machine learning and deep learning applications. *Mechanical systems and signal processing* 147:107077.

Chang, M.& Pakzad, S.N. 2014. Optimal sensor placement for modal identification of bridge systems considering number of sensing nodes. *Journal of Bridge Engineering* 19(6): 04014019.

Childers, B.A., Froggatt, M.E., Allison, S.G., Moore Sr, T.C, Hare, D.A., Batten, C.F. & Jegley, D.C. 2001. Use of 3000 bragg grating strain sensors distributed on four 8-m optical fibers during static load tests of a composite structure. In *Smart structures and materials* 2001: *Industrial and commercial applications of smart structures technologies* (4332): 133–142. SPIE.

Dang, V.H., Vu, T.C., Nguyen, B.D., Nguyen, Q.H. & Nguyen, T.D. 2022. Structural damage detection framework based on graph convolutional network directly using vibration data. *Structures* 38: 40–51.

Downing, S.D. & Socie, D.F.1982. Simple rainflow counting algorithms. *International journal of fatigue* 4(1): 31–40.

Eshkevari, S.S., Pakzad, S.N., Tak´a˘c, and Thomas J Matarazzo. 2020. Modal identification of bridges using mobile sensors with sparse vibration data. *Journal of Engineering Mechanics* 146(4): 04020011,

Eshkevari, S.S., Matarazzo, T., Milardo, S., Dabbaghchian, I., Santi, P., Pakzad, S.N., Ratti, C. & Cronin, L. 2023. Bridging the gap: Commodifying infrastructure condition data with crowdsensing.

Farrar, C.R. & Worden, K. 2012. Structural health monitoring: a machine learning perspective. John Wiley & Sons.

Fatemi, A. & and Yang, L.1998. Cumulative fatigue damage and life prediction theories: a survey of the state of the art for homogeneous materials. *International journal of fatigue* 20(1): 9–34.

Fritzen, C.P. 2005. Vibration-based structural health monitoring–concepts and applications. *Key Engineering Materials* 293: 3–20.

Gonz´alez, A., OBrien, E.J. & McGetrick, PJ. 2012. Identification of damping in a bridge using a moving instrumented vehicle. *Journal of Sound and Vibration* 331(18): 4115–4131.

Gulgec, N.S., Tak´a˘c, M. & Pakzad, S.N. 2019. Convolutional neural network approach for robust structural damage detection and localization. *Journal of computing in civil engineering*, 33(3): 04019005.

Gulgec, N.S., Tak´a˘c, M. & Pakzad, S.N. 2020a. Experimental study on digital image correlation for deep learning-based damage diagnostic. In *Dynamics of Civil Structures, Volume 2: Proceedings of the 37th IMAC, A Conference and Exposition on Structural Dynamics 2019*: 205–210. Springer.

Gulgec, N.S., Tak´a˘c, M. & Pakzad, S.N. 2020b. Structural sensing with deep learning: Strain estimation from acceleration data for fatigue assessment. *Computer-Aided Civil and Infrastructure Engineering* 35 (12): 1349–1364.

Jiao, l., Chen, J., Liu, F., Yang, S., You, C., Liu, X., Li, L. & Hou, B. 2022 Graph representation learning meets computer vision: A survey. *IEEE Transactions on Artificial Intelligence* 4(1): 2–22.

Kim, M. & Song, J. Near-real-time identification of seismic damage by graph neural network based on structural modes. 2023. *14th International Conference on Applications of Statics and Probability in Civil Engineering, ICASP14.*

Kim, S., Pakzad, S.N., Culler, D., Demmel, J., Fenves, G., Glaser, S. & Turon, M. 2007. Health monitoring of civil infrastructures using wireless sensor networks. *In Proceedings of the 6th international conference on Information processing in sensor networks*: 254–263.

Kosti´c, B. & G¨ul, M. 2017. Vibration-based damage detection of bridges under varying temperature effects using time-series analysis and artificial neural networks. *Journal of Bridge Engineering* 22(10): 04017065.

Maeda, H., Sekimoto, Y., Seto, T., Kashiyama, T. & Omata, H. 2018. Road damage detection and classification using deep neural networks with smartphone images. *Computer-Aided Civil and Infrastructure Engineering* 33(12): 1127–1141.

Maes, K. & Lombaert, G. 2021. Monitoring railway bridge kw51 before, during, and after retrofitting. *Journal of Bridge Engineering* 26(3): 04721001.

Maes, K. & Lombaert, G. 2023. Validation of virtual sensing for the reconstruction of stresses in a railway bridge using field data of the kw51 bridge. *Mechanical Systems and Signal Processing* 190: 110142.

Marasco, G., Eshkevari, S.S. & Pakzad, S.N. 2023. Graph convolutional neural networks based strain estimation. 2023. In *Proceedings of the 14th International Workshop on Structural Health Monitoring*.

Martin, D., K¨uhl, N. & Satzger, G. 2021. Virtual sensors. *Business & Information Systems Engineering* 63:315–323.

Matarazzo, T.J., Horner, M., Koser, K. & Pakzad, S.N. 2016. Multiphase mobile sensor network for beam health monitoring. In *Maintenance, Monitoring, Safety, Risk and Resilience of Bridges and Bridge Networks*: 186–186. CRC Press.

Matarazzo, T.J & Pakzad, S.N. 2016. Stride for structural identification using expectation maximization: Iterative output-only method for modal identification. *Journal of Engineering Mechanics* 142(4): 04015109.

Matarazzo, T.J. & Pakzad, S.N. 2016. Structural identification for mobile sensing with missing observations. *Journal of Engineering Mechanics* 142(5): 04016021.

Matarazzo, T.J. & Pakzad, S.N. 2016. Truncated physical model for dynamic sensor networks with applications in high-resolution mobile sensing and bigdata. *Journal of Engineering Mechanics* 142(5): 04016019.

Matarazzo, T.J, & Pakzad, S.N. 2018. Scalable structural modal identification using dynamic sensor network data with stridex. *Computer-Aided Civil and Infrastructure Engineering* 33(1): 4–20.

Matarazzo, T.J, Santi, P., Pakzad, S.N., Carter, K., Ratti, C., Moaveni, B., Osgood, C. & Jacob, N. 2018. Crowdsensing framework for monitoring bridge vibrations using moving smartphones. *Proceedings of the IEEE* 106(4): 577–593.

Matarazzo, T.J., Kondor, D., Milardo, S., Eshkevari, S.S., Santi, P., Pakzad, S.N., Buehler, M.J. & Ratti, C. 2020. Crowdsourcing bridge vital signs with smartphone vehicle trips. *arXiv preprint arXiv*: 2010.07026.

Morgul, E.F., Yang, H., Kurkcu, A., Ozbay, K., Bartin, B., Kamga, C. & Salloum, R. 2014. Virtual sensors: Web-based real-time data collection methodology for transportation operation performance analysis. *Transportation Research Record* 2442(1): 106–116.

Nicoletti, V., Martini, R., Carbonari, S. & Gara, F. 2023.Operational modal analysis as a support for the development of digital twin models of bridges. *Infrastructures* 8(2): 24.

Pakzad, S.N., Fenves, G.L., Kim, S. & Culler, D.E. 2008. Design and implementation of scalable wireless sensor network for structural monitoring. *Journal of infrastructure systems* 14(1): 89–101.

Pakzad, S.N. & Fenves, G.L. 2009. Statistical analysis of vibration modes of a suspension bridge using spatially dense wireless sensor network. *Journal of structural engineering* 135(7): 863–872.

Pakzad, S.N. 2010. Development and deployment of large scale wireless sensor network on a long-span bridge. *Smart Structures and Systems* 6(5-6): 525–543.

Rawat, W. & Wang, Z. 2017. Deep convolutional neural networks for image classification: A comprehensive review. *Neural computation* 29(9): 2352–2449.
Rosso, M.M., Marasco, G., Aiello, S., Aloisio, A., Chiaia, B. & Marano, G.C. 2023. Convolutional networks and transformers for intelligent road tunnel investigations. *Computers & Structures* 275: 106918.
Sarmadi, H., Entezami, A., Yuen, K.V. & Behkamal, B. 2023. Review on smartphone sensing technology for structural health monitoring. *Measurement* 223: 113716.
Siringoringo, D.M. & Fujino Y. 2012. Estimating bridge fundamental frequency from vibration response of instrumented passing vehicle: analytical and experimental study. *Advances in Structural Engineering* 15(3): 417–433.
Wang, Y., Wang, J., Cao, Z. & Farimani, A.B. 2022. Molecular contrastive learning of representations via graph neural networks. *Nature Machine Intelligence* 4(3): 279–287.
Whalen, E. & Mueller, C.2022. Toward reusable surrogate models: Graph-based transfer learning on trusses. *Journal of Mechanical Design* 144(2): 021704.
Wilson, E. 1997. Virtual sensor technology for process optimization. In *Symposium on computers and controls in the metals industry in iron and steel society*.
Yang, Y.B., Lin, C.W. & Yau, JD. 2004. Extracting bridge frequencies from the dynamic response of a passing vehicle. *Journal of Sound and Vibration* 272(3-5): 471–493.
Ying, R., He, R., Chen, K., Eksombatchai, P., Hamilton, W.L. & Leskovec, J. 2018. Graph convolutional neural networks for web-scale recommender systems. In *Proceedings of the 24th ACM SIGKDD international conference on knowledge discovery & data mining*: 974–983.

Bridge Maintenance, Safety, Management, Digitalization and Sustainability – Jensen, Frangopol & Schmidt (eds)
© 2024 The Author(s), ISBN 978-1-032-77040-6
Open Access: www.taylorfrancis.com, CC BY-NC-ND 4.0 license

Innovations in bridge management in Australia to rise to the challenges of today and the future

Nigel G. Powers
National Transport Research Organisation, Melbourne, Australia

ABSTRACT: Australia has a relatively small and dispersed population across a significantly large continent. Its economy is heavily based on the movement of freight which is primarily done on its road network due to capacity and access limitations on other alternatives such as rail, air, and water. The freight task is growing rapidly due to unprecedented population growth, coupled with increased demand from trading partners in Asia and rapid changes in technology, e-commerce, and consumer behavior. To remain competitive in a global market, the movement of freight must be fast, efficient, and effective. This is a significant challenge with an ageing road bridge network designed and built to outdated standards, loads increasing in frequency and mass and more frequent extreme climatic events like floods and bushfires.

Australia's road infrastructure managers are investing in research to seek innovations and practical and implementable improvements. Partnerships between researchers and infrastructure managers are critical to ensure innovations are identified, best practice is furthered, and the ever-increasing risk is appropriately managed. To achieve this and rise to the challenges faced research programs have covered many areas including the refinement of structural assessments, assessing structural risk, identifying innovative materials and maintenance, rehabilitation and strengthening techniques, improved monitoring practices and enhanced testing and analysis. The outcomes of this research will be shared along with recommendations for future investment and research.

1 INTRODUCTION

Australia's freight task is growing at a rapid rate due to unprecedented population growth, coupled with increased demand from our trading partners in Asia and rapid changes in technology, e-commerce, and consumer behavior. Overall, transport logistics was valued at over A$135.5 billion in 2023 and has been steadily increasing since. A significant proportion of freight is transported using the road network and to remain competitive this network needs to facilitate fast, safe, efficient, and effective access.

This is a significant challenge with an ageing bridge network and many of the in-service bridges built to outdated standards and for loads that are less than the allowable loads on the road network. Australia is also a land of temperature and weather extremes with major climatic events quite frequent which constantly tests the resilience of our bridges. When you combine the above with a freight industry constantly pushing to increase access and allowable loads, infrastructure managers have a major challenge to rise to.

In rising to this challenge, Australia's infrastructure managers are being innovative, partnering with industry to conduct research and address the problems they are facing. In partnership with industry and with funding from the State and Federal Governments, there has been significant research and development with the monitoring, assessment, and management of bridges.

DOI: 10.1201/9781003483755-10

2 AUSTRALIA'S FREIGHT TASK

The effective and efficient movement of freight across Australia is critical for the Australian economy. A significant proportion of freight is transported on the Australian road network. This is due to constraints on the rail network and the characteristics of the land not being conducive to using other transport forms like air and sea freight.

It is estimated that the overall transport logistics industry contributed A$135.5 billion to Australia's GDP in 2023. This is expected to grow to 173.8 billion by 2029 (Mordor Intelligience, 2023) thus access across the road network is essential.

2.1 *Population growth*

Australia's population was 26.64 million as of 30 June 2023 (Australian Bureau of Statistics, 2023). Over the last ten years the average annual growth rate was 1.4% and is expected to continue to grow in the decades ahead. By 2071 Australia's population is predicted to reach between 34.3 and 45.9 million people (Australian Bureau of Statistics, 2023).

This increase poses a significant challenge for infrastructure managers. Not only will it result in more vehicles being on the road network but it will also generate freight to provide the infrastructure needed to support such growth.

2.2 *Australia's size*

Australia is the sixth largest country in the world at 7.688 million square kilometers and accounts for 5% of the world's land mass (Geoscience Australia, 2023). The Australian Road Network is estimated to have a total length of 873,573 kilometers. Australia has a low population density with 3 inhabitants per square kilometer (World Data.Info, 2023).

The above aspects combine to create a significant challenge for Australia's road infrastructure managers. The large country size and length of network and the relatively small and dispersed population create the challenge of providing the funding required to build and maintain the network to the required standards.

2.3 *Trade*

Australia's national freight is predominantly generated by our trading partners in Asia. 75% of Australia's goods exports are going to Asia, in particular the booming economies of China and southeast Asia (Infrastructure Australia, 2018). This is expected to continue, if not increase over coming years.

This also poses a challenge to infrastructure managers with Australia's reliance on the road network to transport freight, the increase in trade will increase the quantity of heavy vehicles across the network. With freight operators striving for more efficient movement of freight, often resulting in larger and heavier vehicles, this will create further challenges for infrastructure managers to meet.

2.4 *E-commerce*

As with many countries across the world, e-commerce is booming Australia wide. The predicted revenue for e-commerce in Australia in 2023 is A$71 billion and this is expected to increase to A$94.61 billion by 2023 (ECDB, 2023).

The vast majority of this results in the delivery of parcels across Australia via the road network. Due to the nature of these deliveries, they are generally small and light and thus does not create a structural burden on our bridges but more a capacity issue for our already congested urban road networks.

2.5 *Road freight*

In 2017–2018 Australian freight vehicles moved an estimated 214,789 million tonne-kilometres of freight across Australia's road network (Australian Bureau of Statistics, 2019). This represents a 5.0% increase since 2016.

The majority of road freight transported crude materials (30 per cent) such as stone, sand and gravel, followed by manufactured goods (12 per cent) and food and live animals (11 per cent).

Over 95% of Australia's road freight is carried by vehicles heavier than 4.5 tonnes with the B-Double (Figure 1) accounting for 40% of all frieght movement (ACIL Allen Consulting, 2014). B-Doubles typically carry a load of approximately 68 tonnes. With current frieght industry initiatives across Australia for more high productivity vehicles, such as B-Triples with a mass of up to 85 tonne, this will allow road freight to grow and be a cost effective form of transport. Such large and heavy vehicles create challenges for the road network in terms of safety and bridge capacity.

With such a heavy reliance on road freight for Australia's economic prosperity, it is critical to ensure that our road infrastructure can safely accommodate the movement of frieght across the network.

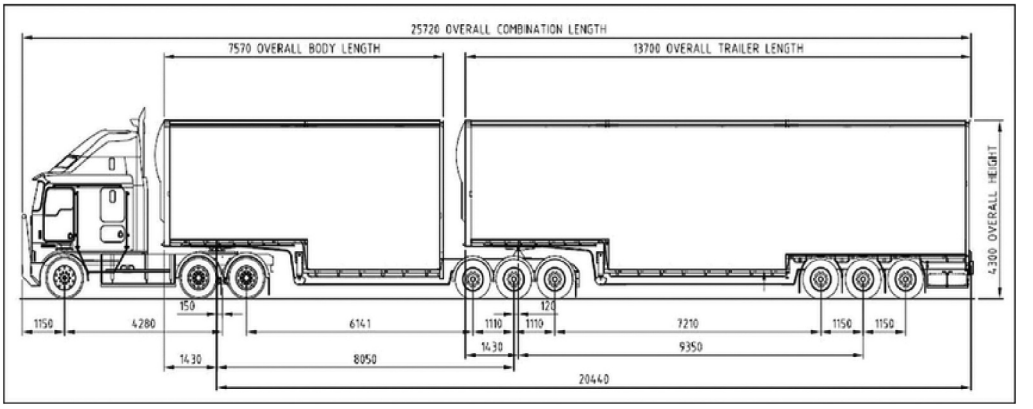


Figure 1. Typical B-Double. dimensions in mm. source: Spark, 2013.

3 AUSTRALIAN BRIDGE NETWORK

3.1 *Background*

Similar to the rest of the world, Australian bridges have developed over recent centuries from timber and masonry structures prior to the 18th century, progressing to steel structures towards the end of the 19th century and the network is now dominated by steel and concrete structures.

Timber bridges have largely been removed from the road network over the years to make way for more modern materials and structures and to carry the loads that are now on the road network. That said, timber structures are still very important on the road network as timber is often the only material readily accessible in the remote parts of Australia. For example, the Queensland Department of Transport and Main Roads still has over 300 timber bridges in service across its network (Austroads, 2018).

This is also the case for masonry structures. While some masonry structures remain in service, many have been removed from service across the network, like Winchelsea Bridge shown in Figure 2, due to condition and uncertainty of structural capacity.

3.2 *Current asset manager information*

In Australia there are approximately 53,000 road bridges (Caprani, 2018). Of these:

- Approximately 23,000 are managed by the State and Territory Road Authorities,
- Approximately 30,000 are managed by Local Government Authorities, and
- A small number are managed by private road operators.



Figure 2. Winchelsea Bridge, Victoria – opened in 1867.

3.3 *Design eras in Australia*

Before 1900, standards for bridge design and loading did not exist. Many were built to withstand the loads from horse and cart and may have been tested using a 16 ton road roller. Some of these bridges are still in service today.

In the early 1900's, bridge design developed, and the loading gradually progressed. In the 1920's and 1930's a loading was specified for the class of road with Class AA roads based on a 20 ton traction engine, Class A roads 15 tons and Class B roads 10 tons.

From 1947, bridge design loading was made uniform across Australia with the adoption of AASHTO and the design loading of H20 S16-44 truck (approximately equivalent to 33 tonne semi-trailer). There was a construction boom across Australia during this period with the current network made up of approximately 50% of bridges built to this standard (Caprani, 2018).

In 1976 – 2004 this progressed to T44 (approximately 47 tonne semi-trailer) with the current network consisting approximately 25% of bridges built to this standard.

With the development of the Australian Standard for Bridge Design, AS5100 – Bridge Design Code, the design load progressed to SM1600 which is equivalent to 2 x 75 tonne semi-trailers, nose to tail. These are estimated to make up 10% of the current bridge network.

4 PARTNERSHIPS WITH INDUSTRY TO MEET THE CHALLENGES OF TODAY AND THE FUTURE

4.1 *National asset centre of excellence*

In 2013 the Department of Transport and Main Roads Queensland (TMR) and the Australian Road Research Board, now National Transport Research Organisation (NTRO), established the National Asset Centre of Excellence (NACOE). NACOE delivers engineering excellence through leading road asset research that welcomes innovation and drives road management practice efficiency, creating fit-for-purpose engineering solutions (NACOE, 2023).

NACOE's research contributes to improving road safety initiatives to help save lives, reduce our carbon footprint, and deliver significant cost savings to the people of Queensland.

The program has a particular emphasis on pavements and materials technology, and covers the following key discipline areas:

- Pavements
- Asset management
- Structures
- Network Operations
- Road Safety
- Heavy Vehicle Management
- Sustainability

4.2 *Western Australian Road Research and Innovation Program*

The Western Australian Road Research and Innovation Program (WARRIP) is a collaborative research initiative between Main Roads Western Australia (MRWA) and NTRO. The WARRIP explores cutting edge research in:

- Pavements and surfacing,
- Asset management,
- Road safety,
- Sustainability, and
- Road structures.

The WARRIP aims to deliver innovative, sustainable, and cost-saving solutions for road infrastructure projects throughout Western Australia. The projects are delivered by subject matter experts in both MRWA and NTRO as well as engaging with industry and academia (WARRIP, 2023)

4.3 *Research projects*

The following outlines a small number of projects delivered under NACOE and WARRIP that have contributed to meeting the challenges of ageing infrastructure and the significant freight task.

4.3.1 *Deck unit bridge deck analysis under live load*

TMR's road network includes approximately 3000 bridges and 4000 culverts. Of these, more than 1900 Deck Unit (DU) bridges (Figure 3) have been built since the 1960's. A DU bridge is a bridge type commonly used in Queensland as it is simple to construct and cost effective for smaller span structures. It consists of individual, pre-cast, prestressed concrete hollow beams units that are connected via Transverse Stressing Bars (TSB). It relies on the TSB for the beams to act in composite as it does not have shear keys or a concrete overlay.

With DU bridges making up approximately 60% of the TMR bridge stock, the accurate analysis of their structural capacity is very important to make informed decision regarding allowable loads. Through the standard numerical analysis of DU bridges possible inadequate



Figure 3. Typical DU bridge. source: NACOE.

capacity was identified. Due to limited documentation and research on DU bridges a four-year project was commissioned to conduct load testing, assess the ultimate capacity of each beam, conduct performance and ultimate load testing of a partial DU bridge and investigation of the effects of TSB damage on the structural performance of a bridge.

The in-service monitoring and load testing in the first year of the project was conducted on a two-span bridge with spans of 8.3m long, each with 13 DUs. The results from the testing showed the bridge superstructure performed better than theoretically predicted with the load transfer like that of a flat slab bridge. This outcome was critical with the results being used to calibrate numerical models and refine capacity assessments.

Destructive testing was conducted on DUs taken from a decommissioned bridge. Tests were conducted on bending and shear on 9.1m long units from a bridge built in the 1970s. The tests concluded that the bending and shear performance was higher than estimated in the design specifications. Testing was also conducted on the concrete and steel which yielded higher values than also estimated in the design specifications.

A partial DU bridge was assembled including six 8.3m long DUs and one Kerb Unit (KU) from a decommissioned bridge, see Figure 4 below. The performance load testing delivered results consistent with the in-service testing and the failure mechanism was predominantly ductile.

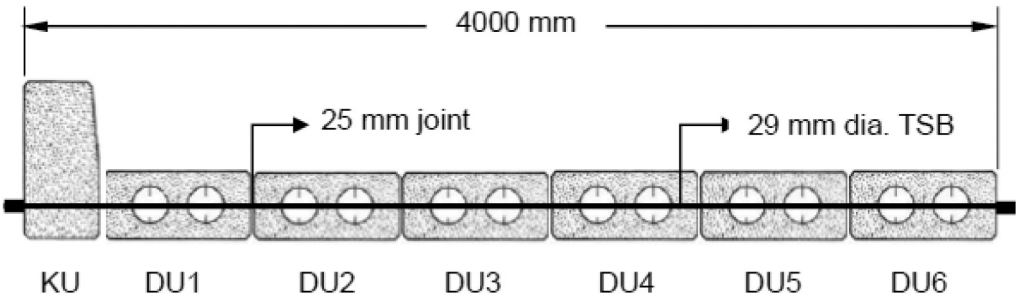


Figure 4. Cross section of the partial DU bridge used for testing. source: NACOE.

Finally, a DU bridge with 16m spans and TSB at 2m (Figure 5) was used to test the effect of TSB damage. Damage was gradually introduced by severing the TSBs and then conducting load tests. The testing showed that extensive TSB damage leads to an 18% increase of the load distribution factor, 32% increase in strain and 30% increase in vertical deflection.

The outcomes of this project have provided TMR with an improved understanding of DU bridges and how they behave under load and with TSB damage. This has helped them to make more informed decisions on the restrictions of heavy vehicle movements and on the maintenance, strengthening and replacement of DU bridges.

4.3.2 *Virtual WiM – enriching WiM and enhancing decisions*

This project was commissioned to explore an opportunity to enhance TMR's existing Weigh-in-Motion (WiM) network by supplementing it with data from other sources. TMR has 60 WiM installations and 126 networked classifier installations across its 33,000km road network. When determining access and planning outcomes, policy decision makers are regularly required to exercise judgment balancing productivity and risk. Decisions must be made with an often-incomplete subset of information and knowledge available. This incomplete knowledge can lead to sub-optimal decisions and utilization of the network.

To enhance the WiM data other sources of data were identified including:

- bridge monitoring,
- automatic number plate recognition,
- GPS tracking of heavy vehicles,
- authority to operate,

- onboard mass management, and
- classifier data.

These sources of data were combined with the WiM data which created a virtual WiM (Figure 6) tracking tool which dramatically increased the range of network covered. This was achieved through extrapolating data from a WiM site and applying it to a classifier site which was statistically similar. This extrapolation methodology was tested by comparing WiM sites where the extrapolated data was compared to the actual data collected which showed strong correlation.

The virtual WiM tracking tool developed was used to track load platforms as these pose the largest risk to TMR's bridges due to their overall mass. The trial was successful and was able to provide TMR with valuable information about specific loads crossing bridges which informed risk assessments and future heavy vehicle access decisions.

The virtual WiM approach enhances data quality, coverage, accessibility and the value of existing WiM datasets. It provides greater volumes of reliable data to make informed decisions on heavy vehicle movements without the need for significant investment in WiM assets across the network.



Figure 5. View of span 9 of test bridge. source: NACOE.

4.3.3 *Timber bridge management*

Across Australia, in particular in rural areas, timber bridges still make up a significant proportion of in-service bridges. The majority of these were built and designed before 1950 to outdated standards and for loads significantly less than current legal loads. Due to this NACOE and WARRIP recently conducted the two below research projects related to the management of timber bridges.

4.3.3.1 In-line timber replacement options

TMR manages over 300 timber bridges across its network. Some of these require replacement or significant rehabilitation in coming years. The replacement often occurs in-line with closure of the bridge and provision of sidetrack and crossing to facilitate safe and efficient construction. To reduce the timeframe for construction TMR was interested in investigating the available rapid construction methods in the industry and understand their compliance with TMR bridge design criteria and specifications.

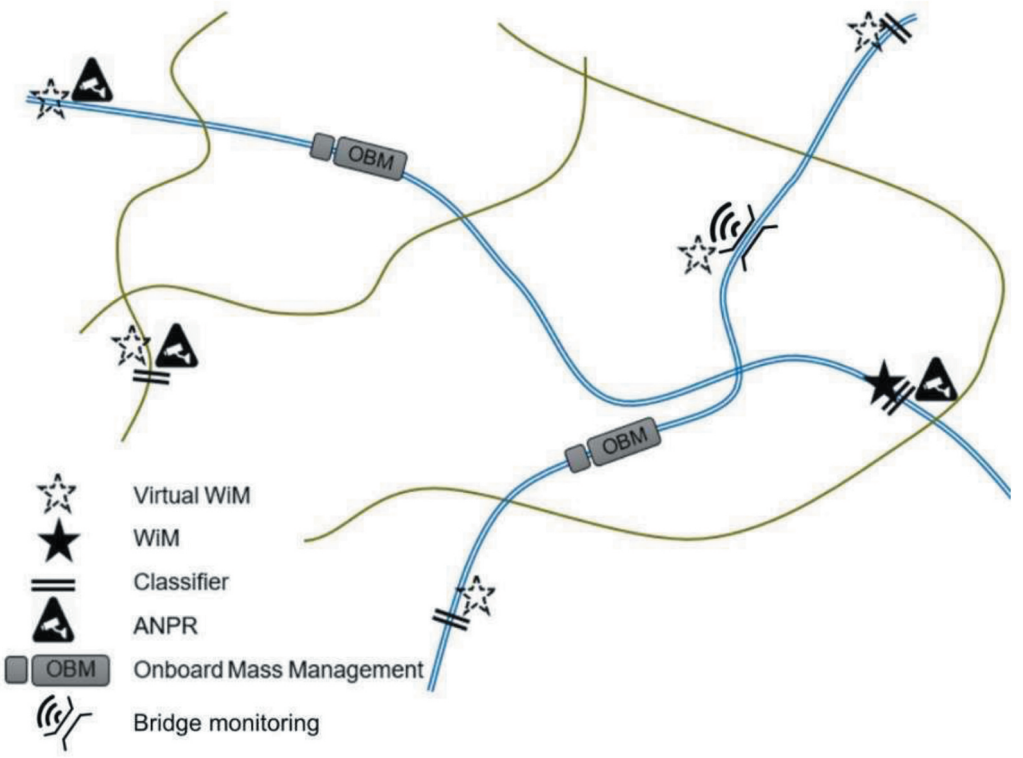


Figure 6. Virtual WiM concept combining various data sources across the network. source: NACOE.

As part of the project, NACOE determined the typical functional requirements for bridge replacement projects and investigated the available market solutions. Six pre-engineered solutions were reviewed to understand their applicability and limitations. A matrix was developed to inform decision makers of the feasible options based on a typical project and product characterization.

The matrix provides details for the following aspects for the available solutions:

- Lengths available
- Widths possible
- Number of lanes
- Number of spans
- Design life
- Design traffic load
- Design standard
- Substructure and superstructure material
- Construction duration
- In-line constructability
- Approximate cost (deck only per sq.m)
- Departures from TMR Standards
- Limitations

To assist TMR with the selection of the available options a decision supporting tool was developed. The selection process was broken into three main steps covering the following areas:

- Site condition screening
- Preliminary section
- Final selection.

The site condition screening step consists of assessing site accessibility, bridge componentry, geometry, design, construction, and resource availability. The output of this assessment is then compared to the solutions available in the market to see which best matches the specific site.

The preliminary selection stage utilizes a matrix that was developed for several advanced parameters against the bridge systems available to further refine the outcome from the site condition screen step. The matrix includes aspects like componentry, typical geometry, design loading and standard, duration of construction, cost and importantly departures from TMR standards.

The final selection step includes a detailed review of data provided for each bridge system which helps TMR to better understand the design criteria and performance of the product.

The decision supporting tool created as part of this project provides a consistent and unbiased approach to the selection of the most appropriate rapid construction system. The tool also provides a significant time saving.

4.3.3.2 Advanced epoxy timber pile repair

MRWA has many bridges across its network with timber piles originally constructed 60-80 years ago. It has been monitoring these structures over time and has identified a common defect pattern due to pile decay (Figure 7). They have been utilizing an epoxy fill solution for their timber piles for approximately 20 years to address this decay and mitigate further localized deterioration. This solution is relatively cost and time effective when compared to other solutions such as pile splicing or full replacement.

A WARRIP opportunity was identified to further develop this solution and investigate whether it could also increase structural capacity. The first stage in the development of this solution was to investigate currently available epoxy resins to see what is most suitable for this method. The resins identified were assessed against key criteria including viscosity,



Figure 7. Trial site showing typical pile decay. source: WARRIP.

permeability, bond characteristics, shrinkage, pot life, cure time and characteristic strength. Based on this criteria epoxy resins were selected for on-site field trials to test and further refine the construction methodology and test the epoxy resins suitability. After two weeks the sections repaired were cut and removed to observe the penetration across the cross-section, see Figure 8 below.



Figure 8. Pile cross-section showing epoxy resin penetration. source: WARRIP.

The trials conducted have led to further refinement of the construction methodology including pile preparation, improvement to formwork and reducing the volume of material required. This has also led to improved selection of the epoxy resin and refinement of the MRWA specification for this work. This research will continue in 2024 to evaluate the mechanical and structural performance of the epoxy resin repair solution.

5 CONCLUSION

Australia is a large country with a dispersed population and its economy is heavily reliant on the road network to transport freight efficiently and effectively to remain competitive in the global market. Those tasked with managing the road network face significant challenges with an ageing road bridge network designed and built to outdated standards, loads increasing in frequency and mass and more frequent extreme climatic events like floods and bushfires.

Australia's road infrastructure managers are investing in research programs such as NACOE and WARRIP to rise to the challenges posed. Through these programs they have been able to improve the assessment, maintenance, and management of their structures to provide the level of service required by the freight industry and the community and support Australia's economy. These programs have also provided a significant return on investment with

Benefit Cost Ratios (BCRs) as high as 14 on some projects and the overall program BCRs being in the range of 3.6 to 5.7. Continued investment in research and programs like NACOE and WARRIP will help Australia to meet the challenges or today and into the future an provide benefit to the Australian economy and community.

ACKNOWLEDGEMENTS

I would like to acknowledge the following:

- IABMAS 2024 Committee for requesting me to deliver a keynote paper and presentation at their conference.
- Department of Transport and Main Roads Queensland for partnering with NTRO under the NACOE Program and for review and input into his paper.
- Main Roads Western Australia for partnering with NTRO under the WARRIP and for the review and input into this paper.

REFERENCES

ACIL Allen Consulting. 2014. The Economic Significance of the Australian Logistics Industry. Australian Logistics Council.

Australia Bureau of Statistics. 2019. Australian Bureau of Statistics. Source: https://www.abs.gov.au/AUSSTATS/abs@.nsf/mediareleasesbyReleaseDate/6006BF6A6CC2F525CA2574B20020D2AB?OpenDocument

Australian Bureau of Statistics. 2023. National, state and territory population. Source: https://www.abs.gov.au/statistics/people/population/national-state-and-territory-population/latest-release

Australian Bureau of Statistics. 2023. Population Projections, Australia. Source: https://www.abs.gov.au/statistics/people/population/population-projections-australia/latest-release#:~:text=Australia's%20population%20in%202022%20(26,between%2043.8%20and%2047.6%20years.

Austroads. 2018. Guide to Bridge Technology Part 1 - Introduction and Bridge Performance. Sydney, Australia: Austroads.

Caprani, C. (2018, August 22). Are Australian bridges safe, and can we do it better? Retrieved from The Conversation: https://theconversation.com/are-australian-bridges-safe-and-can-we-do-better-101825

ECDB. 2023. eCommerce market in Australia. Source: https://ecommercedb.com/markets/au/all

Geoscience Australia, 2023. Australia's size compared. Source: https://www.ga.gov.au/scientific-topics/national-location-information/dimensions/australias-size-compared#:~:text=Australia%20is%20the%20planet's%20sixth,is%20the%20world's%20largest%20island.

Infrastructure Australia. 2018. Australia's Growing Freight Task: Challenges and Opportunities. Source: https://www.infrastructureaustralia.gov.au/listing/speech/australias-growing-freight-task-challenges-and-opportunities

Mordor Intelligence. 2023. Australia Freight and Logistics Market SIZE & SHARE ANALYSIS - GROWTH TRENDS & FORECASTS UP TO 2029 Source: https://www.mordorintelligence.com/industry-reports/freight-logistics-market-in-australia.

NACOE. 2023. About Us. Source: https://www.nacoe.com.au/

Spark, I. 2013. A numerical control algorithm for a B-double truck–trailer with steerable trailer wheels and active hitch angles. Part 2: Reversing. Source: https://www.researchgate.net/figure/Typical-dimensions-of-a-B-double-truck-trailer-vehicle-Lengths-are-in-mm_fig1_258177823

WARRIP. 2023. About Us. Source: https://warrip.com.au/

World Data.Info, 2023. Transport and infrastructure in Australia. Source: https://www.worlddata.info/oceania/australia/transport.php#:~:text=The%20network%20of%20roads%20and,place%20in%20the%20global%20ranking.

MINI-SYMPOSIA

MS 01 - Prediction and extension of the service duration of bridges

Organizers: A. Miyamoto, E. Brühwiler, R. Kiviluoma & A. Yabe


Taylor & Francis
Taylor & Francis Group
http://taylorandfrancis.com

Bridge Maintenance, Safety, Management, Digitalization and Sustainability – Jensen, Frangopol & Schmidt (eds)
© 2024 The Author(s), ISBN 978-1-032-77040-6
Open Access: www.taylorfrancis.com, CC BY-NC-ND 4.0 license

Field tests for remaining life prediction of aged bridges

A. Miyamoto
Prof. Emeritus, Dr. Eng., Yamaguchi University, Ube, Japan

ABSTRACT: The remaining life prediction is a crucial part of the systematization of maintenance planning because it can be used to estimate the end of service duration of the bridges. This paper describes the details of how to predict the remaining life of an aged RC-T girder bridge based on the chloride ion and carbonation tests results of the concrete cores and the cross-section cutting-off girders as the field tests required to determine the performance of concrete from material(durability) point of view. The concrete cores were tested for both carbonation and chloride ions whereas the cross-section cutting-off girders were tested for carbonation only. The results of the concrete cores investigation show that the main factor in the deterioration of the bridge is carbonation and that chloride ion attack has also contributed to the deterioration of the bridge. In order to establish a method of the remaining life prediction based on the chloride ion and carbonation tests results of the concrete cores and the cross-section cutting-off girders, a flowchart is proposed for the remaining life prediction of an RC bridge based on the extent of deterioration due to carbonation and chloride attack. The end of the service life (duration) was defined as the point at which the cumulative amount of steel corrosion reached a critical value which is obtained by a practical bridge management system (J-BMS BREX) to predict the remaining life of the existing concrete bridges.

1 INTRODUCTION

Lifetime management for civil infrastructure is becoming more important issue in sustainable development of societies around the world. In advanced countries the benefits of long-term management of civil infrastructure have been recognized by the experts of the discipline. Integrated lifetime management and maintenance planning includes continuous condition assessment, predictive modeling of performance, maintenance planning and decision-making procedures regarding maintenance action (Sarja 2006). The remaining life prediction is a crucial part of the systematization for maintenance planning because it can be used to estimate the end of bridge's service life(duration). The reinforced concrete (RC) structures such as aged bridges are exposed to the environmental impact and strongly influenced by environmental conditions during their service life resulting in reducing of the remaining life. High level of carbon dioxide as a result of the high traffic volume leads to carbonation process. The chloride attack should be considered as another factor of deterioration if the location of the bridge is near the sea. Either carbonation or chloride attack or both can lead to corrosion of the reinforcing bar. The most serious deterioration mechanisms that occur in RC bridges are associated with corrosion (JSCE 2013).

In case of aged bridges, a bridge management system, J-BMS which integrated with a bridge rating expert sub-system, BREX has developed by the authors for making appropriate safety evaluation and remaining life prediction (Miyamoto & Motoshita 2015, Miyamoto & Asano 2018). Especially, the remaining life prediction by the system needs to be verified through the concrete core tests extracted from some parts on main girders, deck slabs and bridge piers(local), such as compressive strength, carbonation depth, chloride ion concentration, etc., and cross-section cutting-off girder examinations of a target bridge for entire carbonation depth, cover concrete thickness, inside cracking, etc. respectively.

This paper describes a new method for predicting the remaining life of an aged bridge using the limited number of concrete cores, and verify the remaining life prediction results using cross-

DOI: 10.1201/9781003483755-11

section cutting-off girders. Because the remaining life prediction is one of the methods to estimate the end of life of the bridge and moreover to determine how best to make these decisions be made concerning whether to maintain or to demolish/reconstruction the target bridges. The remaining life of both concrete cores and cross-section cutting-off girders was calculated using some equations according to the method to predict the remaining life, with the requirement that the cumulative amount of steel corrosion (Q) equal to 75 mg/cm^2. This value is similar with the remaining life as indicated by the J-BMS BREX system in the evaluation of deterioration of the bridge due to chloride ion attack (Takahashi, et al. 2012). Therefore, the possibilities will be open to identifying the relationships between local evaluation results (were obtained by examining concrete cores), overall structural evaluation results (were obtained from the J-BMS BREX system), and the entire evaluation results (were obtained by examining cross-section cutting-off girders). By expanding the scope of an evaluation from local to the entire structure of the bridge, it may also be possible to enhance testing efficiency by reducing the total number of the concrete cores which are necessary for testing. The main objectives of this study are: ①to develop a method for predicting the remaining life of an aged bridge through the chloride ion and carbonation tests on concrete cores and cross-section cutting-off girders, ②to predict the remaining life and service life from concrete cores and cross-section cutting-off girder. The service life prediction is restricted by a criterion value i.e., cumulative amount of steel corrosion, Q = 75 mg/cm^2 which is obtain by the J-BMS BREX system, ③to verify the remaining life prediction results of the concrete cores with cross-section cutting-off girders.

Although there are various definitions of terms related to service life (duration) for RC structures, in this study the end of the service life was defined as the point at which the cumulative amount of steel corrosion due to carbonation and/or chloride ion attack reached a critical value. Figure 1 shows a schematic illustration of terms related to service life. The service life was divided into four stages: initiation, propagation, acceleration, and deterioration stages. The initiation stage is identified on the basis of the measured carbonation depth and the thickness of remaining concrete cover. The initiation of corrosion occurs when the thickness of remaining concrete cover falls below 10 mm. The propagation stage can be defined as the stage in which cracking occurs due to corrosion. Cracking will occur if the cumulative amount of steel corrosion is approximately 10 mg/cm^2. The acceleration and the deterioration stages are defined with respect to the critical value of the cumulative amount of steel corrosion, which in this study was taken to be 75 mg/cm^2.

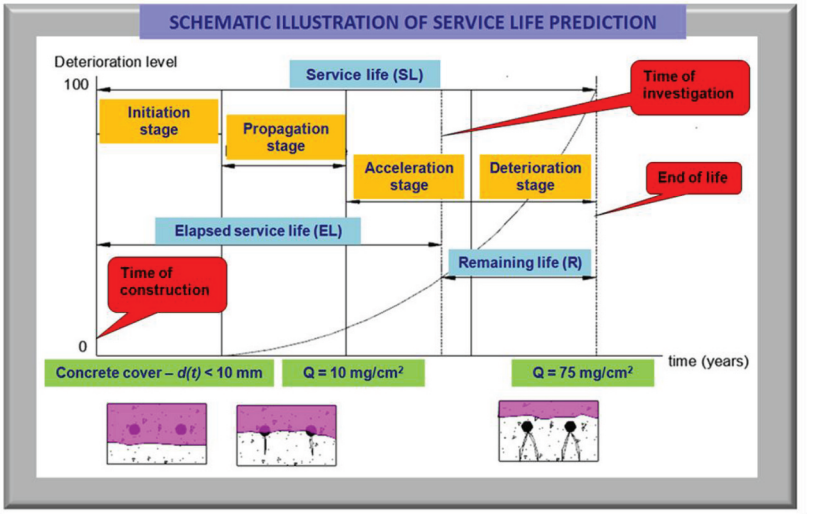


Figure 1. Schematic definition of service life (duration) and remaining life.

2 CONCEPT AND FLOW OF FIELD TESTS FOR REMAINING LIFE PREDICTION

2.1 *Target (Aged) bridge and flow of field tests (*Widyawati 2015)

The target bridge investigated for this study is an aged bridge to be removed ("SK-Bridge" over 72 years old) located on the main route of National Highway No. 2 at the border between Yamaguchi and Hiroshima prefectures, Japan. The SK-bridge has simple supported eight-span reinforced concrete cantilever T-girder (5 girders) structure, total length of 168.3 m and a width of 11.0 m, and was completed in 1942. The bridge was exposed to high level carbon dioxide environment during its service period because of the high traffic volume on the main route, and was located less than 1 km upstream from the Seto Inland Sea. Figure 2 shows the configuration and dimensions of the SK-bridge before removal.

Figure 3 shows the main concept and flow of investigations and inspections for the field tests mainly through close visual inspection and materials (concrete core and cross-section cutting-off girder) test results. According to the flow, at first, close visual inspections in-situ were carried out by professional engineers for predicting quantitatively of remaining life of the target bridge by applying the J-BMS BREX with field inspection data. Then, in order to verify the remaining life prediction result by the system, concrete core tests which extracted from some parts of SK-bridge and cross-section cutting-off girder examinations were carried out from the durability point of view. Finally, as a new bridge health monitoring method for short and medium span bridges, "bus-based monitoring system" using a public bus was conducted along with a safety index, "characteristic deflection" which is relatively free from the influence of dynamic disturbances due to such factors as the roughness of the road surface and a structural anomaly parameter (Miyamoto & Yabe 2012).

2.2 *Concrete core tests*

2.2.1 *Extract of concrete cores*

In this study, concrete cores were extracted from Girder 1 to Girder 5 of Spans 1 and 3 (Figure 2), which are the inspected girder spans. The coring locations are shown in Figure 4 for Spans 1 and 3 with cross dots (⊕), white dots (○) and black dots (●). The concrete cores were extracted from four regions roughly demarcated according to cross beam locations in each span. It was assumed, for purpose of this study that each core shows the average state of internal deterioration in each region (Widyawati 2015). The extracted concrete cores were examined for chloride ion content test called C-series that is identified as ⊕ and "C". The numbers of C-series are 11 specimens for Span 1 and 12 specimens for Span 3. M-series were examined for carbonation test that is identified as ○ and "M". The numbers of M-series are 15 specimens for Span 1 and 20 specimens for Span 3. Furthermore, S-series were examined for both carbonation and chloride ion content tests that is identified as ● and"S"with 6 specimens for both Span 1 and 2.

2.2.2 *Chloride ion test*

The concrete cores of C-series were analysed for chloride ion content. The concrete cores at depth between 0 and 105 mm in depth direction were divided into seven pieces (at interval of 15 mm) and, thus, prepared for analysing the chloride ion content. The measurement was conducted in accordance with JIS A 1154: 2003; "Methods of test for chloride ion content in hardened concrete" and the specimens were examined down to the depth at which the initial chloride ion content could be determined. In the test method, the total amount of chloride ion contained in the powder sample which is extracted with nitric acid, and its mass rate to the sample was measured.

2.2.3 *Carbonation test*

The concrete cores of the M-series were analysed for carbonation test. The measurement of carbonation depth was conducted in accordance with JIS A 1152: 2011; "Method for measuring carbonation depth of concrete". The carbonation test is most commonly carried out by spraying 1% phenolphthalein solution on the surface of the concrete cores. The carbonation depth was assessed using 1% phenolphthalein solution, the indicator that appears pink (or purple) in contact

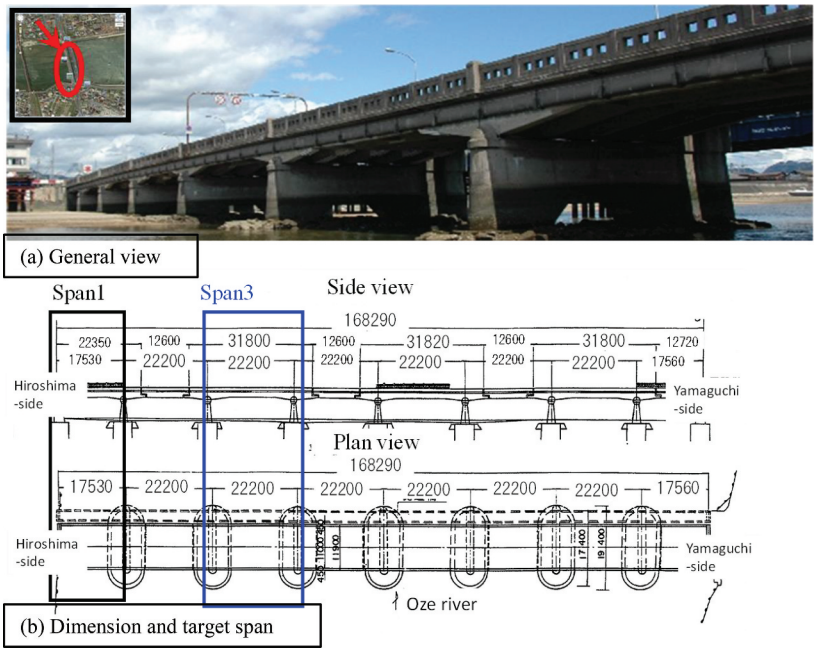


Figure 2. Details of SK-Bridge (before removal) and inspection area (span) (unit: mm).

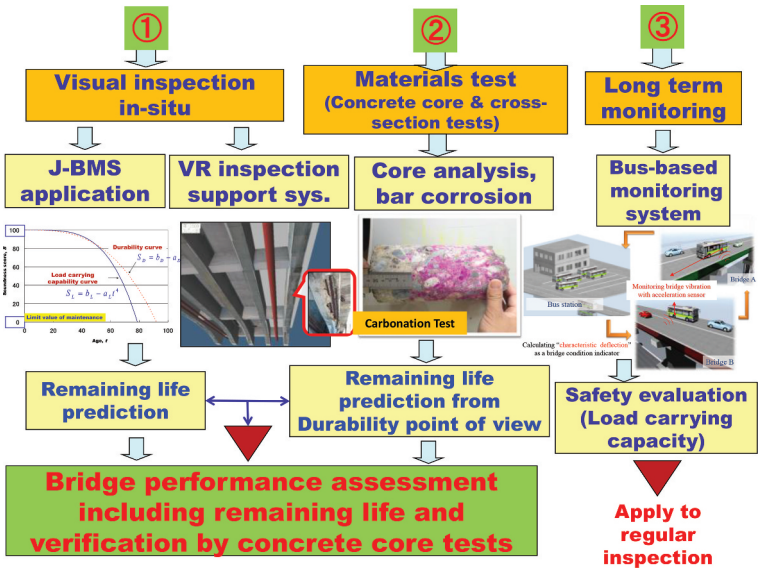


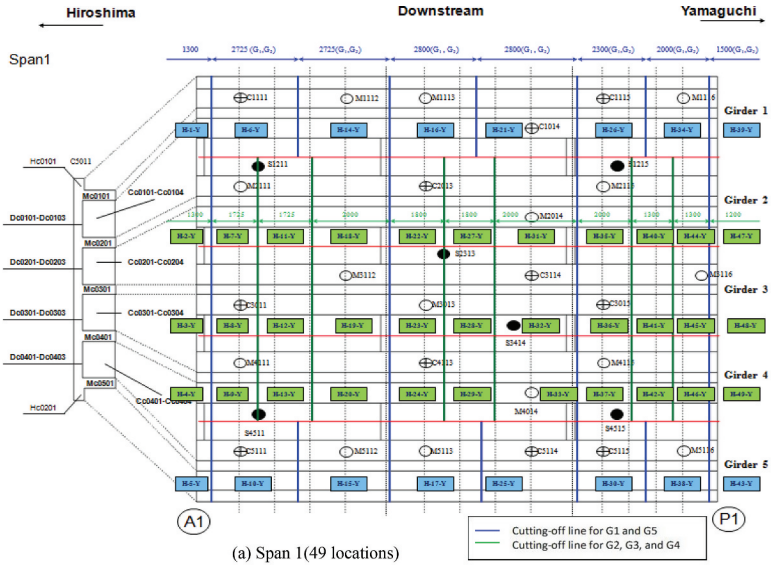
Figure 3. Concept and flow of field tests for remaining life prediction.

with alkaline concrete. Collared area is detected alkaline area, defined as the healthy concrete area (un-carbonated). Collarless area is defined as the carbonation area. To avoid further carbonation on the cutting-off surface, the carbonation test was carried out immediately within 30 minutes after cleaning. Carbonation depth is the distance between the concrete cover surface and the boundary between collared and uncollared areas.

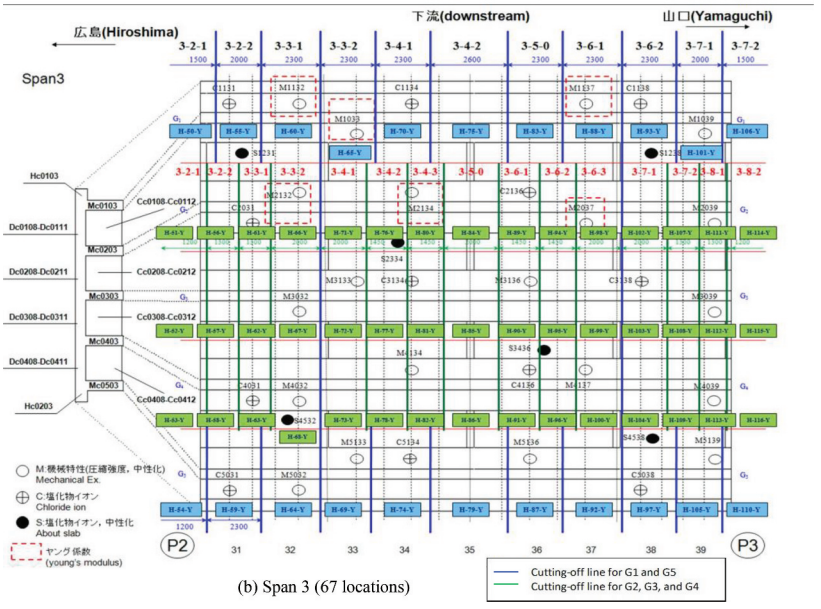
2.3 *Cross-section cutting-off girder examinations*

2.3.1 *Cross-section cutting-off girders*

The demolition of the bridge provided a good opportunity to obtain many types of useful information. Two spans, Span 1 and Span 3, shown in Figure 2, were inspected. Each span consisted of five girders, Girder 1 (G1) through Girder 5 (G5) (see Figure 4). The girders had been cut into pieces with the maximum weight approximately 10 tons, in order to move from the bridge location to the demolishing place. The cross-section cutting-off girders locations with the identification symbol for each cross-section cutting-off girders are shown in Figure 4(a) for Span 1 and Figure 4(b) for Span 3. Figure 5 shows an example of cross-section cutting-off girder after



(a) Span 1(49 locations)



(b) Span 3 (67 locations)

Figure 4. Location of concrete cores extracted and cross-section cutting-off girders.



Figure 5. Example of cross-section cutting-off girder of SK-bridge.

spraying phenolphthalein. The total number of cross-section cutting-off girders of Span 1 and Span 3 were 49 and 67, respectively. Each cross-section cutting-off girders has an identification symbol. It was given the identity as: H-number-Y, where "H" is Hiroshima side and "Y" is Yamaguchi side. "Number" is the number of cross-section cutting-off girders, 1 to 116 pieces.

2.3.2 *Examination of cross-section cutting-off girders*

The demolition of SK-Bridge began with the removal of each span of the main girders of the bridge. The first girder removed was the outer girder on the mountain side, G5. The outer girder on the sea side, G1, was removed next, and then the inner girders, G4, G2, and G3 were removed.

After the girders were removed from the bridge, they were placed on a temporary bridge. The cutting process used the special equipment for cutting concrete called a wire saw machine with the diamond wire. The cross-section cutting-off girder was cut with a maximum weight approximately 10 tons, it is the maximum weight that could be moved by a truck to a particular place to be demolished.

2.3.3 *The thickness of concrete cover measurement*

The cross-sections cutting-off girders were examined to measure the thickness of the concrete cover on the reinforcement. The thickness of the concrete cover is very important because the concrete cover serves to protect the reinforcing bars from damage due to environmental exposure. Among the environmental effects that may cause corrosion in reinforcing bars are attacked by carbon dioxide, acid, and salt (Papadakis, et al. 1991). As well known, corrosion in the reinforcing bar affected the deterioration of the reinforced concrete structures. Therefore, the thickness of concrete cover should be controlled to meet the minimum requirements needed. The thickness of concrete cover is the thickness of concrete between the concrete cover surface and the outer reinforcing bar. In this investigation, the location of embedded reinforcing bars is quite varied. Then, the value of thickness of concrete cover was assumed by average values of the measurement. This was measured for the sea sides, bottom sides, and mountain sides of the girders.

2.3.4 *Carbonation depth measurement*

Carbonation tests are most commonly carried out by spraying a phenolphthalein solution on freshly exposed surfaces of concrete or on concrete cores. In this study, this carbonation test method was applied to the cross-section surfaces of the cross-section cutting-off girders. To avoid further carbonation of the cut surfaces, the carbonation tests were conducted within 30 minutes of the cross-section surfaces being cleaned and prepared for testing. In accordance with Japanese Industrial Standard JIS A 1152, the carbonation depth was assessed by examining the area of the surface that appeared pink or purple after application of the phenolphthalein solution. The concrete in areas where this coloring appears is alkaline and is considered to be healthy and to have experienced no carbonation. The concrete in areas that remain collarless is not alkaline and is considered to be concrete that has experienced carbonation. The carbonation depth of the cross-section cutting-off girders was also measured. The carbonation depth is the distance between the concrete cover surfaces and the boundary between the collared and uncollared areas.

3 TEST RESULTS AND REMAINING LIFE PREDICTION

3.1 *Results of the thickness of concrete cover measurement*

Table 1 shows the thickness of concrete cover measurement results for the cross-section cutting-off girders from Spans 1 and 3. The results shown are the averages of the values obtained by measuring the distances between the concrete cover surface and the outer reinforcing bars. In an RC bridge, the most serious deterioration mechanisms are those that lead to corrosion of the reinforcing bars, resulting in a reduction in the effective cross-sectional area of the reinforcing bars and in spalling of the concrete cover. The nature of the deterioration in an RC bridge may be chemical, such as reinforcing bar corrosion due to carbon dioxide and chloride attack on the concrete. Concrete cover serves to protect the reinforcing bars from environmental exposure that leads to corrosion. In the deterioration process caused by carbonation, the thickness of concrete cover affects the time required for carbon dioxide to reach the reinforcing bars. A thicker concrete cover increases the diffusion time of carbon dioxide in the concrete.

Table 1. Thickness of concrete cover and carbonation depth (average) of Spans 1 and 3.

		Thickness of concrete cover			Carbonation depth		
No.	Girder SPAN 1	Sea side mm	Bottom side mm	Mountain side mm	Sea side mm	Bottom side mm	Mountain side mm
1	G1	56.44	49.06	51.25	65.49	27.39	58.76
2	G2	68.33	55.35	61.05	51.57	38.71	49.25
3	G3	47.17	54.92	50.38	61.05	49.68	64.90
4	G4	52.83	52.58	48.72	75.15	63.19	82.13
5	G5	48.92	63.41	68.00	69.84	46.57	72.13
+Average		54.74	55.06	55.88	64.62	45.11	65.43
	SPAN 3						
6	G1	49.79	45.59	42.70	59.88	22.29	55.83
7	G2	64.98	45.82	49.06	62.43	25.17	57.78
8	G3	40.38	56.15	76.81	58.36	43.33	50.81
9	G4	82.10	53.28	43.63	72.02	50.01	64.71
10	G5	59.85	51.47	62.96	55.72	43.83	56.18
Average		59.42	50.46	55.03	61.68	36.93	57.06

3.2 *Carbonation depth measurement results and carbonation rate coefficient*

The carbonation depth measurement results for the cross-section cutting-off girders from Spans 1 and 3 are also shown in Table 1. The results shown are the averages of the values obtained from five to ten measurement points. The carbonation rate, which can be obtained from the carbonation depth measurements, can be used to predict the carbonation depth in future years. The thickness of concrete cover and the carbonation depth can be used to predict the initiation of corrosion due to carbonation. The initiation of corrosion is frequently identified from the remaining concrete cover, i.e., the difference between the thickness of concrete cover and the carbonation depth. In previous studies (JSCE 2013), researchers have concluded that the initiation of corrosion occurs when the remaining concrete cover falls below 10 mm. Thus, the remaining cover affects the initiation of corrosion.

The carbonation rate coefficient, A can be determined from measurements of the carbonation depth, $d(t)$ in mm at time (t) in years. The change in the carbonation depth over time is calculated according to the $\sqrt{t}$ rule, as shown in Eq. (1):

$$d(t) = A\sqrt{t} \tag{1}$$

The carbonation depth results are the averages of the values obtained from eight to sixteen measurements from the cross-section cutting-off girders from each span.

3.3 *Chloride ion content and main deterioration factor*

Table 2 shows the chloride ion data obtained from the concrete core tests on the SK-Bridge. The apparent chloride ion diffusion coefficient was calculated from the following equation:

$$C(x,t) = C_0 \cdot \left(1 - erf\left[\frac{x}{2\sqrt{(D_{ap} \cdot t)}}\right]\right) + C_i(x,0) \quad (2)$$

Table 2. Results of chloride ion content analysis.

Girder No.	Core specimen No.	Surface chloride ion content C_0 (kg/m^3)	Apparent diffusion coefficient x 10^{-8} D_{ap} (cm^2/s)	Initial chloride ion content $C_i(x, 0)$ (kg/m^3)	Chloride ion content at reinforcement location $C(x,t)$ (kg/m^3)
SPAN 1					
1	C1014	1.10	0.60	0.60	1.00
	C1111	0.60	0.50	0.40	0.60
	C1115	0.80	0.60	0.60	0.90
2	C2113	2.30	0.90	0.65	1.80
3	C3011	2.50	1.80	0.90	2.50
	C3015	2.60	1.80	0.50	2.10
	C3114	3.80	1.50	0.80	3.00
4	C4113	3.10	0.40	0.40	1.30
5	C5111	3.90	1.80	0.80	3.20
	C5114	1.80	1.80	0.60	1.70
	C5115	1.40	1.80	0.30	1.20
SPAN 3					
1	C1131	0.70	0.40	0.40	0.60
	C1134	0.70	0.08	0.30	0.30
	C1138	0.90	0.40	0.30	0.55
2	C2031	2.50	0.40	0.50	1.20
	C2136	1.90	0.40	0.65	1.20
3	C3134	1.00	0.40	0.10	0.40
	C3138	0.70	0.10	0.15	0.18
4	C4031	0.90	0.08	0.18	0.20
	C4136	1.20	0.05	0.12	0.12
5	C5031	1.30	0.05	0.20	0.20
	C5134	1.10	0.05	0.12	0.12
	C5038	0.80	0.05	0.30	0.30

where $C(x,t)$ is the chloride ion content at depth x at time t, C_0 is the chloride ion content at the concrete surface, D_{ap} is the apparent chloride ion diffusion coefficient, and $C_i(x,0)$ is the initial chloride ion content in the concrete. Table 2 also summarizes the results of the

chloride ion content tests (i.e., $C(x,t)$, C_0, and $C_i(x,0)$) of the concrete cores. The apparent chloride ion diffusion coefficient, D_{ap} is an unknown parameter in Eq. (2) and is determined from the results of the chloride ion content tests. The results obtained for depths of 30–45 mm in the concrete cores were used as the chloride ion contents at the reinforcement depth, $C(x,t)$.

According to the Standard Specifications for Concrete Structure Maintenance of the Japan Society of Civil Engineers (JSCE) (JSCE 2013), corrosion due to carbonation typically begins when the thickness of remaining concrete cover falls below 10 mm. This means that remaining concrete cover is an indicator of the degree of influence of carbonation. Table 1 shows the results of the concrete cover thickness and carbonation depth measurements. The average carbonation depths in the main girders of both Span 1 and Span 3 are greater than the average of the thickness of concrete cover, except for the bottom side of Span 3, which has received some repair work. The maximum carbonation depth was 60 mm or greater in more than half of the cross-section cutting-off girders, which is considerably greater than the thickness of the concrete cover.

The average chloride ion content determined from the tests on the concrete cores taken from the SK-Bridge was 1.07 kg/m^3, as shown in Table 2. This value is lower than the critical chloride ion content for steel corrosion of 2.0 kg/m^3. Table 2 also shows that only four of the 23 points on the bridge had chloride ion contents higher than the critical content for steel corrosion, and these contents were only slightly higher than the critical chloride ion content. Based on these results, it was concluded that the main cause of the deterioration of the SK-Bridge was carbonation because the carbonation depth was considerably greater than the thickness of concrete cover. The average chloride ion content did not exceed the critical chloride ion content for steel corrosion. However, given that the bridge is located less than 1 km upstream from the mouth of the Sagawa River that it spans, which empties into the Seto Island Sea, chloride ion attack is believed to have also contributed to the deterioration of the bridge.

3.4 *Service life prediction*

In this study, the end of the service life was defined as the point at which the cumulative amount of steel corrosion due to carbonation and chloride ion attack reached a critical value of Q = 75 mg/cm^2. This value was obtained from the J-BMS BREX system, which is used in cases in which the main deterioration factor is chloride attack.

The service life, SL in years can therefore be expressed as the sum of the elapsed service life, EL (in this case, 72 years) and the remaining service life, R in years, as shown in Eq. (3):

$$SL = EL + R \tag{3}$$

Although carbonation was concluded to have been the main factor in the deterioration of the SK-Bridge, based on its location, approximately 1 km upstream from the mouth of the river it spans, chloride ion attack was concluded to also have affected the deterioration of the bridge.

Figure 6 shows a flowchart of the service life prediction method for the case in which the deterioration is mainly caused by carbonation but is also affected by chloride ion attack. Initial corrosion due to carbonation is assumed to begin when the remaining concrete cover, i.e., the thickness of the concrete cover minus the carbonation depth, is 10 mm or less.

The carbonation depth at 72 years was obtained from the measurements of the cross-section cutting-off girders. The carbonation rate coefficient, A was calculated from the carbonation depth, $d(t)$ at time t using Eq. (1).

Eq. (4) is used to calculate the steel corrosion rate, V if the remaining concrete cover is 10 mm or less. If the remaining concrete cover at time t is greater than 10 mm, Eq. (5) should be used.

$$V = 1.32(Cl - 1.2)k \tag{4}$$

$$V = (0.840W - 0.145C + 1.32Cl + 0.0293W \cdot C - 0.0917C \cdot Cl + 0.658Cl \cdot W - 2.52)k \tag{5}$$

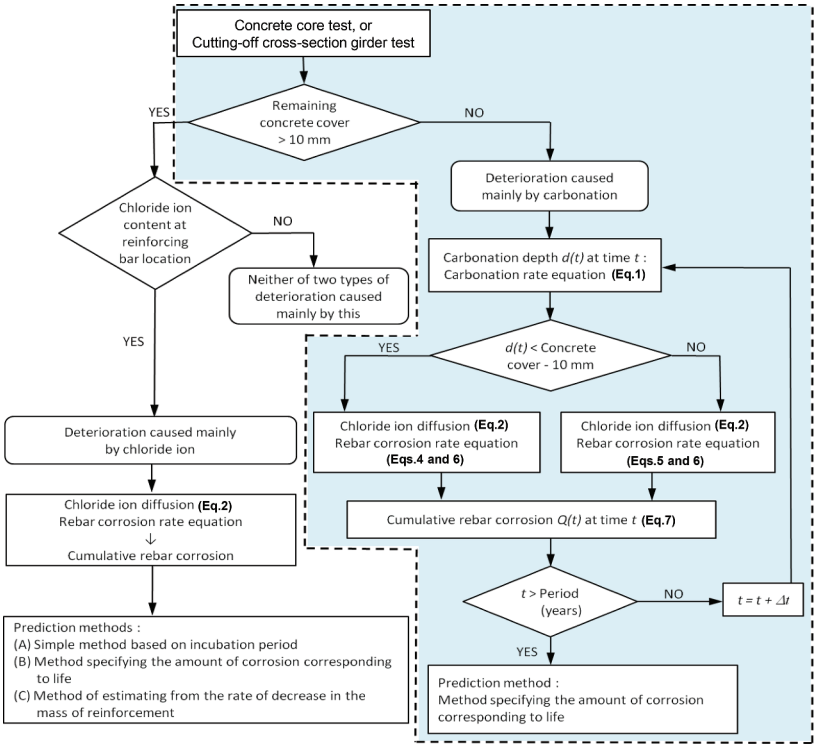


Figure 6. Flowchart of remaining life prediction.

where, V (mg/cm^2/year) is the steel corrosion rate, Cl (kg/m^3) is the chloride ion content at the reinforcement location, C (mm) is the remaining concrete cover, W (%) is the moisture content of the concrete surface, and k is a correction for the temperature parameter, tmp (°C), which can be calculated from Eq. (6):

$$k = 1 + 0.0381(tmp - 20) \tag{6}$$

The cumulative amount of steel corrosion, $Q(t)$ at time t, in kg/mm^2, can be calculated from the steel corrosion rate, $V(t)$ at time t and the integration time step, dt using Eq. (7):

$$Q(t) = Q(0) + \sum_{t=dt}^{t=X} \left(\frac{dt}{2} \left(V\left(t - \frac{dt}{2}\right) + V\left(t + \frac{dt}{2}\right) \right) \right) \tag{7}$$

where, $Q(0)$ can be calculated using Eq. (8):

$$Q(0) = \frac{dt}{4} \left(V(0) + V\left(\frac{dt}{2}\right) \right) \tag{8}$$

As in a previous study (Widyawati 2015), the remaining life, R of the SK-Bridge, as indicated by the results of the tests on the concrete cores, was calculated as the life expectancy, X in years minus the period of service, N in years. In this study, the service life, SL was calculated based on the time $t = t_1$ elapsed before the total amount of steel corrosion, calculated using Eq. (7), reaches the critical value, $Q(t)$ = 75 mg/cm^2, which was taken to be the indicator of the end of the service life. This is the critical value for the total amount of steel corrosion used in the prediction method of the J-BMS BREX system.

Based on the schematic illustration of the service life prediction (Figure 1), the propagation stage can be defined as when cracking occurs due to corrosion. Cracking will occur if the cumulative amount of steel corrosion exceeds approximately 10 mg/cm^2, which is considered to be the critical amount of corrosion corresponding to initial cracking. The deterioration stages are defined by the critical value of the total amount of steel corrosion, i.e., 75 mg/cm^2. Service life prediction was conducted for the cross-section cutting-off girders listed in Figure 4. The values used for *tmp* in Eq. (6) and *W* in Eq. (5) were 16 °C (mean temperature) and 4%, respectively.

Table 3 shows the results of the service life prediction. These results show that the time before reaching the critical amount of corrosion for initial cracking for the sea sides, bottom sides, and mountain sides of the girders were, on average, 55.6 years, 104.6 years, and 56.3 years, respectively. The service life prediction, based on the cumulative amount of steel corrosion reaching 75 mg/cm^2, were, on average, 81.5 years, 142.6 years, and 81.2 years for the sea sides, bottom sides, and mountain sides of the girders, respectively. As these results show that the predicted service life varies from -33.6 years to 217.7 years.

Table 3. Results of service life prediction for both span 1 and span 3 (on average).

Span	No.	Girder No.	Seaside			Bottom side			Mountain side		
			Q=10mg/cm^2	Q=75 mg/cm^2		Q=10mg/cm^2	Q=75 mg/cm^2		Q=10mg/cm^2	Q=75 mg/cm^2	
			Cracking limit	Service life	Remaining life	Cracking limit	Service life	Remaining life	Cracking limit	Service life	Remaining life
			(years)	*SL* (years)	*R* (years)	(years)	*SL* (years)	*R* (years)	(years)	*SL* (years)	*R* (years)
Span 1	1	G1	52.1	72.8	0.8	131.9	217.7	145.7	43.5	64.6	-7.4
	2	G2	97.5	116.8	44.8	98.9	135.2	63.2	94.3	112.1	40.1
	3	G3	28.9	41.9	-30.1	55.0	88.0	16.0	31.7	47.0	-25.0
	4	G4	28.5	48.4	-23.6	49.1	68.0	-4.0	21.5	38.4	-33.6
	5	G5	25.7	39.3	-32.7	77.7	96.2	24.2	46.6	63.6	-8.4
Span 3	6	G1	42.3	75.6	3.6	136.0	147.8	75.8	30.3	56.9	-15.1
	7	G2	64.8	84.3	12.3	196.5	250.8	178.8	40.1	58.4	-13.6
	8	G3	49.2	79.8	7.8	191.6	231.1	159.1	177.1	220.4	148.3
	9	G4	78.7	123.2	51.2	71.6	117.8	45.8	34.7	72.5	0.5
	10	G5	87.9	133.2	61.2	38.0	73.0	1.0	43.0	78.0	6.0
Average (years)			**55.6**	**81.5**	**9.5**	**104.6**	**142.6**	**70.6**	**56.3**	**81.2**	**9.2**

3.5 *Discussions*

3.5.1 *Result of service life prediction*

The service life prediction shown in Table 3 are based on the cumulative amount of steel corrosion reaching 75 mg/cm^2, which is the same as the criterion used in the J-BMS BREX system, which is used in cases in which the main cause of deterioration is chloride attack. The service life prediction were almost the same for the sea sides and mountain sides of the girders, i.e., 81.5 years and 81.2 years, respectively. This means that for the sea side and the mountain side of the SK-Bridge, the service life prediction is approximately 81 years. The service life prediction for the bottom side is much longer, approximately 142 years, because of repair work done on the bottom side. This repair work was proven to work well. It effectively extended the service life by approximately 60 years, compared with that for the sea side and the mountain side.

3.5.2 *Comparison between service life prediction by concrete cores test and cross-section cutting-off girders examination*

Concrete cores were extracted from all of the girders in Spans 1 and 3, but only on the sea and mountain sides. On the bottom side, it was quite difficult to extract concrete cores because of the reinforcing bars embedded in the bottoms of the girders. In a previous study (Takahashi, et al. 2014), the service life prediction of the SK-Bridge, based on tests on concrete cores, was found to be approximately 77 years (remaining life of approximately 7 years). This service life prediction is similar to the values predicted in this study for the sea and mountain sides of the bridge, based on tests on the cross-section cutting-off girders, i.e., approximately 81 years (remaining life of

approximately 9 years). Service life prediction based on concrete cores represents the locations from which the cores were extracted. In contrast, service life predictions based on cross-section cutting-off girders represent the entire girders. The two sets of service life prediction were compared. The results are shown in Figures 7 and 8. The relationships between the service life predictions from the concrete cores and those from the cross-section cutting-off girders had correlation coefficients of 0.73 and 0.71 for Spans 1 and 3, respectively, on the sea side and 0.57 and 0.59 for Spans 1 and 3, respectively, on the mountain side. These correlation coefficients indicate good correlation. The service life predictions obtained on the basis of the core testing were similar to those obtained based on the testing of the cross-section cutting-off girders, which represent the entire span of the bridge.

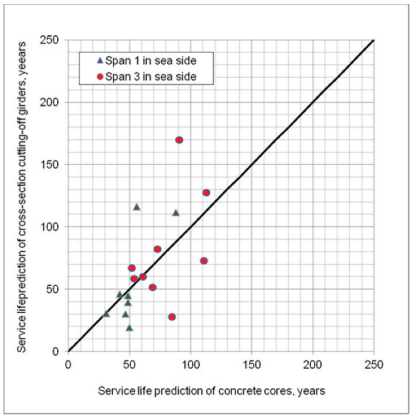


Figure 7. Relationship between service life prediction of concrete cores and cross-section cutting-off girders at 72 years on the sea side (on averages).

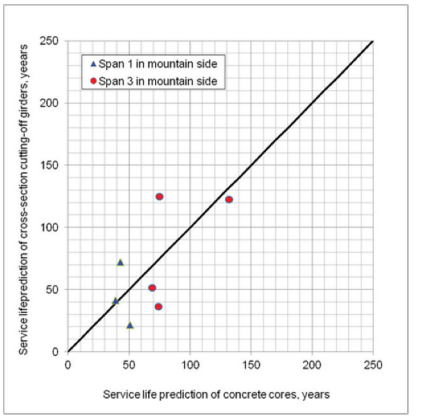


Figure 8. Relationship between service life prediction of concrete cores and cross-section cutting-off girders at 72 years on the mountain side (on averages).

4 CONCLUSIONS

This paper presents the details of carbonation tests and proposes a method to predict the remaining life of an RC bridge (72 years in service) based on the extent of deterioration related to corrosion of the reinforcing bars due to carbonation and chloride attack. Main conclusions of the paper are summarized as follows:

1) The results of the carbonation tests showed that the main factor in the deterioration of the bridge has been carbonation associated with corrosion of the reinforcing bars. However, because the bridge is located less than 1 km upstream from the mouth of the river it spans, which flows into the sea, chloride ion attack should be considered as another factor in the bridge's deterioration.
2) The end of the service life of the bridge was defined as the point at which the total amount of steel corrosion reached a critical value of Q = 75 mg/cm^2. The predicted service life of the SK-Bridge was predicted to be approximately 81 years (remaining life = 81 years – 72 years = 9 years) for the sea side and mountain side, and approximately 142 years (remaining life = 142 years – 72 years = 70 years) for the bottom side. The predicted service life for the bottom side was longer than for the other side because of repair work done on the bottom side.
3) The extent of carbonation is typically assessed by conducting visual inspections or examining concrete cores. However, in this study it was possible to conduct carbonation tests on cross-section cutting-off from girders from an existing bridge. The carbonation tests yielded a considerable amount of information, but the results exhibited some variability. Therefore, the results of the carbonation tests of the cross-sections cutting-off girders were verified by conducting carbonation tests on concrete cores. The service life estimates

obtained on the basis of the core testing were similar to those obtained on the basis of the testing of the cross-section cutting-off girders, which represent the entire span of the bridge.

4) The results of comparison between service life prediction for the case in which the deterioration is mainly caused by carbonation and also affected by chloride ion attack and for the case in which the deterioration is caused only by carbonation in the sea sides and mountain sides of the girders on both cases were almost similar, approximately 80 years. This caused by the differences in the requirements and thresholds used in determining the end of life on these cases and the different equations were used.

REFERENCES

Japan Society of Civil Engineers (JSCE), 2013. Standard Specifications for Concrete Structures: Maintenance, (in Japanese), *JSCE Guidelines for Concrete*, Japan Society of Civil Engineers (JSCE), Tokyo.

Miyamoto, A. and Yabe, A. 2012. Development of Practical Health Monitoring System for Short- and Medium-span Bridges based on Vibration Responses of City Bus, *Journal of Civil Structural Health Monitoring*, 2, pp.47–63.

Miyamoto, A., Motoshita, M. 2015. Development and Practical Application of a Bridge Management System (J-BMS) in Japan, *Civil Engineering Infrastructures Journal*, 48(1), pp.189–216.

Miyamoto, A., Asano, H. 2018. Application of J-BMS to Performance Evaluation and Remaining Life Prediction of an Existing RC Bridge, *Civil Engineering Infrastructures Journal*, 51(2), pp.311–337.

Papadakis, V. G., Vayenas, C. G. and Fardis, M. N. 1991. Physical and Chemical Characteristics Affecting the Durability of Concrete, *ACI Materials Journal*, Title no. 88-M24, March-April, pp.186–196.

Sarja, A. 2006. Predictive and Optimized Life Cycle Management, *Building and Infrastructure*, Taylor & Francis, UK.

Takahashi, J., Emoto, H. and Miyamoto, A. 2012. A Proposal on Bridge Soundness Evaluation System's Verification Method based on Concrete Core Testing, *Proceedings of the Japan Concrete Institute*, 34 (2), pp.1399–1404.

Takahashi, J., Widyawati, R., Emoto, H. and Miyamoto, A. 2014. Remaining Life Prediction of an Aged Bridge based on Concrete Core Test, Proc. of the Japan Concrete Institute, 36(2), pp.1339–1344.

Widyawati, R. 2015. Development of a Method of Remaining Life Prediction for an Aged Bridge based on Concrete Cores and Cross-section Cutting-off Girders", *PhD Thesis at Yamaguchi University*, Yamaguchi, Japan.

Bridge Maintenance, Safety, Management, Digitalization and Sustainability – Jensen, Frangopol & Schmidt (eds)
© 2024 The Author(s), ISBN 978-1-032-77040-6
Open Access: www.taylorfrancis.com, CC BY-NC-ND 4.0 license

Behavior analysis of an integrated column by multiple steel pipes using monitoring measurement

S. Akamatsu & M. Hattori
Hanshin Expressway Research Institute for Advanced Technology, Osaka, Japan

Y. Taniguchi, M. Nishimura & Y. Aoki
Hanshin Expressway Company Limited, Osaka, Japan

S. Miyata
Dia Nippon Engineering Consultants Co., Ltd., Tokyo, Japan

K. Sugiura
Graduate School of Engineering, Kyoto University, Kyoto, Japan

ABSTRACT: Monitoring measurements have been conducted on an integrated columns by multiple steel pipe applied to actual bridges to verify that the pier behave according to the concept assumed in the design. In this measurement, the response is measured for both ordinary conditions and small earthquake conditions. This study proposes a method for verifying the performance of an integrated column by multiple steel pipe using the measured data, and evaluated the performance of the piers using the measured data obtained so far. For ordinary conditions, the measured data were used to verify that the behavior of the piers was as assumed in the design, and for small earthquake conditions, the validity of the analysis model was verified by reproduction analysis using observed waveforms.

1 INTRODUCTION

In the Hanshin-Awaji Earthquake of 1995, piers collapsed or were severely damaged, and it took a long time to restore them. Therefore, Hanshin Expressway developed an integrated column by multiple steel pipes that have higher earthquake resistance than reinforced concrete piers or steel piers, and can be restored easily and quickly.

An integrated column by multiple steel pipes is a single column composed of four steel pipes connected by shear links that incorporate shear panels with historical damping functions. In this structure, vertical loads such as dead and live loads are supported by steel pipes, and horizontal loads such as seismic forces are resisted by shear links. In the event of Level2 earthquake, which is specified in the Specifications for Highway Bridges, Part V Seismic Design [1], the damage is concentrated in the shear panels so that the steel pipes remain sound, allowing vehicles to pass through quickly after the earthquake. In addition, during emergency inspections after an earthquake, the shear panels are damaged before other members, thus limiting the number of members to be inspected. Furthermore, in the event of damage that requires restoration, performance can be restored simply by replacing the shear panels, thereby contributing to the reduction of seismic life-cycle costs.

These concepts have been verified through analysis and experimentation and applied to actual structures such as the Ebie Junction and Nishi-Senba Junction on the Hanshin Expressway. However, it has not been verified whether the columns behave according to the concepts in the actual structure. In response, a monitoring plan based on the structural characteristics of integrated column by multiple steel pipes was developed, and the behavior of the actual bridge has been measured since April 2021.

In this study, we proposed a method for evaluating the performance of integrated columns by multiple steel pipes using the measured data. Furthermore, an example of the performance evaluation of integrated column by multiple steel pipes is shown using the data measured so far.

DOI: 10.1201/9781003483755-12

2 TARGET STRUCTURE AND MEASUREMENT

2.1 *Target structure*

The integrated column by multiple steel pipes targeted for evaluation was applied to the PD4 of the D-ramp (1), which is the crossing line from the Kobe Route to the Yodogawa-sagan Route at the Ebie JCT. A plan view of the D-ramp (1) is shown in Figure 1 (processed from an aerial photograph). The D-ramp (1) bridge including PD4 is a 5-span continuous steel box girder bridge with orthotropic steel deck between PD1 and PD5 (92.7 + 60.5 + 50.5 + 49.0 + 78.9 = 331.6 m). The end bearings are movable at PD1 and fixed at PD5, and the piers between them are rigidly connected. The height from the ground surface to the superstructure of PD4 is about 30 m, the highest of all the piers on the D-ramp (1), and is a location where the characteristics of the integrated column by multiple steel pipes can be fully utilized. The piers other than PD4 are conventional rectangular section steel piers.

A structural drawing of the PD4 is shown in Figure 2. PD4 consist of four steel pipes, connected by shear links in four cross-sections. A caisson foundation with a diameter of 7000 mm was adopted due to site constraints, and diameter of steel pipe and shear link dimension were determined from the caisson diameter. From the top of the caisson to a height of 13 m, including the second shear link from the bottom, the steel pipes are filled with concrete filling as in the case of conventional steel piers.

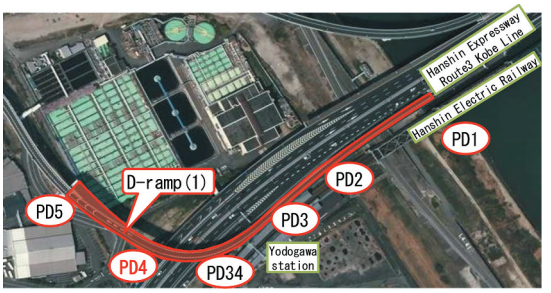


Figure 1. Bridge plan view of D-ramp (1).

2.2 *Measurement items*

The measurements based on the monitoring plan have been taken since April 2021. Figure 3 shows the locations of the measurement equipment and the names of the measuring points, and Figure 4 shows the installation status of the equipment.

The measurement cross section of the strain gauges was set at the base of the piers at 100 mm from the protective concrete, and at the top of the piers at a minimum distance of 100 mm from the fillet between the superstructure and the piers to avoid the effect of the stress concentration. Strain gauges were attached to each steel pipe at four points in the longitudinal and transverse direction and at 16 points per cross-section, and the direction of measurement was vertical direction. Accelerometers were set 100 mm below the ground surface and above each shear link of Pipe B, for a total of five locations. The measurement directions were the longitudinal direction, the transverse direction, and the vertical direction regarding the integrated column by multiple steel pipes.

Table 1 shows the frequency and duration of measurements. The effect of live load is measured once a year for about three days in spring, when traffic is average, and the effect of wind load is measured once a year for about one days when strong winds, such as typhoons. The effect of temperature load is affected by atmospheric temperature, so it is measured four times a year for about one week in spring, summer, fall, and winter. In the case of an earthquake, a trigger is determined by an accelerometer installed at the base of the steel pipe, and measurement is started when a certain level of acceleration occurs. In this measurement, the threshold value is set to 1 gal so that data can be obtained even for small seismic motions.

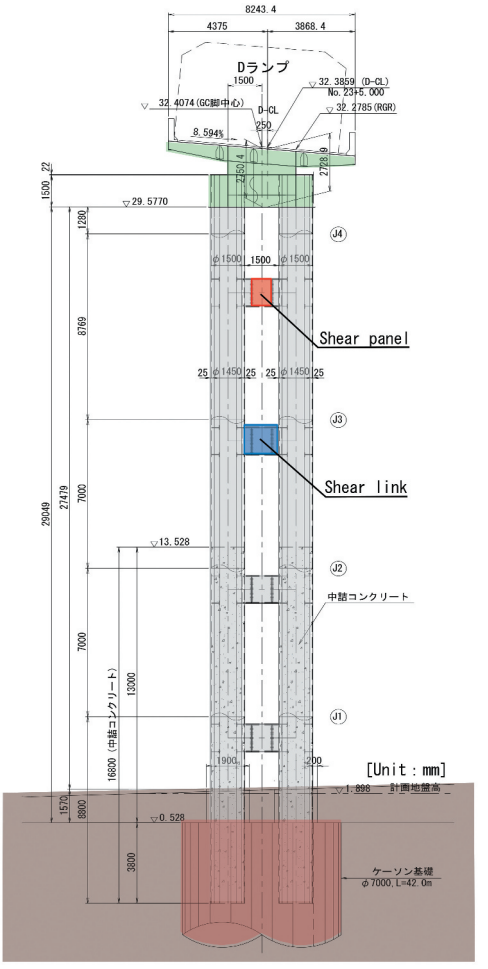


Figure 2. Structural drawing of PD4.

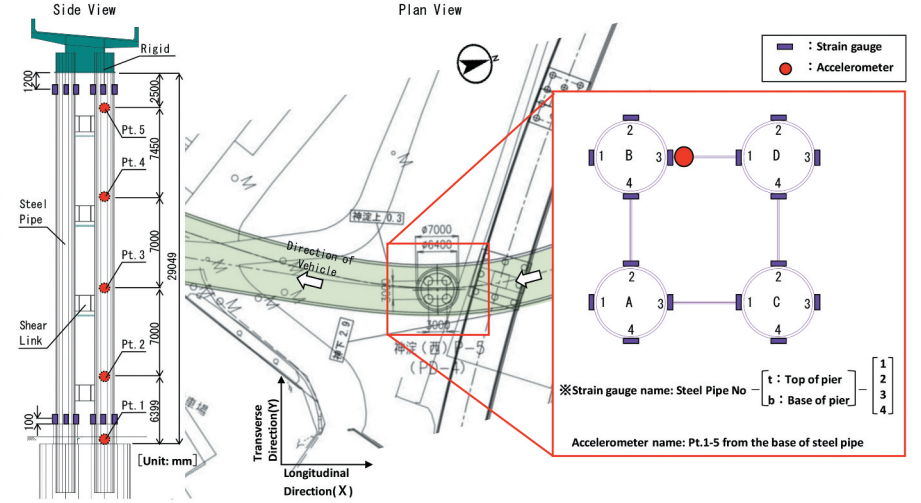
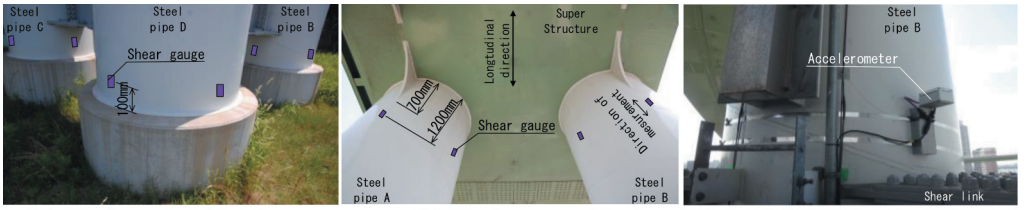


Figure 3. Locations of the measurement equipment and names of the measuring points.



(a) Strain gauge (Base) (b) Strain gauge (Top) (c) Accelerometer

Figure 4. Installation status of the equipment.

Table 1. Interval and duration of measurements.

Situation		Number of times and timing of measurements	Measurement Period
Ordinary Condition	Live Load	Once a year(Spring)	About 3 days
	Wind Load	Once a year(typhoon)	About 1 days
	Temperature Change	Four times a year (Spring・Summer・fall・winter)	About 1 week
Earthquake Condition	Level 1 Earthquake	At the time of earthquake	300 seconds after earthquake
	Level 2 Earthquake		
	Over Level 2 Earthquake		

3 PROPOSAL FOR PERFORMANCE EVALUATION USING MONITORING RESULTS

Figure 5 shows the performance evaluation flow using the measurement results. In this flow, when the performance can be evaluated directly from the measurements, the performance is evaluated by organizing and analyzing the measurement data. On the other hand, when the performance cannot be evaluated directly from the measurements, the performance is evaluated indirectly by reproducing the behavior of the structure through analysis. When using analysis, the reproducibility of the model is first verified by comparing the responses at the measured positions in the analytical model with the measured actions. If there is a discrepancy between the measurements and the analysis results, the analytical model is reviewed after analyzing the factors that may cause the discrepancy, and the performance of the integrated column by multiple steel pipes is evaluated using the analytical model whose reproducibility is verified. Here, we show an example of analysis based on these two evaluation methods.

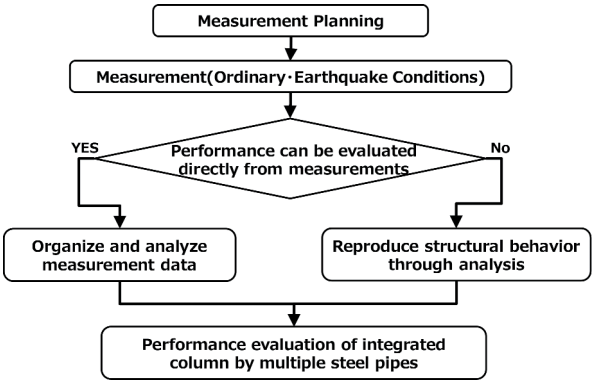


Figure 5. The flow of the proposed performance evaluation.

3.1 *Performance evaluation using measured data*

The following is an example of performance evaluation based on measured data for behavior under temperature change. The Integrated column by multiple steel pipes is assumed to "Four steel pipes resist horizontal loads as a single column". In contrast, since it is suspected that each steel pipe resists discretely, the behavior was analyzed using measured data during temperature change.

Among the measured data, the lowest outside temperature was 3.6°C at 5:38 on January 23, 2022, and the highest outside temperature was 39.1°C at 16:04 on July 23, 2022. Figure 6 shows the amount of change in pipe strain resulting from this temperature change (+35.5°C). Focusing on the strain at the base of steel pipes, the strain at the outer transverse direction of pipes B and D (B-b-2 and D-b-2) changed by +617 με and +649 με, respectively, and the strain at the outer transverse direction of pipes A and C (A-b-4 and C-b-4) changed by -350 με and -524 με, respectively. This is considered to capture the behavior of PD4 being pushed outward out of the curve due to the extension of the superstructure caused by the +35.5°C temperature change. And the strain at the outermost edge in the direction of extrusion is the maximum and minimum, respectively. In this manner the strain distribution behaves like a single column, so it was confirmed that the four steel pipes resist as a single column. On the other hand, the strain at the top of the steel pipes did not show the same tendency as that at the base of the pipes. This is because the strain at the top of the steel pipes includes not only the strain caused by the horizontal behavior due to temperature change but also the vertical strain caused by the live load.

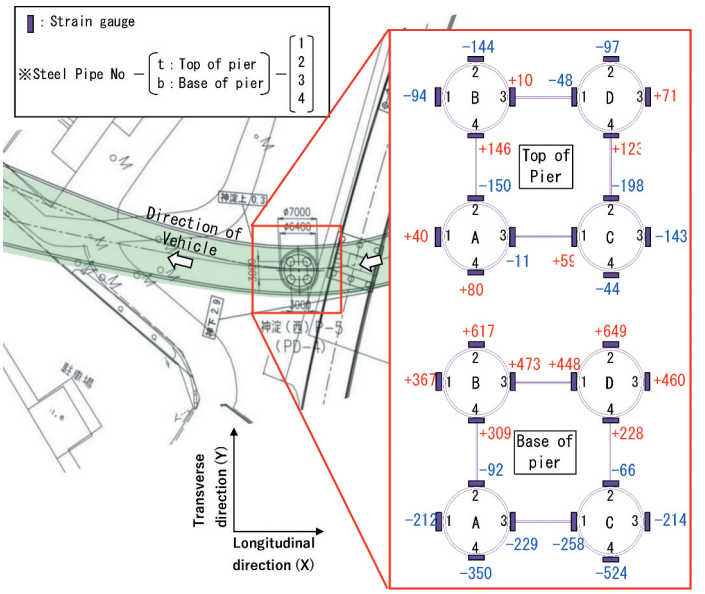


Figure 6. Change in steel pipe strain with temperature change (+35.5°C).

3.2 *Performance evaluation using analysis*

At 23:34 on March 31, 2022, a magnitude M4.3 earthquake occurred with its epicenter in the southern part of Kyoto Prefecture, recording a maximum intensity of 4 near Kameoka City, Fushimi-ku, Kyoto Prefecture. The seismic intensity of 2 was observed in Fukushima-ku, Osaka City, where Ebie JCT is located, and seismic observation data was obtained with the installed measurement equipment.

The integrated column by multiple steel pipes is designed to behave elastically in the event of small to medium-sized earthquakes. However, this behavior is difficult to evaluate from the limited number of measurement points shown in Figure 4 and from visual observation, so it is

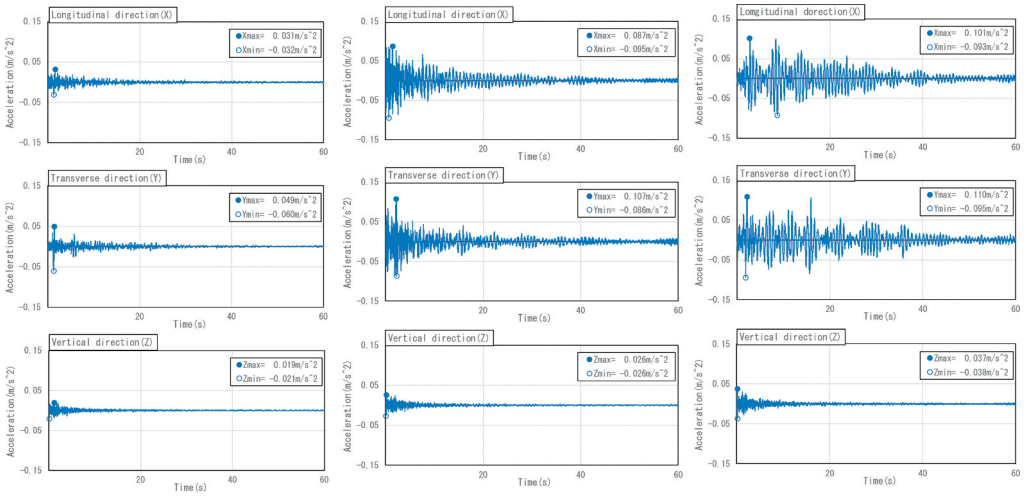
necessary to reproduce the behavior of the integrated column by multiple steel pipes during an earthquake by time history response analysis and to evaluate the behavior using the analytical model. On the other hand, it has been reported that the nonlinear dynamic analysis models generally used in seismic design do not match the behavior of small- and medium-scale earthquakes. Therefore, since the acceleration during the earthquake could be measured, although it was a small earthquake, we first used this observation data to confirm the reproducibility of the behavior using a general nonlinear dynamic analysis model.

3.2.1 *Observation waveform*

The time history waveforms of the acceleration at the measured points and the acceleration response spectra with 5% damping are shown in Figures 7 and 8. The points at the base of the pier (Pt. 1), the second shear link from the base (Pt. 3), and the fourth shear link from the base (Pt. 5) are shown here as representative points among the accelerometers shown in Figure 6.

3.2.2 *Modeling of target bridges*

The analytical model was a fiber model that can account for biaxial bending moments, axial force variation, and geometric nonlinearity for the entire system of D-ramp (1). Figure 9 shows the 3-D frame model of the entire bridge system and the modeling method for the integrated column by multiple steel pipes. The fiber elements of the steel pipe cross section of the PD4 piers were divided into 64 sections in the circumferential direction and 2 sections in the thickness direction.



(a) Pt.1 (b) Pt.3 (c) Pt.5

Figure 7. Observed acceleration response time history waveform.

The function separating type bridge supporting of the PD1 are modeled with linear spring elements in the longitudinal and transverse directions.

Since the purpose of this study is to analyze the behavior of the actual bridge, the yield strength of each member is based on the actual strength. For the PD4 piers, the yield strength was set based on the material tests, σ_y = 377 N/mm^2 for steel pipes (standard value: σ_y = 315 N/mm^2) and σ_y = 229 N/mm^2 for shear panels (standard value: σ_y = 225 N/mm^2). The yield strength of the pier members, except for the PD4 piers, was the average value of the statistical data, based on the results of the statistical data survey.

3.2.3 *Reproducibility of small earthquakes*

A dynamic analysis was conducted using the acceleration measured at Pt.1 as the input earthquake motion to confirm the reproducibility of the acceleration measured at Pt.3, Pt.4, and

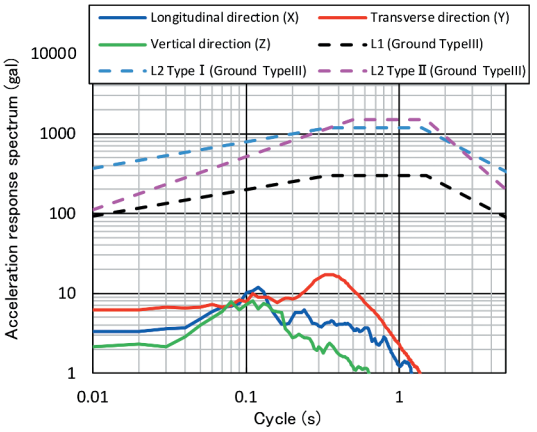


Figure 8. Acceleration response spectra of observed waveform (Pt.1).

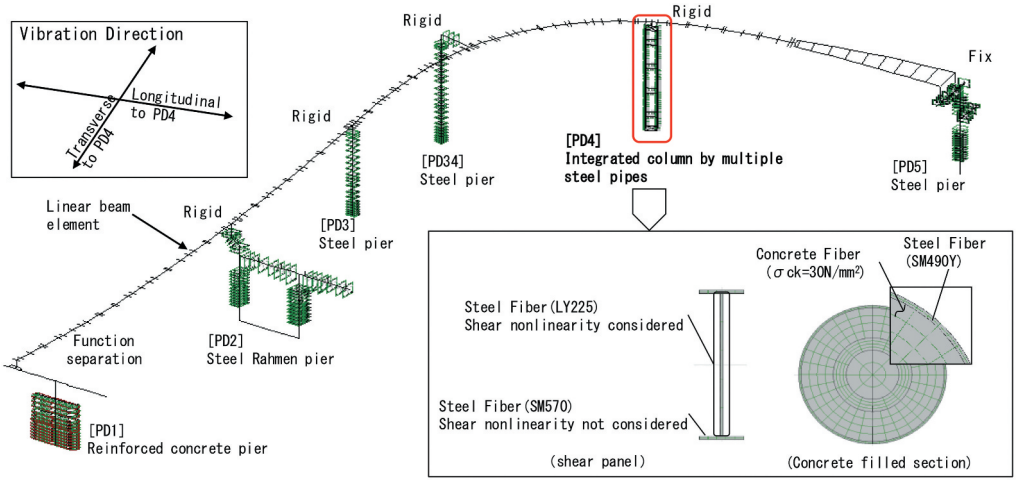


Figure 9. Analytical model of D-ramp (1) and the integrated column by multiple steel pipes.

Pt.5. Pt.1 is an accelerometer installed at the base of the PD4 pier, and this acceleration is the response acceleration waveform affected by the seismic response of the foundation structure and the interaction between the foundation structure and the ground. To use this response acceleration waveform as the input seismic motion, the boundary condition of the analytical model was fixed at the base of the piers, and the seismic motion was applied to the base of the pier. The earthquake motion was applied to the PD4 in three directions simultaneously: longitudinal, transverse, and vertical, in accordance with the direction of measurement. The general-purpose structural analysis program SeanFEM was used for the analysis.

Figure 10 shows a comparison of the observed and analyzed acceleration response time history waveforms in the longitudinal and transverse direction for Pt. 3, Pt. 4, and Pt. 5. In terms of the maximum acceleration, the observed waveform tends to be larger than the analytical result at Pt. 3, while the results at Pt. 4 and Pt. 5 are almost identical. However the acceleration response time history waveforms did not match, and there were some points where they were in opposite phase.

Figure 11 shows the Fourier spectrum of Pt. 5. Focusing on the lowest dominant frequency in the longitudinal direction, the observed waveform is 1.28 Hz, while the analytical result is 1.11 Hz. Similarly, in the transverse direction, the analytical results show a shift to the low frequency side (long period side) compared to the observed waveform. This is because the stiffness

of the superstructure of the analytical model does not take into account the stiffness of the concrete balustrade and pavement, and the stiffness of the concrete balustrade, especially when the width is narrow and the girder height is low, as in the case of a ramp bridge, is considered to have a large impact. In addition, because this is a curved bridge, the out-of-plane stiffness of the concrete balustrade is expected to affect both the longitudinal and transverse directions.

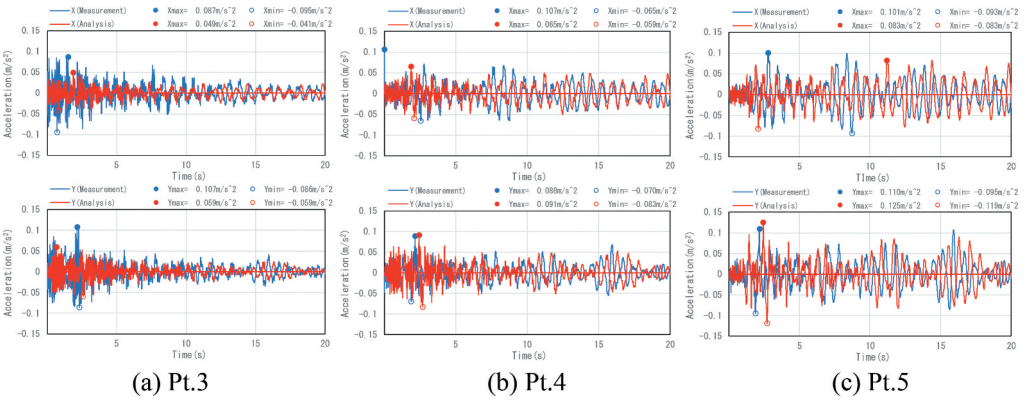


Figure 10. Comparison of observed and analyzed acceleration response time history waveforms (Upper row: bridge longitudinal direction, lower row: transverse direction).

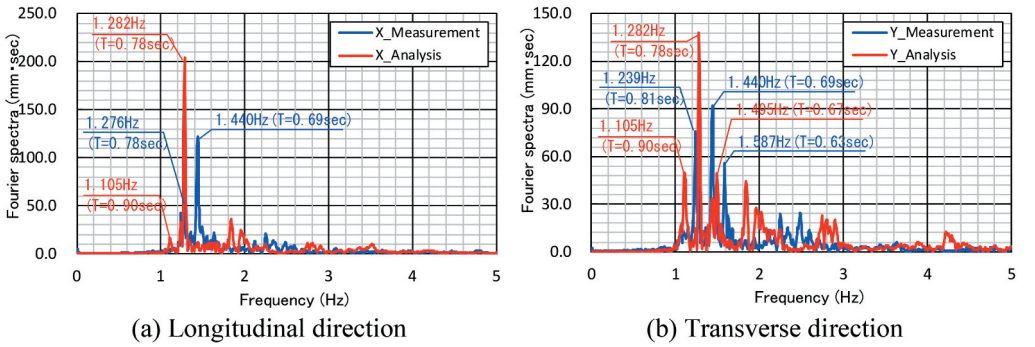


Figure 11. Comparison of Fourier spectra of observed and analyzed waveforms (Pt. 5).

Thus, it is necessary to check the reproducibility of the behavior of the measured positions using the analytical model, and if the measured values differ from the analytical values, the analytical model should be updated after analyzing the factors causing the discrepancy. It is effective to evaluate items that are difficult to evaluate from measurement data and visual observation, such as whether the entire steel pipe and all shear panels behave elastically, using an analytical model whose reproducibility has been confirmed.

4 CONCLUSION

This study proposes a method for evaluating the performance of integrated columns by multiple steel pipes using measurement data and an example of performance evaluation using the measurements obtained so far. The findings are as follows.

(1) An evaluation flow was proposed for cases in which the performance can be directly evaluated from the measurements, and for cases in which it cannot.

(2) As an example of the case where direct evaluation is possible from the measurements, the strain at the base of the steel pipe measured when the temperature changes was analyzed, and it was confirmed that the four steel pipes resisted as a single column as assumed in the design.
(3) As an example of a case that cannot be directly evaluated from the measurements, the measured acceleration during a small earthquake was used to verify the reproducibility of a general nonlinear dynamic analysis model. As an example of a case that cannot be directly evaluated from the measurements, the measured acceleration during a small earthquake was used to verify the reproducibility of a general nonlinear dynamic analysis model. The results showed that the analysis tended to be long-period in both the longitudinal and the transverse direction. This is thought to be due to the stiffness of the concrete balustrade, which is not considered in the analytical model.

In the future, it is necessary to analyze the causes of the discrepancy between the actual behavior and the behavior of the analytical model, and to evaluate the performance with a matched model. It is also necessary to evaluate the performance of the integrated column by multiple steel pipes piers when subjected to larger actions, using the measurement data obtained.

ACKNOWLEDGEMENTS

The authors would like to thank Hanshin Expressway Engineering Co., Ltd. and Naigai Kozo Co., Ltd. for their cooperation in measuring the behavior of an integrated column by multiple steel pipes.

REFERENCES

[1] Japan Road Association: Specifications for Highway Bridges, Part V Seismic Design, 2017.

Bridge Maintenance, Safety, Management, Digitalization and Sustainability – Jensen, Frangopol & Schmidt (eds)
© 2024 The Author(s), ISBN 978-1-032-77040-6
Open Access: www.taylorfrancis.com, CC BY-NC-ND 4.0 license

Prediction of bridge service duration for CBM by the indirect monitoring using vehicles

Akito Yabe
Kozo Keikaku Engineering Inc., Tokyo, Japan

ABSTRACT: Recently, the structural maintenance way is transforming from the time-based maintenance (TBM) to the condition-based maintenance (CBM). On the other hand, to be realized the CBM, the end of service duration must be predicted and be decided taking measures by applying the state-of-the-art digitalized technologies. But it is impossible to carry the technologies for all huge number of bridges, cause to need huge budget. For solving the issues many kinds of solution were proposed. The most effective method is to narrow down the target by screening. By using vehicles such as city bus, the road roughness condition, bridge condition, and underground condition and so on will be measured frequently. And these are given us for analyzing as big data to evaluate the road condition. This result can indicate the end of service, even if the deterioration mechanism is unknown.

1 INTRODUCTION

A huge number of bridges exist all over the world. And now, a lot of bridge is constructed. From long ago, life cycle bridge maintenance has been widely discussed for establishing the rational maintenance strategies of existing bridges based on the end of bridge service duration. The service duration of a bridge the period during which people and vehicles can safely pass through it. And the safety indicators like as bending, shear or deflection capacity are relation with the end of bridge service duration. Also, it is a key technology for holistic bridge maintenance decisions. For evaluating durability, load carrying capacity and remaining service duration state-of-the-art digitalized technologies like as smart monitoring systems, non-destructive testing and digital twins are needed.

However, the safety indicator is composed highly complex and multi-oriented issue (JSCE2022). Because the safety indicator is influenced each other by material deterioration, maintenance condition, traffic condition, environment change, disaster damage, and so on. Therefore, an important point is surely notice that the bridge is coming on reaching the end of service duration.

And recently, the structural maintenance way is transforming from the time-based maintenance (TBM) to the condition-based maintenance (CBM). To be realized the CBM, the end of service duration must be predicted and be decided taking measures by applying the state-of-the-art digitalized technologies. And in the case of based on the operation by CBM for near the end of service bridge, it will be needed that more frequently inspection and investigating bridge condition. Because near the end of service bridge condition may change unexpectedly and rapidly bad. If inspection and investigating bridge condition are emptied many years, it become sever accident like collapse. But it is impossible to carry and to operate frequently the technologies for all huge number of bridges, cause to need huge budget.

For solving the issues many kinds of solution were proposed. The most effective method is to narrow down the target by screening. For monitoring methods that aim to screen a large number of bridges over a wide area, it is desirable to use general indicators, such as deflection, that are not dependent on bridge and deterioration type. Additionally, a mobile indirect monitoring system is more reasonable than a monitoring system installed on each bridge (Konstantinos Gkoumas et al. 2021).

DOI: 10.1201/9781003483755-13

In this paper, as one of the utilities of the indirect monitoring using vehicles is introduced. By using vehicles such as city bus, the road roughness condition, bridge condition, and underground condition will be measured frequently. And these are given us for analyzing as big data to evaluate the road condition. This result can indicate the end of service, even if the deterioration mechanism is unknown.

Figure 1 shows the relationship between current inspection operation and proposed system. In this study the monitoring system is designed specifically to detect fatal damage signs of relatively large changing at the acceleration and deterioration stages to be used in conjunction with a continuous monitoring system using periodic inspections and structural health monitoring (SHM) . This system assumes the use of especially buses of a kind of large vehicles. This is because,

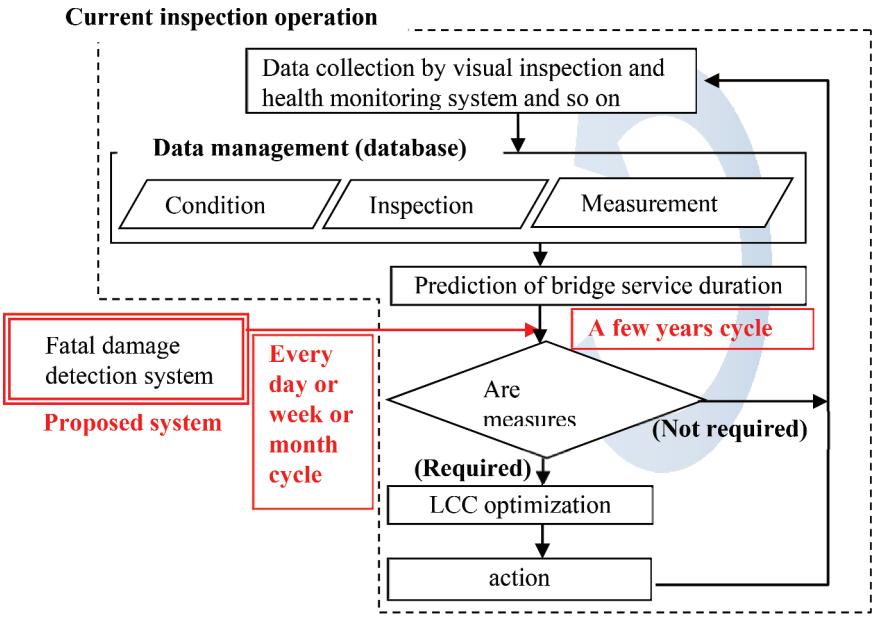


Figure 1. The relationship between current inspection operation and proposed system.

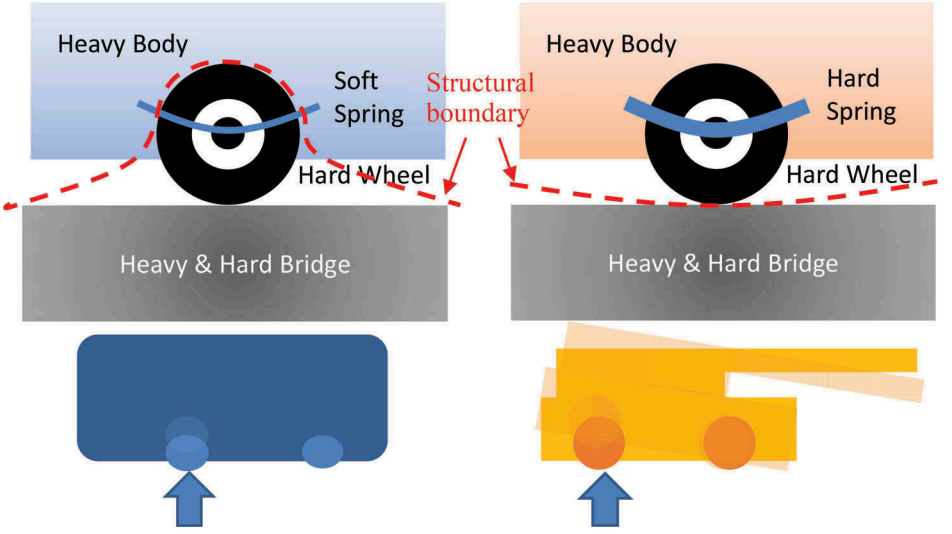


Figure 2. The structural feature of bus and others.

as shown in Figure 2, the structural boundary is unlike other large vehicles, the body of a bus for transporting people is structurally insulated from the wheels using soft springs (Akito Yabe 2020).

Figure3 shows the monitoring system using city bus. An acceleration sensor is installed on the center of the rear axle and connected to a data logger at the rear of the bus. Power is supplied from the bus. Acceleration data is saved together with location information obtained by the GPS sensor. After measuring, GPS data is used for extracting running on the bridge data, and the indicator of the end of bridge service be calculated.

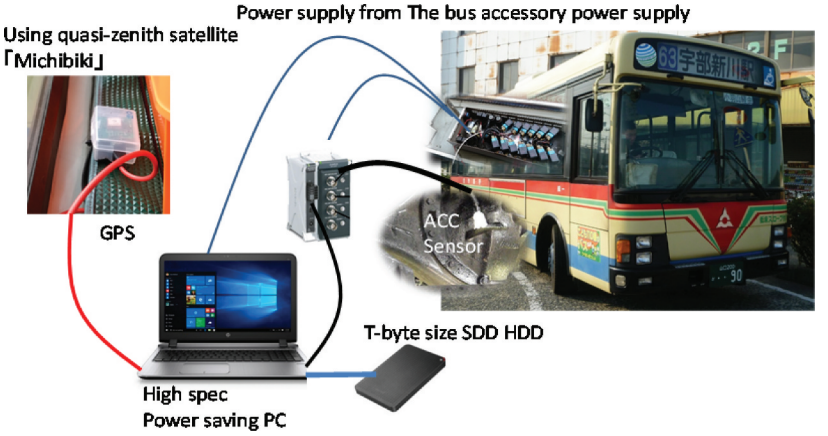


Figure 3. The monitoring system using city bus.

2 PRINCIPLE OF THE INDIRECT MONITORING USING VEHICLES

When a vehicle passes over a bridge, its mechanics model can be expressed as a dynamic interaction between the equation of motion of the bridge, expressed by Equations (1), and the equation of motion of the vehicle, expressed by Equations (2) (Kawatani, M. and Shimada, R 1988). The method of formulating a bridge structure model and a vehicle structure model as separate equations of motion and expressing their interaction at joints with input and output vectors is called the "substructure method".

$$M_m\ddot{u}_m + C_m\dot{u}_m + K_m u_m = \begin{Bmatrix} R_s \\ R_m \end{Bmatrix} \tag{1}$$

$$M_s\ddot{u}_s + C_s\dot{u}_s + K_s \begin{Bmatrix} u_{s_f} \\ u_{s_g} \end{Bmatrix} = \begin{Bmatrix} 0 \\ R_s \end{Bmatrix} \tag{2}$$

where the parameters are as follows
$M_mC_mK_m$, $M_sC_sK_s$: mass/damping/stiffness matrix for bridge and for vehicle,

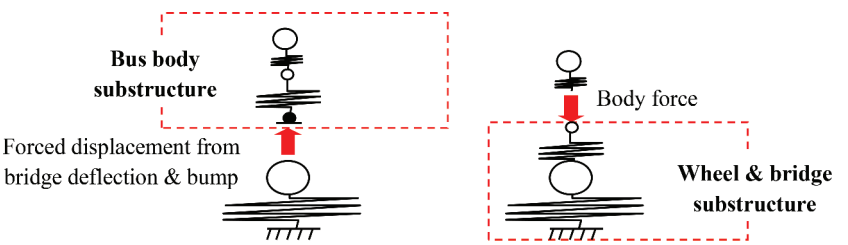


Figure 4. Substructures for modeling bridge and bus body.

$\ddot{u}_m \dot{u}_m u_m, \ddot{u}_s \dot{u}_s u_{s_f}$: response acceleration/velocity/displacement vector for bridge and for vehicle,
u_{s_g}: input forced displacement vector for vehicle, and
$R_m R_s$: support reaction vectors for bridge and vehicle.

For bridge–vehicle interactions, the vehicle wheel reaction to the bridge is input as the load vector R_s, and the bridge deflection ($\delta(t) \in u_m$) and road surface unevenness ($\lambda(t)$) are input to the vehicle as the force displacement vector u_{s_g}. Changes in bridge stiffness Km are reflected in the measurement results for both the bridge system and the vehicle system. Then, it can be concluded that, because structural anomalies of the bridge due to deterioration, etc. are reflected in changes in the nodal response $\ddot{u}_s \dot{u}_s u_{s_f}$ of the vehicle system, anomalies of the bridge, in theory, can be detected from the vehicle.

Here, let us consider substructure segmentation based on the bus body–wheel–bridge concept, as shown in Figure 4. First, let us take a look at the bus body–wheel system. In a mechanics problem in which the difference method approximation holds true, when forced displacement including the bridge deformation $\delta(t)$ is input to the wheel of the bus, the equation of motion can be approximated, as shown in Equations (3), by using the proportionality constant *P*, which is dependent on physical quantities that remain unchanged in the system, such as time, stiffness, damping and mass, and the state constant Co (known) before time t obtained by a Taylor expansion, etc.[22] This means that the system's response to the input vector is allocated proportionately depending on the system-dependent constants.

$$u_{s_f} \cdot P(M_s, C_s, K_s, t) + Co(M_s, C_s, K_s, t) = F(t) \tag{3}$$

where the parameters are
$M_s C_s K_s$: mass/damping/stiffness matrix for the vehicle,
u_{s_f}: displacement vector,
Co: known value before time t obtained by Taylor expansion, etc.,
$F(t)$: input vector to vehicle system, and
P: proportionality constant dependent on system.

Next, let us consider wheel–bridge vibration transmitted from the bus body. The response of the wheel and the bridge to the input from the bus body is allocated proportionately depending on the physical constants of the system. Let A_b represent the response vector of the bridge, and A_s, the wheel response vector of the bus. Then, we have matrix *P* expressed as shown below:

$$A_b = \mathbb{P}^{-1} A_s \mathbb{P} \tag{4}$$

This means that if Equations (4) holds true in a mechanics problem in which the difference method approximation holds true, then the vibration behavior of the bridge is proportional to the wheel vibration of the bus, and changes in A_b due to bridge anomalies are reflected proportionately in changes in wheel vibration, A_s, of the bus.

3 THE INDICATOR FOR THE END OF SERVICE

Next, let us explain the rationale behind the method for extracting damage/deterioration-related information from measured rear wheel vibrations of a bus without being affected by the dynamic characteristics of the bridge and the vehicle or the road surface profile. The rear wheel vertical vibration $\delta_a(t)$ of a bus running at a constant speed can be expressed as the sum of static displacement $\delta_{sa}(t)$, which is dependent on the measured rear wheel vertical vibration of the bus, and dynamic displacement $\delta_{da}(t)$, which is dependent on the road surface profile and the vibration characteristics of the bridge and the vehicle:

$$\delta_a(t) = \delta_{sa}(t) + \delta_{da}(t) \tag{5}$$

If it is assumed that the unevenness of the road surface can be expressed as a steady-state random Gaussian process with an average value of 0 and that dynamic displacement including

bridge–vehicle interaction is ergodic and Fourier-series-expandable, the dynamic displacement $\delta_{da}(t)$ can be expressed as their sum:

$$\delta_{da}(t) = S_r(\Omega, t) + \int_{-\infty}^{+\infty} X(f) \cdot e^{2\pi f t i} df \tag{6}$$

where the parameters are
$S_r(\Omega, t)$: density function for unevenness of road surface,
Ω: spatial frequency of road surface profile, and
$X(f)$: Fourier coefficient.

In Equations (6), the sample mean in the second term is 0. The mean of a sufficient number (N) of samples obtained from $\delta_{da}(t)$ can be expressed as

$$\frac{\sum_{t=1}^{N} \delta_{da}(t)}{N} 0 \tag{7}$$

Because the sample mean follows a normal distribution in accordance with the central limit theorem, $\overline{\delta a(t)}$ converges to a certain value (μ_a). For the sample mean $\delta_a(j)$ of a sufficient number (n) of samples, sampling is performed so that there is no overlap in the samples. If N is sufficiently large for $nk = N$ and $t = 1 \sim N$, the following equation holds true:

$$\mu_a = \frac{\sum_{i=1}^{n} \overline{\delta a(t)}_i}{n} = \frac{\sum_{i=1}^{nk} (\delta_a(j))_i}{nk} \frac{\sum_{t=1}^{N} \delta_a(j)_t}{N} = \frac{\sum_{t=1}^{N} \delta_{sa}(t)}{N} \tag{8}$$

This means that the mean displacement of the rear axle of the bus passing over the bridge obtained from a sufficient number (N) of samples can be extracted as a value, μ_a (referred to as characteristic deflection for short "CD"), that is relatively free from the influence of the vibration characteristics of the bridge and the vehicle and the dynamic displacement due to the unevenness of the road surface. On the basis of a similar assumption, the mean of the deflection $\delta_b(t)$ at a given point on the bridge during the passage of the vehicle converges to a certain value (μ_b) that is relatively free from the influence of dynamic deflection. By using static deflection $\delta_{sb}(t)$, μ_b can expressed. If similarity holds true between $\delta_{sa}(t)$ and $\delta_{sb}(t)$ as discussed earlier, and values extracted from measurements taken after the occurrence of deterioration or damage are represented by $\mu_a'$and μ_b', then the following equation can be defined:

$$\alpha = \frac{\mu_b'}{\mu_b} = \frac{\mu_a'}{\mu_a} \tag{9}$$

The rate of change α expressed by Equations (9) is defined as the structural anomaly parameter. After a given value of α is set, the characteristic deflection is monitored continuously. When CD has exceeded a certain limit, it can be judged that the bridge of interest has moved from the acceleration stage on to the deterioration stage.

4 LONG-TERM MONITORING EXPERIMENT TEST

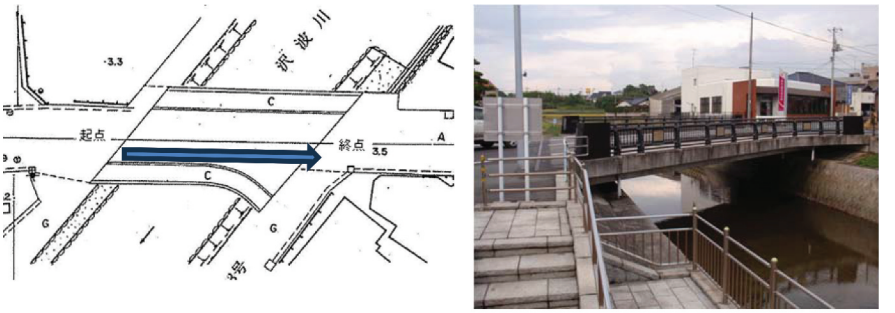
The CD component is removed from the acceleration data acquired by the system in Figure 3 and converted to displacement data. From these data, the data when running on the center of the bridge is extracted and the characteristic deflection value is calculated.

Figure 5 shows the long-term monitoring experiment test field at Ube in Yamaguchi Pref. Japan. It was constructed 1998. From 2010 to 2014 the long-term monitoring experiment test was done for short and medium bridge. This bridge is "Prestressed Concrete Bridge". If it loses 50% of prestress force, a stiffness reduction rate is 0.5. and if it loses 90% of prestress force, a stiffness

reduction rate is 0.35 (Akito YABE, Ayaho Miyamoto, et al. 2013). Therefore, a structural anomaly parameter was calculated using dynamic interaction analysis between the bridge, road surface condition and moving vehicle by FEM shown Figure 6. The results are shown Table 1.

The acceleration stage was decided 1.93 as the prediction sign for coming on reaching the end of service duration soon and a structural anomaly parameter of the end of bridge service was decided 2.86.

Figure 7 shows the result of long-term monitoring experiment test. Blue dots are shown each characteristic deflection value. Yellow line is shown the acceleration stage criterion. Red line is shown the end of bridge service criterion. It was confirmed that there were no major structural changes during the experimental period. In the future, if the characteristic deflection value is over the yellow line, that is a sign of coming on reaching the end of service duration soon. And when will reach the end of bridge service can be predicted by the changes of characteristic deflection value like a blue dots line.



Span 23.6m Width 11.7m PC Girder Bridge Constructed in 1998

Figure 5. The long-term monitoring experiment test field.

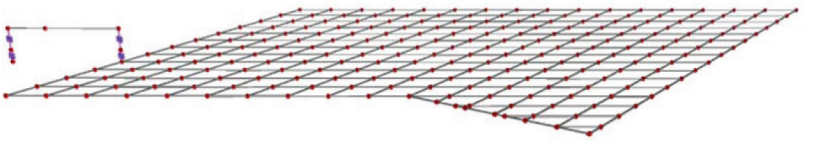


Figure 6. FEM for calculation a structural anomaly parameter.

Table 1. Results of the structural anomaly parameter by FEM.

speed	Sound condition	Loses 50%%	Loses 90%
30km/h	-1.61 mm	-3.10 mm	-4.59 mm
40km/h	-1.60 mm	-3.10 mm	-4.60 mm
50km/h	-1.61 mm	-3.11 mm	-4.61 mm
average	-1.61 mm	-3.10 mm	-4.60 mm
a structural anomaly parameter		1.93	2.86

5 CONCLUSIONS

Main conclusions are summarized as follows:

1) It was shown that the bus is especially an effective large vehicle to be predicting when the bridge is coming on reaching the end of service duration for CBM.

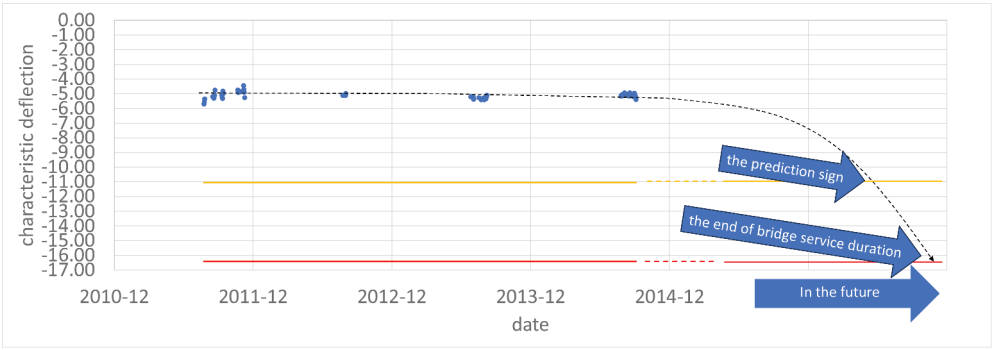


Figure 7. Result of the long-term monitoring experiment test.

2) The vibration behavior of the bridge is proportional to the wheel vibration of the bus. Based on this principle, a calculated "characteristic deflection" is one of indicator to notice the bridge condition.
3) On the long-term monitoring experiment test to a prestressed concrete bridge, it was assumed that the end of bridge service duration when prestress force will lose 90%. And it was assumed that the time when prestress force will lose 50% is the prediction sign for coming on reaching the end of the bridge service duration soon. Based on this assumption, a structural anomaly parameter of the acceleration stage could be decided 1.93 as the prediction sign for coming on reaching the end of bridge service duration soon by FEM.
4) The long-term monitoring experiment is shown that it is able to predict when coming on reaching the end of the bridge service duration soon by using bus.

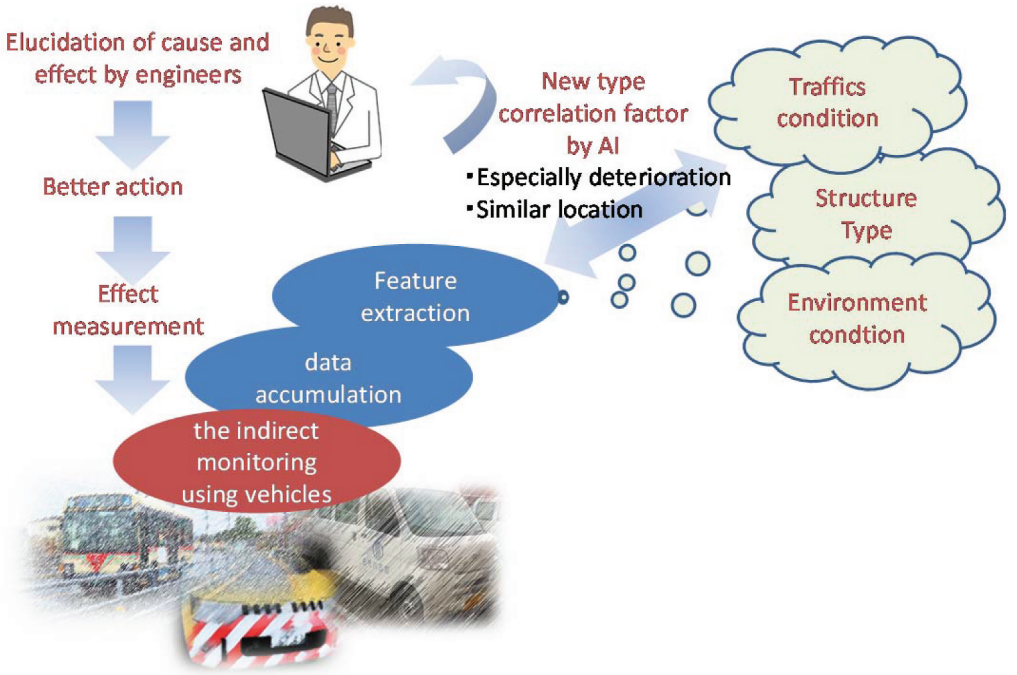


Figure 8. Future of the indirect monitoring using vehicles for CBM.

6 FUTURE OUTLOOK ON RESEARCH

This system has problems concerning data management. In this monitoring experiment measurement data have been picked up offline. Because measurement data is huge, so this system is not connected to online systems like internet. Currently, the development of inexpensive, high-speed, large-capacity wireless communication networks and cloud services is progressing. In the future, these services effectively applying is necessary for this system.

Figure 8 shows one of the indirect monitoring operation using vehicles for CBM. Not only this system but also other monitoring data will be connecter to internet and cloud services at real-time. And AI will help us to predict the end of the bridge service duration by detecting new type correlation factors from the complex cause-and-effect . Engineers have to play an important role in determining the rationality of such causal relationships.

REFERENCES

- Konstantinos Gkoumas, Kyriaki Gkoktsi, Flavio Bono, Maria Cristina Galassi and Daniel Tirelli (2021). The Way Forward for Indirect Structural Health Monitoring(iSHM) Using Connected and Automated Vehicles in Europe. Infra Structures.
- Japan Society of Civil Engineers (JSCE), 2022. Standard Specifications for Concrete Structures: Maintenance, (in Japanese), JSCE Guidelines for Concrete, Japan Society of Civil Engineers (JSCE), Tokyo.
- Akito Yabe 2020. Bridge Maintenance, Safety, Management and Life-Cycle Optimization, CRC Press (A Balkema Book), IABMAS'2020, Sapporo, JAPAN
- Kawatani, M. and Shimada, R.: "Nonstationary random response and impact of girder bridges under moving vehicles", Proceedings of the Japan Society of Civil Engineers, No. 398/I-10, pp. 385–394, October 1988.
- Lin C.W. and Yang Y.B. 2005. Use of a passing vehicle to scan the fundamental bridge frequencies: an experimental verification. Engineering Structures, 27, 1865–1878.
- Ayaho Miyamoto, Akito Yabe: Bridge Condition Assessment based on Vibration Responses of Passenger Vehicle, Journal of Physics(CS), Vol.305(1), pp.1–10, 2011 7..
- Akito YABE, Ayaho Miyamoto, Satoshi Isoda and Nobuyuki TANI: DEVELOPMENT OF BRIDGE MONITORING SYSTEM FOR SHORT- AND MEDIUM-SPAN BRIDGES BASED ON BUS VIBRATION, Journal of JSCE F4, Vol. 69, No. 2, 102–120, 2013.

Bridge Maintenance, Safety, Management, Digitalization and Sustainability – Jensen, Frangopol & Schmidt (eds)
© 2024 The Author(s), ISBN 978-1-032-77040-6
Open Access: www.taylorfrancis.com, CC BY-NC-ND 4.0 license

Combining monitoring information and UHPFRC strengthening to extend bridge service duration

Numa Bertola* & Eugen Brühwiler
Laboratory for Maintenance and Safety of Structures, Swiss Federal Institute of Technology (EPFL), Lausanne, Switzerland

ABSTRACT: As many bridges are approaching the end of their supposedly theoretical service duration, finding novel technical solutions to extend their service duration is crucial, also for reasons of sustainability. In this article, two strategies (structural performance monitoring, and strengthening with ultra-high-performance fiber-reinforced cementitious composite (UHPFRC)) are introduced to avoid prematurely replacing structures. The case study of the Ferpècle road bridge (Valais, Switzerland) is presented since the two strategies were combined in 2023 to extend its service duration. This bridge is one of the first prestressed concrete bridges in Switzerland. Built in 1958, the structure consists of a single girder with a 34.5-meter span resting on abutments in the form of reinforced concrete piers. As the deck has a width of only 5.3 meters, bridge owners have decided to widen it to 7.9 meters in order to include two road lanes and a pedestrian way. Despite its good condition, the bridge must be strengthened as its load-bearing capacity (bending moment at mid-span) would be largely insufficient with the new deck width. To increase its load-bearing capacity while widening the bridge deck by 50%, an intervention with UHPFRC has been made. The innovative intervention enables clamping the abutments with the bridge deck to modify the static system to obtain a semi-rigid frame to reduce the bending moment at mid-span. Two load tests using the latest sensing technologies, before and after the intervention, have enabled the quantification of the design capacity and the validation of this pioneering intervention. This case study demonstrates the potential of novel technologies to extend bridge service duration, thereby improving the sustainability of the construction sector.

1 INTRODUCTION

High-performance fiber-reinforced cementitious composite (UHPFRC) has been used in structural designs for over twenty years in many countries (Graybeal et al., 2020). The UHPFRC mix consists of a matrix composed of fine-coarse particles (cement, sand, and silica fumes up to 1 mm in size), water, additives, and a large number of short and slender steel fibers (Brühwiler and Denarié, 2013). Steel fibers (accounting for at least 3 vol-%) give this material its specific mechanical properties and high durability due to its impermeability in service (Brühwiler, 2016).

The mechanical properties of UHPFRC are summarized by (Brühwiler, 2020). UHPFRC has significant characteristic tensile strength (up to 16 MPa) and compressive strength (up to 150 MPa). The elastic modulus is 45-50 GPa, and the material exhibits strain-hardening behavior in tension until 2 ‰. Tensile strength is usually increased by the addition of reinforcing bars (called R-UHPFRC), as for traditional reinforced-concrete structures (Oesterlee, 2010). Technical specification SIA 2052 ("Technical Leaflet on UHPFRC: Materials, Design and Application," 2016) is used to design UHPFRC elements, as well as reinforced concrete (RC) - R-UHPFRC composite elements.

With over 350 applications, Switzerland is a forerunner in using R-UHPFRC both for the construction of strengthening existing structures and new structural designs (Bertola et al., 2021b).

*Corresponding author: numa.bertola@epfl.ch

DOI: 10.1201/9781003483755-14

Regarding the strengthening of existing structures, R-UHPFRC has been used on numerous occasions to improve the load-bearing capacity of bridges, such as the Chillon Viaduct (Brühwiler and Bastien Masse, 2015), the Guillermaux Bridge (Hajiesmaeili et al., 2019) and, more recently, the Riddes Viaduct (El Jisr et al., 2023).

This article presents a recent application of R-UHPFRC for the rehabilitation, strengthening, and widening of a prestressed concrete bridge in Switzerland. The project involves widening the simply-supported bridge deck from 5.3 m to 7.9 m (+50%) by only intervening on the deck. The idea behind the reinforcement is to modify the static system by clamping the abutments to form a monolithic structure. This elegant intervention significantly strengthens the bridge through the parsimonious use of R-UHPFRC while preserving the existing structure. Monitoring campaigns before and after the intervention have enabled the validation of the intervention design.

2 BRIDGE EXAMINATION

2.1 *Presentation*

The Ferpècle Borgne Bridge is a prestressed reinforced concrete double-girder structure (TT cross-section) located in the Swiss Alps in the small village of Les Haudères (Valais) at an altitude of 1450 meters. The bridge was built in 1958 according to the plans drawn up by the engineering firm B.Deléglise - P.Tremblet in Sion, who took over Robert Maillart's engineering office in Geneva, which became Bureau Tremblet, now T Groupe.

The static system is a simply-supported beam with a 34.5-meter span, resting on abutments with side walls approximately 7 meters long (Figure 1). With a beam height of 1.75 meters, the slenderness of 1/20 is audacious for a simple beam. Visual inspection of the structure using the risk approach (Bertola and Brühwiler, 2021) showed that the bridge was in "defective" condition (rating of 3 out of 5), while structural elements are in "acceptable" condition.

2.2 *Structural examination*

With regard to the strength of materials, a C45/55 concrete grade (updated from the C30/37 at the construction) has been selected, leading to a compressive strength of $f_{cd} = 26\ MPa$. The tensile strength of the "Box-Tor-Caron" reinforcing steel was accepted at $f_{sd} = 300\ MPa$. For prestressed bars, an ultimate strength of $f_{pd} = 730\ MPa$ was assumed. Load levels are defined in the Swiss standards for existing structures SIA 269 (Swiss Society of Engineers and Architects, 2011). Structural safety is evaluated based on the concept of the degree of compliance n (Brühwiler et al., 2012) using design values of both structural resistance R_d and action effects E_d.

$$n = Capacity/Demand = \frac{R_d}{E_d} \tag{1}$$

A three-dimensional finite-element model was made in DIANA software to examine the structural safety. This modeling was carried out as realistically as possible, taking into account non-structural elements such as curbs and the asphalt pavement. In addition, each rebar and prestressing tendon have been included in the model. Prestressing is taken from the resistance side.

This model allows the calculation of stresses directly in reinforcing bars and prestressing tendons (Figure 3). For the ultimate limit state (ULS), traffic loads are placed at the most unfavorable locations (at mid-span for bending verifications and close to supports for shear verifications). The stresses in critical prestressing tendons are almost equal to their yield point. Using the numerical model, it is possible to determine the overall degree of compliance by progressively increasing the live-load until failure. A degree of compliance for the mid-span bending verification n_M equal to 1.05 was obtained, showing that the structural safety of the structure in its current state is guaranteed. Analogously, the degree of compliance for the shear verification n_V is equal to 1.10.

Nonetheless, it can be anticipated that after widening (from 5.3 m to 7.9 m), this structural safety will no longer be satisfied. A strengthening scheme will be necessary.

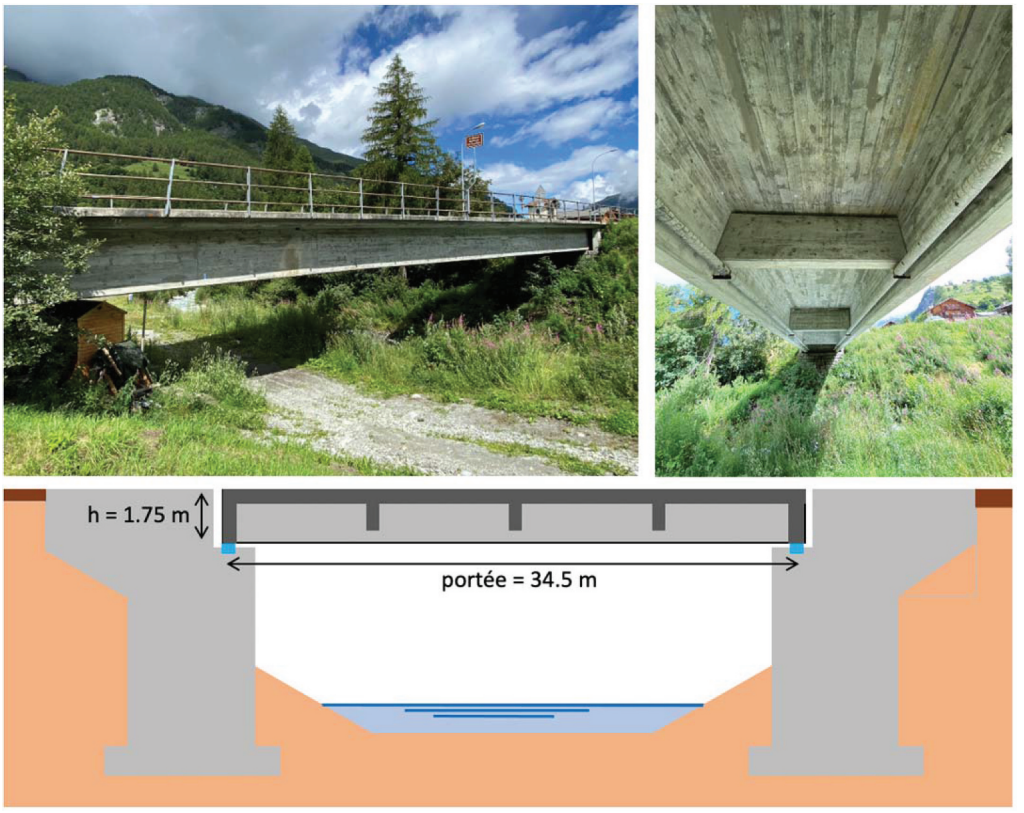


Figure 1. Presentation of the Ferpècle Bridge.

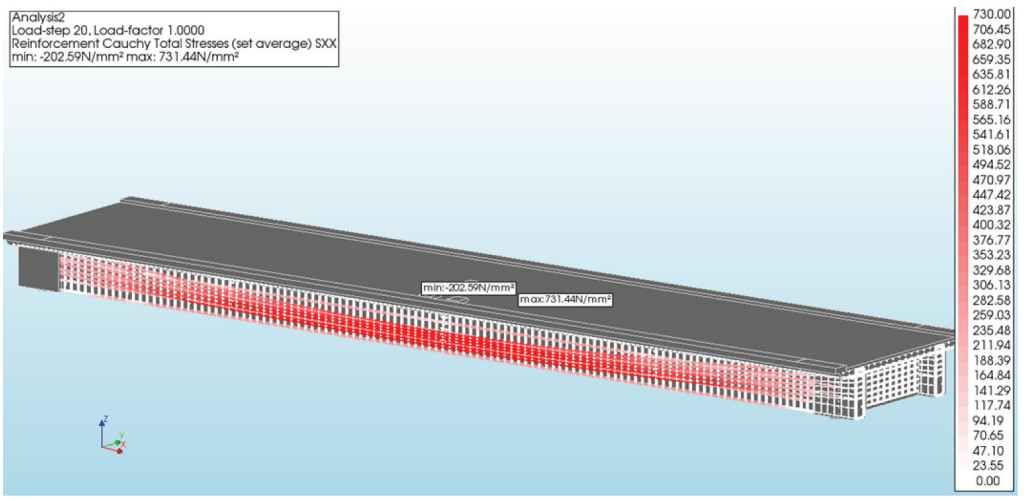


Figure 2. Finite element model and stress in prestressing tendons at ELU 2 (maximal bending at midspan).

3 INTERVENTION SCHEME

The widening of the deck from 5.3 m to 7.9 m, is made through a cantilevered full slab with a variable thickness, in R-UHPFRC (type UB; $f_{Utud} = 6.9MPa,\ E = 45\ GPa$), that is anchored

in the existing structure. At midspan, the deck thickness is increased from 25 to 27.5 cm (Figure 3). 20 mm of concrete from the existing slab is hydro-jetted, and the UHPFRC layer of 45 mm is poured on site. Transverse and longitudinal reinforcing bars (ϕ14 @ 150 mm) have been included in the UHPFRC layer. The RC – R-UHPFRC structure works as a composite element.

At the bridge supports, a thicker layer of R-UHPFRC (70 mm) is cast. Moreover, significant reinforcement steel bars (ϕ22 @100 mm) are included to increase the positive bending capacity. To achieve a monolithic structure, the abutments are clamped with traditional reinforced concrete to the superstructure, connecting the two prestressed beams with the deck, the abutment bottom wall the side walls (Figure 4). This intervention thus eliminates the need for expansion joints. The concept behind this clamping in the longitudinal intervention is (1) to create a semi-integral structure and (2) (partially) connect the beam in the abutments. These abutments also act as "counterweights" to take up the positive bending moment at supports.

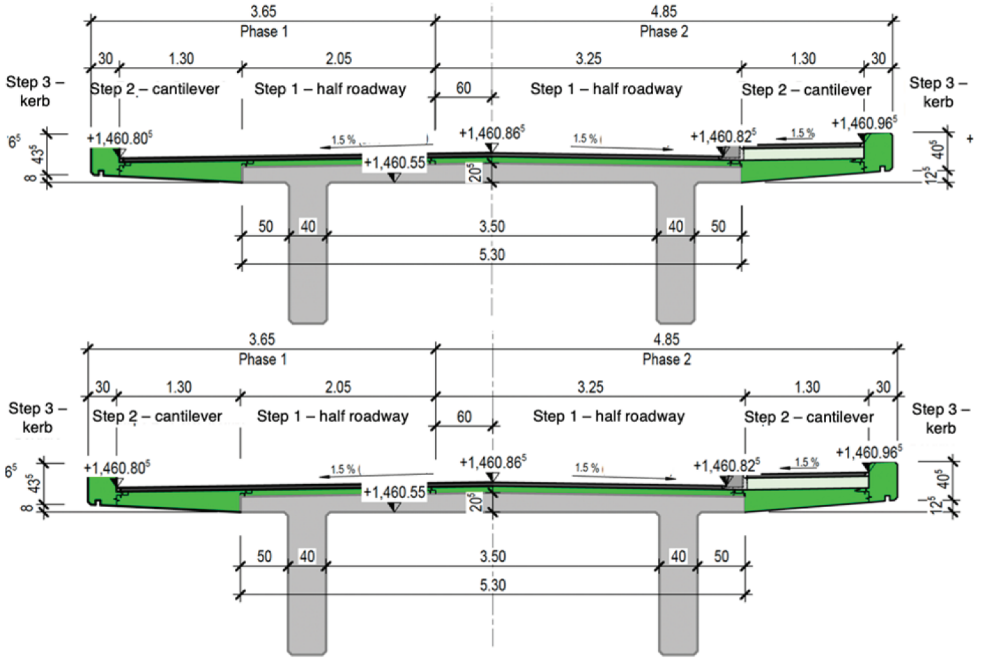


Figure 3. Cross-sections (in span and on supports) with new UHPFRC shown in green.

The concept of the intervention is to redistribute the bending-moment deficit at midspan to the supports. In this way, the static system is modified to form a semi-integral bridge with flexural rigidity at the supports, enabling it to take up this action. The new layer of reinforced UHPFRC (70 mm with (ϕ22 @100 mm) is used to create the necessary bending resistance at supports.

The numerical model is modified to predict the structural behavior after the intervention (Figure 5). For reliable predictions, the abutments are modeled and linked to the superstructure with UHPFRC. This model is used to verify the stresses in the UHPFRC tensile chord, beam compressive action, and abutment tensile reinforcements. Non-linear analyses are needed to effectively predict the strain-hardening behavior of UHPFRC in tension.

This new numerical model is used to evaluate structural safety. The overall degree of compliance obtained is 1.15. Model predictions show that the maximum stress in the new rebars at support is around 280 MPa, well below the yield point. However, some of the rebars in the abutment have stresses up to their yield stress at ULS, showing that this is a decisive factor in the design. In addition, the stresses in the UHPFRC (tension) and in the girder reinforced concrete

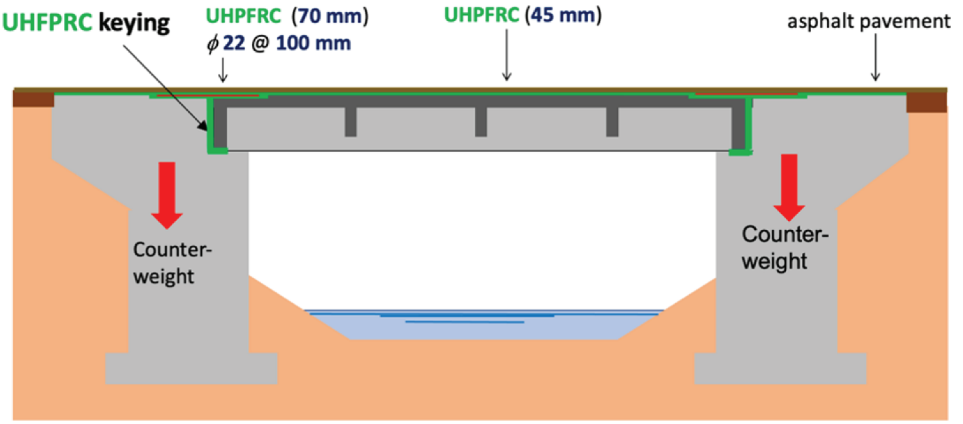


Figure 4. Scheme of the intervention (strengthening in the longitudinal direction).

(compression) are lower than their respective strengths. This difference is due to a greater participating width according to the numerical model than according to an analytical model.

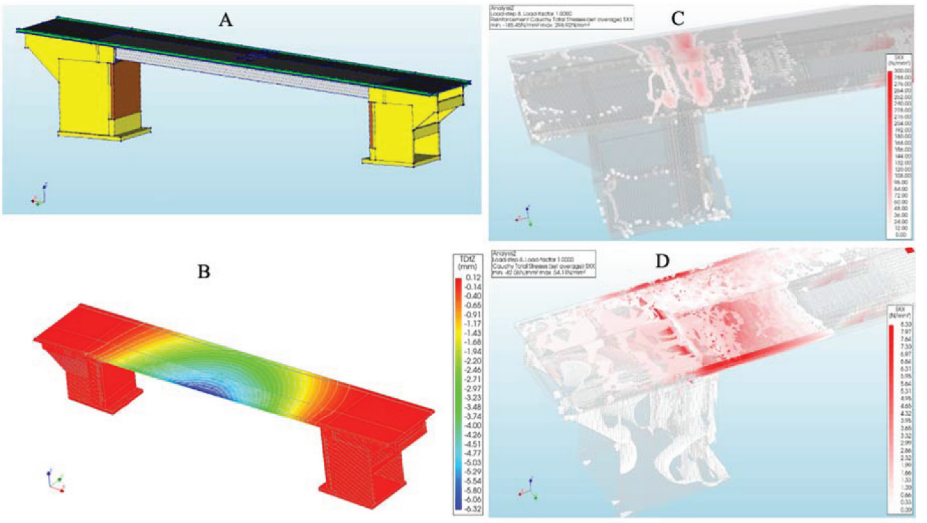


Figure 5. A) Finite element model of the bridge structure after intervention, B) Deformation under SLS load level; C) Tensile stresses in slab reinforcing bars at ULS; D) Tensile stresses in UHPFRC at ULS.

4 INTERVENTION WORK

The intervention was completed between April and November 2023. The work was carried out in two phases (upstream and downstream), enabling alternating traffic flow throughout the work.

In the first stage, scaffolding was erected, the asphalt pavement was removed from the entire deck, and the upstream curb was cut. Then, the formwork for the UHPFRC cantilever and the new curb was installed, and a new RC transition slab was poured. The UHPFRC is prepared directly on site. The deck and the new cantilever were cast in 3 stages (Figure 6), then the curb was cast in a single stage. Finally, the abutments were clamped. The work was then repeated on the downstream part of the structure.

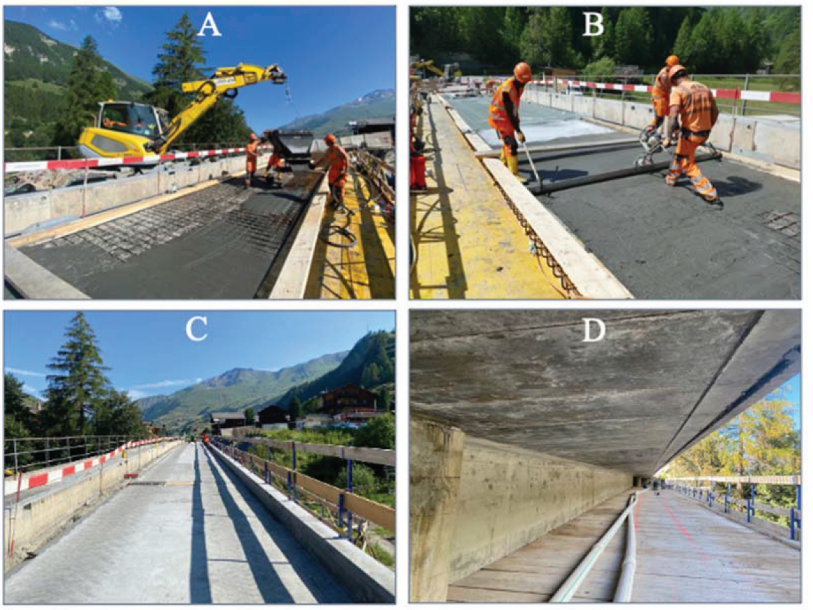


Figure 6. Photographs of the construction work. A, B) UHPFRC casting, C,D) results of the UHPFRC interventions.

5 VALIDATION THROUGH MONITORING

Two monitoring campaigns were performed prior to and after the structural intervention. The aim is to validate the change of the static system (from a simply supported beam to a fixed beam) and to update the material properties, such as the material elastic moduli. Each monitoring involves both static and dynamic excitations that are combined to model updating.

The first monitoring campaign (Phase 1) involved 3 static load tests with a 3-axle truck of 26,5 tons placed at quarter-spans and midspan. The second monitoring campaign (Phase 2) involved 5 static load tests with either one truck (to reiterate previous load tests of Phase 1) or two trucks to maximize the deflections. Additionally, dynamic load tests, which consist of a truck passing over the bridge at a given speed, were performed on both phases of the monitoring campaign.

In Phase 1, the monitoring system involved 10 deflection measurements made from the deck with a total station and targets on the bridge (supports, quartier spans, and midspan), and 10 accelerometers at the same locations. In Phase 2, the monitoring system involved 6 LVDT sensors on one side of the bridge on both girders.

Table 1. Measurements collected during monitoring campaigns.

Measurement	Before intervention	After intervention
1st modal frequency [Hz]	3.42	5.58 (+63 %)
Maximum deflection (extrapolation) [mm]	7.82	2.01 (-38.7 %)

Main data collected during these monitoring campaigns are shown in Table 1, where measurements prior to and after intervention are compared. As the first modal frequency is increased and deflections are reduced, it can be concluded that the rigidity of the structure has been increased significantly. After performing model updating (developed in later studies), it is shown that the global bridge behavior is significantly modified (Figure 7). Deformations predicted by the numerical models prior to and after monitoring match the measurements collected during load tests.

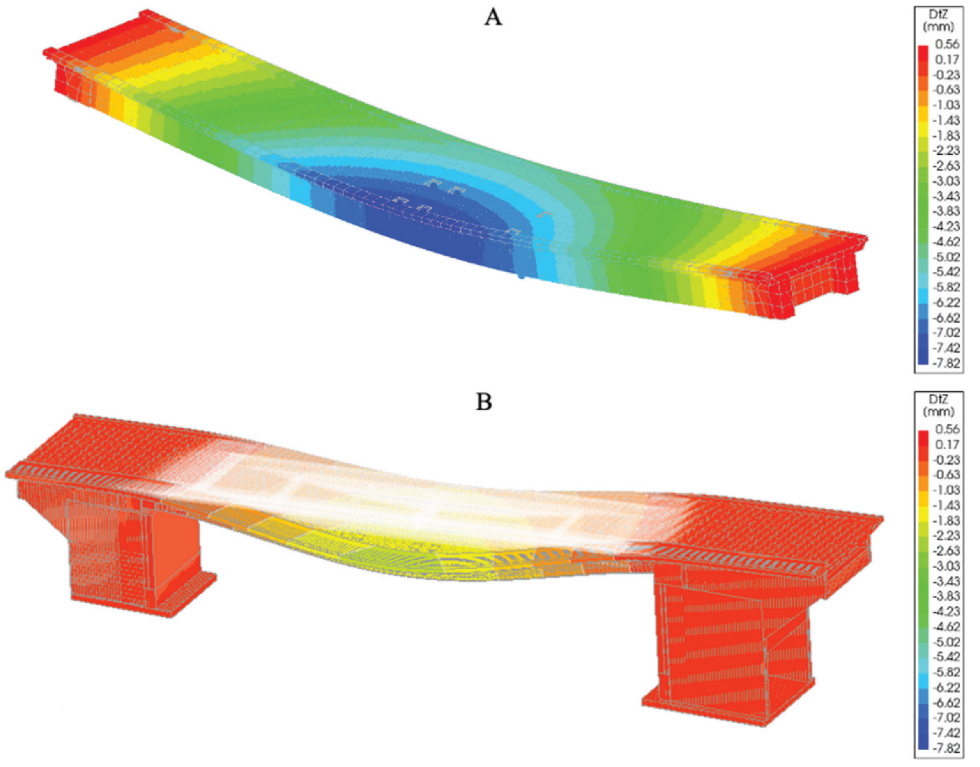


Figure 7. Bridge deflection behavior. A) Prior to monitoring; B) After monitoring.

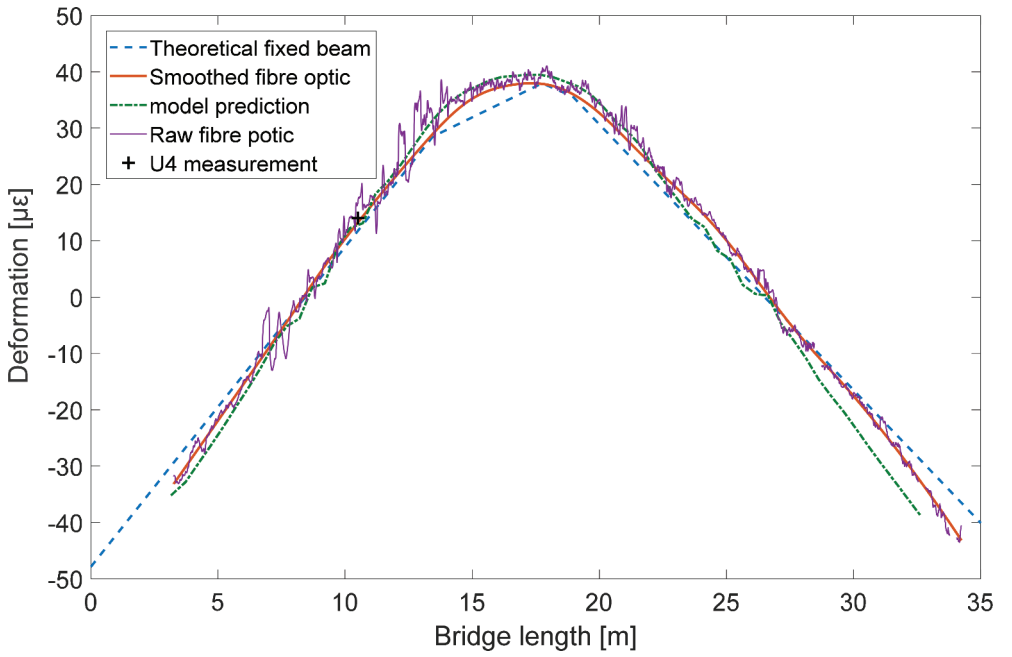


Figure 8. Comparison of model predictions, optical fiber strain measurements, and deformation of a theoretical fixed beam.

Two 32m-long optical fibers (SMARTprofile II from Smartec and a LUNA data acquisition system) were glued along both girders to validate the change of the static system. These optical fibers measure strain every approx. 3 mm along virtually the entire length of the structure. This corresponds to the equivalent of around 11,000 strain gages installed in series on each girder, enabling a much more detailed analysis than is usually the case where only a few strain gages are placed along the length of the bridge. Measurements are taken at a frequency of 5 Hz.

Strain predictions are compared with fiber optic measurements in Figure 8. The values in the cracks are removed from the fiber measurements ("raw fiber optic"). These values are then smoothened ("smoothed fibre optic") to remove local variations in the measurements and enable easier comparison. The theoretical deformation of a fixed beam with three concentrated loads (corresponding to the truck's three axles) is also presented. It can be seen that the predictions are very close to both the fiber optic measurements and the theoretical deformation. The average error is around 2 με. It can thus be concluded that the intervention resulted in the modification of the static system, where the bridge superstructure is being clamped to the abutments, creating a monolithic behavior of the structure. More in-depth analyses of the fiber-optic data will be made in future work.

6 CONCLUSIONS

This article presents the design, execution, and monitoring of the UHPFRC intervention on the Ferpècle bridge, one of the first prestressed concrete bridges in Switzerland. The project involved widening the bridge deck from 5.3 to 7.9 m (increase of about 50 %). The resulting need for reinforcement was met by redistributing actions (from midspan to the supports) based on the theory of plasticity at ULS. Strengthening only the top of the deck increases the structure's flexural load-bearing capacity by 44 %, while widening and rehabilitating the bridge. This case study demonstrates that UHPFRC can effectively strengthen existing structures by changing the static system. Compared with the demolition-reconstruction initially envisaged, the project is considerably less costly (-75 %) and has smaller associated carbon-dioxide emissions (- 55 %). The intervention was validated through an innovative monitoring scheme involving strain, acceleration, and deflection data. Measurements collected during load tests match the predictions of the finite-element models and correspond to the behavior of a fixed beam.

ACKNOWLEDGEMENTS

The authors are thankful to the Küpfer Geometres SA (M. Vaïk Küpfer) and IRMOS companies (Dr. Panagiotis Martakis and Dr. Yves Reuland) for the data acquisition during the load tests.

REFERENCES

Bertola, N., Brühwiler, E., 2021. Risk-based methodology to assess bridge condition based on visual inspection. Structure and Infrastructure Engineering 0, 1–14. https://doi.org/10.1080/15732479.2021.1959621

Bertola, N., Küpfer, C., Kälin, E., Brühwiler, E., 2021a. Assessment of the Environmental Impacts of Bridge Designs Involving UHPFRC. Sustainability 13, 12399. https://doi.org/10.3390/su132212399

Bertola, N., Schiltz, P., Denarié, E., Brühwiler, E., 2021b. A Review of the Use of UHPFRC in Bridge Rehabilitation and New Construction in Switzerland. Frontiers in Built Environment 7, 155. https://doi.org/10.3389/fbuil.2021.769686

Brühwiler, E., 2020. UHPFRC technology to enhance the performance of existing concrete bridges. Structure and Infrastructure Engineering 16, 94–105. https://doi.org/10.1080/15732479.2019.1605395

Brühwiler, E., 2016. "Structural UHPFRC": Welcome to the post-concrete era !, in: International Interactive Symposium on Ultra-High Performance Concrete. Iowa State University Digital Press, Des Moines, Iowa, USA, pp. 1–16. https://doi.org/10.21838/uhpc.2016.key

Brühwiler, E., Bastien Masse, M., 2015. Strengthening the Chillon viaducts deck slabs with reinforced UHPFRC [WWW Document]. IABSE Conference Geneva 2015 "Structural Engineering: Providing Solutions to Global Challenges." URL http://infoscience.epfl.ch/record/212773 (accessed 12.4.20).

Brühwiler, E., Denarié, E., 2013. Rehabilitation and Strengthening of Concrete Structures Using Ultra-High Performance Fibre Reinforced Concrete. Structural Engineering International 23, 450–457. https://doi.org/10.2749/101686613X13627347100437

Brühwiler, E., Vogel, T., Lang, T., Lüchinger, P., 2012. Swiss standards for existing structures. Structural Engineering International 22, 275–280.

El Jisr, H., Moreillon, L., Menétrey, P., 2023. Strengthening of the Riddes Viaduct Through UHPFRC-Based Rehabilitation. Structural Engineering International 0, 1–9. https://doi.org/10.1080/10168664.2023.2194898

Géhin, D., Brühwiler, E., Bertola, N., Widmer, L., 2022. Design and Construction of the" Chaumény" Footbridge in Posttensioned UHPFRC, in: IABSE Symposium Prague 2022. IABSE, pp. 285–292. https://doi.org/10.2749/prague.2022.0285

Graybeal, B., Brühwiler, E., Kim, B.-S., Toutlemonde, F., Voo, Y.L., Zaghi, A., 2020. International Perspective on UHPC in Bridge Engineering. Journal of Bridge Engineering 25, 04020094. https://doi.org/10.1061/(ASCE)BE.1943-5592.0001630

Hajiesmaeili, A., Pittau, F., Denarié, E., Habert, G., 2019. Life Cycle Analysis of Strengthening Existing RC Structures with R-PE-UHPFRC. Sustainability 11, 6923. https://doi.org/10.3390/su11246923

Oesterlee, C., 2010. Structural response of reinforced UHPFRC and RC composite members. EPFL, Lausanne, Switzerland.

Swiss Society of Engineers and Architects, 2011. Existing structures, SIA 269, 269/1-269/7. Swiss Society of Engineers and Architects, Zurich, Switzerland.

Technical Leaflet on UHPFRC: Materials, Design and Application, 2016.

Trinh, N.T., Bertola, N., Garcia, E., Brühwiler, E., 2022. Short Span UHPFRC Railway Bridge in Switzerland-From Design to Implementation, in: IABSE Symposium Prague 2022. IABSE, pp. 277–284. https://doi.org/10.2749/prague.2022.0277

Bridge Maintenance, Safety, Management, Digitalization and Sustainability – Jensen, Frangopol & Schmidt (eds)
© 2024 The Author(s), ISBN 978-1-032-77040-6
Open Access: www.taylorfrancis.com, CC BY-NC-ND 4.0 license

UHPFRC technology for the extension of the service duration of bridges

Eugen Brühwiler*
Laboratory for Maintenance and Safety of Structures, Swiss Federal Institute of Technology (EPFL), Lausanne, Switzerland

ABSTRACT: UHPFRC (Ultra High Performance Fiber Reinforced Cementitious Composite), complemented by reinforcement steel bars, is used for the rehabilitation and strengthening of existing bridges by adding a layer of UHPFRC, often on top of the bridge deck slab in reinforced concrete. Basic principles of the method and recent project realizations in Switzerland are presented. The underlying design concepts and issues of dimensioning and detailing are introduced, and main experiences in casting UHPFRC onsite are mentioned by means of three recent application examples.

UHPFRC interventions are cost effective and contribute in lowering the environmental impact because existing concrete structures are preserved and remain in service, rather than demolished and replaced. The service duration of bridges is thus extended significantly while responding to the demand of future use of bridges. The UHPFRC Technology allows to improve sustainability of bridges.

1 INTRODUCTION

The problems of insufficient durability of reinforced concrete bridges are known for several decades already, in particular in regions using deicing salts in winter and near the sea. So-called "retrofit" implies traditional repair methods, often leading to high intervention and user costs as well as limited durability. Novel intervention methods are urgently needed to improve existing reinforced concrete bridges.

UHPFRC stands for Ultra-High-Performance Fiber Reinforced Cementitious Composite materials. UHPFRC is composed of cement and other reactive powders, additions, hard fine particles, low amount of water, admixtures and very high amount of relatively short and slender steel fibers. The composition of UHPFRC is optimized with respect to compaction of particles leading to a waterproof material up to a tensile strain of about 0,1 %. The tensile strength of UHPFRC typically is about 12 MPa and the material shows significant strain-hardening behavior in tension. UHPFRC has compressive strength typically of 150 MPa. UHPFRC is nowadays used in many countries, mostly in the domain of new construction (Graybeal et al. 2021).

The author and his team have developed the UHPFRC rehabilitation and strengthening technology over the last 25 years by means of scientific research and applications (Bertola et al. 2021, Brühwiler 2020). In Switzerland (8,7 million inhabitants, area of 41′000 km2) there are currently more than 400 reinforced concrete structures, mainly bridges, that have been improved using the UHPFRC Technology, since 2004. This is the by far highest UHPFRC application rate in the world with respect to the size of the country.

The main reason for this successful implementation of a new technology in practice is that compared to traditional methods using concrete, mortar and epoxy coatings, the UHPFRC Technology is economic in terms of costs and material use, allows for an accelerated construction process and provides durable structures for further use reducing or eliminating maintenance costs.

*Corresponding author: eugen.bruehwiler@epfl.ch

DOI: 10.1201/9781003483755-15

By applying a UHPFRC reinforcement and waterproofing layer, the use of the existing RC bridge can continue. In this way, new requirements of use are accommodated in an economical, environmentally friendly and socially responsible manner. The UHPFRC Technology is also particularly suitable for bridges of high cultural values, since interventions are usually not visible.

2 DESIGN CONCEPTS TO IMPROVE BRIDGES

UHPFRC is used as a high-performance building material to improve existing bridges in traditional reinforced concrete with the aim of remedying, through a targeted supplement with UHPFRC, the known deficiencies of reinforced concrete.

2.1 *Basic principle of UHPFRC-concrete composite elements*

The basic idea of reinforcing structural RC bridge elements with UHPFRC is to monolithically connect, as a function of the project requirements, a 25 to 80 mm thick UHPFRC layer with the RC cross-section. The resulting UHPFRC-concrete composite element consists of a RC cross-section and a layer of UHPFRC or R-UHPFRC (incorporating steel reinforcement bars) according to Figure 1.

The term "strengthening" used here includes the increase in resistance and rigidity of structural bridge elements. At the same time, the UHPFRC layer also provides the protection function by a watertight barrier to shield reinforced concrete from direct contact with water and chloride ions.

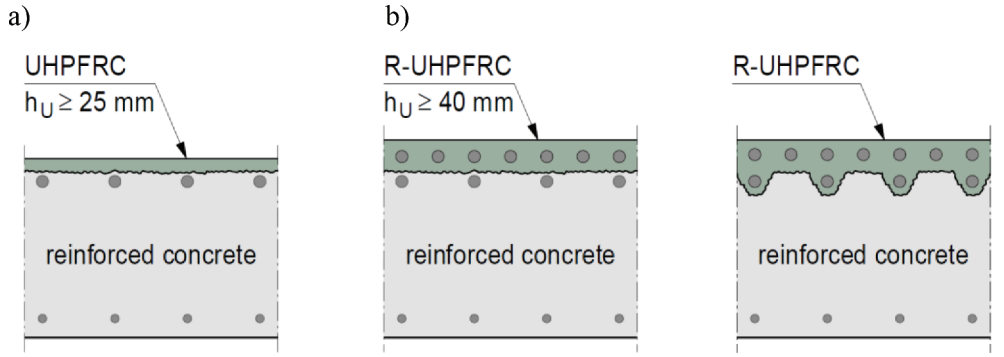


Figure 1. Basic configurations of the UHPFRC-concrete composite construction: a) protective function and increase in rigidity under service conditions, b) protective function and increase in element rigidity and ultimate resistance.

The essentials of UHPFRC-concrete composite behavior and required relevant UHPFRC material properties are summarized in (Brühwiler 2020). UHPFRC is used as material to rehabilitate and restore damaged reinforced concrete elements, thereby replacing inferior materials like repair mortars or epoxy coatings.

In the following, concepts are presented to increase structural resistance of R-UHPFRC improved RC bridges (FEDRO 2023):

2.2 *Project objective 1: Restoring and increasing the resistance of bridge deck slabs*

Bridge deck slabs made of reinforced concrete are subject to particularly high loading due to traffic loads and environmental influences. Accordingly, there is a high demand for intervention to restore and increase the structural resistance of deck slabs.

Figure 2 shows the basic strengthening concept of bridge deck slabs by applying a R-UHPFRC layer to the existing concrete slab. Bridge deck slabs carry loads and forces

mainly in the transverse direction. Correspondingly, a distinction is made between the sagging moment zone (positive bending moments) and the hogging moment zone (negative bending moments) above the webs of beams and box girders.

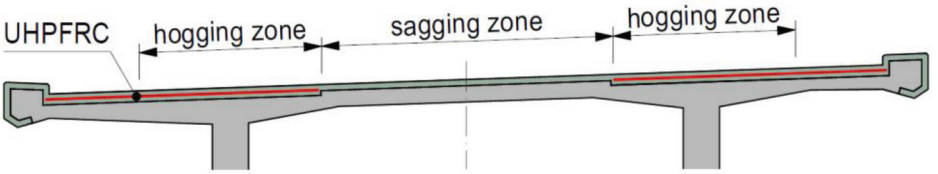


Figure 2. Concept of increasing the resistance of the original RC deck slab by means of the R-UHPFRC layer forming a strong R-UHPFRC tension chord in the hogging moment zone.

The concept is to significantly increase the flexural resistance in the hogging moment zone by forming a strong R-UHPFRC tension chord allowing for moment redistribution from the sagging to the hogging moment zone at ULS (ultimate limit state) according to the plasticity theory, given that the UHPFRC layer subjected to compressive stress in the sagging moment zone only leads to a comparatively small increase in flexural resistance.

The R-UHPFRC tension chord must be compensated by a correspondingly strong compression zone. In order to ensure the balance of the tensile and compressive forces acting in the bending cross-section, the effective concrete compressive strength is exploited, which has usually increased considerably (i.e. by 20 to 50 % compared to the 28-day compressive strength) during the bridge's service duration, often of several decades. This well-known time-dependent increase in strength is estimated using analytical expressions given in related scientific literature and standards, and verified by means of non-destructive testing on the structure. In this way, strengthening of the compression zone can usually be avoided.

By creating a R-UHPFRC tension chord, the ultimate shear resistance is significantly increased in the hogging moment zone, such that the shear force check is usually fulfilled. By the R-UHPFRC reinforcement, the slab rigidity is also significantly increased, which greatly reduces fatigue stresses in the steel reinforcement bars and concrete of the original RC element. The fatigue safety check is therefore usually fulfilled with margin.

2.3 *Project objective 2: Increasing the resistance of bridge girders*

The targeted use of R-UHPFRC, in particular as a R-UHPFRC tension chord, enables a significant increase in the load-bearing capacity of bridge girders in the longitudinal direction without significantly increasing the self-weight of the structure (by the additional R-UHPFRC layer) and without the intervention becoming visible. Also, modification of the static system is usually appropriate and highly effective. Two basic principles are described as follows.

2.3.1 *Principle 1: Reinforcement of continuous beams by means of a R-UHPFRC layer*

In statically indeterminate systems such as continuous beams, the bending resistance in the hogging moment zone is greatly increased by the creation of a strong R-UHPFRC tension chord allowing to carry out plastic moment redistribution from the sagging to the hogging moment zones at ULS, similar to the concept related to deck slabs (Figure 3).

However, this moment redistribution is only possible if the bending cross-sections are sufficiently ductile, which must be verified. For this purpose, a non-linear finite element analysis is often useful if the empirical rules of standards are not satisfied.

This principle is efficient in that an increase in the load-bearing capacity (ultimate resistance) of 15 to 30% (and in extreme cases up to 50%) can be obtained. In this way, for example, even severe damage such as failure of prestressing cables due to corrosion can be compensated without having to install costly additional tendons.

As in the sagging moment zone of a bridge girder, the R-UHPFRC layer only leads to a small increase of the flexural resistance, a need for additional reinforcement of the tension

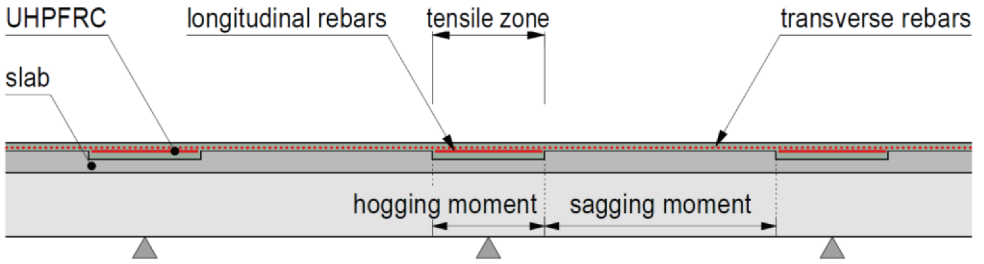


Figure 3. Principle of increasing the ultimate resistance of continuous RC bridge girders using a R-UHPFRC layer with the formation of astrong R-UHPFRC tension band in the hogging regions.

zone at the bottom side of simple and continuous beams can be accommodated for example by CFRP (carbon fiber reinforced plastic) lamellas on the underside of the bottom flange or by additional external posttensioning tendons.

2.3.2 *Principle 2: Creation of hyperstatic systems by force-locked closure of dilation joints*
For existing short and medium span RC bridges with lengths up to 80 m, all dilatation joints can be eliminated using UHPFRC. Force-fit joint closure leads to hyperstatic systems of increased structural rigidity.

Particularly, the structural behavior of the modified abutments needs to be investigated applying recent knowledge in the area of integral RC bridge structures. In the case of existing bridges, the dilation movement to be considered is limited to that due to changes in temperature alone, since girder deformation due to final shrinkage and creep of the existing concrete is negligible.

Bridges consisting of a series of simple beams that are force-fitted monolithically in the support zone by R-UHPFRC, are converted into a continuous beam and are thus analyzed like continuous beams according to Principle 1.

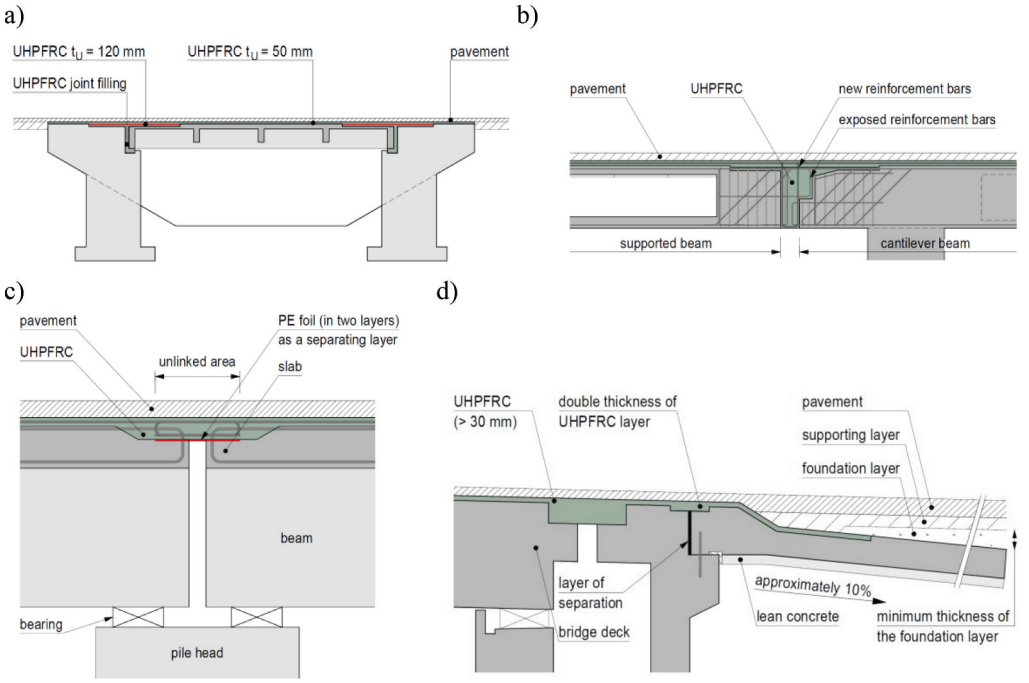


Figure 4. Principle of UHPFRC joint closure: a) in the abutment zones of a single span bridge to create a half-frame, b) force-locked girder joint, c) partial joint closure for beam chains, also called "link slab", and d) creation of a semi-integral bridge end.

Figure 4a shows the concept of joint closure in the abutment area of a single span beam. In the case of pier-like abutments with large dimensions, a semi-frame structure is created. By modifying the end zones of the beam to frame corners, the bending stress is redistributed from the sagging zone to the frame corners and thus relieved. By installing the R-UHPFRC tension chord in the abutment zones and a UHPFRC layer over the entire deck, the dilation joints are eliminated and the reinforced concrete is protected from chlorides and water. The stress flow in the frame corners has to be carefully analyzed.

Figure 4b shows the constructional detail of a force-locked girder joint, which is bending and shear resistant. The UHPFRC lock is anchored into the existing RC bridge structure with rebar inserts on both sides to connect. In the case of single span girders in series, the partial joint closure at the level of the deck slab shown in Figure 4c can be suitable. A relatively massive unbonded slab in R-UHPFRC, called "link slab", is anchored in the adjacent RC deck slabs to connect two adjacent bridge girders by a continuous deck slab. The length of the connecting UHPFRC slab is designed such that temperature related deformations are absorbed by deformation of the "link slab". The static functioning of the original simple beams is not modified by this intervention. This "link slab" principle can also be implemented in the transition from the bridge to the road for dilations up to ±10 mm.

Figure 4d shows the design of a semi-integral abutment by means of a R-UHPFRC lock connecting the bridge deck slab to the transition (or approach) slab, thereby waterproofing the bridge end zone and eliminating the dilation joint above the bridge bearing.

By forming force-locked UHPFRC connections, the structure is stiffened, which usually also increases structural resistance. Obviously, the stresses in the entire strengthened structure and in particular the UHPFRC-locked zone must be analyzed accordingly and the force flow in the modified structure must be carefully verified.

3 FOUR SELECTED RECENT APPLICATIONS

Among numerous UHPFRC application projects (Bertola et al. 2021) with involvement of the author in conceptual design, dimensioning, project proof and quality control, three recent projects are selected and briefly described in the following:

3.1 *Riddes Road Viaduct, Switzerland – Strengthening to restore structural resistance*

The 1,2 km long road viaduct (Figure 5a) consisting of a twin continuous box girder in posttensioned concrete built in 1976 is a major road overpass over a railway line, highway and a river.

a) b)

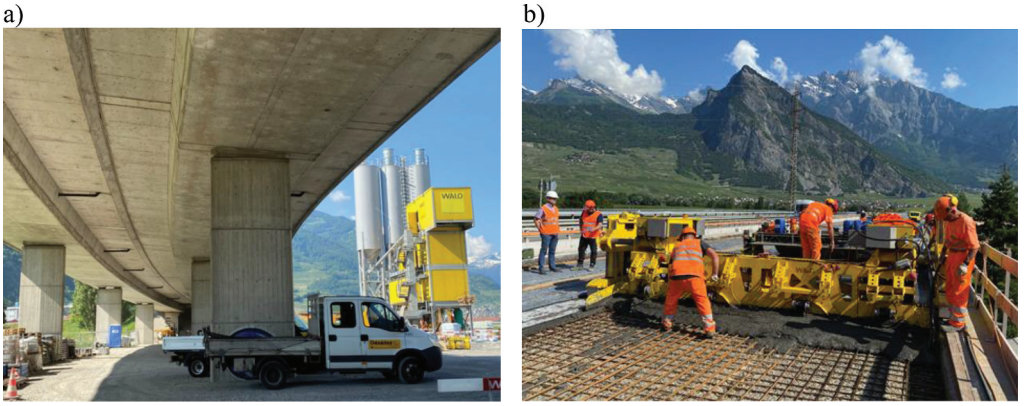


Figure 5. a) UHPFRC ready mix plant next to the Riddes Viaduct, b) UHPFRC casting on the deck slab.

RC damage including corrosion of prestressing tendons and steel rebars as well as alkali-aggregate reaction lead to a significant deficit in structural resistance. Strengthening intervention was urgently needed. The objective of the intervention was to over-strengthen the girder for flexural resistance to accommodate for (1) potential loss of 1/3 of post-tensioning, (2) 30% AAR-related and forecasted concrete strength reduction as well as (3) local damage of the deck slab.

The R-UHPFRC intervention method was found to be most cost-effective and rapid to rescue the viaduct's post-tensioned concrete structure. The concept and design of strengthening was following the principle shown in Figure 6 and the design provisions of the Swiss UHPFRC standard (SIA 2052) including detailed non-linear FE analyses (El Jisr et al. 2023). The UHPFRC layer was cast in 2021 on the deck slab of the viaduct using a casting machine (Figure 5b).

3.2 *Aare Bridge Schinznach, Switzerland – Strengthening and deck widening*

This 120 m long three span road bridge for bi-directional road traffic and with a pedestrian walkway was built in 1954. This bridge belongs to the first generation of steel-concrete composite bridges and has significant cultural and aesthetic values (Figure 6a).

The cross section consists of two main steel girders and the RC deck slab acting in composite action. The RC slab showed usual steel rebar corrosion damage, and the pedestrian walkway had to be widened to accommodate for future user demand. In addition, examination of the composite structure and the deck slab revealed deficits in structural capacity and thus structural strengthening was required.

The realized strengthening consisted in adding a 60 mm thick layer of UHPFRC incorporating steel reinforcement bars in orthogonal directions to waterproof and protect the RC slab as well as to increase the resistance of the slab in the transverse direction and the hogging moment capacity over the piers in the longitudinal direction. The UHPFRC casting works of the roadway were realized in two days in Summer 2022 (Figure 6b).

The R-UHPFRC strengthening was optimized such that strengthening of the two steel girders could be avoided, reducing the intervention on the main structure in steel to the renewal of the corrosion protection coating only.

a) b)



Figure 6. a) View of the steel-concrete composite bridge after R-UHPFRC strengthening, b) casting of UHPFRC with immediate application of curing compound.

3.3 *Viaducts Pont d'Ouche, France – Strengthening of kerb zone for impact forces*

Built as part of a vast motorway program in the 1960s, the 504 m long Pont d'Ouche twin viaducts are one of the major elements of the A6 motorway in France (Figure 7a). At the time of their construction, they were unique by its geometric characteristics, since built entirely in curves and in slope, and by the structure being made up of prestressed prefabricated isostatic beams with spans of 36 m with cast-in-place connecting slabs. This rational structural system for RC viaducts, which was very often realized in France and worldwide, allowed realization in a record time of 20 months, and the inauguration of the viaducts was in October 1970.

Installation of a robust water proofing layer in UHPFRC on the entire slab and all kerbs, repair of rebar corrosion damage and structural strengthening of the slab zone near the curbs to resist possible vehicle impact forces on the new vehicle retaining system, were the main reasons for realizing the UHPFRC project. The UHPFRC layer on the deck slab of the first viaduct was cast in 2022 using a casting machine (Figure 7b). The same UHPFRC intervention was realized in 2023 on the adjacent viaduct.

a) b)

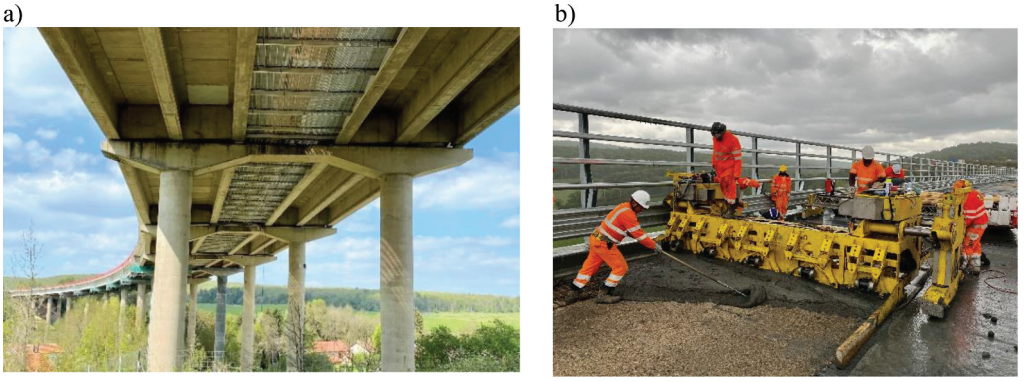


Figure 7. a) View of the twin viaduct structure with triple PC-girder cross section, b) casting of UHPFRC and curing with a plastic foil.

3.4 *Ferpecle Road Bridge, Switzerland – Strengthening and deck widening*

The Ferpècle Bridge is a prestressed reinforced concrete double-girder structure (TT cross-section) from 1958, thus belonging to the first generation of prestressed bridges. The bridge is located in the Swiss Alps. The original static system was a simply-supported beam with a 34,5-meter span, resting on abutments with side walls approximately 7 meters long (Figure 8a). With a beam height of 1,75 meters, the slenderness of 1/20 is audacious for a simple beam.

The bridge condition was acceptable, except for the usual rebar corrosion damage of the top zone of the deck slab and the kerbs.

To accommodate for future road and pedestrian/bike demands, the bridge deck was widened from 5,3 m to 7,9 m, leading to a significant demand in structural resistance of about 60% compared to the original capacity.

The widening was realized by means of a cantilevered full slab of variable thickness in R-UHPFRC, that is anchored in the existing structure. The strengthening was done following the concept shown in Figure 4a to create a half-frame structure starting from a single beam system (Bertola & Brühwiler, 2024):

- In the sagging zone (with positive bending moments in the longitudinal direction), the deck thickness was increased from 25 to 27,5 cm; i.e. 20 mm of concrete from the existing slab was removed by hydro-jetting, and a UHPFRC layer of 45 mm was cast. Transverse and longitudinal reinforcing bars (ϕ14 @ 150 mm) have been incorporated in the UHPFRC layer.
- At the beam supports, a thicker layer of R-UHPFRC (70 mm) was cast. Moreover, significant reinforcement steel bars (ϕ22 @100 mm) are included. To achieve the necessary monolithic half-frame corners, the abutment zones were force-locked, connecting the beams with the abutments. In this way, the required hogging zone of high structural resistance was realized.
- Additionally, this intervention also eliminates any costly dilation joint and its high maintenance cost.

The works were carried out in summer 2023 in two phases (upstream and downstream), enabling alternating traffic flow throughout the works. The UHPFRC casting was realized according to confirmed methods, without any particularity.

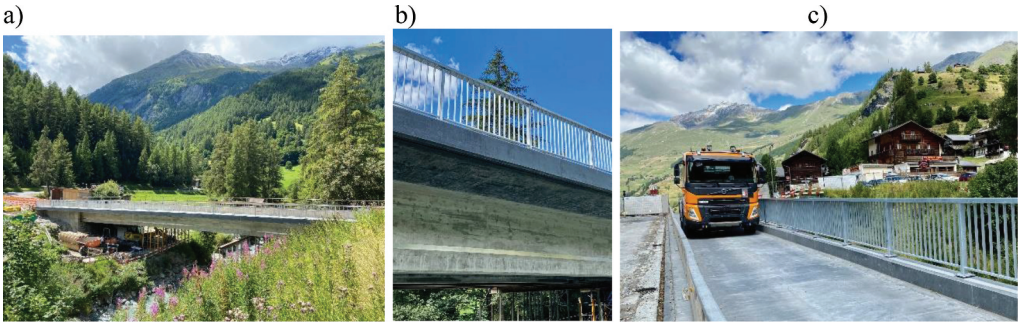


Figure 8. a) Ferpecle Bridge in Alpine surrounding, b) traffic on the bridge half already built using UHPFRC, c) original concrete in bright grey and UHPFRC cantilever slab in dark grey.

4 UHPFRC TECHNOLOGY AND SUSTAINABILITY

The two technically most efficient building materials are steel and cement. They are currently criticized as being particularly harmful to the environment. This ignores the fact that it depends on how these building materials are used. UHPFRC contains relatively high quantities of cement and steel, such that the energy input and greenhouse gas emissions per kg of UHPFRC are obviously relatively high compared to most other building materials.

Nevertheless, the principles of sustainability can be well respected through the targeted use of UHPFRC. This is because UHPFRC is a high-performance building material with which the required technical performance of structures is achieved with installing small material quantities on the existing structure, thereby preserving the existing structure.

In addition, "eco"-UHPFRC mixtures have already been developed and will be used in the near future, allowing for a reduction of the environmental impact of the UHPFRC material alone. Also, UHPFRC can be decomposed and recycled at the end of its use.

When dealing with existing structures, the use of UHPFRC follows the principle: *"Improve instead of replace!"* UHPFRC Technology is able to rehabilitate and strengthen, actually to salvage, existing RC structures. In this way, material resources and grey energy already in use are further utilized, thanks to a relatively small amount of UHPFRC. The existing structure is valorized and upgraded in an economic manner.

Estimations show that this approach has about an order of magnitude less environmental impact (and is significantly less expensive) than the still practiced demolition-replacement approach, also called "end-of-life approach", which obviously is outdated nowadays. Contrary to humans, structures don't have an end of life.

5 CONCLUSIONS

The UHPFRC Technology provides effective solutions to rehabilitate and strengthen existing bridges with little use of materials to upgrade them for future utilization. When dealing with existing bridges, the use of UHPFRC leads to: *"Improve instead of replace!"*

The UHPFRC Technology allows to rehabilitate and strengthen, actually to salvage, existing RC structures. In this way, already used material resources are further utilized. The existing bridge is valorized and upgraded in an economic manner. This follows the principle of sustainability to preserve material resources and their embodied energy, are already in use, thereby limiting greenhouse gas emissions to a minimum.

The UHPFRC Technology has already been implemented in practice. Recently, the Swiss Federal Roads Office has published a documentation to facilitate the use of the UHPFRC Technology for the preservation existing and the construction of new engineering structures of the road infrastructure (FEDRO 2023).

REFERENCES

Bertola, N. et al. "A Review of the Use of UHPFRC in Bridge Rehabilitation and New Construction in Switzerland." *Frontiers in Built Environment*, vol. 7, 2021, p. 155.

Bertola, N., Brühwiler, E., Combining monitoring information and UHPFRC strengthening to extend bridge service duration, Proceedings, IABMAS'24 Copenhagen, 2024.

Brühwiler, E., "UHPFRC Technology to Enhance the Performance of Existing Concrete Bridges." *Structure and Infrastructure Engineering*, vol. 16, no. 1, 2020, pp. 94–105.

El Jisr, H., Moreillon, L., Menétrey, P., 2023. Strengthening of the Riddes Viaduct Through UHPFRC-Based Rehabilitation. Structural Engineering International 0, pp. 1–9.

FEDRO Documentation: UHPFRC for the preservation and construction of structures of the road infrastructure (author: E.Brühwiler), Swiss Federal Roads Office, Bern, Switzerland (in German and French), March 2023.

Graybeal, B. et al. "International Perspective on UHPC in Bridge Engineering." *ASCE Journal of Bridge Engineering*, vol. 25, no. 11, Nov. 2020, 16p.

SIA Standard 2052 „UHPFRC materials, dimensioning and execution", Swiss Society of Engineers and Architects, Zurich Switzerland, 2016 (revised version 24 Dec 2021).

Bridge Maintenance, Safety, Management, Digitalization and Sustainability – Jensen, Frangopol & Schmidt (eds)
© 2024 The Author(s), ISBN 978-1-032-77040-6
Open Access: www.taylorfrancis.com, CC BY-NC-ND 4.0 license

Interpreting monitored responses of an orthotropic steel deck using FEM

S. Ye
Arup, Hong Kong

R. Gibson
Arup, London

N. Yeung & S. Kite
Arup, Hong Kong

ABSTRACT: The actual response of a bridge deck under heavy vehicles is of great interest for bridge assessment. To better understand this, strain and displacement monitoring technologies have been deployed on many bridges around the world to measure their responses, particularly for stress histories under heavy vehicle events. For orthotropic steel decks (OSD) of highway bridges, it remains a key technical challenge to process and interpret these monitored stress responses. This is due to the uncertainties in vehicle weave (transverse axle position), axle load, axle type and vehicle configuration. Fatigue performance governs the life of OSD, and efficient processing of monitoring data would significantly improve the ease of assessing its health. In this paper, the outputs from detailed finite element modelling (FEM) are used to interpret the monitored heavy vehicle responses from the OSD of a long span suspension bridge. The FEM investigates the effects of different weave positions and axle arrangements on stress histories at locations equivalent to those monitored on the bridge. Responses from heavy vehicle events are also extracted from the high frequency strain gauge monitoring data. Through engineering interpretation, key features of the generated responses under different types and locations of heavy vehicles are identified. It is envisaged that this interpretation could be automated through machine learning, which ultimately could be linked back to local fatigue assessments and bridge inspections to correlate processed monitoring data with fatigue health.

1 INTRODUCTION

1.1 *Background and motivation*

Orthotropic steel decks (OSD) are adopted for many bridges around the world as it is a highly efficient method for providing a lightweight deck, particularly for long span bridges. It has been used since 1950s and has remained relatively unchanged, incorporating only a small number of variations. The OSD system uses steel only where it is necessary, with the main stiffness required in the longitudinal direction. The system consists of a flat deck plate with U-shaped longitudinal trough stiffeners welded to the underside. The deck plate and troughs sit on regularly spaced cross girders. The trough spacing is typically 600 mm and the cross girders at 3-4 m spacing.

The design of OSD is governed by fatigue rather than strength. The continuous passage of heavy trucks and buses provides the most onerous condition for fatigue local to the tyre tracks. Small vehicles such as cars do not have a significant effect. Looking at

DOI: 10.1201/9781003483755-16

existing steel bridges, a significant amount shows signs of fatigue cracking after only 10-30 years of service life. This suggests a lack of understanding of the fatigue effects in OSD in the past. Detailed analysis techniques have been developed by Arup, which calculate a representative level of stress that results in damage predictions correlating well with cracking found on the bridges in this timescale. The fatigue assessment uses a detailed finite element (FE) model of the bridge deck to generate stress histories of heavy vehicle passage events at different vehicle weaves (transverse axle positions) at each weld location. The stress histories are then cycle counted in order to perform damage prediction calculations.

However, the current fatigue assessment process is time-consuming and requires a very detailed and sophisticated approach. We propose a new approach of assessment which involves interpreting strain monitoring data of OSD to enable more efficient assessment of fatigue health. The strain gauge data taken from the OSD is interpreted by comparing with the stress histories obtained from the finite element method (FEM). Each vehicle type, such as double-decker bus (DDB) and heavy goods vehicle (HGV), will have a signature stress history.

The proposed approach also requires some historic correlation with actual damage found on bridges in order to provide validation and calibration of assessment results. As the strain gauge measurements are not taken from the weld itself, there is no fatigue calculation that can be directly performed. Therefore, to make best use of the interpreted data requires correlation with the performance data of similarly configured OSD (e.g., plate thickness and trough stiffener shape). This must be based on normalised truck numbers to remove differences in demand between bridges.

In this paper, we present the identification of double-decker bus (DDB) passage events and their weave positions using FEM results. This is carried out through manual comparison with FEM outputs and engineering interpretation. It is envisaged that ultimately this can be automated through machine learning in order to perform the interpretation on thousands of heavy vehicle events.

1.2 *Long Span Bridge and its structural monitoring*

The paper uses the OSD of a long span suspension bridge as the case study, hereinafter referred to as the Long Span Bridge (LSB). The bridge deck of the LSB consists of orthotropic deck plates, and carries multiple road traffic lanes in each direction.

On the LSB, a structural health monitoring (SHM) system has been deployed, with sensors such as strain gauges, displacement transducers, GPS rover stations, accelerometers, anemometers and temperature sensors. The SHM system was designed to measure input loadings (e.g., wind, temperature, traffic), output responses (e.g., strain, displacement) and structural properties (e.g., modal frequencies, mode shapes).

1.3 *Data used in this study*

In this study, data collected from five strain gauges at the OSD of upper deck was used, referred to as Strain Gauge 1 (SG-1) to Strain Gauge 5 (SG-5). The sensor layout is shown in Figure 1. These five sensors are located under the slow lane where heavy vehicles travel. SG-1, SG-3 and SG-5 measure strain in the longitudinal direction, and SG-2 and SG-4 measure strain in the vertical direction. Each strain gauge collects data continuously at around 50 Hz, which gives over 4 million data points per day. To facilitate the data analysis and interpretation, strain data was converted to stress data using $\Delta\sigma = E\Delta\varepsilon$, assuming E = 210 GPa for steel.

Ideally, 100 Hz is adopted for fully capturing the stress history under each heavy vehicle event, but 50 Hz may be good enough. In addition, as shown in Figure 2, it has been discovered that SG-1 has relatively large data noise (about ± 4 με). These factors need to be considered when interpreting the monitored heavy vehicle responses.

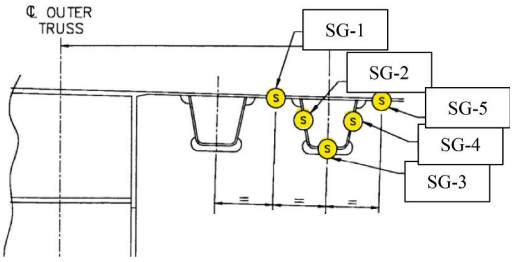


Figure 1. Five strain gauges at orthotropic steel deck.

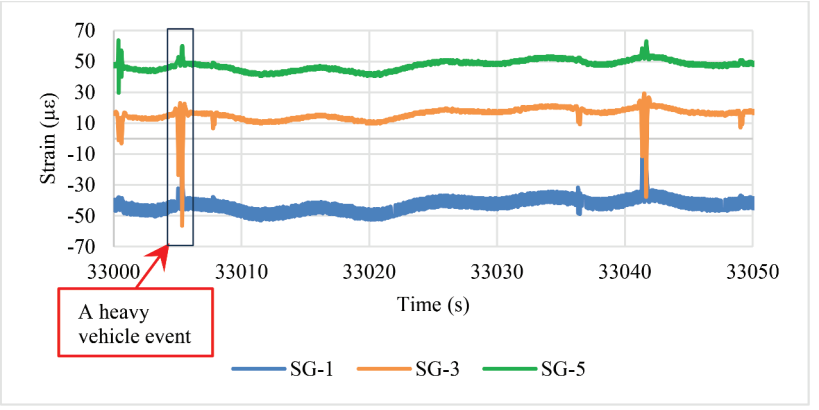


Figure 2. Example plot of collected strain data (at 33000-35000 s of a day).

2 METHODOLOGY

2.1 *Extraction of heavy vehicle events from strain monitoring data*

Individual heavy vehicle events were first extracted from the strain monitoring data using machine learning (support vector machine) and statistical methods (moving average-based algorithms). More information on the methods was provided in Ye et al. (2023).

2.2 *Finite element modelling and analysis*

The fatigue assessment of the LSB OSD was performed using a detailed local 3D linear elastic FE model. It was analysed using *MSC Nastran*, and the fatigue calculation was performed using software written by Arup specifically for assessing bridge decks. For the purpose of this study, the fatigue software was used to generate stress histories of double-decker buses (DDB) passing over the deck for comparison with the strain monitoring data.

The FE model was a multi-scale model. A detailed local region of the bridge deck section, which consisted of shell elements, was embedded into the global region, as shown in Figure 3. The global model consisted of beam elements with equivalent shell elements for the deck.

The local region was 27 m long and included six 4.5 m cross frame bays. The full width of the bridge was included. The "cut-section" ends of this local region were rigidly constrained to the global region. The mesh density in the fine detailed region was such that stress concentrations (other than those generated by the weld profiles) were adequately predicted. This means a mesh size in the order of the thickness of the deck plate or trough.

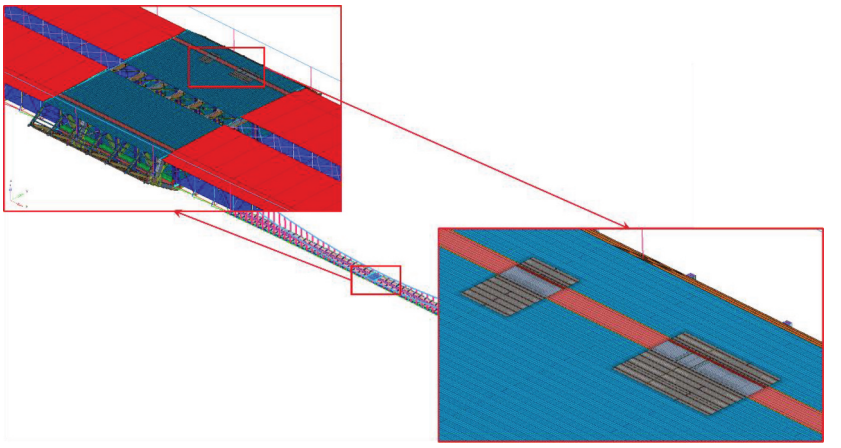


Figure 3. Finite element model of orthotropic steel deck in NASTRAN.

Fatigue damage in OSD is caused by the passage of heavy trucks and buses. There are many variations of truck configuration, however, there are not many bus types that travel on the LSB. To keep the process straightforward, this initial study was based on the type of double-decker bus (DDB) which was prevalent at the time of monitoring data collection. The DDB consists of three axles (see Figure 4). The front steering axle has a single tyre each side, known as an A-axle. The rear two axles have pairs of tyres each side, known as a B-axle. This study assumed the maximum bus weight of 27 tonnes, as specified by the manufacturer. The load was positioned so that the second axle was longitudinally in-line with the strain gauges.

In order to find matching responses between the detailed FE model and monitoring data, the analysis was run for ten different transverse bus positions, or weaves, relative to the strain gauges (see Figure 5). The bus load was incrementally moved along the model to generate stress histories from elements at each gauge location, one bus passage per weave.

The strain gauge locations are previously shown in Figure 1. They are attached to the underside of the deck plate (SG-1 and SG-5), sides of the trough stiffener (SG-2 and SG-4)

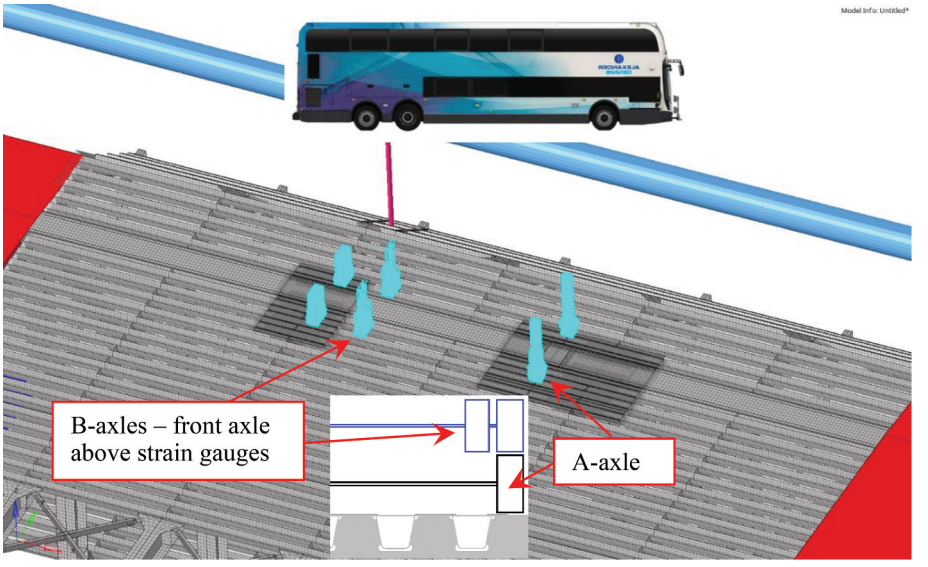


Figure 4. Application of environ 500 bus loading on orthotropic steel deck.

and beneath the trough (SG-3). Outputs from SG-2 and SG-4 were not used, as they are not typical of OSD behaviour. The main outputs were taken from SG-1 and SG-5, as they show distinctive stress patterns, with clear indications of bus location. SG-3 was found to be less sensitive to bus location but useful for correlation.

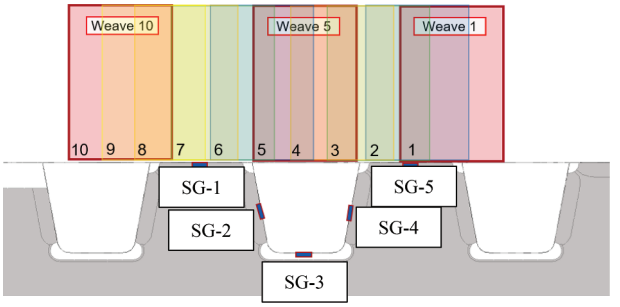


Figure 5. Application of bus load at different weave positions.

3.3 *Interpretation of monitored responses using FEM output*

Looking at the strain monitoring data alone from the bridge, it is unknown what vehicles passed or where they passed over. However, the stress histories from the FE model, at different weave positions, are known. They can be compared with the monitored responses (i.e., matching response patterns) to ascertain the bus passage event and bus location.

3 RESULTS AND INTERPRETATION

3.1 *FEM outputs*

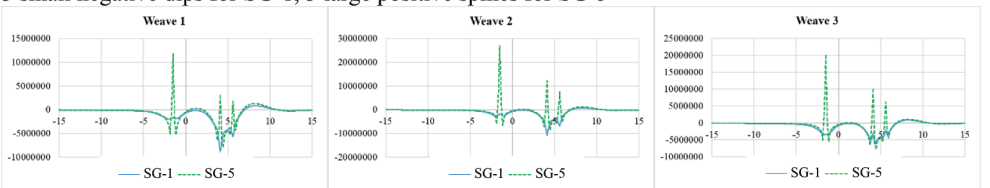
The stress histories from the FE model, under the DDB nominal loading at different weave positions (weaves 1 to 10), are summarised in Table 1, which shows that four distinctive response patterns can be identified. As for the relationship between weave positions and sensor locations, as shown previously in Figure 5, weave 2 is directly above SG-5, weave 8 is approximately directly above SG-1, and weave 5 is directly above the trough stiffener.

A number of observations and interpretations can be made from the response patterns:

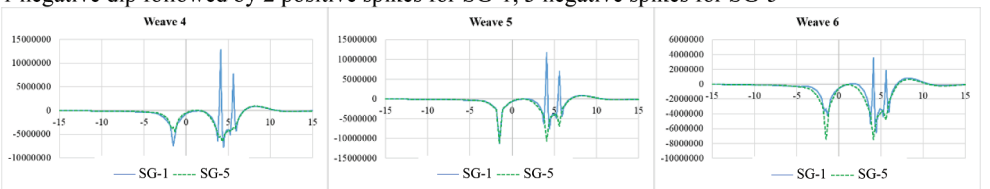
- The stress history includes global response of the deck and local response of the deck plate or trough stiffener, with an influence length approximately the distance between cross frames.
- For A-axle (single tyre), when the tyre is directly above SG-5 (refer to response pattern 1), which is located at the deck plate between two adjacent trough stiffeners, it results in a tension response due to local bending (large positive spikes) of the deck plate. Likewise for SG-1 (refer to response pattern 3).
- For A-axle, when the tyre is slightly away from SG-5 (refer to response patterns 2-4), it results in a global compression response (relatively small negative dips) of the deck. Likewise for SG-1 (refer to response patterns 1, 2 and 4).
- For response pattern 10, the tyres are much closer to SG-1 than SG-5. This is illustrated by the higher in magnitude and the definition of dips for each axle for SG-1.
- For B-axle (double tyres), it results in a combination of the above-mentioned two types of response. For example, for SG-1 in response pattern 2, the front A-axle results in global compression response while the rear B-axles results in a combination of global compression (due to the outer tyre) and local tension (due to the inner tyre).

Table 1. Different response patterns from FEM outputs.

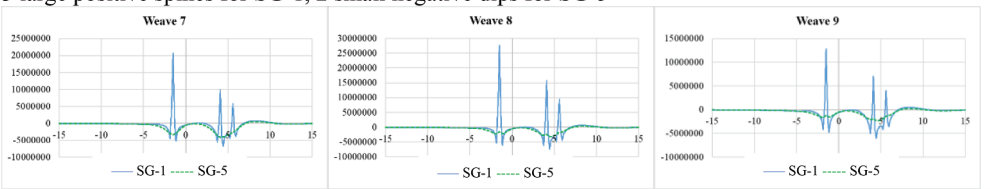
FEM response pattern 1 (weaves 1 to 3):
3 small negative dips for SG-1, 3 large positive spikes for SG-5



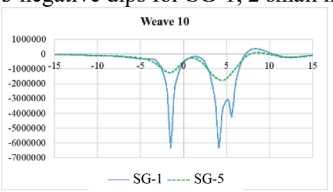
FEM response pattern 2 (weaves 4 to 6):
1 negative dip followed by 2 positive spikes for SG-1, 3 negative spikes for SG-5



FEM response pattern 3 (weaves 7 to 9):
3 large positive spikes for SG-1, 2 small negative dips for SG-5



FEM response pattern 4 (weave 10):
3 negative dips for SG-1, 2 small negative dips for SG-5



3.2 *Interpretation of monitored responses using FEM output*

The following graphs show examples of monitored responses (refer to Figures 6–9). As discussed in the previous section, the deck plate strain response spikes very sharply when the tyre is directly above the gauge. This provides a guidance as to where the vehicle is located. Also, the number and spacing of spikes provides an indication of axle arrangement. It should be noted that the data frequency is around 50 Hz, and the SG-1 response contains relatively large noise, as previously explained in section 1.3.

The monitored response pattern I in Figure 6 has sharp peaks in SG-1 response, indicating that the vehicles are located around weaves 7-9. The peaks suggest the vehicles have two axles. Although the axle count is different, the shapes are similar to response pattern 3 in Table 1. SG-5 shows negative dips which represent the global response from axles further away. SG-3 at the bottom of the trough is less sensitive to sharp peaks, but the response indicates that the rear axle is heavier than the front axle.

The monitored response pattern II in Figure 7 has sharp peaks in SG-5 for the rear tyre only, suggesting a B-axle located outside of weave 1. The inner tyre generates the large stress response in SG-5. The peaks suggest that the vehicles have two axles. SG-1 shows negative dips which represent the global response.

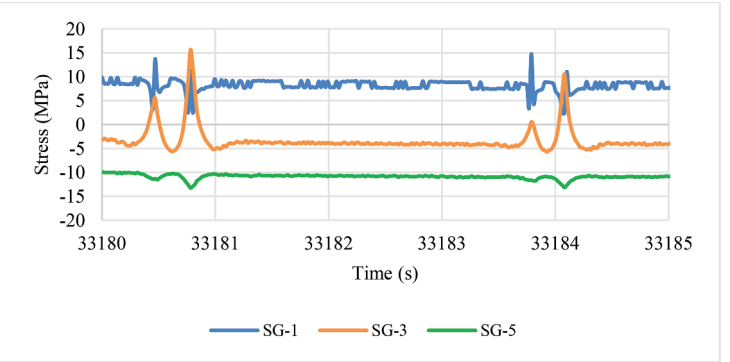


Figure 6. Monotored response pattern I.

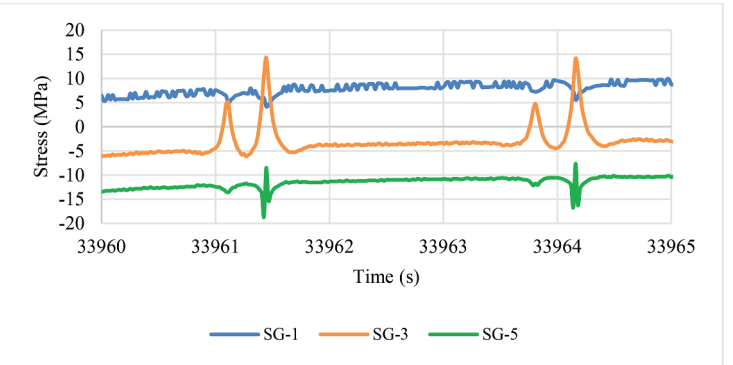


Figure 7. Monotored response pattern II.

The monotored response pattern III in Figure 8 has sharp peaks in the SG-1 response, but only for the rear tyres. This indicates that the vehicles are on weaves 4-6, for which only the B-axle with inner tyres generate the large spiked stress response in SG-1. The response shows a double peak which means the vehicles have three axles. Again, SG-5 shows negative dips with no peaks which represents the global response. SG-3 at the bottom of the trough has a larger rear peak as there are two closely spaced axles.

The monotored response pattern IV in Figure 9 has sharp peaks in the SG-5 response, indicating that the vehicles are located around weaves 1-3. The peaks suggest the first vehicle has three axles and the second has four. SG-1 shows negative dips which represent the global response.

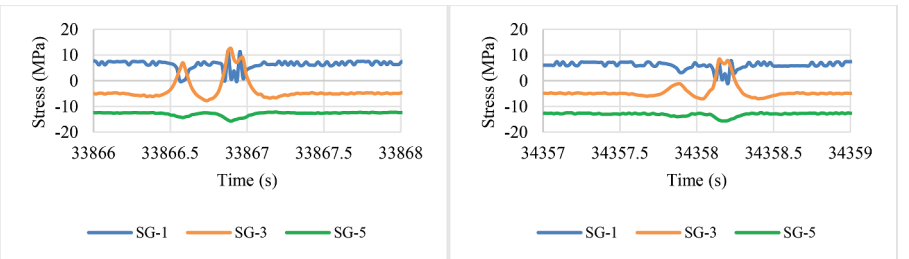


Figure 8. Monotored response pattern III.

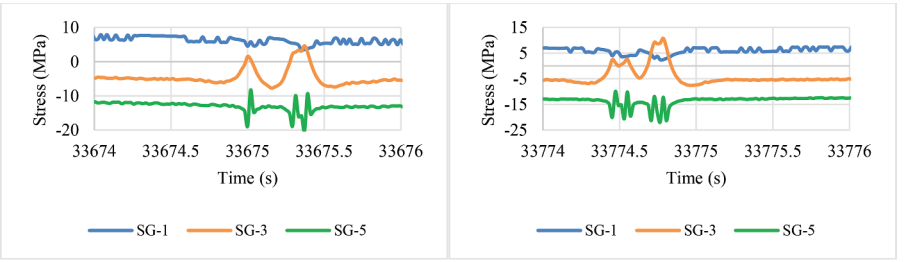


Figure 9. Monitored response pattern IV.

4 DISCUSSION

This study has demonstrated the technical feasibility of interpreting monitored heavy vehicle responses using FEM outputs, and in particular, inferring axle arrangement and vehicle weave from the response data. It is envisaged that the outcomes of this study can be used to develop a physics-guided machine learning algorithm for recognising the responses of different types of heavy vehicles at different weave positions, which is useful information in fatigue assessment. This could become a general tool for analysing the monitoring data under heavy vehicles, linking input loading data to output response data, and thus better understanding the behaviour and response of OSD. Ultimately, this could be linked to local fatigue assessments and bridge inspections to correlate processed monitoring data with fatigue health.

5 CONCLUSIONS

In this paper, we have demonstrated the technical feasibility of interpreting monitored heavy vehicle responses of orthotropic steel deck (OSD) using finite element method (FEM) analysis results, and in particular, the identification of axle arrangement and vehicle weave (transverse axle position). The study has used the OSD of a Long Span Bridge (LSB) as the case study, which has strain gauges installed at the deck plates and trough stiffeners, with continuous data collection at around 50 Hz. The FEM results of stress response under the type of double-decker bus (DDB) that travelled frequently on the LSB, at 10 different weave positions were generated using a detailed FE model. Four distinctive response patterns were identified from the FEM outputs, which were interpreted from a structural behaviour perspective. These FEM response patterns served as the reference patterns to interpret the monitored heavy vehicle responses. It is envisaged that this interpretation could be automated through machine learning in order to perform the interpretation on thousands of heavy vehicle events and enable more efficient and accurate fatigue assessment.

REFERENCES

Ye, C., Yeung, N., Vishnoi, P. & Kite, S. 2023. A machine learning-based methodology of integrating loading data and load effect data for long span bridge assessment. In *IABSE Congress New Delhi 2023*, 20-22 September 2023. Paper ID: 184.

Bridge Maintenance, Safety, Management, Digitalization and Sustainability – Jensen, Frangopol & Schmidt (eds)
© 2024 The Author(s), ISBN 978-1-032-77040-6
Open Access: www.taylorfrancis.com, CC BY-NC-ND 4.0 license

Predicting time history response of bridges under vehicle load using CNN

Huile Li & Tianyu Wang
Key Laboratory of Concrete and Prestressed Concrete Structures of the Ministry of Education, School of Civil Engineering, Southeast University, Nanjing, China
National and Local Joint Engineering Research Center for Intelligent Construction and Maintenance, Southeast University, Nanjing, China

ABSTRACT: Vehicles represent the main operational loadings of bridge structures since they are designed and constructed to sustain passing vehicles. Among others, structural responses due to the moving vehicles play a crucial role in bridge health monitoring, condition assessment, maintenance. Traditionally, vehicle-induced dynamic responses can be obtained through a variety of numerical computational models. Depending on the complexity of existing models, they could become either computationally expensive or hard to be implemented in regular engineering practice. Moreover, as physical-based methods, a good number of parameters associated with materials, mechanics, and geometry are required to establish a reliable model reflecting the physical structure behaviour. Recently, the literature has seen an increasing research efforts in dynamic response estimation of civil structures subjected to vehicle, seismic, or wind load using machine learning techniques. This paper presents an investigation of predicting dynamic responses of bridges by neural network under vehicle loadings. Representative analysis model is employed to create training data pairs for learning parameters in the network. The state-of-art deep learning technique, namely, convolutional neural network is adopted to develop the metamodel of the vehicle and bridge system, capable of delivering time history response to be compared with results from numerical experiments. The results show that the predictive model yields high prediction accuracy and is robust to data noise.

1 INTRODUCTION

Structural dynamic response of bridges plays a crucial role in the entire bridge life cycle, such as planning, design, operation & maintenance, inspection, and monitoring. These responses can be obtained by field measuring or numerical computation. For vibration measurement, sensors need to be installed in the structural components or cross-sections of interests (Carey et al., 2017; Mostafa, 2021; Xia et al., 2013). However, the campaign is still labor intensive and cost-ineffective. Although long-term bridge health monitoring can provide continuous data of bridges (Hu et al., 2013; Cahill, 2016; Sun et al., 2020), this type of monitoring system is rarely applied to the bridges with regular spans. These bridges account for the vast majority of the bridge inventory.

Recently, artificial neural network (ANN) has been regarded as a quite promising soft computing algorithm in dynamic analysis of large-scale civil structures (Adeli, 2001; Adeli, 2020; Vaidyanathan et al., 2005). The development of deep learning techniques provides new tools for structural response prediction due to dynamic loadings (Adeli, 2020; Feng et al., 2021; Kim et al., 2020). As a data driven approach, ANN models can be constructed by using labeled data as input and output respectively. For example, Lagaros & Papadrakakis (2012) used neural network for dynamic response prediction of buildings under seismic load.

DOI: 10.1201/9781003483755-17

Joghataie & Farrokh (2008) used a feedforward neural network to perform dynamic analysis involving seismic excitation. Oh et al. (2020a) realized the prediction of the maximum response of structures based on conventional multi-layer perceptron under artificial earthquakes. In addition, many researchers have studied the application of deep neural networks in estimating the dynamic response of structures caused by ground motion (Xu et al., 2021; Wu et al., 2019; Kim et al., 2019; Peng et al., 2021; Oh et al., 2020b; Torky & Ohno, 2021;).

While ANN based surrogate models have gained more and more attention in the literature related to earthquake-induced structural dynamic response analysis, limited research has been reported focusing on the response prediction of bridges under vehicular loads by the neural network algorithms (Li et al., 2020, 2021, 2022, and 2023a). To this end, this work aims to present an investigation of adopting deep neural networks to analyze vehicle-induced bridge vibrations and the efficacy of the state-of-art machine learning techniques under consideration. A representative model namely, moving load model is established in this study. The model is able to capture the main dynamic characteristics of the vehicular loads. A deep convolutional neural network (CNN) model is proposed to predict the time-histories of bridge dynamic response. The deep learning architecture is developed based on the bridge equation of motion governing the structural vibration in generalized coordinates. A comparison of time-history curve and peak error are carried out to evaluate the estimation capacity of proposed model.

2 MOVING LOAD MODEL

In this paper, a simple model of vehicular loads, namely moving load model, is considered to simulate the dynamic responses. As shown in Figure 1, the inertia force of vehicle can be ignored and the vehicular load can be simplified as a moving concentrated force *P*. Additionally, the track irregularity excitation is also neglected herein (Li et al., 2023b). When the force P passes the bridge at the speed of v, the partial differential equation of the bridge vibration can be written as

$$EI_{\mathrm{b}}\frac{\partial^4 Z_{\mathrm{b}}(x,t)}{\partial x^4}+\bar{m}\frac{\partial^2 Z_{\mathrm{b}}(x,t)}{\partial t^2}+c\frac{\partial Z_{\mathrm{b}}(x,t)}{\partial t}=P\delta(x-vt) \tag{1}$$

Where Z_{b} is the bridge displacement; I_{b}, $\bar{m}$, and c are the moment of inertia, mass per unit length, and damping coefficient of the bridge respectively; E is the modulus of elasticity; and δ is the Dirac delta function.

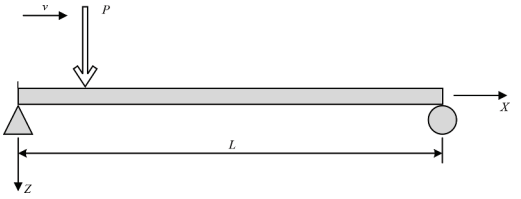


Figure 1. Moving load model.

Equation (1) can be solved through modal decomposition technique. Accordingly, the solution of Equation (1) is expressed in the following form (Li et al., 2023c):

$$Z_{\mathrm{b}}(x,t)=\sum_{i=1}^{\infty}q_i(t)\phi_i(x) \tag{2}$$

where $q_i(t)$ is the generalized mode coordinates and $\phi_i(x)$ is the function of the ith vibration mode. For a simply-supported bridge, the function of vibration mode can be written as

$$\phi_i(x) = \sin\frac{i\pi x}{L} \tag{3}$$

Then, the ith order generalized equation of motion of the simply-supported beam is given by

$$\ddot{q}_i(t) + 2\varsigma_i\omega_i\dot{q}_i(t) + \omega_i^2 q_i(t) = \frac{2}{\bar{m}L}P\sin\frac{i\pi vt}{L} \tag{4}$$

where ω_i and ς_i are the ith frequency and damping ratio. The solution of Equation (4) can be written as

$$q_i(t) = e^{-\varsigma_i\omega_i t}(A_i\cos\omega_{id}t + B_i\sin\omega_{id}t + D_i\cos\omega_{iv}t) \tag{5a}$$

$$C = \frac{2P}{\omega_i^2\bar{m}L}\frac{1-(\omega_{iv}/\omega_i)^2}{\left[1-(\omega_{iv}/\omega_i)^2\right]^2 + [2\varsigma_i(\omega_{iv}/\omega_i)]^2} \tag{5b}$$

$$D = \frac{2P}{\omega_i^2\bar{m}L}\frac{-2\varsigma_i(\omega_{iv}/\omega_i)}{\left[1-(\omega_{iv}/\omega_i)^2\right]^2 + [2\varsigma_i(\omega_{iv}/\omega_i)]^2} \tag{5c}$$

where $\omega_{iv} = i\pi v/L$ and $\omega_{id} = \omega_i\sqrt{1-\varsigma_i^2}$. A_i and B_i are the undetermined constants which can be identified by the initial condition. Therefore, the response of bridge can be expressed as

$$Z_b(x,t) = \frac{2P}{\bar{m}L}\sum_{i=1}^{\infty}[e^{-\varsigma_i\omega_i t}(A_i\cos\omega_{id}t + B_i\sin\omega_{id}t) + C_i\sin\omega_{iv}t + D_i\cos\omega_{iv}t]\sin\frac{i\pi vt}{L} \tag{6}$$

3 DEEP CNN FOR RESPONSE PREDICTION

Deep CNN is a type of classical deep learning model which is specialized in processing data with grid structure. In this paper, the time history data of the generalized force is adopted as input. A deep CNN model is proposed to predict the time history response of the bridge.

3.1 *CNN*

Since the input of the neural network is usually considered to be high-dimensional, resulting in large model size and thus considerable computational burden, the feature extraction layers are introduced into the deep learning model to reduce the dimensionality of data and to improve the fitness of model. Convolutional layer is a widely used feature extraction layer in deep learning models. In a convolutional layer, the convolutional operation and nonlinear activation function are used together to extract the feature from the input $\mathbf{X}$. Convolutional operation can be expressed as

$$\mathbf{O}_{i,j,k} = (\mathbf{X} * \mathbf{V})_{i,j,k} = \varphi\left(\sum_{m,n,l} X_{(i-1)s+m,(j-1)s+n,l}V_{m,n,l,k}\right) \tag{7}$$

where $X_{i,j,l}$ is the input component at the i^{th} row, j^{th} column, and l^{th} input channel; $V_{m,n,l,k}$ is the component of convolutional kernel $\mathbf{V}$ at the m^{th} row and n^{th} column, connecting the l^{th} input

channel and k^{th} output channel; $\mathbf{O}_{i,j,k}$ is the output component at the i^{th} row, j^{th} column, and k^{th} output channel; s is strides defining that the convolutional operation is carried out every s data point in each direction; $\varphi()$ is the activation function; and $*$ is the convolution operator. As shown in Figure 2, several convolutional operations are usually carried out in parallel, each of which can be regarded as a linear filter.

To extract advanced features from the input data, nonlinear activation functions such as sigmoid function, hyperbolic tangent function, and rectified linear unit (ReLU) are usually used after the convolutional operation to improve the ability of nonlinear mapping. The expressions of the activation functions, sigmoid, tanh, and ReLU are given as

$$Sigmoid(x) = \frac{1}{1+e^{-x}} \tag{8}$$

$$tanh(x) = \frac{e^{x}-e^{-x}}{e^{x}+e^{-x}} \tag{9}$$

$$ReLU(x) = \begin{cases} x & x>0 \\ 0 & x \le 0 \end{cases} \tag{10}$$

Another operation in CNN is the pooling operation which includes mean pooling and max pooling to calculate the mean value or max value of all the data in the pooling domain respectively. Figure 2 shows how the mean pooling can reduce the input data size.

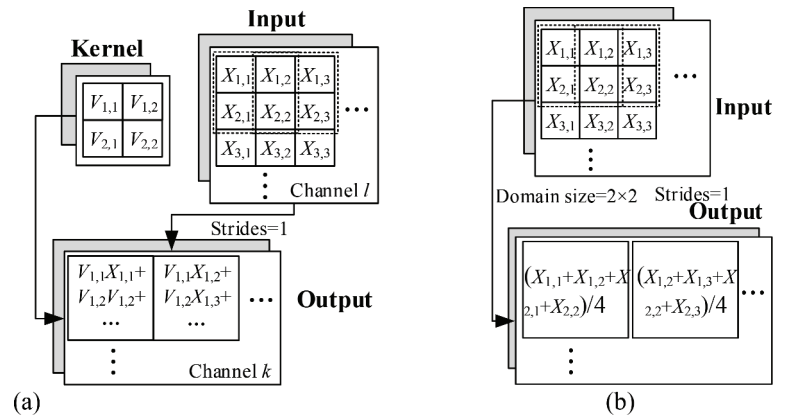


Figure 2. The CNN algorithm: (a) convolutional operation; and (b) pooling operation.

3.2 *Proposed CNN model for time history prediction*

According to Equation (4), the input of the CNN model is determined as the generalized force associated with the ith mode of vibration. To predict the dynamic bridge response in terms of discrete time, the network input can be expressed as

$$X_{i,j} = \sin\left(\frac{i\pi v t_j}{L}\right), \quad i = 1,2\ldots n, \quad j = 1,2\ldots m \tag{11}$$

where $X_{i,j}$ is the element in the input matrix $\mathbf{X}$ at the ith column and jth row; $t_j = j\Delta t \in [0, T]$; n is the number of vibration modes considered in response calculation; Δt is a constant which represents the time interval related to the sampling frequency; T is the time needed for the vehicle

to cross the bridge in the present analysis; and $m=T/\Delta t$ is the number of data points associated with one vehicle passing event.

The deep CNN model with the architecture shown in Figure 3 is proposed to realize the time history response prediction of bridge displacement, velocity, and acceleration.

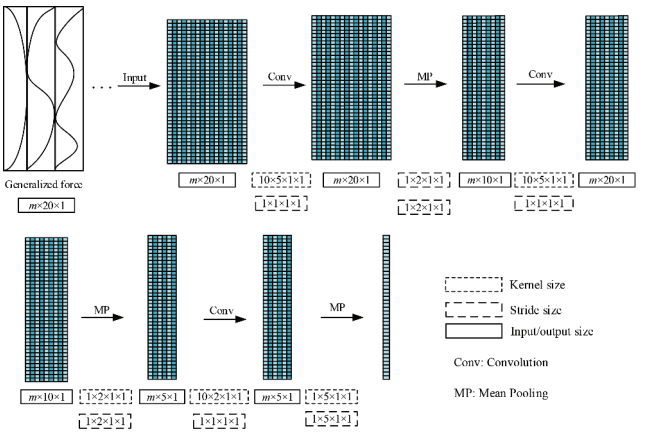


Figure 3. Architecture of the proposed deep CNN model for time history response prediction.

4 NUMERICAL EXAMPLE

To validate the proposed deep CNN model in time history response prediction, a numerical example is used. A vehicle-bridge system in the railway (Li et al., 2021) is simplified as the moving load -bridge model. The model parameters are shown in Table 1.

Table 1. Parameters of the vehicle-bridge system.

Parameter	Value
Bridge span L	23.1 m
Mass per unit length $\bar{m}$	2.12×10^4 kg
Elastic Module E	3.45×10^4 MPa
Moment of inertia I_b	6.78 m^4
damping ratio	0.02
Central force P	5.49×10^5 N

4.1 *Bridge response*

Figure 4 shows the displacement, velocity, and acceleration response of the bridge mid-span when the train speed is 300km/h.

4.2 *CNN training*

In this paper, 600 samples are generated by the moving load with random vehicle speeds between 250 km/h to 300 km/h. Among these examples, 500 samples are selected as training samples and the remaining 100 samples are used as validation datasets. For the model input, modal forces associated with 20 vibration modes are considered in this example. Mean square error (MSE) is utilized as the loss function given by

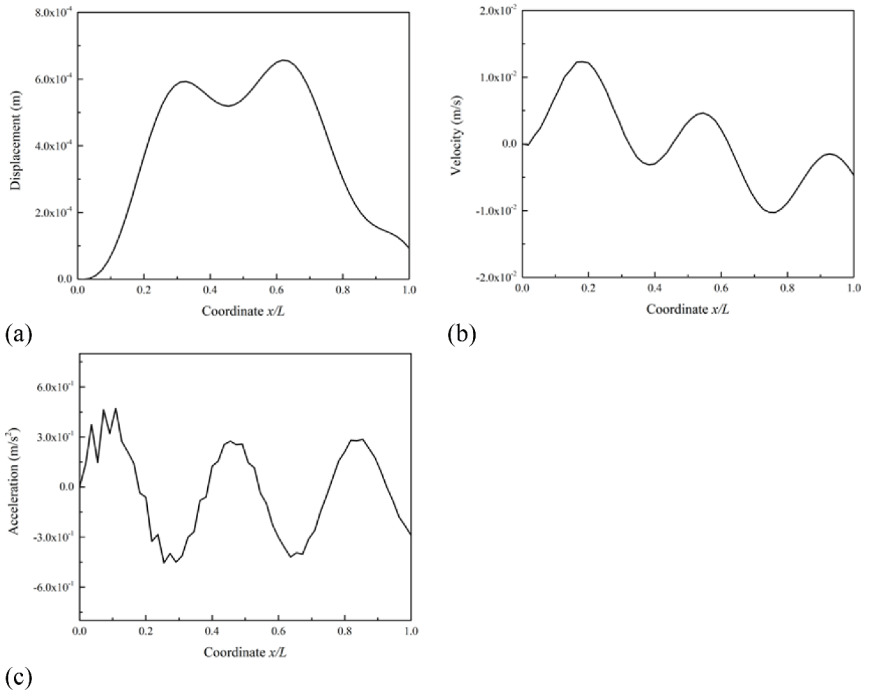


Figure 4. Sample of bridge response at mid-span with train speed of 300km/h: (a) displacement; (b) velocity; and (c) acceleration.

$$MSE = \frac{1}{M_{\mathrm{b}}} \sum_{i}^{M_{\mathrm{b}}} \left(X_i - \hat{X}_i \right)^2 \tag{12}$$

where X_i and $\hat{X}_i$ are the predicted value and target value of deep learning model; and M_{b} is the number of samples in a training batch.

In this example, root mean square prop (RMSprop) algorithm with initial learning rate of 0.0001 is utilized to train the proposed deep neural network model. The MSE of training samples and validation samples varying with the training epochs are presented in Figure 5.

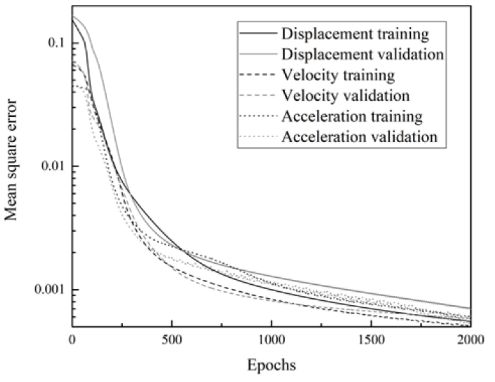


Figure 5. The variation of MSE with training epochs.

4.3 *Response prediction results*

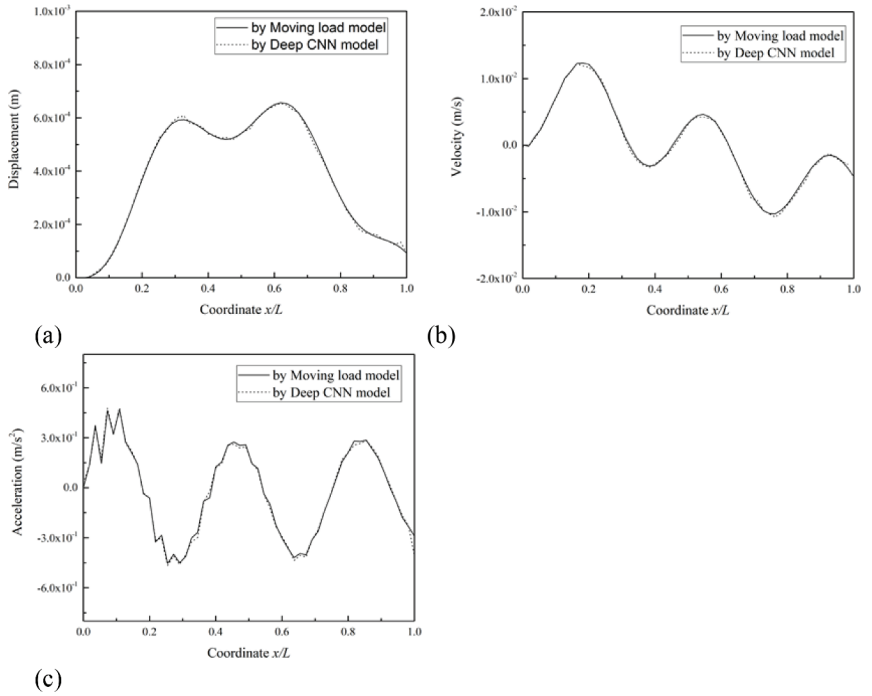


Figure 6. Comparison of time history response resulting from the deep learning model and moving load model: (a) displacement; (b) velocity; and (c) acceleration.

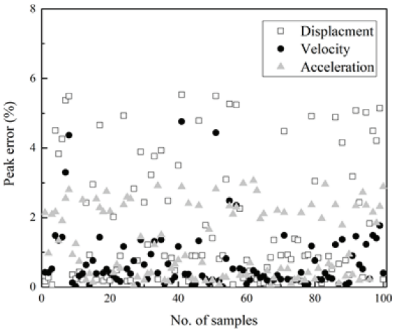


Figure 7. The peak error of predicted response prediction.

Figures 6 (a)-(c) present the comparison of time history response of the bridge under moving load while the moving speed is 300 km/h. One can observe from the figures that the prediction result is close to the analysis result from the moving load model.

Figure 7 displays the peak error (PE) of response prediction result of 100 new samples. As it is shown, for most samples, PE is less than 3%. Some samples have a larger value in PE and yet all the PE of tested samples are less than 6%. Therefore, the results show that the proposed deep learning model can make the response prediction under different moving speeds.

To examine the robustness of the proposed deep CNN model, different levels of noise, namely 1%, 2%, 5% and 10% are added to the input generalized force. The data noise can also

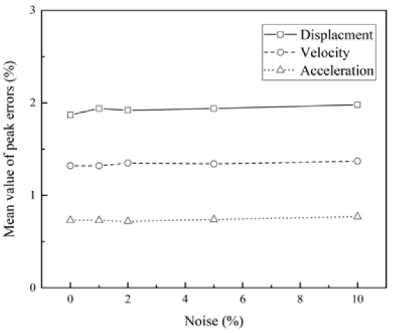


Figure 8. Mean value of peak errors varies with input noise.

be regarded as the inaccuracy of the input data. Figure 8 shows the variation of the mean PE of 100 samples with the input data. From the figure, it can be seen that the mean PE slightly increases with the rise of the noise level. Even under 10% noise, the PE value of the predicted result is less than 2%. Therefore, the developed prediction model is adaptable to varying input data quality.

5 CONCLUSIONS

In this paper, a deep CNN model is proposed to predict the bridge response under vehicular loads. Moving load model is used to obtain the bridge dynamic response samples. The generated samples are utilized to train the proposed deep CNN model for response prediction. The following conclusions can be drawn.

(1) Time-history responses including displacement, velocity, and acceleration can be predicted by the proposed CNN model.
(2) The peak error of response prediction result can be controlled to below 6%. Therefore, the proposed CNN model can be utilized to predict the peak response with satisfactory accuracy.
(3) The proposed deep CNN model is robust. Under the noise level up to 10%, the proposed model can predict the peak value of the response.

ACKNOWLEDGEMENTS

This research was partially supported by the National Natural Science Foundation of China (Grant No. 51708112).

REFERENCES

Adeli, H. 2001. Neural networks in civil engineering: 1989-2000. *Computer-Aided Civil and Infrastructure Engineering* 16(2): 126–142.

Adeli, H. 2020. Four decades of computing in civil engineering. In CIGOS 2019, Innovation for sustainable infrastructure (pp. 3–11). Springer, Singapore.

Cahill, P., Jaksic, V., Keane, J., O'Sullivan, A., Mathewson, A., Ali, S. F. & Pakrashi, V. 2016. Effect of road surface, vehicle, and device characteristics on energy harvesting from bridge-vehicle interactions. *Computer-Aided Civil and Infrastructure Engineering* 31(12): 921–935.

Carey, C., OBrien, E. J., Malekjafarian, A., Lydon, M. & Taylor, S. 2017. Direct field measurement of the dynamic amplification in a bridge. *Mechanical Systems and Signal Processing* 85: 601–609.

Feng, Y., Wang, H., Yang, H. & Wang, F. 2021. Time-continuous energy-conservation neural network for structural dynamics analysis. *Neurocomputing* 456: 450–460.
Hu, X., Wang, B. & Ji, H. 2013. A wireless sensor network-based structural health monitoring system for highway bridges. *Computer-Aided Civil and Infrastructure Engineering* 28(3): 193–209.
Joghataie, A. & Farrokh, M. 2008. Dynamic analysis of nonlinear frames by Prandtl neural networks. *Journal of Engineering Mechanics* 134(11): 961–969.
Kim, T., Kwon, O. S. & Song, J. 2019. Response prediction of nonlinear hysteretic systems by deep neural networks. *Neural Networks* 111: 1–10.
Kim, T., Song, J. & Kwon, O. S. 2020. Pre- and post-earthquake regional loss assessment using deep learning. *Earthquake Engineering & Structural Dynamics* 49(7): 657–678.
Lagaros, N. D. & Papadrakakis, M. 2012. Neural network based prediction schemes of the non-linear seismic response of 3D buildings. *Advances in Engineering Software* 44(1): 92–115.
Li, H.L., Wang, T.Y. & Wu, G. 2021. Dynamic response prediction of vehicle-bridge interaction system using feedforward neural network and deep long short-term memory network, *Structures* 34: 2415–2431.
Li, H.L., Wang, T.Y. & Wu, G. 2022. A Bayesian deep learning approach for random vibration analysis of bridges subjected to vehicle dynamic interaction, *Mechanical Systems and Signal Processing* 170: 108799.
Li, H.L., Wang, T.Y. & Wu, G. 2023a. Probabilistic safety analysis of coupled train-bridge system using deep learning based surrogate model, *Structural and Infrastructural Engineering* 19(8): 1138–1157.
Li, H.L., Wang, T.Y. & Yan, H. 2023b. Online prediction of dynamic irregularity and acceleration of HSR bridges using modified LSGAN and in-service train, *Smart Structures and Systems* 31(5): 501–516.
Li, H.L., Wang, T.Y. & Wu, G. 2023c. Deep learning models for time-history prediction of vehicle-induced bridge responses: A comparative study, *International Journal of Structural Stability and Dynamics* 23(1): 2350004.
Li, H.L., Wu, G. & Cui, M.D. 2020. A machine learning based approach for efficient safety evaluation of the high speed train and short span bridge system, *Latin American Journal of Solids and Structures* 17: e319.
Mostafa, N., Di Maio, D., Loendersloot, R. & Tinga, T. 2021. Extracting the time-dependent resonances of a vehicle-bridge interacting system by wavelet synchrosqueezed transform. *Structural Control and Health Monitoring* e2833.
Oh, B. K., Glisic, B., Park, S. W. & Park, H. S. 2020a. Neural network-based seismic response prediction model for building structures using artificial earthquakes. *Journal of Sound and Vibration* 468: 115109.
Oh, B. K., Park, Y. & Park, H. S. 2020b. Seismic response prediction method for building structures using convolutional neural network. *Structural Control and Health Monitorin*g 27(5): e2519.
Peng, H., Yan, J., Yu, Y. & Luo, Y. 2021. Time series estimation based on deep Learning for structural dynamic nonlinear prediction. *Structures* 29: 1016–1031.
Sun, L., Shang, Z., Xia, Y., Bhowmick, S. & Nagarajaiah, S. 2020. Review of bridge structural health monitoring aided by big data and artificial intelligence: From condition assessment to damage detection. *Journal of Structural Engineering* 146(5): 04020073.
Torky, A. A. & Ohno, S. 2021. Deep learning techniques for predicting nonlinear multi-component seismic responses of structural buildings. *Computers & Structures* 252: 106570.
Vaidyanathan, C. V., Kamatchi, P. & Ravichandran, R. 2005. Artificial neural networks for predicting the response of structural systems with viscoelastic dampers. *Computer-Aided Civil and Infrastructure Engineering* 20(4): 294–302.
Wu, R. T. & Jahanshahi, M. R. 2019. Deep convolutional neural network for structural dynamic response estimation and system identification. *Journal of Engineering Mechanics* 145(1): 04018125.
Xia, Y., Chen, B., Zhou, X. Q. & Xu, Y. L. 2013. Field monitoring and numerical analysis of Tsing Ma Suspension Bridge temperature behavior. *Structural Control and Health Monitoring* 20(4): 560–575.
Xu, Y., Lu, X., Cetiner, B. & Taciroglu, E. 2021. Real-time regional seismic damage assessment framework based on long short-term memory neural network. *Computer-Aided Civil and Infrastructure Engineering* 36(4): 504–521.

Bridge Maintenance, Safety, Management, Digitalization and Sustainability – Jensen, Frangopol & Schmidt (eds)
© 2024 The Author(s), ISBN 978-1-032-77040-6
Open Access: www.taylorfrancis.com, CC BY-NC-ND 4.0 license

Behavior of CFST piers with compound concrete under cyclic lateral loading

Ji-Ji Wang*, Jun-Lei Fu, Su-Gong Cao, Hao Hu & Hao Tian
Zhejiang Scientific Research Institute of Transport, Hangzhou, China

ABSTRACT: Compound concrete, which refers to fresh concrete partly replaced with coarsely crushed demolition concrete (recycled concrete lumps or RCLs hereafter), is a simpler recycling process than the reuse of recycled concrete aggregates. The inherent weakness of the interface between RCLs and fresh concrete can be suppressed when a substantial amount of confinement can be provided as that in concrete-filled steel tubular (CFST) columns. The local buckling of CFST columns can be further delayed or suppressed when fibre-reinforced polymer (FRP) is used to jacket the steel tubes. The potential use of the composite column is as piers in rebuilt bridges. The paper presents and interprets the results of an experimental study on the mechanical behavior of CFST piers with compound or normal concrete subjected to combined axial compression and cyclic lateral loading. Four large-scale piers were tested, including a reinforced-concrete (RC) pier, a CFST pier, two GFRP-jacketed CFST piers with or without RCLs, to investigate the influence of parameters such as confinement types and concrete types. The test results indicate that the seismic behavior of the GFRP-jacketed CFST pier with compound concrete is comparable to that of fresh concrete; the use of GFRP jackets is effective in delaying the local buckling failure at the end of a cantilevered pier; the ductility and lateral load-carrying capacity of the RC pier can be significantly enhanced due to confinement.

1 INTRODUCTION

Compound concrete, which refers to fresh concrete partly replaced with coarsely crushed demolition concrete (recycled concrete lumps or RCLs hereafter), is a relatively new technique for recycling concrete. It has several advantages over traditional ways of recycling concrete aggregates, including its simplicity, cost-effectiveness and increased recycling ratio of demolition concrete. However, the non-uniformity and weak interfaces between RCLs and fresh concrete have detrimental effect on the mechanical performance of the compound concrete. Teng et al. (2016) conducted an experimental study on the compressive behavior of fibre-reinforced polymer (FRP) tubes filled with compound concrete. They found that with a significant level of confinement, the ultimate axial stress and the ultimate axial strain of the compound concrete with RCLs are comparable to those of the fresh concrete, regardless of the strength of the old concrete. Thereafter, many studies have been conducted experimentally and analytically on compound concrete with different type of confinements (Yu and Wu 2019; Zhao et al. 2020; Zhou et al. 2021; Chen et al. 2022, .etc).

Concrete-filled steel tubular (CFST) columns are widely used in new construction and can provide superior ductility over traditional reinforced concrete columns under seismic loading, especially when the local buckling issue can be delayed or suppressed by wrapping FRP sheets over steel tubes (Hu et al. 2011). The FRP-confined CFST columns with compound concrete has the potential to be used as bridge piers where low-capacity bridges should be demolished and rebuilt. Zhao et al. (2020) conducted axial compression tests on this kind of composite

*Corresponding author: wangjiji2009@qq.com

DOI: 10.1201/9781003483755-18

columns and obtained the axial stress-strain behavior of the compound concrete. The seismic performance of this kind of columns has not been studied yet.

The paper presents and interprets the results of an experimental study on the behavior of CFST columns with compound or normal concrete subjected to combined axial compression and cyclic lateral loading. Four large-scale piers were tested, including a reinforced-concrete (RC) pier, a CFST pier, two GFRP-jacketed CFST piers with compound or normal concrete, to have a deeper understanding on the seismic performance of the composite column and investigate the influence of parameters such as confinement types and concrete types.

2 EXPERIMENTAL PROGRAM

2.1 *Specimen details*

The experimental program consisted of four large-scale test specimens, one CFST column, one reinforced concrete (RC) column and two GFRP-jacketed CFST columns with compound concrete or normal concrete. All the specimens had a circular section with a diameter of 406 mm, except that the RC column was 440 mm in diameter and its concrete cover was 40 mm measured from the outer side of longitudinal steel bars. All the specimens were 1575 mm in length from the point of lateral loading to the top of the reinforced concrete (RC) footing with a dimension of $1500\times1500\times800$ mm. The steel tubes were rolled from Q235 steel plate with a longitudinal seam weld. All steel tubes had an outer diameter of 406 mm and a thickness of 6 mm. Each specimen was given a name, which starts with "GC/SC/RC" to represent the GFRP-confined CFST column, CFST column, or RC column, respectively, followed by "NC/CC" to represent normal or compound concrete. For instance, specimen GC-NC was a GFRP-confined CFST column that filled with normal concrete. Specimen details were summarized in Table 1.

Table 1. Specimen details.

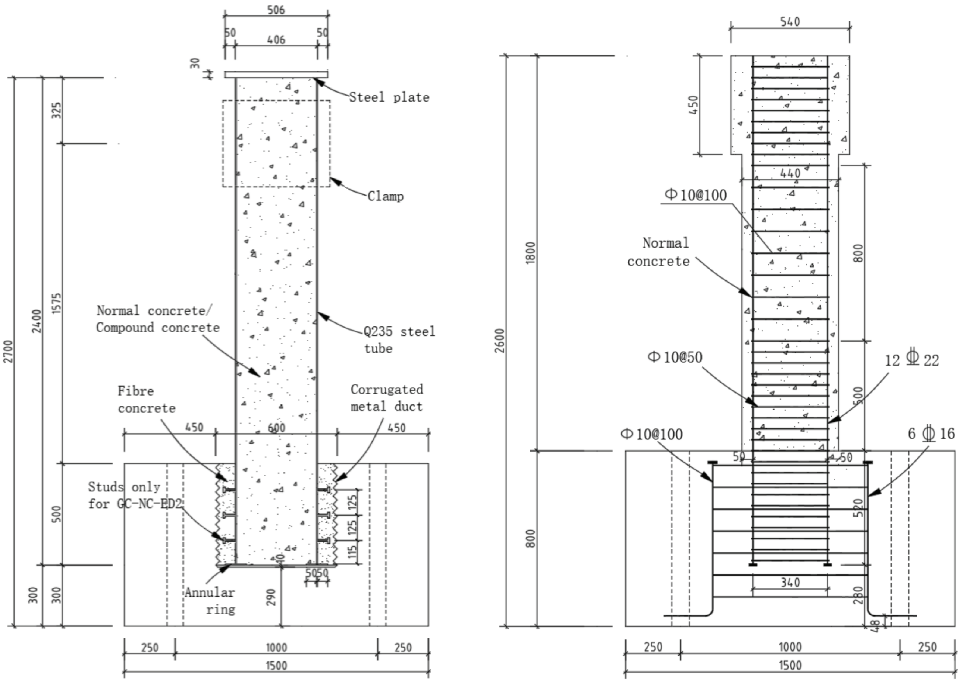
Specimen label	Concrete type	Number of GFRP layer	Type
GC-NC	Normal concrete	2 plies	GFRP-jacketed CFST columns
GC-CC	30% RCLs (volume ratio)	2 plies	GFRP-jacketed CFST columns
RC-NC	Normal concrete	N/A	RC columns
SC-NC	Normal concrete	N/A	CFST columns

The three specimens with steel tubes were embedded in the footing 500 mm in depth. The corrugated metal duct was used to increase bonding force and provide confinement to concrete in the connection region, in which fiber-reinforced concrete was filled after the steel tube was temporarily supported in the footing. Studies found that welding annular rings at the bottom of steel tubes significantly increased the shear resistance of joints when the extending width was between 8 to 16 times the thickness of the steel tube (Stephens et al. 2015; Zhu 2017). This design detail was adopted in the present study, with the annular ring extending a width of 50 mm to both inside and outside of the steel tube (Figure 1a).The RC specimen was connected to the footing with longitudinal reinforcement. Totally 12 evenly distributed 22 mm HRB400 steel bars were fixed by steel wire to the steel cages in the footing.The anchoring length of the longitudinal reinforcement extending into the column and footing was 520 mm according to the requirements in GB 50010-2010 for headed steel bar (see Figure 1b).

2.2 *Preparation of specimens*

Specimens were constructed in sequence of footings, connections and columns (see Figure 2).

(a) Firstly, the steel cages of the footing were put in the molds. Corrugated metal ducts or steel cages of the connection were temporally supported in the footing, and the footings were cast with C30 normal concrete.



(a) Specimens with steel tubes (b) RC specimen

Figure 1. Design details of specimens.

(b) For specimens with steel tubes, steel tubes were put in the ducts and temporarily supported with 4 steel bars, after which fiber-reinforced concrete was cast in the ducts. For the RC specimen, the steel tube mold was put above the footing and was adjusted to vertical state with four steel bars.

(c) Steel tubes or the steel mold were poured with concrete in three layers and each layer was carefully vibrated. For specimen with compound concrete, the RCLs were made from C30 steel cubes and were put in water to absorb water for over 24 hours. For each layer, the RCLs were thrown into the steel tube together with the normal concrete.

(d) Thick steel plates were welded on top of the steel tubes to sustain axial compression. Two layers of GFRP sheets were horizontally wrapped on the steel tubes in the lab.



(a) Steel cages installed with strain gauges (b) Concrete casting (c) FRP wrapping and top plates welding

Figure 2. Preparation of specimens.

2.3 *Material properties*

In total, three batches of concrete were prepared for the footings, columns and the connections, respectively. 6 mm-length PVA fiber with a content of 1.8kg/m^3 was added in the concrete batch for the connection. For each batch of concrete, at least three 150 mm cubes were prepared and tested in accordance with GB/T 50081-2019. The average compressive strengths of 150 mm cubes were 47.3 MPa, 61.3 MPa, and 49.0 MPa for concrete in the footings, the columns and the ducts, respectively, at the age of about three months. Compound concrete with recycled concrete volume ratio of 30% was used in specimen GC-CC. The RCLs were crushed from 150 mm cubes whose average compressive strength was 59.2 MPa at the age of 28 days. The characteristic length of the RCLs was 50~150 mm. Cylinders 200 mm in diameter and 400 mm in length were also prepared for the compound concrete and the normal concrete (the same batch concrete for columns), whose average cylinder compressive strengths were 36.8 MPa and 45.8 MPa, respectively.

Three steel coupons were cut from a steel tube which was exactly the same as those in the columns. The steel tube had an elastic modulus of 201 GPa, a yield stress of 275.4 MPa, and an ultimate stress of 390.1 MPa. The steel reinforcement has an elastic modulus of 203 GPa, a yield stress of 441.1 MPa, and an ultimate stress of 654.1 MPa. The GFRP jacket used had an elastic modulus of 100 GPa and an ultimate strain of 2.5% according to the manufacturer.

2.4 *Instrumentation*

Strain gauges and transducers were employed to monitor the behaviour of specimens (see Figure 3a). A number of bi-directional strain gauges were used to measure the axial and hoop strain distributions of the column at 9 different column heights, namely, the circumferences at 50 mm, 170 mm, 290 mm and 410 mm from the column bottom surface, and 50 mm, 170 mm, 290 mm, 490 mm and 690 mm from the column footing top surface, respectively. For No. 5~7 layer of strain gauges, eight strain gauges were evenly installed around the circumference. The other heights were expected to be outside the plastic hinge region, so a smaller number (i.e. four) of strain gauges were used for each circumference. The gauge length of the strain gauges attached to the steel tubes was 10 mm while that of the strain gauges attached onto the FRP jackets was 20 mm.

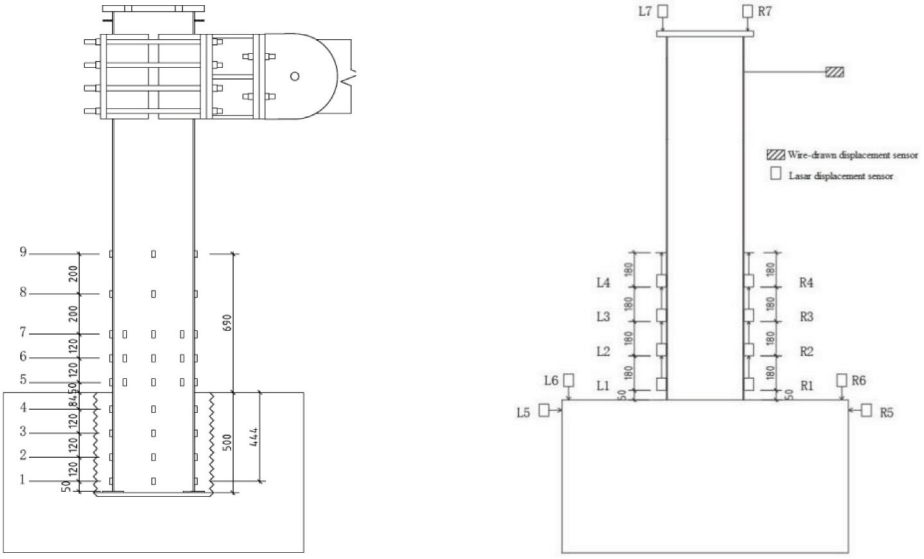
Eight linear variable displacement transducers (LVDTs) were installed on the two sides of the loading plane (i.e. the western side and the eastern side, see Figure 3b) of the column at intervals of 180 mm starting from the column end (i.e. the top surface of the footing). These LVDTs were installed on the column surface through pre-fixed nuts. In addition, two pairs of LVDTs (each pair consisted of one vertical and one horizontal transducer) were used on the two sides of the foundation to monitor the movement it could experience during the test. A wire-drawn displacement sensor was installed at the center of the clamp connected to the lateral laod actuator to measure the lateral displacement. The rotation of the column head and the shortening of the column were measured by two LVDTs on the top steel plate.

2.5 *Testing frame*

All the tests were conducted using a testing frame at the Structural Engineering Laboratory of Zhejiang Scientific Research Institute of Transport. Figure 4 shows a photo of the testing frame. The testing frame includes a vertical actuator (capacity: 1000 kN) connected to a relatively large steel beam and rollers are provided between the actuator and the beam so that during the test the horizontal locations of the actuator can be adjusted. In addition, a horizontal actuator (capacity: 500 kN in tension and compression) is provided which can apply horizontal loading through a hinge joint. The positions of both actuators can be controlled manually. Both actuators can apply not only compression but also tension forces. In the test, the specimen was fixed to a strong floor using eight sets of screws (80 mm in diameter) and nuts.

2.6 *Loading scheme*

Pre-loading procedure was conducted before formal loading to reduce the gap between the specimens, basement and actuators, and to make sure the measuring instruments were in



(a) Strain gauges installed on tubes (b) Transducer layout

Figure 3. Preparation of specimen.



Figure 4. Testing frame

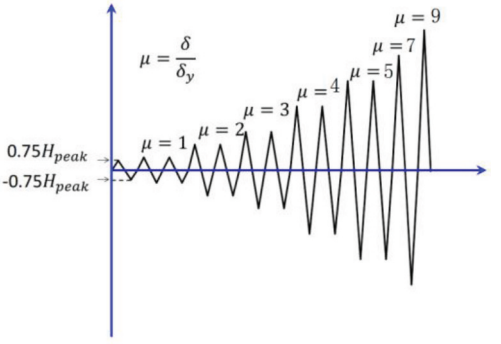


Figure 5. Loading scheme

correct status. After pre-loading, a constant axial load of 700 kN was applied to each column. The lateral load scheme was conducted following the practice of existing studies (Yamao et al. 2002; Zhang 2014). The yield displacement was used to control the lateral cyclic loading. The yield displacement of the column was defined in the following way: (1) load the column to a level which is 0.75 times the maximum lateral load H*peak*; *Hpeak* was estimated through a sectional analysis method and was found to be 350 kN; (2) the yield displacement δ_y is defined as the elastic limit of an equivalent elastic-perfectly plastic curve with a reduced stiffness being equal to the secant stiffness at 75% of the peak lateral load. The lateral load was applied in the following scheme (see Figure 5):

(a) Before 0.75H*peak*: the specimens were pushed to one side with a loading rate of 100 kN/min and stopped when the lateral force was 250 kN. Calculate the displacement δ_{y1} at H*peak*. Reverse the loading direction and obtain the displacement δ_{y2}. The yield displacement used to control the following lateral loading scheme was the average of the absolute value of two displacements.

(b) After 0.75H*peak*: the lateral cyclic loading was controlled by a maximum displacement of $\pm\delta_y$, $\pm 2\delta_y$, $\pm 3\delta_y$, $\pm 4\delta_y$, $\pm 5\delta_y$, $\pm 7\delta_y$, etc., and consisted of two cycles at each displacement level before $5\delta_y$. The loading rate was 9 mm/min. Loading was stopped for 5 minutes at each maximum displacement before observing the status of the specimen.

3 EXPERIMENTAL RESULTS AND DISCUSSIONS

3.1 *Test observations*

The failure mode of GFRP-confined CFST column specimens GC-NC/CC: firstly, transverse inter-layer cracks appeared at the bottom of the column in GFRP, and then the steel pipe bulged at the bottom of the column. The composite material gradually fractured near the bulge of the steel pipe, and finally the steel pipe buckled at a distance of 50mm from the bottom of the column, resulting in a significant decrease in bearing capacity.

The failure mode of CFST column specimen SC-NC: The steel tube is bulging and bending at the bottom of the column. Due to weld defects, the tensile test weld of the steel tube breaks prematurely, and there is no tearing failure of the steel tube.

The Failure mode of RC column specimen RC-NC: The concrete protective layer at the bottom of the column peels off extensively, the exposed longitudinal bars buckle, the core concrete at the bottom of the column falls off, and the test is terminated when the horizontal force drops by more than 15%.

Take specimen GC-NC as an example to introduce the failure process in detail. The specimen experienced GFRP damage in the tensile side first, after which the steel tube buckled. There was a sharp drop in horizontal force for specimen GC-NC during the first positive cycle of $7\delta_y$ when the steel tube on the tensile side was damaged (see Figure 6).

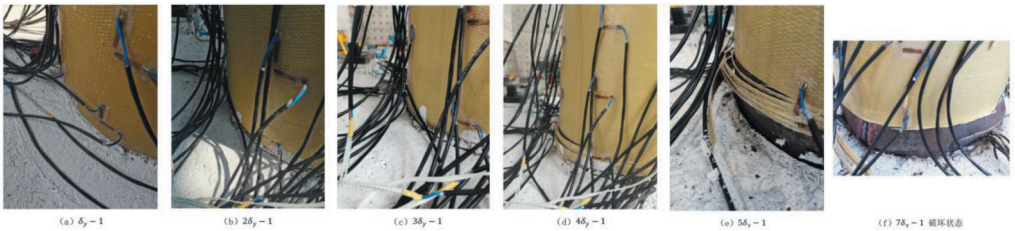


Figure 6. Failure process of specimen GC-NC.

3.2 *Lateral load–lateral displacement curve*

The envelope lateral load-lateral displacement curve was shown in Figure 7. Several observations can be drawn from the figure:

(a) The horizontal bearing capacity and ductility of CFST specimen or GFRP confined CFST specimens are greater than those of reinforced concrete pier column specimens. The experimental phenomenon shows that the concrete in the plastic hinge area at the bottom of RC column specimen peeled off and was damaged severely. Although the concrete in the plastic hinge area of other specimens also showed crushing failure, due to the constraints of steel pipes and composite materials, the concrete inside the column still maintained vertical compressive bearing performance.
(b) The seismic behavior of the GFRP-jacketed CFST pier with compound concrete is comparable to that of fresh concrete. The bearing capacity of specimen GC-CC is a little weaker than its counterpart, as the cylinder test showed that the compressive strength of the compound concrete was 36.8 MPa, smaller than that of normal concrete (45.8 MPa).

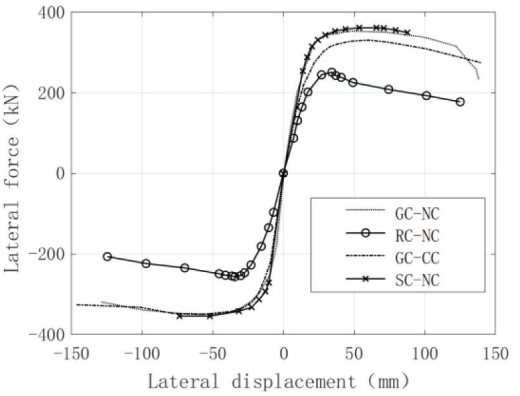


Figure 7. Envelope lateral load-displacement curve.

3.3 *Ductility*

Table 2 shows the ductility factor of each specimen. The ductility factor of specimen RC-NC is the smallest, indicating that the ductility of RC columns is worse than that of composite column specimens. The reason for the low ductility of specimen SC-NC (CFST column) is due to earlier failure in the weld seam compared to those in GFRP-confined CFST columns.

Table 2. Ductility of specimens.

Specimen		Yield displacement (mm)	Yield load (kN)	Ultimate displacement (mm)	Load at ultimate displacement (kN)	Ductility factor μ	Ductility factor (Mean)
GC-	+	22.0	326.7	121.9	316.1	5.54	5.60
NC	-	22.8	317.3	128.9	319.2	5.66	
RC-	+	17.8	210.0	66.9	221.4	3.90	4.26
NC	-	23.1	219.4	106.6	209.9	4.62	
GC-	+	21.9	275.1	132.7	280.8	6.07	6.35
CC	-	22.1	319.2	146.5	326.0	6.62	
SC-NC	+	20.1	315.4	87.6	349.2	4.36	4.31
	-	17.3	313.0	73.8	354.1	4.26	

4 CONCLUSIONS

The paper presents and interprets the results of an experimental study on the mechanical behavior of CFST piers with compound or normal concrete subjected to combined axial compression and cyclic lateral loading. By comparing and analyzing the failure mode, bearing capacity and ductility of each specimen, the influence of confining type and concrete type on the seismic performance of the specimens is studied. Through the analysis of experimental phenomena and results, the following conclusions can be drawn:

(1) GFRP-confined CFST columns have superior ductility over RC and CFST columns. The ductility and lateral load-carrying capacity of the RC pier can be significantly enhanced due to confinement.
(2) The seismic behavior of the GFRP-jacketed CFST pier with compound concrete is comparable to that of fresh concrete. The use of GFRP jackets is effective in delaying the local buckling failure at the end of a cantilevered pier.

ACKNOWLEDGMENTS

The authors would like to acknowledge the supports of Independent Research and Development Projects of Zhejiang Scientific Research Institute of Transport (Grant No. ZK202301, ZK202302, ZK202412).

REFERENCES

Chen, G. M., Zhang, J. J., Lin, G., Wu, Y. F., and Jiang, T.(2022). Behavior of different-sized frp-confined square compound concrete columns containing recycled concrete lumps. *Journal of composites for construction*(2), 26.

GB/T 50081-2019, Standard for Test Methods of Concrete Physical and Mechanical Properties, Standardization Administration of China, China, 2019.

Hu Y M, Yu T, Teng J G. FRP-confined circular concrete-filled thin steel tubes under axial compression. *Journal of Composites for Construction*, 2011, 15(5): 850–860.

Teng, J. G., Zhao, J. L., Yu, T., Li, L. J., & Guo, Y. C. (2016). Behavior of FRP-confined compound concrete containing recycled concrete lumps. *Journal of Composites for Construction*, 20(1), 04015038.

Wu, B., Yu, Y., Chen, Z., & Zhao, X. (2018). Shape effect on compressive mechanical properties of compound concrete containing demolished concrete lumps. *Construction and Building Materials*, *187*, 50–64.

Stephens MT, Lehman DE, Roeder CW. (2015). *Concrete-Filled Tube Bridge Pier Connections for Accelerated Bridge Construction*. Department of Civil and Environment Engineering, University of Washington.

Yu, Yong, and Bo Wu. Discrete element mesoscale modeling of recycled lump concrete under axial compression. *Materials* 12.19 (2019): 3140.

Zhang B. *Hybrid FRP-Concrete-Steel Double-Skin Tubular Columns under Static and Cyclic Loading*, PhD Thesis, The Hong Kong Polytechnic University, 2014.

Zhao, J., Xu, C., Sun, L., and Wu, D. (2020). Behaviour of FRP-confined compound concrete-filled circular thin steel tubes under axial compression. *Advances in Structural Engineering*, 23(9), 1772–1784.

Zhu, H.Q. (2017). *Seismic behavior of embedded concrete-filled steel tubular pier-to-reinforced concrete beam connections*. PhD Dissertation. Wuhan University of Technology. (in Chinese).

Zhou, J. K., Guan Lin, and J. G. Teng. Stress-strain behavior of FRP-confined concrete containing recycled concrete lumps. *Construction and Building Materials* 267 (2021): 120915.

Bridge Maintenance, Safety, Management, Digitalization and Sustainability – Jensen, Frangopol & Schmidt (eds)
© 2024 The Author(s), ISBN 978-1-032-77040-6
Open Access: www.taylorfrancis.com, CC BY-NC-ND 4.0 license

Extending the service duration of bridges by means of (R-)UHPFRC

S. De Maria & D. Briccola
University of Applied Sciences and Arts of Southern Switzerland (SUPSI), Mendrisio, Switzerland

ABSTRACT: Ultra-High-Performance Fiber Reinforced Cementitious Composite (UHPFRC) and Reinforced UHPFRC (R-UHPFRC) are mainly used to improve the performance of aging bridge structures against increasing traffic, aggressive environmental scenarios, and demanding operational conditions. The growing number of applications in this field requires a robust numerical modeling technique to quantify the load carrying capacity and ductility response of arbitrary-shaped cross-section reinforced with (R-)UHPFRC layers under axial load and bending moments. The application of a well-codified approach, based on (i) the discretization of a cross-section in iso-parametric subdomains, (ii) equilibrium and compatibility equations, and (iii) numerical integration to solve (ii), allows to easily evaluate the frontier of interaction domains and moment-curvature diagrams. In this way, different refurbishment solutions can be compared highlighting the advantages of each of them in terms of load-carrying capacity and durability. This approach can aid practicing engineers, breaking down the last barrier to the widespread use of this promising material.

1 INTRODUCTION

Reinforced and prestressed concrete structures such as existing bridges and viaducts, when subjected to large stresses or cyclic actions, as well as to severe environmental conditions, show deficits in terms of mechanical strength and durability. Traditionally, numerous rehabilitation works have been carried out using ordinary concrete. Despite its wide use, the limited durability of concrete combined with the harsh exposure conditions jeopardize the effectiveness of traditional renovation techniques, resulting in the need to intervene again few years after.

Research in the field of engineered materials for use in civil engineering structures has brought to the development of Ultra-High-Performance Fiber Reinforced Concrete (UHPFRC). Thanks to its extraordinary mechanical properties, UHPFRC is nowadays in Switzerland the first choice for carrying out rehabilitation works on existing reinforced concrete (RC) and prestressed concrete (PRC) structures.

The material exhibits outstanding mechanical properties: extremely high compressive and tensile strengths respectively in the range of 150 - 200 MPa and 7 - 10 MPa in the elastic range, up to 14 MPa in the strain hardening domain as reported in Brühwiler, E. (2019). More in detail, 10-15 mm steel fibres, added in a dosage of at least 2- 3 % in volume to a specific mixture of cement, minerals, and water, are responsible of the increased tensile capabilities of the material. Moreover, thanks to its composition, UHPFRC exhibits an ultra-low permeability with a permeability coefficient in non-cracked conditions about 50 times lower than that of ordinary concrete, as reported in Charron, J.P. (2006). That ensures an increased performance in terms of durability.

For these features, UHPFRC represents a valuable method both to create a protective layer for reinforced concrete elements and to increase the load carrying capacity of existing bridges

DOI: 10.1201/9781003483755-19

and viaducts. Therefore, an extensive laboratory and on-field research carried out over the past 20 years mainly in Switzerland have led to a comprehensive knowledge of UHPFRC and a reduced time-to-market. It has been demonstrated in Habert, G. (2012) that producing UHPFRC generates half of the amount of CO2 emissions than ordinary concrete. To aid practitioner engineers in their daily activities in 2016 the Technical Leaflet SIA 2052 was published. An additional aid to the widespread use of such an innovative material in rehabilitation and strengthening of existing RC and PC bridges could be an easy-to-use sectional analysis program to evaluate the strength and ductility of (R-)UHPFRC-RC/PC cross-sections under bending and axial forces. Therefore, the goal of this research is to apply the numerical approach presented in Quagliaroli, M. (2015) to determine the interaction domains and moment-curvature diagrams of R-UHPFRC-RC sections subjected to axial load and bending moment. A critical comparison of interaction domains and moment-curvature diagrams can help identifying effective methods to extend the service duration of existing bridges based on materials data durability and structural properties.

2 A CONVENIENT APPROACH TO ASSESS THE BEHAVIOR OF (R)UHPFRC-RC CROSS SECTIONS

To highlight the advantages UHPFRC can offer to existing bridges and viaducts in terms of extended service duration, e.g. increased durability and load carrying capacity, multiple layer/ reinforcement configurations based on two different cross-section geometry have been scrutinized.

The configurations exploited can be grouped into two main categories: solutions for (a) protection, where only a thin layer of material is placed on the top of the cross-section to secure it from aggressive environments thanks to UHPFRC outstanding permeability characteristics, avoiding the penetration of chlorides due to deicing agents; (b) strengthening, where the additional UHPFRC layer is reinforced with steel bars to increase both resistance and ductility of cross-sections. For each arbitrary-shaped composite cross-section made of UHPFRC applied as a protective or strengthening layer on existing RC sections, the kinematic assumption valid for slender elements and the perfect bond of materials allow to assess their structural response.

The presence of multiple materials characterized by different constitutive laws makes it convenient to apply the subdomain discretization approach introduced by Malerba, P.G. (1984). According to Briccola, D. (2013), two types of scenarios allow to numerically assess its structural response (strength and ductility): (i) given a deformation state, determine the corresponding stress state (direct problem); (ii) given the stress state, determine the cross-section kinematics. The first scenario allows drawing the axial force- bending moment interaction envelope for limit state design by iteratively changing the applied deformation state. Instead, the second problem allows determining the moment-curvature diagrams under service condition given a defined axial force. Sectional equilibrium and compatibility equations, written in a general matrix form, enable handling both scenarios.

From the numerical point of view, the first problem, written explicitly, involves a simple quadrature approach to solve the stress functions integral over the cross-section. Instead, the second one involves a numerical strategy for solving systems of nonlinear equations, namely the Newton- Raphson procedure.

The kernel of the problem is the integration of the terms of the stiffness matrix of the section arising from the algebraization of the abovementioned equations. By subdividing the cross-section into parametric subdomains and using different types of Gauss integration rules, an effective numerical integration strategy allows for solving the problems and drafting interaction domains and moment-curvature diagrams. Figure 1 shows graphically the subdivision and integration steps of the numerical procedure. For details on the numerical integration procedure and the analytical formalism, the reader can rely on Quagliaroli, M.(2015).

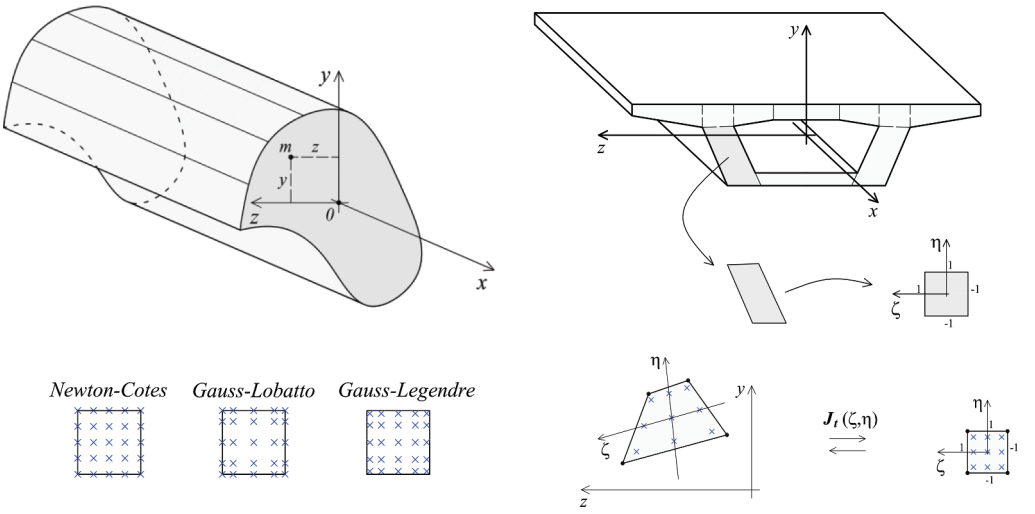


Figure 1. Integration strategies. The section is divided into subdomains and the integration works sampling in a parent domain by using parametric transformations.

3 APPLICATIONS AND MAIN FINDINGS

The numerical approach described has been applied to: (i) a reinforced concrete square section [RCsq] strengthened with a 40mm-depth UHPFRC layer with [RU-RCsq] or without [U-RCsq] reinforcing bars or, in alternative, with a traditional concrete layer with [RC-RCsq] or without [C-RCsq] reinforcing bars; (ii) a reinforced concrete two-cell box girder section [RCbg] strengthened with a 40mm-depth UHPFRC layer with [RU-RCbg] or without [U-RCbg] reinforcing bars or, in alternative, with a traditional concrete layer with [RC-RCbg]

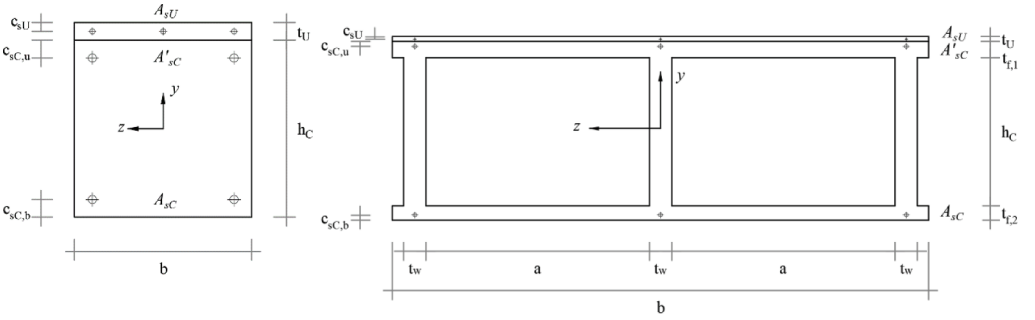


Figure 2. Square section (left) and two-cells box girder deck section (right).

Table 1. Geometrical properties of square section (1) and two-cells box girder deck section (2).

Section	c_{sU}	$c_{sC,u}$	$c_{sC,b}$	t_U	h_C	b	A_{sU}	A'_{sC}	A_{sC}
	[mm]						[mm^2]		
1	20	40	40	40	400	400	235.6	402.1	402.1

Section	c_{sU}	$c_{sC,u}$	$c_{sC,b}$	t_U	$t_{f,1}$	$t_{f,2}$	h_C	t_w	a	b	A_{sU}	A'_{sC}	A_{sC}
	[mm]										[mm^2]		
2	20	20	20	40	180	160	1660	250	2625	6000	5655	36091	12931

or without [C-RCbg] reinforcing bars as in Figure 2. More in detail, 8 subdomains have been used for section (i) and 42 for (ii). As per the integration points a Gauss-Lobatto scheme was selected and with 7 sampling points on each subdomain, considering the outcomes in Quagliaroli, M. (2015).

3.1 *Bending moment – axial force interaction envelope*

Figure 3 shows the frontier of the bending moment-axial force interaction envelope for both the square (left) and box-girder (right) cross section considering different strengthening configurations.

By adding a UHPFRC strengthening layer, even unreinforced, for both sections, the bending moment-axial force interaction envelope assume a pronounced asymmetric shape with a remarkable positive bending moment-negative axial force region. The application of a 40mm-layer of UHPFRC on the top of a RC cross-section significantly increases the positive bending moment for limit state design under compressive axial force due to the UHPFRC high resistance under compression. Reinforcing the layer of UHPFRC with steel bars, for instance adding 3ϕ10 to the reinforced square concrete section, does not provide a meaningful strength increase to the positive bending moment under compression with respect to the unreinforced UHPFRC strengthening option. Indeed, the additional (R-)UHPFR-layer provide a remarkable strength gain in negative bending moment under compressive and tensile axial force.

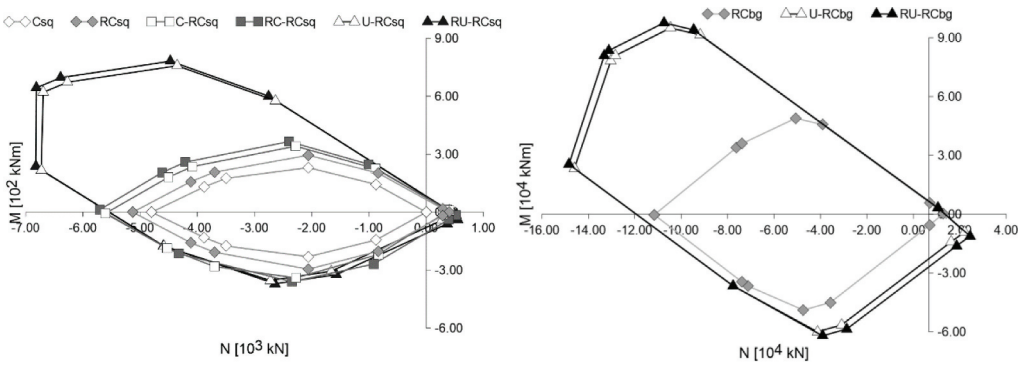


Figure 3. Bending moment - axial force interaction envelope of square cross-section (left) and of two-cells box girder deck section (right) for different strengthening configurations.

3.2 *Moment – curvature diagrams*

Figure 4 shows bending moment-curvature diagrams referring to different configurations of the square section under several levels of axial force for comparing strength and ductility values. Point A, B, C belong to the Csq section bending moment-axial force interaction envelope corresponding to the following failure conditions: point A) $\varepsilon = \varepsilon_{cu}$ at the top fiber, $\varepsilon = 0$ at the bottom reinforcement line; point B) $\varepsilon = \varepsilon_{cu}$ at the top fiber, $\varepsilon = \varepsilon_{sy}$ at the bottom reinforcement line; point C) $\varepsilon = \varepsilon_{cu}$ at the top fiber, $\varepsilon = \varepsilon_{su}$ at the bottom reinforcement line.

An additional level of axial force (N = -2400 kN), far away from failure of Csq section, was selected for further investigations. For all levels of axial force, it is evident that by adding a layer of UHPFRC, reinforced or unreinforced, the section becomes stiffer as the observed

reduction in curvature demonstrates. Moreover, the higher the material strength, the greater the sectional strength.

Conversely, for all levels of axial force and cross-section configurations, it is evident that the maximum bending moment a section can withstand decreases drastically with respect to the ultimate bending moment attained by (R-)UHPFRC-RC section. That highlights the great contribution in terms of strength that even a thin layer of UHPFRC provides to a reinforced concrete cross-section.

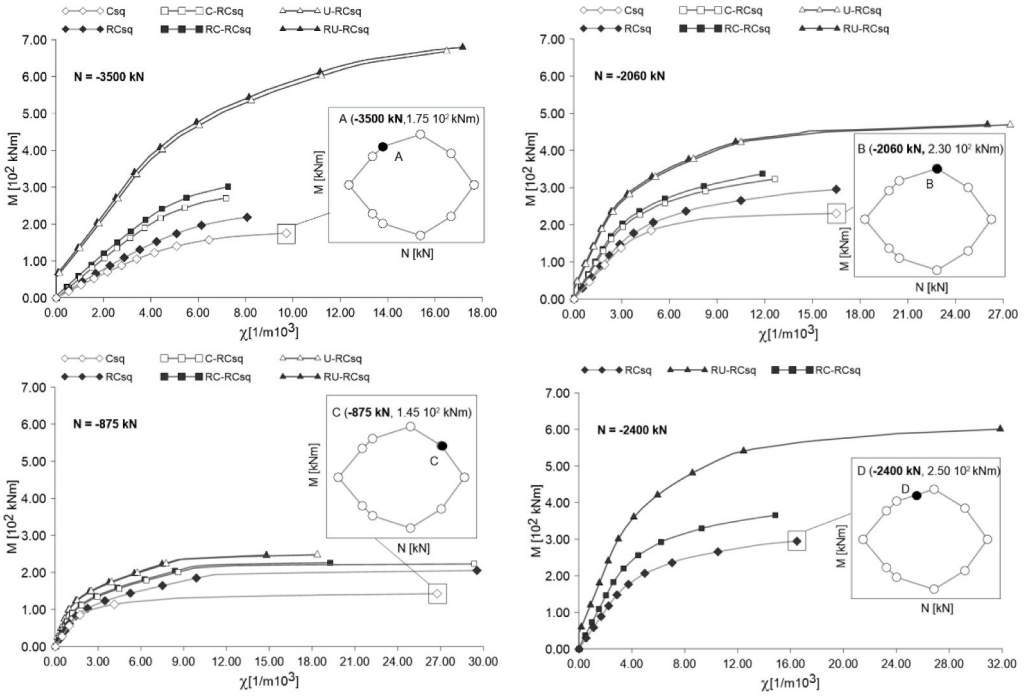


Figure 4. Moment - curvature diagrams comparison for the square section under different level of axial force for several strengthening configurations.

4 DISCUSSION

By further elaborating the results obtained, a synthetic measure of the load carrying capacity gain on average according with limit state design philosophy can be introduced. This measure, named α, shown in Figure 5 and 6 respectively for the square and box-girder deck section, corresponds to the ratio between the area beneath the bending moment-axial force interaction envelope in case of (R)UHPFRC-RC section and that beneath the bending moment-axial force interaction envelope of the original RC section.

The parameter α enables a fast comparison among different UHPFRC solutions under several loading scenarios. It is easy to note that this load carrying capacity gain is more pronounced where UHPFRC mechanical properties are best adapted, that is under positive/negative or negative/positive axial force and bending moment. In fact, in the N+/M- field of interaction the added layer of UHPFRC is stretched and can manifests its higher strength in tension with respect to traditional concrete. Similarly, in the N-/M+ field of interaction the added UHPFRC layer is shortened and can manifests its higher strength in compression with respect to traditional concrete.

As a result, it is evident that even in its protective version UHPFRC increase the load-carrying capacity of the original section, but of course this beneficial effect is even more evident in case of R-UHPFRC.

By comparing Figure 5 and 6 the impact of this increase depends on the cross-section shape and geometry, and on the amount of reinforcement steel. Considering the bending moment-axial force interaction envelope of the RC square cross-section under N+/M- the load carrying capacity gain is about 75% and for the RC two-cell box girder deck section is about 26%. Similarly, under N-/ M+ the load carrying capacity gain is about 3.6% for RC square section, and about 3.5% for the two-cell box girder deck section.

Of course, if material degradation was considered, the load carrying capacity gain magnitude would be different. Nevertheless, in case of structures with a good condition state the values obtained in this study represent a good esteem of the increased structural performance. As a result, it appears evident that UHPFRC repair and/or strengthening strategies to cope with more demanding future traffic conditions is a rewarding source of benefits for extending the service duration of road networks.

A numerical assessment considering different mechanical reinforcement ratios is out of the scope of this study but potentially can affect the load carrying capacity gain jeopardizing the effectiveness of UHPFRC strengthening configurations on protective ones.

5 CONCLUSIONS

The application of a well-codified computational approach to derive bending moment-axial force interaction envelopes and moment-curvature diagrams can aid practicing engineers and favoring the widespread use of this promising material. The procedure adopted can be easily extended to incorporate the contribution of prestressing steel and/or other kind of material. Additionally, biaxial bending moment-axial force interaction domain helpful for instance to

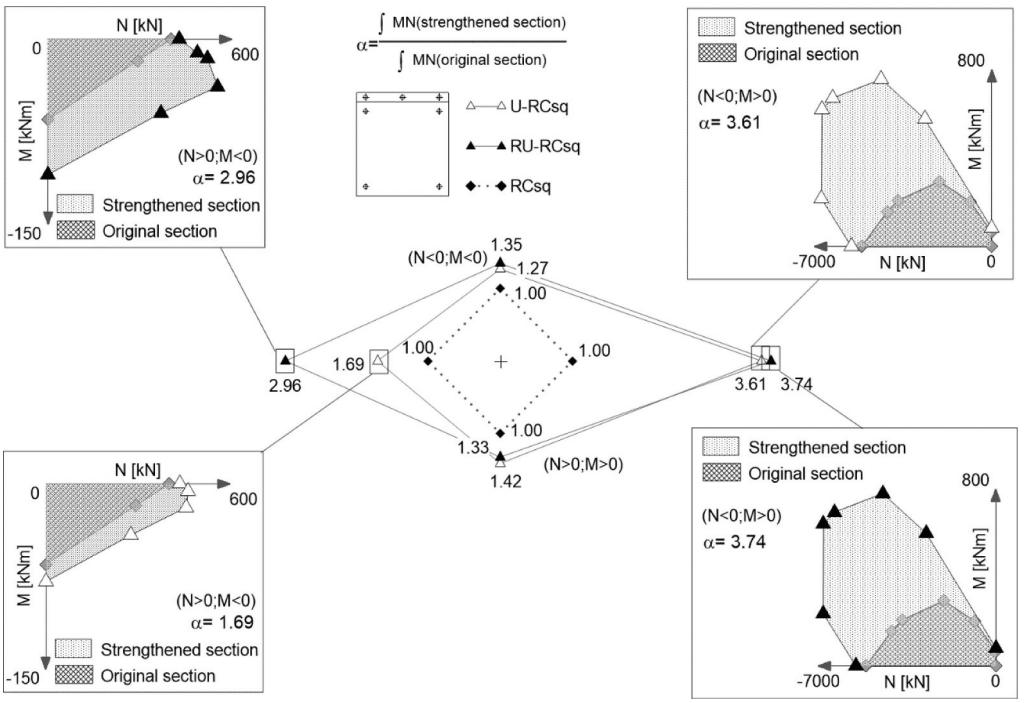


Figure 5. Load carrying capacity gain on average measure according with limit state design philosophy for RC, U-RC and RU-RC square section configurations.

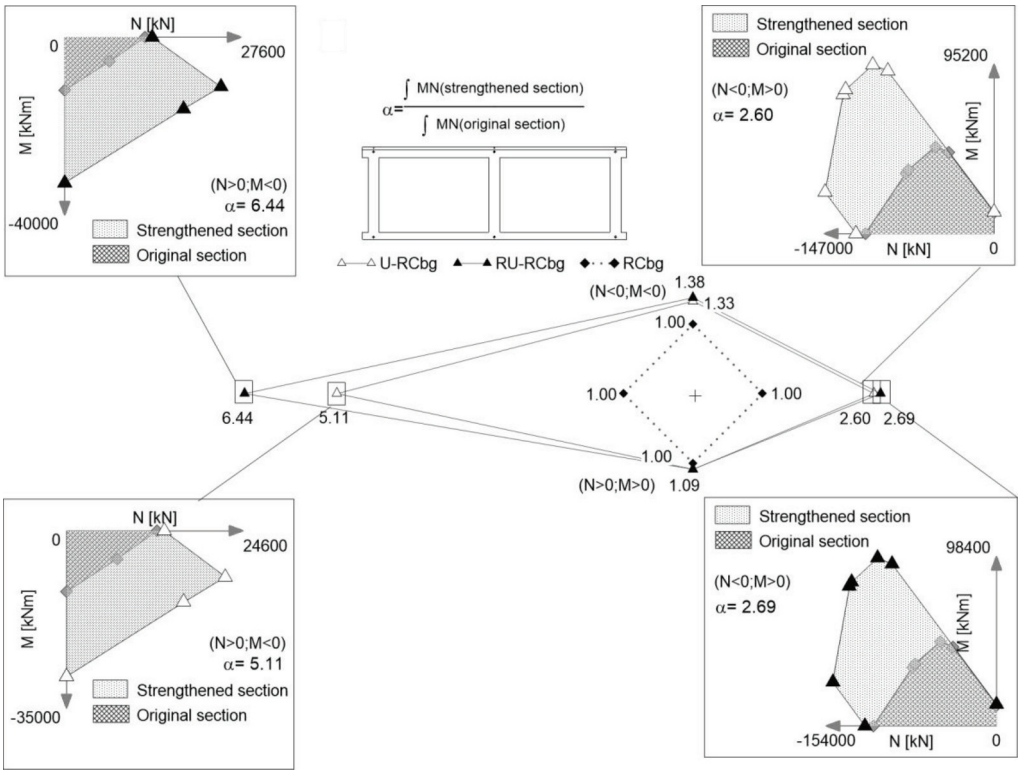


Figure 6. Load carrying capacity gain on average measure according with limit state design philosophy for RC, U-RC and RU-RC two-cells box girder deck section configurations.

study the load carrying capacity of stressed-ribbon footbridges can be straightforward derived by imposing cross-sectional equilibrium and compatibility, relying on perfect bond between different materials.

UHPFRC represents an advantageous material for strengthening aging infrastructures while increasing their durability, therefore achieving the goal of extending the service duration of existing bridges and viaducts. The technology has been implemented and widely used in Switzerland, but it worth to further application in other countries where prestressed reinforced concrete bridges and viaducts represent a huge portion of the total road infrastructural network.

Moreover, it has been demonstrated that besides its noticeable durability due to its incredibly low permeability, this innovative material is more sustainable than traditional one, representing a good candidate for repairing works.

The study carried out support several interesting reflections highlighting the structural performance advantages due to the application over a RC cross-section of a UHPFRC layer both for protective and strengthening purposes. These advantages can be summarized as follow:

- high load carrying capacity and exceptional ductility can be easily achieved on average.
- increasing axial force due to external loads do not drastically reduce ductility and strength.
- the load-carrying capacity gain is higher if the cross-section undergoes positive/negative or negative/positive axial force and bending moment.

Finally, further developments on the topic can be drafted. A rigorous approach to define the actual load carrying capacity of existing bridges must necessarily consider the material

degradation mechanism induced by carbonation, corrosion, exc. The implementation of such degradation models could reveal a limited rotational capacity at the sectional level jeopardizing the benefits of the added protective/strengthening UHPFRC layer.

Moreover, given the advancement in UHPFRC technology, it could be interesting to exploit the material not only where its mechanical properties are best adapted (that means when N +/M- or N-/M+) but everywhere across the deck to profit of the limited displacement of (R) UHPFRC-RC cross-section with respect to RC ones as it can be inferred by looking at the moment-curvature diagrams for fixed internal actions. In fact, the lower the curvature under a given axial force and bending moment, the lower the structural deflection.

REFERENCES

Briccola D., Conti E., Malerba P.G.& Quagliaroli M. 2013 Multiaxial Interaction Domains of R.C: sections derived through a parametric subdomains discretization. *World Congr. on Advances in Structural Eng. And Mechanics*.

Brühwiler, E. 2013. Rehabilitation and Strenghtening of Concrete Structures Using Ultra-High Performance Fibre Reinforced Concrete. *Structural Engineering International*.

Brühwiler, E. 2019. UHPFRC technology to enhance the performance of existing concrete bridges. *Structures and Infrastructure Engineering*.

Charron, J.P. 2006. Permeability of ultra high performance fiber reinforced concretes (UHPFRC) under high stresses. *Materials and structures (2007)* .

Habert, G. 2012. Lowering the global warming impact of bridge rehabilitations by using Ultra High Performance Fibre Reinforced Concretes. *Cement & Concrete Composites.*

Quagliaroli, M. 2015. A parametric subdomain discretization for the analysis of the multiaxial response of reinforced concrete sections. *Advanced in Engineering Software*.

Malerba, P. 1984. Aspetti numerici dell'analisi di sezioni in C.A. soggette a sforzo normale. *Atti del IV Congresso C.T.E.*

Bridge Maintenance, Safety, Management, Digitalization and Sustainability – Jensen, Frangopol & Schmidt (eds)
© 2024 The Author(s), ISBN 978-1-032-77040-6
Open Access: www.taylorfrancis.com, CC BY-NC-ND 4.0 license

Optimization study on wet joints construction of steel plate composite beams

B. Wang
Anhui Transportation Holding Group Co., Ltd, Anhui, China

Z.Q. Liu
Tongji University, Shanghai, China

ABSTRACT: To improve the construction efficiency of the steel plate composite beam bridge deck and reduce the construction steps of wet joints, this paper proposes a method to eliminate shear studs and internal prestressing in wet joints of steel plate composite beams. This significantly enhances the construction efficiency of the steel plate composite beam bridge. By establishing a spatial finite element analysis model and comparing it with a traditional bridge deck in terms of stress analysis, the results show that the two optimized structures have minimal impact on the stress distribution of the bridge deck. In particular, the stress increase in the bridge deck with eliminated wet joint shear studs is less than 4%, and the reduction in stress reserve due to the absence of transverse prestressing in wet joints is only 1 MPa.

Keywords: Wet joints, steel plate composite beam, finite element simulation, structural optimization

1 INSTRUCTIONS

Due to its simple structure, clear force transmission, and efficient construction, the steel plate composite beam bridge has the potential for standardized and industrialized construction, and is often used in the construction of municipal bridges(Zhang, Y., et al. 2020; Tawfic, Y. R., et al. 2021; Hassan, A. D. M., et al. 2020; Du, H., et al. 2020).

In urban bridge construction, the construction of steel plate composite beam bridges often involves the prefabrication of steel main beams and segmental bridge decks in factories, followed by on-site hoisting. Subsequently, wet joints are cast on-site, and prestressing is applied to the bridge deck. While the prefabrication of most components in factories and the mechanized hoisting construction greatly enhance construction efficiency, the welding of shear studs on steel main beams and the subsequent tensioning of prestressing in bridge decks usually require a large workforce, posing a key challenge to the standardization and industrialization of steel plate composite beam construction(Nie, J., et al. 2019; El-Sisi, et al. 2021; Zhao, Y. et al. 2020; Wang, Y. H., et al. 2020).

To further advance the construction efficiency of steel plate composite beam bridges, many scholars have explored the structural construction in-depth. For instance, Huang D and others (Huang, D., et al. 2023) proposed the U-shaped reinforcement wet joint construction, which involves setting the internal straight overlapping reinforcement in wet joints as U-shaped reinforcement, eliminating the need for welding and significantly improving construction efficiency. Additionally, He Shuan-Hai and others (Shuan-hai, H. E., et al.2021) directly improved structural construction efficiency by eliminating wet joints in composite beams. They used high-strength concrete as the bridge deck for I-shaped composite beams, enhancing the structural strength of the bridge deck and eliminating the wet joint construction. Full-scale model tests showed reasonable force distribution and feasible construction.

DOI: 10.1201/9781003483755-20

Based on the comprehensive analysis of the above studies, wet joint construction, due to its complexity, is indeed one of the key research objects affecting the construction efficiency of steel plate composite beams. This paper proposes an optimized method by studying and analyzing the shear studs and transverse prestressing inside wet joints, suggesting the elimination of shear studs and transverse prestressing at wet joint locations, significantly improving the construction efficiency of steel plate composite beams.

2 OPTIMIZATION OF WET JOINT SHEAR NAILS

2.1 *Model establishment*

The study focuses on a 3×40m double main beam steel plate composite beam bridge with a bridge width of 12.5m. A three-dimensional finite element model was established using finite element analysis software. The steel beam element type is SHELL63, and the concrete bridge deck element type is SOLID45. The steel material is Q345, with an elastic modulus of 2.1×10^5 MPa, density of 7850 kg/m³, Poisson's ratio of 0.3, and linear expansion coefficient of 1.2×10^{-5}. The concrete is C50, with an elastic modulus of 3.45×10^5 MPa, density of 2600 kg/m³, and Poisson's ratio of 0.2. Additionally, it is considered that there might be some bonding slip between the concrete bridge deck and the steel beam. This interaction is simulated by establishing spring elements COMBIN14 to model the elastic connection between them.

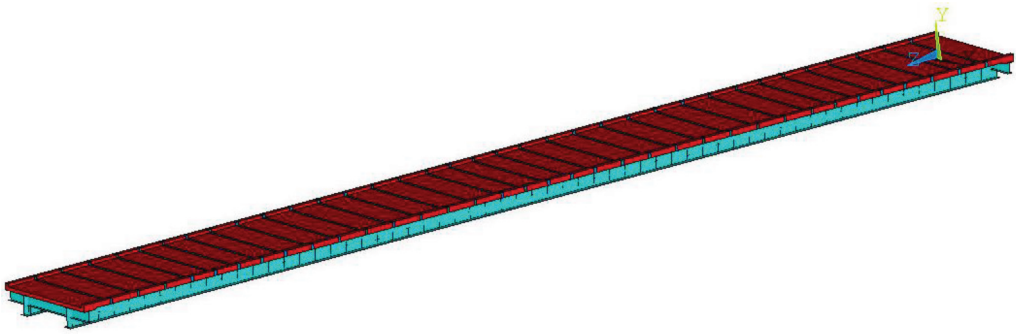


Figure 1. Finite element analysis model.

2.2 *The influence of the number of wet joint shear nails on the structure*

By reducing the number of shear studs in the wet joint area by 0% to 40%, the changes in the structural performance of the entire steel plate composite bridge under its self-weight were compared. As shown in Figure 2, under the self-weight, the structural deformation shows a linear upward trend, and when the number of wet joint shear studs is reduced by 40%, the maximum deformation of the structure increases by 0.12%, with a relatively small change.

Additionally, the impact of reducing the number of shear studs on the stress of the steel main beam is compared, as shown in Figure 3. Similarly, the reduction of shear studs in the wet joint area increases the maximum stress on the lower edge of the steel main beam while decreasing the maximum stress on the upper edge. The overall trend also shows a linear variation. Comparing the magnitude of changes, it is observed that the change in the lower edge is extremely small, less than 0.1%, which can be neglected. The variation in stress on the upper edge of the steel main beam is greater than that on the lower edge, approximately 6.4%.

Overall, the reduction in the number of shear studs in the wet joint area has minimal impact on the deformation and stress of the structure. In the cooperative force-bearing work of the steel main beam and the bridge deck, the shear studs on the bridge deck play a primary role.

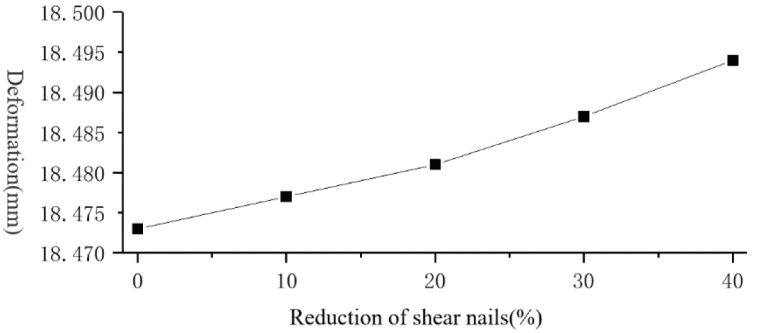


Figure 2. The reduction in shear studs has an impact on the deformation of the steel main beam.

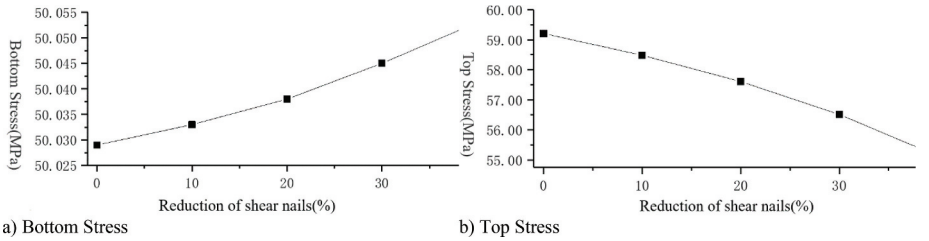


Figure 3. The reduction in shear studs has an impact on the stress of the steel main beam.

2.3 *Optimization of eliminating shear studs in wet joints*

Based on the above research, it is evident that the variation in the number of shear studs in wet joints has minimal impact on the steel main beam. Therefore, considering the elimination of shear studs in wet joint locations, the stress variation of the bridge deck under extreme mid-span and eccentric loading conditions is observed(Wei, C., et al. 2022)). The load is applied at the mid-span position and supports, as shown in Figure 4.

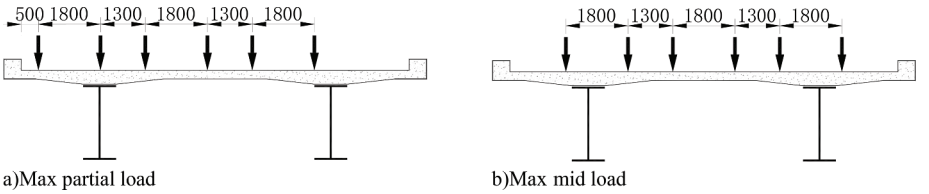


Figure 4. Location of load application.

The model calculation results, as shown in Figure 5, are clear. It is evident that after eliminating shear studs in wet joint locations, the stress on the bridge deck increases under various vehicle loading conditions. The stress increase is more significant for the end transverse beam's extreme vehicle loading condition than for the mid-span extreme vehicle loading condition. However, overall, the stress increase in the bridge deck under various conditions averages less than 4%. The maximum variation occurs in the case of eccentric loading at the support, where the maximum tensile stress in the bridge deck was 6.6 MPa with shear studs in wet joint locations. After eliminating the shear studs, the maximum tensile stress increases to 6.86 MPa, representing a numerical increase of 3.94%.

Therefore, the elimination of shear studs in wet joint locations has an impact on the stress of both the steel main beam and the bridge deck of less than 5%. Considering that the welding of shear studs in wet joint locations significantly affects construction efficiency and conflicts

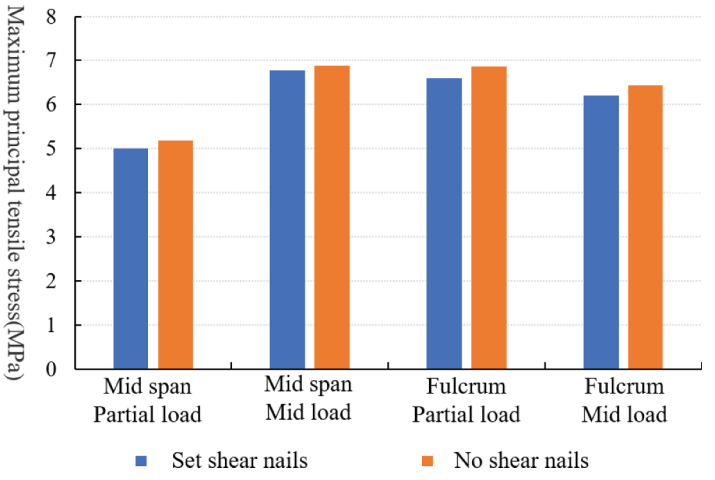


Figure 5. Before and after the cancellation of wet joint shear nails stress comparison.

with the arrangement of reinforcement in wet joints, it is advisable to consider omitting shear studs in wet joint locations during the design and construction process.

3 WET JOINT TRANSVERSE PRESTRESSING OPTIMIZATION

3.1 *Model establishment*

In practical engineering, to enhance durability, transverse prestressing can be applied to the bridge deck of a steel box girder. To study the increase in compressive stress on the bridge deck due to this prestressing, the same 12.5m double main girder steel box girder is taken as the research object, and a local segment model is established, as shown in Figure 6. The model considers the bridge deck, wet joint, steel beams, and prestressing, where the bridge deck and wet joint use Solid45 elements, the steel beams use Shell63 elements, and the prestressing uses Link8 elements.

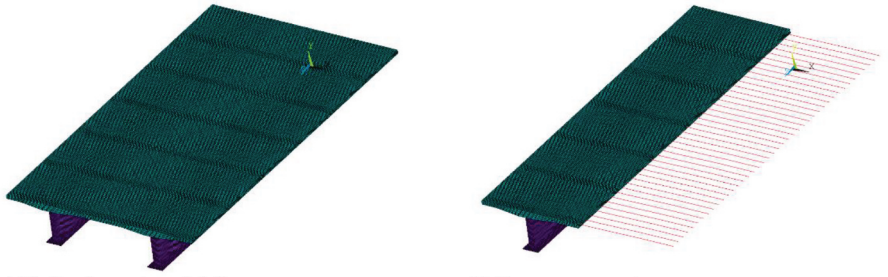


Figure 6. Finite element model of transverse prestressing.

Calculation Conditions Simulating Actual Construction Sequence

The calculation conditions simulate the actual construction sequence. Firstly, the bridge deck is activated, and prestressing is applied. Then, the wet joint is cast, and the prestressing in the wet joint is applied. In the model without prestressing, only the wet joint is activated.

Because the lateral force is the main consideration, the steel beams are supported with simple supports, accounting for the gravity of the bridge deck, considering the prestressing of the bridge deck, and considering the creep loss coefficient. The magnitude of the prestressing in the bridge deck is 1116MPa.

3.2 *Optimization of transverse prestressing in wet joints*

According to the calculation results, the extracted stress conditions of the bridge deck before and after the tensioning of the wet joint pre-stress are shown in Figure 7. It can be seen that the pre-stress tensioning of the wet joint significantly improves the compressive stress on the upper edge of the cantilever region and the lower edge of the central region, reaching a level of 1 MPa.

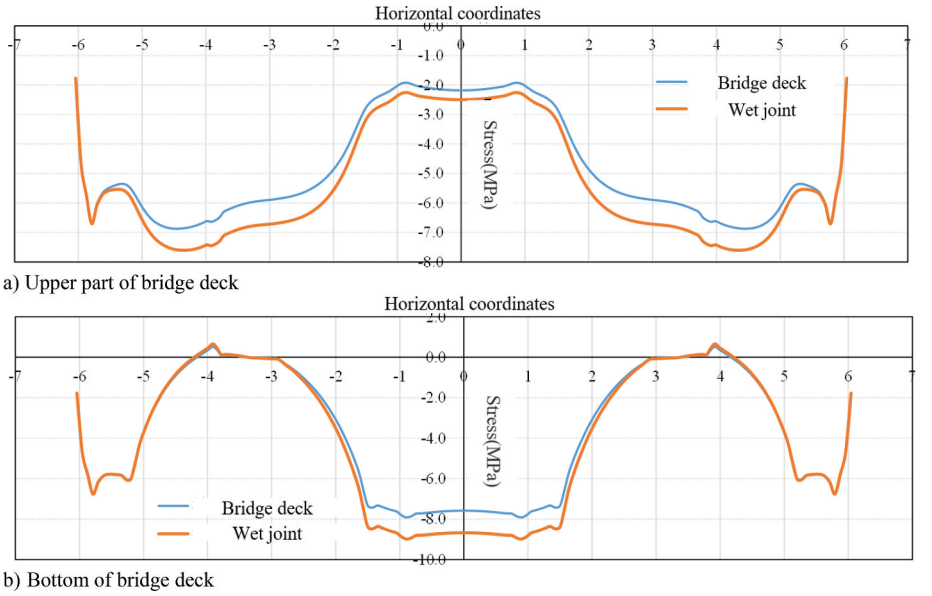


Figure 7. The Influence of wet joint tensioning and pre stressing on the stress of bridge deck.

Examining the stress reserve situation after the pre-stress tensioning of the wet joint itself, as shown in Figure 8, it can be observed that the reserve compressive stress at the root of the cantilever of the wet joint is around 1 MPa, and the reserve compressive stress around the central lower edge is also around 1 MPa. This stress level is relatively low.

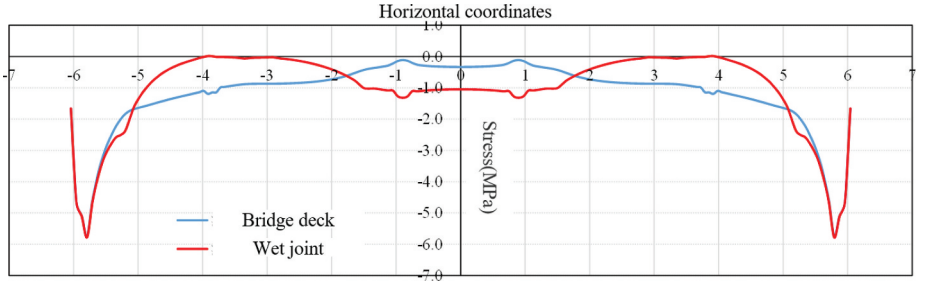
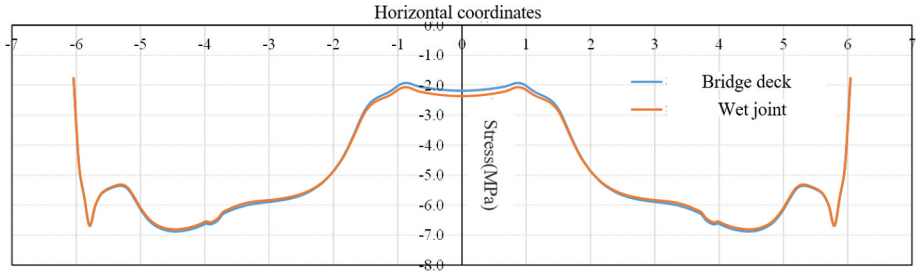
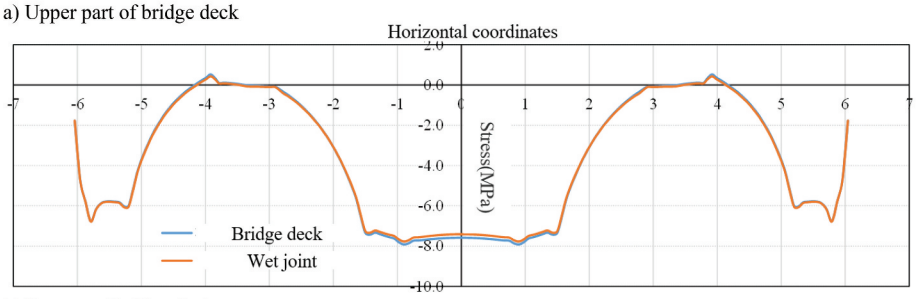


Figure 8. Stress distribution of wet joint after pre-stress tensioning.

If the wet joint is not pre-stressed, after casting the wet joint, the stress of the bridge deck remains essentially unchanged, with a pre-stress of 7MPa at the root of the cantilever, and a reserved compressive stress of 8MPa at the central lower edge. The wet joint is basically not stressed, with stress at around 0.3MPa.



a) Upper part of bridge deck



b) Bottom of bridge deck

Figure 9. The lack of pre-stressing in the wet joint has little impact on the stress of the bridge deck.

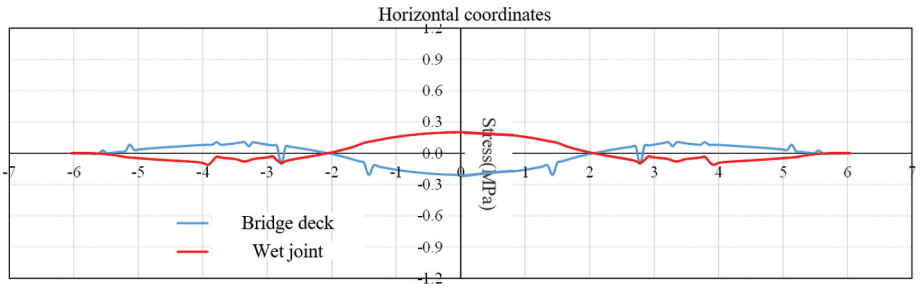


Figure 10. Illustrates the stress distribution in the wet joint after the absence of pre-stressing.

In conclusion, a comparative analysis was conducted using the solid finite element method for wet joint scenarios with and without pre-stressing. The results indicate that the pre-stressing in the wet joint is shared between the wet joint and the bridge deck, leading to an increase of approximately 1 MPa in compressive stress on the bridge deck, and an effective compressive stress of around 1 MPa in the wet joint. The introduction of pre-stressing does not effectively improve the crack resistance of the wet joint, but rather adds complexity to on-site construction, reducing construction efficiency. This approach contradicts the principles of industrialized construction. In practical engineering, it may be considered to eliminate the arrangement of transverse prestressed tendons and optimize the wet joint structure.

4 CONCLUSION

This article analyzes the performance improvement rate of internal shear nails and prestress in the wet joint of a 12.5m bridge wide double main beam steel plate composite beam, and draws the following conclusions:

An analysis of the quantity of internal shear studs in the wet joint indicates that the impact of wet joint shear studs on the deformation of the bridge structure is minimal. The elimination of the arrangement of wet joint shear studs has an impact of less than 5% on

the force distribution of both the main steel girder and the bridge deck. Therefore, it may be considered to omit the placement of shear studs in the wet joint during the design and construction process.

An analysis of the transverse prestressing in the wet joint reveals that the prestress set in the wet joint is shared between the wet joint and the bridge deck. The effective compressive stress generated by the wet joint is approximately 1 MPa. However, this prestressing does not provide effective improvement in crack resistance for the wet joint. Instead, it adds complexity to on-site construction, reducing construction efficiency. This contradicts the principles of industrialized construction. In practical engineering, it may be considered to eliminate the arrangement of transverse prestressed tendons and optimize the wet joint structure.

REFERENCES

Du, H., Hu, X., Meng, Y., Han, G., & Guo, K. (2020). Study on composite beams with prefabricated steel bar truss concrete slabs and demountable shear connectors. Engineering Structures, 210, 110419.

El-Sisi, A. A., Hassanin, A. I., Shabaan, H. F., & Elsheikh, A. I. (2021). Effect of external post-tensioning on steel–concrete composite beams with partial connection. Engineering Structures, 247, 113130.

Hassan, A. D. M., & Nimnim, H. T. (2020, November). Experimental study of steel-concrete composite beams with slab opening. In IOP Conference Series: Materials Science and Engineering (Vol. 928, No. 2, p. 022110). IOP Publishing.

Huang, D., Nie, X., Zeng, J., & Jiang, Y. (2023). Experimental and numerical analysis on flexural behavior of improved U-bar joint details for accelerated bridge construction. Engineering Structures, 289, 116328.

Nie, J., Wang, J., Gou, S., Zhu, Y., & Fan, J. (2019). Technological development and engineering applications of novel steel-concrete composite structures. Frontiers of Structural and Civil Engineering, 13, 1–14.

Shuan-hai, H. E., Jie, C. H. E. N., Zhao, Z. H. U., Yi-fan, S. O. N. G., & Yuan, L. I. (2021). Experiment on Load Transversal Distribution of High Strength Concrete I-beams Without Wet Joints. China Journal of Highway and Transport, 34(11), 83.

Tawfic, Y. R., A Soltan, A. N., & B Saddek, A. (2021). CHARACTERISTICS OF STEEL PLATE-REINFORCED CONCRETE COMPOSITE BEAMS SUBJECTED TO FLEXURAL STRESSES. Journal of Advanced Engineering Trends, 41(2), 41–53.

Wang, Y. H., Yu, J., Liu, J. P., Zhou, B. X., & Chen, Y. F. (2020). Experimental study on assembled monolithic steel-prestressed concrete composite beam in negative moment. Journal of Constructional Steel Research, 167, 105667.

Wei, C., Zhang, Q., Yang, Z., Li, M., Cheng, Z., & Bao, Y. (2022). Flexural cracking behavior of reinforced UHPC overlay in composite bridge deck with orthotropic steel deck under static and fatigue loads. Engineering Structures, 265, 114537.

Zhao, Y., Zhou, X., Yang, Y., Chen, Y. F., & Gurupackiam, S. (2020). Stiffness and cracking behavior of new U-shaped steel and concrete composite beam under negative bending. Journal of Structural Engineering, 146(5), 04020046.

Zhang, Y., Cai, S., Zhu, Y., Fan, L., & Shao, X. (2020). Flexural responses of steel-UHPC composite beams under hogging moment. Engineering Structures, 206, 110134.

Bridge Maintenance, Safety, Management, Digitalization and Sustainability – Jensen, Frangopol & Schmidt (eds)
© 2024 The Author(s), ISBN 978-1-032-77040-6
Open Access: www.taylorfrancis.com, CC BY-NC-ND 4.0 license

Analysis of the effect of hoop prestressed steel wire rope reinforcement on bridge piers and the loss of prestress

D.H. Sun
Anhui Transportation Holding Group Co., Ltd, Anhui, China

Z.Q. Liu & B. Huang
Tongji University, Shanghai, China

ABSTRACT: During the use of pier structures, vertical cracks can develop under the influence of complex factors such as stress, temperature, and corrosion. To suppress the generation and development of vertical cracks in piers and enhance structural durability, a method of reinforcing piers with a circular prestressed steel wire rope system was proposed. Studies on the stress and strain of solid and hollow pier structures under different loads, diameters, and steel wire rope spacings were carried out, verifying the reinforcement effect. Through parametric analysis, the effects of various factors on the reinforcement were explored, and the method was optimized. A study on the prestress loss of the circular prestressed steel wire rope was conducted. A complete method was proposedd. This research can provide a basis for the design of the circular prestressed system and the development of anchors and other structures, and serve as a reference for similar engineering projects.

Keywords: Annular prestress, wire rope, pier, reinforcement

1 INSTRUCTIONS

In the process of using bridge pier structures, vertical cracks can occur due to complex factors such as forces, temperature, and corrosion, severely impacting the durability of the structure. Traditional methods of bridge pier reinforcement include direct repair, increasing cross-sectional area, adhesive reinforcement, and embedded reinforcement. These methods are passive reinforcement approaches and cannot fundamentally inhibit the development of cracks and the formation of new cracks (Reggia et al. 2020; Cadenazzi et al. 2020; Czaderski et al. 2021). External prestressing reinforcement, as an active reinforcement method, can effectively address this issue with superior efficiency (Zhang et al. 2021; Zhu et al. 2015).

Traditional external prestressing reinforcement for bridges is mostly applied to bending components such as main girders. The *Specifications for Strengthening Design of Highway Bridge (JTG/TJ22-2008)* only provides relevant regulations for girder reinforcement, and external prestressing reinforcement for bridge piers is still in the research stage (JTG/T J22-2008). Guo conducted experimental research on semi-circular prestressed steel hoop reinforcement of bridge piers. The study indicated that when the effective prestress on a 5mm thick steel hoop reached 110MPa, it could significantly enhance the ultimate bearing capacity of the pier (Guo et al. 2015). Zhang investigated the axial compression performance of concrete cylinders reinforced with prestressed steel straps. The research demonstrated that with an effective prestress of 465MPa on a 0.9mm thick steel strap, the maximum bearing capacity of C20 concrete specimens increased by 224.5%, and C30 specimens increased by 208.5% (Zhang et al. 2021). Zhou explored the seismic performance of concrete circular piers reinforced with

DOI: 10.1201/9781003483755-21

prestressed CFRP strips. The study showed that prestressed CFRP strip reinforcement could effectively alter the failure mode of the specimen, greatly improve the bearing capacity, displacement ductility, and energy dissipation capacity of circular piers, but the prestress should not exceed 1113MPa (Zhou et al. 2015). However, these studies are limited by material properties and difficulties in tensioning and anchoring, resulting in relatively low effective prestress (El-Hacha and Soudki 2013; Kueres et al. 2020). Research has mainly focused on the impact on the ultimate axial compression bearing capacity and seismic performance of piers, with less emphasis on the local stress and strain that affect the durability of piers. The complex construction process and high material costs also limit the economic feasibility of large-scale use.

Prestressed steel wire rope, characterized by high strength, easy bending and processing, and simple tensioning and anchoring, can better exploit the external prestressing reinforcement effect (Liu et al. 2022; Wu et al. 2014). Circular prestressed steel wire ropes are widely used in the reinforcement of building structures. However, there is a lack of relevant research on larger bridge piers with greater structural dimensions and reinforcement loads. The prestress effect and prestress loss, crucial to the reinforcement effectiveness, remain unclear. In order to improve the stress and strain on the structure surface, inhibit the generation and development of vertical cracks in bridge piers, and enhance structural durability, this paper investigates the prestress effect and prestress loss in the reinforcement of bridge piers with circular prestressed steel wire ropes.

2 ANALYSIS OF RING PRESTRESSING EFFECT

The circular prestressing system can generate radial pressure on the structure. When the pressure is evenly distributed on the structure, traditional Lamé's formula can be used. However, when reinforcing bridge piers with circular prestressed steel wire ropes, the pressure is distributed at intervals on the structure, making it impractical to use traditional methods for calculation. In order to investigate the effect of prestressing on the structure, finite element analysis was conducted.

2.1 *Analysis of single-ring prestressed effects*

The pressure exerted on the concrete by tensioning the circular prestressed steel wire rope can be calculated using Equation (1).

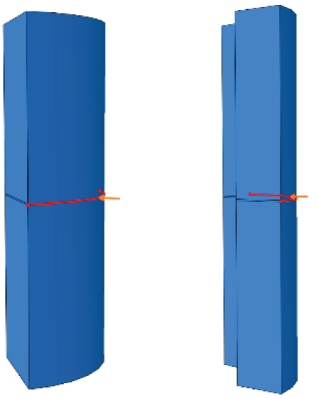
$$p = \frac{A_y \cdot \sigma_{pe}}{r \cdot d_m} \tag{1}$$

where p is the radial pressure on the structure, A_y is the cross-sectional area of the steel wire rope, σ_{pe} is the effective prestress, d_m is the loading width of the steel wire rope on the structure, and r is the radius of the structure. The application of equivalent circular pressure on the structure can simulate the effect of prestressed steel wire rope.

When p acts on the structure, it generates circumferential compressive stress on the pier surface, directly contributing to the suppression of pier cracks. To investigate the influence of p value, whether the pier is hollow or solid, and the pier diameter on the circumferential compressive stress on the surface, a parametric finite element analysis was conducted. The set parameters are outlined in the following Table 1. Applying a single-ring prestress load to the

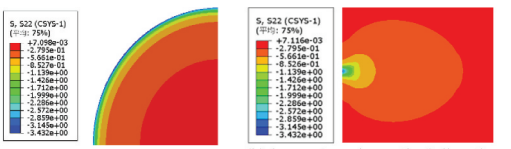
Table 1. Finite element model parameters.

Parameter	Scope	Interval	Number of values
p	6MPa~12MPa	2MPa	4
structure type	hollow or solid	/	2
diameter	1m~3m	0.5m	5



(a) solid pier model. (b) hollow pier model.

Figure 1. Single ring prestressed model.



(a) hoop stress on plane. (b) hoop stress in vertical direction.

Figure 2. Hoop stress (unit: MPa).

column, the material for the column is C50 concrete. The finite element model is as shown in Figure 1.

With a diameter of 2 meters and p=10MPa, the circumferential compressive stress on the surfaces of the solid bridge pier is depicted in Figure 2. It can be observed that the circumferential compressive stress at the edge of the planar surface is maximum, reaching -3.43 MPa and gradually decreasing inward. At a distance of 20 cm from the surface, it has decreased to -1 MPa. The max occurs at the vertically loaded area and diminishes along the vertical direction. By a distance of 10 cm from the loading position, it has decreased to 1 MPa.

The maximum circumferential compressive stress for solid and hollow bridge piers is summarized in Tables 2 and 3. It can be observed that for the same type of pier, the max gradually decreases with an increase in radius. Similarly, under the same load and radius conditions, the stress generated in the solid pier is greater than that in the hollow pier. Given that the tensile strength standard value for C50 concrete is 2.65 MPa, in order to suppress the generation of longitudinal cracks in the pier, the circumferential compressive stress on the structure surface should not be less than 2.65 MPa. Considering factors such as the weakening due to the spaced arrangement of steel wire ropes and prestress loss, the p should not be less than 10 MPa. The pre-tension can be calculated based on Equation (1).

Table 2. Maximum hoop compressive stress of solid bridge pier (unit: MPa).

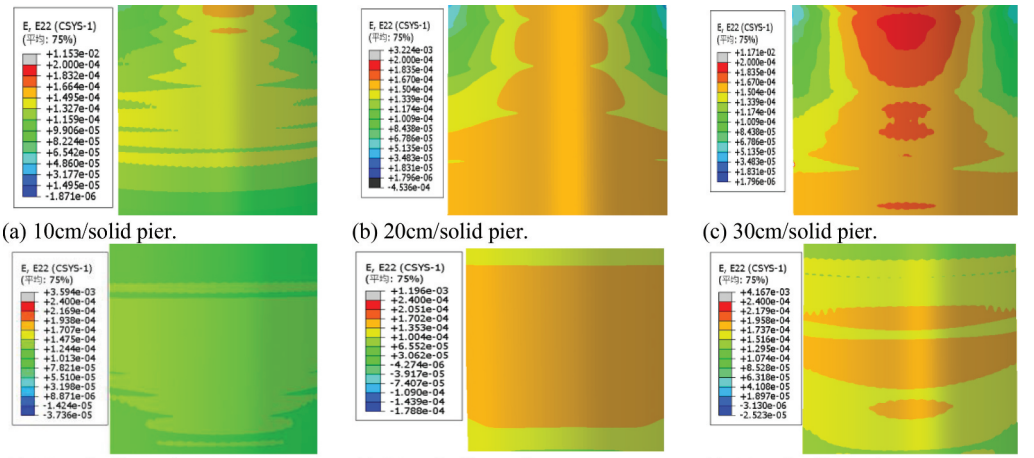
	Prestressed load p			
Diameter	6MPa	8MPa	10MPa	12MPa
1m	2.34	3.07	3.82	4.61
1.5m	2.15	2.83	3.56	4.27
2m	2.1	2.73	3.43	4.11
2.5m	2.04	2.68	3.32	4.01
3m	2.02	2.62	3.29	3.93

Table 3. Maximum hoop compressive stress of hollow bridge pier (unit: MPa).

	Prestressed load p			
Diameter	6MPa	8MPa	10MPa	12MPa
1m	2.31	3.05	3.74	4.44
1.5m	2.15	2.81	3.41	4.12
2m	1.94	2.51	3.14	3.77
2.5m	1.84	2.49	3.05	3.61
3m	1.72	2.42	2.94	3.4

2.2 *Analysis of multi-ring prestressing effects*

To study the effect of multi-ring prestressing on bridge piers, solid and hollow bridge piers with a diameter of 2 meters were considered. The p was set at 10 MPa, and prestressing intervals were varied at 10 cm, 20 cm, and 30 cm. The analysis focused on the effect under axial loading, applied through displacement loading with strain control set at 0.001. Other settings remained consistent with the details mentioned earlier. The finite element analysis results are shown in Figure 3.



(a) 10cm/solid pier. (b) 20cm/solid pier. (c) 30cm/solid pier.

(e) 10cm/hollow pier. (e) 20cm/hollow pier. (e) 30cm/hollow pier.

Figure 3. Hoop strain after reinforcement.(unit:ε).

Following reinforcement and comparison with the unreinforced structure, for solid structures with reinforcement spacings of 10cm, 20cm, and 30cm, there is a reduction in the average strain ratio of 28%, 22%, and 11%, respectively. Similarly, for hollow structures, the reduction ratio is 35.6%, 27%, and 14.9%, respectively. These findings indicate that circumferential prestress can distinctly diminish the tensile strain on the surface of both solid and hollow structures induced by axial loading, effectively suppressing the initiation of vertical cracks. Moreover, the reinforcement efficiency is superior for hollow structures compared to solid structures. 30cm is deemed excessive, Considering a comprehensive evaluation involving factors such as reinforcement efficacy and economic benefits, 20cm emerges as an optimal choice.

3 PRESTRESS LOSS ANALYSIS

The principal pre-stress losses in the reinforced bridge pier with circular prestressed steel wire ropes are as follows: pre-stress loss due to frictional resistance between the steel wire ropes and the structural; loss resulting from elastic compression during staged

tensioning of concrete; loss due to deformation of the anchorages; loss caused by relaxation of the steel wire ropes; pre-stress loss resulting from the creep and shrinkage of concrete. Frictional loss, staged tensioning loss, and anchorage deformation loss are instantaneous losses, while relaxation loss and creep and shrinkage loss of concrete are long-term losses. Calculation methods for various pre-stress losses are proposed (Bonopera et al. 2020; Cao et al. 2021; Kang et al. 2021). The following conditions were employed for calculating: the reinforced structure is a C50 concrete pier with a diameter of 2 meters, a structural age of 5 years, utilizing 6×36WS+IWR steel core wire ropes with a nominal diameter of φ26mm, an elastic modulus of 1.95×105 MPa, a strength of 1870 MPa, a nominal breaking force of 450 kN, and a control stress of 1200 MPa.

3.1 *Analysis of frictional resistance and prestress loss*

The pre-stress loss resulting from the frictional resistance between the steel wire ropes and the structural during the tensioning is calculated using Equation (2).

$$\sigma_{l1} = \sigma_{con}[1 - e^{-(\mu\theta)}] \tag{2}$$

In the equation, σ_{l1} represents the pre-stress loss due to frictional resistance, σ_{con} is the tensioning control stress, μ is the friction coefficient between the steel wire ropes and the structural, and θ is the relative angle between the tensioning end and the calculation position. When employing a single-ring bidirectional tensioning method, The maximum value of θ is 180°. It can be observed that pre-stress loss increases with the roughness of the contact surface. When μ is 0.2, the maximum pre-stress is 540 MPa, constituting 45% of the control stress.

3.2 *Analysis of prestressed loss in batch tensioning*

In the incremental tensioning of circular prestressed steel wire ropes, the subsequent tensioning of the wires induces contraction in the previously tensioned concrete locations, resulting in a loss of prestress, as calculated by Equation (3).

$$\sigma_{l2} = \frac{\alpha_e \sigma_p}{2} \tag{3}$$

In the equation, σ_{l2} represents the incremental tensioning pre-stress loss, α_e is the ratio of the elastic modulus of the steel wire rope to that of the concrete, and σ_p is the radial compressive stress exerted by the subsequently tensioned steel wire rope on the previously tensioned concrete. According to the finite element analysis discussed earlier, the spacing between the steel wire ropes has a significant impact on the incremental tensioning pre-stress loss. Smaller spacing results in greater pre-stress loss. With a wire rope spacing of 20cm, considering the cumulative effect, the pre-stress loss caused by incremental tensioning is 6.72 MPa, approximately 0.6% of the control stress.

3.3 *Analysis of anchorage deformation and prestress loss*

After tensioning and anchoring, the deformation of the anchorage induces a retraction of the steel wire ropes, leading to pre-stress loss, as calculated by Equation (4):

$$\left.\begin{aligned} \varphi_0 = \frac{1}{\mu}\ln\left[1 - \sqrt{\frac{aE_s}{\sigma_{con}} \times \frac{\mu}{1000r}}\right]^{-1} \\ 0 \le \varphi \le \varphi_0 : \sigma_{l3} = \sigma_{con} e^{-\mu\varphi}[1 - e^{-2\mu(\varphi_0 - \varphi)}] \\ \varphi \ge \varphi_0 : \sigma_{l3} = 0 \end{aligned}\right\} \tag{4}$$

In the equation, σ_{l3} represents the pre-stress loss caused by the deformation of the anchorage and the retraction of the steel wire ropes. φ_0 is the angle of the reverse frictional influence zone,

a is the value of the anchorage deformation and steel wire rope retraction, which can be empirically determined or experimentally measured. E_s is the elastic modulus of the steel wire rope, r is the bending radius, and φ is the angle from the tensioning end to the calculation section. Other parameters remain consistent with the preceding text. The pre-stress loss is maximal at the tensioning end, with an empirically chosen a value of 5mm, resulting in a maximum pre-stress of 32 MPa. The loss accounts for approximately 2.7% of the control stress.

3.4 *Analysis of prestressed loss during relaxation of prestressed steel wire ropes*

The pre-stress loss caused by stress relaxation in prestressed steel wire ropes under continuous action is calculated according to Equation (5).

$$\left.\begin{array}{c} \sigma_{con} \leq 0.7 f_{ptk}: \\ \sigma_{l4} = 0.125\left(\frac{\sigma_{con}}{f_{ptk}} - 0.5\right)\sigma_{con} \end{array}\right\} \tag{5}$$

In the equation, σ_{l4} represents the pre-stress loss caused by the relaxation of the steel wire ropes, and f_{ptk} is the tensile strength of the prestressed steel wire ropes. The calculated pre-stress loss is 21.3 MPa, constituting approximately 1.8% of the control stress. Since the relaxation effect is more pronounced in the early stages, controlling the tensioning time can eliminate a significant portion of the pre-stress loss.

3.5 *Analysis of prestress loss in concrete shrinkage and creep*

The radial shrinkage of concrete components due to concrete shrinkage results in a loss of prestress, which can be calculated using Equation (6).

$$\sigma_{l5} = \frac{\varepsilon_{cs}(t, t_s) E_s}{2} \tag{6}$$

In the equation, σ_{l5} represents the pre-stress loss caused by concrete shrinkage, and $\varepsilon_{cs}(t,t_s)$ is the shrinkage strain of concrete from time t_s to t. It can be calculated according to the relevant specifications (JTG 3362—2018).

Prestress loss over the 10-year period for the reinforced concrete bridge pier at 5 years of age is 6.77 MPa. When the controlling tension stress is 1200 MPa, the proportion of prestress loss is 0.55%.

When the circular prestressing is applied to a compressed member, there is both axial and circumferential creep. The calculation of lateral expansion due to axial creep is given by Equation (7).

$$\varepsilon_1(t_1, t_2) = \frac{\sigma_z}{E_c}[\varphi(t_0, t_2) - \varphi(t_0, t_1)]\nu \tag{7}$$

In the equation, $\varepsilon_1(t_1,t_2)$ represents the lateral expansion creep due to axial pressure from t_1 to t_2, σ_z is the axial stress, E_c is the elastic modulus of concrete, $\varphi(t_0,t_n)$ is the creep coefficient from time t_0 to t_n at the loading time, which can be calculated according to the relevant specifications (JTG 3362—2018), and ν is the material Poisson's ratio. During the circumferential creep process, stress continually changes. According to the linear theory of creep, the incremental creep strain for each time period is given by Equation (8).

$$\left.\begin{array}{c} \Delta\varepsilon_2(t_n, t_{n-1}) = \sum_{j=1}^{n-1} \frac{\Delta\sigma_c(t_j)}{E_c}\left[\varphi(t_n, t_j) - \varphi(t_{n-1}, t_j)\right] \\ \Delta\sigma_c(t_j) = \frac{\Delta\varepsilon_2(t_j, t_{j-1}) \times E_s \times A_y}{2r \times d_m} \end{array}\right\} \tag{8}$$

In the equation, $\Delta\varepsilon_2(t_n,t_{n-1})$ represents the circumferential creep strain increment from t_{n-1} to t_n, $\Delta\sigma_c(t_j)$ is the stress increment at time t_j. $\varphi(t_n,t_j)$ is the creep coefficient from t_j to t_n,

calculated using the relevant specifications. Under the conditions mentioned earlier, the recursive solution program can be developed by fitting the creep coefficient. The lateral expansion creep and lateral contraction creep are combined, and the prestress loss is calculated according to Equation (9).

$$\sigma_{l6}=\frac{(\Delta\varepsilon_1+\Delta\varepsilon_2)\times E_s}{2} \tag{9}$$

In the equation, σ_{l6} represents the prestress loss caused by concrete creep. Through program calculation, after 10 years of reinforcement, the prestress loss caused by creep is 10.3 MPa, with a loss proportion of 0.9%.

4 PRESTRESS LOSS TEST

Through the analysis of prestress loss, the most significant loss in the circular steel wire rope prestressing system is caused by the friction, accounting for over 70% of the total loss. Experimental verification of this loss is conducted.

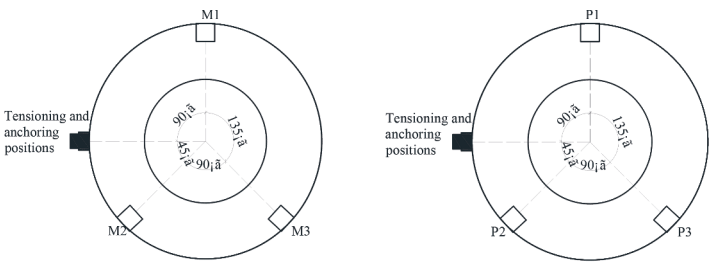
A hollow bridge pier is designed with an outer diameter of 1.2 meters, an inner diameter of 0.63 meters, and a height of 2 meters. The pier is constructed using C50 concrete. circular prestressed steel wire ropes are tensioned on the pier in Figure 4. Magnetic flux sensors are installed on the steel wire rope, and pressure sensors are embedded in the pier, as shown in Figure 5, to measure the prestress loss along the circumference.

In the experiment, tension loading is applied to the steel wire rope. Initially, it is loaded incrementally in 10kN increments up to 50kN, then in 50kN increments up to 150kN, and finally in 10kN increments up to 200kN. After stabilizing the measured data, tension anchoring is performed, followed by an analysis of the measured data.



(a) Test structure front view. (b) Side view of test structure.

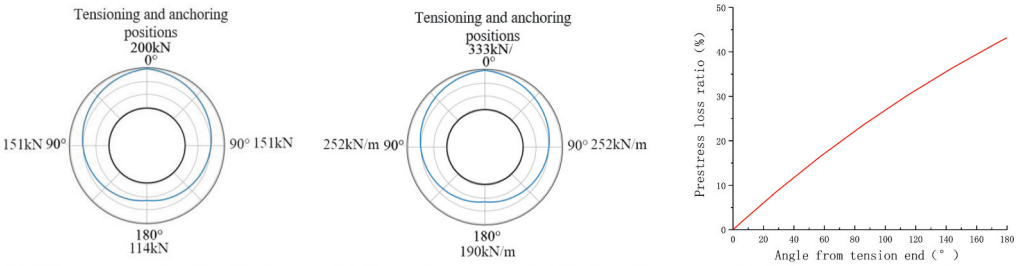
Figure 4. Test structure view.



(a) Magnetic flux sensor settings. (b) Pressure sensor settings.

Figure 5. Sensor settings.

The maximum tension load on the steel wire rope is 200kN. The tension force data of the steel wire rope at different positions is measured through magnetic flux sensors. By using Equation (2), the friction coefficient is calculated as μ=0.18. The tension of the wire rope, the pressure received by the bridge pier, and the prestress loss are shown in Figure 6.



(a) Wire rope tension distribution diagram.

(b) Concrete pressure distribution diagram.

(c) Prestress loss proportion diagram.

Figure 6. Test result.

Due to the friction, the tension in the steel wire rope is unevenly distributed along the circumference. At the tensioning end, it is maximum, reaching 200 kN, and at a position 180° away from the tensioning end, it is minimum, at 114 kN. The pressure distribution pattern on the bridge pier corresponds to the tension distribution pattern on the steel wire rope. At the tensioning end, the maximum pressure is 333 kN/m, gradually decreasing as one moves away from the tensioning end, reaching a minimum of 190 kN/m at the 180° position. As the distance from the tensioning end increases, the prestress loss gradually increases, with the maximum prestress loss percentage reaching 43% at 180° away from the tensioning end. This fully demonstrates that the prestress loss caused by frictional resistance is significant, representing the primary type of loss in the circular prestressed steel wire rope system. It also validates the calculation method proposed in the preceding text.

5 CONCLUSION

This paper conducted a study on the reinforcement of bridge piers using circular prestressed steel wire ropes through finite element analysis. It proposed types and calculation methods for prestress losses, which were then validated through relevant experiments. The main conclusions are as follows:

The maximum circumferential compressive stress generated on the surface of the structure by a single-ring prestress is crucial for reinforcing the vertical cracks in the structure. The maximum circumferential compressive stress decreases as the structure diameter increases. For C50 concrete structures, the radial pressure generated by prestressed steel wire ropes should not be less than 10MPa.

The application of multiple-ring prestress can effectively reduce the circumferential tensile strain on the surface of the structure caused by axial loads, providing inhibition to the development of vertical cracks. The effectiveness decreases with the increase in the spacing between the steel wire ropes. With a 20cm spacing, the reinforcement of solid and hollow structures reduces the maximum tensile strain by 22% and 27%, respectively. The reinforcement efficiency of hollow structures is greater than that of solid structures.

The paper proposes types of prestress losses and their corresponding calculation methods. The calculations under the specified conditions indicate that the prestress loss due to friction between the steel wire ropes and the structure is the most significant, accounting for over 70% of the total losses. Experimental validation of the frictional loss was conducted, revealing that, under μ=0.18, the frictional loss represents 43% of the control stress. Effectively reducing the frictional resistance between the steel wire ropes and the structure is crucial for enhancing the reinforcement efficiency.

REFERENCES

Bonopera, M., Chang, K. C., & Lee, Z. K. (2020). State-of-the-art review on determining prestress losses in prestressed concrete girders. Applied Sciences, 10(20), 7257.

Cadenazzi, T., Dotelli, G., Rossini, M., Nolan, S., & Nanni, A. (2020). Cost and environmental analyses of reinforcement alternatives for a concrete bridge. Structure and infrastructure engineering, 16(4), 787–802.

Cao, R., Zhao, Y., Wang, Y., & Pi, J. (2021). Structural and Mechanical Characteristics of Double-Hoop Unbonded Annular Anchor Lining. ACI Structural Journal, 118(3), 61–70.

CCCC FIRST HIGHWAY CONSULTANTS CO.LTD 2008. Specifications for Strengthening Design of Highway Bridge (JTG/T J22-2008).Beijing: China Communications Press.

CCCC HIGHWAY CONSULTANTS CO.,LTD 2018. Specifications for Design of Highway Reinforced Concrete and Prestressed Concrete Bridges and Culverts (JTG 3362—2018). Beijing: China Communications Press.

Czaderski, C., Shahverdi, M., & Michels, J. (2021). Iron based shape memory alloys as shear reinforcement for bridge girders. Construction and building materials, 274, 121793.

El-Hacha, R., & Soudki, K. (2013). Prestressed near-surface mounted fibre reinforced polymer reinforcement for concrete structures—A review. Canadian Journal of Civil Engineering, 40(11), 1127–1139.

Guo, Z., Huang Q., Hao J., Chen J., & Lai Y. (2015). Experimental study on the axial compression performance of RC bridge piers reinforced with prestressed steel ferrules. Journal of Central South University: Natural Science Edition, 46(8), 3100–3107.

Kang, J., Cao, R., & Liu, L. (2021, October). Numerical Modeling Method and Experimental Verification of Prestressed Lining with Unbonded Annular Anchors. In IOP Conference Series: Earth and Environmental Science (Vol. 861, No. 3, p. 032030). IOP Publishing.

Kueres, S., Will, N., & Hegger, J. (2020). Shear strength of prestressed FRP reinforced concrete beams with shear reinforcement. Engineering Structures, 206, 110088.

Liu, Z. Q., Guo, Z. X., & Ye, Y. (2022). Flexural behaviour of RC beams strengthened with prestressed steel wire ropes polymer mortar composite. Journal of Asian Architecture and Building Engineering, 21(1), 48–65.

Reggia, A., Morbi, A., & Plizzari, G. A. (2020). Experimental study of a reinforced concrete bridge pier strengthened with HPFRC jacketing. Engineering Structures, 210, 110355.

Wu, G., Wu, Z., Wei, Y., Jiang, J., & Cui, Y. (2014). Flexural strengthening of RC beams using distributed prestressed high strength steel wire rope: theoretical analysis. Structure and Infrastructure Engineering, 10(2), 160–174.

Zhang B., Yang Y., & Xia Z. (2021). Axial compression performance test of concrete cylinders reinforced with prestressed steel strips. Bulletin of the Chinese Ceramic Society, 40(7).

Zhou C., Li H., Zeng X., & Tian T. (2015). Finite element analysis of hysteretic performance of concrete cylinder reinforced with prestressed carbon fiber strips. Journal of Applied Fundamentals and Engineering Sciences, 23(3), 586–595.

Bridge Maintenance, Safety, Management, Digitalization and Sustainability – Jensen, Frangopol & Schmidt (eds)
© 2024 The Author(s), ISBN 978-1-032-77040-6
Open Access: www.taylorfrancis.com, CC BY-NC-ND 4.0 license

Development and application of anti-differential disturbance concrete for widening bridge

D.H. Chen
Guangdong Provincial Freeway Co., Ltd., Guangzhou, China

J. Song & C.Y. Zhu
Department of Bridge Engineering, Tongji University, Shanghai, China

ABSTRACT: When the bridge splicing connection is carried out without interrupting the traffic, the differential vibration deformation will occur at the splicing position under the action of vehicle-bridge coupling vibration. It will affect the long-term performance of splicing joints. Therefore, it is necessary to develop a new type of concrete material that can satisfy the requirements of shear deflection and vibration disturbance. Combined with the vibration monitoring and simulation of the actual bridge, the vibration characteristics of the existing old bridge are analyzed to obtain the development requirements of anti-differential disturbance concrete. The vertical shaking table was applied to test the performance of proposed material. After the implementation in the widened bridge, a standardized pouring process for anti-differential disturbance concrete was formed. A series of detection methods were proposed as well. The complete set of construction technology and quality inspection technology of the anti-difference disturbance concrete are established.

1 INTRODUCTION

The traffic flow of the existing freeway is growing rapidly and needs to be reconstructed or widened (Zhou, 2020; Mahboubi, 2021; Jeong, 2018). Based on the reconstruction and widening project of freeway in Guangdong Province, China, the research on splicing of widened bridge without interruption of traffic is carried out. The hollow slab beam bridge which accounts for a large proportion on Shenhai Freeway is mainly focused (Chen, 2023). The widened bridge is mainly including three parts: the existing old bridge, the widening new bridge and the splicing joint. The typical cross-section form of widened bridge is shown in Figure 1.

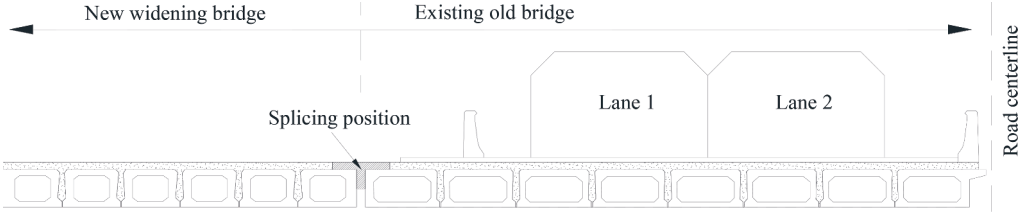


Figure 1. Typical cross-section of the widened bridge (Unit: cm).

When the existing old bridge and the widening new bridge is spliced, the differential vibration deformation will occur in the splicing joint under the action of vehicle-bridge coupling vibration (Cui, 2019). It will influence the quality of the joint concrete. However, due to the

DOI: 10.1201/9781003483755-22

lack of splicing materials to resist vibration and deflection difference, it is faced with the situation of interrupting traffic to splice, which will affect the current road traffic and the long-term performance of splicing joint. Therefore, the splicing of the widened bridge should be carried out without interrupting the traffic.

A number of studies have been carried out on the performance of concrete after disturbance (Yang, 2021; Zhang, 2019a & 2019b). Zeng (2023) proposed a new type of concrete which can resist the vibration disturbance and applied it in the splicing connection of widened bridge without interrupting traffic in freeway. The material performance was tested with the shaking table and concluded that the compressive strength can be improved by 10% to 20% after the disturbance. Liu (2021) evaluated the effect of vehicle–bridge coupled vibration on the mechanical properties of composite concrete. It can be concluded that the vibration has slightly influence on the flexural strength of specimen. Wang (2022) studied the influence of vibration on the steel fiber disturbance in UHPC material, and the mechanical performance of UHPC specimens were tested with shaking table. It can be concluded that vibration amplitude and frequency are the key parameters affecting the flexural and tensile strength of material. However, these studied are mostly based on the laboratory test, the practical application of the material and the related construction technology have not been carried out obviously.

In this article, the vibration characteristics of the existing old bridge are tested for 48 hours. The bridge-vehicle coupling vibration simulation method is adopted. The simulation results are compared with the experimental results, and the key parameters of material development were obtained. Two different types of anti-differential disturbance concrete are developed by adopting test equipment based on vertical shaking table. In addition, the standard construction process are proposed as well, which is verified by the application of anti-differential disturbance concrete in the field test section.

Based on the field test of the real widened bridge project, different types of anti-differential distribute concrete with resilient and ductile performance have been developed by combining laboratory vibration test with field application and optimization. In addition, a complete set of technology for splicing the widened bridge without interrupting traffic is proposed as well.

2 VIBRATION CHARACTERISTICS OF WIDENED BRIDGE

2.1 *Analysis of bridge vibration characteristics based on field test*

In order to obtain the key parameters for the development of anti-disturbance concrete, the vibration characteristic of widened bridges have been tested. The typical case of K3387 +424.551 Middle Bridge, Shenhai Freeway is selected as shown in Figure 2. The key parameters of vibration amplitude and frequency at the splicing of the widened bridge were obtained without interrupting traffic (Răcănel, 2021).



Figure 2. Field test of bridge vibration characteristics.

The sections of *l*/4-span, *l*/2-span and 3*l*/4-span were monitored for 48 hours. The peak value of dynamic deflection and acceleration are presented in Figure 3. For the *l*/2-span section with the most unfavorable deformation, the maximum dynamic deflection is 1.085 mm, and the maximum acceleration is 1.302m/s^2. While the average value of these two parameters are 0.564 mm and 0.487m/s^2, which is much smaller than the peak value. In addition, it can be also obtained from the field test that the first-order natural frequency of the tested bridge is 8.496 Hz.

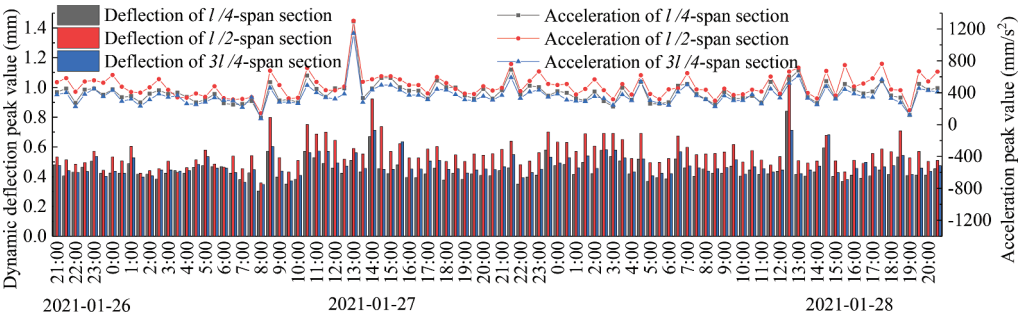


Figure 3. The peak values of bridge vibration characteristics within 48 hours.

2.2 *Vehicle-bridge coupling vibration simulation based on random traffic flow*

The cellular automaton is introduced to microscopic simulation of vehicles (Huang, 2019). By considering the traffic rules, the operation characteristics of vehicles on the bridge can be realized.

On the basis of vehicle-bridge coupling vibration theory, the mass, damping and stiffness matrices have been applied to the vehicle cell extracted from the microscopic simulation model of vehicles. The dynamic equation of vehicle-bridge coupling can be solved by the Newmark-β method. By introducing the data of random traffic flow into the dynamic analysis model, the vehicle-bridge coupling vibration simulation based on random traffic flow can be realized. The basic analysis process of bridge-bridge coupling vibration simulation is shown in Figure 4.

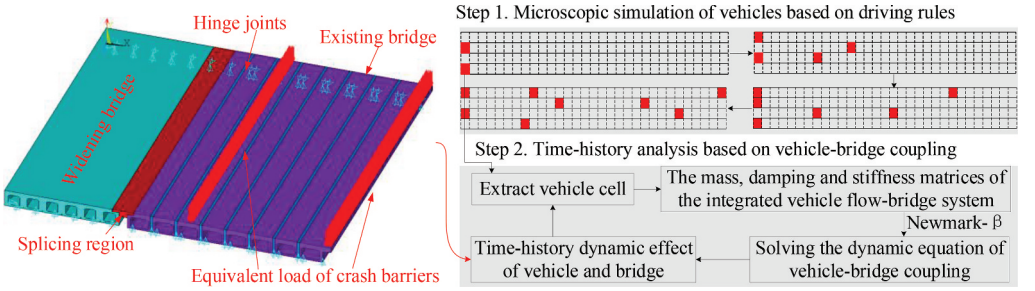


Figure 4. Basic analysis process of bridge-bridge coupling vibration.

In order to reduce the difference between the actual stiffness and the theoretical value of the widened bridge caused by factors such as materials and construction, the simulation results of vehicle-bridge coupling vibration are compared with the field test results. The reliability of the proposed random traffic flow-bridge coupling vibration simulation method can be verified. Different time periods of results are compared as shown in Figure 5. From the comparison results, it can be seen that the simulation results are in good agreement with the test data.

In the case of daytime traffic (from 8:00 to 20:00), the existing old bridge shows obvious vibration deflection characteristics. However, in the case of nighttime traffic (from 0:00 to 8:00 and from 20:00 to 24:00), the intensity of vibration deflection of the existing old bridge is reduced, and the peak vibration deflection is slightly reduced as well.

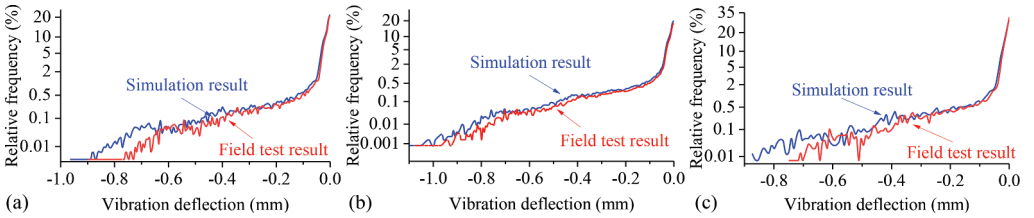


Figure 5. Simulation result of the bridge-vehicle coupling vibration: (a) 0:00 ~ 8:00, (b) 8:00 ~ 20:00, (c) 20:00 ~24:00.

3 DEVELOPMENT OF ANTI-DIFFERENTIAL DISTRIBUTE CONCRETE

According to the vibration characteristic of widened bridge, different types of anti-differential distribute concrete have been developed: the type of resilient and the type of ductile. The anti-differential disturbance resilient concrete is suitable for the case of that the bridge span is less than 20 m and the vibration amplitude is shorter than 6 mm. The anti-differential disturbance ductile concrete is suitable for the case of that the bridge span is in range of 20 m to 40 m and the vibration amplitude is less than 10 mm.

3.1 *Development of anti-differential disturbance resilient concrete*

The experimental device was designed based on the vertical shaking table as presented in Figure 6. The specimen is installed on the static side and the vibration side respectively. The shaking table is opened before the anti-differential disturbance resilient concrete pouring in the specimen mold, so that the concrete in the specimen can be divided into three segments during the condensation hardening process.

The proposed anti-differential disturbance resilient concrete is mainly composed of customized powder, fine sand, gravel, customized admixture, water and high-strength steel fiber. The customized powder is conducive to the formation of early strength of materials. The proposed concrete can be denser by increasing the sand ratio in the mix ratio. In addition, the tensile strength can be significantly improved by adding steel fiber.

The most obvious material characteristic is that the proposed anti-differential disturbance resilient concrete has the ability of reducing the time difference between initial setting and final setting to 95 min. Compared with other traditional products that directly reducing the initial setting or final setting time, the proposed concrete can reduce the time to be disturbed.

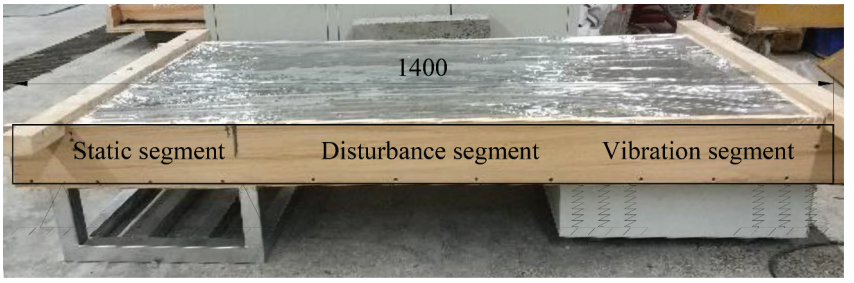


Figure 6. Test setup for the development of anti-differential disturbance resilient concrete.

3.2 *Development of anti-differential disturbance ductile concrete*

Similarly, the experimental device for the development of anti-differential disturbance ductile concrete is also designed based on the vertical shaking table as presented in Figure 7. The specimen can be divided into two precast blocks and one joint segment. The precast block is made of normal concrete of C50 in advance, and the joint segment is poured with the anti-differential disturbance ductile concrete during the test.

The proposed anti-differential disturbance ductile concrete is mainly composed of customized powder, quartz sand, coal fly ash, water reducing admixture and customized polypropylene fiber. The proposed anti-differential disturbance resilient concrete has excellent fracture resistance ability. It can improve the interfacial adhesive performance between the splicing joint and the widened bridge. The tensile properties of the splicing joint can still be maintained after vibration disturbance.

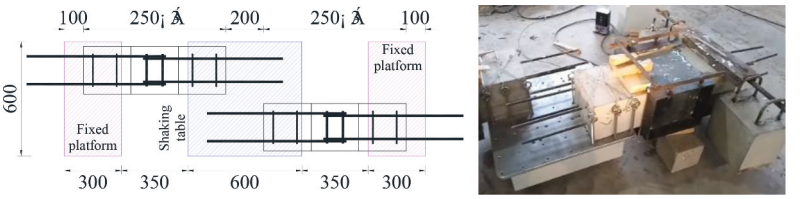


Figure 7. Test setup for the development of anti-differential disturbance ductile concrete (unit: mm).

4 PROPOSAL OF STANDARD CONSTRUCTION PROCESS

4.1 *General requirement*

Before the application of the anti-differential disturbance concrete, the technology index should be checked firstly and then determined the suitable concrete type. The checking process is listed as follows:

Firstly, the on-site monitoring of the deflection difference between the existing old bridge and the widening new bridge should be carried out. The monitoring time should not be less than 48 hours. The maximum difference of deflection and the frequency of its occurrence should be included in the collected data. And the maximum deflection difference with frequency greater than 5 % is adopted as the material selection standard.

Secondly, temporary control measures should be also proposed according to the actual needs of the splicing construction. Such as closing the lane close to the splicing joint, limiting the speed of the vehicle, limiting the weight of the vehicle, and temporarily connecting the existing old and widening new bridges. All these measures can reduce the deflection between the existing old bridge and the widening new bridge during the splicing construction process.

In addition, the anti-differential disturbance concrete selected should fit the following requirement as well. The anti-differential disturbance concrete can still maintain high material properties after the differential disturbance. The retention rate of tensile strength and splitting strength should not less than 80% of the corresponding strength under standard conditions, which should also greater than the design value.

4.2 *Construction scheme design*

Before the splicing construction, the special construction scheme for the splicing joint should be formulated in advance according to construction environment, volume of pouring concrete and so forth. The special scheme should include following contents: the construction preparation, the splicing construction method, and the construction quality inspection and evaluation method.

When making the scheme of construction preparation, the construction schedule needs to be determined according to the construction plan. The use plan of construction machinery and labor needs to be formulated. The construction machinery should be organized and provided on schedule. The assembly-line method for the splicing construction of widened bridge is recommended as follows.

- The splicing construction process should be divided into different construction stages.
- In each construction stage, the dominant construction steps should be determined. And the professional construction staff should be organized.
- The splicing construction project should also be divided into several segments.

- Calculate the flowing rhythm and ensure that it can meet the period requirements of the splicing construction and the resource constraints of the existing investment. The flowing rhythm can be obtained according to Equation 1.

$$t = p/R \cdot b \tag{1}$$

where is p is the number of labor or machinery required in a certain construction segment; R is the number of labor or machinery available; b denotes the number of teams that can participate in the construction in one day; and m represents the number of construction stages divided according to the assembly-line method.

- Calculate the flow spacing between different construction stages.

In addition, the splicing construction method includes the methods of the reinforcement connection, the concrete mixing, the concrete pouring, the concrete maintenance. In which, the concrete mixing method should be designed according to mixed design of anti-differential disturbance concrete. And the weighing scheme, mixing feeding sequence scheme, mixing time control method can be determined. In addition, the concrete pouring method should include the control of vibration time and vibration sequence.

4.3 *Construction preparation*

The existing old should be strengthened before the splicing construction operation, and the widening new bridge should also complete the construction of the main structure according to the design document.

If the design height of the existing old bridge is lower than the design document after widening, the existing old bridge should be jacked up in advance. When the splicing joint is completed, the height of the widened bridge cannot be adjusted any more.

Before the splicing construction operation, the cast-in-place work of the integral layer of the existing old bridge and the widening new bridge needs to be completed in advance. When the main girder structure is T-shape beam, it is necessary to connect the diaphragm between the existing old and widening new bridges in advance.

Each interface of the splicing joint needs to be chiseled and cleaned in advance. The interface that needs to be disposed is presented in Figure 8, it mainly including three parts: the side of the integrated layer (1), the top and side surface (2 and 3) of boundary beam connected to the splicing joint.

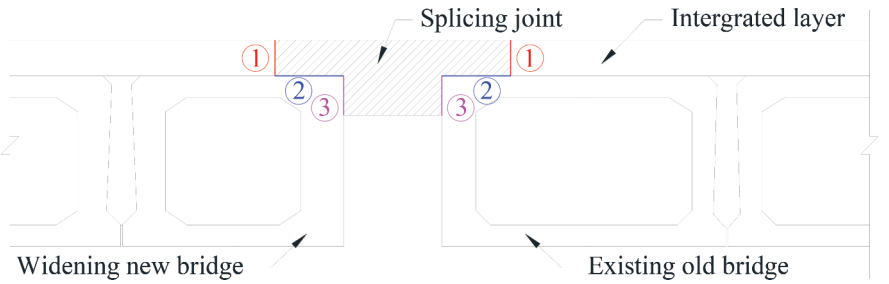


Figure 8. Interfaces need to be treated.

4.4 *Splicing construction operation*

4.4.1 *Reinforcement and formwork project*

The reinforcement should be connected before pouring the anti-differential disturbance concrete. The lap length of the reinforcements in the splicing joint should meet the relevant requirements of the design document. In particular, it is necessary to use the method of planting to connect the reinforcements lapped with the boundary beam of the existing old bridge.

The support of the bottom formwork of the splicing joint should be completed in advance according to the design document. The following requirements should be followed:

Firstly, the formwork should be located accurately.

Secondly, the formwork should have sufficient strength, stiffness and stability. To prevent the displacement of the formwork during pouring concrete, it should be able to withstand various loads generated during the construction process.

Thirdly, after the installation of the formwork is completed, its size and position should be checked according to the design document.

Finally, measures to prevent slurry leakage can be adopted at the joint position between the formwork and the concrete. There should be no slurry leakage between the girders and the formwork.

4.4.2 *Concrete project*

The construction of anti-differential disturbance concrete for widening bridges should be carried out in the following order: verification of mix ratio and operation process before construction → concrete mixing → concrete pouring → concrete vibration → concrete maintenance.

The mix ratio of anti-differential disturbance concrete should be verified before splicing construction. The anti-differential disturbance concrete that does not meet the design documents should not be adopted. However, the design mix ratio of concrete can be adjusted appropriately according to the properties of raw materials, so that the design requirements of concrete performance can be met.

When mixing anti-differential disturbance concrete, raw materials should be put in accordance with the prescribed order: fine aggregate → steel fiber → partial mixing water → coarse aggregate → powder → admixture → residual mixing water. It is advisable to mix fine aggregate and steel fiber uniformly without water, and the mixing time should not less than 60s. Then, add the coarse aggregate and mix them with part of mixing water, and the mixing time should be 30s to 60s. Finally, coarse aggregate and admixture were added and mixed with residual mixing water until uniform, and the mixing time should be about 120s.

The transportation distance and time from the anti-differential disturbance concrete mixing site to the pouring site should be controlled to prevent the surface water loss and hardening of the anti-differential disturbance concrete during transportation.

It is advisable to choose the pouring time reasonably. Combined with the hardening characteristics of anti-differential disturbance concrete, the time period from initial setting to final setting of concrete should be consistent with the period of relatively small traffic flow on the widened bridge.

During the vibration operation of anti-differential disturbance concrete, the uniformity and compactness of concrete should be controlled. There should be no obvious under-vibration and over-vibration, and the vibration operation time should be controlled within 30s at each point.

After the completion of the anti-differential disturbance concrete pouring, it should be covered in time to reduce the water loss of the joint concrete. After the final setting of anti-differential disturbance concrete, continuous wet curing should be started immediately, and the curing process should last at least 48 hours.

After 7 days of continuous wet curing, the concrete in splicing joint can fully reach the design strength state. Before removing the template, it is still necessary to measure the vertical deformation difference on both sides of the splicing joint. When the deformation difference is less than 1mm, it can be considered that the concrete in the joint can work together with the widened bridge and the new bridge.

4.5 *Construction quality inspection and performance verification*

4.5.1 *Construction quality inspection method*

The construction quality inspection scheme should be proposed according to the material performance and the vibration characteristic of the existing old bridge. The appearance quality and concrete strength of the anti-differential disturbance concrete should be checked after the maintenance of splicing joint.

In the appearance quality inspection, following items should be include: the size of the splicing joint after the construction, the surface smoothness of the splicing joint concrete, the apparent quality of the concrete, the crack distribution of the joint concrete, etc. For the top surface of the splicing joint, concrete cracking is not allowed. While for the interface between the splicing joint and the integral layer, the number of cracks per span is not allowed to exceed one, the crack width is not allowed to exceed 0.15 mm, and the crack length is not allowed to exceed 1/10 of the span.

The strength detection method of the anti-differential disturbance concrete mainly include the following three kinds: the laboratory method with standard specimens, the direct measurement of on-site concrete strength of the splicing joint, and the indirect measurement of specimens cured under the same conditions.

4.5.2 *Joint performance verification method*

The performance of anti-differential disturbance concrete in widened joints can be verified by the method of curing model specimens under the same conditions. The model specimen contains three parts: the precast blocks A and B, and the joint segment C, as shown in Figure 9. The precast blocks A and B should be prepared before splicing the joint and made of the same standard concrete as widened bridge. The reinforcement with the same standard as that in the splicing joint of widened bridge should be used in the joint segment C.

Before pouring the concrete of the joint segment C, the interface between the precast block and joint segment should be treated in the same way as that of the widened bridge. Before pouring the splicing joint of the widened bridge, the precast blocks A and B should be installed on the existing old bridge and the widening new bridge in advance. The formwork of the joint segment C should be installed before pouring the splicing joint of the widened bridge.

When pouring the concrete of the splicing joint of the widened bridge, the joint segment C should be poured synchronously. The same maintenance condition is adopted for the joint segment C, and the formwork can be removed after 7 days of maintenance. After 28 days of maintenance, the connectors between the model specimens and the widened bridge can be removed. Then, the model specimens can be tested with four-point flexural loading test to verify the material performance of anti-differential disturbance concrete and mechanical properties of the splicing joint.

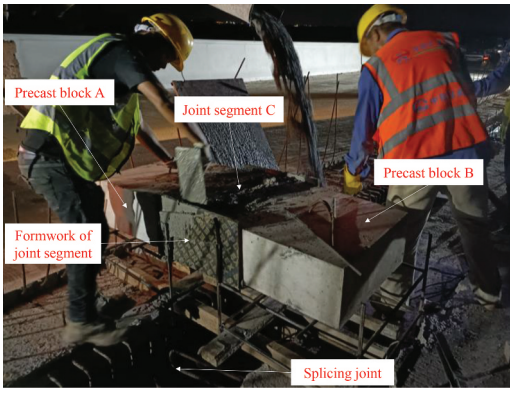


Figure 9. Model specimens cured under the same conditions of the splicing joint.

5 VERFICATION OF FIELD TEST SECTION

The typical case of K3387+424.551 Middle Bridge, Shenhai Freeway is selected as the field test section. According to the optimized on-site mix ratio of anti-differential disturbance concrete, the splicing joints are operated without interrupting the traffic. The pouring process and performance are presented in Figure 10.

The anti-differential disturbance resilient concrete was adopted in this field test section. The mix proportion of the adopted concrete is shown as follows: 400- 500 pieces of customized powder, 700-900 pieces of fine sand, 900-1200 pieces of gravel, 2.5-7.5 pieces of customized admixture, 135-180 pieces of water and 25-75 pieces of high-strength steel fiber. It is a kind of type of performance-improving concrete material, in which steel fiber was added to increase the anti-disturbance performance. The designed standard of this concrete is still the Grade of C50, with designed compressive strength of 50 MPa.

The concrete standard test block was made and cured under the same conditions on site. The compressive strength of the standard test blocks was tested, and the test results are listed in Table 1. It can be learnt from the test results that the compressive strength of adopted anti-differential disturbance resilient concrete can meet the design requirement of material performance.

Table 1. Tested compressive strength of the standard test block.

No.	Tested compressive strength	Ratio to designed compressive strength
HY-3235	57.8 MPa	116 %
HY-3282	58.7 MPa	117 %
HY-3382	67.0 MPa	134 %
HY-3590	56.0 MPa	112 %
HY-3676	60.7 MPa	121 %

After the application of anti-differential disturbance resilient concrete in the field test section, drilling core sampling and core sample CT scanning are carried out on the splicing joint (Liu, 2017). According to the scanning results, the crack depth of centerline of the splicing joint is less than 1 mm. And there is no crack appears on the interface between the splicing joint and bridge girder. There is no aggregate subsidence in the splicing joint. The distribution of steel fibers in the centerline of splicing joint is relatively uniform, and there is no obvious hole or gap in the core sample.

The material properties are verified by the application in field test section and the proposed anti-differential disturbance concrete is optimized. The complete set of construction technology and quality assurance technology of the anti-difference disturbance concrete are established.



(a) (b) (c)

Figure 10. Field test section of anti-differential disturbance concrete: (a) before pouring concrete; (b) concrete pouring and vibrating; (c) after maintenance.

6 CONCLUSION

The anti-differential disturbance concrete was developed for widening bridge, and the material application based on field test section was carried out. The main conclusions are as follows:

1. Based on the field vibration test of existing old bridges, the vibration amplitude and frequency are defined. The random vehicle-bridge coupling vibration simulation method is

introduced and verified the reliability of simulation model by comparing with the test results.
2. Two kinds of anti-differential disturbance concrete, resilient type and ductile type, are developed based on the on-site vibration test, laboratory material test. The proposed concrete can be applied to widened bridges with different span lengths and vibration amplitudes.
3. The material performance of anti-differential disturbance concrete is verified by the implementation of the test section, the standard construction process is summarized. The complete set of construction technology and quality assurance technology of the anti-difference disturbance concrete are established.

ACKNOWLEDGMENTS

This research was funded by the Science and Technology Plan Project of Guangdong Province (Grant No. 2021B1111610002) and the Key Technology Research Project of Expressway Reconstruction and Extension in Guangdong Province (Grant No. MJKJ-SY-001).

REFERENCES

Chen, D.H.; Zhu, C.Y. & et al. 2023. Influence of Random Vehicle–Bridge Coupling Vibration on the Anti-Disturbance Performance of Concrete Materials. *Applied Sciences* 13(13), 7584.

Cui, C.J.; Chen, A.R. & et al. 2019. Fatigue life estimation for suspenders of a three-pylon suspension bridge based on vehicle–bridge-interaction analysis. *Materials* 12, 2617

Huang H.Y.; Zhou J.Y. & et al. 2019. Effects of revised toll-by-weight policy on truck overloading behavior and bridge infrastructure damage using weigh-in-motion data: a comparative study in China. *Advances in Civil Engineering*, 5910463.

Liu, S.J.; Yu, L. & et al. 2021. Effect of vehicle–bridge coupled vibration on the performance of magnesium phosphate cement repair materials. *Materials* 14, 7743.

Liu, X.F.; Wang, J. F. & et al. 2017. Pore-scale characterization of tight sandstone in Yanchang Formation Ordos Basin China using micro-CT and SEM imaging from nm- to cm-scale. *Fuel* 209: 254–264.

Jeong, Y.; Kim, W.S. & et al. 2018. Bridge inspection practices and bridge management programs in China, Japan, Korea, and U.S. *Journal of Structural Integrity and Maintenance* 3(2), 126–135

Mahboubi S.; Kioumarsi M. 2021. Damage assessment of RC bridges considering joint impact of corrosion and seismic loads: a systematic literature review. *Construction and Building Materials* 295, 123662

Răcănel, I.R.; Răcănel, V.D. 2021. Probabilistic estimation of the strength capacity of existing concrete bridges. *Structures* 33, 769–775

Wang, S.F.; Yu, L. & et al. 2022. Effect of steel fiber distribution on the mechanical properties of UHPC caused by vehicle-bridge coupling vibration. *Composites Part B* 245, 110201.

Yang, Z.H.; Liu, S.J. & et al. 2021. A comprehensive study on the hardening features and performance of self-compacting concrete with high-volume fly ash and slag. *Materials* 14, 4286.

Zeng, G.S.; Shi X.F. & et al. 2023. Material performance of anti-differential disturbance concrete based on the vehicle–bridge coupling vibration theory. *Buildings* 13(06), 1486.

Zhang, X.D.; Liu, S.G. & et al. 2019. Effects of vehicle-induced vibrations on the tensile performance of early-age PVA-ECC. *Materials* 12, 2652.

Zhang, X.D.; Liu, S.G. & et al. 2019. Effects of traffic vibrations on the flexural properties of newly placed PVA-ECC bridge repairs. *Materials* 12, 3337.

Zhou J.Y.; Li, T. & et al. 2020. Safety assessment of widened bridges considering uneven multilane traffic-load modeling: case study in China. *J. Bridge Eng*. 25(9), 05020008

Bridge Maintenance, Safety, Management, Digitalization and Sustainability – Jensen, Frangopol & Schmidt (eds)
© 2024 The Author(s), ISBN 978-1-032-77040-6
Open Access: www.taylorfrancis.com, CC BY-NC-ND 4.0 license

Safety performance evaluation of suspension bridge tunnel anchor structure

W. Dou
Anhui Transport Consulting and Design Institute CO., LTD., Anhui, China

Z.Q. Liu & J. Song
Tongji University, Shanghai, China

ABSTRACT: The construction of tunnel-anchored suspension bridge by using rock slope in mountainous area has significant economic benefits. However, uncertainties in lithology and geological conditions have high risks to the long-term performance of bridges. Based on Xiaochuan Bridge in Xin 'anjiang, Huangshan City, the research on tunnel anchorage structure is carried out. Using the three-dimensional fast Lagrangian analysis program, the tunnel anchor excavation and the backfill of the anchor plug body are simulated to clarify the stress characteristics and ensure the construction safety. Then, the influence of rock mass parameters on the stability of the bridge is analyzed. Finally, the feasibility of anchor measures to solve the instability risk is evaluated. This study provides an analysis method for the safety risk assessment of the tunnel anchor of the suspension bridge, which can be used as a reference for similar projects.

1 INTRODUCTION

As the bridge type with the strongest spanning capacity, the suspension bridge is often used for long-span bridges in mountainous areas. The tunnel anchorage mainly transmits the main cable force to the anchor plug body through the steel bundle, and transmits the force to the mountain body by means of the bonding between the anchor body and the surrounding rock. This structure can give full play to the connection between the anchor body and the surrounding rock and the mountain, and improve the bearing capacity of the bridge (Zhao, H.Q et al. 2014).

At present, many scholars have studied the structure and stability of tunnel anchors (He, S. et al. 2023; Han, Y.F. et al. 2023; Seo, S. et al. 2021; Xu, D.D. et al. 2021), such as: mechanical analysis of super-long-span tunnel anchors; the physical model of structural failure is obtained by analyzing the mechanical behavior of tunnel anchorage. The damage of tunnel anchorage structure of suspension bridge is evaluated by scale model. In addition, there are studies on the interaction between the anchor plug and the surrounding rock, and the reasonable action form of the structure is obtained (Xia, Q.Y.et al. 2021; Liu, S.W et al. 2020; Li, N.N. et al. 2020; Wang L.B. et al. 2019).

However, the uncertainty of mountain strata and geology has a great influence on the construction and use stage of the bridge. Therefore, it is still necessary to analyze the overall structural stability of the Xiaochuan Bridge. Firstly, this paper analyzes the structural stability and ensures the construction safety by simulating the two stages of tunnel anchor excavation and anchor plug backfill. Secondly, it analyzes the structural stability of the use process, and finally checks whether the structure meets the requirements of the specification under overload.

DOI: 10.1201/9781003483755-23

2 ENGINEERING SITUATIONS

The tunnel anchor of Xiaochuan Bridge in Xin ‘anjiang mainly includes four parts: open-cut tunnel, saddle chamber, anchor plug body and rear anchor chamber. The open-cut tunnel is 9m long, the saddle chamber is 16.77m long, the length of the anchor plug is 24m, the length of the rear anchor chamber is 2m, the axis angle of the anchor plug is 40 °, and the front and rear anchor surfaces are 6.7m × 8m and 9m × 12m (width × height) respectively. Two tunnel anchor structures are set on one side of the bridge. The distance between the two tunnel anchor axes is 13.5 m, and the distance between the nearest soil of the rear anchor chamber is 4.5 m. The structure of structure is shown in Figure 1.

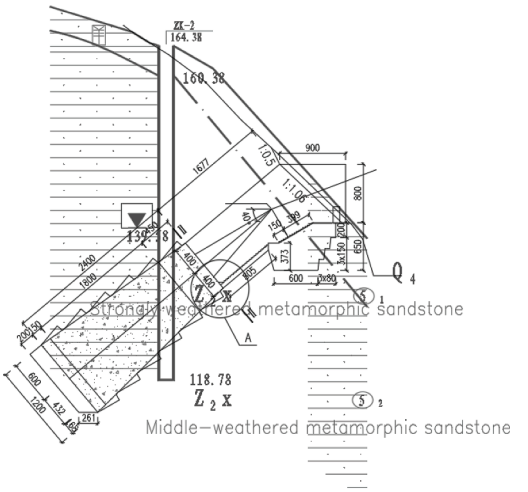


Figure 1. Anchorage structure.

3 CALCULATION METHOD AND CALCULATION MODEL

3.1 *Rationale*

FLAC3D is a three-dimensional fast Lagrangian analysis program. It is a numerical analysis method based on explicit finite difference method. It can simulate the three-dimensional structural mechanical behavior of rock and soil materials, especially the plastic rheological properties when reaching the yield limit. It is more convenient and effective in simulating nonlinear problems, large deformation problems or dynamic problems. Therefore, this simulation uses FLAC3D6.0 to analyze the stability of tunnel anchor excavation and the stress of tunnel anchor (Mahmoudi, M., & Rajabi A.M. 2023; Li, H.T et al. 2023; Xing, B. et al. 2021; Zhu, D.P. et al. 2011).

The Mohr-Coulomb criterion is essentially a shear stress strength criterion, which reflects the strength characteristics of rock more comprehensively, and can make good use of the characteristic that the tensile strength of rock is far less than the compressive strength. According to the results of field sampling and rock mechanics experiments, when the load reaches the strength limit, the rock mass is destroyed. During the post-peak plastic flow process, the residual strength of the rock mass gradually decreases with the development of deformation. Therefore, the Mohr-Coulomb yield criterion is used in the calculation to judge the failure of rock mass.

3.2 *Modeling*

The size of the model is determined to be 150m × 120m × 120m (x × y × z), and the orientation of the tunnel anchor is x-axis. Constraints are applied around the model, which is fixed in the normal direction, fixed constraints are applied at the bottom, and a contact surface is set between

the anchor plug body and the rock mass. Because the tunnel anchor is a shallow buried tunnel, its tectonic stress field is very small and can be almost ignored, so only the effect of gravity stress field is considered in the simulation analysis. The calculation model and initial stress of tunnel anchor are shown in Figure 2 and Figure 3.

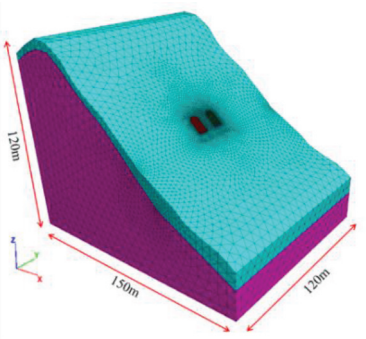


Figure 2. Simulation model.

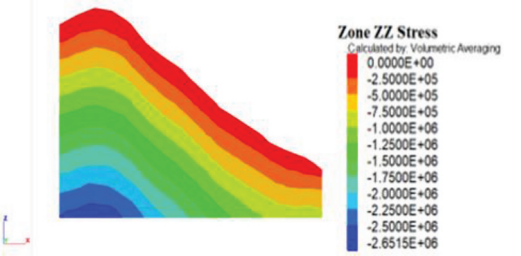


Figure 3. Initial vertical stress cloud diagram.

3.3 *Design conditions*

The location of tunnel anchor is mainly two kinds of strong and medium weathered metamorphic sandstone. Combined with the engineering geological reference materials, the soil parameters of the tunnel anchor area, the C40 and C30 concrete used in the anchor plug body, the scattered saddle foundation part and the concrete lining layer are obtained. The geological parameters are shown in Table 1.

Table 1. Calculation of physical and mechanical parameters of materials.

lithology	density / Kg/m3	deformation modulus /GPa	poisson's ratio	cohesion / KPa	internal friction angle /°	tensile strength / MPa
Strongly weathered metamorphic sandstone	2000	0.8	0.38	180	25	0.39
Middle-weathered metamorphic sandstone	2300	3.0	0.3	500	33	0.77
C30 concrete	2400	3.0	0.2	—	—	—
C40 concrete	2500	3.25	0.2	—	—	—

4 SIMULATION OF TUNNEL ANCHOR CONSTRUCTION

The excavation process of tunnel anchor is complicated. In order to ensure the stability of tunnel anchor excavation, the left and right tunnel anchors will be excavated at the same time based on the most unfavorable situation. This simulation is divided into two states: no support after excavation and timely support after excavation.

4.1 *Analysis of unsupported after excavation*

4.1.1 *Displacement analysis*

The tunnel anchor chamber is excavated without support, and the vertical displacement cloud diagram of the tunnel is shown in Figure 4. Under the condition of no support, with the

deepening of excavation, the settlement increases first and then decreases, and the maximum settlement at the top of the anchor body is 2.19 mm. The maximum uplift displacement at the bottom of the tunnel anchor is 2.98 mm, and the vertical displacement is parabolic, which expands from the excavation face to the rock mass.

The bottom of the front anchor chamber moves due to the weight of the concrete, and the maximum displacement is 0.53 mm. Due to the extrusion of the soil at the top of the rear anchor chamber, the displacement in the negative direction of the X axis is generated, and the maximum value is 0.73 mm. The displacement in the Y direction is mainly concentrated in the tunnel anchor chamber near the rock mass side, and the displacement of the middle rock mass is small, with a maximum displacement of 1.1 mm.

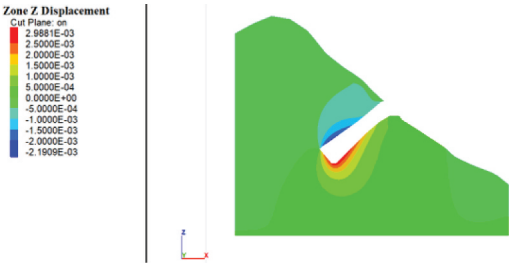


Figure 4. Displacement cloud diagram after tunnel anchor excavation.

4.1.2 *Stress analysis*

After the excavation of the tunnel, the stress of the rock mass has changed significantly. The excavation face is in a low pressure state due to the free boundary. After excavation, the rock mass is still in a state of compression, and the local stress concentration occurs at the top corner of the rear anchor chamber. The maximum principal stress is − 0.6 ~ − 0.8MPa (compressive stress), and the minimum principal stress is − 2.0 ~ − 3.0MPa (compressive stress). Because the rock mass is in a state of compression, there is obvious stress concentration in the vault section of the rear anchor chamber. The minimum principal stress value is greater than other parts, indicating that when the excavation is carried out to the bottom position, it is necessary to strengthen the support of the surrounding rock at the top.

4.2 *Analysis of timely support after excavation*

4.2.1 *Displacement analysis*

Support is carried out in time after excavation. The maximum vertical displacement settlement is 1.46 mm, which is 0.73 mm lower than that of unsupported excavation, about 33 %. In addition, the bottom of the tunnel anchor is uplifted and concentrated in the position of the anchor plug and the rear anchor chamber. The maximum uplift is 2.35 mm, which is slightly larger than the vertical settlement displacement of the top of the tunnel. Compared with the unsupported state, the uplift displacement is reduced by 0.63 mm, about 21.14 %.

4.2.2 *Stress analysis*

After excavation, the rock mass is still under compression, which is similar to the unsupported state. Local stress concentration occurs at the top corner of the rear anchor chamber. The maximum principal stress is − 0.4 ~ − 0.8MPa (compressive stress), and the minimum principal stress is − 1.6 ~ − 2.4MPa (compressive stress). Compared with the unsupported state, the stress is reduced.

The plastic zone of the intermediate rock mass is less, and the area of the plastic zone is greatly reduced compared with the unsupported state. It is mainly concentrated in the contour position of the rear anchor chamber and the anchor plug body, and it is basically in the

shear flow plastic state, indicating that the intermediate rock mass of the two tunnel anchors is not damaged.

4.3 *Anchor plug backfill simulation*

4.3.1 *Analysis of rock mass displacement after backfilling*

After the pouring of the anchor plug body is completed, it is found that there is still displacement at the top and bottom of the tunnel. The weight of the anchor plug body has an inhibitory effect on the uplift at the bottom of the tunnel. The uplift changes from 2.35 mm to 2.01 mm, and the maximum settlement of the rock mass is 1.75 mm. After the backfill of the anchor plug, the subsidence of the surrounding rock at the top increases, and the maximum increase is more than 0.2 mm. The vertical displacement is still parabolically diffused from the top and bottom of the anchor plug to the surrounding soil. Due to the weight of the anchor plug body in the X direction, there is a more obvious displacement in the negative direction of the X axis, and the displacement is small, which is 0.3mm.

4.3.2 *Analysis of rock mass stress after backfilling*

The rock mass is still in a low stress state after the backfill of the anchor plug body, and there is no big change compared with the previous stage. The maximum principal stress range of the rock mass is-0.823 MPa ~ 0.195 MPa, and the minimum principal stress range is-0.005 MPa ~ 2.6 MPa. The backfill of the anchor plug body has little effect on the stress distribution of the surrounding rock. In addition, due to the squeezing effect of backfill, the local shear stress concentration at the bottom of the rear anchor chamber is intensified.

5 STABILITY AND BEARING CAPACITY ANALYSIS

5.1 *Analysis of the impact of rock mass strength on stability*

5.1.1 *Without considering the reduction of rock mass*

Under the action of design load, the overall displacement of the longitudinal section of the surrounding rock mass is small. The maximum displacement is 0.42 mm at the foundation of the splay saddle. The displacement change is mainly gradually decreasing from the anchor plug to the surrounding rock mass. The vertical displacement along the Z axis mainly occurs at the bottom of the anchor plug, and the displacement along the X axis mainly occurs at the top of the anchor plug.

Due to the interaction between the steel strand and the anchor plug body, local compressive stress appears at the bottom of the anchor plug body, and large tensile stress is generated at the contact surface between the two sides of the anchor plug body and the rock mass. The change of the minimum principal stress cloud diagram of the whole model is small, and the whole rock is in a state of compression. The maximum principal stress range is-0.82 MPa ~ 2.35 MPa, and the minimum principal stress range is-0.006 MPa ~ -2.64 MPa.

5.1.2 *Considering the reduction of rock mass*

To simulate the loosening effect of blasting construction on surrounding rock, the strength of rock mass is reduced in the stage of main cable load application, and the parameters such as modulus and tensile strength are reduced according to the proportion of 10 %, 20 % and 30 %. The maximum displacements of rock mass from non-reduction to reduction of 10 %, 20 % and 30 % are 0.32 mm, 0.46 mm, 0.53 mm and 0.60 mm, respectively. The variation increases gradually, and the maximum displacement appears in the foundation part of the scattered cable saddle, which bears the force of the main cable perpendicular to the foundation of the scattered cable saddle. The displacement cloud diagrams under different reduction strengths are similar, and they are all parabolically diffused outward along the central axis of the anchor plug body, as shown in Figure 5.

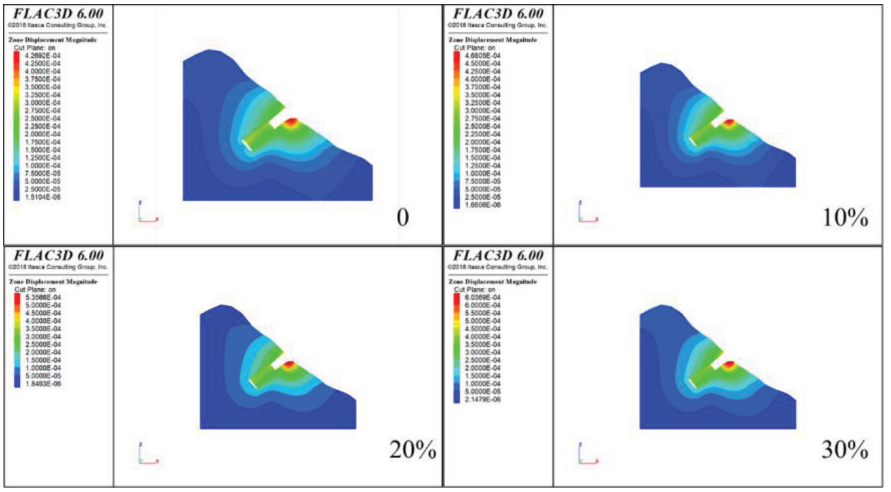


Figure 5. Displacement cloud diagram of different reduction strength (longitudinal section).

5.2 *Analysis of the impact of anchor rods on stability*

On the basis of the original concrete layer, bolt and steel arch support are added. The bolt adopts Φ25 hollow grouting bolt with a length of 3m, and the arrangement is @ 60 × 80cm. The steel arch adopts L16 I-beam with a longitudinal spacing of 60cm.

5.2.1 *Analysis of structure under design load*

Under the action of design load, the reduction of rock mass strength and rock mass strength parameters are reduced by 10 %, 20 % and 30 % respectively without considering the reduction of rock mass strength after the application of anchor rod. The displacement structure shows that the displacement changes of the two are small, both within the range of a few millimeters. In the case of strength reduction of 30 %, the maximum displacement of the two is consistent, both of which appear at the position near the top of the anchor chamber after the tunnel anchor, and the maximum value is 0.898 mm.

According to the failure of the plastic zone, it can be seen that after the replacement of the support scheme, the plastic zone has a certain reduction. Compared with the previous scheme, the plastic zone changes little, and after the strength reduction is more than 20 %, the plastic zone area is basically unchanged, and the main failure mode is shear failure.

5.2.2 *Analysis of stability in limit state*

According to the requirements of the suspension bridge design specification, the anti-slip stability of the anchor body is required to be 2.0, and the stability of the surrounding rock is required to be 4.0. Therefore, considering the application of 4.0 times the main cable force, the strength of the rock mass is not reduced, and the stability of the tunnel anchor is investigated.

Under the action of 4P limit state, the maximum total displacement of rock mass is 1.73 mm, and the maximum horizontal displacement is 1.38 mm. The vertical displacement mainly occurs at the bottom of the tunnel anchor and the foundation of the scattered cable saddle. The foundation of the scattered cable saddle sinks and the bottom of the tunnel anchor arches.

Under the action of 4P load, the plastic zone mainly appears at the bottom corner of the top of the bottom surface of the tunnel anchor chamber, and there is a slight plastic zone on both sides of the rear anchor chamber, and there is no large plastic zone damage and penetration.

5.3 *Analysis of ultimate load stability of tunnel anchor*

By applying different multiples of main cable load to the tunnel anchor, the deformation of the tunnel anchor under the action of 1P (design load), 3P (overload 3 times), 5P (overload 5

times) and 10P (overload 10 times) is compared. The deformation cloud diagram is shown in Figure 6.As the load increases, the overall deformation of the anchor plug body increases, and the maximum deformation occurs at the contact surface between the top of the anchor plug body and the surrounding rock. The distribution law of deformation in different load stages is basically the same, and it diffuses from the surrounding rock between anchors to both sides. The maximum displacement increased exponentially, and the displacements were 0.42 mm, 1.27 mm, 2.13 mm, and 4.27 mm, respectively.

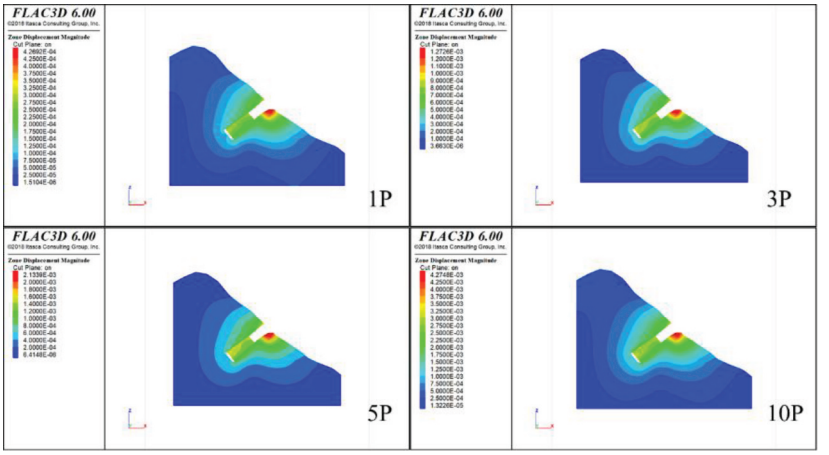


Figure 6. Displacement cloud diagram of different reduction strength (longitudinal section).

With the increase of overload, the displacement of the steel strand will also increase, and the internal compressive stress value of the anchor plug will also increase, and the steel strand at the free end will be elongated, so that it will have a large deformation difference with the anchor plug. With the increase of the depth of the steel strand, the deformation of the joint will gradually decrease. The maximum deformation of the steel strand under the load of 1P, 3P, 5P and 10P is 3.2cm, 9.0cm, 16.2cm and 32cm respectively, and the minimum deformation of the anchorage section is 1.4cm, 4.3cm, 7.3cm and 14.5cm respectively.

6 CONCLUSION

By fully utilizing natural resources to build bridges, ecological harmony can be achieved. However, the uncertainty of geological conditions can bring safety risks. Therefore, a study was conducted on an anchor suspension bridge in a certain tunnel. Through the analysis of the structural stability in the process of excavation and backfilling of tunnel anchor, the following conclusions are drawn:

Under the condition of no support, the displacement change of the top of the tunnel anchor mainly occurs at the top of the anchor plug body. With the deepening of excavation, the settlement increases first and then decreases, and the maximum settlement is 2.19 mm. The uplift at the bottom of the tunnel anchor is concentrated at the bottom of the anchor plug and the rear anchor chamber, and the maximum displacement is 2.98 mm;

Under the condition of timely support, the maximum settlement of tunnel anchor after excavation is 1.46 mm, and the maximum bottom heave is 2.35 mm. The influence range of plastic zone after excavation is small, and there is no obvious plastic penetration failure in the middle soil of the two tunnels;

The backfill pouring of the anchor plug has little effect on the deformation and stress change of the rock mass. The self-weight of the anchor plug body inhibits the uplift at the bottom of

the tunnel, from 2.35 mm to 2.01 mm, and the maximum settlement of the rock mass is 1.75 mm. The squeezing effect of the backfill of the anchor plug body leads to the intensification of the local shear stress concentration at the bottom of the rear anchor chamber;

After applying the design load of the main cable, the maximum displacement of the tunnel anchor is 0.29 mm, and the deformation of the whole rock mass extends outward in a parabolic way along the axis of the anchor plug body. Under the action of twice the design load of the main cable, there is no obvious relative deformation between the anchor plug body and the tunnel, which meets the requirement that the anti-sliding stability coefficient of the anchor plug body is greater than 2.0;

When the load is less than 4 times the design load, the structural deformation is very small. There is a small range of plastic zone inside, but there is no obvious diffusion phenomenon in the plastic zone. The displacement of the rock mass is less than 1.73 mm, which meets the requirement that the stability of the tunnel anchor cofferdam is greater than 4.0;

The overall deformation of the tunnel anchor hole area is small, and the maximum deformation does not exceed 1mm, which has good overall stability. However, the influence of bedding slope and contact between beddings is not considered in the simulation calculation. Therefore, the field investigation should be strengthened during the implementation period. If there is an interlayer or weak layer, reasonable support should be considered at the exit of the tunnel.

REFERENCES

Zhao, H. Q., He, X. J., Zhao, M. et al. (2014).On the Development and Innovation of Modern Suspension Bridge in China. Applied Mechanics and Materials(587-589), 1435–1438.

He, S. H., He, J.X., Ma, J. F., et al. (2023).Mechanical Behavior of Anchor Bolts for Shallow Super-Large-Span Tunnels in Weak Rock Mass. Materials (Basel, Switzerland)(17).

Han, Y. F., Liu, X. R., Du, L. B., et al. (2023). Physical model test on the mechanical behavior and progressive failure of tunnel-type anchorages. International Journal of Rock Mechanics and Mining Sciences.

Han, Y. F., Liu, X. R., Zhou, X. H., et al. (2023).Experimental study on the progressive failure behaviour of shallow tunnel-type anchorage in soft-rock strata using digital image correlation. Measurement.

Han, Y. F., Liu, X. R., Li, D. L., et al. (2020).Model test on the bearing behaviors of the tunnel-type anchorage in soft rock with underlying weak interlayers. Bulletin of Engineering Geology and the Environment(2), 1023-1040.

Seo, S., Lim, H., &Chung, M.(2021).Evaluation of failure mode of tunnel-type anchorage for a suspension bridge via scaled model tests and image processing. GEOMECHANICS AND ENGINEERING(5), 457-470.

Xu, D. D., Wu, A. Q., Lu, B, et al. (2021).Study on failure mechanism of tunnel-type anchorage using discontinuous deformation analysis method. IOP Conference Series: Earth and Environmental Science(3).

Xia, Q. Y., Zhu, X. G., Zhang, G. F., et al. (2021).The Improved Theory of Synergetic Action Between Anchor Support System and Surrounding Rock-I · L · 4S Mechanism Theory and Its Application in Tunnel Support Engineering. Geotechnical and Geological Engineering(5), 1-10.

Li, N. N., Zhou, Y. Q., Zhao, Y. Q., et al. (2020).Analysis of suspension bridge tunnel-type anchorage construction on the stability of surrounding rock.E3S Web of Conferences02006.

Liu, S.W., He, D. Y., & Fu, M. X. (2020).Experimental investigation of surrounding-rock anchoring synergistic component for bolt support in tunnels. Tunnelling and Underground Space Technology incorporating Trenchless Technology Research.

Wang L.B., & Shu D. Y. (2019).Static and dyna mic analysis the influence of underlying tunnel construction on surrounding rock of existing tunnel-type anchorages. IOP Conference Series: Earth and Environmental Science(2), 022048-022048.

Mahmoudi, M., & Rajabi A. M. (2023).A numerical simulation using FLAC3D to analyze the impact of concealed karstic caves on the behavior of adjacent tunnels. Natural Hazards(1), 555-577.

Li, H. T., &Zhou, L. C. (2023). Numerical Simulation and Analysis of Double Row Pile Anchor Composite Support Structure based on FLAC3D.Journal of Progress in Civil Engineering(8).

Xing, B., & Cao R. L. (2021). Evaluation on Application of Numerical Software in Stability Analysis of Tunnel Engineering. IOP Conference Series: Earth and Environmental Science(3).

Zhu, D. P., Yan, C., Hu, G. X., et al. (2011).Revival Deformation Mechanism of Hefeng Landslide in the Three Gorges Reservoir based on FLAC3D Software. Procedia Engineering(C), 2847-2851.

Bridge Maintenance, Safety, Management, Digitalization and Sustainability – Jensen, Frangopol & Schmidt (eds)
© 2024 The Author(s), ISBN 978-1-032-77040-6
Open Access: www.taylorfrancis.com, CC BY-NC-ND 4.0 license

A review of the durability of concrete wet joints under the loading and corrosion

Yi Wang, Yin Shen & Yu Wang
College of Civil Engineering, Tongji University, Shanghai, China

ABSTRACT: Reinforced concrete bridges suffer from significant durability issues. The increased use of prefabricated assembled components with the development of accelerated bridge construction methods has led to the construction joints having an increasingly negative impact on the concrete durability. Wet joints, as a type of joints, possess a larger interface concrete porosity that promotes the transmission of harmful substances and consequently causes accelerated corrosion to reinforcement. Meanwhile, loads and environment corrosion also cause cracking and degradation of pore structures, leading to diminished concrete durability. This paper focuses on a review of durability of concrete wet joints considering the impact of loads and environment corrosion. The study includes the methods for testing the durability of concrete joints, performance related to their degradation, and the numerical models that account for joints. It also describes the potential study on impact of loads and environment corrosion on bridge construction joints.

1 INTRODUCTION

Concrete is a commonly utilized material in the bridges engineering. The presence of numerous construction joints in bridges is necessary due to the structure design and construction requirements. Concrete cannot generally be poured at once to complete for bridges. So sequentially segmental cast-in-place method or prefabricated assembled connections are used, resulting in the concrete interface. Precast concrete bridges comprise various construction joints, including wet joints, epoxy joints, and mortar bedding joints, etc. The AASHTO specification divides joints into two types: type A and type B. Type A joints include wet joints and epoxy joints, while Type B joints include dry joints.

According to Chinese *Technical Specifications for Construction of Highway Bridges and Culverts*, concrete wet joint refers to the joint that adopts sequential pouring of concrete to connect the structure as a whole, which is commonly found in segmental pouring construction, layer pouring construction, hinge joints and rigid joints of prefabricated assembled bridges, etc. It is generally placed in the part that is subjected to less shear force and bending moment and is convenient for construction. Usually, after the concrete has reached the design strength and has been roughed, cleaned, wetted and supplemented with anchoring reinforcement, the subsequent concrete is poured to form wet joints. Due to the wall effect and other effects, the cement mortar content at joints is higher, the water-cement ratio increases, and the water seepage phenomenon in the subsequent pouring concrete and the interface area gathered many pores and cracks make the wet joints are not as dense as the monolithic concrete. Therefore, wet joints are the weak part of the concrete, and become a channel for the external corrosive substances to enter the concrete.

During the mid-20th century, a significant number of concrete structures experienced premature failure due to diverse durability defects, resulting in failure to accomplish their designated service life. Structure is subject to carbonation and chloride attack, as well as other

DOI: 10.1201/9781003483755-24

erosion. These processes cause corrosion in the reinforcement and expansion, cracking and peeling on concrete. As a result, the bearing capacity of the structure is degraded. Due to corrosion problems leading to concrete structure failures, the United States spent over 100 billion dollars on operation and maintenance on bridges at the beginning of the 21st century. With China's recent rapid infrastructure development, numerous concrete bridges will likely face severe durability issues.

Previous research has not paid attention to the durability of concrete wet joints, and the bridge operation and maintenance process is mostly judged by the strength of the joints, ignoring the environmental corrosion. This paper overview the current research on the environmental corrosion resistance of concrete joints under various loads. It includes an introduction to durability testing methods for concrete joints under loads, a summary of trends in the performance of wet concrete joints under loads and environment, and a concise overview of numerical simulation methods for the corrosion effects on concrete joints.

2 TEST METHODS TO MEASURE THE COMBINED EFFECTS OF ENVIRONMENTAL CORROSION AND LOADING

2.1 *Test methods for monolithic concrete under corrosion and loads*

The progress of durability damage in concrete structures under natural circumstances is very slow and typically replicated in the laboratory through rapid durability tests, such as rapid carbonation test, chloride salt immersion test and rapid freeze-thaw cycle (FTC) test. Despite an absence of uniform standards for testing procedures under the combined impact of environmental corrosion and loading, three testing method are generally used in research. The first method is one-time alternating simulation test in which the specimen is subjected to loading, followed by a durability test or an environmental corrosion test, followed by loading. Although easier to operate, this type test may not accurately reflect the actual damage sustained by a concrete structure. The second method is multiple alternating simulation tests, in which the specimen undergoes alternating loading and durability tests several times. The third method is simultaneous testing of both mechanical loads and environmental corrosion.

Numerous experiments have studied the durability of monolithic concrete specimens under various stress conditions. Static load application methods on concrete specimens have become diverse. The compressive stress state is mainly produced by applying prestressing force (Figure 1a), usually by post-tensioning method (Tian et al., 2010, Wang et al., 2011). Tensile stress state is often achieved by applying bending moments for two primary reasons. Firstly, test equipment limits the test, such as the size of the carbonation chamber. Secondly, most concrete structures in actual bridge create tension through bending. Bending loads are commonly achieved using two or more concrete prismatic specimens anchored to each other in four-point bending (Mu et al., 2002), as shown in Figure 1b.

In addition, loading machines have also applied tensile and compressive stresses (Yao et al., 2016, Chen et al., 2022) when only a part of the concrete specimen surface undergoes environmental corrosion (Figure 1c). Chen et al. (2022) established a compression-bending state construction for freeze-thaw cycling testing. In some instances, specimens have been put in salt spray to simulate natural conditions such as coastal air (Vera et al., 2009, Wang et al., 2011).

Due to fatigue loads caused by vehicles, bridge structures may experience microcracks and increased porosity in the concrete, leading to the intrusion of external corrosive substances (Liu et al., 2023). Considering the complexity of the fatigue loading and the environment combined effect, most of the researches have been conducted through a one-time alternating approach. Li et al. (2015) set up four different test conditions, including flexural fatigue, freeze-thaw cycle, both at the same time and alternating test using an environmental test chamber (Figure 1d). Ren et al. (2015) put reinforced concrete beams in chloride salt solution to carry out flexural fatigue testing. Lu et al. (2017) determined the remaining compressive load-bearing capacity of concrete through axial compressive fatigue loading of concrete prismatic cylinders and subsequent carbonation testing.

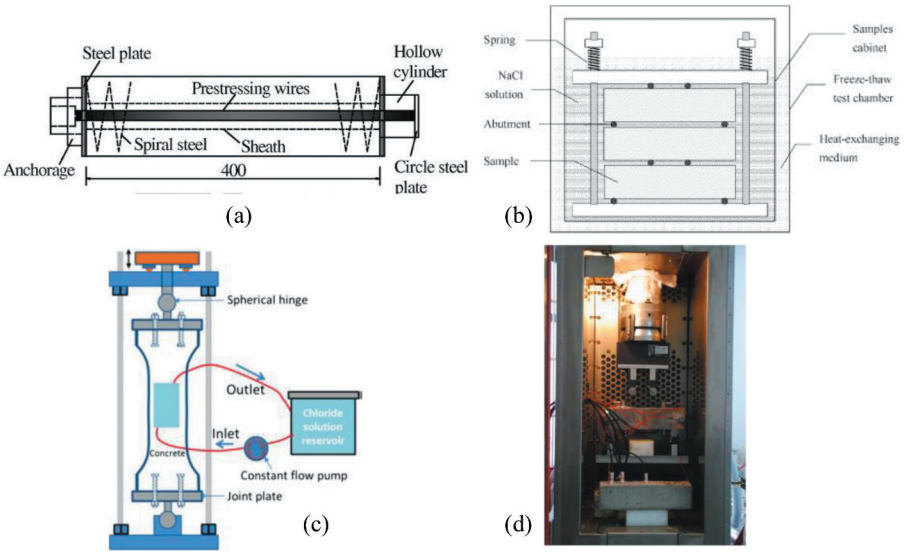


Figure 1. Monolithic concrete test methods. (a) Compressive specimen (Wang et al., 2011); (b) Four-point bending test (Mu et al., 2002); (c) Tensile specimen (Yao et al., 2017); and (d) FTC test (Li et al., 2015).

2.2 *Test method for concrete with joints under corrosion and loads*

In recent years, segmental casting and prefabricated assembling methods have become the predominant construction methods for bridges. As a result, the issue of construction joint durability has become increasingly significant and has garnered the attention of researchers. The method of applying stress state in the concrete specimens with joints is similar to that of monolithic concrete.

Due to significant differences in the construction methods of bridge joints, most previous studies have compared various joint types. Li et al. (2018) analysed the durability of direct wet joints, roughened wet joints, dry joints, and epoxied joints through exposure to chloride erosion, carbonation, and freeze-thaw cycling. Some test specimens were also subjected to compressive stress and monitored for reinforcing steel corrosion. Technical abbreviations are explained whenever necessary throughout the text. Shen et al. (2019) conducted an investigation into the durability of these joint types in concrete specimens subjected to cyclic freezing and thawing. Three compressive stress parameters of 0, 0.3 f_{ck}, and 0.5 f_{ck} were explored. Similar researches were undertaken by, Zhang et al. (2019) and Shen et al. (2023). The fabrication of specimens with joints generally involved three steps. 1) Pouring began at both ends before proceeding to the middle. 2) After disassembling the internal formwork, the joint interface was fabricated in accordance with the construction requirements. 3) Finally, the middle section was filled with concrete (Figure 2a).

Cold joints specimens are produced in a similar way to direct wet joints test samples. Cold joint is a discontinuous surface forms on the concrete surface after hardening following a delay in the working time. Yoo & Kwon (2016) assessed the resistance of cold joints to chloride erosion by applying stress to samples after they had been immersed for 28 and 91 days. Koh et al. (2019) researched the resistance of cold joints to carbonation by applying stress to specimen after a period of rapid carbonation. The specimens for compressive stress were prepared using prismatic moulds, while specimens for tensile stress were prepared using cylindrical moulds for splitting tests. To create cold joints, the concrete was placed in one half and exposed to indoor conditions for 24 hours before pouring the other half. The joints were all perpendicular to the bottom of the column.

Höffgen et al. (2023) conducted an experiment to determine the resilience of concrete joints exposed to three types of environment corrosion: carbonation, chloride attack, and FTC. The age gap between old and new concrete on both sides of the joints was 7 days. The specimens were prepared differently based on the environment exposed to, with carbonation specimens

being created from 100 mm cubes and the chloride specimens extracted by drilling cores from the cubes. The joints of the carbonation and chloride specimens were perpendicular to the bottom of the cylinders, while those for the freeze-thaw cycle specimens were parallel to the bottom of the columns. Qin et al. (2023) investigated the deterioration tendencies of cold joints exposed to wet and dry sulphate cycling. To improve joint strength, key teeth were added to the cold joints and the age of the joints varied from 0-28 days. Compressive stress was applied after wet and dry cycling (Figure 2b).

The joints aforementioned were composed of an equal quantity of concrete material on both sides, whereas certain concrete structures had varying strengths and admixtures on either side of the joints, such as the concrete requiring repair after local damage or reinforcement due to insufficient stresses in prefabricated construction. Yan et al. (2023) examined the impact of joint types (direct wet joint, roughened wet joint, and interfacial joint) and joint materials (M5 mortar, M10 mortar, and grout) on the pattern of chloride erosion. The study used typical concrete and limestone powdered concrete on both sides of the joints. Zhang et al. (2023) investigated the corrosion of steel reinforcement at UHPC interfaces under chloride attack and compared it with normal concrete and high-performance concrete interfaces.

There is a scarcity of research pertaining to the durability of joints under fatigue loading. Zhao & Li (2022) have devised an auxiliary truss unit (Figure 2c) to carry out fatigue tests. A ring of watertight glass adhesive around the edge of the penetrated specimen surface was applied to create a container for simulation of chloride infiltration in wet and dry conditions.

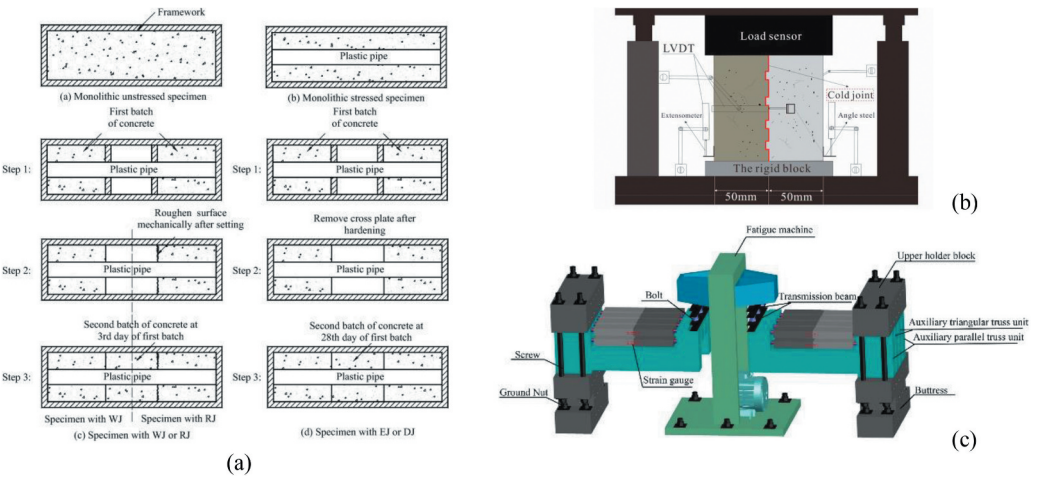


Figure 2. Concrete with joints test methods. (a) Steps for making different joints (Shen et al., 2019); (b) Specimen with teeth (Qin et al., 2023); and (c) Auxiliary truss unit for fatigue load (Zhao & Li (2022).

At present, there are initial outcomes for researching the durability of concrete joint components. In recent years, the test method has evolved from a single durability test to a coupled test with multiple corrosion effects and loads, from static loads to fatigue loads, and from monolithic concrete members to actual joint members in real engineering, gradually innovative and diverse. Mu et al. (2002) and Zhang et al. (2019) have provided a solution to the problem of multiple corrosion; Yao et al. (2016) can accurately apply the stresses and at the same time reduce the test cost. Zhao & Li (2022) through the auxiliary unit applying fatigue loads saves test time and ensures that the members are in the same environment. However, the majority of results concerning specimens with joints can only serve as reference. It is essential to closely examine the actual situation regarding component size and joints treatment adopted in real projects. To reinforce the connection, rebars must be increased on both sides of the joints, and consider the specimen to apply stress and other major factors affecting the structure of the research. These studies also lack

a developed theoretical framework to guide the planning and execution of projects and continue to utilize specifications for monolithic concrete for the purpose of design, construction, operation and maintenance currently.

3 DETERIORATION OF CONCRETE JOINT PARTS UNDER ENVIRONMENTAL CORROSION AND LOADS

3.1 *Deterioration of wet joints under corrosion*

The degradation mechanisms of concrete durability are different under environmental exposures. Carbonation and chloride ion erosion are the main reason for reinforcement deterioration. Carbonation reduces the pH value of the solution, adjacent to the rebar, destabilizing the surface passivation film and leading to corrosion. Chloride ions have strong depassivation properties that cause battery-like corrosion of the steel reinforcement. The concrete strength and stiffness diminish when subjected to the physical processes of concrete cracking and surface spalling caused by the freeze-thaw cycle. Moreover, the concrete matrix also undergoes cracking from the expansion products resulting from sulphate attack.

Concrete properties (such as water-cement ratio, concrete strength, admixtures, etc.) and environmental factors (such as temperature, humidity, dry and wet cycles, exposed environments, etc.) are significant factors that influence concrete durability. Among these, the type of loading and stress level play a important role in determining concrete durability. In recent times, stress is usually employed rather than strain to reflect the loading state of concrete (Ai et al., 2021). Compressive stress enhances the carbonation resistance and resistance to chloride erosion in concrete. It also closes internal micro-cracks and restricts the diffusion of external corrosive substances into the concrete. Conversely, tensile stress diminishes these properties, and increases porosity and cracking in concrete. Corrosive substances can undergo faster chemical reactions and reach the surface of the reinforcement on the rebar much earlier. The durability indicator of carbonization is mainly the depth of carbonization (Shen et al., 2023); the durability indicator chloride attack is measured by the diffusion coefficient of chloride ions or the time when the chloride ions start to corrode the surface of the reinforcement (Zhang et al., 2023); for freeze-thaw cycles, the number of freeze-thaw cycles and the dynamic elastic modulus are used as service period indicators (Shen et al., 2019, Zhang et al., 2019).

Mun & Kwon (2016) and Yang et al. (2018)found that the chloride ion diffusion coefficient at joints did not differ significantly from that of cracked concrete under varying tensile stress levels, indicating that joints and cracks have comparable effects. However, under compressive stress, the chloride ion diffusion coefficient of concrete joints was elevated in comparison to cracks. Koh et al. (2019) revealed that concrete carbonation occurs at a greater depth in cold joints than non-joint concrete. Additionally, the rate of concrete carbonation under tensile stress increases linearly with the level of stress.

Shen et al. (2023) proposed the joint influence factor γ_{Joint}, i.e., the ratio between the depth at the joint section and the depth of monolithic concrete. By testing a bridge in Shanghai, China, which was demolished after 30 years of service, it was found that the carbonation depth of the joints were 2.1 times that of the monolithic concrete due to the setting of a partially prestressed with a small tensile stress, and the web with the largest tensile stress, which made the carbonation depth of the joints were 2.4 times that of the monolithic concrete, suggesting that the durability of concrete bridge joints is far inferior to that of monolithic concrete. And according to the carbonization depth distribution curve derived from the test, it is considered that durability improvement measures are needed in the range of 2 times the carbonization depth of the joint on both sides of the joint.

By examining the carbonation depth and chloride ion corrosion depth, it was found that the concentration of corrosive materials and their byproducts in the wet joints followed an inverted V shape. This means the corrosion depth at the joint was highest when compared to the specimen without joints. Additionally, the impact of the joints on the distribution of corrosive materials on the specimen remained significant within a certain distance from the joint

but decreased thereafter. There is no longer a significant effect with the increase in distance from the joints (Shen et al., 2023, Yan et al., 2023).

Fatigue loading also has a significant effect on the durability of fatigue distressed concrete. For example, when the number of fatigue cycles is low, the compressive stress suppresses microcracking or microporosity in the compression zone and inhibits the carbonation process (Vicente et al., 2018). However, once the compressive fatigue damage reaches a certain level, the carbonation process also increases significantly. Residual strain (Jiang et al., 2017), dynamic modulus of elasticity, number of fatigue cycles and pore microstructure (Song et al., 2020) are the main indicators to characterize the fatigue damage of concrete.

3.2 *Comparison of the durability of different construction joints*

The comparison of the durability of various types of construction joints is a key area of research. Each type of joints exhibits different resistance to chloride ions, carbonation, freeze-thaw cycles characteristics. These properties, however, are consistently inferior to those of the monolithic concrete structure, and thus the joints can be identified as the weak points of the concrete structure (Li et al., 2012a, Li et al., 2012b). The joints can accelerate the diffusion and infiltration of external ions. Li et al. (2018) studied various compressed and unstressed joints and found that roughened wet joints generated microcracks on the surface of old concrete, resulting in damage. In terms of durability, roughened wet joints were inferior to direct wet joints. Epoxy joints did not display satisfactory durability, while dry joints had the poorest durability due to a macroscopic gap in the joints. It is believed that implementing a particular level of pre-compressive stress will have two effects. Primarily, the pore structure of the concrete within the joints will compact. Secondly, the micro-cracks caused by the roughing process will expand further. The combined effect of the two leads to the durability indexes of the roughened wet joints with the application of pre-compressive stresses have the same stochastic nature.

Zhang et al. (2019) conducted research into the carbonation resistance and freeze-thaw resistance of precast segmental girder joints and discovered that epoxy joints exhibited superior carbonation resistance. In contrast, direct wet joints showed the worst carbonation resistance, with monolithic moulded concrete joints performing better but still ranking second to epoxy joints. Yan et al. (2023) conducted a comparison between wet joints and mortar joints and discovered that direct wet joints had the highest concentration of chloride ions. Similarly, roughened joints exhibited greater chloride ion concentration than mortar joints.

The test results indicate that wet joints are significantly impacted by stress levels and that appropriate compressive stress can enhance the durability of concrete specimens by reducing pores and closing microcracks within the concrete. However, higher levels of compressive stress can have an adverse effect on concrete durability, potentially due to lateral tensile stresses arising from Poisson's effect and unstable variations in the internal pores of the concrete.

Roughened wet joints eliminate the negative effect caused by the more permeable cement mortar matrix at the joint interface. However, microcracks that emerge during chipping cause concrete damage at the joints, and such damage is usually greater than the impact of removing the cement mortar matrix. Moreover, roughened wet joints are not as resistant to chloride ions and carbonation as direct wet joints. Under FTCs, chipping had no significant effect on the freeze-thaw resistance of joints (Li et al., 2018).

The type of joints led to a negative effect on concrete durability. Epoxy joints, wet joints, and roughened wet joints had slightly different adverse effects on durability. Tensile strain directly and adversely affects the durability of concrete. Thus, when designing concrete structures under high pressure or tensile stress, a particular safety margin is mandatory to ensure the concrete durability.

4 NUMERICAL SIMULATION METHOD FOR CONSTRUCTION JOINTS

Numerical simulations concerning the durability of concrete have progressed from traditional empirical formulas and macroscopic simulations to meso-scale simulations. Empirical models

typically summarized from experiments and theory from experimentation and theory. Monteiro et al. (2012) proposed a model to predict carbonation depth based on more than 100 measurements of multiple structures with service years ranging from 4-99 years, which takes into account the age of the structure, the effect of paint, the compressive strength of the concrete, and the exposure conditions. The empirical model shows that carbonation depth is directly proportional to the square root of time, with varying carbonation rate constants and indices for different factors influencing the process. The empirical model has some limitations and it is difficult to take into account all factors affecting durability, such as aggregate distribution and concrete variability.

4.1 *Macroscopic model of concrete construction joints*

Macroscopic numerical simulations will treat concrete as an isotropic homogeneous substance. Vagelis G. Papadakis & Michael (1991) acquired a theoretical solution of his proposed system of differential equations for the carbonation process through some simplifying assumptions, which can also be solved numerically. Anna V. Saetta & Renato (1993) and Saetta et al. (1993) formulated a numerical model combining temperature, moisture, diffusion, and the kinetics of the carbonation reaction, taking into account only the carbonation reaction between CO_2 and $Ca(OH)_2$. Tian et al. (2015) developed a three-dimensional multifactor coupled concrete carbonation model, which is able to consider a series of factors such as environmental conditions, concrete material properties, and structural shape. Yan et al. (2023) examined the simulation of macroscopic concrete components featuring construction joints, for the transport of chloride ions. The study considers the decay effect of the chloride ion diffusion coefficient with time and the joints thickness of the protective layer on the durability of concrete elements in a chloride salt environment.

All of these numerical models treat concrete as a macroscopic homogeneous material and do not consider the distinct behaviour exhibited by individual concrete components in relation to the degradation of the overall properties of concrete.

4.2 *Meso-scale model of concrete construction joints*

The durability of concrete at the meso-scale has become a prominent subject recently. At the meso-scale level, the concrete's inhomogeneous distribution of aggregates in the cement paste is considered. The concept of the meso-scale of concrete is proposed by Zaitsev & Wittmann (1981), dividing the concrete into cement paste, aggregates, and the interface transitional zone (ITZ) between them. Pan et al. (2012) and Ruan & Pan (2012) formulated a numerical model for carbonation in concrete at meso-scale, accounting for the influence of aggregate distribution. In relation to the macroscopic model, the depth of concrete carbonation was reduced by the dilution effect and distortion effect of aggregates. The uneven distribution of aggregates caused the depth of carbonation to appear inhomogeneous. Qin et al. (2019)studied the interfacial fracture toughness and water infiltration behaviour of old and new concrete, and developed model at the macroscopic, meso and nano scales. Shi et al. (2022)used meso-scale numerical model to categorise concrete into uncarbonated, semi-carbonated, and fully-carbonated zones. They applied axial loads and found that both compression and tension can result in significant damage to the concrete and the creation of CO_2 diffusion paths. It is worth noting that once these paths are formed, Fick's law no longer applies.

Meso-scale numerical models consider factors such as changes in the external environment of the structure, the concrete structure's shape and internal structure, and can be applied to calculate concrete durability under complex conditions. Currently, research on meso-scale concrete joint simulation primarily centers on concrete structure repair. Concrete construction joints are considered to be a distinct component of concrete. To model construction joints and their response to combined environmental corrosion and load effects, meso-scale numerical model is a recommended approach.

5 CONCLUSION

The effects of corrosive environments and loading effects on concrete structural joints have garnered considerable interest. Current research focuses primarily on the effects of static and fatigue loading on concrete carbonation, chloride transport, FTCs and other environmental effects on monolithic concrete and concrete with construction joints. Models that take into account loading and corrosion have been developed. However, there are still some directions that need to be further explored and researched on this topic:

(1) Current durability studies focus on the properties of the concrete material while ignoring structural aspects, including the impact of construction joints. The excessive use of precast components impedes the continuity of concrete, leading to a porous structure during the initial bridge construction phase which is not as good as the concrete cast-in-place. Construction joints are present in the cement mortar matrix, which is not as dense as the monolithic concrete, becoming a weak part of the concrete, making it easier for external harmful substances to enter the concrete, accelerating the corrosion of concrete. Currently, there are limited studies on construction joints, particularly in terms of environmental corrosion and loading, which can significantly guide the design of actual bridge engineering structures.
(2) Bridge structures are often subjected to fatigue loads caused by vehicles. Previous research has primarily focused on the impact of fatigue loading on carbonation and chloride ion transportation in monolithic concrete, as well as the damage state of concrete when subjected to fatigue loading with FTCs. In addition, some chloride intrusion models considering the effect of fatigue loading have been established. However, the durability performance of the construction joints under the combined effect of fatigue loading and environmental corrosion is limited and still needs to be further studied.
(3) There is potential for enhancing test methods under the effects of fatigue loading and corrosive environments. Alternative test methods that account for these simultaneous interactions need to be explored. The typical approach in most studies employs a one-time alternating simulation test method. In reality, fatigue loading and corrosion occur simultaneously. As fatigue loading increases, concrete damage and the deterioration of microporosity and microcracks drastically accelerate salt erosion process. At the structural level, the acceleration of erosion caused by chloride salt due to fatigue damage results in corrosion deterioration of steel reinforcement embedded in concrete. Corrosion leads to decreased cross-sectional area of the reinforcing steel material, consequently reducing its fatigue resistance. The combined effect of fatigue and corrosion causes the steel reinforcement to deteriorate more rapidly, significantly reducing the service life of reinforced concrete structures. Therefore, it is crucial to establish the degradation characteristics of reinforced concrete when subjected to the joint effects of environmental corrosion and loading.
(4) Concrete structures are exposed to various environmental corrosion factors, often more than one. Studied combinations include carbonation and chloride ion erosion. Further study is needed into the performance degradation mechanism of concrete structures under the combined effect of multiple environmental factors and loads.

ACKNOWLEDGMENT

This work was supported by the National Natural Science Foundation of China, Grant/ Award Number: 51778468.

REFERENCES

Ai, Z., Yang, S., Ruan, F., Shen, Y. & Li, G. 2021. A review of the durability of joints in concrete structures. *Bridge Maintenance, Safety, Management, Life-Cycle Sustainability and Innovations*. CRC Press.

Anna V. Saetta, R. V. S. & Renato, V. V. 1993. Analysis of Chloride Diffusion into Partially Saturated Concrete. *ACI Materials Journal*, 90.
Chen, D., Liu, S., Shen, J., Sun, G. & Shi, J. 2022. Experimental study and modelling of concrete carbonation under the coupling effect of freeze-thaw cycles and sustained loads. *Journal of Building Engineering*, 52, 104390.
Höffgen, J. P., Mohs, M., Lamparter, S., Malárics-Pfaff, V. & Dehn, F. 2023. Experimental methods for the analysis of the durability behavior of concrete joints. *Structural Concrete*, 24, 423–433.
Jiang, C., Huang, Q., Gu, X. & Zhang, W. 2017. Experimental investigation on carbonation in fatigue-damaged concrete. *Cement and Concrete Research*, 99, 38–52.
Koh, T.-H., Kim, M.-K., Yang, K.-H., Yoon, Y.-S. & Kwon, S.-J. 2019. Service life evaluation of RC T-girder under carbonation considering cold joint and loading effects. *Construction and Building Materials*, 226, 106–116.
Li, G., Hu, H. & Cai, R. 2012a. Resistance of Segmental Joints to Carbonation. *ACI Materials Journal*, 114.
Li, G., Hu, H. & Cai, R. 2012b. Resistance of Segmental Joints to Chloride Ions. *ACI Materials Journal*, 113.
Li, G., Hu, H., Ren, C., Zhou, S. & Li, J. 2018. Study on durability of joints in concrete bridge structures. *China Civil Engineering Journal*, 51, 98–103.
Li, W., Jiang, Z., Yang, Z., Jiang, J., Sun, W. & Deng, Z. 2015. Interactive Effect of Mechanical Fatigue Load and the Fatigue Effect of Freeze-Thaw on Combined Damage of Concrete. *Journal of Materials in Civil Engineering*, 27, 04014230.
Liu, D., Wang, C., Gonzalez-Libreros, J., Guo, T., Cao, J., Tu, Y., Elfgren, L. & Sas, G. 2023. A review of concrete properties under the combined effect of fatigue and corrosion from a material perspective. *Construction and Building Materials*, 369, 130489.
Lu, J., Guo, L., Liu, Y. & Zhu, K. 2017. Experimental study of the damage on concrete subjected to combined act ion of fat igue loading and carbonat ion. *Conrete*, 327, 63-66+70.
Monteiro, I., Branco, F. A., Brito, J. d. & Neves, R. 2012. Statistical analysis of the carbonation coefficient in open air concrete structures. *Construction and Building Materials*, 29, 263–269.
Mu, R., Miao, C., Luo, X. & Sun, W. 2002. Interaction between loading, freeze–thaw cycles, and chloride salt attack of concrete with and without steel fiber reinforcement. *Cement and Concrete Research*, 32, 1061–1066.
Mun, J.-M. & Kwon, S.-J. 2016. Evaluation of Chloride Diffusion Coefficients in Cold Joint Concrete Considering Tensile and Compressive Regions. *Journal of the Korea Concrete Institute*, 28, 481–488.
Pan, Z., Ruan, X. & Chen, A. 2012. Numerical simulation of concrete carbonation process on meso-scale. *Journal of Tongji University (Natural Science)*, 40, 900–905.
Qin, R., Hao, H., Rousakis, T. & Lau, D. 2019. Effect of shrinkage reducing admixture on new-to-old concrete interface. *Composites Part B: Engineering*, 167, 346–355.
Qin, Y., Men, B., Liang, D., Geng, K., Zhang, X., Zhou, H. & Liu, R. 2023. Energy evolution of concrete with cold joint under the action of sulfate dry-wet cycles with loading. *Journal of Building Engineering*, 68, 106098.
Ren, Y., Huang, Q., Liu, Q. Y., Sun, J. Z. & Liu, X. L. 2015. Chloride ion diffusion of structural concrete under the coupled effect of bending fatigue load and chloride. *Materials Research Innovations*, 19, S1-181-S1-184.
Ruan, X. & Pan, Z. 2012. Mesoscopic simulation method of concrete carbonation process. *Structure and Infrastructure Engineering*, 8, 99–110.
Saetta, A., Schrefler, B. A. & Vitaliani, R. V. 1993. The carbonation of concrete and the mechanism of moisture, heat and carbon dioxide flow through porous materials. *Cement and Concrete Research*, 23, 761–772.
Shen, Y., Liu, J., Zhou, S. & Li, G. 2019. Experimental investigation on the freeze–thaw durability of concrete under compressive load and with joints. *Construction and Building Materials*, 229, 116893.
Shen, Y., Wang, Y., Xu, X. & Ruan, F. 2023. Study on carbonation of construction joints through field tests on a 30-year-old bridge and accelerated carbonation tests. *Case Studies in Construction Materials*, 19, e02231.
Shi, X., Zhang, C., Liu, Z., Van den Heede, P., Wang, L., De Belie, N. & Yao, Y. 2022. Numerical modeling of the carbonation depth of meso-scale concrete under sustained loads considering stress state and damage. *Construction and Building Materials*, 340, 127798.
Song, L., Liu, J.-l., Cui, C.-x., Yu, Z.-w., Fan, Z.-w. & Hou, J. 2020. Carbonation Process of Reinforced Concrete Beams under the Combined Effects of Fatigue Damage and Environmental Factors. *Applied Sciences*, 10, 3981.
Tian, F., Li, G. & Zhang, C. 2015. Long-term mechanical performence analysis of concrete bridges in atmospheric environment. *Journal of Tongji University (Natural Science)*, 43, 483–489.

Tian, H., Li, G., Liu, J. & Wu, Y. 2010. Experimental Research on Carbonation of Forced Concrete Specimens. *Journal of Tongji University (Natural Science)*, 38, 200-204+213.
Vagelis G. Papadakis, C. G. V. & Michael, N. F. 1991. Physical and Chemical Characteristics Affecting the Durability of Concrete. *ACI Materials Journal*, 88.
Vera, R., Villarroel, M., Carvajal, A. M., Vera, E. & Ortiz, C. 2009. Corrosion products of reinforcement in concrete in marine and industrial environments. *Materials Chemistry and Physics*, 114, 467–474.
Vicente, M. A., González, D. C., Mínguez, J., Tarifa, M. A., Ruiz, G. & Hindi, R. 2018. Influence of the pore morphology of high strength concrete on its fatigue life. *International Journal of Fatigue*, 112, 106–116.
Wang, H., Lu, C., Jin, W. & Bai, Y. 2011. Effect of External Loads on Chloride Transport in Concrete. *Journal of Materials in Civil Engineering*, 23, 1043–1049.
Yan, Y., Si, Y., Lu, C., Gao, S. & Liu, X. 2023. Research on transport mechanism of chloride ion in concrete with joint. *Journal of Architecture and Civil Engineering*, 40, 49–56.
Yang, H.-M., Lee, H.-S., Yang, K.-H., Ismail, M. A. & Kwon, S.-J. 2018. Time and cold joint effect on chloride diffusion in concrete containing GGBFS under various loading conditions. *Construction and Building Materials*, 167, 739–748.
Yao, Y., Wang, L., Wittmann, F. H., De Belie, N., Schlangen, E., Eguez Alava, H., Wang, Z., Kessler, S., Gehlen, C., Yunus, B. M., Li, J., Li, W., Setzer, M. J., Xing, F. & Cao, Y. 2016. Test methods to determine durability of concrete under combined environmental actions and mechanical load: final report of RILEM TC 246-TDC. *Materials and Structures*, 50, 123.
Yao, Y., Wang, L., Wittmann, F. H., De Belie, N., Schlangen, E., Gehlen, C., Wang, Z., Alava, H. E., Cao, Y., Md Yunus, B. & Li, J. 2017. Recommendation of RILEM TC 246-TDC: test methods to determine durability of concrete under combined environmental actions and mechanical load. *Materials and Structures*, 50, 155.
Yoo, S.-W. & Kwon, S.-J. 2016. Effects of cold joint and loading conditions on chloride diffusion in concrete containing GGBFS. *Construction and Building Materials*, 115, 247–255.
Zaitsev, Y. B. & Wittmann, F. H. 1981. Simulation of crack propagation and failure of concrete. *Matériaux et Construction*, 14, 357–365.
Zhang, L., Yu, D., Xu, Y., Zhao, Z. & Yang, H. 2019. Experimental Study on Mechanical Properties ofJoints of Prestressed Concrete Beam. *Journal of Hebei Institute of Architecture and Civil Engineering*, 37, 1–6.
Zhang, X., Wang, H., Zhang, Y. & Wang, L. 2023. Corrosion of steel rebars across UHPC joint interface under chloride attack. *Construction and Building Materials*, 387, 131591.
Zhao, J. & Li, F. 2022. Chloride Transport in Interfacial Zone of New–Old Concrete Joints of Precast Prestressed Concrete Bridges under Fatigue Load. *Journal of Materials in Civil Engineering*, 34, 04022263.

Bridge Maintenance, Safety, Management, Digitalization and Sustainability – Jensen, Frangopol & Schmidt (eds)
© 2024 The Author(s), ISBN 978-1-032-77040-6
Open Access: www.taylorfrancis.com, CC BY-NC-ND 4.0 license

PC-PINNs: Physics-informed neural networks for solving the phase-field model of pitting corrosion

Nanxi Chen, Rujin Ma & Airong Chen
Department of Bridge Engineering, Tongji University, China

Chuanjie Cui
Department of Engineering Science, University of Oxford, Oxford, UK

ABSTRACT: Physics-informed neural networks (PINNs) have recently emerged as a promising tool for resolving partial differential equations. However, when confronting complex multi-physics problems, conventional PINNs suffer from substantial challenges. In this study, we present an advanced PINN framework tailored for the phase-field model of pitting corrosion (PC-PINNs) , effectively navigating the complexities of the rigidly coupled Allen-Cahn and Cahn-Hilliard equations. The main ingredients of PC-PINNs include: 1) an NTK-based adaptive weighting strategy to balance the multiple loss terms arising from coupled equations, 2) a generalized adaptive sampling scheme complemented by dual criteria to accurately track the corrosion interface, 3) a random-batch technique to accelerate the weight calculation, and 4) a cross-scale sampling technique to ensure the veracity of convergence. We evaluate the PC-PINNs against two phase-field corrosion benchmarks, using various strategy permutations to validate the effectiveness of the proposed theory. Results demonstrate that the PC-PINNs successfully overcome the limitations of the conventional PINNs, delivering simulations with high fidelity.

1 INTRODUCTION

Pitting corrosion, a form of localized corrosion, poses a significant threat to alloys in various service environments. Its occurrence can result in the development of perforations and cracks on components, ultimately leading to the deterioration and failure of engineering structures (Mai et al., 2016). Consequently, conducting comprehensive investigations into the evolution process of pitting corrosion is imperative for the purpose of reliability assessment and health monitoring of structures.

The simulation of pitting evolution using the phase field method has been intensively studied (Mai et al., 2016). The phase-field method is a computational approach widely utilized in material science to simulate the evolution of complex microstructures (Chen, 2002). It is characterized by the ability to capture dynamic processes of phase transitions by representing the material's microstructure as a continuous field variable. The problem can then be formulated as a set of coupled partial differential equations (PDEs) that govern the evolution of the phase-field variable. This eliminates the necessity of explicitly tracking interfaces and circumvents the imposition of boundary conditions on moving interfaces (Mai et al., 2016), thereby streamlining the implementation of simulations through computational programs. When solving the PDEs associated with the phase-field model, various numerical methods, including finite difference, finite element, finite volume methods, etc., have conventionally served as the principal options (Zhao et al., 2023).

However, in recent years, physics-informed neural networks (PINNs) have emerged as a promising approach for solving PDEs. By integrating the residuals of governing equations into the neural network's loss function, PINNs combine the strengths of both numerical methods and

DOI: 10.1201/9781003483755-25

machine learning. Thus, PINNs can be viewed as a self-superimposed learning strategy that does not require any labeled data, such as results of prior simulations or experiments (Cuomo et al., 2022). This novel computational framework exhibits numerous advantages. On one hand, well-established program frameworks for deep learning, such as PyTorch and TensorFlow, along with computational platforms like CUDA, enable highly parallelized computational processes. On the other hand, the governing equations are embedded into the loss function as part of a multi-objective optimization, facilitating the coupling of physical fields. Furthermore, compared to discrete conventional numerical methods, PINNs are mesh-free and continuous, thereby naturally avoiding a range of numerical challenges resulting from improper discretization (Wu et al., 2023).

In this study, we present a refined PINN framework for solving the phase field model of pitting corrosion. This phase field model is characterized by strong stiffness and sharp interface transition. Section 2 describes this PC-PINN framework in detail, including the specially designed NTK matrix-based weighting strategy for the coupled equations and the strategy for adaptive sampling, as well as a series of related techniques. Section 3 gives illustrative examples of solving typical pitting problems to validate the effectiveness of the framework.

2 PHYSICS-INFORMED NEURAL NETWORK FOR PITTING CORROSION (PC-PINN)

In this section, we first present a theoretical background for the modeling of the pitting problem using the phase field method. A PINN model is constructed based on the phase field theory. To ensure the convergence and accuracy of the PINN, several techniques, such as loss weighting and adaptive sampling, are discussed in detail.

2.1 *Phase field model of pitting corrosion*

The key idea of the phase field method for pitting corrosion is to introduce a phase field variable to describe the formation and evolution process of corrosion pits. By employing the phase field equations and boundary conditions, this approach enables the simulation of pit expansion and shape variation, thereby facilitating quantitative prediction and analysis of pitting corrosion.

Specifically, the phase field model is governed by coupled Allen-Cahn and Cahn-Hilliard equations, which are given by

$$\text{Allen-Cahn}: \frac{\partial \phi}{\partial \mathrm{t}}(x,\mathrm{t}) = -\mathrm{L}\left(\frac{\partial \mathrm{f}}{\partial \phi} - \alpha_\phi \nabla^2 \phi\right) \tag{1}$$

$$\text{Cahn-Hilliard}: \frac{\partial \mathrm{c}}{\partial \mathrm{t}}(x,\mathrm{t}) = \nabla \cdot \mathrm{M} \nabla \frac{\partial \mathrm{f}}{\partial \mathrm{c}} \tag{2}$$

In the above equations, ϕ represents the phase field variable, c represents the normalized concentration, and f represents the local free energy density. The relevant equations and parameters involved in this study can be found in Ref. (Mai et al., 2016)

2.2 *Sampling strategies*

The careful selection of a suitable dataset is a crucial and pivotal stage in the training of neural networks, as it fundamentally influences their convergence and accuracy. In the context of PINNs, the dataset consists of the sampling points within the spatiotemporal domain D. Therefore, conducting a thorough analysis of the sampling strategies becomes imperative when training PINNs.

In this study, the sampling points can be categorized into three main groups:

1. Common collocations $\boldsymbol{S}_c$: These points are sampled within the domain D and are representative of the overall behavior of the system.
2. Adaptively sampled collocations $\boldsymbol{S}_a$: These points are sampled and dynamically adjusted to accurately capture the sharp interface transitions that occur during the evolution of the system.
3. Initial/boundary collocations $\boldsymbol{S}_i$,$\boldsymbol{S}_b$: These points are sampled on the initial and boundary conditions of the problem.

It is worth noting that the collocations used to compute the loss term of the governing equations (namely in-domain collocations) are formed by the union of common collocations and adaptively sampled collocations, denoted as $S_f = S_c \cup S_a$. At the beginning of the training process, each category of points is sampled using specific strategies. Subsequently, the sampling points are periodically resampled and updated to ensure that they effectively capture the evolving behavior of the system. Further details regarding these sampling strategies will be discussed in the subsequent sections.

2.2.1 *Cross-scale sampling for continuous initial collocations*

When solving the phase field governing equations, conventional numerical methods typically involve meshing the domain and imposing discrete initial conditions on the mesh. Then interpolation is conducted to obtain the initial conditions at any position within the domain. In the context of pitting corrosion, it is sufficient to declare the initial position of the corrosion interface using conditional syntax, without explicitly specifying the detailed profile of the diffuse phase-field interface. For instance, in a one-dimensional problem, a common form to express the initial condition is as follows:

$$\hat{u}(x_0, 0) = \begin{cases} 1 & x_0 \geqslant 0 \\ 0 & x_0 < 0 \end{cases} \tag{3}$$

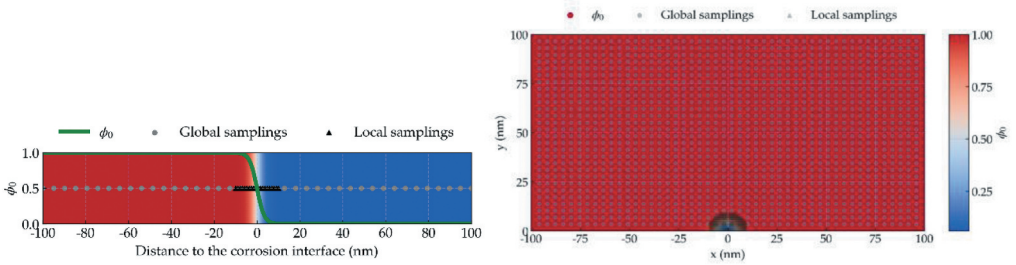
Since PINNs are meshless and continuous, the neural network will learn and fit the initial condition at any position when $t = 0$. Therefore, if the initial condition is solely defined by specifying the position of the corrosion interface at the initial moment using conditional syntax, PINNs may capture a discrete and abrupt interface. This contradicts the fundamental concept of diffuse interfaces in the phase field method. Therefore, it is necessary to incorporate a refined phase-field profile with an analytical expression.

In this regard, (Kim et al., 1999) proposed a smooth interpolation function for the equilibrium phase-field profile, which is given by:

$$\phi_0(x) = \frac{1}{2}\left[1 - \tanh\left(\frac{\sqrt{\omega}}{\sqrt{2\alpha_\phi}}x\right)\right] \tag{4}$$

$$c_0(x) = h[\phi_0(x)]c_S^e + \{1 - h[\phi_0(x)]\}c_L^e \tag{5}$$

In phase-field modeling, the interface of the phase transition between the solid and liquid phases is typically confined to an extremely narrow region (see Figure 1a). When sampling collocation points for initial conditions solely at a global scale, only a limited number of scatters are distributed over the diffuse interface. Consequently, the phase field and concentration profiles described in Equations 4 and 5 may pose challenges for PINNs to learn. Furthermore, when simulating pitting corrosion conducted in two dimensions and higher, the initial pits typically occupy a very small portion of the spatial domain (see Figure 1b). Employing single-scale sampling in such scenarios would result in a significant imbalance in the number of scattered samples representing the solid and liquid phases. This imbalance would lead to the failure of PINNs in learning the initial conditions.



(a) (b)

Figure 1. Examples for cross-scale sampling of continuous initial conditions: (a) One-dimensional case; (b) Two-dimensional case.

Consequently, a cross-scale sampling strategy is employed to address the issue. Given that the gradients of the physical fields are all zero in the region outside the phase transition, it is reasonable to cover the entire spatial domain at time $t = 0$ using global sampling with a relatively low density. However, in the vicinity of the corrosion interface at the initial moment, the local spatial domain needs to be sampled more densely.

2.2.2 *Adaptive sampling strategy*

In the simulation of pitting problems, it is common to observe extremely high gradients in the physics field near the corrosion interface. To address this issue, a residual-based adaptive sampling strategy was initially introduced in Ref. (Lu et al., 2021).The fundamental concept behind this strategy involves incorporating sampling points with the highest residual term, in relation to the governing equations, into the training of the subsequent iteration.

This study summarizes the general scheme for performing adaptive sampling in PINNs when dealing with coupled governing equations, as shown in Algorithm 1. The key concept of this algorithm is the choice of the criterion for the computation of the indicating values $\{R\}$. In particular, two kinds of effective criteria are proposed for the adaptive sampling of the phase field model.

Algorithm 1. General scheme of adaptive sampling.

Step1:	Conduct a sufficiently dense and random sampling of $N_{a,b}$ points within the spatiotemporal domain D, thereby establishing the base set of adaptively sampled points $S_{a,b}$;
Step2:	Input the complete base set into the PINN model and obtain the corresponding solution $\hat{u}$;
Step3:	Compute several groups of indicating values $\{\mathcal{R}\}$ based on a pre-defined criterion, as described in Equations 6-11
Step4:	Select the points corresponding to the highest k from each set of indicating values and subsequently merge any duplicate points from different sets to obtain the final set of adaptively sampled points S_a

Residual criterion: Points corresponding to the highest k absolute residual values of the governing equations are selected, expressed as

$$S_{a,\mathrm{AC}} = \arg_{(x_j,t_j)} \mathrm{TopK}\left|\mathcal{F}_{AC}\left[x_j, t_j, \hat{u}(x_j, t_j)\right]\right| \quad (x_j, t_j) \in S_{a,b} \tag{6}$$

$$S_{a,\mathrm{CH}} = \arg_{(x_j,t_j)} \mathrm{TopK}\left|\mathcal{F}_{AH}\left[x_j, t_j, \hat{u}(x_j, t_j)\right]\right| \quad (x_j, t_j) \in S_{a,b} \tag{7}$$

$$S_a = S_{a,\mathrm{AC}} \cup S_{a,\mathrm{CH}} \tag{8}$$

where $S_{a,\mathrm{AC}}$,$S_{a,\mathrm{CH}}$ and $\mathcal{F}_{AC}$, $\mathcal{F}_{CH}$ denote the adaptively sampled points and the residuals of the Allen-Cahn and Cahn-Hilliard equations, respectively.

Residual criterion: Points corresponding to the highest k absolute gradient values with respect to the spatial and temporal coordinates are selected, expressed as (in one-dimensional cases)

$$S_{a,x} = \arg_{(x_j,t_j)} \mathrm{TopK} \left| \frac{\partial \hat{u}(x_j,t_j)}{\partial x_j} \right| \quad (x_j,t_j) \in S_{a,b} \tag{9}$$

$$S_{a,t} = \arg_{(x_j,t_j)} \mathrm{TopK} \left| \frac{\partial \hat{u}(x_j,t_j)}{\partial t_j} \right| \quad (x_j,t_j) \in S_{a,b} \tag{10}$$

$$S_a = S_{a,x} \cup S_{a,t} \tag{11}$$

2.3 *NTK-based adaptive weighting strategy with random-batch technique*

In the context of the phase field model governed by coupled equations, the loss function consists of four terms: (1) the loss for the Allen-Cahn equation, (2) the loss for the Cahn-Hilliard equation, (3) the loss for the initial condition, and (4) the loss for the boundary condition. Consequently, the training process of PINNs can be viewed as a multi-objective optimization problem (Bischof and Kraus, 2021). To ensure the convergence and accuracy of the PINNs model, it is crucial to assign appropriate weights to the combination of these competitive loss terms.

In this study, an NTK-based weighting strategy is employed (Wang et al., 2022) to conduct the adaptive weighting of the loss terms. In addition, to improve the efficiency of the NTK-based weighting strategy, a random-batch technique is introduced to reduce the computational cost of the NTK calculation.

Let $\boldsymbol{J}_{\mathrm{AC}}(s)$,$\boldsymbol{J}_{\mathrm{CH}}(s)$,$\boldsymbol{J}_{\mathrm{IC}}(s)$,$\boldsymbol{J}_{\mathrm{BC}}(s)$ be the Jacobian matrices of the left sides of the PDE with respect to the network parameters $\boldsymbol{\theta}$ at iteration s. The NTK matrices of the four loss terms can be expressed as

$$\boldsymbol{K}_j = \boldsymbol{J}_j(s)\boldsymbol{J}_j(s)^T \tag{12}$$

where the subscript j can represent any of the four loss terms, i.e. AC, CH, IC, BC. The weight of each loss term can then be calculated as inversely proportional to the mean values of the corresponding traces, which can be expressed as

$$\omega_j(s) = \frac{N_j}{\mathrm{tr}(\boldsymbol{K}_j(s))} \left[\frac{\mathrm{tr}(\boldsymbol{K}_{\mathrm{AC}}(s))}{N_{\mathrm{AC}}} + \frac{\mathrm{tr}(\boldsymbol{K}_{\mathrm{CH}}(s))}{N_{\mathrm{CH}}} + \frac{\mathrm{tr}(\boldsymbol{K}_{\mathrm{IC}}(s))}{N_{\mathrm{IC}}} + \frac{\mathrm{tr}(\boldsymbol{K}_{\mathrm{BC}}(s))}{N_{\mathrm{BC}}} \right] \tag{13}$$

Here, j = AC,CH,IC,BC and $\omega_j(s)$ denotes the weight of each loss term at iteration s.

In order to facilitate the calculation process of NTK-based weights for large-scale samplings, a random-batch technique is proposed in this study. Instead of using all the samplings to calculate the weights, the random-batch technique reduces the requirements for computational cost by randomly sampling a small batch of points to represent the entire sampling set.

Let us consider the elements on the main diagonal of the NTK matrices as random variables, denoted as X_{AC}, X_{CH}, X_{IC} and X_{BC}, corresponding to the four loss terms. Specifically, we have:

$$X_j = \mathrm{diag}(K_j) = \left[x_{j,11}, x_{j,22}, \cdots, x_{j,N_jN_j}\right] \tag{14}$$

The ratio of the trace of the NTK matrix to the matrix dimension, $\mathrm{tr}(K_j)/N_j$, represents the mean of the population, denoted as $\mu_{X\mathrm{j}}$. Consequently, each weight ω_j in Equation 13 can be expressed as a linear combination of the means of the population of the four random variables:

$$\omega_j = \frac{1}{\mu_{X_j}} \sum \mu_{X_j} = \frac{1}{\mu_{X_j}} \left(\mu_{X_{\mathrm{AC}}} + \mu_{X_{\mathrm{CH}}} + \mu_{X_{\mathrm{IC}}} + \mu_{X_{\mathrm{BC}}}\right) \tag{15}$$

According to the central limit theorem, the mean of a sufficiently large number of random samples approaches the mean of the population (Dinov et al., 2008), i.e.

$$\lim_{b_j \to N_j} \mu_{Y_j} = \mu_{X_j} \tag{16}$$

where Y_j represents the random selected subset of X_j with a batch size of b_j. Therefore, for an appropriate batch size b_j, the mean of the random samples μ_{Yj} can be used to approximate the mean of the population μ_{Xj}. The above analysis indicates the rationality of using the random-batch technique to calculate the NTK-based weights.

3 RESULTS

To validate the effectiveness of the PC-PINN framework, we employ it to solve two illustrative phase-field pitting corrosion problems, namely one-dimensional and two-dimensional diffusion-controlled corrosion problems. The reference solution is obtained using the finite element method implemented in the Python package FeniCS (Logg and Wells, 2010).

3.1 *One-dimensional diffusion-controlled corrosion*

In this case, the spatial domain spans from –50 to 50 nm, while the temporal domain ranges from 0 to 100 s. The initial and boundary conditions are depicted in Figure 2. At the initial moment, the corrosion interface is positioned at x = 40 nm.

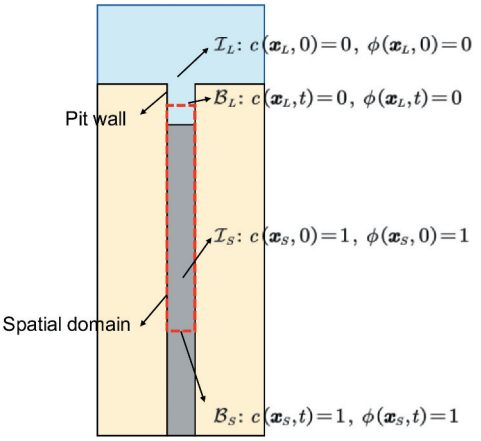


Figure 2. Schematic of the initial and boundary conditions for the one-dimensional diffusion-controlled corrosion problem.

In this model, we employ a neural network architecture consisting of 8 hidden layers, each containing 16 neurons. For the sampling process, we utilize 900 common collocations, with 30 collocations allocated on each coordinate. Both the number of initial collocations and boundary collocations are set to 128. 4,000 adaptive samplings are selected from a base set comprising a total of 30,000 points. For the weighting process, the NTK-based weighting strategy with the random-batch technique is adopted with a batch size of 512. The samplings and weights are updated once every 1,000 iterations. We train the model for 50,000 iterations with a learning rate of 50×10^{-4}.

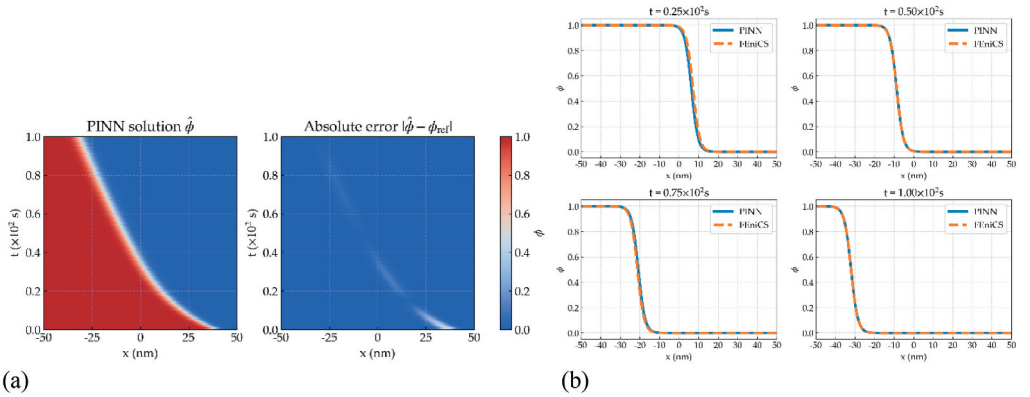


Figure 3. Evaluation of the baseline model for the one-dimensional diffusion-controlled corrosion problem: (a) The PINN solution $\hat{\phi}$ and absolute error $|\hat{\phi} - \phi_{\text{ref}}|$; (b) Time snapshots of the reference solution and the PINN solution.

The comparative solution obtained using the PINN and the reference solution is presented in Figure 3. Figure3a presents the distribution of PINN solution $\hat{\phi}$ and the absolute error $|\hat{\phi} - \phi_{\text{ref}}|$. The MSE value of the PINN solution is 8.769×10^{-4}, indicating the good performance of the PINN model on the overall accuracy across the entire spatiotemporal domain. Figure 3b demonstrates the agreement of the PINN solution and the reference solution at some specific moments.

3.2 *Two-dimensional diffusion-controlled corrosion*

In this case, the spatial domain is set to [–50, 50] × [0, 50] nm and the temporal domain ranges from 0 to 50 s. The initial and boundary conditions are depicted in Figure 2. At the initial moment, the center of the corrosion interface is positioned on a semicircle arc with a radius of 5 nm and a center of (0,0).

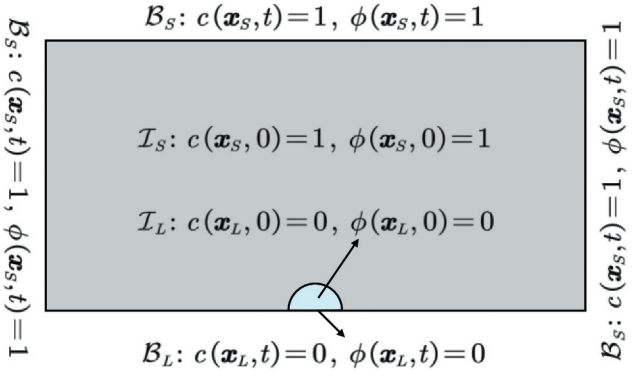


Figure 4. Schematic of the initial and boundary conditions for the two-dimensional diffusion-controlled corrosion problem.

In this model, we employ a neural network architecture consisting of 8 hidden layers, each containing 16 neurons. For the sampling process, we utilize 3375 common collocations, with 15 collocations allocated on each coordinate. The numbers of initial collocations and boundary collocations are set to 128 and 256, respectively. The residual criterion is employed to adaptively sample 8,000 points from a base set comprising a total of 60,000 points. For the weighting process, the NTK-based weighting strategy with the random-batch technique is adopted with a batch size of 512. The samplings and weights are updated once every 1,000 iterations. We train the model for 50,000 iterations with a learning rate of 1.0×10^{-3} and then continue training for another 50,000 iterations with a learning rate of 1.0×10^{-4}.

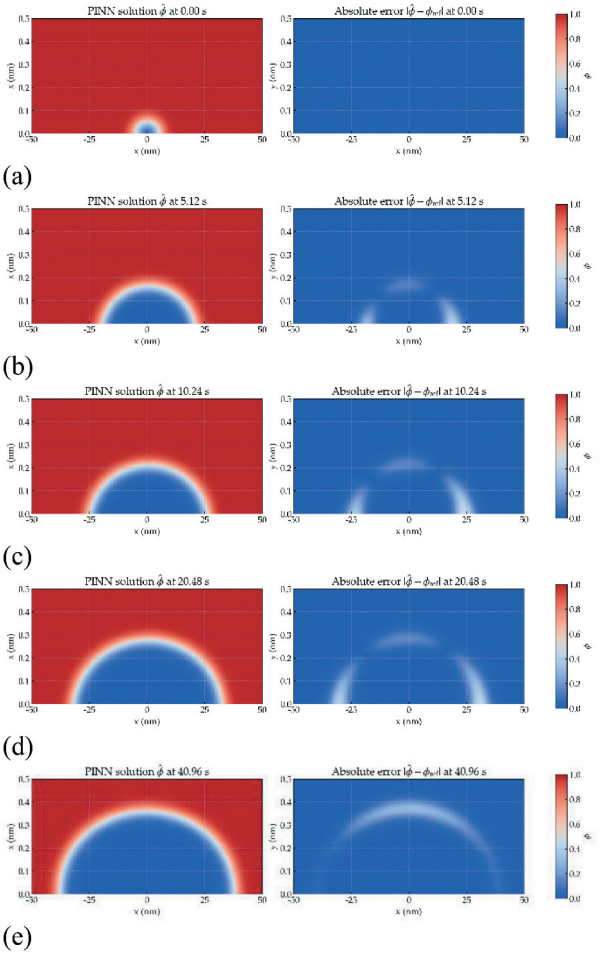


Figure 5. Time snapshots of the reference solution and the PINN solution. (a) t = 0.00 s; (b) t = 5.12 s; (c) t = 10.24 s; (d) t = 20.48 s; (e) t = 40.96 s.

Figure 5 presents the distributions of the PINN solution $\hat{\phi}$ and the absolute error $\left|\hat{\phi} - \phi_{\text{ref}}\right|$ at specific moments. The mean value of the mean squared error (MSE) at each moment is 6.658×10^{-4}, indicating the excellent performance of the PINN model in terms of overall accuracy across the entire spatiotemporal domain.

4 CONCLUSION

A new PINN framework (PC-PINN) is proposed to solve the phase-field model of pitting corrosion in real-world physical contexts. The PC-PINN model addresses the challenges posed by the high stiffness and sharp interface transition of the coupled Allen-Cahn and Cahn-Hilliard equations by incorporates adaptive strategies and techniques for weighting and sampling.

We successfully solve two representative phase-field pitting corrosion problems using the proposed framework. The obtained results clearly demonstrate the high accuracy of the PC-PINN model in predicting the evolution of the phase-field variable and the corrosion interface. This serves as a strong validation of the effectiveness of the PC-PINN framework.

ACKNOWLEDGEMENT

The authors acknowledge financial support from the National Natural Science Foundation of China (grants No.52178153 and No.52238005), National Key R & D Program of China (grant No. 2021YFF0501003). Chuanjie Cui additionally acknowledges financial support from the UKRI Horizon Europe Guarantee MSCA Postdoctoral Fellowship (grant EP/Y028236/1).

REFERENCES

Bischof, R., Kraus, M., 2021. Multi-Objective Loss Balancing for Physics-Informed Deep Learning.

Chen, L.-Q., 2002. Phase-Field Models for Microstructure Evolution. Annu. Rev. Mater. Res. 32, 113–140.

Cuomo, S., di Cola, V.S., Giampaolo, F., Rozza, G., Raissi, M., Piccialli, F., 2022. Scientific Machine Learning through Physics-Informed Neural Networks: Where we are and What's next.

Dinov, I.D., Christou, N., Sanchez, J., 2008. Central Limit Theorem: New SOCR Applet and Demonstration Activity. J. Stat. Educ. 16.

Kim, S.G., Kim, W.T., Suzuki, T., 1999. Phase-field model for binary alloys. Phys. Rev. E 60, 7186–7197.

Logg, A., Wells, G.N., 2010. DOLFIN: Automated finite element computing. ACM Trans. Math. Softw. 37, 1–28.

Lu, L., Meng, X., Mao, Z., Karniadakis, G.E., 2021. DeepXDE: A deep learning library for solving differential equations. SIAM Rev. 63, 208–228.

Mai, W., Soghrati, S., Buchheit, R.G., 2016. A phase field model for simulating the pitting corrosion. Corros. Sci. 110, 157–166.

Wang, S., Yu, X., Perdikaris, P., 2022. When and why PINNs fail to train: A neural tangent kernel perspective. J. Comput. Phys. 449, 110768.

Wu, C., Zhu, M., Tan, Q., Kartha, Y., Lu, L., 2023. A comprehensive study of non-adaptive and residual-based adaptive sampling for physics-informed neural networks. Comput. Methods Appl. Mech. Eng. 403, 115671.

Zhao, Y., Xing, H., Zhang, L., Huang, H., Sun, D., Dong, X., Shen, Y., Wang, J., 2023. Development of Phase-Field Modeling in Materials Science in China: A Review. Acta Metall. Sin. Engl. Lett. 36, 1749–1775.

Bridge Maintenance, Safety, Management, Digitalization and Sustainability – Jensen, Frangopol & Schmidt (eds)
© 2024 The Author(s), ISBN 978-1-032-77040-6
Open Access: www.taylorfrancis.com, CC BY-NC-ND 4.0 license

Sensitivity analysis on the fatigue factors for fatigue reliability evaluation

M.Z. Mili, K. Sugiura, Y. Kitane & R. Matsumoto
Graduate School of Engineering, Kyoto University, Kyoto, Japan

ABSTRACT: This study focuses on fatigue reliability in steel bridges, a critical concern due to increasing traffic loads. Employing the *S-N* curve method, a Stochastic Sensitivity Analysis (SSA) is conducted to assess the impact of input parameters. Miner's rule and fracture mechanics are compared for fatigue assessment, considering uncertainties through stochastic sensitivity analysis. Material-related factors and the equivalent stress range are identified as pivotal contributors to fatigue reliability. The study emphasizes the importance of understanding influential parameters for improved design and predictive insights in structural behavior.

1 INTRODUCTION

Fatigue in steel bridges is a common issue caused by increasing traffic loads (Kala 2019, Kwon & Frangopol 2011, Ye et al. 2014). Repeated exposure to external loads is the root cause of this phenomenon, i.e., cyclic load, which can engender local or global failure of the structure. It is estimated that fatigue is the cause of 38% of steel bridges collapse (Kuzawa et al. 2018). In this context, there is growing interest in assessing and predicting the remaining fatigue life of components and structures.

Several studies and research focused on the evaluation and prediction of fatigue damage. Researchers employed two different approaches. The first method is Miner's linear damage rule, also known as Miner's rule or the *S-N* curve method. (e.g., Kwon & Frangopol 2011). It stipulates that fatigue damage accumulates linearly with the number of cycles experienced at a given stress level. The fatigue life of a material can be estimated by summing damage contributions from each load cycle, normalized by the material's fatigue strength at that stress level. The second one is the fracture mechanics approach. It is a crack-based method based on the Paris-Erdogan law. Here, the focus is on the crack initiation and propagation considering the stress intensity at the crack tip (e.g. Kala 2019a, b, Kwon &Frangopol 2011, Leander & Al-Emrani 2016). The *S-N* curve method is used for the fatigue design and life assessment of existing bridges. The fracture mechanics method is an effective way to evaluate fatigue life related to crack propagation, as well as for inspection and maintenance planning (Chryssantopolos & Righiniotis, 2006; Kwon & Frangopol, 2011).

Both methods involve parameters related to loads and materials, introducing significant uncertainties. Treating these parameters as deterministic entities does not account for their inherent and time-dependent variability. As a result, probabilistic approaches are adopted for fatigue evaluation (Kala 2019a, b, Leander & Al-Emrani 2016, Ye et al. 2014).

Whether conducting a fatigue assessment for structural design or predictive purposes, it is crucial to comprehend the influence of fatigue factors related to loads and materials on structural fatigue performance. Sensitivity Analyses (SA) are often conducted in engineering to assess the influence of the inputs on the outputs of a process or a system. To account for the uncertainties of inputs, researchers turn to Stochastic Sensitivity Analyses (SSA) (Kala 2019a, b, Leander & Al-Emrani 2016).

DOI: 10.1201/9781003483755-26

From a management perspective, identifying the influential parameters affecting fatigue reliability is crucial. This determination not only facilitates the enhancement of design but also enhances the predictive understanding of the structure's behavior across various scenarios (Pan et al. 2020). Leander & Al-Emrani (2016) and Kala (2019a, b) identified key factors crucial for fatigue assessment through the application of the fracture mechanics approach. In this paper, an SSA is conducted to evaluate important factors for the fatigue reliability of a steel bridge using the *S-N* curve method. The monitoring data throughout the service life is simulated and the statistical parameters of the fatigue factors are assumed based on the results and recommendations of previous research. Several SSA methods are compared in the determination of the influential fatigue factors quantitatively and qualitatively. In all cases, the material-related material factors and the equivalent stress range are found to be the most important factors.

2 FATIGUE RELIABILITY ANALYSIS

2.1 *Limit state function*

In the general case, the limit state function is given by Equation 1:

$$G(R, Q) = R - Q \tag{1}$$

where R is the resistance and Q is the load effect. This implies that if the resistance R is greater than the load Q ($G \geq 0$), the structure performs normally under the given load condition. However, if the load effect Q exceeds the structure's resistance ($G<0$), the safety of the structure is compromised. In the particular case of fatigue assessment based on the Miner's rule and the Japanese standards, the limit state function is written as follows (Kwon & Frangopol 2011, JRA 2012):

$$g(X) = \Delta - e\frac{N_{total}}{C_0}\left(SR_{eq}\right)^m \tag{2}$$

$$SR_{eq} = \left(\sum_{i=1}^{k} \frac{n_i}{N_{total}}.SR_i^m\right)^{1/m} \tag{3}$$

where Δ is the Miner's critical damage accumulation index, e is the error factor, N is the number of stress cycles, C_0 is the fatigue detail coefficient for each category, m is the slope of the *S-N* curve, SR_{eq} is the equivalent stress range given by Equation 3, n_i is the number of observations in the i^{th} predefined stress range bin SR_i, and N_{total} is the total number of recorded cycles up to the k^{th} range.

2.2 *The uncertainties of resistance factors* Δ, C_0, *and* m

Miner's rule assumes that the fraction of total fatigue life consumed by multiple stress cycles at a specific stress level is proportional to the overall number of cycles, with fatigue failure occurring when the sum of contributions from all stress ranges equals Δ (usually assumed equal to one). Experiments show that Miner's rule reasonably predicts fatigue life under random loadings, but its deterministic nature overlooks the scatter of fatigue experimental results. A more accurate description of fatigue failure considers that fatigue damage (D) exceeds the critical damage accumulation index Δ.

$$\sum_{i=1}^{k} \frac{n_i}{N_i} = D \geq \Delta \tag{4}$$

The fatigue tests employed to establish S-N curves are recognized for yielding scattered results even under identical loading conditions (Wirsching 1984, Wirsching et al. 1991). The S-N curves proposed by the design codes are lowered for the sake of safety. In other words, joints are more likely to endure more cycles than specified by the design code (Leander & Al-Emrani 2016). For

instance, studies indicate that a coefficient of variation of the fatigue detail C_0 ranges from 0.45 to 1.35, highlighting the significance of uncertainties in factors derived from S-N curves (Wirsching 1984, Wirsching et al. 1991, Kwon & Frangopol 2011). To address these uncertainties, C_0 is treated as a random variable. The slope of the *S-N* curve (m) is kept deterministic in this study as the material uncertainties in *S-N* curves are addressed through the fatigue detail coefficient C_0.

2.3 *The load factors*

Field monitoring data are crucial in the fatigue evaluation regardless of the adopted method. This data provides insight into the load condition of the structure. Using Hook's law and the rain-flow counting method, the monitored strain data provide the equivalent stress range bin histogram and the number of cycles, i.e. N, n_i, and N_{total}. In addition, this data is used to gain information on the variability of load volume and intensity over time when a long-term monitoring system is used (Kwon & Frangopol 2011).

2.4 *Error factor e*

The error factor permits accounting for modeling errors. The main source of error is the strain gauges (Kwon & Frangopol 2011, Wirsching 1984). These errors are revealed by the sensors' manufacturer or investigated by researchers. Frangopol et al. (2008) have reported that electrical strain gauges have an error margin of 1-4%. The coefficient of variation COV(e) ranges between 3-4% (Kwon & Frangopol 2011, Frangopol et al. 2008, Leander, Al-Emrani 2016).

2.5 *Fatigue reliability model FRM*

Figure 1 schematizes the fatigue reliability model used in this research. The statistical parameters of the average daily truck traffic ADTT and strain are obtained for the monitoring data. Using Hooke's law, strain is transformed into stress and the stress range bin histogram is established by rain-flow counting. The equivalent stress range is derived by Equation 3. The statistical parameters and the distribution type of the rest of the parameters are determined based on the previous studies (Wirsching 1984, Wirsching et al. 1991, Frangopol et al. 2008, Kwon & Frangopol 2011). The probability of failure P_f is the ratio between the number of times that failure occurs $S(G<0)$ and the total number of simulations (S). P_f is given by Equation 5 (Nowak & Collins 2013).

$$P_f = \frac{S(G<0)}{S_{Total}} \tag{5}$$

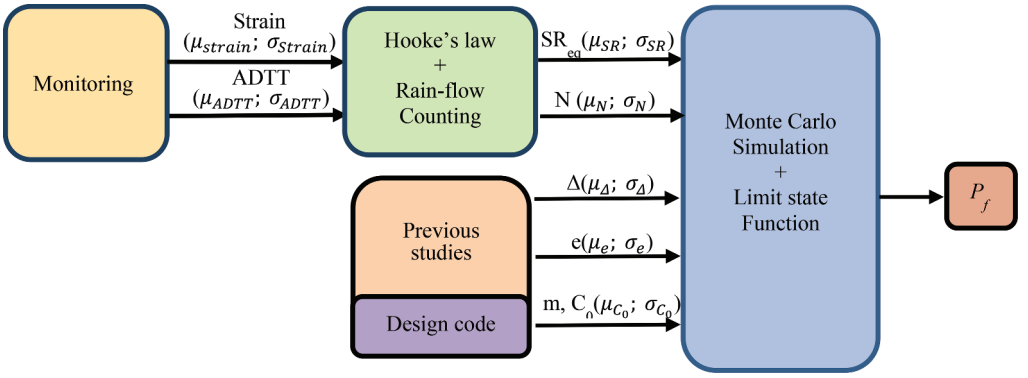


Figure 1. Scheme of the fatigue reliability analysis.

3 SENSITIVITY ANALYSIS

Many studies have looked into sensitivity methods, exploring how they work and where they can be used. Some examples include Borgonovoa & Plischke (2016), Pan et al. (2021), and Novák et al. (2017). Sensitivity methods are classified into two types: global and local sensitivity methods. A local sensitivity method assesses how sensitive a system or model is to changes in its input variables at a specific point or region. Instead of examining the overall impact across the entire system, it focuses on understanding the influence of variations in input parameters near a particular condition or scenario. A global sensitivity checks additionally how input variables interact with each other across the whole system. The Sobol indices method is a well-developed tool to analyze sensitivity. However, the calculation of the Sobol indices with the Monte Carlo method is still quite demanding in terms of computational effort (Pan et al. 2021). In addition, Pan et al. (2021) proved through examples that the local sensitivity methods, that is the local analysis of variation, present a good agreement with the results of Sobol indices method. Considering the scope of this study and the computational constraint, the following local sensitivity methods are considered.

3.1 *The local perturbation method*

The local perturbation method also called the one-at-a-time (OAT) method is a straightforward sensitivity analysis approach. It involves changing one input variable at a time while keeping others constant and observing the resulting impact on the model's output. This method provides a quick and practical way to understand the influence of individual factors on the overall system response (Pan et al. 2021, Borgonovoa & Plischke 2016).

3.2 *Local analysis of variation*

This method aims to assess the influence of the variance of a given input variable on the variance of the system. This consists on calculating the variance of the model response while setting the i^{th} variable at its mean and all the other variables free to vary. The sensitivity indicator S_i is given by Equation 6 (Pan et al. 2021).

$$S_i = 1 - \frac{CoV_i}{CoV_{original}} \tag{6}$$

Here CoV_i is the standard deviation of the response if the i^{th} input is fixed at the mean and $CoV_{original}$ is the standard deviation of the response when all the random variables are free to vary. A value of S_i close to 1 indicates that the variability of the system is generated essentially by the i^{th} variable.

3.3 *The omission sensitivity factor*

The omission sensitivity analysis was presented by Madsen (1988), and used by Lander & Al-Emrani (2016) in their fatigue sensitivity analysis based on fracture mechanics. The omission Sensitivity Factor is defined as the ratio between the output of a system or mathematical model (i.e. the probability of failure or the reliability index) when all the random variables are free to vary and the response when the i^{th} is set at its mean as denoted by Equation 7.

$$O_i = \frac{F_{original}}{F_{Xi}} \tag{7}$$

Here F_{Xi} is the response when X_i is set at its mean and $F_{original}$ is the response when all the random variables are free to vary. A value near 1 suggests that the random variable can be effectively set to its mean, indicating minimal impact on the output. Conversely, the interpretation of O_i values varies depending on the type of response. For example, the significance of

these factors changes based on whether the response relates to the reliability index or the probability of failure.

3.4 *The correlation coefficient*

The correlation coefficient (ρ), also called Pearson correlation coefficient, indicates the degree of linear dependence between two random variables (Novak & Collins 2013). In the context of sensitivity analysis, the correlation coefficient has been used to measure the relative effect of each basic random variable on the structural response (Iooss & Lemaître 2015, Novák et al. 2017). With values ranging between 1 and -1, the correlation matrix provides an intuitive insight on the relation between the response and the input random variables. This is a straightforward and uncomplicated method that demands no additional computational effort, particularly when employing Monte Carlo simulations (Novák et al. 2017).

4 SIMULATION PROCESS AND SENSITIVITY ANALYSIS

4.1 *Modeling assumption and initial values*

In this study, the monitoring data throughout the service life (i.e. strain data and ADTT) is simulated by assuming their initial statistical parameters. It is assumed that the yearly increase of traffic volume and the traffic load (GVW) are 3% and 1% respectively. The relative variability of the strain and the average daily traffic is kept constant during the service life. Young's modulus and the slope of the *S-N* curve *m* are considered as deterministic. The values of the deterministic inputs are summarized in Table 1.

Table 1. The initial values of deterministic inputs.

Deterministic inputs	Value
Service life (years)	50
e_t	3%
e_{Strain}	1%
Number of samples (MC simulation)	500 000
Young's Modulus (GPa)	210
Joint category	D
m	3

In this study, the coefficient of variation (CoV) is considered for the random variable instead of the standard deviation for two reasons. Firstly, CoV is advantageous for variables with diverse units or scales. Normalizing variability relative to the mean and providing a standardized, percentage-based measure that facilitates meaningful comparisons independently of specific units or scales. Furthermore, assessing the variation of a random variable using its Coefficient of Variation becomes more rational, especially when the variable follows a skewed distribution, such as a lognormal distribution in this context.

The statistical parameters of all random variables are derived from previous studies. It is assumed that all the input random variables are uncorrelated. The details of the input variables are summarized in Table 2.

Regarding ADTT and strain, the references mentioned in Table 2 provides the CoV. The means were considered in a subjective manner. As for C_0, it was calculated using Equation 8 in accordance with Japanese standards (JRA 2012).

$$C_0 = 2 \times 10^6 \times \Delta SR^m_{allow} \tag{8}$$

Table 2. Statistical parameters of random variables.

Random variable	Distribution	Mean	CoV	Source
ADTT (truck/day)	Normal	1000	10%	Nowak & Collins 2013
Strain	Normal	0.0012	10%	Fu et al. 2022
Δ	Lognormal	1.0	30%	Wirsching 1984, Kwon & Frangopol 2011
Error	Lognormal	1.0	3%	Wirsching 1984, Frangopol et al. 2008, Kwon & Frangopol 2011, Leander & Al-Emrani 2016
C_0 (Detail D)	Lognormal	2E+13	45%	Wirching 1984, Wirsching et al. 1991, JRA 2012

Here ΔSR_{allow} is the basic allowable stress range for each category. The mean was computed utilizing the bias factor introduced by Wirsching (1984) and Wirsching et al. (1991). These references have also identified that the Coefficient of Variation (CoV) for the fatigue coefficient C_0 ranges from 0.45 to 1.35. In this study, the minimum value within this range was assumed. The same value was adopted by Kwon & Frangopol (2011) in their corresponding study.

4.2 *Sensitivity analysis*

The initial values and the statistical parameters depicted in Table 1 and Table 2 represent the reference scenario of this study. The probability of failure is computed using the Monte Carlo simulation and Equations 2 and 5. The sensitivity analysis is performed at the end of the service life (year 50). The initial probability of failure, hereafter referred to as $P_{foriginal}$, is found equal to 0.0204. The CoV of the output variable, i.e. G, equals to 50.4%.

4.2.1 *The input perturbation sensitivity analysis*

The mean of each input random variable is first increased by 10% and then lowered by 10%. The effect of such a variation on the probability of failure P_f is calculated and compared to $P_{foriginal}$. It was observed that SR_{eq} exerts the most significant influence on the probability of failure. This observation can be mathematically explained by the fact that SR_{eq} is raised to the power of m (where m=3). The second and the third important parameters are respectively Δ and C_0. The results of the input perturbation sensitivity analysis are presented in Figure 2.

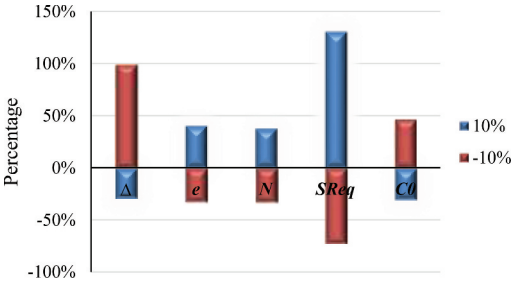


Figure 2. Results of the input perturbation SA.

4.2.2 *Local analysis of variation sensitivity analysis*

The sign of S_i signifies that when the associated random variable is set to its mean value, there is a reduction in output variability for positive values, and an increase in variability for negative values. Therefore, sensitivity is assessed based on the absolute values S_i. The outcomes of this sensitivity analysis presented in Table 3 reveal that the most influential input variables are Δ, C_0, and $SReq$.

Table 3. Local analysis of variation outcomes.

	S_i	Rank
Δ	0.462	1
e	0.001	5
N	0.004	4
$SReq$	0.108	3
C_0	-0.307	2

4.2.3 *The omission sensitivity factor*

When the response is the probability of failure, O_i values greater than 1 suggest that reducing uncertainties associated with the i^{th} variable leads to a decrease in the probability of failure. Conversely, values lower than 1 indicate that replacing the i^{th} variable with its mean value raises the probability of failure, and maintaining uncertainties in this variable contributes to improving the structural performance. According to this sensitivity indicator, SR_{eq} is identified as the parameter exerting the most significant influence on the probability of failure, followed by Δ and C_0. Similarly, consistent with previous methods, the number of cycles and the error factor exhibit an insignificant impact on the probability of failure. The results are shown in Table 4.

Table 4. Omission sensitivity factor.

	O_i	Rank
Δ	2.22	1
e	1.02	5
N	1.01	4
$SReq$	3.90	2
C_0	0.40	3

4.2.4 *The correlation coefficient matrix*

The correlation coefficients are presented in Table 5. Positive values indicate the random variable enhances the response, reducing the failure probability, while negative values imply a decrease in the response, elevating the failure probability. Notably, it is observed that ρ is positive for material-related parameters, such as Δ and C_0, and negative for the other parameters. The most important parameter here is Δ followed by SR_{eq} and C_0.

Table 5. The correlation coefficients.

	G	Δ	e	N	$SReq$	C_0
G	1	0.899	-0.021	-0.027	-0.281	0.251
Δ	0.899	1	-0.001	0.001	0.001	-0.001
e	-0.021	-0.001	1	-0.002	-0.001	0.000
N	-0.027	0.001	-0.002	1	0.001	0.001
$SReq$	-0.281	0.001	-0.001	0.001	1	-0.001
C_0	0.251	-0.001	0.000	0.001	-0.001	1

5 DISCUSSION AND CONCLUSION

A probability-based sensitivity analysis of fatigue reliability was undertaken, employing the *S-N* curve method for evaluating and predicting fatigue damage. Various sensitivity analysis methods were applied to assess the sensitivity of input parameters. Each method measured the significance of the input parameters and established a ranking, which is presented in Table 6.

Based on the results, it has been established that the material-related variables and the stress factor are of utmost importance. In simpler terms, an increase in traffic volume (N) has a lesser impact on the bridge than an increase in load spectrum (SR_{eq}). Additionally, it can be

Table 6. The sensitivity ranking of the input variables with different SA methods.

	Input perturbation	Local analysis of variation	The omission sensitivity factor	The correlation coefficient
Δ	2	1	1	1
e	4	5	5	5
N	5	4	4	4
$SReq$	1	3	2	2
C_0	3	2	3	3

deduced that the accuracy of sensors in the context of fatigue assessment does not significantly impact the evaluation of fatigue life. This aligns with the conclusions drawn by Kala (2019a, b) and Leander & Al-Emrani (2016), despite the different fatigue reliability assessment methods employed in the two studies, namely the fracture mechanics method.

It is also noted that the outcomes of sensitivity analysis are method-dependent, potentially leading to misleading estimations of the most critical parameters. Pan et al. (2021) proved, through various examples, that different sensitivity analysis methods can diverge in identifying the most influential parameter. This discrepancy is attributed to the unique characteristics inherent in each sensitivity analysis method.

However, these methods are simpler and more straightforward to implement compared to the well-developed Sobol indices method. Depending on the objectives of the sensitivity analysis, these methods can provide sufficient insights into the crucial parameters for a given model, offering a convenient initial assessment.

REFERENCES

Borgonovoa, E., Plischke, E. 2016. Sensitivity analysis: A review of recent advances. *European Journal of Operational Research* 248: 869–887.

Chryssanthopoulos, M.K., Righiniotis, T.D. 2006. Fatigue reliability of welded steel structures. Journal of Constructional Steel Research 62 (11): 1199–1209.

Frangopol, D. M., Strauss, A., Kim, S. 2008. Bridge reliability assessment Based on Monitoring, *Journal of Bridge Engineering 13*.

Fu, H., Zhou. X, Zhou, Q., Xiang, P., Zhou, Z. Fu, Q. 2022. An Improved Model for Design Fatigue Load of Highway Bridges Considering Damage Equivalence. *MDPI* 12: 217.

Iooss, B., Lemaître, P. 2015. A review on global sensitivity analysis methods. *Algorithms and Applications*. Springer.

Japan Road Association, 2012. Specification for highway bridges – Part II steel bridges.

Kala, Z. 2019a. Global sensitivity of reliability of structural bridge system. *Engineering Structures* 194: 36–45.

Kala, Z. 2019b. Probability based global Sensitivity analysis of fatigue reliability of steel structures. *Material science and Engineering* 668. (012015).

Kużawa, M., Kamiński, T., Bień, J. 2018. Fatigue assessment procedure for old riveted road bridges. *Archives of Civil and Mechanical Engineering* 18: 1259–1274.

Kwon, K., Frangopol, D. M. 2011. Bridge fatigue assessment and management using reliability-based crack growth and probability of detection models. *Probabilistic Engineering Mechanics* 26: 471–480.

Leander, J., Al-Emrani, M. 2016. Reliability-based fatigue assessment of steel bridges using LEFM – A sensitivity analysis, *Int. J. of Fatigue* 93: 82–91.

Madsen, H. O. 1988. Omission sensitivity factors, *Structural Safety* 5: 35–45.

Novák, D., Lehký, D., Cao, M, Pan, L. 2017. Methods of sensitivity analysis and their role in engineering. *Advances in Engineering Research* 134. Atlantis Press.

Nowak, A. S., Collins, K. R. 2013. Reliability of structures, second edition, CRC Press.

Pan, L., Novák, L., Lehký, D., Novák, D., Cao, M. 2021. Neural network ensemble-based sensitivity analysis in structural engineering: Comparison of selected methods and the influence of statistical correlation. *Computers and Structures* 242.

Wirsching, P. H. 1984: Fatigue reliability for offshore structures. *Journal of Structural Engineering* 110.

Wirsching, P.H., Torng, T.Y., Martin, W.S. 1991. Advanced fatigue reliability analysis. *Int. J. Fatigue* 13: 389–394.

Ye, X. W., Su, Y. H., Han, J. P. 2014. A state of the art review on fatigue life assessment of steel bridges. (956473).

Bridge Maintenance, Safety, Management, Digitalization and Sustainability – Jensen, Frangopol & Schmidt (eds)
© 2024 The Author(s), ISBN 978-1-032-77040-6
Open Access: www.taylorfrancis.com, CC BY-NC-ND 4.0 license

Structural analysis of dapped-end beams through machine learning techniques

V. Picciano, G. Santarsiero, A. Masi & A. Digrisolo
School of Engineering, University of Basilicata, Potenza, Italy

ABSTRACT: Dapped-end beams (or half-joints) are extensively used in both reinforced concrete bridge structures and roofs and flooring for prefabricated buildings. Due to their geometric configuration, they represent discontinuity regions where high stresses concentrate. Therefore, it is crucial to evaluate the load-bearing capacity of these elements which may depend on various parameters, such as the strength of materials, the quantity and the different layouts of the used reinforcements which also significantly influence their failure mode. For this purpose, a literature review led to the creation of an experimental tests database used to conduct an in-depth statistical analysis, considering the influence of various parameters on the ultimate load capacity and failure mode of dapped-end beams. The collected database has been also used to train a regression model with supervised machine learning techniques in order to predict the ultimate capacity of dapped-end beams.

1 INTRODUCTION

Dapped-end beams have some advantages related to construction speed as connections are represented by half-joints (Figure 1) which facilitate the installation operations. In bridge structures, dapped-end beams are used as part of the cantilever bridges (also called Gerber bridges) for their capability of absorbing small settlements along with a convenient stress distribution. Geometrical details of dapped-end regions make them disturbed regions in which the Bernoulli theory cannot be applied to evaluate stresses and carry out the due safety checks, requiring purposely set-up assessment methods.

In fact, the load-bearing capacity of dapped-end beams can be assessed through different analytical and numerical methods. For example, strut-and-tie models (Mattock 2012, EN 1992-2 2005), eventually accounting for deterioration (Desnerck et al. 2018), are among the lower-bound methods, capable of providing conservative assessments.

The strut-and-tie method (STM) is based on the definition of a truss model that must be consistent with the behavior of dapped-ends observed during experiments in order to idealize the force flow in the recessed part of the beam end. STM trusses that better approximate the force flow in a structural component allow the design of an efficient reinforcement layout increasing the specific failure load and minimizing the occurrence of cracks under the service loads (Mattock 2012). Eurocode 2 (EN 1992-2 2005) provides two alternative models and related reinforcement layouts (one considering only horizontal and vertical bars while the other accounts for the inclined reinforcement also) which can be combined to evaluate to overall strength of a half-joint.

A design method is also reported in the PCI Design Handbook (2010) mainly devoted to precast elements belonging to buildings. This method is based on an experimental investigation in which several potential failure modes were highlighted. In particular, the safety checks of different reinforcement devices are made concerning five specific possible failure modes which can affect both the undapped and the dapped regions of the half-joint. The PCI method has some limitations compared to STM since does not consider inclined rebars and is valid for cases where the shear

DOI: 10.1201/9781003483755-27

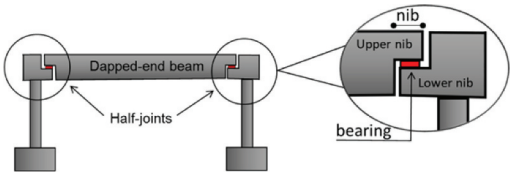


Figure 1. Typical dapped-end beam and half-joint detail.

span-to-depth ratio does not exceed 1.0. For these reasons, it is hardly helpful in the assessment of existing dapped-end elements.

Besides STM and PCI methods, kinematic methods can be used to predict the peak strength of half-joints. These methods assume that the failure mode is governed by the opening of a crack according to a selected pattern (e.g. diagonal cracking starting from the re-entrant corner) and impose that the static equilibrium is guaranteed by the steel crossing it. For example, the model proposed by Rajapakse et al. (2021) is based on the knowledge of the crack angle developing from the re-entrant corner assuming that the failure is governed by flexure stress. Moreover, the model considers the crack width as well as the amount of dapped-end reinforcement, along with the crack length and the rotation about the crack tip. This model was applied to a database of 47 experimental tests providing good prediction results compared to actual values.

A further option to assess the capacity of half-joints is represented by numerical methods consisting of refined finite element models based on nonlinear fracture mechanics (Bazant & Oh 1983). Moreover, there are modelling procedures which can explicitly account for corrosion propagation inside the member during a given period, allowing to perform durability analyses (Santarsiero et al. 2021).

In order to deepen the structural behaviour of dapped-end beams, this study describes a literature review on experimental tests of such elements, leading to the construction of a database of 210 specimens. Following a brief description of the half-joints' typical details and failure modes, a statistical analysis of the main collected parameters was conducted to observe their variability and highlight correlations, such as those between specific failure modes and certain reinforcement layouts. Finally, the database was used to train different regression models using supervised machine learning techniques to predict the ultimate strength of the specimens. These techniques helped identify the best-performing regression model that can be employed to quickly assess dapped-end beams.

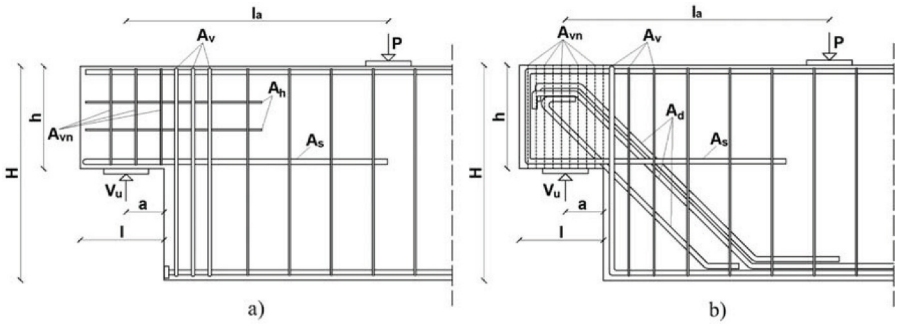


Figure 2. Different half-joint reinforcement layouts a) involving only vertical and horizontal reinforcement and b) also with inclined ones.

2 TYPICAL DETAILS AND FAILURE MODES

Due to their geometry, half-joints represent a discontinuity zone from the perspective of stress distribution, and, as previously illustrated, they require specific design and assessment methods. From a construction detailing point of view also, they represent singular elements

since the arrangement of reinforcements necessary for external load absorption can vary. In particular, considering both the upper and lower nib (Figure 1) as statically equivalent, the two most commonly used reinforcement layouts are illustrated in Figure 2.

Figure 2a illustrates a reinforcement layout mainly related to building structures, where only vertical and horizontal rebars are used. In this case, the absorption of external vertical forces occurs through the formation of an inclined concrete strut in the nib, which, for equilibrium purposes, requires the presence of a vertical tie, represented by the vertical stirrups A_v, and a horizontal tie through the presence of the A_s reinforcements, to which the contribution of horizontal secondary reinforcements A_h can be added, arranged within the nib as illustrated. The nib vertical stirrups A_{vn} have the purpose of confining the inclined concrete strut, thereby increasing its resistance and ductility. Therefore, the reinforcements form a truss mechanism, allowing for the absorption of external loads.

The alternative layout depicted in Figure 2b also involves the presence of inclined reinforcements A_d, providing an additional contribution to the truss mechanism. In particular, this second type of reinforcement layout is widely used within the Gerber saddles of existing bridges, especially in Europe. Inclined reinforcements, besides enhancing the overall half-joint's strength (Desnerck et al. 2016), also limit re-entrant corner cracking under service loads thus limiting the ingress of polluting agents such as chlorides, which can cause reinforcement corrosion (Santarsiero & Picciano 2023).

As for the dapped-end's ultimate behaviour, it is worth emphasizing that there can be different collapse modes depending on the adopted reinforcement layout. In particular, according to the PCI Design Handbook (2010), five potential failure modes are observed in half-joints under vertical loads (Figure 3). Mode 1 involves nib vertical cracking due to flexure and axial tension; mode 2 results from direct shear at the junction of the nib and the undapped region; mode 3 is caused by re-entrant corner diagonal tension; mode 4 represents nib shear failure, and mode 5 is due to diagonal tension in the undapped portion.

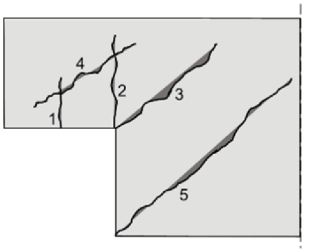


Figure 3. Possible half-joint failure modes according to the PCI Design Handbook (2010).

3 EXPERIMENTAL CAMPAIGNS AND DATABASE COLLECTION

In order to characterize the typical detailing, the failure modes and structural performances, a review of experimental research on half-joints has been conducted and partially illustrated in Santarsiero et al. (2023). This review activity allowed the collection of 147 experimental tests on dapped-end beams which have been recently updated to a total of 210, gathering information from 22 different research projects in the literature, briefly described in the following, for which several parameters were recorded. In particular, the amount and yielding stress of steel reinforcement at any position (stirrups, main vertical and horizontal, inclined) was annotated as well as the detailed geometry, concrete grade and, finally, the load test scheme along with the experimental peak load and failure type obtained during the test.

Mattock & Chan (1979) tested 8 dapped-end beam specimens all provided with the same geometry and different amounts of reinforcement in the vertical and horizontal direction along the re-entrant corner. In Kumaraguru (1992), 12 dapped-end beams were tested to find the capacity of the nibs for different locations of the support reaction and therefore with

different values of the shear span-to-depth ratio. Lu et al. (2003) conducted an experimental program to study the behaviour of high-strength concrete dapped-end beams testing 12 specimens with the same geometry and different detailing and concrete strength. The effect of different amounts of principal horizontal and vertical reinforcement, the shear span-to-depth ratio and the concrete strength on the specimens' shear capacity was analysed by Lin et al. (2003) testing 24 high-strength concrete dapped-end beams. Tests on 18 dapped-end specimens were selected from Wang et al. (2005). In this paper, the specimens' resistance was investigated as a function of dapped-end height, the reinforcement layout, in particular related to the presence of inclined rebars which is found to influence the load-bearing capacity. Taher (2005) experimentally tested 3 specimens having identical geometry but different detailing. They were used as control specimens in an experimental campaign devoted to testing various strengthening techniques. 7 specimens were selected from Herzinger (2008) that investigated the efficiency of studs with single or double heads for reinforcing the dapped-ends. This latter prevents premature failure caused by inadequate anchorage of conventional reinforcement and an experimental campaign was set up in order to make a comparison with the behaviour of conventionally reinforced dapped-end beams. Lu et al. (2012) tested 24 specimens having different geometry, concrete grades and amount of reinforcement in order to find the influence of these parameters on the load capacity and failure mode. Ahmad et al. (2013) tested 4 reinforced concrete dapped-end beams divided into two groups with different depth values. The research aimed to investigate the effectiveness of STM in predicting the failure load finding that, in the case of lower depth dapped-end beams, unconservative solutions were obtained. Moreno-Martínez & Meli (2014) conducted a research program to evaluate the performance of a dapped-end solution for a railway bridge with respect to both service and ultimate loads, to explore solutions that can enhance the component's performance. The study conducted by Mata-Falcón (2015) provides a set of 60 tests on dapped-ends (among which 8 have been selected for the database), corresponding to 30 different configurations in which parameters such as the amount and layout of reinforcement were studied. Lu et al. (2015) investigated the shear strength of 24 reinforced concrete dapped-end beams with shear span-to-depth ratios larger than unity. Aswin et al. (2015) experimentally investigated the shear response of 4 large-scale RC dapped-end specimens to find out the influence of the amount of nib reinforcements, the main flexural reinforcements, and concrete type at the dapped-end area. Atta & Taman (2016) studied the effectiveness of strengthening systems applied to dapped-end beams. Therefore, they also tested a control specimen. Desnerck et al. (2016) studied the behaviour of 4 half-joint specimens to find out the effect of local reductions in reinforcing bars and cracking in the anchorage zone on the load-bearing capacity. Desnerck et al. (2018) studied the tuning of STMs for deteriorated RC half-joints through an experimental campaign. 2 specimens out of 12 were used as control specimens and were included in this database. Hussain & Shakir (2019) tested several dapped-end specimens two of which are collected in the database. The study aimed to find the effect of repeated loads and the influence of increased shear span-to-depth ratio. Mata-Falcón et al. (2019) proposed simplified strut-and-tie models which were experimentally validated through static tests on 15 dapped-end beam specimens. The database also considered 24 dapped-end beams among the 27 specimens experimentally tested by Mohamed et al. (2020). They investigated the effect of a shear span-to-depth ratio larger than 1.0 finding that the PCI approach for the evaluation gave an underestimation with respect to experimental capacity values. The study conducted by Rajapakse et al. (2022) involved the execution of 8 large-scale dapped-end tests to investigate the influence of the amount of reinforcement in terms of the ratio of dapped-end horizontal to vertical reinforcement area. This variable was correlated with the dapped-end's resistance, crack control, and rotation capacity. Di Carlo et al. (2023a,b) investigated the impact of reinforcement corrosion on the strength and failure mode through the implementation of an experimental campaign on dapped-end beams, of which 4 control specimens have been selected for this database.

In summary, most of the experimental research programs here investigated are devoted to analysing the effect of different shear span-to-depth ratios, alternative reinforcement layouts and amounts as well as the influence of concrete grades adopted. Therefore, the database has a wide variability of governing parameters to allow an in-depth statistical analysis.

First of all, a brief overview of the collected parameters' variability is illustrated. In particular, referring to the geometric scheme depicted in Figure 2, Table 1 reports the minimum, maximum and mean values also with the standard deviation of the main specimens' geometric features, namely the dapped-end's width b, the ratio between the nib depth and the full beam depth h/H, the nib length-to-nib depth ratio l/h, the shear span-to-depth ratio a/h and the lever arm adopted during the experimental test in terms of l_a/H ratio.

Furthermore, over 60% of the specimens exhibit a full depth exceeding 500 mm, a share of 25% less than 500 mm and upper than 250 mm, and only 13% have a lower depth. As indicated by the mean value in Table 1, the majority of specimens have an a/h ratio below 1, while only 9% fall into the category where it exceeds unity. Turning to the strength characteristics of the specimens, the variability in both concrete and steel strength was analysed. Specifically, most of the specimens exhibit a mean value of cylindrical concrete compressive strength exceeding 20 MPa, and a share of 45% is classified as high-strength concrete specimens with $f_c > 40$ MPa. The steel used for tested dapped-ends has different grades for horizontal, vertical and stirrup rebars. Considering the average strength value among the different grades used for each specimen, more than 50% of them have a rather low yielding strength ($f_{ym} < 320$ MPa), 40% have $320 < f_{ym} \leq 450$ MPa and only 8% have a yielding strength upper than 450 MPa.

Regarding the failure mode, in 204 out of 210 tests included in the database, it was possible to attribute the collapse mode to one of the 5 types indicated in the PCI Design Handbook (2010) or a combination of them. Considering that only 36 tests are provided with inclined reinforcements, while 168 present only vertical and horizontal rebars, it has been observed that in the former case, the most frequent failure mode (30%) is associated with a combination of modes 3 and 4 (Figure 3), followed by mode 5 (22%) and mode 3 (13.9%), while pure mode 4 is almost absent. In the absence of inclined reinforcements, the tested dapped-ends mostly failed through modes 3 and 4 or a combination of them. Therefore, the presence of inclined reinforcements seems to prevent failure mode 4 related to shear stresses in the nib.

Table 1. Boundary range of the specimens' geometric features.

Parameter	Min	Max	Mean	St.dev
b (mm)	120	1000	208.9	99.2
h/H (-)	0.43	0.77	0.53	0.07
l/h (-)	0.46	2.50	1.20	0.47
a/h (-)	0.13	1.33	0.59	0.27
l_a/H (-)	0.64	3.79	1.32	0.64

4 DATABASE ANALYSIS AND DISCUSSION

Data from individual experimental tests were employed to train a Machine Learning algorithm aimed at predicting the load-bearing capacity of any half-joint. In fact, supervised learning techniques take a known set of input data (the training set) and known responses to the data (output), and train a model to generate reasonable predictions employing new input data. These techniques are widely used in the field of civil engineering, particularly to predict specific responses, representing a reliable alternative to analytical models based on the use of a few control parameters that may not be representative of the whole studied phenomenon (Koya et al. 2022).

In this case, supervised learning techniques were employed to train a regression algorithm based on information from 210 literature experimental tests on dapped-ends. The input data are geometric and mechanical parameters, as well as construction details in terms of reinforcement layouts and amount. The output data consisted of the ultimate strength of each test.

Figure 4 provides a detailed illustration of the input and output parameters used for model training. Specifically, 10 input parameters were considered, involving geometric parameters

such as dapped-end width b, nib depth h, full beam depth H and shear span a. Regarding mechanical parameters and construction details, concrete strength f_c was taken into account, along with the strength's contributions of each reinforcement layout. This involved the product of the reinforcement area and the average yielding strength of the corresponding steel rebars. Therefore, referring to the scheme in Figure 2, the strength associated with the main horizontal bars is calculated as $R_s = A_s \cdot f_{ym,s}$, the contribution of the main vertical stirrups is $R_v = A_v \cdot f_{ym,v}$, the inclined reinforcements contribute $R_d = A_d \cdot f_{ym,d}$, and finally, the contribution of secondary horizontal and vertical stirrups in the nib are determined as $R_h = A_h \cdot f_{ym,h}$ and $R_{vn} = A_{vn} \cdot f_{ym,vn}$, respectively.

The training of the predictive algorithm was carried out using the MATLAB software (The MathWorks Inc. 2023a), specifically through the Statistics and Machine Learning Toolbox (The MathWorks Inc. 2023b). This toolbox allows for the utilization of the Regression Learner App, which interactively trains, validates, and tunes regression models.

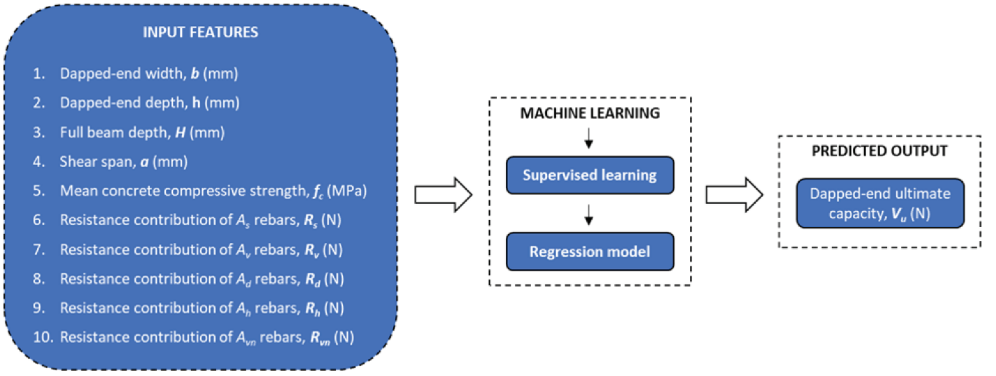


Figure 4. Adopted input and output variables for predicting the dapped-end ultimate capacity with machine learning algorithms.

The entire database of 210 observations was divided into a training set containing 80% of the samples (168 samples) and a test set comprising the remaining 20% (42 samples). This operation was performed automatically within the application to randomly partition the database based on the provided size. This latter ensures the random selection of observations used for the test dataset and avoids any bias introduced by manual selection.

The training set represents the data on which the regression model is trained, while the test set is used to check the accuracy of predictions and other statistical measures, aiming to prevent inaccurate results due to overfitting of data.

The Regression Learner App allowed for training and evaluating the predictive capability of different regression models, including Linear Regression, Nonlinear Regression, Gaussian Process Regression Model, SVM Regression, Generalized Linear Model, and Regression Tree. In order to identify the model with the best predictive capacity, the coefficient of determination R^2 was employed as a performance indicator. It can be calculated as follows:

$$R^2 = 1 - \frac{\sum_{i=1}^{N} \left[V_{upredicted} - V_{uexperimental}\right]^2}{\sum_{i=1}^{N} \left[V_{upredicted} - \overline{V_{uexperimental}}\right]^2} \quad (1)$$

Based on this performance indicator, the regression model with the best predictive capability is the Rational Quadratic Gaussian Process Regression (GPR), which exhibited an R^2 value of 0.984 for the test dataset and a value of 0.958 for the training set.

In particular, the GPR model represents a nonparametric regression method designed to accommodate more complex regression curves without specifying the relationship between the response and the predictors through a predetermined regression function (Rasmussen & Williams 2006). Figure 5 shows the results of the trained model in terms of comparison between

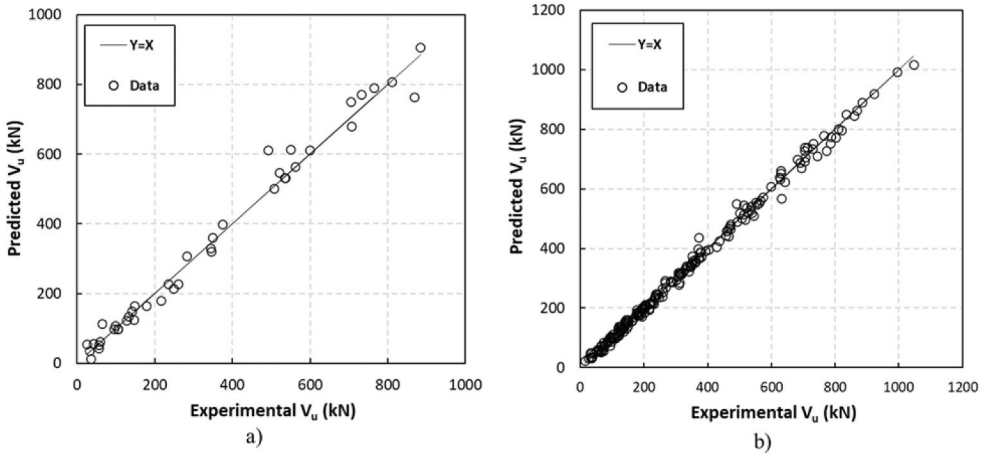


Figure 5. Comparison of the experimental and predicted dapped-end ultimate capacity a) for the test dataset only and b) considering all data.

the experimental values of dapped-end ultimate capacity and the predicted ones, considering only the test dataset (Figure 5a) as well as the prediction obtained based on the entire dataset of 210 specimens (Figure 5b). Although the trained model has shown a rather high value of the performance indicator R^2, it is worth highlighting that the accuracy of the model depends on the size of the dataset. On the other hand, this study has shown a rapid method which can be useful to obtain an accurate response for purposes such as condition assessment and preventive retrofitting measures for existing half-joints.

To make the predictive model available, a repository (https://github.com/Picciano-unibas/ML_HalfJoints) has been created, which includes the MATLAB code. This code can be used to retrain the model based on a new database, structured as illustrated in this study. Additionally, a "struct" array is included in the repository, containing the trained model, which can be employed to make predictions with new input data.

5 CONCLUSIONS

This paper is aimed at studying the half-joints' structural behaviour through the collection of a series of experimental results by various authors, allowing to building of a database including more than 200 tests. From each test, the main specimens' features were taken such as geometrical data, material properties related to concrete and reinforcing steel as well as regarding the amount and layout of reinforcement. These properties were represented by ten variables whose influence on the ultimate resistance of the half-joints was investigated through machine learning algorithms. These latter were aimed at predicting the load-bearing capacity of the half-joints considered in this study. The best performing algorithm was found to be the Rational Quadratic Gaussian Process Regression (GPR), which gave a high correlation between experimental and predicted strength values over both the test set and the entire dataset. The trained algorithm is freely available through a public repository and can be used for the preliminary assessment of reinforced concrete half-joints. In the future, ML classification algorithms will be used to predict the failure mode and ductility features of half-joints to provide a comprehensive analysis tool.

ACKNOWLEDGMENTS

The studies presented here were carried out as part of the activities envisaged by the Agreement between the Italian Department of Civil Protection and the ReLUIS Consortium (DPC-ReLUIS

project 2022-24, WP5-Task 5.4 "Upgrading and retrofitting interventions of existing bridges"). The contents of this paper represent the authors' ideas and do not necessarily correspond to the official opinion and policies of DPC.

REFERENCES

Ahmad, S., Elahi, A., Hafeez, J., Fawad, M., & Ahsan, Z. (2013). Evaluation of the shear strength of dapped ended beam. *Life Science Journal*, *10*(3), 1038–1044.

Aswin, M., Mohammed, B. S., Liew, M. S., & Syed, Z. I. (2015). Shear failure of RC dapped-end beams. *Advances in Materials science and engineering*, *2015*.

Atta, A., & Taman, M. (2016). Innovative method for strengthening dapped-end beams using an external prestressing technique. *Materials and Structures*, *49*(8), 3005–3019.

Bažant, Z. P., & Oh, B. H. (1983). Crack band theory for fracture of concrete. *Matériaux et construction*, *16*, 155–177.

Desnerck, P., Lees, J. M., & Morley, C. T. (2016). Impact of the reinforcement layout on the load capacity of reinforced concrete half-joints. *Engineering Structures*, *127*, 227–239.

Desnerck, P., Lees, J. M., & Morley, C. T. (2018). Strut-and-tie models for deteriorated reinforced concrete half-joints. *Engineering Structures*, *161*, 41–54.

Di Carlo, F., Meda, A., Molaioni, F., & Rinaldi, Z. (2023a). Experimental evaluation of the corrosion influence on the structural response of Gerber half-joints. *Engineering Structures*, *285*, 116052.

Di Carlo, F., Molaioni, F., Meda, A., & Rinaldi, Z. (2023b). Structural Behaviour of Gerber Half-Joints Subjected to Steel Corrosion. In *International Symposium of the International Federation for Structural Concrete* (pp. 322–331). Cham: Springer Nature Switzerland.

EN 1992-2. (2005). Eurocode 2: *Design of concrete structures – Part 2: Concrete bridges – Design and detailing rules*. Belgium: European Committee for Standardization.

Herzinger, R. (2008). *Stud Reinforcement in Dapped Ends of Concrete Beams*. PhD thesis, University of Calgary, Calgary, Alberta, Canada, 2008, 139–228.

Hussain, H. N., & Shakir, Q. M. (2019). Experimental Study of the Behavior of Reinforced Concrete Beams with Composite Dapped End under Effect of Static and Repeated Loads. *International Journal of Applied Science*, *2(1)*.

Koya, B. P., Aneja, S., Gupta, R., & Valeo, C. (2022). Comparative analysis of different machine learning algorithms to predict mechanical properties of concrete. *Mechanics of Advanced Materials and Structures*, *29*(25), 4032–4043.

Kumaraguru, P. (1992). *Strength of dapped end beams*. MSc Thesis, University of Calgary, Calgari, Alberta, Canada, 1992.

Lin, I. J., Hwang, S. J., Lu, W. Y., & Tsai, J. T. (2003). Shear strength of reinforced concrete dapped-end beams. *Structural engineering and mechanics: An international journal*, 16(3), 275–294.

Lu, W. Y., Chen, T. C., & Lin, I. J. (2015). Shear strength of reinforced concrete dapped-end beams with shear span-to-depth ratios larger than unity. *Journal of Marine Science and Technology*, *23*(4), 5, 431–442.

Lu, W. Y., Lin, I. J., & Yu, H. W. (2012). Behaviour of reinforced concrete dapped-end beams. *Magazine of concrete research*, *64*(9), 793–805.

Lu, W. Y., Lin, I. J., Hwang, S. J., & Lin, Y. H. (2003). Shear strength of high-strength concrete dapped-end beams. *Journal of the Chinese Institute of Engineers*, *26*(5), 671–680.

Mata-Falcón, J. (2015). *Serviceability and Ultimate Behaviour of Dapped-end Beams* (In Spanish Estudio del comportamiento en servicio y rotura de los apoyos a media madera). PhD Thesis, Universitat Politècnica de València, Valencia, 2015, 747.

Mata-Falcón, J., Pallarés, L., & Miguel, P. F. (2019). Proposal and experimental validation of simplified strut-and-tie models on dapped-end beams. *Engineering Structures*, *183*, 594–609.

Mattock, A. H. (2012). Strut-and-tie models for dapped-end beams. *Concrete International*, *34*(2), 35–40.

Mattock, A. H., & Chan, T. C. (1979). Design and behavior of dapped-end beams. *PCI journal*, *24*(6), 28–45.

Mohammed, B. S., Aswin, M., & Liew, M. S. (2020). Prediction of failure load of RC and R-ECC dapped-end beams. *Case Studies in Construction Materials*, *13*, e00433.

Moreno-Martínez, J. Y., & Meli, R. (2014). Experimental study on the structural behavior of concrete dapped-end beams. *Engineering Structures*, *75*, 152–163.

PCI Design Handbook. (2010). *Precast and Prestressed Concrete*. Sixth Edition.

Rajapakse, C., Degée, H., & Mihaylov, B. (2021). Assessment of failure along re-entrant corner cracks in existing RC dapped-end connections. *Structural Engineering International*, *31*(2), 216–226.

Rajapakse, C., Degée, H., & Mihaylov, B. (2022). Investigation of shear and flexural failures of dapped-end connections with orthogonal reinforcement. *Engineering Structures*, *260*, 114233.
Rasmussen, C. E., & Williams, C. K. (2006). *Gaussian processes for machine learning* (Vol. 1, p. 159). Cambridge, MA: MIT press.
Santarsiero, G., & Picciano, V. (2023). Durability enhancement of half-joints in RC bridges through external prestressed tendons: The Musmeci Bridge's case study. *Case Studies in Construction Materials*, *18*, e01813.
Santarsiero, G., Masi, A., & Picciano, V. (2021). Durability of Gerber saddles in RC bridges: Analyses and applications (Musmeci Bridge, Italy). *Infrastructures*, *6*(2), 25.
Santarsiero, G., Picciano, V., & Masi, A. (2023). Structural rehabilitation of half-joints in RC bridges: a state-of-the-art review. *Structure and Infrastructure Engineering*, 1–24.
Taher, S. D. (2005). Strengthening of critically designed girders with dapped ends. *Proceedings of the Institution of Civil Engineers-Structures and Buildings*, *158*(2), 141–152.
The MathWorks Inc. (2023a). *MATLAB version: 23.2.0 (R2023b)*, Natick, Massachusetts: The MathWorks Inc. https://www.mathworks.com
The MathWorks Inc. (2023b). *Statistics and Machine Learning Toolbox: 23.2 (R2023b)*, Natick, Massachusetts: The MathWorks Inc. https://www.mathworks.com
Wang, Q., Guo, Z., & Hoogenboom, P. C. (2005). Experimental investigation on the shear capacity of RC dapped end beams and design recommendations. *Structural Engineering and Mechanics*, *21(2)*, 221–235.

Bridge Maintenance, Safety, Management, Digitalization and Sustainability – Jensen, Frangopol & Schmidt (eds)
© 2024 The Author(s), ISBN 978-1-032-77040-6
Open Access: www.taylorfrancis.com, CC BY-NC-ND 4.0 license

Assessment of the efficiency of the base-isolation for a bridge structure

T. Zhelyazov
National Institute of Geophysics, Geodesy and Geography, Bulgarian Academy of Sciences, Sofia, Bulgaria

S. Ólafsson & R. Rupakhety
Earthquake Engineering Research Centre, University of Iceland, Selfoss, Iceland

ABSTRACT: Various types of models of a lead core rubber bearing are discussed in this contribution. This includes an analytical model defining the overall behavior of the isolator and a finite element model in which constitutive relations are formulated for the constituencies (rubber, lead, and steel). The models are being developed for implementation in the finite element model of a seismically protected structure. The presented ongoing study aims to simulate the dynamic response of a base-isolated bridge during a strong ground motion. On the one hand, the focus is on the LRB model, and the bridge structure is being described with relatively few details. On the other hand, both the analytical and the finite element models are to be implemented in the finite element model of the bridge. Comparison of the dynamic response of the bridge obtained with the LRB models will enable the assessment of the analytical model validity domain.

1 INTRODUCTION

Lead core Rubber Bearings (LRBs) are frequently used devices for seismic isolation. Compared to other types of seismic isolators, such as friction-pendulum systems, they reportedly possess higher energy dissipation capacity, which makes them a preferred option for structures like hospitals, nuclear power plants, and bridges.

The main goal of their implementation is to decouple the superstructure from the ground, thus reducing the damage induced during an earthquake event. Seismic isolation is expected to minimize accelerations, velocities, and displacements in the isolated structure. Also, forces developed in structural elements are expected to be smaller due to the seismic isolation; this reduces the demand and leads to a more efficient design, at least for earthquake scenarios. More generally, limiting displacement amplitudes minimizes the probability of damage to vibration-sensitive equipment.

It is widely accepted that the accurate assessment of the dynamic response of structures during a strong ground motion is a prerequisite for a safe and efficient design. If the seismic isolation of a large structure is to be assessed, it might seem mandatory to simplify the analysis procedures as much as possible. In line with this, one may choose models proven not to be extremely computationally demanding. Further in the text, such models are referred to as 'light' models. However, to assess their adequacy, a comparison with the provided output may be required. Such model validation can be performed by using either empirical data obtained via monitoring of the behavior of an instrumented bridge during a strong ground motion or by using numerical data acquired in the analysis of a structure containing a detailed model of the bearing device. Herein and further in the text, finite element models are referred to as 'detailed' models.

The contribution outlines some aspects of an ongoing study in which both 'light' and 'detailed' models of an LRB are being developed with the aim of being used in the numerical analysis of the dynamic behavior of a seismically isolated structure.

DOI: 10.1201/9781003483755-28

The LRB analytical models have been developed since the first implementation of the device in New Zealand. A number of research works have contributed to a better understanding of the global dynamic response of the LRB (see, among others, Robinson 1982, Kalpakidis & Constantinou 2009a, b, Kumar et al.2014, Eem & Hahm 2019, Liu et al. 2021). Some earlier theories still find their application (Bouc 1967, Wen 1976).

The 'detailed' models appear as an alternative. Instead of defining the global response of the LRB, constitutive relations are formulated for its compound materials (steel, lead, and rubber). The most challenging part is to model the response of the rubber, which is inherently a hyperelastic material; the Mooney-Rivlin model is employed (Ogden 1998). A bilinear model is postulated for the lead, assuming isotropic hardening after yielding. Although the same approach can be used for steel, its behavior is presumed linear, elastic, and isotropic for simplicity.

The study focuses on LRB response modeling. For this reason, the model of the seismically protected structure (a base-isolated bridge) is modeled by minimizing, as much as possible, the details considered. For this purpose, finite elements defined with fewer nodes are preferred for the model of the isolated structure. Finite elements of type structural solid are employed to generate the finite element mesh for the 'detailed' LRB model; on the other hand, finite elements of type beam and shell are used to develop the model of the bridge.

Both a model of the bridge containing a 'detailed' LRB model and a model of the bridge with implemented 'light' models are being developed.

2 MODELING THE LRB

The modeled LRB consists of 8 rubber layers, 16 mm in thickness, separated by seven 3 mm steel shims. A 100 mm in diameter cylindrical lead core is mounted in a central hole. The device contains a top and bottom steel plate with a cross-section of 460x460 mm and a thickness of 30 mm (Figure 1).

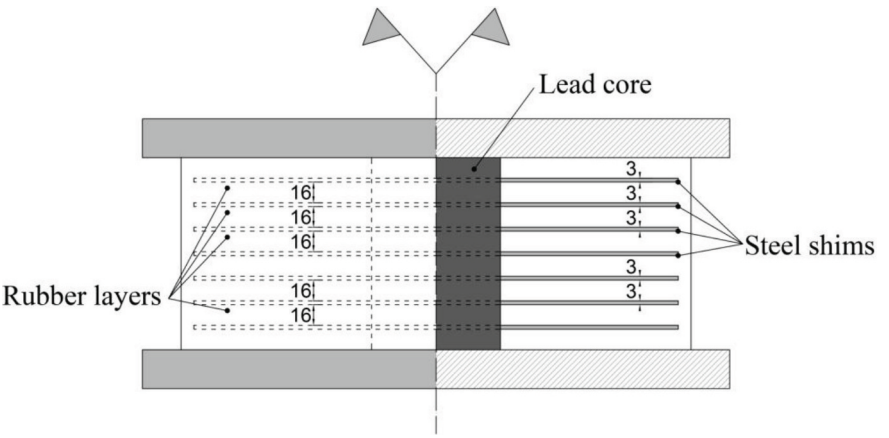


Figure 1. The LRB geometry.

Two models are being developed: a finite element (or detailed) model and an analytical (or light) model.

2.1 *The finite element model*

In the finite element model, besides the detailed geometrical representation (Figure 1), constitutive relations are defined for all the compound materials: steel, lead, and rubber. The material for the steel shims and the top and bottom steel plates is assumed to have linear elastic behavior with Young's modulus E_s=200000 MPa and Poisson's ratio v=0.3. For the lead core, a bilinear constitutive relationship is defined. The initial elasticity modulus is set to E_l=18000 MPa, and

the Poisson's ratio – to 0.43; the yield stress is assumed to be 14 MPa, and the tangent modulus is 100 MPa. A 3-parameter Mooney-Rivlin model is defined for the rubber. Additionally, a Prony model is employed to account for the viscoelastic phenomena in the rubber behavior.

Constitutive modeling is validated by simulating a characterization performed on the LRB. Nodes generated on the bottom steel plate are fixed (i.e., all nodal displacements are restrained), whereas displacements (in the function of the assumed testing protocol) are applied. The dynamic response of the LRB is obtained by performing a transient analysis. A tentative 'shear force-displacement' relationship is shown in Figure 2.

Generally, the identification of model constants involved in the constitutive relations should be based on empirical data obtained in characterization tests performed on small-scale specimens made of the corresponding materials.

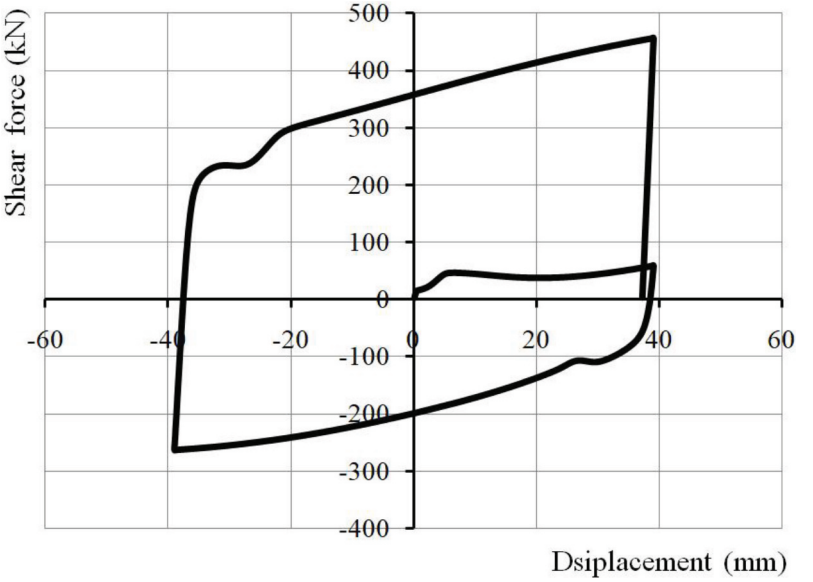


Figure 2. Characterization test on the LRB: results obtained by finite element analysis.

2.2 *The 'light' model*

Typically, the analytical models describing the LRB response consist of an equation defining a 'skeleton' curve and a second equation giving the hysteresis variable evolution. Historically, among the first analytical approaches, the smooth bilinear model (Robinson 1982) and the Ramberg-Osgood model can be cited. Approaches referred to as 'differential equation models' (Wen 1976, Ozdemir 1976) have also been proposed. The research carried out in this field led to more sophisticated models that take into consideration the temperature increase (Kalpakidis & Constantinou 2009a, b), strength degradation (Kumar et al.2014, Liu et al. 2021), and strain hardening (Eem & Hahm 2019).

The model employed herein is defined by the following two equations (Bouc 1967, Wen 1976)

$$F_r = \alpha \frac{f_y}{u_y} u(t) + (1-\alpha) f_y z(t), \tag{1}$$

$$\frac{dz}{dt} = \frac{1}{u_y}\left[A\frac{du}{dt} - \gamma\left|\frac{du}{dt}\right| z(t)|z(t)|^{n-1} - \beta\frac{du}{dt}|z(t)|^n\right]. \tag{2}$$

In Equation (1), F_r denotes the restoring force generated in the LRB, u is the current value of the applied displacement, α is the post-yielding to initial stiffness ratio (i.e., defines the tangent stiffness of the isolator after yielding), u_y is the displacement at yielding, and f_y is the

yield shear (or restoring) force. Equation (5) defines the evolution of the hysteresis variable z(t) in the function of the model constants γ, β, and *n*; the first two are expected to control the size and the shape of the hysteresis loops, and the third one – the curve smoothness upon transition between response in and out of the elastic domain.

3 MODELING A SEISMICALLY ISOLATED BRIDGE

3.1 *Geometry*

A three-span seismically isolated bridge consisting of a continuous steel deck mounted on steel girders is being studied. By assumption, the seismic isolation consists of LRBs under the steel girders placed on the caps of the reinforced concrete piers. The geometry of the structure is depicted in Figure 3 (Hedayati Dezfuli & Alam 2018).

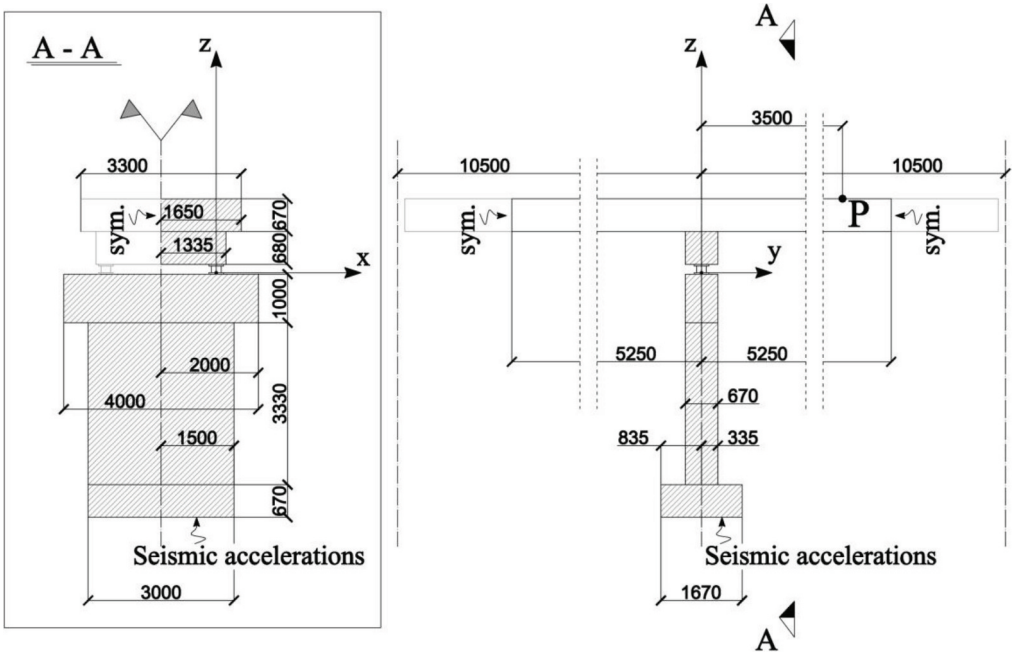


Figure 3. The bridge geometry.

3.2 *Model*

An evident strategy would be the development of a lighter model of the bearing device and its further implementation into the seismically isolated structure. However, an alternative option is employed herein. Focusing on the explicit model of the bearing device, it is inserted in the model of the seismically isolated structure.

In the developed finite element model of the bridge, the footing, the pier, the pier cap, and the girder are meshed with beam elements (BEAM188), whereas the bridge deck is modeled with shell elements (SHELL281).

For simplicity, to all structural elements, except for the LRB, linear, elastic, and isotropic materials are attributed. Young's modulus and Poisson's ratio for the bridge structural elements in steel are assumed to be identical to those of the steel shims and plates in the LRB. The elasticity modulus and Poisson's ratio for the reinforced concrete pier and the footing are 29700 MPa and 0.2, respectively. To include inertia effects, mass densities for steel and concrete are set to 7850 kg/m^3 and 2500 kg/m^3.

No soil-structure interaction is considered.

3.3 *Boundary conditions*

The response of the bridge is obtained by performing a time-history analysis. Acceleration time series recorded in an Mw5.4 earthquake is employed. Symmetries are defined in the structure and are taken into account in the simulations by modeling only a part of the bridge and postulating symmetry boundary conditions, as shown in Figure 3.

3.4 *Transient analysis*

The response of the superstructure is then obtained by performing a full transient analysis as the acceleration time series are applied to the footing. This implies the integration of a differential equation which, in its most general form, reads

$$[M]\{\ddot{u}\} + [D]\{\dot{u}\} + [K]\{u\} = \{F(t)\}. \tag{3}$$

In equation (3), $\{\ddot{u}\}$, $\{\dot{u}\}$, and $\{u\}$ are the nodal acceleration vector, the nodal velocity vector, and the nodal displacement vector, respectively; [M] denotes the mass matrix, [D] is the damping matrix, and [K] is the stiffness matrix.

4 NUMERICAL RESULTS

The response of the bridge structure to seismic load is shown in Figure 4-5. More precisely, displacement- and acceleration- components obtained for a specified point on the bridge deck are plotted.

Figure 4-a), b) displays the y- and z-components of the displacement time-history at location P (Figure 3). Acceleration components are shown in Figure 5– a), b).

5 CONCLUSIONS

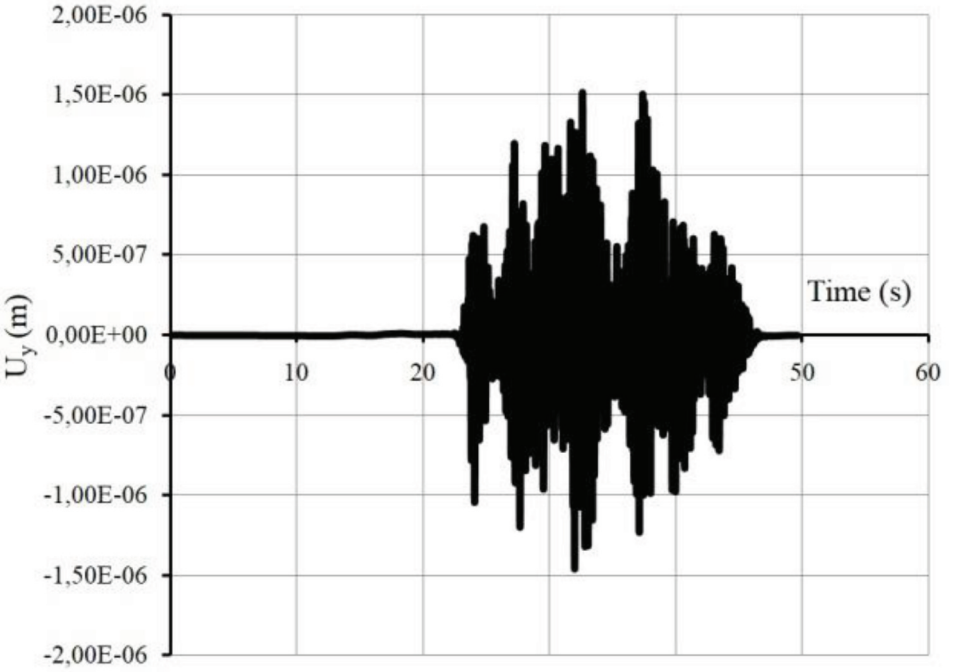
Elements of ongoing research work focused on the evaluation of the dynamic response of a bridge equipped with base isolation have been reported. Two approaches to model the devices for seismic isolation (LRB) have been discussed, specifically – a detailed (finite element model) and a light (analytical) model.

The detailed model is expected to capture more accurately the dynamic behavior of the seismic isolator and better reproduce the bridge dynamics. On the other hand, the detailed model is more resource-demanding. Using the light model within a finite element analysis might appear more efficient in terms of required computational time.

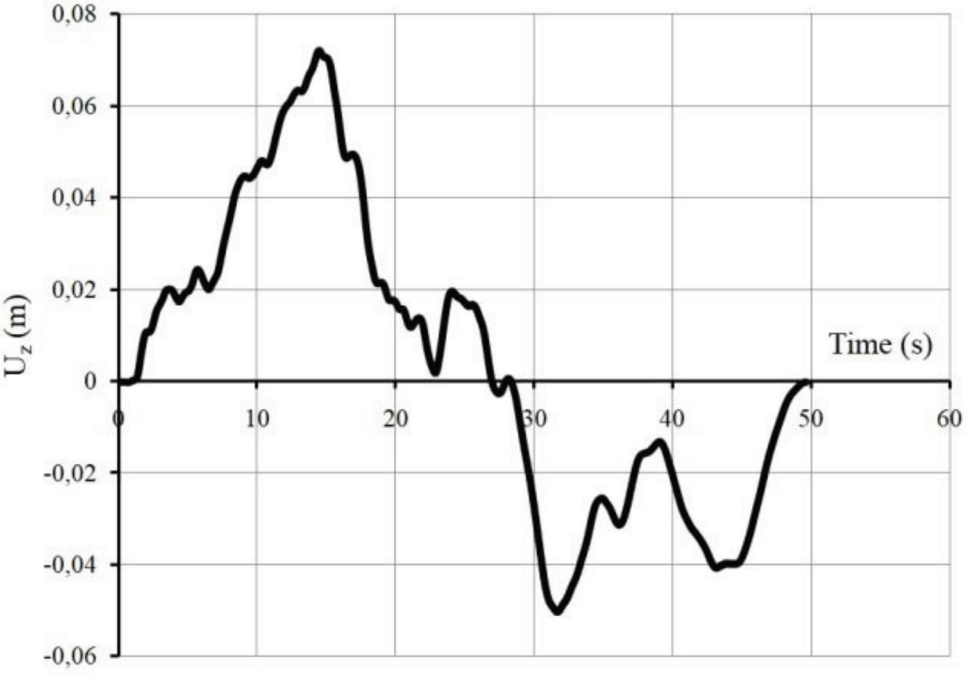
Clearly, the best solution to calibrate the analytical model is to have access to data acquired from an instrumented seismically isolated bridge. Given that this is not always possible, the accurate representation of all bridge structural elements, including the devices for base isolation, appears appealing.

It should also be noted that tuning the analytical model for the LRB based solely on the LRB characterization test might not be sufficient to explore the entire space containing the design variables of the device. Therefore, the detailed model implementation can fill such possible gaps.

In the context of this ongoing study, a comparison of the bridge response obtained using various LRB models, either detailed finite element models or 'light' analytical models, can shed light on the adequacy and efficiency of the latter. As an outcome, possible limitations on the 'light' models implementation can be formulated: should they be relied on in the design, or should they be used only in searching for a compromise between the accuracy and the fast design process.

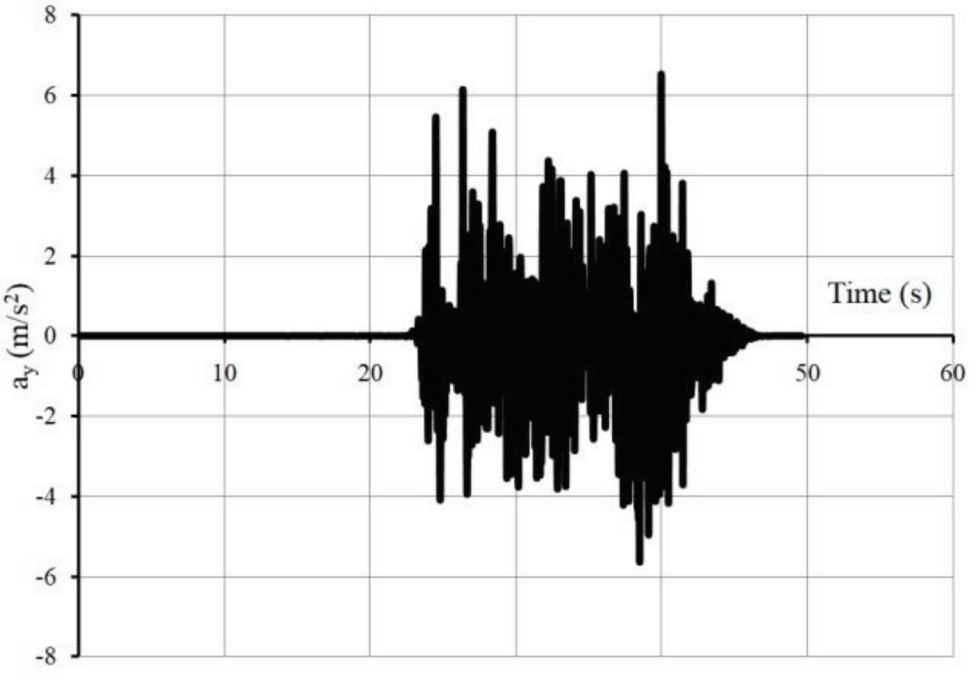


(a)

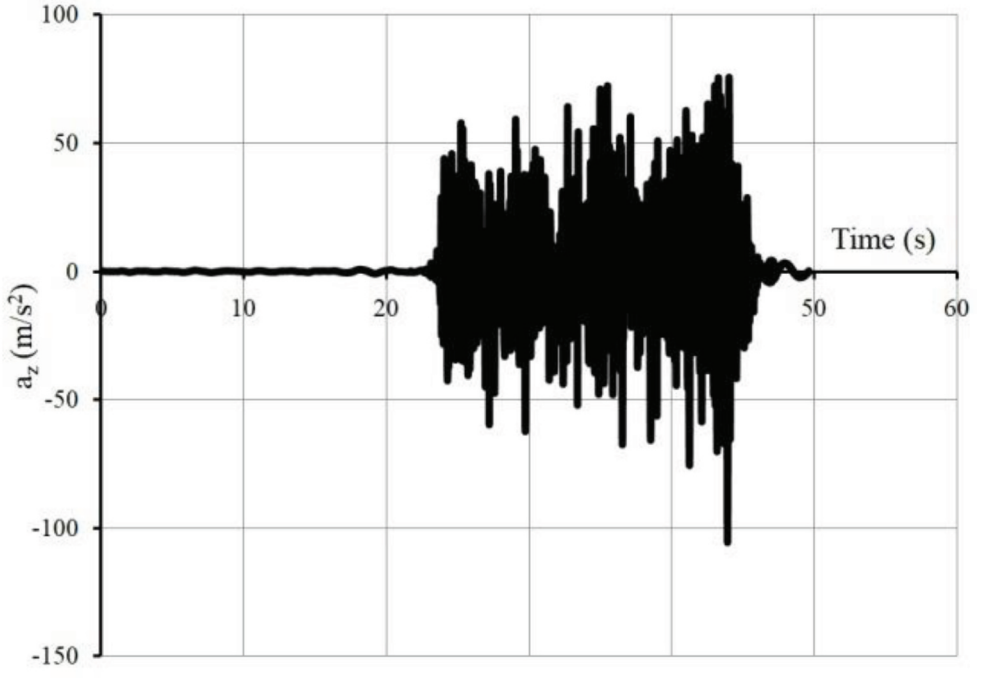


(b)

Figure 4. Response of the bridge deck (specified location) in terms of displacement y- and z- components time-history, a) and b), respectively.



(a)



(b)

Figure 5. Response of the bridge deck (specified location) in terms of acceleration y- and z- components time-history, a) and b), respectively.

REFERENCES

Bouc, R. 1967. Forced vibration of mechanical systems with hysteresis. *Proc. of the 4th Conf. on Nonlinear Oscillations*.

Constantinou M.C. & Tadjbakhsh M. 1985. Hysteretic Dampers in base isolation: random approach. *Journal of Structural Engineering* 111(4): 705–721.

Eem, S., Hahm, D. 2019. Large strain nonlinear model of lead rubber bearings for beyond design basis earthquakes. *Nuclear Engineering and Technology* 51(2): 600–606.

Hedayati Dezfuli, F., & Alam, M.S. 2018. Smart lead rubber bearings equipped with ferrous shape memory alloy wires for seismically isolating highway bridges. *Journal of Earthquake Engineering* 22(6): 1042–1067.

Kalpakidis, I.V. & Constantinou, M.C. 2009a. Effects of heating on the behavior of lead-rubber bearings. I: Theory. *Journal of Structural Engineering* 135(12): 1440–1449.

Kalpakidis, I.V. & Constantinou, M.C. 2009b. Effects of heating on the behavior of lead-rubber bearings. II: Verification of theory. *Journal of Structural Engineering* 135(12): 1450–1461.

Kumar, M., Whittaker, A.S., Constantinou, M.C. 2014. An advanced numerical model of elastomeric seismic isolation bearings. *Earthquake Engineering & Structural Dynamics* 43(13): 1955–1974.

Liu, Y., Zhong, W., Mercan, O., Tan, P., Zhou, F. 2021. A new nonlinear model to describe the degradation law of the mechanical properties of lead-rubber bearings under high-speed horizontal loading. *Structural Control and Health Monitoring* 28(12): e2836.

Ogden, R.W. 1998. *Non-Linear Elastic Deformations*. Dover.

Ozdemir, H. 1976. Nonlinear transient dynamic analysis of yielding structures. PhD dissertation, University of California, Berkeley, California.

Rivlin R.S. 1948. Large Elastic Deformations Isotropic Materials. IV. Further Developments of the General Theory. *Philosophical Transactions of the Royal Society A* 241(835): 379–397.

Robinson, W.H. 1982. Lead-rubber hysteretic bearings suitable for protecting structures during earthquakes. *Earthquake Engineering & Structural Dynamics* 10(4): 593–604.

Selvadurai, A.P.S. 2006. Deflections of a Rubber Membrane. *Journal of the Mechanics and Physics of Solids* 54(6):1093–1119.

Song J, & Der Kiureghian A. 2006. Generalized Bouc–Wen model for highly asymmetric hysteresis. *Journal of Engineering Mechanics ASCE* 132(6): 610–618.

Wen, Y.-K. 1976. Method for random vibration of hysteretic systems. *J. Engrg. Mech. ASCE* 102(2): 249–263.

Bridge Maintenance, Safety, Management, Digitalization and Sustainability – Jensen, Frangopol & Schmidt (eds)
© 2024 The Author(s), ISBN 978-1-032-77040-6
Open Access: www.taylorfrancis.com, CC BY-NC-ND 4.0 license

Fracture toughness of structural steel in Swedish bridges

M. Ablahad & H. Pétursson
Trafikverket, Sweden

ABSTRACT: The toughness of older steel structures is of crucial interest for the remaining lifespan and safety assessment of aging structures. Many structures in operation today were constructed during times when safety requirements regarding fracture toughness were not specified. This means that very little was known about the defect tolerance of such structures under various loading conditions. It is widely recognized that the toughness of common structural steels is strongly dependent on temperature and loading rate. Since the early 1990s, the Swedish Transport Administration (Banverket and Vägverket now Trafikverket) has conducted more than 600 fracture toughness tests on several hundred old steel bridges. The testing procedures were developed by the late Kjell Eriksson, who was affiliated with Luleå Technical University. The university has also conducted the majority of the fracture mechanics testing presented in this paper. This article will provide an overview of the fracture toughness testing conducted by the Swedish Transport Administration. The research leading to and background of the method used will be described. An example how the method is used for assessment of the load bearing capacity of older steel bridges in view of the toughness properties.

1 INTRODUCTION

Many of the approx. 500 steel bridges in the Swedish national railway network were erected before 1960. The toughness of older steels in railway bridges and similar structures of the same age in public service, e.g. road bridges, has been addressed from time to time in Sweden as well as many other countries during the last decades. Often, surprisingly low notch toughness figures are reported, of the order 2-5 J, in view of the fact that Williams & Ellinger (1953) reported brittle fracture in base materials from fractured ships with up to some 15J Charpy notch toughness. Such low toughness values seem to be common knowledge of many investigators and also of those responsible for the use of older steels. This and the observations a) that the common toughness requirement, 27J Charpy notch toughness according to the Bonhommerecommendation, strictly applies to structural steels intended for welding and b) that failures due to fracture in bridges of riveted and rolled members on the whole are very rare, have risen the question "What minimum toughness is necessary to ensure present safety requirements in older nonwelded structures?"

Since the beginning of the 90:s Kjell Eriksson has worked with this question on behalf of first Swedish Rail Administration (Banverket) that became the Swedish Transport Administration. He developed the method described here. Kjell Eriksson was active in the field until his unfortunate passing in 2021.

2 PREVIOUS WORK

Kjell Eriksson did a number of publications and a few of them are mentioned here.

With the possible exception of the most brittle older steels, fracture is preceded by plastic deformation to such an extent that the conditions for small scale yielding fracture mechanics are not fulfilled Eriksson (1990).

DOI: 10.1201/9781003483755-29

It was found experimentally that Charpy testing alone of older and inhomogeneous steels might be misleading. All steels tested were tougher according to fracture toughness (Jc) tests than to Charpy (Cv) tests compared to the corresponding relationship for homogeneous steels. The steels in Eriksson (1990) investigation might be divided into two groups depending upon the relation between Jc and Cv.

In the first group the steels are twice to four times tougher according to Jc and to Cv. The steels in this group are brittle both according to Charpy-V notch toughness and to fracture toughness.

In the second group the steels are more than ten times tougher according to Jc and Cv. The steels are in fact brittle according to Cv and ductile according to Jc. This is because the toughness of these steels is (very) inhomogeneous, particularly in the second group.

It was concluded from the investigation that full thickness specimens are required to obtain the effective toughness of a structural element. The fracture toughness of a full-scale structure can be predicted from small specimens provided the constraint is similar in both cases. It was also concluded that fatigue crack growth rate does not increase with decreasing toughness.

Eriksson (1991) discusses the historical use of the Charpy test, dating back to 1905, for qualitative assessments of the brittle-to-ductile transition temperature of structural steels. Before World War II, there was no rational basis for predicting structural behavior or calibration against service performance. However, after the Liberty ship disasters in the early 1940s, it became evident that the transition temperature of a cracked body was critical for the loss of strength.

The text also highlights the inadequacy of using notch toughness alone as an indicator of defect tolerance. Notch toughness underestimates the effective toughness of a structural element, leading to conservative estimates of material quality.

Three examples were provided to illustrate these points: inhomogeneous steel with varying transition temperatures, pressure vessel steel susceptibility to embrittlement after cold forming and welding, and weld metals with poor fracture toughness despite acceptable notch toughness.

In conclusion, the text demonstrates that there is no universal correlation between notch toughness and fracture toughness. Empirical relationships may underestimate fracture toughness, especially for inhomogeneous materials, and relying solely on notch toughness for weld metal may not ensure the desired safety against fracture.

In Eriksson (1992a) the emphasis is on the safety of structures containing potentially brittle materials. The paper incorporated a blend of laboratory experiments, full-scale testing, and statistical analysis to establish appropriate toughness criteria.

Eriksson's work from 1992 also delves into a method for estimating the remaining fatigue life of structural steel members subjected to service-related damage and corrosion. This approach is rooted in the Palmgren-Miner damage accumulation rule and takes into account factors such as field-recorded stress patterns, stress concentration effects, and the influence of corrosion. Its application is vital for evaluating the structural integrity of aging infrastructure like railway bridges.

There are several key situations where an evaluation of a structure's remaining lifespan becomes necessary:

a) When the structure approaches its anticipated service life,
b) When there are alterations in loading conditions, and
c) When the structure is damaged.

Historically, inspections of older bridges have yielded favorable results, with only a minimal number of cracks being identified. However, the focus of the paper is shifted towards comprehending the consequence of common types of damage, such as scratches and impacts from road traffic, on the residual longevity of these structures.

Eriksson's 1992 work presents a straightforward model based on Palmgren-Miner's rule to quantify the potential effects of corrosion and stress concentration on the remaining lifespan of corroded areas affected by scratches or impacts. The analysis underscores that these factors can substantially diminish the fatigue life expectancy of old steel structures.

Furthermore, Eriksson (1992a) also explores the computation of damage and introduces an algorithm for calculating damage in various scenarios. He introduces fatigue strength

reduction factors tailored to different surface conditions and provides illustrative calculations for different damage types.

In Eriksson (1992b) an experimental and theoretical investigation is described. The deformation and fracture of a precracked HEB400 steel beam (St37 class D) is investigated through various methods, including full-scale testing, numerical computation of the J-integral, analytical estimations, and fracture toughness testing of small specimens. The study aims to understand how fracture properties obtained from small-scale specimens apply to full-scale structures.

Key findings and observations from the paper include: The study aimed to assess the transferability of fracture data obtained from laboratory specimens to full-scale structural elements. It found that fracture toughness data from different types of specimens correlate reasonably well. The materials used in the study were heterogeneous, with considerable scatter in mechanical properties. Some materials were taken from structures that had been in service for several decades, while others were made from steel not manufactured to current standards. The fracture toughness of the materials ranged from very low for some specimens (around 10 kN/m) to much higher for others (greater than 100 kN/m). The scatter in fracture toughness was significant but relatively consistent between laboratory and full-scale specimens.

The paper includes detailed experimental observations, including load-displacement relationships, strain measurements, temperatures, and crack mouth opening displacements for each beam. The results showed that fracture did not occur for crack lengths shorter than approximately 40 mm, even for brittle materials, indicating a threshold crack length for fracture initiation. The paper discusses the use of the J-integral and CTOD (Crack Tip Opening Displacement) to characterize fracture toughness and presents critical values for different specimens. It also presents a residual strength diagram that illustrates the borderline between "long" and "short" cracks, where "long" cracks led to fracture, and "short" cracks only resulted in plastic deformation but no crack growth.

In summary, the paper focuses on the fracture behavior of structural steel beams with preexisting cracks at low temperatures. It evaluates the transferability of fracture data obtained from laboratory specimens to full-scale structures and provides insights into the influence of crack length and material properties on fracture toughness.

Eriksson (1994) presented a method for calculating fracture toughness requirements for ordinary structural steel, particularly focusing on older and potentially inhomogeneous steels found in various structures such as bridges. The main objective was to ensure the safety and structural integrity of these older materials.

The key findings and processes outlined by Eriksson include:

There are numerous old steel structures in Sweden and around the world, some dating back to early 20th century, raising concerns about the toughness of the materials used in these structures.

Testing of older steel samples revealed two distinct groups - one group that met safety requirements and another that did not. In particular, some older steels displayed a surface layer with ductile properties and a brittle core.

Full-scale testing of structural elements and laboratory specimens was conducted to assess the transferability of results. The behavior of beams could be predicted from extracted specimens provided the constraint was similar in both cases.

The text discusses the development of a method for calculating fracture toughness requirements based on assumed crack sizes and typical loading conditions. This method aims to maintain safety standards in structures with older materials.

Two fracture toughness levels are suggested - a lower level requiring immediate replacement and an upper level that ensures satisfactory safety. The upper level is approximately equivalent to a Charpy notch toughness of 27 Jc.

The text concludes that Charpy testing alone may be insufficient for assessing older and inhomogeneous steels. Full-thickness specimens are necessary to accurately estimate structural element toughness, and fracture toughness of full-scale structures can be predicted from small specimens with similar constraint conditions.

Lorentzon & Eriksson (1995) examines the influence of quasistatic loading rate and temperature on the fracture toughness of older structural steel. The research was aimed to assess the integrity and applicability of the steel in older structures.

The results indicated that the fracture toughness of structural steel significantly decreases at common loading rates encountered in practice compared to standard fracture toughness tests. This implies that reliable fracture toughness data for structures exposed to quasi-static loading rates require testing at appropriate speeds.

The study's conclusions suggest that the impact of loading rate on fracture toughness can be predicted using data from laboratory tests with extracted small specimens. The results also emphasize that increased material toughness leads to improved safety at lower loading rates.

Lastly, the study underscores the importance of understanding the influence of loading rate on structural safety, particularly for future structures intended for high-speed train traffic.

3 TRAFIKVERKET CODES REGARDING FRACTURE TOGHNESS OF STEELS IN BRIDGES

There are two documents provided by Trafikverket explaining the procedure of testing the fracture toughness of structural steel, both are written in Swedish, (Trafikverket (2023) and Trafikverket (2014).

The fracture toughness of the steel in the main structure of a bridge is tested if the bridge is built before 1970. Before that year it was not a standard procedure to do Charpy-V tests on steels that were used in bridges.

The median is considered to be lowest fracture toughness value of three to five specimens or the second lowest fracture toughness value of six to eight specimen orthe third lowest fracture toughness value of nine or more samples.

The material testing consists of chemical analysis and fracture toughness. In order to determine each toughness value, three tests are conducted using different test specimens. The specimen can be, three-point-bend specimens with a rectangular cross section, three-point-bend specimens with broken edges (Figure 1) or CT-specimen or CT-round specimen.

A complete chemical analysis is made for the following substances, C, Si, Mn, P, S, Cr, Ni, Cu, Mo, V and N.

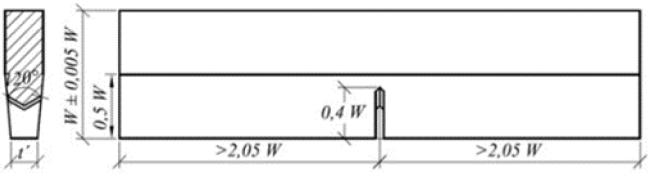


Figure 1. CT-specimen with broken edges.

The specimens are cooled to -30° C when testing and a fracture toughness is evaluated for each specimen. The loading speed of the test is chosen depending on the speed of the traffic over the bridge and the length of the influence line.

The load case during testing mimics a 50 mm deep elliptical surface crack in a comparatively substantially larger geometry. If the test shows Jc>50 kN/m, then fatigue failure will not occur for cracks shorter than 50 mm. The fracture toughness should fulfill the requirements according to level one in Table 1.

Table 1. Basic requirements.

Terms	f_v[MPa]	J_c [MPa]
Accepted	220	30
without special	260	40
measurements	290	50

If the measured toughness of the steel is lower than in Table 1, then level two is applied according to Table 2 where the maximum nominal stress in tension in serviceability limit state (σ_{nom}) is stated depending on the J_c value. If J_c is less than 20 kN/m, then a special investigation has to be made in order to verify the bridge capacity.

Table 2. Maximum allowed stress in tension with regard to steels toughness value.

Fracture toughness [kN/m]	Maximum allowed σ_{nom} [MPa]
$20 < J_c < 30$	$\sigma < 100 + 6{,}7\ (J_c - 20)$
$30 < J_c < 40$	$\sigma < 167 + 3\ (J_c - 30)$
$40 < J_c < 50$	$\sigma < 197 + 2{,}3\ (J_c - 40)$

4 CONDUCTED TESTS

The fracture toughness of structural steel has been tested on 587 different samples from different bridges. This could be seen in Figure 2 that shows the year of construction for each bridge and its Jc value. Furthermore, the results can also be seen in Table 3 from a general point of view and Table 4 from a more specific point of view where Jc < 20, 30, 40 and 50 is presented for the bridges.

In Table 3 it can be seen that one column has a max value for Jc of 50 kN/m this is due to the fact that the upper limit of this value is set to 50 kN/m and therefore Jc >50 is not of interest.

The calculation of Jc is done using equation 1 which includes the thickness (t), widtht (W) and the crack length of the specimen (a).

$$J_c = \frac{2U}{t(W-a)} \tag{1}$$

Table 3. General results of J_c for conducted tests on steel bridges.

Year of construction	Average [kN/m]	Average (max 50 kN/m)	Std deviation
Before 1910	192	40	217
After 1910	133	40	174

Table 4. Specific results of Jc for conducted tests on steel bridges.

Year of construction	Quantity	<20	<30	<40	<50
Before 1910	45	1	14	19	20
After 1910	463	57	143	203	250

The railway bridge Testeboån, was constructed in 1942 and replaced by a new bridge in 2013. From the demolished bridge structure, 7 I-beams of type Dip 32 were preserved for fracture mechanical testing. Additionally, a new HEB 320 beam was acquired for comparative testing. The fracture mechanical testing was conducted in two phases. In the first phase, the beams were tested at full scale in three-point bending. Subsequently, three three-point bending test specimens were produced per beam, using material taken from the beam flanges, totaling (7 + 1) x 3 = 24 test specimens. In the second phase, testing was carried out using the three-point bending test specimens. The testing temperature for both beam elements and test specimens was -30°C.

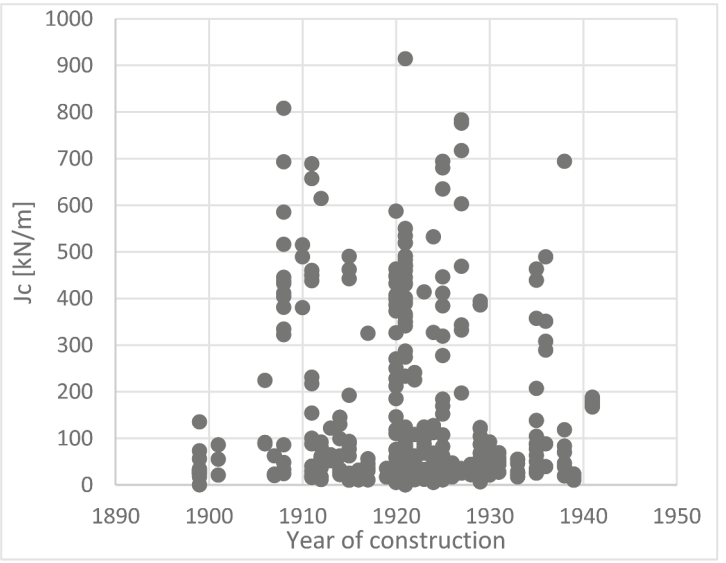


Figure 2. Results from fracture toughness evaluations in relation to age of the steel.

The fracture mechanical testing was performed following the guidelines outlined in Trafikverket (2014).

The fracture mechanical testing was conducted at two different loading rates, a low rate for three beam elements from the current bridge and a high rate for the remaining four beam elements and the newly acquired beam. The low loading rate is quasi-static and representative of structural elements with a large influence length, approximately 20 meters and larger, typical for components such as lower chord members in truss structures. The high loading rate corresponds to shorter influence lengths, on the order of 3-5 meters, as encountered in long beams and crossbeams at train speeds of 80-100 km/h. The test results are presented in Table 5.

Table 5. Test results.

Test beam	Whole beam Jc [kN/m]	Test specimen Jc [kN/m]
B1	66	19
B2	70	20
B5	23	14
B3	40	17
B4	37	12
B6	61	18
B7	41	16
New	67	37

5 EXAMPLE ASSESMENT AND TESTING OF TOUGHNESS REQUIREMENTS OF A RAILWAY BRIDGE

Fracture toughness tests have been conducted on a lot of bridges as mentioned, one bridge is "Ludvika ström" which is a simply supported bridge with three spans of 3.2m, 17.2m and 17.2m, see Figure 3 (left). The bridge is located by a stream in the town Ludvika in Sweden. It was first built in 1874. The superstructure was replaced in 1924.

The maximum load bearing capacity corresponds to line category E3 (CEN 2021) in ultimate limit state.

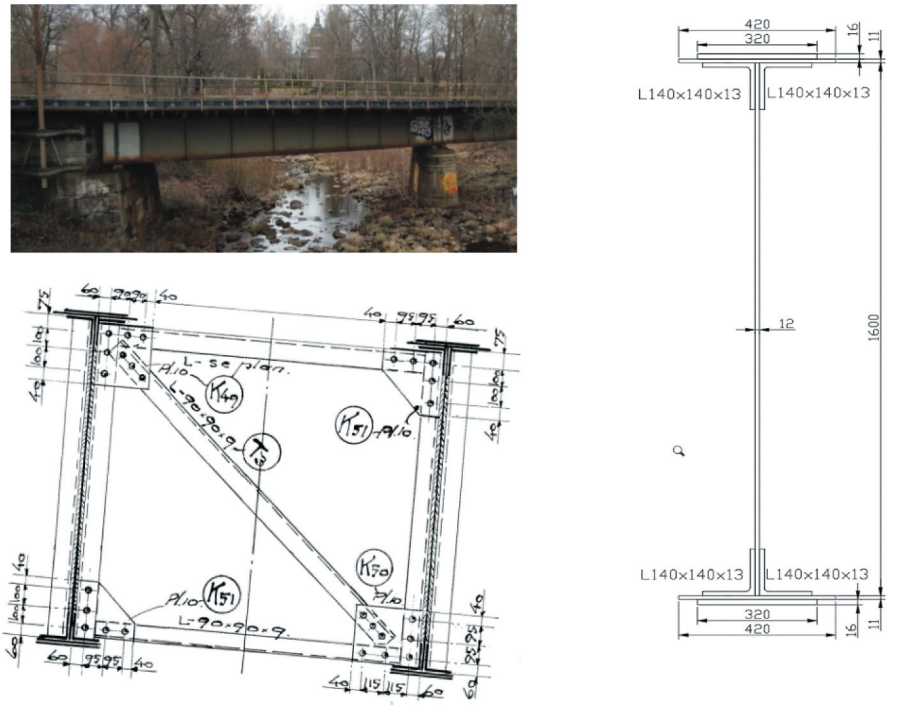


Figure 3. The bridge, Ludvika ström and bridge section (left). Beam used for samples (Right).

The fracture toughness testing of this bridge required a total of 12 specimens, six from the web and six from the flange that were taken out from the beam seen in Figure 3 (right). The test that was conducted on the specimens gave low results regarding the fracture toughness of the steel. This resulted in a need to calculate of the tension stresses in order to ensure the capacity of the bridge according to Table 1 and 2 in chapter 3.

The lowest fractur toughness turned out to be J_c = 21kN/m for the flange and the steel has fy =216 MPa, meaning that the steels require J_c>30 to be regarded to be safe without further

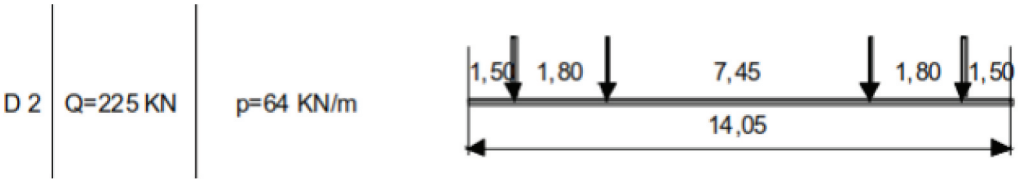


Figure 4. Train load corresponding to line category D2.

Table 6. Parameters used for calculation of tension. Loads on one (of two) bridge girders.

Parameter	quantity	unit
Steel yield strength	216	[MPa]
Dead weight	7.9	[kN/m]
Wind load (horizontal)	6	[kN/m]
Wind load (vertical)	±7.7	[kN/m]
Side support	54.6	[kN]
Dynamic factor	1.12	
Eccentricity of train load	50	[mm]

analysis. The tension stress must be less than 106.7MPa. This was not the case. The line category was lowered to D2 in order to fulfill the requirement, see Figure 4.

The parameters in Figure 3 (right) are used to calculate the bending moment in the serviceability limit state, moment of inertia and the area in order to further calculate the stress in tension was calculated to be σ D2 = 86 MPa. The requirement is now fulfilled, meaning that will a longer lifespan for the bridge is possible.

6 CONCLUSION

Kjell Eriksson's research started in the 1990s and forms the basis for the regulations used by the Swedish Transport Administration today to secure older steel bridges. This paper has described some of the research that has led to the rules, results from hundreds of tests from steels in old bridges and an example of how the regulations are use in practice. The fundaments of the regulations are the following:

a) To estimate the median fracture toughness with a 87.5% confidence level, a minimum of three test specimens are required. The estimated value of the median is the lowest of the three fracture toughness values.
b) A reasonable requirement for the fracture toughness of structural steel in load-bearing structural elements is that the standard safety is not exceeded even if a defect or crack of a certain size occurs in the most heavily loaded cross-section of the structure. As a typical case for a load-bearing railway bridge's main girder, the scenario of a wide-flange beam subjected to bending with an edge crack in the tension flange has been considered.
c) Taking into account the risk of escaping detection in inspections using common nondestructive testing methods, a crack with a depth of 50-100 mm is a reasonable starting point.
d) The variability in fracture toughness for common types of structural steel is significant, necessitating the establishment of two levels, a lower and an upper limit.
e) Steel with fracture toughness greater than the upper limit can be used without restrictions, while steel with fracture toughness lower than the lower limit is not allowed in load-bearing structural components. For steel with fracture toughness between the upper and lower limits, an individual assessment is made.
f) Limits for the fracture toughness of structural steel:
   Lower limit: Jc = 20 kN/m
   Upper limit: Jc = 50 kN/m
   At the lower limit and a crack length of 50 mm, the safety is at least equivalent to the Accident Load, and at the upper limit and a crack length of 100 mm, it is at least equivalent to Safety Class 3.
g) That full thickness specimens should be used for fracture toughness tests.
h) The fracture toughness of a full-scale structure can be predicted from small specimens provided the constraint is similar in both cases.
i) Fatigue crack growth rate does not increase with decreasing toughness.

REFERENCES

CEN-EUROPEAN COMMITTEE FOR STANDARDIZATION, (2021), EN 15528:2021 Railway applications – Line categories for managing the interface between load limits of vehicles and infrastructure

Eriksson, K., (1990) "Toughness requirements for older structural steels", Proceedings of the IABSE Workshop on "Remaining Fatigue Life of Steel Structures", IABSE, Zürich,

Eriksson K. (1991), "On the Correlation Between Charpy Notch Toughness and Fracture Toughness of Base and Weld Metal", Mechanical Effects of Welding pp 175–180, IUTAM Symposium Luleå Sweden 1991

Eriksson, K, (1992a) "Fatigue life assessment of service damaged and corroded members of structural steel", Fatigue design 1992: Helsinki, Finland, 19-22 May, 1992

Eriksson K., (1992b), “The deformation and failure at -30 °C of cracked broad flange beams of ordinary structural steel in bending”, Shallow crack fracture mechanics, toughness tests and applications, TWI V00, PAPER 10 Cambridge, UK 23-24 September 1992
Eriksson, K., (1994) “A fracture mechanics assessment method for older structural steels”,
Leander J. (2024) “Utmattningsprovning av detaljer från järnvägsbron över Söderström”,
Lorentzon M. and Eriksson K, (1995) “Influence of quasi-static loading rate and temperature on the fracture toughness of older structural steel” IABSE Symposium, San Francisco 1995
Williams, M.L. and Ellinger, G.A. (1953), The Welding Journal, Vol. 32, No. 10, Research Suppl, 1953, pp 498–527.
Trafikverket (2014) (Swedish Transport administration), TDOK 2012:23 Brottseghet och kemisk analys av konstruktionsstål (In Swedish) (Toughness and chemical analysis of structural steel), https://trvdokument.trafikverket.se/fileHandler.ashx?typ=showdokument&id=b3614afc-4cf5-4d00-8fb3-4b0e0bde5189
Trafikverket (2023) (Swedish Transport administration), TRVINFRA-00228 Bro och broliknande Konstruktion Brounderhåll (in Swedish) (Bridge and Bridgelike Structures Bridge maintenance), Trafikverkets infrastrukturregelverk, https://puben.trafikverket.se/dpub/visa-dokument/07e4b809-637f-453d-bc6c-b7ad2b7ba383

MS02: Field testing of existing bridges

Organizers: E. Lantsoght, G. Sas & J. Schmidt


Taylor & Francis
Taylor & Francis Group
http://taylorandfrancis.com

Bridge Maintenance, Safety, Management, Digitalization and Sustainability – Jensen, Frangopol & Schmidt (eds)
© 2024 The Author(s), ISBN 978-1-032-77040-6
Open Access: www.taylorfrancis.com, CC BY-NC-ND 4.0 license

Collapse test of prestressed concrete slab-between-girder bridge

S.W.H. Ensink
Concrete Structures, Delft University of Technology, Delft, The Netherlands

E.O.L. Lantsoght
Concrete Structures, Delft University of Technology, Delft, The Netherlands
Politécnico, Universidad San Francisco de Quito, Quito, Ecuador

M.A.N. Hendriks
Concrete Structures, Delft University of Technology, Delft, The Netherlands
NTNU, Trondheim, Norway

ABSTRACT: In the Netherlands, there are about 70 prestressed T-girder bridges with cast-in-between decks, constructed post-World War II. While they have low ratings upon assessment, inspections reveal no distress. This research aims to understand the structural behavior of the full system compared to isolated T-girders. Experiments were conducted on the original structure, as well as on the structure with the deck sawn to test individual girder behavior. The main insight is that the system behavior at the ultimate limit state is driven by compressive membrane action in the deck as well as compressive arching action in the girders, and that simplified distribution factors for shear derived from linear elastic behavior do not properly reflect the distribution and load path at the ultimate. These results can be used for a better assessment of the existing pre- stressed T-girder bridges.

1 INTRODUCTION

In the decades following the Second World War, the Dutch road network underwent a large ex- pansion. This expansion also involved the construction of a large number of bridges. These bridges are now reaching the end of their originally devised service life (Lantsoght et al. 2013). Upon assessment, engineers are confronted with the fact that the live loads that are currently prescribed by NEN-EN 1991-2:2003 (CEN 2003) are heavier than prescribed by the previous national codes, and that at the same time the shear capacity calculated from the current code pro- visions in NEN-EN 1992-1-1:2005 (CEN 2005) is lower than in the previous national codes (Dutch Institute for Normalization 1962). As a result, a large number of existing bridges are ana- lytically found to be insufficient for shear.

One subset of the Dutch bridge stock consists of prestressed T-girder bridges with cast-in-between decks. About 70 of these structures are present in the Netherlands. Even though the analytical assessment for shear results in the conclusion that these bridges are not sufficient, typically no signs of distress are found upon inspection. A possible explanation for this observation is that additional load-carrying mechanisms are activated, which are traditionally not considered in assessment. In particular, for prestressed T-girder bridges with cast-in-between decks, the structural capacity could benefit from the effect of compressive membrane action in the deck, compressive arching action in the girder, the effect of the diaphragms acting as intermediate supports, and of transverse distribution from the analysed girder to the adjacent girders.

Experimental data that quantify the transverse distribution for shear in prestressed T-girder bridges with cast-in-between decks is limited. Moreover, the available experimental data were obtained through diagnostic load tests, or the distribution factors were derived based on

DOI: 10.1201/9781003483755-30

linear finite element analyses. For girder bridges, the test data are limited to slab-girder bridges, for which the deck is cast on top of the girders instead of in between the girders (Arockiasamy and Amer 1998, Jáuregui and Barr 2004, Wekezer et al. 2004, Mordak and Manko 2008, Idriss and Liang 2010). Additional difficulties for the assessment of the existing prestressed T-girder bridge with cast-in-between decks in the Netherlands are the very low shear reinforcement ratios, and the presence of diaphragms (Cai et al. 2002).

For design, the distribution factors from AASHTO §4.6.2.2 (AASHTO 2015) can be used.

Different distribution factors are determined for bending moment and shear, and for interior and exterior girders. The distribution factor (DF) for an interior girder for shear is as follows:

$$DF = 0.36 + \frac{S}{25.0} \tag{1}$$

with S the spacing of the beams in [ft]. Guidelines are available for flexure on how to use field tests to determine the distribution factors (ACI Committee 342 2016). However, it is not known if the distribution changes as the load is increased and the structural behaviour changes from linear elastic to the ultimate limit state. With this in mind, this paper will use the described test results on a prestressed concrete slab-between-girder bridge to evaluate if the distribution factors can be used to describe the system behaviour, and, if not, which mechanisms contribute to the system behaviour.

2 DESCRIPTION OF VECHT BRIDGE

2.1 *Location, structural system, and geometry*

One example of a T-girder prestressed concrete bridge with cast-in-between decks is the Vecht Bridge near the town of Muiden in the province of Noord Holland in the Netherlands. This bridge was built in 1962, and consisted of nine simply supported spans of which one span contains a movable bridge over the Vecht river. Two parallel bridges were built, one per driving direction. The bridge was situated in the A1 highway. This highway is rerouted, so that it became possible to test the bridge to failure in two spans prior to its demolition. A partial overview of the bridge structure is given in Figure 1 showing the western approach ramp. Figure 1 also marks the inves- tigated spans. On span 3 (see Figure 1) an extensive investigation into the material properties of the concrete (drilled cylinders) and the prestressing tendons has taken place.

All spans are 24 m long, and consist of 15 identical prestressed girders with diaphragms at 8 m intervals. An overview of the transverse cross-section is given in Figure 2. The center-to-center distance between the girders is 1225 mm. The thickness of the cast-in-between decks is equal to the height of the top flange of 180 mm. The girders were prefabricated on-site and pretensioned after which the ducts were grouted.

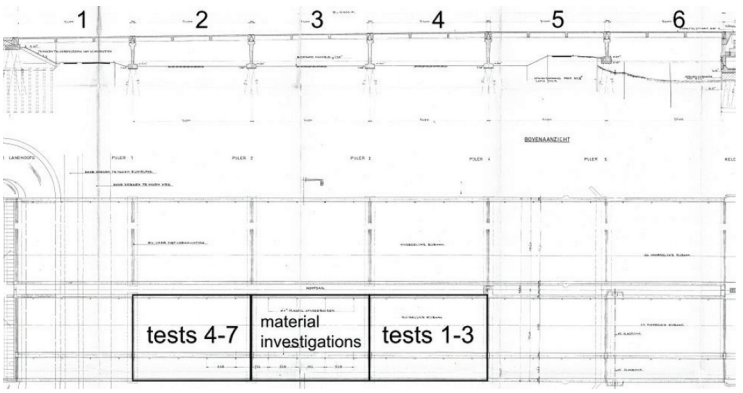


Figure 1. Partial overview of Vecht Bridge, longitudinal section (top) and top view (bottom).

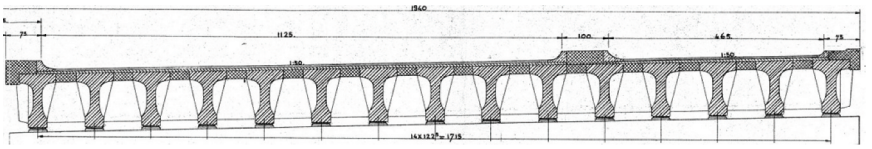


Figure 2. Cross-section of Vecht Bridge (measurements in cm).

2.2 *Material properties and reinforcement*

The longitudinal prestressing in the girders consists of seven 12ø7 mm (A_p = 462 mm^2) tendons per girder. The transverse prestressing consists of 12ø7 mm (A_p = 462 mm^2) per tendon, with a total of 59 transverse prestressing tendons per span. A detail of the curved prestressing tendons close to the support is shown in Figure 3. Prestressing steel qualities QP150 and QP170 were used during the era of construction of the Vecht Bridge. Documents from the archives suggest the use of QP170, so that f_{pk} is estimated as 1754 MPa. Extensive material research in span 3 identified the yield strength of the prestressing steel as 1505.4 MPa and the ultimate strength as 1769.5 MPa. Mild steel reinforcement is present in the deck and girders. In the bottom flange of the girders, 3ø10 mm bars are present at 1107 mm from the face of the top flange and 2ø10 mm at 980 mm. In the web, 2ø10 mm are present at 785 mm, 560 mm and 300 mm, see also Figure 4. The shear reinforcement consists of ø8 mm at 500 mm on center. The mild steel is QR24 with a character- istic yield strength f_{yk} estimated at 280 MPa and confirmed with the extensive material investigation as 287.7 MPa. With the exception of the transverse prestressing, there is no steel reinforce-ment connecting the cast in-between slab to the girder.

The average concrete cube compressive strength $f_{ck,cube}$ on the original drawings is 50 MPa. From this value the average cylinder strength f_{cm} is estimated as 64 MPa. From the extensive material research, the average cylinder strength was found as 87.7 MPa (based on 30 cores) in the T-beams and 60.3 MPa in the integrated deck slab.

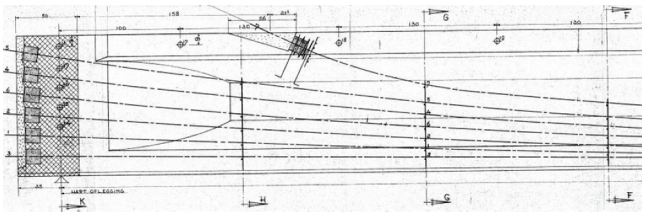


Figure 3. Detail of curved prestressing tendons in T-girder close to the support.

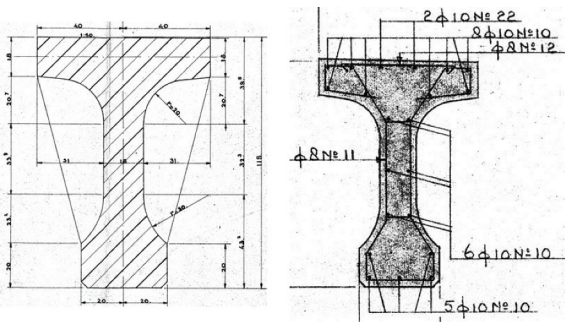


Figure 4. Cross-section of girder (left) and steel reinforcement (right) (measurements in cm).

3 TEST SETUP

3.1 *Load positions*

Three experiments were carried out on span 4, and four experiments in span 2, see also Figure 1 and Table 1. In span 4, the original structural system is unchanged. In test 1 and 2 at least four girders are present between the tested girder and the edge of the bridge. Therefore, in these tests a significant load distribution to the adjacent girders will take place. In test 3 the edge girder itself is loaded. Finally, in span 2, the deck is sawn, so that the individual behaviour of the girders could be tested. Also three of the four cross-beams, with the exception of the one on the opposite side, are sawn. The load position at 4000 mm is chosen because of the position of the cross-beams. The load position at 2250 mm is chosen as the weakest cross-section for an individual girder because of the position of the prestressing tendon anchored in the top flange (see Figure 3). By comparing the structural system to the individual girder behaviour, the system behaviour can be observed.

Table 1. Overview of tests.

Test	Span	Distance from support [mm]	Structural system	Type of test
1	4	4000	not changed	Intermediate girder
2	4	2250	not changed	Intermediate girder
3	4	2250	not changed	Edge girder
4	2	2250	sawn	Individual girder
5	2	2250	sawn	Individual girder
6	2	2250	sawn	Individual girder
7	2	4000	sawn	Individual girder

3.2 *Loading system*

The load is applied through a single concentrated load of 400 mm × 400 mm. The full loading system consist of a 25 m steel spreader beam with ballast on top. The load is then gradually applied from the steel spreader beam to the bridge by using a hydraulic jack. Additionally, a sliding system was provided to easily change the loading position, given the large number of tests planned on site. This system is shown in Figure 5. For the isolated beams in span 2, holes were drilled through the deck through which steel chains were placed and anchored in place by a steel beam, so that the beam would fall into the chains at failure instead of onto the ground.

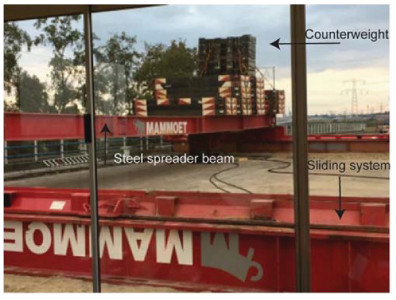


Figure 5. Load application system.

4 TEST RESULTS

4.1 *Failure loads*

Table 2 gives an overview of the results of the seven experiments. The table includes the test number and span of the experiment, with experiments in span 4 on the connected system and in

span 2 of the disconnected girders. The *a/d* distance is the ratio of the shear span *a* to the effective depth *d* of the girder. The maximum load in the experiment is indicated as F_{max} and the maximum deflection in the experiment is indicated as δ_u. The shear at failure is calculated by considering the sectional shear due to the dead weight, the prestressing, and the externally applied load.

The table also gives the Failure mode. For tests 1 and 2, Figure 6 illustrates the failure in the girder and Figure 7 illustrates the failure in the deck, which is the initial failure. Test 3 was an experiment on an edge girder. As there were safety concerns regarding the stability of the tower of counterweight upon failure of the edge girder, this experiment was limited to a maximum load of 250 tons. All experiments on the disconnected T-beams resulted in a flexural shear failure, see Figure 8. The load-deflection diagram of the connected girders is shown in Figure 9 and of the disconnected girders in Figure 10.

Table 2. Results of experiments.

Test	Span	a/d	F_{max} (kN)	V_R (kN)	δ_u (mm)	Failure mode
1	4	2.8	3004	1188	21	Punching of deck and shear failure of girder
2	4	4.8	3444	1525	14	Punching of deck and shear failure of girder
3	4	2.8	2506	998	11	Not tested to failure
4	2	2.8	1678	1301	79	Flexural shear T-girder
5	2	2.8	1703	1323	65	Flexural shear T-girder
6	2	2.8	1774	1385	74	Flexural shear T-girder
7	2	4.8	1022	774	132	Flexural shear T-girder



Figure 6. Shear failure of T-girder in test 1. The diaphragm is located on the left side and the end support on the right side.



Figure 7. Punching failure of the deck slab in test 1, showing top view and measurements in cm (left) and bottom view (right).

4.2 *Comparison of connected and disconnected girders*

It is not straightforward to compare the results of the shear at failure of the disconnected and connected girders, see Figure 11. A first reason why comparison is not simple is related to the load distribution. In the connected girders, load distribution results in a change of failure



Figure 8. Flexural shear failures in test 4 and 5.

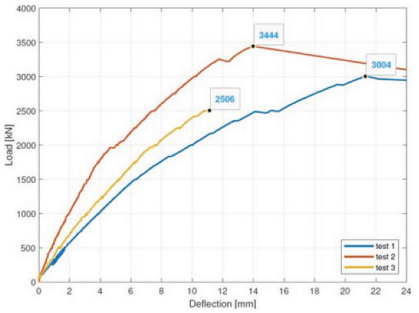


Figure 9. Load-deflection diagrams of girders in connected system.

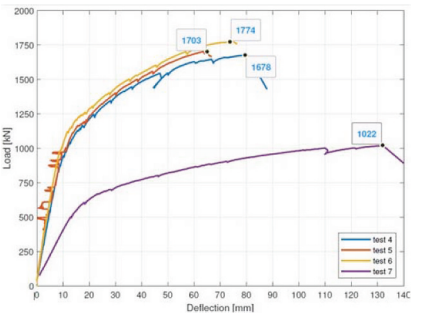


Figure 10. Load-deflection diagrams of girders in disconnected system.

mode from flexural shear for the individual girders to shear-tension for the case of the connected girders. Moreover, an important difference between the connected and disconnected girders can be at- tributed to system behavior represented by arching action in the girder and the deck. For the con- nected girders, the constraints provided by the surrounding members result in significant addi- tional compressive normal forces in the girder and in the development of compressive membrane action in the deck slab (Taylor et al. 2007, Collings and Sagaseta 2015, Amir et al. 2016). Finally, the presence of the diaphragms increases the capacity, as the diaphragm works almost as an in- ternal support.

In addition, using the shear distribution factor from Eq. (1), a factor of 0.52 is found for the interior girders of the Vecht bridge. For an *a/d* distance of 2.8, the maximum load in the connected system is 3004 kN, which would correspond to a maximum load on the tested girder of 1562 kN according to this distribution factor. This value can be compared to the average failure load of the three experiments of disconnected girders with $a/d = 2.8$ of 1718 kN. For $a/d = 4.8$ the maximum load in the connected system is 3444 kN, which would give a maximum load on the tested girder of 1791 kN. The failure load in test 7 was 1022 kN. This brief comparison shows that the AASHTO distribution factors cannot capture the complex system behavior and different shear failure mechanisms that occur in the system at the ultimate limit state.

5 DISCUSSION

This article describes the seven experiments to failure carried out on the Vecht Bridge. As can be seen from the comparison of the maximum load and the sectional shear at failure for the connected bridge system and the disconnected girders, a one-on-one comparison between the two cases is not straightforward. The reasons for the complexity of the comparison is the system behaviour of the connected system, in which compressive membrane action in the deck occurs and compressive arch action in the prestressed girder. Moreover, these two arching mechanisms need to be analysed

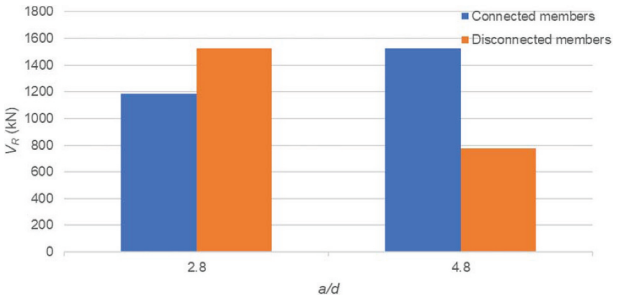


Figure 11. Comparison between sectional shear force at failure for connected and disconnected members from Table 2. Note that the average result of tests 4-6 is used in this comparison.

together. As a result, the flow of forces and the failure mode is significantly different in the connected system as compared to in the individual girders. A full analysis of system behaviour applied to this case study, as well as linear elastic finite element calculations typically used in assessment and non-linear finite element calculations used to further study the experiment can be found in (Ensink 2024).

One important aspect that can already be highlighted here with regard to the system behaviour is that in these experiments, compressive membrane action occurred, even though the load was placed right over the girder. These experiments are the first experiments that demonstrate that compressive membrane action can also be activated when the load is not in the middle of the deck, but right over the girder.

The comparison of the maximum loads also shows that the AASHTO shear distribution factors do not give good results at the ultimate limit state, as these factors are based on linear elastic analyses. The relation between the transverse distribution and the load level requires further re- search. It needs to be verified if the simplified load distribution factors gave good results for the lower load levels in the experiments on the Vecht Bridge, and it can be recommended to carry out research into transverse distribution factors that are representative of the ultimate limit state.

While collapse testing of bridges is expensive (order of magnitude of 400k€), the cost savings for the service life extension of the other slab-between-girder bridges (where replacement would cost over 10m€) is significant (approximately 45% cost savings on a 100-year time horizon when comparing annual equivalent costs). Moreover, indirect cost savings from avoid traffic delays and ecological cost savings related to material use and transportation are obtained.

A final step of this research, which is foreseen for future work, is the extension of this study to encompass all geometries encountered in the slab-between-girder bridges in the Netherlands. For these geometries, the system behaviour needs to be studied in more detail. Once this information is available, a method can be developed to improve the assessment of the existing prestressed T- girder bridges in the Netherlands.

6 SUMMARY AND CONCLUSIONS

This paper introduces seven experiments that were carried out on the Vecht Bridge, a slab-between-girder bridge in the Netherlands with diaphragms at the end and at one third of the span, and with post-tensioned girders. Three experiments were carried out on the connected system and four experiments were carried out on the bridge in which the deck and diaphragms were cut so as to study the behavior of the disconnected girder. The goal of the experiments was to compare the behavior of the connected system and individual members. Based on the described experiments, we can draw the following conclusions:

- The overall system behaves in a much stiffer way than the individual girders.
- The maximum load in the case of the overall system is significantly larger, indicating system behavior in these bridges.

– The failure mode changes from flexure-shear in the individual girders to punching of the deck with a shear-tension failure of the girder for the connected system.
– The system behavior can be attributed to compressive arch action in the girders and compressive membrane action in the deck, and cannot be represented properly by the AASHTO shear distribution factors.

Overall, these failure tests on a real bridge, with all its original details, has provided unique in- sights into the behavior and failure mode of existing slab-between-girder bridges.

ACKNOWLEDGMENT

The authors wish to express their gratitude and sincere appreciation to the Dutch Ministry of Infrastructure and the Environment (Rijkswaterstaat) for financing this research work. The contributions and help of our (former) colleagues Dick Hordijk, Rutger Koekkoek, Marco Roosen, Fred Schilperoort, Cor van der Veen, and Yuguang Yang, and of student Thomas Harrewijn of Delft University of Technology are gratefully acknowledged. The fruitful discussions with Ane de Boer, Sonja Fennis, and Herbert van der Ham from the Dutch Ministry of Infrastructure and the Environment, with Frank Linthorst and Danny den Boef of Witteveen+Bos, responsible for logistics and safety during the test, and with Otto Illing and the late Chris Huissen of Mammoet, responsible for applying the load during the collapse test, are also acknowledged.

REFERENCES

AASHTO 2015. *AASHTO LRFD bridge design specifications*, *7th edition with 2015 interim specifications*, Washington, DC, American Association of State Highway and Transportation Officials.

ACI Committee 342 2016. ACI 342R-16: Report on Flexural Live Load Distribution Methods for Evaluating Exisiting Bridges. Farmington Hills, Michigan: American Concrete Institute.

Amir, S., Van der Veen, C., Walraven, J.C. & De Boer, A. 2016. Experiments on Punching Shear Behavior of Prestressed Concrete Bridge Decks. *Aci Structural Journal*, 113, 627–636.

Arockiasamy, M. & Amer, A. 1998. Load Distribution on Highway Bridges Based On Field Test Data: Phase III.

Cai, C. S., Shahawy, M. & Peterman, R. J. 2002. Effect of Diaphragms on Load Distribution of Prestressed Concrete Bridges. *Transportation Research Record*, 1814, 47–54.

CEN 2003. Eurocode 1: Actions on structures - Part 2: Traffic loads on bridges, NEN-EN 1991-2:2003. Brussels, Belgium: Comité Européen de Normalisation.

CEN 2005. Eurocode 2: Design of Concrete Structures - Part 1-1 General Rules and Rules for Buildings. NEN-EN 1992-1-1:2005. Brussels, Belgium: Comité Européen de Normalisation.

Collings, D. & Sagaseta, J. 2015. A review of arching and compressive membrane action in concrete bridges. *Institution of Civil Engineers – Bridge Engineering*, 169, 271–284.

Dutch Institute for Normalization 1962. NEN 1009:1962 Provisions Reinforced Concrete.

Ensink, S. W. H. 2024. *System behaviour in prestressed concrete T-beam bridges*. PhD. Thesis, Delft University of Technology.

Idriss, R. L. & Liang, Z. 2010. In-Service Shear and Moment Girder Distribution Factors in Simple-Span Prestressed Concrete Girder Bridge - Measured with Built-in Optical Fiber Sensor System. *Transportation Research Record*, 2172, 142–150.

Jauregui, D. V. & Barr, P. J. 2004. Nondestructive Evaluation of the I-40 Bridge over the Rio Grande River. *Journal of Performance of Constructed Facilities*, 18, 195–204.

Lantsoght, E. O. L., Van der Veen, C., De Boer, A. & Walraven, J. C. 2013. Recommendations for the Shear Assessment of Reinforced Concrete Slab Bridges from Experiments Structural Engineering International, 23, 418–426.

Mordak, A. G. & Manko, Z. 2008. Static Load Tests of Posttensioned, Prestressed Concrete Road Bridge over Reservoir Water Plant. *Transportation Research Record*, 2050, 90–97.

Taylor, S. E., Rankin, B., Cleland, D. J. & Kirkpatrick, J. 2007. Serviceability of bridge deck slabs with arching action. *ACI Structural Journal*, 104, 39–48.

Wekezer, J., Kwaiewski, L. & Malachowski J. 2004. Analytical and experimental evaluation of existing Florida DOT bridges.

Bridge Maintenance, Safety, Management, Digitalization and Sustainability – Jensen, Frangopol & Schmidt (eds)
© 2024 The Author(s), ISBN 978-1-032-77040-6
Open Access: www.taylorfrancis.com, CC BY-NC-ND 4.0 license

Bridge load testing: Recent advances in research, collaboration, and codes

E.O.L. Lantsoght
Universidad San Francisco de Quito, Quito, Ecuador
Delft University of Technology, Delft, The Netherlands

J.W. Schmidt
Aalborg University, Aalborg, Denmark

G. Sas
Luleå University of Technology, Luleå, Sweden

ABSTRACT: Bridge load testing is one of the tools engineers are using for the assessment of existing bridges, which is becoming increasingly important to manage the existing bridge stock in a sustainable manner. Over the past years, various research groups have worked on theoretical and practical research regarding load testing. Moreover, various international committee work on load testing recommendations. This paper provides an overview of recent research efforts in Denmark, the Netherlands, and Sweden. The way in which recent research efforts are implemented in new committee reports and guidelines is highlighted. Overall, the efforts have focused on combining load testing with insights in structural behavior, applying improved instrumentation techniques, combining with numerical analyses, and providing a probabilistic substantiation. In conclusion: bridge load testing is a dynamic field of research that benefits from international collaboration. Further improvements to existing codes and guidelines will be forthcoming in the next years.

1 INTRODUCTION

In Europe, the decades after the end of the Second World War marked a time of economic expansion and growth, which is reflected, among other aspects, by the expansion of the transportation network. As a result, many of the existing bridges in Europe are from the 1950s to 1970s (Lantsoght *et al.* 2013). These bridges are reaching the end of their originally devised service life. Replacing bridges at the end of their service life is however not a wise decision: the economic cost and CO_2 emissions are high, the impact on traffic flows creates a high indirect economic cost, and natural resources are dwindling. In short, to manage the existing bridge stock sustainably, it is important to assess existing bridges and decide how and in which way the service life of the existing bridges can be extended (Yang *et al.* 2019).

Load testing of bridges can be a valuable method for assessment when uncertainties regarding the overall behavior of the bridge are large (Alampalli *et al.* 2021). Often these uncertainties are dedicated to the contributions from certain mechanisms (such as the effect of support boundary conditions, transverse distribution when strong bands of reinforcement are used for the sidewalks, or to quantify the contribution of the non-structural elements), which are difficult to quantify analytically. Typically, two types of load tests can be distinguished: diagnostic load tests and proof load tests. In a diagnostic load test, a known live load is applied and the resulting structural responses are compared to analytically determined responses to better

DOI: 10.1201/9781003483755-31

understand the overall bridge behavior. Ultimately, a field-validated model can be developed and used for assessment. In a proof load test, a load representative of the factored live load is applied directly to the bridge to demonstrate in the field that the bridge fulfills the code requirements. As high loads are involved, the load needs to be applied incrementally, and at each load level, the structural responses need to be compared to pre-determined thresholds, the so-called stop criteria (Lantsoght *et al.* 2019; Christensen *et al.* 2022). When a stop criterion is reached, further increasing of the load is not permitted. A final type of field test is a collapse test, in which a bridge is loaded to failure, which can give a full insight into the structural behavior of the bridge and all its load-carrying mechanisms.

2 PROOF LOADING ASSESMENT

2.1 *General*

Proof loading methods used as a means to capacity-upgrade existing concrete structures are, at present state, highly country dependent. However, proof load testing assessments seem to be limited by procedure uncertainty, lack of consistent methodologies, guidelines and codes. Often reluctance towards proof loading is present since safety measures and traffic disturbances occur during testing. Short testing time and environmental conditions could influence the result acquisition. This challenge, combined with a possibility of structural collapse, provides an important bridge owner caution that has to be addressed to ensure confidence in proof loading methods.

2.2 *Denmark*

A comprehensive concrete bridge-proof loading research project in Denmark has been ongoing for approximately half a decade. The project collaborators are the Danish Road Directorate, the Technical University of Denmark (DTU), Aalborg University (AAU), and COWI A/S.

The proof loading concept has its basis in the Danish classification system, where specified axle loads are given for each classification vehicle (Vejdirektoratet - The Danish Road Directorate 2017; Schmidt *et al.* 2020). The heavy vehicles' positioning is described, where a classification vehicle A is placed in the desired position on the bridge. Adjacent to the vehicle A, a stable vehicle B load is applied. A bridge has sufficient resistance if the bridge class is higher than the class of the passing vehicle. The research includes a multidisciplinary approach that combines experimental testing, theoretical response evaluations, and probabilistic assessments. Bridges on a road stretch between Herning and Holstebro in Denmark were initially tested in the Danish bridge testing project. Some of the weakest bridges were seen to have significantly larger resistance than predicted theoretically (Schmidt *et al.* 2018). Several pilot-proof loadings were performed during the research project to verify the developed methods and to get unique experience with the in-situ response- and handling of sensitive equipment. It was experienced that in-situ proof load can be very challenging compared to laboratory testing due to the environmental and practical conditions which may affect result acquisition. This aspect is combined with a short testing time demand to reduce related costs and traffic disturbances. Advanced testing equipment should thus be efficiently optimized and reduced to an extent that meets these challenges and generates the desired output. The outcome aims to accommodate a satisfactory evaluation of deformations, stop criteria, target loads, etc., to ensure a sufficient proof load decision basis.

Experiences and findings from the Danish proof loading research project have generated input for a Danish bridge proof loading guideline, which is expected to be published soon. The guideline describes how to perform proof loading on one-span bridges with a background in the Danish classification system. A pilot project was initiated to verify whether the guideline procedure was possible. Four class 80 bridges were identified on a chosen road stretch, which was aimed to be upgraded to class 100 using the developed proof loading method. The bridges

were tested successfully in three days, (including a manageable traffic disturbance (Christensen *et al.* 2023)). Consequently, the road stretch was upgraded to class 100, and the results could be integrated into the Danish strategic road network.

2.3 *The Netherlands*

In the Netherlands, research related to assessment of existing concrete bridges originally focused mostly on reinforced concrete slab bridges, as a large number of these bridges form the 1960s and 1970s were found to be insufficient for shear upon assessment according to the newly introduced Eurocodes (Lantsoght *et al.* 2013; Lantsoght *et al.* 2017a). These efforts were in line with the development of the Dutch Guidelines for the Assessment of Existing Bridges (RBK) (Rijkswaterstaat 2013).

Assessment of existing bridges in the Netherlands is carried out at four different Levels of Approximation (LoA). The first LoA is usually a spreadsheet-based hand calculation, which compares the factored load effect in a simplified way with the factored capacity from the code. If the Unity Check, i.e. the ratio of demand to capacity, is more than one, the assessment is taken to the next level. If not, it is found with a simplified approach that the critical cross-section, and by extent, the bridge, fulfills the requirements. At the next LoA, a linear finite element analysis is used for finding the factored load effect, and the factored capacity is again determined using the code expressions. Then, if a next level is necessary, a nonlinear finite element analysis may be considered, following the Dutch Guidelines for Nonlinear finite element analysis of concrete structures (Rijkswaterstaat 2012). Finally, if none of the analytical approaches can demonstrate that the bridge fulfills the code requirements, and it is expected that additional sources of capacity can be activated, a proof load test may be considered.

Proof load testing in the Netherlands is not a common method of assessment. At this moment, a series of pilot proof load tests have been carried out (Lantsoght *et al.* 2017b). These pilot proof load tests showed the feasibility of proof load testing for the assessment of existing reinforced concrete bridges in the Netherlands, both for flexure and shear. However, it was decided to first carry out fundamental research to determine stop criteria for shear and to develop a probabilistic substantiation of proof load testing in line with the current code requirements before proof load testing can be carried out by market parties.

2.4 *Sweden*

Sweden owns approximately 30,000 bridges, of which about 4,000 are railway bridges and the remaining are road bridges BaTMan (Trafikverket 2023). Some 70% of these bridges are owned by the Swedish Transport Administration (Trafikverket), while the rest, exclusively road bridges, are owned by regional counties. Very few railway bridges are also owned by private companies. The bridge population is relatively young, with many built after the Second World War, and their design lifetimes vary. As codes have evolved and the quality of materials and workmanship has improved, many bridges have been designed with longer lifetime expectations. It is also acknowledged that the quality of the bridges is high. To the authors' best knowledge, failures or service impairments have been seldom encountered. Currently, capacity assessment is conducted using a national code issued by the Swedish Transport Administration (TRVINFRA-00331 2023), based on the European Norms (Eurocodes), incorporating adjustments from the previous Swedish national codes.

The assessment of the bridges is largely undertaken by consulting companies, supervised by 10 bridge specialists from Trafikverket. The initial assessment step involves automated worksheets or simple linear elastic calculations based on design values, complemented by verification through inspection reports in BaTMan. If the capacity conditions are met, no further steps are taken. If not, Trafikverket may contract more detailed analysis, which can include non-linear finite element simulations, in-depth inspections, and structural health monitoring. Sweden has a relatively short history of proof load testing of bridges.

According to (Elfgren *et al.* 2018), thirteen full-scale bridges have undergone testing in the past three decades, with five tested to the point of failure. The objectives of these proof load tests varied, including monitoring the bridge under controlled loads, validating advanced calculations, verifying strengthening methods, or checking for settlements. The tests conducted to the point of failure aimed to collect data for verifying and comparing capacities in shear of concrete and prestressed concrete bridges under concentrated loads, using methods like finite element modeling (FEM). The results consistently showed discrepancies between code estimates, test results, and numerical simulations, thus prompting further developments.

3 RECENT RESEARCH

3.1 *Denmark*

The bridge proof loading project's first version (V1) succeeded with significant in-situ test experience and descriptions of a test setup and related design. The optimized multidisciplinary approach seemed to work well where advanced monitoring could be optimized and reduced to an extent that enabled several pilot-proof loading tests. In addition, testing and theoretical evaluations also revealed sufficient interaction between OT elements under in situ and laboratory conditions. Thus, desirable slab behavior was obtained, enabling more optimized calculation methods and capacity upgrading of several bridges, see Figure 1.

Findings and results from the V1 project provided a good basis for continuing the Danish proof loading project based on the classification system. A good foundation for classification-based proof loading, which is economically competitive, seemed to be provided. The V1 project dealt with one-span bridges and seems to provide an excellent background for an extension to the second version 2 (V2), which will research methods to proof-load multi-span bridges. In addition, further evaluation and optimization of stop criteria is ongoing in the V2 project. This evaluation will be one of the main scopes since an open question remains concerning stop criteria related to the potentially brittle behavior of non-shear reinforced (shear-critical) slabs and prestressed concrete bridges. The extension to V2 was deemed to work in excellent synergy with upcoming international activities, ensuring an even more significant gain. One of the main aims is to extend the Danish guideline with the findings of the V2 project.

a) b)



Figure 1. a) Laboratory OT-slab point loading testing (behind glass screen) with acoustic emission, digital image correlation, LVDTs, etc. b) In-situ pilot testing using representative classification vehicles.

3.2 *The Netherlands*

Recent and current research in the Netherlands on proof load testing has mostly focused on fundamental research to support the proof load testing practice. This research has focused on

developing stop criteria for shear for use during proof load testing of reinforced concrete members without shear reinforcement, and on deriving a probabilistic substantiation of proof load testing.

The research on stop criteria encompasses two series of experiments. A first series consists of 25 experiments in flexure and shear on 6 reinforced concrete slabs of 5m × 2.5 m × 0.3 m subjected by a proof load testing protocol first, and then tested stepwise to failure. A second series, ongoing at the time of writing this paper, consists of 8 skewed reinforced concrete slab specimens, see Figure 2. To develop these stop criteria, first shear stop criteria for slab strips have been developed, and then these stop criteria are extended to reinforced concrete slabs. The shear stop criteria for beams can be found in (Zarate Garnica *et al.* 2024), whereas the shear stop criteria for slabs are under development. The second series of experiments has the following goals: 1) validate the developed shear stop criteria for straight slabs for the situation of skewed slabs, and 2) validate current assessment procedures for skewed slab bridges, and in particular the way in which the load effect is determined in the obtuse corner.



Figure 2. Skewed slab testing at TU delft.

The research on the probabilistic substantiation of proof load testing is addressing the following aspects: 1) time-dependent probabilities of failure (de Vries *et al.* 2022), 2) state of information and the effect of the type of prior selected (de Vries *et al.* 2023), 3) using stop criteria and measurements during proof load testing for the probabilistic analysis (de Vries *et al.* 2024), and 4) spatial variability.

3.3 *Sweden*

During the last 30 years about fifteen tests on bridges have been conducted in Sweden, primary led by Luleå University of Technology (LTU) (Elfgren *et al.* 2018). The most recent work on proof loading of bridges in Sweden aims at contributing to the sustainability challenge by identifying the True Capacity of the existing bridges. This is done by developing tools



Figure 3. Concept used at Luleå University of Technology (LTU) for life extension of existing structures.

and methods for life cycle assessment in areas of SHM, prediction simulations and tests, see Figure 3.

A 65-year-old prestressed box-girder concrete bridge in Kalix, northern Sweden, was demolished in 2022. Prior to this, an experimental campaign was conducted to enhance our understanding of the behavior of such bridges. The work focused on three aspects: (1) condition assessment of the bridge using non-destructive testing (NDT), (2) development of a proof loading method for assessing service limit conditions with standard convoys and Structural Health Monitoring (SHM) sensors, (3) formulation of controlled demolition methods for prestressed concrete bridges. The results have shown that NDT tools are promising for identifying defects, though they require further field validation and a comprehensive understanding of the bridge's design and construction principles. The proof loading method incorporated tests with new technologies, including Fiber Optic Sensors (FOS), acoustic emission testing, and various techniques for measuring prestressing forces. The developed demolition process was successfully executed, ensuring safety and environmental cleanliness.



Figure 4. View of the midspan of the Kalix bridge under proof loading.

New research related to railway bridges began in 2021 with an investigation into potentially increasing axle loads from 30 tons to 32.5 and 35 tons on one of the most heavily utilized railway lines, the Iron Ore Line in Northern Sweden. Approximately 50% of the bridges on this line are trough-type, comprising two side beams and a slab that form a U-shaped structure filled with ballast. The study (1) verifies the existing standard load distribution model by monitoring pressure distribution between the ballast and the concrete deck and beams, and (2) assesses the impact of increased axle loads on the lifespan of these bridges. Of high interest is the development of criteria for the fatigue assessment. Experiments are conducted on a full-scale model bridge (7 m × 4 m) in the LTU laboratory, Figure 5. A suite of sensors, including standard strain gauges, Linear Variable Differential Transformers (LVDTs), Fiber Optic Sensors (FOS) on the internal reinforcement and concrete surface, and photogrammetry for crack detection and mapping, has been deployed. The data collected will be utilized for benchmarking numerical analyses and subsequent parametric stochastic validation.



Figure 5. View of the full-scale trough bridge tested at the LTU lab.

Research into developing proof loading methods for railway bridges has included analysis, condition assessment based on autonomous crack detection, and instrumentation of four bridges of various designs: trough, composite steel girder - concrete slab, concrete arch, and portal frame bridges. Sensors have been strategically placed in areas deemed critical for assessing bridge performance. Controlled train loads have been applied in both dynamic and static tests under varying seasonal conditions. These tests aim to understand how temperature fluctuations and humidity levels over a year affect the interaction between the bridges and their support structures.

3.4 *State of collaboration*

Current research in Denmark, the Netherlands, and Sweden focuses in broad lines on the following common themes: modeling of existing concrete structures, automated condition assessment, improved instrumentation methods for field measurements, and probabilistic aspects, see Figure 6. Moreover, field testing occurs under constraints of time and budget. As such, sharing experiences is to the benefit of all. In particular, a synergy of activities can be found between the three countries for the following topics: solving practical challenges related to application of loading and sensors when multiple spans need to be tested, determination of the required number of positions and proof load for the test, extrapolation of results from one span to another span for an assessment, evaluation of the choice of testing a lower number of positions under a higher load, versus a higher number of positions under a lower load, and the practical repercussions of such a choice, and developing considerations for different types of bridges, and those that are multiply statically determinate versus statically indeterminate bridges.

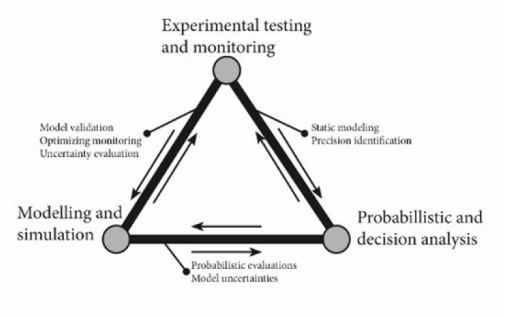


Figure 6. Synergy between research topics.

4 RECENT GUIDELINE AND ADVANCED IN INTERNATIONAL COLLABORATION

Recent research efforts related to proof load testing as illustrated above, as well as carried out by colleagues internationally, have resulted in the publication of a number of technical documents, codes and guidelines that may be of relevance to the reader. The first relevant document is a recent *fib* Bulletin of TG 3.2 (fib TG 3.2 2024), which includes a section related to proof load testing of existing structures, and in particular existing concrete bridges. For existing reinforced concrete buildings, the new ACI 437.2M-22 (ACI Committee 437 2022) code is a major development as compared to ACI 437.2M-13 (ACI Committee 437 2013), as the current version of the code includes the option to proof load test buildings for shear. For bridges, the upcoming version of the AASHTO Manual for Bridge Evaluation includes a new Chapter 8 on Load Testing, which is aligned with the contents of the TRB e-circular 257 (Alampalli *et al.* 2019).

Besides the recently published documents mentioned in the previous section, various international committees have included or are including load testing recommendations in their reports and guidelines. In particular, within IABMAS, the IABMAS Bridge Load Testing

committee is working together with *fib* COM 3 on the development of a guidance document related to proof load testing of existing concrete bridges. Moreover, the members of the IABMAS Bridge Load Testing committee meet twice a year virtually, as well as in hybrid mode at the IABMAS symposia. Interested readers can find the minutes of the activities of the technical committee on the IABMAS website (IABMAS 2021), as well as find the mission, goals and membership of the committee reported.

5 CONCLUSION

This paper shows how assessment of existing concrete bridges is carried out in Denmark, the Netherlands, and Sweden, and how proof load testing is used in these countries as part of the assessment. The paper also gives a summary of recent research insights from the three countries. A summary of the research efforts show that these efforts have been focused on combining load testing with better insights in structural behavior, applying improved instrumentation techniques in the field, combining measurements with numerical analyses, and providing a probabilistic substantiation of the practice. Synergy in the research efforts is identified by looking at the broad categories of practices applied in the three countries, even though assessment and proof load testing practices are driven by national differences. In conclusion: bridge load testing is a dynamic field of research that benefits from international collaboration. It is expected that further improvements to existing codes and guidelines will be forthcoming in the next years.

REFERENCES

ACI Committee 437 (2013) Code Requirements for Load Testing of Existing Concrete Structures (ACI 437.2M-13) and Commentary Farmington Hills, MA.

ACI Committee 437 (2022) Code Requirements for Load Testing of Existing Concrete Structures (ACI 437.2-22) and Commentary Farmington Hills, MA.

Alampalli, S., Frangopol, D.M., Grimson, J., Halling, M.W., Kosnik, D.E., Lantsoght, E.O.L., Yang, D. and Zhou, Y.E. (2021) 'Bridge Load Testing: State-of-the-Practice', Journal of Bridge Engineering, 26(3), 03120002, available: http://dx.doi.org/doi:10.1061/(ASCE)BE.1943-5592.0001678.

Alampalli, S., Frangopol, D.M., Grimson, J., Kosnik, D., Halling, M., Lantsoght, E.O.L., Weidner, J.S., Yang, D.Y. and Zhou, Y.E. (2019) Primer on Bridge Load Testing, TRANSPORTATION RESEARCH CIRCULAR E-C257.

Christensen, C.O., Damsgaard, K.D.S., Sørensen, J.D., Engelund, S., Goltermann, P. and Schmidt, J.W. (2023) 'Reliability-Based Proof Load Factors for Assessment of Bridges', Buildings, 13(4), 1060.

Christensen, C.O., Zhang, F., Garnica, G.Z., Lantsoght, E.O.L., Goltermann, P. and Schmidt, J.W. (2022) 'Identification of Stop Criteria for Large-Scale Laboratory Slab Tests Using Digital Image Correlation and Acoustic Emission', Infrastructures, 7(3), 36.

de Vries, R., Lantsoght, E.O.L., Steenbergen, R.D.J.M. and Fennis, S.A.A.M. (2022) 'Reliability assessment of existing reinforced concrete bridges and viaducts through proof load testing', in IABMAS 2022, Barcelona, Spain.

de Vries, R., Lantsoght, E.O.L., Steenbergen, R.D.J.M., Hendriks, M.A.N. and Naaktgeboren, M. (2024) 'Structural reliability updating using in-situ load testing and laboratory test results', in IABMAS 2024.

Elfgren, L., Täljsten, B., Blanksvärd, T., Sas, G., Nilimaa, J., Bagge, N., Tu, Y., Puurula, A., Häggström, J. and Paulsson, B. (2018) 'Load-testing used for quality control of bridges', in Workshop of COST TU 1406 in Wroclaw, Poland, March 1-2, 2018, 1–6.

fib TG 3.2 (2024) Modelling Structural Performance of Existing Concrete Structures: State-of-the-Art Report, Bulletin: fédération internationale du béton.

IABMAS (2021) IABMAS Technical Committee on Bridge Load Testing, available:http://iabmas.org/ [accessed November 16th 2021].

Lantsoght, E.O.L., De Boer, A. and Van der Veen, C. (2017a) 'Levels of Approximation for the shear assessment of reinforced concrete slab bridges', Structural Concrete, 18, 143–152.

Lantsoght, E.O.L., Van der Veen, C., De Boer, A. and Hordijk, D.A. (2017b) 'Proof load testing of reinforced concrete slab bridges in the Netherlands', Structural Concrete, 18(4), 597–606.
Lantsoght, E.O.L., van der Veen, C., de Boer, A. and Walraven, J.C. (2013) 'Recommendations for the Shear Assessment of Reinforced Concrete Slab Bridges from Experiments ', Structural Engineering International, 23(4), 418–426.
Lantsoght, E.O.L., Yang, Y., van der Veen, C., Hordijk, D.A. and de Boer, A. (2019) 'Stop Criteria for Flexure for Proof Load Testing of Reinforced Concrete Structures', Frontiers in Built Environment, 5 (47), available: http://dx.doi.org/10.3389/fbuil.2019.00047.
Rijkswaterstaat (2012) Guidelines for Nonlinear Finite Element Analysis of Concrete Structures.
Rijkswaterstaat (2013) Guidelines Assessment Bridges - assessment of structural safety of an existing bridge at reconstruction, usage and disapproval (in Dutch), RTD 1006:2013 1.1, Utrecht, the Netherlands.
Schmidt, J.W., Halding, P.S., Jensen, T.W. and Engelund, S. (2018) 'High Magnitude Loading of Concrete Bridges', Special Publication, 323.
Schmidt, J.W., Thöns, S., Kapoor, M., Christensen, C.O., Engelund, S. and Sørensen, J.D. (2020) 'Challenges Related to Probabilistic Decision Analysis for Bridge Testing and Reclassification', Frontiers in Built Environment, 6, available: http://dx.doi.org/10.3389/fbuil.2020.00014.
Trafikverket (2023) BaTMan database., available:https://batman.trafikverket.se/ [accessed 21/12/2023].
TRVINFRA-00331 (2023) Bro och broliknande konstruktion, Bärighetsberäkning, available: Available at: https://bransch.trafikverket.se/for-dig-i-branschen/teknik/Tekniska-dokument/Nyhetsarkiv-Tekniska-dokument/2022/trvinfra-00331-bro-och-broliknande-konstruktion-barighetsberakning/ [accessed 21/12/2023].
Vejdirektoratet - The Danish Road Directorate (2017) DS/EN 1991-2 DK NA:2017, Annex A: Lastmodeller for klassificering og bæreevnevurdering (Models of special vehicles for road bridges).
Yang, D.Y., Frangopol, D.M. and Teng, J.-G. (2019) 'Probabilistic life-cycle optimization of durability-enhancing maintenance actions: Application to FRP strengthening planning', Engineering Structures, 188, 340–349, available: http://dx.doi.org/https://doi.org/10.1016/j.engstruct.2019.02.055.
Zarate Garnica, G.I., Lantsoght, E.O.L., Yang, Y. and Hendriks, M.A.N. (2024) 'Shear stop criteria for reinforced concrete slab strips', in IABMAS 2024.

Bridge Maintenance, Safety, Management, Digitalization and Sustainability – Jensen, Frangopol & Schmidt (eds)
© 2024 The Author(s), ISBN 978-1-032-77040-6
Open Access: www.taylorfrancis.com, CC BY-NC-ND 4.0 license

Reliability of I-girder PC bridges through proof load testing: Preliminary results

Gianmarco Addonizio
Department of Structures for Engineering and Architecture, University of Naples Federico II, Naples, Italy

Rein de Vries
Faculty of Civil Engineering and Geosciences, Delft University of Technology, Delft, The Netherlands
Structural Reliability, Netherlands Organization for Applied Scientific Research, Delft, The Netherlands

Eva O.L. Lantsoght
Faculty of Civil Engineering and Geosciences, Delft University of Technology, Delft, The Netherlands
College of Sciences and Engineering, Universidad San Francisco de Quito, Quito, Ecuador

Daniele Losanno
Department of Structures for Engineering and Architecture, University of Naples Federico II, Naples, Italy

ABSTRACT: Structural assessment of existing bridges is one of the most challenging aspects for the correct and sustainable management of civil infrastructures that emerged in the last few years. Specifically, Italy has a substantial number of bridges over 50 years old, mainly represented by simply supported prestressed concrete I-girder-type with a cast-in-situ deck. Proof load testing represents an empirical alternative to the standard calculation methods commonly adopted for safety assessment of existing structures. This article investigates the reliability of a bridge in different configurations including damaged and undamaged scenario through site-specific traffic data collected by Weigh-In-Motion (WIM) systems in the Netherlands. Assuming a target load corresponding to characteristic load combination according to Eurocode provisions, the proof load test resulted into slightly reduced reliability indexes during the test while achieving higher values under successful completion. Preliminary results contribute to demonstrate proof load test can represent a valuable method for assessment of existing bridges.

1 INTRODUCTION

1.1 *Motivation for proof load testing*

Looking at the high number of ageing structures, management and safety assessment of existing bridges have emerged as increasingly crucial global concerns. Taking into account mainly the European and North American panorama (Calvi, et al., 2019), a pervasive imperative has arisen to understand the condition of our infrastructure to create prioritisation for good asset management and ensure ongoing safety and efficiency. Many bridges are reaching their nominal design life in the short term. For example, in Italy, the majority of the modern road network (total 840,000 km) was built during the two decades from 1955 to 1975 (Pinto & Franchin, 2010). Moreover, the intricate topography of Italy is a cause of a dense distribution of bridges (Calvi, et al., 2019), with an approximate frequency of one every two kilometres of highways (Miluccio, Losanno, Parisi, & Cosenza, 2021). Additionally, in (ANSFISA, 2022) it is possible to see that the Italian road network is mainly owned by Municipalities (~80%). Similar considerations for ageing bridges can be made in the Netherlands and the United States (Lantsoght, 2023).

DOI: 10.1201/9781003483755-32

In such a challenging framework, different safety assessment methods should be evaluated for the existing bridges (Lantsoght, 2023). This paper focuses on Proof Load Testing (PLT), i.e. a complementary method to the numerical desk-study assessment for evaluating bridges' structural safety against traffic loads. Basically, through a prescribed static loading protocol, the aim is to check actual bridge conditions by monitoring its structural response and at the same time obtaining a minor of its capacity. PLT assumes particular relevance when standard calculation methods encounter limitations, such as in case of lacking original plans (Shenton, J.Chajes, & J.Huang, 2007) (Anay, Cortez, Jáuregui, ElBatanouny, & Ziehl, 2015) or when numerical models are limited by a number of assumptions regarding structural analysis. Moreover, sometimes analytical safety checks are too demanding and time-consuming for several local authorities, when the level of knowledge is low and the number of bridges is very high with a limited budget for an in-depth safety assessment. In this case, exceptional vehicles that passed over the bridge during the past would represent a proof load and could be taken into account for reliability assessment in absence of deterioration phenomena.

1.2 *Codes and state-of-art overview*

As regards international code provisions, mainly two approaches can be acknowledged all over the world. The former approach is typical in the USA and is highlighted by the Manual for Bridge Evaluation (MBE) (AASHTO, 2011), which prescribes the so-called "Proof Load Test" to demonstrate the ability of the bridge to carry some "magnified" live load that is correlated to a specific load rating vehicle. The second approach is more typical in Europe, where an "acceptance" load test after bridge completion or extraordinary maintenance operations is conceived and it is based on an equivalent sectional effect between the load applied during the test and the design unfactored live load. Unfortunately, a fragmented outline persists in the European scenario regarding codes and guidelines for PLT (Lantsoght, 2023). For example, the Italian Building Code (Italian Ministry of Infrastructures and Transportation, 2018) only prescribes the so-called "acceptance" test. Recently, in 2020, the Italian High Council of Public Works (HCPW) issued new guidelines for classification and risk management, safety assessment, and structural health monitoring of existing bridges (Italian High Council of Public Works, 2020) introducing a "temporary operational" condition to be proved by load testing. Nevertheless, this PLT has to be followed by a conventional, i.e. analytical-based, safety assessment (to be completed within 60 days from the test). In (AASHTO, 2011) the calibration of proof load factors is based on literature review, (Lichtenstein, 1993) and (Transportation Research Board, 1998). In the European framework (Casas & Gómez, 2013), a methodology to calibrate proof loads to be applied to existing highway bridges was proposed, based on available WIM data for traffic modelling. Several modifications have been recently proposed by (de Vries, Lantsoght, & Steenbergen, 2023) to improve the PLT practice.

1.3 *Research objective*

After reviewing the current literature on PLT, this study aims to highlight the potential of an empirical alternative to the standard calculation methods commonly adopted for the safety assessment of existing I-girder PC bridges, linking proof load testing and structural reliability. Based on restricted but realistic hypotheses, theoretical benefits in terms of increasing reliability have been proved for different traffic load combinations and damage scenarios.

2 PROOF LOADING RELIABILITY

According to (Melchers & Beck, 2018), structural reliability is related to the probability of a limit state being exceeded for an engineered structural system at any stage during its life. The main concern of PLT is the calibration of the load to be applied in order to achieve target reliability, assuming that a trade-off between collapse risk during the test and posterior benefit regarding proved capacity has to be found. Indeed, the use of relatively high target loads entails an increased risk during the test itself, but once the test has been successfully completed

the reliability of the structure would be higher. For this reason, a reliability-based approach is required for a research-oriented analysis and calibration of proof load targets, stop criteria and methodology (Spaethe, 1994). In a probabilistic framework, all types of uncertainties and randomness affecting initial assumptions can be accounted for. The nominal probability of failure P_f (Melchers & Beck, 2018) and the relative Reliability Index β at a structural element level can be considered exhaustive safety measures. Considering all the variables as mutually independent, an example of general limit state function equation Z before any proof load test, adopted in (de Vries, Lantsoght, & Steenbergen, 2023) and (de Vries R., Lantsoght, Steenbergen, & Fennis, 2023), is represented by Equation 1:

$$Z = [\theta_R R - \theta_E G] - \theta_E C_{0T} T = R' - \theta_E C_{0T} T \quad (1)$$

where R represents a capacity measure, G is the permanent load (i.e. the self-weight plus the load due to non-structural elements) and T is the traffic live load. Both for resistance and loads, model uncertainties (θ_R; θ_E) may be considered in the analysis to account for approximation when calculating resistance and load effects, respectively. Finally, the random variable C_{0T} may account for time-independent uncertainties of traffic trend effects. During the PLT, Z_{PL} of Equation (2) may be considered as a limit state function, assuming that in the meantime of the test, the bridge is closed to traffic:

$$Z_{PL} = [\theta_R R - \theta_E G] - \theta_{E,PL} Q_{PL} = R' - \theta_{E,PL} Q_{PL} \quad (2)$$

where R, G, T, θ_R and θ_E are the same as Equation (1) and Q_{PL} represents the effect due to the proof load PL and $\theta_{E,\ PL}$ is the model uncertainty for the controlled proof load effect. Both Q_{PL} and $\theta_{E,\ PL}$ can be modelled as random or deterministic variables. Looking at the posterior analysis, at the state-of-the-art, different ways exist to consider the actual benefit due to a PLT in a reliability framework. The most consolidated and spread approach is to consider the effect generated by a specific load as a lower bound of the actual capacity of the bridge through a truncation of its probability distribution (Christensen, et al., 2023), (Transportation Research Board, 2019), (Casas & Gómez, 2013) and (Faber, Val, & Stewart, 1999). For instance, Equation (1) may still be considered valid with a truncate distribution of R'. Other methods to consider the additional knowledge about the bridge behaviour, such as a bayesian updating, can be found in (K. Nishijima, 2006), (Schmidt, et al., 2020), (Kapoor, Christensen, Schmidt, Sørensen, & Thons, 2021) and (de Vries R., Lantsoght, Steenbergen, & Fennis, 2023).

3 CASE STUDY BRIDGE

3.1 *General description*

The I-girder prestressed concrete (PC) deck archetype represents a significant number of Italian roadway bridges built during past decades. Most of the bridge stock is represented by simply supported decks of 30 to 40 m span with PC girders designed according to an allowable stress method in force at the time (Pinto & Franchin, 2010; Borzi, et al., 2015). In (Miluccio, Losanno, Parisi, & Cosenza, 2021) and (Miluccio, Losanno, Parisi, & Cosenza, 2022), the authors investigated the traffic-load fragility of a portfolio of I-girder PC bridges assumed to be representative of many existing bridges. At the Ultimate Limit State (ULS), the case-study bridges showed higher vulnerability (i.e. higher values of conditional failure probability) to flexural mechanisms rather than shear under traffic load model 1 (TLM 1) (Comité Européen de Normalisation, 2003). Grounding on these preliminary results, the authors of this paper assumed a case study bridge built during the '60s along an important highway in the South of Italy. With a span length of 42m and a total length of around 1km, the bridge is simply supported and it is composed of 3 m high PC I-girders, a cast in situ concrete slab (variable thickness between 0.20 and 0.30m) and four diaphragms (Figure 1).

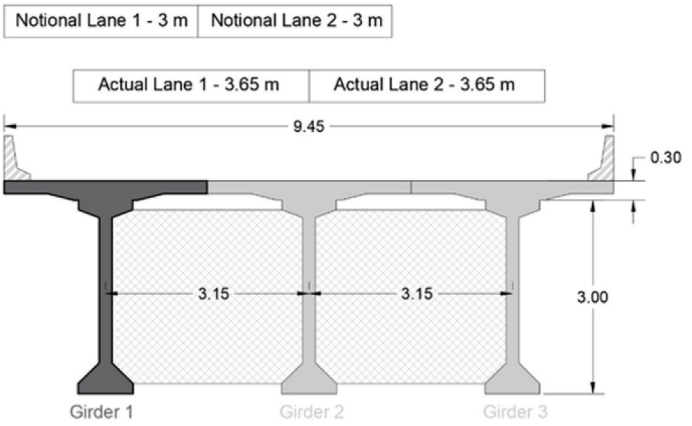


Figure 1. Deck cross-section including traffic load configurations.

Due to the deteriorating state of the viaduct, retrofit interventions were designed in the last few years in order to restore the full bearing capacity of the bridge. Original design and retrofit plans were made available. Additionally, an acceptance load test (i.e. imposed traffic load) after restoration was recently performed to reproduce the TLM1 bending moment. This effect was achieved with four steps of loading, each with two 42t heavy trucks. In the final loading configuration, the eight trucks were arranged according to the notional configuration of traffic (Figure 1). The structural response during the PLT was monitored through displacement transducers, demonstrating linear behaviour and no damage upon unloading.

3.2 *Capacity modelling*

At ULS, the flexural capacity model M_R (Equation 3) has been adopted by considering contributions from both prestressing steel area A_{sp} and reinforcing steel area A_s to be lumped in their centroid with internal lever arm $d \approx 0.9h_{section}$, being $f_{p,\,01}$ the conventional yield strength of prestressing steel and f_y the yield strength of mild steel:

$$M_R = d \cdot \left(A_{sp}f_{p,01} + A_s f_y\right) \tag{3}$$

During on-site visual inspections, different corrosion scenarios were detected in a number of girders prior to retrofitting. In the following analyses, both undamaged and damaged configurations have been assumed; in the latter case the most severe corrosion was considered in terms of 10% loss of total prestressing steel area (i.e. 8 out of 80 strands in total) and total loss of reinforcing steel area at the bottom of the beam (Table 1). Based on original plans, mechanical properties f_y and $f_{p,\,01}$ were assumed as lognormal random variables defined in the next section.

Table 1. Deterministic geometric variables.

Undamaged	Reinforcing steel area Prestressing steel area	A_s A_{sp}	6ϕ10 + 7ϕ20 80 strands*	2670 mm^2 7440 mm^2
Damaged	Reinforcing steel area Prestressing steel area	$A_{s,\,dam}$ $A_{sp,dam}$	- 72 strands*	0 mm^2 6696 mm^2

*1 strand = 7 wires 1/2''.

Safety checks in terms of internal bending moment accounting for partial safety factors at ULS yielded capacity-to-demand ratios (CDR) equal to 1.36 and 1.26 in undamaged and damaged configuration, respectively. The PLT was performed on the retrofitted bridge whose intervention aimed at restoring the original undamaged safety level (i.e., CDR =1.36).

3.3 *Load distribution factors*

Load distribution due to traffic load is paramount in assessing existing structures. In a few circumstances, simplification may be assumed. Because of the presence of a discrete number of diaphragms, the Engesser-Courbon method (Raithel, 1978) was adopted to calculate load distribution factors for the case study bridge. Basically, the deck deflection profile of the deck is assumed to be rigid in the transverse direction and defined in terms of downward displacement plus rotation only. The primary torsional stiffness of the single girder is neglected therefore deck torsional stiffness is associated with flexural stiffness of the girders. Additionally, the vertical displacements obtained during the load tests validated this assumption with a maximum error of less than 5%. Due to equal girders and traffic load eccentricity, the maximum bending moment M was expected at midspan in the edge right girder (i.e. girder 1) located beneath the slow lane where trucks primarily drive (Figure 1). Two different lane configurations were considered, one having notional lanes (3m width) and one with actual lanes (3.65m width) (Figure 1). In both cases, two load lanes are assumed to obtain maximum effects from the analysis. The effects of each lane in terms of distribution load factors of the edge girder are summarised in Table 2.

Table 2. Load distribution factors.

Lane configuration	Factor lane 1	Factor lane 2
Notional	0.83	0.35
Actual	0.64	0.03

3.4 *Traffic effect modelling*

Acknowledging the present absence of robust Italian Weigh-In-Motion (WIM) data and the methodological purpose of this article, for the present case study a statistical characterisation of traffic load is derived from WIM measurements, utilising an extensive dataset from the Netherlands. Preliminary WIM data from Italian highways is going to be made available in the near future also due to new guidelines promoting traffic monitoring of existing bridges, (Iervolino, et al., 2023) and (Cosenza & Losanno, 2021). WIM recording stations considered in this study are strategically positioned in the Netherlands along high-intensity highway locations and are assumed representative of the traffic load on the case study bridge. Considering that Netherlands traffic is some of the heaviest in Europe (O'Brien, O'Connor, & Arrigan, 2012), the former hypothesis could be considered conservative in terms of intensity and loads. Data from four specific locations (highways A16L, A27L, A50L, A67L) featuring 2-3 traffic lanes were selected due to their high quality. The weekly block maxima of the load effect were obtained to determine the distribution of the load effect in terms of maximum bending moment at midspan. Subsequently, the Gumbel extreme value distribution was fitted to the data using the maximum likelihood estimation (MLE) method. A threshold value (probability of exceedance S = 0.25) was selected to capture the linearly descending right tail of the distribution on the log scale. Lastly, the distribution of weekly maxima was converted to the distribution of annual maxima (de Vries, Lantsoght e Steenbergen 2023). Considering the load distribution factors of Table 2, the simulation was conducted for both notional and actual lane configurations, yielding two sets of parameters for the Gumbel distributions (Table 3), represented in Table 4 as T_{Not} and T_{Act}, respectively. The mean value of the traffic load in the

Table 3. Load effects due to Gumbel distributions for notional and actual traffic lane configurations.

Lane configuration	Annual mean [MNm]	COV [-]
Notional	9.13	0.039
Actual	6.63	0.019

notional lane configuration significantly exceeds that in the actual configuration due to higher eccentricity. Furthermore, contributions from the second lane amplify the coefficient of variation. The realism of the notional lane configuration is a subject of inquiry, especially when considering the layout of the bridge, including the presence of guardrails. Such a configuration would be code-compliant that rarely happens.

3.5 *Permanent load effect modelling*

Permanent load G (Table 4) is considered to model deck self-weight plus non-structural components. The mean value of the associated bending moment (11.70 MNm) is assumed to be equal to the value computed deterministically considering original plans, with a CoV supposed to be equal to 0.10.

3.6 *Proof load effect modelling*

The effect due to a proof load PL, α is modelled both deterministically and probabilistically. The Deterministic Proof Load (DPL) initial assumption considers $Q_{PL,\ \alpha}$ as a deterministic variable equal to α times the value M_{LM1}, which represents the unfactored TLM1 effect (Comité Européen de Normalisation, 2003). According to Italian code provisions for acceptance test (Italian Ministry of Infrastructures and Transportation, 2018), M_{LM1} was computed considering the notional configuration (Figure 1) with tandem (Q1K, Q2K) and distributed loads (q1k, q2k) for the first and the second lane, respectively. A remaining area uniformly distributed load qrk has been considered for the unfavourable parts of the influence lane. $\theta_{E,\ PL}$ is modelled as a deterministic variable equal to 1. For the posterior analysis, DPL truncates the lower tail of the random variable $R' = \theta_R R + \theta_G G$ at the value $\alpha * M_{LM1}$ and uses this distribution when computing Z. Two different values of α (1 and 1.5) are taken into account to investigate the influence of a PLT with a target effect equal to 100% and 150% LM1, respectively. The Probabilistic Proof Load (PPL) initial assumption considers $Q_{PL,\alpha}$ as a normal random variable with a mean equal to α times the value M_{LM1} computed as in the case of DPL. A CoV equal to 0.05 is considered to account for geometric uncertainty when positioning the trucks. $\theta_{E,\ PL}$ is modelled as a normal variable with mean and CoV respectively equal to 1 and 0.10. In the posterior evaluation of reliability, PPL considers only samples for which there is no failure during the PLT.

3.7 *Probabilistic models*

All the random variables used in the analysis are defined in Table 4. Bending moment probability distribution functions are displayed in Figure 2 without model uncertainties.

Table 4. Random variables.

Variable	Symbol	Unit	Mean	CoV	Distribution
Yield strength mild steel	f_y	*MPa*	440	0.075	Lognormal
Yield strength prestressing steel	$f_{p,\ 01}$	*MPa*	1600	0.050	Lognormal
Resistance Model Uncertainty	θ_R	-	1.00	0.050	Lognormal
Load Model Uncertainty	θ_E	-	1.00	0.100	Lognormal
Proof Load Model Uncertainty	$\theta_{E,\ PL}$	-	1.00	0.100	Lognormal
Time-independent Traffic Load Uncertainty	C_{0T}	-	1.10	0.100	Lognormal
Notional Maxima Traffic Load Effect	T_{Not}	*MNm*	9.13	0.039	Gumbel
Actual Maxima Traffic Load Effect	T_{Act}	*MNm*	6.63	0.019	Gumbel
Permanent Load Effect	G	*MNm*	11.70	0.100	Normal
Proof Load Effect (α=1)	QPL, 1	*MNm*	12.58	0.050	Normal
Proof Load Effect (α=1.5)	QPL, 1.5	*MNm*	18.87	0.050	Normal

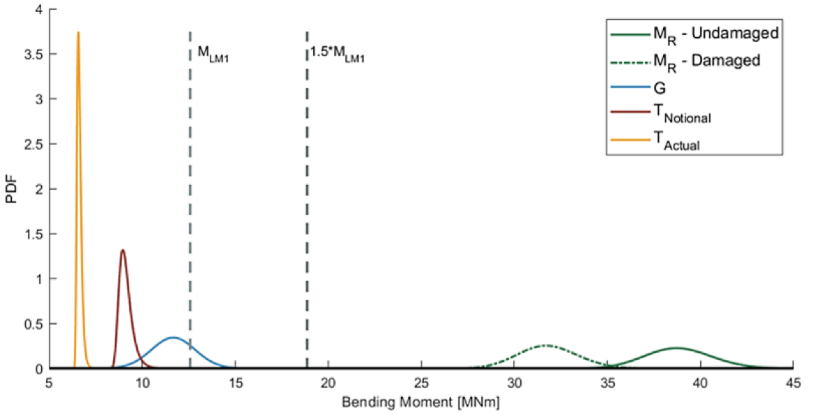


Figure 2. Distribution of bending moment demand due to different loads and capacity scenarios.

Considering the random variable $R' = \theta_R R - \theta_G G$ (undamaged) with mean value μ_R' and standard deviation $\sigma_{R'}$, Table 5 displays proof load magnitudes and mean values of traffic load distributions.

Table 5. Distances of load random variables from the mean value of R' undamaged.

$\mu_{Q_{PL,1}} = \mathrm{M_{LM1}}$	12.58 MNm	$\mu_{R'} - 4.7\ \sigma_{R'}$
$\mu_{Q_{PL,1.5}} = 1.5 \cdot \mathrm{M_{LM1}}$	18.87 MNm	$\mu_{R'} - 2.7\ \sigma_{R'}$
$\mu_{T_{Not}}$	9.13 MNm	$\mu_{R'} - 5.8\ \sigma_{R'}$
$\mu_{T_{Act}}$	6.63MNm	$\mu_{R'} - 6.0\ \sigma_{R'}$

3.8 *Methodology and results*

Before and during the PLT, P_f has been estimated as the probability of the limit state functions Z and Z_{PL} being not positive. After the PLT, the nominal probability of failure P_f (Melchers & Beck, 2018) has been estimated through the Monte Carlo Simulation (MCS) method for a time-invariant analysis, counting the number of successes over the total number of simulations. Considering the two Proof Load Effect Modelling (PPL and DPL), P_f at ULS has been estimated for each traffic load configuration, before, during and after the PLT, in both undamaged and damaged scenarios. Once P_f was estimated, reliability indexes β were calculated and are summarised in Tables 6 and 7. Percentage variations of β are computed according to Equation 4 and reported in Tables 6 and 7.

$$\Delta\beta_i\ [\%] = \left(\beta_i - \beta_{before}\right)/\beta_{before} \tag{4}$$

where β_{before} is the reliability indexes before the PLT and β_i is the reliability index during or after the PLT.

Table 6. Reliability indexes for undamaged scenario.

			During PLT				After PLT			
Traffic	Before PLT	α	PPL	[%]	DPL	[%]	PPL	[%]	DPL	[%]
Notional	4.25	1	3.67	-14	4.80	+13	4.58	+8	4.28	+1
Notional	4.25	1.5	1.95	-54	2.83	-33	5.88	+38	4.96	+17
Actual	5.26	1	3.67	-30	4.80	-9	> 6.0	> +14	5.61	+7
Actual	5.26	1.5	1.95	-63	2.83	-46	> 6.0	> +14	> 5.5*	> +5

*e10 trials without failure samples

Table 7. Reliability indexes for damaged scenario.

			During PLT				After PLT			
Traffic	Before PLT	α	PPL	[%]	DPL	[%]	PPL	[%]	DPL	[%]
Notional	2.79	1	2.13	-24	2.80	0	3.56	+28	2.99	+7
Notional	2.79	1.5	0.41	-85	0.55	-80	5.60	+101	4.93	+77
Actual	3.77	1	2.13	-44	2.80	-26	5.92	+57	4.67	+24
Actual	3.77	1.5	0.41	-89	0.55	-85	> 6.0	> +59	> 5.5*	> +46

*e10 trials without failure samples

It can be seen that the higher the value of the PLT, the higher the posterior value of β compared to its initial value. Assuming a PLT with $Q_{PL,\ 1}$ in the PPL hypothesis, in the case of undamaged configuration, the variation of β with the notional and actual lane is equal to +8% and more than +14%, respectively. Limited effectiveness in the case of a notional lane can be explained in terms of CDR larger than unit (1.36). In the case of lower CDRs as per damaged configuration, this benefit increased up to +28% and +57% for notional and actual lanes, respectively. As regards the differences between PPL and DPL, data indicates slight differences with higher values in case of PPL. Considering variability during the proof load test PPL results in lower reliability than neglecting proof load model uncertainty in DPL. As a matter of fact, for the notional configuration and according to DPL the reliability index doesn't reduce during the PLT. The lower risk during the PLT is reflected in a lower benefit after that, i.e. there is always a positive difference between β_{after} computed probabilistically and deterministically compared to β_{before}. This outcome suggests that the model uncertainty may have important effects on reliability and more investigation is needed.

4 CONCLUSIONS

Proof load testing is a powerful empirical method for the assessment of existing bridges, especially when the level of knowledge of the structure is limited. Specific considerations have to be drawn in terms of damage prevention during the test, target PLT and reliability levels during and after the test as well as in terms of feasibility. The paper presented a preliminary study on the positive impact of a PLT on an existing I-girder PC bridge deck, considering different traffic load combinations and both undamaged and damaged girder conditions. The higher the imposed proof load, the lower the reliability index during the test but the higher the benefit once it is passed successfully. In contrast to CDRs showing a relative difference of less than 10% between undamaged and damaged configurations, the impact of the PLT in terms of posterior reliability would be significantly higher. The methodology could be particularly effective for those bridges interested by exceptional traffic loads during the past which did not report any damage. Even if the preliminary results address the positive impact of PLT on existing bridges, a number of limitations have to be acknowledged from the present study. Further refinement of capacity modelling is recommended considering different failure mechanisms and limit states, such as shear mechanism and cracking. Experimental tests, including laboratory testing on prototype girders, could represent a benchmark for calibrating the PLT and reducing model uncertainties. Dynamic amplification factors should be taken into account when calculating the live load effects. WIM data represent a major breakthrough in traffic modelling to be developed in the near future for the reliability assessment of existing bridges.

ACKNOWLEDGMENT

This study was developed within the CSLLP-ReLUIS project, funded by the Italian High Council of Public Works.

REFERENCES

AASHTO. (2011). *Manual for Bridge Evaluation*. American Association of State Highway and Transportation Officials, Washington, D.C.

Anay, R., Cortez, T. M., Jáuregui, D. V., ElBatanouny, M. K., & Ziehl, P. (2015). On-Site Acoustic-Emission Monitoring for Assessment of a Prestressed Concrete Double-Tee-BeamBridge without Plans. *Journal of Performance of Constructed Facilities*.

ANSFISA. (2022). *Relazione annuale sulla sicurezza delle ferrovie e delle instrastrutture stradali e autostradali.* Agenzia Nazionale per la Sicurezza delle Ferrovie e delle Infrastrutture Stradali ed Autostradali, Roma.

Borzi, B., Ceresa, P., Franchin, P., Noto, F., Calvi, G. M., & Pinto, P. E. (2015). Seismic Vulnerability of the Italian Roadway Bridge Stock. *Earthquake Spectra*.

Calvi, G. M., Moratti, M., O'Reilly, G. J., Scattarreggia, N., Monteiro, R., Malomo, D., Pinho, R. (2019). Once upon a Time in Italy: The Tale of the Morandi Bridge. *Structural Engineering International*.

Casas, J., & Gómez, J. (2013). Load Rating of Highway Bridges by Proof-loading. *KSCE Journal of Civil Engineering*.

Christensen, C. O., Damsgaard, K. D., Sørensen, J. D., Engelund, S., Goltermann, P., & Schmidt, J. W. (2023). Reliability-Based Proof Load Factors for Assessment of Bridges. *Buildings*.

Comité Européen de Normalisation. (2003). EN1991-2 - Eurocode 1: Actions on structures - Part 2: Traffic loads on bridges. Brussels.

Cosenza, E., & Losanno, D. (2021). Assessment of existing reinforced-concrete bridges under road-traffic loads according to the new Italian guidelines. *Structural Concrete*.

de Vries, R., Lantsoght, E. O., Steenbergen, R. D., & Fennis, S. A. (2023). Time-dependent reliability assessment of existing concrete bridges with varying knowledge levels by proof load testing. *Structure and infrastructure engineering*.

de Vries, R., Lantsoght, E., & Steenbergen, R. N. (2023). Proof Load Testing Method by the American Association of State Highway and Transportation Officials and Suggestions for Improvement. *Journal of Transportation Research Record*.

Faber, M. H., Val, D. V., & Stewart, M. G. (1999). Proof load testing for bridge assessment and upgrading. *Engineering Structures*.

Iervolino, I., Baltzopoulos, G., Vitale, A., Grella, A., Bonini, G., & Iannaccone, A. (2023). Empirical distributions of traffic loads from one year of weigh-in-motion data. *Scientific Data*.

Italian High Council of Public Works. (2020). *Linee guida per la classificazione e gestione del rischio, la valutazione della sicurezza ed il monitoraggio dei ponti esistenti*. Rome, Italy.

Italian Ministry of Infrastructures and Transportation. (2018). DM 17/01/2018. Aggiornamento delle "Norme tecniche per le costruzioni'. Rome, Italy.

K. Nishijima, M.F. (2006). Bayesian approach to proof loading of quasi-identical multi-components structural systems. *Civil Engineering and Environmental Systems*.

Kapoor, M., Christensen, C. O., Schmidt, J. W., Sørensen, J. D., & Thons, S. (2021). Decision analytic approach for the reclassification of concrete bridges by using elastic limit information from proof loading. *Reliability Engineering & System Safety*.

Lantsoght, E. O. (2023). Assessment of existing concrete bridges by load testing: barriers to code implementation and proposed solutions. *Structure and Infrastructure Engineering*.

Lichtenstein, A. (1993). Bridge Rating Through Nondestructive Load Testing - NCHRP 12-28(13)A.

Melchers, R. E., & Beck, A. T. (2018). *Structural Reliability Analysis and Prediction*. Wiley.

Miluccio, G., Losanno, D., Parisi, F., & Cosenza, E. (2022). Fragility analysis of existing prestressed concrete bridges under traffic loads according to new Italian guidelines. *Structural Concrete*.

Miluccio, G., Losanno, D., Parisi, F., & Cosenza, E. (2021). Traffic-load fragility models for prestressed concrete girder decks of existing Italian highway bridges. *Structural Concrete*.

O'Brien, E., O'Connor, A., & Arrigan, J. (2012). Procedures for Calibrating Eurocode Traffic Load Model 1 for National Conditions. *Bridge Maintenance, Safety, Management, Resilience and Sustainability*.

Pinto, P., & Franchin, P. (2010). Issues in the Upgrade of Italian Highway Structures. *Journal of Earthquake Engineering*.

Raithel, A. (1978). *Ponti a travata*. Napoli: Liguori Editore.

Schmidt, J. W., Thöns, S., Kapoor, M., Christensen, C. O., Engelund, S., & Sørensen, J. D. (2020). Challenges Related to Probabilistic Decision Analysis for Bridge Testing and Reclassification. *Frontiers in Built Environment*.

Shenton, H. W., M. J. Chajes, & J. Huang. (2007). Load Rating of Bridges Without Plans. *Journal of Performance of Constructed Facilities*.

Spaethe, G. (1994). Die Beeinflussung del Sicherheit eines Tragwerkes durch Probebelastung. *Bauingenieur*.

Transportation Research Board. (1998). Manual for Bridge Rating Through Load Testing. (234).

Transportation Research Board. (2019). Primer on Bridge Load Testing (E-C257)

Bridge Maintenance, Safety, Management, Digitalization and Sustainability – Jensen, Frangopol & Schmidt (eds)
© 2024 The Author(s), ISBN 978-1-032-77040-6
Open Access: www.taylorfrancis.com, CC BY-NC-ND 4.0 license

Danish concrete bridge proof loading procedure and considerations

J.W. Schmidt & C.O. Christensen
Department of the Built Environment, Aalborg University, Aalborg, Denmark

R. Bang & C. von Scholten
The Danish Road Directorate, Fløng, Denmark

P. Goltermann
Department of Civil and Mechanical Engineering, Technical University of Denmark, Kgs. Lyngby, Denmark

S. Engelund
COWI A/S, Aalborg, Denmark

ABSTRACT: A Danish concrete bridge proof loading project (V1) was initiated in 2016 and followed by a project extension (V2) initiated primo 2023. A main scope of the project V1 was to provide a classification-based proof loading procedure in accordance with the Danish classification system. In addition, significant CO2 and societal economical savings was deemed possible. A multidisciplinary approach was used for the evaluations involving multi-scale testing, theoretical capacity evaluations and probabilistic assessments. The project resulted in various novel testing and theoretical developments as well as significant experience gain. Several bridges were classified to a higher capacity through pilot projects, using the developed proof load test procedure. A Danish national guideline is expected to be published soon based on the findings, just as an excellent basis for the V2 project was established. Several main results from the V1 project leading to the background for initiating the V2 proof loading project, will be presented.

1 INTRODUCTION

The Danish bridge testing project (V1) was commenced to investigate the load-carrying capacity of existing concrete bridge structures through advanced evaluation, load testing, and probabilistic analysis (Schmidt et al., 2020) as it potentially could provide significant economic, CO2 and societal savings through enhanced understanding.

As an integrated project scope, the project aimed to establish a proof-loading test method tailored for one-span bridges in accordance with the Danish classification system (Vejdirektorat (The Danish Road Directorate), 2017). The Danish road bridges are classified through this unique system based on the weight and axle configurations from specified heavy classification vehicles. Figure 1a illustrates three examples of the vehicles outlined in the system. A heavy classification vehicle can cross a bridge if the bridge class is higher than the vehicle class. Failure to meet this criterion necessitates either a detour or a rearrangement of goods on the vehicle. A comprehensive literature study revealed a consistent trend of capacities being higher in practice than what was theoretically estimated during the design. Some of the reasons for this were deemed to be; 1) more desirable material parameters due to time dependency, 2) boundary conditions, 3) interaction between structural elements, and 4) redistribution of stresses, etc. (Bakht & Jaeger, 1990; Goodpasture & Burdette, 1973; Saraf & Nowak, 1998; Schmidt et al., 2018).

Nevertheless, the existing literature showcased a wide array of unique test approaches, predominantly tailored to specific bridge types, rendering them unsuitable as a universal foundation for the Danish project (Bagge et al., 2018). Furthermore, no prior testing had been

DOI: 10.1201/9781003483755-33

conducted in accordance with the Danish classification system. The project objective, however, was not only to evaluate the behavior of a specific bridge type but to develop a more standardized methodology for performing load-carrying capacity tests. Based on this knowledge, the following main research objectives were generated at the initiation of the V1 project:

- Carrying out several in-situ load-carrying capacity tests that will form the basis of an upgrading of the bridge class on which the tests were carried out.
- Perform capacity tests which can be used to identify- and evaluate the critical failure mechanisms in a bridge classification test perspective.
- Generate a link between applied theoretical- and monitoring methods and thus form a basis for a future strategy for non-destructive load testing of existing bridges.
- Develop calculation models that conform and verify the monitoring results from the full-scale testing.
- Provide optimized test set-ups that can reduce advanced methodologies into representative more simplified methods for evaluating the bridge class of one-span bridges.

Throughout this paper, the main findings and milestones related to these objectives will be discussed and an initial insight into the research perspectives of a newly initiated project extension, version 2 (V2), initiated primo 2023 will be revealed.

2 SAFETY MARGIN AND STOP CRITERIA

When performing in-situ bridge load testing, uncertainty regarding a sufficient safety margin seems to be a main concern (Christensen et al., 2023; Lantsoght et al., 2017). In previous studies, the authors suggested that a multidisciplinary approach may be required. Such an approach may involve; 1) representative testing combined with advanced monitoring, 2) initial calculation estimates sometimes followed by advanced modelling and simulation, and 3) probabilistic and decision analysis, see Figure 1b. These research field interfaces represent a transfer of information, that can help improve the evaluation approach within each field. Often the research fields 1,2 and 3 are not equally represented in research projects, since their substance often depends on the available information and scope of the project. The probabilistic research area 3, is often reduced and more focus dedicated to 1, and 2, if research projects contain well defined material- and structural information. However, 1 and 3 may be more in focus if little information concerning the material and structure is available and theoretical model uncertainties are relatively high. The latter often providing the basis for proof loading assessment. Consequently, the multidisciplinary research field synergy may help to improve initial considerations regarding proof loading and safety margin.

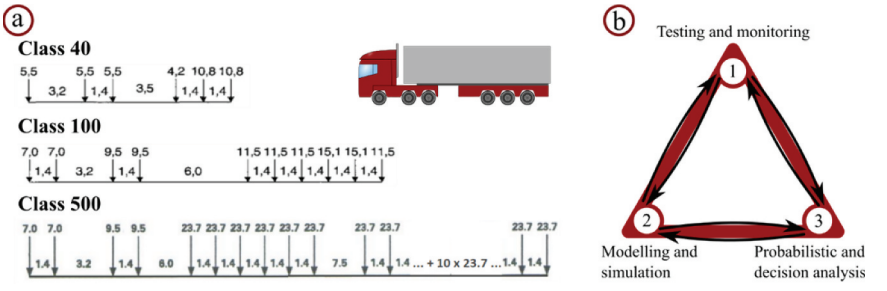


Figure 1. A) An example of the vehicles described in the Danish classification system. Axel loads in tons b) Schematic multidisciplinary research synergy overview (Schmidt et al., 2020).

The true in-situ behavior of a bridge structure may however only be revealed through load testing. Following a proof-load test, the multidisciplinary interactions between research fields may be updated in accordance with the obtained proof loading output. However, to do so, the response uncertainty and bridge collapse concerns must be considered beforehand, and measures must be

taken to avoid these. Monitoring-based stop criteria may be used to achieve this. Such thresholds may provide indications of irreversible damage during proof loading. Note that an effective stop criterion should provide a sufficient margin of safety but also not be overly conservative (Lantsoght et al., 2019). It is essential to use sufficient monitoring and loading schemes to ensure that the bridge response regimes are well depicted in the data acquisition. Only few countries have provisions that describe stop criterion thresholds but recent work in this field has aimed to combine the information given in the guidelines to provide a flexure stop criterion threshold (Lantsoght et al., 2019). Work is still ongoing regarding suitable stop criteria in general, but especially those relating to shear failure mechanisms and pre-stressed concrete structures are still up for discussion. Typical stop criterion values relate to strain, crack width, stiffness reduction, etc. which are quantitative values where a qualitative outcome can be deformation profiles, load-deflection curves, crack detection, and overall structural behavior (Schmidt et al., 2022). Digital image correlation (DIC) measurements have been a superior measurement tool in the Danish bridge testing project combined with conventional monitoring (LVDTs, Strain gauges, distance lasers). Especially a wide-angle 2D system was investigated to provide high-resolution monitoring and facilitate a short installation time. However, due to out-of-plane movement, the 2D DIC system measures too large strain values and must be corrected (Halding et al., 2019). It should be noted that a large distance from the camera to the surface reduces the error and that for pure out-of-plane movement, the error is always on the safe side when monitoring towards stop criteria. A common stop criterion is monitoring of crack widths. The following are some examples of stop criteria provided in literature for crack width in flexure:

- The German guideline where the crack width has to be within, $w_{max} \leq 0.5$ mm for new cracks and $w_{max} \leq 0.3$ mm for existing cracks (DAfStb, 2000).
- A more theoretically based criterion is presented in (Lantsoght et al., 2019) where crack widths are proposed to be within $w_{max} \leq 0.11$ mm and $w_{max} \leq 0.19$ mm, based on the considered bridges. It is also stated that crack widths less than 0.05 mm should not be considered as a crack.
- Using EN 1992-1-1 (EC2) maximum crack widths in the serviceability limit state are $w_{max} \leq 0.2$ mm for pre-stressed members with bonded tendons and $w_{max} \leq 0.3$ mm for non-prestressed structures.

Quantifying the stop criteria thresholds still requires further research where failure mode, monitoring precision, loading approach, etc. must be evaluated in a theoretical and/or probabilistic perspective. An additional constraint that can have a significant effect on an in-situ proof load testing project is engineering judgment and related experience. A link that provides a desired connection between laboratory- and in-situ testing seems extremely important but is challenging due to the different environmental and test conditions, related equipment, and crew capabilities (Christensen, Halding, et al., 2022). Nevertheless, such projects are often tied up in delivering robust advanced methods that provide consistency and sufficient precision which can generate a proof loading decision basis. In addition to monitoring-based stop criteria related to damage states, the definition of a relevant target load may also be considered a stop criterion. The magnitude of the target load must be determined so that the test gives grounds to conclude that the bridge has sufficient reliability, ensuring it can withstand actual load effects anticipated on the bridge. Multiple approaches exist for determining the target load (Casas & Gómez, 2013), but most require input from resistance models. However, bridges with poor information on the resistance are the ones most relevant for proof-load testing. As part of the Danish bridge testing project, an alternative approach to target load has been presented (Christensen et al., 2023), where the target load is determined based on representative standard vehicles from the Danish classification system (Vejdirektoratet (The Danish Road Directorate), 2017) and associated probabilistic design guideline.

3 V1 IN-SITU TESTING

Throughout the V1 project, several in-situ tests have been performed and different approaches have been applied for load application and monitoring setup. The tests comprise full-scale high magnitude load tests, subcomponent tests, and proof-load testing.

3.1 *High magnitude load testing*

Several bridges were tested on a road stretch in Denmark in 2016 (Schmidt et al., 2018). The most critical of these bridges were OT (upside down T-beam)-slab bridges and they were originally evaluated to class 40. To test these bridges, a novel high-magnitude load testing rig was needed. The classification vehicle for class 40 has a maximum axle load of 10.8 tons. The test setup was designed as a cradle system with cross-beams, hydraulic pistons, and wheel pressures reflecting the Danish classification system and with a significant capacity reserve compared to the original bridge class. However, when testing these bridges, the axle load capacity for the test setup of 100 tons was reached. At this time, no visible cracks were seen. The axle load level was approximately 4 times higher than the highest axle loads in the Danish classification system, belonging to the class 500 vehicle. The results indicated that significant capacity reserve may be present when dealing with concrete OT-slab bridges. In addition, the tests provided significant experience with high-magnitude load testing. In addition to the full-scale in-situ tests, several subcomponent tests were performed. Slab strips were cut from the bridge deck and tested in-situ with the same test rig setup, and beams were cut to be tested in the laboratory. These tests provided some of the same indications of available capacity reserve but also provided more information for the identification of stop criteria. The link between in-situ testing and laboratory testing was, however, identified as one of the major challenges, because in-situ testing often involves: 1) A short testing time window, where preparations should be made to limit the effect on traffic, and 2) Challenging environmental conditions that differ significantly from the laboratory. The valuable information gained in all these initial tests provided the background for later pilot tests of four single-span bridges which were upgraded from class 80 to class 100 through the developed in-situ test approach. In addition, it provided an important basis for the later approaches developed in the project.

3.2 *Proof-load testing*

Based on the initial findings and application of the multidisciplinary approach used in the project, (Figure 1b), a national guideline, expected to be published soon, on proof load testing was developed (Vejdirektoratet (The Danish Road Directorate), 2021). To verify the concepts of the guideline, an in-situ pilot proof load project was arranged. For this project, a more time-effective test method was developed. This method involved the use of special vehicles reflecting the Danish classification system with individually hydraulically controlled axle loads. Such vehicles are shown in Figure 2a along with a concept drawing and the classification vehicles.

The pilot project scope was to show that the developed method could be used as a basis for upgrading the bridges on a class 80 road stretch into a class 100. If the project succeeded, the road way could be included in the existing traffic roadway system where Class 100 heavy vehicles can drive freely without applying for a Danish permit.

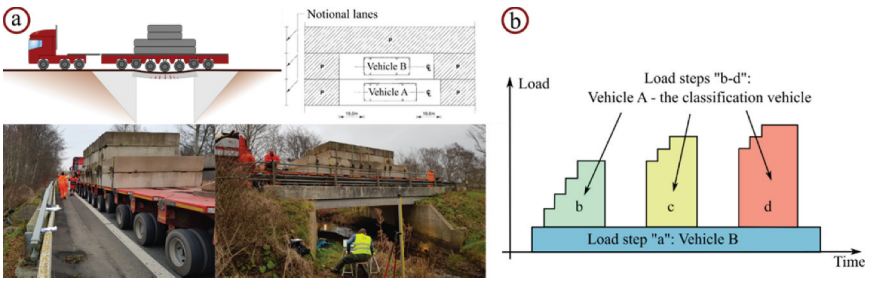


Figure 2. A) Example of testing using special heavy vehicles with hydraulic axle control. b) Example of a loading scheme for proof load testing.

The target load was defined according to a reliability-based method (Christensen et al., 2023) and was applied in load steps with increments as seen in Figure 2b. Monitoring was applied according to the provisions of the Danish proof loading guideline with output from a land surveyor, hydraulic output of the test vehicles and real-time DIC (Christensen et al., 2021;

Christensen, Zhang, et al., 2022). All four bridges were successfully tested to the designated target load. An example of a response curve can be seen in Figure 3a. The maximum deflections of the bridges were 0.45 mm, 2.0 mm, 0.63 mm, and 0.65 mm, respectively, and no visible signs of distress were observed. This was supported by the real-time DIC, where no signs of crack initiations or critical deformations were measured. Consequently, the road stretch was upgraded from a class 80 to a class 100 road stretch. The pilot project thus indicated the applicability of the Danish guideline which applies for one-span bridges with a span from 2m to up to 12m.

4 LABORATORY TESTING AS A REFERENCE

In order to perform the proof load testing and provide the basis for the national guideline, significant background knowledge was required. A part of this knowledge, was gained through several advanced laboratory tests, with a large array of monitoring equipment (Christensen, Halding, et al., 2022) applied. The laboratory tests reflected the experiences and gains from the in-situ testing throughout the V1 project and provided additionally directions for important areas of improvement. For instance, in-situ conditions were implemented in the laboratory for the DIC system with no artificial lighting and camera distances similar to the in-situ bridges. Additionally, supporting the tested slabs along three edges was used to mimic a continuous slab and to test the shear transfer capabilities of the construction joints between the OT-elements. The primary components of the laboratory test setup are depicted in Figure 3b. The setup components included (1) multiple load-carrying columns with three stiffeners, (2) horizontal I-profiles along three edges for support along with pinned bearings between the profiles and the slab surface, (3) the primary actuator used for load application, and (4) the OT-slab. The described setup provided a transverse span of approximately 1.6 m and a longitudinal span of approximately 7.5 m.

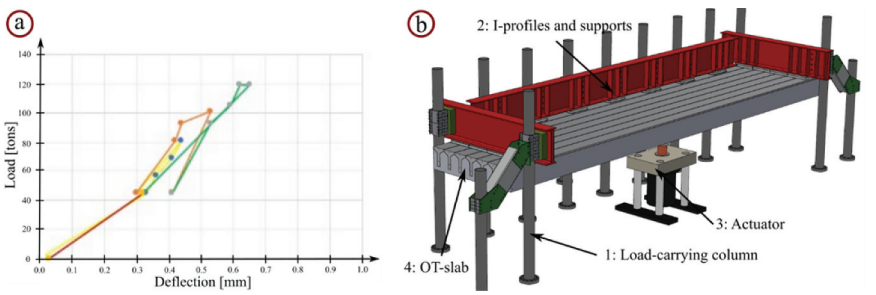


Figure 3. A) Response curve from a proof load test. b) Laboratory test setup for testing of OT-slabs.

A large monitoring setup of approximately 60 sensors of at least 8 different types was applied (LVDTs, strain gauges, wire potentiometers, load cells, inclinometers, distance lasers, DIC, and AE (Acoustic emission). The evaluation included a comparison of sensor output and establishing the relevance of the different sensors. The 2D DIC camera was placed at a distance of 3.8 m to provide a correlation with the in-situ tests. The surface was covered in a black speckle contrast pattern and no additional light except for the laboratory overhead lighting was applied (Christensen et al., 2021). It should be noted that the application of a surface pattern generates an extra working procedure compared to direct measurements on the concrete surface. However, the used application method and optimized pattern seemed applicable for in-situ testing as well, and was deemed to provide a more optimized measurement consistency; this was later verified in the proof load testing. The AE sensors were placed based on the test results from the first slab test in the critical zone. AE analysis was performed in collaboration with colleagues from TU Delft (Christensen, Zhang, et al., 2022). Since AE measures inside the structural component and DIC on the surface, they are independent, and the combination of the two methods may be a desirable monitoring method for future

application. Figure 4a shows the load/deflection curve from two laboratory OT-slab tests. Markers are placed for crack detection and fully developed yield lines. The crack patterns of these two stages are additionally depicted in Figure 4a.

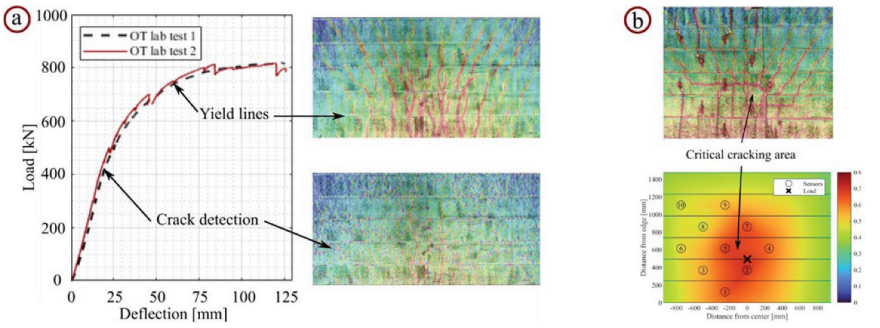


Figure 4. A) Results from OT-slab tests. I) Response curve, ii) Crack pattern at crack detection, iii) crack pattern with developed yield lines. B) Comparison of DIC crack pattern and AE activity contour (calm ratio). AE sensors are numbered 1-10.

The tests supported previous indications of sufficient interaction between the OT-beam elements to provide slab behavior. In terms of 2D DIC, it was seen that crack detection occurs in the linear elastic regime before any stiffness change. Directly measured values (without correction for out-of-plane movement) from a distance of 3.8 m, resulted in a crack detection between 0.2 mm and 0.3 mm. However, after correcting for out-of-plane movements, the crack widths ranged from 0.080 to 0.132mm which is below the EC2 SLS threshold. When combining the DIC crack pattern and acoustic emission (AE) a good correlation was found. High AE activity was seen in the areas with extensive cracking and much less activity in the lesser- and un-cracked areas (Christensen, Zhang, et al., 2022), Figure 4b. The results indicated that the DIC seemed efficient as an independent monitoring technique, whereas AE may be more advantageous to use in conjunction with other monitoring techniques. However, to ensure optimal proof loading, it seems beneficial to apply several independent monitoring methods in conjunction with a sufficient loading scheme, as described in the, soon published, Danish proof loading guideline (Vejdirektoratet (The Danish Road Directorate), 2021) and in associated research paper (Christensen et al., 2023).

5 UPCOMING ACTIVITIES

The upcoming activities of the V2 project reflect the achievements and conclusions of V1 but also involve the shortcomings. So far, the proof-loading guideline facilitates proof-load testing of specific bridge types. However, further refinement for stop criteria assessment is required and the guideline must be expanded, to facilitate testing of more bridge types. For the V2 project, the Danish Road Directorate has opened opportunities to perform in-situ tests on a series of bridges. The primary bridges are multi-span bridges set for demolition due to a highway expansion from two to three lanes. However, other bridge tests on both single-span and multi-span bridges may also present themselves in the project duration. A special focus will be dedicated to four wing bridges which are almost identical and highly relevant for the Danish bridge testing project. Example drawings of the concrete wing bridges are depicted in Figure 5 with a plan view (Figure 5a), a side view (Figure 5b), and a section view (Figure 5c). The concrete bridges are constructed with prestressed in-situ cast main girders and slabs which terminate sideways with cantilever wings. The full three span bridges are evaluated to a sufficient classification capacity and are relevant for testing in several localized areas for different test purposes. Ideally, the middle span could be used for in-situ testing, however, due to passing traffic in the middle span during demolition, the focus is initially dedicated to the side

spans, see Figures 5a and b. Figure 5c governs additionally initial thoughts on how testing may be performed. Work in regards to a suitable monitoring setup is presently ongoing. However, it should be noted that the descriptions are very early test considerations and may be adjusted before the final test approaches are settled upon. It is the aim to cut the slabs between the main girders of the full bridge in a way that enables in-situ slab testing of representative slab subcomponents. Such a cut-out is shown in Figure 5c.

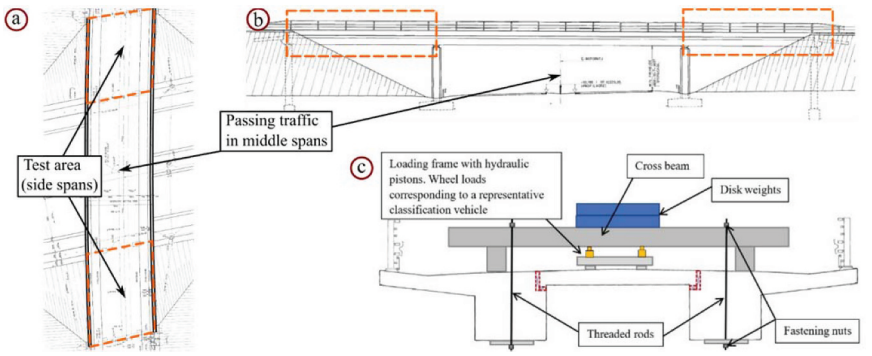


Figure 5. A) Plan view with marked test areas, b) side view with marked test locations, and c) Section view with initial thoughts on a load rig.

The slab length is aimed to be approximately 10m. A vertical and horizontal cut may separate these from the longitudinal main girders. This ensures more relevant support boundary conditions toward single-span non-shear-reinforced slab bridges. The slabs may be tested using the loading frame setup also illustrated in Figure 5c. Drilled holes through the longitudinal main girders enable mounting of the threaded rods to the loading frame and underneath the main girders. Underneath the cross beams, the loading frame may be placed for the representation of loads of the Danish classification system. The load will be applied using hydraulic pistons between the cross-beams and the loading frame and potentially counteracting disk weights. In addition, material and subcomponent testing will be performed which may include beams and slabs that are cut from the middle span during the demolition process. As part of the investigations, the authors aim to evaluate structural failure modes of the tested specimens and evaluate potential brittle or ductile behavior further. Identification of sufficient stop criteria related to obtained failure modes and multi span bridges will additionally be a primary investigation. Based in the V2 project findings it is the aim to update the Danish proof-loading guideline.

6 CONCLUSIONS AND PROJECT OUTLOOK

It can be concluded that the significant experience with the multidisciplinary approach was gained. The V1 project succeeded in performing representative testing in accordance with the Danish classification system. The project identified capacities which was significantly higher than predicted theoretically in the in-situ test and desirable interaction between the OT slab-elements, to provide slab behavior, was identified. Consequently, plate behavior with yield lines occurred in the laboratory tests and provided comparable DIC and EA results when evaluating the crack pattern. Based on in-situ -and laboratory testing an optimized monitoring method was developed including real time evaluations during testing. The findings and experiences from the V1 project provided a good basis for the upcoming Danish guideline on proof load testing of concrete bridges. The guideline was thus used as basis for upgrading a road stretch with four bridges, from class 80 to class 100, in a pilot project. The research additionally provided knowledge which revealed areas where more knowledge is needed which is included in the V2 research scope. Investigations of stop criteria thresholds related to relevant failure mechanisms of non-shear reinforced slabs for both single and multi-span bridges, will be investigated. It is the aim to update the Danish proof-loading guideline, accordingly.

ACKNOWLEDGEMENT

Special thanks to the Danish Road Directorate for their pivotal role in the Danish concrete bridge testing project. We are grateful for your support and are looking forward to our continued collaboration on load testing practices in Denmark. Additional thanks are addressed to all collegues and partners, who has taken part in the Danish bridge testing project - technicians, workers and scientists, thank you. Your knowledge and competence have been instrumental for our shared success.

REFERENCES

Bagge, N., Popescu, C., & Elfgren, L. (2018). Failure tests on concrete bridges : Have we learnt the lessons ? *Structure and Infrastructure Engineering*, *2479*, 292–319. https://doi.org/10.1080/15732479.2017.1350985

Bakht, B., & Jaeger, L. G. (1990). Bridge Testing—A Surprise Every Time. *Journal of Structural Engineering*, *116*(5). https://doi.org/10.1061/(asce)0733-9445(1990)116:5(1370)

Casas, J. R., & Gómez, J. D. (2013). Load rating of highway bridges by proof-loading. *KSCE Journal of Civil Engineering*. https://doi.org/10.1007/s12205-013-0007-8

Christensen, C. O., Damsgaard, K. D. S., Sørensen, J. D., Engelund, S., Goltermann, P., & Schmidt, J. W. (2023). Reliability-Based Proof Load Factors for Assessment of Bridges. *Buildings*, *13*(4), 1060. https://doi.org/10.3390/buildings13041060

Christensen, C. O., Halding, P. S., Schmidt, J. W., & Goltermann, P. (2022). Large-scale OT-slab tests Laboratory measurements and evaluation. *11th International Conference on Bridge Maintenance, Safety and Management*, 2099–2106. https://doi.org/10.1201/9781003322641-260

Christensen, C. O., Schmidt, J. W., Halding, P. S., Kapoor, M., & Goltermann, P. (2021). Digital Image Correlation for Evaluation of Cracks in Reinforced Concrete Bridge Slabs. *Infrastructures*, *6*(7), 99. https://doi.org/10.3390/infrastructures6070099

Christensen, C. O., Zhang, F., Garnica, G. Z., Lantsoght, E. O. L., Goltermann, P., & Schmidt, J. W. (2022). Identification of Stop Criteria for Large-Scale Laboratory Slab Tests Using Digital Image Correlation and Acoustic Emission. *Infrastructures*, *7*(3), 36. https://doi.org/10.3390/infrastructures7030036

DAfStb. (2000). *DAfStb-Guideline: Load Tests on Concrete Structures*. Deutscher Ausschuss für Stahlbeton.

Goodpasture, D. W., & Burdette, E. G. (1973). Full Scale Tests to Failure of Four Highway Bridges. *American Railway Engineering Association*, *74*(643), 454–473.

Halding, P. S., Christensen, C. O., & Schmidt, J. W. (2019). Surface Rotation Correction and Strain Precision of Wide-Angle 2D DIC for Field Use. *Journal of Bridge Engineering*, *24*(4). https://doi.org/10.1061/(ASCE)BE.1943-5592.0001358

Lantsoght, E. O. L., Yang, Y., Tersteeg, R. H. D., Van Der Veen, C., & De Boer, A. (2017). Development of stop criteria for proof loading. *Life-Cycle of Engineering Systems: Emphasis on Sustainable Civil Infrastructure - 5th International Symposium on Life-Cycle Engineering, IALCCE 2016*. https://doi.org/10.1201/9781315375175-135

Lantsoght, E. O. L., Yang, Y., Veen, C. Van Der, & Hordijk, D. A. (2019). Stop Criteria for Flexure for Proof Load Testing of Reinforced Concrete Structures. *Frontiers in Built Environment*, *5*(April). https://doi.org/10.3389/fbuil.2019.00047

Saraf, V., & Nowak, A. S. (1998). Proof Load Testing of Deteriorated Steel Girder Bridges. *Journal of Bridge Engineering*, *3*(2). https://doi.org/10.1061/(asce)1084-0702(1998)3:2(82)

Schmidt, J. W., Halding, P. S., Jensen, T. W., & Engelund, S. (2018). High Magnitude Loading of Concrete Bridges. *ACI Structural Journal*, *323*, 9.1–9.20.

Schmidt, J. W., Sørensen, J. D., & Christensen, C. O. (2022). In Situ Concrete Bridge Strengthening Using Ductile Activated NSMR CFRP System. *Buildings*, *12*(12). https://doi.org/10.3390/buildings12122244

Schmidt, J. W., Thöns, S., Kapoor, M., Christensen, C. O., Engelund, S., & Sørensen, J. D. (2020). Challenges Related to Probabilistic Decision Analysis for Bridge Testing and Reclassification. *Frontiers in Built Environment*, *6*(February). https://doi.org/10.3389/fbuil.2020.00014

Vejdirektoratet (The Danish Road Directorate). (2017). DS/EN 1991-2 DK NA:2017, Annex A: Lastmodeller for klassificering og bæreevnevurdering (Models of special vehicles for road bridges). In *(The Danish Road Directorate)*.

Vejdirektoratet (The Danish Road Directorate). (2021). *Vejledning for prøvebelastning af broer (Guideline for proof-loading of bridges)*.

Bridge Maintenance, Safety, Management, Digitalization and Sustainability – Jensen, Frangopol & Schmidt (eds)
© 2024 The Author(s), ISBN 978-1-032-77040-6
Open Access: www.taylorfrancis.com, CC BY-NC-ND 4.0 license

A comparative study of proof load configurations related to bridge classification

K.D.S. Damsgaard & S. Engelund
COWI A/S, Aalborg, Denmark

J.D. Sørensen, J.W. Schmidt & C.O. Christensen
Aalborg University, Aalborg, Denmark

C. von Scholten
Vejdirektoratet, the Danish Road Directorate, Copenhagen, Denmark

ABSTRACT: Proof load testing is increasingly used to assess existing road bridges. The load configuration of a proof load test is however an open research question and approaches vary in the literature. To the author's knowledge, a comprehensive comparison of different load configuration approaches is not available in the literature. As part of a Danish bridge testing project a literature study has been carried out regarding proof load configurations. This paper presents part of this study with an emphasis on comparison between the Danish approach and approaches using the Eurocodes LM1. A brief state-of-the-art is presented. Following this, proof load configurations calculated from Danish codes and guidelines are compared with LM1 approaches. The results indicate numerous benefits of a bridge classification system like the Danish. The research may inspire a common European bridge classification system, ultimately paving the way for better utilization of bridges through proof loading.

1 INTRODUCTION

For the assessment of existing bridges where traditional assessment methods fail to show sufficient load-bearing capacity or for which there is little to no documentation, proof load tests may be carried out to prove the desired capacity. Many of the European bridges in use today were erected in the 60s and 70s. In many cases theoretically determined load bearing capacities prove insufficient for allowance of the heavier vehicles of today, especially regarding special transports. These are transports exceeding legal weight limits, which therefore need to apply for permits for travelling on roads and crossing bridges. Practices for issuance of these permits vary greatly within Europe (European Commission, 2008) and the practice is highly related to the traffic load models adopted. Commonly, the first approach to assessing bridges along the desired route of the special heavy transport is to compare the load effects, bending and shear, of the special transport to the load effects of the traffic load model, for which the bridges were designed or later classified (Bundesministerium für Verkehr und digitale Infrastruktur, 2016; Correia & Branco, 2006; Statens Vegvesen, 2023; Trafikverket, 2011; Vigh & Kollár, 2007). If this proves insufficient, a following approach is commonly to carry out direct assessment of the bridge for the special transport applied for. It is of course desirable to reduce the number of direct assessments or proof load tests. Therefore, the load applied in a proof load test should be chosen, such that an appropriate number of future permits can be granted through the first approach.

A common approach to proof load testing, is to calculate proof load factor to be multiplied by a chosen load model, such that the posterior reliability of the bridge, after a successful test, is proven equal to or higher than the target reliability. Throughout the years, different methods

DOI: 10.1201/9781003483755-34

to determine proof load factors have been reported, some without consideration of a code traffic load model (Faber et al., 2000) and some with the consideration of predetermined traffic load models but with uncertainty modelled based on probabilistic guidelines (Christensen et al., 2023; Lantsoght et al., 2017; Saraf & Nowak, 1998) or traffic measurements (Casas & Gómez, 2013). Some of these studies consider a resistance model, while others omit them.

In this paper, comparisons are made between Danish approaches to proof load configurations and approaches using the Eurocode Load Model 1 (LM1). Danish proof load factors are calculated both with and without inclusion of a resistance model to investigate the research questions:

- What are the advantages and disadvantages of applying proof loads based on Danish codes and guidelines compared to using LM1?
- What is the gain from including knowledge on a resistance model when calculating proof load factors?

2 STATE-OF-THE-ART ON PROOF LOAD CONFIGURATIONS

2.1 *Theoretical background for proof loading*

The goal of a proof load test is typically to prove that the reliability of the structure is at least equal to the target reliability. Prior to a proof load test, when there is knowledge on the resistance, the probability of failure, P_f, is calculated as the probability of the load effect, S, being higher than the resistance, R, (Thoft-Christensen & Baker, 1982), $P_f=P(R<S)$, see Figure 1a. If the target reliability is not reached through this evaluation, a proof load test can be carried out, where the structure is loaded to a desired load effect S_p. With the knowledge that the resistance is at least equal to S_p, the resistance can be truncated to give R^* (Nowak & Tharmabala, 1988), see Figure 1b. The probability of failure may then be calculated as $P_f=P(R^*<S)$. If there is no knowledge on the resistance, the probability of failure may be calculated as the probability that the actual traffic load effect, Q_{actual}, is higher than the proof load effect, Q_{proof}, (Christensen et al., 2023), $P_f=P(Q_{proof}<Q_{actual})$, as the actual dead load, G_{actual}, is deterministic and present both during and after the test, see Figure 1c.

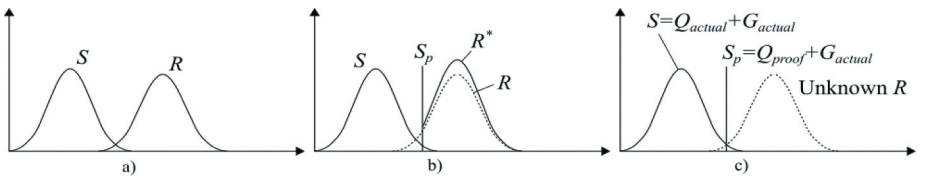


Figure 1. Probability density functions for a) probabilistic assessment b) proof load assessment with a resistance model and c) proof load assessment without a resistance model.

2.2 *Traffic load modelling*

When modelling traffic loads, the Eurocodes use LM1 (European Committee for Standardization (CEN), 2003). LM1 is based on Weigh-In-Motion (WIM) data from 1986, from which the heaviest vehicle measured had a gross weight of roughly 75 tonne (Sedlacek et al., 2008). LM1 contains both a tandem axle and distributed load in each lane, see Figure 2. A limitation is that this load configuration does not reflect the complex axle configuration of real heavy vehicles, which usually consist of multiple axle groups. Instead, it is determined from influence lines to give the 1000-year extreme moment and shear for different bridge spans as extrapolated from the WIM-data.

In Denmark, a bridge classification system is adopted, where both special transports and bridges are classified based on a set of standard vehicles (Ravn et al., 2006). When a special transport permit is applied for, the special transport is classified by determining the shear and moment along simply supported beams of different lengths which is then compared to the

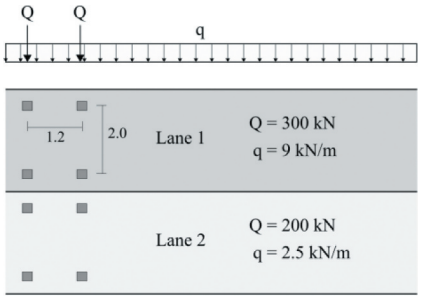


Figure 2. Eurocode LM1. (European Committee for Standardization (CEN), 2003).

same load effect of the different standard vehicles. The standard vehicles range from class 10 to class 500 denoting roughly their gross weight in tonne (Vejdirektoratet, 2017). Examples of three standard vehicles are given in Table 1. Compared to LM1, the use of such standard vehicles may better resemble the axle configurations of real heavy vehicles.

Table 1. Danish standard vehicles. (Vejdirektoratet, 2017).

Class	Axle configuration (loads in [t], spacings in [m])
100	7,0 7,0 — 1,4 — 3,2 — 9,5 9,5 — 1,4 — 6,0 — 11,5 11,5 11,5 15,1 15,1 11,5 — 1,4 1,4 1,4 1,4 1,4
150	7,0 7,0 — 1,4 — 3,2 — 9,5 9,5 — 1,4 — 6,0 — 7 × 17,8 — 1,4 1,4 1,4 1,4 1,4 1,4
200	7,0 7,0 — 1,4 — 3,2 — 9,5 9,5 — 1,4 — 6,0 — 8 × 21 — 1,4 1,4 1,4 1,4 1,4 1,4 1,4

2.3 *Proof loading*

As part of the EU ARCHES-project, (Casas & Gómez, 2013) determined proof load factors to be applied to the design LM1 load model. The goal of the ARCHES project was to raise the standard of the highway structures of Central Eastern European Countries (CEEC). CEEC proof load factors were based on WIM-data from the Czech Republic, Poland, Slovenia, and Slovakia. Dutch data was also used to calculate proof load factors for comparison. The WIM-data contained both normal traffic and special transports weighing up to 165 ton. Proof load factors were calculated both with and without resistance models for different 50-year lifetime reliability indexes, β_{target} = 2.3, 3.6 and 5.0, and for different bridge spans between 10 and 35 m.

When a resistance is assumed to be known and is included when determining the proof load factor, the ratio between the modelled resistance and load effect will influence the resulting proof load magnitude i.e., if R in Figure 1b is shifted left, S_p must be shifted right for $P(R^*<S)$ to still be equal to the target failure probability. To describe this shift (Casas & Gómez, 2013) introduced a parameter R/R_n, which is varied between 0.5 and 1.0. R_n is deterministic and is equal to the design load effect such that R_n is the resistance needed for the design equation to give a utilization of 1. R is the stochastic resistance, which is modelled with a bias = 1.12 for the chosen R/R_n and COV = 0.14.

In The Netherlands, viaduct de Beek was proof load tested using a test rig simulating only the tandem axles of LM1 (Lantsoght et al., 2017). The magnitude of the proof load from the tandem axles was determined such that the resulting maximum sectional force was equal to that of the combined LM1 tandem axles and distributed load including a proof load factor.

In Denmark a bridge was classified from class 80 tonne to class 100 tonne through proof loading with axle spacings corresponding to the rear axle group of the standard vehicle (Christensen et al., 2023). The proof loading magnitude was determined without including a resistance model based on the old probabilistic guideline (Vejdirektoratet, 2004). Presently, a new probabilistic guideline is being prepared and is expected to be published shortly (Vejdirektoratet, 2024).

3 PROOF LOAD FACTORS CALCULATED FROM DANISH CODES

3.1 *Calculation basis*

The proof load factors in the following calculations are calculated for proof loading of an existing bridge in CC3 for bending, which can be assumed to give warned failure without capacity reserve. This results in an annual target reliability of $\beta_{target} = 4.8$ (Vejdirektoratet, 2010). Proof load factors are calculated for class 100, 150 and 200, both with and without a resistance model. An existing Danish single span concrete bridge with 10 m span is used as a base case to model the resistance, R_{basis}, and the dead loads. For simplicity, the bridge is modelled as a 3 m wide beam corresponding to the notional lane within the Danish classification system and the Eurocode.

Comparably to the R/R_n approach by (Casas & Gómez, 2013), in the following, proof load factors with resistance are determined for different values of the reciprocal of the design utilization, $R_d/R_{d,req}$ or R_d/S_d, where R_d is the design resistance, $R_{d,req}$ is the required design resistance and S_d is the design load effect, see Figure 3. R can then be modelled as $R_d/S_d \cdot R_{req}$, given that R and R_{req} have the same coefficient of variance (COV) and that R_d and $R_{d,req}$ correspond to the same quantile. R_{req} is determined from the resistance model of the base case bridge as $R_{req} = z \cdot R_{basis}$, where z is determined from the design equation such that $z \cdot R_{d,basis} = S_d$.

For the resulting proof load factor to be sensible when a resistance model is included, the prior probability $P(R<S)$ must give $\beta < \beta_{target}$. Therefore, another parameter, $(R/S)_{prob}$, is introduced and is determined from such that $P((R/S)_{prob} \cdot R_{req} < S)$ gives $\beta = \beta_{target}$. Then $R_d/S_d < (R/S)_{prob}$ for the proof load to be sensible. For the calculations in this paper, R_d/S_d has been varied in the range $0.75 \le R_d/S_d \le 0.95 \cdot (R/S)_{prob}$.

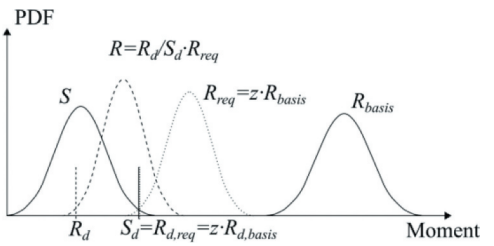


Figure 3. Approach to determine R for different values of R_d/S_d based on R_{basis}.

3.2 *Design equation*

z is determined from the design equation (1) for which variables are listed in Table 2.

Table 2. Variables in the design equation, Equation (1).

Variable	Description	Value
f_{yk}	Characteristic reinforcement yield strength	550 MPa
γ_s	Reinforcement partial safety factor	1.2
f_{ck}	Characteristic concrete compressive strength	25 MPa
γ_c	Concrete partial safety factor	1.45
K_{FI}	Consequence factor	1.1 for CC3
Q_k	Characteristic vehicle weight (same as μ_W)	Class 100: 109.2t Class 150: 157.6t Class 200: 201t
φ_k	Dynamic factor	1.228 for L_{inf}=10m
γ_Q	Traffic load partial safety factor	1.25
G_k	Characteristic structural dead load (concrete)	25 kN/m3
G_{wk}	Characteristic additional dead load (1.2 m gravel)	18 kN/m3
γ_G	Dead load partial safety factor	1.00

$$z \cdot R_{d,basis}\left(\frac{f_{yk}}{\gamma_s}, \frac{f_{ck}}{\gamma_c}\right) = S_d\Big(Q_k \cdot \varphi_k \cdot \gamma_Q \cdot K_{FI},\ (G_k + G_{wk}\Big) \cdot \gamma_G \cdot K_{FI}) \tag{1}$$

3.3 *Prior probabilistic assessment*

$(R/S)_{prob}$ is determined from the limit state equation (2) such that $\beta = \beta_{target}$. Variables of the equation are listed in Table 3.

$$g = z \cdot (R/S)_{prob} \cdot R_{basis}\big(f_y \cdot I_{fy}, f_c \cdot I_{fc}\big) - S\big(Q \cdot I_Q \cdot (1 + S_t), G + I_G, G_W + I_{G_W}\big) \tag{2}$$

The stochastic models used are based on the Danish probabilistic guideline (Vejdirektoratet, 2024). In accordance with the guideline, the material model uncertainties, I_{fy} and I_{fc}, are calculated including the model uncertainty on the computational model, material identity and determinataion of material parameters. The annual extreme vehicle weight, Q, is calculated based on the vehicle weight, W, and the number of vehicles per year, N, see Equation (3).

$$F_{max}(q) = \exp(-N(1 - F(w))) \tag{3}$$

Table 3. Variables for the probabilistic assessment, see Equation (2) and (3). Variables are based on (Vejdirektoratet, 2024).

Variable	Description	Distribution	Mean, μ	Std. deviation, σ
f_y	Reinforcement yield strength	LogNormal	590 MPa	25 MPa
I_{fy}	Model uncertainty for f_y	LogNormal	1	0.104
f_c	Concrete compressive strength	LogNormal	32.1 MPa	$0.15{\cdot}\mu_{fc}$
I_{fc}	Model uncertainty for f_c	LogNormal	1	0.153
W	Standard vehicle weight	Normal	Class 100: 109.2t Class 150: 157.6t Class 200: 201t	Class 100: 6.6t Class 150: 7.1t Class 200: 7.0t
N	Annual number of vehicles (Main roads)	Deterministic	Class 100: 200 Class 150: 100 Class 200: 100	
I_Q	Model uncertainty, traffic load	Normal	1	0.1
S_t	Dynamic supplement	Normal	$D_{base}{\cdot}D_{extra}$	$D_{base}{\cdot}D_{extra}$
G	Structural dead load	Normal	25 kN/m^3	$0.05{\cdot}\mu_G$
I_G	Model uncertainty of G	Normal	0	$0.05{\cdot}\mu_G$
G_w	Additional dead load	Normal	18 kN/m^3	$0.1{\cdot}\mu_{GW}$
I_{Gw}	Model uncertainty of G_w	Normal	0	$0.05{\cdot}\mu_{GW}$

$D_{base} \cdot D_{extra}$ from Table 3 is calculated from Equation (4) and (5), where W is the vehicle weight in kN and L is the influence length, which is 10 m.

$$D_{base} = \frac{41.5}{\sqrt{W \cdot 1000}} \cdot \left(\frac{5}{L}\right)^{0.2} \tag{4}$$

$$D_{extra} = 1 + 0.12 \cdot L^{0.4} - 0.03 \cdot \frac{W/10 - 50}{10} \tag{5}$$

3.4 *Proof load factor with resistance*

While the added load from the proof load test is deterministic, as the dead loads are modelled stochastically in this paper, the combined load effect, S_p, during the proof load test is also stochastic. Therefore, R, cannot be truncated at a single value of S_p as in Figure 1b. Instead, the posterior probability of failure can be determined as the probability of failure due to actual loading, event A, conditional on a successful proof load test, event B. The posterior probability of failure is calculated by Equation (6) in which the proof load factor, $\eta_{w/}$, is introduced with *w/* denoting that the proof load factor is calculated *with* resistance. $\eta_{w/}$ is multiplied to the design traffic load and is determined such that the annual $\beta = \beta_{target}$.

$$\begin{aligned} &\mathrm{P_f} = \Phi(-\beta) = \mathrm{P}(A|B) = \tfrac{\mathrm{P}(A\cap B)}{\mathrm{P}(B)} \\ &A:\ R = z\cdot R_d/S_d\cdot R_{basis}\left(f_y\cdot I_{fy}, f_c\cdot I_{fc}\right) < S\left(Q\cdot I_Q\cdot(1+S_t), G+I_G, G_W+I_{G_W}\right) \\ &B:\ R = z\cdot R_d/S_d\cdot R_{basis}\left(f_y\cdot I_{fy}, f_c\cdot I_{fc}\right) > S_p\left(\eta_{w/}\cdot Q_k\cdot\varphi_k\cdot\gamma_Q, G+I_G, G_W+I_{G_W}\right) \end{aligned} \tag{6}$$

3.5 *Proof load factor without resistance*

Proof load factors without resistance are determined similarly to the approach by (Christensen et al., 2023) but from the new probabilistic guideline, see the limit state Equation (7). Here the proof load factor, $\eta_{w/o}$, is introduced with *w/o* denoting that the proof load factor is calculated *without* resistance. Again, the proof load factor is determined such that $\beta = \beta_{target}$.

$$g = Q_{proof} - Q_{actual} = \eta_{w/o}\cdot Q_k\cdot\varphi_k\cdot\gamma_Q - Q\cdot I_Q\cdot(1+S_t) \tag{7}$$

4 RESULTS

This section presents the results of the described analyses. Figure 4 shows proof load factors calculated from the Danish codes and guidelines both with and without resistance. $\eta_{w/o}$ is constant in Figure 4, as the factor is nondependent on the resistance and therefore also on R_d/S_d.

For the resulting proof load factors to be comparable to those from (Casas & Gómez, 2013), additional proof load factors are calculated with a 50-year reliability index of β_{target}=3.2, instead of the annual reliability of 4.75 as specified from the Danish Code. To get the 50-year extreme traffic load N in equation (3) is multiplied by 50. The maximum moments calculated for a -10 m bridge span from both these Danish proof load factors and from proof load factors in (Casas & Gómez, 2013) are shown in Figure 5. The cut-off points for $\eta_{w/}$ is at R_d/S_d = $0.95\cdot(R/S)_{prob}$.

The axle loads of the class 150 vehicle and of $\mathrm{LM1_{CEEC}}$ at R_d/S_d = 0.6 are shown in Figure 6 along with the associated moment distribution. The tandem axle load of $\mathrm{LM1_{NL}}$ is determined, such that the resulting maximum moment is equal to that from the combined tandem axle and distributed load, as proposed by (Lantsoght et al., 2017).

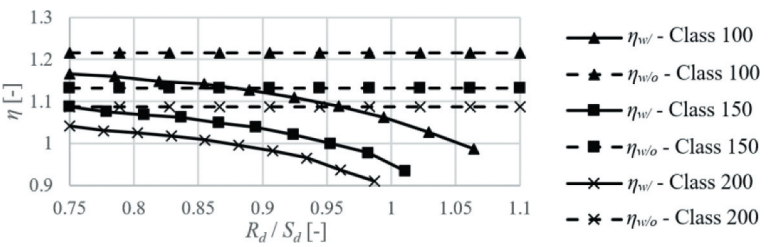


Figure 4. Proof load factors calculated from Danish codes and guidelines.

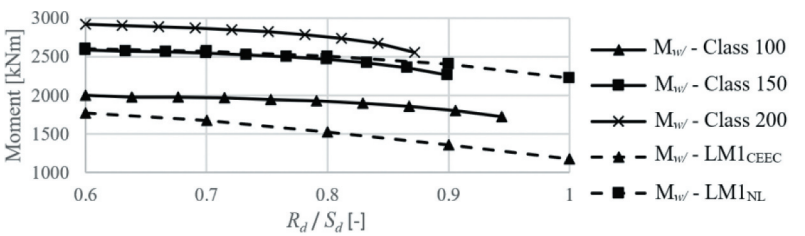


Figure 5. Danish proof load moments and proof load moments from (Casas & Gómez, 2013).

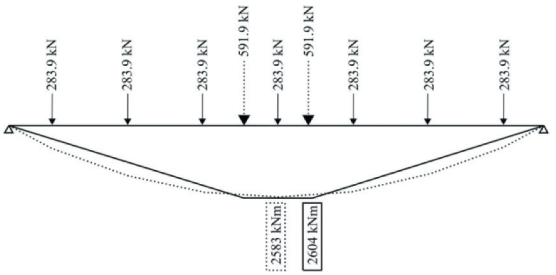


Figure 6. Class 150 (full) and $LM1_{NL}$ (dashed) axle configurations at R_d/S_d=0.6 in Figure 5.

5 DISCUSSION

Before carrying out a proof load test, it should be clear how the knowledge, that a bridge has survived the proof loading, can be used i.e., which vehicles can be allowed crossing. Here the Danish system seems to have an advantage as the standard vehicles were produced with special transport permitting in mind. When a bridge is proven for a certain class, then all special transports in the same class or lower can be permitted crossing. LM1 is determined from extrapolation of WIM-data with the heaviest vehicle measured weighing roughly 75-tonne. LM1 seems therefore not linked to special transport allowance. Using WIM-data containing special transports weighing up to 165-ton, (Casas & Gómez, 2013) calculated CEEC and Dutch proof load factors to be applied to LM1. These proof load factors, although to be applied to LM1, were thus determined with higher consideration for future special transport allowance. Still, the proof load factors were based on 1000-year extreme load effect extrapolated from past measurements, meaning that only one load level, which is meant to encapsulate all special transports, can be chosen. In the Danish system a different load level can be chosen for each bridge based on the desired bridge class. This can be an advantage, as the class can be chosen lower or higher depending on the special transport classes planned to be allowed crossing or depending on the expected bearing capacity of the bridge. This difference can be seen from Figure 5, where only one proof load moment is plotted for either CEEC or The Netherlands, whereas different levels are plotted for Denmark.

The Danish standard vehicles compared to LM1 seem to have a higher resemblance to real vehicles. The standard vehicles are designed with increasing number of axles and increasing axle weight with increasing class, whereas LM1 consists of one axle tandem and a distributed load. In practice this distributed load may be hard to simulate in a proof load test. Therefore, (Lantsoght et al., 2017) proposed to increase the tandem axle load, such that the resulting section forces are equal to that of the combined tandem axle and distributed load. However, this may lead to unreasonably large axle loads and as a result exaggerated local effects compared to the load effects resulting from real special transports. This phenomenon may be seen from Figure 6, which shows significantly higher axle loads for $LM1_{NL}$ compared to those of the class 150 standard vehicle, although the two load configurations result in comparable moments in Figure 5.

In the literature, proof load tests have been reported using proof load factors calculated both with and without resistance. Figure 4 shows that $\eta_{w/o}$ approaches $\eta_{w/}$ with decreasing z_{proof}/z_d, which means that the higher the utilization from the partial safety method, the smaller the value of resistance information becomes. However, due to the inclusion of a resistance, the results for $\eta_{w/}$ are highly case dependent, whereas the results for $\eta_{w/o}$ are more universal and may be constant along road stretches. Furthermore, the precision of the model uncertainty on the computational resistance model, and thus also $\eta_{w/}$, can be questioned (Schmidt et al., 2020). In the Danish proof loading project, failure tests will be carried out on concrete slab bridges to quantify the model uncertainty of given resistance models and thus, hopefully, give rise to better stochastic resistance modelling. It shall be noted that the calculations in this paper are carried out as an academic exercise, where a bridge with only one lane is used as base case, which may not be representative of too many bridges. Future work in the project will be to determine proof load configurations for multiple-lane bridges using real traffic data.

6 CONCLUSION

This paper compares Danish approaches to proof load configuration with approaches using the Eurocodes Load Model 1. For comparison with LM1 proof load configurations from the literature, Danish proof load factors both with and without resistance are calculated based on the Danish probabilistic guideline. A seemingly clear advantage of the Danish bridge classification system compared to LM1 is the higher resemblance of the traffic load configuration to real special transports. It was found that using LM1 may result in unreasonably high axle loads to be applied in a proof load test, which, although giving reasonable beam moment and shear, may lead to exaggerated local effects. As an example, to reach a moment of roughly 2600 kNm in a 10 m beam, the axle load magnitude to be applied to prove LM1 is 59 tonne, while for the Danish class 150 standard vehicle it is only 28 tonne.

It was found that the gain from including a resistance model is higher for lower design utilizations. The highest difference between the proof load factors calculated with and without resistance is roughly 20 %, while the lowest difference is roughly 5 %. However, as was discussed, the method including a resistance model is more case dependent and may suffer from questionable precision of the resistance model. Therefore, this may not conclusively prove one method to be superior to the other.

ACKNOWLEDGEMENT

The financial support from the Danish Road Directorate, Innovation Fund Denmark and COWIfonden is greatly appreciated.

REFERENCES

Bundesministerium für Verkehr und digitale Infrastruktur. (2016). *Regelungen und Richtlinien für die Berechnung und Bemessung von Ingenieurbauten (BEM-ING) - Teil 3 - Berechnung von Straßenbrücken im Bestand für Schwertransporte*.

Casas, J. R., & Gómez, J. D. (2013). Load rating of highway bridges by proof-loading. *KSCE Journal of Civil Engineering*, *17*(3), 556–567. https://doi.org/10.1007/s12205-013-0007-8

Christensen, C. O., Damsgaard, K. D. S., Sørensen, J. D., Engelund, S., Goltermann, P., & Schmidt, J. W. (2023). Reliability-Based Proof Load Factors for Assessment of Bridges. *Buildings*, *13*(4), 1060. https://doi.org/10.3390/buildings13041060

Correia, J. P. R. R., & Branco, F. A. B. (2006). New Methodology: Permit Checking of Vehicular Overloads. *Journal of Bridge Engineering*, *11*(3), 274–281. https://doi.org/10.1061/ASCE1084-0702200611:3274

European Commision. (2008). *Abnormal Road Transport: European Best Practice Guidelines*.

European Committee for Standardization (CEN). (2003). *EN1991-2. Eurocode 1: Actions on structures - Part 2: Traffic loads on bridges*.

Faber, M. H., Val, D. V., & Stewart, M. G. (2000). Proof load testing for bridge assessment and upgrading. *Engineering Structures*, *22*, 1677–1689.

Lantsoght, E. O. L., van der Veen, C., de Boer, A., & Hordijk, D. A. (2017). Required proof load magnitude for probabilistic field assessment of viaduct De Beek. *Engineering Structures*, *148*, 767–779. https://doi.org/10.1016/j.engstruct.2017.07.010

Nowak, A. S., & Tharmabala, T. (1988). BRIDGE RELIABILITY EVALUATION USING LOAD TESTS. *Journal of Structural Engineering*, *114*(10), 2268–2279.

Ravn, D. L., Attrup, P., Stoltzner, E., & Linneberg, P. (2006). Load Capacity Rating and Overweight Permitting. *IABSE Symposium Report*, *91*, 94–101.

Saraf, V., & Nowak, A. S. (1998). Proof Load Testing of Deteriorated Steel Girder Bridges. *Journal of Bridge Engineering*, *3*(2), 82–89.

Schmidt, J. W., Thöns, S., Kapoor, M., Christensen, C. O., Engelund, S., & Sørensen, J. D. (2020). Challenges Related to Probabilistic Decision Analysis for Bridge Testing and Reclassification. *Frontiers in Built Environment*, *6*. https://doi.org/10.3389/fbuil.2020.00014

Sedlacek, G., Merzenich, G., Paschen, M., Bruls, A., Sanpaolesi, L., Croce, P., Calgaro, J. A., Pratt, M., Jacob, Leendertz, M., de Boer, A., Vrouwenvelder, A., & Hanswille, G. (2008). Background document

to EN 1991- Part 2 - Traffic loads for road bridges - and consequences for the design. *JRC Scientific Technical Rep*.
Statens Vegvesen. (2023). *Spesialtransport - Utdrag fra forskrift om bruk av kjøretøy kap. 5*.
Thoft-Christensen, P., & Baker, M. J. (1982). *Structural reliability theory and its applications*. Springer-Verlag.
Trafikverket. (2011). *Dispenstransporter - en handbok*.
Vejdirektoratet. (2004). *Reliability-Based Classification of the Load Carrying Capcity of Existing Bridges*.
Vejdirektoratet. (2010). *Vejledning Til Belastnings- Og Beregningsgrundlag*.
Vejdirektoratet. (2017). *DS/EN 1991-2 DK NA:2017, Annex A: Lastmodeller for klassificering og bæreevnevurdering (Models of Special Vehicles for Road Bridges)*.
Vejdirektoratet. (2024). *Reliability-Based Classification of the Load Carrying Capcity of Existing Bridges*. Unpublished.
Vigh, A., & Kollár, L. P. (2007). Routing and Permitting Techniques of Overweight Vehicles. *Journal of Bridge Engineering*, *12*(6).

Bridge Maintenance, Safety, Management, Digitalization and Sustainability – Jensen, Frangopol & Schmidt (eds)
© 2024 The Author(s), ISBN 978-1-032-77040-6
Open Access: www.taylorfrancis.com, CC BY-NC-ND 4.0 license

Static and dynamic monitoring of bridges with contactless techniques

T. Moser & W. Lienhart
Institute of Engineering Geodesy and Measurement Systems, Graz University of Technology, Austria

F. Schill
i3mainz – Institute for Spatial Information and Surveying Technology, University of Applied Sciences Mainz, Germany

ABSTRACT: Modern geodetic sensors are capable of capturing static and dynamic monitoring data of civil structures with up to several hundred Hertz. In order to assess the potential of such sensors, a comparative field study at a multi span highway bridge in Austria was performed. In the field tests different geodetic sensors such as robotic total stations (RTS) and terrestrial laser scanners (TLS) both in 3D and profile configuration were used to observe the structural behaviour during controlled static and dynamic load tests. Two trucks were placed at different positions on the steel-concrete composite bridge and the displacements of two bridge decks were observed. Additionally, both trucks were crossing the bridge at constant speeds (5 km/h and 30 km/h). In this study it is shown that remote sensing techniques are an appropriate tool for bridge monitoring and can ensure undisturbed operation of civil structures, as well as high accurate deformation measurements.

1 INTRODUCTION

While geodetic sensors such as robotic total stations (RTS) are mostly used for static-only measurements, the development of more advanced instruments enables the possibility to capture dynamic phenomena of objects as well (Lienhart et al. 2023). Other sensors as accelerometers or tilt sensors could either derive static or dynamic information but rarely could gather both details at a time. These drawbacks could be overcome by modern geodetic remote sensors, as the instruments can capture static deformations, but as well dynamic behavior with up to several hundred Hertz. However, geodetic sensors are not commonly used yet for dynamic monitoring. Among the few examples are GNSS based monitoring of bridges and high-rise buildings (Schönberger et al. 2022, Shen et al. 2019, Im et al. 2013, Yi et al. 2013) and RTS or terrestrial laser scanner (TLS) based monitoring of bridges (Lienhart et al. 2017, Psimoulis et al. 2008). In all these publications only few different technologies are being used and often under uncontrolled loading of the structures.

This paper presents a comparative study and investigates how different sensor technologies complement each other. Furthermore, the achievable accuracy difference between static and dynamic measurements is investigated. Geodetic sensors in the form of Profile Laser Scanners (PLS), 3D TLS and RTS are used to observe a multi-span highway bridge with different loading scenarios. The geometrical and temporal performance of capturing the bending of a bridge girder is examined. It shall be shown, that with geodetic sensors not only static deformations, but as well dynamic movements of the object can be captured when used in dynamic mode.

Remote sensors do not need sensor installation on objects, but there are some remote sensing methods that need installation of passive elements such as targets for tracking. Thus, the sensor is classified as a semi-remote sensor. Other sensors such as laser scanners or terrestrial

DOI: 10.1201/9781003483755-35

Table 1. Sensors and their capabilities.

Sensor	Max. Measurement rate	Dimension	Sensitive direction	Remote
RTS	20	3D	3D	Semi
Profile Laser Scanner	200 profiles/s	2D	2D, in a profile	Yes
Terrestrial Laser Scanner	1/60	3D	3D	Yes
Interferometric Radar	200	1D	LoS*	Yes
GNSS	20	3D	3D	No
Telescopic Camera	500	2D	2D, Orth. to LoS*	Yes
Accelerometer	20000	1D	1D	No
Tilt Sensors	1/60	1D	1D	No

*Line of Sight

radars are completely remote and no targets at the structure are needed. A list of different sensor types and their capabilities can be seen in Table 1.

2 LOAD TESTING AT AN AUSTRIAN HIGHWAY BRIDGE

The Austrian Brenner highway is part of the European route E45 and crosses Europe in north-south direction from north of Finland to the south of Italy. The passage across the Austrian alps is a crucial part of the route and as well crucial to the European transnational movement of goods. The highway passage across the alps was mainly build in the 1960s, and in this time also the Gschnitztalbrücke was build.

The structure itself is a steel-concrete composite and is shaped as a 7-span continuous beam, whereas the outer two spans are 70 m long, all the others have a length of 84 m. The total length therefore is 560 m long. The monitoring of the load test focused on the two spans (span 6 and span 7) next to the south bearing of the bridge, as seen in Figure 1.

2.1 *Test procedure*

Part of this monitoring was a load test which was carried out in May 2023. One direction of the highway bridge was temporarily closed to place two trucks on it, each weighing more than 50 tons, to create different load scenarios. Thereby, the trucks were put statically on span 6, then one of the trucks moved on to span 7 and after that, the second truck followed to span 7, so that there are 3 load scenarios, as shown in Figure 2. Additionally, four dynamic tests took place, where the trucks passed the bridge with speeds of 5 or 30 km/h on the first and second lane.

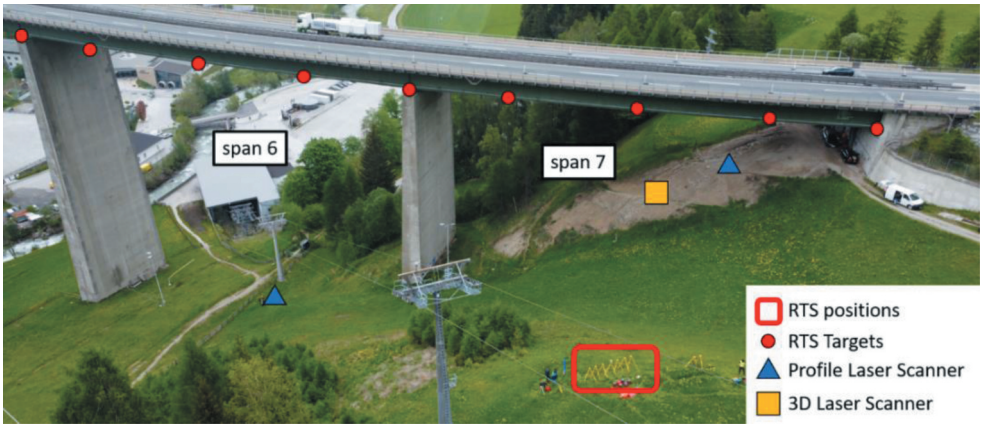


Figure 1. Overview image of the two observed spans of the bridge with the position of the remote sensors.

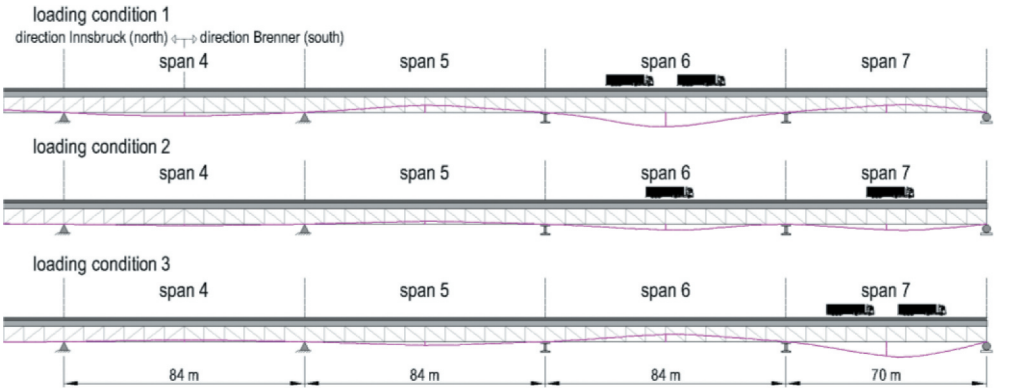


Figure 2. Schematic side view of the bridge with three loading scenarios of static load tests and schematic bending lines of the structure.

2.2 *Test setup*

Six Leica MS60 RTS were set up next to each other to follow the movement of six monitoring prisms mounted directly on the steel girder at span 6 and 7, see Figure 1. In addition, a Leica TM50 RTS is used to take successive measurements on the prisms mentioned above as well as on the prisms attached directly to the bearings of the bridge.

A PLS was located under each of the two observed spans, enabling both dynamic and static observations. At span 7 a Z+F Imager 5016 3D laser scanner is used in profile mode, and a Z +F Profiler 9012 is used at span 6. Additionally, a Leica RTC360 is located at span 7 for 3D static observations, as the measurement takes around 60 seconds.

3 USED SENSORS

The focus of this study is on RTS and TLS, as well as PLS (Schill & Eichhorn 2019), which are very similar in terms of their basic operating principle. All instruments gather polar coordinates consisting of angles in vertical and horizontal directions as well as distances to the observed point. A crucial difference between the instruments is, that RTS follows a single target, and take measurements to this exact point with a nominal measurement rate of up to 20 Hz (Leica 2020), while a TLS or PLS measures in consecutive angles and takes measurements to the surface itself that is in line of sight. The used TLS can measure 1 - 2 million points per second. In case of the PLS this is combined with up to 200 profiles per second (Zoller + Fröhlich 2017). Because of the operating principle, PLS can only detect 2D displacements in a profile, while the RTS and TLS measurements provide 3D information of the observed prism or the object surface.

3.1 *Robotic Total Station (RTS)*

The dynamic measurements of the six RTS are taken with the Leica Streaming App with a nominal measurement rate of 20 Hz. As a result, a data entry for each measurement with information of horizontal and vertical angles, distance measurement, compensator, and a time stamp is generated. This time stamp is a continuous counter in milliseconds from the moment of turning on the instrument. As the time stamps are only internal times, the different RTS need to be synchronized to each other. This synchronization is realized with a 360° prism on a pole and performing a significant movement while all the RTS are tracking the prism. Additionally, a GNSS receiver is mounted above the prism to capture the movement via dynamic GNSS measurements. These captured movements serve as a correlation pattern to not only synchronize the different RTS to each other, but also set the measurements into a global time system provided by the GNSS.

3.2 *Terrestrial Laser Scanner (TLS)*

TLS capture millions of points in the entire visible environment, resulting in a 360° panorama in the form of a point cloud. The laser beam emitted and reflected by the object being measured is analyzed and contactless distance measurements are carried out. As the angles of the emitted laser beam are known, three-dimensional coordinates can be derived.

The sequential acquisition is realized by rotating simultaneously in 2 directions: the laser beam is deflected by a high-frequency rotating mirror and the TLS is rotating around its standing axes.

3.2.1 *Profile Laser Scanner (PLS)*

If TLS are used in profile mode (Schill et al. 2019), the instrument only uses the high-frequency rotating mirror, but in contrast to 3D TLS does not rotate around its standing axis, so that the laser beam gets deflected into the same profile repeatedly.

By reducing the spatial resolution to such a single profile, the temporal resolution can be increased significantly. In this way, PLS can be used either to record dynamic and spatially distributed motion behavior, such as displacements of objects of interest. Or to statically capture the surface geometry within a profile with increased precision by time averaging the measurements taken while the structure is not moving. With more than one epoch of statically recorded surface profiles, static displacements can be derived with high spatial resolution and high precision.

For both applications, a spatial approximation of the profiles measured on the object surface takes place. In the simplest case, it is realized based on a spatial averaging of the closely spaced profile points. By doing so, the system accuracy can be increased for both applications.

4 RESULTS

4.1 *Robotic Total Station*

4.1.1 *Dynamic Robotic Total Station*

It must be considered that the single measurements of the RTS are not done uniformly regarding timing. Also, the time differences are not normally distributed, but rather gather in groups that have spacings of the minimal time difference of about 50 ms. Additionally, there is a time drift in the data of the RTS. There were made multiple time correlations with 4 RTS, whereas the drift of 3 of them is rather similar with a time drift of about 40 ppm. One instrument shows a bigger drift in the beginning of 115 ppm which later comes down to a drift of 60 ppm. The change in drift could be due to heating effects of the instrument (Gojcic et al. 2018), but needs further investigation to determine the specific systematics.

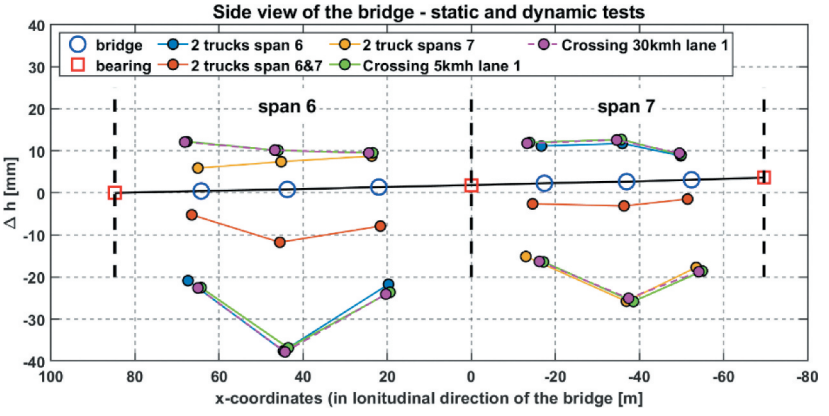


Figure 3. Deformations derived with RTS from dynamic measurements of static and dynamic (green & magenta) load tests. Prisms of bearings are only measured during static load tests.

In general, the drift creates a time delay of a about 1 s over a time span of 5 hours. Depending on the desired synchronization accuracy, the drift problem could either be overcome by correlating the instruments more often, or just apply a predetermined time drift for each individual RTS, as the drifts do vary from one to the other instrument.

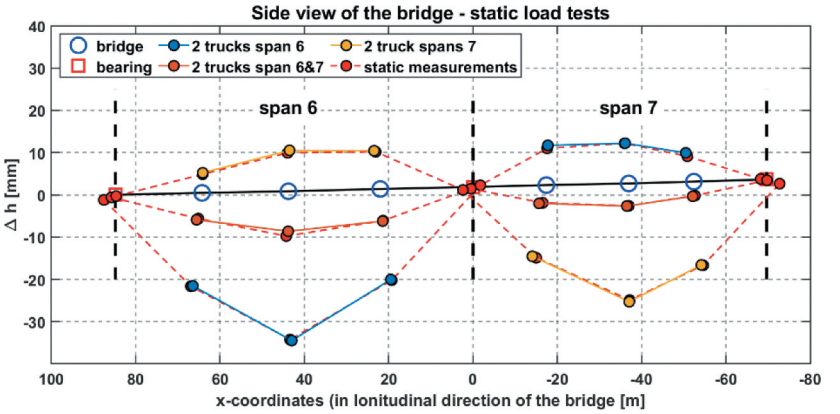


Figure 4. Deformations during static load tests derived from static (red) and dynamic measurements.

The most important results that should be obtained from the measurements are displacements in the form of height changes. As the RTS takes angle and distance information of every single point, not only the change of elevation can be detected, but as well a change of position can be derived. This supports the understanding of the structural system and its reaction to loading.

The maximum and minimum deformation of height caused by two trucks passing the bridge with 5 km/h and 30 km/h can be seen in Figure 3 together with the static load tests. To obtain the deformation of the static load test, the measurements are averaged over the time where the bridge is statically loaded. The left and middle prism in span 6 is significantly differing between static and dynamic tests. This comes from the crossing of the trucks because span 6 gets lifted when the trucks are passing span 5, therefore the maximum height change differs if dynamic and static load tests are carried out. Considering this, the extreme values of the displacements of Figure 4, the dynamic measurements can capture the same displacement in a drive by test, as the static measurements during static loading.

4.1.2 *Static Robotic Total Station*

During the static load tests, one RTS takes measurements in multiple sets of all mounted prisms sequentially. The measurements are taken once without any loading of the bridge as a reference measurement, all following measurements are set in respect to this reference.

As the static measurements include all prisms, not only the bending and displacement of the steel girder, but also the movement at the bearings can be calculated. Additionally, the strain between the prisms can be derived of the change of its 3D positions. Comparing the results of static and dynamic measurements of the same load tests, as shown in Figure 4, the variations are rather small.

4.2 *Terrestrial Laser Scanning (TLS)*

4.2.1 *3D TLS*

The static load tests were recorded with three different TLS. A PLS and a 3D TLS in profile mode were used, which are described in more detail in section 4.2.2. Additionally, a Leica RTC360 was used to record the static tests epoch wise in 3D for span 7, see also Figure 1.

In Figure 5 the underside of the bridge and the results of an exemplary static load test are presented. The vertical displacements were calculated with the M3C2 algorithm (Lague et al.

2013) and are color coded from blue (negative) to red (positive). Every epoch was recorded with one laser scan, leading to a precision of the displacements in the lower millimeter range. The maximum deformation (blue) occurs approximately in the center of span 7 and spreads symmetrically from the edge.

One advantage of acquisition with a 3D TLS is the high spatial resolution; not only the one main beam can be observed, but the entire visible structure. Further information can therefore be derived from the measurement data, e.g. that the maximum deformation of the cantilevered carriageway is in the order of approx. 10 mm greater than the main beam, see right side of Figure 5.

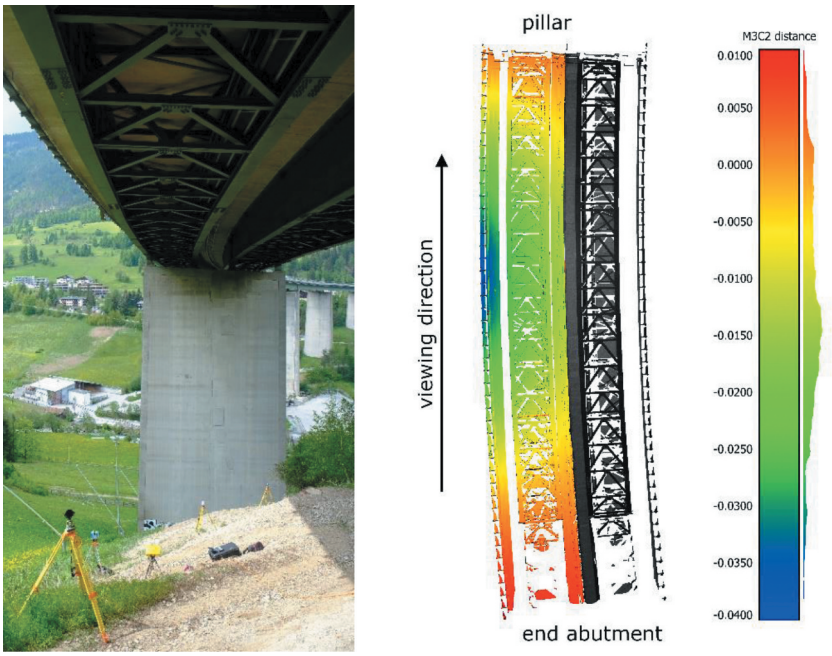


Figure 5. Left: Photograph of the underside of span 7; right: Color coded vertical displacements of an exemplary static load test of span 7, with both trucks at the outer edge in the middle of span 7, compare with Figure 2. The other direction of travel is shown as an intensity visualization, as this direction of travel was not closed to traffic. The viewing direction of the photograph is visualized with an arrow in the middle.

4.2.2 *Dynamic Profile Laser Scanning (PLS)*

A disadvantage of 3D acquisition with TLS, on the other hand, is the long measuring time, so this method can only be used for static load tests, as seen above. In addition to the static load tests four dynamic tests were performed, that cannot be analyzed with a 3D TLS. As explained in section 3 it is possible to overcome this issue by reducing the spatial resolution to a single profile to get a temporal resolution of up to 200 Hz. In addition, the profile approximation can be used to increase the precision of displacement detection in the submillimeter range (Schill et al. 2022).

Shows the exemplary results of one dynamic experiment, where both trucks are passing the bridge with 5 km/h. The upper graph shows a time series measured with the PLS approximately at the position of the center prism at span 7. In accordance with Figure 2, the rising and lowering of the bridge deck can be seen, starting when the two trucks are in span 4, leading to a slight rise in the height for span 7. Subsequently, the points in time can be recognized when the trucks are in the spans 5 (lowering), 6 (blue, maximum rise) and 7 (red, maximum lowering).

In the lower graph the spatially distributed displacement measurements of the profile scanner are shown for the latter two points in time, which are also marked in the upper graph in

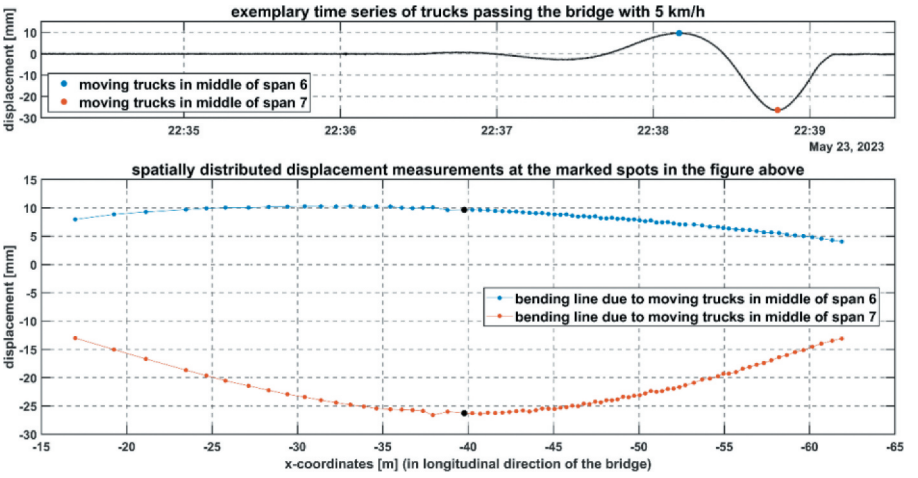


Figure 6. Dynamically captured bridge displacements of PLS measurements on span 7. The lower figure shows the bending line of the steel girder at the time of the marked points in the same color in the upper figure. The x-coordinates correspond to Figure 4.

corresponding colors. These two exemplary points in time are designed to illustrate the potential of just one PLS. In this example, up to 80 spatially distributed displacement time series can be derived with sub-millimeter accuracy and a temporal resolution of under 0.02 seconds.

4.2.3 *Static Profile Laser Scanning (PLS)*

PLS can also be used to analyze static load tests, further increasing precision and spatial resolution through additional time averaging during the load holding phases. In Figure 7 the results of three repeated load test scenarios are shown. Approximately 600 displacement values could be derived in a profile area of just under 50 meters. Most of the mutual deviations from two completely independent experiments are in the order of 0.1 mm and below. Only the load position with one truck on span 6 and one truck on span 7 shows larger deviations. However, these deviations can also be caused by slightly different positions of the trucks on the bridge between tests.

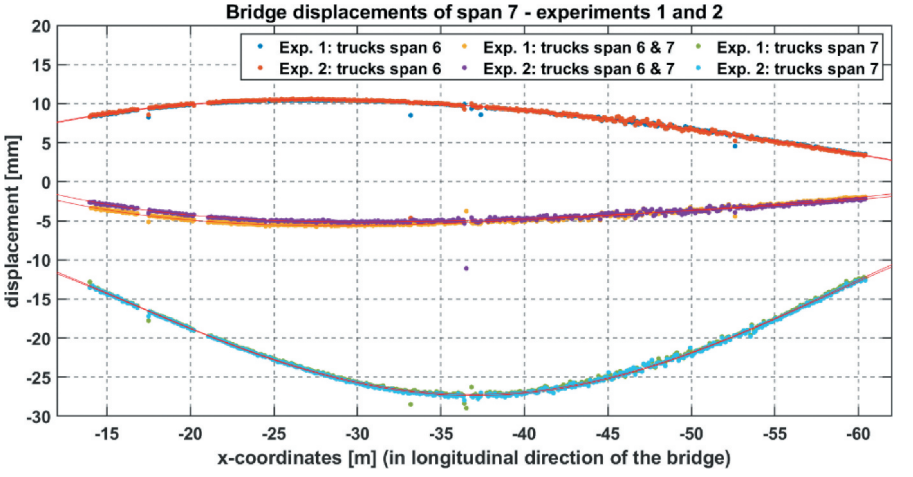


Figure 7. Bridge displacements captured by profile laser scanner. Two identical experiments with 3 load conditions (see also Figure 2) are shown.

5 CONCLUSION

It could be shown, that both RTS and PLS are highly capable of detecting static and dynamic deformations of bridges. If both, static and dynamic results are compared, the performance of the sensors is promising in both applications.

RTS can capture single points with a measurement rate up to 20 Hz and can gather real 3D deviations of this point with high accuracy. Nevertheless, the temporal drift of each individual sensor hast to be considered, in particular when its used for a longer period at a time, as the drift can accumulate up to 1 s after 5 hours.

3D TLS capture its full surroundings in a period of about 60 seconds, which can be used for static 3D deformation analysis of structures, with millimeter precision. When the rotation of the TLS around the standing axis is suppressed, a profile remains as measurand. In doing so, the temporal resolution can be increased significantly, and up to 200 profiles per second can be captured. With temporal or spatial averaging, the accuracy of the recorded profile increases to the sub-millimeter range. In addition, a large number of spatially distributed displacement values can be derived.

Overall, a comprehensive understanding of bridge displacements under static and dynamic load scenarios can be achieved with relatively little effort. The use of geodetic remote sensors can therefore address the challenges of an ageing infrastructure by providing more actually measured information. The next step should be a comprehensive integration of these remote measurements into digital twins to enable an integrated analysis accompanying the life cycle of infrastructure buildings. With precise knowledge about the bridge system it may be possible to contribute to moving force identification (Firus 2022) using dynamic remote sensors.

ACKNOWLEDGEMENTS

We want to acknowledge the support of the Austrian Highway Agency (ASFINAG), especially Peter Augschöll for the possibility of performing a load test on the bridge.

REFERENCES

Firus, A. 2022. A contribution to moving force identification in bridge dynamics. Technische Universität Darmstadt. Dissertation. https://doi.org/10.26083/tuprints-00020293

Gojcic, Z. & Kalenjuk, S. & Lienhart, W. 2018. A Routine for Time Synchronization of Robotic Total Stations. *AVN 125 (10)*: 299-307

Im, S. B. & Hurlebaus, S., & Kang, Y. J. 2013. Summary review of GPS technology for structural health monitoring. Journal of Structural Engineering, 139(10), 1653–1664. https://doi.org/10.1061/(ASCE)ST.1943-541X.0000475

Lague, D. & Brodu, N. & Leroux, J. 2013. Accurate 3D comparison of complex topography with terrestrial laser scanner: Application to the Rangitikei canyon (N-Z). *ISPRS Journal of Photogrammetry and Remote Sensing*, 82, 10–26. https://doi.org/10.1016/j.isprsjprs.2013.04.009.

Lienhart, W. & Schill, F. & Moser, T. 2023. Dynamic bridge monitoring with remote sensing techniques. Structural Health Monitoring 2023: Designing SHM for Sustainability, Maintainability and Reliability (pp. 184–191). https://doi.org/10.12783/shm2023/36736

Lienhart, W. & Ehrhart, M. & Grick, M. 2017. High frequent total station measurements for the monitoring of bridge vibrations. *Journal of Applied Geodesy*, vol. 11, no. 1, 2017, pp. 1–8. https://doi.org/10.1515/jag-2016-0028

Leica 2018. Leica RTC360 Datenblatt, Leica Geosystems AG, Heerbrugg, Switzerland, 2p.

Leica 2020. Leica TS60/MS60/TM60 User Manual Version 4.0, Leica Geosystems AG, Heerbrugg, Switzerland, 94p.

Psimoulis, P.A. & Stiros S. C. 2008. Experimental Assessment of the Accuracy of GPS and RTS for the Determination of the Parameters of Oscillation of Major Structures. Computer-Aided Civil and Infrastructure Engineering, 23: 389–403. https://doi.org/10.1111/j.1467-8667.2008.00547.x

Schill, F. & Sviridova, A. & Eichhorn, A. 2019. Deformation monitoring of noise barriers with profile laser scanning. *Conference: 4th Joint International Symposium on Deformation Monitoring (JISDM)* Athen

Schill, F. & Eichhorn, A. 2019. Deformation Monitoring of Railway Bridges with a Profile Laser Scanner. *ZFV - Zeitschrift für Geodäsie, Geoinformation und Landmanagement*. 144. 109–118. https://doi.org/10.12902/zfv-0248-2018.

Schill, F. & Michel, C. & Firus, A. 2022. Contactless Deformation Monitoring of Bridges with Spatio-Temporal Resolution: Profile Scanning and Microwave Interferometry. *Sensors* 2022, *22*, 9562. https://doi.org/10.3390/s22239562

Schönberger, C. & Lienhart, W., & Moser, T. 2022. Dynamic monitoring of civil infrastructures with geodetic sensors. In 5th Joint International Symposium on Deformation Monitoring: JISDM 2022, pp. 537–543. https://dx.doi.org/10.4995/JISDM2022.2022.16057

Shen, N. & Chen, L. & Liu, J. & Wang, L. & Tao, T. & Wu, D. & Chen, R. (2019). A review of global navigation satellite system (GNSS)-based dynamic monitoring technologies for structural health monitoring. Remote Sensing, 11(9), 1001. https://doi.org/10.3390/rs11091001

Zoller + Fröhlich. 2017. Datasheet Profiler 9012. Zoller + Fröhlich, Germany, 2p.

Yi, J., Zhang, J. W., & Li, Q. S. 2013. Dynamic characteristics and wind-induced responses of a super-tall building during typhoons. Journal of Wind Engineering and Industrial Aerodynamics, 121, 116–130. https://doi.org/10.1016/j.jweia.2013.08.006

Bridge Maintenance, Safety, Management, Digitalization and Sustainability – Jensen, Frangopol & Schmidt (eds)
© 2024 The Author(s), ISBN 978-1-032-77040-6
Open Access: www.taylorfrancis.com, CC BY-NC-ND 4.0 license

Shear stop criteria for reinforced concrete slab strips

G.I. Zarate Garnica
Delft University of Technology, Delft, The Netherlands
Ney & Partners, Delft, The Netherlands

E.O.L. Lantsoght
Delft University of Technology, Delft, The Netherlands
Universidad San Francisco de Quito, Quito, Ecuador

Y. Yang
Delft University of Technology, Delft, The Netherlands

M.A.N. Hendriks
Delft University of Technology, Delft, The Netherlands
NTNU, Norway

ABSTRACT: Proof load testing for assessment can involve a large risk due to the high loads. Stop criteria can reduce this risk. Stop criteria are necessary for shear, which is a brittle failure mode. This paper describes the development of shear stop criteria for slab strips. The shear stop criteria are developed by combining theoretical concepts related to cracking, as well the relationship between bending- and shear-critical regions, along with insights from the Critical Shear Crack Theory and the Critical Shear Displacement Theory. The shear stop criteria are validated with fourteen beam tests. The result is a set of shear stop criteria in a "traffic light system" with a green light level related to serviceability, and yellow and red light related to the ultimate limit state for shear. These stop criteria serve as the basis for a global approach for proof load testing of reinforced concrete bridges.

1 INTRODUCTION

Proof load testing for assessment has gained recognition in the past years as a promising method for bridges for which capacity reserves are expected that cannot be demonstrated with an analytical assessment (Alampalli et al., 2021; Lantsoght, 2023). During a proof load test, a load representative of the factored live load is applied to the bridge. These high loads imply high risks. Therefore, stop criteria are used. Stop criteria are thresholds to the measured responses of the bridge. Once these thresholds are reached, the proof load test should be stopped and further loading is not allowed, as it could result in irreversible damage or potentially even collapse of the bridge.

In the Netherlands, a large number of reinforced concrete slab bridges require assessment, and some of these are good candidates for proof load testing (Lantsoght et al., 2017). However, to come to a wide adoption of the practice of proof load testing for assessment of existing reinforced concrete slab bridges, stop criteria for shear are necessary, as a large number of the existing reinforced concrete slab bridges are found to be shear-critical upon an analytical assessment (Lantsoght et al., 2014).

Theoretically derived stop criteria for flexure are available and validated (Lantsoght et al., 2019). For shear, stop criteria have been proposed based on a small number of experiments (Lantsoght et al., 2018; Yang et al., 2018), but more profound theoretical research was deemed necessary in combination with experiments. The current research on shear stop criteria consists of two steps: 1) theoretically deriving shear stop criteria for reinforced concrete slab strips and validating these criteria with experiments on beams without stirrups, and 2) extending these stop criteria to

DOI: 10.1201/9781003483755-36

slabs and validating these stop criteria on straight and skewed slabs. This paper reports the findings of the first stage.

2 THEORETICAL STOP CRITERIA FOR SHEAR

2.1 *Indicator based on simplified aggregate interlock expression*

Aggregate interlock is one of the main shear-carrying mechanisms. A stop criterion based on aggregate interlock should be linked to a measurable parameter. Crack width is considered as the most suitable measurable parameter to link to aggregate interlock. For the stop criterion, the simplified aggregate expression of the Critical Shear Displacement Theory, CSDT, (Yang et al., 2016) is used. This theory leans on the critical shear displacement Δ, which is difficult to measure during a proof load test. Therefore, a proposal that is based on the crack width w at the level of the tension steel and the acting shear stress τ at the cracked section has been proposed (Yang et al., 2018). Moreover, it is assumed that the aggregate interlock capacity V_{ai} can be taken as a lower bound for the shear capacity V. As a result, the shear capacity expression becomes the expression of the aggregate interlock capacity:

$$V = f_c^{0.56} s_{cr} b \frac{0.03}{w - 0.01}\left(-978\Delta^2 + 85\Delta - 0.27\right) \tag{1}$$

In Eq. (1), f_c is the concrete compressive strength, s_{cr} is the height of a fully developed crack, b is the member width, w is the nominal crack width at the level of the steel reinforcement, and Δ is the shear displacement. Rearranging terms so that all measurable parameters in a proof load test are on the left-hand side of the equation and replacing the shear displacement Δ by the critical shear displacement Δ_{cr} results in:

$$V(w - 0.01) = 0.03 f_c^{0.56} s_{cr} b\left(-978\Delta_{cr}^2 + 85\Delta_{cr} - 0.27\right) \tag{2}$$

with the critical shear displacement Δ_{cr} as:

$$\Delta_{cr} = \frac{25 d_l}{30610\phi_{eq}} + 0.0022 \leq 0.025 \tag{3}$$

and the equivalent rebar diameter ϕ_{eq} can be determined as:

$$\phi_{eq} = \frac{\Sigma\phi_i^2}{\Sigma\phi_i} \tag{4}$$

The height of the fully developed crack can be determined as:

$$s_{cr} = \left(1 + \rho n - \sqrt{\rho n + (\rho n)^2}\right) d_l \tag{5}$$

with ρ the reinforcement ratio, n the ratio between the Young's modulus of the steel and the Young's modulus of the concrete, and d_l the effective depth to the longitudinal reinforcement. The lefthand side of Eq. (2) can be simplified into the shear indicator I_{CSDT} relating the shear stress τ and nominal crack width w as follows:

$$I_{CSDT} = \frac{V(w - 0.01)}{bs} \approx \frac{V(w - 0.01)}{bd} = \tau(w - 0.01) \tag{6}$$

The critical shear indicator $I_{s,cr}$ then becomes:

$$I_{CSDT,cr} = 0.03 f_c^{0.56} \frac{s_{cr}}{d} \left(-978\Delta_{cr}^2 + 85\Delta_{cr} - 0.27\right) \tag{7}$$

with Δ_{cr} from Eq. (3) and s_{cr} from Eq. (5).

2.2 *Indicator based on Critical Shear Crack Theory*

In the Critical Shear Crack Theory, CSCT, (Muttoni & Fernández Ruiz, 2008), the shear strength depends on the crack width and roughness of a critical shear crack (expressed as a function of the maximum aggregate size d_g). In other words, the CSCT considers aggregate interlock as the main shear-carrying mechanism. One of the main assumptions in the theory is that the critical crack width w can be taken as proportional to the multiplication of longitudinal strain ε_x and indication of crack spacing d at a control depth of $0.6d$ from the top fiber. Using these considerations, the shear strength V_R is expressed as:

$$\frac{V_R}{bd\sqrt{f_c}} = \frac{1}{6} \frac{2}{1 + 120 \frac{\varepsilon_x d}{16 + d_g}} \tag{8}$$

with f_c the concrete compressive strength (in MPa), b the width, d the effective depth, ε_x the longitudinal strain at the control depth derived from the bending moment demand in the critical section, and d_g the maximum aggregate size in mm. Replacing the shear resistance V_R by the sectional shear V, an indicator can be derived with f_c in MPa and d_g in mm:

$$\begin{aligned} I_{CSCT} &= \tfrac{V}{bd\sqrt{f_c}} = \tfrac{1}{6} \tfrac{2}{1+120\frac{\varepsilon_x d}{16+d_g}} = \tfrac{1}{3} \tfrac{1}{1+120\frac{w}{d_g}} \\ I_{CSCT} &= \tfrac{V}{bd} \left(1 + 120 \tfrac{w}{d_g}\right) = \tau \left(1 + 120 \tfrac{w}{d_g}\right) \leq \tfrac{\sqrt{f_c}}{3} \end{aligned} \tag{9}$$

In this expression, the measurable parameters are V (as a function of the applied load) and ε_x, which can be derived from the strain at the level of the tension reinforcement and assuming a linear strain distribution as:

$$\varepsilon_x = \frac{0.6d - c}{d - c} \varepsilon_{x,rebar} \tag{10}$$

with d the effective depth and c the height of the compression zone.

2.3 *SLS crack width limit*

In addition to the considerations, the crack width limitation from the serviceability limit state (SLS) as prescribed by NEN EN 1992-1-1:2005 (CEN, 2005) is studied. The limiting crack width is a function of the exposure class. For reinforced concrete bridges, the SLS limit for crack width is w_{SLS} = 0.3 mm. Using the consideration from the previous section, the average crack width w_{avg} can be determined, and compared to the SLS limit as:

$$w_{avg} = \frac{\varepsilon_{c,average} l_g}{n_{cr}} \leq 0.3mm \tag{11}$$

The number of cracks n_{cr} represents the average number of cracks within the gauge length l_g. The difference between the crack spacing between major cracks and secondary cracks at the reinforcement level is considered using a factor of 0.5, resulting in:

$$n_{cr} = \frac{l_g}{0.5 l_{crm}} \tag{12}$$

with l_{crm} the average crack spacing.

An indicator of the Serviceability Limit State (SLS) is crucial as it serves as a signal for potential repairs after proof loading. Exceeding the SLS limit state can cause limited damage, however, the crack width is restricted so that it will not impair the proper functioning or durability of the structure.

3 EXPERIMENTS

Slab strips of 10 m length × 0.3 m width, and with heights of 500, 800 and 1200 mm were tested to validate the proposed shear stop criteria (Koekkoek & Yang, 2016; Yang, 2021). The slab strips were simply supported and subjected to a single concentrated load. The span length was 9 m, and the distance between the load and the support varied among the experiments. Only one experiment was carried out per beam. The load was applied with a hydraulic jack in displacement-controlled way with a loading speed of 0.02 mm/s. The load was increased stepwise until failure. Figure 1 shows the test setup used in these experiments.

The concrete class was C65/80. The reinforcement consisted of ribbed bars with f_{ym} = 550 MPa. Figure 2 shows the reinforcement layout in the beams. It can be seen that one span is provided with stirrups, to avoid an unexpected failure mode.

Table 1 gives an overview of the parameters of the fourteen selected experiments. The table reports the cube concrete compressive strength $f_{c,cube}$, the rebar configuration, the reinforcement ratio ρ_l, the shear span a, the effective depth to the longitudinal reinforcement d_l and the shear span to depth ratio a/d_l. The naming system of the specimen relates to H for high members, the reinforcement ratio (roughly), and the last digit refers to the number of the identical specimen. The table also includes the test results as P_u, which refers to the load level at which the specimen failed in shear, or for the case of the specimens with low a/d, the load at which the critical shear crack opens.

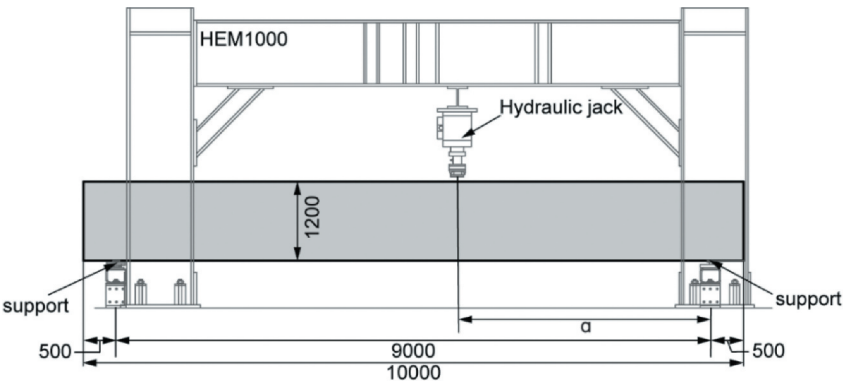


Figure 1. Sketch of test setup. Units in [mm].

The instrumentation on the specimens consisted of traditional sensors such as linear variable differential transformers (LVDTs), laser triangulation sensors (lasers), and the load cell at the hydraulic jack. The structural responses that were measured are deformations in horizontal and vertical direction with the LVDTs as well as deflection under the concentrated load with the lasers. The load cell is sued to report the applied load. Moreover, two-dimensional digital image correlation (2D DIC) is used to monitor the crack pattern and the full displacement field. The displacement field is obtained by using the MatchID (MatchID, 2022) software, as

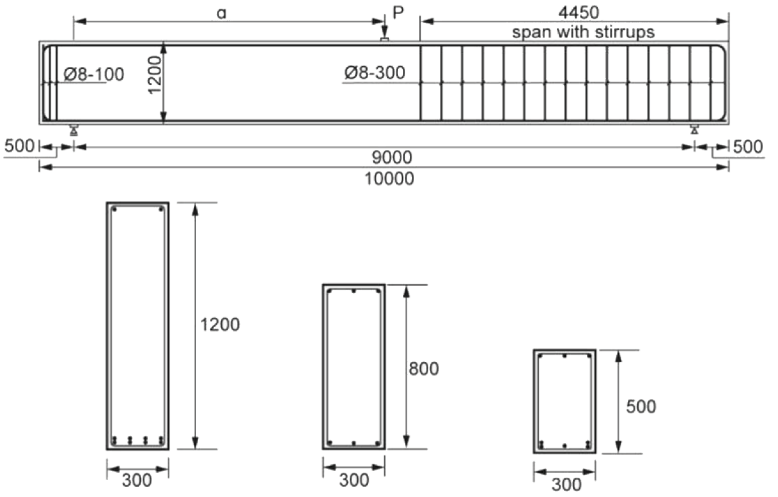


Figure 2. Reinforcement layout of the tested beams. Units in [mm].

Table 1. Parameters of experiments.

Test name	$f_{c,cube}$ (MPa)	Rebar	ρ_l (%)	a (mm)	d_l (mm)	$\lambda=a/d_l$	P_u
H602	86	4Ø25 R	0.57	4500	1158	3.89	306
H401	81	3Ø25 R	0.42	4500	1158	3.89	264
H403	82	3Ø25 R	0.42	4500	1158	3.89	350
H404	82	3Ø25 R	0.42	4000	1158	3.45	269
H121	84	8Ø25 R	1.14	3000	1145	2.62	341
B501A1	81	5Ø20 R	1.15	2500	455	5.5	277
B501B1	76	5Ø20 R	1.15	1500	455	3.3	210
B502B1	77	3Ø20 R	0.68	1750	455	3.8	155
E801A1*	84	3Ø25 R	0.64	2000	770	2.6	213
E801B1	91	3Ø25 R	0.64	2000	770	2.6	205
E802A1	76	6Ø20 R	0.83	2000	740	2.7	219
E802B1*	76	6Ø20 R	0.83	2000	740	2.7	270
E803A1	83	6Ø20 R	0.82	3500	760	4.6	279
E803B1	83	6Ø20R	0.82	3500	760	4.6	308

R for ribbed bars
* specimens with $P_u = P_{cr}$ (load level at which the critical shear crack opened)

well as a Matlab (The Mathworks, 2019) script to obtain the crack pattern, the crack kinematics, and the average strain measurements. The crack pattern and crack kinematics are obtained using the automated detection and crack measurement (ACDM) software (Gehri et al., 2020).

Figure 3 shows the crack numbering and crack width determination as applied to H602.

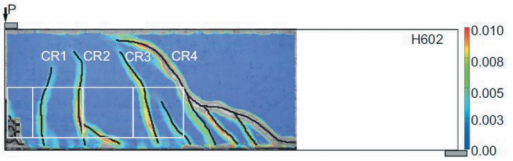


Figure 3. Numbering of cracks, as applied to H602.

4 COMPARISON BETWEEN EXPERIMENTS AND STOP CRITERIA

In order to simulate a real-world measurement of a proof load test, in which the location of the critical cross-section is not known beforehand. The stop criteria are determined at a series of cross-sections of the listed beams along the longitudinal axis. Here the value of crack width or longitudinal strain of a given cross section is determined by a virtual LVDT obtained from the DIC results. The load level when the stop criterion at a given cross-section is reached is noted as P_{ind}. The value of P_{ind} is compared to the measured shear load when shear failure (P_{cr}) is obtained from the test. In general, the ratio between P_{ind}/P_{cr} and M/Vd follows a parabolic trend, see for example Figure 4. In the figure, the factor $\lambda=a/d_l$ for each specimen is given in parenthesis. Overall, the stop criteria related to the shear theories were reached closer to failure in the regions with $M/Vd < 2$. In the region near the loading point between $1d$ and $0.5d$, where the M/Vd is the largest, this corresponds to the area influenced by the largest bending moments and the crack opening and the stop criteria were reached first. This is in line with the model described in CSDT, that a cracked section with smaller M/Vd tends to be more difficult to reach shear failure.

To facilitate the comparison between the various beam experiments with different a/d_l, the M/Vd ratio was normalized by the factor $\lambda= a/d_l$, as shown in Figure 5. This normalization allowed the identification of two main regions: 1) the region corresponding to l_{crm} from the support (larger M/Vd ratios) where the shear resistance is mainly influenced by the crack opening, and 2) the region with the lowest M/Vd which corresponds to shear failure, and where the shear resistance is governed by the shear displacement and the inclination of the cracks.

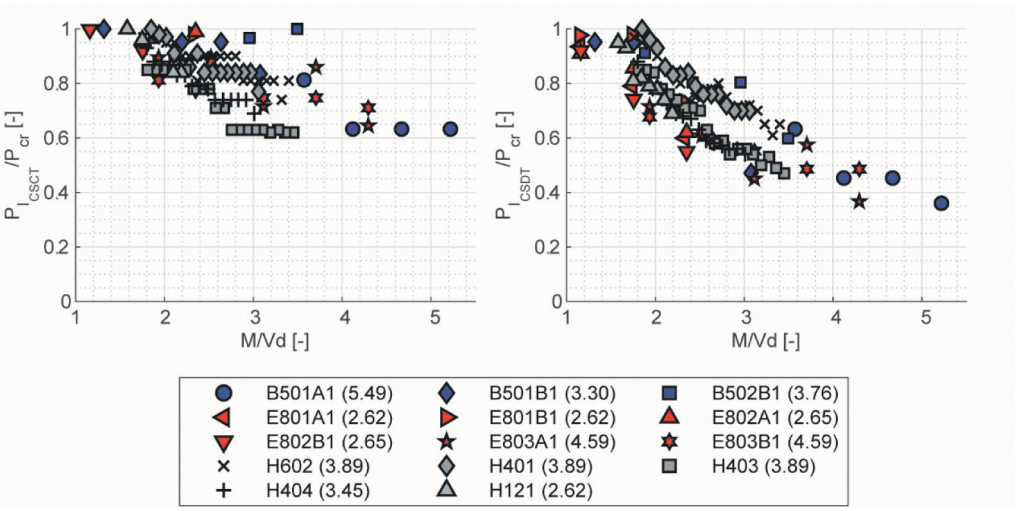


Figure 4. Results of the indicator based on the Critical Shear Crack theory and the Critical Shear Displacement Theory as a function of M/Vd.

The summary of the results of the comparison between the stop criteria and the measurements, subdivided into these regions can be found in Table 2. The results of large M/Vd include the measurements between $0.8<M/Vd\times(1/\lambda)<1$ and the low M/Vd consists of the measurements with $M/Vd\times(1/\lambda)<0.7$. Overall, the results of this comparison show that the cracking indicator is reached first, as expected. For the shear indicators, the indicator based on the CSDT is reached generally before the indicator of the CSCT, and both indicators present similar values for the associated coefficient of variation. Generally, the stop criteria in the low M/Vd region are reached around 84% of the failure load, which would be too close to the critical load for application in proof load tests. However, the stop criteria in this region could serve as

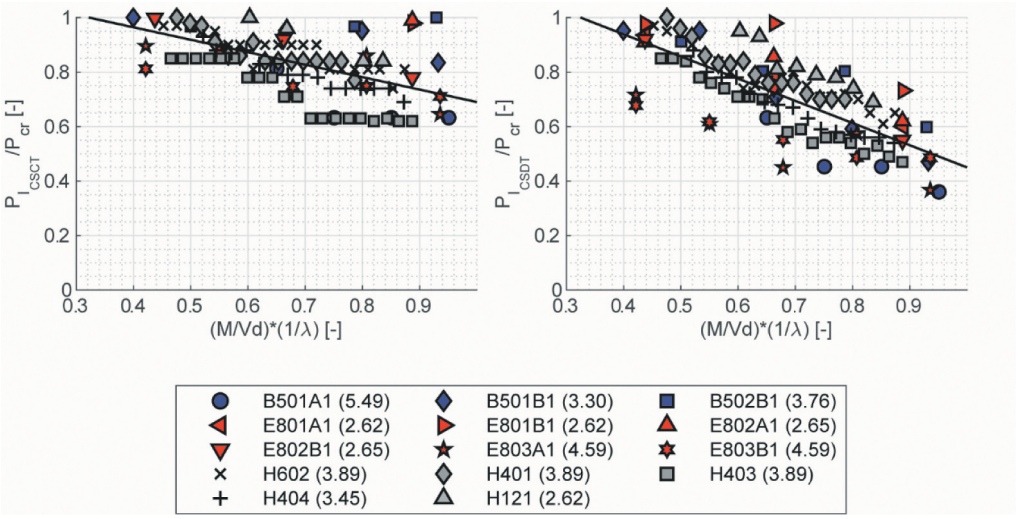


Figure 5. Results of the indicator based on the Critical Shear Crack theory and the Critical Shear Displacement Theory as a function of M/Vd normalized by factor λ.

warning signals for imminent failure. Overall, the proposed stop criteria are suitable for the reinforced concrete slab strips tested and they provide a different margin of safety as a function of the location along the shear span.

The Serviceability Limit State (SLS) crack width limit was, on average, reached at 51% of the failure load in the large M/Vd region, with a standard deviation of 0.11 and a coefficient of variation of 0.22. In the low M/Vd region, it was reached at an average of 74% of the failure load, with a standard deviation of 0.15 and a coefficient of variation of 0.21.

Table 2. Comparison between experiments and proposed stop criteria.

	Large M/Vd			Low M/Vd
	$0.8<M/Vd\times(1/\lambda)<1$			$M/Vd\times(1/\lambda)<0.7$
	I_{CSDT}	I_{CSCT}	I_{CSDT}	I_{CSCT}
AVG	55%	77%	80%	88%
STD	0.10	0.13	0.12	0.08
COV	0.18	0.16	0.13	0.12

5 RECOMMENDATIONS FOR SHEAR STOP CRITERIA FOR SLAB STRIPS

To better understand the risk associated with reaching a stop criterion, the stop criteria are organized in a traffic light system, as also used by (Zhang, 2022). The system uses the following colors and interpretations: 1) green light corresponds to serviceability limit state and is related to cracking in the region close to the load l_{crm}, 2) yellow light corresponds to the ultimate limit state for shear and potential irreversible damage, and is related to the increase in the crack opening or the average longitudinal strain, as well as the opening of the critical shear crack in the low M/Vd region, and 3) red light corresponds to imminent failure for the ultimate limit state for shear, and is based on the indicator of increase in crack opening and the shear failure criteria from the theoretical shear models. It is recommended to monitor these regions using traditional measuring techniques such as LVDTs or 2D DIC to obtain measurements of crack widths or longitudinal strains. The recommended gauge length is $0.8d$. Detailed information about the study of the optimal gauge length can be found on (Zarate Garnica

et al., 2022). These regions and the different levels of the stop criteria are also indicated in Figure 6.

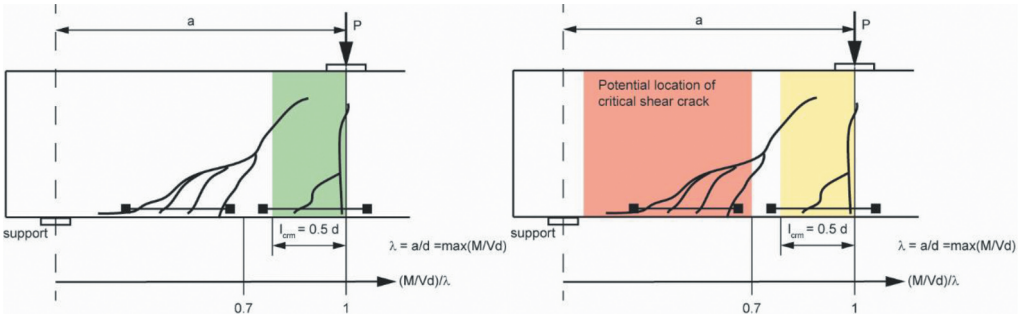


Figure 6. Overview of stop light system for shear stop criteria for RC slab strips.

6 SUMMARY AND CONCLUSION

This paper shows the development of stop criteria for the ultimate limit state for shear and for the serviceability limit state for cracking from theoretical principles. These stop criteria are then compared to the experimental results from fourteen beams, and different critical regions in the shear span are identified. Finally, a traffic light system for the stop criteria is proposed.

From this research, the following conclusions can be drawn:

- A serviceability limit state cracking indicator can be used as a stop criterion in the region of the shear span close to the load to identify the beginning of flexural cracking.
- The two theoretically derived shear stop criteria, based on the Critical Shear Displacement Theory and the Critical Shear Crack Theory, perform equally well, with the stop criterion based on the CSDT generally being reached first.
- The shear stop criteria can be used to warn for imminent danger for collapse in the region corresponding to the lowest M/Vd.
- It is recommended to monitor the shear span using LVDTs or 2D DIC to obtain measurements of crack width or longitudinal strain.

ACKNOWLEDGMENT

The authors wish to express their gratitude and sincere appreciation to the Dutch Ministry of Infrastructure and the Environment (Rijkswaterstaat) for financing this research work. We are deeply indebted to our colleague Albert Bosman for his work in the laboratory, and design of the test setup. Thanks also to Jakub Pawlowicz for his work in the laboratory during the phase of the testing.

REFERENCES

Alampalli, S., Frangopol, D. M., Grimson, J., Halling, M. W., Kosnik, D. E., Lantsoght, E. O. L., Yang, D., & Zhou, Y. E. (2021). Bridge Load Testing: State-of-the-Practice. *Journal of Bridge Engineering*, *26*(3), 03120002. https://doi.org/doi:10.1061/(ASCE)BE.1943-5592.0001678

CEN. (2005). Eurocode 2: Design of Concrete Structures - Part 1-1 General Rules and Rules for Buildings. NEN-EN 1992-1-1:2005. In (pp. 229). Brussels, Belgium: Comité Européen de Normalisation.

Gehri, N., Mata-Falcón, J., & Kaufmann, W. (2020). Automated crack detection and measurement based on digital image correlation. *Construction and Building Materials*, *256*, 119383.

Koekkoek, R. T., & Yang, Y. (2016). *Measurement Report on the transition between flexural and shear failure of RC beams without shear reinforcement*.

Lantsoght, E. O. (2023). Assessment of existing concrete bridges by load testing: barriers to code implementation and proposed solutions. *Structure and Infrastructure Engineering*, 1–13.
Lantsoght, E. O. L., Van der Veen, C., De Boer, A., & Hordijk, D. A. (2017). Proof load testing of reinforced concrete slab bridges in the Netherlands. *Structural Concrete*, *18*(4), 597–606.
Lantsoght, E. O. L., Van der Veen, C., & Hordijk, D. A. (2018). *Proposed stop criteria for proof load testing of concrete bridges and verification* IALCCE 2018, Ghent, Belgium.
Lantsoght, E. O. L., Van der Veen, C., Walraven, J., & De Boer, A. (2014). *Recommendations for the Shear Assessment of Reinforced Concrete Solid Slab Bridges* IABMAS 2014, Shanghai, China.
Lantsoght, E. O. L., Yang, Y., van der Veen, C., Hordijk, D. A., & de Boer, A. (2019). Stop Criteria for Flexure for Proof Load Testing of Reinforced Concrete Structures [Original Research]. *Frontiers in Built Environment*, *5*(47). https://doi.org/10.3389/fbuil.2019.00047
MatchID. (2022). *User manual*. https://www.matchid.eu/Software.html
Muttoni, A., & Fernández Ruiz, M. (2008). *Shear strength in one- and two-way slabs according to the Critical Shear Crack Theory* International FIB Symposium 2008, Amsterdam, The Netherlands.
The Mathworks, I. (2019). *Matlab R2019a, User's Guide*. In
Yang, Y. (2021). *Shear Capacity of RC Slab Structures with Low Reinforcement Ratio - an Experimental Approach* fib symposium 2021, Lisbon (online).
Yang, Y., Den Uijl, J. A., & Walraven, J. (2016). The Critical Shear Displacement theory: on the way to extending the scope of shear design and assessment for members without shear reinforcement. *Structural Concrete*, *17*(5), 790–798.
Yang, Y., Zárate Garnica, G., Lantsoght, E. O. L., & Hordijk, D. A. (2018). *Calibration of the shear stop criteria based on crack kinematics of reinforced concrete beams without shear reinforcement* fib conference 2018, Melbourne, Australia.
Zarate Garnica, G. I., de Vries, R., & Lantsoght, E. O. L. (2022). *Analysis report of reinforced concrete slabs for stop criteria*.
Zhang, F. (2022). *Acoustic emission-based indicators of shear failure of reinforced concrete structures without shear reinforcement* Delft University of Technology].

Bridge Maintenance, Safety, Management, Digitalization and Sustainability – Jensen, Frangopol & Schmidt (eds)
© 2024 The Author(s), ISBN 978-1-032-77040-6
Open Access: www.taylorfrancis.com, CC BY-NC-ND 4.0 license

Development of a guideline for proof loading of bridges

S. Engelund
COWI A/S, Aalborg, Denmark

J.D. Sørensen & J.W. Schmidt
Aalborg University, Aalborg, Denmark

C. von Scholten & R. Bang
The Danish Road Directorate, Copenhagen, Denmark

ABSTRACT: The Danish Road Directorate has developed a guideline for proof loading of road bridges. The guideline ensures that proof load tests are planned and executed in a consistent manner and that test results may be used to update the load-carrying capacity of the considered bridge. The guideline describes how proof load tests may be planned, executed, and interpreted to demonstrate that the considered bridge can withstand a given load with sufficient reliability. One of the primary hypotheses is that many bridges have a load-carrying capacity that may be larger than the one determined by traditional computational analysis. This is mainly because the computational models, that are used to determine the load carrying capacity, of a given bridge does not predict the actual response of the considered bridge with sufficient accuracy. Most models are inherently conservative and underestimates the actual load carrying capacity of the considered bridge. Load testing is a cost-effective method to demonstrate that a given bridge has a sufficient load carrying capacity.

1 INTRODUCTION

The Danish Road Directorate has since 2016 led a research project concerned with proof loading of bridges. The purpose of the project is to make proof loading of bridges a useful tool that may be used to update the load-bearing capacity of bridges. The Danish Road directorate has published a guideline for proof loading of bridges, (Vejdirektoratet, 2023b). The guideline has been prepared with a view to ensuring that proof load tests are carried out on a consistent basis, that test loads can be carried out safely and that test loads provide a sufficient basis for an update of the load-bearing capacity of the considered bridge.

The proof-loading methods were developed to comply with the unique Danish guidelines, (Vejdirektoratet, 2017), (Vejdirektoratet, 2010) and (Vejdirektoratet, 2023a) for classification of the load carrying capacity of existing bridges. The provisions enable consistent administration and handling of heavy vehicles in Denmark.

The guideline has been developed using the results of several research projects that focused on the following topics:

- The use of non-destructive methods to register the state of the bridge during the load testing (Christensen et al., 2021) and (Christensen et al., 2022)
- Evaluation of the magnitude of the proof load on the basis of probabilistic methods, (Christensen et al., 2023) and (Schmidt et al., 2020)
- The use of advanced analytical methods to predict the load carrying capacity of concrete slap bridges, (Jensen, 2019)

DOI: 10.1201/9781003483755-37

These topics have also been subject to much attention by various research teams. The use of non-destructive methods has also been investigated by (Alam et al., 2015) and (Lantsoght et al., 2019). Evaluation of the magnitude of the proof load has been investigated by (Faber et al., 2000) and (Lantsoght et al., 2017).

2 THE DANISH CLASSIFICATION SYSTEM AS BACKGROUND FOR GUIDELINE

In Denmark, a unique classification system is used by the administration of the permits that must be issued to the owners of heavy vehicles that wish to travel by a given route. The heavy vehicle is permitted to use a given route given that all the bridges on the given route have a bridge class that is larger than the vehicle class. If this requirement is not met, an alternative route must be found, or the goods are rearranged to meet the required vehicle class.

The bridge class is determined using several standard vehicles with a given axle configuration and axle loads. The bridge class is defined as the heaviest standard vehicle the bridge can carry with sufficient reliability (together with a class 50 vehicle in the other lane if the bridge carries more than one lane), see (Vejdirektoratet, 2017).

The vehicle class is found by comparing the sectional forces introduced by the considered vehicle in a simply supported beam to the sectional forces introduced in a simply supported beam by the standard vehicle. The vehicle class is defined as the vehicle that provides the same sectional forces in the beam as the considered vehicle. The classification of a bridge deck naturally depends on the span of the considered bridge. Further, different elements of the same bridge may have different bridge classes.

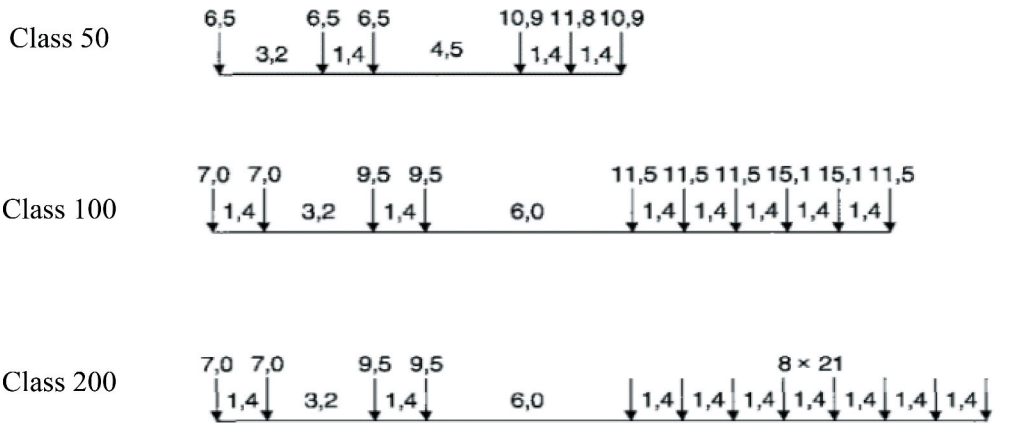


Figure 1. Examples of axle configurations of classification vehicles (weights are given in tons), see (Vejdirektoratet, 2017).

Examples of the lowest (class 50), strategic roadmap vehicle (class 100), and the class 200 vehicle are shown in Figure 1. There are 22 different bridge classes ranging from class 10 to class 500. The bridge class is roughly equal to the total weight in tons of the largest standard vehicle that is allowed to pass the given bridge.

The Danish Road Directorate has developed the so called "strategic road map" which shows all roads where vehicles up to class 100 can drive safely without applying for a permit.

3 PLANNING OF PROOF LOAD TESTS

The Danish proof loading guideline concerns the planning and execution of proof loading of concrete bridges. General guidance on proof lading of concrete bridges with a span of 2 m – 12 m is given in the guideline to ensure that proof loading is done consistently. The results

generated using the guideline should thus provide a sufficient background to update the load carrying capacity of the considered bridge.

3.1 *Bridge inspection*

Prior to the load test an initial inspection of the condition of the considered bridge must be carried out. The focus should be on the following:

- Review of the geometry of the structure to determine whether it corresponds to the provided drawings and static documentation.
- Assessment of the structural behaviour and boundary conditions
- Assessment of the size of natural loads that cannot be controlled in connection the execution of a proof loading. This includes e.g. wind load and water pressure
- Registration of cracks, deflection and other conditions that may be of significance in connection with the assessment of the test's stop criteria.
- Registration of any deterioration mechanisms that may affect the load-bearing capacity of the structure.

3.2 *Initial assessment of the load carrying capacity*

The planning of a proof load test of a given bridge must be based on an initial assessment of the load carrying capacity of the bridge using analytical methods. Based on the initial assessment the load carrying capacity of the bridge with respect to several different failure modes (bending, shear, punching etc.) may be demonstrated. Further, the critical failure mode(s) and the critical load configuration(s) that is (are) decisive for the load carrying capacity of the bridge may be identified. By this initial assessment it should also be determined whether the critical failure mode is a ductile or a brittle failure mode. I the critical failure mode is a brittle failure it should be considered whether a proof load test should be carried out. By the initial assessment all relevant information gained from the bridge inspection should be considered.

3.3 *Acceptance criteria*

According to prEN1990-2 (CEN, 2021b) B.5.2 load testing may be used to update the failure probability of a structure based on a known load. The target test load, defined as the load the structure must carry in addition to the self-weight and permanent load and other acting loads if relevant, should be determined such that:

- the probability that the action effect is not lower than the action effect caused by the applied test load corresponds to the target reliability if no prior knowledge on the resistance is available; or
- the updated probability of failure given survival of the action effect caused by the applied test load corresponds to the target reliability if prior knowledge on the resistance is available.

The guideline developed by the Danish Road Directorate is based on the first mentioned of the two approaches given above. This approach has been chosen because the proof load tests that have been performed so far show that the actual load carrying capacity of the bridges is significantly larger than the load carrying capacity predicted using analytical models (even when using mean values of the material parameters). This shows that the analytical models do not predict the load carrying capacity of the considered bridges with sufficient accuracy but are highly conservative. The models are subject to a considerable model uncertainty and the mean value of the model uncertainty is not equal to one. When no accurate model for the prediction of the load carrying capacity is available it is difficult to take information concerning the resistance of the bridge into account.

3.4 *Load configuration and magnitude*

In planning a proof load test, using the simplest load configuration, which produces a given load effect in the structure may seem attractive. Suppose the critical failure mechanism of

a given bridge is bending failure at the midspan of the bridge deck. In that case, it may seem attractive to perform a proof load test where a point load is applied at midspan and determine the target load such that the probability that the load effect introduced by actual loads is higher than the load effect introduced by the point load (proof load) corresponds to the target reliability. This approach fails to consider that one of the significant reasons why proof load tests often reveal a higher load-carrying capacity of the considered structure is that the actual load effects introduced in the structure are different from the load effects predicted based on the computational models.

Let m_a denote the model uncertainty related to a given computational model that is used to predict the load effect of the actual traffic load acting on the considered bridge and let m_p denote the model uncertainty related to the same computational model when it is used to predict the load effect of the proof load. If the model uncertainty related to the computational model is independent of the load configuration the model uncertainty m_a will be equal to the model uncertainty m_p. In this case it will be possible to determine a configuration of the proof load that introduces the same load effects in the structure as the actual loads acting on the structure. However, in general the model uncertainty will depend on the load configuration implying that it is not possible to determine a simple load configuration that may be used by a proof load test. A proof load test should generally be performed such that the load configuration used by a proof load test, to the greatest possible extent, reflects the configuration of the actual loads acting on the considered structure.

In the guideline for proof loading of bridges developed by the Danish Road Directorate it is recommended that the proof load test of bridges is carried out using loads that represent the actual traffic loads. The proof load is designed such that it represents the axle loads from two vehicles. An example of the load configuration is shown in Figure 2 below.

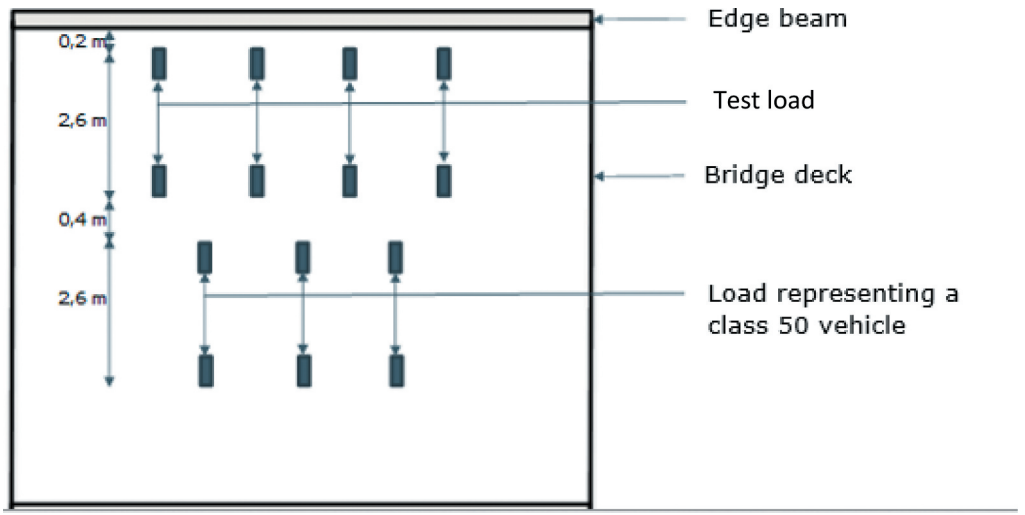


Figure 2. Load configuration for proof load testing.

The magnitude of the load is determined on the basis of the acceptance criteria given in section 33 using the probabilistic models for probabilistic classification of bridges developed by the Danish Road Directorate, (Vejdirektoratet, 2004) and (Vejdirektoratet, 2023).

3.5 *Positioning of the load*

When planning a proof loading test, the location of the reinforcement in the bridge deck needs to be considered. Additional longitudinal and shear reinforcement could be present, meaning that the most critical test location may differ from the locations where the maximum section forces occur. Consequently, the essential failure mechanisms may initiate at other

locations where the bridge has less resistance. The most undesirable location of the applied classification vehicle load will typically be as close to the edge beam as possible. On bridges with a width less than 5.4 m, where the vehicle load is placed in one lane only, a distance of 0.2 m to the edge beam should be used. The distances correspond to a loaded lane width of 3.0 m and a vehicle width of 2.6 m, (Vejdirektoratet, 2017), see Figure 2. The vehicle should be placed in the same position on bridges widths larger than 5.4 m. a standard class 50 vehicle should be placed in the adjacent lane. The actual conditions should be evaluated before prof-loading to ensure the loading procedure is possible.

3.6 *Stop criteria*

Stop criteria define the threshold between acceptable and unacceptable conditions when proof loading. The stop criteria can be defined for ductile failure mechanisms. For brittle failures no such threshold can be defined. The stop criteria must be defined for any relevant failure mechanism and reflected in the applied monitoring. Accordingly, these values should be measurable and available in real-time during proof loading to ensure they can be overseen during testing. Identification and use of the stop criteria shall prevent bridge damage when performing proof loading and thus ensure that the safety level is acceptable.

3.7 *Monitoring*

Stop criterion values can relate to the structural response, crack widths, deformations, target load, etc., which are primary parameters that should be measured in connection with proof loading. Such parameters can be measured using land surveyors, LVDTs, Laser sensors, digital image correlation, etc., and supported by measurements such as rotation, strain gauge, optical fibers, etc. It should, however, be noted that environmental conditions can influence equipment placement and influence the results significantly, which should be accounted for. The crack stop criteria have identical values as described in the serviceability limit state described in DS/EN-1992-2 DK NA, where the maximum crack widths are 0.3 and 0.2 mm for non-prestressed and prestressed bridges, respectively. In addition, the Danish guideline allows settlements at the supports up to 2 mm. Unloading the structure to an extent that enables evaluation of permanent plastic deformations should be possible. It is thus essential to ensure linearity of deformations during proof loading. It should be noted that such deformations can be affected by the loading procedure, crack formations, geometric conditions, boundary conditions, foundation conditions, etc., which should be reported if present.

4 EXECUTION OF A PROOF LOAD TESTS

A proof loading project was arranged in southern Denmark to evaluate the procedure given in the guideline on actual structures. During this project load tests were carried out on five bridges. Each load test was carried out within a period of few hours. Based on the experience from these load tests it is the authors belief that a load test may be performed within a period of about one hour.

One of the tests was performed on a concrete bridge with a span of 6.5 m carrying two traffic lanes. Prior to the test the load carrying capacity of the bridge was estimated to comply with bridge class 80. The bridge is shown in 3 below.

The planned test setup for the bridge is shown in Figure 4 below. The loading consists of a variable load that represents the classification vehicle and a fixed load representing a class 50 vehicle. The class 50 vehicle has axle loads of approximately 17 tonnes. The load configuration is not identical to the load configuration shown in Figure 2. However, the actual load configuration must be adjusted according to the materiel used by the test.

In Figure 5 below the actual test setup is shown. Loading was applied using advanced heavy vehicles, where the axle loads are adjustable Notice that three axles provide the loading on the bridge and that the two axles adjacent to the three axles providing the loading on the bridge are retracted and provide no loading.



Figure 3. Concrete bridge with 6.5 m span.

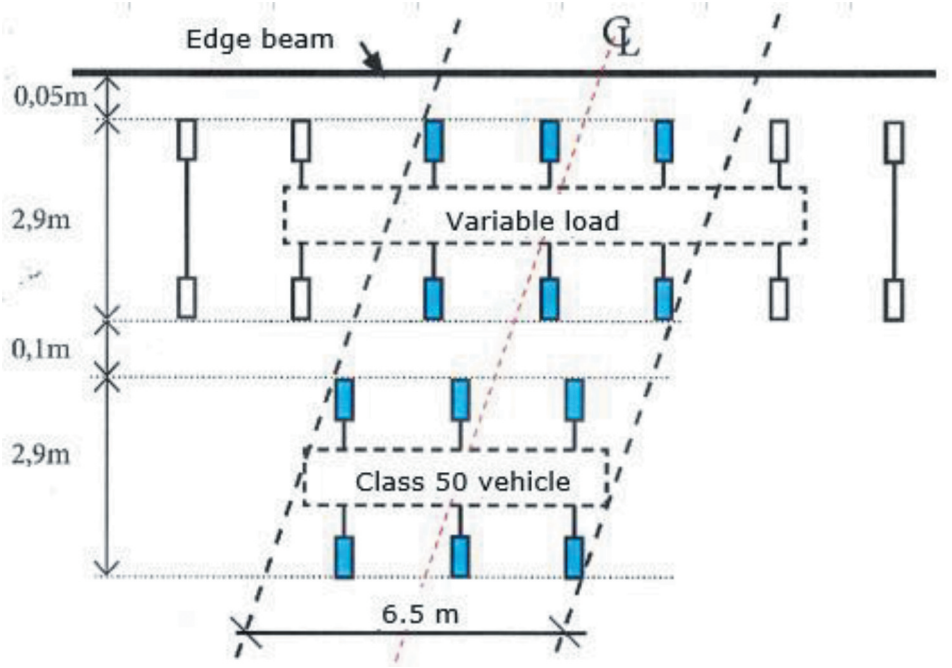


Figure 4. Test setup, see (Christensen et al., 2023).



Figure 5. Actual test setup.

During the testing the load was increased in steps and the response of the bridge was measured after each load step. The monitoring was conducted using Digital Image Correlation to detect cracks in the concrete. Further, the deformations of the structure were determined by a surveyor.

The measured response of the structure did not exceed the stop criteria and the structure showed a linear relation between the load and the response during the load test. The bridge was subject to axle loads of 29 tonnes which shows that the bridge has (at least) a load carrying capacity corresponding to class 100.

5 DISCUSSION AND CONCLUSION

The combination of the ongoing research project worked well as an input generator for the Danish proof loading guideline of concrete bridges. However, one of the main factors that enabled this synergy was the Danish classification system, which describes well-defined load models of heavy vehicles. The classification system and related provisions made it possible to approach a consistent multidisciplinary direction throughout the guideline document addressing the load effects, placing of vehicles, schematics of proof loading procedures, monitoring, etc., leading to a method that can be used for proof loading. A successful pilot project was initiated to prove the guideline's concept. An example of the outcome was shown when proof loading of an actual bridge was compared with values depicted in the guideline. This guideline method upgraded the road stretch from class 80 to class 100. In addition, experiences and outcomes have already been used as input for the upcoming Eurocode background document, prEN1990-2, Basis of assessment and retrofitting of existing structures: general rules and actions. However, some of the document's shortcomings relate to testing structures with potentially brittle failure mechanisms, such as non-shear reinforced slabs, punching shear, etc.

Consequently, the document concerns proof loading of structures deemed susceptible to bending failure and ductile behavior. Further research related to stop criterion thresholds of potentially brittle structures is researched in an ongoing project initiated by the Danish Road

Directorate, COWI, Technical University of Denmark, and Aalborg University. One of the aims of this project is to provide output that can be used to extend the Danish guidelines.

ACKNOWLEDGEMENT

Special thanks to the Danish Road Directorate for their pivotal role in the Danish concrete bridge testing project. We are grateful for your support and look forward to our continued collaboration on load testing practices in Denmark. Additional thanks are addressed to all colleagues and partners who participated in the Danish bridge testing project - technicians, workers, and scientists. Your knowledge and competence have been instrumental in our shared success.

REFERENCES

Alam, S.Y., Loukili, A., Grondin, F., Rozière, E. (2015), *Use of the digital image correlation and acoustic emission technique to study the effect of structural size on cracking of reinforced concrete*. Eng. Fract. Mech. 2015, 143, 17–31.

Christensen, C.O., Zhang, F., Garnica, G.Z., Lantsoght, E.O.L., Goltermann, P., Schmidt, J.W. (2022), *Identification of Stop Criteria for Large-Scale Laboratory Slab Tests Using Digital Image Correlation and Acoustic Emission*. Infrastructures 2022, 7, 36

Christensen, C.O., Schmidt, J.W., Halding, P.S., Kapoor, M., Goltermann, P. (2021), *Digital Image Correlation for Evaluation of Cracks in Reinforced Concrete Bridge Slabs*. Infrastructures 2021, 6, 99.

Christensen, C. O., Damsgaard, K. D. S., Sørensen, J. D., Engelund, S., Goltermann, P., & Schmidt, J. W. (2023). *Reliability-Based Proof Load Factors for Assessment of Bridges*. *Buildings*, *13* (4), 1060. https://doi.org/10.3390/buildings13041060

Faber, M. H., Val, D. V., & Stewart, M. G. (2000). *Proof load testing for bridge assessment and upgrading*. Engineering Structures, 22, 1677–1689.

Jensen, T. W. (2019) *Modelling the load carrying capacity of reinforced concrete slap bridges*, PH.D. Thesis R-417, Department of Civil Engineering, Technical University of Denmark.

Lantsoght, E. O. L., van der Veen, C., de Boer, A., & Hordijk, D. A. (2017). *Required proof load magnitude for probabilistic field assessment of viaduct* De Beek. Engineering Structures, 148, 767–779. https://doi.org/10.1016/j.engstruct.2017.07.010

Lantsoght, E.O.L., Yang, Y., Van Der Veen, C., Hordijk, D.A., De Boer (2019), A. *Stop Criteria for Flexure for Proof Load Testing of Reinforced Concrete Structures*. Front. Built Environ. 2019, 5, 47.

Schmidt, J. W., Thöns, S., Kapoor, M., Christensen, C. O., Engelund, S., & Sørensen, J. D. (2020). *Challenges Related to Probabilistic Decision Analysis for Bridge Testing and Reclassification*. Frontiers in Built Environment, 6. https://doi.org/10.3389/fbuil.2020.00014

Vejdirektoratet. (2004). *Reliability-Based Classification of the Load Carrying Capcity of Existing Bridges*.

Vejdirektoratet. (2010). *Vejledning Til Belastnings- Og Beregningsgrundlag*.

Vejdirektoratet. (2017). *DS/EN 1991-2 DK NA:2017, Annex A: Lastmodeller for klassificering og bæreevnevurdering (Models of Special Vehicles for Road Bridges)*.

Vejdirektoratet. (2023a). *Reliability-Based Classification of Existing Bridges*. Unpublished.

Vejdirektoratet. (2023b). *Prøvebelastning af broer* (in danish), not yet published.

Bridge Maintenance, Safety, Management, Digitalization and Sustainability – Jensen, Frangopol & Schmidt (eds)
© 2024 The Author(s), ISBN 978-1-032-77040-6
Open Access: www.taylorfrancis.com, CC BY-NC-ND 4.0 license

Load testing on existing prestressed concrete bridges to determine long-term effects on strain measurement

Harald Burger, Thibault Tepho & Oliver Fischer
Technical University of Munich, Munich, Germany

Nicholas Schramm
Büchting + Streit AG, Munich, Germany

ABSTRACT: Structural Health Monitoring is an effective tool for extending the life of aging bridges with load-bearing capacity deficits. To interpret and verify the data from sensor systems on structures, in-field load tests for calibration can be used. Such tests were performed for a long-term monitoring project on two prestressed highway slab bridges in Munich. The sensor system was designed to detect fractures in prestressing steel and concrete cracks and to derive a site-specific traffic load model. To achieve this, fiber optical sensors based on the Rayleigh backscattering technology were used for crack detection, while permanent strain gauges provided continuous traffic load measurements. For calibration purposes, it was possible to compare the results from different sensor types. The strain levels recorded are low and the test results indicate that strain gauges are highly accurate under different environmental conditions, while fiber optic sensors are less accurate. During the calibration process, long-term effects were identified that did not significantly affect the data.

1 INTRODUCTION

Around 50 % of bridges on German federal highways are over 50 years old (BASt 2023). Since then, traffic and permitted axle load increased. Technical knowledge has developed, and the relevant standards have been updated to address specific issues. For these reasons, some bridges have a deficiency in their load-bearing capacity, even though they were built correctly at the time, and are now in good structural condition with no significant damage.

Prestressing steel with a risk of stress corrosion cracking is one such problem. Stress corrosion cracking can cause brittle fracture of the prestressing steel. In this case, there would be no warning in the event of a component failure. Until 1978, prestressing steel with these properties was produced in West Germany (mainly trade names Neptun and Sigma Oval). In East Germany, Henningsdorf steel was used until the early 1990s, which had a risk of stress corrosion cracking. Recommendations for dealing with this problem were published in the 1990s and continuously updated. These recommendations were included in a guideline (HA SpRK 2011), which provides a calculative proof of sufficient warning behavior as a crack before structural failure (crack-before-failure).

The guideline includes defining inspection instructions to guarantee a sufficient level of safety. The inspection interval should exceed the standard three-year interval (DIN 1076). Alternatively, a long-term monitoring system can be installed and operated. In this case, it is important to calibrate the sensor system to obtain reliable data, especially for long-term measurements. Schacht (2019) and Bolle (2017) describe monitoring applications and the performance of load tests for calibration for this use case.

A monitoring system is in operation on two bridges in Munich with prestressing steel sensitive to stress corrosion cracking since 2021. The monitoring system differs from those

DOI: 10.1201/9781003483755-38

mentioned in Schacht (2019). In addition to strain gauges, distributed fiber optical sensors (DFOS) for measurement technology based on the Rayleigh backscattering are used for crack detection. There are currently no guidelines for an in-field calibration of these sensor types, despite their numerous applications (e.g., Bado 2021, Bednarski 2022). This study aims to demonstrate the feasibility of in-field calibration for various strain measurement sensors used in long-term monitoring and to investigate long-term effects on the data.

2 KREUZHOF BRIDGES

2.1 *Description*

The "Kreuzhof" bridges (BW 40/45 and BW 40/46) are located southwest of Munich at the link to the A95 federal highway as interchange to a four-lane road. Figure 1 illustrates the bridges. BW40/45 carries the four main lanes in opposite directions and a separate ramp with two lanes. The second ramp, with a total of two lanes, is carried by BW40/46. The bridges were completed in 1967 as part of an infrastructure project for the 1972 Olympics. Currently, the bridges span a four-lane road. Both bridges are three-span slab bridges with longitudinal tubular voids and a maximum total length of 76.0 m. The concrete slabs are prestressed by the bonded post-tensioning system according to the approval of the company Polensky und Zöllner.

The bridge BW 40/45 is 37.5 m wide with a varying skew angle from 13° to 26°. The outer spans are between 19.9 m and 21.8 m, the midspan's length is between 29.9 m and 31.6 m. The cross-section is structurally decoupled with a longitudinal joint into two slabs with a variable height of 1.10 m to 1.40 m. The bridge BW 40/46 is partly curved in plan and 8.0 m wide. The span lengths are around 20.5 m – 29.0 m – 20.5 m. The cross-section is 1.15 m high.

2.2 *Stress corrosion cracking*

The bridges are in good structural condition but have calculative deficits due to the prestressing steel. The type of steel used is inadequate regarding stress corrosion stability. This material problem has led to failures in older constructions in the past. Therefore, improvements to the robustness and durability of prestressed structures were introduced in 1995. These improvements are based on the concept that cracks are a warning of collapse. The steel grades concerned are no longer certified, but existing structures still incorporate such prestressing steel (fib 2003).

The national authorities in Germany have developed a regulation for existing bridges on how to handle these structures (HA SpRK 2011). The regulation includes a proof of robustness, which involves a crack-before-failure analysis not only on individual cross-sections, but also on the overall structural system on a stochastic basis. This is done in two steps. The remaining prestressing steel in a cross-section is calculated when the first crack appears under frequent combination in service limit state. Then, the safety of the structure must be proven with the reduced steel amount under characteristic load combination.

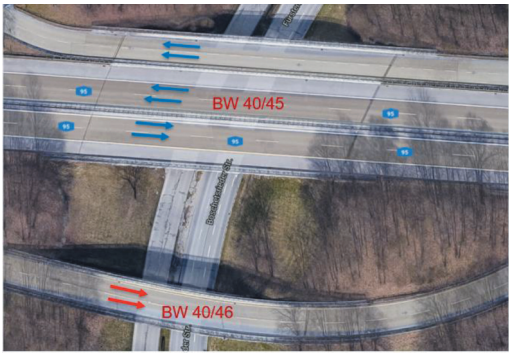


Figure 1. "Kreuzhof" bridges with traffic direction display (taken from [www.google.com/maps]).

The proof for the two "Kreuzhof" bridges was unsuccessful. A large number of wires would have to break before a crack would be detectable and the result would be a complete failure. The remaining amount of prestressing steel is not sufficient to support the characteristic load combination. Verifications were provided positive for inner supports and the inner span. However, it is not possible to detect cracking in the area of the inner supports due to the existing bridge deck. Detailed inspection instructions must be defined for all areas, including those with calculative warning behavior. Based on these results, a monitoring concept was developed for both bridges.

2.3 *Monitoring concept*

In particular, the monitoring pursues the following objectives:

1. detection of potential prestressing steel fractures
2. detection of cracks or damage to the structure
3. derivation of site-specific traffic load model

Acoustic emission sensors were installed to detect steel fractures directly (1). These sensors have been continuously recording data since their installation in 2021. If an acoustic emission (AE) event is detected, local and global structural response (2) will be checked along with webcam data. Inclinometers and distributed fiber optical sensors (DFOS) are installed for this purpose. Inclinometer data was continuously recorded. DFOS measurement data is collected every three to four months or in the event of an AE occurrence using Rayleigh backscattering technology. This redundant sensor system enables the exclusion of errors in the data analysis.

With the use of a site-specific traffic load model (3), the design check according to chapter 2.2 can be updated. Moreover, a more accurate estimation of the number of acceptable steel fractures before failure of the structure is possible. The data on traffic actions were provided from different sensor types: Strain gauges record the structural stress in the longitudinal direction, laser scanners are used to detect, count, and classify vehicles passing over the bridge. Additionally, accelerometers and temperature sensors were installed to identify unknown effects during data interpretation. The system continuously recorded data for one and a half years.

Strain measurement plays a major role in this monitoring system. The use of two different sensor types (DFOS and strain gauge) allows data comparison during calibration. However, calibration still requires a known reference value. To achieve this, load tests were conducted using trucks.

3 LOAD TESTS AND INSTRUMENTATION

The test load concept of the bridges is based on the specifications of the (COST 323) final report, which provides sample timetables and tests during different environmental conditions for calibrating and testing Weigh-in-Motion (WIM) systems. The reliability of the results increases with the number of load conditions available for testing. The scope of a test load is always dependent on the project's boundary conditions.

The test loads on the "Kreuzhof" bridges were primarily necessary to calibrate the sensor system for derivation of a site-specific traffic load model. During the load test on the bridges, also the structural condition was monitored. For this reason, the maximum permissible vehicle load per lane was used to detect any existing cracks or damage.

3.1 *Load test*

A total of four tests were performed over four different days including driving with trucks in moving traffic (dynamic test) and stopping a truck at nine designated locations along closed lanes (static test). Dynamic and static testing was conducted in December 2021 and May 2022, respectively, using three different vehicles listed in Table 1. LKW 3 only participated in the May 2022 test. The axle load of the trucks (listed in Table 1) was weighed and varied minimally in each test.

Dynamic tests were carried out using LKW 1 and LKW 2. The trucks drove across the bridge at speeds ranging from 20 km/h to 65 km/h over a hundred times on both days. The tests investigated various vehicle configurations, including driving one behind the other and driving side by side. The static test consisted of three phases, with the lane used for the test being closed in each investigated road segment. During the first phase, LKW 1 stopped at the designated stop locations. Figure 2 (top) shows four of the nine locations. In December 2021, only one truck was used. During the first phase in the second static test in May 2022, LKW 3 drove with moving traffic at a maximum speed of 20 km/h in lane two. LKW 1 was stationed at one of the stops per direction. The aim was to apply the highest permissible vehicle load to detect any cracks resulting from damage.

In the second phase, the LKW 1 drove backward at walking speed across the entire bridge. In the last phase, the truck drove forward, also at walking speed, across the bridge.

Table 1. Approximate weight in ton per axle for the used vehicles.

name	axles	A1	A2	A3 (– A5)	Total (maximum)
LKW 1	5	6.9	10.3	24.1	41.3
LKW 2	3	8.6	10.7	6.7	26.0
LKW 3	5	7.6	9.0	24.3	40.9

3.2 *Strain sensor setup*

This study focuses on analyzing and presenting the results of the southern slab of the bridge BW40/45. Due to the limited measurement frequency, DFOS data collection was restricted to static tests. he DFOS measuring device (Odisi 610x) had a limited number of channels, allowing only one simultaneous measurement with four fiber optic sensors. Figure 2 (bottom) shows the location of the relevant DFOS and strain gauges on the bottom of the slab.

The DFOS are BRUSens V9 sensors embedded in a groove. Detailed information about the application method can be found in (Burger et al. 2023). The concrete strain gauge used is the

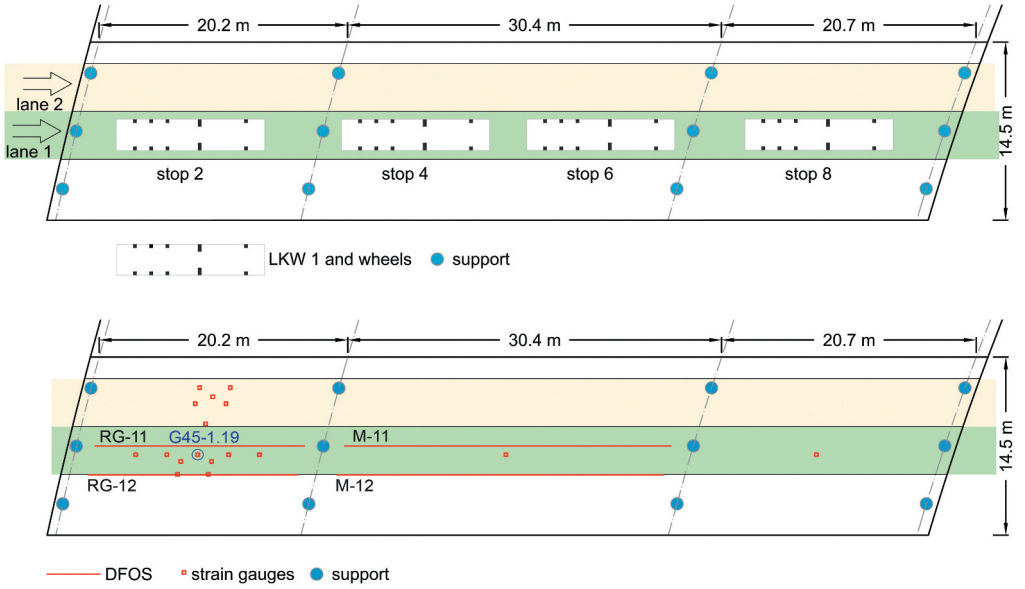


Figure 2. Layout of the southern slab of bridge BW40/45 with different stops during static load test (top) and relevant strain sensors during the static load test (bottom).

PL-120-11 from TML company, which is 120 mm long. These gauges are positioned in various locations below the lanes to determine the number, distance, weight, and lateral distribution of axle loads.

A 120 mm long strain gauge can be compared with approximately 46 datapoints along the DFOS, as shown in Figure 3. The 46 DFOS points can be statistically evaluated for each time stamp. This evaluation is graphically illustrated at the top right of Figure 3. Thus, a general measurement noise over time can be minimized within DFOS data, and extract further information simultaneously. The distance between the DFOS and the neutral axis is about 3 mm smaller. This theoretically results in 0.5 % less elongation for the DFOS.

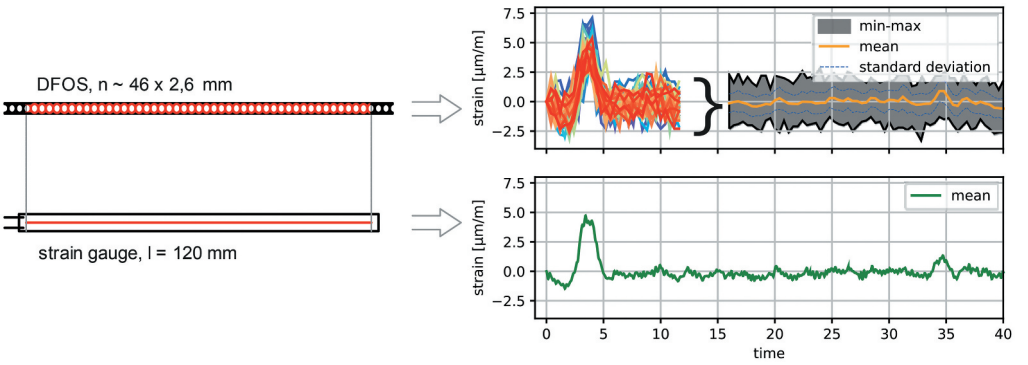


Figure 3. Concept of comparison data from DFOS and strain gauge.

4 EXPERIMENTAL RESULTS

This study shows only a brief excerpt of the static load test results. Specifically, the measurement data from DFOS RG-11 and RG-12, as well as the strain gauge G45-1.19 (blue marked in Figure 2) in the outer span, were analyzed. The measured signals from strain gauges correspond to the strain influence line at the location of the gauge. The data was set to zero for the evaluation at the start of the test load. The temperature is approximately constant over the test period. A constant temperature ensures the consideration of only mechanical load under different ambient conditions.

All strain measurements recorded with fiber optic sensors have been performed at 2.5 Hz, while data from strain gauges are recorded at 400 Hz. Strain gauge data is already filtered using the third order Butterworth filter as a low pass filter with a frequency cutoff of 4.5 Hz, adapted from (Nowak et al. 2023). This value corresponds approximately to the natural frequency of the slab.

4.1 *Comparison DFOS and strain gauge*

During load testing, even minor errors can significantly influence the evaluation due to the shallow strain level. Figure 4 shows the results of the static load test in December 2021. Phase one lasted from t = 37 sec until 290 sec. The stops one, two, and three are located in the outer span where the strain gauge G45-1.19 is installed. The strain remained constant during the stops. The three plateaus until t = 125 sec represent the three stops with a maximum strain measured by the strain gauge at stop two, about 6 µm/m (0.006 ‰). At the beginning of every plateau, a short oscillation appears due to the vehicle's braking process. Stops four, five, and six plausibly cause negative strains, but they cannot be distinguished. The strain from the last three stops is difficult to identify due to the high stiffness of the structure.

During phase two, which lasted from t = 336 sec until 431 sec, the load vehicle drove backward to its starting position in front of the bridge at approximately 3 km/h. During phase 3, from t = 466 sec until 515 sec, the vehicle drove forward over the structure at an approximate

speed. 8 km/h. The highest strain resulted in a maximum difference of 1.23 µm/m (0.00123 ‰) between the strain gauge and DFOS (distance between red and yellow graph in Figure 4, top). Whereby the standard deviation per time stamp for data along the DFOS is already 1.87 µm/m (0.00187 ‰; blue line in Figure 4, bottom). The values are very high considering the maximal strain measured.

During the measurement period, various smaller peaks stand out from the noise. These peaks were caused by heavy vehicles in lane 2 during the test and can be filtered for evaluation. Signals from light traffic (cars) are difficult to detect due to the shallow strain level. However, they have a minor role in determining a site-specific traffic load model. The signal characteristics are essentially the same as those calculated on the three-field beam (20.5 m – 30.0 m – 20.5 m). In addition, the strain gauges signal from phase three has nearly identical characteristics and amplitudes to that observed in the dynamic tests.

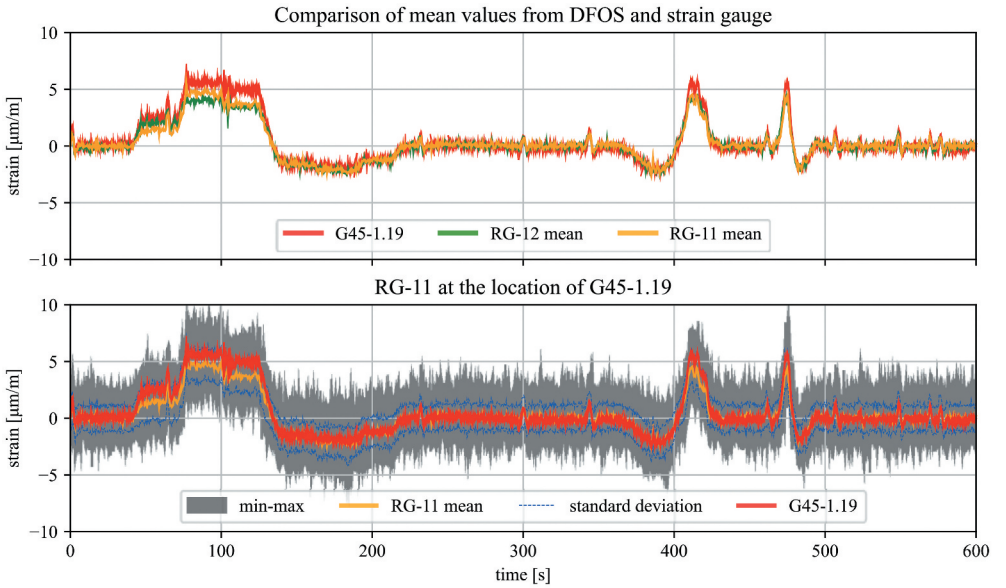


Figure 4. Results of strain gauge and DFOS during static load test.

4.2 *Determination of long-term effects*

To determine long-term influences, it was necessary to reproduce the boundary conditions from the first test were reproduced on the second test day. The same vehicle, LKW 1 (Table 1), was used, but the total weight was 1 % lower in May due to lower cargo load. The locations of the stops in lane 1 were the same, considering specific tolerances when driving a 12-meter-long truck. Weather conditions were different. The temperature on the bottom of the bridge deck during the static load test in December 2021 was 2.8° C on average without sunshine. During the load test in May 2022, the temperature was significantly higher and averaged 20.2° C with clear skies and sunshine. The temperature at the top of the bridge was higher due to solar exposure.

To compare the results from December 2021 and May 2022, the highest strain of the sensors during the static load test is considered. In stop two of phase one of the test, the truck stopped directly above the strain gauge G45-1.19, resulting in the highest strain measured by both sensor types. The stop lasted for at least $\Delta t = 20$ sec. During Δt, the strain only changes due to the load on the lane 2 and measurement noise. Therefore, minimal and maximum values, the median and the mean are considered. Table 2 shows the results for the strain gauge G45-1.19. Note that this level of accuracy cannot be achieved with the fiber optic measurement system. Figure 5 illustrates the median recorded at the two load tests. A comparison of each strain gauge along the DFOS shows an average of 1.00 µm/m (0.001 ‰) higher strain in May 2022

and a maximum difference of 4.45 µm/m (0.00445 ‰). The standard deviation of the difference is 1.27 µm/m (0.00127 ‰). Additionally, the mean scattering width between the minimum and maximum during Δt is 1.18 µm/m (0.00118 ‰) higher in May.

The orange graph in Figure 5 displays the side-by-side configuration of LKW 1 and LKW 3 in May 2022. The maximum strain measured is not exactly double. This load distribution corresponds to the results of the dynamic tests. All the results indicate linear elastic structural behavior of the bridge slab without any observed damages such as cracks.

Table 2. Results of strain in µm/m (10^{-3} ‰) during static load tests, phase 1, stop 2, measured by strain gauge G45-1.19.

Δt = 20 sec	Median	Mean	Max	Min
December	5.61	5.62	5.98	5.34
May	5.65	5.63	6.02	5.28
Δε	0.04	0.01	0.04	0.06

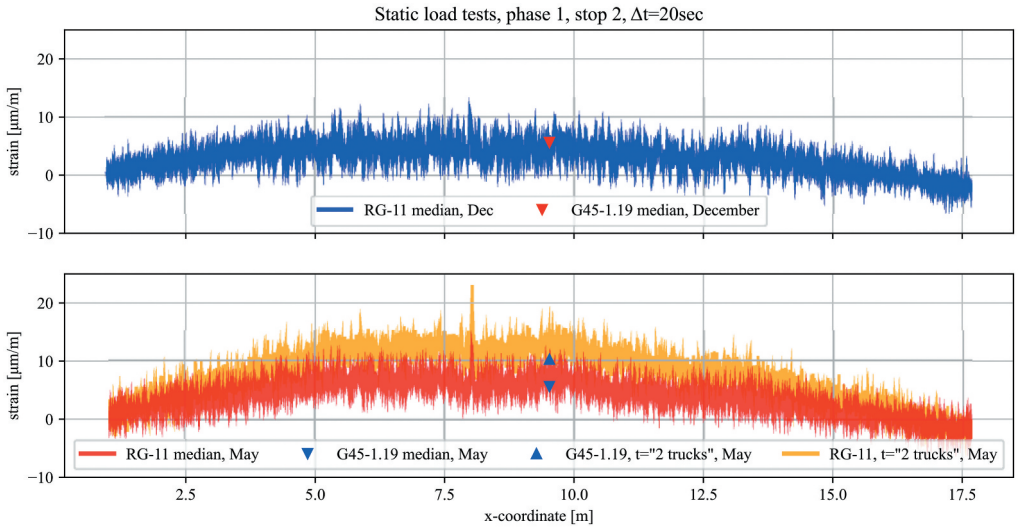


Figure 5. Results of strain gauge and DFOS during static load test in December 2021 (top) and May 2022 (bottom).

5 CONCLUSIONS

To effectively operate a long-term strain-monitoring system, it is necessary to calibrate the sensor system. The test load concept should be adjusted to the project's specific boundary conditions, such as the structure's geometry, monitoring run time, expected loads, etc.. If strain gauges and DFOS are used for strain measurement, it is useful to compare the results in order to validate the data, as it is also done in laboratory tests with DFOS and different measurement systems (Berrocal 2021, Herbers 2023).

To ensure the long-term functionality of the sensors, load tests must be conducted under various environmental conditions. This suggestion is also mentioned in (COST 323) and (Bolle 2017). In the case of the test loads on the "Kreuzhof" bridges, no significant long-term effects were found from different environmental conditions, which provides a functional monitoring system. The obtained monitoring strain data can be further used to update a structural model, similar to the approach used in (Agredo Chávez 2023).

ACKNOWLEDGEMENT

The authors would like to thank the Department of Civil Structures of the City of Munich for the project assignment and the pleasant cooperation.

REFERENCES

Bundesanstalt für Straßenwesen (BASt) [online]. *Brueckenstatistik 01.09.2023*. Retrieved December 3, 2023, from https://www.bast.de/DE/Statistik/Bruecken/Brueckenstatistik.pdf?__blob=publicationFile&v=21

Handlungsanweisung Spannungsrisskorrosion (HA SpRK 2011) *Handlungsanweisung zur Überprüfung und Beurteilung von älteren Brückenbauwerken, die mit vergütetem, spannungsrisskorrosionsgefährdetem Spannstahl erstellt wurden.* Bundesministerium für Verkehr, Bau und Stadtentwicklung – Abteilung Straßenbau. Version: 06/2011.

DIN 1076. *Engineering structures in connection with roads - inspection and test*. German version: 11/1999

Schacht, G.; Kaeding, M.; Bolle G.; Marx S. (2019) *Concepts for the assessment of bridges with the risk of stress corrosion cracking* In German. Beton- und Stahlbetonbau 114, H.2, S. 85–94. https://doi.org/10.1002/best.201800087

Bolle, G.; Mertzsch O.; Marx S. (2017) *Structural monitoring for safeguarding the remaining life time of a bridge building endangered by stress corrosion cracking* In German. Beton- und Stahlbetonbau 112, H. 2, S. 75–84. https://doi.org/10.1002/best.201600067

Bado, M.F.; Casas, J.R. (2021) *A Review of Recent Distributed Optical Fiber Sensors Applications for Civil Engineering Structural Health Monitoring*. In Sensors 2021, 21, 1818. Basel, Switzerland.https://doi.org/10.3390/s21051818

Bednarski L.; Sienko R.; Howiacki T.; Zuziak K. (2022) *The Smart Nervous System for Cracked Concrete Structures: Theory, Design, Research, and Field Proof of Monolithic DFOS-Based Sensors*. Sensors 2022, 22, 8713. https://doi.org/10.3390/s22228713Construction Documents BW40/45 and BW40/46: *inspection reports, drawings, structural calculations*.

fib bulletin No. 22. (2003) *Influence of material and processing on stress corrosion cracking of prestressing steel: State-of-art report.* Lausanne: International Federation for Structural Concrete.

COST 323 (2002) *Weigh-in-Motion of Road Vehicles: final report, Appendix 1: European WIM Specifications*. Paris: Laboratoire Central des Ponts et Chaussées.

Burger, H; Tepho, T.; Fischer, O.; Schramm, S. (2023) *Performance assessment of existing prestressed concrete bridges utilizing distributed optical fiber sensors*. Biondini, F.; et al. [edit.] Life-Cycle of Structures and Infrastructure Systems. London: CRC Press.

Luna, Inc. [online*]. ODiSI 6000 Optical Distributed Sensor Interrogators.* Retrieved December 3, 2023, https://lunainc.com/sites/default/files/assets/files/data-sheet/Luna%20ODiSI%206000%20Data%20Sheet.pdf

Keil, S. (2017) *Technology and Practical Use of Strain Gages*. Berlin: Wilhelm Ernst & Sohn.

Nowak, M.; Fischer, O.; Tepho, T.; Willberg, U. (2023) *Traffic Monitoring on a Highway Bridge – Data collection on local traffic characteristics as a basis for site-specific traffic load models.* In German. Beton- und Stahlbetonbau 118 H., 9, S. 636–648. https://doi.org/10.1002/best.202300043

Berrocal C.; Fernandez I; Bado, M.; Casas J.; Rempling R. (2021) *Assessment and visualization of performance indicators of reinforced concrete beams by distributed optical fibre sensing*. Structural Health Monitoring Volume 20, Issue 6. https://doi.org/10.1177/1475921720984431

Herbers M.; Richter B.; Gebauer D.; Classen M.; Marx S. (2023) *Crack monitoring on concrete structures: Comparison of various distributed fiber optic sensors with digital image correlation method*. Structural Concrete Volume 24, Issue 5. https://doi.org/10.1002/suco.202300062

Agredo Chávez, A.; Gonzalez-Libreros, J.; Elfgren, L.; Sas, G. (2023) *Structural model updating of an existing concrete bridge based on load testing and monitoring data*. Biondini, F.; et al. [edit.] Life-Cycle of Structures and Infrastructure Systems. London: CRC Press.

Agredo Chávez, A.; Gonzalez-Libreros, J.; Elfgren, L.; Sas, G. (2023) *Structural model updating of an existing concrete bridge based on load testing and monitoring data.* Biondini, F.; et al. [edit.] Life-Cycle of Structures and Infrastructure Systems. London: CRC Press.

Bridge Maintenance, Safety, Management, Digitalization and Sustainability – Jensen, Frangopol & Schmidt (eds)
© 2024 The Author(s), ISBN 978-1-032-77040-6
Open Access: www.taylorfrancis.com, CC BY-NC-ND 4.0 license

Load testing and evaluation of inverted T-section slabs in road bridges

C.O. Christensen & J.W. Schmidt
Department of the Built Environment, Aalborg University, Aalborg, Denmark

R. Bang & C. von Scholten
The Danish Road Directorate, Copenhagen, Denmark

P. Goltermann
Department of Civil and Mechanical Engineering, Technical University of Denmark, Kgs. Lyngby, Denmark

K.D.S. Damsgaard & S. Engelund
COWI A/S, Aalborg, Denmark

ABSTRACT: OT-slab road bridges and their capacity were investigated in a comprehensive Danish research project. Such bridges are constructed with prefabricated prestressed overturned T-section beams with in-situ concrete cast on top and are combined with transverse reinforcement for shear load transfer. Often existing bridges suffer from low capacity evaluations insufficient to meet current and future traffic-load requirements. However, recent studies indicate higher capacities than predicted in applied theory. This capacity increase seems to be due to slab behavior rather than strip behavior where insufficient interaction between the OT-elements is presumed. This paper presents evaluations of OT-bridge slabs, based on results from a Danish bridge testing project, (V1), initiated in 2016. The study evaluates capacities in relation to the strip method and yield line theory where Danish standard classification vehicle loads are applied. The results indicate that the strip method may underestimate the capacity of the tested OT-slabs that the yield line theory may be a more suitable assessment method up to the demonstrated load magnitudes.

1 INTRODUCTION

In the Danish Road network, the existing OT-slab concrete road bridges, or inverted T-section slab bridges, stand out as a frequently used short-span bridge type with problematic bridge classifications that often fail to meet today's traffic load requirements. These bridges are constructed using prefabricated and prestressed Overturned T-section (OT) beams, complemented by an in-situ concrete layer poured on top. Additional transverse reinforcement is strategically placed to ensure transverse shear load transfer (Ostenfeld & Jønson, 1950). OT-slab bridges are found in various countries, but it's important to note that they may include different variations of OT-beams (Aadnesen & Husevaag, 1982; Sriskandan, 1977).

In the last decades, numerous studies have undertaken the task of identifying the in-situ behavior and capacity of the existing bridge stock. A common observation from these studies is that the current evaluation methods are conservative and that the actual capacity is usually higher than predicted theoretically (Bagge et al., 2018; Bakht & Jaeger, 1990; Christensen et al., 2023). The capacity of OT-slab bridges has traditionally been evaluated using the strip method (Hillerborg, 1974). However, recent studies in a Danish bridge testing project have

DOI: 10.1201/9781003483755-39

indicated that such an assumption may provide an underestimation of the slab capacity; this hypothesis is indicated by previous studies as well (Halsey & Miller, 1996; Mirtalaei, 1991). In these studies, however, the number of full-scale experiments was limited.

The Danish bridge testing project (V1) was initiated in 2016 to investigate the load-carrying capacity of existing short-span bridges in Denmark and to establish a proof load test method representative of the Danish bridge and vehicle classification system (Vejdirektoratet (The Danish Road Directorate), 2017). The project applied a multidisciplinary approach involving three main research areas: 1) Experimental testing and monitoring, 2) Modelling and simulation, and 3) Probabilistic and decision analysis (Schmidt et al., 2020). Out of the considered bridges, one of the main bridge types in focus was the OT-slab bridge.

Consequently, since 2016, several test results have been generated on OT-slabs. The test results are applied in numerous studies related to the bridge testing project. This paper will provide a comparison in a broad perspective and relate the measured capacities and behavior to known evaluation methods. Based on this, the following research questions have been defined:

- How do the OT-structures perform with regard to the standard vehicles in the Danish classification system?
- How do the OT-structures perform with regard to the evaluation methods of yield line theory and the strip method?
- How can the presented results be used to consider OT-slab structures in the future?

2 EVALUATION METHODS

For a concrete slab, OT-slabs are quite complex since they consist of prefabricated and prestressed beams with in-situ cast reinforced concrete (RC) on top. All interfaces between the OT-beams and the top concrete may be considered a concrete joint. Factory concrete and in-situ concrete typically have different properties as well. Because of this, capacity evaluation of OT-slabs has been governed by the strip method, which may be applied as a lower-bound solution. An upper-bound solution could be hypothesized to be the use of yield line theory. Cross-sectional evaluations for both methods have been carried out using the FAGUS software (cubus, 2023).

The strip method applied considers a strip in the span direction, which is treated as statically independent from adjacent beam elements. In this case, it is assumed that no shear capacity between the elements is present and that the in-situ cast concrete does not provide any contribution to the capacity and is considered as dead load only. In doing this, the evaluation may be based on a common beam evaluation, which for OT-slabs includes an OT-beam with top concrete attached. The determined capacity may be scaled to a desired width. In this paper, the width for full-scale bridges is assumed to be the width of a notional lane (3 m) in the Danish classification system.

For the applied yield line theory, yield moments in the transverse direction are considered along with the yield moments in the longitudinal direction. The transverse reinforcement is thus assumed to be able to redistribute the applied load through the concrete interfaces (up to its bending capacity), and the shear bearing capacity is assumed higher than the bending capacity. In the considered OT-slabs, a reinforcement net is present in the top concrete. This is necessary to evaluate using the yield line method. All yield line evaluations are performed in the software Optum MP, (Optum, 2023).

3 IN-SITU BRIDGE AND SUBCOMPONENT TESTS

Three full-scale bridge tests on OT-slab bridges have been carried out (Schmidt et al., 2018). The bridges were set for decommissioning, and the tests were planned as potential failure tests. However, they all reached higher capacities than anticipated in the given calculation basis. As a result, one of the bridges was cut into strips and tested again (Christensen et al.,

2021). In these tests, more of the response and behavior was revealed. Another bridge had beam elements cut out, which were tested in the laboratory. In addition, a single proof load test has also been performed (Christensen et al., 2023). Since this was a proof load test, the load levels were significantly lower than in the failure tests.

3.1 *The test bridges*

The test bridges had different characteristics and dimensions but were of the same OT-type. Photographs of some of the tested bridges are shown in Figure 1abc. A typical cross-section of the used OT-beams and a combined bridge cross-section is shown in Figure 1d (from bridge 1576), for general bridge characteristics see Table 1. All evaluations in this paper are based on mean values for material strengths. The evaluations are thus meant for comparison with the real bearing capacity and not the design value. For the in-situ bridges, material strengths were found through material testing of bridge 1576. The most significant parameters are: 1) pre-cast concrete $f_{cm} = 72$MPa, 2) in-situ top concrete $f_{cm} = 41$MPa, prestressed tendon yield and ultimate strengths $f_{ym}\tilde{1}500$MPa, and $f_{um}\tilde{1}800$MPa. The regular reinforcement was not tested, and the yield strength, $f_{ym}\tilde{5}90$MPa, is thus based on drawings.

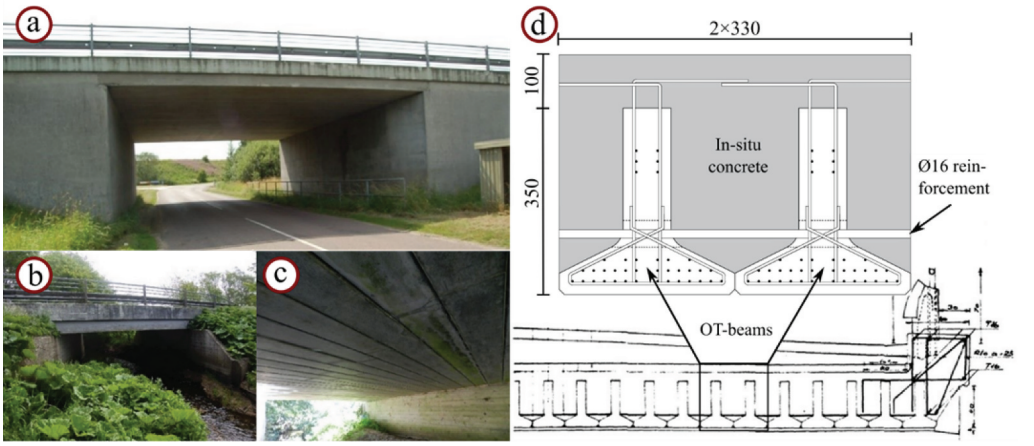


Figure 1. A) Bridge 1577 before testing. b) Bridge 3700 before testing. c) The bottom surface of Bridge 3700. d) Cross-section and combined cross-section of Bridge 1576.

Table 1. Bridge characteristics of the in-situ test bridges.

Bridge number	1577	1727	Strip 1 (1727)	Strip 2 (1727)	1576	3700
Span [m]	11	9	-	-	6.6	6.5
Skewed [deg.]	-	-	-	-	32	29.5
OT-beams	37	37	11	11	72	34
OT-height [mm]	450	450	-	-	350	350
OT-width [mm]	330	330	-	-	330	330
Prestress tendons	32	32	-	-	36	22
Road build-up [m]	0.45	0.45	0.45	0	1.2	0.4

3.2 *Cut-out beams from Bridge 1576*

The simplest test in the test matrix was the beams cut from bridge 1576. These consisted of two adjacent beams, including top concrete (L = 5.3 m). The beams were tested in four-point bending with 1.4 m between the loading points (axle distance of the Danish system). The response curves for the five specimens are shown in Figure 2a along with a beam evaluation

and two wheel loads of a class 500 ton vehicle of the Danish classification system (the heaviest vehicle in the Danish classification system).

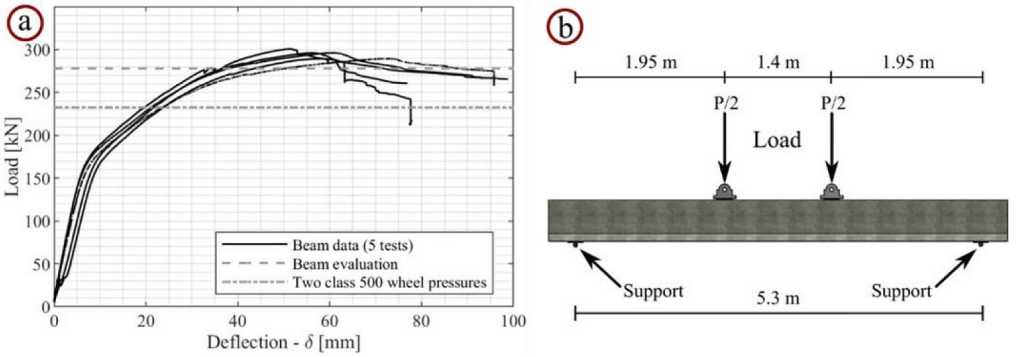


Figure 2. A) Response curves for the five OT-elements. Original results presented in (Jensen et al., 2018). b) Cross-section of the tested beams with two OT-beams, transverse reinforcement, and in-situ concrete.

It is seen that the beam evaluation fits well with the experimental results and that the beams are stronger than the wheel pressures of the class 500 ton vehicle (the largest of the system). Figure 2b shows the cross-section of the tested beams. The average ultimate capacity was 294 kN. The beam evaluation was 278 kN.

3.3 *In-situ test methods*

The high-magnitude failure tests were performed using a novel high-magnitude load testing rig, designed for controlled loading of short-span slab bridges (up to 12 m). The test setup was designed to facilitate loading with wheel and axle load configurations representative of the Danish standard vehicles (Vejdirektoratet (The Danish Road Directorate), 2017). It utilized a cradle system with loading frames simulating wheel pressures. Ballast and hydraulic pistons were used for the load application of the primary vehicle, Vehicle A. The secondary vehicle, Vehicle B was a passive fixed load. The test setup can be seen in Figure 3a. On bridges 1577, 1727, 1576, and 3700, both vehicles A and B were applied. The two strip tests of bridge 1727 had a total width of 3.63 m and were thus too narrow for both vehicles. Therefore, only vehicle A (the classification vehicle) was applied. The single proof load test on an OT-slab bridge utilized special heavy vehicles with hydraulic control of individual axles for load application (Christensen et al., 2023). Such vehicles are seen in Figure 3b.

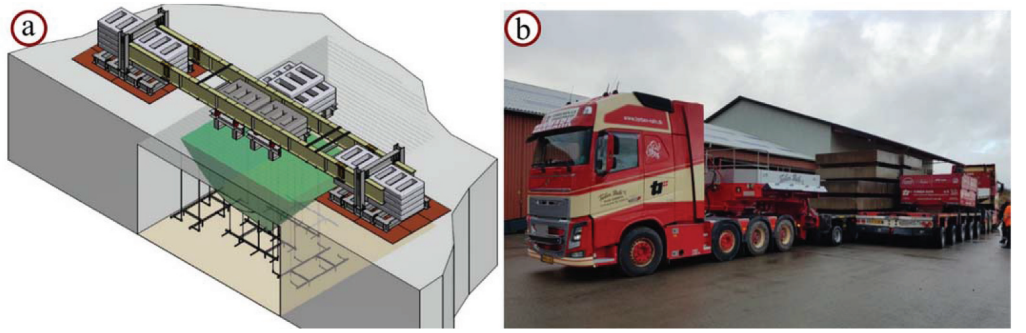


Figure 3. A) Novel high-magnitude loading rig first presented in (Halding et al., 2017). b) Special heavy vehicles with hydraulic control.

In both load setups, the load is applied according to the Danish classification system and in one case using actual heavy vehicles that drive the Danish road network. This is deemed more representative than e.g., the application of Load Model 1 (LM1) of the Eurocode (European Committee for Standardization (CEN), 2003), which may require significantly higher wheel pressures that do not reflect the vehicles of the Danish classification system.

3.4 *In-situ results and evaluation*

Using the characteristics in Table 1 and the described evaluation methods, the bridge capacities have been determined. Note that the following assumptions have been made: 1) The road build-up has not been included in the capacity evaluation, neither as self-weight nor as a contribution to the capacity. In addition, no load distribution has been applied through the road build-up. Table 2 shows the estimated capacities along with the design loads of a class 500 ton vehicle and the applied test loads. Note that all loads describe the total applied load on the bridges and that the total mean load of vehicle B was 330 kN.

The response curves for the two strip tests are shown in Figure 4. They should not be mistaken for full-scale tests since they are more correctly described as wide beam tests, which are dependent on some interaction between OT-beam elements. If there is no interaction, only the beams underneath the wheel pressures can be activated, therefore both a calculation for the full width and the beams underneath the wheel pressures have been included. It is seen that the full-width beam evaluation fits well with the strip tested without asphalt, while the strip with asphalt seems stronger. In addition, the strips were much stronger than the mean loads of a class 500 ton vehicle.

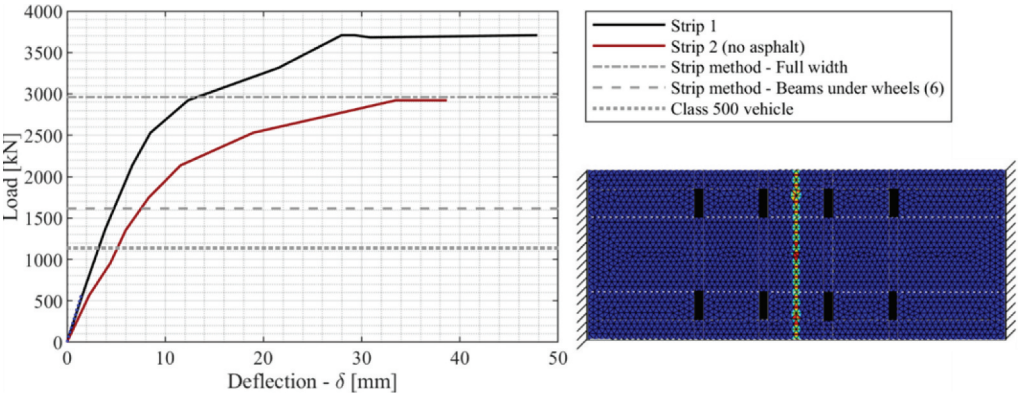


Figure 4. Response curves for the two in-situ strip tests. Original results in (Christensen et al., 2021).

The response curves of the full-scale bridge tests are shown in Figure 5. Figure 5a shows Bridge 1577, Figure 5b shows Bridge 1727, Figure 5c shows Bridge 1576, and Figure 5d shows Bridge 3700. The evaluated capacities and classification vehicle are also depicted.

Bridges 1577, 1727, and 1576 appear much stronger than the mean values for the class 500 ton vehicle while the proof loaded bridge 3700 only just reaches this load. No, failure or visible cracks were observed at the applied maximum loads. However, with a deflection of only 2 mm, it seems safe to say that the capacity is much higher. The first three bridges all surpass the strip method results, but none reach the yield line results. Everything in the performed tests points at a sufficient load distribution.

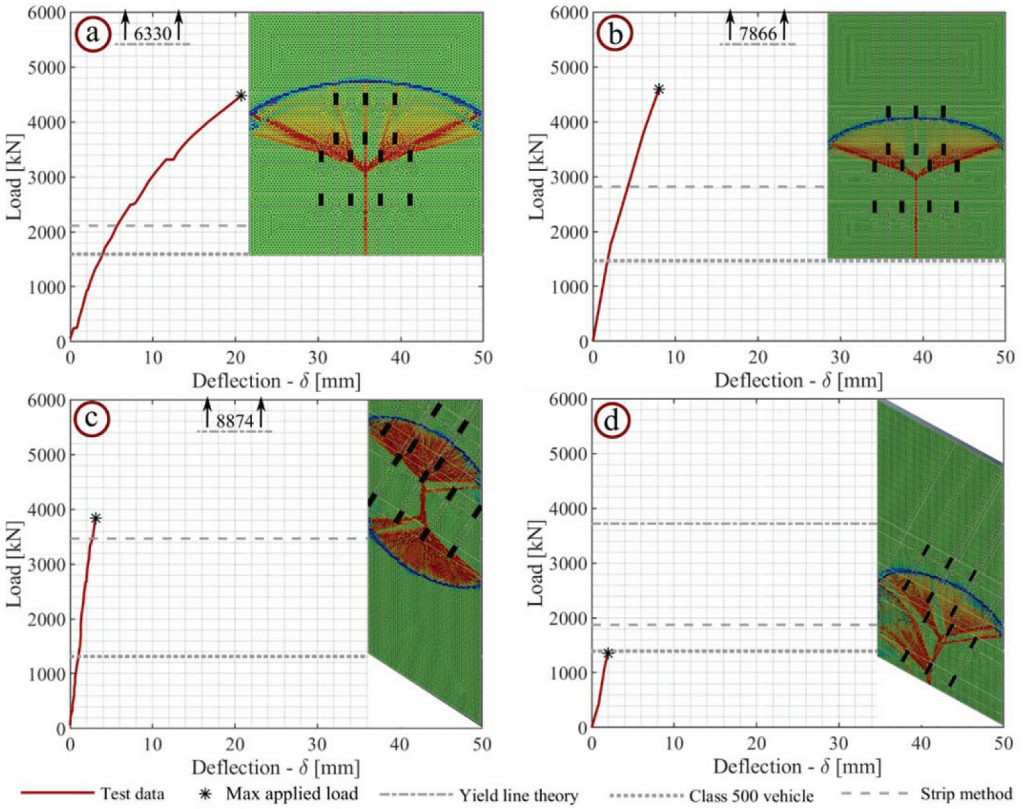


Figure 5. Response curves and load placement for four tested in-situ bridges. a) Bridge 1577. b) Bridge 1727. c) Bridge 1576. d) Bridge 3700. Original results in (Christensen et al., 2023; Schmidt et al., 2018).

Table 2. Estimated bridge capacities, a class 500 vehicle, and test results. All loads and capacities in kN.

Bridge number	1577	1727	Strip 1 (1727)	Strip 2 (1727)	1576	3700
Strip method	2110	2816	974*		3464	1872
Yield-line theory	6330	7866	2962**		8874	3718
Class 500	1594	1468	1138		1314	1392
Applied load	4481	4600	2922	3708	3842	1354

*Determined as the capacity of the beams directly under applied wheel pressures (no redistribution).
**Determined for the full width of the strip (3.63 m).

4 SCALED LABORATORY TESTS

A good interaction between OT-beam elements was observed in the in-situ bridge tests. The topic was assessed to require further investigation; this because a more verified interaction could open an opportunity to assume slab behavior and apply yield line-based methods.

A test was designed for the laboratory that could serve as an evaluation of the shear interaction between the OT-beam while providing data on the response until failure. The test setup was designed to utilize three-sided support of an OT-slab with seven downscaled OT-beams. Figure 6 shows the test setup and cross-section (Figure 6a) and proposed behavior (Figure 6b).

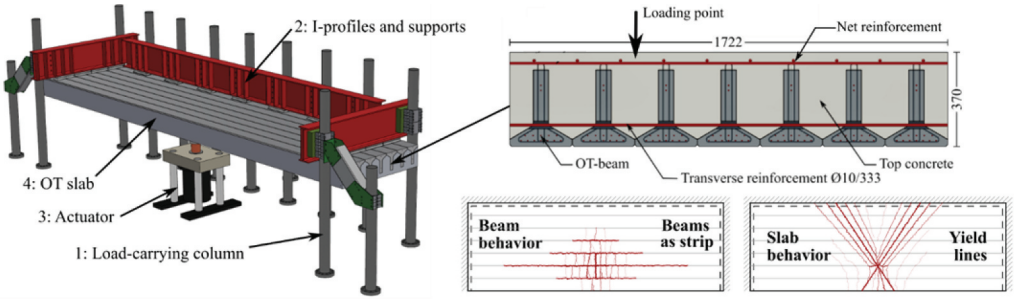


Figure 6. A) Laboratory test setup and OT-slab cross-section consisting of seven OT-beams. b) Suggested behavior extremes; beam behavior and slab behavior (Christensen, Halding, et al., 2022).

The slabs had dimensions of 8.40m x 1.72m x 0.37m and were loaded with a single point load between the second and third beams. For more information on downscaling, etc., see (Christensen, Halding, et al., 2022). The response curves of the two tests can be seen compared to yield line theory and beam evaluation in Figure 7 and to a class 500 ton vehicle wheel load. Even for these down-scaled slabs, the capacity is higher than beam evaluations and class 500 ton wheel loads. The revealed crack patterns showed both beam behavior and slab behavior, but the capacity was equivalent to slab behavior and yield line theory (Christensen, Halding, et al., 2022).

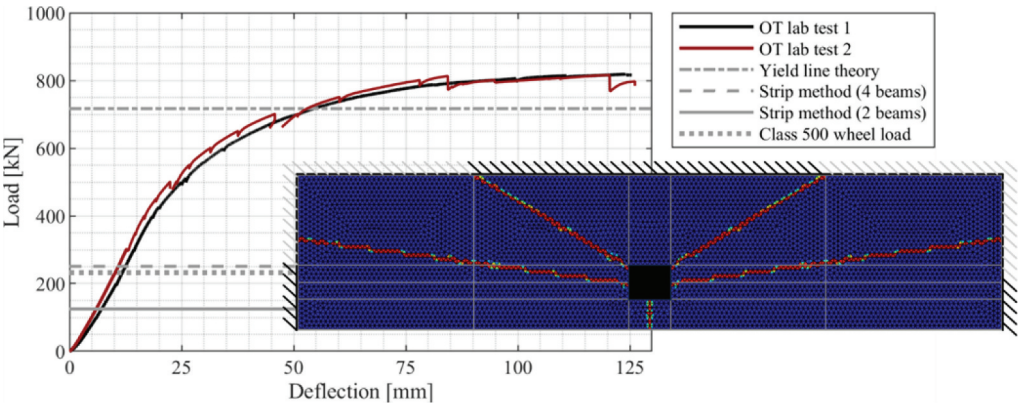


Figure 7. Load/deflection curve for the two OT-slab tests. Original results presented in (Christensen et al., 2021; Christensen, Zhang, et al., 2022). At maximum load, the support conditions changed due to slab behavior causing a lift of the corners; this is included in the yield line model, see areas marked with grey.

5 DISCUSSION

To some extent, the results of the full-scale bridge tests (Table 2 and Figure 5) appear to go towards the applied upper-bound solution of yield line theory. However, the full-scale tests did not reveal the full plastic regime of the OT-slabs; this for two reasons: 1) Unexpected high loads and available ballast ran out, and 2) Proof loading purposes limited the load application. In this situation, the strip tests of Bridge 1727, beam tests of Bridge 1576, and laboratory slab tests related to Bridges 1577 and 1727 provide strong indications of the capacity potential of the tested bridges.

All tested structures exhibited slab behavior until the applied maximum load. For instance, the laboratory OT-slabs which were designed as an ultimate capacity test of the concrete

interface between the OT-beams, showed significant cracking. This observation indicates that the transverse reinforcement actually ensures the desired slab behavior. The results thus support previous findings of two comparative studies (Halsey & Miller, 1996; Mirtalaei, 1991). Consequently, it can be justified that the interface between OT-beams and the associated transverse load transfer may provide sufficient capacity to generate a yield line formation (if properly constructed).

All tests showed capacities significantly higher than the mean values for the largest vehicle in the Danish classification system (Class 500 ton) and its axle loads; this even for the strips with reduced width (Figure 4). The beam tests with two OT-beams carried loads larger than the design value of two wheel loads of the class 500 vehicle ton (Figure 2) and the OT-slab supported along three edges (Figure 7) showed that even a load almost four times the class 500 wheel load could be transversely transferred through the beam interfaces from a single loading point. It should be noted that in a classification or proof loading situation, the loads of a class 500 ton vehicle will be significantly higher, but in the present paper, only a comparison of capacities is performed. As standard vehicles and associated load configurations are used for both classification of bridges and granting of special vehicle permits, the applied loads are assumed to sufficiently represent the extreme load effects that may be experienced by a bridge.

The results from the strip tests of Bridge 1727 with a width of 3.63 m and the beam tests in the laboratory of Bridge 1576 showed that the strip method/beam evaluation adequately estimates the actual capacity of the structures. The full-scale tests showed that the strip method largely underestimates the capacity of OT-structures because load redistribution is not included. In addition, the extreme stress test in the laboratory using a single point load showed that the concrete interface in similar OT-structures has sufficient transverse capacity. Therefore, with the knowledge that there most likely will be a capacity reserve, the strip method may be used as a first estimate but seems inadequate as a definite solution. The yield line method seems to be a more suitable approach to evaluate OT-slabs if sufficient transverse capacity between the OT-beams is considered.

6 CONCLUSION

The Danish bridge testing project V1 has provided significant insight into OT-slab bridges and their behavior. The results show that the OT-slabs generally exhibit slab behavior (linear until high capacities) and are therefore more correctly evaluated by taking into account more transverse capacity than previously anticipated; this facilitating the use of the yield line method. The test results are insufficient to conclude that this can be done until maximum capacity, however, the measured capacities have a magnitude that indicates that the OT-slabs do not seem to represent a challenge in relation to the heaviest vehicle in the Danish classification system (Class 500 ton) - Loads which are much higher than the structures original classification. Consequently, it is likely that OT-bridges capacity poses a reduced challenge in the Danish road network.

ACKNOWLEDGEMENT

Special thanks to the Danish Road Directorate for their pivotal role in the Danish concrete bridge testing project. Additional thanks to Assistant Professor, Philip Skov Halding, at the Technical University of Denmark, for his part in data collection and documentation during his time as a Postdoc.

REFERENCES

Aadnesen, L., & Husevaag, E. (1982). Standard prefabricated culverts and bridges in Norway. *Nordisk Betong*, *25*(1982: 2–4).

Bagge, N., Popescu, C., & Elfgren, L. (2018). Failure tests on concrete bridges : Have we learnt the lessons ? *Structure and Infrastructure Engineering*, *2479*, 292–319. https://doi.org/10.1080/15732479.2017.1350985

Bakht, B., & Jaeger, L. G. (1990). Bridge Testing—A Surprise Every Time. *Journal of Structural Engineering*, *116*(5). https://doi.org/10.1061/(asce)0733-9445(1990)116:5(1370)

Christensen, C. O., Damsgaard, K. D. S., Sørensen, J. D., Engelund, S., Goltermann, P., & Schmidt, J. W. (2023). Reliability-Based Proof Load Factors for Assessment of Bridges. *Buildings*, *13* (4), 1060. https://doi.org/10.3390/buildings13041060

Christensen, C. O., Halding, P. S., Schmidt, J. W., & Goltermann, P. (2022). Large-scale OT-slab tests Laboratory measurements and evaluation. *11th International Conference on Bridge Maintenance, Safety and Management*, 2099–2106. https://doi.org/10.1201/9781003322641-260

Christensen, C. O., Schmidt, J. W., Halding, P. S., Kapoor, M., & Goltermann, P. (2021). Digital Image Correlation for Evaluation of Cracks in Reinforced Concrete Bridge Slabs. *Infrastructures*, *6*(7), 99. https://doi.org/10.3390/infrastructures6070099

Christensen, C. O., Zhang, F., Garnica, G. Z., Lantsoght, E. O. L., Goltermann, P., & Schmidt, J. W. (2022). Identification of Stop Criteria for Large-Scale Laboratory Slab Tests Using Digital Image Correlation and Acoustic Emission. *Infrastructures*, *7*(3), 36. https://doi.org/10.3390/infrastructures7030036

cubus. (2023). *FAGUS - Cross Sections Definition and Analyses*. Retrieved December 20, 2023, from https://www.cubus-software.com/Guests/Produkte/Fagus/e_main.html

European Committee for Standardization (CEN). (2003). *EN1991-2. Eurocode 1: Actions on structures - Part 2: Traffic loads on bridges*.

Halding, P. S., Schmidt, J. W., Jensen, T. W., & Henriksen, A. H. (2017). Structural response of full-scale concrete bridges subjected to high load magnitudes. *Fourth Conference on Smart Monitoring, Assessment and Rehabilitation of Civil Structures*.

Halsey, J. T., & Miller, R. (1996). Destructive testing of two forty-year-old prestressed concrete bridge beams. *PCI Journal*, *41*(5). https://doi.org/10.15554/pcij.09011996.84.93

Hillerborg, A. (1974). *Strip Method of Design* (C. and C. Association, Ed.). Transport and Road Research Laboratory (TRRL).

Jensen, T. W., Poulsen, P. N., & Hoang, L. C. (2018). Finite element limit analysis of slabs including limitations on shear forces. *Engineering Structures*, *174*. https://doi.org/10.1016/j.engstruct.2018.07.007

Mirtalaei, K. (1991). How to attain full continuity and standardization in composite prestressed multi-beam bridges. *American Concrete Institute, ACI Special Publication*, SP-128. https://doi.org/10.14359/2885

Optum. (2023). *Optum MP*. Retrieved December 20, 2023, from https://optumce.com/products/optum-mp/

Ostenfeld, C., & Jønson, W. (1950). Forspændte betonkonstruktioner i Danmark. In *Beton-Teknik: Vol. Hæfte 16*.

Schmidt, J. W., Halding, P. S., Jensen, T. W., & Engelund, S. (2018). High Magnitude Loading of Concrete Bridges. *ACI Structural Journal*, *323*, 9.1–9.20.

Schmidt, J. W., Thöns, S., Kapoor, M., Christensen, C. O., Engelund, S., & Sørensen, J. D. (2020). Challenges Related to Probabilistic Decision Analysis for Bridge Testing and Reclassification. *Frontiers in Built Environment*, *6*(February). https://doi.org/10.3389/fbuil.2020.00014

Sriskandan, K. (1977). Standard bridges as highway overcrossings (United Kingdom). *IABSE Structures*, *C-1/77*, 14–15.

Vejdirektoratet (The Danish Road Directorate). (2017). DS/EN 1991-2 DK NA:2017, Annex A: Lastmodeller for klassificering og bæreevnevurdering (Models of special vehicles for road bridges). In *(The Danish Road Directorate)*.

Bridge Maintenance, Safety, Management, Digitalization and Sustainability – Jensen, Frangopol & Schmidt (eds)
© 2024 The Author(s), ISBN 978-1-032-77040-6
Open Access: www.taylorfrancis.com, CC BY-NC-ND 4.0 license

Lessons learnt from load testing in the UK

D.P. Cousins
Accolade Measurement, Welwyn Garden City, UK

ABSTRACT: Accolade Measurement have been conducting load testing in the UK since 1993. Notable examples include suspended trusses of the Cleveland Bridge in Bath, reinforced concrete deck hinge joints of the M4 Usk River Bridge after they were strengthened by post-tensioning, a jetty at Jarrow and a vehicle parking floor at Luton. Tests have involved load application by rolling heavy vehicles, concrete kentledge blocks and water bags. Measurements of displacements and strains have used permanent structural health monitoring systems, temporarily fixed sensors, total stations and digital image correlation; each of which have their advantages and limitations. Other tests on cantilevers, parapets, lifting systems, buildings and mezzanine floors have addedto the body of knowledge. Where numerical assessments are unsuitable and leave uncertainties, proof load tests have demonstrated capacity for vehicle loading. This paper draws on experience of Accolade and the author's career, to present some interesting cases and highlight lessons learnt.

1 BACKGROUND

Load testing of bridges is only occasionally conducted in the UK and never routine. Guidance from National Highways (the owner and operator of all trunk road bridges in England), sets the standard for bridge management in the UK, widely accepted also as the benchmark for bridges owned by other highway regions, Network Rail, local authorities and private bridge owners. Document CS 463 (National Highways, 2019) enables the use of load testing to 'assist in the strength assessment of bridges', stating:

> Load testing of a bridge shall only be undertaken after calculated assessments using the best available methods and information. . .fail to show it to comply with the assessment standards.

The guidance continues to describe two forms of load testing as:

- Supplementary load testing: where controlled loads applied are less than the normal daily working loads of the structure, no greater than 90% of the unfactored serviceability limit state (or 60% in steel-concrete composite bridges) and remain within the bridge's elastic limit. This is to be used for calibrating or correcting assessment calculations and models. Long established 'Guidance for Supplementary Load Testing of Bridges' is still in regular use (ICE, 1998). In other countries this may be called 'diagnostic testing'.
- Proving load testing: (elsewhere termed 'proof load test', including this paper) where the test replaces numerical assessment by imposing a larger load than permitted traffic, but is only allowed for bridges which would otherwise be closed to traffic or demolished. To date, no further guidance on the use of proof load testing for bridges is recognised in the UK, reliant instead on the experience of the testing contractor. Guidance for proof load testing from other countries, including the USA (Transport Research Board, 2019), may be referenced at the engineer's discretion.

Unlike other countries (for instance France (Sétra, 2004)), 'acceptance load tests' are not required in the UK for new bridges, though may be specified for substantially novel or large bridges

DOI: 10.1201/9781003483755-40

(see Queensferry Crossing, below). Confusingly, the ICE guidance (ICE, 1998) calls this a 'proof load' – but which this author suggests should be removed from UK engineering terminology.

Increasingly, proof load tests are required for existing bridges of incalculable capacity or uncertain load distribution, hoping to maintain load carrying capacity, extend service life and minimise expensive, environmentally damaging strengthening or reconstruction. This author is familiar with bridge owners or consultants seeking examples and evidence of past experience before deciding to conduct a load test. There is assumed to be a lack of precedence or procedures for technical approval needed in the UK. It is hoped that this paper provides some of that guidance.

2 CASE STUDIES

2.1 *Cleveland Bridge*

A single span highway bridge constructed originally in 1826 of five cast-iron arches, was reconstructed in 1928 retaining the arches, alternating with four reinforced concrete trusses, to support a new concrete deck (Figure 1a). Each truss is suspended at both ends on eleven steel bars of 31.75mm diameter, found to suffer from corrosion. Assessment calculations assumed the arches to be no longer structural. In 2021, the bridge was temporarily closed to traffic for safety.

Installed sensors for long-term measurement include: 16 displacements at truss ends, using linear variable displacement transducers (LVDT); 42 vibrating wire strain gauges on selected hanger bars; 1 LVDT at a notable group of cracks in reinforced concrete; and 2 cameras for digital image correlation (DIC) monitoring of seventeen finer crack movements in the same zone.

A supplementary load test was conducted overnight in October 2022, with normal traffic limited to one lane of the carriageway in contraflow. Two gritter trucks were applied, of 10.2 tonnes and 17.8 tonnes (Figure 1b), with their positions measured by a laser distance gauge and fed into the same data acquisition unit, thus avoiding manual records.

Data collected was later displayed as influence lines for each vehicle passing the bridge. Load sharing relationships between the four trusses were evidenced from vertical deformations. Vehicle load supported in the trusses was calculated from the strains, evidencing additional contribution of the cast-iron arches despite not directly monitoring them.

No damage was detected in the load test and no irreversible deformations were measured. This, combined with ongoing remote monitoring, which is assisted by anomaly detection using machine learning, enabled the bridge managers to reopen the bridge in both directions for vehicles up to 18 tonnes.



Figure 1. Cleveland Bridge a) Section view and b) load application for supplementary test.

2.2 *Usk River Bridge*

A five-span motorway underbridge totalling 135m length, carries the M4 motorway over the Usk River. Constructed in 1967, it includes flexible hinge joints in reinforced concrete beams at four contraflexure positions providing freedom of rotation yet maintaining shear connection. Beam depth is reduced to 1/3 of the typical depth for just 38mm in length. Reinforcement bars pass through the reduced depth including horizontal dowels and flanking diagonals (Figure 2a). As the hinge rotates due to beam deflections, these bars are highly stressed.

In cold temperatures, the bridge deck can be subject to horizontal tension meaning there to be no reliable compression through the joint (unlike 'Mesnage' or 'Freyssinet' hinge joints in

compression columns (Schacht & Steffen, 2015)). On rotating, the joint cracks through concrete and deck surfacing, allowing chlorinated road water to pass directly down into the hinge joint, which had led to pitting corrosion on reinforcement at the critical centre, confirmed by intrusive investigations. Fatigue assessment and laboratory model testing were conducted extensively between 2005 and 2010 (Cousins, 2017), which sparked this author's excitement in complex deteriorated structures. Repairs were conducted in 2017 which led to the joints being externally post-tensioned to create a constant compression across the hinge joints. The bridge was subject to supplementary load tests by Cardiff University and Accolade Measurement at multiple stages during investigations and after the strengthening:

- In 2005, a mobile crane of 60 tonnes mass was applied, but measurements focused on the external faces which were later shown unrepresentative of internal hinge joints.
- In 2007, the test was repeated with a 96 tonne mobile crane. Additional sensors were used to compare the rotations of internal and external hinges. The vertical profile of the deck was measured by total station extensively. These were used to calibrate finite element models for the bridge assessment.
- In 2020, a repeat test was conducted with a 60 tonne vehicle (Figure 2b) to investigate the influence of the post-tensioning on hinge stiffness, comparable to the 2005 test. Results demonstrated no detriment from the works to the load distribution in the bridge.

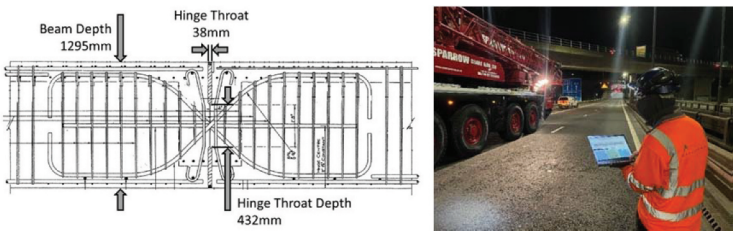


Figure 2. Usk River Bridge a) Deck hinge concrete details and b) Loading and live data displays, 2020.

2.3 *Union Chain Bridge hanger caps*

The Union Chain Bridge was constructed in 1820, crossing the River Tweed between England and Scotland. In celebration of its 200-year anniversary, the bridge was partially dismantled for refurbishment. Cast iron, components known as 'hanger caps' sit on the main chains and support vertical hanger bars. Some of these were found by magnetic particle inspection to include cracks in their top surface emanating from the concave corners of the centre hole.

It was possible to replace all hanger caps with new steel parts formed by computer numerical control (CNC) machining, but which would have been expensive and wastefully disposed of these original parts. An opinion was given that the cracks were superficial, probably existent from original casting and should not pose a risk of fracture in future service. In order to investigate this, a proof load test was conducted on five hanger caps (Figure 3a).

Caps were supported imitating the bridge chain and vertical load imposed by jacking onto a steel wedge insert, similar in shape to the hangers. Force was applied equal to five times the maximum service load of a hanger bar. Crack widening was measured with vibrating wire strain gauges. Conducted inside a shipping container provided safety in case it were to fragment.

In all cases, the cracks were seen to widen up to a maximum of 0.1mm, but fully return to their starting condition when load was removed, which evidenced no propagation of the cracking even under extreme loading. Hanger caps were deemed suitable to return to the bridge and remain in service, maintaining these historical parts.

2.4 *Queensferry Crossing, Edinburgh*

Load testing of the Queensferry Crossing was conducted in August 2020, which is described in detail by Cousins, et al. (2022). Three vertical towers hold suspension cables of the main spans, crossing the tidal estuary. Two road traffic lanes plus a hard-shoulder flow in each direction,

straddling the towers and cables. The bridge hosts what is believed to be the world's largest structural health monitoring system, consisting of 2184 physical sensors, reading at up to 1000Hz.

A supplementary load test was required in the construction specification to demonstrate the functionality of the structural health monitoring and confirming behaviour of the bridge.

The test was conducted overnight, when traffic was minimally disrupted and there was less variation in temperature. Six 44-tonne trucks passed over the bridge in formation three vehicles wide. Position of the vehicles was recorded by one GNSS rover unit on the lead vehicle. Normal traffic in the direction of the test load were held back temporarily by police vehicles. Traffic in the opposing direction remained free flowing. Consideration was given to the possibility of complete closure of the bridge for the load test, but the traffic management, expense and disruption caused would have been unfavourable. It was determined acceptable to have short duration closures in one direction only, and the 'noise' from other traffic was not obtrusive to the results.

Results showed that the bridge stiffness was within 10% of design estimations.

2.5 *River Tyne jetty*

A concrete jetty supported on piled foundations in the River Tyne at Jarrow was to be repurposed. A new pipe bridge from shore to the jetty would be constructed landing onto two pile caps of the existing structure. A proof load test in January 2022 demonstrated capacity (Figure 3b).

Localised poor areas of the concrete deck were alleviated by placing steel plates over, which concentrated loading on selected piles beneath and avoided punching shear. Loading by concrete kentledge blocks totalling 80 tonnes was applied in 7 increments, installed by mobile crane. Due to unfavourable weather, the two-day testing was truncated. After 16 tonnes was applied, wind speeds rose meaning the crane could no longer operate, progress was halted and not restarted until 40 days later. There was good evidence that at this small load, no creep developed.

Monitoring consisted of digital levelling of the jetty top surface, relative to a static marker on river bank with tolerance of ±0.2mm. The maximum movement seen in the test was only 2.56mm, but this in an upward direction and consistent across all monitored positions on the jetty. This confused the team at the time, and did not to correlate to applied load. Later a better correlation was found to the tide level in the estuary. No damage was noted to the piles and results were deemed to have demonstrated sufficient strength in the piled foundations.



Figure 3. a) Hanger cap from Union Chain Bridge, in proof load test and b) Kentledge loading of 80 tonnes on the River Tyne jetty.

2.6 *Luton vehicle parking floor*

A structural floor for vehicle parking with an aged concrete deck could not be assessed numerically due to a lack of recorded information and subsequent deterioration. Instead, it was proof load tested in January 2016, by applying water weights. Though not a bridge, the principles of testing remain the same, as has been conducted on roofs and floors of many buildings. Confined water sacks were used to apply universally distributed loads to the surface in regions up to the ultimate limit state at 8.2kN/m^2 in eight increments, to a maximum of 316 tonnes (Figure 4a).

Loading zones were sequenced to create hog and sag effects in the deck. By measuring the water flow rate, it was possible to ensure the load is controlled and equally applied in multiple bags. A small amount of water leaked as is common in such tests and normally of no problem to clear, but in the winter conditions this froze, making the working area temporarily slippery. At one point, the temperature dropped further such that hoses became frozen and testing was delayed.

LVDTs measured vertical deformation of the deck and supporting beams at 17 locations, using plumb bobs suspended on Invar wire (for temperature stability) (Figure 4b). Prior identified cracks were monitored for width at five locations. Loads were held for up to 2 hours. A maximum of 2.08mm displacement was measured in beams and observation of hysteresis patterns during the test supported that the test had caused no permanent deformation.



Figure 4. a) Water weights used for load testing at Luton and b) plum bob and LVDT measurements.

2.7 *Millbrook and Redbridge parapets*

Not all load tests are vertically applied. Parapets of the Millbrook and Redbridge Flyovers on the A33 at Southampton were identified as deficient when an impact occurred. Precast concrete parapet units of 2m length are attached to the bridge cantilever edges by a cast in-situ joint. Subsequent to the fault, strengthening was designed and implemented by joining parapet units together at their top edge. Load testing was required to demonstrate the improved resistance.

Accolade Measurement applied horizontal proof load tests in a static representation of the impact force. Overturning moment equivalent to 13kNm/m was applied to the parapet units and held for 5 minutes, demonstrating stiffness and elastic recovery.

To minimise disruption, test equipment was mounted to a low loader trailer of 39 tonnes mass (Figure 5a). The test was applied to 219 locations distributed throughout both bridges, conducted in just 6 night-shifts between March and May 2018. Only three locations showed signs of distress, seen in cracking at the parapet base joint; one test was stopped before reaching maximum load for safety reasons. Improvements needed were thus minimised.

2.8 *Upper Teesdale bridges*

Load testing is equally applicable to the smallest of bridges. In the North-East of England, five small bridges provide a route to the source of the River Tees. When revetment works to the river banks required haulage vehicles to transport heavy rocks up the mountain, the track needed to be uprated from the sign-posted 3 tonnes weight limit. The cause for imposing such signage was not known, and records of the bridges were not available for numerical assessment. Investigation and material sampling, followed by numerical assessment calculations would have been prohibitively long and likely result in ambiguous or very conservative conclusions.

Instead, proof load tests were conducted for all five bridges over five days in June 2023 (Figure 5b). Load application involved concrete blocks of 1.2 tonnes on a flat-bed trailer, driven on and off the bridges, up to 33 tonnes. Measurements of vertical deformation were taken by LVDTs on vertical poles and live DIC, demonstrating small deflections and elastic behaviour. All bridges were upgraded for the construction work, permitting specific vehicles up to 25.5 tonnes capacity.



Figure 5. a) Parapet load test at Redbridge flyover and b) Proof load test at upper Teesdale.

3 LESSONS SHARED

3.1 *Risk*

Proof load testing can be a high-risk task. The uncertainty of the structural capacity, which has led to the need for physical testing, is cause for concern. The test must be conducted:

- By suitably experienced engineers – notably this is plural, to check each other's work. Guidance (ICE, 1998) defines the role of Test Controller, who must be a Chartered Engineer and experienced in load testing, and CS 463 (National Highways, 2019) requires the 'supervision of a Chartered Engineer with specialist expertise in bridge strength assessment or design'.
- With stop criteria defined and their rationale explained in advance,
- Incrementally increasing loads and checking for the signs of distress including on unloading,
- With the ability to identify stop criteria being breached to avoid damage,
- Without requiring access for personnel onto or under the bridge,
- Conscious of external factors which may increase the risks or alter the measurements taken, including tides, rain, snow, ice, wind and change in temperature during the test, and
- For tests exceeding 12 hours, with two equally capable teams handing over comprehensively.

While supplementary load testing is less dangerous, appropriate caution is still necessary. The design or assessment model should be investigated before testing, to predict results. Stop criteria is still defined and monitored live, though it less likely they be reached in the test.

3.2 *Measurements*

Measurements of global deformation and local distress (such as crack widening) need to be taken at a suitable scale and sample rate. The resolution of measurements should be no larger than 1/100 of the typical magnitudes expected. Repeatability (or maximum noise level) should be less than 1/10 of the typical magnitudes expected.

Readings on all sensors should be taken at a sample rate sufficiently fast to capture peak events. In most tests, the load is applied and withdrawn slowly to avoid dynamic excitations, so measurements once every second suffices. If the load or effects are dynamic or of vibrations (for instance footbridges), then measurements should be taken at a time interval 1/10 of the wave's time period. If the test is for the effects of a moving vehicle, but where the resonant response of the structure is not of interest, then the sample rate should be 1/10 of the time period for the influence line of the vehicle passing over the component. When measuring the local effects of cross beams (particularly on rail underbridges) this can mean that very high sample rates are required, since the wheel load is only influential on the cross beam momentarily.

High sample rates require anti-alias filtering. Alternating current power supplies create a signal at 50Hz, which is undesirable and is best removed by electrical filters before the analogue signal reaches the data logger. Computational post-processed filtering is possible, but less effective.

Time synchronisation of all readings (including load applied) is necessary, ideally collected on one acquisition system, otherwise a common clock using PTP or NTP protocol is necessary. Manual merging of datasets after the test is prone to errors.

Measurements should be zeroed at the start of testing with no applied load and thereafter not zeroed again. Relative measurements can be offset like a re-zero in post-processing, but the underlying dataset should remain unchanged.

Accolade Measurement include additional 'reference sensors' which are fixed such to give no response to the structural behaviour, located close to the primary measurements, using similar sensors, cabling and data acquisition. Observation of reference data can confirm the influence of thermal effects, electrical interference or other undesirables, often verifying that unexplained measurements in the data are real or not.

Digital image correlation (DIC) provides the ability to take displacement readings in locations unsuitable for physical sensors. Access to the structure is often still required to install targets for suitably accurate measurements. Whilst this is an emerging technology, Accolade Measurement supplement this with physical sensors, which provides some verification.

A permanent structural health monitoring system can be suitable for collecting the measurements. It is common that the system will need to have other sensors added for the test and the sample rate increased. Design for this expansion at initial stages is a necessary consideration, which can increase cost, data transmission requirements and power consumption.

3.3 *Loading*

Load application can be vehicles, water weights or kentledge blocks. It is necessary that the loads can be applied, and more importantly removed, quickly. During the test, load changes are the slowest task and hence any ability to hasten this is favourable.

It is often not necessary to close the road to all traffic for a supplementary load test. Where the controlled load is of larger magnitude and held constant for a longer duration than passing traffic spends on the bridge, then the interference of passing traffic can be seen distinctly as spikes, allowing selected periods of the test to be removed from the analysed data set.

Supplementary load tests need not apply a very large load. The Queensferry Crossing is capable at serviceability limit state to take many heavy vehicles, but the load test used only 264 tonnes of live loading (6no x 44 tonnes). This was sufficient, even with the uncontrolled traffic on the opposite carriageway, to measure the structural response. Where trust in the design, modelling, materials and construction is sufficient, this supplementary test can replace acceptance load tests, that otherwise require greater loading approaching the serviceability limit state.

If the structure's response is not instantaneous (as with all concrete bridges due to creep), the loading rate and hold times must be consistent, otherwise results appear like non-linear behaviour.

3.4 *Conditions*

External influences may have effects on the results. If possible, tests are conducted at stable temperatures and (for more flexible bridges) at low wind speeds; overnight is normally good and this usually coincides with low public traffic and therefore minimal disruption. For tests outdoors and lasting longer than 1 hour, temperature is likely to be influential on the instrumentation and must be minimised. In tidal or varying waters, the planning must consider whether this increases risks and/or will alter the readings. Any external factors which are suspected to influence, should be measured directly to correlate and correct for.

3.5 *Scale*

Where a particular component or assembly from a bridge is identified as critical and it can be removed (temporarily or replaced), then a load test can be conducted on the component away from the bridge, so long as suitably similar restraint conditions can be replicated. The hanger clamps from the Union Chain Bridge were detachable and selected units were load tested safely in isolation. Conversely, the Southampton parapets could only be tested on the bridge, as their fixing to the bridge deck was critical for performance.

An alternative, as per the research programme for the Usk River Bridge, is to replicate the components in a laboratory. In that case, two replica reinforced concrete hinge joints were created at 75% scale – and at an inverse square ratio, loading could be reduced to 56%. Nearly 100 strain gauges were fixed to steel reinforcement bars before casting into the concrete.

Smaller is generally better in load testing. Reducing the load, reducing the duration, and reducing the extents, all contribute to reducing the safety risks and disruption. However, we must ensure that the right data is collected sufficiently. Some failure modes are reliant on the coincidence of loads across the whole structure and hence reducing the extents is not appropriate for such proof load tests. A good way to envisage this is to produce from the theoretical model an influence surface of the bridge deck for the location or component considered.

3.6 *Data handling and analysis*

In a short term (few days) load test it is normal to collect and keep all data, enabling the reviewer to detect all patterns later. It is normal that one or more engineer is on site continuously throughout the test, providing the ability to resolve problems should they occur.

When the monitoring duration extends longer, it may be that the instrumentation is left unsupervised. 'Edge processing' the data, extracts details and reduces the uploaded data. It can be that a duplicate of the full data is kept on site and manually retrieved at intervals.

It is important that all data is backed up on separate devices as soon as possible. Duplicates may be sent away live during testing (preferrable) or taken physically at intervals.

It is necessary to display data live during any test to check for stop criteria. Visualisations include readings shown numerically or graphically, and present comparable measurements.

We have heard suggestions that warning lights or alarms should be installed based on readings exceeding thresholds. However, in our experience, only certain stop criteria can be quantified so neatly as to use in mathematical thresholds (criteria such as, maximum deformation). Stop criteria like indication of plastic deformation and creep are better spotted by the experienced test engineers' observation of graphical data. We prefer this more manual approach for collectively considering all stop criteria and maybe even those which cannot be foreseen.

4 CONCLUSIONS

Over 30 years' experience of load testing for bridges and structures is summarised in selected examples and the notable lessons are shared for the benefit of safe delivery of future tests. Other examples have been left out due to limited space, including proof load testing for an access bridge in the London Olympic Park, destructive tests of crossheads on the M4 Elevated Roadway, monitoring and testing of hinge joints with a retrofitted support system of the River Ebbw bridge, and supplementary load tests on steel-composite viaducts, but their lessons learnt are included.

It is hoped that supplementary and proof load tests will continue to be used for determining the performance of bridges for many years. With the sharing of good practice, this might be more readily available as a technique for design improvements, assessment of existing structures and extension of asset life. Updates to guidance and the inclusion of proof load testing would benefit the engineering community in the UK and abroad.

REFERENCES

Cousins, D. P., 2017. Reinforced-concrete beam hinge joint fatigue assessment. London: Proceedings of the Institution of Civil Engineers - Bridge Engineering.

Cousins, D. P., McAra, D. & Hill, C., (available pre-print) 2022. Monitoring of the Queensferry Crossing, Scotland. Proceedings of the Institution of Civil Engineers - Bridge Engineering.

ICE, 1998. Guidelines for the Supplementary Load Testing of Bridges. London: Thomas Telford Publications, The Institution of Civil Engineers, National Steering Committee for the Load Testing of Bridges.

National Highways, 2019. Load Testing for Bridge Assessment. Revision 0 ed. London: National Highways (formerly Highways England), Design Manual for Roads and Bridges.

Schacht & Steffen, 2015. Concrete hinges in bridge engineering. London: Proceedings of the Institution of Civil Engineers - Engineering History and Heritage.

Sétra, 2004. Guide Technique-Épreuves de chargement des ponts-routes et passerelles piétonnes. Paris: s.n.

Transport Research Board, 2019. Primer on Bridge Load Testing. Washington D.C.: Transport Research Board.

Bridge Maintenance, Safety, Management, Digitalization and Sustainability – Jensen, Frangopol & Schmidt (eds)
© 2024 The Author(s), ISBN 978-1-032-77040-6
Open Access: www.taylorfrancis.com, CC BY-NC-ND 4.0 license

Long-term monitoring of ASR deteriorated bridges after reinforcement

M. Tsuda & S. Kagatani
Department of Civil Engineering, National Institute of Technology, Ishikawa College, Ishikawa, Japan

S. Ura
Kokudo Kaihatsu Center Company Limited, Ishikawa, Japan

K. Torii
Central Nippon Highway Engineering Nagoya Company Limited, Ishikawa, Japan

ABSTRACT: Deterioration due to alkali-aggregate reaction (ASR) began to be observed on bridges about 10 years after opening for service, due to the use of aggregate with high ASR reactivity. Serious ASR deterioration was also found at the time of seismic retrofitting in underground footings. Moreover, rebar rupture was recognized in 13 of the deteriorated bridges. ASR-related retrofitting of these bridges has therefore been conducted continually in conjunction with large-scale repair and seismic retrofitting projects since 1998. Furthermore, crack displacement gauges were fixed to strengthened bridges to automatically monitor the crack behavior over a long time for more than a decade. This study revealed that the ASR expansion rate was significantly reduced after retrofitting and that changes in the crack width have a strong correlation with temperature changes. Underground ASR reactivity was also investigated by accelerated expansion tests simulating an underground environment and outdoor exposure tests.

1 INTRODUCTION

The Noto Satoyama Kaido Expressway (former Noto Toll Road) spanning 82.9 km came into full operation as an arterial high-standard highway in 1982 to connect Kanazawa, the capital of Ishikawa, and the Noto area, the peninsular part of the prefecture and was designated as a primary emergency transport road to ensure preferential traffic in times of disaster.

With their wide distribution throughout the Noto area, volcanic rocks including andesite are important sources of aggregate for concrete in the area where gravel resources are in short supply. Meanwhile, serious deterioration due to alkali-silica reaction (ASR) has been recognized in concrete made using crushed andesite. The risk of ASR is also considered to be potentially high all over Japan, a land of volcanoes, as layers of the Neogene period containing large percentages of ASR-causing activated silica are widely distributed over the country.

The basic policy of Japan's ASR-suppressing measures is to control the total alkali content of materials (3 kg/m^3). However, it has been pointed out that alkali elusion from crushed andesite with a high volcanic glass content from the Noto area can cause long-term ASR deterioration.

From the viewpoint of "local production for local consumption" and "reduction of environmental load", it is not realistic to select aggregates with no risk at all for ASR. It is considered rather important to create concrete structures with no ASR by formulating rules for ASR-suppressing measures suitable for aggregate from each locality to make the most of local materials. In the Noto area, crushed andesite has currently been replaced by crushed limestone, while ASR-suppressing measures using fly ash concrete have become widely used.

DOI: 10.1201/9781003483755-41

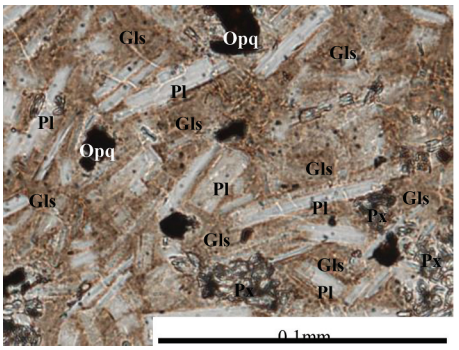


Photo 1. Polarizing microscope photograph by the foil sample of the crushed andesite.

Table 1. State of Deterioration and repair/retro fitting methods of bridges under study.

Bridge under study		Year of con-struction	Year of retro-fitting	Substructure style	Height	Pier cross-section	ASR deterioration	State of hoops	Repair/ retrofitting method
E	Pier P2	1982	2007	Cantilever pier	33.0 m	4.1×9.1 m	Cracking in cross beam of pier and top of footing	Rupture	Hoop restoration + RC jacketing of pier + RC jacketing of footing by RC Standard Spec. structural calculation
I	Pier P1	1980	2002 - 2004	Cantilever pier (hollow near the base)	26.5 m	3.8 ´ 3.8 m	Large cracking in the corner near pier base	Rupture	Hoop restoration (flare welding)
	Pier P2				26.5 m	3.8 ´ 3.8 m	Large cracking in the corner near pier base	Unconfirmed	Prestressed concrete jacketing
L	Piers P1 to P5	1977	1998 - 2000	Two-column gate-type rigid frame			Map cracking in entire pier	Rupture	Reinforced concrete jacketing + through prestressing bars
M	Piers P1 to P8	1980	1997 - 2000	Cantilever pier			Cracking in pier (vertical) and top of footing	Rupture	Prestressed concrete jacketing
O	Pier P1	1978	2005 – 2006	Hollow cantilever pier	42.1 m	4 ´ 4 m	Vertical cracking in pier	Sound	Steel panel jacketing + re-placement of girders
	Abut-ment A1			Rigid frame abutment	5.9 m	10.7 ´ 0.6 m	Cracking in the direction of main bars	Sound	No treatment except crack injection
P	Pier A1	1978	2007	Wall pier	29.5 m	10 ´ 3 m	Very large cracking in the corner of pier	No connec-tion since construction	Prestressed concrete jacketing
R	Abut-ments A1 & A2	1976	1998 - 1999	Changed from cantilever pier to abutment	8.8 m	-	Large cracking in the corner of footing	Rupture	Jacketing of footing + construction of box culverts in side-spans to change the structure

This paper reports on a study in which ASR-deteriorated concrete structures strengthened by various methods were subjected to long-term monitoring using crack displacement gauges to check the progress of deterioration, while verifying the effect of each repair/retrofitting method in suppressing ASR expansion.

2 OUTLINE OF BRIDGES AND REPAIR/ RETROFITTING METHODS

2.1 *Lithological characteristics and alkali-silica reactivity of aggregates used for bridges*

As shown in Photo 1, coarse aggregate used for the bridges under study is mostly crushed andesite, or two-pyroxene andesite to be precise, produced from Okunoto, Ishikawa Prefecture, which contains a relatively high percentage of volcanic glass as a reactive mineral.

Alkalis have been eluted into concrete over a long time from volcanic glass, clay minerals, etc., contained in crushed andesite used for these bridges.

2.2 *Bridge overview, state of damage, and repair/retrofitting methods*

2.2.1 *Bridge overview and state of damage*

Figure 1 and Table 1 show the locations and speci-fications, respectively, of ASR-deteriorated bridges along the Noto Satoyama Kaido Expressway. The construction of bridges on this expressway concen-trated in the 1970s and early 1980s, when fresh or slightly modified andesite, which formed after the Miocene of the Tertiary Period in the Northern Noto area, became available on the market for concrete aggregate with the infrastructure development in the

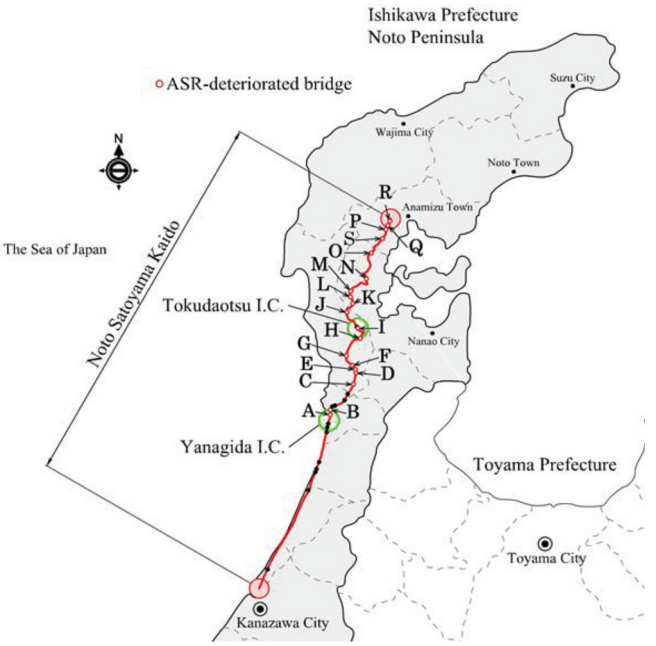


Figure 1. Location map of ASR-deteriorated bridge on Noto Satoyama Kaido.



Photo 2. The pier corner part cracking situation (Bridge P).



Photo 3. The footing with map cracking situation(Bridge E).

Noto area. Also, due to the opening of the entire No-to Satoyama Kaido in 1982, none of the bridges was subject to the "temporary measures against ASR" of-ficially established in 1986.

With this construction background, 19 bridges north of the Yanagida Interchange on the expressway out of 25, nearly 80% of the bridges, suffered ASR-deterioration. Furthermore, 13 of these ASR-deteriorated bridges (nearly 70%) underwent reinforcing bar rupture.

Photo 2 shows an instance of damage. Cracks exceeding 1 mm in width were frequently found in the corners of members of damaged bridges, mainly due to ASR expansion. Map cracking was also found in the entire top surfaces of footings as shown in Photo 3.

2.2.2 *Bridge repair methods*

Table 1 lists the investigated bridges, which were repaired/strengthened primarily by jacketing with prestressed concrete (PC), reinforced concrete (RC), or steel panels. Deteriorated footings were also repaired/strengthened by PC and RC jacketing, with some being also vertically tightened. Some of the bridges underwent significant deterioration both in the super- and substructure, leading to changes to their structural systems.

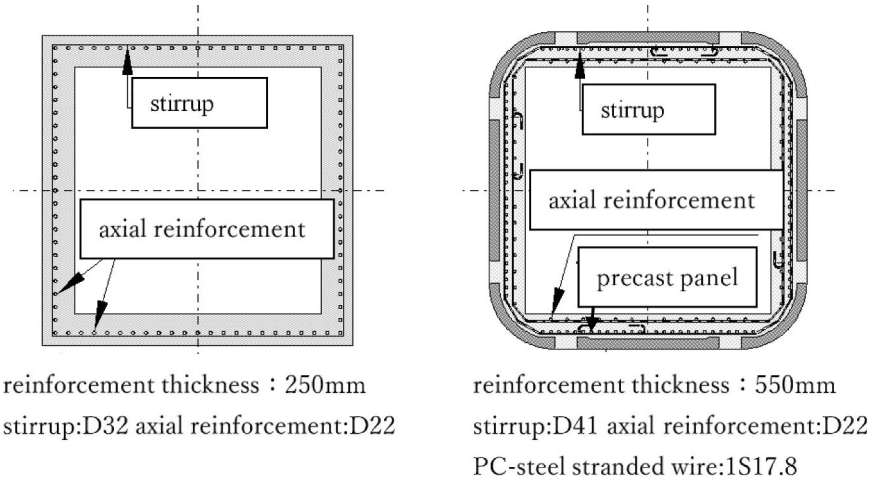


Figure 2. Outline of retrofitting carried out (Bridge I).

Repair/retrofitting of these bridges began around 1998 along with seismic retrofitting. The methods were selected not only based on the results of seismic calculation and economic efficiency but also in consideration of the degree of ASR deterioration and the functional recovery of hoop reinforcement.

- Repair method for Bridge I
  Repair/retrofitting of Piers P2 and P3 of Bridge I was designed and executed in 2003 and 2004 by PC jacketing (Figure 2) for the purpose of restraining ASR expansion and retrofitting against an earthquake. This technique comprises placing precast prestressed concrete panels around the existing piers, setting prestressing steel through the panels, and tensioning the steel in the circumferential direction.
  Repair/retrofitting of Piers 1 and 4 through 8, which was designed and executed in 2007, was required to be completed within the fiscal year, as it coincided with the recovery project from the earthquake off the coast of Noto Peninsula. Since simultaneous projects were expected at many other bridges, concern arose of a shortage of contractors for the PC jacketing, which is a special method. For this reason, RC jacketing (Figure 2) with proven results requiring fewer work processes was adopted.
- Repair method for Bridge P
  Bridge P constructed in 1978 is a simple pretensioned PC bridge consisting of a T-beam part and a four-span continuous rigid T-frame part. The cross-sectional shape of the

existing piers was rectangular. Pier PA1 is located at the joint between the two parts. Cracking occurred in the corner of this pier in the pier axis direction. The pier was subjected to seismic performance verification by seismic horizontal load-carrying capacity testing and dynamic analysis and was also found to fail to meet the seismic requirements. Comparison was therefore made among three methods: RC-, PC-, and steel panel jacketing. As a result, the pier was strengthened by PC jacketing, which provides a stronger effect of reuniting concrete and a higher cost performance.

2.3 *Service conditions of bridges*

The bridges under study were constructed almost in the same period, being in service for over 30 years. Moreover, roughly 5 kg/m² of NaCl is sprinkled over the bridges every winter to prevent freezing, whereby roadway drainage containing the deicer seeps through the expansion joints throughout the year. This forms an environment prone to accelerate ASR.

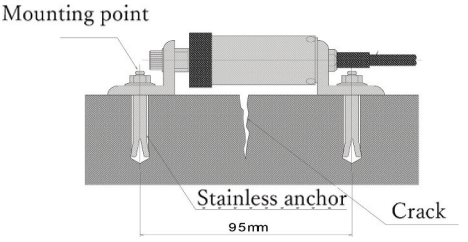


Figure 3. Detail of crack displacement transducers.

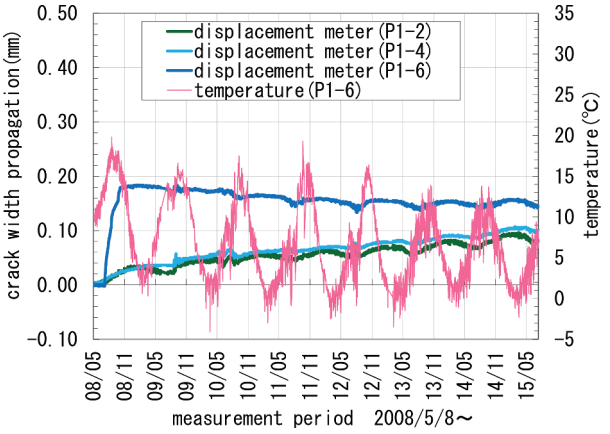


Figure 4. The results of crack propagation monitoring after the retrofitting (Bridge I・Pier P1).



Photo 4. The setting situation of crack displacement transducers.

3 CRACK MONITORING USING CRACK DISPLACEMENT GAUGES

Figure 3 and Photo 4 show crack displacement gauges with a sensitivity of 1/1,000 mm and measurement range of ± 5 mm attached to cracks to monitor changes in the crack width, thereby monitoring the crack propagation due to ASR. In view of long-term monitoring, each gauge was encased in a plastic box filled with grease, with the cracking being sealed with a resilient sealant to prevent contact with seepage from other cracks. This treatment is considered to enable the long-term monitoring to be discussed later in this paper.

A thermocouple was also placed at each monitoring point for temperature correction of the strain values. On one of the piers, multiple crack displacement gauges were placed at segments with different environmental conditions, such as in the soil and in the air, to examine the effect of temperature difference.

4 RESEARCH RESULTS AND DISCUSSION SO FAR

4.1 *Bridge I*

Figure 4 shows the results of measurement at the pillar of Pier P1, Bridge I, which was strengthened by RC jacketing. Seven years have passed since the beginning of monitoring in May 2008 upon completion of the retrofitting work. Though the crack width tends to gradually increase at an early stage of monitoring, the peak values of the fluctuations due to annual temperature changes themselves remaine nearly constant, with the increments in the crack width due to ASR expansion being not more than around 0.01 mm/year at the greatest. At P1-6 near the ground surface, the displacement increases significantly at the beginning of monitoring, presumably because of localized action of ASR expansion on the upper surface due to the increased restraining reinforcement ratio on the bottom surface. However, the values do not increase thereafter or rather tend to decrease since 6 months after the beginning, apparently having converged at the present stage.

The periodic lowering of the thermocouple readings can be attributed to the insulating effect of surrounding vegetation. Figure 5 shows the results of monitoring at the Pier P2, Bridge I, for 10 years since PC jacketing. The crack width annually fluctuates with the temperature, rising from spring to summer and falling from autumn to winter. The annual peak displacements tend to decrease from the beginning of monitoring, demonstrating that ASR expansion has been effectively restrained more by PC jacketing than by RC jacketing.

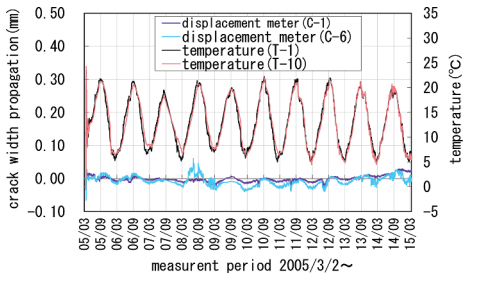


Figure 5. The results of crack propagation monitoring after the retrofitting (Bridge I・Pier P2).

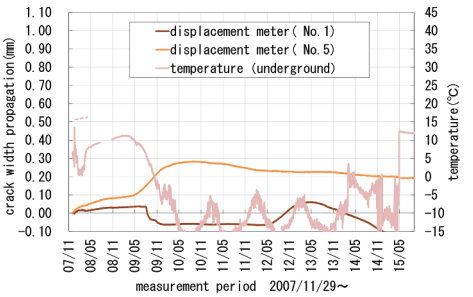


Figure 6. The results of crack propagation monitoring after the retrofitting (Bridge P・Pier PA-1).

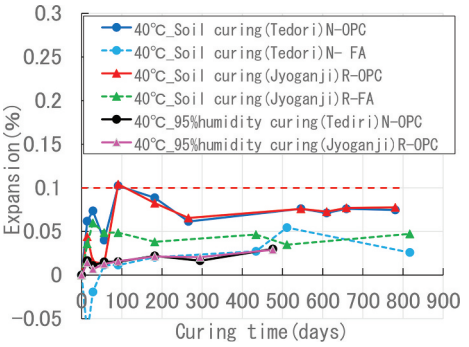
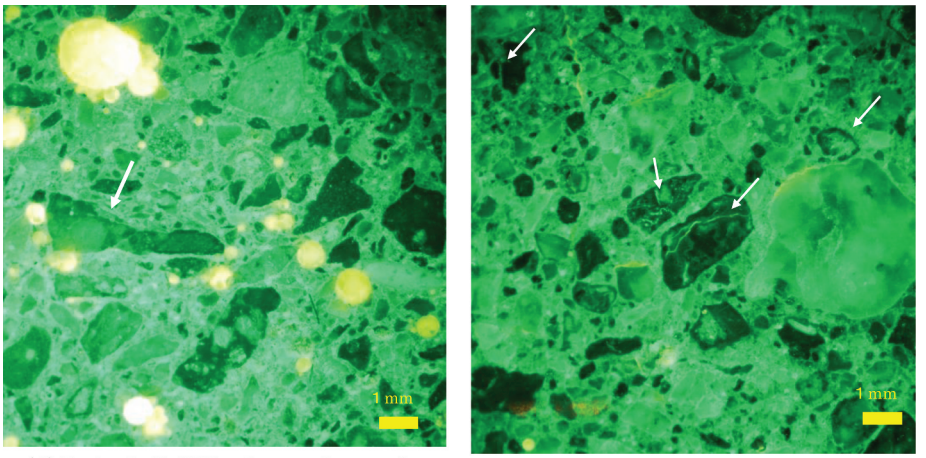


Figure 7. Results by the mortar bar method.

4.2 *Bridge P*

Figure 6 shows the measurements of crack displacement gauges on Pier PA-1, Bridge P, including those of the gauge set underground. The thermocouple measurements have shown no periodicity since 2 years after installation, presumably due to deterioration of the device. The crack displacement of Gauge No. 5 underground on the inbound lane side tends to increase for 3 years since installation but subsequently turns to decreasing tendencies, leveling off thereafter. Expansion due to ASR is therefore smaller underground than that in the air, which is more strongly affected by sunlight, precipitation, and deicers. At the time of pier retrofitting, its footing was excavated to apply a waterproofing layer on all surfaces excluding the bottom. This is also considered to contribute to suppression of the progress of ASR.



(1) Tedori N-OPC Expansion rate 0.0747(%)

(2) Jyoganji R-OPC Expansion rate 0.0776(%)

Photo 5. Fluorescence microscope observation (cross-sectional view).

5 OUTLINE AND RESULTS OF INDOOR TESTS SIMULATING UNDERGROUND ENVIRONMENT

River sands from Tedori River, Ishikawa Prefecture, and Joganji River, Toyama Prefecture, were used for the tests as non-ASR reactive and ASR-reactive sands, respectively. The difference in their ASR reactivity is derived from the component rates of reactive rocks (andesite and rhyolite) and nonreactive rocks (granite and diorite) in the aggregates. To simulate an environment (sandy soil) near an ASR-deteriorated underground structure, silica sand from Toyoura (former JIS Z 8801 Toyoura standard sand) was filled in test tanks and saturated with tap water.

Figure 7 shows the expansion rates of specimens at a curing temperature of 40°C. The curing tank was kept at a relative humidity exceeding 95%. The expansion rates of specimens without fly ash fluctuated at the beginning of curing, but ultimately increased to over 0.07% by a curing age of 781 days, regardless of the reactivity of aggregate, showing similar expansion behavior throughout the period. Their expansion rates in this sandy soil are higher than those of specimens tested by the mortar bar procedure specified in JIS A 1146 at the same 40°C, presumably being affected by alkalis eluted from the sandy soil and specimens. The expansion rates of specimens containing fly ash are lower than those of specimens without fly ash, demonstrating the expansion-suppressing effect of fly ash.

Photo 5 shows the results of fluorescence microscopy. The specimen made using ASR-reactive aggregate from Joganji River containing no fly ash shows wide cracks due to ASR gel derived from sand particles. On the other hand, a number of small cracks are observed in the

specimen made using non-reactive aggregate from Tedori River containing no fly ash. Although their expansion rates are similar at less than 0.08%, their cracking characteristics are thus found to differ from each other.

6 CONCLUSIONS

Major results of this study are summarized as follows:

(1) ASR-deteriorated bridge piers were strengthened by jacketing with reinforced concrete and prestressed concrete along with seismic retrofitting. Both methods were proven effective in suppressing ASR expansion.
(2) ASR-deteriorated footings were coated with a waterproofing layer. Subsequent ASR expansion was found to be small by crack width measurement. The waterproofing was proven effective in suppressing the progress of ASR.
(3) Indoor ASR-accelerating tests were conducted simulating an underground environment involving groundwater. As a result, the expansion rate of specimens in sandy soil was found to be higher, at the same curing temperature, than that of specimens in a moist environment with a relative humidity of more than 95%.
(4) The expansion rate of specimens containing fly ash was lower than that of specimens containing no fly ash, demonstrating the ASR-suppressing effect of fly ash.
(5) When verifying the effect of measures against ASR, it is considered important to assume long-term monitoring for more than 10 years to incorporate changes over a long time. To this end, it is considered essential to ensure the durability of monitoring equipment.
(6) This method should be used to investigate underground structures that use aggregates with high ASR reactivity and are located in alkali-containing soils. While this method can more accurately reproduce in-situ environmental conditions and accurately determine ASR-related risks, it requires the cost of soil investigation and construction of a test site, as well as a long testing time.

ACKNOWLEDGMENT

The authors thank Ph.D. M. Asada, ARS Consultants Company Limited, for his advice in the experiment

REFERENCES

Alkali aggregate reaction restraint measure (Civil engineering structure) Implementation Guidelines. 2002 (in Japanese).

Minato,T. & Torii,K.2010. ASR-deteriorated bridges and rock type of reactive aggregate on Noto expressway. *Journal of the Society of Materials Science*, Japan 59(10):781–786 .(in Japanese).

Torii,K. & Hashimoto,T. 2014. We Should Now Use The Fly ash Concrete in The Hokuriku District Why Don`t You Use It?. *Cement and Concrete* 810:18–23.

Torii, K. Nomura, M. & Minami,Y. 2006. Alkali-Silica Reactivity and Alkalis Releasing Property of River Sands Produced In Hokuriku District. *Cement and Concrete Research* 60:390-395(in Japanese).

Tsuda, M. Amin, K,A,R.nakata,Y. & Torii, K. 2019.Suppressing Effect of Alkali Silica Reaction in Chloride Attack Environment by Classified Fine Fly ash.*Proceedings of 4th International Symposium on Concrete and Structures for Next Generation*:108-117.

Yamada, K. Kawabata, Y. Kubo, Y. Goda, H. Sagawa, Y. & Hirono, S. 2014.Technical Committee on Diagnosis of ASR-affected Structures. *JCI-TC115FS [On-line]*. On: www.jci-net.or.jp/ (in Japanese).

Bridge Maintenance, Safety, Management, Digitalization and Sustainability – Jensen, Frangopol & Schmidt (eds)
© 2024 The Author(s), ISBN 978-1-032-77040-6
Open Access: www.taylorfrancis.com, CC BY-NC-ND 4.0 license

The use of smart bridge bearings for railway bridge monitoring

P. Olaszek, A. Sakowski & N. Kur
Road and Bridge Research Institute, Warsaw, Poland

M. Smoliński
B2 Sp. z o.o., Warsaw, Poland

ABSTRACT: The load control of the bridge structure can be an important element of structural health monitoring (SHM). The paper presents the use of smart bridge bearings (SBB) for load monitoring. SBB was developed as an adaptation of Pot Bearings (Confined Elastomeric Bearings) integrated with special force sensors which were used to monitor reaction forces. The force sensor takes advantage of the properties of the encapsulated virtually incompressible elastomer in the cylinder, which is similar to those of a viscoelastic fluid. SBBs are placed instead of all standard bearings on which the monitored span is supported. Monitoring system with SBB has been tested in laboratory and next implemented on a test basis on a plate girder bridge with short span length and with intensive traffic of passenger trains. Numerical analysis were also performed to assess the compliance of the measured time histories of reaction forces with those determined theoretically.

1 INTRODUCTION

Structural health monitoring (SHM) of railway bridges is beginning to use more and more innovative sensors. The load control of the bridge structure can be an important element of such systems. In recent years, monitoring systems for bridge structures using intelligent components such as expansion joints, bearings or dampers used in seismic protection have been presented, Savioz et al. (2018), Islami et al. (2016). The advantages of a bearing-integrated sensor are presented in a publication discussing bridge bearing developments by Kazi et al. (2018). The idea of determining the support reactions in bridge structures by measuring deformations in concrete bearing pads located directly under the bearings is presented by Salamak & Klikowicz (2014).

The previously presented applications related to the measurement of reaction forces apply only to the measurement of slow-change loads. The sensors developed and presented here allow full analysis of dynamic phenomena and an automatic procedure for distinguishing dynamic (fast-variable) from static (slow-variable) phenomena. To analyze the accuracy of the smart bridge bearings (SBB), laboratory tests and a trial implementation on a railway bridge were carried out. Numerical analyzes were also performed to evaluate and calibrate the numerical model of the structure based on the monitoring results of this bridge.

There is a trend in current monitoring systems to process and visualize data on remote servers. Internet of Things (IoT) and Cloud Computing solutions are being used – Imam et al. (2021). The principle is to transfer virtually the entire burden of data processing, software and computing power to the server, and to allow constant access to this processed data through client computers. Thus, after transmission of only pre-processed data from the measurement sensors, further data processing and visualization is done on the server. Such a concept is also used in the developed monitoring system with SBB.

The monitoring systems used SBB could be integrated with the system of bridge vibration and displacement monitoring using inertial sensors presented by Olaszek et al. (2020). They could be the basic elements of a "Future Smart Bridge" that will control both the amount of load and the structure's response to that load – Olaszek (2024).

DOI: 10.1201/9781003483755-42

2 SBB DESEIGN

2.1 *Adaptation of pot bearings*

SBB was developed as an adaptation of Pot Bearings (Confined Elastomeric Bearings) integrated with special force sensors which were used to monitor reaction forces. Such force sensor (pressure sensor) takes advantage of the properties of the encapsulated virtually incompressible elastomer in the cylinder, which is similar to those of a viscoelastic fluid. SBBs are placed instead of all standard bearings on which the monitored span is supported. In addition, the SBBs were equipped with a bi-directional inclinometer and a thermometer. The view of SBB components is presented at Figure 1.

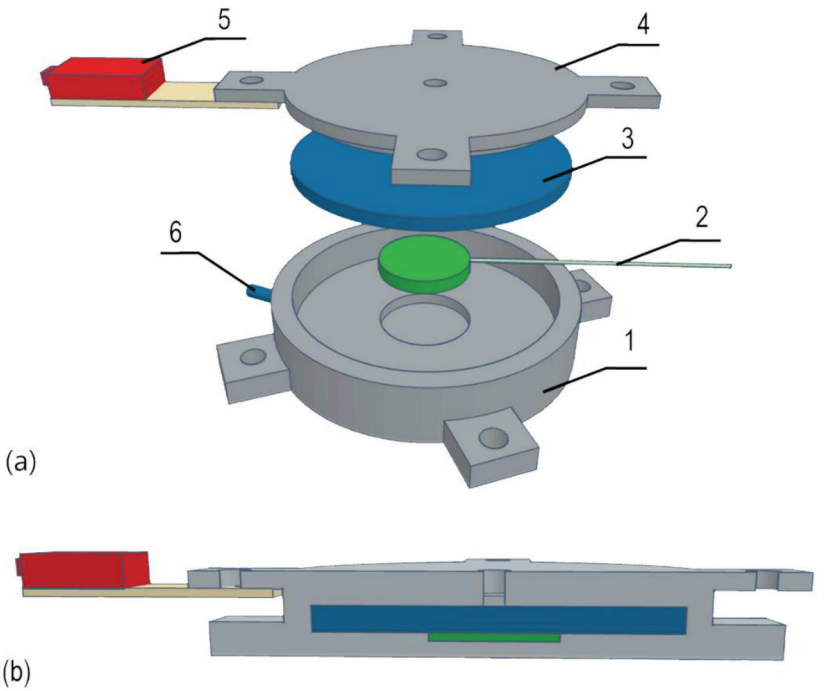


Figure 1. The view of smart bridge bearings (SBB): (a) components: 1 – pot plate, 2 – pressure sensor with cable, 3 – elastomeric disc, 4 – piston plate; 5 – inclination sensor, 6 – temperature sensor; (b) cross-section of the assembled bearing.

2.2 *Laboratory tests*

The developed prototype of the bearing with sensors passed laboratory tests. Laboratory tests included testing smart bearings for static loads. A compression machine with a high-accuracy force sensor was used for testing. The tests included scaling the force sensor and then checking its accuracy. During checking accuracy, axial and non-axial loads were carried out causing significant rotation of the bearing piston (Figure 2). The accuracy of measurement of the bearing loading force was tested with individual scaling and with a theoretically determined scaling factor based on the scaling of bearings with sizes other than the tested bearing.

The main conclusions of the research were as follows:

- The use of an elastomer pressure sensor to measure the bearing force is characterized by high measurement accuracy at pressure forces exceeding 20%-30% of the maximum force.
- The developed prototypes of an intelligent bearing with a pressure force sensor showed relatively high accuracy and resistance to non-axial loads causing significant piston rotation.



Figure 2. The view of bearing during laboratory tests on a compression machine; visible wedge plate enabling examination of reaction force indications with the piston plate twisted (Photo A. Matysek).

– Individual scaling of each sensor-bearing system ensures deviations from reference measurements (at a load close to 50% of the range) of 0.7%-1.2%.
– Scaling the sensor-bearing system based on the scaling of bearings of other sizes provides deviations from reference measurements (at a load close to 50% of the range) of 0.9%-1.1%.

2.3 *The monitoring system intelligence – signal analysis*

Based on the positive results of laboratory tests, a decision was made to undertake further work in order to obtain a product that is a fully intelligent bearing. It was necessary to develop a system for local and remote analysis of measurement results performed by a bearing installed in the bridge structure. The analysis of measurement results should be carried out taking into account two types of bridge bearing loads:

1) static load – from the structure's own weight;
2) dynamic load – from the moving load of the structure.

Figure. 3 shows a diagram of the system's operation, including the phases of signal processing and analysis. At the level 1, the reaction force signals are sampled at a frequency of 200 Hz. It takes place in a transducer built next to the bearing. Then the signal is transmitted via cable to a local computer located at the monitored bridge. The local computer collects data from all installed SBBs and is responsible for data processing at level 2. Special computer software on the local computer enables separate analysis of static and dynamic phenomena and limits the GSM transmission to the required minimum data. In order to assess dynamic phenomena, reaction force measurement is performed continuously at a frequency of 200 Hz and stored in a buffer. In the event of a load entering the bridge (which will be detected by a rapid increase in the measured reaction force), the entire reaction force time history during the train passage is copied from the buffer, stored and next transmitted to the server, along with a 5-second period before and 10 seconds after the train departure. To analyze static phenomena, the collected data on force, angles and temperature are averaged over 10 second time intervals and next transmitted to the server. At level 3, dynamic charts corresponding to all registered train journeys and static charts corresponding to daily, weekly, 30- and 90-day registration periods are automatically created on the server. Access for end-user to monitoring results is possible from level 4. It is possible to view charts using a web browser or download data using the FTP mechanism and use your own data processing algorithms.

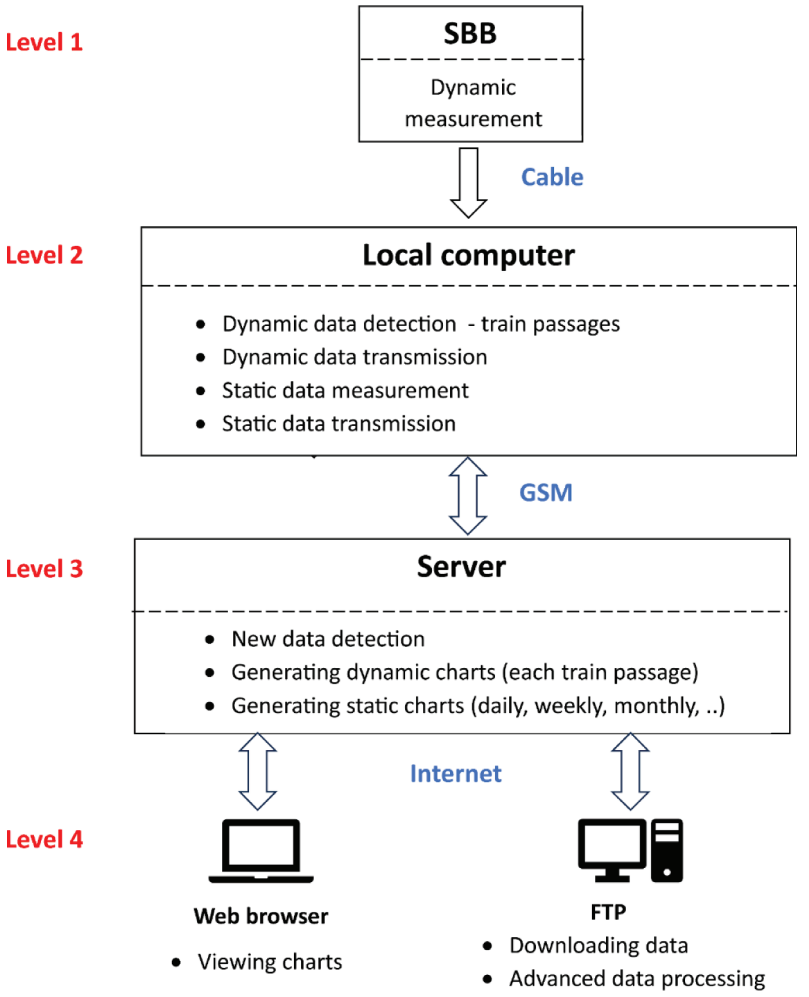


Figure 3. Diagram of the monitoring system use SBB.

3 EXAMPLE IMPLEMENTATION

3.1 *The tested bridge with SBB*

Due to the size and proportion of dynamic to static loads occurring on railway structures, a prototype of a monitoring system using SSB was developed and installed on the railway bridge.

For the test implementation of the monitoring system using SBBs, a six-span double-track bridge that was rebuilt in 1964 was selected. SBBs were installed on the extreme free-supported span of a steel structure with two plate girders. The theoretical span is equal to 7.45 m and the girder height is 0.86 m. Four SBBs were installed as shown in Figure 4. By the time the paper was prepared (December 2023), the bridge had been monitored for almost 2 years. Example results from dynamic and static analyzes will be presented below.

3.2 *Sample dynamic monitoring results*

Figure 5 Shows an example of the recorded reaction forces and the determined course of the total load from the passage of a passenger train consisting of an one locomotive and 5 passenger cars. The data relating to the locomotive are as follows: total weight: 80 tons, maximum axle load: 20 tons, overall length: 15,915 m, wheelbase for terminal axles: 11,600 m, bogie wheelbase: 3,050m.



Figure 4. The view of monitored plate girder bridge; the numbers of the bearings and their possible directions of movement were marked, and views of the bearings S1 and S3 at the first support and S2 and S4 at the second support were added. (central photo – before mounting the SBB).

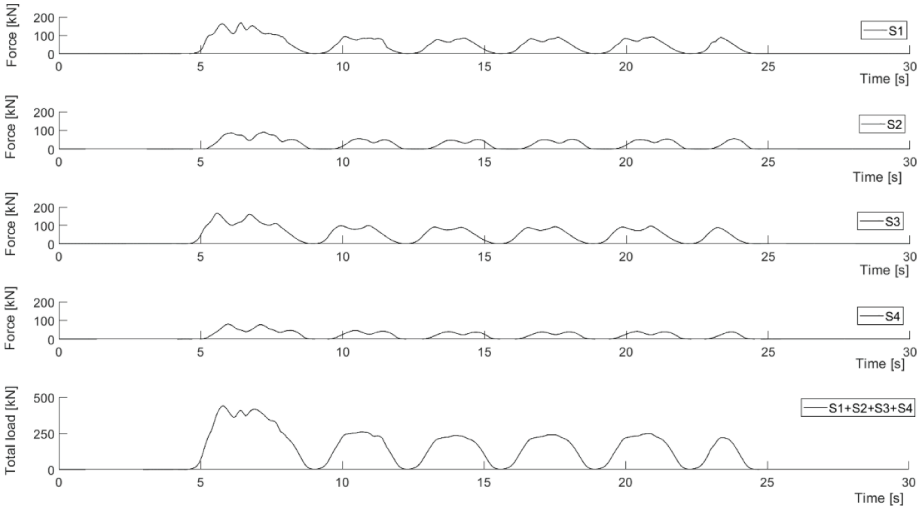


Figure 5. The passage of a passenger train consisting of one locomotive and 5 passenger cars; from the top: recorded reaction forces S1, S2, S3 & S4 and the determined time histories of the total load.

Figure 6 shows all the determined extreme values of the reaction forces on the S1 bearing for all train passages during one week of monitoring.

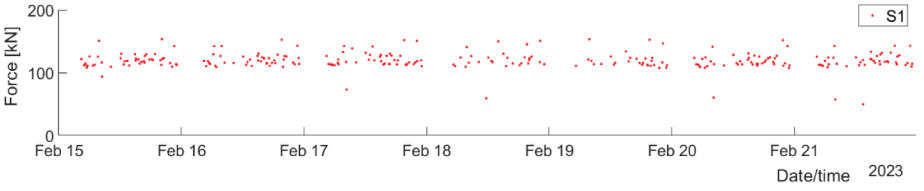


Figure 6. The determined extreme values of the reaction forces on the S1 bearing for all train passages during one week of monitoring.

3.3 *Sample static monitoring results*

Figure 7 shows an example of static impact analysis over a period of one week. The waveforms of changes in the measured reaction forces of the selected bearing (a bearing moving in

both directions) as a function of time and temperature were analyzed. The determined correlation coefficient (Stuart and Ord 1995) $\rho(R_s, T)$ of reaction force from temperature was equal to $\rho(R_s, T) = -0.94$.

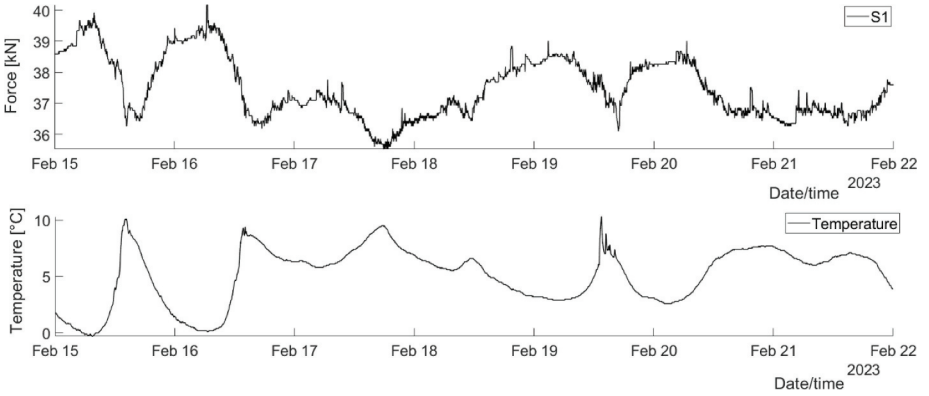


Figure 7. Recorded static waveforms of reaction force on one of the bearings and temperature during one week of monitoring.

3.4 *Measurements using monitoring and numerical analyses*

Computational analyzes of reaction force courses were performed using two numerical models:

- a two-dimensional bar model of a simply supported bridge span;
- a three-dimensional shell model of a simply supported span with a connection through the railway track to the embankment and the adjacent span.

In the latter case, rounded and non-linear waveforms of reaction forces were obtained, which were similar in shape to measured waveforms. Figure 8 shows the determined time histories of the reaction force of the S1, S2 bearings and time histories of the sum of all reaction forces using these two models and measured by SBB, for the train passage from Figure 5.

The extreme recorded weight of the front bogie of the locomotive passage in relation to the calculated data with the use of the bridge two-dimensional bar model equals about 109% and the average about 116%. Using a three-dimensional shell model, the ratios of measured and calculated values were respectively equal to about 88% and the average about 89%. It should be added that the measured average weight of the locomotive's front bogie is 100.1% consistent with the theoretical value from the locomotive's catalog data. In the case of a dozen or so other trains the deviations of measured average weight of the locomotive's bogie in relation to catalog values were below 2%.

4 CONCLUSIONS

SBB laboratory tests confirmed relatively high accuracy and resistance to non-axial loads causing significant piston rotation. Individual scaling of each sensor-bearing system ensures deviations from reference measurements (at a load close to 50% of the range) of 0.7%–1.2%. The use of an elastomer pressure sensor to measure the bearing force is characterized by high measurement accuracy at pressure forces exceeding 20%-30% of the maxi-mum force. Further work related to the development of the use of the pressure sensor in an SBB should be related to the study of the non-linear operation of the bearing at a load below 30% of the range.

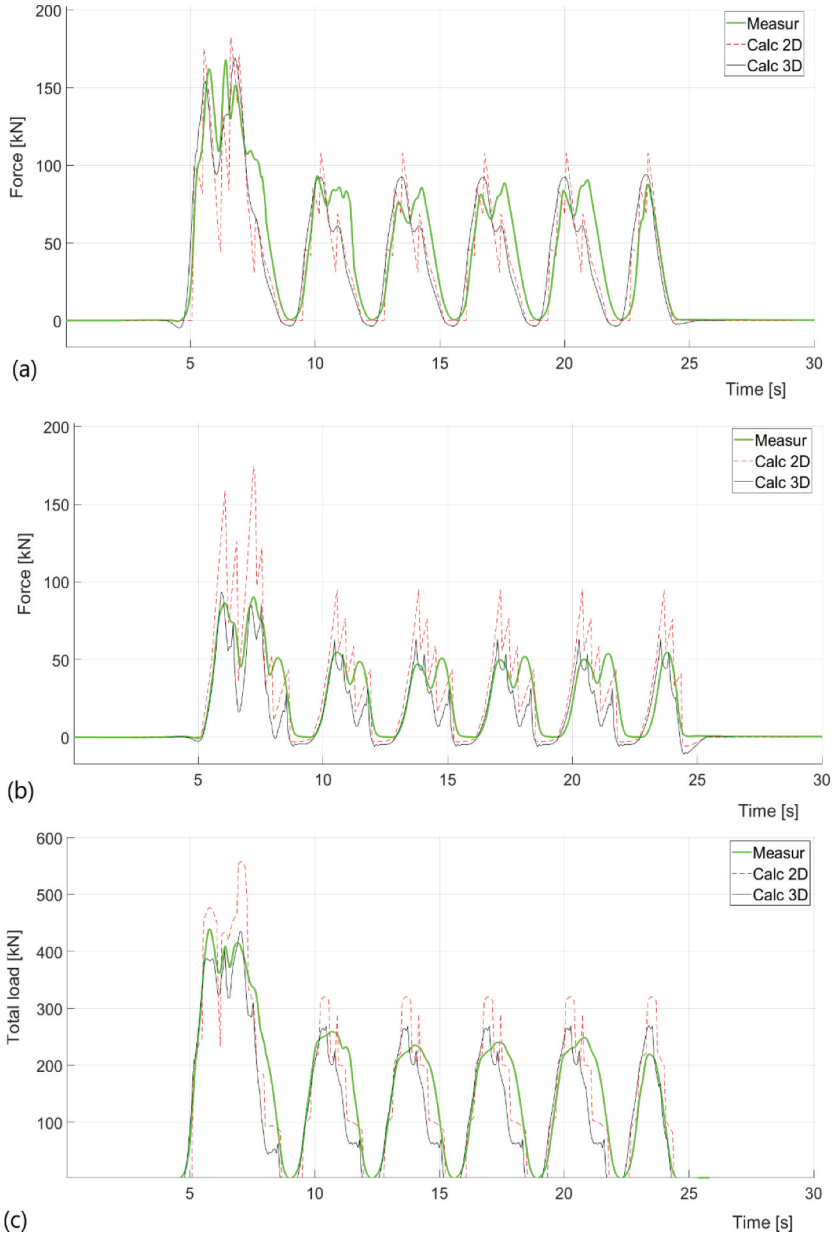


Figure 8. The determined using two models (Calc 2D & Calc 3D) and measured time histories for one locomotive and 5 passenger cars passage (from Figure 5): (a) the reaction force of the S1 bearing, (b) the reaction force of the S2 bearing and (c) the total load (sum of all reaction forces).

The monitoring system tests with the application of SBB carried out at the railway bridge confirmed the system's ability to monitor dynamic and static loads. It is possible to use the system to control the axle loads of passing trains as well as the total weight of passing trains. Deviations of measured average weight of the locomotive's bogie in relation to catalog values were below 2%. During the next tests, it is planned to compare the results with the actual, not catalog, weight of the locomotives.

Due to significant discrepancies between numerical analyzes and monitoring results it is planned to conduct further numerical analysis related to the simply supported bridge span with a connection through the railway track to the embankment and the adjacent span.

Integrating the data from SBB monitoring system with the results of the displacement and acceleration monitoring system will enable a reliable assessment of the behavior of the bridge structure. Such an assessment is particularly useful for monitoring old structures raising doubts about their load-bearing capacity and new structures raising doubts about their behavior under loads with significant speeds. In the future, it seems possible to combine the system for analyzing monitoring results with the train control system. Analysis of monitoring results over long periods confirmed their suitability for analyzing changes induced by static loads. It is possible to use the system to control possible bearing failures and support settlements.

ACKNOWLEDGMENTS

The presented project was subsidized by the Polish Agency for Enterprise Development (PARP) within Smart Growth Operational Programme 2014-2020, co-financed by the European Regional Development Fund.

The authors would like to thank the members of the team who completed the presented projects from the Road and Bridge Research Institute from Warsaw & Kielce; B2 Sp. z o.o.; Adaptronica Sp. z o.o.; ZEPWN sp. z o.o. sp.k., SHM System Sp. z o.o. Sp. kom. and Railway Track Development and Construction Unit of PKP Polskie Koleje Państwowe S.A.

REFERENCES

Imam, M., P. Savioz, and C. O'Suilleabhain. 2021. IoT Bridge Components–Specialized Smart Monitoring Solutions to Address User-Specific Needs. In *Bridge Maintenance, Safety, Management, Life-Cycle Sustainability and Innovations*, 882–889. CRC Press.

Islami, K., N. Meng, and C. O'Suilleabhain. 2016. Smart Bridge Components (Expansion Joints, Bearings and Seismic Devices) for Intelligent Infrastructure. In *Proc. 19th IABSE Congress*.

Kazi, S.N., V.V. Ghodke, and C. Sarmiento. 2018. Advances in Materials and Further Improvements in Bridge Pot Bearings. In *Maintenance, Safety, Risk, Management and Life-Cycle Performance of Bridges*, 2277–2284. CRC Press.

Olaszek, P. 2024. New Sensors and Digital Data Processing Algorithms for Monitoring Railway Bridges. In *Digital Railway Infrastructures. Editors D. Ribeiro, P. Montenegro, A. Andersson, M. Martinez-Rodrigo*. Springer Book Edition.

Olaszek, P., I. Wyczałek, D. Sala, M. Kokot, and A. Świercz. 2020. Monitoring of the Static and Dynamic Displacements of Railway Bridges with the Use of Inertial Sensors. *Sensors* 20, no. 10 (May 12): 2767.

Salamak, M., and P. Klikowicz. 2014. Indirect Determination of Support Reactions in Concrete Bridge Elements. In . LIBEREC 2014.

Savioz, P., K. Islami, and V.V. Ghodke. 2018. "Smart" Bridge Expansion Joints Enabling Optimized Decision-Making at Different Life-Cycle Stages. In *Maintenance, Safety, Risk, Management and Life-Cycle Performance of Bridges*, 2269–2276. CRC Press.

Stuart, Alan, and John Keith Ord, eds. 1995. Kendall's Advanced Theory of Statistics. 2: Classical Inference and Relationship/Alan Stewart & J. Keith Ord. - 5. Ed., 2. [Pr.]. London: Griffin.

Bridge Maintenance, Safety, Management, Digitalization and Sustainability – Jensen, Frangopol & Schmidt (eds)
© 2024 The Author(s), ISBN 978-1-032-77040-6
Open Access: www.taylorfrancis.com, CC BY-NC-ND 4.0 license

Development of a proof loading method for railway bridges with masonry abutments

C. Wang, J. Gonzalez-Libreros, L. Elfgren & G. Sas
Division of Structural and Fire Engineering, Luleå University of Technology, Luleå, Sweden

C. Daescu
Faculty of Civil Engineering, Politehnica University Timisoara, Timisoara, Romania

O. Enoksson & T. Hojsten
Trafikverket, Luleå, Sweden

ABSTRACT: Railway bridges with masonry abutments represent a significant portion of aging infrastructure in north Sweden. The assessment of their structural integrity is crucial to ensure safe and efficient railway operations. This paper presents the development of a proof loading method tailored specifically for railway bridges with masonry abutments. Before conducting loading tests, the bridge condition was assessed through visual inspections using ground-based photogrammetry and Ground Penetrating Radar (GPR). Realistic loads were simulated using a carefully chosen train fleet during the tests to evaluate load-carrying capacity and structural integrity. Comprehensive data, including strains, displacements, temperature, and acceleration measurements, were collected to gain insights into the bridges' behavior under real-life loading conditions. This data played a crucial role in making accurate predictions and guiding maintenance decisions for targeted rehabilitation efforts. To enhance capacity assessments, finite element models were calibrated using the test results, enabling confident predictions of how the bridges would respond to various loads. This rigorous approach ensures the safe operation of these historic bridges during planned heavy transports while adhering to safety standards. By employing the proposed proof loading method and utilizing advanced monitoring techniques, railway authorities can effectively manage the maintenance and preservation of these crucial structures.

1 INTRODUCTION

The proof load method for railway bridges is a vital procedure to confirm their capability to withstand significant loads, to assess the feasibility of increasing load capacity, or to evaluate the bridge's performance under operational conditions (Lantsoght et al, 2017; Lantsoght, 2019; Duvnjak et al, 2019). This method becomes particularly crucial in situations where there are doubts about the bridge's condition, possibly due to missing structural plans, material degradation, or when solely relying on analytical methods does not yield conclusive information regarding the bridge's performance.

Vitån Bridge, an integral component of Northern Sweden's transportation network along the Haparanda railway line, connects Boden and Morjärv. Special transports exceeding the line capacity are planned with axle loads equal to 30 tons. This line was refurbished several years ago but has not been loaded with heavier axle loads than about 22.5 tonnes per axle, although the allowable load is 25 tonnes. As the expected loads are higher, it is crucial to progressively test the bridge's capacity in the railway line to handle heavier traffic up to 30 tonnes per axle.

DOI: 10.1201/9781003483755-43

This study delves into the bridge's condition assessment, leveraging ground-based photogrammetry and Ground Penetrating Radar (GPR) to inform maintenance and structural integrity evaluations. A 3D digital model was generated from photogrammetry, enabling detailed analysis and damage detection. GPR scanning provided insights into the abutments and soil structure.

Furthermore, proof load tests using a specialized train fleet were conducted to simulate operational conditions and assess the bridge's performance. These investigations offer valuable insights into maintaining and evaluating similar structures, emphasizing the Vitån Bridge's role in regional infrastructure and engineering practices.

2 BRIDGE DESCRIPTION

Vitån Bridge is an essential transportation link along the Haparanda railway line, as shown in Figure 1. This bridge has significantly contributed to the movement of people and goods between Boden and Morjärv, and has become a critical component of Northern Sweden's infrastructure.

Spanning 21.1 m in length and 4.5 m in width, Vitån Bridge's superstructure is a composite beam design. This design features steel beams, fully braced and securely attached to a reinforced concrete slab using shear studs. This integration enables the steel and concrete to function as one single composite section. The composite beam is simply supported by the masonry abutments, with one end of the superstructure fixed to prevent the longitudinal movement, and the other end allowed some freedom in the same direction. The masonry abutments were constructed in 1900, while the superstructure is constructed in 2006.



Figure 1. Vitån bridge.

3 INVESTIGATION PRIOR TESTING

To gather information about the condition of the bridges before conducting the proof load tests, activities related to the visual inspection of the bridge condition trough ground-based photogrammetry, and use of Ground Penetrating Radar (GPR) were performed.

3.1 *Preliminary condition assessment using photogrammetry*

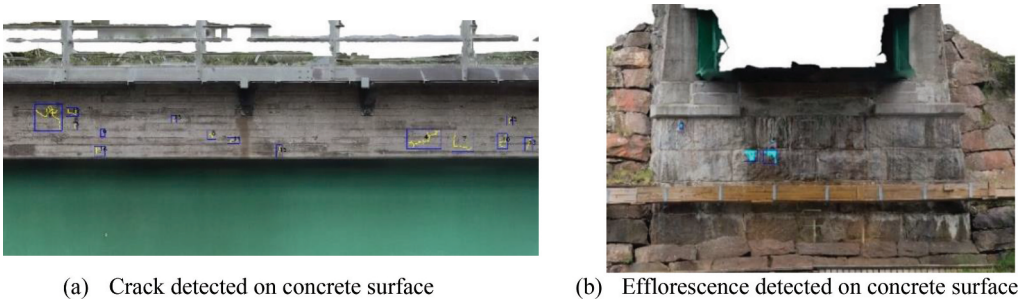
Photogrammetry is a technique employed to obtain precise measurements and 3D models of objects and their surroundings. It involves capturing images of the object or area of interest from multiple angles and the use of software to analyze and reconstruct the data.

For Vitån bridge, a comprehensive dataset of 496 photographs was captured, encompassing the entire structure from multiple perspectives. These photographs were meticulously processed to generate a precise 3D digital model of the bridge, as shown in Figure 2, serving as a foundational tool for the analysis. Utilizing advanced computer vision techniques and



Figure 2. 3D digital model of Vitån bridge.

machine learning algorithms, the model is systematically analyzed to detect surface damages. The detected damages are shown in Figure 3. This 3D model is used to define the instrumentation layout and position, Finite element model (FEM), etc.



(a) Crack detected on concrete surface (b) Efflorescence detected on concrete surface

Figure 3. Damage detection of Vitån bridge: Cracks are marked in yellow, and efflorescence is marked in blue.

3.2 *Subsurface detection using GPR*

GPR is an electromagnetic technique in which a high-frequency electromagnetic pulse is emitted into the ground, and reflections are recorded. The pulse (wave) propagates in the media (soil and bedrock) and when it encounters objects or layers with differing electrical properties, a portion of the wave energy is reflected back to the ground surface, where it is subsequently detected.

Since the masonry abutments in Vitån bridge were constructed over a century ago, their thickness and depth are unclear from existing documentation. To address this, GPR scanning was conducted before the proof load tests. The measurements also help detect any voids or other anomalies present in the bridges' abutments. In addition, GPR was used to collect information related to the soil stratification in the transition zone between the ballasted track and the bridges.

GPR scanning was performed on top of the rails and cross-sectional measurements on the abutment walls. In the radargram retrieved with a 160 MHz antenna (see Figure 4), two layers

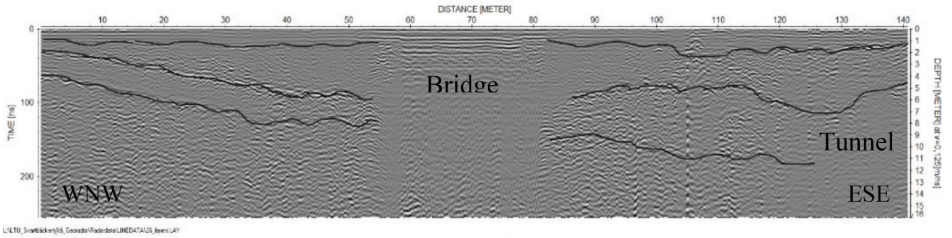


Figure 4. Radargram on different layers in track system.

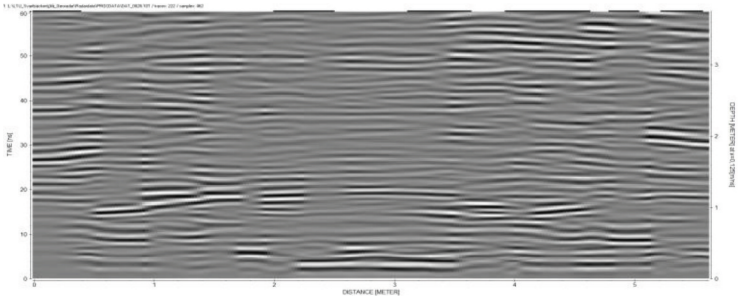


Figure 5. Radargram on first row of the northern abutment.

of filling can be identified on top of the original ground surface. The rock surface follows the shape/dip of the ground surface on the western part, slightly dipping towards the east. Soil depth is about 2 m on the western side but increases to about 4 m on the eastern side. The abutment measurements are presented in Figure 5.

4 PROOF LOAD TESTS

4.1 *Instrumentation*

A comprehensive measurement plan was developed to estimate the bridges' behavior as accurately as possible. This section summarizes the instrumentation used to measure variations of key variables during the proof load test.

The main variables assessed were strains, displacements, temperature, and acceleration of the bridges. Data was acquired from all instruments described in this section throughout the entire testing schedule, unless otherwise stated.

For Vitån bridge, four accelerometers (T-A1~A4) were instrumented in Phase I. In Phase II, two additional strain gauge (S1, S2) were added. The location of instrumentation is illustrated in Figure 6, with sensors from Phase I marked in blue and those from Phase II in red. The LVDTs were placed to measure both the vertical and horizontal deformation in masonry abutments; the accelerometers measure accelerations in the superstructure induced by the moving train. The strain gauges, which were welded to the steel girder, measure the strain induced by the loading train. Figure 7 shows the accelerometers, LVDTs, and strain gauges instrumented in Vitån bridge.

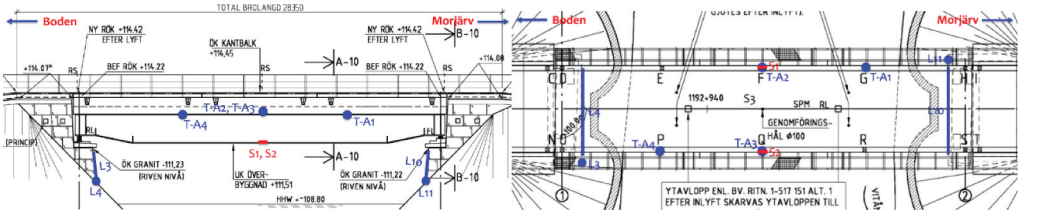


Figure 6. Instrumentation of Vitån bridge.

4.2 *Vehicle*

In the proof load tests, a train fleet (comprised of a locomotive and wagons), with specific axle loads, distribution, and configuration, is utilized to apply load on the bridge structure. The train fleet has to be carefully chosen to obtain a desired loading scenario that reflects real-life situations and simulates actual operating conditions.

The axle load and speed of the train serve as the primary variables to assess the bridge structure's performance under different loading. The train moves across the bridge at various controlled



Figure 7. Strain gauges, LVDTs, accelerometers deployed in Vitån bridge.

and consistent speeds, ensuring that dynamic load effects are taken into account during the testing process. Additionally, the train stops at specific positions on the bridge to conduct static tests, allowing for a thorough evaluation of the structure's response under stationary loads.

For the proof load tests, a 71.73 m long freight train fleet consisting of one locomotive, two coupling wagons, and four Uno wagons was employed, as displayed in Figure 8. It can be observed that the locomotive is connected to the Coupling Wagon, and adjacent Uno Wagons are connected to each other. The coupling Wagon serves to connect the locomotive and the Uno wagon. The wheelsets of the train fleet are labeled from P1-1 to P7-4.

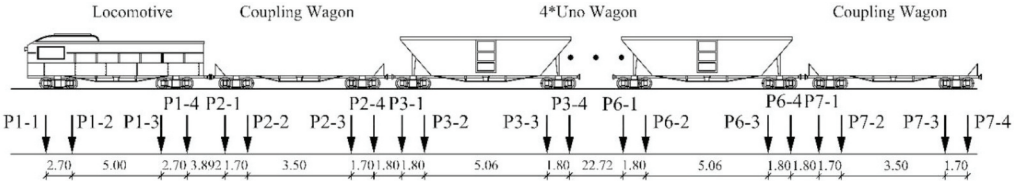


Figure 8. Geometry of the proof loading train (Unit: m).

The axle load of the locomotive and coupling wagons are fixed as 19.5 tons and 9 tons respectively under different loading scenarios. The axle load of the Uno wagons varies from 22.5 tons to 30 tons. In Phase I, 22.5 tons and 25 tons were adopted as the axle loads of the Uno wagons. In Phase II, the axle load increased to 26.5 tons, 28 tons and 30 tons in steps.

4.3 *Loading tests*

The trains are positioned in the bridges with the aim of producing maximum loads in the superstructure and substructure:

- Near the supports: For maximum shear and maximum load on the foundations
- Midspan: For maximum bending moment

The initial evaluation of the stress state for the bridge was performed using the AxisVM software. The reinforcement and masonry abutment were not introduced in this initial 3D linear analysis. Based on this initial analysis, the loading positions that induce maximum bending moment and maximum reaction force were determined. Based on the initial 3D linear analysis, the loading positions were marked before the proof load tests, as shown in Figure 9.

Five axle load levels were included in the proof loading test program. The axle load of the Uno wagons varied from 22.5 tons to 30 tons. In each load level, the train was stopped at two specific positions on the bridge to generate maximum bending moment in the superstructure and maximum reaction force in the substructure. The exact loading positions during static tests are recorded in Table 1.

During the dynamic tests, the train crosses the bridge at various controlled and consistent speeds, at load levels that match those of the static tests. In this way, it is ensured that

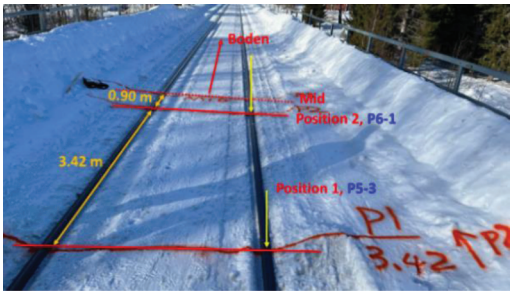


Figure 9. Marking loading positions for Vitan bridge.

dynamic load effects are incorporated into the testing process. The freight train used have a maximum speed of approximately 60 km/h. For each load level, dynamic tests were performed at different speed. Table 2 presents the dynamic load cases executed during the proof loading of the bridges. In the table, the speed, direction, and axle load of the Uno wagons date are summarized.

Table 1. Static load tests of Vitån bridge.

Phase	Axle Load (tons)	Loading Position (cm)	Wheel Set
I	22.5	-432.0	P5-3
		-83.0	P6-1
	25.0	-449.0	P5-3
		-108.0	P6-1
II	26.5	-439.0	P5-3
		-90.0	P6-1
	28.0	-432.0	P5-3
		-100.0	P6-1
	30.0	-367.0	P5-3
		-90.0	P6-1

Table 2. Dynamic load tests of Vitån bridge.

Phase	Speed (km/h)	Axle Load (tons)	Direction
I	54.0	22.5	Boden-Morjärv
	55.0	25	Boden-Morjärv
II	58.2	26.5	Boden-Morjärv
	57.0	28	Boden-Morjärv
	60.0	30	Boden-Morjärv
	55.2	30	Boden-Morjärv
	30.0	30	Morjärv-Boden
	45.0	30	Morjärv-Boden

5 CAPACITY ASSESSMENT

5.1 *Finite element modeling*

Finite Element (FE) Analysis was adopted for the structural assessment of Vitån bridge. is a pivotal technique for structural assessment. The analysis uses DIANA version 10.6 software and integrates empirical proof load tests with theoretical FEM analysis for a comprehensive assessment. The structural model includes the superstructure, foundation/substructure, track system, and soil, with each component modeled using 3D solid elements. Reinforcement in

concrete is represented by 1D beam elements with full interaction, using DIANA's 'embedded reinforcement' feature (Diana, 2022).

Accuracy is ensured through the comparison of structural drawings, 3D point cloud data, and Ground Penetrating Radar (GPR) scanning. The bridge's masonry walls and surrounding terrain are detailed using point cloud data and GPR scans, with soil modeling simplified based on GPR data. Figure 10 shows the finite element model of Vitån bridge used in the structural analyses.

Nonlinear material properties for concrete are simulated using total strain-based crack models with specific behavior curves for compression and tension. Soil material simulation considers various constitutive models, with the Mohr-Coulomb elasto-plastic model chosen for abutment materials, requiring parameters for soil elasticity and plasticity. An advanced Hardening-Soil model was also considered but not fully adopted due to its complexity. In addition to soil and concrete, linear material properties were assigned to the rail steel and sleeper concrete, and reinforcements were modeled with a linear Young's modulus and a Von Mises plasticity model. This comprehensive approach facilitates a realistic and accurate assessment of the bridge's structural integrity.

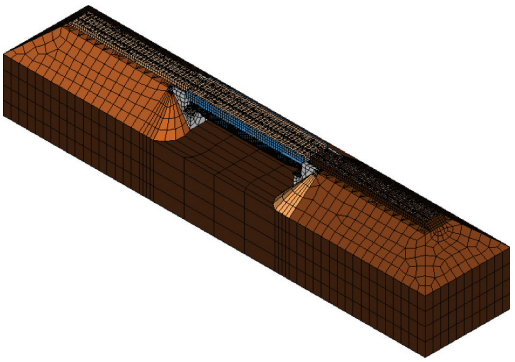


Figure 10. 3D FE model of Vitån bridge.

5.2 *Loading*

The bridge was subjected to two primary loads: the self-weight of the bridge and the proof loading from the train fleet. In the analysis, the self-weight of reinforcements was deemed negligible compared to that of the concrete and thus was not considered. The software calculated the total weight of the concrete, which was then applied as a dead load in the initial step of the analysis.

In applying the load, the FE model employed both load-control and displacement-control strategies. The displacement-control strategy proved to be more stable than the load control. In this approach, the displacement at each loading area was regulated by its center point using the TYING method in Diana (Diana, 2022). To align the applied displacement with the structural deformation, a statically determined system of rigid beams was used to distribute the vehicle point loads accurately from the nodes of prescribed displacement. The loading points' nodes were tied to the end nodes of these rigid beams to ensure identical displacements. Additionally, another rigid beam connected the center of two beams on the first level, also employing the tying method. The number of beam levels depended on the bridge's loading points, with constraints on translation along the beams and rotation around the beams' axes. Vertical point loads were applied to the central node of the top rigid beam via prescribed deformation. Finite element analysis.

5.2.1 *Static analysis*

FE analyses were carried out with axle load of 26.5, 28 and 30 tons for two loading positions in the static case. The results of analyses are presented in Table 3.

Table 3. FE results for static loading cases.

Axle load (tons)	Maximum Vertical Deformation (mm)		Maximum Reaction Force (kN)	
	Position 1	Position 2	Position 1	Position 2
26.5	-29.0	-30.1	970.9	972.3
28	-29.3	-30.5	972.1	973.6
30	-29.7	-31.1	973.7	975.2

Increasing the loading on the Vitån bridge structure led to a rise in both the maximum vertical deformation and the support reaction. Figure 11 illustrates the maximum vertical deformation under an axle load of 30 tons at P2 loading position.

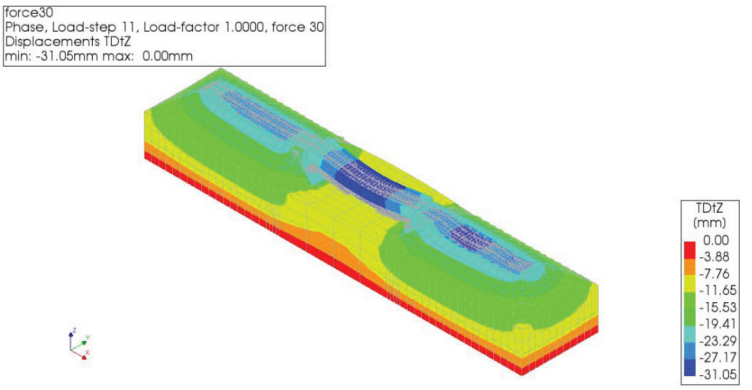


Figure 11. Static vertical displacement due to the axle load of 30 tons.

The bridge is experiencing a settlement of approximately 30 mm or more across all loading scenarios. This significant displacement is observed both at the midpoint of the bridge span and in the soil adjacent to the right abutment. Such extensive deformation is of considerable concern and could potentially lead to structural issues. Hence, ongoing monitoring of the bridge's overall deformation is recommended.

An additional scenario was investigated to determine the maximum capacity of the Vitån bridge. This analysis utilized a displacement-control loading scheme, designed to stress the structure to its failure point. This evaluation was conducted with a single loading position, as

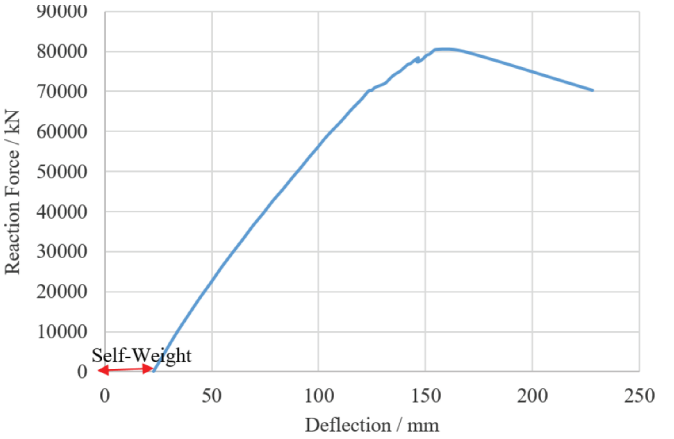


Figure 12. Reaction force versus deflection showing the elastic and plastic states of structure.

the distance between positions P1 and P2 does not markedly affect the structure's ultimate stage. The results of this analysis are presented in Figure 12, with the reaction force indicating the total load imposed on the entire structure.

5.2.2 *Dynamic analysis*

Transient dynamic analyses were conducted to assess the dynamic behaviors of the Vitån bridge under arbitrary time-dependent loads, following the moving load approach. Modal analysis was also carried out to ascertain the damping factors. This analysis aimed to identify the eigenfrequencies for the first ten modes.

The lowest and highest eigenfrequencies for the first 10 modes were 2.83 Hz and 4.56 Hz, respectively. Rayleigh damping parameters were then calculated, $\alpha = 0.52114\ s^{-1}$ and $\beta = 0.00116\ s^{-1}$ The calculated Rayleigh damping parameters, α and β, were then added to the material properties in the FE model.

To simulate the moving train loads on the bridge, a common method, incorporating the application of moving loads in the form of pulse time histories for each node is utilized. The method simply works based on the time of load arrival and node discretization.

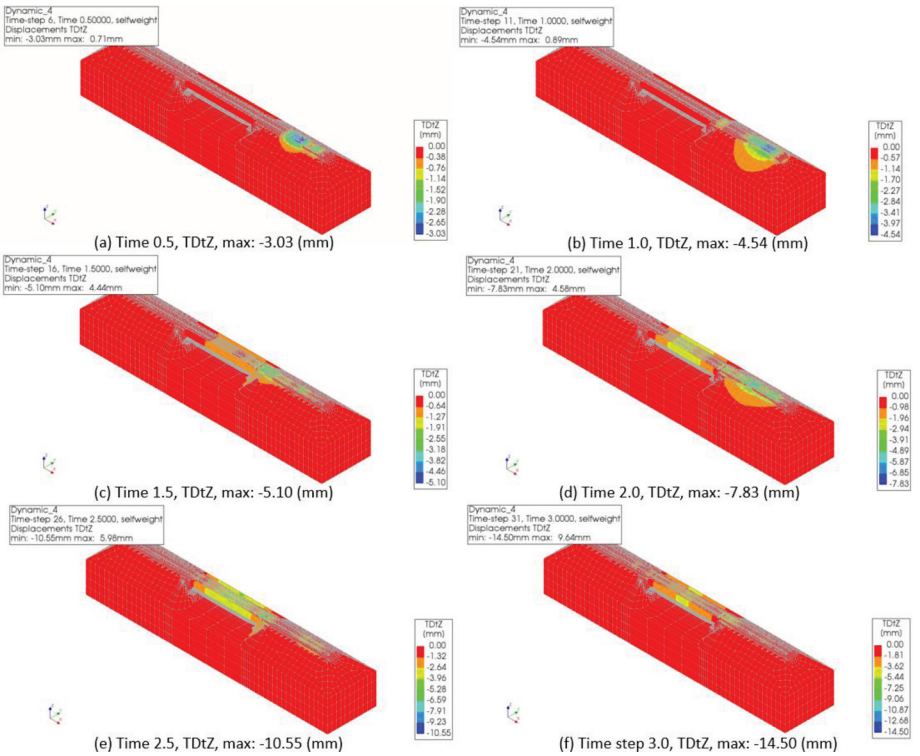


Figure 13. Vertical displacement in every 5 time-step of transient dynamic analysis.

The moving load was simulated using a triangular force distribution by Gharad and Sonparote (2016), as well as Wang et al (2016, 2020). Notably, the latter researchers linked the triangular force function at each node to the diameter and velocity of the moving train. Furthermore, Sánchez-Haro et al (2023) explored the moving load force function utilizing three distinct shapes: rectangular, triangular, and sine squared. Their findings indicated that while the rectangular shape is not suitable for the Finite Element (FE) model, both triangular and sine shapes yield favorable outcomes.

As illustrated in Figure 13, the analysis demonstrates the influence of the moving load on the bridge structure. The results reveal a maximum deflection of -27.93 mm caused by the moving load at time 5.3 s. Additionally, the maximum stress observed in the reinforcement

reaches 18.31 MPa at time 5.6 s, indicating that the stress remains comfortably below the yield strength of the reinforcing steel. These findings collectively affirm the structural integrity of the bridge under the dynamic loading scenario.

6 CONCLUSIONS AND FUTURE RESEARCH

In this study, the Vitån Bridge underwent a detailed structural evaluation using proof load tests integrated with finite element analysis, particularly under challenging winter conditions. The findings affirm the bridge's capacity to support an axle load of 30.0 tons, with no significant structural damage or major deformations noted. However, the minor deformations in the masonry abutments observed under these specific conditions underscore the necessity for further refinement of our finite element model. Moreover, the study mentioned the critical role of temperature variations in influencing the structural properties and behavior of the bridge's masonry abutments. This insight points to the importance of expanding the assessment parameters to include a range of climatic conditions, ensuring a comprehensive understanding of the bridge's structural integrity throughout the year. Key points for the future research can be drawn as:

- Model Calibration and Refinement: Enhance the finite element model, particularly the masonry substructures, to better reflect observed deformations, ensuring increased accuracy in structural assessments.
- Temperature Effect Analysis: Conduct extensive studies on how temperature changes affect the bridge's components, focusing on the masonry substructures to ensure reliable load-bearing capacity assessments year-round.
- Advanced Load Testing: Implement comprehensive load tests under diverse temperature conditions to validate potential increases in allowable axle loads and identify any latent structural vulnerabilities.

ACKNOWLEDGEMENTS

The authors gratefully acknowledge the measurement support from Mats Petersson, Erik Andersson and other colleagues from LTU, in-situ test support from BDX, and acknowledge the financial support from Trafikeverket.

REFERENCES

Lantsoght, E.O.L., Koekkoek, R.T., Hordijk, D. and de Boer, A., 2018. Towards standardisation of proof load testing: pilot test on viaduct Zijlweg. *Structure and Infrastructure Engineering*, *14(3)*, pp.365–380.

Lantsoght, E.O.L, 2019. *Load testing of bridges: Proof load testing and the future of load testing*. CRC Press.

Duvnjak, I., Damjanović, D., Bartolac, M., Frančić Smrkić, M. and Skender, A., 2019. Monitoring and diagnostic load testing of a damaged railway bridge. *Frontiers in built environment*, *5*, p.108.

Diana. (2022). *User's Manual – Release 10.6*. Diana FEA, Retrieved from https://manuals.diana-fea.com/d106/Diana.html.

Wang, C., Wang, Z., Zhang, J., Tu, Y.M., Grip, N., Ohlsson, U. and Elfgren, L., 2016. FEM based research on the dynamic response of a concrete railway arch bridge. *In 19th IABSE Congress Stockholm, 21-23 September 2016* (pp. 2472–2479).

Wang, C., Zhang, J., Tu, Y., Sabourova, N., Grip, N., Blanksvärd, T. and Elfgren, L., 2020. Fatigue assessment of a reinforced concrete railway bridge based on a coupled dynamic system. *Structure and Infrastructure Engineering*, *16(6)*, pp.861–879.

Sánchez-Haro, J., Lombillo, I. and Capellán, G. (2023). Modelling criteria proposal for dynamic analysis of beam bridges under moving loads using fem models. *Structures, Vol. 50*, pp.651–669.

Gharad, A.M. and Sonparote, R.S. (2016). Assessment of resonance effects on railway bridges under moving loads. *i-Manager's Journal on Structural Engineering*, *5(4)*, p.38.

Bridge Maintenance, Safety, Management, Digitalization and Sustainability – Jensen, Frangopol & Schmidt (eds)
© 2024 The Author(s), ISBN 978-1-032-77040-6
Open Access: www.taylorfrancis.com, CC BY-NC-ND 4.0 license

Structural reliability updating using monitoring data from in-situ load testing and laboratory test results

R. de Vries
Faculty of Civil Engineering and Geosciences, Delft University of Technology, Delft, The Netherlands
Reliable Structures, Netherlands Organization for Applied Scientific Research (TNO), Delft, The Netherlands

E.O.L. Lantsoght
Faculty of Civil Engineering and Geosciences, Delft University of Technology, Delft, The Netherlands
College of Sciences and Engineering, Universidad San Francisco de Quito (USFQ), Quito, Ecuador

R.D.J.M. Steenbergen
Reliable Structures, Netherlands Organization for Applied Scientific Research (TNO), Delft, The Netherlands
Faculty of Engineering and Architecture, Ghent University (UGent), Ghent, Belgium

M.A.N. Hendriks
Faculty of Civil Engineering and Geosciences, Delft University of Technology, Delft, The Netherlands
Department of Structural Engineering, Norwegian University of Science and Technology (NTNU), Trondheim, Norway

M. Naaktgeboren
Rijkswaterstaat, Ministry of Infrastructure and Water Management, Utrecht, The Netherlands

ABSTRACT: Given the ageing infrastructure, verifying the reliability of existing structures is crucial. Field testing presents a viable approach to evaluating a structure's current condition, particularly proof load testing. In a proof load test, a large load is applied to assess its reliability. Structures in sound condition are expected to display satisfactory behaviour under average load intensities. Can good structural performance under moderate load levels already prove sufficient structural reliability? The proposed method utilises data from laboratory tests on similar structural elements. A case study was conducted on a bridge to illustrate the effectiveness of the method. Data acquired from laboratory tests were pre-processed to provide the required input for the reliability updating. It reveals that sufficient reliability can be demonstrated without excessive load levels by incorporating laboratory data. However, the actual capacity of the bridge and the uncertainty associated with the laboratory data remain important factors.

1 INTRODUCTION

Ensuring the reliability of bridges and viaducts is an ongoing effort involving inspections, structural assessments, and maintenance practices. As the infrastructure ages and experiences increased traffic loads and intensities, accurate assessment methods are required to account for the changing conditions. Load testing may be used to verify a bridge or viaduct's current structural integrity. A load test conducted to prove a structure's ability to withstand future traffic loads is referred to as a 'proof load test' (Alampalli et al., 2021; Faber et al., 2000; Lantsoght et al., 2017). The magnitude of the load to be applied in the test, commonly called the target load, is pivotal in proof load testing. If the structure can resist a large load without any

DOI: 10.1201/9781003483755-44

issues, it proves it is sufficiently reliable for future use. The magnitude of the target load is directly related to the reliability requirements. Often, such reliability requirements result in relatively large loads being applied to the structure (De Vries et al., 2023a). A potential solution to this problem is to probabilistically consider all relevant information about the structural resistance, especially the performance indicators during testing. Then, load testing can demonstrate the same reliability level with lower test loads, making it a cost-effective alternative to other evaluation methods.

The current article presents a novel reliability updating method that integrates information from two distinct sources: the survival of the applied load during the proof load test and the indicator value observed throughout the testing process. When a proof load test is conducted, the load is gradually applied in small steps until the target is reached to prevent unwanted damage. Measurement of displacements, crack widths and so on usually cannot instantly tell us about the structural performance. Therefore, corresponding stop criteria interpret the structural behaviour rather than the measurements directly (Zarate Garnica & Lantsoght, 2021). For example, strains may be interpreted via sectional analysis to identify a critical value. The type of expected damage and failure mechanism will define the specific stop criteria that should be used.

2 METHOD

2.1 *Reliability updating using two information sources*

When a particular load is resisted in a proof load test, the structure's resistance is at least equal to the load effect achieved during the test ($R \geq E_{PL}$). The load effect consists of permanent loads and the load applied within the test ($E_{PL} = G + Q_{PL}$). This results in a truncation of the resistance distribution (Lin & Nowak, 1984). Naturally, there will be some uncertainty associated with this load effect. When accounted for, the truncation will be more gradual, still assigning some probability density to values lower than the intended (mean) proof load effect ($m_{E,PL}$) (Brüske, 2018). This truncation results in the first source of information following from successfully withstanding the applied load (Figure 1, point 1).

The in-situ measurements and stop criteria introduced in the previous section are commonly used to prevent structural failure. The novel method described herein uses the measurement data to *predict* the structure's resistance at moderate load levels. This prediction gives rise to the second source of information following a load step in the proof load test. The prediction may be achieved using suitable data that links observed damage to the applied loading for similar structural elements. In this context, the measurements normally conducted within the application of stop criteria are called indicators. The strain calculated from displacement measurements at the bottom of a beam or slab is an example of such an indicator. From the data obtained in the

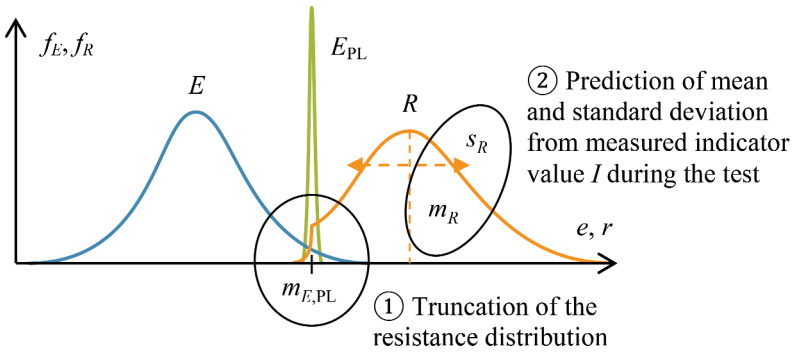


Figure 1. General principle of updating the resistance distribution from two sources of information.

laboratory tests and the indicator value observed during the in-situ test, the corresponding mean and standard deviation of the resistance may be inferred (Figure 1, point 2).

2.2 *Probabilistic model for updating*

The structural reliability is determined by evaluating a limit state function (Z), which results in a negative value when failure occurs. The limit state function for the assessment of a bridge (or viaduct) subjected to traffic load has been formulated in line with the Probabilistic Model Code (JCSS, 2015) and *fib* Bulletin 80 (fib, 2016):

$$Z = \theta_R R - \theta(G_{Dl} + G_{SDL} + C_{0Q}Q \tag{1}$$

where R is the resistance, θ_E is the model uncertainty of the load effect calculation, G_{DL} is the dead load, G_{SDL} is the superimposed dead load, C_{0Q} is the time-invariant part of the live load, and Q is the time-variant part of the live load. Here, θ_R accounts for the statistical model uncertainty in which in-situ testing is coupled with laboratory experiments. This uncertainty is small when the laboratory specimens are representative of the structure under consideration. However, large uncertainty should be expected if the structures are dissimilar or the measurement techniques and data post-processing differ. Real-world experience with the proposed method will give insight into appropriate model uncertainty values. The uncertainty in predicting the resistance from a measured indicator value will be contained in the ratio X and follows from the statistical processing of the laboratory data.

Each time the structure successfully resists a new load level, the distribution function of R may be updated to reflect the newly obtained information (Section 2.1). The updated distribution of R may be written as a multiplication of the ratio X and the load effect produced during the last successful load test cycle ($R = X E_{\mathrm{PL}}$). Since the proof load is survived, this indicates $R \geq E_{\mathrm{PL}}$ and therefore $X = R/E_{\mathrm{PL}} \geq 1$. However, this does not imply that the resistance distribution is truncated at a fixed value because of the uncertainty in the proof load effect (E_{PL}) (Figure 1). The resulting distribution of R does not follow a regular distribution since it follows from the multiplication of X and E_{PL}, of which the latter is also a product of other random variables. The resistance R may be expanded and inserted into Equations (1), giving:

$$Z = \theta_R X[\theta_E(G_{DL} + G_{SDL}) + \theta_{E,PL}] - \theta_E(G_{DL} + G_{SDL} + C_{0Q}Q) \tag{2}$$

where $\theta_{E,\mathrm{PL}}$ is the model uncertainty applicable for calculating the load effect from the applied proof load, and Q_{PL} is the load effect following from the applied load in the test. Because of the controlled conditions during the test, the uncertainty in calculating the load effect from the proof load is expected to be smaller than for the other loads. The calculation model and method will likely be the same for both; thus, a strong correlation exists between $\theta_{E,\mathrm{PL}}$ and θ_E. For simplicity, it may be assumed that they are the same ($\theta_{E,\mathrm{PL}} = \theta_E$), effectively eliminating them from the limit state equation:

$$Z = \theta_R X(G_{DL+}G_{SDL+}Q_{PL}) - (G_{DL} + G_{SDL} + C_{0Q}Q \tag{3}$$

Although the permanent loads ($G_{\mathrm{DL}} + G_{\mathrm{SDL}}$) appear in both the resistance and the load effect, they cannot be eliminated from the equation. Yet, it can be difficult to estimate them when the original drawings and calculations are lost or the structure has been modified. It is seen that the permanent load terms lead to an increase in the resistance since $X \geq 1$ must be satisfied to survive the proof load. Conservatively, the permanent load terms may be removed:

$$Z = \theta_R X Q_{\mathrm{PL}} - C_{0Q}Q \tag{4}$$

For structures where the permanent loads are relatively small compared to the live load, Equations (4) results in similar reliability values as Equations (3). It may also be observed that with

$X = 1$, the lower bound approximation is recovered, which is discussed in De Vries et al. (2023b). The lower bound approximation forms the basis of the probabilistic background for the proof load testing method in the MBE (AASHTO, 2018), as described by Lichtenstein (1993).

2.3 *Distribution of the resistance ratio (X)*

A relation between indicator values and the resistance ratio, random variable X in Equations (2), may be deduced from the laboratory tests. Therefore, the laboratory measurements are post-processed to determine the resistance ratio for each load step. The maximum indicator value observed up to each load step is used instead of the actual indicator value for each load step. This approach mitigates the noise and erratic response in the crack-forming process. When specimens have failed the ratio is 1, reflecting that the resistance is at least equal to the current load effect but not higher (Figure 1, point 1). Once the ratios X_i from the laboratory test are obtained for each chosen indicator value, the data points may be analysed using the established knowledge of sample testing, e.g. Annex D of EN 1990 (CEN, 2019). Student's t-distribution is used to account for the typically small number of tests (Gosset, 1908). Of use here is the so-called *prediction distribution* for an assumed normally distributed population (Geisser, 1993):

$$X_{n+1} = M + TS\sqrt{1 + \frac{1}{n}} \tag{5}$$

where X_{n+1} is the next to-be-observed value, M is the sample mean, S is the sample standard deviation, n is the number of samples and T follows Student's t-distribution with $v = n - 1$ degrees of freedom. The sample mean and standard deviation, including Bessel's correction $(n - 1)$, are obtained through the well-known statistical formulas (Wasserman, 2004). Because the prediction distribution of X is used, the actual variation is more significant than solely indicated by the standard deviation.

3 APPLICATION TO A REINFORCED CONCRETE SLAB BRIDGE

3.1 *Description*

To demonstrate how the proposed method would be applied in practice, the structural reliability of a reinforced concrete slab bridge is considered. The bridge is fictional but characterises typical Dutch slab bridges without shear reinforcement. Deep beams representing strips of such a slab were tested in the laboratory to determine the shear resistance (Figure 2). Because the bridge is fictional and no actual load test was performed, a load test result must be assumed. In reality, indicator values following from actual measurements would be used.

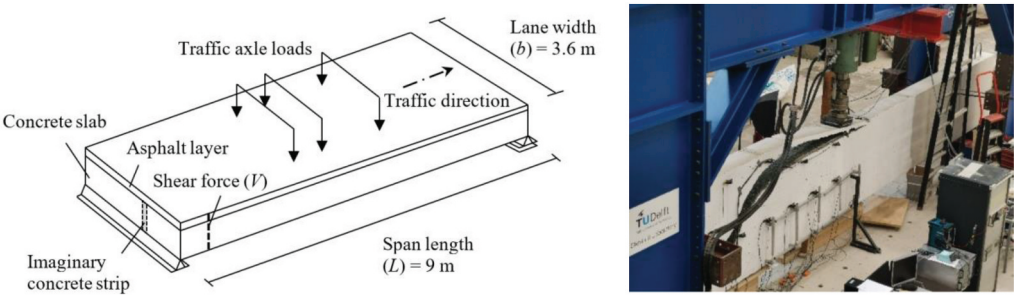


Figure 2. Reinforced concrete slab bridge considered in the case study, with (a) its schematic drawing and (b) a picture of one of the concrete strips tested to failure.

To simplify calculations only the first lane is considered, whilst in reality reinforced concrete slab bridges will typically have multiple lanes. The traffic load effect of the first lane is based on Weigh-In-Motion (WIM) measurements (FHWA, 2018) obtained from Dutch highways. The load effect in this case study is the shear force occurring at 1 m from the support ($E = V$). Loads applied at a smaller distance from the support are expected to travel directly to the support. For a span length of 9 m, the annual mean shear force is m_Q = 390 kN with a coefficient of variation V_Q = 0.035 (De Vries et al., 2023b).

The laboratory measurements used in this case study were initially designed to study the shear behaviour of reinforced concrete beams without shear reinforcement (Yang et al., 2021). The H-variants (H121, H401, H403, H404, H602) were used from the test series. These strips, or deep beams, had a height of 1.2 m and a width of 0.3 m. The simply supported beams were loaded by a single jack close to the middle of the span and resulted in shear failure close to the support. Given the assumed lane width, there are 3.6/0.3 = 12 strips within the considered slab.

3.2 *Laboratory data post-processing*

During the tests, Digital Image Correlation (DIC) was used to identify and follow the formation of cracks in the concrete (Jones & Iadicola, 2018). From the DIC results, the nominal crack width may be obtained for many locations (Gehri et al., 2020). The locations may be chosen arbitrarily, but DIC data must be available over the virtual gauge length. The gauge length that delivered the best results in this study was $0.8d$, where d is the distance from the top of the beam to the middle of the longitudinal reinforcement. For each chosen location, the nominal crack width is calculated at the reinforcement level. In order to assign greater meaning to cracks forming near the supports, a weighted crack width is introduced where the nominal crack width is multiplied by the factor Vd/M where V and M are the shear force and bending moment at the considered location, respectively. Over the entire length of the beam, the maximum nominal crack width ($w_{\max}$) and maximum *weighted* nominal crack width may be determined ($w_{\max,w}$). The corresponding resistance ratio $X = V/V_u$ for both indicators was plotted for each load step (Figure 3).

The data was further post-processed to yield the sample mean and standard deviation for each considered indicator value (Figure 4). It is observed that the standard deviation of the data is smaller with the maximum weighted nominal crack width indicator ($w_{\max,w}$), making it the best choice for further modelling. The data points with $w_{\max,w} < 0.08$ mm result in very high mean and standard deviation values. This could result from noise in the DIC measurements for very small displacements. In general, the mean and standard deviation show some erratic behaviour considering different values of the indicator $w_{\max,w}$. Therefore, an analytical model was fit to the result, which also describes the convergence towards reaching the true resistance with higher loads (Figure 4):

$$m_{V_u/V}(w_{\max,w}) = \begin{cases} 1 + 1.6\,(w_{\max,w} - 0.85)^2 & w_{\max,w} < 0.85 \\ 1 & w_{\max,w} 0.85 \end{cases} \tag{6a}$$

$$s_{V_u/V}(w_{\max,w}) = \begin{cases} 0.3 - 0.3 w_{\max,w} & w_{\max,w} < 1 \\ 0 & w_{\max,w} 1 \end{cases} \tag{6b}$$

A direct consequence of Equations (6a) and (6b), is that for $w_{\max,w} \geq 1$ mm the method provides no benefit over proof load testing using the lower bound approximation (De Vries et al., 2023b).

3.3 *Assumed load testing results*

Section 3.1 describes the bridge under consideration as hypothetical and has not been tested in real life. However, an indication of reasonable indicator values is desired. The characteristic value

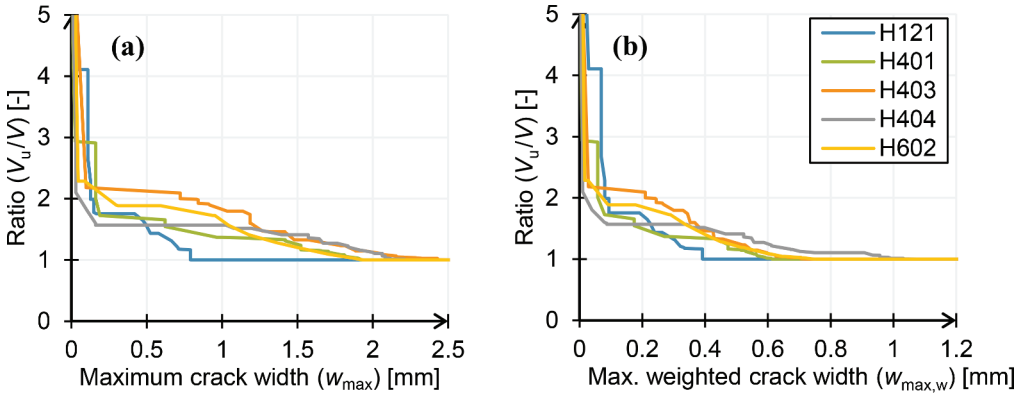


Figure 3. Shear resistance ratio versus (a) the maximum nominal crack width and (b) the maximum weighted nominal crack width.

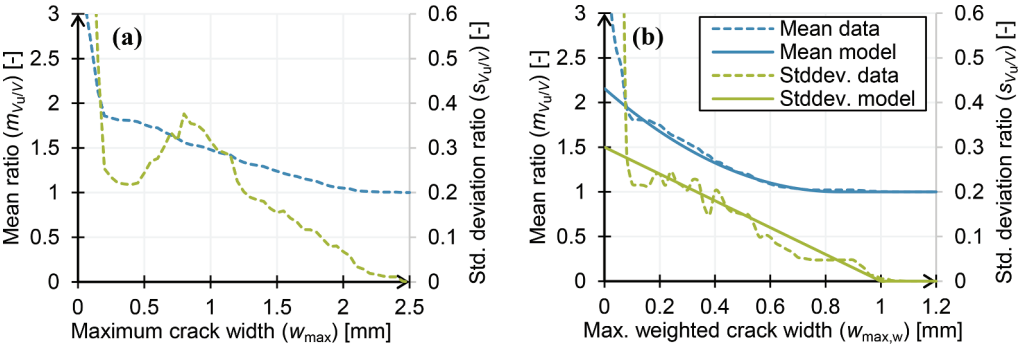


Figure 4. Mean and standard deviation of the shear resistance ratio versus (a) the maximum nominal crack width and (b) the maximum weighted nominal crack width.

of the traffic load multiplied by a factor serves as a helpful target load. Given the target loads, the laboratory test may provide reasonable indicator values (Table 1). When applied in practice, this step would not be necessary. The sensitivity to this input is described in the discussion (Section 5). It should be noted that the structure outside will already have the superimposed dead load (G_{SDL}) included in the measurements – i.e. the starting point of the measurements is different. Therefore, the values in Table 1 for the case $G_{DL} + G_{SDL}$ should be added to the values obtained during field testing to relate them to the laboratory experiments.

Table 1. Expected indicator readings given proof load.

Proof load test	Loadsacting on structure	Expected shear force [kN]	Maximum crack width, weighted by position ($w_{max,w}$) [mm]					
			H121	H401	H403	H404	H602	Average
-	G_{DL}	30.0	0	0	0	0	0	0
-	$G_{DL} + G_{SDL}$	34.9	0.004	0.002	0.002	0.002	0.010	0.004
1	$G + Q_k$	73.0	0.069	0.058	0.019	0.010	0.016	0.034
2	$G + 1.2Q_k$	80.6	0.069	0.058	0.023	0.010	0.029	0.038
3	$G + 1.4Q_k$	88.2	0.069	0.071	0.026	0.016	0.058	0.048
4	$G + 1.6Q_k$	95.9	0.069	0.135	0.158	0.032	0.087	0.096

4 RESULTS

4.1 *Probabilistic model*

In this section, the case study of Section 3 is continued with reliability calculations following the method outlined in Section 2. Given the average indicator values from Table 1, the mean and standard deviation of the resistance ratio may be obtained from Equations (6a) and (6b), see Table 2. For each proof load test, a reliability analysis is performed using the random variables specified in Table 3. The mean and coefficient of variation are based on the Probabilistic Model Code (JCSS, 2015) and *fib* Bulletin 80 (fib, 2016). A small coefficient of variation (0.02) is used for model uncertainty of the resistance because the laboratory tests are assumed to be representative.

Table 2. Mean and standard deviation of the resistance ratio for each proof load test.

Proof load test	Mean PLeffect, strip ($m_{Q,\mathrm{PL,s}}$) [kN]	Mean PLeffect, lane ($m_{Q,\mathrm{PL}}$) [kN]	Indicator value ($w_{\max,\mathrm{w}}$) [mm]	Mean ratio ($m_{V\mathrm{u}/V}$) [-]	Std. deviation ratio ($s_{V\mathrm{u}/V}$) [-]
1 (Q_k)	38.1	457.4	0.034	2.07	0.290
2 ($1.2Q_\mathrm{k}$)	45.7	548.8	0.038	2.06	0.289
3 ($1.4Q_\mathrm{k}$)	53.3	640.3	0.048	2.03	0.286
4 ($1.6Q_\mathrm{k}$)	61.0	731.8	0.096	1.91	0.271

4.2 *Reliability calculation results*

The annual reliability in the first year after the proof load test is calculated using the various limit state functions presented in Section 2 (assuming survival). In addition, the reliability is calculated using the lower bound approach that ignores permanent loads and additional resistance (i.e. $X = 1$ and $\theta_R = 1$). The calculations were performed with SORM (Hohenbichler et al., 1987), which approximately accounts for the non-linearity encountered in the limit state functions (Table 4). The results show that the calculated reliability indices are much higher compared to the lower bound approach. This reliability gain is the result of taking into account the measurements during proof load testing in the analysis (information source 2 in Figure 1). Even when the permanent loads are excluded from the limit state function, a target load of about $1.2Q_{\mathrm{k,WIM}}$ would still be sufficient to satisfy annual $\beta = 4$ requirement for CC3 (Steenbergen & Vrouwenvelder, 2010).

Table 3. Overview of random variables in the limit state function.

Var.	Description	Distribution	Mean	COV [-]
θ_R	Model uncertainty of the resistance	Lognormal	1	0.02
X	Resistance to current load effect ratio	Student's t, Equations (5)	(varies)	(varies)
G_DL	Dead load effect	Normal	356 kN	0.05
G_SDL	Superimposed dead load effect	Normal	59.3 kN	0.1
C_{0Q}	Time-invariant part of traffic load effect, including traffic trend	Lognormal	1.1	0.1
Q	Traffic load effect, annual maximum	Gumbel	390 kN	0.035
Q_PL	Load effect achieved by proof load	Normal	(varies)	0.02

Table 4. Mean and standard deviation of the resistance ratio for each proof load test.

Characteristic load effect, WIM ($Q_{k,WIM}$) [kN]	Characteristic load effect, LM1 ($Q_{k,LM1}$) [kN]	Annual reliability (β) [-]		
		Incl. permanent loads, Equations (3)	Excl. permanent loads, Equations (4)	Lower bound approach
1	0.78	3.21	3.02	0.70
1.2	0.93	4.11	4.02	2.31
1.4	1.09	5.03	5.00	3.66
1.6	1.24	5.86	5.85	4.78

5 DISCUSSION

In the laboratory data post-processing in Section 3.2, the model does not fit the data well for $w_{max,w} < 0.08$ mm. In the reliability calculations that follow, this region of minuscule cracks is used in the resistance prediction. Therefore, it may be questioned if the results can be trusted. Fortunately, as displayed in Figure 3, the data shows very high resistance ratios in this region with positive distribution skew. However, careful consideration must be made with regard to the similarity to the in-situ tested structure and the lab results. In the case study, it is assumed that the response of the bridge slab is similar to the response of the strips tested in the laboratory – presumably a conservative assumption, but it should still be validated.

An average response based on the laboratory measurements was assumed for the reliability calculations. In reality, the structure that is being tested may give a very different response and different measurement data post-processing may be necessary. When its strength is larger than expected and its condition is excellent, smaller indicator values are expected. When the assumed indicator values are divided by 10, the annual reliability indices increase by approximately 0.2. For structures that immediately display large crack widths under small loads, lower reliability is expected. When the indicator values are multiplied by 10, the reliability indices decrease by approximately 0.5 to 1. However, the reliability indices still remain higher than when calculated using the lower bound approach.

6 CONCLUSIONS

The proposed reliability updating method involves updating the resistance distribution using two sources of information: (1) the survival of the applied load in the proof load test and (2) the indicator value observed during the test, leading to an updated resistance distribution. A probabilistic model for updating the resistance distribution was presented, considering model uncertainties and permanent loads. The application of the proposed method was demonstrated through a case study of a reinforced concrete slab bridge. Laboratory data post-processing, including the consideration of weighted crack widths, provided insight into the resistance ratios considering different target loads. Reliability calculations based on the proposed method indicated a significant improvement compared to the lower bound approach, highlighting the importance of incorporating measured data.

The study addresses potential difficulties, particularly in fitting the model to data for small crack widths. It also recognizes the variability in real-world responses compared to assumed average values. Despite these considerations, the results consistently showed higher reliability indices than conservative estimates based on live loads alone. Real-world validation is recommended to enhance the robustness of the proposed approach. The next steps in the research will consider Bayesian approaches to include prior information in addition to the measurement data. Modelling choices and the application of the method with other types of resistance modes and measurements will be further reviewed.

REFERENCES

AASHTO. (2018). The manual for bridge evaluation. *Standard*, *3rd Edition. Washington, D.C., USA*.

Alampalli, S., Frangopol, D. M., Grimson, J., Halling, M. W., Kosnik, D. E., Lantsoght, E. O. L., Yang, D. Y., & Zhou, E. (2021). Bridge Load Testing: State-of-the-Practice. *Journal of Bridge Engineering*, *26*(3).

Brüske, H. (2018). Structural test design with value of information. *PhD Thesis (Report 401)*, *DTU, Kongens Lyngby, Denmark*.

CEN. (2019). Eurocode 0: Basis of structural design. In *Standard, EN 1990+A1+A1/C2:2019*. Brussels, Belgium: European Committee for Standardization.

De Vries, R., Lantsoght, E. O. L., Steenbergen, R. D. J. M., & Fennis, S. A. A. M. (2023a). Time-dependent reliability assessment of existing concrete bridges with varying knowledge levels by proof load testing. *Structure and Infrastructure Engineering, In press*.

De Vries, R., Lantsoght, E. O. L., Steenbergen, R. D. J. M., & Naaktgeboren, M. (2023b). Proof Load Testing Method by the American Association of State Highway and Transportation Officials and Suggestions for Improvement. *Transportation Research Record*.

Faber, M. H., Val, D. V., & Stewart, M. G. (2000). Proof load testing for bridge assessment and upgrading. *Engineering Structures*, *22*, 1677–1689.

FHWA. (2018). Weigh-in-motion pocket guide - Part 1: WIM technology, data acquisition, and procurement guide. *Federal Highway Association, FHWA-PL-18-015*, *Washington D.C., USA*.

fib. (2016). *Partial factor methods for existing concrete structures*. Retrieved from Lausanne, Switzerland:

Gehri, N., Mata-Falcón, J., & Kaufmann, W. (2020). Automated crack detection and measurement based on digital image correlation. *Construction and Building Materials*, *256*.

Geisser, S. (1993). *Predictive inference: An introduction*. New York: Chapman & Hall.

Gosset, W. S. (1908). The probable error of a mean. *Biometrika*, *6*(1), 1–25.

Hohenbichler, M., Gollwitzer, S., W.,K., & Rackwitz, R. (1987). New light on first- and second-order reliability methods. *Structural Safety*, *4*, 267–284.

JCSS. (2015). Probabilistic model code. Retrieved from https://www.jcss-lc.org/jcss-probabilistic-model-code/.

Jones, E. M., & Iadicola, M. A. (2018). *A good practices guide for digital image correlation*. Retrieved from https://doi.org/10.32720/idics/gpg.ed1/print.format

Lantsoght, E. O. L., van der Veen, C., de Boer, A., & Hordijk, D. A. (2017). State-of-the-art on load testing of concrete bridges. *Engineering Structures*, *150*, 231–241.

Lichtenstein, A. G. (1993). *Bridge rating through nondestructive load testing*. Retrieved from Washington, D.C., USA:

Lin, T. S., & Nowak, A. S. (1984). Proof loading and structural reliability. *Reliability Engineering*, *8*, 85–100.

Steenbergen, R. D. J. M., & Vrouwenvelder, A. C. W. M. (2010). Safety philosophy for existing structures and partial factors for traffic loads on bridges. *Heron*, *55*(2), 123–139.

Wasserman, L. (2004). All of statistics: A concise course in statistical inference. *Book*, *Springer*.

Yang, Y., Van der Ham, H. W. M., & Naaktgeboren, M. (2021). Shear capacity of RC slab structures with low reinforcement ratio – An experimental approach. *fib Symposium*, *Lisbon, Portugal*.

Zarate Garnica, G. I., & Lantsoght, E. O. L. (2021). Stop criteria for proof load testing of reinforced concrete structures. *Proceedings of the 2021 session of the 13th fib International PhD Symposium in Civil Engineering*, 195–202.

Bridge Maintenance, Safety, Management, Digitalization and Sustainability – Jensen, Frangopol & Schmidt (eds)
© 2024 The Author(s), ISBN 978-1-032-77040-6
Open Access: www.taylorfrancis.com, CC BY-NC-ND 4.0 license

Load testing of the first stress ribbon bridge in Slovenia

Đ. Đukić, D. Hekič, M. Kosič, R. Vezočnik & A. Anžlin
Slovenian National Building and Civil Engineering Institute, Ljubljana, Slovenia

A. Štrukelj
Faculty of Civil Engineering, Transportation Engineering and Architecture, University of Maribor, Maribor, Slovenia

M. Pipenbaher & T. Weingerl
Ponting inženirski biro, Maribor, Slovenia

ABSTRACT: Paper presents selected results of the diagnostic load testing of a newly-built footbridge in Novo Mesto, Slovenia. The bridge is significant as the first bridge in Slovenia being built with the stress ribbon technology. The diagnostic load testing took place in March 2023 and comprised of three-stage static load testing, dynamic testing with a light truck driving over artificial obstacles, and measurement of ambient vibrations. The consistency between the actual response of the bridge and the response of the finite element (FE) model, used in the design, was evaluated by comparing vertical displacements from the static load testing, natural frequencies and mode shapes. The comparison of the results indicates a satisfactory agreement between the measurements and the response of the FE model, confirming the appropriateness of the employed FE model.

1 INTRODUCTION

A newly built pedestrian bridge in the village of Irča Vas, near Novo Mesto, is the first bridge in Slovenia built using stress-ribbon technology. The bridge is a slender catenary-shaped structure with concrete precast segments placed over prestressed steel ribbons that function as scaffolding during bridge construction (Strasky & Pirner, 1986). Forces from the stress ribbons are transferred through well foundations and geotechnical anchors on both sides of the bridge to load-bearing soil.

In March 2023, a diagnostic load test was conducted using 18 3.9-tonne trucks, representing approximately 60% of the design load. Proof load tests in the USA should be performed using guidelines set by the Manual for Bridge Evaluation (2018). Similar approach was utilised in the case of Irča Vas bridge. To validate the designer's calculations, an extensive measurement campaign was undertaken. It is comprised of sensors installed for long-term monitoring and sensors installed for diagnostic load tests, designated as short-term measurements. The following measurements were performed: measurement of rotations using inclinometers and 3-axial MEMS accelerometers, acceleration measurements using single and 3-axial MEMS accelerometers, and deflection measurements using a total station and 3D laser scanner. Additionally, force in the geotechnical anchors was measured. This article outlines the most important results of the diagnostic load testing with a focus on short-term sensor data and compares with the calculated response from the bridge designer's finite element (FE) model.

2 BRIDGE DESCRIPTION

A new pedestrian bridge crosses the Krka river with a span of 131 m, as shown in Figure 1. The maximum longitudinal slope of the bridge is 6%, as the structure has an inbuilt radius, where its lowest point is around 8 m above the river surface.

DOI: 10.1201/9781003483755-45



Figure 1. Bridge on the day of the diagnostic load test.

The bridge deck is supported with abutments, which rest upon the well foundations. The tensile forces from prestressing tendons are carried over by geotechnical anchors and transferred in load-bearing soil (Figure 2).

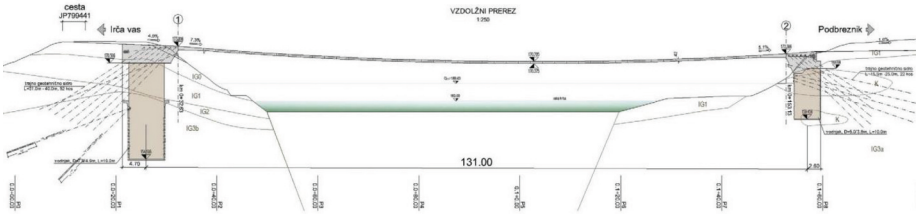


Figure 2. Longitudinal section of the bridge.

The cross-section of the bridge is shown in Figure 3. Precast concrete elements are 4.0 m wide and 2.4 m long. Element thickness varies in a transverse direction from 0.42 m at the edges to 0.18 m in the middle. The usable width of the bridge is 3.5 m. Precast elements are built offsite using C45/55 concrete. More in-depth information about the bridge geometry and building process is available in Weingerl et al. (2023).

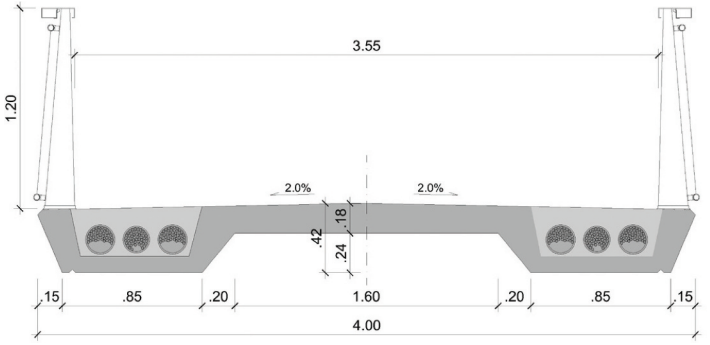


Figure 3. Cross-section of the bridge.

3 MEASUREMENTS

The bridge's diagnostic load test comprised static (trucks stationary on the bridge) and dynamic (trucks passing an artificial bump on the bridge) testing. In addition, vibrations

under ambient excitation before and after the testing campaign were captured. 6 phases were performed overall:

- Phase 0: Resting phase before loading (zero state).
- Phase 1: 9 trucks at the 2/2 of the bridge (half-load).
- Phase 2: 18 trucks across the entire bridge (full load of 70.4 tonnes overall, Figure 4).
- Phase 3: 9 trucks at the 1/2 of the bridge (half-load).
- Phase 4: Resting phase after loading (release state).
- Phase 5: Dynamic test – trucks passes artificial bump on the bridge.



Figure 4. In the static load test (Phase 2), all 18 trucks with an overall 70.4 tonnes were present on the bridge.

Axle loads and distance of statically-weighted 18 trucks are presented in Table 1.

Table 1. Axle load data for each truck used during the load test.

Truck number	Axle distance[m]	1st axle load[kg]	2nd axle load[kg]	SUM[kg]
1	4.35	1700	2200	3900
2	3.65	1600	2400	4000
3	3.65	1400	2800	4200
4	3.65	1500	2300	3800
5	3.00	1700	2200	3900
6	3.60	1600	2300	3900
7	4.35	1700	2300	4000
8	3.65	1300	2900	4200
9	3.65	1300	2900	4200
10	3.65	1400	2700	4100
11	3.65	1300	2900	4200
12	3.65	1500	1900	3400
13	3.65	1300	2700	4000
14	4.35	1700	1800	3500
15	3.65	1300	2700	4000
16	4.35	1700	1700	3400
17	3.65	1500	2300	3800
18	3.65	1500	2600	4100

During phase 0, zero state was measured with both total stations, 3D laser scanner, MEMS accelerometers (for inclinations) and inclinometers. Moreover, ambient vibrations were measured with MEMS accelerometers for a duration of approximately 20 minutes.

Phase 1 was conducted by placing the first 9 trucks on the 2nd half of the bridge, between the mid-span and end (left, according to Figure 4) abutment. Phase 2 was conducted without load relief by adding 9 additional trucks to the 1st half of the bridge, between the first abutments and the mid-span. Phase 3 of the static load test was performed by removing the 9 trucks from bridge such that trucks were only present in the 1st half of the bridge, between the right(according to the the Figure 4) abutment and the mid-span. In phase 4, the bridge was fully relieved. For Phase 1 – Phase 4 the vertical displacements of the deck and horizontal displacements of the abutments were measured with both total stations. Additionally, the inclinations of the deck were measured with MEMS accelerometers and the inclinations of the abutments with inclinometers. 3D laser scans were performed only for Phase 2 and Phase 4. Ambient vibrations using MEMS accelerometers were measured only in phase 4.

The aim of the dynamic test was to excite the structure such that modal parameters could also be determined with uniaxial accelerometers (presented in Chapter 4), which are permanently installed on the bridge, and not only with the MEMS accelerometers. During this test, a truck was driving over the four equally-distant wooden obstacles near the mid-span. In the first measurement, the truck crossed the bridge from right to left (according to Figure 4) abutment with 20 km/h. Afterwards, a truck drove in the reverse direction across the same obstacles at 10 km/h. In the last phase, the truck drove over the bridge in both directions at 10 km/h.

4 INSTRUMENTATION

The considered bridge has a built-in permanent monitoring system which is capable of continuous measurement of bridge accelerations and rotations of the abutments, as shown in Figure 5.

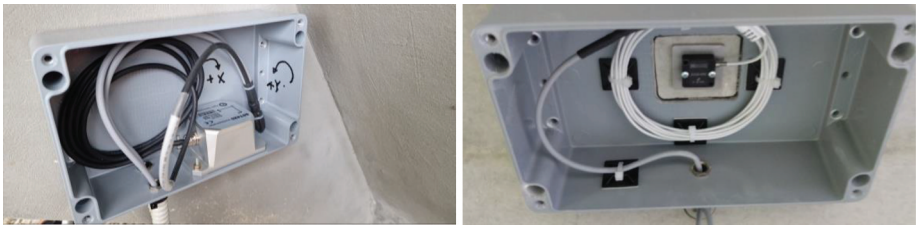


Figure 5. Sensors used for the permanent monitoring: biaxial inclinometer (left) and uniaxial accelerometer (right).

The permanent monitoring system is designed such that it allows for remote access to the measured data. Each abutment is equipped with one biaxial inclinometer (type Vigor Technology SST420), which allows for the measurement of support rotation (INCL_01 and INCL_02 in Figure 6). Uniaxial accelerometers used in permanent monitoring (type Silicon Designs 2220-002) are placed on the bottom side of the precast concrete elements of the bridge deck. They were placed before the precast elements in the construction phase due to the difficulty of access afterward. Three pairs of two accelerometers were placed at the narrower part of the bridge deck (ACC_01 – ACC_06 in Figure 6). Using those accelerometers, three cross-sections were instrumented (First quarter, middle quarter, and third quarter of the span). Due to vandalism which occurred after the construction and before the load test of the bridge, connection to accelerometer ACC_06 and inclinometer INCL_01 was lost, and it was impossible to re-establish after the end of the construction.

During the load test of the bridge, all working sensors that are part of the permanent monitoring system were used. Additionally, the bridge was temporarily equipped with 12 triaxial MEMS accelerometers (type DEWESoft IOLITEi 3xMEMS-ACC), designated with green dots in Figure 6). These accelerometers were placed in pairs every 20 m of the bridge and were used to identify modal parameters in Phase 0 and Phase 4.

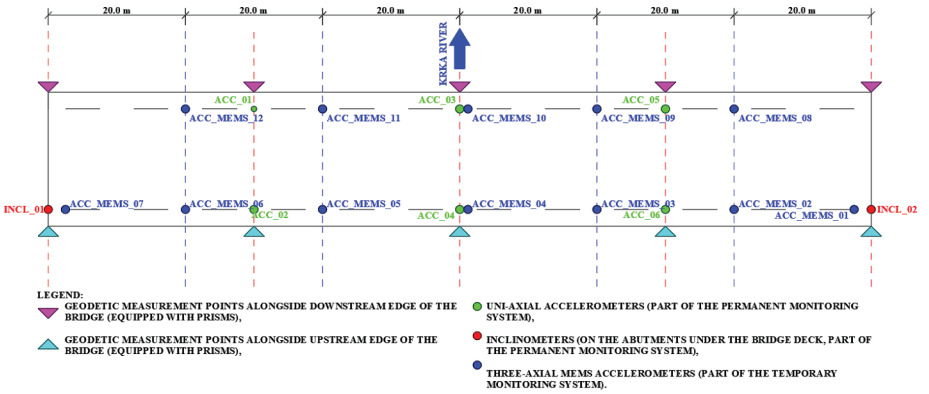


Figure 6. Sensor disposition (permanent and temporary monitoring systems).

During the static load test, vertical displacement along the upstream and downstream edge of the bridge was measured using two total stations and a laser scanner (Figure 7). Vertical displacement measurement points were placed along the upstream and downstream edges of the bridge deck at quarter, middle and three-quarters of the bridge span. Rotation of the abutments, horizontal displacements and rotations at the abutments were measured for all phases of the static load test.

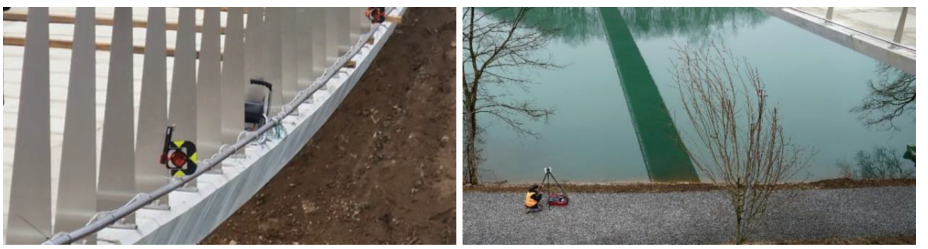


Figure 7. Geodetic measurement points along the downstream edge of the bridge deck (left) and position of the laser scanner (right).

Laser scanning was carried out with a Leica RTC360 laser scanner situated at the upstream river bank. From this location, the instrument's range managed to include about 80 m of the bridge, reaching well beyond the structure's lowest point in the middle of the bridge (60 m). Due to such limited scanning geometry, the highest scanning resolution was selected (3 mm at a distance of 10 m), resulting in roughly 3000 points per square meter at the location of the lowest bridge point. The 3D point accuracy of this scanner at a distance of 60 m is about 5 mm. One should note, however, that since only relative displacements in the vertical direction were of primary interest, this value is not completely representative.

5 MEASUREMENT RESULTS AND COMPARISON

Each of the measured parameters was calculated by the designer during the design phase of the project. A detailed FE model was created in SOFISTIK software. Before the load test phase, the designers also calculated the vertical displacement of the deck, abutment rotations and horizontal abutment displacement for each of the three phases of the static load test. Alongside the displacements, the designer calculated modal characteristics, namely the natural frequencies and mode shapes, beforehand. Below are the most important results, i.e., a comparison of the mid-span

deflection and modal characteristics measurements. More in-depth analysis exceeds the scope of this paper.

A comparison between the calculated and measured bridge deck vertical displacements for all three static load cases is shown in Table 2. The values shown represent the average displacement of the downstream and upstream edges of the bridge deck.

The scanning was carried out in three consecutive time moments, i.e. before the loading (T1 designating Phase 0), at the time of the maximum load (T2 designating Phase 2), and after unloading (T3 designating Phase 3). Two distinct point profiles (P1 and P2) were selected from these three point clouds on each side of the bridge deck, forming the basis for further bridge displacement analysis. The P1 point profile consists of points near the upstream edge of the deck, and the P2 point profile consists of points near the downstream edge of the deck. Both profiles are 5 centimetres wide. The shape of each profile in the vertical domain was modelled using polynomials since they best fitted the profile points. Figure 8 shows the deformation line of the bridge deck's downstream edge for all three static load test phases.

Table 2. A comparison between the average measured and calculated values of mid-span vertical displacement of the bridge deck.

Phase	Total station [mm]	Laser scanner* [mm]	FE model [mm]
1	65.0	/	69.5
2	129.0	127.3	145.5
3	70.1	/	64.5
4	9.9	7.6	/

* average values of profiles P1 and P2

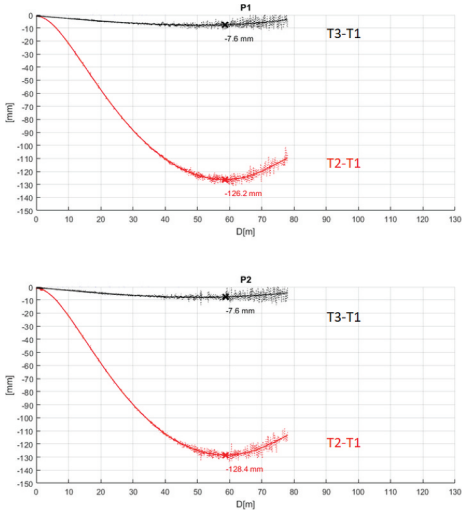


Figure 8. Measured deformation line of the downstream edge of the bridge deck for all three phases of static load test.

As shown in Table 2, the values of measured and calculated displacements match well for all three phases of the static load test. Measured displacements were smaller than calculated. Values measured by a laser scanner and total station differ by 2 mm. Figure 9 shows the point cloud measured with the laser scanner.

Table 3 shows the measured and calculated natural frequencies which correspond to the vertical mode shapes of the structure. Table 4 shows the measured and calculated mode

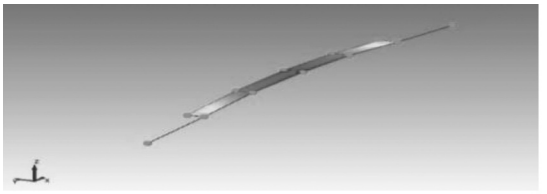


Figure 9. Point cloud measured with a laser scanner.

Table 3. First three measured and calculated natural frequencies [Hz].

Vertical mode shape	Measured – FDD	FE model
1	0.68	0.70
2	0.98	1.09
3	1.51	1.66

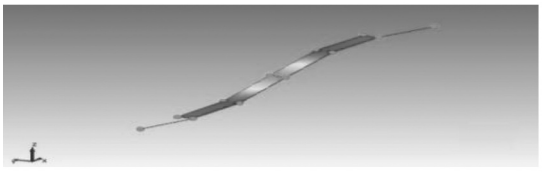
Table 4. Comparison between measured and FE model mode shapes.



1st measured mode shape: f_1 = 0.68 Hz



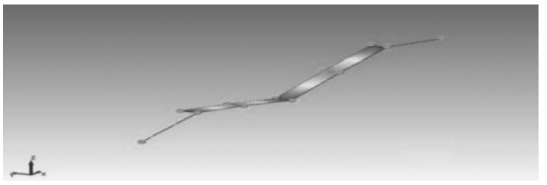
1st FE model mode shape: f_2 = 0.70 Hz



2nd measured mode shape: f_2 = 0.98 Hz



2nd FE model mode shape: f_3 = 1.09 Hz



3rd measured mode shape: f_3 = 1.51 Hz



3rd FE model mode shape: f_3 = 1.66 Hz

shapes. Measured modal parameters were extracted with the Frequency Domain Decomposition (FDD) method (Brincker et al. 2000) using the ARTeMIS Modal (Structural Vibration Solutions 2023) software package for modal identification of structures.

As shown in Table 4, modal parameter identification methods give satisfactory estimates of natural frequencies. The best matching between measurements and the numerical model was recorded for the first mode shape. For the second and third mode shapes, natural frequencies were overestimated. Natural frequencies calculated using numerical models are for the first three mode shapes higher than those measured, which indicate the higher stiffness of the model. At most, measured and calculated natural frequencies differ by 11.2 % for the second mode shape.

6 CONCLUSIONS

The paper presents selected results of load testing of the newly built stress ribbon pedestrian bridge near Novo Mesto, Slovenia. The bridge is significant as the first bridge in Slovenia to be built using stress ribbon technology. Diagnostic load testing of the bridge consisted of three-phase static load testing, dynamic load testing performed with truck driving over artificial obstacles and ambient vibration measurements. Static response of the structure was recorded using two electronic total stations and a laser scanner. The dynamic response of the structure was measured using the permanent monitoring system, which includes uniaxial accelerometers and biaxial inclinometers, and a temporary monitoring system, which consists of 12 triaxial MEMS accelerometers. Furthermore, MEMS accelerometers were used to measure the response under ambient excitation before and after the load test.

Only the selected results are shown in this paper, mainly from the short-term measurements i.e. vertical displacement at the mid-span of the bridge and three vertical mode shapes and their corresponding natural frequencies. The matching between measured and calculated values of vertical displacement was satisfactory in all three phases of static load testing. Measured displacements were smaller than calculated ones. However, the order of magnitude was comparable. Additionally, satisfactory matching was also achieved between measured and calculated vertical mode shapes and their corresponding natural frequencies.

The findings of the load test confirm correct modelling and assumptions during the design of the bridge. For a better understanding of the complex static and dynamic response of the bridge, additional data analysis and calculations are required.

REFERENCES

American Association of State Highway Transportation Officials. 2018. The Manual for Bridge Evaluation, Standard, 3rd ed. AASHTO, Washington, D.C.

Brincker, R., Zhang, L. & Andersen, P. 2000. Modal identification from ambient responses using frequency domain decomposition. Proceeding of the International Modal Analysis Conference – IMAC, 7-10 February 2000, San Antonio, Texas, USA.

Strasky J. & Pirner, M. 1986. DS-L Stress-ribbon footbridges, Dobravni stavby, Olomouc, Czechoslovakia.

Structural Vibration Solutions. 2023. ARTeMIS Modal Pro [online]. Available from: https://www.svibs.com/artemis-modal-pro/ [Accessed 26 Dec 2023].

Weingerl, T., Pipenbaher, M., Gotovčević, T. & Filipič, A. 2023. Prvi most, grajen po tehnologiji nateznega traku v Sloveniji (in Slovene). Gradbeni vestnik letnik 72: 206–216.

Bridge Maintenance, Safety, Management, Digitalization and Sustainability – Jensen, Frangopol & Schmidt (eds)
© 2024 The Author(s), ISBN 978-1-032-77040-6
Open Access: www.taylorfrancis.com, CC BY-NC-ND 4.0 license

Damage evaluation of a road bridge subjected to an avalanche

H. Naito
Tohoku University, Sendai, Miyagi, Japan

A. Uchida
Nippon Geophysical Prospecting Co., Ltd., Tokyo, Japan

K. Yoshinaga
Hirose Hokyodo Co., Ltd., Tokyo, Japan

A. Kamura & M. Kazama
Tohoku University, Sendai, Miyagi, Japan

ABSTRACT: A road bridge in Japan's Mt. Fuji area was damaged by a large avalanche in 2021. In this study, damage evaluation was conducted on a RC beam and the foundation of the bridge. Shear cracks in the RC beam were observed with the naked eye. From reliability assessment using a Monte Carlo simulation, the equivalent impact load of the avalanche was estimated over 3-4 times the design load from weights of the superstructure and vehicles. Moreover, cracks and damages in the footing and piles were also detected from forced vibration testing using a portal vibrator and hammering impact echo inspection. Using both non-destructive testing methods, damage locations of the invisible piles under the ground were identified. The effectiveness of reliability assessment and non-destructive testing for concrete bridges damaged by accidental loads (e.g., avalanches) was indicated.

1 INTRODUCTION

Roads play important roles in rescue activities for serious natural disasters. These civil structures need to have high safety performance and remain serviceable in case of disasters. The standard specifications for concrete structures were revised (Japan Society of Civil Engineers 2022), containing safety performance verification for accidental loads, such as tsunamis, floods, landslides, rockfalls (Biagi et al. 2020, Mougin et al. 2005), impact loads of trains, airplanes (Arros & Doumbalski 2007), or ships (Consolazio et al. 2005). Studies on dynamic responses (Pham & Hao 2017), damage and failure processes, and safety design of structures for impact loads (Nataraja et al. 1999, Tachibana et al. 2010) have been investigated. However, compared to the seismic design, further data and analyses are needed to improve safety design of structures for accidental loads.

Roads are required to be in service within a short period of time after disasters. However, inspection of bridges subjected to accidental loads has a difficulty in detecting invisible cracks and damages. It is necessary to examine the effectiveness of non-destructive testing to detect invisible cracks and damages caused locally by impact loads.

In this study, reliability assessment and non-destructive testing were conducted on a road bridge to collect data for improving safety design and inspection of civil structures. The bridge was in Japan's Mt. Fuji area and was damaged by a large avalanche in March 2021, as shown in Figure 1. The reliability analyses using a Monte Carlo simulation were conducted for evaluating the relationship between load level and failure probability of the RC beam subjected to an avalanche. Moreover, forced vibration testing (Naito & Bolander 2019, Naito et al. 2020) and impact

DOI: 10.1201/9781003483755-46



Figure 1. Shakunage Bridge before the avalanche. (Provided by Yamanashi Prefecture).

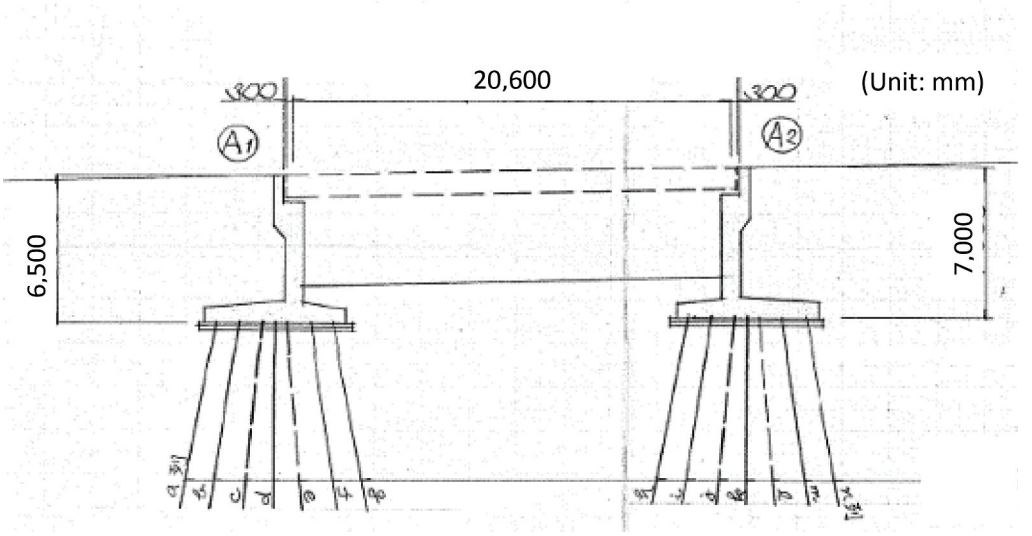


Figure 2. Layout of Shakunage Bridge. (Provided by Yamanashi Prefecture).

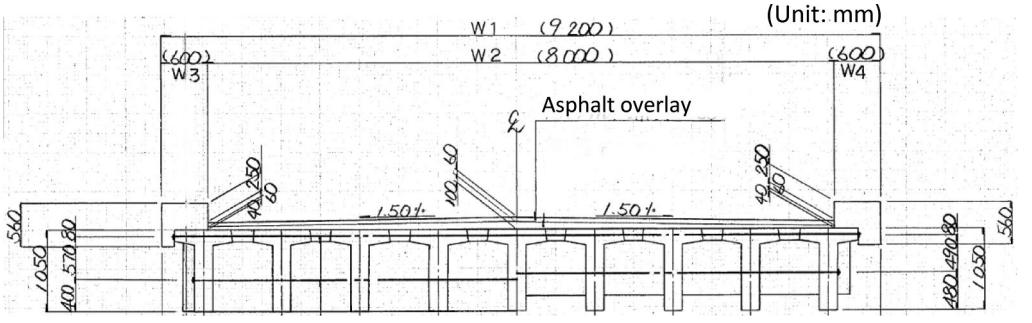


Figure 3. Cross-section of the superstructure. (Provided by Yamanashi Prefecture).

echo inspection (Schubert et al. 2008) with elastic waves were conducted on the invisible piles from the top surface of the footing.

2 DAMAGE CONDITIONS OF THE BRIDGE

Figure 1 shows a road bridge before the avalanche. The layout of the bridge and the cross-section are shown in Figures 2 and 3. It was constructed in 1993, with a span of 20.6 m and

a width of 9.2 m. The superstructure had nine RC beams with a sectional height of 1050 mm. The RC beams were supported at both sides. Figure 4 shows a diagram of cracks on the outer beam after the avalanche. Shear cracks were observed in the beam through eye inspection. It was thought that the impact location was around the left quarter of the span, as shown in Figure 4.

In addition, cracks were observed in the left abutment (A1). The crack in the abutment was caused by a horizontal load during the avalanche. The damage conditions indicated that a large vertical load was applied to the superstructure. In addition, a large horizontal load and moment were applied to the abutment and foundation from the superstructure through bearings at both sides of the beams.

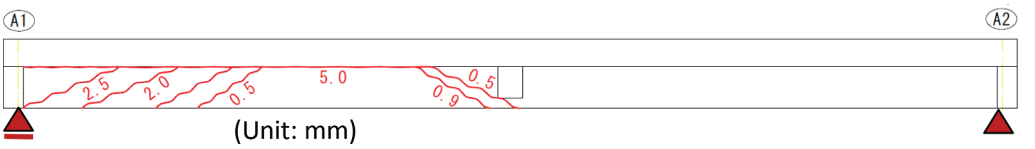


Figure 4. Crack diagram in the RC beam side view. (Provided by Yamanashi Prefecture).

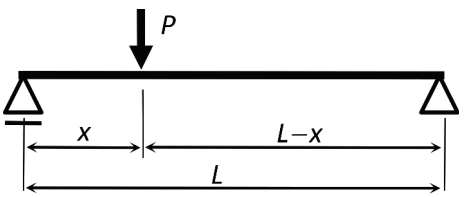


Figure 5. Beam model.

Table 1. Failure probabilities for the design load, P_d.

Failure probability of shear mode, $P_{f,s}$	Failure probability of flexural mode, $P_{f,f}$	Reliability index of shear mode, β_s	Reliability index of flexural failure, β_f
below 10^{-5}	1×10^{-5}	4.82	5.02

3 RELIABILITY ANALYSES ON THE RC BEAM

Failure probabilities of shear and flexural modes were calculated on the RC beam using a Monte Carlo simulation. Figure 5 shows a beam model of the bridge. For simplicity, the design load ($P = P_d$) of the beam was given as a concentrated load from weights of the superstructure and vehicles, that was applied to the center of the span (at $x = L/2$).

In the Monte Carlo simulation, normal distributions were assumed for the flexural and shear load capacities of the beam. The limit state functions of flexural and shear failures were given from the Japanese design code (Japan Society of Civil Engineers 2022). The mean of the flexural moment capacity M_u was given as $P_d L/2$, where M_u was set to twice the moment of $P_d L/4$ at the center of the span for a flexural failure safety factor of 2.0. The mean of the shear load capacity V_u was given as $1.8\ M_u \times 2/L$, where the ratio of shear to flexural capacities was set to 1.8. Coefficient of variations of the flexural and shear capacities were assumed as 10 % and 15 %, respectively. The two parameters (M_u and V_u) were changed randomly in the Monte Carlo simulation having 100,000 trials. During the 100,000 calculations, the number of flexural failures N_f and the number of shear failures N_s of the beam were counted. The failure probabilities of flexural and shear modes were obtained as $P_{f,f} = N_f/100{,}000$ and $P_{f,s} = N_s/100{,}000$, respectively.

In addition, a reliability index is obtained as $\beta = m(Z)/\sigma(Z)$, where Z is the performance function given as $Z=R–S$. β_f and β_s are the reliability indices of failure and shear modes, respectively. They were calculated from resistances R (the moment capacity M_u and the shear capacity V_u) and the subjected force S obtained from moment and shear force distributions in Figure 5.

The failure probabilities and reliability indices of flexural and shear modes calculated from the Monte Carlo simulation are shown in Table 1, when the vertical load ($P = P_d$) was applied to the center of the span (at $x = L/2$). Both failure probabilities of flexural and shear modes were low and safe. Both reliability indices of failure and shear modes were close to 5.0. These results indicated high safety performance of the beam for the design load P_d, when it was applied at $x = L/2$.

Figure 6 shows the relationship between loading location x and failure probabilities. On the x-axis in the figure, the locations $x = 0$ and $0.5L$ were at the left support and center of the span, respectively. The failure probability of shear mode increased as the loading location was closer to the left support.

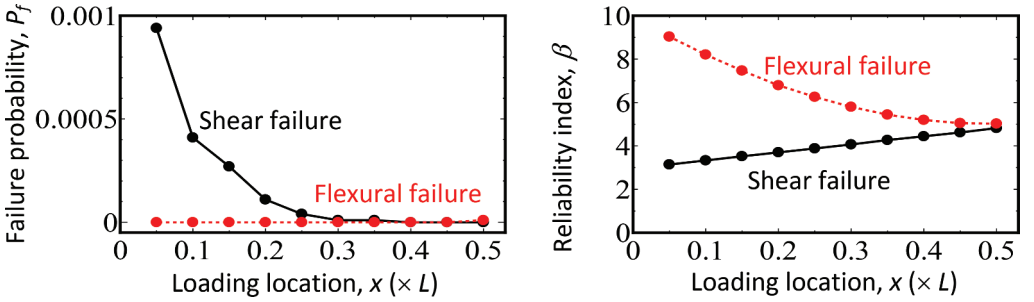


Figure 6. Failure probabilities and reliability indices with changes in loading location.

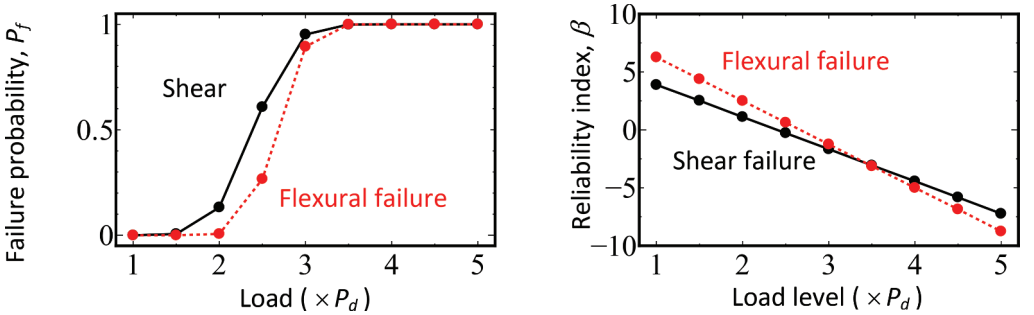


Figure 7. Failure probabilities and reliability indices with changes in load.

Referring to the reliability indices, the β_s of shear mode decreased to 3.14 (at $x = 0.05L$) from 4.82 (at $x = 0.5L$), when changing the loading location toward the support. On the other hand, the β_f of flexural mode increased to 9.03 near the support (at $x = 0.05\ L$), because the moment around the pin-support was very small. The center of the impact load of the avalanche was considered at $x = 0.25L$ from Figure 4. The failure probability $P_{f,s}$ and reliability index β_s at the location $x = 0.25\ L$ were still safe. Results indicated the load level of the avalanche was much higher than the design load P_d.

The relationship between load level and failure probabilities are shown in Figure 7, with the loading location fixed at $x = 0.25\ L$. The probabilities of flexural and shear failures converged to 1.0 when the load P was higher than $3P_d$. The safety β_s of shear mode was lower than that of flexural mode β_f. Moreover, these reliability indices were switched between 3.0 P_d and 4.0 P_d.

From the conditions set in the calculation model, the vertical load P by the avalanche was estimated over 3 to 4 times the design load P_d from weights of the superstructure and vehicles.

4 NON-DESTRUCTIVE TESTING ON THE FOUNDATION

4.1 *Forced vibration testing*

4.1.1 *Experimental program*

Cracks in the bridge abutment were observed through visual inspection, indicating large horizontal and moment had affected the abutment through bearings of the beams. Moreover, it was likely that the horizontal force had also affected the foundational footing and piles. However, it is difficult to detect damage in the footing and piles under the ground.

In this study, forced vibration testing (Naito & Bolander 2019, Naito et al. 2020) and impact echo inspection were conducted on the piles. The ground around the foundation was composed of volcaniclastic debris mixed with gravel and scoria. The foundation was a group pile structure (root piles), with 68 micropiles. The piles had a diameter of 131 mm and a length of 8.5 m. Cement milk was filled around a 51mm diameter deformed steel bar.

As shown in Figure 8, the abutment had been removed in the site test. Two non-destructive testing were conducted from the top surface of the footing to apply elastic waves into the piles. Figures 9 shows the measurement locations from the top surface of the footing, where the black marks were 20 measured piles. The measurement locations Nos. 1 to 20 were determined from the design drawings. A schematic diagram of the elastic wave testing is shown in Figure 9. The elastic waves were applied into the pile from the top surface of the footing, for obtaining reflected waves from the bottom of the pile. During these site tests, forced vibration testing and impact echo inspection were conducted.



Figure 8. The top surface of the footing.

An electric-magnetic vibrator was used in the forced vibration testing. The vibrator has a mass of 9.5 kg, frequency range of 20 to 20,000 Hz, a maximum excitation force of 49 N, and a maximum acceleration of 377 m/s^2. In the site test, white noise was applied to the piles for saving test duration. The white noise was generated at a power spectral density of 15 (m/s^2)^2 /Hz in a frequency range of 50 to 500 Hz, where the root mean square (RMS) of the acceleration waveform was 82 m/s^2. Response acceleration waveforms were measured with a piezoelectric accelerometer with a mass of 4.6 g, and a sensitivity of 10 mV/G in a frequency range of 1 to 30 kHz. The accelerometer was placed on the top surface of the footing approximately 100 mm away from the excitation location. Frequency response functions with a resolution of 1 Hz were obtained.

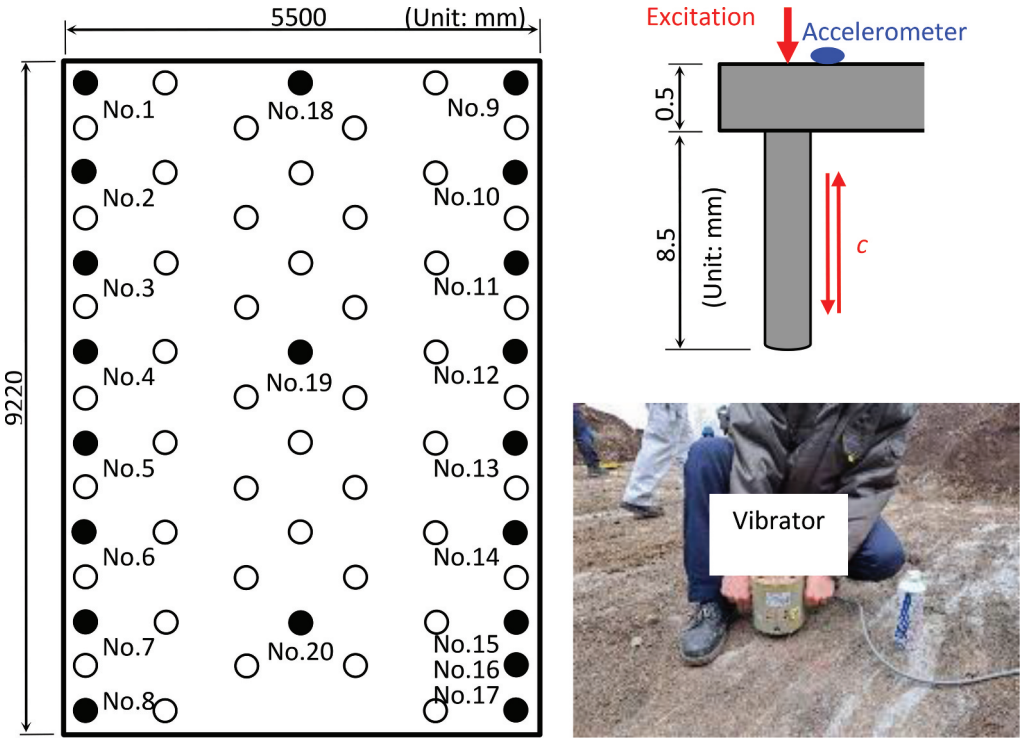


Figure 9. Measurement locations in the forced vibration tests.

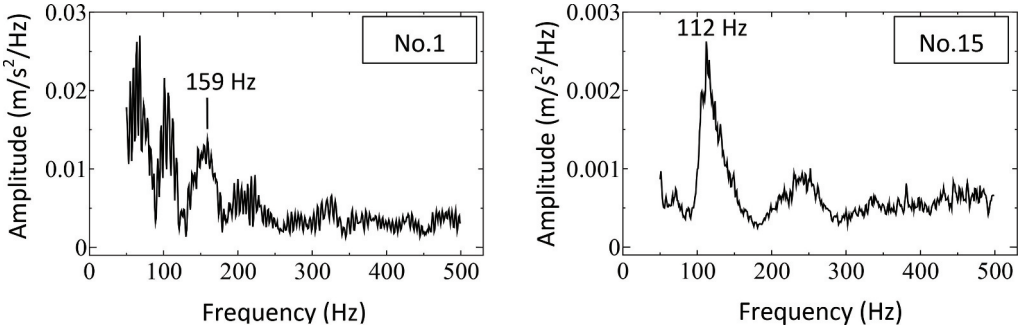


Figure 10. Frequency response functions from the forced vibration tests.

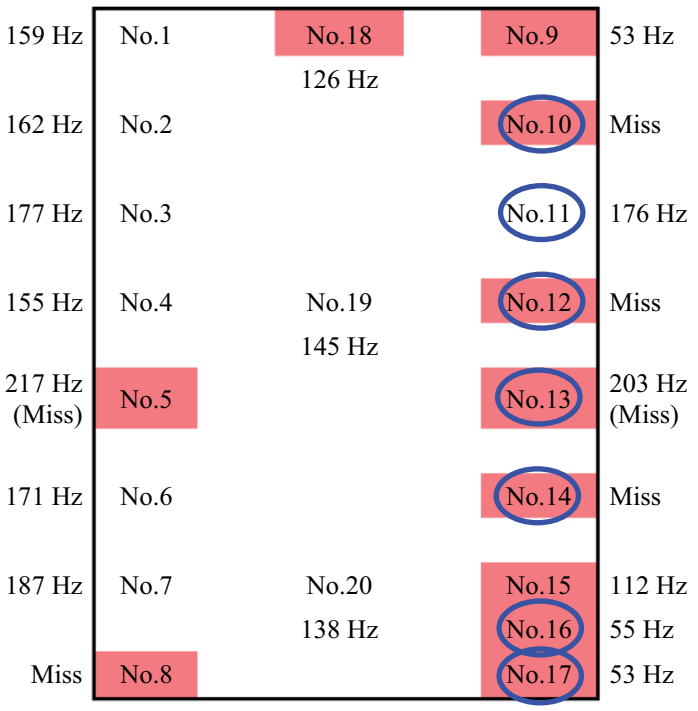
A longitudinal vibration of the pile was excited with the vibrator, as shown in Figure 9. The resonant frequency f_0 of an intact pile was obtained as $f_0 = c/(2L)$, where c is the speed of sound within the pile, and L is the vibration length. The vibration length L was given as 9.0 m, from the pile length of 8.5 m and the footing thickness of 0.5 m. The speed of sound was assumed as 3700 m/s, as well as that within concrete. In addition, a reduction factor of 0.80 was given in considering influence of the footing mass (Naito et al. 2017). The modified speed of sound c was given as $c = 0.80 \times 3700 = 3000$ m/s. The resonant frequency $f_0 = 166$ Hz was calculated. Moreover, considering a coefficient of variation $\sigma = 10$ %, resonant frequency of the intact pile was in the range of 130 to 200 Hz, from f_0 (1 +/– 2σ) in normal distribution.

However, resonant frequency (stiffness) decreases when cracks are contained within the pile. From the forced vibration testing, measured resonant frequencies were defined as frequencies corresponding to amplitude peaks in frequency response functions. The measured resonant frequencies in the range of 50 to 130 Hz were determined to be in "Damaged condition". Those in the range of 130 to 200 Hz were determined to be in "Intact condition". In addition, measurement locations were labeled as "Miss", when the measured resonant frequencies were higher than 200 Hz. This has a possibility of damage, having complex wave propagation characteristics with diffracted and reflected waves around cracks within the pile.

4.1.2 *Experimental result*

Frequency response functions of No. 1 and No. 15 are shown in Figure 10. The frequency response of No. 1 was labeled "Intact condition", since one of the amplitude peaks was observed at 159 Hz, within the intact range of 130 to 200 Hz. On the other hand, the frequency response of No. 15 had no amplitude peak in the intact range of 130 to 200 Hz. It was labeled as "Damaged condition" since the longitudinal resonant frequency (stiffness) of the pile decreased due to cracks and damages. Indeed, cracks and damage were observed around the joints of the footing and piles, after removing soil around the measurement locations Nos. 15 to 17.

Figure 11 shows the measured resonance frequencies and condition labels for Nos. 1 to 20. Conditions "Damaged" and "Miss" are colored in red. Most of Nos. 1 to 7 on the left side of the footing were labeled "Intact condition". The statistical values of the resonant frequencies from Nos. 1 to 7 except for No. 5 were: a mean of 169 Hz, and a coefficient of variation of 7.2 %. The mean value of 169 Hz showed agreement with the calculated frequency f_0 = 166 Hz.



*Red areas (from the forced vibration testing) and blue circles (from the impact echo inspection) indicate damaged piles.

Figure 11. Damage evaluation results.

On the other hand, most of the piles Nos. 9 to 17 on the right side of the footing had been labelled "Damaged condition" or "Miss", out of the intact range of 130 to 200 Hz. It was thought the piles had cracks and damage. As described above, the footing and piles of Nos. 15 to 17 were damaged, through visual inspection after soil removal.

Measured resonant frequencies from Nos. 18 to 20 on the center line of the footing were lower than those of the left side (Nos. 1 to 8). However, it was thought the piles of Nos. 18 to 20 were lightly damaged since the thickness on the center line of the footing was higher than that of the left side shown in the drawings.

4.2 *Impact echo inspection*

During the site test, impact echo inspection was also conducted on the piles. Impact loads were applied to the pile with a hand-held hammer from the top surface of the footing, as shown in Figure 12. The hammer had a mass of 1.4 kg. The accelerometer had a sensitivity of 50 mV/G ina frequency range of 0.7 to 9000 Hz.

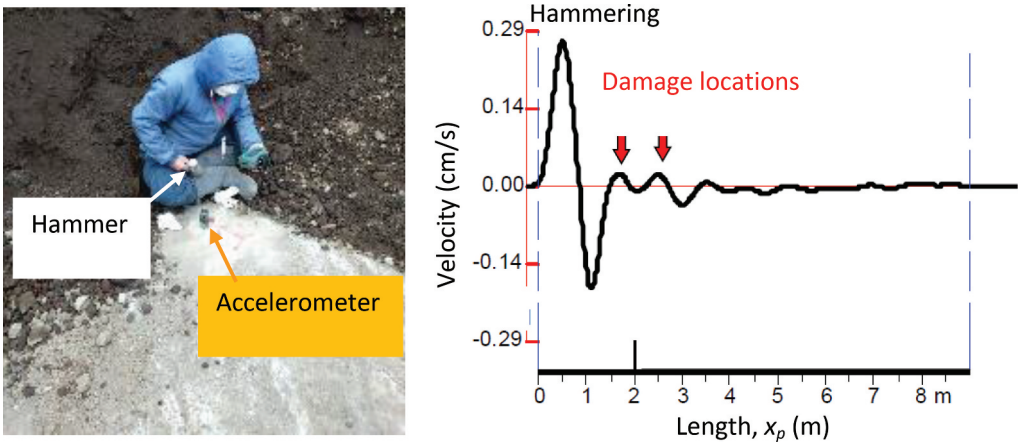


Figure 12. Impact echo inspection and measured waveform.

Figure 12 shows a schematic diagram of waveform analysis in the impact echo inspection. The time records of acceleration were integrated into velocity waveforms. The x-axis in Figure 12 was converted to a distance from the top surface of the footing in the longitudinal direction. This is given as $x_p = ct/2$, where x_p is the distance from the top surface of the footing, t is the time, and c is the speed of sound within the pile, assuming the modified value of c = 3000 m/s as in the forced vibration testing. The arrows at velocity peaks in Figure 12 indicate reflected waves from horizontal cracks within the pile.

Figure 11 shows the results of damage evaluation from the impact echo inspection. The 20 measurement locations were the same as those of the forced vibration tests. Damaged piles evaluated from the impact echo inspection were indicated with blue circles in Figure 11. Most of the piles were damaged on the right side of the footing. Comparing the results from the forced vibration tests, both non-destructive testing methods were in agreement. The effectiveness of using and comparing different testing methods for detecting damage in non-visible structures covered in soil was observed.

5 CONCLUSIONS

In this study, damage evaluation of a road bridge subjected to an avalanche was conducted, using reliability analyses and non-destructive testing. These findings were observed:

1) Shear cracks occurred in the RC beam due to a vertical load of the avalanche. From visual observation, the loading location of the center of the avalanche was thought to be around a quarter of the span.
2) A failure probability and reliability index for shear failure were evaluated using a Monte Carlo simulation. From the calculated result, the impact load of the avalanche was estimated to be over 3 to 4 times the design load from weights of the superstructure and vehicles.
3) Forced vibration testing and impact echo inspection were conducted on the foundation. The results from these two methods were in agreement. Piles on the left side of the footing were almost intact, whereas those on the right side were seriously damaged. It was thought that a large horizontal load was applied to the abutment and foundation during the avalanche.

The effectiveness of reliability assessment and non-destructive testing was shown through the examples of damage evaluation of a bridge subjected an avalanche. Further studies applying these methods on various types of accidental loads are needed to improve design and inspection processes for civil structures.

ACKNOWLEDGEMENTS

A part of this research was conducted with the support of JST FOREST Program (Grant Number JPMJFR2150, Japan), and the Japan Society for the Promotion of Science (Grant Number 22H01568). In addition, we thank the staff of the Road Maintenance Division, Yamanashi Prefecture, for providing their reports and document materials.

REFERENCES

Arros, J. & Doumbalski, N. 2007. Analysis of aircraft impact to concrete structures. *Nuclear Engineering and Design* 237: 1241–1249.

Biagi, V.D., Marchelli, M. & Peila, D. 2020. Reliability analysis and partial safety factors approach for rockfall protection structures. *Engineering Structures* 213: 110553.

Consolazio, G.R., Cowan, D.R., Biggs, A., Cook, R.A., Ansley, M. & Bollmann, H.T.2005. Full-Scale Experimental Measurement of Barge Impact Loads on Bridge Piers. *Transportation Research Record: Journal of the Transportation Research Board* 1936 (1): 81–93.

Japan Society of Civil Engineers. 2022. Standard specifications for concrete structures.

Mougin, J.-P., Perrotin, P., Mommessin, M., Tonnelo, J. & Agbossou, A. 2005. Rock fall impact on reinforced concrete slab: an experimental approach. *International Journal of Impact Engineering* 31: 169–183.

Naito, H. & Bolander, J.E. 2019. Damage detection method for RC members using local vibration testing. *Engineering Structures* 178: 361–374.

Naito, H., Sugiyama, R. & Bolander, J.E. 2020. Local vibration testing and damage evaluation for RC bridge decks. *Journal of Structural Engineering* 146 (9), ASCE: 04020168.

Naito, H., R. Sugiyama, T. Matsumoto, S. Horimi, & M. Suzuki. 2017. Inspection for RC structures using forced vibration testing. *Proceedings of Annual Conference of the Japan Society of Civil Engineers* 72: 283–284. (in Japanese)

Nataraja, M.C., Dhang, N. & Gupta, A.P. 1999. Statistical variations in impact resistance of steel fiber-reinforced concrete subjected to drop weight test. *Cement and Concrete Research* 29: 989–995.

Pham, T.M. & Hao, H. 2017. Effect of the plastic hinge and boundary conditions on the impact behavior of reinforced concrete beams. *International Journal of Impact Engineering* 102: 74–85.

Schubert, F. & Kohler, B. 2008. Ten lectures on impact-echo. *Journal of Nondestructive Evaluation* 27: 5–21.

Tachibana, S., Masuya, H. & Nakamura, S. 2010. Performance based design of reinforced concrete beams under impact. *Natural Hazards and Earth System Sciences* 10: 1069–1078.

Bridge Maintenance, Safety, Management, Digitalization and Sustainability – Jensen, Frangopol & Schmidt (eds)
© 2024 The Author(s), ISBN 978-1-032-77040-6
Open Access: www.taylorfrancis.com, CC BY-NC-ND 4.0 license

In-situ, lab testing and FE simulations historical steel-concrete bridge decks

A. de Boer, B. Renckens & L. Ha
Engineering Office, City of Amsterdam, The Netherlands

ABSTRACT: Before 1950 steel-concrete bridges are built without a dowel connection between the steel and concrete part of the bridge deck. The steel part of this bridge type is a common steel I-type girder. The concrete part has no bearing capacity reinforcement. The span length vary from 5-15 meter. The assessment of those structures aren't covered by the Eurocode, a dowel connection between the steel and concrete part is missing. Slip behaviour of the bonded connection between steel and concrete is unknown. In-situ cycle loading tests, ULS cycle and ULS lab tests with Eurocode TS load configurations are executed on 5 samples, constructed in 1938. They show the bonded behaviour. Solid3D FE model simulations confirm the test measurements. This process leads to a practical engineering re-examination assessment protocol based on a simple Shell2.5D FE model. The historical view of the city of Amsterdam can be saved and reduces the renovation costs.

1 INTRODUCTION

After the publication of the steel-concrete Eurocode 4 part 2[CEN 2005] and the introduction of the set of Eurocodes in the Netherlands in 2012 it wasn't allowed anymore to design steel concrete bridge decks without dowels between the steel girders and the concrete bridge decks. However the inner cities of "old" towns like Amsterdam have a large number of steel concrete bridge decks.



Figure. 1. Overview inner city of Amsterdam.



Figure. 2. Overview 3-span steel concrete bridge.

The city of Amsterdam counts more than 800 road traffic bridges, where more than 200 in the inner city, which are mostly steel concrete bridge decks. Their technical design lifetime of 80 years is already passed, so the assessment of those bridge decks could have a problem. However the bridge decks are still in operational, sometimes with restrictions to the vehicle weight, but even with these restrictions there was a need to have an additional guideline to the

DOI: 10.1201/9781003483755-47

Eurocode 4 part 2. The so called historical steel concrete bridge decks are designed on the theory of Joseph Melan[Melan1884]. These bridge decks are well known as the bridges based on the Melan System. The system contains common steel profiles embedded as reinforcement into a concrete deck. No additional reinforcement with a bearing capacity role was included in the deck, only shrinkage reinforcement was later on added at the top of the bridge deck. Later on, Wapenhans and Kind[Wapenhans1987] have published the Melan System again with some additions in a practical form for design engineers.

An additional guideline to the Eurocode means setting up experiments of these types of historical steel concrete bridges. The renovation program of the city of Amsterdam shows some bridges where the bridge deck should be removed, so this was an opportunity to setup some in-situ experiments. When the in-situ experiments show reasonable results, parts of the bridge deck could be transported to a laboratory environment, where similar or extended experiments could be done with an extended number of sensors in relation to the in-situ. Parallel to these experiments FE simulations can be done with solid 3D models to predict the real behaviour of the experiments. Later on, the solid 3D model can be simplified to a 2.5D shell model, which is more convenient for the practical engineering offices, which are involved to make the assessment re-examinations of the structures.

2 DESCRIPTION OF THE BRIDGE

The 3-span steel concrete bridge is already shown in Figure 2. The bridge counts 2 side spans and 1 main span; the span length of the side span is 5.8 meter, where the main span counts 7.55 meter.

The west side of the 3 spans can be used for experiments, while this is the first part which will be replaced in the renovation process. The basic cross section of the bridge is given in Figure 3.

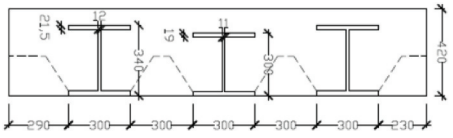


Figure 3. Basic cross section steel concrete bridge parts of the bridge deck.

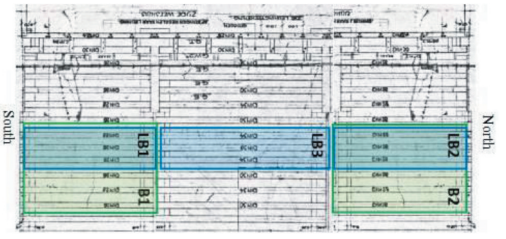


Figure 4. Top overview in-situ and lab experiment parts of the bridge deck.

Figure 3 shows 3 steel girders which are with the web and top flange full embedded in the concrete part of the bridge deck. The center to center dimension is 600 mm. Figure 3 shows also that there are 2 different steel profiles embedded, a so called DIN260 and a DIN280. The main span has a longer span, so the steel profiles are in this part a DIN300 and a DIN340. Concrete cores are taken from all 3 spans, which gives information about the concrete strength. Also some samples are taken out of the steel girders to get information about the steel quality and the steel strength and yield limit. There is shrinkage reinforcement embedded at the top of the concrete part, but this reinforcement part is neglected in Figure 3 and also in the Solid and Shell FE simulations. The abutments of the spans are given as a steel plate with a width of the bottom flange width of the steel profile and have a length of 700 mm on each side. The foundation isn't part of the experiments, it is a masonry structure on wooden piles. The restriction of the in-situ loadings is 475 kN to keep the foundation in the right condition after the experiments.

Figure 4 shows the parts of the bridge deck, which are used for the in-situ experiments (green area; B1 and B2) and the lab experiments(blue area; LB1, LB2 and LB3). The width of

the in-situ experiments counts 6 steel girders with the belonging concrete part, where the width of the lab experiments counts 3 steel girders with the belonging concrete part. As the in-situ experiments were scheduled first, the concrete of the 6 girder width part was sawn separately from the rest of the bridge deck, to get a simple supported slab environment. Only the side spans could be used for the in-situ experiments, while the transport over water in the inner city should be on going. When the in-situ experiments were finished the 3 girder width part was sawn again to make the transport of these part easier over water to the lab.

3 IN-SITU EXPERIMENTS

The in-situ experiments show a cyclic behaviour of a wheel print area load, which is located on the top of the concrete deck between the girder 3 and 4 of the 6 girder width of the side

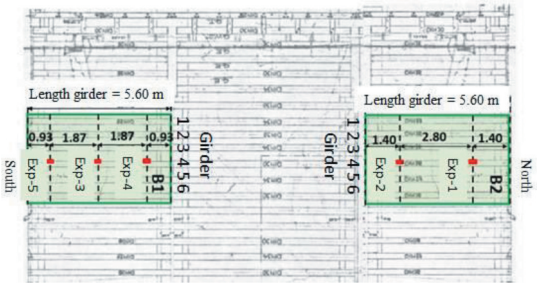


Figure 5. Wheel print load locations (red dots).

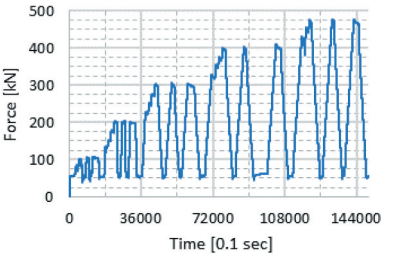


Figure 6. Cyclic loading scheme.

span. In total there were 5 locations of the wheel print, midspan, 1/4L, 3/4L, 1/6L and 5/6L. Figure 5 shows the locations of the side spans. The cyclic loading scheme is given in Figure 6.

An overview of the minimum of sensors is used at the in-situ experiments. Figure 7 shows the wheel print load sensor location in red, the strain sensors at the bottom girder flange in blue, the

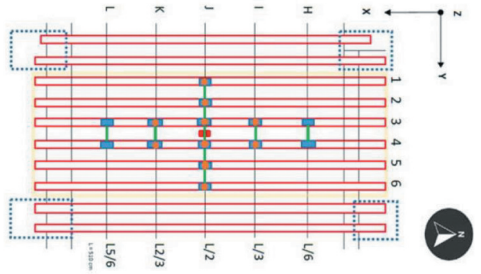


Figure 7. Sensor equipment bridge deck.

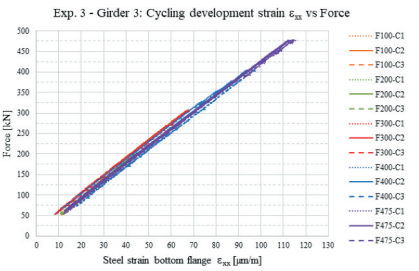


Figure 8. Strain ε $_{xx}$ cycle development.

displacement sensors of some bottom flange girders in orange and the sensors over the width to measure the displacement between the bottom flanges of the steel girders in green.

The strain εxx cycle development of girder 3 in Figure 8 shows a linear behaviour, which corresponds also with the inspections afterwards of this specific experiment, that there were no cracks seen at the bottom of the concrete bridge deck. Another important conclusion is coming from the distribution ratios of the wheel print midspan load over all 6 girders, which is given in Figure 9.

Figure 9 shows that girder 3 and 4 have almost the same distribution ratio related to the strain and the displacement in the same row with sensors at the midspan location of the wheel print load.

Further on, Figure 10 shows a possible hidden bending moment at the slab support lines. This result is neglected in the setup of the FE simulations, a simple supported span is simu-

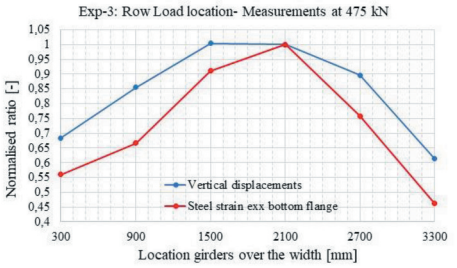


Figure 9. Distribution wheel print load.

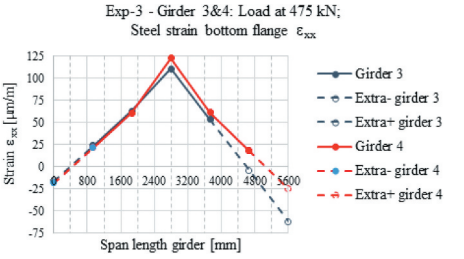


Figure 10. Hidden bending moment supports.

lated in FE. The last result of the in-situ experiments is coming from the sensors over the width of the 6 girder part. They measure a sudden jump at different load levels at different load cycles. This result is given in Figure 11.

Main result is of course, that a wheel print load capacity of 475 kN shows enough reliability related to the Eurocode, with a maximum wheel print load of 150 kN.

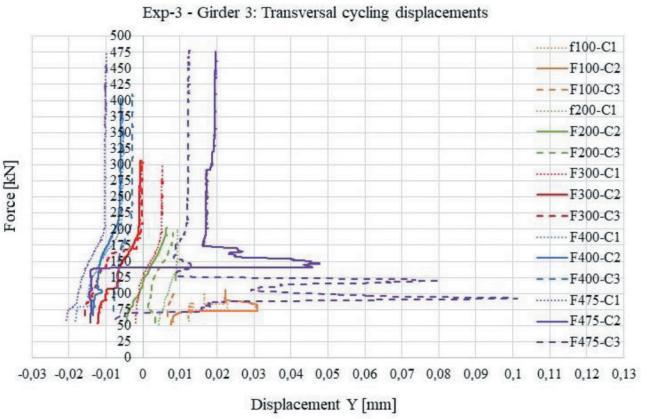


Figure 11. Transversal displacement girder 3.

Conclusion of this result given in Figure 11, shows that there is a reset of transversal displacements between the steel girder and the belonging concrete at low levels of the wheel print load at different cycles.

An interface behaviour between the steel girder and the belonging concrete should be included in the Solid FE simulations.

4 LAB EXPERIMENT WITH CYCLE LOADING

To get more information about the cycling behaviour, one of the side spans with a width of 3 steel girders with the belonging concrete gets also a cycling load scheme, but now in the laboratory, where more sensors can be installed. In total there were more than 100 sensors for

the displacements, strains, etc. The load is related to the tandem configuration of the Eurocode LM1, where both axles of the vehicle are simulated by a distributed beam over the width

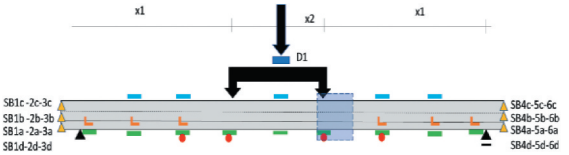


Figure 12. Side view of the lab experiment with sensor locations.

of the experiment. Also the Digital Image Correlation(DIC) method is partly installed at the concrete part underneath the location of one axle location. A side view with the sensors is given in Figure 12 and a top view with the s7ensors in Figure 12.

Figure 12 shows not only the strain sensors of the steel girders(green), vertical displacement sensors of the steel girders(red) or concrete deck(blue), but also the horizontal displacement sensors over the height of the experiment of the heads at every girder and belonging concrete.

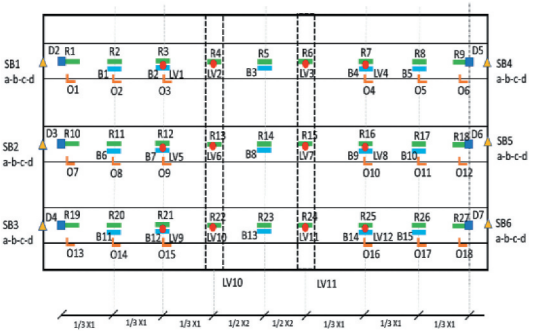


Figure 13. Top view of the lab experiment with all sensor locations.

The last mentioned sensors should measure the possible disconnecting behaviour between the steel girders and the belonging concrete. The light blue rectangle under the right load location shows the DIC area. Figure 13 shows an additional top overview of the sensor locations.

The load is attached in 2 stages, the first stage comes to a load level of 1400 kN and the second stage goes to the ULS load level. Every stage has some intermediate load levels with 3 cycles similar to the in-situ experiment. Also the breaks of the basic load level or the

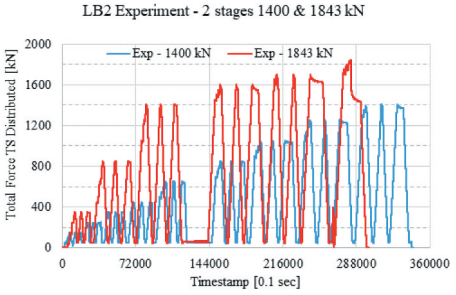


Figure 14. Loading scheme 2 stages LB2.

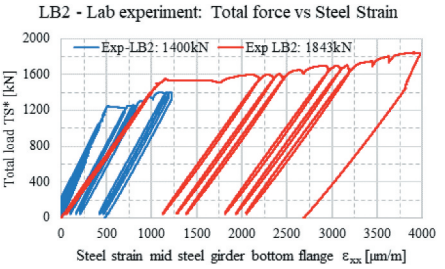


Figure 15. Strain ε_{xx} development 2 stages LB2.

intermediate load levels are similar in time duration. Figure 14 shows the load behaviour of the 2 stages, Figure 15 shows the strain of the bottom flange of the mid girder(DIN260) development of the 2 stages at the load location at the left axle.

Both stages in Figure 14 shows a break between 12.000 and 14.000 seconds, which is the lunch break in the laboratory. Also the overall duration of the experiments is very long and counts 8-10 hours. The strain development at the bottom flange beneath the left axle of the distributed load shows at the first stage a yielding behaviour at the load level of 1200 kN and at the second stage a yielding behaviour at the load level of 1500 kN. The reason is related to the hardening behaviour of the steel girder, which increases the ductility of the overall structure when overloading would be occur. The strain with a value of 500 micron at a load level of 1200 kN is in relation to the in-situ experiment much larger where the strain is 110 micron at a load level of 475 kN. Both diagrams have a linear development.

The load level of 1200 kN is 2 times the Eurocode vehicle LM1 with a load of 600 kN. Of course, there is also a Eurocode distributed vehicle load, but the span length is only 5.8 meter, so the overall distributed load counts for 160 kN, which is spread over 3 meter width or in this case at least 5 steel girders. The in-situ experiment shows already that one wheel print load will be carried by 2 steel girders, so there is sufficient bearing capacity in these type of historical bridge decks with already a technical lifetime of 80 years. Reason to follow up with ULS verifications with real wheel print load areas between the steel girders on the remaining spans. Restriction is of course the 3 girder wide spans, but still there is space to locate both wheel print locations between 2 steel girders.

5 VERIFICATION ULS EXPERIMENTS

Still there are a side span and a main span of the steel concrete bridge to verify the bearing capacity of the historical bridge decks. The assumptions from the cycle experiments are the following:

a) There is slip behaviour between the concrete part and the steel girder at a lower load level, so to be conservative the slip level is reached at a load level of 100 kN tandem axle configuration;
b) The installation of the bridge deck shows a stage with steel girders and green concrete, which implies that the steel girders are preloaded by the dead weight of steel and concrete. This means that the belonging stress by this dead weight load reached a level of 20 N/mm^2, which is ± 10% of the yield stress limit of the steel girders;

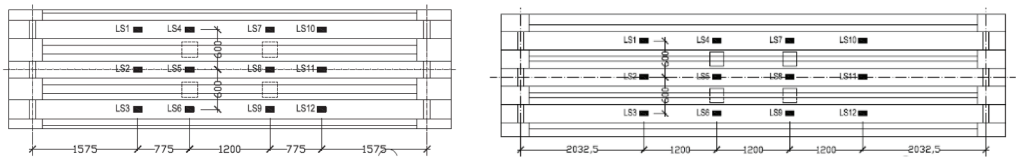


Figure 16. Topview load scheme wheel print load locations side span(left) and main span(right).

c) A restriction has to be made in case of the wheel print locations center to center distance, where the Eurocode shows a distance of 2 meter and the remaining 2 spans have a distance of 0.6 meter. This aspect shows a second conservatism. This top view of the load scheme wheel print load locations is given in Figure 16.

Both remaining spans show a similar equipment of sensors like the cycle LB2 experiment. Only the concrete decks show in this experiment no LVDT to measure the strain of the concrete but there are optic fibres installed. Also the DIC method is part of the measurements and located between a support and an axle location. The load scheme in time of both spans is shown in Figure 17 and 18. Again there is a short break around the 12.000 seconds. At that

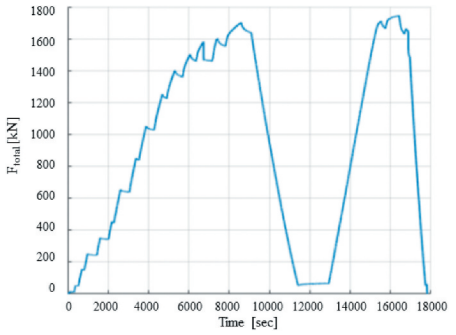


Figure 17. Load scheme side span.

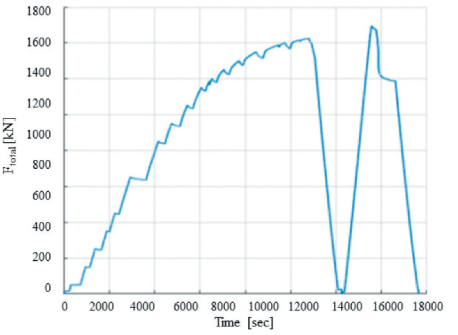


Figure 18. Load scheme main span.

moment the load was reduced to a small load level to make it possible to remove the DIC installation to avoid damage to these expensive installation.

The side span shows at the ULS load level slip behaviour between the steel girder and the concrete at one head of the experiment. Both experiments show a lot of crushing concrete at the top of the bridge deck between the axle locations. However, the ULS load level of the side span was 1744 kN and for the main span 1494 kN(1410 kN in a stable stage).

6 FINITE ELEMENT SIMULATIONS

All prediction and postdiction calculations of the experiments are based on Solid 3D element models. The basic steel girder and the belonging concrete shows the same element configuration in the cross-sectional area, which is given in Figure 19 as an extension of Figure 3, where the basic is given of a 3 girder cross section. In longitudinal direction the area between the

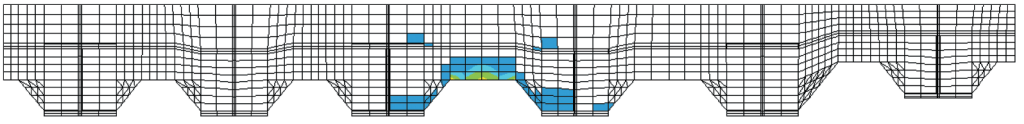


Figure 19. Cross sectional area of the 6 girder width in-situ experiment.

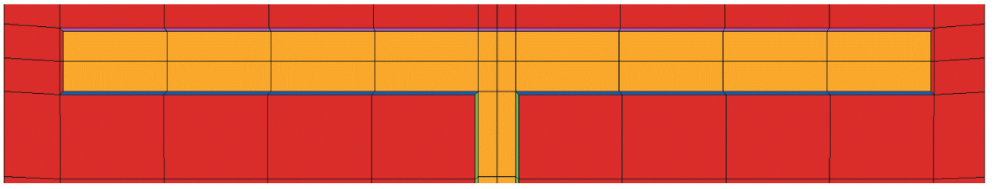


Figure 20. Interface surfaces between the steel girder and the belonging concrete.

loading lines is divided in element sizes of 100 mm. In transversal direction there are always 4 elements in the top and bottom flange of the steel girder, where the concrete between the steel girder shows maximum element sizes of 35 mm. All elements are quadratical elements. Between the steel girders surfaces and the belonging concrete surfaces with interface elements are modelled to simulate the slip behaviour. Figure 20 shows the interface surfaces, which have their own physical properties for the top and bottom of the top flange, the top of the bottom flange, the longitudinal side of the top flange and the web. The used FE program is the Dutch DIANA software [DIANAFEA 2021].

Table 1. Physical properties of the FE simulations.

Physical property	Symbol	Value
Concrete		
Young's modulus	E	37900 N/mm^2
Poisson ratio	ν	0.15
Density	ρ	2400 kg/m^3
Type curve softening	Hordijk	
Mean tensile strength	fctm	3.88 N/mm^2
Fracture energy	Gf	105 N/m
Crack bandwidth method	Govindjee	
Reduction Poisson ratio	Damage based	
Type curve compression	Parabolic	
Mean compression strength	fcm	54.6 N/mm^2
Compressive fracture energy	Gc	32 000 N/m
Reduction lateral cracks	Yes	
Minimum reduction factor	0.4	
Influence lateral locking	Yes	
Steel		
Young's modulus	E	210000 N/mm^2
Poisson ratio	ν	0.3
Density	ρ	7850 kg/m^3
Yield stress	σ	235 N/mm^2
Hardening method	Strain, EN1993-1-5	

Table 2. Additional slip properties.

```
: Normal and Shear Stiffness LE
   DSNZ 7.50E+03
   DSSX 1.00E+01
   DSSY 1.00E+0
: Additional nonlinear stiffness
: Displacement –Stress Diagram
: Normal Z direction
   DUSTNZ -1.0E+01 -7.50E+05
                1.0E-12 7.50E-09
                1.0E+02 7.51E-08
: Transversal X direction
   DUSTSX -8.00E+01 -2.40E+02
               -0.25E-02 -0.25E-01
                0.25E-02 0.25E-01
                8.00E+01 2.40E+02
: Transversal Y direction
DUSTSY -8.00E+01 -2.40E+02
           -0.25E-02 -0.25E-01
            0.25E-02 0.25E-01
            8.00E+01 2.40E+02
```

Table 3. Results experiments & solid and shell fe simulations.

Model	LB2	LB1	LB3
F_{exp}	1843	1744	*1410*
FE_{3D}	1828	1680	1330
$FE_{2.5D600}$	n/a	1410	1190
$FE_{2.5D300}$	n/a	1410	1190

The physical properties of the FE models are given in Table 1, and are related to the fib ModelCode2010[fib2012], the NLFEA Guideline of the Delft University of Technology[Hendriks2020]. Making it easier for practical engineering offices also a shell FE model based on beam grid theory is setup. Here the concrete is divided in cross beams with a width of 600 mm, based on the transversal cracks center to center distance of 600 mm of the lab tests. The FE simulations got the name $FEA_{2.5D600}$ and $FEA_{2.5D300}$. Here the center to center dimension is reduced till 300 mm. An extension of the guideline for the beam grid models is part of the re-examination process.

7 CONCLUSIONS

The following conclusions can be drawn:

a) The in-situ experiments show at least a bearing capacity distribution of the wheel print load over 2 neighboring steel girders;
b) The cycle lab experiment shows a decrease of the stiffness of the overall structure, which should be related to cracking of the concrete;

c) Bond(slip) behaviour between the steel and concrete part of the historical bridge decks is less relevant for the bearing capacity of the historical steel concrete bridge decks;
d) The linear behaviour of the steel strains till a load level of 1200 kN show a lot of confidence to allow heavy traffic with some restrictions in the inner city of Amsterdam;
e) All FE simulations, the Solid 3D model and the Shell 2.5D models, show a conservative ULS load level related to the experiments;
f) The Shell 2.5D FE simulations show also a conservative ULS load level related to the Solid 3D FE simulations, so if there is a need for a maximum bearing capacity, a 3D FE simulation is recommended;
g) The speed of the Shell 2.5D FE simulations is mostly 10 times faster than the speed of the Solid 3D FE simulations;
h) Re-examination work can be done easily, quicker & cheaper by Shell FE 2.5D simulations.

ACKNOWLEDGEMENT

The authors wish to express their gratitude and sincere appreciation to the Programme Bridges and Quay Walls of the Engineering Office of the Municipality of Amsterdam for their support of the project "Steel-Concrete Bridge Decks(Verbundträger)". Beside these thanks we like to thank also our other project team members and external partners, which were involved in the in-situ tests (TNO Research, MFPA Leipzig, Mammoet, Dekker, Bouwrisk) and the laboratory experiments (TNO Research, Delft University of Technology) for their contribution.

REFERENCES

CEN, 2005, European Committee for Standardization. EUROPEAN STANDARD English Version Eurocode 4 - Design of composite steel and concrete structures-Part 2: General rules and rules for bridges. Tech. rep. 2005

Melan, J., 1884. Beitrag zur Berechnung statisch unbestimmter Stabsysteme, in: Zeitschrift des Österreichischen Ingenieur- und Architekten-Vereines 36 (1884), pp. 100–108. (German)

Wapenhans, W. & Kind, S., 1987, Verbundkonstruktionen aus Stahl und Beton: Vorbemessung für Stahlprofilblech-Verbunddecken, Verbundträger im Hochbau, Verbundstraßenbrücken, Berlin: Bauinformation DDR, (German)

DIANAFEA, 2021, Users's Manual, Release 10.5, DIANA FEA BV, Delft, the Netherlands

fib 2012. ModelCode2010, Final Draft, International Federation for Structural Concrete (fib), Lausanne, Switserland

Hendriks, M.A.N. & Roosen, M., 2020, "Guidelines for Nonlinear Finite Element Analysis of Concrete Structures", Rijkswaterstaat-Centre for Infrastructure, Report RTD:1016-1:2020, version 2.2, Rijkswaterstaat, the Netherlands

Bridge Maintenance, Safety, Management, Digitalization and Sustainability – Jensen, Frangopol & Schmidt (eds)
© 2024 The Author(s), ISBN 978-1-032-77040-6
Open Access: www.taylorfrancis.com, CC BY-NC-ND 4.0 license

Practical experience with proof loading – examples from 3 bridges

J.H. Roldsgaard, J.K. Nørregaard, C. Pedersen & J. Vig
Monitoring & Analysis of Existing Structures, Transport, Ramboll DK A/S, Denmark

A. O'Connor
Trinity College Dublin, Dublin, Ireland

ABSTRACT: Practical examples of how proof loading of bridges is approached and applied by consultants with the goal of increasing the bearing capacity of existing bridges, are still limited. The present paper presents the proof loading of 3 bridge located on a route where a heavy special transport with a total weight of >500 tonnes and an axle weight of >20 tonnes. The main outcomes of the theoretical deterministic assessment before the proof loading were decided upon, determination of the proof load together with all the considerations in the planning phase including how the proof loading can be carried out will be presented. Especially the planning phase of the proof load is essential to mitigate all significant risks and ensure a successful project for both bridge owners, users and the project team. At the end some learnings from the proof loadings will be shared and the results presented.

1 INTRODUCTION

The proof loading of bridges is a crucial and highly relevant process in the field of structural engineering, serving as a comprehensive method to validate the safety and performance of a bridge structure(s). This procedure involves applying controlled and incremental loads to the bridge, often exceeding the design loads, to assess its response and behavior under extreme conditions. Proof loading provides valuable insights into the structural integrity, load-carrying capacity, and overall resilience of the bridge. By subjecting the bridge to loads beyond its expected operational conditions, potential weaknesses can be identified, effectiveness of structural components can be assessed, and it can be ensured that safety margins are appropriate. Proof loading can contribute to the optimization of bridge design/assessment and ensure that structures meet structural safety requirements. This paper presents the methodology for determination of appropriate proof loading levels for a number of bridges in Denmark. The bridges were intended to carry exceptional loads which were to be transported along their route. Traditional deterministic structural assessment failed to demonstrate adequate capacity, due in part to the absence of sufficient structural information, and as a result it was necessary to undertake proof loading to validate that the structures had sufficient structural safety to carry the loads. The paper first describes the specifics of the exceptional heavy loads to which the structures were to be subjected. This is followed by a description of the specific structures and their critical limit states for the considered loads. The process or determining, probabilistically the level of proof load to be applied, to provide for sufficient structural safety, relative to prescribed limits, is detailed along with discussion of important aspects such as the definition of stop criteria. Finally, the methodological process of carrying out the proof loading is detailed. Ultimately, the value of proof loading for validation of sufficient structural capacity it demonstrated.

DOI: 10.1201/9781003483755-48

1.1 *Heavy special transports*

The proof loading of the 3 bridges presented in the present paper has been initiated as it is wished to drive a heavy special transport from Brande to Hvide Sande (Denmark), which is from the middle of Jutland to the west coast as shown in Figure 1. The heavy special transport consists of a truck with 8 axles of 8t-10t each and a flatbed truck with >20 axles of >20t with a spacing of 1.5m and hydraulic equalization between the axles. This gives a total weight of well above 500t.

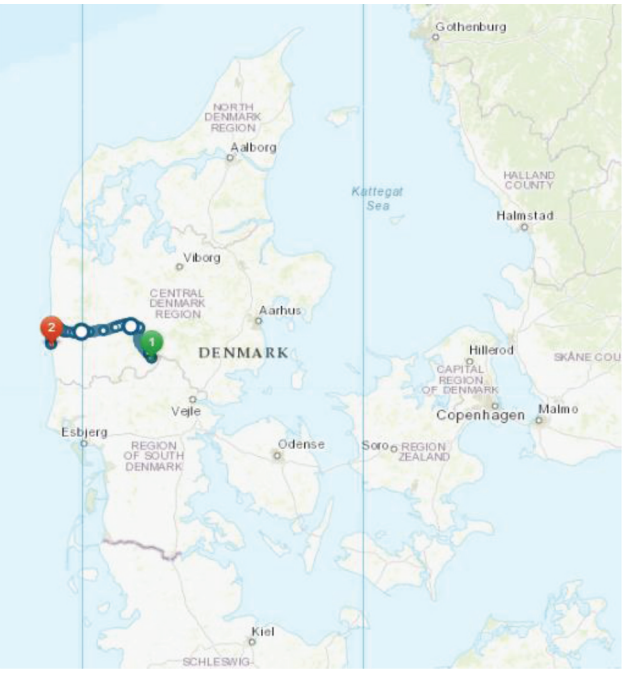


Figure 1. Route for the heavy special vehicle indicated on the map of Denmark.

2 BRIDGES SUBJECT FOR PROOF LOADING

Proof loading of the 3 bridges presented here all failed to prove adequate capacity of the sub-structure in the deterministic assessment (partial safety factor method) according to Danish Road Directorate (2017). However, for all 3 bridges the superstructures showed adequate capacity with the normal safety factor method, hence the proof loading could be tailored for the sub-structure.

For a bridge to be fit for proof loading a number of criteria should be fulfilled. The following is not a comprehensive list but some of the considerations carried out before it was decided to proof load the 3 bridges presented here.

2.1 *Rind Å - failure mechanism*

The bridge across Rind Å is a reinforced concrete beam/plate bridge with a grillage cross-section built in the 1930's. The bridge was widened in 1992 to the south with a separate pedestrian/bicycle bridge. The main span is approx. 10m and the bridge is about 9m wide carrying one lane of road traffic in each direction with a pedestrian/bicycle lane one side. Extracts of the original drawings of the bridge across Rind Å are shown in Figure 2.

All capacity checks in the ultimate limit state for the superstructure proved adequate capacity for the heavy transport to pass the bridge, however, the capacity check of the piles failed short of capacity. During the capacity assessment of the piles, it was assessed that the data

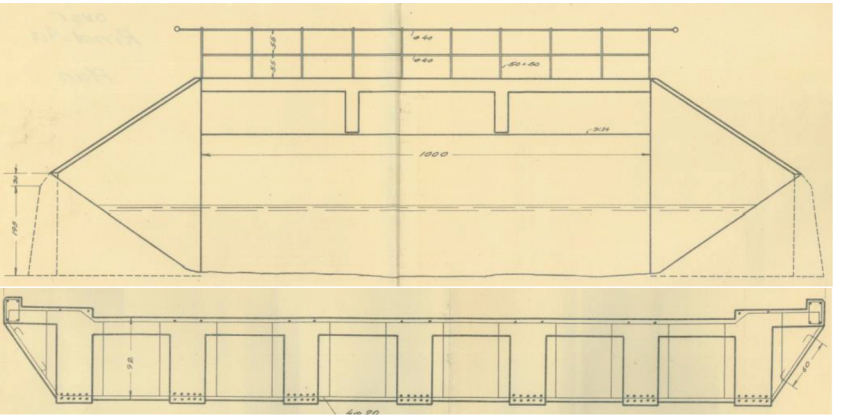


Figure 2. Original drawings of Rind Å showing the plan and cross-section.

processing of the soil samples was somehow conservative, furthermore, it was suspected that for this particular bridge the standard also was conservative. Hence, it was decided to carry out proof loading of the substructure if found possible.

An important consideration of the failure mechanism was performed before it was decided to perform proof loading of the bridge to prove the capacity of the bridge for the heavy special vehicle. From the analysis it was found that failure of one or more piles would lead to deformation/settlement of the walls supporting the bridge deck, hence a very slow a ductile failure mode, and not a sudden brittle failure.

2.2 *Vorgod Å - failure mechanism*

The bridge across Vorgod Å is a reinforced concrete 3-span beam/plate bridge with a cross-section consisting of 7 T-beams, the bridge is built in the 1950's. The main span is approx. 8m and the two side spans are approx. 7.3m with a width of about 9m wide carrying one lane of road traffic in each direction. Extracts of the original drawings of the bridge across Vorgod Å are shown in Figure 3. One thing to notice is that a mistake on the original drawing was found, it only showed 6 T-beams, but from the inspections 7 T-beams were found. A special inspection of the bridge confirmed the rest of the information from the drawings.

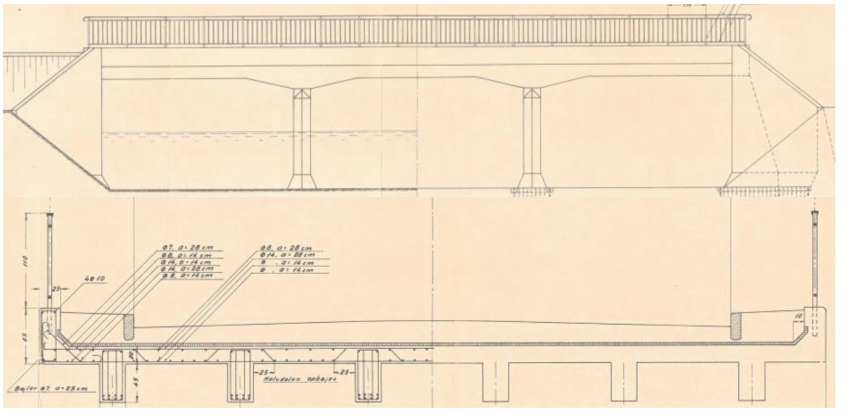


Figure 3. Original drawings of Vorgod Å showing the plan and cross-section.

All capacity checks in the ultimate limit state for the superstructure proved adequate capacity for the heavy transport to pass the bridge, however, the capacity check of the piles was

rather difficult as none of the original drawing or documentation stated the pile lengths. This bridge over Vorgod Å was key for the transport of the heavy special vehicle as it is a spanning over multiple supports and the total length is above 20m, making it very laborious and expensive to temporary replace or strengthen for the vehicle to pass and maybe even impossible without total replacement. Hence, it was decided to carry out proof loading of the substructure if found possible.

An important consideration of the failure mechanism was performed before it was decided to perform proof loading of the bridge to prove the capacity of the bridge for the heavy special vehicle. From the analysis it was found that failure of one or more piles would lead to deformation/settlement of the walls supporting the bridge deck, hence a very slow a ductile failure mode, and not a sudden brittle failure.

2.3 *Skjern Å - failure mechanism*

The bridge across Skjern Å is a reinforced concrete beam/plate bridge with a cross-section consisting of 8 T-beams, the bridge is built between 1945 and 1954, but the precise year is unknown. The main span is approx. 8m and with a width of about 9m wide carrying one lane of road traffic in each direction. Extracts of a sketch of the bridge from a military measurement in Figure 4, however, these should only serve as indicative as they often are found inaccurate for use in a detailed capacity assessment.

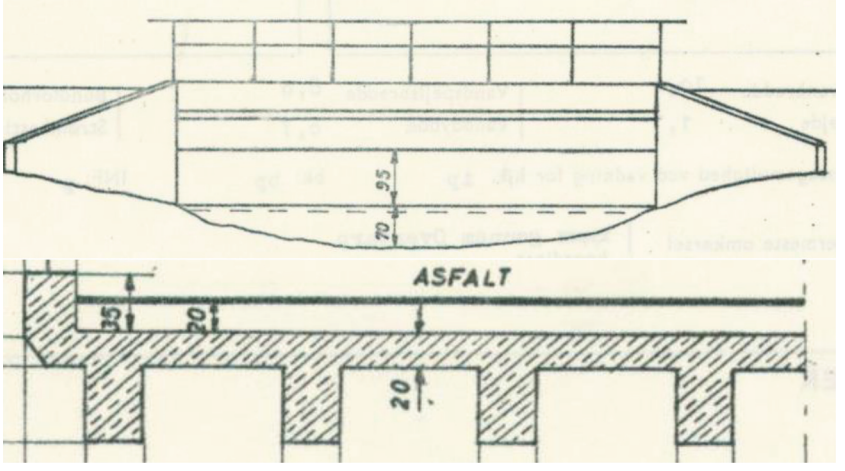


Figure 4. Sketch of Skjern Å shown plan and cross-sectional shape.

As no drawings or documentation material existed a special inspection was performed, where the geometry of the bridge deck was established together with the layout of the reinforcement by scrapping the concrete covering layer away such that the reinforcement was exposed for visual inspection and measurements. Regarding the quality such as concrete strength and yield strength of the reinforcement the typical building material for this period was assumed. The year of construction was established by archive photos and found to be between 1945-1954. Assumptions around the materials were taken conservatively, however, it was possible to show adequate capacity of the superstructure for the heavy special vehicle to pass the bridge.

About 50m away an almost similar (type, span and materials) bridge is placed, however, not longer in service as the road layout was changed during the period 1945-1954, where the bridge in question was built. The neighboring bridge was built in the 1930's and the original drawings of this bridge are available. From the drawings this bridge is direct founded, hence, as the soil test samples showed that the soil conditions for the two neighboring bridges are very similar it was assumed that the bridge in question also is built with direct foundations. However, as the assumptions around the substructure are made with high uncertainty it was

decided to proof load this bridge to show that the capacity of the substructure was adequate for the heavy special vehicle to pass.

It was assessed that the failure mechanism of the direct foundation is ductile until about a deformation of approx. 10mm, for which sudden brittle failure could happen. Hence, the loading scheme for the proof loading was made extra carefully and the stop criteria allowing only very small deformations to ensure that a sudden brittle failure would not occur.

3 PREPARATION

The level of the proof load for which the bridges should be tested is determined in accordance with Christensen et al (2023) and the next version of the guideline for reliability-based classification of existing bridges, Danish Road Directorate (2024).

The heavy special vehicle will pass the bridges with a speed equal to or lower than 10 km/h at the most favourable position on the bridge without any other traffic, hence, in accordance with Danish Road Directorate, 2017 and DS/EN 1991-2 (2003) including Danish national annex this is classified as conditional passage type 3, which means that it is assumed there is no dynamic amplification.

3.1 *Probabilistic estimation of the proof loading load*

For the 3 bridges it is the substructure and especially the uncertainty about the construction of the substructure which is uncertain. Hence, in the estimation of the proof load all the safety is put on the variable load side which essentially means that the bridges should be proof load with a load having the probability of occurrence as the safety level requires. The required safety level for existing bridge with a ductile failure mode is given in Danish Road Directorate (2017) and Danish Road Directorate (2024) as:

$$p_f = 10^{-6}$$

where p_f is the probability of failure

To determine the level of the proof load for the 3 bridges the distribution for the annual extreme vehicle weight is established according to Danish Road Directorate (2024):

$$F_p = \exp(-N_i(1 - F_W(x))$$

where N_i is the number of yearly heavy special transports and $F_W(x)$ is the distribution of the weight of the heavy vehicle.

The number of annual heavy special vehicles is conservatively assumed to 10, where the client has informed Ramboll it is less than half of this. As for the distribution of the weight of the heavy vehicle only the number of axles actually affecting the failure mode is included which for the bridges presented here is between 3-4. On this basis the uncertainty is interpolated from [guideline] and found in the order of 7-8% depending on the number of axles, where the uncertainty of the total weight of the axles decreases with increasing number of axles. The proof load factors found for the 3 bridges are shown in Table 1.

Table 1. Proof load factors and total proof load.

Bridge	Proof load factor [-]	Proof load [tons]
Rind Å	1.33	139.8
Vorgod Å	1.34	108.4
Skjern Å	1.34	108.4

3.2 *Safety of the superstructure for the proof loading load*

The capacity assessment of the superstructure is as the first step checked against the following load combination:

$$E_d = K_{FI} \cdot \left(\sum (\gamma_{Gi} \cdot G_i) + \gamma_q \cdot Q_k \right)$$

where E_d is the design load effect, $K_{FI} = 1.1$ and related to the consequence class, which for all bridges in Denmark above 6m is CC3. $\gamma_{Gi} = 1.0$ is the partial safety factor for the self-weight and the superimposed deadload and G_i is the actual load effect from self-weight or superimposed deadload. $\gamma_q = 1.20$ is the partial safety factor for the heavy special vehicle, this is to be used when the actual axle configuration and weight is known before the transport and Q_k is the load effect from the heavy special vehicle. The above load combination is to verify that the superstructure has the required safety during the actual transport according to the Eurocode with Danish national annexes [ref].

The superstructure does not only need to show adequate capacity during the actual transport with the heavy special vehicle but also during the proof loading, where more load is applied to the bridge than for the actual situation as a result of "putting" all the safety on the load side in the determination of the proof load level as described in Section 3.1. Hence, the capacity of the superstructure is shown adequate for the following load combination:

$$E_d = K_{FI} \cdot \left(\sum (\gamma_{Gi} \cdot G_i) + \gamma_{q_W} \cdot Q_{k_W} \cdot \gamma_{PF} \right)$$

where $\gamma_{q_W} = 1.15$ as the weight of the proof load vehicle is known exactly (weighed), Q_{k_W} is the load effect from the proof loading load, and γ_{PF} is the proof load factor found in Section 4.1.

3.3 *Stop criteria*

The stop criteria for the proof loading were carefully selected to ensure no failure of the bridges. In general deformation above 5mm of the supporting wall was highly undesirable, however, not a hard criterion. Whereas continuously deformation for the same load was a very hard stop criterion and if this particular situation would arise the proof loading would have been called off. The superstructures were also monitored during the proof loading even though their capacity had been shown adequate with the partial safety factor method as described in Section 3.2.

An example of the intended measuring points for Vorgod Å is shown in Figure 5.

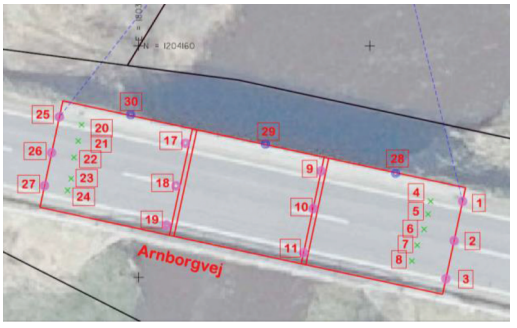


Figure 5. Example of intended measuring points for Vorgod Å.

4 EXAMPLES

For all 3 bridges more than one critical location is tested, meaning all supporting walls were subject to proof loading as well as behind the bridges for Skjern Å and Rind Å. This is to ensure that eventual difference in the foundation conditions or soil conditions critical for the capacity of the bridge is uncovered by the proof loading.

4.1 *Load stepping*

The paradigm for the load stepping was the same used for all 3 bridges. The stepwise procedure is listed below:

1) Reference measurement of the bridge without load by the surveyor. The surveyor measured approx. 10 points for the two smaller bridges and approx. 25 points for the 3-span bridge with a precision of about ±0.2mm.
2) The front end of the truck with 3x10t axles is positioned at the bridge at the marked locations on the asphalt.
3) The surveyor measures potential deformations of the bridge. This is performed again after 5 min to ensure eventual deformations do not continue.
4) The flatbed truck with 16.5t axles per 1.5m is positioned at the bridge.
5) Step 3) is repeated.
6) The load on the axles is increased by 2t.
7) Step 5) – 6) is repeated until the proof loading load is reached.
8) The bridge is onloaded and step 3) repeated before moving on to the next location.

4.2 *Rind Å*

Proof loading of Rind Å was carried out in December 2023 was a success and the capacity of both the super- and substructure of the bridge is assessed to be adequate for passing of the heavy special vehicle maintaining the required safety level. The maximum deformation for the supporting walls was approx. 2mm and 1mm for the superstructure, which both were well within the acceptable limits.



Figure 6. Photos from the proof loading of Rind Å.



Figure 7. Photos from the proof loading of Rind Å of the flatbed truck.

Figure 6 shows the flatbed truck on the bridge with the surveyor measuring the potential deformations of the bridge. Figure 7 is showing the configuration of the flatbed truck with the extra heavy steel on top to create the desired proof load and the marking of the asphalt to ensure the truck is located as assumed in the theoretical analysis.

4.3 *Vorgod Å*

The proof load of Vorgod Å was a success and the capacity of both the super- and substructure of the bridge is assessed to be adequate for passing of the heavy special vehicle maintaining the required safety level. The maximum measured deformation during loading was 2.5mm, however, the deformation after unloading was maximum 0.7mm. As the concern is permanent deformations of the substructure the type of loading during proof loading is more conservative than for the heavy special transport passing the bridge, as the proof loading lasted much longer time than it will take the heavy special transport to pass the bridge.



Figure 8. Photos during proof loading of Vorgod Å.

Figure 8 to the left shows the flatbed truck on the bridge and to the right some of the measuring points are shown with the surveyor measuring the potential deformations of the bridge. Figure 8 is showing the configuration of the flatbed truck with the extra heavy steel on top to create the desired proof load and the marking of the asphalt to ensure the truck is located as assumed in the theoretical analysis.

4.4 *Skjern Å*

The proof loading of Skjern Å was a success and the capacity of both the super- and substructure of the bridge is assessed to be adequate for passing of the heavy special vehicle maintaining the required safety level. The maximum deformation for the supporting walls was approx. 2mm and 1mm for the superstructure, which both were well within the acceptable limits. Photos from the actual proof loading of Skjern Å are shown in Figure 9. On the photo to the right, it can be seen from the compression of the tires, that the axles deliver different load to the bridge – from the left to the right it is approx. 5 – 40 – 25 – 25 tonnes. This is possible due to the hydraulic system of the flatbed truck and enables much freedom in the design of the proof loading.

5 CONCLUSIONS

This paper presented 3 practical examples of proof loading of 3 reinforced concrete bridges built between 1930-1955. The bridges all showed adequate capacity of the superstructure, but all suffered with too low capacity of the substructure or too high uncertainty of the actual foundation. Before the proof loading of the bridges was carried out careful considerations about the failure



Figure 9. Photos from the proof loading of Skjern Å.

mechanism, loading scheme, stop criteria etc. had been performed. Such that it was ensure that any potential failure would be a ductile failure with warning, allowing for decisions gates on whether to continue to the next load step or to stop.

The proof loading of all 3 bridges was a success and the capacity of both the super- and substructure of the bridge is now assessed to be adequate for passing of the heavy special vehicle maintaining the required safety level.

REFERENCES

Christensen, C.O., Damsgaard, K.D.S., Sørensen, J.D., Engelund, S., Goltermann, P., Schmidt, J.W. 2023. Reliability-Based Proof Load Factors for Assessment of Bridges. In Buildings 2023, 13, 1060.

Danish Road Directorate, 2017. Vejledning til belastnings- og beregningsgrundlag for broer, Vejregel.

Danish Road Directorate, 2024 DRAFT. Reliability-Based Classification of Existing Bridges, Vejregel.

DS/EN 1991-2, 2003. Eurocode 1: Actions on structures – Part 2: Traffic loads on bridges incl. Danish national annex.

Bridge Maintenance, Safety, Management, Digitalization and Sustainability – Jensen, Frangopol & Schmidt (eds)
© 2024 The Author(s), ISBN 978-1-032-77040-6
Open Access: www.taylorfrancis.com, CC BY-NC-ND 4.0 license

Integrated utilization of infrared and ultrasound technologies for bridges

I. Alqurashi & M. Debees
Department of Civil, Environmental, and Construction Engineering, University of Central Florida, Orlando

Masato Matsumoto
NEXCO West USA Inc. Vienna

A. Alqarfi
Department of Industrial Engineering and Management Systems, University of Central Florida, Orlando

F. Necati Catbas
Department of Civil, Environmental, and Construction Engineering, University of Central Florida, Orlando

ABSTRACT: This study assesses the effectiveness of integrating infrared thermography (IR) and ultrasound (UT) technologies for the non-destructive testing of concrete bridges, addressing the critical need for advanced assessment methods amidst the deteriorating state of U.S. infrastructure. By combining the rapid, surface-level scanning capabilities of IR with the precise, in-depth analysis offered by UT, our research demonstrates a comprehensive approach to identifying subsurface anomalies such as delaminations, voids, and corrosion of reinforcement. The findings underscore the complementary strengths of IR and UT, highlighting their potential to significantly enhance the accuracy of infrastructure evaluations, optimize maintenance strategies, and ensure public safety. This integrated methodology proposes a balanced, efficient inspection process, advocating for further development in data collection, processing, and analysis techniques to improve the longevity and reliability of critical public works.

1 INTRODUCTION

The United States' civil infrastructure, which is fundamental to its economic success and the quality of life of its citizens, is facing severe challenges due to aging and wear. This infrastructure includes vital structures such as bridges, roads, dams, water treatment systems, and public transportation networks. These elements are essential for society's daily functioning but deteriorate over time. However, these systems are in poor condition and need urgent investment and innovation. The country's infrastructure received a dismal rating of C- from the American Society of Civil Engineers (ASCE) in their 2021 Report Card (ASCE 2021). Given that many of these structures are over 50 years old and continue to function beyond their intended lifespan, their critical state is reflected in their grade. Their deterioration puts public safety in danger and costs the country billions of dollars in missed growth and productivity. We are in a race against time because, in the absence of prompt intervention, the state of these systems is only predicted to worsen. According to ASCE projections, the country will need to invest $2.59 trillion by 2029 to close the infrastructure gap and maintain a good level of service.

Non-Destructive Testing (NDT) and Non-Destructive Evaluation (NDE) are becoming indispensable methods for addressing infrastructure deterioration. Without inflicting any harm to infrastructure elements like roads and bridges, these approaches allow for the detection of inherent flaws or vulnerabilities in them. They act as a preventative measure by

DOI: 10.1201/9781003483755-49

enabling the early identification of problems and expediting prompt repairs. But even with their drawbacks, industry standards for concrete testing continue to rely heavily on traditional techniques like visual examination and sounds. A metal rod or hammer is used to tap the concrete surface, and the sound that is created is listened to. Examining the concrete surface visually entails searching for fractures, spalling, or other indications of damage. Although easy to use, affordable, and straightforward, these methods have a number of disadvantages. They are subjective, unreliable, and only detect surface defects. They cannot reveal the internal condition of the concrete, which corrosion, delamination, voids, or other hidden flaws may compromise (Hiasa, Birgul, and Catbas 2017). Therefore, there is a need for more advanced and objective techniques that can provide a comprehensive assessment of the concrete's integrity. Infrared thermography (IR) and ultrasound (UT) can detect subsurface defects and provide quantitative data for analysis. Implementing IR and UT in maintenance routines can significantly reduce repair costs and enhance public safety. Such practices are instrumental in guiding investments and ensuring essential public works' structural integrity and longevity. With the strategic use of IR and UT, the nation can effectively manage its infrastructure assets, sustain its operation, and ensure it meets safety standards for the long term.

Infrared Thermography (IR) is a non-destructive testing method that uses thermal imaging to detect subsurface anomalies in concrete structures (Watase et al. 2015). It measures the infrared radiation emitted from the surface and converts these measurements into temperature values using the Stefan-Boltzmann law (Starnes, Carino, and Kausel 2003), which states that the radiant flux W emitted per unit area is proportional to the fourth power of the absolute temperature T of the target, modulated by the emissivity ϵ and the Stefan-Boltzmann constant σ. Mathematically, this relationship is expressed as

$$\mathrm{W} = \sigma \times \in \times \mathrm{T}^4 \tag{1}$$

In this formula, σ is the Stefan-Boltzmann constant (5.67×10-8 W/m2/K4), and W is the radiant flux emitted per unit area in watts per square meter (W/m2), ϵ denotes the unitless emissivity value of the concrete, and T stands for the absolute temperature of the target in kelvins (K). These parameters allow IR devices to generate a temperature map revealing dis-parities due to defects like cracks, voids, or delamination. Although environmental factors may influence the precision of IR, it remains an effective first step in assessing the structural integrity of concrete by identifying potential areas that warrant further, more detailed investigation.

Ultrasound, an advanced NDT (Non-Destructive Testing) technique, uses high-frequency sound waves ranging from 16 kHz to 500 MHz (Pham et al. 2009) that are inaudible to the human ear to probe beneath the surface of materials. This technology is deeply rooted in the early experiments of Lazzaro Spallanzani in 1794, who first utilized these waves to understand how bats navigate in darkness. Over the centuries, ultrasound has evolved significantly and is now indispensable in various industries, including medicine, which aids in diagnostics and engineering and ensures structural integrity. The underlying science of ultrasound in NDT is encapsulated in two fundamental equations, "Wave propagation" and "Acoustic impedance." These equations are paramount for detecting internal anomalies guiding the precise calibration and application of ultrasound equipment:

$$\mathrm{V} = \mathrm{f} \times \lambda \tag{2}$$

$$\mathrm{Z} = \rho \times \mathrm{v} \tag{3}$$

where, v = wave velocity; ρ = material density; λ = wavelength; f = frequency; Z= acoustic impedance

Mastery of these equations allows for identifying minute defects essential for maintaining the safety and functionality of critical infrastructure and medical diagnostics. Effectively using the "Wave propagation" equation (1) is crucial for selecting the appropriate frequency and transducer for the examined material. On the other hand, the "Acoustic impedance" equation

(2) is vital for evaluating the material's properties, such as density and elasticity, which affect how ultrasound waves are transmitted and reflected. This information is critical in determining the location, size, and nature of any defects present within the material. The precision with which these principles are applied directly impacts the reliability and accuracy of ultrasound inspection, making them a cornerstone of NDT practices. Through the diligent application of these scientific principles, ultrasound remains a cornerstone of non-destructive testing, enabling the discovery of defects that are not otherwise visible and ensuring the longevity and safety of various structures and systems critical to modern life.

2 METHODOLOGY

2.1 *Infrared inspection*

Two systems by ("NEXCO-West USA, Inc." n.d.) were employed for the infrared inspection: the Deck Top Scanning System (DTSS) and the Universal Surface Scanning System (U3S). The DTSS, a vehicle-mounted system including an infrared thermography camera and two line-scanning cameras, rapidly scanned the deck-top surface, Figure 1. The IR camera captures a 15-foot swath, while the line-scanning cameras cover a 13-foot swath, totaling 18 feet with overlapping areas for image stitching. The DTSS's high-speed capability (up to 70 mph) allows for quick scanning without traffic disruptions. The U3S system, adaptable for use on various platforms, scanned the bridge's underneath, girders, and bents, focusing on predefined critical areas to maximize coverage within the project's limited timeframe. Both systems operated best during temperature transitions, highlighting subsurface defects due to their distinct thermal signatures compared to sound material. Visual data, complementing IR, were collected in clear weather to identify visible deficiencies like



Figure 1. The Deck Top Scanning System (DTSS).

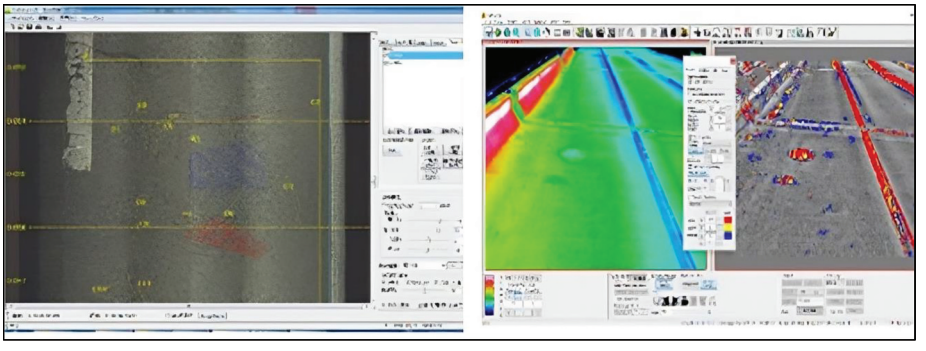


Figure 2. Software JeEditor (left) and software Ir-BAS (right).

cracks and spalls. For analysis, software such as IrBAS, JeEditor, and Kuraves integrated sensor data to create a comprehensive map of the bridge's condition (Figure 2).

2.2 *Ultrasound inspection*

Upon identifying critical spots with IR, an in-depth evaluation was conducted using Ultrasonic Testing (UT). Figure 3 shows the MIRA 1040A 3D, an ultrasonic pulse-echo tomograph, was utilized for its advanced A-DPC® sensor technology, enabling high-resolution 3D FMC/TFM imaging. This portable device can connect to a tablet wirelessly and has 32 active dry point contact transducers. The system works within a material sound velocity range from 1,000 to 4,000 m/s and is operable across a broad temperature spectrum.



Figure 3. UT setup overview.

The UT process involved scanning the areas marked by IR, using the MIRA system to generate B, C, and D scans for a detailed analysis of the concrete's internal structure. This allowed for the precise localization and characterization of flaws, as depicted in Figure 4, informed by raw and SAFT-processed data, significantly improving resolution by synthesizing signals from multiple transducers. The illustrated UT signals and their interaction with the concrete slab demonstrate the method's effectiveness. The UT's capability to focus on all directions simultaneously via SAFT provides an in-depth understanding of the defect's nature and severity, which is crucial for the structural assessment and subsequent maintenance planning.

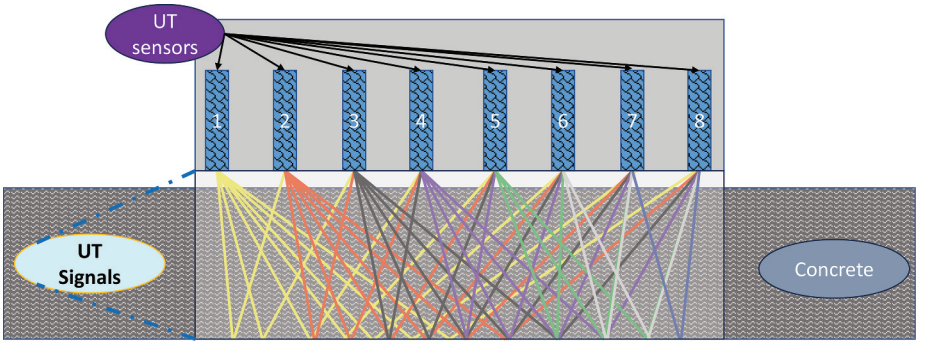


Figure 4. The work sequence of the 32 transducers.

3 RESULTS

3.1 *Bridge deck*

In Figure 5A, the green dots on the IR data for bridge deck spans 1-10 suggests potential subsurface anomalies in the concrete, identified by irregular thermal patterns, which could signify a range of structural concerns from delamination to possible voids or corrosion of reinforcement. The precise thermal signatures captured in this phase of rapid scanning are critical as they guide the subsequent in-depth analysis, highlighting areas that warrant closer inspection to ensure the bridge's safety and longevity.

Following the IR survey, targeted Ultrasonic Testing (UT) detailed scanning was performed on some areas of interest. Figures 5D and 5E show that the results correspond to spans #04 and #10, where the initial IR screening indicated potential anomalies. These UT scans give more detailed findings to the IR scans, offering a deeper look into the integrity of the concrete. The ultrasound data provides a comprehensive image of the internal features of Span #04, describing the depth, shape, and orientation of the detected irregularities. A cut of the 3D image is shown in Figure 5D. Similarly, Figure 5E showcases the ultrasound data for Span #10, providing crucial information about the size and severity of the anomalies within.

The information collected from the UT scans is valuable. It confirms the presence of anomalies and characterizes them, revealing the details of their dimensions and thus allowing for an accurate assessment of the bridge deck's condition. Moreover, these findings enable engineers to prioritize areas for repair to the sections where the structural integrity is most compromised. Therefore, the multi-dimensional insights gained from the UT scans complement the initial IR data and enhance the understanding of the bridge deck's health, laying a solid foundation for any necessary retrofit work to ensure the structure's resilience and reliability.

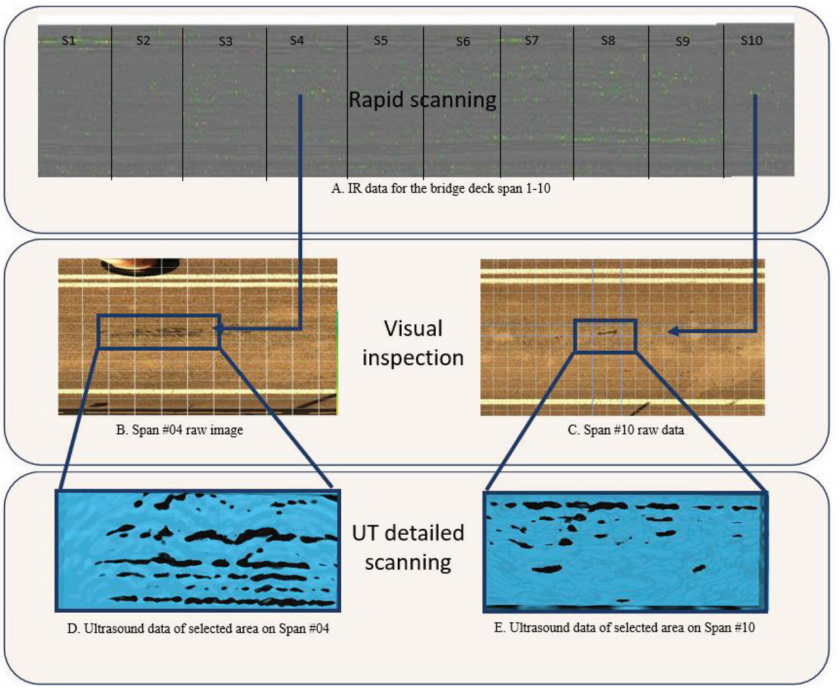


Figure 5. Bridge deck results.

3.2 *Beam*

In Figure 6a, a detailed description of the structural scan conducted on beam #1 span #1 of a bridge, employing both Infrared (IR) and Ultrasonic Testing (UT) to examine the integrity of the concrete and its internal reinforcements. The IR imagery, specifically the data from NEXCO in (A), visually captures the thermal footprint of the internal steel rebar, distinguishing it from the surrounding concrete material. The variations in green on a predominantly grey background correspond to the rebar, offering insight into its layout and condition. Such imaging is essential to ensure that the rebar is correctly positioned and intact, as any inconsistencies could impact the bridge's structural integrity. The processed IR data in (C) enhances the visual distinction of these areas, providing a more detailed and high-contrast view that makes the rebar's presence more detectable. This processing aids in detecting potential issues with coverage or anomalies in the rebar itself, which might not be apparent in standard visual inspections.

On the other side of the analysis, the UT scans in Figures 6B, 6D, and 6E offer a complementary and more in-depth look into the concrete's subsurface. UT technology utilizes high-frequency sound waves to penetrate the material and reflect information about the internal state of the concrete. The scan results, represented by vibrant blue visuals, reveal the acoustic profile of the beam's interior. Brighter areas within the blue gradient indicate differences in material density, which often signify flaws such as delamination, where the concrete may have begun to separate from the reinforcement. This separation is a critical concern for structural engineers as it can significantly reduce the load-bearing capacity of the beam. The longitudinal views provided in the UT setup overview in Figures 6D and 6E map out these potential delamination zones along the beam's span. The scans can detect subtle changes in the internal structure, such as cracks, voids, or other anomalies that could compromise the bridge's integrity. Understanding the extent and location of such defects is crucial for any structural evaluation and subsequent intervention, as it allows for a targeted approach to address these concerns, aiming to restore the beam to its optimal condition and ensure the long-term durability and safety of the bridge.

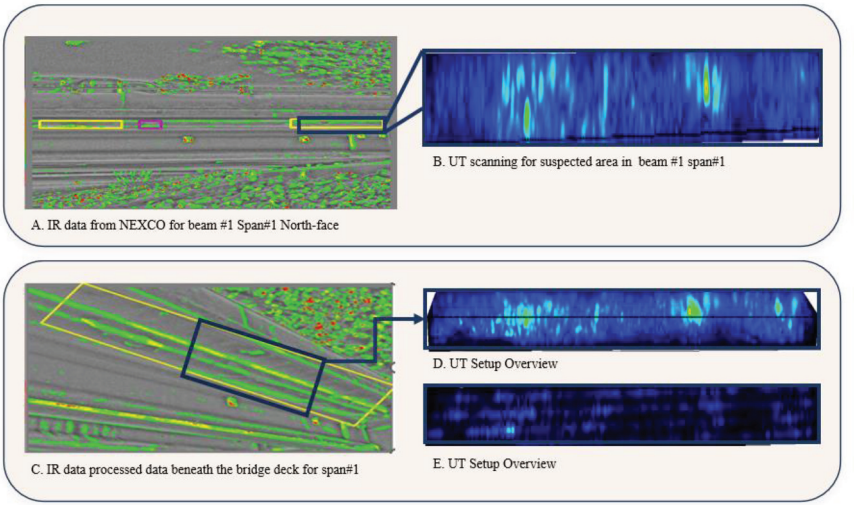


Figure 6. Beam results.

4 CONCLUSION

The inspection of the bridge deck and beam #1 span #1, as illustrated in Figures 5 and 6, highlights the process of structural assessment under the presence of complicating factors such as asphalt overlays. Figure 5A shows that asphalt overlays may prevent accurate scans of the underneath beam's condition, potentially obscuring the true state of the concrete beneath.

The IR imagery thus predominately reflects the deterioration of the asphalt, requiring additional scanning methods like Ultrasonic Testing (UT) to obtain a clear picture of the concrete's deck health.

For a more accurate understanding, targeted UT detailed scanning was employed, as represented in Figure 5D, 5E, on areas initially identified by IR as potentially deteriorated. This UT analysis provides an essential view past the asphalt, bringing to light the internal composition and anomalies within the concrete. Specifically, the UT imaging in Figure 5D delivers an in-depth look at the internal state of Span #04, while Figure 5E in Span #10, explains the extent of the detected irregularities.

Addressing the previous oversight, Figure 6 focuses on the beam itself, particularly span #1. The visual inspection and detailed UT scanning for span #1, shown in Figure 6, comprehensively evaluate the beam's subsurface condition. The UT data in Figure 6D provides a definitive acoustic profile of the interior, detecting issues such as delamination or voids that the IR method could not discern through the asphalt layer. These findings from the UT scans are pivotal for identifying precise areas of concern within the beam, areas where the structural integrity could be compromised, thereby guiding targeted and efficient rehabilitation efforts.

Although UT scanning provides detailed information about the structural element, it requires more time and effort to conduct these scans. On the other hand, IR is a rapid method to scan a structure to get the condition status of the structure. Hence, optimizing the usage of both systems is crucial to gather enough information about the structure's condition while saving time and labor efforts.

ACKNOWLEDGMENT

The author extends sincere gratitude to NEXCO for their invaluable contributions to the data collection process pertinent to this information retrieval research. Their support and collaboration have been instrumental in advancing this study.

REFERENCES

ASCE. 2021. "A COMPREHENSIVE ASSESSMENT OF AMERICA'S INFRASTRUCTURE." www.infrastructurereportcard.org.

Hiasa, Shuhei, Recep Birgul, and F Necati Catbas. 2017. "Effect of Defect Size on Subsurface Defect Detectability and Defect Depth Estimation for Concrete Structures by Infrared Thermography" 36: 57. https://doi.org/10.1007/s10921-017-0435-3.

"NEXCO-West USA, Inc." Rapid Scanning Final Report 2022.

Pham, Thuy Duong, Reena Amatya Shrestha, Jurate Virkutyte, and Mika Sillanpää. 2009. "Recent Studies in Environmental Applications of Ultrasound." *Canadian Journal of Civil Engineering* 36 (11): 1849–58. https://doi.org/10.1139/L09-068/ASSET/IMAGES/LARGE/L09-068F2.JPEG.

Starnes, Monica A., Nicholas J. Carino, and Eduardo A. Kausel. 2003. "Preliminary Thermography Studies for Quality Control of Concrete Structures Strengthened with Fiber-Reinforced Polymer Composites." *Journal of Materials in Civil Engineering* 15 (3): 266–73. https://doi.org/10.1061/(ASCE)0899-1561(2003)15:3(266).

Watase, Azusa, Recep Birgul, Shuhei Hiasa, Masato Matsumoto, Koji Mitani, and F. Necati Catbas. 2015. "Practical Identification of Favorable Time Windows for Infrared Thermography for Concrete Bridge Evaluation." *Construction and Building Materials* 101 (December): 1016–30. https://doi.org/10.1016/J.CONBUILDMAT.2015.10.156.

Bridge Maintenance, Safety, Management, Digitalization and Sustainability – Jensen, Frangopol & Schmidt (eds)
© 2024 The Author(s), ISBN 978-1-032-77040-6
Open Access: www.taylorfrancis.com, CC BY-NC-ND 4.0 license

Determining load distribution in a riveted railway bridge through controlled field testing

B. Imam, S. Biswal & M.K. Chryssanthopoulos
School of Sustainability, Civil and Environmental Engineering, University of Surrey, UK

P. Wildbore
Network Rail, The Quadrant, Elder Gate, Milton Keynes, UK

ABSTRACT: This paper summarizes results obtained from the field testing of an open deck plate-girder riveted metallic bridge removed from service in the UK and load-tested under controlled conditions. A purpose-built loading frame was constructed around the bridge for the application of the loading, which was applied in a form that represents typical passenger train axle loading; this included single and pairs of 10-ton axle loads. Testing was carried out under different axle load positions on the bridge with and without the timber deck to quantify load distribution effects on the bridge components. The response was measured via approximately 40 displacement transducers and 30 strain gauges. It was concluded that the presence of timber beams is significant both in terms of the maximum strains reached under a typical train axle load, as well as in terms of the load experienced by adjacent elements when the axle is directly over a specific cross-girder. Moreover, the effect of irregularities in the solid timber beams, e.g. in the form of unintended camber, can play a significant role in the recorded response. Minor geometric asymmetries, e.g. the location of transverse offset stiffeners on the two main girders, can introduce noticeable effects on the U-frame action, whose quantification is an important factor in bridge assessment guidelines. These observations will be utilized in updating adjustment factors for simplified fatigue assessments based on stress ranges estimated from idealized train passages over the bridge.

1 INTRODUCTION

Many metallic railway bridges in the UK (and in other countries) are characterised by an open deck construction form, with the main girders restrained laterally through a secondary system comprising cross girders (sometimes also including stringer beams running in the main girder direction). These elements are inter-connected through riveted connections (in the older bridge stock, mid-19th to mid-20th century) or welded connections (for more recently constructed bridges). The response of these bridges to live loading is dependent on the behaviour of the connections, i.e., cross-to-main girder and stringer-to-cross-girder connections, both in terms of the fatigue performance of individual members/connections as well as the overall U-frame action developed on such bridge forms. The connections are typically built-up using plates, angles and rivets with parts of them being hidden and therefore difficult to access in an inspection. Although the response of such bridges has been studied through numerical modelling (Al-Emrani & Kliger, 2003; Imam & Righiniotis, 2010) and static/fatigue component testing (Al-Emrani, 2005; Bertolesi et al., 2021), there is little information from field measurements on actual bridges, especially under controlled conditions.

The value of bridge load testing has been recognized for many years, as evidenced by early work (Bakht & Jaeger, 1990), where emphasis was placed on the shortcomings of then

DOI: 10.1201/9781003483755-50

available mathematical models; as well as the recent state-of-the-practice review (Alampalli et al., 2021) which focused on newly developed protocols and interpretation of results for various types of load testing (diagnostic, proof) undertaken for different purposes (current rating/reliability, remaining service life). Within published literature, of note to this study are investigations on testing of historical bridges, such as the wrought-iron riveted bowstring arch truss in Virginia, USA (Moen et al., 2013) and the bolted "Model 1936" Swiss military bridge (Fleming, 2022). In the former, tests were aimed at establishing the lateral stiffness provided to the arches by an innovative underslung bracing system and quantifying its influence on the global response of the bridge. The latter focused on connection stiffness parameters, which were used to calibrate a finite element model of the bridge, thus demonstrating the value that can be added to modelling through load testing, particularly in accounting for unaccounted interactions between members.

The purpose of the work described in his paper is to add to contributions on the response of historical bridges by undertaking field testing on a decommissioned 19th-century open deck riveted railway bridge with the following objectives: (1) to provide load-displacement measurements of the main bridge members (main-girders and cross-girders) that are compared with in-service monitoring measurements obtained under actual railway loading, (2) to provide evidence on the U-frame action in the bridge, and (3) to assist towards the development and calibration of a global numerical bridge model to be used for subsequent fatigue assessment calculations.

2 EXPERIMENTAL SET UP

2.1 *Structure tested*

The Yetminster bridge was taken out of service in February 2020, as part of programmed replacement aiming at asset renewal that leads to reduced maintenance requirements. The bridge was delivered to the University of Surrey (Figure 1) in order to carry out research on various aspects of the behaviour of old riveted railway under-bridges (U-frame action, connection stiffness, remaining fatigue life). The bridge was constructed approximately in the 1880/90's, with its main girders, rivets and connection angles made of wrought iron whereas the cross-girders made from early steel. Double angle riveted connections are used to connect the cross-girders with the main girders. The bridge, which has offset stiffeners with respect to the main to cross-girder connections, has been in service for approximately 130 years, sitting on masonry abutments. It carried a railway track which was fixed on top of solid timber beams (0.432×0.375×12 m) placed on top of the cross-girders, as shown in Figure 1(right). The bridge was delivered to an open land with thick concrete flooring where it was placed on four solid prestressed concrete blocks (Figure 1) sitting on an in-situ constructed concrete slab. Here it was subjected to quasi-static load testing, through controlled loads applied to the cross-girders with the displacement and strain response recorded at several points of interest. Upon completion, the bridge was cut into several large sub-assemblies which are currently undergoing static and fatigue testing.

2.2 *Loading arrangement*

The testing was carried out on the bridge, first, in the presence of the timber deck beams (Figure 1(left)), as well as after removing the timber deck beams (Figure 1(right)) to understand the load distribution on metallic members in both cases. For the application of loading, a reaction framework was constructed and was anchored into the concrete surface using 16mm threaded rods into expansion anchors, as shown in Figure 2. A total of 30 such anchors were used. Vertical loads were applied through a hydraulic jack and four load cells (LC1 to LC4). In the presence of timber beams, the vertical loads were applied onto the timber beams through loading plates. After the timber beams were removed, the loads were applied directly onto the cross-girder top flanges through loading plates. The maximum distributed pressure

force applied on the top surface of each loading plate was 50 kN, representing a typical wheel load of the passenger train type that ran on the Yetminster bridge route. The loads were applied incrementally in steps of 10 kN. A total of 25 loading scenarios were considered in the testing representing different positions of a train axle or bogie on the bridge. In this paper, a smaller number of the key loading scenarios are presented.



Figure 1. (left) Bridge with timber deck; (right) bridge with timber deck removed.



Figure 2. (left) Loading frame constructed for load application; (right) threaded anchors.

2.3 *Instrumentation*

A total of 38 linear varying displacement transducers (LVDTs) and 30 strain gauges (linear and rosettes) were used. The locations of LVDTs for measuring vertical and horizontal displacement are shown in Figure 3 and Figure 4 respectively. Strain gauges were selectively installed on the bottom flanges of cross-girders CG2, CG3 and CG4 (midspan location) and the bottom flange of the main girders. The vertical deflection measurements allowed the

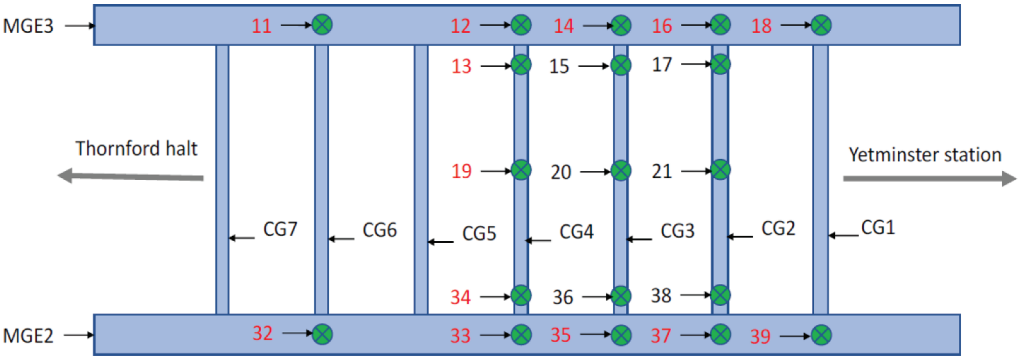


Figure 3. LVDT locations for vertical displacement measurement.

creation of longitudinal profiles for the main girders and transverse profiles for three cross-girders. The horizontal displacement measurements are aimed at longitudinal profiles of the main girder flange and selected profiles along the depth of the main girder web (U-frame action), taking into account web stiffener positions.

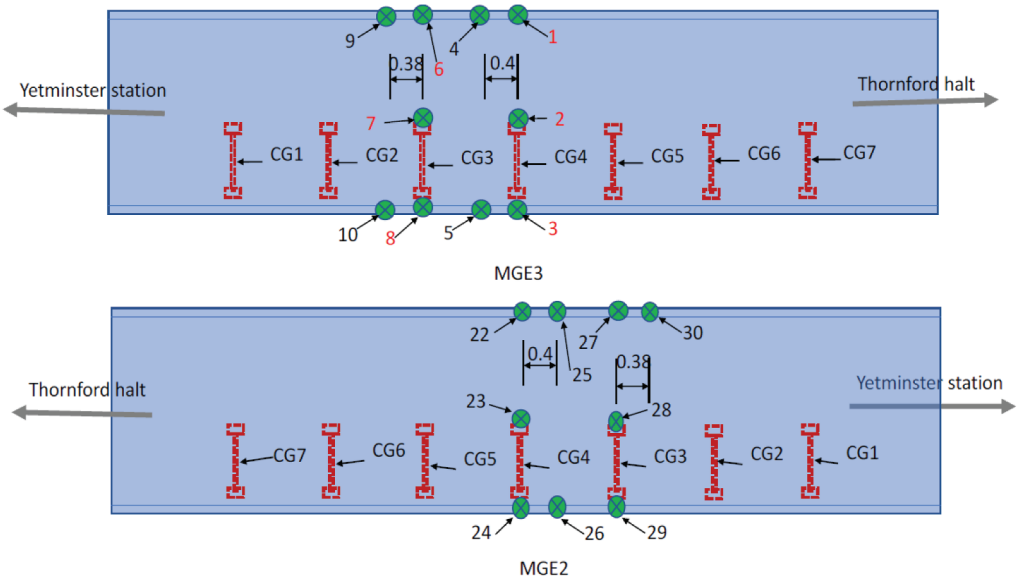


Figure 4. LVDT locations for horizontal displacement measurement (dimensions in m).

3 RESULTS AND DISCUSSION

3.1 *Load application*

Strains and displacements for two loading scenarios shown in Figure 5, with the timber deck (loading scenario A) and without the timber deck (loading scenario B) are presented herein. The load time histories of the four load cells for the two loading scenarios are shown in Figure 6. Due to stiffness variations and load application asymmetries, it can be seen that there is a variability in the actual load being applied (compared to the nominal value which should be increasing in steps of exactly 10 kN). This variability is also scenario dependent, with the case that includes timber beams producing higher variability than the one without. For load vs deformation (displacement or strain) plots involving sensors located on a plane passing through the main axis of a cross girder, the total load is taken as the sum of all the load cell measurements placed on that cross girder. For load vs deformation plots involving sensors located at all other locations, the total load is taken as the sum of all the load cell measurements present in the relevant load scenario.

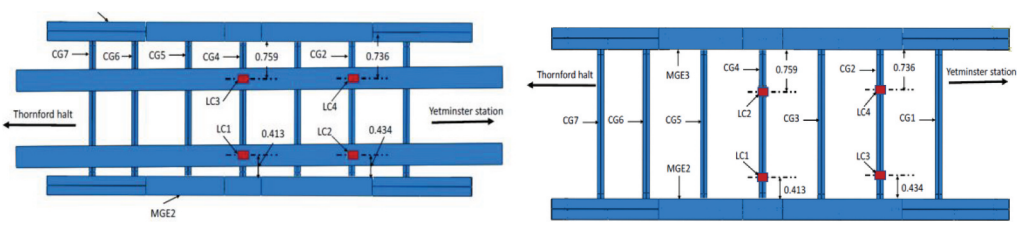


Figure 5. (left) Loading scenario A; (right) Loading scenario B (all dimensions in m).

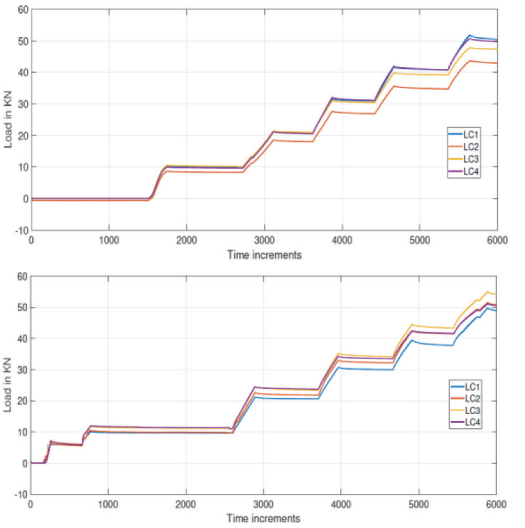


Figure 6. Load time histories for (left) scenario A, with timber deck; (right) scenario B, w/o timber deck.

3.2 *Vertical displacement measurements*

The vertical displacement measurements on the LVDTs located on the loaded cross-girders (CG4 and CG2) are shown in Figure 7. The presence of the heavy timber beams is seen to contribute to the stiffness of the structure, though the effect varies both across a single cross-girder as well as between cross-girders. On the side connected to MGE3 (LVDTs 13 and 17), the difference in stiffness between the with and without timber cases is the greatest (~50%), whereas on the side connected to MGE2 (LVDTs 34 and 38) the difference is roughly halved (22%). The smallest difference is recorded at the centre of the cross-girder, indeed it is negligible for deflections up to 1mm.

3.3 *Strain measurements*

Table 1 summarises the strain measurements obtained on the top and bottom flanges of the main girders for both with (scenario A) and without the timber deck present (scenario B), at the maximum load applied. At the MGE3 bottom flange, three strain gauges across the width of the flange were installed to measure any potential torsional effects on the member. Overall, the removal of the timber deck beams results in higher strains being recorded at the same load level, the increase ranging between 16-35% (average ~27%). This is important, especially taken in conjunction with the previous comment on stiffness, considering that numerical (e.g. grillage, FE) or simplified mechanical models do not account for the effect of timber superstructure in estimating the response; e.g. the timber deck was absent in the numerical model considered by Moen et al. (2013).

3.4 *Load distribution*

To estimate load sharing by adjacent cross girders when the load acts directly on any particular cross girder four identical scenarios with and without timber were selected (Table 2). In the absence of timber beams (cases I & VII), the indirectly loaded cross girders record a very small amount of strain (less than 10% of the corresponding value on the directly loaded girder). A similar trend can be observed for cases III & V. This could be attributed to: (i) out of plane bending of the main girders imposing rotational moments at the ends of the cross girders, and (ii) the differential displacement of the two main girders caused by the asymmetrical (offset with respect to the centre line) loading applied on the bridge. However, in the presence of timber beams (case II), the indirectly loaded cross girder CG2 experiences ten

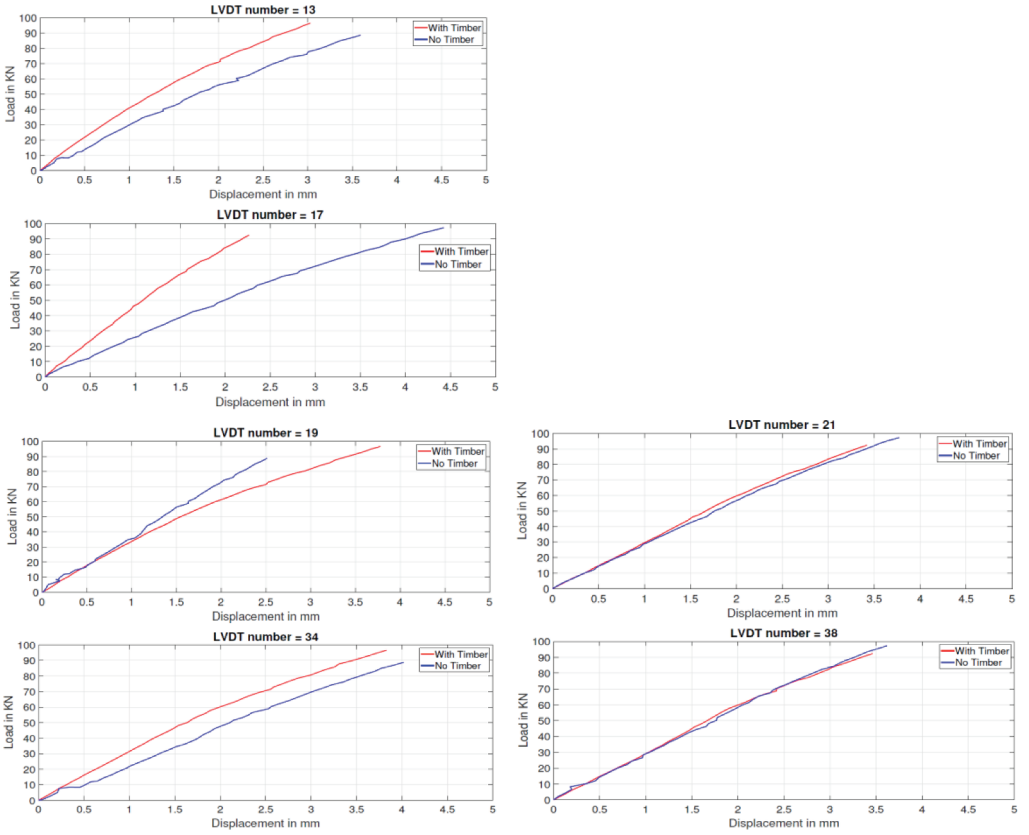


Figure 7. Vertical displacements on LDVTs located on (left) CG4 and (right) CG2.

Table 1. Longitudinal strains (in με) at top and bottom flanges of MGE2 and MGE3.

Location		With timber deck	Without timber deck
MGE3 top flange (midspan)		-59	-70
	Inside	73	39
MGE3 bottom flange (midspan)	Mid	63	92
	Outside	49	122
MGE2 top flange (midspan)		-73	-89
MGE2 bottom flange (midspan)		82	115

times more strain than the directly loaded cross girder CG4. Similarly for cases IV, VI and VIII, the load shared by the indirectly loaded cross girders varies depending on the position of applied loads on the timber beams. This can be attributed to a pre-existing camber in the timber beams, prior to testing. The maximum camber at the center of the timber beam close to MGE2 was measured to be 24 mm. Thus, for the loading scenarios with timber beams the pre-existing camber affects significantly load sharing by the adjacent indirectly loaded cross girders. As a result, load sharing estimates are subject to a degree of variability due to particularities that can only be revealed through a bridge survey.

3.5 *U-frame action*

The U-frame action was recorded at three sections, as shown in Figure 8. Sections A-A and C-C pass through the longitudinal axis of CG4 and CG3 respectively, whereas section

Table 2. Strains at bottom flanges of CG2, CG3 and CG4 corresponding to an average load of 50 kN/cell.

Case identifier	Loading type	Strain in CG2 (με)	Strain in CG3 (με)	Strain in CG4 (με)
I	Two 50 kN loads on CG4(without timber deck)	4	16	164
II	Two 50 kN loads on CG4 (with timber deck)	8	12	79
III	Two 50 kN loads on CG4 and two 50 kN loads on CG2 (without timber deck)	150	32	153
IV	Two 50 kN loads on CG4 and two 50 kN loads on CG2 (with timber deck)	115	78	42
V	Two 50 kN loads on CG3 and two 50 kN loads on CG1 (without timber deck)	22	143	5
VI	Two 50 kN loads on CG3 and two 50 kN loads on CG1 (with timber deck)	90	71	8
VII	Two 50 kN loads on CG2 (without timber deck)	153	15	2
VIII	Two 50 kN loads mid-length between CG4 and CG3 and two 50 kN loads midlength between CG2 and CG1 (with timber deck)	100	73	25

B-B passes through the web T-stiffeners at mid-length of the bridge. The displacement profiles, scaled up by a factor of 50, are shown in Figure 9 for three loading scenarios with and without timber beams. The maximum horizontal displacements for the same loading scenarios are given in Table 3.

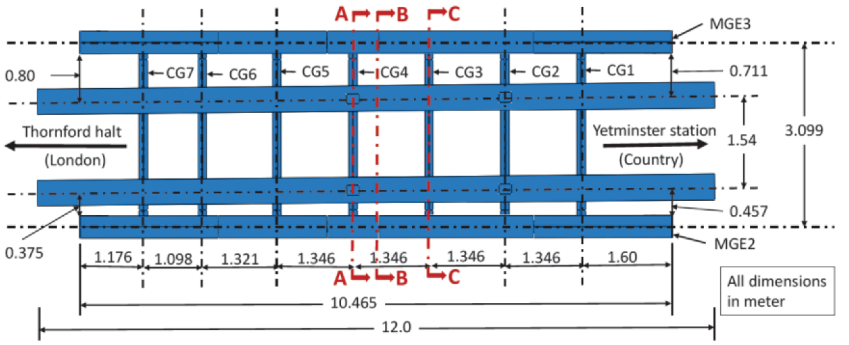


Figure 8. Top view of the bridge with details of the sections at which U-frame action was recorded.

The profiles in Figure 9 indicate that, for all cross-sections considered, sway behaviour of the bridge under vertical load is present. This can be attributed to an eccentricity in the vertical load, i.e. load which is not applied at the centre of the main girders, due to the eccentric location of the timber girders. It is also worth noting that the diagrams do not appear to conform with the usual assumption of symmetry between left and right main girders. In fact, the main girders are not identical due to the different location of transverse web stiffeners along their length. Additionally, three of the cross-girders have been stiffened in the flanges over only part of their length, which introduces a further asymmetry. As a result, it seems that the U-frame action does not introduce the same effect on the two sides of the bridge. On the other hand, the results with and without timber beams are generally consistent, with the latter showing a small magnification compared to the former in most cases. In line with conclusions reached in earlier studies (e.g. Flemming, 2022), establishing an understanding of the global behaviour of a particular bridge based on full-scale testing, provides valuable information as to whether modelling simplifications could be adopted without introducing bias and/or significant uncertainty. In addition, local effects also need to be considered (e.g. local corrosion and connection

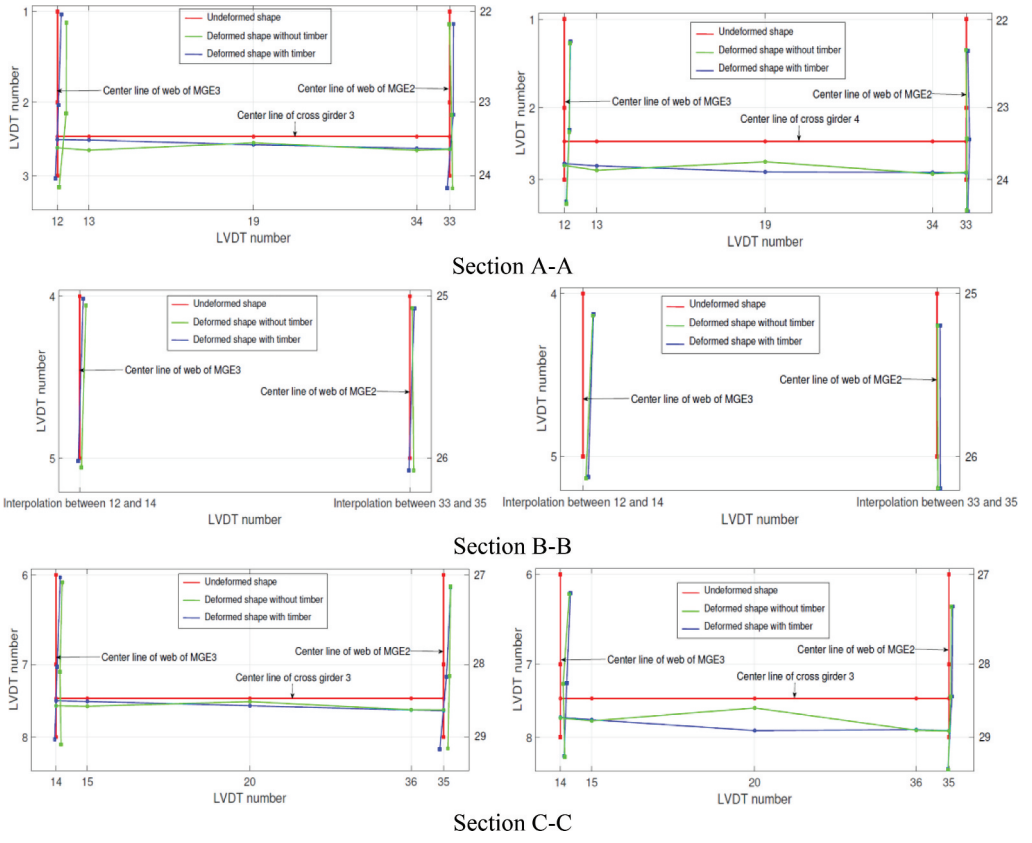


Figure 9. U-frame action (left) CG4 two 50 kN loads; (right) CG4 two 50 kN & CG2 two 50 kN loads.

Table 3. Comparison of maximum horizontal displacements (in mm) with and without timber beams.

		Two 50 kN loads on CG4		Two 50 kN loads on CG4 and two 50 kN on CG2	
LVDT No	Identifier	Without timber	With timber	Without timber	With timber
1	MGE3-CG4	-0.711	-0.315	-0.822	-0.658
2	MGE3-CG4	-0.696	-0.082	-0.548	-0.476
3	MGE3-CG4	-0.137	0.160	-0.285	-0.188
4	MGE3-T	-0.573	-0.319	-0.727	-0.551
5	MGE3-T	-0.147	0.157	-0.197	-0.204
6	MGE3-CG3	-0.489	-0.327	-0.730	-0.478
7	MGE3-CG3	-0.302	-0.081	-0.470	-0.344
8	MGE3-CG3	-0.398	0.108	-0.327	-0.213
22	MGE2-CG4	-0.026	0.297	0.130	0.245
23	MGE2-CG4	0.152	0.280	0.377	0.465
24	MGE2-CG4	0.219	-0.205	0.090	0.129
25	MGE2-T	0.221	0.407	0.333	0.372
26	MGE2-T	0.350	-0.091	0.236	0.234
27	MGE2-CG3	0.542	0.557	0.476	0.457
28	MGE2-CG3	0.458	0.223	0.107	0.242
29	MGE2-CG3	0.331	-0.316	0.087	-0.272

* For LVDTs 1 to 10 and 22 to 29 +ve for outward displacement and -ve for inward displacement.

factors, such as rivet clamping forces) in order to help explain with greater confidence observations from diagnostic tests (Alampalli, 2021) such as the ones conducted in this bridge.

4 CONCLUDING REMARKS

This paper summarised results obtained from field testing of an open deck riveted metallic railway bridge removed from service and tested under controlled conditions. Load distribution with and without the timber deck and the structure's U-frame action were assessed through a series of diagnostic tests using quasi-static loading. The main conclusions are as follows:

- Testing of real structures reveals unforeseen effects arising from unintended factors, such as imperfections and minor asymmetries, as well as deterioration and changes during service.
- Numerical models can take account of such factors especially if the performance of such models can be compared with results from diagnostic testing, as carried out herein.
- For this class of metallic riveted bridges, the effect of superstructure, such as the timber deck, was found to be quite important. Neglecting its presence in numerical models would result in conservative assessment results (in terms of strains/stresses and displacement) but this has to be carefully assessed with respect to the purpose of the analysis/assessment.
- Even relatively small asymmetries in the geometry of a bridge (i.e. the transverse offset web stiffeners on the main girders) can introduce noticeable effects on its global response.

The study re-affirms one of Bakht and Jaeger's (1990) principal conclusions, namely that "some aspects of bridge behavior, because they never enter design considerations, can escape the attention of even experienced bridge designers and analysts". It is hoped that this study has thrown a useful light on such aspects in the context of old open deck riveted metallic railway bridges.

REFERENCES

Alampalli, S., Frangopol, D.M., Grimson, J., Halling, M.W., Kosnik, D.E., Lantsogt, E.O.L, Yang, D. and Zhou, Y.E. (2021). Bridge load testing: State-of-the-practice. *J. Bridge Eng*., 26(3):03120002.

Al-Emrani M. & Kliger R. (2003). FE analysis of stringer-to-floor-beam connections in riveted railway bridges. *J. Constr. Steel Research*, 59(7): 803–818.

Al-Emrani M. (2005). Fatigue performance of stringer-to-floor-beam connections in riveted railway bridges. *J. Bridge Eng*., 10(2):179–185.

Bakht, B. & Jaeger, L.G. (1990). Bridge testing – a surprise every time. *J. Struct. Eng*., 116(5):1370–1383.

Bertolesi, E., Buitrago, M., Adam, J.M. & Calderon, P.A. (2021). Fatigue assessment of steel riveted railway bridges: Full-scale tests and analytical approach. *J. Constr. Steel Research*, 182: 106664.

Fleming, P.H. (2022). Full-scale testing and stringer connection fatigue analysis of a historical Swiss military bridge for the Rhaetian railway. *J. Bridge Eng*., 27(9):05022007.

Imam, B.M. & Righiniotis, T.D. (2010). Fatigue evaluation of riveted railway bridges through global and local analysis. *J. Constr. Steel Research*, 66 (11): 1411–1421.

Moen, C.D., Shapiro, E.E. & Hart, J. (2013). Structural analysis and load test of a nineteenth-century iron bowstring arch-truss bridge. *J. Bridge Eng*., 18(3):261–271.

Bridge Maintenance, Safety, Management, Digitalization and Sustainability – Jensen, Frangopol & Schmidt (eds)
© 2024 The Author(s), ISBN 978-1-032-77040-6
Open Access: www.taylorfrancis.com, CC BY-NC-ND 4.0 license

Field assessment of a vibration-based damage identification procedure

J. Raedersdorff & A. Chateauneuf
CIDECO, Clermont-Ferrand, France

D. Clair & A. Bouchaïr
Clermont Auvergne INP, CNRS, Institut Pascal, Université Clermont Auvergne, Clermont-Ferrand, France

ABSTRACT: This paper presents the assessment of a damage identification procedure applied to a multi-span prestressed concrete bridge equipped with accelerometers. In addition, the central span is equipped with LVDT sensors recording local displacements from which two structural states of the bridge are defined. Using the acceleration measurements, the corresponding modal characteristics are determined from an output-only modal identification procedure including a clustering step to compute mean values of the identified mode shapes. Damage detection and localization is performed by combining the use of damage indicators and the updating of a simplified finite element model. The damage pattern obtained in the central span is consistent with the information available from the LVDT sensors. In the side spans, the evolution between the two structural states seems to correspond to an increase in stiffness. This point requires further investigation. Improvements to the present method, including a statistical analysis, are also being considered.

1 INTRODUCTION

Vibration-Based Methods (VBMs) for Structural Health Monitoring (SHM) of bridges have been widely developed over the last 30 years (Sohn 2003, An 2019). They are promising as they potentially lead to identify damage occurrence related to structural evolution over time, such as changes in stiffness due to modifications in the connections between structural members, or degradation of material properties. Nevertheless, field applications of VBMs are not straightforward for several reasons: measurements are subject to uncertainties and noise, the number of sensors is limited, the ambient excitation due to traffic is variable and unknown. It is therefore of crucial importance to evaluate their performance in practical cases. The two first objectives of the SHM of bridges are the qualitative detection of damage and its localization. As recently recalled in the review by Karakostas & al. (Karakostas 2023) one classical approach to achieve this relies in a two steps data driven procedure consisting in the identification of natural frequencies and modal shapes in both undamaged and damaged states followed by the computation of damage indicators based on these modal data. Another possibility is to use a model-based method including a model updating. A third solution is to combine both previous approaches to build a hybrid method. This paper presents a field assessment of a Vibration-Based damage identification procedure applied to a multi-span prestressed concrete bridge subjected to thermal gradient variations. The bridge is equipped with 24 accelerometers. In addition, the central span is equipped with LVDT sensors which allow the definition of the structural states corresponding to the evolution of the bridge structure, due to the loss of prestressing of the joints causing a local loss of stiffness. The two reference states will be hereafter referred to as State S1 and State S2. In order to track the differences between these two states, a hybrid method is proposed that combines the use of damage indicators with the model updating of a simplified finite element model.

DOI: 10.1201/9781003483755-51

2 METHODOLOGY

The proposed approach is summarized on Figure 1. The acceleration signals from the sensors are filtered using a Singular Spectral Analysis procedure (Golyandina, 2020) leading to the reduction of measurement noise. The modal characteristics of the bridge are determined using an output only modal identification procedure, based on the combination of Random Decrement (RD) technique with an improved Ibrahim Time Domain (ITD) method. After a clustering step, the modal identification leads to the determination of two sets of modal characteristics:

$$\left(\tilde{\omega}_i^{S1}, \tilde{\xi}_i^{S1}, \tilde{\phi}_i^{S1}\right)_{m'} i = 1, \ldots, n; m = 1, \ldots m_{sk} \text{ in state } Sk, k = 1, 2 \quad (1)$$

After averaging, these modal data are used to calculate damage indicators enabling the detection and localization of damage. The possible location of damage is then used as an input to a finite element updating procedure using a simplified model of the bridge. Each step is briefly presented in the following sub-paragraphs. This hybrid approach has several advantages. Firstly, its spatial resolution depends mainly on the spatial resolution of the finite element model and is therefore enhanced compared to a purely data driven approach where the spatial resolution is correlated with the number of sensors. Secondly, the solution of the inverse problem of updating is simplified compared to a purely model based method as the number of parameters to update is reduced thanks to the damage indicator-based damage detection and localization.

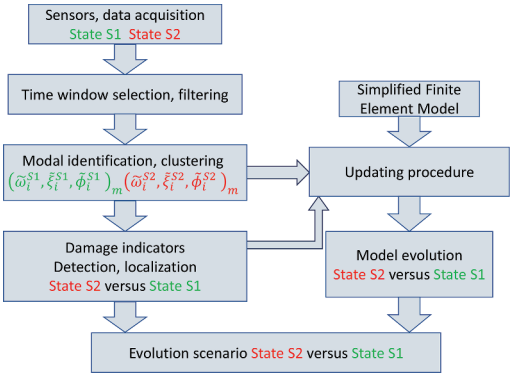


Figure 1. Methodology.

2.1 *Modal identification procedure*

The modal characteristics are determined using an output-only modal identification procedure, based on the combination of Random Decrement (RD) technique with an improved Ibrahim Time Domain (ITD) method (Ibrahim, 1977). The procedure also includes a clustering step and a statistical analysis of the obtained modal characteristics. Starting from the observation measured by the accelerometers at N locations on the bridge, the modal identification procedure leads to the determination of the identified modes $\tilde{\phi}_i \in R^N$ with $||\tilde{\phi}_i|| = 1$, pulsations $\tilde{\omega}_i$, and modal damping $\tilde{\xi}_i$, for $i = 1, \ldots, n$ where n is the number of identified modes. Compared to a finite element model giving high dimensional mass normalized modes, reduced information is therefore available.

2.2 *Damage indicators*

The considered damage indicators are based on two sets of modal characteristics identified for states S1 and S2. The objective here is limited to damage localization and the results of the damage indicators must not be interpreted in a quantitative way. The reason is that, as many authors have pointed out, the probability of false alarms is high when using damage indicators

and a reliable use of their prediction requires the definition of thresholds that are rather complicated to estimate (Alvandi 2006, Erduran 2021).

2.2.1 *Modal flexibility based index*

The Modal Flexibility method uses mass-normalized modal vectors to estimate an n-approximation F_n of the flexibility matrix F. Using only the first identified unit norm mode of reduced dimension $\tilde{\phi}_1$, the damage indicator $D_F(j)$ is defined as:

$$D_F(j) = \frac{max|\Delta F(i,j)|}{a},\ i = 1, \ldots, N \tag{2}$$

with $\Delta F = \tilde{F}_1^{S2} \tilde{F}_1^{S1} \tilde{F}_1^{Sk} = \frac{\tilde{\phi}_1^{Sk} \tilde{\phi}_1^{SkT}}{\omega_1^{Sk2}}$ and, $a = \left(\sum_{j=1}^{n} max|\Delta F(i,j)|^2 \right)^{1/2}$

2.2.2 *Modal interpolation error indicator*

The modal interpolation error, proposed by Limongelli (Limongelli, 2011), is a damage indicator based on the use of a cubic spline function interpolating the modal shapes of the structure. At the j[th] location of the structure, the accuracy of the interpolation is computed for the i[th] mode from the interpolation error E_{ji}, that is the magnitude of the difference between the identified component of the i[th] modal shape at that location $\tilde{\phi}_{ji}$ and the interpolated value $\hat{\phi}_{ji}$ of the same component.

The modal interpolation error in the state Sk at location j is defined as:

$$E_{ji}^{Sk} = \left| \tilde{\phi}_{ji}^{Sk} - \hat{\phi}_{ji}^{Sk} \right| \tag{3}$$

The damage indicator D_I is then defined as:

$$D_I(j) = \left| E_j^{S2} - E_j^{S1} \right| \tag{4}$$

where $E_j^{Sk} = \sqrt{\sum_{i=1}^{n} E_{ji}^{Sk\ 2}}$ is the interpolation error in the state Sk at the j[th] location.

Following the idea of Limongelli (Limongelli 2016), a threshold is fixed for the detection and localization of damage resulting in a binary indicator: 0 (no damage) or 1 (damage) defined by:

$$DS_P(j) = (sign(D_P(j) - \bar{D}_P - \sigma_{DP}) + 1)/2 \tag{5}$$

where $\bar{D}_P$ and σ_{DP} are respectively the mean and standard deviation of $D_P, P = F$ or I.

2.3 *Model updating*

Damage is simulated by varying the stiffness of the finite elements. The mass matrix M is considered as a constant and the following parameterization of the stiffness matrix is adopted:

$$\Delta K = K^{S2} - K^{S1} = -\sum_{p=1}^{n_d} d_p K_p \tag{6}$$

where K^{Sk} is the stiffness matrix in the state Sk, K_p is the contribution of the undamaged element p to stiffness matrix, d_p denotes the damage of element p, and n_d is the number of potentially damaged elements chosen using the damage indicators results.

It should be noted that the spatial resolution of the search for damage using the update procedure is associated with the spatial resolution of the finite element model and is therefore finer than that the one obtained from the accelerometers placed on the bridge. The originality of this procedure is that it updates the selected model parameters so that the modal differences between state S1 and S2 numerically calculated fits the experimentally identified ones.

The updating procedure consists in minimizing the following objective function:

$$J(d) = \left\| \sum_{i=1}^{n} \left[\left(\overset{\vee}{\phi}_i^{S2} - \overset{\vee}{\phi}_i^{S1} \right) - \left(\tilde{\phi}_i^{S2} - \tilde{\phi}_i^{S1} \right) \right] \right\|^2 \tag{7}$$

where $\overset{\vee}{\phi}_i^{Sk}$ are the unit norm vector obtained from the finite element model.

The model updating is performed using the CMA-ES algorithm (Hansen 2016) to find:

$$d_{S2/S1} = \text{argmin}(J(d)), d_{S2/S1} \in R^{n_d} \tag{8}$$

3 CASE STUDY: THE BRIDGE OF LONGUES

3.1 *Description and sensor equipment of the bridge of longues*

The bridge of Longues (Figure 2a) is a prestressed concrete bridge consisting of 3 spans. The total length of the structure is approximately 162m, and its width is about 12m. The structure is equipped with 24 accelerometers referenced as $a_k,\ k = 1, \ldots, 24$ (Figure 2b) placed at regular intervals of approximately 6.5m (Figure 3). The abutments are not equipped. However, 2 sensors are placed at the locations of the intermediate piers. The sensors are arranged vertically on the central web separating the 2 chambers (Figure 4). The temporal signal is acquired at a sampling frequency of 250Hz over a duration of 20s. Additionally, LVDT sensors are positioned on three different abscissae denoted L1, L2 and L3 identified as subject to decompression due to thermal gradient.



a b

Figure 2. External and internal views of the bridge structure.

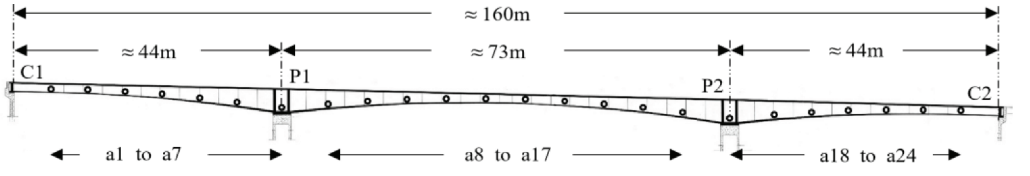


Figure 3. Overall dimensions of the bridge in longitudinal cross-section and location of accelerometers.

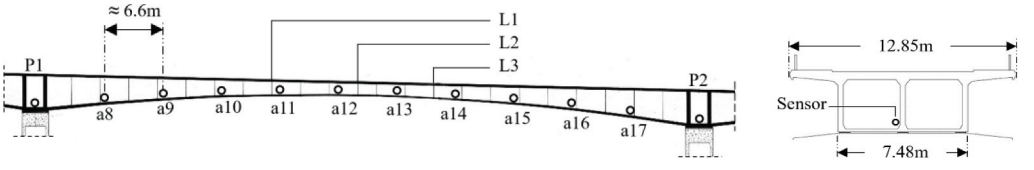


Figure 4. Location of the accelerometers on the central span (a8 to a17) and voussoir joints equipped with CEREMA's LVDT sensors (L1 to L3). Location of accelerometers on a transversal cross-section.

Recorded signals of LVDT sensors enable to identify the time windows to consider for detecting a structural modification of the bridge associated in the present case to a decompression of the intrados. Consequently, the state of the bridge on April 3, 2023 is chosen as state S1 and on April 9, 2023 as state S2. Within each of the two time-windows defined in Figure 5, two subgroups of data are selected to carry out a comparative analysis on two separate datasets corresponding to the same state of the bridge and assess the robustness of the modal identification procedure. Time windows T1.1 and T1.2 correspond to the state S1, and T2.1 and T2.2 correspond to the state S2.

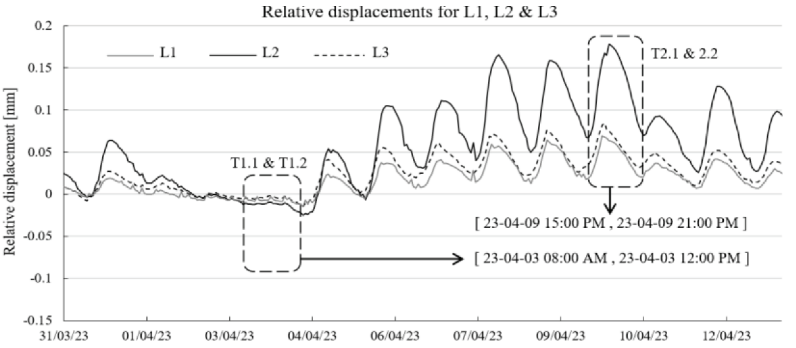


Figure 5. Selection of time windows, considering relative displacement measured by LVDT sensors L1, L2 and L3.

3.2 *Application of the damage identification procedure*

3.2.1 *Modal identification*

The modal identification procedure is applied to the data sets derived from the four temporal sub-windows T1.1 and T1.2 corresponding to the state S1, and T2.1 and T2.2 the state S2. As

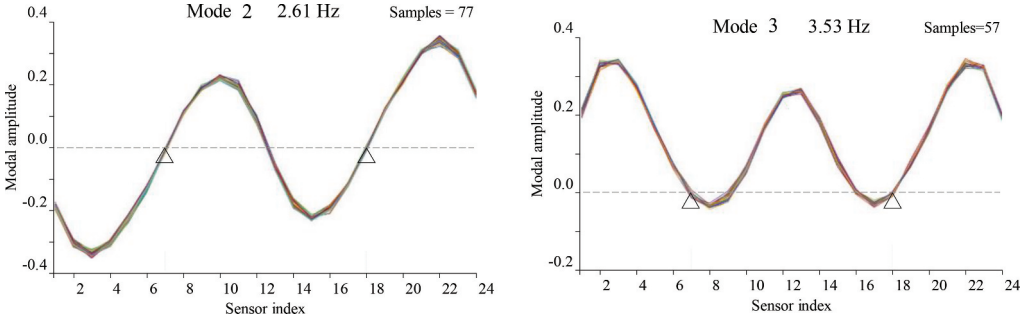


Figure 6. Illustration of two mode sets identified from the temporal sub-window T1.1.

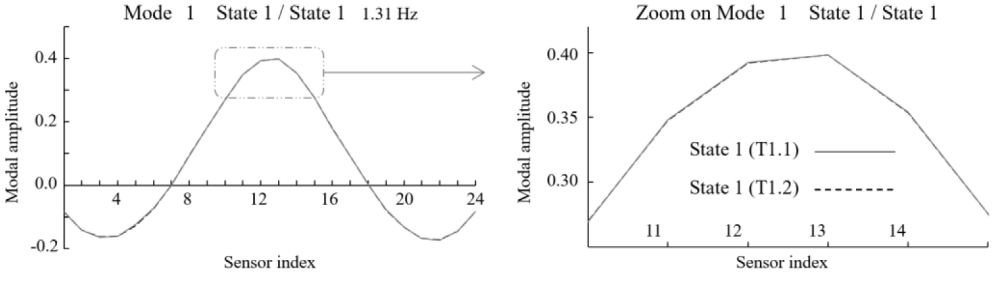


Figure 7. Comparison of mode 1 for two distinct instances of S1 (T1.1 & T1.2).

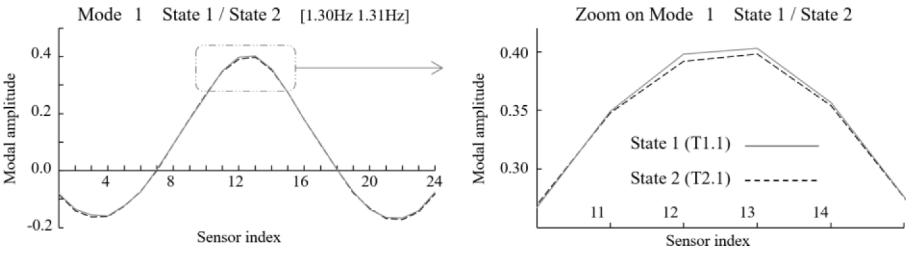


Figure 8. Comparison of mode 1 for two distinct instances of S1 and S2 (T1.1 & T2.1).

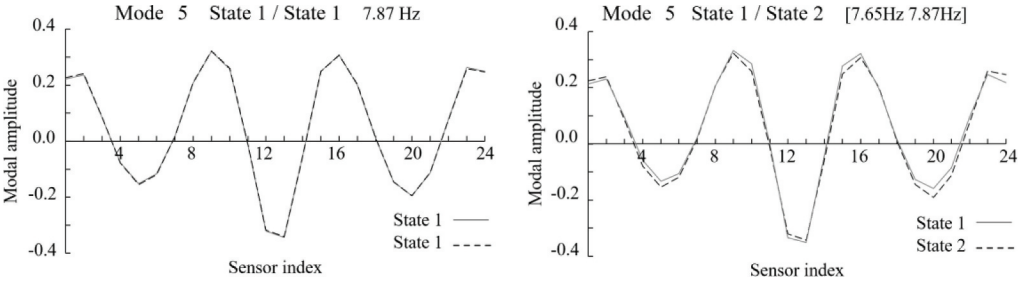
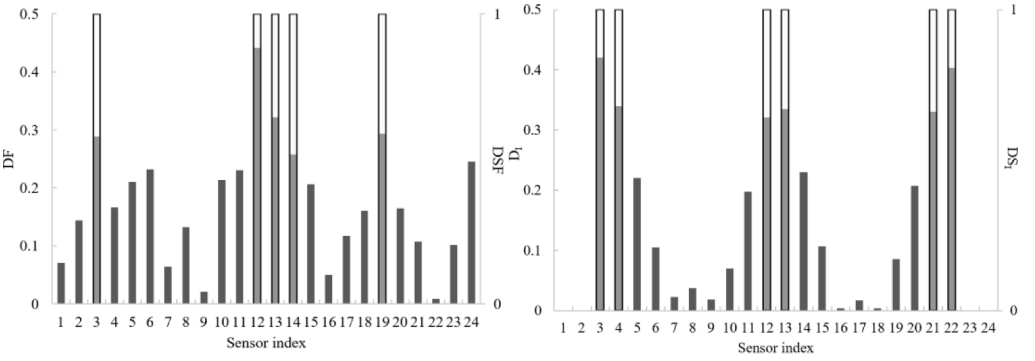


Figure 9. Superposition of mode 5 for two distinct instances of S1 (T1.1 & T1.2) and two distinct instances of S1 and S2 (T1.1 & T2.1).

an illustration, Figure 6 shows the distribution of 2 modes identified from the sub-window T1.1. Figures 7, 8 and 9 compare the average of modes 1 and 5 derived from sets of time sub-windows related to the same state (S1: T1.1 with T1.2 or S2: T2.1 with T2.2), and then to states S1 and S2. The modes obtained from the same state are very close assessing the robustness of the modal identification. The evolution of the modes between states S1 and S2 confirm the structural changes in the bridge, also detected by the LVDT sensors.

3.2.2 *Damage detection and localization*

Figures 10a and 10b show respectively the results obtained with the indicators D_F, DS_F and D_I, DS_I. Both indicators detect a modification of the bridge behavior that is in good accordance with the observations made thanks to the LVDT sensors placed in the central span. They also seem to indicate that other modifications of the bridge occur also in the left and right span. This information cannot be checked as only the central span is equipped with LVDT sensors, but a complementary analysis is possible using the updating results.



a. Flexibility: D_F and DS_F b. Interpolation (n=5): D_I and DS_I

Figure 10. Damage indicators.

3.3 *Model updating*

3.3.1 *Model description*

The proposed model is a simplified finite element model of the bridge made of 156 Euler-Bernoulli beam elements of variable moment of inertia and cross-sectional area following the design of the bridge. The Young's modulus is homogeneous, and its value is chosen equal to that of concrete.

3.3.2 *Updating*

The potentially damaged zones and the updating results are represented in Figure 11. The obtained damage pattern in the central span is consistent with the damage indicators and measurement obtained from the LVDT sensors. In the left and right span of the bridge, the evolution between states S1 and S2 seems to correspond to an increase of stiffness. This point has to be further investigated in order to determine whether it is linked to effective modification of the bridge or not. Figure 12 present the comparison between the quantities $\overset{\vee}{\phi}_i S2 - \overset{\vee}{\phi}_i S1$ and $\tilde{\phi}_i^{S2} - \tilde{\phi}_i^{S1}$ showing a good agreement between experimental and numerical results.

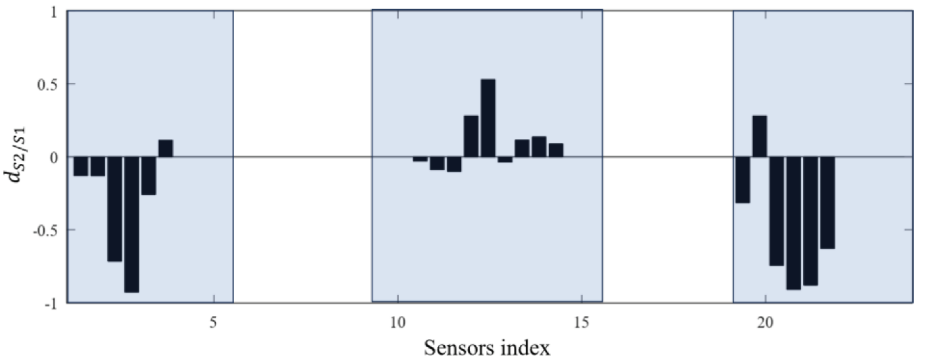
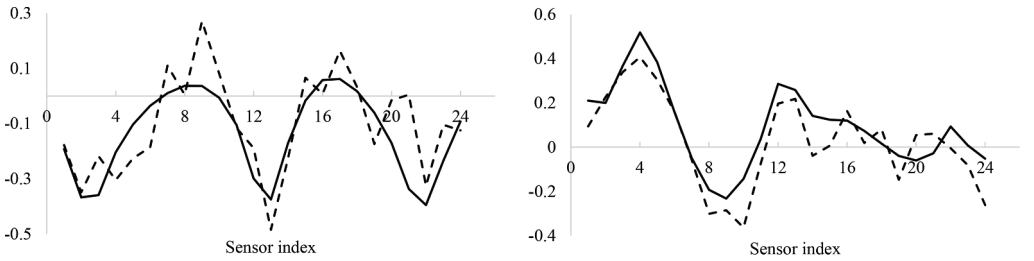


Figure 11. Updated damage between state S1 and S2.



a. Mode 1 b. Mode 4

Figure 12. Comparison of $\overset{\vee}{\phi}_i S2 - \overset{\vee}{\phi}_i S1$ ( ) and $\tilde{\phi}_i^{S2} - \tilde{\phi}_i^{S1}$(—) obtained by the model and identified from the recorded data.

4 CONCLUSION

The aim of this paper was to demonstrate the potentiality of the proposed hybrid methodology for the identification of the damage of a real bridge. The combined use of modal identification, damage indicators and simplified finite element model has enabled the detection and localization of damage on the central span that are in accordance with the information from the LVDT

sensors. Furthermore, other damage locations that were not expected have been detected by indicators and confirmed by model updating. This point has to be further investigated on the bridge by new measurements. The equipment of the bridge with complementary LVDT sensors and additional accelerometers is planned.

The advantage of the proposed strategy, compared to a classical model updating procedure, relies in the reduction of the number of model parameters to be updated on the base of the results of damage indicators. The originality of the updated procedure is that it updates the selected model parameters so that the modal differences between state S1 and S2 numerically calculated fits the experimentally identified ones.

The methodology presented in section 2 can be applied to other types of bridges as for example truss bridges. In that case, other damage indicators as for example Damage Locating Vectors (DLVs) proposed by Bernal (Bernal 2002) and an adapted simplified finite element model have to be employed. This point and other improvements to the present method, including statistical analysis, are also under consideration. This further research will enlarge the scope and improve the robustness of the proposed methodology.

ACKNOWLEDGMENT

The project CI3S received a grant from the call for projects *Ponts Connectés* funded by the French Government and led by Cerema which aims to improve bridge management by using the most recent techniques in terms of monitoring, data transfer and data processing. Moreover, the authors would like to thank Cerema for organizing this call for projects and for its scientific involvement in the follow-up of the project and for sharing the data of the LVDTs on the bridge of Longues.

REFERENCES

Alvandi, A. & Cremona C. 2006. Assessment of vibration-based damage identification techniques. *Journal of Sound and Vibration*. 292: 179–202.

An, Y. & Chatzi, E. & Sim, S.H. & Laflamme, S. & Blachowski, B. & Ou, J. 2019. Recentprogress and future trends on damage identification methods for bridge structures. *StructuralControl Health Monitoring*.

Bernal, D. 2002. Load vectors for damage localization, *Journal of Engineering Mechanics, ASCE*,128, 1: 7–14.

Erduran E, Ulla FK, Næss L. A Framework for Long-Term Vibration-Based Monitoring of Bridges. *Sensors* (Basel). 2021 Jul 11;21(14):4739. doi: 10.3390/s21144739. PMID: 34300479; PMCID: PMC8309670.

Golyandina, N. & Zhigljavsky, A. 2020. SSA for Forecasting, Interpolation, Filtering andEstimation. Singular Spectrum Analysis for Time Series. *SpringerBriefs in Statistics*. Berlin, Heidelberg: Springer.

Hansen, N. 2016. The CMA evolution strategy: A tutorial. *arXiv preprint arXiv*:1604.00772 .

Ibrahim, S.R. 1977. Random Decrement Technique for Modal Identification of Structures.*Journal of Spacecraft and Rockets.*14, 11: 696–700.

Karakostas, C. & Quaranta, G. & Chatzi, E. & Zülfikar, A. & Çetindemir, O & De Roeck, G. &Döhler, M. & Limongelli, M.P. & Lombaert, G. & Apaydin, N. & Pakrashi, V. &Papadimitriou, C. & Yesilyurt, A. 2023. Seismic assessment of bridges through structural health monitoring: a state-of-the-art review. *Bulletin of Earthquake Engineering*. 1–49.

Limongelli, M.P. 2011. The interpolation damage detection method for frames under seismic excitation. *Journal of Sound Vibration*. 330: 5474–5489.

Limongelli, M. P., Chatzi, E., Döhler, M., Lombaert, G., & Reynders, E. 2016, July. Towards extraction of vibration-based damage indicators. *In EWSHM-8th European workshop on structural health monitoring*.

Limongelli, M. P. 2019. Vibration-based structural health monitoring: Challenges and opportunities. *In Advances in Engineering Materials, Structures and Systems: Innovations, Mechanics and Applications-Proceedings of the 7th International Conference on Structural Engineering, Mechanics and Computation*, (pp. 1999–2004). CRC Press/Balkema.

Sohn, H. & Farrar, C.R. & Hemez, F. M. & Shunk, D.D. & Stinemates, D.W. & Nadler, B.R. & Czarnecki, J.J. 2003. A review of structural health monitoring literature: 1996-2001. *USA: Los Alamos National Laboratory*. 1, 16.

Bridge Maintenance, Safety, Management, Digitalization and Sustainability – Jensen, Frangopol & Schmidt (eds)
© 2024 The Author(s), ISBN 978-1-032-77040-6
Open Access: www.taylorfrancis.com, CC BY-NC-ND 4.0 license

Road overpasses with Gerber half-joints: Field tests and numerical models

D. De Domenico, M. Mazzeo, D. Messina & A. Recupero
Department of Engineering, University of Messina, Italy

ABSTRACT: This contribution presents a combined experimental-numerical investigation on road overpasses with Gerber half-joints. The analysis is focused on a series of existing overpasses of the A20 highway, Sicily, Italy, built more than 50 years ago and characterized by a Niagara-type Gerber deck with prestressed concrete girders and transverse diaphragms. The structural health of the overpass deck is assessed by diagnostic field tests combined with numerical simulation. First, dynamic free-vibration tests under the transit of trucks are conducted in situ to determine the bridge deck modal characteristics (frequencies and modal shapes) through a recently developed identification strategy. The experimental results are used to calibrate a finite element model, which is finally used to simulate the deflection response of the deck under static load tests. The results of this study are useful to develop field-validated digital twins of real bridge structures and for performing parametric analysis when designing repair interventions, where necessary.

1 INTRODUCTION

The Italian Road system includes around 840,000 km of highways, provincial and municipal roads (Cosenza & Losanno 2021) with more than 50,000 bridges. A large number of such bridge structures were built more than 50 years ago with concrete or prestressed concrete schemes. Because of ageing and lack of periodic inspection and maintenance, several bridges are undergoing material deterioration that, combined with structural defects related to design or construction errors or caused by the aggressive environment, may lead to catastrophic collapses (Nuti et al. 2020). The critical situation observed in Italy, with 15 bridge collapses in the last 10 years and a total of 52 fatalities and 38 injured (Palmisano et al. 2022), requires efficient methodologies to assess the health conditions of existing bridges and, if critical aspects are identified, to define the most suitable repair or intervention actions in a cost-effective manner. The structural safety of existing bridges can be comprehensively assessed through suitable experimental investigations assisted by numerical calculations. In this context, diagnostic field tests are very useful for the structural health assessment of existing bridges, as they provide rapid information on the overall response of the structure under either dynamic or static loads (Lantsoght 2023) and can be exploited to develop a field-validated numerical model of the bridge (De Domenico et al. 2022).

Among the various static schemes of decks, several existing bridges built in Italy in the 1960s and 1970s are realized with a half-joint, also called Gerber joint or dapped-end beam in the literature (Desnerck et al. 2018). This scheme has the advantage of covering a longer span (space between intermediate piers) than decks with simply supported girders and was indeed widely used for road overpasses for spans of approximately 45 m, which are typically those associated with two separate road carriageways separated by a central traffic island. Similar to the simply supported scheme, bridges with Gerber half-joints have a statically determinate scheme, which is not sensitive to differential settlements and thermal variations (that instead typically affect multi-span continuous girder bridges). Besides these advantages, there are also well-known disadvantages related to the Gerber joints, including potential brittle shear failure

DOI: 10.1201/9781003483755-52

due to the reduced height in the half-joint (Moreno-Martínez et al. 2014), defective leakage of water through the joint (Santarsiero et al. 2021) that causes concrete deterioration and reinforcement corrosion in the protruding nib (di Prisco et al. 2023), as well as difficulty of visual inspection and defect detection. The collapse of a section of the de la Concorde Overpass in Quebec, Canada in 2006, and the more recent collapse of the Annone Brianza overpass in Italy in 2016 occurred in an exceptional, sudden manner, and revealed the inherent vulnerability of these kind of structures (Mitchell et al. 2011). Consequently, it is of paramount importance to develop efficient procedures for the structural assessment of half-joint bridges by exploiting experimental data and diagnostic field tests (Spinella et al. 2022).

This contribution deals with a set of road overpasses belonging to the A20 highway in Sicily, Italy, built in the early 1970s and with a Niagara-type Gerber prestressed concrete (PC) deck. Aim of this work is to illustrate a combined experimental-numerical framework to assess the structural health conditions of these road overpasses through interconnected field tests and numerical simulation. First, a comprehensive experimental campaign is conducted for characterization of materials. A rational, well-established procedure for assessing the structural health conditions under service loads consists in the comparison between modal characteristics retrieved from in-situ tests and numerical values obtained from digital models. To this aim, we use free vibration tests, which allow a quick and cost-effective determination of dynamic structural features using a sparse network of few sensors and avoiding long-lasting monitoring campaigns. The peculiarities of the modal shapes of this kind of structures are illustrated and critically discussed against alternative continuous-girder or simply-supported deck schemes. The experimental dynamic features of the bridge deck from free vibration tests are then compared to those identified by a finite element model (FEM). The inherent material uncertainties, identified from the previous experimental campaign, are included in the numerical simulation by using three different values of the concrete elastic modulus based on the pertinent statistical distribution. Field tests also include static load tests performed on the overpass decks under heavy trucks. The FE models, previously calibrated through the dynamic test results, are then validated against the static load tests by comparison in terms of deflections.

2 ANALYZED ROAD OVERPASSES

A family of 18 road overpasses of the A20 Messina-Palermo highway (Sicily, Italy), built in the early 1970s, are analyzed in this work. The deck is realized with a Niagara-type Gerber scheme (Figure 1), with two symmetric lateral spans having length of 29.0 m, including a segment of 22.0 m from the abutment to an intermediate pier and another cantilevered segment of 6.5 m with dapped beam at the end. The dapped end of the cantilever span is the support of a complementary dapped end of a central (suspended) span of 31.0 m length: this connection is termed half joint and can be viewed as an internal hinge realizing a statically determinate scheme, with an overall length between the intermediate piers of 44.0 m. Although the entire set of 18 overpasses analyzed are characterized by the same static scheme with identical span lengths, the deck width is variable from 6.5 m to 17.0 m depending on the number of I-shaped post-tensioned prestressed concrete (PC) girders, ranging from 3 to 8, respectively, all equally spaced at 2.0 m from each other. The majority of the overpasses analyzed (12 out of 18) are composed by 5 girders and have a deck width of 10.0 m.

The girders are tapered, having a variable height ranging from 1.3 m (at the abutments) to 1.7 m (above the intermediate piers and along the cantilevered segment) and are mutually collaborating through transverse diaphragms and an overlying reinforced concrete (RC) slab 0.16 m thick. The girders are reinforced with prestressing cables, having parabolic configuration to follow the bending moment profile, and made of cold-drawn Ø7 steel wires: in the lateral spans there are 4 cables, 3 of which (anchored at the dapped end) have 32 wires and 1 (the uppermost, anchored at the abutment) have 42 wires; in the central span, there are 3 cables, all made of 32 wires, 2 of which anchored at the left dapped end and the remaining one anchored at the right dapped end. Additional ordinary reinforcement of girders consists of transverse web reinforcement Ø12/15 cm, 6Ø10 longitudinal bars both in the top flange and

central web, and 13Ø12 in the bottom flange. The dapped end, with depth 0.90 m and width 0.75 m, is reinforced with 2Ø24 hangers, 4Ø24 diagonal bars and 6Ø24 longitudinal (top and bottom) steel bars properly anchored, stirrups and longitudinal skin reinforcement Ø14/15 cm. The overlying RC slab is reinforced with 4Ø14 longitudinal bars in the central part (over the I-shaped girder flange) and 3Ø8 longitudinal bars (top and bottom) at either external side of the deck, plus Ø10/25 cm horizontal bars for the entire slab width.

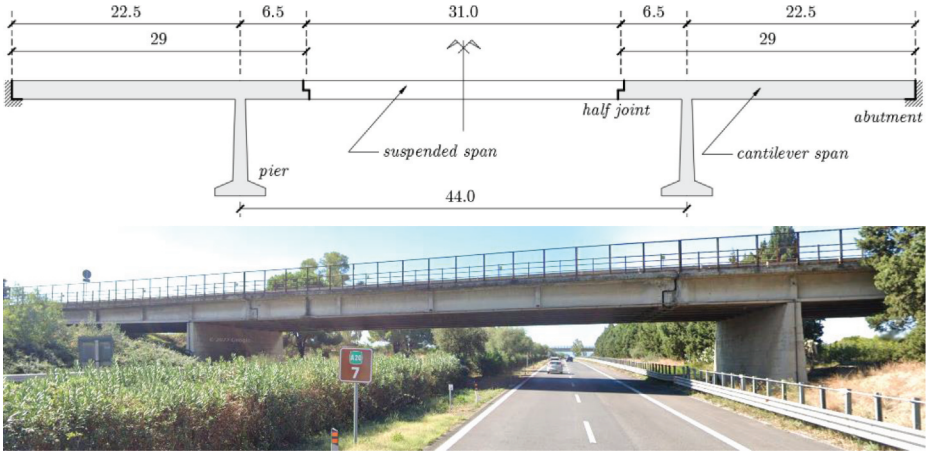


Figure 1. Longitudinal configuration (top) (measures in [m]) and photograph of a typical road overpass of the A20 Messina-Palermo highway (bottom).

An extensive in-situ test campaign has been performed, including coring, SonReb and pull-out tests for concrete strength of different structural members (foundations, abutments, piers, girders, diaphragms and slabs). Of particular relevance for the aims and scope of this paper, the concrete compressive strength data resulting from destructive and non-destructive tests have been grouped all together and processed statistically by fitting a log-normal probability density function (PDF). Indeed, the concrete strength f_c is an important parameter that affects the concrete elastic modulus E_c and, in turn, the structural response under serviceability loads explored in the dynamic and static field tests. It has been considered that two different classes of concrete were used for the realization of girders and of slabs + diaphragms, and two log-normal PDFs have been fitted accordingly (Figure 2).

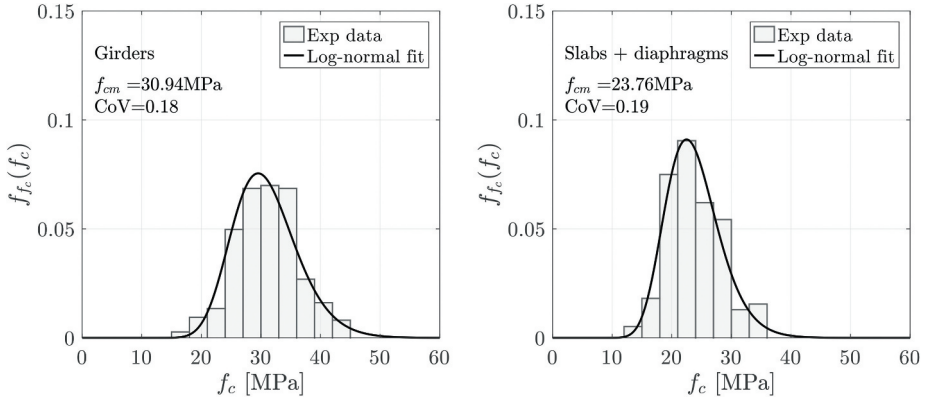


Figure 2. Statistical processing and log-normal fitting of concrete strength data for girders (left) and slabs + diaphragms (right).

3 FIELD TESTS AND NUMERICAL SIMULATION

3.1 *Dynamic load tests*

Dynamic field tests serve to identify modal characteristics of a structure, and in this work are used to assess the overall structural health conditions of the overpass deck. To this aim, free vibration tests are conducted on the analyzed overpasses and results, in terms of natural frequencies and modal shapes identified in situ, are compared to estimates obtained by a FEM assuming ideal conditions (no ongoing cracking or damage phenomenon, perfect restraints, etc.). As shown in Figure 3, a network of 8 accelerometric uniaxial sensors (labeled S1-S8) are anchored to the bridge deck to measure the vertical accelerations, of which 6 within the suspended span and the remaining 2 in the two cantilever spans. The free vibrations are triggered by the transit of a heavy truck (gross weight of 400 kN, approximately) along the deck at an average speed of 50 km/h, and the accelerometric measurements are acquired once the truck has left the overpass. The signals are sampled at a frequency of 1 kHz and are preliminarily processed through a third-order Butterworth filter by cutting off frequencies beyond the range [0.5-15] Hz.

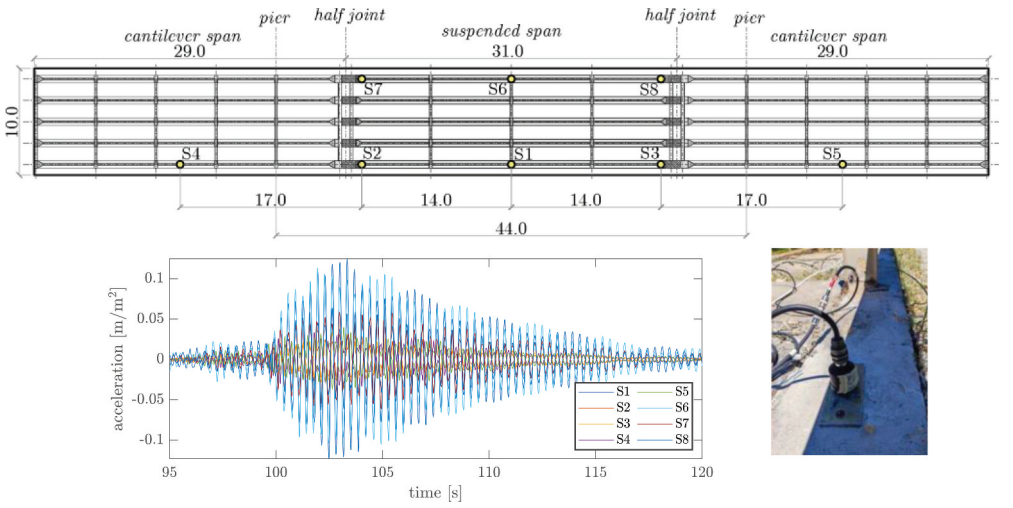


Figure 3. Arrangement of accelerometric sensors (S1-S8) on the overpass deck (top) during the dynamic load tests (measures in [m]) and representative signal array recorded during the free vibration tests (bottom).

Modal parameters of the overpass deck are identified from free-vibration-test results through the method proposed by Mazzeo et al. (2023), which exploits the Variational Mode Decomposition (VMD) to extract the intrinsic mode functions (IMFs) of the processed signals. The central frequencies of the IMFs are assumed as estimates of the natural frequencies, while the mode shapes are determined based on the phase shifts of the various synchronous sensor recordings.

Natural frequencies and modal shapes from the field tests are compared with numerical predictions by a FEM realized with the software SAP2000® (Computers and Structures Inc. 2016). In particular, different levels of accuracy are considered in the numerical simulation, by performing a parametric analysis to investigate various kinds of boundary conditions and modeling assumptions. Only a limited set of results of this parametric analysis are reported in this paper for the sake of brevity. The first model is made of 1D beam elements with six degrees of freedom per node for both girders and diaphragms, with the collaborating RC slab portion incorporated in the girder cross-section. This model underestimated the stiffness of the deck, as the numerical natural frequencies were systematically lower than those obtained from the experimental tests, Hence, a second, more refined model is set up, with 1D beam elements for girders and diaphragms, but with the RC slab being explicitly modeled with 2D shell elements, by introducing rigid links

combined with joint offsets to account for the actual difference between the slab mid-plan and the centroid of the girders, as per previous papers (De Domenico et al. 2022). The deck present Mesnager hinges at the abutments. It has been observed that clamping restraints at the abutments are the most appropriate boundary conditions to simulate the actual response of the deck, as the Mesnager hinges behave as real clamp restrains if the neighboring concrete areas is uncracked.

Figure 4 illustrates a comparison between experimental and numerical natural frequencies and mode shapes for the first three vibration modes. In particular, the first and second mode, having experimental natural frequencies of 2.82 Hz and 3.17 Hz, respectively, are related to the flexural and torsional vibration of the suspended span, respectively, while the third mode, with frequency 4.82 Hz, corresponds to a flexural behavior of the cantilever spans with the suspended span following rigidly the vertical deflections of the lateral parts with a cusp (abrupt change of rotation) at the half-joint. It can be observed that these mode shapes are quite peculiar and different from those typically observed in simply-supported bridge decks. A good agreement is observed between experimental and numerical natural frequencies and mode shapes. In particular, the accuracy of the FEM in terms in terms of frequency prediction is demonstrated by relative errors lower than 10%, while the accuracy of the FEM in terms of mode shape prediction is quantitatively demonstrated by modal assurance criterion (MAC) factors higher than 0.98 for all investigated cases. The error (interval) markers associated with the experimental bars in the histogram of Figure 4 identify the range of variation between minimum and maximum frequency from all sensors and analyzed overpasses (having the same number of girders), which are reasonably negligible, whereas the error markers associated with the numerical bars indicate the lower and upper bounds of the frequencies obtained by the FEM simulation using the 5% and 95% fractiles of the

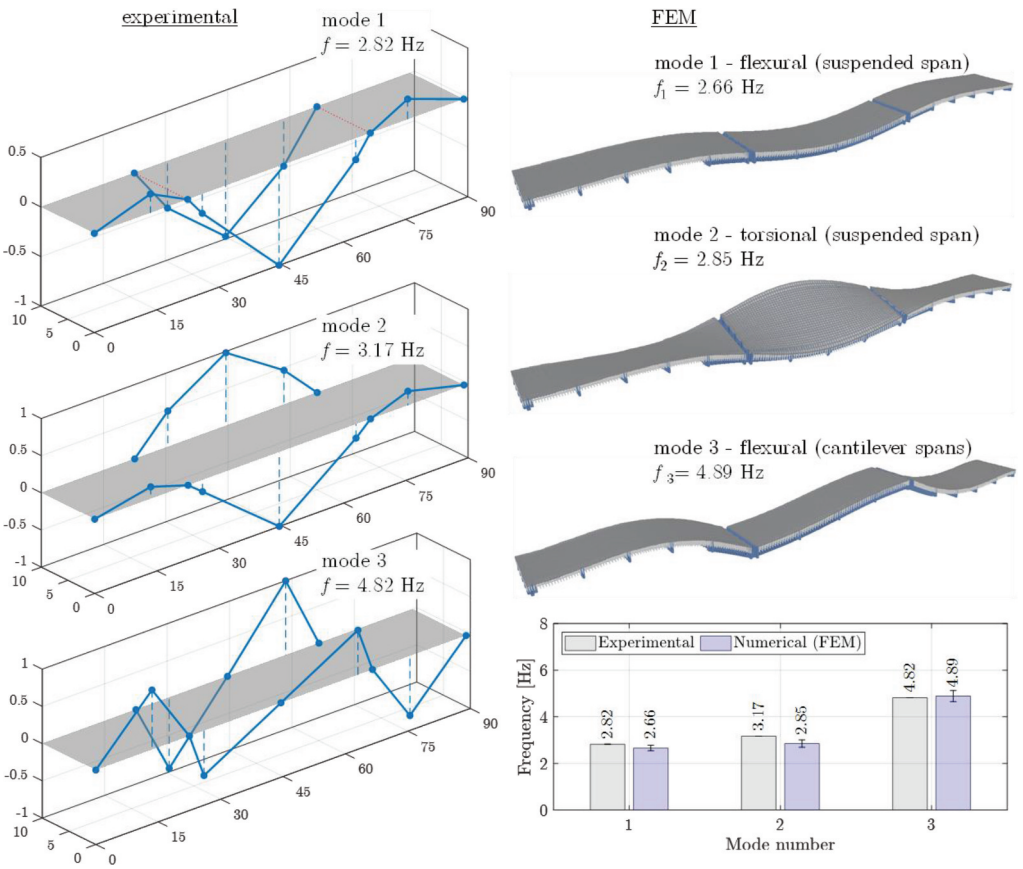


Figure 4. Comparison between experimental and numerical frequencies and mode shapes of overpass deck.

elastic modulus distribution determined by statistically processing the concrete strength data of the experimental campaign. In this simplified manner, it is possible to consider the impact of the inherent material uncertainties in the critical analysis of the numerical simulation results. Based on the obtained results, no damage spots or significant discrepancy between the FEM results (with idealized, uncracked material properties) and the experimental findings are noted, which may suggest that no damage process is taking place in the overpass deck under service conditions.

3.2 *Static load tests*

In addition to dynamic load tests, the structural health of the overpass deck under maximum serviceability load has been also assessed through static load tests. The tests are performed on 8 out of the 18 overpasses analyzed, all having 5 girders (deck width 10.0 m). The loads are applied through two trucks with four axles, whose weight and location has been designed to reproduce the same mid-span bending moment resulting from the load model 1 of the Eurocode 1-Part 2 (European Committee for Standardization 2003). The aim of these tests is to evaluate the deflection response of the deck under traffic loads that are different from those prescribed by the standards in force at the time of bridge construction; more importantly, 50 years of service life may have generated material deterioration and stiffness degradation, which can be evaluated by comparison between theoretical deflection under the assumed truck loads (e.g., via calibrated FEM) and actual experimental deflection. The location of the trucks is illustrated in Figure 5: the weight of each truck is 400 kN, and the pair of trucks are eccentrically placed so as to trigger not only flexural deflection (in the suspended span) but also torsion behavior of the deck. The deflections are measured by 7 linear variable displacement transducers (range ±50 mm, accuracy 0.01 m), denoted with letters A-G in Figure 5, fixed on aluminum rods via rigid connections and pointing towards the deck soffit.

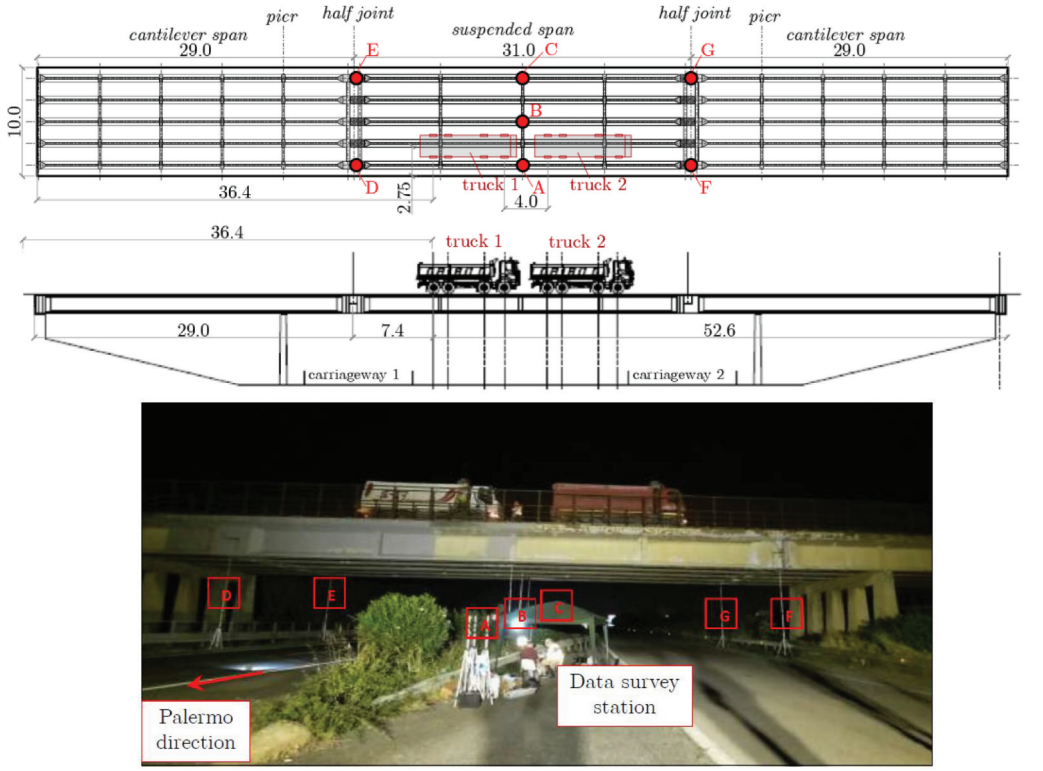


Figure 5. Arrangement of trucks and of 7 deflection sensors (A-G) on the overpass deck (top) during the static load tests (measures in [m]) and photograph taken during a representative field test (bottom).

The FEM previously calibrated against the dynamic tests is used to simulate the deflection response of the deck subjected to the truck loads, and the deflection profile is shown in the top part of Figure 6. The average experimental deflections (among the eight investigated overpasses) are reported as solid lines with circle markers in the bottom part of Figure 6, accompanied by error bars that denote the interval of variations from overpass to overpass. The quantitative value of the deflection and the corresponding interval of variation is reported as text label besides each measurement point. As reasonably expected, the maximum deflection is obtained at the mid-span in the loaded side (18.45 mm), while the maximum average deflection is 15.89 mm.

To critically analyze the experimental deflection response and to incorporate the inherent material uncertainties in the numerical simulation in a simplified way, three values of the concrete elastic modulus are used in the FEM, namely the mean value E_{cm} and the 5% and 95% fractiles of the corresponding probability distribution $E_{c,5\%}$ and $E_{c,95\%}$, respectively. The latter values can be associated with lower and upper bounds of the overpass deck stiffness, which produce the upper and lower bounds of the deflection response, respectively. By inspection of the results in Figure 6, it can be seen that the FEM is really accurate in capturing the deflection response of the deck not only along the longitudinal profile in the most loaded side (alignment of sensors D-A-F) but also along the transversal profile (alignment of sensors C-B-A). Moreover, it is clearly noted that the range of variation of the experimental findings is encompassed by the estimates of the deflection response resulting from the FEM with the lower and upper bound value of the elastic modulus. It can be concluded that the FEM results obtained in the simulation of the static load tests are consistent with those obtained during the field tests.

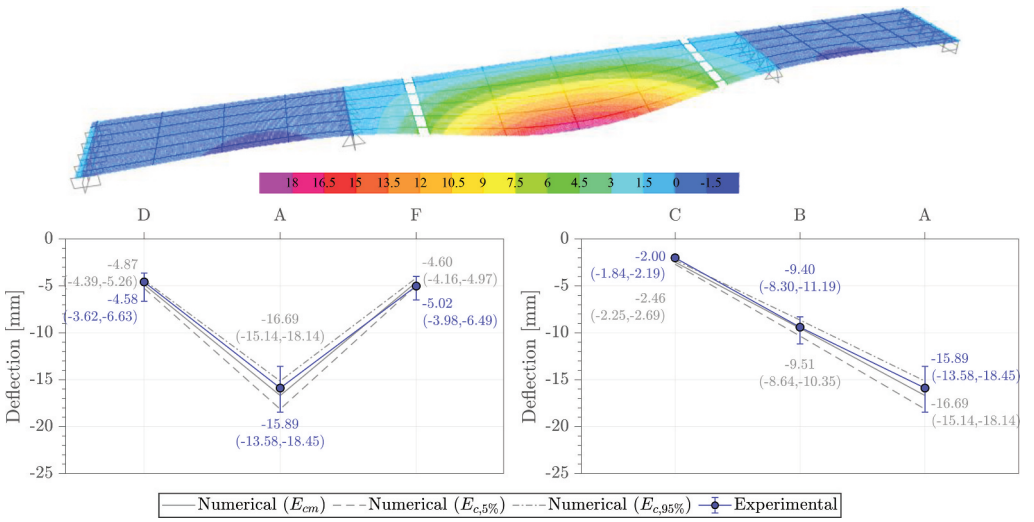


Figure 6. Deflection profile obtained by the calibrated FEM (top) and comparison between experimental and numerical deflections using three values of concrete elastic modulus (bottom).

4 CONCLUSIONS

This contribution has presented a combined experimental-numerical investigation on road overpassed located in the A20 highway Messina-Palermo (southern Italy) built around 50 years ago and whose deck is realized in prestressed concrete with a Niagara-type Gerber scheme. Starting with an extensive experimental campaign for the material characterization (only briefly described in this work, for the sake of brevity), an accurate FEM has been calibrated to simulate the results of field tests including dynamic and static load tests. Coupling information obtained from original design drawings and a parametric analysis to select the

most suitable boundary conditions and element types, a critical comparison between experimental and numerical results has led to the following conclusions: 1) the overpasses are not experiencing any evident damage or cracking process responsible for a variation of their modal parameters under service loads, as the estimates of natural frequencies and modal shapes obtained by the numerical simulation assuming ideal material properties are well aligned with the experimental findings from the dynamic field tests; 2) the overpasses remain uncracked under the maximum serviceability load prescribed by the load model 1 of the current Eurocode 1-Part 2, and the deflection response is consistent with that obtained by the numerical simulation. A simple procedure underlying a basic statistical processing of the concrete strength data for the determination of mean and relevant fractiles of the concrete elastic modulus makes it possible to incorporate the inherent material uncertainties in the critical analysis of the FEM results. The proposed method is general and is particularly useful when dealing with a family of bridges sharing similar structural scheme age and materials, to incorporate material uncertainties in the processing of diagnostic test data and to rationally exploit static and dynamic tests for an overall structural health assessment.

ACKNOWLEDGEMENTS

The authors express their gratitude to the Italian High Council of Public Works (CC.SS.LL.PP.) and the Network of University Laboratories of Seismic Engineering (RELUIS). The results of this study were achieved in the national agreement for implementing the agreement pursuant to art. 15 law 7 August 1990, No. 241 between the Superior Council of Public Works and RELUIS.

REFERENCES

Computers and Structures Inc. CSi Analysis Reference Manual for SAP2000®. Berkeley: CA, USA; 2016.

Cosenza, E., Losanno, D. 2021. Assessment of existing reinforced concrete bridges under road-traffic loads according to the new Italian guidelines. *Struct Concr* 22(5): 2868–2881.

De Domenico, D., Messina, D., & Recupero, A. 2022. Quality control and safety assessment of prestressed concrete bridge decks through combined field tests and numerical simulation. *Structures* 39: 1135–1157.

Desnerck, P., Lees, J. M., and Morley, C. T. 2018. Strut-and-tie models for deteriorated rein-forced concrete half-joints. *Engineering Structures* 161: 41–54.

di Prisco, M., Colombo, M., & Martinelli, P. 2023. Structural Aspects of the Collapse of a RC Half-Joint Bridge: Case of the Annone Overpass. *Journal of Bridge Engineering* vol. 28, Issue 11.

European Committee for Standardization. 2003. Eurocode 1: Actions on structures – Part 2: Traffic loads on bridges.

Lantsoght, E. O. 2023. Assessment of existing concrete bridges by load testing: barriers to code implementation and proposed solutions. *Structure and Infrastructure Engineering*, 1–13.

Mazzeo, M., De Domenico, D., Quaranta, G., & Santoro, R. 2023. Automatic modal identification of bridges based on free vibration response and variational mode decomposition technique. *Engineering Structures* 280: 115665.

Mitchell, D., Marchand, J., Croteau, P., & Cook W.D. 2011. Concorde Overpass Collapse: Structural Aspects. *Journal of Performance of Constructed Facilities*. Vol. 25, Issue 6.

Moreno-Martínez, J. Y., & Meli, R. 2014. Experimental study on the structural behavior of concrete dapped-end beams. *Engineering Structures* 75, 152–163.

Nuti, C., Briseghella, B., Chen, A., Lavorato, D., Iori, T., & Vanzi, I. 2020. Relevant outcomes from the history of Polcevera Viaduct in Genova, from design to nowadays failure. *Journal of Civil Structural Health Monitoring* 10: 87–107.

Palmisano, F., Asso, R., Chiaia, B., Marano, G. C., & Pellegrino, C. 2022. Structural assessment of existing RC half-joint bridges according to the new Italian guidelines. *Journal of Civil Structural Health Monitoring*, 1–25.

Santarsiero, G., Masi, A., & Picciano, V. 2021. Durability of Gerber saddles in RC bridges: Analyses and applications (Musmeci Bridge, Italy). *Infrastructures* 6(2): 25.

Spinella, N., Messina D. 2022. Load-bearing capacity of Gerber saddles in existing bridge girders by different levels of numerical analysis. *Structural Concrete*. 24(1): 211–226.

MS03: Life-cycle performance assessment of existing bridges in an aggressive environment
Organizers: M. Akiyama, D.M. Frangopol & H. Matsuzaki


Taylor & Francis
Taylor & Francis Group
http://taylorandfrancis.com

Bridge Maintenance, Safety, Management, Digitalization and Sustainability – Jensen, Frangopol & Schmidt (eds)
© 2024 The Author(s), ISBN 978-1-032-77040-6
Open Access: www.taylorfrancis.com, CC BY-NC-ND 4.0 license

Self-healing performance of aged bacteria-based cementitious materials: An overview

Naru Kim, Seonhyeok Kim & H.K. Lee
Korea Advanced Institute of Science and Technology (KAIST), Daejeon, South Korea

ABSTRACT: The use of bacteria to impart self-healing capabilities to cementitious materials has garnered attention in addressing crack propagation issues within Submerged Floating Tunnel structures. Recent investigations into the self-healing performance of bacteria-based cementitious materials have highlighted challenges related to declining bacterial viability, attributable to adverse conditions and limited nutrients within the cementitious materials. This study presents a comprehensive overview of recent literature addressing the self-healing performance of aged bacteria-based cementitious materials, focusing on diverse bacterial strains, carrier for bacteria, and curing conditions for cementitious materials. In addition, a preliminary study examines the bacterial viability and self-healing performance of cementitious materials with different binders.

1 INTRODUCTION

The advent of Submerged Floating Tunnel (SFT) presents a possible solution for addressing challenges of waterway crossings, characterized by its consistent construction cost and weather-free operability (Zhang et al., 2010). However, the structural integrity of SFT faces potential threats due to the inherent susceptibility of cementitious materials to tensile loads and irreversible crack propagation (Kim et al., 2021), adding to the complexity on the repair work in underwater conditions (Iovane et al., 2023). Against this backdrop, the utilization of bacteria capable of self-healing in the cementitious materials emerges as a viable solution to mitigate cracks in underwater structures, addressing both environmental and economic considerations (Iovane et al., 2023). Consequently, researchers have explored the incorporation of bacteria into cementitious materials as a promising approach to recover the cracks on them (Vijay et al., 2017).

Preceded investigations into bacteria-based cementitious materials and their self-healing capabilities often overlooked the influence of curing age (Zheng and Qian, 2020). The inherently unfavorable conditions within cementitious materials, such as high alkalinity and pore sizes smaller than the bacteria, contribute to the gradual decline in bacterial viability over time (Kim et al., 2021, Zheng and Qian, 2020). Consequently, recent research has shifted focus on investigating the self-healing behaviors of aged cementitious materials and the various factors affecting them (Skevi et al., 2021).

Therefore, the present study aims to provide a comprehensive overview of recent research exploring the bacterial viability and self-healing performances of aged bacterial-based cementitious materials. Bacterial strains, carrier types, and curing conditions within these materials have been identified as key areas of interest across multiple studies. In addition, a preliminary study evaluates the impact of binder systems on bacterial viability and their subsequent self-healing performances (Kim et al., 2024).

DOI: 10.1201/9781003483755-53

2 LITERATURE REVIEW

2.1 *Bacterial strains*

The bacterial viability and self-healing performances in aged cementitious materials can be influenced by the genus species, and inherent characteristics of bacterial strains, as individual strains possess different conditions favoring $CaCO_3$ precipitation mechanism (Kim et al., 2021). For instance, ureolytic and non-ureolytic bacteria contribute to $CaCO_3$ precipitation through ureolysis and denitrification, respectively (Kim et al., 2021).

One typical non-ureolytic bacteria genus used for granting self-healing capacity on cementitious materials is *Bacillus* strain (Justo-Reinoso et al., 2021). Studies involving *Bacillus* species, including *B. pseudofirmus*, *B. cohnii*, and *B. halodurans* demonstrated varying degrees of spore viability and healing ratios after 7 days of encapsulation (Ivaškė et al., 2023). The test result showed that the bacterial spore viability decreased with time, and the spores of *B. halodurans* exhibited the highest viability exceeding 5% after 56 days (Ivaškė et al., 2023). Meanwhile, the healing ratio, defined as the ratio of covered crack width over initial crack width, was shown to be comparable among three species as 0.466 to 0.497, after 56 days of healing (Ivaškė et al., 2023). Regarding the results, Ivaškė et al. (2023) asserted that the carrier type or curing conditions may have affected more significantly than the species of bacteria on the healing performance of aged bacteria-based cementitious materials (Ivaškė et al., 2023).

Comparative studies between spore-forming (e.g., *Bacillus* strains) and non-spore forming bacteria (i.e., *Arthrobacter luteolus*, *Chryseomicrobium imtechense*, and *Corynebacterium efficiens*) in cementitious materials was performed by Shaheen et al. (Shaheen et al., 2023). The tested non-spore forming bacteria were alkaliphilic and calcifying thus having potentials to be used in self-healing cementitious materials (Shaheen et al., 2023). Spore-forming bacteria (i.e., *Bacillus* bacteria strains) exhibited slightly higher healing properties compared to the non-spore forming bacteria, in terms of crack enclosure, regain in compressive strength, permeability, and chloride resistance (Shaheen et al., 2023). Nevertheless, the non-spore forming bacteria showed significant recovery of these properties compared to bacteria-free samples, indicating the potential of both types of bacteria for healing at 90 days of curing (Shaheen et al., 2023).

2.2 *Carrier type*

The carrier type significantly influences bacterial viability within cementitious materials. Ordinary Portland cement, due to its alkalinity and dense microstructure, poses challenging conditions for bacterial survival. Specifically, the pH of ordinary Portland cement often exceeds the favorable pH range of alkaliphilic bacteria (Henze and Randall, 2018). Thus, the use of protective carrier for bacterial survival has been investigated in depth so far.

Studies by Ivaškė et al. (2023) encapsulated the self-healing bacteria within 2% sodium alginate, peptone, and meat extract. The initial bacterial viability was shown to be reduced in post-encapsulation (Ivaškė et al., 2023). However, the survival rate of bactera exceeded that of non-encapsulated bacteria (Ivaškė et al., 2023). Furthermore, the survival rate of bacteria spores in cement paste and cement mortar was also assessed, and it was revealed that the percentage of alive spore was higher in the cement paste (Ivaškė et al., 2023). It was claimed that the mortar might accompany rigid microstructure and compress the capsules with higher extent than the paste (Ivaškė et al., 2023).

The use of other encapsulating materials was explored by Wang et al. (2014), and Zheng & Qian (2020). The former study (Wang et al., 2014) tested the bacterial spores encapsulated in hydrogels. It was confirmed that the bacterial spores in hydrogel were hardly destroyed in the high alkaline cement and the bacterial viability was sustained by the encapsulation in hydrogel (Wang et al., 2014). In detail, the water stored in hydrogel was able to proceed the autogenous healing by bacterial spores, resulting in the higher healing ratio of the cement samples (Wang et al., 2014). The latter study (Zheng and Qian, 2020) delved into the cementing materials as carriers, namely potassium magnesium phosphate cement (MKPC) and sulphoaluminate

cement (SC), contributing to their low alkalinity. Consequently, the bacterial survival rate and area repair rate at 180 days of curing were greatly enhanced by the encapsulation of spores in both materials, while the use of SC achieved slightly higher survival rate and healing performance than that of MKPC (Zheng and Qian, 2020). It was asserted that the higher protective effect of SC can be due to the favorable pore characteristics for bacterial survival (Zheng and Qian, 2020).

2.3 *Curing conditions*

Curing conditions of cementitious materials significantly impact the survival and performances of bacteria. For instance, the outer temperature and salinity can offer significant impact on the survival of bacteria. Ivaškė et al. (2023) tested the temperatures of 20, 40, and 80 ˚C as curing temperatures of mortar samples with *B. pseudofirmus* bacteria for 3 days, and then cured at 20 ˚C for the rest of curing time (Ivaškė et al., 2023). The bacterial viability at 28 days of curing was observed to be approximately 10, 2, and 0%, respectively (Ivaškė et al., 2023). The results accorded with the bacterial growth rate with respect to temperature, which showed sharp decrease above 40 ˚C (Membré et al., 2005). Thus, the curing temperature of bacteria-based cementitious materials can be a crucial factor to sustain their healing performances for a long duration, regardless of the bacteria strains.

Furthermore, studies involving different temperatures (10, 20, and 30 ˚C) and salinity levels (0.5, 2, and 3.5%) for cementitious materials incorporating *Sporosarcina pasteurii* were performed (Kim et al., 2020). The growth rate and maximum optical density of bacteria were increased by the increase in temperatures from 10 to 30 ˚C (Kim et al., 2020). In addition, salinity addressed a positive relationship with bacterial growth but displayed less profound effects than temperature changes (Kim et al., 2020). These findings suggest that the selection of curing temperature and consideration of salinity levels are critical in sustaining long-term bacterial healing performances in bacterial-based cementitious materials (Kim et al., 2020, Lowe et al., 1993, Ivaškė et al., 2023).

3 A PRELIMINARY STUDY

A preliminary study was conducted to assess the bacterial viability and self-healing performances of aged bacteria-based cementitious materials using different binder types. The binder types used in the study are ordinary Portland cement and calcium sulfoaluminate cement. The bacteria strain of *S. pasteurii* was employed due to its ureolysis capabilities and high biomineralization rate (Achal et al., 2009). The assessment of these binder systems was conducted by the means of pH measurements, microscopic examination of cracks, and analysis of nutrient concentrations in cultured media containing granulated samples. Further details regarding the test methodologies and results will be thoroughly elucidated in Kim et al. (2024).

4 CONCLUDING REMARKS

The present study comprehensively reviewed literature on the bacterial viability and self-healing performance of aged bacteria-based cementitious materials. Investigations into extending bacterial lifespan within cementitious materials involved examining various factors such as bacterial strain, carrier type, and curing conditions. The bacterial viability and self-healing performances declined with increasing curing age of the cementitious materials, showing insignificant changes according to different bacterial strain (Ivaškė et al., 2023, Shaheen et al., 2023). Meanwhile, the utilization of low-alkaline carriers and maintaining temperatures within the range of 20 to 30 ˚C notably enhanced self-healing performances during later stages (Wang et al., 2014, Zheng and Qian, 2020, Kim et al., 2020). Therefore, for the successful integration of bacteria as self-healing agents in SFT, the choice of low-alkaline carriers and

careful consideration of temperature conditions will be pivotal in ensuring the longevity and efficacy of bacteria-based cementitious materials. Moreover, the results of preliminary study showed the enhancement in bacterial viability and self-healing performances in later stages of curing by the use of calcium sulfoaluminate cement instead of ordinary Portland cement as a binder.

ACKNOWLEDGEMENT

This study was supported by a grant from the National Research Foundation (NRF) of Korean government (No.2021R1A2C3006382) funded by the Korean government.

REFERENCES

Achal, V., Mukherjee, A., Basu, P. & Reddy, M. S. 2009. Strain improvement of Sporosarcina pasteurii for enhanced urease and calcite production. *Journal of industrial Microbiology and Biotechnology*, 36, 981–988.

Henze, J. & Randall, D. G. 2018. Microbial induced calcium carbonate precipitation at elevated pH values (> 11) using Sporosarcina pasteurii. *Journal of Environmental Chemical Engineering*, 6, 5008–5013.

Iovane, G., Kim, H., Tizzano, D., Mazzolani, F. M., Landolfo, R., Park, S., Faggiano, B. & Lee, H. 2023. Cementitious materials with biological additive for enhanced durability in marine environment. *ce/papers*, 6, 251–257.

Ivaškė, A., Gribniak, V., Jakubovskis, R. & Urbonavičius, J. 2023. Bacterial Viability in Self-Healing Concrete: A Case Study of Non-Ureolytic Bacillus Species. *Microorganisms*, 11, 2402.

Justo-Reinoso, I., Heath, A., Gebhard, S. & Paine, K. 2021. Aerobic non-ureolytic bacteria-based self-healing cementitious composites: A comprehensive review. *Journal of Building Engineering*, 42, 102834.

Kim, H., Son, H., Park, S., Seo, J. & Lee, H.-K. 2020. Effects of temperature and salinity on concrete-surface treatment by bacteria in marine environment. *ACI Materials Journal*, 117, 57–65.

Kim, H., Son, H., Seo, J. & Lee, H.-K. 2021. Recent advances in microbial viability and self-healing performance in bacterial-based cementitious materials: A review. *Construction and Building Materials*, 274, 122094.

Kim, N., Cho, A. & Lee, H.-K. 2024. Microbial viability under binder type and microbial dosage of aged cementitious materials. *In preparation*.

Lowe, S. E., Jain, M. K. & Zeikus, J. G. 1993. Biology, ecology, and biotechnological applications of anaerobic bacteria adapted to environmental stresses in temperature, pH, salinity, or substrates. *Microbiological reviews*, 57, 451–509.

Membré, J.-M., Leporq, B., Vialette, M., Mettler, E., Perrier, L., Thuault, D. & Zwietering, M. 2005. Temperature effect on bacterial growth rate: quantitative microbiology approach including cardinal values and variability estimates to perform growth simulations on/in food. *International Journal of Food Microbiology*, 100, 179–186.

Shaheen, N., Khushnood, R. A., Memon, S. A. & Adnan, F. 2023. Feasibility assessment of newly isolated calcifying bacterial strains in self-healing concrete. *Construction and Building Materials*, 362, 129662.

Skevi, L., Reeksting, B., Gebhard, S. & Paine, K. Bacteria Based Self-healing of Later-Age Cracks in Concrete. International RILEM Conference on Early-age and Long-term Cracking in RC Structures, 2021. Springer, 367–376.

Vijay, K., Murmu, M. & Deo, S. V. 2017. Bacteria based self healing concrete–A review. *Construction and building materials*, 152, 1008–1014.

Wang, J., Snoeck, D., Van Vlierberghe, S., Verstraete, W. & De Belie, N. 2014. Application of hydrogel encapsulated carbonate precipitating bacteria for approaching a realistic self-healing in concrete. *Construction and building materials*, 68, 110–119.

Zhang, K., Xiang, Y. & Du, Y. 2010. Research on tubular segment design of submerged floating tunnel. *Procedia Engineering*, 4, 199–205.

Zheng, T. & Qian, C. 2020. Self-healing of later-age cracks in cement-based materials by encapsulation-based bacteria. *Journal of Materials in Civil Engineering*, 32, 04020341.

Bridge Maintenance, Safety, Management, Digitalization and Sustainability – Jensen, Frangopol & Schmidt (eds)
© 2024 The Author(s), ISBN 978-1-032-77040-6
Open Access: www.taylorfrancis.com, CC BY-NC-ND 4.0 license

Degradation prediction of FRP bars within concrete bridge decks in service

X.L. Zhao, Q. Zhao, I. Keitai, J.G. Dai & M.F. Kai
Department of Civil and Environmental Engineering, The Hong Kong Polytechnic University, Hong Kong, China

ABSTRACT: FRP bars are chemically anti-corrosive to chloride salts, and suitable to reinforce concrete structures in offshore and coastal regions. Some FRP bar-reinforced concrete structures have been in service for decades. As service time increases, FRP bar-reinforced concrete structures (FRPRC) will undergo degradations in different environments. The aim of this paper is to study the effects of service environments on the deterioration process of FRP bar-reinforced concrete structures. A fully coupled mesoscale physical-chemical-mechanical model was developed to simulate the ingress of moisture and carbon dioxide (CO_2) in concrete reinforced by FRP bars. The resultant effect of ingress on the mechanical deterioration of concrete was evaluated, such as carbonation depth and pH values. The predicted results were also compared and verified with field data after 15 years of service. In addition, the dominant factors from different service environments which degraded the FRP-concrete structures were discussed.

1 INTRODUCTION

The steel corrosion in concrete due to the use of deicing salts posed a severe safety risk to the bridges. As an alternative to steel reinforcement in concrete structures, fiber-reinforced polymer (FRP) bars are not sensitive to chloride salts, and they have been used to reinforce concrete in bridge decks since 1990s (Gooranorimi and Nanni 2017). Until now, many FRP-reinforced concrete structures have been in service for several decades. However, the long-term performance evaluations of these structures under natural atmospheric environments are rarely studied and reported.

To study the long-term performance of FRP bars, many accelerated experiments have been carried out by previous researchers, including exposure to wet-dry cycles, high relative humidity conditions, and immersion in water, seawater, acid and alkaline solutions (Chen et al. 2007; Wu et al. 2015; Zhao et al. 2021). However, these simulated conditions are usually much harsher than the actual service environments of FRP bars embedded in concrete. In other words, FRP bars in concrete will not degrade as fast as those exposed in these experiments. Thus, it is essential to propose an equation that can relate the accelerated data with the actual service life of FRP bars in concrete.

In this paper, the simulations of moisture ingress and CO_2 transport in concrete in the Sierrita de la Cruz Creek Bridge after 15 years of service were performed using the weather records in Amarillo, Texas, from 2000 to 2020. Firstly, the carbonation depth and pH were compared with the test data in the case study conducted by Gooranorimi and Nanni (Gooranorimi and Nanni 2017) to verify the accuracy of numerical simulations. Then, a relationship between the accelerated degradation rate in pore solution and the actual degradation rate of the relative humidity conditions in pores of concrete was proposed. Thus, the deterioration of GFRP bars embedded in concrete under a natural atmospheric environment can be evaluated by combining the chemical etching rate-based model with the moisture ingress and CO_2 transport in concrete cover.

DOI: 10.1201/9781003483755-54

2 MATERIALS AND SOFTWARE

Sierrita de la Cruz Creek Bridge was built in 2000, and it is located 40 km northwest of Amarillo, Texas (Phelan et al. 2003). The compressive strength of the concrete used in the bridge is 41.4 MPa. Two types of GFRP bars were used in the bridge. The DuCOM, an integrated coupled multi-scale platform (Maekawa et al. 2003a; b), was adopted to simulate the moisture and CO_2 ingress in concrete under the local atmospheric environment from 2000 to 2015.

3 MOISTURE INGRESS AND CO_2 TRANSPORT IN CONCRETE

The relative humidity (RH) in the pores of concrete structures varied with the atmospheric environment. The weather records from 2000 to 2015 in Amarillo, Texas, were collected. A concrete model with a size of 50 mm × 50 mm × 100 mm was built, as shown in Figure 1. Average temperatures and RHs per month from 2000 to 2015 in Amarillo, Texas, were used to carry out the moisture and CO_2 transport in the concrete bridge deck reinforced by GFRP bars. The time interval for simulation is 8 hours. The CO_2 concentration in the atmosphere was assumed to remain at 350 ppm. The RH and pH simulation results are illustrated in Figure 2 and Figure 3. The cracks due to traffic loading were not considered in the simulation.

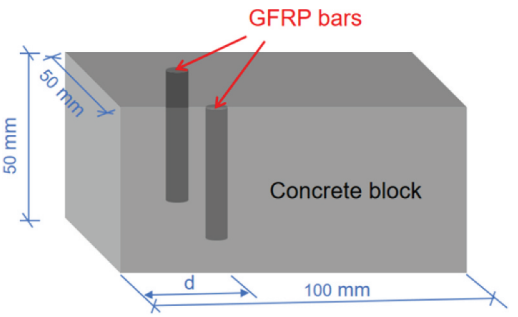


Figure 1. Size of concrete block for simulations.

From Figure 2, it can be observed that the RHs in concrete pores remained at 1.0 during the concrete casting and cement hydration period. However, the RHs in concrete pores fluctuatingly decreased to around 0.5 after 15 years of service. It is interesting to notice that the RHs of concrete pores near the surface are more likely to be affected by the atmosphere. The RH values of

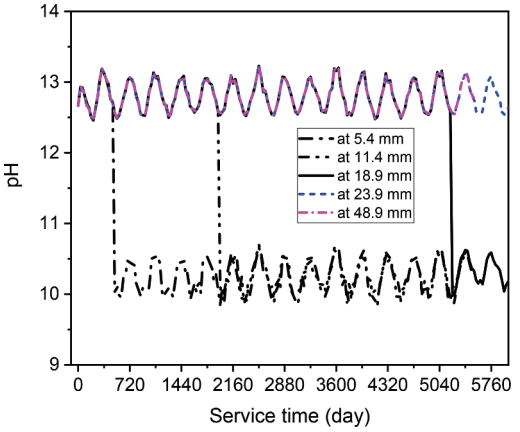


Figure 2. RH variations in concrete pores during service.

concrete pores near the concrete surface decreased much faster than those of internal pores in concrete. For instance, the RH at a depth of 5.4 mm decreased to 0.62, 0.56, and 0.64 after 30, 90 and 5400 days, respectively. By contrast, the RH values remained 0.98, 0.97, and 0.51 at a depth of 48.9 mm. In other words, the RHs near the concrete surface changed more quickly to the values approximate to those of the atmosphere than the internal parts of the concrete block, which is in accordance with the observed data.

CO_2 ingress has a significant effect on the pH values of concrete pore solution, as shown in Figure 3. The initial pH values of concrete pore solution remained around 13.0 after 28 days. As more CO_2 penetrated the concrete from the atmosphere, the pH values began to decrease, and carbonation occurred accordingly.

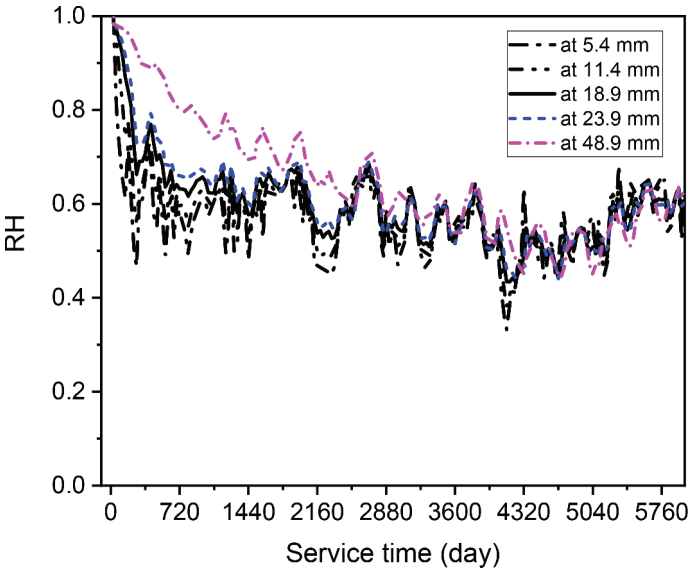


Figure 3. pH variations of concrete pore solution during service.

The pH values at five different points were compared, and their carbonation depths were evaluated after 15 years of service, as shown in Figure 4. After 540 days, the pH value at the depth of 5.4 mm decreased below 10.0. Thus, the maximum carbonation depth after 1.5 years of

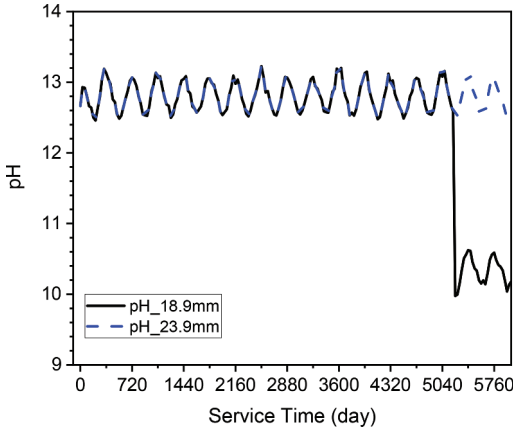


Figure 4. Carbonation evolution with service time.

service should be 5.4 mm. Similarly, the maximum carbonation depths after 2010 and 5220 days (5.8 and 14.5 years) of service reached 11.4 and 18.9 mm, respectively. According to the case study by Gooranorimi and Nanni (Gooranorimi and Nanni 2017), irregular carbonation fronts were observed in three tested samples after 15 years of service, varying between 25 and 32 mm. Considering the fact that the cracks due to traffic loads and the imperfections in construction were not considered in this simulation, the carbonation predictions are still valuable and reasonable, and these results can be referenced by engineers and maintainers for public infrastructures.

4 DEGRADATION MODEL OF FRP BARS IN SERVICE

4.1 *Gas-liquid environment shift equation*

Considering the contact probability of water molecules with FRP bars, the degradation rate of FRP bars in air at a given relative humidity (RH) can be related to that exposed in the pore solutions through Equation (1).

$$v_{RH} = v_{sol} \times \frac{\rho_{sat}}{\rho_{liq}} \times F_{gls} \times RH \tag{1}$$

where v_{RH} denotes the degradation rate in RH conditions; v_{sol} denotes the degradation rate of GFRP bars exposed in solution; ρ_{liq} is the density of the liquid solution and ρ_{sat} is the maximum vapor water content in the unit volume of air at a given temperature; F_{gls} is the reaction participation ratio considering the different states of vapor and liquid water.

4.2 *Chemical etching rate-based model*

The chemical etching rate-based model (CEM) proposed by Zhao et al. (Zhao et al. 2021, 2022) can be summarized below, as shown in Equations (2) ~ (4):

$$v_{sol} = r_{sf_m} V_m + r_{sf_f} V_f \tag{2}$$

$$R_{dg} = \int_0^t v dt \tag{3}$$

$$f_t = \frac{\left[R_0 - \left(A_1 e^{\frac{-E_{a_m}}{RT}} \times \frac{1}{N} \times V_m + A_2 e^{\frac{-E_{a_f}}{RT}} \times V_f\right) \times c[OH^-] \times t\right]^2}{{R_0}^2} f_0 \tag{4}$$

$$c[OH^-] = 10^{pH-14} \tag{5}$$

where v denotes the normal etching rate to GFRP bars exposed to pore solution. r_{sf_m} and r_{sf_f} are the reaction rates of hydrolysis of the matrix and the etching to glass fibers, respectively. V_f and V_m are molar volumes of fibers and matrix. $c[OH^-]$ denotes the concentration of hydroxyl ions. A_1 and A_2 are the pre-exponential factors of matrix and glass fiber, respectively. E_{a_m} and E_{a_f} are the active energy of matrix and glass fiber. N is the number of ester groups in the unit element of the matrix. f_t and f_0 are the residual tensile strength and initial tensile strength of GFRP bars. R_0 and R_{dg} are the bar diameter and degradation depth.

4.3 *Degradation of GFRP bars in concrete*

Based on the CEM and the proposed formula in Equation (1), the degradation of GFRP bars in concrete during service can be evaluated. The predicted degradation depths of GFRP bars are plotted against service time in Figure 5. Here, the saturated water vapor content is around 30 grams at 25ºC, while the water density is 1000 kg/m^3. The gas-liquid shift factor F_{gls} was taken as 1000 in the simulation, further research is needed to determine more accurate F_{gls}.

The degradation of GFRP bars in concrete is very minor after 15 years of service, with a degradation depth of 0.0135 and 0.0142 mm at the depth of 18.9 and 23.9 mm from the surface. It means that the tensile strength retentions of GFRP bars at the two positions are 99.7% and 99.6% after 15 years. The extracted GFRP samples showed that almost no degradation occurred. The simulation results agree well with the field data. It should be noted that carbonation is beneficial to GFRP bars in concrete because the pH values of the pore solution after carbonation will decrease (Zhao et al. 2021).

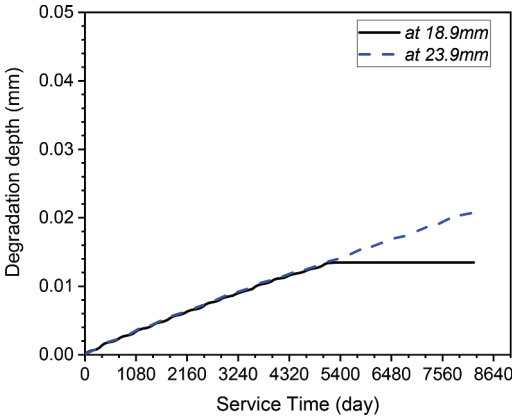


Figure 5. Degradation depth of GFRP bars during service.

5 CONCLUSION

The paper provided a degradation modeling of GFRP bars in service. Based on the chemical etching model and gas-liquid environment formula and the moisture and CO_2 ingress in concrete, the degradation of GFRP bars in the Sierrita de la Cruz Creek Bridge was evaluated during the service using local weather records from 2000 and 2015. Some conclusions can be drawn as follows.

- The distributions of moisture (RH) and pH values in concrete during service were provided using the DuCOM, and then the pH values and carbonation depth were compared and verified with field data.
- A gas-liquid environment shift equation was proposed to relate the accelerated degradation rate in solution and the normal degradation rate in air.
- The degradation of GFRP bars in concrete was predicted during the service period from 2000 to 2015. The simulation results agreed well with the test data from the extracted GFRP samples after 15 years of service.

ACKNOWLEDGEMENTS

The authors want to express our sincere appreciation to Dr. Sandra Rayne from the Climate Sciences and Services Division of NOAA's National Centers for Environmental Information for her kind guidance to help us obtain the weather records in Amarillo, Texas from 2000 to 2022.

REFERENCES

Chen, Y., J. F. Davalos, I. Ray, and H. Y. Kim. 2007. "Accelerated aging tests for evaluations of durability performance of FRP reinforcing bars for concrete structures." *Compos. Struct.*, 78 (1): 101–111. https://doi.org/10.1016/j.compstruct.2005.08.015.

Gooranorimi, O., and A. Nanni. 2017. "GFRP Reinforcement in Concrete after 15 Years of Service." *J. Compos. Constr.*, 21 (5): 04017024. https://doi.org/10.1061/(asce)cc.1943-5614.0000806.

Maekawa, K., T. Ishida, and T. Kishi. 2003a. "Multi-scale Modeling of Concrete Performance." *J. Adv. Concr. Technol.*, 1 (2): 91–126. https://doi.org/10.3151/jact.1.91.

Maekawa, K., A. Pimanmas, and H. Okamura. 2003b. *Nonlinear Mechanics of Reinforced Concrete*. CRC Press.

Phelan, R. S., W. P. Vann, and J. Bice. 2003. *FRP reinforcement bars in bridge decks Field instrumentation and short-term monitoring*. Lubbock, TX.

Wu, G., Z.-Q. Dong, X. Wang, Y. Zhu, and Z.-S. Wu. 2015. "Prediction of Long-Term Performance and Durability of BFRP Bars under the Combined Effect of Sustained Load and Corrosive Solutions." *J. Compos. Constr.*, 19 (3): 04014058. https://doi.org/10.1061/(asce)cc.1943-5614.0000517.

Zhao, Q., D. Zhang, X.-L. Zhao, and S. Sharma. 2021. "Modelling damage evolution of carbon fiber-reinforced epoxy polymer composites in seawater sea sand concrete environment." *Compos. Sci. Technol.*, 108961. https://doi.org/10.1016/j.compscitech.2021.108961.

Zhao, Q., D. Zhang, X. Zhao, and W. Wang. 2022. "Experimental and modelling studies on damage evolution of epoxy-based GFRP bars in pore solution environment of seawater sea-sand concrete." *China Civ. Eng. J.*, 55 (9): 25–41. https://doi.org/10.15951/j.tmgcxb.21080781.

Bridge Maintenance, Safety, Management, Digitalization and Sustainability – Jensen, Frangopol & Schmidt (eds)
© 2024 The Author(s), ISBN 978-1-032-77040-6
Open Access: www.taylorfrancis.com, CC BY-NC-ND 4.0 license

Load-bearing capacity assessment of RC beams using corrosion crack widths

Takehiro Adachi, Mitsuyoshi Akiyama, Taiki Yamada, Satoru Nakamura & Zhejun Xu
Waseda University, Tokyo, Japan

Dan M. Frangopol
Lehigh University, Bethlehem, PA, USA

ABSTRACT: In chloride-laden environment, steel corrosion in RC members leads to their structural performance deterioration. Inspection methods using unmanned aerial vehicle (UAV) have attracted attention as an alternative method of classical visual inspection. Corrosion crack width detected by UAV could be an effective information to evaluate the structural condition. However, since the relationship between steel corrosion and crack widths is complex and uncertain due to associated parameters such as structural details, this observational information has not been used to evaluate the structural performance of in-situ concrete structures. In this study, the load-bearing capacity of deteriorated RC members is probabilistically evaluated using the observational corrosion cracks obtained by UAV, in addition to finite element analysis, stochastic field theory, and machine learning. A case study is presented to investigate the effect of the different measurement method of corrosion crack widths between UAV shooting and close-up shooting with digital camera on the load-bearing capacity.

1 INTRODUCTION

For reinforced concrete (RC) members located in a chloride-laden environment, corrosion of steel bars causes cover concrete cracking and structural performance degradation. Quantitative assessment of the structural performance of deteriorated RC structures is of great importance in maintenance. However, it is difficult to confirm the corrosion status of steel bars inside RC members directly using nondestructive detection techniques. Since corrosion-induced cracks are caused due to expansion pressure from corrosion products, they could be useful information for estimating steel weight loss inside the RC members. However, predicting the structural performance based on crack information remains challenging due to the uncertain nonlinear relationship between steel corrosion and corrosion cracks (Lim et al. 2017). Zhang et al. (2021) and Srivaranun et al. (2023) presented a probabilistic framework for estimating the load-bearing capacity of deteriorated RC members with the corrosion crack width distribution, using machine learning, stochastic simulation, nonlinear finite element analysis (Non-FEA) and Monte Carlo simulation (MCS). In their framework, the database for training machine learning models was developed numerically as a relationship between corrosion crack width and steel weight loss. In order to apply their framework of load-bearing capacity assessment to on-site corroded concrete structures, it is necessary to develop techniques for obtaining corrosion cracks.

Recently, images taken by Unmanned Aerial Vehicles (UAVs) have been utilized for crack detection of concrete structures (Ding et al. 2023). However, it is not yet widely used for structural capacity assessment. Figure 1 shows a proposed probabilistic framework for estimating the load-bearing capacity of corroded RC members using observational information of corrosion

DOI: 10.1201/9781003483755-55

cracks obtained by UAV. In addition to the application of UAVs, a database of the relationship between corrosion crack width and corrosion product thickness for training the machine learning model is developed in this study. To ensure that the numerical database can reflect the information obtained from the actual corroded RC beams, a new corrosion expansion model considering the difference in corrosive conditions is presented. After obtaining the corrosion crack distributions by remote shooting by UAV, the load-bearing capacity of deteriorated RC beams is finally estimated by utilizing the machine learning model and MCS-based FEA.

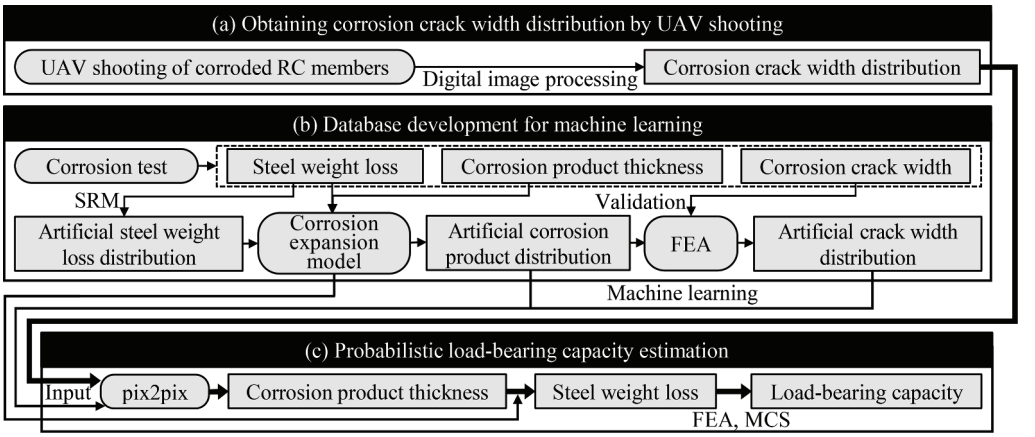


Figure 1. Probabilistic framework for estimating the load-bearing capacity of corroded RC beams using observational information on corrosion cracks obtained by UAV.

2 MEASUREMENTS OF CORROSION CRACK WIDTHS WITH UAV

2.1 *Accelerated corrosion test*

To simulate the inspection of deteriorating concrete structures using UAVs, large-scale RC beams are cast and corroded by the galvanostatic (GS) method. Table 1 shows details of the RC beam. The specimen has a cross-section of 370 mm × 450 mm and a length of 6,000 mm. Three tensile rebars, referred to as L, C, and R (left, center, and right, respectively), are arranged. In the corrosion test, the direct current (i.e., 500 $\mu A/cm^2$) is applied only to the specified corrosion region (2,800 mm ~ 3,200 mm from the left end of the RC beam, same as the pure bending region) by placing a water-absorbing sponge immersed in the 3% NaCl solution under the RC beam.

After the loading test, the steel weight loss of the tensile rebars removed from the RC beam is measured at 10 mm intervals in the longitudinal direction of the corrosion region in the RC beam using digital calipers. Figure 2 shows the steel weight loss distribution.

2.2 *Measurement of corrosion crack width with UAV and close-up shooting*

After the completion of the corrosion test, UAVs are used to take a picture of corrosion cracks on the bottom surface of the RC beam. Close-up shooting with a digital camera is also conducted to compare the measurement accuracy of the corrosion crack width. Table 2 shows the performance of the camera used in each shooting method. The UAV navigates longitudinally beneath the specimen with its camera lens pointing vertically upward. The shooting distance is approximately 0.45 m. Figure 3 shows corrosion crack width distributions and corresponding images obtained by each shooting method. The corrosion crack widths were measured with 10 mm intervals using digital image processing.

Table 1. Structural details and corrosive conditions of the large-scale RC beam.

Beam	Cover (mm)	Rebar spacing (mm)	Rebar diameter	Stirrup (mm)	Compressive strength (28 days) (MPa)	Target maximum corrosion crack width (mm)
A-1	20	95	DB19	DB10@200	41.7	0.3 ~ 0.6

Table 2. Performance of cameras.

Shooting method	UAV shooting	Close-up shooting
Sensor	1/2.3 inch	1/2.93 inch
Sensor size	6.2 mm × 4.7 mm	4.8 mm × 3.6 mm
Image resolution	3040 × 4056	3024 × 4032
Focal length*	23	28
F-number	f/2.8	f/1.8

*Focal length represents 35mm equivalent focal length.

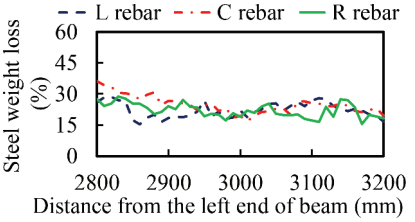


Figure 2. Steel weight loss distribution.

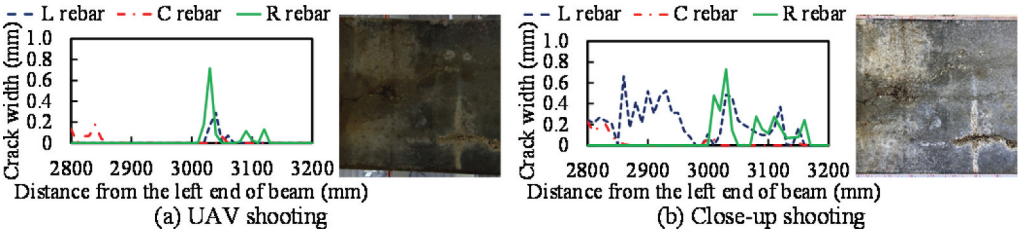


Figure 3. Corrosion crack width distribution and corrosion crack images.

2.3 *Effect of shooting method*

The effects of each shooting method on the measurement accuracy of corrosion crack width are compared. As a benchmark of the measurement, the number of pixels corresponding to corrosion cracks measured manually at certain intervals in the longitudinal direction were converted to the corrosion crack width.

Table 3 shows a comparison of the mean values of corrosion crack widths. Despite the same degree of image resolution, the corrosion crack width obtained by the UAV shooting was smaller than that obtained by the close-up shooting. Possible reasons include: 1) UAVs photographed the bottom of the specimen, which was not illuminated; and 2) the stability of UAV was disturbed by the wind reflected from the bottom of the specimen, which resulted in a blurred image. Therefore, when image processing of the crack images taken by the UAV is performed, it will be difficult to obtain the corrosion crack width from a concrete surface contaminated with rust fluid.

Table 3. Comparison between mean corrosion crack widths obtained by two shooting methods and correct value.

	Mean corrosion crack widths		
Beam	Correct value (mm)	UAV shooting (mm)	Close-up shooting (Digital image processing) (mm)
A-1	0.132	0.019	0.100

3 DEVELOPMENT OF NUMERICAL DATABASE FOR MACHINE LEARNING

3.1 *Modeling of corrosion product*

For reproducing the characteristics of corrosion-induced crack width distributions, a new model of steel corrosion product is developed in this study using the test specimens listed in Table 4 (Nakamura et al. 2022). The specimen had a cross-section of 300 mm × 160 mm and a length of 1460 mm. Three tensile rebars were arranged and exposed to the accelerated corrosion.

The corrosion expansion model is proposed considering the effect of current density. To develop a corrosion expansion model, corrosion product thickness is obtained every 5 mm in the longitudinal direction and every 30° within the cross-section using X-ray photography and digital image processing. The corrosion product thickness *Tcp* is modeled and expressed by:

Table 4. Structural details of the RC beams for developing the model of steel corrosion product.

Beam	Cover (mm)	Rebar spacing (mm)	Rebar diameter	Stirrup (mm)	Current density ($\mu A/cm^2$)	Compressive strength (28 days) (MPa)
B	20	95	DB13	DB6@100	100	45.0
C	20	57	DB13	DB6@100	500	47.8
D	20	57	DB19	DB6@100	100	45.7
E	20	95	DB13	DB6@50	100	46.6
F	20	57	DB13	DB6@100	100	44.9

$$Tcp = \alpha(\theta) \times MTcp_l \tag{1}$$

$$\alpha(\theta) = 1.884 \times \exp[-\{(\theta - 180)/91.69\}^2] + 0.1241 \tag{2}$$

$$MTcp_l = n \times (R - R') \tag{3}$$

$$n = \left\{(R + R')/R^2\right\} \times (2.873 - 2.372 \times 10^{-3} I_{corr}) \tag{4}$$

where R (mm) and R' (mm) are the rebar diameters before and after the corrosion test, respectively. α is the angle parameter representing the shape of corrosion products, which typically accumulate predominantly on the bottom of the RC beams. $MTcp_l$ (mm) is the mean value of corrosion products per cross-section. The constant n depends on the corrosive environments.

3.2 *Stochastic simulation of steel weight loss*

Based on the steel weight loss distributions inside the RC beams shown in Table 4, stochastic parameters for the spectral representation method (SRM) are derived (Srivaranun et al. 2021). In his stochastic simulation, the spatial correlation of steel weight loss distributions in the longitudinal and transverse directions are represented by the auto-spectral density function (auto-SDF) and the coherence function, respectively.

3.3 *Development of database*

Figure 4 Shows a procedure to obtain the relationship between distributions of steel weight loss and corrosion crack width. From the steel weight loss distribution simulated by SRM, corrosion product thickness is determined and provided as imposed displacement at the location of tensile rebars in the Non-FEA for obtaining the corresponding corrosion crack width.

4 PREDICTION OF CORROSION DISTRIBUTION USING MACHINE LEARNING

Using the database developed in Section 3, a machine learning model is constructed to predict the corrosion product distribution from corrosion crack width distribution. The pix2pix model is

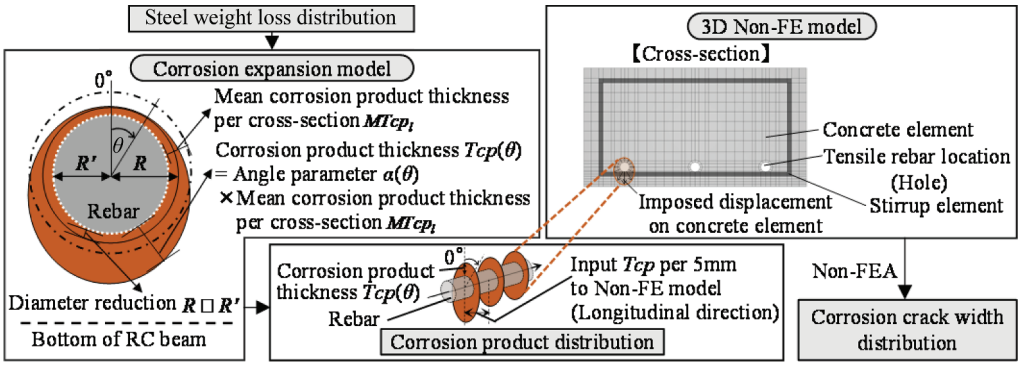


Figure 4. Application of corrosion expansion model to Non-FE model.

selected in this study to consider the two-dimensional spatial variability of the steel weight loss. To construct the pix2pix model, corrosion crack width distributions and corrosion product distributions with 41 values (10 mm interval) per rebar and the structural details (i.e., rebar diameter and rebar spacing) are linearly converted to a luminance value (0 to 255), respectively. Then, 8-bit color images with corrosion crack width distributions and structural details are given as R, G, and B channels, respectively, and the 8-bit grayscale images of the corrosion product distributions can be generated. In the estimation of corrosion product distribution from corrosion crack width distribution using pix2pix, the epoch number is set to 50 and 240 images are used for training.

The model error ε_{test} associated with pix2pix is quantified as the difference between the testing data and predicted results of steel weight loss. The details of pix2pix and corresponding model error quantification are provided in Srivaranun et al. (2023).

5 CASE STUDY: PROBABILISTIC ESTIMATION OF LOAD-BEARING CAPACITY OF CORRODED RC BEAMS USING MCS

5.1 *Corrosion crack information for load-bearing capacity assessment*

As the case study, the corrosion crack width distributions of the large-scale RC beam shown in Table 1, obtained by UAV shooting and close-up shooting, are used in the pix2pix model to predict the steel weight loss distribution. Since there is a difference in load-bearing capacity between the experimental and 3D Non-FE results, the model error ε_{FE} associated with 3D Non-FEA is quantified using the previous loading test results. ε_{FE} is assumed to follow a normal distribution. Considering the pix2pix model error ε_{test} and the Non-FE model error ε_{FE}, Monte Carlo-based Non-FEA is performed to obtain the load-bearing capacity.

5.2 *Results and discussion*

Figure 5 shows a comparison of the yield load between the experimental and computational results of the A-1 specimen. In the case of close-up shooting, the experimental yield load is located near the mean value of the estimated probability density function (PDF). With the estimation results by UAV shooting, the assessed PDF of flexure capacity was overestimated compared to the loading test result. This result suggests that the measurement accuracy of corrosion crack width has a significant impact on the estimation of the load-bearing capacity of deteriorated RC structures.

The minimum visible scale width which was obtained by using the crack scale attached to the bottom of the RC beam, depends significantly on the shooting method; the minimum visible scale width was 0.05 mm for close-up shooting and 0.20 mm for UAV shooting. In order to estimate the load-bearing capacity of deteriorated RC structures with sufficient accuracy using UAV shooting, the quality of the image is should be equivalent to that of the close-up image.

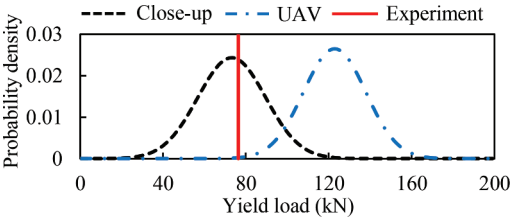


Figure 5. Experimental result and estimated probability density functions of yield load.

6 CONCLUSIONS

1. A framework, which consists of digital image processing, machine learning, stochastic field theory, nonlinear finite element analysis, and Monte Carlo simulation, was proposed to calculate the PDF of the load-bearing capacity of corroded RC members based on images of corrosion cracks taken by a UAV.
2. A database for pix2pix machine learning model to predict steel weight loss from corrosion crack width was developed using a proposed corrosion expansion model.
3. The quality of corrosion crack images required for load-bearing capacity assessment of corroded RC members was discussed. It is clarified that the images which can capture the crack width of 0.05 mm is required for the UAV inspection of the deteriorating concrete structures.

ACKNOWLEDGEMENTS

This research was supported by a research grant from Japan Construction Information Center (JACIC).

REFERENCES

Ding, W., Yang, H., Yu, K., and Shu, J.: Crack detection and quantification for concrete structures using UAV and transformer, *Automation in Construction*, 152: 104929, 2023.

Lim, S., Akiyama, M., Frangopol, D.M. and Jiang, H.: Experimental investigation of the spatial variability of the steel weight loss and corrosion cracking of RC members: Novel X-ray and digital image processing techniques, *Structure and Infrastructure Engineering*, 13(1): 118–134, 2017.

Nakamura, S., Yamada, T., Shintani, M., Surivaranun, S., Akiyama, M.: Database improvement for machine learning and application to structural capacity estimation of deteriorated RC members using observational corrosion crack distributions, *Informatics and Infrastructure*, 3 (J2), 117–127, 2022. (in Japanese)

Srivaranun, S., Akiyama, M., Bocchini, P., Christou, V., Frangopol, D.M., Fukushima, H. and Masuda, K.: Effect of the interaction of corrosion pits among multiple tensile rebars on the reliability of RC structures: Experimental and numerical investigation, *Structural Safety*, 93: 102115, 2021.

Srivaranun, S., Akiyama, M., Taiki, Y., Frangopol, D.M., and Xin, J.: A novel combined experimental-machine learning approach to estimate the probabilistic capacity of RC beams with spatially correlated rebar corrosion in transverse and longitudinal directions, *Engineering Structures*, 279: 115588, 2023.

Zhang, M., Akiyama, M., Shintani, M., Xin, J. and Frangopol, D.M.: Probabilistic estimation of flexural loading capacity of existing RC structures based on observational corrosion-induced crack width distribution using machine learning, *Structural Safety*, 91: 102098, 2021.

Bridge Maintenance, Safety, Management, Digitalization and Sustainability – Jensen, Frangopol & Schmidt (eds)
© 2024 The Author(s), ISBN 978-1-032-77040-6
Open Access: www.taylorfrancis.com, CC BY-NC-ND 4.0 license

Probabilistic structural identification using time-dependent deflection of prestressed concrete bridges

Siyi Jia & Mitsuyoshi Akiyama
Waseda University, Tokyo, Japan

Dan. M. Frangopol
Lehigh University, Bethlehem, PA, USA

ABSTRACT: This paper presents a probabilistic structural identification (SI) framework using the time-dependent deflection of prestressed concrete bridges (PSCBs). The framework involves a stochastic volatile model (SVM) that considers the full ranges of the unobserved state variables affecting the time-dependent deflection of PSCBs, namely, structural rigidity, creep, shrinkage, prestress level and dead load level, along with the volatility parameters associated with the deterioration path of structural rigidity, which is modeled via the Wiener process. Exploiting the latent structure of the SVM, a cyclic Markov chain Monte Carlo sampler is proposed to draw samples from the joint posterior distribution of the unobserved state variables and volatility parameters. In an illustrative example, deflection measurements of an existing bridge are used as the target information for SI. The updated model can reveal the accumulated damage of the case bridge over the monitoring period.

1 INTRODUCTION

The time-dependent deflection of prestressed concrete bridges (PSCBs) features low-cost acquisition and contains low-entropy evidence about multiple structural states, including damage accumulation, creep and shrinkage behaviors of concrete. Structural identification (SI) using the time-dependent deflection is of practical importance for PSCBs, because it avoids the calibration of mass and damping ratio as required in vibration-based SI (Buda and Caddemi, 2007). Previous studies on SI using the time-dependent deflection of bridges have been primarily output-only analyses that focus on discerning anomalous data outside of expected bounds (Hedegaard et al., 2017; Reynders et al., 2013). However, output-only damage detection is subject to large uncertainties due to changing environmental conditions and time-dependent material behaviors such as creep and shrinkage, which can mask subtle changes in damage (Hedegaard et al., 2017). Therefore, more reliable SI conditioned on time-dependent deflection requires a model-based inverse analysis that is anchored on mechanical models. On the other hand, the uncertainties in the time-dependencies of state variables associated with time-dependent deflection are rarely considered in the previous studies. It is necessary to consider these uncertainties since the time-dependencies of state variables can vary significantly with changing environments. By modelling the stochastic time-dependencies of state variables, the inverse analysis conditioned on time-dependent deflection is converted to a stochastic volatility model (SVM), in which both the unobserved state variables and their time-dependencies are subject to inference (Jacquire et al., 1994).

This paper presents a probabilistic SI framework for an SVM conditioned on the time-dependent deflection of PSCBs. As illustrated in Figure 1, the SI considers the full ranges of the unobserved state variables affecting the time-dependent deflection of PSCBs, namely, structural rigidity, creep, shrinkage, prestress level and dead load level, along with the volatility parameters associated with the deterioration path of structural rigidity, which is modeled

DOI: 10.1201/9781003483755-56

by the Wiener process. A rate-type time-dependent finite element model (FEM) is constructed considering the effects of the state variables. In view of the latent structure of the SVM, a cyclic Markov chain Monte Carlo (CMCMC) sampler is proposed to draw samples from the joint posterior distribution of the unobserved state variables and volatility parameters. As an illustrative example, the proposed framework is applied to the SI of an existing PSCB.

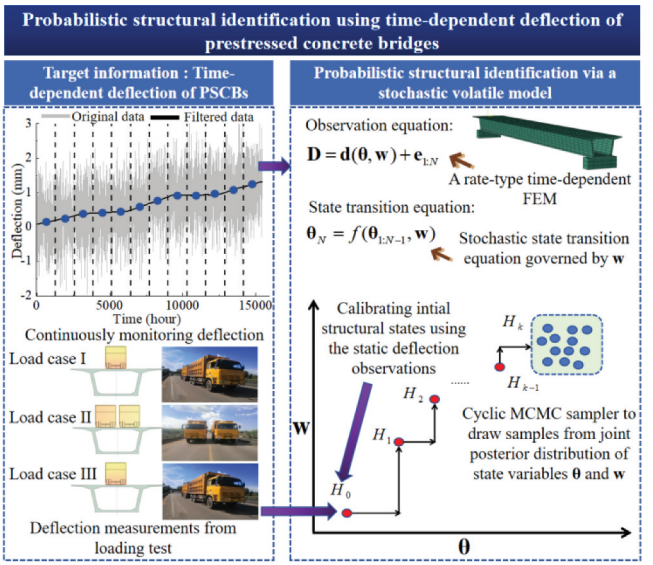


Figure 1. Flowchart of probabilistic structural identification of PSCBs.

2 METHOD

2.1 *Inference Frame of the SVM*

The SVM involves an observation equation that links the deflection measurements $\mathbf{D}_{1:N}$ from time 1 to time N with the unobserved time series of state variables $\boldsymbol{\theta}_{1:N}$:

$$\mathbf{D}_{1:N} = \mathbf{d}(\theta_{1:N}, \mathbf{w}) + \mathbf{e}_{1:N} \tag{1}$$

where $\mathbf{d}$ denotes the time-dependent deflection of the PSCB as computed using a physical model. $\mathbf{e}_{1:N}$ is the error term that follows a normal probability distribution N(0, σ). σ is the standard deviation of the model. The stochastic transition density of $\boldsymbol{\theta}$ is determined by a stochastic hyperparameter vector $\mathbf{w}$:

$$\boldsymbol{\theta}_N = f(\boldsymbol{\theta}_{1:N-1}, \mathbf{w}) \tag{2}$$

The joint posterior distribution of $\boldsymbol{\theta}_{1:N}$ and $\mathbf{w}$ conditioned on $\mathbf{D}_{1:N}$ is provided by Bayes theorem (Jacquire et al., 1994):

$$p(\boldsymbol{\theta}_{1:N}, \mathbf{w}|\mathbf{D}_{1:N}) = \frac{L(\mathbf{D}_{1:N}|\boldsymbol{\theta}_{1:N}, \mathbf{w})p(\boldsymbol{\theta}_{1:N}|\mathbf{w})p(\mathbf{w})}{\int L(\mathbf{D}_{1:N}|\boldsymbol{\theta}_{1:N}, \mathbf{w})p(\boldsymbol{\theta}_{1:N}|\mathbf{w})p(\mathbf{w})d\mathbf{w}} \tag{3}$$

where $p(\mathbf{w})$ is the prior probability density of $\mathbf{w}$. $p(\boldsymbol{\theta}_{1:N}|\mathbf{w})$ is the prior distribution of $\boldsymbol{\theta}$ given a deterioration path defined by $\mathbf{w}$. L denotes the likelihood function, which can be formulated as a Gaussian density of the error term $\mathbf{e}$.

2.2 *State variables and their time-dependencies*

Time-dependent deflection of PSCBs is initiated by the dead loads that are not offset by the prestress, which are magnified by the creep effects of concrete. Shrinkage and damage accumulation also contribute to the time-dependent deflection. Accordingly, $\boldsymbol{\theta} = (\theta_{cr}, \theta_{sh}, \theta_q, \theta_{ps}, \theta_e)^T$ in which θ_{cr} and θ_{sh} represent the ratios between the actual creep compliance J and shrinkage strain ε_{sh}, with respect to those computed from prescribed by the B3 model, denoted as J_0 and $\varepsilon_{sh,0}$, respectively (Bažant and Baweja, 1995):

$$J = \theta_{cr} J_0, \varepsilon_{sh} = \theta_{sh} \varepsilon_{sh,0} \tag{4}$$

Similarly, θ_q, θ_{ps} denote the ratios between actual dead load p_q and prestress p_{ps} of PSCBs, with respect to their designed values $p_{q,0}$ and $p_{ps,0}$, respectively:

$$p_q = \theta_q p_{q,0}, p_{ps} = \theta_{ps} p_{ps0} \tag{5}$$

θ_e represents the reduction in structural rigidity, which is characterized in terms of the reduction of the global stiffness matrix $\mathbf{k}_e$ (Cheung and Beck, 2009):

$$\mathbf{k}_e = \theta_e \mathbf{k}_e{}^0 \tag{6}$$

where $\mathbf{k}_e{}^\circ$ is the nominal global stiffness matrix calculated based on the design values of material elasticity and structural geometry.

For aging PSCBs, the statistics of $\boldsymbol{\theta}$ need to be re-calibrated because they can largely deviate from their prior distributions. Specifically, $\boldsymbol{\theta}_0 = (\theta_{cr,0}, \theta_{sh,0}, \theta_{q,0}, \theta_{ps,0}, \theta_{e,0})^T$ is calibrated using the static deflection measurement $\mathbf{D}_0$ before the continuous monitoring:

$$p_0(\boldsymbol{\theta}_0) = \frac{L(D_0|\boldsymbol{\theta}_0) p(\boldsymbol{\theta}_0)}{\int L(D_0|\boldsymbol{\theta}_0) p(\boldsymbol{\theta}_0) d\boldsymbol{\theta}_0} = c_0{}^{-1} L(D_0|\boldsymbol{\theta}_0) p(\boldsymbol{\theta}_0) \tag{7}$$

The calibrated statistics of θ_{cr}, θ_{sh}, θ_q and θ_{ps} are assumed to remain time-invariant, while the time-dependency of $\boldsymbol{\theta}_e$ should be considered and calibrated by the continuously monitoring deflection data, due to the accumulation of structural damage. In this paper, the decrement in structural rigidity over a time increment Δt, $\Delta\theta_e(t) = \theta_e(t+\Delta t) - \theta_e(t)$, is assumed to be independent of $\theta_e(t)$ and modeled as a Gaussian variable:

$$\Delta\theta_e(t) \sim \mathrm{N}(\beta \Delta\Lambda(t), \alpha^2 \Delta\Lambda(t)) \tag{8}$$

where β and α denote the mean and standard deviation, respectively, of each increment. $\Delta\Lambda(t) = \Lambda(t+\Delta t) - \Lambda(t)$ is the increment in a monotonically increasing function of time $\Lambda(t) = t^q$ (Peng et al., 2014), where q is the exponential factor.

2.3 *Rate-type time-dependent FEM*

A step-by-step time-dependent FEM is constructed to compute $\mathbf{d}$ in Equation (1), which reduces the time-dependent computation to a sequence of elastic analyses based on the creep increment in each time step (Jia et al., 2023). To remove the dependencies among creep increments and the history stress in previous time steps, a rate-type formulation is adopted, in which the creep compliance J at time τ is approximated by an m-order Dirichlet series

$$J(\tau, t') = \sum_{l=1}^{m} a_l(t') [1 - e^{-\kappa_l(\tau - t')}] \tag{9}$$

where $\boldsymbol{\kappa}_l$ is the exponent associated with the l-th Dirichlet basis. t' is the age of loading. The undetermined parameters a are calibrated based on the observed creep/shrinkage curve. The time-dependent FEM is processed in ABAQUS using users' subroutines USDFLD and

EXPAN, which convert the creep and shrinkage increments at each time-step into the thermal strain applied to the concrete. Detailed formulations of the time-dependent FEM can be found in Jia et al. (2023).

A Kriging surrogate model of the time-dependent FEM is built to improve the computation efficiency for the samplers, in which $\mathbf{d}$ is modeled as a Gauss process determined by input $\boldsymbol{\theta}$, centered on the best linear unbiased estimate $\mu_d(\boldsymbol{\theta})$, with variance $\sigma^2{}_d(\boldsymbol{\theta})$ (Santner et al., 2003)

$$\mathbf{d}(\boldsymbol{\theta}) \sim \mathrm{N}(\mu_d(\boldsymbol{\theta}), \sigma^2{}_d(\boldsymbol{\theta})) \tag{10}$$

2.4 *Samplers for the posterior distribution*

The analytical solution for the joint posterior distribution $p(\mathbf{w}, \boldsymbol{\theta}_{1:N} | \mathbf{D}_{1:N})$ in Equation (3) is generally intractable. Alternatively, a sampler is constructed to draw samples from $p(\mathbf{w}, \boldsymbol{\theta}_{1:N} | \mathbf{D}_{1:N})$, and the samples are used to approximate the statistics of the distribution. Considering that the conditional distributions between $\boldsymbol{\theta}_{1:N}$ and $\mathbf{w}$ are readily available, a CMCMC sampler is designed as a Gibbs-type sampler that alternatively draws samples from $\boldsymbol{\theta}_{1:N}$ and $\mathbf{w}$ in the augmented state space $(\boldsymbol{\theta}_{1:N}, \mathbf{w}) \in H$ (Jacquire et al., 1994).

As illustrated in Figure 2, the CMCMC sampler starts at the point H_0 $(\boldsymbol{\theta}_0, \mathbf{w}_0)$, which is obtained by the Bayesian inference in Equation (7). Each step of the Markov chain involves alternating sampling from the two conditional densities $p(\boldsymbol{\theta}_{1:N}|\mathbf{w}, \mathbf{D}_{1:N})$ and $p(\mathbf{w}|\boldsymbol{\theta}_{1:N}, \mathbf{D}_{1:N})$, which are derived through Bayesian inference conditioned on the deflection measurements $\mathbf{D}_{1:N}$:

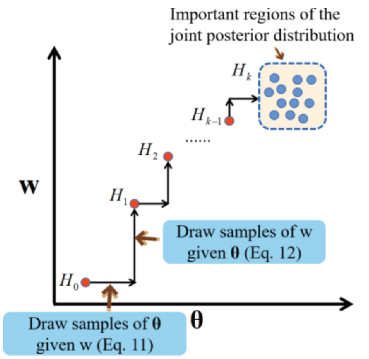


Figure 2. Flowchart of the CMCMC sampler.

$$p(\boldsymbol{\theta}_{1:N}|\mathbf{w}, \mathbf{D}_{1:N}) \propto L(\mathbf{D}_{1:N}|\mathbf{w}, \boldsymbol{\theta}_{1:N}) p(\boldsymbol{\theta}_{1:N}|\mathbf{w}) \tag{11}$$

$$p(\mathbf{w}|\boldsymbol{\theta}_{1:N}, \mathbf{D}_{1:N}) \propto L(\mathbf{D}_{1:N}|\mathbf{w}, \boldsymbol{\theta}_{1:N}) p(\mathbf{w}|\boldsymbol{\theta}_{1:N}) \tag{12}$$

where $p(\boldsymbol{\theta}_{1:N}|\mathbf{w})$ refers to the prior distribution of $\boldsymbol{\theta}_{1:N}$ under a certain degradation path that is specified by $\mathbf{w}$. $p(\mathbf{w}|\boldsymbol{\theta}_{1:N})$ is readily available from the Bayesian treatment of linear models with specified samples of $\boldsymbol{\theta}_{1:N}$ (Jacquire et al., 1994). The drawn samples gradually populate the important regions in posterior distribution $p(\mathbf{w}|\boldsymbol{\theta}_{1:N}, \mathbf{D}_{1:N})$ after a sufficient number of iterations.

3 NUMERICAL APPLICATION

3.1 *Case description*

The bridge analyzed herein is a posttensioned single box-girder PSCB built in 1985. Figure 3 presents the geometry and monitoring scheme of the bridge.

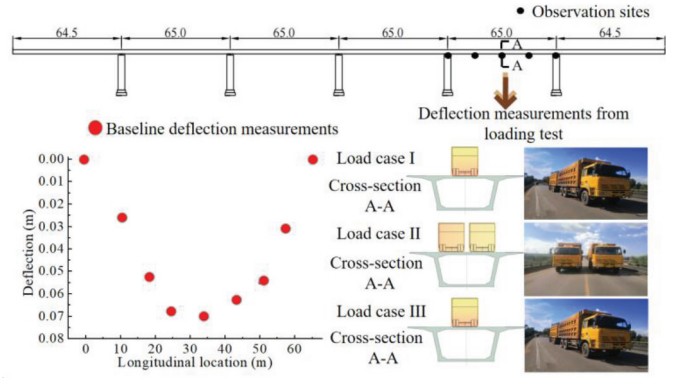


Figure 3. Geometry and monitoring scheme of the case bridge (unit: m).

3.2 *Inference results before the continuous monitoring*

As formulated in Equation (7), $\boldsymbol{\theta}_0 = (\theta_{cr,0}, \theta_{sh,0}, \theta_{q,0}, \theta_{ps,0}, \theta_{e,0})^T$ is calibrated by the Bayesian inference conditioned on deflection measurements $\mathbf{D}_0$ before the continuous monitoring. As shown in Figure 3, $\mathbf{D}_0$ includes heterogeneous deflection measurements obtained from a static loading test and baseline static deflection measured by the electronic level, which were used to update $\boldsymbol{\theta}_0$ in a sequential manner. The marginal posterior distributions of the components of $\boldsymbol{\theta}_0$ approximately follow Gaussian distributions, with their means and standardized deviations (STDEV) provided by Figures 4 a), b), c), d) and e). The posterior average of $\theta_{e,0}$ shows noticeable reduction from the undamaged state (θ_e =1), which suggests the damage accumulation in case bridge. The updated statistics of $\theta_{cr,0}$ and $\theta_{sh,0}$ suggest that the standard model (θ_{cr} ~ N(1, 0.23), θ_{sh} ~ N(1, 0.34)) (Bažant and Baweja, 1995) overestimates the development of creep and shrinkage for the case bridge, and the uncertainties associated with θ_{cr} and θ_{sh} can be significantly reduced after updating.

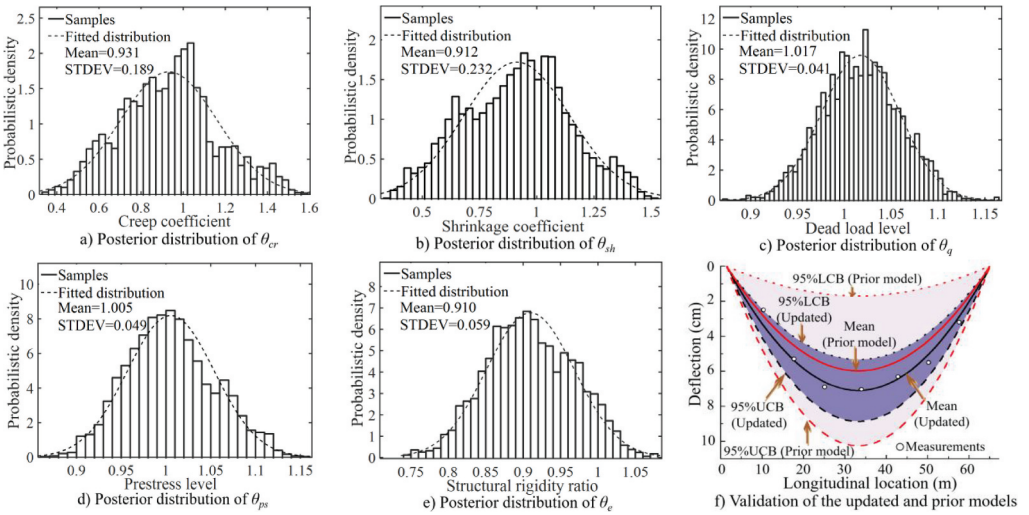


Figure 4. Inference results before the continuous monitoring.

Figure 4 (f) shows the deflection outputs of the updated and prior models, in which the average and the 95% upper confidence bounds (UCBs) and lower confidence bounds (LCBs) of deflection are presented. It can be observed that the average deflection output from the model with the updated parameters can fit the deflection measurements better than the prior standard

model. Additionally, the variance of the predictions is greatly reduced after the update, while the updated 95%-confidence interval can still capture most of the deflection measurements.

3.3 *Inference results based on the continuous monitoring deflection*

Continuous monitoring of the case bridge started in 2018 and lasted for two years. Angle-measuring inclinometers were used to collect the static and dynamic deflection of the bridge at 1/4-span, mid-span and 3/4-span of the bridge. A multiresolution discontinuous wavelet transformation (DWT) analysis was conducted on the original deflection signal to filter out the influence of temperature variation (Mallat, 1999). As presented in Figures 5 a), b) and c), the low-pass components with characterized period (T > 3072 h) were retained and averaged every two-month intervals. The averages were used as the target information in further Bayesian inference of $\boldsymbol{\theta}_e$.

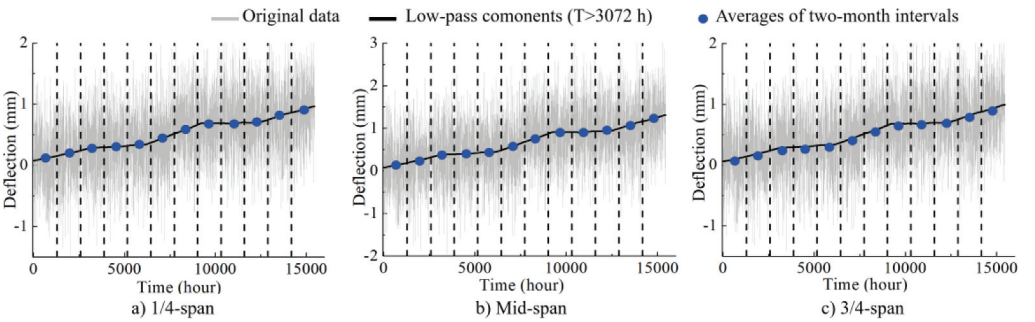


Figure 5. Wavelet analysis of the continuously monitoring deflection.

Figure 6 (a) presents the marginal posterior distributions of $\boldsymbol{\theta}_e$ that are derived using the CMCMC sampler, in which $\boldsymbol{\theta}_e$ is averaged in each two-month interval. All components of $\boldsymbol{\theta}_e$ approximately follow a Gaussian distribution, and the mean values of the samples exhibit a clear deterioration path over time. During the two-year monitoring period, the average level of structural rigidity dropped from 0.91 to 0.905. The reduced structural rigidity is a phenomenological representation of the damage accumulated during the monitoring period.

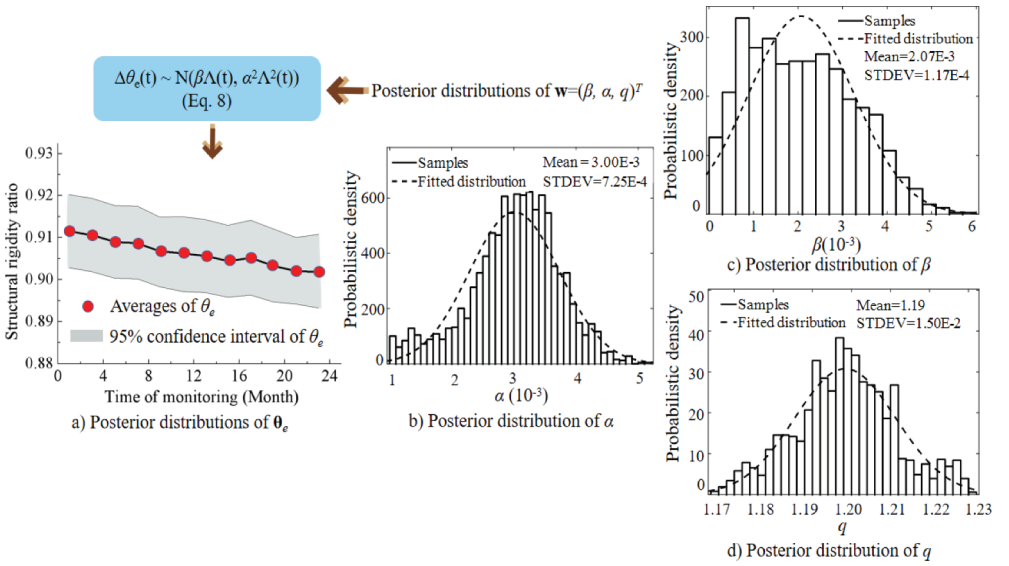


Figure 6. Inference results based on the continuous monitoring deflection.

The CMCMC sampler was also used to update $\mathbf{w}=(\beta, \alpha, q)^T$ that governs the deterioration path of $\boldsymbol{\theta}_e$ using the Wiener process formulated in Equation (8). As presented in Figures 6 b) and c), the posterior distributions of β and α are truncated Gaussian distributions since the values of these parameters must be nonnegative to ensure a nondecreasing deterioration path. As shown in Figure 6 d), the posterior distribution of q approximately follows a Gaussian distribution centered on the average of 1.198, which produces a nearly linear degradation path for this PSCB, which has been in service for 36 years.

4 CONCLUSIONS

The proposed probabilistic SI framework can identify the state variables associated with the time-dependent deflection of PSCBs, along with their time-dependencies. Specifically, damage-insensitive factors (i.e., creep, shrinkage, dead load, and prestress) can be calibrated based on static measurements before the start of continuous monitoring, whereas the damage-sensitive state variable (i.e., structural rigidity), together with its degradation path as specified by the Wiener process, can be updated based on continuously monitored deflection data.

REFERENCES

Bažant, Z.P. & Baweja, S. 1995. Creep and Shrinkage Prediction Model for Analysis and Design of Concrete Structures: Model B3. *Materials and Structures* 28(6):357–365.

Buda, G. & Caddemi S. 2007. Identification of concentrated damages in Euler-Bernoulli beams under static loads. *Journal of Engineering Mechanics* 133(8): 942–956.

Cheung, S.H. & Beck, J.L. 2009. Bayesian model updating using hybrid Monte Carlo simulation with application to structural dynamic models with many uncertain parameters. *Journal of Engineering Mechanics* 135(4):243–255.

Hedegaard, B.D., French, E.W. & Shield, C.K. 2007. Long-term monitoring strategy for time-dependent deflections of posttensioned concrete bridges. *Journal of Bridge Engineering* 22: 04017095.

Jacquire, E., Polson, N.G. & Rossi, P.E. 1994. Bayesian analysis of stochastic volatility models. *Journal of Business and Economic Statistics* 12(4): 69–87.

Jia, S., Akiyama, M., Han, B., Xie, H., & Frangopol, D. M. 2023. Structural identification via the inference of the stochastic volatility model conditioned on the time-dependent bridge deflection. *Structural Safety* 100: 102279.

Peng, W., Li, Y.F., Yang, Y.J., Huang, H.Z. & Zuo, M.J. 2014. Inverse Gaussian process models for degradation analysis: a Bayesian perspective. *Reliability Engineering and System Safety* 130(1): 175–189.

Reynders, E., Wursten, G. & De Roeck, G. 2013. Output-only structural health monitoring in changing environmental conditions by means of nonlinear system identification. *Structural Health Monitoring* 13(1): 82–93.

Santner, T., Williams, B. & Notz W. 2003. *The design and analysis of computer experiments*. New York: Springer.

Bridge Maintenance, Safety, Management, Digitalization and Sustainability – Jensen, Frangopol & Schmidt (eds)
© 2024 The Author(s), ISBN 978-1-032-77040-6
Open Access: www.taylorfrancis.com, CC BY-NC-ND 4.0 license

Advanced framework for degradation modeling of operating structures

M.E.A. Ben Seghier, A. Jiménez Rios & J. Dai
Oslo Metropolitan University, Oslo, Norway

V. Plevris
Qatar University, Doha, Qatar

ABSTRACT: The safe operation of steel structures, such as bridges, is of paramount importance to mitigate potential issues. Consequently, the continuous and thorough monitoring of their operational conditions is imperative to uphold their safety and reliability. However, the inexorable process of corrosion, catalyzed by environmental conditions, leads to the inevitable deterioration of structural integrity over time. This research endeavors to predict the extent of corrosion in the primary cables of bridges through the application of advanced methodologies based on machine learning techniques. The execution of the proposed model necessitates the utilization of an extensive database encompassing diverse characteristics pertaining to the environmental properties of the surrounding region. The performance of the proposed models is rigorously assessed using a comprehensive suite of statistical and graphical metrics. The findings of this investigation underscore the effectiveness of the recommended solutions, surpassing previously established methodologies in addressing this pressing issue. The demonstrated success of the proposed model augurs favorably for its potential utility in furthering research into the dependability assessment of suspension bridge main cables.

1 INTRODUCTION

Suspension bridges rely on main cables made of high-strength carbon steel with a zinc protection layer (Barton Scott et al., 2000) to carry traffic loads and maintain structural stability. These cables are susceptible to corrosion, which depends on manufacturing and environmental factors (Chavel & Leshko, 2012). Current inspection methods involve removing the external cover to assess internal wire condition, but this provides limited information due to practical constraints and budget limitations (Mayrbaurl & Camo, 2004). Accurate prediction of the annual corrosion rate in these cables is crucial for ensuring safety, determining remaining useful life, and optimizing maintenance and replacement efforts while minimizing costs (Ben Seghier, Corriea, et al., 2021).

Corrosion growth on steel structures poses a formidable challenge, with substantial cost implications (El Amine Ben Seghier et al., 2018; Hussein Farh et al., 2023). Bridge cables, in particular, endure harsh environmental conditions, experiencing fluctuating temperatures and varied weather patterns over their lifespan (Kim et al., 2002). Numerous studies have delved into the critical environmental factors affecting metal corrosion in bridge cables, highlighting temperature (T), pH levels, humidity duration, contaminant and ion concentrations, and extended wetness periods as the key determinants (Saha, 2012). Bettie et al. (Betti & Yanev, 1999) discovered that pH values below 4 can result in water infiltration into internal cables in New York City suspension bridges, while Eiselstein and Caligiuri (Eiselstein & Caligiuri, 1987) emphasized the significance of water contaminant accumulation within the cables. Stahl

DOI: 10.1201/9781003483755-57

(Stahl & Gagnon, 1995) pointed out that issues could also be linked to imperfections in protective coatings or cable manufacturing. Further investigations (Deeble Sloane Matthew et al., 2013; Suzumura & Nakamura, 2004) have as well demonstrated the pivotal role of humidity and temperature fluctuations during the day in corrosion rates acceleration within main cables under ambient conditions. Collectively, these findings underscore the detrimental impact of environmental factors on bridge cable corrosion rates, emphasizing the need of appropriate advanced models for predicting corrosion rates using available environmental data from inspection reports.

The power-law model (Romanoff, 1957), is commonly used to predict corrosion rates in steel structures, including carbon steel wires. It relies on time and constant variables derived from simple fitting methods based on experimental data. However, its efficiency is limited, especially in terms of its applicability and precision to a larger database, resulting in inaccurate corrosion rate estimations in various scenarios (Kamrunnahar & Urquidi-Macdonald, 2010). Recently, the research community has turned its attention to machine learning techniques, recognizing their potential to effectively capture the intricate relationships through the implementation of complex anomaly detection algorithms (Jiménez Rios et al., 2023). Karanci and Betti (Karanci & Betti, 2018a) were pioneers in this area, implementing artificial intelligence (AI) models to model the annual corrosion rate in suspension bridge main cables. They compared linear regression, artificial neural networks (ANN), and support vector regression (SVR) to tackle the problem, but their approaches yielded less-than-ideal results, attributed to the complexity of the database and the limited generalization capabilities of the AI models. Ben Seghier et al. (Ben Seghier, Corriea, et al., 2021) optimized the single machine learning (ML) model control parameters using more advanced AI-models such as hybrid-ML techniques with meta-heuristic algorithms (i.e. marine predators algorithm (MPA)). When compared to single-ML models, their results were more accurate. This highlights the pressing need for more advanced AI models to enhance the predictive accuracy of such complex problems.

The primary objective of this research is to introduce a new predictive model designed to estimate the annual corrosion rate by analyzing environmental conditions from a global dataset. To address this challenge, we assess the performance of different ensemble learning models, namely, decision tree (DT), random forest (RF), adaptive boosting (ADB), and extreme gradient boosting (XGB). Furthermore, these models' performance is compared against four conventional regression techniques, i.e. multiple linear regression (MLR), ridge regression (RR), lasso regression (LR), and elastic net regression (ER). Various evaluation criteria are applied to assess the performance of ensemble and regression models in term of efficiency and accuracy.

2 METHODOLOGY

2.1 *Database description*

In this paper, we delve into an in-depth analysis of the intricate patterns of corrosion rate in suspension bridge main cables, which exhibit nonlinear behaviors contingent upon the environmental factors at play. To accomplish this, we draw upon a comprehensive database meticulously compiled by Karanci and Betti (Karanci & Betti, 2018a, 2018b). The database encompasses over 250 testing sites distributed across 33 countries (e.g. USA, Germany, Norway, Mexico, …, etc). Within this extensive collection, an uncover 309 distinct measurements are used, which shed light on the annual corrosion rate of carbon steel specimens, each subjected to diverse atmospheric conditions over the course of a year. The tests consisted on exposing carbon steel specimens to different atmospheric circumstances.

This study considers the impact of six crucial environmental factors, which serve as input variables. Specifically, these factors encompass temperature (T, °C), relative humidity (RH,%), the duration of moisture on the metal's surface (TOW, %), annual precipitation (P, mm), rainwater pH (pH), and chloride ion concentration (Cl^-, mg/L). These variables collectively represent the surrounding environmental conditions. The primary focus of this investigation centers on the annual corrosion rate (mm/year), which is regarded as the principal output parameter and is observed in the main cable wires. Table 1 presents a statistical summary of the database,

including the mean (X_{Mean}), standard deviation (X_{STD}), the minimum value (X_{Min}) and the maximum value (X_{Max}). Figure 1 shows the Pearson correlation matrix of the studied parameters. It can be seen that there is moderate to low correlation between the input variables and the target output, indicating that all the utilized variables are suitable to be included in the models' development.

Table 1. Dataset description of the input and output variables.

Type	Variables	X_{Mean}	X_{STD}	X_{Min}	X_{Max}
Inputs	Temperature, °C	15.30	8.75	-3.10	29.82
	RH, %	0.46	0.18	0.00	0.98
	TOW, %	68.70	14.10	33.30	91.10
	Precipitation, mm	882.43	486.83	13.00	3677.00
	pH	4.99	0.87	3.45	7.37
	Cl^-, mg/L	12.35	27.17	0.01	192.73
Outputs	Corrosion rate, μm	38.53	43.76	3.30	376.70



Figure 1. Pearson correlation matrix of the input and output variables.

2.2 *Regression models*

Four conventional regression techniques were implemented in this study as follows:

- Multiple linear regression (MLR): a statistical technique used in data analysis and modeling to examine the relationship between a dependent variable (or response variable) and two or more independent variables (or predictor variables).

- Ridge regression (RR): also known as L2 regularization, it is a linear regression technique used in statistics and machine learning to address the problem of multicollinearity and overfitting in MLR.
- Lasso regression (LR): an abbreviation for "Least Absolute Shrinkage and Selection Operator" regression, which is a linear regression technique used in statistics and machine learning for variable selection and regularization.
- Elastic net regression (ER): it is a linear regression technique that combines both Lasso (L1 regularization) and Ridge (L2 regularization) regression methods to address the limitations of each individual approach.

2.3 *Ensemble learning models*

Ensemble Learning (EL) models are machine learning (ML) techniques that combine the predictions of multiple individual models (base models or learners) to improve overall predictive performance, generalization, and robustness. The idea behind ensemble learning is that by aggregating the predictions of multiple models, the ensemble can often produce more accurate and reliable results than any single model on its own. One base model and three ensemble learning models were employed in this work, as follows:

- Decision tree (DT) –Base model-: used for both classification and regression tasks. It is a versatile and interpretable model that can be represented graphically as a tree structure.
- Random forest (RF) –EL-model-: a technique that combines the predictive strength of multiple DT to produce more accurate and robust results.
- Adaptive boosting (ADB) -EL-model-: a technique that designed to improve the performance of weak learners (classifiers that perform slightly better than random guessing) by combining them into a strong ensemble model.
- Extreme gradient boosting (XGB) -EL-model-: an extension of the gradient boosting machine (GBM) algorithm, designed to be highly optimized, scalable, and capable of delivering excellent predictive performance.

Besides, a k-fold cross-validation was used to prevent over-fitting of all EL-models and regression approaches. The data were divided into 70% for building the predictive models, while 30% were attributed for the validation of the developed predictive models. The performance of all models was measured based on comparative statistical indicators as described in the following (Ben Seghier, Gao, et al., 2021; Ben Seghier, Kechtegar, et al., 2021):

1. Root mean square error (RMSE):

$$RMSE = \frac{1}{n}\sum_{i=1}^{n}\left(C_{rate,i}^{Act} - C_{rate,i}^{Pre}\right)^2 \tag{1}$$

2. Mean absolute error (MAE):

$$MAE = \frac{1}{n}\sum_{i=1}^{n}\left|C_{rate,i}^{Act} - C_{rate,i}^{Pre}\right| \tag{2}$$

3. Coefficient of determination (R^2):

$$R^2 = 1 - \frac{\sum_{i=1}^{n}\left(C_{rate,i}^{Act} - C_{rate,i}^{Pre}\right)^2}{\sum_{i=1}^{n}\left(C_{rate}^{Avg} - C_{rate,i}^{Pre}\right)^2} \tag{3}$$

4. Confidence interval (CI):

$$CI = WI \times NSE \tag{4}$$

$$WI = 1 - \frac{\sum_{i=1}^{n}\left(C_{rate,i}^{Act} - C_{rate,i}^{Pre}\right)^2}{\sum_{i=1}^{n}\left(\left|C_{rate,i}^{Pre} - C_{rate}^{Avg}\right| + \left|C_{rate,i}^{Act} - C_{rate}^{Avg}\right|\right)^2} \quad (5)$$

$$NSE = 1 - \frac{\sum_{i=1}^{n}\left(C_{rate,i}^{Act} - C_{rate,i}^{Pre}\right)^2}{\sum_{i=1}^{n}\left(C_{rate,i}^{Act} - C_{rate}^{Avg}\right)^2} \quad (6)$$

5. U95:

$$U95 = 1.96 \times \sqrt{Standard\ deviation^2 - RMSE^2} \quad (7)$$

Where $C_{rate,i}^{Act}$, $C_{rate,i}^{Pre}$ and C_{rate}^{Avg} are the actual, predicted, and average values of the i-th annual corrosion rate from the test result measurements. The lower the RMSE, MAE, and U95 values, the higher the projected values by the utilized model, and the higher the CI and R^2 values, the higher the model accuracy.

3 RESULTS AND DISCUSSION

3.1 *Predictive regression models*

The performance evaluation of the four regression models implemented in this study is presented in Table 2. It can be seen from the obtained results that the best performing regression model among the utilized ones is the ER. This latter yielded the lowest RMSE, MAE and U95 values flowed by LR, while the MLR yielded the lowest performance during both phases, training, and testing. In addition, the highest obtained R^2 value is 0.825 and 0.742 by the EL during the training and testing sets respectively. The overall results show low adaptation to the complexity of the used database, indicating the drawbacks of the used regression models.

Table 2. Performance evaluation of the four regression models.

Phase	Models	RMSE	MAE	R^2	CI	U95
Training	MLR	22.991	16.331	0.758	0.530	46.134
	RR	23.528	15.707	0.780	0.479	47.107
	LR	21.910	15.236	0.803	0.516	43.899
	ER	**19.859**	**14.328**	**0.825**	**0.576**	**39.673**
Testing	MLR	29.421	16.391	0.543	0.239	58.225
	RR	20.442	14.480	0.679	0.457	40.545
	LR	18.834	13.427	0.727	0.481	37.743
	ER	**18.245**	**13.310**	**0.742**	**0.501**	**36.565**

* Bold numbers represent the best results.

Furthermore, Figure 2 presents the scatter plots of the different employed regression models. Besides from the relatively low prediction capacity of the regression models explored in this paper, another important drawback worth highlighting is the fact that such models could result into negative values of annual corrosion rate (see dots plotted below the horizontal axis, close to the origin), which does not hold any physical meaning. Thus, the applicability of such models can result on misleading values of the annual corrosion rate.

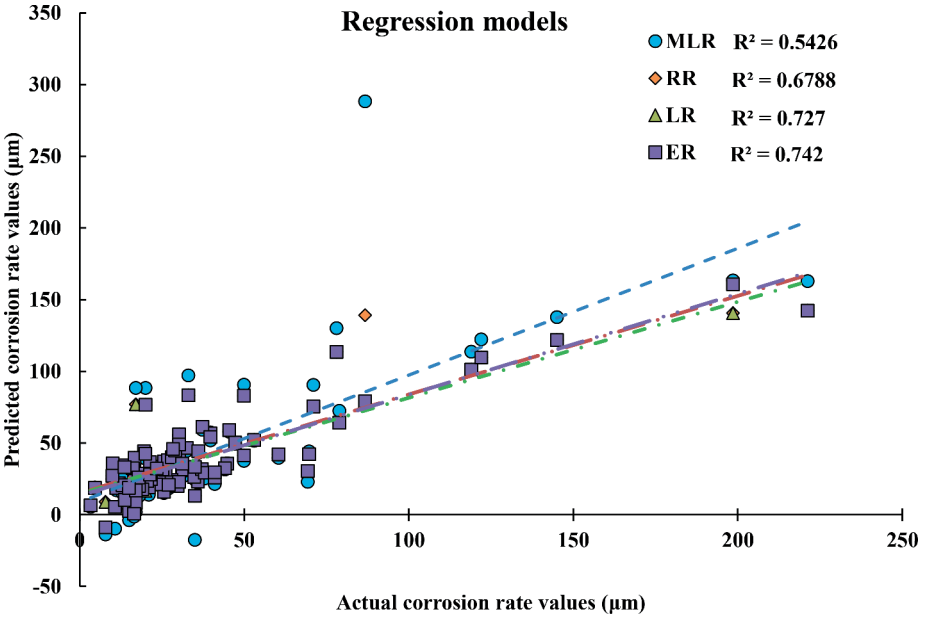


Figure 2. Scatter plots of the regression models.

3.2 *Predictive ensemble learning models*

The performance evaluation of the single based models (i.e. DT) and the three ensemble learning models (i.e. RF, ADB and XGB) implemented in this study are presented in Table 3. According to the results, the DT model showed perfect results during the training phase, whereas the model yielded the lowest results during the testing phase, indicating an overfitting and inaccurate results obtained by this technique a single base model. The DT results are obtained as follow: RMSE = 37.999 µm/year, MAE=16.997 µm/year and CI=-0.117, which is the lowest among all other ensemble learning models. The best performing ensemble learning algorithm is the XGB, where this observation is based on all the utilized statistical indicators, including the obtained R^2 value (0.999 and 0.941 for the training and testing sets respectively). These results highlight the suitability of ensemble learning models to be implemented in annual corrosion prediction tasks.

Table 3. Performance evaluation of the three ensemble learning models.

Phase	Models	RMSE	MAE	R^2	CI	U95
Training	DT**	0.000	0.000	1.000	0.750	0.000
	RF	9.579	5.245	0.970	0.684	19.770
	XGB	**1.604**	**1.145**	**0.999**	**0.746**	**4.010**
	ADB	11.030	8.492	0.954	0.694	20.897
Testing	DT	37.999	16.997	0.380	-0.117	74.978
	RF	14.876	10.966	0.863	0.549	29.784
	XGB	**8.858**	**6.733**	**0.941**	**0.678**	**18.315**
	ADB	14.562	12.173	0.887	0.582	25.936

* Bold numbers represent the best results.
** DT shows perfect results due to the overfitting problem.

Similar to the previous section, Figure 3 presents the scatter plots of the base single model (i.e. DT) and the different ensemble learning models using the testing phase results. Besides from the higher performance already commented, it can be observed that under no

circumstances, ensemble learning models provide negative values of annual corrosion rate, thus respecting the physical meaning of the task at hand. In addition, the performance of the models can be ranked as follows: XGB>ADB>RF>DT.

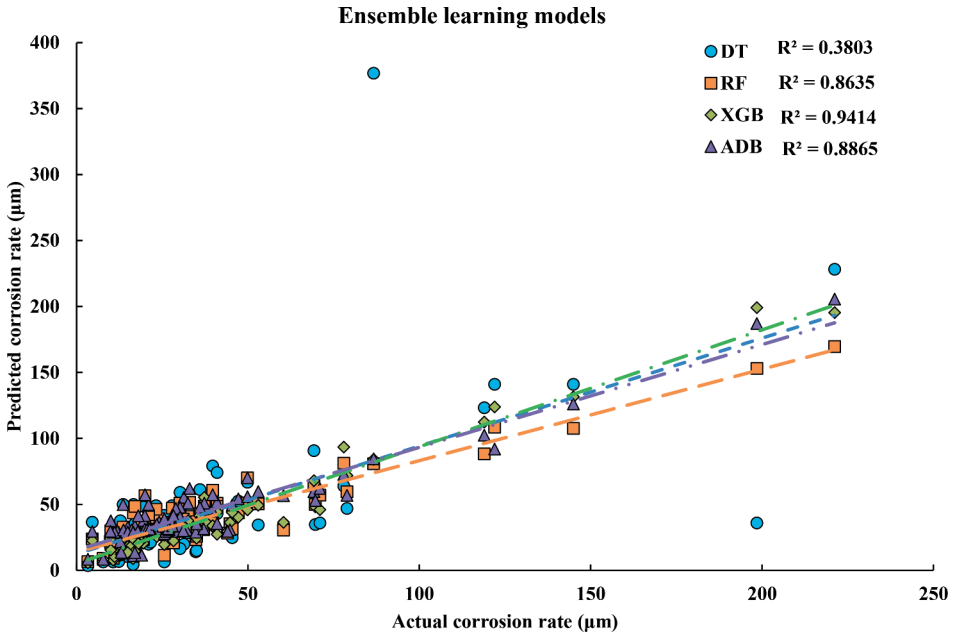


Figure 3. Scatter plots of the ensemble learning models.

4 CONCLUSION

The prediction of the annual corrosion rate in suspension bridge main cables presents a complex and nonlinear issue characterized by chaotic patterns and stochastic tendencies. In this paper, we have assessed the performance of different ensemble learning models, namely, decision tree (DT), random forest (RF), adaptive boosting (ADB), and extreme gradient boosting (XGB), to predict annual corrosion rates using a comprehensive database composed of 309 measurements of annual corrosion rate of carbon steel specimens as a function of diverse atmospheric conditions over the course of a year, distributed across 33 countries. Furthermore, these models' performance was compared against four conventional regression techniques, i.e. multiple linear regression (MLR), ridge regression (RR), lasso regression (LR), and elastic net regression (ER).

In general, except for the DT model, the ensemble learning models presented a better performance than the conventional regression models. XGB was the best performing ensemble learning algorithm with R^2 values reaching 0.999 and 0.941 for the training and testing sets, respectively. Moreover, all ensemble learning models respected the physical meaning of the predicted outcome parameter and none of them resulted in negative estimated values.

REFERENCES

Barton Scott, C., Vermaas Garry, W., Duby Paul, F., West Alan, C., & Betti, R. (2000). Accelerated Corrosion and Embrittlement of High-Strength Bridge Wire. *Journal of Materials in Civil Engineering*, *12*(1), 33–38. https://doi.org/10.1061/(ASCE)0899-1561(2000)12:1(33)

Ben Seghier, M. E. A., Corriea, J. A. F. O., Jafari-Asl, J., Malekjafarian, A., Plevris, V., & Trung, N.-T. (2021). On the modeling of the annual corrosion rate in main cables of suspension bridges using combined soft computing model and a novel nature-inspired algorithm. *Neural Computing and Applications*, *33*(23), 15969–15985. https://doi.org/10.1007/s00521-021-06199-w

Ben Seghier, M. E. A., Gao, X.-Z., Jafari-Asl, J., Thai, D.-K., Ohadi, S., & Trung, N.-T. (2021). Modeling the nonlinear behavior of ACC for SCFST columns using experimental-data and a novel evolutionary-algorithm. *Structures*, *30*, 692–709. https://doi.org/10.1016/j.istruc.2021.01.036

Ben Seghier, M. E. A., Kechtegar, B., Nait Amar, M., A.F.O. Correia, J., & Trung, N.-T. (2021). Simulation of the ultimate conditions of fibre-reinforced polymer confined concrete using hybrid intelligence models. *Engineering Failure Analysis*, *128*, 105605. https://doi.org/10.1016/j.engfailanal.2021.105605

Betti, R., & Yanev, B. (1999). Conditions of Suspension Bridge Cables: New York City Case Study. *Transportation Research Record*, *1654*(1), 105–112. https://doi.org/10.3141/1654-12

Chavel, B. W., & Leshko, B. J. (2012). *Primer for the Inspection and Strength Evaluation of Suspension Bridge Cables* (FHWA-IF-11-045). U.S. Department of Transportation Federal Highway Administration. https://www.fhwa.dot.gov/bridge/pubs/if11045.pdf

Deeble Sloane Matthew, J., Betti, R., Marconi, G., Hong Ah, L., & Khazem, D. (2013). Experimental Analysis of a Nondestructive Corrosion Monitoring System for Main Cables of Suspension Bridges. *Journal of Bridge Engineering*, *18*(7), 653–662. https://doi.org/10.1061/(ASCE)BE.1943-5592.0000399

Eiselstein, L. E., & Caligiuri, R. D. (1987). *Atmospheric corrosion of the suspension cables on the Williamsburg Bridge*. ASTM International. https://www.astm.org/stp25841s.html

El Amine Ben Seghier, M., Keshtegar, B., & Elahmoune, B. (2018). Reliability analysis of low, mid and high-grade strength corroded pipes based on plastic flow theory using adaptive nonlinear conjugate map. *Engineering Failure Analysis*, *90*, 245–261. https://doi.org/10.1016/j.engfailanal.2018.03.029

Hussein Farh, H. M., Ben Seghier, M. E. A., Taiwo, R., & Zayed, T. (2023). Analysis and ranking of corrosion causes for water pipelines: a critical review. *npj Clean Water*, *6*(1), 65. https://doi.org/10.1038/s41545-023-00275-5

Jiménez Rios, A., Plevris, V., & Nogal, M. (2023). Bridge Management through Digital Twin-based Anomaly Detection Systems: A Systematic Review. *Frontiers in Built Environment*. https://doi.org/10.3389/fbuil.2023.1176621

Kamrunnahar, M., & Urquidi-Macdonald, M. (2010). Prediction of corrosion behavior using neural network as a data mining tool. *Corrosion Science*, *52*(3), 669–677. https://doi.org/10.1016/j.corsci.2009.10.024

Karanci, E., & Betti, R. (2018a). Modeling Corrosion in Suspension Bridge Main Cables. I: Annual Corrosion Rate. *Journal of Bridge Engineering*, *23*(6), 04018025. https://doi.org/10.1061/(ASCE)BE.1943-5592.0001233

Karanci, E., & Betti, R. (2018b). Modeling Corrosion in Suspension Bridge Main Cables. II: Long-Term Corrosion and Remaining Strength. *Journal of Bridge Engineering*, *23*(6), 04018026. https://doi.org/10.1061/(ASCE)BE.1943-5592.0001234

Kim, H.-K., Lee, M.-J., & Chang, S.-P. (2002). Non-linear shape-finding analysis of a self-anchored suspension bridge. *Engineering Structures*, *24*(12), 1547–1559. https://doi.org/10.1016/S0141-0296(02)00097-4

Mayrbaurl, R. M., & Camo, S. (2004). *Guidelines for Inspection and Strength Evaluation of Suspension Bridge Parallel Wire Cables*. The National Academies Press. https://doi.org/10.17226/23338

Romanoff, M. (1957). *Underground corrosion* US Government Printing office. https://nvlpubs.nist.gov/nistpubs/Legacy/circ/nbscircular579.pdf

Saha, J. K. (2012). *Corrosion of constructional steels in marine and industrial environment: frontier work in atmospheric corrosion*. Springer Science & Business Media. https://link.springer.com/book/10.1007/978-81-322-0720-7

Stahl, F. L., & Gagnon, C. P. (1995). *Cable corrosion in bridges and other structures: Causes and solutions*. American Society of Civil Engineers (ASCE).

Suzumura, K., & Nakamura, S.-i. (2004). Environmental Factors Affecting Corrosion of Galvanized Steel Wires. *Journal of Materials in Civil Engineering*, *16*(1), 1–7. https://doi.org/10.1061/(ASCE)0899-1561(2004)16:1(1)

Bridge Maintenance, Safety, Management, Digitalization and Sustainability – Jensen, Frangopol & Schmidt (eds)
© 2024 The Author(s), ISBN 978-1-032-77040-6
Open Access: www.taylorfrancis.com, CC BY-NC-ND 4.0 license

Modeling the deterioration of road bridges at the provincial level in Lao PDR

H. Silimanotham, A. Amir & M. Henry
Shibaura Institute of Technology, Tokyo, Japan

ABSTRACT: Deterioration is one of the key concerns in assessing bridge performance and is necessary to understand how bridges degrade with age for optimal maintenance budget allocation. The rate of deterioration varies across bridge types, with Laos predominantly featuring aging concrete slab bridges, concrete girder bridges, and steel truss bridges. It is imperative to ascertain the deterioration rate of these bridge types for effectively determine maintenance costs. This paper analyzes available inspection data from the Ministry of Public Works and Transport (MPWT), employing linear regression analysis to find the trend of deterioration rates of different types of bridges with time. Focusing on concrete slab, girder, and steel truss bridges in the 18 provinces of Laos, the study forecasts the deterioration rates over bridges' service life. The results can inform various bridge management tasks, including maintenance planning and asset evaluation, contributing to more effective decision-making for the preservation and safety of Laos' bridge infrastructure.

1 INTRODUCTION

Efficient road transport is the backbone of a country's economy, and bridges constitute a crucial and costly component of the road network that necessitates a timely and effective management plan. This plan should involve allocating the available budget to specific structures (bridges) based on their condition and the prescribed maintenance and rehabilitation requirements (Amir et al., 2023). Several factors contribute to the deterioration of these bridges such as axle load, aging, and environmental factors. Many bridge management departments around the world have been developing and improving a variety of bridge management systems (BMS) for decades to provide timely and effective bridge maintenance, repair, and rehabilitation (MR&R) by collecting and analyzing technical-condition data and performance evaluations on a continuous basis (DeStefano and Grivas, 1998, Archila, 1999, Calvert et al., 2020, Madanat et al., 1997, Medina and Gonzalez, 2022, Nurmuhametov et al., 2021).

Laos has over 3,500 bridges constructed within its road network, which is classified into national, provincial, district, urban, rural, and specific roads (JICA, 2021). According to the Ministry of Public Works and Transport (MPWT), annually only 1 percent of the road annual budget goes to the maintenance of these bridges, which also covers site inspection and surveying. Since Laos lacks a maintenance management strategy, decision-making regarding which bridges should be maintained is usually based on coordination meetings between authorities without considering and evaluating technical factors. It is because of this that maintenance budgets are usually spent only on urgent cases, and that routine and periodic maintenance is generally neglected. Furthermore, there is a lack of a data-driven maintenance strategy that incorporates bridge deterioration modeling for budget optimization, necessitating the need to analyze the historical data of these bridges. This analysis is crucial for developing models that can be integrated into maintenance planning to address such issues effectively.

In recent years, bridge deterioration modeling has been developed by many researchers for predicting the bridge condition with time. Various deterministic deterioration modeling studies were conducted using both the national and state bridge inventories. Transportation Research Center of the U.S. Department of Transportation (DOT) used linear regression to correlate bridge condition

DOI: 10.1201/9781003483755-58

ratings with other bridge characteristics recorded in the NBI database (Busa et al., 1985). Similarly, the Wisconsin Department of Transportation and the New York State Department of Transportation used an improved piecewise linear regression (Fitzpatrick et al., 1981, Hyman and Hugles, 1983) and developed a bridge deterioration model using two methods: 1) rates of change and 2) average condition ratings of all bridges in New York City Metropolitan area (Yanev and Chen, 1993). Similarly, In Laos, the infrastructure primarily comprises old bridges. Therefore, there is a need to develop a strategy for assessing the rate of deterioration of these bridges with time.

The Lao PDR is one of the timber-exporting countries in Southeast Asia, and a significant portion of timber exports to China and Vietnam is through the Northern and Southern Road networks of Laos. However, due to heavy transport, both these roads and bridges undergo deterioration with time. Most of the bridges in these areas fall into three types that's include concrete slab, concrete girder, and steel truss. Recognizing that bridge type can be a crucial factor influencing deterioration rate, this research focused on utilizing existing data from the Ministry of Public Works and Transport (MPWT) to develop and compare the rate of deterioration across different bridge types by utilizing the statistical approach such as the linear regression method.

2 METHODOLOGY

2.1 *Data preparation*

This research uses the bridges database of the year 2018 obtained from the MPWT which includes bridge inspection and bridge characteristics data. In the bridge database, there are six classifications of road as national, provincial, district, urban, rural, and specific road. However, approximately 24% of the total number of bridges (3,580 bridges) in Laos are located on national roads. Moreover, the collected data from the MPWT was incomplete and lacked characteristics and information about the years of construction for the entire road classification network. Consequently, the research narrowed its focus to compare the rates of deterioration of different types of bridges classified under one road category, specifically, national roads in different areas such as the Northern (8 provinces), Central (6 provinces), and Southern area (4 provinces). The areas' descriptions are mentioned in Table 1. The classification of Northern, Central, and Southern areas is based on their respective geographical locations. The Northern region is predominantly mountainous, the Central region consists of flat areas, and the Southern region encompasses both mountainous and flat terrain. Most of the timber transportation to the neighboring countries of Laos is carried out on the Northern and Southern areas road network.

Table 1. The regions of Laos.

Northern area	Central area	Southern area
Phongsaly province	Vientiane capital	Saravan province
Houaphane province	Vientiane province	Xekong province
Xiengkhouang province	Xaisomboun province	Champasak province
Louang Prabang province	Bolikhamxai province	Attapeu province
Xaiyabouly province	Khammouan province	
Oudomxai province	Savannakhet province	
Bokeo province		
Louangnamtha province		

The national road network has around 844 bridges with 3 main bridge types that included concrete slab, concrete girder, and steel truss. Due to data limitations, complete information was available for only 735 bridges in the three different areas. Among these, there are 190 bridges of concrete slab, 452 bridges of concrete girder, and 93 bridges with steel truss, as shown in Figure 1. The analysis was done based on the bridge service period (age) and bridge conditions. The bridge conditions were classified into 5 categories in the data obtained, with 0 showing "no damage" to the 4 representing the "severe damage" of the bridge as shown in Table 2.

Table 2. Condition ratings.

Code	Bridge Condition
0	No damage, element as new
1	Insignificant damage, no repair needed
2	Minor damage, repair when convenient
3	Damage, repair soon
4	Severe damage, repair immediately

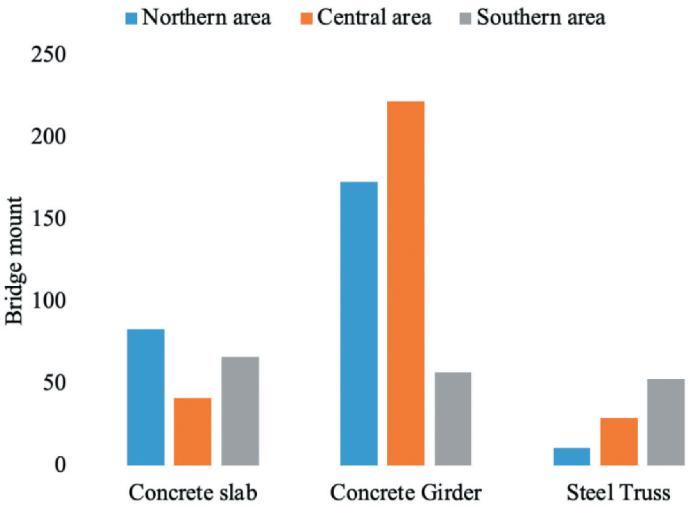


Figure 1. Number of three bridge types on the national road.

2.2 *Methodology*

The data consisted of 735 bridges. During the pre-processing of data, it was found that several bridges have the same service life (age), hence average bridge condition was calculated for different years of service life (age). The linear regression was performed by taking the average bridge condition as the dependent variable and the service life (age) as the independent variable for estimating the trends of deterioration rate with time by the equation below:

Linear regression:

$$Y = a + bX \tag{1}$$

Where,
Y represents the dependent variable (average bridge condition),
a is the intercept,
b is the slope, and
X signifies the independent variable (bridge service period or age).

In equation 1, the slope b offers insights into the rate of deterioration. A positive b implies a positive relationship between the variables which means that as the independent variable increases (e.g., as the bridge ages), the dependent variable also increases (e.g., indicating deterioration in bridge condition). Similarly, when comparing the rate of deterioration in different areas using linear regression, a higher slope for a particular area suggests more rapid deterioration in the average bridge condition as the bridge service period or age increases in that specific area.

3 RESULTS AND DISCUSSIONS

3.1 *Regression modeling of deterioration by bridge type and region*

3.1.1 *Concrete slab bridges*

The results of the linear regression are shown in Figures 2, 3, and 4, which illustrate the deterioration rate of concrete slab bridges over bridge service life in different areas. These figures represent the relationship between the bridge's average condition and bridge service period. It was observed from the analysis that there is a higher rate of deterioration for concrete bridges in the Northern area as compared to the Central and Southern areas (Figure 2). This increased rate of deterioration is evident through the larger slope value (0.0485) in the Northern area. In contrast, the deterioration slope values are 0.0278 in the Central area and 0.009 in the Southern area, as illustrated in Figures 3 and 4, respectively.

Furthermore, the values associated with these linear regression analyses provide information about how well the model fits for each area's data. For the Northern and Southern areas, the R^2 values were 0.7432 and 0.5126, indicating that 74.3% and 51.2% of the variability, respectively, is explained by the regression analysis. However, the R^2 value for the Central region was the lowest (0.1529), signifying only 15% variability explained. This lower R^2 value may be attributed to the limited amount of available data for the Central region. Despite this limitation, the model can still be utilized for finding the trend of bridge deterioration rates in the Central area (Lu et al. 2016).

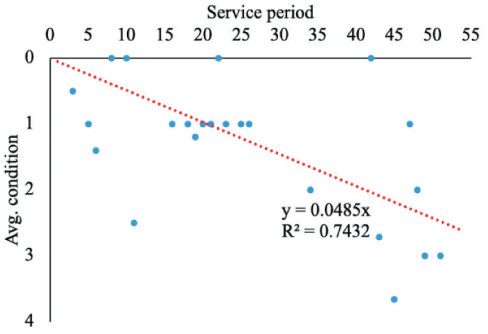


Figure 2. The deterioration rate of concrete slab bridges in Northern area.

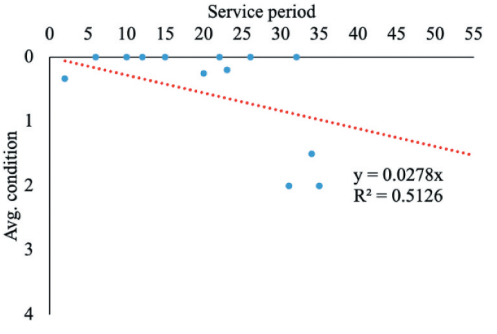


Figure 3. The deterioration rate of concrete slab bridges in Central area.

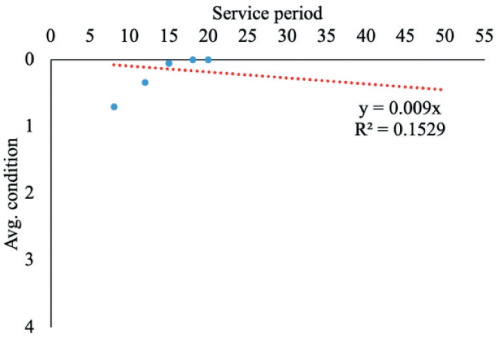


Figure 4. The deterioration rate of the concrete slab bridges in the Southern area.

3.1.2 *Concrete girder bridges*

Figures 5, 6, and 7 show the deterioration rate of concrete girder bridges in the Northern, Central, and South areas. It has been observed from the analysis that the rates of deterioration of concrete girder bridges in the Southern and Northern areas were almost similar (y= 0.0377

and 0.0358) and higher than the concrete girder bridges in the Center area (y=0.0225). Similarly, the R^2 values obtained for these models were 0.5965, 0.4312, and 0.584 indicating 59.6%, 43.1%, and 58.4% of variability explained for the Northern, Southern, and Central areas bridges data respectively.

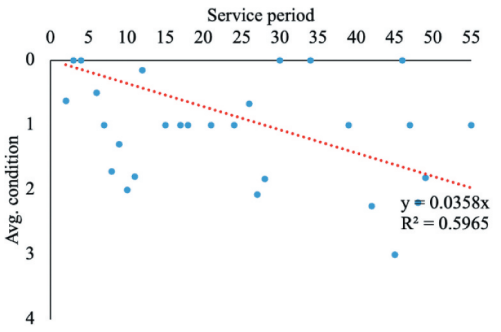


Figure 5. The deterioration rate of concrete girder bridges in Northern area.

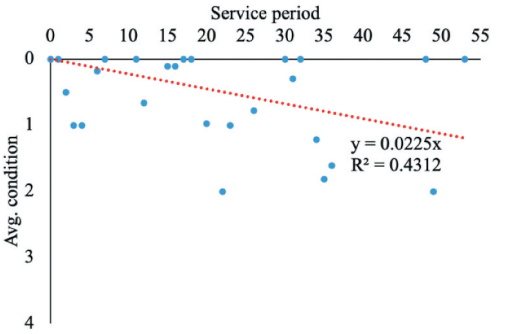


Figure 6. The deterioration rate of concrete girder bridges in Central area.

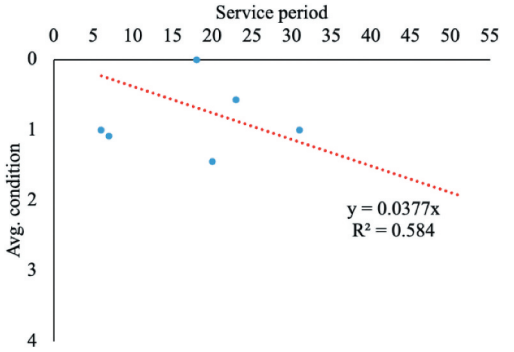


Figure 7. The deterioration rate of concrete girder bridges in Southern area.

3.1.3 *Steel truss bridges*

The results of the linear regression model for steel truss bridges are shown in Figures 8, 9, and 10, illustrating the deterioration rating of concrete slabs in different areas by examining the relationship between bridge average condition and bridge service period. It was observed that the rate of deterioration of steel truss bridges in the Northern areas is higher, as evident by the elevated slope value (y=0.0578, Figure 7), while steel bridges in the Central areas exhibit the slowest rate of deterioration (y=0.0315, Figure 9). The R^2 values obtained from the analysis showed the lowest value for the Central area with 0.2215 indicating the 22% variability explained by the bridge data of central areas.

3.2 *Comparison of the bridge deterioration rates between different areas*

Figure 11 shows the comparison of deterioration rates of three types of bridges such as concrete slab, concrete girder, and steel truss in the Northern, Center, and Southern areas. The comparison of bridge deterioration rates among different areas reveals distinct patterns. It was observed that the Northern areas exhibit higher rates of deterioration across all three bridge types. It may be due to the heavy axle loading in this region. However, for concrete

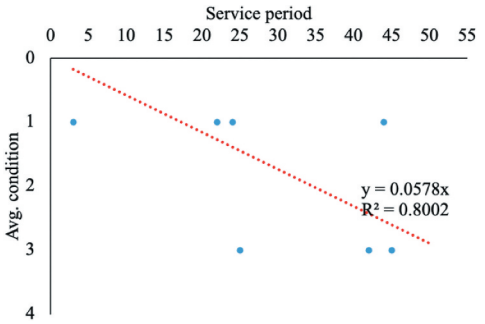


Figure 8. The deterioration rate of steel truss bridges in Northern area.

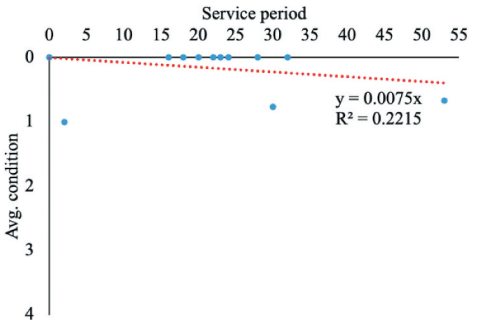


Figure 9. The deterioration rate of steel truss bridges in Central area.

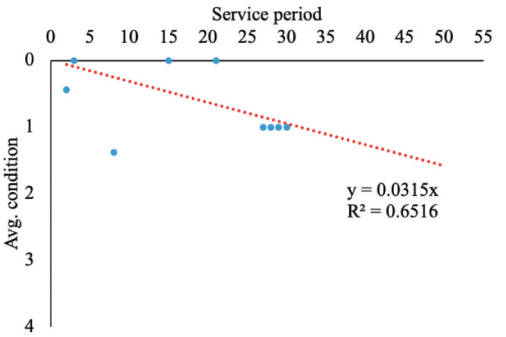


Figure 10. The deterioration rate of steel truss bridges in the Southern area.

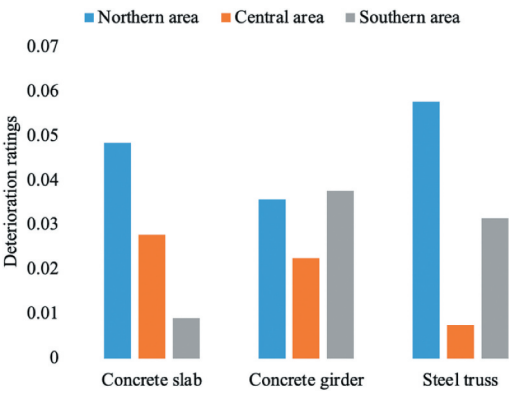


Figure 11. Bridge deterioration rating in three areas.

girder bridges, the rates are almost equal in both Northern and Southern areas. Conversely, the Central area, characterized by predominantly flat terrain, showed low rates of bridge deterioration for all three bridge types. In light of these findings, it is evident that geographical variations, specifically the type of traffic usage can influence the rates of bridge deterioration for three bridge types in different terrains. It could be attributed to the presence of heavy axle traffic in the Northern and Southern areas, given that a substantial portion of the road network is utilized for transporting timber with heavy axle loads.

4 CONCLUSIONS

This research aimed to evaluate and compare the trends of bridge deterioration based on available data from the Ministry of Public Works and Transport (MPWT) in the national road network of Laos. Linear regression methods were applied to three types of bridges, namely concrete slab, concrete girder, and steel truss, to estimate deterioration rates for effective maintenance planning. The results were thoroughly analyzed and compared, revealing different rates of deterioration among the three bridge types in different geographical areas.

It was observed that the Northern area exhibited a higher bridge deterioration rate compared to the Central and Southern regions. This discrepancy suggests a higher frequency of required bridge maintenance in the Northern areas, which can be attributed to the prevalent heavy axle traffic associated with timber transportation. Conversely, the analysis for the Central area showed the slowest bridge deterioration rates, reducing overall maintenance frequency is suggested. The findings emphasize the substantial influence of geographical variations on bridge deterioration rates. The future research can be extended by incorporating additional factors into the bridge data for finding more robust factors affecting the rate of deterioration.

ACKNOWLEDGEMENT

The Authors would like to extend their gratitude to Japan International Cooperation Agency (JICA) for their support through the Road Asset Management Program, to Shibaura Institute of Technology (SIT), Tokyo for providing the environment for the research, and to Ministry of Public Works and Transport (MPWT) in Lao PDR, for sharing the data and information needed.

REFERENCES

Amir, A. and Henry, M., 2023. Reverse Engineering of Maintenance Budget Allocation Using Decision Tree Analysis for Data-Driven Highway Network Management. *Sustainability*, 15(13), p.10467.

Archilla, A.R., 1999. Method for Estimating Transition Probability in Bridge Deterioration Models. Discussion and Closure. *Journal of Infrastructure Systems*, 5(2).

Busa, G., Cassella, M. and Gazda, W., 1985. *A National Bridge Deterioration Model, Transportations Systems Center*. Report SS-42-U5-26, Cambridge, MA: US Department of Transportation.

Calvert, G., Neves, L., Andrews, J. and Hamer, M., 2020. Multi-defect modelling of bridge deterioration using truncated inspection records. *Reliability Engineering & System Safety*, 200, p.106962.

DeStefano, P.D. and Grivas, D.A., 1998. Method for estimating transition probability in bridge deterioration models. *Journal of infrastructure systems*, 4(2), pp.56–62.

Fitzpatrick, M.W., Law, D.A. and Dixon, W.C., 1981. Deterioration of New York State Highway Structures. *Transportation Research Record*, (800).

Lu, P., Pei, S. and Tolliver, D., 2016, April. Regression model evaluation for highway bridge component deterioration using national bridge inventory data. In *Journal of the Transportation Research Forum* (Vol. 55, No. 1, pp. 5–16).

Hyman, W.A. and Hughes, D.J., 1983. *Computer model for life-cycle cost analysis of statewide bridge repair and replacement needs* (No. 899).

JICA (2021). The Project For Capacity Development On Bridge Maintenance and Management in Lao PDR. *Work Process*.

Madanat, S.M., Karlaftis, M.G. and McCarthy, P.S., 1997. Probabilistic infrastructure deterioration models with panel data. *Journal of infrastructure systems*, 3(1), pp.4–9.

Medina, P.A. and González, J.L., 2022. Reinforced concrete long-term deterioration prediction for the implementation of a Bridge Management System. *Materials Today: Proceedings*, 58, pp.1265–1271.

Nurmuhametov, K., Zinnurov, T. and Sadykov, D., 2021, April. Implementation of the Decision-Making Algorithm in the Bridge Management System. In *International Scientific Conference on Socio-Technical Construction and Civil Engineering* (pp. 31–37). Cham: Springer International Publishing.

Yanev, B. and Chen, X., 1993. Life-cycle performance of New York City bridges. *Transportation Research Record, 1389*, p.17.

Bridge Maintenance, Safety, Management, Digitalization and Sustainability – Jensen, Frangopol & Schmidt (eds)
© 2024 The Author(s), ISBN 978-1-032-77040-6
Open Access: www.taylorfrancis.com, CC BY-NC-ND 4.0 license

Experimental investigation on shear behaviour of corroded and repaired prestressed concrete beams

B. Belletti, S. Ravasini & A. Sirico
Department of Engineering and Architecture, University of Parma, Parma, Italy

J. Sanchez Montero, J. Torres & N. Rebolledo
CSIC – Institute of Construction Science of Spain, Eduardo Torroja (IETCC), Madrid, Spain

P. Saura
Department of Architectural Constructions, University of Alicante, Alicante, Spain

ABSTRACT: In this paper, an investigation on the shear capacity of naturally corroded prestressed concrete (PC) beams without transversal reinforcement is presented. At first, to estimate the corrosion level, a visual inspection was carried out to detect concrete spalling and cracking, together with chloride concentration, as well as potential, resistivity, and corrosion rate measurements. Moreover, in the damaged areas, measurements of cross-section and weight loss for reinforcement were carried out. Then, the beam was repaired, and full-scale tests were conducted. To evaluate the effectiveness of the repairing system for shear capacity, full-scale tests were conducted by applying a concentrated load close to the ends of the beam - where the strands were subjected to corrosion - and close to the central part of the beam - where strands were uncorroded. The experimental results highlight that, since the repairing system is not able to restore prestress, the shear capacity is strongly reduced also after reparation.

1 INTRODUCTION

Reinforcement corrosion is one of the main causes of deterioration for reinforced concrete structures, which results in significant damages and intervention costs all over the world (Soutsos 2010; Hansson 2011; Menga et al. 2022). This detrimental effect can strongly reduce the bearing capacity of reinforced concrete elements, due to the decrease in the cross-sectional area of reinforcements and the reduced bond stiffening action between reinforcement and concrete. Hence, corrosion can pose severe risks to safety of reinforced concrete structures, being also responsible for the modification of collapse mechanisms from ductile to brittle (Ravasini et al. 2023). In the most critical cases, corrosion can provoke the failure of the structure, even under dead loading (Belletti et al. 2019; Soltani et al. 2019).

In the case of prestressed concrete (PC) elements, the risk of failure becomes higher than in ordinary reinforced members due to the intrinsic higher susceptibility of this kind of prestressed members to corrosion phenomena. Indeed, the bond decay in PC structures causes the de-tensioning and the loss of prestressing force that anticipate brittle failures, often related to shear resistance. However, the scientific literature lacks of experimental tests on shear resistance of naturally corroded PC beams, while it is more focused on ordinary reinforced concrete beams, often artificially corroded (Li et al. 2011; Vecchi et al. 2020; Vereecken et al. 2021). Few experimental test results on naturally corroded beams (Recupero and Spinella 2019) can be found in the literature, and none of them, except the ones by the authors (Belletti et al. 2020; Vecchi et al. 2020), focus on PC beams without transversal reinforcement.

In this paper, the shear behaviour of a PC beam without transverse reinforcement subjected to natural corrosion, induced by chloride exposition of strands is analysed. The tested beam

DOI: 10.1201/9781003483755-59

comes from a group of beams that were part of a thermal power plant located on the Spanish Mediterranean coast and were exposed to wetting and drying cycles with marine water. The environmental aggressivity and the deficiencies in the strand's protection at the ends of the PC beams, caused a fast propagation of corrosion in strands and, for some of them, shear failures.

The visible damage induced by volume expansion and consequent reduction of the cross-sectional area, was longitudinal splitting cracking and cover spalling. The detected damage caused a decay of the bond resistance between concrete and strands that negatively influences flexural and shear capacity of the PC beams (Vecchi et al. 2021; Franceschini et al. 2022).

The paper deals with verifying the effectiveness of patch repairing and other interventions aimed at re-activating the pull-out resistance of strands on the shear capacity of PC beams. The methodology adopted in this research simulates engineering practices for in situ inspections and repairing planning, when no detailed information on the corrosion morphology along the length of the strands is available. Firstly, non-destructive methods were adopted to assess the level of corrosion, such as crack mapping, chloride concentration, potential, resistivity, and corrosion rate measurements. Secondly, based on the in-situ measurement outcomes, a patch repair was applied to deteriorated zones located at both ends of the beam together with specific interventions to reactivate the pull-out resistance of strands along the transmission length. Finally, the shear capacity of the PC beam was experimentally investigated by performing three-point bending tests in three different positions of the beam: at the ends of the beam - where the strands were corroded and then the beam was repaired - and in the central zone - where the strands were uncorroded and then the beam was unrepaired.

2 CORROSION MEASUREMENTS AND REPAIRING SYSTEM

2.1 *Geometry and mechanical properties of the investigated PC beam*

The beam under investigation had a cross-section (b x h) of 150 x 300 mm and a length of 5.21 m. The prestressed beam was characterized by a lower reinforcement formed by two seven-wire strands. The outer wires' diameter is 4.26 mm and the inner one is 4.38 mm, resulting in a total nominal diameter equal to 12.9 mm. The upper reinforcement consisted of two bars with a diameter of 5 mm, whereas the beam did not contain transversal reinforcement. The concrete cover is 50 mm on each side of the beam. The assessment of residual prestress was not experimentally measured but the prestressing stress at the time of testing can be estimated to be equal to 1095 MPa, by considering long-term effects for an age equal to 13 years old and by using the formulations proposed in the literature (fib 2013). The same Standard Code was used also to evaluate the transmission length, which results equal to 365 mm, approximately 30 times the strands' diameter. The mechanical properties, which are summarized in Table 1, were assumed according to the findings on companion beams previously investigated (Belletti et al. 2020; Vecchi et al. 2020).

Table 1. Assumed mechanical properties of concrete, bottom and top reinforcement.

Concrete			Bottom reinforcement			Top reinforcement		
f_c [MPa]	f_{ct} [MPa]	E_c [GPa]	E_p [GPa]	f_{pu} [MPa]	ε_{pu} [%]	E_s [GPa]	f_{sy} [MPa]	ε_{su} [%]
45.4	3.36	35.6	195	1901.75	5	195	435	18

2.2 *Damage mapping*

As the first step, before testing, a visual inspection was conducted to evaluate any type of damage observed on the surface of the beams caused by corrosion. The beam was photographed to find signs of cracks, rust stains, and spalling of concrete cover. Figure 1 shows the most important damages found during the inspection of the beam. With this data, as shown in Figure 2, a damage map was created, which reports also crack opening widths. Significant

damage was found in the concrete cover near the left end of the beam, together with splitting longitudinal cracks along the surface in correspondence with the strands. Moreover, on the top of the right side of the beam in correspondence with the top reinforcement, a longitudinal crack with a maximum width of 0.7 mm was recognized.



Figure 1. Representative damages found during visual inspection.

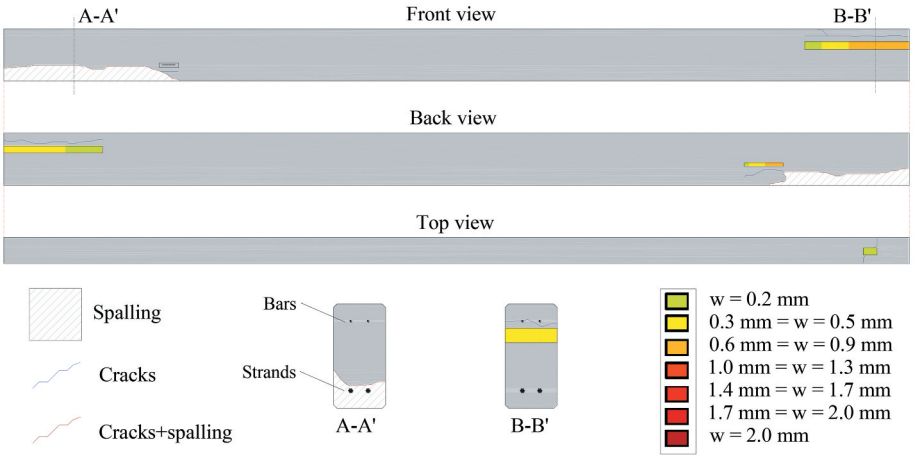


Figure 2. Damage and crack width mapping.

2.3 *Non-destructive electrochemical tests for corrosion assessment*

To assess the corrosion and degradation state of the reinforcement within the beams, various non-destructive tests using electrochemical methods were conducted. These tests include corrosion potential, resistivity, and corrosion rate measurements.

Table 2. Corrosion risk based on potential (ECORR measurements) and resistivity.

Risk of corrosion	Potential - CuSO4 (sat. Cooper sulfate)	Resistivity
Negligible	Ecorr > - 274 mV	> 100 kΩcm
Moderate	- 274 mV > Ecorr > - 424 mV	50 – 100 kΩcm
High	Ecorr < - 424 mV	10 – 50 kΩcm

Corrosion potential mapping was conducted on the lateral surfaces of the beam at 18 points, each 0.30 m apart. Two measurements, at the two sides, placed at the level of strands, were carried out by using the portable GECOR10 corrosimeter. It is important to note that the reference electrode for this equipment is $Cu/CuSO_4$, and the threshold value according to the UNE 112083 Standard for active corrosion (with an assumed risk of corrosion of 50%) is -274 mV, as shown in Table 2. Then, at the same points and by using the same system, resistivity mapping was created.

This measurement provides indirect information about the porosity of the medium and its level of saturation. It is worth noting that lower resistivity values indicate an increased probability of corrosion, as shown in Table 2. The results of the corrosion potential and resistivity mapping of the beams can be observed in Figure 3 and indicate that there is a considerable risk of corrosion near the ends of the beams, confirming the findings of visual inspections.

The corrosion rate was measured at 3 positions on the lateral faces of the beams by means of the portable GECOR10 corrosimeter, with two measurements at the ends and one at the centre of the beam. A corrosion rate (Icorr) of 0.1 μA/cm² or higher indicates active corrosion. The results reported in Figure 4 indicate that the probability of corrosion is higher near the ends of the beam; as previously highlighted.

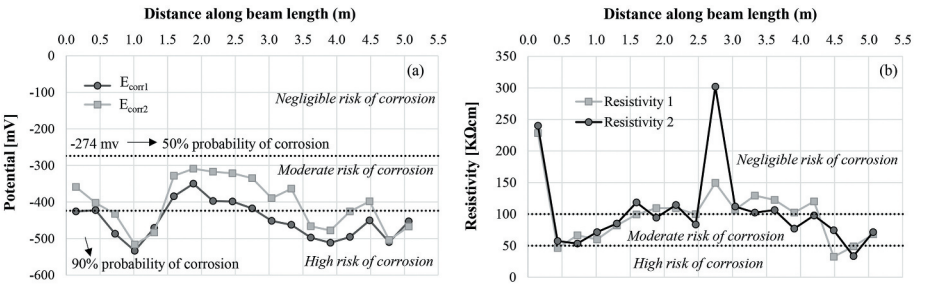


Figure 3. Corrosion measurements: (a) potential and (b) resistivity mapping along the beam length.

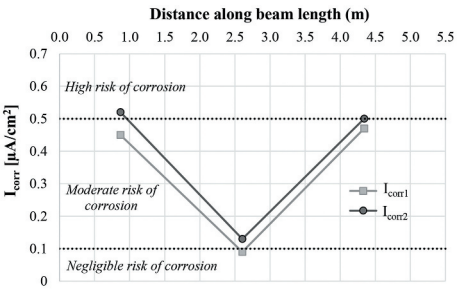


Figure 4. Corrosion rate measurements along the beam length.

2.4 *Chloride concentration*

The measurement of chloride concentration in the concrete was conducted by evaluating the chloride concentration at the reinforcement level. This measurement was carried out by extracting a powdered sample by means of a drill from one side of the beam. The analyses were conducted twice, and then the values obtained were averaged, distinguishing only between the non-cracked and cracked areas. By assuming a cement content of 350 kg/m^3, the percentage of chloride by weight of cement was found to be equal to 2.85% and 2.73%, for cracked and not-cracked areas, respectively. These values are much higher than the limit set by standards, where a value of 0.6% by weight of cement, is the threshold value set for active reinforcement.

2.5 *Measurements of cross-section and weight loss for reinforcement*

The measurement of cross-section loss and weight loss was carried out on both bottom and top reinforcement. The reinforcements were stripped using an acid solution (with eurotropine) to remove corrosion products and allow accurate measurements. A calibre was used to measure the remaining section in the reinforcement areas with cover loss, and an analytical balance was used for weighing. Weight loss values of over 15% have been measured in areas with active corrosion as measured by electrochemical techniques, reaching values of up to 40% in areas where cracking has occurred.

2.6 *Repairing system*

After the visual inspection, a repairing system was designed to be applied to the beam, with the aim of restoring the pull-out resistance of strands. The corrosion of the strands and the related rust volume expansion resulted in cracking and spalling of the concrete cover, especially at the beam extremities, which in turn caused the bond loss, refer to Figure 2. Hence, at beam ends the concrete-to-strands interaction was lost and the beams resulted without residual prestressing force.

At first, the part of the concrete cover affected by cracks caused by reinforcement corrosion was removed by using manual and mechanical methods (Figure 5a). After this removal, the exposed concrete surface was cleaned of dirt and rust residues, leaving the strands clean up to the non-corroded area. For a thorough cleaning, a mechanical sandblasting method was used on both the concrete and steel surfaces. The final clean-up to remove any remaining sand residues was done by using a metal bristle brush and a plastic bristle brush.

Then, at the bottom extremity of the beam where spalling of concrete cover and cracks had been found, 304L stainless steel sleeves designed on purpose (Figure 6) were installed to restore the pull-out resistance of strands. The severely deteriorated parts of the strands were cut, and they were connected to the sleeves by using epoxy resin, as shown in Figure 5b. The diameter of the tubular sleeves was greater enough with respect to that of strands to ensure that the chemical anchoring worked correctly. Then, these sleeves were embedded within a repair mortar used for the patch repairing to re-establish the structural integrity, i.e. the original shape of the transversal cross-section. To this aim, formworks were placed around the beam, and the repair mortar Sika Monotop 4200 Multiflow was used, as seen in Figure 5c. It is worth noting that this type of mortar does not require a bonding bridge with the base concrete. Once poured, compacted, and manually trowelled, the mortar was cured for one day before removing the formwork.



Figure 5. (a) Mechanical cleaning of the beam; (b) placement of metallic sleeves on reinforcement; (c) pouring of repair mortar for the replacement of the beam section and final state after 28 days of curing.

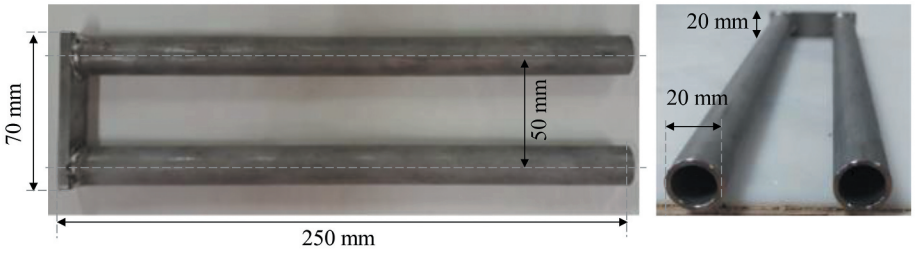


Figure 6. Photos of metallic sleeves for bonding renewal.

3 SHEAR TESTS AND DISCUSSION

3.1 *Experimental setup*

The experimental tests were performed at the "Instituto de Ciencias de la Construccion Eduardo Torroja" in Madrid. The shear behaviour of the corroded and repaired PC beam was investigated by means of three-point bending tests, which were performed thrice: at the two extremities - where the strands were corroded, and the beam was repaired - and in the central zone - where the strands were uncorroded and the beam was unrepaired. Therefore, three experimental tests were carried out on the same specimen. More in detail, the beam was firstly tested on the left end zone (Test 1), then it was tested on the right end zone (Test 2), and finally also in the central part (Test 3).

All three tests were performed by adopting the same ratio between the applied load position, "a" (equal to 750 mm), and the effective depth "d" of the beam (equal to 250 mm), so obtaining a shear span-to-effective depth ratio (a/d) equal to 3. The sketch of the setup of the three tests is reported in Figure 7. The experimental tests were carried out under displacement control, to control the tests during critical phases, as such load drops, sudden cracking, or brittle failure. A quasi-static loading rate of 0.50 mm/min was applied by means of a servo-hydraulic actuator with a loading capacity of 200 kN. The load was applied on the beam by means of steel plates with dimensions 100 mm x 150 mm x 20 mm, while supports were made by roller and 200 mm x 150 mm x 20 mm steel plates. Two linear variable displacement transducers (LVDTs) were utilized for measuring deflections at mid-span and under the loading point.

3.2 *Shear-displacement curves and failure mechanisms*

Figure 8 Shows the shear vs. deflection response, measured under the loading point as well as the crack pattern at failure for the three tests performed.

As can be seen in Figure 8a, the shear resistance of the PC beam tested in the uncorroded central zone (Test 3) was almost double with respect to that obtained in the corroded and repaired areas (Test 1 and Test 2).

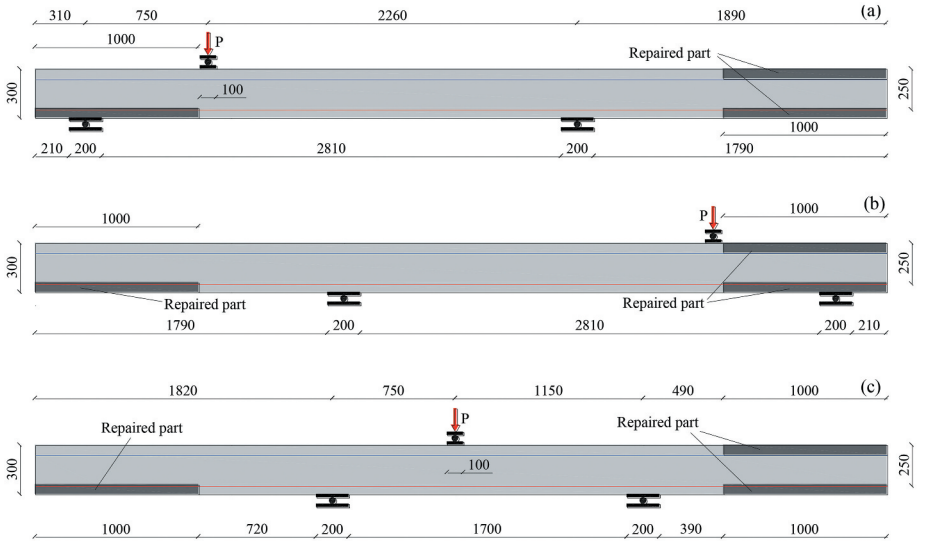


Figure 7. Three-point bending tests performed: (a) at the left end zone (Test 1); (b) at the right end zone (Test 2); (c) in the central zone (Test 3).

More in detail, in Test 3, where the load was applied in the uncorroded and un-repaired central region, flexural cracks developed for a higher value of applied load than Test 1 and Test 2, thanks to the active prestressing force. A main shear diagonal crack suddenly developed causing the failure of the beam (Figure 8d).

In Tests 1 and Test 2 the failure mode of PC beam was similar and characterised by the formation of an inclined shear crack in a region previously cracked in bending. However, in these cases, the anticipated formation of vertical cracks in bending which lead to the premature shear failure, was caused by the loss of residual prestressing force - due to concrete cover spalling during corrosion propagation and concrete removal during cleaning and repairing.

The shear resistance, attributed to the concrete in PC beams without transversal reinforcement, can dramatically decrease when the residual prestressing force is lost by corrosion and/or repairing interventions and the transversal area of strands is reduced due to the formation of pits. The repairing system can effectively protect the strands and re-activate the pull-out resistance but cannot re-introduce the prestressing level previously acting in the uncorroded PC beam. Therefore, particular attention must be paid during the repairing of PC members because patch repairing and other solutions dealing with pull-out strengthening cannot solve the problems related to the loss of the prestressing force.

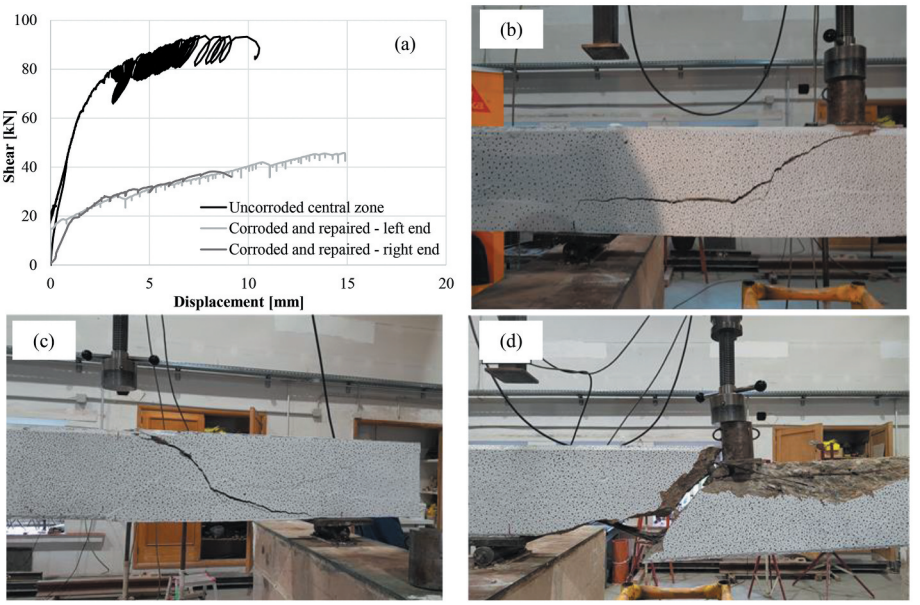


Figure 8. Results in terms of: (a) shear vs. deflection curve; (b-c) crack pattern at failure for the corroded and repaired beam, tested at the left (Test 1) end and at the right end (Test 2), respectively; (d) crack pattern at failure for the test performed at the uncorroded central zone (Test 3).

4 CONCLUSIONS

In this paper, the results regarding the shear behaviour of naturally corroded and repaired PC beams are presented. According to the results obtained, the following conclusions can be drawn.

- The visual inspection is important to highlight longitudinal cracks and concrete cover spalling that reveal corrosion. However, electrochemical tests are required to detect corrosion also in zones without defeat visible to the naked eye and asses the corrosion level distribution along the length of PC elements.
- The presence of corroded strands in PC beams without transversal reinforcement is particularly dangerous since the loss of prestressing force affects the shear resistance attributed to concrete.
- The shear resistance of the PC beam tested in the uncorroded and un-repaired central region was almost double with respect to the shear resistance in the corroded and repaired zones, since the corrosion propagation and the cover removal during repairing caused the total loss of prestressing force.

- The risk of failure in repaired PC members could be even higher than in damaged members because the patch repairing could hide the pre-existing damage, such as splitting cracking or cover spalling that is a sentinel warning of prestressing force loss.

ACKNOWLEDGEMENTS

This study was developed within the PRIN project FIRMITAS "multi-hazard assessment, control and retroFIt of bridges for enhanced Robustness using sMart IndusTriAlized Solutions", which was funded by the Italian Ministry of University and Research.

REFERENCES

Belletti, B., Rodríguez, J., Andrade, C., Franceschini, L., Sánchez Montero, J. and Vecchi, F. 2020. Experimental tests on shear capacity of naturally corroded prestressed beams. *Structural Concrete* 21 (5): 1777–1793.

Belletti, B., Vecchi, F., Bandini, C., Andrade, C. and Montero, J.S. 2019. Numerical evaluation of the corrosion effects in prestressed concrete beams without shear reinforcement. *Structural Concrete* 21(5): 1794–1809.

Conforti, A., Minelli, F. and Plizzari, G.A. 2017. Shear behaviour of prestressed double tees in self-compacting polypropylene fibre reinforced concrete. *Engineering Structures* 146: 93–104.

fib. 2013. fib Model Code for Concrete Structures 2010.

Franceschini, L., Belletti, B., Tondolo, F. and Sanchez, J. 2023. A simplified stress-strain relationship for the mechanical behaviour of corroded prestressing strands: the SCPS-model. *Structural Concrete* 24 (1): 189–210

Hansson, C.M. 2011. The impact of corrosion on society. *Metallurgical and Materials Transactions A: Physical Metallurgy and Materials Science* 42(10): 2952–2962.

Li, F., Yuan, Y. and Li, C.Q. 2011. Corrosion propagation of prestressing steel strands in concrete subject to chloride attack. *Construction and Building Materials* 25(10): 3878–3885.

Menga, A., Kanstad, T., Cantero, D., Bathen, L., Hornbostel, K. and Klausen, A. 2023. Corrosion-induced damages and failures of posttensioned bridges: A literature review. *Structural Concrete*: 24: 84–99.

Ravasini, S., Franceschini, L. and Belletti, B. 2023. Simplified analytical method for moment-curvature response of corroded prestressed concrete beams. *IALCCE 2023 Eighth International Symposium on Life-Cycle Civil Engineering*, July 2-6 2023, *Milan, Italy.*

Recupero, A. and Spinella, N. 2019. Experimental tests on corroded prestressed concrete beams subjected to transverse load. Structural Concrete 20(6): 2220–2229.

Soltani, M., Safiey, A. and Brennan, A. 2019. A state-of-the-art review of bending and shear behaviors of corrosion-damaged reinforced concrete beams. *ACI Structural Journal 116(3)*: 53–64.

Soutsos, M. 2010. Concrete durability: a practical guide to the design of durable concrete structures. *Thomas Telford Ltd.*

Vecchi, F., Belletti, B., Franceschini, L., Andrade, C., Rodriguez, J. and Montero, S.J. 2020. Flexural Tests on Prestressed Beams Exposed to Natural Chloride Action. *Proceedings of the 2nd CACRCS Workshop*, *Parma, Italy*: 205-212.

Vecchi, F., Franceschini, L., Tondolo, F., Belletti, B., Sánchez Montero, J. and Minetola, P. 2021. Corrosion morphology of prestressing steel strands in naturally corroded PC beams. *Construction and Building Materials* 296: 123720.

Vereecken, E., Botte, W., Lombaert, G. and Caspeele, R. 2021. Assessment of corroded prestressed and posttensioned concrete structures: A review. *Structural Concrete* 22(5): 2556–2580.

Bridge Maintenance, Safety, Management, Digitalization and Sustainability – Jensen, Frangopol & Schmidt (eds)
© 2024 The Author(s), ISBN 978-1-032-77040-6
Open Access: www.taylorfrancis.com, CC BY-NC-ND 4.0 license

Risk-based retrofit optimization of deteriorating reinforced concrete bridge columns subjected to corrosion and earthquakes

Sunyong Kim & Yanzhi Yang
Wonkwang University, Iksan, Republic of Korea

Dan M. Frangopol
Lehigh University, Bethlehem, PA, USA

ABSTRACT: This paper presents an approach for risk-based retrofit optimization of reinforced concrete (RC) bridge columns. The proposed approach consists of (a) time-variant seismic performance assessment, (b) time-variant risk assessment, and (c) retrofit optimization. The bridge performance is represented by the time-variant exceedance probability, which indicates the probability of an RC structure exceeding a specific damage state under a given ground motion intensity over time. The effect of corrosion on the exceedance probability is addressed. The damage states of an RC bridge column are defined using the displacement at the top of the column. A 3-dimensional finite element model of the bridge is used to simulate the seismic responses of the RC columns with and without retrofitting. In order to reduce the computational cost for the time-variant exceedance probability, a machine learning technique is adopted. For the time-variant risk assessment, the consequences associated with a specific damage state and associated occurrence probabilities are estimated. The risk assessment is used to formulate the optimization problem for determining the retrofit time for RC bridge columns. The optimization is based on maximizing the benefit ratio during a predefined lifetime.

1 INTRODUCTION

Maintaining the safety of existing bridges under various environmental stressors, deterioration mechanisms, and natural hazards is crucial for ensuring public safety and infrastructure longevity. Over the last several decades, risk has been treated as a rational performance indicator to integrate the occurrence probability of an adverse event for deteriorating bridges and the resulting monetary loss (Zhu & Frangopol 2012; Dong & Frangopol 2015; Frangopol & Kim 2022). Accordingly, several approaches to assess the risk of deteriorating individual bridges and bridge networks have been developed, considering earthquakes, floods, hurricanes, and climate conditions (Stein et al. 1999; Padgett & DesRoches 2007; Decò & Frangopol 2011; Saydam et al. 2013; Zoubir & McAllister 2016; Yang & Frangopol 2019). Based on these approaches, it is necessary to optimize the bridge retrofit for reducing the risk and extending the service life.

In this paper, an approach for risk-based retrofit optimization of reinforced concrete (RC) bridge columns is presented. This approach requires (a) time-variant seismic performance assessment, (b) time-variant risk assessment and (c) retrofit optimization. The seismic performance indicates the probability of exceeding a specific damage state under a given ground motion intensity, where the corrosion propagation is considered. The damage states of an RC bridge column are determined by the displacement at the top of the column. To estimate the effect of retrofit on the seismic responses of the RC columns with and without retrofitting, a 3-dimensional (3D) finite element (FE) model of the bridge is adopted. Through a machine learning (ML) technique, the time-variant seismic performance is computed cost-effectively. Using

DOI: 10.1201/9781003483755-60

the computed time-variant exceedance probability for each damage state, the time-variant risk can be obtained for formulating the optimization problem to determine the retrofit times for RC bridge columns. The optimization is based on maximizing the cost-benefit ratio during a predefined lifetime.

2 TIME-VARIANT SEISMIC PERFORMANCE

The seismic performance can be considered the probability of exceeding a specific damage state under a given peak ground acceleration (PGA). This exceedance probability is expressed as a fragility function at time t

$$P(Dmg(t)|PGA) = \Phi\left[\frac{ln(Med_d(t)) - ln(Med_c(t))}{\sqrt{(\sigma_d(t))^2 + (\sigma_c(t))^2}}\right] \tag{1}$$

where $Dmg(t)$ = damage state of a bridge at time t; $\Phi(\cdot)$ = standard normal cumulative distribution function (CDF); $Med_d(t)$ = median of the seismic demand; $Med_c(t)$ = median of the seismic capacity; $\sigma_d(t)$ = standard deviation (SD) of the seismic demand; and $\sigma_c(t)$ = SD of the seismic capacity. $Med_d(t)$ is estimated using the nonlinear time-history analysis with a 3D FE model. $Med_c(t)$ is predefined for the damage states to be considered. In this study, the denominator in Eq. (1) is assumed to be 0.5 (HAZUS 1999; Banerjee & Ganesh 2013). The effect of corrosion on the fragility function is addressed in estimating $Med_d(t)$.

2.1 *Corrosion initiation and propagation*

The corrosion in the bridge column consists of corrosion initiation and propagation. The corrosion initiation time t_{ini} can be estimated as indicated in Mortagi & Ghosh (2020). Based on both uniform and pitting corrosion propagation models, the remaining reinforcement area $A_r(t)$ at time t can be estimated as indicated in Ghosh & Sood (2016). Finally, the yield strength $f_y(t)$ and ultimate strength $f_u(t)$ of the reinforcement, and compressive strength of the cover concrete $f_{c,cov}(t)$ at time t can be expressed as indicated in Coronelli & Gambarova (2004).

2.2 *Effect of bridge column retrofit on seismic performance*

A bridge column plays a crucial role in providing support and stability to a bridge structure, especially during seismic events. To enhance the seismic performance of bridge columns, retrofitting techniques such as the use of wraparound jackets have been adopted. These jackets, commonly made of materials including steel, carbon fiber, and glass fiber, are applied to existing columns to strengthen and confine them, improving their resistance to earthquakes. Assuming that bridge column jacketing increases the median of PGA resulting in a particular damage state, the logarithm of the median of the seismic demand after bridge column jacketing $ln(Med_d^*(t))$ is expressed as

$$ln\left(Med_d^*(t)\right) = ln(Med_d(t)) \cdot (1 - r_{rt}) \quad \text{for } ln(Med_d(t))0 \tag{2a}$$

$$ln\left(Med_d^*(t)\right) = ln(Med_d(t)) \cdot (1 + r_{rt}) \quad \text{for } ln(Med_d(t)) < 0 \tag{2b}$$

where r_{rt} is the reduction factor associated with retrofit. In this paper, the carbon fiber composite (CFC) jacket is used as a bridge column retrofit. The seismic demand of the bridge column is characterized by the displacement ductility, defined as the ratio between the maximum displacement at the top of the column and the displacement at the same location when the reinforcement attains its yield strength.

3 TIME-VARIANT SEISMIC RISK AND COST-BENEFIT ANALYSIS

Risk is an effective bridge performance indicator for addressing both the probability of occurrence of a specific adverse event and the associated monetary loss (Frangopol & Kim 2022). Based on risk, the cost-benefit analysis can be performed to optimize the bridge column retrofit.

3.1 *Time-variant risk assessment*

The expected seismic risk can be expressed as (Padgett et al. 2010)

$$R(t) = \int_{P_l}^{P_u} R(t|PGA = x)\left|\frac{dP_{exd}(x)}{dx}\right|dx \tag{3}$$

where P_u and P_l are the upper and lower bounds of PGA, respectively; $R(t|PGA = x)$is the seismic risk for a specific PGA equal to x at time t, and $P_{exd}(x)$ is the annual probability of exceeding PGA = x. The annual exceedance probability $P_{exd}(x)$ can be determined by the seismic hazard analysis with the historical earthquake data for a region. The seismic risk $R(t|PGA = x)$ can be computed as (Dong & Frangopol 2015)

$$R(t|PGA = x) = \sum_{i=1}^{N_D} C_{lss,i}(t) \cdot P(Dmg_i(t)|PGA = x) \tag{4}$$

where $C_{lss,i}(t)$ = monetary loss for the ith damage state; $P(Dmg_i(t) \mid PGA = x)$ = fragility function associated with the ith damage state; and N_D is the number of damage states. The fragility function $P(Dmg_i(t) \mid PGA = x)$ is estimated using Eq. (1). The monetary loss $C_{lss,i}(t)$ can be computed as

$$C_{lss,i}(t) = C^{dir}_{lss,i}(t) + C^{ind}_{lss,i}(t) \tag{5}$$

where $C^{dir}_{lss,i}(t)$ and $C^{ind}_{lss,i}(t)$ are the direct and indirect monetary loss, respectively, for the ith damage state at time t.

3.2 *Cost-benefit analysis based on risk*

The cost-benefit analysis for application of the bridge column retrofit can be based on risk assessment. The retrofit reduces the risk by improving the resistance of bridge columns to earthquakes. The cost-benefit can be analyzed by comparing the risk with and without bridge column retrofit. Therefore, the cumulative benefit C_{ben} by applying the retrofit can be expressed as (Padgett et al. 2010; Mondoro & Frangopol 2018)

$$C_{ben} = \int_0^{t_{tg}} [R_0(t) - R_{rt}(t)]dt \tag{6}$$

where t_{tg} is the predefined target time; and $R_0(t)$ and $R_{rt}(t)$ are the expected seismic risk without and with retrofit, respectively. When the cumulative benefit C_{ben} in relation to retrofit cost is investigated, the cost-benefit ratio R_{ben} can be used, which is expressed as (Padgett et al. 2010; Mondoro & Frangopol 2018)

$$R_{ben} = \frac{C_{ben}}{C_{rt}} \tag{7}$$

where C_{rt} is the retrofit cost. In this study, the optimum seismic retrofit for RC bridge columns is based on maximizing the cost-benefit ratio R_{ben}.

4 APPLICATION TO AN EXISTING BRIDGE

The approach presented in this paper is illustrated with an existing RC bridge located in South Korea. In this paper, the bridge columns are treated as a critical bridge component under seismic events (Akiyama et al. 2011; Abbasi & Moustafa 2019). Details of the bridge configuration and associated 3D FE model can be found in Ge et al. (2023).

4.1 *Time-variant fragility analysis using machine learning*

For the time-variant fragility analysis, the four damage states (i.e., slight, moderate, extensive, and complete states) are defined by the displacement ductility of the bridge column. The median of the seismic capacity of the displacement ductility for slight, moderate, extensive, and complete damage states are 1.0, 2.9, 4.6, and 5.0, respectively (Banerjee & Ganesh Prasad 2013). They are used to compute the exceedance probability of Eq. (1). The displacement ductility of the bridge column is computed through the nonlinear time-history analysis of the 3D FE model, where the effects of corrosion on the cross-sectional area of the bridge column, degradation of the yield and ultimate strengths of reinforcement and loss of cover concrete strength are addressed. The nonlinear time-history analysis for estimating the time-variant median value of seismic demand is performed with the response spectrum based on the Korean seismic design code (MOLIT 2018). The logarithmic median value of seismic demand at time t can be expressed as (Hwang et al. 2001)

$$ln(Med_d(t)) = \alpha(t) + \beta(t) \cdot ln(PGA) \tag{8}$$

where $\alpha(t)$ and β (t) are the regression coefficients to represent the relation between ln(PGA) and $ln(Med_d(t))$.

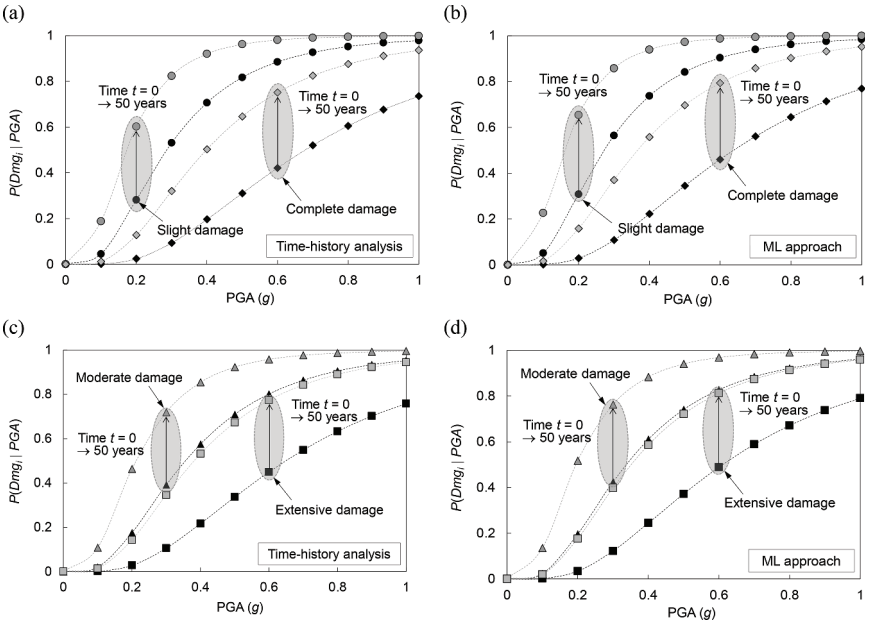


Figure 1. Fragility curves at 0 and 50 years: (a) time-history analysis for slight and complete damage states; (b) ML approach for slight and complete damage states; (c) time-history analysis for moderate and extensive damage states; and (d) ML approach for moderate and extensive damage states.

In order to obtain the coefficients $\alpha(t)$ and β (t) at a specific time t, multiple times of nonlinear time-history analyses should be performed. As the number of times to be investigated for the

time-variant fragility analysis increases, a higher computational cost is required. Recently, ML techniques have been recognized for enhancing the computational efficiency of fragility analysis (Huang & Huang 2020). In this paper, the ML approach based on XGBoost is used. As a result, the coefficients $\alpha(t)$ and $\beta(t)$ in Eq. (8) are expressed in the form of a second-order polynomial as:

$$\alpha(t) = 0.001 \cdot t^2 + 0.0057 \cdot t + 1.02 \tag{9a}$$

$$\beta(t) = 3 \times 10^{-5} \cdot t^2 - 0.0004 \cdot t + 1.89 \tag{9b}$$

Figure 1 shows the fragility curves based on the nonlinear time-history analysis and ML approach at time t = 0 and 50 years for slight, moderate, extensive, and complete damage states. Using Eqs. (8) and (9), the fragility curves at any time t for four damage states can be obtained, and furthermore is used to compute the risk and formulate the optimization for bridge column retrofit.

4.2 *Risk assessment with bridge column retrofit*

The bridge column retrofit using CFC can reduce (a) the seismic demand, which is represented by the reduction factor r_{rt} [see Eq. (2)], (b) the probability of exceeding a specific damage state under a given PGA [see Eq. (1)], and (c) the expected seismic risk [see Eq. (3)]. In order to determine the reduction factor r_{rt}, the relation between $ln(Med_d(t))$ and $ln(Med^*_d(t))$ in Eq. (2) is computed through the nonlinear time-history analysis based on 3D FE model, where the mechanical properties of CFC provided in Chandrasekaran & Banerjee (2016) are used. As a result, the reduction factor r_{rt} is determined as 0.485. Figure 2 shows the seismic risk $R(t|PGA = 0.3g)$ with and without retrofit. It is assumed that the bridge column retrofit is applied to an entire area of the columns, and corrosion of the bridge column continuously propagates after retrofit. The details for the risk assessment are provided in Kim et al. (2023).

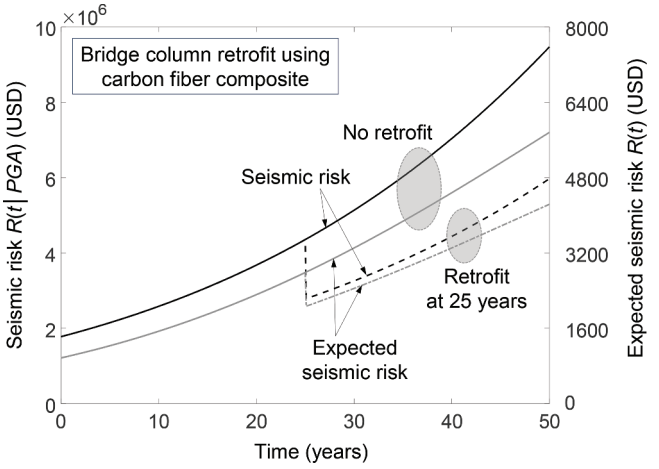


Figure 2. Seismic risk under PGA = 0.3g and expected seismic risk without and with retrofit applied at 25 years.

The expected seismic risk profiles without and with retrofit applied at 25 years are also shown in Figure 2. As indicated in Eq. (3), estimation of the expected seismic risk $R(t)$ requires the annual probability of exceeding a specific PGA, which is based on the seismic hazard analysis for the bridge location. According to Nakajima et al. (2007) and Park et al. (2021), it is estimated as $P_{exd}(x)$ = 0.005·exp[-15x], where x is the PGA ranging from 0g to 1.0g. From

Figure 2, it can be seen that the bridge column retrofit using CFC reduces both the seismic risk for a given PGA and the expected seismic risk.

4.3 *Optimum bridge column retrofit*

The optimum bridge column retrofit using CFC determines the retrofit time to maximize the cost-benefit ratio R_{ben} during the predefined lifetime of 50 years. The cost-benefit ratio R_{ben} is defined as the ratio between the cumulative benefit C_{ben} and retrofit cost C_{rt}, as indicated in Eq. (7). Figure 3 shows the cumulative benefit C_{ben} and cost-benefit ratio R_{ben}, when the retrofit application time t_{rt} ranges from zero to 50 years. The maximum cumulative benefit C_{ben} can be obtained by immediately applying the CFC bridge column retrofit (i.e., t_{rt} = 0 years). The application of the CFC bridge column retrofit at 26.9 years maximizes the cost-benefit ratio R_{ben}.

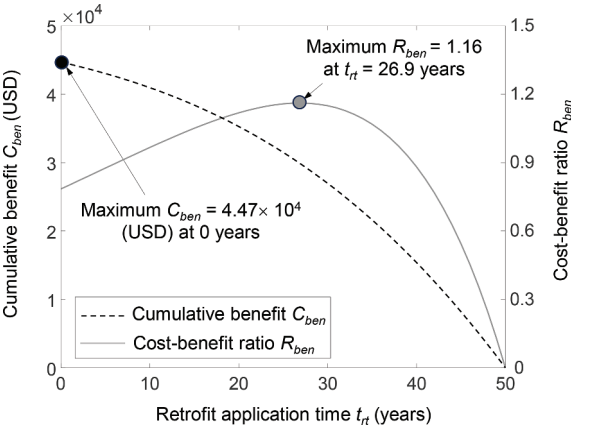


Figure 3. Relation between cumulative benefit and retrofit application time, and between cost-benefit ratio and retrofit application time.

5 CONCLUSIONS

This paper presents an approach to optimize the retrofit of bridge columns. This approach consists of (a) time-variant seismic performance prediction, (b) time-variant risk assessment with and without retrofit, and (c) optimization to determine the retrofit time. The seismic performance is represented by the fragility of a bridge column. The retrofit can reduce the expected seismic risk associated with corroded bridge columns. In the example presented, the cumulative benefit obtained from the retrofit is positive over 50 years. However, it continuously decreases over time. Therefore, to maximize the cumulative benefit, an immediate application of the bridge column retrofit is required. When both the cumulative benefit and retrofit cost are considered, the objective of maximizing the cost-benefit should be adopted for the optimum bridge column retrofit.

ACKNOWLEDGEMENTS

The support by grant from National Research Foundation (NRF) of Korea NRF-2023R1A2C1007097 is gratefully acknowledged. The opinions presented in this paper are those of the authors and do not necessarily reflect the views of the sponsoring organizations.

REFERENCES

Abbasi, M., & Moustafa, M.A. 2019. Time-dependent seismic fragilities of older and newly designed multi-frame reinforced concrete box-girder bridges in California. *Earthquake Spectra*, 35(1): 233–266.

Akiyama, M., Frangopol, D.M., & Matsuzaki, H. 2011. Life-cycle reliability of RC bridge piers under seismic and airborne chloride hazards. *Earthquake Engineering & Structural Dynamics*, 40(15): 1671–1687.
Banerjee, S., & Ganesh Prasad, G. 2013. Seismic risk assessment of reinforced concrete bridges in flood-prone regions. *Structure and Infrastructure Engineering*, 9(9): 952–968.
Chandrasekaran, S., & Banerjee, S. 2016. Retrofit optimization for resilience enhancement of bridges under multihazard scenario. *Journal of Structural Engineering*, 142(8): 1–12.
Coronelli, D., & Gambarova, P. 2004. Structural assessment of corroded reinforced concrete beams: Modeling guidelines. *Journal of Structural Engineering*, 130(8): 1214–1224.
Decò, A., & Frangopol, D.M. 2011. Risk assessment of highway bridges under multiple hazards. *Journal of Risk Research*, 14(9): 1057–1089.
Dong, Y. & Frangopol, D.M. 2015. Risk and resilience assessment of bridges under mainshock and aftershocks incorporating uncertainties. *Engineering Structures*, 83: 198–208.
Frangopol, D.M. & Kim, S. 2022. *Bridge Safety, Maintenance and Management in a Life-Cycle Context*. Boca Raton: CRC Press.
Ge, B., Yang, Y., and Kim, S. 2023. Time-dependent multi-hazard seismic vulnerability and risk assessment of deteriorating reinforced concrete bridges considering climate change. *Structures*, 55: 995–1010.
Ghosh, J., & Sood, P. 2016. Consideration of time-evolving capacity distributions and improved degradation models for seismic fragility assessment of aging highway bridges. *Reliability Engineering & System Safety*, 154: 197–218.
HAZUS 1999. *Earthquake Loss Estimation Methodology*. Technical Manual SR2. Washington, DC: Federal Emergency Management Agency through agreements with National Institute of Building Science.
Huang, C., & Huang, S. 2020. Predicting capacity model and seismic fragility estimation for RC bridge based on artificial neural network. *Structures*, 27, pp. 1930–1939.
Hwang, S.H., Mangalathu, S., Shin, J., and Jeon, J.S. 2021. Machine learning-based approaches for seismic demand and collapse of ductile reinforced concrete building frames. *Journal of Building Engineering*, 34: 101905.
Kim, S., Yang, Y., & Frangopol, D.M. 2023. Optimum seismic retrofit of deteriorating RC bridge columns based on risk, cost-benefit and real option analyses. *ASCE-ASME Journal of Risk and Uncertainty in Engineering Systems*, *Part A: Civil Engineering*, under review.
MOLIT. 2018. *General seismic design* (*KDS 17 10 00*). Ministry of Land, Infrastructure and Transport, (MOLIT), Korea (in Korean).
Mondoro, A., & Frangopol, D.M. 2018. Risk-based cost-benefit analysis for the retrofit of bridges exposed to extreme hydrologic events considering multiple failure modes. *Engineering Structures*, 159: 310–319.
Mortagi, M., & Ghosh, J. 2020. Climate change considerations for seismic vulnerability assessment of aging highway bridges. *ASCE-ASME Journal of Risk and Uncertainty in Engineering Systems, Part A: Civil Engineering*, 6(1): 04020005.
Nakajima, M., Choi, I.K., Ohtori, Y., & Choun, Y.S. 2007. Evaluation of seismic hazard curves and scenario earthquakes for Korean sites based on probabilistic seismic hazard analysis. *Nuclear Engineering and Design*, 237(3): 277–288.
Padgett, J.E., & DesRoches, R. 2007. Bridge functionality relationships for improved seismic risk assessment of transportation networks. *Earthquake Spectra*, 23(1): 115–130.
Padgett, J.E., DesRoches, R., & Nilsson, E. 2010. Risk-based seismic life-cycle cost–benefit (LCC-B) analysis for bridge retrofit assessment. *Structural Safety*, 32: 165–173.
Park, S., Hong, T.K., & Rah, G. 2021. Seismic hazard assessment for the Korean peninsula. *Bulletin of the Seismological Society of America*, 111(5): 2696–2719.
Saydam, D., Bocchini, P. & Frangopol, D.M. 2013. Time-dependent risk associated with deterioration of highway bridge networks. *Engineering Structures*, 54: 221–233.
Stein, S., Young, G.K., Trent, R.E., & Pearson, D.R. 1999. Prioritizing scour vulnerable bridges using risk. *Journal of Infrastructure Systems*, 5(3): 95–101.
Yang, D.Y., & Frangopol, D.M. 2019. Physics-based assessment of climate change impact on long-term regional bridge scour risk using hydrologic modeling: application to Lehigh river watershed. *Journal of Bridge Engineering*, 24(11): 4019099.
Zoubir, L. & McAllister, T.P. 2016. Risk-based decision making for sustainable and resilient infrastructure systems. *Journal of Structural Engineering*, 142(9): F4016005.
Zhu, B. & Frangopol, D.M. 2012. Reliability, redundancy and risk as performance indicators of structural systems during their life-cycle. *Engineering Structures*, 41(8): 34–49.

Bridge Maintenance, Safety, Management, Digitalization and Sustainability – Jensen, Frangopol & Schmidt (eds)
© 2024 The Author(s), ISBN 978-1-032-77040-6
Open Access: www.taylorfrancis.com, CC BY-NC-ND 4.0 license

Life-cycle assessment of riverine bridges under flood and corrosion

R.K. Arora, S. Banerjee & A. Kumar
Department of Civil Engineering, Indian Institute of Technology Bombay, Powai, Mumbai, India

ABSTRACT: Global bridge failure statistics highlight that hydraulic actions, particularly hydrodynamic forces and scour, contribute significantly to bridge failures. Previous incidents reveal that extreme floods can lead to complete inundation, resulting in collapse of bridges. Recent studies underscore the vulnerability of the superstructure during flood events. Despite prior research, understanding the impact of flood-induced hydraulic forces on diverse bridge components, particularly in life-cycle analysis with gradual degradation from chloride-induced corrosion, remains limited. This study utilizes computational fluid dynamics (CFD) simulations through ANSYS Fluent. It evaluates hydrodynamic forces on superstructure of a typical RC riverine bridge, accounting for gradual performance degradation due to corrosion. The study considers flood-induced scour and conducts finite element (FE) analyses at different stages of the bridge's lifespan, offering insights into its life-cycle performance under diverse flood scenarios. These findings inform strategies to mitigate the enhanced flood vulnerability of inland RC river bridges facing future intense flood events.

1 INTRODUCTION

Bridges play a crucial role in network connectivity, serving as essential links across various landscapes such as valleys, rivers, and roads to facilitate efficient transportation. Among them, riverine bridges face unique challenges, particularly related to flood hazards. Cook et al. (2015) and Wardhana and Hadipriono (2003) highlight that over 60% of bridge failures result from hydraulic-related issues, such as hydrodynamic forces, debris forces, and scour. Hydrodynamic forces, specifically drag and lift, are predominant factors influencing bridge components and depend on factors like inundation ratio, force coefficients, water velocity, and cross-sectional area. Most of the past research has explored hydrodynamic forces on bridge superstructures in isolation and are categorized into three categories: experimental, numerical, and empirical studies. Experimental studies, exemplified by Bushra (2010), Dean (2020), and Kerenyi et al. (2009), involve scaled models in experimental flumes to compute hydrodynamic forces for different submergence levels. Numerical simulations, as seen in studies by Greco and Lonetti (2022), Istrati and Hasanpour (2022), and Pregnolato et al. (2022), employ computational fluid dynamics (CFD) to calculate hydrodynamic forces on submerged bridge superstructures. Empirical studies by Arora and Banerjee (2023) and Mondoro and Frangopol (2018) considered empirical formulae given by international bridge design codes. However, these studies have yet to examine the combined effect of hydrodynamic forces and scour comprehensively. Therefore, the study addresses this research gap by considering the simultaneous action of hydrodynamic forces and scours on riverine bridges. Additionally, the study includes a life-cycle assessment focusing on the deterioration of reinforcement bars due to chloride-induced corrosion, as discussed in the following paragraph.

Owing to the presence of microcracks, aggregate particles, and interconnected pores in concrete, chloride ions can permeate the material when its surface is exposed to a corrosive environment. As concrete possesses alkaline properties, it can withstand chloride exposure up to

DOI: 10.1201/9781003483755-61

a certain concentration. The duration it takes for chloride ions to initiate corrosion on reinforcing bars after intrusion is termed as corrosion initiation time. Prolonged corrosion activity leads to the development of hemispherical pits on the surface of reinforcements. These pits may exhibit non-uniform distribution along the length of the rebar and vary in depth. Consistent pit creation with similar depths across the rebar length is termed as uniform corrosion, whereas uneven pit development is referred to as pitting corrosion. The procedure for uniform corrosion is rather straightforward, entailing reduction of rebar diameter to compute the decrease in the cross-sectional area. The corrosion intensity is influenced by multiple factors incorporated in the corrosion rate formulation. Devendiran and Banerjee (2023) presented a detailed understanding of the reduced area calculation due to pitting corrosion. The next section discusses the methodology adopted for this study.

2 METHODOLOGY

This study used a systematic approach to examine how flood-related issues affect different bridge components (Figure 1). The process begins by establishing extreme flood scenarios to be considered for the study. Ideally, this should be based on a site-specific investigation, but since data for the site was unavailable, different combinations of water velocity and water height were considered, as these are the key factors influencing bridge components during floods. The next step involves developing a finite element (FE) model of the bridge and assessing the forces acting on its components. Computational fluid dynamics (CFD) is employed for the superstructure, while a code-based formula is used for the piers. However, most bridge design codes have defined formulas for pier forces; only AS 5100.2 (2017) and CD 356 (2020) provide hydrodynamic force definitions for the superstructure. Additionally, scour depth is calculated using the empirical formula from Arneson et al. (2001). Subsequently, all computed forces are applied to the FE bridge model at varying scour depths, and the response of the bridge components is recorded. Finally, to consider the bridge's life cycle, the corrosion model is integrated into the study, accounting for reduced cross-sectional area and material properties of reinforcement bars.

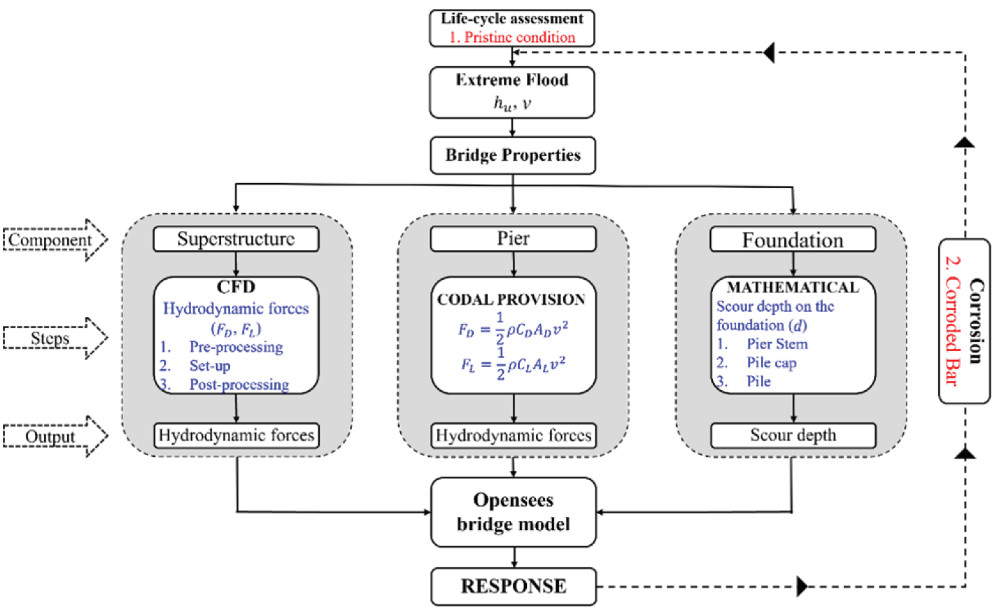


Figure 1. Numerical framework for analyzing the bridge under flood hazard.

3 BRIDGE MODEL

A representative bridge located in the Shetrunji River in Gujarat, India, was chosen as a case study (Figure 2). The bridge is 3-span simply supported with a span length of 20m and a width of 10.1m. The bridge deck is upheld by five concrete T-girders positioned on elastomeric bearings. The bridge consists of two bents, each featuring two piers measuring 0.75m in diameter. The foundations include a pile cap beneath each pier supported by eight circular piles, each with a diameter of 0.46m. A finite element bridge model is developed in OpenSees using Concrete07 for concrete and Steel02 for reinforcement bars. For bridge superstructure, rather than using a single beam stick model, a deck grillage was developed, which can distribute the hydrodynamic load more efficiently. The entire superstructure was modeled as linear elements due to the high lateral stiffness of the bridge. The validity of deck grillage model is cross-checked with an experimental study performed by Song et al. (2016), and the outcomes align favorably with the study at hand. Furthermore, elastomeric bearings with dimensions 0.451×0.146×0.060m are modeled. The bearing pad was modeled as an elastic material, whereas the bars in bearings were modeled as perfectly plastic material. Similar properties are assigned to the bearing in both horizontal directions. Elastomeric bearing is highly stiff in the vertical direction. The cross-section of the pier has 14 number 32mm diameter reinforcing bars, which are modeled as displacement-based fiber elements that consider distributed plasticity. The bridge has two seat-type abutments on both sides with soil modeled as bilinear hysteretic behavior. Further impact elements are also modeled in the bridge between 2 adjacent spans and between span and abutments. At last, the foundation was modeled, which has a 1m thick pile cap with dimensions shown in Figure 2. The soil surrounding the piles is simulated using p-y, t-z, and q-z springs in accordance with the API (2000) recommendations. The p-y spring characterizes soil properties in both horizontal directions. In contrast, the t-z spring represents the vertical soil properties, and the q-z spring signifies the lowermost spring at the piles. The subsequent section describes the hydrodynamic forces considered for this study on different bridge components.

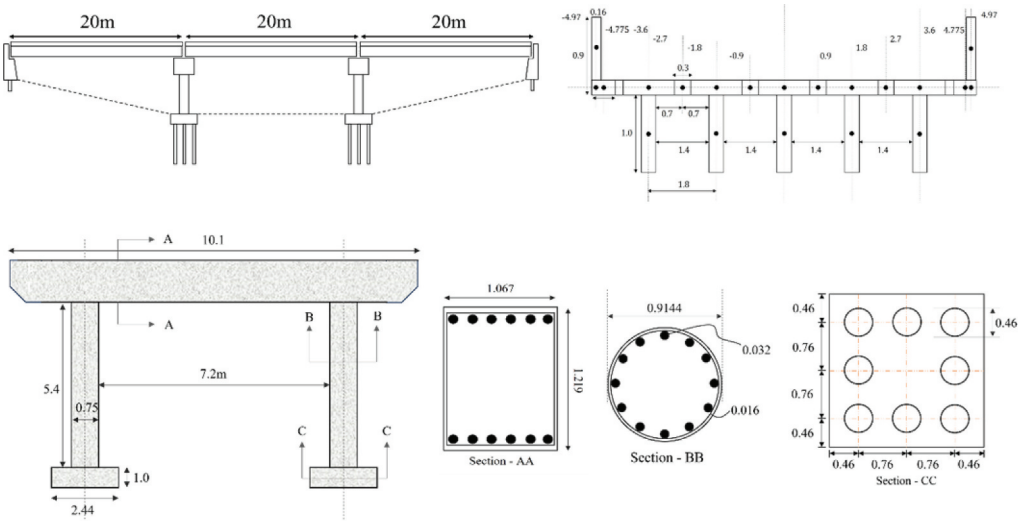


Figure 2. Bridge model considered in the study.

3.1 *Hydrodynamic loads on piers*

This research focused on analyzing the hydrodynamic loads, specifically the drag and lift forces, exerted on bridge components during extreme flood conditions. The hydrodynamic forces exerted on bridge piers were computed in accordance with established bridge design

codes, as these codes typically provide clear guidelines for calculating hydrodynamic loads on piers. Based on major design codes, the following expressions are used in this study to compute the drag (F_d) and lift (F_l) forces on piers.

$$F_d = \frac{1}{2}\rho.C_d.A_d.v^2 \tag{1}$$

$$F_l = \frac{1}{2}\rho.C_l.A_l.v^2 \tag{2}$$

In this context, ρ represents the density of water, and v represents the mean flow velocity. The variables A_d and A_l denote the respective cross-sectional areas that experience drag and lift forces. However, concerning the bridge superstructure, detailed information on hydrodynamic loads is only mentioned in AS5100.7 (2017) and CD356 (2020); other codes lack comprehensive descriptions in this regard. Therefore, numerical modeling approach has opted to compute the forces on superstructure.

3.2 *Hydrodynamic forces on superstructure*

To compute the hydrodynamic forces exerted on the bridge superstructure, a Computational Fluid Dynamics (CFD) simulation is employed, and Ansys Fluent is selected among various available software for this purpose. The superstructure model detailed in Section 2 is recreated in ANSYS Fluent at a reduced scale of 1:40. In Ansys, the κ – ε turbulence model is widely used for fully submerged superstructures. The Shear Stress Transport (SST) κ – ω turbulence model combines the advantages of κ – ε and κ – ω models, enhancing boundary layer behavior and flow separation capture. Past studies employed the Volume of Fluid (VoF) transient multiphase model for free surface tracking (Kerenyi et al., 2009). In this study, VoF multiphase (air and water) with κ – ω SST turbulence model is applied. Inlet, outlet, and free surface boundary conditions, including velocity and submergence, are detailed further. The hydrodynamic forces acting on superstructures are influenced by various crucial parameters, with water height and water velocity being two key determinants. Water height is alternatively expressed as the inundation ratio, defined as the ratio of the difference between the water level (h_u) and the soffit level of the girder (h_b) to the thickness of the superstructure (s) (Equation 3).

$$h^* = \frac{h_u - h_b}{s} \tag{3}$$

Essentially, it signifies the degree of submergence of the superstructure relative to water. In this study, two scenarios are examined: one involving partial submergence ($h^* = 0.5$) and the other a full submergence ($h^* = 2$). The water velocity range selected in this study was based on prior research done on submerged superstructures and varies from 1 to 3 m/s, For the CFD simulations aimed at calculating hydrodynamic forces, an interval of 0.25 m/s is employed. Further, to ensure accuracy, a mesh convergence study is conducted using three distinct meshing schemes: single-face, double-face, and multi-block meshing. The validation of these meshing strategies is cross-checked by Kerenyi et al. (2009), with the double-face meshing method being adopted for this study in accordance with Kerenyi's findings. Additionally, a time-step convergence study is carried out, and a time step of 0.005 seconds is chosen for the subsequent analysis.

3.3 *Life-cycle consideration*

To assess the life cycle deterioration of the bridge, corrosion initiation time (T_{ini}) was computed using Equation 4.

$$T_{ini} = \left\{ \frac{X^2}{4k_e k_c D_{cl,0} (t_0)^{n_{cl}}} \left[\text{erf}^{-1} \left(\frac{C_s - C_{th}}{C_s} \right) \right]^{-2} \right\}^{\frac{1}{(1-n_{cl})}} \quad (4)$$

The variation of corrosion rate over time for pitting corrosion is illustrated in Figure 3. The correction parameter for curing (k_c) is 0.16, and environmental influences (k_e) is 0.68, X (50.8 mm) is the concrete cover of the exposed component, $D_{cl,0}$ (473 mm/year) denotes the reference diffusion coefficient, C_s (9.5 kg/m^3) denotes the surface chloride concentration of the bridge component (Dey & Sil, 2021), C_{th} is the chloride concentration threshold, which is set at 0.52 kg/m^3 (Caltrans, 2018), and n_{cl} (0.65) is an age exponent that represents the susceptibility of reinforcing bars to corrode owing to cement densification caused by hydration. The initiation time for this study comes out to be 7.7 years. The time-varying area reduction ratio of rebar (Reduced Area/Original Area) due to pitting corrosion is shown in Figure 4. After the computation of reduced area, the area of reinforcement in the T-girder is reduced in the FE (Finite Element) model for that particular year, and the modified degraded bridge is used for further analysis.

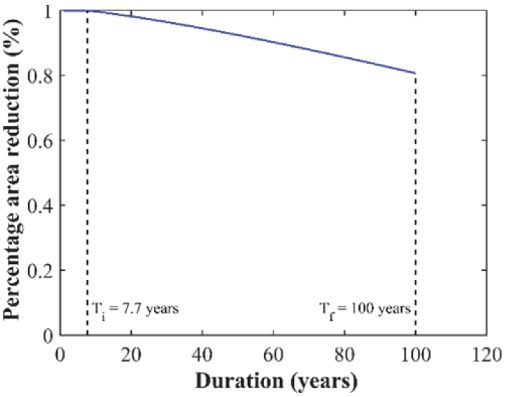


Figure 3. Percentage area reduction vs time.

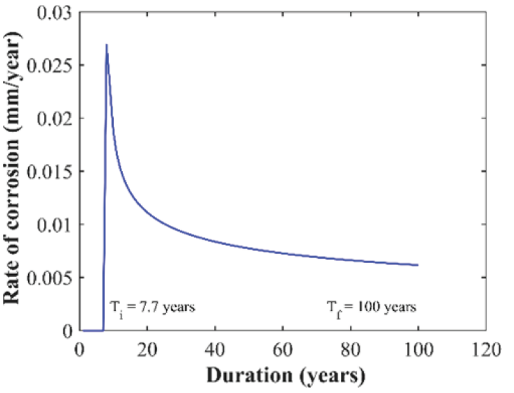


Figure 4. Rate of corrosion vs time.

3.4 *Damage states associated with different bridge components*

Once the bridge model, hydrodynamic forces, and corrosion model is done, the subsequent step involves defining the damage states linked to various bridge components. Specifically, damages to the bridge superstructure are evaluated in relation to the bearing dimensions (which are 25%, 50%, and 75% of half of bearing length), as the bridge girders rely on these bearings for support. The bearing damage states are adopted from Yilmaz et al. (2016). To define the damage state associated with pier, curvature ductility is selected as the governing parameter as they are generally designed as flexural components. Moment-curvature analysis is performed for the pier section to compute the curvature ductility associated with each damage state. Based on this, the actual moment-curvature curve is established. Further, based on the actual moment-curvature curve, an idealized curve is derived. In this context, four damage states are defined. The curvature associated with rebar yielding (ϕ_y) marks the initiation of piers' plastic deformation representing minor damage. Pier failure occurs when the core concrete crushes (i.e., at $\phi_{cu\text{-}core}$) representing a failure scenario. Between yielding and collapse, two intermediate damage (namely moderate and major) thresholds are defined: one when the concrete cover crushes ($\phi_{cu\text{-}cover}$) and the other when two-thirds of the ultimate core crushes ($\phi_{2/3cu\text{-}core}$). Table 1 provides detailed curvature ductility values (both upper and lower bounds) for each damage state. Identifying such damage states is crucial for determining post-event recovery measures for piers.

Table 1. Damage states for different bridge component.

S.no	Damage states	Superstructure lateral displacement [Δ_S] (mm)	Bearing lateral displacement [Δ_B] (mm)	Pier curvature ductility [ϕ]
1	Minor	*≤ 56*	*30 – 88*	*1.0 – 3.82*
2	Moderate	*56 – 113*	*88 – 282*	*3.82 – 9.91*
3	Major	*113 – 169*	*282 – 335*	*9.91 – 14.38*
4	Collapse	*169 ≥*	*335 ≥*	*14.38 ≥*

4 RESULTS AND DISCUSSION

Figure 5a illustrates the lateral displacement of the superstructure under inundation levels 0.5 and 2, pertaining to water velocity under no scour conditions. The lateral response exhibits a positive correlation with velocity, attributed to the increase in hydrodynamic forces as water velocity rises. While the displacement is minimal at lower velocities, it escalates rapidly once the velocity surpasses 1.5m/s. The maximum displacement under pristine conditions occurs at a velocity of 3.5m/s, reaching 32mm. In contrast, the response for a corroded section under inundation level 2 is 37mm. Figure 5b depicts similar plots for a 5m scour case. The maximum response under pristine conditions for inundation level 2 is 40.5mm, whereas, for a corroded section, the superstructure response is approximately 46mm. It is worth noting that the Opensees bridge model experiences failure under inundation level 2 for a velocity of 4m/s in both scour cases. This basically represents that superstructure is undergoing minor damage and moderate damage for a velocity of around 3.6m/s. There is a noticeable contrast in the superstructure lateral displacement between the two scour scenarios.

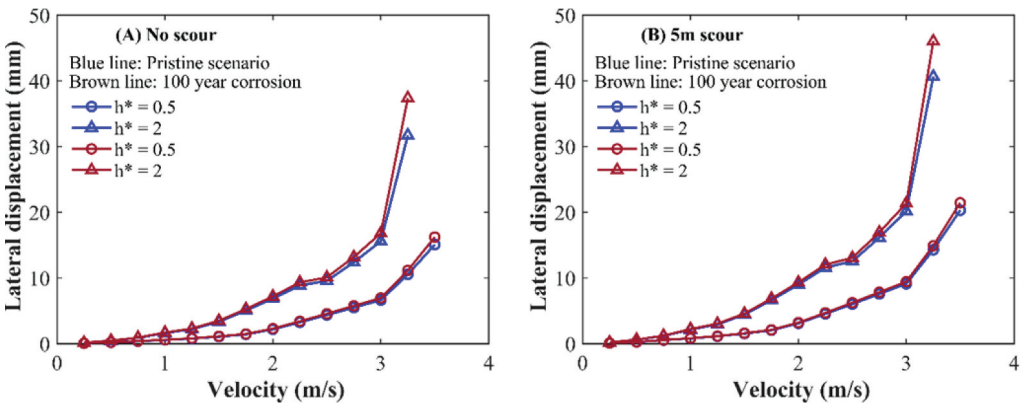


Figure 5. Lateral displacement of the superstructure for different inundation levels and corrosion scenarios (a) No scour and (b) 5m scour.

Figure 6 depicts the lateral displacement of the bearing across various scour scenarios, considering both pristine and a 100-year corrosion case. The recorded displacements for the bearings are notably minimal or no change, even in the presence of scour. Additionally, the marginal difference in response between the two inundation levels suggests that bearings are not susceptible components under hydrodynamic loading and even for maximum scour.

Figure 7 depicts the bridge pier response in terms of curvature ductility for different inundation levels and pristine and 100-year corroded section. The pier response depicted in Figure 7 shows a resemblance in both scour scenarios concerning the specified inundation levels. In each case, the maximum curvature ductility is observed at 3.5m/s, exceeding a value of 2, signifying minor damage to the piers resulting from hydrodynamic forces. This also represents that the pier is the second most vulnerable component in the bridge model due to hydrodynamic forces.

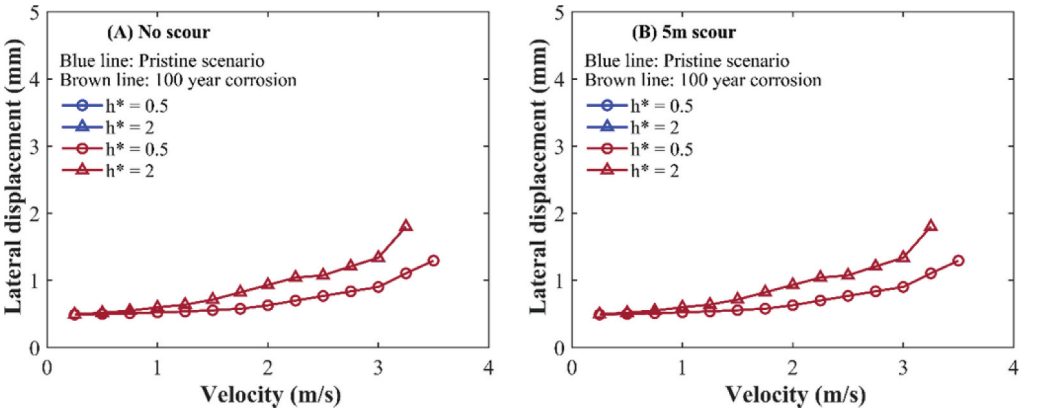


Figure 6. Lateral displacement of the bearings for different inundation levels and corrosion scenarios (a) No scour and (b) 5m scour.

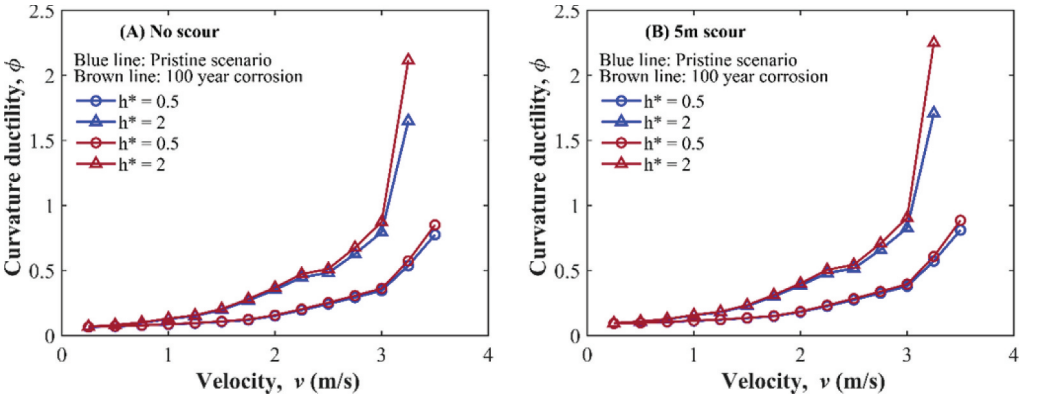


Figure 7. Curvature ductility of the pier for different inundation levels and corrosion scenarios (a) No scour and (b) 5m scour.

The methodology employed in this research draws from both code-based and computational dynamics simulations. To the best of the author's knowledge, no prior study has utilized a comparable approach. While individual studies have explored code-based and numerical methods, this novel methodology requires further refinement, and the results obtained using this approach warrant additional assessment.

5 CONCLUSIONS

This study considers the effect of hydrodynamic forces and scour on riverine bridges at various inundation levels. Additionally, this study conducted a life-cycle analysis that considered the gradual degradation of reinforced concrete (RC) bridges over 100 years. A representative bridge on the Shetrunji River in Gujarat region of India is selected for this study. The bridge is modeled in Opensees with superstructure as deck grillage, pier as fiber-based element and soil below the ground is modeled using p-y, t-z and q-z spring properties following API recommendations. The hydrodynamic forces for the superstructure are computed based on CFD simulations in Ansys fluent, whereas for substructure, these forces are computed using code provisions. These forces are exerted on the bridge model developed in OpenSees, leading to several conclusions drawn from the analysis, which are outlined below.

1) In the context of life-cycle analysis, the onset of pitting corrosion occurred at 7.7 years. Additionally, the cross-sectional area of the rebar, designed for a 100-year lifespan, was reduced by 20%.
2) The maximum superstructure displacement was observed at a velocity of 3.5m/s for 5m scour cases at inundation level 2 under pristine conditions, measuring 40.5mm. In contrast, for the 100-year corrosion scenario, it was recorded as 46mm. Further, the maximum response for superstructure can go up to moderate damage at a velocity of 3.6m/s. The bridge bearings exhibit minimal response to hydrodynamic forces, indicating no damage.
3) The OpenSees bridge model experiences failure at inundation level 2 at velocity 4m/s for both scour cases. This failure primarily pertains to the bridge superstructure, as neither the bearings nor the piers exhibit specific damage.
4) Pier responses were evaluated based on curvature ductility, and various damage states were computed using moment-curvature analysis. Under 5m scour and a corroded section subjected to maximum water velocity, the pier experienced minor damage.

In the future, this study can be extended to explore the uncertainties linked to both flow properties and structural properties.

REFERENCES

API. 2000. *Recommended Practice for Planning, Designing and Construction Fixed Offshore Platforms-Working Stress Design*.

Arneson, L.A.M., Zevenbergen, L.W., Lagasse, P.F, & Clopper, P.E. 2001. *Evaluating scour at bridges, Hydraulic Engineering Circular (HEC) No. 18*, *Publication No. FHWA-HIF-12-003.* Federal Highway Administration, Department of Transportation, Washington, DC, U.S.

Arora, R.K. & Banerjee, S. 2023. Reliability-based approach for fragility assessment of bridges under floods. *Structural Engineering and Mechanics*, 88(4): 311–322.

AS 5100.2. 2017. *Bridge Design, Part 2: Design loads*. www.standards.org.au

Bushra, A. 2010. Computational fluid dynamics of hydrodynamic forces on inundated bridge decks and the effect of scaling. [PhD Thesis]. University of Nebraska.

CD 356. 2020. Design of highway structures for hydraulic action. Highway England.

Cook, W., Barr, P.J., & Halling, M. W. (2015). Bridge Failure Rate. *Journal of Performance of Constructed Facilities*, 29(3). https://doi.org/10.1061/(asce)cf.1943-5509.0000571

Dean, M.T. 2020. Laboratory Study of Hydrodynamics of Submerged Bridges. [MSc Thesis]. University of Texas.

Devendiran, D.K. & Banerjee, S. 2023. Influence of Combined Corrosion–Fatigue Deterioration on Life-Cycle Resilience of RC Bridges. *Journal of Bridge Engineering*, 28(5). https://doi.org/10.1061/jbenf2.beeng-5708

Greco, F. & Lonetti, P. 2022. Vulnerability Analysis of Structural Systems under Extreme Flood Events. *Journal of Marine Science and Engineering*, 10(8): 1121. https://doi.org/10.3390/jmse10081121

Istrati, D. & Hasanpour, A. 2022. Numerical investigation of bam break-induced extreme flooding of bridge superstructures. *3rd International Conference on Natural Hazards and Infrastructures*, July.

Kerenyi, K., Sofu, T., & Guo, J. 2009. Hydrodynamic Forces on Inundated Bridge Decks. Federal Highway Administration Publ. No. In Report No. FHWA-HRT-09-028 (Issue May). http://www.fhwa.dot.gov/publications/research/infrastructure/hydraulics/09028/

Mondoro, A. & Frangopol, D.M. 2018. Risk-based cost-benefit analysis for the retrofit of bridges exposed to extreme hydrologic events considering multiple failure modes. *Engineering Structures*, 159, 310–319. https://doi.org/10.1016/j.engstruct.2017.12.029

Pregnolato, M., Winter, A.O., Mascarenas, D., Sen, A.D., Bates, P., & Motley, M.R. 2022. Assessing flooding impact to riverine bridges: An integrated analysis. *Natural Hazards and Earth System Sciences*, 22(5): 1559–1576. https://doi.org/10.5194/nhess-22-1559-2022

Song, X., Melhem, H., Li, J., Xu, Q., & Cheng, L. 2016. Effects of Solar Temperature Gradient on Long-Span Concrete Box Girder during Cantilever Construction. *Journal of Bridge Engineering*, 21(3), 1–16. https://doi.org/10.1061/(ASCE)BE.1943-5592.0000844

Wardhana, K. & Hadipriono, F.C. 2003. Analysis of recent bridge failures in the United States. *Journal of Performance of Constructed Facilities*, 17(3): 144–150. https://doi.org/10.1061/(ASCE)0887-3828(2003)17:3(144)

Yilmaz, T., Banerjee, S., & Johnson, P.A. 2016. Performance of Two Real-Life California Bridges under Regional Natural Hazards. *Journal of Bridge Engineering*, 21(3). https://doi.org/10.1061/(asce)be.1943-5592.0000827

Bridge Maintenance, Safety, Management, Digitalization and Sustainability – Jensen, Frangopol & Schmidt (eds)
© 2024 The Author(s), ISBN 978-1-032-77040-6
Open Access: www.taylorfrancis.com, CC BY-NC-ND 4.0 license

Life-cycle cost-benefit analysis of an SMA-steel reinforced bridge under earthquakes

Jing Qian & Tong Guo
School of Civil Engineering, Southeast University, Nanjing, People's Republic of China

You Dong
Department of Civil and Environmental Engineering, The Hong Kong Polytechnic University, Hong Kong, People's Republic of China

Yue Zheng
College of Civil Engineering, Tongji University, Shanghai, People's Republic of China

ABSTRACT: The shape memory alloy (SMA) is a type of advancing material with flag-shaped hysteretic behavior. Compared with the conventional bridge, the SMA-steel reinforced bridge can mitigate seismic hazards due to its self-centering characteristics. The economic cost and carbon dioxide emissions of producing the SMA material are relatively higher compared with conventional steel. Within the life cycle of bridges, multiple earthquakes and continuous deterioration can occur resulting in accumulated consequences. It is necessary to conduct a cost-benefit analysis in a life-cycle context. In this study, the life-cycle earthquakes are modeled using a stochastic process. The deterioration is modeled to compute the time-dependent seismic fragility by considering the chloride attack. The life-cycle benefit of the SMA-steel reinforced bridge is computed in terms of sustainability (e.g., social, economic, and environmental aspects) and resilience. The economic and environmental cost of constructing the novel bridge is obtained from historical data. The life-cycle cost-benefit analysis is finally conducted. The advantages of the novel bridge are revealed in a life-cycle context, which can aid the design of bridges for a sustainable and resilient future.

1 INTRODUCTION

Within the service life of bridges, multiple earthquakes can occur and cause consecutive structural damage, resulting in accumulated consequences in social, economic, and environmental aspects. In the meantime, bridges can deteriorate over time in a marine environment due to chloride exposure, resulting in time-variant performance.

Self-centering characteristics are important for structures to mitigate damages under earthquakes, the concrete walls equipped with friction devices were developed, and their effectiveness of self-centering capability and damage mitigation has been confirmed (Guo et al. 2017, 2018). The shape memory alloy (SMA) is a type of advancing material associated with self-centering characteristics and corrosion resistance (Fang et al. 2022, 2017, 2014, Xiang et al. 2020, Billah & Alam 2012). A novel bridge design equipped with SMA-steel reinforcement has been developed for the purposes of mitigating the consequences by adapting compound earthquakes and corrosion (Fang et al. 2021, Li et al. 2021, Muntasir Billah & Alam 2015, Xiang et al. 2020, Zheng & Dong 2019). The construction of the SMA-steel reinforced bridge needs higher construction cost and produces more carbon dioxide emissions compared with the conventional bridge. Due to the risk associated with climate change, decision-makers have invested tremendous attention in carbon dioxide emissions to achieve the goal of carbon neutrality (Anderson & Peters 2016, Wang et al. 2021). The benefit of an adaptation measure is

DOI: 10.1201/9781003483755-62

event-dependent and can be accumulated from multiple events over time. The performance of SMA-steel reinforced bridge has been assessed (Qian et al. 2022b).

However, the cost-benefit analysis in a life-cycle context for the SMA-steel reinforced bridge has not been well conducted. In this study, a life-cycle cost-benefit analysis covering the criteria of sustainability and resilience is developed. Then, it is implemented on an SMA-steel reinforced bridge. New insights on the cost-benefit results of the novel bridge are provided in a life-cycle context.

2 AN SMA-STEEL REINFORCED BRIDGE

The SMA is a type of advancing material associated with the characteristics of super elasticity. The SMA bars are found to present a flag-shaped constitutive behavior upon loading and unloading. Due to the self-centering capacity, the SMA bar can almost return to its pre-loading position after experiencing considerable deformation. Additionally, the SMA material is associated with superior corrosion resistance, it can be used in a marine environment to prevent the corrosion induced by chloride penetration. Considering the advantages of self-centering characteristics and corrosion resistance, the SMA material can be implemented into structures for adapting to earthquakes and corrosion in a life-cycle context.

The SMA bars have been used in the plastic hinge of the pier to develop the SMA-steel reinforced bridge. Within the service life, bridges can experience multiple stochastic earthquakes and time-dependent corrosion. Under compound earthquakes and corrosion, the sustainability and resilience of the SMA-steel reinforced bridge can be improved compared with the conventional bridge (Qian et al. 2022b), while the construction cost and carbon dioxide emissions of the SMA-steel reinforced bridge are much higher. It is essential to conduct a cost-benefit analysis in a life-cycle context to facilitate the decisions of future implementation.

3 LIFE-CYCLE COST-BENEFIT ANALYSIS: SUSTAINABILITY AND RESILIENCE

3.1 *Deterioration and earthquakes within the service life of bridges*

The bridges can deteriorate along with the service life in a marine or deicing salt environment. The chlorides can propagate through the concrete cover and contact with reinforcing steel, initiating corrosion. The corrosion initiation time for the deicing salt environment is expressed as (Enright & Frangopol 1998)

$$T_{i,deicing} = \frac{x^2}{4D_C}\left[erf^{-1}\left(\frac{C_s - C_{cr}}{C_s}\right)\right]^{-2} \tag{1}$$

where x is the cover concrete depth; D_C is the diffusion coefficient; C_s is the equilibrium chloride concentration at the concrete surface; C_{cr} is the critical chloride concentration; and the *erf* is the Gaussian error function.

The corrosion can cause the loss of steel area over time. The time-dependent area of the steel considering uniform corrosion can be calculated as (Enright & Frangopol 1998, Shekhar et al. 2018)

$$A_U(t) = \begin{cases} \frac{\pi}{4}D_i^2 & \text{for } t \le \mathrm{T_i} \\ \frac{\pi}{4}\left[D_i - 2\int_{T_i}^{t} r_{corr}(t_p)dt_p\right]^2 & \text{for } 2\int_{T_i}^{t} r_{corr}(t_p)dt_p < D_i \\ 0 & \text{for } D_i \le 2\int_{T_i}^{t} r_{corr}(t_p)dt_p \end{cases} \tag{2}$$

where D_i represents the diameter of the original steel bar; r_{corr} is the corrosion rate; and T_i is the corrosion initiation time.

In real observations, the area loss of the steel was found to be nonuniform, deep pits can appear along the length of the steel. To incorporate the nonuniform corrosion effects, the

pitting corrosion model was developed (Zandi Hanjari et al. 2011). A pitting factor is used to describe the relative area loss of pitting corrosion conditioned on uniform area loss.

Rust is produced due to the corrosion of steel, resulting in an increased volume of steel bars. Concrete cracks or even spalling can occur due to the expansion effects. In this circumstance, the concrete strength can be modeled in a time-dependent manner (Rao et al. 2017, Shekhar et al. 2018).

Within the life cycle of bridges, the occurrence time, the number, and the intensity of the earthquakes are uncertain. The probabilistic occurrence time of the earthquakes is generally modeled using a stochastic process. The Brownian passage-time (BPT) renewal process is considered herein to model the nonstationary arrival process of earthquakes (Li et al. 2020, Matthews et al. 2002). The probabilistic inter-arrival time of earthquakes is modeled using a probability density function (PDF) of BPT distribution as

$$f_W(x) = \left(\frac{\mu}{2\pi\alpha^2 t^3}\right)^{1/2} \exp\left\{-\frac{(t-\mu)^2}{2\mu\alpha^2 t}\right\} \tag{3}$$

where μ and α are the mean and coefficient of variation, respectively.

The ground motion prediction models (GMPMs) can be used to output the probabilistic distribution of earthquake intensity (Boore et al. 2014). The GMPMs are expressed as the functions of several characteristic parameters (e.g., magnitude, distance, fault type, etc.). By integrating the stochastic process model and GMPM, the probabilistic earthquake scenarios within the service life of the bridges can be simulated.

3.2 *Sustainability and resilience*

Sustainability is measured by social, economic, and environmental criteria (Dong et al. 2013). The social metric can be expressed as the number of fatalities due to the collapse of the structures. The economic metric can be calculated as the sum of the direct and indirect losses. The direct loss is related to the repair cost of the damaged structures. The indirect loss consists of time loss and running cost which is induced by the loss of functionality of the bridge due to damage. For instance, the traffic capacity and speed can be limited once the damage occurs on the bridges. Some vehicle users may follow the original route by reducing the speed on the damaged transportation network or following the detour to destinations, resulting in additional running cost and time loss (e.g., wage and compensation). The detailed quantification method of the time-dependent social and economic metrics can be found in a previous study (Dong et al. 2013). The environmental metric is considered as carbon dioxide emissions. In the context of carbon neutrality, carbon dioxide which is a greenhouse gas has been receiving increasing attention. It can cause global warming and bring enormous adverse effects to society. The carbon dioxide emissions associated with the repair activities of the damaged bridge can be quantified based on the amount of repair materials used and the relevant transportation conditions.

The time-dependent carbon dioxide emissions induced by the detour traffic is quantified as

$$EN_{DT}(t, IM) = \sum_{i=1}^{4} P_{DS_i}(t, IM).ADTD_{DS_i}.D_l.d_{DS_i}.[Enp_{car}.(1-T) + Enp_{Truck}.T] \tag{4}$$

where $P_{DSi}(t, IM)$ is the probability of being in damage state i given time t and intensity IM; $ADTD_{DSi}$ is the daily traffic following detour for damage state i; D_l is the detour length; d_{DSi} represents the time of detour for damage state i; T is the average daily truck traffic ratio; Enp_{car} and Enp_{Truck} represent the carbon dioxide emitted per unit distance for cars and trucks, respectively.

Resilience is the other emerging indicator that can be used to measure the capability of the systems to withstand, adapt, and recover from extreme events (Timmerman 1981, Yang & Frangopol 2019). The time-dependent resilience loss index is expressed as (Qian et al. 2022a)

$$R_L(t, IM) = \frac{t_h.100\% - \int_{t_i}^{t_i+t_h} Q(t_r|t)dt_r}{t_h} \tag{5}$$

where t_h is the investigated recovery time horizon of interest; and $Q(t_r|t)$ is the time-dependent functionality of the bridge after the hazard event.

3.3 *Life-cycle cost-benefit analysis*

The construction cost and carbon dioxide emissions of the SMA-steel reinforced bridge are higher than those of the conventional bridge. Cost-benefit analysis should be conducted in a life-cycle context to account for the accumulated consequences under multiple events. The long-term sustainability or resilience loss is computed by accumulation (Zheng et al. 2018)

$$L = \sum_{k=1}^{N_h(t_L)} L_k(t_k).e^{-rt_k} \tag{6}$$

where t_L is the considered service time of a system; $N_h(t_L)$ is the number of disruptions within t_L; L is the long-term sustainability or resilience loss; $L_k(t_k)$ is the sustainability or resilience loss induced by event k at time t_k; and r is the monetary discount rate. The monetary discount rate becomes zero for computing the non-monetary metrics of long-term sustainability and resilience.

The relative reduction of long-term loss by implementing a measure is expressed as (Bastidas-Arteaga & Stewart 2015)

$$\Delta L(T_s) = \frac{L_{exicisting}(T_s) - L_{adaptation}(T_s)}{L_{exicisting}(T_s)} \tag{7}$$

where T_s is the service time of the bridge; $L_{existing}(T_s)$ and $L_{adaptation}(T_s)$ are the long-term loss for the existing bridge and the bridge with adaptation measures, respectively.

In cost-benefit analysis, the cost is the cost of implementing an adaptation measure, and the benefit is the reduction of the loss by implementing an adaptation measure. The cost-benefit index (CBI) is expressed as (Bastidas-Arteaga & Stewart 2015)

$$CBI(T_s) = \frac{L_{exicisting}(T_s)\Delta L(T_s)}{C_{adaptation}} \tag{8}$$

where $C_{adaptation}$ is the cost of implementing the adaptation measure for reducing the long-term loss $\Delta L(T_s)$. The cost-benefit index provides information for decision making, an adaptation measure is considered to be cost-effective if the CBI exceeds unity. The CBI depends on the service time of the bridges. An adaptation measure may not be cost-effective in the short term due to the high adaptation cost, it may be cost-effective from a life-cycle perspective as the benefit can be accumulated over service time. The uncertainties associated with the earthquakes and corrosion are considered in this study resulting in probabilistic CBI. The probability that an adaptation measure is cost-effective is expressed as Pr(CBI>1).

4 ILLUSTRATIVE EXAMPLE

The developed approach is illustrated on an SMA-steel reinforced bridge under earthquakes and deterioration. The configuration of the bridge is presented in Figure 1.

The deterioration process of the bridge is modeled following the approach in section 3.1. The life-cycle earthquake scenarios incorporating the stochastic occurrence time and

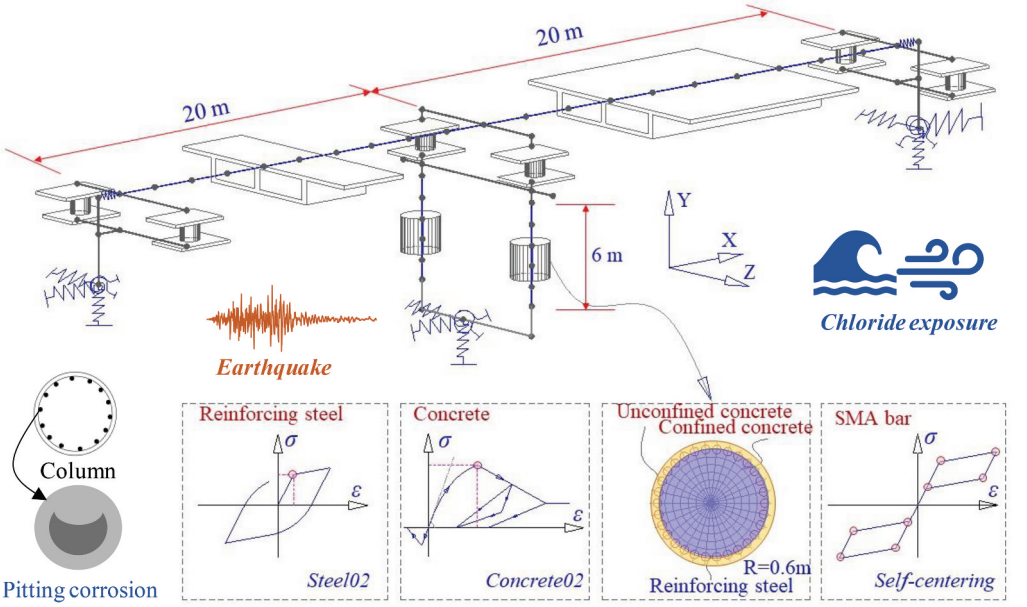


Figure 1. Configuration of the modeling bridge.

intensities are simulated following the procedures in section 3.1. The deteriorated bridge realizations are generated and paired with selected ground motion records. Finite element models are established in the software OpenSees and nonlinear time history analysis is performed for the deteriorated bridge. After computing the probabilistic seismic demand model, the time-dependent seismic vulnerability of the bridge can be computed. By considering the consequences induced by multiple possible events for an investigated time horizon, the long-term sustainability and resilience are computed. The long-term expected number of fatalities and resilience loss of the conventional bridge and the SMA-steel reinforced bridge are presented in Figure 2. The SMA-steel reinforced bridge is associated with less long-term expected number of fatalities and resilience loss compared with the conventional bridge, and the difference increases over service time.

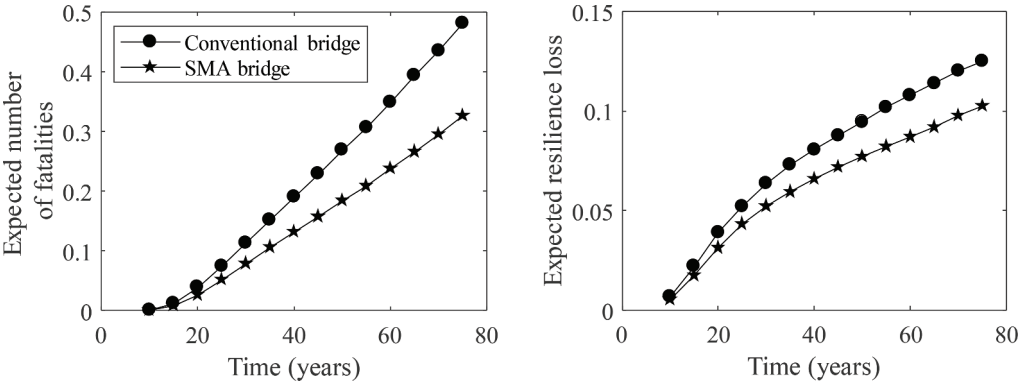


Figure 2. Long-term expected number of fatalities and resilience loss.

Following the approach in section 3.3, the probabilistic cost-benefit indices (CBIs) in terms of economic loss (ECO) and carbon dioxide emission (CDE) are computed and the expected values are presented in Figure 3. Due to the extra construction cost and carbon dioxide

emissions associated with the SMA-steel reinforced bridge, the CBIs are less than 1 for the short term. The expected CBIs increase over the service life of the bridges, as multiple extreme events can occur with the service life and the benefit can be accumulated over time. For the service time of 75 years, the expected CBIs of the ECO and CDE are 2.85 and 48.20, respectively. It is worth noting that an adaptation measure is considered to be cost-effective if the CBI exceeds 1.

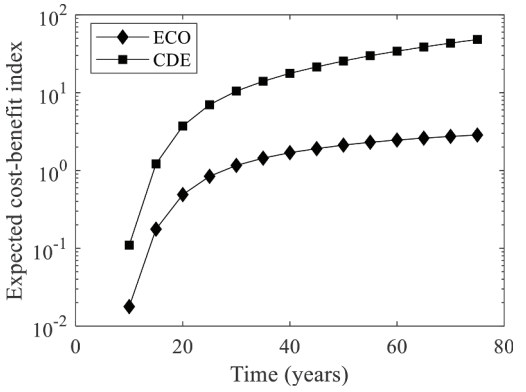


Figure 3. Expected cost-benefit index in terms of economic loss (ECO) and carbon dioxide emission (CDE) over the bridge service life.

The probability of the novel bridge being cost-effective over the bridge service life is presented in Figure 4. The novel bridge is associated with a lower probability of being cost-effective in the short term. Due to the accumulation of benefits within the service life, it is associated with a higher probability of being cost-effective considering the criteria of economic loss and carbon dioxide emissions in a life-cycle context. In addition to the economic loss and carbon dioxide emissions, it is worth noting that the SMA-steel reinforced bridge can also bring benefits in terms of resilience and fatalities which cannot be directly measured by monetary values.

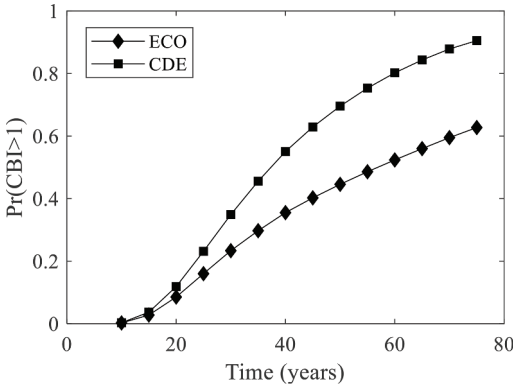


Figure 4. The probability of the novel bridge being cost-effective over the bridge service life.

5 CONCLUSIONS

This study develops a life-cycle cost-benefit analysis approach for structures under earthquakes and corrosion. The earthquakes and deterioration occurring within the life cycle of structures are modeled incorporating uncertainties. The long-term sustainability and resilience loss are computed under the sudden earthquakes and continuous deterioration. The life-cycle

cost-benefit index can be computed by considering the economic loss and carbon dioxide emissions.

The developed approach is implemented on an SMA-steel reinforced bridge under earthquakes and deterioration. As the construction cost and carbon dioxide emissions associated with the SMA-steel reinforced bridge are higher than those of the conventional bridge, the expected CBIs are less than 1 for the short term. The expected CBIs increase over the service life of the bridges, as multiple extreme events can occur with the service life and the benefit can be accumulated over time. The novel bridge is associated with a lower probability of being cost-effective in the short term. Due to the accumulation of benefits within the service life, it is associated with a higher probability of being cost-effective considering the criteria of economic loss and carbon dioxide emissions in a life-cycle context. Besides, the SMA-steel reinforced bridge is associated with benefits in terms of resilience and fatalities which is vital for the society and cannot be directly measured by monetary values. Overall, the SMA-steel reinforced bridge is cost-effective in a life-cycle context under earthquakes and deterioration.

REFERENCES

Anderson, K., Peters, G., 2016. The trouble with negative emissions. Science 354, 182–183.

Bastidas-Arteaga, E., Stewart, M.G., 2015. Damage risks and economic assessment of climate adaptation strategies for design of new concrete structures subject to chloride-induced corrosion. Structural Safety 52, 40–53.

Billah, A.H.M.M., Alam, M.S., 2012. Seismic performance of concrete columns reinforced with hybrid shape memory alloy (SMA) and fiber reinforced polymer (FRP) bars. Construction and Building Materials 28, 730–742.

Boore, D.M., Stewart, J.P., Seyhan, E., Atkinson, G.M., 2014. NGA-West2 equations for predicting PGA, PGV, and 5% damped PSA for shallow crustal earthquakes. Earthquake Spectra 30, 1057–1085.

Dong, Y., Frangopol, D.M., Saydam, D., 2013. Time-variant sustainability assessment of seismically vulnerable bridges subjected to multiple hazards. Earthq Eng Struct Dyn 42, 1451–1467.

Enright, M.P., Frangopol, D.M., 1998. Probabilistic analysis of resistance degradation of reinforced concrete bridge beams under corrosion. Eng Struct 20, 960–971.

Fang, C., Ping, Y., Zheng, Y., Chen, Y., 2021. Probabilistic economic seismic loss estimation of steel braced frames incorporating emerging self-centering technologies. Engineering Structures 241, 112486.

Fang, C., Wang, W., He, C., Chen, Y., 2017. Self-centring behaviour of steel and steel-concrete composite connections equipped with NiTi SMA bolts. Engineering Structures 150, 390–408.

Fang, C., Wang, W., Qiu, C., Hu, S., MacRae, G.A., Eatherton, M.R., 2022. Seismic resilient steel structures: A review of research, practice, challenges and opportunities. Journal of Constructional Steel Research 191, 107172.

Fang, C., Yam, M.C.H., Lam, A.C.C., Xie, L., 2014. Cyclic performance of extended end-plate connections equipped with shape memory alloy bolts. Journal of Constructional Steel Research 94, 122–136.

Guo, T., Xu, Z., Song, L., Wang, L., Zhang, Z., 2017. Seismic resilience upgrade of RC frame building using self-centering concrete walls with distributed friction devices. Journal of Structural Engineering 143, 04017160.

Guo, T., Wang, L., Xu, Z., Hao, Y., 2018. Experimental and numerical investigation of jointed self-centering concrete walls with friction connectors. Engineering Structures 161, 192–206.

Li, S., Wang, J., Alam, M.S., 2021. Seismic performance assessment of a multispan continuous isolated highway bridge with superelastic shape memory alloy reinforced piers and restraining devices. Earthquake Engineering & Structural Dynamics 50, 673–691.

Li, Y., Dong, Y., Frangopol, D.M., Gautam, D., 2020. Long-term resilience and loss assessment of highway bridges under multiple natural hazards. Structure and Infrastructure Engineering 16, 626–641.

Matthews, M. V, Ellsworth, W.L., Reasenberg, P.A., 2002. A Brownian model for recurrent earthquakes. Bulletin of the Seismological Society of America 92, 2233–2250.

Muntasir Billah, A.H.M., Alam, M.S., 2015. Seismic fragility assessment of concrete bridge pier reinforced with superelastic shape memory alloy. Earthquake Spectra 31, 1515–1541.

Qian, J., Dong, Y., Frangopol, D.M., 2022a. Probabilistic long-term resilience of bridges under seismic and deterioration processes. In: Proceedings of the Institution of Civil Engineers-Bridge Engineering. pp. 1–12.

Qian, J., Zheng, Y., Dong, Y., Wu, H., Guo, H., Zhang, J., 2022b. Sustainability and resilience of steel–shape memory alloy reinforced concrete bridge under compound earthquakes and functional deterioration within entire life-cycle. Eng Struct 271, 114937.

Rao, A.S., Lepech, M.D., Kiremidjian, A.S., Sun, X.-Y., 2017. Simplified structural deterioration model for reinforced concrete bridge piers under cyclic loading. Structure and infrastructure Engineering 13, 55–66.

Shekhar, S., Ghosh, J., Padgett, J.E., 2018. Seismic life-cycle cost analysis of ageing highway bridges under chloride exposure conditions: Modelling and recommendations. Structure and Infrastructure Engineering 14, 941–966.

Timmerman, P., 1981. Vulnerability resilience and collapse of society. A Review of Models and Possible Climatic Applications. Toronto, Canada. Institute for Environmental Studies, University of Toronto.

Wang, Fang, Harindintwali, J.D., Yuan, Z., Wang, M., Wang, Faming, Li, S., Yin, Z., Huang, L., Fu, Y., Li, L., others, 2021. Technologies and perspectives for achieving carbon neutrality. The Innovation 2, 100180.

Xiang, N., Chen, X., Alam, M.S., 2020. Probabilistic seismic fragility and loss analysis of concrete bridge piers with superelastic shape memory alloy-steel coupled reinforcing bars. Engineering Structures 207, 110229.

Yang, D.Y., Frangopol, D.M., 2019. Life-cycle management of deteriorating civil infrastructure considering resilience to lifetime hazards: A general approach based on renewal-reward processes. Reliab Eng Syst Saf 183, 197–212.

Zandi Hanjari, K., Kettil, P., Lundgren, K., 2011. Analysis of mechanical behavior of corroded reinforced concrete structures. ACI Struct J 108, 532–541.

Zheng, Y., Dong, Y., 2019. Performance-based assessment of bridges with steel-SMA reinforced piers in a life-cycle context by numerical approach. Bulletin of Earthquake Engineering 17, 1667–1688.

Zheng, Y., Dong, Y., Li, Y., 2018. Resilience and life-cycle performance of smart bridges with shape memory alloy (SMA)-cable-based bearings. Construction and Building Materials 158, 389–400.

Bridge Maintenance, Safety, Management, Digitalization and Sustainability – Jensen, Frangopol & Schmidt (eds)
© 2024 The Author(s), ISBN 978-1-032-77040-6
Open Access: www.taylorfrancis.com, CC BY-NC-ND 4.0 license

Probabilistic assessment of corrosion initiation in RC structures under chloride attack

G.H. Vieira & L.C. Meneghetti
University of São Paulo, São Paulo, Brazil

R.M. Teixeira & M.A. Silva
Federal University of Pará, Belém, Pará, Brazil

ABSTRACT: Chloride-induced corrosion is one of the main deteriorating mechanisms of reinforced concrete structures. This paper presents a probabilistic study to assess and quantify the impact of key variables during corrosion initiation phase. Evaluations were performed on a bridge pier section under constant and time-dependent surface concentrations, investigating the impacts of both exposure conditions on corrosion initiation. A sensitivity analysis was conducted by testing different values for each variable and quantifying their impact on corrosion initiation. During this analysis, the key variables were identified and discussed. The analyses utilized a probabilistic tool that performs Monte Carlo simulations with a one-dimensional analytical diffusion model. Results highlighted greater significance of surface chloride content in early ages than in later ages, with diminished influence of concentration steps near corrosion initiation time. This paper underscores the importance of considering surface chloride content time-dependency and its impact on corrosion initiation, providing valuable insights for corrosion modeling.

1 INTRODUCTION

During the service life, concrete structures are influenced by various mechanisms, impacting their performance and durability. Chloride-induced corrosion stands out as one of the most significant degradation mechanisms in reinforced concrete structures (Frangopol et al. 1997, Khan et al. 2017). In regions with intense environmental exposure, chloride ions penetrate the concrete and are transported to its interior by different mechanisms (Poulsen & Mejlbro 2006). The transport of chloride ions within the concrete depends on various factors, including the chloride content in the environment, concrete porosity, geometry, type of cement and additives (Mehta & Monteiro 2014). When a critical concentration is reached on the reinforcement, the passivated layer breaks, initiating corrosion, which can be divided into two main phases: initiation, where ion transport occurs, and propagation, where corrosion effectively takes place (Tuutti 1982) and causes the loss of steel area, concrete cracking and spalling of the concrete cover, impacting structural capacity.

During the design phase, durability is usually approached with a technological emphasis, where parameters such as concrete cover and concrete properties are standardized in accordance with environmental exposure classes (ACI 2019, CEN 2004, ABNT 2023). This approach, however, lacks precision in quantifying how the structure's performance is affected over its service life, making it difficult to plan interventions (Biondini & Vergani 2015). To fully address structural degradation effects, models explicitly considering degradation mechanisms are necessary.

This paper introduces a probabilistic study of the corrosion initiation phase, where the transport of chloride ions is simulated. Utilizing an analytical model for chloride diffusion and a real bridge pier section, the different variables are assessed to identify and quantify their respective impacts on the time required for corrosion initiation.

DOI: 10.1201/9781003483755-63

2 CHLORIDE DIFFUSION SIMULATION

2.1 *Diffusion model*

Diffusion is the most relevant chloride transport mechanism in concrete and can be properly modeled using Fick's second law (Bertolini et al. 2004). For an isotropic medium, with homogeneous material, constant diffusivity throughout space and unidimensional flow, Equation 1 is utilized (Crank 1975):

$$\frac{\partial C(x,t)}{\partial t} = D(t).\nabla^2 C(x,t) \tag{1}$$

where: C [wt%/cem] = chloride content; D [m²/s] = chloride diffusivity; x [m] = evaluated point; and t [s] = time.

Solutions to the diffusion problem depend on the adoption of initial conditions, represented by an initial concentration profile, $C_0(x)$, within the element, and boundary conditions, represented by a known surface chloride content function, $C_S(t)$, within the element surface.

2.2 *One-dimensional error function-based solutions*

Analytical solutions are available only under specific initial and boundary conditions (Titi & Biondini 2016). In the case of one-dimensional diffusion in a semi-infinite medium, error function-based solutions are common (Crank 1975, Frederiksen et al. 2008). If chloride diffusivity and surface chloride content are assumed constant, the solution is denoted by Equation 2:

$$C(x,t) = C_s.erfc\left(\frac{x}{2\sqrt{D.(t-t_0)}}\right) \tag{2}$$

where: Cs [wt%/cem] = surface chloride content; and t_0 [s] = exposure time.

Modified versions of Equation 2 allow for the consideration of variable diffusivity and surface chloride content in time. By defining an average diffusivity, D_{av}, according to Equation 3, Equation 2 can be utilized by substituting the instantaneous diffusivity, D, with D_{av}.

$$D_{av}(t) = \frac{1}{t-t_0}\int_{t_0}^{t} D(\tau).d\tau \tag{3}$$

where: D_{av} [m²/s] = average diffusivity.

FIB "Model Code for Service Life Design" (FIB 2006) presents a version of Equation 2 considering the average diffusivity, the presence of an initial chloride content, C_0, and a convection zone, Δ_x, which is a region where transport is not governed by diffusion but by capillarity.

$$C(x,t) = C_0 + (C_s - C_0).\left[1 - \text{erf}\left(\frac{x-\Delta x}{2.\sqrt{D_{av}(t).(t-t_0)}}\right)\right] \tag{4}$$

where: C_0 [wt%/cem] = initial chloride content; and Δx [m] = convection zone depth.

For variable surface content, Poulsen & Mejlbro (2006) employ the superposition of constant surface content solutions, approximating the surface chloride content function with a step function. For the solution presented in Equation 4, Equation 5 is obtained:

$$C(x,t) = C_0 + \sum_{j=1}^{n} C_{sj} \cdot H\left(t - t_{j-1}\right) \cdot \left[1 - \text{erf}\left(\frac{x-\Delta x}{2.\sqrt{D_{av}(t).\left(t-t_{j-1}\right)}}\right)\right] \tag{5}$$

where: C_{sj} [wt%/cem] = surface chloride content step; t_j = step time; and H = Heaviside function.

2.3 *Chloride diffusivity*

Chloride diffusivity measures the speed at which ions are transported inside the concrete, reflecting the porosity of the concrete. Diffusivity's time-dependency is caused by the continuous hydration of the cement and increase in chloride binding capacity (Andrade 2005, Helene 1993, Khan et al. 2017), and is usually modeled by correcting diffusivity at a reference time by an exponential function that increases with the inverse of exposure time raised to an aging coefficient. FIB "Model Code for Service Life Design" (FIB 2006) presents Equation 6 for calculating the average diffusivity over time. This equation introduces the chloride migration coefficient obtained from laboratory tests, D_{RCM}, that can be transformed into the diffusivity at reference time by multiplying it by the test factor, k_t. The environmental factor, k_e, corrects the test temperature to the actual temperature acting on the structure.

$$D_{av}(t) = k_e.k_t.D_{RCM}.\left(\frac{t_{ref}}{t}\right)^m \tag{6}$$

where: D_{RCM} [m²/s] = chloride migration coefficient; k_e [-] = environmental factor; k_t [-] = test factor; t_{ref} [s] = reference time (test time); and m [-] = aging coefficient.

2.4 *Corrosion initiation time*

Reinforcement depassivation occurs when the concentration of chloride ions at the edges of the rebar reaches a critical chloride content, C_{crit}. FIB "Model Code for Service Life Design" (FIB 2006) recommends a value of C_{crit} = 0.60 wt%/cem. The instant when C_{crit} is reached sets the initiation of corrosion. The calculation of the corrosion initiation time for the solution of Equation 4 is given by:

$$t_i = C^{-1}(x_r, C_{crit}) = \left[\frac{(c-\Delta x)^2}{4.k_e.k_t.D_{RCM}.t_{ref}^m} \cdot \text{erf}^{-1}\left(\frac{C_s - C_{crit}}{C_s - C_0}\right)^{-2}\right]^{\frac{1}{1-m}} \tag{7}$$

where: t_i [s] = corrosion initiation time; C_{crit} [wt%/cem] = critical chloride content; x_r [m] = rebar position; and c [m] = concrete cover.

3 CORROSION INITIATION ANALYSIS

The assessment of corrosion initiation will be conducted on a pier section from the Rio Torto Bridge, Italy, as presented by Pugliese et al. (2022). The pier has a hollow circular section with an external diameter of 1.50 m and a wall thickness of 0.30 m, subjected to chloride exposure on the external face. The problem will be addressed through a one-dimensional diffusion model.

The analyses utilize a tool developed in MATLAB™ that performs one-dimensional diffusion analysis based on the analytical solution (Eq. 4) and the diffusivity expression (Eq. 6) proposed by FIB "Model Code for Service Life Design". For time-dependent chloride surface content, the tool employs an approximation using a step function, as per Equation 5. The results obtained from the analysis include the chloride content history at the point corresponding to the concrete cover and the corrosion initiation time, obtained through Equation 7 for constant surface chloride content and through linear interpolation of the concentration profiles for time-dependent surface chloride content.

The tool performs both deterministic and probabilistic analyses. Therefore, in addition to the mean values of each variable, it receives the parameters that define their probability distributions. Probabilistic analyses were conducted through conventional Monte Carlo simulation, where the tool generates random values for each variable based on input data and performs the analysis for each set of values. In probabilistic analyses, an additional factor θ is introduced, multiplying the concentration results to account for model uncertainty (Cui et al. 2018).

3.1 *Probabilistic corrosion initiation time*

In the probabilistic analysis of the corrosion initiation time, two cases are considered: one with constant surface chloride content and another with time-dependent surface chloride content. The time-dependent concentration is equivalent to the constant concentration adopted for the first case, using the same ratios of variable to constant concentration as Poulsen & Mejlbro (2006). The function has an initial step equivalent to 70% of the constant concentration. At the subsequent steps, occurring at 20 and 40 years, the increases are equivalent to 50% and 40%, respectively, of the constant concentration. A Spearman correlation analysis is also conducted based on the probability distributions obtained from the analysis, providing an initial assessment of the impact of each variable on the corrosion initiation time. The parameters adopted in the analysis are obtained from Pugliese et al. (2022) and are presented in Table 1.

Table 1. Statistical distributions of the parameters in the probabilistic corrosion initiation time analysis.

Variable	Description	Distribution	Distribution Parameters
D_{RCM} [m²/s]	Chloride migration coefficient	Normal	$\mu = 15.80 \times 10^{-12}$; $\sigma = 0.20\mu$
m [-]	Aging coefficient	Beta	$\mu = 0.30$; $\sigma = 0.12$ lb = 0.00; ub = 1.00
C_{crit} [wt%/cem]	Critical chloride content	Beta	$\mu = 0.50$; $\sigma = 0.15$; lb = 0.20; ub = 2.00
c [m]	Concrete cover	Lognormal	$\mu = 0.04$; $\sigma = 0.008$
C_S [wt%/cem]	Surface chloride content	Normal	Cs = 1.30; μ = Cs; $\sigma = 0.30\mu$
C_{Sj} [wt%/cem]	Surface chloride content step	Normal	Csj = [0.70, 0.50, 0.40].Cs Csj = [0.91, 0.65, 0.52] μ = Csj; $\sigma = 0.30\mu$
θ [-]	Model uncertainty	Lognormal	$\mu = 1.00$; $\sigma = 0.05$
k_e [-]	Environmental factor	Gamma	$\mu = 0.676$; $\sigma = 0.114$
k_t [-]	Test factor	Deterministic	1
Δx [m]	Convection zone depth	Deterministic	0
C_0 [wt%/cem]	Initial chloride content	Deterministic	0
t_j [yr]	Step time	Deterministic	[0, 20, 40]
t_{ref} [yr]	Reference time	Deterministic	0.0767
t_0 [yr]	Exposure time	Deterministic	0.0767

Table 2. Statistical distributions of the parameters in the sensitivity analysis

Variable	Description	Distribution	Distribution Parameters
D_{RCM} [m²/s]	Chloride migration coefficient	Normal	μ = [1.0, 2.5, 5.0, 10.0, 12.5, 15.0, 20.0, 25.0] $\times 10^{-12}$ $\sigma = 0.20\mu$
m [-]	Aging coefficient	Beta	μ = [0.05, 0.10, 0.20, 0.40, 0.50, 0.60, 0.70, 0.80] $\sigma = 0.12$; lb = 0.00; ub = 1.00
C_{crit} [wt %/cem]	Critical chloride content	Beta	μ = [0.30, 0.40, 0.60, 0.70, 0.80, 0.90, 1.00] $\sigma = 0.15$; lb = 0.20; ub = 2.00
c [m]	Concrete cover	Lognormal	μ = [0.03, 0.035, 0.045, 0.050, 0.055, 0.060] $\sigma = 0.008$
C_S [wt%/cem]	Surface chloride content	Normal	μ = [1.00, 1.15, 1.40, 1.70, 2.00, 3.00] $\sigma = 0.30\mu$
C_{Sj} [wt %/cem]	Surface chloride content step	Normal	$C_{S1} = 0.70.C_S$; $C_{S2} = 0.50.C_S$; $C_{S3} = 0.40.C_S$ μ = Csj; $\sigma = 0.30\mu$
Δx [m]	Convection zone depth	Deterministic	[0.0025, 0.0050, 0.0075, 0.0100]
C_0 [wt%/cem]	Initial chloride content	Deterministic	[0.05, 0.10, 0.15, 0.20]

3.2 *Sensitivity analysis*

After conducting a probabilistic analysis of corrosion initiation time, a sensitivity analysis was carried out for both cases (constant and time-dependent surface chloride contents). Different values were adopted for each variable, while keeping the other variables at the same values used in the base cases (Table 1). The objective of this analysis was to identify the most relevant variables and how each one impacts the corrosion initiation, complementing the results obtained from the Spearman correlation analysis. The new analysis also allows the evaluation of variables such as the depth of the convection zone and the initial chloride content, which were not considered in the previous analysis. The values adopted for each variable were chosen within a range of possible values (FIB 2006) and are presented in Table 2. In the time-dependent surface chloride content cases, each concentration step C_{Sj} was treated as an individual variable. Therefore, the values for each concentration step were assessed while keeping all other variables, including the other concentration steps, constant and with the same values of the base case. The values for each step were calculated based on the range of possible values adopted for the constant surface chloride content, C_S, following the same ratios of variable to constant concentration utilized in the base case.

4 RESULTS

4.1 *Corrosion initiation time*

Figure 1 Presents histograms of the corrosion initiation time and empirical cumulative probability functions for both base cases. The results reveal a substantial impact of the time-dependency of surface chloride content, with the mean corrosion initiation time increasing from 20 years to approximately 28.3 years, representing a 41% rise. Theoretically, surface concentration is always time-dependent, influenced by factors such as exposure conditions and concrete properties (Yang et al. 2021). Assuming constant surface chloride content, while prioritizing safety, may lead to excessively conservative estimates of corrosion initiation time. Figure 2 illustrates the results of the Spearman correlation analysis for the same cases. These results highlight a greater impact of the aging coefficient, followed by cover depth and critical and surface chloride contents. The significance of these variables was expected, as they are directly associated with decreasing diffusivity over time, the distance chloride ions need to travel, and environmental exposure. The analysis further validates observations derived from the corrosion initiation time distributions, suggesting a greater significance of surface chloride content during early ages, i.e. those more distant from corrosion initiation time. Conversely, its importance diminishes in the later ages, i.e. those near corrosion initiation.

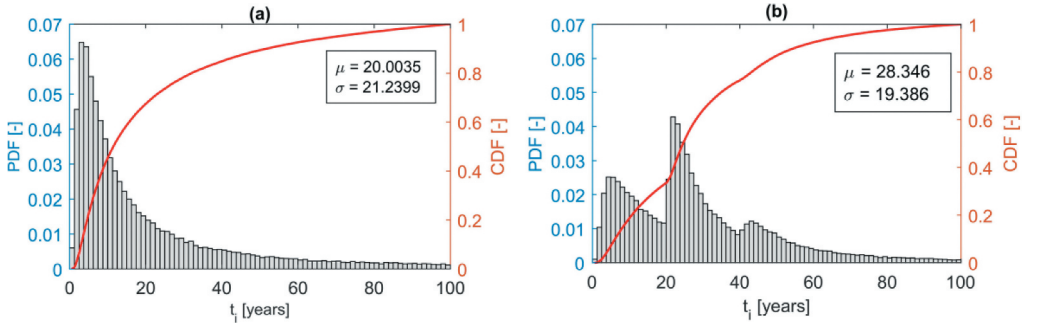


Figure 1. Histograms and empirical cumulative probability functions of corrosion initiation time for constant surface chloride content (a) and time-dependent surface chloride content (b).

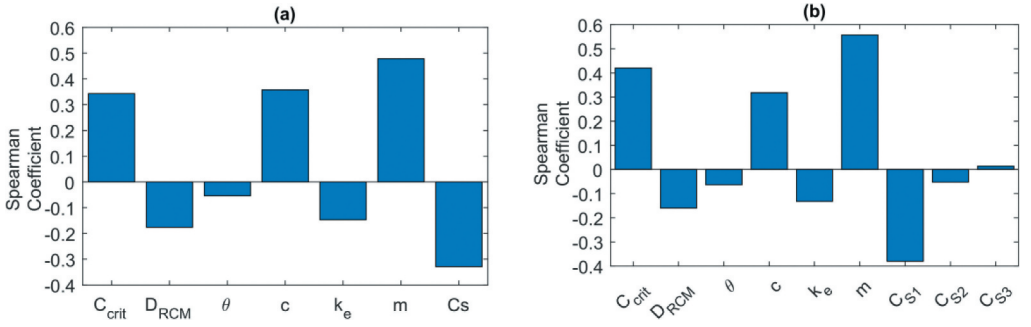


Figure 2. Spearman correlation analysis for constant surface chloride content (a) and time-dependent surface chloride content (b).

4.2 *Sensitivity analysis*

Figures 3-7 present the results obtained in the sensitivity analysis for both constant and time-dependent surface chloride content, illustrating the mean corrosion initiation time, a two-standard deviation confidence interval, and box plots, where red markers identify the outliers. These results confirm those initially obtained in the Spearman correlation analysis and quantify the impact of each variable. Notably, the chloride migration coefficient (Figure 3a) stands out as the most relevant variable, causing variations in the corrosion initiation time in a range of 10 to 70 years. This behavior was expected since this parameter defines the ion transport velocity. In the correlation analysis, the evaluated values of the migration coefficient were around the mean value of 15.8×10^{-12} m/s², a region where small variations do not significantly impact the corrosion initiation time, justifying the reduced influence observed in that initial analysis. The aging coefficient (Figure 3b) also showed a high impact on corrosion initiation time, which was also observed in the correlation analysis. As previously stated, this can be explained because the parameter considers the decrease of diffusivity over time, directly affecting diffusion speed.

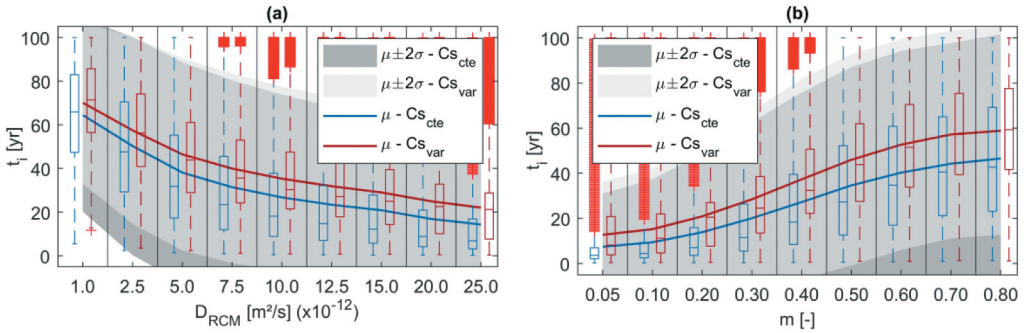


Figure 3. Sensitivity analysis – Impact of chloride migration coefficient (a) and aging coefficient (b).

The concrete cover depth, which assumes low values and has a significant impact on the corrosion initiation time (Figure 4a), is of great importance since it can be easily neglected during execution. A decrease of 0.5 cm, for instance, can lead to a reduction of 4 years in the corrosion initiation time. A similar conclusion is valid for the convection zone depth (Figure 4b), as values of about 10 mm can be easily established depending on the exposure condition, resulting in a reduction of about 5 years in corrosion initiation time. The initial chloride content (Figure 5a) did not show a significant variation for the tested values; however, it should be considered that some standards allow elevated levels of this variable, up to 0.3 wt%/cem (ABNT 2023). When the contribution of all these different factors is combined, the service life of the structure can be significantly impacted.

Both the critical chloride content and the surface chloride content (Figs 5b, 6a) showed a high impact on corrosion initiation time, confirming the results initially obtained during the correlation analysis. This impact was expected, as these parameters measure the chloride content necessary for depassivation and the environmental exposure, respectively. Results from Figures 6-7 also confirm and quantify the conclusions drawn in previous analyses. It was observed that the impacts of the constant surface chloride content and of the first step of time-dependent surface chloride contents are similar, leading to reductions of about 15 years within the range of tested values. The impact of the second step of time-dependent surface chloride content is smaller, causing reductions of up to 5 years in depassivation, while the impact of the third step is negligible. If these steps occurred at early ages, e.g. $t_2 = 10$ and $t_3 = 15$ years, a more significant relevance should be expected due to a greater distance to corrosion initiation. The comparison between results with constant and time-dependent surface chloride content (Figs. 3-5) showed that considering the time-dependency resulted only in a translation of the mean initiation time curve, which remained almost parallel for both cases in all variables tested. This result indicates that the surface chloride content time-dependency does not directly affect how each variable impacts corrosion initiation.

In the cases with constant surface chloride content, the boxplots showed a reduction in dispersion and an increase in kurtosis for lower corrosion initiation times, consistent with the shape of the histogram for constant surface chloride content (Figure 1a). In these situations, a higher positive skewness was also observed, reflected in a greater deviation of the median from the mean. In the cases with time-dependent surface chloride content, a similar behavior is observed, except for the situations where the mean corrosion initiation times are slightly higher than the ages when the concentration steps occur. In these situations, the histogram of corrosion initiation time approximates the shape of Figure 1b, resulting in a boxplot showing lesser skewness, with a smaller deviation of the median from the mean.

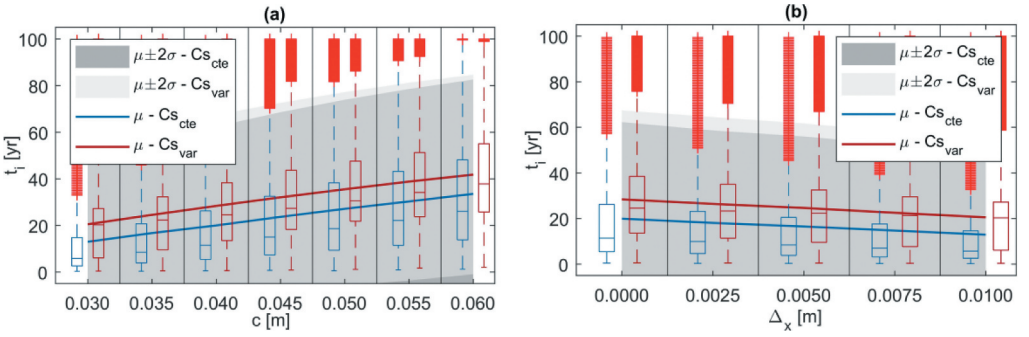


Figure 4. Sensitivity analysis – Impact of concrete cover (a) and convection zone depth (b).

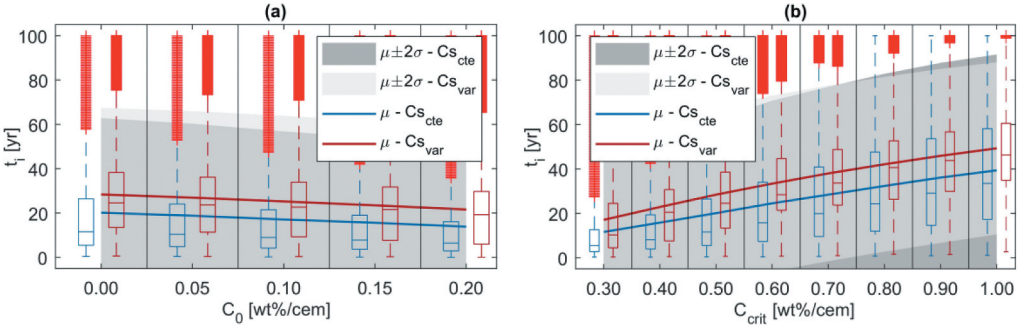


Figure 5. Sensitivity analysis – Impact of initial chloride content (a) and critical chloride content (b).

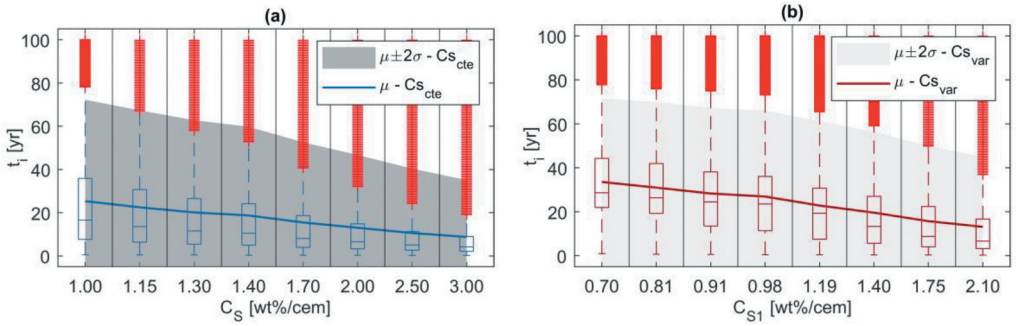


Figure 6. Sensitivity analysis – Impact of constant surface chloride content (a) and surface chloride content step 1 (b).

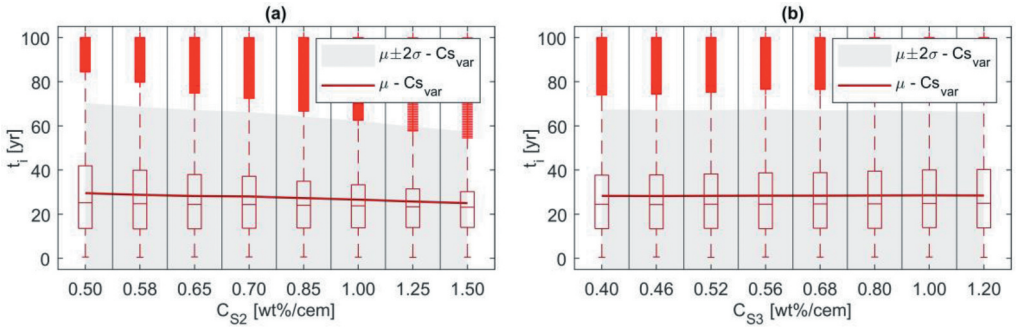


Figure 7. Sensitivity analysis – Impact of surface chloride content steps 2 (a) and 3 (b).

5 CONCLUSIONS

This article addressed the corrosion initiation due to chloride ion attack and conducted a probabilistic analysis to improve the understanding and quantify the impacts of each variable in this phase. In the first stage of this analysis, results from the cases with constant and time-dependent surface chloride content highlighted the significant relevance of this temporal variation, often ignored in diffusion models. At this stage, variables with the greatest impact on the corrosion initiation time were identified, a result that was complemented by the sensitivity analysis. The variables that proved most relevant were the chloride migration and the aging coefficients. The cover depth was also important, as its reduction during execution can accelerate the onset of corrosion. During this analysis, surface chloride content in the early ages proved to be more relevant than in later ages, as the influence of concentration steps near corrosion initiation time diminished. Thus, the accurate assessment of the surface chloride content is essential for precise predictions of corrosion initiation. Constant surface chloride content is usually estimated based on long historical data, resulting in higher values than the actual concentrations in early ages. This may lead to excessively conservative estimates of corrosion initiation time. When surface chloride content is experimentally obtained in the early ages, e.g. immediately after construction, assuming constant concentration throughout time may lead to contrary to safety predictions, since it may ignore important concentration build-up before corrosion initiation.

The study explicitly evaluated corrosion initiation, in contrast to the purely technological approach defined by standards. Since one-dimensional diffusion models were utilized, the results obtained in this study can be extrapolated to other geometries under the hypothesis of

one-dimensional diffusion. Future work will explore the effects of bidimensionality on the evaluated section, as well as the impacts of different boundary conditions, e.g. a real surface chloride content function, in contrast to the step function approximation (Author, in prep.).

REFERENCES

ACI 2019. *ACI 318-19 Building Code Requirements for Structural Concrete*. Farmington Hills: ACI.

ABNT 2023. *NBR6118*: *Projeto de estruturas de concreto – Procedimento*. Rio de Janeiro: ABNT.

Andrade, C. 2005. Concepts on the chloride diffusion coefficient. In C. Andrade (ed), *Third international RILEM Workshop on testing and modeling chloride ingress into concrete; Proc. intern. symp., Madrid, 9-10 September 2002*. Bagneux: RILEM Publications S.A.R.L

Bertolini, B. et al. 2004. *Corrosion of steel in concrete: Prevention, diagnosis, repair*. Weinheim: Wiley.

Frangopol, D. M. et al. 1997. Reliability of reinforced concrete girders under corrosion attack. *Journal of Structural Engineering* 123(3): 286–297.

Biondini, F. & Vergani, M. 2015. Deteriorating beam finite element for nonlinear analysis of concrete structures under corrosion. *Structure and Infrastructure Engineering* 11(4): 519–532.

Crank, J. 1975. *The mathematics of diffusion*. London: Oxford University Press.

Cui, F. et al. 2018. Seismic fragility analysis of deteriorating RC bridge substructures subjected to marine chloride-induced corrosion. *Engineering Structures* 155: 61–72.

CEN 2004. *Eurocode 2: Design of concrete structures – Part 1-1: General rules and rules for buildings*. Brussels: CEN.

FIB 2006. *FIB Bulletin 34 – Model code for service life design*. Lausanne: International Federation for Structural Concrete.

Frederiksen, J. et al. 2008. *Fick's 2nd law – Complete solutions for chloride ingress into concrete*. Lund: Lund Institute of Technology.

Helene, P. 1993. *Contribuição ao estudo da corrosão em armaduras de concreto armado*. São Paulo: Escola politécnica da Universidade de São Paulo.

Khan, M. U. et al. 2017. Chloride-induced corrosion of steel in concrete: An overview on chloride diffusion and prediction of corrosion initiation time. *International Journal of Corrosion* 2017(3): 1–9.

Mehta, P. & Monteiro, P. 2014. *Concrete: Microstructure, properties and materials*. New York: McGraw-Hill.

Poulsen, E. & Mejlbro, L. 2006. *Diffusion of chloride in concrete: Theory and application*. Abingdon: Taylor & Francis.

Pugliese, F. et al. 2022. Reliability assessment of existing RC bridges with spatially variable pitting corrosion subjected to increasing traffic demand. *Reliability Engineering and System Safety* 218(108137).

Titi, A. & Biondini, F. 2016. On the accuracy of diffusion models for life-cycle assessment of concrete structures. *Structure and Infrastructure Engineering* 12(9): 1202–1215.

Tuutti, K. 1982. *Corrosion of steel in concrete*. Stockholm: Swedish Cement and Concrete Research Institute.

Yang, L. et al. 2021. Time-varying behavior and its coupling effects with environmental conditions and cementitious material types on surface chloride concentration of marine concrete. *Construction and Building Materials*. 303(124578).

Bridge Maintenance, Safety, Management, Digitalization and Sustainability – Jensen, Frangopol & Schmidt (eds)
© 2024 The Author(s), ISBN 978-1-032-77040-6
Open Access: www.taylorfrancis.com, CC BY-NC-ND 4.0 license

Why is maintenance and management of rails so important to railway bridges?

J. Wuorenjuuri
Sweco Finland Oy, Finland

ABSTRACT: Answer to the question is simple. Disasters can happen. Worst-case scenario is derailments and failures of bridge superstructure. The railways bridges can be categorized in two types: bridges with ballast and bridges without ballast. Ballastless bridges have many sub-types such as old wooden sleepers and more new age embedded rails. General public can see only sleepers and rails on railway bridges, but each type of rail also has many details and special solutions, that are very critical to the behavior of the bridges. Rail structures also include the rails, guard rails and their fastenings, expansion joints, and transitions zones.

1 INTRODUCTION

The railway is a very aggressive environment for a bridge. One of the challenges with track structures on bridges is the high precision demands due to safety. On high-speed lines defects are measured in millimeters. Even on slower track lines, there is very little room for failures of tracks. All defects on the track may be harmful for the bridge and for the trains. Of course, the worst-case scenario is derailments and failures of bridge superstructure.

The other challenge is related to the maintenance procedures. There are no specialists or experts in this field anymore. Usually bridge engineer and inspectors of bridges do not know how to evaluate these structures and leave it to the track maintenance personnel. The track maintenance personnel usually are not very interested in the bridges because they are special structures to them. The track superstructure has so many different components that it really would need experts who understand the rails.

One of the challenges is that many rail solutions on bridges are unique. From a maintenance point of view, every time some new rail innovation comes along and is implemented into the track, it means that the maintenance needs more expertise. Every component requires special maintenance, and management. Track -bridge interaction requires special expertise, for both bridge and track maintenance crews. This makes the detail so important to be maintained and managed optimally.

The great thing about the rail that it is monitored many times a year on every bridge as track measurement vehicles run through the lines. Valuable information is gathered many times aa year to ensure the safety of the tracks for trains. But challenges come up if there is a problem with the measurements. Where is the problem? On the track? On the bridge? Does the track work on the bridge correctly? What are the corrective actions? When is the track superstructure aged? When is it beneficial to do renewal instead of maintenance? Can the track be modernized somehow? After all the technology is in many cases from the 1800 century.

2 BALLAST AND SLEEPERS

The first railway tracks on bridges were ballastless tracks, where wooden sleepers were attached to the steel of wooden bridge. One of the advantages of wooden sleepers was that it was soft, gentle for both the train and the bridge. It softened the impacts of the train to the

DOI: 10.1201/9781003483755-64

bridge, but also softened the impacts to the train's bogeys. Also, the easy maintenance of these wooden sleepers has been an advantage.

Later in the start of 1900's railways developed, and railway engineers wanted to have continuous ballast layers over the bridge. This meant that bridges started to be built out of stone, masonry or later with concrete. Larger bridges were still built with "old" rail technology as the span lengths of stone or concrete bridges were limited for some decades.

Up to these days railway bridges are ballastless or with ballast. The quality of ballast has of course developed from sand to stone. Also, sleepers are mainly concrete these days on mainlines. But still on many steel bridges the wooden sleepers are fixed to the steel girders.

In the recent years however, new technology has come along. In Europe the wooden sleepers have been handles with creosote. Now this is banned for environmental reasons and new materials have been developed for sleepers on bridges. New composite sleepers are introduced into the market. This may be a good solution but for now it has been much more expensive than the wooden sleepers. There are also uncertainties with these composite sleepers.

First, we know that the steel bridges have defects, we know they have rivets. How much can these composite sleepers be prefabricated or is there a way to fit them on a bridge? How are the possible uneven surfaces of the steel plates fixed? Current idea is to use fitting pieces. How much can the maintenance personnel correct the rail defects if something comes up? How does the composite sleeper behave in cold weather in the long term? Also, the noise levels of composite sleepers on steel bridges are yet to be tested.

Also ballasted tracks with sleepers have been replaced by different kinds of embedded rails. This means that the track is glued onto a bridge deck with several kinds of solutions. One advantage of embedded rail is said to be the maintenance free track, but on a short bridge, the transition from embedded track on a bridge to the softer transition zone on the embankment is difficult for maintenance. Usually, it must be done manually with tamping machines, which of course is not so high-quality maintenance.

On steel bridges, the traditional wooden sleepers are fixed to the bridge with vertical and horizontal bolts. traditionally these bolts have required a lot of maintenance as the wooden sleeper expands and decreases in size during time and in different weather conditions. And there are many new innovations for this fastening, which again means that it is a challenge for the maintenance.

3 RAILS AND GUARD RAILS

Over the history of railways, rails have also developed. The profile of the rail has grown and In Finland, new rails on mainline are mainly 60 kg/m rails. Every time the rail profile grows, also the fastening to the sleepers also changes. The fastening depends on the rail profile, but also on the length of the bridge. There are different kinds of washer plates, springs, and screws for rails, and it is not the same which kind of fastening the maintenance uses.

One of the challenges is the different fastening for maintenance. In many cases, the cause of rail defects is that wrong fastenings are used. The rail behaves uncontrollably. It is very understandable that the maintenance personnel are call to fixed a problem on the bridge, and take the first available spare parts from the warehouse. But not making sure that they are the right parts.

All misuse of rail parts can influence the bridge and finally its load capacity or fatigue loads. That is why the maintenance of rails is so important on the bridge.

On longer bridges there is usually also another set of rails on a bridge. The additional rails are guard rails, and they are supposed to prevent a derailment of a train to cause extra damage to the bridge or for the people on the train. In Finland guard rails are used mainly on bridges over 30 meters long and that have a greater risk of derailment to have serious consequences.

Table 1. Requirements for guard rail in Finland.

Bridge type/rail type	Bridge length L < 30 m	Bridge length L ≥ 30 m
Concrete bridge. Edge beam is higher rail, and further than 2500mm to rail	Not required	Not required
Concrete bridge. The ballast layer is more than 450mm and edge beam is further than 2400mm	Not required	Not required
Concrete bridge. The ballast layer is more than 450mm and edge beam is no more than 2400mm	Not required	Required
All bridges. The ballast layer is less than 450mm/or no ballast layer	Not required	Required
Steel girder bridge with thin deck structure	Required	Required
All bridges. Rail has additional structures to prevent derailments	Not required	Not required
All bridges. Bridge has expansion joints	Required	Required
All Bridges. Bridge or embankments have curve less than 300m	Required	Required

In Finland the theory is that the locomotive is the part of the train that derails. But in some rail networks, the theory is that one of the wagons may be derailed on a long train and may cause damage to the bridge. For this there is special devices to lift a derailed wagon on to the rails before coming on to the bridge.

The maintenance of the guard rail is as important as that of the main rail. It must function properly in case of a derailment. But unfortunately guard rails are many times fastened with secondary fastening and not very much attention to this is paid by maintenance. We have been lucky not to have had any incidents that have been caused by guard rails being maintained poorly.

Guard rails are sometimes used also on a normal track where for example a overpass and its foundations need to be protected from possible derailment. From a maintenance point of view, this is not a very good solution again because maintenance must either remove the guard rails before tamping or do the maintenance of the tracks manually. And of course, the guard rails require a special sleeper, which make a guard rail a costly protective system. The best solution would be to choose the bridge type to be such that there would not be any extra risk in case of a derailment. This is true for both underpasses and over passes.

4 EXPANSION JOINTS AND DEVICES

In the first decades of railways, the track superstructure of the railway networks were mainly short rails. As continuous rail technology developed, there was a need for rail expansion joints. In Finland, by the 1960's and 1970's, the first rail expansion joints had been developed so that they were already in use on the Finnish railway network.

Rail expansion joints are as critical to maintain properly as the switches and the crossings on the track yards. Rail expansion joints are mainly used on long bridges with continuous rails and occasionally in other special structures. The expansion joint device must allow the longitudinal movements occurring on the bridge with their extreme values without changing the track width. It must also withstand the longitudinal forces of the track. The need for a rail expansion device is determined by the type of bridge and the expansion length of a bridge. The rail expansion device is always a point of discontinuity on the track and for that reason, very critical to work and be maintained properly. Many times, in the bridge design phases, it is possible to find a solution that reduces the expansion length of a bridge, and the use of rail expansion devices can be replaced with ordinary rail systems.

Rail expansion device requires a lot of maintenance. The old 54 kg/m rail expansion device requires constant maintenance and checking of the adjustments. In addition, the structure of the device has a quality that there is a lot of wear in the running surface of the rail. It does not remain as good for as long as with new devices. In Finland after 1990, many of these old expansion devices have been removed from the railway bridges during the renovation of railway sections. By using solutions such as sliding fastening, it has been possible to remove devices even from bridges where the total length of the bridge deck would otherwise not have allowed it.

The first rail expansion devices of the new era began to appear in the early 1990s. The new rail moving devices were of manufactured as elements. The same element contained the rail expansion device for both rail lines. The first rail expansion device of this type for a 60 kg/m rail was installed on the Halssila bridge in Jyväskylä in 1996. The official type of number of this device was SA60-200, where 200 means the allowed expansion length of the device. The finished battened element also includes protective guard rails.

Types of certified rail expansion joints used:

- 54E1/69-L100
- 54E1/69-L160
- 54E1 SA-54-200
- 60E1 SA-60-200

There is a city tram bridge being built now to Helsinki. It will have a rail expansion joint, with expansion capacity of 800 mm. The rail network has also many new big bridges being renewed in the near future. There bridges will have a new age rail expansion joint with more challenges for both designers and maintenance crews.

As a rule, these new-age rail expansion devices are designed as a combination of a support rail and a tongue rail. The operating principle is that the support rail, the outer rail is sliding, and the inner rails stay in place. When the device is working normally, the track width remains unchanged.

The rail expansion device is usually shown in the design documents of the bridge, and the installation of the device is usually made into an installation drawing. The device must have a nameplate that shows the manufacturer, type number of the device, serial number and year of manufacture, so that the device can be identified, and in maintenance the correct spare parts can be obtained later if necessary.

There are different types of expansion joints for different superstructures and bridge lengths. The most important selection criteria when choosing an expansion device are the length of the bridge, the total length of the decks affecting the same expansion joint, and the location of the decks and fixed support bearings.

Table 2. Rail expansion joints on Finnish Railway Bridges.

Bridge name	Bridge length	Year	Type of expansion joint
Iloharju bridge	156	1972	SA60E1-300B
Syrjäsalme bridge	117	1967	54E1/69-L160
Saimaan kanava bridge	200	2017	NYA
Mansikkakoski bridge	200	2017	NYA
Luhdanmäki bridge	548,4	2005	NYA
Rööpakka northern bridge	106,75	2005	NYA
Pukinkallio bridge	377	2005	NYA
Lukkokoski bridge	154,4	2005	NYA
Rööpakka southern bridge	105	2005	NYA
Kemijoen pääväylä bridge	308	1942	54E1/69-L100
Jarkko bridge	124,2	1979	54E1/69-L160
Rautiola bridge	123	1979	54E1/69-L160
Ounaskoski bridge	403,5	1951	54E1/69-L160
Ounaskoski bridge	403,5	1951	NYA
Iijoki bridge	188	1949	54E1/69-L160
Päiväkumpu bridge	6,5	1977	NYA
Pätkinlahti bridge	191,5	1976	60E1/SA60-200
Punkasalmi bridge	60	1976	54E1/69-L100
Kyrönsalmi bridge	204	1908	54E1/69-L100
Halssila bridge	188	1973	60E1/SA60-200
Pohja eastern bridge	163	1972	NYA
Pohja western bridge	166,9	1972	NYA
Vaalansalmi bridge	179,7	1929	SA60-200H
Penttilä bridge	350,05	2008	NYA

The rail expansion device divides the running rail forms an almost uniform running surface for the train wheels. This is made possible by a longitudinally moving support rail and an almost stationary tongue rail.

It is recommended to install and maintain the prefabricated rail expansion device element at temperatures where the factory 0 setting can be directly utilized. The expansion device can be moved in advance according to the prevailing conditions, but the need for moving power is great. The rail expansion is preset at the factory and locked with a transport lock. Before the installation of the device, it is ensured that the equipment does not have a transport lock that prevents the operation of the device.

Installations of modern expansion equipment have generally been successful and there have been no problems with their operation on the track network and the bridges. The biggest problem in the installations has been caused by the fact that the bridge designer has left the expansion joint of the bridge unnecessarily large. Unnecessarily increasing the expansion joint of the bridge increases the tensions and vertical displacement of the running rail.

In some cases, the ballast also must have a device in the joint and it must be installed in the same expansion joint. There are different types of ballast gutting devices and usually vertical ribs may cause the distance between the sleepers to increase too much. In these areas, special solutions with the bridge designer and the superstructure designer to reach a good result. There are cases on the Finnish railway network where the installation requires removing the manufactured structures to fit sleepers in the right places.

As a rule, cleaning and lubrication are necessary for the inspection and maintenance of expansion device. Other important items in maintenance are:

- the running surface and running edges of the rail of the expansion device,
- sliding rail attachments between the washer of the expansion device and the movement joint of the bridge
- inspection of rail anchors
- the expansion device must be cleaned, for example with a pressure washer,
- inspection of the tightening torque of tie screws and fasteners

The timing of inspections is important. It would be important that in the summer periods, at the highest possible temperatures, inspection measurements, inspection of devices and rail anchoring, and general maintenance are carried out. Correspondingly during the winter period, inspection measurements should be made at temperatures as low as possible.

The first inspection should be done 6-8 weeks after commissioning, which includes at least the following measures:

- removing the burr formed in the tongue and support rails by sanding.
- tightening of all screw connections without cotter protection with the prescribed torque
- visual inspection of all shocks and structural parts

Follow-up inspections, which must be carried out annually after the first inspection, include the following minimum measures:

- track width inspection
- checking the tips of the tongue with the help of an interpreter tool
- visual inspections, observations on the running surfaces, the appropriateness of all screw connections, observations on the plate fastenings of the bridge joints, the condition of the flexible rib washers

To ensure the proper functioning of the rail expansion device, the operation of the bridge and the expansion device must be monitored. In connection with the installation, it is important to use a inspection form, that should have the history of the inspections starting from the installation. There are special inspection measurements forms for the rail expansion devices in the maintenance contracts.

It must be remembered that a malfunctioning rail expansion device is a potential place for train derailments, as are faulty switches. On the Finnish rail network there are approximately

30 rail expansion devices on the bridges. This makes it a special maintenance point for any contractor.

5 CONCLUSIONS

Ballast, sleepers, rails, and expansion devices are all very important part of a bridge. Failure of any of these can have crucial consequences. That is why more maintenance and management should be focused on these rail elements on bridges.

In Finland the maintenance companies are mainly responsible for the maintenance of these structures. There is not enough know-how of bridge inspectors about these structures. The number of experts of this field is diminishing in both design and maintenance phases. But the experts taking care of these parts of the railway network are true experts. There is a definite need in the future for more people to understand the bridge and rail interactions to keep the rails on bridges safe.

REFERENCES

Finnish Transport Infrastructure Agency. Manual for Railway Bridges *RATATEKNISET OHJEET (RATO) osa 8, Rautatiesillat, 2020*. Helsinki

Finnish Transport Infrastructure Agency. Bridge managements system, Helsinki

Hämäläinen R. 2023. Railway Magazine 03/2023. Article. *Päällysrakenteen erikoislaitteet - kiskonliikuntalaite*

Bridge Maintenance, Safety, Management, Digitalization and Sustainability – Jensen, Frangopol & Schmidt (eds)
© 2024 The Author(s), ISBN 978-1-032-77040-6
Open Access: www.taylorfrancis.com, CC BY-NC-ND 4.0 license

Retrofit of PRC bridges by external post-tension under different corrosion scenarios

G. Santarsiero, V. Picciano, A. Masi & G. Ventura
School of Engineering, University of Basilicata, Potenza, Italy

ABSTRACT: Prestressed reinforced concrete bridges with post-tensioned strands are subjected to heavy corrosion deterioration problems due to injection defects and chloride ingress by de-icing salts or sea airborne. The peculiarity of this prestressing system is recognized by the new italian guidelines on existing bridges prescribing special assessment procedures. Therefore, these bridges need reliable strengthening techniques able to enhance durability reducing the risk of collapse. This paper examines the application of post-tension to rehabilitate pc bridges with injected cables, considering corrosion initiation and propagation, estimated through a chloride ingress model included in the finite element models. Assuming a high chlorides surface concentration, a case study bridge is investigated to design an external post-tension intervention evaluating the time evolution of the capacity-demand ratio under gravity and traffic loads. The capacity loss is estimated depending on the considered corrosion period also assessing the response in terms of cracking and deformation.

1 INTRODUCTION

Following the Second World War, Italy witnessed a growing development of its infrastructure network, so much that it could compete with the main European cities. The majority of the bridges along the road networks were constructed during that period and, as a result, they are now in a state of obsolescence and degradation due to reaching the end of their design service life (Di Prisco 2019).

During those years, the most used technologies for bridge construction were reinforced concrete and prestressed reinforced concrete with post-tensioned cables, which presented significant issues related to degradation due to cable corrosion. In fact, due to the execution deficiencies of this technique, which was still in its early stages during those years, a widespread error was primarily associated with the incorrect or sometimes complete lack of grout injection into the ducts (Smith & Wood 2001), resulting in the creation of voids that facilitated chloride ingress due to the use of de-icing salts or marine aerosol, subsequently initiating and promoting tendon corrosion (Gjørv 2009).

Another critical aspect is that, for this type of structure, is difficult to detect ongoing corrosion phenomena through simple visual inspection or the most common non-destructive diagnostic techniques. Therefore, they may be in a significantly degraded condition not visible from the outside, which can lead to the sudden collapse of the structure (Godart 2015).

For these reasons, within the Italian code for existing bridges, namely the Guidelines on risk classification and management, safety assessment and monitoring of existing bridges (Ministry of Infrastructure, CSLP 2020), prestressed concrete bridges with post-tensioned cables are classified as structures that require accurate assessments and the implementation of special inspections, given their inherent vulnerability.

Therefore, an accurate assessment of safety levels and residual functionality is of fundamental importance, primarily for bridges that are clearly in a state of degradation, but also for bridges that, while appearing to be in optimal preservation conditions, may still exhibit obsolescence, even if only in terms of regulatory compliance, as they were designed according to the specifications of older technical standards (Santarsiero et al. 2023).

DOI: 10.1201/9781003483755-65

Following the safety assessments required by current regulations, most of the existing bridges and viaducts show an actual capacity lower than the demand generated by current traffic loads, which are significantly higher than those considered at the design time of each structure. Therefore, it is necessary to take action through strengthening measures to restore the lost load-bearing capacity due to current degradation conditions and/or the gap in terms of the capacity-demand ratio to satisfy safety verifications.

The purpose of this study is to evaluate the effectiveness of a rehabilitation intervention for existing bridges with a prestressed reinforced concrete girders deck, employing external post-tensioning cables. Specifically, using nonlinear numerical analyses conducted with the finite element software ATENA (Červenka et al. 2021), the overtime decay of the load-bearing capacity of the most stressed beam was first evaluated, considering different time scenarios of damage associated with the onset of chloride-induced corrosion phenomena.

Subsequently, following the innovative approach underlying the new Italian Guidelines, an accurate assessment of the beam's residual capacity was performed by comparing it with the maximum expected stresses, in order to determine the potential need for a static rehabilitation intervention. As for the proposed intervention, the key aspects influencing its design and, consequently, its effectiveness were highlighted.

Thanks to nonlinear finite element simulations, it was possible to conduct a long-term analysis that simultaneously takes into account both the effect of the intervention and the overtime evolution of degradation induced by corrosion. Therefore, the novelty of the proposed approach is to accurately assess the overtime variation of the load-bearing capacity of the beam, even when subjected to an intervention, in order to quantify its long-term effectiveness as well as the whole durability.

2 FINITE ELEMENT ANALYSIS OF THE CASE STUDY BEAM

2.1 *Modelling*

The analysed case study is represented by an edge beam of a highway bridge with a simply supported span system, built in 1966 using prestressed reinforced concrete technology with post-tensioned cables. The bridge deck has an overall length of 32.80 m and a width of 11.05 m, consisting of 5 prestressed reinforced concrete beams with a height of 1.7 m, spaced at a distance of 2.20 m (Figure 1a). The 5 beams are connected at the top by a reinforced concrete slab with a thickness of 20 cm and by 5 reinforced concrete transverse beams. Furthermore, crucial information for the analysis, related to the arrangement of the beam and slab reinforcement, as well as the prestressing cable layout, was derived from the design documents (Figure 1b).

The software used for finite element analysis is ATENA (Červenka et al. 2021), which allows for detailed analysis by constructing three-dimensional models. Additionally, the software accounts for concrete and reinforcement nonlinear behaviour. Specifically, for concrete a constitutive model capable of reproducing its behaviour under both compressive (crushing) and tensile (cracking) loading was utilized (Bazant & Oh 1983). Further details on the constitutive model used can be found in the work conducted by (Santarsiero et al. 2021). As for the reinforcement and prestressing cables, an elastic-plastic hardening constitutive model for steel was employed (Ministry of Infrastructure 2018).

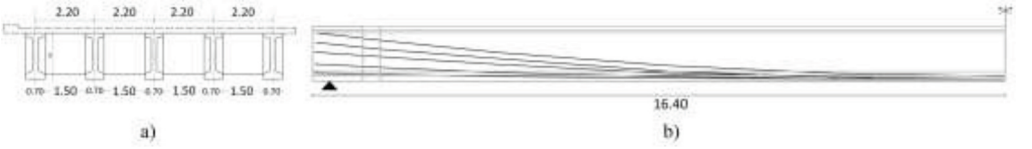


Figure 1. a) Bridge deck's cross-section; b) longitudinal profile of the beam and layout of the post-tensioning cables for half length.

To determine the mechanical properties of reinforcement bars, prestressing cables, and slab concrete, a reference to literature studies was made. However, to estimate the prestressing applied to the cables and the concrete class of the beam, the approach followed was that of "simulated design". This type of approach involves the ability to follow the design phases of the structure, using the regulatory tools of the time, in order to have an understanding of the materials used and construction details, even in the absence of explicit information.

Regarding the reinforcements of the slab and the beam, two types of steel, namely "TOR50" and "AQ50", were used. Given the steel types, it was possible, with the studies of Masi & Digrisolo (2013) and Verderame et al. (2011), to deduce the mean and characteristic values of the parameters necessary for modelling, such as yielding and ultimate tensile strength and strain. In order to conduct safety verifications in accordance with the current regulations (Ministry of Infrastructure 2018), the design strengths used in the software were calculated from these values (Table 1), as specified in the Italian Guidelines (Ministry of Infrastructure, CSLP 2020). In particular, the design values are derived through the following expression:

$$f_d = \min\left(\frac{f_m}{CF \cdot \gamma_m}; \frac{f_k}{CF}\right) \tag{1}$$

where γ_m represents the material safety factor (equal to 1.15 for steel and 1.5 for concrete) (Ministry of Infrastructure 2018), while the term CF represents the confidence factor, which depends on the level of knowledge of the structure (Circolare No. 7/C.S.LL.PP 2019), and has been assumed equal to 1.

As for the prestressing cables, reference was made to the studies by Jacinto et al. (2012) to obtain the characteristic values of strength at 0.1% deformation and rupture ($f_{p0.1k}$ = 1632 MPa, f_{ptk} = 1860 MPa, ε_t = 5%) and, from these, design strengths used within the modelling were derived. Furthermore, in order to model the presence of the protective duct for the prestressing cables (Corven & Moreton 2013), reproducing a certain delay in the onset of cable corrosion during the degrading simulations, the cross-sectional area of each cable has been increased by an amount equal to the cross-sectional area of the duct itself. Therefore, the strength values were reduced to ensure equivalence in terms of force within each cable. Knowing that each cable is made up of 44 strands with a 6 mm diameter and that the duct has a thickness of 0.3 mm, the reduced yield strength values were obtained as $f'_{p0.1d}$ = 1362.54 MPa and ultimate tensile strength as f'_{ptd} = 1552.9 MPa.

Table 2 presents the main strength characteristics of the concrete in the slab and the beam. In the first case, the mean and characteristic strength values were obtained referring to the study by Miluccio et al. (2021). In the second case, the minimum compressive strength value f_{ck} was calculated to ensure that the maximum compressive stress within the beam, subjected to self-weight and cables' prestress, did not exceed the allowable value equal to 48% of the cubic compressive strength, as specified by the regulations in force at the time of design (Circolare No. 384 of 1962). In both cases, once the mean and/or characteristic strength were known, Young's modulus and tensile strength were determined using expressions from the current regulations (Ministry of Infrastructure 2018), while the fracture energy was calculated following the guidelines provided in the Model Code 2010 (Fib, Fédération Internationale du Béton 2010).

Table 1. Strength characteristics of ordinary reinforcement.

	AQ50	TOR50
Young's modulus, E	200 GPa	200 GPa
Design yielding stress, f_{yd}	321.02 MPa	306.55 MPa
Failure stress, f_{td}	475.53 MPa	442.99 MPa
Failure strain, ε_t	0.26 (-)	0.255 (-)

Table 2. Concrete properties for nonlinear simulations.

	Beam	Slab
Design compressive strength, f_{cd}	32 MPa	20.81 MPa
Design tensile strength, f_{td}	2.34 MPa	1.59 MPa
Young's modulus, E	35,220.46 MPa	31,953.76 MPa
Fracture energy, G_F	1.47E−4 MN/m	1.38E−4 MN/m

The assessment of prestressing forces within the cables was carried out by retracing the design phases prescribed by the regulations of that time, in order to achieve a state of integral compressive stress (Leonhardt 1979) within the beam, both when subjected only to self-weight and in operational condition considering permanent and traffic loads (Circolare No. 384 of 1962). In doing so, a value of the prestress applied to the individual cable was obtained, equal to $\sigma_{p,i}$ = 1090 MPa, which is approximately 80% of the cables' yield strength.

Figure 2 shows the 3D finite element model of the analysed beam, discretized into finite elements (3000 hexahedral elements, 49,387 tetrahedral elements, 1824 linear elements, for a total of 22,868 nodes). In particular, taking advantage of the beam's symmetry, only half of it was modelled. Load conditions were applied through a plate located at the midpoint of the beam, while the lower plate transferred the boundary conditions to the model. Both plates were modelled using linear elastic steel behaviour.

The analysis considered the initiation and development of reinforcement and prestressing cable corrosion due to chloride ingress. In fact, the ATENA software allows for mechano-chemical analyses that take into account chloride diffusion inside the concrete, accelerated by the presence of cracking generated by applied loads on the beam. These analyses quantify the time of corrosion initiation and the percentage of corrosion, understood as a reduction in the cross-sectional area, on the reinforcement and prestressing cables. The model was described in detail in Santarsiero et al. (2021) and Santarsiero & Picciano (2023). In particular, by appropriately selecting the values of the main model parameters (surface chlorides concentration C_s, chlorides diffusion coefficient D_{ref}, and critical chlorides content C_{crit}) to consider an aggressive environment due to the use of de-icing salts (Hájková et al. 2018), it was possible to simulate a common degradation condition within bridge beams, where the most deteriorated areas are evident at the locations of water drainage systems and the ends of the beams.

In this way, several analyses were implemented to assess the beam's capacity in as-built conditions and under degraded conditions following time scenarios of 56, 86, and 106 years, which respectively correspond to the current age of the bridge and an additional 30 and 50 years of corrosion development. In each analysis, different intervals can be distinguished as follows: from the first to the fifth interval, the self-weight of the beam and the prestressing force $\sigma_{p,i}$ in each of the 5 prestressing cables are applied; in the sixth interval, the weight of the slab and permanent loads are applied; in the analyses with corrosion simulation, the seventh interval corresponds to the application of the mechano-chemical model; in the final interval, through a displacement-controlled analysis, the beam is brought to failure to assess its ultimate capacity.

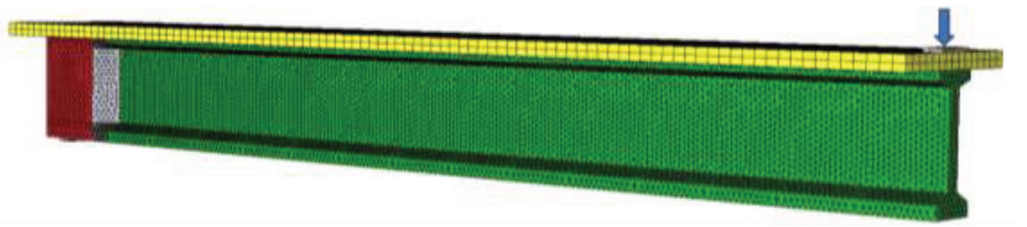


Figure 2. Finite element model of the beam.

2.2 *Analyses' results and verifications*

Thanks to the finite element analyses, it was possible to assess the overtime progression of the beam's load-bearing capacity following the considered corrosion scenarios. The beam's capacity was evaluated in terms of flexural strength, resulting in a value of 15,130 kNm in the as-built condition. This capacity undergoes reductions of approximately 10.7% (M_{rd} = 13,520 kNm), 46.5% (M_{rd} = 8100 kNm), and 55.3% (M_{rd} = 6771 kNm), following corrosion development scenarios respectively of 56, 86, and 106 years. As shown in Figure 3, which represents the overtime progression of the maximum corrosion percentage on the prestressing cables, the variations in the beam's strength are justified by a reduction in the cross-sectional area of the cables, ranging from a minimum of 20.5% to a maximum of 36.5% after 56 years, between 30.1% and 67.1% after 86 years, and between 36.2% and 82% following 106 years of corrosion development.

It is worth noting that the mechano-chemical model implemented takes into account the presence of cracks, which increase the possibility of chloride ingress. Furthermore, due to the specific arrangement of the cables within the beam, they are subject to different initiation times, and therefore, the function representing the corrosion progression does not maintain the same concavity throughout the structure's life. This also results in terms of the beam strength variation, showing a nonlinear trend, as demonstrated by the different values of the decay rate obtained in the various time intervals considered. In particular, the first 56 years show a decay of 0.19%, compared to 1.34% between 56 and 86 years, and 0.82% between 86 and 106 years (Figure 4).

Subsequently, to perform the flexural strength verification of the beam, the demand in terms of flexural stress was calculated considering the application of traffic and permanent loads according to the current Italian regulations (Ministry of Infrastructure 2018). Regarding the traffic ones, load pattern No. 1 for global verification includes both tandem concentrated loads Q_{ik} and distributed ones q_{ik}, arranged in 3 conventional lanes with a width of 3 m, as shown in Figure 5. Proceeding with the transverse load distribution procedure by Courbon Engesser (Raithel 1977), a load of 40.62 kN/m on the edge beam is obtained. Using the ultimate limit state combination, this value is combined with structural permanent loads (self-weight of the beam, slab, and concrete curbs) and non-structural permanent loads (pavement and safety devices), resulting in an overall load value on the edge beam of 99.6 kN/m, which produces a maximum midspan flexural demand, for a simply supported beam, of M_{ed} = 13,391.15 kNm.

Figure 4 shows the overtime progression of the ratio between the beam's capacity, assessed through numerical simulations considering the corrosion-induced degradation, and the demand assessed according to current regulations. As can be seen, the flexural verification is satisfied in the as-built condition, with a value of ζ = 1.13, and in the current condition (t = 56 years), although with a very limited safety margin (ζ = 1.01), which leads to exceeding the capacity in subsequent periods (ζ = 0.60 at t = 86 years and ζ = 0.51 at t = 106 years). Therefore, in the next section, the design of a strengthening intervention is carried out.

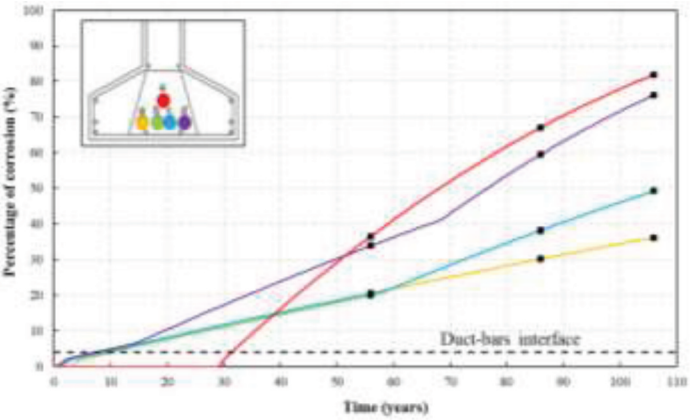


Figure 3. Progression of maximum prestressing cables' corrosion over time.

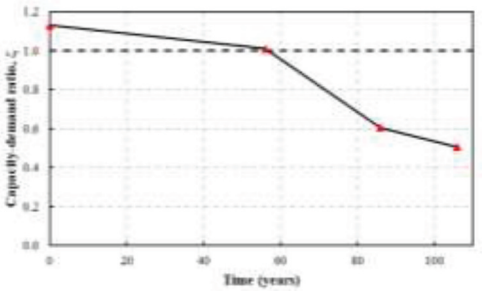


Figure 4. Capacity-demand ratio as a function of time.

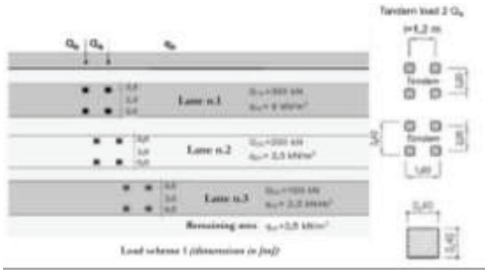


Figure 5. Load pattern No. 1 according to Ministry of Infrastructure (2018).

3 DESIGN AND MODELLING OF EXTERNAL POST-TENSION INTERVENTION

The intervention consists of 2 post-tensioned external cables appropriately arranged along the lateral surfaces of the beam and anchored to it through anchoring plates and deviator plates required for the transfer of the imposed load state. Through cables' tensioning, a compressive force is applied to the structure, increasing its flexural capacity, reducing deflection, and partially or fully recovering existing crack patterns, improving both the serviceability and ultimate limit state performance (Daly & Witarnawan 1997).

In this case, the strengthening system was designed by evaluating the cable prestressing force required to compensate for the deficit in terms of the beam's flexural resistance, as assessed in the previous section. In addition, the assessment of the design prestressing value also depends on the cable's geometry, by evaluating its inclination and eccentricity at the deviator plates. Through iterative steps, the design force of each cable was evaluated equal to T = 1733.13 kN, considering an inclination of 11 degrees and an eccentricity value of 1760 mm. Based on the calculated design force, a cable consisting of 12 strands with a 15 mm diameter was selected from a commercial catalogue, with a yielding strength of $f_{y,e}$ = 1550 MPa, an ultimate tensile strength of $f_{t,e}$ = 1770 MPa, and a failure load of 3180 kN. According to the procedure proposed by MacGregor et al. (1989), the designed cable must also be verified against the increased force to which it would be subjected following a possible failure of the beam, considering a collapse mechanism with the formation of a plastic hinge at midspan. In the end, taking into account this additional verification, a cable prestressing stress of $\sigma_{p,e}$ = 963 MPa was obtained.

Figure 6 shows the 3D model of the beam with the intervention, in which 3 C-plates in S275JR ordinary steel (EN 1993-1-1 2005) have been inserted to anchor the cables at the beam's head and at the locations where they change direction. Therefore, a preliminary nonlinear analysis was implemented to assess the capacity of the reinforced beam, considering that the intervention was applied at t = 56 years, during which the corrosion progression was simulated as seen earlier. Subsequently, two additional scenarios were analysed in which, following the intervention, the beam was subjected to further 30 and 50 years of corrosion development.

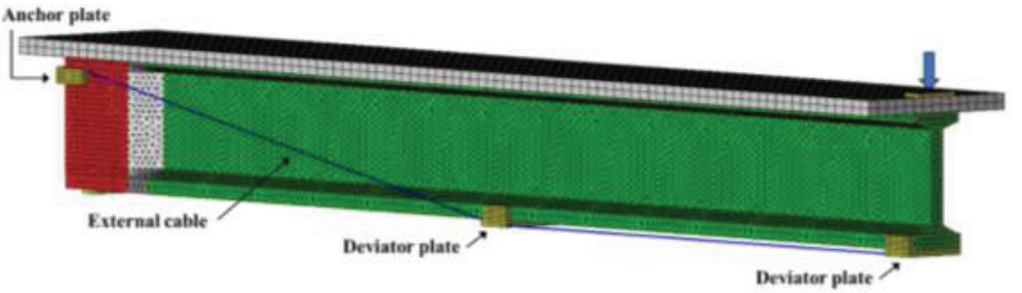


Figure 6. Finite element model of the beam with the intervention.

4 MAIN RESULTS AND DISCUSSION

The implemented nonlinear analyses allowed for the evaluation of the overtime evolution of the beam's capacity-demand ratio, both with and without the strengthening intervention using post-tensioned external cables, as shown in the graph of Figure 7. As can be observed, compared to the conditions without intervention at t = 56 years (current bridge conditions), there is an increase in flexural capacity of approximately 46%, which goes from a value of 13,520 kNm to 19,758 kNm. Additionally, thanks to the intervention, the beam's capacity remains higher than the demand even during the subsequent years of simulated corrosion progression, unlike the case without intervention. In particular, capacity-demand ratio values ζ are 1.48, 1.15, and 1.10, respectively at t = 56, 86, and 106 years with intervention. Another result that can be deduced from the graph is that there is a delayed decrease in strength over time. This is evident from the shallower slope of the lines with the intervention compared to those in as-built corroded conditions in the periods between 56 and 86 years and between 86 and 106 years. In fact, there is an annual decay rate of 0.73% compared to 1.34% without intervention in the first period, while there is a decay of 0.23% compared to 0.82% without intervention in the second one.

Furthermore, the intervention allows for a reduction in the extent of cracking observed at the beam's failure condition. In fact, nonlinear simulations enable the quantification of the maximum crack width, which, in the degraded condition after 56 years of corrosion development, amounts to 2.4 cm (corresponding to reaching a flexural capacity of 13,520 kNm). Conversely, under similar degradation conditions but with the intervention, the maximum crack width is reduced to 1.1 cm (with a flexural capacity of 19,758 kNm), resulting in a 54% reduction. The beneficial effect of external post-tensioning is also evident in terms of beam deformation, reaching a maximum displacement at failure of 16.3 cm, compared to the value of 33.4 cm achieved without intervention and under similar degradation conditions.

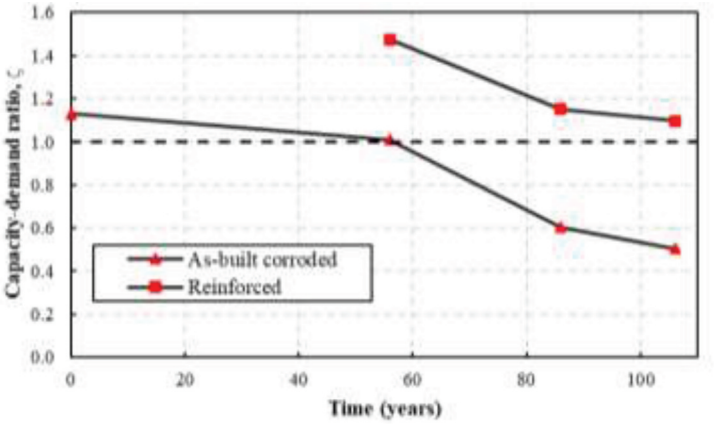


Figure 7. Overtime evolution of capacity-demand ratio in the presence and absence of intervention.

5 CONCLUSIONS

In this study, the structural behaviour of a prestressed reinforced concrete bridge beam built in the 1960s was analysed. The beam was assessed using the finite element software ATENA, which is capable of conducting nonlinear analyses and durability assessments, taking into account chloride-induced corrosion through an advanced mechano-chemical model. The primary objective was to initially evaluate the time-dependent evolution of the structure's capacity under various corrosion scenarios, simulating the current condition of the bridge as well as an additional 30 and 50 years of degradation. Subsequently, this evaluation was compared

to the demand derived from traffic loading patterns in accordance with current Italian regulations. This comparison revealed the need for a strengthening intervention. Therefore, an intervention was designed and modelled, involving the use of external post-tensioned cables. The effectiveness of this intervention was evaluated through a long-term analysis, subjecting the beam to the same corrosion scenarios as before. The results indicate that the intervention increases the flexural capacity of the beam by 46%, raising the capacity-demand ratio from 1.01, in the absence of intervention, to 1.48 in the current state, and maintaining this ratio above 1 even after additional 50 years of degradation. This highlights the effectiveness of the intervention over the long term. Additionally, the beam experiences beneficial effects in terms of cracking and deformation at failure, reducing the maximum crack width and mid-span displacement by 54% and 51%, respectively.

ACKNOWLEDGMENTS

The studies presented here were carried out as part of the activities envisaged by the Agreement between the Italian Department of Civil Protection and the ReLUIS Consortium (DPC-ReLUIS project 2022-24, WP5-Task 5.4 "Upgrading and retrofitting interventions of existing bridges"). The contents of this paper represent the authors' ideas and do not necessarily correspond to the official opinion and policies of DPC.

REFERENCES

Bazant, Z. P., & Oh, B. H. (1983). Crack Band Theory for Fracture of Concrete. *Materials and Structures*, *16*(3), 155–177

Červenka, V., Jendele, L., & Jan Červenka, J. (2021). ATENA Program Documentation, Part 1, *ATENA Theory Manual*, 2000-2021.

Circolare n. 384 del 1962 del Ministero LL.PP. "*Norme relative ai carichi per il calcolo dei ponti stradali*" (Ministero dei Lavori Pubblici). (in Italian).

Circolare n 7.C.S.LL.PP. del 21/01/2019. (2019). *Istruzioni per L'applicazione dell'"Aggiornamento Delle Norme Tecniche per le Costruzioni*" di cui al Decreto Ministeriale 17 Gennaio 2018. (in Italian).

Corven, J., & Moreton, A. J. (2013). *Post-tensioning tendon installation and grouting manual* (No. FHWA-NHI-13-026). Federal Highway Administration (US).

Daly, A. F., & Witarnawan, W. (1997). Strengthening of bridges using external post-tensioning. In *Conference of eastern Asia society for transportation studies* (October 1997), Seoul, Korea.

Di Prisco, M. (2019). Critical infrastructures in Italy: State of the art, case studies, rational approaches to select the intervention priorities. In *fib Symposium 2019: Concrete-Innovations in Materials, Design and Structures* (pp. 49–58). International Federation for Structural Concrete.

EN 1993-1-1 (2005) (English): *Eurocode 3: Design of steel structures - Part 1-1: General rules and rules for buildings* [Authority: The European Union Per Regulation 305/2011, Directive 98/34/EC, Directive 2004/18/EC]

Fib, Federation Internationale du Beton. (2010). *Model Code 2010* First Complete Draft, Fib Bulletin n. 55, vol. 1, Lausanne, Switzerland, 2010

Gjørv, O. E. (2009). *Durability Design of Concrete Structures in Severe Environments*. Taylor & Francis: London, UK; New York, NY, USA.

Godart, B. (2015). Pathology, appraisal, repair and management of old prestressed concrete beam and slab bridges. *Structure and Infrastructure Engineering*, *11*(4), 501–518.

Hájková, K., Šmilauer, V., Jendele, L., & Červenka, J. (2018). Prediction of reinforcement corrosion due to chloride ingress and its effects on serviceability. *Engineering Structures*, *174*, 768–777.

Jacinto, L., Pipa, M., Neves, L. A., & Santos, L. O. (2012). Probabilistic models for mechanical properties of prestressing strands. Construction and Building Materials, 36, 84–89.

Leonhardt, F. (1979). *C.a. & c.a.p.: calcolo di progetto & tecniche costruttive*. Edizioni di scienza e tecnica.

MacGregor, R.J.G., Kreger, M.E., Breen, J.E. (1989). *Strength and Ductility of a Three-Span Externally Post-Tensioned Segmental Box-Girder Bridge Model*. Research Report 365-3F, Project 3-5-85/8-365, Centre for Transportation Research, Bureau of Engineering Research, The University of Texas at Austin, January.

Masi, A., & Digrisolo, A. (2013). Analisi delle caratteristiche meccaniche di acciai estratti da edifici esistenti in cemento armato. In *Proceedings of the ANIDIS XY Conference" L'Ingegneria Sismica in Italia"*, Padova (Vol. 30).

Miluccio, G., Losanno, D., Parisi, F., & Cosenza, E. (2021). Traffic-load fragility models for prestressed concrete girder decks of existing Italian highway bridges. *Engineering Structures*, *249*, 113367.

Ministry of Infrastructure, CSLP. (2020). *Guidelines on Risk Classification and Management, Safety Assessment and Monitoring of Existing Bridges*. Ministry of Infrastructure: Rome, Italy, 2020 (in Italian).

Ministry of Infrastructure. (2018). *Aggiornamento delle Norme tecniche per le costruzioni*. Ministry of Infrastructure, DM 17 Gennaio 2018, Suppl. or. n.30 alla G.U. n.29 del 4/2/2008. (in Italian).

Raithel, A. (1977). *Costruzioni di ponti*. Napoli (in Italian).

Santarsiero, G., & Picciano, V. (2023). Durability enhancement of half-joints in RC bridges through external prestressed tendons: The Musmeci Bridge's case study. *Case Studies in Construction Materials*, *18*, e01813.

Santarsiero, G., Albanese, P., Picciano, V., Ventura, G., & Masi, A. (2023). Level 3 Assessment of Highway Girder Deck Bridges according to the Italian Guidelines: Influence of Transverse Load Distribution. *Buildings*, *13*(7), 1836.

Santarsiero, G., Masi, A., & Picciano, V. (2021). Durability of Gerber saddles in RC bridges: Analyses and applications (Musmeci Bridge, Italy). *Infrastructures*, *6*(2), 25.

Smith, L. J., & Wood, R. (2001). Grouting of external tendons-a practical perspective. *Proceedings of the Institution of Civil Engineers-Structures and Buildings*, *146*(1), 93–100.

Verderame, G. M., Ricci, P., Esposito, M., & Sansiviero, F. C. (2011). Le caratteristiche meccaniche degli acciai impiegati nelle strutture in ca realizzate dal 1950 al 1980. *XXVI Convegno Nazionale AICAP*.

Bridge Maintenance, Safety, Management, Digitalization and Sustainability – Jensen, Frangopol & Schmidt (eds)
© 2024 The Author(s), ISBN 978-1-032-77040-6
Open Access: www.taylorfrancis.com, CC BY-NC-ND 4.0 license

Life-cycle environmental impact assessment of bridge designs considering maintenance strategy

S.H. Lee
Seoul National University, Seoul, Republic of Korea

L.S. An
FAMU-FSU College of Engineering, Tallahassee, USA

H.K. Kim
Seoul National University, Seoul, Republic of Korea & Institute of Construction and Environmental Engineering, Seoul, Republic of Korea

ABSTRACT: The growing emphasis on carbon neutrality and sustainability within the global infrastructure sectors exerts a profound influence on the decision-making processes concerning construction materials. Now, it become imperative to select the primary construction materials not only based on economic feasibility but also by taking into account the quantified environmental impact in terms of life-cycle assessment. The cost and environmental impact may vary significantly depending on the maintenance strategy during operation and the recycling rate after the end-of-life stage. In this study, life-cycle assessments were conducted on steel plates and pre-stressed concrete girder bridges under identical structural conditions. We systematically quantified the effects of primary construction materials and environmental conditions on the overall environmental impact.

1 INTRODUCTION

The relationship between the infrastructure industry and its environmental impact has been a focal point of discussions, addressing key concerns such as energy consumption, greenhouse gas emissions, raw material depletion, and waste generation (Barbhuiya and Das, 2023). Notably, 90% of CO_2 emissions within the infrastructure sector are concentrated in the product stage of construction material (Blanco et al., 2021). The crux of mitigating the environmental impact of the infrastructure industry lies in the engineer's sustainable conceptual design decision and optimized designs (Kanyilmaz et al., 2023). Alongside life-cycle performance assessment (LCPA), ensuring sustainability based on quantitative life-cycle impact assessment (LCIA) is paramount. Precedent studies have conducted comparative LCIA of alternative designs for several types of infrastructure, including bridges (Du et al., 2014, Gervásio and da Silva, 2008) and buildings (Desai and Bheemrao, 2022, Katebi et al., 2023).

Infrastructures inevitably experience structural performance deterioration over time due to their lengthy design life (Biondini and Frangopol, 2016). The extent of performance deterioration can be significantly influenced by environmental conditions to which the structure is exposed and long-term climate changes (Cai et al., 2018, Xie et al., 2018). Both the life-cycle environmental impact and cost can be affected by the maintenance scenarios and strategies employed to address performance deterioration (Kere and Huang, 2019, Orcesi et al., 2010). For instance, if technical actions such as member replacement or reinforcement are integrated into the maintenance strategies, notable differences can emerge in the environmental performance and cost throughout the life cycle (Cadenazzi et al., 2020, Han et al., 2021). Moreover, the incorporation of a construction material recycling strategy introduces complexity and challenges to the life-cycle assessment (LCA), as investigated by Kanyilmaz et al. (2023) Therefore, it is essential to establish appropriate

DOI: 10.1201/9781003483755-66

maintenance strategies and understand their implications through time-variant performance analysis from a life-cycle perspective (Alfredo and TANG, 2007, Strauss et al., 2008).

This study systemically quantified the life-cycle environmental impact of bridge design alternatives of different primary construction materials (concrete and steel) while maintaining identical conditions in all other aspects. A two-step LCA framework was employed. First, a time-variant LCPA was conducted, accounting for the deterioration of structural components induced by corrosion. The influence of corrosive environments on the final environmental impact was investigated by considering three distinct corrosive environments. Second, by integrating the information on technical actions derived from LCPA into LCIA, the environmental impacts associated with bridge construction materials were quantified. The outcomes of case studies provide insights into the environmental impact of bridge design alternatives, taking into the interplay of bridge deterioration, time-variant performance, and material recycling.

2 LCA FRAMEWORK

2.1 *LCPA*

LCPAs were conducted on the flexural capacity of the maximum positive moment section under the design truck load, extending up to the target service life of 100 years for the service limit state according to AASHTO LRFD guidelines (AASHTO, 2020). The structural performance degradation due to corrosion was considered. Three corrosive environmental conditions were investigated; rural, urban, and marine environments (Albrecht and Naeemi, 1984). Throughout the use stage, the maintenance strategies for the bridge were categorized into preventive (patching, repainting, etc.) and essential maintenance (girder replacement, reconstruction, etc.) each involving different technical actions (Biondini and Frangopol, 2016). In this study, the preventive maintenance interval (t_m) was set as 10 years. Essential maintenance of deteriorated girder replacement was set to occur when the probability of failure (P_f) reached 0.6% of target P_f according to AASHTO MBE (AASHTO, 2018). Figure 1 illustrates the LCPA framework.

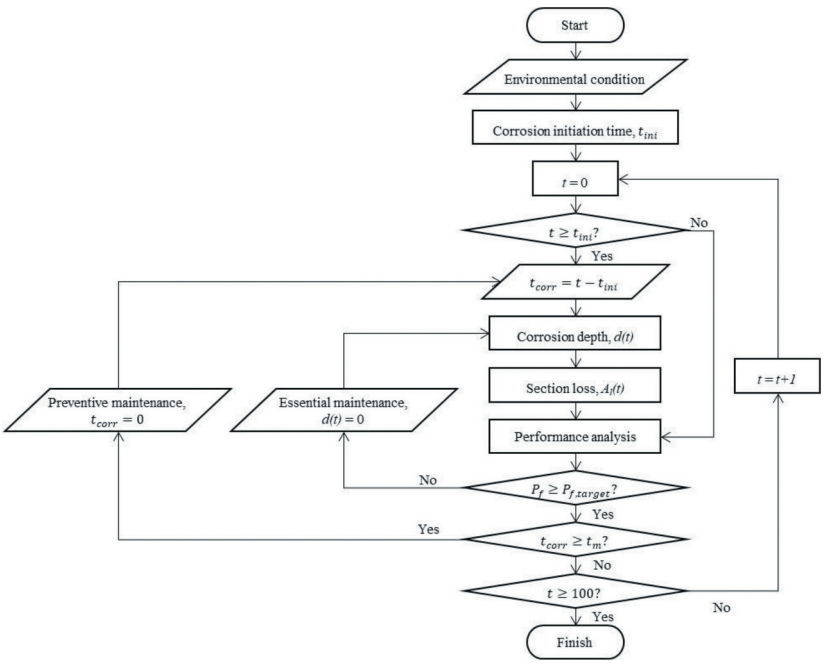


Figure 1. LCPA flowchart.

2.2 *LCIA*

The bridge LCA of alternative designs under identical structural conditions were carried out in accordance with ISO 14040 (ISO, 2006a), 14044 (ISO, 2006b), and 21930 (ISO, 2017) standards. The system boundary was defined as cradle-to-grave, including the potential benefits and loads of a circular economy. For the assessment of the circular economy of steel, adherence to ISO 20915 (ISO, 2018) is crucial to accurately evaluate industry-specific data and the losses and benefits associated with recycling processes. The OpenLCA (GreenDelta, 2023), utilizing the ecoinvent database (DB) (RIVM, 2016), was employed for the LCIA. In cases where products were absent in the ecoinvent DB, the industrial environmental product declaration (EPD) DB registered in TOTAL (KEITI, 2023), a Korean LCA program, was utilized. Environmental data related to all included materials throughout the bridges' lifetimes were gathered and characterized using the ReCiPe 2016 method (RIVM, 2016), yielding results for the six environmental categories (Table 1). Environmental impacts, considering loss and benefits from the recycling of steel, were determined based on data provided by Korean industries and environmental reports (ME, 2023).

Table 1. Environmental categories.

Impact category	Reference unit
abiotic depletion potential (ADP).	10 kg Cu eq
eutrophication potential (EP)	kg PO43- eq
global warming potential (GWP)	t CO2 eq
ozone-layer depletion potential (ODP)	g CFC11 eq
acidification potential (AP)	kg SO2 eq
photochemical ozone-creation potential (POCP)	10 kg NOx eq

3 CASE STUDY

3.1 *Target Bridge*

The target bridge for design consist of two one-way bridges, each with widths of 12.3 m (B1) and 15.9 m (B2), and a total length of 175 m (5 spans at 35 m each). LCAs were conducted for two types of bridge design alternatives: one with pre-stressed concrete (PSC) girders and the other with steel plate girders. The same framework was applied to both alternatives. Figure 2 illustrates the plane view of the bridge.

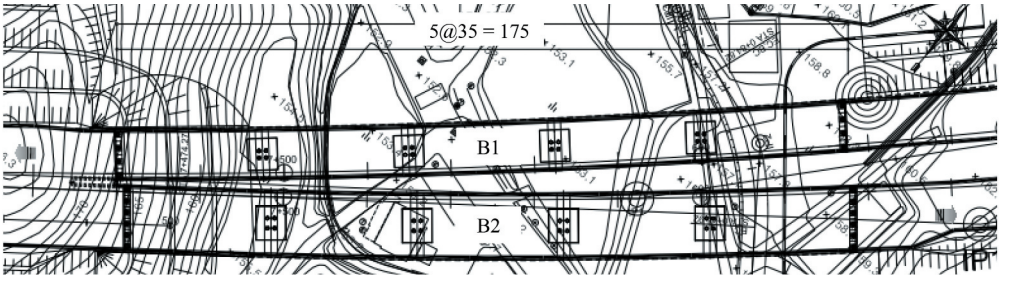


Figure 2. Plane view of target bridge.

3.2 *Results of LCPA*

Performance deterioration of the PSC girder bridge was evaluated according to the chloride-induced corrosion model under different environmental conditions (Vu and Stewart, 2000) considering a chloride penetration scenario where chloride infiltration into the tendon leads to

corrosion (Al-Mosawe et al., 2022). The corroded cross-sectional shape and loss model of the tendon were applied by Yoo et al. (2018). For the steel plate girder bridge, the corrosion progression model was adopted based on Kayser (1988), and the cross-sectional loss model was applied according to Kere and Huang (2019).

The LCPA results considering two maintenance strategies are shown in Figure 3. Depending on environmental conditions, the rural case did not require replacement for both PSC girder and steel plate girder bridges. However, in the urban case, the replacement was projected to be necessary twice for PSC girder and not at all for the steel plate girder, while the marine case predicted seven replacements for PSC girder and two for the steel plate girder. It is noted that the frequency of the maintenance could vary based on the chosen maintenance strategies and structural deterioration model.

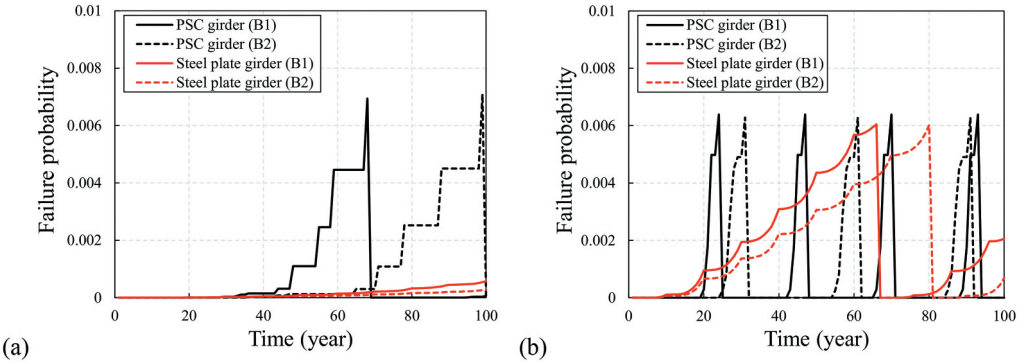


Figure 3. LCPA results for environmental conditions: (a) urban case; and (b) marine case.

3.3 *Results of LCIA*

The frequency of technical actions calculated in Section 3.2 was considered in conjunction with maintenance and disposal amounts to conduct LCIA. Figure 4 illustrates the results of LCIA for the marine case. A recycling rate of steel was commonly applied as 40.1% in Republic of Korea (BIR, 2022). The environmental impacts of the PSC girder bridge, which was evaluated with a relatively higher frequency of technical actions, consistently showed higher values.

Figure 5 presents the sensitivity analysis results for recycling rates ranging from 0% to 100%. It was observed that the proportion of environmental impacts that can be reduced in a circular economy varies significantly based on the recycling rate of steel, with the greatest reduction observed in EP, AP, and GWP, in that order.

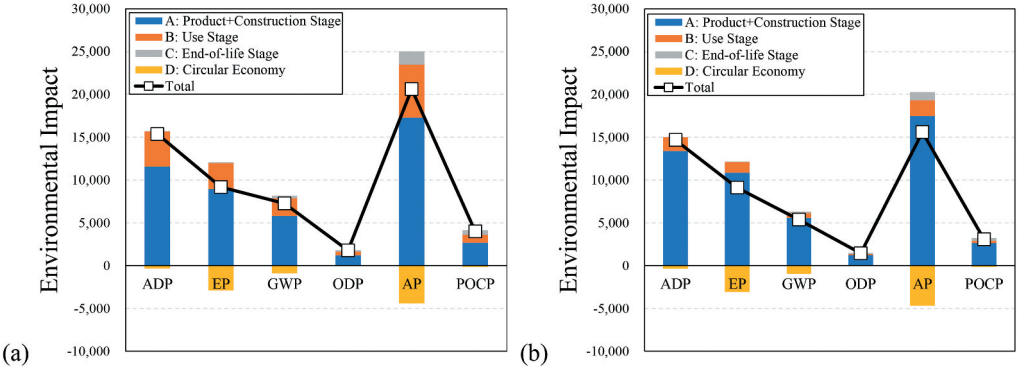


Figure 4. LCIA results for marine case: (a) PSC girder bridge; and (b) steel plate girder bridge.

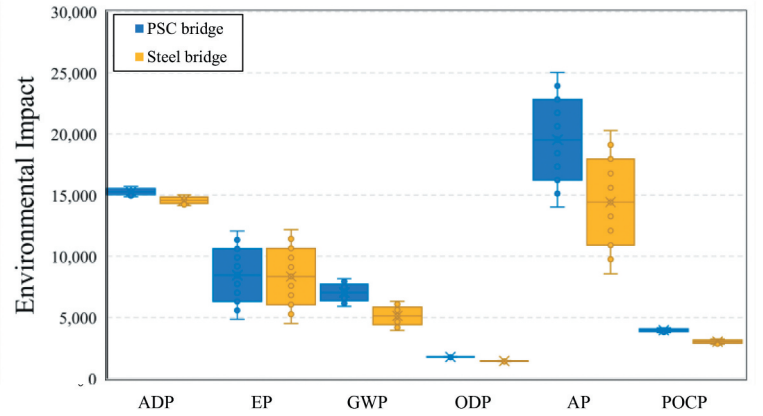


Figure 5. Influence of steel recycling rate into the environmental impact categories.

4 CONCLUSIONS

This study conducted LCPA considering structural performance degradation due to corrosion and LCIA case studies for two types of bridge designs: PSC girder bridge and steel plate girder bridge. Depending on the environmental conditions, it was calculated that the PSC girder may require a maximum of 7 replacements, while steel plate girder may need a maximum of 2 replacements. The tendon corrosion scenario was found to be particularly critical for the performance deterioration of the PSC girder bridge. Technical actions for maintenance strategies, such as girder replacement, demonstrated a significant impact on the overall LCIA results. Additionally, sensitivity analysis on recycling rates of steel revealed that the effect of circular economy plays a crucial role in reducing the final environmental impact.

ACKNOWLEDGMENTS

This work is supported by the Korea Agency for Infrastructure Technology Advancement (KAIA) grant funded by the Ministry of Land, Infrastructure and Transport (Grant RS-2023-00250727) through the Korea Floating Infrastructure Research Center at Seoul National University.

REFERENCES

AASHTO 2018. AASHTO The Manual for Bridge Evaluation. Washington, D.C., USA: American Association of State Highway and Transportation Officials (AASHTO).

AASHTO 2020. AASHTO LRFD Bridge Design Specification. Washington, D.C., USA: American Association of State Highway and Transportation Officials (AASHTO).

Al-Mosawe, D., Neves, L. & Owen, J. Reliability analysis of deteriorated post-tensioned concrete bridges: The case study of Ynys-y-Gwas bridge in UK. Structures, 2022. Elsevier, 242–259.

Albrecht, P. & Naeemi, A. H. 1984. Performance of weathering steel in bridges. *NCHRP report*.

Alfredo, H. & Tang, W. H. 2007. Probability concepts in engineering. *Planning*, 1, 1–3.

Barbhuiya, S. & Das, B.B. 2023. Life Cycle Assessment of construction materials: Methodologies, applications and future directions for sustainable decision-making. *Case Studies in Construction Materials*, e02326.

Biondini, F. & Frangopol, D. M. 2016. Life-cycle performance of deteriorating structural systems under uncertainty. *Journal of Structural Engineering*, 142, F4016001.

BIR 2022. WORLD STEEL RECYCLING IN FIGURES 2017 – 2021: Steel Scrap – a Raw Material for Green Steelmaking. Brussels, Belgium: Bureau of International Recycling.

Blanco, J., Engel, H., Imhorst, F., Ribeirinho, M. & Sjodin, E. 2021. Call for action: Seizing the decarbonization opportunity in construction. M. Company (ed.).
Cadenazzi, T., Dotelli, G., Rossini, M., Nolan, S. & Nanni, A. 2020. Cost and environmental analyses of reinforcement alternatives for a concrete bridge. *Structure and infrastructure engineering*, 16, 787–802.
Cai, Y., Zhao, Y., Ma, X., Zhou, K. & Chen, Y. 2018. Influence of environmental factors on atmospheric corrosion in dynamic environment. *Corrosion Science*, 137, 163–175.
Desai, A. & Bheemrao, N. 2022. Life cycle assessment of construction materials and its environmental impacts for sustainable development. *Materials Today: Proceedings*, 65, 3866–3873.
Du, G., Safi, M., Pettersson, L. & Karoumi, R. 2014. Life cycle assessment as a decision support tool for bridge procurement: environmental impact comparison among five bridge designs. *The International Journal of Life Cycle Assessment*, 19, 1948–1964.
Gervásio, H. & Da Silva, L. S. E. 2008. Comparative life-cycle analysis of steel-concrete composite bridges. *Structure and Infrastructure Engineering*, 4, 251–269.
GREENDELTA 2023. OpenLCA Nexus. GreenDelta GmbH: GreenDelta.
Han, X., Yang, D. Y. & Frangopol, D. M. 2021. Optimum maintenance of deteriorated steel bridges using corrosion resistant steel based on system reliability and life-cycle cost. *Engineering Structures*, 243, 112633.
ISO 2006a. ISO 14040 International Standard. *Environmental Management – Life Cycle Assessment – Principles and Framework*. Geneva, Switzerland: International Organisation for Standardization.
ISO 2006b. ISO 14044 International Standard. *Environmental Management – Life Cycle Assessment – Requirements and Guidelines*. Geneva, Switzerland: International Organisation for Standardization.
ISO 2017. ISO 21930 International Standard. *Core Rules for Environmental Product Declarations of Construction Products and Services*. Geneva, Switzerland: International Organisation for Standardization.
ISO 2018. ISO 20915 International Standard. *Life Cycle Inventory Calculation Methodology for Steel Products*. Geneva, Switzerland: International Organisation for Standardization.
Kanyilmaz, A., Dang, V. H. & Kondratenko, A. How does conceptual design impact the cost and carbon footprint of structures? Structures, 2023. Elsevier, 105102.
Katebi, A., Tushmanlo, H. S. & Asadollahfardi, G. 2023. Environmental life cycle assessment and economic comparison of different roof systems. *Journal of Building Engineering*, 76, 107316.
Kayser, J. R. 1988. *The effects of corrosion on the reliability of steel girder bridges*, University of Michigan.
Keiti 2023. TOTAL. Korea Environmental Industry and Technology Institute: KEITI.
Kere, K. J. & Huang, Q. 2019. Life-cycle cost comparison of corrosion management strategies for steel bridges. *Journal of Bridge Engineering*, 24, 04019007.
Me 2023. Guidelines for Environmental Product Declaration by Product Category. Sejong-si, Republic of Korea: Ministry of Environment.
Orcesi, A. D., Frangopol, D. M. & Kim, S. 2010. Optimization of bridge maintenance strategies based on multiple limit states and monitoring. *Engineering Structures*, 32, 627–640.
RIVM 2016. ReCiPe 2016. National Institute for Public Health and the Environment: RIVM.
Strauss, A., Bergmeister, K., Hoffmann, S., Pukl, R. & Novák, D. 2008. Advanced life-cycle analysis of existing concrete bridges. *Journal of Materials in Civil Engineering*, 20, 9–19.
Vu, K. A. T. & Stewart, M. G. 2000. Structural reliability of concrete bridges including improved chloride-induced corrosion models. *Structural safety*, 22, 313–333.
Xie, H.-B., Wang, Y.-F., Gong, J., Liu, M.-H. & Yang, X.-Y. 2018. Effect of global warming on chloride ion erosion risks for offshore RC bridges in China. *KSCE Journal of Civil Engineering*, 22, 3600–3606.
Yoo, C.-H., Chul Park, Y. & Kim, H.-K. 2018. Modeling corrosion progress of steel wires in external tendons. *Journal of Bridge Engineering*, 23, 04018098.

Bridge Maintenance, Safety, Management, Digitalization and Sustainability – Jensen, Frangopol & Schmidt (eds)
© 2024 The Author(s), ISBN 978-1-032-77040-6
Open Access: www.taylorfrancis.com, CC BY-NC-ND 4.0 license

Damage assessment and expert system for the repair of ageing reinforced concrete components

F. Binder
Asfinag Baumanagement GmbH, Vienna, Austria

U. Schneck
CITec Concrete Improvement Technologies GmbH, Dresden, Germany

A. Strauss
Institute of Structural Engineering, University of Natural Resources and Life Sciences, Vienna, Austria

ABSTRACT: In the face of the limited development of the transport infrastructure, maintaining the condition of the existing structures is becoming more and more important. The majority of structures are made of reinforced or prestressed concrete. Due to their intensive use and the harsh environmental conditions, they are exposed to increased aging. This results in a progressive form of degradation. The application of durable repairs at the optimum time for rehabilitation is a key challenge. The decision to select repairs is often made under unclear conditions. The information from preliminary investigations can be misinterpreted in many ways and the reduction to purely visually detectable damage can lead to wrong conclusions. The aim is to use systematized damage assessments to make decisions on the type of repair more objective and focused on scientific knowledge and expertise. Using a multimodal approach to measure the degradation of reinforced concrete components, the assessment is systematized so that the condition is always objective, comprehensive, and accurate. For this purpose, the results obtained from preliminary investigations are transformed into four damage classes and an objective and by weighting representative condition index. The developed fuzzy logic decision algorithm uses the condition index as input parameter for the selection of optimal repair methods. Hence, this assessment methodology is Fuzzy-Logic (FL), which treats and combines input data in not clear-cut borderlines to choose an optimal maintenance measure. A case study will proof the method to deal with lack of knowledge and uncertainty in this fuzzy decision process.

1 INTRODUCTION

Accurate information on road structure conditions is crucial for safety, maintenance planning, and route availability. Corrosion of reinforced concrete, primarily caused by reinforcement corrosion, poses economic challenges. Globally, five tons of steel corrode every second, amounting to about 6% of a developed country's GDP. To ensure optimal preservation within budget constraints, estimating remaining service life and understanding degradation progression is vital. Existing guidelines in Austria rely on visual assessments, overlooking issues like chloride penetration and carbonation that lead to hidden corrosion. An objective condition assessment is needed to bridge the gap between visual perception and the actual state, enhancing the effectiveness of mandatory inspections.

Developing a practical and objective method for assessing the preservation of reinforced concrete components is the goal of this work. The method aims to determine the preservation state through simple yet objective means, enabling a preselection of targeted and sustainable repair methods. The effectiveness and duration of repair systems are considered, taking into account the current preservation state and component exposure.

DOI: 10.1201/9781003483755-67

2 METHODOLOGY

Road infrastructures face increased degradation from various damaging effects, with exposure to chlorides being a major driver, particularly at the rebar level. Concrete degradation occurs when chlorides surpass a threshold the concrete can no longer absorb, leading to indicators like cracking and a drop in electrochemical potential. This chapter presents objective assessments of reinforced concrete degradation, utilizing examinations that align with established standards and literature (Casas 2017). Results categorize degradation indicators into four damage classes, mirroring long-standing practices in road condition assessment. While such classification is common for asphalt and concrete roads, its application in reinforced concrete construction is still evolving, and this paper serves as a foundational guide for the development of indicators based on measured values.

Detecting corrosion in concrete-reinforced steel is challenging due to various overlapping factors, often requiring indirect methods like potential measurement. Degradation signs may not be immediately visible on the surface, demanding high qualifications for accurate interpretation. Chloride-induced corrosion is a key driver of degradation, necessitating preliminary surveys for a comprehensive assessment.

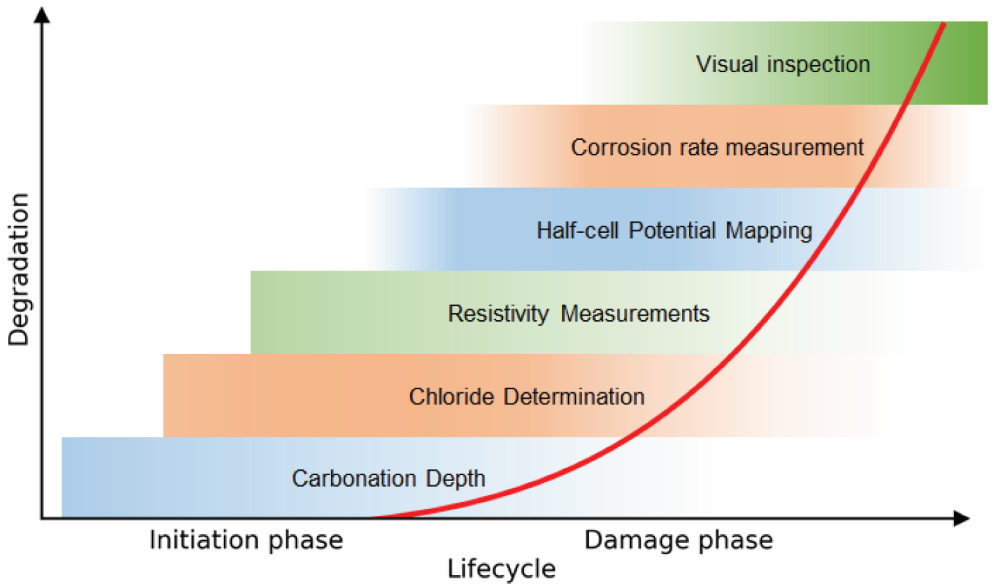


Figure 1. Effectiveness of different condition survey methods for condition assessment depending on the state of degradation based on (Pailes & Gucunski 2015).

Figure 1 shows the efficiency of condition survey techniques as a function of the condition state. For example, a determined investigation for a specific problem, such as half-cell potential mapping, does not provide more accurate information about the state of preservation until parts of the reinforcement are already affected by corrosion and the concrete components can be therefore already in the damage phase. Furthermore, the figure shows an important insight for the engineer, that with single visual condition assessment, damage is detected very late. Therefore, it is of enormous importance to know when and how accurate a possible degradation can be detected.

The examination techniques mentioned in Figure 1 are established procedures and allow to obtain acceptable good and quantitatively sufficient results with sufficient monetary expenditure. It is always important that the procedures enable and support the increase of knowledge of the overall objective of the condition analysis.

As already mentioned, it is difficult to determine the true dimension of damage only based on visual appearance of the concrete component. Nevertheless, different condition survey techniques are available depending on the stage of degradation (see Figure 1).

2.1 *Indicators for degradation*

The condition, which is initially determined mainly visually, as well as the development of damage due to corrosion over time, is serving as the basis for decisions regarding the time and intensity of repair. A simple and objective method for assessing the condition of concrete structures is of decisive economic interest.

Based on all available results from preliminary examinations, the condition of the structural element should be determined simply and objectively. The primary basis in the procedure for objectifying and standardizing the results of condition assessment is a thorough and, above all, complete inspection, which thus makes it possible to take further steps towards classification and indexing of the results obtained. The indicators obtained individually from the various pre-liminary inspections are of varying degrees of importance for degradation. Therefore, the indicators were subjected to weighting via an analytical hierarchy process (AHP) before being synthesized into a condition index.

Additionally, the results of condition assessments are often not clearly interpretable, as they also contain a subjective perspective. This results in unclear decisions regarding the maintenance strategy. Therefore, a fuzzy logic expert system is introduced which can deal with this vague decision space.

Table 1. Indicator for degradation and their levels.

			Degradation indicator level			
Degradation Ind.	Akr.	Unit	1 Negligible	2 Low	3 Moderate	4 High
Visual appearance	Vis	[mm]	< 1	≥ 1 - 4	≥ 4 - 10	≥ 10
Carbonation depth	X_{CO}	[mm]	0% C	≤ 75% C	> 75% C	≥ C
Chloride content	X_{Cl}	[m%]	≤ 0,2	0,2 - 0,6	0,6 - 1,0	> 1,0
Concrete resistivity	ρ	[Ωm]	> 1000	500 - 1000	100 - 500	< 100
Corrosion potential[1]	E_{corr}	[mV]	> -200	-200 - -350	-350 - -500	< -500
Corrosion state	KG	[-]	0 < 1	≥ 1 - 2	≥ 2 - 3	≥ 3 - 4

[1] using Cu/CuSO4 reference electrode
C means thickness of the concrete cover

2.2 *Condition index*

For the determination of a condition index, all available results from preliminary investigations at the evaluation time, such as carbonation depth and chloride content at the reinforcement level, are divided into classes. From these, information is obtained that can provide information on the current state, respectively the intensity of the damage due to corrosion. The index is divided into four classes as follows:

1.= no damage and negligible or no corrosion,
2.= minor damage and low corrosion,
3.= moderate damage and moderate corrosion,
4.= high damage and high corrosion.

The corrosion damage index (CDI) is obtained by first transferring measured values to Corrosion indicator levels, see Table 1. These scenarios represent common evaluation approaches which have to be proven and possibly updated in practical use. The mean of the corrosion indicator levels results in the "Corrosion Damage Index":

$$CDI_{Mean} = \sum_i^n \frac{Degradation\ indicator\ level_i}{n} \quad (1)$$

here n is the number of corrosion indicators used, according to Table 1.

The mean value is calculated for simplification purposes. In principle, it is possible to assign more importance to individual indicators.

A weighting can be based on the type of measurement on the one hand and on the significance of the indicator on the other. The indicators carbonation, visual appearance, chloride content at reinforcement level and cracks are all indicators that provide indirect information about the degradation, whereas potential, corrosion rate or cross-section loss of the rebar represent direct measured values related to the corrosion of the reinforcement and may therefore weighted stronger. A method for determining the weights, the analytical hierarchy process (AHP) (Saaty 1977). The calculation of the condition index when weighted indicators are used is as follows:

$$CDI_{AHP} = \sum_i^n Degradation\ indicator\ level_i \cdot w_i \quad (2)$$

where w_i is the weighting factor for the particular degradation indicator used.

The method enables transparent traceability of how prioritization was calculated and, thus, strengthens the understanding and acceptance in decision making. Thus, a comprehensible and expert based weighting is achieved. The approach of the method is to simplify the problem by breaking it down into a hierarchical system and to form a systematic procedure to structure and solve the decision processes. Which indicators are used in particular and how they are ranked and prioritized can be seen in Table 2. Therefore, the corrosion indicator chloride content is two times more important than the corrosion potential (X_{Cl}) and seven times more influential than the carbonation depth (X_{CO}). This additional information is processed in the AHP algorithm and derives the weighting in percent, which is given in the last column of Table 2 labeled as priority.

Table 2. Weights of the degradation indicators to determine the condition index.

		Importance						
Degradation indicator DI	Rank	1	2	3	4	5	6	w_i [%]
Chloride content	**1**	1	3	4	5	7	8	**43,7**
Corrosion potential	**2**	1/2	1	2	3	6	7	**23,9**
Concrete resistivity	**3**	1/3	1/2	1	2	5	6	**15,7**
Corrosion state	**4**	1/4	1/3	1/2	1	4	5	**10,3**
Carbonation depth	**5**	1/7	1/6	1/5	1/4	1	2	**3,8**
Visual appearance	**6**	1/8	1/7	1/6	1/5	1/2	1	**2,7**

The CDI is thus a measure of the direct quantifiable damage due to corrosion the reinforcement has undergone, combined with the expected corrosion progress. The result is therefore a measure that provides information about damage already caused and describes the current status of the degradation. The level of the index (CDI) shows the extent of the damage that has already occurred. The higher the damage index, the greater the damage and extent of the degradation. By using AHP the decision problem is decomposed into a hierarchy of more easily comprehensive sub-problems, which can be analyzed independently. Once the hierarchy is built, the process consists of systematically evaluate the elements and determine their interrelations and by comparing them to each other with respect to their impact on an element above them in the hierarchy. In making the comparisons, concrete data about the elements can be used to enhance the judgments about the elements' relative meaning and importance. The AHP converts these evaluations to numerical values that can be processed and compared

over the entire range of the proposed problem. Finally, a numerical weight or priority is derived for each element of the hierarchy, allowing diverse and often incommensurable elements to be compared in a rational and consistent way. After incorporating these judgments this yields to a set of overall priorities for the hierarchy. With every kind of pairwise comparison, inconsistencies can also occur. For the examination of these inconsistencies a so called Consistency Ratio (CR) is used, where CR < 10 % is considered to be acceptable. For the examination of these inconsistencies a so called Consistency Ratio (CR) is used, where CR < 10 % is considered to be acceptable (Saaty 1990).

2.3 *Fuzzy-logic decision support system*

It is indeed difficult to perform a quantitative evaluation of the effectiveness of repairs. This problem has many sources. They include environmental influences, time pressure during implementation, lack of root cause analysis, price wars among repair companies and poor execution quality.

It is not possible to evaluate the effectiveness of repair procedures quantitatively. Complex tests on site and in the laboratory are required for realization.

It is more appropriate to use an expert system so that knowledge can be made available to experts. A rule-based expert system (RES) models an expert who can handle the system instead of the system to be operated. This makes the expert knowledge accessible to non-experts, who can thus make decisions with the help of the RES. Furthermore, the conception of a RES enables the knowledge of the experts, which is intuitive and empirical, to be readable and processable by computers.

Fuzzy RES are based on qualitative (fuzzy) expert statements and thus on (fuzzy) stored qualitative knowledge. In addition to the use of linguistic variables and operators, an essential concept is the method of defuzzification. In this paper, it is shown how the effectiveness of individual repair measures can be estimated as a function of the damage classes or corrosion indicators using the fuzzy logic approach.

The simplest form of a fuzzy logic application is a fuzzy controller. This takes input, then performs calculations and finally provides an output value. Fuzzy sets were first applied by (Zadeh 1965). The following steps must be gone through:

- Setting the input and output values as linguistic variables,
- Definition of the fuzzy sets of input and output values,
- Converting the input values into fuzzy values (fuzzyfication),
- Formulation of the rules and store in the knowledge base,
- Applying the rules to the fuzzy values (inference),
- Convert obtained statements into numerical form (defuzzyfication).

Figure 2 illustrates the basic structure of a fuzzy logic expert system with focus of the presented problem.

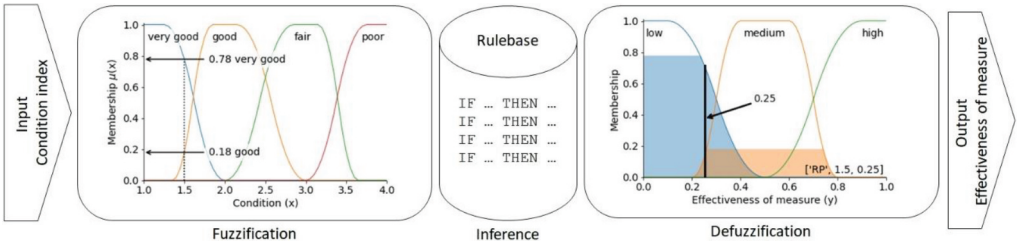
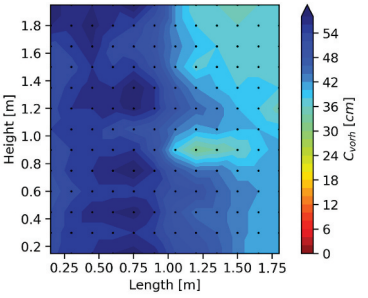


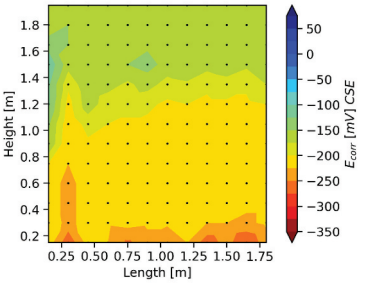
Figure 2. Illustration of the fuzzy logic process to determine the effectiveness of repair measure based on the condition index (CDI = 1.5).



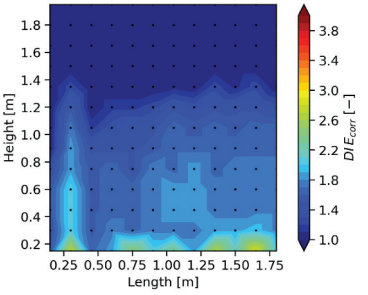
a) Visual appearance of the component.



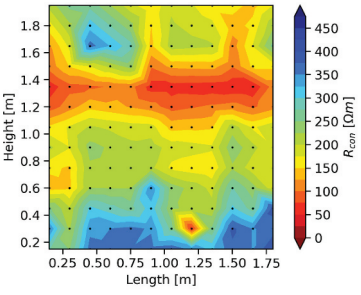
b) Concrete cover C_{exg} represented as surface plot.



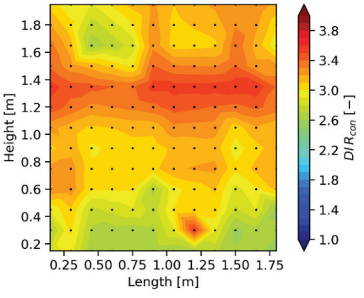
c) Measurement results of the potential measurement.



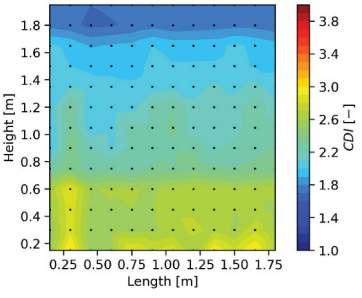
d) Representation of the corrosion potential as Degradation indicator ($DI\,E_{corr}$).



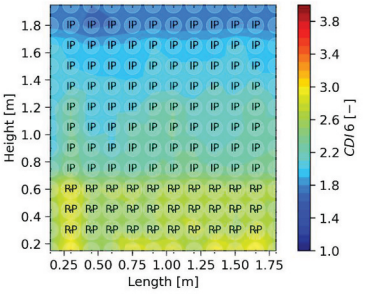
e) Measurement results of the concrete resistivity



f) Representation of the concrete resistivity as Degradation indicator ($DI\,R_{con}$).



g) Representation of the condition indicator (CDI).



h) Representation of the condition indicator (CDI) including the by the FL-algorithm proposed repair measure.

Figure 3. Representation of the in-situ measurements from the preliminary surveys and their degradation indicators to obtain the overall condition indicator (CDI) which is serving as an input parameter to derive the optimal repair measure by using the developed Fuzzy Logic algorithm.

3 FIELD STUDY

The survey was undertaken on a retaining wall situated in Vienna at the Austrian motorway network of ASFiNAG. The retaining wall is 3.80 m beside the motorway lane. The wall is 133 m long and between 0.5 m and 5.90 m of height. It is retaining a slope before an overpass. Taking into account that the surveyed structure is 38 years old, the evaluation of the conditions shows already degradation phenomena, like delamination, cracks and particularly corrosion of the reinforcement. The preliminary survey shows a mean carbonation depth of 2.4 cm and chloride contamination over 1 % Chloride per mass binder up to approximately 4 cm in the concrete surface (see Figure 3).

4 CONCLUSIONS

The paper presented a methodology to assess the condition of concrete components. The condition is determined from real and therefore objective values which are suitable to indicate degradation. The obtained data is mainly derived from condition surveys and may also monitoring data, like humidity, electrical resistivity, and corrosion potential.

The demand of an exact as possible determination of the condition state is a key mission for the asset management to decide which maintenance measure is the best for a certain condition at certain time. This is considered by using objective indicators (degradation indices) to derive an overall performance index. This condition indicator (CDI) is handled through an analytic hierarchy process (AHP) for the sake of objectivity and comprehensibility.

The AHP was utilized in this paper to develop a useful tool for determining the corrosion damage condition of a reinforced concrete bridge component based on different corrosion indicators. AHP method was used to help determine weight factors for different indicators relative to the determination of the final corrosion condition. AHP method can reduce the influence of certain expert's mistakes in the judgment by using pairwise comparison method. A final and more accurate CDI value can be obtained.

The condition index has been transformed into a fuzzy logic system. An overview of the whole fuzzy logic process for determining the effectiveness of repairs based on the condition index CDI was given. A simple expert-based decision rule regime was used to determine the effectiveness of individual repair principles.

At first, membership functions of the sharp input, here condition index, and output variables, here theoretical effectiveness of repair, are conceived. Fuzzy ranges of values are created. These values are related in the inference via a rule database, which was designed empirically and based on expert knowledge. After defuzzification, the effectiveness of the respective maintenance principle is the output to the corresponding condition index CDI.

In Figure 3.h it can be seen that the effectiveness of a certain maintenance measure is not completely ineffective or fully effective in any of the cases. The developed decision algorithm can reliably represent the state of knowledge of experts in the field of repair of reinforced concrete structures. The structure of the system is deliberately kept simple and the reconstruction of the decisions is also clearly comprehensible.

In addition, the fuzzy logic expert system can be extended with respect to the degradation indicators forming the condition index. Furthermore, the developed system is machine-readable, therefore simultaneously applicable to a collective of reinforced concrete components or even entire infrastructure networks.

The methodology was evaluated, proofed, and demonstrated within the case study. If enough data from the condition assessment is available, it can provide a more accurate condition overall and so serve for more profound input for the Fuzzy Logic expert system to choose an optimal repair measure.

The strict rely on only visual inspection data for condition assessment to manage repair measures is considered as critical by the authors.

The paper presents a comprehensive methodology for structural monitoring with the aim of showing how directly usable results from monitoring can be, obtained in the long term for service life prognosis, asset management and maintenance with acceptable effort.

In addition, with the application of this approach on a larger, representative building stock, the perspective of an even more reliable service life prognosis will take place. Therefore, the data already acquired, but also future data, can be described as valuables. In the future better forecasts will be possible based on more precise condition assessments. An important point is that uncertainties on both the impact and the resistance side can be concretized or reduced through dense NDT in time and space, or monitoring.

5 OUTLOOK

The transfer of damage to reinforced concrete components into damage classes can be extended to include indicators for freeze-thaw attack or sulfate attack. Also, such damage classifications can be applied to other materials, such as steel by extension. The application of the degradation indicators allows an objective representation of the state and contributes to the homogenization of the data.

With this more accurate data, at the structure level, the fuzzy logic algorithm can serve as a decision support tool in choosing the optimal repair method. In addition, the fuzzy logic expert system can be extended with regard to the degradation indicators forming the condition index. In addition, the developed system is also applicable to a collective of components, structures or even entire infrastructure networks.

At the network level, the fuzzy logic algorithm can provide more accurate results when calculating the budget requirements of future maintenance activities. This allows to take full advantage of the optimal rehabilitation at the optimal time and so effectiveness of financial resources.

REFERENCES

Casas, J.R. & Matos, J.C. 2017. Standardization of quality control plans for highway bridges in Europe: COST Action TU 1406. In *IOP Conf. Ser.: Mater. Sci. Eng* 236. https://doi.org/10.1088/1757-899X/236/1/012051

Pailes, B.M. & Gucunski, N. 2015. Understanding Multi-modal Non-destructive Testing Data Through the Evaluation of Twelve Deteriorating Reinforced Concrete Bridge Decks. In *J Nondestruct Eval* 34, 14. https://doi.org/10.1007/s10921-015-0308-6

Saaty, T.L. 1990. How to make a decision: The analytic hierarchy process. In *European Journal of Operational Research* 48, 9–26. https://doi.org/10.1016/0377-2217(90)90057-I

Saaty, T.L. 1977. A scaling method for priorities in hierarchical structures. In *JMP* 15, 234–281–234–281. https://doi.org/10.1016/0022-2496(sci77)90033-5

Zadeh, L.A. 1965. Fuzzy sets. *Information and control* 8, 353. https://doi.org/10.1016/S0019-9958(65)90241-X


Taylor & Francis
Taylor & Francis Group
http://taylorandfrancis.com

MS04: Life-cycle redundancy, robustness and resilience of bridges and infrastructure networks under multiple hazards

Organizers: F. Biondini & D.M. Frangopol


Taylor & Francis
Taylor & Francis Group
http://taylorandfrancis.com

Bridge Maintenance, Safety, Management, Digitalization and Sustainability – Jensen, Frangopol & Schmidt (eds)
© 2024 The Author(s), ISBN 978-1-032-77040-6
Open Access: www.taylorfrancis.com, CC BY-NC-ND 4.0 license

Connectivity of road network with bridges and slopes under rainfall

Zhengying He
Tongji University, Shanghai, China
Waseda University, Tokyo, Japan

Putri S. Firdaus & Mitsuyoshi Akiyama
Waseda University, Tokyo, Japan

Dan M. Frangopol
Lehigh University, Bethlehem, PA, USA

Hiroshi Matsuzaki
National Defense Academy of Japan, Kanagawa, Japan

ABSTRACT: Bridge damage and landslide resulting from rainfall significantly disrupt transportation systems. To enhance the performance and resilience of road networks due to torrential rainfall events, it is essential to assess the connectivity of road network while considering the failure of bridges and slopes. This study presents a methodology for probabilistic connectivity assessment of road network incorporating the potential failure of bridges and slopes under rainfall hazard. The proposed method selects surface runoff as a critical parameter to establish a spatial correlation model for the hazard intensities exerted on bridges and slopes. As an illustrative example, the proposed method is applied to a hypothetical road network in Yamagata Prefecture, Japan, susceptible to rainfall-induced floods and landslides.

1 INTRODUCTION

The devastating consequences of torrential rainfall events (e.g., concurrent flooding and landslides) have not only caused individual structural damage but also disrupted road networks (Ario et al., 2022; Dave et al., 2021; Mori and Ono, 2019). In July 2020, Kyushu island in Japan experienced torrential rain, resulting in floods and various geo-disasters (e.g., slope failures and road subsidence). These led to substantial damage to road infrastructure with 10 bridges washed away by floods, and road closures due to landslides (Mukunoki et al., 2021). Therefore, a methodology assessing road network connectivity considering failure of bridges and slopes due to rainfall is imperative.

Fragility assessments of bridges and slopes exposed to rainfall hazards has become a focal point (Donnini et al., 2017; Loli et al., 2022; Zhang et al., 2023). Traditional studies, however, focus on road disruption, often considering only a singular structure type. Furthermore, despite the well-established concept of spatial correlation in seismic hazard assessment (Baker and Chen, 2020; Jayaram and Baker, 2009), its application to bridge damage and slope failure resulting from rainfall remains limited. During heavy rainfall, flow discharge associated with surface flow serves as the hazard intensity measure leading to bridge damage (Mondoro and Frangopol, 2018), while infiltration into the slopes influences the slope stability (Huang and He, 2023; Xu et al., 2021). With spatially correlated hazard intensities exerted on bridges and slopes, a framework for assessing road network connectivity should be developed.

Under uncertainties associated with hazard intensity and structural fragility, probabilistic connectivity of origin-destination (OD) pairs can be an effective indicator to quantify the performance of road networks in post-disaster activities (Bocchini and Frangopol, 2013, 2011).

DOI: 10.1201/9781003483755-68

This assessment involves measuring the simultaneous occurrence of hazard intensity among spatially distributed bridges and slopes. Spatially correlated hazard intensity is determined based on physical properties associated with hazard characteristics and random field simulations. Therefore, a comprehensive methodology for probabilistic connectivity assessment of road network considering simultaneous failure of bridges and slopes under rainfall hazard should be established to evaluate the performance of the road networks.

This study presents a methodology for probabilistic connectivity assessment of road networks considering failure of bridges and slopes under rainfall hazard. The hazard intensity exerted on bridges and slopes is modeled through a key hydrological parameter (i.e., surface runoff resulting from rainfall). As an illustrative example, the proposed method is applied to a hypothetical road network with bridges and slopes in Yamagata Prefecture, Japan.

2 PROBABILISTIC CONNECTIVITY ASSESSMENT OF ROAD NETWORK CONSIDERING FAILURE OF BRIDGES AND SLOPES UNDER RAINFALL HAZARD

Figure 1 shows the proposed methodology for estimating the probabilistic connectivity of road network considering failure of bridges and slopes under rainfall hazard.

2.1 *Definition of road network*

The configuration of the initial road network, denoted as G_0, involving both bridges and slopes is defined as follows:

$$G_0(\mathbf{V}, \mathbf{E}),\ \mathbf{E} \subseteq \{uv | v \in \mathbf{V}, u \neq v\} \tag{1}$$

where vertices **V** represent OD pairs, bridges, slopes, and highway intersections; edges **E** define road segments connecting vertices; and *uv* is a subset of edges.

2.2 *Spatially correlated hazard assessment*

Surface runoff is chosen as the key parameter to establish the spatial correlation model for the hazard intensities exerted on bridges and slopes. After generating the annual maximum rainfall intensities based on the Gamma distribution and historical rainfall daily data, the spatial correlated run off is modelled by Geographically Weighted Regression (GWR).

The hazard intensity for bridges is assessed with flow discharge (Mondoro and Frangopol, 2018; Firdaus et al., 2023). The time series of flow discharges is generated using Soil and

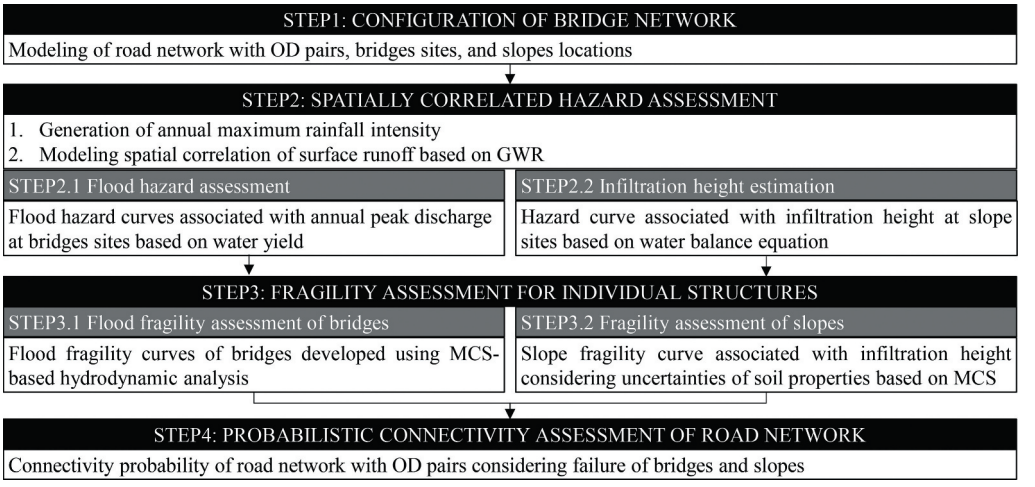


Figure 1. Framework for connectivity of road network with bridges and slopes under rainfall hazard.

Water Assessment Tool (SWAT) considering spatially correlated surface runoff. Since this study focuses on hazards induced by heavy rainfall, only the water balance components when the discharge reaches its annual peak (i.e., annual peak flow) are extracted for further analysis. The hazard intensity for slopes is estimated by spatially correlated change of soil wetting (i.e., infiltration height) based on the water balance performed in SWAT. The probability distribution of the initial infiltration height, calculated at each grid, is used. Subsequently, the mean infiltration height at slope locations can be calculated.

2.3 *Fragility assessment*

Firdaus et al. (2023) developed fragility curves of bridges under flood hazard based on Monte Carlo simulation-based hydrodynamic analysis. Their fragility curve for a bridge at site j is expressed as:

$$P_{vb,j} = P\left(g_{Fm,j} \leq 0 | Q = q_{vb,j}\right) \tag{2}$$

where $P\left(g_{Fm,j} \leq 0 \mid Q = q_{vb,j}\right)$ is the conditional failure probability of bridge given flood hazard intensity $Q = q_{vb,j}$; and m represents multiple failure modes of a bridge including flexural failure in bridge columns and washout of the superstructure. The details about the performance functions of bridge can be found in Firdaus et al. (2023).

The slope fragility curve is calculated using the infinite slope model, considering the uncertainties associated with soil parameters and slope geometry. The fragility curve for any slope at site k given infiltration heights is expressed:

$$P_{vs,k} = P\left(g_{H,k} \leq 0 | H = h_{vs,k}\right) \tag{3}$$

where $P\left(g_{H,k} \leq 0 \mid H = h_{vs,k}\right)$ is the conditional failure probability of slope given infiltration height $H = h_{vs,k}$ resulting from rainfall. The detail of performance function of slope $g_{H,k}$ can be found in Phoon (2014).

2.4 *Probabilistic connectivity assessment of road network*

The probabilistic connectivity of the road network accounting for failure of bridges and slopes caused by rainfall is assessed based on the Monte Carlo simulation (MCS) considering the spatial correlation of hazard intensities. The states of a structure following a heavy rainfall event can be expressed as a binary variable (Bocchini and Frangopol 2011):

$$S_{v,n} = \begin{cases} 1, & \text{if } P_{ve,n}(\mathbf{g}_n \leq 0 | \gamma_n) > r_{v,n} \\ 2, & \text{if } P_{ve,n}(\mathbf{g}_n \leq 0 | \gamma_n) \leq r_{v,n} \end{cases} \tag{4}$$

where $s_{v,n}$ is the service state of bridge or slope at site n given the corresponding hazard intensity γ_n (i.e., $h_{vb,n}$ for bridges and $h_{vs,n}$ for slopes); $P_{ve,n}$ (i.e., $P_{ve,n} = P_{vb,n}$ for bridges and $P_{ve,n} = P_{vs,n}$ for slopes) is the failure probability given γ_n; $\mathbf{g}_n$ is the performance function of a bridge or slope at site n; and $r_{v,n}$ is a uniformly distributed random number between 0 and 1 associated with hazard-induced damage. The states of a structure (i.e., 1 or 0) correspond to the impassable and passable states of road segment, respectively.

Following a heavy rainfall event, the vertices describing bridge and slope sites within the road network fail to maintain the connection between road elements. The new road network after a heavy rainfall event, denoted as G_R, is defined by:

$$G_R(\mathbf{V}_R, \mathbf{E}_R) = \left(\mathbf{V} - \left\{v_{s,n} \in \mathbf{V} | s_{v,n} = 1\right\}, \mathbf{E} - \left\{u v_{s,n} \in \mathbf{E}, u \in \boldsymbol{V}\right\}\right) \tag{5}$$

where $\mathbf{V}_R$ is the set of vertices in the road network excluding sites of bridges and slopes (i.e., $v_{s,n}$); $\mathbf{E}_R$ is the set of edges in the road network excluding road segments that are connected to $v_{s,n}$; $\mathbf{V}$ and $\mathbf{E}$ represent the vertices and edges, respectively, before the occurrence of the rainfall hazard event; and u is a vertex joining bridge $v_{s,n}$.

The probability of road network disconnection between OD pairs is determined by evaluating the presence of disconnected links, which is expressed as:

$$P_{f,OD} = 1 - \frac{1}{M}\sum_{m=1}^{M} L_{OD}(\exists \text{ OD connectivity} \in G_m \text{ is true}) \quad (6)$$

where M is the total number of the MCS. If there is at least one route G_R between OD pair in the road network after the event in the m-th MCS trials (i.e., $\exists$ OD connectivity $\in G_m$ is true), L_{OD} =1; otherwise, L_{OD} =0.

3 ILLUSTRATIVE EXAMPLE

3.1 *Analyzed region and road network*

The connectivity probability of an OD pair within a hypothetical road network, spanning the Mogami and Miomote watersheds in Yamagata Prefectures, Japan, is estimated herein. Figure 2 illustrates the schematic road network with specified OD pair, and the locations of bridges and slopes. Table 1 shows the reach slope, stream network and channel type at bridge sites.

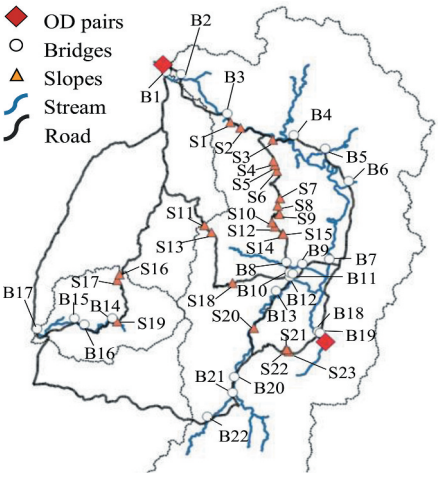


Figure 2. Schematic of analyzed road network.

Table 1. Reach slope and channel type at bridge sites.

Bridge ID	Slope (%)	Stream network	Channel type
B1, B2	1.94×10^{-6}	Mogami	Main
B3	7.82×10^{-1}	Mogami	Tributary
B4	1.39×10^{-1}	Mogami	Main
B5	4.52×10^{-1}	Mogami	Tributary
B6	5.70×10^{-1}	Mogami	Tributary
B7	1.00×10^{-1}	Mogami	Main
B8, B9	9.46×10^{-1}	Mogami	Tributary
B10, B11, B12, B13, B20	2.02×10^{-1}	Mogami	Main
B18, B19	3.06×10^{-1}	Mogami	Tributary
B21, B22	5.06×10^{-1}	Mogami	Tributary
B14, B15, B16	7.22×10^{-1}	Miomote	Main
B17	1.64×10^{-1}	Miomote	Main

3.2 *Spatially correlated hazard assessment*

Figure 3 depicts the flood hazard curves associated with annual peak flow at the bridge sites. Flood hazard intensities at B1, B2, B4, and B7 are significantly higher than those at other bridge sites. Figure 4 illustrates the hazard curves associated with infiltration height at slope sites. The infiltration heights at S1, S2, S3 S18 and S20 are markedly higher than those at other slope sites. It should be noted that the locations with the maximum flood hazard intensity and the maximum infiltration height are not necessarily closer due to difference in soil properties and other factors.

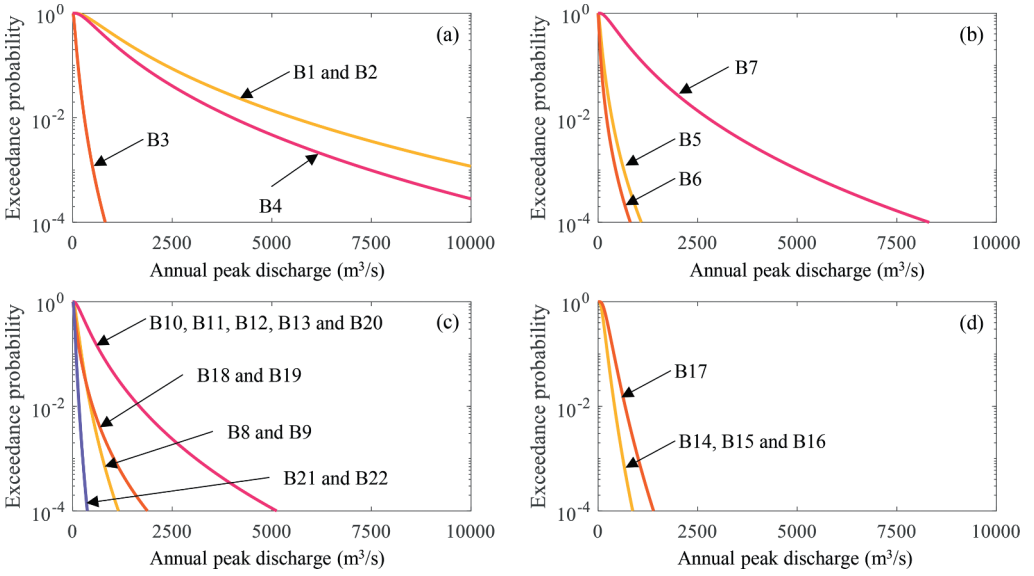


Figure 3. Flood hazard curves at each bridge location.

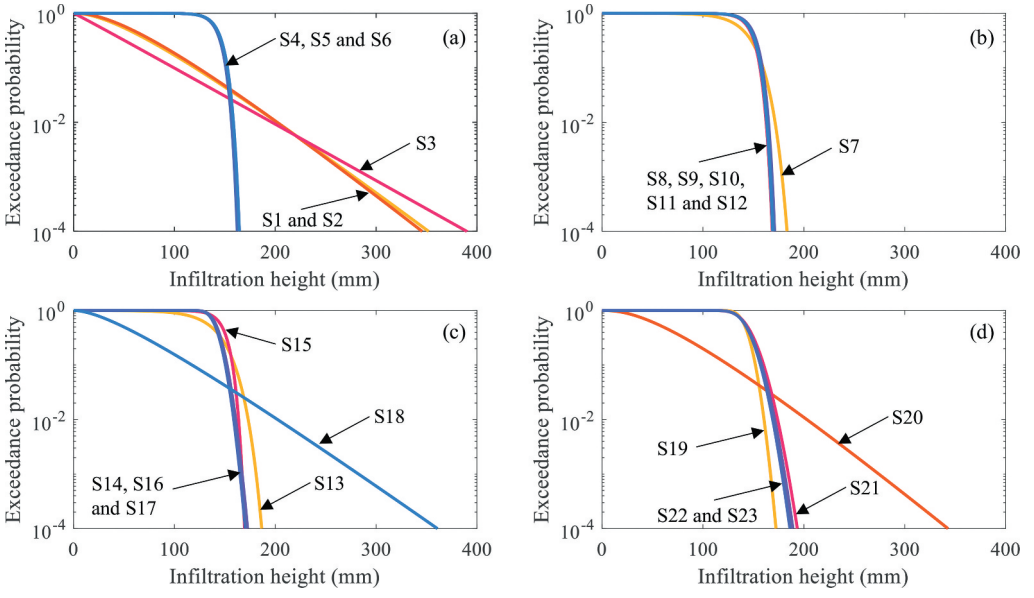


Figure 4. Hazard curves associated with infiltration height at each slope location.

3.3 *Fragility and reliability assessment*

The bridge models presented by Firdaus et al. (2023) and an infinite slope model modified from Phoon (2014) are used in this illustrative example. Figure 5 (a) to (d) and (e) depict the bridge fragility curves given annual peak discharge and slope fragility curve given infiltration height, respectively. The results reveal how vulnerability is affected by reach slope characteristics.

Bridges on steeper slopes and narrow spans are vulnerable to damage in columns, while those on lower slopes and wider spans face susceptibility to superstructure washout due to flooding. Steeper slopes with narrow spans indicate a more larger flow velocity.

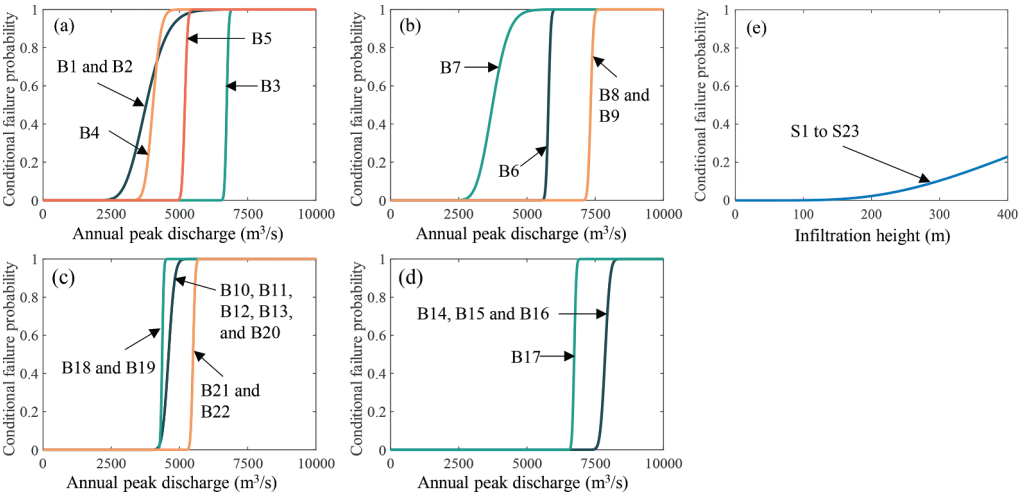


Figure 5. (a) to (d) Flood fragility curves of bridges; and (e) fragility curve of slope given infiltration height.

3.4 *Probabilistic connectivity assessment of road network*

The probabilistic probability of road network, taking into account spatially correlated hazard intensities, is assessed under perfect and independent correlation assumptions for bridge and slope damage states. With 10,000 MCS trials, the connectivity probability of the road network is 0.27 when the damage states of bridges and slopes are perfectly correlated, and 0.23 when they are independent.

4 CONCLUSIONS

Conclusions are as follows:

- A procedure for probabilistic connectivity assessment of road network considering failure of bridges and slopes under rainfall hazard is presented. As an illustrative example, the proposed method is applied to a hypothetical road network in Yamagata Prefecture, Japan.
- Surface runoff is identified as the critical parameter for establishing a spatial correlation model for hazard intensities (i.e., flooding intensity and infiltration height) exerted on bridges and slopes. Spatially correlated flood intensity and infiltration height are evaluated based on water yield and water balance equations, respectively.
- The probabilistic connectivity of road network depends on the spatial relationship of runoff and infiltration, and fragility of bridges against flooding and slopes exposed to infiltration height.

ACKNOWLEDGEMENTS

This research was supported by JSPS KAKENHI (grant number: 23H00217), and JST-JICA-SATREPS (grant number: JPMJSA2009).

REFERENCES

Ario, I., Yamashita, T., Tsubaki, R., Kawamura, S., Uchida, T. Watanabe, G., Fujiwara, A. 2022. Investigation of Bridge Collapse Phenomena due to Heavy Rain Floods: Structural, Hydraulic, and Hydrological Analysis. *Journal of Bridge Engineering* 27: 04022073.

Baker, J.W., Chen, Y. 2020. Ground motion spatial correlation fitting methods and estimation uncertainty. *Earthquake Engineering and Structural Dynamics* 49: 1662–1681.
Bocchini, P., Frangopol, D.M. 2013. Connectivity-Based Optimal Scheduling for Maintenance of Bridge Networks. *Journal of Engineering Mechanics* 139: 760–769.
Bocchini, P., Frangopol, D.M. 2011. Generalized bridge network performance analysis with correlation and time-variant reliability. *Structural Safety* 33: 155–164.
Bondy, J.A., Murty, U.S.R. 1976. *Graph Theory with Applications*.
Dave, R., Subramanian, S.S., Bhatia, U. 2021. Extreme precipitation induced concurrent events trigger prolonged disruptions in regional road networks. *Environmental Research Letters* 16: 104050.
Donnini, M., Napolitano, E., Salvati, P., Ardizzone, F., Bucci, F., Fiorucci, F., Santangelo, M., Cardinali, M., Guzzetti, F. 2017. Impact of event landslides on road networks: a statistical analysis of two Italian case studies. *Landslides* 14: 1521–1535.
Firdaus, P.S., Matsuzaki, H., Akiyama, M., Aoki, K., Frangopol, D.M. 2023. Probabilistic connectivity assessment of bridge networks considering spatial correlations associated with flood and seismic hazards. *Structure and Infrastructure Engineering*. (published online: November 10, 2023).
Giani, G., Rico-Ramirez, M.A., Woods, R.A. 2022. Are moments of rainfall spatial variability useful for runoff modelling in operational hydrology? *Hydrological Sciences Journal* 67: 1466–1479.
Huang, Y., He, Z., 2023. Rainfall-oriented resilient design for slope system: Resilience-enhancing strategies. *Soils and Foundations* 63: 101297.
Jayaram, N., Baker, J.W. 2009. Correlation model for spatially distributed ground-motion intensities. *Earthquake Engineering and Structural Dynamics* 38: 1687–1708.
Loli, M., Kefalas, G., Dafis, S., Mitoulis, S.A., Schmidt, F. 2022. Bridge-specific flood risk assessment of transport networks using GIS and remotely sensed data. *Science of The Total Environment* 850: 157976.
Mondoro, A., Frangopol, D.M. 2018. Risk-based cost-benefit analysis for the retrofit of bridges exposed to extreme hydrologic events considering multiple failure modes. *Engineering Structures* 159: 310–319.
Mori, S., Ono, K. 2019. Landslide disasters in Ehime Prefecture resulting from the July 2018 heavy rain event in Japan. *Soils and Foundations* 59: 2396–2409.
Mukunoki, T., Suetsugu, D., Sako, K., Murakami, S., Fukubayashi, Y., Ishikura, R., Hino, T., Sugimoto, S., Wakinaka, K., Ito, S., Koyama, A. 2021. Reconnaissance report on geotechnical damage caused by a localized torrential downpour with emergency warning level in Kyushu, Japan. *Soils and Foundations* 61: 600–620.
Phoon, K.-K. 2014. Reliability-Based Design in Geotechnical Engineering: Computations and Applications. *CRC Press*, London.
Xu, X., Xing, Y., Guo, Z., Huang, Y. 2021. Stability Analysis of Rainfall-Triggered Toe-Cut Slopes and Effectiveness Evaluation of Pile-Anchor Structures. *Journal of Earth Science* 32: 1104–1112.
Zhang, Y., Ayyub, B.M., Gong, W., Tang, H. 2023. Risk assessment of roadway networks exposed to landslides in mountainous regions–a case study in Fengjie County, China. *Landslides* 20: 1419–1431.

Bridge Maintenance, Safety, Management, Digitalization and Sustainability – Jensen, Frangopol & Schmidt (eds)
© 2024 The Author(s), ISBN 978-1-032-77040-6
Open Access: www.taylorfrancis.com, CC BY-NC-ND 4.0 license

Measuring the extreme risk of coastal bridges under tropical cyclones

Y. Li*
Department of Construction and Quality Management, Hong Kong Metropolitan University, Hong Kong, China

D. Zhu & Y. Dong
Department of Civil and Environmental Engineering, The Hong Kong Polytechnic University, Hong Kong, China

ABSTRACT: Coastal bridges are susceptible to the compounding effects of storm surge and waves in tropical cyclone-prone areas. Over the long term, the vulnerability and risk of bridges may increase due to the uncertain storm conditions under climate change. Thus, evaluating the long-term risk of these bridges can be significant for mitigating financial and societal losses and minimizing interruptions to transportation systems. However, previous studies mainly highlighted bridge reliability, neglecting loss assessment and long-term risk under the uncertain frequency and intensity of cyclones. Particularly, the potential extreme risk has not been investigated. This study aims to develop a framework to assess the extreme risk of coastal bridges subjected to storm waves and surge in a life-cycle context. Within the framework, risks of different failure modes will be investigated and compared. In addition to the conventional deck unseating failure, a failure mode that considers dynamic structural response will be analyzed by incorporating component damage, thereby comprehensively combining the effects of wave load time histories, bearing connections, and overturning moment. Given vulnerabilities to different failure modes, the long-term risk and the associated extreme loss can be calculated based on a stochastic non-homogeneous Poisson process considering the non-stationary frequency and intensity of cyclones. The developed framework will be applied to a coastal highway bridge to identify the extreme risk and long-term performance under cyclone hazards.

1 INTRODUCTION

In cyclone-prone coastal zones, bridge infrastructures are inherently at risk from the synergistic impacts of storm surge and wave forces. The necessity for risk assessment is highlighted by the potential growing vulnerability under the climate-induced alterations in behavior of tropical cyclones. Therefore, assessing the long-term risks posed to bridges is vital for reducing potential financial losses, minimizing harm to communities, and preventing disruptions to transportation networks. Existing literature has mainly concentrated on the structural reliability of bridges and vulnerability modeling. Though few studies looked at the loss assessment of coastal systems (Liu et al. 2022), the long-term risk considering uncertainties associated with stochastic nature of cyclone frequency and intensity is rarely discussed (Alhamid et al. 2022). Especially, the hazard-induced extreme risk of systems in the long time horizon has been ignored.

Thus, this study seeks to formulate a framework to assess the extreme risk of coastal highway bridge structures within their entire operational lifespan, taking into account the confluence of wave and surge forces. Beyond the conventional deck unseating failure mode, this

*Corresponding author: yahli@hkmu.edu.hk

DOI: 10.1201/9781003483755-69

study investigates the overturning failure mode, incorporating a dynamic assessment of structural responses considering the cumulative effects of wave-induced forces, bearing integrity, and the propensity for overturning. The long-term risk and extreme risk measure of these two failure modes are investigated and computed. The introduced risk assessment framework employs a stochastic non-homogeneous Poisson process to capture the non-stationary uncertainties of cyclonic events in both frequency and intensity dimensions, thereby enabling a quantification of long-term assessment. By introducing the time-varying occurrence rate in the non-homogeneous Poisson model, the impact of climate change on frequency and intensity can be easily considered in the stochastic occurrence model. The proposed framework can be introduced to coastal bridge and civil infrastructure systems to manage the structural susceptibility to extreme risk and enhance resilience over the long-term against tropical cyclones.

2 VULNERABILITY MODELING UNDER STORM WAVES

For superstructure failure of coastal highway bridges, current methodologies for assessing bridge risk subjected to tropical cyclone waves and surge impact mainly focus on deck unseating and overturning moment failure. For instance, deck unseating is caused by vertical wave load exceeding deck weight (Ataei and Padgett 2013, Mondoro et al. 2017), while the failure can also occur due to wave induced overturning moment and bearing constraints (Zhu et al. 2021). In this study, both the two types of failure models are considered for risk measurement.

For the detailed assessment of vulnerability, uncertainties associated with wave height and surge height should be considered. Due to limited measured data, the surge height used to determine structural demand was assumed to follow a uniform distribution of ±20% (Saeidpour et al., 2019). The wave height distribution was modeled using a Weibull-Generalized Pareto (WGP) model based on observations in shallow water (Wu et al., 2016). The detailed surge height and wave impact modeling directly uses the three-dimensional model established in Zhu et al. (2021).

Vulnerability modeling of highway bridges relies on computation of probability failure. The structural failure probability P_f can be described as the probability of structural capacity C is smaller than the demand D

$$P_f = P[C < D] \tag{1}$$

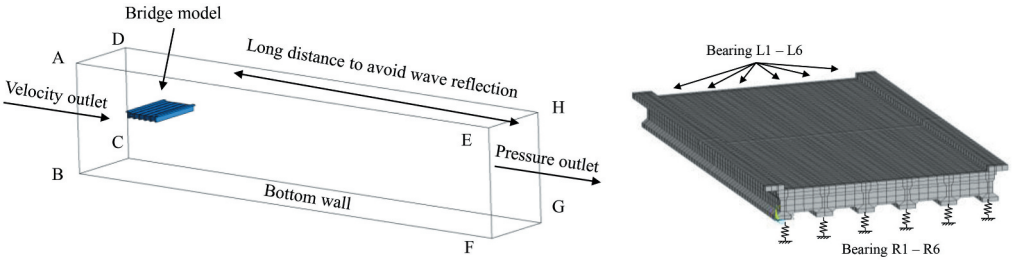
In terms of deck unseating failure, the bridge's capacity to resist vertical loads is provided by the self-weight Ws of the bridge deck itself (Li et al. 2020).

$$W_s = \left(d_b W_0 + A_g n_g\right)\gamma l \tag{2}$$

where d_b = deck thickness W_0 = deck width, A_g = the total cross-sectional area of bridge girders; n_g = girder numbers; γ = unit weight of the construction material; and l = length of bridge span.

As for the overturning failure mode, the structural damage state is defined that bearing constraints were damaged are damaged due to wave and surge impacts. In this study, the bridge's structural capacity C_M was calculated to be 7696 kNm based on a finite element model of the bridge (Zhu et al. 2021). This capacity value took into account the functional state of the bearings in the model.

The demands associated with the two failure modes should be analyzed by the established three-dimensional computational fluid dynamics (CFD) model and the finite element bridge model to assess the probabilistic demand for wave forces and overturning moments acting upon the bridge deck. The model illustrated in Zhu et al. (2021) is adopted as an illustrative example here. Figure 1 shows the developed CFD model and the finite element model. The bridge model examined is 15.85 m long and 9.6 m wide. The deck has a thickness of 0.18 m and contains 6 evenly spaced I-shaped girders with a height of 1.37 m each. Prior to the arrival of the storm surge and waves, the initial water depth is set at 12.5 m below the bridge, with a 4 m clearance from the water to the bottom of the bridge deck.



(a) (b)

Figure 1. (a) The established CFD model and (b) the finite element bridge model with bearing constraints.

3 LONG-TERM RISK ASSESSMENT AND EXTREME RISK

Following the vulnerability analysis, the cyclone-induced losses can be assessed by multiplying the failure probability and the consequence. Over the service life $(0, t_{\text{int}}]$ of the infrastructure, hazard occurrence can be modeled as a stochastic non-homogeneous process $\{N(t_{\text{int}}), t_{\text{int}} > 0\}$. The arrival times of hazards are defined as random variables $\{T_1, T_2, \ldots, T_k\}$. The time between hazard arrivals, known as inter-arrival times, are $\{W_1, W_2, \ldots, W_k\}$, with T_k equal to the sum of the inter-arrival times $(W_1 + W_2 + \ldots + W_k)$. When a hazard occurs at time T_k, it results in damage loss L_k for the infrastructure system due to necessary repairs. The traditional homogeneous Poisson process with a stationary occurrence rate λ may not be appropriate to represent the time-varying frequency associated with the tropical cyclones under changing climate conditions. Therefore, a non-homogeneous Poisson process with a time-varying occurrence rate $\lambda(t)$ is more suitable when modeling hazard risk considering climate change effects. An illustrative figure of a NHPP is shown in Figure 2.

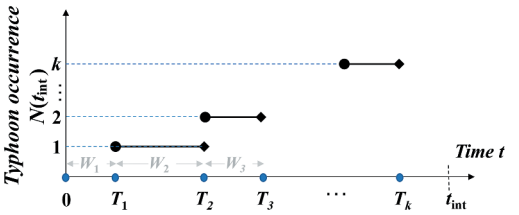


Figure 2. Tropical cyclones occurrence modeled by the stochastic non-homogeneous Poisson process.

The stochastic model describing The NHPP model provides the expected number of hazard events over the lifetime as:

$$E[N(t_{\text{int}})] = \int_0^{t_{\text{int}}} \lambda(t)dt \tag{3}$$

Accordingly, the distribution of the number of hazard events within the lifetime can be

$$\mathrm{P}[N(t_{\text{int}}) = k] = \frac{\left(\int_0^{t_{\text{int}}} \lambda(t)dt\right)^k \exp\left(-\int_0^{t_{\text{int}}} \lambda(t)dt\right)}{k!}, k = 1, 2, \cdots \tag{4}$$

Given these parameters, the long-term loss $DL(t_{\text{int}})$ of the bridge due to damages caused by hazards can be formulated as

$$DL(t_{\text{int}}) = \sum_{k=1}^{N(t_{\text{int}})} L_k e^{-rT_k} \tag{5}$$

where r = discount rate to obtain the present loss value. L_k = damage loss and can be computed from multiplying the repair cost and failure probability.

4 EXTREME RISK

Previous studies focused only on the expected value of total loss. However, since the long term loss $DL(t_{\text{int}})$ is a random variable, then only the expectation does not fully characterize the uncertainty information about the loss assessment. This study examines the probabilistic distribution of $DL(t_{\text{int}})$ along with other statistical indicators - variance, skewness, and kurtosis. These metrics provide additional insights beyond the mean risk. They can be assessed using Monte Carlo simulation or analytically derived from the moment generating function (MGF). This comprehensive analysis of the long-term loss distribution gives a more complete picture of the range of possible losses. The MGF of the long-term loss can be defined as (Li et al., 2020)

$$M_{DL(t_{\text{int}})}(\xi) = \exp\left[\int_0^{t_{\text{int}}} \lambda(s)[M_L(\xi e^{-rs}) - 1]ds\right] \tag{6}$$

By taking derivatives at zero, statistical moments of the long-term loss can be assessed. For instance, the expectation of $DL(t_{\text{int}})$ can be computed as by taking the first derivative at zero. Similarly, the αth order moments of the risk can be calculated by taking derivatives of the MGF

$$E[DL^{\alpha}(t_{\text{int}})] = \frac{dM_{DL(t_{\text{int}})}{}^{\alpha}(\xi = 0)}{d\xi^{\alpha}} \tag{7}$$

This study introduces using quantiles to assess the "worst case" of long-term loss as the extreme risk. The quantile represents tail risk - events with low probability but potentially high losses. While the expected risk is the average case, quantiles characterize extreme cases by focusing on the distribution tail. However, quantile risk measures are most relevant for risk-averse decision makers. Risk-neutral parties may only consider the expected total risk. The quantile of the risk can be defined as:

$$[R_{WC}(t_{\text{int}})] = Quantile_{\sigma}(DL(t_{\text{int}})) \tag{8}$$

where σ indicates the risk level deemed acceptable for the worst-case scenario. It refers to the σth quantile of the random variable $DL(t_{\text{int}})$. As illustrated in Figure 4, the quantile focuses on the tail of the loss distribution. Usually, the worst case of loss is much higher than the mean value.

5 ILLUSTRATIVE EXAMPLE

A highway bridge vulnerable to deck unseating in tropical cyclones is used as an example to demonstrate the extreme risk assessment. The bridge is at risk from storm surges and waves. Several inputs are needed for the NHPP model: the annual occurrence rate for cyclones and the analysis period. Given the NHPP results, the loss distribution and discount rate are used to quantify the long-term loss and the extreme risk. The cost to replace the bridge superstructure is assumed to be 1.283 million US dollars (USD). The bridge service life is taken as 150 years. This cost estimate is derived from previous studies on bridge replacement costs (Mondoro et al. 2017). The first four statistical moments (mean, variance, skewness, kurtosis) of $DL(t_{\text{int}})$ can then be calculated. Ultimately, the full distribution of $DL(t_{\text{int}})$. is obtained, enabling worst case analysis. The initial inputs for this illustration are based on a prior study by Li (2020). For the investigated case, with a maximum hurricane wind speed of 60 m/s subjected to tropical cyclone hazards, the failure probability of deck unseating is 0.53 while that for overturning moment failure mode is 0.72.

Given inputs, the four statistical indicators of $DL(t_{\text{int}})$ for deck unseating failure can be calculated as mean 8.5848×10^6 USD, standard deviation 2.4367×10^6 USD, skewness 0.55, and kurtosis 3.45, respectively. The 5% "worst-case" risk subjected to this mode is 26.1400×10^6 USD. In contrast, the four values for overturning moment failure can be mean 1.1659×10^7 USD, standard deviation 3.3052×10^6 USD, skewness 0.55, and kurtosis 3.46, respectively. The "worst-case" risk for this overturning mode is 35.4713×10^6. The long-term loss distribution and the associated extreme risk of the two investigated failure modes are shown in Figure 3. It shows that the expected long-term losses for the two cases do not vary substantially while the associated extreme risks are significantly different. Analysis of the two cases reveals that although the expected long-term losses are relatively similar, the associated extreme risks diverge considerably. While the mean losses remain similar, examination of the tail risk quantified through the 95% worst case scenario may increase over 30%. This disparity highlights the value of quantile-based risk measures, able to capture risks of catastrophic loss that expectations alone fail to reveal.

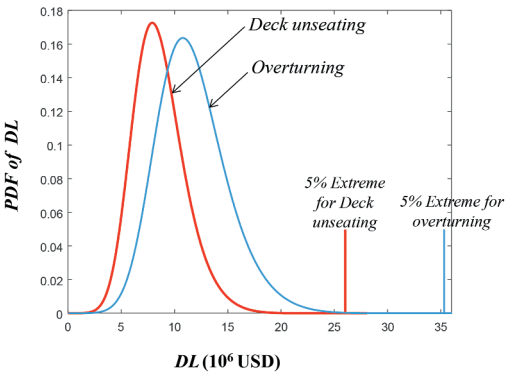


Figure 3. Loss distribution and extreme risk associated with the deck unseating failure and the overturning failure.

6 CONCLUSIONS

In conclusion, this study presents a comprehensive framework to evaluate the extreme risk of coastal highway bridges over their lifetime, considering both wave and surge forces. The analysis goes beyond just deck unseating failures to also investigate overturning modes, incorporating dynamic structural response, cumulative wave loading, bearing integrity, and overturning potential. Both the expected long-term loss and extreme risks are quantified for the failure modes using stochastic modeling. A non-homogeneous Poisson process captures non-stationary cyclone occurrence in frequency and intensity, enabling robust long-term risk assessment. This proposed approach can help manage bridge susceptibility to extreme events and improve resilience against tropical cyclones and can be applied to investigate other hazards. Analysis reveals that while two investigated failure modes may have similar expected losses, their extreme risks can diverge substantially. Although the expected losses stay relatively similar between the two failure modes, analyzing the extreme tail risks using the 95th percentile worst case scenario indicates that catastrophic losses could rise over 30%. This highlights the value of quantile-based measures, able to reveal risks of catastrophic losses that expectations alone miss. The framework provides a powerful quantitative tool for understanding and mitigating coastal infrastructure risk.

REFERENCES

Alhamid, A. K., Akiyama, M., Aoki, K., Koshimura, S., & Frangopol, D. M. (2022). Stochastic renewal process model of time-variant tsunami hazard assessment under nonstationary effects of sea-level rise due to climate change. *Structural Safety*, *99*, 102263.

American Concrete Institute (ACI) (2005). Building Code Requirements for Structural Concrete and Commentary (ACI 318R-05). Detroit, MI: American Concrete Institute.

Ataei, N., & Padgett, J. E. (2013). Probabilistic modeling of bridge deck unseating during hurricane events. *Journal of Bridge Engineering*, *18*(4), 275–286.

Li, Y., Dong, Y., & Qian, J. (2020). Higher-order analysis of probabilistic long-term loss under nonstationary hazards. *Reliability engineering & system safety*, *203*, 107092.

Li, Y., Dong, Y., & Zhu, D. (2020). Copula-based vulnerability analysis of civil infrastructure subjected to hurricanes. *Frontiers in Built Environment*, *6*, 571911.

Liu, M., Qin, J., Lu, D. G., Zhang, W. H., Zhu, J. S., & Faber, M. H. (2022). Towards resilience of offshore wind farms: A framework and application to asset integrity management. *Applied Energy*, *322*, 119429.

Mondoro, A., Frangopol, D. M., & Soliman, M. (2017). Optimal risk-based management of coastal bridges vulnerable to hurricanes. *Journal of Infrastructure Systems*, *23*(3), 04016046.

Saeidpour, A., Chorzepa, M. G., Christian, J., & Durham, S. (2019). Probabilistic hurricane risk analysis of coastal bridges incorporating extreme wave statistics. *Engineering Structures*, *182*, 379–390.

Wu, Y., Randell, D., Christou, M., Ewans, K., & Jonathan, P. (2016). On the distribution of wave height in shallow water. *Coastal engineering*, *111*, 39–49.

Zhu, D., Li, Y., Dong, Y., & Yuan, P. (2021). Long-term loss assessment of coastal bridges from hurricanes incorporating overturning failure mode. *Advances in Bridge Engineering*, *2*, 1–15.

Bridge Maintenance, Safety, Management, Digitalization and Sustainability – Jensen, Frangopol & Schmidt (eds)
© 2024 The Author(s), ISBN 978-1-032-77040-6
Open Access: www.taylorfrancis.com, CC BY-NC-ND 4.0 license

Resilience-based countermeasure strategy for bridges under multiple hazards

H. Ishibashi
Nihon University, Koriyama, Japan

M. Akiyama
Waseda University, Tokyo, Japan

S. Koshimura
Tohoku University, Sendai, Japan

ABSTRACT: This paper presents a methodology for identifying optimal pre-disaster strategies for bridges subjected to ground motion and tsunami. The seismic and tsunami hazard curves are estimated based on the Monte Carlo simulation considering the uncertainties associated with fault movement. The seismic and tsunami fragility curves of a bridge pier and bearing are developed by numerical methods. The optimization problem for maximizing the benefit-cost ratio and the resilience is solved to identify the bridges necessary to be retrofitted before the event or replaced immediately after the event and find the optimal countermeasures based on the post-disaster road network functionality depending on the damage state of individual bridges. The application to the road network in Wakayama City expected to be affected by the anticipated Nankai Trough earthquake demonstrates that the proposed method can provide the optimal strategies for bridge management to enhance the road network resilience under budget constraints.

1 INTRODUCTION

Seismic and subsequent tsunami impacts can cause various failure modes to bridges, such as flexural and shear failures of piers and washout of superstructures. The failure mode is determined by the vulnerability of structural components, such as bridge pier and bearing, and the seismic and tsunami intensities. In addition, the effects of damage to bridges on road network functionality after an earthquake depends on the failure mode. For example, in case the bridge superstructure is washed away by tsunami, the reconstruction work would take a very long time, causing significant economic loss and delays in the recovery process. The optimal bridge countermeasure plans should be taken before an earthquake considering the potential failure mode of individual bridges and the negative social impacts caused by damage to bridges.

Optimization techniques on bridge management contribute to improving the cost-effectiveness of countermeasures and enhancing the resilience of communities affected by natural disasters. As examples of studies on the optimization problems for bridge management, Bocchini & Frangopol (2012) proposed a genetic algorithm (GA)-based optimization procedure for the restoration activities for bridges damaged by ground motion considering the transportation network resilience, restoration time and cost. Dong et al. (2015) developed a framework for reducing the extent of earthquake damage to society, economy, and environment (i.e. sustainability) with minimum total retrofit costs of bridge networks. Although the techniques on optimal bridge management have developed, studies considering the effects of multiple hazards on bridges and the associated social impacts are scarce in the literature. In addition, a resilience-based framework for identifying optimal bridge countermeasures before an earthquake is needed to achieve a rapid recovery process.

DOI: 10.1201/9781003483755-70

This paper presents a methodology for developing the optimal pre-disaster countermeasure strategies for bridges under seismic and tsunami hazards. Uncertainties associated with hazard intensity and structural vulnerability are considered based on the Monte Carlo simulation (MCS) to compute the failure probabilities of piers and bearings. The structural vulnerabilities of bridges against tsunamis are estimated considering the effects of seismic damage on the reduction in tsunami capacity. A GA-based optimization approach is adopted to identify which bridges should be retrofitted before the event or replaced immediately after the event to maximize cost-effectiveness and resilience. Resilience is defined in this study as the time-normalized integral of road network functionality (Frangopol & Bocchini 2011), which is quantified based on the damage state of individual bridge piers and bearings. In an illustrative example, the proposed method is applied to the road network with bridges affected by the anticipated Nankai Trough earthquake to investigate optimal pre-disaster countermeasure strategies for bridges under multiple hazards.

2 PROCEDURE FOR DETERMINING OPTIMAL COUNTERMEASURE STRATEGY

2.1 *Hazard assessment*

Probabilistic seismic and tsunami hazard analyses are performed based on the MCS given the occurrence of an earthquake. The average stress drop, which is a key parameter associated with dislocation and moment magnitude of the fault movement, is considered a random variable when estimating hazard curves. In the seismic hazard assessment, the maximum velocity on the engineering bedrock at each bridge location is obtained using the attenuation relationship provided by Si & Midorikawa (1999). Peak ground velocity (PGV) is then estimated by multiplying the maximum velocity on the engineering bedrock with the amplification factor calculated using the empirical formula proposed by Fujimoto & Midorikawa (2006). The model errors associated with these formulas used in the estimation process of PGV are also considered in the MCS.

Inundation depth is used as a tsunami intensity measure in the tsunami hazard assessment. The initial tsunami water level due to fault movement is repeatedly calculated using the formulas developed by Okada (1985) considering the uncertainty associated with average stress drop. Horizontal 2D tsunami propagation simulations based on nonlinear longwave theory (Goto et al. 1997) are then performed using the values of initial water level to estimate tsunami hazard curves at all the locations of individual bridges.

2.2 *Fragility curve*

Sequential nonlinear seismic and tsunami response analyses are performed to develop seismic and tsunami fragility curves of a pier and bearing considering the effects of seismic damage on reducing tsunami capacity. Horizontal force due to ground motion and tsunami and vertical tsunami force are used to assess the horizontal and vertical structural vulnerabilities of the pier and bearing, respectively. The maximum displacement and shear force of the pier are investigated to determine the damage state after an earthquake when estimating the fragility curves of the pier. For the bearing, both horizontal and vertical failure directions due to ground motion and tsunami hydrodynamic and uplift forces are considered in the vulnerability assessment. The damage states of a pier and bearing are defined based on the recovery time required after an earthquake and divided into three levels: none ($=DS_1$), moderate ($=DS_2$) and complete ($=DS_3$).

Seismic waves observed during past earthquakes in Japan are used to perform MCS-based nonlinear seismic response analyses. Horizontal and vertical tsunami forces obtained using the empirical formulas from the Subcommittee on Analysis of Damaged Bridges due to the Great East Japan Earthquake (2015) are used in the tsunami response analyses considering seismic damage to the pier and bearing. The uncertainties associated with material properties and model errors of empirical formulas used in the fragility assessment are considered random variables in the MCS.

Seismic and tsunami fragility curves are developed by a log-normal cumulative distribution function below:

$$P_{fi}(DS_i|\Gamma = \gamma) = \int_0^{\gamma} \frac{1}{\sqrt{2\pi}\sigma_i(x - l_i)} \exp\left[-\frac{\{\ln(x - l_i) - \mu_i\}^2}{2{\sigma_i}^2}\right] dx \quad (1)$$

where DS_i is the damage state, $P_{fi}(DS_i|\gamma)$ is the conditional failure probability that the damage state becomes greater than or equal to DS_i given the hazard intensity $\Gamma=\gamma$, and μ_i, σ_i and l_i are parameters. The natural logarithm of X-l_i is normally distributed with mean μ_i and variance σ_i^2. Although l_i is commonly set to zero when developing fragility curves, it is considered to improve the fitting of the estimated fragility curves to the discrete results of MCS-based response analyses.

2.3 *Optimization problem for pre-disaster bridge countermeasure strategy*

Horizontal and vertical failure probabilities of individual bridge piers and bearings are estimated using the seismic and tsunami hazard, and fragility curves for horizontal and vertical directions, respectively. The road network is assumed to be impassable at the location of bridges that have a pier or bearing with moderate or complete damage states. The MCS-based road network analysis is performed considering recovery time and cost of damaged bridge piers and bearings, and traffic speed of the road network after an earthquake.

NSGA-II (Deb et al. 2002) is adopted to determine the optimal pre-disaster countermeasure strategies for bridges under multiple hazards. Two objectives, benefit-cost ratio (*BCR*) and resilience, are considered in the optimization problem. *BCR* is defined as follows:

$$BCR = \frac{L_{none} - L_{mea}}{C_{mea}} \quad (2)$$

where C_{mea} is the total countermeasure cost, L_{none} is the mean of total economic loss of recovery cost of damaged bridges and indirect loss due to deterioration of road network functionality when no countermeasures are taken for all bridges, and L_{mea} is the mean of total economic loss when countermeasures are taken for some or all bridges.

The resilience R is defined as follows (Frangopol & Bocchini 2011; Ishibashi et al. 2021):

$$R = \frac{1}{t_h} \int_{t_0}^{t_0+t_h} Q(t)dt \quad (3)$$

where t_0 is the time at which the earthquake occurs, t_h is the investigated time horizon, and $Q(t)$ is the road network functionality at time t. $Q(t)$ is calculated based on the indirect loss due to the earthquake. The increase in resilience by countermeasures compared to no countermeasures is considered the objective of the optimization problem.

3 ILLUSTRATIVE EXAMPLE

3.1 *Analyzed road network*

A megathrust earthquake along the Nankai Trough (i.e. the Nankai Trough earthquake) would cause strong ground motion and tsunami in the Pacific coastal region of Japan in the near future (HERP 2013). The proposed method is applied to the road network in Wakayama City, which is expected to be affected by the Nankai Trough earthquake. Figure 1 shows the analyzed road network. In this illustrative example, the road network functionality is assessed based con the transportation between six origins and nine destinations. The data on the location and construction year of bridges are provided by the Ministry of Land, Infrastructure, Transport and Tourism (MLIT) (2022). The analytical conditions on traffic information, such as traffic volume, speed and truck ratio, are determined based on the national road traffic census (MLIT 2015).

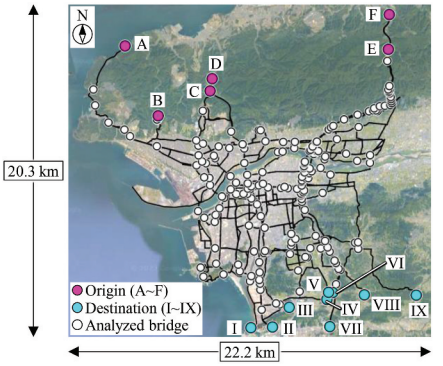


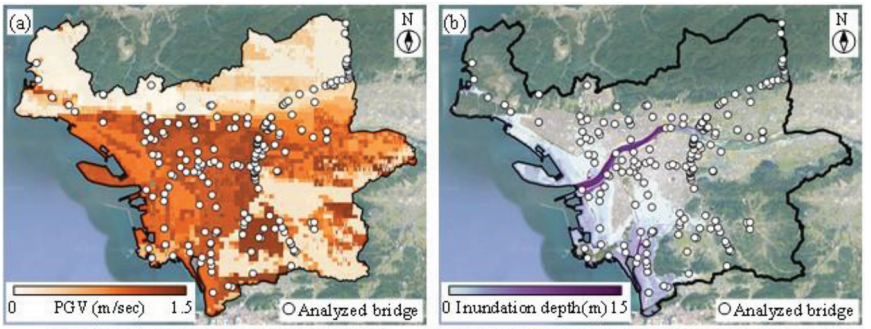
Figure 1. Analyzed road network in Wakayama City.

3.2 *Hazard assessment*

Figure 2 shows the contours associated with mean PGV and inundation depth in Wakayama City. Two seismic and eleven tsunami fault models provided by the Cabinet Office, Government of Japan (2012) are used to estimate seismic and tsunami hazard intensities, respectively, considering the uncertainty associated with large-slip areas. The average stress drop is modeled as a truncated lognormal distribution with a mean of 2.1 MPa and a standard deviation of 1.1 MPa based on the past earthquake data provided by the Cabinet Office, Government of Japan (2012) when estimating seismic hazard curves. In the tsunami hazard assessment, a truncated lognormal distribution with a mean of 1.9 MPa and a standard deviation of 1.9 MPa is assumed (Murotani 2013).

3.3 *Fragility curves*

Four types of bridges are designed according to the Japanese seismic specifications published in 1964, 1971, 1990 and 1996 and applied to investigate the effects of the upgrade of seismic specifications on their performance. Herein, these bridges are referred to as the 1964, 1980, 1990 and 1996 bridges, respectively. The seismic and tsunami fragility curves of the 1996 bridges are shown in Figure 3. The 1996 bridge has seismic performance equivalent to the current Japanese seismic design code. The pier height is assumed to be 6 m regardless of bridge locations. Hence, tsunami forces act on the bearings when the inundation depth exceeds 6 m.



(a) Contours associated with the mean PGV (b) Contours associated with the mean inundation depth

Figure 2. Contours associated with (a) mean PGV and (b) inundation depth in Wakayama City.

3.4 *Optimal countermeasure strategy*

Figure 4 shows the horizontal failure probability of non-retrofitted piers and the vertical failure probability of non-retrofitted bearings. The optimal countermeasure for each bridge depends on

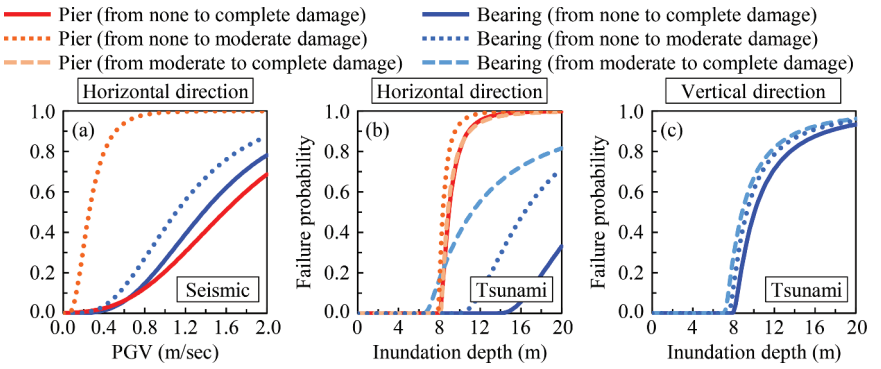


Figure 3. Fragility curves of 1996 bridge: (a) seismic fragility curves, (b) tsunami fragility curves (hori-zontal direction) and (c) tsunami fragility curves (vertical direction).

the potential failure mode, and post-disaster recovery cost and time. In the optimization problem, seismic retrofitting and pre-disaster preparation of temporary bridge girders for vertical damage to bearings are considered countermeasures. The fragility curves of the 1996 bridge are applied to retrofitted bridges. The seismic retrofitting can reduce the failure probability of the pier and bearing, while the preparation of temporary bridge girders decreases the recovery time required for reconstruction of the superstructure washed away by the tsunami.

Figure 5 shows the solutions associated with countermeasures obtained using NSGA-II. The estimation results of optimal countermeasure strategies (i.e., five Pareto solutions in Figure 4)

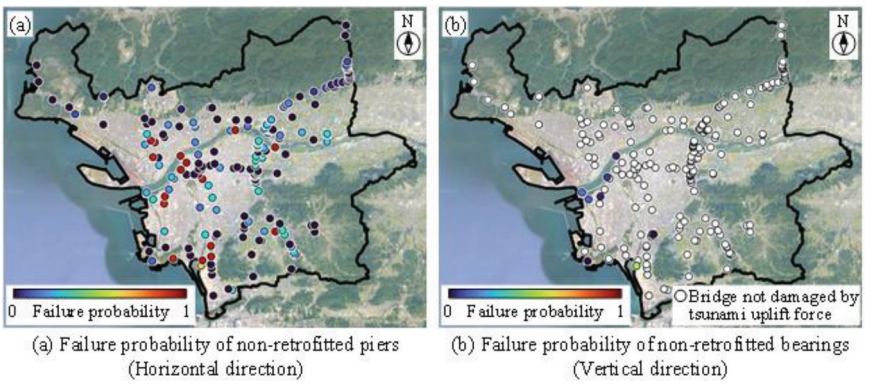


Figure 4. (a) Horizontal failure probability of non-retrofitted piers and (b) vertical failure probability of non-retrofitted bearings.

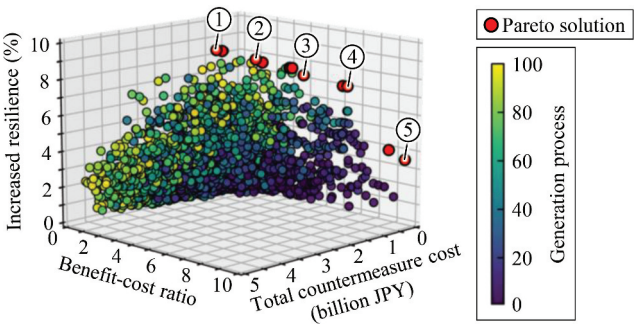


Figure 5. Solutions associated with countermeasures for bridges in road network.

Table 1. Estimation results of optimal countermeasure strategies.

No	BCR	Increased resilience (%)	Countermeasure cost (billion JPY)	Number of bridges with countermeasures*		
				Type 1	Type 2	Types1 and 2
1	3.410	9.339	2429.560	48	0	2
2	4.560	8.821	1860.220	29	0	1
3	6.088	7.982	1222.565	27	0	1
4	8.078	7.623	972.405	26	0	0
5	9.870	3.585	185.465	9	0	0

* Type 1: Seismic retrofitting.
Type 2: Pre-disaster preparation of temporary bridge girders.
Types 1 and 2: Both seismic retrofitting and pre-disaster preparation of temporary bridge girders.

are listed in Table 1. In this study, t_h in Equation (3) is set to 60 days. Seismic retrofitting is an effective countermeasure for analyzed bridges. However, the preparation of temporary girders for some bridges assuming washout of superstructures can significantly increase resilience. The proposed method provides optimal strategies to maximize *BCR* and resilience.

4 CONCLUSIONS

A framework for determining the optimal pre-disaster countermeasure strategies for bridges subjected to ground motion and tsunami is proposed. The failure probabilities of bridge piers and bearings in horizontal and vertical directions are estimated based on hazard and fragility curves obtained considering various uncertainties in the MCS. NSGA-II is adopted to solve the optimization problem for maximizing the *BCR* of bridge countermeasures and road network resilience. Seismic retrofitting and preparation of temporary bridge girders are considered pre-disaster countermeasures for bridges against an earthquake. The illustrative example of the road network with bridges in Wakayama City affected by the anticipated Nankai Trough earthquake demonstrates that the proposed method can facilitate decision-making for cost-effective pre-disaster bridge management strategies to enhance road network resilience.

In this paper, the recovery time of damaged bridges is assumed to depend only on the damage state. Constraints on the recovery process should be included in the optimal problems when assessing the economic loss and resilience considering the post-disaster severe situation.

ACKNOWLEDGMENT

This work was supported by JSPS KAKENHI Grant Number JP21K14235, the Project Grant in 2023 from the Co-creation Center for Disaster Resilience, International Research Institute of Disaster Science (IRIDes) at Tohoku University, and the Council for Science, Technology and Innovation (CSTI), Cross-ministerial Strategic Innovation Promotion Program (SIP), the 3rd period of SIP "Smart Infrastructure Management System" Grant Number JPJ012187 (Funding agency: Public Works Research Institute).

REFERENCES

Bocchini, P. & Frangopol, D.M. 2012. Restoration of bridge networks after an earthquake: Multicriteria intervention optimization. *Earthquake Spectra* 28(2): 427–455.

Cabinet Office, Government of Japan. 2012. Investigative commission on the modeling of giant earth-quake caused by Nankai Trough earthquake: Modeling of seismic fault (in Japanese).

Deb, K., Pratap, A., Agarwal, S., & Meyarivan, T. 2002. A fast and elitist multiobjective genetic algorithm: NSGA-II. *IEEE Transactions on Evolutionary Computation* 6(2), 182–197.

Dong, Y., Frangopol, D.M., & Sabatino, S. 2015. Optimizing bridge network retrofit planning based on cost-benefit evaluation and multi-attribute utility associated with sustainability. *Earthquake Spectra* 31 (4): 2255–2280.

Frangopol, D.M. & Bocchini, P. 2011. Resilience as optimization criterion for the bridge rehabilitation of a transportation network subject to earthquake. *Proceedings of the ASCE Structures Congress 2011*: 2044–2055.
Fujimoto, K. & Midorikawa, S. 2006. Relationship between average shear-wave velocity and site amplification inferred from strong motion records at nearby station pairs. *Journal of Japan Association for Earthquake Engineering* 6(1): 11–22 (in Japanese).
Goto, C., Ogawa, Y., Shuto, N. & Imamura, F. 1997. Numerical method of tsunami simulation with the leap-frog scheme. IUGG/IOC Time Project.
MLIT (Ministry of Land, Infrastructure, Transport and Tourism). 2015. National road traffic census. https://www.mlit.go.jp/road/census/h27/ (in Japanese)
MLIT (Ministry of Land, Infrastructure, Transport and Tourism). 2022. National road facility inspection database. https://road-structures-map.mlit.go.jp/ (in Japanese)
Murotani. S., Satake. K., & Fujii. Y. 2013. Scaling relations of seismic moment, rupture area, average slip, and asperity size for M~9 subduction-zone earthquakes. *Geophysical Research Letters* 40(19): 5070–5074.
Okada, Y. 1985. Surface deformation due to shear and tensile faults in a half-space. *Bulletin of the Seismological Society of America* 75(4): 1135–1154.
Si, H. & Midorikawa, S. 1999. New attenuation relationships for peak ground acceleration and velocity considering effects of fault type and site condition. *Journal of Structural and Construction Engineering* 64(523): 63–70 (in Japanese).
Subcommittee on Analysis of Damaged Bridges due to the Great East Japan Earthquake, Japan Society of Civil Engineers. 2015. Final report. Part II: Damage analysis due to tsunami. 1–391 (in Japanese).

Bridge Maintenance, Safety, Management, Digitalization and Sustainability – Jensen, Frangopol & Schmidt (eds)
© 2024 The Author(s), ISBN 978-1-032-77040-6
Open Access: www.taylorfrancis.com, CC BY-NC-ND 4.0 license

Enhancing seismic resilience of aging highway bridges using FRP retrofit

V. Singh
Research Scholar, Indian Institute of Technology Mandi, India

S. Shekhar
Assistant Professor, Indian Institute of Technology Mandi, India

N. Kotoky
Assistant Professor, National Institute of Technology Meghalaya, India

ABSTRACT: Environmental degradation mechanisms such as corrosion can have a significant impact on the resilience of the reinforced concrete (RC) highway bridges present near the harsh marine environment within high seismic zones. This study aims to evaluate the effectiveness of fiber-reinforced polymer (FRP) jackets in enhancing the seismic resilience of deteriorated highway bridges. A representative case-study non-seismically designed highway bridge located close to marine sources within the seismic active region of Gujarat, India is selected. Time-dependent chloride-induced corrosion deterioration of bridge pier is evaluated considering non-uniform pitting corrosion. FRP jacket is used to retrofit the deteriorated bridge pier, and pushover analysis results reveal a significant increase in the damage state thresholds of the FRP retrofitted deteriorated bridge pier. Seismic fragility curves of as-built, 75-year aging and FRP retrofitted bridges are developed and combined with suitable loss and recovery models to calculate the seismic resilience of bridges for varying earthquake intensity. From the result, it is observed that the resilience of the bridge decreases with an increase in earthquake intensity and FRP retrofit significantly enhances the seismic resilience of deteriorated bridge.

1 INTRODUCTION

Highway bridges are the key component of transportation systems and play a significant role in the sustainable economic growth of the nation. Most of the highway bridges are built using antiquated design standards and experience degradation from age-related corrosion. According to the report card for American Infrastructure (2021), there are about 617,000 bridges in the United States, and 42% of them are over 50 years old, and currently, 7.5% of the nation's bridges are classified as structurally deficient, whereas in India, out of 14,500 bridges on the national highway, 1700 bridges are reportedly in need of repair and restoration (Wakchaure and Jha 2011). Corrosion degradation results in an increase in the failure probability of these bridges when located in regions of moderate to high seismicity as observed during the Bhuj earthquake 2001 (Madabhusi and Haigh 2001). In the context of India, inadequate highway bridge performance has been observed in the past earthquake events (Cachar earthquake 1984, Jabalpur earthquake 1997, Chamoli earthquake 1999, and Bhuj earthquake 2001). Past studies highlighted the high vulnerability of existing older bridges in India due to the absence of ductile detailing principles in the seismic standards (Shekhar et al. 2020). Bridge damage caused by such disasters greatly affects transportation networks, reducing their functionality, and as a result, affecting emergency response and socioeconomic recovery activities across the region after the hazard occurrence.

DOI: 10.1201/9781003483755-71

Seismic resilience has been recognized as an important metric to evaluate the performance of infrastructure systems such as bridges considering vulnerability, losses, and post-event recovery. Previous studies on the seismic resilience assessment of aging bridges have observed a reduction in resilience due to corrosion degradation (Vishwanath and Banerjee 2019, Huang and Huang 2021). Seismic retrofitting is a preferred methodology used by several transportation departments to enhance bridge performance during earthquake occurrences. Application of retrofit interventions can significantly reduce post-earthquake losses, improve overall disaster preparation, and lessen the negative effects of seismic occurrences on transportation infrastructure. Several research studies have been conducted in the past on assessing the seismic resilience enhancement of the as-built structures using retrofit methodologies (Venkittaraman and Banerjee 2014; Chandrasekaran and Banerjee 2016; Anwar and Dong 2020), however, there is limited understanding of the seismic resilience enhancement of deteriorating highway bridges using retrofit measures. Qiu et al. (2023) have estimated the effect of FRP wraps on the seismic resilience of aging highway bridges including repair cost and repair time, however, this study does not consider the non-uniform chloride-induced deterioration process.

This study evaluates the effectiveness of using carbon fiber reinforced polymer (FRP) jackets in enhancing the seismic resilience of aging highway bridges. The next section of the paper describes the framework for the estimation of seismic resilience with the help of fragility, losses, and recovery models. Next, the selection of a case-study bridge designed as per outdated seismic design guidelines and located in the Gujarat region is presented followed by a discussion on the time-dependent corrosion model. This section also discusses the bridge pier's FRP retrofit design and a detailed finite element model for the aging and FRP retrofitted bridges. The subsequent section of the study presents the seismic capacity evaluation of the aging and FRP retrofitted bridge pier using nonlinear static pushover analysis. In the final section of the paper, seismic resilience is evaluated for the aging and FRP retrofitted bridge pier using developed fragility curves, losses, and recovery models. The paper finishes with the conclusion and suggestions for future work.

2 SEISMIC RESILIENCE ASSESSMENT FRAMEWORK FOR BRIDGES

Previous research has developed and computed the resilience of several lifeline systems, such as transportation networks (Amdal and Swigart 2010; Cimellaro et al. 2010). In general, resilience is described as a dimensionless measure showing the rapidity with which a system may recover from a damaged state and resume its pre-damaged functionality level. Losses that occurred due to the extreme event and post-event recovery path are the two main factors used to measure the resilience of civil infrastructure systems. Seismic resilience for a single earthquake event can be expressed as (Cimmeralo et al. 2010):

$$R = \int_{(t_{0E})}^{(t_{0E}+T_{LC})} \frac{Q(t)}{T_{LC}}\,dt \tag{1}$$

where t_{0E} is the time when an event E occurs, T_{LC} is the control time and $Q(t)$ denotes the time-dependent functionality of the system and can be represented as:

$$Q(t) = 1 - [L(I, T_{RE}) \times \{H(t - t_{0E}) - H(t - (t_{0E} + T_{RE}))\} \times f_{RE}(t, t_{0E}, T_{RE})] \tag{2}$$

where $L(I,T_{RE})$ represents the loss function, $H(.)$ is the Heaviside step function, f_{RE} is the recovery function, T_{RE} is the time required for recovering the functionality of the damaged bridge. Figure 1 (a) represents the seismic resilience diagram of degrading bridges, which can be calculated from the normalized area under the functionality curve from the time of the seismic event (t_{0E}) to a subsequent time instant ($t_{0E} + T_{LC}$).

Figure 1 (b) shows the framework for the evaluation of enhancement in seismic resilience of the aging bridges using FRP retrofitting. The overall framework is divided into six steps. Step

(A) of the framework involves the assessment of chloride-induced corrosion deterioration of the bridge, with detailed discussion provided in Section 3. Step (B) involves the development of the finite element (FE) model of the bridge incorporating deterioration effects. Next, in Step (C) time-dependent seismic fragility curves are developed using a suite of site-specific ground motions. The seismic fragility curves can be expressed for the damage state *DS* as:

$$Pf_{DS|IM} = \Phi\left[\frac{\ln(IM/med_{DS})}{\zeta_{DS}}\right] \tag{3}$$

where $Pf_{DS|IM}$ denotes the probability of failure associated with the damage state *DS* conditioned on intensity measure *IM*. Φ represents the standard normal distribution function, med_{DS}, and ζ_{DS} represents the median and dispersion of the fragility curves, respectively. Step (D) of the framework involves the calculation of seismic resilience for aging bridge utilizing seismic losses and recovery function. The loss function comprises direct and indirect loss resulting from seismic event. Direct losses arise from the cost associated with the post-event repair and restoration and are computed by multiplying the failure probability determined by fragility curves (Equation 3) by the damage ratios (HAZUS-MH MR4 2003). The indirect losses occur due to various factors such as traffic delays, network outages, and casualties during the system's recovery. The ratio between indirect loss and direct loss ranges from 5-20 (Denneman 2009). For this study, the indirect losses are considered to be 13 times that of direct losses (Venkitraman and Banerjee 2014). The recovery function (f_{RE}) represents the path that should be followed after an event to restore bridges. However, the lack of precise data makes it challenging to trace the accurate recovery path. Cimmeralo et al. (2010) introduced simple mathematical models such as linear and exponential functions as the recovery path of the system. According to Jonas (2007), sigmoidal curves can also be used to represent recovery path and are adopted in this study. The time required for post-event recovery (T_{RE}) for different damage states is adopted from HAZUS (HAZUS-MH MR4 2003).

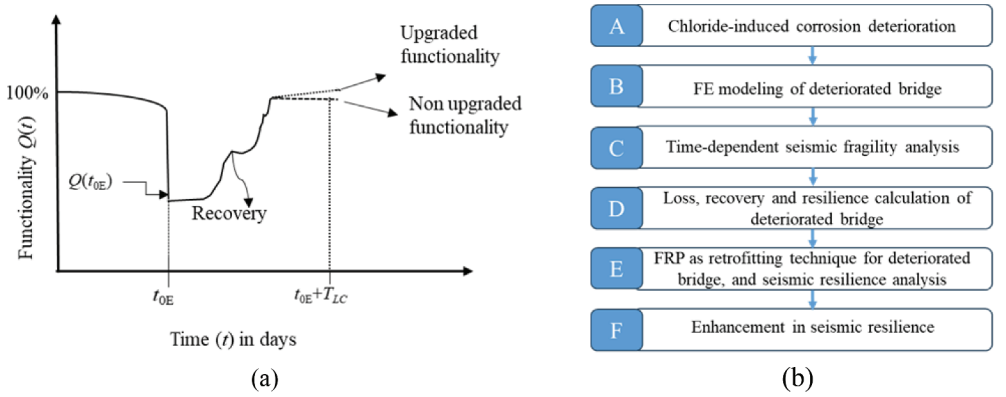


Figure 1. (a) Schematic illustration of seismic resilience of the aging bridge (b) framework for the evaluation of enhancement in seismic resilience of aging bridge after retrofitting.

3 REPRESENTATIVE CASE-STUDY BRIDGE

To investigate the effect of FRP jacket on the seismic resilience of the aging highway bridge, a semi-integral bridge is assumed to be situated in Gujarat, India region which is near the coastline and comes under seismic zone V (IS 1893: 2016). The deck of the bridge is 20 m long and 7.5 m wide resulting in a gravity load of 4000 kN on the reinforced concrete (RC) bridge pier. The height (*H*) and diameter (*D*) of the bridge pier are adopted as 5.0 m and 1.4 m,

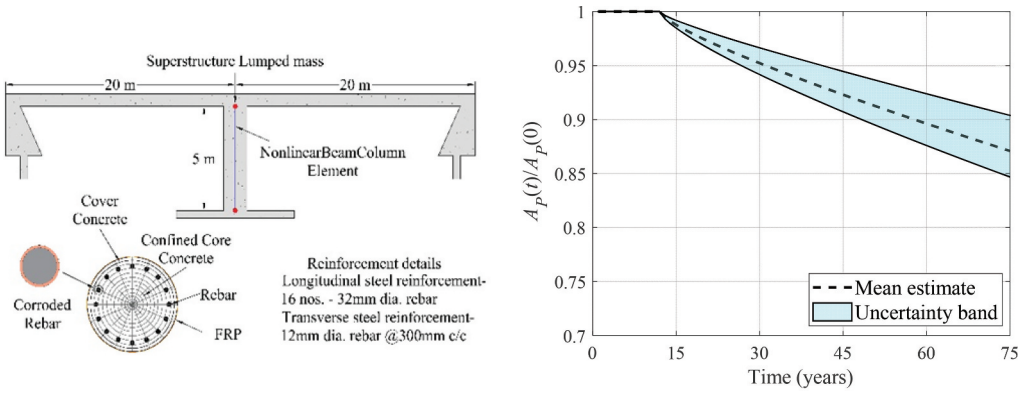
respectively. The bridge is designed according to outdated seismic design standards; therefore, the pier is primarily designed for gravity loads and negligible lateral forces. The reinforcement detailing of the bridge pier depends on the minimum reinforcement criteria because of the absence of ductile detailing provisions in the seismic standards (Shekhar et al. 2020). Figure 2 (a) shows the general layout of the bridge along with the reinforcement details of the pier.

3.1 *Time dependent corrosion modeling of the bridge pier*

For RC bridges, chloride-induced corrosion deterioration has become a major concern for bridge owners (Choe et al. 2008). During their design life, several bridge components continuously deteriorate due to corrosion. The deterioration of bridge piers due to corrosion significantly affects the seismic response of the bridge (Andisheh et al. 2016). The corrosion deterioration in the RC structures commences after a time gap which is denoted as corrosion initiation time (T_i). Throughout this period, chloride ions progressively penetrate the concrete cover, depassivating the reinforcement and starting the corrosion process. The corrosion initiation time depends on parameters such as chloride diffusion coefficient, surface chloride concentration, critical chloride concentration, and concrete cover depth, among others, and can be evaluated using Fick's second law of diffusion. The statistical distribution of the above-mentioned parameters considering marine splash zone is adopted from Duracrete (2000). The mean corrosion initiation time for the case-study bridge structure has been calculated as 12 years. After initiation, the corrosion propagation phase begins with the depassivation of steel. Steel area loss during this phase is greatly influenced by the rate of corrosion and is calculated based on the model proposed by Vu and Stewart (2000). The time-dependent non-uniform pitting corrosion can be calculated as (Dizaj et al. 2023):

$$A_P(t) = \beta A_{ave}(t) \tag{4}$$

where, $A_P(t)$ represents the time-dependent cross-sectional area of reinforcement, including pitting corrosion effects, $A_{ave}(t)$ is the average time-dependent cross-sectional area of steel reinforcement, and β is the pitting coefficient. The statistical distribution of the pitting coefficient is adopted from Dizaj et al. (2023). After considering the uncertainties in the corrosion degradation process, Figure 2 (b) illustrates the decrease of mean reinforcing steel area with time, as well as the lower and upper bounds, corresponding to the 5th and 95th percentile. Apart from the reduction of reinforcing steel area, corrosion deterioration can also cause several secondary effects such as a reduction in cover and core concrete strength, and steel rebar strength and ductility. These secondary effects are calculated based on past literature (Du et al. 2005; Biondini and Vergani 2015).



(a) (b)

Figure 2. (a) General layout of case study bridge and details of FE modeling, and (b) variation of mean reinforcement steel area over time, and the uncertainty bands.

3.2 *FRP retrofit design and details of the bridge pier*

To enhance the seismic resilience of the deteriorated non-seismically designed bridge pier, this study uses carbon fiber reinforced polymer (FRP) as retrofit jacket material for the bridge pier which is widely used for retrofitting structures. Carbon FRP is chosen for its high strength to weight ratio, ease of implementation, and resistance towards corrosion. It consists of unidirectional or bidirectional high-strength fibers. The carbon FRP used in this study has tensile strength and elastic modulus of 3000 MPa and 230 GPa, respectively (He et al. 2019). The thickness of one ply FRP is 0.167mm and for this study, two ply of FRP is applied over the full length of the bridge pier. An adequate amount of jacket thickness plays a significant role in retrofitting, as it prevents the lateral expansion of the concrete which increases load bearing capacity and ductility of the structure.

3.3 *FE modeling of aging and retrofitted bridge piers*

The seismic performance of semi-integral bridges is mainly governed by the response of bridge piers, wherein the RC piers are connected monolithically with the deck (Kolias et al. 2012). The analytical model of the bridge in this study considers the 2D beam-column element representing the bridge pier with the mass of the superstructure lumped at the top of the bridge pier. The bridge pier's boundary condition is modeled to be fixed, assuming that the pier is located on firm soil. The finite element (FE) model of the bridge pier is developed in OpenSees (Mckenna et al. 2000) by utilizing a nonlinear beam column element using a fiber section approach with distributed plasticity which consists of circular concrete patches along with circular layers of reinforcement. The unconfined and confined concrete is modeled using *Concrete01*, where the confined concrete properties are derived using the model obtained from Mander et al. (1988). A *uniaxialmaterial Hysteretic* material is used to model the longitudinal steel reinforcement. The loss in steel area due to corrosion is modeled as the reduction in diameter of rebar which includes the time-dependent uncertainty caused by corrosion rate. The pier elements are divided into five integration points, and separate fiber sections are assigned at each integration point considering the spatial and temporal variability of the pitting corrosion. Based on the lognormal distribution as suggested by Kashani et al. (2013), samples of pitting coefficients are generated and assigned randomly to rebars at fiber sections. The secondary effects due to corrosion deterioration are also included in the FE modeling of the deteriorated bridge pier. The FRP confined concrete is modeled using *ConfinedConcrete01* material to precisely represent the concrete confinement caused by the use of FRP.

4 SEISMIC CAPACITY OF THE AGING AND RETROFITTED BRIDGE PIER

The seismic fragility of the structure requires information on demand and capacity which involves the assessment of demand through non-linear time history analyses (NLTHAs) and comparing it to particular capacity estimates or thresholds of various *DS*s (Slight, Moderate, Extensive, and Complete). Due to the corrosion, lateral load capacity may be reduced with respect to time. The present study evaluates the time-dependent capacity of *DS*s for the aging and FRP retrofitted bridge pier using pushover analyses. The *DS* thresholds in terms of drift ratio (*DR*) for various *DS*s are derived using concrete and steel material strain criteria.

Figure 3 depicts the threshold value for different *DS*s shown on the pushover curve of as-built (0-year), 75-year corroded, and 75-year corroded bridge pier retrofitted with FRP. For the bridge pier, Slight *DS* threshold is considered as *DR* corresponding to the idealized yield point determined analytically through elastoplastic idealization of the pushover curve (Ni Choine 2014). For the as-built and aging bridge pier, the Moderate *DS* threshold occurs either at the concrete spalling or when the residual crack width reaches 1mm. Concrete spalling is considered to occur when the strain value of extreme compressive fiber in cover concrete attains a value of 0.003 (Bae and Bayrak 2003), while initiation of residual crack width occurs at a strain value of 0.015 in reinforcement (Kowalsky 2000). In the case of retrofitted bridge

pier, Moderate *DS* threshold is achieved either at the loss of aggregate interlocking or FRP delamination. The aggregate interlocking loss and FRP delamination are considered to occur at strain values of 0.004 and 0.008 of cover concrete, respectively (Bakis et al. 2002). Complete *DS* threshold for both cases is attained when any of the following conditions are met - crushing of core concrete, buckling of the rebar, or fracture of rebar. For retrofitted bridge pier, the assumed strain value for core concrete crushing is 0.035 (Parghi and Alam 2017). The strain value for fracture and buckling of the longitudinal bar is obtained from the expression given by Berry and Eberhard (2008). The Extensive *DS* threshold is considered at the geometric mean of the Moderate and Complete *DS*s. From Figure 3, it is observed that corrosion caused a reduction of 32.8% in load-carrying capacity of the 75-year deteriorated pier as compared to the as-built state. After retrofitting it has been seen that there is slight increase in load carrying capacity, but the drift capacity of the deteriorated bridge pier has increased considerably. At Complete *DS*, the drift capacity of the 75-year deteriorated bridge pier retrofitted with FRP is 118% higher than the 75-year deteriorated bridge pier.

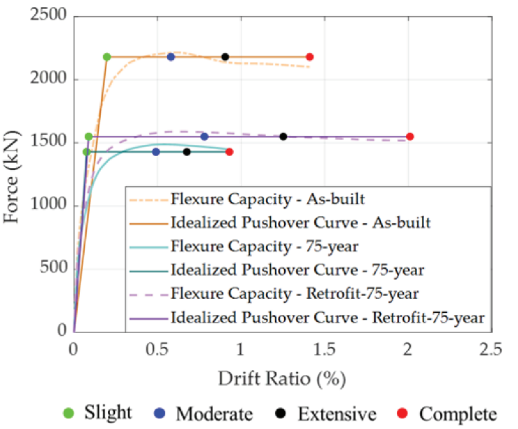


Figure 3. Pushover curve showing damage state thresholds for the as-built, 75-year corroded, and 75-year FRP retrofitted bridge piers.

5 SEISMIC RESILIENCE OF THE AGING AND RETROFITTED BRIDGE

Seismic fragility curves indicate the probability of exceedance of damage state for the specific ground motion intensity measure. Peak ground acceleration (*PGA*) is used as an intensity measure (*IM*) to develop the seismic fragility curves. Seismic fragility curves for as-built, corroded, and FRP retrofitted bridges are derived using Step (C) of the previously defined framework.

Figure 4 (a) demonstrates the seismic fragility curves of as-built (0-year), 75-year corroded, and 75-year FRP retrofitted bridge piers for Complete *DS*. It is observed that there is an increase in the vulnerability of the 75-year bridge pier when subjected to chloride exposure compared to the as-built state. The median *PGA* (corresponding to 50% failure probability) for 75-year deteriorated bridge is 37.8% lower compared to the as-built bridge. The FRP retrofitting of the 75-year deteriorated bridge results in a significant decrease in the vulnerability, with a 47.42% increase in the median *PGA* compared to the corroded state. Similarly, trends in fragility curves are observed for other *DS*s, which are further used in seismic resilience assessment.

Following the development of fragility curves, seismic losses are computed. Damage specific recovery functions (f_{RE}) and control time are utilized to compute the functionality, and seismic resilience of the bridge is calculated using Step (D) of the framework (Equations (1) and (2)). Using Step (E) and Step (F) of the framework, enhancement in seismic resilience is evaluated using carbon FRP retrofit. Figure 4 (b) represents the seismic resilience for a range of *PGA* for as-built, 75-year corroded, and FRP retrofitted 75-year corroded bridge. It is found that with the increase in *PGA*, seismic resilience is reduced, and this reduction is higher for the

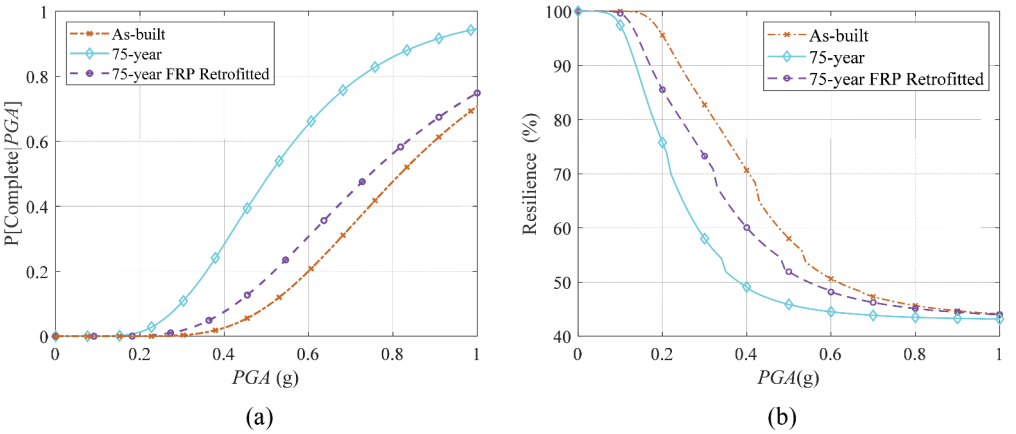


Figure 4. (a) Comparison of seismic fragility curves for Complete *DS* for as-built, 75-year corroded, and 75-year FRP retrofitted bridge piers, and (b) Comparison of seismic resilience curves for as-built, 75-year corroded, and 75-year FRP retrofitted bridge piers.

75-year deteriorated bridge. At 0.4g *PGA,* the loss in seismic resilience of the as-built and 75-year corroded bridges are 29.4% and 50.9%, respectively. The FRP retrofitting of the 75-year deteriorated bridge increases the seismic resilience, and for 0.4g *PGA*, the resilience loss is 40%, which is less than the corroded bridge highlighting the effectiveness of FRP in improving the resilience of corroded bridges.

6 CONCLUSION

The current study investigates the effectiveness of FRP retrofitting in improving the seismic resilience of deteriorating highway bridges. A semi-integral bridge located near the coastline of high seismicity Gujarat region is selected as the case-study bridge, and the corrosion deterioration path incorporating non-uniform pitting corrosion under marine splash chloride exposure condition is estimated for the bridge pier. Carbon FRP is selected for retrofitting the corrosion-deteriorated bridge pier. FRP retrofitting of the deteriorated bridge pier (t=75 years), results in an increase in the Complete damage state drift capacity. To develop the seismic fragility curves, a full probabilistic approach is conducted considering the different sources of uncertainty. Results obtained from the seismic fragility analysis indicate that the seismic vulnerability increases significantly for the deteriorated bridge pier and vulnerability is reduced after retrofitting the bridge pier. For the Complete *DS*, the median *PGA* for a 75-year deteriorated bridge is 37.8% lower as compared to the as-built bridge and for FRP retrofitted 75-year deteriorated bridge, the median *PGA* is increased by 47.42% as compared to the 75-year deteriorated bridge. Next, seismic resilience is evaluated with the help of the information obtained from the seismic fragility, direct and indirect losses, and the recovery model. Results reveal that seismic resilience decreases with the increase in *PGA.* For 0.4g *PGA*, the loss in seismic resilience for the as-built bridge is 29.4% which is increased to 50.9% because of the corrosion-induced deterioration at 75-year, and after retrofitting the bridge the reduction in seismic resilience reduced to 40%, which highlights the effectiveness of applying FRP retrofit to enhance the seismic resilience of aging bridge. Future work will consider the influence of different retrofitting techniques in enhancing the seismic resilience of multi-span simply supported aging highway bridges.

ACKNOWLEDGMENTS

The authors acknowledge the financial assistance provided by the Science and Engineering Research Board (statutory body under the Department of Science and Technology, India) through Grant No. SRG/2021/001574 for this research.

REFERENCES

ACI 440.2R-02 (2002). "Guide for the Design and Construction of Externally Bonded FRP Systems for Strengthening Concrete Structures" Reported by ACI Committee 440.

Afsar Dizaj, E., Salami, M. R., & Kashani, M. M. 2023. Impact of asymmetrical corrosion of piers on seismic fragility of aging irregular concrete bridges. Structure and Infrastructure Engineering, 1–20.

Amdal, J. R., & Swigart, S. L. 2010. Resilient Transportation Systems in a Post-Disaster Environment: a Case Study of Opportunities Realized and Missed in the Greater New Orleans Region. In October, 49.

Andisheh, K., Scott, A., & Palermo, A. 2016. Seismic Behavior of Corroded RC Bridges: Review and Research Gaps. International Journal of Corrosion, 2016(3).

Anwar, G. A., & Dong, Y. 2020. Seismic resilience of retrofitted RC buildings. Earthquake Engineering and Engineering Vibration, 19, 561–571.

Bae, S., & Bayrak, O. 2003. Early Cover Spalling in High-Strength Concrete Columns. Journal of Structural Engineering, 129(3), 314–323.

Berry, M. P., & Eberhard, M. O. 2008. Performance Modeling Strategies for Modern Reinforced Concrete Bridge Columns Performance Modeling Strategies for Modern Reinforced Concrete Bridge Columns. Montana The Magazine of Western History, April.

Biondini, F.,& Vergani M. 2015. Deteriorating beam finite element for nonlinear analysis of concrete structures under corrosion. Structure and Infrastructure Engineering, 11(4), 519–532.

Chandrasekaran, S., & Banerjee, S. 2016. Retrofit optimization for resilience enhancement of bridges under multihazard scenario. Journal of Structural Engineering, 142(8)

Choe, D. E., Gardoni, P., Rosowsky, D., & Haukaas, T. 2008. Probabilistic capacity models and seismic fragility estimates for RC columns subject to corrosion. Reliability Engineering and System Safety, 93(3), 383–393.

Cimellaro, G. P., Reinhorn, A. M., & Bruneau, M. 2010. Framework for analytical quantification of disaster resilience. Engineering Structures, 32(11), 3639–3649.

Dennemann, K.L. 2010. "Life-cycle cost-benefit (LCC-B) analysis for bridge seismic retrofits." Rice University.

Du, Y. G., L. A. Clark, and A. H. C. Chan. 2005. "Residual capacity of corroded reinforcing bars." Mag. Concr. Res. 57 (3): 135–147.

Duracrete. 2000. "General guidelines for durability design and redesign." Report Number BE95-1347/R17 Prepared for DuraCrete: Probabilistic Performance-Based Durability Design of Concrete Structures, The European Union – Brite EuRam III.

Federal Emergency Management Agency (FEMA). (2003). "HAZUS-MH MR4 Multi-Hazard Loss Estimation Methodology – Earthquake Model: Technical Manual." Department of Homeland Security. Federal Emergency Management Agency, Washington, DC.

He, Z., Ou, X., Li, J., & Ou, J. 2019. Collapse safety margin-oriented seismic retrofit strategy for corroded reinforced concrete frames using fibre reinforced plastics. Structure and Infrastructure Engineering, 15(8), 1025–1035.

Huang, C., & Huang, S. 2021. Seismic resilience assessment of aging bridges with different failure modes. In Structures (Vol. 33, pp. 3682–3690).

IS: 1893 (part 1)-2016, ,Indian Standard Criteria for Earthquake Resistant Design of Structures, Bureau of Indian Standards, New Delhi, India, 2016.

Jónás, T. 2007. Sigmoid functions in reliability based management. Periodica Polytechnica Social and Management Sciences, 15(2), 67–72.

Kashani, M.M., Crewe, A.J., & Alexander, N.A. (2013). Nonlinear stress–strain behaviour of corrosion-damaged reinforcing bars including inelastic buckling. Engineering Structures, 48, 417–429.

Kolias, B., Fardis, M.N., Pecker, A., & Gulvanessian, H. 2012. "Designers guide to Eurocode 8: design of bridges for earthquake resistance." Designers' Guide to Eurocodes.

Madabhushi, S. P. G., & Haigh, S. K. 2005. The Bhuj, India Earthquake of 26th January 2001; A FIELD REPORT BY EEFIT. Society, 44(January 2001), 207–235.

Mander, J.B., Priestley, M.J., & Park, R. 1988. "Theoretical stress-strain model for confined concrete." Journal of Structural Engineering, 114(8), 1804–1826.

McKenna, F., Fenves, G., & Scott, M. 2000. "Open system for earthquake engineering simulation." Berkeley, CA: Univ. of California.

Parghi, A., & Alam, M. S. 2017. Seismic collapse assessment of non-seismically designed circular RC bridge piers retrofitted with FRP composites. Composite Structures, 160, 901–916.

Qiu, Z., Prabhakaran, A., Su, L., & Zheng, Y. 2023. Performance-based seismic resilience and sustainability assessment of coastal RC bridges in aggressive marine environments. Ocean Engineering, 279, 114547.

Report Card for America's Infrastructure 2021. https://infrastructurereportcard.org/cat-item/bridges-infrastructure.

Shekhar, S., Ghosh, J., & Ghosh, S. 2020. Impact of Design Code Evolution on Failure Mechanism and Seismic Fragility of Highway Bridge Piers. Journal of Bridge Engineering, 25(2), 1–19.
Shekhar, S., Ghosh, J., & Padgett, J. E. 2018. Seismic life-cycle cost analysis of aging highway bridges under chloride exposure conditions: modelling and recommendations. Structure and Infrastructure Engineering, 14(7), 941–966.
Venkittaraman, A., & Banerjee, S. 2014. "Enhancing resilience of highway bridges through seismic retrofit." Earthquake Engineering & Structural Dynamics, 43(8), 1173–1191.
Vishwanath, B. S., & Banerjee, S. 2019. "Life-Cycle Resilience of Aging Bridges under Earthquakes." Journal of Bridge Engineering, 24(11), 1–12.
Vu, K. A. T., & Stewart, M. G. 2000. "Structural reliability of concrete bridges including improved chloride-induced corrosion models." Structural Safety, 22(4), 313–333.
Yang, J., & Wang, J. 2018. "Seismic Performance of Shear-Controlled CFRP-Strengthened High-Strength Concrete Square Columns under Simulated Seismic Load." Journal of Composites for Construction, 22(6), 04018061

Bridge Maintenance, Safety, Management, Digitalization and Sustainability – Jensen, Frangopol & Schmidt (eds)
© 2024 The Author(s), ISBN 978-1-032-77040-6
Open Access: www.taylorfrancis.com, CC BY-NC-ND 4.0 license

Fragility curves for regular and irregular RC bridges via non-linear static analysis

H. Rezaei
Islamic Azad University, Tehran, Iran

E.M. Dehcheshmeh
University of Science and Technology, Tehran, Iran

Y. Tsompanakis
Technical University of Crete, Chania, Greece

ABSTRACT: The main objective of this study is to present an efficient method for developing seismic fragility curves for regular and irregular reinforced concrete (RC) bridges based on the capacity spectrum assessment, i.e., FRACAS method. Accordingly, 3D models of unbalanced, skewed, and curved irregular bridges were considered, taking into account uncertainties related to geometry, material as well as seismic excitation characteristics. In the presented methodology, the FRACAS method, which was initially developed for buildings, was appropriately modified to become suitable for the 3D analysis of the examined bridges, reducing also the demand error compared to -computationally demanding- non-linear time-history analysis (NTHA) approach. For this purpose, the fragility curves obtained from the proposed 3D FRACAS were compared with those obtained via NTHA. Results illustrate that the 3D FRACAS approach can be efficiently used for developing the fragility curves for regular and irregular bridges in a computationally efficient and accurate manner.

1 INTRODUCTION

Undoubtedly, the seismic behavior of bridges is strongly influenced by various types of irregularities in their geometry. The main types of irregularities are related to curved, skewed, and unbalanced bridges (e.g., Rezaei et al. (2022a); Rezaei et al. (2023)). In recent years, bridge irregularities have been thoroughly studied (e.g., Mangalathu et al. (2019); Rezaei et al. (2022b); Rezaei et al. (2023)). As it is commonly reported in relevant studies, the increased complexity of the seismic behavior of irregular bridges compared to simpler regular bridges. Moreover, uncertainties related to mechanical, geometric and seismic excitation characteristics further increase the difficulty to assess the seismic performance and vulnerability of such bridges. In addition, due to the excessive computational cost required for the dynamic analyses of real-life bridges, necessitates the development of simple and fast methods that are capable of accurately assessing the complex seismic response of regular and -mainly- irregular bridges.

The Capacity Spectrum Method (CSM) is a non-linear static technique for obtaining structural response for different seismic hazard scenarios. To perform structural capacity assessment, CSM uses non-linear static pushover analysis. Structural capacity is derived via modal analysis in the form of a spectral acceleration versus spectral displacement curve, whereas spectral demand is derived using acceleration-displacement response spectrum (ADRS). Due to the direct comparison of spectral capacity with spectral demand curves, an estimation of the structural response can be obtained, the so-called performance point. Generally, CSM-based methods can be considered as a very efficient tool in integrity assessment for various types of structural systems under seismic

DOI: 10.1201/9781003483755-72

loads that require repeated and time-consuming dynamic analyses, due to their reduced computational cost and sufficient accuracy in estimating structural capacity.

Within this framework, Rossetto et al. (2016) proposed a fragility through capacity spectrum assessment approach, the so-called FRACAS method, which is capable of considering record-by-record variability and was effectively applied to develop fragility curves of buildings. Herein, the standard FRACAS method has been modified for 3D irregular bridge models and further improved to reduce the demand error compared to non-linear time-history analysis (NTHA) approach. The main aim of this work is to provide a computationally efficient method, i.e., 3D FRACAS method, which can accurately and reliably estimate the dynamic non-linear response of regular and irregular bridges and facilitate the generation of the fragility curves of various bridge components for several damage levels without the need to perform computationally expensive non-linear time-history analyses.

2 PROPOSED 3D FRACAS METHODOLOGY

In this paper, unbalanced, skewed and curved irregular bridges, considering geometry, material and seismic excitation uncertainties have been examined. For each bridge type, regular configurations as well as with slight, moderate and extreme irregularities have been studied. Three-dimensional (3D) numerical models have been developed for all cases utilizing the advanced capabilities of OpenSees finite-element software. Non-linear time-history analyses (NTHA) have been performed for 160 ground motions. The NTHA results have been used to validate the fragility results obtained via the proposed 3D capacity spectrum assessment fragility methodology (3D FRACAS). In particular, the error distribution functions of the 3D FRACAS method were estimated for each bridge class. To determine the error distribution functions, a normal distribution is fitted on the difference between the responses of the "accurate" NTHA method and 3D FRACAS method for each EDP. The obtained error distribution functions were used to develop the probabilistic seismic demand models, which in turn were used to develop the fragility curves of important bridge components as well as for the whole bridge system. The obtained fragility curves of the improved 3D FRACAS were compared with those derived via NTHA method.

The error of the estimated demand is calculated and included in the improved method to reduce the estimation error. Hence, in the improved 3D FRACAS approach, an appropriate distribution function $\varepsilon\ (\mu, \sigma)$ is obtained for each EDP and used for developing the fragility curves. In the proposed framework, the obtained seismic demand and the fitting error are compared with the capacity distributions of the bridge components to generate the fragility curves. In brief, 3D FRACAS analysis is conducted via the following main steps:

1. First, a 3-D numerical model of the bridge structure is constructed and the pushover curve of the structure is calculated, both in longitudinal and transverse directions. The pushover loading pattern is in accordance with the sum of the modal shapes, utilizing at least 90% of the total mode participation. In order to determine the seismic demand values, the deformations of the structural components are recorded at each step of the pushover process.
2. Second, the goal is to simplify the 3-D structure of the bridge with an equivalent 3DOF system with equivalent mass and capacity curve for the examined bridge in both directions.
3. Third, the time-history analysis of the 3DOF system is performed for a ground motion scaled to the desired IM level. The orthogonal components of the earthquake are randomly applied along bridge longitudinal and transverse directions. The 3DOF system represents the capacity in both directions according to the previous step.
4. Fourth, the performance point of the structure (i.e., the intersection of the capacity curve with the response spectrum) is determined in both directions.
5. For each direction, the demand of all bridge components -at the stage equivalent to the performance point in pushover analysis- is recorded as the engineering demand parameter (EDP). The Square-Root-of-Sum-of-Squares (SRSS) of the EDPs along the two directions is considered as the EDP for each ground motion.

6. Based on the normalized fitting function of the error (ε_{EDP}), a large random number n_t (i.e., 10^6) is generated and added to the demand value (EDP_{IM}) obtained from the fifth step.
7. For a given limit state, n_t random numbers are generated for each bridge component based on the distribution assumed for that component capacity (given in Rezaei et al. (2023)). The $EDP_{IM} + \varepsilon_{EDP}$ values and resulting capacity are compared to generate a $n_t \times 1$ vector consisting of 1's and 0's, wherein "1" indicates survival (Demand < Capacity) and "0" denotes failure (Demand > Capacity). The probability of failure is the ratio of n_f to n_t (where n_f is the number of failures).
8. Steps 6 and 7 are repeated to obtain the failure probability for all IM levels. Lastly, the fragility curve parameters (median and dispersion) are estimated by logarithmic fitting of IM values versus collapse probability.

3 NUMERICAL MODELING OF IRREGULAR BRIDGES

In this study, multi-span continuous box girder RC bridges with irregularities are investigated. These irregularities include unbalanced stiffness, skewness and horizontal curvature. The examined bridges have 2, 3, and 4 spans and bents with different number of columns. Seat-type abutments with elastomeric bearing pads have been used. The bridge deck placement on elastomeric bearing pads can lead to collision and deck unseating. The structural details and the calculation of the element properties for the bridge models are typical for bridges in California, as defined by Ramanathan (2012).

Table 1. Four cases of pier heights for the unbalanced bridges, i.e., α_{U1}, α_{U2}, α_{U3} are height factors for 1st, 2nd, and 3rd bents, respectively.

Irregularity	Two-span bridge			Three-span bridge				Four-span bridge				
	Class name	subclass	α_{U1}	Class name	subclass	α_{U1}	α_{U2}	Class name	subclass	α_{U1}	α_{U2}	α_{U3}
Regular	R2	R2	1	R3	R3	1	1	R4		1	1	1
Slight	-		-	U3	US3	1	1.5	U4	US4	1	1.5	2
Moderate	-		-		UM3	1	2		UM4	1	2	3
Extreme	-		-		UI3	1	3		UI4	1	3	4

Table 2. Four cases of skewness angle, α_S, for the skewed bridges.

Irregularity	Two-span bridge			Three-span bridge			Four-span bridge		
	Class name	subclass	α_S	Class name	subclass	α_S	Class name	subclass	α_S
Regular	R2	R2	0°	R3	R3	0°	R4	R4	0°
Slight	S2	SS2	15°	S3	SS3	15°	S4	SS4	15°
Moderate		SM2	30°		SM3	30°		SM4	30°
Extreme		SI2	45°		SI3	45°		SI4	45°

Table 3. Four cases of deck radius, R, for the curved bridges.

Irregularity	Two-span bridge				Three-span bridge				Four-span bridge			
	Class name	subclass	α_C	R(m)	Class name	subclass	α_C	R(m)	Class name	subclass	α_C(m)	R
Regular	R2	R2	0°	∞	R3	R3	0°	∞	R4	R4	0°	∞
Slight	C2	CS2	45°	265	C3	CS3	45°	265	C4	CS4	45°	265
Moderate		CM2	90°	132		CM3	90°	132		CM4	90°	132
Extreme		CI2	135°	66		CI3	135°	66		CI4	135°	66

With respect to unbalanced bridge configurations, four height factors have been considered for the piers, while each factor corresponds to a certain level of irregularity. The height ratios of columns (α_U) for 2-, 3-, and 4-span bridges are given in Table 1. Evidently, there is no

unbalanced pier in 2-span models, as there is only one pier. Table 2 presents the skew angle (α_S) values, i.e., 0° (for straight bridges) 15°, 30°, and 45°; for 2-, 3-, and 4-span skewed bridges. Lastly, the main parameter for the curved bridges is the radius of the deck in the horizontal plane. Four curved bridge subclasses have been analysed with different deck radii varying from infinity, representing a straight bridge, to a sharp curve radius. Table 3 lists the radius of the curved deck (α_C) and deck radius (R) for 2-, 3-, and 4-span bridges. The subtended angle is defined as the length ratio of the bridge to its curvature radius.

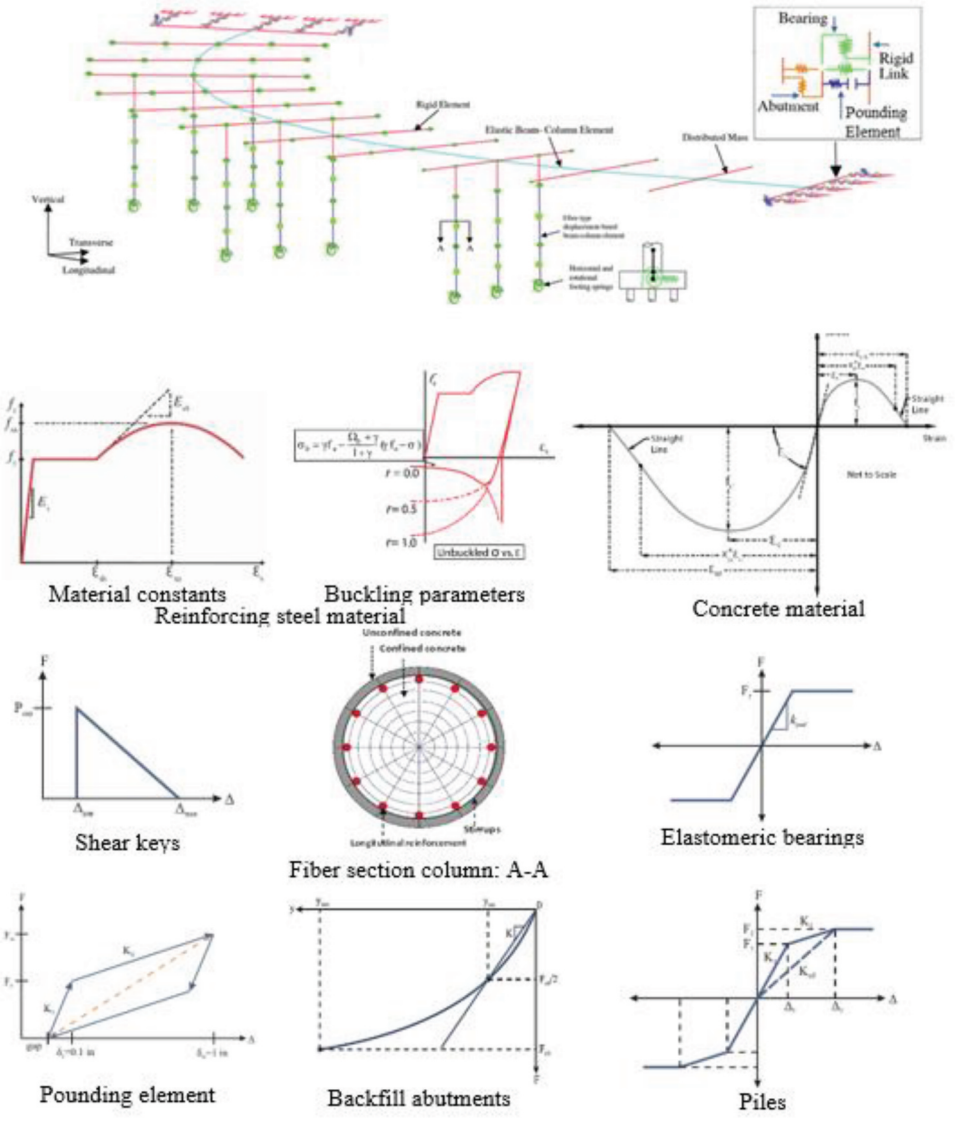


Figure 1. Finite element modeling details of bridge components.

The dynamic non-linear analyses of the bridges have been performed by modeling different bridge components as shown in Figure 1, using OpenSees software (McKenna, 2011) and considering the non-linear response of the materials. In addition, geometrical non-linearities have also been included in the analyses. Inherent damping is modeled utilizing Rayleigh damping. Other sources of damping (hysteretic) have been explicitly modeled due to non-linear force-deformation

properties. The results are presented as the seismic demand of the bridge components. The numerical modeling of bridge elements is briefly described in the sequence, while more details can be found in Rezaei et al. (2020). It should be noted that the validity of the adopted computational approaches for modeling various bridge components has been proven in several relevant studies (e.g., Rezaei et al. (2020, 2022a); Moayeddi et al. (2023)).

The 160 earthquake records used in this investigation are derived from Baker et al. (2011). These ground motions represent uncertainties with respect to potential earthquake (e.g., soil type, magnitude and focal depth) and are divided into four sub-groups, thus, each set includes forty unscaled records. More details about these four suites can be found in Baker et al. (2011). In the present study, the spectral acceleration for one second period for 5% of critical damping, S_a (1.0s), has been adopted as IM. This selection is in accordance with the extensive studies conducted by Ramanathan (2012) to derive the appropriate IM for bridges in California.

The input data of the examined bridge models are derived based on the distribution functions of the random variables. The bridge models are randomly subjected to 160 pairs of excitations in both directions. In the next step, the preferable irregularity level for each bridge class is selected and the irregular models are generated. Accordingly, 4320 non-linear time-history analyses have been conducted and the resulting EDP values have been obtained for each pair of bridge-ground motion models. These results are used for validating the proposed simplified approach. More specifically, the improved 3D FRACAS method has been applied to estimate the EDP values for each simulation. The differences between each 6 EDPs for the different bridge classes are calculated and a suitable distribution function is used for their fitting. Subsequently, these error distribution functions are used to improve the 3D FRACAS method. Lastly, the results of the proposed 3D FRACAS methodology are compared with those derived from NTHA to assess its accuracy and computational performance.

Table 4. Mean and standard deviations of the fitted normal distribution functions for the examined EDPs.

Bridge Class	CCD		SUA		EBD		APD		AAD		ATD	
	μ	σ	μ	σ	μ	σ	μ	σ	μ	σ	μ	σ
R2	0.83	0.21	0.83	0.49	0.67	0.28	1.73	0.78	1.42	1.34	1.90	1.18
R3	0.82	0.20	0.85	0.51	0.69	0.32	1.70	0.80	1.44	1.42	1.99	1.14
R4	0.86	0.23	0.85	0.50	0.73	0.33	1.77	0.82	1.45	1.46	1.89	1.17
U3	0.84	0.22	0.85	0.50	0.72	0.32	1.79	0.77	1.36	1.29	1.84	1.18
U4	0.88	0.24	0.84	0.48	0.73	0.32	1.84	0.78	1.42	1.36	1.76	1.15
C2	0.82	0.20	0.85	0.50	0.73	0.34	1.71	0.80	1.26	1.17	2.16	1.13
C3	0.84	0.22	0.92	0.54	0.76	0.35	1.72	0.80	1.38	1.33	2.07	1.13
C4	0.85	0.23	0.90	0.53	0.76	0.35	1.73	0.80	1.28	1.23	1.95	1.16
S2	0.83	0.21	0.80	0.46	0.68	0.30	1.72	0.80	1.27	1.21	1.88	1.20
S3	0.83	0.21	0.87	0.51	0.71	0.31	1.75	0.79	1.43	1.33	1.93	1.17
S4	0.84	0.23	0.85	0.50	0.72	0.32	1.72	0.80	1.27	1.26	1.80	1.18

4 RESULTS AND DISCUSSION

As described in Section 2, in order to improve the standard 3D FRACAS methodology, it is necessary to determine the error histogram of EPDs. The mean values (μ) and standard deviations (σ) of the fitted normal distribution functions for the examined EDPs are shown in Table 4, in which the first index denotes the bridge type, while the number corresponds to bridge spans. More specifically, indexes R, U, C and S correspond to regular, unbalanced, curved and skewed bridges, respectively. According to the obtained results, the normalized fitting distributions on the errors exhibit better fitting for SUA, CCD and EBD demand parameters. In contrast, the fitting distribution functions on APD, AAD, and ATD errors exhibit higher dispersion. Hence, the obtained values for APD, AAD and ATD seismic responses

have slight differences with the corresponding ones of the NTHA method. It is stressed that the results in Table 4 can be generalized to all bridges with similar characteristics, i.e., they can be used in future studies without needing to perform NTHA again.

In the sequence, the fragility curves corresponding to the damage states presented in Rezaei et al. (2023) are presented. Indicatively, Figure 2 displays the fragility curves for all EDPs (i.e., CCD, SUA, EDB, APD, AAD and ATD) of the S3 bridge. Regarding the other bridge classes, due to space limitations, error statistics are presented and compared. It is observed that the improved 3D FRACAS method effectively improves the estimation of fragility curves for different limit states. This is more pronounced in estimating CCD, SUA and EBD, compared to APD, AAD and ATD parameters. The mean of percentage differences of fragility parameters has also been investigated via comparisons with NTHA results. The improved 3D FRACAS method has a mean percentage difference of approximately 18% in estimating all EDP parameters.

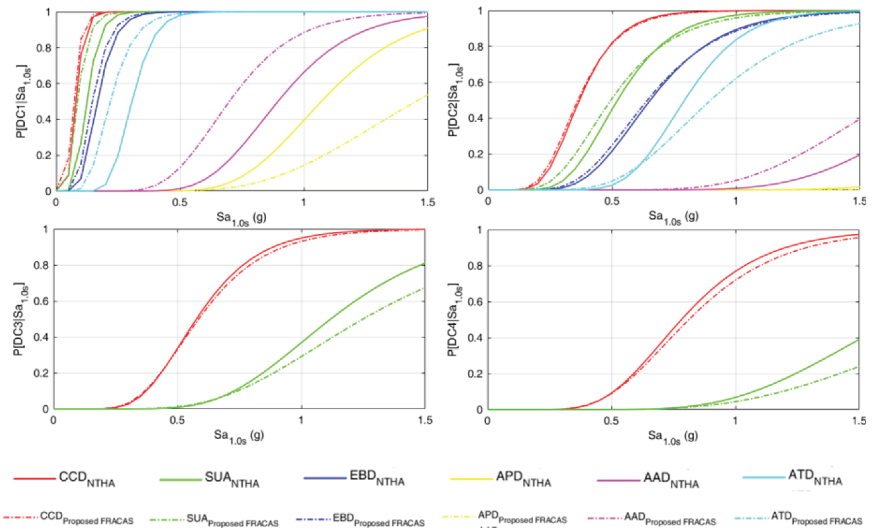


Figure 2. Comparison of fragility curves for S3 bridge for different damage states.

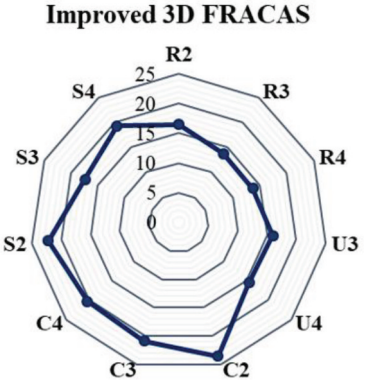


Figure 3. Mean error percentage of the median of fragility curves for all bridge classes.

Figure 3 presents a comparison of the mean error percentage of the median of fragility curves (utilizing NTHA results) for the improved method for all bridge classes. In this comparison, all four damage states and number of spans are taken into account. The average

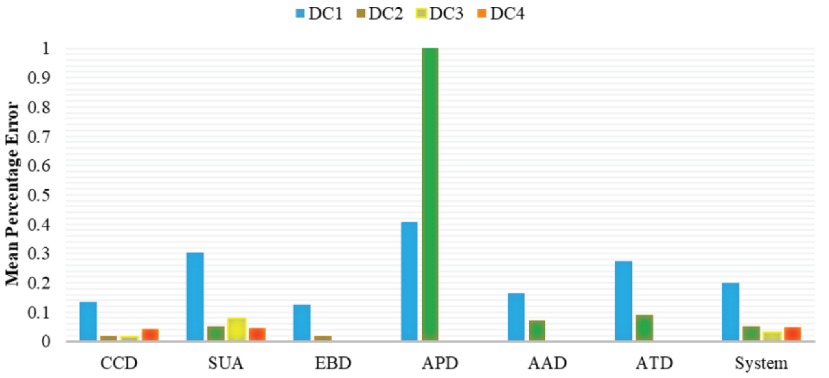


Figure 4. Mean percentage error of the improved 3D FRACAS compared to NTHA method.

error values for the improved method are 14.7, 15.8, 21.6, and 19.6%, respectively. It should be noted that this difference is mainly due to the abutment-related parameters. By ignoring the abutment parameters, the mean error of the improved method is 8%. Considering the complexities of irregular bridges simulations, as well as material, geometry and ground motion uncertainties, the obtained results are considered satisfactory.

Figure 4 depicts the mean percentage error of fragility median value of the improved 3D FRACAS compared to NTHA method based on different damage levels and EDPs. The comparison of the entire bridge system fragility shows that the average error of 8% in improved 3D FRACAS, while in the three damage levels of DC 2, 3 and 4, the error is less than 5%. A comparison of system fragility for bridge class S3 is shown in Figure 5.

Finally, the comparison of computational effort required in this study shows that, using the same computational environment, the computing time ratio of the improved 3DFRACAS method versus NTHA is equal to approximately 0.13. More specifically, the time of a NTHA is on average equal to 1796 seconds, while the duration of the analysis is substantially reduced to 240 seconds when using the improved 3DFRACAS method, i.e., the proposed method achieves a 87% reduction in computational cost for each analysis. Moreover, it should be stressed that in order to calculate the total computational cost, the number of considered IMs for the generation of fragility curves should be multiplied with the time needed for a single analysis.

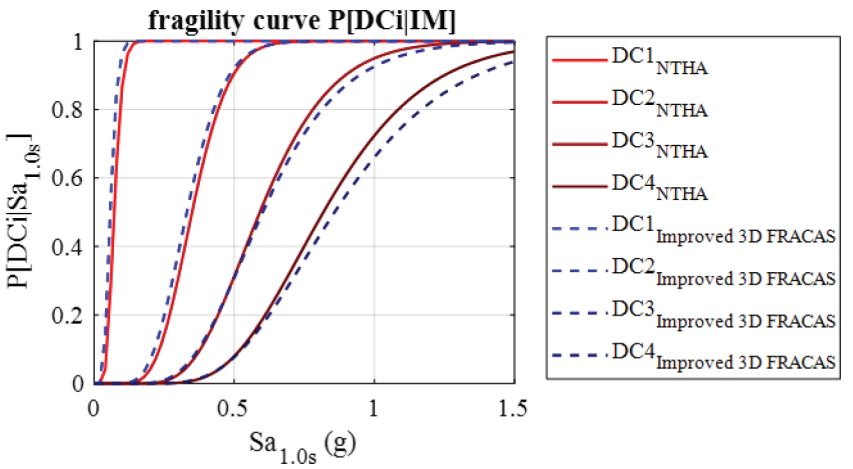


Figure 5. Comparison of system fragility curves for S3 bridge for different damage states.

5 CONCLUSIONS

This study aims to establish an efficient methodology for the development of fragility curves for regular and irregular RC Bridges using non-linear static analysis in a probabilistic manner, by achieving an optimal balance among efficiency, accuracy and computational cost. Accordingly, an efficient 3D FRACAS method has been proposed and implemented for the seismic fragility analysis of box-girder highway bridges. Three types of irregularities including unbalanced, horizontally curved, and skewed bridges have been examined, for three irregularity levels (slight, moderate and extreme). Furthermore, uncertainties related to mechanical, geometrical and ground motion characteristics have been considered.

In total, 4320 NTHA analyses have been conducted for the examined two-, three-, and four-span bridge models and the 160 records. For each EDP, an appropriate distribution function is fitted on the error. Accordingly, an efficient methodology is utilized for developing seismic fragility curves using the obtained error distribution functions. The presented results justify that the improved method can reliably estimate the EDPs with acceptable accuracy and substantially smaller computational cost compared to NTHA, i.e., approximately 87% less computing time per analysis on average.

The proposed method can provide an acceptable estimation of fragility curves for unbalanced, skewed, and curved bridges despite all complexities involved. It should be noted that the improved 3D method has been examined herein only for box-girder RC bridges. Thus, in future extensions other bridge types can be investigated as well as other structures, e.g., irregular buildings. Furthermore, the improved 3D FRACAS method needs to be further enhanced in order to estimate more accurately the response in terms of parameters related to abutments, which presented the highest errors, by considering support conditions for the simplified equivalent structure that are more suitable with the characteristics of the abutments.

REFERENCES

Baker, J.W., Lin, T., Shahi, S.K. & Jayaram, N. 2011. New ground motion selection procedures and selected motions for the PEER transportation research program. PEER Report, Pacific Earthquake Engineering Research Center, CA.

Ramanathan, K.N. 2012. Next generation seismic fragility curves for California bridges incorporating the evolution in seismic design philosophy. PhD Thesis, Georgia Institute of Technology, GA.

Rezaei, H., Arabestani, S., Akbari, R. & Noroozinejad Farsangi, E. 2022a. The effects of earthquake incidence angle on the seismic fragility of reinforced concrete box-girder bridges of unequal pier heights. Structure and Infrastructure Engineering, 18(2): 278–293.

Rezaei, H., Zarfam, P., Golafshani, E. M. & Amiri, G. G. 2022b. Seismic fragility analysis of RC box-girder bridges based on symbolic regression method. Structures, 38: 306–322.

Rezaei, H., Moayyedi, S. A. & Jankowski, R. 2020. Probabilistic seismic assessment of RC box-girder highway bridges with unequal-height piers subjected to earthquake-induced pounding. Bulletin of Earthquake Engineering, 18(4): 1547–1578.

Rezaei, H., Zarfam, P., Golafshani, E. M. & Amiri, G. G. 2023. Development of seismic demand prediction models for bridges based on probability approach using symbolic regression method. Computers & Structures, 282, 106991.

Rossetto, T., Gehl, P., Minas, S., Galasso, C., Duffour, P., Douglas, J. & Cook, O. 2016. FRACAS: A capacity spectrum approach for seismic fragility assessment including record-to-record variability. Engineering Structures, 125: 337–348.

McKenna, F. 2011. OpenSees: a framework for earthquake engineering simulation. Computing in Science & Engineering, 13(4): 58–66.

Moayyedi, S. A., Rezaei, H., Kalantari, A. & Jankowski, R. 2023. Effects of deck-abutment pounding on the seismic fragility curves of box-girder highway bridges. Journal of Earthquake Engineering, https://doi.org/10.1080/13632469.2023.2283004.

Bridge Maintenance, Safety, Management, Digitalization and Sustainability – Jensen, Frangopol & Schmidt (eds)
© 2024 The Author(s), ISBN 978-1-032-77040-6
Open Access: www.taylorfrancis.com, CC BY-NC-ND 4.0 license

Connectivity of post-earthquake bridge networks under aging of isolators

H. Matsuzaki
National Defense Academy of Japan, Yokosuka, Japan

ABSTRACT: In this study, the effects of improving the seismic performance of existing bridges by seismic isolation on the post-earthquake connectivity of a road network were investigated. As a result, it was shown that the bridge which should be retrofitted to improve the seismic performance in terms of reducing the probability of disconnection between the Origin-Destination (OD) pair is significantly affected not only by the seismic hazard but also by the spatial correlation of the intensity of ground motions, which depends on the distance between the bridge sites.

1 INTRODUCTION

Road networks play important roles during the post-earthquake rescue and recovery in the communities. Bridges are the most vulnerable components of road networks and susceptible to seismic damage (Gidaris et al., 2017). Seismic isolation is one of the key technologies for improving the seismic performance of existing bridges and maintaining the traffic function after the seismic events. During the 2011 Tohoku earthquake and the 2016 Kumamoto earthquake, rupture of laminated rubber bearings and large cracks in lead rubber bearings occurred at several bridges (Akiyama et al., 2020; Takahashi & Hoshikuma, 2013). Matsuzaki (2022) showed that the seismic safety of seismically isolated bridges can be improved by setting an adequate capacity ratio between the isolator and the column, as it can avoid the rupture of the isolator under extreme ground motions even if the aging deterioration of isolators is considered.

However, it is necessary to investigate the effects of improving the seismic performance of existing bridges by seismic isolation on maintaining the traffic function as a road network. In this study, the effects of improving the seismic performance of existing bridges by seismic isolation on the probabilistic post-earthquake connectivity of a road network (Firdaus et al., 2023) will be discussed.

2 A BRIDGE NETWORK ANALYSED

2.1 *Road network with bridges*

A hypothetical road network in Yamagata Prefecture, Japan shown in Figure 1 was analysed in this study. The hypothetical road network is located near the northern part of the western boundary fault zone of the Yamagata basin, which would cause an earthquake with a moment magnitude of 6.8 (National Research Institute for Earth Science and Disaster Resilience, 2023). The locations and fault distances of the bridges are listed in Table 1.

2.2 *Bridges*

The existing non-isolated bridges (ENI) analysed are multi-span continuous steel girder highway bridges on the stiff soil with an $AVS30$ of 400 m/s, all assuming identical bridge configurations shown in Table 2. The effects on the post-earthquake connectivity of the road network are evaluated by retrofitting only one of the nine bridges at the site shown in Table 1 with the isolators shown in Table 3. The capacity ratio of Bridges I-570 and I-700 calculated based on Matsuzaki (2022) is 0.91 and 1.25, respectively.

DOI: 10.1201/9781003483755-73

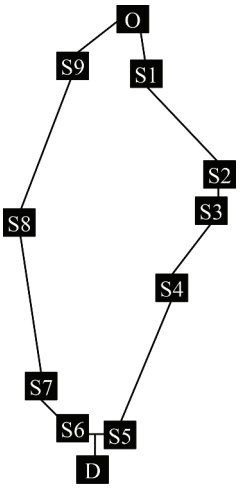


Figure 1. Road bridge network analysed.

Table 1. Location of the bridges and fault distance.

Bridge site	Longitude	Latitude	Fault distance (km)
S1	38.694826	140.311336	4.9
S2	38.611432	140.388223	7.8
S3	38.581771	140.380052	8.0
S4	38.519421	140.337769	6.6
S5	38.397693	140.283116	6.0
S6	38.404320	140.233099	4.2
S7	38.438538	140.199967	5.5
S8	38.572931	140.176912	9.8
S9	38.701724	140.233756	9.2

Table 2. Configurations of the existing reinforced concrete bridge columns.

Section size (m)	Height (m)	Mass (ton)	Longitudinal reinforcement ratio (%)	Volumetric ratio of tie (%)
3.2 × 2.6	14.0	397	1.2	1.0

Table 3. Configurations of the isolators.

Bridge	Effective size (mm)	Total thickness of rubber (mm)	Lead plug	Primary shape factor	Secondary shape factor
I-570	570 × 570	84	4 × ϕ80	6.8	6.8
I-700	700 × 620	96	4 × ϕ100	5.1	6.5

3 SEISMIC HAZARD AND SEISMIC FRAGILITY ASSESSMENT

3.1 *Seismic hazard assessment*

The spatial correlation of seismic hazard intensity at the bridge site is needed to discuss the connectivity of the road network. Wang and Takada (2005) discussed the microspatial correlation of the intensity of ground motions. The variability of the intensity of ground motions at

different sites during an earthquake can be expressed using a predicted component and a residual component for each sites as:

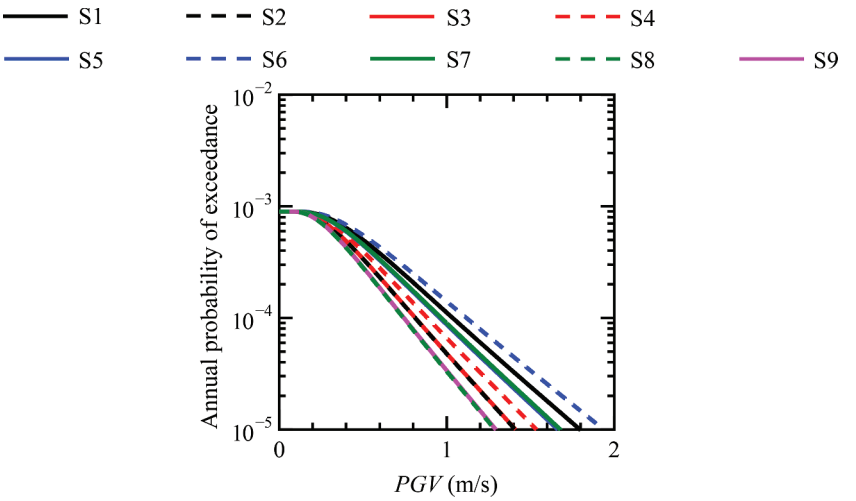


Figure 2. Seismic hazard curves at the bridge sites.

$$\log PGV_i = \log \overline{PGV} + \varepsilon_i \tag{1}$$

where $\overline{PGV}$ is the trend component and ε_i is a normal random function at bridge site i with mean zero and the standard deviation σ_{PGV}.

The trend component at the ground surface $\overline{PGV}$ is calculated as:

$$\overline{PGV} = AF_i \cdot \overline{PBV} \tag{2}$$

where $\overline{PBV}$ is the trend component at the engineering bedrock and AF_i is the amplification factor at the bridge site i calculated as:

$$\log AF_i = -0.852 \log\left(AVS30_i / V_{S,B}\right) \tag{3}$$

where $AVS30_i$ is the average shear-wave velocity in the subsurface from the surface to a depth of 30 m at the bridge site i. $V_{S,B}$ is the shear-wave velocity at the engineering bedrock.

Using the attenuation equation proposed by Si and Midorikawa (1999), the trend component at the engineering bedrock $\overline{PBV}$ is calculated as:

$$\log \overline{PBV} = 0.58M_w + 0.0038D - 1.29 - \log\left(X + 0.0028 \times 10^{0.50M_w}\right) - 0.002X \tag{4}$$

where M_w is the moment magnitude, D is the fault depth at the fault center, and X is the fault distance. The engineering bedrock in Equation (4) is defined as a shear-wave velocity of 600 m/s ($V_{S,B}$ = 600 m/s) and σ_{PGV} is treated as 0.23 (Si & Midorikawa, 1999).

The seismic hazard curves associated with the fault distance shown in Table 1 are shown in Figure 2.

Wang and Takada (2005) proposed an exponential decay function to model the site-to-site correlation of the intensity of ground motions during an earthquake expressed as:

$$\rho_{ij} = \exp\left(-\Delta_{ij}/b_c\right) \tag{5}$$

where ρ_{ij} is a correlation coefficient between bridge sites i and j, Δ_{ij} is the distance between bridge sites i and j, and b_c is the correlation distance. b_c = 30 km was adopted as the correlation distance in this study, as it has been reported that the correlation distance is approximately 30 km if the peak velocity at the engineering bedrock is used as the seismic intensity (Sokorov & Wenzel, 2013; Wang & Takda, 2005).

To calculate the site-to-site correlated intensity of ground motions, the correlation matrix **C** can be expressed as:

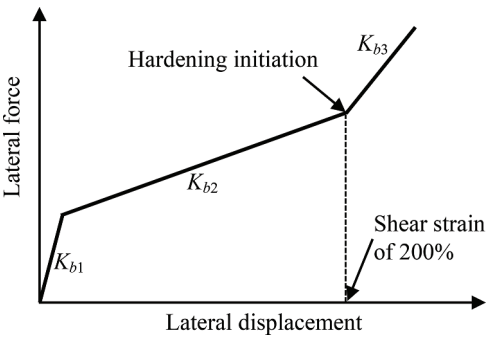


Figure 3. Skeleton of the lateral force–lateral displacement relationship of lead rubber bearings.

$$\mathbf{C} = \begin{pmatrix} 1 & \rho_{12} & \cdots & \rho_{1n} \\ \rho_{21} & 1 & \cdots & \rho_{2n} \\ \vdots & \vdots & \ddots & \vdots \\ \rho_{n1} & \rho_{n2} & \cdots & 1 \end{pmatrix} \tag{6}$$

where n is the total number of the bridge sites (n = 9 in this study).

A lower triangular matrix is obtained by using Cholesky decomposition as:

$$\mathbf{C} = \mathbf{L}\mathbf{L}^T \tag{7}$$

The residual error ε_i in Equation (1) is calculated as:

$$\varepsilon = \mathbf{L}\mathbf{r} \tag{8}$$

where **r** is a vector containing independent normal random variables with the mean zero and the standard deviation equal to σ_{PGV}.

3.2 *Seismic fragility assessment*

In the seismic fragility assessment, dynamic nonlinear response analysis was conducted in the longitudinal direction by idealizing a reinforced concrete column with isolators as a two-degree-of-freedom model. Lead rubber bearings were idealized based on a tri-linear model considering strain hardening of rubber, as shown in Figure 3. In Figure 3, the ratio of K_{b1} to K_{b2} was set as 6.5:1 based on the Japan Road Association (2018) and the ratio of K_{b3} to K_{b2} was set based on Naito et al. (2017). The skeleton and hysteresis of reinforced concrete columns were idealized based on bi-linear model and Takeda degrading stiffness model by Takeda et al. (1970), respectively. The evaluating method for the performance of isolators considering aging deterioration is based on Matsuzaki (2022).

The ultimate displacement of the column and the rupture strain in shear of rubber layer of isolators were adopted as the structural capacity in the seismic fragility assessment.

$$g_1 = \chi_{ls3}\delta_{ls3} - \delta_{\max} \tag{9}$$

$$g_2 = \chi_{rup}\gamma_{rup} - \gamma_{\max} \tag{10}$$

where δ_{ls3} is the ultimate displacement of the column (Japan Road Association, 2017), χ_{ls3} is the model uncertainty associated with the ultimate displacement (Japan Road Association, 2023), γ_{rup} is the rupture strain in shear, χ_{rup} is the model uncertainty associated with the rupture strain in shear (Adachi, 2002), and $\delta_{\max}$ and $\gamma_{\max}$ are the peak responses of the column and isolator, respectively. If g_1 in Equation (9) or g_2 in Equation (10) is negative, the bridge cannot be restored immediately after the seismic event and is considered to be impassable. Uncertain factors considered in the seismic fragility assessment are listed in Table 4.

Table 4. Uncertain factors considered in the seismic fragility assessment.

Uncertain factor		Distribution	Characteristic value	Coefficient	
				Mean	C.O.V
Superstructure	Mass	Normal	600 ton	1.05	0.05
Isolator	Yield strength	Normal	Calculated based on Japan Road Association (2018)	1.13	0.18
	Shear stiffness	Normal	Calculated based on Japan Road Association (2018)	1.04	0.04
	K_{b3}/K_{b2}	Normal	–	3.1	0.09
	Rupture strain	Normal	250%	1.34	0.11
Column	Compressive strength of concrete	Normal	23.5 N/mm^2	1.20	0.10
	Section area of steel bar	Normal	Nominal value	0.97	0.01
	Yield strength of steel bar	Normal	345 N/mm^2	1.20	0.07
	Young's modulus of steel bar	Normal	2.06×10^5 N/mm^2	0.97	0.01
	Mass	Normal	397 ton	1.05	0.05
	Ultimate displacement δ_{ls3}	Normal	Calculated based on Japan Road Association (2017)	1.32	0.23

A total of 25 horizontal components of observed ground motions with a peak ground velocity of 0.50 m/s or higher recorded at stiff soil in Japan selected in Matsuzaki (2022) were used in this study and were adjusted to the required peak ground velocity by varying amplitude properties in the seismic fragility assessment.

The seismic fragility curves of the existing non-isolated bridges (ENI) and retrofitted bridges by seismic isolation (I-570 and I-700) are shown in Figure 4. Hereinafter, I-size of the isolator-*N*y denotes that the bridge I-size of the isolator of time after construction of *N* years. Although Bridge I-570, which is retrofitted by seismic isolation, has improved seismic safety compared to the existing non-isolated bridge ENI, it has a high probability of rupture at the isolators due to an inadequate capacity ratio of 0.91, and the probability of failure at the isolator is further increasing with aging deterioration of the isolator. On the other hand, Bridge I-700, with a sufficient capacity ratio of 1.25, has a sufficiently low probability of rupture at the isolator and is not susceptible to aging deterioration of the isolator.

4 PROBABILISTIC CONNECTIVITY ANALYSIS OF THE ROAD NETWORK

In the probabilistic connectivity analysis, the service state of individual bridges should be expressed. Bocchini and Frangopol (2011) represented the in/out service state of the bridges as binary variables. The service state (s_{Bi}) of the bridge at site *i* can be expressed by using the fragility curve (P_{Bi}) of the bridge at site *i* as:

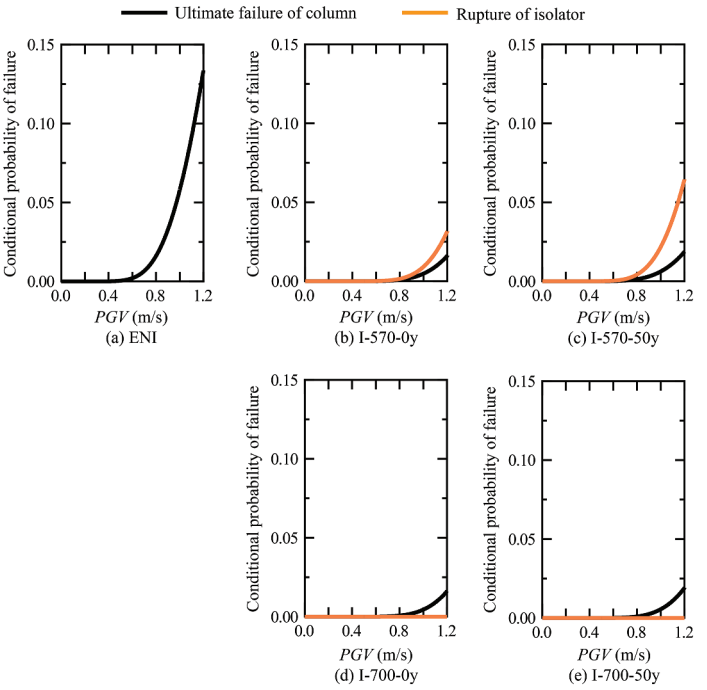


Figure 4. Fragility curves.

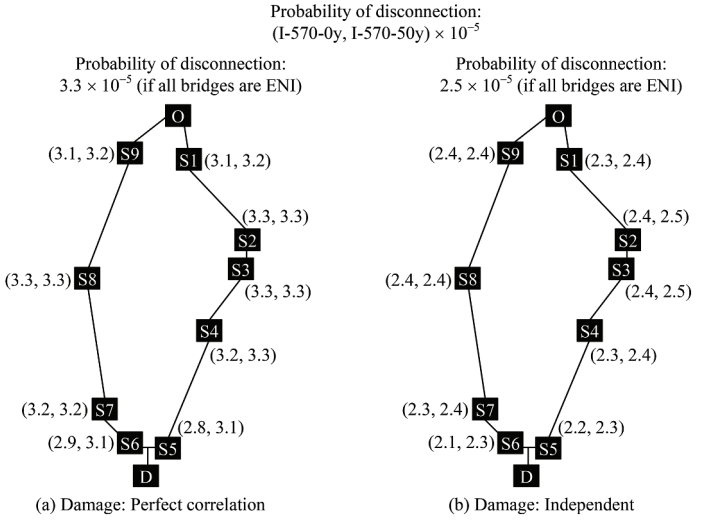


Figure 5. Effects of the bridge site where the existing non-isolated bridge is retrofitted by seismic isolation as Bridge I-570 on the probability of disconnection between the OD pair.

$$s_{Bi} = \begin{cases} 1, \text{if } P_{Bi}(PGV_i|g \le 0) q_{vBi}(\text{impassable}) \\ 0, \text{if } P_{Bi}(PGV_i|g \le 0) < q_{vBi}(\text{passable}) \end{cases} \tag{11}$$

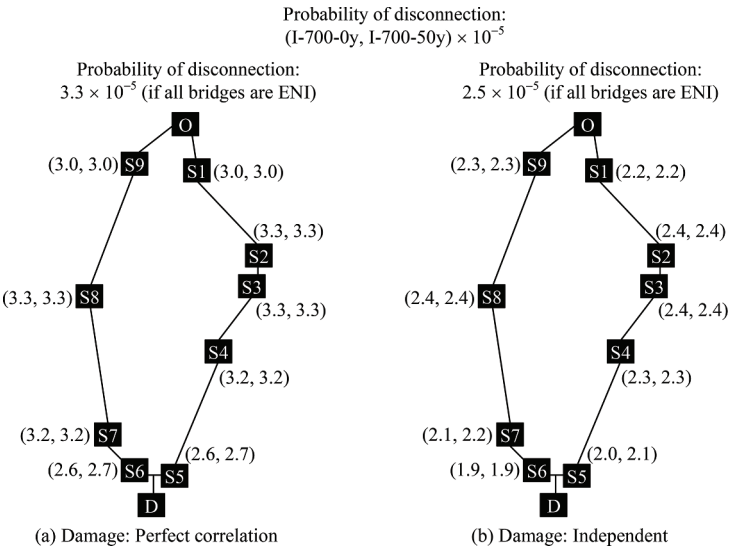


Figure 6. Effects of the bridge site where the existing non-isolated bridge is retrofitted by seismic isolation as Bridge I-700 on the probability of disconnection between the OD pair.

where g is the performance function in Equations (9)–(10), which results in the traffic closure after seismic events, q_{vBi} is the uniformly distributed random number between 0 and 1 associated with the seismic damage. The value of q_{vBi} is assumed perfectly correlated or independent among the bridges analysed. The probability of disconnection between the OD pair can be calculated by adopting the algorithm proposed by Dijkstra (1959) based on Monte Calro simulation by eliminating the impassable route.

Figures 5 and 6 show the effects of the bridge site where the only one existing non-isolated bridge (ENI) is retrofitted by seismic isolation on the probability of post-earthquake disconnection between the OD pair. The target road network has two routes between the OD pair, route O-S1-S2-S3-S4-S5-D and route O-S9-S8-S7-S6-D. The most severe seismic hazard sites within each route are identified as S1 and S6 from Figure 2. Regardless of whether the spatial correlation of damage is perfectly correlated or independent, improving the seismic performance of the bridge at S6 on the route O-S9-S8-S7-S6-D contributes to reducing the probability of post-earthquake disconnection between the OD pair. On the other hand, the results shown in Figures 5 and 6 indicate that the seismic performance of the bridge at S5 should be improved instead of the bridge at S1, where the seismic hazard is the highest on the route O-S1-S2-S3-S4-S5-D. This is due to the fact that in route O-S1-S2-S3-S4-S5-D, even S2, which is closest to S1, the distance between S1 and S2 is 11.4 km, while S6, which is on a different route from the route including S5, is only 4.4 km away from S5, which is significantly influenced by the spatial correlation of intensity of ground motions.

Furthermore, it was confirmed that if the capacity ratio between the isolator and the column is insufficient, the probability of post-earthquake disconnection between the OD pair is affected by the aging deterioration of the isolators, but if the capacity ratio is sufficient, the aging deterioration of isolators has little effect on the probability of post-earthquake disconnection between the OD pair.

5 CONCLUSIONS

Effects of improving the seismic performance of existing bridges by seismic isolation on the post-earthquake connectivity of a road network were investigated in this study. The following conclusions can be drawn:

1. The bridge which should be retrofitted to improve the seismic performance in terms of reducing the probability of post-earthquake disconnection between the OD pair is significantly affected not only by the seismic hazard but also by the spatial correlation of the intensity of ground motions, which depends on the distance between the bridge sites.
2. It was confirmed that if the capacity ratio between the isolator and the column is insuffi-cient, the probability of disconnection between the OD pair is affected by the aging deterioration of the isolators, but if the capacity ratio is sufficient, the aging deterioration of isolators has little effect on the probability of disconnection between the OD pair.

ACKNOWLEDGEMENTS

This study was supported by JSPS KAKENHI Grant Number 23K04018. It is appreciated that strong ground motions were provided by K-NET and KiK-net of NIED, JMA, JAEE and NGA databases of PEER.

REFERENCES

Adachi, Y. 2002. Reliability analysis and limit state design method for isolated bridge structures under extreme ground motions. Doctoral thesis, Kyoto University, Japan.

Akiyama, M., Frangopol, D.M. & Ishibashi, H. 2020. Toward life-cycle reliability-, risk- and resilience-based design and assessment of bridges and bridge networks under independent and interacting hazards: emphasis on earthquake, tsunami and corrosion. *Structure and Infrastructure Engineering* 16(1): 26–50.

Bocchini, P. & Frangopol, D.M. 2011. Generalized bridge network performance analysis with correlation and time-variant reliability. *Structural Safety* 33(2): 155–164.

Dijkstra, E.W. 1959. A note on two problems in connexion with graphs. *Numerische Mathematik* 1(1): 269–271.

Firdaus, P.S., Matsuzaki, H., Akiyama, M., Aoki, K. & Frangopol, D.M. 2023. Probabilistic connectivity assessment of bridge networks considering spatial correlations associated with flood and seismic haz-ards. *Structure and Infrastructure Engineering*. doi: 10.1080/15732479.2023.2276373

Gidaris, I., Padgett, J.E., Barbosa, A.R., Chen, S., Cox, D., Webb, B. & Cerato, A. 2017. Multiple-hazard fragility and restoration models of highway bridges for regional risk and resilience assessment in the United States: State-of-the-art review. *Journal of Structural Engineering* 143(3): 04016188.

Japan Road Association 2017. *Design Specifications for Highway Bridges V Seismic Design*. Tokyo: Maruzen.

Japan Road Association 2018. *Bearing Handbook for Highway Bridges*. Tokyo: Maruzen.

Japan Road Association 2023. *References of seminar on Design Specifications for Highway Bridges*. Tokyo: Maruzen.

Matsuzaki, H. 2022. Time-dependent seismic reliability of isolated bridges considering ageing deterioration of lead rubber bearings. *Structure and Infrastructure Engineering* 18(10-11): 1526–1541.

Naito, N., Mazda, T., Uno, H. & Kawakami, M. 2017. Seismic performance evaluation of LRB considering Mulllins effect and hardening. *Journal of Japan Society of Civil Engineers*, Ser. 1, 73(4): I_499–I_510.

National Research Institute for Earth Science and Disaster Resilience 2023. Japan Seismic Hazard Information Station. https://www.j-shis.bosai.go.jp/en/

Si, H. & Midorikawa, S. 1999. New attenuation relationships for peak ground acceleration and velocity considering effects of fault type and site condition. *Journal of Structural and Construction Engineering (Transactions of AIJ)*, 64(523): 63–70.

Sokolov, V. & Wenzel, F. 2013. Further analysis of the influence of site conditions and earthquake magnitude on ground-motion within-earthquake correlation; analysis of PGA and PGV data from the K-NET and the KiK-net (Japan) networks. *Bulletin of Earthquake Engineering* 11(6): 1909–1926.

Takahashi, Y. & Hoshikuma, J. 2013. Damage to road bridges induced by ground motion in the 2011 Great East Japan Earthquake. *Journal of JSCE* 1(1): 398–410.

Takeda, T., Sozen, M.A. & Nielsen, N.N. 1970. Reinforced concrete response to simulated earthquakes. *Journal of the Structural Division* 96(12): 2557–2573.

Wang, M. & Takada, T. 2005. Macrospatial correlation model of seismic ground motions. *Earthquake Spectra* 21(4): 1137–1156.

Bridge Maintenance, Safety, Management, Digitalization and Sustainability – Jensen, Frangopol & Schmidt (eds)
© 2024 The Author(s), ISBN 978-1-032-77040-6
Open Access: www.taylorfrancis.com, CC BY-NC-ND 4.0 license

Computational analysis of resilience in reinforced concrete railway bridge

A.L. Gamino, R.R. Santos, T.N. Bittencourt & M.M. Futai
Department of Structural and Geotechnical Engineering, School of Engineering, University of Sao Paulo, Sao Paulo, Brazil

ABSTRACT: This paper deals with a proposal for determining and quantifying the structural resilience of railway bridges in reinforced concrete using a computational modeling technique. In the technical literature, structural resilience is a quantitative parameter related to the ability of an asset or its parts to resist eventual damage events (explosions, impacts, fires, or overloads) to be efficiently rehabilitated in the face of loss of performance caused by fortuitous events. Thus, three-dimensional computational models were developed based on real explosion events (unusual disturbance) that caused damage to some structural elements of the evaluated asset using CSi-Bridge v. 21. A FNA (Fast Non-Linear Analysis) dynamic time history analysis was used, which, according to the technical literature, produces greater accuracy and efficiency when compared to the direct integration technique. Damping was also used for all vibration modes. A soil-structure interaction law was applied to the asset's foundations with elastic springs calibrated according to the geometric characteristics of the foundation and soil elements, which produced confinement in the infrastructure elements. The elastic supports in neoprene bridge bearings were modeled using Winkler springs according to the characteristics of the elements used in the construction of the asset and the law of representation of stiffness. The results obtained allowed quantification of the resilience of the degraded structural elements through the dynamic responses obtained in the passage of the railway composition due to the time used during rehabilitation and reinforcement. In this way, the capacity of the structural elements affected by the explosion unusual event was measured and the recovery capacity was evaluated. The proposed proposal opens new horizons for a quantitative assessment of the resilience of structural elements of railway bridges due to unusual degradation events, repair time, and efficient recovery.

1 INTRODUCTION

1.1 *Structural resilience*

Resilience consists of a metric to assess the capacity of a system to withstand unexpected disruptions and to recover efficiently from the induced damage. For civil infrastructure, resilience is typically associated with its capability to maintain a specific service level despite the occurrence of an extreme event and to recover the desired functionality thereafter (Bocchini et al. 2014). The structural resilience study proposed in this work was based on the research developed by Bocchini et al. (2014). Therefore, structural resilience can be determined from a loss of functionality related to a performance reduction due to a fortuitous event (explosions, fires, or impact loads).

In this way, resilience can be associated with displacement, acceleration, velocity, or natural frequency quantified in the structure by computational dynamic analysis techniques, which was the methodology applied in the present paper.

Bocchini et al. (2014) analyzed the concept of resilience applied to the construction and operational costs of road bridges in a more comprehensive way. The basic concept was to analyze maintenance costs combined with the useful life of the asset and its parts using assumptions regarding the flow of vehicles over the bridge. In this study, different types of damage to

DOI: 10.1201/9781003483755-74

the asset were considered; the authors concluded that the joint study between resilience and sustainability should be done using probability techniques.

Uehan (2023) analyzed recent advances in the study of dynamic effects on high-speed railway bridges. In this sense, the author evaluated the dynamic effects of wind action on the bridge structure as well as the support conditions of the superstructure and the behavior of the vehicle on the asset. Additionally, the effects of road irregularities were verified with a monitoring system on board the vehicle. The results obtained were used in computer simulations using the finite element method. The computational results obtained were compared with experimental responses of the asset; the displacements along the span showed an excellent correlation, demonstrating that recent advances in the study of dynamic effects are relevant to the topic.

The integration of the structural resilience concept into the digital twin of an infrastructure asset was proposed by Kaewunruen et al. (2022). The authors used an evolutionary concept between levels of detail of information about railway bridges located in the United Kingdom. The first level corresponds to drawing information (CAD), followed by two-dimensional and three-dimensional details until the integration between engineering and architecture (BIM). The last level of detail corresponds to the digital twin of the asset, which integrates numerical and analytical results, promoting a framework for determining the structure life-cycle and resilience.

Fernandes et. al. (2022) present relevant work related to the resilience of steel bridges. In this study, the authors evaluated the asset conditions of exposure, its failure modes, and the bridge degradation process. Therefore, the bridge performance was evaluated by considering various levels of maintenance, the repair and strengthening costs involved, as well as resilience to different scenarios linked to recovery time. The results obtained by the authors demonstrated that the 50% resilience was not affected by the rehabilitation time, considering a linear resilience function. On the other hand, log-normal resilience functions displayed a reduction of approximately 5% in the bridge resilience, considering repair times of 180 days and 270 days.

In this context, the present paper aims to determine and quantify the structural resilience of a reinforced concrete railway bridge employing computational modeling techniques. The proposed study opens new horizons for a quantitative assessment of the resilience of structural elements of railway bridges due to unusual degradation events, repair time, and efficient recovery.

1.2 *Asset description*

The asset studied in this paper was a six-pan reinforced concrete railway bridge with 180 meters in total length, built in the 80s and located in the northern region of Brazil (Figure 1). The bridge comprises two continuous sections: the first includes two 25-meter spans, and the second has four 25-meter spans. Each section ends with abutments. The bridge presents a hyperstatic configuration, with the superstructure consisting of two longitudinal beams with rectangular cross-sections, transverse beams, and a concrete deck with variable cross-sections. The superstructure is supported on the pile caps by neoprene bridge bearings. The infrastructure comprises pile caps and caissons supported by a rock layer.

The smallest section of the bridge, which is composed of a continuous section with two spans, had one of its piers subjected to an explosion during an act of vandalism that occurred on October 18, 2016. Therefore, due to this unforeseen event, this region was considered for the resilience study proposed in this paper. The damage effect on the asset was taken to the computational model produced in the CSiBridge 21 software by penalizing the stiffness of the affected elements (thickness of the shell elements and Young's modulus) as shown in Figure 2.

Specific details related to numerical modeling calibration, natural frequencies, and vibration modes can be checked in Gamino et. al. (2023). The geometric and mechanical properties used in the computational model of the railway bridge can be found in Table 1.

The stiffness values used in the foundation elements were determined from the soil-structure interaction (SSI) model by Morrison (1993) according to the local characteristics of the soil. Linear springs were applied to represent the lateral confinement effect of the soil. The existing neoprene bearing pads on the pile caps located in axes 4 and 5 (Figure 2) had Winkler spring stiffness using Guerreiro (1993) technique. Table 2 presents the spring stiffness values used in these regions.



Figure 1. Case study bridge: (a) Bridge details, (b) Geometric configuration of the studied region.

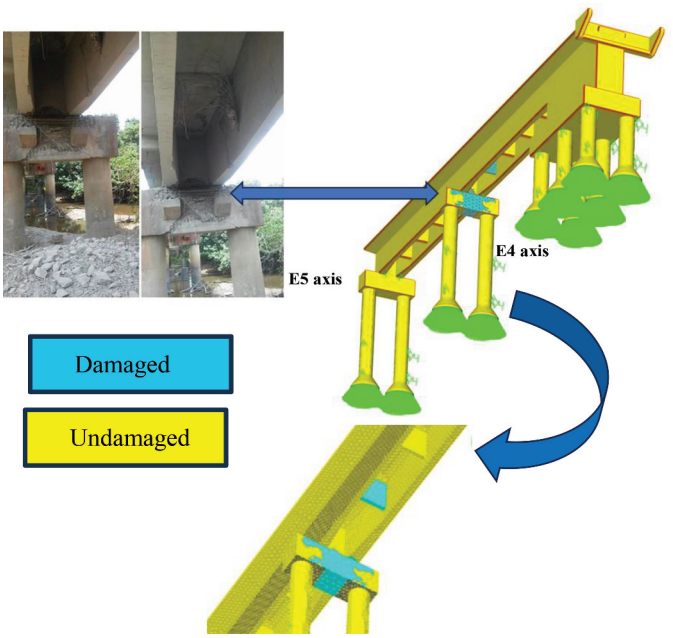


Figure 2. Asset damage and computational strategy.

Table 1. Physical and mechanical parameters are used in the computational model.

Asset part	Concrete Strength (MPa)	Youngs's Modulus (MPa)	Thickness (mm)
Superstructure	18	24091	200
Infrastructure	15	21797	150
Damaged elements	0.5	10	5

Table 2. Winkler spring stiffness values.

Asset region*	Kx (tf/m)	Ky (tf/m)	Kz (tf/m)	Kθx (tf.m/rad)
Caissons top	8134	8134	- - -	- - -
Caissons bottom	10780	10780	- - -	- - -
Neoprene pads E5	3.3	- - -	2120	10.5
Neoprene pads E4	7.8	- - -	8131	55.7

* x axis (longitudinal), y axis (transverse), z axis (vertical)

1.3 *Computational analysis*

Nonlinear time history analysis was used with 200-time steps and an increment of 0.1 s. The damping used in the asset (3.6% for all vibration modes) was obtained from a monitoring campaign carried out by a third-party company. The load conditions of the railway vehicle traveling over the asset at a speed of 60 km/h were used.

The computational model was initially calibrated based on experimental data (Gamino et al. 2023) and subsequently, the imposition of damage to the asset was carried out as shown in Figure 2 and Table 1. Shell finite elements were used throughout the model and an unstructured mesh (Figure 2). Finally, the FNA (Fast Nonlinear Analysis) technique implemented in the CSiBridge v. 21 program was used to obtain the time history traces.

2 DETERMINATION OF STRUCTURAL RESILIENCE

2.1 *Technique employed*

The technique for determining structural resilience in this paper was based on the formulation presented by Bocchini et al. (2014). In this context, resilience can be determined based on the loss of functionality $F(t)$ of the asset or its parts. Functionality can be related to displacements, speeds, accelerations, or even natural frequencies.

The residual functionality after the adverse event (earthquake, explosion, impacts, fires) determines the robustness $Ro(t)$ of the asset. Thus, the loss of functionality $F(t)_{loss}$ will be given by:

$$F(t)_{loss} = 1 - Ro(t) \tag{1}$$

Resilience depends on the asset's recovery time due to $F(t)_{loss}$. Thus, using t_0 for the start time of the rehabilitation of structural elements and t_f the end time, the angular coefficient of the asset recovery function can be defined with a linear approximation:

$$R(t) = \frac{F(t)_{loss}}{t_f - t_0} \tag{2}$$

where $R(t)$ is the rapidity with which the asset was recovered from the fortuitous event and the losses of identified functionalities.

Finally, the resilience triangle can be determined from the geometric figure generated vertically by $F(t)_{loss}$ and horizontally by $F(t)_{loss}/R(t)$.

$$Res(t) = 1 - 0.5\ F(t)_{loss}\ \frac{F(t)_{loss}}{R(t)} \tag{3}$$

where $Res(t)$ represents the resilience of the asset.

2.2 *Loss of functionality using computational modeling*

The assessed loss of functionality refers to the longitudinal velocities (direction "x") in the pile cap located on the damaged E4 axis following an explosion that occurred in 2016 (Figure 2). Two computational models were developed, one with the original undegraded configuration and the other with the degraded elements based on the photographic record obtained during the asset inspection. The dynamic analysis used is detailed in item 1.3 of this paper.

3 RESULTS

3.1 *Computational results*

Figure 3 shows the longitudinal velocities of the damaged and intact pile cap according to the description of the dynamic analysis carried out on the asset. Speed peaks for vehicle passage close to 5s of analysis can be seen.

Table 3 presents the speed peaks obtained in the computational models and the results of loss of functionality and robustness of the asset.

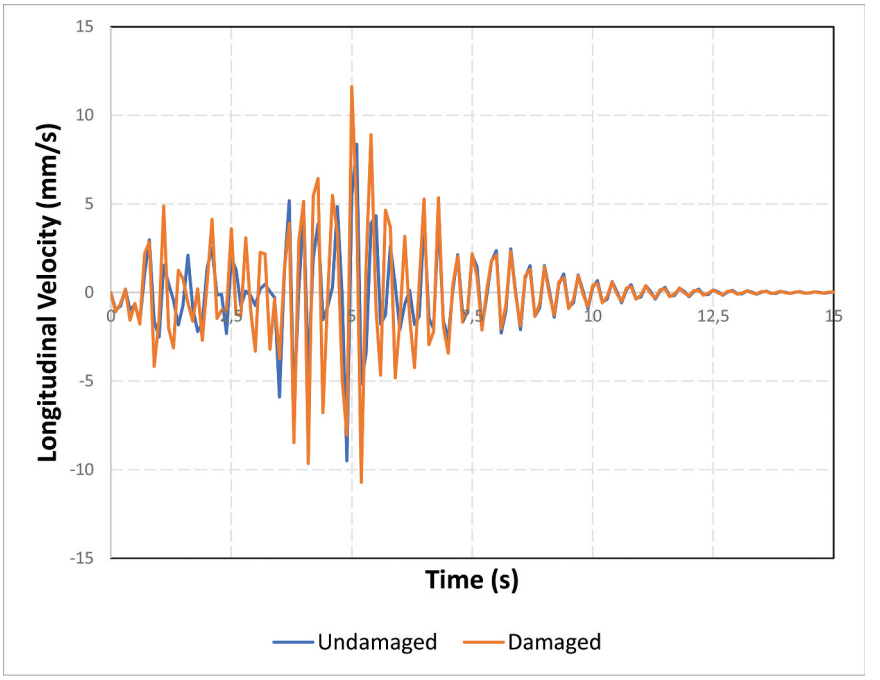


Figure 3. Variation over time of velocities in the studied pile cap.

Table 3. Loss of functionality and robustness.

Computational model	Vx_{peak} (mm/s)	$F(t)_{loss}$ (%)	Ro(t) (%)
Original asset	8.37	- - -	- - -
Damaged asset	11.62	39	61

From a documentary analysis of the asset, related to the identification of the recovery period, it was noticed that the time t_0 corresponded to the date of November 11, 2016, and the time t_f on May 17, 2017. Thus, based on the loss of functionality identified in Table 3 and the recovery time of the asset, we have the resilience triangle as illustrated in Figure 4.

Finally, the resilience of the railway bridge evaluated from Equation 3 was 64% as shown in Table 4. The results for the resilience variables were found based on reliable documents related to the rehabilitation of the asset for local conditions. The studied railway bridge is in an area of difficult access; there was a need to develop a specific reinforcement project in addition to mobilizing trained personnel to rehabilitate the asset.

Table 4. Determination of structural resilience.

Resilience parameter	$t_f - t_0$ (days)	R(t) (%/day)	Res (%)
Value	187	0.208	64

Finally, the effect of asset recovery time was studied, considering official documents and the calibrated computational model developed. The restoration process was performed in three stages:

a. Stage 1: Pile caps recovery (140 days).
b. Stage 2: Recovery of floor beams (spans between girders, 28 days).
c. Stage 3: Recovery of girders (19 days).

Stage 3 was executed with the asset in its original configuration, before the damage event. Computational models were developed that simulated the recovery steps as shown in Figure 5.

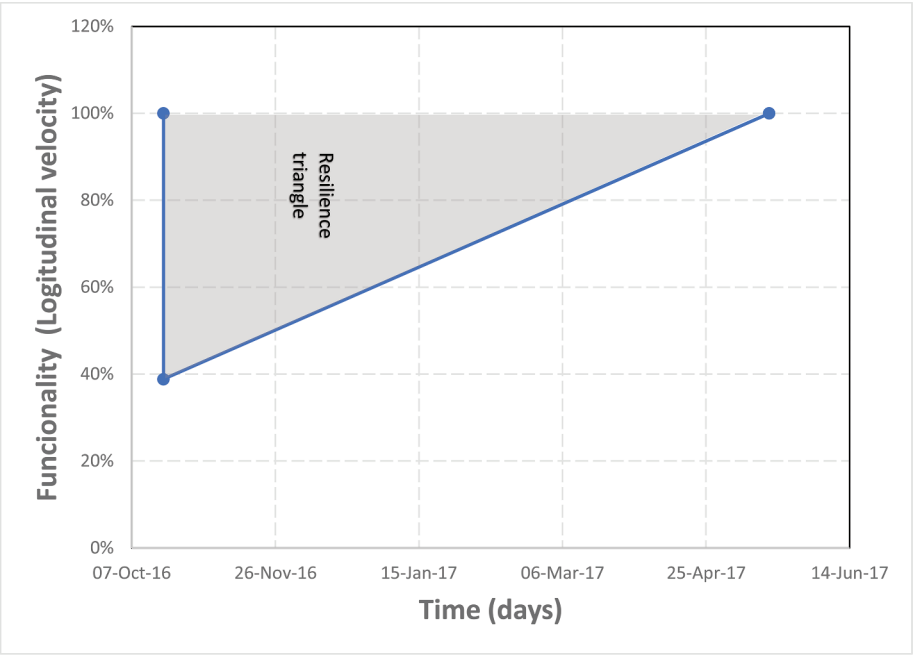
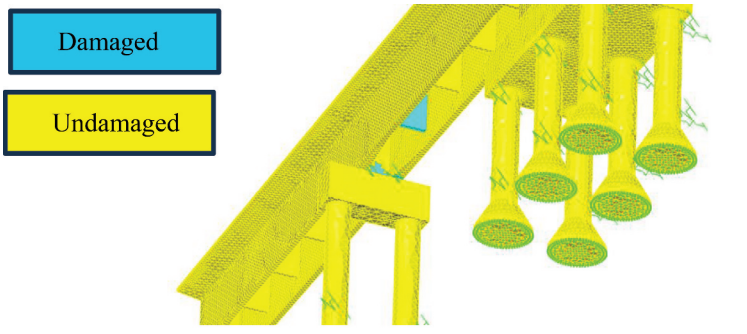
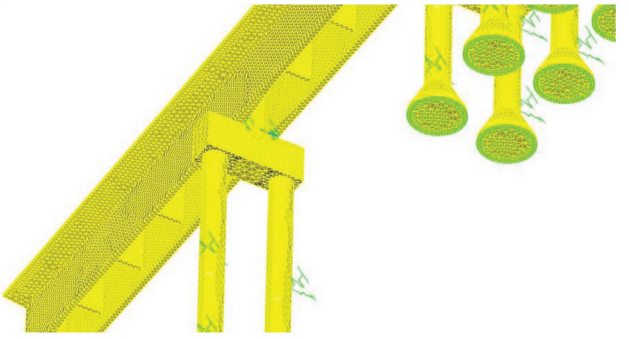


Figure 4. A resilience triangle was obtained for the damaged bridge pier.



a. Stage 1 (pile caps recovery).



b. Stage 2 (girders recovery).

Figure 5. Simulation of asset recovery in computational models.

Velocities peaks were taken from each recovery stage and resilience was calculated over time based on the performance of the asset obtained considering a linear recovery time and the real one obtained from official documents (Figure 6).

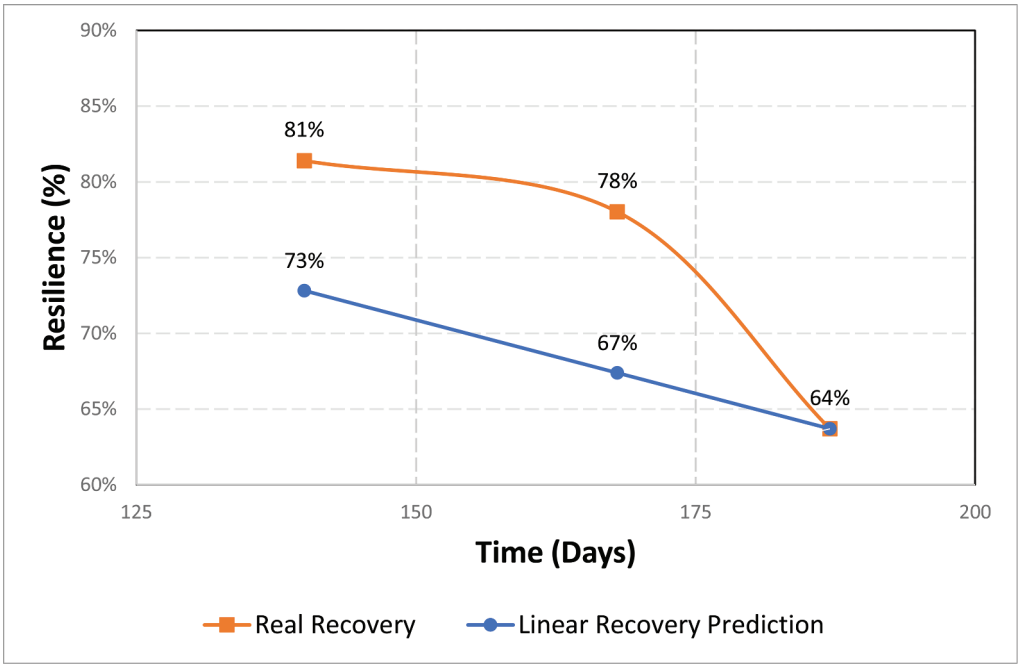


Figure 6. Effect of recovery time on structural resilience.

The results obtained demonstrate a non-linear relationship between resilience and asset recovery time. In the technical literature, probability functions simulate the uncertainties about these variables in the process of determining resilience. In the present work, it was found that linear variations in recovery times do not convey reliability to the resilience obtained.

4 CONCLUSIONS

Considering the results obtained in this paper from the proposed computational model, it is possible to identify the following conclusions:

- The proposed computational model, previously calibrated with experimental results previously obtained in an instrumentation and monitoring campaign (Gamino et. al. 2023), proved capable of predicting the loss of functionality of the asset in the event of an explosion.
- The resilience determined in this paper was directly impacted by the recovery time due to the adverse location of the railway bridge and all the work carried out in generating the reinforcement project and construction team.
- The loss of functionality can be explored in other results from dynamic analysis, such as displacements, accelerations, and natural frequencies; in this way, the minimum resilience of the asset can be determined.
- The recovery time of damaged elements directly affects the resilience of the asset according to a non-linear relationship between these variables.

- Considering the computationally determined loss of 39% for longitudinal velocities in the pile cap and a recovery time of 187 days, a structural resilience of 64% was obtained.
- The Winkler springs used in the soil-structure interaction modeling strategy were fundamental for calibrating the asset and obtaining structural resilience results.

ACKNOWLEDGEMENT

This paper was funded by VALE Catedra Under Rail, FAPESP (grant #2020/02350-2, The São Paulo Research Foundation), and CNPq (The National Council for Scientific and Technological Development, grant #163757/2020-8).

REFERENCES

Bocchini, P., Frangopol, D. M., Ummenhofer, U. & Zinke, T. 2014. Resilience and sustainability of civil infrastructure: Toward a unified approach. *J. Infrastruct. Syst*. 20(2): 1–16.

Fernandes, J. N. D., Matos, J. C., Sousa, H. S. & Coelho, M. R. F. 2022. Life cycle analysis of a steel railway bridge over the operational period considering different maintenance scenarios: Application to a case study. *Advances in Civil Engineering* 2022: 1–18.

Gamino, A. L., Santos, R. R., Bittencourt, T. N., Futai, M. M. & Carvalho, H. 2023. *Computational analysis of a reinforced concrete railway bridge considering the soil-structure interaction. Oxfordshire*: *Taylor & Francis.*

Guerreiro, L.A. 2003. *A borracha na concepção anti-sísmica. Faculdade de Engenharia da Universidade do Porto*. Porto: FEUP.

Kaewunruen, S., AbdelHadi, M., Kongpuang, M., Pansuk, W. & Remennikov, A. M. 2023. Digital twins for managing railway bridge maintenance, resilience, and climate change adaptation. *Sensors* 23 (252): 1–22.

Morrison, N. 1993. Interacción suelo-estructuras: semi-espaço de Winkler. *MSc. Dissertation; Universidad Politécnica de Cataluña*. Barcelona: UPC.

Uehan, F. 2023. Recent Research on Railway-specific Dynamic Issues. *QR of RTRI* 64(2): 81–85.

Bridge Maintenance, Safety, Management, Digitalization and Sustainability – Jensen, Frangopol & Schmidt (eds)
© 2024 The Author(s), ISBN 978-1-032-77040-6
Open Access: www.taylorfrancis.com, CC BY-NC-ND 4.0 license

Assessment of honeycomb cushion for enhancing bridge deck impact protection

H. Mraih, J. Hashemi, R. Kalfat, R. Al-Mahaidi & G. Lu
Swinburne University of Technology, Melbourne, Australia

ABSTRACT: This study examines the suitability of honeycomb panels as a viable protective cushioning system to mitigate the impact of over-height vehicle collisions on bridge girders. Two honeycomb specimens, composed of aluminium alloy 3003 and sharing cross-sections of 300 × 300 mm, with thickness variations of 300 and 150 mm were tested. These panels underwent static load testing to explore their capacity for energy absorption. The findings serve as a proof-of-concept, confirming the potential effectiveness of honeycomb panels as a promising choice for structural applications, particularly as sacrificial anti-impact cushions.

1 INTRODUCTION

The frequency of over-height vehicle collisions with bridge superstructures, specifically girders, poses a significant threat to the infrastructure networks and road users. It can lead to potentially catastrophic consequences that affect public safety and infrastructural integrity. Xu et al. (2012) stated that the percentage of overpasses in Beijing, China, that experienced collisions is around 50%, and the over-height vehicle collisions are approximately 20%. This impact event is also considered a fundamental problem in the USA. Hite (2007) states that the damage of over-height vehicle collisions to the interchange bridges in the USA is estimated to be 61%. Further, Nguyen (2018) claims that a report from the transportation department in the United Kingdom illustrates a significant increase in collisions involving over-height vehicles and bridge girders, rising from 729 incidents in 1990 to 1870 in 1994. This impact event can cause severe damage to the bridge girders (Figure 1-a) or a complete bridge collapse, as occurred to the footbridge on a motorway in Kent, UK (Figure 1-b).



Figure 1. Real-life over-height vehicle collisions with bridge girders: (a) Michigan, USA, 2023 (Pair, 2023); and (b) Kent, UK, 2016 (Nguyen, 2018).

DOI: 10.1201/9781003483755-75

Thus, different impact prevention strategies were defined to mitigate the collision effects on the bridge girders, such as rerouting, warning systems, clearance augmentation (e.g., steel pedestals) (Hite, 2007), and energy-absorber (Yang, 2006, Yang and Qiao, 2008, Yang and Qiao, 2010). While each mitigation strategy has limitations and advantages, energy-absorbing systems can be effectively designed with reduced cost, effort, and installation requirements. These systems need to be designed to absorb as much energy as possible and reduce the translated loads to the protected girder. The repairs may involve replacing the damaged cushion pieces, resulting in lower costs and effort.

In the existing literature, a limited number of studies were identified that explored the application of cushion materials in mitigating over-height vehicle collisions (Sharma, 2010, Xu et al., 2022, Yang and Qiao, 2010). Notably, honeycomb structures, characterised by their hexagonal cell arrangement, have demonstrated remarkable energy-absorbing capabilities. The manufacturing process of honeycomb structures involves bonding thin sheets of material, such as aluminium or composite materials, to create a rigid and lightweight core. When subjected to external forces, the honeycomb's cellular walls collapse in a controlled manner, deforming and absorbing energy through plastic deformation. This controlled deformation efficiently disperses impact energy throughout the structure, preventing concentrated damage and reducing the transmitted forces to the protected components.

Yang and Qiao (2010) adopted one type of honeycomb cushion with an energy-absorbing capacity of 147.2 kJ. Based on their analytical and experimental investigation, they confirmed that their innovative cushion system could be used to protect the girder from impact loads of 4.5 tons (the top part of the over-height vehicles that are involved in the impact event) travelling with 60 km/h (truck's velocity during impact) which was based on the assumption that there is a loss of the applied impact energy due to a bounce back of the impacting project. This paper presents an experimental and analytical assessment of one main component of a proposed hybrid cushion protective system. It is an initial step toward developing the next generation of impact-resistant cushions to protect bridge girders from collisions involving over-height vehicles.

2 EXPERIMENTAL PROGRAM

In this study, two honeycomb panels with hexagonal-shaped cells were tested under static loads. The honeycomb panels were made from aluminium alloy 3003 and manufactured by Foshan City Linwell Honeycomb Hardware Co. (2024). The detailed process of manufacturing honeycomb panels from aluminium involves a series of precise steps. The initial phase is the precision cutting of the solid aluminium alloy into plates. These plates are then stacked together using adhesive to form a consolidated block. The next step involves subjecting this block to hot pressing within a specialised machine. This process facilitates the fusion and melting of the adhesive, forming a solid composite structure. The block is carefully segmented into various heights, which are determined based on the thickness required for the honeycomb samples. The final stage of the manufacturing process is expanding the honeycomb structure. This expansion is a crucial step, and given the substantial thickness required for both the current study and practical applications, the manufacturer emphasises the challenge of achieving uniform expansion across the samples and their cells.

The two honeycomb specimens, with similar cross-sections of 300 $\times$ 300 mm, have respective heights of 150 mm and 300 mm, and both specimens share a foil thickness of 0.06 mm. The measured weights of the samples were 1.673 kg and 2.895 kg, resulting in densities of 124 kg/m^3 and 107 kg/m^3 for the small and large specimens, respectively. This density variance occurred due to the difficulties during the expanding phase for such a high panel's thickness.

The static test was performed using the Instron 5MN Four-column Static Testing Machine at the Smart Structures Laboratory at Swinburne University of Technology, Melbourne, Australia (Figure 2-a). Figure 2-b provides a view of the height of the two test samples. To ensure a stress distribution across the entire area of the samples, two steel plates measuring 400 $\times$ 400 $\times$ 40 mm were positioned on both the top and bottom of each sample, as depicted in Figure 2-c and d. The compression load was applied by moving the upper plate towards the lower one.

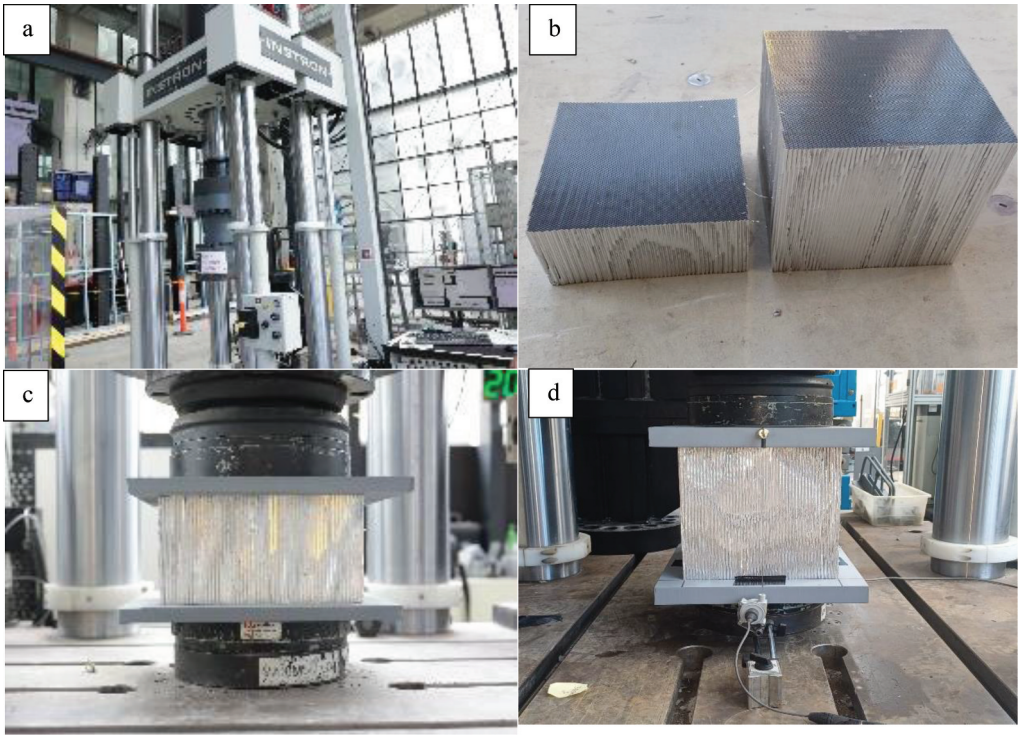


Figure 2. Static test apparatus and samples' placement: (a) Testing Machine – Instron 5MN; (b) Two tested samples; (c) Small specimen – 150 mm thick; and (d) Large specimen – 300 mm thick.

3 RESULTS AND DISCUSSION

This section covers the results of the static load testing of the cushions. Generally, and as defined in Ashby and Medalist (1983), the behavior of the honeycomb panel can be described in three regions: (i) the elastic zone, when all the panels resist the load without any permanent deformation; (ii) the plateau stress, where the layers of the honeycomb undergo deformation gradually; and (iii) the densification stage when the panel still deform but requires large corresponding loads. Figure 3-a, b, and c visually depict these three structural performance phases. In the first stage (Figure 3-a), the specimen is loaded, and the overall geometry of the panels was involved in withstanding the load until the first layer of the panel (close to the top steel plate was deformed). Then, Figure 3-b illustrates the middle of the consecutive deformation of the layers. Finally, when the total panel thickness was compressed, the specimen reached its densification stage (Figure 3-c).

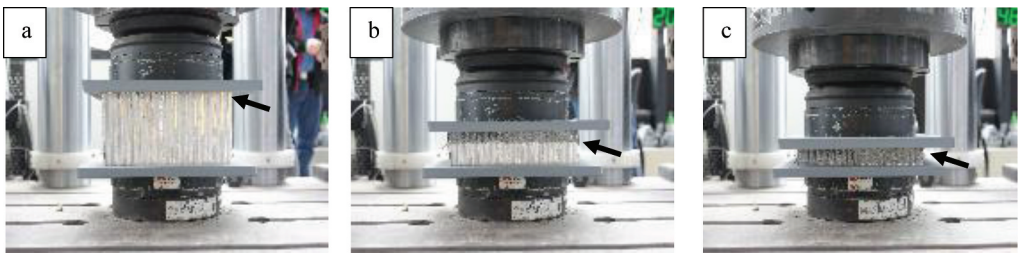


Figure 3. Loading stages on the honeycomb panel – 150 mm thick: (A) Starting of the plastic zone; (B) Within plateau loading stage; and (C) Starting to densification stage.

The pictures in Figure 3 above were captured using a Canon EOS R6 Mark II camera, which was automatically adjusted to capture one picture per second. The camera was synchronised with the testing machine, enabling the identification of images' locations on the load-displacement curve, as shown in Figure 4. It can be observed that the total panel resisted the compression load within the elastic zone (684 kN at 2.8mm). The sudden drop of force (103 kN at 3 mm) represents the failure of the first layer of the panel. Subsequently, the specimen's stiffness was re-exhibited until the failure of the subsequent layer. This phenomenon is evident as a load fluctuation along the displacement and test time. The fluctuation range is particularly noticeable in the early stages of the plateau force zone. With the consistent application of load and the continuous, consecutive failure of layers, the fluctuation range can be reduced until it becomes nearly a constant load. Finally, the final red dot depicts the starting point of the densification zone, in which the panel still undergoes displacement under high applied load, potentially translating the load to the protected members.

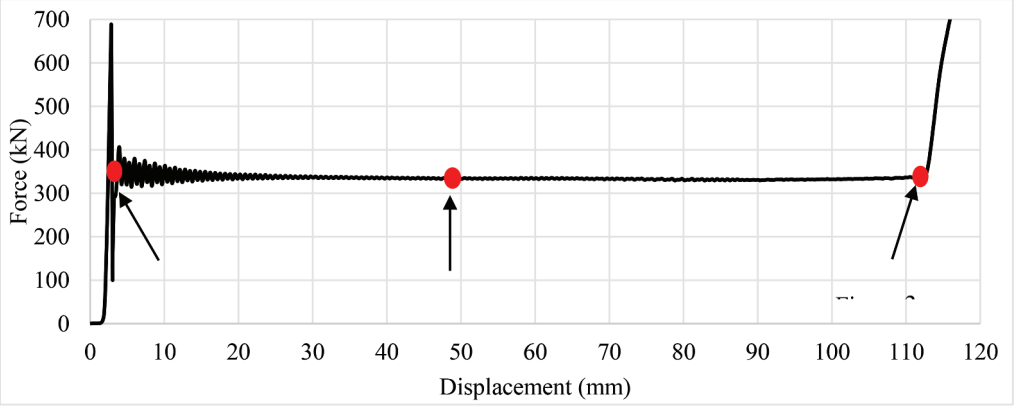


Figure 4. Load-Displacement curve of the honeycomb panel -150 mm.

The load-displacement curve of the two tested panels is presented in Figure 5; it is apparent that the density affects the energy-absorbing capacity of the overall system. However, due to the gradual deformation of the panel's layers along the thickness, the plateau stress continues for longer distance and duration, resulting in a total energy absorbing capacity of the large panel equal to 58.7 kJ compared to 38.3 kJ for the small panel.

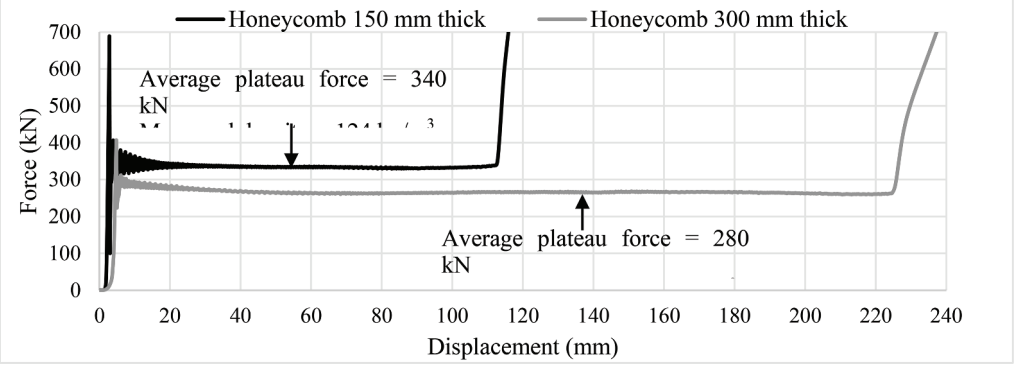


Figure 5. Load-displacement curve of the two tested panels.

4 ANALYTICAL ASSESSMENT OF HONEYCOMB PANELS

The energy absorbing capacity of the honeycomb sandwich panel was calculated using the procedure of Ashby and Medalist (1983) and Lu and Yu (2003). The relative density of the panel as it called cellular materials (ρ_c) can be obtained for general cellular materials. The relative density was experimentally demonstrated to be the significant factor that affects the mechanical properties of the cellular materials, including plateau stress, Young's Modulus, and densification strain, which governs the energy-absorbing capacity of these materials. The relationship model between the density and the mechanical properties of cellular materials was developed by Ashby and Medalist (1983), and it is known as the Gibson-Ashby Model. Like other cellular materials, honeycombs undergo three stress zones: elastic, plateau, and densification stress. The corresponding densification strain represents the point when the material absorbs energy, but transfers stress to the protected structure. Therefore, the energy-absorbing capacity of the panels was estimated by computing the area under these three regions of the stress-strain curve.

A regular honeycomb panel was used in this study, which has hexagonal cell shapes with equal side lengths and the angle of the cells ($\theta = 30^{o}$), the following equations (1- 4) were adopted to determine the relative density, plateau stress, and densification strain, which were used to estimate the energy-absorbing capacity of the panels.

$$\frac{\rho_c}{\rho_s} = \frac{2}{\sqrt{3}}\frac{t}{l} \tag{1}$$

$$\sigma_c = 5.6\ \sigma_s\left(\frac{t}{l}\right)^{\frac{5}{3}} \tag{2}$$

$$\varepsilon_D = \rho_c = 1 - \ 1.4\ \frac{\frac{t}{l}\left(\frac{h}{l}+2\right)}{2\cos\theta\left(\frac{h}{l}+\sin\theta\right)} \tag{3}$$

$$\mathrm{W}_\omega = \int_0^{\varepsilon} \sigma(\varepsilon)d\varepsilon \tag{4}$$

where ρ = density; E = modulus of elasticity; and σ = yield strength. Substrate "$_c$" is the corresponding property for the cellular structure. In contrast, the substrate "$_s$" refers to solid materials. ε_D = densification strain of the cellular product; t = foil's thickness; and h and l = the side lengths of the cell of the cellular structures in the in-plane direction; and W_ω = energy absorbing limit of the cellular material per unit volume.

In Table 1 below, a comparison is presented between the analytical approach to highlight the density and corresponding energy-absorbing capacity (EAC) in contrast to the experimental results of this study. Considering that the analytical approach is based on optimal panel properties, such as the exact hexagonal shape of the cells, foil thickness, and precise panel dimensions, a slight difference between the analytical and experimental results was observed.

For the large specimen, which has a measured density of 107 kg/m^3, close to the calculated analytical density of 103.4 kg/m^3, the experimental energy-absorbing capacity of the panel (58.7 kJ) is almost the same as the analytical value (60 kJ). However, the larger actual density of the small specimen resulted in a greater gap between the analytical and experimental values.

Table 1. Analytical and experimental comparison of two aluminium honeycomb panels.

Panel dimensions	Analytical approach		Experimental results	
mm	Density (kg/m^3)	EAC (kJ)	Density (kg/m^3)	EAC (kJ)
300 × 300 × 300	103.4	60.1	107	58.7
300 × 300 × 150	103.4	30.05	124	38.3

5 CUSHION APPLICATION IN PRACTICE

The results obtained in this study highlight the potential efficacy of employing honeycomb structures as a cushioning system to protect bridge girders from collisions with over-height vehicles. The energy-absorbing capacity of the honeycomb panels, as revealed in the small and large samples, is noteworthy. Specifically, a 150 mm thick panel demonstrated an energy absorption of 38.3 kJ, while a larger panel with a slightly reduced density exhibited 58.7 kJ.

It is essential to recognise that real-world collisions involving over-height vehicles can vary significantly in mass, ranging from a few kilograms to several tons. A parametric study by Yang and Qiao (2010) explored the impact mass of over-height materials from large trucks, ranging from 30.2 kg to 4.6 tons. Table 2 summarises the practicality of this study's panels regarding the actual cost, the total materials required, and associated prices for protecting a specific length of bridge girders. Additionally, the table presents the corresponding weights of the entire system, serving as a superimposed dead load on the structures. The cost for the required materials to protect 22 m of the susceptible bridge stands at 2000 US$, establishing the application of honeycomb structures as an attractive solution due to their efficiency, cost-effectiveness, and ease of installation.

Table 2. Cushion-related features for practical applications.

Property	Large panel 300 ×300 × 300	Small panel 300 ×300 × 150
Density (kg/m3)	107	124
Energy absorbing capacity (kJ)	58.7	38.33
Cost of single panel (US$)	53	26.5
Mass of a single panel (kg)	2.895	1.673
Number of panels/cubic meter	37	74
Protected Bridge width (m)	11	22
Cost of the materials (US$)	1963	1963
Superimposed dead load (kN)	1.07	1.24

The large panel's practical properties, as detailed in Table 2, are illustrated in Figure 6 below. The bridge girder section in this figure represents the protected end girder of a susceptible low-clearance bridge. In practice, it is not necessary to incorporate all 11 meters (37 panels) on a single bridge. However, the total length was utilised for explanation purposes. It is essential to note that the total cost in the figure solely represents the cost of the materials, excluding considerations for transportation and installation phases. Additional materials, such as adhesive for bonding the panels to the girder, are also required to implement the protective system in practice.

To illustrate the practical application of honeycomb cushions, Figure 7 is presented, showcasing the efficiency of two different-sized honeycomb panels across various impact scenarios. It is worth mentioning that the analysis assumes that only the over-height portion of vehicles engaged in the collision with the bridge girders and the standard impact width is set at 2.5 m (width of the truck). The findings indicate that large panels can effectively protect a bridge girder against impacts up to 489.1 kg, sufficient to withstand the energy generated by a two-ton mass moving at 22 m/s (79.2 km/h). Meanwhile, the smaller cushion proves adequate for impacts up to 319.4 kJ, protecting girders from a 1.5-ton object travelling at 18 m/s (65 km/h).
where: Impact energy = $0.5mv^2$, energy absorbing capacity of large and small panels (489.1 and 319.4) kJ results from multiplying the capacity of the individual panel by the standard width of the truck (2.5 m) and divided by the width of the unique panel (0.3) m.

It is essential to highlight that the establishment of Figure 7 assumes that all the impact kinetic energy from over-height vehicles is transferred to the impacting cushion and requires absorption. However, a significant portion of energy may be dissipated due to the rebound of the impacting object (restitution coefficient's effects) and the loss of energy during indentation,

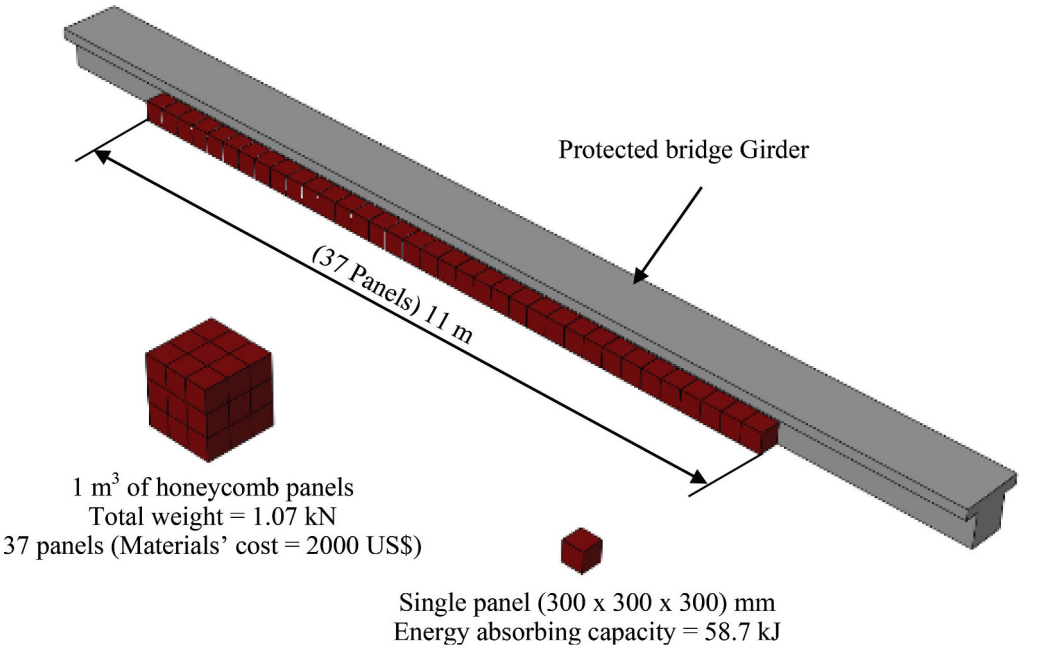
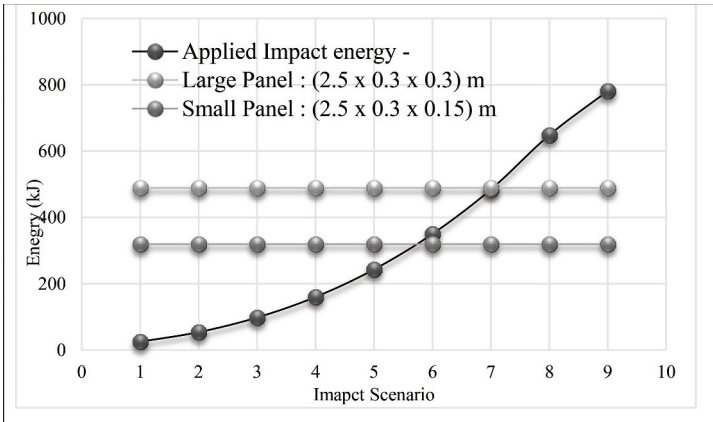


Figure 6. Illustration of the required materials, cost, and weight to protect 11 m length of bridge.



Impact scenario	Mass (kg)	Velocity (m/sec)
1	500	10
2	750	12
3	100	14
4	1250	16
5	1500	18
6	1750	20
7	2000	22
8	2250	24
9	2500	25

Figure 7. Energy absorbing capacity of two honeycomb panels against different impact scenarios.

as studied by Yang and Qiao (2010). Consequently, the cushion's effectiveness is evaluated against a conservative estimate of applied kinetic energy.

6 CONCLUSION

This study explores the potential use of aluminium honeycomb panels as sacrificial protection for bridge girders against impact from over-height vehicles. Two-panel sizes underwent quasi-static testing to determine their energy absorption capacity, which was then compared to analytical predictions. The alignment between observed and analytical results confirms the effectiveness of honeycomb cushions in mitigating impact loads on bridge girders. Panel density emerged as a critical factor affecting energy absorption. For example, a 300 × 300 × 150 mm

panel with a density of 124 kg/m^3 absorbed 38.3 kJ, while a larger 300 × 300 × 300 mm panel with a density of 107 kg/m^3 absorbed 58.7 kJ. Standardising panel density and refining manufacturing processes can enhance quality control in estimating energy absorption capacity for honeycomb cores with large thicknesses. This study represents a significant step in evaluating cushioning systems for practical use, contributing to the safety assessment of bridge infrastructure against over-height vehicle collisions. Its implications for transportation safety underscore its importance in advancing bridge safety measures.

REFERENCES

Ashby, M. F. & Medalist, R. M. 1983. The mechanical properties of cellular solids. Springer.

Foshan City Linwell Honeycomb Hardware Co., L., China. 2024. Available: http://www.linwellchina.com/ [Accessed 2023].

Hite, M. C. 2007. *Evaluation of the performance of bridge steel pedestals under low seismic loads*. Georgia Institute of Technology.

Lu, G. & Yu, T. 2003. *Energy absorption of structures and materials*, Elsevier.

Nguyen, B. 2018. *Vision-based over-height vehicle detection for warning drivers*. University of Cambridge.

Pair, J. 2023. *Eastbound I-94 closes when semi-truck hits overpass near Ann Arbor* [Online]. Ann Arbor. Available: https://www.mlive.com/news/ann-arbor/2023/03/semi-truck-hits-overpass-on-eastbound-i-94-near-ann-arbor.html [Accessed].

Sharma, H. 2010. *Design of a bridge bumper to protect bridge girders against collisions of overheight vehicles*. Texas A & M University.

Xu, D., Yuan, X., Ozdagli, A. I., AgÜero, M., Nasimi, R., Wang, T. & Moreu, F. 2022. Over-height truck collisions with railway bridges: attenuation of damage using crash beams. *Earthquake engineering and engineering vibration*, 21, 237–252.

Xu, L., Lu, X. Z., Smith, S. T. & He, S. 2012. Scaled model test for collision between over-height truck and bridge superstructure. *International Journal of Impact Engineering*, 49, 31–42.

Yang, M. 2006. *Impact mechanics of elastic and elastic-plastic sandwich structures*. University of Akron.

Yang, M. & Qiao, P. 2008. Quasi-static crushing behavior of aluminum honeycomb materials. *Journal of Sandwich Structures & Materials*, 10, 133–160.

Yang, M. & Qiao, P. 2010. Analysis of cushion systems for impact protection design of bridges against overheight vehicle collision. *International Journal of Impact Engineering*, 37, 1220–1228.

Bridge Maintenance, Safety, Management, Digitalization and Sustainability – Jensen, Frangopol & Schmidt (eds)
© 2024 The Author(s), ISBN 978-1-032-77040-6
Open Access: www.taylorfrancis.com, CC BY-NC-ND 4.0 license

Multi-hazard resilience-based bridge prioritization for aging bridge networks in a changing climate

L. Jafari & F. Biondini
Politecnico di Milano, Milan, Italy

ABSTRACT: Engineering structures and infrastructures are exposed to various hazards throughout their service life. When subjected to natural disasters, such as earthquake sequences and riverine floods, bridges emerge as highly vulnerable elements within transportation networks, which are important infrastructure facilities. The ongoing rise in greenhouse gas emissions, particularly carbon dioxide (CO_2), is widely regarded as the underlying cause of global warming and climate change that are posing a significant threat to various types of structures, including bridges. Studies have provided evidence that climate change is responsible for a rise in the frequency and magnitude of hydrological extremes. Intensified future design floods have been observed to lead to higher likelihood of increased scouring around river crossing bridge piers. Also, global warming and climate change accelerate aging and deterioration processes of materials and structural components. This paper presents a probabilistic resilience-based prioritization framework for aging bridges and bridge networks under multiple hazards, including seismic sequences, floods, and corrosion processes, in a changing climate. The proposed approach exploits multi-objective optimization to identify optimal solutions, determining the best retrofit methods, and prioritizing repair activities. The results of the application to a six-bridge transportation network address cost-effective enhancement of resilience by strategically managing rehabilitation activities.

1 INTRODUCTION

Over the lifespan of bridges within a transportation network, they may face not only a single hazard but a combination of hazards that can occur either sequentially or simultaneously (Argyroudis et al. 2020). Additionally, climate change poses significant impacts on both existing and future bridges' functionality, necessitating a comprehensive assessment of these effects in their lifetime. Fluctuations in precipitation intensity and quantity, coupled with temperature and humidity variations, stand out as the most evident indicators of climate change. As a bridge ages, its vulnerability due to corrosion becomes more distinct compared to its early years in service (Biondini & Frangopol 2016). These factors have the potential to amplify the vulnerability of structures when confronted with other hazards such as earthquakes and flooding (Milić & Marić 2023). The increase in the amount and intensity of precipitation leads to increase in higher level and frequency of floods and change in groundwater and geomechanical conditions. These outcomes lead to the activation of landslides, erosion, and soil liquefaction, which can also exacerbate the intensity of earthquakes and risk of scour (Harasti et al. 2021, Milić & Marić 2023). The altered precipitation patterns, additionally contribute to material degradation, a situation further compounded by the insufficient capacity of the drainage system. The increase in temperature and humidity can influence the structural dynamics, particularly in the case of steel bridges. Additionally, high temperatures may induce concrete cracking due to excessive stresses, potentially significantly reducing the lifespan of a structure, especially when exposed to aggressive environmental conditions (Nasr et al. 2020, Milić & Marić 2023, Nava et al. 2023). As stated, bridges may face various hazards, and it is imperative to mitigate consequences by deploying effective preventive and rehabilitation measures. The concept of resilience is extensively utilized to evaluate a system's capacity to mitigate

DOI: 10.1201/9781003483755-76

the impacts of hazards and recover, returning to its necessary functionality with both effectiveness and efficiency (Bruneau et al. 2003). Effectively managing rehabilitation interventions involves damage evaluation and condition assessment of structures. To ensure efficient decision-making, life-cycle resilience assessment and optimal resource allocation are crucial for bridges as vulnerable components of transportation networks. Resource allocation needs to take into account limitations related to the budget and availability of manpower and equipment for interventions. The adverse effects of climate change can be managed through adaptation measures and by implementing appropriate interventions to prevent or minimize the potential damage that such effects may cause (Figueiredo et al. 2023).

Numerous studies have suggested resilience-based approaches for prioritizing rehabilitation activities, whether post-event or pre-event, when exposed to single hazards (Capacci et al. 2022). Jafari et al. (2023a, b) developed a probabilistic framework that prioritizes both pre- and post-event interventions for bridge networks, accounting for aging and deterioration effects within mainshock-aftershock sequences. This probabilistic framework is extended in this paper to incorporate multiple hazards, specifically seismic sequences and floods as natural hazards, along with the environmental hazard of aging bridges affected by corrosion. The consideration of climate change effects on hazards and deterioration processes is also included. The proposed approach utilizes multi-objective optimization to identify optimal solutions, determining the best retrofit methods and prioritizing the initial time of repair activities. This aims to maximize aging bridge network resilience against prescribed multiple hazards while minimizing associated costs. Vulnerability assessment considers fragility curves, accounting for retrofitting, aging, deterioration, climate change and damage accumulation from previous hazards. The bridge network functionality is assessed using a traffic flow congestion metric, which considers travel time delays and distance increases during periods of reduced bridge traffic capacity caused by damage. The proposed approach is applied to a six-bridge transportation network including riverine bridges facing seismic scenarios and floods. The results address cost-effective enhancement of resilience by strategically managing rehabilitation activities. Considering that future climate change projections in bridge planning enables authorities to proactively prepare for a changing landscape, the implementation of the adaptation measures and rehabilitation strategies resulting from the proposed approach could be beneficial to reduce the potential impact of climate change on bridges, enhancing their resilience and functionality in the face of multiple hazards.

2 VULNERABILITY TO MULTIPLE HAZARDS

The vulnerability of a transportation bridge in the face of hazards is frequently assessed through fragility functions. These functions provide the likelihood of the bridge exceeding specified damage levels at given hazard intensity, such as peak ground acceleration (PGA) in earthquakes or parameters like water discharge or scour depth in floods (Nielson 2005, Argyroudis & Mitoulis 2021). There has been some research dedicated to creating fragility curves for multiple hazards irrespective of whether or not climate change is considered. Argyroudis and Mitoulis (2021) developed fragility surface for a typical river-crossing bridge exposed to flood and seismic hazard, considering the effect of scour, debris accumulation, and hydraulic forces along with seismic forces. Ghimire et al. (2022) developed fragility curves for earthquake and scouring scenarios, and their findings indicated that overlooking scouring conditions may lead to an underestimation of fragility across all damage states, highlighting the substantial impact of scouring if left unaccounted for. Mortagi and Gosh (2020) developed fragility curves for steel girder bridges exposed to earthquakes taking into consideration the effects of aging due to chloride-induced corrosion deterioration, and the impact of climate change on both the initiation time and rate of corrosion. Since the reference temperature T_0 and reference humidity RH_0 are taken as 20°C and 75%, respectively to predict initiation time and rate of corrosion, the study identified that the alterations in temperature T and relative humidity RH brought about by climate change are contributing factors to changes in the initiation time and rate of corrosion. The study also highlights that aging, along with the effects of climate change, exacerbates bridge vulnerability, emphasizing the critical importance of considering the influence of

initial temperature and relative humidity on seismic fragility estimates for aging highway bridges. Guo et al. (2019) introduced a scour-dependent empirical seismic fragility modeling approach, aiming to establish a fragility surface for earthquake and flood hazards. Their study underscores the significant influence of scour depth on the seismic performance of the investigated bridge system, especially regarding its contribution to severe damage. Different retrofit methods can be utilized to reduce the vulnerabilities of susceptible components in bridges, towards hazards. Various retrofit techniques for decreasing seismic vulnerability may involve seismic isolator bearings, seat extender, shear keys, different kinds of jacketing such as concrete, steel, fiber reinforced polymer (FRP), engineered cementitious composite (ECC), and fabric reinforced cementitious matrix (FRCM) jacketing. Riprap is one of the main approaches selected to minimize scour damage in the occurrence of flooding (Argyroudis et al. 2019). Additionally, the research illustrated that bridges equipped with seismic isolators exhibit lower vulnerability compared to non-isolated bridges when subjected to multiple hazards, including earthquakes and floods (Argyroudis & Mitoulis 2021, Billah & Iqbal 2022).

A fragility surface considering exposure to earthquake sequences and flood hazards as well as potential conditions of aging, climate change and retrofitting giving rise to as-built, retrofitted, state-dependent, and time-dependent fragility curves, can be formulated as follows (Argyroudis et al. 2019, Skokandić et al. 2022):

$$P[S_b \geq s_b|\hat{s}_b, r_b, i_b, t_b, Sc_b] = \Phi\left[\frac{\ln(i_b)-\ln(MF_a(s_b,t_b,T,RH)\cdot MF_{Sc}(s_b,Sc_b)\cdot MF(s_b,\hat{s}_b,r_b)\cdot MF_{Sc,r}(s_b,r_b,Sc_b)\cdot i_{b,m}(s_b))}{\zeta_{s,b}(s_b)}\right], \quad s_b > \hat{s}_b \tag{1}$$

where S_b is a variable denoting the damage state of the b-th bridge in the network, taking on values s_b = 0, 1, 2, 3, 4 corresponding to no damage, slight damage, moderate damage, extensive damage, and complete damage state, respectively; $\hat{s}_b$ represents the pre-existing damage state; r_b denotes the retrofit method, taking the value 1 for a non-retrofitted bridge, and values 2, 3, and so forth for various types of retrofit interventions; i_b signifies the seismic intensity at the b-th bridge site; Sc_b is scour depth at the b-th bridge site; $i_{b,m}$ (s_b) represents the median intensity measure leading to the exceedance of a given damage state s_b; $\zeta_{s,b}(s_b)$ is the standard deviation of the natural logarithm of the intensity measure leading to the exceedance of a given damage state s_b; t_b stands for bridge age; MF_a (s_b, t_b, T, RH) represents the modification factor for median values of fragility curves for damage state s_b, considering the bridge age t_b at the occurrence time of hazards integrating the consequences of anticipated shifts in temperature T and relative humidity RH, with MF_a (s_b, t_b, T, RH) ≤1. MF_{Sc} (s_b, Sc_b) functions as the factor that addresses the influence of scour depth on the vulnerability of bridges; MF (s_b, $\hat{s}_b$, r_b) denotes the modification factor for median values of fragility curves for damage state s_b, considering retrofit measure r_b and pre-existing damage state $\hat{s}_b$; $MF_{Sc,r}$ (s_b, r_b, Sc_b) is the modification factor utilized to incorporate the impact of riprapping or isolating on improving the fragility surface. Figure 1 shows typical trends of modification factors. Figure 2 shows typical fragility surface for combined earthquake and flood hazards considering the effect of deterioration and climate change (Figure 2a) and retrofits (Figure 2b). For $s_b = \hat{s}_b$, P [$S_b \geq s_b \mid \hat{s}_b$, r_b, i_b, t_b, Sc_b] = 1, and for s_b = 5, P [$S_b \geq s_b \mid \hat{s}_b$, r_b, i_b, t_b, Sc_b] = 0. Additional information can be found in Jafari et al (2023a, b).

The evaluation of the occurrence probability of damage state s_b on bridge b is therefore conducted using fragility curves in the following manner:

$$P[S_b = s_b|\hat{s}_b, r_b, i_b, t_b, Sc_b] = P[S_b \geq s_b|\hat{s}_b, r_b, i_b, t_b, Sc_b] - P[S_b \geq s_b + 1|\hat{s}_b, r_b, i_b, t_b, Sc_b], \quad s_b \geq \hat{s}_b \tag{2}$$

When $s_b < \hat{s}_b$, the probability of being in damage state s_b is null (P [$S_b = s_b \mid \hat{s}_b$, r_b, i_b, t_b, Sc_b] = 0). To quantify the damage level l_b for each bridge affected by earthquakes and flood, the average occurrence probabilities of different damage states can be utilized (Bocchini & Frangopol 2011):

$$l_b = E(S_b) = \sum_{s_b \geq \hat{s}_b}^{4} s_b \cdot P[S_b = s_b|\hat{s}_b, r_b, i_b, t_b, Sc_b] \tag{3}$$

The damage level l_b is limited to the interval [0, 5) ⊂ R. Bridges within a transportation network that are exposed to earthquakes and flood may experience varying levels of damage. The combination of these damage levels represents the overall damage state of the bridge network. In order to obtain a discrete number of damage combinations representative of bridge network damage state s, the damage levels l_b are rounded down to the nearest smaller integer, which takes the values 0, 1, 2, 3 and 4. More details can be found in Jafari et al. (2023a, b).

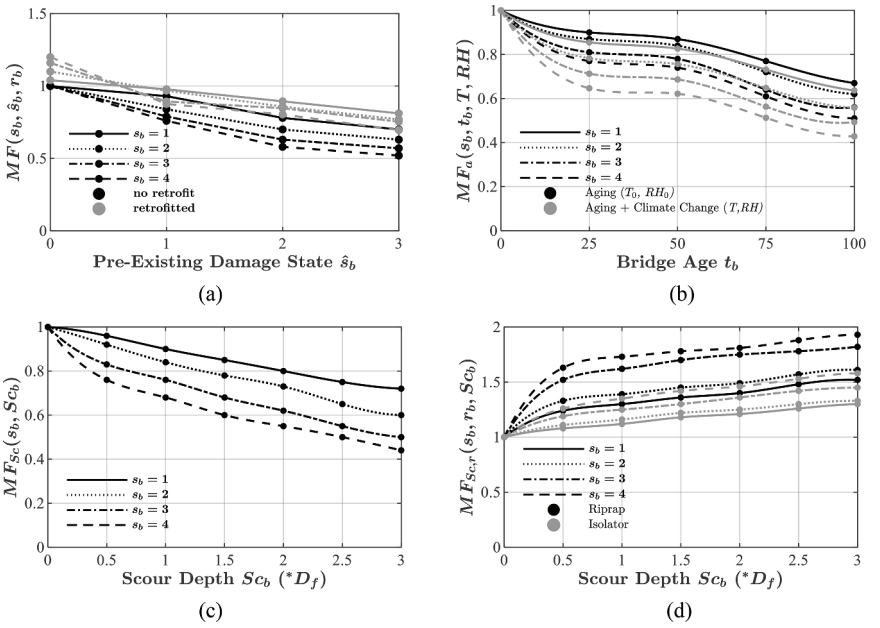


Figure 1. Typical trends for Modification Factors: (a) MF (s_b, $\hat{s}_b$, r_b); (b) MF_a (s_b, t_b, T, RH); (c) MF_{Sc} (s_b, Sc_b); (d) $MF_{Sc,r}$ (s_b, r_b, Sc_b).

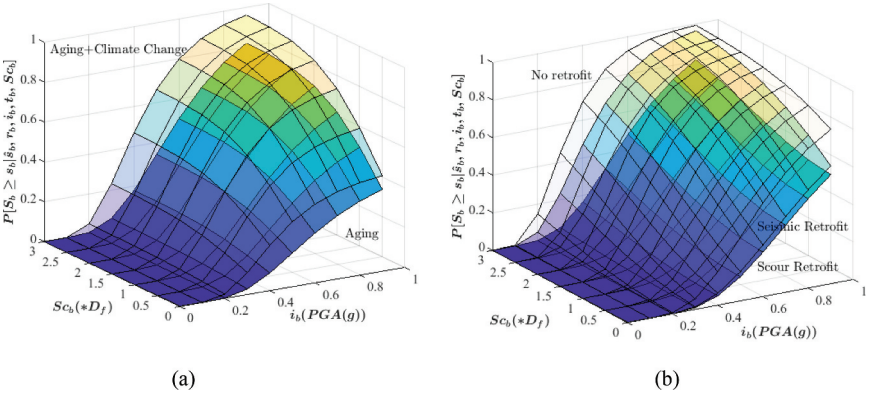


Figure 2. Typical fragility surfaces: (a) considering deterioration with and without the effect of climate change; (b) considering retrofit effects.

3 METHODOLOGY

A prioritized management plan for rehabilitation activities on aging bridges vulnerable to multiple hazards under climate change is established in order to maximizing network resilience R and simultaneously minimizing associated retrofit C_{Ret} and repair C_{Rep} costs. Resilience is characterized as the assessment of a network's reaction to hazards, encompassing qualities

such as robustness, rapidity of recovery process, resourcefulness, and redundancy in the face of potential threats. The resilience R can be quantitively defined by the integral mean of the functionality profile over a time horizon extending from the event occurrence time t_0 to a fixed horizon time $t_{\square}$. The functionality of the bridge network at each damage state s ($Q_i(s)$) is assessed using a metric defined by the increase in both total travel time $TTT(s)$ and total travel distances $TTD(s)$ resulting from the utilization of alternative routes when bridges are partially or fully closed. To assess resilience within the designated time frame, the network functionality is evaluated at each time step Δt_i of total number of steps N_t taking into account the damage status of bridges influenced by the impact of retrofit measures and the extent of repair. It is assumed that each bridge will recover from one damage state to the next within a given time interval. Damage state of bridges is evaluated by employing relevant fragility surfaces, as discussed previously. Three decision variables are considered for each bridge, including seismic retrofit r_b, flood retrofit $r_{b,Sc}$, and initiation time of repair activities $tInt_b$. Restrictions on the maximum number of repair activities occurring simultaneously $N^t{}_{SiAct}$ and the maximum duration of concurrent repair activities $N^T{}_{month}$ on various bridges are imposed due to resource limitations. The optimization problem is formulated as follows:

$$
\begin{aligned}
&\text{find}: \quad r_b,\, r_{b,Sc},\, tInt_b \\
&\text{so that}: \ \max R = \frac{1}{t_h - t_0} \sum_{i=0}^{N_t} Q_i(s) \cdot \Delta t_i;\ \min C = C_{\text{Ret}} + C_{\text{Rep}} \\
&\text{Constraints}: \\
&r_b \in \{1, 2, ..., N_{rb}\},\ r_{b,Sc} \in \left\{N_{rb}+1, N_{rb}+2, ..., N_{rb,Sc}\right\},\ tInt_b \in \{0 : \Delta t_i : t_h\} \quad \forall b = 1, 2, ..., N_b \\
&N^t_{SiAct} \le N^{\max}_{SiAct},\ N^T_{month} \le N^{\max}_{month}
\end{aligned}
\tag{4}
$$

This multi-objective constrained problem is solved using the NSGA-II meta-heuristic algorithm (Deb et al. 2002) with penalty functions. Decision-makers have the flexibility to choose optimal solutions from the Pareto-Front, which is derived by addressing the optimization problem, taking into account their specified resilience criteria, budget considerations, and available resources. Further details on how to exploit Pareto-Fronts can be found in Jafari et al. (2023a, b).

4 APPLICATION

The proposed approach is implemented on a hypothetical bridge network, shown in Figure 3a. It is assumed that B1 and B5 are multi-span continuous (MSC) concrete girder bridges, B2 is MSC steel girder bridge, B3 is multi-span simply supported (MSSS) steel girder bridge, and B4 and B6 are MSSS concrete girder bridges. The network is assumed to be situated in a seismic region with a considerable flood risk, expected to experience an increase in precipitation, attributed to climate change projections. A hazard scenario involving mainshock-aftershocks occurring at 0, 6, and 10 months, with magnitudes of 6.9, 7.5, and 6.0, respectively, is considered. The flood hazards are assumed to impact riverine bridges B1, B4, and B5 within the network. The seismic intensity i_b in PGA, obtained through attenuation law (Bindi et al. 2011), and flood hazard intensity in scour depth are illustrated in Figures 3b and 3c, respectively. At the occurrence of the mainshock, the six bridges are aged 50, 20, 40, 100, 70, and 80 years, respectively. The modification factor MF_a (s_b, t_b, T, RH) depicted in Figure 1b is applied to account for the average impact of variations in temperature (T) and relative humidity (RH) due to climate change on fragility curves of aged bridges. The effect of scouring is considered by applying modification factor MF_{Sc} (s_b, Sc_b) in Figure 1c. The possible seismic retrofits that can be applied on bridges are assumed to be steel jackets, elastomeric isolation bearings, restrainer cables, seat extenders, shear keys, concrete jacketing, ECC jacketing, CFRP jacketing and FRCM jacketing. The details for developing fragility curves of as-built and retrofitted bridges and required modification factor MF (s_b, $\hat{s}_b$, r_b) can be found in Jafari et al (2023a, b). The

flood retrofit methods include riprap and elastomeric isolation bearings and their associated modification factor $MF_{Sc,r}$ (s_b, r_b, Sc_b) are depicted in Figure 1d. The coordinates of nodes in the bridge network and the number of vehicles either originating from or being attracted to each node are listed in Table 1. Additional information regarding traffic characteristics, detours and traffic analysis of the bridge network, aimed at determining the network functionality under each damage state $Q(s)$, along with the necessary recovery time for each damage state of every bridge type, retrofit, and repair costs, can be found in Jafari et al. (2023a, b).

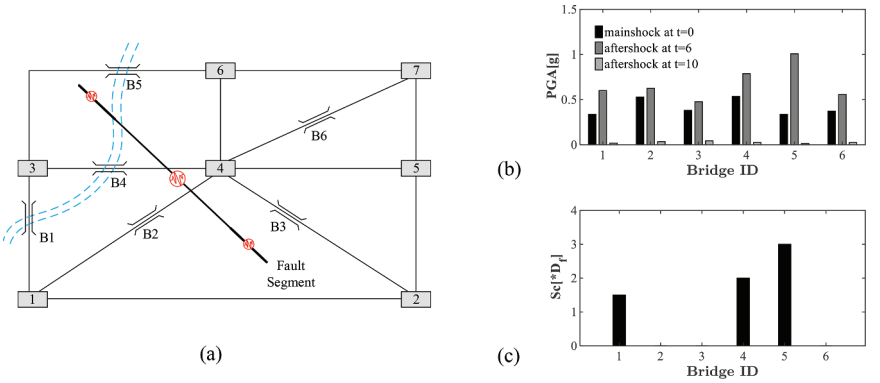


Figure 3. Six-bridge transportation network: (a) Bridge network layout; (b) Seismic demands at bridge sites associated with mainshock and aftershocks; (c) Scour depth (multiple of foundation depth D_f).

Table 1. Node characteristics of bridge network.

Node	1	2	3	4	5	6	7
X [km]	0	32	0	15	32	15	32
Y [km]	0	0	14	14	14	25	25
Originated vehicles [cars/h]	15400	16000	17000	28000	16500	19000	18500
Attracted vehicles [cars/h]	15400	16000	17000	28000	16500	19000	18500

The proposed methodology is applied to the network shown in Figure 3a and and resilience is computed over a 2-year horizon considering a time step of 0.2 month. Initial times of repair intervention are chosen from a 2-year horizon, allowing for a maximum of three simultaneous repair activities with a 12-month time interface on different bridges. Seismic retrofits r_b are chosen from {1,2, . . .,12}, representing no retrofit, steel jackets, elastomeric isolation bearings, restrainer cables, seat extenders, shear keys, restrainer cables & shear keys, seat extenders & shear keys, concrete jacketing, ECC jacketing, CFRP jacketing, and FRCM jacketing. Flood

Table 2. Details of selected pareto-front solutions.

#	Seismic retrofit/Flood retrofit interventions [ID]						Initial time of repair interventions [months]						Resilience [%]	Cost [M$]
	B1	B2	B3	B4	B5	B6	B1	B2	B3	B4	B5	B6		
1	1	1	1	1	1	1	24.0	24.0	24.0	24.0	24.0	24.0	4.5	0.0
	1	1	1	1	1	1								
2	5	1	1	11	1	1	24.0	24.0	24.0	24.0	24.0	24.0	23.3	0.15
	1	1	1	13	1	1								
3	3	5	12	11	1	11	3.6	24.0	24.0	0.0	24.0	24.0	69.5	2.86
	13	3	1	13	1	1								
4	3	8	12	11	3	11	10.0	0.2	8.2	0.0	24.0	1.0	93.6	6.97
	13	3	1	13	13	3								

retrofits $r_{b,Sc}$ are selected from {1,3,13}, corresponding to no retrofit, elastomeric isolation bearings, and ripraps, respectively. The optimal Pareto-Front solutions is illustrated in Figure 4a. The details of selected solutions are presented in Table 2, featuring network functionality (Figure 4b) and bridge damage profiles (Figure 4c) with corresponding repair schedules (Figure 4d). These results provide key information for decision-makers.

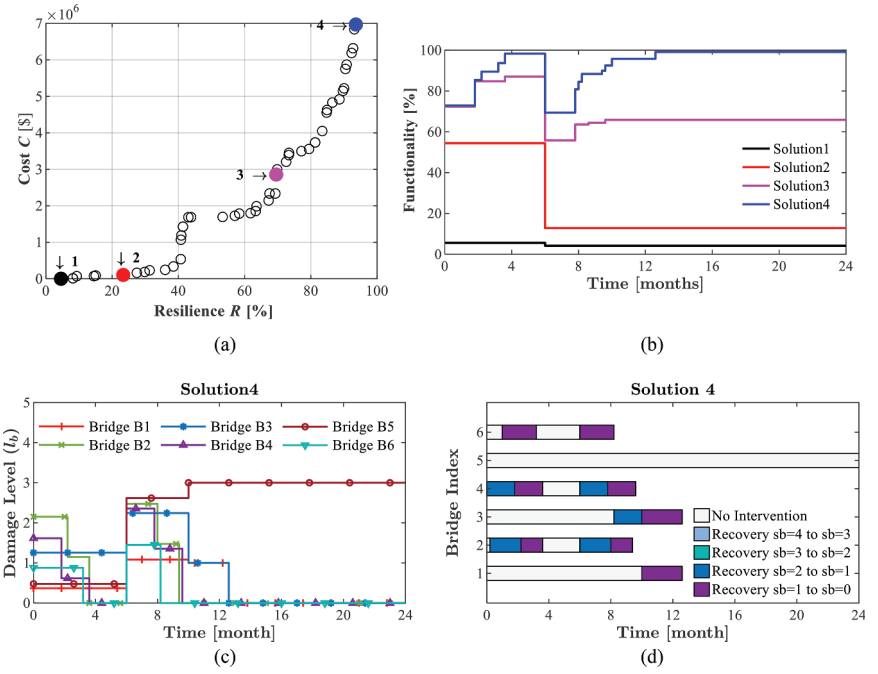


Figure 4. Solution of the optimization problem: (a) Pareto-Front with a selection of four optimal solutions; (b) Network functionality with recovery profiles of the four selected solutions; (c) Damage levels profile for solution #4; (d) Repair schedules associated with solution #4.

5 CONCLUSIONS

A framework for life-cycle management of aging bridge networks exposed to multiple hazards in a changing climate has been presented. The hazard scenario includes earthquake mainshock, aftershocks, floods, and deterioration processes influenced by climate change. Separate retrofit methods associated to each type of hazard implemented as pre-event activities are considered as decision variables to enhance the resilience of bridge network. Additionally, decision variables include the initial times of interventions on bridges, offering insights into effective post-event recovery. The prioritization of rehabilitation activities is determined by evaluating potential damages to each bridge, considering factors such as its location, exposure to hazards, importance, and its impact on traffic flow, along with considerations of time delay and distance increase. The vulnerability of bridges is estimated using fragility surfaces for multiple hazards. Resource limitations are addressed through constraints on the number of simultaneous rehabilitation activities and their duration on a limited number of bridges. The overarching goal is to maximize resilience while minimizing associated intervention costs. The results have been presented through Pareto- Fronts, providing decision-makers and managers with a range of solutions aligned with their budgetary constraints and resource availability, including labor and equipment. Future research can be dedicated on improving multiple hazards models and climate change projections, enhancing fragility surfaces, and developing comprehensive and realistic recovery models, to reach more effective management plan in the face of multiple hazards under a climate change.

REFERENCES

Argyroudis, S.A., Mitoulis, S.A., Winter, M.G. & Kaynia, A.M. 2019. Fragility of transport assets exposed to multiple hazards: State-of-the-art review toward infrastructural resilience. *Reliability Engineering & System Safety* 191:106567.

Argyroudis, S.A., Mitoulis, S.A., Hofer, L., Zanini, M.A., Tubaldi, E. & Frangopol, D.M. 2020. Resilience assessment framework for critical infrastructure in a multi-hazard environment: Case study on transport assets. *Science of the Total Environment* 714: 136854.

Argyroudis, S.A. & Mitoulis, S.A. 2021. Vulnerability of bridges to individual and multiple hazards-floods and earthquakes. *Reliability Engineering & System Safety* 210:107564.

Billah, A.M. & Iqbal, A. 2022. Effect of seismic isolation on fragility of bridges with scoured foundations. *Journal of Structural Engineering* 148(6): 04022062.

Biondini, F. & Frangopol, D.M. 2016. Life-cycle performance of deteriorating structural systems under uncertainty: *Review Journal of Structural Engineering*, *ASCE* 142(9): F4016001.

Bocchini, P. & Frangopol, D.M. 2011. A stochastic computational framework for the joint transportation network fragility analysis and traffic flow distribution under extreme events. *Probabilistic Engineering Mechanics* 26(2):182–193.

Bruneau, M., Chang, S. E., Eguchi, R. T., Lee, G. C., O'Rourke, T. D., Reinhorn, A. M., Shinozuka, M., Tierney, K., Wallace, W. A. & Von Winterfeldt, D. 2003. A framework to quantitatively assess and enhance the seismic resilience of communities. *Earthquake Spectra* 19(4): 733–752.

Capacci, L., Biondini, F. & Frangopol, D.M. 2022. Resilience of aging structures and infrastructure systems with emphasis on seismic resilience of bridges and road networks: Review. *Resilient Cities and Structures* 1(2): 23–41.

Figueiredo, E., Santos, L.O., Moldovan, I., Kraniotis, D., Melo, J., Dias, L. & Coelho, G.B. 2023. A Roadmap for an Integrated Assessment Approach to the Adaptation of Concrete Bridges to Climate Change. *Journal of Bridge Engineering*, *ASCE* 28(6): 03123002.

Ghimire, R., Pradhan, P. & Gautam, D. 2022. Multi-hazard fragility analysis of RC bridges for high seismicity and high scouring scenarios. *The Journal of Engineering* 2022(6): 618–628.

Guo, X., Badroddin, M. & Chen, Z. 2019. Scour-dependent empirical fragility modelling of bridge structures under earthquakes. *Advances in Structural Engineering* 22(6): 1384–1398.

Harasti, A., Gilja, G., Potočki, K. & Lacko, M. 2021. Scour at bridge piers protected by the riprap sloping structure: A review. *Water* 13(24): 3606.

Jafari L., Capacci L., Biondini F. & Khanmohammadi, M. 2023a. Resilience-based optimal management of aging bridge networks under mainshock-aftershock sequences. *Eighth International Symposium on Life-Cycle Civil Engineering* (IALCCE 2023), Milan, Italy, July 2-6, 2023. In: Biondini, F., Frangopol, D.M., (Eds.), 2023. *Life-Cycle of Structures and Infrastructure Systems*. CRC Press, Taylor & Francis Group, London, UK (Open Access): 1869–1876

Jafari, L., Khanmohammadi, M., Capacci, L. & Biondini, F. 2023b. Resilience-based optimal seismic retrofit and recovery strategies of bridge networks under mainshock-aftershocks sequences. *Journal of Infrastructure Systems*, *ASCE* (submitted).

Milić, P. & Kušter Marić, M. 2023. Climate change effect on durability of bridges and other infrastructure. *Građevinar* 75(09.): 896–906.

Mortagi, M. & Ghosh, J. 2020. Climate change considerations for seismic vulnerability assessment of aging highway bridges. *ASCE-ASME Journal of Risk and Uncertainty in Engineering Systems, Part A: Civil Engineering* 6(1): 04020005.

Nasr, A., Kjellström, E., Björnsson, I., Honfi, D., Ivanov, O.L. & Johansson, J. 2020. Bridges in a changing climate: A study of the potential impacts of climate change on bridges and their possible adaptations. *Structure and Infrastructure Engineering* 16(4): 738–749.

Nava, G.V., Capacci, L., Biondini, F. & Casti, L., 2023. Life-cycle structural reliability of RC bridge piers under corrosion in a changing climate. *Eighth International Symposium on Life-Cycle Civil Engineering* (IALCCE 2023), Milan, Italy, July 2-6, 2023. In: Biondini, F., Frangopol, D.M., (Eds.), 2023. *Life-Cycle of Structures and Infrastructure Systems*. CRC Press, Taylor & Francis Group, London, UK (Open Access): 1625–1633

Nielson, B.G. 2005. Analytical fragility curves for highway bridges in moderate seismic zones. *Georgia Institute of Technology*.

Skokandić, D., Vlašić, A., Kušter Marić, M., Srbić, M. & Mandić Ivanković, A. 2022. Seismic assessment and retrofitting of existing road bridges: state of the art review. *Materials* 15(7): 2523.

Bridge Maintenance, Safety, Management, Digitalization and Sustainability – Jensen, Frangopol & Schmidt (eds)
© 2024 The Author(s), ISBN 978-1-032-77040-6
Open Access: www.taylorfrancis.com, CC BY-NC-ND 4.0 license

Probabilistic capacity model for concrete-filled steel tubes

A. Aloisio
Department of Civil, Construction-Architectural and Environmental Engineering, University of L'Aquila, L'Aquila, Italy

A. Contento & J. Xue
College of Civil Engineering, Fuzhou University, Fuzhou, China

G. Quaranta
Department of Structural and Geotechnical Engineering, Sapienza University of Rome, Rome, Italy

P. Gardoni
Department of Civil and Environmental Engineering, University of Illinois at Urbana-Champaign, Urbana-Champaign, USA

B. Briseghella
College of Civil Engineering, Fuzhou University, Fuzhou, China

ABSTRACT: Concrete-filled steel tubular (CFST) columns are increasingly used around the world due to their significant structural and economic advantages. Although considerable research and several experimental tests have been carried out on CFST col-umns, there are no mechanics-based probabilistic models of their axial capacity. The present paper proposes a mechanics-based probabilistic capacity model for the assessment of the ultimate axial capacity of CFST columns. The accuracy of the numerical predictions obtained with the proposed formulation is compared with that of existing capacity equations already in use within technical standards and available in the literature.

1 INTRODUCTION

Concrete-filled steel tubular (CFST) columns are largely employed around the world because they offer two significant advantages. The first one is the composite action of the steel tube and infilled concrete, which enhances the strength and ductility of the columns. The steel tube effectively confines the concrete core, thereby providing a highly ductile response under compression and increasing the overall energy dissipation capacity (Johansson, 2002). The second advantage is the use of the steel tube as a permanent formwork for concrete casting, which helps to reduce construction time and costs. In the last decades, multiple experimental findings (O'Shea and Bridge, 2000; Giakoumelis and Lam, 2004; Zeghiche and Chaoui, 2005; van de Lindt and Gupta, 2006) proved that the axial capacity of CFST columns N_u is generally higher than the sum of the axial capacities of their components, which are the steel tube and the concrete core. This mechanical behaviour is represented by the following inequality:

$$N_u - \left(f_c A_c + f_y A_s\right) > 0, \tag{1}$$

where f_c is the concrete compressive strength, f_y is the steel yielding strength, whereas A_c and A_s are the cross-sectional areas of concrete and steel, respectively. This behavior is attributable to the confinement effect provided by the steel tube on the concrete core. This confinement

DOI: 10.1201/9781003483755-77

effect, originally highlighted in (Gardner and Jacobson, 1967) determines an increment of the compressive strength of the concrete (Richart, Brandtzæg and Brown, 1928) that varies during the loading process of the CFST columns. The loading process of the CFST columns can be divided into three phases (Johansson and Gylltoft, 2001; Shanmugam and Lakshmi, 2001; Susantha, Ge and Usami, 2001; De Nardin, El Debs, and others, 2004; Sakino *et al.*, 2004).

According to the mechanical behaviour of CFST (Xue, Briseghella, and Chen, 2012), N_u can be estimated as the sum of the axial capacities of steel tube and confined concrete core using specific correction factors as follows:

$$N_u \simeq \left(f_{cc}A_c + \alpha_s f_y A_s\right), \tag{2}$$

where α_s is the factor that accounts for the reduction of the axial capacity due to the presence of the biaxial stress state inside the steel tube, and f_{cc} is the compressive strength of the confined concrete. Following a Mohr-Coulomb strength condition, the resistance of the confined concrete core can be obtained as follows:

$$f_{cc} = f_c + \alpha_c k_c \sigma_{c,r}, \tag{3}$$

in which α_c is a reduction factor related to the geometry of the concrete core, k_c is the confinement coefficient, and $\sigma_{c,r}$ is the radial compression stress.

In the literature, α_c is sometimes referred to as scale factor, and it is usually a function of the outer diameter of the CFST column D, as in (Morino, 2002) and (Hassanein *et al.*, 2018) where it is defined as

$$\alpha_c = \left(1.67D^{0.112}\right)^{-1}. \tag{4}$$

The values adopted for k_c vary within the different formulations available in the literature. While Richart et al. (Richart, Brandtzæg and Brown, 1929) suggested assuming a constant value in the range 4 − 4.1, Saatcioglu and Razvi (Saatcioglu and Razvi, 1992) showed that k_c can take values in the range 2.5 − 7, which decreases when the radial compression stress increases. Consequently, they proposed a formulation where k_c depends on $\sigma_{c,r}$ as follows:

$$k_c = 6.7(\sigma_{c,r})^{-0.17}. \tag{5}$$

The maximum confinement stress can be obtained from Barlow's formula (Timoshenko, 1983), assuming that the maximum tensile stress in the steel tube equals the steel yielding strength, and reads

$$\sigma_{c,r} = \frac{2t}{D} f_y, \tag{6}$$

where t is the thickness of the steel tube. By introducing the expressions for f_{cc} (Eq. 3) and $\sigma_{c,r}$ (Eq. 6) into Eq. (2), the axial capacity of CFST columns can be written as follows:

$$N_u \simeq \left\{1 + \left[\alpha_c k_c \left(\frac{2t}{D}\right)\frac{f_y}{f_c}\right]\right\} f_c A_c + \alpha_a f_y A_s. \tag{7}$$

In a more compact form, Eq. (7) can be rewritten as follows:

$$N_u \simeq f_c A_c (1 + \alpha_c k_c \psi + \alpha_a \xi), \tag{8}$$

where $\psi = (2t/D)\,/(f_y/f_c)$ and $\xi = f_y A_s / f_c A_c$. In technical standards and the literature, Eq. (7) is often presented as

$$N_u \simeq \alpha'_c f_c A_c + \alpha_a f_y A_s \tag{9}$$

assuming a constant value for α'_c. The values of α_s, α_c, k_c, and α'_c vary among the available formulations.

2 THEORETICAL BACKGROUND

Following (Gardoni, Der Kiureghian, and Mosalam, 2002), the proposed form of the axial capacity and reduction factors is written as follows:

$$T[C(\mathbf{x},\Theta)] = T\left[\hat{C}(\mathbf{x})\right] + \gamma(\mathbf{x},\theta) + \sigma\varepsilon, \tag{10}$$

where $T(\cdot)$ is a variance stabilizing transformation, $C(\mathbf{x},\Theta)$ is the dimensionless capacity, $\mathbf{x}$ are the measurable capacity variables, and $\Theta = \{\theta,\sigma\}$ are unknown model parameters. On the right side of Eq. (10), $\hat{C}(\mathbf{x})$ is a deterministic model based on mechanics rules (also borrowed directly from technical standards), $\gamma(\mathbf{x},\theta)$ is a correction term based on mechanics rules and evidence derived from the experimental data. The product $\sigma\varepsilon$ is the model error, with model standard deviation σ and normally distributed random variable ε. The model is based on three assumptions: additivity (i.e., the additivity of $\sigma\varepsilon$); homoskedasticity (i.e., the independence of σ from $\mathbf{x}$); normality (i.e., the normality of ε). Through a suitable choice of $T(\cdot)$, such assumptions can be approximately satisfied in the transformed space, within the range of the data used to calibrate the model. The correction term $\gamma(\mathbf{x},\theta)$ is selected as a linear combination of n dimensionless explanatory functions $h_i(\mathbf{x})$ and reads

$$\gamma(\mathbf{x},\theta) = \theta^{\mathrm{T}} \cdot \mathbf{h}(\mathbf{x}). \tag{11}$$

The set of explanatory functions $\mathbf{h}(\mathbf{x}) = \{h_1(\mathbf{x}),..,h_n(\mathbf{x})\}$ is constructed starting from physical variables not included in $\hat{C}(\mathbf{x})$ that may be relevant for the described physical phenomenon, but also from those included in $\hat{C}(\mathbf{x})$ and the effect of which should be recalibrated in light of the available experimental data. The parameters collected into Θ are calibrated using the Bayesian approach (Box and Tiao, 1992). It combines the prior knowledge on the parameters, which is contained in the prior distribution of Θ, $f'(\Theta)$, with the information provided by the data, which is contained in the likelihood function, $L(\Theta)$. The posterior distribution of the parameters $f''(\Theta)$ is defined as follows:

$$f''(\Theta) = kL(\Theta)f'(\Theta), \tag{12}$$

and it is obtained by dividing the product $L(\Theta)f'(\Theta)$ by the evidence k, which is the following normalizing constant:

$$k^{-1} = \left[\int_{\Omega_\Theta} \mathcal{L}(\Theta)f'(\Theta)\mathrm{d}\Theta\right], \tag{13}$$

where Ω_Θ is the parameters space.

The posterior distributions $f''(\Theta)$ obtained after the calibration can be used to find a point estimate for the model by ignoring the epistemic uncertainties in the model parameters. An alternative approach is used in the present study, which also accounts for the epistemic uncertainties in the model parameters. This alternative approach assumes Θ as random variables and find a predictive estimate of $C(\mathbf{x},\Theta)$ in agreement with (Gardoni, Der Kiureghian, and Mosalam, 2002) as follows:

$$\tilde{C}(\mathbf{x}) = \int_{\Omega_\Theta} C(\mathrm{x};\Theta)f''^{(\Theta)}\mathrm{d}\Theta. \tag{14}$$

Since an analytical solution for Eq. (16) is often missing, it is opportune to find a numerical approximation of the distribution of $\tilde{C}(\mathbf{x})$ by sampling from $f''(\Theta)$ and finding the corresponding realizations of $C(\mathbf{x};\Theta)$. In this way, it is possible to assume the sample mean of such realizations as predictive estimate and define the $\alpha\%$ confidence interval, where the lower and upper bounds are given by:

$$\{0.5(100-\alpha),\ [100-0.5(100-\alpha)]\}. \tag{15}$$

In this specific case, non-informative priors are chosen in the form of Gaussian distribution with zero means and large variance for all the parameters. In order to facilitate the use of the model and its possible implementation into technical standards, it should be parsimonious (i.e., with a correction term constructed using a limited number of explanatory functions n) and as accurate as possible (i.e., with a small value of standard deviation σ). However, a reduction of n usually entails a higher value of σ. Stepwise deletion allows finding a compromise between parsimony and accuracy. There are several procedures to apply stepwise deletion, and they mostly differ in the deletion criteria, such as the stepwise deletion based on p-values (Stone, 1996).

The stepwise deletion process used in this paper starts with a model that includes all the candidate explanatory functions, and at each step removes the explanatory function with the highest coefficient of variation (COV) of the corresponding θ_i, as proposed in (Gardoni, Der Kiureghian, and Mosalam, 2002). Once an explanatory function is removed, the model is re-calibrated and the deletion process repeated. The deletion process ends when either σ grows beyond an undesirable threshold, or the increment of σ is too large compared to the reduction of the model complexity.

3 THEORETICAL BACKGROUND

The model of the axial capacity of CFST columns follows the form presented in Eq. (10). The modeled non-dimensional capacity parameter is $C(\mathbf{x}, \Theta) = \tilde{N}_u(\mathbf{x}_u, \Theta_u)/N_c$, i.e., the ratio between the axial capacity of CFST columns $\tilde{N}_u(\mathbf{x}_u, \Theta_u)$ and the total compressive strength of the concrete core $N_c = f_c A_c$. For this model, the measurable capacity variables are $\mathbf{x}_u = \mathbf{s}$, and $\Theta_u = \{\theta_u, \sigma_u\}$ is the set of unknown model parameters. The variance stabilizing transformation used to approximately satisfy the additivity, normality, and homoskedasticity assumptions is the natural logarithm $T(\cdot) = \ln(\cdot)$ (Box and Tiao, 1992). The chosen deterministic model is the ratio between the plastic compression resistance $N_{pl} = f_c A_c + f_y A_s$ and N_c, i.e., $\hat{C}(\mathbf{x}) = N_{pl}/N_c = 1 + \xi$. Consequently, Eq. (10) is rewritten as

$$\ln\left[\frac{\tilde{N}_u(\mathbf{x}_u, \Theta_u)}{N_c}\right] = \ln(1+\xi) + \gamma_u(\mathbf{x}_u, \theta_u) + \sigma_u \varepsilon, \tag{16}$$

or, equivalently, as

$$\ln\left[\frac{\tilde{N}_u(\mathbf{x}_u, \Theta_u)}{N_{pl}}\right] = \gamma_u(\mathbf{x}_u, \theta_u) + \sigma_u \varepsilon \tag{17}$$

Through this formulation, the axial capacity of the CFST column is expressed as follows:

$$\tilde{N}_u(\mathbf{x}_u, \Theta_u) = N_{pl} \mathrm{e}^{[\gamma_u(\mathbf{x}_u, \theta_u) + \sigma_u \varepsilon]}, \tag{18}$$

and the exponential factor derived from the correction term assumes the meaning of Strength Index (SI), which is a dimensionless parameter that quantifies the strength improvement of CFST columns due to the confinement effect and defined as the ratio N_u/N_{pl} (Wang, Fan, and Lai, 2022). Given the normality assumption, a 67% confidence interval for $\ln\left[\tilde{N}_u(\mathbf{x}_u, \Theta_u)/N_c\right]$ can be found as follows:

$$\{\ln(1+\xi) + \gamma_u(\mathbf{x}_u, \theta_u) - \sigma_u, \ln(1+\xi) + \gamma_u(\mathbf{x}_u, \theta_u) + \sigma_u\}, \tag{19}$$

whereas the corresponding confidence interval for $\tilde{N}_u(\mathbf{x}_u, \Theta_u)$ is

$$\left\{N_{pl} e^{[\gamma_u(\mathbf{x}_u, \theta_u) - \sigma_u]}, N_{pl} e^{[\gamma_u(\mathbf{x}_u, \theta_u) + \sigma_u]}\right\}. \tag{20}$$

Table 1 shows the set of non-dimensional candidate explanatory functions $h_{ui}(\mathbf{x}_u)$ used in the initial step of the stepwise deletion process. The first explanatory function $h_{u1}(\mathbf{x}_u)$ takes into account a possible constant bias. The second and third explanatory functions, $h_{u2}(\mathbf{x}_u)$ and $h_{u3}(\mathbf{x}_u)$, are suggested by the formulation proposed by the Eurocode 4 (Eurocode 4, 2004) and are used to evaluate the possible effects of the relative slenderness λ_r defined as follows:

$$\lambda_r = \left(\frac{N_{pl}}{N_{cr}}\right)^{\frac{1}{2}}, \tag{21}$$

where

$$N_{cr} = \frac{\pi^2 EI_{eff}}{L^2} \tag{22}$$

is the elastic critical normal force for the relevant buckling mode, L is the length of the CFST column, and EI_{eff} is the characteristic value of the effective flexural stiffness of the cross-section given by

$$EI_{eff} = E_s I_s + 0.6 E_c I_c. \tag{23}$$

Herein, I_s and I_c are the second moments of area of the steel tube and concrete core, respectively. Moreover, E_s and E_c are the Young modulus of steel and concrete, respectively.

Table 1. Set of non-dimensional candidate explanatory functions $h_{ui}(\mathbf{x}_u)$ used in the initial step of the stepwise deletion process.

Explanatory functions		
$h_{u1}(\mathbf{x}_u) = 1$	$h_{u6}(\mathbf{x}_u) = \psi$	$h_{u10}(\mathbf{x}_u) = \xi$
$h_{u2}(\mathbf{x}_u) = \lambda_r$	$h_{u7}(\mathbf{x}_u) = \lambda_r \psi$	$h_{u11}\ (\mathbf{x}_u) = \lambda_r \xi$
$h_{u3}(\mathbf{x}_u) = \lambda^2{}_r$	$h_{u8}(\mathbf{x}_u) = \lambda_r^2 \psi$	$h_{u12}(\mathbf{x}_u) = \lambda_r^2 \xi$
$h_{u4}(\mathbf{x}_u) = \lambda$	$h_{u9}(\mathbf{x}_u) = \lambda \psi$	$h_{u13}(\mathbf{x}_u) = \lambda \xi$
$h_{u5}(\mathbf{x}_u) = \frac{t}{D}$	—	$h_{u14}(\mathbf{x}_u) = \frac{t}{D} \xi$

Similarly, $h_{u4}(\mathbf{x}_u)$ explores the possible contribution of the geometric slenderness ratio $\lambda = L/D$, whereas $h_{u5}(\mathbf{x}_u)$ reflects the contribution of the relative thickness of steel tube and concrete core. The explanatory functions $h_{u6}(\mathbf{x}_u)$-$h_{u9}(\mathbf{x}_u)$ and $h_{u10}(\mathbf{x}_u)$-$h_{u14}(\mathbf{x}_u)$ search for the interactions between the same effects relevant for the explanatory functions $h_{u1}(\mathbf{x}_u)$-$h_{u5}(\mathbf{x}_u)$ and the contributions due to the confinement effect and steel tube (i.e., ψ and ξ, respectively). The model $\tilde{N}_u(\mathbf{x}_u, \boldsymbol{\Theta}_u)$ is calibrated with records from the database analysed in (Thai *et al.*, 2019). The database contains tests conducted on both rectangular and circular CFST columns and includes data obtained from specimens with high-strength materials and slender sections. Some of the data are collected from tests where the normal force is applied in an eccentric position (i.e., tests where the members are subjected to combined axial compression and bending moment). Only data from tests without eccentricity of the applied axial loads and CFST columns with circular cross-section are herein used for the calibration of $\tilde{N}_u(\mathbf{x}_u, \boldsymbol{\Theta}_u)$, thereby resulting in a total of 815 records. Figure 1 presents the results of the stepwise deletion process for the axial capacity model. For each step, the figure shows the value for the posterior mean of σ_u, which is represented by a square, and the coefficients of variation of the θ_{ui}'s related to the h_{ui}'s included at that step, which are represented by dots. The dots with a cross denote the coefficients of variation of the terms that are dropped. The red line represents the value of σ_u at the first step, and it is used to facilitate the comparison with the values of σ_u in the following steps. The figure also explicitly shows the values of σ_u at some selected steps.

In the first step, the selection process removes h_{u4}, which is the term associated with the parameter that has the largest coefficient of variation, θ_{u4}, being $\mathrm{COV}_{\theta_{u4}} = 1.57$. One term is removed at each step up to Step 10, which leads to the elimination of θ_{u12} and a 5% cumulative increase in σ_u. The process stops at Step 11 because removing h_{u1}

would result in a cumulative increase in σ_u higher than 10%, which is deemed excessive, and because the additional step would entail an increase in σ_u equivalent to the cumulative increase of the first 10 steps. The 10% threshold is chosen to have a parsimonious model that could be adopted in technical standards. Moreover, the difference in accuracy between the reduced model and the full model (i.e., the model obtained without applying the stepwise deletion process) is limited. The reduced model resulting from the selection process has $\gamma_u(\mathbf{x}_u, \theta_u)$ in the following form:

$$\gamma_u(\mathbf{x}_u, \theta_u) = \theta_{u0} + \theta_{u2}\lambda_r + \left(\theta_{u10} + \theta_{u14}\frac{t}{D}\right)\xi \ . \tag{24}$$

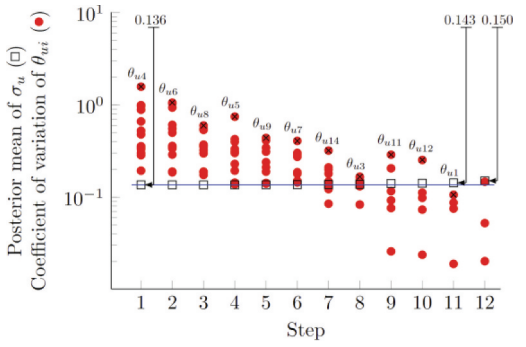


Figure 1. Stepwise deletion process for the axial capacity model.

This formulation suggests that there may be a systematic bias in the deterministic predictions obtained with N_{pl} because h_{u1} is retained in the model. It also shows that λ_r plays a significant role in reducing the axial capacity of CFST columns. The combined effect of h_{u10} and h_{u14} likely accounts for the confinement effect, which is proportional to the compressive strength of the steel column and depends on the t/D ratio. Table 4 gives the posterior statistics of the five model parameters. Figure 2 shows the predicted versus measured capacity for each test. The closer the data points are to the 1:1 lines (i.e., the continuous lines in the figure), the more accurate are the predictions. Figures 2(a) and 2(b) compare predictions made considering the plastic resistance to compression.

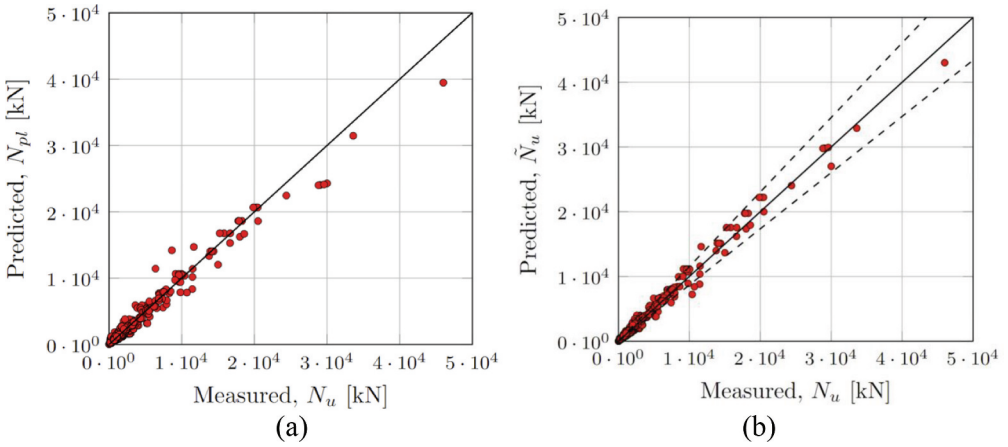


Figure 2. Predicted versus measured values of the axial capacity: (a) predictions with plastic resistance to compression; (b) predictions with proposed probabilistic model.

4 COMPARISON BETWEEN STANDARDS AND LITERATURE FORMULATIONS

Figure 3 presents a comparative assessment of the axial capacity of CFST columns in terms of the ratio between numerical predictions and corresponding experimental values $r_u = N_u pre/N_u exp$. The figure presents both predictions made with code-conforming formulations (ACI Committee 318, 1995; Eurocode 4, 2004; AISC Committee and others, 2010; GB 50923-2013, 2013) and with formulations from the literature (Goode and Narayanan, 1997; Giakoumelis and Lam, 2004; Ho and Le, 2021). A short presentation of these formulations is provided in Appendix. This assessment is intended to analyse the differences between the formulations and should not be considered as a competitive evaluation of their accuracy. This is because the existing formulations considered for the present comparative assessment might have been developed on a testing dataset instead of the complete dataset, or because the code-conforming formulations require design values and are not intended for mean values, or even because the considered formulations may not be valid for the intervals of the parameters in the considered dataset. Table 2 shows the statistics of the distributions of r_u obtained from the different formulations considered in the comparative assessment.

Table 2. Comparison between literature and technical standards, where S.D stands for Standard Deviation while M.S.E. for Mean Square Error.

Formulation	Mean	S.D.	M.S.E.
EC4	1.084	0.593	0.359
AISC	1.091	0.472	0.231
ACI	1.033	0.453	0.206
Goode et al. (1997)	0.627	0.284	0.219
Giakoumelis and Lam (2004)	1.293	0.546	0.384
Xue et al. (2013)	0.912	0.189	0.044
Ho and Le (2021)	1.188	0.230	0.056
Proposed	1.011	0.155	0.024

It can be observed from Figure 3 and Table 2 that all code-conforming formulations tend to underestimate the axial capacity of CFST columns. The formulations collected from the existing literature show a progressive increment of accuracy in time. Particularly, the formulation proposed by Ho and Le (Ho and Le, 2021) based on support vector machine and the one proposed

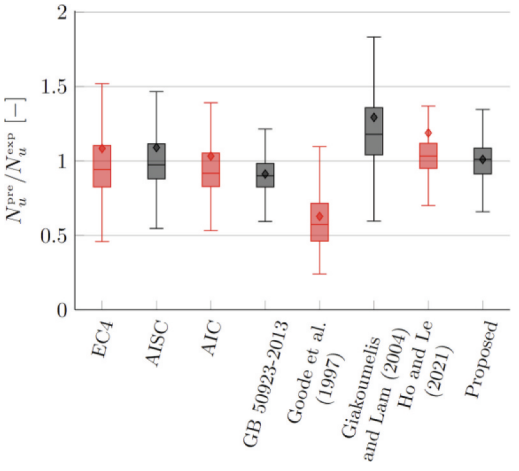


Figure 3. Comparison among predictions of the axial capacity of CFST columns in terms of box plot of the ratio between numerical predictions and corresponding experimental values $N_u pre/N_u exp$ (complete dataset of 815 samples).

in the present study show comparable levels of accuracy. The main difference with the earliest formulations (Goode and Narayanan, 1997; Giakoumelis and Lam, 2004) is the lack of the confinement effect, which is either not considered (in (Goode and Narayanan, 1997)) or overestimated (in (Giakoumelis and Lam, 2004)).

5 DERIVATION OF UNCERTAINTY FACTORS FOR DESIGN APPLICATION

The potential use of the proposed formulation for practical applications requires the definition of an uncertainty factor γ_{Nd} for the calculation of the design value of the axial capacity. Such uncertainty factor is needed to avoid the underestimation of the axial capacity due to the involved uncertainties, in such a way that the design can ensure a safety margin in compliance with code regulations. The code-format design axial capacity can be defined as follows:

$$N_{ud} = \frac{\eta}{\gamma_{Nd}} \tilde{N}_u(\mathbf{x}_{ud}, \Theta_u), \tag{25}$$

where η is a conversion factor that depends on the technical standard (Eurocode 4, 2004) and $\mathbf{x}_{ud}$ is the vector of the design values of the capacity variables. In a similar fashion, for CFST columns with axial load applied in eccentric position or with debonding, the code-format design axial capacity reads

$$N_{ud} = \frac{\eta}{\gamma_{Nd}} \tilde{k}_e(\mathbf{x}_{ed}, \Theta_e) \tilde{N}_u(\mathbf{x}_{ud}, \Theta_u), \tag{26}$$

and

$$N_{ud} = \frac{\eta}{\gamma_{Nd}} \tilde{k}_d(\mathbf{x}_{dd}, \Theta_d) \tilde{N}_u(\mathbf{x}_{ud}, \Theta_u), \tag{27}$$

respectively. The estimation of γ_{Nd} is performed by assuming that the design value is less than the corresponding experimental value with a probability equal to p as

$$P\left[N_{ud} < N_u^{exp}\right] = p. \tag{28}$$

The value of p depends on the reference technical standard. The estimation of γ_{Nd} is performed with $\eta = 1$ and characteristic values of compressive concrete strength and steel yielding stress equal to those in the experimental database used for the model calibration. The ratio of the number of samples for which $N_{ud} > N_u^{exp}$ and the total number of samples is used to estimate $P[N_{ud} < N_u^{exp}]$ and the corresponding value of γ_{Nd}. Table 3 compares the values of γ_{Nd} obtained for three different technical standards, namely Eurocodes, AASHSTO, and GB50923-2013.

The European building code sets p as $\Phi(\alpha_R \beta_{LS})$, where $\Phi(\cdot)$ is the standard Normal cumulative distribution function, α_R is the sensitivity factor for the capacity, and β_{LS} is the safety index relevant to the considered limit state. Assuming a 50-years reference period and an ultimate limit state, $\Phi(\alpha_R \beta_{LS})$=0.9988. For AASHSTO, the value of p is derived as $p = \Phi(3.5) = 0.9997$ because $\beta = 3.5$ is the target reliability index. Following the specifications of the GB50923-2013 technical standard, the value of p is derived assuming a ductile failure and the 2nd safety level, which lead to $p = \Phi(3.2) = 0.9993$. The calibration of γ_{Nd} is performed with all available data, including those with eccentric applied axial load and debonding. The accuracy in approaching the target values of p and, consequently, in defining an accurate value of γ_{Nd} is determined by both the number of available samples and the distribution of N_u^{exp}. Since 1006 tests are used, the probability values closer to the target values of p are $p^* = 1004/1006 = 0.9980$, $p^* = 1005/1006 = 0.9990$, and $p^* = 1006/1006 = 1.000$. The values of γ_{Nd} corresponding to the target values of p are obtained by linear interpolation. Table 3 shows the results of the calibration.

The higher values of γ_{Nd} derived for the AASHTO compared to those obtained for the Eurocode 4 and GB50923-2013 are due to both the higher target reliability index and the higher design values of the compressive concrete strength and steel yielding stress.

Table 3. Model uncertainty factors for γ_{Nd} for the proposed axial capacity derived according to the three different technical standards.

Technical Standard	Target p value	γ_{Nd} p=0.998	γ_{Nd} p=0.999	γ_{Nd} p=1.000	γ_{Nd} Interp.
EC4	0.9988	1.599	1.815	—	1.772
AASHTO	0.9997	—	2.276	3.128	2.872
GB50923-2013	0.9993	—	1.642	2.484	1.895

6 CONCLUSIONS

The beneficial interaction between steel tube and infilled concrete core has promoted the large diffusion of CFST columns in many projects over the years. To begin with, the concrete core prevents the inward local buckling of the steel tube. At the same time, the steel tube confines the concrete core. Such synergy results in high load-carrying capacity and enhanced ductility, that come together with economic and construction efficiency benefits due to the use of the steel tube as permanent formwork. Motivated by these attractive features, a large amount of experimental, analytical, and numerical studies about CFST columns under axial load have been performed in the last decades, but a probabilistic capacity model has not been proposed yet. Hence, the present study is meant at filling this gap and, to this end, proposed a comprehensive probabilistic model for the axial capacity of CFST columns. The probabilistic models for the axial capacity is derived by means of a Bayesian approach taking into rational account, both, model parsimony and model accuracy. The predictive performance of the proposed probabilistic capacity models are discussed within a comparative assessment that involves existing formulations collected from some available technical standards and previous researches. To foster the use of the proposed formulation for design purposes, the paper also provides uncertainty factors calibrated to meet the reliability levels required by three different technical standards.

REFERENCES

ACI Committee 318 (1995) 'Building Code Requirements for Structural Concrete: (ACI 318-95)'.

AISC Committee and others (2010) 'Specification for structural steel buildings (ANSI/AISC 360-10)'.

Box, G. E. P. and Tiao, G. C. (1992) *Bayesian Inference in Statistical Analysis*. John Wiley & Sons, Ltd.

Eurocode 4 (2004) 'Design of composite steel and concrete structures-Part 1.1: General rules and rules for buildings'.

Gardner, N. J. and Jacobson, E. R. (1967) 'Structural behavior of concrete-filled steel tubes', in *Journal Proceedings*, pp. 404–413.

Gardoni, P., Der Kiureghian, A. and Mosalam, K. M. (2002) 'Probabilistic capacity models and fragility estimates for reinforced concrete columns based on experimental observations', *Journal of Engineering Mechanics*, 128(10), pp. 1024–1038.

GB 50923-2013 (2013) 'Technical Code for Concrete-filled Steel Tube Arch Bridges'.

Giakoumelis, G. and Lam, D. (2004) 'Axial capacity of circular concrete-filled tube columns', *Journal of Constructional Steel Research*, 60(7), pp. 1049–1068.

Goode, C. D. and Lam, D. (2011) 'Concrete-Filled Steel Tube Columns-Tests Compared with Eurocode 4', in *Composite Construction in Steel and Concrete VI*, pp. 317–325.

Goode, C. D. and Narayanan, R. (1997) 'Design of concrete filled steel tubes to EC4′, in *Proceedings of the ASCCS Seminar on Concrete Filled Steel Tubes—A Comparison of International Codes and Practice*, pp. 1–25.

Hassanein, M. F. *et al.* (2018) 'Finite element analysis of large diameter high strength octagonal CFST short columns', *Thin-Walled Structures*, 123, pp. 467–482.

Ho, N. X. and Le, T.-T. (2021) 'Effects of variability in experimental database on machine-learning-based prediction of ultimate load of circular concrete-filled steel tubes', *Measurement*, 176, p. 109198.

Johansson, M. (2002) 'The efficiency of passive confinement in CFT columns', *Steel and Composite Structures*, 2(5), pp. 379–396.

Johansson, M. and Gylltoft, K. (2001) 'Structural behavior of slender circular steel-concrete composite columns under various means of load application', *Steel and Composite Structures*, 1(4), pp. 393–410.
van de Lindt, J. W. and Gupta, R. (2006) 'Damage and damage prediction for wood shearwalls subjected to simulated earthquake loads', *Journal of performance of constructed facilities*, 20(2), pp. 176–184.
Morino, S. (2002) 'Concrete-filled steel tube column system: recent research and construction in Japan', in *Proceeding of the 1st Fib Congress*, pp. 1–16.
De Nardin, S., El Debs, A. and others (2004) 'An experimental study of connections between I-beams and concrete filled steel tubular columns', *Steel and Composite Structures*, 4(4), p. 303.
O'Shea, M. D. and Bridge, R. Q. (2000) 'Design of circular thin-walled concrete filled steel tubes', *Journal of Structural Engineering*, 126(11), pp. 1295–1303.
Richart, F. E., Brandtzæg, A. and Brown, R. L. (1928) *A study of the failure of concrete under combined compressive stresses*.
Richart, F. E., Brandtzæg, A. and Brown, R. L. (1929) *Failure of plain and spirally reinforced concrete in compression*.
Saatcioglu, M. and Razvi, S. (1992) 'Strength and ductility of confined concrete', *Journal of Structural Engineering*, 118:6.
Sakino, K. *et al.* (2004) 'Behavior of Centrally Loaded Concrete-Filled Steel-Tube Short Columns', *Journal of Structural Engineering*, 130(2), pp. 180–188.
Shanmugam, N. E. and Lakshmi, B. (2001) 'State of the art report on steel-concrete composite columns', *Journal of Constructional Steel Research*, 57(10), pp. 1041–1080.
Stone, C. J. (1996) *A course in probability and statistics*. Belmont: Duxbury Press.
Susantha, K. A. S., Ge, H. and Usami, T. (2001) 'A capacity prediction procedure for concrete-filled steel columns', *Journal of Earthquake Engineering*, 5(04), pp. 483–520.
Thai, S. *et al.* (2019) 'Concrete-filled steel tubular columns: Test database, design and calibration', *Journal of Constructional Steel Research*, 157, pp. 161–181.
Timoshenko, S. (1983) *History of strength of materials: with a brief account of the history of theory of elasticity and theory of structures*. Courier Corporation.
Wang, X., Fan, F. and Lai, J. (2022) 'Strength behavior of circular concrete-filled steel tube stub columns under axial compression: A review', *Construction and Building Materials*, 322, p. 126144.
Xue, J.-Q., Briseghella, B. and Chen, B.-C. (2012) 'Effects of debonding on circular CFST stub columns', *Journal of Constructional Steel Research*, 69(1), pp. 64–76.
Zeghiche, J. and Chaoui, K. (2005) 'An experimental behaviour of concrete-filled steel tubular columns', *Journal of Constructional Steel Research*, 61(1), pp. 53–66.


Taylor & Francis
Taylor & Francis Group
http://taylorandfrancis.com

MS06: AI and robotics for bridges: Monitoring, assessment, and maintenance

Organizers: Y. Dong, D.M. Frangopol, B. Wang & X. Lei


Taylor & Francis
Taylor & Francis Group
http://taylorandfrancis.com

Bridge Maintenance, Safety, Management, Digitalization and Sustainability – Jensen, Frangopol & Schmidt (eds)
© 2024 The Author(s), ISBN 978-1-032-77040-6
Open Access: www.taylorfrancis.com, CC BY-NC-ND 4.0 license

Bridge condition assessment with full-scale view and computer vision methods

Xiaoming Lei & You Dong
Department of Civil and Environmental Engineering, Hong Kong Polytechnic University, Hung Hom, Kowloon, Hong Kong

Dan M. Frangopol
Department of Civil and Environmental Engineering, ATLSS Engineering Research Center, Lehigh University, Pennsylvania, USA

ABSTRACT: Bridge condition assessment is vital for ensuring the safety and reliability of transportation infrastructure. Traditional inspection methods have limitations in terms of efficiency and coverage, motivating the exploration of innovative technologies. Our methodology introduces a robust image stitching approach, which enables the creation of full-scale views of target structures by seamlessly combining a vast number of single images from different vantage points. To facilitate efficient defect detection, segmentation techniques are used to automatically identify target structural surfaces and associated defects. This streamlined process significantly reduces the need for manual intervention, making the inspection more efficient and reliable. The advantages of the full-scale view-based approach lie in its ability to cover large bridge span with a single panoramic image, thus reducing the inspection time and enhancing safety by minimizing the need for inspectors to work in hazardous locations. The paper concludes by highlighting the significant impact of full-scale image-based assessment on bridge inspection, offering a cost-effective and reliable solution for infrastructure management. By leveraging advanced computer vision and deep learning techniques, the proposed approach represents a promising step towards ensuring the long-term integrity and safety of the transportation infrastructure.

1 INTRODUCTION

Bridges serve as essential components of transportation infrastructure, playing a crucial role in ensuring efficient connectivity and safe passage for vehicles and pedestrians(Lei et al., 2023). The assessment of bridge conditions is paramount to maintaining their structural integrity and, consequently, guaranteeing public safety (Lei et al., 2022, Dong et al., 2013). Traditional methods of bridge inspection often rely on visual assessments, which are not only time-consuming but also subject to human bias (Morgenthal et al., 2019). As the demand for more efficient and reliable inspection techniques grows, this study introduces a pioneering approach that combines full-scale view imaging and advanced computer vision methods for comprehensive bridge condition assessment.

The proposed methodology addresses the limitations of conventional inspection practices by leveraging a robust image stitching technique. This process seamlessly integrates numerous single images captured from diverse vantage points, creating expansive full-scale views of the target bridge structure. To enhance defect detection accuracy and streamline the inspection process, segmentation techniques are employed to automatically identify structural surfaces and associated anomalies (Gul et al., 2015). This innovative approach significantly reduces the reliance on manual intervention, thereby improving the efficiency and reliability of bridge assessments.

DOI: 10.1201/9781003483755-78

One of the key advantages of the full-scale view-based methodology is its ability to cover extensive bridge spans with a single panoramic image (Hu et al., 2023). This not only accelerates the inspection process but also enhances safety by minimizing the need for inspectors to work in hazardous locations. The amalgamation of advanced computer vision and deep learning techniques further contributes to the efficiency of defect identification and classification.

This paper aims to shed light on the transformative impact of full-scale image-based assessment on bridge inspections. By offering a cost-effective and reliable solution for infrastructure management, the proposed approach represents a significant advancement in ensuring the long-term integrity and safety of transportation infrastructure. Through the integration of cutting-edge technologies, this study contributes to the evolving landscape of bridge condition assessment, emphasizing the potential for improved accuracy, efficiency, and overall reliability in the evaluation of critical transportation assets.

2 OVERALL FRAMEWORK

The first step in our framework involves the application of a robust image stitching technique to seamlessly combine multiple images captured from diverse vantage points. This process aims to create comprehensive full-scale views of the target bridge structure. Advanced algorithms for image registration and feature matching will be employed to ensure the accurate alignment of images, resulting in a panoramic representation of the entire bridge span.

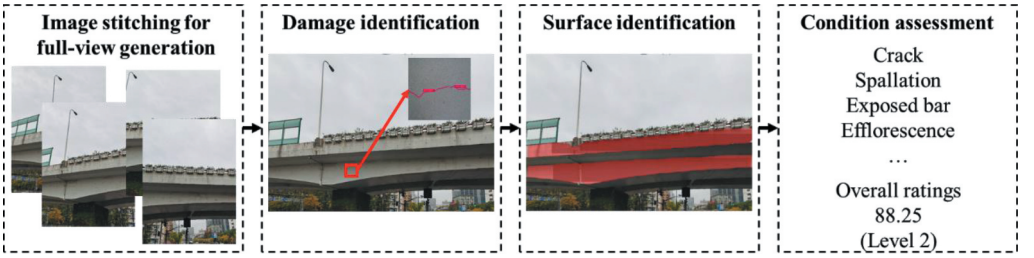


Figure 1. Full-view generation of bridge.

Following the generation of full-scale views, the next stage focuses on the automatic identification and segmentation of damaged areas on the bridge structure. Computer vision algorithms will be applied to analyze the visual data and detect anomalies or defects. These algorithms will be trained to recognize patterns associated with common types of structural damage, such as cracks, corrosion, or deformations. The output of this step is a segmented representation highlighting regions of potential damage.

To enhance the precision of defect detection and analysis, the framework includes a bridge surface segmentation process. This step involves the automatic identification and delineation of distinct structural surfaces within the bridge, such as decks, piers, and abutments. Accurate segmentation is crucial for isolating specific areas of interest, enabling focused assessments and reducing false positives in damage detection. Computer vision techniques, including semantic segmentation, will be employed to achieve reliable and detailed surface segmentation.

The final step of the framework involves a comprehensive structural assessment based on the segmented data. By integrating the information obtained from image stitching, damage segmentation, and bridge surface segmentation, the framework facilitates a holistic evaluation of the bridge's overall condition. Advanced algorithms, possibly incorporating machine learning models, will be employed to analyze the structural health and identify potential risks. The output will provide a detailed assessment report, highlighting the condition of different structural components and recommending necessary maintenance or repair actions.

By incorporating these four steps into our framework, we aim to establish a systematic and efficient approach to bridge condition assessment. The integration of image stitching, damage segmentation, bridge surface segmentation, and structural assessment leverages the capabilities

of computer vision methods to enhance the accuracy and reliability of the inspection process, ultimately contributing to the safety and longevity of critical transportation infrastructure.

3 IMAGE STITCHING METHOD

Image stitching is a computer vision technique used to combine multiple images into a larger, seamless panorama. This method is commonly employed to create panoramic photographs or to produce wide-angle views of scenes that cannot be captured in a single shot. The process involves aligning and blending overlapping images to create a cohesive and visually continuous result. Here is a step-by-step description of the image stitching method:

1) Image Acquisition: Capture a series of images of a scene, ensuring that each image overlaps with the adjacent ones. These images are usually taken from different viewpoints or angles.
2) Feature Extraction: Identify distinctive features in each image, such as corners, edges, or keypoints. These features serve as reference points for aligning and matching images.
3) Image Alignment: Align the images by matching the extracted features. This step involves adjusting the position, rotation, and scale of each image to ensure a precise overlap. Techniques like geometric transformation or homography are often used for this purpose.
4) Image Blending: Blend the aligned images seamlessly to create a smooth transition between them. This involves adjusting pixel intensities along the overlapping regions to avoid visible seams. Various blending algorithms, such as feathering or gradient-based blending, can be applied to achieve a natural and continuous appearance.
5) Panorama Composition: Combine the aligned and blended images into a single panoramic image. The resulting panorama provides a wide-angle view that encompasses the entire scene captured in the input images.
6) Color and Exposure Adjustment: Ensure consistent color and exposure across the panorama by applying adjustments to match the tones and lighting conditions of the original images. This step enhances the overall visual coherence of the stitched panorama.
7) Output: The final output is a seamless and visually cohesive panoramic image that represents a wider field of view than any of the individual input images. This stitched image provides a comprehensive representation of the captured scene.

4 DAMAGE SEGMENTATIONS

Damage segmentation with the YOLOv8 (You Only Look One-level) method involves employing a state-of-the-art object detection algorithm to identify and delineate areas of structural damage within images. YOLOv8 is part of the YOLO family of real-time object detection models, known for their speed and accuracy.

5 STRUCTURAL SURFACE SEGMENTATIONS

Structural surface segmentation with the YOLOv8 method involves leveraging the capabilities of the YOLOv8 object detection algorithm to automatically identify and delineate distinct structural surfaces within images of bridges. The final output includes visual representations of the original image with overlaid bounding boxes and segmentation maps, highlighting the identified structural surfaces. These visual outputs offer a clear and detailed overview of the different components, aiding in further analysis and assessment.

6 CONDITION ASSESSMENT

Condition assessment for bridges using full-view images involves a comprehensive analysis of the visual data captured through panoramic or full-scale images. Apply image stitching



Figure 2. Image capturing for the full-view stitching.



Figure 3. Full-view generation of bridge.

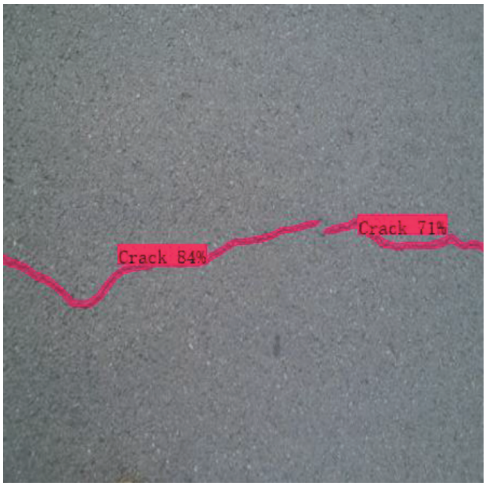


Figure 4. Damage segmentation.



Figure 5. Structural surface segmentations.

methods to seamlessly combine the individual images into a single, panoramic view. This creates a comprehensive representation of the entire bridge, allowing for a detailed inspection without the need for inspectors to physically traverse the structure. Perform quantitative analysis on the full-view images to assess parameters such as cracks, voids, spallation, etc. This involve comparing current conditions to baseline data or industry standards to determine the severity of identified issues.

Generate comprehensive reports and visualizations based on the analysis of the full-view images. This includes detailed maps of detected defects, the condition of structural components, and any recommended maintenance or repair actions. Visualization tools can assist in conveying complex information to stakeholders in an accessible manner. Integrate the findings from the full-view image assessment into broader infrastructure management systems. This allows for long-term tracking of the bridge's condition, facilitates maintenance planning, and supports decision-making for asset management.

7 CONCLUSIONS

In conclusion, the integration of full-view images and advanced computer vision methods for the condition assessment of bridges represents a significant leap forward in the field of infrastructure inspection. This study introduced a comprehensive framework that leverages panoramic images to provide a holistic view of bridge structures and employed sophisticated computer vision techniques, including image stitching, damage segmentation, and structural surface segmentation, to automate and enhance the assessment process.

REFERENCES

Dong, Y., Frangopol, D.M. & Saydam, D. 2013. Time-variant sustainability assessment of seismically vulnerable bridges subjected to multiple hazards. *Earthquake Engineering & Structural Dynamics*, 42, 1451–1467.

Gul, M., Catbas, F.N. & Hattori, H. 2015. Image-Based Monitoring of Open Gears of Movable Bridges for Condition Assessment and Maintenance Decision Making. *Journal of Computing in Civil Engineering*, 29.

Hu, H., Wang, J.J., Dong, C.Z., Chen, J.Q. & Wang, T. 2023. A hybrid method for damage detection and condition assessment of hinge joints in hollow slab bridges using physical models and vision-based measurements. *Mechanical Systems and Signal Processing*, 183.

Lei, X., Dong, Y. & Frangopol, D.M. 2023. Sustainable Life-Cycle Maintenance Policymaking for Network-Level Deteriorating Bridges with a Convolutional Autoencoder–Structured Reinforcement Learning Agent. *Journal of Bridge Engineering*, 28, 04023063.

Lei, X.M., Xia, Y., Dong, Y. & Sun, L.M. 2022. Multi-level time-variant vulnerability assessment of deteriorating bridge networks with structural condition records. *Engineering Structures*, 266.

Morgenthal, G., Hallermann, N., Kersten, J., Taraben, J., Debus, P., Helmrich, M. & Rodehorst, V. 2019. Framework for automated UAS-based structural condition assessment of bridges. *Automation in Construction*, 97, 77–95.

Bridge Maintenance, Safety, Management, Digitalization and Sustainability – Jensen, Frangopol & Schmidt (eds)
© 2024 The Author(s), ISBN 978-1-032-77040-6
Open Access: www.taylorfrancis.com, CC BY-NC-ND 4.0 license

Data-driven prediction models for extreme wave impacts on coastal bridges

Deming Zhu, Jiaxin Zhang & You Dong
Department of Civil and Environmental Engineering, The Hong Kong Polytechnic University, Hong Kong, China

ABSTRACT: Coastal bridges are susceptible to extreme waves during coastal natural hazards like tropical cyclones and tsunamis. The investigation of the structural performance of coastal bridges under extreme wave impacts plays a central role in the development of coastal communities. In recent years, deep neural networks based methods emerge and shown promising performance for these hydrodynamic problems. However, their interpretability and generalization remain a major challenge, especially for the complex uncertainties within the hydrodynamic process. In this study, the authors propose to combine the advantages of both experimental studies and deep neural networks for such investigations, so as to achieve reliability, network interpretability, and effectiveness simultaneously. Specifically, laboratory experiments are conducted to test the wave impacts on coastal bridges under various wave scenarios and hydrological environments. The measured wave profiles and wave loads are divided into a multivariate time series and used as the input of a Long-Short-Term-Memory (LSTM) model. Such a prediction method helps to reduce errors caused by experimental uncertainty by substituting every set of the collected data during the repeated experiments into the training set. In summary, the proposed scheme is effective and interpretable, and the comparisons with experimental results demonstrate its superior performance in predicting the structural performance of coastal bridges under wave impacts.

1 INTRODUCTION

Coastal bridges, serving as crucial elements within transportation systems in cities near shore, face significant safety risks due to the adverse natural environment. The rising sea levels and increasing intensity of hazards resulting from global climate change (e.g., tropical cyclones and tsunami-induced waves) have led to substantial damage to low-lying bridges in recent decades. A post-hazard survey reported that during Hurricane Ivan in 2004, 58 bridge spans became dislodged from their piers, and 66 spans experienced misalignment (Meng and Jin 2007). Afterward, Hurricane Katrina inflicted severe damage on the US 90 highway bridge over Biloxi Bay once again (Robertson et al. 2011). Among the critical failure modes observed in coastal bridges, the failure of deck unseating has been identified as a significant concern. Thus, this has motivated a number of studies to assess to magnitudes of wave loads and bridge failure mechanisms to improve the design and maintenance of coastal bridges.

The study of wave-bridge interactions faces a significant challenge concerning the limited availability of time series analysis of wave loads. While experimental tests and numerical simulations have been conducted to measure wave loads, most of these studies have primarily focused on capturing the maximum vertical and horizontal forces, neglecting the evolving process of external loads on the bridge surface (Jin and Meng 2011; Seiffert et al. 2016). Consequently, the structural performance of coastal bridges subjected to these extreme waves may lack accurate structural demand input, which merely compares the maximum load with the

DOI: 10.1201/9781003483755-79

static capacity of the bridge. This approach fails to fully predict the potential risks associated with periodic wave impacts during actual storm hazards, misleading maintenance and management strategies for high-risk bridges (Zhu et al. 2021b). To address this issue, this study measures the time histories of vertical and horizontal wave forces under different wave intensities. These measurements not only provide an intuitive reflection of the effects of different wave parameters but also serve as datasets for training prediction models.

Experimental methods are reliable for obtaining wave forces on coastal bridges but can be prohibitively expensive and challenging to conduct on a large scale (Xu et al. 2022). In an attempt to overcome these challenges, researchers and engineers have sought to develop full-scale numerical models to approximate wave forces under various hazard scenarios. However, the computational cost associated with creating a sufficiently large database often makes this approach impractical, particularly for reliability and life-cycle analyses that involve extensive computations (Jia et al. 2022; Xiao and Huang 2008). To address these limitations, machine learning (ML) methods have been employed to establish the relationship between input hazard intensities and output structural responses. For instance, Xu et al. (2022) found that ML models exhibited superior capabilities in estimating maximum wave forces, while more datasets were necessary to enhance model quality. Zhu et al. (2021a) utilized ML models to replace time-consuming simulations, facilitating risk assessment and the proposal of mitigation measures, and achieved satisfactory results. However, a common issue is that existing ML technologies primarily focus on peak values, while investigations into the effects of time series data are limited (Hu et al. 2023). Besides, numerical simulations remain the primary source of training data, limiting the wider applications of ML methods. To address this gap, the present study develops a Long Short-Term Memory (LSTM) network based on experimentally measured wave force time histories. Different hyperparameters are tuned and validated to enhance the accuracy of the model.

Overall, this study examines the effects of wave impacts on coastal bridge superstructures and develops data-driven ML techniques for predicting time series results. Laboratory experiments are conducted to investigate the time histories of wave forces. Based on the measured results, LSTM models are established to forecast wave impacts. The optimized LSTM model demonstrates favorable performance in forecasting wave forces under different wave scenarios. This model could provide more accurate load inputs for addressing the engineering challenge of coastal bridge interactions.

2 EXPERIMENT DESIGN FOR WAVE-BRIDGE INTERACTION

Laboratory tests are conducted in conjunction with activities at the Hydraulics Laboratory of the Hong Kong Polytechnic University, as shown in Figure 1(a). The 1:30 scale experiment is designed according to the open channel Froude similarity, which is suitable for phenomena where gravity and inertial forces are dominant, particularly for free surface flows (e.g., coastal structures and waves) (Yuan et al. 2022). The wave channel is 27 m in length, 1.5 m in width, and 1.5 m in depth. Solitary waves and regular waves are generated using a wave generator at one end of the channel. These two types of waves are used to study the extreme waves generated by the tsunami and tropical cyclone natural hazards, respectively. The storm-induced waves are highly periodic in nature, while tsunami waves are often caused by the displacement of a significant volume of water under the sea. For the regular waves, 5 different water depths D (0.48 m, 0.50 m, 0.52 m, 0.54 m, and 0.56 m) are selected. Four different wave heights H (0.10 m, 0.12 m, 0.14 m, 0.16 m) are paired with 6 different wave periods T (1.0 s, 1.2 s, 1.4 s, 1.6 s, 1.8 s, and 2.0 s) and tested under each water depth. With respect to the solitary waves, 6 different wave heights (0.10 m, 0.12 m, 0.14 m, 0.16 m, 0.18 m, and 0.20 m) are tested under the aforementioned 5 water depths. The selection of these wave parameters not only takes into account the performance of the wave generator but also satisfies the requirement that being converted to a prototype size can simulate the wave intensity in real disasters.

The dimensions of the investigated bridge specimen are plotted in Figure 1(b), which is a typical reinforcement concrete simply supported bridge in practical design (Robertson et al.

2007). The selected bridge span has a length of 15.85 m and a width of 10.8 m. The girder height is 1.37m and the deck thickness is 0.18 m. The overlength out of the two sides of the deck is taken as 0.5 m. To measure the external loads acting on the tested specimen, a three-axis force sensor is equipped. The sampling rate is set as 20 Hz. Each case is repeatedly tested 5 times to avoid experimental monitoring deviations. Figure 1(c) and 1(d) show two snapshots captured during the experiment, depicting specific moments in the specimen's behavior. Figure 1(c) corresponds to the moment just before the arrival of the wave, while Figure 1(d) captures the moment when the specimen is being subjected to wave impacts.

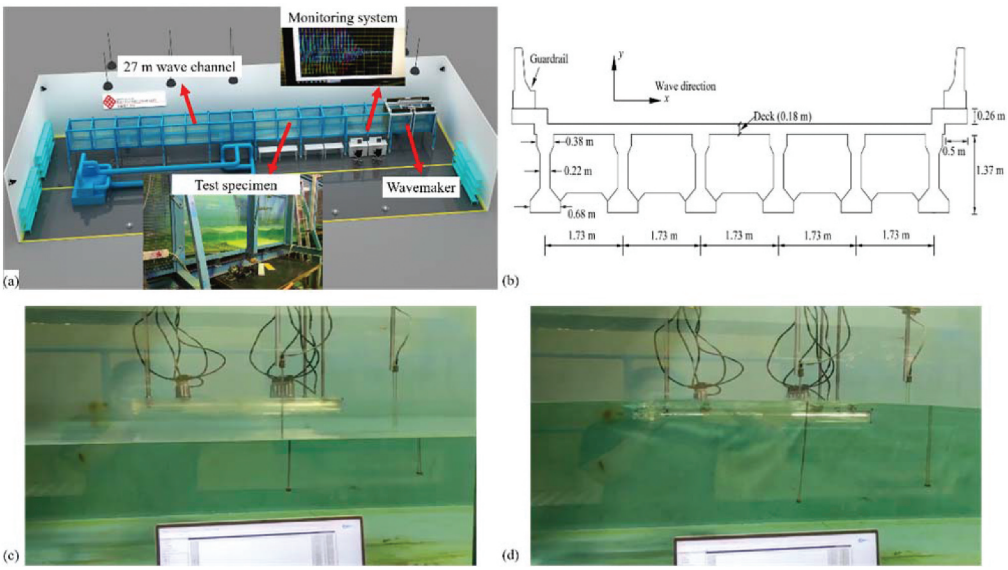


Figure 1. (a) Schematic diagram of the hydraulics laboratory and photos of experimental facilities; (b) dimensions of the investigated bridge superstructure model; (c) snapshots of the specimen before wave arrives; and (d) snapshots of the specimen under wave impacts.

3 LSTM PREDICTION METHOD FOR WAVE LOAD TIME HISTORIES

An LSTM network is employed in this study to predict wave force time series based on measured wave profiles. The LSTM network is an extension of the RNN architecture, incorporating four states within a single recurrent structure, which could overcome the limitations of conventional neural network architectures in handling input sequences that rely on the interdependence of information (Sherstinsky 2020; Zhang et al. 2021). These states enable the network to retain and manage input information over longer sequences. Each layer of the LSTM network consists of one recurrent structure, and the frequency of self-updates is determined by the input data dimensions and the number of cycles. This design allows the current LSTM layer to compute a single recurrent unit instead of multiple consecutive units, improving computational efficiency. In the trained LSTM cell, several components are involved in processing the input data. The input gate regulates the amount of current network input data that is stored in the unit at the current time step. The forget gate determines the extent of the transition from the previous state to the current state. Finally, the output gate controls the output of the current unit state. To assess the prediction performance of the LSTM models, two commonly used metrics are employed: mean squared error (MSE) and the R^2-score. MSE is a loss function that is typically minimized during network training. However, one limitation of MSE is that it does not account for the variability of the data since it assumes numerical values without normalization. To address this limitation, the R^2-score is utilized to evaluate the

predictive power of the model. The R^2-score measures the model's predictive performance compared to a trivial model that always forecasts the mean value of the observed data (where $R^2 = 0$). The R^2-score is widely used because it provides a normalized version of the R^2, making it a valuable metric for assessing the performance of the model. These two indicators are calculated as

$$MSE = \frac{1}{N}\sum (y - y')^2 \tag{1}$$

$$R^2 = 1 - \frac{\sum (y - y')^2}{\sum (y - \bar{y})^2} \tag{2}$$

where y = the measured data in the experiment; y' = the predicted value using LSTMs; and $\bar{y}$ = mean of the truth data.

4 WAVE-INDUCED LOADS ON THE BRIDGE SPECIMEN

To obtain more insight into wave force characteristics, time histories of vertical and horizontal wave forces are presented and discussed in this section. By collecting the measured results from the load cell, Figure 2(a) shows the time series results of the solitary wave case with D = 0.52 m and H = 0.18 m. Both the vertical wave force F_y and horizontal wave force F_x increase to a maximum value and then decrease as the propagation of the solitary wave. The maximum value of F_y is 101.36 N, and the maximum F_x is 44.78 N. The minimum forces occur at around 19 s, with F_y being -41.23 N and F_x being -14.56 N. Generally, the peak values of F_y and F_x in the positive directions (uplift and wave forward directions) are much larger than those in the negative directions. Figure 2(b) presents the time-dependent wave force acting on the specimen under a regular wave case with D = 0.52 m, H = 0.14 m, and T = 1.6 s. The wave forces also exhibit periodic fluctuations as the water surface rises and falls, but the differences in peak values between positive and negative directions are smaller compared to solitary waves. The maximum values of F_y and F_x are 43.24 N and 31.58 N, respectively, while the minimum values are -28.30 N and -12.63 N, respectively.

During the experimental tests, each wave case is repeated five times to mitigate monitoring deviations. Although the input parameters remain the same for repeated tests of the same wave case, there may still be slight variations in wave heights and waveforms during propagation, leading to deviations in the experimental measurements due to associated uncertainties. For example, in the repeated tests of a solitary wave case with D = 0.50 m and H = 0.20 m, the maximum vertical force ranges from 85.34 N to 89.17 N, and the horizontal force ranges from 50.03 N to 54.54 N. To address these deviations and uncertainties, the LSTM-based AI methods

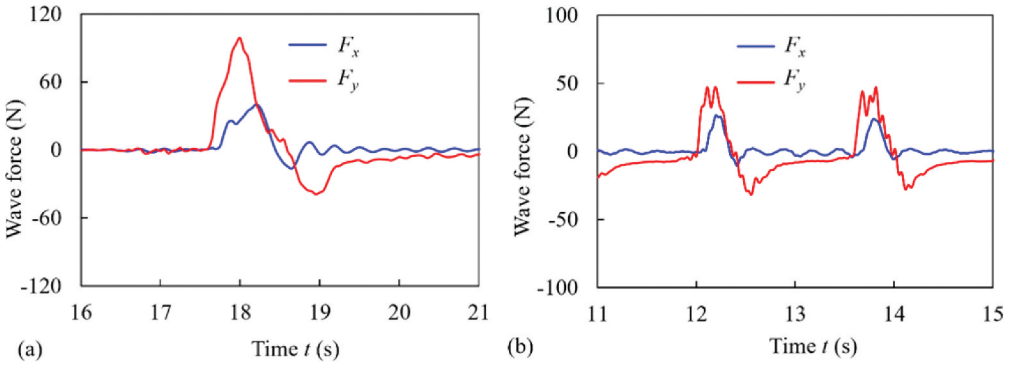


Figure 2. (a) Wave force time histories for the solitary wave case with D = 0.52 m and H = 0.18 m; and (b) wave force time histories for the regular wave case with D = 0.52 m, H = 0.14 m, and T = 1.6 s.

utilize all the test results in the training set. By directly relating the time histories of wave loads to the time-dependent water surface, the effects caused by changing wave profiles during wave propagation can be effectively mitigated. This approach overcomes the limitations of averaging the results after removing outliers, as is commonly done in experimental measurements, and provides a more comprehensive understanding of the wave load characteristics.

5 TRAINING OF THE LSTM MODEL

5.1 *Development of LSTM models*

In this study, the LSTM models are trained using experimental measured wave load time histories as the training database. The values of parameters water depth D, wave height H, and wave period T are chosen based on the experimental requirements to meet the wave-making conditions in the laboratory facilities. However, future studies may explore other value methods, such as stratified sampling and Latin Hypercube sampling techniques, to construct datasets with higher levels of independence. The changing wave profiles collected from the wave gauges are used as input to the LSTM models, while the wave force time series are used as the output. The training process utilizes 70% of the raw data as the training set, 15% as the test set, and the remaining 15% as the validation set. One potential advantage of this approach is that the LSTM prediction results can help reduce deviations caused by repeated tests since it incorporates all the available datasets.

After several trials, 128 hidden neurons are selected for the LSTM model. Each node in the fully connected layer is connected to all preceding nodes and plays a role in integrating the salient characteristics learned from earlier layers and capturing the hidden patterns in the time series. In this study, considering both computational efficiency and model accuracy, it is determined that 64 nodes in the fully connected layer are sufficient. The learning rate, a critical hyperparameter in supervised and deep learning, determines the speed at which the objective function converges to a local minimum. An optimal learning rate ensures that the objective function is resolved within a reasonable timeframe. Through rigorous experimentation, the optimal learning rate for this study is determined to be 0.005. The network training is conducted using TensorFlow, an open-source symbolic math library developed by the Google Brain team for machine learning applications. TensorFlow offers a flexible data flow architecture, enabling high-performance training of various neural network types on multiple platforms, including CPUs, GPUs, and TPUs. The simulations in this study are performed on a desktop computer equipped with 12th Intel Core i7-12700K CPUs and an NVIDIA GTX 1080Ti GPU card. The model training process takes approximately 10 hours to complete.

It is important to note that although the structure of the LSTM models is similar for both the solitary wave and regular wave cases, their hyperparameters, such as weights and biases,

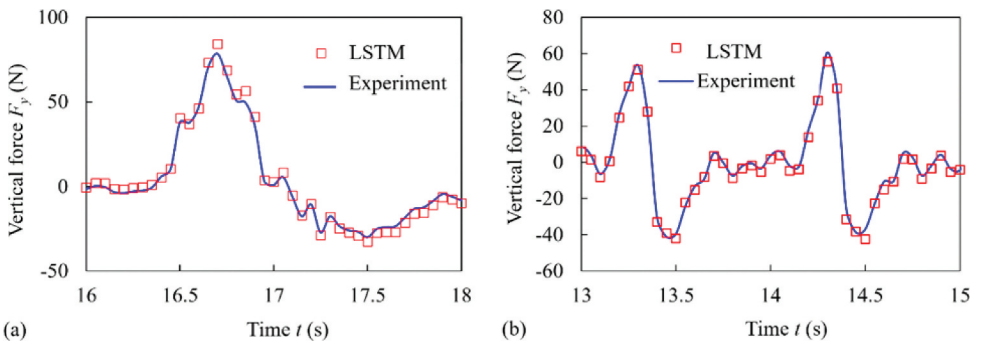


Figure 3. Comparisons between LSTM predicted wave force time histories with experimental measurements (a) solitary wave case with D = 0.50 m and H = 0.16 m; and (b) regular wave case with D = 0.50 m, H = 0.16 m, and T = 1.0 s.

are different due to the distinct characteristics of their input data. Figure 3 presents comparative results between the LSTM prediction of wave loads and the experimental measurements. It is worth mentioning that the cases shown in Figure 3 are all from the test set, not the training set. This means that the LSTM model has not been exposed to these specific cases during the training process. The high accuracy achieved in predicting these unseen cases demonstrates the model's generalization capability. The small loss value observed after 600 iterations and the good convergence observed in the comparisons further validate the prediction performance of the developed LSTM models. These results indicate that the LSTM models effectively capture the relationships between the wave profiles and wave forces, leading to accurate predictions of wave loads.

5.2 *Hyperparameter tuning*

In this section, the impact of hyperparameter configurations on the performance of the LSTM models is explored. Specifically, the effect of learning rate and dropout settings on the model's prediction results is investigated. Hyperparameter tuning is essential in optimizing machine learning models, and understanding the effect of individual hyperparameters on the model's performance is crucial for customizing the model for a specific task. In this study, the learning rate and dropout rate are considered as the hyperparameters of interest. The learning rate is varied from 10^{-4} to 10^{-2}, while the dropout values range from 0.2 to 0.7. Two performance indicators, mean squared error (MSE) and coefficient of determination (R^2), are used to assess the influence of hyperparameters on the model's prediction results. These metrics provide a reliable approach for evaluating the model's predictive capability compared to the actual observations.

For the LSTM model predicting solitary wave loads, Figure 4(a) and 4(b) depict the variation in predictive performance with different learning rates, while keeping the dropout values constant. The analysis reveals a quadratic relationship between the model's predictive ability and the learning rate, resulting in a single-peak curve in the model performance graph. The optimal

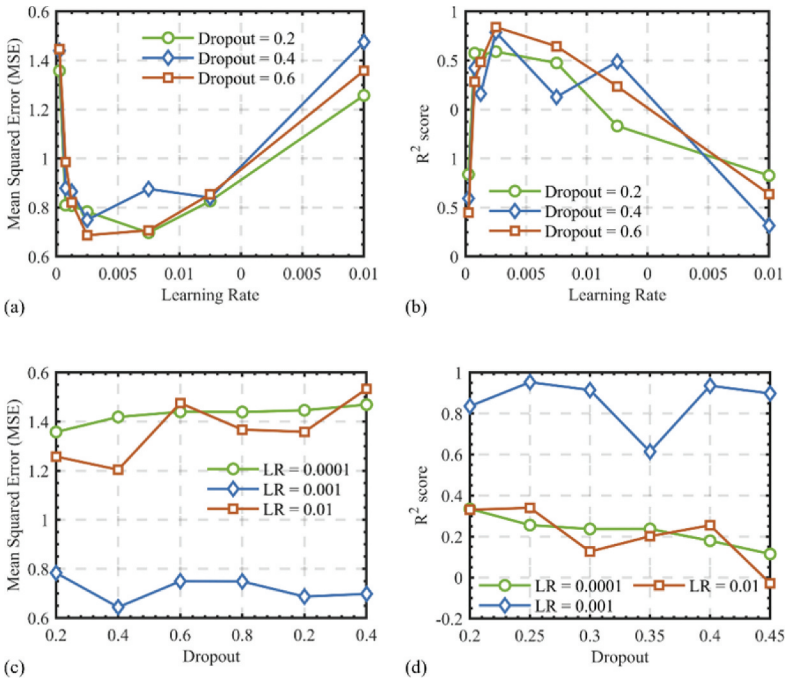


Figure 4. Comparisons between LSTM predicted wave force time histories with experimental measurements (a) solitary wave case with D = 0.50 m and H = 0.16 m; and (b) regular wave case with D = 0.50 m, H = 0.16 m, and T = 1.0 s.

learning rate is found to be approximately 0.001. These findings emphasize the importance of selecting an appropriate learning rate to optimize the model's prediction capability. On the other hand, Figure 4(c) and 4(d) illustrate the change in predictive performance with different dropout values, while keeping the learning rate constant. Interestingly, no clear trend is observed in the model performance curve, suggesting that the impact of dropout on the model's performance is relatively minor. However, it is worth noting that a dropout value of 0.5 typically yields the worst predictive performance, and it is advisable to avoid using it in practical applications. Furthermore, the analyses indicate that when the learning rate is low (around 0.001 to 0.003), the effect of dropout on the model's predictive accuracy is minimal. This finding is significant as it suggests that in certain scenarios, the specific value of the dropout rate may not be critical to the overall performance of the model when the learning rate is sufficiently low.

6 CONCLUSIONS

This study introduces a hydrodynamic experiment focused on studying the interaction between waves and bridges, as well as the development of LSTM-based data-driven techniques for forecasting wave forces in time series data. The experiment involves the use of a 1:30 scale bridge superstructure specimen subjected to wave tests in a wave channel. Various solitary wave and regular wave conditions are considered. During the experiment, measurements of wave profiles and wave-induced forces are recorded, forming the basis of the dataset used to train LSTM models. Through the tuning of different hyperparameters, high-performance LSTM prediction models are developed.

To optimize the forecasting performance for wave-induced forces, LSTM models with specific configurations are developed. These models consist of 128 hidden neurons, with each connected layer containing 64 nodes. They are trained using a learning rate of 0.001. Through the investigation of different hyperparameters, it is observed that when the learning rate is low, ranging from 0.001 to 0.003, the impact of dropout on the model's predictive accuracy is relatively minimal. The LSTM prediction models, based on experimental data, offer several advantages, including reduced deviation and improved efficiency. The LSTM models demonstrate satisfying performance, with R^2 scores close to 0.98 and low MSE values at the order of 10^{-1}. These well-trained models can accurately predict the time series of wave forces based on the wave profiles within seconds. The developed LSTM models provide effective prediction methods for wave load time histories, offering more accurate load inputs for engineering problems related to wave-bridge interactions.

Furthermore, it should be noted that these LSTM models can be enhanced by incorporating additional datasets from different test points, incorporating underlying mechanical mechanisms of wave-bridge interactions through physics-informed machine learning models, and conducting further examinations on bridge structures with varying dimensions.

ACKNOWLEDGMENTS

The study has been supported by the Research Grants Council of Hong Kong (PolyU 15225722 and PolyU 15221521), the Department of Civil and Environmental Engineering of the Hong Kong Polytechnic University (1-WZ0B), and the Environment and Conservation Fund Committee of the Hong Kong Government (2022-42). The support is gratefully acknowledged. The opinions and conclusions presented in this paper are those of the authors and do not necessarily reflect the views of the sponsoring organizations.

REFERENCES

Hu, P., Cheng, W., Xu, G., Han, Y., Yan, N., & Wang, N. (2023). Prediction of buffeting responses of the thin plate under joint action of wave and wind using LSTM and transfer learning. *Applied Ocean Research*, *134*, 103514.

Jia, L., Zhang, Y., Zhu, D., and Dong, Y. (2022). 3D Numerical Modeling and Quantification of Oblique Wave Forces on Coastal Bridge Superstructures. *Journal of Marine Science and Engineering*, *10*(7), 860.

Jin, J., and Meng, B. (2011). Computation of wave loads on the superstructures of coastal highway bridges. *Ocean Engineering*, *38*(17–18), 2185–2200.

Meng, B., and Jin, J. (2007). Uplift wave load on the superstructure of coastal bridges. *New Horizons and Better Practices*, 1–10.

Robertson, I. N., Yim, S., and Tran, T. (2011). Case study of concrete bridge subjected to hurricane storm surge and wave action. *Solutions to Coastal Disasters 2011 - Proceedings of the 2011 Solutions to Coastal Disasters Conference*, 728–739.

Seiffert, B. R., Cengiz Ertekin, R., and Robertson, I. N. (2016). Effect of Entrapped Air on Solitary Wave Forces on a Coastal Bridge Deck with Girders. *Journal of Bridge Engineering*, *21*(2), 4015036.

Sherstinsky, A. (2020). Fundamentals of Recurrent Neural Network (RNN) and Long Short-Term Memory (LSTM) network. *Physica D: Nonlinear Phenomena*, *404*, 132306.

Xiao, H., and Huang, W. (2008). Numerical modeling of wave runup and forces on an idealized beach-front house. *Ocean Engineering*, *35*(1), 106–116

Xu, G., Wei, H., Xue, S., Wang, J., and Li, Y. (2022). Predicting wave forces on coastal bridges using genetic algorithm enhanced ensemble learning framework. *Ocean Engineering*, *266*, 112963.

Yuan, P., Zhu, D., Dong, Y., & Xu, G. (2022). Response-based bridge deck limit state considering component-level failure under extreme wave. *Marine Structures*, *83*, 103184.

Zhang, W., Li, H., Li, Y., Liu, H., Chen, Y., and Ding, X. (2021). Application of deep learning algorithms in geotechnical engineering: a short critical review. *Artificial Intelligence Review*, *54*(8), 5633–5673.

Zhu, D., Li, Y., and Dong, Y. (2021a). Reliability-based retrofit assessment of coastal bridges subjected to wave forces using 3D CFD simulation and metamodeling. *Civil Engineering and Environmental Systems*, *38*(1), 59–83.

Zhu, D., Yuan, P., and Dong, Y. (2021b). Probabilistic performance of coastal bridges under hurricane waves using experimental and 3D numerical investigations. *Engineering Structures*, *242*, 112493.

Bridge Maintenance, Safety, Management, Digitalization and Sustainability – Jensen, Frangopol & Schmidt (eds)
© 2024 The Author(s), ISBN 978-1-032-77040-6
Open Access: www.taylorfrancis.com, CC BY-NC-ND 4.0 license

Digital twin for intelligent maintenance towards sustainable bridges

J. Heng[#]
Department of Civil Engineering, University of Birmingham, Birmingham, UK

L. Lai & Y. Dong*
Department of Civil and Environmental Engineering, The Hong Kong Polytechnic University, Hong Kong, China

S. Kaewunruen & C. Baniotopoulos
Department of Civil Engineering, University of Birmingham, Birmingham, UK

ABSTRACT: Aging steel bridges constitute a significant portion of transportation infrastructure, requiring more efficient and intelligent maintenance to enhance their sustainability. This work presents a digital twin (DT) framework for the intelligent maintenance of aging steel bridges subject to time-dependent deterioration, by fully exploiting the prediction model and the data from monitoring and inspection. A tied-arch bridge, subjected to prominent corrosion fatigue (CF) in its hanger system, is selected as a case study. The DT framework comprises three modules: digital data perception, deterioration prognosis, and condition-based decision making. First, a finite element (FE) model of the bridge is developed as the mechanical backbone of the DT, based on the design document and updated with the latest inspection result. Then, the traffic data collected by the structural health monitoring (SHM) system are converted into fatigue stress spectra. Next, the stress spectra and site-specific environmental data are integrated to perform a hybrid deterioration prognosis using a time-variant probability-stress-life model. Finally, optimal maintenance actions are determined based on the prognosis results, by constructing a stochastic environment and adopting a customized deep learning-based solution algorithm. The research outcome demonstrates the value of incorporating SHM data in deterioration prognosis and maintenance planning, and provides a promising framework for the interoperable DT of aging structures at the mechanistic level. The result reveals the nonlinear evolution of C-F deterioration in steel bridge hangers, with increasing failure probability and dispersity. Consequently, different strategies are recommended by the proposed DT framework, such as regular repairs in the early life and frequent inspections and timely replacement in the late life. Furthermore, the present DT framework suggests that the appropriate use of SHM systems can effectively reduce the life-cycle costs and risks, with a value of information that exceeds the initial investment.

Keywords: Steel Bridge, Deterioration, Digital Twin, (DT), Intelligent Maintenance, Decision making, Suitability

[#]: Presenting author; *: Main author

DOI: 10.1201/9781003483755-80

1 INTRODUCTION

1.1 *Background and motivation*

The need for condition-based maintenance (CBM) (Lai et al. 2023) of steel bridge hangers is underscored by their critical role in transferring vehicle loads from the deck system to the main structural member of bridges, such as the main arch or cable. These steel hangers are continuously subjected to vehicle-induced fatigue deterioration and environmental-assisted corrosion, leading to a synergistic corrosion fatigue (CF) coupled deterioration (Zhang & Yuan 2014). This degradation poses significant risks, as evidenced by the reduced service life of hangers in suspended arch bridges, often ranging from 10 to 15 years, and in extreme cases, even less than 10 years (Yao et al. 2021). This issue calls for an intelligent maintenance strategy tailored to the current deterioration state and future evolution of hangers, emphasizing the urgent need for proactive and informed maintenance approaches to ensure the longevity and safety of steel bridge hangers. As a result, it can be of the first priority to address two parallel research concerns: (i) obtaining current-to-future prognosis of CF deterioration in steel bridge hangers through integrating models and site-specific data, and (ii) stipulating an automatic and intelligent DIM policy based on the prognosis results.

1.2 *State-of-the-art overview*

Current standards, including JTG-D64 (MOT 2015), Eurocodes (CEN 2003), and AASHTO (AASHTO 2020), typically employ a fatigue load model (FLM) derived from national traffic statistics, which may not accurately reflect site-specific conditions. To address this, in-situ monitoring data, including weight-in-motion (WIM) data (MacLeod & Arjomandi 2023), has become increasingly integral in deterioration prognosis. For instance, studies by Deng et al. (2019), Li and Feng (2023), and Jiang et al. (2020) have utilized WIM data for fatigue stress and damage estimation in bridge hangers and stay cables, noting significant acceleration in fatigue deterioration above certain corrosion degrees, potentially leading to premature failure of critical components. This situation underscores the necessity of shifting from traditional corrective maintenance to more proactive CBM (Stenström et al. 2016), relying on sophisticated decision models for maintenance actions. Early decision models, typically based on decision trees (Rasouli & Timmermans 2014), segment structures based on components and damage, making decisions based on discriminative conditions at each node. However, these models lack dynamic adaptability. To overcome this, Bayesian networks (Heng et al. 2019) have been employed to balance risk and action costs, although they face limitations in scalability. An alternative, the Markov decision process (MDP) (Lei et al. 2023), and its adaptation, the partially observable MDP (POMDP) (Lai et al. 2023), offer more robust and flexible tools for managing stochastic deterioration in large-scale systems. POMDPs, in particular, have been applied across various infrastructure assets, demonstrating technical superiority in asset management. Based on the above theoretical progress, the innovative method of digital twins (Heng et al. 2023) is now gradually applied in the management of infrastructure assets, which is especially evidenced with a fast pace with the recent rapid advances in sensing, internet of things (IoT), computing, artificial intelligence (AI), numerical simulation, etc. Regarding the application of digital twins in bridge maintenance, the focus has been on two main aspects: geometric reconstruction and establishing physical-to-digital connections for real-time interaction. While computer vision technologies are successfully employed for creating geometric models of structures, efforts are ongoing to enhance the bidirectional link between physical assets and their virtual counterparts. Despite growing interest in using digital twins for bridge maintenance, much of the current research still remains conceptual. There is a pressing need for practical advancements in areas like physical-virtual communication and AI-assisted decision-making to fully realize the potential of digital twins in infrastructure maintenance.

1.3 *Research gaps and aim of the study*

This study identifies key research gaps in the field of bridge maintenance, particularly in applying digital twins and condition-based maintenance (CBM) strategies for aging bridges.

Despite the significant advances in understanding the deterioration mechanisms of bridge components and the integration of in-situ monitoring data for more accurate prognosis, there remain substantial gaps in practical application and scalability. Current models, while theoretically robust, often fall short in addressing real-world complexities, particularly in large-scale bridge networks. Moreover, the application of digital twins in bridge maintenance is still largely conceptual, with limited practical implementations. This study aims to bridge these gaps by developing an advanced, scalable model that integrates digital twins and CBM for effective bridge maintenance. The focus is on creating a practical framework that not only enhances the understanding of bridge deterioration processes but also provides actionable insights for maintenance and risk management. This study seeks to contribute to the body of knowledge by providing a comprehensive, real-world applicable model that combines the latest in sensor technology, data analytics, and AI algorithms, setting a practical instance in intelligent bridge maintenance and management.

2 METHODOLOGY

2.1 *Selection of the bridge for case studies*

The selected case study for this research is a concrete-filled steel tube (CFST) tied-arch bridge, as shown in Figure 1, an essential component located in the urban highway network of Chengdu, China. This bridge is uniquely characterized by its three tied-arches, each supporting the deck system with 21 steel hangers. These hangers are crucial for the bridge's structural integrity but are highly prone to corrosion fatigue, necessitating a shift towards condition-based inspection and maintenance strategies. The bridge's location further complicates maintenance efforts, with a busy railway running underneath, imposing strict limitations on the timing of maintenance activities. To address these challenges, a comprehensive Structural Health Monitoring (SHM) system has been installed. This system consists of a weight-in-motion (WIM) module to capture traffic loads and a vibrational measurement module, which tracks the acceleration and natural frequency of structural components, including the hangers. This setup not only aids in ongoing maintenance but also provides valuable data for this research.



Figure 1. The case-study bridge. (photo on courtesy of Dr Junlin Heng).

Traffic data over a year has been categorized into six types based on functionality and axle count, revealing that two-axle cars constitute a significant portion of the traffic, while heavy trucks, which have a more substantial impact on corrosion fatigue, account for a smaller fraction. Vehicle lane preferences have also been observed, with lighter passenger cars predominantly using the fast lane and heavier trucks favoring the middle and slow lanes. In addition to traffic load, the ambient conditions surrounding the bridge are monitored through a micro meteorological station. Key environmental factors, including temperature, humidity, and airborne salinity, indicate a subtropical climate conducive to steel corrosion. The presence of industrial activities in the

vicinity introduces moderate levels of sulphury dioxide, further influencing corrosion rates. Considering the susceptibility to anchor flooding, a conservative approach has been adopted in the study, using an adjusted average humidity value higher than the actual measurements to ensure a comprehensive assessment of the corrosion risks faced by the steel bridge hangers.

2.2 *General framework*

Figure 2 presents the general framework the digital twins for intelligent bridge maintenance, aimed at optimizing the trade-off between cost and risk in the maintenance of steel hangers on the case-study bridge. This comprehensive framework integrates four key modules: digitalization, prediction, prognosis, and AI-aided decision. The process initiates with the development of a numerical bridge model based on design documents, which is then fine-tuned using vibrational data collected from the monitoring system. This model underpins the hybrid simulations, where monitored traffic loads serve as inputs to a finite element (FE) model, enabling the assessment of fatigue stress spectra on the hangers. These spectra are projected into future states using a Bayesian dynamic linear model (BDLM) (Zhang et al. 2021), enhancing the accuracy of the deterioration prognosis. Following this, the framework engages in the prognosis quantifying uncertainties associated with the deterioration process of hangers through the application of partially observable Markov decision processes (POMDPs). This module assimilates both inspection results and maintenance action effects, offering a holistic view of the hanger condition over time. The final stage of the framework employs the asynchronous advantage actor-critic (A3C) algorithm (Shen et al. 2023), a deep reinforcement learning (DRL) strategy, to identify the most effective maintenance strategy within the POMDP environment. The framework does not merely replicate the physical bridge in a digital format but also facilitates a critical digital-to-physical interaction by advising on the optimal maintenance policy.

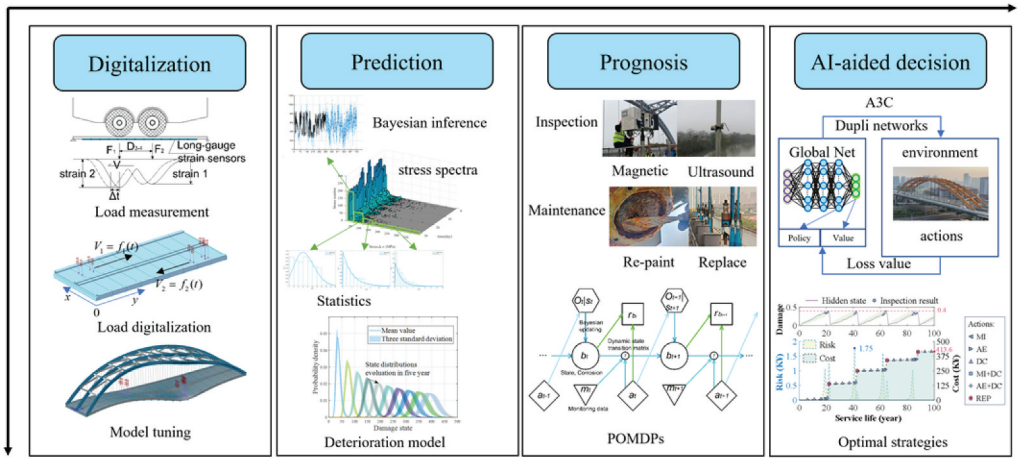


Figure 2. General framework of the digital twins for intelligent bridge maintenance.

3 RESULT AND DISCUSSION

3.1 *Digital twins of case-study bridge*

The implementation of digital twins for the case-study bridge marks a significant advancement in the domain of intelligent bridge maintenance. The first step of the digital twins focuses on analyzing and predicting the fatigue stress spectra of the steel hangers in the case-study bridge, which are critical to its structural integrity. Thus, a comprehensive and accurate virtual model of the bridge has been created, as shown in Figure 3. This model is based on detailed design

documents and is continuously refined using real-time data gathered from various sensors installed on the bridge. These sensor-monitored key parameters such as traffic loads, vibrational frequencies, and environmental conditions, providing an inclusive view of the operational state of the bridge.

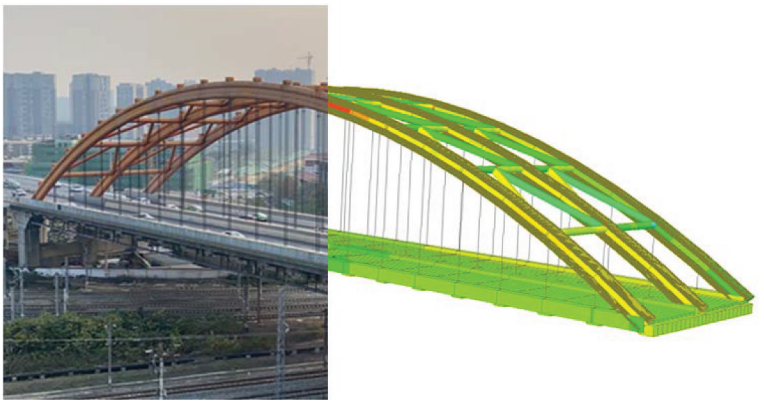


Figure 3. Virtual mirror of the case-study bridge by finite element modelling and tuning.

With this model, hybrid simulations are conducted to evaluate the fatigue stress spectra of the steel hangers. Figure 4 illustrates the fatigue stress spectra (during one month) predicted for the most critical hanger of the case-study bridge. These simulations use the monitored traffic load data as input for a (FE) model, allowing for a detailed assessment of the load effects on the hangers. The output of FE models can be then used to predict the future states of the stress spectra for the hangers, by utilizing advanced predictive techniques, i.e., the BDLM in the present work. To this end, the above digital twins not only help in identifying current stress levels but also in forecasting future deterioration trends.

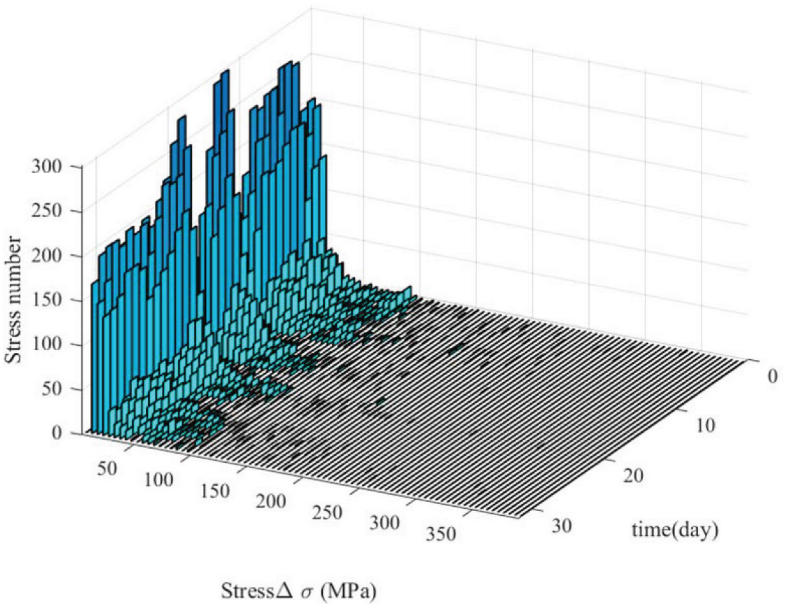


Figure 4. Fatigue stress spectra of the most critical hanger (for one month).

3.2 *Reliability evolution*

Based on the digital twins-based method stated above, the probabilistic prognosis can be carried out for various hangers in the case-study bridge, which effectively combines available data with the physical model to create a comprehensive understanding of the deterioration process over time. Figure 5 provides an insightful comparison of service reliability for hangers 9 and 11, incorporating scenarios in both corrosive and non-corrosive (in-air) environments. A failure limit, denoted as $\beta = 2$, is applied to determine the unreliability threshold.

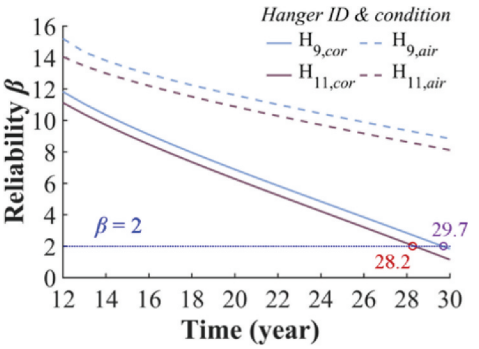


Figure 5. Reliability evolution of critical hangers (in-air versus corrosive).

In general, the nonlinear pattern in the C-F deterioration of steel bridge hangers is evidenced by the observed behavior under varying environmental conditions. The accelerated decline in reliability under corrosive conditions, as opposed to the more stable performance in non-corrosive environments, clearly demonstrates the increasing likelihood of failure and variability in deterioration over time. Initially, the reliability curves for both environments exhibit high values. However, under corrosive conditions, there is a noticeably accelerated decline in reliability compared to the non-corrosive environment. In the latter scenario, the curve remains well above the unreliability threshold, indicative of sustained robustness against deterioration. Conversely, in a corrosive environment, the reliability curve of hanger 11 approaches the limit after approximately 28.2 years, followed closely by hanger 9 at 29.7 years. These observations underscore the significant impact of environmental corrosivity on the fatigue deterioration of hangers, while also highlighting the variation in deterioration rates among hangers located in different parts of the bridge. The above variance emphasizes the need for a nuanced approach to maintenance actions, tailored to the specific conditions and deterioration rates of individual hangers.

3.3 *Optimal strategy*

As discussed above, the digital twin-based prognosis offers a detailed understanding of the current and future deterioration states of the hangers, thereby facilitating optimal maintenance strategies. The study evaluates four maintenance methods: acoustic emission (AE), magnetic inspection (MI), drainage and coating (DC), and replacement (REP), with a total of six envisioned actions due to possible combinations. The costs of these actions have been determined through industrial consultation and existing guidelines (MOT 2020), with an additional cost consideration for replacements due to the railway beneath the bridge. The results of MI and AE inspections are assumed to follow a normal distribution centered around their mean values, with standard deviations set at 0.1 and 0.025, respectively. The DC method is considered a partial repair, assumed to enhance corrosion resistance for an additional five years per effort. In contrast, the REP action is viewed as a full repair, resetting the hanger to its intact state. The study conducts a projective analysis into the future status evolution of the hangers in a stochastic space, assuming a 100-year design life for the bridge. Figure 6 illustrates the analysis result for the most critical hanger, considered critical, showing both the predicted hidden state and inspection results within a 2σ confidence interval.

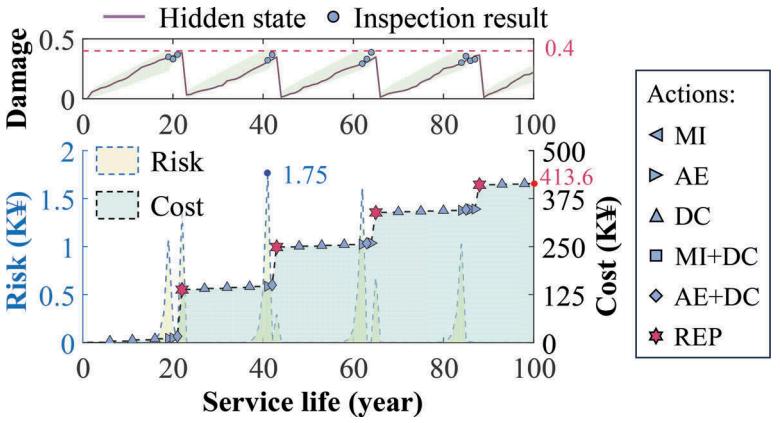


Figure 6. Life-cycle maintenance planning of the most critical hanger.

The digital twins approach proposes scheduling maintenance actions to minimize both cost and risk, as shown in the lower part of Figure 6. The optimal strategy suggests four REP actions approximately every 20 years throughout the design life of the bridge. Between REP actions, the digital twins approach recommends repeating the DC action every five years to reduce the deterioration rate of the hanger. This results in a linear increment in the damage factor, with intensive inspections scheduled before each REP action for well-informed decision-making. The total maintenance budget over the 100-year design life is estimated as 413,600 (in CNY). The proposed maintenance policy aims to maintain the damage factor generally below 0.4, which remarks a faulty warning that requires a mandatory shutdown and replacement. REP actions are advised when the damage factor approaches the limit of $D = 0.4$, maximizing the service life of the hanger within a safe margin. The risk is maintained at a moderate level throughout, peaking at 1,750 CNYs in year 40, coinciding with an inspection result indicating a critical state for the hanger, thereby justifying the need for a REP action.

4 CONCLUDING REMARKS

Based on the above study, the major findings can be drawn as below.

- A nonlinear pattern has been identified in the corrosion-fatigue deterioration of steel bridge hangers. This pattern is characterized by an increasing likelihood of failure and a growing variability in the deterioration process over time.
- According to the result of digital twins, the intelligent algorithm advocates regular repair work during the early stages of the lifecycle and more frequent inspections coupled with timely replacements as the hangers near the end of their service life.
- The result also underscores the importance of a tailored approach to bridge maintenance, one that adapts to the changing conditions of the bridge components over time and utilizes advanced monitoring techniques to inform maintenance decisions.
- The present work in generally, contribute to a comprehensive understanding of bridge maintenance, particularly emphasizing the role of advanced monitoring and predictive modeling in enhancing the safety, and cost-effectiveness of bridge management.
- For the future study, more in-depth cost-benefit analyses of SHM systems are suggested across different bridges. Besides, it is also worth exploring to integrate more sophisticated machine learning algorithms or deep learning techniques to improve the prediction accuracy and goodness of optimization.

ACKNOWLEDGEMENT

The Marie Curie Fellowship via URKI (EP/X022765/1) and ROYAL SOCIETY (IES\R1 \221036) and (IES\R1\211087) are gratefully acknowledged by the authors.

REFERENCES

AASHTO, 2020. AASHTO LRFD Bridge Design Specifications. 9th ed. Washington, DC: American Association of State Highway and Transportation Officials.

CEN, 2003. Eurocode 1: Actions on structures - Part 2: Traffic loads on bridges. Brussels: European Committee for Standardization.

Deng, Y., Li, A. and Feng, D., 2019. Fatigue performance investigation for hangers of suspension bridges based on site-specific vehicle loads. Structural Health Monitoring, 18(3), pp.934–948.

Heng, J., Zheng, K., Kaewunruen, S., Zhu, J. and Baniotopoulos, C., 2019. Dynamic Bayesian network-based system-level evaluation on fatigue reliability of orthotropic steel decks. Engineering Failure Analysis, 105, pp.1212–1228.

Heng, J., Zhang, J., Kaewunruen, S., Dong, Y. and Baniotopoulos, C., 2023. Digital Twin-Based Deterioration Prognosis of Steel Wind Turbine Towers in Modular Energy Islands. ce/papers, 6(3-4), pp.1111–1118.

Jiang, C., Wu, C., Cai, C.S., Jiang, X. and Xiong, W., 2020. Corrosion fatigue analysis of stay cables under combined loads of random traffic and wind. Engineering Structures, 206, p.110153.

Lai, L., Dong, Y. and Smyl, D., 2023. SHM-informed life-cycle intelligent maintenance of fatigue-sensitive detail using Bayesian forecasting and Markov decision process. Structural Health Monitoring, p.14759217231160412.

Li, J.A. and Feng, D., 2023. Fatigue life evaluation of bridge stay cables subject to monitoring traffic and considering road roughness. Engineering Structures, 293, p.116572.

Lei, X., Dong, Y. and Frangopol, D.M., 2023. Sustainable life-cycle maintenance policymaking for network-level deteriorating bridges with a convolutional autoencoder–structured reinforcement learning agent. Journal of Bridge Engineering, 28(9), p.04023063.

MacLeod, E. and Arjomandi, K., 2023. Dynamic bridge weigh-in-motion using estimated modal parameters from ambient vibration tests. Engineering Structures, 289, p.116254.

Ministry of Transport of the People's Republic of China (MOT), 2015. Specifications for Design of Highway Steel Bridge JTG D64-2015. Beijing: China Communications Press.

Ministry of Transport of the People's Republic of China (MOT), 2020. Highway bridge maintenance project budget quota JTG/T 5612-2020. Beijing: China Communications Press.

Rasouli, S. and Timmermans, H.J., 2014. Using ensembles of decision trees to predict transport mode choice decisions: Effects on predictive success and uncertainty estimates. European Journal of Transport and Infrastructure Research, 14(4), pp.412–424.

Shen, H., Zhang, K., Hong, M. and Chen, T., 2023. Towards Understanding Asynchronous Advantage Actor-critic: Convergence and Linear Speedup. IEEE Transactions on Signal Processing.

Stenström, C., Norrbin, P., Parida, A. and Kumar, U., 2016. Preventive and corrective maintenance–cost comparison and cost–benefit analysis. Structure and Infrastructure Engineering, 12(5), pp.603–617.

Yao, G.W., Yang, S.C., Zhang, J.Q. and Leng, Y.L., 2021. Analysis of corrosion-fatigue damage and fracture mechanism of in-service bridge cables/hangers. Advance in Civil Engineering, 6633706.

Zhang, W. and Yuan, H., 2014. Corrosion fatigue effects on life estimation of deteriorated bridges under vehicle impacts. Engineering Structures, 71, pp.128–136.

Zhang, Y.M., Wang, H., Bai, Y., Mao, J.X., Chang, X.Y. and Wang, L.B., 2021. Switching Bayesian dynamic linear model for condition assessment of bridge expansion joints using structural health monitoring data. Mechanical Systems and Signal Processing, 160, p.107879.

Bridge Maintenance, Safety, Management, Digitalization and Sustainability – Jensen, Frangopol & Schmidt (eds)
© 2024 The Author(s), ISBN 978-1-032-77040-6
Open Access: www.taylorfrancis.com, CC BY-NC-ND 4.0 license

Structural damage detection approach using input-output monitoring system and transfer learning

Liangfu Ge
Department of Civil and Environmental Engineering, Western University, London, Canada

Danhui Dan
School of Civil Engineering, Tongji University, Shanghai, PR China

Ayan Sadhu
Department of Civil and Environmental Engineering, Western University, London, Canada

ABSTRACT: Damage detection stands as a pivotal subject in bridge health monitoring. As the actual structures and their theoretical models inevitably have differences in structural parameters, it is practically challenging to detect damages in the absence of precise baseline information. In this regard, this paper introduces a baseline-free damage detection framework that combines measurements of moving loads with acceleration responses. Specifically, the moving loads are extracted using computer vision techniques while the acceleration is measured by distributed sensing. For each measured moving load, the same loading process is applied to the finite element models with different structural parameters and ambient noise. With simulated structural responses, an advanced 1d convolutional neural network is proposed for damage detection. Theoretical derivation reveals the proposed framework is applicable for damage detection without initial structural parameters. The proposed framework is validated to be effective on both damage localization and quantification.

1 INTRODUCTION

Damage detection (DD) is one of the most important concerns for structural health monitoring and has been a long endeavor in structural engineering for several decades (Doebling et al. 1996; Das et al. 2016; Li et al. 2023). Most of the previous efforts were on output-only approaches using measurements such as acceleration, strain, displacement, tilt, etc. The main barrier to output-only methodologies is that they highly rely on the baseline model quality, which was influenced by ambient environmental changes, such as traffic load, thermal effect and wind loading. Also, to mitigate the challenges posed by incomplete information, output-only methods typically necessitate the deployment of many sensors. Therefore, DD methods that introduce input information have also garnered widespread attention in recent years.

The approach based on Influence lines (ILs) is a representative method with both input and output information. An early study explored video recording and strain sensors to calculate strain influence lines (SILs) and then used them to detect damage in a bridge model (Zaurin & Catbas 2011). Displacement influence lines (DILs) were also validated applicable to damage localization and quantification on laboratory bridge models (He et al. 2018; Le et al. 2019). Since DILs have lower sensitivity to damage around the supports, rotational influence lines (RILs) were also considered promising for damage detection. Zhou et al. (2018) proposed a damage localization method by finding an abrupt change in RILs. Farhad et al. (2020) carried out experimental validations on a RILs based method in the laboratory and field. To combine the advantages of DILs and RILs, Breccolotti & Natalicchi (2022) proposed an

DOI: 10.1201/9781003483755-81

estimation method for flexural bending rigidity using the information from a FE model and validated it through numerical simulations.

Computer vision techniques have been used in recent years for measurements of vehicle trajectories and bridge displacements (Ge et al. 2020; Wang et al. 2023; Ge et al. 2024). With the combined information, DILs or RILs can be calculated in the field. For instance, Dong et al. (2019) implemented a field system for measuring the DIL of a small real truss bridge. Martini et al. (2022) identified the DIL of a steel beam for the purpose of finite element model updating. Even though the above vision systems are attractive to obtain ILs for real bridges, they are rarely applied to damage detection. Khuc & Catbas (2018) reported a successful experiment on the existence detection of damage. For damage localization, Ge et al. (2023) proposed a high-precision visual measurement system and successfully applied it to identify various damages. The two studies introduced a prototype for the input-output DD, however, these advancements primarily focus on static effects, and the exploration of input-output methodologies tailored for scenarios involving dynamic vehicle-induced responses remains an uncharted area of research.

Signal processing techniques, such as wavelet transform (WT) and Hilbert-Huang Transform (HHT), are widely used in DD research using vehicle-induced displacement or acceleration. Hester et al. (2012) suggested an improved WT using wavelet energy content at each bridge section and successfully detected damage in a bridge model with its acceleration response. Roveri & Carcaterra (2012) applied HHT to displacements to identify damage locations along beam structures. Nguyen et al. (2020) combined the WT with a deep learning network to detect multiple cracks in a beam. Basically, these approaches localize damage with some indicators (e.g., wavelet coefficient or Lipschitz exponent), but the physical correspondence between these indicators and the damage is not clear, resulting in natural limitations in damage quantification. Transfer learning, which is a branch of deep learning technologies, has also been applied recently in DD. For example, Teng et al. (2023) generated different digital models in simulation and trained a damage classification model with their response to random excitation force. Wang et al. (2021) created a free vibration dataset through finite element analysis and applied them to train a densely connected network to detect damages in a frame structure. Transfer learning approaches make baseline-free DD possible, but they are rarely seen in the existing DD related to vehicle-induced responses.

Regarding the limitations summarized from the existing DD approaches, this paper proposed a novel DD method using an input-output measurement system and transfer learning with vehicle-induced structural accelerations. This method does not require prior knowledge of structural initial parameters and can be used in both damage localization and quantification. In the following of this paper, the mapping relationship of the accelerations before and after damage is first introduced, followed by a demonstration of the proposed transfer learning framework. Then, Section 4 gives a numerical validation of the proposed approach. Section 5 presents conclusions.

2 MAPPING BETWEEN ACCELERATIONS BEFORE AND AFTER DAMAGE

To unveil the theoretical foundation behind using transfer learning for DD, this section derives the mapping relationship between the structural acceleration responses before and after damage.

Considering a linear discrete structure with n elements, if each node accounts for l degree of freedom (l=1∼6), then the structural governing equation can be expressed as:

$$M_{l(n+1)\times l(n+1)}\ddot{X}_{l(n+1)\times 1} + C_{l(n+1)\times l(n+1)}\dot{X}_{l(n+1)\times 1} + K_{l(n+1)\times l(n+1)}X_{l(n+1)\times 1} = P_{l(n+1)\times 1} \quad (1)$$

Where M is the mass matrix, K the stiffness matrix, P the vector of external force, and X the displacement vector for all nodes. The Rayleigh damping is adopted while it is assumed that the damping ratio ξ of the lower-order modes is identical. The damping matrix is given by

$$C = \alpha M + \beta K\left(\alpha = \frac{2\xi\omega_i\omega_j}{\omega_i + \omega_j}; \beta = \frac{2\xi}{\omega_i + \omega_j}\right) \quad (2)$$

ω_i and ω_j are the minimum and maximum frequencies analyzed. It is assumed that the damage state can be represented by stiffness reduction matrix D_K and mass reduction matrix D_M, both of which have dimensions of l(n+1)×l(n+1). Then, the stiffness and mass matrices after damage are

$$K_d = D_K K,\ M_d = D_M M \tag{3}$$

Substituting Equations (2) and (3) into Equation 1 yields the structural acceleration after damage:

$$\begin{aligned}\ddot{X}_d &= M^{-1}D_M^{-1}(RP - D_K KX - \alpha D_M M\dot{X} - \beta D_M K\dot{X}) \\ &= \left[M^{-1}D_M^{-1}RM, M^{-1}D_M^{-1}D_K M, E, M^{-1}D_M^{-1}D_K M\right]\left[M^{-1}P, -M^{-1}KX, -\alpha\dot{X}, \beta M^{-1}K\right] \\ &= \mathbf{T}\left[M^{-1}P, -M^{-1}KX, -\alpha\dot{X}, \beta M^{-1}K\right]^T\end{aligned} \tag{4}$$

In this equation, R is a $l(n+1)\times l(n+1)$ diagonal matrix representing the ratio coefficients of vehicle loads observed before and after damage, which is known in the input-output measurement system. E represents an equally sized identity matrix. For the undamaged state, the structural acceleration can be given by

$$\begin{aligned}\ddot{X}_d &= [E, E, E, E]\left[M^{-1}P, -M^{-1}KX, -\alpha\dot{X}, -\beta M^{-1}K\right] \\ &= \mathbf{T}_0\left[M^{-1}P, -M^{-1}KX, -\alpha\dot{X}, -\beta M^{-1}K\right]\end{aligned} \tag{5}$$

It can be seen from the above equation that the difference in acceleration of the structure at any time t, before and after damage, is determined by the difference in $\mathbf{T}$ and $\mathbf{T}_0$. $\mathbf{T}$ is named to as the damage mapping matrix. Furthermore, since the matrices K and M are basically assembled with the element stiffness K^e and M^e, respectively. If the stiffness and mass reduction coefficients of the element k are denoted as $d_{K,k}$ and $d_{M,k}$,K_d and M_d then can be expressed as

$$K_d = D_K K = \sum_{k=1}^{n} d_{K,k} G_k^T K_k^e G_k,\ M_d = D_M K = \sum_{k=1}^{n} d_{M,k} G_k^T K_k^e G_k \tag{6}$$

where $d_{M,k}, d_{K,k} \in (0, 1]$. It can be seen from Equations (4) and (6) that, $\mathbf{T}$ can be expressed by the following high-dimensional mapping

$$\mathbf{T} = F(d_{K,1}, d_{K,2}, \ldots d_{K,n}, d_{M,1}, d_{M,2}, \ldots d_{M,n}, M_1^e, M_2^e, \ldots, M_n^e, R) \tag{7}$$

It is important to emphasize that, since the element mass M^e is constant, this information is not required when comparing $\mathbf{T}$ and $\mathbf{T}_0$. Therefore, with R known, $\mathbf{T}$ is uniquely corresponding to the structural damage.

3 INPUT-OUTPUT TRANSFER LEARNING FRAMEWORK

3.1 *Overview*

The theoretical derivation demonstrates that when the spatiotemporal distribution of vehicle loads is measurable, the structural damage state can be uniquely determined by the acceleration response. Based on this core principle, Figure 1 illustrates the proposed transfer learning damage identification framework. Within this framework, the moving loads acting on the actual structure can be observed by vision-based load monitoring systems (Ge et al. 2020; Ge et al. 2023), while the structural effects are measured by synchronized accelerometers.

In this framework, the loads measured on the actual structure are applied to the finite element model with the same magnitude and location. The finite element model is parameter-variable, with changing parameters including the initial structural model parameters, damage parameters,

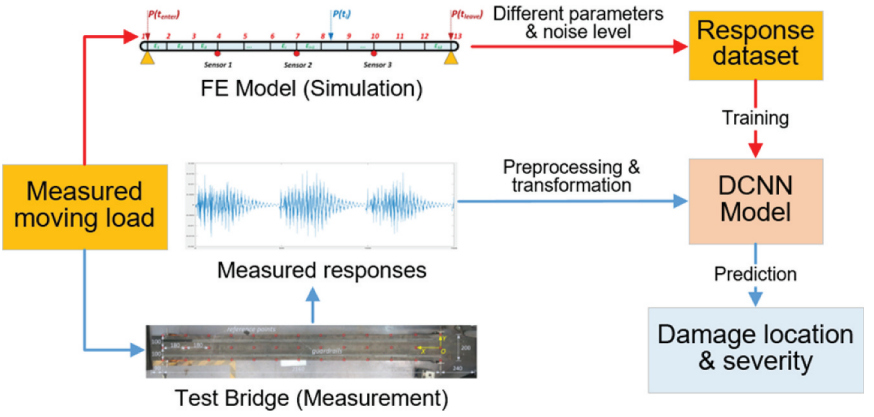


Figure 1. The transfer learning framework for damage detection.

and noise parameters. By continuously altering these three types of parameters, it is aimed to simulate structural effects under different parameter combinations as extensively as possible to create a simulated database. Both measured and simulated structural effects include acceleration signals before and after damage. Since the damage mapping matrix corresponds uniquely to the damage, theoretically, similar matrices **T** can be extracted from both simulated and measured signals for the same damage. Due to the high-dimensional and complex nature of the damage mapping matrix parameter space, it is advised to use deep learning methods for extraction in the proposed framework. Figure 1 displays the measured acceleration time history, which generally requires noise reduction and filtering processing before being input into the deep learning model.

3.2 *1D Efficient-V2 damage detection model*

To elaborate in greater details on the use of the damage identification framework, this section will introduce a deep convolutional neural network model and describe its application in time-domain signal damage identification. For the framework in Figure 1, the data input to deep learning models can be either time series or other forms post processing such as images. Since the input data is generally from simulation or ideally designed experiments, they are paired with a damage vector that reflects the states of all the elements. For example, in case a beam structure with n elements, the damage vector is defined as $\mathbf{d}=(d_1,d_2,, d_n)$, $(0 < d_i \leq 1)$. After the put data undergoes forward propagation through the network, a predicted damage vector $\mathbf{d}^{\mathbf{p}}$ of the same dimension is outputted. By using both $\mathbf{d}^{\mathbf{p}}$ and **d**, the loss function can be calculated, thereby ascertaining the accuracy of damage prediction.

This study proposes an adapted EfficientV2 network as the fundamental architecture of the deep learning model. The EfficientNetV2, introduced by Tan & Le (2021), was optimized using Neural Architecture Search (NAS) technique so that having a rational configuration of network depth, the number of channels, and network width. Considering data volume and training speed, this section focuses on modifying the smaller parameter version, EfficientNetV2-S, of which the structure is as presented in Table 1. More details of the listed modules can be found in the reference (Tan & Le 2021).

After undergoing a series of computations through Stages 0-7, the EfficientNetV2-S ultimately outputs a 1×1280 feature vector. In the original EfficientNetV2, the vector was used to calculate a one-hot encoded vector for image classification. However, the following modifications have been made in this study.

1) Labels: the labels of input data are revised into double-precision vectors from one-hot vectors.
2) Loss function: while cross-entropy is often used to evaluate the similarity between two vector distributions in image classification problems rather than regression problems, it is replaced with the Mean Squared Error function.
3) Activation function: the original Swish activation function is changed to the Tanh.

Table 1. Network structure of efficientNetV2-S.

Stages	Operations	Strides	Channels	Layers
0	Conv3×3	2	24	1
1	Fused-MBConv1, k3×3	1	24	2
2	Fused-MBConv1, k3×3	2	48	4
3	Fused-MBConv1, k3×3	2	64	4
4	MBCConv4, k3×3, SE0.25	2	128	6
5	MBCConv6, k3×3, SE0.25	1	160	9
6	MBCConv6, k3×3, SE0.25	2	256	15
7	Conv1×1 & Pooling & FC	-	1280	1

In this study, multi-point acceleration signals from bridge structures are used as input and the adapted EfficientNetV2-S is employed as the core of the DCNN model to localize and quantify the damage.

4 NUMERICAL VALIDATION

The steps using the proposed DD framework are:

1) Measure the real acceleration and moving loads. The simulation uses randomly generated load segments based on the traffic load models from (Ge et al. 2022), with acceleration responses computed by an initialized FE model.
2) Develop a simply supported model with variable structural parameters.
3) Apply real moving loads to the FE model to calculate accelerations. The model parameters, such as stiffness, mass, damage states, and noise levels, are varied to cover as many structural scenarios as possible. The "real" structure in the simulation is set as a FE model with random yet constant initial parameters to mimic the uncertainties in real-world.
4) Validate the predictive accuracy of actual structural damage using "measured" acceleration data, which are derived from finite element analysis of the "real" structure.

Figure 2 Presents a schematic diagram of the moving loads, FE model and the observation of acceleration involved in the simulation. The FE model is a 12-elements simply supported beam, with the following parameters: beam length of 2.16m, elastic modulus $2.06 \times 10^5 GPa$, moment of inertia $I = 3600mm^4$, and density $\rho = 7.8 \times 10^3 kg/m^3$. For the moving load, a 5-second segment is randomly generated with the distributions of headway, vehicle weight and speed obtained in (Ge et al. 2022). The load is simplified as a concentrated force moving uniformly from node 1 to node 13, with a load updating step of 0.01 seconds. Three measurement points are designed at the bottom of the beam to capture the structural acceleration under the load, calculated using *Newmark* β method with the computation step same as the load updating step. The figure illustrates the time history of the acceleration responses at the three measurement points under the 5-second moving load segment.

The numerical simulation considers only single damage scenarios. To acquire training data under various structural states, the initial FE model is repeatedly modified in the damage location, damage extent, and noise level. Specifically, the damage location is divided into 12 possible scenarios based on the element number. The damage extent involves reductions in element stiffness and mass, considering reductions at ratios of (10%, 20%, ... 50%) across 6 levels. Noise is added to the original signal at five levels: 2%, 4%, 6%, 8%, and 10%. The noise signal is calculated by

$$noise = \boldsymbol{e}_{N\times 1} \frac{N(0,1) \times noise\ level}{\sqrt{mean\ (signal^2)}} \tag{8}$$

where $\boldsymbol{e}_{N\times 1}$ represents a $N\times 1$ unit vector with the same size as the signal.

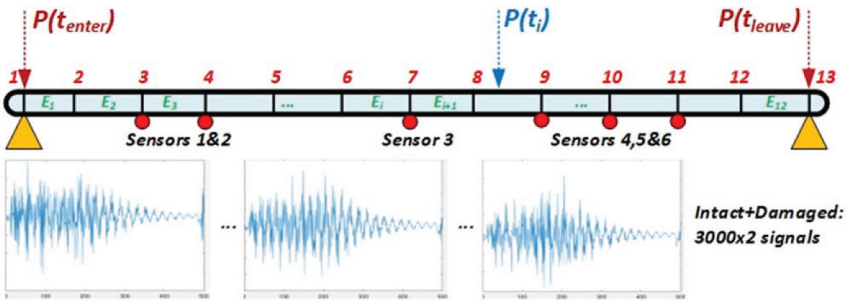


Figure 2. Diagram for the moving load, FE model and structural responses in simulation.

Further, to simulate the scenario of unknown initial structural parameters, the initial element stiffness is set as the product of the design value and a random coefficient within the range of 80%-120%. It is assumed that the mass of the elements remains unchanged, while the structural damping is determined based on the first three modal frequencies and their damping ratios. Assuming the first three modes have the same damping ratio $\xi = 0.03$, a total of 52,000 acceleration arrays with dimensions of 500×6 are obtained after 80 iterations varying the damage location, extent and noise levels. These arrays are concatenated with corresponding undamaged state signals to form 3000×2 arrays. These data are then input into different channels of the network, row by row, and divided into a training set and a test set in a 9:1 ratio for training the deep learning model.

The trained model was tested on a validation set containing 6, 500 signal arrays. These signals, derived from calculations under two different moving loads in both damaged and undamaged conditions, contain structural initial parameters and random noise that are completely distinct from the training data. This makes them ideal for validating the generalization capabilities of the proposed method. Figure 3 presents the accuracy of damage localization under various scenarios involving different damage positions and levels of damage extent. It can be observed that, even without a baseline model, the proposed method achieves an average accuracy of over 90% in locating damages at different positions, with a slight decrease in precision near the support location (element 11). When the stiffness reduction exceeds 20%, the accuracy of damage localization by the proposed method exceeds 98%. However, when the stiffness reduction is around 10%, the accuracy decreases to approximately 80%. This outcome is attributed to the lower signal-to-noise ratio in the structural response near the

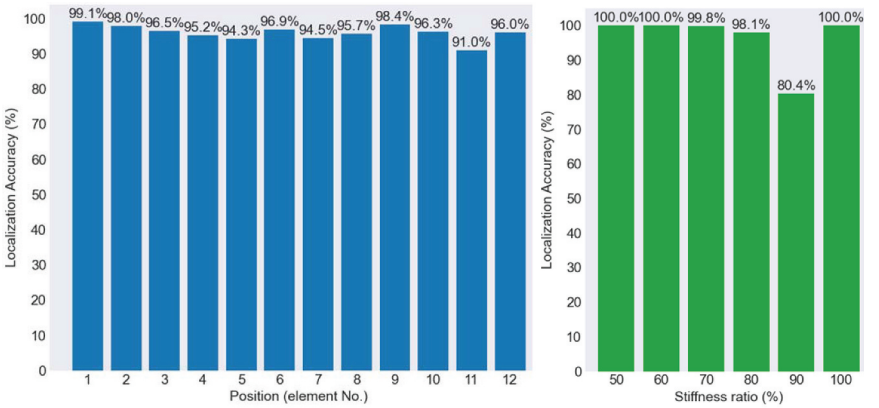


Figure 3. The accuracy of damage localization with respect to different positions and extents.

supports, where changes due to stiffness reduction might be more challenging to detect. Similarly, the smaller the damage, the more difficult it is to detect changes in structural response.

Furthermore, to validate the damage quantification capability of the proposed method, the relative error of predicted stiffness reduction for different damage scenarios is calculated on the validation set. The relative error is defined as

$$Er = \frac{\left|d_{i,pred} - d_{i,real}\right|}{d_{i,real}} \times 100\% \tag{9}$$

Figure 4 Presents the average relative error in predicted stiffness reduction for various positions and degrees of damage. The results demonstrate that the proposed method maintains a quantitative relative error of less than 10% for most damage scenarios. Similar to damage localization, a higher relative error is observed in elements 11 and 12, which are closer to the support positions. However, even with smaller degrees of stiffness reduction, the quantitative error in damage estimation remains at a relatively low level.



Figure 4. The absolute relative errors of damage quantification.

After the numerical validations and discussions presented above, it is reasonable to conclude that the proposed input-output framework can achieve both damage localization and quantification without the need for a baseline model. However, the applicability of this method still requires further experimental validation. In the model experiments, two points need to be noted. First, the consistency between the numerical model and the actual distribution of structural parameters should be considered. Although the method described in this paper can rely on numerical simulations to generate a large amount of training data, the distribution of this data should be similar to that of the actual structure. Therefore, in practical applications, a preliminary assessment and modification of the parameter space of the numerical model are necessary. Second, for actual structures, most cases of damage result in stiffness reductions of less than 10%, and the structural forms are more complex. The performance of the proposed framework for smaller damages and in more complex structures remains to be further explored.

5 CONCLUSIONS

In this paper, an input-output structural damage detection framework is proposed from a dynamic perspective. The framework constructs physical model information through the measured acceleration effects and moving loads on the bridge, and a digital model of the actual structure is created using FE modeling. The digital and physical models are connected by the measured moving loads. Under the action of these loads, the digital model generates a simulated acceleration effect database that encompasses various structural states. The

acceleration responses are comprehensively simulated for different damage locations, extents and noise levels, and are used to train an adapted one-dimensional EfficientNetV2 convolutional neural network model to detect damage in the physical model. Numerical experiments demonstrate that the framework preliminarily possesses the capability to locate and quantify structural damage using vehicle-induced acceleration signals.

REFERENCES

Breccolotti, M., & Natalicchi, M. (2022). Bridge damage detection through combined quasi-static influence lines and weigh-in-motion devices. *International Journal of Civil Engineering*, *20*(5), 487–500.

Das, S., Saha, P., & Patro, S. (2016). Vibration-based damage detection techniques used for health monitoring of structures: a review. *Journal of Civil Structural Health Monitoring*, *6*(3), 477–507.

Doebling, S. W., Farrar, C. R., Prime, M. B., & Shevitz, D. W. (1996). Damage identification and health monitoring of structural and mechanical systems from changes in their vibration characteristics: a literature review.

Dong, C. Z., Bas, S., & Catbas, F. N. (2019). A completely non-contact recognition system for bridge unit influence line using portable cameras and computer vision. *Smart Struct. Syst*, *24*(5), 617–630.

Ge, L., Dan, D., & Li, H. (2020). An accurate and robust monitoring method of full-bridge traffic load distribution based on YOLO-v3 machine vision. *Structural Control and Health Monitoring*, *27*(12), e2636.

Ge, L., Dan, D., & Sadhu, A. (2024). A Benchmark Data Set for Vision-Based Traffic Load Monitoring in a Cable-Stayed Bridge. *Journal of Bridge Engineering*, *29*(2), 04723001.

Ge, L., Koo, K. Y., Wang, M., Brownjohn, J., & Dan, D. (2023). Bridge damage detection using precise vision-based displacement influence lines and weigh-in-motion devices: Experimental validation. *Engineering Structures*, *288*, 116185.

Ge, L., Dan, D., Liu, Z., & Ruan, X. (2022). Intelligent simulation method of bridge traffic flow load combining machine vision and weigh-in-motion monitoring. *IEEE Transactions on Intelligent Transportation Systems*, *23*(9), 15313–15328.

He, W. Y., Ren, W. X., & Zhu, S. (2017). Baseline-free damage localization method for statically determinate beam structures using dual-type response induced by quasi-static moving load. *Journal of Sound and Vibration*, *400*, 58–70.

Hester, D., & González, A. (2012). A wavelet-based damage detection algorithm based on bridge acceleration response to a vehicle. *Mechanical Systems and Signal Processing*, *28*, 145–166.

Khuc, T., & Catbas, F. N. (2018). Structural identification using computer vision–based bridge health monitoring. *Journal of Structural Engineering*, *144*(2), 04017202.

Le, N. T., Thambiratnam, D. P., Nguyen, A., & Chan, T. H. T. (2019). A new method for locating and quantifying damage in beams from static deflection changes. *Engineering Structures*, *180*, 779–792.

Li, Z., Lin, W., & Zhang, Y. (2023). Drive-by bridge damage detection using Mel-frequency cepstral coefficients and support vector machine. *Structural Health Monitoring*, 14759217221150932.

Martini, A., Tronci, E. M., Feng, M. Q., & Leung, R. Y. (2022). A computer vision-based method for bridge model updating using displacement influence lines. *Engineering Structures*, *259*, 114129.

Nguyen, T. Q., Vuong, L. C., Le, C. M., Ngo, N. K., & Nguyen-Xuan, H. (2020). A data-driven approach based on wavelet analysis and deep learning for identification of multiple-cracked beam structures under moving load. *Measurement*, *162*, 107862.

Roveri, N., & Carcaterra, A. (2012). Damage detection in structures under traveling loads by Hilbert–Huang transform. *Mechanical Systems and Signal Processing*, *28*, 128–144.

Tan, M., & Le, Q. (2021, July). Efficientnetv2: Smaller models and faster training. In *International conference on machine learning* (pp. 10096–10106). PMLR.

Teng, S., X. Chen, G. Chen, & L. Cheng, Structural damage detection based on transfer learning strategy using digital twins of bridges. Mechanical Systems and Signal Processing, 2023. 191.

Wang, M., Xu, F., Xu, Y., & Brownjohn, J. (2023). A robust subpixel refinement technique using self-adaptive edge points matching for vision-based structural displacement measurement. *Computer-Aided Civil and Infrastructure Engineering*, *38*(5), 562–579.

Wang, R., J. Li, S. An, H. Hao, W. Liu, & L. Li, Densely connected convolutional networks for vibration based structural damage identification. *Engineering Structures*, 2021. **245**: p. 112871.

Zaurin, R., & Necati Catbas, F. (2011). Structural health monitoring using video stream, influence lines, and statistical analysis. *Structural Health Monitoring*, *10*(3), 309–332.

Bridge Maintenance, Safety, Management, Digitalization and Sustainability – Jensen, Frangopol & Schmidt (eds)
© 2024 The Author(s), ISBN 978-1-032-77040-6
Open Access: www.taylorfrancis.com, CC BY-NC-ND 4.0 license

Data fusion in structural health monitoring: Integrating computer vision and strain gauges for enhanced inspection

K. Aminfar, M. Ghyabi, Y. Shen & D. Lattanzi
George Mason University, USA

G. Ciaramella, M. Gherlone & C. Surace
Politecnico di Torino, Italy

ABSTRACT: In the evolving field of Structural Health Monitoring (SHM), the integration of diverse sensing techniques is pivotal for comprehensive structural analysis. This study introduces a novel data fusion methodology that synergizes the precision of strain gauges with the broad coverage of computer vision techniques. Aimed at advancing SHM practices, our approach facilitates a detailed understanding of structural behavior by concurrently analyzing strain fields and displacement signals captured through video streams. We employ Physics Informed Neural Networks (PINNs) to refine measurements and ensure physical plausibility in our data interpretation. Our methodology's effectiveness is validated through laboratory experiments on a simplified structural model, demonstrating enhanced accuracy and reliability in SHM. This paper highlights the potential of integrating traditional and contemporary sensing techniques in infrastructure monitoring, setting a new benchmark in the field.

1 INTRODUCTION

Structural Health Monitoring (SHM) is vital for ensuring the integrity and safety of key infrastructures. Conventionally, SHM has heavily relied on direct sensor installations like strain gauges (Mousa et al., 2021). These sensors are indispensable as they not only detect, localize, and quantify unusual structural behaviors but also project current and future structural predictions (Glisic, 2022). Nevertheless, their deployment poses logistical challenges and often require multiple sensors for single-point displacement estimation (Ma et al., 2023), prompting the need for alternative methods.

Shifting focus, non-contact methods like utilizing video streams offer a valuable alternative. These methods capture displacement fields, reflecting the overall stiffness of structures and providing an accurate assessment of structural conditions (Feng & Feng, 2018). Despite their precision, vision-based techniques are not without drawbacks, including high computational demands and sensitivity to lighting conditions (Ma et al., 2023). Alone, these methods may fall short of the accuracy and consistency achieved through sensor-based approaches.

To address these challenges, our study proposes a multi-modal sensor fusion strategy. Traditional fusions generally combine accelerometers with either strain sensors or vision cameras (Ma et al., 2023). Our approach goes further, merging strain gauge data with computer vision outputs. This fusion integrates the precision of strain measurements with the extensive spatial analysis offered by video-based techniques. The aim is to develop a robust analytical framework that correlates strain and visual data, thus enriching SHM with a more comprehensive understanding of structural behavior.

Further advancing our methodology, we introduce Physics-Informed Neural Networks (PINNs) (Raissi et al., 2019) into our vision-based SHM framework. PINNs represent

DOI: 10.1201/9781003483755-82

a significant evolution from traditional machine learning models, as they offer enhanced interpretability and conform more closely to physical principles (Faroughi et al., 2023). By incorporating physical laws into the neural network architecture, PINNs ensure that the model's predictions are not only accurate but also physically plausible. Their application in SHM is multifaceted: for instance, they have been effectively utilized in modeling stress and displacement under varying conditions, an aspect central to understanding structural behaviors (Henkes et al., 2022). Furthermore, PINNs show promise in accurately simulating the behavior of materials under different strain rates and temperatures, a factor crucial for assessing the long-term durability and resilience of infrastructure (Arora et al., 2022). Importantly, PINNs have the capability to refine wave velocity estimations from displacement data, enhancing the precision of structural imaging and enabling the early detection of potential structural failures (Rathod & Ramuhalli, 2022). Additionally, their adeptness in solving complex differential equations relevant to structural dynamics positions them as an invaluable tool in SHM, particularly for analyzing intricate structural responses under varied load conditions (Kollmannsberger et al., 2021).

Overall, this study presents a novel approach in SHM by leveraging the combined strengths of both strain gauges and computer vision, further augmented by the analytical prowess of PINNs. This unique combination not only promises to bolster the accuracy and reliability of structural assessments but also signifies a substantial advancement in the application of machine learning within the domain of infrastructure monitoring.

2 METHODOLOGY

2.1 *Theoretical foundation*

In SHM, leveraging the strengths of different sensors is key to achieving comprehensive monitoring. Strain sensors offer high-precision local measurements, crucial for detecting minute changes in structural integrity. In contrast, vision-based methods provide extensive spatial coverage, enabling the capture of broader deformation patterns. This fusion approach is vital for a holistic understanding of structural condition.

A core aspect of our methodology involves shape sensing, which reconstructs a structure's displacement field using discrete surface strain measurements (Gherlone et al., 2018). According to the Bernoulli-Euler theory of pure bending, there is a direct correlation between axial strain and the curvature of the beam (Ko et al., 2007). This relationship is mathematically expressed as $\kappa = d^2w/dx^2$, where κ represents the curvature, and $w(x)$ denotes the beam's deflection along its longitudinal axis. The axial strain (ϵ) at any point is linked to curvature by $\epsilon = -y\kappa$, with 'y' being the distance from the neutral axis.

Using this principle, curvature is deduced from localized strain measurements. Subsequent numerical integration allows us to calculate the beam's slope (dw/dx) and overall deflection ($w(x)$). The precision of these estimations hinges on the density of strain data points, the accuracy of the numerical integration method, well-defined boundary conditions, and an exact characterization of the beam's properties and loading.

Utilizing the strain data recorded by our sensors, we augment our analysis by contrasting these sensor-derived displacement values at specific sensory points against the displacement data acquired through vision-based displacement measurement techniques.

2.2 *Image based displacement measurement*

To facilitate vision-based displacement measurement, the Demons algorithm is employed. The Thirion's image matching algorithm (Thirion, 1998), known as the Demons algorithm, is a linear complexity technique for nonrigid image registration, crucial in applications requiring intense value preservation. The proposed algorithm consists of estimation of the demon forces for every demon (more precisely, the result of the application of a force during one iteration step, that is a deformation field), and update of the transformation based on the calculated forces (Sotiras et al., 2013).

The core of the Demons algorithm lies in its optical flow component, which calculates pixel displacements by comparing sequential images. This comparison relies on the assumption of constant brightness over time, enabling accurate estimation of pixel movement between images. Essentially, the algorithm computes the displacement needed at each pixel (treated as a "demon") to align the moving image with the reference image. This calculation involves analyzing intensity gradients and differences between pixels.

In implementing this method, our study involved converting each frame into grayscale to standardize intensity values, followed by applying normalization techniques to ensure uniformity across images, countering variations in illumination. This preprocessing set the stage for the effective application of the Demons algorithm.

For enhanced efficiency and accuracy, a pyramidal approach is employed. This involves performing multiple iterations at progressively coarser image resolutions, starting with a low-resolution overview and gradually refining the displacement field at finer scales. This multi-scale approach balances computational efficiency with detailed displacement estimation (Zitová & Flusser, 2003).

2.3 *Physics informed neural network*

Physics-Informed Neural Networks (PINNs) (Raissi et al., 2019) operate by incorporating physical laws into the neural network architecture and its loss function, and aim to approximate solutions that closely match both the training data and the underlying physical equations. Here, the SciANN (Haghighat & Juanes, 2021), a Keras/TensorFlow wrapper is employed to create the PINN model.

2.3.1 *Network architecture and data fitting*

The architecture of the PINN is based on a standard feed-forward neural network (Kollmannsberger et al., 2021). The network is designed to predict displacement and strain as a function of the position along the beam, taking into account the beam's length (L), applied load (P), and material properties such as the modulus of elasticity (E) and moment of inertia (I).

To train the network, a synthesized dataset is created using analytical solutions for displacement and strain under various loading conditions. The data is further augmented by adding Gaussian noise, to mimic the real scenario. The data-fitting loss, L_{data}, is formulated as the mean squared error between the network's predictions and the actual values from the dataset. It is expressed as:

$$L_{data} = \left(\frac{1}{N}\right) \sum_{1}^{N} \left(\hat{d}_{(x_i)} - d_{data(x_i)}\right)^2 + \left(\hat{\varepsilon}_{(x_i)} - \varepsilon_{data(x_i)}\right)^2$$

where N is the number of data points, $\hat{d}$ and $\hat{\varepsilon}$ are the network's predictions for displacement and strain, respectively, and subscript *data* refers to the corresponding true values.

2.3.2 *Incorporation of physical laws*

The distinct feature of a PINN is its ability to integrate physical laws into the learning process. This is achieved by adding terms to the loss function that represent the governing equations of the system being modeled.

For a cantilever beam under a point load P, the Euler-Bernoulli beam theory provides the necessary physical laws. The physics-based loss for deflection, $L_{deflection}$, ensures the network's compliance with the deflection equation of the beam. It is given by:

$$L_{deflection} = \left(\frac{1}{M}\right) \sum_{1}^{M} \left(\hat{d}_{(x_i)} - \frac{P x_i^2}{6EI}(3L - x_i)\right)^2$$

Strain in a beam is directly related to its curvature, and the curvature at any point along the beam is mathematically represented by the second derivative of displacement with respect to

the position. Similarly, the physics-based loss for strain, L_{strain}, enforces the correct strain profile as per the beam theory. It is calculated as:

$$L_{strain} = \left(\frac{1}{M}\right) \sum_{1}^{M} \left(\hat{\varepsilon}_{(x_i)} - \frac{d^2 \hat{d}}{dx^2}(x_i) \right)^2$$

where the term corresponding to the second derivative of the predicted displacement, indicates the curvature of the beam.

2.3.3 *Total loss function and training*

The overall loss function, L, for the PINN is a weighted sum of the data-fitting loss and the physics-based losses. It is defined as:

$$L_{total} = \alpha L_{data} + \beta L_{deflection} + \gamma L_{strain}$$

Here, α, β, and γ are coefficients that balance the importance of fitting the data and adhering to the physical laws.

2.4 *Data fusion*

The process begins with the calculation of the beam displacement field from the image sequence, designated as $v(z)$. This computation is conducted first through conventional image pre-processing, encompassing image cropping, selection of the Region of Interest, black weight artifact removal, and illumination correction. Following these initial steps, the punctual displacements are determined using the Demon algorithm, as previously stated. Then, the longitudinal strain field, termed $\varepsilon(z)$, is derived directly from the previously calculated displacement field, $v(z)$.

The refinement process involves enhancing the strain field, now referred to as $\varepsilon_{fix}(z)$, utilizing data from strain gauges. The displacement field, denoted as $v_{fix}(z)$, is then fine-tuned by numerically integrating this enhanced strain field, $\varepsilon_{fix}(z)$. An important assumption is the consideration of zero displacements at the beam ends. The interpolation of the displacement field employs smoothing splines. This stage is followed by a re-interpolation process, wherein an adjusted smoothing parameter is utilized to give precedence to data smoothness.

The computation of $\varepsilon(z)$ involves transforming the displacement data into strain data, guided by the principles of Hooke's and Navier's laws. The strain field, $\varepsilon_{fix}(z)$, is then calculated using a smoothing spline interpolation function. This function is designed to fit the data accurately and detect changes in slope, ensuring adherence to these changes. The computation of the refined displacement field is achieved through the double integration of linear functions. This process necessitates the imposition of boundary and continuity conditions.

2.5 *Experimental setup and testing procedure*

Our experimental investigation was conducted on a 6063 Aluminum beam, with dimensions of 50.80 mm width, 18.50 mm height, 1.60 mm thickness, and 2414.6 mm length. The beam was instrumented with six Type I strain gauges, arranged in a half-bridge configuration at intervals of L/4, L/2, and 3L/4 along the beam (Figure 1). This configuration, known for its high sensitivity and ability to compensate for temperature variations, ensured accurate strain measurement. Data from the strain gauges were captured using an NI cDAQ-9188 system, complemented by an optoNCDT 1420 laser sensor and an industrial-grade Ueye camera for deflection and motion tracking. To enhance image processing, the beam was marked with a colored speckle pattern, facilitating optical flow computations, and was positioned against a whiteboard for optimal contrast (Figure 2). The laser sensor acted as ground truth data for the investigations.

The experimental procedure involved a series of controlled static load tests with pinned ends to simulate hinge connections. The objective was to examine the beam's structural response to different load intensities, focusing on consistency and repeatability. Each test was conducted thrice to ensure the reliability of the data. The testing scenarios included 0.05, 0.2 and 0.5 kg load the beam's midpoint.

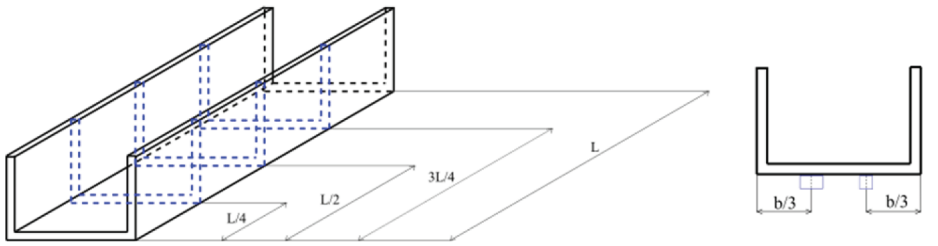


Figure 1. Beam section and strain gauge locations.

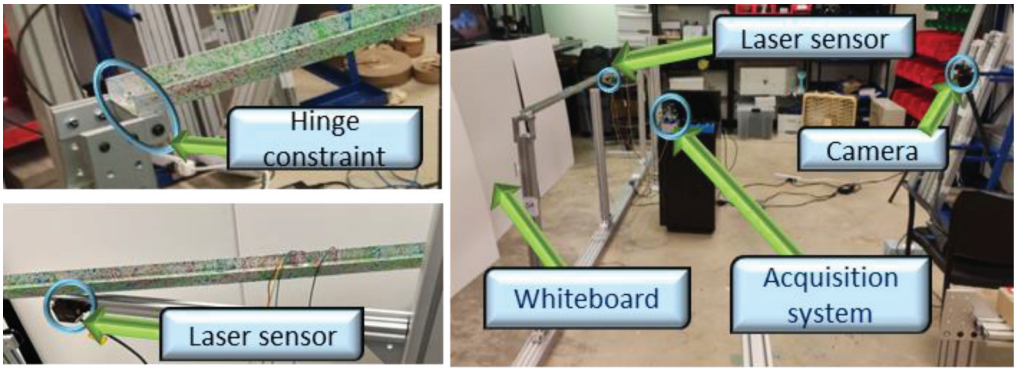


Figure 2. Experimental setup.

3 RESULTS AND DISCUSSION

This section presents the findings from our experimental tests, focusing on displacement and strain measurements under a 0.2 kg load at the centerline of the beam (Case 2), as these were typical for all conducted experienced. The results are illustrated in Figures 3 to 6.

Figure 3 displays the displacement curve obtained using the Image-based Measurement (IIm) method for Case 2. This graph results from iterative interpolation using smoothing splines, with the exclusion of residuals exceeding a set tolerance. The graph features an error measure focusing on data point fitting to the spline, along with a roughness measure:

$$p\sum_i w_i(y_i - s(z_i))^2 + (1-p)\int \lambda\left(\frac{d^2s}{dz^2}\right)^2 dz$$

Figure 4 illustrates the strain curve derived from both strain gauge readings and the analytical approach for Case 2. The stress-displacement relationship is characterized as

$$\frac{d^2v(z)}{dz^2} = -\frac{\varepsilon(z)}{Y}$$

by assuming zero second derivatives at the beam's extremes. This accounts for the beam's properties as slender, elastic, and isotropic, with shear effects neglected.

The results of the corrected strain field, integrating strain gauge measurements, are presented in Figure 5. The process involves iterative and weighted interpolation with smoothing splines, exclusion of data points that degrade the distribution, and enforcement of interpolation at strain gauge measurements. Correction is applied based on the boundary condition of zero strain at the clamp section.

The comparison of the neural network's performance with and without the inclusion of the physics-based loss function is depicted in Figure 6. It is evident that the incorporation of the physics-based loss function enhances the model's generalizability and alignment with the physical phenomena for both strain and deflection.

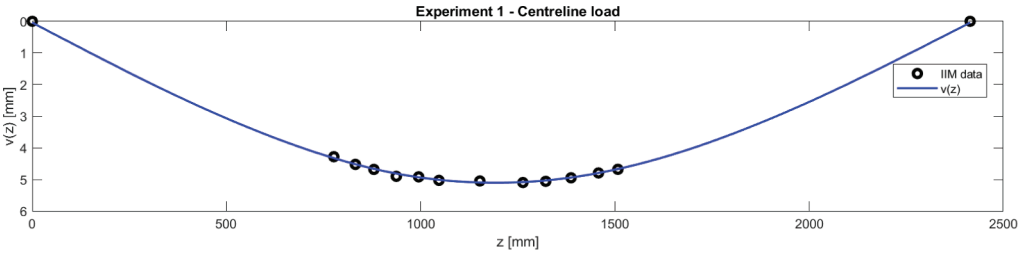


Figure 3. Image-based displacement measurement.

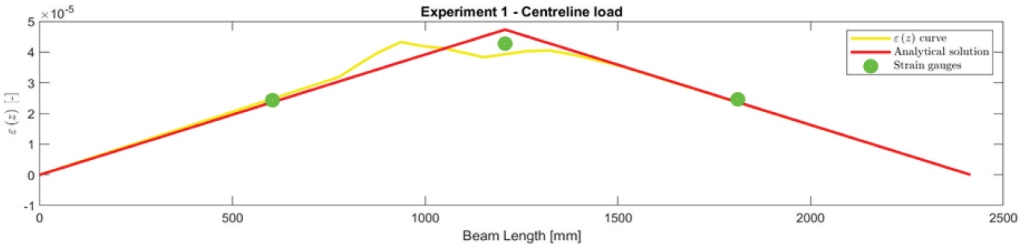


Figure 4. Strain analysis with strain gauges and analytical method.

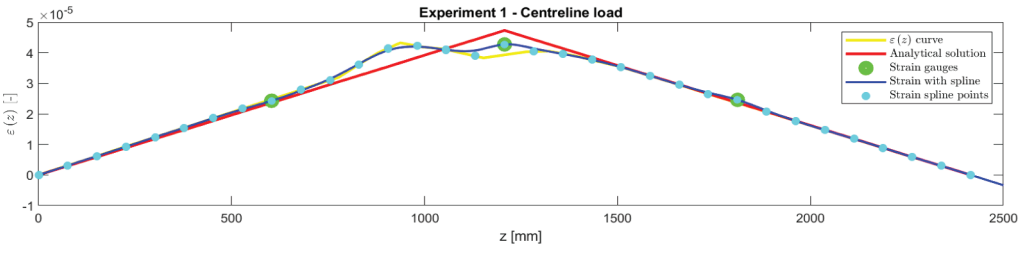


Figure 5. Corrected strain field with strain gauge measurements.

4 CONCLUSION

This study introduces an innovative approach that effectively combines strain gauge data and computer vision with an underlying physical formulation. Our method represents a significant advancement over traditional SHM techniques, particularly in its ability to accurately assess

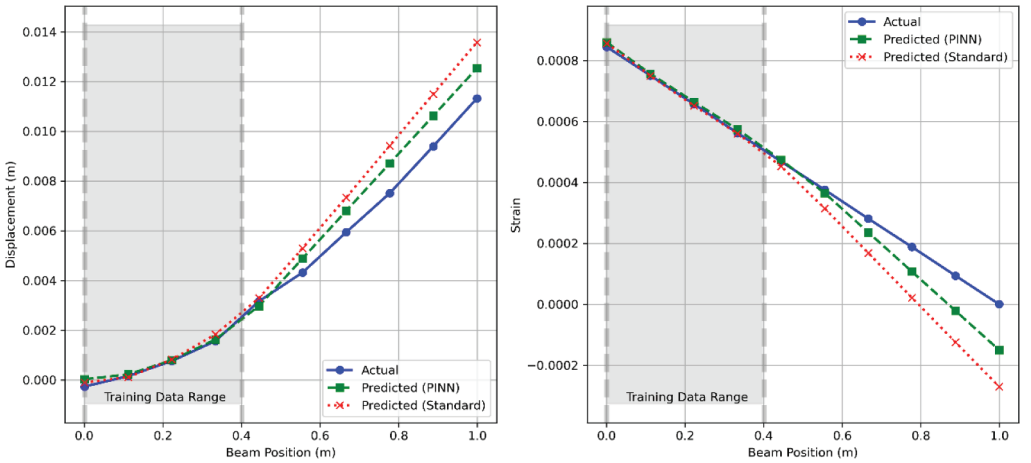


Figure 6. Neural network performance with and without physics-based loss function.

structural integrity. This is achieved by correlating displacement and strain data through corrected measurements. The incorporation of Physics-Informed Neural Networks (PINNs) substantially enhances the accuracy and physical plausibility of the predictions, ensuring close alignment with actual structural responses under various load conditions. While our approach is effective in standard configurations, future work could aim to further enhance and integrate the model's accuracy in more complex structural scenarios, particularly through the application of PINNs. Such advancements promise to broaden the applicability of this innovative approach in the field of SHM.

REFERENCES

Arora, R., Kakkar, P., Dey, B., & Chakraborty, A. (2022). *Physics-informed neural networks for modeling rate- and temperature-dependent plasticity* (arXiv:2201.08363). arXiv. https://doi.org/10.48550/arXiv.2201.08363

Faroughi, S. A., Pawar, N., Fernandes, C., Raissi, M., Das, S., Kalantari, N. K., & Mahjour, S. K. (2023). *Physics-Guided, Physics-Informed, and Physics-Encoded Neural Networks in Scientific Computing* (arXiv:2211.07377). arXiv. http://arxiv.org/abs/2211.07377

Feng, D., & Feng, M. Q. (2018). Computer vision for SHM of civil infrastructure: From dynamic response measurement to damage detection – A review. *Engineering Structures*, *156*, 105–117. https://doi.org/10.1016/j.engstruct.2017.11.018

Gherlone, M., Cerracchio, P., & Mattone, M. (2018). Shape sensing methods: Review and experimental comparison on a wing-shaped plate. *Progress in Aerospace Sciences*, *99*, 14–26. https://doi.org/10.1016/j.paerosci.2018.04.001

Glisic, B. (2022). Concise Historic Overview of Strain Sensors Used in the Monitoring of Civil Structures: The First One Hundred Years. *Sensors*, *22*(6), Article 6. https://doi.org/10.3390/s22062397

Haghighat, E., & Juanes, R. (2021). SciANN: A Keras/Tensorflow wrapper for scientific computations and physics-informed deep learning using artificial neural networks. *Computer Methods in Applied Mechanics and Engineering*, *373*, 113552. https://doi.org/10.1016/j.cma.2020.113552

Henkes, A., Wessels, H., & Mahnken, R. (2022). Physics informed neural networks for continuum micromechanics. *Computer Methods in Applied Mechanics and Engineering*, *393*, 114790. https://doi.org/10.1016/j.cma.2022.114790

Ko, W. L., Richards, W. L., & Tran, V. T. (2007). *Displacement Theories for In-Flight Deformed Shape Predictions of Aerospace Structures*.

Kollmannsberger, S., D'Angella, D., Jokeit, M., & Herrmann, L. (2021). Physics-Informed Neural Networks. In S. Kollmannsberger, D. D'Angella, M. Jokeit, & L. Herrmann (Eds.), *Deep Learning in Computational Mechanics: An Introductory Course* (pp. 55–84). Springer International Publishing. https://doi.org/10.1007/978-3-030-76587-3_5

Ma, Z., Choi, J., & Sohn, H. (2023). Structural displacement sensing techniques for civil infrastructure: A review. *Journal of Infrastructure Intelligence and Resilience*, *2*(3), 100041. https://doi.org/10.1016/j.iintel.2023.100041

Mousa, M. A., Yussof, M. M., Udi, U. J., Nazri, F. M., Kamarudin, M. K., Parke, G. A. R., Assi, L. N., & Ghahari, S. A. (2021). Application of Digital Image Correlation in Structural Health Monitoring of Bridge Infrastructures: A Review. *Infrastructures*, *6*(12), Article 12. https://doi.org/10.3390/infrastructures6120176

Raissi, M., Perdikaris, P., & Karniadakis, G. E. (2019). Physics-informed neural networks: A deep learning framework for solving forward and inverse problems involving nonlinear partial differential equations. *Journal of Computational Physics*, *378*, 686–707. https://doi.org/10.1016/j.jcp.2018.10.045

Rathod, V. T., & Ramuhalli, P. (2022). Physics-informed neural networks for identification of material properties using standing waves. *Nondestructive Characterization and Monitoring of Advanced Materials, Aerospace, Civil Infrastructure, and Transportation XVI*, *12047*, 179–188. https://doi.org/10.1117/12.2607314

Sotiras, A., Davatzikos, C., & Paragios, N. (2013). Deformable Medical Image Registration: A Survey. *IEEE Transactions on Medical Imaging*, *32*(7), 1153–1190. https://doi.org/10.1109/TMI.2013.2265603

Thirion, J.-P. (1998). Image matching as a diffusion process: An analogy with Maxwell's demons. *Medical Image Analysis*, *2*(3), 243–260. https://doi.org/10.1016/S1361-8415(98)80022-4

Zitová, B., & Flusser, J. (2003). Image registration methods: A survey. *Image and Vision Computing*, *21*(11), 977–1000. https://doi.org/10.1016/S0262-8856(03)00137-9

Bridge Maintenance, Safety, Management, Digitalization and Sustainability – Jensen, Frangopol & Schmidt (eds)
© 2024 The Author(s), ISBN 978-1-032-77040-6
Open Access: www.taylorfrancis.com, CC BY-NC-ND 4.0 license

A smart robotic system for autonomous inspection of large-scale concrete girder

Yujie Cui, Yue Pan, Dalei Wang & Mazeyu Ji
Tongji University, Shanghai, China

Sugong Cao
Zhejiang Scientific Research Institute of Transport, Hangzhou, China

ABSTRACT: Inspecting concrete box girders is crucial for bridge maintenance. Challenges in accessibility and working conditions often hinder effective internal inspections, posing a serious threat to bridge operational safety. This paper proposes a solution using a lightweight and cost-effective robotic device for the automated collection of apparent internal defects in bridge box girders. Emphasizing the bridge environment and the lightweight nature of the device, we optimized mapping, path planning, and tracking schemes. Our robot, equipped with consumer-grade sensors, successfully mapped a hundred-meter-long box girder within a bridge at meter-level accuracy. Path planning covered the entire box girder, collecting defect information from the top and side walls.

1 INTRODUCTION

Concrete box girders in bridge engineering commonly exhibit defects like spalling, exposed reinforcement, and cracks over extended service periods. Manual visual inspections, the prevailing method for inspecting these girders, have inherent drawbacks such as subjectivity, inefficiency, and limited defect detection. The increasing labor costs and inspection volumes have spurred a shift toward automated methods for inspection support (Tung, 2002; M La, 2013; Lei, 2018).

Despite the growing trend towards automation, the distinct environment within concrete box girders complicates the direct application of automation solutions developed for bridge surfaces and exteriors. Weak GPS signals within the girders impede stable robot positioning using GPS, while alternative wireless positioning methods necessitate fixed base stations, adding both cost and inconvenience.

Simultaneous Localization and Mapping (SLAM) technology has witnessed significant development in scene perception over the past two decades, with researchers applying SLAM to bridge inspection (Jung, 2020; Phillips, 2019). However, existing SLAM methods encounter challenges in effectively addressing mapping and localization tasks within box girders. Visual SLAM struggles due to low light conditions and a lack of textured concrete surfaces on inner walls, while traditional laser SLAM faces difficulties in accurate mapping due to the absence of sufficient terrain features.

Another significant hurdle in the system pertains to path planning and coverage detection. While precise mapping simplifies path planning and coverage detection in box girders with simple terrain features, large concrete box girders in expansive bridge structures necessitate the introduction of multi-robot collaborative detection for enhanced efficiency.

Hence, considering the limitations of the box girder environment, this paper enhances existing methods and introduces a fully automated inspection framework specifically tailored for the interior of concrete box girders, as depicted in Figure 1. To address the dim and

DOI: 10.1201/9781003483755-83

feature-limited conditions within box girders, the paper optimizes the laser SLAM algorithm to construct a 2D grid map. Subsequently, the paper partitions the work area for multiple robots on the 2D grid map and employs an optimized Spanning Tree Coverage algorithm to generate efficient work trajectories. Finally, a tracked robot control scheme is proposed to guide the robot in achieving path navigation, image capture, and defect localization.

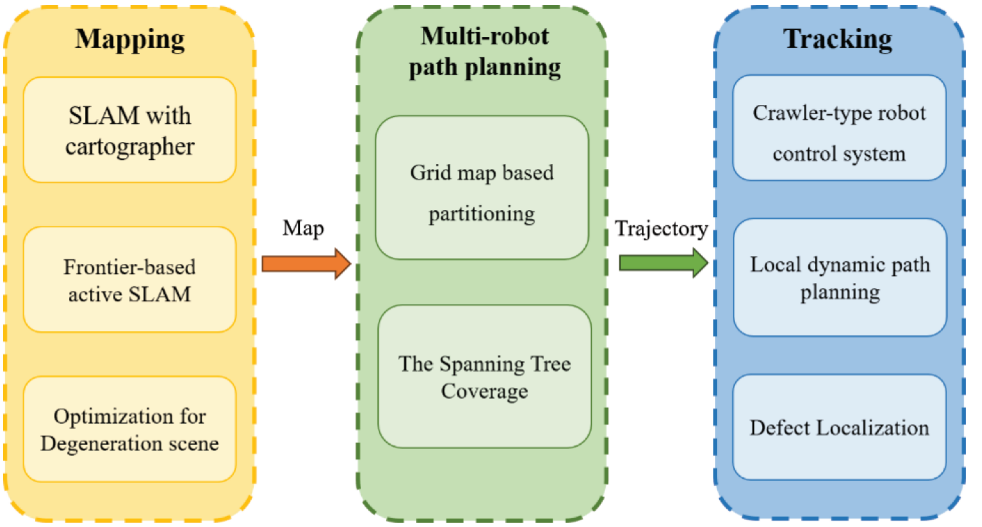


Figure 1. Overview of the novel robotic system for autonomous inspection.

2 FRAMEWORKS

2.1 *Mapping*

SLAM, a method addressing the challenge of simultaneous robot position determination and map construction in environments lacking prior knowledge, proves particularly effective for mapping tasks within box girders. In this framework, information from various sensors, commonly LiDAR scan data and odometry information, is processed. These represent the point cloud from laser LiDAR environmental scans and the recorded positional data of the robot. Merging these data types enables real-time map generation and accurate estimation of the robot's current pose.

The paper utilizes the Cartographer algorithm, a sophisticated open-source 2D laser SLAM algorithm (Hess, 2016). Cartographer optimizes the robot's pose vector $(\xi_x, \xi_y, \xi_\theta)^T$ through both local and global optimization, where the first two parameters denote translation, and the third represents rotation. Global optimization, involving loop closure detection, eliminates cumulative errors. Local optimization optimizes a cost function by matching laser scan points with the map and updating submaps.

To achieve full automation, active SLAM is introduced, allowing the robot to autonomously explore unknown environments. The Frontier-based Exploration method (Yamauchi, 1997) selects boundaries in unexplored regions to acquire map and localization information simultaneously. This method guides the robot in selecting the next exploration target point with the highest information gain, balancing exploration performance and map information gain.

However, mapping issues arise due to the lack of sufficient environmental terrain features within the box girder, particularly in degraded scenes with long corridors and minimal terrain

features. Different frames scanning the scene exhibit extreme similarity, and odometry accumulates errors, leading to significant mapping inaccuracies.

In the foundational SLAM framework, Correlative Scan Matching (CSM) requires manual parameter tuning and does not consider the impact of degraded scenes and different environments. To address this, we design an environment-sensitive CSM method based on real-time results. This method dynamically adjusts motion weights, achieving autonomous adaptability to various environments (Shi.2023).

The Principal Component Analysis (PCA) method is employed to decentralize the normal vectors of all scanned points in the environment. The first and second eigenvectors, denoted as v_1 and v_2, are determined. The ratio $k = \frac{v_1}{v_2}$, $k \in (1, +\infty)$ is then mapped onto (0, 1) with $\beta = -\frac{1}{k} + 1$, yielding the degradation coefficient β. A value closer to 1 indicates a higher degree of environment degradation.

In SLAM algorithms, the probability distribution of the motion model is typically calculated and represented by a Gaussian distribution $\mathrm{x_i} \sim N(\mu, \sigma^2)$, where x_i represents the estimated robot poses, μ is the initial guess for the pose based on x_{i-1} and $\mathrm{u_i}$, and σ determines the weight of the initial pose. In a series of algorithms based on CSM, the motion score $\mathrm{S_{mot}}$ for each x_i is often calculated using the following formula. In this equation, the basic motion weight σ is replaced with the dynamic weight σ/β, allowing the adjustment of motion weight through the degeneration coefficient.

$$\Delta \mathrm{x_i} = (\Delta \mathrm{x}, \Delta \mathrm{y}, \Delta\theta)^{\mathrm{T}} = \mathrm{x_i} - (\mathrm{x_{i-1}} + \mathrm{u_i}) \tag{1}$$

$$p(x_i|x_{i-1}, u_i) \propto S_{\mathrm{mot}} = \exp\left(-\frac{\beta^2\left(\sqrt{\Delta x^2 + \Delta y^2} + |\Delta\theta|\right)^2}{\sigma^2}\right) \tag{2}$$

2.2 *Multi-robot path planning*

Upon achieving accurate mapping, to enhance the efficiency of detection in large box girder scenes, we can opt for the introduction of multiple robots collaboratively performing the inspection task. Thus, we need to devise path planning for the traversal of the scene by multiple robots, as illustrated in Figure 2. Firstly, this paper conducts down sampling of the grid map based on the robot's radius. Subsequently, the approximate rectangular box girder area is uniformly partitioned and assigned to each robot. After preprocessing the grid map, the paper employs the Spanning Tree Coverage (STC) algorithm to generate loop detection paths, ensuring each robot can access all locations on the map without redundancy. (Kapoutsis.2017)

The map is represented as a grid map, where the number of cells in the map signifies both the required spatial resolution and the transmission ability of the robot. Let's define a sequence set X with a neighboring connectivity length of m. The position of robot $\mathrm{x_i(t)} = (\mathrm{x_i}, \mathrm{y_i}) \in \mathrm{L}$ (where L is the traversable area), and the path length of $\mathrm{X_i}$ is denoted as $|\mathrm{X_i}|$.

The Spanning Tree Coverage (STC) algorithm is able to construct a minimum path covering all the manipulation area L starting from any obstacle-free cell. Each large unit is first split into four small units, which is done to make it easier to form a loop so that the robot can complete the traversal and return to the origin. The non-blocking region is then considered as a node, and neighboring nodes introduce an edge. Next, a minimum spanning tree is constructed using the STC algorithm. Finally, the path formed by each large unit is transformed into a connected loop formed by every group of four small units.

The original mCPP (Multi-robot Coverage Path Planning) problem can be simplified to generate paths L_i for each robot in the non-blocked area, satisfying the problem of minimizing the maximum path length $|L_i|$. This can be expressed mathematically as:

$$\begin{cases} \mathrm{L_i} \cap \mathrm{L_j} = \emptyset, \forall i, j \in 1, \ldots, \mathrm{n_r}, i \neq j \\ L_1 \cup L_2 \cup \cdots \cup L_{n_r} = \mathcal{L} \\ |L_1| \approx |L_2| \cdots \approx |L_{n_r}| \\ L_i \ \text{ is connected} \, \forall i \in 1, \ldots, n_r \\ X_i(t_0) \in L_i \end{cases} \tag{3}$$

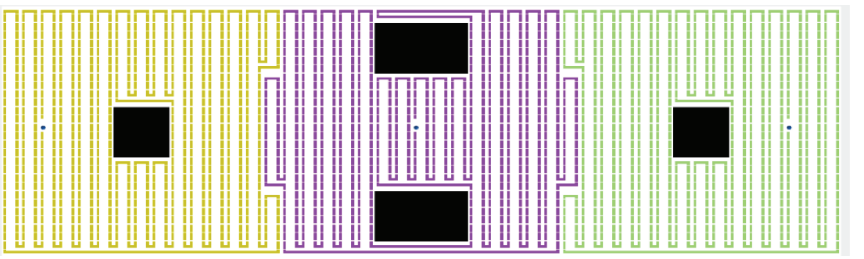


Figure 2. Illustration of multi-robot path planning: The diagram depicts the starting positions of three robots as indicated by blue dots, obstacles represented by black rectangles, and the paths planned by the three robots in yellow, purple, and green. The paths are evenly distributed.

2.3 *Tracking*

In the process of trajectory navigation, the control of tracked robots and the elimination of dynamic map errors during specific travel play crucial roles. The control scheme for tracked robots influences the trajectory strategy, particularly the transition strategy between different target points along the path. Additionally, the paths generated by the global planner need dynamic adjustments based on real-time discoveries of local changes during the trajectory process.

Opting for tracked robots to conduct exploration tasks within bridge box girders offers several advantages, including robust off-road capability, strong load-bearing capacity, and smooth traversal. Tracked robots can adapt to the terrain within box girders, carry additional sensors, and maintain stable operation.

A tracked robot, with one side of its track equivalently viewed as an infinite number of small wheels, ensures uniform rotational speed across these wheels. Therefore, the steering mechanism of a tracked robot aligns with that of a four-wheel-drive robot, involving sliding steering. (Martínez.2004)

In practical operations, precision in-place rotation and straight-line movement can be achieved using a tracked vehicle. Thus, controlling the tracked vehicle involves maintaining consistent wheel speeds, with opposite or identical directions. The magnitude of speed only affects the speed of rotation and forward movement, without introducing tracking errors.

After completing mapping and route planning within the box girder, deviations may occur due to errors in mapping, route planning, or changes in the internal environment during the trajectory process. Consequently, local path adjustments are essential, incorporating real-time navigation planning to achieve obstacle avoidance.

Upon determining the path, if it encounters obstacles, we establish start and target points before and after the obstacle. Utilizing the Time Elastic Band (TEB) algorithm (Rösmann,2012), we connect these points, allowing the path to deform. The deformation criterion involves treating all constraints as external forces acting like rubber bands, enabling the path to circumvent obstacles and avoid disruptions.

$$\mathrm{f(B)} = \sum\nolimits_{\mathrm{k}} \gamma_{\mathrm{k}} \mathrm{f_k(B)} \tag{4}$$

$$B^* = \text{argmin}_B f(B) \tag{5}$$

The objective function $f(B)$ represents a weighted sum of various components and is indicative of the optimization goals. Here, B^* denotes the optimized Time Elastic Band (TEB). The objective function is divided into two categories: penalties expressed through penalty functions, encompassing velocity and acceleration constraints, as well as trajectory-related objectives such as the shortest or fastest path, and objectives related to obstacle distances. The penalty functions employ a piecewise continuous and differentiable cost function to calculate penalties for violating constraints.

$$e_\Gamma(x, x_r, \in, S, n) \simeq \begin{cases} \left(\frac{x-(x_r-\in)}{S}\right)^n & if\ x > x_r - \in \\ 0 & otherwise \end{cases} \tag{6}$$

where x_r is the limit value, S denotes the scaling, n denotes the polynomial order, $\in$ denotes a small offset near the approximation, and $S, n, \in$ affects the accuracy of the approximation.

After the robot reaches each waypoint following the trajectory, it proceeds to perform data collection. The global path planning provides the coordinates of each waypoint, and if the trajectory is modified by TEB, the waypoint coordinates are adjusted accordingly. Once the coordinates of the waypoints are determined, the position of the imaging inside the box girder is derived by combining the gimbal angle at the time of shooting, the lens position, and the distance from the shooting plane to the lens. The gimbal angle is determined by sensors in the servo, while the shooting distance is measured by multiple parallel infrareds ranging sensors mounted on the lens.

3 APPLICATION

3.1 *Robot-design*

We have developed a robotic system for automated detection, as illustrated in Figure 3. The robot consists of three main components: the perception layer, the power layer, and the control layer. The perception layer is equipped with sensors to perceive the environment and collect data. Essential sensors include a laser rangefinder for laser SLAM mapping and a camera for capturing information on the interior walls of the concrete box girder. The power layer comprises essential motion components and energy storage elements, including batteries, motors, and wheels. The control layer is the core part, responsible for algorithm execution and driving various components. Considering the task difficulty and cost, microcontrollers such as STM32 and Raspberry Pi can be used.

In the experiments conducted on the Su-Tong Yangtze River Highway Bridge in Jiangsu Province, China, the perception layer utilized an industrial 4K camera from Hikvision with 32x optical zoom, mounted on a 2-DOF dual-servo gimbal for high-definition imaging of the box girder's interior walls. The perception layer also integrated a 2D laser rangefinder capable of scanning coverage with a minimum measurement distance of 0.05mm.

The power layer includes two batteries with a capacity of 9800mAh each, weighing 0.36kg each. The theoretical robot's rated power allows it to operate for 12 hours. The chassis has a carrying capacity of 3-4kg.

The control layer employs a 16GB Raspberry Pi as the main control board, orchestrating various components of the robot and storing the core algorithms used in this paper. Additionally, two STM32 microcontrollers are used to drive the chassis and the gimbal, respectively.

3.2 *Mapping*

In the testing phase, we conducted on-site mapping at the Su-Tong Yangtze River Highway Bridge in Jiangsu Province, China. The robot employed a 360° LiDAR with a scanning radius of 4 meters. The controller utilized a tracked two-wheel differential drive system with

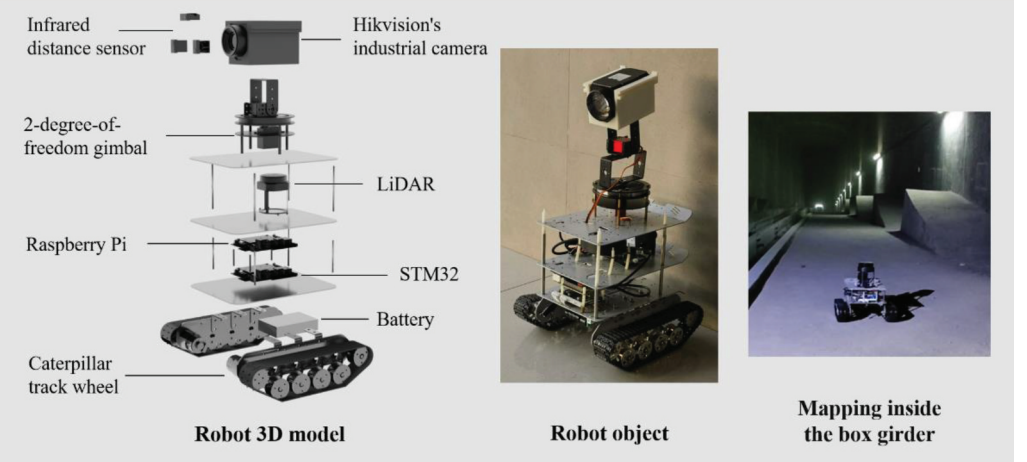


Figure 3. Three-dimensional exploded view of the robot's structure, a physical representation of the robot, and on-site mapping images of the robot within the box girder of the Su-tong Yangtze River Highway Bridge in Jiangsu Province, China. During the mapping process, the robot utilized only the functionality layer equipped with the LiDAR.

a maximum speed of 0.2 m/s. The mapping focused on the northern section of the first continuous rigid box girder in the navigation channel of the bridge, with a length of 139.6 meters, as illustrated in Figure 4.

During mapping, we collected datasets from all sensors and manually adjusted the relevant parameters of Correlative Scan Matching (CSM) within the SLAM framework. Multiple mapping iterations were conducted using the acquired data, as illustrated in Figure 5. In Figure 5 (a), we manually decreased the parameteσ, enhancing the confidence of the observation model primarily based on the laser radar, while lowering the confidence in the motion model. Conversely, in Figure 5 (b), we increased σ, resulting in higher confidence in the motion model and lower confidence in the observation model. It was observed that (a) performed poorly in similar segments of degraded environmental radar scans, while (b) exhibited deviations in describing features in rich environmental areas.

Our optimized algorithm, capable of adapting to the degree of environmental degradation, yielded the best mapping results in Figure 5 (c).

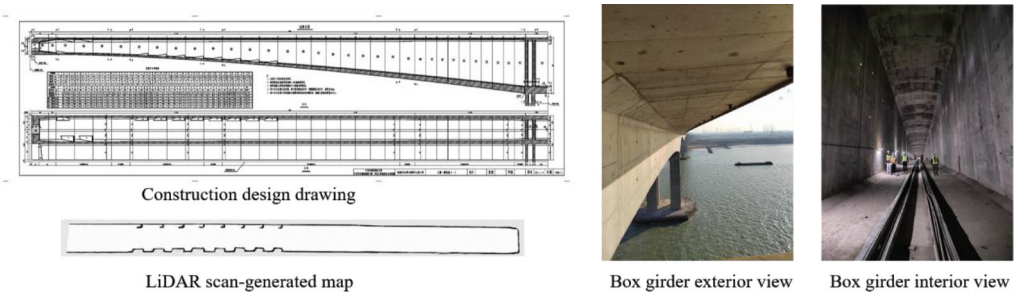


Figure 4. Construction design drawing, LiDAR scan-generated map, exterior view and interior view of the box girders in the navigable channel of the Su-Tong Yangtze River Highway Bridge. The construction design drawing includes side view and top view.

3.3 *Path-planning and tracking*

Once precise mapping results are obtained, path planning on the map becomes feasible. Considering the map's size and obstacles in the actual terrain, we selected an appropriate number

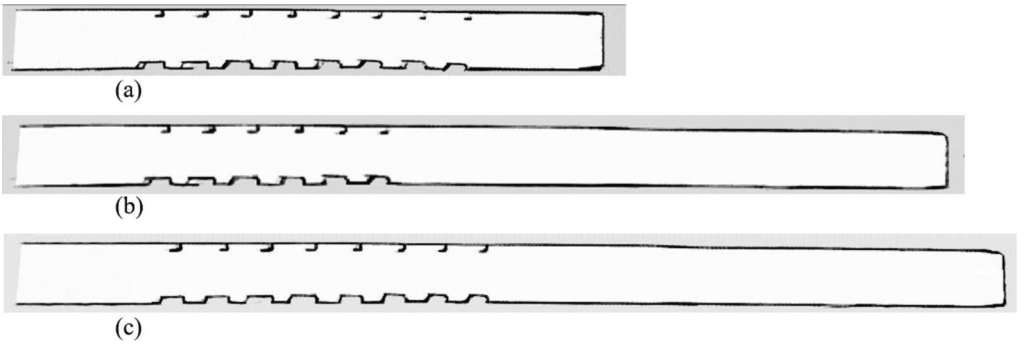


Figure 5. Mapping results under different parameters within the box girder of the Su-tong Yangtze River Highway Bridge in Jiangsu Province, China. (a) and (b) represent manually adjusted parameter results in Correlative Scan Matching (CSM). In (a), $\sigma = 0.1$ while in (b), $\sigma = 0.7$. (c) displays the mapping results of our algorithm, which can adapt to environmental features.

of robots and interval between working points to accomplish path planning, as depicted in Figure 6. It is evident that in multi-robot planning, effective terrain coverage is achieved with an even distribution of scanning workload for each robot. Additionally, Figure 6 showcases partial stitching results of scanned images along working points, utilizing a feature point matching algorithm to achieve seamless integration.

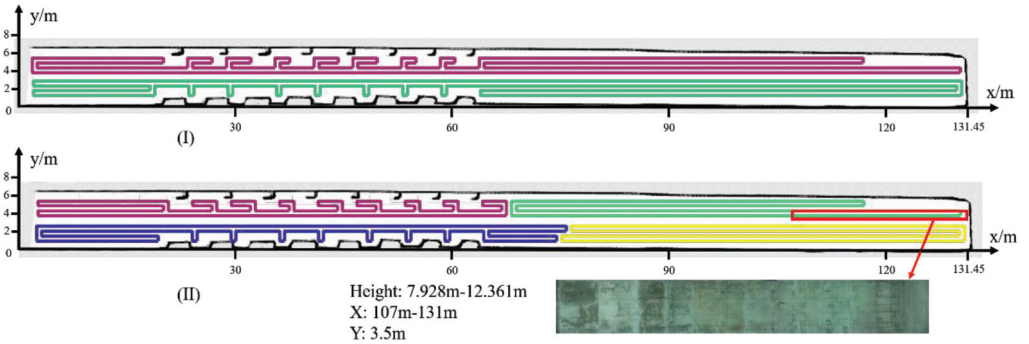


Figure 6. The path planning results for two robots and four robots, along with the stitched images from collecting data at selected working points.

3.4 *Detection*

During tracing, the robot captures images of the top and side walls at each working point, ensuring a capture range diameter approximately equal to the distance between working points for a comprehensive scan of the box girder. At a working point (x_0, y_0), the angles of the two gimbal servos θ_1, θ_2 and the distances d_1, d_2, d_3 from three infrared sensors (determining the distance from the lens to the capture plane) are synchronized and recorded with the captured images. This process facilitates determining the position of each image within the box girder, as illustrated in Figure 7.

The robot traverses the path during the data collection process of inspecting box girder's defects. To visually represent the location information of defects more intuitively, two surface images of beams obtained directly above two working points were selected, as shown in the right part of Figure 7. In the actual inspection procedure, when the machine learning algorithm identifies a relatively severe defect, the specific location of the defect within the beam can be pinpointed through the location information associated with the image. This assists human operators in detecting and repairing the defects.

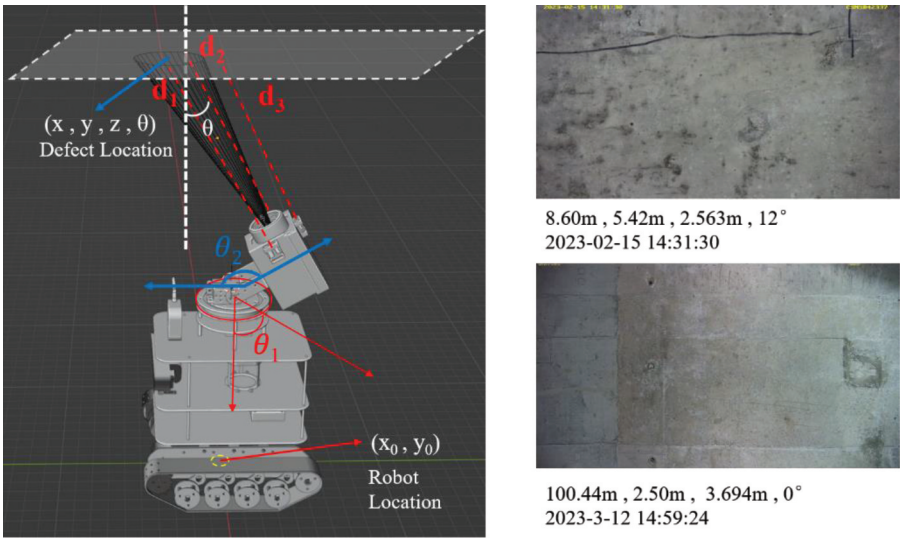


Figure 7. Schematic diagram illustrating the principle of concrete surface defects localization within the box girder. Two examples of defect location are also illustrated.

4 CONCLUSION

In this study, we developed a robotic autonomous inspection system tailored for the interior of large concrete box girders. The key contributions include the design of the robot body, synchronous mapping and localization (SLAM) within an unknown box girder environment, as well as a solution for path planning and tracking. Preliminary experimental validation was conducted on the Su-tong Yangtze River Highway Bridge. For mapping and localization, we employed the Frontier-based Exploration method for autonomous active SLAM and the Cartographer algorithm optimized for degraded scenes, resulting in higher precision in mapping and localization within the box girder. Multi-robot collaborative path planning was employed for increased efficiency. A robust track-based robot control strategy, using the TEB algorithm for dynamic obstacle avoidance and tracking, was implemented. The autonomous inspection system collected images of surface defects within the concrete box girder, obtaining accurate information for semantic segmentation and subsequent post-processing.

This comprehensive solution enables the fully automated collection of defect data, providing clear and intuitive records of the location and severity of box girder defects. This system greatly facilitates tasks such as box girder warning and maintenance.

In the future, we plan to deploy multiple robotic systems in actual box girder environments to more accurately reflect the advantages and limitations of the proposed methods. We will address any shortcomings through targeted improvements and enhancements.

ACKNOWLEDGEMENTS

This research was financially supported by National Natural Science Foundation of China (Grant No. 52208198), National Key R&D Program of China (Grant No. 2021YFF0501004), and Research and Development Center of Transport Industry of New Generation of Artificial Intelligence Technology (Grant No. 202201H).

REFERENCES

Pi-Cheng Tung, Yean-Ren Hwang, and Ming-Chang Wu. The development of a mobile manipulator imaging system for bridge crack inspection. Automation in construction, 11(6):717–729, 2002.

Hung M La, Ronny Salim Lim, Basily B Basily, Nenad Gucunski, Jingang Yi, Ali Maher, Francisco A Romero, and Hooman Parvardeh. Mechatronic systems design for an autonomous robotic system for high-efficiency bridge deck inspection and evaluation. IEEE/ASME Transactions on Mechatronics, 18(6):1655–1664, 2013.

Bin Lei, Ning Wang, Pengcheng Xu, and Gangbing Song. New crack detection method for bridge inspection using UAV incorporating image processing. Journal of Aerospace Engineering, 31(5):04018058, 2018.

Jung S, Choi D, Song S, et al. Bridge inspection using unmanned aerial vehicle based on HG-SLAM: Hierarchical graph-based SLAM[J]. Remote Sensing, 2020, 12(18): 3022.

Phillips S, Narasimhan S. Automating data collection for robotic bridge inspections[J]. Journal of Bridge Engineering, 2019, 24(8): 04019075.

Hess W, Kohler D, Rapp H, et al. Real-time loop closure in 2D LIDAR SLAM[C]//2016 IEEE international conference on robotics and automation (ICRA). IEEE, 2016: 1271–1278.

Yamauchi B. A frontier-based approach for autonomous exploration[C]//Proceedings 1997 IEEE International Symposium on Computational Intelligence in Robotics and Automation CIRA'97.'Towards New Computational Principles for Robotics and Automation'. IEEE, 1997: 146–151.

Shi W, Li S, Yao C, et al. Dense Normal Based Degeneration-Aware 2-D Lidar Odometry for Correlative Scan Matching[J/OL]. IEEE Transactions on Instrumentation and Measurement, 2023: 1–16. http://dx.doi.org/10.1109/tim.2022.3231326. DOI:10.1109/tim.2022.3231326.

Kapoutsis A C, Chatzichristofis S A, Kosmatopoulos E B. DARP: divide areas algorithm for optimal multi-robot coverage path planning[J]. Journal of Intelligent & Robotic Systems, 2017, 86: 663–680.

Martínez J L, Mandow A, Morales J, et al. Kinematic modelling of tracked vehicles by experimental identification[C]//2004 IEEE/RSJ International Conference on Intelligent Robots and Systems (IROS) (IEEE Cat. No. 04CH37566). IEEE, 2004, 2: 1487–1492.

Rösmann C, Feiten W, Wösch T, et al. Trajectory modification considering dynamic constraints of autonomous robots[C]//ROBOTIK 2012; 7th German Conference on Robotics. VDE, 2012: 1–6.

Bridge Maintenance, Safety, Management, Digitalization and Sustainability – Jensen, Frangopol & Schmidt (eds)
© 2024 The Author(s), ISBN 978-1-032-77040-6
Open Access: www.taylorfrancis.com, CC BY-NC-ND 4.0 license

LSTM-based structural pattern recognition for floating bridges

S. Ryu, S. Min, Y.J. Kang & S. Kim
Korea University, Seoul, Korea

ABSTRACT: This study introduces a deep learning approach to identify patterns in floating bridges, specifically employing the Long Short-Term Memory (LSTM) algorithm to analyze time-domain data. Wind, wave, and displacement that have been measured in the Bergsøysund bridge between the years 2014 and 2018 were used for the pattern recognition. For the feasibility study, the LSTM-based model was trained to recognize the complicated relation between the variables including the environmental conditions and induced response. After that, the response predicted by the trained model was directly compared to the measured one to evaluate the pattern model. According to this study, the proposed method can effectively recognize the structural pattern of a floating bridge from measured data. In addition, the pattern analysis-based structural health monitoring method can be used for early detection of the structural condition change of the floating bridge.

Keywords: Floating bridge, structural pattern recognition, deep learning, wave, wind

1 INTRODUCTION

Recently, several types of offshore structures have been actively developed for various purposes, such as sea crossing transportation and renewable energy facilities, as well as conventional offshore oil and gas facilities. (Min et al., 2023a) Among these, the floating bridge is one of the general structural systems in the world as a prospective sea crossing transportation system. The fundamental concept of floating bridges, believed to have first emerged around 2000 BC(Watanabe, 2003), has gained recognition in recent times as a vital component of infrastructure. Floating bridges offer significant advantages, particularly in reducing transportation time, thereby proving to be a crucial infrastructure solution in specific geographical and logistical contexts. In conventional infrastructure management, regular and systematic inspections are a generalized norm for identifying potential damages. These routine inspections are often complemented by detailed structural surveys and evaluations, especially when there is a need for an in-depth assessment of structural integrity and performance. In the case of large-scale infrastructures, real-time sensors are attached to the structures. These sensors facilitate the collection of response data crucial for both short-term and long-term Structural Health Monitoring (SHM). (Min et al., 2023b) Floating bridges, categorized as significant transportation infrastructures in marine environments, are similarly expected to benefit from a SHM system based on real-time data acquisition. An effective SHM system is critical in assessing structural health, thereby playing a key role in preventing structural deterioration and averting catastrophic events, such as collapses. (Min et al., 2023c)

However, in contrast to traditional bridges, floating bridges present a challenge in the realm of SHM. With only around 20 such structures installed worldwide (Kvåle et al., 2016), floating bridges are relatively scarce. This rarity limits the availability of measurement cases, posing significant challenges in acquiring comprehensive external and response data essential for SHM analysis. Consequently, there are relatively few studies investigating the feasibility and effectiveness of SHM systems in the context of floating bridges. In the specific instance of the Bergsøysund Bridge, a comprehensive sensor system has been implemented to monitor dynamic responses. Kvale et al.

DOI: 10.1201/9781003483755-84

(2023) provided data obtained from these sensors, which include metrics on acceleration, displacement, external sources, and sensor locations. (Kvåle et al., 2016) The current study leverages this rich dataset to evaluate the potential application of SHM analysis to floating bridges, utilizing the real-time data collected from the Bergsøysund Bridge.

2 PATTERN RECOGNITION-BASED IDENTIFICATION OF STRUCTURAL CONDITION

2.1 *Overview*

Structural responses are influenced by external sources as well as by the structural characteristics, which are defined by the geometry, material properties, and boundary conditions of the structure. This indicates that the responses of structures to external sources are inherently determined by these characteristics. Therefore, if we can successfully recognize and model the behavioral patterns of a structure, then it becomes feasible to estimate or predict structural responses in advance using a pattern model. (Min et al., 2023c, Lee et al., 2020) However, when working with actual measurement data, the challenge lies in the numerous of external sources affecting the structure. Accounting for all these sources may not be feasible. To overcome these limitations, our methodology focuses on recognizing structural patterns using previously measured structural responses and a limited range of measurable external sources.

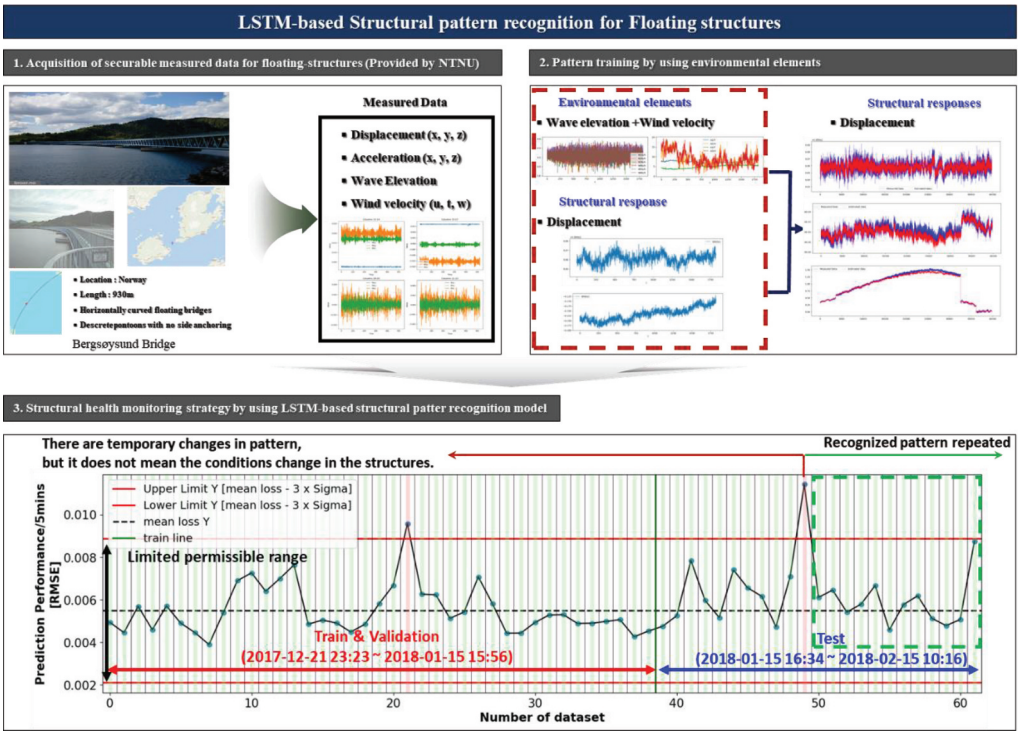


Figure 1. Overview of the proposed method for structural condition change recognition.

Figure 1 illustrates our methodological framework for detecting structural condition changes. We begin by analyzing a comprehensive dataset of the Bergsøysund Bridge's structural responses to identify behavior patterns. This analysis is conducted using the Long Short-Term Memory (LSTM) algorithm, well-suited for time-series data. The next step involves comparing the model's predicted responses with real data from structure-mounted sensors. If

the structure is stable and undamaged, the estimated data typically aligns closely with the actual measurements. However, significant differences between these datasets can indicate major changes in structural conditions or the presence of damage, aiding in continuous monitoring of the structure's integrity.

In this study, the three-sigma rule was utilized to define a threshold for the acceptable range of variance between the predicted and actual measured structural responses, serving as an indicator of changes in structural condition. The three-sigma rule, grounded in the principles of normal distribution, asserts that approximately 99.7% of data lies within ±3 standard deviations from the mean. To apply this rule, we initially calculated the prediction error for the structural response from the data trained. Subsequently, the mean and standard deviation of this prediction error were determined, setting the bounds for an acceptable range of difference in the test data. Finally, in this study, variation in structural conditions was detected and pattern analysis was performed based on the threshold calculated through three-sigma.

2.2 *Measured data details for patter recognition of floating bridges*

The Bergsøysund Bridge, a 930-meter-long horizontally curved pontoon bridge located in Norway, presents a unique structural design. Unlike most floating bridges, which are typically designed as continuous pontoon girder types with reduced flexibility due to side anchoring, Bergsøysund stands out as one of the few discretely pontoon bridges in the world. (Kvåle and Øiseth, 2017) As part of a project by the Norwegian Public Roads Administration (NPRA), Kvale et al. are making publicly available monitored dynamic response data of the Bergsøysund Bridge.(Kvåle et al., 2023) This dataset, stored in a hierarchical metadata structure, contains a variety of measurements such as acceleration, displacement, wave height, and wind speed.

These measurements were recorded from 2014 to 2018 at sampling rates of 2 Hz and 10 Hz. Once the threshold is exceeded, data measurement begins and lasts for 30 minutes. Therefore, we verified that data was missing for some periods where the threshold was not met. The available measurement data of Bergsøysund Bridge are shown in Figure 2. This study used the data on the period during which the GNSS Sensor was installed since we are focusing on the pattern recognition of structural responses such as displacement.

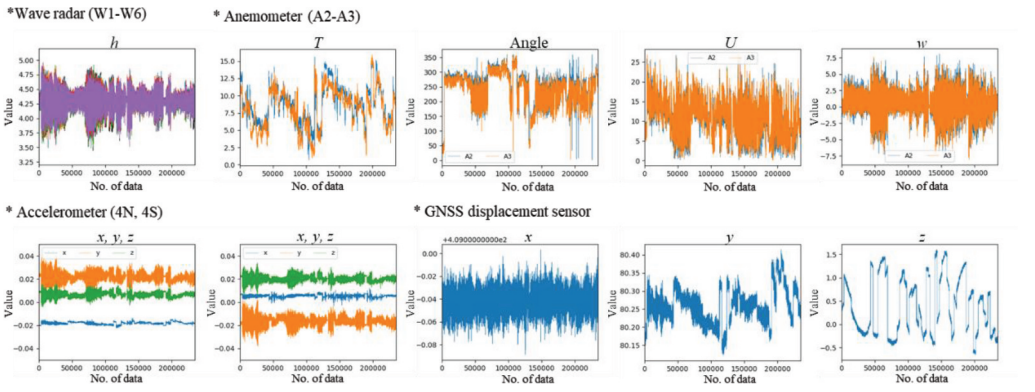


Figure 2. Available measurement data of bergsøysund bridge.

3 PATTERN RECOGNITION USING LSTM ALGORITHM

3.1 *LSTM architectures*

Many studies have been conducted on damage detection using various deep learning algorithms such as deep neural networks (DNNs), convolutional neural networks (CNNs), recurrent neural networks (RNNs), and long short-term memory (LSTM). (Carden and

Brownjohn, 2008, Gulgec et al., 2017, Moradi et al., 2023)Among these, LSTM algorithms are a special kind of Recurrent Neural Network (RNN) designed to address the vanishing gradient problem associated with standard RNNs. The core idea of LSTM is its ability to maintain long-term dependencies in sequential data, making it exceptionally well-suited for time series analysis, speech recognition, and similar tasks.

The dynamic response dataset from the Bergsøysund Bridge offers two sets of data sampled at 2 Hz and 10 Hz. In this study, the 2 Hz dataset was chosen, considering the balance between memory usage and computational speed. The focus of the study was on displacement as a primary structural response, hence data collected during the period the GNSS sensor was operational was utilized. The period from 2017-12-21 23:23 to 2018-01-15 15:56 was used as training and validation data for learning. Following this, the testing phase was divided into two distinct segments to assess the long-term effects. The first segment spanned from 2018-01-15 16:34 to 2018-01-16 03:54, and the second segment was conducted to 2018-02-15 10:16. From the available data - acceleration, wave height, wind speed, temperature and displacement - wind speed and wave height, temperature were selected as external sources, and displacement was selected as the structural response for the LSTM-based pattern recognition. The displacement measured via GNSS was the primary focus, so data from sensors near the center, where the GNSS was installed, was applied in this analysis. The LSTM architecture configuration used in this study is shown in Table 1 and the used data in study is shown in Figure 3.

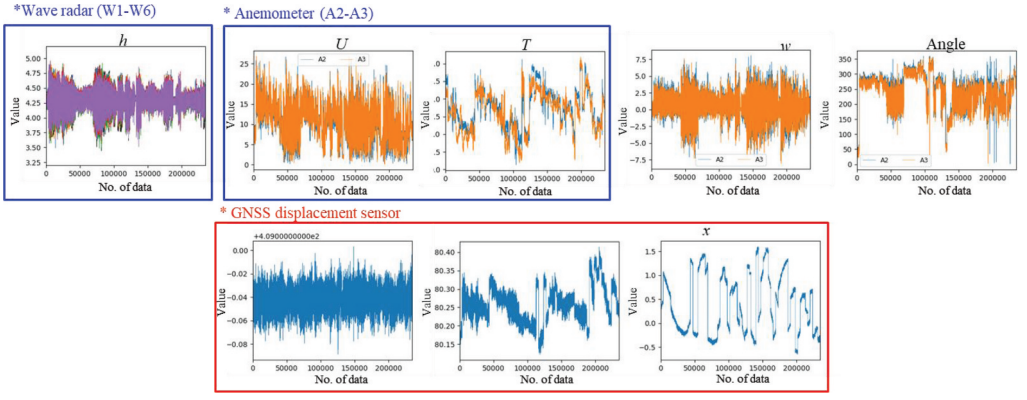


Figure 3. Used measurement data in SHM analysis.

Table 1. LSTM model hyperparameters for structural pattern recognition.

Hyperparameter	LSTM (Limited external sources & structural response)
Input variables	Wind velocity, Wave elevation, Temperature, Displacement
Output variables	Displacement
Batch size	4,000
Number of hidden layers	1
Epoch	100
Number of units in hidden layer	200
Optimizer	Adam
Learning rate	0.001
Loss function	MSE
Activation function in hidden layer	ReLU
Weight initializer	glorot_uniform

3.2 *Pattern recognition using wave elevation, wind velocity and GNSS data*

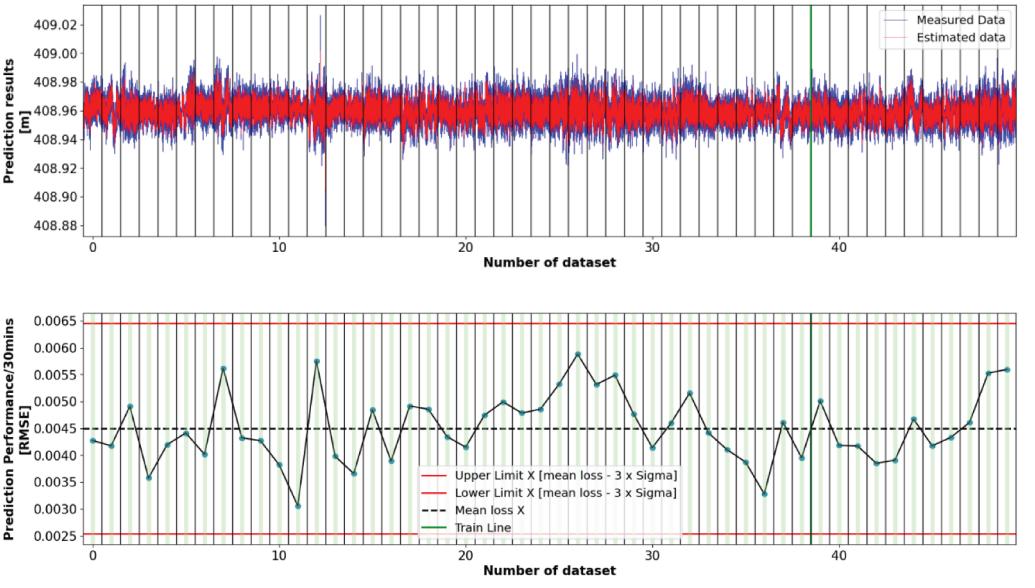
The methodology proposed in this study is predicated on the utilization of a deep learning algorithm that demonstrates robust predictive performance. Owing to its capacity to effectively capture the time-series characteristics of data, LSTM is particularly adept at processing sensor data that exhibits temporal features. To assess the predictive performance of the LSTM-based model employed in this study, regression performance metrics such as Mean Absolute Error (MAE) and Root Mean Squared Error (RMSE) were applied to the test data. As a result, confirmed through regression performance indicators in Table 2, The target main responses, longitudinal and lateral positions, and heave were confirmed to have high average performance with MAE of 0.0135 and RMSE of 0.0179.

Table 2. MAE, RMSE performance of LSTM-based model.

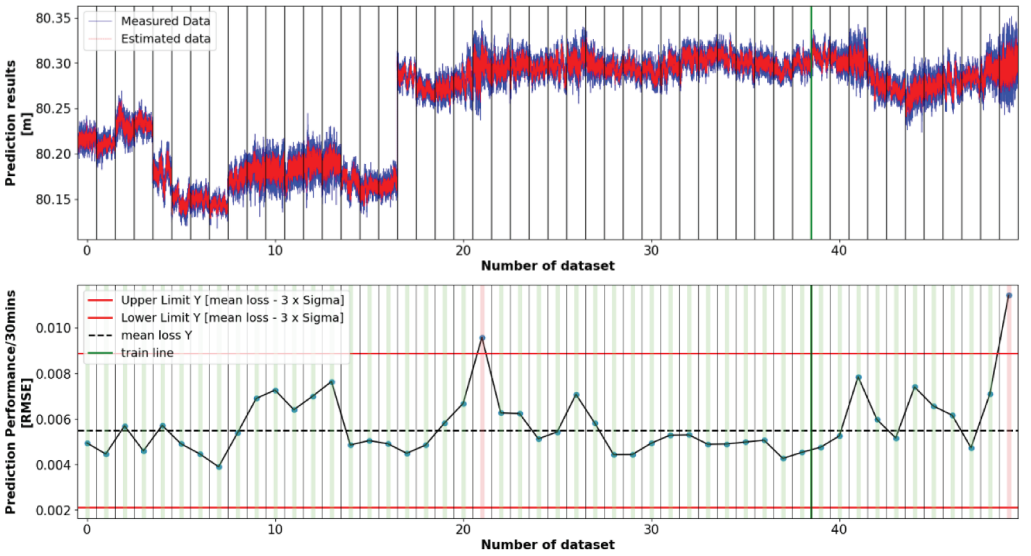
	MAE	RMSE
Position	m	m
Longitudinal	0.0034	0.0044
Lateral	0.0053	0.0067
Vertical (Heave)	0.0317	0.0427

The results of prediction and pattern analysis are shown in Figure 4. Pattern analysis in this study was conducted using a recognized pattern through LSTM. To evaluate the performance, a graph was plotted with time on the x-axis and prediction performance on the y-axis. The y-value at any point on this graph represents the average difference between the predicted and directly measured data over a thirty-minute interval, serving as an indicator of pattern recognition performance. A red line on the graph delineates the calculated threshold through the three-sigma rule.

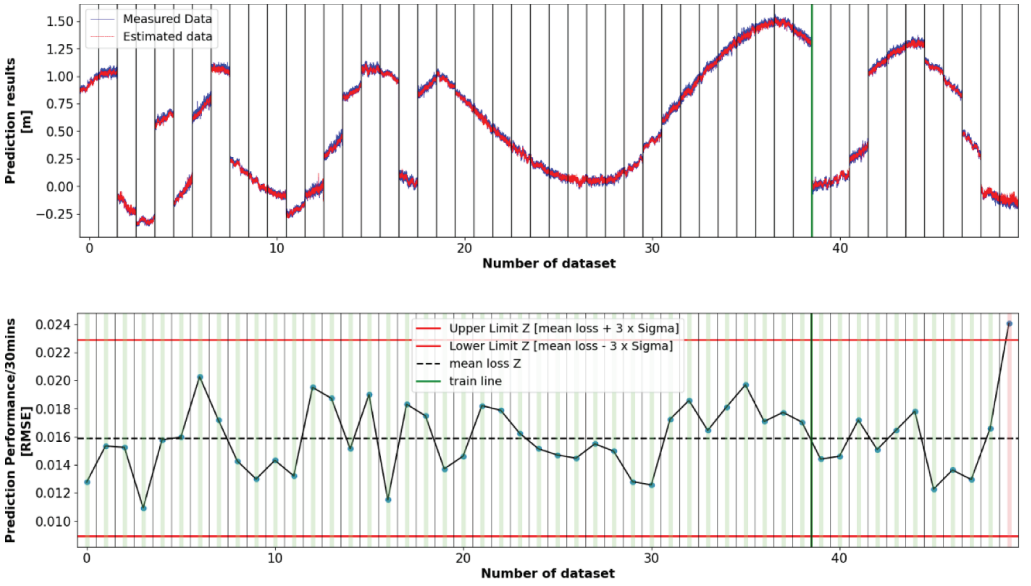
As you can see on the Figure 4, the pattern analysis results reveal that the majority of displacement values within the test section fall within the established limited permissible range. This observation leads to the inference that the structural condition of the bridge remained without variation throughout the test period, which spanned 2018-01-15 16:34 to 2018-01-16



(a) Long-term estimated performance and pattern analysis (RMSE, Longitudinal position)



(b) Long-term estimated performance and pattern analysis (RMSE, Lateral position)



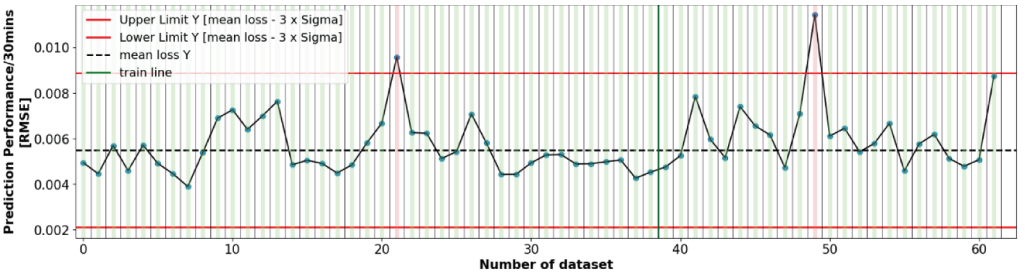
(c) Long-term estimated performance and pattern analysis (RMSE, Heave)

Figure 4. Long-term estimated performance by recognized pattern

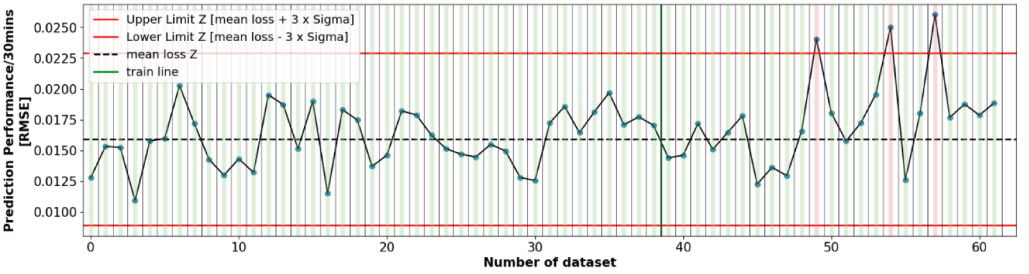
03:54. In the case of lateral position and heave, some values did exceed this permissible range. However, these instances are considered to represent temporary fluctuations in the pattern rather than indicative of any significant changes in the structural conditions or damages to the bridge.

To verify that the deviations observed were merely temporary, this study extended the pattern analysis to a longer test period while applying the same recognized pattern. The pattern analysis results for lateral position and heave about prolonged test periods are shown in Figure 5. The prolonged analysis confirmed that the values eventually returned to within the

limited permissible range, conforming to the recognized pattern. This outcome suggests that the instances of values exceeding the permissible range were simply transient anomalies and did not signify any significant changes in the structural condition. On the other hand, a consistent pattern of values exceeding the limited permissible range, if observed repeatedly, could signify a change in the structural condition, potentially indicative of damage or the risk of catastrophic events such as a collapse.



(a) Long-term estimated pattern analysis (RMSE, Lateral position)



(b) Long-term estimated pattern analysis (RMSE, Heave)

Figure 5. Long-term estimated performance by recognized pattern.

This study suggests that the proposed methodology has the potential to effectively detect variations in structural conditions by directly comparing measured responses with those predicted from the recognized pattern. Although this data-driven approach may not precisely identify the specific causes of structural changes, it acts as a reliable tool for determining whether a structure is experiencing degradation or alterations in condition without extensive investigative procedures.

4 CONCLUSION

In this study, we trained and evaluated the LSTM models to predict structural responses using long-term measurement data from Bergsøysund Bridge to detect changes in the structural conditions. We confirmed that LSTM model effectively estimates structural response since the data shows time series characteristics. This model was employed to analyze the variations in the predictive performance and structural response patterns using actual data measured in Bergsøysund Bridge. In addition, a methodology was proposed to identify variations in the condition of the structure. The results of this study can be summarized as follows:

(1) The methodology adopted in this study relies on a model that demonstrates substantial learning and high predictive performance. The Long Short-Term Memory (LSTM) algorithm, known for its effectiveness with time-series data, was employed. The trained LSTM model exhibited impressive performance in estimating structural responses. The primary responses targeted, namely Longitudinal and lateral positions, and Heave showed high

average performance, with a Mean Absolute Error (MAE) of 0.0135 and a Root Mean Squared Error (RMSE) of 0.0179.

(2) The application of the LSTM model for pattern analysis facilitated the identification of the structural response pattern. Throughout the testing phase, it was observed that the majority of the predictive performance remained within the established threshold. This consistency implies that structural condition continues without notable variation. Although there were instances where some values exceeded the permissible range, these occurrences were interpreted as temporary fluctuations, not as indicators of a permanent change in the structural condition.

Pattern recognition was conducted using an LSTM model trained with data from a floating bridge, leading to the development of a methodology for verifying structural condition changes. This approach enables the assessment of structural conditions by directly comparing the measured responses with those predicted from the recognized pattern. However, it's important to note that the data used in this study did not encompass major structural changes such as damage or collapse, resulting in a largely consistent overall pattern. However, because the data used in this study did not include major condition changes in the structure, such as damage or collapse, the overall pattern was maintained. Therefore, research is needed to confirm changes in the pattern by simulating situations where damage occurs by adding noise to measured data.

CONFLICT OF INTEREST

The authors declare that the study was conducted in the absence of any commercial or financial relationships that could be construed as potential conflict of interest.

ACKNOWLEDGEMENTS

This work is supported by the Korea Agency for Infrastructure Technology Advancement (KAIA) grant funded by the Ministry of Land, Infrastructure and Transport (Grant RS-2023-00250727) through the Korea Floating Infrastructure Research Center at Seoul National University.

FUNDING

This work is supported by the Korea Agency for Infrastructure Technology Advancement (KAIA) grant funded by the Ministry of Land, Infrastructure and Transport (Grant RS-2023-00250727) through the Korea Floating Infrastructure Research Center at Seoul National University.

REFERENCES

Carden, E. P. & Brownjohn, J. M. 2008. ARMA modelled time-series classification for structural health monitoring of civil infrastructure. Mechanical systems and signal processing, 22, 295–314.

Gulgec, N. S., TakãČ, M. & Pakzad, S. N. Structural damage detection using convolutional neural networks. Model Validation and Uncertainty Quantification, Volume 3: Proceedings of the 35th IMAC, A Conference and Exposition on Structural Dynamics 2017, 2017. Springer, 331–337.

Kvçle, K. A., Fenerci, A., Petersen, Ø. W., Rúnnquist, A. & Øiseth, O. 2023. Data Set from Long-Term Wave, Wind, and Response Monitoring of the Bergsøysund Bridge. Journal of Structural Engineering, 149, 04723002.

Kvçle, K. A. & Øiseth, O. 2017. Structural monitoring of an end-supported pontoon bridge. Marine Structures, 52, 188–207.

Kvçle, K. A., Sigbjørnsson, R. & Øiseth, O. 2016. Modelling the stochastic dynamic behaviour of a pontoon bridge: A case study. Computers & Structures, 165, 123–135.

Lee, Y., Jang, M., Kim, S. & Kang, Y.-J. 2020. A study on the long-term measurement data analysis of existing cable stayed bridge using ARX model. International Journal of Steel Structures, 20, 1871–1881.
Min, S., Jeong, K., Lee, Y., Jung, D. & Kim, S. 2023a. Estimation of reaction forces at the seabed anchor of the submerged floating tunnel using structural pattern recognition. Computers and Concrete, 31, 405–417.
Min, S., Jeong, K., Lee, Y. & Kim, S. 2023b. Estimation of unmeasured structural responses of submerged floating tunnels using pattern model trained via long short-term memory. Ocean Engineering, 277, 114284.
Min, S., Lee, Y., Byun, Y.-H., Kang, Y. J. & Kim, S. 2023c. Merged LSTM-based pattern recognition of structural behavior of cable-supported bridges. Engineering Applications of Artificial Intelligence, 125, 106774.
Moradi, M., Broer, A., Chiachïo, J., Benedictus, R., Loutas, T. H. & Zarouchas, D. 2023. Intelligent health indicator construction for prognostics of composite structures utilizing a semi-supervised deep neural network and SHM data. Engineering Applications of Artificial Intelligence, 117, 105502.
Watanabe, E. 2003. Floating Bridges: Past and Present. Structural Engineering International, 13, 128–132.

Bridge Maintenance, Safety, Management, Digitalization and Sustainability – Jensen, Frangopol & Schmidt (eds)
© 2024 The Author(s), ISBN 978-1-032-77040-6
Open Access: www.taylorfrancis.com, CC BY-NC-ND 4.0 license

Vision-based structural displacement measurements using deep learning and super-resolution

Mubarak F. Abu Zouriq & Daniel G. Linzell
Department of Civil and Environmental Engineering, University of Nebraska-Lincoln, Lincoln, NE, USA

Roya Nasimi
Department of Engineering, California State University East Bay, Hayward, CA, USA

ABSTRACT: Vision-based displacements can be used to measure response of structures subjected to dynamic loading. The accuracy of these measurements can be dependent on a number of factors, with image resolution being one of the most critical factors. This study focuses on improving the accuracy of displacement measurements via tests of a dynamically loaded, reduced scale, cantilevered beam using a consumer-grade camera. The effectiveness with which a deep learning based Super-Resolution approach improved image quality was studied by training an Enhanced Super Resolution Generative Adversarial Network (ESRGAN). ESRGAN aims to construct artificial high-resolution frames by upscaling original frames to twice their dimensions with sharper details, leading to enhanced measurement accuracy. ESRGAN was selected for study because of its reported ability to generate detailed and realistic images. To examine SR model accuracy, displacement measurements from the original frames and from SR-extracted frames were compared to reference displacements measurements taken using a contact sensor. Results showed that root mean square errors (RMSEs) of the measured dynamic displacements were smaller when SR image enhancement was used.

1 INTRODUCTION

Structures can be subjected to various loads and environmental conditions, which may make it necessary to periodically monitor their health to maintain operational safety (Farrar & Worden, 2007; Feng et al., 2016). Increased need for safe, efficient, and economical monitoring solutions makes non-contact, computer-vision (CV) techniques a compelling option, particularly using low-cost cameras (Lydon et al., 2019).

Research examining image utilization to accurately measure structural displacements has encompassed three main areas: tracking movement of predefined templates (Xu et al., 2021; Du et al., 2022; Azimbeik et al., 2023); special feature point matching (Dong & Catbas, 2019; Franco et al., 2017; Brox & Malik, 2010); and optical flow techniques (Nie et al., 2022).

Employing low-cost cameras to extract dynamic displacements can potentially provide a simple, cost-effective data collection option (Wang et al., 2023). However, a perceived limitation is video quality as subtle deformation changes may not be adequately captured (Feng & Feng, 2016).

Super-Resolution (SR) can enhance images beyond original camera capabilities. the technique uses original images to generate artificial High Resolution (HR) images, which can be utilized to mitigate consumer-grade camera limitations (Yue et al., 2016). SR encompasses two prominent approaches, interpolation-based techniques and deep learning-based methods (Zhang & Yu, 2022). Interpolation-based SR embeds additional pixels in original Low-Resolution (LR) images to generate upscaled images by creating artificial pixels between original ones, with their values estimated using interpolation algorithms, such as bicubic or bilinear interpolation

DOI: 10.1201/9781003483755-85

(Gilman et al., 2008). Although interpolation-based methods provide a quick and computationally efficient SR approach, resulting images lack fine details or high-frequency components (Zhang & Yu, 2022). Deep learning-based SR leverages advanced neural network models, greatly enhancing image resolution. Deep learning models such as Convolutional Neural Networks (CNNs) and Generative Adversarial Networks (GANs) map between LR and HR pairs that can capture complex patterns and features when trained on extensive datasets, allowing the generation of upscaled, detail-rich HR images (Hoque et al., 2019).

The application of deep learning in SR has significantly advanced the accuracy and visual fidelity of upscaled images, finding widespread use in various domains. Many researchers have investigated the efficacy of SR models for crack detection, using techniques that include Attention-Dense Residual and Generative Adversarial Network (ADRAGAN) (Zhou et al., 2022), and Cycle Generative Adversarial Network (CycleGAN) (Zhang et al., 2020). The incorporation of these techniques substantially improved crack detection performance and growth tracking. Using SR methods with cameras to reduce structural displacement measurement error has seen more limited research activity. The effectiveness with which Super-Resolution Generative Adversarial Networks (SRGAN) improved displacement measurements using SR has shown considerable promise under static and dynamic loads (Sun et al., 2022), but the scope of dynamic evaluation needs more investigation as the performance of the SR under variable structure-to-camera distances, angle of the camera with respect to the structure, and the surrounding circumstances such as the lighting have not been investigated.

The study summarized herein provides some preliminary results related to the effectiveness of using deep learning-based Enhanced Super-Resolution Generative Adversarial Networks (ESRGAN) for image improvement when applied to the measurement of dynamic displacements. Outcomes of the study can serve as a foundation for subsequent research, potentially facilitating expansion of the ESRGAN deep learning technique into image based SHM and helping address increases demand for high-quality and accurate image-based monitoring that would effectively support more informed infrastructure management.

2 METHODOLOGY

This study utilized the multi-stage methodology presented in Figure 1 to extract improved, vision-based, vertical displacement measurements of a reduced scale, cantilevered beam. The primary concept revolves around generating HR images through transformation of captured LR counterparts and subsequently utilized these enhanced images to determine displacements. The subsequent sections summarize each stage provided in the figure.

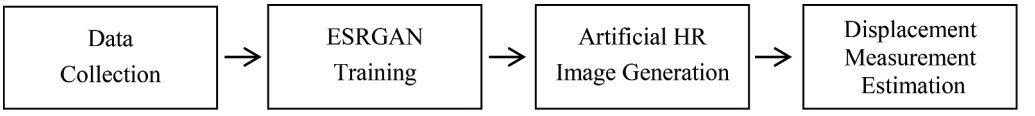


Figure 1. Proposed methodology.

2.1 *Data collection*

To create the ESRGAN model, the proposed methodology necessitated acquiring two types of image-based data. These were: 1) low-resolution video recordings of the cantilevered beam under dynamic excitation using an inexpensive, stationary camera; and 2) high-resolution images taken using a camera from a mobile device.

2.2 *ESRGAN training*

To train the ESRGAN model, an area that includes the region of interest (ROI) and its surroundings was cropped from the HR images to reduce computational needs. Corresponding LR images

were then developed by artificially degrading the HR dataset acquired using Python's OpenCV package via downscaling images to half their original size, imposing Gaussian white noise, and blurring the images by replacing each pixel value with the average value of its neighboring eight pixels. ESRGAN was developed and trained using Python by mapping features from degraded images to corresponding HR images.

2.3 *Artificial HR image generation*

The trained ESRGAN model was utilized to generate artificial HR images from extracted video frames that captured structural response. Before feeding the video frames to the ESRGAN model, a frame cropping operation was performed so that a smaller section of the frames containing the ROI could be analyzed.

2.4 *Displacement measurement estimation*

Displacements were extracted from the artificial HR images and the original LR frames by employing target-free feature tracking, which was selected due to its ability to extract feature motion at sub-pixel accuracy when coupled with an appropriate tracking algorithm. Necessary steps included lens distortion correction using intrinsic and extrinsic camera parameters, defining ROI for the target location on the structure, extracting the Speeded-Up Robust Features (SURF) from the ROI in the video frame prior to system excitation, and tracking movement of SURF features through the video frames with respect to a reference object appearing in the background using the Kanade-Lucas-Tomasi (KLT) algorithm. Average resulting motion of important features was then calculated in pixel coordinates and converted to displacements using a scale factor obtained via a dimensional relationship of a known object size to pixel sizes in the image.

3 EXPERIMENTAL SETUP

A simple, reduced scale, cantilevered beam was used as the test article. The beam, constructed of mild steel and 1100 mm long, 76 mm wide, and 6.5 mm thick, was made thicker in an arbitrarily selected ROI via the addition of wood blocks. Features within this ROI were enhanced using colored tape, which provided additional texture and contrast.

The beam was manually excited vertically using a steel rod affixed perpendicular to its longitudinal axis by pushing the rod downward and upward by hand. Reference vertical displacements were measured using a Linear Variable Differential Transformer (LVDT) at mid-length of the beam Image-based displacements were captured using a low-cost camera on a tripod 4.5 m away from the beam. A 20 mm checkerboard was used to find the corresponding scale factor and convert units of displacements from pixels to millimeters. An overview of the test is shown in Figure 2.

For ESRGAN model training, 250 HR images were collected at varying orientation and positions with respect to the beam using a high-resolution smartphone. As discussed previously, collected HR images were degraded by downscaling, imposing noise, and blurring to create corresponding LR images for ESRGAN training. Figure 3(a) shows a sample of an artificially degraded image and Figure 3(b) shows its corresponding, original, HR counterpart. Image pairs such as these were used to train the ESRGAN model.

4 RESULTS

After training the ESRGAN model using the image pairs, it was utilized to process the video frames and enhance the quality of the video data collected using the low-cost camera. A sample, cropped, LR frame, and its corresponding SR-generated image are shown in Figure 4.

The beam dynamic displacement time histories were calculated using both the original LR frames from the low-cost camera and enhanced SR artificial frames created using ESRGAN.

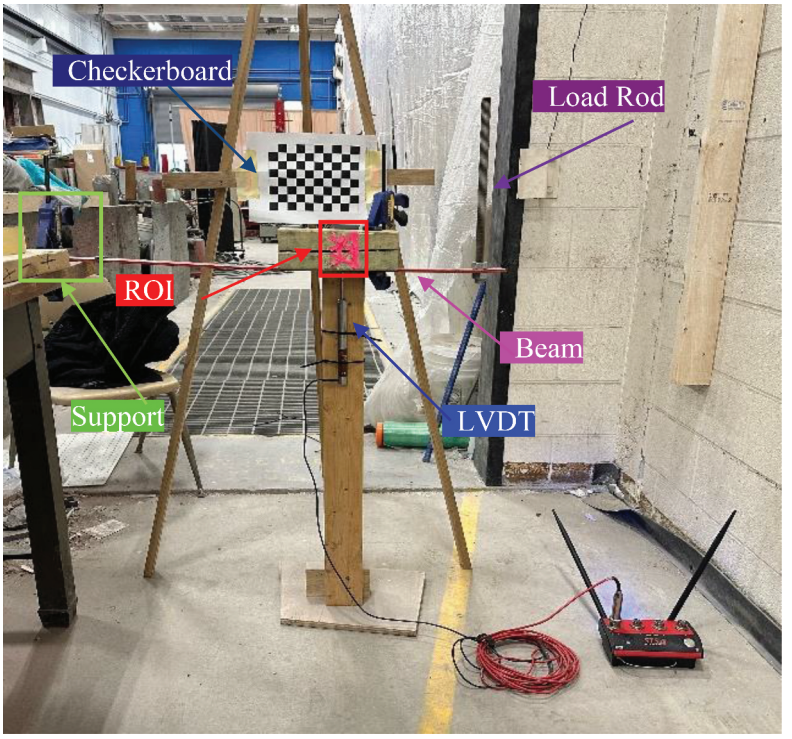
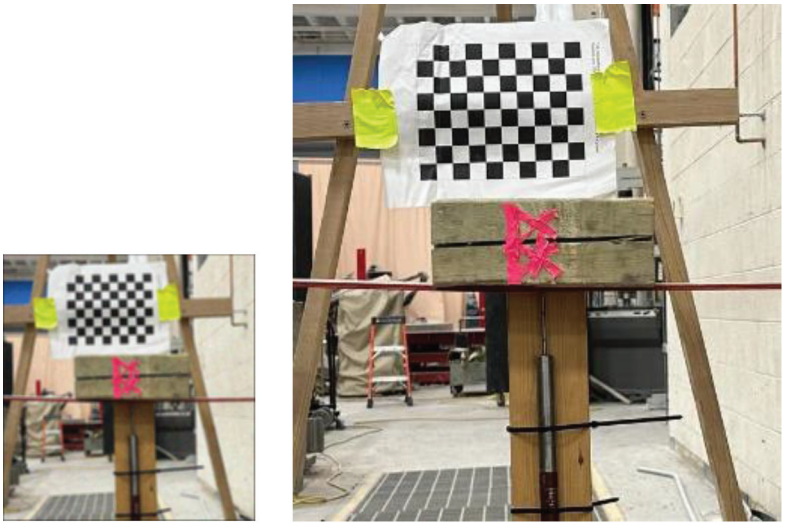


Figure 2. Experimental setup.

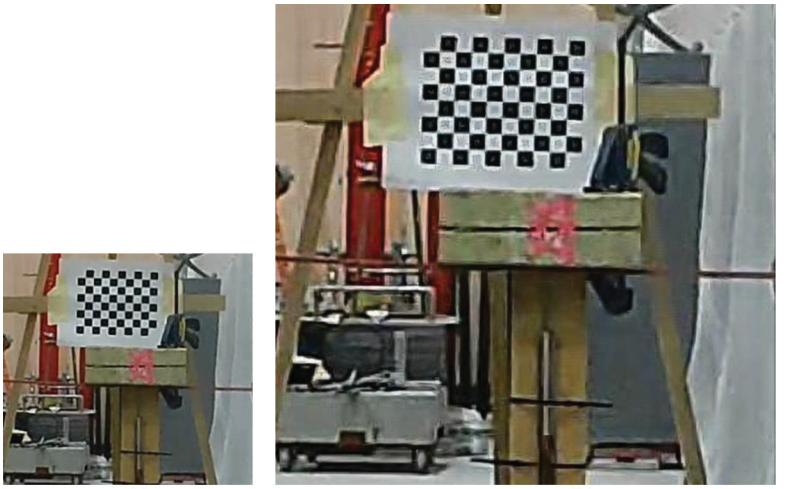


(a) (b)

Figure 3. Sample of HR-LR pairs; (a) LR image; (b) HR image.

Calculated displacements were compared to those measured using the LVDT. A sample time-history comparison is shown in Figure 5. Results indicate that extracted structural displacement accuracy was improved using the generated SR images, as it shows more pronounced alignment with LVDT measurements, when compared to response extracted using the original LR images.

Measurement accuracy was further examined using Root Mean Square Error (RMSE) values between the SR and LR displacement measurements and the reference LVDT values. The results showed that, for this test, using enhanced images for displacement measurement resulted in reducing the RMSE from 0.24 mm for LR measurements to 0.17 mm for SR measurements (a 29% reduction). This level of error reduction mimicked what was observed for all tests and can potentially highlight the efficacy of the proposed enhancement methodology for refining displacement measurement precision using low-cost cameras.



(a) (b)

Figure 4. Processed image samples; (a) LR frame; (b) SR-extracted frame.

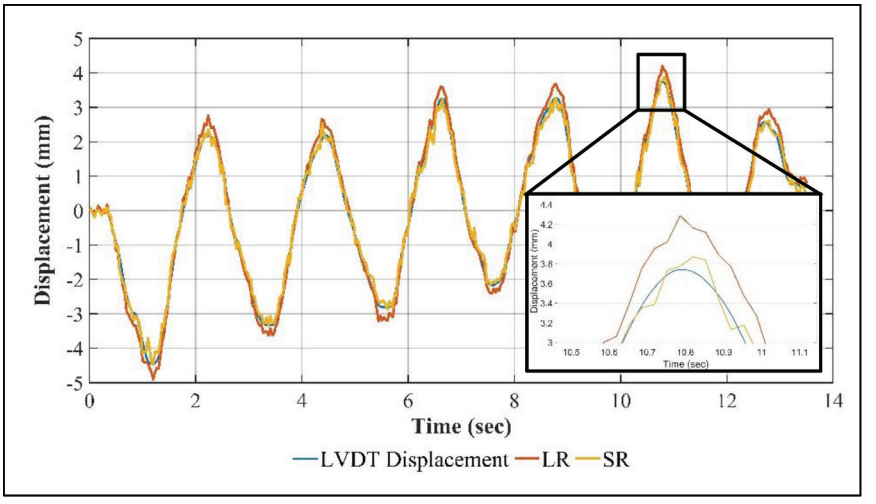


Figure 5. Vertical displacement measurements for the two types of frames.

5 CONCLUSIONS

This study investigated the efficacy of deep learning-based SR image enhancement for SHM dynamic displacement measurements captured using low-cost cameras. The ESRGAN model was selected and an architecture developed whose accuracy was examined using simple reduced scale cantilevered beam dynamic tests. The process used to develop and examine the

SR application involved acquisition of HR images using a high resolution mobile phone camera and videos using a low-cost camera, training the ESRGAN model using the high-quality images, and subsequently applying this trained model to enhance the frames from LR video that captured the beam movement. Vertical displacement time histories were extracted using the post-processed ESRGAN artificial high-resolution images and original LR images captured from the low-cost camera. Displacement measurements from both set of images were compared to one another and LVDT measurements.

Results indicate that using the artificial SR images leads to an accuracy improvement in vertical displacement extraction as a result of frames quality refinement. These results show that SR may be able to adequately improve low-cost camera resolution to the point where extracted displacements could be used within an SHM system.

ACKNOWLEDGEMENT

The authors would like to acknowledge support provided by the US Army Corps of Engineers, Engineering Research and Development Center, grant W912HZ21C0060 –Multilevel Analytics and Data Sharing for Operations Planning (MADS-OPP). The authors also gratefully acknowledge the assistance, access, computing resources, data, and expertise provided by the University of Nebraska's Holland Computing Center.

REFERENCES

Azimbeik, K., Mahdavi, S. H., & Rofooei, F. R. (2023). Improved Image-Based, Full-Field Structural Displacement Measurement using Template Matching and Camera Calibration Methods. Measurement, 112650.

Brox, T., & Malik, J. (2010). Large displacement optical flow: descriptor matching in variational motion estimation. IEEE transactions on pattern analysis and machine intelligence, 33(3), 500–513.

Dong, C. Z., & Catbas, F. N. (2019). A non-target structural displacement measurement method using advanced feature matching strategy. Advances in Structural Engineering, 22(16), 3461–3472.

Du, W., Lei, D., Hang, Z., Ling, Y., Bai, P., & Zhu, F. (2022). Short-distance and long-distance bridge displacement measurement based on template matching and feature detection methods. Journal of Civil Structural Health Monitoring, 1–18.

Farrar, C. R., & Worden, K. (2007). An introduction to structural health monitoring. Philosophical Transactions of the Royal Society A: Mathematical, Physical and Engineering Sciences, 365(1851), 303–315.

Feng, D., & Feng, M. Q. (2016). Vision-based multipoint displacement measurement for structural health monitoring. Structural Control and Health Monitoring, 23(5), 876–890.

Feng, D., Feng, M. Q., Ozer, E., & Fukuda, Y. (2015). A vision-based sensor for noncontact structural displacement measurement. Sensors, 15(7), 16557–16575.

Franco, J. M., Mayag, B. M., Marulanda, J., & Thomson, P. (2017). Static and dynamic displacement measurements of structural elements using low cost RGB-D cameras. Engineering Structures, 153, 97–105.

Gilman, A., Bailey, D. G., & Marsland, S. R. (2008, January). Interpolation models for image super-resolution. In 4th IEEE International Symposium on Electronic Design, Test and Applications (delta 2008) (pp. 55–60).

Hoque, M. R. U., Burks, R., Kwan, C., & Li, J. (2019, October). Deep learning for remote sensing image super-resolution. In 2019 IEEE 10th Annual Ubiquitous Computing, Electronics & Mobile Communication Conference (UEMCON) (pp. 0286–0292). IEEE.

Kromanis, R., Forbes, C., & Borah, S. (2019). Super-resolution images for measuring structural response. In SMAR 2019-Fifth Conference on Smart Monitoring, Assessment and Rehabilitation of Civil Structures. Potsdam, Germany (pp. 1–8).

Lydon, D., Lydon, M., Taylor, S., Del Rincon, J. M., Hester, D., & Brownjohn, J. (2019). Development and field testing of a vision-based displacement system using a low cost wireless action camera. Mechanical Systems and Signal Processing, 121, 343–358.

Nie, G. Y., Bodda, S. S., Sandhu, H. K., Han, K., & Gupta, A. (2022). Computer-Vision-Based Vibration Tracking Using a Digital Camera: A Sparse-Optical-Flow-Based Target Tracking Method. Sensors, 22(18), 6869.

Sun, C., Gu, D., Zhang, Y., & Lu, X. (2022). Vision-based displacement measurement enhanced by super-resolution using generative adversarial networks. Structural Control and Health Monitoring, 29(10), e3048.
Wang, M., Koo, K. Y., Liu, C., & Xu, F. (2023). Development of a low-cost vision-based real-time displacement system using Raspberry Pi. Engineering Structures, 278, 115493.
Wang, X., Yu, K., Wu, S., Gu, J., Liu, Y., Dong, C., & Change Loy, C. (2018). Esrgan: Enhanced super-resolution generative adversarial networks. In Proceedings of the European conference on computer vision (ECCV) workshops.
Xu, Y., Zhang, J., & Brownjohn, J. (2021). An accurate and distraction-free vision-based structural displacement measurement method integrating Siamese network based tracker and correlation-based template matching. Measurement, 179, 109506.
Yue, L., Shen, H., Li, J., Yuan, Q., Zhang, H., & Zhang, L. (2016). Image super-resolution: The techniques, applications, and future. Signal processing, 128, 389–408.
Zhang, J., Qian, S., & Tan, C. (2022). Automated bridge surface crack detection and segmentation using computer vision-based deep learning model. Engineering Applications of Artificial Intelligence, 115, 105225.
Zhang, J., Qian, S., & Tan, C. (2023). Automated bridge crack detection method based on lightweight vision models. Complex & Intelligent Systems, 9(2), 1639–1652.
Zhang, K., Zhang, Y., & Cheng, H. D. (2020). Self-supervised structure learning for crack detection based on cycle-consistent generative adversarial networks. Journal of Computing in Civil Engineering, 34(3), 04020004.
Zhang, Y., & Yu, W. (2022). Comparison of DEM Super-Resolution Methods Based on Interpolation and Neural Networks. Sensors, 22(3), 745.
Zhou, H., Liu, Y., Liu, Z., Zhuang, Z., Wang, X., & Gou, B. (2022). Crack Detection Method for Engineered Bamboo Based on Super-Resolution Reconstruction and Generative Adversarial Network. Forests, 13(11), 1896.

Bridge Maintenance, Safety, Management, Digitalization and Sustainability – Jensen, Frangopol & Schmidt (eds)
© 2024 The Author(s), ISBN 978-1-032-77040-6
Open Access: www.taylorfrancis.com, CC BY-NC-ND 4.0 license

Multimodal data collection using mobile robotics for rapid structural assessment

Furkan Luleci, Abdulrrahman AlGadi & F. Necati Catbas
Department of Civil, Environmental, and Construction Engineering, University of Central Florida, USA

ABSTRACT: This study focuses on assessing civil engineering systems lacking documentation, a common challenge in assessing old systems. Using tools like cameras and LiDARs to generate 3D models of the structure is a useful implementation; however, it becomes difficult when these systems are off-limits due to disaster-induced structural risks. Using mobile robots emerges as a promising solution to this limitation. Thus, this study employs a wheeled Unmanned Ground Vehicle (UGV) equipped with cameras, LiDARs, and other sensors (e.g., accelerometers) to collect multimodal data, including visual and monitoring. The study demonstrates using the UGV to collect data from a mechanical room of a building. The UGV navigates the room, collecting various data such as images, LiDAR scans, and vibration data while generating the interior mapping of the room in real-time. This study presents some of the collection results and highlights the significance of using mobile robotics for rapid assessments of civil systems.

1 INTRODUCTION

1.1 *Background*

The condition assessment techniques of existing civil engineering structures and infrastructure systems are vital as these systems age and undergo deterioration over time. Typically, these assessments involve traditional techniques like chain drag or hammer tapping to identify issues such as delamination and voids in concrete, often relying solely on visual inspections. However, these conventional methods are labor-intensive, time-consuming, and subjective. To address these challenges, Structural Health Monitoring (SHM) has been introduced and explored in research for its practical application (Aktan et al., 1996; Housner et al., 1997).

In essence, SHM is a methodology designed to monitor and assess the performance of civil structures by gathering and analyzing diverse data through various sensors. The goal of SHM is to track the responses of existing civil structures, enabling the determination of their condition through damage diagnosis and prognosis. This involves analyzing, visualizing, and interpreting sensor data collected from structures. The insights gained from SHM contribute to establishing a dependable foundation for decision-making regarding the operation and maintenance of civil structures (Aktan et al., 2000; Farrar & Worden, 2007).

SHM methods are typically categorized based on their application levels, either local or global (Dong & Catbas, 2021). Local-level SHM aims to diagnose specific defects, utilizing Non-Destructive Tools (NDT) such as ultrasound, ground penetration radar, and electromagnetic devices. On the other hand, global-level applications employ fixed setup systems like accelerometers, strain gauges, and potentiometers. Non-Contact Tools (NCT), including computer vision tools like various cameras and LiDAR, play a role in both local (e.g., crack or spalling detection) and global (e.g., displacement and acceleration monitoring) applications (Catbas et al., 2022; Catbas & Khuc, 2018; Dong & Catbas, 2019; Feng & Feng, 2018;

DOI: 10.1201/9781003483755-86

Gucunski et al., 2010; Gul & Catbas, 2008; Kaartinen et al., 2022; Luleci, Catbas, et al., 2022; Luleci & Catbas, 2023; Morozova et al., 2023).

A recent trend in the SHM field is the growing interest in robotic-based experiments (Charron et al., 2019; Van Nguyen et al., 2018; Zhu et al., 2012). Robotic applications can operate at both global and local levels. For instance, an Unmanned Ground Vehicle (UGV) equipped with vision sensors can gather acceleration (vibration) data for global-level modal analysis while simultaneously performing image-based defect detection at the local level. Accelerometers installed on the UGV enhance the spatial resolution of data collection, aiding in identifying local damage within the structure (McLaughlin et al., 2020; Mei et al., 2020; Tian et al., 2022). Similarly, an Unmanned Aerial Vehicle (UAV) can be utilized for image-based damage detection at the local level, and a group of UAVs can measure displacement or acceleration at the global level through vision sensors, presenting a new dimension to civil SHM with increased mobility and diverse sensor applications (Cha & Kang, 2018; Ribeiro et al., 2021).

1.2 *Challenge, objective, and scope*

One significant obstacle in the assessment of existing civil structures/infrastructure systems lies in the assessment of those lacking structural documentation, blueprints, or data. This challenge becomes more pronounced, particularly when conducting condition assessments of old systems.

Using cameras (e.g., regular digital camera, stereocamera, etc.) and 3D scanners (e.g., structured-light or time-of-flight 3D scanners, LiDARs - e.g., time-of-flight or phase LiDARs) come out as one of the most precise and reliable technologies to capture/scan and provide the 3D digital model of the existing civil structures (Hosamo & Hosamo, 2022; Kaile'a Moseley et al., 2021; Luleci et al., 2024; Luleci, Li, et al., 2022; Thelen et al., 2022; Xue et al., 2020). The 3D digital model can be in the form of a point cloud, mesh (textured point cloud), and numeric models generated from the point cloud (Catbas et al., 2024; Wang et al., 2023). This comes as very useful in assessing the existing civil systems with incomplete information, as it enables experts involved in the assessment process to have a complete understanding of the integrity of the structure/infrastructure system. However, one particular challenge related to gathering data for 3D model creation is that these systems may not be allowed for human occupancy nor near human presence due to disaster or other external stressors -caused structural, electrical, or mechanical risks. Therefore, the use of mobile robots, such as wheeled Unmanned Ground Vehicle (UGV), equipped with various sensors (LiDARs, cameras, and other types of sensors) is a very promising application for this challenge.

In light of the discussion given in the previous paragraph, the study herein aims to present a brief demonstration of using a UGV for rapid visual data acquisition from a research building structure located on the campus of the University of Central Florida (UCF). In doing so, different data modalities, including visual (LiDAR scans and camera captures) and monitoring data (vibration), are collected in a mechanical room of the research building. Some of the data gathered during the collection process are presented herein, and the subsequent studies will include full-scale 3D models along with further analysis of the mechanical room.

The study herein first introduces the UGV, presenting its configuration and sensors briefly. Then, the methodology of the study is presented, including the test location (the mechanical room of the research building), the data collection procedure via UGV, and some of its outputs. Subsequently, the conclusion of the study is given.

2 UNMANNED GROUND VEHICLE

The UGV, named Cypector (Cyber + Inspector), is a Husky model robot manufactured by Clearpath Robotics. Husky is a 4-wheeled UGV operating on a wheeled chassis. Including Husky, Cypector used in this study contains additional accessories, where some are installed on the plate, and some are under, as shown in Figure 1. The accessories are 2 VLP-16

LiDARs from Velodyne, an ADK Infrared Camera and 2 Blackfly S Cameras from FLIR, GPS-18x from Garmin, a ZED 2 Stereo Camera from Stereolab, an Omni 60 360 Camera from Occam, Wireless Router from Gigabit, and GPU-enabled Mini-ITX computer and IMU (Inertial Measurement Unit) from Microstrain, which are placed under the plate.

Robot Operating System (ROS) serves as a middleware framework in communicating with Cypector, offering a suite of open-source tools and libraries. ROS functions as a middleware layer, abstracting hardware intricacies and facilitating communication between software components and physical devices installed on the robot, like the accessories of Cypector. It achieves this communication by including device drivers that interface with various hardware components. For the User-Cypector connection, the User simply connects to the SSID (Service Set Identifier) broadcasted by Cypector's access point (router), which is linked to the robot's internal computer. After the connection, the User's computer is granted an IP address via static or DHCP ways. Users can now SSH into the Cypector's computer to control its operation.

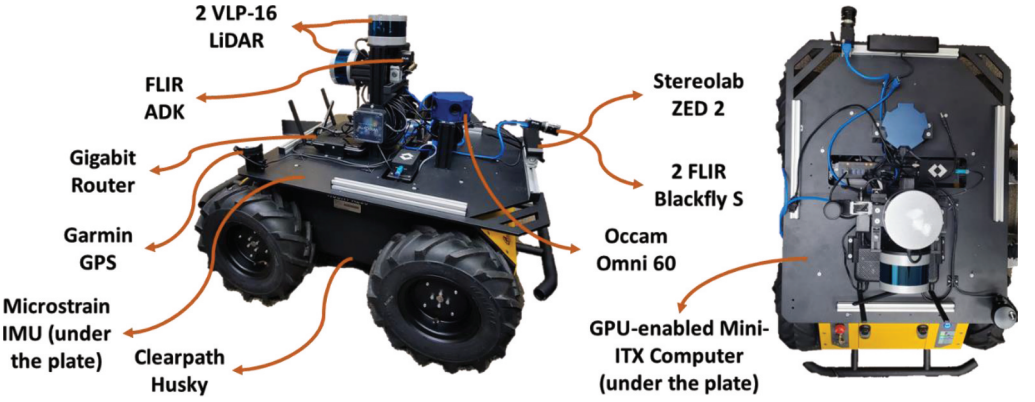


Figure 1. Cypector and its configurations.

3 METHODOLOGY

3.1 *The mechanical test room*

The mechanical room within the research building serves as a critical hub for maintaining the structural and environmental integrity of the facility. Dominated by an intricate network of industrial machinery, the room houses an array of essential components responsible for the building's operational functionality, such as the HVAC system for maintaining optimal conditions within the building. Robust piping, suspended from the ceiling and attached to the walls, facilitates the distribution of vital fluids such as coolant and heating agents throughout the facility. In Figure 2, the images of the mechanical room are given. The data collection efforts are centered on deploying the UGV in addition to TLS in this environment.

3.2 *Data collection via UGV*

The data collection procedure via Cypector is illustrated in Figure 3. The whole data collection process took around 5 minutes. During the collection, Cypector (the UGV) is navigated through the mechanical room following the route depicted in the figure. Note that the route in the figure is not the exact trajectory Cypector took but shows the overall route. Throughout the rover, Cypector collected various types of data samples constantly, such as image data via 360-degree images, depth, confidence, and stereo views, LiDAR scans via horizontal and vertical LiDARs as well as point clouds generated real-time by the depth images using ZED 2.



Figure 2. The mechanical room in the research building.

These data samples through the collection are also viewed online in rviz (a 3D visualization platform for the Robot Operating System - ROS), as shown in Figure 3. In addition to the image data, vibration data of the room is collected through different acceleration sensors, such as the IMU and ZED 2's internal sensors. For that reason, at one point during the collection, Cypector is commanded to stop for a brief period in order to collect the acceleration data, as the noises from the rover could disrupt the monitoring data quality. During vibration data collection, it is also possible to view the Fast Fourier Transform (FFT) of the sets of vibration data instances in real-time, as shown in the figure.

In addition to the visual data, monitoring data of the room could reveal critical characteristics of the operating conditions of the machinery equipment in the mechanical room for different scenarios (e.g., pre and post-disasters). Lastly, using the horizontal and vertical LiDAR scans, the environment of the mechanical room, which is unknown to Cypector, is 2D mapped in real-time. For that, Google's Cartographer Simultaneous Localization and Mapping (SLAM) is utilized (Hess et al., 2016b). In short, SLAM is a technique that allows robots to create and update a map of their environment while simultaneously determining their own location within that environment (Dwijotomo et al., 2020; Hess et al., 2016a; Sobczak et al., 2022; Weerakoon et al., 2022).

3.3 *Some results*

While this study "only" explores the rapid mobile robot-based data collection exemplar application for generating the 3D models of civil systems, the real-time generated 2D mapping of the surroundings of the mechanical room by Cypector using SLAM is presented in Figure 4. As depicted in the figure, the general visual accuracy, when compared with the actual environment (floor plan of the room), exhibits a commendable level of precision while having some loop closure issues at some edges, such as near the entrance to the room. Generating mappings of the interior as well as exterior is important for autonomous applications, providing essential information for navigation, obstacle avoidance, human interaction, and overall situational awareness in interior environments during the data collection for structural assessment procedures.

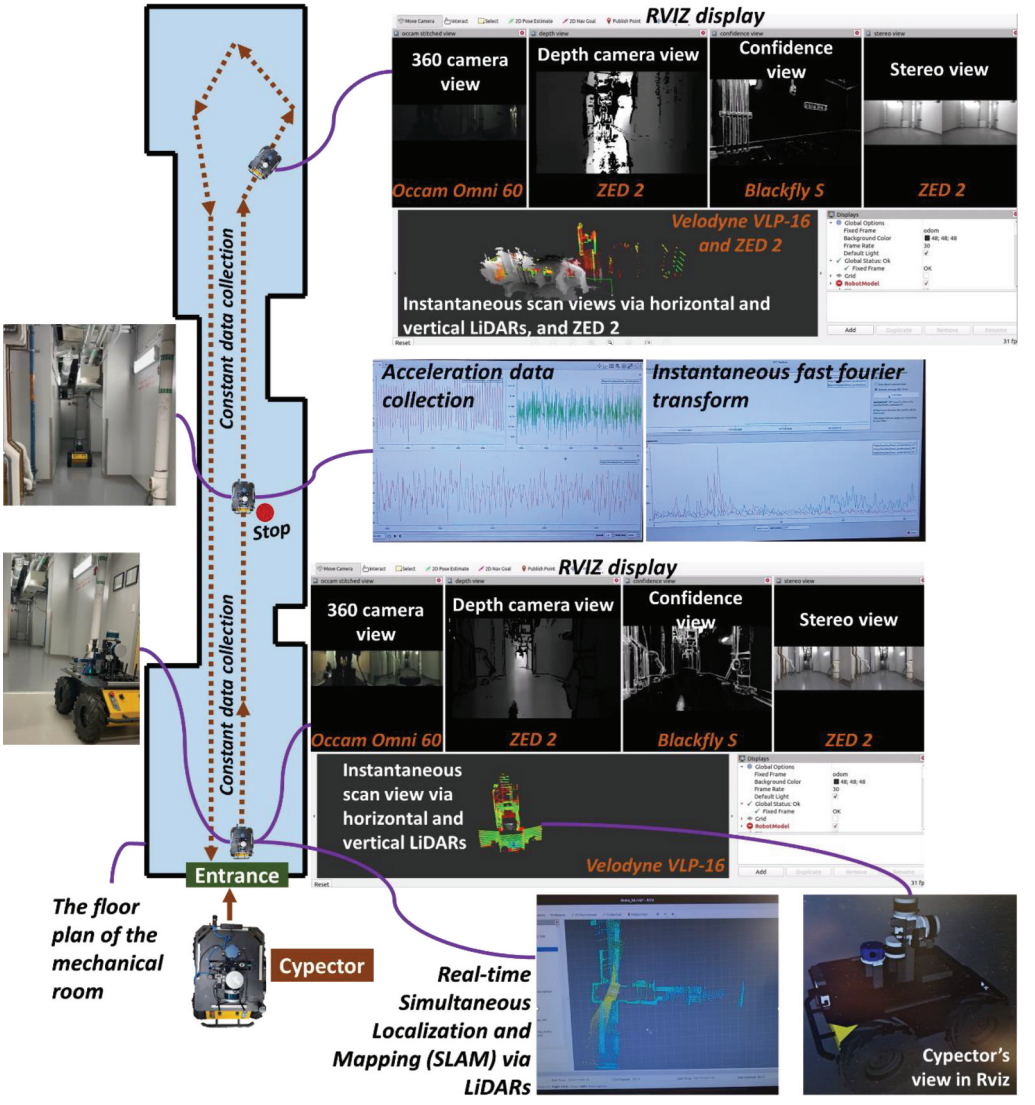


Figure 3. The overview of the data collection procedure carried out by Cypector in the mechanical room.

The generated 2D map can also be extended to 3D models, enabling a more comprehensive understanding of the physical environment in three dimensions, and Cypector is capable of doing so as it is equipped with horizontal and vertical LiDARs as well as stereo camera (ZED 2), enabling depth sensing to generate the 3D representation of the environment. Yet, this is computationally more demanding, especially when processing dense 3D point clouds, occasionally interfering with the generated 3D map quality. The subsequent studies will encompass the development of comprehensive 3D models on a full scale, accompanied by additional analysis of the assessment data, just like the 3D model of a pedestrian bridge structure generated by registering multiple LiDAR scans, as shown in Figure 5 (Catbas et al., 2024; Luleci et al., 2024).

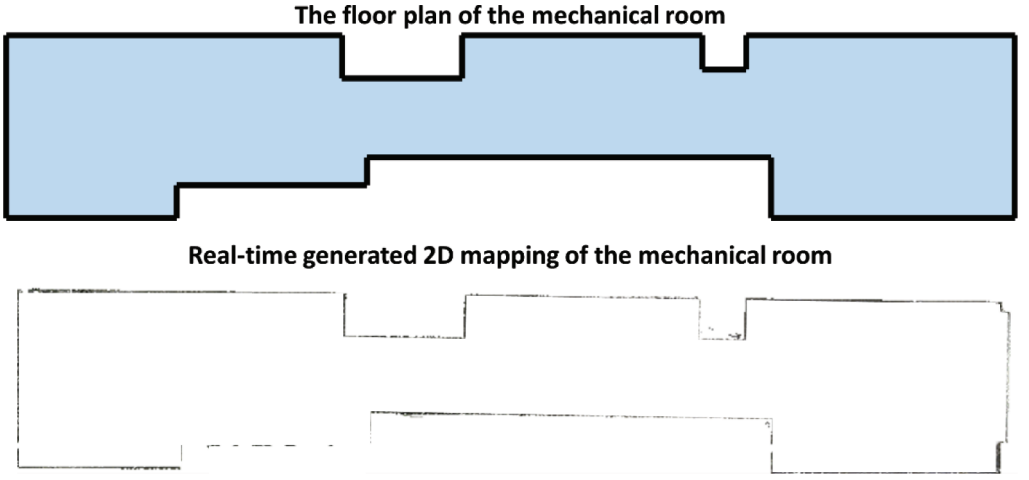


Figure 4. The floor plan of the mechanical room (top) and the generated 2D map via SLAM (bottom).

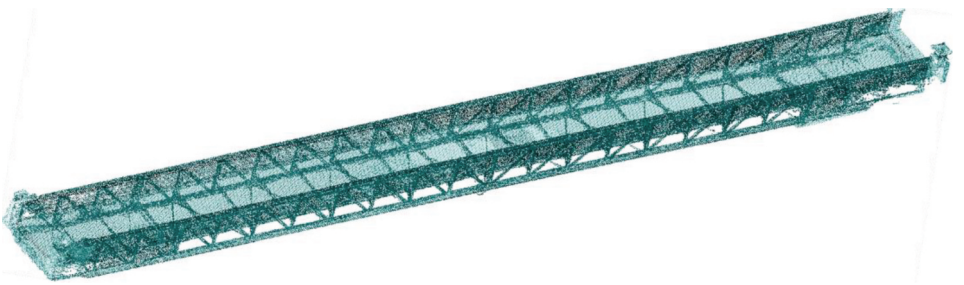


Figure 5. An example 3D model of a bridge formed by multiple LiDAR scans (Catbas et al., 2024).

This study holds significant importance in addressing the challenging task of assessing existing civil structures with insufficient documentation. By employing mobile robots equipped with advanced sensors like LiDARs and cameras, the research aims to overcome obstacles posed by inaccessible or hazardous environments, ensuring a non-intrusive yet comprehensive approach to data acquisition. The emphasis on creating 3D digital models from collected data allows for a thorough structural integrity assessment, particularly relevant for historical or aged civil systems. Integrating multiple data modalities, including visual and monitoring data, enhances the depth of structural assessments. The real-world application of this methodology in a mechanical room underscores its practical viability. Moreover, the study sets the groundwork for future research endeavors, promising further development and analysis of full-scale 3D models.

4 CONCLUSION

In conclusion, this study highlights the significance of addressing the challenging task of assessing aging civil structures and infrastructure systems that lack proper documentation. Mobile robots equipped with advanced sensors like LiDARs and cameras play a crucial role, particularly in data acquisition within hazardous environments in civil systems affected by disasters or external stressors. The emphasis on creating 3D digital models from collected data enables a comprehensive approach to structural integrity assessment, which is particularly beneficial for historical or aged civil systems facing limitations in traditional assessment methods.

Through the use of robotics, integrating multiple data modalities, including visual and monitoring data, provides valuable insights into structural assessments. The real-world application of this methodology in a mechanical room demonstrates its practical viability. The subsequent studies will include in-depth data analysis and full-scale 3D models. Overall, this study showcases the potential for mobile robotics for rapid structural assessments of civil systems.

REFERENCES

Aktan, A. E., Catbas, F. N., Grimmelsman, K. A., & Tsikos, C. J. (2000). Issues in Infrastructure Health Monitoring for Management. *Journal of Engineering Mechanics*, *126*(7), 711–724. https://doi.org/10.1061/(ASCE)0733-9399(2000)126:7(711)

Aktan, A. E., Farhey, D. N., Brown, D. L., Dalal, V., Helmicki, A. J., Hunt, V. J., & Shelley, S. J. (1996). Condition Assessment for Bridge Management. *Journal of Infrastructure Systems*, *2*(3), 108–117. https://doi.org/10.1061/(ASCE)1076-0342(1996)2:3(108)

Catbas, F. N., Cano, J. A., Luleci, F., Walters, L. C., & Michlowitz, R. (2024). On the Generation of Digital Data and Models from Point Clouds: Application on Pedestrian Bridge Structure. *Infrastructures*.

Catbas, F. N., & Khuc, T. (2018). Computer vision-based displacement and vibration monitoring without using physical target on structures. In *Bridge Design, Assessment and Monitoring* (1st ed.). Taylor Francis.

Catbas, F. N., Luleci, F., Zakaria, M., Bagci, U., LaViola, J. J., Cruz-Neira, C., & Reiners, D. (2022). Extended Reality (XR) for Condition Assessment of Civil Engineering Structures: A Literature Review. *Sensors*, *22*(23), 9560. https://doi.org/10.3390/s22239560

Cha, Y.-J., & Kang, D. (2018). Damage detection with an autonomous UAV using deep learning. In H. Sohn (Ed.), *Sensors and Smart Structures Technologies for Civil, Mechanical, and Aerospace Systems 2018* (p. 4). SPIE. https://doi.org/10.1117/12.2295961

Charron, N., McLaughlin, E., Phillips, S., Goorts, K., Narasimhan, S., & Waslander, S. L. (2019). Automated Bridge Inspection Using Mobile Ground Robotics. *Journal of Structural Engineering*, *145*(11), 04019137. https://doi.org/10.1061/(ASCE)ST.1943-541X.0002404

Dong, C.-Z., & Catbas, F. N. (2019). A non-target structural displacement measurement method using advanced feature matching strategy. *Advances in Structural Engineering*, *22*(16), 3461–3472. https://doi.org/10.1177/1369433219856171

Dong, C.-Z., & Catbas, F. N. (2021). A review of computer vision–based structural health monitoring at local and global levels. *Structural Health Monitoring*, *20*(2). https://doi.org/10.1177/1475921720935585

Dwijotomo, A., Abdul Rahman, M. A., Mohammed Ariff, M. H., Zamzuri, H., & Wan Azree, W. M. H. (2020). Cartographer SLAM Method for Optimization with an Adaptive Multi-Distance Scan Scheduler. *Applied Sciences*, *10*(1), 347. https://doi.org/10.3390/app10010347

Farrar, C. R., & Worden, K. (2007). An introduction to structural health monitoring. *Philosophical Transactions of the Royal Society A: Mathematical, Physical and Engineering Sciences*, *365*(1851), 303–315. https://doi.org/10.1098/rsta.2006.1928

Feng, D., & Feng, M. Q. (2018). Computer vision for SHM of civil infrastructure: From dynamic response measurement to damage detection – A review. *Engineering Structures*, *156*, 105–117. https://doi.org/10.1016/j.engstruct.2017.11.018

Gucunski, N., Romero, F., Kruschwitz, S., Feldmann, R., Abu-Hawash, A., & Dunn, M. (2010). Multiple Complementary Nondestructive Evaluation Technologies for Condition Assessment of Concrete Bridge Decks. *Transportation Research Record: Journal of the Transportation Research Board*, *2201*(1), 34–44. https://doi.org/10.3141/2201-05

Gul, M., & Catbas, F. N. (2008). Ambient Vibration Data Analysis for Structural Identification and Global Condition Assessment. *Journal of Engineering Mechanics*, *134*(8), 650–662. https://doi.org/10.1061/(ASCE)0733-9399(2008)134:8(650)

Hess, W., Kohler, D., Rapp, H., & Andor, D. (2016a). Real-time loop closure in 2D LIDAR SLAM. *2016 IEEE International Conference on Robotics and Automation (ICRA)*, 1271–1278. https://doi.org/10.1109/ICRA.2016.7487258

Hess, W., Kohler, D., Rapp, H., & Andor, D. (2016b, May 16). Real-Time Loop Closure in 2D LIDAR SLAM. *In Proceedings of the IEEE International Conference on Robotics and Automation (ICRA)*.

Hosamo, H. H., & Hosamo, M. H. (2022). Digital Twin Technology for Bridge Maintenance using 3D Laser Scanning: A Review. *Advances in Civil Engineering*, *2022*, 1–15. https://doi.org/10.1155/2022/2194949

Housner, G. W., Bergman, L. A., Caughey, T. K., Chassiakos, A. G., Claus, R. O., Masri, S. F., Skelton, R. E., Soong, T. T., Spencer, B. F., & Yao, J. T. P. (1997). Structural Control: Past, Present, and Future. *Journal of Engineering Mechanics*, *123*(9), 897–971. https://doi.org/10.1061/(ASCE)0733-9399(1997)123:9(897)

Kaartinen, E., Dunphy, K., & Sadhu, A. (2022). LiDAR-Based Structural Health Monitoring: Applications in Civil Infrastructure Systems. *Sensors*, *22*(12), 4610. https://doi.org/10.3390/s22124610

Kaile'a Moseley, Furkan Luleci, & Necati Catbas. (2021). Investigation of Tablet and Terrestrial LiDAR and Photogrammetry Applications to Structural Engineering. In *Conference: Scholar Symposium - UCFAffiliation: University of Central Florida*. https://www.researchgate.net/publication/353242704_Investigation_of_Tablet_and_Terrestrial_LiDAR_and_Photogrammetry_Applications_to_Structural_Engineering

Luleci, F., & Catbas, F. N. (2023). A brief introductory review to deep generative models for civil structural health monitoring. *AI in Civil Engineering*, *2*(1), 9. https://doi.org/10.1007/s43503-023-00017-z

Luleci, F., Catbas, F. N., & Avci, O. (2022). A literature Review: Generative Adversarial Networks for Civil Structural Health Monitoring. *Frontiers in Built Environment*, *8*(1027379). https://doi.org/10.3389/fbuil.2022.1027379

Luleci, F., Chi, J., Cruz-Neira, C., Reiners, D., & Catbas, F. N. (2024). Fusing Structural Health Monitoring Data in Point Cloud: An Application on Pedestrian Bridge. *Automation in Construction*.

Luleci, F., Li, L., Chi, J., Reiners, D., Cruz-Neira, C., & Catbas, F. N. (2022). Structural Health Monitoring of a Foot Bridge in Virtual Reality Environment. *Procedia Structural Integrity*, *37*, 65–72. https://doi.org/10.1016/j.prostr.2022.01.060

McLaughlin, E., Charron, N., & Narasimhan, S. (2020). Automated Defect Quantification in Concrete Bridges Using Robotics and Deep Learning. *Journal of Computing in Civil Engineering*, *34*(5). https://doi.org/10.1061/(ASCE)CP.1943-5487.0000915

Mei, Q., Gül, M., & Shirzad-Ghaleroudkhani, N. (2020). Towards smart cities: crowdsensing-based monitoring of transportation infrastructure using in-traffic vehicles. *Journal of Civil Structural Health Monitoring*, *10*(4), 653–665. https://doi.org/10.1007/s13349-020-00411-6

Morozova, N., Shibano, K., Shimamoto, Y., Tayfur, S., Alver, N., & Suzuki, T. (2023). Frost damage evaluation of concrete irrigation structure by X-ray CT and AE energy release trend at the initial loading stage. *Case Studies in Construction Materials*, e02088. https://doi.org/10.1016/j.cscm.2023.e02088

Ribeiro, D., Santos, R., Cabral, R., Saramago, G., Montenegro, P., Carvalho, H., Correia, J., & Calçada, R. (2021). Non-contact structural displacement measurement using Unmanned Aerial Vehicles and video-based systems. *Mechanical Systems and Signal Processing*, *160*, 107869. https://doi.org/10.1016/j.ymssp.2021.107869

Sobczak, Ł., Filus, K., Domańska, J., & Domański, A. (2022). Finding the best hardware configuration for 2D SLAM in indoor environments via simulation based on Google Cartographer. *Scientific Reports*, *12*(1), 18815. https://doi.org/10.1038/s41598-022-22938-y

Thelen, A., Zhang, X., Fink, O., Lu, Y., Ghosh, S., Youn, B. D., Todd, M. D., Mahadevan, S., Hu, C., & Hu, Z. (2022). A comprehensive review of digital twin — part 1: modeling and twinning enabling technologies. *Structural and Multidisciplinary Optimization*, *65*(12), 354. https://doi.org/10.1007/s00158-022-03425-4

Tian, Y., Chen, C., Sagoe-Crentsil, K., Zhang, J., & Duan, W. (2022). Intelligent robotic systems for structural health monitoring: Applications and future trends. *Automation in Construction*, *139*, 104273. https://doi.org/10.1016/j.autcon.2022.104273

Van Nguyen, L., Gibb, S., Pham, H. X., & La, H. M. (2018). A Mobile Robot for Automated Civil Infrastructure Inspection and Evaluation. *2018 IEEE International Symposium on Safety, Security, and Rescue Robotics (SSRR)*, 1–6. https://doi.org/10.1109/SSRR.2018.8468642

Wang, B., Li, Z., Xu, Z., Sun, Z., & Tian, K. (2023). Digital twin modeling for structural strength monitoring via transfer learning-based multi-source data fusion. *Mechanical Systems and Signal Processing*, *200*, 110625. https://doi.org/10.1016/j.ymssp.2023.110625

Weerakoon, L., Herr, G. S., Blunt, J., Yu, M., & Chopra, N. (2022). *Cartographer_glass: 2D Graph SLAM Framework using LiDAR for Glass Environments*.

Xue, F., Lu, W., Chen, Z., & Webster, C. J. (2020). From LiDAR point cloud towards digital twin city: Clustering city objects based on Gestalt principles. *ISPRS Journal of Photogrammetry and Remote Sensing*, *167*, 418–431. https://doi.org/10.1016/j.isprsjprs.2020.07.020

Zhu, D., Guo, J., Cho, C., Wang, Y., & Lee, K.-M. (2012). Wireless Mobile Sensor Network for the System Identification of a Space Frame Bridge. *IEEE/ASME Transactions on Mechatronics*, *17*(3), 499–507. https://doi.org/10.1109/TMECH.2012.2187915


Taylor & Francis
Taylor & Francis Group
http://taylorandfrancis.com

MS08: Sustainable and efficient monitoring and digitization-based decision-making models

Organizers: A. Strauss & D.M. Frangopol


Taylor & Francis
Taylor & Francis Group
http://taylorandfrancis.com

Bridge Maintenance, Safety, Management, Digitalization and Sustainability – Jensen, Frangopol & Schmidt (eds)
© 2024 The Author(s), ISBN 978-1-032-77040-6
Open Access: www.taylorfrancis.com, CC BY-NC-ND 4.0 license

Human role in existing bridge digital twin frameworks, towards Industry 5.0

A. Jiménez Rios
Oslo Metropolitan University, Oslo, Norway

V. Plevris
Qatar University, Doha, Qatar

M. Nogal
Delft University of Technology, Delft, The Netherlands

ABSTRACT: Regardless of the current challenges and limitations of Digital Twins, there seems to be only one school of thought and a consensus toward their future adoption for design, construction, management, operation, and decommissioning of bridges. This novel paradigm surged within the Industry 4.0 context and was fostered by evolving technologies such as artificial intelligence, internet of things, big data, among others. Digital twins have now been recognized as an enabling technology towards the development and adoption of Industry 5.0 principles. Such principles are human-centrism, resilience, and sustainability. In this paper we explore the increasingly important role that humans will have within existing bridge digital twin frameworks and how the human-centrism principle could be better implemented within such context. Moreover, we also discuss how a successful implementation of human centrism could uphold and maximize the resilience and sustainability of existing bridges, especially those with cultural heritage value.

1 INTRODUCTION

Most bridges in Europe were constructed after 1945. Originally designed with a lifespan of 50-100 years, many have already begun to deteriorate (Gkoumas et al., 2021). In fact, it is estimated that 10% of these bridges suffer from structural deficiencies (Wenzel, 2009). On another note, numerous historic European bridges hold significant cultural value, with seven of them being listed on the United Nations Educational, Scientific and Cultural Organization (UNESCO) World Heritage List (UNESCO WHC, 2023). Besides the human and economic losses, the damage or collapse of a historical bridge also signifies the painful loss of a cultural asset.

In recent times, the field of bridge engineering has greatly benefited from technological advancements associated with Industry 4.0. These include the use of digital twins (DT) and building information modeling (BIM) to enhance bridge management (Tita et al., 2023), the application of DT for enriched structural health monitoring of bridges and other infrastructure assets (Pillai et al., 2022), the utilization of DT to aid during the construction process of bridges (Hu et al., 2022), the implementation of advanced anomaly detection algorithms to optimize the management and operation of bridges within a DT framework (Jiménez Rios et al., 2023a), among others.

As observed by the non-exhausting list of examples mentioned, the development and adoption of DT is particularly noteworthy to various stakeholders in the Architecture, Engineering, Construction, Management, Operation, and Conservation (AECMO&C) industry. DT are virtual replicas of physical assets capable of real-time performance monitoring and the early identification of potential issues, ultimately enhancing safety and reducing maintenance costs (Schleich et al., 2017). Within the context of cultural heritage bridges, DT can as well be used to validate the proposal of novel intervention techniques (Jiménez Rios & O'Dwyer, 2019; Zampieri et al., 2023) before they are applied in the asset thus preventing incompatibility damages.

DOI: 10.1201/9781003483755-87

The consensus in the industry is strong, as there is widespread agreement on the value of DT for all phases of the life cycle of bridges, including design, construction, management, operation, and decommissioning. Nevertheless, creating Industry 4.0 DT presents several significant challenges, among which, i) the lack of compatibility among various proprietary and open-source software used in the DT model generation process, ii) lack of consensus regarding the development of macro-DT that combine DT models of individual assets, and iii) the absence of Findable, Accessible, Interoperable, and Reusable (FAIR, (Wilkinson et al., 2016)) benchmark databases suitable for prototyping and validating digital twins (Jiménez Rios et al., 2023b, 2023c).

While the concept of Industry 4.0 has driven an increased industrial digitalization and higher productivity, it has also brought about unanticipated challenges (European Commission, 2020). These challenges include the environmental impact of intensified industrial activities (United Nations, 2023) and the potential risks posed by an increasingly automated industrial system to the human element within the socio-economic chain (Ellingrud et al., 2023). Regrettably, as emphasized in the United Nations (UN) Emissions Gap Report 2022 (United Nations, 2022), insufficient action has been taken so far to address the global climate crisis. There is an urgent need for a rapid transformation in the energy supply, industry, transport, and buildings sectors to meet the goals of the Paris Agreement (United Nations, 2015). This transformation is also supported by the European Union (EU) and promoted through the European Green Deal (EGD) (European Commission, 2019).

Consequently, Industry 4.0 is now considered insufficient to achieve European goals by 2030 (European Commission, 2022), leading to the emergence of a new paradigm, Industry 5.0, primarily built upon three core principles (European Commission, 2021): i) human-centrism, resilience, and sustainability. Moreover, DT and simulations have been recognized as one of the key enabling technologies of this transformative vision. Despite being a relatively recent concept, Industry 5.0 has quickly attracted the interest of many researchers. They have conducted in-depth analysis of its fundamental principles and the technologies that make it possible (Maddikunta et al., 2022). Additionally, researchers have put forth fresh frameworks for its application (Yang et al., 2022) and have begun to create practical applications across various domains, including manufacturing, education, data privacy, food security, and wind energy infrastructure (Chen et al., 2021). However, it's worth noting that the AECMO&C industry has yet to explore, let alone implement, Industry 5.0 principles.

A plausible framework for Industry 5.0 principles implementation is the one proposed by an augmented digital twin, also referred to as a human-centric digital twin (see Figure 1). In this novel framework, an additional "human asset" (besides from the Industry 4.0 components corresponding to the "physical asset" and "digital asset") component is considered. This component is composed by the series of digital technologies capable of enhancing human stakeholders' performances, which could ultimately result into a sustainable and resilient built environment. The different digital tools proposed include exoskeletons, augmented reality, virtual reality, wearable trackers, intelligent personal assistants, collaborative robots, social networks, and big data analytics, all of which have been thoroughly discussed elsewhere (Mourtzis et al., 2022).

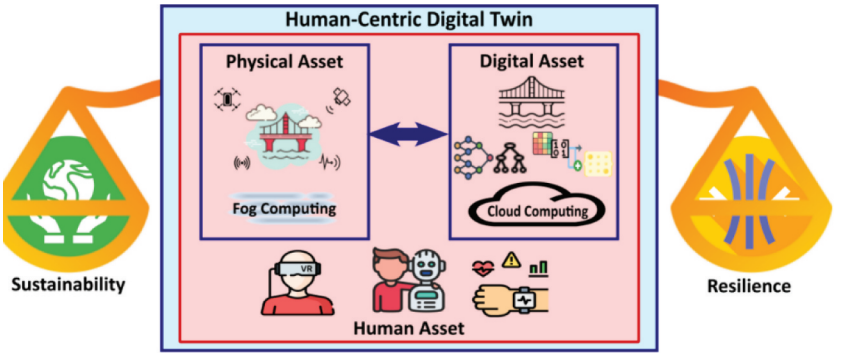


Figure 1. Novel Industry 5.0 Human-Centric digital twin framework.

In this paper, we explore the increasingly important role that humans will have within existing bridge DT frameworks and how the human-centrism principle could be better implemented within such context. We carried out a six-steps stakeholder analysis and discuss how a successful implementation of human centrism could uphold and maximize the resilience and sustainability of existing bridges, especially those with cultural heritage value.

2 METHODOLOGY

A system analysis approach has been applied to analyze the complex adoption of Industry 5.0 principles by different stakeholders of the AECMO&C industry. The stakeholder analysis method proposed by Enserik et al. (Enserink et al., 2022) has been followed. More specifically, this methodology has been implemented in a study case involving the conservation of existing bridges, in particular those with a cultural heritage value, in the city of Oslo, Norway. The case study presented assumes the educational institutions of the city to be the "*problem owners*".

The problem was first clearly formulated through the construction and interpretation of a means-ends diagram. A means-ends diagram was built by first identifying a dissatisfaction about an actual situation. A verb sentence was used to expresses the desired situation (end). Then a series of consecutive "why" questions related to the identified desired situation were asked. Answers were again placed in rectangles linked through arrows (pointing upwards). When no meaningful answer could be given anymore, a "back propagation" process started asking "how" each one of the identified ends could be achieved (means). This process allowed to map a comprehensive view of the situation and helped to select, together with appropriate spatial and temporal demarcations, an adequate level of analysis. The selected problem was then re-written in the form of a focal objective, which was no longer a "verb" phrase, but a "noun" one.

As the focal objective obtained from the means-ends diagram usually has an abstract nature or involves different complex aspects, it must be further refined by the means of an objectives tree. Objectives trees help to simplify the problem by operationalizing it into lower-level objectives and providing measurable criteria parameters. Once the problem has been defined and the factors related to it identified, the effect of each factor in the outcome (and in other factors) can be qualitatively observed through a causal relation diagram, also known as a causal map. Means-ends analysis, objectives tree, and the casual map are all summarized by the means of a system diagram. The path between means and external factors was traced to qualitatively assess their influence in the system criteria. Such influences were summarized in consequence tables.

The following step was to create an inventory of involved stakeholders. To do this, two different identification techniques were followed, so that, although partially overlapping, individual results could complement each other. The techniques followed were: i) positional approach where actors were identified based on their formal position in policymaking, and ii) opinion leadership approach where stakeholders with an influence on others were identified and included. Stakeholders' information on rights, responsibilities, and organizational charts along with established procedures, legislation, and laws, was collected to draw a formal chart. In this chart it was possible to visualize the mutual relations between different stakeholders and to sketch the arena within which they could interact to solve the problem under study.

The main characteristics of the inventoried stakeholders were then studied based on their interests, objectives, and perceptions. In this context, interests represent stakeholder's matters of importance and point towards a fixed direction, objectives are dynamic and indicate stakeholders wishes under the current problem context, and perceptions are stakeholder's interpretations of the situation. A stakeholder overview table tool was developed and extended with each stakeholders' resources, importance, and replaceability level. With all this information and based on a systematic comparison, stakeholders' dependencies were determined, and finally presented in the form of a power-interest grid.

3 RESULTS AND DISCUSSION

The adoption of Industry 5.0 principles could be described as an "*untamed*" problem in the classification proposed by (van de Graaf & Hoppe, 1996) as it requires a large degree of social

consensus and involves a high degree of technological uncertainty. Thus, this problem requires a multi-actor engagement and agreement to be solved. Why should Industry 5.0 principles be adopted? This question leads to a series of positive outcomes among which are the achievement of emissions neutrality, to increase industry competitiveness, and to improve working conditions. Ultimately, the question "why all these should be done?" leads to the end of generating economic, ecologic, and societal value. But what are the means needed for the adoption of Industry 5.0 principles? According to our analysis, this problem could be tackled if efforts are put in four different aspects: i) the modification of current business models, ii) the investment on enabling technologies (mainly in the implementation of the discussed human-centric digital twin), iii) the establishment of interdisciplinary collaborations between diverse stakeholders, and iv) the up-skilling/re-skilling of the AECMO&C industry workforce. The means-ends diagram developed to support the system delimitation for the study case selected is presented in Figure 2.

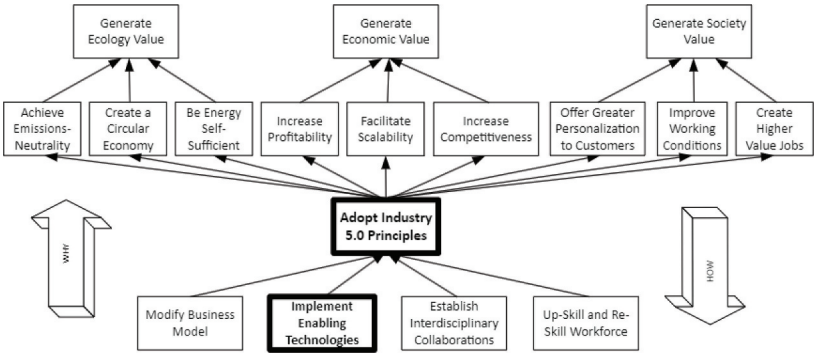


Figure 2. Means-Ends diagram on the adoption of industry 5.0 (It is not limited to the study case under discussion, But it is of general application character).

We can now re-write the problem under study in the form of a focal objective such as that we obtain "Adoption of sustainability, resilience, and human-centrism". This objective should be achieved while aiming at avoiding a series of undesirable side effects. A key issue for our study case is the hampering of technology development. An objective tree was created (not shown here for the sake of brevity) to identify the outcomes of interest on achieving this focal objective through the implementation of human-centric digital twins. These items were formulated as measurable criteria. Namely, high return of investment [profit/initial cost], high regulatory compliance [days/regulatory approval], low energy consumption [watts/hour], high acceptation [perception level], many jobs generated [jobs generated/year].

The relationship between means (see Figure 2) and identified measurable criteria was better understood thanks to the creation of a causal map (not shown here for the sake of brevity). Eventually, both means-end diagram and casual map were used to depict a conceptual model of the study case analyzed through a system diagram, as presented in Figure 3. In this diagram a more elaborated structure of the problem can be observed. Means are placed in the left side of the boundary. We focus our attention on the implementation of enabling technologies (i.e. human-centric digital twins, the detail analysis of the remaining means is outside of the scope of this paper) and their effect on internal system factors and the identified criteria, which are placed on the right border of the diagram. The path from means to criteria is qualitatively assessed based on the arrow connectivity and sign. These causal pathways are tabulated in the consequence table shown in Table 1.

Table 1. Consequence table on the implementation of enabling technologies for the case under study.

Means/Criteria	Return of Investment	Generated Jobs	Acceptation	Energy Consumption	Regulatory Compliance
Implement Enabling Technologies	+, +, -	-, -	+, +	+, - and +, +	+, -

From these results it can be observed that the adoption of Industry 5.0 principles by the educational institutions of the city would bring with it higher complications to comply with regulatory frameworks. Moreover, such regulations may not even be in place now, but being under development, such as the discussed European Union legislation on Artificial Intelligence (Madiega, 2023). It can also be said that initially the adoption of Industry 5.0 principles would negatively affect the return of investment of the problem owners. Nevertheless, it has been shown that early adoptions require of small monetary investments, whereas that to maintain competitiveness, later adopters require higher amounts of investment (Della Seta et al., 2012). On the other hand, positive impacts are expected in terms of job generation and perception level. Whereas that the energy consumption criteria would receive mixed inputs. From one point of view, an enhanced technological efficiency would reduce the amount of energy consumption. The proposed human-centric digital twin technology would require great amounts of data processing/storages, which would ultimately be reflected on a higher energy consumption.

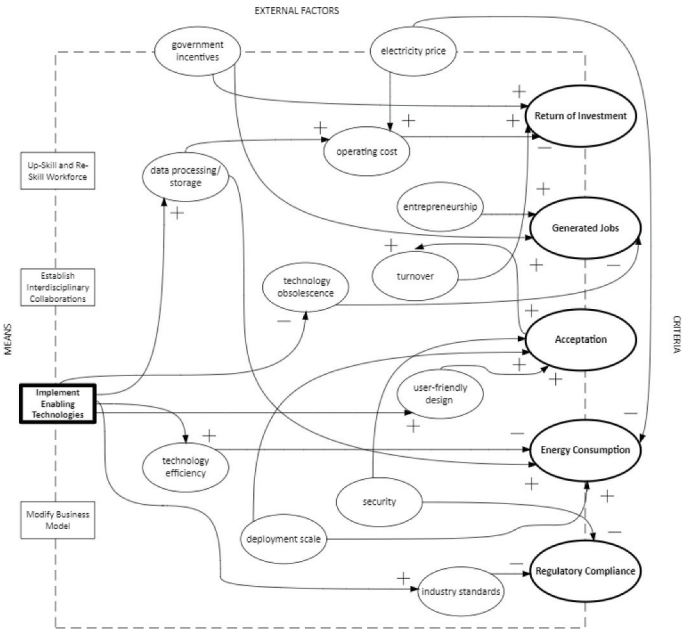


Figure 3. System diagram.

The adoption of such an important paradigm shift is a complex problem that cannot be fixed in isolation by the problem owner itself. Therefore, an inventory of relevant stakeholders which may contribute to reach a solution was created. Stakeholders at international (lately discarded as deemed irrelevant for the case study), regional, national, and local level were identified and clustered in accordance with their issues of interest into governance, infrastructure, conservation, education/R&D, industry, and society. More importantly, the formal relationships among them were map through a formal chart, as shown in Figure 4.

The two stakeholders in Oslo offering educational programs specialized on the AECMO&C industry, and considered on this study, are Oslo Metropolitan University (OsloMet, through its Department of Built Environment) and the Oslo School of Architecture and Design (AHO). They obtain research funding both from European and National institutions and can participate in the co-creation and delivery of teaching/research projects with two important stakeholders involved in the conservation of cultural heritage: the Norwegian Institute for Cultural Heritage Research (NIKU) and the National Trust of Norway (Fortidsminneforeningen). Interdisciplinary research and professional practices can be performed between these education institutions and the main players in the infrastructure sector at national level (Statens Vegvesen, who is responsible for the management of two protected bridges in Oslo under the National Conservation Plan for

the Norwegian Public Roads Administration) (Klima- og miljødepartementet, 2022). Finally, these Universities can play a key role in the up-skilling and re-skilling of the AECMO&C industry workforce (represented by some consulting and contracting companies in Figure 4).

The key players identified for the adoption of Industry 5.0 principles in the context of conservation of existing bridges with cultural heritage value in Oslo, Norway (see Figure 5), are those of governance nature both at national and local level. The ministry of Transport and the Ministry of Climate and Environment with their subordinate agencies, Statens Vegvesen and Riksantikvaren respectively, along with Oslo Komunne and its Cultural Heritage Office Agency possess the monetary and authority irreplaceable resources to adopt such principles while incentivizing the remaining stakeholders to follow.

It is hypothesized that if such resources are driven towards a suitable business model, the adoption of human-centric digital twins as enable technology, the establishment of interdisciplinary collaborations between the identified stakeholders, and the up-skilling/re-skilling of the

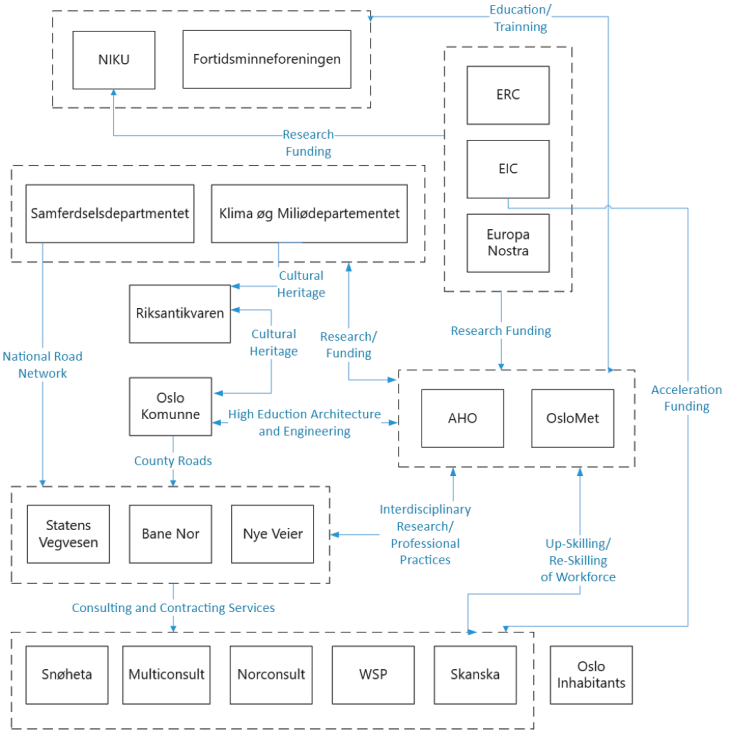


Figure 4. Formal chart.

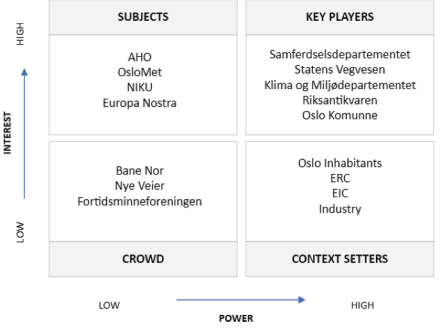


Figure 5. Power-Interest matrix.

AECMO&C industry a successful adoption could be achieved. These efforts would ultimately result in the creation of economic, ecological, and societal value.

4 CONCLUSION

Industry 5.0 has recently surged as a novel paradigm to tackle the unforeseen negative consequences of its predecessor and is rapidly being adopted in different sectors. In this paper, we explored how the human-centrism principle fostered by Industry 5.0 could be better implemented within the context of bridge engineering. The work was carried out following a six-steps stakeholder analysis methodology which was applied in a study case involving the conservation of existing bridges, in particular those with a cultural heritage value, in the city of Oslo, Norway. The educational institutions of the city were assumed to be the "*problem owners*".

Despite of the pragmatic and systematic nature advantages of stakeholder analysis, it does not come without cons. Some limitations of this methodology include the fact that stakeholder classification is static while in the real world stakeholders evolve constantly and dynamically, its lack of specificity and the reliability of the information upon which it is constructed (Hermans & Thissen, 2009). Luckily its main drawback could be greatly mitigated through a participatory approach. The involvement of different stakeholders and citizens in scientific research and/or knowledge production through a co-creation workshop for example, could significantly enhance the outcomes of this kind of work (Fritz et al., 2019).

REFERENCES

Chen, X., Eder, M. A., Shihavuddin, A. S. M., & Zheng, D. (2021). A human-cyber-physical system toward intelligent wind turbine operation and maintenance [Article]. *Sustainability (Switzerland)*, *13*(2), 1–10, Article 561. https://doi.org/10.3390/su13020561

Della Seta, M., Gryglewicz, S., & Kort, P. M. (2012). Optimal investment in learning-curve technologies. *Journal of Economic Dynamics and Control*, *36*(10), 1462–1476. https://doi.org/10.1016/j.jedc.2012.03.014

Ellingrud, K., Sanghvi, S., Dandona, G. S., Madgavkar, A., Chui, M., White, O., & Hasebe, P. (2023). *Generative AI and the future of work in America*. https://www.mckinsey.com/mgi/our-research/generative-ai-and-the-future-of-work-in-america

Enserink, B., Bots, P., van Daalen, E., Hermans, L., Kortmann, R., Koppenjan, J., Kwakkel, J., Ruijgh, T., Thissen, W., & Slinger, J. (2022). *Policy Analysis of Multi-Actor Systems* (2nd ed.). TU Delft OPEN. https://doi.org/10.5074/T.2022.004

European Commission. (2019). *The European Green Deal*. https://eur-lex.europa.eu/resource.html?uri=cellar:b828d165-1c22-11ea-8c1f-01aa75ed71a1.0002.02/DOC_1&format=PDF

European Commission. (2020). *Enabling Technologies for Industry 5.0: results of a workshop with Europe's technology leaders*. https://data.europa.eu/doi/10.2777/082634

European Commission. (2021). *Industry 5.0: Towards a sustainable, human-centric and resilient European industry*. https://data.europa.eu/doi/10.2777/308407

European Commission. (2022). *Industry 5.0: A transformative vision for Europe*. https://research-and-innovation.ec.europa.eu/knowledge-publications-tools-and-data/publications/all-publications/industry-50-transformative-vision-europe_en

Fritz, S., See, L., Carlson, T., Haklay, M., Oliver, J. L., Fraisl, D., Mondardini, R., Brocklehurst, M., Shanley, L. A., Schade, S., Wehn, U., Abrate, T., Anstee, J., Arnold, S., Billot, M., Campbell, J., Espey, J., Gold, M., Hager, G., … West, S. (2019). Citizen science and the United Nations Sustainable Development Goals. *Nature Sustainability*, *2*(10), 922–930. https://doi.org/10.1038/s41893-019-0390-3

Gkoumas, K., dos Santos, F. L. M., & Pekar, F. (2021). *Research in bridge maintenance, safety and management: An overview and outlook for Europe* [Conference Paper]. 10th International Conference on Bridge Maintenance, Safety and Management, IABMAS 2020, https://doi.org/10.1201/9780429279119-239

Hermans, L. M., & Thissen, W. A. H. (2009). Actor analysis methods and their use for public policy analysts. *European Journal of Operational Research*, *196*(2), 808–818. https://doi.org/10.1016/j.ejor.2008.03.040

Hu, W., Lim, K. Y., & Cai, Y. (2022). Digital Twin and Industry 4.0 Enablers in Building and Construction: A Survey. *Buildings*, *12*(11). https://doi.org/10.3390/buildings12112004

Jiménez Rios, A., & O'Dwyer, D. (2019). *External Post-tensioning System for the Strengthening of Historical Stone Masonry Bridges* [Book Chapter]. RILEM Bookseries, https://doi.org/10.1007/978-3-319-99441-3_168

Jiménez Rios, A., Plevris, V., & Nogal, M. (2023a). Bridge Management through Digital Twin-based Anomaly Detection Systems: A Systematic Review. *Frontiers in Built Environment*. https://doi.org/10.3389/fbuil.2023.1176621

Jiménez Rios, A., Plevris, V., & Nogal, M. (2023b). *Synthetic data generation for the creation of bridge digital twins what-if scenarios* 9th International Conference on Computational Methods in Structural Dynamics and Earthquake Engineering (COMPDYN), Athens, Greece. https://doi.org/10.7712/120123.10760.21262

Jiménez Rios, A., Plevris, V., & Nogal, M. (2023c). *Uncertainties in the synthetic data generation for the creation of bridge digital twins* 5th International Conference on Uncertainty Quantification in Computational Science and Engineering (UNCECOMP), Athens, Greece. https://doi.org/10.7712/120223.10323.20020

Forskrift om endring i forskrift om fredning av statens kulturhistoriske eiendommer, (2022). https://lovdata.no/dokument/LTI/forskrift/2022-11-17-1976

Maddikunta, P. K. R., Pham, Q. V., B, P., Deepa, N., Dev, K., Gadekallu, T. R., Ruby, R., & Liyanage, M. (2022). Industry 5.0: A survey on enabling technologies and potential applications [Review]. *Journal of Industrial Information Integration*, *26*, Article 100257. https://doi.org/10.1016/j.jii.2021.100257

Madiega, T. (2023). *Artificial intelligence act* (EU Legislation in Progress, Issue. E. P. R. Service. https://www.europarl.europa.eu/RegData/etudes/BRIE/2021/698792/EPRS_BRI(2021)698792_EN.pdf

Mourtzis, D., Angelopoulos, J., & Panopoulos, N. (2022). Operator 5.0: A survey on enabling technologies and a framework for digital manufacturing based on extended reality [Article]. *Journal of Machine Engineering*, *22*(1), 43–69. https://doi.org/https://doi.org/10.36897/jme/147160

Pillai, S., Iyengar, V., & Pathak, P. (2022). Monitoring Structural Health Using Digital Twin. In *Digital Twin Technology* (pp. 125–139). https://doi.org/10.1002/9781119842316.ch8

Schleich, B., Anwer, N., Mathieu, L., & Wartzack, S. (2017). Shaping the digital twin for design and production engineering [Article]. *CIRP Annals - Manufacturing Technology*, *66*(1), 141–144. https://doi.org/10.1016/j.cirp.2017.04.040

Tita, E. E., Watanabe, G., Shao, P., & Arii, K. (2023). Development and Application of Digital Twin-BIM Technology for Bridge Management. *Applied Sciences*, *13*(13). https://doi.org/10.3390/app13137435

UNESCO WHC. (2023). *World Heritage List*. UNESCO WHC. Retrieved 08/11/2023 from http://whc.unesco.org/en/list/

United Nations. (2015). *The Paris Agreement*. https://unfccc.int/process-and-meetings/the-paris-agreement

United Nations. (2022). *Emissions Gap Report 2022*. https://www.unep.org/resources/emissions-gap-report-2022

United Nations. (2023). *The Intergovernmental Panel on Climate Change (IPCC) Assessment Report 6 Synthesis Report: Climate Change 2023*. https://www.ipcc.ch/report/ar6/syr/

van de Graaf, H., & Hoppe, R. (1996). *Beleid en Politiek. Een Inleiding tot de Beleidswetenschap en de Beleidskunde*. Bussum: Coutinho. https://hdl.handle.net/11245/1.127073

Wenzel, H. (2009). *Health Monitoring of Bridges*. John Wiley & Sons, Ltd. https://doi.org/10.1002/9780470740170

Wilkinson, M. D., Dumontier, M., Aalbersberg, I. J., Appleton, G., Axton, M., Baak, A., Blomberg, N., Boiten, J.-W., da Silva Santos, L. B., Bourne, P. E., Bouwman, J., Brookes, A. J., Clark, T., Crosas, M., Dillo, I., Dumon, O., Edmunds, S., Evelo, C. T., Finkers, R., … Mons, B. (2016). The FAIR Guiding Principles for scientific data management and stewardship. *Scientific Data*, *3*(1), 160018. https://doi.org/10.1038/sdata.2016.18

Yang, C., Tu, X., Autiosalo, J., Ala-Laurinaho, R., Mattila, J., Salminen, P., & Tammi, K. (2022). Extended Reality Application Framework for a Digital-Twin-Based Smart Crane [Article]. *Applied Sciences (Switzerland)*, *12*(12), Article 6030. https://doi.org/10.3390/app12126030

Zampieri, P., Piazzon, R., Ferroni, R., & Pellegrino, C. (2023). The application of external post-tensioning system to a damage masonry arch. *Procedia Structural Integrity*, *44*, 605–609. https://doi.org/10.1016/j.prostr.2023.01.079

Bridge Maintenance, Safety, Management, Digitalization and Sustainability – Jensen, Frangopol & Schmidt (eds)
© 2024 The Author(s), ISBN 978-1-032-77040-6
Open Access: www.taylorfrancis.com, CC BY-NC-ND 4.0 license

Overview of assessment for bridges affected by HS2 tunnelling, UK

J. Tsekhanskiy
Arup, New York, USA

A. Bariyya, G. Ledsham-James & D. Shapley
Arup, Birmingham, UK

Y. Li
Arup, London, UK

ABSTRACT: The HS2 tunnelling works in the United Kingdom required extensive ground movement assessment (GMA) for existing third party bridges to identify which assets might be susceptible to damage and require mitigation measures, and to provide a basis for screening out structures likely to suffer negligible damage. This paper presents an overview of the GMAs conducted on approximately 80 existing bridges located above the future twin-bored, tunnelled, HS2 route, focusing on the challenges faced, methodologies employed, and findings obtained. The GMAs ensured that detrimental effects of HS2 construction on existing assets were identified early and impacts to those assets were minimized, reducing overall project expenditure with risk-based damage assessment. This paper shares the learning points from assessing a large sample of bridges of various ages and structural types under the influence of tunnel-induced ground movement. Findings include recommended monitoring, remedial works, or mitigation outcomes grouped by bridge type.

1 INTRODUCTION

The development of high-speed railways brings numerous opportunities for economic growth and improved transportation networks. In the United Kingdom, the construction of the High Speed 2 (HS2) railway is a flagship project aimed at enhancing capacity, stimulating growth to connected cities, and reducing carbon emissions. Once operational, HS2's trains will journey between London and the Midlands in the UK.

This paper focuses on the S1/S2 contracts of HS2 delivered by Skanska Costain Strabag (SCS) Joint Venture, with design support from Design House Joint Venture (Arup, Typsa, & Strabag). The S1/S2 contracts cover the first portion of Phase 1, shown in Figure 2, trains running largely in tunnel from Euston station in Central London to West Ruislip on the edge of the conurbation. The new twin-bored, tunnelled, HS2 route is largely constructed using an Earth Pressure Balance (EPB) tunnel boring machine (TBM). While TBM construction has proved to be safe and controlled, inherent volume loss at the face can cause vertical and horizontal ground displacements along the tunnel paths, as seen in Figure 1. As part of this contract, SCS were required to undertake GMAs of existing infrastructure with a moderately conservative volume loss (VL) modelled at 1% for tunnel boring machine type (EPB) and 1.5% for sprayed concrete lining (SCL) tunnel construction.

Tunnelling construction below London and consideration of VL on existing surface assets is well documented, particularly for building structures. For the HS2 project, a similar GMA methodology has been adopted as described by Lazarus & Jung (2018) for the construction of Crossrail (now the Elizabeth Line) which focused largely on the impact of tunnelling on

DOI: 10.1201/9781003483755-88

buildings. GMA methodologies specifically for bridges have been previously described for London projects including Crossrail (Bradley et al., 2015; McCarthy, 2016) and Channel Tunnel Rail Link (CTRL) (Jacobsz et al., 2006). The HS2 S1/S2 packages of work are unique in that they contain a relatively large sample of bridge structures undergoing ground movement assessment. This paper presents a summary of the GMA methodology, findings grouped by bridge type, and observations or conclusions that may be useful for future bridge GMAs. Please note that due to the sensitive nature of the project, any identifying information about specific assets has been removed, and results are only presented in amalgamation.

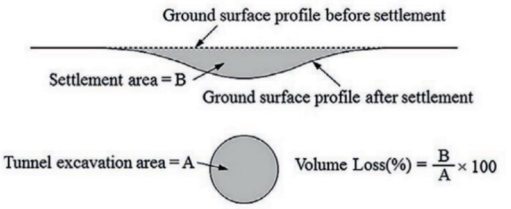


Figure 1. Definition of volume loss as shown in Lazarus & Jung (2018).

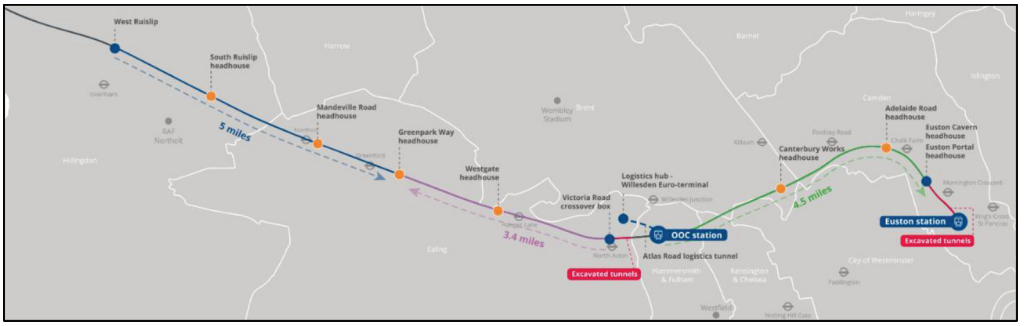


Figure 2. Proposed Hs2 route largely in tunnel below London (SCSJV, 2023).

2 OBJECTIVES

The GMA identified the degree of intervention required for each bridge asset to safeguard it from the effects of HS2 tunnelling. The analyses aimed to identify potential risks associated with ground movement due to permanent works and temporary works dewatering, and to highlight where mitigation measures might be necessary to ensure the safety and durability of these critical assets. The three main outcomes for each bridge asset were monitoring only, remedial works, and mitigation, described in more detail in Section 4 of this paper. The assessment mitigated the risk to the project while reducing its potential carbon footprint by eliminating the need for extensive asset replacement. Bridge assets are considered critical infrastructure and the consequences of ultimate limit state or service limit state failure causing closure of the bridge are expensive and could result in harm to the public. By completing a GMA, time and resources are saved by employing a risk-based approach that initially screens out assets that will remain unaffected by construction activity. Some assets that are affected by construction activity but experience negligible movement are concluded to require monitoring only. Those assets moderately impacted by construction activity but that can withstand the impact may only require remedial works after the completion of construction. Only those assets which are deemed impacted by construction and the movements may impact the

ability of the asset to function as intended are recommended for proactive mitigation measures. This ranked approach reduces risk while utilising project funds effectively.

3 METHODOLOGY

The ground movement assessment involved a multi-disciplinary and phased approach, combining geotechnical investigations and structural analysis. The phased approach allowed for many of the assets to be reviewed quickly and at a high level to rule out the need for mitigation interventions. However, as bridge assets are considered "critical" infrastructure, bridges inside the zone of influence (ZoI) were pushed to the most in-depth level of assessment. The GMAs considered the vertical and horizontal ground movements across all phases of construction. Defining the most impactful ground movements and structural checks to be carried out is dependent on bridge type and required engineering judgement. The primary purpose of the GMA was to establish what impact (if any) the HS2 construction has on the existing bridges. The philosophy for the GMA was to demonstrate by the simplest means possible whether the bridges can accommodate the HS2 tunnel-induced ground movements or if mitigation measures are required to do this. A GMA is therefore *not* the same as a live load assessment where the objective is to determine the load capacity of all structural elements.

On occasion, limited information was available for some structures, such as no as-built drawings or lack of records of repairs or alterations to the structure. Topographical surveys and Inspections for Assessment were carried out on behalf of SCS to gain the necessary information to confirm assumptions about the bridges.

The initial steps of analysis for a GMA were often relatively simple, comprising hand calculations and structural analysis models using prescribed displacements from the ground movement models. Where simpler methods did not enable a conclusion to be reached about the need for mitigation measures, then more sophisticated analytical methods were employed.

For arch structures, a specific methodology was developed and is described in a separate paper - 'Ground movement assessment method for arch bridges affected by HS2 tunnelling' by Saavedra Justo et al. (2024).

Due to considerable interfaces between bridge assets and adjacent buildings, utilities, rail, and other asset types, extensive coordination ensures the GMA is completed with a multi-disciplinary approach in mind. The complexity of asset interfaces could be the subject of another paper and will only be touched on briefly here. In coordination with a geotechnical team, each bridge asset was modelled in Oasys XDisp, a ground movement software, along with the proposed tunnel design and alignment, cross passages, vent shafts, and other excavations that could impact the ground movement near the asset. The Oasys XDisp software utilises a methodology of sub-surface greenfield ground movements that can be calculated using empirical methods, as demonstrated by Mair et al. (1993) and Taylor (1995), where a settlement trough perpendicular to the new tunnel can be estimated using an inverted normal probability curve (Gaussian curve). The three-dimensional form of movement is calculated using the Attewell & Woodman (1982) methodology. The software models the longitudinal "bow wave" settlement data around the tunnel and transforms it to vertical and horizontal displacements at the bridge location. The "bow wave" in the context of this paper refers to ground movement at the face of the TBM, which behaves similarly to the wave that forms at the bow of a ship when it moves through the water. As the ship's bow wave spreads out, it defines the outer limits of a ship's wake, which is the analogy for the ground movement ZoI in this paper.

Due to prevailing ground conditions in certain areas of the project, it has been identified that some locations along the construction route will require temporary works dewatering to enable their construction, such as some vent shafts and cross passages between tunnels. Settlement due to tunnelling is permanent, whereas settlement due to temporary works dewatering is a transient effect. It is anticipated that full or partial reversal of the additional settlement will occur after the dewatering systems are switched off as the water levels recover and effective stress returns to its original state. Temporary works dewatering will result in additional

vertical settlement only in areas where it is deployed due to the increase in vertical effective stress. No horizontal movement is predicted to occur due to dewatering.

The Oasys XDisp ground movement software allows the settlement analysis to be carried out along different phases of construction. This enabled detailed analysis of displacements on structures at various stages of construction, including the impact of temporary works dewatering, and progressive shaft, tunnelling, and cross passage construction on the structure. In many cases the worst-case movement on the structure did not take place at the final stage, but at an interim stage where differential settlement peaked due to offset Up Line and Down Line TBM progression.

4 POTENTIAL OUTCOMES

The GMA work identified the degree of intervention required on a bridge asset to safeguard it from the effects of HS2 tunnelling. This was achieved by splitting the assets into several predicted outcomes: monitoring only, remedial works, or mitigation, based on their individual risk profiles (due to condition, age, predicted impact, etc.). Where the identified need for intervention was minimal – for example, monitoring only – then this also helped to reduce the risk profile for SCS and reduce the carbon footprint by avoiding any mitigation works to the structure.

4.1 *Instrumentation and monitoring*

All bridges within the ZoI, regardless of GMA outcome, require an instrumentation and monitoring (I&M) plan. The objectives of I&M are:

- To record ground movements and deflections of assets within the ZoI of the works and allow checks that these are in accordance with calculations;
- To provide evidence that the VL due to tunnelling is in accordance with the modelling assumptions; and
- To determine the effects of the construction works on third party assets and provide early warning of any need for additional mitigation measures if required.

After a period of baseline monitoring to establish seasonal effects, monitoring will continue for the duration of the HS2 tunnelling works and for a period after completion to confirm that the behaviour of the tunnel linings complies with the design intent and ground movements diminish as expected.

Based on predicted movement, asset-specific trigger values were calculated to alert the project if actual movements approach (or even exceed) the calculated values. A robust Monitoring Action Plan is in place with agreed actions relating to various levels of specified trigger values.

4.2 *Remedial works*

It was often recommended that remedial works could be required to repair minor damage after completion of HS2 tunnel construction. Examples of minor defects that might occur include spalling of concrete or cracking to masonry.

4.3 *Mitigation*

If the GMA for a bridge asset resulted in a suggested mitigation outcome, specialist mitigation solutions were recommended to protect the asset and ensure continued service on which the pedestrians, rail, vehicles, etc. rely. An example of one such mitigation solution for the HS2 S1/S2 project can be seen in the paper by Carlucci & Godden (2022).

5 FINDINGS

As expected, the data confirmed that generally bridge assets experienced lower overall ground movements if they were located further away from the tunnels (Figure 3), where distance is three-dimensional (measuring both plan distance and depth beneath ground level). In fact, of the assets reviewed, primarily in London Clay with an excavated tunnel diameter between 8.53m - 9.84m and ranging from approximately 5m to 50m below ground level, no assets greater than 20m in plan from the tunnels required mitigation, regardless of asset age or structural type. Foundation position relative to the tunnels influences ground movements experienced by the asset. An asset with a deep foundation (piles) and directly above the tunnels in plan is expected to experience higher vertical settlements than the same asset with a shallow foundation at the same location. However, an asset positioned on the edge of the Gaussian settlement curve with a deep foundation may experience smaller ground movement than an asset with a shallow foundation. This is because deep foundations may potentially be founded in ground that is only minimally affected by the tunnels. A visual example of this can be seen in Figure 4.

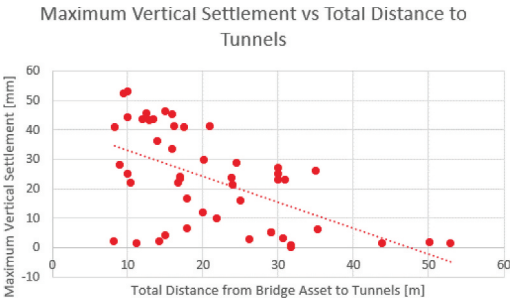


Figure 3. Plot of maximum vertical settlement versus total distance from the bridge asset to the tunnels. trend line verifies the correlation.

Due to the scope and complexity of assessing such a large quantity of structures, it was invaluable to have a set of standard diagrams and templates for presenting information. Clear report templates and automated tools to create graphical outputs helped illustrate the information in a consistent and easy to understand format. The output could then be easily compared against similar bridge types for a quick comparison between other similar structures to pick up any anomalies in their analysis as a way of further validating the results on top of the usual check and review process. One such example is the vertical settlement curves used to illustrate the ground settlement at all construction stages shown concurrently with structure and tunnel depth (see Figure 4).

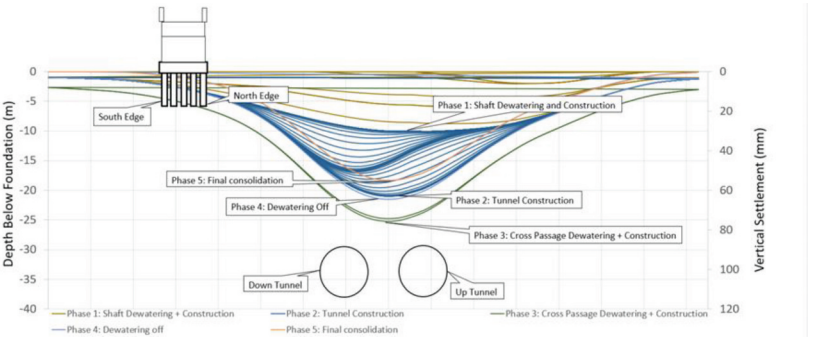


Figure 4. Vertical settlement curve across the bridge (including the effects of temporary works dewatering). key construction stages are labelled.

Figure 4 shows the vertical settlement curve across a bridge, which shows the settlement imposed by the passing of the Down Line and Up Line tunnels individually as a series of blue curves. The Down Tunnel passes first leading to a shallow settlement curve adjacent to the bridge. When the Up Tunnel passes, the settlement curve widens and becomes centred over the tunnels. Throughout the phases, differential settlement from the offset tunnel progression was found to be the most prevalent issue, particularly in structures with limited ability to accommodate the additional movement. Another notable outcome of the modelling process was the impact of the TBM on the structure before it reaches the asset. The tunnel settlement bow wave impacts the asset before the TBM is directly below the asset and continues to impact the asset until it is several tunnel diameters past. This early- and late-stage settlement can be seen in the diagram of the tunnel progression in Figure 5.

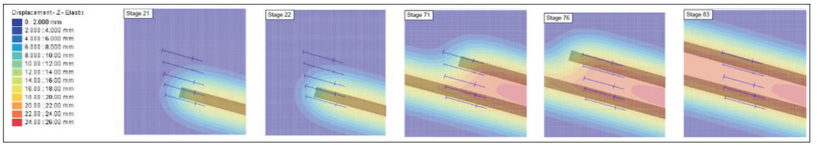


Figure 5. Vertical settlement at key construction stages. bridge piers are shown as blue lines with tunnels in brown.

Figure 6 below shows the split of suggested interventions per structure type. Some general trends can be observed, one of which is that arch structures in the study proved to be more resilient than steel girder bridges. This may be because, for many steel girder bridges, relative displacement of adjacent piers led to bearing and expansion joint tolerance exceedance as aging bridges normally have limited residual capacities for bearings and expansion joints. The specific arch analysis methods are detailed in 'Ground movement assessment method for arch bridges affected by HS2 tunnelling' by Saavedra Justo et al. (2024).

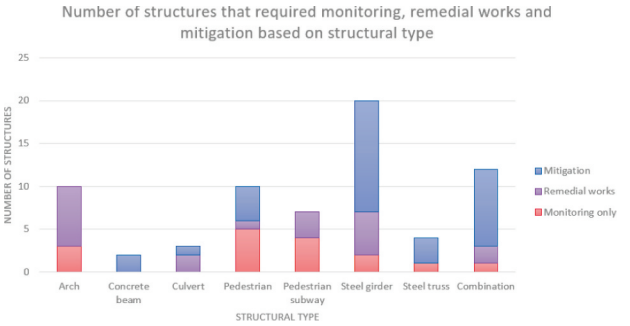


Figure 6. Number of structures that required monitoring, remedial works, and mitigation, grouped by structural type. n.b. combination structures are those that were added onto over time (e.g. road widening). [work is still progressing on gma refinement and may result in updated recommendations, changing the values presented above].

In Figure 6, the "combination" grouping of structures represents the assets, of those analysed, that were originally constructed in one bridge structural form, then added onto with one or more different structural types over time. These "combination" type assets proved to be prone to mitigation recommendations as the interfaces between the different structural types were not adaptable to differential settlement.

Interestingly, as can be seen in Figure 7 below, no clear difference can be interpreted from the bridge data based on foundation type. There was no discernible favour between shallow foundations and deep foundations in terms of resiliency against ground movement. This may

be due to the limited number of deep foundation assets available to study and the fact that settlement for bridges with deep foundation can be higher or lower depending on their relative location to the tunnel alignment. Mitigation was the suggested outcome for approximately half of both shallow and deep foundation type assets.

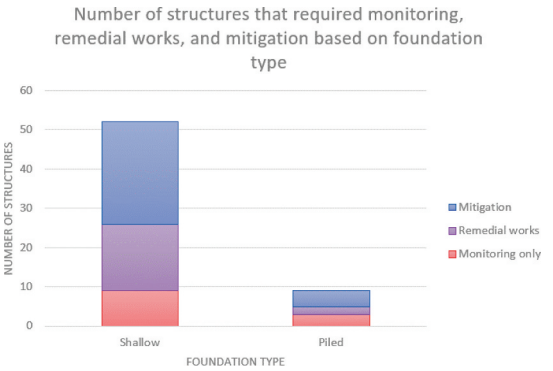


Figure 7. Number of structures that required monitoring, remedial works, and mitigation based on foundation type. [work is still progressing on gma refinement and may result in updated recommendations, changing the values presented above].

At the start of the ground movement assessment work, it was unclear if age of asset would relate to recommended asset outcome. Estimating how much ground movement a historic bridge can accommodate can be difficult because of historic approaches to bridge articulation, and sometimes a lack of records. For instance, one asset had combination pin/roller bearings where the roller base was completely encased and therefore difficult to visually confirm the range of allowable movement. Only a note on the drawings indicated the ability of the bearing to accommodate longitudinal movement. Some of the newer bridges with designed mechanical bearings (e.g. rocker bearings, sliding bearings) analysed as part of the GMAs were least able to accommodate ground movements due to their limited articulation ranges. Lead plate bearings fared better at accommodating horizontal movement, however, could induce a friction force into the structure due to the movement. An advantage of some older bridge forms, notably arch structures, was better accommodation for ground movements than some newer bridges with bearings with prescribed movement ranges. However, as can be seen in Figure 8, date of construction/age of structure was not a strong indicator of mitigation outcomes.

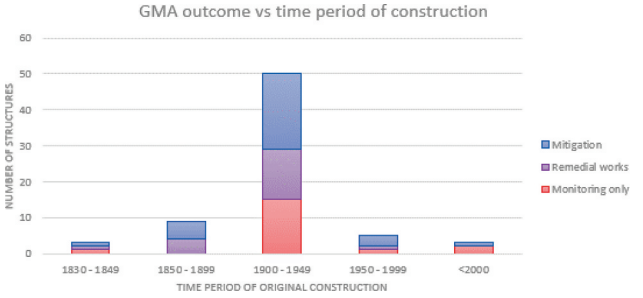


Figure 8. Number of structures that required monitoring, remedial works, and mitigation based on date of original asset construction. [work is still progressing on gma refinement and may result in updated recommendations, changing the values presented above.]

While it can be related to asset age but is not necessarily linked (assets that are well-maintained over their lifespan can potentially perform very well in old age), condition of the asset was another key indicator for GMA outcome. Poor asset condition or reduced existing

capacity of a structure was often more critical than the effects of ground movements. There were bridges where ground movements had negligible effect, but there were health and safety concerns because of underlying and pre-existing issues with the bridge.

6 CONCLUSIONS

The HS2 ground movement assessment programme has provided valuable insights into the potential challenges and risks associated with tunnelling under a major city. Key indicators for mitigation outcomes included bridge vicinity to tunnelling works, foundation depth (favourable or unfavourable depending on the location among the Gaussian settlement curve), and bridge type (arches were found to be more adaptable to ground movement than steel girder bridges, "combination" bridges were more susceptible to ground movement than single-structural-type assets). Age of asset and foundation type did not strongly correlate to a specific recommended outcome, but asset condition was even more important than the effects of ground movement. The findings underscore the importance of thorough structural assessments, continuous monitoring, and appropriate mitigation measures to ensure the safety and resilience of aging bridge infrastructure adjacent to tunnelling projects. With careful consideration, project risk can be reduced with sustainable outcomes.

REFERENCES

Attewell, P. B. and Woodman, J. P (1982) 'Predicting the dynamics of ground settlement and its derivatives caused by tunnelling in soil', *Ground Engineering*.

Bradley, B., Callaghan, D., Moore, T., Reaney, A. and Sevilla, J. (2015) 'Lord Hill's Bridge Mitigation Works'. In: Black, M., Dodge, C. and Lawrence, U., eds. *Crossrail Project: Infrastructure design and construction*. London: ICE Publishing, pp. 253–270. Available at: https://www.icevirtuallibrary.com/doi/abs/10.1680/cpid.60784.017 (Accessed: 21 November 2023).

Carlucci, A. and Godden, S. (2022) 'Mitigating the effects of tunnelling under Euston Bridge 7′, *HS2 Learning Legacy*.

Jacobsz, S., Bowers, K.H., Moss, N.A. and Zanardo, G. (2006) 'The effects of tunnelling on piled structures on the CTRL'. The International Society for Soil Mechanics and Geotechnical Engineering. Available from: 10.1201/NOE0415391245.ch12 (Accessed: 21 November 2023).

Lazarus, D. and Jung, H. (2018) 'Damage assessment and monitoring for buildings on the Elizabeth Line', The Structural Engineer. Vol. 96 (Issue 7), pp. 14–24. Available at: http://dx.doi.org/10.56330/IXSM2164 (Accessed: 21 November 2023).

Mair, R., Taylor, R.A. & Bracegirdle, A. (1993) 'Subsurface settlement profiles above tunnels in clay', *Geotechnique*, Vol. 43 (No. 2), pp. 315–320.

McCarthy, J. (2016) 'Lindsey Street Bridge - a structural solution to settlement mitigation'. In: Black, M., ed. *Crossrail Project: Infrastructure design and construction*, Vol. 3. London: ICE Publishing, pp 265–282. Available at: https://www.icevirtuallibrary.com/doi/abs/10.1680/cpid.61293.265 (Accessed: 21 November 2023).

Saavedra Justo, A. et al. (2024), 'Ground movement assessment method for arch bridges affected by HS2 tunnelling', *IABMAS Conference*, June 2024, Copenhagen.

SCSJV (2023) SCSJV. Available at: https://scsjv.co.uk/about-us/ (Accessed: 28 November 2023).

Taylor, R. N. (1995), 'Tunnelling in soft ground in the UK'. *Underground construction in soft ground*. Fujita, K and Kusakabe, O (Eds). Balkema. pp 123–126.

Bridge Maintenance, Safety, Management, Digitalization and Sustainability – Jensen, Frangopol & Schmidt (eds)
© 2024 The Author(s), ISBN 978-1-032-77040-6
Open Access: www.taylorfrancis.com, CC BY-NC-ND 4.0 license

Comparison of modal parametric and nonparametric vibration-based techniques

A. Dia & N. Makhoul
ESTP - Ecole Spéciale des Travaux Publics, Cachan, France

ABSTRACT: Ensuring the structural integrity of bridges is of paramount importance for public safety and the longevity of these critical infrastructures. Early detection and assessment of damage are essential to prevent catastrophic failures and optimize maintenance efforts. Vibration-based methods have emerged as effective tools for structural health monitoring (SHM) in bridge structures due to their non-intrusive nature and sensitivity to subtle changes in structural behavior. In this study, we present a comprehensive comparative analysis between two prominent vibration-based (VB) approaches: modal parametric and nonparametric methods, for damage characterization in bridges. The modal parametric approaches rely on interpreting the variation of the dynamic response of the structure based on identified modal parameters like natural frequencies and damping ratios sensitive to damage. While modal parametric approaches require system identification for damage characterization, these non-parametric methods involve extracting features from raw signals that are sensitive to damage, utilizing time series modeling techniques. After conducting a brief and comprehensive literature review, data collected from tests conducted on bridge cables were analyzed using both modal parametric and data-driven VB damage identification techniques. We then evaluate their performance in terms of sensitivity to damage characterization.

Keywords: SHM, damage, parametric methods, nonparametric methods, bridges

1 INTRODUCTION

The safety of daily users and the continuous operation of economic activities in cities depend on the proper and sound functioning of infrastructures such as bridges and their load-bearing components, such as metallic cables. These cables are exposed to cyclic mechanical, chemical, and thermal loads that can lead to damage resulting from pathologies, mainly corrosion and fretting fatigue (Dieng et al., 2009). Therefore, it is essential to integrate Structural Health Monitoring (SHM) and nondestructive techniques (NDT) into the management of structures to achieve a comprehensive characterization of damage and ensure the long-term safety and functionality of the bridges' cables. In response to these needs, several NDT techniques have been adopted such as visual inspection, ultrasonic methods, electromagnetic field methods, acoustic emission, and vibration-based methods. Vibration-based (VB) NDT allow the extraction, from measurements, of the global parameters of a mechanical system or a structure. Indeed, a change in the structural parameters (mass loss, stiffness, damping) leads to a change in the global modal parameters such as natural frequencies, mode shapes, and damping coefficients. This variation can also be reflected in the signals that can be recorded such as accelerations, velocities, or displacements. VB techniques can then be classified into two categories: parametric-based ones and non-parametric methods. Parametric methods refer to those based on system identification (Yan et al., 2019), i.e. the variation of modal and physical parameters such as frequencies, mode shapes, and damping ratios for modal parameters and/or stiffness, mass, and damping for physical parameters. As for non-parametric methods, they refer to methods that use statistical means, time series modeling tools, to characterize damage directly from recorded accelerations, displacements and/or velocities signals (Avci et al., 2021).

DOI: 10.1201/9781003483755-89

These methods make it possible to overcome the local nature of certain methods (acoustic emission, ultrasound, electromagnetic methods) and allow us to have an overview of the global health state of a structure with limited measurement points. Therefore, VB methods are qualified as global methods; even if a network of closely spaced measurement points (sensors) can, in some cases, provide local information. These vibration measurements are mainly carried out on a structure for four reasons that can be summarized as follows (Cremona, 2005):

1. perform vibration tests to assess the resistance of a structure to possible events that may solicit it during its operation such as strong winds, shocks, etc.
2. perform structural analysis for a better design through numerical model updating.
3. perform comfort measurements to measure the vibration levels of the structure.
4. and/or perform monitoring and diagnosis to reveal defects occurring in the structure.

The approach adopted in the context of this study falls within this last point and much research in damage characterization using VB techniques has been widely developed and documented (Das et al., 2016).

These literature reviews make it possible to identify different dynamic methods and their fields of application. The interest of this study, in addition to applying these methods on cable-type structures, a case study rarely addressed in the literature, is to indicate among the four levels of damage's characterization (Rytter, 1993), those that are achieved by these VB techniques (detection, location, quantification, and prediction of the structure's residual lifetime).

Also in this study, using experimental data obtained on cables and addressed in our previous study (Dia et al., 2021), we will go further and discuss the comparison of damage characterization through parametric and non-parametric methods.

2 METHODS AND MATERIAL PRESENTATION

2.1 *Methods description*

The global VB NDT techniques can be classified into different categories depending on the approaches, parameters, and tools used to perform analysis on vibration responses of monitored structures. As stated in the introduction, in this study we focused on classifying these techniques depending on the extracted parameters to perform damage characterization: modal parameters and non-(modal)-parameters. Whatever the used technique, the first step in damage identification is modal identification for parametric-based (P-based) techniques or time series modeling for the non-parametric (NP) approach. Thus, the following tree (Figure 1) gives a glance at those steps and their ramification allowed by technologies (sensors, computing, storage) advances.

The development of computational capabilities and reliable algorithms first led to classical modal parameters identification techniques known as experimental modal analysis (EMA) where both input (excitation force) and output (measured response, e.g., accelerations) data are used for modal parameters identification. This procedure can be applied in the frequency domain, through frequency response functions (FRFs), in the time domain, based on impulse response functions (IRFs) or in the time-frequency domain (TFD), through wavelet analysis. Depending on these domains respectively, Linefitting, PolyMAX - *Polyreference Least-Squares Complex Frequency-domain* or Hilbert-Huang Transform (HHT) are examples of each of these system identification techniques (Orlowitz & Brandt, 2017; Yang et al., 2021).

To address the main drawback of these EMA techniques regarding large-scale civil structures in operating conditions, i.e. the need for a known input force, operational modal analysis techniques (OMA) were developed. These refer to methods where the input force is not known or not measurable. The idea of OMA is thus to replace the artificial excitations used up to now with natural excitations such as wind, traffic, waves, etc. However, OMA and EMA methods share a common theoretical background. The main difference lies in the formulation of the input, which is known in EMA while it is random and unmeasured in OMA. Thus, while EMA procedures are developed in a deterministic framework, OMA methods can be considered as their stochastic counterpart (Rainieri & Fabbrocino, 2014). As a result, for OMA,

instead of FRFs, *power spectral densities* (PSDs) or *Singular Values Decomposition* (SVD) (Brincker et al., 2001) will be used and autocorrelation functions (ACFs) instead of IRFs. These mathematical transformations lead to algorithms such as the *Enhanced Frequency Domain Decomposition (EFDD),* the *covariance-driven Stochastic Subspace Identification)* (Peeters & Roeck, 2001). Given the fact the above-mentioned natural excitations cannot be always modeled as white noise, the supposed behavior of the input force in OMA methods, researchers have proposed systems identification techniques based on transmissibility functions (TFs) such as the *polyreference Transmissibility-based OMA (pTOMA)* (Weijtjens et al., 2014).

Modal analysis-based damage detection techniques rely on the identification and estimation of modal parameters. However, these techniques face several challenges, particularly in detecting early-stage damage where modal parameters variation is very low to be detected. Thus, particular attention has been paid to non-parametric methods to detect structural defects directly from the recorded signals using statistical and probabilistic tools (Tseng & Naidu, 2002). These techniques are mainly based on time series modeling (TSM) and extracting damage-sensitive features (parameters) from the models. In the field of SHM with VB techniques, autoRegressive (AR) and moving average (MA) models and their variants: AutoRegressive moving average (ARMA), AutoRegressive eXogenous (ARX), etc. have been the most widely used for signals modeling . For damage sensitive features extraction using NP-based tools, machine learning (ML) algorithms have been also used, alone or combined with AR-MA models, i.e., Gaussian Mixture Models (GMM), Principal Component Analysis (PCA), Genetic Algorithm (GA) (Silva et al., 2016).

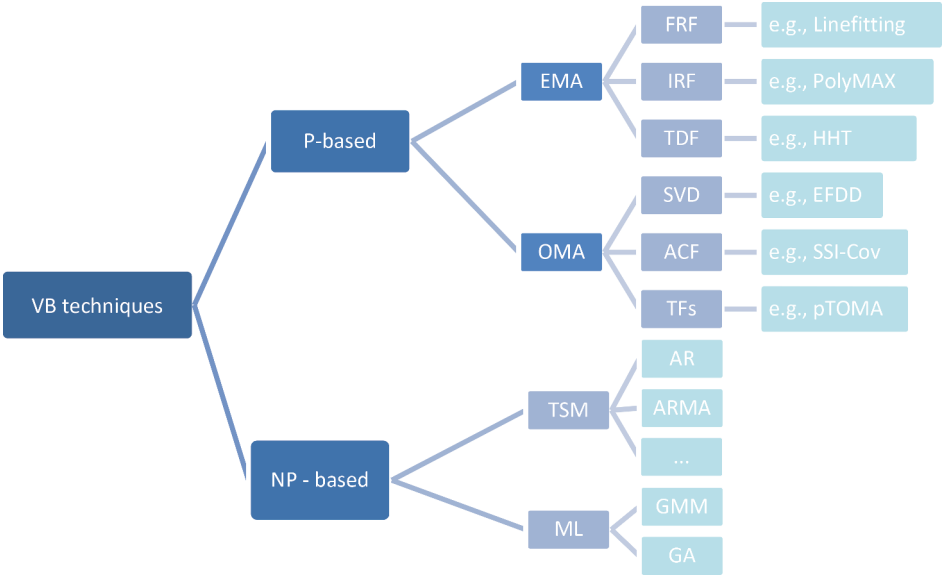


Figure 1. Modal analysis and time series features identification techniques.

Whatever the technique used, the final objective of each of these methods is to be able to detect damage and its level of severity to deduce the actions that must be taken. Thus, after the identification of parameters, the next step is to define indicators based on these parameters, which allows to identify the presence or not of damage and their possible severities for the structures' lifespan. Hence, in the following Table 1, we give some of the defined indicators/criteria in the literature for damage characterization and the performance achieved concerning to detection (D), localization (L), and severity estimation (S). For each of the mentioned indicators in Table 1, we only mentioned the main principle behind the most defined indicators in the literature and the interested reader can find more details in these references: (Silva et al., 2016; Yang et al., 2021).

In the following section, considering bridges' cables, we will discuss damage detection using well-established modal analysis techniques and ARMA-based methods.

Table 1. Damage characterization indicators and criteria from P-based and NP-based methods.

VB technique	Indicators	Definition and performance	Pros (+) and Cons (-)
P-based	Δf_s^d	• Structures' frequencies variation between safe (s) and damaged (d) state. • D, S	+: frequencies are easy to determine and sensitive to damage. -: sensitive to thermal variations
	ΔDR_s^d	• Damping ratios (DR) variation • D (eventually)	-: important variability, difficult to measure
	$\Delta \Phi_s^d$	• Mode shapes variation • D, L, S	+: sensitive to damage, less sensitive to thermal variations -: more difficult to identify, need more sensors
	ΔSE_s^d	• Strain energy (SE) variation • D, L, S	+: Stability when noisy signals -: Not efficient for small damage, need more sensors
	ΔTF_s^d	• Transfer functions variation (transmissibility functions or FRFs) • D, L, S	+: use of a range of frequencies and mode shapes (not only the resonant poles as for the above indicators) -: High computational demand, sensitive to ambient conditions
NP-based	MSD	• Mahalanobis (Squared) Distance between mean values features. • D, S, L	+: ability to identify outliers; use in real scenarios. -: Assume a Gaussian distribution, slow training phase, can be sensitive to operational and environmental variability
	$D_{centroids}$	• Distances of clusters' centroids • D, L, S	+: ability to identify outliers. -: computational cost, and stabilization issues depending on the used algorithm, can be sensitive to operational and environmental variability

2.2 *Experimental setup: Case study*

The above-described techniques were applied to data collected from tests conducted on a bilayer cable. Its geometric and mechanical characteristics are given in Table 2.

Table 2. Geometric and mechanical characteristics of the used bilayer cable.

Cable	Length (mm)	Young's modulus (MPa)	Density (g/cm^3)	Breaking strength (kN)
Bilayer	6230	200	7.8	513

The cable is installed on a load test bench with a capacity of 300 kN and wedge anchor sockets have been used to fasten it to the load test bench with the help of a tensioning hydraulic jack. The loads are applied with an instrumented hammer.

The vibration data are stored as displacements using contact-less laser sensors so that additional masses are not impacting the global mass of the cable. The eight laser sensors are coupled with QuantumX MX 1615B and 1610 data acquisition systems and the CATMAN software. The arrangement of the laser sensors on the cable is shown in Figure 2.

Considering these means, the tests are first done on a safe cable considered as the reference state of the cable and the damage are introduced later by cutting wires gradually in the indicated position in Figure 2. The chosen experimental procedure can then be summarized in these six steps:

- Step 1. Tension of the cable at 30 % of its maximum breaking loads
- Step 2. Lasers and data acquisition systems mounting

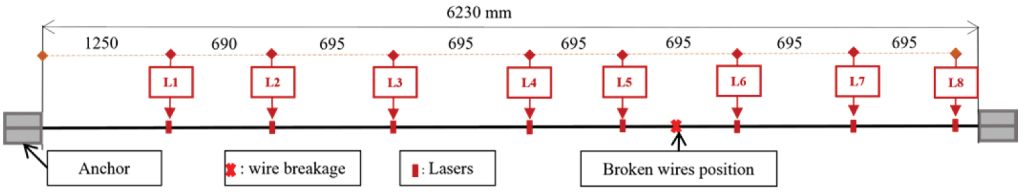


Figure 2. Laser arrangement on bilayer cable.

- Step 3. Excitation of the cable by hammer impacts and data storage at the sampling rate of 300 Hz for 45 seconds. Near each sensor, we repeat the impact four times.
- Step 4. Removal of the acquisition system and introduction of damage (wire breaks)
- Step 5. After a wire break, the tension of the bilayer cable is maintained at its post-breakage values, i.e. the cable is not re-tensioned to the initial tension value.
- Step 6: data analysis.

3 RESULTS COMPARISON AND DISCUSSION

3.1 *Extraction of modal and signal-based parameters*

Either method used, one should make sure that the parameters are correctly extracted from the raw signal. For parametric VB techniques, based on the FRFs curves, the cables dynamic natural frequencies and mode shapes are determined. This step is carried out using the Line-Fitting method (Ewins, 2000) which gives stable results according to modal assurance criterion (MAC) coefficients (for mode shapes) and coefficients of variation (for natural frequencies). The MACs are defined as:

$$MAC(\phi_A, \phi_B) = \frac{\left|\{\phi_A\}^T\{\phi_B\}\right|^2}{\left(\{\phi_A\}^T\{\phi_A\}\right)\left(\{\phi_B\}^T\{\phi_B\}\right)} \tag{1}$$

where ϕ_A and ϕ_B represent mode shapes extracted from data collected under same conditions (e.g., safe) at distinct points A and B on the cable. The coefficients of variation are defined as:

$$C_v(\%) = 100 \times \frac{\sigma_\omega}{\mu_\omega} \tag{2}$$

σ_ω and μ_ω represent the standard deviation and mean of natural frequencies obtained for the same vibration mode from different excitation data.

For non-parametric VB techniques, correct signal modeling is also a must, as from extracted features, will be performed damage characterization. Therefore, before fitting the displacement signal (X) from a sensor with the Python statsmodels module, they are first normalized $(\tilde{X})$:

$$\tilde{X}(t) = \frac{X(t) - \mu}{\sigma} \tag{3}$$

After normalizing the data, we use stationarity tests to ascertain whether further transformations are required to make the time series data stationary (mean, variance and autocorrelation are constant over time). The augmented Dickey-Fuller (ADF) test's p-values are employed for this purpose. The ADF test assesses the null hypothesis that a unit root exists in a time series. If the p-value is less than 0.05, we can reject the null hypothesis and conclude that the time series is stationary.Once the initial data preprocessing is complete, the optimal $ARMA(p, q)$ model order and its coefficients are estimated:

$$\tilde{X}(t) = \sum_{i=1}^{p} \varphi_i \tilde{X}(t-i) + \sum_{i=1}^{q} \theta_i \varepsilon(t-i) + \varepsilon(t) \tag{4}$$

where φ_i and θ_i are the model parameters and ε_i are the error terms.

For the best model order selection, we fit many $ARMA(p, q)$ models with different combinations of values for p and q. The best model is selected according to the Akaike information criterion (AIC), and we assess its viability by analyzing its residuals (difference between actual and modeled values of signals) which should be like white noise: uncorrelated and normally distributed.

Once all these steps have been taken, for P-based and NP-based techniques, we can then proceed to damage characterization.

3.2 *Damage characterization with P-based and NP-based techniques*

Using the natural frequencies thus obtained, we first performed the detection of wire breaks in the bilayer cable with five broken wires. The detection is based on the variation of the natural frequencies between the safe and the damaged cable $\left(C_i^{s-d}(\%)\right)$:

$$C_i^{s-d}(\%) = 100 \times \frac{f_n^s - f_n^d}{f_n^s} \tag{5}$$

In Figure 3, the C_i^{s-d} values increase with the severity of the damage (number of cut wires). This combined with the low variability of the natural frequencies observed with the coefficients of variation ($C_v < 1\%$), we can conclude that these parameters (C_i), of the order of 3% for one cut wire $\left(C_i^{s-1d}\right)$ and greater than 6% for two or more cut wires, allow to detect the presence of damage, whatever the chosen frequency mode.

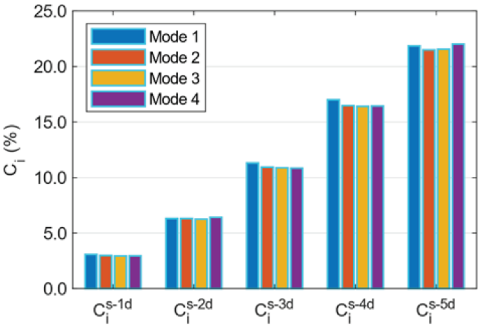


Figure 3. Evolution of C_i^{s-d} coefficients from one (1d) to five (5d) broken wires.

For NP-based analysis, for the same excitation, after choosing the best model order (the optimal values of p and q) based on the data recorded on one sensor, this order is applied to the data recorded on the other seven sensors. Once the best model order is selected and the parameters determined, inspired by the work of (Nair et al., 2006), we contribute by suggesting two new parameters based on damage sensitive features (DSF). The first one (Equation 6) is a generalization of the (Nair et al., 2006) formula, which considered the first 3 AR), by considering the p AR coefficients from the best model, the φ_i in equation 4:

$$DSF_{AR} = \frac{\varphi_1}{\sqrt{\sum_{i=1}^{p} \varphi_i^2}} \tag{6}$$

The second proposed parameter (Equation 7) is based on the q MA coefficients, the θ_i in equation 4. This damage sensitive features are defined as:

$$DSF_{MA} = \frac{\theta_1}{\sqrt{\sum_{i=1}^{p} \theta_i^2}} \tag{7}$$

According to these two parameters, the results for the safe and damaged cable (with 2 to 4 cut wires) are given in Figure 4. From this latter, the DSF_{AR} parameters (at left) do not show any

correlation with the severity of the damage. However, the DSF_{MA} parameters do show an upward trend with increasing damage severity for almost all the sensors (L1 to L8). This suggests that the DSF_{MA} parameters may be a more effective way to detect and quantify damage in cables. Nevertheless, in their current state, these DSF_{MA} factors cannot be used to reliably attest the presence of defects in the cable. Indeed, their variances remain quite high as shown with the error bar for the safe cable values on sensor L1.

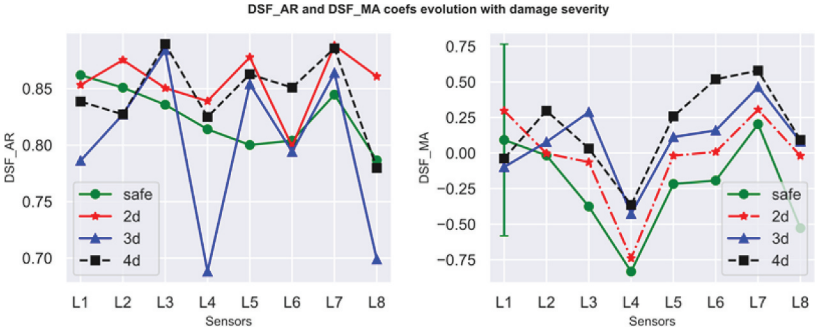


Figure 4. Evolution of damage sensitive features (DSF_{AR} & DSF_{MA}) with damage severity.

These results from DSF show the need to fit all data from each sensor to search for its own best model even if the data are collected from one excitation force and in the same conditions, as each location point of the sensor may have its specificities. Based on this observation, preliminary studies to improve the models are conducted. Each 45-second signal from each sensor is divided into 3-second segments (a total of 15 segments for one sensor signal) and the transformations mentioned in the previous chapter are applied to each of these segments. The results of the ADF stationarity tests show that the p-values are slightly higher than 0.05 for some 3-second segments (see Figure 5). Using $ARIMA(p, d, q)$ modeling techniques the best model is found for each of these stabilized chunks. The $ARIMA(p, d, q)$ models add the integration order d in the process to make time series stationary. The preliminary results are promising as shown in Figure 6. As with Figure 4, these results shows also that DSF_{MA} values are more suitable for damage characterization as the Euclidian distance between DSF_{MA} of safe and damaged cable is superior to that between DSF_{AR} values.

4 CONCLUSION

This study emphasizes the significance of vibration-based methods in ensuring bridge structural integrity, offering a comprehensive and concise review of modal parametric and non-parametric approaches. Through a case study on cables, while modal parametric methods

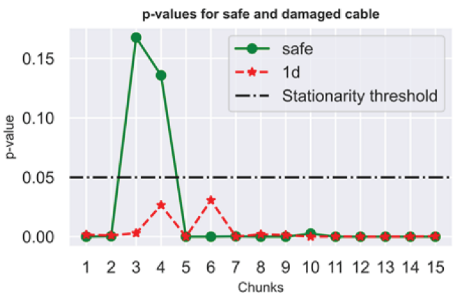


Figure 5. P-values of signal chunks.

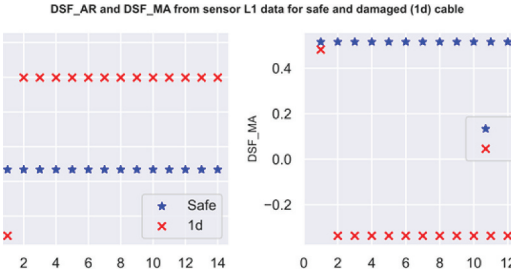


Figure 6. DSF_AR and DSF_MA values for each L1 data chunk.

exhibit sensitivity to damage severity, non-parametric techniques, especially those based on moving averages coefficients (DSF_{MA}), show promise in capturing damage trends, better than those based on autoregressive ones. This new suggested parameter improved the results and contribute to the stat of arts in this field. However future ongoing research will focus on refining non-parametric methods modeling, considering sensor location specificity, and exploring hybrid approaches. Extending the study to diverse structural components and real-world applications will further validate and enhance the practicality of these approaches in advancing bridges' structural health monitoring.

REFERENCES

Avci, O., Abdeljaber, O., Kiranyaz, S., Hussein, M., Gabbouj, M., & Inman, D. J. (2021). A review of vibration-based damage detection in civil structures: From traditional methods to Machine Learning and Deep Learning applications. In *Mechanical Systems and Signal Processing* (Vol. 147). Academic Press. https://doi.org/10.1016/j.ymssp.2020.107077.

Brincker, R., Ventura, C. E., & Andersen, P. (2001). Damping estimation by frequency domain decomposition. *Proceedings of the International Modal Analysis Conference - IMAC*, *1*, 698–703.

Cremona, C. (2005). Qu'est-ce qu'une évaluation dynamique ?. *Revue Européenne de Génie Civil*, *9*(1–2), 11–42. https://doi.org/10.1080/17747120.2005.9692745.

Das, S., Saha, P., & Patro, S. K. (2016). Vibration-based damage detection techniques used for health monitoring of structures: a review. *Journal of Civil Structural Health Monitoring*, *6*(3), 477–507. https://doi.org/10.1007/s13349-016-0168-5.

Dia, A., Dieng, L., & Gaillet, L. (2021). Vibration-based non-destructive techniques for a 3-level characterization of damages in cables. *Conference Proceedings of the Society for Experimental Mechanics Series*. https://doi.org/10.1007/978-3-030-47709-7_16.

Dieng, L., Périer, V., Gaillet, L., & Tessier, C. (2009). Mécanismes de dégradation et moyens de protection des câbles du génie civil. *Mécanique & Industries*, *10*(1), 33–42. https://doi.org/10.1051/meca/2009030.

Ewins, D. J. (2000). *Modal testing: theory, practice, and application*. (R. S. Press, Ed.; 2nd ed.). Research Studies Press.

Nair, K. K., Kiremidjian, A. S., & Law, K. H. (2006). Time series-based damage detection and localization algorithm with application to the ASCE benchmark structure. *Journal of Sound and Vibration*, *291*(1–2), 349–368. https://doi.org/10.1016/j.jsv.2005.06.016.

Orlowitz, E., & Brandt, A. (2017). Comparison of experimental and operational modal analysis on a laboratory test plate. *Measurement*, *102*, 121–130. https://doi.org/10.1016/j.measurement.2017.02.001.

Peeters, B., & Roeck, G. De. (2001). Stochastic system identification for operational modal analysis: A Review. *Journal of Dynamic Systems, Measurement and Control, Transactions of the ASME*, *123*(4), 659–667. https://doi.org/10.1115/1.1410370.

Rainieri, C., & Fabbrocino, G. (2014). Output-only Modal Identification. In *Operational Modal Analysis of Civil Engineering Structures: An Introduction and Guide for Applications*. (pp. 103–210). Springer New York. https://doi.org/10.1007/978-1-4939-0767-0_1.

Rytter, A. (1993). *Vibrational Based Inspection of Civil Engineering Structures*. Dept. of Building Technology and Structural Engineering, Aalborg University.

Silva, M., Santos, A., Figueiredo, E., Santos, R., Sales, C., & Costa, J. C. W. A. (2016). A novel unsupervised approach based on a genetic algorithm for structural damage detection in bridges. *Engineering Applications of Artificial Intelligence*, *52*, 168–180. https://doi.org/10.1016/J.ENGAPPAI.2016.03.002.

Tseng, K. K. H., & Naidu, A. S. K. (2002). Non-parametric damage detection and characterization using smart piezoceramic material. *Smart Materials and Structures*, *11*(3), 317. https://doi.org/10.1088/0964-1726/11/3/301.

Weijtjens, W., De Sitter, G., Devriendt, C., & Guillaume, P. (2014). Operational modal parameter estimation of MIMO systems using transmissibility functions. *Automatica*, *50*(2), 559–564. https://doi.org/10.1016/J.AUTOMATICA.2013.11.021.

Yan, W. J., Zhao, M. Y., Sun, Q., & Ren, W. X. (2019). Transmissibility-based system identification for structural health Monitoring: Fundamentals, approaches, and applications. *Mechanical Systems and Signal Processing*, *117*, 453–482. https://doi.org/10.1016/J.YMSSP.2018.06.053.

Yang, Y., Zhang, Y., & Tan, X. (2021). Review on Vibration-Based Structural Health Monitoring Techniques and Technical Codes. *Symmetry 2021, Vol. 13, Page 1998*, *13*(11), 1998. https://doi.org/10.3390/SYM13111998.

Bridge Maintenance, Safety, Management, Digitalization and Sustainability – Jensen, Frangopol & Schmidt (eds)
© 2024 The Author(s), ISBN 978-1-032-77040-6
Open Access: www.taylorfrancis.com, CC BY-NC-ND 4.0 license

Limits of digital twin modelling

Andre Beigel & Alfred Strauss
University of Natural Resources and Life Sciences, Vienna Department of Civil Engineering and Natural Hazards, Vienna, Austria

Dan M. Frangopol
Lehigh University, ATLSS Engineering Research Center, Bethlehem, PA, USA

Maosen Cao
Hohai University, Nanjing, China

ABSTRACT: Digital models are often only used in the construction process of a structure and lose their meaning after completion. The goal is to continue to use these models during the operational phase and for maintenance, to generate added value from them. The continuous use of a digital model as a digital twin is a viable approach to specifically analyze the relevant structure components and simulate effects from changing conditions such as the long-term behavior of the structure. However, the development of numerical digital twins reaches its limits very easily due to a lack of information about boundary conditions or material properties and their development over time as well as the lack of suitable monitoring systems. In this study, the development of a digital twin of a tunnel profile is presented, in which analyses regarding suitable monitoring systems for the SLS and ULS behaviour of the profile were also carried out. It was also of particular interest to show the added value that can be generated by the detailed digital twin in terms of safety or safety formats.

1 INTRODUCTION

In infrastructure sector, planners and operators invest a lot of time and money in the creation of analysis models to document the design of tunnels and rock drives and to carry out simulations. However, once the construction phase is complete, construction models are often only used to a very limited extent. An important goal is to continue using these highly complex models as digital twins during the operating phase for monitoring and maintenance. In particular, any extensions or changes can be effectively considered in the existing models. By using a virtual model in parallel as a digital twin during operation, all important structural elements can be visualized and specific calculations can be carried out. In addition, a detailed understanding of the long-term behavior of the structural and functional components of e.g. tunnels and the rock formations during operation is obtained. This allows new scenarios to be simulated and more targeted measures to be taken before damage occurs. In addition, a proof load can be carried out to reduce the model uncertainty of the structural behavior. It enables robust statements about structural safety, the interaction of structural elements, the influence of damages and the effectiveness of previous repair measures (Model Code 2020).In cooperation between the University of Natural Resources and Life Sciences, Vienna, the Austrian Federal Railways and the Vienna University of Technology, a test load was applied to a tunnel pilot using a combination of modern monitoring systems (Strauss et al., 2020, Strauss et al., 2018, Neuner et al., 2022, Strauss et al., 2022, "MONTUN" project). Based on these findings, the opportunities, challenges and limitations of digital twins are highlighted. In this project, the digital twin was set up as a non-linear finite element model and analyzed with the measurement results of the test loads.

DOI: 10.1201/9781003483755-90

As indicated previously, the monitoring systems play a very important role in the development of digital twins. Therefore, in the first phase of the project, monitoring systems were put into operation under laboratory conditions and subjected to various test procedures. The focus was on determining the noise level, identifying possible drift phenomena and recording processes as well as the influence of magnetic fields. The second phase comprised the installation of the measuring systems in the tunnel-like test pilot in the outdoor area. For this purpose, a so-called mouth profile with a length of 2.7 m, an opening of around 2 m and a total weight of 9.5 tonnes was designed and built. This phase was divided into a long-term monitoring study, which lasted around three months, and a short-term capacity study. In the long-term study, the long-term stability of the monitoring systems and the influence of atmospheric parameters and weather conditions were analysed. The accuracy in detecting changes in the range of a few tenths of a millimetre up to 1.5 cm was quantified by means of a proof loading of the mouth profile. A laser tracker and a total station served as reference measuring systems. Based on various criteria for accuracy, robustness, technical and economic cost estimation and expertise, the monitoring systems were evaluated and further recommendations were formulated, including the setup of the digital twin. Overall, all these procedures, including the analysis of the monitoring system, were used to create and gradually optimise the digital twin of the mouth profile and to check its suitability for extended safety formats.

2 CHARACTERISTICS OF THE DIGITAL TWINS

2.1 *General details*

This study presents the design of the digital twins with the measurement systems in the tunnel-like test pilot in the outdoor area. The details of the preliminary laboratory tests on the monitoring systems used to set up the digital twins are reported in Neuner et al. (2022). A reinforced HABA concrete profile 3600mm/2250mm was used as the tunnel test pilot, see Figure 1(a). The pilot profile was manufactured according to ÖNORM EN 1916 and ÖNORM B5074 and has a similar geometry to real tunnel profiles. In order to reduce the bending stiffness of the profile and allow to induce significant deformations, the cross-section was configured with slots measuring 30 cm in depth and 20 cm in width, strategically placed in the crown region as well as the upper and lower strut areas. The load was applied in stages via tension rods and hydraulic cylinders running through the cross-section, see Figure 1(a).

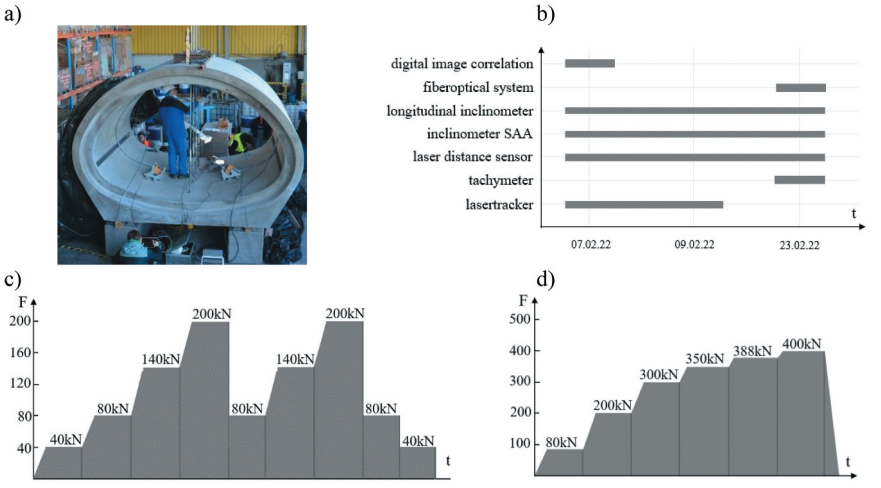


Figure 1. Characteristics of the tunnel digital twins, a) test object, b) chronological overview of the monitoring systems, c) load plan 09.02.22 and d) 23.02.22.

2.2 *Proof loading procedures*

The proof loading procedures on the tunnel pilot was carried out on a total of three different days. Figures 1(c) and 1(d) present the proof loading steps/plan from 9 February 2022 and 23 February 2022. In order to record the pilot reaction in a comprehensive manner, various monitoring systems were used. An overview of the use of the monitoring systems during the test period is shown in Figure 1(b). The load test on 7 February 2022 was carried out with a maximum load of 80 kN (4 x 20 kN threaded rod load), with the main objective being to record the response of the elastic system and the profile stiffness information to create the digital twin. The load test on 9 February 2022 was carried out with a maximum load of 200 kN (4 x 50 kN threaded rod load) (Figure 1(c)). The load configuration with load cycles was intended to generate a non-elastic system reaction and initiate cracks in order to compare the occurring behavior and the existing crack distribution with the NLFEM. In addition, the ability of the measurement systems used to detect cracks and plastic deformations, which are also of great importance for the alignment of digital twins, was investigated. Visible cracks on the inside and outside of the profile occurred at approximately 120 kN.

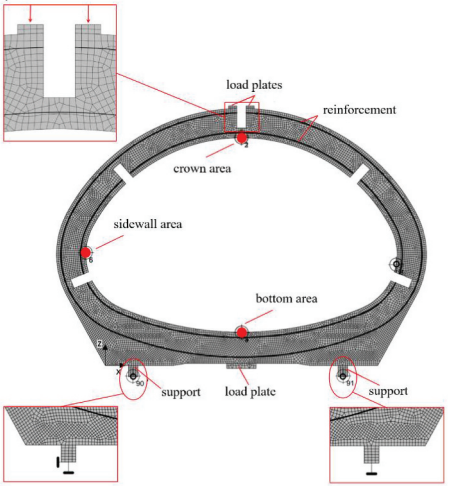
The aim of the test on the last day, 23 February 2022, was to generate high deformations and thus initiate significant cracks in the profile in order to validate the digital twin in the area of load-bearing capacity. Therefore, it was analyzed to what extent the states of reduced stiffness characterized by local bending stresses can be simulated with the NLFEM and what accuracies can be achieved.

3 MODELLING OF DIGITAL TWINS

3.1 *General details*

A dual modelling approach was chosen to create the digital twin of the tunnel twin pilot. On one hand, a replica of the mouth profile was created using a digital 2D model of non-linear finite elements and, as a second approach, the model was reproduced using a non-linear 3D twin of finite elements. This two-part procedure was chosen to gain an understanding of the important elements in the development of the digital twin in the first phase and to analyse the model update procedure using the monitoring information in 2D and then transferring it to the 3D model. The focus of the presented analysis is on the 2-dimensional modelling and the chances and limitations. The primary aim of the modelling was, in a first step, to simulate the load paths resulting from the circula proof loading and to compare these model results with

a)



b)

Parameter	Value
f_{cu}	50 MPa
Young modulus E	30000 MPa
Poisson-ratio μ	0,2
Tension strength f_t	3,598 MPa
Compressive strength f_c	-39 MPa
Fracture energy (MC2010)	$1{,}237*10^{-4}$ MN/m

Material	Model
concrete	non-linear 3D cement model plane deformation state
reinforcement	linear material model

Figure 2. Details of the digital twin models, a) boundary conditions and b) material parameters.

the results of the monitoring systems, for which the ATENA Science software from Červenka Consulting (Červenka et al., 2013) was used. Subsequently, the crack formation developments were also included in the modelling of the digital twin.

A common first step in digital twin modelling is the definition of the geometric boundary conditions and the material parameters. An overview of the defined boundary conditions of the supports, the geometry and location of the reinforcement (solid black lines) as well as a first approximation of the loading type of the model can be seen in Figure 2(a). The concrete material was modelled using the non-linear 3D cement model in ATENA 2D and plane strain properties, a bi-linear material model was used for the reinforcement, as is generally the case. An overview of the selected material models, parameters and values is given in Figure 2(b).

3.2 *Updating processes*

Additional steps were necessary in addition to the classic procedure of updating the model of the material properties and support conditions, for example using sequential updating procedures or sensitivity analyses (Figure 3). As the position of the reinforcement and the load shape have a major influence on the simulation results, additional geometric adjustment steps were necessary. For example, the geometric positions of the circumferential reinforcement in the profile and the depth of the cut-outs in the crown area and in the side wall areas of the profile were updated. An essential part of the construction of the digital twin was also to model the proof load application effectively and realistically in order to be able to simulate the load paths resulting from the test days. To this end, various approaches to load application (force- and displacement-controlled) were analysed and a model update was carried out. The data from the laser tracker and total station monitoring systems from the various load phases served as a reference for the modelling results.

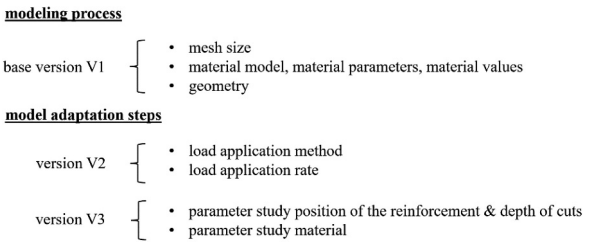


Figure 3. Digital twin, process of modeling.

Figure 4(a) shows the analyzed load scenarios with (1) the force-controlled approach, (2) the displacement-controlled approach and (3) the approach with two externally applied tendons, whereby a displacement-controlled variant with temperature loading and a force-controlled loading approach with a prestressing force were investigated. For the planned analyses of the load paths, the approaches must also fulfill the possibility of precise load control and effective analysis in addition to the results obtained. Due to the fact that no maximum load levels can be precisely simulated with the displacement-controlled load approaches, only the force-controlled approaches meet the requirements. With displacement-controlled approaches, it is not possible to control load levels without manual intervention and adjustment of the displacement variable, which leads to a more time-consuming simulation and makes automated sensitivity analyses significantly more complicated. In the process of modeling, it became clear that the forming inner lever arm between the reinforcement and the lower edge of the cut-outs has a considerable influence on the model behavior. Since the exact position of the reinforcement on the test object could not be clearly localized on site, parametric studies were carried out with various lever arm enlargements. For this purpose, concrete elements were modeled in the cuttings, which serve to enlarge the lever arm (Figure 4(b)). For these concrete elements, the modulus of elasticity is scattered in a range of 10000 N/mm² -

40000 N/mm², which causes the lever arm to be activated at high values or to drop out at low modulus of elasticity.

The simulation analyzed below is based on the force-controlled loading approach using two externally applied prestressed tendons, whereby the prestressing force is increased in predefined steps. By specifically controlling the desired maximum load, load cycles such as those carried out as a result of the test load on 09.02.2022 (Figure 1(c)) can be simulated and any non-elastic system reactions that occur can be investigated. In addition, this loading approach best reflects the test setup by directly coupling the crown and base areas of the cross-section.

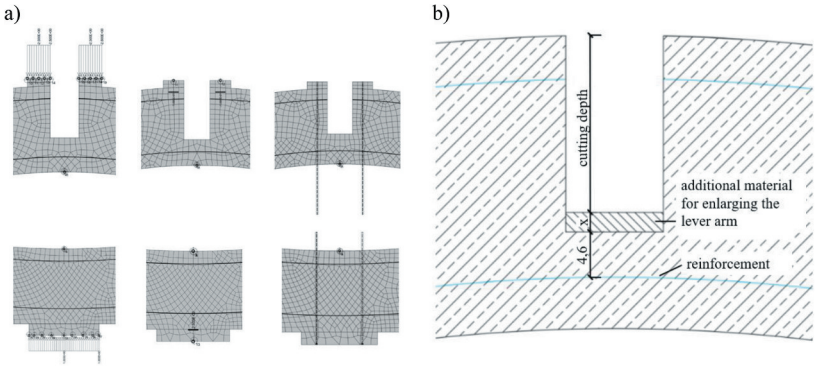


Figure 4. Updating of the a) load scenarios and b) lever arm.

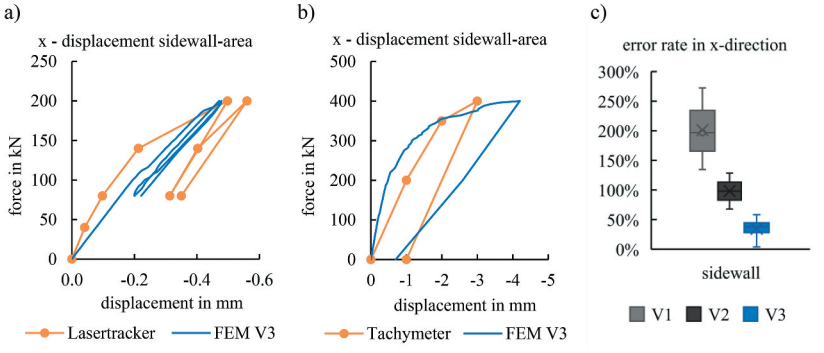


Figure 5. Findings in the horizontal displacements in the sidewall area a) 09.02.2022 and b) 23.02.2022 and the error rate in this area.

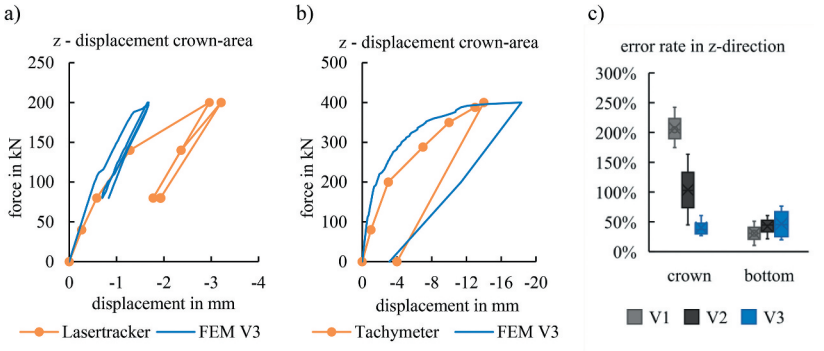


Figure 6. Findings in the vertical displacements in the crown area a) 09.02.2022 and b) 23.02.2022 and c) the error rate in this area.

3.3 *Findings*

The results of the simulation are compared below with the results of the reference monitored values and their percentage deviation per simulation version is shown. As shown in Figure 3, Version 1 represents the basic version of the simulation. Version 2 corresponds to the modelling with updated load model and version 3 represents the digital twin with updated lever arm distance and material parameters.

The horizontal displacements in defined areas of the profile were of great interest in connection with the deformation of the profile. Detailed information about the deformation behavior of the profile along the entire load path was generated. Of particular interest was the possible formation of yield joints or rigid body movements. Figure 5 displays the results of the horizontal displacements in the side wall area of the simulation and reference from (a) 9 February 2022 and (b) 23 February 2022. It can be seen that the deviations of the digital twin from the reference measurement of the laser tracker are very small and therefore very good results were achieved. The model behavior in Figure 5(a) is slightly less rigid than the real deformation. The unloading and reloading paths show a good correlation with the measurement results. A stiffer model behavior can be seen in Figure 5(b), whereby the stiffness only decreases in the high load range. Figure 5(c) shows the deviations from the reference for each simulation version along the load paths. It can be seen that a significant increase in accuracy was achieved by updating the model from Version 1 to Version 3.

Apart from the horizontal displacements in the areas of interest, the vertical displacements were also of great importance for the model update. Figure 6 shows the vertical displacements in the crown area as a force-displacement diagram from (a) 09.02.2023 and (b) 23.02.2022. It can be seen, that in Figure 6(a) the deviations of the FE simulation from the reference measurement at a load of 140 kN ranges in the tenth of a mm. The highest deviation of 1.28 mm occurs at 200 kN. After the first unloading to 80 kN, a plastic deformation can be recognized. The calculated gradient of the unloading and reloading paths correlates very well with the measured values. The simulation of the load path up to 400 kN shows a slightly stiffer model behavior compared to the reference. A larger model deformation is recognizable in the high load range. Figure 6(c) shows the deviations from the reference for each simulation version along the load paths. Similar to the results in the horizontal direction, it is recognizable that with a continuous model update both the error size and the range of the errors occurring could be reduced.

4 LIMITS OF DIGITAL TWIN MODELING

4.1 *General aspects regarding the level of approximation*

All digital models used to calculate individual elements or complex structures represent an approximation of the real behavior of the studied object. These simplifications can be categorized into different levels of accuracy. The level of approximation approach is a step-by-step design strategy in which the accuracy of a model output is gradually improved through refined physical parameter inputs (Model Code, 2020). Applied to the modeling presented here, initial estimates using analytical formulas can represent the first level of accuracy. The next level of accuracy is the numerical calculation using non-linear finite element modeling. By refining the load application as well as geometry and material updates, the modeling can be categorized in the third accuracy level. A possible increase in accuracy is the extension to a probabilistic analysis. Figure 7 compares these steps with the time required for information gathering, model building as well as calculation and the achievable accuracy. The information on accuracy and time expenditure may vary from project to project and represents an expert estimate. An increase in accuracy is accompanied by an increase in effort, therefore the curve flattens out, reflecting the low information gain with constantly increasing time input.

4.2 *Limitations*

However, each model update must be assessed critically, as a model update does not automatically lead to an increase in accuracy. The evaluation of the various simulations has shown, for

example, that a refinement of the loading approach does not necessarily lead to a better output (Figure 6(c)). Basically, models are optimized for areas of particular interest, in terms of either location or load range. It should also be mentioned that the 2D modeling can be limited regarding the level of detail (Figure 8). As a result of the test load, significant cracks appear in the inner area of the crown area between the holes of the threaded rods. This aspect cannot be simulated in the 2D model due to the lack of dimension. If these holes, which act as weak points, are not taken into account in the simulation, a large number of hairline cracks occur at this point in the 2D simulation. A 3D simulation with simulated discontinuities removes this limitation and could be relevant for subsequent installations in building structures. As modelling and digital twins become increasingly refined, the number of detailed questions that can only be answered with assumptions in the modelling increases. In these cases, the effort no longer increases linearly, but almost exponentially, as, for example, not only the actual condition of the structure, but also the historical, e.g. curing, creep and shrinkage conditions, must be considered.

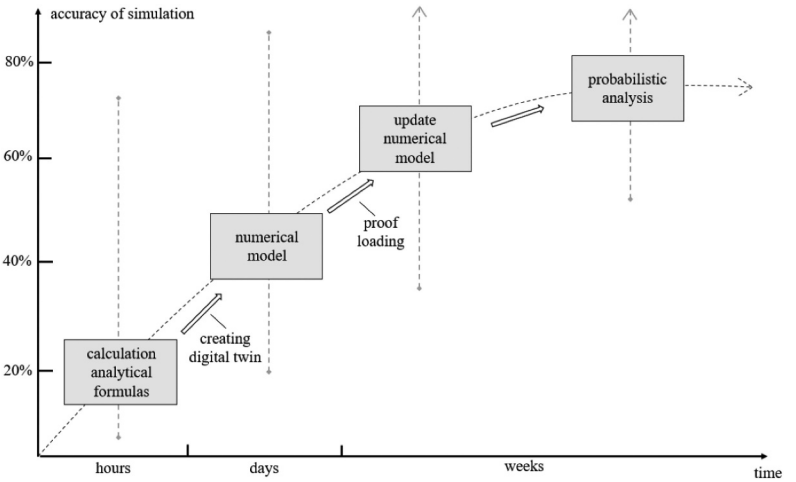


Figure 7. Level of approximation approach, time expenditure of information gathering, model building & calculation.

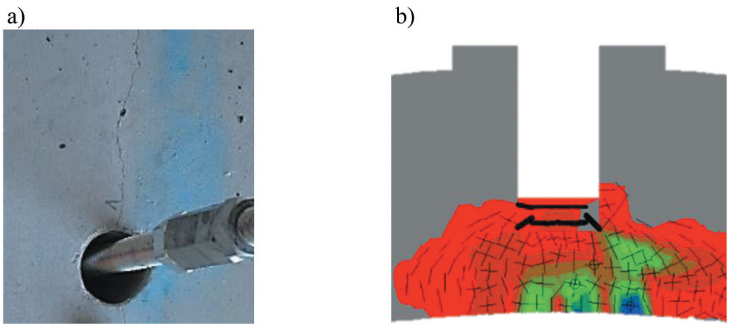


Figure 8. Model uncertainties due to crack distribution in a) in reality versus b) 2D-digital-twin versus.

4.3 *Modeling vs. extended safety formats*

The digital twins, which have been developed in this research with varying degrees of complexity, were used to determine the increase in reliability and safety associated with the modelling effort. In the case of the tunnel digital twin profile, there was an increasing capacity growth, which can

be seen in Table 1, but this may not always be the case. As with structurally unstable systems, an increasing level of modelling complexity can also lead to a reduction in load-bearing capacity.

Table 1. Computed reliability index in terms of the level of detailing of the digital twin.

	Analytical model	Numerical model (FORM)	Updated numerical model (FORM)	Probabilistic model
Reliability Index	4.7	5.3	5.4	5.7
Time	hours	days	days	weeks

5 CONCLUSIONS

By means of a tunnel pilot equipped with several monitoring systems, it was shown how the development of a digital twin is not a simple optimisation process, e.g. in the material parameters and support conditions. The chosen proof loading concept and the extensive monitoring concept made it possible to show that the digital twin development requires a complex interaction between modelling and system responses via different loading regimes. It was also possible to show the time required for modelling at different levels of detail vs. the changes in the reliability level and safety format.

ACKNOWLEDGEMENTS

The authors thank the ÖBB Infra for funding the MONTUN Research Project. The authors also thank the Czech Science Foundation, Czech Republic, under MAPA project number 22-00774S.

REFERENCES

Beigel, A. 2023. Digitale Zwillinge und Sensorüberwachung für alpine Ingenieurbauwerke: Anwendung auf Tunnels. Vienna, Universität für Bodenkultur.

Červenka, V. Jendele, L. & Červenka, J. 2013. ATENA Program Documentation, Part I, Theory, Czechia: Červenka Consulting

fib Model Code 2020, "Model Code for Concrete Structures", (under review), 2022

Neuner, H., Kostjak, V., Linzer, F., Loderer, W., Seywald, C., Strauss, A., Rigler, M. & Polt, M. 2022. Assessing Deformation Monitoring Systems For Supporting Structural Rehabilitation under Harsh Conditions. EGU General Assembly 2022. Vienna.

Strauss, A., Neuner, H., Rigler, M., Polt, M., Seywald, C., Kostjak, V., Linzer, F. & Loderer, W. 2022. Verification of the performance of reinforced concrete profiles of alpine infrastructure systems assisted by innovative monitoring. EGU General Assembly 2022. Vienna.

Strauss, A., Beigel A., Sattler, F., Täubling-Fruleux, B., Seywald, C., Neuner, H., Kostjak, V., Frangopol, D. M. 2023. Digital Twins and Sensor Monitoring for Alpine Engineering Structures: Applications for Tunnels. Life-Cycle of Structures and Infrastructure Systems, 4100–4106.

Strauss, A., Sattler, F., Täubling-Fruleux, B., Seywald, C., Neuner, H., Kostjak, V., Frangopol, D. M. 2023.Sensor monitoring for engineering structures: Applications to tunnels. Life-Cycle of Structures and Infrastructure Systems, 1737-1744.

Montun-report, Entwicklung von Monitoringsystemen für das geotechnische Sicherheitsmanagement bei Erneuerungsmaßnahmen unter Bahnbetrieb,(under review),2023

Spyridis, P. & Strauss, A. 2020. Robustness Assessment of Redundant Structural Systems Based on Design Provisions and Probabilistic Damage Analyses. Buildings, 10, 213.

Zimmermann T., Strauss A., Bergmeister K. 2012. Structural behavior of low-and normal-strength interface mortar of masonry. Materials and Structures/Materiaux et Constructions, 45 (6), pp. 829–839, DOI: 10.1617/s11527-011-9801-2

Zimmermann T., Strauss A., Bergmeister K. 2010. Numerical investigation of historic masonry walls under normal and shear load. Construction and Building Materials, 24 (8), pp. 1385–1391, DOI: 10.1016/j.conbuildmat.2010.01.021

Bridge Maintenance, Safety, Management, Digitalization and Sustainability – Jensen, Frangopol & Schmidt (eds)
© 2024 The Author(s), ISBN 978-1-032-77040-6
Open Access: www.taylorfrancis.com, CC BY-NC-ND 4.0 license

Vehicle impacts on reinforced concrete railway bridges

Michael Reiterer
REVOTEC gmbh, Department of Structural Dynamics, Vienna, Austria

Alfred Strauss & Benjamin Täubling
Vienna Department of Civil Engineering and Natural Hazards, University of Natural Resources and Life Sciences, Vienna, Austria

Dan M. Frangopol
Lehigh University, ATLSS Engineering Research Center, Bethlehem, PA, USA

ABSTRACT: In many European cities there are a considerable number of railway bridges with a minimum height above road overpasses. The number of impacts increases on these road overpasses, which automatically results in the closure of the railway operation. A procedure supported by non-linear finite element analysis (NLFEA) and monitoring systems has been developed which, through a detailed analysis of the impact energy, the impact effects, and the structural resistance behaviour, identifies the actual impact value that has occurred and determines the impact limit value that triggers the closure of the railway operation. Finally, guidelines can be proposed for calculating the impact limit values and the arrangement of intelligent monitoring systems to prevent interruptions to operations.

1 INTRODUCTION

One major problem with railway bridges is the impact of vehicle induced collision events on the superstructure, e.g. on reinforced concrete slabs or girder systems, as this usually leads to a temporary suspension of train operations in accordance with the provisions of railway law and a closure of the bridge. In the event of an vehicle impact, the bridge and its operation can only be released in accordance with the current alarm chain after a police report and visual inspection by a bridge expert, which can take a significant amount of time. In view of the increasing train traffic and also the very high frequency on the routes of the Trans European Network (TEN), the impact events and also the current alarm process chain are a relevant restriction and can lead to very large impairments of the railway lines. Impact processes are increasingly occurring in inner-city areas where the clearance heights are usually kept to the minimum permitted by law, which is not always in agreement with the railway operator. As surveys show, such bridge objects are not uncommon, as there are often complex interrelationships with other infrastructure systems. The obvious question is therefore whether there are monitoring systems that make it possible to prove the actual energy and shock input due to a vehicle impact and thus have a good basis for deciding whether railway traffic can continue to operate after an impact on the railway structure or whether operation must be interrupted and the classic alarm and testing process chain initiated. The surveys carried out have shown that monitoring systems for recording impact loads on railway bridges are not conventional or documented, as there is also a risk of the monitoring system failing. In-depth NLFEM analyses and dynamic test loads were therefore proposed in detailed discussions with experts in order to specify the possibilities of monitoring and also to determine those areas and components of the bridges in which the energy input of an impact can best be determined. The executed bridge specific bearings and regions around were characterised as the most suitable for determining the energy input from a vehicle impact and are identified as potential zones for the characterization of key performance indicators that can be monitored. The aim of this paper is to present the

DOI: 10.1201/9781003483755-91

initial results and procedural steps of the analytical and numerical investigations carried out, which enable the impact problem on railway bridges and the associated alarm process chain to be re-evaluated from a holistic system perspective.

2 MOTIVATION

Vehicle impacts on the superstructure of railway bridges occur particularly in urban areas in those cases where the permissible clearance height of driving road vehicles is not maintained (Schönfeld 2015, Ozdagli et al 2020). If vehicles collide with the superstructure of a railway bridge, structural damages are expected and thus, an immediate report is always made to the person responsible for the maintenance of the bridge structure, who in the first step orders the train traffic to be blocked. Hence, vehicle impacts on railway bridges currently lead to an immediate blockage of train traffic and thus to a restriction in route availability, regardless of the intensity of the impact. In this study information about the extent to which structural damage and/or permissible object-specific bearing forces occur on railway bridges as a result of a vehicle impact is obtained by carrying out "quasi-static" numerical calculations of the impact on a railway bridge. Exceeding the object-specific bearing forces is defined as decisive and in these cases, blockage of the train traffic is necessary. The aim is therefore to determine whether, for an existing railway bridge in Austria on route 2052, km 13.011, assuming a vehicle impact defined in accordance with current standards, the structural damage and/or bearing forces reach values that affect the railway bridge to continue to be used for train traffic. In addition, "quasi-static" impact calculations with increased impact loads are also to be carried out, from which the permissible sizes of the impact loads or impact forces specific to the considered bridge are determined. From the results obtained an assessment is made with regard to any necessary measures or unrestricted release for train traffic after an impact event occurs. For the Austrian Federal Railways as contracting body of the research project, the implementation of the research results has the advantage that impact events on railway bridges are assessed with regard to structural damage and/or exceeding permissible bearing loads and that measures such as the closure of the railway route are not necessary in all cases, i.e. availability of the route remains unrestricted even after an impact event.

3 NATIONAL AND INTERNATIONAL REGULATIONS

3.1 *National regulations*

The analysis and assessment of vehicle impact on the superstructure of railway bridges is regulated in the following national standards:

- ÖNORM EN 1991-1-7, Eurocode 1 - Actions on structures, Part 1-7: General actions - Extraordinary actions, edition: 2014-09-01.
- Background Document Eurocode 1, Part 1.7, Accidental Actions, January 2005.
- Designers' Guide to Eurocode I: Actions on Bridges. EN 1991-2, EN 1991-1-1, -1-3 to -1-6 and EN 1990 Annex A2.

Table 1. Equivalent static design forces due to vehicle impact on superstructures of railway bridges according to ÖNORM EN 1991-1-7.

Category of traffic	Equivalent static design force F_{dx} [a]
	kN
Motorways and country national and main roads	500
Country roads in rural area	375
Roads in urban area	250
Courtyards and parking garages	75

[a] x = direction of normal travel.

ÖNORM EN 1991-1-7 define the equivalent static design forces due to vehicle impact on superstructures of railway bridges as listed in Table 1. Impact calculations needs to be carried out on bridges with a clearance height of ≤ 6 m. It is seen from Table 1, that the equivalent static design force of F_{dx} = 250 kN must be applied for the category roads in urban areas, which is the suitable category for the railway bridge considered in this study.

3.2 *International regulations*

International regulations regarding the assessment of vehicle impact on the superstructure of railway bridges are:

- UIC-KODEX 777-1, Measures to protect railway bridges against impacts from road vehicles, and to protect rail traffic from road vehicles fouling the track (in German), 2nd Edition, June 2002
- DIN 1055-9, Actions on structures - Part 9: Extraordinary actions, Edition: 2003-08.
- Swiss Guideline, Impact of road vehicles on structural parts of engineering buildings (in German), Extension to Code SIA 261, Edition 2005

UIC 777-1 define the vehicle impact loads to be applied for overelevated vehicles with 500 kN in horizontal direction (driving direction) and 250 kN in vertical direction. With respect to urban areas the size of the impact load in horizontal direction is two times higher than the load defined in ÖNORM EN 1991-1-7, but UIC 777-1 does not distinguish between road categories. According to UIC 777-1 no impact calculation needs to be carried out on bridges with a clearance height of more than 6 m, i.e. this regulation is identical with ÖNORM EN 1991-1-7.

DIN 1055-9 defines the size of the "quasistatic" impact load for so-called frontal crash with 1000 kN for the category country roads in rural area, which is around 4 times higher than the value defined in ÖNORM EN 1991-1-7, see Table 1.

3.3 *Discrepancy of regulations in standards and mechanical impact equations*

As shown in section 4, the design forces according to national and international regulations are low in comparison to the result obtained by evaluating the mechanical impact. The discrepancy of mechanical impact equations and regulations in current standards needs deeper research.

4 THEORETICAL BACKROUND TO VEHICLE IMPACT LOADS

The impact of vehicles on the superstructure of railway bridges represents a shock-like load, where the size of the resulting interaction force (impact force) F_S depends on the impact mass (vehicle mass) m_F, the vehicle speed v_F, the impact duration Δt and the vehicle stiffness k_F. Annex C of ÖNORM EN 1991-1-7 specifies an analytical calculation method for determining the interaction forces (impact forces) F_S resulting from a vehicle impact, and a distinction is made between an impact as a "hard" and a "soft" impact. According to ÖNORM EN 1991-1-7 an impact is referred to as a "hard impact" if the impact energy is mainly dissipated by the impact object (vehicle). A "soft impact", on the other hand, is characterized by the fact that the object (railway bridge) that is impacted deforms and thereby absorbs impact energy and then dissipates it. In the case of railway bridges, however, the supporting structure itself only deforms negligibly in the direction of impact, and therefore the "hard impact" is considered to be decisive. The reality, however, will lie between a "hard" and a "soft" impact, since in the case of a structure supported on elastomeric bearings, a horizontal deformation of the bridge structure will take place and the impact energy will be partly dissipated. Assuming "hard" impact is on the safe side, the energy dissipation occurs exclusively through the impact object (vehicle).

Annex C of ÖNORM EN 1991-1-7 states that in the event of a hard impact, the equivalent static (quasistatic) forces according to Table 1 may be applied. Alternatively, a dynamic approximation calculation can be carried out using a simplified mechanical impact model, and this approximation procedure is presented for the "hard" impact.

In the event of a "hard" impact, the structure to be impacted is assumed to be completely rigid, i.e. there is no energy dissipation through the structure, while the impact object deforms

"linearly" and dissipates the impact energy. The maximum dynamic interaction force (upper limit) is expressed as:

$$F_S = v_F \sqrt{k_F m_F} \tag{1}$$

where F_S defines the quasistatic impact force, v_F the speed of the vehicle upon impact, m_F the mass of the vehicle and k_F the equivalent elastic stiffness of the impact object, i.e. the ratio of the impact force F_S to the total deformation w_F of the impact object. The impact process can be considered as a sudden square-wave impulse (Figure 1) acting on the superstructure to be impacted, e.g. the superstructure of a railway bridge, and equation (1) can be rewritten as:

$$F_S \cdot \Delta t = v_F m_F \tag{2}$$

If the impact duration Δt is known, equation (2) can also be used to directly determine the impact force

$$F_S = \frac{v_F m_F}{\Delta t} \tag{3}$$

In equations (2) and (3), the impact duration Δt now appears as an explicit quantity and is defined as:

$$\Delta t = \sqrt{\frac{m_F}{k_F}} \tag{4}$$

Equation (3) can also be interpreted as the impact object vibration period or reciprocal of the fundamental frequency of the impact object (vehicle).

Due to the variability of the actual vehicle stiffness k_F, the exact determination of the impact duration represents a major challenge when considering a real vehicle in practice and can only be solved approximately. A very short impact duration consequently leads to equally high impact forces, which can reach implausible values. In the case of a completely rigid impact object and a rigid supporting structure, an infinitely high impact force would result.

If it is possible to model the impact object as an equivalent elastic body with a uniform cross-section, in this case the following equations can be used to determine the equivalent vehicle stiffness and mass

$$k_F = \frac{EA}{L} \tag{5}$$

$$m_F = \rho A L \tag{6}$$

where E is the equivalent modulus of elasticity, A is the equivalent cross-sectional area of the impact object, L is the equivalent vehicle length and ρ is the equivalent mass density of the impact object. Figure 1 shows the mechanical model for the approximate calculation of the impact force F_S in the case of a "hard" impact. Since the impact duration Δt can only be determined very imprecisely based on purely theoretical considerations, so-called crash tests are carried out in practice to determine the impact forces F_S and the equivalent stiffness k_F of impacting vehicles. Table C.1, ÖNORM EN 1991-1-7 provides a deterministic value for the equivalent vehicle stiffness of k_F = 300 kN/m, and assuming a total vehicle weight of a multi-axle lorry of 25 t (m_F = 25,000 kg) results the impact duration Δt = 0.29 seconds from Equation (4). For an assumed vehicle speed of v_F = 50 km/h (realistic speed in urban areas), this results in an impact force of F_S = 1202.81 kN, see calculation and graphical representation in Figure 2.

The calculation results illustrated in Figure 2 for the impact force F_S determined in accordance with Annex C of ÖNORM EN 1991-1-7 show that, according to this conservative mechanical model of the "hard" vehicle impact, even light vehicles already exceed the impact loads defined in ÖNORM EN 1991-17 (Table. 1). For urban areas (applies to the railway bridge considered here to be examined for vehicle impact) a static equivalent impact force of F_{dx} = 250 kN must be applied according to ÖNORM EN 1991-1-7. Contrary, the impact force determined using the "hard" impact approximation method according to Annex C of ÖNORM EN 1991-

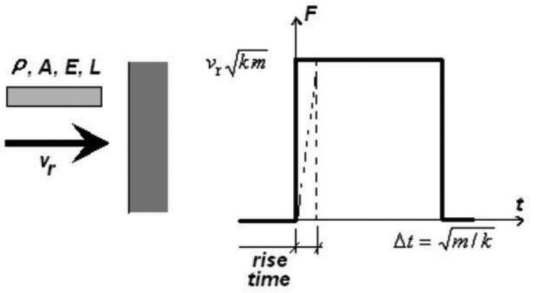


Figure 1. Mechanical model for approximate calculation of impact force F_S in the case of a "hard" impact according to Annex C, ÖNORM EN 1991-1-7.

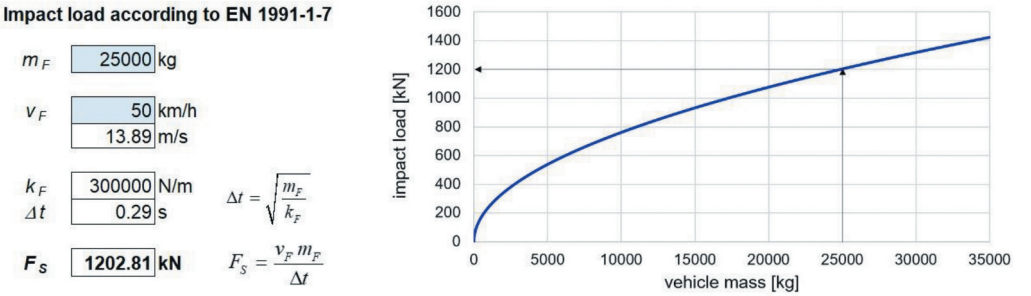


Figure 2. Determination of impact force F_S with assumed input parameters and graphical representation of impact force depending on the vehicle mass m_F.

1-7 for a 25,000 kg heavy truck is approximately 5 times higher. This discrepancy between normative regulations and mechanical impact models needs deeper research. It is assumed that railway bridges necessitate much higher requirements than road bridges because of their accuracy requirements regarding the rail position and track position stability.

5 RAILWAY BRIDGE EXAMINED FOR VEHICLE IMPACT

5.1 *General aspects*

Figure 3 shows photos of the railway bridge examined regarding the vehicle impact. It is located in Austria on route 2052, km 13.011. It is a two-track single span inclined bridge structure with a span of 9.49 m (measured along the bridge axis) and 8.45 m (normal to the abutment axis). The crossing angle is 63°. Figure 4 shows a cross section and ground view with bearing scheme of the railway bridge. The existing clearance height (headroom) is 3.23 m. The bridge deck plate (superstructure) is separated in the middle to the adjacent plate by a longitudinal joint, i.e. there are two individual bridge deck plates that each carry the traffic loads from one track. In the numerical calculation of the vehicle impact, only a single deck plate is therefore considered. With regard to the bearing construction, it can be seen that one roundly fixed and transversely fixed bearing as well as 4 roundly movable bearings are for each individual bridge deck plate. In the event of a vehicle impact, the resulting transverse impact force is therefore carried by the roundly fixed bearing and transversely fixed bearing. The forces used when dimensioning the bearing structures are as follows: load in longitudinal direction H_x = 700 kN (roundly fixed bearing) and load in transverse direction H_y = 280 kN (roundly fixed and transverse fixed bearing).



Figure 3. Photos of railway bridge examined for vehicle impact, located in Austria on route 2052, km 13.011.

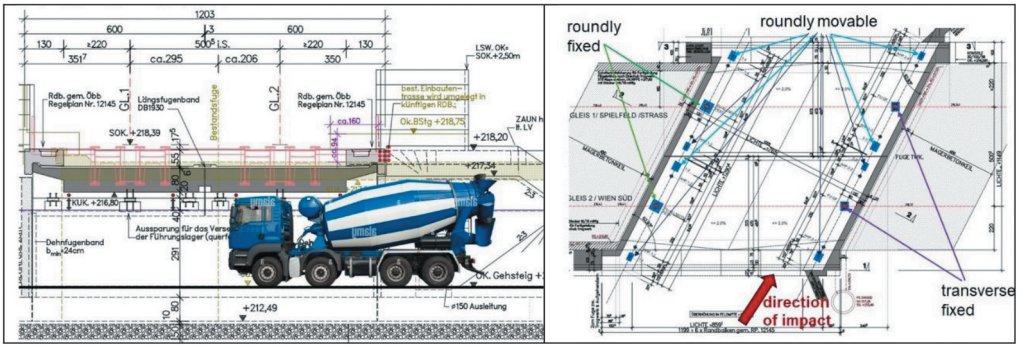


Figure 4. Cross section and ground view with bearing scheme of railway bridge examined for vehicle impact.

It is noted that the mentioned bearing loads are design values including partial safety factors that were determined by the responsible structural engineer in the ULS verification and specified for the bearing design. The bearing static resulted for the fixed bearing the proof "weld seam around the block shear connector" being decisive (calculated equivalent stress σ_v = 206 MPa < allowable equivalent stress $\sigma_{v,zul}$ = 241 MPa). For the transversely fixed bearing, the proof of "welded seams around the lower block shear connector" resulted to be decisive (calculated equivalent stress σ_v = 170 MPa < allowable equivalent stress $\sigma_{v,zul}$ = 241 MPa).

5.2 *Numerical digital twin analysis*

The modelling of the collision impact on the railway bridge on route 2052, km 13.011 was carried out using the ATENA Scientific 3D software to analyse the energy input, the force propagation and the resulting bearing force. The plan data served as the basis for the modelling is shown in Figure 4. Figure 5 shows the correspondingly high level of detail of the modelling and the selected macro zoning as well as the bearing arrangement and the position of impact in the centre of the bridge span. Figure 5 shows that the stiffness of the bearings has a significant influence on the transmission of the impact force to the bearings. It can be seen from the illustrated diagrams that on average approx. 70 % of the impact force is transferred to the fixed bearing for the optimal impact position in the bridge centre. If the bearing had already been designed for an average value of 700 kN, it could therefore accommodate an impact load of 1000 kN.

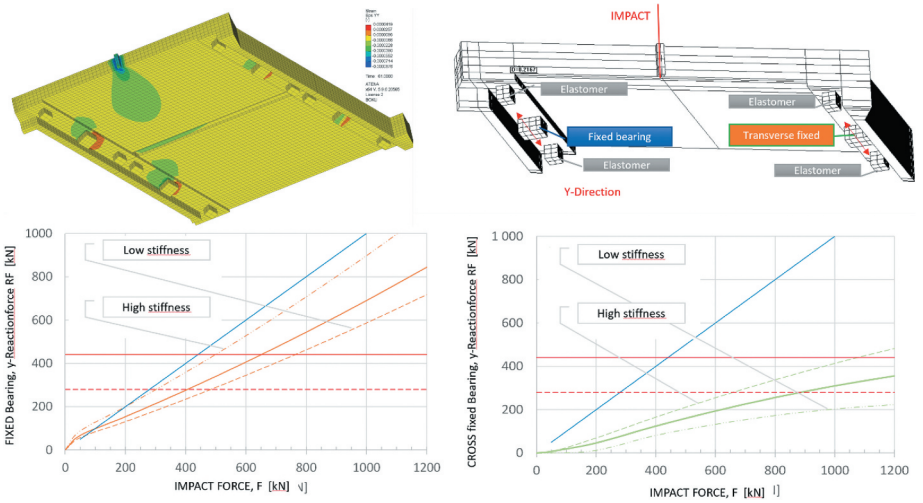
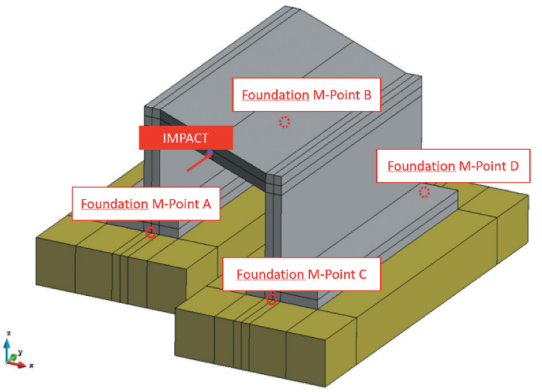


Figure 5. Fixed bearing reaction force vs. impact force in the theoretically optimal vehicle driving direction on the road under the superstructure (fixed bearing and transverse fixed bearing).

(a)



(b)

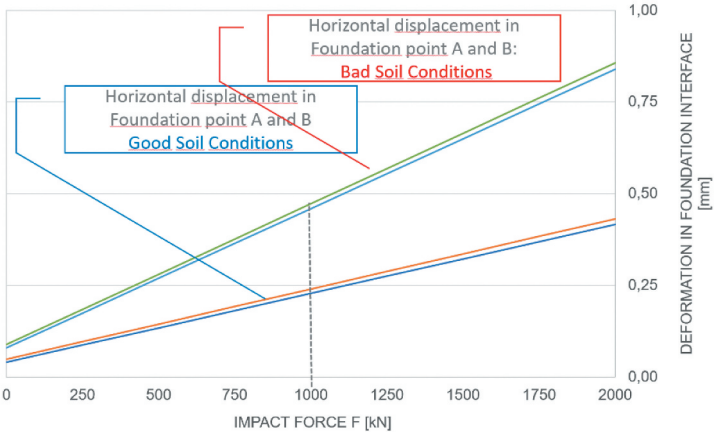


Figure 6. Analysis of the bridge system (a) adapted frame system with monitoring points in the foundation, and (b) impact vs. displacements in the foundation monitoring points A and B.

In addition to the investigations of the supported superstructure, the overall stability of the bridge system in terms of soil interaction was analysed for different soil conditions, as shown in Figure 6. For this purpose, as shown in Figure 6(a), an adapted spatial frame system was used, and monitoring points were placed in the foundation to analyse the "quasistatic" impact load induced displacements and stresses. Figure 6(b) shows that the maximum horizontal displacements of the foundation at an impact of 1000 kN are in a range of maximum 0.25 mm to 0.50 mm depending on different soil conditions. In all cases the static friction of the bridge system is not exceeded by far, which proves the structural stability and shows that no critical displacements for a rail closure occur.

6 CONCLUSIONS

The analyses conducted on the reinforced concrete railway bridge show that the impact forces can be absorbed by the executed bearings. If the up to 3-fold vehicle impact load (250 kN for the impact load in urban areas according to ÖNORM EN 1991-1-7 times 3, i.e. 750 kN), which is very likely to occur under unfavourable conditions, is applied, the numerical calculations carried out shows that only around 70% of the impact force can be absorbed by the executed bearings. The bearing forces resulting from the impact load of 750 kN should already be taken into account when planning the bearings. Nevertheless, a non-linear pre-analysis of the impact situation with alarm monitoring is generally strongly recommended. Based on the results, the design of the bridges could be reconsidered and adapted so that the impact loads can be safely absorbed.

ACKNOWLEDGEMENTS

This publication was produced on the basis of a commission from ÖBB-Infrastruktur AG (Austrian Federal Railways). The opinions and conclusions presented in this paper are those of the writers and do not necessarily reflect the views of the sponsoring organization. The authors would like to thank the expert team Thomas Simandl, Richard Zedlacher, Alfred Hüngsberg, Maximilian Autengruber and Josef Schorn of Austrian Federal Railways, bridge construction department, for their support.

REFERENCES

Background Document Eurocode 1, Part 1.7, Accidental Actions, January 2005.

Designers' Guide to Eurocode I: Actions on Bridges. EN 1991-2, EN 1991-1-1, -1-3 to -1-6 and EN 1990 Annex A2.

DIN 1055-9, Actions on structures - Part 9: Extraordinary actions, Edition: 2003-08.

Ozdagli, A.I., Moreu, F., Xu, D., Wang, T. 2020. Experimental analysis on effectiveness of crash beams for impact attenuation of overheight vehicle collisions on railroad bridges. Journal of Bridge Engineering, 25(1), 04019133.

ÖNORM EN 1991-1-7, Eurocode 1 - Actions on structures, Part 1-7: General actions - Extraordinary actions, edition: 2014-09-01.

Schönfeld S. 2015. Development of a methodology for risk assessment of impact safety on existing steel railway overpasses in urban areas (In German). Master-Thesis.

Swiss Guideline, Impact of road vehicles on structural parts of engineering build-ings (In German), Extension to Code SIA 261, Edition 2005.

UIC-KODEX 777-1, Measures to protect railway bridges against impacts from road vehicles, and to protect rail traffic from road vehicles fouling the track (in German), 2nd Edition, June 2002.

Strauss A. 2016, Numerical and monitoring based Markov Chain approaches for the fatigue life prediction of concrete structures. Engineering Structures, 112, pp. 265–273, DOI: 10.1016/j.engstruct.2016.01.020.

Zambon I., Vidović A., Strauss A., Matos J. 2019 Condition prediction of existing concrete bridges as a combination of visual inspection and analytical models of deterioration. Applied Sciences (Switzerland), 9 (1), art. no. 148, DOI: 10.3390/app9010148.

Bridge Maintenance, Safety, Management, Digitalization and Sustainability – Jensen, Frangopol & Schmidt (eds)
© 2024 The Author(s), ISBN 978-1-032-77040-6
Open Access: www.taylorfrancis.com, CC BY-NC-ND 4.0 license

Advanced modelling methods of the Jauntal railway bridge

Alfred Strauss & Benjamin Täubling-Fruleux
Department of Civil Engineering and Natural Hazards, University of Natural Resources and Life Sciences, Vienna, Austria

Lukáš Novák & Drahomír Novák
Institute of Structural Mechanics, Brno University of Technology, Brno, Czech Republic

Alexander Oplustil & Michael Kaulfus
KOB ZT Ges.m.b.H., Vienna, Austria

Herwig Steiner, Richard Zedlacher, Alfred Hüngsberg & Gerhard Oberlerchner
Austrian Federal Railways, Vienna, Austria

Dan M. Frangopol
Lehigh University, ATLSS Engineering Research Center, Bethlehem, PA, USA

ABSTRACT: The increasing need for mobility is fuelling interest in extending the service life of existing bridges. In case of the Jauntal Bridge, one of the highest railway bridges in Europe, a new structure with two tracks is placed on the existing massive concrete columns with a hight of almost 100 m compared to the old structure with one track. Non-linear innovative numerical analyses and advanced safety considerations were used to examine whether the significantly higher bearing-column forces can be sustained by the existing columns and column heads. This paper shows how the advanced modelling methods can be applied to ensure that the existing structures, can be safely maintained over their planned lifetime in service for sustainability reasons.

1 INTRODUCTION

The Jauntal Bridge in Carinthia, shown in Figure 1, crossing 96m above the Drau River valley, the single-track bridge with a total length of almost 430 meters has stood the test of time in remaining one of Europe's highest railway bridges. It was built in 1961 and is currently being replaced by a new structure with a double-track line and a footpath and cycle path underneath. In the construction work, the old steel structure was coupled with the new one and both were moved together in the longitudinal direction in order to bring the new structure in its final position. The new deck above the steel structure has already been partially erected and the reinforced concrete deck is being concreted with formwork carriages. An extensive monitoring system has already been installed on the bridge, monitoring both the construction phases and the operational phases and allowing a comprehensive performance assessment.

Planning and construction of the new structure, shown in Figure 2, was processed by the engineering office KOB and ÖBB Infra and accompanied by the scientific partners in the dynamic analyses and some detailed verifications of the bearings using shock transmitters. As can be seen in Figure 2(c) at the bottom of the bearing sketch is a special moving bearing system in which the braking and earthquake forces are absorbed by shock transmitters. Another special feature with respect to this bearing system was the analysis of the bridge as a continuous welded rail system with special track interaction situations due to the shock transmitter solution.

DOI: 10.1201/9781003483755-92



Figure 1. Jauntal Bridge in Carinthia: New structure under construction with a double-track line and a footpath and cycle path underneath. (ÖBB, 2023).

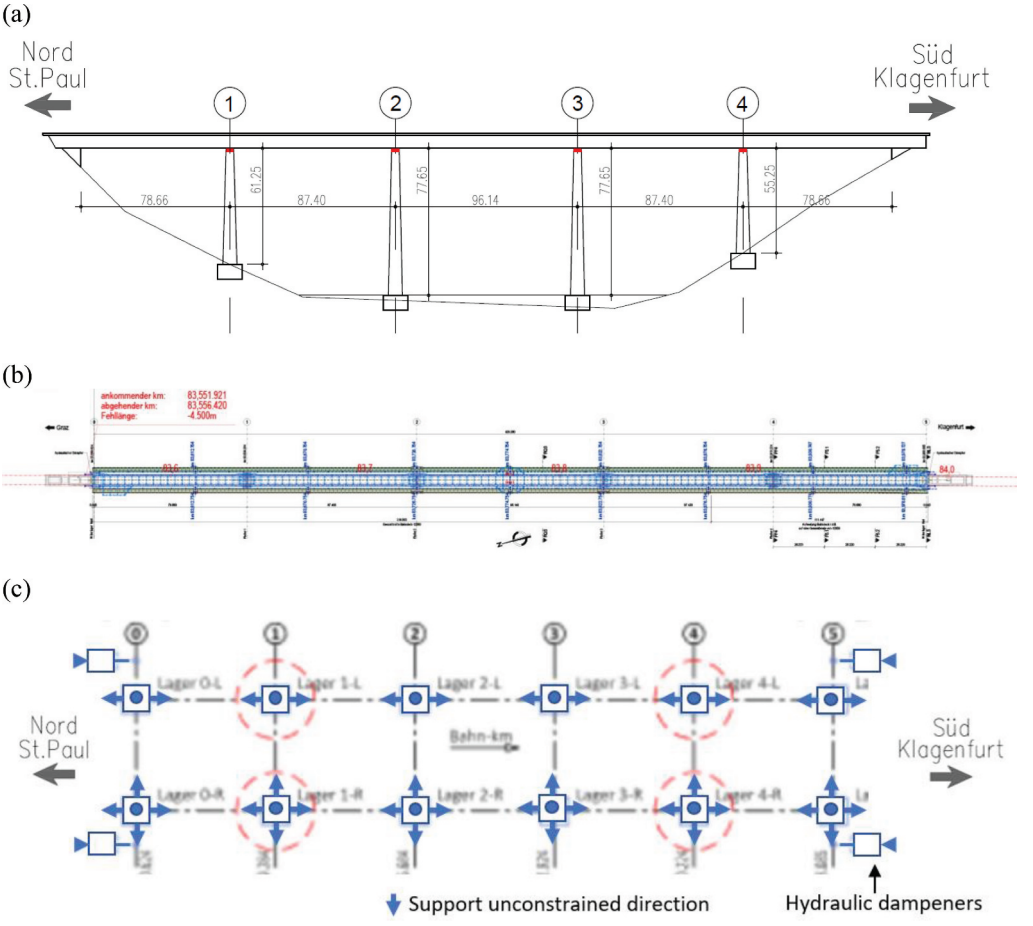


Figure 2. Jauntal Bridge in Carinthia, Austria (a) side view south, (b) top view on the double-track line of the new bridge, (c) bearing system of the bridge.

In addition to the numerous innovative solutions that were necessary to place the double-track line on the existing columns and to continue operating it in terms of sustainability, special investigations and, in some cases, reinforcements of the column heads were also required. This study deals with the discussion of these investigations and analyses. It is shown how the load-bearing capacity of the historical support heads can be verified using a reliable

procedure, which also had to be approved by an external expert, and analysed using innovative Level III methods and extended safety format concepts.

2 HEAD PERFORMANCE OF EXISTING COLUMNS

2.1 *General aspects*

The new supporting structure, a reinforced concrete-steel composite structure, is a continuous girder system supported by the columns with a steel truss as the main girder under the track slab. The loads of the new structure must be transferred to the old existing reinforced concrete columns via the bearings and bearing bases, as shown in Figure 3a to 3c. The bearing force at design level, which results from the self-weight, the removal loads and the live loads of the structure, is a design load of 50 MN. The partial area pressure verifications for new concrete bearing bases on old concrete column heads, shown in Figure 3, are usually interpreted very differently by the experts in accordance with EN 1992 (ASI, 2018) and sometimes lead to very unrealistic results. The planners and the client were therefore very interested in having the verifications and thus the load-bearing capacity of the bearings/columns checked using reliable methods. As a result, the scientific partners created a real-life digital twin in line with the possible verification procedures of level III of MC2020 (fib, 2024(expected)) and B4008 Part 2 (ASI, 2019) using non-linear finite element methods. Moreover, due to significant uncertainties involved, probabilistic approaches to verify the existing capacity and the existing safety were used. As can be seen in Figure 3d, the column head was additionally reinforced with appropriate tension rods to create a confinement and increase the load-bearing capacity of the column head; the effects of these rods have to be taken into account in the analyses.

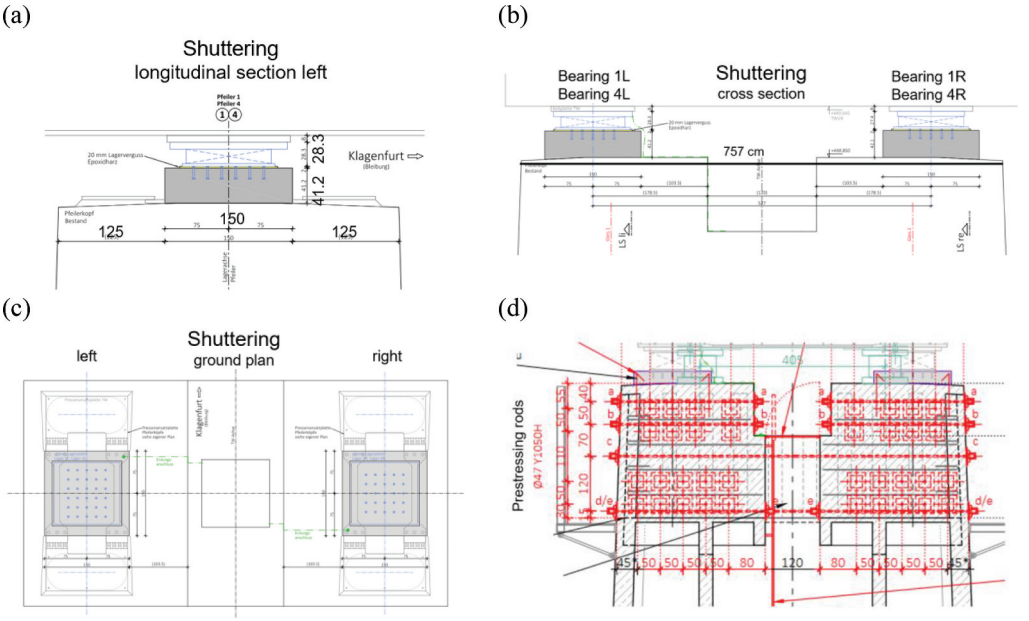


Figure 3. New concrete bearing bases associated with the new steel-concrete composite structure of the Jauntal bridge: (a) side view on the concrete bearing bases, (b) longitudinal view on the concrete bearing bases, (c) top view on the concrete bearing bases and (d) confinement to increase the load-bearing capacity of the column head.

The material parameters of the old concrete from the columns, the results of the conformity check of the new concrete and the detailed reinforcement drawings were provided. In the

subsequent analysis, verification steps were defined as follows: (a) checking the use of the correct material laws in the modelling for the old and new concrete, (b) modelling of the column head without strapping, (c) modelling of the column head with confinement but without prestressing, and (d) modelling of the column head with confinement and prestressing. In addition to these validation steps, the crack width of 0.1 mm was defined as the decisive load-bearing capacity criterion, i.e. the maximum load of 50 MN must not cause a crack width larger than 0.1 mm.

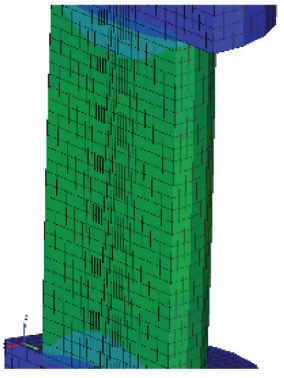
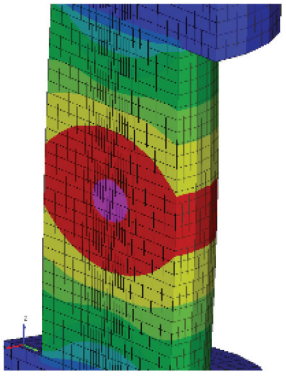
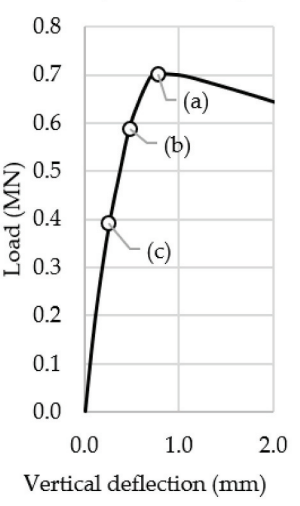
2.2 *Characterisation of material models – step a*

The concrete properties of the existing column heads were experimentally determined with a characteristic cube compressive strength of f_{ck} = 29 MPa. Using the concrete model CC3DNonLinCementitious2 based on the CEB-fib Model Code 90 (CEB-FIB, 1993)

Table 1. Material properties of existing column concrete.

Material parameter of old concrete	value	unit
Modulus of elasticity E	33253.6	MPa
Compressive strength f_c	-37.0	MPa
Tensile strength f_{ct}	2.83	MPa
Poisson's-ratio μ	0.2	-
Fracture energy G_f	0.00014	MN/m
Plastic strain at strength f_c ε_{cp}	-0.00133	-
Onset of crushing f_{c0}	-5.95	MPa
Critical compressive displacement w_d	-0.0005	m

Table 2. Development of the maximum load when creating models using cylinder compressive strength.

95% (667,6 kN) σ = 37.8 N/mm²	100 % (702,7 kN) σ = 39.8 N/mm²	
		

(a) Max. Value = N_{cm} = 702.7 kN, (b) Characteristic Value = N_{ck} = 586.5 kN, (c) Design Value = N_{cd} = 391.0 kN

Note: 100% chosen according to maximum in the load displacement diagram

available in the ATENA (Červenka, 2016) programme package, see Table 1, it was possible to take into account the material and geometric non-linearity as well as the material degradation due to crack development with the help of this material model. The concrete properties of strength class C40/50 according to ÖNORM EN 1992-1-1 were used for the new structural concrete.

The results of the analysis with the concrete properties determined for the existing column head are shown in Table 2. The properties are based on the experimental tested cylindrical specimens. The principal normal stresses determined step by step for 95% and 100% of the maximum load are shown, whereby the load was applied in about 250 load steps. The stress curves concentrate in the centre of the longitudinal axis of the cylinder as the load increases. The maximum load carrying capacity of 702.7 kN was also reached when the first cracks appeared. These results are consistent with the experimentally observed behaviour of the samples and confirm the appropriateness of the chosen material laws. The computational modelling showed almost no cracking up to the maximum value of 702.7 kN, as can be seen in Table 2, and only then significant cracks occurred, which also corresponded very well with the tests carried out. The characteristic and design values indicated in Table 2 show a very good agreement with the standard concrete strength C30/35 of the concrete of the existing column, so that the modelling and discretisation of the cylinder could be assumed to be validated.

2.3 *Column head performance with confinement and prestressing - step d*

After the characterisation and validation of the material laws, the column heads and the bearing base interaction were modelled in steps (b) and (c) without and with prestressing and confinement, as briefly outlined in Section 2.1. Finally, in step (d), the real-world structure was modelled with prestressing and confinement of the column head, as shown in Figure 4. The pre-stressing force was set at P = 1275 kN. To simplify matters, no bond between the bar tendons and the concrete structure was assumed. A linear elastic material with an elastic modulus of steel was adopted for the pressure distribution plates. The material parameters used are shown in Table 3. The main normal stresses obtained step by step and the crack developments are shown for 95% and 100% of the load, where the load was applied in approximately 250 load steps. As can be seen from Figure 5, the maximum load capacity is around 141.1 MN.



(a) (b)

Figure 4. FE model of the pier head: (a) presentation of the pier head model with prestressed FE mesh; (b) presentation of detail of the prestressing system.

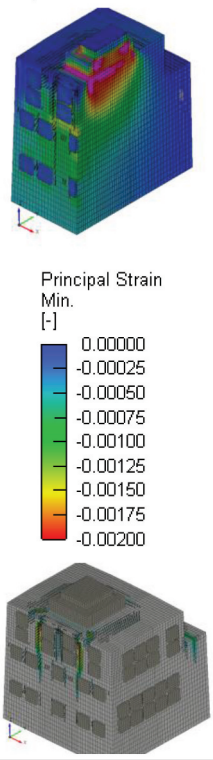
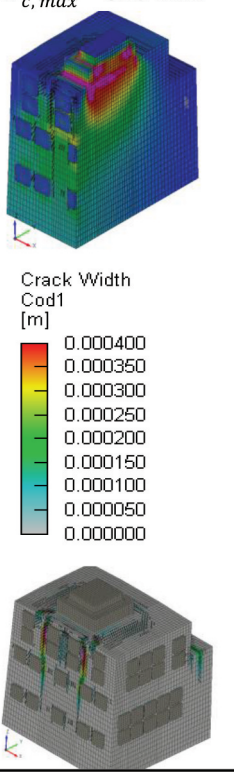
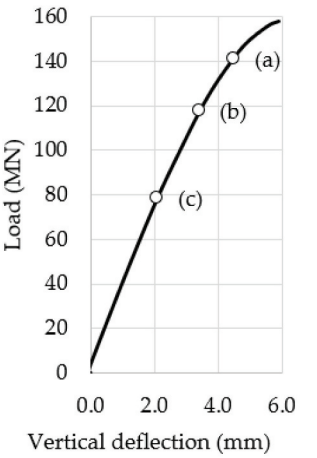
Table 3. Material parameters of pre-stressing rods.

Parameter	Value	Unit
Modulus of elasticity E	200000	MPa
Diameter d	47	mm
Yield strength YS	950	MPa
Strain at bar rupture	0.025	-
Stress at bar rupture	1050	MPa

2.4 *Non-linear finite element digital twin analyses of stages (b) to (d)*

The analysis results of stages b, c and d are presented in Table 4 and Figure 5. In Table 4 the derived force mean value (N_{cm}), characteristic value (N_{ck}) and design value (N_{cd}) are shown.

Table 4. Real world digital twin of the column head - load capacity curve vs. the crack width development.

95% (134.05 MN)	100 % (141.10 MN)	
$\sigma = 59.6$ MPa $w_{c,max} = 0.38$ mm	$\sigma = 62.7$ MPa $w_{c,max} = 0.49$ mm	
		
		(a) Max. Value = N_{cm} = 141.1 MN, (b) Characteristic Value = N_{ck} = 117.7 MN, (c) Design Value = N_{cd} = 78.5 MN

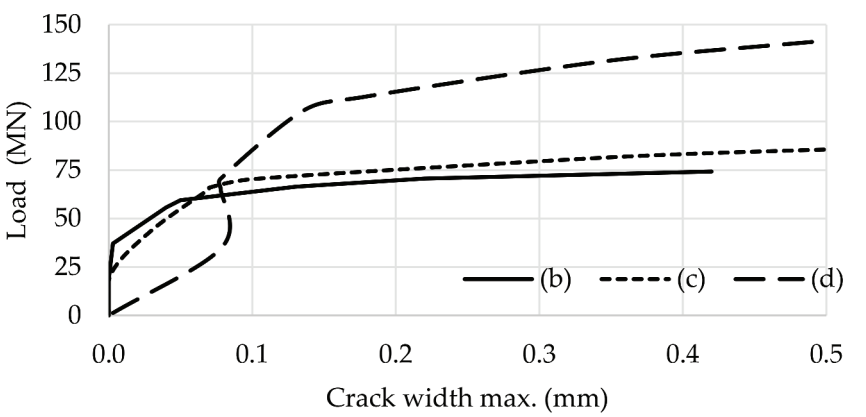


Figure 5. Load vs max. crack width diagram for pier head models: (b) modelling without reinforcement, (c) modelling with non-tensioned reinforcement, (d) modelling with prestressing.

The values in Table 4 were used to formulate and evaluate a limit state in which a maximum crack width of 0.1 mm was defined. Figure 5 compares the load with the crack width max. results of the three stages. The rebound in the long dashed curve in Figure 5 also shows the interesting effect that the cracks formed during prestressing close again due to the increasing load and larger cracks form elsewhere. On the whole, this real-world digital twin of the column head demonstrated that the interaction of the load-bearing base with the old concrete allows a maximum bearing load of 141 MN while maintaining a crack width of maximum 0.5 mm.

3 CONCLUSIONS

In this study, an application-oriented development of a real digital twin of the structural column interaction of the Jauntal bridge (new/old concrete interaction) was demonstrated. With the non-linear finite element-based real digital twin, an iterative adaptation of the constitutive laws of the existing concrete was carried out in stage I by simulating the drilled core specimens. In a further step, a systematic step-by-step procedure has to be used to show how the complex 3D prestressing of existing columns could be realistically included in the real digital twin calculations and finally how the maximum load-bearing capacity could be characterized using a crack width criterion.

ACKNOWLEDGEMENTS

This publication was produced on the basis of a commission from ÖBB-Infrastruktur AG (Austrian Federal Railways). The opinions and conclusions presented in this paper are those of the writers and do not necessarily reflect the views of the sponsoring organization. The authors would like to thank the expert team from Austrian Federal Railways, bridge construction department, for their support. Czech authors acknowledge the support from the Czech Science Foundation, project No. 22-00774S and co-financed by European Union within the framework of programme Austria-Czech republic 2021-2027, project No. ATCZ00068/IREC.

REFERENCES

Austrian Standards International (ASI). 2018. ÖNORM EN 1992-1-1: *Eurocode 2: Design of concrete structures – Part 1-1: General rules and rules for buildings*.

Austrian Standards International (ASI). 2019. ÖNORM B 4008-2: *Assessment of load capacity of existing structures – Part 2: Bridge construction*.

Červenka V., Jendele L., Červenka J. 2016. ATENA Program Documentation Part 1, Theory

fib Fédération internationale du béton. 1993. CEB-FIP Model Code 1990: Design.

fib Fédération internationale du béton. 2024(expected). fib Model Code 2020.

ÖBB Infra 2023. ÖBB Webcam ´Baustelle Tragwerks Erneuerung Jauntalbrücke`.

Strauss A. 2016. Numerical and monitoring based Markov Chain approaches for the fatigue life prediction of concrete structures. Engineering Structures, 112, pp. 265–273, DOI: 10.1016/j.engstruct.2016.01.020.

Strauss A., Šomodíková M., Lehký D., Novák D., Bergmeister K. 2018. Nonlinear finite element analysis of continuous welded rail–bridge interaction: Monitoring-based calibration. Journal of Civil Engineering and Management, 24 (4), pp. 344–354, DOI: 10.3846/jcem.2018.3050.

UIC 2002. UIC-KODEX 777-1, Measures to protect railway bridges against impacts from road vehicles, and to protect rail traffic from road vehicles fouling the track (in German), 2nd Edition.

Zambon I., Vidović A., Strauss A., Matos J. 2019. Condition prediction of existing concrete bridges as a combination of visual inspection and analytical models of deterioration. Applied Sciences (Switzerland), 9 (1), art. no. 148, DOI: 10.3390/app9010148.

Zimmermann T., Strauss A., Bergmeister K. 2010. Numerical investigation of historic masonry walls under normal and shear load. Construction and Building Materials, 24 (8), pp. 1385–1391 DOI: 10.1016/j.conbuildmat.2010.01.021.

Bridge Maintenance, Safety, Management, Digitalization and Sustainability – Jensen, Frangopol & Schmidt (eds)
© 2024 The Author(s), ISBN 978-1-032-77040-6
Open Access: www.taylorfrancis.com, CC BY-NC-ND 4.0 license

Generation of digital twins for bridges of medium spans - Schwindegg Bridge pilot project

J. Wimmer & T. Braml
Institute for Structural Engineering, University of the Bundeswehr Munich

ABSTRACT: In the coming years, bridge maintenance will be an essential task for the upkeep of the infrastructure. Especially in the case of bridges with small and medium spans in the municipal road network, in many cases there are no longer sufficient personnel available for the inspection and maintenance of structures. Therefore, it will be necessary in the future to develop concepts for a partially automated bridge inspection. If information is available from the actions and resistances of structures, the measured values contain important information on the condition of the structure. One concept for this can be digital twins. Based on digital twins and the information they contain; intelligent maintenance management can be implemented. In this paper, we present the challenges and chances of implementing the digital twin concept on a single-span prestressed concrete frame bridge.

1 INTRODUCTION

The construction industry, like many other fields, faces a dearth of proficient labour. According to a recent statistic from the German IAB (Bossler & Popp 2023), the labour market has been becoming increasingly constrained since 2010. The private individual's most noticeable effect of this situation is the long wait times for appointments with craftsmen. Moreover, the absence of workforce is perceptible in the public sector as well, resulting in long wait times for building applications among other things. Not only individuals, but also critical infrastructure such as bridges, experience prolonged wait times due to the shortage of skilled workers in many office positions (Böhme 2022). Consequently, the maintenance of bridges falls into backlog and their structures deteriorate at a faster pace. Notably, broken bridges do not only cause inconvenience to private citizens, but also imperil a country's economic performance (Vorländer 2023). A potential solution to saving valuable labour lies in the simplification and digitalisation of planning processes using intelligent technologies, according to Böhme (Böhme 2022). In recent decades, extensive research has been conducted on digitalisation within the construction industry. In Germany, the first step towards digitalisation is the implementation of ASB-ING, which regulates the mapping infrastructure structures in databases (Bundesministerium für Verkehr, Bau- und Stadtentwicklung 2013). This led to the development of the SIB-BW software, which can create a structure book for each bridge structure, documenting its condition, including any damage. The database resulting from this endeavour serves as a documentation of the structure's condition, particularly in cases of damage. However, it does not possess any intelligent capabilities.

Based on Building Information Modelling (BIM), there are efforts towards digitally mapping processes. The process initiates with the planning of new bridge constructions with BIM. To use the created up to7-dimensional models (Kainz & Wolf 2023) over the life cycle, it is imperative to integrate maintenance and damage management. For German systems, the semantics again rely on ASB-ING since logic has already been specified here. BIM models are not usually available for existing buildings, so current efforts focus on researching the

DOI: 10.1201/9781003483755-93

semantic segmentation of 3D point clouds (Schellen, et al. 2023). Furthermore, ASB-ING approaches are implemented in this area. Investigative efforts are directed towards syntax, enabling semantic assignment of processes and data management to the models via the Semantic Web (Hagedorn, et al. 2023). The next step in this process is to develop an automated real-time evaluation system for the structure's condition and subsequent control. In the field, the notion of digital twin has gained prominence, with increasing application in the construction industry. However, a transition to the digital shadow frequently does not occur (Hindersmann, et al. 2023). This can be attributed to various factors, such as the inadequacy of BIM systems in handling real-time data, gained by Structural Health Monitoring (SHM). Practitioners have thus explored alternatives in linked data frameworks (Naraniecki, et al. 2023). Industry 4.0 (I4.0) systems are designed objectively with predictive maintenance in mind, processing data in a streamlined manner. Commercial software is traditionally implemented for monitoring and controlling machines. Additionally, Asset Administration Shells (AAS) are being researched, mainly using open source. Braml et al. have introduced the AAS configurator, known as BridgeBox (BBox), to create AAS for bridge structures (Braml, et al. 2022). In the following sections, we will outline the potential opportunities and tasks related to digital twins, assess the relevance of AAS in this context, and categorize them through a practical case study of the digital bridge prototype in Schwindegg (Germany) shown in Figure 1.



Figure 1. Western view of the Isenbridge in Schwindegg (Wimmer & Braml 2023a).

2 DIGITAL TWINS AND ITS BENEFITS

2.1 *Definitions*

The definition of a digital twin depends on its intended use. Siemens defines an industrial digital twin as a virtual replica for real-world products and processes, contributing to improved comprehension and prediction of performance (Siemens Digital Industries Software 2019). It utilises multi-physics simulation, data analytics, and machine learning for the purpose of enhancing design, usage scenarios, and environmental conditions, thus reducing the requirement for physical prototypes and augmenting the quality of final products or processes. By using real-time sensor data from physical objects, digital twins can update themselves continuously during the product's lifespan. They define three types of twins: Product, Production, and Performance twins (Siemens Digital Industries Software 2019). Further definitions are summarized in (Schleich, et al. 2017; Stavropoulos & Mourtzis 2022). However, digital twins are defined as interconnected and interacting models that are suitable for predicting the behaviour of products, rather than as a singular model. To maximize advantages, they must be fed with all available data (Schleich, et al. 2017). Company-specific philosophies vary

regarding whether they should be mapped for processes, product life cycles, or products (Schleich, et al. 2017). This is shown in Figure 2 as application levels.

The definition of a digital twin's maturity is currently absent, despite knowing what it can be and how it is used in I4.0. Kritzinger et al. have categorised digital models, digital shadows, and digital twins, based on the extent of data integration, however, shown in Figure 2 (maturity level)(Kritzinger, et al. 2018). Meanwhile, the I4.0 platform developed AAS, which differ in the communication of digital twins amongst themselves (Plattform Industrie 4.0 2021). There are three types of AAS: passive type 1, reactive type 2, and proactive type 3 (Figure 2, maturity level) (Plattform Industrie 4.0 2021; Jacoby, et al. 2023).

In the construction sector, the life cycle of buildings provides a means of translating these definitions. Kosse et al. identify four components of the life cycle: Planning, detailed design, fabrication or construction and operation and maintenance (Kosse, et al. 2022). It is clear that for structures that are intended to endure, the long-term factor is of utmost significance. An example of this can be found in the notably shorter lifespan of industrial tools in comparison to the components of bridge structures.

After defining digital twins and their requirements, Ye et al. examined three approaches for handling measurement data from Structural Health Monitoring (SHM): data-driven, physics-based, and data-centric engineering (Ye, et al. 2019). The data-centric approach combines both physics- and data-driven digital twins within a single framework, and specifically addresses building construction and operation. In (Danwitz, et al. 2023), this approach is referred to as the "Hybrid Digital Twin". This comprises a data-driven model, a model based on physics, a model with reduced dimensions and a basic model, all working in conjunction to represent a level of modelling, shown in Figure 2 with the modelling level.

Progressive literature on digital twins in the construction industry incorporates the definitions of I4.0, but there is often a conflation of the terms digital model, digital shadow, and digital twin. This issue is also observed in I4.0 literature (Kritzinger, et al. 2018).

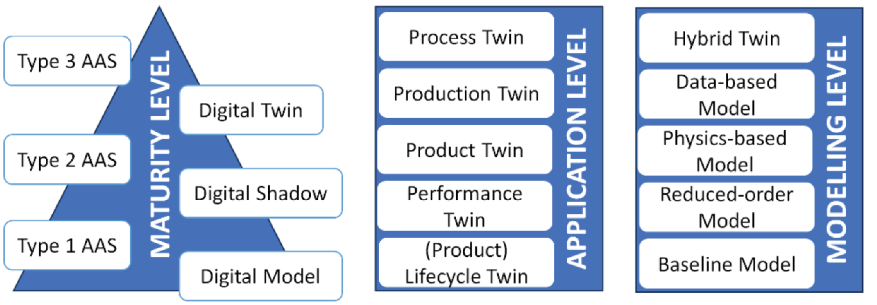


Figure 2. Maturity level, degree of application and degree of modelling as alternatives to the definition of a digital twin.

2.2 *Use of digital twins*

Digital twins are not limited to I4.0; progress in the concept is also evident in healthcare and smart cities. Reviews of the respective sectors summarise the use cases. Within I4.0, the manufacturing industry stands out for exploiting digital twins to enhance production, alter and simulate prototypes or demonstrate the product life cycle (Kenett & Bortman 2022). However, limitations arise during the development of a cyber-physical system as existing software encounters difficulties in logically linking the data and utilizing it as a factual digital twin. Currently, real digital twins are utilized to support physical experiments. Kenett & Bortman offer digital twins of I4.0 in their text (Kenett & Bortman 2022), showcasing gear fault diagnosis using the digital twin of a rotating machine, electronics, material properties, and production process. Additionally, (Stavropoulos & Mourtzis 2022) explore further digital twin applications such as personalised manufacturing, ergonomic production, or human-machine interaction.

The healthcare sector has experienced a significant surge in scientific literature concerning digital twin technology in recent years. According to reviews, hospitals' and devices' digital twins have achieved exceptional development due to their proximity to the industry. Nevertheless, these digital twins remain restricted to specific areas of concern (Machado & Berssaneti 2023). For digital twins of patients and processes, however, political paths need to be paved first, as described in scientific papers. No report of a digital twin of a physical body has been published yet, as per (Machado & Berssaneti 2023). Other reviews, like (Sun, et al. 2023), discuss specific use cases of digital twins. They describe various aspects, including gene composition, diagnosis, and treatment, as well as measurement data from examinations or patient data at the patient level. These features are integrated into the digital twin, providing clinical decision support, personalised recovery paths, real-time monitoring, a mechanism model, opportunities for scientific research, and educational support (Sun, et al. 2023).

The concept of Smart Cities is gaining traction in urban planning. The term Urban Digital Twin or City Digital Twin is increasingly being used synonymously (Shahat, et al. 2021; Weil, et al. 2023). The main challenges revolve around the integration and analysis of data from diverse sources. Once resolved, City Digital Twins have the potential to significantly enhance the quality of life of city residents. For example, measuring commuter flows enables the optimisation of public transport and adaptation of traffic lights in response to traffic flows. This leads to more efficient energy systems (Shahat, et al. 2021). Nevertheless, publications also address environmental sustainability, as well as resources (workforce, finance) and ethics (Weil, et al. 2023). The resilience of the city is another application; for example, preparing for natural hazards or man-made dangers (Therias & Rafiee 2023). Digital twins of bridges and other critical infrastructure provide results that can be classified in this field and enhance the city's digital twin's sensory data or structural condition information. In seismic zones in Vancouver, for example, SHM is already being employed to gather measurement data from bridge monitoring projects (Kaya & Ventura 2019). Just like City/Urban Digital Twins, overcoming numerous challenges is crucial for its success. These will be presented in the following section.

2.3 *Challenges and chances on the way to a bridge's digital twin*

As there is ongoing basic research into digital twins of bridges, only some aspects of the concept have been standardised. The full benefits of a digital twin are realised when all accessible information can be gathered, accessed, and integrated automatically throughout the entire lifecycle. Robust measurement technology is necessary for installation and long-term stability. Additionally, freely available, standardised, and durable data formats that are both human- and machine-readable are needed. Intelligent data processing is required to compress large amounts of information, and bidirectional interfaces with other digital twins of bridges, routes, or even cities are necessary.

Several solutions exist for each of these technical building blocks of a digital twin, but a combination of the steps is paired with a proprietary solution. As most stakeholders of the elements do not cover all solutions, e.g., the large number of measurement principles available and used on the market, standardised interfaces are required. Braml et al. propose a concept from the perspectives of both research and industry, categorising the components into data collection, transfer, storage, and analysis (Braml, et al. 2023).

If the obstacles that have been faced are surpassed, enabling a digital twin to be established and operated effortlessly, and the whole process can act as a "plug and play" solution, then the digital twin's complete potential could be exploited. Intelligent maintenance management implementation takes priority in achieving this objective, intended specifically to support the infrastructure operators who are working to capacity. At best, this approach enables early recognition and repair of damage, thus extending the service life in accordance with predictive maintenance principles. The employment of metaverse approaches, whereby users can interact with pertinent data, is similarly plausible (Yaqoob, et al. 2023). The resulting increase of the bridge's service life could decrease (Wimmer & Braml 2023a).

3 MULTIUSE OF DIGITAL BRIDGE SCHWINDEGG – PROOF OF CONCEPT

3.1 *The bridge and the motivation to make it a digital bridge*

The Isenbridge, a single-span prestressed concrete frame bridge spanning approximately 20m, is located in Schwindegg, Germany (Figure 1). The main supporting structure comprises precast beams with in-situ concrete supplements and abutments founded on bored piles. The bridge facilitates the passage of a two-lane district road over the river Isen in Schwindegg, and it is connected to the local infrastructure via an overpass for power and telecommunications supply lines. The bridge's dimensions, geographical position and favourable environment create the ideal requirements for continuous measurement data gathering and transmission. The dtec.bw RISK.twin study on digital twins motivated the selection of this bridge as a living lab. Construction finalisation took place in 2022 and the sensors were installed simultaneously. The concepts of installation, monitoring, and measurement, along with the encountered challenges and corresponding findings during construction, were previously disclosed in (Wimmer & Braml 2023c). Details of the sensors used and installation process are displayed in (Wimmer, et al. 2023). Successful implementation guaranteed data collection from the outset of operation.

The aim of this project is to provide a proof of concept by showing the applicability of the sensors and their installation in construction operations. Additionally, it will demonstrate how multiple sources of measurement data can be connected to the BBox and then transmitted as a digital shadow to the AAS. The gathered measurement data will enable the development of intelligent evaluation methods, such as those based on principal component analysis, allowing for expedient feedback, fewer data transmissions, and the undertaking of later assessments of the bridge. The resulting Structural Health Information Patterns (SHIPs), as discussed in (Varabei, et al. 2022), will be used accordingly.

3.2 *Proof of concept*

By integrating the sensors and instrumentation into the site planning, the installations for operating the sensors are already in place. The ample provision of space allows for future installation of additional sensors, and cables can be safely laid within a secure environment (see Figure 3a). The analysis of the current sensors is used to define appropriate measurement

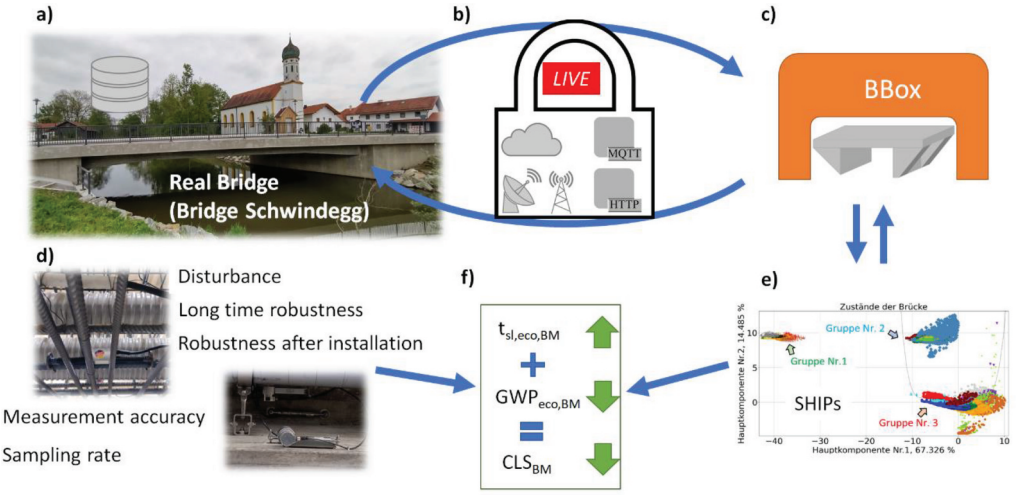


Figure 3. Chances and opportunities for data analysis using the digital Bridge (a) due to standardisation of data transfer with live connection (b) to the asset administration shell BBox (c), use of appropriate sensory systems (d) and intelligent analysis methods (here: SHIPs, (Varabei, et al. 2022)), extension of service life $t_{sl,eco,BM}$, reduction of GWP, lower utilisation of the climate limit state (CLS) (Wimmer & Braml 2023a)(f).

chains for installation and data provision. The categories of "robustness after installation," "measurement accuracy," "sampling rate," "disturbance," and "long time robustness" are distinguished (refer to Figure 3d). As of now, positive findings regarding robustness after installation are the only ones that can be reported, due to the short running time of less than a year. However, all commercially available sensors have exhibited suitability for their intended application. After extended use, the long-term stability of the measurement data (i.e. deviations) can also be determined by the use of various sensors and measurement systems.

Trials for data transmission between sensors and measuring devices through cable and wireless will be carried out. Spacious pathways have been designed to enable the testing of future systems with any technical advancements. The data flow shown in Figure 3b, linking real bridge and digital twin (BBox), is also under investigation, with a focus on data transmission media, data size, and transmission speed, for possibly suitable transmission protocols. Further details can be found in (Braml, et al. 2023).

The data collected is fed into the AAS BBox without any filtering to ensure there is no loss of information. Only a **preliminary plausibility check is conducted, which includes a functional** examination of the sensors or the correct indication of measured values. In the digital experimental environment, diverse analytical, statistical, and artificially intelligent processing techniques are employed to analyse the data. An instance of this is the SHIPs illustrated in Figure 3e, highlighted in (Varabei, et al. 2022). The generated patterns are based on principal component analysis and interpret the combined measurement data comprehensively. Any irrelevant sensors are identified and removed for further assessment.

Numerous sensors were installed in areas of static significance. A finite element model was formed for the structure, utilising load assumptions from structural calculations. Subsequent investigations involve examining various characteristic values, such as strains, temperatures, and pressures, through target/actual comparison.

For the first time, the measurement data is automatically entered in real-time rather than being manually entered into BBox after a measurement campaign (as explained in (Braml, et al. 2022)). This required the creation of various interfaces for the different measurement chains. We also analysed the handling of the measurement data in case of connection failure or power outage. In case of the former, the data is stored locally for a temporary period (Figure 3a). In the event of the latter, it is advisable to have an emergency power supply. Minor power outages can be easily resolved with the aid of the built-in battery packs. Another crucial aspect to consider is the sensor localisation in its digital image. The physical localisation is accomplished by georeferencing the sensors in the Gauss-Krüger coordinate system (Wimmer & Braml 2023b), while the digital localisation is carried out through separate submodels for the metering points in the AAS. The use of BIM to visualise the metering points is being investigated.

Finally, this analysis considers the potential for a digital twin to improve the carbon footprint of the bridge, starting from the moment it is opened to traffic. To assess this potential, we compare it against the Climate Limit State (CLS) concept presented in (Haist, et al. 2022), which verifies the structural climate compatibility of a given structure. On the one hand, the choice of materials for new construction affects this compatibility. Figure 3f displays the Global Warming Potential ($GWP_{eco,BM}$), which the Isenbridge prototype does not immediately provide results for. If new, more material-efficient construction methods are under investigation, a digital twin can effectively record the potential savings or construction method potential. Another variable, which is more apparent, is the extension of the service life ($t_{sl,eco,BM}$, Figure 3f). Predictive maintenance enables the building to have a longer service life, reducing the CLS and thus the carbon footprint (Wimmer & Braml 2023a).

4 CONCLUSION AND OUTLOOK

This paper examines prevalent definitions of digital twins within industry and categorises them based on maturity, application, and modelling levels. The definitions are found to be complementary. Examples of digital twin applications are presented in industry, healthcare, and infrastructure as smart cities. The assessment of digital twin approaches in bridge construction indicates that

most of the maturity lies in the digital shadow, but it is hard to scale due to proprietary closed solutions. Therefore, standardisation is crucial. The challenges of the digital twin are exemplified by Isenbridge Schwindegg in Germany, which utilises the Industry 4.0 platform Asset Administration Shell (AAS). On one hand, selecting appropriate sensors and establishing connections for collecting and transferring measurement data to the AAS, and on the other hand, intelligently processing data prior to and following data collection needs to be investigated. These elements, which may help to achieve predictive maintenance, are described in a proof of concept. Their potential for significantly reducing a building's carbon footprint is highlighted.

The collection of measurement data has been ongoing since December 2022 and is presently secured for an indefinite period. Currently, algorithms are being developed to detect and compress the relevant measurement data simultaneously. This process is carried out with the use of existent sensors. However, the potential of alternative sensors, such as distributed fiber optic sensors, is also under investigation. Research is currently being conducted into the characteristics of the current bridge condition and their evaluation. The potential added value that this information could provide for building operators, engineers, or even smart cities remains largely theoretical. Nevertheless, the Isenbridge in Schwindegg is a valuable source of data from the moment it is opened to traffic.

ACKNOWLEDGEMENTS

This research is funded by dtec.bw – Digitalization and Technology Research Center of the Bundeswehr which we gratefully acknowledge [project RISK.twin]. dtec.bw is funded by the European Union – NextGenerationEU.

REFERENCES

Böhme, H. 2022. Behörden suchen Bauingenieure: Keine Planer, keine Projekte. *NDR* [online]. https://www.ndr.de/nachrichten/schleswig-holstein/Behoerden-suchen-Bauingenieure-Keine-Planer-keine-Projekte,fachkraefte268.html. [accessed on: 28.10.2023].

Bossler, M.; Popp, M. 2023. Arbeitsmarktanspannung aus beruflicher und regionaler Sicht: Die steigende Knappheit an Arbeitskräften bremst das Beschäftigungswachstum. IAB - Institut für Arbeitsmarkt- und Berufsforschung: IAB-Kurzbericht (12|2023).

Braml, T. et al. 2022. Digitaler Zwilling: Verwaltungsschale BBox als Datenablage über den Lebenszyklus einer Brücke. *Bautechnik*. 99 2: 114–122.

Braml, T. et al. 2023. Standardisierung im Structural Health Monitoring (SHM) – Konzeptvorschlag. In Krieger, Jürgen. 2. Fachkongress Digitale Transformation der Verkehrsinfrastruktur. Ostfildern. 20.06.2023. Tübingen: Expert Verlag: 71–81.

Bundesministerium für Verkehr, Bau- und Stadtentwicklung 2013. ASB-ING[online]. https://www.bast.de/BASt_2017/DE/Publikationen/Regelwerke/Ingenieurbau/Erhaltung/ASB-ING.html. [accessed on: 23.06.2023].

Danwitz, M. von et al. 2023. Hybrid Digital Twins: A Proof of Concept for Reinforced Concrete Beams. *PAMM*. 22 1.

2021.Functional View of the Asset Administration Shell in an Industrie 4.0 System Environment. Berlin. Plattform Industrie 4.0

Hagedorn, P. et al. 2023. BIM-Enabled Infrastructure Asset Management Using Information Containers and Semantic Web. *Journal of Computing in Civil Engineering*. 37 1.

Haist, M. et al. 2022. Nachhaltig konstruieren und bauen mit Beton. In Bergmeister, Konrad; Fingerloos, Frank; Wörner, Johann-Dietrich. *Nachhaltigkeit, Digitalisierung, Instandhaltung*. Berlin: Ernst & Sohn a Wiley brand: 421–531.

Hindersmann, I. et al. 2023. Monitoring on federal highways bridges: current situation, future opportunities & digital implementation. *ce/papers*. 6 5: 654–660.

Jacoby, M. et al. 2023. Open-Source Implementations of the Reactive Asset Administration Shell: A Survey. *Sensors (Basel, Switzerland)*. 23 11: 5229.

Kainz, C.; Wolf, G. 2023. Use of data from BIM method for new and existing concrete bridges – Practical report and possible improvements. In Osaka Metropolian University. GJBS 2023. Osaka. 29.08.2023 - 30.08.2023: 431–438.

Kaya, Y.; Ventura, C. 2019. Seismic Structural Health Monitoring of Bridges in British Columbia, Canada. *Seismic Structural Health Monitoring*: 31–49.
Kenett, R. S.; Bortman, J. 2022. The digital twin in Industry 4.0: A wide-angle perspective. *Quality and Reliability Engineering International*. 38 3: 1357–1366.
Kosse, S. et al. 2022. Digital Twin Framework for Enabling Serial Construction. *Frontiers in Built Environment*. 8.
Kritzinger, W. et al. 2018. Digital Twin in manufacturing: A categorical literature review and classification. *IFAC-PapersOnLine*. 51 11: 1016–1022.
Machado, T. M.; Berssaneti, F. T. 2023. Literature review of digital twin in healthcare. *Heliyon*. 9 9: e19390.
Naraniecki, H. et al. 2023. Concept for a digital twin of railway bridges on the example of the new Filstal bridges. *ce/papers*. 6 5: 711–717.
Schellen, M. et al. 2023. Annotation rules and classes for semantic segmentation of point clouds for digitalization of existing bridge structures. *EC3 Conference 2023*. 4: 0.
Schleich, B. et al. 2017. Shaping the digital twin for design and production engineering. *CIRP Annals*. 66 1: 141–144.
Shahat, E. et al. 2021. City Digital Twin Potentials: A Review and Research Agenda. *Sustainability*. 13 6: 3386.
Siemens Digital Industries Software 2019. Digital Twin | Siemens [online]. https://www.plm.automation.siemens.com/global/en/our-story/glossary/digital-twin/24465. [accessed on: 27.10.2023].
Stavropoulos, P.; Mourtzis, D. 2022. Digital twins in industry 4.0. *Design and Operation of Production Networks for Mass Personalization in the Era of Cloud Technology*: Elsevier: 277–316.
Sun, T. et al. 2023. Digital twin in healthcare: Recent updates and challenges. *Digital health*. 9: 1–13.
Therias, A.; Rafiee, A. 2023. City digital twins for urban resilience. *International Journal of Digital Earth*. 16 2: 4164–4190.
Varabei, Y. et al. 2022. Ingenieurbauwerke als intelligente Systeme – Erhaltungsmanagement mit Structural Health Information Patterns (SHIPs). *Beton- und Stahlbetonbau*. 117 7: 472–487.
Vorländer, B. 2023. Wie marode Brücken die Wirtschaft bedrohen. *tagesschau.de* [online]. https://www.tagesschau.de/wirtschaft/konjunktur/bruecken-marode-wirtschaftliche-folgen-100.html. [accessed on: 28.10.2023].
Weil, C. et al. 2023. Urban Digital Twin Challenges: A Systematic Review and Perspectives for Sustainable Smart Cities. *Sustainable Cities and Society*. 99: 104862.
Wimmer, J. et al. 2023. Digitale Zwillinge für Brücken mittlerer Stützweite – Pilotprojekt Brücke Schwindegg – Teil 1: Sensorik. *Beton- und Stahlbetonbau*. 118 12.
Wimmer, J.; Braml, T. 2023a. Digital Bridge Schwindegg: Ab initio bridge monitoring for a sustainable lifecycle management. In International Association for Bridge and Structural Engineering (IABSE). IABSE Congress New Delhi 2023. New Delhi, India. 20-22 September 2023.
Wimmer, J.; Braml, T. 2023b. Geo-referenced localisation of SHM sensors on new bridge construction based on the example of the digital bridge Schwindegg (Germany). In Osaka Metropolian University. GJBS 2023. Osaka. 29.08.2023 – 30.08.2023: 394–402.
Wimmer, J.; Braml, T. 2023c. Permanent Structural Health Monitoring of a new prestressed concrete bridge. *ce/papers*. 6 5: 691–700.
Yaqoob, I. et al. 2023. Metaverse applications in smart cities: Enabling technologies, opportunities, challenges, and future directions. *Internet of Things*. 23: 100884.
Ye, C. et al. 2019. Structural health monitoring 2019. Lancaster, Pennsylvania: DEStech Publications, Inc.

Bridge Maintenance, Safety, Management, Digitalization and Sustainability – Jensen, Frangopol & Schmidt (eds)
© 2024 The Author(s), ISBN 978-1-032-77040-6
Open Access: www.taylorfrancis.com, CC BY-NC-ND 4.0 license

ANYTWIN – standardizing monitoring-based safety assessments of bridges and the integration into Digital Twins

A. Lazoglu
MKP GmbH, Hannover, Germany

J.-H. Bartels
Institute of Concrete Structures, Technical University of Dresden, Germany

R. Stein
GMG Ingenieurgesellschaft, Dresden, Germany

M. Maibaum
Department of Conceptual and Structural Design – Steel Construction, Technical University of Berlin, Germany

L. Puttkamer
Federal Highway Research Institute (BASt), Bergisch Gladbach, Germany

L. Ulbrich
Hentschke Bau GmbH, Bautzen, Germany

ABSTRACT: Normative specifications and guidelines for the supplementary use of sensor-based monitoring in the assessment of road bridges are currently insufficient. This leads to heterogeneous approaches in measurement-based recalculations. In the research project ANYTWIN, standardized measurement and analysis concepts are being developed for selected structural safety verifications. Engineers will benefit from recommendations for actions that can be applied to structures with similar issues. To ensure sustainable and interoperable usage, concepts for integrating structural safety verifications into Digital Twins are created. This will enable information to be interoperably utilized across generations. The automated and standardized integration and analysis of measurement data prospectively establish a crucial core functionality of Digital Twins in infrastructure. The concepts are validated with extensive data from the model bridge of the research project IDA-KI and the Digital Twin of the Köhlbrand Bridge. The ANYTWIN research project commenced in September 2023 and is funded for three years by the Federal Ministry of Digital and Transport (BMDV). Approaches and initial results are presented in this paper.

1 INTRODUCTION

The transportation infrastructure is both a cornerstone and a vulnerability of Germany's economy. Due to the high age of structures and the significant increase in heavy traffic, in 2020 approximately 12% of bridge surfaces were in an insufficient condition (Bast 2023). Reinforced concrete, prestressed concrete and steel bridges account for approximately 83% of the total bridge stock in the federal highway network. Over 80% of the damages observed on these bridges can be attributed to cracks, deformations, and welding seam issues. (Schnellenbach-Held et al. 2015) (Bartels et al. 2022). These damages may result from deficient maintenance

DOI: 10.1201/9781003483755-94

management or planning deficiencies in construction and structural analysis. Examples include the use of prestressing steels susceptible to stress corrosion cracking and the inadequate design of coupling joints in the sectional construction of prestressed concrete bridges.

Safety-relevant failure mechanisms that remain partly hidden and result in a sudden component failure pose a challenge. Therefore, a structural analysis is indispensable. However, the prevailing lack of information on existing bridges leads to conservative calculation assumptions. For the preservation of structures, especially those with high strategic importance in the infrastructure network, more innovative research approaches are required. Sensor-based monitoring can be utilized to conduct more realistic analyses and detect changes early on within the framework of continuous monitoring. The goal of the ANYTWIN project is to conceptualize a Digital Twin that enables a measurement-based structural safety assessment for road bridges. The project focuses on vulnerable areas of structures and typical deficiencies in structural analyses.

2 STANDARDIZATION OF MEASUREMENT-BASED VERIFICATIONS

Structures are based on the design calculations performed by structural engineers. These calculations are also conducted to assess the probability of specific failure mechanisms. The verifications are considered valid, and the structures are deemed structurally sound only as long as the initial computational assumptions remain applicable. Inadequacies in the original design approaches, changes in the structural condition, and variations in external influences, such as the increase in heavy traffic, often necessitate the reassessment of existing bridges. For German road bridges, there is a guideline for this purpose known as the recalculation guideline (BMVBS 2011). The procedure is structured in stages, with each stage increasing the computational effort and, consequently, the accuracy of the calculations (Figure 1).

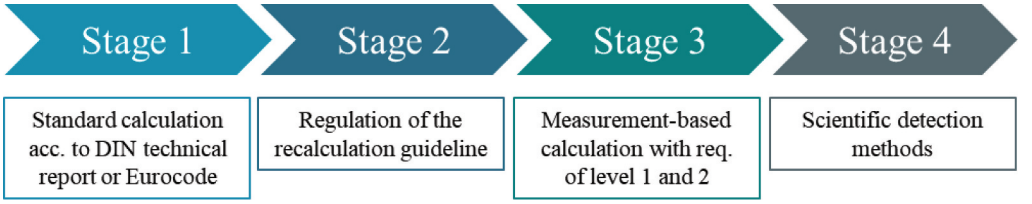


Figure 1. Stages of the recalculation guideline.

In Stage 3, additionally, sensor-based measurements of external influences or structural behavior can be integrated into a so-called monitoring- or measurement-based calculation. The verification result can extend the assessed lifespan of bridges without necessitating restrictions through traffic compensatory measures or costly reinforcement interventions (DBV 2018). While there are numerous practical examples for Stage 3, the recalculation guideline does not provide sufficient information on procedures. ANYTWIN aims to standardize these procedures.

2.1 *Examined failure mechanisms*

In (Fischer et al. 2016) and (Neumann & Brauer 2018), verification results of concrete, steel, and composite bridges were analyzed, evaluating the cause and effect of significant deficiencies. These analyses in ANYTWIN are used to determine the failure mechanisms to be investigated.

To verify and update these analyses and capture the impact of the optimized verification formats introduced since the implementation of the recalculation guideline, ANYTWIN will

conduct a survey of infrastructure operators in December 2023. This survey will gather the experiences and challenges of operators with existing regulations and frequently encountered verification deficiencies. Furthermore, infrastructure operators will be surveyed regarding their current handling of Stage 3 and potential support in the application of measurement technology in the context of bridge reassessment.

Initial results of the analyses indicate that the most common deficiencies in verifications arise from the following five failure mechanisms:

- Failure of Couplings in Coupling Joints (Fischer et al. 2016)
- Stress Corrosion Cracking (Fischer et al. 2016)
- Shear Cracking (Fischer et al. 2016)
- Plate Buckling (Neumann & Brauer 2018)
- Fatigue (Neumann & Brauer 2018)

These five failure mechanisms will be further examined in the ANYTWIN project.

2.2 *Investigation of optimization opportunities through sensor-based monitoring*

The failure mechanisms can be described by limit state equations. The parameters included in the equations are examined regarding their impact on the results (sensitivity analysis) and their measurability through sensor-based methods. In the development of standardized measurement concepts, reference is made to the sensitive parameters that have a significant impact on the failure mechanism.

As an example, the limit state equation for fatigue verification at coupling joints is formulated as follows, see Equation (2.1).

$$g(x) = D_{limit} - D \tag{2.1}$$

This is based on the Palmgren-Miner rule, which requires the stress amplitudes $\Delta\sigma$ of all crossings to determine the damage sum D and is described by Equation (2.2).

$$D = \sum_i D_i = \sum_i \frac{n_i}{N_i} = \sum_i \frac{n_i}{\frac{\Delta\sigma_{Rsk}^m \cdot N^*}{\Delta\sigma_i^m}} = \frac{1}{\Delta\sigma_{Rsk}^m \cdot N^*} \cdot \sum_i n_i \cdot \Delta\sigma_i^m \tag{2.2}$$

If strains are directly measured on the prestressing steel, they can be converted into stresses and directly integrated into Equation (2.2). However, this approach requires exposing the tendons, which is not always desired due to the additional damage it causes (Steffens 2019). As an alternative, it is possible to determine the damage sum according to (Zilch et al. 2001) using Equation (2.3), where the prestressing steel stress is calculated, for example, using a finite element model. It should be noted that the basic moment (M_0) in a prestressed concrete cross-section influences the stress range due to the non-linear structural behavior of prestressed concrete according to Figure 2.

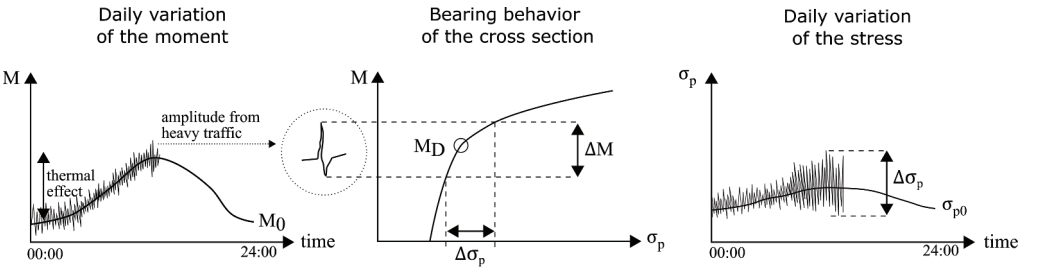


Figure 2. Stress amplitude ranges depending on the daily variations in temperature and vehicle loading.

As a result, the moment-stress relationship must be correctly recorded in the finite element model. Additionally, the actual basic moment is required to determine the stress range according to Equation (2.4).

The basic moment includes effects from dead loads, prestressing, settlements, and temperature. Whereby these can be assumed to act as constants, except for the cyclic temperature loading.

The influence of the basic moment on the stress range requires different temperature conditions to be considered when calculating partial damage from traffic-related alternating stresses (Krohn 2014).

$$g(x) = D_{limit} - N_{tot} \cdot \sum_{\Delta T=\min\Delta T}^{\Delta T=\max\Delta T} \left(\sum_{i=1}^{j} \left(\sum_{h=1}^{24} \lambda_{V,h} \cdot \lambda_{T,\Delta T,h} \cdot p_i \cdot D_{\Delta T,i} \right) \right) \tag{2.3}$$

$$\Delta\sigma(M_i) = \sigma\left(M_{perm} + M_{\Delta T} + M_{Q,max,i}\right) - \sigma\left(M_{perm} + M_{\Delta T} + M_{Q,min,i}\right) \tag{2.4}$$

where D_{limit} = limit of the total damage sum; N_{tot} = number of heavy vehicles in the period of use; $\lambda_{V,h}$ = share of heavy traffic during hour h in the total daily traffic volume; $\lambda_{T,\Delta T,h}$ = probability of the temperature gradient ΔT occurring during hour h of the day; p_i = share of vehicle type i; $D_{\Delta T,i}$ = partial damage of vehicle type i with simultaneous temperature gradient ΔT analogous to (2.2) by determining the stress ranges $\Delta\sigma_i$ according to (2.4).

Sensor-based measurements are primarily related to variable loads or stresses, as these represent measurable quantities affected by changing conditions. Nevertheless, the measurement of constant residual stresses typically entails significant effort. In the fatigue failure mechanism of the couplings, variable influences such as heavy traffic and temperature changes affect the magnitude of the stress range. Through long-term monitoring, the actual temperature gradients and traffic loads influences can be recorded. Traffic influences can be subsequently converted to the service life period, with or without considering traffic developments, as outlined in (Steffens & Geißler 2021). Furthermore, through short- or long-term measurements, it is possible to measure the behavior of the real structure, evaluate the basic moment and adjust the moment-stress relationship used for recalculation, as shown in (Zilch & Penka 2014) and (Weiher et al. 2015).

2.3 *Development of standardized measurement and analysis concepts*

For the measurement-based verification of failure mechanisms, standardized measurement concepts are developed. These include information on the type, scope, and location of sensors, as well as the respective measurement periods, sampling rates, and requirements for data processing. The challenge of standardization is to separate the measurement requirements from the uniqueness of each structure. To ensure the cross-structure usability of the measurement concepts, parameterized finite element models are developed, and influences on the choice of concept parameters are examined.

Like the approach of the recalculation guideline (Figure 1), ANYTWIN follows a stagewise progression in the measurement concepts, in which the complexity of the measurement task gradually increases. For example, in the case of coupling fatigue, in the first stage, over a limited period in summer (high temperature gradients) and under real traffic conditions, only the crack width of the coupling joint and the concrete strain in the uninterrupted area immediately adjacent to the coupling joint are measured and compared. Significant differences would indicate "joint breathing" and thus a potential fatigue problem. In subsequent stages, the scope and duration of the measurements can be expanded to pursue more complex approaches for calibrating the basic moment and the occurring temperature gradients and traffic loads. Figure 3 shows an exemplary excerpt from a measurement report with the positions of temperature sensors and displacement transducers, as well as exemplary data trends.

Evaluation concepts are intended to establish processes and conditions for substituting the verification-relevant physical parameters with a value based on raw measurement data. In the

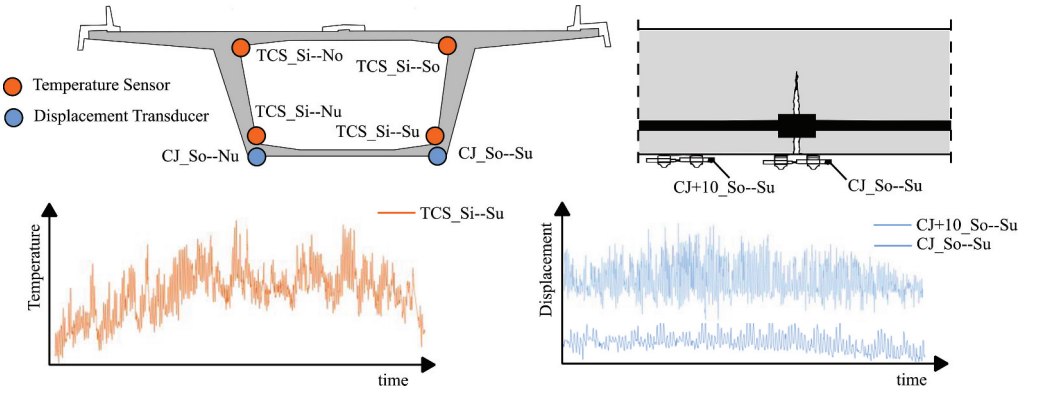


Figure 3. Exemplary measurement layout and corresponding data trends.

present example in Figure 3, this would involve converting the data from individual temperature sensors into a resulting vertical temperature gradient. Both the measurement and evaluation concepts need to be developed by the normative safety requirements of Eurocode 0.

3 CONCEPT OF A DIGITAL TWIN

Germany's sustainability strategy (BMVI 2020) is aligned with the 17 Sustainable Development Goals of the UN Agenda 2030. Goal 9 includes the establishment of a "resilient transportation infrastructure." The strategy prioritizes "maintenance over expansion and new construction" and the optimization of traffic flow. The German "BIM Master Plan" for Federal Highways (BMVI 2021) envisions the future scenario of maintenance and operation based on Digital Twins. After Building Information Modelling (BIM) has been established in the planning and manufacturing phases, the development and testing of Digital Twins are intended to create a "Master Plan" for Digital Twins. This perspective also includes integrating verifications of failure mechanisms, conducted either as a one-time assessment or continuously through sensor-based monitoring, into a Digital Bridge Twin. In ANYTWIN, a concept is being developed as a basis for this. The focus lies on the operational phase, where Digital Twins enable real-time monitoring.

3.1 *Definition and characterization of the Digital Twin*

The term "Digital Twin" originated in 2002 and 2003 when Grieves and Vickers described it as a "conceptual ideal for the product lifecycle management" using the example of a motor vehicle (Grieves & Vickers 2017). Today, the user-specific definition of a Digital Twin varies across different industries:

In the wind energy industry, the Digital Twin is primarily understood as a three-dimensional finite element model calibrated with real-time information for structural assessment (Solman, et al., 2022). In mechanical engineering, the Twin is defined as a virtual assistance system in connection with Mixed Reality in plant operations, enabling remote monitoring and maintenance of critical machine components (Schweiger-Recksiek et al. 2020).

In the construction industry, despite the ongoing digitization and the introduction of BIM, there are no uniform standards for the terms and definitions of Digital Twins. Additionally, there are no standardized definitions for linking with BIM and utilizing it in maintenance management. In bridge construction, the combination of real-time data with a BIM model is increasingly used to create Digital Twins (Lazoglu et al. 2023) (Ye et al. 2019).

The common element of collecting and evaluating information about the actual structure is shared in all definitions. Publications related to construction, like the one by (Boje et al. 2020), offer a general overview of progress in this field.

For most applications in construction, it is not necessary to digitize the physical object with all its information. For example, the use of sensors in construction is currently mainly event-driven, focusing on critical areas and specific damage or failure mechanisms of an object and its surroundings. Abstraction can be achieved through the definition of maturity levels (ARUP 2019). The choice of the maturity level to be developed depends on the engineers' and operators' individual requirements, considering the complexity of the object and its specific safety and relevance to society and the environment. Thus, infrastructure with high operational importance for the transportation network is particularly suitable for developing Digital Twins with higher maturity levels.

The first use cases of the Digital Twin were elaborated in (Nieborowski et al. 2023), serving as a basis for identifying use cases in ANYTWIN.

3.2 *Data integration, management, and provision in the Digital Twin*

The definition of use cases for Digital Twins requires consideration of relevant structural and environmental data. In the context of verifying failure mechanisms, these include e. g. computational results from finite element analysis, primarily evaluated measurement data and sensor states. The quality of this data significantly influences valid structural safety information. It is also necessary to integrate existing conditions and state information (such as damages and material properties) as they have a direct impact on the failure mechanism.

The challenge in data integration lies in the diversity of the heterogeneous data sources, some of which are not digital, machine-readable, or decentralized. In the ANYTWIN project, the current state is being explored, and based on use cases, proposals for data formats, quality requirements, and metadata, especially for monitoring data, are being developed.

In ANYTWIN, the Digital Twin is considered a Single Source of Truth, functioning as a database system where all relevant data, including BIM model information, is digitally stored. To address the size limitation of IFC-files, alternative approaches for integrating extensive monitoring data into Digital Twins are being investigated. Linked and Embedded Data methods are often favored in practice, where BIM structural and domain models are updated in a Common Data Environment (CDE). Additional databases may exist to link dynamic data (Wedel et al. 2022).

Efficient storage, management, and processing require the development of a data structure model, especially at higher levels of automation. In ANYTWIN, a generalized data structure model is being designed based on use cases, serving as the foundation for the development of a flexible database system. The focus is on cross-structure applicability and scalability for potential future use cases.

Approaches are being developed in ANYTWIN for the intuitive provision of relevant condition information in the Digital Twin. These approaches aim to deliver data based on user needs, providing maximum flexibility and efficiency. This supports engineers in making informed decisions about repair measures. It also enables rapid responses to change in structural conditions, with visualizations tailored to various user groups such as infrastructure operators, structural engineers, and the public.

4 VALIDATION OF THE CONCEPTS

4.1 *SmartBRIDGE Hamburg – monitoring system of the Köhlbrand bridge*

In the "smartBRIDGE Hamburg" project, a Digital Twin of the Köhlbrand bridge has been developed with continuous update through data from an extensive monitoring system with approximately 800 sensors (Grabe et al. 2020) (Wenner et al. 2021). The structure comprises a cable-stayed bridge with a steel superstructure and adjacent bridges with prestressed

concrete superstructures. Verifications for failure mechanisms such as shear failure, coupling fatigue, steel fatigue, and buckling have been successfully conducted in higher verification stages (including Stages 3 and 4). For the piloting of the Digital Bridge Twin these failure mechanisms have been monitored through measurements for nearly 2.5 years.

For example, strain gauges distributed on the steel box girder capture the stresses within the steel plates. These stresses contribute to an automated, probabilistically guided buckling verification, analogous to (Herbrand et al. 2021). The evaluation is automated by determining a failure probability expressed as a reliability index with a reference period of 50 years ($\beta_{50\,Y}$). This index, along with other condition indicators, is imported into the database of the Digital Twin and made available through the "Condition Control" platform (Herbrand et al. 2022).

The extensive dataset in the Digital Twin of the Köhlbrand bridge allows for the validation of concepts developed in ANYTWIN. Due to the collaboration of some authors in the conception and testing of fundamental concepts in smartBRIDGE Hamburg, synergies can be leveraged across projects.

4.2 *OpenLAB – research bridge in Bautzen, Germany*

As part of the research project IDA-KI, a research bridge, the "openLAB," was constructed as an open research structure (see Figure 4). It is approximately 45 meters long, 4.5 meters wide, and consists of three spans, made of prestressed concrete with tendons in immediate composite action. Additionally, post-tensioning strands were incorporated to enable the replication of a coupling joint issue. Specific structural vulnerabilities, such as damaged tendons, gravel nests, voids, and areas with reduced shear capacity, were deliberately included. To capture changes in condition, measurement technology was installed during the production of the components. A significant portion of the monitoring is conducted using distributed fiber optic sensors (DFOS).

Along the coupling joint, the arrangement of DFOS was carried out in a way that allows the capture of joint opening profiles and strain profiles across the entire cross-section. The extensive measurement equipment of the openLAB, the existing IT infrastructure, and the implementation of a Digital Twin enable the validation of concepts in ANYTWIN. For this purpose, the existing measurement and loading concept from IDA-KI is expanded to meet the requirements of ANYTWIN. Finally, there is the possibility of integrating the measurement data into the existing BIM-based Digital Twin of the openLAB. Further information on the research project IDA-KI and the openLAB can be found in (Herbers et al., in press).



Figure 4. Virtual representation of the research bridge IDA-KI (Hentschke Bau GmbH).

5 SUMMARY AND OUTLOOK

In the research project ANYTWIN, which commenced in September 2023, holistic measurement and evaluation concepts are being developed for the structural assessment of bridge structures and their integration into Digital Twins. Following initial research, the focus for standardizing measurement-based verification is placed on failure mechanisms such as buckling and fatigue in steel bridges, as well as stress corrosion cracking, coupling- and shear failure in prestressed concrete bridges. Standards are being developed for the entire verification process, ranging from sensor requirements (including necessary metadata) to data cleansing and integration into failure equations. The conceptual development for the verification of coupling fatigue is the starting point.

This article presents the results of an initial investigation into the definition and existing concepts and implementations of cross-industry Digital Twins. Subsequently, ANYTWIN aims to develop a data structure model for the Digital Twin, based on which the collected and analyzed data can be stored in a flexible database system and visualized appropriately for different user groups. This approach ensures the full utilization of the benefits of the Digital Twin, providing effective support for infrastructure operation. Standardization requires a comprehensive systematic compilation of ideas and concepts, as well as the implementation of numerous Digital Twins that must be carefully evaluated through pilot projects. ANYTWIN will play a crucial role in this process.

ACKNOWLEDGEMENT

This article presents the results of the research project ANYTWIN (Standardizing Monitoring Based Safety Assessments of Bridges and the Integration into Digital Twins), funded by the German Federal Ministry for Digital and Transport within the mFUND funding program (grant number: 19FS2248A-F).

REFERENCES

ARUP 2019. *Digital Twin – Toward a meaningful framework*. London: ARUP.

Bartels, J.-H., Naraniecki, H. & Marx, S. 2022. *Schadenspriorisierungsanalyse bei Eisenbahnbrücken – Priorisierung von Brückenschäden bei der Deutschen Bahn nach dem Prinzip der FMEA*. Bautechnik, 99, Issue 11, 825–834. https://doi.org/10.1002/bate.202100119

BMVBS 2011. *Richtlinie zur Nachrechnung von Straßenbrücken im Bestand (Nachrechnungsrichtlinie)*. Bundesministerium für Verkehr, Bau und Stadtentwicklung (BMVBS). Berlin, 05/2011.

BMVI 2020. *Bericht des BMVI zur Nachhaltigkeit 2020.* Bundesministerium für Verkehr und digitale Infrastruktur (BMVI). Berlin, 05/2020.

BMVI 2021. *Masterplan BIM Bundesfernstraßen.* Bundesministerium für Verkehr und digitale Infrastruktur (BMVI). Berlin, 09/2021.

Boje, C., Guerriero, A., Kubicki, S. & Rezgui, Y. 2020. *Towards a semantic Construction Digital Twin: Directions for future research*. Automation in Construction, Volume 114. https://doi.org/10.1016/j.autcon.2020.103179.

Bast 2023. *Brückenstatistik*. Bundesanstalt für Straßenwesen (Bast). [Online 01.09.2023] Available at: https://www.bast.de/DE/Statistik/Bruecken/Brueckenstatistik.html.

DBV 2018. *"Brückenmonitoring - Planung, Ausschreibung, Umsetzung"*. Deutscher Beton- und Bautechnik-Verein e. V. DBV-Merkblatt. Berlin, 08/2018.

Fischer, O., Lechner, T., Wild, M., Müller, A. & Kessner, K. 2016. *Nachrechnung von Betonbrücken - systematische Datenauswertung nachgerechneter Bauwerke*. Berichte der Bundesanstalt für Straßenwesen, Reihe B: Brücken- und Ingenieurbau, Heft 124.

Grabe, M., Ullerich, C., Wenner, M. & Herbrand, M., 2020. *smartBridge Hamburg – prototypische Pilotierung eines digitalen Zwillings*. Bautechnik 97, Issue 2, 118–125. https://doi.org/10.1002/bate.201900108

Grieves, M. & Vickers, J., 2017. *Digital Twin: Mitigating Unpredictable, Undesirable Emergent Behavior in Complex Systems.* In: Transdisciplinary Perspectives on Complex Systems - New Findings and Approaches. Switzerland: Springer.

Herbers, M., Naraniecki, H., Jesse, F. & Smarsly, K., in press. *openLAB - Eine Forschungsbrücke zur Entwicklung eines digitalen Brückenzwillings.* Beton- und Stahlbetonbau.

Herbrand, M., Lazoglu, A., Ullerich, C., Marx, S. & Zehetmaier, G. 2022. *Aggregation von Zustandsindikatoren aus Inspektions- und Monitoringdaten im Brückenbau*. Bautechnik 99, Issue 2, S. 95–103. https://doi.org/10.1002/bate.202100095

Herbrand, M., Wenner, M., Ullerich, C., Rauert, T., Zehetmaier, G. & Marx, S. 2021. *Beurteilung der Bauwerkszuverlässigkeit durch Bauwerksmonitoring – Probabilistischer Beulnachweis der Hamburger Köhlbrandbrücke*. Bautechnik 98, Issue 2, 93–104. https://doi.org/10.1002/bate.202000094

Krohn, S. 2014. *Messwertgestützte Ermüdungsnachweise an bestehenden Straßenbrücken*, Book Series of the Department of Civil Engineering, Technische Universität Berlin, 16. Aachen: Shaker.

Lazoglu, A., Naraniecki, H., Zaidman, I. & Marx, S. 2023. *A monitoring based digital twin for the Filstal bridges*. Proceedings of the 8th International Symposium on Life-Cycle Civil Engineering (IALCCE 2023).

Neumann, W. & Brauer, A. 2018. *Nachrechnung von Stahl- und Verbundbrücken - Systematische Datenauswertung nachgerechneter Bauwerke*. Berichte der Bundesanstalt für Straßenwesen, Reihe B: Brücken- und Ingenieurbau, Heft 144

Nieborowski, S.; Windmann, S.; Bednorz, J.; Hindersmann, I. & Zinke, T. 2023 Digitaler Zwilling Brücke im Betrieb. Bautechnik 100, Issue 2, 86–93. https://doi.org/10.1002/bate.202200089

Ruhrberg, R. 1994. *Schäden an Brücken und anderen Ingenieurbauwerken: Dokumentation 1994*. Verkehrsblatt-Verlag, 1994.

Schnellenbach-Held, M., Peeters, M. & Miedzinski, G. 2015. *Intelligente Brücke - Schädigungsrelevante Einwirkungen und Schädigungspotenziale von Brückenbauwerken aus Beton*. Berichte der Bundesanstalt für Straßenwesen, Reihe B: Brücken- und Ingenieurbau, Heft 110.

Schweigert-Recksiek, S., Trauer, J., Engel, C, Spreitzer, K., Zimmermann, M. 2020. *Conception of a digital twin in mechanical engineering – A case study in technical product development*. Proceedings of the Design Society: DESIGN Conference. 2020, 1, 383–392. https://doi.org/10.1017/dsd.2020.23

Solman, H., Kirkegaard, J. K., Smits, M., Vliet, B. V., Bush, S. 2022. *Digital twinning as an act of governance in the wind energy sector*, Environmental Science & Policy, Volume 127, 2022, 272–279. https://doi.org/10.1016/j.envsci.2021.10.027.

Steffens, N. 2019. *Sicherheitsäquivalente Bewertung von Brücken durch Bauwerksmonitoring*, Book Series of the Department of Civil Engineering, Technische Universität Berlin, 26. Düren: Shaker.

Steffens, N. & Geißler, K., 2021. *Standortspezifisches Ziellastniveau und objektspezifische Lastmodelle für die Nachrechnung auf der Basis von Bauwerksmonitoring*. Bautechnik 98, Issue 10, 720–735. https://doi.org/10.1002/bate.202100051

Wedel, F., Opitz, D., Tiedemann, C. & Meyer-Westphal, M., 2022. *Das 3-D-Modell als Grundlage des digitalen Zwillings*. Bautechnik 99, Issue 2.

Weiher, H., Runtemund, K. & Ullerich, C., 2015. *Monitoringbasierter Nachweis der Spannstahlermüdung an den Koppelfugen der Köhlbrandbrücke*. Beton- und Stahlbetonbau, 110, H. 8.

Wenner et. al. 2021. *The Concept of Digital Twin to Revolutionise Infrastructure Maintenance: the Pilot Project smartBRIDGE Hamburg*, 27th ITS World Congress, Hamburg, Germany.

Ye, C. & Butler, L. & Calka, B. & Iangurazov, M. & Lu, Q. & Gregory, A. & Girolami, M. & Middleton, C. 2019. *A Digital Twin of Bridges for Structural Health Monitoring*. https://doi.org/10.12783/shm2019/32287.

Zilch, K., Hennecke M. & Buba, R. 2001. *Kombinationsregeln für Ermüdung - Grundlagen für Betriebsfestigkeitsnachweise bei Spannbetonbrücken*. Forschung Straßenbau und Straßenverkehrstechnik, 10 Heft, 824. https://doi.org/10.1080/15732479.2012.761247

Zilch, K. & Penka, E. 2014. *Fatigue resistance evaluation for couplers of existing post tensioned, concrete bridges*, Structure and Infrastructure Engineering, Volume 10, Issue 7, Pages 901–910.

Zilch, K., Kriechbaum, M., Maurer R., Heinrich, J., Weiher, M. & Runtemund K. 2023. *Integration der Handlungsanweisungen Spannungsrisskorrosion und Koppelfugen in die Nachrechnungsrichtlinie*. Berichte der Bundesanstalt für Straßenwesen, Reihe B: Brücken- und Ingenieurbau, Heft 186.

Bridge Maintenance, Safety, Management, Digitalization and Sustainability – Jensen, Frangopol & Schmidt (eds)
© 2024 The Author(s), ISBN 978-1-032-77040-6
Open Access: www.taylorfrancis.com, CC BY-NC-ND 4.0 license

Condition assessment of mechanical fasteners by use of smart bolts

M. Reiterer & R. Thukbatullin
REVOTEC gmbh, Department of Structural Dynamics, Vienna, Austria

ABSTRACT: The maintenance of the preload force in mechanical fasteners is of great importance to ensure the load bearing capacity and durability of engineering structures that are executed with bolted connections. An innovative method for condition assessment of mechanical fasteners is presented in this paper, the smart bolts. The special features of the smart bolts are that the bolt or nut itself is the measuring device, i.e. the bolt or nut is modified to a smart component, and that the smart bolts are complete wireless without any permanent power supply. Beside the development of the smart bolts the applied data-driven method is presented aiming to compute the Remaining Useful Lifetime (RUL) for preloaded mechanical fasteners based on the permanent recorded smart bolt data. An already executed application of the developed smart bolts to ripped base plates for rail fastening is also presented and indicates the high potential of smart bolts for permanent condition assessment and RUL estimation of mechanical fasteners.

1 INTRODUCTION

Mechanical fasteners are widely used when connecting two components, e.g., connecting steel girders with cover plate joints, or when connecting between a component and another construction material (concrete, masonry, etc.). In steel structures, the execution of preloaded screwed fasteners is well established, and the controlled introduction of the preload force is of great importance to ensure the load-bearing capacity, durability, and fatigue safety (VDI 2230, 2015). Thereby, it is of central importance to achieve a defined size of preload force after initial tightening and to maintain this force over the service life of the structure, especially in dynamically stressed steel structures. The controlled pretension of the mechanical fastener leads to a force and frictional connection between the connected components. This results in significantly lower fatigue stress ranges under dynamic loading compared to a non-preloaded connection (Reiterer 2019, Reiterer et al 2020, Schiborr 2016, Schiborr & Stranghöner 2017, Dümpelmann 2020). The positive effect of preloading under dynamic load actions in terms of reducing the force and stress variation range is described in detail in Schiborr (2016) for connections in steel structures and in DAfStb-Heft 541 (2003) for fastening elements in concrete structures.

Various visual and sensor-based methods are currently used to test and monitor the actual size of the preload force in mechanical fasteners, e.g., direct tensioning indicators (Schiborr & Stranghöner 2017), ring force sensors (Tränkler & Reindl 1998) and ultrasonic measuring devices (Schiborr 2016, Reiterer 2021). However, the visual methods allow just a rough estimation of the actual preload condition, and the sensor-based methods, e.g. ring force sensors, show several disadvantages like their high costs, wired design as well as their influence on the clamp length and support surface friction of the mechanical fastener. Hence, the installation of ring force sensors is not recommended because it results a completely different fastening systems, that differs from the origin system with regard to the setup and present preload force.

This contribution introduces an innovative complete passive and wireless smart bolt (*e-Bolt*®) for condition assessment and RUL prognosis of mechanical fasteners. The basic idea of the developed smart bolt is that an already present component of the screw set (screw or nut) itself is modified and expanded into a measuring component. This results in an intelligent, talking component that can temporarily or permanently communicate its current

DOI: 10.1201/9781003483755-95

preload force condition to a hand-held reader unit or a receiver device with internet connection. The steps carried out to develop and calibrate the smart bolts are presented. In addition, the applied data-driven method for condition assessment and RUL estimation is introduced and an application example of the smart bolts is presented.

2 DEVELOPMENT OF SMART BOLTS

2.1 *Mechanical operating principle of bolted connections*

The applied preload of a screw set presses several components together. The individual parts are thus connected to form a component by the force and friction connection. When the screw set is tightened by application of the tightening moment M_A, an installation preload force F_{SM} is generated (Figure 1). The installation preload force is equal to the preload force, i.e. $F_{SM} = F_V$. In the balance of forces in the assembly state, this is identical to the clamping force F_K in the components in the joints of the components (Figure 1).

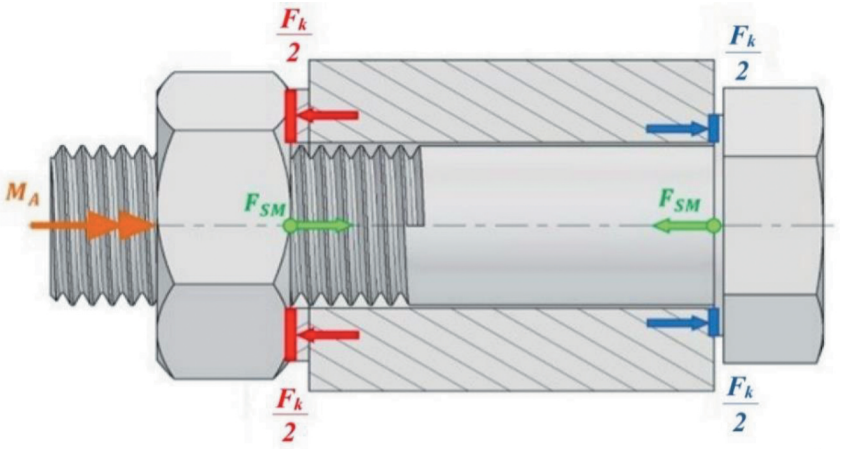


Figure 1. Principle of force equilibrium in a bolted connection.

The relation between the applied tightening moment M_A and the preload force F_V is given in Wittel et al (2019) and defined as follow,

$$M_A = F_V \cdot \left(\frac{d_2}{2} \cdot \tan(\varphi + \varsigma') + \mu_k \cdot \frac{d_k}{2} \right) \tag{1}$$

where d_2 = Pitch diameter of the screw thread; φ = pitch angle of the thread; ς' = thread friction angle; μ_k = friction coefficient in the headrest of the nut; and d_k = effective friction diameter in the nut pad. It is seen from equation (1) that the friction coefficient μ_k and the thread friction angle ς' highly influence the size of preload force that is generated by applying the tightening moment. In practice, the exact value of friction is not known and hence, applying the same size of tightening moment results in different sizes of the preload force in mechanical fasteners. This fact is important with respect to preload condition monitoring systems, that starts from different initial values although the identical tightening moment was applied.

Bolted engineering structures are very often dynamically loaded, e.g. through wind loads, rotating machines, traffic, or earthquakes, and hence the preload force in mechanical fasteners varies dynamically, i.e. a force variation range ΔF_V occurs and induces fatigue damages. The force variation range ΔF_V is therefore the effective fatigue stress for which proof of the durability or fatigue strength of the bolted connection must be carried out during the design phase. In the case of a preloaded bolted connection the dynamic load induced force variation range ΔF_V is significantly lower than in non-preloaded connections.

The prestressed bolted connection can only offer its advantage of low ΔF_V when the joint between the components is closed or over pressed. If the acting operating force is excessively high or the preload force is too low, the parting line can gap, causing the additional preload force to increase disproportionately. After exceeding the withdrawal limit the operating force-bolt force curves for the preloaded and non-preloaded connections are identical.

Based on the presented operating principle of bolted connections it is summarized, that a defined size of the preload force in mechanical fasteners is of great importance to keep fatigue damages as small as possible and to ensure the load bearing capacity over the total service life of bolted engineering structures. However, it is evident that the initial applied preload force decreases over the lifetime of structures, in dependence of the loading and boundary conditions. Because of this fact it is important to check the actual present size of the preload force periodically and a permanent method for condition assessment of mechanical fasteners, would enable both monitoring of the actual preload force and computing the Remaining Useful Lifetime (RUL) of bolted connections by application of data-driven methods.

2.2 *Development of smart bolts*

The basic idea of the developed smart bolts was to modify a standard worldwide used building product, in particular the screw and nut of the typical screw set, to an intelligent talking component. The aim was to avoid any cable connections to the smart component, i.e. wireless, and to apply a physical principle that enables a contactless energy transmission through air, i.e. no permanent power supply and battery are necessary to install to the smart bolt. After transmission of energy the actual measurement should be automatically carried out on the bolt and the data should be transmitted again through air. It is noted that two different smart components were developed, the smart bolt-bolt (*e-Bolt*®-*b*) illustrated in Figure 2a and the smart bolt-nut (*e-Bolt*®-*n*) illustrated in Figure 2b. A reader unit (Figure 2c) is used to transfer the energy through air and to receive the measured preload force from the smart bolt. Usually, depending on the boundary conditions of the structure to be equipped with smart bolts, either the *e-Bolt*®-*b* or the *e-Bolt*®-*n* is used as intelligent component.

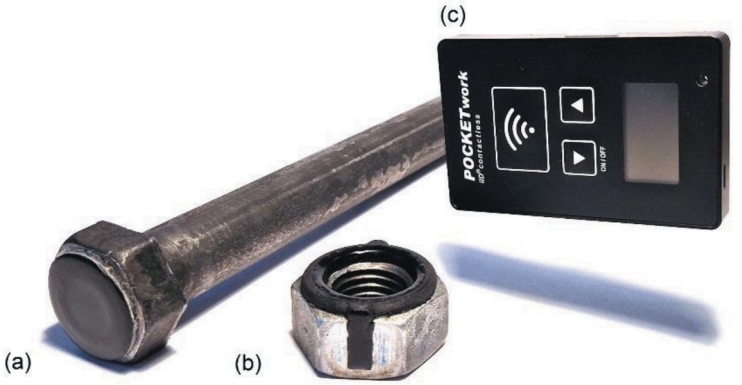


Figure 2. Photo of developed smart bolts: (a) smart bolt-bolt (*e-Bolt*®-*b*), (b) smart bolt-nut (*e-Bolt*®-*n*), (c) reader unit.

The physical principle that is applied for contactless energy and data transmission from a reader unit to the smart bolt and vice versa is in principle the Radio Frequency Identification (RFID) technology, but this principle was extended to be able to not only identify the components of mechanical fasteners, but also to carry out accurate measurements of the actual preload force. As a contactless identification and data transmission technology, RFID tags has been widely applied for access control and information tracking in logistics and industrial processes (Weinstein 2005). However, the application of the RFID technology for detecting the physical parameters of tagged structures, i.e. smart sensing, is currently very rare, and not common.

In our application the standard RFID tag is integrated with electronic components, i.e. sensors, Analogue-Digital Converter (ADC), and a Micro-Controller Unit (MCU) to get an integrated passive RFID-Sensor-Transponder module on the smart bolt. Thereby the RFID-Sensor-Transponder is used as a communication interface for data transmission. The modified RFID tag harvest the Radio-Frequency (RF) energy from RF radiation to power the circuit and carry out the measurement of the actual preload force, then save the measured data in the RFID chip to be accessed by the reading unit. The standard RFID reading unit as illustrated in Figure 2c is a handheld device and it needs a person to carry out discrete measurements, e.g. one measurement per day or per month. To avoid any personnel expenses and to record the preload data of the smart bolts continuously over time, e.g. one value per hour, a special low energy radio transducer that contains the electronic components of the reading unit and is powered by a battery has been developed.

2.3 *Calibration of smart bolts*

The developed smart bolts (*e-Bolt®-b* or the *e-Bolt®-n*) determine the actual preload force of the mechanical fastener through strain measurements, i.e. special configurated strain gauges are installed at defined locations on the smart bolts, and they measure the strain development during preloading of the bolt. In the case of the *e-Bolt®-b* so called submersible strain gauges are implanted in a 2.0 mm centric borehole of the bolt and connected to the RFID-electronic. In the case of the *e-Bolt®-n* strain gauges are installed to the side surfaces of the screw nut and connected to the RFID-electronic. For the *e-Bolt®-b* the preload force can in principle be calculated from measured strains by application of Hooke´s law. However, the material specific Young's modulus shows a scattering and the strain gauge in the borehole needs to be calibrated. For the *e-Bolt®-n* the measured strains on the side surface cannot assigned to a defined compressed area of the nut and hence, it is not possible to compute the preload force by applying Hooke´s law. Hence, the *e-Bolt®-n* needs in every case a calibration to deliver accurate preload force values.

Based on the mentioned facts, a special tightening test stand for calibration of smart bolts has been developed and is illustrated in Figure 3. The aim of the test stand is to determine the actual relation between the preload force F_V and the electrical voltage measured by the smart bolts during preloading. The test stand consists of an electric motor with planetary gear able to apply a torque moment up to 2000 Nm which is measured by a high-accurate calibrated torque sensor. An overload clutch prevents damages of the tested bolts in the case of uncontrolled torque moments generated from the electric motor. The smart bolts to be calibrated are installed to the torque support steel construction which is supported by a linear guiding. A high-accurate calibrated axial force transducer measures the preload force development during the preload process.

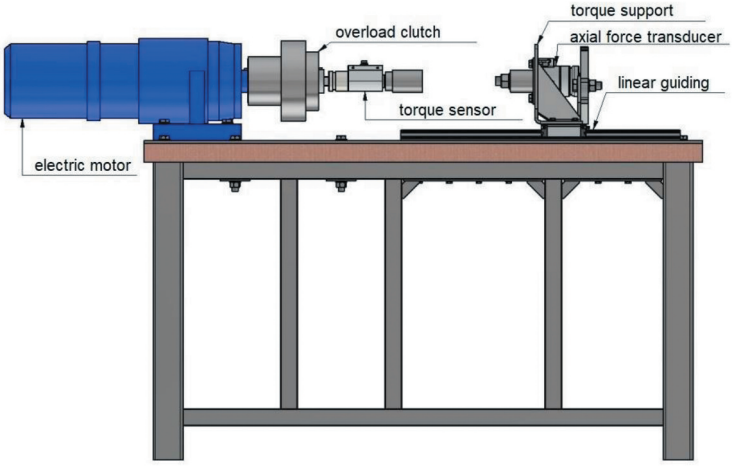


Figure 3. Principle sketch of the tightening test stand for calibration of smart bolts.

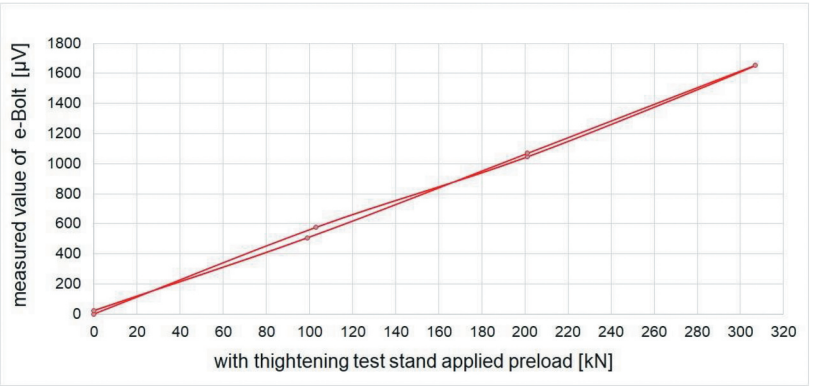


Figure 4. Calibration of *e-Bolt*®-*n* by use of the tightening test stand.

Figure 4 illustrates the result of a smart bolt calibration by use of the tightening test stand, carried out for the *e-Bolt*®-*n*. An almost linear relation between the voltage signal of the smart bolt and the preload force is indicated. It is noted that the two lines in Figure 4 depict tighten and untighten of the tested *e-Bolt*®-*n*. The determined calibration curve of the tested *e-Bolt*®-*n* is transmitted and saved to the Micro-Controller Unit (MCU) of the smart bolt and hence, the measured values are directly recorded as preload forces in Newton. In addition to the force calibration a temperature compensation of the measured preload is also taken into account and a correction curve is saved on the MCU. Therefore, temperature tests of smart bolts are carried out in climate chambers.

3 REMAINING USEFUL LIFETIME (RUL) ESTIMATION BASED ON SMART BOLT SENSOR DATA

Permanent recording of the actual preload condition of mechanical fasteners via application of smart bolts (*e-Bolt*®-*b* or *e-Bolt*®-*n*) in combination with low energy radio transducers for automatic data transmission allow to predict the Remaining Useful Life (RUL) of the degrading fatigue sensible parts of the bolted connection. Predicting RUL from permanent recorded sensor data is a central goal of predictive-maintenance algorithms (Kamariotis et al 2024). These RUL predictions form the basis for optimizing maintenance planning in a predictive maintenance paradigm. The task of optimal maintenance planning informed by the prognostic model output is known as health management.

Typically, the RUL of a structure or a component is estimated by developing a model that can perform the estimation based on the time evolution or statistical properties of condition indicator values, e.g. degradation model. Predictions from such models are statistical estimates with associated uncertainty. They provide a probability distribution of the RUL for the structure or component of interest.

Degradation models extrapolate past behavior to predict the future condition of the structure or component. This type of RUL calculation fits a linear or exponential model to the degradation profile of a condition indicator. It then uses the degradation profile of the test component to statistically compute the remaining time until the indicator reaches some defined threshold. These models are most useful when there is a known value of the condition indicator that indicates a critical state or failure.

In the case of dynamically loaded smart bolts the preload force is defined as a single condition indicator and critical losses of the preload are defined, in which case the fatigue damage would increase exponentially, i.e. a cumulative degradation occurs after a defined number of load cycles. Hence, for computing the RUL of smart bolts an exponential degradation model is chosen that describes the degradation behavior of the bolt as an exponential stochastic process with an offset term. If the amplitude of the degradation signal was observed (measured)

at discrete points in time, the amplitude at a given sampling epoch $A(t_i)$ is defined according to Gebraeel (2006) as,

$$A(t_i) = \phi + \theta \exp^{\beta t_i + \varepsilon(t_i) - \frac{\sigma^2}{2}} = \phi + \theta \exp^{\beta t_i} \exp^{\varepsilon(t_i) - \frac{\sigma^2}{2}} \quad (2)$$

where ϕ = is a constant deterministic parameter; θ = random variable; β = random variable; $\varepsilon(t_i)$ = normally distributed random error term with mean 0 and variance σ^2. In our case the amplitude of the degradation signal corresponds to the preload force measured by the installed smart bolts. It is noted that the random variable θ is lognormal-distributed and β is Gaussian-distributed. At each time step t_i, the distribution of the random variables θ and β is updated to the posterior based on the latest recorded preload measurement data of $A(t_i)$. It could be shown that $E[exp^{\varepsilon(ti)- \sigma^2/2}] = 1$ and, consequently, $E[A(t_i) \mid \theta, \beta] = \phi + \theta\, exp^{\beta(ti)}$.

The application of equation (2) for estimating the RUL of a smart bolt monitored connection used for a ripped base plate fasting system is demonstrated in section 4.

4 APPLICATION EXAMPLE: RIPPED BASE PLATE FOR RAIL FASTENING

4.1 *Smart bolt application to ripped base plates for rail fastening*

The application example presented in this paper shows the smart bolt nut (*e-Bolt®-n)* installation to ripped base plates fastening locations on a two-span railway steel bridges with a total length of 60 m span. Ripped base plates are used to support the rail clamps and during train crossing high dynamic loads act on all components of the rail fastening system. Every 0.65 m a ripped base plate is fastened by four M24 10.9 bolts to lateral steel girders and for installation a defined tightening moment of 1000 Nm is applied to the bolts (Figure 3). In case of the considered railway bridge with a length of 60 m a total of around 750 M24 bolts are executed at both rails and by application of the tightening moment of 1000 Nm an initial preload force in the range of 200 to 300 kN arises. The big spreading of the arising preload force results from the present thread friction and support surface friction, which always show a high spreading and directly influences the arising preload force in bolted connections. Hence, it is understandable that the application of the same tightening moment always leads to different values of the preload force in bolted connections.

It has been observed that due to the dynamic load actions some of the installed bolts lose their initial present preload rapidly and this may lead to critical conditions for crossing trains and railway users, respectively. Hence, the bolted connections must undergo a periodic check of the actual preload condition and to carry out this checks the railway track must be closed which lead to unwanted interruptions. In this project the *e-Bolt®-n* are installed to just 3 ripped base plates located at the beginning, end, and center of the railway bridge, i.e. 12 *e-Bolt®-n* are installed in total.



Figure 5. Photo of smart bolt nut (*e-Bolt®-n)* installed to the ripped base plates of a railway bridge and photo of fitted transducers for automatic preload data transmission.

Every of the installed *e-Bolt*®-*n* is equipped with a fitted radio transducer (Figure 3) for automatic data transmission to a nearby receiver unit with internet connection, i.e. it is not necessary to enter the railway track for getting the actual preload force value. The installation of the 12 *e-Bolt*®-*n* at 3 ripped base plates was carried out on 7th December 2022. It is noted that during the first 205 days after installation of the *e-Bolt*®-*n* only periodic preload measurements – once a month – were carried out by the hand-held reader unit (Figure 2c), and no permanent measurements were performed within this period. The radio transducers for permanent transmission of the preload force were installed on 1st July 2023, i.e. 205 days after installation of the *e-Bolt*®-*n*, and from this date, the estimation of RUL was carried out by application of equation (2). It is noted that the actual preload force of the installed *e-Bolt*®-*n* was measured and transmitted every 6 hours, i.e. 4 preload force values per day and per smart bolt.

4.2 *Results of data-driven Remaining Useful Lifetime (RUL) prediction*

The automatic preload data recording of the installed *e-Bolt*®-*n* offers the possibility to compute the Remaining Useful Lifetime (RUL) of the ripped base plate bolts according to the process described in section 3 and by application of equation (2). It is noted that in our considered application example the estimated RUL do not define the fatigue collapse of the installed bolts but a 40% loss of the initial preload value. The 40% threshold was chosen according to expertise knowledge regarding an unwanted increase of the fatigue stress variation range $\Delta\sigma_E$ in the smart bolts of the ripped base plate.

Figure 6a illustrates the computed result of the preload loss estimation based on 164 days of permanent reading of the actual preload force of the installed *e-Bolt*®-*n* (No. 41). It is again noted that the installation of the *e-Bolt*®-*n* was carried out on 7th December 2022 and the permanent measurements of the preload force did start around half a year later on the 1st of July 2023 after installation of the fitted radio transducers. Hence, the 164 days of permanent sensor signal reading run until 11th December 2023 and based on this data the RUL until 40% loss of the preload force occurs is computed by application of equation (2). It is seen from Figure 6 that the defined threshold of 40% preload loss is reached 383 days after the 11th of December 2023, i.e. on the 27th of December 2024. The total days until the 40% occurs, counting from the date of *e-Bolt*®-*n* installation on the 7th of December 2022 thus results to 752 days. Figure 6b shows the Probability Density Function (PDF) of the RUL computed based on 164 days of permanent reading of the *e-Bolt*®-*n* preload data.

In Figure 6a the horizontal red line defines the threshold of 40% preload loss. The dark blue line depicts the actual preload loss measured by the installed *e-Bolt*®-*n* and the light blue line is the computed exponential function of the considered degradation model. The confidence interval is defined by the red dashed lines. In Figure 6b the light blue line depicts the PDF of the RUL, and the red line defines the estimated RUL. The light green line defines the confidence interval.

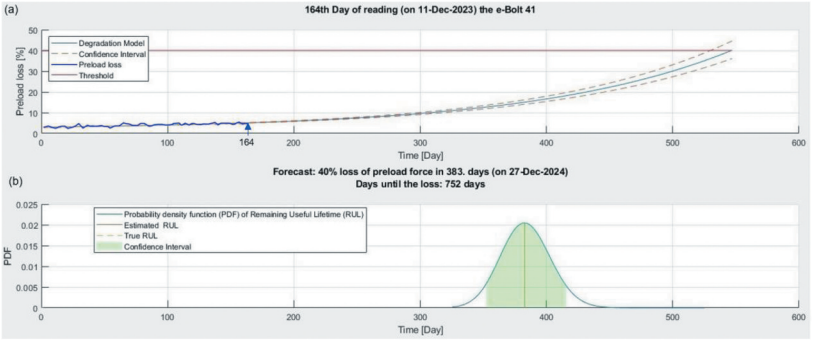


Figure 6. Preload loss estimation (a) and probability density function (b) of Remaining Useful Lifetime (RUL) until 40% loss of preload occurs.

5 CONCLUSION

Innovative passive and wireless smart bolts (*e-Bolt*®) were introduced for condition assessment and RUL prognosis of dynamically stressed mechanical fasteners. Two different smart bolts execution variants were presented, the smart bolt-bolt (*e-Bolt*®-*b*) and the smart bolt-nut (*e-Bolt*®-*n*). Usually, depending on the boundary conditions of the structure to be equipped with smart bolts, either the *e-Bolt*®-*b* or the *e-Bolt*®-*n* is used as intelligent component in mechanical fasteners. It was shown that either a hand-held reader unit or a fitted radio transducer can be used to transfer the energy through air to the smart bolt for carrying out the measurement and to transmit the actual preload force to the reader unit or transducer, respectively. The application of the radio transducer allows to carry out permanent measurements of the actual preload force and using of recorded data for predictive maintenance of bolted connections.

Besides the introduction of the *e-Bolt*® and its calibration, the applied data-driven method for condition assessment and prediction of RUL of the mechanical fasteners were also presented. Finally, to demonstrate the process of estimating the remaining RUL of bolted connections by use of smart bolts an application example of the *e-Bolt*®-*n* installed to ripped base plates of rail fasteners was presented. In this example a threshold of 40% of the loss of preload was chosen as condition indicator to be monitored and to be used for estimating the RUL. The permanent preload force measurements did start on the 1st of July 2023 and were considered until 11th December 2023. Based on these 164 days of permanent reading of the actual preload force of the exemplary considered *e-Bolt*®-*n* the RUL until 40% loss of the preload occurs turned out to 383 days, i.e. based on the actual available preload force measurement data maintenance work (re-tightening) of the installed *e-Bolt*®-*n* is necessary on the 27th of December 2024.

It is concluded that the installation of the developed smart bolts (*e-Bolt*®) in combination with radio transducers for permanent measurement of the actual preload force provide an optimal data basis for application of data-driven methods to estimate the RUL of bolted connections and effectively plan maintenance work, i.e. re-tightening of bolted connections.

REFERENCES

Dümpelmann, C. 2020. Erfassung der Strukturintegrität durch Messung der zeitabhängigen Vorspannkraft in Schraubenverbindungen. Dissertation, University of Siegen, ISBN 978-3-96182-074-0.

DAfStb-Heft 541. Das Ermüdungsverhalten von Dübelbefestigungen. Deutscher Ausschuss für Stahlbetonbau, Beuth Verlag GmbH, 2003.

European Patent EP4007857B1. Intelligente Schraubenmutter. REVOTEC zt gmbh, Erfinder: Michael Reiterer und Gergely Gulyás, Anmeldenummer: 20756745.4, Anmeldetag: 04.08.2020, Patenterteilung: 27.09.2023.

Gebraeel, N. 2006. Sensory-Updated Residual Life Distributions for Components with Exponential Degradation Patterns. In IEEE Transactions on Automation Science and Engineering 3(4), 382–393.

Kamariotis, A., Tatsis, K., Chatzi, E., Goebel, K. & Straub, D. 2024. A metric for assessing and optimizing data-driven prognostic algorithms for predictive maintenance. In Reliability Engineering & System Safety 242, 109723, ISSN 0951–8320. https://doi.org/10.1016/j.ress.2023.109723

Reiterer, M. 2019. Experimentelle Untersuchung von Lärmschutzwandstehern und deren Befestigung auf Kunstbauten, Teil 1 - Ermüdungsverhalten. In Stahlbau 88(10), 988–1003.

Reiterer, M., Stranghöner, N. & Jungbluth, D. 2020. Experimentelle Untersuchung von Lärmschutzwandstehern und deren Befestigung auf Kunstbauten, Teil 2 - Vorspannverhalten. In: Stahlbau 89(02), 1–15.

Reiterer, M. 2021. Innovative methods for testing and controlling preload forces in mechanical fasteners. In Civil Engineering Design 3, Issue 1-2, 23–34.

Schiborr, M. 2016. Anwendung von direkten Kraftanzeigern in vorgespannten Verbindungen. Dissertation, Institute for Metal and Lightweight Construction at the University of Duisburg-Essen.

Schiborr, M. & Stranghöner, N. 2017. Application of direct tension indicators in preloaded bolted connections. In Steel Construction 10 (2017), No. 2, 176–188.

Tränkler, H.R. & Reindl, L.M. 1998. Sensortechnik. Springer Vieweg. DOI 10.1007/978-3-642-29942-1

VDI 2230. Systematic calculation of highly stressed bolted joints, Joints with one cylindrical bolt. In VDI-Richtlinien, November 2015.

Weinstein, R. 2005. RFID: A technical overview and its application to the enterprise. In IT Professional, 7 (3), 27–33.

Wittel, H., Jannasch, D. & Spura, C. 2019. Roloff/Matek Maschinenelemente Formelsammlung. Springer Vieweg. https://doi.org/10.1007/978-3-658-25469-8

MS09: Novel technologies and information fusion for structural health monitoring of bridges

Organizers: C.-W. Kim, V. Sarhosis, J. Li & Y. Zhang


Taylor & Francis
Taylor & Francis Group
http://taylorandfrancis.com

Bridge Maintenance, Safety, Management, Digitalization and Sustainability – Jensen, Frangopol & Schmidt (eds)
© 2024 The Author(s), ISBN 978-1-032-77040-6
Open Access: www.taylorfrancis.com, CC BY-NC-ND 4.0 license

Real-time scour depth estimation of a pier using vibration monitoring

D. Kawabe & C.W. Kim
Kyoto University, Kyoto, Japan

V. Sarhosis
University of Leeds, Leeds, UK

ABSTRACT: This study is intended to discuss a statistical real-time scour depth estimation by use of vibration monitoring of a railway bridge pier. Recently, scour has been one of the most critical threats for bridges crossing rivers around the world because of intensive rainfalls. One novel technology to assess the ground condition around the pier during a swollen river water period is to identify its natural frequency from microtremors. To make a fast and accurate decision for bridge operation during the swollen river water period, a way of providing real-time information on scour depth, which is intuitively acceptable, estimated from identified frequency and Finite Element Model is proposed. Long-term vibration monitoring data of in-service railway bridge pier is used to investigate the possibility of scour progress timely during a flood period and a proposed method demonstrated that the probability that scour progresses beneath the footing is extremely low.

1 INTRODUCTION

Scour is the localized erosion that undermines bridge foundations during flooding and is considered as one of the most critical threats for bridges crossing rivers around the world. Nearly 21,000 bridges are reported to be susceptible to having their foundations undermined during extreme storm events (ASCE, 2021). It is particularly difficult to visually determine the scour risk of a bridge over a river, as the condition of the ground beneath the water surface of a pier cannot be directly visualized. To keep bridges as sustainable as possible, a quantitative assessment of the scour is needed.

Bridge authorities have conducted several inspection methods for assessing the condition of the bridge foundation to help manage such risk (Briaud et al., 2009). Many Japanese railway companies have adopted a vibration-based method by means of the impact test that excites the pier by dropping a weight to identify the natural frequency of the rocking mode of the target pier as a promising scour detection method (RTRI, 2007, Bao and Liu, 2017). However, the impact test is a laborious and time-consuming method, and it is inapplicable for real-time scour monitoring to make a proper decision on the train operation during high water level. Therefore, when rivers start to rise, the authorities suspend operations until they deem conditions safe. However, the longer the suspension period is, the greater the economic loss and user disruption are likely to be.

A real-time monitoring scheme utilizing ambient vibrations, thus, has been studied as an alternative method for scouring assessment during flooded rivers. In addition, a cloud-based remote sensing system using the Internet of Things (IoT) has been developed to enable high-precision structural identification to provide information on the natural frequency of monitored pier in real-time (Prendergast and Gavin, 2014). Kim et al (2020, 2021) demonstrated

DOI: 10.1201/9781003483755-96

the possibility of real-time scour monitoring by developing a remote sensing system in a real railway bridge pier as a practical application of ambient vibration-based scour detection.



Figure 1. Monitoring bridge overview.

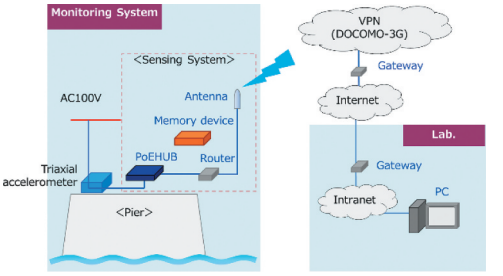


Figure 2. Remote sensing system.

In addition to scouring detection, real-time information on structure performance, such as scour depth, is also crucial for faster and more accurate decision-making on suspending or resuming traffic under uncertainties. It is, therefore, expected that the identified frequencies will be used to update numerical models to estimate the structural performance of the pier. However, there is insufficient study to propose a real-time scour assessment method that uses the modal parameters of the pier to provide information on the performance and safety of the structure.

This study proposes a way of estimating the scour depth around the vibration-monitored bridge pier for real-time assessment during the swollen river water period. A finite element model (FEM) is being built to express a soil-structure interaction and clarify the relationship between soil spring stiffnesses and the frequency of the rocking mode of the pier. Since the identified frequency of the real bridge pier using ambient vibration has a significant uncertainty due to weak signal responses, this study introduces the Bayesian model updating method to express the uncertainty of its properties. Assuming that the soil spring stiffness decreases with scour progression, the relationship between eigenvalues and scour progression is determined. Finally, the multivariate probability density function (PDF) to estimate the probability of scour depth is approximated using the polynomial curve fitting. The proposed method using the long-term vibration-monitored data of a railway bridge pier is applied to the observed data during the flood period. This study also discusses the probability of scour progress during the flood period. It is noted that this study only focuses on the spread footing type as many older railway bridges adopt spread footings.

2 MONITORING BRIDGE

2.1 *Target bridge pier and monitoring system*

The Target bridge is a steel plate girder railway bridge with a single railway track, and the span length of the bridge is 22.5m. The monitoring pier is one of its piers with a height of 9 m and a width of 3 m as shown in Figure 1. Two accelerometers were installed on top of the pier, one on the upstream and another on the downstream sides. The sampling frequency was 200Hz. For a real-time scour assessment, the remote monitoring system shown in Figure 2 was instrumented at the bridge. A long-term vibration monitoring was started in September 2017 and 24-hour measurements were conducted. The result of the impact test conducted before the long-term monitoring campaign was 9.2Hz, which is called "target frequency" of the rocking mode of the pier.

2.2 *Long-term monitoring of the identified frequency of the pier in normal condition*

A swollen river water period was observed on 3rd July 2019. Therefore, this study focuses on a monitoring period from 12th June to 3rd July 2019. Since there was no significant high water level period in June, this period is defined as a normal condition. The natural frequencies of the pier under normal conditions using ambient vibration, excluding train-induced vibration,

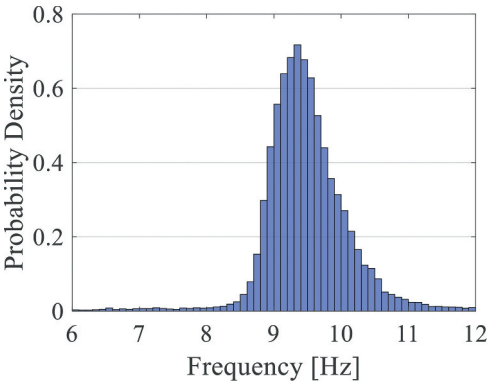


Figure 3. Identified frequency in normal condition.

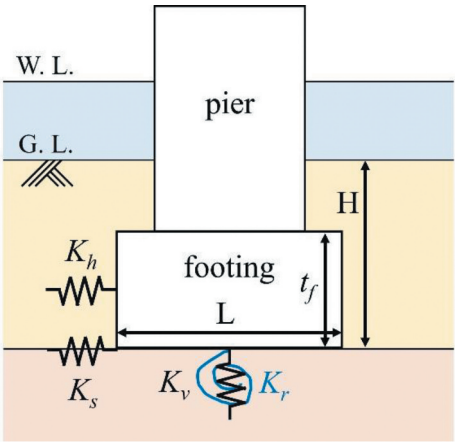


Figure 4. Location in soil springs of FEM.

were accumulated and are shown in Figure 3. A Fast Bayesian FFT (Au 2012a, b) is used to identify the target modal properties. The identified frequency ranges from 6 Hz to 12Hz, showing a wide range, and the variation is significant. This is considered that the high rigidity of the concrete pier results in small signal responses and the signal-to-noise ratio becomes relatively small. The normal distribution is considered as probability distribution function of the observed frequency, and the maximum likelihood estimation is used to estimate the parameters, such as mean value and variance. Eq. (1) shows the estimated parameters.

$$X_n \sim \mathcal{N}(9.47,\ 0.56) \tag{1}$$

3 FINITE ELEMENT MODEL

3.1 *Soil spring stiffnesses*

To estimate the scour progression of the target bridge pier, FEM is being developed in this study. The target pier is modeled with three-dimensional beam elements. Material properties are assigned to the model based on the given design code of materials. The superstructure is simplified as a point mass and attached to the pier top. The footing is modeled as a rigid body.

Adding springs are common modeling and analyzing method for the soil-structure interaction. In most cases, the foundation soil has a finite stiffness and springs can be applied in appropriate positions of the structure to present the finite stiffness of foundation soil. Horizontal, shear, vertical, and rotational springs denoted respectively as k_h, k_s, k_v, and k_r are considered following the Japanese design document (RTRI, 2012) and standard penetration test in 2015. The modeling scheme of the pier with footing is shown in Figure 4 and the dimension is summarized in Table 1. k_v and k_r are set at the center of the bottom of the footing, while the location of k_h is the same as center of gravity of the footing and k_s is located at the next to the bottom of the footing. The spring constants are summarized in Table 2.

The rocking frequency obtained from the eigenvalue analysis was around 9.57Hz which is a bit higher than the impact test and long-term monitoring result as shown in Eq. (1). To reduce this difference, the model will be updated for calibration of the soil spring parameters. Sensitivity analysis is firstly conducted. Figure 5 shows the sensitivity analysis results, in which the horizontal axis shows each soil spring stiffness, and the vertical axis indicates rocking frequency by eigenvalue analysis. Sensitivity analysis demonstrates that the rotational soil spring stiffness has a stronger influence on changes in the rocking frequency of the pier than the other springs. Therefore, the value of rotational soil spring stiffness is updated and updated rotational soil spring stiffness is shown in Table 3, while other springs use the same values in Table 2.

Table 1. Key sizes of the target bridge.

Size name	Character	Value	Unit
Footing length	L	7.8	m
Footing width	B	4.5	m
Footing height	t_f	2.0	m
Length below grade	H	3.5	m

Table 2. Soil spring stiffnesses.

Soil spring	Character	Value of Stiffness	Unit
Horizontal	k_h	7.225×10^4	N/mm
Shear	k_s	2.842×10^6	N/mm
Vertical	k_v	8.528×10^6	N/mm
Rotational	k_r	4.324×10^{14}	$N \cdot mm$

Table 3. Updated rotational soil spring stiffness.

Soil spring	Character	Value of Stiffness	Unit
Rotational	k_r	5.600×10^{13}	$N \cdot mm$

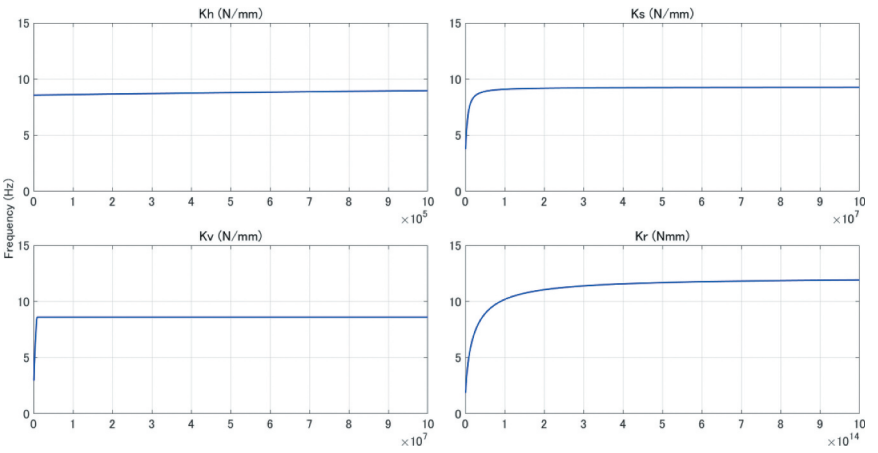


Figure 5. Sensitivity analysis result: rotational soil spring stiffness of the right bottom figure has a stronger influence than other stiffnesses.

3.2 *Identifying uncertainty of rotational soil spring stiffness by MCMC*

Since identified frequencies show a probability distribution as shown in Figure 3, the Bayesian model updating approach (Beck and Katafygiotis, 1998, Katafygiotis and Beck, 1998) that considers uncertainty of properties attributable to measurement noise and modeling error is used in this study. Based on sensitivity analysis results, the contribution of the rotational soil spring to the rocking frequency is significantly larger than the contribution of other springs. This study, therefore, considers it only as the parameter distribution.

As a sampling procedure of the Bayesian model updating, the Markov chain Monte Carlo (MCMC) sampling algorithm is utilized (Mosegaard and Tarantola, 1995, Tierney, 1994). Although there are several adaptable algorithms to cope with intensive computational cost, this study employs the Metropolis-Hastings (MH) algorithms (Metropolis et al., 1953, Hastings, 1970) which is one of the fundamental algorithms within the MCMC framework as the

uncertain parameter is only rotational spring. The target frequency from the updated model is calculated and expressed in Eq. (2).

$$X_n^{upd} \sim \mathcal{N}(9.50,\ 0.24) \tag{2}$$

Although the standard deviation from the updated model is still smaller than that of identified frequencies in the field, the eigenvalue results by the updated model can express the uncertainty. Figure 6 portrays a marginal distribution of the updated spring stiffness, in which the red line represents a PDF of updated rotational soil spring stiffness as the normal distribution shown in Eq. (3).

$$K_r \sim \mathcal{N}\left(6.72 \times 10^{13},\ 7.21 \times 10^{12}\right) \tag{3}$$

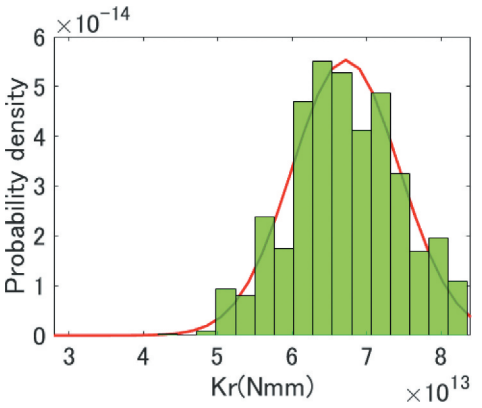


Figure 6. Marginal distribution of rotational soil spring stiffness and PDF of normal distribution.

3.3 *Assumption of the relationship between soil stiffnesses and scour progression*

Scour progression can be divided into two stages. The scenario where the scour progresses above the bottom of the footing is defined as Stage 1 shown in Figure 7b), and the scenario where the scour erodes under the footing is defined as Stage 2 shown in Figure 7c). At Stage 1, horizontal spring stiffness k_h is strongly affected by scour progress. On the other hand, k_v and k_s are assumed to have little effect on scour progression, as most of the resistance area is occupied by the bottom of the footing and has not yet been eroded. Therefore, this study assumes that values of k_v and k_s do not change at Stage 1. At Stage 2, since scour progresses under the bottom of the footing and the resistance area is reduced, k_v and k_s assume decreasing.

For k_r, the resistance area includes the bottom and front side of the footing, and the front side of the pier under the ground. If scour progressed within stage 1, the resistance area of the front side of the footing and that of the pier would be reduced. Therefore, it is assumed that k_r would be decreased following the decreasing ratio of the resistance area. It is noted that the resistance area also includes the top surface area of the footing, but since the pressure due to soil cover is small and negligible, the resistance area of the top surface of the footing is neglected. Furthermore, it is difficult to predict how the variation in k_r, shown in equation (3), will change as the scour progresses. Therefore, it is assumed that the standard deviation of the rotational spring stiffness remains constant regardless of scour stages. All assumptions are summarized in Figure 8.

3.4 *Probability of scour depth given identified frequency*

Figure 9 shows the relationship between the amount of scour progression and target frequency obtained from eigenvalue analysis from soil spring stiffnesses assumed in Figure 8. In Stage 1, the decreasing trend in frequency is relatively gradual, but this trend increases in Stage 2. Furthermore, the variance in frequency becomes larger at Stage 2. A deterioration function is

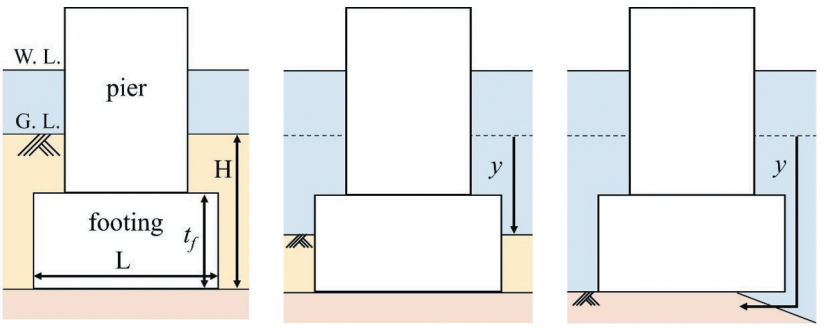
considered to explain these trends. A joint probability distribution model of scour progression y and identified frequency x is calculated in Eq. (4).

$$f(y,x) = \frac{1}{\sqrt{2\pi}\beta(y)} e^{-\frac{1}{2}\left(\frac{x-\alpha(y)}{\beta(y)}\right)^2} \tag{4}$$

Here, hyperparameters α and β are obtained from a procedure of fitting a polynomial curve. The optimal order of the polynomials for the hyperparameters is chosen taking into account the convergence of the root mean square error and is shown in Eqs. (5) and (6), including the identified coefficients.

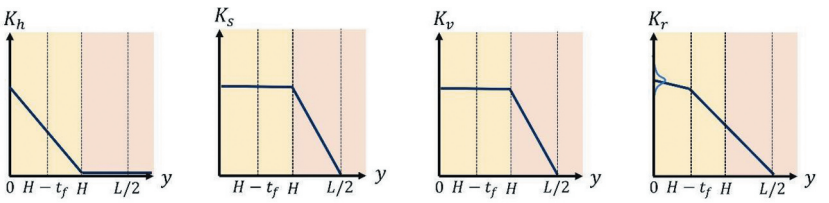
$$\alpha(y) = 0.017y^3 - 0.161y^2 + 0.687y + 8.335 \tag{5}$$

$$\beta(y) = -5.000 \times 10^{-4}y^4 - 5.000 \times 10^{-3}y^3 + 0.048y^2 - 0.137y + 0.389 \tag{6}$$



a) Intact condition. b) Stage 1: Scour depth above the bottom of footing. c) Stage 2: Scour erodes under footing.

Figure 7. Scour progression stages: y represents the scour progression.



a) K_h b) K_s c) K_v d) K_r

Figure 8. Assumption for decreased trends of each soil spring stiffness following scour progression.

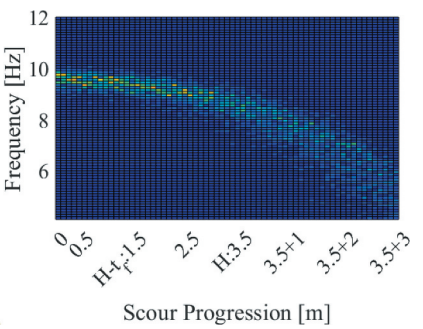


Figure 9. Estimated relationship between identified frequency and scour progress.

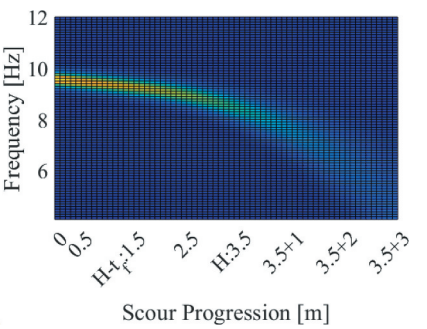


Figure 10. The relationship is approximated utilizing polynomial curve fitting.

Finally, the multivariate PDF in Eq. (4) is shown in Figure 10. The probability of a designated scour progress y_t given identified frequency x_t at a time t can be calculated by Eq. (7).

$$f(y_t, x_t) = 1 - \int_0^{y_t} \frac{1}{\sqrt{2\pi}\beta(y)} e^{-\frac{1}{2}\left(\frac{x_t - \alpha(y)}{\beta(y)}\right)^2} dy \tag{7}$$

4 REAL-TIME SCOUR DEPTH ESTIMATION

To investigate the performance of the proposed method, the ambient vibration monitored on 3rd July 2019 when there was intensive rainfall around the region is examined. Figure 11a) shows the time series of the identified target frequency plotted as black dots and its 30-minute moving average drawn as a red line with the time series of water level drawn as a blue line. As the water level rises, the scattering of the identified frequencies tends to decrease because the river water flow strongly excited the bridge pier, i.e. the signal-to-noise ratio was improved.

Figure 11b) shows the probability that scour depth reaches the bottom of the footing of the target pier expressed as $f(y_t = 3.5, x_t)$. It means the probability that the scour reaches Stage 2. The probability of scour is estimated to be almost less than 0.2 when the water level falls, and the probability converges to zero even though there are several outliers when the water level has stabilized enough. Therefore, it is concluded that the probability of scour reaching Stage 2 is extremely low in this event.

One of the advantages of the proposed method is a flexibleness of setting scour depth. A bridge authority might request an alert the scour progression within Stage 1 considering social impacts. Then, the proposed method can address such requests by setting the value of $y_t = 2$, for example.

5 CONCLUSION

This study proposes a way of estimating the probability of scour depth by means of ambient vibration monitoring of the bridge pier during the swollen river water period. The proposed method, firstly, builds FEM to grasp the relationship between the rocking frequency of the pier and the soil stiffnesses modeled as springs, and investigates springs having a strong influence on changes in the rocking frequency of the pier. Then, as the variance of identified

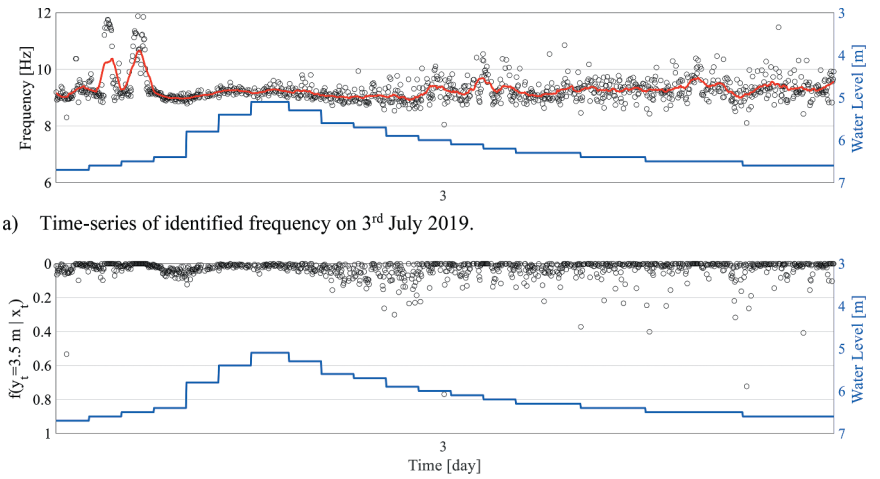


Figure 11. The result in the proposed probability of scour depth estimation when the water level is high.

frequency is significant when ambient vibration of the bridge pier is used, the marginal distributions of the investigated springs are identified utilizing the Bayesian model updating. This study applied MH algorithms and the PDF of rotational soil spring stiffness is updated modeling its uncertainty. Finally, the relationship between soil springs taking into account the footing resistance and the scour depth are assumed, and the deterioration function representing decreasing trend of the natural frequency following the scour progression is estimated utilizing polynomial curve fitting.

The proposed method was applied to the ambient vibration of the bridge pier where the remote sensing system had deployed and estimated the probability that scour depth reaches the bottom of the footing of the pier timely during the swollen river water period. The results of the probability were estimated to be almost less than 0.2 when the water level falls, while the probability converged to zero when water level had stabilized enough. It demonstrates that the probability that scour progresses under the bottom of the footing is extremely low during the considered flood event.

ACKNOWLEDGMENT

This work was supported by a Japanese Society for the Promotion of Science (JSPS) Grant-in -Aid for Scientific Research (B) under project No. 22H01576 and the CDRI fellowship program 2022-23, which are greatly appreciated.

REFERENCES

American Society of Civil Engieers, 2021. ASCE's 2021 Infrastructure Report Card. available at: *https://infrastructurereportcard.org/cat-item/bridges-infrastructure/* (accessed 11 November 2023).

Au, S. K. 2012a. Fast Bayesian ambient modal identification in the frequency domain, Part I: Posterior most probable value. *Mechanical Systems and Signal Processing*, 26, 60–75.

Au, S. K. 2012b. Fast Bayesian ambient modal identification in the frequency domain, Part II: Posterior uncertainty. *Mechanical Systems and Signal Processing*, 26, 76–90.

Bao, T. & Liu, Z. 2017. Vibration-based bridge scour detection: a review. *Structural Control and Health Monitoring*, 24, e1937.

Beck, J. L. & Katafygiotis, L. S. 1998. Updating models and their uncertainties. I: Bayesian statistical framework. *Journal of Engineering Mechanics*, 124, 455–461.

Briaud, J. L., Govindasamy, A. V., Kim, D., Gardoni, P. & Olivera, F. 2009. Simplified method for estimating scour at bridges. Texas. Dept. of Transportation. Research and Technology Implementation Office.

Hastings, W. K. 1970. Monte Carlo sampling methods using Markov chains and their applications. *Biometrika*, 57(1), 97–109.

Katafygiotis, L. S. & Beck, J. L. 1998. Updating Models and Their Uncertainties. II: Model Identifiability. *Journal of Engineering Mechanics*, 124, 463–467.

Kim, C. W., Yoshitome, J., Qi, J., Kitagawa, S., Hamada, Y. 2020. Vibration based long-term scour monitoring of railway bridges, *International Conference on Structural Dynamics*, *EURODYN*, *Athens*, *23-26 November*.

Kim, C. W., Qi, J., Kitagawa, S. 2021. Ambient vibration monitoring for scour assessment of railway bridge, *SHMII10, Porto*, *30-2 July*.

Metropolis, N., Rosenbluth, A. W., Rosenbluth, M. N., Teller, A. H. & Teller, E. 1953. Equation of state calculations by fast computing machines. *The journal of chemical physics*, 21, 1087–1092.

Mosegaard, K. & Tarantola, A. 1995. Monte Carlo sampling of solutions to inverse problems. *Journal of Geophysical Research: Solid Earth*, 100, 12431–12447.

Prendergast, L. J. & Gavin, K. 2014. A review of bridge scour monitoring techniques. *Journal of Rock Mechanics and Geotechnical Engineering*, 6, 138–149.

Railway Techinical Research Institute. 2007. *Railway structures maintenance management standard and commerntary* (*structural edition*), Tokyo, Maruzen Shuppan.

Railway Techinical Research Institute. 2012. *Design Standards for Railway Structures and Commentary (Substructures)*, Tokyo: Maruzen Shuppan.

Tierney, L. 1994. Markov chains for exploring posterior distributions. *the Annals of Statistics*, 1701–1728.

Bridge Maintenance, Safety, Management, Digitalization and Sustainability – Jensen, Frangopol & Schmidt (eds)
© 2024 The Author(s), ISBN 978-1-032-77040-6
Open Access: www.taylorfrancis.com, CC BY-NC-ND 4.0 license

Structural integrity estimation of bridges based on acceleration measurement

Hanliang Yu & Chul-Woo Kim
Department of Civil and Earth Resources Engineering, Kyoto University, Kyoto, Japan

ABSTRACT: As the ages of bridges in Japan continue to increase, the demand for monitoring these bridges is also increasing. However, there might be some problems while conducting BSHM. Practically, collecting displacement data is much more challenging than collecting acceleration data. In terms of theoretical analysis, FE models are very complex. Both creating datasets and updating models require a significant amount of computational resources. To solve these problems, this study uses accelerometers to identify the displacement of bridges for structural integrity estimation. A scaling factor is developed to solve the problems of discrepancies between measured physical response and FEA response, and help to create a model that can reduce the computation time of updating. Finally, the damage detection is achieved by a CVAE which uses displacement data as its interface. The feasibility of the proposed method is verified through an in-house experiment.

1 INTRODUCTION

1.1 *Background*

There are currently about 730,000 bridges in Japan, of which about 660,000, or more than 90%, are managed by local governments and local public agencies. Approximately 34% of them are over 50 years old. This is expected to increase to about 59% in 10 years. Of the 27,938 bridges constructed between 2018 and 2021, 13,833 (49.5%) bridges have been identified as having abnormal deformation, and they need to be observed for a certain period. Therefore, the maintenance of bridges is a crucially important technical issue. Currently, according to the guidelines of the Ministry of Land, Infrastructure, Transport and Tourism (MLIT) in Japan, close-up visual inspections should be carried out on each bridge once every five years. Periodic close-up visual inspections require experience although the accuracy of this method is not high enough. However, the time and cost of visual inspection are considerably high. A more efficient and accurate method of bridge inspection is required. A challenge is to establish a method that can diagnose damage on bridges with lower cost, higher efficiency, and higher accuracy.

1.2 *Vehicle drive-by test*

Utilizing the bridge responses under traffic is popular in BSHM, and vehicle drive-by test provides more accurate and organized data although it needs to interrupt the traffic. To conduct a vehicle drive-by test, sensors are set on the structures to collect real-time acceleration, displacement, or strain when the vehicle traveling on the bridge. Then, a data-driven model (DDM) could be established based on the data. Among all the indicators, displacement is one of the most useful responses because it contains the most direct information on the structural behavior. However, practically, collecting displacement data is not an easy task as displacement transducers or high-definition cameras always need a stable platform to set. Utilizing

DOI: 10.1201/9781003483755-97

accelerometers is an alternative of the displacement transducer if displacement is accurately identified using acceleration because accelerometers could be directly instrumented on the bridge. In this study, displacement is estimated based on the acceleration measurement.

1.3 *Data-driven FE model*

To assess the current performance of the bridge, the finite element method (FEM) based SHM has become very popular in the last decades (Singh 2022). FEM is a general numerical method to solve partial differential equations. It divides large systems into smaller, simpler parts called finite elements (FE). The simple equations of each element are assembled into a larger system of equations to model the entire problem completely. In general, FEM involves creating a simplified 2D or 3D model of the structure on a FEM solver and obtaining a unique solution. The FE models are often simplifications of real structures while ensuring the accuracy of the calculation. Data-driven modeling (DDM) (Solomatine 2008) is another commonly used method. DDM uses the collected data as a model and does not pay too much attention to the principle of the structural system. Instead, it predicts possible future changes in the structure based on experience. This model has been very successful in weather prediction (Ashesh 2022). It handles uncertain errors better than physical models.

1.4 *Existing problems*

Acceleration is often used in BSHM to estimate the modal frequency, modal damping, and mode shapes of bridges. Displacements and rotation angles are commonly used to assess the bridge's structural integrity. However, in practice, monitoring displacements accurately can be challenging. Specifically, for long-term monitoring, factors such as labor cost, equipment maintenance expenses, and equipment stability need to be considered, leading to a limited number of feasible methods that can be implemented (Gosliga 2022). Several techniques support direct displacement measurement. The use of high-precision physical displacement transducers enables long-term data collection. However, these sensors often require a relatively fixed platform or reference for device placement, making them unsuitable for bridges crossing rivers and seas. Thus, if displacement could be estimated through acceleration, those problems would be solved.

In FEM-based damage detection, several FE models are created based on multiple assumed damage scenarios (Nizar 2018). The difference between the FE models is achieved by changing the area of the section, changing the bending stiffness, or eliminating elements. In practical engineering, the internal parameters of the structure change over the years due to various reasons such as material degradation, crack, or creep. Timely updating of the FE model is an important process to keep generating highly comparable structural responses with the actual structure. Detecting the damage and deciding how to update the FE models may not be difficult, but calculations must be performed on all updated models. Computing time for each model will also rise drastically due to increasing complexity.

Surrogate models, also called metamodels, are common in DDM. A surrogate model aims to create a mapping from the input to the output, while the inner workings of the code remain unknown. If there is no damage to the structure, it is impossible to obtain the structural response under damage states. Therefore, the training data for damage states of the structure cannot be generated from the measured data. Recent research hopes to use the surrogate model as a replacement for the FE model (Hoffer, 2021) expecting that updating the surrogate model could be simpler, less time-consuming, and more practical to use. However, it is difficult to control changes to internal parameters.

This study aims to solve the following problems in damage detection by BSHM: a) to develop a method to estimate deformation using acceleration; b) to solve the problems of discrepancies between measured physical response and FEA response; c) to create a numerical model that can reduce the computation time of updating; and d) to develop a surrogate model which can detect damage and uses displacement data as its interface.

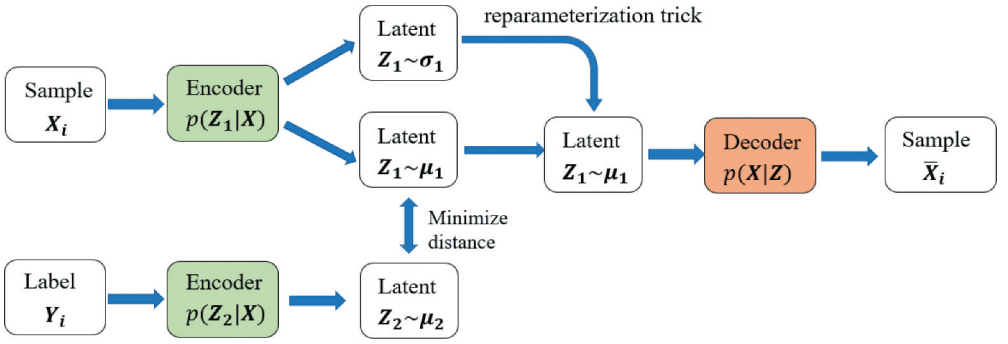


Figure 1. Algorism of CVAE.

2 METHODOLOGY

2.1 *Displacement estimation in vehicle drive-by test*

In the vehicle drive-by test, the rotation angle of one point on a bridge is a binary function of position and time. If the shape function of the bridge rotation is continuous and could fit a polynomial, the deflection $\delta_z(x, t)$ can be an integral along location x of rotation angle $\theta(x, t)$ shown in Equation (1).

$$\delta_z(x,t) = \int_L \theta(x,t)dx = \int_L \arctan\left(\frac{\hat{a}_x(x,t)}{g}\right)dx \tag{1}$$

where $\hat{a}_x(x,t)$ denotes the acceleration in the horizontal direction

The shape function of the bridge rotation is fit by a polynomial as:

$$\boldsymbol{Y} = \boldsymbol{\theta}(\boldsymbol{X}) = a_0 + a_1\boldsymbol{X}^1 + a_2\boldsymbol{X}^2 + \ldots + a_{m-1}\boldsymbol{X}^{m-1} + a_m\boldsymbol{X}^m = \boldsymbol{aX} \tag{2}$$

The boundary condition could be determined by physical knowledge. For a simply supported beam of length L, the boundary condition would be:

$$[\boldsymbol{M}, \boldsymbol{D}]^T\boldsymbol{a} = \boldsymbol{b} \tag{3}$$

where $\boldsymbol{M}$ denotes the boundary condition given by the moment, $\boldsymbol{D}$ denotes the boundary condition given by the displacement, and $\boldsymbol{b} = \{\boldsymbol{0}, \boldsymbol{0}, \boldsymbol{0}, \boldsymbol{0}\}$ when the beam is simply supported. According to the least-squared method, the best-fitted polynomial could be calculated by minimizing the Equation 4:

$$L(a_0, \ \ldots, \ a_m) = \frac{1}{2}\sum_{i=1}^{n}\left(\theta(x_i) - \hat{\theta}_i\right)^2 = \left|\left|\boldsymbol{Xa} - \widehat{\boldsymbol{\theta}}\right|\right| \tag{4}$$

The physical boundary condition acts as a strong constraint of the DDM. If there exists a $\boldsymbol{c}$ such that the equation holds, the coefficients $\boldsymbol{a}$ of the polynomial could be calculated according to Karush-Kuhn-Tucker (KKT) equations:

$$\begin{bmatrix}\boldsymbol{a}\\ \boldsymbol{c}\end{bmatrix} = \begin{bmatrix}\boldsymbol{X}^T\boldsymbol{X} & [\boldsymbol{M}, \boldsymbol{D}]\\ [\boldsymbol{M}, \boldsymbol{D}]^T & \boldsymbol{0}\end{bmatrix}^{-1}\begin{bmatrix}\boldsymbol{X}^T\widehat{\boldsymbol{\theta}}\\ \boldsymbol{b}\end{bmatrix} \tag{5}$$

Once the expression for the rotation angle is obtained, deflection shape functions can be directly computed by integrating the polynomial. In this process, we avoid using numerical integration to reduce noise.

2.2 *Conditional Variational Auto-Encoder (CVAE)*

A CVAE is used in damage detection using the identified displacement from the acceleration. It is generally an auto-encoder, a kind of neural network specialized in recognition and random generating (Kingma 2022). The encoder creates a mapping from the deformation response to the latent layer, and the decoder creates a mapping from the latent layer to the deformation response.

In a Variational Autoencoder (VAE), for the encoder, assuming all samples are drawn from the prior distribution $p(\boldsymbol{Z})$, there exists a posterior distribution $p(\boldsymbol{Z}|\boldsymbol{X_i})$ for each sample $\boldsymbol{X_i}$. Assuming this posterior distribution $p(\boldsymbol{Z}|\boldsymbol{X_i})$ follows a normal distribution $N(\mu_i,\ \sigma_i^2)$, the generator $\boldsymbol{X} = g(\boldsymbol{Z})$ can reconstruct $\boldsymbol{X_i}$ from a sample $\boldsymbol{Z_i}$ drawn from the distribution $p(\boldsymbol{Z}|\boldsymbol{X_i})$. This process extracts a set of information of $p(\boldsymbol{Z}|\boldsymbol{X_i})$ from the real sample $\boldsymbol{X_i}$ and reconstructs $\widehat{\boldsymbol{X}}_i$ through sampling. Hence, we can train a neural network by minimizing the distance between $\boldsymbol{X_i}$ and the reconstructed $\widehat{\boldsymbol{X}}_i$. Typically, this distance is measured using Kullback–Leibler divergence (KL divergence).

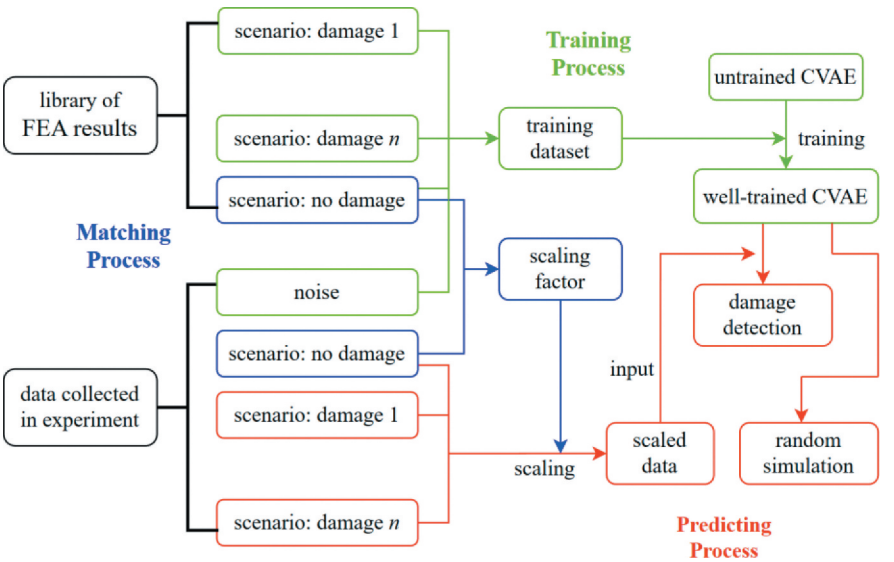


Figure 2. Flow chart of training a data-driven FE model.

In this study, the actual structural response data is treated as sample $\boldsymbol{X}$. Through training the encoder $\boldsymbol{Z}_1 = f_1(\boldsymbol{X})$, the mean of the sample is obtained. Simultaneously, the structural damage field is set as the label $\boldsymbol{Y}$ and, by training the encoder $\boldsymbol{Z}_2 = f_2(\boldsymbol{Y})$, features of the label are obtained. Then we assume this posterior distribution $p(\boldsymbol{Z}|\boldsymbol{Y_i})$ follows a normal distribution $N(\mu_i^*,\ 1)$. Therefore, during the training of the VAE, we achieve directed training of the latent layer. The VAE is now a conditional variational auto-encoder (CVAE) as shown in Figure 1. Making these two normal distributions as close as possible results in an advanced formula for KL divergence as Equation (6).

$$KL(N(\mu_i,\ \sigma_i^2)||N(\mu_i^*,\ 1)) = \int \frac{1}{\sqrt{2\pi\sigma_i^2}} e^{-(x-\mu_i)^2/2\sigma_i^2} \log\left\{ \frac{e^{-(x-\mu_i)^2/2\sigma_i^2}/\sqrt{2\pi\sigma_i^2}}{e^{-(x-\mu_i^*)^2/2}/\sqrt{2\pi}} \right\} dx \qquad (6)$$

The loss could be written as:

$$L_{KL} = \frac{1}{2}\sum_{i=1}^{n}\left[\left(\mu_i - \mu_i^*\right)^2 + \sigma_i^2 - \log\left(\sigma_i^2\right) - 1\right] \tag{7}$$

2.3 *Data-driven FE model*

The flow chart of training a data-driven FE model is shown in Figure 2. In the 'Training process', finite element analysis (FEA) is carried out to provide a dataset for training the CVAE. Within the finite element model, the structure is divided into multiple regions. Structural damage is defined as a reduction in the stiffness (EI) of these regions, and damage fields are randomly generated. FEA is performed for each randomly generated damage field, producing structural displacement response curves. The displacement response serves as the training dataset for the CVAE, and the directed training of the CVAE is accomplished using the damage fields. The noise collected during the experiment is analyzed. According to the distribution of the signal, the noise data could be generated randomly. Training data is then obtained by applying random noise to the FEA results. This method is a solution to the problem of insufficient training data. After the training is completed, the inner parameter of the CVAE will never change. In this case, the encoder can detect the damage in the FE model.

In the 'Matching process', due to the discrepancies between the FEA results and the measured data, the measured data cannot be used directly as input to the CVAE. A scaling factor is used for the assimilation of two data sets: the FEA results of a scenario with no damage, and the data collected in a 'current' state. The encoder is then able to detect the change in the

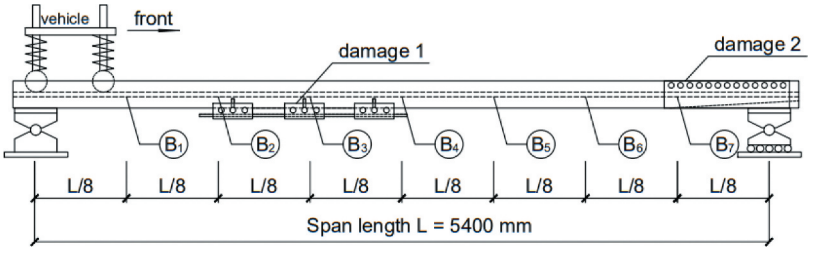


Figure 3. Model bridge.

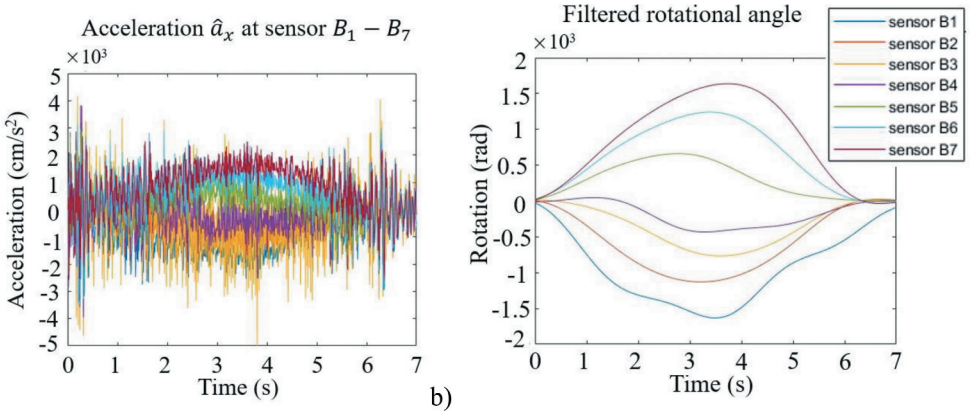


Figure 4. Time histories of acceleration and rotation in scenario dmg00: a) acceleration; b) rotation.

damage and compare it to the current state. When damage happens, instead of updating the FE model or CVAE, the current state and scaling factors are updated. The scaling factor $\boldsymbol{H}$ could be obtained by using the element-wise operation given by Equation (8).

$$H_{ij} = \frac{X_{ij,FEM}}{X_{ij,Exp}} \tag{8}$$

In the 'Predicting process', after the scaling factor has been obtained, it is used to scale all of the collected data to resolve the discrepancies. The scaled data is used as input to the VAE. The output results of the latent layer will show the prediction of the damage. We can also predict structural behavior under different damage conditions by sampling from the latent layer to obtain results for various damage scenarios.

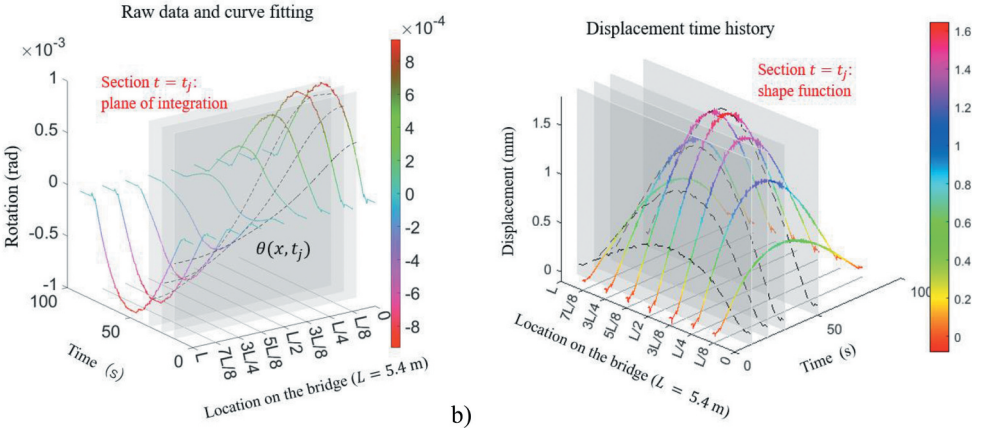
In summary, FEA computation time is reduced by avoiding FE model updates. Discrepancies between measured physical response and FEA response are solved using a scaling factor. Damage detection could be achieved without the need for data collection through the creation of a library of FEA results. The FEA and the training of the CVAE are performed only once. Updating the model is achieved by updating the scaling factor, which is completely independent of the CVAE and the FE model.

3 DEFLECTION ESTIMATION

3.1 *In-house experiment*

An experiment is carried out on a simply supported steel beam in the laboratory. Figure 3 shows the experimental bridge with sensor deployment. The bridge has a length of 5600 mm, a span of 5400 mm, a width of 287 mm, and a height of 66 mm. The support on one side is a pin and the support on the other side is a roller.

The cross-section of the model bridge is an "H" shaped section. The Area of cross-section (A) is 6.5483×10^{-3} m^2, the second moment of area (I) is 5.7480×10^{-7} m^4, and the material of the bridge is SS400 steel whose Young's modulus (E_0) is 206 GPa, density is 7850 kg/m^3, and Poisson's ratio is 0.34. When the vehicle moves on the bridge, accelerometers set at location $B_1 \sim B_7$ collect real-time acceleration.



a) b)

Figure 5. Estimation of deformation: a) integration of rotation; b) displacement field.

There are two reinforcements on the bridge, marked as damage 1 and damage 2, and this state is denoted as a "no damage" state. When each of the reinforcement is removed, the bridged is considered to be damaged and denoted as "damage 1" and "damage 2" states respectively.

3.2 *Rotation estimation*

The horizontal acceleration ($\hat{a}_x(x,t)$) time history obtained from the sensor is shown in Figure 4 a). The sampling frequency was 200 Hz. By applying a Butterworth lowpass filter with a cut-off frequency of 0.5 Hz, the noise in the signal was well eliminated. The filtered signal is shown in Figure 4 b).

3.3 *Displacement estimation*

In the test, after filtering, the motion of the vehicle on the bridge can be considered quasi-static. The sampling frequency during the experimental process is 200Hz. At each time plane $t = t_j$, constrained least squares curve fitting is applied to the collected data. This process yields the relationship between the bridge's rotation angle and position at the current moment, denoted as $\theta(x, t_j)$ shown in Figure 5 a).

Once the rotation-position curve $\theta(x, t_j)$ is obtained, the displacement shape function $\delta(x, t_j)$ can be obtained by integrating the position in that plane. After performing integration calculations in each plane, a displacement field $\delta(x, t)$ could be obtained, which contains the displacement information of the whole structure at any time increment.

On the plane $x = x_i$ ($i \in [0, L]$, $i \in \mathbb{R}$, continuous), the displacement-time history $t - \delta(x_i)$ at a point x_i on the bridge under the moving vehicle can be obtained. Dividing it by the vehicle weight will provide the influence line of displacement. On the plane $t = t_j$ ($j \in [0, L/v]$, $j \in \mathbb{R}$, continuous), the displacement shape function $x - \delta(t_j)$ at a specific time increment t_j when the vehicle travels on the bridge can be obtained as shown in Figure 5 b).

4 DAMAGE DETECTION IN THE EXPERIMENT

4.1 *FEM simulation*

In the FEM simulation, the bridge is divided into 20 elements. A random damage field is applied to the structure. The displacement time history at the location from B_1 to B_7 is selected to be the input data. Figure 6a) shows the FE model and an example of a randomly generated damage field.

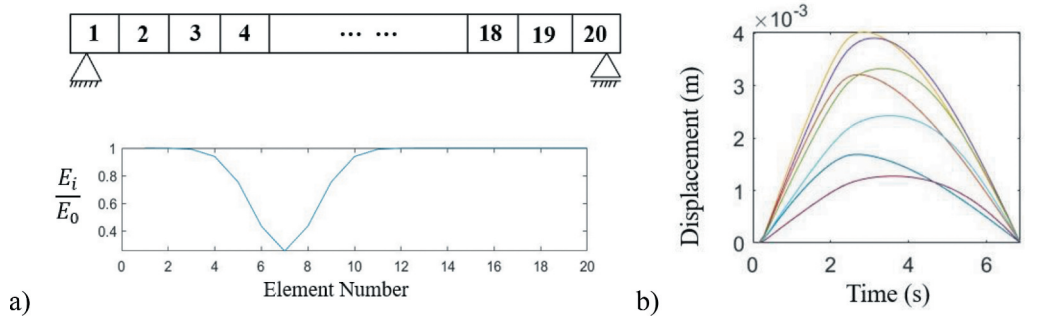


Figure 6. FE model: a) Damage field; b) result of FEA.

4.2 *Damage detection*

Figure 7 Depicts the CVAE's discrimination of damage on the test dataset. The color bar displayed on the right side indicates the location with the highest likelihood of damage occurrence. It can be observed that the entire latent variable exhibits a radial distribution in space. As the severity of damage is random during the generation of

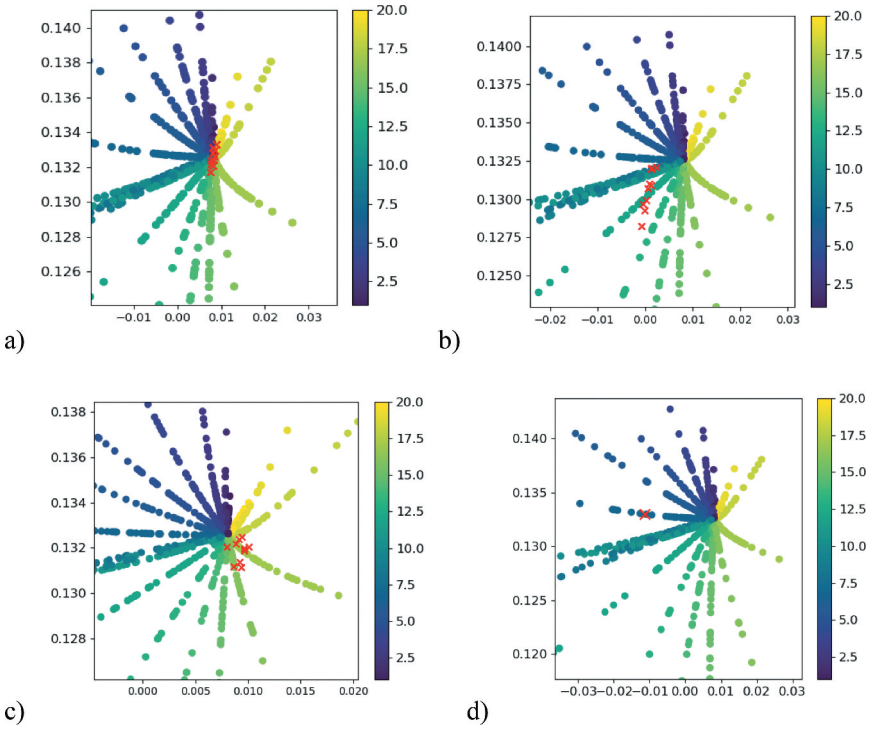


Figure 7. distribution of variable in latent layer **Z**: a) scenario: no damage; b) scenario: damage 1; c) scenario: damage 2; d) a sample for the generator (the example in 4.1).

damage fields, determining minor damage conditions is more challenging, naturally leading to proximity to the central region. It is clear that the CVAE successfully detects two types of damage, and also it does not interfere with the no damage scenario.

4.3 *Scenario generation*

For the experimental data, after modifying it with a scaling factor, the distribution of the data in the latent space after encoding is shown in Figure 7 d). We can obtain a specific damage field by sampling values from the latent space (Figure 7 d)). This value, once decoded, can output a predicted structural response. Comparing it with the finite element calculation results for this damage field is illustrated in Figure 8. It can be concluded the estimation is quite comparable.

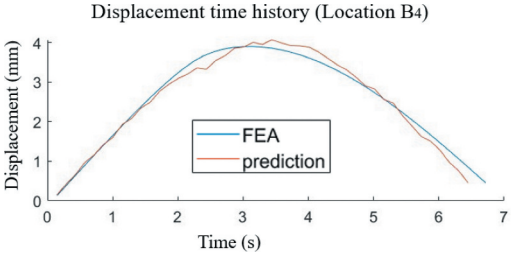


Figure 8. Displacement time history at location $\boldsymbol{B}_4$.

5 CONCLUSION

This study investigates a method that estimates displacement using only acceleration data. The deformation could be used for damage detection, aiming to improve existing FEM model updating methods. To solve the discrepancies between the FEA results and the real data. This study solves the problem by establishing a mapping called scaling factor to map the real data set to the result generated by the FEA. In this way, CVAE can also be used for damage detection on real data.

Next step for this study is feasibility of damage detection with reduced number of sensors. If this can be achieved, the practical value of this method would significantly increase. It is noted that the latent layer of the CVAE is used to visualize the classification results. If Bayesian theory can be applied to the post-processing of the data, the specific determination of the damage location can be converted into a probability of occurrence of damage at each location. The results would then be expected to be more intuitive.

ACKNOWLEDGMENT

This work was supported by a Japanese Society for the Promotion of Science (JSPS) Grant-in -Aid for Scientific Research (B) under project No. 22H01576 which is greatly appreciated.

REFERENCES

Ashesh, C., Mustafa, M., Pedram, H., Eviatar, B. & Karthik, K., 2022. Towards physics-inspired data-driven weather forecasting: integrating data assimilation with a deep spatial-transformer-based U-NET in a case study with ERA5, *Geosci. Model Dev*.

Kingma, D. P. & Welling, M., 2022. Auto-Encoding Variational Bayes, arXiv:1312.6114v11

Gosliga, J., Hester, D., Worden, K., & Bunce, A., 2022. On population-based structural health monitoring for bridges, *Mechanical Systems and Signal Processing*, 173:108919

Hoffer, J.G., Geiger, B.C., Ofner, P., & Kern, R., 2021. Mesh-Free Surrogate Models for Structural Mechanic FEM Simulation: A Comparative Study of Approaches, *Appl. Sci*, 11: 9411

Nizar F., Maosen C., Yufeng Z., Mahmoud B., & Zhongqing S., 2018. Structural damage detection using finite element model updating with evolutionary algorithms: a survey, *Neural Computing and Applications* 30: 389–411

Singh, T., Sehgal, S., Prakash, C., & Dixit, S, 2022. Real-Time Structural Health Monitoring and Damage Identification Using Frequency Response Functions along with Finite Element Model Updating Technique, *Sensors*, 22(12):10.3390/s22124546

Solomatine, D., See, L.M. & Abrahart, R.J., 2008. Data-Driven Modelling: Concepts, Approaches and Experiences. *Practical Hydro informatics*, pp.17–30.

Bridge Maintenance, Safety, Management, Digitalization and Sustainability – Jensen, Frangopol & Schmidt (eds)
© 2024 The Author(s), ISBN 978-1-032-77040-6
Open Access: www.taylorfrancis.com, CC BY-NC-ND 4.0 license

Research on application of real-time dynamic safety monitoring system for medium and small span bridges

Hua Hong, Su-gong Cao, Jun-lei Fu & Yue-kai Xu
Zhejiang Scientific Research Institute of Transport, Hangzhou, China
Key Laboratory of Road and Bridge Inspection and Maintenance Technology of Zheng jiang Province, Hangzhou, China

ABSTRACT: In view of the lack of economic and practical structural health monitoring system for medium and small span bridges in china, A new idea of health monitoring for small and medium span bridges based on displacement is proposed. The economical bridge health monitoring system with displacement monitoring combined with heavy vehicle capture as the main monitoring content has been designed and developed, The application research of practical bridge was carried out. A 2×25m span prestressed reinforced concrete T beam is selected as the research object, Real-time monitoring of vertical displacement of beam, Statistics of out of limit quantity, Record the out of limit value. The response law of bridge structure under external load during operation period is discussed and the trend of structural bearing capacity is monitored. The results showed that: The R&D system can accurately capture the effect of causing structural overrun response, and conduct real-time early warning for emergencies; The monitoring and analysis results can effectively guide the scientific management and maintenance of the bridge.

1 INTRODUCTION

By the end of 2021, In china's highway bridge operation system, the medium and small span bridges account for 85%[1]. However, Due to the aging, corrosion, fatigue and other factors of medium and small span bridges, the increasing traffic flow, construction quality and maintenance attention, the safety factor of medium and small span bridges is much lower than that of large span bridges, and the probability of sudden damage, collapse and other safety accidents is much higher than that of large span bridges[2~3]. Therefore, It is extremely necessary to monitor the structural health status of small and medium span bridges in real time, The evaluation of structural safety and operational stability should be included in the daily management of bridge operation.

Scholars at home and abroad have conducted some useful research on the dynamic safety monitoring of bridges. Zhang Jian-long et al. [4] proposed a bridge health monitoring and early warning platform based on neural network. The platform has the functions of data collection, transmission, persistence, etc., and also supports multiple types and quantities of bridge data visual interaction and bridge health assessment functions. David et al. [5] combined the global positioning system (GPS) and linear variable differential sensor (LVDT) to monitor the structural deformation of the bridge, and finally determined some slight displacements of the bridge in the horizontal direction. Xin Guang-tao et al.[6] systematically analyzed the requirements of structural health monitoring system for long-span bridges, and introduced the design principles of the system from the aspects of software and hardware design and development. Roshandeh A M et al.[7] summarized the bridge big data platform as data entry module, data display module, data exit module and data early warning module, and introduced the functions of each module. Ren Pu et al.[8] proposed a bridge health monitoring system platform based on big data. The system platform utilizes a distributed file system with high fault tolerance and a parallel data processing engine with high

DOI: 10.1201/9781003483755-98

computational efficiency, which has high reliability, availability and storage efficiency, and is easy to expand, and can provide real-time early warning for bridge safety.

The existing research results on bridge health monitoring mostly focus on the research and development of long-span bridge monitoring system and monitoring equipment, while few research on real-time online early warning system for small and medium span bridges. However, the current situation of bridges in china is that the proportion of medium and small span bridges is large, and the probability of safety accidents is high. Therefore, the research on real-time online monitoring of medium and small span bridges at important nodes is of great significance. In view of the current situation that there is no economical and practical structural health monitoring system for medium and small span bridges, this paper proposes a new idea of health monitoring for medium and small span bridges only based on displacement. At the same time, a bridge health monitoring system based on displacement monitoring combined with heavy vehicle capture is designed, which is quite economical. To achieve the reasonable, practical and cost-effective goals of the structural monitoring system for medium and small span bridges.

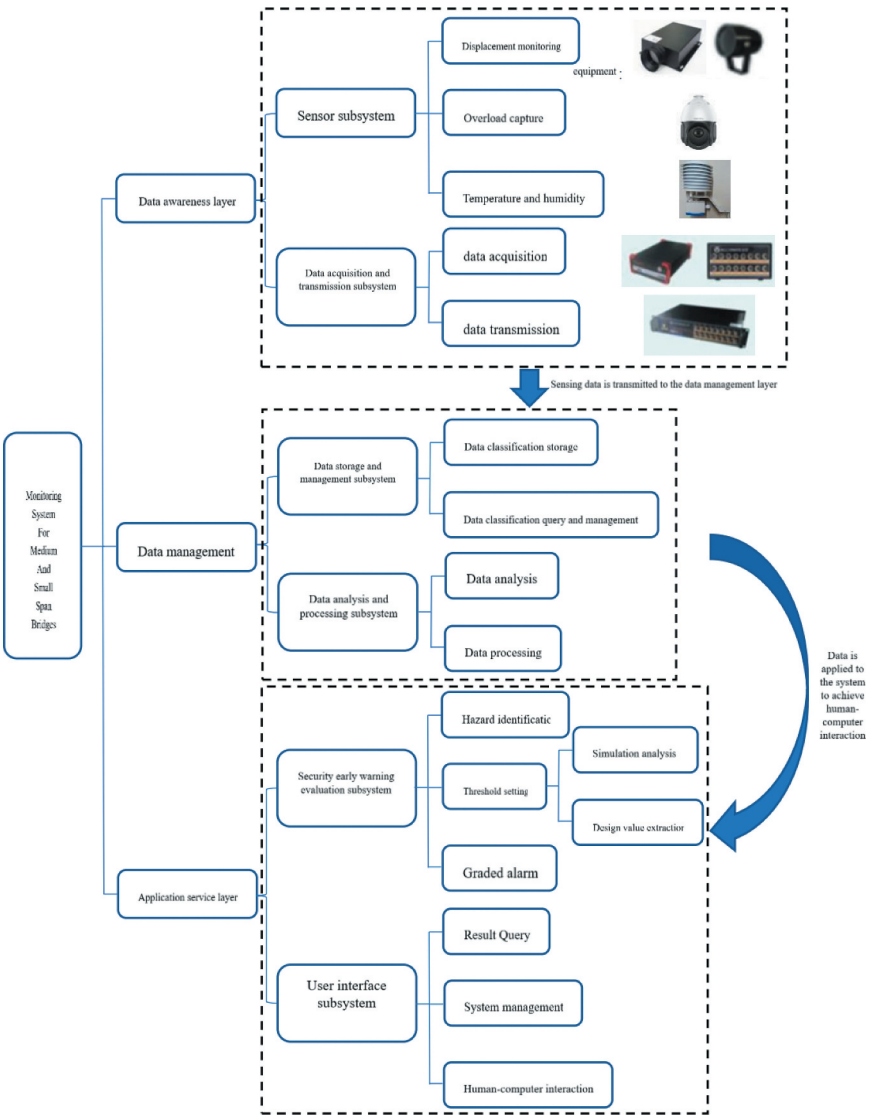


Figure 1. Design idea map.

2 DESIGN IDEAS

The basic connotation of the bridge health monitoring system is to use modern sensing and communication technology to real-time monitor the structural response of the bridge under various environmental conditions during the operation stage, Obtain various information reflecting structural conditions and environmental factors, From this, the health status of the structure is analyzed and the reliability of the structure is evaluated, To trigger the early warning signal when the operation condition of the bridge is abnormal, To trigger the early warning signal when the operation condition of the bridge is abnormal, At the same time, it provides scientific basis for bridge management and maintenance decision.

Based on this, the overall design of monitoring system for medium and small span bridges should include three functional layers, namely, data perception layer, data management layer and application service layer. Among them, the data sensing layer is the underlying structure, including the sensor subsystem, data acquisition and transmission subsystem, Displacement acquisition should be the main objective, supplemented by overload linkage capture, environmental temperature and humidity monitoring; The data management layer is the middle layer, including the data storage and management subsystem, the data processing and analysis subsystem and the data reporting subsystem; The application service layer is the top-level structure, including the security early warning evaluation subsystem and the user interface subsystem. The design idea diagram is shown in figure 1.

3 SYSTEM LAYOUT

The main user of the system is the bridge management and maintenance institution, It is one of the key contents of system interface design to establish the management and visual display of various data of the system. At the same time, combined with the current situation and stress characteristics of medium and small span bridges, Considering the economy and practicality of the system, The main monitoring content of the system design is displacement monitoring combined with heavy vehicle capture. Based on this, the visual display of the monitoring system, data analysis, early warning, linkage capture and evaluation are considered in the system layout.

3.1 *System display*

Provide friendly interactive graphical user interface, The main display screen includes the system home page, structure home page, etc; Display of data, including: 3D model, measuring point position, attributes, real-time historical curve and other information; Heavy load capture display, including: synchronous display of heavy load capture overrun monitoring curve,



Figure 2. System display interface.

capture image and dynamic deflection; Display of other statistical data, Including: display of statistics of times of different warning levels. The system display interface is shown in Figure 2.

3.2 *Early warning setting*

For this system, settings are made from the following aspects: early warning method design, early warning threshold confirmation, early warning value configuration, early warning push and early warning history.

The early warning method is designed from the threshold value, data deviation, data change rate and joint analysis between different data, The monitoring structure is simulated and analyzed by numerical simulation, Combined with the corresponding provisions of 《Technical Specifications for Structure Monitoring of Highway Bridges》(JT/T 1037-2022), Determine the threshold corresponding to different warning levels of each monitoring parameter.

It provides the editing of batch alarm and single point alarm, According to the different alarm level information is pushed to different roles and users by sms, email and other means, and the existing alarm information is counted.

3.3 *Linkage capture arrangement*

Moving load is the main load of small and medium span bridge during operation, Vehicle overload is the main cause of structural damage.Using the structural deflection response feedback, linkage with the capturing camera, When the deflection exceeds the corresponding threshold of different levels, record the measured data of heavy vehicles crossing the bridge and the relative deformation caused only by vehicle load, Capture images of heavy vehicles crossing the bridge, It can provide data guidance for maintenance inspection work and load supervision and control work.

4 REAL BRIDGE APPLICATION

4.1 *Bridges overview*

The total length of the bridge is 342.0m, with a total of 20 spans, The layout of the bridge span is: 10 × 16m+2 × 25m+8 × 16m, This project requires Establish long-term health monitoring for the 2×25m span (11th and 12th spans). The upper structure of this unit is prestressed reinforced concrete T-beam, and the structure is discontinuous. The lower structure is double column pier and bored Pile foundation, and the bridge deck is paved with asphalt concrete pavement. The transverse arrangement of the bridge is: 0.5m(guardrail)+11.8m(carriageway)+0.5m(guardrail), and the edge plate is equipped with concrete anti-collision guardrail.

4.2 *Structural theory analysis*

4.2.1 *Calculation model*

Design load class: Highway - Class I.

Based on the short-term action effect calculation method of the limit state of normal use, Mainly according to the bridge construction specifications, The content of this checking calculation is formulated according to the "Design Specification for Highway Reinforced Concrete and Prestressed Concrete Bridges and Culverts"(JTG 3362-2018).

4.2.2 *Warning value setting*

According to the principles of hierarchical early warning and security control, Combined with the requirements of the "Technical Specifications for Highway Bridge Structure Monitoring" (JT/T 1037-2022), Implement second-level security early warning control for this bridge, The basis and values for setting up early warning values are as follows:

Table 1. Setting of warning value.

Serial Number	Warning level	early warning value	Unit	Establishment basis
1	Second level	4.88	mm	Meet the requirement of 0.8 times the effect of Class I moving load on highways
2	first level	6.1	mm	Meet the requirements for the effect of Class I moving load on highways

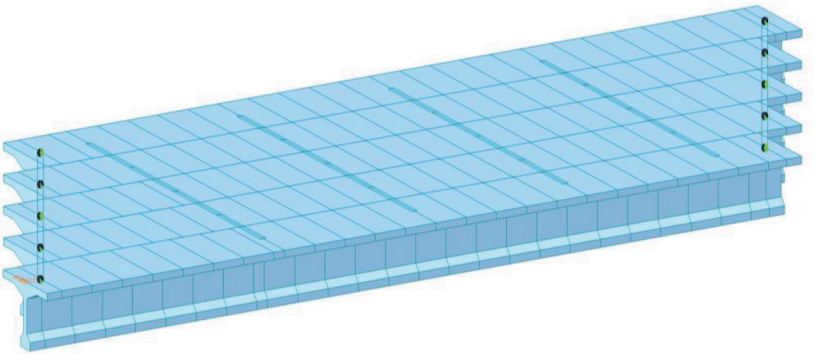


Figure 3. Calculation model.

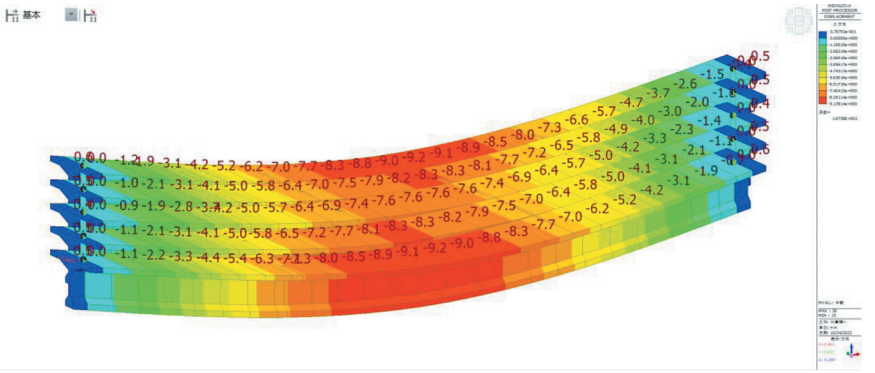
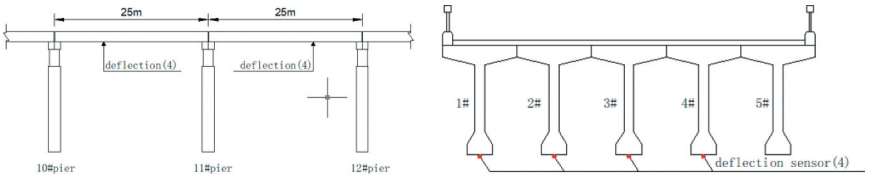


Figure 4. Calculation results of deflection.

4.3 *Monitoring point layout*

The layout of monitoring points plays an important role in the Structural health monitoring of bridges, The quality and scientificity of the layout of measurement points directly affect whether the monitoring data can accurately reflect the actual state of the bridge. For this bridge combined with the actual situation on site, the layout of monitoring points is shown in Figure 5.



(a) Elevation Diagram of Measuring Point Layout

(b) Schematic Diagram of Cross Section of Measuring Point Arrangement

Figure 5. Layout diagram of monitoring points.

4.4 *Monitoring results*

4.4.1 *Data presentation*

Real time monitoring of the structural deflection of the main beam under moving loads, To evaluate the overall stiffness characteristics of the structure, It provides the basis for the evaluating of the overall health status of bridge structure, the verification of bridge design theories and the standardization of operation management. The system provides real-time data query function, as shown in Figure 6. According to the results of the monitored data, the data can be traced online and the corresponding data can be analyzed longitudinally, as shown in Figure 7.



Figure 6. Real-time data.



Figure 7. Historical data in any period.

4.4.2 *Overlimit linkage capture*

Triggered by structural deflection response, Linkage capture camera, When the dynamic deflection exceeds the threshold set for the corresponding level, record the deflection of the bridge when the heavy vehicle crosses the bridge, and capture the image when the heavy vehicle crosses the bridge. The bridge adopts the capturing system and monitoring deflection linkage to capture and record heavy vehicles. The results are as follows:

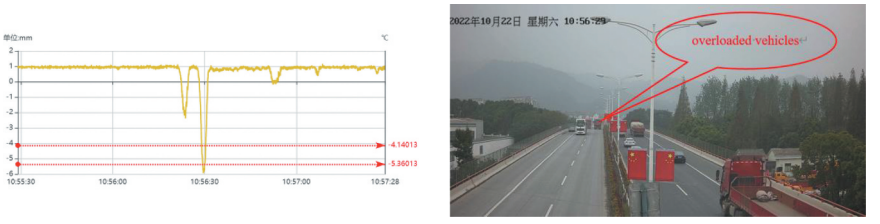


Figure 8. Real-time capture of early warning at 10:56:29 on October 22, 2022.

4.4.3 *Early warning statistical*

For this bridge, According to the statistical data from October 18, 2022 to November 17, 2022, A total of 203 first-level warnings and 764 second-level warnings have been monitored. The results are as follows:



(a) Statistics Results of Level I Early Warning

(b) Statistical Results of Level II Early Warning

Figure 9. Statistics of early warning results.

4.5 *Data analysis*

4.5.1 *Statistical analysis*

Conduct statistical analysis on the alarm data from October 18, 2022 to October 25, 2022, The results are shown in the following figure.

For this bridge, Based on the following statistical data, it can be inferred that:

(1) Only 8 days from October 18, 2022 to October 25, 2022, The number of alarms has reached 470 times, with frequent alarms. According to the results of the scene capture, the cause of alarm was caused by heavy-duty truck. Frequent alarm in a short period of time can easily lead to fatigue of in-service structure, seriously affect the durability and then affect its bearing capacity.
(2) According to the monitoring statistical results, there are often alarms in the evening, indicating that there are still excessive loads crossing the bridge at night.
(3) Since October 23, 2022, the number of alarms has significantly decreased, indicating: Based on the monitoring data of the system, reasonable control and guidance measures can effectively suppress overloading.

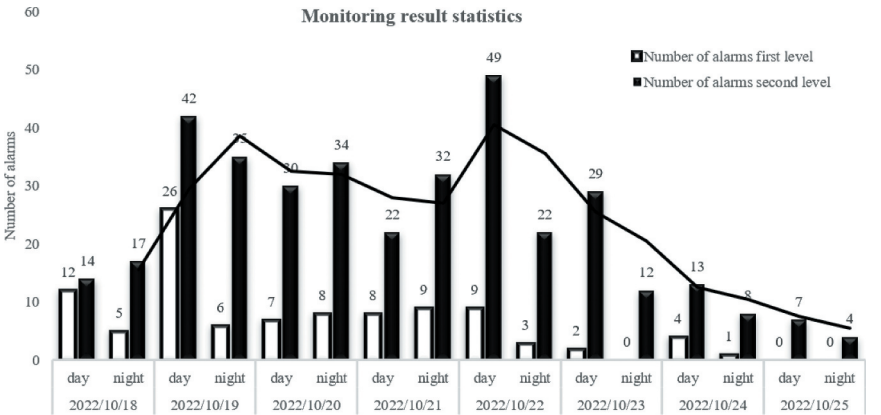


Figure 10. Statistical analysis of monitoring results.

4.5.2 *Trend analysis*

Based on the system monitoring and early warning data from October 18, 2022 to November 17, 2022, Trend analysis was conducted on the "Level one alarm" data, and the results are as follows:

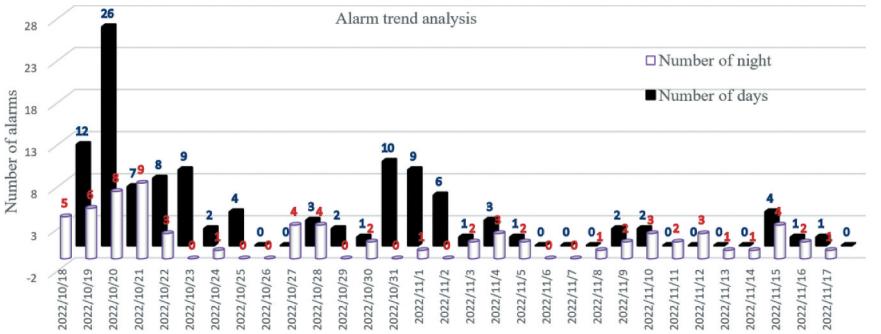


Figure 11. Alarm trend analysis.

Based on the trend analysis results of early warning data, it can be inferred that:

(1) Starting from October 23, 2022, on-site control measures will be taken, From October 23 to October 29, the number of first-level alarms during the day and night decreased significantly, with the maximum number of alarms being 4 and the minimum number of alarms being 0; However, during the period from October 30th to November 1st, the situation was abnormal, with the maximum number of alarms reaching 10.

(2) Starting from November 2nd, on-site control will be strengthened, From November 2nd to November 17th, The number of alarms has significantly decreased, the maximum number of alarms is 4 times, the minimum number of alarms is 0 times, However, during this period, there was an obvious trend of more alarm times at night than in the day, indicating that the overload at night was more serious than in the day, and overload control at night was relatively severe.

4.5.3 *Analysis of occurrence interval*

In order to understand the concentrated time range of overload occurrence, Perform interval probability statistical analysis on the overload data after control (October 23rd to November 17th), and obtain the time range of concentrated overload occurrence. The analysis results are as follows:

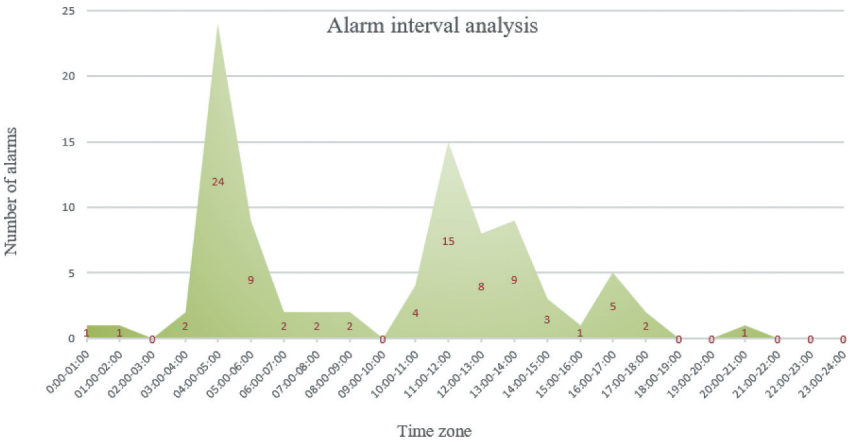


Figure 12. Analysis of overload occurrence interval.

Based on the above analysis results, it can be inferred that: Overloading is prone to occur between 04:00~06:00 and 11:00~14:00, The number of overloads that occurred between 04:00 and 06:00 reached 33, accounting for 36.3% of the total number of overloads, The number of overloads that occurred between 11:00 and 14:00 reached 32, accounting for 35.2% of the total number of overloads, They account for 71.5% of the total overload times.

5 CONCLUSION

This article is based on the self-developed health monitoring system for small and medium-sized span bridges, Real bridge application research on real-time dynamic safety monitoring of small and medium span Bridges is carried out, The rationality, practicability and advancement of this system applied to real bridge are discussed. The main conclusions are as follows:

(1) The R&D system can accurately capture the effects that cause the structure to respond beyond the limit, Real-time early warning for emergencies;
(2) Monitoring and analysis results can effectively guide the scientific management of real bridge, For example, the conclusion that the overload of bridge is serious (470 overload times in only 8 days), the increase trend of overload at night, and the occurrence of overload is easy to occur at 04:00~06:00 (36.3% probability) and 11:00~14:00 (35.2% probability) can timely and effectively guide the field scientific management.
(3) Using displacement monitoring big data, real-time statistical analysis is made on the change trend of the monitoring deflection value, the analysis results can be used to infer the trend of structural stiffness changes, and then determine the change law of the structural bearing capacity, providing data support for the safe operation of small and medium-sized span Bridges.

ACKNOWLEDGEMENTS

This research was supported by the Independent research and development project of Zhejiang Scientific Research Institute of Transport (ZK202301).

REFERENCES

[1] Ministry of Transport.2022. 《Statistical Bulletin of Transport Industry Development in 2021》.Beijing:*Comprehensive Planning Department of the Ministry of Transport*.
[2] Jing Ya-biao. 2022. Design and Research on Structural Health Monitoring System of Small and Medium Span Bridges. *Science & Technology Information* 20(17):106–108.
[3] Chen Yu-zhe. 2014. Research and Application of Small and Medium Span Bridge Health Monitoring System based on Sensor Network. *Hu nan:Hunan University*.
[4] Zhang Jian-long,Zhao Dong-yue,Li Yi-wen,et al.2022. Research on Bridge Health Monitoring and Alarming Platform Based on Neural Network. *Computer Technology and Development* 32(4):205-209.
[5] David M S,Bakaonem. 2021 Dynamic deformation moni-toring of lotsane bridge using global positioning systems (GPS) and linear variable diferential transducers (LVDT). *Journal of Data Analysis and Information Processing* 9(1):30–50.
[6] XIN Guang-tao,ZHAO Jian. 2020 Design and research of long-span bridge structure health monitoring system. *Journal of Highway and Transportation Research and Development(Application Technology Edition)* 16(10):288-290.
[7] Roshandeh A M,Poormirzaee R,Ansari F S.2014. Systematic data management for real-time bridge health monitoring using layered big data and cloud computing. *International Journal of Innovation and Scientific Research* 2(1):29–39.
[8] Ren Pu,Ding You-liang,Li Ya-dong,et al.2019. Data storage and early-warning methods of bridge health monitoring system based on big-data. *Science Technology and Engineering* 19(12):266–270.

Bridge Maintenance, Safety, Management, Digitalization and Sustainability – Jensen, Frangopol & Schmidt (eds)
© 2024 The Author(s), ISBN 978-1-032-77040-6
Open Access: www.taylorfrancis.com, CC BY-NC-ND 4.0 license

Enhancing structural performance evaluation of PC girder bridges through Bayesian model updating

D.B. Chen & C.W. Kim
Department of Civil and Earth Resources Engineering, Graduate School of Engineering, Kyoto University, Kyoto, Japan

ABSTRACT: This study aims to improve the evaluation of structural performance in prestressed concrete (PC) girder bridges by employing a calibrated FE model. This is achieved through Bayesian model updating, utilizing measured responses in the elastic stress state. Bayes' theorem is employed to quantify uncertainties in FE model parameters by inferring the joint posterior probability density function (PDF). The Transitional Markov Chain Monte Carlo (TMCMC) sampler is utilized to generate samples for estimating the posterior PDFs of model parameters. The selection of a suitable model class is guided by sensitivity analysis of model parameters and a comprehensive discussion of the updating outcomes from linear models. The nonlinear static simulation results obtained through the calibrated model are rigorously compared with the measured crack pattern and load-deflection curve to validate the effectiveness of Bayesian model updating. Observations showed that structural damage resulting from concrete cracking minimally affects the 1st bending frequency. Consequently, vibration characteristics exhibit specific limitations in their application for assessing damages caused by concrete cracking. The proposed high-fidelity model updating approach, driven by multi-source data, establishes a reliable digital twin model suitable for SHM of PC bridges.

1 INTRODUCTION

The proportion of bridge infrastructures in Japan that have been in service for over 50 years is experiencing a rapid increase. Approximately 45% of existing bridges in Japan adopt prestressed concrete (PC) (Road Bureau 2020). Instances of deterioration, such as inadequate grout filling, corrosion, and rupture of PC tendons, have been documented. Many aging PC bridges necessitate inspection and maintenance to address potential degradation damages. However, lack of experienced inspectors and the rise in maintenance costs pose inevitable challenges in bridge maintenance. Consequently, there is an urgent need to develop a quantitative method for evaluating the structural integrity of these aging bridges. To this end, obtaining validated finite element (FE) models is crucial for bridge health monitoring and inspection. In contrast to direct model calibration, data-driven model updating based on Bayesian inference methods may offer a promising way to acquire validated models.

In recent years, Bayesian model updating has gained prominence owing to its ability to derive posterior probability density functions (PDFs) for model parameters. Beck and Katafygiotis (1998) formulated the Bayesian model updating framework, encompassing model class selection for structures and probability models for characterizing system errors. Subsequent investigations in this domain have been pursued by other researchers. The Bayesian model updating approaches have found application in reliability analysis and damage detection

DOI: 10.1201/9781003483755-99

across numerous instances, encompassing both laboratory experiments and real-world engineering structures (Zhou et al. 2022).

Given the limitations inherent in the one-dimensional (1D) beam model, Yoshida et al. (2021) recommended employing an FE model capable of simulating three-dimensional (3D) features when assessing the load-carrying capacity of PC girder bridges. Due to continuous advancements in computational performance, the creation of geometric digital twin models faithfully replicating intricate structural features has become achievable. Furthermore, studies on advanced 3D numerical modeling, incorporating Bayesian model updating techniques, are of great importance for the realization of a physical digital twin.

2 METHODOLOGY

2.1 *Bayesian model updating framework*

The posterior PDF of the uncertain parameter vector θ ($\theta \in \mathbf{R}^{N_\theta}$) conditioned on the system response D and specific model class M can be expressed as Equation (1).

$$P(\theta|D, M) = \frac{P(D|\theta, M)P(\theta|M)}{P(D|M)} \tag{1}$$

Under the assumptions that the measurements D_k (for k=1, …, n) are independently and identically distributed (iid), and that the error term $\boldsymbol{e}$ between the observation and the model prediction follows a zero-mean Gaussian distribution with fixed variance, the likelihood function for model updating is expressed as Equation (2).

$$P(D|\theta, M) = \prod_{k=1}^{n} P(D_k|\theta, M) = ce^{-J(\theta)/2\sigma^2} \tag{2}$$

where $J(\theta)$ denotes the goodness-of-fit function used to minimize errors as shown in Equation (3).

$$J(\theta) = \sum_{i=1}^{N_m} \left((1 - \langle \varphi_i(\theta), \hat{\varphi}_i \rangle)^2 + \left(1 - f_i(\theta)/\hat{f}_i\right)^2 \right) + \sum_{i=1}^{N_d} \left(1 - \delta_i(\theta)/\hat{\delta}_i\right)^2 \tag{3}$$

where $f_i(\theta)$ and $\varphi_i(\theta)$ represent the frequencies and mode shapes derived from the eigenvalue analysis using FEM, respectively; $\hat{f}_i$ and $\hat{\varphi}_i$ denote the measured modal properties obtained from the experiment, respectively; $\delta_i(\theta)$ and $\hat{\delta}_i$ denote the simulated deflection using FEM and the measured deflection, respectively.

2.2 *Computational tool*

In practical applications with multiple parameters, the computation of joint and marginal PDFs often involves solving high-dimensional integrals, making sampling methods a common choice. In this study, the Transitional Markov Chain Monte Carlo (TMCMC) algorithm is employed to estimate the parameters of the FE model by generating samples from the posterior PDFs of model parameters. The principle of TMCMC involves generating intermediate PDFs in a series that progresses from the prior PDF to the posterior PDF (Ching & Chen 2007). The transitional distributions are defined as presented below.

$$P^j \propto P(\boldsymbol{D}|\boldsymbol{\theta})^{\beta_j} \cdot P(\boldsymbol{\theta}) \tag{4}$$

where j denotes the transition step number, and β_j signifies the tempering parameter, which takes values such that $\beta_0 = 0 < \beta_1 < \beta_2 < \cdots < \beta_m = 1$.

3 EXPERIMENT ON PC BOX GIRDER

3.1 *Specimen design*

The test specimen prototype is a post-tensioned PC box girder bridge, designed according to the specifications for highway bridges. As illustrated in Figure 1, the specimen represents a 1/2 scale simply supported box girder with a span length of 7.5 m and a girder height of 1000 mm. The prestressing tendons positioned on the web (No. 1 to No. 6 in Figure 1(c)) curve upward at the beam's end, while the prestressing tendons located on the bottom plate (No. 7 in Figure 1(c)) are arranged in a straight line.

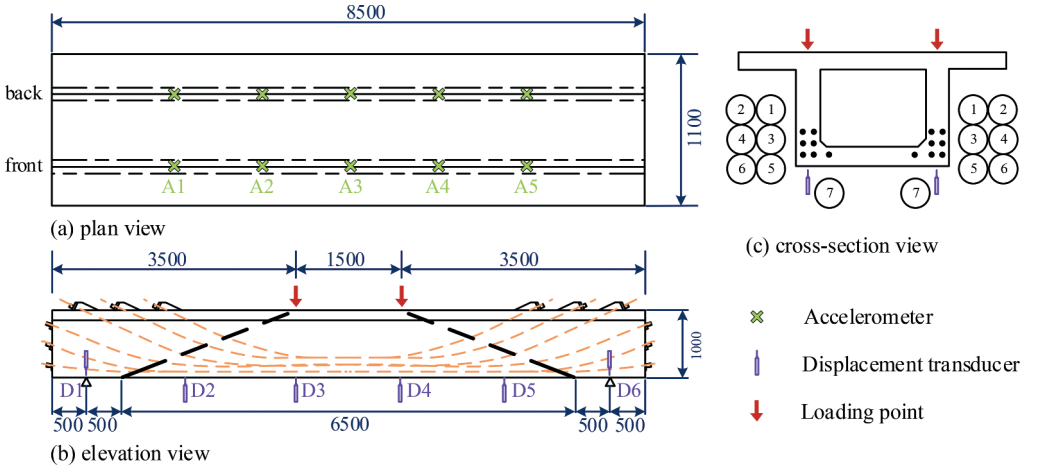


Figure 1. Specimen design and sensor locations (unit: mm).

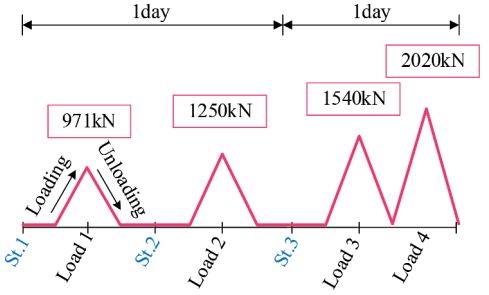


Figure 2. Loading procedures..



Figure 3. Photo of static loading test.

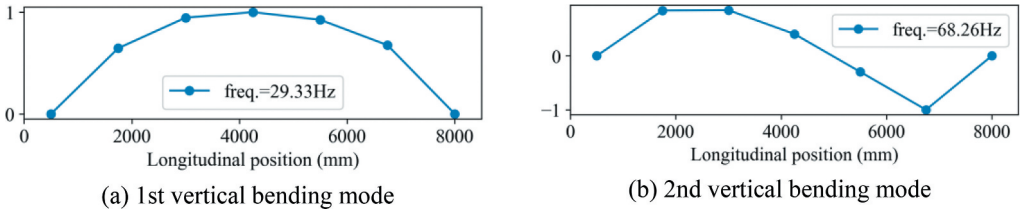
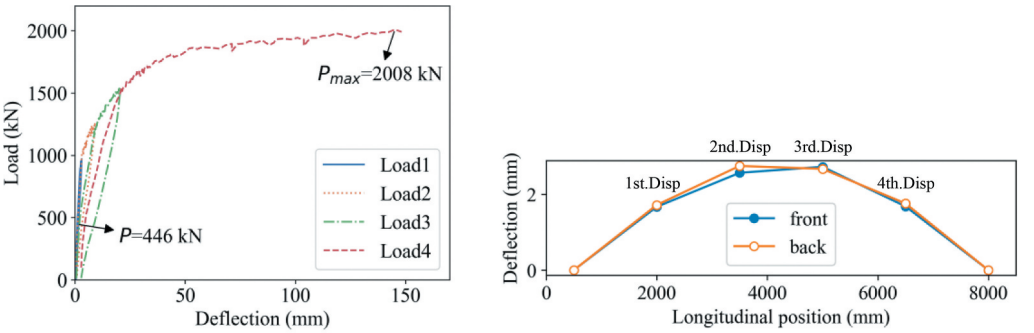


Figure 4. Frequencies and mode shapes identified from vibration test.



(a) load-deflection curve

(b) deflection diagram (P=446 kN)

Figure 5. Experimentally measured deflection.

3.2 *Static loading and vibration test*

As shown in Figure 1, the specimen was subjected to a four-point concentrated static load. Displacement transducers were placed at the five equidistant points along the span. The loading procedures, illustrated in Figure 2, involved four distinct phases: initial cracking load (Load 1), shear cracking load (Load 2), stirrup yield load (Load 3), and ultimate load (Load 4). To assess vibration characteristics simultaneously, three vibration tests (St. 1~3) were conducted. Ten accelerometers, each with a sampling frequency of 2000 Hz, were positioned at the six equidistant points of the span, with five accelerometers on each side. The specimen was excited with an impact hammer, and the same excitation was replicated ten times at each accelerometer position. Figure 3 shows the photo of the static loading test.

The modal parameters for the first two bending modes are shown in Figure 4, which are extracted from the frequency response function (FRF) using acceleration data measured at St. 1. The load-deflection curves measured experimentally, along with the deflection diagram illustrating measurements under a 446-kN load, are presented in Figure 5. At this load level, the PC girder stays within its elastic stress range.

4 MODEL UPDATING

4.1 *Finite element model*

A three-dimensional (3D) finite element (FE) model is established using Diana 10.6 for model updating, as shown in Figure 6. The concrete beam is modeled using 8-node hexahedral solid elements, while rebars and prestressing tendons are represented by line elements embedded in the concrete, assuming a perfect bond between the reinforcement and the surrounding concrete. Rotational and translational constraints at supports are included using springs, as illustrated in Figure 7. To address the influence of the self-weight of the steel loading beam on the free vibration of the PC girder during the vibration test, additional concentrated masses are introduced at the loading points.

4.2 *Sensitivity analysis*

Potential candidates for updating parameters include modulus of elasticity of concrete (E_c), mass density of concrete (ρ_c), modulus of elasticity of rebar (E_r), modulus of elasticity of prestressing tendon (E_p), spring constant of rotational spring (K_r) and spring constant of translational spring (K_t).

The results of the sensitivity analysis revealed that the modulus of elasticity and mass density of concrete significantly affect the frequencies. Nevertheless, these two parameters hardly

affect the Modal Assurance Criterion (MAC), a normalized measure employed to evaluate the similarity between two mode shapes. The modal parameters are insensitive to changes in the modulus of elasticity of the rebar and prestressing tendon.

It is noted that increasing the spring constants of both rotational and translational springs at supports will lead to higher frequencies. However, the experimentally measured frequencies for bending modes were smaller than those simulated using the initial FE model. Therefore, careful consideration should be given to the decision of whether to employ springs or not to the supports in the eigenvalue analysis.

Deflection is exclusively responsive to variations in the modulus of elasticity of concrete, with density changes exerting no influence. Moreover, deflection remains largely unresponsive to shifts in the modulus of elasticity of the rebar and prestressing tendon. The addition of rotational and translational springs to the boundary conditions has only a marginal effect on deflection, unlike the modal parameter.

Based on the sensitivity analysis results, the selected uncertain parameters for the model update comprise the modulus of elasticity of concrete (E_c), mass density of concrete (ρ_c), spring constant of rotational spring (K_r), and spring constant of translational spring (K_t).

4.3 *Model class selection and updating scenarios*

This study explores three model classes: M_1, characterized by four parameters (E_c, ρ_c, K_r, K_t), M_2, distinguished by three parameters (E_c, ρ_c, K_r), and M_3, defined by two parameters (E_c, ρ_c). The model responses employed for model updating are categorized into two groups. Exp 1 incorporates the frequencies and mode shapes of 1st and 2nd vertical bending modes (Figure 4) into the goodness-of-fit function. Meanwhile, Exp 2 includes the frequency and mode shape of the 1st vertical bending mode, along with elastic deflection (Figure 5 (b)), in the goodness-of-fit function.

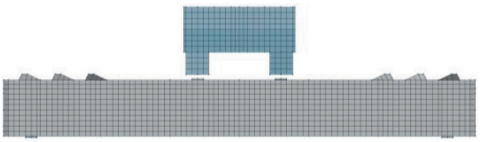


Figure 6. 3D FE model established in Diana.



Figure 7. Additional rotational and translational constraints of boundary conditions.

Table 1. Comparison between MPVs and reference values for model parameters.

Scenario		E_c (MPa)	ρ_c (t/mm^3)	K_r (N/mm^2/rad)	K_t (N/mm^2)
Reference value		3.40×10^4	2.50×10^{-9}	0.0001	0.0001
Exp1_R1_T1	Upd. value	1.74×10^4	1.81×10^{-9}	-1.641	0.485
	Upd. deviation	-48.74%	-27.68%	–	–
Exp1_R1_T0	Upd. value	1.76×10^4	1.65×10^{-9}	5.531	–
	Upd. deviation	-48.15%	-33.82%	–	–
Exp1_R0_T0	Upd. value	1.72×10^4	1.26×10^{-9}	–	–
	Upd. deviation	-49.33%	-49.52%	–	–
Exp2_R1_T1	Upd. value	3.27×10^4	2.45×10^{-9}	0.406	-1.616
	Upd. deviation	-3.69%	-2.19%	–	–
Exp2_R1_T0	Upd. value	3.33×10^4	2.49×10^{-9}	-1.079	–
	Upd. deviation	-2.10%	-0.40%	–	–
Exp2_T0_R0	Upd. value	3.32×10^4	2.47×10^{-9}	–	–
	Upd. deviation	-2.32%	-1.32%	–	–

Table 2. Comparison between measured and simulated responses.

Scenario		1st.Freq (Hz)	1st. MAC	2nd.Freq (Hz)	2nd. MAC	3rd.Disp (mm)	4th.Disp (mm)
Exp. value		29.33		68.26		1.06	0.64
Exp1_R1_T1	Value	29.94	0.99	68.49	0.96	1.44	0.83
	Error	2.07%	1.25%	0.33%	3.99%	36.12%	28.96%
Exp1_R1_T0	Value	28.62	0.99	70.91	0.84	1.64	0.95
	Error	-2.44%	1.18%	3.88%	15.70%	54.68%	48.24%
Exp1_R0_T0	Value	27.85	0.99	72.95	0.81	2.00	1.20
	Error	-5.06%	0.91%	6.86%	19.17%	88.90%	87.03%
Exp2_R1_T1	Value	29.43	0.99	74.32	0.79	1.08	0.65
	Error	0.31%	0.88%	8.88%	20.95%	2.09%	1.05%
Exp2_R1_T0	Value	29.30	0.99	74.14	0.79	1.07	0.65
	Error	-0.13%	0.87%	8.60%	21.27%	1.28%	0.36%
Exp2_T0_R0	Value	29.37	0.99	74.36	0.79	1.07	0.65
	Error	0.13%	0.87%	8.93%	21.26%	1.52%	0.60%

Note: Exp.: Experimental, Upd.: Updated.
R: Rotational spring, T: Translational spring, 1: Indicates the use of springs, 0: Indicates no use of springs.
e.g. Exp1_R1_T1 indicates that the model utilizes both rotational and translational springs, incorporating the frequencies and mode shapes from Exp 1 scenario into the goodness-of-fit function.

4.4 *Model updating results*

Table 1 compares the most probable values (MPVs) of model parameters and their corresponding reference values. Furthermore, Table 2 provides a summary that includes both experimentally measured responses and simulated responses obtained by applying the MPVs of model parameters. The 1st. Freq (MAC) and 2nd. Freq (MAC) in Table 2 correspond to the 1st and 2nd bending modes, respectively. Additionally, the 3rd. Disp and 4th. Disp represent the deflection data measured by the 3rd and 4th sensors, as illustrated in Figure 5 (b). As an illustrative example, Figures 8 and 9 display histograms of samples for scenarios Exp1_R1_T1 and Exp2_R0_T0.

It is inferred that the identification error for the 2nd bending mode is relatively large compared to the 1st bending mode. The potential sources of this error can be attributed to two factors. Firstly, the specimen's cross-sectional dimensions are scaled in alignment with the static experiment, resulting in a significantly large overall bending stiffness for the main girder. Consequently, the higher stiffness leads to elevated frequencies, making it more challenging to induce vibration during the experiment. Secondly, environmental noise has exhibited a noticeable impact on the vibration characteristics.

Owing to the notable disparity between the observed modal parameters for the 2nd bending mode and the computed values from the FE model, the MPV values for the concrete's modulus of elasticity and the mass density in the calibrated models of three Exp 1 scenarios substantially deviate from their reference values.

The utilization of static-dynamic data, encompassing the 1st bending mode and elastic deflections, in the model updating process for the three Exp 2 scenarios has yielded accurate estimates of material parameters that closely align with the reference values. Furthermore, the computed responses from the calibrated model exhibit excellent agreement with the measured data.

Upon comparing the updated results of the three Exp 2 scenarios, it can be concluded that the additional constraints at the supports have a negligible effect on the model responses compared to the material properties. This is attributed to the consistency of the boundary conditions in the 3D FE model with the experiments, in contrast to the 1D beam model, which simplifies the constraints at the supports. Therefore, the calibrated FE model in scenario Exp2_T0_R0, characterized by its adoption of the simplest model class, is utilized for subsequent analysis and discussion.

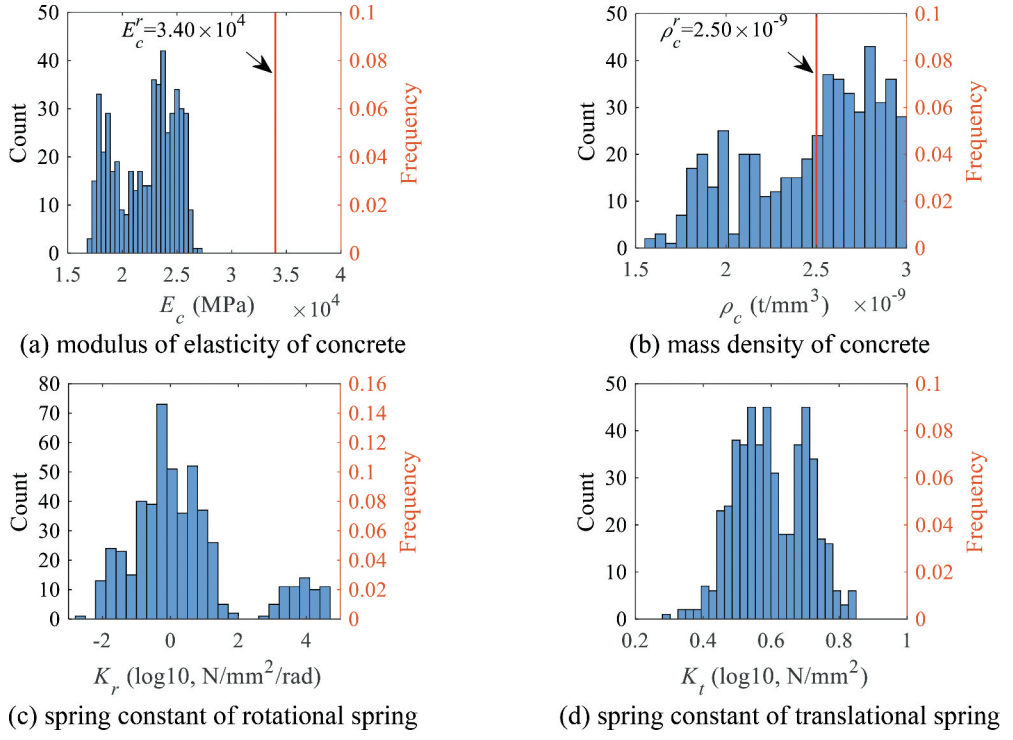


Figure 8. Histogram of samples for scenario Exp1_R1_T1.

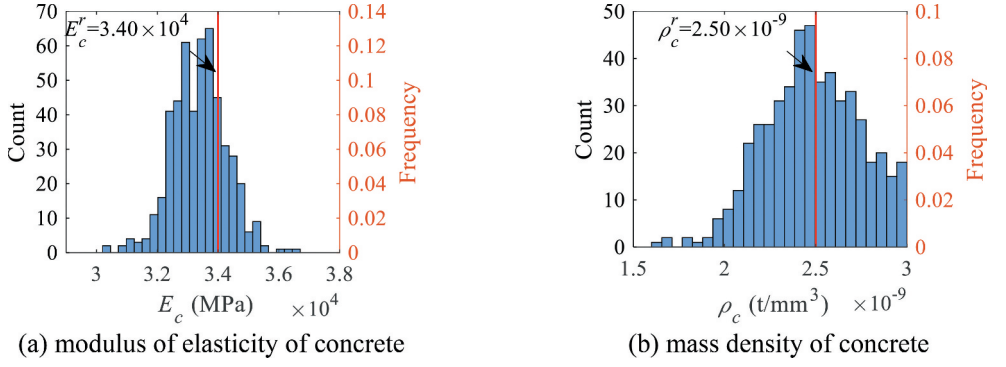
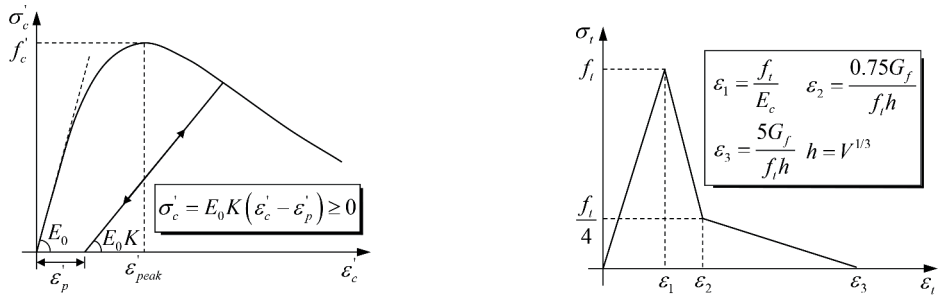


Figure 9. Histogram of samples for scenario Exp2_R0_T0.

Table 3. Comparison of 1st bending frequencies between intact and cracked states.

Unit: Hz	St.1	St.2	St.3
Exp. (FRF)	29.33	29.24	29.12
Exp. (BAYOMA)	29.27	28.38	28.45
Upd.	29.37	29.37	29.36



(a) compressive constitutive model (b) tensile constitutive model

Figure 10. Nonlinear constitutive model of concrete.

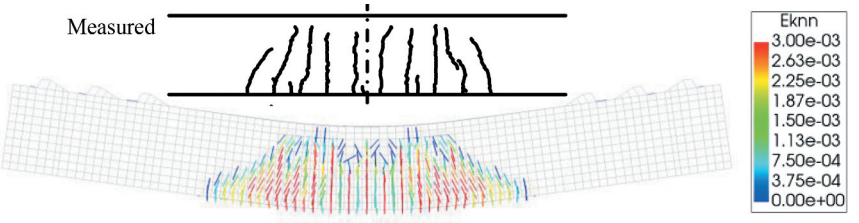
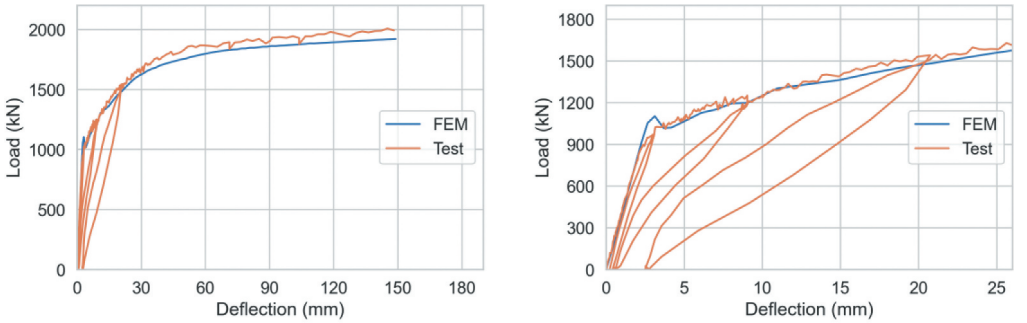


Figure 11. Comparison of measured and simulated crack patterns (at Load 2).



(a) load-deflection curve (b) enlarged view

Figure 12. Comparison of measured and simulated load-deflection curves.

4.5 *Structural performance assessment using the calibrated FE model*

Model-based structural health monitoring (SHM) requires high-fidelity FE models to accurately predict the performance of structures throughout their service life. Following the Bayesian model updating with measured data from the elastic stress state, the calibrated FE model is then utilized for assessing structural performance in subsequent states. It is crucial to validate the model's effectiveness in capturing nonlinear stress states to ensure the reliability of the model updating process.

Table 3 presents a comparison of 1st bending frequencies obtained from both the experiment and the calibrated FE model across intact (St.1) and cracked (St.2 and St.3) states. The table incorporates the frequency response function (FRF) and Bayesian operational modal analysis (BAYOMA) as two distinct methods employed for identifying modal parameters

based on measured acceleration signals. It has been discovered that structural damage resulting from concrete cracking has minimal impact on the 1st bending frequency. The calibrated model, using measured data from St.1, accurately calculates the frequencies of post-cracking states.

The nonlinear behavior of concrete is described using the total strain crack model with the Maekawa cracked concrete curves (Maekawa et al. 2003), as illustrated in Figure 10. Additionally, the uniaxial stress-strain curves of rebars and prestressing tendons are characterized by the simplified quadratic plastic flow model and trifold elasto-plasticity model, respectively.

Figure 11 and Figure 12 show a compassion of measured and simulated crack patterns and load-deflection curves, respectively. The simulation results generated by the calibrated FE model demonstrate a favorable alignment with the experimental outcomes. This underscores the capability of the FE model, updated by the model responses of the elastic state, to accurately predict the nonlinear structural responses of PC girders. As a result, it establishes a reliable digital twin model suitable for SHM.

5 CONCLUSIONS

This study proposes a new approach to improve the structural performance assessment of PC girder bridges using a Bayesian model updating method. A high-fidelity 3D FE model was developed, and its parameters were updated based on measured responses in the elastic stress state. The selection of an appropriate model class was informed by sensitivity analysis of model parameters and a comprehensive discussion of linear model updating outcomes. Our findings demonstrate that the calibrated FE model exhibits notable efficacy in predicting nonlinear structural behavior, particularly in capturing crack patterns and bending stiffness. As a result, it serves as a reliable digital twin model for SHM applications in PC girder bridges. Additionally, our case study reveals that structural damage induced by concrete cracking has minimal impact on the 1st bending frequency, and operational modal parameters are susceptible to noise interference, thereby highlighting specific limitations in their applicability for model updating purposes.

REFERENCES

Ching, J. & Chen, Y.C. 2007. Transitional Markov chain Monte Carlo method for Bayesian model updating, model class selection, and model averaging. *Journal of Engineering Mechanics* 133(7): 816–32.

Katafygiotis, L.S. & Beck, J.L. 1998. Updating models and their uncertainties. II: model identifiability, *Journal of Engineering Mechanics* 124(4): 463–67.

Maekawa, K., Okamura, H., & Pimanmas, A. 2003. Nonlinear Mechanics of Reinforced Concrete. Spon Press, 2003.

Road Bureau, 2020. Annual Statistical Report of Roads, Current conditions of bridges categorized by the material used for superstructure in each prefecture (general road), Ministry of Land, Infrastructure, Transport and Tourism (MLIT). (in Japanese)

Yoshida, E., Oshima, Y., Ishida, M., Yamamoto, T., Hattori. A, Takahashi, Y. 2021. Effect of cable rupture near anchorage zone on load bearing performance of PC box girder bridge, *Journal of JSCE E2 (Material & Concrete Structures)* 77(4): 210–29. (in Japanese)

Zhou, X., Kim, C.W., Zhang, F.L., Chang, K.C. 2022. Vibration-based Bayesian model updating of an actual steel truss bridge subjected to incremental damage, *Engineering Structures* 260, 114226.

Bridge Maintenance, Safety, Management, Digitalization and Sustainability – Jensen, Frangopol & Schmidt (eds)
© 2024 The Author(s), ISBN 978-1-032-77040-6
Open Access: www.taylorfrancis.com, CC BY-NC-ND 4.0 license

Framework of UAV bridge inspection with computer vision and deep learning

Kuan Yen & Chia-Ming Chang
Department of Civil Engineering, National Taiwan University

ABSTRACT: Bridge integrity is one of the most critical issues for infrastructure. Natural disasters or aging problems can cause damage to the structure and even affect safety, while regular inspection is one practical approach to affirm the current conditions of bridges. Because sophisticated inspectors are short with respect to the number of bridges, traditional visual inspection should be improved to be efficient and address the drawbacks of being time-consuming and labor-intensive. Additionally, specific bridge components have accessibility problems for inspection, e.g., abutments and bottom of bridge decks. Unmanned aerial vehicles (UAVs) have significantly enhanced the efficiency of bridge inspection in recent years. Therefore, this study proposes a systematic framework for bridge visual inspection utilizing UAVs in conjunction with deep learning and computer vision. This framework involves image localization, defect recognition, and damage quantification as three sequential tasks in bridge visual inspection. By shooting azimuths and camera-to-objective depths, bridge surface images captured from UAVs can be localized from the camera coordinates to the global coordinates (e.g., aligned with the GPS coordinates). Then, the defects on a bridge are detected by a deep learning model featuring instance segmentation, which enables cracks, spalling concrete areas, and exposed reinforcements to be highlighted in images. These images are also tagged with a point of interest and linked to the global coordinates. Moreover, the geometric parameters of these defects can also be interpreted through photogrammetry based on available azimuth and depth, and these defects are consequently quantified. An example using the proposed framework for bridge visual inspection is provided in this study for demonstration. As shown in the results, this framework further improves the efficiency of bridge inspection with added information, such as the three-dimensional locations, types, and geometric quantities of defects.

1 INTRODUCTION

Bridge inspections are crucial for maintaining the integrity and safety of infrastructure. Traditionally, these inspections have relied mainly on manual visual assessments, which, while fundamental, present several limitations (Moore et al., 2001). The efficiency of these inspections is often hampered by the subjectivity inherent in human judgment, insufficient inspection capacity due to a shortage of qualified personnel, and the visual limitations of manual inspections. These factors contribute to a lack of accurate and complete data collection, challenging the integrity of historical data. However, advancements in AI, as shown by Yoshikura et al. (2022), have the potential to address these limitations. Moreover, the manual approach is labor-intensive and time-consuming, compounding the high bridge maintenance and repair costs.

In recent years, Unmanned Aerial Vehicles (UAVs) have emerged as a significant innovation in bridge inspection practices (Gong et al., 2023), offering several advantages over traditional methods (Kim and Irizarry, 2020). UAVs provide superior three-dimensional mobility, enabling access to hard-to-reach areas of bridges, such as abutments and the underside of bridge decks. These UAVs are also capable of digitizing collected data, which enhances the efficiency of inspections and reduces costs and traffic disruptions. The ability to operate autonomously and capture

DOI: 10.1201/9781003483755-100

high-quality images from various angles represents a considerable leap forward in bridge inspection techniques using UAVs, allowing for more comprehensive and less intrusive inspections.

Integrating Artificial Intelligence (AI), particularly deep learning, in bridge inspections marks a transformative step in identifying and quantifying structural defects (Zhou et al., 2022). AI algorithms, trained on extensive datasets of bridge images, have demonstrated remarkable proficiency in detecting a broad spectrum of bridge defects, such as cracks, spalling, and exposed rebar (Liu et al., 2022; Munawar et al., 2022). This technology not only surpasses the limitations of human visual inspection in terms of accuracy and objectivity but also provides a quantitative basis for assessing the severity and extent of detected defects. This advancement in defect detection is crucial for effective bridge maintenance, facilitating the prioritization of repair efforts based on the severity of the detected defects.

This study contributes to the evolving field of bridge inspection by proposing a comprehensive framework that synergizes UAV technology with advanced computer vision and deep learning techniques. By employing UAVs for data collection and utilizing AI for defect detection and quantification, this framework addresses the challenges of traditional inspection methods (Savino and Tondolo, 2022) and enhances the overall efficiency, safety, and cost-effectiveness of bridge inspections. The study demonstrates the practical application of this framework through detailed case studies, highlighting its effectiveness in real-world scenarios. This integrated approach streamlines the inspection process and aligns with standard inspection protocols, resulting in a valuable tool for bridge engineers and inspectors.

2 SMART BRIDGE INSPECTION FRAMEWORK

Through the integration of Unmanned Aerial Vehicles (UAVs) with advanced computer vision and deep learning technologies, the proposed method introduces a systematic approach to bridge inspection. This method is intended to address the limitations of traditional bridge inspection techniques, particularly in terms of efficiency, data accuracy, and accessibility.

2.1 *Framework of proposed method*

As shown in Figure 1, the framework for smart bridge inspection is proposed in this study. This framework consists of three main components: automated data collection with UAVs, establishing a bridge defects detection model using deep learning techniques, and connecting the detection results to a bridge assessment scale. By combining automated data collection, deep learning-based defect detection, and linking detection results to a bridge assessment scale, the proposed framework enables more efficient and accurate bridge inspections. Facilitating this framework reduces manual inspections, improves inspection coverage, and provides objective and quantitative information for better maintenance decision-making.

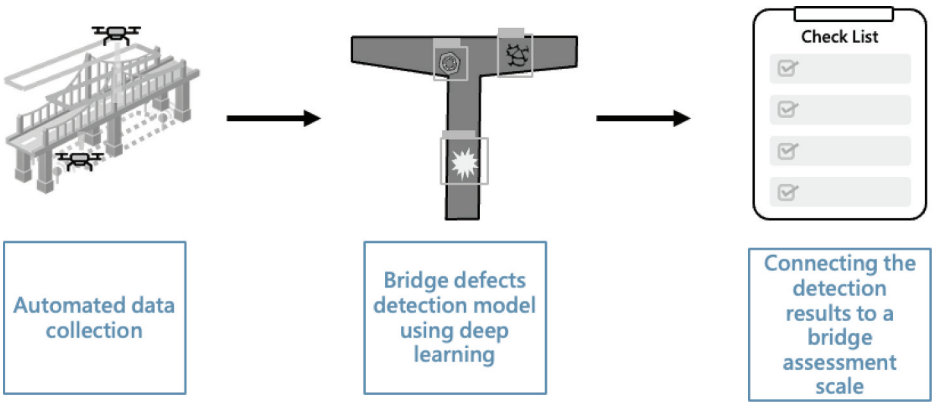


Figure 1. Smart bridge inspection framework.

2.2 *Data collection with UAV*

The first stage of the framework involves automated data collection using UAVs. UAVs are programmed to fly predetermined routes, capturing high-resolution images of various components from a bridge. Due to the lack of GNSS (Global Navigation Satellite System) signals under a bridge, a UWB network needs to be established to provide critical structural images of the beam, transverse diaphragm, and support (i.e., bearings) for the UAV. In this operational scheme, the establishment of the UWB positioning network consists of multiple UWB transmitters. These fixed-ground UWB transmitters create virtual GNSS coordinate signals to replace the real GNSS signals that may be unavailable due to structural obstruction. The relative coordinates are calculated and translated to the mobile aerial UWB, allowing the UWB device on the UAV to obtain absolute coordinates and complete spatial positioning.

This study chose to use open-source route planning software, i.e., the Mission Planner, as a tool for creating UAV-readable flight paths (Chintanadilok et al., 2022). Figure 2 shows the route planning procedure for UAV imaging acquisition, in which the images should contain the required scale and geometric transformations, coordinate data for subsequent safety assessment, and further plan the UAV's flight path. This study requires capturing images of the bridge deck, sides, and underside to establish a dataset for detecting bridge components.

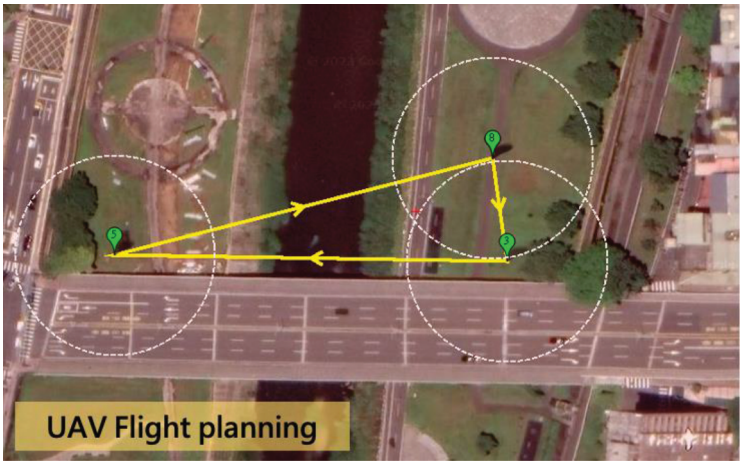


Figure 2. Flight route planning.

2.3 *Establish bridge defects detection model with deep learning*

This study primarily collects data through self-acquired sources and bridge inspection data provided by a consulting company. These sources include public datasets and self-collecting datasets. The public datasets mainly consist of street photos, including bridge images and are provided by the Mapillary Vistas (Neuhold et al., 2017). To be used in this research, only those images with clear and complete bridges are selected as training data. The self-collecting datasets are provided by the consulting sectors and mainly consist of images from previous manual inspections of bridges. In these datasets, over 10,000 bridge inspection images are included, e.g., steel bridges and concrete bridges, covering the important vehicle and pedestrian bridges and river crossings in Taipei City. Because this research targets concrete bridges, only concrete cracks, concrete spalling, and exposed rebar are considered as bridge defects. After selection, a total of 739 images featuring these defects, as shown in Table 1.

In this study, the bridge visual inspection deep learning model is constructed using the Detectron2 object detection library, which is open-sourced by Facebook Artificial Intelligence Research (FAIR) (Paszke et al., 2019). The model utilizes the Mask R-CNN

framework (He et al., 2018), and its hyperparameter settings are detailed in Table 2. These hyperparameters play a regulating role during the training process of deep learning. Specifically, the batch size refers to the number of training samples used for computing gradients and updating model weights through the loss function. The loss function evaluates the error between predicted results and actual observations, with the goal of minimizing this error to improve model accuracy. The learning rate controls the magnitude of weight updates, where it is multiplied by the computed gradient for weight updates. The optimization process of the model adjusts based on the value of the loss function. This study also adopts the warmup approach, which initially sets the learning rate to zero during training and gradually increases it to the default learning rate as the number of training iterations increases. The optimal combination of hyperparameters is usually determined through multiple experimental evaluations. Finally, the performance evaluation of the model uses the Average Precision (AP) metric, which is commonly used for object detection and instance segmentation. It comprehensively evaluates precision and recall at different thresholds and visualizes these data as a two-dimensional curve, with the area under the curve representing the AP value.

Table 1. Number of bridge defects datasets.

Types of defects	number	comment
Crack	300	Includes surface cracks on concrete piers.
Spalling	305	Deterioration of bridge structure and parapet
Exposed rebar	134	Includes exposed rebar in the concrete part of the steel bridge

Table 2. Hyperparameter values.

Parameters	Value
Batch size	4
Learning rate	0.0001(warmup)
Epochs	1000 epochs

2.4 *Connection to the detection scale for identification results*

According to the 'Highway Bridge Inspection and Strengthening Specifications' in Taiwan, the widely adopted assessment standard is the D.E.R.&U. visual inspection. The assessment process of this criterion takes into account four main factors: "Degree," "Extent," "Relevancy" to bridge structural safety and serviceability, and "Urgency" of maintenance. These factors not only streamline the inspection work but also focus on critical components of the bridge and their impact on overall structural safety. D.E.R.&U. divides bridges into 21 inspection items and evaluates the degree of deterioration, scope, impact on safety, and urgency of maintenance, as shown in Table 3. Through integrating image processing, computer vision, and deep learning in artificial intelligence, this study has developed a specialized identification process for bridge components and defects. After analyzing the identification results, the specific location of the defect is determined. Based on the rating criteria set in the specifications, the corresponding DER&U value is calculated. Based on this value, an assessment of structural safety severity is conducted, and a classification of urgency is determined. The classification results will be used to prioritize inspection operations and prioritize the formulation of maintenance plans for more severe situations. After the identification stage, the study will conduct a thorough analysis of the D, R, and U values. Based on the reference values set in the specification table, the range and appearance features of the defect are

determined based on existing image data and past rating reports. Concrete DER&U values are provided for subsequent evaluation and management. Due to the significant differences in shape, size, color, and location of bridge components, it may be necessary for professional engineers to make rule adjustments or add exception judgment conditions based on specific situations to ensure the accuracy of identification in practical applications.

Table 3. DER&U assessment method testing project.

(1) Approach embankment	(8) Friction layer	(15) Bearing/Bearing pad
(2) Approach guardrail	(9) Bridge deck drainage facilities	(16) Shock block/Tie rod
(3) River channel	(10) Curb and sidewalk	(17) Expansion joint
(4) Approach slope protection measures	(11) Railing and parapet	(18) Main component (Main beam)
(5) Abutment foundation	(12) Pier protection facilities	(19) Secondary component (Crossbeam)
(6) Abutment	(13) Pier foundation	(20) Bridge deck plate/Hinge plate
(7) Wing wall/Retaining wall	(14) Pier body/Cap beam	(21) Others

3 FIELD INSPECTION OF IN-SERVICE BRIDGE

This study selected the open field area of Pinghu No. 7 Bridge as the testing site. The total length of the bridge is 85 meters, with a maximum width of 12 meters and 2 lanes. The bridge has a total of 2 spans. The structure type is a beam bridge, where girders are prestressed concrete I-beams. Due to the lowest clearance height of 1.2 meters under the bridge, large machinery and vehicles are inaccessible, and UAVs are an excellent alternative for inspection.

3.1 *Prediction results of bridge inspection model*

This study employs deep learning techniques to analyze data obtained from unmanned aerial vehicle (UAV) inspections. The objective is to develop a Mask R-CNN segmentation model tailored for the visual detection of three distinct types of structural deficiencies in bridges: "cracks," "concrete spalling," and "exposed rebar." The model's performance is assessed based on the ability to identify and categorize these deficiencies from the UAV-collected imagery accurately.

Compared to traditional inspection methods, unmanned drone inspections have significant advantages. Not only does it reduce labor costs, but it also shortens maintenance and repair time. Drones can easily reach terrains and angles that are difficult for traditional inspections, as shown in Figure 3. Utilizing UAVs can comprehensively capture the perimeters of bridges, including the sides and railings that are difficult to inspect manually.

Figure 4 demonstrates the effectiveness of a deep learning model in detecting defects on bridges. This model can automatically pinpoint the specific defect locations. In Figure 4(a), a blue square is used to highlight the presence of cracks on a bridge pier. This type of defect is often overlooked during manual inspections, and the deep learning model becomes an invaluable tool. Figures 4(b) and (c) display spalling and exposed rebar. These defects are denoted by red and green squares. With the deep learning-based approach, these defects can be accurately identified without any subjectivity that may arise during manual inspections. By relying on data-driven machine learning algorithms, this method of defect identification offers more objectivity and accuracy, and more reliable results in bridge inspections are then successfully acquired.



(a). (b).

Figure 3. (a) Visual inspection, (b) AI with UAV inspection comparison.



(a). (b). (c).

Figure 4. AI detection results of three defects.

3.2 *Bridge ratings based on deep learning results*

Take the example of Pinghu No. 7 Bridge to compare the use of UAVs combined with AI automatic deterioration recognition technology and manual visual inspection. The experimental results are shown in Table 4, which indicate that the automated deterioration recognition technology can provide comprehensive monitoring of the bridge from different angles and distances. It can also detect areas that cannot be reached by manual visual inspection, thereby compensating for the limitations of manual inspection.

As seen in Figure 5, visual inspection has limitations regarding angle and field of view, resulting in missing defects. On the other hand, the combination of unmanned drones and artificial intelligence offers high maneuverability and can detect more defects. Suppose the AI model has omissions or errors in recognizing certain defects. In that case, these data can be fed back to the model through human judgment and labeling, further improving the model's accuracy. Figure 5 presents the detection and assessment results for the Pinghu No. 7 bridge. The results show the quantitative values for each parameter (Degree, Extent, Relevancy, Urgency) for the components of the bridge. These values help determine the level of deterioration, the extent of deterioration, the impact on safety and functionality, and the urgency of maintenance required for each component. The higher the values, the more critical the component's deterioration is, indicating a higher urgency for maintenance. It necessitates assessments solely for elements exhibiting deterioration, thereby omitting evaluations for components in satisfactory condition.

Table 4. Comparison between visual inspection and UAV inspection.

Components	Visual inspection	AI detection with UAV
Main bean	0	8
Pier/Cap beam	0	2
Bridge guardrail	1	1
Bridge abutment	6	4
Bridge deck	0	3

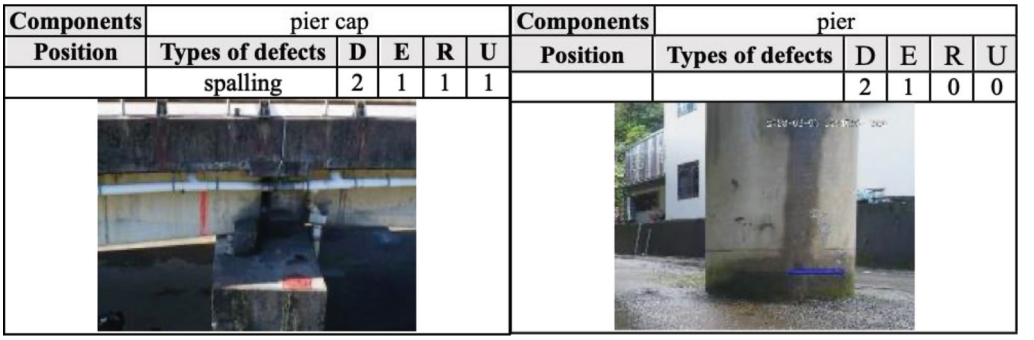


Figure 5. Bridge assessment scale.

4 CONCLUSIONS

This study developed an automated inspection framework using UAVs as patrol tools. In data collection, this research comprehensively assembled images of crucial bridge inspection components through a complete UAV flight planning process. The autonomous image collection was accomplished by UAVs using a UWB network. Through the Mission Planner, the UAVs can automatically operate and collect data along a predefined route. All the collected images were tagged with positions and recognition outcomes (i.e., defects, if any). Finally, these data and information were mapped to a bridge rating system, and the current condition of the bridge was determined. Moreover, the proposed framework was implemented on the Pinghu No. 7 Bridge. In the beginning, a UWB network was established through multiple UWB anchors and transmitters. A UAV with a consumer-graded camera was exploited to collect images over this bridge and also autopiloted using a predefined inspection route. A number of images were then collected and analyzed by a well-trained defect detection model. Various types of defects were identified and informed with locations. These detection results are finally interpreted by a rating system and converted into the DERU scores defined by the inspection code. As compared to the traditional approach, the proposed framework provided more detailed information and efficiency for bridge inspection.

REFERENCES

Chintanadilok, J., Patel, S., Zhuang, Y., & Singh, A. (2022). Mission Planner: An open-source alternative to commercial flight planning software for unmanned aerial systems. EDIS, 2022(4).

Zhou, F., Wen, G., Qian, G., Ma, Y., Pan, H., Liu, J., & Li, J. (2022). A high-efficiency deep-learning-based antivibration hammer defect detection model for energy-efficient transmission line inspection systems. *International journal of antennas and Propagation*, *2022*.

Gong, Y., Zhou, W., Wang, K., Wang, J., Wang, R., Deng, H., & Liu, G. (2023). Defect detection of small cotter pins in electric power transmission system from UAV images using deep learning techniques. *Electrical Engineering*, *105*(2), 1251–1266.

He, K., Gkioxari, G., Dollár, P., & Girshick, R. (2017). Mask R-CNN. In *Proceedings of the IEEE International Conference on Computer Vision* (pp. 2961–2969).

Kim, S., Kim, D., Jeong, S., Ham, J. W., Lee, J. K., & Oh, K. Y. (2020). Fault diagnosis of power transmission lines using a UAV-mounted smart inspection system. *IEEE Access*, *8*, 149999–150009.

Moore, M., Phares, B. M., Graybeal, B., Rolander, D., Washer, G., & Wiss, J. (2001). Reliability of visual inspection for highway bridges, Volume I (No. FHWA-RD-01-105). Turner-Fairbank Highway Research Center.

Munawar, H. S., Ullah, F., Shahzad, D., Heravi, A., Qayyum, S., & Akram, J. (2022). Civil infrastructure damage and corrosion detection: An application of machine learning. *Buildings*, *12*(2), 156.

Neuhold, G., Ollmann, T., Rota Bulo, S., & Kontschieder, P. (2017). The mapillary vistas dataset for semantic understanding of street scenes. In *Proceedings of the IEEE International Conference on Computer Vision* (pp. 4990–4999).

Paszke, A., Gross, S., Massa, F., Lerer, A., Bradbury, J., Chanan, G., ... & Chintala, S. (2019). Pytorch: An imperative style, high-performance deep learning library. *Advances in Neural Information Processing Systems*, *32*.

Savino, P., & Tondolo, F. (2023). Civil infrastructure defect assessment using pixel-wise segmentation based on deep learning. *Journal of Civil Structural Health Monitoring*, *13*(1), 35–48.

Liu, Y., Dong, J., Li, Y., Gong, X., & Wang, J. (2022). A UAV-based aircraft surface defect inspection system via external constraints and deep learning. *IEEE Transactions on Instrumentation and Measurement*, *71*, 1–15.

Yoshikura, M., Minami, T., Fukuoka, T., Fujiu, M., & Takayama, J. (2022, March). Assessment of bridge engineers on output display size in automatic detection of free lime using deep learning. In *7th International Conference on Road and Rail Infrastructure*.

Bridge Maintenance, Safety, Management, Digitalization and Sustainability – Jensen, Frangopol & Schmidt (eds)
© 2024 The Author(s), ISBN 978-1-032-77040-6
Open Access: www.taylorfrancis.com, CC BY-NC-ND 4.0 license

Vision-based optimal sensor selection for full-field displacement reconstruction

Y.F. Weng, S.T. Quek & K.W. Yeoh
Department of Civil and Environmental Engineering, National University of Singapore, Singapore

X.L. Lu
College of Civil Engineering, Tongji University, Shanghai, China

ABSTRACT: Computer vision-based methods provide dense and accurate structural displacement measurements, countering the limitations of traditional contact-type sensors. However, storing the extensive data generated by full-field measurements, where each pixel acts as a sensor, poses a challenge. To address this, an optimal sensor selection strategy is proposed. First, the improved phase-based optical flow (IPBOF) method, which is resistant to illumination changes and phase wrapping, is used for displacement measurement. Subsequently, the obtained displacement matrix is decomposed into tailored bases through Singular Value Decomposition (SVD), and QR decomposition is then applied to determine the best pixels for reconstruction. The efficacy of the proposed method was verified using a laboratory video capturing the vibration of a 6-story building model. The results validate the method's ability to robustly reconstruct full-field dynamic displacement with high precision and a notable compression rate. This approach offers a solution to handle extensive data, retaining accurate full-field displacement information for long-term structural monitoring purpose.

1 INTRODUCTION

Structural displacement is an important indicator to assess the health condition of the structure. In the field of structural health monitoring (SHM), dynamic displacement signal can be utilized to obtain insights into the structural behavior and detect potential damage and risk of civil infrastructure at an early stage. Traditional displacement measurement approaches include linear variable differential transformer (LVDT), laser Doppler vibrometer (LDV) and global positioning system (GPS) (Celebi, 2000). LVDT requires one end to be being fixed on a stationary object as reference, which limits its application in actual practice. LDV can remotely measure the displacement with high resolution and accuracy but is restricted to limited measurement points and not cost-efficient. GPS is an indirect measurement approach and can provide the displacement signal without the need for a reference point. However, general GPS data can only provide centimeter level accuracy and a more accurate measurement, such as differential global positioning system (DGPS), usually comes at a high cost.

Over the past decade, computer vision-based structural vibration measurement has become a wide research topic with the rapid development of the computational hardware and the proliferation of high-quality low-cost cameras in the market. Compared to traditional sensors, vision-based approach is more cost-efficient and easier to instrument. Moreover, vision-based method provides the possibility of measuring the structural displacement remotely and densely. Each image pixel can be regarded as a virtual sensor, thus making the approach efficient for simultaneous multi-point measurement. Recently, Chen et al. (2015) developed the phase-based optical flow (PBOF) algorithm to estimate the displacement of a steel cantilever beam, which matched well with the reference provided by the laser vibrometer. The approach

DOI: 10.1201/9781003483755-101

was then successfully applied to measure the vibration of an antenna with a distance of over 175 meters in outdoor environment (Chen et al., 2017). Compared with the intensity-based methods, such as the Kanade-Lucas-Tomasi (KLT) tracker, the PBOF algorithm is more robust with respect to changes in contrast, scale, orientation, and speed (Fleet et al., 1990; Barron et al., 1992). The PBOF algorithm has been demonstrated to have the capacity of accurately measuring movements even with an amplitude of hundreds of times smaller than a single pixel (Diamond et al., 2017). However, conventional PBOF approach is prone to illumination changes and phase wrapping issue. Phase unwrapping techniques could potentially resolve this issue but require higher computational cost (Cai et al., 2023). Therefore, a more robust PBOF algorithm is urgently needed. In addition, since each pixel can be regarded as a virtual sensor, the full-field displacement data obtained using the PBOF algorithm requires a significantly large storage space, which is challenging especially for long-term monitoring.

To address these challenges, an improved phase-based optical flow (IPBOF) method and an optimal sensor selection strategy are proposed herein. First, the full-field displacement data is measured using the proposed IPBOF, which is invariant to illumination changes and phase wrapping. Subsequently, the displacement matrix is decomposed into a set of tailored bases using singular value de-composition (SVD), and the QR decomposition is applied to these tailored bases to determine the optimal number and locations of pixels that will be utilized for reconstructing the full-field displacement data. Finally, the tailored bases and the displacement data of the selected pixels are stored to compress the data size and facilitate full-field displacement reconstruction. The efficacy of the proposed approach was validated using a laboratory video capturing the vibration of a base-excited 6-story building model. The results demonstrated that the proposed method can robustly reconstruct the full-field dynamic displacement with high accuracy and compression rate.

2 METHODOLOGY

Figure 1 illustrates the workflow of the proposed vision-based displacement measurement and reconstruction method. This framework comprises two primary steps: vision-based full-field displacement measurement and optimal sensor selection for reconstruction. Further details for each step are elaborated below.

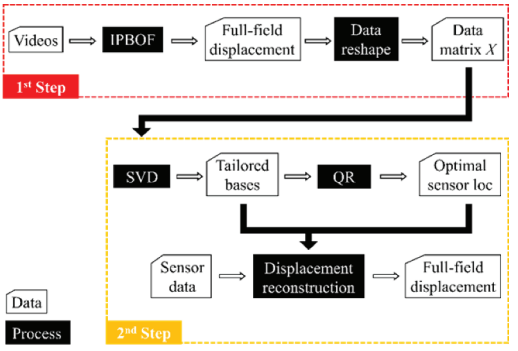


Figure 1. Workflow of the proposed vision-based displacement measurement and reconstruction method.

2.1 *Vision-based full-field displacement measurement*

Over the last decade, phase-based optical flow (PBOF) method has shown potential in measuring displacement up to a hundredth of a pixel. The PBOF is built on the theory that constant contours of the image local phase as a function of time correspond to the displacement signal, which can be expressed as

$$\phi_\theta(x, y, t) = c \tag{1}$$

where θ is a specified orientation at each pixel location (x, y) at time t, and c is the phase constant.

A quadrature pair of complex filters $G_2^\theta + iH_2^\theta$, where G_2^θ and H_2^θ have the same frequency response but differ in phase by 90°, is used to obtain the local phase information. The second derivative of a Gaussian function and its Hilbert transform approximation, as specified by Freeman et al. (1991), are employed herein for G_2^θ and H_2^θ, respectively. The video frame $I(x, y, t)$ is then spatially convolved with this nine-by-nine tap complex filter to obtain the amplitude $A_\theta(x, y, t)$ and phase $\phi_\theta(x, y, t)$ as

$$A_\theta(x, y, t)e^{\phi_\theta(x,y,t)} = \left(G_2^\theta + iH_2^\theta\right) \otimes I(x, y, t) \tag{2}$$

where (x, y) are the pixel locations, and t is the time index. By evaluating the filter $G_2^\theta + iH_2^\theta$ at $\theta = 0$, $\theta = \pi/2$ and substituting in Eq. (2), the local phase in the horizontal and vertical directions, respectively, are obtained.

The amplitude image, $A_\theta(x, y, t)$, contains edge strength information, while the phase image, $\phi_\theta(x, y, t)$, is sensitive to small motion. By differentiating Equation (1) with respect to time and setting the derivative in the orthogonal direction to zero, the local motion in pixels between two video frames can be expressed as

$$d_x(x, y, t) = \left(\frac{\partial \phi_0(x, y, t)}{\partial x}\right)^{-1} \frac{\partial \phi_0(x, y, t)}{\partial t} \tag{3}$$

$$d_y(x, y, t) = \left(\frac{\partial \phi_{\frac{\pi}{2}}(x, y, t)}{\partial y}\right)^{-1} \frac{\partial \phi_{\frac{\pi}{2}}(x, y, t)}{\partial t} \tag{4}$$

where d_x and d_y denote the local motions (velocities) in the horizontal and vertical direction, respectively.

However, conventional PBOF suffers from measurement error induced by possible illumination changes and phase wrapping. In response to these challenges, this study introduces an improved phase-based optical flow (IPBOF) algorithm. Initially, the mean intensity of each video frame within the region of interest (ROI) is standardized to mitigate the impact of uniform illumination changes. The ROI represents an m pixel area around each specific pixel location. In this context, the region size m is set at 9, aligning with the size of the complex filter utilized for convolution. The intensity adjustment process can be represented by

$$I'(x, y, t) = I(x, y, t) - [\bar{I}(t) - \bar{I}(1)] \tag{5}$$

$$\bar{I}(t) = \frac{\sum_{\mathrm{ROI}}[M(x, y) \cdot I(x, y, t)]}{\sum_{\mathrm{ROI}}[M(x, y)]} \tag{6}$$

where $\bar{I}(t)$ is the ROI mean intensity at time step t; M is a pixel mask employed to select areas with good contrast because displacement signals in textureless regions are usually noisy and should be discarded. Herein, the initial amplitude image $A_\theta(x, y, 1)$ is used to determine the pixel mask, which can be expressed as

$$\begin{cases} M(x, y) = 1 & \text{if } A_\theta(x, y, 1) \geq A_t \\ M(x, y) = 0 & \text{if } A_\theta(x, y, 1) < A_t \end{cases} \tag{7}$$

where A_t is the amplitude threshold set to be half of the median of the 30 pixels with the largest amplitude.

Subsequently, the phase information is obtained by spatially convolving the intensity adjusted images $I'(x, y, t)$ with the complex filter $G_2^\theta + iH_2^\theta$, as indicated in Equation (2). The phase derivatives $\partial\phi_0/\partial x$, $\partial\phi_{\frac{\pi/2}{2}}/\partial y$ and $\partial\phi_\theta/\partial t$ can be computed via

$$\frac{\partial\phi_0(x,y,t)}{\partial x} = angle\left(\frac{A_0(x+1,y,t)}{A_0(x,y,t)}e^{i[\phi_0(x+1,y,t)-\phi_0(x,y,t)]}\right) \tag{8}$$

$$\frac{\partial\phi_{\frac{\pi}{2}}(x,y,t)}{\partial y} = angle\left(\frac{A_{\frac{\pi}{2}}(x,y+1,t)}{A_{\frac{\pi}{2}}(x,y,t)}e^{i\left[\phi_{\frac{\pi}{2}}(x,y+1,t)-\phi_{\frac{\pi}{2}}(x,y,t)\right]}\right) \tag{9}$$

$$\frac{\partial\phi_\theta(x,y,t)}{\partial t} = angle\left(\frac{A_0(x,y,t)}{A_0(x,y,1)}e^{i[\phi_0(x,y,t)-\phi_0(x,y,1)]}\right) \tag{10}$$

where $angle(\cdot)$ is the four-quadrant inverse tangent operator. By computing phase variations before taking the inverse tangent operation, the proposed method can avoid potential phase wrapping caused by the intrinsic phase.

2.2 *Optimal sensor selection for full-field displacement reconstruction*

Vision-based sensors offer accurate and dense displacement measurements compared to conventional contact-type sensors. However, they possess larger dimensions and require more storage space for data. For instance, an image with a resolution of 1920×1080p encompasses 2,073,600 dimensions, as each pixel acts as a virtual sensor. Storing such large displacement datasets can pose challenges, especially in the context of long-term monitoring. To tackle this issue, an optimal sensor selection strategy is employed to compress the full-field displacement data by leveraging its sparse data structure. The high-dimensional full-field displacement $\mathbf{d}_t$ at time step t can be efficiently represented as a superposition of a set of structural vibration modes $\mathbf{\Psi}$, as illustrated below:

$$\mathbf{d}_t = \mathbf{\Psi}\mathbf{s}_t \tag{11}$$

where $\mathbf{d}_t$ represents an n dimensional displacement vector at time step t, $\mathbf{\Psi}$ is a $n \times n$ transformation basis containing all potential structural vibration modes, and $\mathbf{s}_t$ denotes an n dimensional sparse coefficient vector at time step t, wherein most elements are either zero or close to zero.

By discarding the structural vibration modes corresponding to zero or near-zero elements in the sparse vector, a $n \times r$ tailored transformation basis $\mathbf{\Psi}_r$ can be constructed. Consequently, Equation (11) can be reformulated as:

$$\mathbf{d}_t = \mathbf{\Psi}_r\mathbf{a}_t \tag{12}$$

where $\mathbf{a}_t$ is an r dimensional sparse coefficient vector at time step t that corresponds to the non-zero elements in $\mathbf{s}_t$.

Given that the tailored basis $\mathbf{\Psi}_r$ has a much lower rank compared to the original transformation basis $\mathbf{\Psi}$, retaining data from only r sensors (pixels) can significantly reduce the storage space for displacement data, as illustrated below:

$$\mathbf{y}_t = \begin{bmatrix} \mathbf{d}_{t,\gamma 1} & \mathbf{d}_{t,\gamma 2} & \cdots & \mathbf{d}_{t,\gamma r} \end{bmatrix} = \mathbf{C}\mathbf{d}_t = \mathbf{C}\mathbf{\Psi}_r\mathbf{a}_t \tag{13}$$

where $\mathbf{y}_t$ denotes the displacement data from the r selected sensor locations γ, $\mathbf{C}$ is a $r \times n$ sensor selection matrix.

With Equation (13), the full-field displacement vector $\mathbf{d}_t$ can be reconstructed as

$$\mathbf{d}_t = \mathbf{\Psi}_r(\mathbf{C}\mathbf{\Psi}_r)^{-1}\mathbf{y}_t \tag{14}$$

To robustly and accurately reconstruct the full-field displacement using Equation (14), the optimal determination of the tailored basis $\mathbf{\Psi}_r$ and sensor selection matrix $\mathbf{C}$ is crucial. According to the Eckart-Young theorem, singular value decomposition (SVD) offers the best least-squares approximation to the matrix reconstruction for a given rank r (Eckart & Young, 1936). Hence, the proper orthogonal decomposition (POD) modes $\mathbf{U}_r$ obtained via SVD of the full-field displacement matrix $\mathbf{D}$ can serve as the tailored basis $\mathbf{\Psi}_r$, as illustrated below:

$$\mathbf{D} = [\ \mathbf{d}_1 \quad \mathbf{d}_2 \quad \cdots \quad \mathbf{d}_t\ ] \approx \mathbf{U}_r \mathbf{\Sigma}_r V_r^T = \mathbf{\Psi}_r \mathbf{\Sigma}_r V_r^T \tag{15}$$

$$\sum_{i=1}^{r} \sigma_i / \sum_{i=1}^{n} \sigma_i > \varepsilon \tag{16}$$

where σ_i denotes the ith singular value of $\mathbf{\Sigma}_r$, and ε is the threshold used for determining the rank.

The determination of the sensor selection matrix $\mathbf{C}$ can be achieved by optimizing the condition number of the matrix $\mathbf{C\Psi}_r$ to ensure greater robustness in its pseudoinverse. However, direct optimization of $\mathbf{C\Psi}_r$ using its determinant or trace poses computational challenges. Manohar et al. (2018) demonstrated that QR decomposition with column pivoting can yield a near-optimal condition number, thereby providing r sensors that efficiently sample the tailored basis $\mathbf{\Psi}_r$,

$$\mathbf{\Psi}_r^T C^T = \mathbf{QR} \tag{17}$$

where $\mathbf{Q}$ is an orthogonal matrix and $\mathbf{R}$ is an upper triangular matrix.

Finally, with Equation (14) to (17), the n dimensional full-field displacement data can be reconstructed by using solely r dimensional sparse data.

3 VALIDATION

3.1 *Experimental setup*

A six-story shear building model with a weight of 2.8 kg per story, as shown in Figure 2, was employed for the validation. The model was affixed to a uniaxial shaking table and white noise excitation was applied to excite the model at both the beginning and end of the experiment. Modal frequencies for the first six modes were measured using accelerometers and recorded as follows: 1.657 Hz, 5.038 Hz, 8.138 Hz, 10.833 Hz, 12.930 Hz, and 14.339 Hz. The structural vibration was recorded using a DSLR camera with a resolution of 1570×430p and a frame rate of 59.94 fps.

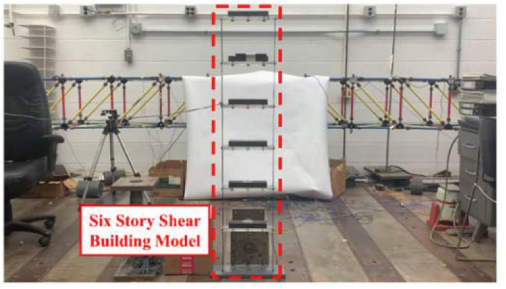


Figure 2. Six-story shearing building model used for laboratory validation.

3.2 *Experimental results*

The left column of the building model was selected, and its deformation was measured using the proposed IPBOF algorithm. The resulting valid measurement points consisted of 2925

pixels, and their corresponding displacement time histories are depicted in Figure 3. Subsequently, by conducting SVD on the obtained full-filed displacement matrix and truncating it a rank of six, the six POD modes can be generated and visualized as shown in Figure 4. Using Equation (17), the optimal sensor locations were determined through pivoting QR decomposition of the obtained tailored transformation basis. Figure 5 illustrates the distribution of the six optimal sensor locations and their corresponding displacement signals. The optimally obtained sensor positions closely match the positions on each story, aligning closely with the empirical judgment of civil engineers regarding sensor placements.

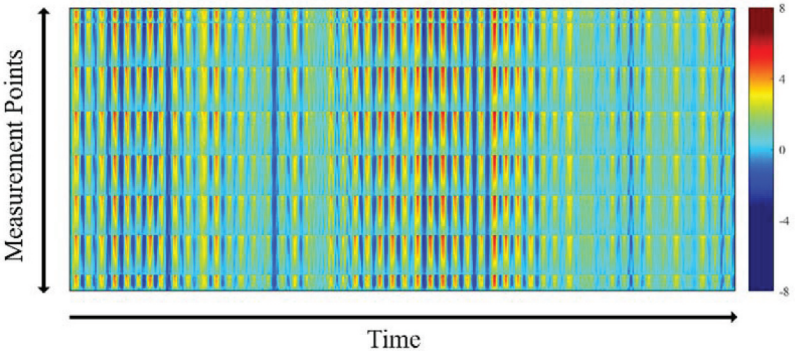


Figure 3. Visualization of the obtained full-field displacement matrix.

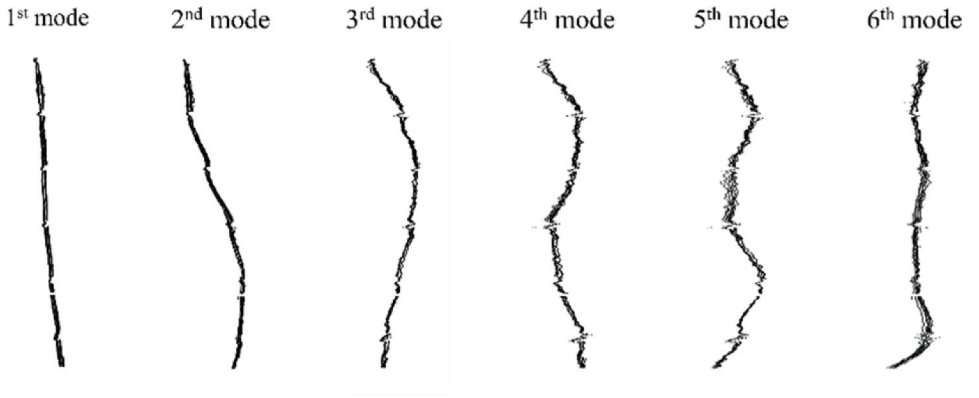


Figure 4. Visualization of the six POD modes.

To further assess the accuracy of the proposed displacement reconstruction method, the full-field displacement matrix is reconstructed utilizing the tailored basis and the displacement signals from the six optimal sensor locations, by employing Equation (14). Figure 6 shows the calculated reconstruction error and the average normalized root mean square error (NRMSE) yield a value of 1.07%. The results demonstrate the capability of the proposed method to compress high-dimensional displacement data at a remarkable compression rate of 0.33% while retaining a recovery rate of up to 98.93%.

4 CONCLUSION

This study presents an optimal sensor selection strategy to reduce storage space needed for full-field displacement data computed by the proposed improved phase-based optical flow

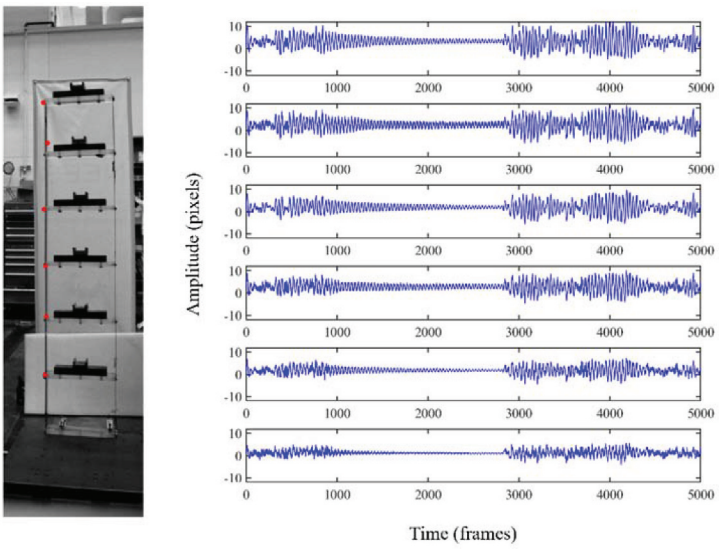


Figure 5. Six optimal sensor locations determined by the proposed method and their corresponding displacements.

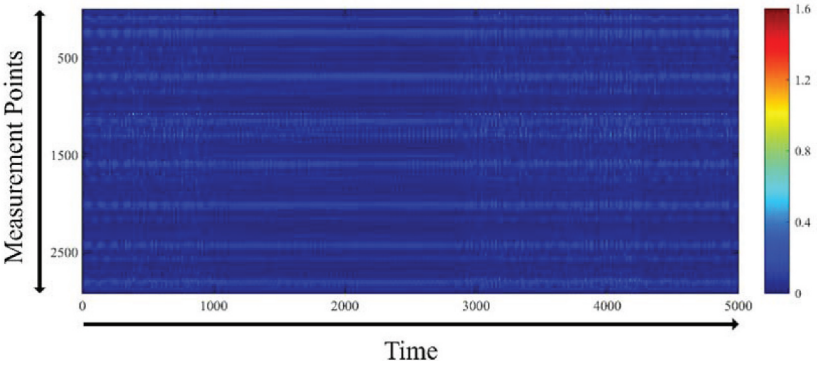


Figure 6. Full-field displacement reconstruction error.

(IPBOF) method. First, the method performs an SVD transformation on the full-field displacement matrix to construct a tailored transformation basis. Subsequently, a QR decomposition with column pivoting is used to determine the optimal sensor locations. Finally, the displacement signals of the selected pixels, as well as the tailored basis are stored and used to reconstruct the full-field displacement.

The effectiveness and accuracy of the proposed method are then verified using the video of a vibrating six-story shear building model in the laboratory. The results demonstrate the capability of the proposed method to compress high-dimensional displacement data significantly, achieving a compression rate of 0.33%, while retaining a recovery rate of up to 98.93%. Thus, the proposed method exhibits potential for vision-based long-term displacement monitoring.

REFERENCES

Barron, J. L., Fleet, D. J., Beauchemin, S. S. & Burkitt, T. A. 1992. Performance of optical flow techniques. *IEEE Computer Society Conference on Computer Vision and Pattern Recognition*, *IEEE Computer Society Press*, *Champaign, IL, USA*, *1992* . pp. 236–24

Cai, E., Zhang, Y., Ji, X., Lu, X., Xie, L., Zhuang, Y., Zhao, T. & Lin, G. 2023. Estimating small structural motions from multi-view video measurement. *Engineering Structures*. 275, 115259.

Celebi, M. 2000. GPS in dynamic monitoring of long-period structures. *Soil Dynamics and Earthquake Engineering*. 20(5), 477–83.

Chen, J. G., Wadhwa, N., Cha, Y.-J., Durand, F., Freeman, W. T. & Buyukozturk, O. 2015. Modal identification of simple structures with high-speed video using motion magnification. *Journal of Sound and Vibration*. 345, 58–71.

Chen, J. G., Davis, A., Wadhwa, N., Durand, F., Freeman, W. T. & Buyukozturk, O. 2017. Video camera-based vibration measurement for civil infrastructure applications. *Journal of Infrastructure System*. 23(3), B4016013.

Diamond, D. H., Heyns, P. S., & Oberholster, A. J. 2017. Accuracy evaluation of sub-pixel structural vibration measurements through optical flow analysis of a video sequence. *Measurement*. 95, 166–172.

Eckart, C., & Young, G. 1936. The approximation of one matrix by another of lower rank. Psychometrika, 1(3), 211–218.

Fleet, D. J., & Jepson, A. D. 1990. Computation of component image velocity from local phase information. *International Journal of Computer Vision*. 5(1), 77–104.

Freeman, W. T., & Adelson, E. H. 1991. The design and use of steerable filters. *IEEE Transactions on Pattern Analysis and Machine Intelligence*. 13(9), 891–906.

Manohar, K., Brunton, B. W., Kutz, J. N., & Brunton, S. L. 2018. Data-driven sparse sensor placement for reconstruction: Demonstrating the benefits of exploiting known patterns. *IEEE Control Systems Magazine*. 38(3), 63–86.

Bridge Maintenance, Safety, Management, Digitalization and Sustainability – Jensen, Frangopol & Schmidt (eds)
© 2024 The Author(s), ISBN 978-1-032-77040-6
Open Access: www.taylorfrancis.com, CC BY-NC-ND 4.0 license

Domain adaptation for bridge health monitoring via physics-informed generative adversarial learning

Liangfu Ge & Ayan Sadhu
Department of Civil and Environmental Engineering, Western University, London, Canada

ABSTRACT: Structural health monitoring (SHM) plays an important role in assessing bridge safety and detecting anomalies. However, significant discrepancies exist in the domain distribution of physical parameters between digital models and real structures. As a result, many bridge health monitoring theories struggle to be effective in practice, even if they perform perfectly in simulation. This paper proposes an unsupervised domain adaptation approach based on a physics-informed generative adversarial network (GAN), focusing on the mapping of structural responses for the mutual conversion between digital and physical models. To enhance the learning capability of the generative model for inherent characteristics of structures, physical constraints derived from the governing equations are incorporated in the time domain. Through a large number of free vibration tests on a simply supported bridge model, it was verified that the proposed approach can accurately complete the conversion between the measured responses and simulated responses in both time and frequency domains.

1 INTRODUCTION

Structural health monitoring (SHM) is essential for the safety management of infrastructure and cost-effective structural maintenance. Data from field measurement is the premise of SHM, but in most cases, obtaining sufficient data from real structures is labor-intensive and expensive. With this challenge, simulations are frequently employed, offering insights into potential structural behaviors across various scenarios. However, a notable obstacle in practical SHM is that the simulation data obtained by various theoretical models exhibits unpredictable discrepancies when compared with the measurements from actual structures, i.e., domain drifts. The domain drifts between simulation and real-world measurement often stem from modeling simplifications, variability in material properties, and impacts of the operating environment. Historically, model updating techniques have been favored to bridge these domain drifts for their clear physical interpretation (Ren & Chen 2010; Ferrari et al. 2019; Mao et al. 2020), however, they often requires iterative optimization, which can become computationally intensive as the complexity of structures increases. Also, these methods possibly get trapped in local optima when dealing with complex parameter spaces with limited experimental data.

Deep learning techniques (Seventekidis et al. 2020; Sony et al. 2021; Sony et al. 2022; Ge et al. 2023), which have recently garnered increasing attention due to exceptional robustness and generalization capability to real-world applications, provide another choice to cope with domain drifts of simulation and measurement. These approaches mostly adopt the strategy of exploring the parameter space in simulations, subsequently using the simulated data to train the latent mapping between observed responses and structural parameters. For instance, Yuan et al. (2023) trained a generative adversarial network (GAN) with simulated acceleration responses of a steel-concrete bridge tower under various combinations of structural parameters. The trained GAN was used to predict the structural parameter with the measured acceleration as input. Teng et al. (2023) generated digital twin models and their responses to random excitation force with different parameter distributions for the training of a damage

DOI: 10.1201/9781003483755-102

classification convolutional neural network (CNN). Similarly, Wang et al. (2021) successfully detected damages in a frame structure by using DenseNet trained from a simulated free vibration dataset. The aforementioned methods can predict the parameters of actual structures by leveraging computational results from numerous numerical models under different states. They can effectively bridge the domain drifts between simulations and measurements when the parameter range of the actual structure is determinable. However, the simulation using a large number of models with different initial parameters and even damage states requires a huge computational cost, rendering the training of deep learning models challenging to be finished within a practical timeframe.

Another strategy that has attracted significant interest recently is to conduct domain adaptation on the structural responses. Domain adaptation (DA) is a special case of transfer learning, which focuses on reducing the discrepancies between different data distributions from source and target domains (Singhal et al. 2023). For instance, Gardner et al. (2022) used a domain-adopted Gaussian mixture model for aligning frequency features in bridge data, while Wang & Xia (2022) developed a re-weighted adversarial domain adaptation network for finite element models. Similarly, Martakis et al. (2023) used Domain Adversarial Neural Networks for transferring simulation knowledge to real data for damage classification in building models. These methods have proven effective in aligning data distributions across domains and enhancing classifier performance on simulated data. However, they primarily function as "black boxes", labeling features without directly producing post-DA structural responses, which are essential for dynamic structural analysis.

Generative adversarial learning makes it possible for DA to present the changes in structural responses. Luleci & Catbas (2023) applied the Domain-Generalized Cycle-Generative model to perform DA on the responses of two prestressed bridge FE models with different parameters under the same excitation of Gaussian noise. The results showed that the translated bridge state has similar frequencies and mode shapes to the target bridge. Following this study, Luleci et al. (2023) modified the CycleGAN into a DA model for 1D time series and then employed it to translate acceleration responses from undamaged to damaged states. Gatti et al. (2023) applied a Representation GAN to simulate and assess the transient dynamic responses of shear-type multi-story buildings under earthquake loading, enabling accurate damage classification and severity assessment. The DA in these studies has achieved some success in the state translation among multiple FE models or varying states of a singular real structure. However, there is a very limited exploration of generative approaches to facilitate DA between simulated and actual structures, which can lead to more pronounced and unpredictable domain drifts.

Given the limitations identified in the above literature review, this research introduces an adapted CycleGAN. The proposed model uniquely integrates governing equations as physical constraints and the transformer for self-attention modules. Experiments show that the improvements not only offer better global feature extraction capability but also assures greater training stability compared to the original CycleGAN.

2 PHYSICS-INFORMED AND SELF-ATTENTION-ENHANCED CYCLEGAN

GANs are one of the most transformative ideas of deep learning that lie in two neural networks: the generator and the discriminator. They are used to generate samples with the input information and evaluate the generated samples, respectively. Specifically, the generator aims to produce synthetic data that the discriminator cannot distinguish from real data, while the discriminator aims to improve its ability to identify fake data. CycleGAN is a variant of traditional GAN to avoid the requirement of paired training data. CycleGAN can translate the datasets from two domains simutinously without labels, thus it is suitable for SHM applications where the data annotation is always costly. Different from GANs, the loss function of CycleGAN includes the adversarial loss $\mathcal{L}_{adv}$, cycle consistency loss $\mathcal{L}_{cycle}$ and identity loss $\mathcal{L}_{idt}$. For the mapping function $S(\cdot) : X \mapsto Y$ and its corresponding discriminator D_Y, $\mathcal{L}_{adv}$ can be expressed as (Zhu et al. 2017):

$$\mathcal{L}_{adv}(S, D_Y, X, Y) = \lambda_{aS}\mathbb{E}_{\ddot{x}\sim p_{data}(\ddot{x})}\left[(D_Y(S(\ddot{x})) - 1)^2\right] + 0.5\Big(\mathbb{E}_{\ddot{x}\sim p_{data}(\ddot{x})}\left[D_Y(S(\ddot{x}))^2\right] + \mathbb{E}_{\ddot{y}\sim p_{data}(\ddot{y})}\left[(D_Y(\ddot{y}) - 1)^2\right]\Big) \quad (1)$$

where λ_{aS} represents the weight for the adversarial loss of the generator S and $\mathbb{E}_{\ddot{x}\sim p_{data}(\ddot{x})}$ denotes the expectation computed over all acceleration data in domain X that follows the statistical distribution $p_{data}(\ddot{x})$. The first term on the right side of Equation (1) is utilized for training the generator, while the second term is for training the discriminator.

The cycle consistency loss is for restricting the mapping functions to be cycle-consistent: for each acceleration sequence $\ddot{x}$ from domain X, the transformation cycle should be able to bring $\ddot{x}$ back to the original values, i.e., $\ddot{x} \to S(\ddot{x}) \to T(S(\ddot{x})) \approx \ddot{x}$, where $S(\cdot)$ and $T(\cdot)$ are mapping functions. Similarly, the domain adaptation from domain Y to domain X should also be cycle-consistent. To this end, $\mathcal{L}_{cycle}$ is given by:

$$\mathcal{L}_{cycle}(S, T) = \lambda_{cS}\mathbb{E}_{\ddot{x}\sim p_{data}(\ddot{x})}[\|T(S(\ddot{x})) - \ddot{x}\|_1] + \lambda_{cT}\mathbb{E}_{\ddot{y}\sim p_{data}(\ddot{y})}[\|S(T(\ddot{y})) - \ddot{y}\|_1] \quad (2)$$

where λ_{cS} and λ_{cT} represent the respective weights for the cycle consistency losses.

The identity loss is designed to constrain the generator to retain the primary features of the input data while preventing unnecessary modifications. It is defined as:

$$\mathcal{L}_{idt}(S, T) = \lambda_{iS}\mathbb{E}_{\ddot{x}\sim p_{data}(\ddot{x})}[\|S(\ddot{x}) - \ddot{x}\|_1] + \lambda_{iT}\mathbb{E}_{\ddot{y}\sim p_{data}(\ddot{y})}[\|T(\ddot{y}) - \ddot{y}\|_1] \quad (3)$$

where λ_{iS} and λ_{iT} are weights for the identity losses of S and T. Then, the training objective of CycleGAN is to minimize the sum of the above three loss fuctions.

CycleGAN may struggle to effectively learn the global features of input data, potentially leading to unstable training, when directly applied to long time series. Therefore, this paper introduces two improvements to the original CycleGAN: modifying the network architecture and updating the loss function. Figure 1 presents the network structure and the forward propagation process for the transformation from domain X to domain Y. The input to the generator is an N×C×L tensor from domain X, where N stands for the batch size, C for the number of channels, and L represents the length of the time series. The generator outputs a tensor of the same dimensions as the input, which is anticipated to align with the feature distribution of domain Y. The proposed model integrates an additional transformer encoder in the preliminary layers of both the generator and discriminator, enhancing the ability to learn global features. The transformer is noted for handling long-range dependencies in data without any significant loss in performance due to its self-attention mechanism (Vaswani et al. 2017). In addition, the transformer has flexibility regarding the length of the input time series. In this study, all the time series with a length of L are uniformly encoded into feature vectors of length 200 and noted as input embedding. To make use of the order of the time series and learn temporal dependencies, position encodings are separately assigned to each element of the input embedding using sine and cosine functions. The model uses a four-head attention module, followed by residual connections, normalization, and a dropout rate of 0.1. The transformer outputs embeddings going through convolutional blocks (ConvBlock), residual network blocks (ResNetBlock), and transpose convolutional blocks (TConvBlock), with the ReLU activation function replaced by LeakyReLU. The number of filters, convolution kernel size, padding, and stride are denoted as f, kz, p and s, respectively.

Besides the self-attention modules, the inclusion of a physical loss is the second highlight of the proposed DA model. For linear structural systems, the structural response can be obtained by modal superposition. The responses of the i^{th} mode $r_i(t)$ can be described by,

$$m_i\ddot{r}_i(t) + c_i\dot{r}_i(t) + k_i r_i(t) = p_i(t) \quad (4)$$

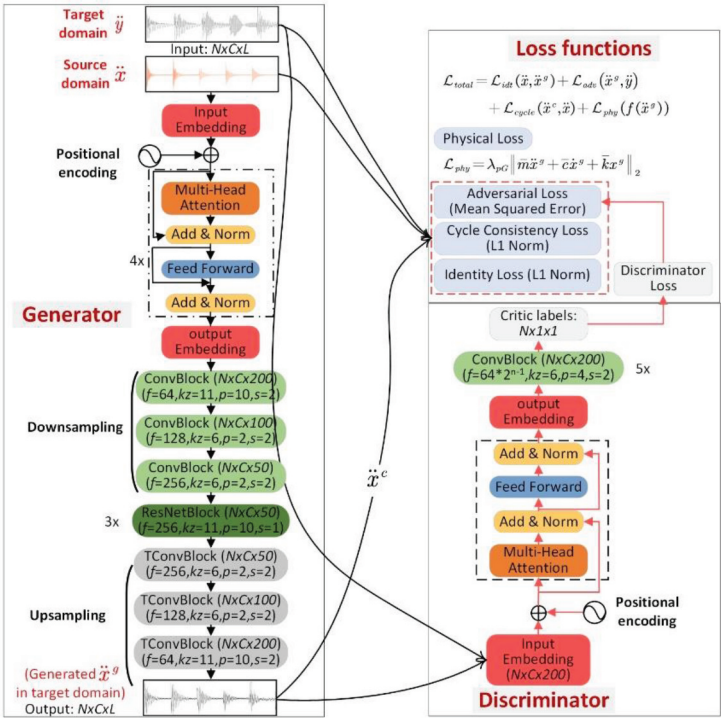


Figure 1. Structure of the single network from domain X to domain Y.

where m_i, c_i and k_i represent the modal mass, damping and stiffness, respectively, while p_i denotes the generalized force. In most cases, the structural response can be represented by the linear superposition of a few dominant modes. To describe the averaged effect of dominant modes, it is assumed that there exists an equivalent mode that satisfies

$$\bar{m}\ddot{r}(t) + \bar{c}\dot{r}(t) + \bar{k}r(t) = p(t) + \varepsilon(t) \tag{5}$$

In this equation, $\bar{m}$, $\bar{c}$ and $\bar{k}$ are equivalent parameters that are trainable in the DA model. $r(t)$ and $p(t)$ are the sums of the responses and generalized force of n dominant modes, i.e., $r(t) = \sum_{i=1}^{n} r_i(t)$ and $p(t) = \sum_{i=1}^{n} p_i(t)$. $\varepsilon(t)$ denotes the errors that can be physically regarded as a virtual time-varying force. The physical loss is to minimize $\|\varepsilon(t)\|_2$. For the free vibration, the $p(t)$ becomes zero. Then, by replacing $r(t)$ in Equation (4) with x, physical loss is defined as

$$\mathcal{L}_{phy}(S,T) = \lambda_{pS}\mathbb{E}_{\ddot{x}\sim p_{data}(\ddot{x})}\left[\left\|\bar{m}_S\ddot{x}^g + \bar{c}_S\dot{x}^g + \bar{k}_S x^g\right\|_2\right] + \lambda_{pT}\mathbb{E}_{\ddot{y}\sim p_{data}(\ddot{y})}\left[\left\|\bar{m}_T\ddot{y}^g + \bar{c}_T\dot{y}^g + \bar{k}_T y^g\right\|_2\right] \tag{6}$$

where λ_{pS} and λ_{pT} are weights respectively for the generator S and T. It should be noted that the displacement and velocity data in Equation (5) can generally be obtained through the integration of acceleration. Then, the total loss can be obtained by

$$\mathcal{L}_{total} = \mathcal{L}_{adv}(S, D_Y, X, Y) + \mathcal{L}_{adv}(T, D_X, Y, X) + \mathcal{L}_{cycle}(S,T) + \mathcal{L}_{idt}(S,T) + \mathcal{L}_{phy}(S,T) \tag{7}$$

3 EXPERIMENTAL VALIDATION

3.1 *Laboratory experiments for target domain dataset*

A simply supported beam with cantilevers at ends is selected for free-vibration tests. As shown in Figure 2, the test structure is a steel beam with dimensions of 2.49m × 20cm × 6mm and a 2.16 m distance between the supports. Six Opal wireless sensors are used for acceleration measurements. They are installed beneath the beam at positions of 1/6, 1/4, 1/2, 2/3, 3/4 and 5/6 spans, respectively, as shown in Figure 2(a) and (c) and are synchronized with a docking station before installation. The data streams from different sensors are transferred to the access point wirelessly and then recorded by the Motion Studio, a software suite bundled with the APDM monitoring system, as shown in Figure 2(b). The impact force was acted at around 5/12 span using a test hammer shown in Figure 2(d). A total of 100 repeated free vibration tests are carried out to obtain attenuation responses under different impact forces. The sampling frequency of accelerators is set as 128 Hz while the measurement range of $-2 \sim 2$g.

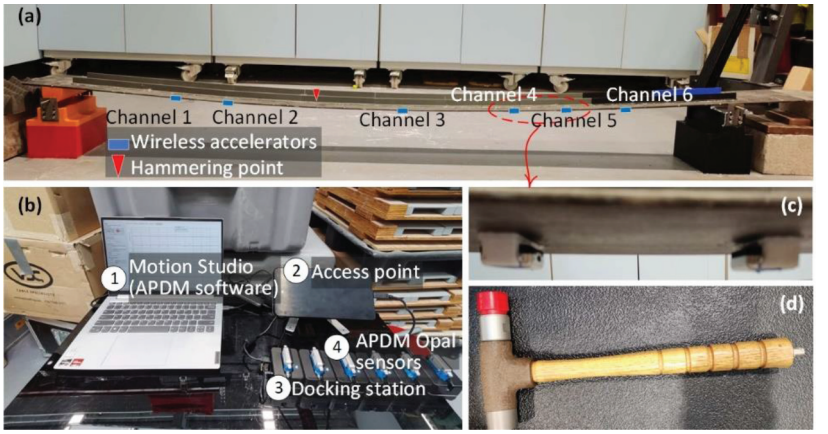


Figure 2. Experiment setup for the free vibration tests: (a) steel beam; (b) APDM system; (c) installed sensors; (d) test hammer.

Six measurement points are used to collect the vertical acceleration subjected to impact forces. The signals from different channels are well synchronized and exhibit typical patterns of free decaying. To eliminate the response segment during the contact period between the test hammer and the structure, the response at the mid-span is taken as the reference. The signal is truncated starting from the third peak, and the length of the signal is uniformly set to 3500 sample points. During the 100 repeated hammering tests, the magnitude of the applied force is left uncontrolled to reproduce unknown initial amplitudes of attenuation responses in real-world structures. However, for model training, it is still necessary to standardize the input responses to mitigate any adverse effects resulting from varying scales. Once again, Channel 3 is selected as the reference. The responses in Channel 3 from different tests are first individually normalized by dividing their maximum values, and then the responses of other channels are scaled by the same proportion. In this way, a dataset for the target domain is obtained, containing 100 sets of normalized time series from 6 channels in size of 3500×1.

3.2 *Numerical simulations for source domain dataset*

Real-world structures are generally regarded homogeneous with their FE models. The difference in data distributions between actual and simulated structures arise due to assumptions of material properties, boundary conditions and load patterns, etc. For the specific test beam, the FE model simplified it into a standard simply supported beam, omitting the cantilever at both ends. As shown in Figure 3, the model consists of 12 constant-sectional beam elements,

using an impulse force to simulate hammer loads. Six nodes are selected to analyze decaying responses responding to signals from six laboratory sensors.

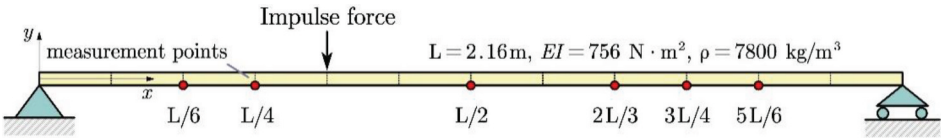


Figure 3. Finite element model of the simply supported beam.

The FE model is built with the parameters shown in the figure, incorporating Rayleigh damping with a damping ratio $\xi = 0.02$ for the first three modes. Acceleration responses are calculated using the Newmark β method at a 1/128 second interval, matching the sampling frequency of accelerators. The numerical simulation is also repeated by 100 times using the peak accelerations from Channel 3 as the impulse force for each iteration. To account for observational errors, white noise at levels of 1%, 5%, and 10% is added to the responses from the six channels, followed by normalization. This created a simulated dataset in the source domain with the same size as the measurements in the target domain data.

3.3 *Model training*

Experimental and FE simulation samples are used to train DA models. The proposed model enables bidirectional conversion between measurement and simulation domains in a single training session, benefiting from the idea of cycle consistency. To initially evaluate the correctness of the FE model and the distribution of simulated data, frequency analysis for structural responses in both domains is conducted. Table 1 presents the first three vertical bending frequencies of the test beam and the FE model with different bending stiffnesses. Their frequencies are shown close, indicating the modelling is reliable. However, as DA for such small differences is relatively easy and not ideal to demonstrate the performance of DA models, this section uses the FE model with 20% stiffness for the training and testing to increase the domain drifts.

Table 1. Modal frequencies of the test beam and FE models.

Model (Stiffness)	ω_1	ω_2	ω_3
FE model (EI)	3.07 Hz	11.81 Hz	24.03 Hz
Test beam (unknown)	3.09 Hz	10.77 Hz	26.42 Hz
FE model (20% EI)	1.37 Hz	5.39 Hz	11.90 Hz

The measured and simulated datasets are divided into training and test sets in a 9:1 ratio, and the size of each sample is 6×3500, representing the number of channels and data length, respectively. The parameters in Table 2 are used for the model training. The proposed model is trained for 250 epoches on a computer equipped with an Nvidia RTX A6000 GPU. Regarding the DA

Table 2. Hyperparameters for the training of the DA models.

λ_{aS}	20
$\lambda_{aT}, \lambda_{cS}, \lambda_{cT}, \lambda_{pS}, \lambda_{pT}$	10
$\lambda_{iS}, \lambda_{iT}$	0
Discriminator updating frequency	1 time per 5 epochs
Learning rate for Generators	0.0001
Learning rate for Discriminators	0.0001
Batch size	5

from simulation to measurement is more difficult than that in the opposite direction, the following discussion only focuses on the training from simulations to measurements.

3.4 *Model evaluation*

A 10% subset of the dataset is used for model testing. Differing from the training process, model testing involves utilizing single-domain data as input to generate synthetic samples while using the other domain data to assess the synthetic outputs. As discussed in Section 3.3, the DA from measurement to simulation tends to yield favorable results. Hence, to provide more robust validation, this section focuses on the testing of the trained DA model for the DA process from simulation to measurement, considering varying levels of noise. Figure 4 shows clips of the mid-span (Channel 3) acceleration responses before and after DA. It can be seen in Figure 4(a) that the simulated acceleration (with 5% additional noise) is significantly different from the measurement. However, when applying the trained DA model to the simulated data, a synthetic response, which is shown in good agreement with the measured one, can be obtained, as shown in Figure 4(b). Correspondingly, the value of the Mean Square Error is greatly reduced.

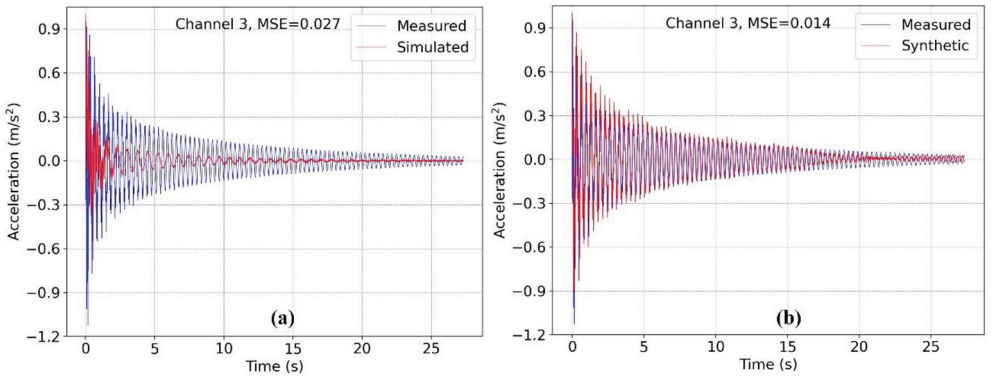


Figure 4. Comparison of the acceleration responses: (a) before DA; (b) after DA.

Besides the comparison in the time domain, Figure 5 presents the Fourier spectrums of acceleration responses. It is shown that the proposed DA model successfully generates synthetic responses on different noise levels, which have similar frequencies as the actual measurements.

Accordingly, the Mean Magnitude Squared Coherence (MMSC) scores, of which defination can be found in (Luleci et. Al 2023), are significantly increased. However, it is still noticeable that there are errors in the peak values of the frequencies, which may affect the accuracy of mode shapes.

For further investigation, modal identification is conducted on both the measured and synthetic responses using SSI-Cov algorithm (Reynders 2012). Figure 6 gives the identified mode shapes for 5% noise. It can be seen that the first two mode shapes identified from the generated responses are in good agreement with those from the measured ones. The third mode is possibly a torsional mode and cannot be reflected in the beam-like FE model, but it was still successfully reconstructed, suggesting the proposed model well learned the data characteristics of the measurement domain. The fourth mode has the smallest energy and is almost indistinguishable in Figure 5, resulting in more differences in the identification results of the mode shapes. To quantify the differences, the modal assurance criterion (MAC) is calculated for all modes and noise cases, of which the results are listed in Table 3. It is evident that using ten sets of synthetic samples can effectively identify the first three modes while maintaining a high degree of similarity with the measured mode shapes. However, the recognition rate (the rate of correctly identifying the mode shapes) and MAC for the fourth mode shape experienced a slight decrease. It is worth noting that noise has less influence on low-order modes with high energy proportion but more significant influence on high-order modes. Therefore, it is recommended to only focus on the few dominant modes in practical applications.

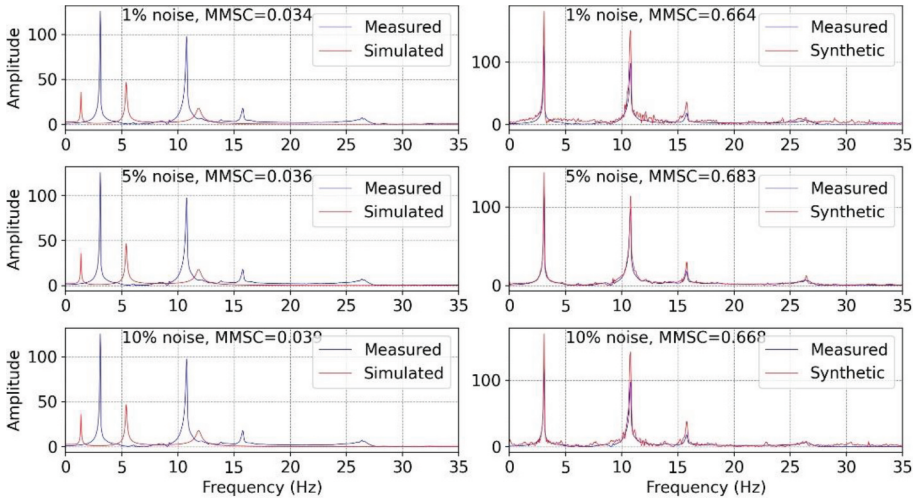


Figure 5. Frequency domain comparison of Channel 3 responses for different levels of noise.

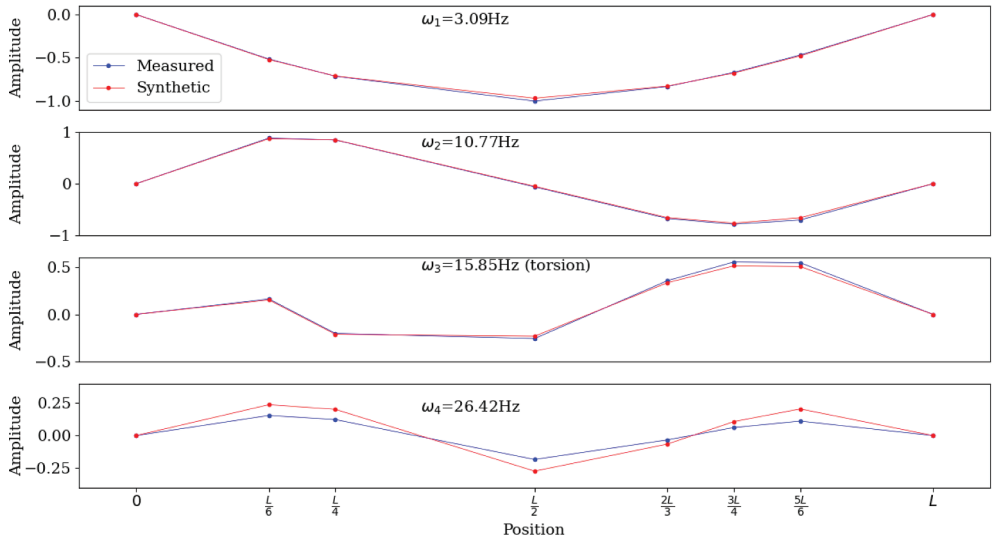


Figure 6. Comparison of the mode shapes identified from measured and synthetic responses.

4 CONCLUSIONS

In this paper, a novel generative DA model is proposed to achieve DA between the FE models and real engineering structures. The DA approach was verified effective through free-vibration tests on a steel beam model. The structure exhibits substantial discrepancies in structural parameters compared to its FE model. Nonetheless, the proposed DA model successfully learned the mapping relationships between the simulation and measurement domains and delivered good performance on previously unseen test data. The proposed method exhibits superior performance in the DA of low-order modal responses compared to higher-order models. Additionally, it demonstrates reduced sensitivity to noise interference. The proposed DA approach is demonstrated on the structures in unchanged structural states. For future endeavors, it is recommended to conduct DA research among multiple structural states to serve model updating and damage detection in SHM.

Table 3. Averaged MAC values between the measured and synthetic mode shapes.

Noise level	1st mode	2nd mode	3rd mode(torsion)	4th mode
1%	0.9997	0.9992	0.9912	0.9539
5%	0.9997	0.9995	0.9992	0.9899
10%	0.9994	0.9996	0.9804	0.9089
Recognition rate	100%	100%	100%	90%

REFERENCES

Ferrari, R., D. Froio, E. Rizzi, C. Gentile, & E.N. Chatzi, Model updating of a historic concrete bridge by sensitivity-and global optimization-based Latin Hypercube Sampling. *Engineering Structures*, 2019. 179: p. 139–160.

Gardner, L.A. Bull, N. Dervilis, & K. Worden, Domain-adapted Gaussian mixture models for population-based structural health monitoring. *Journal of Civil Structural Health Monitoring*, 2022. 12 (6): p. 1343–1353.

Gatti, F., L. Rosafalco, G. Colombera, S. Mariani, & A. Corigliano, Multi-storey shear type buildings under earthquake loading: Adversarial learning-based prediction of the transient dynamics and damage classification. *Soil Dynamics and Earthquake Engineering*, 2023. 173: p. 108141.

Ge, L., K.Y. Koo, M. Wang, J. Brownjohn, & D. Dan, Bridge damage detection using precise vision-based displacement influence lines and weigh-in-motion devices: Experimental validation. *Engineering Structures*, 2023. 288: p. 116185.

Luleci, F., & Catbas, Condition transfer between prestressed bridges using structural state translation for structural health monitoring. *AI Civil Eng*, 2023. 2(1): p. 7.

Luleci, F. Necati Catbas, & O. Avci, CycleGAN for undamaged-to-damaged domain translation for structural health monitoring and damage detection. *Mechanical Systems and Signal Processing*, 2023. 197.

Mao, J., H. Wang, & J. Li, Bayesian finite element model updating of a long-span suspension bridge utilizing hybrid Monte Carlo simulation and kriging predictor. *KSCE Journal of Civil Engineering*, 2020. 24(2): p. 569–579.

Martakis, P., Y. Reuland, A. Stavridis, & E. Chatzi, Fusing damage-sensitive features and domain adaptation towards robust damage classification in real buildings. *Soil Dynamics and Earthquake Engineering*, 2023. 166.

Ren, W.-X., & H.-B. Chen, Finite element model updating in structural dynamics by using the response surface method. *Engineering structures*, 2010. 32(8): p. 2455–2465.

Reynders, E., System identification methods for (operational) modal analysis: review and comparison. *Archives of Computational Methods in Engineering*, 2012. 19: p. 51–124.

Seventekidis, P., D. Giagopoulos, A. Arailopoulos, & O. Markogiannaki, Structural Health Monitoring using deep learning with optimal finite element model generated data. *Mechanical Systems and Signal Processing*, 2020. 145: p. 106972.

Sony, S., K. Dunphy, A. Sadhu, & M. Capretz, A systematic review of convolutional neural network-based structural condition assessment techniques. *Engineering Structures*, 2021. 226: p. 111347.

Sony, S., S. Gamage, A. Sadhu, & J. Samarabandu. *Vibration-based multiclass damage detection and localization using long short-term memory networks*. in *Structures*. 2022. Elsevier.

Singhal, P., R. Walambe, S. Ramanna, & K. Kotecha, Domain Adaptation: Challenges, Methods, Datasets, and Applications. *IEEE Access*, 2023. 11: p. 6973–7020.

Teng, S., X. Chen, G. Chen, & L. Cheng, Structural damage detection based on transfer learning strategy using digital twins of bridges. *Mechanical Systems and Signal Processing*, 2023. 191.

Vaswani, A., N. Shazeer, N.Parmar, J. Uszkoreit, L. Jones, A.N. Gomez, ... I. Polosukhin, Attention is all you need. *Advances in neural information processing systems*, 2017. 30.

Wang, & Y. Xia, Knowledge transfer for structural damage detection through re-weighted adversarial domain adaptation. *Mechanical Systems and Signal Processing*, 2022. 172.

Wang, R., J. Li, S. An, H. Hao, W. Liu, & L. Li, Densely connected convolutional networks for vibration based structural damage identification. *Engineering Structures*, 2021. 245: p. 112871.

Yuan, Z.-Q., Y. Xin, Z.-C. Wang, Y.-J. Ding, J. Wang, D.-H. Wang, & Y. Yang, Structural Nonlinear Model Updating Based on an Improved Generative Adversarial Network. *Structural Control and Health Monitoring*, 2023. 2023: p. 1–21.

Zhu, J.-Y., T. Park, P. Isola, & A.A. Efros. *Unpaired image-to-image translation using cycle-consistent adversarial networks*. in *Proceedings of the IEEE international conference on computer vision*. 2017.

Bridge Maintenance, Safety, Management, Digitalization and Sustainability – Jensen, Frangopol & Schmidt (eds)
© 2024 The Author(s), ISBN 978-1-032-77040-6
Open Access: www.taylorfrancis.com, CC BY-NC-ND 4.0 license

Anomaly detection of bridges by Bayesian method with optimized sensor placement

C.W. Kim & Y. Hirate
Department of Civil and Earth Resources Engineering, Kyoto University, Kyoto, Japan

ABSTRACT: This study aims to investigate the effectiveness of a Bayesian hypothesis-based damage detection using sensor arrangement optimized by the effective independence (EFI) method. The feasibility of Bayesian anomaly detection is verified using vibration and damage experimental data on an actual steel plate girder bridge. It was found that the same vibration frequencies could be identified with the optimally located three sensors as when all sensors were used. Observations demonstrated that it is possible to detect damage and to identify the damage location approximately even with optimally arranged three sensors. In addition, the EFI method was also useful in Bayesian anomaly detection.

1 INTRODUCTION

Maintenance of aging bridges has become a major issue globally. However, considering the shortage of engineers who inspect bridges and the time and cost required for visual inspection, a more efficient and quantitative bridge inspection method is required. Structural health monitoring (SHM) has been studied as an alternative method to visual inspection (Ko & Ni 2005, Doehler et al. 2014). Vibration-based SHM is a useful technique if the modal parameters of a bridge can be identified effectively (Magalhaes et al. 2012), and the ambient vibration induced by wind and traffic is an effective way to monitor the bridge as it requires no traffic control. On actual bridges, however, traffic-induced vibrations presumably include unsteady noise that affects the identification results of the modal parameters (Kim et al. 2012). Therefore, pre-processing and post-processing should be applied carefully to improve the accuracy of modal parameter identification.

To avoid troublesome procedures in signal processing, direct decision-making methods have been investigated using damage indicators that are converted directly from acceleration, instead of the modal properties. Nair et al. (2006) investigated a damage indicator consisting of univariate autoregressive (AR) coefficients because the AR coefficients vary as the modal properties vary. The feasibility of the damage indicator has been examined for a modeled bridge (Kim et al. 2012) and an actual steel truss bridge (Goi & Kim 2017). Goi & Kim (2017) investigated a hypothesis-testing method using a vector autoregressive (VAR) model to support decision-making for bridge maintenance. Although those methods indicate changes in VAR models, noisy operational conditions in the field still hinder their practical use. One difficulty is that stochastic models involve epistemic uncertainty caused by a gap separating the models from actual phenomena. In other words, regressive parameters involve variance that is unrelated to a change in modal parameters, and handling uncertainty caused by operational conditions constitutes the primary difficulty.

Another keen issue in the SHM of bridges is how to reduce the number of sensors because it is necessary to install a large number of sensors in order to identify modal parameters and detect damage accurately. However, considering the huge amount of bridge stocks it is not always possible to instrument many sensors, and many researchers have investigated in terms

DOI: 10.1201/9781003483755-103

of sensor optimization aiming to reduce the number of sensors without sacrificing the performance of damage detection (Kammer 1991, Heo et al. 1997, Papadopoulos & Garcia 1998, Friswell & Castro-Triguero 2015, Li et al. 2020).

Bayesian theory enables quantification of the uncertainty involved in parametric models (Dzunic et al. 2017). This study thus adopts Bayesian theory to quantify the uncertainty involved in the model. The VAR model is adopted for Bayesian inference without MCMC, and input from the traffic was assumed Gaussian white noise even though it is non-stationary random loadings. Thus, non-stationary vehicle loads lead to biased estimates of the regression parameters. For robust damage detection, it is desirable to extract parameters related to damage-sensitive modal characteristics and exclude other parameters from damage detection. This study applies PCA to the input subspace of the VAR model for prompt modal identification. Bayes factor (Kass & Raftery 1995), which is defined as the marginalized likelihood ratio, is adopted as the anomaly indicator. The PCA enables the formulation of the Bayes factor to detect changes in damage-sensitive parameters. Therefore, measured acceleration is converted seamlessly to the anomaly indicator to detect changes in the modal properties.

This study aims to investigate the effectiveness of a Bayesian hypothesis-based damage detection using a small number of sensors. The minimal sensors arrangement is investigated using the effective independence (EFI) method (Kammer 1991). A parameter from the coefficient matrix of the VAR model of measured acceleration responses is adopted as damage sensitive feature. A Bayesian hypothesis test is used to detect anomalies as an outlier analysis. Vibration data from a damage experiment giving cracks in the steel plate girder bridge are used to verify the validity of the proposed approach. To examine the effect of the number of sensors, relationships between the number of sensors and the accuracy of the anomaly detection are investigated utilizing the Bayes factor (BF), which is a damage index in the Bayesian hypothesis test.

2 BAYESIAN ANOMALY DETECTION

2.1 *Vector autoregressive (VAR) model*

Let $\boldsymbol{y}_k \in \mathbb{R}^{m\times 1}$ denote a column vector of the discrete-time series of measured acceleration whose components correspond to m measurement locations. The following VAR model idealizes the linear time series with sufficient model order p and noise term (Kim et al. 2012).

$$\boldsymbol{y}_k = \sum\nolimits_{i=1}^{p} \alpha_i \boldsymbol{y}_{k-i} + \boldsymbol{e}_k \tag{1}$$

where, $\boldsymbol{\alpha}_i \in \mathbb{R}^{m\times m}$ is an autoregressive coefficient matrix of order i, and $\boldsymbol{e}_k \in \mathbb{R}^{m\times 1}$ is a time series of white Gaussian noise vectors. To simplify the discussion, transform Equation (1) as follows.

$$\boldsymbol{y}_k = \mathbf{W}\begin{bmatrix} \boldsymbol{y}_{k-1} \\ \vdots \\ \boldsymbol{y}_{k-p} \end{bmatrix} + \boldsymbol{e}_k = \mathbf{W}\boldsymbol{\phi}_k + \boldsymbol{e}_k \tag{2}$$

where, $\boldsymbol{\phi}_k \in \mathbb{R}^{mp\times 1}$ is a column vector. Furthermore, when $\boldsymbol{\Sigma}$ represents a covariance matrix of the noise vector $\boldsymbol{e}_k$, the probability density function of $\boldsymbol{y}_k$ is expressed as follows.

$$p\left(\boldsymbol{y}_k|\boldsymbol{\phi}_k, \boldsymbol{W}, \boldsymbol{\Sigma}\right) = \mathcal{N}\left(\boldsymbol{y}_k|\boldsymbol{W}\boldsymbol{\phi}_k, \boldsymbol{\Sigma}\right) \tag{3}$$

where, $p(\cdot|\cdot)$ represents the conditional probability density function, $\mathcal{N}(\boldsymbol{x}|\mu, \boldsymbol{\Sigma})$ represents the multivariate normal distribution with the expected value μ and the covariance matrix $\boldsymbol{\Sigma}$.

Consider the problem of estimating the regression coefficient $\boldsymbol{W}$ and the covariance $\boldsymbol{\Sigma}$ of the regression error from the observed value of the target variable $\boldsymbol{y}$ using Bayes' theorem, and a data set consisting of n target variables $\boldsymbol{y}_1, \ldots, \boldsymbol{y}_n$ and their corresponding inputs $\boldsymbol{\phi}_1, \ldots, \boldsymbol{\phi}_n$,

and define $\mathbf{Y} = [\mathbf{y}_1, \ldots, \mathbf{y}_n] \in \mathbb{R}^{m \times n}$ and $\boldsymbol{\phi} = [\boldsymbol{\phi}_1, \ldots, \boldsymbol{\phi}_n] \in \mathbb{R}^{mp \times n}$. Assuming that these data are generated independently, the following likelihood function is obtained for the parameters $\boldsymbol{W}$ and $\boldsymbol{\Sigma}$.

$$p(\boldsymbol{Y}|\boldsymbol{\phi}, \boldsymbol{W}, \boldsymbol{\Sigma}) = \prod_{k=1}^{n} \mathcal{N}(\boldsymbol{y_k}|\boldsymbol{W}\boldsymbol{\phi_k}, \boldsymbol{\Sigma}) \tag{4}$$

The next section explains how to calculate BF from this likelihood function using Bayes' theorem.

2.2 *Bayesian hypothesis test*

The parameters $\boldsymbol{W}$ and $\boldsymbol{\Sigma}$ will be collectively referred to as regression parameters. The posterior distribution of regression parameters is obtained according to the following Bayes' theorem.

$$p(\boldsymbol{W}, \boldsymbol{\Sigma}|\boldsymbol{Y}, \boldsymbol{\phi}) = \frac{p(\boldsymbol{Y}|\boldsymbol{\phi}, \boldsymbol{W}, \boldsymbol{\Sigma}) p(\boldsymbol{W}, \boldsymbol{\Sigma})}{p(\boldsymbol{Y}|\boldsymbol{\phi})} \tag{5}$$

where, $p(\boldsymbol{W}, \boldsymbol{\Sigma})$ on the right side is the prior distribution. $p(\boldsymbol{W}, \boldsymbol{\Sigma}|\boldsymbol{Y}, \boldsymbol{\phi})$ on the left side is the posterior distribution for the regression parameters obtained under the condition of observed accelerations and shows the posterior distribution. In the following discussion, the left side of Equation (5) is abbreviated as $p(\boldsymbol{W}, \boldsymbol{\Sigma}|\boldsymbol{Y})$ for simplicity.

In Bayesian inference, it is known that a closed solution can be obtained for the probability density function of the posterior distribution by assuming a prior distribution as a conjugate prior. Regarding the likelihood function expressed in Equation (4), it is known that the conjugate prior distribution of the regression parameter is the matrix normal inverse Wishart distribution defined by the following equation (Goi & Kim 2023).

$$p(\boldsymbol{W}, \boldsymbol{\Sigma}) = \mathcal{MN}(\boldsymbol{W}|\boldsymbol{M}, \boldsymbol{\Sigma}, \boldsymbol{L}^{-1}) \mathcal{IW}(\boldsymbol{\Sigma}|\psi, \nu) \tag{6}$$

where, $\mathcal{MN}(\mathbf{W}|\mathbf{M}, \boldsymbol{\Sigma}, \mathbf{L}^{-1})$ and $\mathcal{IW}(\boldsymbol{\Sigma}|\boldsymbol{\Psi}, \nu)$ are the matrix normal distribution and the inverse Wishart distribution, respectively,

The parameters $\mathbf{M} \in \mathbb{R}^{m \times mp}$, $\mathbf{L} \in \mathbb{R}^{mp \times mp}$, $\boldsymbol{\Psi} \in \mathbb{R}^{m}$ and $\nu \in \mathbb{R}$ in Equation (6) are the parameters that determine the shape of the prior distribution, so-called hyperparameters. The posterior distribution is expressed as follows (Goi & Kim 2023).

$$p(\boldsymbol{W}, \boldsymbol{\Sigma}|\boldsymbol{Y}) = M\mathcal{N}\left(\boldsymbol{W}|\boldsymbol{M}', \boldsymbol{\Sigma}, \boldsymbol{L}'^{-1}\right) I\mathcal{W}(\boldsymbol{\Sigma}|\boldsymbol{L}', \nu') \tag{7}$$

where,

$$\mathbf{L}' =, \mathbf{L} + \boldsymbol{\phi}\boldsymbol{\phi}^{\mathrm{T}} \tag{8}$$

$$\mathbf{M}' = \left(\mathbf{M}\mathbf{L} + \mathbf{Y}\boldsymbol{\phi}^{\mathrm{T}}\right)\mathbf{L}'^{-1} \tag{9}$$

$$\nu' = \nu + n \tag{10}$$

$$\boldsymbol{\Psi}' = \boldsymbol{\Psi} + \mathbf{Y}\mathbf{Y}^{\mathrm{T}} + \mathbf{M}\mathbf{L}\mathbf{M}^{\mathrm{T}} - \mathbf{M}'\mathbf{L}'\mathbf{M}'^{\mathrm{T}} \tag{11}$$

Since it is difficult to derive a strict non-information prior distribution for the prior distribution in Equation (6), A uniform distribution is assumed. The Bayesian hypothesis test in this study is performed by evaluating the BF defined as the ratio of the likelihood functions. When

$\boldsymbol{D}$ is the observation data set and $\boldsymbol{\theta}$ is the model parameter (regression parameter), the likelihood function of hypothesis H is generated as follows.

$$p(\boldsymbol{D}|\mathrm{H}) = \int p(\boldsymbol{D}|\boldsymbol{\theta}, \mathrm{H}) p(\boldsymbol{\theta}|\mathrm{H}) d\boldsymbol{\theta} \tag{12}$$

where, $p(\boldsymbol{D}|\boldsymbol{\theta}, \mathrm{H})$ and $\boldsymbol{p}(\boldsymbol{\theta}|\mathrm{H})$ represent the likelihood function and prior distribution under hypothesis H, respectively. From Bayes' theorem, the posterior distribution under hypothesis H is described as follows.

$$p(\mathrm{H}|\boldsymbol{D}) = p(\boldsymbol{D}|\mathrm{H}) p(\mathrm{H}) \boldsymbol{p}(\boldsymbol{D})^{-1} \tag{13}$$

If the null hypothesis H_0 denotes "the statistical model according to the observed values is the same as that of a bridge in a healthy state", and then, the alternative hypothesis H_1 denotes "prior information is uncertain about the statistical model that the observed values follow." Taking the ratio of the posterior distribution in each hypothesis obtained from Equation (13), it is expressed as follows.

$$\frac{p(\mathrm{H}_1|\boldsymbol{D})}{p(\mathrm{H}_0|\boldsymbol{D})} = \frac{p(\mathrm{H}_1)}{p(\mathrm{H}_0)} B \tag{14}$$

where B is expressed as BF as follows.

$$B = \frac{p(\boldsymbol{D}|\mathrm{H}_1)}{p(\boldsymbol{D}|\mathrm{H}_0)} \tag{15}$$

Equation (14) means that the ratio of the posterior distribution can be expressed by the ratio of probability distributions of the null hypothesis H_0 and the alternative hypothesis H_1 and the likelihood function assuming that each hypothesis H_0 and H_1. If the prior probabilities for two hypotheses are equivalent, then the BF corresponds to the updated posterior odds. The BF therefore provides evidence to assess whether observed data support the null hypothesis or alternative hypothesis.

Here, the BF when the acceleration data $\boldsymbol{D}$ represents all the sensors is called the Global Bayes factor (GBF). Since GBF uses the information of all the sensors attached to the bridge, it is possible to estimate the presence or absence and degree of abnormality of the entire bridge. On the other hand, the BF in each sensor uses the acceleration expressed by the following equation using the jth element of Equation (1).

$$\boldsymbol{y}_k^{(j)} = \sum_{i=1}^{p} \alpha_i^{(j)} \boldsymbol{y}_{k-i} + \boldsymbol{e}_k \tag{16}$$

where, $\boldsymbol{y}_k^{(j)}$ and $\alpha_i^{(j)}$ are j-th element of $\boldsymbol{y}_k$ and α_i. The BF calculated using the acceleration data of Equation (16) is called the Local Bayes factor (LBF). Since LBF is calculated using the acceleration data of each sensor, it represents the BF of each sensor. Therefore, the damage position can be estimated by comparing the BF values at each location.

In this study, BF is considered on the scale of the natural logarithm, and when $2lnB$ is larger than 10, the basis for rejecting the null hypothesis is "very strong" (Jeffreys 1946). Here, the acceleration data of a healthy bridge is defined as reference data, and that of a bridge with unknown abnormalities is defined as test data. In determining the AR order p, the Bayesian Information Criterion (BIC) (Bishop 2006) was used in this study. The stabilization diagram is used as a method for obtaining the order q that extracts the features sensitive to damage detection.

3 EFFECTIVE INDEPENDENCE METHOD FOR SENSOR LOCATION OPTIMIZATION

As the coefficient matrix of the VAR model contains information on the modal parameters, including the mode shapes of the structure, the optimal sensor placement by applying the EFI method to the regression parameter $\boldsymbol{W}$ is deemed to be effective.

The EFI method is a method for finding the optimum sensor placement using the mode shape matrix $\boldsymbol{\Phi}$, which is a matrix of mode vectors estimated from the measurements and normalized so that the norm is 1. When applying the EFI method, the number of measurement points and the positions at which the mode shape matrix □ is calculated are first determined in advance. Secondly, the mode of interest is determined, and thirdly, the number of sensors to be finally installed, N_0, is determined. When using the EFI method, the number of sensors to be finally determined, N_0 should not be less than the number of mode shapes to be considered (Kammer 1991).

The EFI method determines the sensor arrangement that maximizes the Fisher Information Matrix (FIM), F, shown in Equation (17), leaving the sensor with the largest FIM determinant and reducing the number of sensors one by one. This is repeated until the planned number of sensors is reached. This selection of sensors is determined based on the orthogonal projection matrix E shown in Equation (18).

$$\mathbf{F} = \boldsymbol{\Phi}^T \boldsymbol{\Phi} \tag{17}$$

$$\mathbf{E} = \boldsymbol{\Phi} \mathbf{F}^{-1} \boldsymbol{\Phi}^T \tag{18}$$

The diagonal component E_{ii} of matrix $\mathbf{E}$ represents the influence of the i-th component of the mode shape matrix $\boldsymbol{\Phi}$. In other words, the excluded ith component is removed as the sensor with the least impact on the target mode as shown in Equation (19).

$$\det(\mathbf{F}) = \det(\mathbf{F}_0)(1 - E_{ii}) \tag{19}$$

where $\mathbf{F}_0$ represents the original FIM and $\mathbf{F}$ represents the FIM after the i-th sensor has been removed. Therefore, the FIM determinant decreases as one row is removed from the mode shape matrix Φ, as shown in Equation (19). In this way, the number of sensors is reduced until the pre-determined number of sensors N_0 is reached and the optimum sensor arrangement is determined.

4 FIELD EXPERIMENT ON A STEEL PLATE GIRDER BRIDGE

The target bridge shown in Figure 1 is a simply supported steel plate girder bridge with a total bridge length of 40.5 m, an effective width of 4.0 m, and a depth of 2.0 m. The bridge was constructed in 1957 and was removed in 2017. The state of the bridge before introducing damage is regarded as a healthy state (hereinafter referred to as the INT scenario). The damage location is near sensor A1. In the first stage of damage, a through crack is introduced into the lower flange (hereinafter DMG1 scenario). In the second stage damage through cracks was introduced into the web plate in addition to DMG1 (hereinafter DMG2 scenario). As a safety measure, a bridge collapse prevention device was set at the girder end on the A1 side. Regarding the bearings, the A1 side is the plain sliding bearing and the A2 side is the pivot bearing.

A moving vehicle experiment was conducted and the vertical acceleration response of the bridge was measured. The vehicle speed was 20 km/h. The number of trials for each run is 60 for the INT scenario, 32 for the DMG1 scenario, and 30 for the DMG2 scenario, respectively. The traveling direction reciprocates from A1 to A2, and one way was counted as one trial. The sampling frequency was 200 Hz and the data length was 15 seconds (forced vibration was

five seconds and free vibration was ten seconds). A high-sensitivity accelerometer ARS-10A (Tokyo Instrument Research Institute) was used, and a multi-recorder TMR-200 series (Tokyo Instrument Research Institute) was used for data acquisition. Accelerometers were installed at ten locations as shown in Figure 1 (A1 to A10). The identified modal frequency under different damage scenarios is summarized in Table 1. Mode shapes up to the third bending mode under the INT scenario were identified as shown in Figure 2. These three bending modes are modes of interest in sensor location optimization.

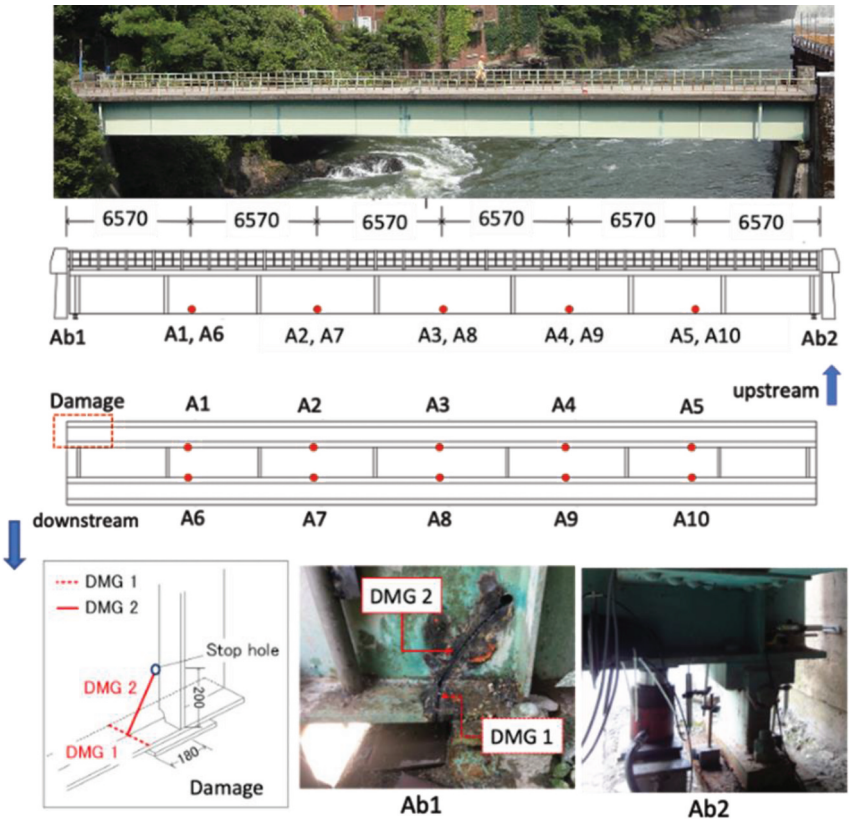


Figure 1. Experiment bridge and sensor deployment.

Table 1. Identified modal frequencies.

Mode		INT	DMG1	DMG2
1st bending	Freq. (Hz)	3.15	3.25	3.28
	CV	0.013	0.011	0.006
	MAC	-	1.000	0.999
2nd bending	Freq. (Hz)	9.53	9.24	8.85
	CV	0.009	0.005	0.005
	MAC	-	0.993	0.975
3rd bending	Freq. (Hz)	21.87	21.87	21.60
	CV	0.005	0.004	0.003
	MAC	-	0.998	0.991

Freq.: Frequency, CV: Coefficient of Variation, MAC: Modal Assurance Criterion

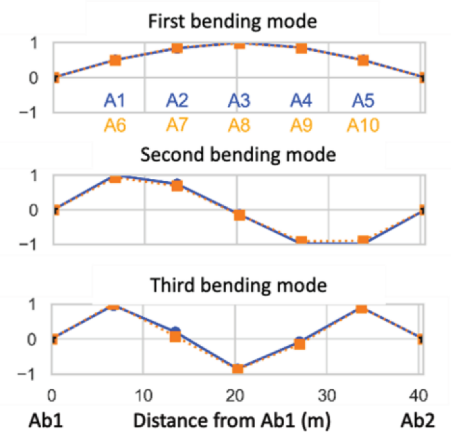


Figure 2. Identified the first three bending modes under the INT scenario.

5 DAMAGE DETECTION WITH OPTIMAL SENSORS

5.1 *Bayesian damage detection using a full number of sensors*

Using the identified posterior probability density autoregressive coefficient matrix from ten sensors, the Bayesian hypothesis test is carried out. Figure 3 shows the plots of the global Bayes factor (GBF) where the horizontal axis denotes the damage scenario and the vertical axis indicates the BF in the log scale. The CV shows the leave-one-out cross-validation (LOOCV) to measure how well the predictions made by the model match the observed data. It demonstrates that the GBF clearly indicates changes in vibration characteristic of the bridge, and even clearly shows higher evidence of supporting the alternative hypothesis H_1. Damage detection using the local Bayes factor (LBF) is summarized in Figure 4. It is obvious that A1 and A6 which are instrumented around the artificial damage at the girder-end show higher LBF, which also supports the feasibility of the LBF in terms of damage detection.

5.2 *Bayesian damage detection using an optimized number of sensors*

As discussed in the previous section, GBF and LBF successfully detected damage in the bridge. In this section optimal sensor location is discussed. The target number of sensors is assumed three. The removed sensor decided by means of the EFI method is summarized in Table 2 which shows the step-by-step reduction of sensors up to three sensors which is the target number of sensors. In other words, sensors A7, A9, A2, A4, A1, A8, and A5 were removed, and the remaining sensors A3, A6, and A10 were selected as the optimal sensors by

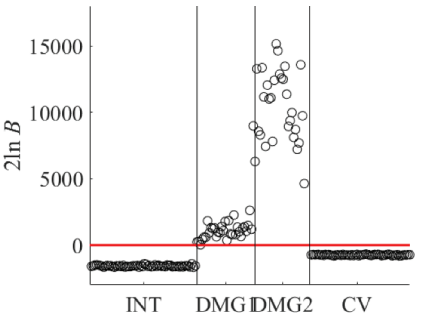


Figure 3. GBF of ten sensors.

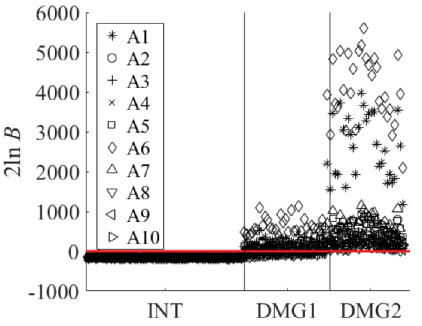


Figure 4. LBF of ten sensors.

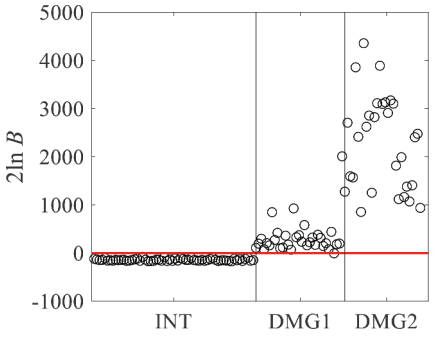


Figure 5. GBF from three sensors optimally placed (A3, A6 and A10).

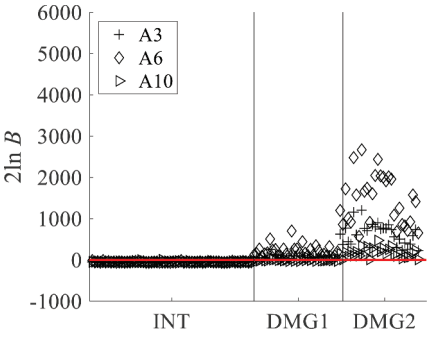


Figure 6. LBF from three sensors optimally placed (A3, A6 and A10).

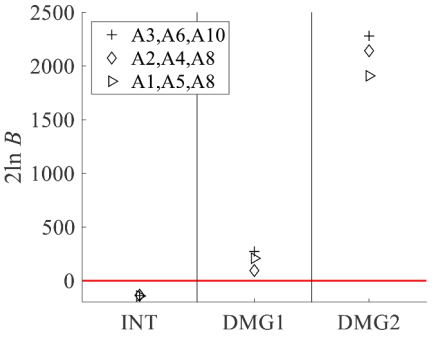


Figure 7. GBFs from optimal sensor group (A3, A6 and A10) and artificially determined sensor groups (A2, A4 and A8, and A1, A5 and A8).

Table 2. Determinant of FIM w.r.t removed sensor by means of EFI.

N_0	10	9	8	7	6	5	4	3
Sensor to be removed	NA	A7	A9	A2	A4	A1	A8	A5
det(**F**)	109.7	86.8	67.3	47.6	33.4	20.1	11.4	6.2

det(**F**): determinant of FIM

means of the EFI method. Those GBF and LBF using optimal three sensors with respect to damage scenarios are summarized in Figures 5 and 6 respectively. The GBF in Figure 5 with three sensors demonstrates that the more severe the damage, the higher the GBF value. For the LBF shown in Figure 6, the A6 sensor which is the nearest sensor at the damage among the three sensors shows the highest LBF. To verify the validity of the optimal sensor group for damage detection, the GBFs of two artificially selected sensor groups are compared to the GBF of the optimal sensor group. Figure 7 shows those comparisons, and demonstrates the optimal sensor group that resulted in the most sensitivity to the damage compared to the other two artificially determined sensor groups.

6 CONCLUSIONS

A Bayesian damage detection method was used to investigate the possibility of estimating the extent and location of damage. A way to reduce the number of accelerometers used for

Bayesian damage detection was also investigated using the EFI method which is an optimal sensor placement method. In the application of the EFI method as the optimal sensor placement method, targeting the first, second, and third bending modes, with the number of sensors set to three. It was found that the same vibration frequencies could be identified with the optimally located three sensors as when all sensors were used. However, the reduced number of sensors resulted in weaker power of the dominant frequency in the PSD curve. Therefore, the damage detection accuracy can be decreased under a strong noise condition. The results of Bayesian damage detection using the sensor information of the optimum sensor arrangement under the above conditions suggest that Bayesian damage detection is effective even with three sensors.

ACKNOWLEDGMENT

This work was supported by a Japanese Society for the Promotion of Science (JSPS) Grant-in -Aid for Scientific Research (B) under project No. 22H01576 which is greatly appreciated.

REFERENCES

Bishop, C.M. 2006. Pattern recognition and machine learning. New York: Springer.

Doehler, M., Mevel, L. & Hille, F. 2014. Subspace-based damage detection under changes in the ambient excitation statistics, *Mech. Syst. Signal Process*., 45: 207–224.

Dzunic, Z., Chen, J.G., Mobahi, H., Büyüköztürk, O. & Fisher, J.W. 2017. A Bayesian state-space approach for damage detection and classification, *Mech. Syst. Signal Process*, 96: 239–259.

Friswell, M.I. & Castro-Triguero, R. 2015. Clustering of sensor locations using the effective independence method, *AIAA J*, 53(5): 1388–1390.

Goi, Y. & Kim, C.W. 2017. Damage detection of a truss bridge utilizing a damage indicator from multivariate autoregressive model, *Journal of Civil Structural Health Monitoring*, 7(2): 153–162.

Goi, Y. & Kim, C.W. 2023. Damage detection of bridges by principal component analysis and Bayesian hypothesis testing utilizing traffic-induced vibration, *Structural Control and Health Monitoring*, Article ID 7986061.

Heo, G., Wang, M.L. & Satpathi, D. 1997. Optimal transducer placement for health monitoring of long span bridge, *Soil Dyn Earthq Eng*., 16: 495–502.

Jeffreys, H. 1946. An invariant form for the prior probability in estimation problems, *Proceedings of the Royal Society of London*, 186: 453–461.

Kammer, D.C. 1991. Sensor placement for on-orbit modal identification and correlation of large space structures, *J Guid Control Dynam*., 14: 251–259.

Kass, R. & Raftery, A. 1995. Bayes Factors, *J of the American Statistical Association*, 90(430): 773–795.

Kim, C.W., Kawatani, M. & Hao, J. 2012. Modal parameter identification of short span bridges under a moving vehicle by means of multivariate AR model, *Structure and Infrastructure Engineering*, 8(5): 459–472.

Ko, J.M. & Ni, Y.Q. 2005. Technology developments in structural health monitoring of large-scale bridges, *Engineering Structures*, 27: 1715–1725.

Li, D., Jiang, Y. & Li, H. 2020. New sensor placement method based on remodeling innovation, *AIAA J*, 58(4): 1–9.

Magalhaes, F., Cunha, A. & Caetano E. 2012. Vibration based structural health monitoring of an arch bridge: From automated OMA to damage detection, *Mech. Syst. Signal Process*., 28, 212-228: 2012.

Nair, K.K., Kiremidjian, A.S. & Law, K.H. 2006. Time series-based damage detection and localization algorithm with application to the ASCE benchmark structure, *J. Sound Vib*., 291: 349–368.

Papadopoulos, M. & Garcia, E. 1998. Sensor placement methodologies for dynamic testing, *AIAA J*, 36: 256–263.

Bridge Maintenance, Safety, Management, Digitalization and Sustainability – Jensen, Frangopol & Schmidt (eds)
© 2024 The Author(s), ISBN 978-1-032-77040-6
Open Access: www.taylorfrancis.com, CC BY-NC-ND 4.0 license

Converting finite element models to irreducible element models for use in population-based SHM

C. O'Higgins
School of Natural & Built Environment, Queen's University Belfast, Belfast, UK

D.S. Brennan
Dynamics Research Group, Department of Mechanical Engineering, University of Sheffield, Sheffield

C. Kent, D. Hester & S.E. Taylor
School of Natural & Built Environment, Queen's University Belfast, Belfast, UK

ABSTRACT: Population-Based Structural Health Monitoring (PBSHM) has emerged as a promising approach to increase the understanding of structural health by leveraging data from a population of structures, surpassing the insights attainable from individual structures alone. For successful knowledge transfer in PBSHM, structural similarities need to be established to prevent negative transfer effects. Irreducible Element (IE) models, combined with graph theory, are the vehicles used within PBSHM to facilitate this process. This paper presents a Finite Element (FE) to Irreducible Element model converter. While FE models are conventional in civil engineering, IE models represent a novel technology tailored for PBSHM, with limited available tools for their creation. This paper details a procedure for transforming FE models into IE counterparts. By enabling the conversion of existing FE models into IE models, this tool mitigates the need for specialised IE model expertise, resulting in more accessibility and ease of adoption of PBSHM. The significance of the FE to IE converter in the field of bridge Structural Health Monitoring is that it can help bridge the gap between conventional SHM and emerging PBSHM. The conversion tool also significantly enhances the accessibility of PBSHM in the civil infrastructure industry. The converter's utilisation holds the potential to accelerate the adoption of PBSHM by enabling the incorporation of an expansive array of structures with pre-existing FE models into the PBSHM framework.

1 INTRODUCTION AND APPLICABILITY OF FINITE ELEMENT (FE) MODELS

PBSHM leverages data from multiple structures within a similar population, providing an understanding and insights into the population and other similar structure (Worden et al., 2020). Populations of bridges can be wide ranging an example of a very similar population may be 2 or more steel truss pedestrian bridges however induvial elements can also be considered such as a population of bridges that all contain a ladder deck. Monitoring a population of structures, PBSHM offers a distinct advantage over traditional single-structure monitoring approaches which is the potential for transfer learning. Transfer learning is a method where knowledge gained from training a model on one task is leveraged to improve the performance on a different but related task. Instead of training a model from scratch for each new task, transfer learning allows pre-trained models to serve as a starting point, with the hope that the knowledge gained from one domain can be beneficial in learning another. However, the effective application of transfer learning between structures within PBSHM, which seeks to harness the knowledge gained from one structure to provide insights into others, hinges on establishing structural similarities that prevent negative transfer. To this

DOI: 10.1201/9781003483755-104

end, Irreducible Element (IE) models, combined with graph theory, serve as a fundamental vehicle in PBSHM, facilitating the identification of structural commonalities and differences. More information about the foundations of PBSHM can be found in (Bull et al., 2021; Gardner et al., 2021; Gosliga et al., 2021; Tsialiamanis et al., 2021).

Concurrently, the field of civil/structural engineering has used Finite Element (FE) models as a fundamental numerical tool for analysing and simulating structural behaviour. FE models have a rich history of application, but as PBSHM is at the early stage of development, there is a growing need to bridge the gap between conventional SHM and emerging PBSHM. This necessitates the development of tools and techniques that promote the use of PBSHM within civil engineering industry.

One of the main challenges lies in the creation of IE models, for which there are currently limited available tools. To address this gap, this paper introduces the concept of an FE to IE model converter. The impact of this converter within the field of PBSHM has the potential to be significant as it empowers the transformation of existing FE models into their IE counterparts. By doing so, it not only mitigates the need for specialised IE model expertise, but also enhances the accessibility and ease of adoption of PBSHM.

This paper, presents a detailed procedure for converting FE models to IE models, encompassing two critical stages: the extraction of relevant information from FE models and the generation of IE models from the extracted data. The utilisation of this conversion tool holds the potential to accelerate the adoption of PBSHM by enabling the incorporation of an expansive array of structures with pre-existing FE models into the PBSHM framework.

2 IE MODEL OVERVIEW

In the second part of the 'Foundations of Population-based Structural Health Monitoring' series, (Gosliga et al., 2021) introduced the concept of an Irreducible Element (IE) model. The IE model is used in PBSHM to represent significant structural components and their interactions. It provides an abstract representation needed to assess the similarity of different structures in the network. The IE model only considers components belonging to the structure and describes where the interactions with external systems are, without providing information on how they interact with a model.

To create an Irreducible Element (IE) model, two lists are needed. The first list encompasses individual elements within a structure, each accompanied by attributes such as material and geometry. The second is a list of relationships which define how each element is connected to each other and the properties of each connection. In essence, an IE model is constructed through these two lists, encapsulating the structural elements and their relationships.

This is an oversimplification of how IE models are created and there are a lot of details that have to be considered when developing a system that is required to model structures ranging from aeroplanes to bridges. A more comprehensive description can be found in (Gosliga et al., 2021).

3 PROCEDURE FOR CONVERTING FE MODELS TO IRREDUCIBLE ELEMENT MODELS

The creation of IE models remains a challenge, as there is a limited availability of tools for their generation. To bridge the gap between conventional Structural Health Monitoring (SHM) and emerging PBSHM, we introduce the concept of a Finite Element (FE) to Irreducible Element (IE) model converter. This converter holds significant potential within the field of PBSHM, as it empowers the transformation of existing FE models into their IE counterparts. By doing so, it not only mitigates the need for specialised IE model expertise but also enhances the accessibility and ease of adoption of PBSHM in the civil infrastructure industry.

In this section, we present a detailed procedure for converting FE models to IE models, separated into two stages: the extraction of relevant information from FE models and the generation of IE models from the extracted data. The idea of this separation is that stage one would be software dependent, and stage two would be a generalised procedure that should work

with any FE software. This division of the procedures means that only stage one would have to be altered if a new FE software is used to create the FE models.

3.1 *Creation of the FE model*

Before the introduction of the conversion procedure, this section provides a brief overview of how an FE model is traditionally created. In FE analysis, structures are discretised into finite elements, which are interconnected to simulate their behaviour under various loading conditions. The Finite Element (FE) software, Lusas (version 19), was used for this research. The creation of an FE model typically involves:

- Geometry and Mesh Generation: Define the geometry of the structure and generate a mesh by dividing it into finite elements.
- Material Properties: Assign material properties to the elements, including information about stiffness, density, and other mechanical characteristics.
- Boundary Conditions: Specify boundary conditions to represent how the structure interacts with its surroundings.
- Loading conditions: Specify which parts of the structure are under loading and the magnitude of this loading.

In the context of this work, the primary difference in creating FE models for conversion to IE models lies in providing the elements with human understandable names, which is required for generating IE models with meaningful structural descriptions.

3.2 *Stage one: Extracting relevant information from the FE model*

To convert an FE model into an IE model, the first stage involves the extraction of key information from the existing FE model, this information includes positional, geometrical and material information for all of the elements. This information is vital for creating an accurate representation of the structure in the IE model. This information is required for any FE simulation and so the only unknown between different FE software is how this information can be extracted from the model. For this research, LUSAS version 19 software was used. After the model had been created in LUSAS there are a number of exported formats, two formats were selected as they contain all the required information. These were a Visual Basic for Applications (VBA) Script File and an Industry Foundation Classes (IFC). These are both common text-based file formats and the latter being an open file format used by Building Information Modelling (BIM) programs. These files were then parsed using Matlab and grouped into the following tables:

Regular Element Information

Contains data related to elements within the FE model that are the 'regular elements' within the IE model, including element name, element type (line/surface), geometry reference, material reference and the coordinates of the vertices. The vertices of a line are the two end points and the vertices of a surface are the 4 corner points.

Ground Element Information

Ground elements are unique to IE models and comprise unique element names to denote the location of where the model interacts with other external systems. At this stage of the process, the location of the support conditions within the FE model are recorded to create a list of equivalent ground elements with unique names.

Relationship Information

This table takes the vertices stored in the 'Regular Element' table and uses the shared vertices to determine which elements are connected to each other. By default, the connections are fully static within the FE model and so that is the default relationship that is defined in the IE model. At this point in the procedure, the algorithm determines which connections are 'perfect'. Perfect relationships within an IE model are defined as 'A relationship that represents the interaction between two elements where the two elements in question could be considered to be the same singular element'. To determine whether there is a perfect relationship there are two tests one for line elements and one for surface elements. For lines, if geometry matches and the lines are connected and parallel (to a defined tolerance), there is a perfect relationship.

For surfaces, if geometry matches and the surfaces share an edge there is a perfect relationship. For the relationships that are determined to be perfect, they are suffixed with an '_P' so they can be identified at a later stage.

Boundary Condition Information

Specifies the support conditions and locations of the boundary conditions applied to the model, such as fully fixed or pinned. These properties while not utilised in the current version of IE models may be implemented in future revisions.

Geometry Information

Includes geometric properties of the elements within the FE model, defining dimensions, shape, and spatial arrangement. At this point, the geometry of each element is matched to a predefined list of allowed geometry types in the IE model schema.

Material Information

Provides data on material properties assigned to each element, encompassing stiffness, density, and other mechanical characteristics. Again, like the geometry information, each unique material is matched to a predefined list of allowed material types in the IE model schema.

General Model Data Information

This table extracts the model properties of the FE model such as the units that are used for dimensions, loads etc and the vertical direction defined in the model.

These tables collectively constitute a comprehensive dataset that captures the essential characteristics of the FE model. The grouping of information into these categories facilitates a systematic and organised approach to the subsequent stages of IE model generation. Stage two in the process involves utilising this extracted information to generate an IE model in the specific format that is required by the IE model schema.

3.3 *Stage two: Generating IE model from extracted information*

Once the relevant information is extracted from the FE model, the second stage involves generating an IE model based on the extracted data. IE models are stored using a Javascript Object Notation (JSON) format. The conversion tool formats all of the information that is described in this section into the correct JSON format as outlined below. This stage includes; defining the structure properties and then defining the IE model section properties, which comprise the type of model, the elements in the model and the relationships between the elements.

Defining Structure Properties

To define the structure properties, three items are needed, the name of the structure, the population that the structure belongs to and the timestamp as to when the model is created. The name and the population field are user inputs, and the algorithm produces the timestamp in the correct format based on the clock of the system being used.

Defining the IE model

The first aspect of the IE model that needs to be defined is the type. This can be either 'free' or 'grounded'. The difference between these types is that the grounded model considers the boundary conditions and the free model does not. The type is selected by the user and if 'free' the information collected regarding the boundary conditions is ignored and if 'grounded', then the boundary condition information is incorporated into the IE model in the sequential steps.

Compiling the elements object

The elements object in an IE model is a list of both ground elements (assuming a 'grounded' model is being created) and regular elements with associated attributes. For the ground elements, the only information required is the name of the ground element a list of which has already been populated in stage one. Therefore, at this point, all that is required is collating all the ground elements in the correct format and adding the 'ground' type to each element.

The regular elements required more information than the ground elements to be valid against the current IE model schema. At a minimum, each regular element in the IE model requires the following information: name, type, contextual, geometry and material. The name and type information are straightforward as the names are extracted from the FE model and the tables extracted during stage 1 have already been separated into either 'ground' or 'regular'.

Further processing of the information extracted during stage 1 needs to be undertaken to determine the contextual, geometry and material properties needed for the regular elements.

The first step is to further divide the regular elements into line objects and surface objects depending on how they have been represented in the FE model. For the line objects the coordinates of the endpoints are used to calculate the length of the line and the vector of the line (compared with the global axis of the FE model). The vector of the line is used to select the context of the element from a predefined list which includes; 'beam', 'column', 'slab', 'cable' and other such contextual entities. The conversion tool has a series of rules to select the most appropriate context such as if a line object is parallel to the ground then its context is a 'beam' if perpendicular to the ground then its context is a 'column'. A similar procedure is then used for the surface elements, the vertices of the surface are used to calculate the centre of the surface and the lengths of each side of the surface. This information, along with other inbuilt rules, is then used to select the most suitable contextual information from the predefined list.

For the geometry properties of the regular elements there needs to be a map of how the geometry of the FE model translates to the allowable geometry type of the IE model schema. For example a 'Rectangular Solid' will be mapped to the IE model type 'beam > rectangular' and a 'Surface' geometry ID in the FE model will map to a 'plate > rectangular' IE model type. The most common types have been mapped in the conversion tool and new items will be added as they arise further into the development.

The material properties are handled in a similar way with a map embedded into the conversion tool that translates a FE material ID to an allowable IE material.

4 ILLUSTRATIVE CASE STUDY

To demonstrate the application of the Finite Element (FE) to Irreducible Element (IE) model conversion process, this section presents a case study featuring a simple bridge structure. This example structure was designed to contain a range of common bridge elements and a range of materials thus showing the range of capabilities of the conversion procedure.

4.1 *Description of structure*

A simple bridge was chosen to have key features of typical of real-world bridges while remaining simple enough to test all the features of the conversion tool without the complexity of a real bridge. While the bridge used here would be unrealistic in the real world it does provide a mix of material and geometric features that show the capabilities of the conversion tool. The bridge has a length of 10 meters and a width of 3 meters. Concrete columns, each with a 500 mm diameter and a height of 2 meters, are located at the four corners of the deck. The bridge deck consists of a 50 mm thick steel surface and is supported by rectangular concrete beams measuring 300 mm in height and 150 mm in width. Three transverse beams span the width of the bridge, and two longitudinal beams running along the deck's length. A schematic of the bridge can be seen in Figure 1.

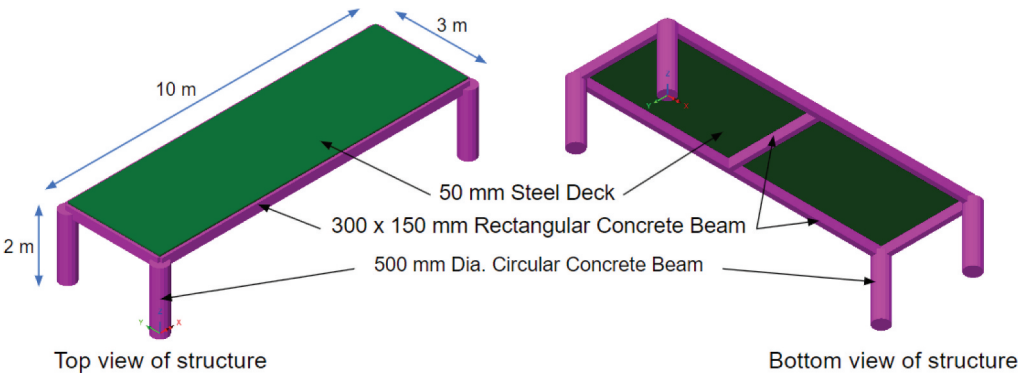


Figure 1. Schematic of simple bridge structure.

4.2 *Simple bridge FE model*

The Finite Element (FE) model of the simple bridge structure described above can be created in the conventional manner. The process involves defining the finite element mesh, geometric dimensions, assigning material properties, and specifying boundary conditions to simulate the structure as accurately as possible. It is noteworthy that creating the FE model for use with the Irreducible Element (IE) conversion tool involves minimal deviation from standard practices.

The key departure lies in the embedding of IE model element names during the creation of the FE model. This step is crucial for ensuring that the subsequent IE model, generated through the conversion process, retains human-understandable names for each element. This adjustment to the FE model means that no additional information is needed by the conversion tool. If this naming of the elements was moved to the conversion tool then the FE model would require no adjustment but the conversion tool would require more user inputs. Figure 2 shows the naming convention used for this simple structure.

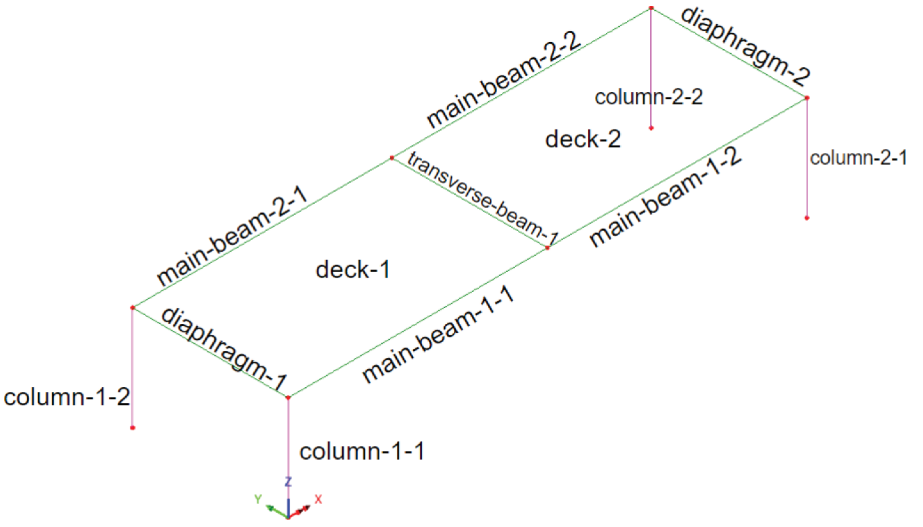


Figure 2. IE naming convention used for simple bridge structure.

Furthermore, the FE model serves another purpose during its creation. Beyond preparing for the IE conversion, it becomes a valuable tool for ensuring the structural behaviour of the model is as intended by the modeller. Deflections, obtained through the FE model, can be cross-referenced against theoretical calculations. Additionally, the model allows for the examination of the bending moment diagram and shear force diagram, providing a means to verify if the structure behaves as expected under various loading conditions. This gives a level of confidence that the structure has been modelled as intended.

4.3 *Application of the FE to IE converter*

4.3.1 *Extraction of relevant information*

After creating the FE model and checking the behaviour of the structure is as expected, the two required files can be exported from the Lusas software. Utilising the previously described in Section 3.2, the relevant information from the FE model is extracted and organised into tables, including Regular Element Information, Ground Element Information, Relationship Information, Boundary Condition Information, Geometry Information, Material Information, and General Modal Data Information. The 'Elements' tables showing the extracted information from the FE model can be seen in Figure 3, with the most significant columns labelled underneath the tables.

Elements

'column-1-1'	'Line'	'2'	[233;239;244]	'LGeo3'	'Concrete'	21x1 double	21x1 cell	1x3 cell	1x3 cell	[]	[]
'column-1-2'	'Line'	'3'	[249;255;260]	'LGeo3'	'Concrete'	21x1 double	21x1 cell	1x3 cell	1x3 cell	[]	[]
'column-2-1'	'Line'	'4'	[265;271;276]	'LGeo3'	'Concrete'	21x1 double	21x1 cell	1x3 cell	1x3 cell	[]	[]
'column-2-2'	'Line'	'5'	[281;287;292]	'LGeo3'	'Concrete'	21x1 double	21x1 cell	1x3 cell	1x3 cell	[]	[]
'main-bea...	'Line'	'24'	[361;367;372]	'LGeo1'	'Concrete'	21x1 double	21x1 cell	1x3 cell	1x3 cell	[]	[]
'main-bea...	'Line'	'23'	[345;351;356]	'LGeo1'	'Concrete'	21x1 double	21x1 cell	1x3 cell	1x3 cell	[]	[]
'main-bea...	'Line'	'21'	[313;319;324]	'LGeo1'	'Concrete'	21x1 double	21x1 cell	1x3 cell	1x3 cell	[]	[]
'main-bea...	'Line'	'22'	[329;335;340]	'LGeo1'	'Concrete'	21x1 double	21x1 cell	1x3 cell	1x3 cell	[]	[]
'diaphragm...	'Line'	'25'	[377;383;388]	'LGeo1'	'Concrete'	21x1 double	21x1 cell	1x3 cell	1x3 cell	[]	[]
'diaphragm...	'Line'	'26'	[393;399;404]	'LGeo1'	'Concrete'	21x1 double	21x1 cell	1x3 cell	1x3 cell	[]	[]
'transverse-...	'Line'	'20'	[297;303;308]	'LGeo1'	'Concrete'	21x1 double	21x1 cell	1x3 cell	1x3 cell	[]	[]
'deck-1'	'Surface'	'4'	[409;415;421]	'SGeo2'	'Steel'	54x1 double	54x1 cell	1x3 cell	1x3 cell	1x3 cell	1x3 cell
'deck-2'	'Surface'	'5'	[426;432;438]	'SGeo2'	'Steel'	54x1 double	54x1 cell	1x3 cell	1x3 cell	1x3 cell	1x3 cell

Element Name
Element Type
Lusas Element Reference
Geometry Reference
Material Reference
Vertex 1 coordinates
Vertex 2 coordinates
Vertex 3 coordinates
Vertex 4 coordinates

Figure 3. Elements table extracted from FE models.

4.3.2 *Generation of IE model*

The extracted information is then processed through the FE to IE converter. The converter transforms the FE data into an Irreducible Element (IE) model using the process outlined in Section 3.3. The generation of the Irreducible Element (IE) requires very limited additional input (structure name and population) from the user beyond the extracted information from the FE model. All pertinent information easily embedded into the IE model is automatically included, allowing a high level of adaptability to future developments of the IE model and similarity comparisons. This approach goes beyond the minimal requirements of the IE model schema, providing a degree of future-proofing by capturing additional data that may prove valuable in evolving applications of the IE models.

Furthermore, the simplicity and efficiency of this conversion process enable easy iteration. In the event of amendments or updates to the FE model, the IE model generation can be repeated with little effort. This adaptability ensures that any modifications made to the underlying structure are seamlessly reflected in the corresponding IE model. The iterative nature of the conversion process allows any changes to the structure in real life to be reflected in the IE model, promoting a dynamic and responsive workflow for ongoing structural health monitoring processes. Figure 4 shows the attributed graph constructed using the IE model file. This graph is a simple form of validation, letting the user easily see if the elements of the IE model are in the correct location.

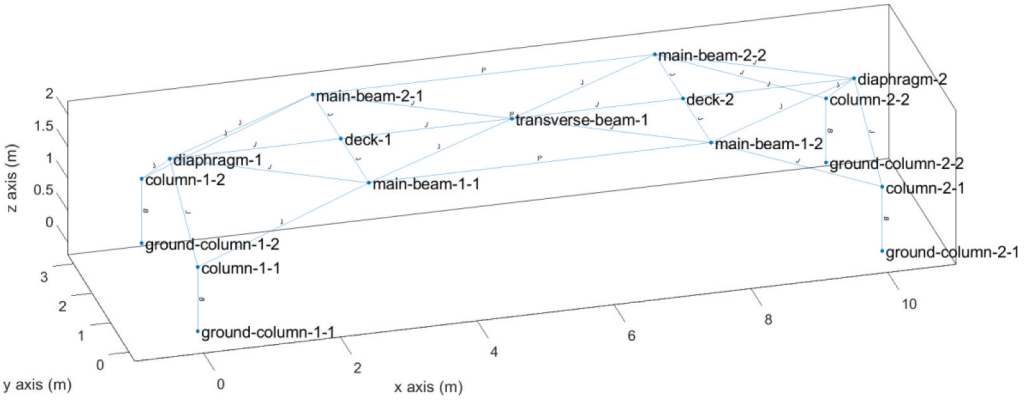


Figure 4. Attributed graph constructed from IE model.

5 CONCLUSION

In addressing the challenges posed by Population-Based Structural Health Monitoring (PBSHM) and the need for effective knowledge transfer among structures within a population, this paper has presented a novel approach through the development of a Finite Element (FE) to Irreducible Element (IE) model conversion tool. The research problem centred around the limitations in existing tools for creating IE models with the aim to bridge the gap between more traditional engineering models (FE) and the new technology of the IE model which can offer population based intelligence for informed decision making by asset owners. The outlined procedure for converting FE models to IE counterparts offers a systematic and accessible solution to developing IE models. The conversion tool was designed to operate with FE models created through standard practices with minimal required amendments to the FE model. The benefits of the FE to IE conversion tool extend beyond mitigating the need for specialised IE model expertise. By encapsulating essential structural information, the tool facilitates the incorporation of an expansive array of structures into the PBSHM framework, thereby accelerating the adoption of PBSHM in the civil infrastructure industry. The creation of an FE model prior to an IE model also has the benefit of allowing checks to be made to the behaviour of the structure. The implications of this conversion tool on PBSHM are significant. It provides a practical means to establish structural similarities among diverse members of a population which is essential in preventing negative transfer effects and enabling more effective knowledge transfer within the PBSHM framework.

REFERENCES

Bull, L. A., Gardner, P. A., Gosliga, J., Rogers, T. J., Dervilis, N., Cross, E. J., Papatheou, E., Maguire, A. E., Campos, C., & Worden, K. (2021). Foundations of population-based SHM, Part I: Homogeneous populations and forms. *Mechanical Systems and Signal Processing*, *148*, 107141. http://dx.doi.org/10.1016/j.ymssp.2020.107141

Gardner, P., Bull, L. A., Gosliga, J., Dervilis, N., & Worden, K. (2021). Foundations of population-based SHM, Part III: Heterogeneous populations – Mapping and transfer. *Mechanical Systems and Signal Processing*, *149*, 107142. http://dx.doi.org/10.1016/j.ymssp.2020.107142

Gosliga, J., Gardner, P. A., Bull, L. A., Dervilis, N., & Worden, K. (2021). Foundations of Population-based SHM, Part II: Heterogeneous populations – Graphs, networks, and communities. *Mechanical Systems and Signal Processing*, *148*, 107144. http://dx.doi.org/10.1016/j.ymssp.2020.107144

Tsialiamanis, G., Mylonas, C., Chatzi, E., Dervilis, N., Wagg, D. J., & Worden, K. (2021). Foundations of population-based SHM, Part IV: The geometry of spaces of structures and their feature spaces. *Mechanical Systems and Signal Processing*, *157*, 107692. http://dx.doi.org/10.1016/j.ymssp.2021.107692

Worden, K., Bull, L. A., Gardner, P., Gosliga, J., Rogers, T. J., Cross, E. J., Papatheou, E., Lin, W., & Dervilis, N. (2020). A Brief Introduction to Recent Developments in Population-Based Structural Health Monitoring. *Frontiers in Built Environment*, *6*. http://dx.doi.org/10.3389/fbuil.2020.00146

Bridge Maintenance, Safety, Management, Digitalization and Sustainability – Jensen, Frangopol & Schmidt (eds)
© 2024 The Author(s), ISBN 978-1-032-77040-6
Open Access: www.taylorfrancis.com, CC BY-NC-ND 4.0 license

Impact factor of a seven span continuous cable-stayed bridge

Shinya Kimura
Eight-Japan Engineering Consultants Inc., Osaka, Japan

Chul-Woo Kim
Kyoto University, Kyoto, Japan

Hiroyuki Sugiyama & Masaaki Isa
Hanshin Expressway, Osaka, Japan

Kazuyuki Ono
Eight-Japan Engineering Consultants Inc., Hyogo, Japan

ABSTRACT: This study aims to investigate the impact factor of a seven span continuous cable-stayed bridge planned for the extension of an expressway by means of a three-dimensional vehicle-bridge coupled vibration analysis. The validity of the three-dimensional analysis was verified comparing the vibration response of a single span steel cable-stayed bridge in service subjected to vehicle running tests with those numerical responses from the three-dimensional analysis. The impact factors of a seven span continuous cable-stayed bridge were found to be less than 1.07 for the main girder, less than 1.03 for the base of the main tower and less than 1.04 for the cable. The impact factor was highest when several vehicles were running at resonant headway.

1 INTRODUCTION

A new cable-stayed bridge construction is planned on the 14.5km-long Osaka Bay Line as a part of extension in Hanshin Expressway. The new bridge is a seven-span continuous cable-stayed bridge with a length of 2,730 m connecting two manmade islands, called Rokko island and Port island in Kobe respectively.

In highway bridge design, dynamic amplification of bridge responses due to traveling heavy vehicles are considered using the impact factor or dynamic amplification factor. In the Japanese highway bridge design code (Japan Road Association, 2017), the impact factor is defined as $i = 20/(50 + \mathrm{L})$ where L indicates the span length in meters. The impact factor is applicable to bridges with a span length of less than 200 m, however, the cable-stayed bridge in this study has a span length of 650m long which exceeds the applicable range of the impact factor. Cable-stayed bridges exhibit more flexible behavior than girder bridges and have more complex vibration characteristics due to their complex structure consisting of beams, cables, and pylons. Dynamic impact effects require evaluation of various factors such as road surface roughness, vehicle speed, vehicle vibrations, vehicle traveling style, and bridge structural type, but few studies examine the impact factor of the cable-stayed bridge with an extremely long span.

This study aims to investigate the impact factor of a seven-span continuous cable-stayed bridge with a maximum span length of 650m. The impact coefficient is estimated using the three-dimensional (3D) vehicle-bridge interaction (VBI) analysis. The validity the validity of the 3D VBI analysis, a moving vehicle experiment on a single span steel cable-stayed bridge in service, and those vibration responses from the experiment are compared to those from the 3D VBI analysis.

DOI: 10.1201/9781003483755-105

2 VERIFICATION OF IMPACT FACTOR ON REAL BRIDGE EXPERIMENT

2.1 *Moving vehicle experiment*

The validity of the 3D VBI analysis was verified through the comparison to the field-test data on girder bridges (Kawatani & Kim et al., 1998, 2005, 2008). However, in order to properly evaluate the impact factor of the cable-stayed bridge by means of the 3D VBI analysis, it is necessary to accurately reproduce the vibration characteristics and responses of cable-stayed bridges through 3D VBI analysis. Therefore, a field experiment on a similar type of the cable-stayed bridge was carried out to examine the validity of the VBI analysis for the cable-stayed bridge. The general layout and cross-sectional view of the target bridge are shown in Figure 1. The bridge is a steel cable-stayed bridge (Ehara et al., 1993) crossing the Aji River at the Hanshin Expressway No. 5 Bayside Route. The total length is 640m long and the span length is 120m+350m+170m long. The bridge consists of six lanes: three inbound lanes and three outbound lanes.

The acceleration of the girder, main tower, and experiment vehicles were measured, and the displacement at the center of the main girder was also measured using a laser displacement transducer. Figure 2 shows the measurement points and the corresponding analysis node numbers. Accelerometers are installed at three points on the top and middle stages of the main tower, and at L/4, L/2, and 3 L/4 of the main girder in the center span and side span. A laser displacement meter was installed under the center of the span between P11 and P12, which can be measured from the ground, and measured the vertical displacement of the girder. Figure 3 shows an overview of the test vehicle and the locations where the accelerometers are installed. The test vehicle was a dump truck with a front axle weight of 54.74 kN and a rear axle weight of 140.68 kN, and total weight was 195.42 kN (□196 kN). Accelerometers were installed near the center axis of the vehicle above and below the front and rear suspensions. Free vibration tests for the test vehicle were measured to identify the bounce frequency and axle hop frequency at the front and rear wheels. The bounce frequency at the front axle was 1.5Hz, and that at the rear axle was 3.5 Hz. For the axle hop frequency, 10 Hz was dominant at both the front and rear wheels. The vehicle speed during the moving vehicle experiment was set 80km/h.

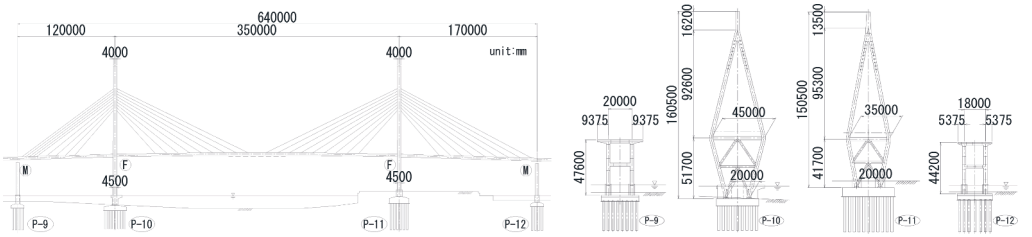


Figure 1. The general layout of the in-service cable-stayed bridge for the experiment (unit: m).

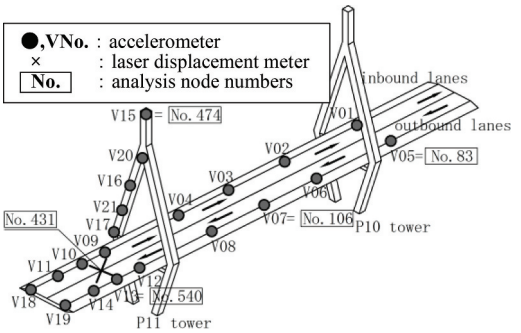


Figure 2. The measurement points and the node numbers in the corresponding analysis.

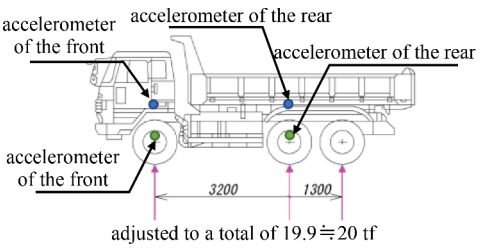


Figure 3. Overview of the test vehicle and the locations of the accelerometers.

2.2 *VBI analysis and impact factor verification*

Dynamic responses of the in-service bridge are obtained taken from 3D VBI analysis (Kim et al., 2005). It is based on the finite element method for the modal analysis using three-dimensional models for both vehicle and bridge. The numerical bridge model is shown in Figure 4 in which the beam element is used to model girders, the truss element is used for cables, and the spring element with two nodes with the same coordinate is adopted to model the elastomeric bearing. The vehicle model is composed of the body, tires, and suspension systems. Details of the vehicle model are shown in Figure 5 and Table 1 along with the eight degrees of freedom to describe its movement (Kawatani & Kim et al., 2005, 2008). The vehicle properties were estimated using the free vibration measurement on a 20 ton dump truck used in the test. Rayleigh damping was adopted in the 3D VBI analysis of the bridge, and the coupled equation of motion for vehicles and bridge interactive system were solved by the Newmark-β method assuming β = 1/4. In the 3D VBI analysis of the bridge, the roadway roughness on the bridge surface is simulated based on the PSD curves (ISO 8608, 1995). Since the road surface properties are not clear, the parameters α = 0.003 (cm^2/(m/c)), β = 0.05 (c/m), and n = 2.00 were assumed.

In the moving vehicle experiment on the bridge, the measured value of the acceleration response is converted into a dynamic displacement using Fourier transform, and the impact factor is calculated. Figure 6 shows the dynamic displacement extracted from the measured acceleration

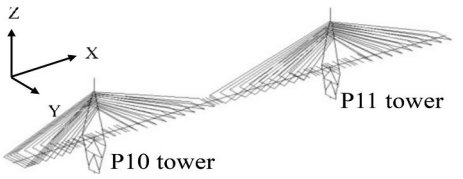


Figure 4. FE models for bridges.

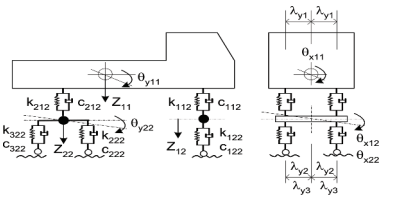


Figure 5. 8DOF Vehicle.

Table 1. Mechanical properties of vehicle.

Total weight (kN)	196.0
Axle weight(kN)	Front: 49.0, Rear: 147.9
Damping ratio	Front: 0.66, Rear: 0.33
Natural frequency(Hz)	Suspension at front (bounce): 1.5, Suspension at Rear (bounce): 3.5, Tyre (hop): 10~20
Damping coefficient of vehicle (kN.s/m)	suspension at front axle: 11.76, suspension at rear axle: 27.83 tyre at front axle: 7.25, at rear axle: 9.20
Spring constant of vehicle (kN /m)	suspension at front axle: 668.36, suspension at rear axle: 5328.3 tyre at front axle: 2518.6, tyre at rear axle: 10071.5

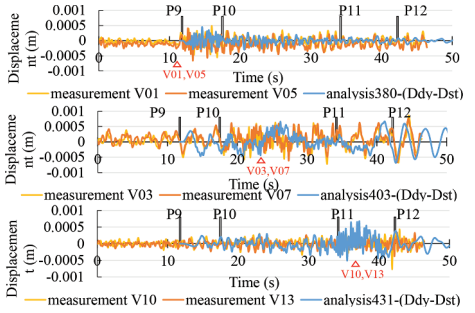


Figure 6. Dynamic displacement at the span center of the girder.

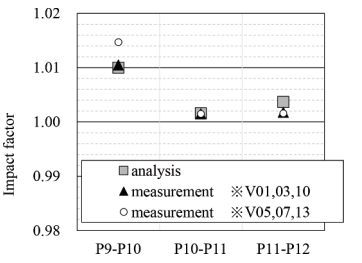


Figure 7. Impact factor.

response at the span center of each girder with the analytical ones, where "Ddy" denotes the response including both static and dynamic components while "Dst" denotes the static displacement. Figure 7 shows the impact factor determined from the dynamic displacement shown in Figure 6. It is observed from Figures 6 and 7 that the response and impact factor obtained from the VBI analysis are comparable with those from experiment, i.e. shows validity of the 3D VBI analysis.

3 3D VBI ANALYSIS AND IMPACT FACTOR OF SEVEN SPAN CONTINUOUS CABLE-STAYED BRIDGE

3.1 *Numerical models*

The general layout and cross-sectional view of the seven span continuous cable-stayed bridge (hereafter called "target bridge") are shown in Figure 8. The bridge is a seven-span continuous cable-stayed bridge. The total length is 2730m long and the span length is 130m+260m+3@650m +260m+130m long. The bridge has four A-shaped steel towers in the longitudinal direction, and has six lanes, three inbound lanes and three outbound lanes, as shown in Figure 8. Dynamic responses of the bridge are taken from the same way as the verification of analysis validity on real bridge experiment described above. The bridge model is shown in Figure 9. Two vehicle speeds, 80 km/h and 60 km/h, are considered in the 3D VBI analysis. The roadway roughness on the bridge surface is simulated based on the PSD curves, in which the roadway roughness is assumed to be categorized as Class A according to the ISO estimate (ISO 8608, 1995).

3.2 *Definition of impact factor*

The impact factor adopted in this study is defined as $DIF = 1 + y_{I,dmax}/y_{stmax}$ where $y_{I,dmax}$ denotes the maximum dynamic amplitude, and y_{stmax} denotes the maximum static amplitude. The definition of the impact factor is also illustrated in Figure 10. The impact factor is calculated based on vertical displacement for the main girder, bending moment for the main tower, and analytical tension for the cable.

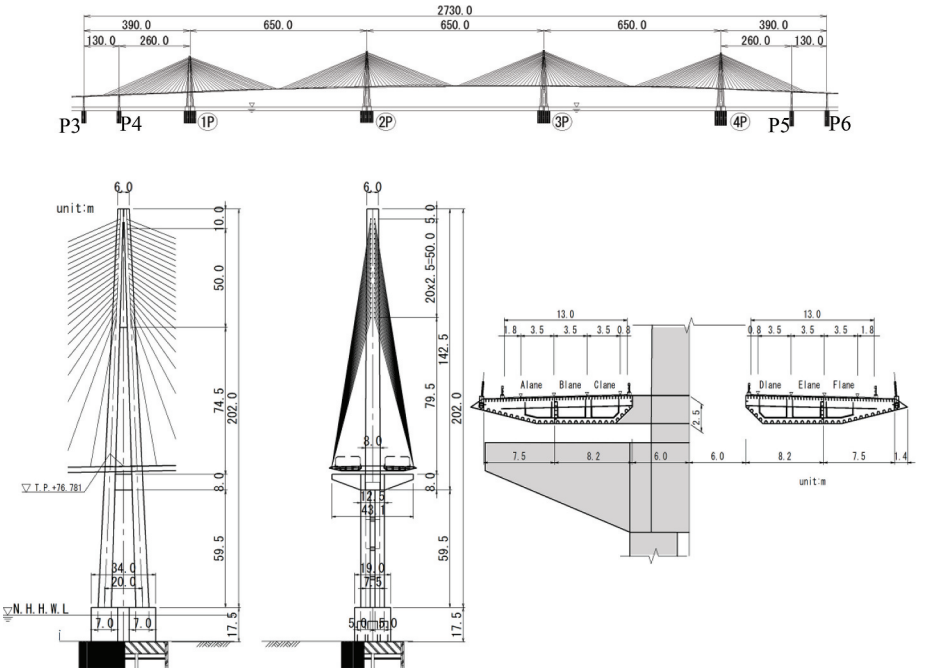


Figure 8. The general layout of the examined a cable-stayed bridge (unit: m).

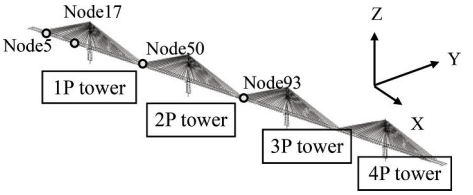


Figure 9. FE models for bridges.

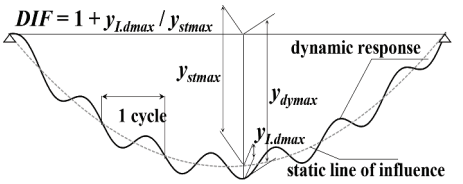


Figure 10. Definition of impact factor.

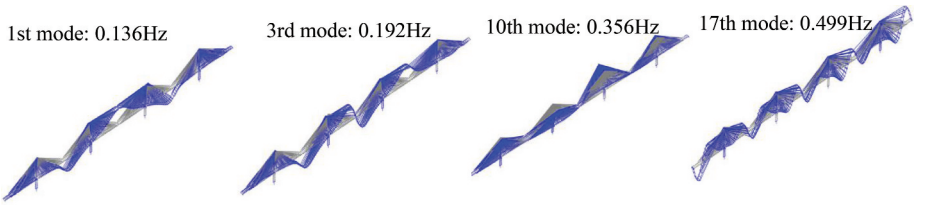


Figure 11. The general layout of the examined a cable-stayed bridge (unit: m).

Table 2. Analysis scenarios for impact factor.

	Driving lane	Vehicle speed (km/h)	No of vehicles	Resonant headway (m)	Road surface roughness
Case1	A to C	80	4/lane	165(=v/f=22.22(m/s)/0.136(Hz))	A-1; α=0.001
Case2	A to C	80	4/lane	165	A-2; α=0.004
Case3	A to C	60	4/lane	125(=v/f=16.67(m/s)/0.136(Hz))	A-1; α=0.001
Case4	A to F	80	4/lane	165	A-1; α=0.001
Case5	A to C	80	1/lane	165	A-1; α=0.001
Case6	A to C	80	10/lane	60	A-1; α=0.001

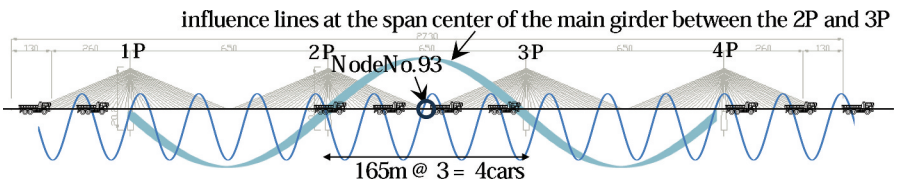


Figure 12. Vehicle placement for Case 1 to Case 4 of the analysis scenario.

3.3 *Eigenvalue analysis*

Selected mode shapes and frequencies of the bridge from the eigenvalue analysis are summarized in Figure 11. Therein, the bending mode of the bridge is observed in the 1st mode (0.136Hz). The 3rd mode (0.192Hz) is the 2nd bending mode of the main girder between the 2P tower and 3P tower. The 10th mode (0.356Hz) shows a sway mode of the main tower, and the 17th mode (0.499Hz) is the 2nd bending mode of all spans.

3.4 *Impact factor of main girders located between 1P and 4P towers*

3.4.1 *Analysis scenarios*

Analysis scenarios are summarized in Table 2 where the resonant headway indicates the distance between two vehicles which produces the most excessive vibration of the bridge. Two road surface roughness profiles denoted A-1 and A-2 are considered in the VBI analysis. The difference

between the A-1 and A-2 road surface roughness profiles is the amplitude of the profile, i.e. the A-1 profile is smoother than the A-2 profile. Since the vertical bending mode of the main girder and the sway mode of the main tower are dominant, the resonant headway is set as L=165m ($L = v/f = 22.22(m/s)/0.136(Hz)$). The number of vehicles traveling on one lane is set to four so that four vehicles with a headway of 165m place on the deflection mode of the main girder as shown in Figure12. Cases 5 and 6, which are vehicle running scenarios without resonance headway, were also employed to investigate the impact of resonant headway on the impact factor.

3.4.2 *Impact factor of the main span*

The estimated impact factors of the main girder are summarized in Figure 13, which shows that the impact factor ranges between 1.01 and 1.05. Although the amplitude of road unevenness is larger than in other scenarios, the impact factor for Case 2 shows the same value as Case 1. One reason is that the bridge vibration is dominated by the first bending mode at 0.136 Hz, and the contribution from the vehicle vibration with a frequency of around 3.5 Hz was extremely weak.

When multiple vehicles with resonant headway are traveling on all lanes like in Case 4, the largest impact factor is observed among six scenarios. On the other hand, lower impact factors were observed for slower vehicle speeds and fewer vehicles, as in Case 3 and Case 5. Even if the vehicle load is large, if there is no resonance, the impact coefficient is low as Case6. Figure 14 shows the maximum value and amplification factor of the dynamic response displacement of the main girder during vehicles traveling on 2P-3P span under the scenarios Case 1, Case 4, and Case 5. In Case 1 and Case 4, the amplification factor of dynamic displacement increases due to the resonance effect of the vehicle, and the impact factor increases.

The impact factors of the main tower at the middle section and tower base are calculated from the bending moment and summarized in Figure 15. The impact factors of cables, which are obtained from analytical tensions, are summarized in Figure 16. The impact factors for the main towers and cables were less than 1.05.

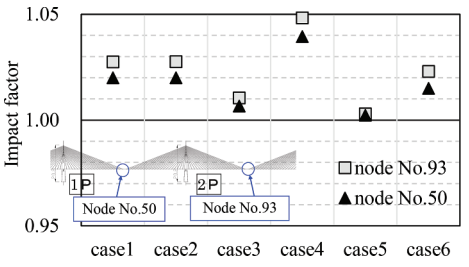


Figure 13. Impactor factor of main girder.

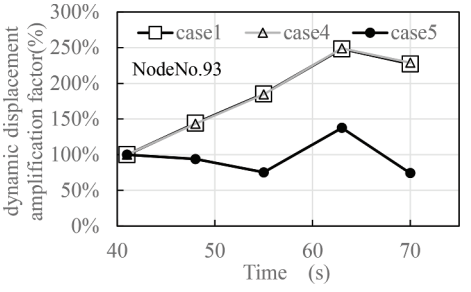


Figure 14. Amplification factor of the dynamic displacement of the main girder during vehicle traveling from 2P to 3P.

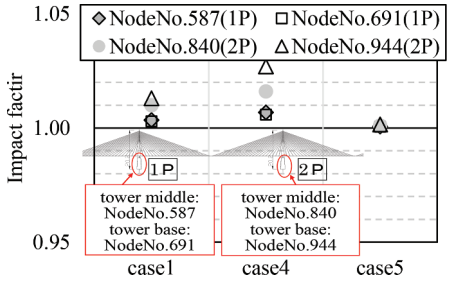


Figure 15. Impactor factor of main tower.

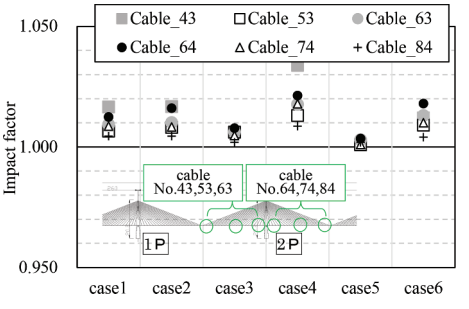


Figure 16. Impactor factor of main cable.

Table 3. Analysis scenarios for impact factor.

	Driving lane	Vehicle speed (km/h)	No of vehicles	Resonant headway (m)	Road surface roughness	hump at EJ
Case7	A to C	80	14+9/lane	46.7(=v/f=22.22(m/s)/0.476(Hz))	A-1; α=0.001	W/O hump
Case8-1	A to C	80	14+9/lane	44.5(=v/f=22.22(m/s)/0.499(Hz))	A-1; α=0.001	W/O hump
Case8-2	A to C	80	14+9/lane	44.5	A-1; α=0.001	W/ hump H=15mm
Case9	A to C	80	14+9/lane	40.2(=v/f=22.22(m/s)/0.553(Hz))	A-1; α=0.001	W/O hump

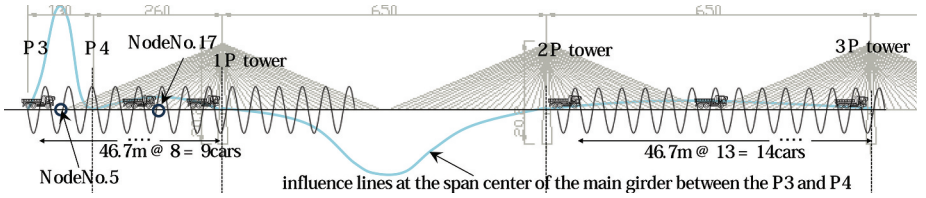


Figure 17. Vehicle placement for Case 7 to Case 9.

3.5 *Impact factor of the main girder at the side span center between P3 and 1P tower*

3.5.1 *Analysis scenarios*

In addition to impact factors of the main span under vehicle loadings considering the 1st bending mode of the main span, it is worth investigating the effect of vehicle loadings considering the dominant bending mode of the side span. The dominant first bending mode of the side span is different from the main span, the first bending mode of the side span observed in the 17th mode (0.499Hz) shown in Figure 11 is considered for the resonant vehicle loading. In addition, bending modes near the 17th mode (0.499Hz), that is the 16th mode (0.476Hz) and the 21st mode (0.553Hz), are also considered in the VBI analysis. Analysis scenarios are summarized in Table 3. The number of vehicles, road surface roughness profiles, and vehicle speed are not changed. Since the vertical bending mode of the main girder is dominant, the resonant headway is considered as L=46.7m for f = 0.476(Hz), L=44.5m for f = 0.499(Hz) and L=40.2m for f = 0.553(Hz). Humps at the expansion joint is considered in the VBI analysis for the side span. Case 8-2 is the scenario with the hump at the expansion joint on P3 located at the entrance of the side span. The depth of the hump was assumed 15mm and the length of the hump was assumed 2500mm. The impulsive vehicle wheel load generated when vehicles pass on the hump travels farther according to vehicle speed, and this study investigates the effect of vehicle speed and hump at the expansion joint on the impact fact of the bridge. Figure17 shows the vehicle placement for Case 7 to Case 9. 23 vehicles with the resonant headway place on the deflection influence line of the main girder.

3.5.2 *Impact factor of the side span*

The estimated impact factor of the main girder under the vehicle loadings considering the dominant bending mode of the side span is summarized in Figure 18. The impact factor between P3-P4 is found to be in the range of 1.05 to 1.07, those of P4-1P tower were found to be in the range of 1.01 to 1.02. The impact factor between P4-1P tower with short span length was smaller than that between 2P-3P towers because the displacement between the 2P and 3P towers is amplified much more due to resonance. The impact factor for Case 8-2 shows the same value as Case 8-1, which indicates that the dynamic responses of the girder at the span center is hardly affected by the hump since the observation point is far from the hump.

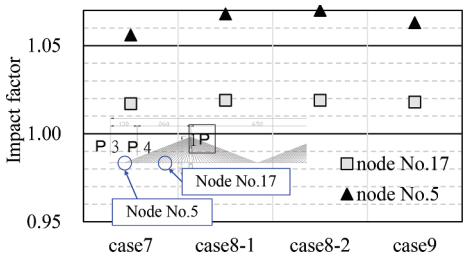


Figure 18. Impactor factor of main girder.

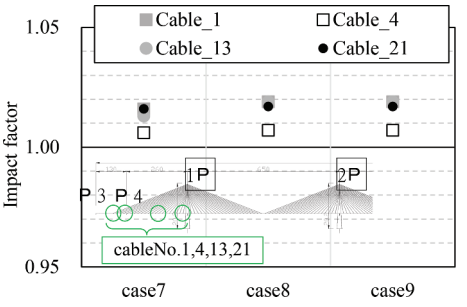


Figure 19. Impactor factor of main cable.

The impact factors of cables, which are obtained from analytical tensions, are summarized in Figure 19. The impact factors for cables were less than 1.05, the same as the main span section.

4 CONCLUSIONS

Impact factors of a seven span continuous cable-stayed bridge planned for the extension of an expressway by means of a three-dimensional vehicle-bridge interaction (VBI) analysis. The validity of the three-dimensional VBI analysis was verified comparing the vibration response of a single span steel cable-stayed bridge in service subjected to vehicle running tests with those numerical responses from the three-dimensional analysis. Impact factors of the seven-span continuous cable-stayed bridge were found to be less than 1.07 for the main girder, less than 1.03 for the base of the main tower, and less than 1.04 for the cable. The largest impact factor was observed when several vehicles are running with resonant headway at higher speeds. Additionally, it was confirmed that the impact coefficient was the largest in the case where multiple vehicles were driven with a resonant headway.

REFERENCES

Ehara, T. & Mori Y., 1993. Actual bridge vibration experiment of Tempozan Bridge, Hanshin Expressway Co., Ltd., Technical Report No. 12, 67–74. (in Japanese)

ISO 8608. 1995. Mechanical Vibration−Road Surface Profiles−Reporting of Measured Data. ISO.

Japan Road Association I. 2017. Specification for highway bridges.

Kawatani, M., Kim, C.W. & Kawada, N. 2005. Three-dimensional finite element analysis for traffic-induced vibration of a two-girder steel bridge with elastomeric bearings, Transportation Research Record; Journal of the Transportation Research Board, CD11-S, 225-233.

Kawatani, M., Kim, C.W., Kawada, N. & Koga, S. 2008. Assessment of traffic-induced low frequency noise radiated from steel box girder bridge, Steel Structures 8, 305–314.

Kawatani, M., Yamada, Y., Kim, C.W. & Kawaki, H. 1998. Estimation of slab's response in traffic-induced vibration of highway bridge by three-dimensional analysis, Journal of Structural Engineering, JSCE, 44A, 827–834. (in Japanese)

Kim, C.W., Kawatani, M., Kawada, N. & Sakata, T. 2005. Effect of vehicle model and initial condition on traffic-induced vibration of short-span girder bridges, Proc. of Construction and Maintenance, Kuala Lumpur, Malaysia, 10-11 October 2005, 313–322.

Kim, C.W., Kawatani, M. & Kim, K.B. 2005. Three-dimensional dynamic analysis for bridge-vehicle inter-action with roadway roughness, Computers and Structures 83(19-20), 1627–1645.

Bridge Maintenance, Safety, Management, Digitalization and Sustainability – Jensen, Frangopol & Schmidt (eds)
© 2024 The Author(s), ISBN 978-1-032-77040-6
Open Access: www.taylorfrancis.com, CC BY-NC-ND 4.0 license

Distributed fiber optic sensors for structural health monitoring of post-tensioned bridges

B. Piątek
Rzeszow University of Technology, Rzeszow, Poland

T. Howiacki
Cracow University of Technology, SHM System, Krakow, Poland

T. Siwowski
Rzeszow University of Technology, Rzeszow, Poland

ABSTRACT: Post-tensioned concrete is currently one of the most common technology used to construct bridges. For decades it was used to build medium-span bridges over the world and now many of them require diagnostics due to their worsening technical condition. One of the novel diagnostic technique for such bridges can be distributed fiber optic sensing (DFOS). It allows the measurements to be taken continuously over the entire structural length, which is especially important in such structures. The advantages of this method have already been proven in civil engineering applications, especially those related to concrete structures. Thanks to their construction distributed fiber optic sensors can be used for both new and existing structures. The paper presents the research on two post-tensioned beams with curvilinear multiwire strands in which optic sensors have been installed before and after concreting. The main aims of the research was to measure strains, stresses, cracks and displacements, to compare results from monolithic sensors embedded in the concrete (for new structures) and those installed in pre-made near-to-surface grooves (for existing structures) and to identify defects in one of the beam thanks to sensors installed inside the cable duct and the strain itself. The DFOS measurements were also compared with reference measurements made with conventional spot techniques, achieving very good compliance. The research proved that a well-designed DFOS-based system, including appropriate measurement techniques, optical sensors, installation methods and post-processing algorithms, is the relevant tool for the diagnostics of post-tensioned concrete bridges.

1 INTRODUCTION

Due to the continuous development of road and railway infrastructure around the world, the number of bridge structures has been steadily increasing year by year, particularly in developing countries. For example over the last 20 years, the count of these structures on national roads in Poland has tripled. Bridges with such superstructure currently represent around half of all road bridges in Poland, whereas in 2002, their share was less than 20%. Presently, the most commonly chosen type of construction for small and medium-span road bridge structures is prestressed concrete (either post-tensioned or pre-tensioned). The increase in the number of prestressed bridges is expected to be driven in the coming years by the further expansion of the national road network and the construction of new railway lines. Similarly, in other countries prestressed bridges constitute an important part of the infrastructure system.

DOI: 10.1201/9781003483755-106

The primary driver behind the dynamic growth of such structures is the fact that properly designed and constructed prestressed bridges rank among the most durable constructions, requiring minimal maintenance during their operational lifespan. These structures undergo the introduction of substantial prestressing forces during construction, making them unfortunately highly sensitive to any design or construction errors. Incorrectly designed or constructed prestressed bridges are susceptible to the detrimental effects of environmental factors, resulting in a shortened operational lifespan and a gradual reduction in load-bearing capacity over time. In extreme cases, this can lead to the failure or catastrophe of these structures (Anania, Badalà, & D'Agata, 2018; Hurlebaus, Hueste, Karthik & Terzioglu, 2016; Powers, Sagues & Virmani, 2002). As a result, prestressed bridges require meticulous control during the construction phase and heightened attention from bridge inspectors during periodic condition assessments during operation. Identifying local damage in prestressed bridges is challenging and highly laborious with current methods due to the localized positioning of the tendons within the concrete cross-section (Mazzatura, Salvatore, Caprili, Celati, Mori & Gammino, 2023). Early-stage diagnostics of damage allow for the prevention of further deterioration to a level threatening the safety of the structure and prompt implementation of remedial measures, which are often less costly at this stage (Frangopol, Saydam, & Kim, 2012). A promising and continually evolving technique in the field of diagnostics and monitoring of concrete structures is the use of distributed fiber optic sensors (DFOS) (Alj et al., 2021; Bado, Casas & Kaklauskas, 2021; Bednarski et al., 2022; Buda-Ożóg et al., 2022).

This article presents research results on the development of a DFOS sensor system for monitoring and diagnosing post-tensioned concrete bridges, addressing the needs of the construction industry in this regard. It aims to fill the current gap in the control and management system for bridge structures during the operational phase. Initial studies have demonstrated that using the DFOS sensor system allows for the detection of damages, primarily voids in the grout inside cable ducts, which are the most common causes of failures (Piątek et al. 2023). By embedding sensors during the manufacturing phase of prestressed elements, valuable insights can be gained into their behavior during concrete pouring, prestressing, and concrete maturation. Additionally, continuous geometric measurements using DFOS sensors provide a comprehensive picture of deformations, displacements, and crack distribution along the length of the element, which is unattainable using typical point sensors (Fischer, Thoma & Crepaz, 2019; Liu, Huang & Yang, 2020).

2 RESEARCH PROGRAM

2.1 *Design of tested beams*

Two post-tensioned concrete beams were tested in order to examine DFOS system and check it's utility for diagnostics, first served as a reference (PT1) and second had simulated damages (PT2). The beams had a trapezoidal shape with a height of 60 cm and a width ranging from 45 to 55 cm (Figure 1). Both beams were made of C40/50 concrete with an experimentally determined compressive strength of 58.1 MPa, tensile strength of 4.7 MPa and elastic modulus of 44.2 GPa. Two cables were applied in each beam, each containing four strands with a diameter of ϕ15.7 mm (Y1860S7 steel). After concrete placement, the cables were prestressed with an initial force of 1500 kN each. The beam included reinforcement in the form of ϕ16 rods at the bottom and top edges, as well as circumferential reinforcement with ϕ10 rods (B500SP steel). Shear reinforcement was also applied using double stirrups with a diameter of ϕ12 mm (B500SP steel). Cross-sectional and longitudinal views of the beams are presented in Figure 1. In the beam with simulated damages during prestressing, the ducts were not fully filled with grout, leaving approximately 1.4 m of free space from the beam ends. This resulted in four unfilled sections of the ducts, the first was left completely empty (real void in the channel). In the second, corrosion simulation was conducted (real void and corroded prestressing tendon), while in the third and fourth sections, partial filling with polyurethane foam was carried out. The schematic of the simulated damages is shown in Figure 2.

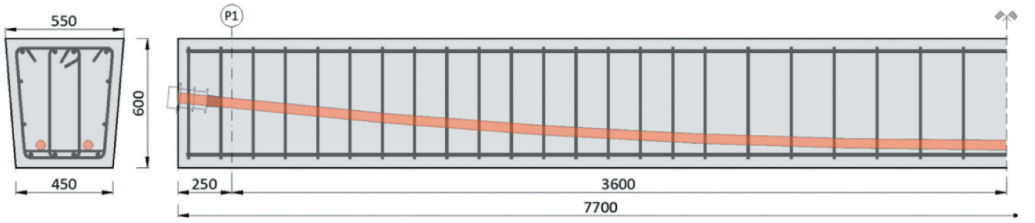


Figure 1. Cross-section and longitudinal section of the beams.

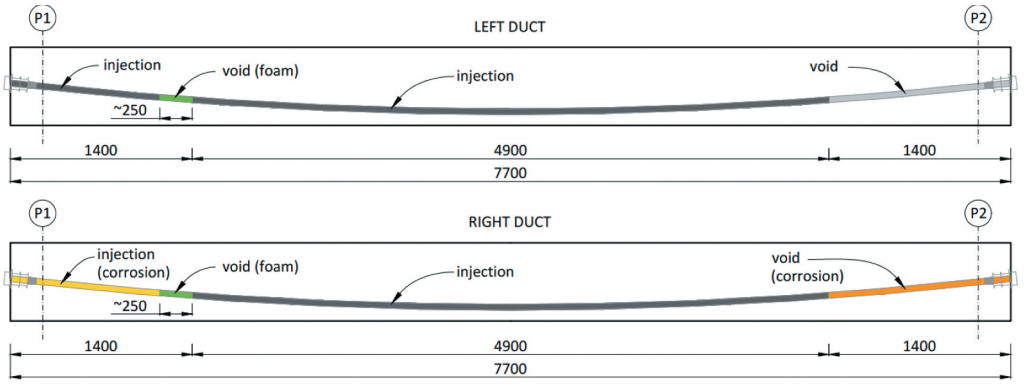


Figure 2. Damages simulated in the second beam (PT2).

2.2 *Test setup and instrumentation*

The beams were subjected to a four-point bending load scheme on specially designed testing stand equipped with two hydraulic actuators with a maximum pressing force of 630 kN placed at a spacing of 1.2 m. The theoretical span of the beams was 7.2 m. View of the beams on the testing stand is presented in Figure 3.

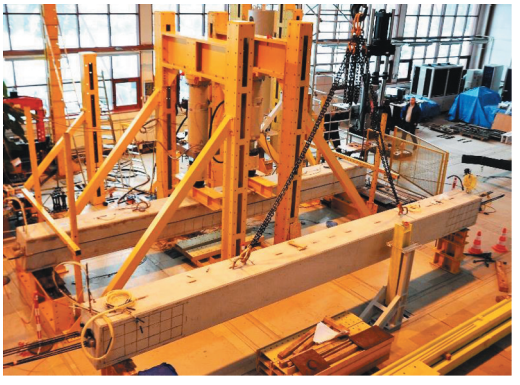


Figure 3. Cross-section and longitudinal section of the beams.

During the tests, the following distributed fiber optic sensors (DFOS) were utilized: EpsilonSensor (ES), 3D displacement sensors, and fiber optic sensors integrated with a prestressing strand, developed as part of the project. EpsilonSensor is made with monolithic

composite material with low elastic modulus (3 GPa) which provides precise strain reading and crack locations. In Figure 4, the markings and numbering of fiber optic sensors in the cross-sections of individual beams are presented. 3D displacement sensors consist of four optical strain fibres precisely positioned on the top and bottom of a rectangular composite core. It allows to determine deflections along the beams knowing the spacing between the fibres and the boundary conditions. Sensors were installed using three methods: embedding inside the concrete (EpsilonSensors), bonding to the surface (3D sensors) and near-to-surface installation inside a pre-made groove (EpsilonSensors). Additionally, reference measurements were conducted for comparison with DFOS techniques. Electro-resistance strain gauges were used for strain measurements, and linear variable displacement transducers (LVDTs) were employed for displacement measurements. Force measurements were carried out using sensors integrated with loading system.

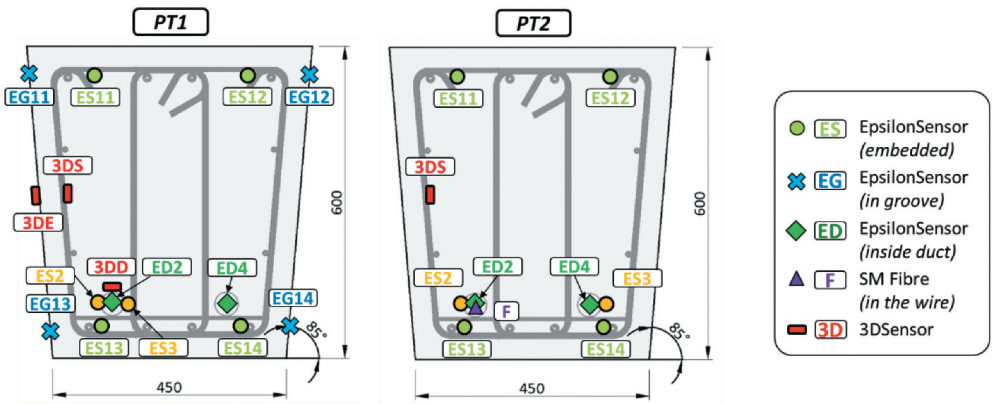


Figure 4. Locations and adopted symbols for sensors in the cross-section of the beams.

The Rayleigh-based method was employed for measurements using the Luna Innovations OBR optical backscatter reflectometer. In the post-processing of the data, a spatial resolution of 10 mm was configured, enabling a strain resolution of 1 με. Spatial resolution of 10 mm translates to 100 measurement points per meter of the DFOS sensor and 770 measurement points along the length of the post-tensioned girder (for a single sensor). With such a large number of points, statistical analysis and interpretation of the measured strain profiles is possible.

3 TEST RESULTS AND ANALYSIS

3.1 *Cracking identification*

In this section, sensor readings installed in exactly the same locations and in the same manner are compared, however, on two different beams: one without damages (PT1) and one with damages (PT2). To facilitate the physical interpretation of the measurements, data for the undamaged beam will be indicated by a dashed line, while data for the damaged beam will be indicated by a solid line. Cross-sectional diagrams with the marked location of the analyzed sensor are included in the charts. Since beam PT2 was not equipped with sensors in near-surface grooves, the results are presented for sensors embedded inside the concrete. Exemplary results of comparison between two beams under load of 350 kN in the upper and lower zone of the beam are presented in Figure 5 and Figure 6, respectively.

Based on the DFOS measurements, it was possible to identify existing cracks in the upper part of the beams, closing under the influence of compression induced by bending as well as new cracks forming in the lower part of the beams due to tensile forces induced by bending.

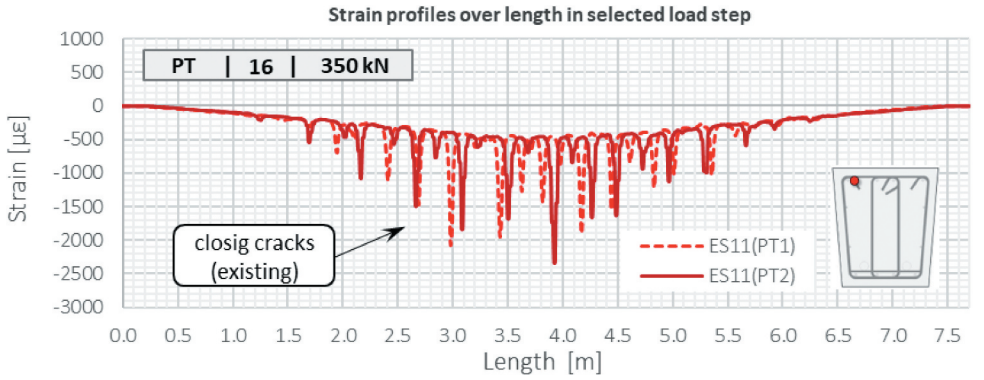


Figure 5. Strain profiles over length measured monolithic sensors ES11 in the upper zone of the beam under force of 350 kN.

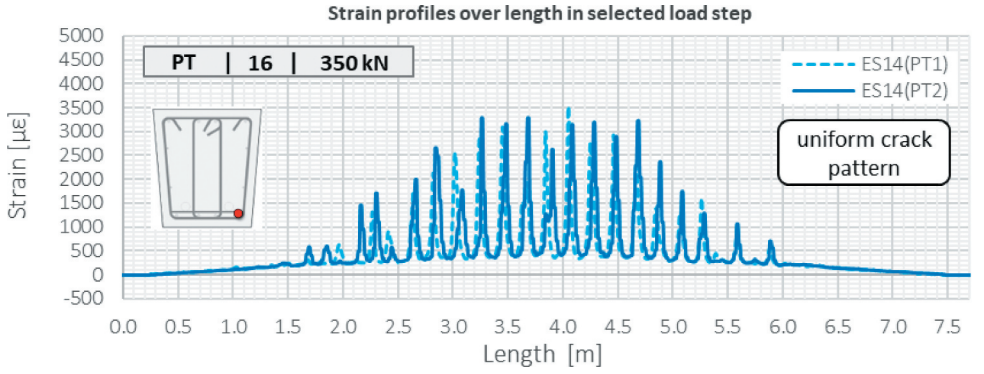


Figure 6. Strain profiles over length measured monolithic sensors ES14 in the lower zone of the beam under force of 350 kN.

The cracks in the upper part of the beams were caused by thermal-shrinkage deformations and under the influence of the compression process, causing stretching of the upper fibers. The characteristic and symmetrical distribution of cracks indicates that mechanical deformations from prestressing had a decisive influence. Despite performing zero measurements when the cracks already existed in the upper part of the beam, the change in deformation under bending allowed for their unambiguous identification. In existing, operational structures, this detection will be additionally supported by thermal deformations of the structural element.

Identification of the new cracks in the lower part of the beams was possible because zero readings were taken just before the test, i.e., after the prestressing of the element, from a measurement perspective, the sensor was subjected to tension from the very beginning (the analysis does not consider compression from prestressing). In the next subsection an analysis aimed at estimating the width of these new cracks is presented.

Since the simulated damages in the PT2 beam were not significant and located only near the end sections of the beams they did not influence on a global behavior and are not visible in Figures 5 and 6 because cracks have a dominant share in the measured values. The analysis of local damages will be discussed in details in subsection 3.3.

3.2 *Calculations of crack widths*

There are several ways to estimate the crack width based on the measured strain profile (Howiacki T. et al., 2023). The basic approach used in this analysis involves integrating (summing up) the strains over the effective length. In the case of a stabilized crack state, this length can be assumed between the midpoints of the segments determined between the cracks. However, it should be noted that this approach relies on the assumption that the strains in the concrete between the cracks are zero, which may not always be true. In reality, at the edge of the crack, the concrete relaxes completely, but as one moves away from the crack, tensile strains may accumulate (up to a value corresponding to the tensile strength of the concrete). The crack widths obtained using the above method will therefore be slightly overestimated, but previous experiences indicate that an accuracy of no worse than 0.05 mm can be safely assumed. From the perspective of the engineering assessment of the structural condition, such accuracy can be considered sufficient. In the case of analyzing a single crack, the effective length will strongly depend on the type of DFOS tool used (optical fiber, layered cable, monolithic sensor), the installation method (adhesive on the surface, embedding inside the concrete), as well as the properties of the concrete itself. In the following calculations, the effective length was defined as 14 cm.

The graphical representation of the example results under load of 350 kN is presented in Figures 7 and 8 for in-groove sensors in beam PT1 and embedded sensors in beam PT2, respectively. The widths of selected cracks are directly indicated in millimeters and are depicted in the pink and blue boxes, while the reference measurements are shown in the white

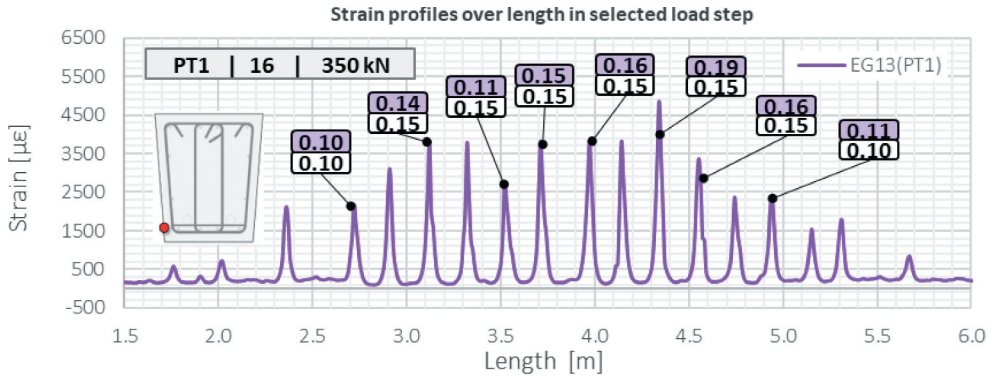


Figure 7. Crack analysis in beam PT1 based on the strain profiles measured by monolithic sensor EG13 installed in near-to-surface groove under force of 350 kN.

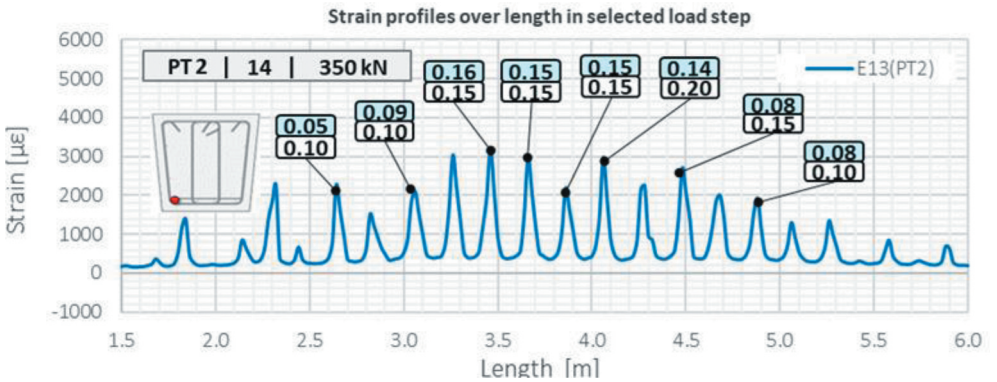


Figure 8. Crack analysis in beam PT2 based on the strain profiles measured by embedded ES13 monolithic sensor under force of 350 kN.

boxes. Reference readings were conducted on the lateral surface of the girder using a plastic plate crackmeter with an accuracy of ±0.05 mm. Due to the different measurement locations and the unpredictable course and width of the cracks, the comparison within the single crack can only be considered approximate. However, the statistical analysis of a larger number of cracks will give a more reliable indication of the range of possible errors.

The differences in the analysis of crack widths between the DFOS technique and conventional measurements are in most cases not greater than 0.05 mm. This value, in practical engineering applications, is sufficient for a proper assessment of the performance of a cracked structure. It is also worth emphasizing that ongoing efforts are being made to optimize computational algorithms, allowing for the estimation of crack widths based on fiber optic strain measurements with even greater precision.

3.3 *Identification of simulated damages*

The damages were simulated only in the initial and final areas of the 1.4 m long beams, i.e. in the areas where no cracking occurred. In these areas, significant differences between two beams can be noticed. Due to the loss of adhesion of the ED2 sensor to concrete in the areas of simulated voids, there is no characteristic, monolithic increase in deformation. On the other hand, in the location of the injection with simulated corrosion (the last 100-120 cm of the girder), the strain increment is accelerated compared to the undamaged girder. The details of the analysis are presented in the following figures. In turn, in the injection site with simulated corrosion (the last 100-120 cm of the beam), the increase in deformations is accelerated compared to the beam without damage. Details of the analysis are presented in Figure 9.

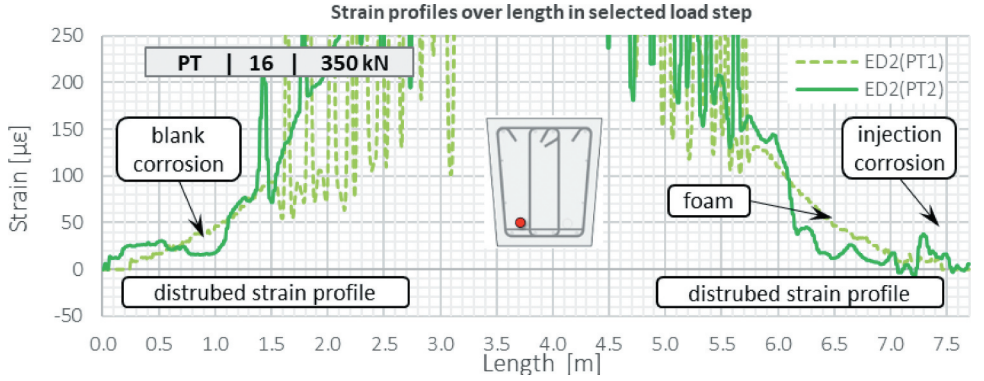


Figure 9. Comparison of strain profiles over length measured monolithic sensors ED2 inside the duct under force of 350 kN.

The analysis of local phenomena in the initial and final areas of the girder allowed for the diagnosis of damages. There is also the possibility of analyzing the global performance of the girder, involving the calculation of statistics (including average values) for selected load steps and comparing them with the results for the undamaged girder at the same forces. For each sensor pair, an increase in average strains was recorded. The smallest increases (of the order of a few percent) were observed for sensors in the compressed and tensioned zones, not located in the immediate vicinity of the simulated damage. On the other hand, the largest increments (of the order of several tens of percent) were shown by ED2 sensors inside the duct and ES2 sensors installed on the duct.

3.4 *Deflections*

Distributed fiber optic sensors can be also used to calculate displacements (deflections, shape changes) of the beams. For this purpose, 3D sensors were used, which contain four optical fibers

arranged around a rectangular core and are dedicated to displacement measurements. Additionally, the concept was employed in which, from the entire structural element equipped exclusively with optical deformation sensors, a displacement sensor is created. This schematic serves as an analogy to the internal structure of a 3DSensor. However, in this case, the composite core is replaced by the cross-section of the element, and the optical fibers are replaced by deformation sensors (EpsilonSensors). Measures from DFOS sensors were compares with reference method using linear variable displacement transducers. Exemplary results are presented in Figure 10.

The average difference between the readings of both DFOS solutions throughout the entire study did not exceed 0.7 mm, and in relation to the reference measurements, the errors were on average less than 1 mm, with measured absolute values at the level of several millimeters. The agreement is therefore considered accurate.

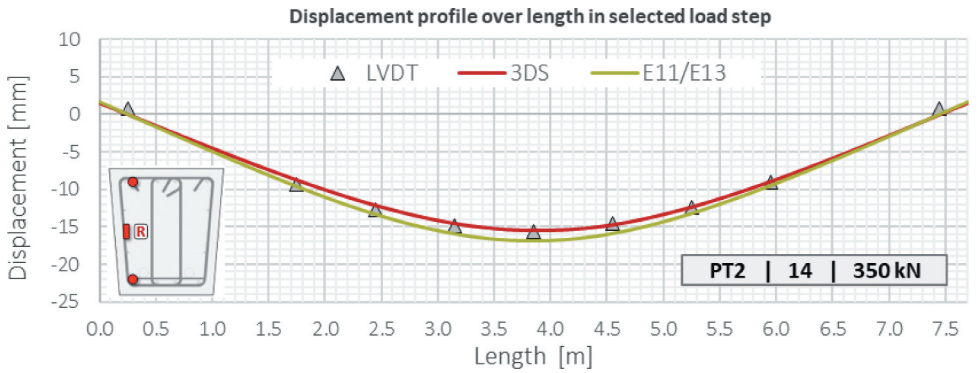


Figure 10. Comparison of displacement measured using 3D sensor (3DS), EpsilonSensors (E11 and E13) and linear variable displacement transducers (LVDTs) in beam PT2 under force of 350 kN.

4 CONCLUSIONS

Distributed fiber optic sensors can provide valuable information about the performance of the post-tensioned girders. A well-designed monitoring system using these sensors can be employed for periodic checking of strains and displacements in bridge structures, allowing inferences about their technical condition. The key conclusions from the presented research are outlined below.

- The DFOS technique provides information about the deformation changes along the entire length of the sensor (element). In the conducted studies, a spatial resolution of 10 mm was typically adopted, corresponding to one hundred measurement points per meter of the sensor.
- Apart from the global analysis of the sensor's behavior along the entire length of the examined element, the DFOS technique allows for the analysis of local phenomena, such as cracking and damage detection.
- Data from DFOS measurements can be utilized with suitable computational algorithms to accurately determine crack widths and deflections.

The research described in the paper was carried out at the Rzeszow University of Technology, Poland, as part of the R&D project: "Monitoring and diagnostic system for prestressed structures using integrated fibre optic sensors (DFOS)". It was funded by the Podkarpackie Center of Innovation, the grant no.: RPO.RB.22.004 – N3-056.

REFERENCES

Alj, I., Quiertant, M., Khadour, A., Grando, Q., & Benzarti, K. 2021. Environmental durability of an optical fiber cable intended for distributed strain measurements in concrete structures. *Sensors*, 22(1), 141.

Anania, L., Badalà, A., & D'Agata, G. 2018. Damage and collapse mode of existing post tensioned precast concrete bridge: The case of Petrulla viaduct. *Engineering Structures*, 162, 226–244.

Bado, M. F., Casas, J. R., & Kaklauskas, G. 2021. Distributed Sensing (DOFS) in Reinforced Concrete members for reinforcement strain monitoring, crack detection and bond-slip calculation. *Engineering Structures*, 226, 111385.

Bednarski, Ł., Sieńko, R., Howiacki, T., & Zuziak, K. 2022. The smart nervous system for cracked concrete structures: theory, design, research, and field proof of monolithic DFOS-based sensors. *Sensors*, 22(22), 8713.

Buda-Ożóg, L., Zięba, J., Sieńkowska, K., Nykiel, D., Zuziak, K., Sieńko, R., & Bednarski, Ł. 2022. Distributed fibre optic sensing: Reinforcement yielding strains and crack detection in concrete slab during column failure simulation. *Measurement*, 195, 111192.

Fischer, O., Thoma, S., & Crepaz, S. 2019. Distributed fiber optic sensing for crack detection in concrete structures. *Civil Engineering Design*, 1(3-4), 97–105.

Frangopol, D. M., Saydam, D., & Kim, S. 2012. Maintenance, management, life-cycle design and performance of structures and infrastructures: a brief review. *Structure and infrastructure engineering*, 8 (1), 1–25.

Howiacki, T., Sieńko, R., Bednarski, Ł., & Zuziak, K. 2023. Crack shape coefficient: comparison between different DFOS tools embedded for crack monitoring in concrete. *Sensors*, 23(2), 566.

Hurlebaus, S., Hueste, M. B. D., Karthik, M. M., & Terzioglu, T. 2016. *Condition assessment of bridge post-tensioning and stay cable systems using NDE methods*. Transportation Research Board of the National Academies, Texas A&M Transportation Institute: College Station, TX, USA.

Liu, T., Huang, H., & Yang, Y. 2020. Crack detection of reinforced concrete member using rayleigh-based distributed optic fiber strain sensing system. *Advances in Civil Engineering*.

Mazzatura, I., Salvatore, W., Caprili, S., Celati, S., Mori, M., & Gammino, M. 2023. Damage detection, localization, and quantification for steel cables of post-tensioned bridge decks. *Structures* Vol. 57, p. 105314.

Piątek, B., Howiacki, T., Kulpa, M., Siwowski, T., Sieńko, R., & Bednarski, Ł. 2023. Strain, crack, stress and shape diagnostics of new and existing post-tensioned structures through distributed fibre optic sensors. Measurement, 221, 113480.

Powers, R. G., Sagues, A. A., & Virmani, Y. P. (2002). Corrosion of post-tensioned tendons in Florida bridges. In *Proc., 17th US-Japan Bridge Engineering Workshop* (pp. 579–594).

Bridge Maintenance, Safety, Management, Digitalization and Sustainability – Jensen, Frangopol & Schmidt (eds)
© 2024 The Author(s), ISBN 978-1-032-77040-6
Open Access: www.taylorfrancis.com, CC BY-NC-ND 4.0 license

Modeling temperature impact on sensor data in prestressed concrete bridges

V. Coric, C. Wang, J. Gonzalez-Libreros, L. Elfgren & G. Sas
Department of Civil, Environmental and Natural Resources Engineering (SBN) Luleå University of Technology, Lulea, Sweden

ABSTRACT: Prestressed concrete bridges experience complex load scenarios throughout their lifespan which impacts their load capacity and overall performance. To ensure optimal functionality and safety it is crucial to understand the diverse responses from the structure under varying load. By deploying sensors in strategically placed locations, a numerical representation of varying responses can be attained during operation. Variation in temperature can affect the readings of a sensor. This can lead to false positive structural damage responses. Thus, it is important to differentiate between variations in structural properties induced by temperature fluctuations, and variations from structural damage. This paper presents a novel approach for mapping the temperature effect in structural responses. By employing an artificial neural network (ANN) and measurement data from a prestressed concrete bridge located in northern Sweden, a correlation between the temperature and the sensor values is achieved.

1 INTRODUCTION

Prestressed concrete bridges face different dynamic loads that affect their structural health and performance. Knowing how they react to these loads is crucial for their safety and continued use.

Structural Health Monitoring (SHM) of concrete structures involves differentiating the impact of environmental and operational conditions (EOCs) on sensor data from their impact on the structure itself. Thermal stresses caused by temperature fluctuations trough expansion and contraction in the concrete can lead to cracking and accelerated deterioration (Wałach, 2020), particularly in areas with extreme climates. Other environmental factors, such as freeze-thaw cycles and deicing chemicals, also contribute to internal stress and concrete damage. Chemical reactions from sulfate attack and alkali-aggregate reactions, induced by environmental exposure, cause further degradation (Portland Cement Association, 2002; Luo et al, 2013). A study by Shan et al, (2018) found that temperature is a major factor in changing modal frequencies. For instance, the Alamosa Canyon Bridge in USA and Z24 Bridge in Switzerland showed significant frequency variations (up to 18%) due to temperature.

Sensors, both analog and digital, can be affected by harsh conditions and may exhibit mechanical changes or calibration drift over time, leading to inaccurate data measurements (Xiang et al, 2018; Yan et al, 2022). This misrepresentation can result in false diagnostics of the structure's condition. Therefore, it is critical to consider EOCs when interpreting sensor readings, as they can obscure the true state of structural damage. A study by Keshmiry et al, (2023) emphasize the importance of accounting for variables like temperature, humidity, and wind, which can alter sensor responses and hide damage indicators, affecting the dynamic response and physical properties of the structures. Another study by Gianesini et al, (2021) highlighted the use of the electromechanical impedance (EMI) technique in SHM for real-time damage detection. However, EMI is sensitive to temperature changes, which can mimic structural

DOI: 10.1201/9781003483755-107

damage. Showcasing the impact EOCs has on sensors and highlights the importance to handle the EOC impact on sensor data while not removing its effects on the structure itself.

The growth of computational power has significantly changed the use of machine learning (ML) in engineering. With better processing abilities and large datasets, similar to what's seen in big data, engineers are better equipped to handle structural analysis on structures. Research has explored these effects using various techniques, Malekloo et al, (2022) discuss the shift from traditional damage detection to advanced, smart monitoring and decision-making with ML. This enables near real-time damage assessment, enhancing safety and reliability for structures like bridges. Methods like Principal Component Analysis (PCA) have been suggested. Zhang et al, (2013) used PCA to filter out environmental disturbances from sensor data, improving SHM system performance. Their simulations showed that combining PCA with the Hilbert-Huang transformation (HHT) greatly increased SHM accuracy against environmental factors. However, even with these advancements in ML approaches, there's no universal solution and often depends on the engineer's expertise (Zinno et al, 2022).

Operational conditions like traffic and environmental factors such as wind and ice accumulation present challenges in SHM. Traffic and wind alter the load on a structure, causing different stress responses, while ice adds weight, complicating the analysis. Sensors capture these varying responses, but accurate interpretation is key; not all recorded changes point to damage. Correctly categorizing these operational and environmental impacts is critical for reliable SHM (Keshmiry et al, 2023). Unaccounted EOCs can lead to misidentification of structural damage, resulting in inaccurate damage assessments. Properly distinguishing between actual damage and EOC effected values is essential for the safety and longevity of structures. By effectively filtering these effects, we can allocate maintenance resources more efficiently, focusing on real structural issues rather than false alarms.

Another challenge today is integrating ML into SHM systems. Effective SHM requires high-quality data, but many structures aren't built with ML principles in mind, leading to poorly placed sensors and inadequate data. Preprocessing this data for ML use is complex, particularly for those without expertise in structural engineering or ML (Flah et al, 2021). This creates a barrier to adopting advanced ML techniques for SHM, required specialized training or significant time and resource investment.

This article introduces a novel method to understand and track the impact of temperature on prestressed concrete bridges using an ANN. The method is demonstrated on data recorded from a bridge in Northern Sweden. The study finds a strong correlation between temperature and sensor values indicating the temperature variations and the bridge's structural behavior.

1.1 *EOC effects on structural sensor data*

Addressing the effects of EOCs is crucial in SHM. This not only optimizes resource utilization but also ensures the structural integrity of important public infrastructures like bridges. Accurate SHM data is vital for making informed decisions about necessary repairs, preventing minor problems from developing into major failures, thus maintaining both public safety and confidence in these structures (Gharehbaghi et al, 2022; Kaloop et al, 2018).

2 METHOD

2.1 *Regression analysis and artificial neural networks*

Building on the challenges presented by the impact of EOCs on measurement data in SHM systems is crucial to explore how modern ML techniques can revolutionize this field. These advanced methods have the potential to significantly reduce the need for domain-specific knowledge and can be tailored to fit various structures, making them highly versatile. One such method is regression analysis.

Regression analysis, a fundamental technique in ML, excels in establishing relationships between variables. In SHM, this translates to correlating sensor data with indicators of

structural health. The essence of regression lies in its mathematical foundation, where the goal is to find the best-fit line or curve that models the relationship between independent variables, such as values from sensors on the structures, and a dependent variable, which in this case is the temperature.

The process typically begins with defining a regression function. For instance, in linear regression, the simplest form, this function is a straight line described by Eq 1.

$$y = \beta_0 + \beta_1 x + \varepsilon \tag{1}$$

Here, y represents the structural health indicator, x is an EOC factor, β_0 is the y-intercept, $\beta_1 x$ is the slope of the line, and ε accounts for deviations in the data. The objective here is to determine the values of β_0 and $\beta_1$that best fit the observed data, a process known as Ordinary Least Squares (OLS).

Multiple regression is used when we deal with many variables affecting an outcome. It adjusts to include each variable and measures its specific impact. This makes regression models versatile for analyzing different structures and EOCs, providing a custom solution for monitoring structural health.

Regression analysis is also valuable for its predictive abilities. It helps predict how EOC changes could affect structural integrity, guiding the planning of maintenance and repairs. It can separate the influence of different variables using techniques like multivariate analysis. This ensures that the effect of each EOC is clearly understood, which is essential for accurate health assessments of structures.

The clear results from regression analysis support informed decision-making for maintenance and repairs, giving precise information about the impact of each EOC. This allows for focused interventions and efficient resource allocation to the most critical structural issues.

ANNs add another layer to SHM. Unlike simpler models, ANNs can learn complex, non-linear relationships within data. They improve as they process more information, becoming better at predicting structures' responses to various conditions. With enough data, ANNs can uncover subtle patterns, greatly enhancing SHM's precision and dependability.

2.2 *Model overview*

The model used in this study is novel sequential neural network. It is a type of ANN where each layer is arranged in a sequence, with each layer feeding its output directly to the next layer. This ANN is designed for regression learning to predict the temperature of prestressed concrete bridges, utilizing the principles from the previous section. The ANN utilizes input from 15 distinct sensor parameters. This array of sensors captures comprehensive structural data, enabling precise temperature prediction crucial for assessing the bridge's structural health. A simple overview of the model can be seen in Figure 1.

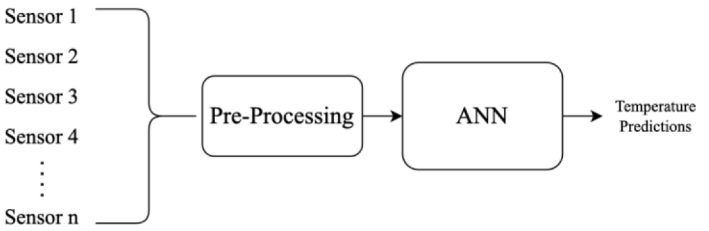


Figure 1. Model overview.

2.3 *Data acquisition and preparation*

Data was collected from a network of sensors installed on a prestressed concrete bridge. The sensor suite included LVDTs, FTGs, and Noptel sensors. LVDTs were utilized to quantify the bridge's deflections, capturing the displacements indicative of the bridge's load-bearing performance. FTGs

measured the strain, relating to the internal stresses under varying loads. Noptel laser sensors provided deformation data.

Upon such an event, the sensors' data is automatically transmitted to a Secure File Transfer Protocol (SFTP) server, from where it is readily accessible via the internet. To facilitate the handling of this data, specialized software was developed to parse and organize the data into an array format. This format is particularly beneficial for feeding into ML algorithms as input data. The data used in this study was gathered over a span of 1 month.

Prior to training the ANN, a preprocessing step involved conducting a covariance analysis on the collected sensor data. This analysis aimed to understand the degree of linear relationship between each sensor parameter and the bridge's temperature. Covariance values were calculated between the temperature and each of the 15 sensor parameters. These values provided insight into how strongly each parameter influenced the temperature, with values closer to ±1 indicating a stronger linear relationship.

The ANN was structured with multiple layers, each designed to process the input data sequentially for precise temperature prediction. A distinctive feature of this ANN is its weight initialization strategy. Instead of random weight assignments typically used in ANNs, this model utilized the covariance analysis results. Initial weights were adjusted to correlate with the covariance values associated with each sensor parameter. Parameters with higher covariance values were assigned greater initial weights, denoting their substantial impact on the ANN's output. This method of weight initialization aimed to enhance the learning efficiency and accuracy of the model from the outset.

2.4 *Training process*

The ANN underwent a supervised learning process using the preprocessed dataset. The training phase involved adjusting the network's weights to minimize the error between the predicted temperatures and the actual measurements. Performance metrics such as mean squared error (MSE) and R-squared were utilized to evaluate the accuracy and effectiveness of the model. A complete process pipeline of the ANN is shown in Figure 2.

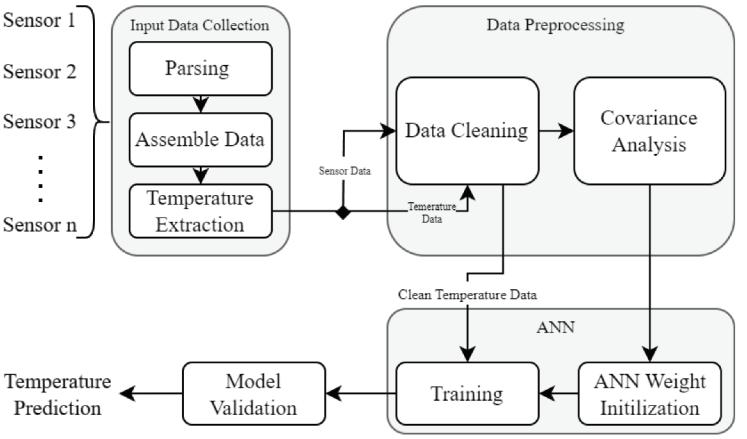


Figure 2. Process overview of the model.

2.5 *Case study – data from autio bridge*

The Autio Bridge, see Figure 3, is a prestressed concrete structure over the Torne River located in Northern Sweden, and was constructed in 1963. It spans a total length of 134.8 meters, with three segments of 36.4, 62.0, and 36.4 meters. Its width measures 7.48 meters. The bridge's beams and deck were made from concrete K450 (C45) and reinforced with Ks40 (400 MPa) and Ks60 (600 MPa) steel. Prestressing strands used were 6 mm BBR with stress ranges 1500/1700 MPa. Specifically, the prestressing reinforcement in the bridge includes curved tendons in steel ducts.

Between 2012-2014 and resuming in 2019, mining-related transport resulted in the bridge bearing loads from trucks totaling 90 tons. Cracks in the beams were observed during time, however it is not clear when they first emerged. The monitoring of crack progression was conducted manually until 2020, when it was supplemented with automated instrumentation using strain gauges and LVDTs. These cracks typically range in width from 0.1 to 0.3 mm and extend longitudinally over time. In November 2020, notable increases in strain gauge readings on the concrete prompted the closure of the bridge to all traffic for safety reasons. To further evaluate the structural integrity, additional strain gauges were installed to the vertical reinforcement bars, leading to a comprehensive assessment of the bridge's fatigue strength (Agredo Chavez et al, 2022).



Figure 3. Prestressed concrete bridge over Torne River at Autio built in 1963.

3 RESULTS AND DISCUSSION

3.1 *Predictive performance*

The sensor suite operates under the trigger of specific load conditions on the bridge, capturing data within a limited timeframe spanning from October to November. Despite the restricted period and conditional data collection, the ANN regression model achieved an R-squared score of 99.8%, suggesting nearly perfect predictiveness in mapping sensor data to external temperature.

3.2 *Analysis of model predictions*

Figure 4 shows a comparison between the actual and predicted temperatures, delineating a congruence as evidenced by the superimposed trend lines. The graph showcases a random sample of the model outputs, further validating the predictive accuracy across the data set.

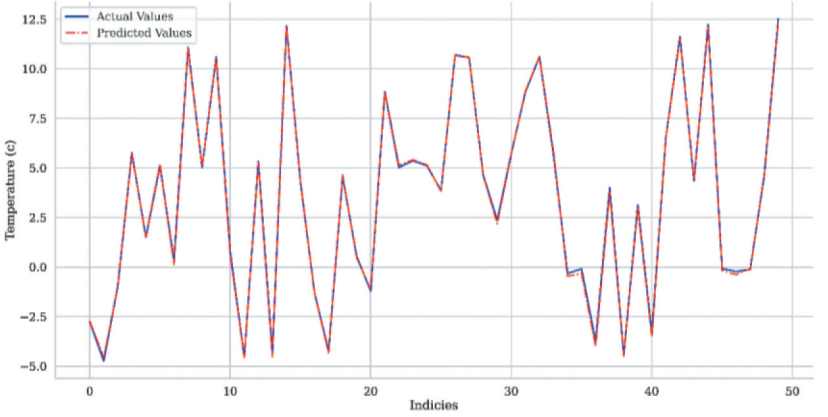


Figure 4. Random sampling of actual vs predictive values.

In Figure 5 the Locally Weighted Scatterplot Smoothing (LOWESS) technique is applied to sensor data associated with temperature fluctuations. This presentation includes a non-parametric smoothed curve and a confidence interval to assess prediction uncertainty. An examination of the residuals and the LOWESS fit reveals a clustering effect near the zero line, indicating minimal and randomly distributed model errors. Furthermore, the absence of any

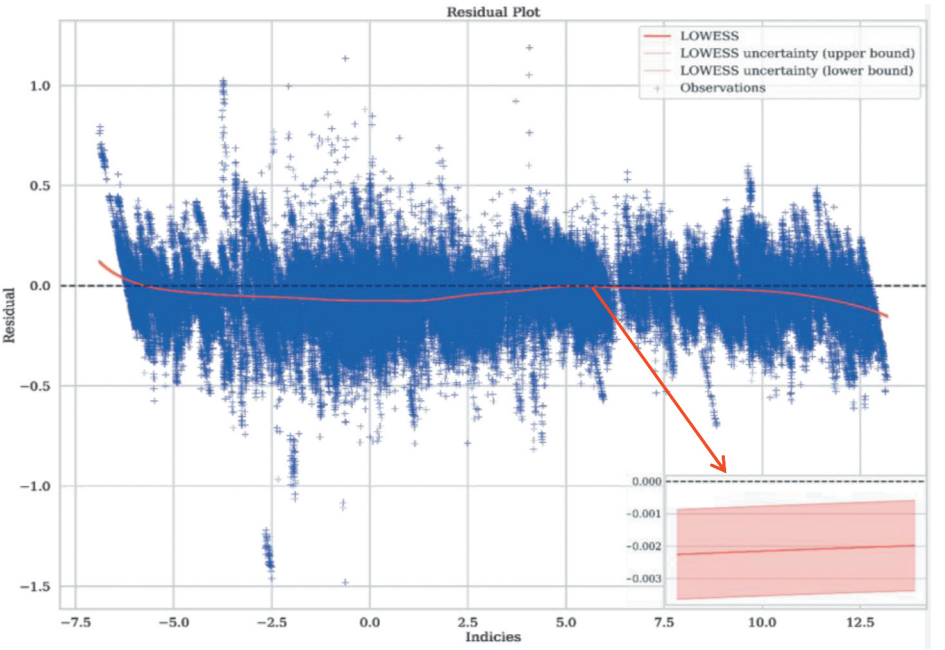


Figure 5. Residual plot with LOWESS representation.

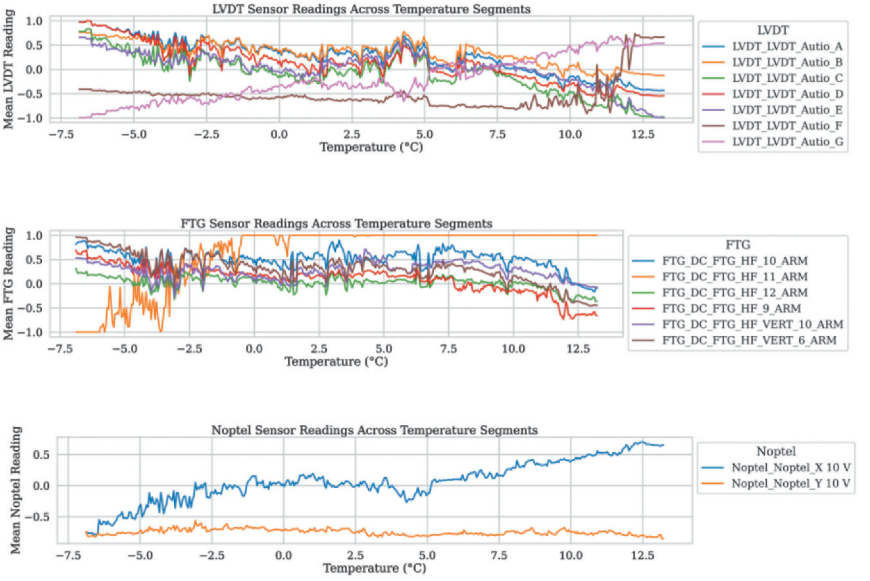


Figure 6. Dynamic sensor response to temperature fluctuations.

discernible systematic pattern in the residuals, which scatter randomly above and below the zero line, confirms the successful capture of the primary trend by the LOWESS method. The inset in the bottom-right corner zooms in on a portion of the residual plot, clearly illustrating the constrained fluctuation range of the residuals and emphasizing the model's precision.

Figure 6 illustrates the responsiveness of the Autio Bridge's monitoring system to ambient temperature variations, as captured by the normalized readings of the installed sensors. The graphical representation synthesizes the behavior of the bridge's instrumentation, including LVDTs, FTGs, and Noptel sensors, under the influence of external temperature changes. By segmenting the temperature data and applying a moving average smoothing algorithm, we have attenuated transient noise, enabling the delineation of more pronounced trends that are indicative of the bridge's thermally induced strain responses.

4 CONCLUSION

In conclusion, this study has demonstrated the use of an artificial neural network (ANN) for analyzing the effects of temperature on a prestressed concrete bridge. The ANN model, supported by comprehensive field data, effectively differentiates temperature-induced structural behaviors from those caused by other factors. This distinction is important for precise structural health monitoring and life-span enhancement of bridges.

The importance of ongoing monitoring is emphasized, highlighting continuous data collection as essential for the analysis and prediction of bridge performance under various environmental conditions. The integration of machine learning and empirical data has shown potential, leading to more efficient and proactive maintenance strategies.

Future research is directed towards expanding the study to different bridge structures and environmental conditions to confirm the model's utility. Enhancements to the ANN model to include additional environmental factors could improve its predictive accuracy. Additionally, the adoption of real-time data processing in bridge management systems is recommended for prompt and informed decision-making.

Lastly, the potential of self-learning algorithms for increasing the durability and adaptability of the model over time is suggested as an important area for further study. These developments are expected to refine model precision and aid in the development of smart infrastructure with enhanced longevity.

ACKNOWLEDGEMENTS

The research presented in this paper was significantly guided by the goals of the SCABEAC (Sustainable Construction and Build Environment in Arctic Climate) project, a component of the Interreg Aurora program. The focus of SCABEAC on sustainable building practices and the longevity of structures in the challenging Nordic climate provided a compelling motivation for our exploration in this field. Their commitment has played a vital role in broadening our understanding of essential new technologies and methods relevant to construction in Arctic conditions. This inspiration has been a key factor in shaping the direction and depth of this study.

REFERENCES

Agredo Chavez, A. M., Gonzalez, J., Andersson, K., Leidzen, J., Andersson, E., Petersson, M., Sas, G., Elfgren, L. & Häggström, J. (2022) Cracking and Fatigue of Heavy Loaded Prestressed Concrete Bridge in Sweden, *IABSE Symposium Prague 2022: Challenges for Existing and Oncoming Structures, Prague, Czech Republic*, May 25-27, *2022*. International Association for Bridge and Structural Engineering.

Portland Cement Association, USA. (2002) Types and Causes of Concrete Deteriation.

Flah, M., Nunez, I., Ben Chaabene, W. & Nehdi, M. L. (2021) Machine Learning Algorithms in Civil Structural Health Monitoring: A Systematic Review. *Archives of Computational Methods in Engineering*, 28(4), 2621–2643.

Gharehbaghi, V. R., Noroozinejad Farsangi, E., Noori, M., Yang, T. Y., Li, S., Nguyen, A., Málaga-Chuquitaype, C., Gardoni, P. & Mirjalili, S. (2022) A Critical Review on Structural Health Monitoring: Definitions, Methods, and Perspectives. *Archives of Computational Methods in Engineering*, 29(4), 2209–2235.

Gianesini, B. M., Cortez, N. E., Antunes, R. A. & Vieira Filho, J. (2021) Method for removing temperature effect in impedance-based structural health monitoring systems using polynomial regression. *Structural Health Monitoring*, 20(1), 202–218.

Kaloop, M. R., Hu, J. W., Elbeltagi, E. & El Refai, A. (2018) Structural Health Monitoring and Assessment: Sensors and Analysis. *Journal of Sensors*, 2018, 9834958.

Keshmiry, A., Hassani, S., Mousavi, M. & Dackermann, U. (2023) Effects of Environmental and Operational Conditions on Structural Health Monitoring and Non-Destructive Testing: A Systematic Review. *Buildings*, 13(4), 918.

Luo, D., Wang, Y. & Niu, D. (2013) Durability environmental regionalization for concrete structures. *Mathematical Problems in Engineering*, 2013.

Malekloo, A., Ozer, E., AlHamaydeh, M. & Girolami, M. (2022) Machine learning and structural health monitoring overview with emerging technology and high-dimensional data source highlights. *Structural Health Monitoring*, 21(4), 1906–1955.

Shan, W., Wang, X. & Jiao, Y. (2018) Modeling of temperature effect on modal frequency of concrete beam based on field monitoring data. *Shock and Vibration*, 2018, 1–13.

Wałach, D. (2020) Analysis of factors affecting the environmental impact of concrete structures. *Sustainability*, 13(1), 204.

Xiang, J., Yang, Z. & Aguilar, J. (2018) Structural health monitoring for mechanical structures using multi-sensor data. *International Journal of Distributed Sensor Networks*, 14, 155014771880201.

Yan, M., Tan, X., Mahjoubi, S. & Bao, Y. (2022) Strain transfer effect on measurements with distributed fiber optic sensors. *Automation in Construction*, 139, 104262.

Zhang, H., Guo, J., Xie, X., Bie, R. & Sun, Y. (2013) Environmental effect removal based structural health monitoring in the internet of things, *2013 Seventh International Conference on Innovative Mobile and Internet Services in Ubiquitous Computing*. IEEE.

Zinno, R., Haghshenas, S. S., Guido, G. & VItale, A. (2022) Artificial Intelligence and Structural Health Monitoring of Bridges: A Review of the State-of-the-Art. *IEEE Access*, 10, 88058–88078.

Bridge Maintenance, Safety, Management, Digitalization and Sustainability – Jensen, Frangopol & Schmidt (eds)
© 2024 The Author(s), ISBN 978-1-032-77040-6
Open Access: www.taylorfrancis.com, CC BY-NC-ND 4.0 license

Field testing of the longest Polish footbridge made of FRP composites using distributed fibre optic sensor system

Maciej Kulpa & Tomasz Siwowski
Rzeszow University of Technology, Rzeszow, Poland

ABSTRACT: Excellent mechanical properties and high durability of fibre reinforced polymer (FRP) composites cause the increasing popularity of using these materials for the construction of pedestrian and bicycle bridges. The spans of bicycle footbridge at the Carpathian Bridge in Rzeszów (Poland) were constructed in the form of sandwich panels. Since FRP composite is a relatively new construction material and the footbridge is of significant size, the structural health monitoring (SHM) system based on distributed fibre optic sensors (DFOS) was designed and implemented for condition assessment. The optical fibres were placed inside the sandwich structure between the fabrics of the selected laminates, before the infusion process. It enables the high durability and reliability of the monitoring system because the sensors are not exposed to damage or the influence of the environment. Before the footbridge was open to public use, the static and dynamic proof load tests were performed. DFOS operation as well as design assumptions and the static and dynamic behavior of the lightweight structure had been checked.

1 INTRODUCTION

Since 2016, when the first bridge in Poland made of FRP composites was built (Siwowski et al. 2017), the popularity of composite bridge structures in Poland has been systematically increasing. The main reason for this is the excellent mechanical properties and high durability of FRP composites. FRP composite structures are most often used in the construction of new pedestrian and bicycle footbridges and in the redecking as well as the widening of existing bridges (e.g. Chróścielewski et al. 2017, Sonnenschein et al. 2016, Kossakowski and Wciślik 2022). In each of these cases the following advantages of FRP composite structures are also important: low weight (lightness) and full prefabrication, as well as the ease and quick assembly on site. Among the several available technologies for manufacturing FRP composite structures, sandwich panels manufactured using the vacuum assisted resin transfer molding (VARTM) method are currently dominant.

The implementation of the FRP bicycle footbridge at the Carpathian Bridge in Rzeszów described in the paper combines the two above-mentioned areas of application: it is a new, individually designed FRP composite structure, placed on the supports of the adjacent bridge and thus widening it. This method of widening bridges is one of the most effective and frequently used worldwide (Radomski & Kasprzak 2017). In such a case, a lightweight and durable FRP composite structure is the optimal technical and economic choice. In addition, the use of built-in and persistent DFOS monitoring further increases the value of such a solution.

2 FRP FOOTBRIDGE STRUCTURE

2.1 *Assumptions for design*

The construction of new bicycle footbridges near existing road bridges has been a long demand of Rzeszów cyclists. There are many bicycle paths in Rzeszów, but the problem is

DOI: 10.1201/9781003483755-108

their lack of continuity over Wisłok river, which prevents smooth and collision-free communication. The three existing bridges in Rzeszów city centre (the Lviv Bridge, the Narutowicz Bridge and the Carpathian Bridge) do not have bicycle paths. Therefore, the municipality authorities decided to build bicycle footbridges next to the mentioned bridges (i.e. to widen them), because it is not possible to isolate bicycle paths on any of these bridges.

The Carpathian Bridge, located along national road No. 94, is the most heavily trafficked bridge in Rzeszów, both by cars and pedestrians. Therefore it was chosen to be widened to include a two-way bicycle path. A FRP composite structure placed on steel cantilevers attached to the existing supports of the bridge turned out to be the optimal solution. Due to the fact that the new footbridge was to be supported on the piers of the existing bridge (from 1973), the designers decided to use a construction solution with minimum dead weight. Of the two design options considered: aluminum and FRP composite, the latter was chosen. The span length of the new bicycle footbridge was determined by the existing piers. This FRP sandwich structure consists of five simply-supported spans of 4.17 + 23.55 + 23.67 + 23.67 + 23.47 m. The total length of the superstructure is 104.95 m, and thus it is believed to be the longest Polish footbridge made of FRP composites. The service width for bicycle path is 2.50 m (Figure 1). Since FRP composite is a relatively new construction material and the footbridge is of significant size, the SHM system based on DFOS was designed and implemented for condition monitoring.

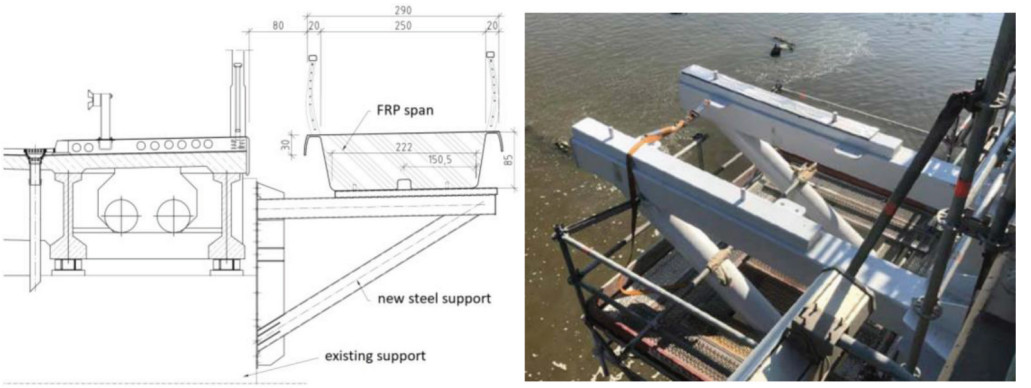


Figure 1. The cross-section of existing bridge and new footbridge (on left) and steel cantilevers mounted on existing piers.

2.2 *Design of the FRP structure*

The initial design of the footbridge assumed a span structure made of two U-shaped composite thin-walled girders, connected with a composite deck slab with a sandwich structure using adhesive joints. Such kind of structure was implemented on one of the first Polish all-composite road bridges (Siwowski et al. 2018). However, on the initiative of the contractor, an alternative design was considered, based on the Dutch InfraCore® Inside FRP composite panel technology (Veltkamp 2019).

The sandwich panel structure of FRP composite spans was proposed by the manufacturer, the Dutch company FiberCore Europe B.V., the creator and main European manufacturer of composite panels using the InfraCore® Inside technology. The panel consists of upper and lower laminates and vertical ribs stiffening the panel core. The laminates and ribs are made of E-glass fibre fabrics and polyester resin. The foam core made of PUR foam with a density of 38 kg/m^3 only serves to fill the panel and is not included in the calculations (Figure 2).

A numerical model built in the SOFiSTiK environment was used to design the FRP composite structure (Figure 3). The laminates and ribs were modeled with 4-node Timoshenko-Reissner shell finite elements with bilinear shape functions with enrichment of the deformation

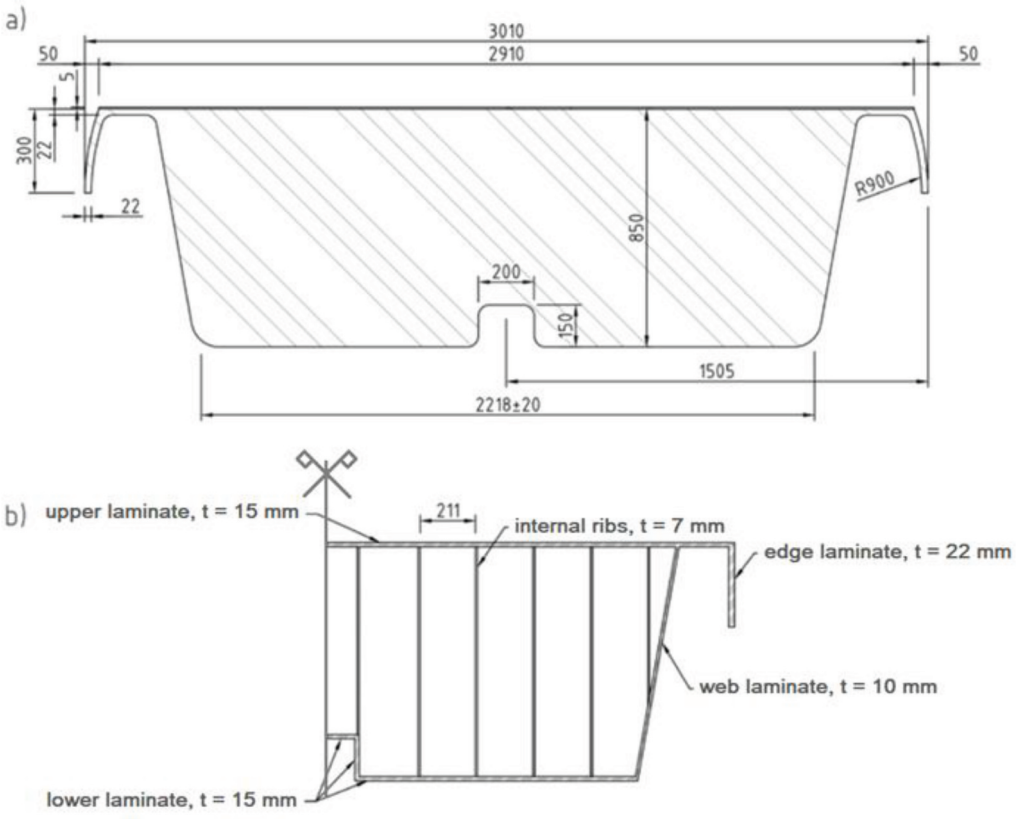


Figure 2. FRP composite span: a) cross-section with general dimensions; b) detailed dimensions of the span components.

state eliminating the locking effect and taking into account the shear effect. The shell elements were assigned a designed thickness and a sequence of arrangement of individual layers in laminates. The properties of the finite elements were assumed based on the results of material tests and the designed lamina sequences in each element. The target global material parameters for individual finite elements were determined as resultants, in accordance with the classical lamination theory. The effect of the core foam as filler material was conservatively omitted from the model. The footbridge load models were adopted in accordance with Eurocode 1 and the limit states of particular FRP components were checked in accordance with the pre-standard EuCIA (2019) .

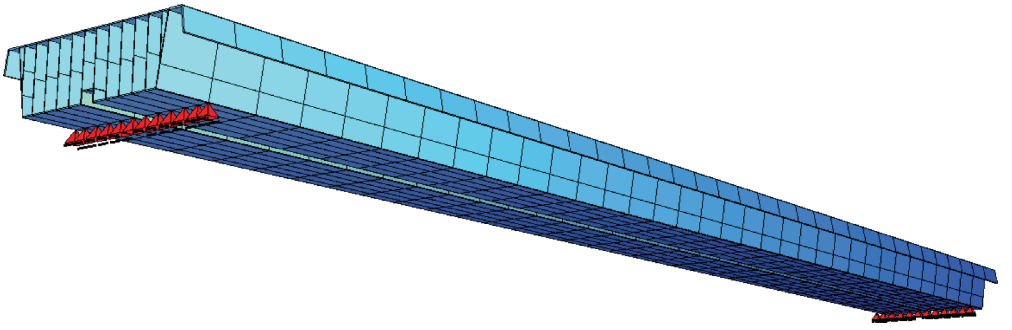


Figure 3. Numerical model of a composite footbridge.

2.3 *Manufacturing technology*

The footbridge spans were manufactured using the VARTM method in the workshop of FiberCore Europe B.V. in Rotterdam, Netherlands. Each of them was created in a special mold in which glass fabrics were arranged in the sequences necessary to obtain the designed thicknesses and strength of the laminates. Core foam elements with a height of 820 mm were placed between the fabrics, the main task of which was to form volume of panels and creating vertical laminates of the internal ribs. After placing all the materials in the mold, it was sealed and then the infusion process began, which involved saturating the content with liquid polyester resin using a vacuum. After filling the mold with resin, its supply was closed and the process of hardening (cross-linking) of the resin began. After complete hardening, the span was pulled out of the mold to a station for finishing and protecting the outer surface of the laminates. A chemically hardened surface was also made at this stage.

After manufacturing, all five spans of the footbridge were transported in two transport sets from the factory in Rotterdam (the Netherlands) to Rzeszów (Poland). Due to the relatively low weight of the spans (the weight of a single span over 24 m is approximately 10 tons), it was possible to transport two spans simultaneously on one truck. The spans were installed on site directly from the truck trailer on previously mounted steel cantilevers, which created direct supports for the spans (Figure 4a). The spans on the supports were stabilized using φ 36 mm steel pins, which were placed in special sockets created in the lower laminates of the spans. Some of the sockets were made "to measure", blocking the structure's ability to move, while others were made with appropriate "clearances", ensuring the free elongation of the spans under the service load and due to temperature. The assembly of a single span of the footbridge took approximately 30 minutes (Figure 4b).



Figure 4. Installation of the footbridge spans (from left): transport of the span; assembly of the span using cranes; all footbridge spans on supports.

2.4 *Monitoring system*

Due to the pioneering nature and size of the FRP composite structure, monitoring of the footbridge's behavior in service was planned. A SHM system based on DFOS fibre optic sensors was chosen. However, it was decided to use in practice the newly designed monitoring system for FRP composite structures using fibre optic sensors integrated with the composite laminates (Kulpa et al. 2020).

Unlike classic measurement sensors, which are mounted on a ready-made structure, in the integrated DFOS system the optical fibres were placed inside the composite between the laminate fabrics, before the infusion process. Therefore, they are not exposed to damage or destruction as a result of environmental influences or acts of vandalism, and the entire measurement system is characterized by high durability. To limit interference in the structure of laminates, fibre optic sensors were used without cover (Figure 5). As a result, the diameter of the sensors was reduced from a few millimeters to 250 μm, limiting the risk of entering structural notches that weaken the laminates. Connection terminals were welded to the measurement fibres and reinforced with yellow covers, which made it possible to lead them out of the structure. During sensors installation, their continuity were checked using laser testers. After infusion of the composite structure, the sensor tips were temporarily protected for transport, and after the span assembling at the construction site, they were placed in a box attached to the structure.

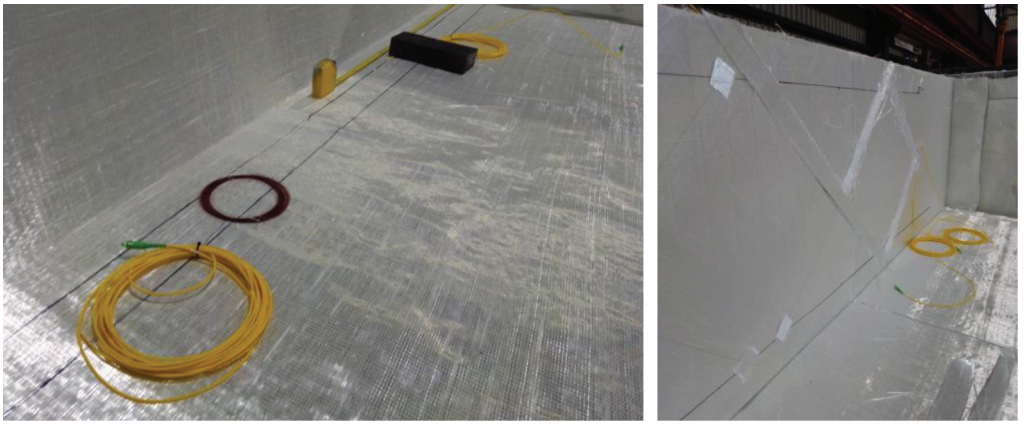


Figure 5. Installation of optical fibres between fabrics of the lower laminate (left) and in vertical ribs (right).

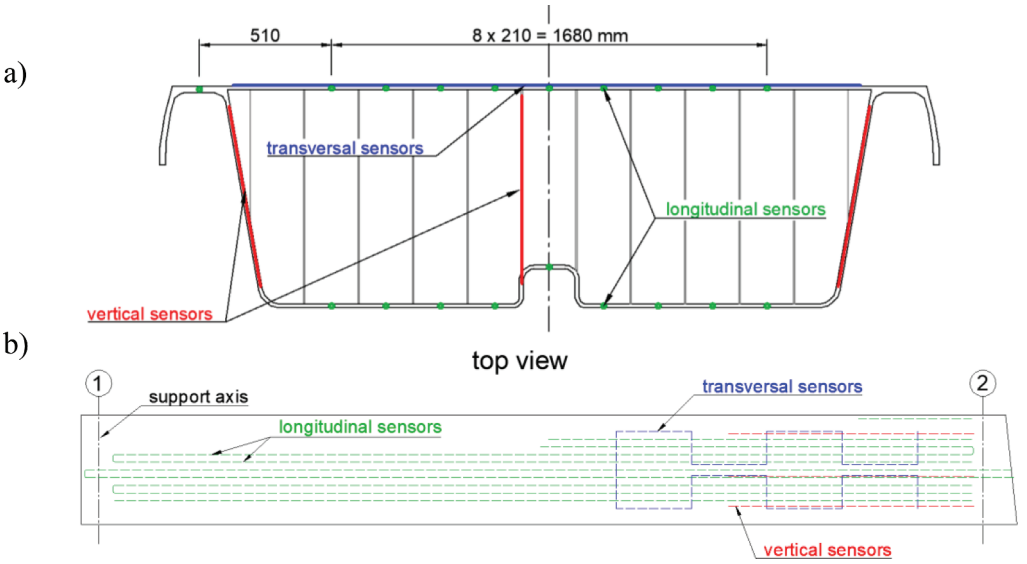


Figure 6. Fibre optic sensor system: a) cross-section; b) top view.

The FRP composite spans of the footbridge were equipped with measurement sensors in the form of single-mode fibres of the SM9/125 type with an acrylic coating. The fibre system was divided according to the orientation of the sensor into longitudinal fibres, transverse fibres and vertical fibres. The first two groups were placed in the plane of the upper and lower face laminates. The vertical fibres were placed in the three ribs and were oriented in the direction of the principal stresses (±45°). The DFOS system is shown in Figure 6. In total, over 200 meters of fibre optic sensors were placed in the structure of a single span. The DFOS system can measure strains of the structure at 5 mm intervals and is equivalent to a measurement system containing over 40,000 single spot sensors. Moreover, thanks to the division of fibre optic sensors, the measurement can be limited to a smaller number of points (e.g. only in critical sections/points) or a local part of the structure (e.g. support zone). This enables flexible measurement depending on demands and reduction of collected data in very complex high-frequency sensor systems.

3 FIELD TESTING

3.1 *Static test*

Concrete slabs with dimensions of 300 × 150 × 15 cm weighing 1,656 kg (corresponding to 16.25 kN) were used to load the structure statically during field test. The test was carried out at night, and the slabs were placed using two cranes from the adjacent, existing road bridge (Figure 7). The slabs were placed in two layers, and there were a maximum of 16 slabs per span. Due to the fact that two footbridge spans are supported on one steel cantilever support, a scheme was also planned in which 32 slabs were placed on two adjacent spans. Static load during field load test was 85% of the characteristic load for which the footbridge was designed (5 kN/m^2).

The tests began with control measurement of unloaded structure and followed by placing the subsequent slabs starting from one of the supports. After placing the first layer of slabs, the measurements were compared with the design values and after a positive result, the second layer was laid. The load on the span was placed for 30 minutes and then removed in the reverse order of installation.



Figure 7. Static load placed on the footbridge: in one layer (left) and in two layers (right).

Figure 8 shows an example of the distribution of axial strains in the upper laminate caused by subsequent loading slabs.

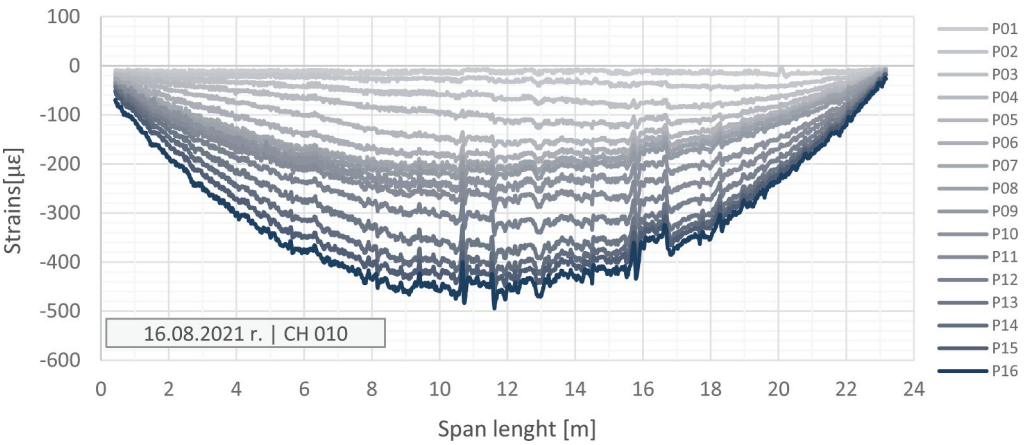


Figure 8. Distribution of axis strain along the length of the upper laminate after placing individual load slab (P1-P16).

Due to the use of distributed sensors running along the entire length of the single span, it was possible to determine not only the strains (measured directly), but also to calculate the vertical displacements of the span (measured in-directly). For this purpose, the laws of mechanics and strength of materials (f.e. the Euler-Bernoulli hypothesis) were used. This calculation procedure was developed and tested in laboratory conditions by Kulpa et al. (2020).

To check and verify the DFOS monitoring system, during the field test, measurements of spans' and piers' displacements were also measured using reference, high-precision geodetic techniques with an accuracy of 0.1 mm. The comparison of vertical displacements under the maximum load along the length of the span determined by the DFOS system and reference, as well as design values is shown in Figure 9.

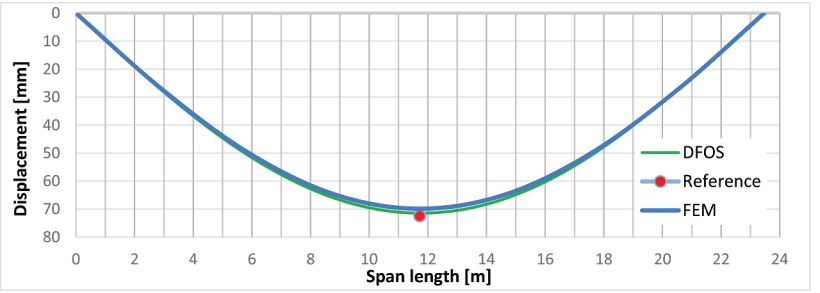


Figure 9. Distribution of vertical displacements along the length of the span measured by DFOS system, reference method and design value.

The elastic deflections in three of the four spans accounted for from 93 to 98% of the design (calculated) values. Only in one span the elastic deflections were greater, reaching 103% and 105% of the design values. This slight exceedance of the design values in one of the spans can be considered acceptable, most likely resulting from the specificity of the composite structure, which was made manually and therefore is characterized by a slight variability of strength and elastic parameters and dimensions inconstancy in individual spans.

3.2 *Dynamic test*

Dynamic identification test included a series of dynamic excitations of the footbridge in order to record its dynamic response. For synchronous excitations, it was necessary to use a tactometer synchronized with the forced natural frequency of the structure. The excitations included, among others: natural passing, synchronized passing, running and jumping of a group of people (1, 2, 3, 4, 12 and 30). A group of 12 and 30 people corresponds to a load density of 0.2 and 0.5 person/m^2 of the deck area, respectively. The latter is treated as a "intense (dense) pedestrian traffic". This type of load may occur occasionally, e.g. during mass events. In total, 29 individual loading patterns were performed (Figure 10).

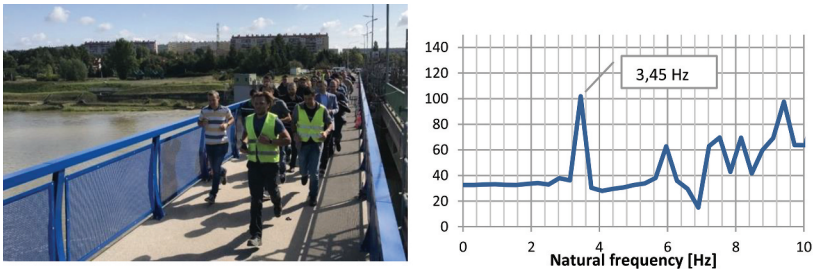


Figure 10. The dynamic tests (left) and an example of the natural frequency spectrum distribution obtained from the DFOS system (right).

During the dynamic test, the DFOS system measured strains in selected sensors with a frequency of up to 250 Hz. From the obtained function of strain over time, fragments when the structure vibrated freely were isolated. Based on this data, the Fast Fourier Transform was performed, and the obtained spectrum identified natural frequencies (Figure 10).

To verify the dynamic measurements performed using DFOS monitoring system, the typical acceleration gauges PCB393A03 were mounted in ½ and ¼ of span length to compare both measurement methods. The first natural frequency measured using the DFOS system (3,45 Hz) and the reference acceleration sensors (3,56 Hz) were very similar to each other, and the slight difference is due to the fact that these values were determined with different types of excitation. Moreover, the measured first natural frequency was very close to the calculated value (3,47 Hz) which proves that the numerical model correctly simulates the behaviour of the FRP composite structure.

4 CONCLUSION

Field test results confirmed the proper behavior of the footbridge under static and dynamic loads. The FRP footbridge structure behaved elastically - permanent deflections of spans did not exceed 6% of the total deflections. The compliance of the measured and calculated displacements for the spans was in the range of 93-98%, which proves the correctness of the numerical model. The slight (3- 5%) exceedances of elastic deflections in one of the tested spans can be considered acceptable, resulting from the specificity of the composite structure.

The installed DFOS monitoring system showed high compliance with conventional measurements carried out during the load test. This confirms correct operation and the possibility of measuring longitudinal strains and based on them accurate calculation of vertical displacements. Thanks to the sensors being placed inside the structure itself, the system is very durable and is planned to operate it for the future.

REFERENCES

Chróścielewski, J., Miśkiewicz, M., Pyrzowski, Ł., Sobczyk, B., & Wilde, K. 2017. A novel sandwich footbridge-Practical application of laminated composites in bridge design and in situ measurements of static response. *Composites Part B: Engineering* 126: 153–161.

De Corte, W., Jansseune, A., Van Paepegem, W., & Peeters, J. 2017. Structural behaviour and robustness assessment of an InfraCore inside bridge deck specimen subjected to static and dynamic local loading. *In Proceedings of the 21st International Conference on Composite Materials*, Xi'an (pp. 1–8).

EuCIA - Prospect for New Guidance in the Design of FRP Structures (Eurocodes). European Composites Industry Association (EuCIA), Brussels, 2019

Veltkamp, M. 2019. Eurocode and the Design, Manufacture and Installation of 62 Clear Span FRP Bridges to the City of Rotterdam (NL). *In*: *9th Australian Small Bridges Conference*, Surfers Paradise, Queensland, Australia

Kossakowski, P. G., & Wciślik, W. (2022). Fiber-reinforced polymer composites in the construction of bridges: Opportunities, problems and challenges. Fibers, 10(4), 37.

Kulpa, M., Howiacki, T., Wiater, A., Siwowski, T., & Sieńko, R. 2021. Strain and displacement measurement based on distributed fibre optic sensing (DFOS) system integrated with FRP composite sandwich panel. *Measurement* 175: 109099.

Radomski, W. A., & Kasprzak, A. 2017. Poszerzanie mostów. Wydawnictwo Naukowe PWN (in Polish)

Siwowski, T., Kaleta, D., & Rajchel, M. 2018. Structural behaviour of an all-composite road bridge. *Composite Structures* 192: 555–567.

Siwowski, T., Rajchel, M., Kaleta, D., & Własak, L. 2017. The first Polish road bridge made of FRP composites. *Structural Engineering International* 27(2): 308–314.

Sonnenschein, R., Gajdosova, K., & Holly, I. (2016). FRP Composites and their Using in the Construction of Bridges. Procedia engineering, 161, 477–482.

Bridge Maintenance, Safety, Management, Digitalization and Sustainability – Jensen, Frangopol & Schmidt (eds)
© 2024 The Author(s), ISBN 978-1-032-77040-6
Open Access: www.taylorfrancis.com, CC BY-NC-ND 4.0 license

Online noise parameters estimation for sigma-point Kalman filter using sequential importance resampling

Weixiang Liu
Master Student, School of Civil and Environmental Engineering, Harbin Institute of Technology, Shenzhen, China

Feng-Liang Zhang*
Professor, School of Civil and Environmental Engineering, Harbin Institute of Technology, Shenzhen, China

ABSTRACT: The sigma-point Kalman filter (SPKF) is a widely-used method for system state and structural parameters estimation. It assumes that the state prediction errors are minimized when the structural parameters correspond to the noise covariance matrices. However, in practice, the covariance matrices for process noise and measurement noise are usually unknown. Arbitrary selection of these covariance matrices may lead to unreliable state predictions and potentially diverging estimation results. To address this problem, we propose a method by integrating the sequential importance resampling algorithm into the traditional SPKF for the estimation of the noise covariance matrices based on the acceleration response measurement. The effectiveness of the proposed Sequential Importance Resampling Sigma-point Kalman Filter (SIR-SPKF) is demonstrated through a numerical application to a bridge structure and a laboratory experiment involving a 3 degrees of freedom model.

Keywords: noise covariance matrices, system identification, sigma-point Kalman filter, sequential importance resampling

1 GENERAL INSTRUCTIONS

In recent decades, online structural health monitoring (SHM) has gained widespread attention and been extensively investigated [1-3]. The sigma-point Kalman filter is one of the promising methods for structural identification using dynamic response measurement. It has demonstrated significant potential in excitation smoothing [4], identification of structural parameters [5], and damage identification [6].

The sigma-point Kalman filter (SPKF) is a method that implements the Kalman filter procedure using a number of sigma points in a sampling manner [7]. Similar to Kalman filter, the determination of the covariance matrices of the process noise and measurement noise remains a critical issue for achieving optimal and stable results [8].

To address these issues, the sequential importance resampling algorithm is integrated with SPKF to simultaneously estimate the covariance matrices of the process noise and measurement noise. In this algorithm, the two covariance matrices are parameterized with the noise parameters. The optimal noise parameters are estimated by calculating the expected value of the candidate noise particles based on their weights, which are related to the most recent measurement at each time step. The effectiveness of the proposed method is demonstrated through a numerical application on a bridge structure and a laboratory experiment involving a 3-degree-of-freedom model.

*Corresponding author: zhangfengliang@hit.edu.cn

DOI: 10.1201/9781003483755-109

2 SEQUENTIAL IMPORTANCE RESAMPLING SIGMA-POINT KALMAN FILTER

Consider the equation of motion of a structural system:

$$\boldsymbol{M}\ddot{\boldsymbol{X}} + \boldsymbol{C}\dot{\boldsymbol{X}} + \boldsymbol{K}\boldsymbol{X} = \boldsymbol{\Gamma}\boldsymbol{f} \tag{1}$$

where $\boldsymbol{M}, \boldsymbol{C}$ *and* $\boldsymbol{K}$ are the mass, damping and stiffness matrix, respectively; $\boldsymbol{X}$ is the generalized displacement vector; $\boldsymbol{\Gamma}$ is the excitation distribution matrix; and $\boldsymbol{f}$ is the unknown external excitation (i.e., the process noise), which is modeled as a zero-mean Gaussian process. The mass matrix $\boldsymbol{M}$ is assumed to be known while the damping and stiffness matrix $\boldsymbol{C}(\boldsymbol{\theta}_c)$ *and* $\boldsymbol{K}(\boldsymbol{\theta}_k)$ are assumed to be unknown and parameterized using the damping parameter vector $\boldsymbol{\theta_c}$ and stiffness parameter vector $\boldsymbol{\theta_k}$. Consequently, the structural parameter vector $\theta \equiv \left[\boldsymbol{\theta}_k^T, \boldsymbol{\theta}_c^T\right]^T$ is defined.

To estimate the system state and uncertain structural parameter vector $\boldsymbol{\theta}$, the augmented state vector $\boldsymbol{Y} \equiv \left[\boldsymbol{X}^T, \dot{\boldsymbol{X}}^T, \boldsymbol{\theta}^T\right]^T$ is defined. Then the augmented state-space equation can be expressed as follows:

$$\dot{\boldsymbol{Y}} = \boldsymbol{A}\boldsymbol{Y} + \boldsymbol{B}\boldsymbol{f} \tag{2}$$

$$\boldsymbol{A} = \begin{bmatrix} \boldsymbol{0} & \boldsymbol{I} & \boldsymbol{0} \\ -\boldsymbol{M}^{-1}\boldsymbol{K}(\boldsymbol{\theta}_k) & -\boldsymbol{M}^{-1}\boldsymbol{C}(\boldsymbol{\theta}_c) & \boldsymbol{0} \\ \boldsymbol{0} & \boldsymbol{0} & \delta\boldsymbol{I} \end{bmatrix}, \boldsymbol{B} = \begin{bmatrix} \boldsymbol{0} \\ \boldsymbol{M}^{-1}\boldsymbol{\Gamma} \\ \boldsymbol{0} \end{bmatrix} \tag{3}$$

where $\boldsymbol{0}$ and $\boldsymbol{I}$ are the zero matrix and identity matrix, respectively; $\delta = -10^{-10}$ is a very small negative number introduced to prevent singularity in the transition matrix $\boldsymbol{A}$. Eq. (2) represents the state-space equation in continuous-time and can be discretized based on sampling frequency *fs* as:

$$\boldsymbol{Y}_{k+1} = \boldsymbol{A}_k\boldsymbol{Y}_k + \boldsymbol{B}_k\boldsymbol{f}_k \tag{4}$$

where $\boldsymbol{Y}_k \equiv \boldsymbol{Y}(k/fs)$; $\boldsymbol{A}_k = \exp(\boldsymbol{A}/fs)$; $\boldsymbol{B}_k = \boldsymbol{A}^{-1}(\boldsymbol{A}_k - \boldsymbol{I})\boldsymbol{B}$; $\boldsymbol{f}_k \equiv (k/fs)$; and the unknown external excitation $\boldsymbol{f}_k$ at the k^{th} time step is Gaussian with zero-mean and covariance matrix $\boldsymbol{Q}_k$.

The observation equation is given by:

$$\boldsymbol{Z}_{k+1} = \boldsymbol{h}(\boldsymbol{Y}_{k+1}) + \boldsymbol{v}_{k+1} \tag{5}$$

where $\boldsymbol{Z}_{k+1}$ is the contaminated measurement vector at the $(k+1)^{th}$ time step. The measurement noise vector $\boldsymbol{v}_{k+1}$ is modeled as Gaussian with zero-mean and covariance matrix $\boldsymbol{R}_{k+1}$.

2.1 *Sigma-point Kalman filter*

The detail formulation of sigma-point Kalman filter can refer to [7]. The overall procedure of sigma-point Kalman filter can be summarize as the follow equations:

2.1.1 *Predicted state and covariance matrix*

A set of N sigma points $\boldsymbol{y}_{i,k|k}$ can be generated through:

$$\boldsymbol{y}_{i,k|k} = fun(\boldsymbol{Y}_{k|k}, \boldsymbol{P}_{\boldsymbol{Y},k|k}) \tag{6}$$

$$\boldsymbol{y}_{i,k+1|k} = \boldsymbol{A}_{k,i}\boldsymbol{y}_{i,k|k} \tag{7}$$

$$\boldsymbol{Y}_{k+1|k} = \sum_{i=0}^{N} w_i\boldsymbol{y}_{i,k+1|k} \tag{8}$$

$$\boldsymbol{P}_{\boldsymbol{Y},k+1|k} = \sum_{i=0}^{N} w_i(\boldsymbol{y}_{i,k+1|k} - \boldsymbol{Y}_{k+1|k})(\boldsymbol{y}_{i,k+1|k} - \boldsymbol{Y}_{k+1|k})^T + \boldsymbol{B}_k\boldsymbol{Q}_k{\boldsymbol{B}_k}^T \tag{9}$$

$$\boldsymbol{y}_{i,k+1|k} = fun(\boldsymbol{Y}_{k+1|k}, \boldsymbol{P}_{\boldsymbol{Y},k+1|k}) \tag{10}$$

where $fun(\cdot)$ is a sigma-point generation function (e.g., unscented transform, cubature transform); w_i and N denote the weight of the corresponding sigma-point and the number of sigma points, respectively, which are determined by the selection of the generation function; $\mathrm{Y}_{k+1|k}$ represents the predicted state vector; and $\boldsymbol{P}_{\boldsymbol{Y},k+1|k}$ denotes the associated covariance matrix.

2.1.2 *Predicted measurements*

The above sigma points $\boldsymbol{y}_{i,k+1|k}$ are propagated as follow:

$$\boldsymbol{z}_{i,k+1|k} = \boldsymbol{h}(\boldsymbol{y}_{i,k+1|k}) \tag{11}$$

$$\boldsymbol{Z}_{k+1|k} = \sum_{i=0}^{N} w_i \boldsymbol{z}_{i,k+1|k} \tag{12}$$

$$\boldsymbol{P}_{\boldsymbol{Z},k+1|k} = \sum_{i=0}^{N} w_i (\boldsymbol{z}_{i,k+1|k} - \boldsymbol{Z}_{k+1|k})(\boldsymbol{z}_{i,k+1|k} - \boldsymbol{Z}_{k+1|k})^T + \boldsymbol{R}_{k+1} \tag{13}$$

2.1.3 *Kalman gain*

The cross-covariance matrix $\boldsymbol{P}_{\boldsymbol{YZ},k+1|k}$ and Kalman gain matrix $\boldsymbol{K}_{k+1}$ can be obtained:

$$\boldsymbol{P}_{\boldsymbol{YZ},k+1|k} = \sum_{i=0}^{N} w_i (\boldsymbol{y}_{i,k+1|k} - \boldsymbol{Y}_{k+1|k})(\boldsymbol{z}_{i,k+1|k} - \boldsymbol{Z}_{k+1|k})^T \tag{14}$$

$$\boldsymbol{K}_{k+1} = \boldsymbol{P}_{\boldsymbol{YZ},k+1|k} \boldsymbol{P}_{\boldsymbol{Z},k+1|k}^{-1} \tag{15}$$

2.1.4 *Updated state and covariance matrix*

Finally, the updated state vector $\boldsymbol{Y}_{k+1|k+1}$ and the associated covariance matrix $\boldsymbol{P}_{\boldsymbol{Y},k+1|k+1}$ are readily obtained:

$$\boldsymbol{Y}_{k+1|k+1} = \boldsymbol{Y}_{k+1|k} + \boldsymbol{K}_{k+1}(\boldsymbol{Z}_{k+1} - \boldsymbol{Z}_{k+1|k}) \tag{16}$$

$$\boldsymbol{P}_{\boldsymbol{Y},k+1|k+1} = \boldsymbol{P}_{\boldsymbol{Y},k+1|k} - \boldsymbol{K}_{k+1} \boldsymbol{P}_{\boldsymbol{Z},k+1|k} \boldsymbol{K}_{k+1}^T \tag{17}$$

2.2 *Sequential importance resampling*

The augmented state vector can be updated according to Eq. (16) and Eq. (17). However, the matrices $\boldsymbol{P}_{\boldsymbol{Y},k+1|k}$ and $\boldsymbol{P}_{\boldsymbol{Z},k+1|k}$ from Eq. (9) and Ed. (13) depend on the process noise covariance matrix $\boldsymbol{Q}_k$ and the measurement noise covariance matrix $\boldsymbol{R}_{k+1}$, respectively, which are typically unknown in practical applications. Inappropriately assigned noise covariance matrices may result in divergence.

The noise covariance matrices can be updated using the noisy responses collected from the dynamic system [8]. Similar to the parameterization of structural stiffness and damping matrix, the noise covariance matrices can be parameterized as: $\boldsymbol{Q}_k = \boldsymbol{Q}_k(\boldsymbol{\varphi}_{\boldsymbol{Q},k})$ and $\boldsymbol{R}_{k+1} = \boldsymbol{R}_{k+1}(\boldsymbol{\varphi}_{\boldsymbol{R},k+1})$. Subsequently, the noise parameter vector is formed as: $\boldsymbol{\varphi}_{k+1} = \left[\boldsymbol{\varphi}_{\boldsymbol{Q},k}^T, \boldsymbol{\varphi}_{\boldsymbol{R},k+1}^T\right]^T$. According to sequential importance sampling and the theorem of large numbers, the expected value of the noise parameter vector can be estimated without knowing the posterior PDF of the noise parameters $p(\boldsymbol{\varphi}_{0:k+1}|\boldsymbol{D}_{k+1})$:

$$\begin{aligned} \boldsymbol{\varphi}_{k+1} = E(\boldsymbol{\varphi}_{0:k+1}) &= \int \boldsymbol{\varphi}_{0:k+1} \frac{p(\boldsymbol{\varphi}_{0:k+1}|\boldsymbol{D}_{k+1})}{q(\boldsymbol{\varphi}_{0:k+1}|\boldsymbol{D}_{k+1})} q(\boldsymbol{\varphi}_{0:k+1}|\boldsymbol{D}_{k+1}) d\boldsymbol{\varphi}_{0:k+1} \\ &\approx \frac{1}{n} \sum_{i=1}^{n} \boldsymbol{\varphi}_{k+1}^{(i)} \omega_{k+1}^{(i)} \end{aligned} \tag{18}$$

where $p(\boldsymbol{\varphi}_{0:k+1}|\boldsymbol{D}_{k+1})$ is the joint PDF; $q(\boldsymbol{\varphi}_{0:k+1}|\boldsymbol{D}_{k+1})$ is an importance density; n indicate the number of the noise parameter particles; and $\omega_{k+1}^{(i)}$ signify the weight of the i^{th} associated noise parameter vector particle. Assuming $q(\boldsymbol{\varphi}_{k+1}^{(i)}\left|\boldsymbol{\varphi}_{k}^{(i)}, \boldsymbol{Z}_{k+1}\right.) = p(\boldsymbol{\varphi}_{k+1}^{(i)}\left|\boldsymbol{\varphi}_{k}^{(i)}\right.)$, the expression for $\omega_{k+1}^{(i)}$ can be reformulated as follows:

$$\omega_{k+1}^{(i)} \propto \omega_{k}^{(i)} \left|\boldsymbol{P}_{\boldsymbol{Z},k+1|k}\right|^{-\frac{1}{2}} \exp\left[-\frac{1}{2}(\boldsymbol{Z}_{k+1} - \boldsymbol{Z}_{k+1|k})^{T} \boldsymbol{P}_{\boldsymbol{Z},k+1|k}^{-1}(\boldsymbol{Z}_{k+1} - \boldsymbol{Z}_{k+1|k})\right] \tag{19}$$

where $\boldsymbol{P}_{Z,k+1|k}$ is the covariance matrix of predicted measurement vector $\boldsymbol{Z}_{k+1|k}$; and $\boldsymbol{Z}_{k+1}$ is the noisy measurement at $(k+1)^{th}$ time step. Then the covariance matrix $\boldsymbol{P}_{\boldsymbol{\varphi},k+1}$ is given by:

$$\boldsymbol{P}_{\boldsymbol{\varphi},k+1} = \sum_{i=1}^{n} \bar{\omega}_{k+1}^{(i)} (\boldsymbol{\varphi}_{k+1}^{(i)} - \boldsymbol{\varphi}_{k+1})(\boldsymbol{\varphi}_{k+1}^{(i)} - \boldsymbol{\varphi}_{k+1})^{T} \tag{20}$$

where $\bar{\omega}_{k+1}^{(i)}$ is the normalized weights.

After a few iteration steps, all but one of the normalized weights are very close to zero, leading to a degeneracy phenomenon. To address this, the current particle set can be replaced with new ones, where particles are distributed according to their normalized weights, and the weights of the particles are reset as $\bar{\omega}_{k+1}^{(i)} = 1/n$.

2.3 *Sequential importance resampling sigma-point Kalman filter*

In this section, the sequential importance resampling method is integrated into the SPKF to jointly estimate the system state, structural parameters and noise parameters. The procedure of the proposed method is outlined in Table 1.

Table 1. Sequential importance resampling sigma-point Kalman filter (SIR-SPKF).

S-1: Set initial value for $\boldsymbol{Y}_{0|0}, \boldsymbol{P}_{\boldsymbol{Y},0|0}, \boldsymbol{\varphi}_0, \boldsymbol{P}_{\boldsymbol{\varphi},0}, \left[\boldsymbol{\varphi}_0^{(1)}, \boldsymbol{\varphi}_0^{(2)}, \cdots, \boldsymbol{\varphi}_0^{(n)}\right]$.
S-2: Calculate the predicted state $\boldsymbol{Y}_{k+1|k}$.
S-3: Generate particles set $\left[\varphi_{l,k+1}^{(1)}, \varphi_{l,k+1}^{(2)}, \cdots, \varphi_{l,k+1}^{(n)}\right] = 2^{r_k * randn(1,n)} . * \left[\varphi_{l,k}^{(1)}, \varphi_{l,k}^{(2)}, \cdots, \varphi_{l,k}^{(n)}\right], r_k = \max(1 + \frac{1}{\sqrt{n}} - \frac{k}{fs}, \frac{1}{32})$.
S-4: Update the noise parameter vector $\boldsymbol{\varphi}_{k+1}$ and the associated covariance matrix $\boldsymbol{P}_{\boldsymbol{\varphi},0}$ by Eqs. (18) and (20).
S-5: Calculate the updated state $\boldsymbol{Y}_{k+1|k+1}$ and covariance matrix $\boldsymbol{P}_{\boldsymbol{Y},k+1|k+1}$ by Eqs. (16) and (17).
S-6: Go to S-2 for the next time step.

where $\varphi_{l,k+1}^{(i)}$ is the l^{th} element of the noise parameters vector $\boldsymbol{\varphi}_{k+1}^{(i)}$.

3 NUMERICAL APPLICATION

In this section, a bridge structure [8] comprising five spans and four piers, as depicted in Figure 1, under stationary response scenarios was considered to showcase the efficacy of the proposed SIR-SPKF. The entire bridge model consisted of 72 degrees of freedom (DOFs), discretized into 28 elements and partitioned into 14 substructures. The length between two adjacent nodes of each span was $26m$, $24m$, $27.5m$, $24m$ and $26m$, respectively, while it was $20m$ for all piers. The material properties and section properties of the bridge are detailed in Table 2.

The Rayleigh damping model in form of $\boldsymbol{C} = \alpha\boldsymbol{M} + \beta\boldsymbol{K}$ was utilized, with the Rayleigh damping coefficients set as $\alpha = 0.0670s^{-1}$ and $\beta = 0.0015s$. The global stiffness matrix of the bridge was parameterized and assembled as $\boldsymbol{K} = \sum_{i=1}^{14} \boldsymbol{\theta}_{ki}\boldsymbol{K}_i$, where $\boldsymbol{K}_i$ represented the known stiffness matrix of the i^{th} substructure and $\boldsymbol{\theta}_{ki}$ denoted the corresponding stiffness parameter. Due to potential discrepancies between design and construction in engineering, the actual stiffness parameters might vary, and thus were assigned different values denoted by

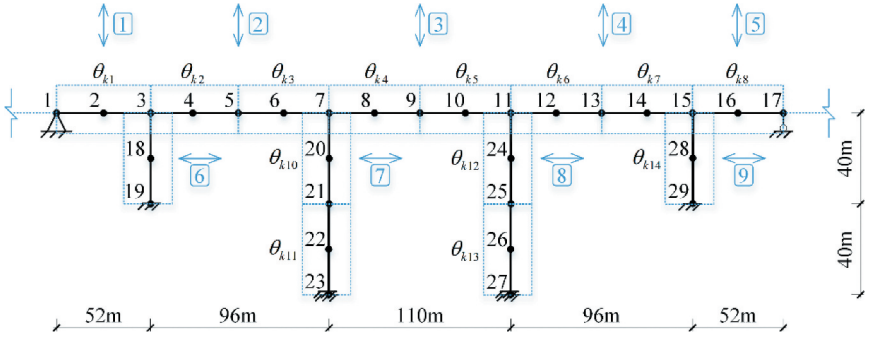


Figure 1. Bridge model.

Table 2. Material properties and section properties of the bridge.

Properties of girder		Properties of pier	
m_g(kg/m^3)	2700	m_p(kg/m^3)	2600
E_g(GPa)	34.5	E_p(GPa)	32.0
A_g(m^2)	9.8	A_p(m^2)	18.5
I_g(m^4)	10.7	I_p(m^4)	55.5

$\bar{\boldsymbol{\theta}}_k = [1.10, 1.15, 1.05, 0.98, 0.90, 0.95, 1.00, 0.97, 1.07, 0.95, 0.98, 0.95, 0.90, 0.90]^T$. Consequently the uncertain structural parameter vector was defined as $\boldsymbol{\theta} = [\boldsymbol{\theta}_k{}^T, \boldsymbol{\theta}_c{}^T]^T = [\boldsymbol{\theta}_k{}^T, \alpha, \beta]^T$.

The bridge was subjected to horizontal ground acceleration of $\boldsymbol{\varphi}_Q = 0.0025$. The stiffness of the 4^{th} and 10^{th} substructures was reduced abruptly to 0.95 and 0.90 at $t = 30s$, respectively. Afterwards, the stiffness of the 13^{th} substructures was reduced to 0.85 at $t = 70s$. The nodes and directions of the acceleration responses collected are depicted in Figure 1, with a sampling frequency of 200 Hz over a period of 150 s. The measurement noise level was set at 5% root-mean-square (RMS) of the noise-free response of the DOF corresponding to the 2^{nd} and 8^{th} sensors for those in the girders and those on the piers, respectively.

The initial noise parameters were assigned with $\boldsymbol{\varphi}_0 = [1, 1, 1]^T$ and $\boldsymbol{P}_{\boldsymbol{\varphi},0} = \boldsymbol{I}_3$. The initial augmented state vector and the associated covariance matrix were determined as follows:

$$\boldsymbol{Y}_{0|0} = [\boldsymbol{\theta}, a_0^{(1)}\bar{\theta}_{k1}, a_0^{(2)}\bar{\theta}_{k2}, \cdots, a_0^{(14)}\bar{\theta}_{k14}, a_0^{(15)}\alpha, a_0^{(16)}\beta]^T \tag{21}$$

$$\boldsymbol{P}_{\boldsymbol{Y},0|0} = diag([10^{-10}\mathbf{1}, (0.1a_0^{(1)}\bar{\theta}_{k1})^2, (0.1a_0^{(2)}\bar{\theta}_{k2})^2, \cdots, (0.1a_0^{(14)}\bar{\theta}_{k14})^2, (0.1a_0^{(15)}\alpha)^2, (0.1a_0^{(16)}\beta)^2]) \tag{22}$$

where $a_0^{(1)}, a_0^{(2)}, \cdots, a_0^{(16)}$ follow the uniform distribution in [0.7,1.3]. The number of the noise parameter particles n was set as 30.

The estimation results of the structural parameters estimated by SIR-SPKF are illustrated in Figure 2. The solid lines denote the values estimated by SIR-SPKF, while the dotted lines indicate their associated 99.7% credible intervals. The dashed lines correspond to the actual values. Figure 2(a)-(g) display some representative estimation results of the stiffness parameters, while Figure 2(h)-(i) depict the estimation results of the damping parameters. The results identified by SIR-SPKF revealed the following: (1) there was a time lag in estimating the abrupt changes of stiffness parameters, as the estimation results at the current step also depended on the historic measurements; (2) the estimated values and credible intervals of the stiffness parameters on the piers fluctuated violently at the time step when the stiffness parameters in the girders suddenly changed, since the reduction of the stiffness in the girders would also lead to reduction in the horizontal constraint of the piers, causing the amplitude of the response on the piers to change rapidly.

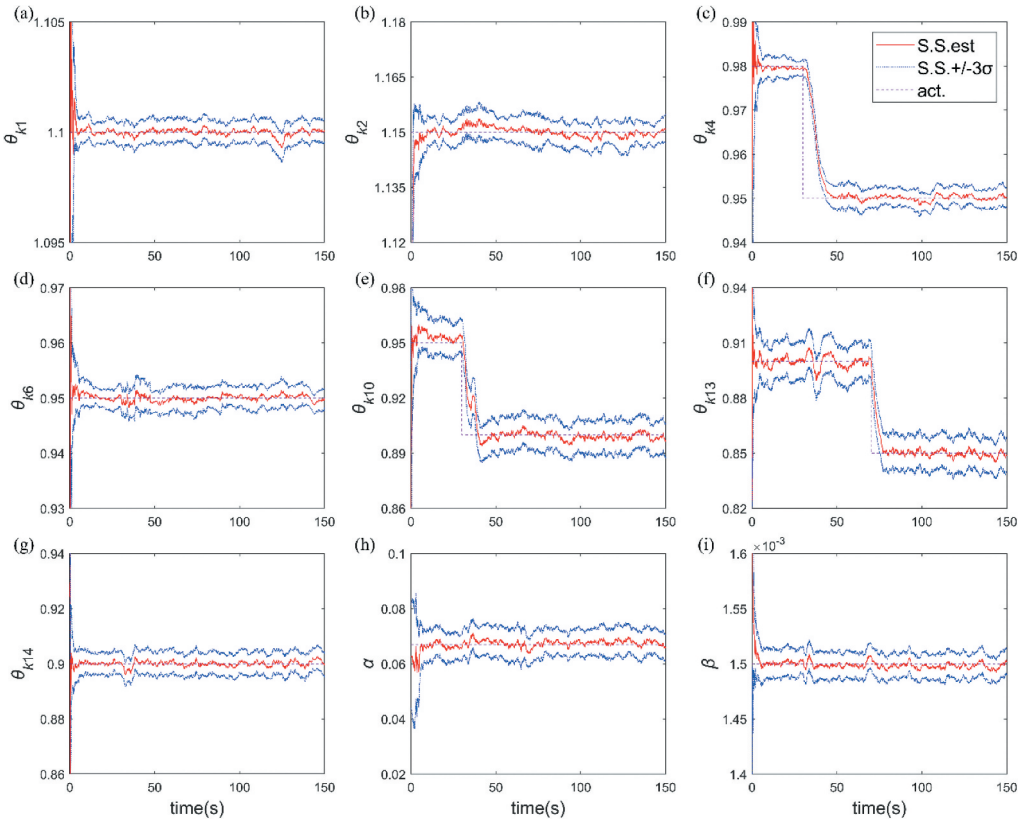


Figure 2. Estimation results of structural parameters by SIR-SPKF (S.S.).

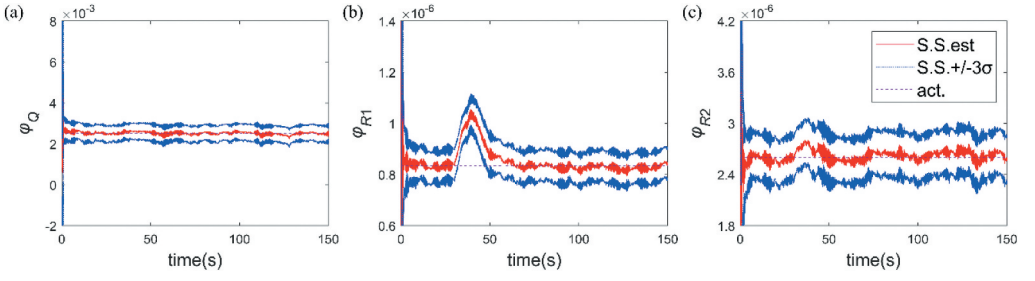


Figure 3. Estimation results of noise parameters by SIR-SPKF (S.S.).

The estimation results of noise parameters, estimated simultaneously by SIR-SPKF, are depicted in Figure 3. Regarding the results obtained thorough SIR-SPKF: (1) the estimated values quickly approached the vicinity of the actual values since the noise parameters particles were generated using a scaling model and updated based on their respective weight; (2) the estimated values φ_{R1} and the corresponding credible intervals deviated from the actual values at the time step that the stiffness parameters suddenly changed, due to the combination impact of the sudden change of the stiffness parameters θ_{k4} and θ_{k10}. Apart from this time interval, the estimated noise parameter values closely matched the actual values, and the 99.7% credible intervals effectively encompassed the actual values.

In summary, the proposed SIR-SPKF method demonstrated the capability to accurately estimate both structural parameters and noise parameters.

4 EXPERIMENTAL STUDY

In this section, the effectiveness of the proposed SIR-SPKF was further validated using experimental data obtained from a three-story shear model [9], which was simplified as a 3-DOF shear model. The mass of each floor was 25.2 kg, and the linear stiffness of each floor were found to be $k_1 = 3.1$ N/mm, $k_2 = 10.4$ N/mm and $k_3 = 11.3$ N/mm.

The experimental study was conducted under ambient conditions. Sensors were connected to a data acquisition system and controlled by a laptop. Acceleration response data were collected for 600 seconds from the first and third floor, with a sampling frequency of 2048 Hz. Subsequently, the data was decimated by a factor of 8 to achieve a frequency of 256 Hz for further analysis. The coefficients $\theta_{ki}(i = 1, 2, 3)$ of the corresponding stiffness parameters k_i were then estimated. Rayleigh damping model in form of $\boldsymbol{C} = \alpha\boldsymbol{M} + \beta\boldsymbol{K}$ was adopted.

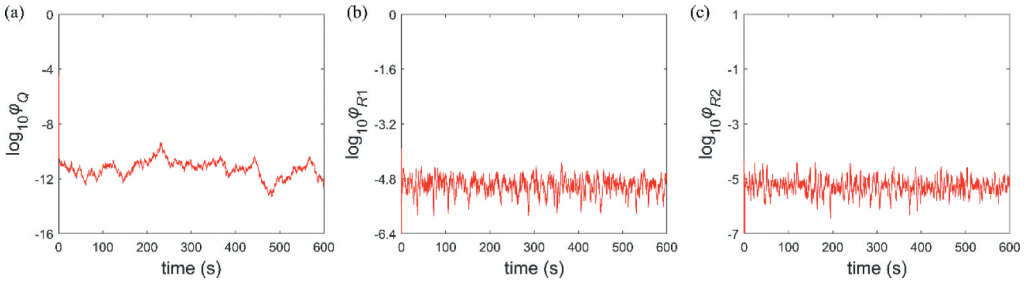


Figure 4. Estimation results of noise parameters in the experimental study.

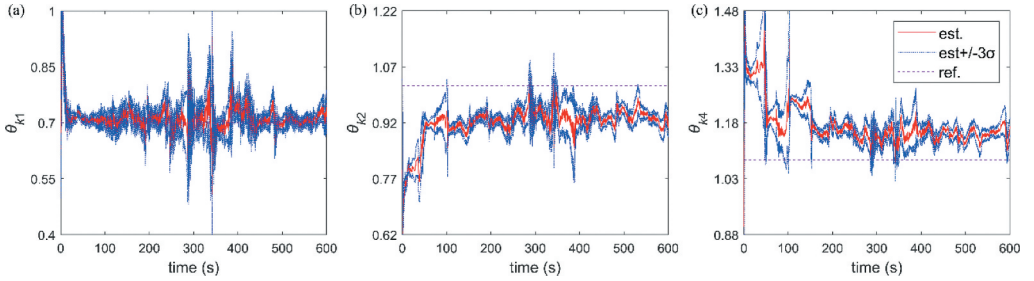


Figure 5 . Estimation results of stiffness parameters of the 3-DOF shear model.

Table 3. Average values of the estimated structural parameters and those in [10].

	θ_{k1}	θ_{k2}	θ_{k3}	ξ_1	ξ_2
Literature [10]	0.709	1.019	1.081	0.00341	0.00169
SIR-SPKF	0.709	0.938	1.148	0.00847	0.00196

The initial conditions were set as the ways as those in Section 3. The unknown noise parameter vector was denoted as $\boldsymbol{\varphi}_{k+1} = \left[\varphi_{Q,k}, \boldsymbol{\varphi}_{R,k+1}^T\right]^T = \left[\varphi_{Q,k}, \varphi_{R1,k+1}, \varphi_{R2,k+1}\right]^T$. A logarithmic plot displaying the estimation results of the noise parameters is presented in Figure 4. It is evident from the plot that the estimated values of the unknown noise parameter are significantly smaller than the initial values [1,1,1].

The estimation results of the stiffness parameters are depicted in Figure 5. The solid lines denote the estimated values, the dotted lines illustrate the 99.7% credible intervals, and the dashed lines indicate the reference values according to [10]. It is noticeable that the estimated values

closely align with the reference values. However the estimated values of the stiffness parameter coefficients θ_{k1} and θ_{k2} consistently deviate to be smaller or larger than the reference values. This deviation may arise from variances in the identification methods. Additionally, it should be noted that the signal-to-noise ratio of the response data on the first and third floors were calculated to be -7 and -3 respectively, based on the estimated measurement noise parameters. This may also contribute to the deviation between the estimated values and the reference values.

The order of magnitude of the estimated value of the process noise parameter is -11, which is reasonable under ambient conditions. The average values of the structural parameters estimated in the latter 350 seconds, along with those mentioned in [10], are listed in Table 3. It is observed that the proposed SIR-SPKF method satisfactorily estimate the structural parameters.

5 CONCLUSION

In this work, a sigma-point Kalman filter based method for system state and structural parameters, which considers modeling error and measurement error, has been developed. The modeling error and measurement error are reflected by the covariance matrices of the process noise and measurement noise in the mathematic framework and are usually unknown in practical scenarios. To address this issue, a sequential importance resampling algorithm is employed. This algorithm facilitates the estimation of noise covariance matrices by utilizing noisy responses obtained from the dynamic system through a set of particles. The particles are then updated using a random walk model. By reliably estimating the noise parameters through the proposed method, reliable system identification can be ensured. The efficacy of the approach is verified through a numerical application to a bridge structure under stationary response scenarios and an experimental study on a shear building model. The results demonstrate that the proposed SIR-SPKF method is effective and robust in identifying the structural system.

ACKNOWLEDGEMENT

This work is funded by the National Natural Science Foundation of China (52278298) and the Shenzhen Science and Technology Innovation Committee (KJZD20230923114310021, GXWD20231130153531001). These generous supports are gratefully acknowledged.

REFERENCES

[1] He J, Guan X, Liu Y. (2012). Structural response reconstruction based on empirical mode decomposition in time domain. Mechanical Systems & Signal Processing. 28, 348–366.
[2] Kammer C D. (1997). Estimation of Structural Response Using Remote Sensor Locations. Journal of Guidance, Control, and Dynamics. 20:3, 501–508.
[3] Zhang F L, Au S K. (2016). Fundamental two-stage formulation for Bayesian system identification, Part I: General theory. Mechanical Systems and Signal Processing. 66-67:31–42.
[4] Maes K, Gillijns S, Lombaert G. (2018). A smoothing algorithm for joint input-state estimation in structural dynamics. Mechanical Systems and Signal Processing. 292–309.
[5] Luengo D, Martino L, Mónica Bugallo. (2020). A survey of Monte Carlo methods for parameter estimation. Journal on Advances in Signal Processing. 2020:1.
[6] Ebrahimian H, Astroza R, Conte JP, Papadimitriou C. (2018). Bayesian optimal estimation for output-only nonlinear system and damage identification of civil structures. Structural Control Health Monitoring. 25:4.
[7] Vercauteren T, Wang X. (2005). Decentralized sigma-point information filters for target tracking in collaborative sensor networks. IEEE Transactions on Signal Processing. 53:8, 2997–3009.
[8] Yuen K V, Liu Y S, Yan W J. (2022). Estimation of time-varying noise parameters for unscented Kalman filter. Mechanical Systems and Signal Processing. 180.
[9] Zhang F L, Au S K. (2016). Fundamental two-stage formulation for Bayesian system identification, Part II: Application to ambient vibration data. Mechanical Systems and Signal Processing. 66-67, 43–61.
[10] Zhang F L, Au S K, Ni Y C. (2021). Two-stage Bayesian system identification using Gaussian discrepancy model. Structural Health Monitoring. 20:2, 580–595.

MS10: MS Application of probabilistic techniques for the assessment and performance prediction of corroding concrete bridges

Organizers: R. Caspeele, W. Botte, R. Vrijdaghs, B. Belletti & J.R. Casas


Taylor & Francis
Taylor & Francis Group
http://taylorandfrancis.com

Bridge Maintenance, Safety, Management, Digitalization and Sustainability – Jensen, Frangopol & Schmidt (eds)
© 2024 The Author(s), ISBN 978-1-032-77040-6
Open Access: www.taylorfrancis.com, CC BY-NC-ND 4.0 license

Bayesian-updated POD of ultrasonic tomography in the inspection of PT bridges

I. Mazzatura
Department of Civil and Industrial Engineering, University of Pisa, Pisa, Italy
Department of Civil and Environmental Engineering, Universitat Politécnica de Catalunya, Barcelona, Spain

J.R. Casas
Department of Civil and Environmental Engineering, Universitat Politécnica de Catalunya, Barcelona, Spain

S. Caprili & W. Salvatore
Department of Civil and Industrial Engineering, University of Pisa, Pisa, Italy

ABSTRACT: The present research aims to furnish a proper methodology for the reliability assessment of non-destructive tests in the particular field of inspection of post-tensioned (PT) structures. The focus is on the Ultrasonic Tomography used in the inspection of grouting defects inside the PT ducts. The presence of such defects is the most dangerous scenario for triggering the mechanism of corrosion in the prestressing steel and, therefore, for structural safety. Many studies exist about the application of ultrasonic tomography (UT) in the inspection of PT structures and bridges. However, the reliability of the technique is still not known when applied to field inspection of existing bridges. This paper explains the execution of a laboratory testing campaign on many specimens presenting different sizes and types of simulated grouting defects. The tested specimens are designed to represent the most typical source of grouting defects (voids, water) and the most spread typology of ducts (metallic and plastic) and post-tensioning elements (strands and bars). The inspection outcomes are modelled through the Probability of Detection (POD) curve, which gives information about the maximum defect size that the inspection method, UT, can miss, stating a certain confidence level. Since the number of tests is limited due to practical issues, as will be also the case in a real bridge, a Bayesian-updating approach is employed to better estimate the model parameters of the POD curve. In this way, the reliability of the inspection methodology can be derived, which is of great importance in the posterior capacity assessment of the existing structure.

1 INTRODUCTION

The investigation of structures with bonded posttensioned (PT) cables is a challenging issue, mainly for the configuration of the system itself. The rise of such technology, jointly with the euphoria of reconstruction after the II World War, and the total confidence in the full prestressing (because of the belief that concrete under compression is watertight) (Godart 2001), led to an underestimation of the durability's issues potentially affecting these structures, as well as to an absence of consciousness in their investigation.

The PT system can be both internal and external, bonded and unbonded. The present research focuses on the investigation of structures with bonded PT system. The core of the system are the high-strength steel cables, which are protected by three layers against corrosion, i.e. the concrete cover, the metallic sheet of the ducts, and the grout. The triggering of corrosion on the cable

DOI: 10.1201/9781003483755-110

happens if the protecting layers are affected by degradation and/or by conditions promoting the formation of an aggressive environment. The carbonation of concrete, and the penetration of aggressive ions (such as chlorides and sulphites) due to the use of de-icing salts jointly with an inappropriate waterproofing system, represent only a few of the conditions promoting corrosion. Also, bad execution of the grouting, as well as the use of an inappropriate mixture, can facilitate damage to the cables. The corrosion of the cables is often associated with voids inside the ducts (Carsana and Bertolini 2015). Possible reasons for the voids' formation are the evaporation of bleed water, poor grouting, and/or poor construction practices (Trejo et al. 2009). While the presence of voids is not a sufficient condition for the trigger of corrosion, in most cases the presence of corrosion is associated with the presence of voids. Thus, associating voids with corrosion is a conservative assumption. Moreover, sudden collapses without any visible deficiencies are documented by the state of the art (Woodward 2001). Therefore, one of the possible approaches in investigating damage (i.e. corrosion) in PT structures, is searching for voids inside the ducts. It's easier to search for air pockets through non-destructive techniques (NDTs), rather than directly the corrosion. Many technologies exist to detect defects inside the ducts, e.g. thermography (Garrido et al. 2020), X-ray (Innocenzi et al. 2022) and gamma-ray imaging (Freij et al. 2021), Impact Echo (IE) (Carino 2004; Muldoon et al. 2007), acoustic emission-based methods (i.e. Ultrasonic Echo (UE) and Ultrasonic Tomography (UT) (Schickert, Krause, and Mü Ller 2003; Terzioglu et al. 2018)). To optimize results and minimize errors, more NDTs can be used (Terzioglu et al. 2018). UT was selected as the reference technique for the present application because of its quick and easy application. Although much research exists on the application of UT in the investigation of voids through PT ducts, a numerical evaluation of its effectiveness is lacking. The application of the Probability of Detection (PoD) model represents a possible way to carry out this evaluation. The PoD evaluation is widely used in the non-destructive evaluation (NDE) of technologies employed in aerospace and nuclear engineering (Gandossi and Annis 2010; Virkkunen et al. 2019), and it is standardized by ASTM and the American Department of Defence (Anon 2009; ASTM International 2015, 2018). This evaluation allows the determination of the largest flaw that the technique can miss, stating a certain confidence level and for a given probability. The basic assumption of the PoD model is that the probability of success of an NDT depends only on a measurable entity, usually the flaw size. All the other parameters, potentially influencing too, are ignored and converge in potential errors in the probabilistic model. Indeed, it is important to carefully discriminate homogeneous cases in constructing a PoD curve. It is also fundamental to dispose of a large number of tests and a representative range of sample sizes. One way to improve the probability of detection by using a small number of samples is to use them with Bayesian inference to update the "a priori" obtained curve.

In the present research, six reinforced concrete walls with several ducts with simulated grouting defects of different sizes were designed and UT was then applied with the aim of analysing its efficiency in defect detection. The Bayesian approach is proposed to compare different scenarios composed of different number of samples.

2 PROBABILITY OF DETECTION

2.1 *Basic framework*

The PoD relates the probability of successfully detecting a flaw to its size (or to other geometrical characteristics). The standard practice offers two variants of PoD estimation, the so-called *â vs a* approach and the *hit/miss* approach. The first one deals with continuous data, while the *hit/miss* approach is based on binary results, which are hits (correctly found flaws) and misses (flaws not found). The focus will be on the latter since it is the approach adopted in the present research.

The PoD curve is solved using a generalized linear model and a chosen link function (typically logistic) that gives the shape of the PoD curve using the maximum likelihood fit of the data (Virkkunen et al. 2019). The response (y) is related to the controlling variables functionally, $y = f(X)$, where X is the value of controlling variables. Binary (hit/miss) data are bounded and discrete, having only 0 (miss) or 1 (hit) as possible values. A Generalized Linear Model

(GLM) overcomes this difficulty by linking the binary response to the explanatory variables through the probability of either outcome, which does vary continuously from 0 to 1. In other words, a function of y is necessary to *link* (through the probability of the outcome) the binary response to the function of X, in other words, $g(y) = f(X)$.

The binary linear regression model can be expressed as a linear function of the explanatory variable x by Equation (1):

$$f(X) = h[PoD(x)] = \Phi^{-1}(p) \tag{1}$$

where the function $h(p) = \Phi^{-1}(p)$ is the inverse Cumulative Distribution Function (CDF), also known as the quantile function of a standard location-scale distribution and is known in the statistical literature as a *link function*. One of the most used link functions is the *logit* (or log-odds) one. Therefore, it is possible to express the PoD as (2):

$$PoD(x) = \frac{e^{\beta_0+\beta_1 x}}{1 + e^{\beta_0+\beta_1 x}} \tag{2}$$

The PoD depends on (x ; β_0, β_1). β_0 is the slope, while β_1 is the intercept of the logistic regression model.

2.2 *The Bayesian approach*

Unlike the frequentist approach, for which the vector parameter θ of a certain distribution is unknown, but a deterministic quantity, the Bayesian approach considers θ as a random variable with a certain probability distribution. Three key components are associated with the parameter estimation: the prior distribution ($P(\theta)$), the likelihood function ($P(y|\theta)$), and the posterior distribution ($P(\theta|y)$), Equation (3):

$$P(\theta|y) \propto P(y|\theta)P(\theta) \tag{3}$$

The likelihood function gives information contained in the sample and these are combined with information about the prior distribution to obtain the posterior distribution. Therefore, the posterior distribution contains all the available knowledge about the parameters in the model as obtained with the samples. The likelihood function for the logistic regression, assuming that the experimental samples are independent of each other, can be written as (4):

$$Likelihood = \prod_{i=1}^{n} P_i^{y_i} \cdot (1 - P_i)^{(1-y_i)} = \prod_{i=i}^{n} \left(\frac{e^{\beta_0+\beta_1 x_i}}{1 + e^{\beta_0+\beta_1 x_i}}\right)^{y_i} \cdot \left(1 - \frac{e^{\beta_0+\beta_1 x_i}}{1 + e^{\beta_0+\beta_1 x_i}}\right)^{(1-y_i)} \tag{4}$$

The prior distribution can be informative or non-informative. It can be assumed that the parameters of the prior distribution are normally distributed, with a certain mean (μ) and standard deviation (σ). The choice of a normal distributions simplifies the calculation.

$$\beta_j \sim Normal\left(\mu_j, \sigma_j\right) \tag{5}$$

The posterior distribution is derived by multiplying the prior distribution over all the parameters by the full likelihood function, so (6):

$$Posterior \propto \prod_{i=1}^{n} \left(\frac{e^{\beta_0+\beta_1 x_i}}{1 + e^{\beta_0+\beta_1 x_i}}\right)^{y_i} \cdot \left(1 - \frac{e^{\beta_0+\beta_1 x_i}}{1 + e^{\beta_0+\beta_1 x_i}}\right)^{(1-y_i)} \times \prod_{j=0}^{p} \frac{1}{\sqrt{2\pi}\sigma_j} exp\left\{-\frac{1}{2}\left(\frac{\beta_j - \mu_j}{\sigma_j}\right)^2\right\} \tag{6}$$

The latter part is the normal distribution for the β_j parameters. The expression has no closed form; therefore, it is necessary to employ a Markov Chain Monte Carlo (MCMC) method or similar (Chib 2001; Hoffman and Gelman 2014a; Roberts and Richardson 1998), to solve and approximate the mean and standard deviation of the posterior distributions for each parameter.

3 THE EXPERIMENTAL CAMPAIGN

3.1 *Samples*

Six concrete walls with a total of 40 embedded ducts, both plastic and metallic, and with pre-stressing strands and bars were realized. Both voids and water defects of different size were simulated in each duct. The voids were realized through the use of polyurethane foam with the actual dimension of the defects (Figure 1a) or by creating a "stopper" for the grouting (Figure 1b). The water defects were simulated using plastic bags filled with water as shown in Figure 1c.



a) b) c)

Figure 1. Samples with simulated defects before deployment in the concrete wall and grouting. a) three defects of different sizes (3, 5, and 8 cm). b) simulation of a defect of 33 cm. c) simulation of a void filled with water.

A total of 40 samples, including samples with perfectly executed grouting for comparison, were produced.

3.2 *Tests' execution*

Two devices (A1040 MIRA and A1040 MIRA3d) were employed, both using he Ultrasonic Shear-wave (MIRA) technique with an array of Dry Point Contact (DPC). The main parameter to be calibrated to perform the investigation are the velocity and the analog and digital gain.

The velocity of the shear waves through the concrete was estimated by the relation (7) (Krautkrämer and Krautkrämer 1990):

$$c_t = \sqrt{\frac{E}{\rho} \cdot \frac{1}{2 \cdot (1+\nu)}} = 2422\ m/s \tag{7}$$

Being the density (ρ) around 2500 $\frac{kg}{m^3}$, the Elastic modulus (E) up 34625 MPa, and the Poisson ratio (ν) of 0.18. The calibration is performed by comparing the actual thickness of the inspected body with the one derived by multiplying c_t . t (where t is the time required for the wave to come back). In addition, it is necessary to choose the proper values for the analog and digital gain. The analog gain is a parameter that increases the analog signal amplitude before the conversion into a digital signal; the digital gain is a parameter that operates directly on the digital signal (ACS Group 2021). A high value of the analog and the digital gain could lead to an irrelevant scan due to the high colour intensity, in fact the Synthetic Aperture Focusing Technique SAFT (Schickert et al. 2003; Stepinski and Lingvall 2010) algorithm provides a colour map representing the difference in acoustic impedance (Δ) between the base material and the object material in the section scanned. By selecting at least two ducts and performing scans for a length of at least 50 cm in the area in which the occurrence of grouting

defects was less probable, the best values of the analog and digital gain could be found by some attempts until the image given from the scans is not amplified continuously. The test was carried out by performing 10 scans per duct, being the chosen pitch equal to 10 cm and the total length to inspect up to 100 cm (Figure 2).

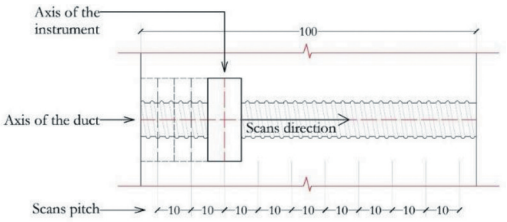


Figure 2. Graphical representation of the tests' execution.

3.3 *Data translation*

The results of the inspection are images computed by the SAFT algorithm. It was necessary to translate the qualitative output in a numerical value by assigning 1 in case the defect was hit by the colour amplification of the scan (i.e. a hit) and 0 if the defect was missed (i.e. a miss), as shown in Figure 3. The colour amplification in between "C" and "B" represents a false positive.

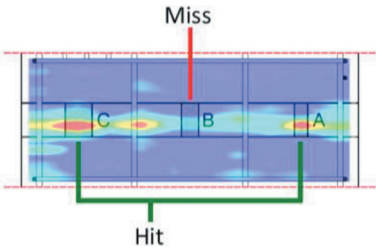


Figure 3. The meaning of "hit" and "miss". Grouting voids A and C are detected, but B is not.

As a consequence of what was presented above, a data set of 110 samples with metallic ducts was therefore considered.

3.4 *Resulting scenarios*

Since the main assumption of the PoD is that the detectability of a flaw depends only on its size, it is of basic importance to correctly discriminate the other potentially influencing parameter. In the present case the tests were divided into 6 scenarios (Table 1) depending on the calibration (i.e. the choice of the analog and digital gain), on the typology of the scan (i.e.

Table 1. Parameters characterizing each scenario.

Id. scenario	Calibration	Geometry	Scan Typology	N° of tests
SC1	1	15 cm	Linear	65
SC2	2	25 cm	Linear	40
SC3	All	15 cm	Linear	89
SC4	All	25 cm	Linear	62
SC5	1	All	Matrix	81
SC6	All	All	Linear	151

linear or matrix, meaning the way in which the sensors are employed by the instruments), and on the eccentricity of the ducts (15 cm or 25 cm).

4 DATA ANALYSIS

4.1 *Description of the hit/miss data*

A total of 232 inspections were performed on 12 flaw lengths from 3 to 100 cm. Figure 4 shows the number of tests for each flaw size. Figure 5 summarizes the percentages of hits and misses at each size. The PoD model seems to be well adapted for the modelling of the reliability and confidence of the inspection results, in fact from the size of 22 cm there are no misses, and for the flaw size less than 22 cm the percentage of misses grows as the length of the flaw decreases.

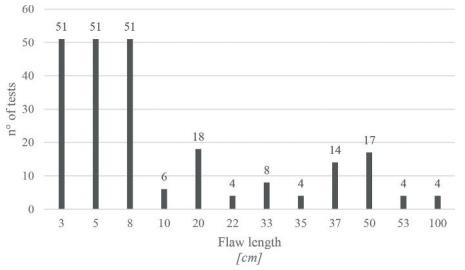


Figure 4. Number of tests in metallic ducts for each flaw length.

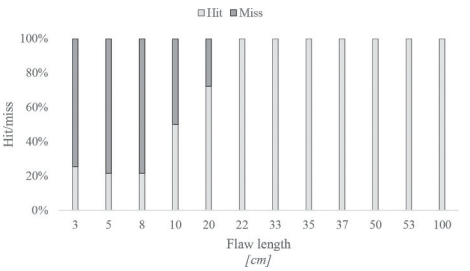


Figure 5. Hit/miss percentage for each flaw length.

4.2 *Construction of the PoDs curves*

A typical PoD is displayed in Figure 6. The most relevant parameters according to (ASTM International 2018) are the critical value of the defects' length for which there is a 50% probability of detection, with a confidence of 50%, to obtain a "hit" (a_{50}); the critical value of the defects' length for which there is the 90% probability, with a confidence of the 50%, to obtain a "hit" (a_{90}) and the critical value of the defects' length for which there is the 90% probability, with a confidence of the 95%, to obtain a "hit" ($a_{90/95}$).

To get comparable results for the different scenarios using different numbers of samples, the Bayesian approach is a solution as presented in (Aldrin, Knopp, and Sabbagh 2013; Kanzler, Müller, and Pitkänen 2013). The Bayesian approach was applied through the Python environment and by the PyMC3 package (Salvatier, Wiecki, and Fonnesbeck 2016). A normal distribution with 0 mean and 10 standard deviation was assumed for both β_0 and β_1 considering the prior distributions as non-informative. The likelihood function representing the probability of observing the actual data given the model parameters as displayed in equation (4) was evaluated. The sampler algorithm employed was the No-U-Turn Sampler (NUTS). This algorithm closely resembled Hamiltonian Monte Carlo (HMC), avoiding the need to choose the problematic number-of-steps parameter (Hoffman and Gelman 2014b). The analyses were performed by running 5 chains of 5000 iterations each. By performing several analyses and varying the number of iterations, it was possible to select 5000 iterations as an appropriate value.

Indeed, considering in the analysis:

$$intercept : \beta_0 \sim N(0, 10)$$

$$slope : \beta_1 \sim N(0, 10)$$

a good representation of a non-informative prior is obtained, as visible from Figure 7, where the mean values of the intercept are obtained for increasing values of the standard deviation

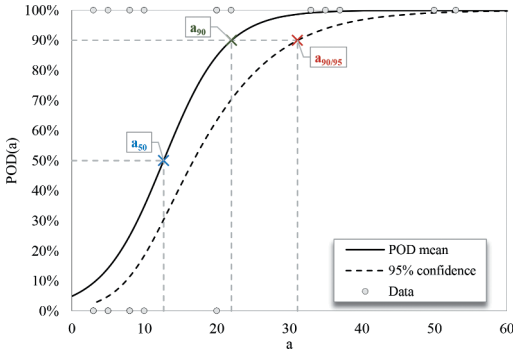


Figure 6. Typical PoD curve showing the most relevant points (a_{50}, a_{90}, $a_{90/95}$).

of the prior (increasing non-information). As seen there, 10 can be considered as the threshold marking the non-informative character of the prior.

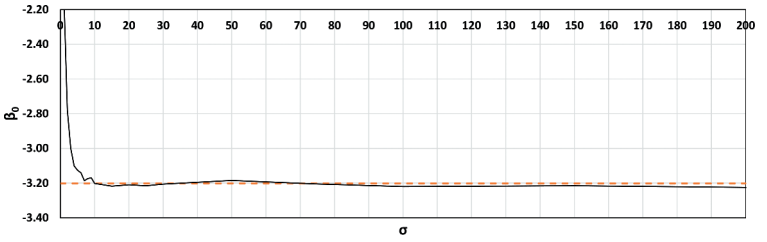


Figure 7. Evolution of the mean value of β_0 with increasing uncertainty of the prior distribution for scenario 1. The dotted line is the value of β_0 parameters considering $\sigma = 10$.

Figure 8 shows the "trace plot" of each chain for the β_0 parameter in the first scenario, i.e. a graph of the sampled parameter values as a function of step in the chain. The upper part in Figure 8 is a smoothed histogram. These plots are useful for a preliminary check of the convergence of the MCMC algorithm: if the traces of each chain in the trace plot overlap each other, then the chains are all representative of the posterior distribution; if any chain were isolated, then the convergence had not been achieved. A similar assessment can be performed on the density plot: if the density plots of the chains overlap, then the chains are producing representative values of the posterior distribution (Kruschke 2014). Similar convergence results were obtained for the rest of the scenarios.

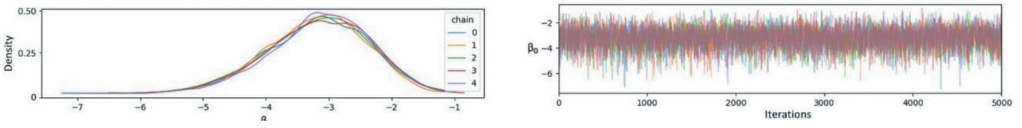


Figure 8. "Density plot" and "trace plot" of the β_0 parameter for scenario 1.

An example of the PoD plot is given in Figure 9, showing the curve obtained for the first scenario for which resulted $\beta_{0_{mean}} = -3.202$ and $\beta_{1mean} = 0.258$.

5 CONCLUSIONS

The main results of the analysis are displayed in Table 2, in term of critical values, i.e. a_{50}, a_{90}, and $a_{90/95}$.

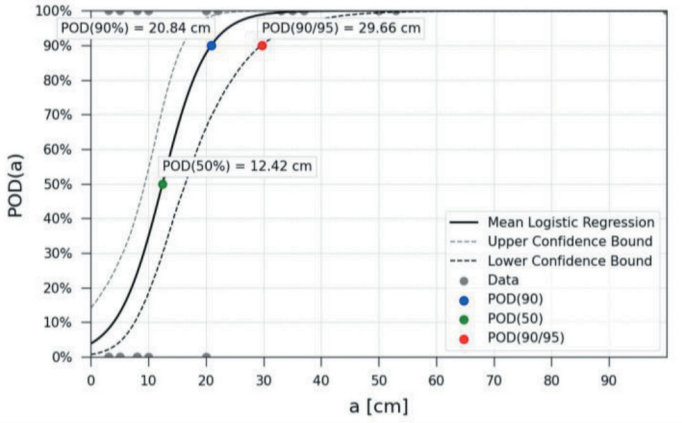


Figure 9. Bayesian PoD of scenario 1.

Table 2. Summary of results by Bayesian analysis.

			Bayesian method		
ID.	n_{hits}	n_{misses}	a_{50} [cm]	a_{90} [cm]	$a_{90/95}$ [cm]
SC1	36	27	12.42	20.84	29.66
SC2	24	16	17.23	23.65	32.46
SC3	47	42	11.02	21.84	32.26
SC4	27	35	16.43	25.65	35.67
SC5	32	49	10.82	24.25	49.50
SC6	74	77	13.23	24.65	32.26

Observing the results, the main conclusions that can be stated are:

- The concrete cover seems to be the most influencing parameter (SC1 vs. SC2, and SC3 vs. SC4). The thicker the cover, the less reliable the test.
- Varying the calibration introduce uncertainty. By comparing SC1 vs. SC3 and SC2 vs. SC4, it can be observed that higher critical voids are determined introducing different calibrations and fixing the other variables (i.e. concrete cover and scan typology).
- Since the most typical ducts' depth is around 15 cm, it seems a correct conclusion that the $a_{90/95}$ to be generally considered is around 30 cm (SC1, SC3, SC6).

The latter is the most important conclusion of the study since it allows to better design the investigation on PT structures. In detail, since is very likely to detect voids larger than 30 cm, the UTs can be performed using a pitch of 30 cm, higher than the one employed in the present research (10 cm), resulting in a significant save of resources.

REFERENCES

ACS Group. 2021. *A1040 MIRA 3D Operation Manual Ultrasonic Low-Frequency Tomograph*.

Aldrin, John C., Jeremy S. Knopp, and Harold A. Sabbagh. 2013. "Bayesian Methods in Probability of Detection Estimation and Model-Assisted Probability of Detection Evaluation." Pp. 1733–40 in *AIP Conference Proceedings*. Vol. 1511. American Institute of Physics Inc.

Anon. 2009. "Nondestructive Evaluation System Reliability Assessment".

ASTM International. 2015. *E3023-15 Standard Practice for PoD for â Versus a Data*.

ASTM International. 2018. *E2862-18 Standard Practice for PoD for Hit/Miss Data*.

Carino, Nicholas J. 2004. “The Impact-Echo Method: An Overview.” in *Structures - A Structural Engineering Odyssey, Structures 2001 - Proceedings of the 2001 Structures Congress and Exposition*.

Carsana, Maddalena, and Luca Bertolini. 2015. “Corrosion Failure of Post-Tensioning Tendons in Alkaline and Chloride-Free Segregated Grout: A Case Study.” *Structure and Infrastructure Engineering* 11 (3):402–11. doi: 10.1080/15732479.2014.887736.

Chib, Siddhartha. 2001. “Markov Chain Monte Carlo Methods: Computation and Inference.” *Handbook of Econometrics* 5:3569–3649.

Freij, Hani, David Dukeman, Christopher L. Alexander, Marcelo D. Ruffolo, Teresita Frigerio, Joaquín Boselli, Mario A. J. Mariscotti, and Alberto A. Sagüés. 2021. “Comparison of Novel Imaging Sensor and Gamma Ray Tomography Imaging of Grout Deficiencies in External Post-Tensioned Structural Tendons.” *NDT and E International* 117(June 2020). doi: 10.1016/j.ndteint.2020.102368.

Gandossi, Luca, and Charles Annis. 2010. *ENIQ TGR Technical Document - Probability of Detection Curves: Statistical Best-Practices*. doi: 10.2790/21826.

Garrido, I., S. Lagüela, R. Otero, and P. Arias. 2020. “Thermographic Methodologies Used in Infrastructure Inspection: A Review—Post-Processing Procedures.” *Applied Energy* 266(February):114857. doi: 10.1016/j.apenergy.2020.114857.

Godart, B. 2001. “Status of Durability of Post-Tensioned Tendons in France.” *Fib Bulletin No. 15 Durability of Post-Tensioning Tendons, Technical Report*, *Proceedings of a Workshop Held at Ghent University on 15–16 November 2001* 25–42.

Hoffman, Matthew D., and Andrew Gelman. 2014a. “The No-U-Turn Sampler: Adaptively Setting Path Lengths in Hamiltonian Monte Carlo.” *Journal of Machine Learning Research* 15:1593–1623. doi: https://doi.org/10.48550/arXiv.1111.4246.

Hoffman, Matthew D., and Andrew Gelman. 2014b. “The No-U-Turn Sampler: Adaptively Setting Path Lengths in Hamiltonian Monte Carlo.” *Journal of Machine Learning Research* 15:1593–1623.

Innocenzi, Raoul Davide, Giulia Pigliapoco, Sandro Carbonari, Fabrizio Gara, and Luigino Dezi. 2022. “Damage Detection of Post-Tensioned Cables in Existing Bridges with Digital Radiography.” Pp. 662–69 in *Lecture Notes in Civil Engineering*. Vol. 200 LNCE. Springer Science and Business Media.

Kanzler, Daniel, Christina Müller, and Jorma Pitkänen. 2013. “Evaluation of Radiographic Testing Performance with an Advanced POD Approach.” in *5th European-American Workshop on Reliability of NDE*.

Krautkrämer, Josef, and Herbert Krautkrämer. 1990. *Ultrasonic Testing of Materials*. Springer Berlin Heidelberg.

Kruschke, John K. 2014. *Doing Bayesian Data Analysis: A Tutorial with* r, JAGS, and *Stan*, *Second* Edition. Elsevier Science.

Muldoon, R., A. Chalker, M. C. Forde, M. Ohtsu, and F. Kunisue. 2007. “Identifying Voids in Plastic Ducts in Post-Tensioning Prestressed Concrete Members by Resonant Frequency of Impact-Echo, SIBIE and Tomography.” *Construction and Building Materials* 21(3):527–37. doi: 10.1016/j.conbuildmat.2006.04.009.

Roberts, Christian P., and Sylvia Richardson. 1998. “Markov Chain Monte Carlo Methods.” in *Robert, C.P. (eds) Discretization and MCMC Convergence Assessment. Lecture Notes in Statistics*. Vol. 135.

Salvatier, John, Thomas V. Wiecki, and Christopher Fonnesbeck. 2016. “Probabilistic Programming in Python Using PyMC3.” *PeerJ Computer Science*. doi: 10.7717/peerj-cs.55.

Schickert, Martin, Martin Krause, and Wolfgang Mü Ller. 2003. “Ultrasonic Imaging of Concrete Elements Using Reconstruction by Synthetic Aperture Focusing Technique.” *Journal of Materials in Civil Engineering* 15(3). doi: 10.1061/ASCE0899-1561200315:3235.

Stepinski, Tadeusz, and Fredrik Lingvall. 2010. “Synthetic Aperture Focusing Techniques for Ultrasonic Imaging of Solid Objects.” Pp. 1–4 in *8th European Conference on Synthetic Aperture Radar*. Aachen.

Terzioglu, Tevfik, Madhu M. Karthik, Stefan Hurlebaus, Mary Beth D. Hueste, Stefan Maack, Jens Woestmann, Herbert Wiggenhauser, Martin Krause, Patrick K. Miller, and Larry D. Olson. 2018. “Nondestructive Evaluation of Grout Defects in Internal Tendons of Post-Tensioned Girders.” *NDT and E International* 99:23–35. doi: 10.1016/j.ndteint.2018.05.013.

Trejo, David, Radhakrishna Pillai, Mary Beth, D. Hueste, and Paolo Gardoni. 2009. “Parameters Influencing Corrosion and Tension Capacity of Post-Tensioning Strands.” *ACI MAterials Journal* 106:144–53.

Virkkunen, Iikka, Tuomas Koskinen, Suvi Papula, Teemu Sarikka, and Hannu Hänninen. 2019. “Comparison of â Versus a and Hit/Miss POD-Estimation Methods: A European Viewpoint.” *Journal of Nondestructive Evaluation* 38(4). doi: 10.1007/s10921-019-0628-z.

Woodward, R. 2001. “Durability of Post-Tensioned Tendons on Road Bridges in the UK.” Pp. 1–10 in *fib Bulletin No. 15 Durability of Post-tensioning Tendons, Technical Report , Proceedings of a workshop held at Ghent University on 15–16 November 2001*, edited by L. Taerwe. Ghent.

Bridge Maintenance, Safety, Management, Digitalization and Sustainability – Jensen, Frangopol & Schmidt (eds)
© 2024 The Author(s), ISBN 978-1-032-77040-6
Open Access: www.taylorfrancis.com, CC BY-NC-ND 4.0 license

Influence of repair interventions on the safety of a reinforced concrete road bridge subjected to chloride ingress

K. Van Den Hende, S. Helderweirt, W. Botte, S. Matthys & R. Caspeele
Ghent University, Ghent, Belgium

G. Lombaert
KU Leuven, Leuven, Belgium

ABSTRACT: Policymakers are increasingly faced with the challenge of managing aging concrete bridges subjected to deterioration. Rebuilding these structures often leads to significant downtime and construction costs. Therefore, repairing and upgrading the existing infrastructure is often preferred instead. Typically, interventions are scheduled after severe signs of deterioration, which might involve significant costs. On the other hand, scheduling preventive interventions during the early stages of chloride-induced corrosion can be highly beneficial as the chloride content at the reinforcement level can be significantly altered. As a result, the structure's lifespan can be extended in a more cost-effective manner compared to a corrective maintenance strategy. This study investigates the impact of the timing of an intervention to the concrete ingress at the concrete surface (e.g. by applying a coating) on the time-dependent safety level of a real-life prestressed bridge girder, which enables to assess the importance of a preventive maintenance strategy.

1 INTRODUCTION

Optimization of repairs and structural intervention in concrete structures is essential to extend the lifetime of deteriorating structures as efficiently as possible. A popular remedy are the so-called preventive strategies, which are repetitive small interventions already applied in an early stage of the structure, ensuring that the safety level of the structure does not drop below a certain threshold over time. In terms of chloride-induced corroding structures, this intervention is typically executed in the initiation phase of the concrete, where the steel is not yet corroding and the chloride concentration is still below a critical threshold. In this work, the repair intervention investigated is related to a complete blockage of chlorides at the surface of the concrete, which is able to slow down the ingress of chlorides, thus extending the initiation period and limiting the duration of the corrosion process.

In the first part of this work, the quantification of the corrosion duration in a probabilistic framework is explained, taking into account blockage of chlorides at the surface for a certain duration. Afterwards, the relation between the corrosion degree and the safety level of a real-life prestressed bridge girder is determined and the effect of the repair intervention is quantified. In the end, conclusions are drawn about the application intervention types and future research topics are proposed.

2 QUANTIFICATION OF INITIATION AND PROPAGATION TIME

2.1 *Without intervention*

Chloride ingress into concrete is a subject which has been investigated thoroughly in previous research, leading to a general consensus regarding the modelling of chloride ingress over time

DOI: 10.1201/9781003483755-111

(fib bulletin 34, 2006). Generally, the one-dimensional diffusion law is used, described by Fick's second law (Crank 1975):

$$C(x,t) = C_s\left[1 - erf\left(\frac{x}{2\sqrt{Dt}}\right)\right] \tag{1}$$

where $C(x, t)$ [*m%cem*] is the concentration at distance from the surface x [m] and time t [y], C_s [*m%cem*] is the constant surface concentration, D [m^2/y] the (apparent) diffusion coefficient and *erf*(.) the Gaussian error function. If the chloride concentration at the level of the reinforcement exceeds a certain critical chloride content C_{crit}, the steel is depassivated, which is generally considered as the starting point of the corrosion process, i.e. the propagation phase.

In order to assess the safety of a structure at a certain time T throughout its lifetime, the propagation time T_{prop} is combined with the expected corrosion rate, which leads to a loss of reinforcement and consequently a reduced safety level. In order to determine the propagation time T_{prop}, one states that the propagation time is equal to the age of the structure subtracted by the initiation time, i.e. $T_{prop} = T - T_{ini}$. The initiation time T_{ini} can be quantified by considering the instant in time at which the corrosion concentration at the reinforcement is equal to the critical chloride content C_{crit}, which has a certain variability due to the uncertain parameters involved.

2.2 *With intervention*

In order to extend the initiation phase, repair techniques are available which can delay the onset of the propagation phase and thus reduce the amount of corrosion over a structure's intended lifetime (fib bulletin 102, 2022). The repair strategy considered in this work is the blockage of new chlorides at the surface of the concrete substrate, which can be the result of a coating at the surface. As a result, the ingress of chlorides slows down and the initiation period is extended. This repair strategy is assumed to function for a limited duration as a coating typically loses its effectiveness after a while, after which the chlorides are able to penetrate again. It must be noted that the effectiveness of the chloride blockage might decrease steadily over time instead of instantly losing all its blockage properties at once. However, this is considered outside of the scope of this work.

Modelling the chloride migration during and after the blockage is done by solving the diffusion equation with the principle of separation of variables (Crank 1975). The boundary and initial conditions for the chloride blockage are:

$$\frac{\partial C(x,t)}{\partial x}|_{x=0} = 0 \tag{2}$$

$$C(x,t)|_{x=h_1} = 0 \tag{3}$$

$$C(x,t)|_{t=0} = \bar{C}(x) \tag{4}$$

and for the free flow with an initial chloride profile:

$$C(x,t)|_{x=0} = Cs \tag{5}$$

$$\frac{\partial C(x,t)}{\partial x}|_{x=h_1} = 0 \tag{6}$$

$$C(x,t)|_{t=0} = \bar{C}(x) \tag{7}$$

where $\bar{C}(x)$ is the initial chloride profile and h_1 the limit of the semi-infinite region, chosen equal to 300 mm in this work. The solution for both problems can be derived in the form of:

$$C(x,t) = C_k + \sum_{n=1}^{\infty} A_n f_n\left(\frac{\lambda_n x}{\sqrt{D}}\right) exp\left(-\lambda_n^2 t\right) \tag{8}$$

with:

$$C_k = \begin{cases} 0 \text{ for chloride blockage} \\ C_s \text{ for free flow} \end{cases} \tag{9}$$

$$f_n(y) = \begin{cases} \cos(y) \text{ for chloride blockage} \\ \sin(y) \text{ for free flow} \end{cases} \tag{10}$$

$$A_n = \frac{2}{h_1} \int_0^{h_1} \left[\bar{C}(x) - C_k\right] f_n\left(\frac{\lambda_n x}{\sqrt{D}}\right) dx \tag{11}$$

$$\lambda_n = \frac{\sqrt{D}}{h_1}\left(n + \frac{1}{2}\right)\pi \tag{12}$$

The number of terms n is practically limited to a finite number, which is chosen as 50 in this work, which has proven to be sufficient for convergence of the solution. In Figure 1 and Figure 2, an example is shown of an intervention which is applied after 20 years and which completely blocked the ingress of new chlorides for another 40 years. The situations with and without interventions are compared, which shows the ingress of chlorides is successfully delayed, extending the initiation period.

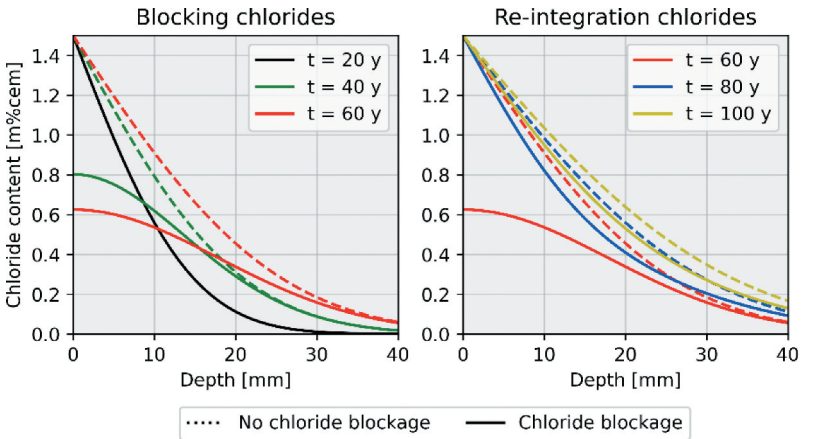


Figure 1. Chloride ingress during and after blockage from 20 to 60 years ($D = 0.2\frac{10^{-12}m^2}{s}$, $C_s = 1.5\ m\%cem$).

Considering the probabilistic properties from Table 1, the distribution of the initiation period T_{ini} is determined by the instant at which the chloride concentration at the cover reaches the critical content, as illustrated in Figure 2. Afterwards, the duration of the corrosion phase T_{prop} is determined at a certain time instant by subtracting the value of T_{ini}. The distribution for the duration of the corrosion phase after 100 years is shown in Figure 3 for a structure without intervention and a structure with chloride blockage applied at an age of 20 years. Three cases are considered, where the effectiveness of the blockage varies from 20 to 60 years. Blocking the chloride ingress at the surface for a certain duration leads to a longer initiation phase and, for this reason, shifts the distribution of the propagation period to smaller values, which shows the benefit of this intervention.

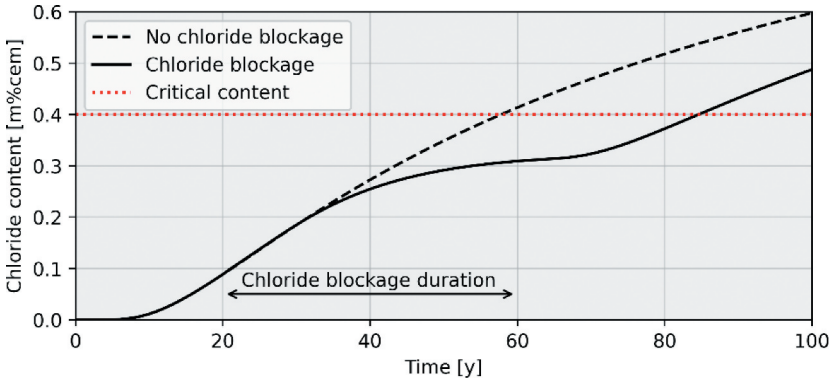


Figure 2. Influence of chloride blockage on chloride concentration over time at a depth of 30 mm after blockage from 20 to 60 years ($D = 0.2\,\frac{10^{-12}m^2}{s}$, $C_s = 1.5\ m\%cem$).

Table 1. Probabilistic models related to the chloride ingress.

Variable	Distr.	μ	V	Source
Concrete cover X [mm]	LN[a]	40	0.20	(fib bulletin 76, 2015)
Diffusion coefficient concrete D [$10^{-12}m^2/s$]	LN	0.1	0.20	(fib bulletin 76, 2015)
Surface concentration C_s [$m\%cement$]	LN	1.5	0.25	(fib bulletin 76, 2015)
Critical concentration C_{crit} [$m\%cement$]	Beta[b]	0.6	0.25	(fib bulletin 76, 2015)

[a] Normal distribution is replaced by LN distribution to avoid negative sample values for concrete cover
[b] With lower limit 0.2 $m\%cem$ and upper limit 2.0 $m\%cem$

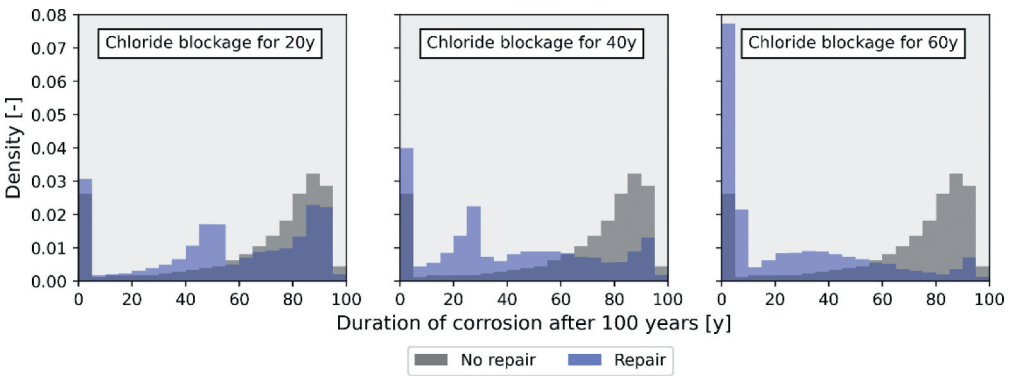


Figure 3. Distribution of duration of corrosion propagation after 100y, with and without chloride blockage at 20y.

3 RELATION BETWEEN SAFETY LEVEL AND PROPAGATION PERIOD FOR A BRIDGE GIRDER

By applying an intervention at an early age, the onset of the propagation period can be delayed significantly, leading to a shorter duration of the propagation period within a given lifetime, as illustrated in the previous section. In order to show how this change in propagation period influences the safety level of a structure, a case study of a prestressed bridge girder

subjected to chloride-induced corrosion is considered. First of all, the relation between the duration of the propagation period and the safety level of the girder is determined. Afterwards, the influence of the intervention discussed previously on the safety level is quantified.

3.1 *Structural capacity of the investigated prestressed girder*

A bridge girder, which is part of an actual bridge superstructure, is considered. The prestressing consists of thirty 52.8 mm^2 strands, leading to a total prestress steel area of 1584 mm^2. The dimensions of the girders are given in Figure 5, where the prestressing strands are assumed to be located at the same location within the cross-section, for simplification purposes. Only the bending failure mode of the prestressed girder is considered to be critical, and the shear capacity of the girder is not evaluated. Moreover, only the location at mid span is considered to be critical and hence this is the only location where the moment capacity is determined. As illustrated in Figure 4, the prestress is applied as an external load and the internal moment resistance is calculated as illustrated in Figure 5. For the concrete, a parabolic-rectangular stress-strain diagram is used with yield limit 2 ‰ and ultimate strain 3.5 ‰. For the prestressing steel, an elastic-perfect plastic stress-strain diagram is used where the ultimate strain is limited to 10 ‰ and the steel is assumed to be yielding in the ultimate limit state. The moment capacity M_R is determined as follows:

$$M_R = M_{R,cs} + M_P + M_0 \tag{13}$$

$$M_P \cong P \cdot 7.25\ m = A_p \cdot \sigma_{p\infty} \cdot sin\left(arctan\left(\frac{357 - 147}{7250}\right)\right) \cdot 7.25\ m \tag{14}$$

$$M_0 = A_p \cdot \sigma_{p\infty} \cdot (0.5\ m - 0.147\ m) \tag{15}$$

where $M_{R,cs}$ is the bending moment capacity of the cross-section analysis, including the model uncertainty of either concrete crushing or steel yielding given in Table 2, M_P the moment due

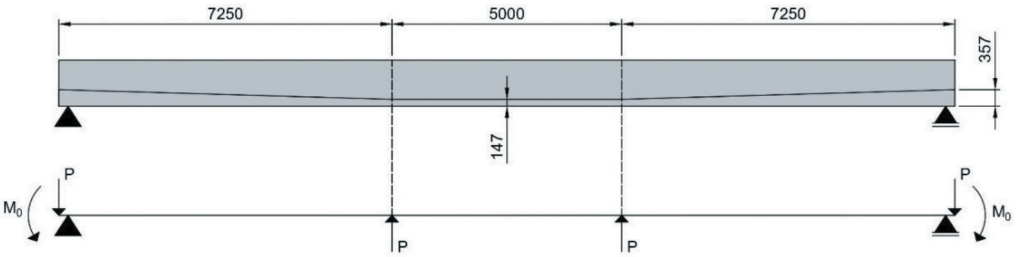


Figure 4. Calculation of prestress as external forces (dimensions in mm).

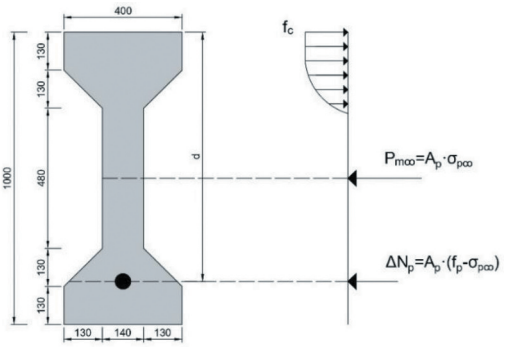


Figure 5. Calculation of internal forces prestressed girder (dimensions in mm).

to the localised force at the draping point and M_0 the external effect of the prestressing at midspan.

Using the probabilistic properties from Table 3, the distribution of the resistance M_R is determined. The resistance is calculated for multiple values of the total prestress area, in order to quantify the effect of corrosion on the resistance of the girder. Note that this is a simplified way of modelling the influence of corrosion, for a more detailed analysis is referred to (Franceschini 2021, 2022a, 2022b) and (Jeon 2019).The results are given in Figure 6, together with their fitted lognormal distribution. As the coefficient of variation V remains more or less constant, and the mean value changes linearly with the number of strands, the following distribution is chosen for the moment resistance of one girder:

$$M_R(A_{p,cor}) = LN\left(\mu = 2097 - 2027\frac{A_{p,cor}}{A_{p0}}\ kNm; \sigma = 0.045\mu\right) \tag{16}$$

where $A_{p,cor}/A_{p0}$ is the ratio of the corroded prestress area over the initial area.

Table 2. Probabilistic models for the variables related to the structural resistance of the investigated prestressed girder.

Variable	Distr.	X_k	μ	V	Source
Concrete strength f_c $[MPa]$	LN	55	65.1[a]	0.10	(MC2020)
Prestress strength f_p $[MPa]$	Normal	1619	$1.04X_k$	0.025	(JCSS, 2001)
Long-term prestress $\sigma_{p\infty}$ $[MPa]$	LN	970	X_k	0.09	(JCSS, 2001)
Prestress area A_p $[mm]$	Det.	1584	X_k	/	/
Effective depth prestress d $[mm]$	LN	853	$[1 - f(X_k)]\ X_k$[b]	$f(X_k)$[b]	(MC2020)
Bending moment resistance model uncertainty steel $\theta_{R,M,s}$	LN	/	1	0.05	(JCSS, 2001)
Bending moment resistance model uncertainty concrete $\theta_{R,M,c}$	LN	/	1.2	0.15	(JCSS, 2001)

[a] chosen such that characteristic value is based on 5-percentile of the distribution

[b] $f(X_k) = 0.05\left(\frac{200}{X_k}\right)^{2/3}$

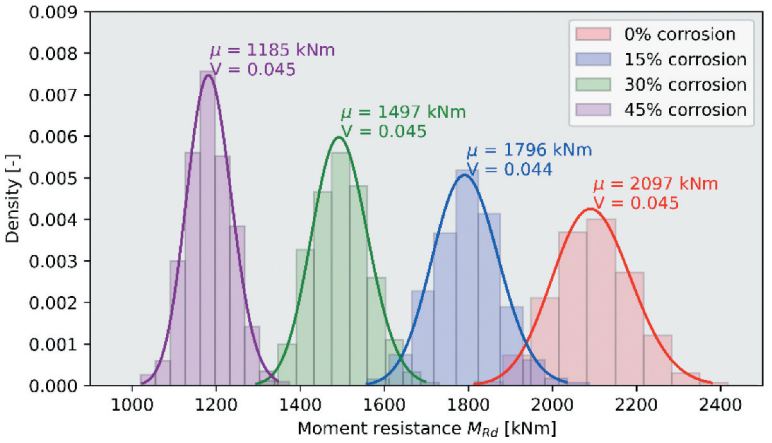


Figure 6. Moment resistance of prestressed girder for different ratios of the corroded prestress area over the initial area.

3.2 *Limit state equation for bending of prestressed girder*

The limit state equation for bending of a bridge girder is described as follows:

$$g_i(\boldsymbol{X}) = M_R\left(A_{p,cor}\right) - \theta_E\left[M_{E,g} + M_{E,p} + C_{0T}M_{E,q}\right] \tag{17}$$

where $M_R(A_{p,cor})$ is the moment resistance of a girder with $A_{p,cor}$ the corroded prestress area defined by Eq. (16) and the other parameters are defined in Table 3. The loads are based on an evaluation of the bridge superstructure subjected to a range of permanent loads and variable traffic loads corresponding to Load Model 1 of EN1991-2.

The corroded prestress area is governed by the propagation period T_{prop} and corrosion rate V_{corr}. The annual failure probability p_f of a girder at a given time instant t can therefore be defined as:

$$p_f(t) = \int_0^t f_{T_{prop}}(\tau)P[g_i(V_{corr}\tau, \boldsymbol{X}) < 0]d\tau \tag{18}$$

In this expression, it is assumed that the corrosion rate is a deterministic value which is expressed in $mm^2/year$. The duration of corrosion propagation has a certain distribution described by a probability density function $f_{T_{prop}}$, as discussed in the first part of this work. Practically, if the annual reliability index β_{1y} needs to be determined at a given time instant t, the distribution $f_{T_{prop}}$ (as illustrated in Figure 3 for $t=100$ years) is determined for this time instant, and applied in Eq. (18).

Table 3. Probabilistic parameters for loads on bridge superstructure.

Variable	Distr.	X_k	μ	V	Source
Self-weight $M_{E,g}$ $[kNm]$	Normal	579.2	X_k	0.04	(MC2020)
Imposed permanent load $M_{E,p}$ $[kNm]$	Normal	228.6	X_k	0.10	(MC2020)
Time-variant component of traffic load $M_{E,q}$ $[kNm]$	Gumbel	832.8	$0.73X_k$[a]	0.075	(MC2020)
Time-invariant component of traffic load C_{0T} $[-]$	LN	/	1.0	0.10	(MC2020)
Load model uncertainty θ_E $[-]$	LN	/	1.0	0.075	(MC2020)

[a] corresponding to a 1-year reference period

3.3 *Influence of repair strategy*

A fictional chloride ingress problem is considered with properties given in Table 1 and a deterministic corrosion rate of 2.5 mm^2/year. From the moment the critical chloride at the cover depth level is exceeded, the corrosion process starts and the amount of prestress area decreases linearly over time. Note that the corrosion process is simplified as all strands are assumed to be located in one place, which is not the case in reality as the strands are distributed over different locations in the cross section.

In Figure 7, the time-dependent annual reliability index of the girder is evaluated over a lifespan of 100 years for a structure that is subjected to a chloride blockage intervention at an age of 20 years. Initially, the annual reliability index of the undamaged girder corresponds to a value of 4.0, which approximates the target reliability level for a structure with consequence class CC2 according to (JCSS 2001, ISO 2394:2015). The duration of the chloride blockage has a large influence on the final safety level of the girder, which shows the importance of the durability of the intervention.

Figure 8 shows the reliability index of the girder at an age of 100 years, for different chloride protection scenarios. Without intervention, an annual reliability value of 2.8 would be reached, which can be significantly improved when the chloride blockage is applied early enough. If the chloride blockage is applied after a lot of chlorides have already migrated into the concrete (e.g. age of 40 years), the benefit is much less compared to the situation where the chlorides are countered from an early age.

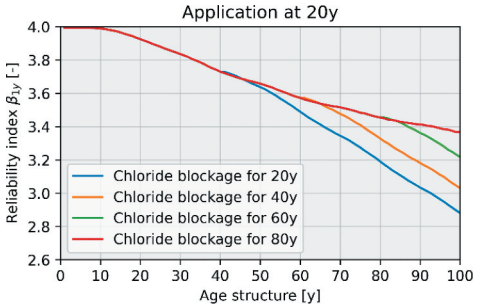


Figure 7. Annual reliability index over time of the bridge girder subjected to an intervention at an age of 20y.

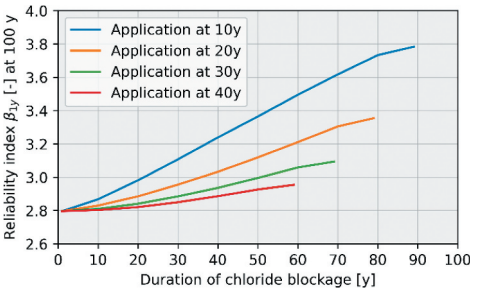


Figure 8. Annual reliability index of the center bridge girder at an age of 100y for interventions at 10y, 20y, 30y, and 40y.

4 CONCLUSIONS AND FURTHER WORK

This work proposes a framework to quantify the influence of a chloride ingress intervention in the initiation phase on the safety level of a structure over time. The framework is applied to a simplified case of an actual prestressed bridge girder. The intervention type considered is a blockage of chlorides at the surface, e.g. by applying a coating, which slows down the migration of chlorides within the concrete substrate. It has been shown that if this intervention is applied early enough in the lifetime of the structure, it is an efficient way to extend the initiation period of a structure and improve the safety level over time. In case the intervention is applied at a later time instant, its effect is much less pronounced as the steel still becomes depassivated by the large amount of chlorides that has already ingressed into the structure.

An important aspect that should be taken into account is the uncertainty regarding the corrosion rate, which is difficult to predict in an initial stage of a structure. However, if one expects a large corrosion rate and notices the ingress of chlorides might cause problems at an early age, the chloride blockage may be a good solution to the safety problems that may arise. In case the corrosion process has already started and one notices a high corrosion rate, other repair strategies might be more beneficial such as the replacement of (part of the) concrete cover in order to re-passivate the steel and stop the corrosion process.

Further work includes the implementation of other repair strategies in order to deal with situations as just described. Moreover, a more realistic corrosion process should be considered, taking into account the fact that the prestressing strands are spatially distributed over the cross-section and the corrosion process in the strands is not uniformly distributed over the strands. Lastly, also the safety level of a complete structure could be assessed, by extending the current analysis of a single bridge girder.

ACKNOWLEDGEMENTS

This research was performed within the framework of FWO SBO project lifeMACS “Multilayer Bayesian life-cycle Methodology for the Assessment of existing Concrete Structures”, supported by FWO-Flanders (FWO-SBO project S001021N).

REFERENCES

CEN. 2003. Eurocode 1 – action on structures – Part 2: Traffic loads on bridges. *European Committee of Standardization*. Brussels.

Crank, J. 1975. The mathematics of diffusion. Oxford University Press. London.

Fib. 2006. Fib Bulletin 34: Model code for service life design. International Federation for Structural Concrete.

Fib. 2015. Fib Bulletin 76: Benchmarking of deemed-to-satisfy provisions in standards: durability of reinforced concrete structures to chlorides. International Federation for Structural Concrete.
Fib. 2022. Fib Bulletin 102: Guide for protection and repair of concrete structures. International Federation for Structural Concrete.
Franceschini L et al. 2021. Analytical method for the evaluation of the residual service life of prestressed concrete beams subjected to corrosion deterioration. Structural Concrete. 23 (1): 121–137.
Franceschini L et al. 2022a. Mechanical behaviour of corroded strands under chloride attack: A new constitutive law. Construction and Building Materials. 316.
Franceschini L et al. 2022b. A simplified stressstrain relationship for the mechanical behavior of corroded prestressing strands: The SCPS-model. Structural Concrete. 24 (1): 189–210.
ISO. 2015. ISO 2394:2015 – General principles on reliability of structures. International Organization for Standardization. Geneva.
JCSS. 2001. Probabilistic model code. Joint Committee on Structural Safety.
Jeon C et al. 2019. Equivalent material model of corroded prestressing steel strand. Journal of Materials Research and Technology. 8(2): 2450–2460.

Bridge Maintenance, Safety, Management, Digitalization and Sustainability – Jensen, Frangopol & Schmidt (eds)
© 2024 The Author(s), ISBN 978-1-032-77040-6
Open Access: www.taylorfrancis.com, CC BY-NC-ND 4.0 license

Probabilistic assessment of the moment-curvature response of PC beams with different corrosion scenarios

B. Belletti, S. Ravasini & S. Sandrini
Department of Engineering and Architecture, University of Parma, Parma, Italy

R. Caspeele & W. Botte
Department of Structural Engineering and Building Materials, Ghent University, Belgium

ABSTRACT: Corrosion of the reinforcement significantly affects the resistance and ductility of concrete members. While various approaches have been proposed to study the sectional response of corroded reinforced concrete structures, the effects of corrosion on prestressed concrete (*PC*) members still poses significant challenges. Therefore, this study focuses on investigating the bending resistance of prestressed concrete sections with different corrosion scenarios through probabilistic assessment using Monte Carlo simulations based on preliminary results of previous work. First, the mechanical properties of the materials and the investigated pit depths have been established as input parameters of the cross-sectional model. To account for corrosion in the constitutive behaviour of the prestressing strands, the Simplified Model for Corroded Prestressing Strands (*SCPS* model) has been adopted. Furthermore, different statistical distributions of the pit depths are derived to represent different corrosion scenarios. Subsequently, Monte-Carlo simulations are utilized to capture the inherent randomness associated with the mechanical properties and pit depths in the sectional response of *PC* elements. Based on the outcome of these simulations, the influence of corrosion on the moment-curvature response as well as the expected failure mode are assessed. Finally, the latter results are investigated for different scenarios of corrosion, providing a comprehensive understanding of the effects of corrosion in *PC* elements and the associated uncertainties. These findings are relevant to researchers, engineers, and practitioners involved in the design, assessment, and maintenance of prestressed concrete structures.

1 INTRODUCTION

The load-bearing capacity assessment of corroded reinforced and prestressed concrete (*RC* and *PC*) structures is a crucial topic in the engineering community. Over the years, the conducted studies have focused on corroded monolithic *RC* structures while few attention has been paid to prestressed structures (Vereecken et al., 2021). In recent literature, both experimental and numerical tests are available (Belletti et al., 2019, 2020; Coronelli et al., 2009; Galano et al., 2023a; Galano et al., 2023b; Rinaldi et al., 2010; Vecchi et al., 2020). Probabilistic studies on the bearing capacity of corroded *PC* members are still lacking, although approaches are available for wires (Lee et al., 2023). This work focuses on the probabilistic assessment - via Monte-Carlo (*MC*) simulations - of the moment-curvature M-χ response of naturally-corroded pre-tensioned concrete beams described in the experimental tests by Belletti et al. (2020) and Vecchi et al. (2020). The work is based on preliminary results of a previous study (Belletti et al., 2023). To consider the chloride-induced corrosion on prestressing strands, the *SCPS* model (Franceschini et al., 2022) is considered. Firstly, different statistical distributions of uncorroded and corroded properties in terms of pit depths are derived and different corrosion scenarios are established. Secondly, a model uncertainty is estimated, and statistical distributions of cracking and ultimate moments are provided and discussed. Finally, a practical estimation of the design resistance of *PC* members subjected to corrosion is carried out. A Matlab code was developed for the purpose.

DOI: 10.1201/9781003483755-112

2 METHODOLOGY, MATERIAL PROPERTIES AND CORROSION SCENARIOS

2.1 *General method*

Monte-Carlo (*MC*) analyses and probabilistic assessment (*PA*) have been carried through the following steps, as already described in a previous work by the authors (Belletti et al., 2023):

1. *MC* simulations are performed with as input data the geometry of the *PC* beam section and the random variation of the mechanical properties of concrete and prestressing strands by establishing corrosion scenarios. Refer to Sections 2.2, 2.3.
2. The output of the *MC* simulations for each scenario are the moment-curvature responses and failure modes. Refer to Section 3.1.
3. The *PA* is performed by evaluating the probability distributions and the design resisting moment based on different percentiles. Refer to Section 3.2.

Details about the number of simulations and corrosion scenarios are reported in Section 2.3.

2.2 *Reference PC beam section geometry and random uncorroded material properties*

The geometrical features of the reference pre-tensioned beam section are reported in Belletti et al. (2020) and Vecchi et al. (2020) and shown in Figure 1(a). The *PC* beam section has width, b, and height, h, equal to 150 and 300 mm, respectively. The lower reinforcement is formed by two seven-wire strands, with outer wires' diameter, ϕ_{out}, equal to 4.26 mm and the inner one, ϕ_{inn}, equal to 4.38 mm, thus a nominal diameter equal to 12.9 mm and total strands' area $A_{p,0}$ equal to 201.06 mm^2. The upper reinforcement, $A_{s,0}$, consists of two bars with a diameter of 5 mm and no transversal reinforcement is provided. The concrete cover is equal to 50 mm. The effective depth of the two strands, d_p, and the eccentricity, e, are equal to 250 mm and 100 mm, respectively.

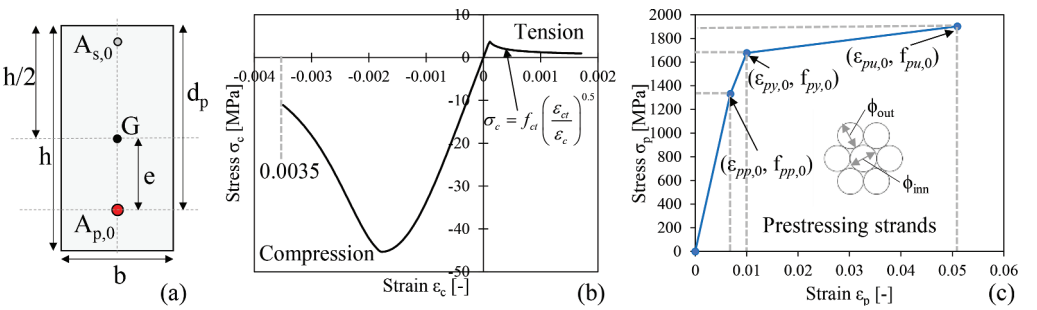


Figure 1. Reference *PC* beam section geometry and stress-strain relations for concrete and prestressing steel strands (Franceschini et al., 2022).

The random variables associated to the mechanical properties of concrete and uncorroded prestressing steel are reported in Table 1. The Thorenfeldt model was adopted for concrete in compression and the power law was used for tensile softening, Figure 1(b). A lognormal distribution was used for the uncorroded properties of concrete and a normal distribution was used for uncorroded prestressing steel (JCSS, 2001). The *SCPS* model (Franceschini et al., 2022) was used for the strands' stress-strain relation (Figure 1(c)). The stresses, $f_{pp,0}$ and $f_{py,0}$, are assumed equal to $0.7 \cdot f_{pu,0}$ and $0.882 \cdot f_{pu,0}$, respectively, while the strains, $\varepsilon_{pp,0}$ and $\varepsilon_{py,0}$, are assumed equal to $f_{pp,0} / E_p$ and 0.01, respectively. By considering only long-term effects, the uncorroded prestressing stress, $\sigma_{p,0}$ was estimated equal to 1171 MPa. The ordinary reinforcement, $A_{s,0}$, has a yield strength equal to 435 MPa. The random variability of the mechanical properties of mild rebars is not considered herein since it does not affect the overall resistance of the section. The relationships between the normal mean and standard deviation with the lognormal one is reported in the Eq. (1) and (2):

$$\lambda = \ln(\mu) - 0.5\zeta^2 \tag{1}$$

$$\zeta = \sqrt{\ln(1 + CoV^2)} \tag{2}$$

where the coefficient of variation, CoV, is the ratio between standard deviation, σ, and mean μ.

Table 1. Uncorroded materials properties random variables and distributions.

Material	Property	Normal distribution (μ, σ)	Lognormal distribution (λ, ξ)
Concrete	f_c [MPa]	45.380, 6.848	3.804, 0.150
	f_{ct} [MPa]	3.808, 0.364	1.332, 0.098
Prestressing steel	$f_{pu,0}$ [MPa]	1901.75, 40.00	-, -
	$\varepsilon_{pu,0}$ [-]	0.051, 0.0035	-, -

2.3 *Random corroded prestressing steel properties and corrosion scenarios*

Table 2 reports the results of the study on the pitting distribution of corroded strands retrieved from the *PC* beams described in the previous Section (Franceschini et al., 2022). Firstly, each corroded strand was scanned, and the distribution of pits was derived by analysing cross-sections along the overall strand every 10 mm spacing. Secondly, for each strand, the maximum pit depth was detected. In this work, as further improvement, linear correlations between the maximum pit depth P_{max}/r_{out} (or P_{max}) and mean and standard deviation values have been constructed, refer to Figure 2. The radius of the exterior wires, r_{out}, is equal to 2.13 mm for the strands. The proposed equations allow to estimate the statistical pit distribution from the knowledge of the maximum pit depth detected along a corroded strand.

Table 2. Maximum pit depth and pit distribution for the strands analysed in Franceschini et al. (2022).

ID Sample	$\varepsilon_{pu,corr,exp}$ [%]	P_{max}/r_{out} [-]	μ [mm]	σ [mm]	$\varepsilon_{pu,corr,an}$ [%]	θ_i [-]
PB9-L(12-82)	0.68	0.803	0.63	0.29	0.81	0.841
PB9-L(426-496)	3.16	0.199	0.20	0.14	1.73	1.828
PB9-R(15-60)	1.07	1.307	0.70	0.38	0.99	1.083
PB10-L(138-208)	0.56	0.277	0.37	0.15	0.76	0.740
PB10-L(445-515)	0.82	1.150	0.42	0.42	0.94	0.872
PB10-R(287-332)	0.69	1.352	0.48	0.36	0.86	0.803
PB11-L(196-266)	0.86	0.658	0.28	0.23	0.94	0.911
PB11-R(6-51)	0.77	0.458	0.34	0.30	0.89	0.860
PB11-R(273-318)	0.47	0.592	0.33	0.35	0.67	0.699
PB12-L(12-82)	0.80	0.730	0.53	0.26	0.87	0.919
PB12-L(124-169)	0.59	0.576	0.30	0.24	0.66	0.888
PB12-R(100-170)	0.36	0.490	0.34	0.21	0.73	0.492
PB13-L(1-46)	0.95	0.685	0.43	0.25	0.82	1.163
PB13-R(0-70)	0.75	0.648	0.50	0.23	0.76	0.982
PB13-L(108-178)	0.81	0.864	0.61	0.46	0.89	0.909
PB13-R(70-115)	1.03	0.510	0.32	0.27	0.86	1.199
PB14-L(10-55)	0.84	1.050	0.65	0.34	0.86	0.981
PB14-R(2-72)	0.62	0.576	0.48	0.26	0.72	0.863
PB14-R(77-122)	-	0.254	0.23	0.12	1.64	-

Firstly, based on the *SCPS* model (Franceschini et al., 2022), a total of four corrosion scenarios (*CSs*), (*S1*, *S2*, *S3* and the uncorroded one *S0*) have been established depending on ultimate corroded strains of the most corroded wire, $\varepsilon_{pu,corr}$, (Figure 3(a) and Table 3)

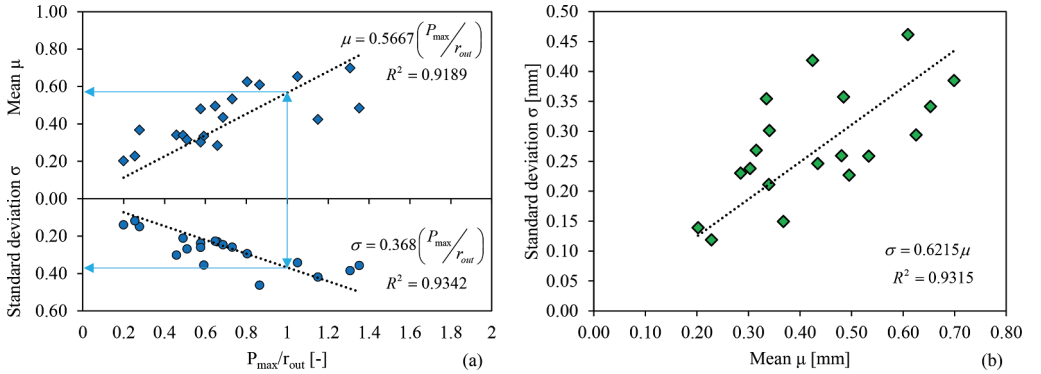


Figure 2. Correlations between P_{max}/r_{out} and mean and standard deviation.

calibrated to fall into the middle of the three ranges of the stress-strain relation. The analytical relation between the ultimate corroded strain and pit depth is reported in Eq. (3), by Franceschini et al. (2022):

$$\begin{cases} \frac{\varepsilon_{pu,corr}-\varepsilon_{py,0}}{\varepsilon_{pu,0}-\varepsilon_{py,0}} = 1 - 3.03\left(\frac{P}{r_{out}}\right) & 0 \le \frac{P}{r_{out}} < 0.33 \\ \frac{\varepsilon_{pu,corr}}{\varepsilon_{py,0}} = 1 - 0.599\left(\frac{P}{r_{out}} - 0.33\right) & 0.33 \le \frac{P}{r_{out}} \le 2.00 \end{cases} \quad (3)$$

The maximum pit depths P_{max} of each *CS* were thus calculated with Eq. (3). Secondly, from the correlations reported in Figure 2, the corresponding statistical distribution can be established, as shown in Figure 3(b) and reported in Table 3. These lognormal distributions of the pits have been adopted for the *MC* simulations as the random pits causing the failure of the most corroded wire. The prestress level decay due to corrosion is accounted for with the formula $\sigma_{p,corr} = \exp(-0.133\mu_{loss})$, where μ_{loss} is the cross-section loss (Ravasini et al., 2023). A total of 2004 simulations were run (500 random plus 1 with average values for each scenario).

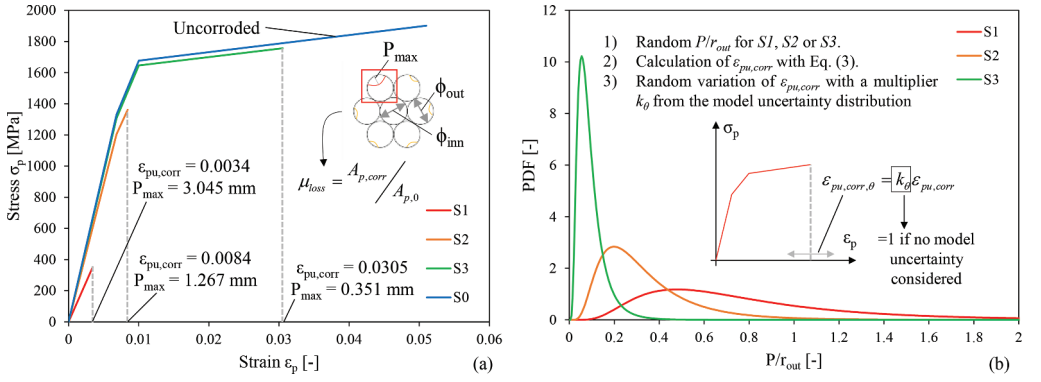


Figure 3. Corrosion scenarios: (a) stress-strain, (b) lognormal distributions of pits and model uncertainty.

The *SCPS* model uncertainty was considered by following the steps (Franceschini et al., 2023):

Table 3. Summary of corrosion scenarios and prestressing strands' random variable.

	Max. pit depth		Distributions of pits used for the *MC* simulations			
Scenario (# sim)	$\varepsilon_{pu,corr}$ [%]	P_{max} [mm]	μ [mm]	σ [mm]	λ	ζ
S1 (501)	0.340	3.045	0.810	0.526	-0.386	0.593
S2 (501)	0.840	1.267	0.337	0.219	-1.263	0.593
S3 (501)	3.050	0.351	0.094	0.061	-2.545	0.593
S0 (501)	5.100	0.000	-	-	-	-

1. For each strand "*i*", the percentile corresponding to $P_{max,i}$ is calculated with the Eq. (4):

$$\xi_{\max,i} = \Phi\left(\ln\left(P_{\max,i}\right) - \lambda_i/\zeta_i\right) \tag{4}$$

2. The average and standard deviation, $\mu_{\xi,max}$ and $\sigma_{\xi,max}$, of the percentiles are calculated.
3. The mean penetration depth for the maximum pit is estimated in a simplified way as the percentile of the distribution of the individual penetration depth measurements by using the Eq. (5):

$$\mu_{P_{\max,i}} = \exp\left(\lambda_i + \zeta_i \Phi^{-1}\left(\mu_{\xi_{\max}}\right)\right) \tag{5}$$

The value of $\varepsilon_{pu,corr,an}$, is re-calculated with Eq. (3) for each specimen and the ratio $\theta_i = \varepsilon_{pu,corr,exp}/\varepsilon_{pu,corr,an}$, is found, refer to Table 2. From the lognormal model uncertainty's distribution, (λ_θ=-0.0956 and ζ_θ=0.2840, or μ_θ=0.946 and σ_θ=0.274)), a coefficient k_θ is randomly used to multiply the ultimate corroded strain calculated with Eq. (3). Refer to Figure 3(b) for clarity.

3 RESULTS

3.1 *Moment-curvature responses and failure modes*

The moment-curvature responses corresponding to the different corrosion scenarios are plotted and shown in Figure 4. Table 4 shows the corresponding statistical parameters for the different corrosion scenarios and distributions, by considering the model uncertainty for cracking and ultimate moments. The normal, lognormal and Generalised Extreme Value (GEV) distributions have been used. For *S3* and *S0* scenarios, all the three distributions fit the numerical results well since the severity of corrosion is low. Based on R^2 value, for *S1* and *S2* scenarios, the *GEV* distribution fits the numerical results better, as observed in the previous work (Belletti et al., 2023).

The red curves in Figure 4 correspond to the analysis with the average values reported in Table 2 and Table 3. In the following, the results with the *GEV* distribution will be shown. Figure 5(a) shows the probability distribution functions (*PDFs*) of cracking and ultimate moments, while Figure 5(b) shows the decay of cracking and ultimate moments vs the normalised pit depth P/r_{out}. It can be observed that there is an increase in the dispersion of moments with increasing corrosion, with σ ranging from 1.49 to 8.18 for M_{cr} and from 1.84 to 11.77 for M_u. The average M_{cr} ranges from 47.36 (*S0*) to 32.15 kN·m (*S1*). A similar trend is observed for the average M_u, from 77.19 (*S0*) to 68.03 kN·m (*S1*). In addition, the effect of the model uncertainty is shown in Table 5 for the ultimate moment, where a higher standard deviation and a lower average value can be observed compared to the case without (k_θ fixed =1) considering the model uncertainty.

The corrosion is also recognized to affect the failure mode of a *RC* or *PC* members. In this study, the sectional failures are attributed to: (i) achieving concrete crushing in compression, (ii) achieving ultimate corroded strain of the most corroded wire of the strand. Table 6 reports the failures of the *CSs*: *S1* showed more than half simulations with strand's failure, while *S0* and *S3* are similar and show concrete crushing failure.

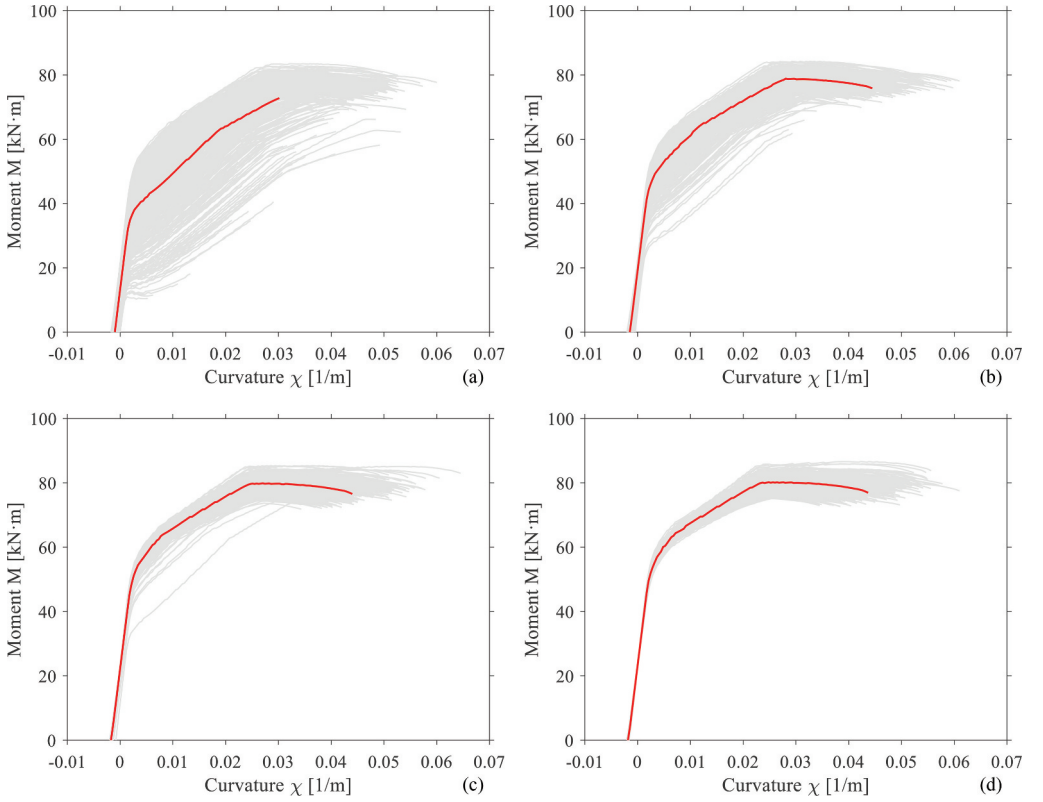


Figure 4. Moment-curvature responses: (a) *S1*, (b) *S2*, (c) *S3*, (d) *S0*.

Table 4. Summary of results for the moment-curvature response considering the model uncertainty.

		Cracking moment M_{cr} [kN·m]				Ultimate moment M_u [kN·m]			
Scenario	Distribution	R^2	μ [kN·m]	σ [kN·m]	CoV [%]	R^2	μ [kN·m]	σ [kN·m]	CoV [%]
	Normal	0.980				0.865			
S1	Lognormal	0.953	32.15	8.18	25.45	0.838	68.03	11.77	17.30
	GEV	0.998				0.950			
S2	Normal	0.976	40.93	4.30	10.51	0.942	75.31	3.53	4.69
	Lognormal	0.965				0.936			
	GEV	0.990				0.953			
S3	Normal	0.998	45.80	2.08	4.55	0.998	76.76	1.88	2.44
	Lognormal	0.997				0.998			
	GEV	0.996				0.997			
S0	Normal	0.998	47.36	1.49	3.15	0.997	77.19	1.84	2.39
	Lognormal	0.997				0.998			
	GEV	0.998				0.998			

3.2 *Design resisting moment estimation*

For practical purposes, the design resisting moment, M_d, can be estimated with the percentile:

$$p = \Phi(-\alpha_R \beta) \tag{6}$$

Table 5. Effect of the model uncertainty on the ultimate moment.

	Without model uncertainty			With model uncertainty		
	μ [kN·m]	σ [kN·m]	CoV [%]	μ [kN·m]	σ [kN·m]	CoV [%]
S1	70.97	9.11	12.83	68.03	11.77	17.30
S2	75.74	2.23	2.94	75.31	3.53	4.69
S3	76.76	1.87	2.44	76.76	1.88	2.44

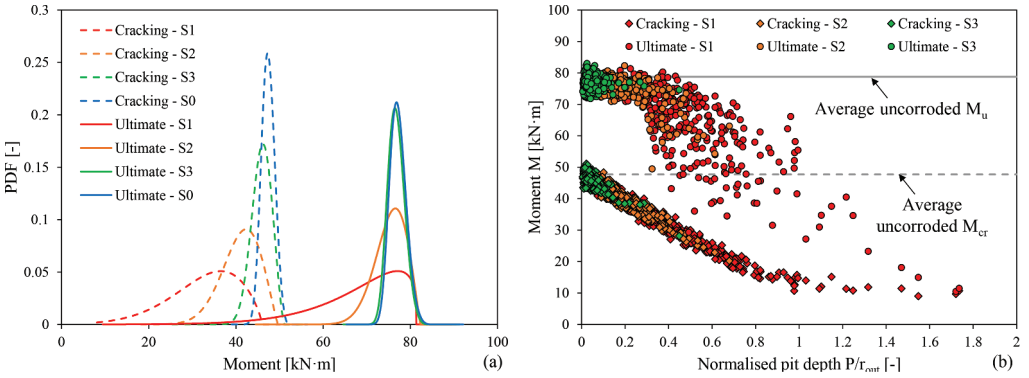


Figure 5. Corrosion scenarios: (a) *PDFs* for cracking and ultimate moments, (b) decay of cracking and ultimate moments vs normalized pit depth.

Table 6. Failure modes of the Monte-Carlo scenarios.

Scenario (# sim)	Concrete crushing [%] (# sim)	Strand failure [%] (# sim)
S1 (501)	48.90 (245)	51.10 (256)
S2 (501)	92.02 (461)	7.98 (40)
S3 (501)	99.80 (500)	0.20 (1)
S0 (501)	100.00 (501)	0.00 (0)

where Φ is the cumulative standard normal distribution. The parameter α_R is the sensitivity factor of the resistance (equal to 0.7 for a reference period of 1 year), while β is the target reliability level (ISO 2394, 2015). In this case, a large relative cost of safety measures with varying consequence classes (*CCs*) is considered to show the variability of M_d with the β value and corrosion scenarios. Figure 6(a) represents the log_{10} plot of the cumulative distribution functions (*CDFs*) and the corresponding intersections with the percentiles and Figure 6(b) represents the trend of corroded to uncorroded M_d as function of percentiles for the different corrosion scenarios.

Table 7 shows the summary for the estimation of M_d based on the different scenarios and by assuming different consequence classes with the corresponding percentiles calculated with the Eq. (6). The corroded design moment ranges from 27.47 to 46.97 kN·m for *S1* case by varying the percentile, while from 72.37 to 73.78 kN·m for *S0* case, highlighting a remarkable dependency of M_d on the severity of corrosion.

4 CONCLUSIONS

In this work, a probabilistic assessment - via Monte-Carlo simulations - of the moment-curvature response of pre-tensioned concrete beams was conducted. The main conclusions are as follows:

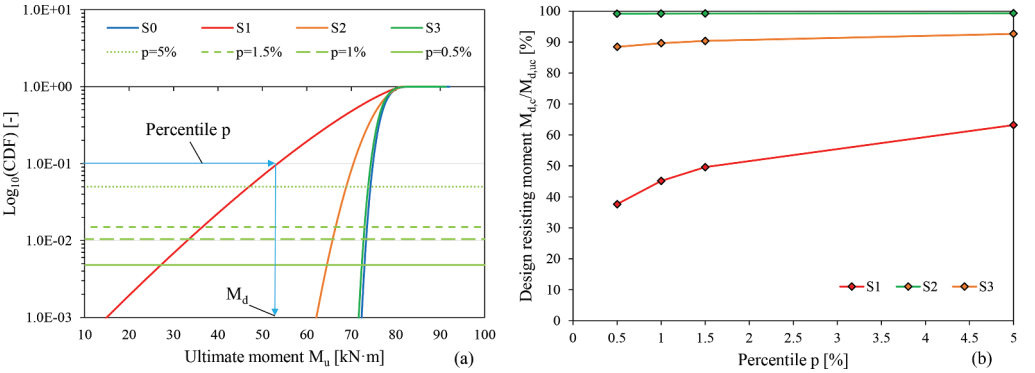


Figure 6. Corrosion scenarios: (a) *GEV CDFs* for ultimate moment and percentiles, (b) normalized corroded to uncorroded ultimate moment.

Table 7. Summary of resisting moment, M_d, for the *GEV* distribution, scenarios, and percentiles.

		Values of M_d [kN·m] for the different scenarios			
Consequence classes (α_R=0.7) (ISO 2394, 2015)	Percentile *p* [%]	S0	S1	S2	S3
CC3 (β=3.7)	0.5	72.98	27.47	64.57	72.37
CC2 (β=3.3)	1.0	73.32	33.10	65.74	72.74
CC1 (β=3.1)	1.5	73.53	36.48	66.46	72.97
-	5.0	74.30	46.97	68.86	73.78

- The *MC* approach highlighted the crucial role of the prestressing steel corrosion severity on the moment-curvature and failure modes of *PC* members. Increasing corrosion led to higher probability of brittle failure of longitudinal reinforcement instead of concrete crushing. Brittle shear failure modes will be investigated in future studies.
- The *GEV* distribution was found to better fit the resistance of corroded *PC* beams, as already stated in the previous study. The model uncertainty, assumed as a random variable with a lognormal distribution, affected the results in terms of ultimate moment M_u, by highlighting a higher dispersion in the probability distribution. Such model uncertainty distribution can be further improved based on additional experimental data.
- The calculation of the design resisting moment M_d was carried out based on the value of different percentiles for a reference period of one year and for the corrosion scenarios. An increasing sensitivity of the M_d was found with increasing corrosion severity. Such observation must be investigated more in detail in future studies.
- Additional distribution parameters for the input random variables such as corrosion of mild rebars and different geometrical features must be investigated in future works.

ACKNOWLEDGEMENTS

The presented study is part of a program of activities funded by the Italian "Consiglio Superiore dei Lavori Pubblici". The results were achieved in the national technical agreement for implementing the agreement pursuant to art. 15 law 7 August 1990, No. 241 between the Superior Council of Public Works and RELUIS. This research has also been made possible through funding from the Research Foundation Flanders (FWO) grant number S001021N (FWO-SBO project lifeMACS.

REFERENCES

Belletti, B., Caspeele, R., Botte, W., Franceschini, L., Ravasini, S., & Sandrini, S. (2023). Probabilistic assessment of the moment-curvature response of PC beams subjected to corrosion. *Capacity Assessment of Corroded Reinforced Concrete Structures, University of Parma, 13th-15th September 2023, Italy*, 1–4.

Belletti, B., Rodríguez, J., Andrade, C., Franceschini, L., Sánchez Montero, J., & Vecchi, F. (2020). Experimental tests on shear capacity of naturally corroded prestressed beams. *Structural Concrete*, *21*(5), 1777–1793.

Belletti, B., Vecchi, F., Bandini, C., Andrade, C., & Montero, J. S. (2019). Numerical evaluation of the corrosion effects in prestressed concrete beams without shear reinforcement. *Structural Concrete*, *21*(5), 1794–1809.

Coronelli, D., Castel, A., Vu, N. A., & François, R. (2009). Corroded post-tensioned beams with bonded tendons and wire failure. *Engineering Structures*, *31*(8), 1687–1697.

Franceschini, L., Belletti, B., Tondolo, F., & Sanchez, J. (2022). A simplified stress-strain relationship for the mechanical behaviour of corroded prestressing strands: the SCPS-model. *Structural Concrete*, *May*.

Franceschini, Lorenzo, Belletti, B., & Tondolo, F. (2022). Study on the Probability Distribution of Pitting for Naturally Corroded Prestressing Strands Accounting for Surface Defects. *Buildings*, *12*(1732), 1–19.

Franceschini, Lorenzo, Caspeele, R., Belletti, B., Tondolo, F., & Sanchez, J. (2023). Partial Safety Factor for the Design Strength Prediction of Naturally Corroded Prestressing Strands. *14th International Conference on Applications of Statistics and Probability in Civil Engineering, ICASP14 Dublin, Ireland*, July 9-13, 2023, 1–8.

Galano, S., Losanno, D., Miluccio, G., & Parisi, F. (2023). Multidimensional nonlinear numerical simulation of post-tensioned concrete girders with different prestressing levels. *Structural Concrete*, *April*, 1–22.

Galano, S., Ravasini, S., Franceschini, L., Losanno, D., Belletti, B., Parisi, F., & Safabakhsh, A. (2023). Numerical simulations of a benchmark reduced-scale post-tensioned concrete bridge girder with corroded strands. In *Capacity Assessment of Corroded Reinforced Concrete Structures*, *University of Parma*, *13th-15th* September 2023*, Italy*.

ISO 2394. (2015). *General Principles of Reliability for Structures*.

JCSS. (2001). *Probabilistic Model Code*. Joint Committee on Structural Safety.

Lee, J., Jeon, C. H., Shim, C. S., & Lee, Y. J. (2023). Bayesian inference of pit corrosion in prestressing strands using Markov Chain Monte Carlo method. *Probabilistic Engineering Mechanics*, *74*(January), 103512.

Ravasini, S., Franceschini, L., & Belletti, B. (2023). Simplified analytical method for moment-curvature response of corroded prestressed concrete beams. In *IALCCE 2023 Eighth International Symposium on Life-Cycle Civil Engineering*, July 2-6 2023, *Milan*, *Italy*.

Rinaldi, Z., Imperatore, S., & Valente, C. (2010). Experimental evaluation of the flexural behavior of corroded P/C beams. *Construction and Building Materials*, *24*(11), 2267–2278.

Vecchi, F., Belletti, B., Franceschini, L., Andrade, C., Rodriguez, J., & Montero, S. J. (2020). Flexural Tests on Prestressed Beams Exposed to Natural Chloride Action. In *Proceedings of the 2nd CACRCS Workshop*, *Parma*, *Italy*.

Vereecken, E., Botte, W., Lombaert, G., & Caspeele, R. (2021). Assessment of corroded prestressed and posttensioned concrete structures: A review. *Structural Concrete*, *22*(5), 2556–2580.

Bridge Maintenance, Safety, Management, Digitalization and Sustainability – Jensen, Frangopol & Schmidt (eds)
© 2024 The Author(s), ISBN 978-1-032-77040-6
Open Access: www.taylorfrancis.com, CC BY-NC-ND 4.0 license

A dynamic Bayesian network approach for multi-component fragility of aging bridges

F. Molaioni
Department of Civil Engineering and Computer Science Engineering (DICII), University of Rome Tor Vergata, Rome, Italy

C.P. Andriotis
Faculty of Architecture and the Built Environment, Delft University of Technology, Delft, The Netherlands

Z. Rinaldi
Department of Civil Engineering and Computer Science Engineering (DICII), University of Rome Tor Vergata, Rome, Italy

ABSTRACT: Assessing life-cycle seismic safety of aging reinforced concrete bridges is a challenging engineering task. Deterioration phenomena reduce structural capacity, exacerbating poor design choices that are typical of old bridges, while also being characterized by major uncertainties. Management of engineering systems in highly uncertain environments can be efficiently addressed through Markov decision processes, which rely on dynamic Bayesian networks to model the deteriorating system's life-cycle. However, there is still a gap in developing virtual environments that can seamlessly fit in such advanced algorithmic decision-making frameworks, especially under life-cycle seismic behavior considerations. In this study, we develop a dynamic Bayesian network capable of incorporating disparate uncertainties related to chloride-induced corrosion and seismic action, aiming at providing fragility curves over the bridge service life. The framework is applied to a prototype bridge encapsulating key risk-prone features. Using a multi-component approach, the developed network provides valuable insights into the fragility evaluation of both the system and individual components. Markovian transitions among component deterioration states are computed by combining corrosion initiation and propagation models with non-stationary Gamma processes. Subsequently, state-dependent fragilities are obtained through probabilistic seismic assessment based on non-linear dynamic analyses and multinomial logistic regression. Results show that the approach sheds light on the risk interplay mechanisms between components and the system, and on how different corrosion scenarios affect the system fragility. Discussion is finally provided on how these risk considerations can be interpreted for decision-making, allowing for better repair and retrofit strategies.

1 INTRODUCTION

Bridges, vital constituents of transport systems, must resist continuous and sudden stresses over time. Their long-term safety and resilience assessment is a challenging task, especially in the case of existing reinforced concrete (RC) bridges, owing to varied uncertainties in materials, deterioration, and design. The copresence of steel rebar corrosion and seismic actions, in particular, can pose significant risks, triggering catastrophic collapses and major network disruptions with high socio-economic impacts. Therefore, in recent years, focus on life extension and management of aging structures has intensified.

DOI: 10.1201/9781003483755-113

Steel corrosion in reinforced concrete occurs in two, largely discrete, phases: (i) initiation, where aggressive agents breach the concrete cover, and (ii) propagation, where steel rebar cross-section decreases due to material mass loss (Bertolini et al. 2004; Tuutti, 1982). Identifying chlorides as one of the most severe aggressive agents for RC structures, studies by Stewart & Rosowsky (1998) and Vu & Stewart (2000) proposed analytical models to be adopted in probabilistic assessment, taking into account both key environmental and structural factors, such as chlorides exposure, concrete cover depth and concrete water cement ratio. Eq. (1) describes initiation based on Fick's law, whereas Eq. (2) models propagation based on Faraday's law.

$$C(x,t) = \chi C_s \left[1 - \mathrm{erf}\left(\frac{x}{2\sqrt{D_c t}}\right)\right] \tag{1}$$

$$\lambda(t) = 0.37 * \frac{\left(1 - \frac{w}{c}\right)^{-1.64}}{x} (t - T_{corr})^{0.29} \tag{2}$$

where x is the concrete cover depth; C_s is the equilibrium chloride concentration at the concrete surface; erf is the Gaussian error function; χ is a factor to account for model uncertainties; t the time in years; w/c is the water cement ratio; and T_{corr} is the time for corrosion initiation in the structure's life-cycle. Corrosion initiation is postulated when the chloride content at the rebar depth $C(x,t)$ reaches a critical value C_{cr}, while $\lambda(t)$ is the uniform corrosion penetration.

Apart from chronic deterioration, extreme events like earthquakes critically impact bridge structural reliability. Knowledge from past earthquakes indicates several types of structural damage, such as deck unseating from bearing failures, column damages, and pounding between deck components (Priestley et al. 1996; Ramirez et al. 2000). Accordingly, several studies have proposed seismic risk assessment frameworks for aging RC bridges (Biondini & Frangopol 2016; Ghosh & Padgett 2010; Nielson & DesRoches 2006; Shekhar & Ghosh 2021). These probabilistic approaches predict time-based risks by merging: (i) probabilistic deterioration assessment, using Eqs. (1)-(2); and (ii) seismic fragility evaluation using nonlinear finite element analysis (NLFEA). This is accomplished initially by predicting the deterioration condition of the structure for designated time-points within the life-cycle. Subsequently, the mechanical properties of the materials are adjusted to conduct fragility analysis under the deteriorated state, aimed at quantifying the seismic risk and its rise at these specific time-points.

However, infrastructure decision-making can be more precise if joint time- and state-based models are considered. This allows for better selection of repair and retrofit actions, but also for updates of uncertainties and fragility functions based on data from monitoring and inspections. Recent advances in algorithmic decision-making reinforces the need for such models, through assimilation of probabilistic models, Bayesian updating, and stochastic optimal control algorithms (Andriotis & Papakonstantinou 2019; 2021; Andriotis et al. 2021). This approach uses partially observable Markov decision processes for inspection and maintenance planning, leveraging upon state-based formulations and dynamic Bayesian networks (DBN). Towards this, in Molaioni et al. (2023), we recently introduced a DBN approach for evaluating the seismic safety of aging bridges throughout their lifespan. This model combines non-stationary transition matrices for corrosion conditions of structural components and consistent, state-dependent seismic fragility functions for both individual components and the entire system. This provides a detailed view of how corrosion and seismic actions affect bridge safety over time. Component and system fragilities, $P_{SDS,t}$, over the life cycle, are computed as:

$$P_{SDS,t} = P(SDS_t \geq s | IM_{0:t}, CDS_{0:t}, SDS_{0:t-1}) \tag{3}$$

where s represents a damage threshold identifying the seismic damage state (SDS); IM is the intensity measure of the seismic action; CDS represents the corrosion damage state; and t is time, considering the structural life-cycle discretized in yearly time-slices.

In this paper, the effectiveness of the proposed approach is further evaluated by applying it to a case study with focus on demonstrating: (i) the method's potential to consider multiple deterioration scenarios within the life-cycle; (ii) the ability to capture how corrosion impacts the seismic safety of the case-study bridge and its components overtime; (iii) its utility in pinpointing vulnerable components and guiding retrofit strategies; (iv) its adaptability potential in incorporating real-time data and its compatibility with Markov decision processes-based decision-making.

2 METHODOLOGY

The DBN introduced by Molaioni et al. (2023) and adopted in this study to quantify aging RC bridges' seismic safety over their life cycle is shown in Figure 1. Variables of the model (blue circles in Figure 1) include: (i) the IM vector of the seismic action, assumed as the peak ground acceleration (PGA); (ii) the CDS vector of structural components, representing the corrosion intensity in a discrete space; (iii) the SDS vector of structural components, encapsulating structural damage of components based on thresholds of Engineering Demand Parameters (EDPs). Transitions among variables (red arrows in Figure 1) represent conditional probabilities among states. These include: (i) the Markovian transition for CDSs over time; and (ii) the state-dependent fragility functions for seismic damage, with the possibility of considering the carry-over effect of damage without repairs (omitted here for simplicity). This way, the adopted approach allows us to break down the problem into smaller, easier to compute segments, by independently analyzing each probabilistic dependency. The aging RC bridge is modeled as a multi-component series system, focusing on the key components, such as columns (COL), High Type Fixed Bearings (HTFB), High Type Expansion Bearings (HTEB), and Low Type Fixed Bearings (LTFB) (Mander et al. 1996; Shekhar & Ghosh 2021). SDSs for these components are classified from "Slight" to "Complete", based on FEMA (2003) definitions and quantified by thresholds from Nielson & DesRoches (2006), as shown in Table 1. CDSs range from "Sound" to "Critical", describing the corrosion intensity and its impact on structural components, as shown in Table 2. Considered corrosion intensity parameters are the average mass loss for steel rebars/bolts, M_{loss} [%], steel plate thickness reduction, PTR [mm], and bearing coefficient of friction, k_{corr} [-].

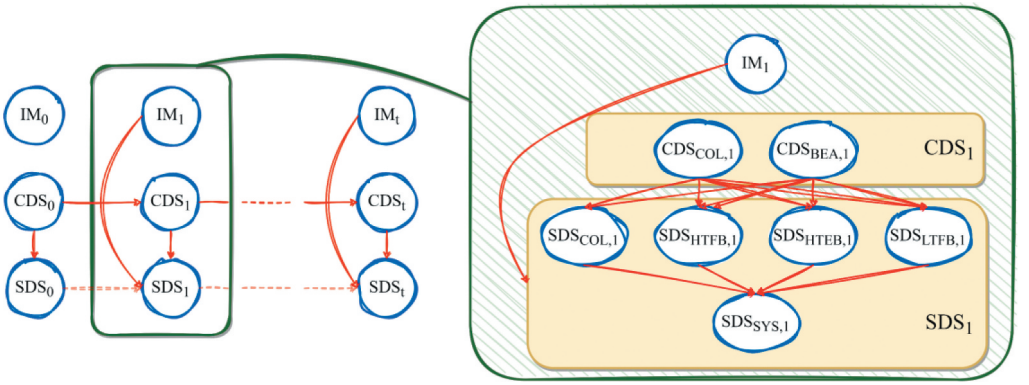


Figure 1. DBN for life-cycle seismic fragility of deteriorating bridges. Left: Model including nodes and transitions. Right: Interactions of components and system states within a single time step.

3 APPLICATION TO A CASE STUDY BRIDGE

The methodology is showcased for a 4-span bridge, typical of many pre-70s seismic-prone and deterioration-susceptible RC bridges in existing transportation networks. The bridge is characterized by poorly detailed RC columns and steel bearings, making it a relevant case study for seismic risk. For detailed information about the case study, its visual representation, and the modeling assumptions for conducting NLFEA, the interested reader is referred to Molaioni et al. (2023).

Table 1. Definition of probabilistic seismic damage states.

		Slight		Moderate		Extensive		Complete	
Component	EDP	M	D	M	D	M	D	M	D
COL	Curvature ductility [-]	1.29	0.59	2.1	0.51	3.52	0.64	5.24	0.65
BEA - Expansion	Displacement [mm]	37.4	0.6	104.2	0.55	136.1	0.59	187	0.65
BEA - Fixed	Displacement [mm]	6	0.25	20	0.25	40	0.47	187	0.65

* M = median of the lognormal distribution, D = Dispersion of the lognormal distribution.

Table 2. Definition of corrosion deterioration states.

CDS		0: Sound	1: Initial	2: Progressive	3: Critical
Component	Parameter	LB-UB	LB-UB	LB-UB	LB-UB
COL	M_{loss} [%]	0-0	0-15	15-30	30-45
BEA	M_{loss} [%]	0-0	0-15	15-30	30-45
BEA	PTR [mm]	0-0	0-3.5	3.5-5.1	5.1-6.5
BEA	k_{corr} [-]	0-0	0-0.35	0.35-0.64	0.64-0.92

* M_{loss} = rebar/bolt mass loss [%], PTR = plate thickness reduction [mm], k_{corr} = additive coefficient of friction for expansion bearings [-].

3.1 *Non-stationary transition matrix for corrosion*

Non-stationary transitions among CDSs are derived using a probabilistic analysis of the corrosion intensity, with respect to rebars/bolts mass loss, M_{loss} [%], over the structure's lifetime, applying Eqs. (1)-(2). These transitions, for initiation and propagation phases, respectively, calculate the conditional probability of moving from CDS=*i* at a given time-slice, *t*, to CDS=*j* at the next one, *t+1*. Monte Carlo simulation is conducted to propagate uncertainties in environmental conditions, material properties and geometry, thus, eventually to evaluate yearly transitions, as in Molaioni et al. (2023):

$$P(CDS_{t+1} = j | CDS_t = i) = \frac{\sum_{samples}(CDS_{t+1} = j \cap CDS_t = i)}{\sum_{samples}(CDS_t = i)} \quad (4)$$

Figure 2 illustrates the resulting non-stationary transition matrices for chloride corrosion under "splash" environmental conditions for the case study components. These matrices, showcasing Markovian probabilities of transitioning from one CDS to another over time, are upper-triangular due to the irreversible nature of damage, as long as no repair interventions are applied. In determining these, crucial is the time of corrosion initiation T_{corr}, calculated using Eq. (1). Among samples, 97.1% experienced corrosion initiation within 100 years, with a mean T_{corr} of 13.7 years and a standard deviation of 20.7 years. Assuming T_{corr} as a lognormally distributed random variable in the propagation model (Eq. (2)) significantly impacts transition probabilities, particularly from state 0 to 0 and from state 0 to 1. Sharp inflection points for these transitions are noted, as T_{corr} statistics suggest corrosion onset is more likely in the early years of the life-cycle.

3.2 *State-dependent fragility curves*

State-dependent and time-invariant fragility functions for both structural components and system have been fitted, corresponding to capacity limit state EDP thresholds, as shown in Table 1. Demand parameters have been obtained from dynamic NLFEA, developing three-dimensional finite element models in OpenSees (McKenna, 2011), incorporating non-linear

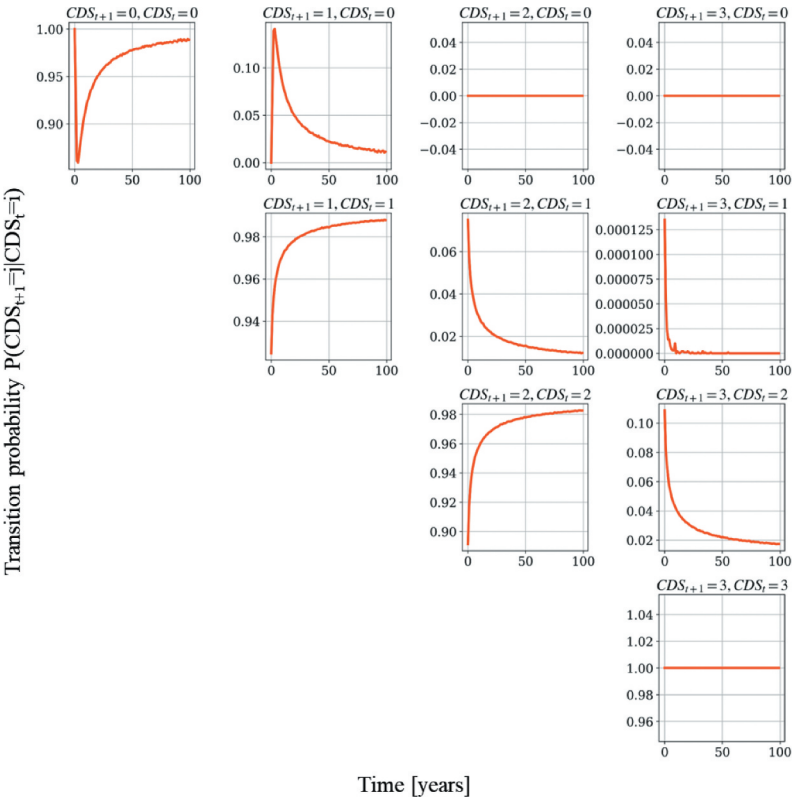


Figure 2. Non-stationary transition matrix for CDSs of components under "splash" conditions.

behavior of key components (COL, HTFB, HTEB, LTFB). A synthetic ground motion suite of 400 records has been applied on 50 statistically varied bridge models, thus propagating uncertainties related to the seismic action, the materials and geometrical properties of the bridge, as well as the corrosion deterioration of components. This way 20'000 EDPs were obtained and then compared with 50 capacity data points sampled from the distributions reported in Table 1, thus eventually creating a set of 1 million SDS labels for each component. A multinomial logistic regression model is trained on this dataset to predict the probability of exceeding a specific SDS as a function of the IM, via the softmax function as in Andriotis & Papakonstantinou, (2018).

For the sake of brevity, in this paper, results related to the "Complete" SDS and corrosion scenarios 00 (As-built), 03 ("Sound" COL, "Critical" corrosion in BEA), 30 ("Critical" corrosion in COL, "Sound" BEA), 33 ("Critical" corrosion in both COL and BEA) are presented. State-dependent fragility curves, shown in Figure 3, reveal that among bridge components, HTEB and COL exhibit the highest fragility across several SDSs and corrosion scenarios, namely, the combination of CDSs for COL and BEA components. Furthermore, a deterioration-driven increase in column fragility is observed due to their own deterioration, while this fragility slightly drops with the onset of corrosion in BEA. Conversely, HTEBs are not significantly influenced by the corrosion of COL alone and do only mildly so due to their own corrosion. This diverse impact of corrosion on the fragility of components leads to an inversion in their hierarchy of strengths. This is evident when comparing the state-dependent curves of scenarios '00' and '03', where the HTEB (dash-dot line) emerges as the most fragile component, with those of scenarios '30' and '33', where COL (thin continuous line) exhibits greater fragility. This highlights the importance of accounting for the multitude of deterioration scenarios that could arise throughout the lifespan of the structure. This understanding is

essential to grasp the potential evolution of the structural behavior, which, in turn, is fundamental in implementing effective enhancements in the bridge's seismic safety through precise retrofit interventions based on the deterioration of components.

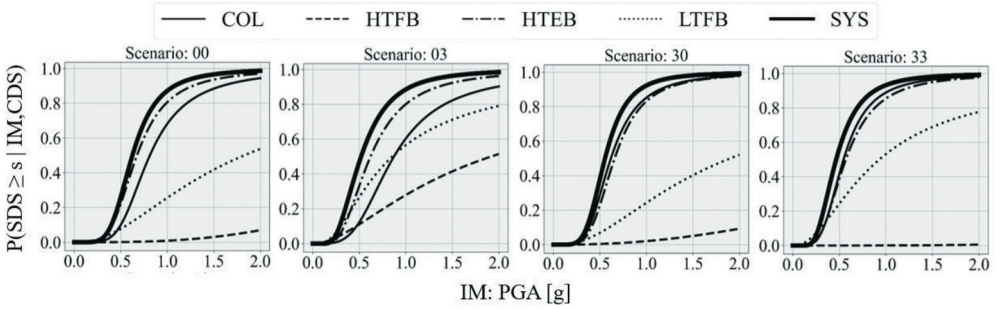


Figure 3. State-dependent fragility curves for both components and system. Corrosion scenarios '00', '03', '30', '33'.

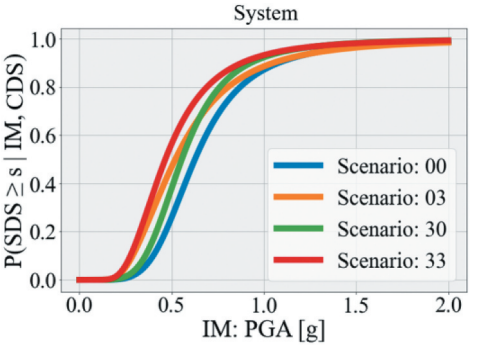


Figure 4. System's state-dependent fragility curves. Corrosion scenarios '00', '03', '30', '33'.

Focusing on the impact of corrosion at the system level, Figure 4 illustrates the system fragilities for these four scenarios. The fragility curves reveal that maximum fragility is consistently observed when corrosion is widespread across the structure (Scenario 33). Additionally, component deteriorations translate into an increase in fragility, which varies according to the deterioration scenario: the system is affected more by corrosion in bearings for PGA < 0.6, and more by the corrosion of columns for PGA > 0.6, as shown in Figure 4 (green and orange curve, respectively). These findings underscore the distinct role each component plays in influencing the system's fragility, reinforcing the utility of the adopted method in retrofit planning.

3.3 *Life-cycle fragility*

The longitudinal fragility of the bridge is determined by marginalizing out the corrosion deterioration state variables, CDSs, for all different components of the system (Figure 4 only displays scenarios 00, 30, 03, 33):

$$\mathrm{P}_t(\mathrm{SDS}{\geq}s|\mathrm{IM}) = \sum_{\mathrm{CDS_{COL}}} \sum_{\mathrm{CDS_{BEA}}} \mathrm{P}(\mathrm{SDS}{\geq}s|\mathrm{IM}, \mathrm{CDS_{COL}}, \mathrm{CDS_{BEA}})\mathrm{P}_t(\mathrm{CDS_{COL}}, \mathrm{CDS_{BEA}}) \quad (5)$$

where P_t (CDS_{COL}, CDS_{BEA}) represents the probability of having a given corrosion scenario (i.e., a combination of CDS for column and bearing components). This can be evaluated by considering the Markovian transitions among CDS and the independence of CDS_{COL} and CDS_{BEA} as:

$$P_t(CDS_{COL}, CDS_{BEA}) = [P_0(CDS_{COL}) \prod_{\tau=0}^{t-1} P(CDS_{COL,\tau+1} \mid CDS_{COL,\tau})][P_0(CDS_{BEA}) \prod_{\tau=0}^{t-1} P(CDS_{BEA,\tau+1} \mid CDS_{BEA,\tau})] \quad (6)$$

To illustrate the evolution of longitudinal fragilities, computations are performed at three time-points throughout the structural lifespan: at the as-built condition (0 years), and subsequently at the 25-, and 100-year time-points. The curves reported in Figure 5, delineating the probability of exceeding specific seismic damage states at specific years and IMs, highlight the significant impact of "splash" environmental conditions on the structural integrity over time. A salient observation is the escalation of fragility curves, notable already at year 25 since construction, a trend that reveals the inadequate component detailing and susceptibility to corrosion. Also, the influence of corrosion manifests differently across the four damage thresholds. In the case of the "Slight" SDS, the increase in fragility over time is relatively modest, in contrast to other damage states, where this increase is more significant. This is linked to the inherent seismic vulnerability of the bridge by design, predisposing the structure to readily exceed the 'Slight' threshold. On the other hand, the progression of corrosion evokes higher nonlinear demands, thereby significantly escalating the probability of exceeding more severe damage states, such as 'Moderate' and 'Extensive'. Furthermore, for all SDSs, an upward trajectory in the bridge fragility over time is evident, reflecting a growing risk of encountering more advanced damage with time. These findings demonstrate the capacity of proposed DBN to propagate corrosion deterioration effects at the component level to the global seismic system risk level over the structural lifespan.

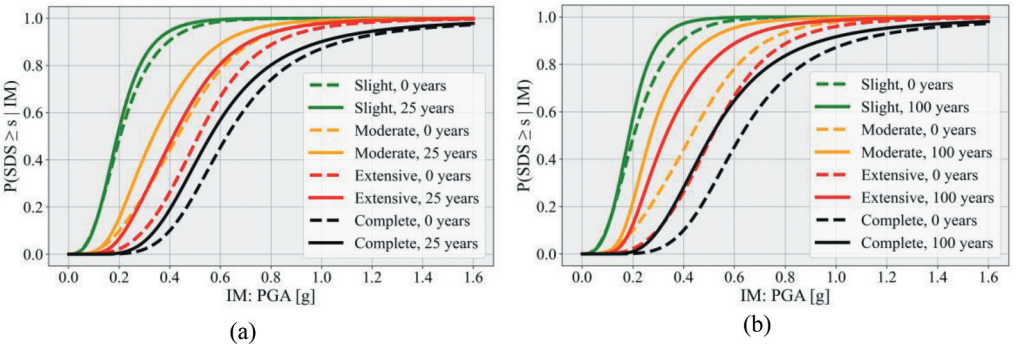


Figure 5. System System fragilities over the life-cycle under "Splash" conditions. (a) 25 years; (b) 100 years.

4 DISCUSSION

The results highlight several advantages of the proposed method. First, its potential to accommodate different deterioration scenarios over the life-cycle of the structure, allows us to define state-dependent fragility functions for possible combinations of component CDSs. This is particularly effective when applying the methodology to real-world bridge structures, which may present non-uniform deterioration distributions across components. For instance, deterioration

may concentrate more on some components than on others, either due to highly differential deterioration phenomena or partial repairs and retrofits applied at different times.

Moreover, the proposed methodology identifies the components' susceptibility to corrosion phenomena, but also how their effects act mutually on the fragilities of the components of the system. As shown by the results in Figure 3, non-uniform deterioration scenarios affect the safety of the structure in several ways. Also, the importance of modeling the bridge as a multi-component system is shown to be key for several insights. Individual component vulnerability can be evaluated through the DBN allowing us to identify the ones most at risk, such as the HTEBs and COLs for this case study. The change in hierarchy of strengths among components can thereby be tracked. This level of detail in the representation of the structural behavior can guide targeted maintenance and reinforcement interventions for the structure.

Finally, the developed DBN can be seamlessly integrated with decision-making frameworks that also involve field observations and actions. The structure of the DBN does not only allow the full description of seismic safety over time through detailed probabilistic transitions among states (i.e., CDS and SDS), but also the observation-based updating of these, which can be in turn propagated to update the fragility functions, together with changes due to repair interventions. This way, the problem can be readily defined as a partially observable Markov decision process and solved through deep reinforcement learning or other appropriate techniques to obtain a near-optimal management policy for the bridge. This has been recently considered in Metwally et al. (2024) which makes use of the realistic bridge system environment proposed here and extends it including repair actions and related costs. The study tests the applicability of multi-agent architectures in identifying dynamic component-level maintenance policies for optimizing system-level cost and reliability objectives and constraints.

5 CONCLUSION

In this paper, a dynamic Bayesian network (DBN) is developed to model the life-cycle seismic fragility of aging RC bridges, with a specific focus on encapsulating the uncertainties associated with corrosion deterioration and seismic actions as stressors to these structures. The methodology conceptualizes the bridge as a multi-component system, considering components that are crucial in determining the global seismic risk, i.e., RC columns and various types of steel bearings. The development of the DBN is facilitated by representing both deterioration and seismic damage in discrete spaces, defining corrosion deterioration states (CDSs) and seismic damage states (SDSs). This way, a structured approach to learning the evolving condition of the bridge components over time is laid out, allowing for efficient description of the complex interplay between deterioration and seismic action for the structural integrity of the bridge. Owing to the DBN properties, this complex learning task is distilled into a neat decomposition consisting of two primary sub-tasks: (i) calculating non-stationary Markovian transitions that portray the progression of CDSs; and (ii) formulating time-invariant and state-dependent fragility curves that capture the probability of exceeding SDSs given the IM and the combination of CDSs of structural components. The approach is applied to a 4-span bridge, which features characteristics typical for pre-70sRC bridges. These include inadequate RC column detailing and steel bearings. The analysis for the case study quantifies the detrimental effect of the environmental "splash" condition, which specifically instigates corrosion with an average onset time of 13.7 years, a critical factor in the structural performance overtime.

The computed time-invariant and state-dependent fragility curves for the case study underscore the high sensitivity of seismic responses to corrosion, providing valuable insights into how corrosion influences the seismic vulnerability of the bridge at various potential scenarios reachable through its life cycle. Furthermore, the approach of mechanically idealizing the bridge as a multi-component system, when combined with the DBN framework, allows us to identify the most at-risk components within the system across a spectrum of corrosion scenarios, which can lend itself to targeted inspection and retrofit intervention planning. Towards this, the capability of the approach to decipher changes in the hierarchy of strength and disentangle complex interactions among components, depending on environmental conditions, ground motion intensities and differential deterioration, provides engineers and decision-makers with insights into the structural

behavior over time. Finally, the presented DBN can be practical in enhancing fragility functions with field observations, thereby allowing for refined seismic risk inference. Due to its structure, it can be also compatible with advanced decision-support systems employing Markov decision processes that enable dynamic structural integrity management. Along these lines, current research trajectories are focused on expanding the capabilities of the DBN model with deep reinforcement learning approaches aimed at optimizing maintenance policies while ensuring structural safety and considering various performance metrics.

REFERENCES

Andriotis, C. P., & Papakonstantinou, K. G. (2018). Extended and Generalized Fragility Functions. Journal of Engineering Mechanics, 144(9), 4018087.

Andriotis, C. P., & Papakonstantinou, K. G. (2019). Managing engineering systems with large state and action spaces through deep reinforcement learning. *Reliability Engineering & System Safety*, *191*, 106483.

Andriotis, C. P., & Papakonstantinou, K. G. (2021). Deep reinforcement learning driven inspection and maintenance planning under incomplete information and constraints. *Reliability Engineering & System Safety*, *212*, 107551.

Andriotis, C. P., Papakonstantinou, K. G., & Chatzi, E. N. (2021). Value of structural health information in partially observable stochastic environments. *Structural Safety*, *93*, 102072.

Bertolini, L., Elsener, B., Redaelli, E., & Polder, R. B. (2004). *Corrosion of Steel in Concrete: Prevention, Diagnosis, Repair*.

Biondini, F., & Frangopol, D. M. (2016). Life-cycle performance of deteriorating structural systems under uncertainty: Review. *Journal of Structural Engineering*, ASCE, 142.

FEMA. (2003). *HAZUS-MH MR1: Technical Manual*.

Ghosh, J., & Padgett, J. E. (2010). Aging Considerations in the Development of Time-Dependent Seismic Fragility Curves. *Journal of Structural Engineering-Asce*, *136*, 1497–1511.

Mander, J.B., Kim, D-K., Chen, S.S., and Premus, G.J. (1996). Response of Steel Bridge Bearings to Reversed Cyclic Loading, Technical Report NCEER-96-0014, National Center for Earthquake Engineering Research.

McKenna, F. (2011). OpenSees: A Framework for Earthquake Engineering Simulation. *Computing in Science & Engineering*, *13*, 58–66.

Metwally, Z., Andriotis, C. P., & Molaioni, F. (2024). Managing aging bridges under seismic hazards through deep reinforcement learning. *IABMAS 2024*, 24-28 June 2024, *Copenhagen, Denmark*.

Molaioni, F., Rinaldi, Z., & Andriotis, C. P. (2023). Assessing life-cycle seismic fragility of corroding reinforced concrete bridges through dynamic Bayesian networks. *Proc. of the eighth Int. Sym. on Life-Cycle Civil Eng. (IALCCE 2023)*, 2-6 July 2023, *Politecnico di Milano, Milan, Italy*. 523–530.

Nielson, B. G., & DesRoches, R. (2006). Seismic fragility methodology for highway bridges using a component level approach. *Earthquake Engineering & Structural Dynamics*, *36*.

Priestley, M. J. N., Seible, F., & Calvi, G. M. (1996). *Seismic Design and Retrofit of Bridges*.

Ramirez, J. A., Frosch, R. J., Sozen, M., & Turk, A. M. (2000). *Handbook for the Post-Earthquake Safety Evaluation of Bridges and Roads*.

Shekhar, S., & Ghosh, J. (2021). Improved Component-Level Deterioration Modeling and Capacity Estimation for Seismic Fragility Assessment of Highway Bridges. *ASCE-ASME Journal of Risk and Uncertainty in Engineering Systems, Part A: Civil Engineering*, *7*, 4021053.

Stewart, M. G., & Rosowsky, D. V. (1998). Time-dependent reliability of deteriorating reinforced concrete bridge decks. *Structural Safety*, *20*, 91–109.

K. Tuutti, Corrosion of Steel in Concrete (Ph.D. thesis), Swedish Cement and Concrete Research Institute, Stockholm, Lund University, 1982, p. 469.

Vu, K. A. T., & Stewart, M. G. (2000). Structural reliability of concrete bridges including improved chloride-induced corrosion models. *Structural Safety*, *22*, 13–333.

Bridge Maintenance, Safety, Management, Digitalization and Sustainability – Jensen, Frangopol & Schmidt (eds)
© 2024 The Author(s), ISBN 978-1-032-77040-6
Open Access: www.taylorfrancis.com, CC BY-NC-ND 4.0 license

Selection of NDT/PDT locations in a box culvert using value of information

Soubhagya Karmakar
Structural Safety, Risk & Reliability (SSRR) Lab, Department of Civil Engineering, Indian Institute of Technology Bombay, Mumbai, India
Department of Atomic Energy, Mumbai, India

Siddhartha Ghosh
Structural Safety, Risk & Reliability (SSRR) Lab, Department of Civil Engineering, Indian Institute of Technology Bombay, Mumbai, India

Saha Dauji
Bhabha Atomic Research Centre, Mumbai, India
Homi Bhabha National Institute, Mumbai, India

ABSTRACT: Concrete box culverts facilitate drainage, railway/road crossing, or subway for transportation networks. Health assessment of box-culverts when distressed, or near end of design life, is generally conducted with non-destructive and/or partially destructive tests (NDT/PDT). The selection of NDT/PDT locations for box-culverts need to consider the inherent low redundancy. In this study, the failure probability of a box-culvert is first estimated using prior knowledge, incorporating the uncertainties in design load/strength, updated later through a Bayesian pre-posterior analysis. The testing expenses and repair costs are associated with the decisions in a value of information (VoI) framework. Proposed approach to select the best possible locations is demonstrated for a square box-culvert by minimizing overall cost. A set of parametric studies have been shown to conclude upon the parameters that may influence the life cycle cost after decision making. Further, the importance of optimizing sampling location has been emphasized with respect to cost of decision making.

1 THE CHALLENGE OF SAMPLING LOCATIONS FOR STRUCTURAL HEALTH ASSESSMENT IN A STRUCTURE

Structural health assessment (SHA) and maintenance of deteriorated structures add up to a huge budget for a nation. With the increasing number of failures of old bridges/structures, SHA is of paramount importance in their life cycle management and reducing uncertainty (Biondini & Frangopol 2016). One of the key aspects of SHA is sampling locations for testing or placement of sensors. Due to lack of clear-cut guidelines, sampling may be conducted without appreciating the objectives of sampling or neglecting the concern of maximum benefit. Despite earlier research (Karmakar et al. 2023; Faroz et al. 2023) highlighting the challenges in selecting test locations in SHA, no standardized method is available till date for practical implementation. A method was proposed for this purpose by Karmakar et al. (2023) for buildings, based on the importance of the different structural elements. However, typical structures such as chimneys, retaining walls, and box culverts would demand special attention.

The concept of value of information (VoI) was used extensively in information technology (Konakli et al. 2015), economics (Willinger 1989), environmental risk management (Yokota & Thompson 2004), and healthcare (Tuffaha et al. 2014). The same has been applied for

DOI: 10.1201/9781003483755-114

structural safety assessment too in the last decade (Konakli & Faber 2014; Khan et al. 2020). A few other notable examples of the application of VoI in civil engineering are: selecting maintenance strategy (Konakli & Faber 2014); and construction management (Zhang et al. 2021). In this article, following concepts of VoI of Konakli & Faber (2014), the importance of different locations in a subway box culvert are quantified using the value of information (VoI) concept in a pre-posterior framework, later used to guide selection of optimum locations for NDT/PDT for a box culvert. This is performed for a particular sample size considering the uncertainties in concrete strength, inherent variability, and material degradation. Multiple case studies for a box culvert are considered in a pre-posterior framework for finding the VoI of different sampling options in a subway box culvert, considering stress-induced degradation.

2 PROBLEM DESCRIPTION AND SAMPLING PROPOSAL

A square box culvert was considered for the study, with sides of 4.4 m, and 7.5 m long. Typical loading considered for estimating the flexural are, a) Dead load on the top slab/ walls, b) Live load on the top slab, and c) Earth pressure from outside. Live load was considered as per Class AA (tracked and wheeled) vehicles (IRC 2017). The seismic load has not been considered during the analysis, as the culvert specified over here is less than 10 m of the span (IRC 2017). Soil weight density was considered as 18 kN/m^3. The functional design life (t_d) of the structure was considered as 50 years. The age at the first inspection was considered as 30 years according to the local municipal act (GoM 2019). Further details are listed in Table 1. Design was governed by wheeled vehicles. For this demonstration, failure probability guided by flexure was considered, but can be extended for other modes or combinations thereof. Design values were used to estimate the initial values of demand, capacity, and failure probability of the culvert.

2.1 *Load combinations and initial capacity*

Moment distribution method was employed for obtaining the bending moment profile for each component (top slab, bottom slab, side walls), the absolute value of which was normalized to the maximum value for each component, independently. Hence, values of maximum demand were kept as μ_S (mean demand) = 1 unit, σ_S (standard deviation of demand) = 0.3 unit in line with Konakli & Faber (2014).

Annual failure probability for civil structures between 10^{-4} to 10^{-3} is generally acceptable (Ghosh & Faroz 2016). Therefore, the initial failure probability is taken as 10^{-4} for the structure; and 5×10^{-5} (half of that of the structure conservatively) for each component (top slab, bottom raft, side wall). According to literature (Konakli & Faber 2014; Khan et al. 2020), taking coefficient of variation (CoV) as 0.1, the design capacity (R) of each component was assumed to be μ_R (mean) = 3.2 unit, and σ_R (standard deviation) = 0.32. Further, both capacity and demand were assigned log-normal distribution (Konakli & Faber 2014). In similar lines, the acceptable limit before maintenance is required, is taken at probability of failure of a component $\leq 5\times10^{-4}$ corresponding to the higher limit of structural failure i.e. $\leq 10^{-3}$.

2.2 *Strength degradation*

Reinforced concrete structures get non-uniformly degraded during their service life due to various factors, such as, environmental, and physical. Here the stress-induced degradation is chosen for demonstration. Higher stress in member lead to higher degradation: carbonation (Liu et al. 2023); changes in pore structure (Tanaka et al. 1999); chloride diffusion (Francois & Maso 1988). Fatigue is a predominant loading in box culverts due to vehicular load and fatigue loading leads to accelerated corrosion (Song et al. 2016). The degradation was therefore taken to be proportional to the stress level (demand/ capacity ratio) of the component. According to literature (Konakli & Faber 2014; Khan et al. 2020), the yearly degradation rate corresponding to the maximum demand/capacity ratio of components is considered 0.01/yr.

2.3 *Sampling of test locations*

In the case study for SHA with fixed sample size (demonstration with one in each component), the overall cost of decision is the sum of maintenance and remaining functional life-cycle failure costs, in addition to the cost incurred in the inspection program. To represent possible different locations on the structure, each component has been sub-divided into 20 sub-components for this study. Finally, the set of sampling locations that yields the lowest overall cost would be selected as the best one.

Table 1. Parameters considered of case studies.

Feature	Types
Prior distribution of capacity parameters	(a) Relatively non-informative, (b) Partially-informative
Age of inspection	30-49 (IS 875-3, 2015).
C_r	(a) 10 unit (Konakli and Faber, 2014), (b) 100 unit
C_{Sf}	1000 unit (Konakli and Faber, 2014)
Maximum mean demand (μ_S)	1 unit (Konakli and Faber, 2014)
The maximum standard deviation (σ_S)	0.3 unit (Konakli and Faber, 2014)
CoV of capacity	0.1 (Konakli and Faber, 2014)
Initial probability of civil structure failure	10^{-4} to 10^{-3}(Ghosh and Faroz, 2016)
Uncorrelated priors of capacity parameters	Used in Lad et al. (2020), Karmakar et al. (2023)
Maximum degradation rate	0.01/ yr (Konakli and Faber, 2014; Khan et al., 2020)
Variation of degradation across sections (Derived hypothesis)	"Highly stressed zone will have higher degradation rate". Corollary from literature (François and Maso, 1988; Tanaka et al., 1999; Song et al., 2016; Liu et al., 2023).
Same initial capacity parameter at all sections	Assumption and limitation
Consideration of Flexural failure only	Limitation

3 METHODOLOGY FOR OBTAINING OPTIMUM SAMPLING LOCATION USING A VOI FRAMEWORK

3.1 *Prior distribution of mean and standard deviation of sub-component capacity parameters*

In the present study, two different priors, (a) relatively non-informative and (b) partial informative, are chosen for the initial distribution of mean and standard deviation of capacity parameters. In the relatively non-informative case, no prior knowledge about the distribution parameters is available. Hence a comparatively wider range uniform prior $u(0.05, 6.05)$ is chosen for the capacity parameters. However, for determining parameters of partial-informative prior, existing literature is used. The value 5×10^{-5} mentioned above is considered as, 5-percentile value for defining the prior mean of component mean capacity, and one order below i.e. 5×10^{-6} is considered as a 95-percentile value. The distribution of prior mean parameters of capacity is considered to follow a normal distribution. These are used to arrive at prior parameters of mean capacity which turns out to be $\mathcal{N}(3.5, 0.182)$. In a similar line, with CoV =0.1, the prior parameter of the standard deviation of mean capacity comes to be $\mathcal{N}(0.35, 0.0182)$. The joint probability of mean and standard deviation of prior parameters can be written as given in Equation 1 considering them to be uncorrelated as used in earlier studies (Lad et al. 2020, Karmakar et al. 2023). These parameters are degraded at the average rate of degradation (of its sub-components) for each of the components of the box culvert and for the remaining life span of the structure to decide upon prior parameters at any age t. The maximum rate of degradation for any sub-component of a component is considered

as 0.01/yr of initial capacity (Konakli & Faber 2014) corresponding to highly stressed zone (lowest capacity to margin ratio) as stated in section 2.

$$f'_{\Theta}(\theta) = P\left(\mu_{R_m}, \sigma_{R_p}\right) = P\left(\mu_{R_m}\right) P\left(\sigma_{R_p}\right) \tag{1}$$

where, $P\left(\mu_{R_m}\right)$ and $P\left(\sigma_{R_p}\right)$ are prior distributions of capacity parameters of m^{th} and p^{th} populations respectively. In the absence of any inspection data cost involved in decision-making can be obtained from prior distribution as written in the form of Equation 2, where, $C(\theta)$ is the cost involved with parameter θ.

$$C' = \int_{\Omega_\Theta} C(\theta) f'_{\Theta}(\theta) d\theta \tag{2}$$

3.2 *Bayesian updating to arrive at the posterior distribution of capacity parameters from its prior distribution*

In light of the test results, the prior distribution of capacity parameters (θ) can be updated to the posterior distribution as given below.

$$f''_{\Theta/\mathrm{x}}(\theta/x) = \frac{L(x|\theta) f'_{\Theta}(\theta)}{\int_{\Omega_\Theta} L(x|\theta) f'_{\Theta}(\theta) d\theta} \tag{3}$$

Similarly, the cost (C'') based on the posterior distribution of θ is

$$C'' = \int_{\Omega_\Theta} C(\theta) f''_{\Theta/x}(\theta/x) d\theta \tag{4}$$

The difference between the costs obtained using prior distribution and posterior information is the value of information as shown below. From the equation it can be said that, these cost values can be correlated as the negative of the value of information.

$$\mathrm{VoI} = C' - C'' \tag{5}$$

3.3 *Cost analysis*

The cost function is defined based on a combination of loss due to structural failure and cost of strengthening/maintenance based on test results. The cost due to structural failure is found by multiplying the cost of structural failure with the probability of its failure (Konakli & Faber 2014). The probability of failure is obtained from the actual demand and capacity parameters of each of the sub-components for each structural component. Bayesian updating is carried out for the capacity parameter with obtained test results as described earlier. The posterior predictive distribution is obtained from the joint posterior distribution of capacity parameters. Next, for the decision-making on maintenance strategy, the strengths are assumed as follows.

1. *Non-tested locations/ sub-components*: The mean and standard deviation of the posterior predictive distribution are assigned.
2. *Tested locations/sub-components*: The actual test value obtained from the experiment at the tested locations is assigned as the mean value of capacity for that location. The standard deviation for capacity is obtained using this capacity mean and CoV is obtained from the posterior predictive distribution.

Next, the probability of failure of any sub-component is obtained using Cornell's reliability method with these assigned mean and standard deviation and actual demand. If

the failure probability values come to be more than the acceptable limit ($P_{fscj}(t_i) \geq 0.0005$) then the strengthening of those locations/ sub-components is carried out. The extent of strengthening is the difference between the desired target mean value (S_t) (Not always the actual S_{at} at that age) to the obtained/ updated capacity mean value (S_{oj}) at the year of decision-making t_i. Readers may note that this strengthening is not the actual required strengthening for all the sub-components except those where inspection/ testing is being carried out. Therefore, after the decision-making on the strengthening scheme the updated actual capacity of the sub-components will be as follows.

1. *Non-strengthened sub-components*: The mean will be the actual (S_{at}) and standard deviation is considered using S_{at} and CoV obtained from posterior predictive distribution.
2. *Strengthened sub-components*: The mean capacity will be the capacity of the sub-component (j) at that age (S_{at}) added with ($S_t - S_{oj}$). However, the CoV is again set to an initial 0.1 (assuming regaining of near initial state) for finding the standard deviation of the capacity of these sub-components.

Hence the overall cost will be the sum of the strengthening cost and the cost of failure in subsequent years, based on updated capacity values. The cost involved in maintenance for one component is calculated as,

$$C_C(t_i) = \frac{C_r}{S_c} \sum_{j=1}^{S_c} \frac{S_t - S_{oj}}{S_t}, \text{if} \left(P_{fscj}(t_i) > 0.0005\right) \tag{6}$$

where, C_r is the cost of fully replacing the component, S_c are the number of sub-components. On the other hand, the cost of failure (C_{lcf}) of the structure based on pre-posterior analysis using the testing results (x) of one component and necessary strengthening can be given by Equation 7. However, for finding the probability of failure for this time, the updated actual capacity distribution is used. This failure probability goes with the assumption that other components in the series have the reliability of 1 and in parallel have the reliability of 0. This assumption is made to simplify the problem and obtain the optimum location component-wise. The obtained optimum sampling locations for individuals can then be compiled to arrive at the optimum test of the location of the complete box culvert. The failure of one component is governed by the failure of any of the sub-components for being correlated systems and placed in series.

$$C_{lcf} = C_{Sf} \sum_{t=t_i}^{t_d-1} \max_{S_c \in all} \left[\frac{P_{fsc}(t_i)}{(1+r)^{(t-t_i)}} \right] \tag{7}$$

C_{Sf} is the cost of complete failure, r discount rate with due consideration to than inflation rate, t_d is the functional design life, t_i is the age of inspection and $P_{fsc}(t_i)$ is the probability of failure of the sub-component in year t_i as given in Equation 8.

$$P_{fsc}(t_i) = P_{fsc}(R_{i+1} < S) - P_{fsc}(R_i < S) \tag{8}$$

where, R_i and S are the capacity and demand in the year 'i'. Finally, the overall cost: $C_{ov}(t_i)$ till the functional service life for the decision in the year t_i can be written as the sum of C_{lcf} and $C_C(t_i)$ as given in Equation 9. The total cost of structural failure is assumed as 1000 units and full replacement cost 10 units in a similar line with earlier works(Konakli et al. 2015; Konakli & Faber 2014).

$$C_{ov}(t_i) = C_{lcf} + C_C(t_i) \tag{9}$$

3.4 *Optimum sampling locations*

In the present problem, capacity parameters for each of the sub-components are considered to be constant and demand is considered to be the highest value in the smallest segment. To find out the optimum sampling location, samples are chosen separately from each of the locations, and comparing the obtained cost of the decision (maintenance and failure), the optimum location is suggested. Ω_Θ is the space containing different possible samples from the overall set of locations. Hence the optimum sampling scheme will be the one giving the lowest value of cost or highest value of information (negative cost) as shown in Equation 10 and Equation 11.

$$S_o = \underset{S \in \Omega_\Theta}{\operatorname{argmax}}(VI) \tag{10}$$

$$S_o = \underset{S \in \Omega_\Theta}{\operatorname{argmin}}\left[\int_{\Omega_\Theta} C(\theta) f''_{\Theta/x}(\theta/x)\, d\theta\right] \tag{11}$$

4 ILLUSTRATION OF THE PROPOSED METHODOLOGY

4.1 *Optimum location for the uniform initial capacity parameters of individual components*

With uniform initial capacity at 3.2 unit, the varying demands at different sub-component, the resulting stress levels also vary. The cost of decision-making was obtained using Equations 6- 9 for each sampling option, and are plotted for the top slab in Figure 1(a) and Figure 1(b) for the remaining service life, respectively for relatively non-informative prior and partially informative prior cases. Similar plots for side walls are presented in Figure 2(a) and Figure 2(b). Plots for the bottom slab were almost similar to the top slab and are not reproduced for brevity. From these figures, it can be observed that: selecting a sampling location corresponding to the lowest initial safety margin would provide the lowest overall life cycle cost; or in other words yield the highest VoI. Studies of these response patterns for different initial parameters are indicated as future scope of research. However, the aspect that application of VoI in selection of sampling location is strongly recommended in optimum decision making to reduce overall life cycle cost.

4.2 *Effect of the year of decision in overall cost thereafter*

Depending on the remaining service life, the effectiveness of the sampling scheme is studied in this section with C_{Sf}=1000 units and C_r = 10 units. The variations of minimum and maximum costs obtained for different sampling schemes with respect to age of structure, for relatively informative and partial informative prior are displayed: for top slab in Figure 3(a) and Figure 3(b); for side walls in Figure 4(a) and Figure 4(b). The reduced cost for higher age arises due to the lesser number of years the structure is to serve based on t_d. Although the cost of maintenance increases in the later phase of decision-making, the total failure cost, being much higher than the maintenance cost, govern the overall cost.

4.3 *Effect of different ratio of total failure cost to replacement cost*

If decision-making happens based on samples collected from highly deteriorated locations and decision is followed based on the obtained result, more cost will be incurred in maintenance. On the other hand, decision based on information from lesser deteriorated portions will lead to higher overall failure costs. Hence, the ratio of overall failure cost to replacement cost could play a major role in the overall life-cycle cost, and decisions. Presently, two different replacement costs for components (10 units, and 100 units) are examined, keeping the overall failure cost same as 1000 units. Similar plots as above are presented: for the top slab in Figure 5(a) and Figure 5(b); for side walls in Figure 6(a) and Figure 6(b). The figures show an increase in the overall cost when samples are collected from lower-margin zones, the effect being more for relatively non-informative prior.

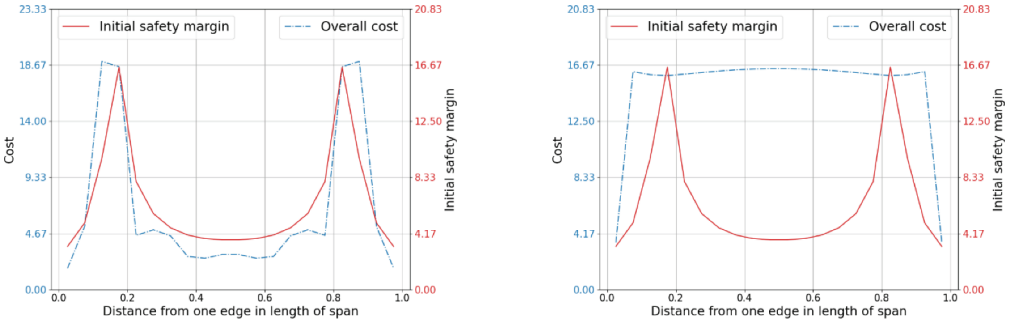


Figure 1. Overall cost and initial safety margin at different sampling location in fraction of length for (a) Relatively non-informative prior and (b) Partial informative prior for top slab.

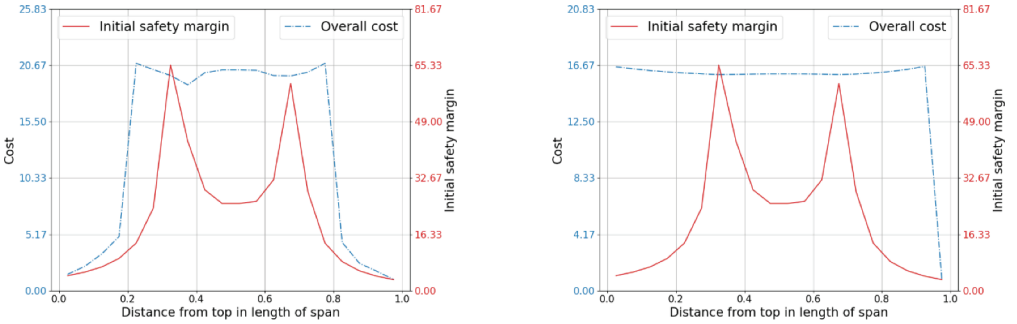


Figure 2. Overall cost and initial safety margin at different sampling location in fraction of length for (a) Relatively non-informative prior and (b) Partial informative prior for side wall.

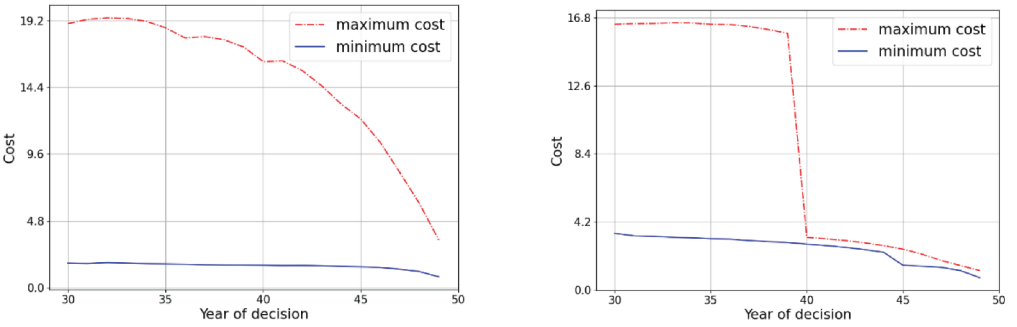


Figure 3. Maximum and minimum overall cost with respect to year of decision for all sample choices for, (a) Relatively non-informative prior and (b) Partial informative prior for top slab.

5 CONCLUSION

This work is the first-of-the-kind study, suggesting locations for NDT/PDT/monitoring for a box culvert, for SHA, in the VoI framework, considering various costs involved. The selection of test locations in the VoI framework would help to achieve overall lowest life-cycle cost for the structure. This case study does not propose a particular sampling location. Rather the work gives

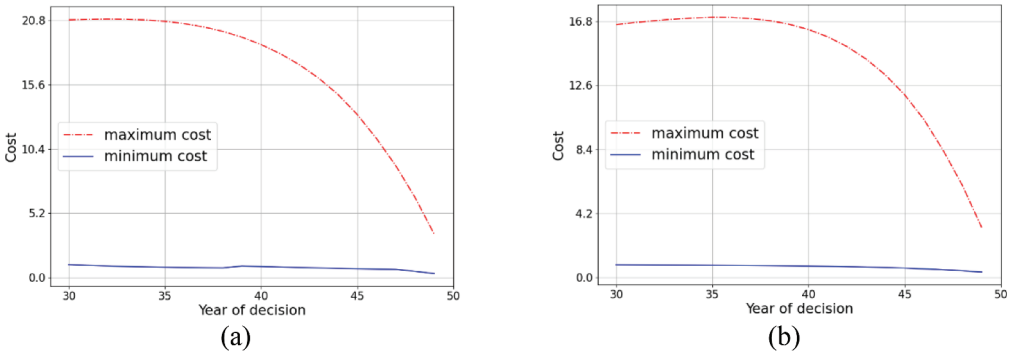


Figure 4. Maximum and minimum overall cost with respect to year of decision for all sample choices for, (a) Relatively non-informative prior and (b) Partial informative prior for side wall.

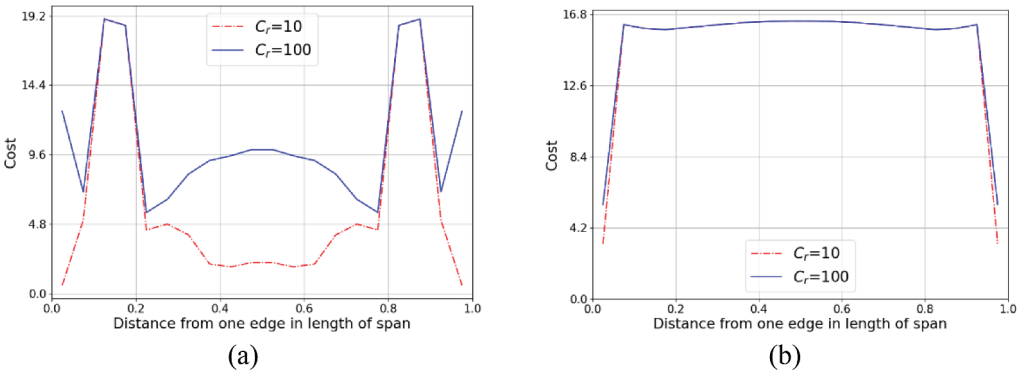


Figure 5. Overall cost at different sampling locations in fraction of length for different C_r values: (a) Relatively non-informative prior and (b) Partial informative prior for top slab.

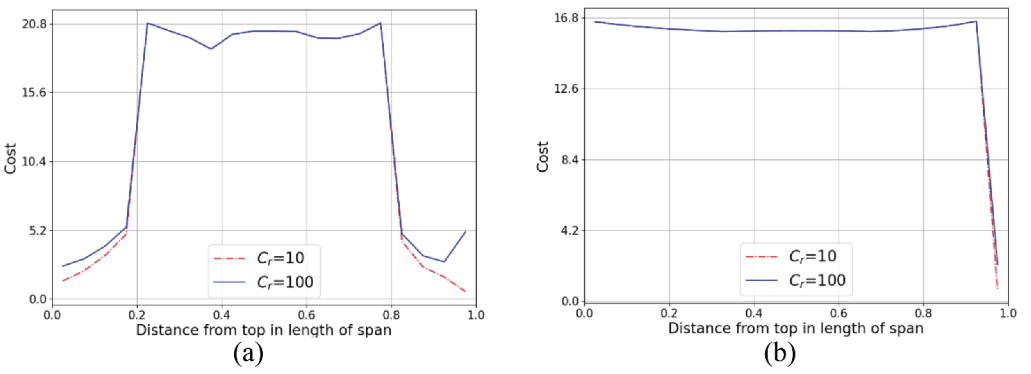


Figure 6. Overall cost at different sampling locations in fraction of length for different C_r values: (a) Relatively non-informative prior and (b) Partial informative prior for side wall.

a methodology to arrive at the optimum sampling location in VoI framework. From the example case studies considered the findings are as follows, a) In pristine conditions, the locations with higher stress would yield highest VoI for test for C_{Sf}=1000 units and C_r = 10 units. b) The age of inspection and functional design life plays role in relative efficacy of this optimization approach, c) The relative cost of repair and cost of failure is an important aspect for choice of location, and detailed rate analysis would be advocated.

The cost, degradation, initial capacity and demand parameters considered in this paper is based on certain values used in earlier literature due to lack of real field data. This is major limitation of the case study. However, the methodology is applicable for both real and normalized parametric values. Hence, obtaining the parameters used in Table 1 experimentally and carrying out the exercise will produce a more realistic picture. Incorporating the effect of imperfect information, effect of correlated prior parameters of capacity can also be examined in future. From the results of such studies, generic guideline for carrying out NDT/PDT/monitoring of box culverts may be formulated in future.

REFERENCES

Biondini, F. & Frangopol, D. 2016. Life-cycle performance of deteriorating structural systems under uncertainty: Review. *Journal of structural engineering* 142, F4016001.

Faroz, S. A., Ghosh, S. & Faroz, A. M. 2023. Tri-level framework for realistic estimation of concrete strength using Bayesian data fusion of UPV and guided coring. *Journal of nondestructive evaluation* 41 (78).

Francois, R. & Maso, J. 1988. Effect of damage in reinforced concrete on carbonation or chloride penetration. *Cement and concrete research 18*(6), 961–970.

Ghosh, S. & Faroz, S. 2016. *Integrating NDT measurements and theoretical model for the failure* assessment *of a corroding girder*, 1st Biennial conference on bridge sustainability.

GoM. 2019. *Bombay Act No. III of 1888: The Mumbai Municipal Corporation Act (Reaffirmed 2019)*. Law and Judiciary department, Government of Maharashtra, Mumbai, India.

IRC-6. 2017. *Standard specifications and code of practice for road bridges, section: II, Load and Load combinations*. Indian Road Congress.

IS-875-3. 2015. *Design Loads Other than Earthquake for Buildings and Structures — Part 3: Wind Load*. Bureau of Indian Standards, New Delhi, India.

Karmakar, S. Ghosh, S. Saha, D. & Faroz, S. A. 2023. Non-destructive and partially destructive test locations in RC structures: A combined spatial optimisation and Bayesian updating approach. *Life cycle of Structures and Infrastructure Systems*, Taylor and Francis, CRC Press, 2355–2362.

Khan, M. S. Ghosh, S. Caprani, C. & Ghosh, J. 2020. Sensitivity of value of information to model and measurement errors. *ASCE-ASME Journal of risk and uncertainty in engineering systems, Part A: Civil Engineering* 6(4), 04020038.

Konakli, K. & Faber, M. 2014. Value of information analysis in structural safety. *Vulnerability*, Uncertainty, *and Risk: Quantification, Mitigation, and Management*, 1605–1614.

Konakli, K. Sudret, B. & Faber, M. 2015. Numerical investigations into the value of information in lifecycle analysis of structural systems. *ASCE-ASME Journal of risk and uncertainty in engineering systems, Part A: Civil Engineering* 2(3), B4015007.

Lad, D. Faroz, S. A. Ghosh, S. 2020. Fusion of rebound number and ultrasonic pulse velocity data for evaluating the concrete strength using Bayesian updating. *Springer, Singapore*, 437–448.

Liu, D. Wang, C. Gonzalez-Libreros, J. Guo, T. Cao, J. Tu, Y. Elfgren, L. & Sas G. 2023. A review of concrete properties under the combined effect of fatigue and corrosion from a material perspective. *Construction and Building Materials* 369, 130489.

Song, Z. Jiang, L. Li, W. Xiong, C. & Chu, H. 2016. Impact of compressive fatigue on chloride diffusion coefficient in OPC concrete: An analysis using EIS method. *Construction and building materials* 113, 712–720.

Tanaka, K. Nawa, T. Hashida, H. & Jeon, J. 1999. Effect of repeated load on micro structure and carbonation of concrete and mortar. *In Eighth International conference on durability of building materials and Components*, 256–265.

Tuffaha, H. Gordon, L. & Scuffham, P. 2014. Value of information analysis in health care: A review of principles and applications. *Journal of medical economics* 17(6): 377–383.

Willinger, M. 1989. Risk aversion and the value of information. *The journal of risk and insurance* 56(2), 320–328.

Yokota, F. & Thompson, K. M. 2004. Value of Information Analysis in Environmental Health Risk Management Decisions: Past, Present, and Future. Risk Analysis 24(3), 635–650.

Zhang, W.H. Lu, D.G. Qin, J. Thons, S. & Faber, M. H. 2021. Value of information analysis in civil and infrastructure engineering: a review. *Journal of infrastructure preservation and resilience* 2(16).

Bridge Maintenance, Safety, Management, Digitalization and Sustainability – Jensen, Frangopol & Schmidt (eds)
© 2024 The Author(s), ISBN 978-1-032-77040-6
Open Access: www.taylorfrancis.com, CC BY-NC-ND 4.0 license

Assessment of a 60-year-old corroded concrete girder through finite-element analysis

L. Soto, M. Noël, B. Martín-Pérez & L. Sanchez
Department of Civil Engineering, University of Ottawa, Ottawa, Ontario, Canada

ABSTRACT: This study implements a two-dimensional nonlinear finite-element approach for the assessment of the shear behavior of a post-tensioned bridge girder whose tendons and reinforcement suffered severe corrosion during its service life of almost 60 years. The girder is lightly reinforced with vertical stirrups and its tendons follow a parabolic profile, with many of them anchored at the top of the girder; as such, the contribution of post-tensioning is significant to its shear capacity. The objective of the study is to understand the various aspects of the progressive damage of the girder due to increased corrosion of its prestressing steel. Through the finite-element modeling tool, different approaches have been considered to model the corrosion of post-tensioning tendons and reinforcement to assess the shear response of the girder in the degraded state.

1 INTRODUCTION

Corrosion of steel in concrete structures is one of the main durability issues that compromises their structural performance; therefore, the assessment of their structural behavior in the degraded state is of significant interest. In the past decades, nonlinear finite element analysis (NLFEA) has proven to be a useful tool in evaluating reinforced concrete (RC) and prestressed concrete (PC) elements affected by corrosion. In the case of PC, several studies may be mentioned that have been dedicated to assessing pretensioned members (Belletti et al. 2020, Huang et al. 2022, Osmolska et al. 2022), while to the knowledge of the authors, NLFEA evaluations of post-tensioned members are practically non-existent.

This study pertains to one of the typical post-tensioned girders from a 60-year-old bridge in Canada, for which detailed field inspections resulted in estimates of 40% to 47% reduction in steel cross-section due to corrosion attack. Although a detailed spatial distribution of corrosion has not been determined, the estimates for the residual capacity calculations of the girder according to current Canadian standards indicated a considerable deficiency in shear.

A numerical approach is implemented herein to incorporate degraded material constitutive models into the assessment of the girder in shear, and to that end, NLFEA have been utilized. The aim of the study is twofold: first, it is of interest to estimate the residual shear capacity and failure mode of the girder by means of an adequate methodology (NLFEA), and through the incorporation of material models that take into account corrosion attack; and second, to obtain insight pertaining to the influence of different degraded material models on the predicted response of the studied member.

2 GIRDER PROPERTIES

The girder used as the basis for this study was part of a decommissioned bridge which had a deck width of 24.08 m and a clear span of 52.43 m. Seven identical parallel girders were used for each span of the superstructure. The girder depth is 3,073 mm and is post-tensioned with 24 tendons, each consisting of 12 -7 mm diameter wires. The tendon layouts are all parabolic, with

DOI: 10.1201/9781003483755-115

13 of them anchored at girder-end and the rest at the top of the girder, as shown in Figure 1. Longitudinal reinforcement is comprised of 4 ϕ10 mm bars in the bottom flange, and 8 ϕ10 mm bars in the top flange. Stirrups at girder ends are ϕ15 mm spaced at 267 mm, while for the rest of the girder ϕ13 mm and ϕ15 mm stirrups are alternated at 800 mm. The thickness of the web varies along the length of the girder, with a maximum of 254 mm at the end of the span.

Concrete compressive strength was measured from drilled cores, and a value of 53.9 MPa was determined for evaluation purposes according to CSA S6-19. Prestressing and reinforcing steel properties were obtained from the original bridge design calculations, with the ultimate tensile strength of tendons being 1,572 MPa and a yield strength for reinforcing steel of 275 MPa.

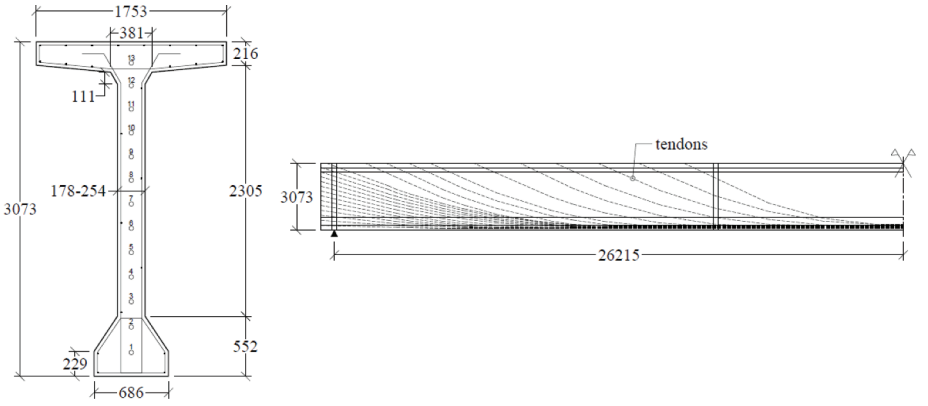


Figure 1. Girder cross-section at end of span, and elevation (dimensions in mm).

Through rigorous inspection campaigns of the bridge through the years, severe corrosion signs in the inclined tendons and bottom tendons were detected, as well as some corrosion of the vertical reinforcing steel. Although a complete assessment of the spatial degree of corrosion has not been possible, it was found that near the mid-span of the girder, the loss of the cross-sectional area of the tendons was approximately 47%. Thus, for the engineering assessment of the girders, a uniform degree of corrosion of 40% area loss was considered. Some of the defects found through the inspections are seen in Figure 2.



Figure 2. Corrosion damage of girder (left: mid-span, right: girder end).

3 FINITE ELEMENT ANALYSIS

Four different degrees of corrosion attack were studied through NLFEA, with 40% area reduction of the steel considered as the most severe scenario. The girder was analyzed considering the application of a concentrated load at a distance of 1.5d from the support.

Furthermore, different degraded material models have been implemented for separate analyses. A total of 19 analyses have been conducted for the girder. The details of the models, analyses, and constitutive models used are found in the next sections.

3.1 *Finite element modeling and analysis*

The girder has been modeled as a plane stress problem using VecTor2 software (Wong et al. 2013), which employs the Modified Compression Field Theory (MCFT) for the analysis of concrete membranes. Given the distribution of the tendons along most of the length of the girder, three-node elements have been used to model concrete and provide a better discretization along the tendons. Two-node truss elements were used to model the tendons in a discrete manner, while stirrup reinforcement has been defined in a smeared approach. Given the large number of tendons near the girder end, they have been modelled in groups of two with equivalent properties to simplify the model mesh. All the different thicknesses and reinforcement ratios in the girder have been explicitly modeled.

The constitutive models were selected from the VecTor2 material library (Wong et al. 2013): for concrete, Popovic's model for pre and post-peak behavior; for prestressing steel, a bilinear model with a transition curve from the elastic to the hardening branch; and for reinforcing steel, a nonlinear strain-hardening branch after the yield plateau. Eligehausen's model has been used for the steel-concrete bond relationship. The finite element model is presented in Figure 3; different colors are used to represent the different concrete web thicknesses ranging from 178-254 mm.

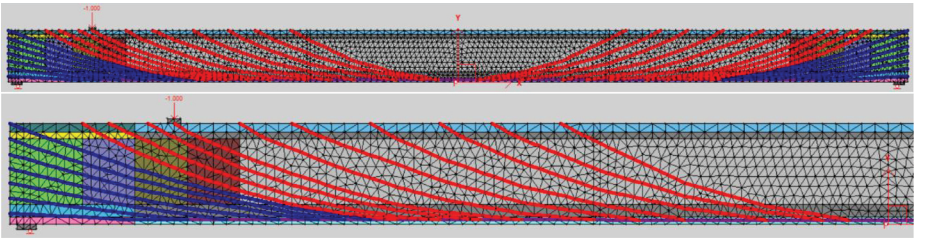


Figure 3. FE model: Complete, and close up of half the girder.

The analysis was carried out in a displacement-controlled manner in two stages: the first one where the effective prestressing forces and self-weight of the girder are applied; and the second, where a downwards displacement is enforced at a distance of 1.5d from the support. A steel plate element was placed under the applied displacement and at support points. The girder is simply supported at its ends.

3.2 *Degraded material constitutive models*

For the analysis of the girder the material models for concrete and steel were modified according to selected degradation models and corrosion degrees. To the knowledge of the authors, no models have been proposed for the degradation of prestressing steel in post-tensioned applications. Under that consideration, three different models were implemented to simulate the degradation of the steel tendons. Furthermore, one model for the degradation of bond properties was also considered.

The compressive strength of concrete has been reduced by applying the compression softening model in the MCFT as used by Coronelli & Gambarova (2004), where the average tensile strain in the transverse direction resulting from corrosion-induced cracking is estimated from the corrosion cracking width in Equation 3 proposed by Molina et al. (1993):

$$f_c^* = f'_c/(1 + K\varepsilon_1/\varepsilon_0) \tag{1}$$

$$\varepsilon_1 = n_{bars} w_{cr} / b_0 \tag{2}$$

$$w_{cr} = \sum u_{i\,corr} = 2\pi(v_{rs} - 1)X \tag{3}$$

where $f'c$ is the compressive strength of undamaged concrete, K is a roughness coefficient, ε_1 is the average strain in the cracked concrete at right angles to the direction of compression, ε_0 is the strain at peak compressive stress, b_0 is the unaffected section width of the girder, n_{bars} is the number of bars in the compression layer, and v_{rs} and X are the ratio of volumetric expansion of oxides and the depth of corrosion attack.

For reinforcing steel, a reduction of the effective area and ductility has been applied according to the degree of corrosion. For prestressing steel, three models have been implemented: 1) by Cairns & Millard (1999) as in Equation 4, 2) by Cairns et al. (2005) as in Equations 5-7, and 3) by Lu et al. (2016) as in Equations 8-10. The models are designated "C&M", "C", and "L" for further differentiations.

$$\varepsilon'_{su} = \varepsilon_{sy} + (\varepsilon_{su} - \varepsilon_{sy})\left(1 - \frac{\alpha_{pit}}{\alpha_{pit,max}}\right) \tag{4}$$

$$f_u = f_{u0}(1 - \alpha_u Q_{corr}) \tag{5}$$

$$f_y = f_{y0}(1 - \alpha_y Q_{corr}) \tag{6}$$

$$\varepsilon_u = \varepsilon_0(1 - \alpha_1 Q_{corr}) \tag{7}$$

$$f'_u = f_s(1 - 2.8\eta_s) \tag{8}$$

$$E'_s = E_s(1 - 1.8\eta_s) \tag{9}$$

$$\varepsilon'_u = \varepsilon_u\left(0.1 + 0.9e^{(-20\eta_s)}\right) \tag{10}$$

In the previous equations α_{pit} is the area reduction due to corrosion, Q_{corr} and η_s, represent the average corrosion degree, and α_u, α_y, α_1 are empirical coefficients depending on experimental conditions. The C&M model allows for a reduction of cross section up to 50%, according to several investigations, while the empirical coefficients of model C have been determined for average corrosion degrees of approximately 30%, and model L has practical application up to a degree of corrosion of approximately 15 to 20%. It is worth noting that model C was developed from experimental tests on artificially corroded strands.

Additionally, a model for bond deterioration between concrete and strands according to Wang et al. (2017) has been employed, denoted as "W". The model considers a reduction of the maximum bond strength τ_{max} as a function of the average corrosion degree η_s calculated in terms of reduction of cross-sectional area. This model may provide practical results up to a degree of corrosion of approximately 15 to 20%.

$$\tau'_{max} = \tau_{max}\left(2.03e^{(-0.118\eta_s)}\right) \tag{11}$$

3.3 *Finite element analyses*

Analyses have been performed for degrees of corrosion of 10, 20, 30, and 40% where the range of applicability of the degradation material model has so permitted according to the limits described in the previous section. The models are labeled according to the degradation models they implement; for example, "C+W" uses prestressing steel degradation by Cairns et al. (2005) and bond degradation by Wang et al. (2017). The summary of conducted analyses is presented in Table 1; where there is no applicability of a model, no analysis has been conducted, and it is denoted as "N/A".

Table 1. Girder FE analyses.

Model	ηs = 10%	ηs = 20%	ηs = 30%	ηs = 40%
C&M*	+	+	+	+
C&M	+	+	+	+
C	+	+	+	N/A
L	+	+	N/A	N/A
C&M+W	+	+	N/A	N/A
C+W	+	+	N/A	N/A
L+W	+	+	N/A	N/A

* No concrete degradation

4 RESULTS

The results regarding the variation of shear resistance for the different analyses are reported in Figure 4 as normalized shear capacity (V_{corr}/V_0) against corrosion degree, where V_0 is the girder capacity in the uncorroded state.

The load-displacement responses for a corrosion degree of 20% are presented in Figure 5; such degree of corrosion represents the limit of applicability in some of the used models, thus providing an interesting point for comparison. In the figure, the response of the undamaged girder is plotted as well.

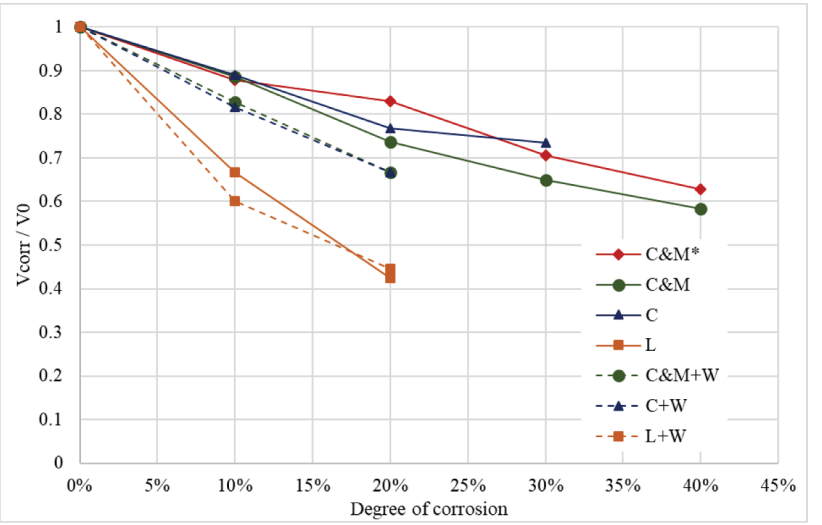


Figure 4. Normalized reduction of shear capacity vs degree of corrosion.

In general, 3 failure modes have been identified throughout the analyses: 1) a combination of wide diagonal cracking to the right of the loading point along the tendons and wide flexural cracking with rupture of some lower tendons, denoted "V-F"; 2) wide flexural cracking in the soffit of the girder in the vicinity of the loading point due to high slippage of tendons, denoted "F-B"; and 3) wide diagonal cracking to the left of the loading point extending to the top of the web where crushing occurs, denoted "V-C". The results are summarized in Table 2, and numbered according to the aforementioned description. The cracking patterns for the identified failure modes are shown in Figure 6, where for clarity only a portion of the girder is shown.

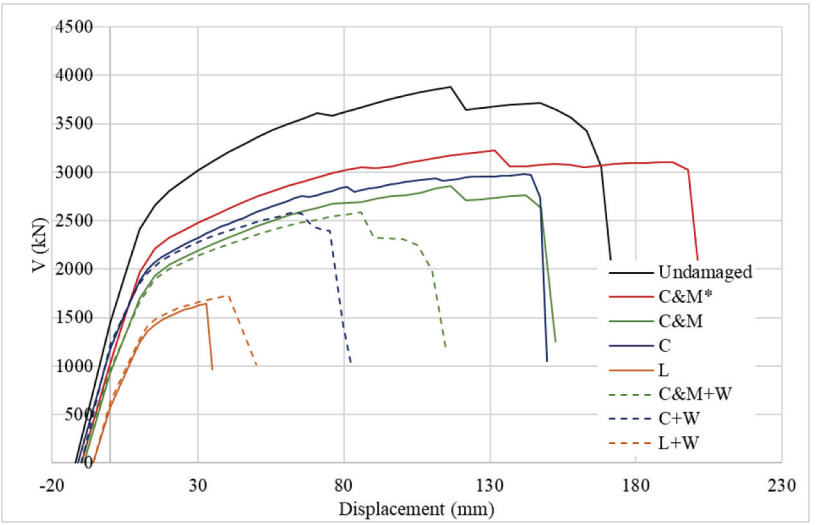


Figure 5. Load-displacement responses of models with 20% corrosion degree.

Table 2. Girder failure modes.

Model	ηs = 10%	ηs = 20%	ηs = 30%	ηs = 40%
C&M*	V-F	V-F	V-F	V-F
C&M	V-F	V-F	V-F	V-F
C	V-F	V-F	V-F	–
L	F-B	F-B	–	–
C&M+W	V-F	V-C	–	–
C+W	V-F	V-C	–	–
L+W	F-B	F-B	–	–

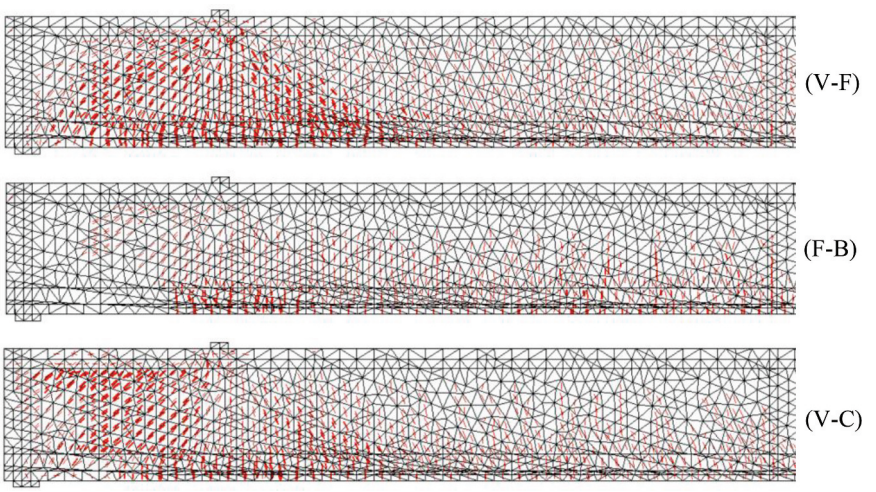


Figure 6. Cracking patterns for different failure modes.

Figure 7 and Figure 8 show the typical stresses in the stirrups and tendons for each type of failure mode; once again, only the relevant portion of the girder is displayed.

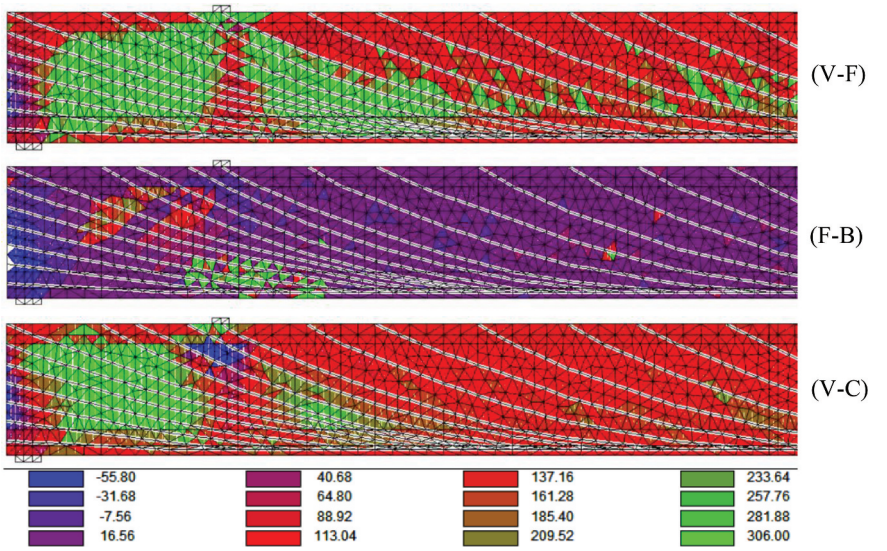


Figure 7. Stresses in stirrups (MPa).

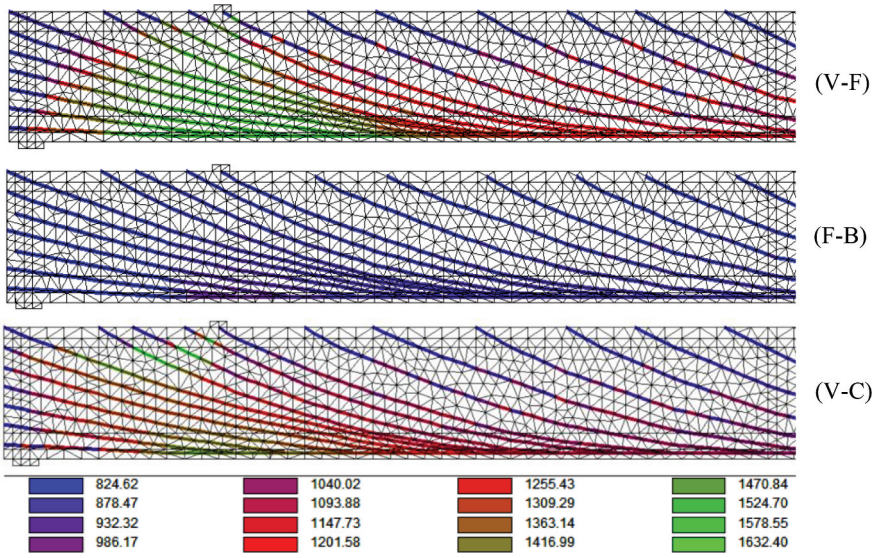


Figure 8. Stresses in tendons (MPa).

5 DISCUSSION

A range for the reduction in shear capacity of the girder has been obtained through the different analyses. By analyzing Figure 4, it is seen that models C&M and C seem to offer an upper bound for the capacity of the girder, while model L provides results on the other side of the spectrum. By comparing results at a degree of corrosion of 20%, both C&M and C models estimate a reduction in capacity of 25%, while L model estimates 55%. Also, it is evident that considering the degradation of concrete has an effect on the behavior of the girder, but it does not seem to be a marked one, perhaps due to the dominant contribution of the steel components to shear resistance. The effect of the reduction of ductility and strength of prestressing steel may be clearly

observed by means of Figure 5, emphasizing its contribution to the shear capacity. Both L and L +W models estimate failure at a much lower vertical displacement, and failure is brittle.

The following observations can be made by examination of the failure modes and stresses in the steel: 1) models C&M and C predict in most cases a failure in which the stirrups and tendons fully engage in the shear response of the girder near ultimate, and failure occurs in the location where stirrup reinforcement is at a minimum and the angle of the tendons decreases; 2) when bond degradation is taken into account, failure due to slippage occurs either at the soffit of the girder or near their anchorage points at the top; 3) when considering model L, the failure is brittle with a very early slippage and rupture of the tendons which have a considerable reduced capacity.

The most evident difference in results occurs when using L model for the reduction of steel properties, and the difference with the other models suggests that further research and experimental work to understand the degradation of post-tensioned steel strands is required.

6 CONCLUSIONS

In this study, estimates of the reduction in shear capacity of a post-tensioned girder were obtained by means of 2D NLFEA according to different degraded material models and degrees of corrosion. At 20% corrosion, shear capacity predictions ranged widely from approximately 45% to 85% that of the undamaged girder. Also, insight into the possible failure modes for each case was obtained, as well as an understanding of the contribution of prestressing steel to the shear response of the girder. NLFEA has proven to be a suitable tool for this evaluation; however, the adequacy of the results will depend on the use of proper material models. Also, it is recognized that further study is needed into the degradation models for implementation in prestressed concrete. Furthermore, it is acknowledged that this type of study would greatly benefit from accurate information pertaining the spatial distribution of corrosion; however, for the problem at hand where a relatively small portion of the member is of interest, the approach followed may prove valuable in the estimation of the shear response of post-tensioned girders.

REFERENCES

Belletti, B., Vecchi, F., Bandini, C., Andrade, C. & Sánchez, J. 2020. Numerical evaluation of the corrosion effects in prestressed concrete beams without shear reinforcement. *Structural Concrete Journal of the fib* 21(5) 1794–1809.

Cairns, J. & Millard, S. 1999. Section 13.2: Reinforcement corrosion and its effect on residual strength of concrete structures. *Proc. 8th Int. Conf. on Structure Faults and Repair*, M. Forde, ed., Engineering Technics Press, Edinburgh, U.K.

Cairns, J., Plizzari, G.A., Du, Y., Law, D.W., & Franzoni, C. 2005. Mechanical Properties of Corrosion-Damaged Reinforcement. *ACI Materials Journal* 102-M29, 256–264.

Coronelli, D., & Gambarova, P. 2004. Structural Assessment of Corroded Reinforced Concrete Beams: Modeling Guidelines. *ASCE Journal of Structural Engineering* 130 (8), 1214–1224.

Huang, L., Liu, J., Wu, Z., Tomlinson, D., Cruz-Noguez, C., Alexander, J. & Li, Y. 2022. Finite element-based parametric analysis of corrosion-induced structural deterioration in prestressed concrete bridge girders. *Canadian Journal of civil Engineering* 49(9) 1543–1558.

Lu, Z., Li, F., Zhao, Y., 2016. An investigation of Degradation of Mechanical Behavior of Prestressing Strands Subjected to Chloride Attacking. *5th International Conference on Durability of Concrete Structures*, 57–65. Shenzhen University, China.

Molina, F.J., Alonso, C. & Andrade, C. 1993. Cover cracking as a function of rebar corrosión: Part 2-Numerical model. *Materials and Structures* 26, 532–548.

Osmolska, M.J., Kanstad, T., Hendriks, M.A.N. & Markeset, G. 2022. Numerical investigation into the effects of corrosion on the shear performance of pretensioned bridge girders with cast-in place slabs. *Structures* (46) 1447–1468.

Wang, L., Zhang, X., Zhang, J., Yi, J. & Liu, Y. 2017. Simplified Model for Corrosion-Induced Bond Degradation between Steel Strand and Concrete. *Journal of Materials in Civil Engineering* 29(4) 04016257–1.

Wong, P.S., Vecchio, F.J. & Trommels, H. 2013. Vector2 & Formworks User's Manual Second Edition. *Technical Report*, *Department of Civil Engineering*, *University of Toronto*, 1–294. Toronto, Ontario, Canada.

Bridge Maintenance, Safety, Management, Digitalization and Sustainability – Jensen, Frangopol & Schmidt (eds)
© 2024 The Author(s), ISBN 978-1-032-77040-6
Open Access: www.taylorfrancis.com, CC BY-NC-ND 4.0 license

Analysis for the bridge fatigue failure and weight limit using the probabilistic machine learning method

Wangchen Yan
College of Civil Engineering, Xiangtan University, Xiangtan, China

ABSTRACT: In this study, a probabilistic machine learning method was proposed as an alternative to the time-consuming finite element simulation method for analyzing the bridge fatigue failure probability under overloading conditions. First of all, the parameters that have great influences on the bridge fatigue failure probability were selected as input variables and the value of the limit state function of the fatigue damage was adopted to be the output variable. Moreover, the feedforward neural network integrated with the Monte Carlo method was employed to predict the bridge fatigue failure probability under different loading conditions. Finally, the influence of different weight limits on bridge fatigue life was explored. Results showed that the machine learning-based approach can serve as an efficient alternative for predicting the fatigue failure probability under different overloading conditions. In addition, the bridge weight limit had a significant impact on the performance of bridges in service for over 45 years. More importantly, it was found that reducing the vehicle gross weight limit from 55 t to 49 t could extend the bridge fatigue life by nearly 40%, indicating the positive effect of posing weight limits on prolonging the fatigue life of bridges.

1 INTRODUCTION

Traffic overloading has been very common around the world because of the quick development of the freight transportation. Truck overloading can pose a great threat to the bridge safety and may even directly result in bridge failure. Hobbacher et al. (Hobbacher et al. 2016) further pointed out that overloading and fatigue were the two main reasons for the damage of composite and steel bridges. As a result, it is of great importance to estimate the fatigue damage of composite girder bridges considering truck overloading.

Many efforts have been made to investigate the bridge fatigue damage caused by vehicular overloading using the deterministic approaches, i.e., finite element (FE) analysis, experiments, site surveys, and test. Cha et al. (Cha et al. 2014) integrated the FE analysis with actual inspection data to assess the influences of vehicular overloading on steel girder bridges. Wang et al. (Wang et al. 2016) evaluated the overloading induced fatigue damage of a new bridge based on the proposed vehicle-bridge coupled vibration system. Deng and Yan (Deng and Yan 2018) used the FE analysis to fulfill the permit checking for bridges in service.

When evaluating the vehicle-induced fatigue damage, scholars primarily focused on equivalent stress. In order to estimate the equivalent stress, a statistical truck model with deterministic parameters was proposed in AASHTO LRFD code (AASHTO 2017) to represent the actual truck traffic. However, the parameters of overloaded trucks were not considered in the AASHTO LRFD code (AASHTO 2017). Lu et al. (Lu et al. 2017) noted that the deterministic configuration of such truck model may not sufficiently capture the variability inherent in truck parameters. Moreover, the bridge fatigue failure is the result of the damage accumulation over time, which can be affected by the uncertainties stemming from truck traffic parameters (Chen et al. 2011). Therefore, probabilistic approaches may be

DOI: 10.1201/9781003483755-116

more suitable to evaluate the vehicle induced fatigue damage (Lu et al. 2017). However, it is known that the probabilistic analysis heavily relies on computation due to the necessity for a large amount of simulations, posing a significant challenge for the efficiency of fatigue damage estimation.

Recently, many advances have been made to improve the efficiency of fatigue damage assessment and machine learning methods are becoming popular owing to its unique advantages. Fathalla et al. (Fathalla et al. 2018) attempted to quickly predict the fatigue life of bridge decks using the artificial neural network (ANN), which was developed based on a large number of crack patterns of bridge deck slabs and the corresponding deck slab fatigue life. Lu et al. (Lu et al. 2017) adopted the support vector regression method to address the fatigue reliability of the bridge deck under the loading of truck models developed based on the weigh-in-motion (WIM) data. It is noted that although the bridge deck slabs directly suffered from the traffic loading, its failure does not lead to the failure of the bridge (Kayser and Nowak 1989). Moreover, despite recent achievements on the fatigue damage evaluation using machine learning, the evaluation of the fatigue failure reliability for steel girder bridges under overloading is still lacked. In this study, the fatigue failure probability of the steel girder bridge was focused on using the machine learning method.

2 TRAFFIC OVERLOADING

Vehicle-induced damage for short-to-medium-span bridges is not only influenced by gross vehicle weight, but also closely related to the vehicle axle load. In this study, the axle-load-based (AL) and gross-weight-based (GW) overloaded trucks were both considered and they were typically represented by the three- and five-axle trucks, respectively, which were shown in Figure 1. In Figure 1, the three-axle overloaded truck model was based on the AASHTO HS 20-44 fatigue design truck, which was developed statistically using the WIM data of 27,000 trucks (Snyder et al. 1985) while the five-axle overloaded truck model was based on the AASHTO type 3S2 truck, which can represent nearly half of heavy vehicles (Mason 1983). Finally, these two kinds of vehicles were used together to reflect the overloaded truck traffic considered in this study.

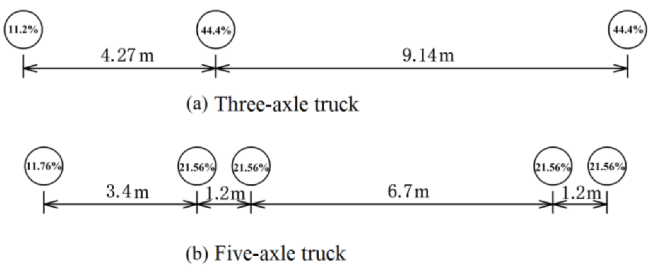


Figure 1. Truck models adopted.

According to Hwang and Nowak (Hwang and Nowak 1991), highway traffic can be typically represented by 20% three-axle trucks and 80% five-axle trucks. In this study, the original overloaded traffic considered was adopted to be the combination of 20% AL-overloaded trucks and 80% GW-overloaded trucks. Moreover, the variable traffic compositions were realized by adjusting the proportions of AL-overloaded trucks or GW-overloaded trucks in this study. Such approach was also adopted by other scholars (Laman and Nowak 1996).

In this study, vehicle weights of AL- and GW-overloaded trucks were regarded as random variables to investigate the influence of traffic overloading on the bridge fatigue failure probability. The corresponding distributions and statistics for the weight of overloaded trucks were adopted from Hwang and Nowak (Hwang and Nowak 1991), as listed in Table 1. It is noted that 320 kN

is the gross weight of both the HS 20-44 truck and type 3S2 truck as specified in AASHTO LRFD code (AASHTO 2017). In this study, in order to simulate the traffic overloading conditions, only the gross weight larger than 320 kN was generated according to Table 1. Moreover, Schilling and Klippstein (Schilling and Klippstein 1977) noted that the gross weight of vehicles larger than 512 kN only accounted for 0.09% according to the surveys for WIM sites, which were not considered in this study. Eventually, the gross weight of AL- and GW-overloaded trucks larger than 320 kN while less than 512 kN were regarded as the effective weight value in this study. Additionally, based on the generated gross weight, the corresponding axle weight of the AL- and GW-overloaded trucks can be calculated according to the distributions shown in Figure 1.

Table 1. Statistics of the gross weight for three- and five-axle trucks (data from Hwang and Nowak 1991).

Truck type	Distribution	Mean value kN	Standard deviation kN
Three-axle	Normal	178	37
Five-axle	Normal	290	76

3 FRAMEWORK

3.1 *Computational framework*

In this study, the main framework was shown in Figure 2, which was conducted according to the following steps. At the first step, the input and output variables were selected carefully. The adopted input variables were randomly generated based on the corresponding distributions, and the value of the limit state function for the accumulative fatigue damage was selected as the output. At the second step, the ANN model was developed based on the

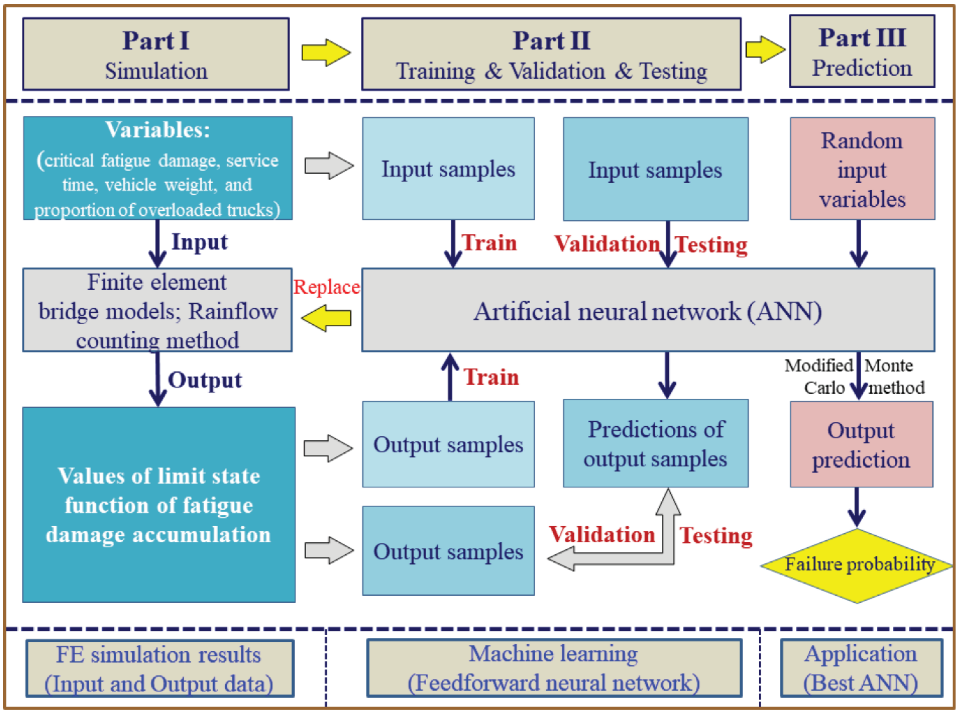


Figure 2. Flowchart for determining vehicle weight limit and making permit decision.

Matlab platform, which was trained, validated, and tested based on the generated input and output data samples. At the third step, the trained ANN model was integrated with the Monte Carlo method to predict the bridge fatigue failure probability under certain overloading conditions.

3.2 *FE bridge model*

In this study, a typical composite steel girder bridge with the concrete deck slab was adopted for illustration. The bridge is 30.48 m in length and 9.75 m in deck width. The cross-section of this bridge model is shown in Figure 3. It should be noted that the adopted bridge model was proved to be a good representative of the simply-supported composite steel girder bridges with concrete deck slabs in the United States and has been employed in many studies for the bridge fatigue damage evaluation (Wang et al. 2016; Wang et al. 2005).

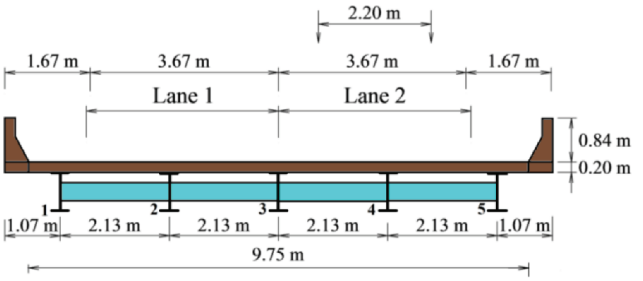


Figure 3. Cross-section of the bridge model.

In the present study, a three-dimensional (3D) FE model of this bridge was built with ANSYS framework. Five identical steel girders were uniformly placed with an interval of 2.13 m in the bridge transverse direction. Two end steel diaphragms and three steel intermediate diaphragms were arranged with a space of 7.6 m in the bridge longitudinal direction. In the FE bridge model, steel girders, the concrete bridge deck, and guardrails were all modeled by solid elements while the steel diaphragms were modeled by shell elements. More detailed bridge parameters can be found in Table 2.

Table 2. Details of the steel girders of the bridge model.

Cross-sectional area	Moment of inertia	Initial Young's modulus	
m^2	m^4	GPa	Poisson's ratio
0.02	0.0011	210	0.25

It is noted that the adopted bridge has a fast lane and a slow lane, which were denoted by Lane 1 and Lane 2 in Figure 3, respectively. Considering the statistics that more than 90% heavy trucks passed through the bridge along the slow lane (Lu et al. 2017), only overloaded trucks traveling in the slow lane were considered in this study, which was also the loading condition suggested by AASHTO LRFD code (AASHTO 2017) when evaluating the bridge fatigue damage.

3.3 *Probabilistic fatigue analysis*

Repetitive overloading can induce increased number of bridge stress cycles and therefore cause accumulated fatigue damage. Generally, the limit state function of the accumulative

fatigue damage, i.e., $g(X)$ as listed in Eq. (1), can be a good indicator of the bridge fatigue reliability, and the condition that the value of $g(X) \leq 0$ indicated the bridge fatigue failure states.

$$g(X)=FD_{\Delta}-\sum_{i=1}^{t} FD(t) \tag{1}$$

where FD_{Δ} is the critical fatigue damage in terms of fatigue resistance and was adopted as a variable in this study; $FD(t)$ denotes the overloading-induced bridge fatigue damage after t years of service.

According to Chen and Li, the critical fatigue damage (FD_{Δ}) usually ranged from 0.5 to 2.0 when the materials failed (Chen and Li 2010). In addition, the parameter FD_{Δ} was assumed to follow the lognormal distribution with a mean value of 1.0 and a coefficient of variation (COV) of 0.15 (Raju et al. 1990). Considering the condition that the overloaded truck traffic can be comprised of trucks with different weights and different proportions of AL- and GW-overloaded trucks, the updated function of $g(X)$ can be found in Eq. (2).

$$g(X)=FD_{\Delta}-Num\cdot t\cdot\left(r_{AW}\cdot\sum_{i}^{t}\frac{n_i\cdot S_i^m}{A}+r_{GW}\cdot\sum_{j}^{t}\frac{n_j\cdot S_j^m}{A}\right) \tag{2}$$

where t is the bridge service time in years, and it was assumed to follow a uniform distribution starting from 1 to any interested year, such as 225 years in this study; Num is the number of passing trucks in one year; r_{AL} and r_{GW} are the proportions of the AL- and GW-overloaded trucks in the truck traffic, respectively; S_i and S_j are the stress range induced by the AL- and GW-overloaded trucks, respectively.

It is noted that the sum of r_{AL} and r_{GW} is always 1. Moreover, it was assumed that the parameter r_{AL} followed a lognormal distribution with a mean value of 0.2 and a COV of 0.15. Regardless of traffic growth, the parameter Num can be calculated based on the average daily truck traffic (ADTT) specified in the AASHTO LRFD code (AASHTO 2017), namely, Num=365 x 2000=730,000. In addition to the distributions for variables of gross weight of AL- and GW-overloaded trucks listed in Table 1, the other distributions of aforementioned variables were listed in Table 3.

Table 3. Distributions of the variables investigated.

Par.	Distribution	Mean value	COV
FD_{Δ}	Truncated lognormal	1.0	0.15
r_{AL}	Truncated lognormal	0.2	0.15
t	Uniform	1 (Minimum)	225 (Maximum)
A	Deterministic	$3.93\text{x}10^{12}$	-
m	Deterministic	3	-

It is noted that the fatigue failure probability of bridges caused by overloaded trucks, as defined in Eq. (3), is closely related to the bridge safety reliability (Melchers and André 2018). In addition, based on the finding by Helmerich et al. (Helmerich et al. 2007), the target reliability of existing bridges usually ranges from 2.0 to 3.5, and the reliability of 2.0 corresponds to a failure probability of 2.3%. Therefore, the value of 2.3% was adopted as the target P_f in this study, which was also employed by other scholars (Lu et al. 2017; Zhu and Zhang 2018).

$$P_f=P(g(X)\leq 0) \tag{3}$$

3.4 *Probabilistic prediction of fatigue failure based on machine learning*

In this section, the feedforward neural network was developed based on the Matlab platform in order to map the relationship between the outputs, i.e., the value of g(X) and the inputs, namely, the gross weight of AL- and GW-overloaded trucks, r_{AL}, service time t, and FD_{Δ}.

The feedforward neural network has an input layer, an output layer, and multiple hidden layers. Each neuron is a basic data processing unit. The data flowed from the input layer and was processed by the neurons in hidden layer, and was finally transferred to the output layer. Each neuron in the hidden layer performed the similar data processing procedures, as shown in Figure 4, and offered the prediction eventually. Once the error between the prediction from the ANN and the actual value met the requirement, the training was complete. The ANN model providing the best predictions was regarded as the trained ANN, which was used to predict the fatigue failure probability with Monte Carlo method in the next section.

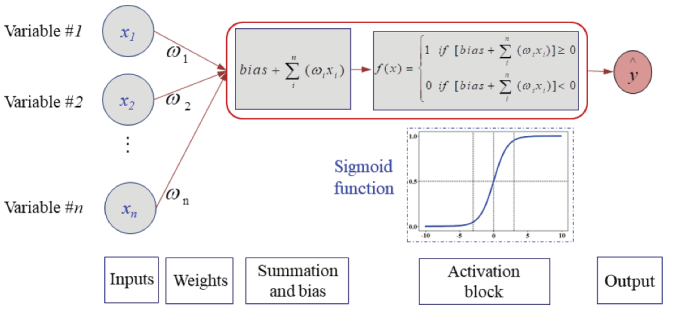


Figure 4. Processing procedure of the neuron in hidden layers.

In order to verify the accuracy of the optimized ANN in this study, differences between the values of $g(X)$ obtained from FE analysis and ANN were compared. The maximum difference was proved to be 0.35%, which demonstrated the reliability and accuracy of the trained ANN.

4 PREDICTION OF THE FATIGUE FAILURE PROBABILITY

Based on the trained ANN model, the bridge fatigue failure probability caused by overloaded truck traffic was studied using the Monte Carlo method. Specifically, a total number of 500,000 sets of input samples were firstly generated randomly according to the distributions summarized in Tables 1 and 3. Then, 500,000 outputs can be predicted using the optimized ANN model. Eventually, the ratio of the number of predicted negative outputs to the total number of outputs predicted, i.e., 500,000, was calculated to be the fatigue failure probability P_f.

In this study, several typical weight limit values were adopted to be the upper limits for *W_AL* and *W_GW*, i.e., 33 t, 41 t, 43 t, 45 t, 47 t, 49 t, 51 t, 53 t, and 55 t. Under these weight limits, the predicted fatigue failure probability was shown in Figure 5. It is necessary to mention that the target fatigue failure probability was selected as 2.3% in this study which corresponds to a target reliability of 2.0 according to Helmerich et al (Helmerich et al 2007).

It can be seen from Figure 5 that under different gross weight limits, the bridge fatigue failure probability varied slightly before the bridge reached its 45th service years. Moreover, the influence of different weight limits became apparent after 45 years of service, which indicated that posing weight limits was more important for the performance of old bridges.

In the early time when the bridge load limit value was not clarified, the vehicle design load value was often mistaken for the bridge load limit value. It was observed from Figure 5 that the fatigue life of the bridge was more than 225 years when the weight limit was adopted to be 33 t. It is noted that 33 t was slightly higher than the vehicle design load value 32 t. This

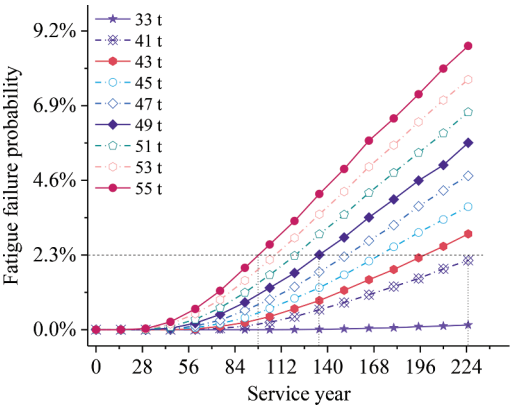


Figure 5. Fatigue failure probability of the bridge under different gross weight limits.

phenomenon clearly indicated that using the vehicle design load value as the bridge weight limit value would significantly underestimate the performance of bridges.

In addition, Under the gross weight limit specified in the "General Specifications for the Design of Highway Bridges and Culverts" (JTG D60-2015), i.e., 55 t, and the maximum allowable total mass of vehicles determined by "External Dimensions, Axle Loads and Mass Limits of Cars, Trailers and Car Trains" (GB1589-2016), i.e., 49 t, the corresponding predicted fatigue life were 98 years and 135 years, respectively. It is noted that the currently used vehicle load limit of 49 t is about 10% lower than the vehicle load limit of 55 t determined in 2015, which could result in nearly 40% extension of the bridge fatigue life. This comparison demonstrated the importance of bridge weight limits in extending the bridge service life.

It is noteworthy that based on the ordinary laptop equipped with Intel® Core™ i7-3520M, the total processing time of the trained ANN for each scenario was only several seconds, which was much less than the time required by performing the FE analysis on the workgroup with Intel® Core™ i7, i.e., 16 hours in this study.

5 CONCLUDING REMARKS

In this study, a method based on the machine learning and Monte Carlo method was proposed to predict the bridge fatigue failure probability considering the effect of overloading. A typical composite steel girder bridge was adopted to illustrate the proposed framework. Results showed that the proposed approach was capable of predicting the fatigue failure probability with high accuracy and efficiency, providing an excellent alternative for finite element analysis-based methods. Moreover, it was found that posing weight limits was more helpful for bridges servicing over 45 years. It was demonstrated that if the weight limit value was decreased from 55 t to 49 t, i.e., 10% reduction, the bridge fatigue life could nearly increase 40%, which indicated the importance of determining rational weight limit to prolong the bridge service life.

ACKNOWLEDGEMENTS

The author gratefully acknowledges the financial support provided by the National Natural Science Foundation of China (Grant No. 52208213), the Excellent Youth Foundation of Education Department in Hunan Province (Grant No. 22B0141), the Xiaohe Sci-Tech Talents Special Funding under Hunan Provincial Sci-Tech Talents Sponsorship Program (2023TJ-X65), and the Science Foundation of Xiangtan University (Grants No. 23QDZ16 and 21QDZ23).

REFERENCES

Hobbacher, A. F., Hicks, S. J., Karpenko, M., Thole, F., & Uy, B. 2016. Transfer of Australasian bridge design to fatigue verification system of Eurocode 3. Journal of Constructional Steel Research, 122, 532–542.

Cha, H., Liu, B., Prakash, A., & Varma, A. H. 2016. Effect of local damage caused by overweight trucks on the durability of steel bridges. Journal of Performance of Constructed Facilities, 30(1), 04014183.

Chen, X., & Li, S. 2010. Fatigue Damage Assessment of the In-Service Bridge Based on the Traffic Investigation. In ICLEM 2010: Logistics For Sustained Economic Development: Infrastructure, Information, Integration (pp. 1537–1543).

Wang, W., Deng, L., & Shao, X. 2016. Fatigue design of steel bridges considering the effect of dynamic vehicle loading and overloaded trucks. Journal of Bridge Engineering, 21(9), 04016048.

Deng, L., & Yan, W. 2018. Vehicle weight limits and overload permit checking considering the cumulative fatigue damage of bridges. *Journal of Bridge Engineering*, *23*(7), 04018045.

American Association of State Highway And Transportation Officials (AASHTO). 2017, LRFD bridge design specifications. Washington, D.C.

Lu, N., Noori, M., & Liu, Y. 2017. Fatigue reliability assessment of welded steel bridge decks under stochastic truck loads via machine learning. Journal of Bridge Engineering, 22(1), 04016105.

Chen, N. Z., Wang, G., & Soares, C. G. 2011. Palmgren–Miner's rule and fracture mechanics-based inspection planning. Engineering Fracture Mechanics, 78(18), 3166–3182.

Fathalla, E., Tanaka, Y., & Maekawa, K. 2018. Remaining fatigue life assessment of in-service road bridge decks based upon artificial neural networks. Engineering Structures, 171, 602–616.

Kayser, J. R., & Nowak, A. S. 1989. Reliability of corroded steel girder bridges. Structural safety, 6(1), 53–63.

Zhu, J., & Zhang, W. 2018. Probabilistic fatigue damage assessment of coastal slender bridges under coupled dynamic loads. Engineering Structures, 166, 274–285.

Snyder, R. E., Likins JR, G. E., & Moses, F. 1985. Loading spectrum experienced by bridge structures in the united states. final report (No. FHWA/RD-85/012).

Mason JR, J. M. (1983). Effect of oil field trucks on light pavements. Journal of Transportation Engineering, 109(3), 425–439.

Hwang, E. S., & Nowak, A. S. 1991. Simulation of dynamic load for bridges. Journal of structural engineering, 117(5), 1413–1434.

Laman, J. A., & Nowak, A. S. 1996. Fatigue-load models for girder bridges. Journal of Structural Engineering, 122(7), 726–733.

Schilling, C. G., & Klippstein, K. H. 1977. Fatigue of steel beams by simulated bridge traffic. Journal of the Structural Division, 103(8), 1561–1575.

Wang, T. L., Liu, C., Huang, D., & Shahawy, M. 2005. Truck loading and fatigue damage analysis for girder bridges based on weigh-in-motion data. Journal of Bridge Engineering, 10(1), 12–20.

Raju, S. K., Moses, F., & Schilling, C. G. 1990. Reliability calibration of fatigue evaluation and design procedures. Journal of Structural Engineering, 116(5), 1356–1369.

Melchers, R. E., & Beck, A. T. 2018. Structural reliability analysis and prediction. John Wiley & Sons, Inc., West Sussex.

Helmerich, R., Kühn, B., & Nussbaumer, A. 2007. Assessment of existing steel structures. A guideline for estimation of the remaining fatigue life. Structure and Infrastructure Engineering, 3(3), 245–255.

Bridge Maintenance, Safety, Management, Digitalization and Sustainability – Jensen, Frangopol & Schmidt (eds)
© 2024 The Author(s), ISBN 978-1-032-77040-6
Open Access: www.taylorfrancis.com, CC BY-NC-ND 4.0 license

Stationary proposal importance sampling for structural reliability of aging RC bridges

L. Capacci
Politecnico di Milano, Milan, Italy

ABSTRACT: Safety assessment of aging bridges may require the modeling of complex deterioration processes, further exacerbating in time the uncertainties involved in the mechanical response of critical members. Simulation-based techniques applied to life-cycle reliability problems may rely on time-consuming structural analyses, leading to untenable computational efforts and impairing the accuracy of the numerical estimates. This paper discusses an efficient computational framework for time-variant failure probability based on Importance Sampling (IS) with Stationary Proposal (SP) distribution. This novel methodology exploits numerical approaches traditionally developed for time-invariant structural reliability problems and extends them into a life-cycle context. Specifically, the simulation density is adaptively selected by minimizing the Kullback–Leibler Cross-Entropy from a chosen family of parametric distributions. The numerical procedure is applied to lifetime structural reliability of a reinforced concrete bridge exposed to chloride-induced corrosion.

1 INTRODUCTION

Traditional simulation-based procedures for structural reliability assessment can be computationally inefficient when time-consuming analyses are required to estimate relatively small failure probabilities (Yang et al. 2017). In life-cycle reliability problems, the computational effort is also affected by factors involved in the evolution in time of physical deterioration phenomena exacerbating uncertainties in structural capacities and performance decay such as functionality and resilience (Capacci et al. 2022). In this context, the impact of environmental aggressiveness and maintenance interventions play a key role in the assessment of structural safety for aging Reinforced Concrete (RC) bridges. Incorporating complex deterioration processes as well as countermeasures adopted to mitigate their impact would further exacerbate uncertainties involved in the time-variant structural capacity assessment of critical members.

Enhancing standard methodologies for the estimation of life-cycle structural safety is an open issue in reliability assessment of structures prone to aging effects. To this purpose, the paper presents a novel numerical framework to efficiently estimate time-variant failure probabilities of deteriorating structural systems, with specific focus on RC bridge decks exposed to chloride-induced corrosion. Random variables and stochastic processes associated to the structural demand and capacity of bridge members are efficiently simulated based on Importance Sampling (IS) from a Stationary Proposal (SP) time-invariant distribution. An adaptive procedure is also implemented to select the optimal SP distribution by identifying the parameters of a prescribed distribution family that minimize the discrepancy with the target density function (Rubinstein 1981). The results in terms of near-optimal sampling distribution parameters and reliability indices highlight the potentialities of the proposed methodology to improve the accessibility of reliability-based design optimization procedures for aging structures as well as to guarantee faster reliability updating frameworks to incorporate additional information available through inspections and maintenance.

DOI: 10.1201/9781003483755-117

2 LIFE-CYCLE STRUCTURAL RELIABILITY ESTIMATE: THE CE-SP-IS APPROACH

2.1 *Monte Carlo Simulation (MCS) and Stationary Proposal Importance Sampling (SP-IS)*

In life-cycle reliability problems, structural capacity evolves in time and underlying uncertainties to deterioration phenomena are described by time-variant Random Variables (RVs) $\mathbf{X}(t)$ with joint Probability Density Function (PDF) $f_{\mathbf{X}(t)}(\mathbf{x})$. The failure probability is formulated based on the mathematical expectation of the indicator function $I(\mathbf{x})$ of limit state function $g(\mathbf{x})$:

$$P_f(t) = E_{f_{\mathbf{X}(t)}}[I(\mathbf{x})] = \int_x I(\mathbf{x}) \cdot f_{\mathbf{X}(t)}(\mathbf{x}) d\mathbf{x} \tag{1}$$

More specifically, the Heaviside step function $I(\mathbf{x})$ is unitary in the failure domain $\{g(\mathbf{x}) \leq 0\}$ and null in the complimentary safe domain$\{g(\mathbf{x}) > 0\}$. Simulation methods are adopted to numerically estimate the multidimensional integral formulated in the failure probability. In traditional Monte Carlo simulation (MCS) for time-variant reliability problems, samples of the indicator function are generated based on the distribution of basic RVs progressively evolving over the system lifetime, requiring one simulation per observation time t. The MCS reliability estimator is the sample mean of the indicator function:

$$p_{MCS}(t) = \frac{1}{N} \sum_{i=1}^{N} I_i(t) \tag{2}$$

where N is the sample size of a single simulation carried out at each observation time t.

Stationary Proposal Importance Sampling (SP-IS) reformulates the failure probability in terms of a *time-invariant* sampling distribution ψ relying on the weighting coefficient W:

$$W(\mathbf{x}|t) = \frac{f_{\mathbf{X}(t)}(\mathbf{x})}{\psi(\mathbf{x})} \tag{3}$$

The SP-IS failure probability refers to the mathematical expectation in terms of the proposal PDF ψ of the product between indicator function I and time-variant weighting coefficients W:

$$P_f(t) = E_{\psi}[I(\mathbf{x}) \cdot W(\mathbf{x}|t)] = \int_{\mathbf{x}} I(\mathbf{x}) \cdot W(\mathbf{x}|t) \cdot \psi(\mathbf{x}) d\mathbf{x} \tag{4}$$

The failure probability is then estimated by the weighted sample mean of the indicator function:

$$p_{IS}(t) = \frac{1}{N} \sum_{i=1}^{N} I_i \cdot w_i(t) \tag{5}$$

The main advantage of SP-IS compared to MCS is that a single simulation is required to estimate probabilities at discrete times t, rather than a single simulation per time instant. Nonetheless, designing the sampling density ψ is a critical issue to effectively retrieve accurate results.

2.2 *Cross-Entropy-based Stationary Proposal Importance Sampling (CE-SP-IS)*

Methodologies based on Cross-Entropy (CE) are conceived to minimize the variance of the reliability estimator obtained by IS, seeking for a near-optimal simulation density ψ from a family of parametric distributions (Rubinstein 1981). This is done by minimizing a discrepancy metrics between a prescribed proposal density ψ with parameters $\mathbf{v}$ and the absolute best distribution p^*. For example, the Kullback-Leibler Cross-Entropy (KL-CE) is formulated as follows:

$$D_{KL} = \int_{\mathbf{x}} p^*(\mathbf{x}) \cdot \ln p^*(\mathbf{x}) d\mathbf{x} - \int_{\mathbf{x}} p^*(\mathbf{x}) \cdot \ln \psi(\mathbf{x}; \mathbf{v}) d\mathbf{x} \tag{6}$$

The optimization problem and the related algorithm to iteratively retrieve the proposal parameters $\mathbf{v}$ minimizing KL-CE are thoroughly described in Kurtz and Song (2013) and Geyer et al. (2019) regarding time-invariant reliability analysis.

In the SP-IS approach, the best possible density $p^*(\mathbf{x})$ is defined over the n_c combinations of (1) n_t discrete times and (2) n_p hazard scenarios affecting the actual PDF $f_{\mathbf{X}}$ as well as (3) n_s investigated limit states affecting the indicator function I (Capacci and Biondini 2023):

$$p^*(\mathbf{x}) = \frac{1}{n_c}\left[\sum_{c=1}^{n_c} \frac{I(\mathbf{x}|c)\cdot f_{\mathbf{X}(c)}(\mathbf{x}|c)}{P_f(c)}\right] \tag{7}$$

where each combination $c=\{t_z,p,s\}$ collects a given pair of z-th time instant t_z, p-th hazard scenario and s-th limit state.

The Gaussian Mixture Model (GMM) is a flexible family of proposal distributions $\psi(\mathbf{x},\mathbf{v})$ and a particularly suitable candidate as proposal density. The PDF of a K-variate is defined as follows as the weighted sum of K variates:

$$\psi(\mathbf{x},\mathbf{v}) = \sum_{k=1}^{K} \pi_k \cdot N(\mathbf{x}|\boldsymbol{\mu}_k,\boldsymbol{\Sigma}_k) \tag{8}$$

where the k-th variate is described by weighting probability π_k, mean vector $\boldsymbol{\mu}_k$, and covariance matrix $\boldsymbol{\Sigma}_k$. For exponential densities such as GMMs, explicit updating rules of their descriptive parameters $\mathbf{v}$ are available (Rubinstein and Kroese 2004). The $(m+1)$-th updating rules for the k-th density are defined as follows (Capacci and Biondini 2023):

$$\pi_k^{(m+1)} = \frac{\sum_{i=1}^{N} \tilde{w}_i \cdot \gamma_{ik}^{(m)}}{\sum_{i=1}^{N} \tilde{w}_i} \tag{9}$$

$$\boldsymbol{\mu}_k^{(m+1)} = \frac{\sum_{i=1}^{N} \tilde{w}_i \cdot \gamma_{ik}^{(m)} \cdot \mathbf{x}_i}{\sum_{i=1}^{N} \tilde{w}_i \cdot \gamma_{ik}^{(m)}} \tag{10}$$

$$\boldsymbol{\Sigma}_k^{(m+1)} = \frac{\sum_{i=1}^{N} \tilde{w}_i \cdot \gamma_{ik}^{(m)} \cdot \left(\mathbf{x}_i - \boldsymbol{\mu}_k^{(m)}\right) \cdot \left(\mathbf{x}_i - \boldsymbol{\mu}_k^{(m)}\right)^{\mathrm{T}}}{\sum_{i=1}^{N} \tilde{w}_i \cdot \gamma_{ik}^{(m)}} \tag{11}$$

where the i-th weight $\tilde{w}_i$ depends on the n_c reliability problems (Capacci and Biondini 2023):

$$\tilde{w}_i = \frac{1}{n_c}\sum_{c=1}^{n_c} \frac{I_i(s)\cdot w_i(\mathbf{w}|t_z,p)}{p_{IS}(t_z,p,s)} \tag{12}$$

3 TIME-VARIANT RELIABILITY OF A STATICALLY INDETERMINATE BEAM

3.1 *Limit states and failure probabilities*

The time-variant structural reliability of a statically indeterminate beam (Capacci and Biotndini 2022) is investigated with respect to two limit states: first plastic hinge formation and collapse. Figure 1a shows the plastic hinge formation mechanism triggering collapse, which is characterized by half-length l=3m and is loaded at midspan by a concentrated force ΘQ. The bending moment diagram sketched in Figure 1b depends on the positive plastic moment M_p^+ at midspan and the negative plastic moment M_p^- at the clamped end. Due to deterioration, the plastic moments are stochastic processes with parameters evolving over the normalized $\tau\in[0,1]$.

Assuming the beam has uniform bending stiffness over its length, elastic analysis allows identifying two safety factors associated to the load multiplier associated to first plastic hinge formation at midspan (i.e., Θ_p^+) and clamped end (i.e., Θ_p^-). The first yielding safety factor is retrieved by the minimum among the safety factors for each potential plastic hinge:

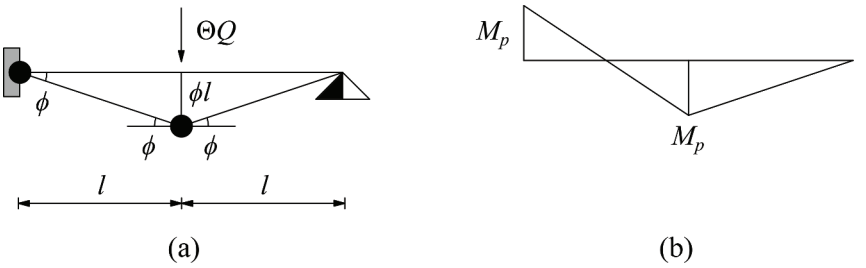


Figure 1. Collapse of a statically indeterminate beam: (a) mechanism; (b) bending moment distribution.

$$\Theta_1(\tau) = \min\left\{\Theta_p^+(\tau), \Theta_p^-(\tau)\right\} = \min\left\{\frac{M_p^+(\tau)}{\frac{5}{16}Ql}, \frac{M_p^-(\tau)}{\frac{3}{8}Ql}\right\} \tag{13}$$

Structural collapse is then evaluated by limit analysis and the related load multiplier is:

$$\Theta_2(\tau) = \frac{2M_p^+(\tau) + M_p^-(\tau)}{Ql} \tag{14}$$

The probabilities of occurrence of each event associated to limit state s=1,...,n_s with n_s=2 is expressed in terms of the related safety factors Θ_s:

$$p_s(\tau) = P[\Theta_s(\tau) \leq 1] \tag{15}$$

3.2 *Statistical dependency and environmental hazard scenarios*

Time-invariant concentrated force Q and time-dependent resisting moment $Mp^{\pm}$ are jointly lognormally distributed with linear coefficient ρ=0.7. Degradation laws in terms of the normalized time τ can be adopted to account for different scenarios for the evolution in time of the plastic moment descriptors. The statistical descriptors of Q and $Mp^{\pm}$ are listed in Table 1. Aging of plastic moments is expressed in terms of the hazard coefficients a_1 and a_2 respectively governing the linearly decaying mean value $\mu_M(\tau)$ and linearly increasing CoV $\delta_M(\tau)$.

Table 1. Statistical descriptors of concentrated force Q and resisting moment M_p.

Random Variable	Mean Value μ	Coefficient of Variation (CoV) δ
Concentrated Force Q	100 kN	0.10
Plastic Moment $M_p^{\pm}$	$(1-a_1\cdot\tau)\cdot$250 kNm	$0.15 + a_2\cdot\tau$

The SP-IS numerical framework effectively allows not only analyzing the evolution in time of multiple reliability problems, but also investigating different hazard and durability scenarios. Two scenarios characterized by "fast" and "slow" deterioration rates are considered and four hazard scenarios n_p=4 are considered by combining the deterioration rates for M_p^+ and M_p^-:

- Scenario "fast-fast": both moments are characterized by "fast" deterioration;
- Scenario "slow-slow": both moments are characterized by "slow" deterioration;
- Scenario "fast-slow": M_p^+ decays faster than M_p^-;
- Scenario "slow-fast", M_p^+ decays slower than M_p^-.

The first two cases are representative of hazard scenarios with different damage propagation rates and uniform aggressiveness over the beam span, whilst the last two scenarios simulate environmental exposure affecting differently the resisting moments at midspan and clamped end. The degradation coefficients a_1 and a_2 for each deterioration rate are collected in Table 2.

Table 2. Degradation coefficient of resisting moment $M_p^{\pm}$ descriptors.

Deterioration Rate	Coefficient a_1	Coefficient a_2
"Fast"	1/3	0.150
"Slow"	1/6	0.075

3.3 *Results of CE-SP-IS methodology*

The optimal proposal density is identified considering multiple time instants n_t, limit states n_s and parametric hazard scenarios n_p. Failure probabilities with respect to the previously discussed n_s=2 limit states are assessed for n_t=21 normalized time instants (i.e., from 0.05 to 1.00 every 0.05). All n_p=4 combinations of correlation and deterioration scenarios are considered, for a total of $\underline{n_c}=\underline{n_t}\cdot\underline{n_s}\cdot\underline{n_p}$=168 reliability problems to be solved.

The simulation is initialized with K=10 Gaussian mixtures with probability π_k=1/K with mean vectors $\boldsymbol{\mu}_k$ randomly simulated from an uncorrelated joint normal distribution standard deviation σ=0.2and centered at the mean vector associated with the final time τ=1 of the "fast-fast" hazard scenario and. Five rounds n_{iter}=5 of pre-sampling with N_{pre}=5′000 are adopted to calibrate the SP optimal density. A simulation with large sample size of N_{final}=25′000 is carried out to obtain the final reliability estimates, for a total of 50′000 structural analyses. Figure 2 shows the results for each aging scenario and time instant for first yielding (Figure 2a) and collapse (Figure 2b) limit states. Regarding first yielding, the most detrimental scenarios correspond to fast aging of end plastic moment M_p^- since scenario "fast-fast" almost overlaps with scenario "slow-fast". Faster degradation pace for midspan moment M_p^+ can lead to larger decay in collapse reliability.

4 TIME-VARIANT RELIABILITY OF A RC BRIDGE DECK

4.1 *Bridge properties and collapse probability*

Figure 3 shows the investigated two-span continuous RC bridge. Each span is l=30 m and it is subjected to both dead load G and live load Q (Figure 3a). The deck is characterized by box-girder cross-section (Figure 3b). The reinforcement layouts S1 and S2 respectively span over the outer deck segments close to the abutments and over the mid-support.

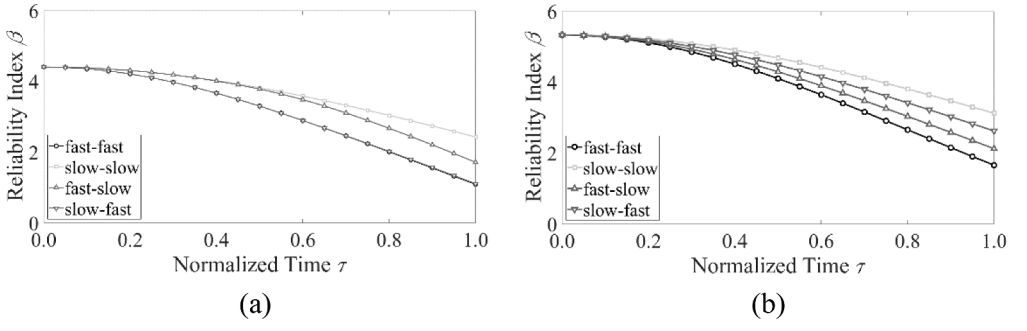


Figure 2. Time-variant reliability index for (a) first yielding and (b) collapse limit states.

The collapse load multiplier of the safety factor can be expressed in terms of the plastic hinge location along the span identified by the local abscissa $z_p \in [0,l]$. The collapse mechanism is retrieved by identifying the plastic hinge location that minimizes the load multiplier obtained by means of the kinematic theorem of limit analysis. Thus, the collapse safety factor Θ_c is:

$$\Theta_c = min_{z_p \in [0,l]} \left[\frac{M_p^- + M_p^+ \cdot \frac{l}{l-z_p}}{Q\frac{l \cdot z_p}{2}} - \frac{G}{Q} \right] \tag{16}$$

The bridge deck is exposed to a chloride diffusive attack that reduces in time the resisting moments $M_p^+(t)$ and $M_p^-(t)$ and, in turn, the collapse safety factor $\Theta_c(t)$ leading to a time-variant failure probability as follows:

$$p_c(t) = P[\Theta_c(t) \leq 1] \tag{17}$$

In pristine conditions, uncertainties are associated to loading conditions informing structural demand (i.e., dead load G and live load Q) and mechanical parameters informing structural capacity (i.e., steel yielding strength f_y and concrete compressive strength f_c). Table 3 summarizes the statistical descriptors of these four lognormally distributed and statistically independent random variables. The collapse probability in pristine conditions is evaluated with a state-of-the-art stand-alone CE-IS, leading to an initial reliability index of $\beta(t=0)=4.7057$.

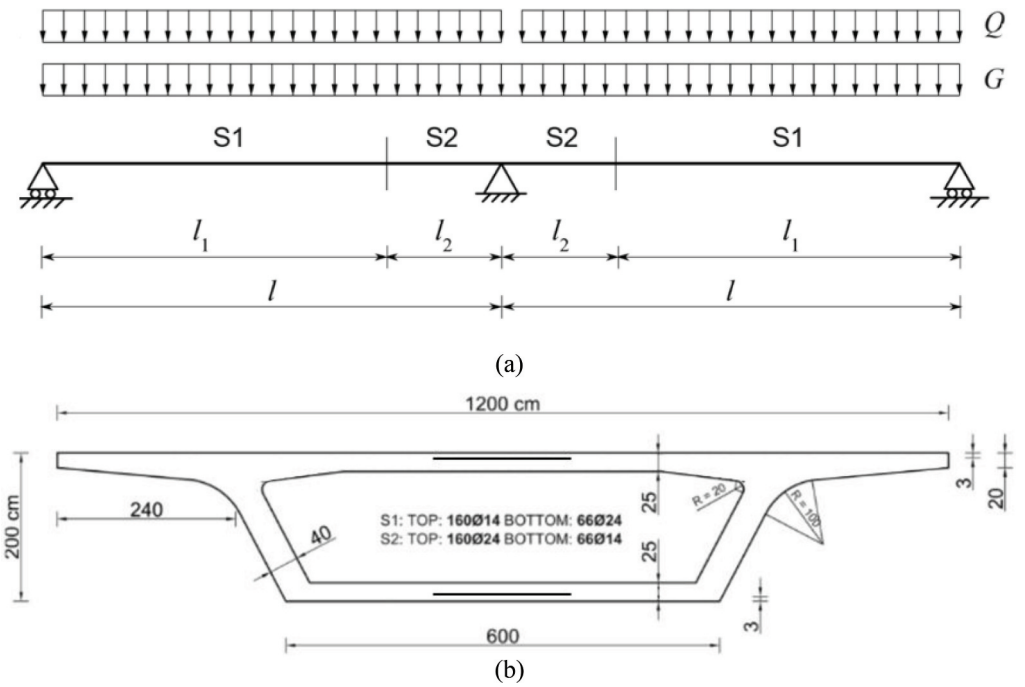


Figure 3. RC bridge: (a) deck static scheme; (b) box girder cross-section geometry and reinforcement.

Table 3. Statistical descriptors of random variables informing pristine structural demand and capacity.

Random Variable	Mean Value μ	Coefficient of Variation (CoV) δ
Dead Load G	100 kN/m	0.05
Live Load Q	150 kN/m	0.20
Steel Yielding Strength f_y	500 MPa	0.10
Concrete Compressive Strength f_c	45 MPa	0.20

4.2 *Corrosion model*

The corrosion initiation phase is governed by environmental aggressiveness and concrete properties. The 1D second Fick's law of diffusion is a suitable model to assess the evolution in time t of steel reinforcement characterized by net cover c from the external surface exposed to a constant concentration C_0:

$$C(c,t) = C_0 \cdot \left[1 - \mathrm{erf}\left(\frac{c}{2\sqrt{D(t)\cdot t}}\right)\right] \tag{18}$$

where erf(·) is the error function and $D(t)$ is concrete diffusivity defined in terms of reference diffusivity coefficient D_e, aging coefficient a, relative humidity RH and temperature T [°C] (Nava et al. 2023):

$$D(t) = D_e \cdot \left(\frac{0.076}{t}\right)^a \cdot \left[1 + \frac{(1-RH)^4}{(1-0.75)^4}\right]^{-1} \cdot e^{\left[\frac{40}{8.314\times10^{-3}}\left(\frac{1}{293}-\frac{1}{273+T}\right)\right]} \tag{19}$$

Corrosion initiates at time t_{cr} a critical concentration C_{cr} is attained at the reinforcing steel bar.

After corrosion onset, the propagation phase deals with the loss assessment of steel area A_s:

$$A_s(t) = [1 - \delta_s(t)] \cdot A_{s0} \tag{20}$$

where the damage index δ_s is the percentage of steel mass loss of a bar with pristine area A_{s0}. The corrosion penetration depth normalized by the diameter of the pristine steel bar ϕ_0 [mm] can be defined in terms of current density i_c [μA/cm^2] and pitting factor R_f (Capacci and Biondini 2022):

$$\delta(t) = \frac{0.0116 R_f}{\phi_0} \cdot \int_{t_{cr}}^{t} i_c(t)dt \quad \text{with } t \geq t_{cr} \tag{21}$$

The current density i_c is adapted from its reference value $i_{c,ref}$ based on temperature, relative humidity, chloride concentration and time from corrosion initiation (Nava et al. 2023):

$$i_c(t) = i_{c,ref} \cdot \left[\frac{0.85}{(t-t_{cr})^{0.29}}\right] \cdot [1 + K_T\ (T-20)] \cdot \left[e^{-6000(RH-0.75)^6}\right] \cdot \left[\frac{Cl(t)+Cl_{cr}}{2\ Cl_{cr}}\right] \tag{22}$$

where K_T=0.025 and 0.073 when temperature is T≤20°C and T>20°C, respectively. Finally, the damage index δ_s is then evaluated in terms of the normalized corrosion depth δ based on the hemispherical pit model proposed in Val and Melchers (1997).

In the proposed case study, the reinforcement layers at top and bottom slabs are subjected to chloride-induced corrosion and, assuming perfect correlation regarding the exposure scenario, steel mass loss of bottom slab reinforcement $\delta_{s,bot}$ and top slab reinforcement $\delta_{s,top}$ can be deterministically related. Therefore, the percentage of steel mass loss $\delta_{s,top}$=δ_s is representative of the bridge cross-section damage and, in turn, of the overall mechanical deterioration suffered by the structural system. Table 4 collects all information regarding random variables governing initiation (i.e., C_s, D_e, a, and C_{cr}) and propagation (i.e., $i_{c,20}$ and R_f). Constant temperature and relative humidity are assumed to be 20°C and 75%, respectively.

Table 4. Probabilistic model of random variables involved in the deterioration process.

Random Variable	Distribution	Mean Value μ	Std. Dev. σ
External Concentration C_0 [%wt./c]	Truncated Positive Normal	μ_C	0.30 μ_C
Reference Diffusivity D_e [10^{-12}m^2/year]	Truncated Positive Normal	μ_D	0.20 μ_D
Aging Parameter a [-]	Uniform Beta	0.30	0.12
Critical Concentration C_{cr} [%wt./c]	Bounded Beta ∈ [0.2-2.0]	0.60	0.15
Current Density at 20°C $i_{c,ref}$ [μA/cm^2]	Lognormal	2.586	1.724
Pitting Factor R_f [-]	Gumbel	7.1	0.17

4.3 *Results of CE-SP-IS methodology*

The CE-SP-IS method is applied to estimate the collapse probability every two years over 50 years of lifetime (i.e., n_t=25). Different environmental aggressiveness scenarios and design strategies for durability are investigated. Five scenarios of external chloride concentrations are investigated, with mean value μ_C increasing from 2.0%wt./c to 4.0%wt./c with steps of 0.5% wt./c and constant mean reference diffusivity μ_D=15·10^{-12}m^2/year. A similar parametric analysis is carried out considering μ_C=3.0%wt./c and five durability scenarios with mean reference diffusivity μ_D equally spaced from 10 to 20·10^{-12} m^2/year. Since one exposure scenario overlaps with one durability scenario, the total number of parametric scenarios is n_p=9 and the total number of structural reliability combinations is n_c=n_t·n_p=225.

The time-variant collapse probability can be evaluated based on the total probability theorem by superposing three components: (1) the pristine failure probability $p_c(t=0)$ scaled by the initiation time PDF $P_0(t)$, (2) the time-variant probability of full damage $P_1(t)$ characterized by certain failure, (3) and most importantly the time-variant failure probability with damage index in the interval between 0 and 1 $\tilde{p}_c(t)$ scaled by $P_\delta(t)$=1–$P_0(t)$–$P_1(t)$:

$$p_c(t) = P_0(t) \cdot p_c(t=0) + P_1(t) + P_\delta(t) \cdot \tilde{p}_c(t) \tag{23}$$

$$\tilde{p}_c(t) = [\Theta_c(t) \leq 1 | \delta_s \in (0,1)] \tag{24}$$

The numerical estimates of the collapse probabilities $\tilde{p}_c(t)$ are obtained by CE-SP-IS. Damage indices are sampled in the simulation space u_δ and transformed into their actual space δ_s as follows:

$$\delta_s = \frac{e^{u_\delta}}{1+e^{u_\delta}} \tag{25}$$

The damage indices δ_s in their actual space are necessary to evaluate the plastic moments adopted in limit analysis for the assessment of the indicator function I_i. Then, weighting coefficients w_i are computed in the simulation space exploiting the inverse transformation.

$$u_\delta = \log \frac{\delta_s}{1-\delta_s} \tag{26}$$

The time-variant actual PDFs of the damage indices in the simulation space $\psi(u_\delta)$ are estimated based on a Gaussian Kernel smoothing function calibrated by MCS involving the deterioration process. Also, $P_0(t)$, $P_1(t)$ and $P_\delta(t)$ are estimated based on such simulation, whilst the pristine failure probability $p_c(t=0)$ is estimated by CE-IS involving the time-invariant random variables (i.e., loading conditions and strength of materials).

The initial GM model constituted by K=20 densities with probability π_k=1/K. The components of mean vectors $\boldsymbol{\mu}_k$ associated to time-invariant random variables are simulated from the actual distribution with standard deviation scaled by σ=3 (Yang et al. 2017). The component of u_δ is analogously simulated from a standard normal variate with scaled standard deviation. The covariance matrices $\boldsymbol{\Sigma}_k$ are then initialized based on the same model adopted for mean vectors initiation.

Five rounds n_{iter}=10 of pre-sampling with N_{pre}=5·10^3 and final simulation with N_{final}=5·10^4, for a total of 10^5 analyses. Figure 4 shows the estimated time-variant collapse reliability indices for all investigated scenarios, spanning between 1.2 and 4.7. The structural reliability decay is more severe when the bridge is exposed to large chloride concentrations (Figure 4a) and larger concrete diffusivity (Figure 4b).

The benefit of CE-SP-IS can be measured by quantitative measures of the degree of estimate accuracy of the failure probability, such as the reliability estimator CoV (Capacci 2024). To give an idea of the accuracy improvement, estimating a reliability index β=4.7 with a CoV=20% by a single traditional MCS would require a sample size of N=(1-p_f)/(CoV^2·p_f)>10^7, which may be practically unfeasible for one out of the 225. The proposed approach leads to very accurate estimates, showing average and maximum CoV of respectively 0.6% and 4.6% over the 225 reliability problems. Therefore, the proposed methodology not only improves the accuracy for low probability estimates as other consolidated IS-based variance reduction techniques, but it also leads to such improvement for multiple reliability problems with a single simulation to explore different hazard scenarios and encompassing the structure lifetime.

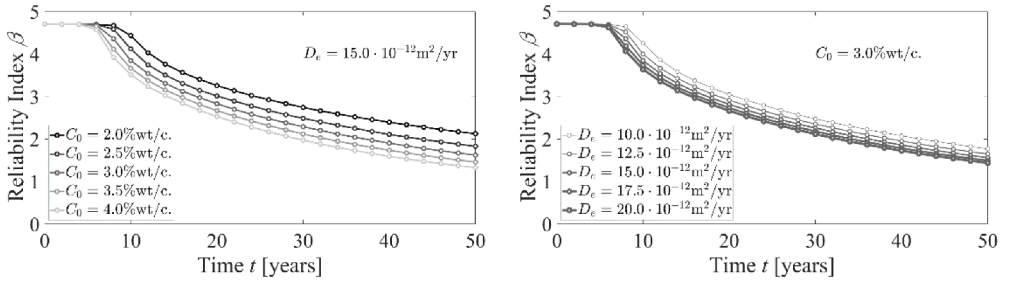


Figure 4. Time-variant collapse reliability index (a) exposure scenarios and (b) durability scenarios.

CONCLUSIONS

Stationary Proposal Importance Sampling (SP-IS) is a novel computational approach to efficiently estimate combinations of structural reliability problems for multiple hazard scenarios and limit states over the system lifetime. In this paper, SP-IS has been applied to aging structures such as a statically indeterminate beam and bridges exposed to chloride-induced corrosion under different environmental aggressiveness scenarios. The methodology is also fostered by a Cross-Entropy-based numerical approach to estimate the near-optimal simulation density to reduce the variance of the reliability estimators over the investigated combination of reliability problems.

The proposed technique is particularly suitable for problems involving time-consuming structural analyses. Typical examples are the calibration of time-variant seismic fragility curves for bridges exposed to chloride-induced corrosion (Capacci and Biondini 2022) and life-cycle seismic risk and resilience assessment of aging infrastructure lifelines such as bridge networks (Capacci 2024). Nonetheless, this approach can be adopted to aid life-cycle reliability-based optimal design of critical structures. Further insight should be devoted to addressing the effective benefit provided by the proposed methodology in comparison to traditional Monte Carlo approaches in terms of computational time and reliability estimator variance.

REFERENCES

Capacci, L. (2024). Seismic risk of aging bridge networks by Cross-Entropy-based Stationary Proposal Importance Sampling. *18th World Conference on Earthquake Engineering* (18WCEE), June 30th–July 5th, 2024, Milan, Italy.

Capacci, L., & Biondini, F. (2022). Efficient sampling techniques for simulation-based life-cycle structural reliability and seismic fragility assessment. *13th International Conference on Structural Safety and Reliability* (ICOSSAR 2021), September 13–17, 2022, Shanghai, China.

Capacci, L., Biondini, F., & Frangopol, D. M. (2022). Resilience of aging structures and infrastructure systems with emphasis on seismic resilience of bridges and road networks. *Resilient Cities and Structures*, 1(2): 23–41.

Geyer, S., Papaioannou, I., & Straub, D. (2019). Cross entropy-based importance sampling using Gaussian densities revisited. *Structural Safety*, 76: 15–27.

Nava, G. V., Capacci, L., Biondini, F., & Casti, L. (2023). Life-cycle structural reliability of RC bridge piers under corrosion in a changing climate. *8th International Symposium on Life-Cycle Civil Engineering* (IALCCE 2023), July 2-6, 2023, Milan, Italy.

Kurtz, N., & Song, J. (2013). Cross-entropy-based adaptive importance sampling using Gaussian mixture. *Structural Safety*, 42: 35–44.

Rubinstein R. (1981). *Simulation and the Monte Carlo methods*. Hoboken (NJ): John Wiley and Sons, Inc.

Rubinstein R., & Kroese D (2004). *The cross-entropy method: a unified approach to combinatorial optimization, Monte-Carlo Simulation, and machine learning*. New York (NY): Springer, Inc.

Val, D. V., & Melchers, R. E. (1997). Reliability of deteriorating RC slab bridges. *Journal of structural engineering*, *123*(12), 1638–1644.

Yang, D. Y., Teng, J. G., & Frangopol, D. M. (2017). Cross-entropy-based adaptive importance sampling for time-dependent reliability analysis of deteriorating structures. *Structural Safety*, *66*: 38–50.

MS11: Towards the realization of the submerged floating tunnels

Organizers: Y. Xiang, H.K. Lee, B. Faggiano, R. Landolfo & L. Martinelli


Taylor & Francis
Taylor & Francis Group
http://taylorandfrancis.com

Bridge Maintenance, Safety, Management, Digitalization and Sustainability – Jensen, Frangopol & Schmidt (eds)
© 2024 The Author(s), ISBN 978-1-032-77040-6
Open Access: www.taylorfrancis.com, CC BY-NC-ND 4.0 license

Coupled dynamic analysis method for wave action on a submerged floating tunnel

B. Huang, W. Luo, X. Cui & S. Wang
School of Civil Engineering, Chongqing Jiaotong University, Chongqing, China

H. Ding, K. Li & L. Cheng
China Merchants Chongqing Communications Technology Research and Design Institute Co., Ltd., Chongqing, China

ABSTRACT: Assessment of hydrodynamic performance of the Submerged floating tunnel (SFT) under wave actions is one of the important factors in the design of the SFT. In this paper, an efficient and accurate theoretical hydrodynamic model is developed to analyze the global spatial dynamic response of the SFT under wave actions. The tube is treated as a more accurate BOEF model with three degrees of freedom, and the new calculation formula of cable-constraint reaction on the BOEF model is proposed. A numerical approach based on potential flow theory and a higher-order boundary element method (BEM) was developed to calculate the wave force on the SFT tube. The numerical results are successfully validated by direct comparison against published numerical data and the calculation results of the finite element model.

1 INTRODUCTION

Submerged floating tunnel (SFT), also known as Archimedes Bridge, is considered an innovative alternative to conventional bridges and underground or immersed tunnels for passing through waterways, lakes, and rivers. A typical SFT generally involves several segments of tubes, which are confined at a certain distance from the sea bed due to residual buoyancy, an anchoring system to restrain large motions of the tube, and revetment structures that act as the connecting device to the shores [1,2]. Since the concept was brought forward, exploration of theoretical methods, small-scale experimental studies and verification, and no prototype has yet been built [3].

Several researchers have performed analyses and experiments for SFT under wave actions. Examples include global performance analysis focused on cable tension and tunnel displacements carried out by Kunisu et al. [4], which disclosed direct proportionality between wave height and cable tension. Remseth et al. [5] discussed the stochastic dynamic response of an SFT to wind-driven waves and time domain earthquake analysis with particular emphasis on fluid-structure interaction. Xu et al. [6] studied the effects of structure parameters on dynamic responses of SFT based on the hydrodynamic environment of Qiandao Lake by an empirical formula called the Morison equation [7]. Xiang and Chao. [8] also applied the Morison equation to solve the fluid force acting on the cables of the SFT, and established a theoretical model for coupled tube-cable vibration to evaluate the SFT structural dynamic response to water current. Oh et al. [9] studied the dynamic response of the SFT with the vertical and inclined mooring cable under the action of regular waves through the physical experimental method. For a simple but accurate estimation of hydrodynamic forces, a theoretical method is proposed by Seo et al. [10] and the tests with physical models in a wave flume were carried out for verification. Luo et al. [11] developed a theoretical hydrodynamic model to describe the coupled dynamic response of a SFT and the cable under regular waves. In this model, wave-induced hydrodynamic loads are estimated by the Morison equation for a moving object. Computational fluid dynamics (CFD) is the analysis of systems involving fluid flow, heat transfer, and

DOI: 10.1201/9781003483755-118

associated phenomena using computer-based simulation, which has been widely used in many offshore engineering fields, such as coastal bridges and offshore platforms [12]. Zou et al. [13] simulated the oceanic internal solitary wave's generation and propagation using the CFD software FLUENT to study the mechanism of interaction between the internal solitary wave and the SFT. At the same time, the cross-section of the SFT tube is optimized by using an artificial neural network and genetic algorithm. Yang et al. [14, 29] developed the vehicle-SFT-current coupling spatial vibration equation based on the Hamilton's principle and Galerkin hybrid method, and further discussed the vehicle-SFT-current coupling vibration.

The traditional empirical formula Morison equation is usually applicable to the calculation of wave forces for small-scale structures, but it cannot guarantee the accuracy of the calculation results for large-scale structures. Although the general CFD method can guarantee the accuracy of calculation, it is difficult to guarantee the solving efficiency. So, some researchers use numerical methods based on potential flow theory to calculate wave forces on large-scale structures. Paik et al. [15] and Ge et al. [16] performed analyses on the fluid-structure interaction of the SFT in wave field by boundary element method (BEM) implementing potential flow theory and investigated dynamic response characteristics of the SFT. Kunisu [17] evaluated the wave forces based on the two-dimension diffraction theory by BEM, and the effects of the size and the shape of the SFT on the wave forces are discussed. Ti et al. [18] developed a numerical approach based on three-dimensional potential flow theory in the frequency domain to study the interaction between surface waves and a flexible bridge pier. A full time-domain two-dimensional numerical model was established by Jin et al. [19] for the coupled dynamic analysis of the SFT structures and a higher-order BEM was applied to discretize the body boundary and the free surface boundary. Huang et al. [20] proposed an analytical method to estimate random wave forces on the box-girder superstructure based on the potential flow theory and the correction parameters, and explore the influence of the peak frequency of the incident wave spectra and the structural configuration on the hydrodynamic performance of the submerged box-girder superstructure.

The finite element method (FEM) or classical dynamics theory is usually used to calculate the tube motion of the SFT under external load. Xiang et al. [21,22] and Lin et al. [23,24] simplified the model of the SFT by using the mathematical analogy method as a beam on an elastic foundation (BOEF) and investigated the global dynamic response of the SFT subjected to external impact, cable break, and vehicle passage. However, the BOEF model proposed by Xiang et al. [21,22] does not consider the wave actions, and the coupling relationship between horizontal displacement and torsional displacement of the SFT tube is not fully considered for the cable-constraint reaction in the BOEF model. Thus, it may not be suitable for the case of large horizontal and torsional displacement of the SFT tube, and needs to be further improved under the wave actions.

Based on the previous research, this paper presents an efficient and accurate theoretical hydrodynamic model in the frequency domain to analyze the global spatial dynamic response of the SFT under linear waves. The new calculation formula of cable-constraint reaction on the BOEF model is proposed, which fully takes into account the coupling relationship between horizontal displacement and torsional angle of the SFT tube due to the constraint effect of the cable, and more suitable for the case where the SFT tube has relatively obvious horizontal displacement or torsional angle. A numerical approach based on potential flow theory and a higher-order BEM was developed to calculate the wave force on the SFT tube. The numerical results are successfully validated by comparisons against published numerical data and the calculation results of the FEM model. On this basis, the effects of the environment and structural parameters on the dynamic response of the SFT under linear waves are studied.

2 THEORETICAL ANALYSIS METHOD

2.1 *Basic assumption and simplified model*

Figure 1 shows a typical SFT structure and the coordinate system. In a global analysis, the cables can be generally regarded as discrete elastic supports with a certain stiffness. To

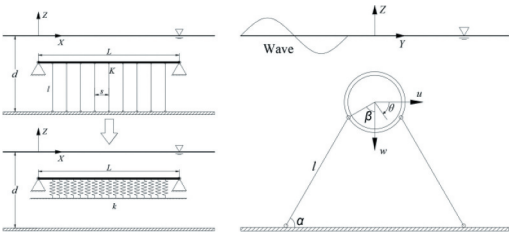


Figure 1. A simplified model of the SFT and the coordinate system.

simplify the SFT model, the cable is assumed to be of the same length, arrangement, material, and spacing, and the SFT tube is considered a BOEF model when the stiffness of the anchoring system and the rigidity of the tube meet the relation of Eq. (1) [25,26].

$$\frac{Ks^3}{24EI} \leq 0.05 \tag{1}$$

Where K is the anchoring stiffness of a pair of cables; s is the longitudinal interval of cable, and the rigidity of the elastic foundation after transforming is uniformly distributed within the interval; EI is the flexural rigidity of the tube. To analyze the tube coupling spatial vibration due to periodic wave action, three further assumptions are given as follows: (a) The tube is a simply-supported Euler-Bernoulli beam with constant sections and equal stiffness. The displacements in the Y and Z directions and the torsion with respect to the X axis are considered. (b) Only the elastic vibration of the SFT tube is considered and assumed that the vibration is small relative to the length of the SFT tube [21]. (c) The incident wave is linear and propagates toward the positive Y-axis. The steady-state wave motion and the structural responses are all harmonic with the same frequency ω under the linear approximation [27].

2.2 *Governing equation of the wave motion in the frequency domain*

In order to obtain an accurate and efficient analysis method for the dynamic response of the SFT, the wave forces on the SFT tube are calculated using the potential flow theory, and the wave forces of the cable are ignored. From the perspective of potential flow theory, the fluid is assumed as an ideal, incompressible, and irrotational material. In addition, the size of the tube length direction of the SFT is much larger than the size of the SFT cross-section, and the vibration of the SFT tube is small compared with the length of the SFT tube. Therefore, two-dimensional linear potential flow theory can be used to solve the wave forces. There is a velocity potential Φ(y, z, t; x) that satisfies the Laplace equation.

The spatial complex velocity potential $\varphi(y, z; x)$ also satisfies the Laplace equation and is subjected to the boundary conditions applied on the seabed, the still water surface, the mean body surface, and far-field, respectively, as:

$$\begin{aligned} &\nabla^2\varphi(y,z;x) = 0 \\ &\begin{cases} \frac{\partial\varphi}{\partial z} = 0 \ (z=-d), \ \text{seabed boundary} \\ \frac{\partial\varphi}{\partial \boldsymbol{n}} = v(y,z;x) \ (\boldsymbol{r}=\partial\Omega_o), \ \text{mean body surface boundary} \\ \frac{\partial\varphi}{\partial z} - \frac{\omega^2}{g}\varphi = 0 \ (z=0), \ \text{still water surface boundary} \\ |\nabla\varphi| < \infty \ (y\to\infty), \ \text{far}-\text{field boundary} \end{cases} \end{aligned} \tag{2}$$

Where d is water depth; $\boldsymbol{n}$ is the normal unit vector of the mean body surface pointing out of the fluid; Ω is all flow field area; $\partial\Omega_o$ represents mean body surface; $\boldsymbol{r}$ is radius vector (x, y, z); v $(y, z; x)$ is the spatial complex velocity of fluid particles in the $\boldsymbol{n}$ direction on the mean body surface; g is the gravitational acceleration. According to the linear characteristics of the above definite solution problem, The spatial complex velocity potential of the wave around the flexible SFT tube is the combination of incident potential (φ_i), diffraction potential (φ_d), and radiation potential (φ_r).

2.3 *Solving the velocity potential and calculating the wave forces of the SFT tube*

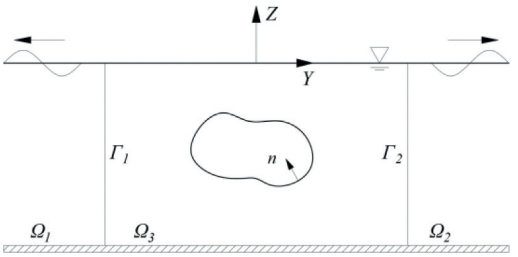


Figure 2. The schematic diagram of calculation of diffraction potential and radiation potential.

Before calculating the wave forces on the SFT tube, the definite solution problems satisfied by φ_d, φ_{u1}, φ_{w1}, and $\varphi_{\theta 1}$ should be solved first. However, due to the irregular shape of the boundary, it is difficult to find analytical solutions for the above velocity potentials. By discretizing the body surface into a finite number of panels, the BEMs provide numerical alternatives to approximate the hydrodynamic solutions for structures with arbitrary geometry [28]. The computational area of the numerical approximation method must be finite, thus the flow field is divided into three regions as shown in Figure 2. Region 3 (Ω_3) is the calculation region, and Region 1 (Ω_1) and Region 2 (Ω_2) are the far-field regions, respectively. Γ_1 and Γ_2 are the interfaces between the calculation region and the far-field region. According to the linear potential flow theory, when the interface is far away from the object surface, the non-propagating term in the potential function can be ignored.

$$\begin{cases} \frac{\partial \varphi_3}{\partial x} + ik\varphi_3 = 0, & (\boldsymbol{r} = \Gamma_1) \\ \frac{\partial \varphi_3}{\partial x} + ik\varphi_3 = 0 & (\boldsymbol{r} = \Gamma_2) \end{cases} \tag{3}$$

Where φ_3 represents one of φ_d, φ_{u1}, $\varphi_{w1,}$ or $\varphi_{\theta 1}$ in the Ω_3. The higher-order BEM associated with Green's function is employed as the solution algorithm to solve the unknown potential function in the Ω_3. Then, The dynamic pressure can be obtained by using the linearized Bernoulli's equation:

$$-\frac{1}{\rho}P(y,z,t;x) = \frac{\partial \Phi}{\partial t} = \frac{\partial}{\partial t}\mathrm{Re}\left[\varphi(y,z;x)e^{-i\omega t}\right] = \mathrm{Re}\left[-i\omega\varphi(y,z;x)e^{-i\omega t}\right] \tag{4}$$

Where $P(y, z, t; x)$ is dynamic pressure in local point (x, y, z) at time t; ρ is the fluid density. Then the wave forces can be expressed as:

$$\begin{cases} F_{fu}(x,t) = \int\limits_{\partial\Omega_o} P \cdot n_y \mathrm{d}s = \mathrm{Re}\left[\int\limits_{\partial\Omega_o} i\omega\rho\varphi n_y \mathrm{d}s \cdot e^{-i\omega t}\right] \\ F_{fw}(x,t) = \int\limits_{\partial\Omega_o} -P \cdot n_z \mathrm{d}s = \mathrm{Re}\left[-\int\limits_{\partial\Omega_o} i\omega\rho\varphi n_z \mathrm{d}s \cdot e^{-i\omega t}\right] \\ F_{f\theta}(x,t) = \int\limits_{\partial\Omega_o} P \cdot (zn_y - yn_z)\mathrm{d}s = \mathrm{Re}\left[\int\limits_{\partial\Omega_o} i\omega\rho\varphi(zn_y - yn_z)\mathrm{d}s \cdot e^{-i\omega t}\right] \end{cases} \tag{5}$$

Where $F_{fu}(x, t)$, $F_{fw}(x, t)$, and $F_{f\theta}(x, t)$ are the horizontal, vertical, and torsional wave forces per unit length of the tube, respectively. According to the assumption in the above section, the wave forces on the structure are also harmonic, and they can also be denoted as:

$$\begin{cases} F_{fu}(x,t) = \mathrm{Re}[f_u(x)e^{-i\omega t}] \\ F_{fw}(x,t) = \mathrm{Re}[f_w(x)e^{-i\omega t}] \\ F_{f\theta}(x,t) = \mathrm{Re}[f_\theta(x)e^{-i\omega t}] \end{cases} \tag{6}$$

Since the curve integral in the above equation can be calculated as a definite number, for convenience, the above equation can be denoted as:

$$\begin{cases} f_u(x) = A_u + v_u B_u + v_w C_u + v_\theta D_u \\ f_w(x) = A_w + v_u B_w + v_w C_w + v_\theta D_w \\ f_\theta(x) = A_\theta + v_u B_\theta + v_w C_\theta + v_\theta D_\theta \end{cases} \tag{7}$$

The wave forces at each point of the SFT tube can be calculated by using Eqs. (6) and (7) according to the vibration amplitude of the SFT tube, v_u, v_w, and v_θ.

2.4 *The cable stiffness of the BOEF model*

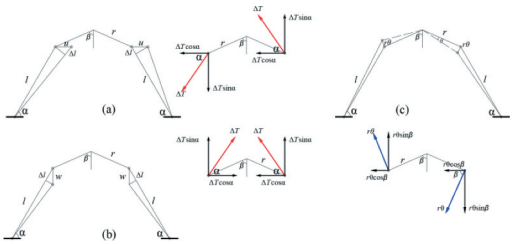


Figure 3. Constraint reaction of the cable due to tube displacement. (a) horizontal displacement; (b) vertical displacement; (c) Torsional displacement.

For discrete elastic supports, the constraint reaction of the cable due to tube displacement with three directions is shown in Figure 3. According to the geometric relation, the stress-strain relation of axial force, Hooke's law, and the symmetric principle, the cable-constraint reaction generated by the horizontal displacement of the SFT tube can be obtained:

$$\Delta T = \frac{E_c A_c \cos\alpha}{l} u \tag{8}$$

For the BOEF model, the constraint reaction of the cable can be evenly distributed in the direction of the SFT tube axis. Thus, the constraint reaction of the cable for the BOEF model due to tube displacement can be expressed as follow:

$$\begin{pmatrix} F_{eu} \\ F_{ew} \\ F_{e\theta} \end{pmatrix} = \begin{bmatrix} k_u & 0 & k_u r(\tan\alpha \sin\beta - \cos\beta) \\ 0 & k_w & 0 \\ k_u r(\tan\alpha \sin\beta - \cos\beta) & 0 & k_\theta - 2k_u r^2 \tan\alpha \sin\beta \cos\beta \end{bmatrix} \begin{pmatrix} u \\ w \\ \theta \end{pmatrix} \tag{9}$$

Where F_{eu}, F_{ew}, and $F_{e\theta}$ are the constraint reaction of the cable of the BOEF model in the horizontal, vertical, and torsional directions per unit length of the SFT tube, respectively.

2.5 *Governing equation of the SFT tube and its solution*

Based on the simplified calculation model in the previous sections, Hamilton Principle is applied to establish the tube-wave coupling spatial vibration equations of the SFT:

$$\delta \int_{t_1}^{t_2} (T - V + W) \mathrm{d}t = 0 \tag{10}$$

The kinetic energy of the tube while moving and twisting can be written as Eq. (11), and a schematic diagram for the positive displacements in three directions of the tube is displayed in Figure 1.

$$T = \frac{1}{2} m_0 \int_0^L \left[\left(\frac{\partial u(x,t)}{\partial t} \right)^2 + \left(\frac{\partial w(x,t)}{\partial t} \right)^2 + a^2 \left(\frac{\partial \theta(x,t)}{\partial t} \right)^2 \right] \mathrm{d}x \tag{11}$$

Where m_0 is the mass per unit length of the tube; L is the span of the SFT; a is the radius of gyration of the tube section. The strain energy of the tube can be represented as Eq. (12).

$$V = \frac{1}{2} \int_0^L \left[EI_w \left(\frac{\partial^2 u(x,t)}{\partial x^2} \right)^2 + EI_u \left(\frac{\partial^2 w(x,t)}{\partial x^2} \right)^2 + GI_p \left(\frac{\partial \theta(x,t)}{\partial x} \right)^2 \right] \tag{12}$$

Where E and G are the elastic modulus and shear modulus of the tube, respectively; I_u and I_w are the moments of inertia of the tube section around the Y axis and Z axis; I_p is the torsional moment of inertia of the tube section. The work of external forces, W, consists of the elastic foundation constraint reaction force, structural damping effect, and wave force, denoted by W_1, W_2, and W_3 respectively as follows:

$$\begin{cases} W_1 = \int_0^L \left[-F_{eu} u(x,t) - F_{ew} w(x,t) - F_{e\theta} \theta(x,t) \right] \mathrm{d}x \\ W_2 = \int_0^L \left[-c_u \frac{\partial u}{\partial t} u(x,t) - c_w \frac{\partial w}{\partial t} w(x,t) - c_\theta \frac{\partial \theta}{\partial t} \theta(x,t) \right] \mathrm{d}x \\ W_3 = \int_0^L \left[F_{fu} u(x,t) + F_{fw} w(x,t) + F_{f\theta} \theta(x,t) \right] \mathrm{d}x \end{cases} \tag{13}$$

Where c_u, c_w, and c_θ are the damping coefficients of the tube in three directions based on the structural material parameter; F_{fu}, F_{fw}, and $F_{f\theta}$ are the horizontal, vertical, and torsional wave forces per unit length of the tube, respectively. The differential equations for three motion components of the SFT tube under wave forces can be obtained. The natural vibration mode can be further simplified as follows:

$$\begin{cases} u(x,t) = \mathrm{Re} \left[\sum_{n=1}^{\infty} U_n \sin \frac{n\pi x}{L} e^{-i\omega t} \right] \\ w(x,t) = \mathrm{Re} \left[\sum_{n=1}^{\infty} W_n \sin \frac{n\pi x}{L} e^{-i\omega t} \right] \\ \theta(x,t) = \mathrm{Re} \left[\sum_{n=1}^{\infty} \Theta_n \sin \frac{n\pi x}{L} e^{-i\omega t} \right] \end{cases} \tag{14}$$

3 NUMERICAL EXAMPLE AND MODEL VERIFICATION

3.1 *Convergence analysis of the proposed method*

The feasibility of the proposed theoretical method depends on the number of vibration modes used in the analysis. Lower modes cannot reflect the vibration characteristics of the structure, but higher modes tend to be less reliable in the vibration. Figure 4(a) shows the horizontal displacements at each point of the SFT tube with a different number of vibration modes. The results obtained by the proposed method with the first nine modes and the first eleven modes are almost the same. Therefore, the first eleven modes of the SFT are adopted in the analysis to ensure computational efficiency and reasonable results. At the same time, as discussed above, the accuracy of solving the velocity potential also depends on the division of the calculation region. For a small computing region, the influence of non-propagating terms cannot be eliminated at the boundary of the region interface, and the calculation accuracy cannot be guaranteed. However, computing resources will be seriously wasted if the computing region is too large. Figure 4(b) shows the horizontal displacements at the position of the longitudinal direction of the SFT tube with different distances (Rc) of from the center of the tube. It's not hard to see that Rc=40 m gives almost the same result as Rc=48 m. Therefore, when Rc is

greater than 48 m, the influence of non-propagating terms on the calculation results can be eliminated to ensure the accuracy of the results.

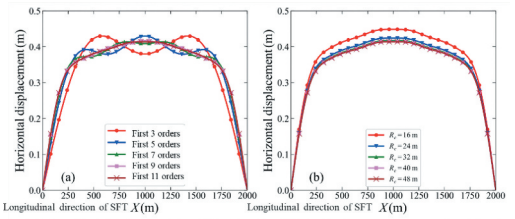


Figure 4. The convergence of the analysis results with the number of modal order terms (series terms) or the convergence of the analysis results.

Accurate calculation of the wave force is the key to obtaining the precise dynamic response of the SFT tube using the proposed method. The proposed method based on the potential flow theory and BEM approximation is validated firstly by the classical problem conducted by Mei and Black [30], and they investigated the transmission coefficient, reflection coefficient, and horizontal and vertical linear wave forces on the rectangular structure. Based on the calculating wave forces part of the proposed method, the dimensionless horizontal, vertical linear wave forces and dimensionless wave moment on the rectangular structure are calculated and compared with the research results conducted by Mei and Black [30] and Li and Teng [31], which is shown in Figure 5. It shows that the wave forces and wave moment based on the proposed BEM approximation method agree very well with the analytical results from Mei and Black [30], which indicates that the estimation of the wave forces and wave torque on the structure using the BEM approximation method is accurate and reliable.

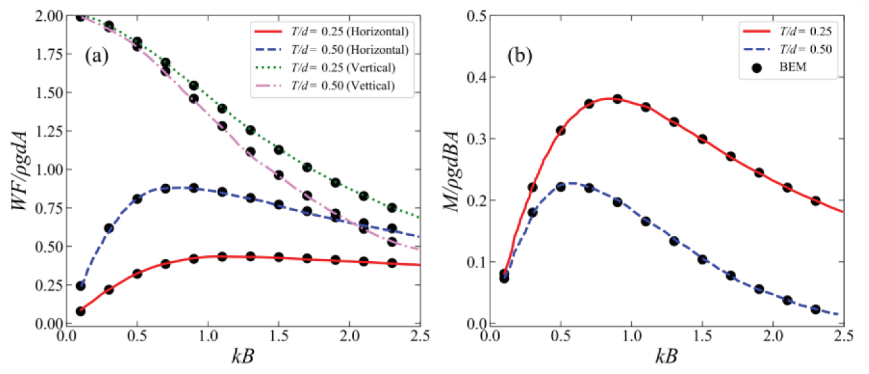


Figure 5. Comparison of nondimensional horizontal and vertical wave forces (a) and dimensionless wave torque (b). The line represents the analytical result conducted by Mei and Black (1969), and the solid point represents the BEM approximate calculation result in this paper.

A finite element analysis (FEA) is conducted to verify the accuracy and applicability of the BOEF model of the theoretical method in this paper. The commercial FEA software, ABAQUS 2020, is used to simulate the vibration process of the SFT, and the dynamic analysis is performed within ABAQUS/Modal dynamics. The basic parameters of the FEA model are the same as the theoretical method, as given in the study conducted by Huang et al. [32]. In the model, the tube of the SFT is modeled with the beam element B31, and the cables are modeled with the truss element T3D2. The connection between the installation point of the cable and the centroid of the SFT section is the MPC/beam. The FEA model is divided into 2,077 nodes and 2,038 elements. When the vibration of the SFT tube reaches a steady state, the wave forces calculated by theoretical methods will be extracted and loaded onto the FEA model in the form of

distributed loads. The maximum horizontal, vertical and torsional displacements at each point of the SFT tube using the BOEF and FEA method are shown in Figure 6.

The SFT tube will produce obvious horizontal displacement under the wave forces. For the wave environments, this study presents a new equation (Eq. (22)) for calculating the constraint reaction of the cable of the BOEF model (called the improved cable-constraint reaction), which is improved from Xiang and Yang [21]. Therefore, Figure 6 also shows the comparison of the calculation results between using the improved cable-constraint reaction and the cable-constraint reaction given by Xiang and Yang [21]. As can be seen from Figure 6, the results calculated by using the improved cable-constraint reaction are in good agreement with those calculated by the FEA model. However, the horizontal and torsional displacements that calculated by using the cable-constraint reaction of Xiang and Yang [21]. are quite different from those calculated by the FEA model. This is because the coupling effect of the horizontal and torsional displacements of the SFT tube under the constraint of the cable increases the displacements in the two directions. Therefore, when the SFT tube appears obvious horizontal or torsional displacement under the action of external wave force, the dynamic response of the SFT tube in the horizontal and torsional directions calculated by using the cable-constraint reaction of Xiang and Yang [21] may be smaller than the actual situation. The calculation results show that the BOEF model using the improved cable-constraint reaction proposed in this paper is accurate and effective, and can be applied to the case of large horizontal and torsional displacement, such as wave environment, horizontal impact, large eccentric vehicle load, and so on.

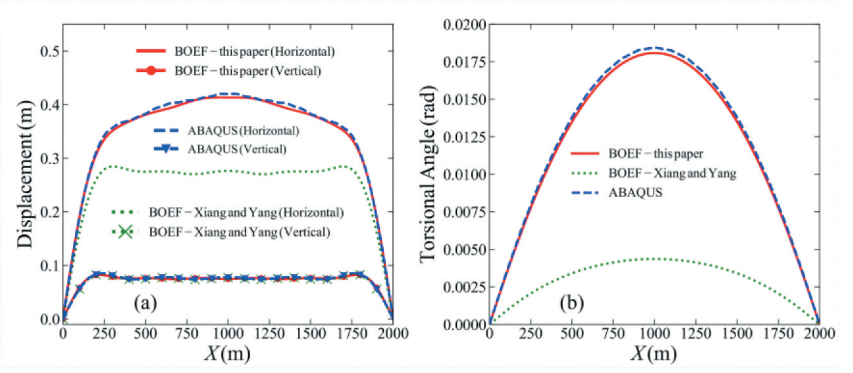


Figure 6. Maximum horizontal, vertical (a), and torsional (b) displacements at each point of the SFT tube.

4 CONCLUSIONS

In this study, an efficient and accurate theoretical hydrodynamic model in the frequency domain is proposed to analyze the global spatial dynamic response of the SFT under linear waves. The calculation results are successfully validated by direct comparison against published numerical data and the calculation results of the FEM model. The main conclusions are as follows:

(1) The proposed theoretical hydrodynamic model based on the BOEF model, potential flow theory, and BEM is efficient and accurate in calculating the dynamic response of the SFT tube under wave actions.
(2) Under the action of periodic wave forces, the peak bending moment and vertical displacement of the SFT tube generally appear near the two ends of the SFT tube, while the peak torsional angle and horizontal displacement generally appear in the midspan position after the SFT tube vibration is stabilized.

REFERENCES

[1] D. Ahrens, Submerged floating tunnels—a concept whose time has arrived, Tunnelling & Underground Space Technology. 12 (1997) 317–336, DOI: 10.1016/S0886-7798(97)90022-5.

[2] H. Østlid, When is SFT competitive?, Process Eng. 4 (2010) 3–11.

[3] Y. Xiang, J. Xue, Study on submerged floating tunnel in the world, China Foreign Highw. 22 (2022) 49–52 (in Chinese).

[4] H. Kunisu, S. Mizuno, Y Mizuno, Study on submerged floating tunnel characteristicsunder the wave condition, In: The fourth International Society of Offshore and Polar Engineers Conference, Osaka, Japan, 1994.

[5] S. Remseth, B. Leira, K. Okstad, K. Mathisen, T. Haukas, Dynamic response and fluid/structure interaction of submerged floating tunnels, Comput. Struct. 72 (1999) 659–685, DOI: 10.1016/S0045-7949(98)00329-0.

[6] L. Xu, F. Ge, Effects of fundamental structure parameters on dynamic responses of submerged floating tunnel under hydrodynamic loads, Journal of mechanics, 2009.

[7] J. Wilson, Dynamics of Offshore Structures. 2, M. John Wiley & Sons Inc (2003) 25.

[8] Y. Xiang, C. Chao, Vortex-Induced Dynamic Response Analysis for the Submerged Floating Tunne! System under the Effect of Currents, Journal of Waterway, Port, Coastal and Ocean Engineering 139 (2013)183-189, DOI: 10.1061/(ASCE)WW.1943-5460.0000175.

[9] S. Oh, W. Park, S. Jang, D. Kim, D. Ahn, Physical experiments on the hydrodynamic response of submerged floating tunnel against the wave action, Proceedings of the 7th International Conference on Asian and Pacific Coasts (APAC) 2013.

[10] S. Seo, H. Mun, J. Lee, J. Kim, Simplified analysis for estimation of the behavior of a submerged floating tunnel in waves and experimental verification, Marine Structures 44 (2015) 142–158, doi:10.1016/j.marstruc.2015.09.002.

[11] W. Luo, B. Huang, Y. Tang, H. Ding, K. Li, L. Cheng, Q. Ren, Numerical simulation of dynamic response of submerged floating tunnel under regular wave conditions, Shock Vib. (2022) 4940091, DOI: https://doi.org/10.1155/2022/4940091

[12] M. Chen, B. Huang, Z. Yang, Q. Ren, B. Zhu, The influence of lateral restraining stiffness on the box-girder superstructure under unbroken solitary waves, Marine Science and Engineering 10 (2022) 1019, DOI: https://doi.org/10.3390/jmse10081019

[13] P. Zou, J. Bricker, W. Uijttewaal, Optimization of submerged floating tunnel cross section based on parametric Bézier curves and hybrid backpropagation - genetic algorithm, Marine Structures 74 (2020) 102807.

[14] Y. Yang, Y. Xiang, H. Lin, Z. Chen, Study on vibration response of submerged floating tunnel considering vehicle eccentric load, Applied Ocean Research, 110 (2021) 102598, doi:10.1016/j.apor.2021.102598.

[15] I.Y. Paik, K. Chang, S. Kwon, Analysis of wave force induced dynamic response of submerged floating tunnel, KSCE Journal of Civil Engineering 8 (2004) 543–550, DOI: 10.1007/BF02899580.

[16] F. Ge, W. Lu, X. Wu, Fluid-structure interaction of submerged floating tunnel in wave field, Procedia Engineering 4 (2010) 263–271.

[17] H. Kunisu, Evaluation of wave force acting on submerged floating tunnels, Procedia Engineering 4 (2010) 99–105.

[18] Z. Ti, Y. Li, S. Qin, Numerical approach of interaction between wave and flexible bridge pier with arbitrary cross section based on boundary element method, Journal of Bridge Engineering 25 (2020) 04020095, DOI: 10.1061/(ASCE)BE.1943-5592.0001628.

[19] R. Jin, Y. Gou, B. Geng, H. Zhang, Y. Liu, Coupled dynamic analysis for wave action on a tension leg-type submerged floating tunnel in time domain, Ocean Engineering 212 (2020) 107600, DOI: 10.1016/j.oceaneng.2020.107600.

[20] B. Huang, W. Luo, Q. Ren, X. Cui, J. Zhang, B. Zhu, Random wave forces on the submerged box-girder superstructure of coastal bridges based on potential flow theory, Ocean Engineering 248 (2022) 110739, DOI: 10.1016/j.oceaneng.2022.110739.

[21] Y. Xiang, Y. Yang, Spatial dynamic response of submerged floating tunnel under impact load, Marine Structures 53 (2017) 20–31, doi:10.1016/j.marstruc.2016.12.009.

[22] Y. Xiang, Z. Chen, Y. Yang, H. Lin, S. Zhu, Dynamic response analysis for submerged floating tunnel with anchor-cables subjected to sudden cable breakage, Marine Structures 59 (2018) 179–191, DOI: 10.1016/j.marstruc.2018.01.009.

[23] H. Lin, Y. Xiang, Y. Yang, Z. Chen, Dynamic response analysis for submerged floating tunnel due to fluid-vehicle-tunnel interaction, Ocean Engineering 166 (2018) 290–301, doi:10.1016/j.oceaneng.2018.08.023.

[24] H. Lin, Y. Xiang, Y. Yang, Vehicle-tunnel coupled vibration analysis of submerged floating tunnel due to tether parametric excitation, Mar. Struct. 67 (2019) 106–120, doi:10.1016/j.marstruc.2019.102646.
[25] M. Sato, S. Kanie, T. Mikami, Structural modeling of beams on elastic foundations with elasticity couplings, Mech. Res. Commun. 34 (2007) 451–459, doi:10.1016/j.mechrescom.2007.04.001.
[26] M. Sato, S. Kanie, T. Mikami, Mathematical analogy of a beam on elastic Supports as a beam on elastic foundation, Appl. Math. Model. 32 (2008) 688–699, DOI: 10.1016/j.apm.2007.02.002.
[27] B. Teng, G. Ying, D. Ning, A higher order BEM for wave-current action on structures—direct computation of free-term coefficient and CPV integrals, China Ocean Eng. 20 (2006), 395–410.
[28] B. Teng, R. Taylor, New higher-order boundary element methods for wave diffraction/radiation, Applied Ocean Research, 17 (1995) 71–77.
[29] Y. Yang, Y. Xiang, C. Gao, Vehicle-SFT-current coupling vibration of multi-span submerged floating tunnel, part I: mode superposition and Galerkin hybrid method, Ocean Eng., 2022, 247, 110746.
[30] C. Mei, J.L. Black, Scattering of surface waves by rectangular obstacles in waters of finite depth, Fluid Mech. 38 (1969) 499–511, doi:10.1017/S0022112069000309.
[31] Y. Li, B. Teng, Wave action on Maritime structures. M. Ocean Press, 2015.
[32] B. Huang, W. Luo, Y. Chen, J. Zhou, H. Ding, K. Li, L. Cheng, D. Zhong, Coupled dynamic analysis for wave action on a tension leg-type submerged floating tunnel in the frequency domain. Ocean Eng., 2024, 296, 116934.

Bridge Maintenance, Safety, Management, Digitalization and Sustainability – Jensen, Frangopol & Schmidt (eds)
© 2024 The Author(s), ISBN 978-1-032-77040-6
Open Access: www.taylorfrancis.com, CC BY-NC-ND 4.0 license

Dynamic substructuring technique for submerged floating tunnels

S. Corazza, F. Foti & L. Martinelli
Department of Civil and Environmental Engineering, Politecnico di Milano, Italy

ABSTRACT: Seabed-anchored Submerged Floating Tunnels (SFTs) are structures made of watertight tubular segments, assembled, and kept floating under the water table by a spread system of anchoring elements connected to the seabed. Due to their inherent flexibility, SFTs are prone to the effect of dynamic loads such as seismic and hydrodynamic loads. These peculiar features have since long lead to the assessment of the SFTs' dynamic response by resorting to the simplified model of a beam on an elastic foundation. This amounts to totally neglect the mass of the anchoring elements and, therefore, their local vibration modes. In this work, the mooring system is modeled as a discrete series of taut-strings possessing axial extensibility, while the tunnel is considered as a continuous Euler-Bernoulli beam. Within this modeling choices, a dynamic substructuring technique is presented and used to obtain both the natural circular frequencies and the mode shapes of the coupled system.

1 INTRODUCTION

Submerged Floating Tunnels (SFTs) are an interesting alternative to long-span bridges and immersed tunnels for crossing deep waterways. Their origin can be traced back to the first patents granted in Norway in 1923-1947 (see (Jacobsen 2010)). Even though a first realization is still missing, preliminary design proposals have been developed for sea straits, fjords and lakes (see, e.g. (Ahrens 1997), (Bruschi et al. 1990)). A distinctive feature of the dynamic behavior of SFTs is the presence of both global vibration modes, that involve significant displacements of the tunnel and quasi-static displacements of the anchoring elements, and local modes, that mainly involve transverse vibrations of the anchors. Dominant global and local modes of the structure are typically associated to well-separated values of the natural frequencies. However, computationally efficient Finite Element (FE) models able to simultaneously capture the main features of both global and local vibration modes with the same degree of accuracy, are inherently hard to set up. To overcome this difficulty, a dynamic substructuring technique for SFTs is here presented. A separate modeling of the two main substructures (i.e. the tunnel and the mooring system) is employed, involving (1) a Reduced Order Model (ROM) of the anchoring elements, which accounts for a generic form of support motion, and (2) a continuous model of the tunnel, which relies on the well-known Euler-Bernoulli beam theory. Within this context, undamped free vibrations of the coupled system are studied, evidencing the influence of a variable mooring stiffness profile on the mode shapes of the SFT, and shedding light on the effect of the mooring system's mass on the global response of the structure. As an illustrative example, the aforementioned approach is applied to the SFT proposal for the Messina's strait crossing, in Italy. On this behalf, the classification of the SFT motion regimes is investigated with regards to the spectral description of hydrodynamic loads, that are assumed to be representative of both service life conditions of the structure and extreme events. The paper is organized as follows: the modeling of the two substructures is presented in Section 2, then the global equations of motion of the SFT are derived in Section 3.

DOI: 10.1201/9781003483755-119

An application example regarding the proposal for the Messina's strait SFT is presented in Section 4, while the conclusions of the work are drawn in Section 5.

2 SUBSTRUCTURES MODELING

2.1 *Preliminaries*

Let us refer to Figure 1a, and consider a tether inclined with an angle θ with respect to the horizontal plane, having initial chord length L_0, external diameter D_o, mass per unit of length γ_s, axial stiffness EA_0 and subject to a static tension $T_0 > 0$ (i.e. a pretension). It is also convenient for the following developments to introduce the non-dimensional load parameter as $\eta_0 = T_0/T_y$, where $T_y = f_y A_0$ is the yielding tensile force and f_y is the yielding stress of the material. The non-dimensional load parameter is directly proportional to the Buoyancy-to-Weight Ratio (BWR) of the tunnel. Moreover, in the case of the vibrations of submerged anchoring elements, the structural linear mass should be modified to account for the mass of the fluid which is moved due to the presence of the anchoring element itself (i.e. the so-called added mass), resulting in "virtual" mass per unit of length given by:

$$\gamma_v = \gamma_s + C_A \gamma_w \tag{1}$$

where γ_w denotes the linear mass of the water moved by a "section" of the tether (i.e. $\gamma_w = \rho_w \pi D_o^2/4$) and C_A denotes the added-mass coefficient, which depends on the cable cross-section. In the case of a circular cross-section, the unit value is usually adopted (i.e. $C_A = 1$) (see, e.g. (Chakrabarti 1987)).

2.2 *Reduced-order model of the anchoring elements*

the anchoring elements of the mooring system are described according to a slightly modified version of the classical taut-string model. Indeed, sag effects and geometrical nonlinearities are neglected, while axial extensibility is accounted for in the present work. It is worth noticing that the well-known elasto-geometric Irvine's parameter (often denoted as λ^2), which is introduced when dealing with the small-sag cable theory, is strictly equal to zero for the present modeling choice, being the initial static configuration coincident with the reference (undeformed) configuration, i.e. the chord of the tether. Let us denote with u_a and w_a the interface-degrees of freedom associated to the top support motion of the anchoring element, according to a classical dynamic substructuring framework, and collect them in a vector $\boldsymbol{r}^k = [u^k{}_a,\ w^k{}_a]^{\mathrm{T}}$, where the superscript k denotes the generic k-th anchoring element. The work-conjugated quantities to the support displacements are the interface forces Fu_a and Fw_a, which can be casted in the following vector: $\boldsymbol{R}^k = [Fu_a{}^k,\ Fw_a{}^k]^{\mathrm{T}}$. In this work, the bottom support is kept fixed to the seabed; however, generalization of the proposed approach to account for soil-structure interaction phenomena is straightforward.

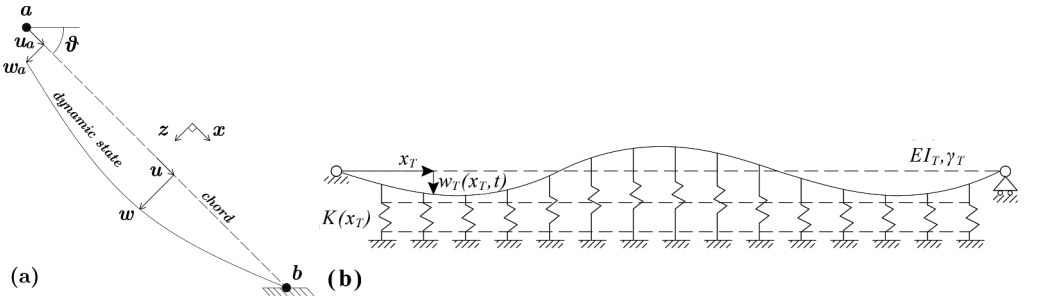


Figure 1. Schematic representation of a generic anchoring element (a), schematic representation of the SFT modeled as an Euler-Bernoulli beam on a Winkler's bed (b).

By following the approach proposed by (Warnitchai et al. 1995), the total motion of the anchoring element is decomposed in a quasi-static component (superscript q) and a modal component (superscript m). The longitudinal and transverse displacement respectively reads:

$$u(x,t) = u^q(x,t) + u^m(x,t) \tag{2}$$

$$w(x,t) = w^q(x,t) + w^m(x,t) \tag{3}$$

At this stage, the quasi-static component of the motion can be related to the support displacements by means of suitable shape functions, whereas the modal part can be expressed as a function of time-varying modal coordinates. Moreover, the axial modal motion can be neglected, being the frequencies of such motion much higher than the ones associated to the flexural motion, i.e.: $u^m(x,t) \ll w^m(x,t)$. One then has:

$$w(x,t) = \sum\nolimits_{s=1}^{N_r} \psi_{w,s}(x) r_s(t) + \sum\nolimits_{m=1}^{M} \phi_m(x) z_m(t) \tag{4}$$

$$u(x,t) = \sum\nolimits_{s=1}^{N_r} \psi_{u,s}(x) r_s(t) \tag{5}$$

The shape functions of the quasi-static component of the motion (i.e. $\psi_{w,s}$ and $\psi_{u,s}$) are linear functions of the interface degrees of freedom r_s, i.e. the entries of the vector $\boldsymbol{r}^k$ (being N_r the total number of interface degrees of freedom. In this case $N_r = 2$), while the modal shape functions are selected as the fixed-base eigenmodes of the taut-string (see e.g. (Irvine 1981)):

$$\phi_m(x) = \sin\frac{m\pi x}{L_0} \tag{6}$$

According to a classical lagrangian approach, the kinetic and potential energy of the generic anchoring element can be respectively expressed as:

$$\mathrm{K}(t) = \frac{1}{2}\gamma_v \int_0^{L_0} \left[\left(\frac{\partial u}{\partial t}\right)^2 + \left(\frac{\partial w}{\partial t}\right)^2 \right] dx \tag{7}$$

$$V(t) = \frac{1}{2} EA_0 \int_0^{L_0} \varepsilon^2(x) dx + \frac{1}{2} T_0 \int_0^{L_0} \left[\left(\frac{\partial u}{\partial x}\right)^2 + \left(\frac{\partial w}{\partial x}\right)^2 \right] dx \tag{8}$$

where, by denoting with an apex the total derivative operator, the axial strain reads:

$$\varepsilon(x) = \frac{\partial u(x,t)}{\partial x} = \sum\nolimits_{s=1}^{N_r} \psi'_{u,s}(x) r_s(t) \tag{9}$$

Substitution of Equations (4), (5) and (9) into Equations (7) and (8) straightforwardly leads to the identification of the entries of both mass and stiffness matrices. The undamped equation of motion (in partitioned form) of the k-th anchoring element simply reads:

$$\begin{bmatrix} \boldsymbol{M}^k{}_{rr} & \boldsymbol{M}^k{}_{rz} \\ \boldsymbol{M}^k{}_{zr} & \boldsymbol{M}^k{}_{zz} \end{bmatrix} \begin{bmatrix} \ddot{\boldsymbol{r}}^k \\ \ddot{\boldsymbol{z}}^k \end{bmatrix} + \begin{bmatrix} \boldsymbol{K}^k{}_{rr} & \boldsymbol{K}^k{}_{rz} \\ \boldsymbol{K}^k{}_{zr} & \boldsymbol{K}^k{}_{zz} \end{bmatrix} \begin{bmatrix} \boldsymbol{r}^k \\ \boldsymbol{z}^k \end{bmatrix} = \begin{bmatrix} \boldsymbol{R}^k \\ \boldsymbol{F}^k{}_z \end{bmatrix} \tag{10}$$

where $\boldsymbol{z}^k$ is vector containing the modal coordinates of the k-th anchoring element, i.e.: $\boldsymbol{z}^k = [z_1,\ldots,z_m,\ldots,z_M]^{\mathrm{T}}$ and $\boldsymbol{F}^k{}_z = [F_1,\ldots,F_m,\ldots,F_M]^{\mathrm{T}}$ is the vector of modal generalized loads, whose components can be obtained through a direct projection on the modal basis of the external forces (e.g. hydrodynamic loads) acting on the k-th element.

2.3 *Tunnel modeling strategy*

The tunnel is modeled as a Euler-Bernoulli beam. Let us denote with L_T and D_T, respectively, the total length of the tunnel and its external diameter, with EI_T its flexural stiffness, and with γ_T its mass per unit of length, which is comprehensive of the added mass of the water moved by the tunnel itself (i.e. $\gamma_T = \gamma_{sT} + \rho_w \pi D_T^2/4$). Then, the vertical (i.e. in-plane, w_T) and horizontal (i.e. out-of-plane, v_T) displacements can be expanded in the modal basis of the decoupled tunnel (free-interface modes):

$$w_T(x_T, t) = \sum_{n=1}^{N_{in}} \phi_n(x_T) q_n(t) \tag{11}$$

$$v_T(x_T, t) = \sum_{n=1}^{N_{out}} \phi_n(x_T) p_n(t) \tag{12}$$

where q_n and p_n denote, respectively, the in-plane and out-of-plane generalized displacements, N_{in} and N_{out} denote, respectively, the in-plane and out-of-plane number of retained basis functions, and:

$$\phi_n = \sin \frac{n\pi x_T}{L_T} \tag{13}$$

being $x_T \in [0, L_T]$ an abscissa spanning the longitudinal dimension of the tunnel (see Figure 1(b)). Entries of both mass and stiffness matrices of the bare tunnel can be easily computed by resorting to classical expressions (see e.g. (Foti et al. 2023)). The undamped equation of motion of the tunnel reads:

$$\boldsymbol{M_T}\ddot{\boldsymbol{q}}_T + \boldsymbol{K_T}\boldsymbol{q}_T = \boldsymbol{F_T} - \sum_{k=1}^{N_A} \boldsymbol{\Phi}_A^k \boldsymbol{F_k} \tag{14}$$

where $\boldsymbol{q}_T = [\boldsymbol{p}, \boldsymbol{q}]^{\mathrm{T}}$ is the vector which collects the out-of-plane and in-plane generalized displacements of the tunnel, $\boldsymbol{F_T}$ is the vector of modal generalized dynamic loads which is obtained by direct projection of the external forces (e.g. hydrodynamic loads), on the modal basis of the tunnel, N_A is the total number of anchoring elements, $\boldsymbol{F_k} = [H_k, V_k]^{\mathrm{T}}$ is the vector containing the horizontal (H_k) and vertical (V_k) forces acting on the tunnel (exchanged by the k-th anchoring element) and $\boldsymbol{\Phi}_A^k$ is the matrix whose entries are defined as follows:

$$\boldsymbol{\Phi}_A^k = \begin{bmatrix} \sin\frac{\pi x_{A,k}}{L_T} & \dots & \sin\frac{n\pi x_{A,k}}{L_T} & \dots & \sin\frac{N_{out}\pi x_{A,k}}{L_T} & 0 & \dots & 0 & \dots & 0 \\ 0 & \dots & 0 & \dots & 0 & \sin\frac{\pi x_{A,k}}{L_T} & \dots & \sin\frac{n\pi x_{A,k}}{L_T} & \dots & \sin\frac{N_{in}\pi x_{A,k}}{L_T} \end{bmatrix} \tag{15}$$

being $x_{A,k}$ the abscissa of the k-th anchoring element in the reference system of the tunnel.

3 EQUATIONS OF MOTION OF THE SFT

In order to couple the equations of motion of the anchoring elements (see section 2.2) and those of the tunnel (see section 2.3), some further advancements are necessary. The interface forces exchanged between the anchoring elements and the tunnel can be expressed in a vectorial form as:

$$\boldsymbol{F^k} = \boldsymbol{T_k}\boldsymbol{R^k} \tag{16}$$

where $\boldsymbol{T_k}$ is the transformation matrix, which permits to pass from the local reference frame of the k-th anchoring element, to the global reference frame of the tunnel, which simply reads:

$$\boldsymbol{T_k} = \begin{bmatrix} \cos\theta_k & -\sin\theta_k \\ \sin\theta_k & \cos\theta_k \end{bmatrix} \tag{17}$$

It is noteworthy that in many SFT design proposals, the angle of inclination $\theta_k = \theta$ is constant for each anchoring element, resulting in a constant transformation matrix $\boldsymbol{T_k} = \boldsymbol{T}$ as well.

By resorting to the description of the displacement field of the tunnel, one can express the vector of interface displacements of the k-th anchoring element according to the following relationship:

$$\boldsymbol{r^k} = \boldsymbol{T}^T \boldsymbol{\Phi}_A^k \boldsymbol{q}_T \tag{18}$$

At this stage, Equation (18) is substituted into the system of Equations (10), and the vector of interface forces acting on the k-th anchor $\boldsymbol{R^k}$ is expressed from the first row. Direct substitution of $\boldsymbol{R^k}$ into Equation (16) allows to obtain the vector of interface forces acting on the tunnel, i.e. $\boldsymbol{F^k}$, which can be finally inserted into Equation (14). The undamped equations of motion of the SFT are then obtained by direct assembling the contributions stemming from all the (N_A) anchoring elements. The system of equations finally reads:

$$\begin{bmatrix} \boldsymbol{M}_T + \boldsymbol{\Phi}_A^T \boldsymbol{T} \boldsymbol{M}_{rr} \boldsymbol{T}^T \boldsymbol{\Phi}_A & \boldsymbol{\Phi}_A^T \boldsymbol{T} \boldsymbol{M}_{rz} \\ \boldsymbol{M}_{zr} \boldsymbol{T}^T \boldsymbol{\Phi}_A & \boldsymbol{M}_{zz} \end{bmatrix} \begin{bmatrix} \ddot{\boldsymbol{q}}_T \\ \ddot{\boldsymbol{z}} \end{bmatrix} + \begin{bmatrix} \boldsymbol{K}_T + \boldsymbol{\Phi}_A^T \boldsymbol{T} \boldsymbol{K}_{rr} \boldsymbol{T}^T \boldsymbol{\Phi}_A & 0 \\ 0 & \boldsymbol{K}_{zz} \end{bmatrix} \begin{bmatrix} \boldsymbol{q}_T \\ \boldsymbol{z} \end{bmatrix} = \begin{bmatrix} \boldsymbol{F}_T \\ \boldsymbol{F}_z \end{bmatrix} \tag{19}$$

where the matrices $\boldsymbol{\Phi_A}$, $\boldsymbol{T}$, $\boldsymbol{M_{rr}}$, $\boldsymbol{K_{rr}}$, $\boldsymbol{M_{zz}}$, $\boldsymbol{K_{zz}}$ and $\boldsymbol{M_{rz}}$ and the vectors $\boldsymbol{F_T}$ and $\boldsymbol{F_z}$ have been assembled by blocks, according to standard procedures (see e.g. (Clough and Penzien 2003)) and $\boldsymbol{z}$ is the vector obtained by queueing the vectors of modal coordinates $\boldsymbol{z_k}$ of each anchoring element. Circular frequencies and mode shapes of the SFT are then found from the following undamped eigenproblem:

$$\left(\boldsymbol{K}_G - \omega^2 \boldsymbol{M}_G\right)\varphi = 0 \tag{20}$$

where the global mass ($\boldsymbol{M_G}$) and stiffness ($\boldsymbol{K_G}$) matrices have been implicitly defined in Equation (19).

4 APPLICATION EXAMPLE

The present section considers an application example regarding the SFT which was proposed for the crossing of the Messina's strait, in Italy (see e.g. (Bruschi et al. 1990), (Perotti et al. 2018)). The considered SFT is designed to connect Sicily to the mainland, crossing a strait characterized by a maximum seabed depth of 325 m (see Figure 2). The total length of the SFT is L_T = 4680 m and the tunnel axis is placed 40 m below the water table. The cross section of the tunnel is defined by the following parameters: D_T = 15.95 m, $EI = 4.383 \cdot 10^{10}$ kNm^2 and γ_T = 368.41 ton/m. The mooring system is made of inclined hollow core circular cross-section tethers, located along 65 mooring stations, with uniform spacing equal to 72 m. For the sake of simplicity, in the present work, the mooring system is considered composed of one hollow circular cross-section only (Type B), leading to a mooring stiffness variability which is only induced by the variation of the seabed depth along the tunnel's abscissa. The cross-section type B is defined by the following parameters: D_o = 1.950 m, s = 0.065 m, A_0 = 0.3849 m^2, γ_v = 6005 kg/m, where s denotes the thickness of the hollow circular profile. The angle of inclination and the non-dimensional loading parameter of the anchoring elements are set respectively to θ= 45° and η_0 = 5%.

In the present work, only in-plane motion of the tunnel is considered, and 100 terms are retained in the series expansion of Equation (11) (i.e. N_{in} =100 and N_{out} = 0). The mooring system is modeled by considering 65 "equivalent" anchoring elements, i.e. characterized by values of both axial stiffness and virtual mass which are representative of the real configuration

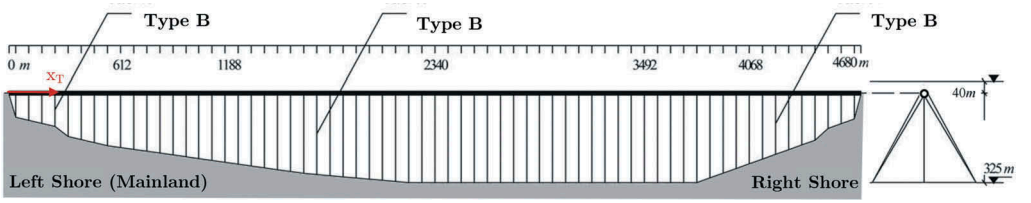


Figure 2. Side view and cross-section of the proposal for the Messina's strait SFT, in Italy.

(which is composed of 4 inclined tethers per mooring section, see again Figure 2). Each "equivalent" tether is then modeled by retaining the first in-plane mode only (i.e. M=1).

Hydrodynamic loads acting on the structure have been modeled starting from the spectral representation of the wave elevation for a certain return period. A general analytical form of the surface wave energy spectrum is (see e.g. (Wilson 1984)):

$$S_\eta(\omega) = C_0 \omega^{-m} e^{-B\omega^{-n}} \tag{21}$$

in which the empirical coefficients C_0, B, m and n define the spectrum. In the most widely used forms, m = 5 and n = 4. Several empirical expressions for the C_0 and B coefficients have been proposed in the literature. In the following, reference is made to the so-called Bretschneider Spectrum, for which C_0 and B coefficients become:

$$C_0 = 0.0081 g^2$$
$$B = 3.11/H_s^2 \tag{22}$$

where g is the gravity acceleration and H_s is the significant wave height. The latter is an important statistical parameter defined as the arithmetic average of the highest one-third of the waves in a wave record (Wilson 1984). Two significant wave heights are considered for the following developments, namely H_s = 5 m and H_s = 16 m, which are tentatively assumed to represent the "operational" wave conditions and extreme hydrodynamic events, respectively.

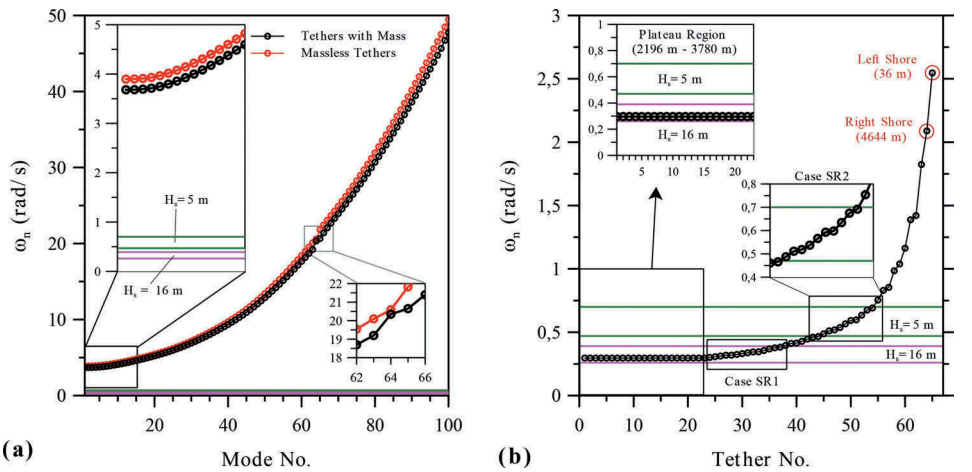


Figure 3. Natural circular frequencies of the tunnel (a) and of the anchoring elements (b) compared to the band of circular frequencies associated to the highest wave elevation spectral ordinates, for two significant wave heights (H_s = 5 m and H_s = 16 m).

Figure 3a depicts the tunnel circular frequencies obtained from the solution of the eigenvalue problem (see Equation (21)) compared to the ones corresponding to the highest spectral ordinates

of the wave elevation spectrum S_η. As a first important comment, it is evident that the response of the tunnel to hydrodynamic excitation can be regarded as quasi-static, being the first natural frequency of the tunnel much higher than the frequency interval associated to the highest spectral ordinates of the wave spectra. Additionally, it is noted that accounting for the anchoring elements' mass, leads to a variation of about 5.5% in the tunnel's circular frequencies, compared to the massless tethers modeling choice. Moreover, around mode 65, an abrupt change in the frequency can be observed. This phenomenon is due to the matching of the wavelength of such mode and the spacing of the anchoring elements, resulting in an activation of the quasi-static motion of the whole mooring system, with a consequent increased global stiffness of the structure.

Figure 3b shows the plot of the anchoring elements circular frequencies, ordered in an ascendent way. The anchoring elements located in the "plateau region" of the seabed (see Figure 2) are characterized by the lowest circular frequencies, being their chord length the longest of the whole mooring system. These anchors might encounter high level of vibrations induced by the motion of the tunnel both for the case of simple resonance, occurring for "extreme" hydrodynamic events, and for the case of parametric resonance, which may arise if "ordinary" waves associated to the service life of the structure are considered. In fact, the frequencies corresponding to the highest spectral ordinates in the wave elevation spectrum (for H_s = 5 m) are close to two times the first natural frequency of these tethers. Proceeding towards the right direction of the abscissa axis, one may find two sets of circular frequencies, respectively denoted as SR1 and SR2. These sets of tethers might be susceptible of simple resonance phenomenon induced respectively by the hydrodynamic motion of the tunnel, whenever "extreme" waves and "ordinary" waves are considered. Finally, the last two circular frequencies correspond to the stiffest anchoring elements, having shortest chord length, which are located very close to the right and left shore, respectively. However, no significant dynamic amplification phenomena are expected in this case, since the natural circular frequencies of these tethers are sufficiently far from the first one of the tunnel. Additionally, it is worth noticing that the first mode of the tunnel is always expected to have a node very close to the position of these two tethers (see Figure 4b).

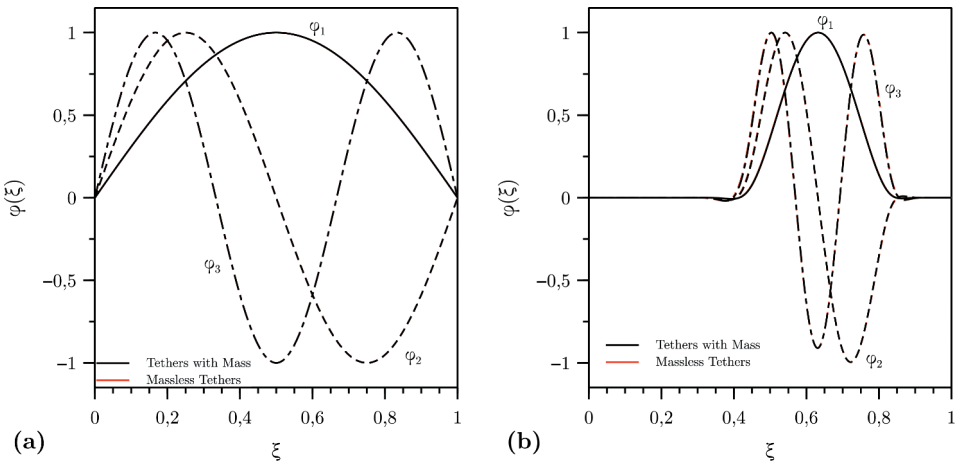


Figure 4. First three mode shapes of the tunnel for a constant (a) and variable (b) seabed depth profile. The non-dimensional abscissa of the tunnel is denoted as $\xi = x_T/L_T$.

Figure 4a and 4b shows the first three global modes of the SFT for a constant and variable seabed depth profile, respectively. As already evidenced in (Foti et al. 2023), the variable seabed profile (which consequently induces a spatially variable mooring stiffness profile) is responsible for the mode localization phenomena, around the region of highest flexibility of the mooring system. As long as the mooring stiffness is constant, localization phenomena do not occur and the mode shapes of the SFT preserve a global character (see Figure 4a). On the contrary, if the mooring stiffness is variable, the mode shapes localize in the range of lowest

stiffness, which is not located symmetrically with respect to the midspan but coincides with the "plateau" region (see Figure 4b – cf. Figure 2).

Moreover, it is noted that the influence of the anchoring elements' mass on the mode shapes is practically negligible for both seabed profiles. This evidence, together with results obtained in Figure 3, permits to conclude that it is feasible to assess the global dynamic response of the SFT by resorting to the simplified model of Euler-Bernoulli beam on a Winkler's bed (possessing a non-homogenous stiffness of the springs), and therefore, neglecting the mass of the tethers (see also (Foti et al. 2022) and Figure 1b).

5 CONCLUSIONS

In this paper, a dynamic substrucuring technique for Submerged Floating Tunnels (SFTs) was presented. The mooring system was modeled as a discrete series of anchoring elements individually described by a taut-string possessing axial extensibility, while the tunnel was modeled as a Euler-Bernoulli beam. The degrees of freedom at the interface between the tunnel and the anchors were evidenced, by expressing their value through the displacements of the tunnel. The inertially-coupled system was assembled and undamped free vibrations of the global structure were studied. The results showed the influence of both the variable mooring stiffness and the anchoring elements' mass on the global modes of the SFT. The classification of the motion regimes for the proposal of the Messina's strait SFT highlighted that the response of the tunnel to hydrodynamic loading conditions can be regarded as quasi-static. For this reason, it is feasible to address the global response of the system by relying on the simplified assumption of mass-less elastic tendon for the anchoring elements, which amounts to consider the tunnel as a Euler-Bernoulli beam resting on a non-homogenous Winkler-type soil. As per the anchoring elements, classification of the motion regimes has revealed the possibility of different resonance phenomena (both simple and parametric) under hydrodynamic loading conditions. Further research is currently ongoing to assess the role of geometrical nonlinearities of the anchoring elements on the global response on the SFT, and to include system coupling due to hydrodynamic loading of the tunnel itself, which may cause parametric excitation (and possibly, parametric resonance) of some tethers.

REFERENCES

Ahrens, D. 1997. Submerged floating tunnels - a concept whose time has arrived. *Tunneling and Underground Space Technology* 12: 318–336.

Bruschi, R. & Giardinieri, V. & Marazza, R. & Merletti, T. 1990. Submerged buoyant anchored tunnels: technical solutions for the fixed link across the strait of Messina, Italy. In J. Krokeborg (ed) *Strait crossings*: 605–612. Rotterdam: Balkema.

Chakrabarti, S.K. 1987. *Hydrodynamics of offshore structures*. Berlin: Computational Mechanics Publications, Springer.

Clough, R. & Penzien, J. 2003. *Dynamics of structures*, 3rd edn. Berkeley: Computers and Structures Inc.

Foti, F. & Martinelli L. & Perotti, F. 2022. A semi-analytical model for the design and optimization of SFTs under seismic loading. In J.R. Casas & D.M. Frangopol & J. Turmo (eds) *Bridge safety, maintenance, management, life-cycle, resilience and sustainability*: 1117–1121. CRC Press.

Foti, F. & Martinelli, L. & Morleo, E. & Perotti, F. 2023. Dynamic response of submerged floating tunnels: an enhanced semi-analytical approach. Submitted to *Ocean Engineering*, p 24.

Irvine, H.M. 1981. *Cable structures*. Cambridge, Massachusetts: The MIT Press series in structural mechanics.

Jakobsen, B. 2010. Design of the submerged floating tunnel operating under various conditions. *Procedia Engineering* 4: 71–79.

Perotti, F. & Foti, F. & Martinelli, L. & Tomasin, M. 2018. SFTs under dynamic loads: new design issues and numerical simulation. In N. Powers & D.M. Frangopol & R. Al-Mahaidi & C. Caprani (eds) *Maintenance, safety, risk, management and life-cycle performance of bridges*: 885–892. CRC Press.

Warnitchai, P. & Fujino, Y. & Susumpow, T. 1995. A non-linear dynamic model for cables and its application to a cable-structure system. *Journal of Sound and Vibration* 187(4): 695–712.

Wilson, J.F. 1984. *Dynamics of offshore structures*. Hoboken: Wiley Inc.

Bridge Maintenance, Safety, Management, Digitalization and Sustainability – Jensen, Frangopol & Schmidt (eds)
© 2024 The Author(s), ISBN 978-1-032-77040-6
Open Access: www.taylorfrancis.com, CC BY-NC-ND 4.0 license

Forming guidelines for software evaluation in bridge structural health monitoring systems

T.A. Bayda, H.W. Shenton & M. Chajes
University of Delaware, Newark, DE, USA

ABSTRACT: With increasing costs of constructing and maintaining infrastructure systems, structural health monitoring (SHM) has seen increased use because it enables owners to evaluate the performance of their systems in real time. To do this, robust, reliable, and intuitive software platforms that can collect, store, manage, process, visualize, and report SHM data are critical. In this study, an evaluation of various existing commercial software platforms was performed using a decision matrix that was developed and used to evaluate the functionality and useability of each platform. Areas evaluated included cost structure, data interpretation, data calculation, software visualization, alarm and report creation, and project management. Ten plus years of experience with the Indian River Inlet Bridge, a fully instrumented cable-stayed bridge, was utilized in developing the decision matrix and evaluating various commercial software platforms.

1 INTRODUCTION

The Charles W. Cullen Bridge, commonly referred to as the Indian River Inlet Bridge (IRIB), is a 533-meter-long reinforced concrete cable-stayed bridge located in Delaware, USA. The IRIB has two 122-meter back spans and a main span of 290 meters to allow for potential future widening of the inlet channel that the bridge spans. Due to its proximity to the Atlantic Ocean, reinforced concrete was chosen as the most durable material to withstand the constant chloride presence in the area. An elevation view looking east towards the IRIB is shown in Figure 1.



Figure 1. Elevation view of the IRIB looking east toward the Atlantic Ocean.

Construction of the bridge was completed in 2012 and included a permanent structural health monitoring (SHM) system with seven different types of sensors to measure strain, tilt, displacement, acceleration, wind speed and direction, chloride content, and temperature. There are over 120 sensors of all types installed at various locations on the bridge (Shenton *et al*, 2017a).

Because of the cooperative efforts between the University of Delaware (UD) and the owner, the Delaware Department of Transportation (DelDOT), the IRIB and the data from its SHM system has been used for multiple research projects. Numerous research papers on the SHM

DOI: 10.1201/9781003483755-120

system and monitoring results have been published (Shenton *et* al, 2017b, Al-Khateeb *et al*, 2018, Al-Khateeb *et al*, 2019). DelDOT also uses the SHM data to catalog and evaluate the performance of the bridge over time.

This paper will provide a methodology to address DelDOT's need for a new SHM data management software platform by describing the creation of a decision matrix that was used to compare the features of platforms from various commercial software vendors.

2 CURRENT SHM SYSTEM STATUS

When the SHM system was installed on the IRIB, SHM was still in its infancy. To meet DelDOT's requirements, a custom software platform was sourced from a commercial vendor. To ensure future reliability and support, DelDOT coordinated with UD to identify and evaluate new software platforms that can perform tasks beyond what the initial platform can do.

Despite some sensors going offline and some limitations of the original software platform, the original SHM system continues to run reliably. The IRIB SHM system has a fiber optic design allowing for fewer cables and corrosion resistance. Located on-site, the raw sensor data is processed by the local computer and then stored on its hard drive. The SHM system regularly

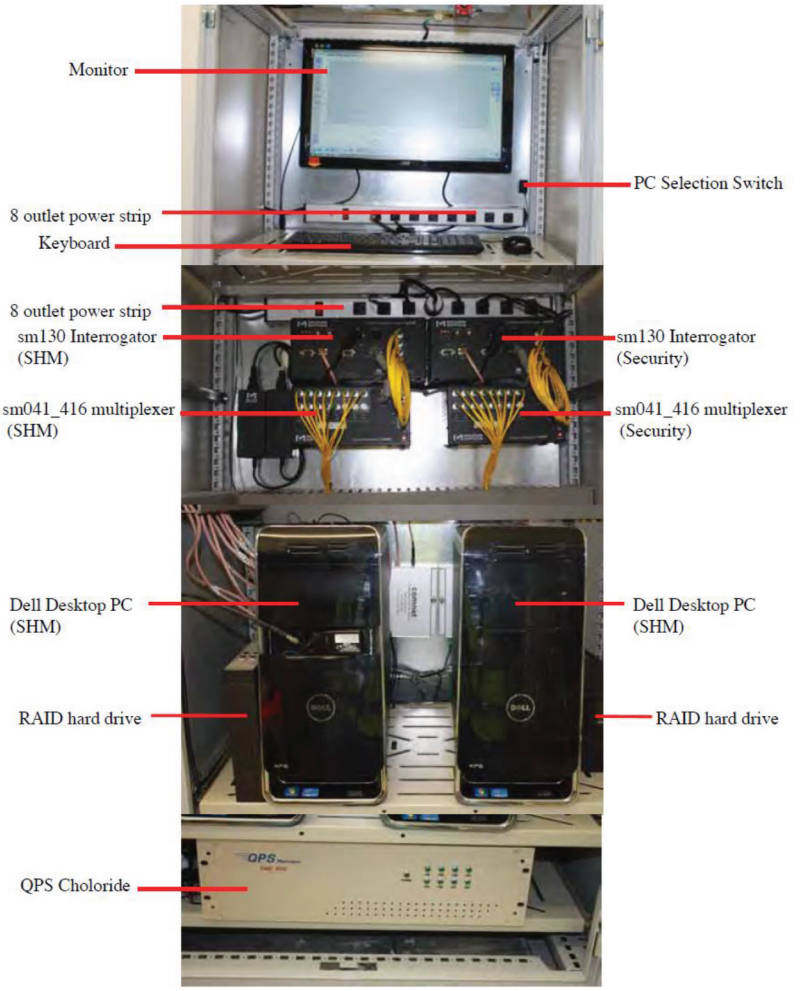


Figure 2. Central processing unit for the IRIB SHM system.

collects data from all sensors at 12.5 Hz and averages 10-minute intervals for strain and temperature data. DelDOT receives the averaged data via file transfer protocol (FTP) that is stored on its secure servers. A depiction of the SHM system's main unit is shown in Figure 2.

3 SOFTWARE PLATFORM EVALUATION METHOD

The IRIB requires a robust and specialized software platform to effectively manage and communicate the substantial data captured by its SHM system. Currently, multiple reputable software companies offer data management software similar to, but more advanced than, the current IRIB SHM system. An initial study evaluated 10 vendors and their respective software platforms to quantify available features and company capabilities. Public documentation and inquiry into each vendor allowed for the development of a feature compatibility checklist. One primary requirement was that a vendor had to have enough staff to have full-time dedication to customer support, usually meaning a staff of 25 or more personnel. Because DelDOT has strict requirements with companies it can do business with on a large scale, only vendors that were based in, or had data servers in, the USA could be selected. Another primary requirement was to source a vendor with at least 20 years of experience in data management software. As was often the case in the early years of SHM, the current software platform was custom-made. Vendors that met the primary requirements were then evaluated based on the features they had available which is outlined in the following section. The 10 vendors were reduced to four who had the most compatibility with DelDOT's requirements. Each of those four vendors were then interviewed and asked to provide a demonstration of their product. After the interviews, three of the vendors were selected, and trial testing of their software was conducted by the UD research team.

The trial testing involved using a simple data logger setup since the actual IRIB SHM data is so extensive. The data logger chosen for this setup was a Campbell Scientific CR6 because of its simplicity and cross-platform compatibility. Three strain gauges were used along with a thermocouple to feed data into the trial software platforms.

All strain gauges were attached to easily bendable objects that allowed for noticeable levels of strain. A thermocouple was positioned in the open air so that the ambient room temperature could be collected easily. Since little energy was required to change any of the readings from the sensors, it was easy to test different features within the software platforms.

The easiest way to get data into the different software platforms was to use FTP. This setup allowed the data logger to automatically send the data files over the Internet to the vendors' respective servers.

Campbell Scientific's programming language for the CR6 data logger is relatively intuitive. The data logger was set to export data via FTP every 10 minutes. Each sensor could be set to sample at rates between every 30 seconds to every two minutes. Ultimately, data was logged every minute for each sensor and then the accumulated data was exported every 10 minutes.

4 THE SOFTWARE DECISION MATRIX

4.1 *Existing decision methods*

After reviewing existing work, three decision-making methods were identified to be most applicable to the IRIB software selection task. Analytical Hierarchy Process (AHP) and Analytical Network Process (ANP) are two similar methods that allow multiple criteria-related problems to be solved using a systematic mathematical theory with weights. ANP differs from AHP in that it allows the evaluator to integrate relationships for relevance and feedback of criteria. ANP has been used to evaluate enterprise risk management and internal auditing software (Lin and Wang, 2011).

Due to the stringent requirements set by DelDOT, however, neither AHP nor ANP could identify the best software platform. All criteria provided by DelDOT would be weighted equally, defeating the purpose of AHP and ANP.

Another option found in the review uses an International Organization for Standardization and International Electrotechnical Commission (ISO/IEC) quality standard. Using ISO/IEC 9126-1 quality standard, the evaluator can compare user requirements and software capabilities (Franch and Carvallo, 2003).

The ISO/IEC 9126-1 quality standard methodology is much more applicable to the IRIB SHM software platform replacement task. A multitude of features present in each vendor's platform can be generalized and then refined to specific attributes. These attributes are then given a metric that can be used to compare between platforms. The IRIB SHM software platform decision matrix primarily uses this methodology as its design template.

4.2 *Understanding DELDOT'S requirements*

From years of using the current software platform, DelDOT was able to determine multiple key features and upgrades that they wanted for the new software platform. Features that were of the highest priority revolved around reporting and figure creation. Of all the desired requirements, the ability of the replacement software to receive full-speed data was the most challenging to accomplish. It is virtually impossible to stream, process, and display the volume of data from the bridge at 12.5Hz with the technology currently available.

In terms of reporting, DelDOT relies on scheduled reports to observe the overall short- and long-term structural health of the IRIB. These reports need to contain text, graphs, and tables that can concisely describe the performance of the bridge. In addition to scheduled reports, DelDOT wants the capability to quickly create a report "on the fly" that may include only certain elements or periods of data.

Bridge safety and data monitoring are also critical aspects that DelDOT requires. The ability to set thresholds on sensor values that could trigger alarms is another invaluable feature. These thresholds can be used to determine both real and error values that could help determine if a sensor is malfunctioning. Any time a threshold is exceeded, an alarm is sent out through multiple channels, such as a text, email, and/or internal software notification, to the key personnel.

The new software graphical user interface (GUI) needed to be able to visualize data in real-time via graphs, tables, dials, and real-time numerical values. All visualized data needs to be able to be created, edited, and/or deleted whenever necessary, allowing the user to see exactly what they want to see. These values, as displayed by the GUI, should be able to recall data for an effective time range that can be changed depending on the situation. DelDOT also specified that the ability to perform basic statistical evaluation on the data is important so that averages and standard deviations, for example, can be quickly calculated.

A feature currently not available in the present system is the ability to create a "virtual variable." This virtual variable allows a new sensor to be created by using raw data from "real" sensors located on the bridge that can then be used to calculate a new variable from one or multiple sensors. This virtual variable does not replace the real sensors on the bridge but compliments them as all data remains real-time and is just funneled through additional calculations to an additional data point on the GUI. If possible, DelDOT and the UD would also like the ability to develop more advanced scripts in programming languages like MATLAB and Python that could be integrated into the software platform.

Since DelDOT wants to have the autonomy to archive its own data outside of the software program, they want to be able to both export and import files and data to and from the software platform. Any charts and reports should be able to be easily exported to common standard formats that can then be manipulated, if necessary, via programs like Microsoft Excel or Word. The likelihood of one employee monitoring and using the software for the entirety of their career at DelDOT is small which is why DelDOT wants to be able to import documentation and other reports to the platform so that anyone that has access can quickly read the necessary materials.

Finally, to avoid some of the current longevity issues that are apparent with the present software solution, DelDOT wants the new platform to be scalable so that it is easy to add additional bridges and personnel to the project. This would involve the software being able to handle many projects and distinguish between each one but house them in the same program. DelDOT wants to be able to have designated login credentials for each user that allows the

user to track changes to the GUI or data, such as addressing alarms from the data. Each user should have individual permissions or be put into groups that have set permissions so that each party has set technical involvement in the software.

4.3 *Development of the software decision matrix*

After evaluating each software platform, a decision matrix was created by combining the similarities of each platform's capabilities and the requirements provided by DelDOT. The following main categories were created to summarize each software platform's features: Cost, Data Management, Calculation, Visualization, Alarms, System Administration, Reporting, and Additional Features.

Each category was then broken down into multiple sub-categories that outlined the platform's capability within a certain feature. For each sub-category, a visual dot rating system was used to distinguish which platforms performed better. The system went from four dots to one dot, with four dots exceeding requirements, three dots meeting requirements, two dots only partially meeting requirements, and one dot failing to meet DelDOT's requirements. The dots served as a quick visual representation of each platform's capabilities and allowed for a quantitative comparison. The average of all sub-categories became the category average. An additional comparative measure was chosen which used the sum of individual sub-category performances to determine a total score for each platform.

Table 1 outlines each sub-category description grouped into each category. By establishing objective sub-categories, the evaluator can consistently describe different features of each platform and how they contribute to the overall requirements of the client, in this case, DelDOT. Since each sub-category is relatively specific, tying each one to an overall category allows the client to see where compromises might need to be made to achieve the highest overall satisfaction with any platform.

Combining this method with the dot rating system allows the client to easily see in which areas each platform excels. Incorporating the actual performance of each sub-category for each platform based on the descriptions listed allows the client to gain a better understanding of why the dot rating was chosen. This can also provide the client with insight into how the evaluator prioritized the requirements provided for each category. Figure 3 provides an example section of the final decision matrix for the IRIB.

5 RESULTS

After evaluating each software platform for a few months, the decision matrix was completed by assigning a metric to each subcategory. A meeting with DelDOT was held in which UD provided quick demonstrations of each software platform and presented the completed software decision matrix. A discussion of the sub-categories which showed the widest range of ratings was presented at the end of the meeting. This greatly helped DelDOT narrow the decision to two vendors. The main differences of each vendor are shown in Figure 4. The decision matrix scored the two vendors selected by DelDOT highest both in terms of total score and average total score.

In addition to selecting two final vendors, DelDOT wanted to see an extended demonstration of each platform. The DelDOT engineer who primarily works with the software platform met with the first author to review the entire list of features available for both platforms. During the meeting, the first author walked through each step of creating and editing features as well as showing any limitations of each feature. Multiple additional questions were generated during these two meetings (one for each software platform) that were then asked to the software vendor to help DelDOT make the best decision.

6 CONCLUSIONS

Critically important to the functionality of any SHM system is having a robust data management software platform. DelDOT's requirement for a new software platform for the IRIB

Table 1. Sub-category descriptions in software decision matrix.

Category	Sub-Category	Description
Cost	Cost	Annual cost structure or total cost as well as alternative costs
Data Management	Data Import	Methods to bring data into platform
	Data Location	Where data can be housed for platform
	Data Export	Ability to export raw data and description of how it's done
	Data Tables	Ability to sort custom sensors into predetermined tables for easy export
	Historic Data	Allows for distinctions in time between data sets
	Data Frequency	How quickly the system can realistically visualize and import data
Calculation	Data Calculations	Calculations that can be per real data sensor
	Virtual Variables	Ability to create additional sensors not physically present and supported calculations available
	Ease of Virtual Variable Creation	Difficulty of creating virtual variable
Visualization	Screen Visualization	Main GUI present in default view of platform and ability to change view
	Dashboard	Ability to see multiple figures at the same time
Alarms	Alarms & Thresholds	Ability to set thresholds for sensors and then assign alarms to each sensor
	Ease of Alarm Setting	Difficulty of creating alarms and alarm types available
	Automatic Alarm Notification	Options for how personnel are notified of alarms
System Administration	User System	Describes the administrative hierarchy of users and permissions
	Multiple Job Sites	Ability of platform to house multiple bridges in one common application and distinguish between them
	General Ease of Use	Qualitative analysis of overall simplicity of platform
	Customer Support	Available customer support present for each platform
Reporting	Reporting Capabilities	Ability of platform to generate reports and any automation capabilities
	Automated Reports	Describes how automation occurs within each platform if possible
	Report Customization	Describes the level of customization allowed by each platform for report development
	Ease of Report Creation	Difficulty of creating a report and ability to change reports once developed
	Figure Development	Ability to create custom figures like charts and tables within the software to then be put in reports or exported
	Document Import	Ability for the system to assign imported documents to sensors or created reports
	Figure Export	Ability to selectively export created figures without creating a report
Additional Features	Custom Scripts	Ability of the platform to interface with advanced coding languages
	Internally Linkable	Ability of the platform to create linkable connections as shortcuts to other features or screen visualizations
	Real Time Webcam	Ability to support a live webcam

bridge was investigated by assessing various commercially available software platforms. An initial set of platforms was chosen due to their ability to satisfy most of the features required by DelDOT. A decision matrix based on existing decision-making methodology was then created to evaluate the various platforms. After scoring each element in the decision matrix, DelDOT was given the final scores and showed a demonstration of each platform. The top two platforms were then extensively evaluated by the DelDOT engineer who interacts with the system the most, and DelDOT is currently making their final decision as to which platform to adopt.

Calculation	Data Calculations	Sensor calibration & offset, virtual variables need to be set up to do additional calculations while still being able to separately see raw sensor data	●●●●	Sensor calibration & offset, virtual variables need to be set up to do additional calculations while still being able to separately see raw sensor data	●●●●	Extensive options for built in code to do data calculations per sensor. Sensors can be linked to create complex calculations involving multiple sensors	●●●●
	Virtual Variables	Very detailed and lots of capability	●●●●	General formulas	●●●	Considered calculated elements can have lots of possibilities	●●●
	Ease of Virtual Variable Creation	Difficult, lots of control over creation, however need to code the variable with an app script in Geocomp's custom language	●	Very easy, functions are slightly limited	●●●●	Very simple, entire menu dedicated to creation	●●●●
	Average Score:	●●●		●●●◐		●●●◐	

Figure 3. Example section of the actual DelDOT IRIB software replacement decision matrix.

Calculation	Ease of Virtual Variable Creation	Difficult, lots of control over creation, however need to code the variable with an app script in Geocomp's custom language	●	Very easy, functions are slightly limited	●●●	Very simple, entire menu dedicated to creation	●●●●
Data Management	Data Import	FTP / Custom Local Upload	●●●●	FTP / Custom Local Upload	●●●●	FTP / Custom Local Upload	●●●●
	Data Location	Cloud Hosted, stored locally if using the custom application	●●●	Cloud Hosted	●●●	Can be locally stored or cloud hosted	●●●●
	Data Frequency	Averages of 30 sec to 1 min displayed continuously - Run background python script on site computer that can detect a threshold and then capture full high speed data for period of time	●●●	Potentially up to 30 sec intervals, started to see compatibility issues	●	Averages over 1 minute - Run background python script that can log full high speed data	●●●
Alarms	Ease of Alarm Setting	New "alarm" job has to be created and alarms are created per each sensor	●●	Done in the alarm configuration, all sensors present in job can be filled out	●●●●	Relatively simple once message center is setup	●●●
System Administration	General Ease of Use	Relatively simple, but limited and clunky	●●●	Very easy and intuitive	●●●●	Initially intimidating, but with some time, easy and intuitive	●●●
	Customer Support	Online user manual, covers some topics	●●●	Relatively extensive online user forum as well as youtube channel	●●●●	Extensive online manual	●●●●
Reporting	Automated Reports	Reports can be emailed to specific people or groups on a scheduled basis by Vendor once format is created	●●●	Reports can be emailed to specific people or groups on a scheduled basis	●●●●	Reports can be emailed to specific people or groups on a scheduled basis	●●●
	Report Customization	Custom reports including sensor data, charts, alerts	●●●●	Custom reports with automated distribution, many features available	●●●●	Custom reports, however limited availability to develop report by user	●
	Ease of Report Creation	Use MS Word pluggin relatively simple	●●●	Through software & very simple	●●●●	Has to be done through Vendor	●
Additional Features	Custom Scripts	Possible through AppScripts, not the easiest to perform	●●●●	Only virtual variables allow for customization, least capability comparatively	●●	Calculated elements allows for custom scripts	●●●
Cost	Cost	Between $20k-30K/yr (closer to$30k), software can be bought out and price will be based on features	●●	Least expensive at tiered price per sensor ~ $11k/yr with reporting	●●●	One time purchase of ~ $44k with support charge per year $2.5k - Option for Vendor to host data, will add $18k/yr	●●●

Figure 4. Prominent differences in the software replacement decision matrix.

REFERENCES

Al-Khateeb, H.T., Shenton III, H.W., Chajes, M.J., and Wenczel, G. 2018. Computing continuous load rating factors for bridges using structural health monitoring data. *Journal of Civil Structural Health Monitoring* 8(5): 721–735

Al-Khateeb, H.T., Shenton III, H.W., Chajes M.J., and Aloupis C. 2019. Structural health monitoring of a cable-stayed bridge using regularly conducted diagnostic load tests. *Frontiers in Built Environment* 5:41

Franch, X. & Carvallo, J.P. 2003. Using quality models in software package selection. *IEEE software* 20(1): 34–41.

Lin, C.W. & Wang, C.H. 2011. A selection model for auditing software. *Industrial Management & Data Systems* 111(5): 776–790.

Shenton III, H.W., Al-Khateeb, H.T., Chajes, M.J., and Wenczel, G. 2017a. Indian river inlet bridge (part a): description of the bridge and the structural health monitoring system. *Bridge Structures* 13(1): 3–13.

Shenton III, H.W., Al-Khateeb, H.T., Chajes, M.J., Wenczel, G., Arndt, J., and Stevens, C. 2017b. Indian river inlet bridge (part b): lessons learned from the design, installation and operation of the structural health monitoring system. *Bridge Structures* 13(1): 15–24.

Bridge Maintenance, Safety, Management, Digitalization and Sustainability – Jensen, Frangopol & Schmidt (eds)
© 2024 The Author(s), ISBN 978-1-032-77040-6
Open Access: www.taylorfrancis.com, CC BY-NC-ND 4.0 license

Nonlinear seismic-response time-history analysis of submerged floating tunnels

Y.Q. Xiang & Y.G. Shen
College of Civil Engineering and Architecture(CCEA), Zhejiang University(ZJU). Hangzhou, China
Research Center for Submerged Floating Tunnel(RCSFT), CCEA,ZJU, Hangzhou, China
Collaborative Innovation Institute of ZJU-Zhejiang Communication Constr. Group, Hangzhou, China

C.F. Chao
Sichuan University of Science & Engineering, Zigong, China
Hangzhou Tongrui Engineering Technology Co., Ltd, Hangzhou, China

L. Deng
Collaborative Innovation Institute of ZJU-Zhejiang Communication Constr. Group, Hangzhou, China

ABSTRACT: Seismic safety of submerged floating tunnel (SFT) is one of the important factors of influencing application of the new structure, so it has important significance to investigate the seismic behaviour of SFTs. In this paper, SFT cable-tube coupling system nonlinear seismic model is established by simplifying the structure of SFT, and the seismic wave propagation mode in cable is constructed. Then, taking the coupling effect between cable vertical vibration and tube lateral vibration into account, the differential equations of the cable and tube coupled motion are derived by using Hamilton principle. In order to evaluate the SFT structural response to seismic events, the time domain dynamic response analysis is carried out by using variable separation approach and modal superposition method. The seismic behaviour of SFT in four cases are analyzed. The result shows that SFT seismic safety needs adequate reserves to ensure the structural safety and the cable vibration can inhibit tube vibration to some extent. The water resistance or damping can effectively weaken the cable vibration, and make the vibration energy of the SFT to be dissipated quickly. The cable maximum displacement tends to decrease with the increase of initial tension and the reasonable tilt angle of anchor cable is about 60°.

1 INTRODUCTION

Submerged Floating Tunnel, is simply called for as "SFT". In Italy, SFT is also known as "Ponte Di Archimede"(PDA) or "Archimede Bridge". It is a new type of transportation structure across the long and deep waterways and straits. It is generally composed of a tubular structure which is submerged in a certain depth of water, a mooring line (or floating tank on the water) anchored in the underwater foundation (it can prevent excessive displacement of the tunnel) and revetment structures connected to the bank in the ends of the waterways and straits Some relevant conceptual designs and application prospects were discussed and analyzed (AHRENS D. 1997, Xiang Y.Q. & Xue J.P. 2002.). Based on this, the application of SFT across straits and bays along the coast of China and the problems that need to be solved were discussed and related problems were studied (Xiang Y.Q. & Chao C.F. 2013, Xiang Y.Q. et al. 2013). Although experts and scholars from all over the world have done a lot of research on the design and analysis of SFT, but so far, no real SFT in the world has been built The reason for this is that there are still many key technical questions that need to be

DOI: 10.1201/9781003483755-121

addressed about how to analyze and design the SFT reasonably for ensuring the safety of the structure.

During the life cycle operation and service of SFT, it is subjected to complex action of the environments and loads around SFT, and the behavior and mechanism of SFT are very complex. Therefore, Xiang Y.Q. et al. (2022) summarized that many scholars from different countries have conducted a series of research related to SFTs from different perspectives in the past more than 20 years. Based on relevant research on bridge and tunnel engineering, Xiang Y.Q. et al. (2020a) also proposed a theoretical framework for the life cycle design of SFT from structural life cycle point of view, and conducted relevant theoretical analysis methods and experimental research, such as the response of SFT to impact loads (Xiang Y.Q. & Yang Y. 2017), the vibration response of SFT due to local anchor cable breakage (Xiang Y.Q. et al. 2020), the vehicle-SFT-fluid coupling vibration response (Xiang Y. Q. et al. 2021), the health monitoring system of SFT (Xiang Y. Q. 2015) and so on.

Due to the fact that earthquakes are one of the important threats to the safety of civil engineering structures, studying the dynamic performance of SFTs under earthquake action is of great significance. Sun S.N. et al. (2006) studied the hydrodynamic pressure acting on a suspended tunnel under seismic shear waves. Di Pilato M. et al. (2008a, b) conducted numerical simulations on the spatial dynamic response of SFT under seismic loads and hydrodynamic excitation. Martinelli L. et al. (2010, 2011), Martinea G. et al. (2010), Chen W.J. & Huang G.J. (2010), Xiao J. & Huang G.J. (2010), Perotti F. et al. (2013), Su Z. etc. (2013), Xiang Y.Q. & Chao C.F. (2015), Lee J.H. (2016), Martinelli L. et al. (2016), Dong M. & Li M.(2016), Mirzapour J. (2017) et al. experts and scholars have also done a lot of research in this area.

Martinelli L. et al. (2010, 2011) proposed a new seismic response spectrum method and a multi support seismic response analysis model for SFT structures, by taking into account the geometric nonlinearity and comprehensive damping effects of anchor cables. Martiera G. et al. (2010) analyzed the seismic dynamic response of SFT scheme in the Messina Strait. Chen W. et al. (2010) analyzed the dynamic response mechanism of SFT under non-uniform seismic excitation. Xiao J. et al. (2010) studied the seismic response of SFT under different forms of revetment connections. Su et al. (2013) established a seismic response model for underwater SFT tethers. Xiang et al. (2015) studied the lateral seismic response analysis considering boundary soil properties based on numerical models. Lee et al. (2016) discussed the impact on the seismic performance of SFTs with rectangular cross-section, including factors such as fluid compressibility, depth of seawater, and position of tunnel structures in water. Dong et al. (2016) studied the influence of SFT span and vertical equivalent stiffness of anchor cables on the dynamic response characteristics of SFT under seismic effect. Martinelli et al. (2016) summarized the dynamic behavior of SFT under seismic motion and emphasized the possibility of mitigating dynamic response through structural control. Mirzapour et al. (2017) studied the seismic response of SFT under support excitation and mainly discussed the influence of model size and anchor stiffness factors on its seismic response characteristics.

In recent years, Chen J.Y.et al. (2021) proposed a vibration control scheme based on plastic deformation dampers arranged side by side with anchor cables, and optimized the number of dampers. Xie J.et al. (2021) proposed a mathematical model, which considered the effect of canyon water transport and analyzed the seismic response of SFT systems. Akbarzadeh et al. (2021) discussed the effects of SFTs under asynchronous support excitation. It takes into account the impact of seismic input non-uniformity due to site differences in the positions of the SFT bank revetments at both ends. Shekari et al. (2022) discussed the impact of seismic wave period and intensity characteristics on the seismic safety performance evaluation of SFT.

Jin & Kim (2021) used a finite element line model to model the SFTs and mooring cables, by taking into account the dynamic/structural deformation capacity of the entire SFT and using the virtual connection mass method and constraint boundary conditions, and the hydrodynamic forces caused by waves and earthquakes were evaluated at the instantaneous node position using the Morison equation. Jin C. et al. (2021, 2022) proposed a new method of installing tuned mass dampers in tunnel pipes to control SFT vibration, carried out the

damper optimization method, and further proposed a passive tuned mass damper by establishing a time-domain dynamic simulation model of SFT and a tuned mass damper (TMD) and considering the interaction of SFT-TMD to slow down and control the resonant motion of SFT in waves and earthquakes.

Xie J. et al. (2023) established a non-uniform input model for seismic motion caused by multi-point excitation (including SFT end revetment points and SFT bottom anchorage points), and used spring elements to simulate the stiffness of joints between pipe segments. Based on harmonic superposition method, the influence of different seismic input modes on the dynamic response of SFT were studied, which improved the universality of problem discussion (Xie, J. 2023).

However, in the above studies, most studies are based on numerical simulations using general programs, while there are relatively few studies using classical analytical methods. The influence of anchor cable on vibration response of SFT under earthquake action is rarely mentioned. In this paper, based on the previous studies, a nonlinear dynamic model of the cable-body coupling system of the SFT is established, and the corresponding dynamic equation is derived. Considering the influence of the cable vibration, the dynamic response of SFTs under seismic action is studied by using time-history analysis method.

2 MATHEMATICAL MODEL

2.1 *Simplification and assumption of the model*

There is a big difference between the dynamic characteristics of the tube body and the cable of the SFT. In order to study the vibration characteristics of the mooring cable-type SFT under earthquake action, the long SFT pipe body is simplified into a beam with simple support at both ends, and the pipe body and the underwater foundation are hinged with mooring anchor cables. Figure 1 shows the simplified calculation model. In the vibration process of SFT, the top of the anchor cable generally moves with the pipe body, and the vertical displacement or strain should be coordinated, while the pipe body can rotate freely at the hinged point, and the bottom end of the anchor cable is fixed. The cross section of the pipe body is to be axially symmetric. At the same time, it is assumed that:

1) The tube body is Bernoulli-Euler beam with equal section and stiffness, and the tube body has no rotational displacement;
2) The pair of cables are equal section, length, stiffness and inclination angle, but the cross section, length, stiffness and inclination angle between the different pairs of cables can be different, and the flexural stiffness of the cables and geometric nonlinearity are ignored, so it can be simplified as a standard string in the model;
3) The earthquake wave input only consider lateral and horizontal seismic acceleration, it is directly acting on the axis line of tube body along the X direction of tube body, that is, is in Y direction of the over-all coordinate is, as shown in Figure 1;
4) Regardless of the traveling wave effect, the two end supports excitation is considered as the consistent excitation;

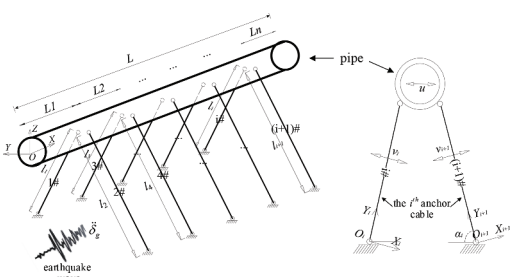


Figure 1. The simplified calculation model of seismic response of submerged floating tunnel.

5) The tube body moves only in the lateral direction (in Y direction). The i^{th} anchor cable moves only in the Xi direction of the local coordinate system.

2.2 *Basic differential equations of motion*

The global coordinate system of the tube body is O-XYZ, and the axis line of the tube body is X-axis. The local coordinate system of the i^{th} anchor cable is $X_iO_iY_i$, located in the inclined plane of anchor cable, and the anchor cable axis line is Y_i axis. Since the space distance between any two anchor cables is generally far, the water flow driven by the anchor cable vibration has basically no influence on the water body at a distance, so the anchor cable vibration cannot affect each other through the water body. Therefore, based on the coordinate system established in Figure 1 and Hamilton's principle, differential equations of the combined structure of anchor cable-tube with respect to u and v_i motion can be obtained:

$$\begin{cases} m_{ci}\ddot{v}_i + c_i\dot{v}_i - (T_i + \Delta T_i)\frac{\partial^2 v_i}{\partial y^2} = -F_{iD} - m_{ci}\ddot{\delta}_{ci} \\ m_{ci+1}\ddot{v}_{i+1} + c_{i+1}\dot{v}_{i+1} - (T_{i+1} + \Delta T_{i+1})\frac{\partial^2 v_{i+1}}{\partial y^2} = -F_{i+1D} - m_{ci+1}\ddot{\delta}_{ci+1} \\ m_b\ddot{u} + c_b\dot{u} + E_bI_b\frac{\partial^4 u}{\partial x^4} + \sum_{i=1}^{(n+1)/2}(\Delta T_i - \Delta T_{i+1})\cos\alpha_i \cdot \delta(x - x_i) = -F_{bD} - m_b\ddot{\delta}_g \\ i = 1, 3, 5, \cdots, n(n\ is\ \text{oddnumber}) \end{cases} \tag{1}$$

Where v_i is the longitudinal displacement of the i^{th} anchor cable perpendicular to the anchor cable axis; u is the lateral displacement at any position x of the pipe body; and m_{ci} is the mass per unit length of the i^{th} anchor cable; c_i is the viscous damping coefficient of the i^{th} anchor cable; $m_b$is the tube body mass per unit length; c_b is the viscous damping coefficient of the tube body; T_i is the initial tension of the i^{th} anchor cable at static equilibrium; ΔT_i is the tension increment of the i^{th} anchor cable during vibration, $\Delta T_i = \frac{E_{ci}A_{ci}}{l_i}\int_0^{l_i}\varepsilon_i \mathrm{d}y$; E_{ci} is the equivalent elastic modulus of the i^{th} anchor cable; A_{ci} is the cross-sectional area of the i^{th} anchor cable; l_i is the actual length of the i^{th} anchor cable; ε_i is the dynamic strain of the i^{th} anchor cable; x_i is the horizontal coordinate of the articulation point between the pipe body and the top of the i^{th} anchor cable; α_i is the tilt angle of the i^{th} anchor cable; E_b is the elastic modulus of the tube body; I_b is the bending stiffness of pipe section; F_{iD} is the sum of the unit length drag force and additional inertial force caused by the longitudinal vibration of the i^{th} anchor cable; F_{bD} is the sum of the unit length drag force and additional inertial force caused by the lateral vibration of the pipe body; $\ddot{\delta}_g$ is the horizontal and lateral acceleration of the earthquake wave; $\delta(x - x_i)$ is the Dirac function.

The dynamic axial strain of anchor cable can be obtained from Green strain:

$$\begin{cases} \varepsilon_i = \frac{u(x=x_i).\cos\alpha_i}{l_i} + \frac{1}{2}\left(\frac{\partial v_i}{\partial y}\right)^2 \\ \varepsilon_{i+1} = -\frac{u(x=x_i).\cos\alpha_i}{l_{i+1}} + \frac{1}{2}\left(\frac{\partial v_{i+1}}{\partial y}\right)^2 \\ i = 1, 3, \ldots n(n\ is\ \text{odd number}) \end{cases} \tag{2}$$

Where $u(x{=}x_i)$ is the displacement of the transverse vibration of the tube body at the articulation point of the i^{th} pair anchor cables.

According to Morison's formula, the dragging force and additional inertial force of water body on the vibrating tube body or anchor cable can be expressed as:

$$F_D = \frac{1}{2}\rho_w D C_D \dot{U}\left|\dot{U}\right| + \frac{\pi D^2}{4}\rho_w C_m \ddot{U} \tag{3}$$

Where C_D is the drag force coefficient; C_m is the additional mass coefficient; U is the displacement of the tube segments relative to the water body; ρ_w is the density of water; D is the

diameter of tube body or anchor cable. For both the pipe body and the anchor cable $C_D = 0.7$ and $C_m = 1.0$.

2.3 *Seismic wave propagation mode in anchor cable*

The propagation of seismic waves in the anchor cable is approximated here as a plane amplitude-varying harmonic shear wave propagating along the anchor cable axis Y axis with velocity V, without considering the reflection of seismic waves. By referring to the wave equation of mechanical waves and considering the effect of viscous resistance on the vibration system, the wave equation of seismic waves in the anchor cable and pipe body can be obtained as follows:

$$\begin{cases} \ddot{\delta}_{ci}(y,t) = \ddot{\delta}_g e^{-\frac{\gamma_i}{2m_{ci}}t}[\sin\omega(t-\frac{y}{V}) + \sin\omega(t-\frac{l_i-y}{V})] \cdot \sin\alpha_i \\ \ddot{\delta}_b(x,t) = \ddot{\delta}_g \\ i = 1,2,\cdots,n \end{cases} \tag{4}$$

Where $\ddot{\delta}_g$ is the seismic acceleration; ω is the seismic wave vibration frequency; $V = \sqrt{\frac{G}{\rho}}$ is the seismic wave propagation speed in the anchor cables; $\gamma = \sqrt{4\beta^2 m_{ci} k_{ci}}$ is the resistance coefficient; G is the shear modulus of the anchor cable material; ρ is the density of the anchor cable material; k_{ci} is the anchor cable stiffness; β is the dimensionless coefficient.

2.4 *Solution of equations*

According to equation (1), for the pipe body and anchor cable with simple support at both ends, the mode superposition method of variable separation can be used to solve the problem, so that:

$$\begin{cases} v_i(y,t) = \sum_{j=1}^{m_i} v_{i,j}(t)\sin(\frac{j\pi y}{l_i}) \\ u(x,t) = \sum_{j=1}^{m} u_j(t)\sin(\frac{j\pi x}{L}) \\ i = 1,3,\cdots,n(n \text{ is odd number}) \end{cases} \tag{5}$$

$$\begin{cases} \ddot{v}_{i,1} + \left[\omega_{i,1}^2 + \frac{E_{ci}A_{ci}\pi^2}{\bar{m}_{ci}{l_i}^3}\cdot u(x=x_i)\cdot\cos\alpha_i\right]\cdot v_{i,1} + 2\xi_{i,1}\omega_{i,1}\dot{v}_{i,1} + \frac{E_{ci}A_{ci}\pi^4}{4{l_i}^4\bar{m}_{ci}}\cdot v_{i,1}^3 = \\ \qquad -\frac{4}{3\bar{m}_{ci}\pi}\rho_w D_i C_{Di}\dot{v}_{i,1}\left|\dot{v}_{i,1}\right| - \frac{m_{ci}}{\bar{m}_{ci}}\cdot e^{-\frac{\gamma_i}{2m_{ci}}t}(B_{1i}\sin\omega t + B_{2i}\cos\omega t)\cdot\ddot{\delta}_g\cdot\sin\alpha_i \\ \ddot{v}_{i+1,1} + \left[\omega_{i+1,1}^2 - \frac{E_{ci+1}A_{ci+1}\pi^2}{\bar{m}_{ci+1}{l_{i+1}}^3}\cdot u(x=x_i)\cdot\cos\alpha_i\right]\cdot v_{i+1,1} + 2\xi_{i+1,1}\omega_{i+1,1}\dot{v}_{i+1,1} + \frac{E_{ci+1}A_{ci+1}\pi^4}{4l_{i+1}^4\bar{m}_{ci+1}}\cdot v_{i+1,1}^3 = \\ -\frac{4}{3\bar{m}_{ci+1}\pi}\rho_w D_{i+1}C_{Di+1}\dot{v}_{i+1,1}\left|\dot{v}_{i+1,1}\right| - \frac{m_{ci+1}}{\bar{m}_{ci+1}}\cdot e^{-\frac{\gamma_{i+1}}{2m_{ci+1}}t}(B_{1i+1}\sin\omega t + B_{2i+1}\cos\omega t)\cdot\ddot{\delta}_g\cdot\sin\alpha_i \\ \ddot{u}_1 + \omega_b^2 u_1 + 2\xi_2\omega_b\dot{u}_1 = -\sum_{i}^{(n+1)/2}\frac{2}{\bar{m}_b L}\left[\frac{2E_{ci}A_{ci}}{l_i}\cdot u(x=x_i)\cdot\cos\alpha_i + \frac{E_{ci}A_{ci}\pi^2}{4{l_i}^2}\cdot v_{i,1}^2 - \frac{E_{ci+1}A_{ci+1}\pi^2}{4{l_{i+1}}^2}\cdot v_{i+1,1}^2\right] \\ \cdot\sin(\frac{x_i\pi}{L})\cdot\cos\alpha_i - \frac{4}{3\bar{m}_b\pi}\rho_w D_{tube}C_D\dot{u}_1|\dot{u}_1| - \frac{4m_b}{\pi\bar{m}_b}\ddot{\delta}_g \\ i = 1,3,5,\cdots,n(n \text{ is odd number}) \end{cases} \tag{6}$$

Where $\omega_{i,1}$ is the first order natural frequency of the i^{th} anchor cable; ${\omega_{i,1}}^2 = \frac{T_i}{\bar{m}_{ci}}\left(\frac{\pi}{l_i}\right)^2$, $\bar{m}_{ci} = m_{ci} + \frac{\pi {D_i}^2}{4}\rho_w C_{mi}$; $\xi_{i,1}$ is the first damping ratio of the i^{th} anchor cable; $B_{1i} = \frac{4\pi V^2(\cos\frac{\omega l_i}{V}+1)}{\pi^2 V^2 - \omega^2 l_i^2}$, $B_{2i} = \frac{4\pi V^2\sin\frac{\omega l_i}{V}}{\pi^2 V^2 - \omega^2 l_i^2}$; ω_b is the first order natural frequency when the tube body is connected without anchor cable; $\omega_b^2 = \frac{E_b I_b}{\bar{m}_b}\left(\frac{\pi}{L}\right)^4$, $\bar{m}_b = m_b + \frac{\pi {D_{tube}}^2}{4}\rho_w C_{mi}$; ξ_2 is the first damping ratio of the tube body.

Tagata G.(1997) pointed out from the test that the basic modes of the tensioned-anchor cable vibration under the end excitation play a dominant role, that is, the displacement response caused by the first-order resonance is the largest. Some research shows that the first mode of the SFT tube body contributes the most to the displacement response, while the higher mode contributes little to the displacement. Therefore, the first-order vibration mode is only taken for both the anchor cable and the tube body in this paper, thus, the differential equations of the motion of the combined structure of the anchor cable-tube body are simplified as equation (6).

Some of studies have shown that when the natural vibration frequency of the pipe body is close to twice the frequency of a certain order vibration of the anchor cable, the structure may produce self-excited resonance phenomenon, also known as parametric vibration (Wang Z.G.& Sun B.N. 2001), and the seismic response of the anchor cables will be amplified several times. The vibration equation of the SFT under earthquake excitation is a nonlinear equation, and there is a nonlinear term of pipe body and anchor cable displacement coupling. Therefore, the vibration of the SFT under earthquake action is nonlinear vibration.

3 NUMERICAL EXAMPLE

3.1 *Numerical examples and benchmark model*

This calculation example is partly taken from the design parameters of SFTs studied in literature (Chen J.Y., Sun S.N. & Su Z.B. 2008). In order to explore the most unfavorable situation under earthquake action, some of structural parameters were artificially changed according to actual possibilities so that the first-order vibration frequency of the pipe body was twice that of the first-order vibration frequency of the anchor cables to generate parametric resonance.

Table 1. Basic model parameters of numerical example.

Structure and medium, Mass or earthquake	Parameter name	symbol	unit	values
1st and 2nd anchor cable	Length	l	m	228.62
	Diameter	D	m	0.489
	Mass per unit length	m_c	kg/m	1474.23
	Density	ρ_c	kg/m^3	7850
	Modulus of elasticity	E_c	MPa	2.1×10^5
	Initial tension	T	kN	6.5×10^4
	Tilt Angle	α	—	45º
Tube body	Length	L	m	90
	Tube diameter	D_{tube}	m	10
	Mass per unit length	m_b	kg/m	1.5×10^5
	Flexural stiffness	I_b	m^4	58
	Modulus of elasticity	E_b	MPa	3.45×10^4
	Density	ρ_b	kg/m^3	2500
Water	Density	ρ_w	kg/m^3	1000
El Centro	Vibration frequency	ω	rad^{-1}	8.98
	Velocity of propagation	V	m/s	3281
	Resistance coefficient	γ	kg/s	150

Here, only a pair of anchor cables is arranged on the pipe body, and the connection point between the pipe body and the pair of anchor cables is located at L/2. The length, cross-sectional area, material and stiffness of two anchor cables are the same. The cable inclination angle α is 45º. The specific values of system parameters are listed in Table 1 and are used as the benchmark model. Newmark method is used for numerical calculation, the parameter

analysis of the seismic response of the SFT based on the benchmark model is realized by Matlab programming.

3.2 *The selection of seismic waves*

Because the structural response of SFT under earthquake is closely related to the time-history characteristics of the input ground motion, the representative El Centro wave occurred in 1940 in the United States is selected in this paper, which is suitable for class III sites. The peak acceleration recorded in the actual ground motion of the seismic wave is converted into the basic intensity, and the single parameter relationship between seismic intensity and ground motion proposed by Hershlcrger is adopted, and the seismic intensity is VIII degree. In the actual calculation of this example, the seismic action adopts the case of laterally acting on the axis line of tube body along the X direction of tube body.

3.3 *Calculation working condition setting*

The four typical working conditions and corresponding parameter settings are selected to use the calculation analysis. The $\xi_{1,1}$ and $\xi_{2,1}$ are the first order damping ratio of 1st, 2nd anchor cables respectively, and ξ_b is the first order damping ratio of tube body, The detailed specific values is seen in Table 2.

Table 2. Work conditions and parameters set.

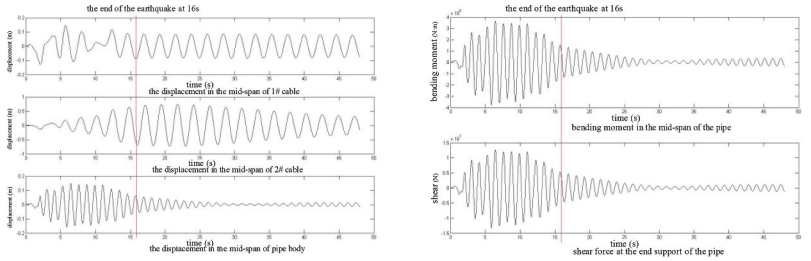
Cases	$\xi_{1,1}$	$\xi_{2,1}$	ξ_b	Remark
1	0.0018	0.0018	0.01	El Centro wave excitation
2	0.0018	0.0018	0.01	El Centro wave excitation, without cable vibration
3	0.0018	0.0018	0.01	El Centro wave excitation, without water damping
4	0.0018	0.0018	0.01	El Centro wave excitation with change of cable inclination

Using dynamic time history analysis method, the displacement time history curves at the center position of anchor cable and mid-span position of tube body were calculated in five different working conditions.

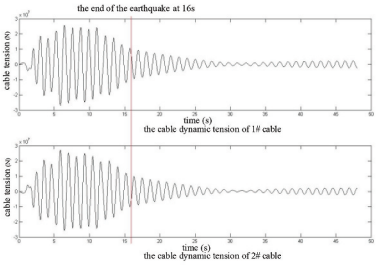
4 NUMERICAL RESULTS AND ANALYSIS

In order to explore the nonlinear seismic response characteristics of the SFT under uniform excitation, the parameters of the SFT are analyzed from the following five cases: (1) The seismic response of the benchmark SFT model; (2) The seismic response of SFT without cable vibration under El Centro wave excitation; (3) The seismic response of SFT without water damping under El Centro wave excitation; (4) The seismic response of SFT with different cable inclination angle under El Centro wave excitation.

It can be seen from Figure 2 that in case 1, under the excitation of El Centro wave, the maximum mid-span displacement of the SFT reaches 0.156m, the maximum mid-span bending moment of the SFT is 3.81×10^5kN.m, and the maximum shear force of the SFT at the end support is 1.33×10^4kN. The maximum displacement of cable span is 0.737m, and the maximum dynamic tension of cable is 2.69×10^4kN, which is 41% of the initial tension. It can be seen that the SFT must reserve enough safety margin to meet the requirements of the SFT safety under the action of earthquake. Under earthquake excitation, due to the large stiffness of the tube body, the seismic response is more significant, so the response of the tube body is the most sensitive, the change of displacement and internal force is basically consistent with the change trend of seismic wave acceleration, and the vibration rapidly attenuates after the earthquake. The vibration response of the anchor cable has a hysteresis effect, and the amplitude continues to increase to the maximum after the earthquake, and then slowly attenuates.



(a) Displacement time history curve (b) The bending moment and shear time history curve of tube



(c) Cable dynamic tension time history curve

Figure 2. Seismic time-response curve of SFT in case one.

Figure 3 shows that in case 2 the maximum displacement in the span of the pipe body reaches 0.167m, which increases by 7.1% compared with the displacement in Figure 3(a). Meanwhile, the vibration attenuation of the pipe body is relatively slow after the earthquake. It can be seen that the cable vibration has a certain inhibition effect on the pipe body, that is, the cable vibration has an "additional damping" effect on the pipe body. This function of the anchor cables are mainly due to the non-synchronous vibration and different direction characteristics of the anchor cables.

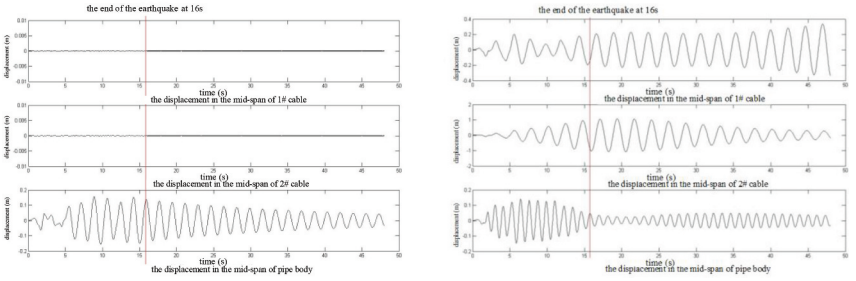


Figure 3. Disp. time-response curve of SFT in case 2 Figure 4. Disp. time-response curve of SFT in case3.

As shown in Figure 4, in case 3, when the effect of water damping on pipe body and anchor cable is not considered, the maximum mid-span displacement of anchor cables reach 1.08m and the maximum mid-span displacement of pipe body is 0.157m. After the end of the earthquake, the pipe body and anchor cable have parametric vibration, and the structural vibration attenuation is slow. Compared with case 1, it can be seen that water damping has a significant effect on inhibiting the maximum vibration displacement of the anchor cable, but cannot inhibit the maximum displacement peak of the pipe body. The vibration energy is consumed by water damping, and the vibration amplitude of the structure is attenuated rapidly.

Cable inclination angle is also one of important parameters in SFT design. Through parameter research, it is found that with the increase of the inclination angle, the maximum vibration

displacement in the span of the cable also tends to decrease on the whole. But at the base inclination angle $\alpha = 45^{\circ}$, that is, when the pipe body and anchor cable have parametric vibration, the peak displacement of 2nd anchor cable reaches the maximum. In addition, when the cable tilts angle $\alpha = 60^{\circ}$, the pipe displacement appears a minimum value, while the cable displacement value is also small. Comprehensive consideration of the cable length, structural vibration and other factors, the reasonable value of the cable tilt angle is about 60°.

5 CONCLUSIONS

This paper only studies the dynamic response of the SFT under the uniform transverse earthquake excitation. By simplifying the SFT structure into a model of simple support at both ends, in which the pipe body of SFT is fixed with the underwater foundation by the anchor cables, the Hamilton principle is used to establish the combined structure model of the anchor cable-pipe body under the earthquake action. The differential equation considering the coupling between the lateral vibration of anchor cables and the transverse vibration of pipe body is derived, and the solution of the equation is given. Based on the above, the vibration response of the cable and pipe body of a SFT is analyzed and studied by setting different design parameters and working conditions of the SFT under uniform transverse seismic excitation. The result shows that SFT seismic safety needs adequate reserves to ensure the structural safety and the cable vibration can inhibit tube vibration to some extent. The water resistance or damping can effectively weaken the cable vibration, and make the vibration energy of the SFT to be dissipated quickly. The cable maximum displacement tends to decrease with the increase of initial tension and the reasonable tilt angle of anchor cable is about 60°.

ACKNOWLEDGEMENTS

This work was supported by the National Natural Science Foundation of China (grant No. 51279178, 51541810), and the Collaborative Innovation Institute of Zhejiang University and Zhejiang Communication Construction Group Co. LTD (2022-009 Co-operation Research and Development Project of SFT).

REFERENCES

Ahrens D. 1997. Submerged floating tunnels—A concept whose time has arrived. *Tunneling and Underground Space Technology*, 12(2): 317–336.

Akbarzadeh, N., Tariverdilo, S. & Emamyari, A. 2021. Vibration of submerged floating tunnels under asynchronous support excitation. *Structures* 30: 329–337.

Chen, W.J. & Huang, G.J. 2010. Seismic wave passage effect on dynamic response of submerged floating tunnels. *Procedia Eng. 4 (ISAB-2010)*: 217–224

Chen, J.Y., Xie, J., Xu, Q. & Ren, B. 2021. Static-dynamic response analysis and vibration control for submerged floating tunnel. *J. Dalian Marit. Univ*. 47 (4): 83–92 (in Chinese).

Chen, J.Y., Sun, S.N. & Su, Z.B. 2008. Dynamic response of submerged floating-tunnel tethers subjected to current. *Eng. Mechanics* 25(10):229-234(in Chinese)

Di Pilato, M., Perotti, F. & Fogazzi, P. 2008a. 3D dynamic response of submerged floating tunnels under seismic and hydrodynamic excitation. *Engineering Structures* 30(1): 268–281.

Di Pilato, M., Feriani, A. & Perotti, F. 2008b. Numerical models for the dynamic response of submerged floating tunnels under seismic loading. *Earthquake Engineering and Structural Dynamics* 37(9): 1203–1222.

Dong, M. & Li, M. 2016. The dynamic responses of the submerged floating tunnel under seismic effect. *Procedia Eng*. 166: 152–159.

Gao, C., Xiang, Y., Yang, Y. & Lin, H. 2022. Transfer matrix method for analyzing dynamic response of multi-span elastically supported SFT under moving load. *Appl. Math. Model* 112: 238–261.

He, R., Yuan, Y. & Fan, Z. et al. 2022. Semi-analytical solutions for seismic responses of tunnel tube in pier-supported submerged floating tunnel under vertical excitation. *Ships & Offshore Struct*. 17 (9): 2082–2102.

Jin, C., Chung, W.C. & Kwon, D. et al. 2021. Optimization of tuned mass damper for seismic control of submerged floating tunnel. *Eng. Struct*. 241:112460.
Jin, C. & Kim, M. 2021. The effect of Key design parameters on the global performance of submerged floating tunnel under target wave and earthquake excitations. *Computer Modeling in Eng. & Sci*. 128 (1): 315–337.
Jin, C., Kim, S.J. & Kim, M.H. 2022.Vibration control of submerged floating tunnel in waves and earthquakes through tuned mass damper, *International J. of Naval Architecture and Ocean Engineering* 14: 100483
Lee, J.H., Seo, S.I. & Mun, H.S. 2016. Seismic behaviors of a floating submerged tunnel with a rectangular cross-section. *Ocean Eng*. 127: 32–47.
Mirzapour, J., Shahmardani, M. & Tariverdilo, S., 2017. Seismic response of submerged floating tunnel under support excitation. *Ships & Offshore Struct*. 12 (3): 404–411.
Martinelli, L., Barbella, G. & Feriani, A. 2010. Modeling of Qiandao Lake submerged floating tunnel subject to multi-support seismic input. *Procedia Eng. 4(ISAB-2010)*:311–318
Martinelli, L., Barbella, G. & Feriani, A. 2011. A numerical procedure for simulating the multi-support seismic response of submerged floating tunnels anchored by cables. *Eng. Struct*. 33 (10): 2850–2860.
Martinelli, L., Domaneschi, M. & Shi, C. 2016. Submerged floating tunnels under seismic motion: vibration mitigation and seaquake effects. *Procedia Eng*. 166: 229–246.
Martirea, G., Faggiano, B. & Mazzolania, F.M. et al. 2010. Seismic analysis of a SFT solution for the Messina Strait crossing. *Procedia Eng. 4(ISAB-2010)*:303–310
Perotti, F., Shi, C., Domaneschi, M. & Martinelli, L. 2013. The nonlinear dynamic response of submerged floating tunnels to earthquake and seaquake excitation. *Proc. of 6th Symp. on Strait Crossing*, 16-19 June 2013. Bergen, Norway
Shekari, M.R., Amiri, S.M. & Zareifard, M.R., 2022. A numerical approach for coupled analysis of the seismic response of a cable-moored submerged floating tunnel. *Mar. Struct*. 83: 103156.
Su, Z. & Sun, S. 2013. Seismic response of submerged floating tunnel tether. *China Ocean Eng*. 27:43–50.
Sun, S.N. & Chen, J.Y. 2006. Hydrodynamic Pressure on Submerged Floating Tunnel under the Earthquake-SV-Wave. *J. of Disaster Prevention and Mitigation Eng*. 26(4):425–430
Tagata, G. 1977. Harmonically forced finite amplitude vibration of a string. *Journal of Sound and Vibration* 51(4): 483–492.
Xiang, Y.Q. & Xue, J.P. 2002.Study on submerged floating tunnels in the world. *Journal of China & Foreign Highway* 22(6):49–52
Xiang, Y.Q. & Chao, C.F. 2013. Vortex-induced Dynamic Response Analysis for the Submerged Floating Tunnel System under the Effect of Currents. *J. of Waterway, Port, Coastal, and Ocean Eng*. 139(3): 183–189.
Xiang, Y.Q., Yang, Y., & Chao, C.F. 2013, Challenges and solutions of future channels construction over straits or bays in China coastal area, *Proc. of 6th Symp. on Strait Crossing*, 16 –19. June, 2013, Bergen, Norway
Xiang, Y.Q., Bai, B. & Zhao, Y. 2020a. Theoretical framework of life cycle design of the submerged floating tunnel. *Proc. of the 10th International Conference on Bridge Maintenance, Safety and Management (IABMAS 2020)*, Sapporo, Japan, Apr. 11–18, 2021
Xiang, Y.Q., Wu, K. S., Yang, Y.S., Jin, L.L., Chen K. 2022. Industry-University-Research Cooperation in China Accelerates the Research and Development of Intelligent SFT. *Proc. of The 10th International Conference on Bridge Maintenance, Safety and Management (IABMAS 2022)*, Barcelona, Spain, 11–15 July, 2022
Xiang, Y.Q., Chen, Z.Y. & Bai, B. et al. 2020b. Mechanical behaviors and experimental study of submerged floating tunnel subjected to local anchor-cable failure. *Eng. Struct*. 212: 110125. DOI:10.1016/j.engstruct.2020.110521.
Xiang, Y. Q., Zhang, K.Q. & Yang, Y. 2015b. Health monitoring system of submerged floating tunnel prototype in Qiandao Lake. *Proceedings of 7th International Conference on Structural Health Monitoring of Intelligent Infrastructure (SHMII-7)*, Torino, Italy 1-3 July,2015
Xiang, Y.Q. & Yang, Y. 2017. Spatial dynamic response of submerged floating tunnel to impact load. *Marine Structures* 53: 20–31.
Xiang, Y. Q., Lin, H.& Bai B. et al. 2021. Numerical simulation and experimental study of submerged floating tunnel subjected to moving vehicle load, *Ocean Eng*. 235. DOI:10.1016/j.oceaneng.2021.109431
Xiang, Y.Q. & Chao, C.F. 2015a. Transverse seismic response analysis of submerged floating tunnel considering boundary soil property. *Proc. of International Conference on Engineering Vibration*, Ljubljana, Slovenia, 7-10 Sept. 2015.
Xiao, J. & Huang, G.J. 2010. Transverse earthquake response and design analysis of submerged floating tunnels with various shore connections. *Procedia Eng. 4(ISAB-2010)* 233–242
Xie, J. & Chen, J. 2021. Dynamic response analysis of submerged floating tunnel- canyon water system under earthquakes. *Appl. Math. Model* 94:757–779.
Xie, J., Li J. & Chen, J., 2023. Seismic response analysis of SFT considering non-uniform excitation and flexible-support boundary effect, *Ocean Eng*. 286: 115468

Bridge Maintenance, Safety, Management, Digitalization and Sustainability – Jensen, Frangopol & Schmidt (eds)
© 2024 The Author(s), ISBN 978-1-032-77040-6
Open Access: www.taylorfrancis.com, CC BY-NC-ND 4.0 license

Experimental investigation for dynamic behavior of the scaled segment model of submerged floating tunnels under waves

H. Ding, L. Cheng, K. Li, D. Zhong & X. Hu
China Merchants Chongqing Communications Technology Research & Design Institute Co., Ltd., Chongqing, China
National Engineering Research Center of Road Tunnel, Chongqing, China

ABSTRACT: Understanding the hydrodynamic behavior of structure under wave loads is essential to improve the safety and stability of the Submerged Floating Tunnel (SFT). Based on the Qiongzhou Strait SFT scheme, the dynamic characteristics of SFT subjected to regular wave were investigated deeply and thoroughly employing experimental tests with a scale of 1:60. The impacts of wave parameters on the dynamic response of the scaled segment model of SFT were discussed in detail. Further prospects for developing experimental research on SFT were given as well. The results show that the acceleration and displacement of the scaled segment model tend to increase nonlinearly with the increase of wave height. The ratio of wavelength to structure size has a significant effect on the dynamic response of the segment model. And the bottom anchor cable provides most of the restraining force for the segment model.

1 INTRODUCTION

Submerged floating tunnel (SFT) is an innovative transportation scheme for crossing deep and large fjord, with prominent advantages in waters with poor geological conditions and high environmental protection requirements. SFTs are surrounded by complex marine conditions, the dynamic response of the structure under multiple external loads is an essential basis for the design of SFT, which has become the research emphasis of many scholars. Tariverdilo et al. (2011) derived an expression for the fluid force acting on the tube based on the potential function of the flow field. Seo et al. (2015) calculated the forces acting on the tube utilizing linear wave theory and Morrison's equations and verified the reliability through a small wave-flume test. Hong et al. (2010), Kang et al. (2016) investigated the vibration characteristics of tube and anchor cables of SFT under the action of wave and current. Martire et al. (2010) and Yuan et al. (2016), Xiang et al. (2018) investigated the influence of traffic inside the tunnel on the dynamic response of SFT by simplifying the traffic loads into homogeneous loads and moving concentrated forces, respectively. Kunisu et al. (1994) and Oh et al. (2013) studied the hydrodynamic characteristics of SFT under the action of regular waves by wave flume tests. Chao et al. (2016) analyzed the effect of impact loading on the structure, and Sun et al. (2008) pioneered the experimental study of the seismic response of SFT. Iovane et al. (2023) summarized the status of experimental research on SFT in detail.

The present research mainly adopted theoretical and numerical analysis to investigate the dynamic response characteristics of SFT under the effects of wave, current and seismic loads, etc. For the model test, the small-scale two-dimensional flume test and pool test were mainly used, and the tube section was primarily modeled by circular. There are fewer studies on large-scale hydrodynamic tests considering three-dimensional effects and the dynamic response characteristics of elliptical section SFT, which lack the support of experimental data.

DOI: 10.1201/9781003483755-122

A hydrodynamic modeling test with geometric scale of 1:60 was conducted in the present study. Section 2 introduced in detail the device of the test, the measuring instruments, and the wave parameters of the regular waves. Section 3 mainly discussed the effects of wave parameters on acceleration, displacement, wave pressure on the surface of the model and anchor cable force. The conclusions and the prospects of the experimental study were presented in Section 4.

2 EXPERIMENTAL SETUP

2.1 *Experimental facility*

The tests were conducted in a wave-current basin at the Underwater Tunnel Laboratory, China Merchants Chongqing Communications Technology Research and Design Institute Co., Ltd., China (CMCT). The wave-current basin is 36 m long, 31 m wide, and 3 m deep. A piston-type wave-making system is equipped at the one side of the basin, generating waves with height ranges from 0.025 to 0.2 m and period ranges from 0.50 to 2.00 s. At the other end of the basin, a series of wave absorbers are installed to reduce the influence of the reflection of incident waves. A large truss truck is mounted above the basin to assist in the installation of SFT scaled segment model (Hereafter referred to as the model) and to provide a platform for testing operations on the water.

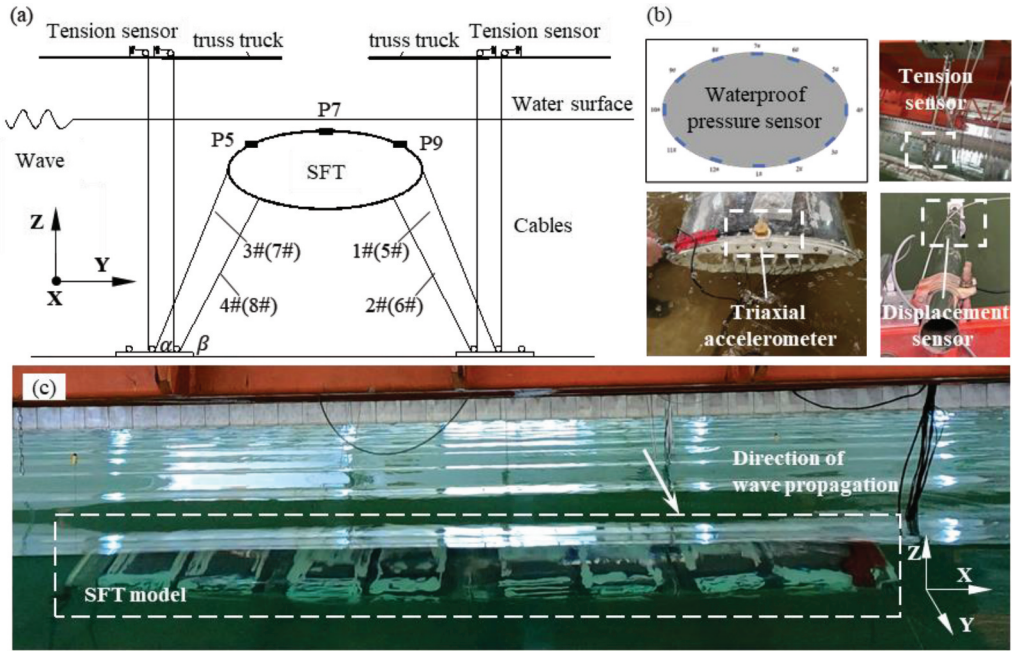


Figure 1. Layout of the test set-up and the submerged floating tunnel model.

2.2 *Model and layout*

The SFT model prototyped from the design plan of Qiongzhou strait passageway proposed by CMCT, and the scale ratio of 1:60 and Froude similarity were used for experiment design. The section of test model is elliptic with a long axis (D_L) of 0.75 m and a short axis (D_S) of 0.317 m, the length is 2 m. The test model was made of polymethyl methacrylate with a thickness of 0.008 m. The buoyancy to weight ratio (BWR) is 1.3. The interior of the model

is padded with lead plates as counterweights according to the center of gravity of the prototype. The coordinate system is illustrated in Figure 1(a), the X-axis (longitudinal direction) aligned with the longitudinal axis of tube, the Y-axis (transverse direction) aligned with wave propagation direction, the Z-axis (vertical direction) aligned with gravity acceleration.

Two pairs of inclined anchor cables symmetrically arranged at each end of the tube, one pair mounted below the tube (bottom cables) and one pair mounted on the transverse side of the tube (side cables). For the sake of distinction, the cables on one side are numbered 1# to 4# and on the other side are numbered 5# to 8#. A series of pulley devices were installed at the bottom of the wave-current basin to fix the cables. The angles between the two pairs cables and the ground are $\alpha = 56^\circ$ and $\beta = 65^\circ$, respectively. The cables were made of stainless-steel wire rope with a diameter of 5 mm. More details on the experimental setup and model can be found in literature written by Ding et al. (2024).

The model was installed at the center of the wave-current basin. The distance separating the model from the wave-generator and wave-absorber is about 12 m and 14 m, respectively. The waves could propagate and develop sufficiently before reaching the model. The three-dimensional effects of waves were considered in this experiment.

2.3 *Measurement*

The time history of model acceleration response was measured by a triaxial accelerometer. This accelerometer was installed above one end of the tube, and its orientation was calibrated to align with the coordinate system illustrated in Figure 1(a) by means of an internal levelling device. The maximum range and accuracy of the accelerometer are 2.0 g and 0.3% respectively. The pull rope displacement sensor with a maximum range of 1000 mm and a sampling rate of 200 Hz was selected to measure the horizontal and vertical displacement. The 4 displacement sensors were grouped into two sets mounted on the two diagonal corners of the model. The circumferential wave pressure of the tube was obtained by 12 waterproof pressure sensors. The measurable pressure ranges from 0 to 20 kPa, the resolution accuracy is 1%, and the sampling rate is 200 Hz. The 12 pressure sensors were evenly installed in the middle of the SFT model as shown in Figure 1(b). Furthermore, the tension sensor with a maximum range of 30 kg was connected to anchor cable through stainless steel collet to monitor cable forces.

2.4 *Test conditions*

The present experimental test focuses on the dynamic response characteristics of SFT model under regular waves. The wave height and period in testing were determined based on long-term observation data of the east coast of China (Huang et al., 2021). Wave heights ranged from 0.05 to 0.1 m, while the wave period varied from 0.8 to 1.10 s. Water depth was kept constant at 2.2 m during the test, which means that the model was 0.4 m below the water surface. The incident wave propagation direction was perpendicular to the longitudinal axis of the SFT model.

The actual wave generated by the wave-making system during the test may be affected by control system errors, basin boundaries or other unknown factors. The reliability of the generated wave field should be examined first before formal test. The actual wave surface without the SFT model was measured by 2 capacitance-type wave gauges installed in the central test area of the wave-current basin. Several wave-generation experimental tests under different wave parameters were conducted, and Figure 2 illustrates the results for typical tests. The measured wave heights showed a relatively good agreement with the calculated values of linear wave theory, with an overall error of less than 3%. The two cases shown above essentially cover the wave condition in tests, including large wave heights as well as large period conditions. Consequently, the wave-current basin can generate a stable and accurate wave field satisfying the requirements of experimental test. All the regular wave parameters are detailed in Table 1.

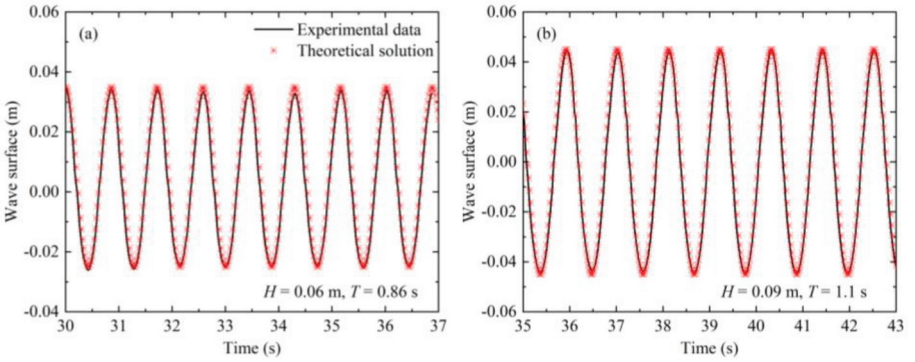


Figure 2. Comparison of regular wave between experimental data and theoretical solution.

Table 1. Regular wave parameters in the tests.

Number	H (m)	T (s)
D01 - D07	0.05	0.8, 0.86, 0.9, 0.96, 1.0, 1.06, 1.10
D08 - D14	0.06	0.8, 0.86, 0.9, 0.96, 1.0, 1.06, 1.10
D15 - D21	0.07	0.8, 0.86, 0.9, 0.96, 1.0, 1.06, 1.10
D22 - D28	0.08	0.8, 0.86, 0.9, 0.96, 1.0, 1.06, 1.10
D29 - D35	0.09	0.8, 0.86, 0.9, 0.96, 1.0, 1.06, 1.10
D36 - D42	0.10	0.8, 0.86, 0.9, 0.96, 1.0, 1.06, 1.10

3 RESULTS AND DISCUSSION

3.1 *Acceleration response*

Figure 3 illustrates the time history of acceleration response in the X, Y, and Z directions (presented in Figure 1(a)) under the wave period of 0.9 s. The longitudinal acceleration of the tube is relatively small, caused mainly by the interaction of the waves with the structure. The transverse acceleration is significantly much greater than the longitudinal acceleration and shows a cyclical pattern consistent with waves. This is primarily due to the wave propagating in the transverse direction, the transverse movement of the water points driving the movement of model. However, when the wave height is small, the curve exhibits a multi-peak phenomenon at the crest. This phenomenon is mainly caused by a combination of wave-reflected wave interactions and wave-structure interactions, indicating a typical nonlinear trend. Compared with the longitudinal and transverse directions, the variation of vertical acceleration response is more complicated. The vertical acceleration shows a multi-periodic variation pattern across the zero point in one wave period, which also indicates that the response frequency of the model in the vertical direction is greater than that in the lateral direction. The multi-peak phenomenon of transverse acceleration becomes attenuated after the wave height greater than 0.07 m, which is because the interaction between the wave and the model strengthened obviously, and it becomes the main influence on the dynamic response of the structure.

Figure 4 shows the time history of the acceleration response under the wave height of 0.08 m with different periods. Under a certain wave height, the multi-peak phenomenon of lateral acceleration weakens as increasing of period and the periodicity of vertical acceleration becomes more significant as well. The reason for this is that the wavelength

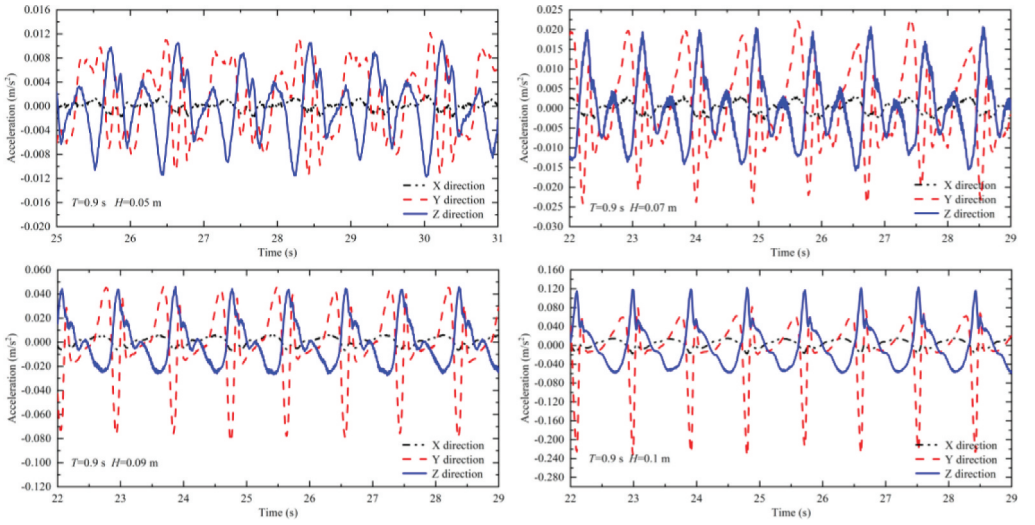


Figure 3. The time history of acceleration response for STF with different wave heights.

increases with increased period, leading to a decrease in wave steepness, which attenuates the energy dissipation of wave breaking. With the increase of wave height and wave period, the amplitude of the negative acceleration in the transverse and vertical directions gradually increases and is much larger than the positive acceleration, and the curve peak of the negative acceleration is also "sharper", which indicates that the speed of the tube changes considerably in a transient time. This is since the transverse and vertical upward movement of the tube is constrained by mooring cable. When the movement of the tube exceeds the permissible range of mooring system, the tube is subjected to a large mooring tension, and the corresponding velocity of the movement will decrease rapidly. It's worth noting that this phenomenon is consistent with the variation of anchor cable tension, which will be further discussed later in Section 3.4.

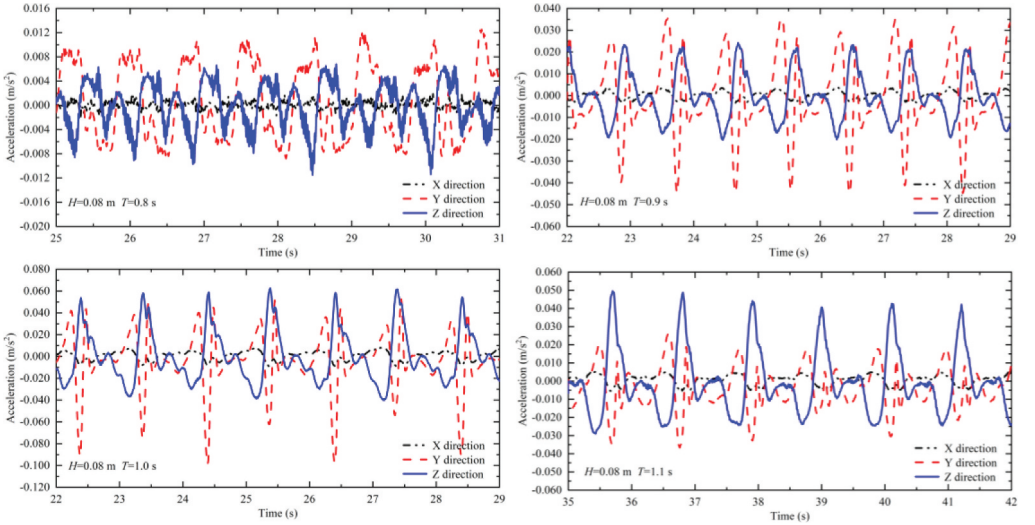


Figure 4. The time history of acceleration response for STF with different wave periods.

To further investigate the influence of wave height as well as wave period on the acceleration response, the extreme values of acceleration response for the model in X, Y and Z directions were extracted. Transverse acceleration is discussed as an example in Figure 5. As the wave height increases, the acceleration responses show a nonlinear increasing trend, indicating that the influence of wave height on the dynamic response of the model is nonlinear. Figure 5 (b) illustrates the variation of acceleration response of tube with wave period. As the period increases, the absolute value of acceleration response increases firstly and then decreases, and reaches the maximum when the wave period is of 1.0 s. The wave period indicates the relative relationship between wavelength and the lateral dimensions of the SFT model. In this test, the wave has the greatest effect on the acceleration response of the tube when the ratio of wavelength to the lateral structure dimensions is approximately 2. Among the different series of data points in Figure 5 (b), the variation of acceleration response with wave period is different in magnitude, indicating that the wave height and wave period play a reciprocal role on the motion response of the structure.

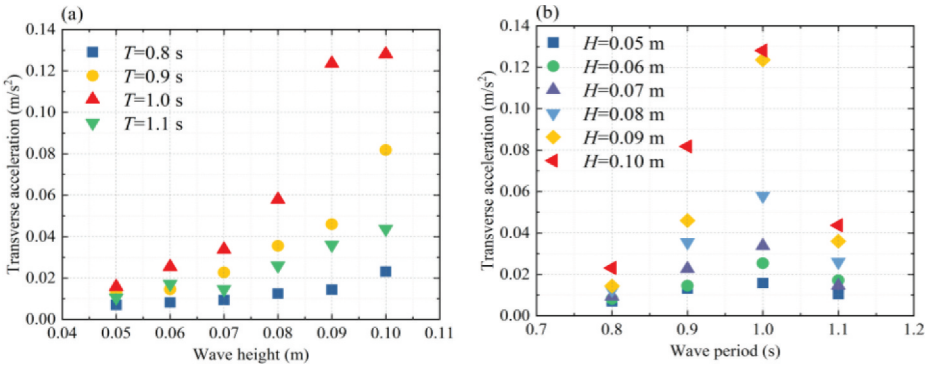


Figure 5. Variation of transverse acceleration maximum with wave height and wave period.

3.2 *Displacement response*

Figure 6 presents the variations of transverse and vertical displacement extremes of the tube with wave height under different wave periods. When the wave period is of 0.8 s, the transverse displacement roughly increases with the increasing of wave height, while the variation regularity of the vertical displacement is relatively weak. Both the vertical and transverse displacements of the tube increase with increasing wave height at wave periods of 0.9, 1.0 and 1.1 s. Meanwhile, it can be found that the vertical and transverse displacements are closer at small wave heights, and the vertical displacement is significantly larger than transverse displacement at large wave heights, indicating the wave height is more significant in influencing the vertical displacement. When the wave period is of 1.0s, i.e., the ratio of wavelength to the transverse structure dimensions is 2, the increase of the displacement for the model increases significantly. It indicates that the wave exerts a significant influence on the kinematic response of the SFT model when the ratio of the wavelength to the structural dimensions is in a certain range. To investigate the effect of wave period on transverse and vertical displacements for the tube, Figure 5 presents the variation of displacement extremes for the tube with wave period. It was found that the displacement of the tube increases firstly and then decreases as the wave period increases (except for wave heights is of 0.05 m). The variation amplitude of the displacement increases significantly when the wave height changes from 0.06 m to 0.1 m. This indicates that the effect of the ratio of wavelength to the structure size on the kinematic response of SFT is more significant at large wave heights.

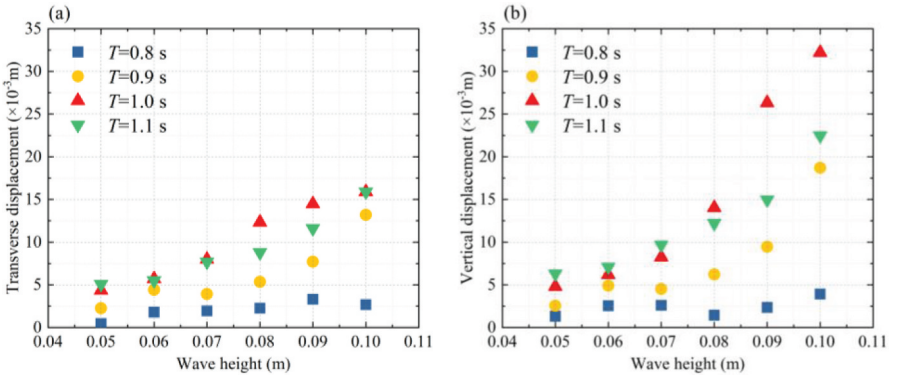


Figure 6. Variations of the displacement extremes of the SFT model with wave height.

3.3 *Wave pressure on the tube*

Taking the case of wave period of 0.8 s as an example, Figure 7 shows the variation of the point pressure at the positions P5, P7 and P9 on the surface of the tube under different wave heights. As presented in Figure 1(b), 5#, 7# and 9# are the midpoint of the wave front, the upper midpoint, and the midpoint of the back wave surface on the SFT model, respectively. As can be seen, the point pressure histories of the three positions show a relatively regular fluctuation phenomenon. Due to the difference in the pressure measurement position, resulting in the wave action time in a sequential order, there is a phase difference in the pressure time histories. The wave pressure is maximum at P5 on the wave front side of the SFT model and minimum at P9 on the leeward side, the former being influenced by both the transverse and vertical movements of the water points. The pressure of P7 at the top of the SFT model is mainly caused by the wave-induced vertical motion of the water points. As the wave height increasing, the energy of the water points increases, it enhances the wave action on the model, and the wave pressures at the three positions show a nonlinear increasing trend, as well as the pressure difference between the three positions decreases progressively. This is distinct from the linear growth trend of the theoretical values calculated using the linearization assumption, indicating the wave-structure interaction has an important effect on the wave force.

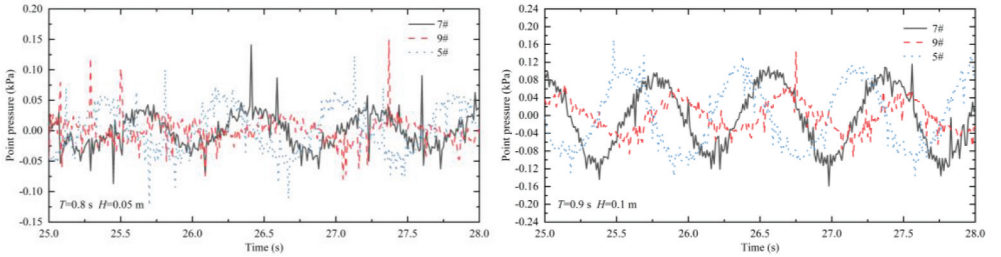


Figure 7. Variation of the point pressure at positions 5#, 7# and 9# on the surface of SFT model.

3.4 *Tension force of cables*

In this test, the anchor cables were symmetrically arranged, and the variations of cable force were comparable. In this section, the 3#~6# anchor cables (see Figure 1(a) for details) were taken as specific examples to discuss the response pattern of the cable force under regular wave. Figure 8 presents the time history of the anchor cable force when the wave height varies from 0.5 to 0.1 m at a wave period of 0.9 s. For small wave heights cases, the four anchor cables' force shows a periodic variation consistent with the wave period, and the order of magnitude for the cable

force is congruent, indicating a uniform distribution of the cable force under the cable arrangement scheme in this test. The variations of the maximum of the cable force with the wave height are given as an example for 3# and 5# anchor cables, which are shown in Figure 9. It should be noted that the measurement equipment failure in the wave height of 0.08m case, so the cable force data is missing. As the increasing of wave height, the cable force of 5# cable (side cables) increased slightly, while the cable force of 3# cable (bottom cables) increased significantly (increased about 6~8 times), and their time history exhibits obvious sharp peaks. As discussed above, with the increase of wave height, the vertical displacement of the tube increases significantly, and the transverse and vertical direction acceleration response curves exhibit obvious "sharp" peaks, when the acceleration response of the tube reaches the maximum, the force of the cables also reaches the maximum at the same time. It is revealed that the anchor cables located below the center of the tube provide most of the restraining force for the structure under large wave height, and more safety allowance is required in the design. The anchor cables located at the side of the tube also play an important role in distributing the force, although the force is smaller. This finding provides an important reference for the selection and design of anchor cable scheme and the safety design of the structure under extreme wave conditions.

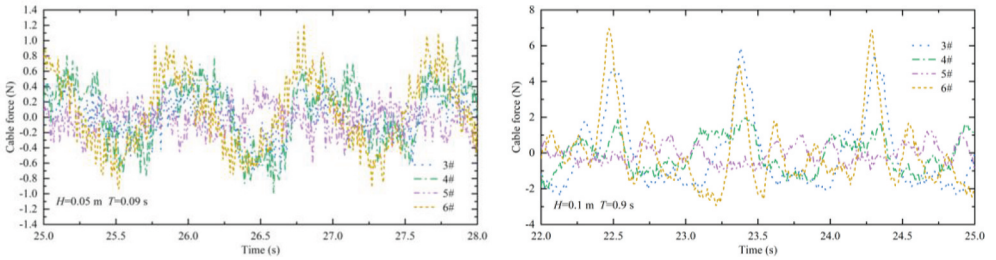


Figure 8. Time history of the anchor cable force with different the wave height.

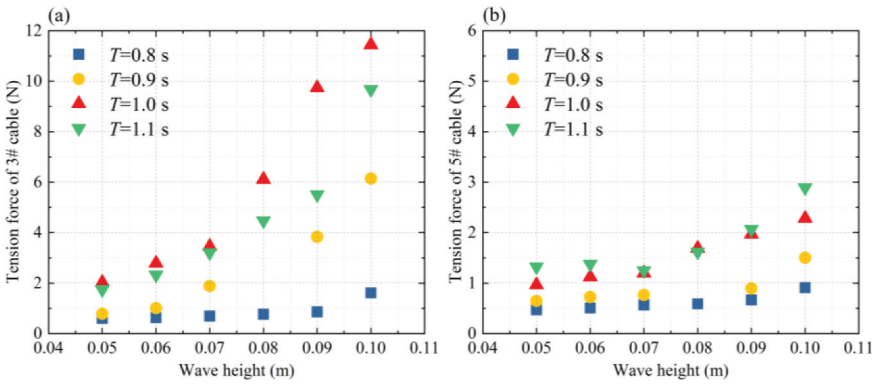


Figure 9. Variations of the maximum of the cable force for 3# and 5# anchor cables.

4 CONCLUSION

In this study, a hydrodynamic experiment of single segment SFT with a geometric scale of 1:60 was conducted based on the Qiongzhou Strait passageway SFT scheme proposed by CMCT. The influence of regular waves on the acceleration, displacement, wave pressure of tube and force of cables were investigated. The results show that:

(1) The acceleration, displacement, wave pressure of the tube and tension force of the cable exhibit a nonlinear increasing trend with the increase of wave height. The acceleration and displacement of the tube firstly increases and then decreases with the increase of wave

period. Wave height and wave period have a reciprocal effect on the kinematic response of the SFT scaled segment model.

(2) The ratio of wavelength to structure size has a significant effect on the dynamic response of SFT. In this test, the wave has a significant effect on the kinematic response of segment model when this ratio is about 2.

(3) With the increase of wave height and wave period, the tension force of the cables below the tube increases significantly and is about twice as much as that of the side anchor cables. The bottom anchor cable provides most of the restraining force for segment model, and the safety allowance for the bottom cable should be increased appropriately in design.

This study can provide an important reference for the structural selection and design of SFT. Further study should be carried out purposely for multi-segment SFT under actual oceanic conditions.

(1) In terms of structure, the influence of neighboring tube sections and boundary constraints should be considered. Special boundary devices should be used in the test to simulate the constraint stiffness. Meanwhile, the characteristics of the joints between tube sections are important factors that reflect and influence the flexible structure characteristics of multiple-segment SFT, which should be emphasized.

(2) In terms of loading conditions, numerical and experimental studies mostly focus on regular waves. However, the actual marine environment is complex, the effects of irregular waves, wave-current coupling, and the coupling of wave-current loads with other loads (impact loads, seismic loads, etc.) on the dynamic response and safety of SFT should be considered as well.

REFERENCES

Chao, C.F., Xiang, Y.Q. & Yang, C. 2016. Experiments on dynamic fluid-structure coupled responses of anchor cables of submerged floating tunnel, *Journal of Vibration and Shock*, *35(3)*, 158–163. (in Chinese)

Ding, H., Huang, B., Cheng, L., Li, K., & Ren, Q. 2024. Hydrodynamic experiment of submerged floating tunnel under regular wave and current actions during construction period. *Marine Structures*, *93*, 103508.

Hong, Y., & Ge, F. 2010. Dynamic response and structural integrity of submerged floating tunnel due to hydrodynamic load and accidental load. *Procedia Engineering*, *4*, 35–50.

Huang, B., Ren, Q., Cui, X., Wan, T., Zhang, C., Zhu, B., & Ding, H. 2021. Wave characteristics and spectrum for Pingtan Strait Bridge location. *Ocean Engineering*, *219*, 108367.

Iovane, G., Mazzolani, F. M., Landolfo, R., Begovic, E., Bilotta, E., & Faggiano, B. 2023. Assessment of experimental tests on SFT small scale specimen. *Applied Ocean Research*, *138*, 103656.

Kang, L., Ge, F., & Hong, Y. (2016). A numerical study on responses of submerged floating structures undergoing vortex-induced vibration and seismic excitation. *Procedia engineering*, *166*, 91–98.

Kunisu, H., Mizuno, S., Mizuno, Y., & Saeki, H. (1994, April). Study on submerged floating tunnel characteristics under the wave condition. In *ISOPE International Ocean and Polar Engineering Conference* (pp. ISOPE–I). ISOPE.

Martire, G., Faggiano, B., Mazzolani, F. M., Zollo, A., & Stabile, T. A. (2010). Seismic analysis of a SFT solution for the Messina Strait crossing. *Procedia Engineering*, *4*, 303–310.

Oh, S.H., Park, W. S., Jang, S.C., Kim, D. H., & Ahn, H. D. 2013. Physical experiments on the hydrodynamic response of submerged floating tunnel against the wave action. In *7th International Conference on Asian and Pacific Coasts, APAC 2013* (pp. 582–587). APAC.

Seo, S. I., Sagong, M., & Son, S. W. 2015. Global response of submerged floating tunnel against underwater explosion. *KSCE Journal of Civil Engineering*, *19*, 2029–2034.

Sun, S.N., & Chen, J.Y. 2008. Hydro dynamic pressure on seabed anchored submerged floating tunnel with oblique incidence of plane P-wave, *Journal of Harbin Institute of Technology*, *40(8)*, 1292. (in Chinese)

Tariverdilo, S., Mirzapour, J., Shahmardani, M., Shabani, R., & Gheyretmand, C. 2011. Vibration of submerged floating tunnels due to moving loads. *Applied Mathematical Modelling*, 35(11), 5413–5425.

Xiang, Y.Q., Lin, H., & Chen, Z.Y. 2018. Dynamic response analysis of submerged floating tunnel under moving load. *Vibration and impact*, *37(4)*, 82–87. (in Chinese)

Yuan, Z., Man-sheng, D., Hao, D., & Long-chang, Y. 2016. Displacement response of submerged floating tunnel tube due to single moving load. *Procedia engineering*, *166*, 143–151.

Bridge Maintenance, Safety, Management, Digitalization and Sustainability – Jensen, Frangopol & Schmidt (eds)
© 2024 The Author(s), ISBN 978-1-032-77040-6
Open Access: www.taylorfrancis.com, CC BY-NC-ND 4.0 license

Numerical simulation of motion response of submerged floating tunnel under wave action

H.B. Jiang, H.D. Zhao & W.D. Chen
The State Key Laboratory of Coastal and Offshore Engineering, Dalian University of Technology, Dalian, People's Republic of China

P.Z. Lin
State Key Laboratory of Hydraulics and Mountain River Engineering, Sichuan University, Chengdu, Sichuan, China

B. Ren
The State Key Laboratory of Coastal and Offshore Engineering, Dalian University of Technology, Dalian, People's Republic of China

ABSTRACT: This paper presents the numerical simulation of the dynamic response of a long-span submerged floating tunnel under wave action. A numerical model for solving the motion of an elliptical cross-section tunnel is established using the commercial software Ansys. The tunnel structure is simulated using multi-point constrained beam elements, and the wave loads are computed using the Morison equation. The hydrodynamic coefficients of the elliptical cross-section are determined using a three-dimensional FDM-VBF-VOF hydrodynamic model that captures the effects of cross-sectional shape. The numerical calculations were conducted to analyze the motion response characteristics of the submerged floating tunnel under the action of different incident wave periods and wave heights. The numerical results indicate a significant correlation between the amplitude of tunnel motion and the structural natural frequency: the closer the incident wave frequency to the structural natural frequency, the greater the amplitude of structural motion.

1 INTRODUCTION

The Submerged Floating Tunnel (SFT) is an innovative marine transport facility characterized by its low environmental impact, stable operation, and consistent costs that remain relatively unaffected by variations in water width and depth. It is suitable for crossing deep and long straits. However, owing to the unique characteristics of its environment, boundary conditions, load capacity, and structural dynamics, the dynamic response of the SFT is very complex, involving the nonlinear interactions of waves, currents, the tunnel structure, anchors, and boundaries. The associated research encompasses nonlinear wave mechanics, vortex dynamics, fluid-structure coupling mechanics, and structural dynamics, among other multidisciplinary fields, so it has become a research hotspot in recent years. (Zhang et al., 2021; Iovane et al., 2023; Xu et al., 2023).

Limited by the development of technology, present model experiments and CFD research of SFT mainly focus on short-span or truncated models. Chen et al. (2023) experimentally studied the motion characteristics of a twin-circular SFT under wave actions. They found when the incident wave frequency was close to twice the natural frequency of the structure, the resonant sway motion with half of the incident wave frequency and a large amplitude would be excited, so they suggested that this resonance phenomenon should be avoided in the design of the structure. The hydrodynamic characteristics of SFT are closely related to its cross-section shape (Li et al., 2018;

DOI: 10.1201/9781003483755-123

Zou et al., 2020). Mandara et al. (2016) compared the dynamic response characteristics of circular and elliptical cross-section SFT for different flow velocities using the Abaqus FSI co-simulation tool. The results show that the elliptical cross-section has better hydrodynamic characteristics. Therefore, this manuscript focuses on the study of SFT with elliptical cross-section.

It is difficult to study the dynamic response characteristics of large-span SFT by experiment and three-dimensional CFD simulation. Therefore, to study the motion response of a large-span elliptical cross-section SFT under the action of regular waves, the Ansys mechanical module is used for structural mechanical analysis and finite element analysis, and the Morrison equation is used to simulate the wave action. The hydrodynamic coefficients of the elliptical cross-section are determined using a three-dimensional FDM-VBF-VOF hydrodynamic model that captures the effects of cross-section shape.

2 NUMERICAL MODEL

2.1 *Ansys numerical model*

The governing equations of dynamics for the structure are described as:

$$[\mathbf{M}]\{\ddot{\boldsymbol{\xi}}\} + [\mathbf{C}]\{\dot{\boldsymbol{\xi}}\} + [\mathbf{K}]\{\xi\} = \{\mathbf{F}\} \tag{1}$$

where [**M**] is the mass matrix; [**C**] is the Rayleigh damping matrix; [**K**] is the stiffness matrix; $\{\ddot{\xi}\}$is the acceleration vector; $\{\dot{\xi}\}$is the velocity vector; [**ξ**] is the displacement vector; {**F**}is the hydrodynamic load vector.

The Newmark-β scheme is used for the time advancements of Equation (1) and the Newton–Raphson technique is adopted for the sub-iteration at each incremental step. The incremental equations for the n+1th incremental step are given as:

$$\begin{aligned} \dot{\xi}_i^{n+1} &= \dot{\xi}_i^{n} + (1-\gamma)\ddot{\xi}_i^{n}\Delta t + \gamma\ddot{\xi}_i^{n+1}\Delta t \\ \xi_i^{n+1} &= \xi_i^{n} + \dot{\xi}_i^{n}\Delta t + \left(\frac{1}{2}-\beta\right)\ddot{\xi}_i^{n}\Delta t^2 + \beta\ddot{\xi}_i^{n+1}\Delta t^2 \end{aligned} \tag{2}$$

where n denotes the time step, the coefficient γ denotes the weight of the effect of the initial and final accelerations on the change in velocity, and the coefficient β denotes the weight of the contribution of the initial and final accelerations to the change in displacement.

2.2 *The FDM-VBF-VOF numerical model*

Based on the fluid-structure interaction model proposed by Wang et al. (2022) and Wang et al. (2023), the incompressible Navier-Stokes equations are adopted as the governing equations for the fluid flow, which are numerically discretized by the finite difference method (FDM). The virtual boundary force (VBF) method proposed by Lin et al. (2016) is used to deal with the boundary conditions at the fluid-solid interface. The volume of fluid (VOF) method is used to capture the water-air interface. The numerical model has been used to investigate the vortex-induced vibration of a circular cylinder with two degrees of freedom (Zhao et al., 2023). The relevant formulas are given as follows:

$$\begin{aligned} \frac{\partial u_i}{\partial x_i} &= 0 \\ \frac{\partial u_i}{\partial t} + u_j\frac{\partial u_i}{\partial x_j} &= -\frac{1}{\rho_f}\frac{\partial p}{\partial x_i} + \nu\frac{\partial^2 u_i}{\partial x_j \partial x_j} + f_{\mathrm{VBF}} \end{aligned} \tag{3}$$

$$\frac{\partial F}{\partial t} + \frac{\partial (u_i F)}{\partial x_i} = 0 \tag{4}$$

where u_i is the fluid velocity in the x_i direction (i, j=1,2 for the x and y directions in the Cartesian coordinate system), t is time, p is pressure, f_{VBF} denotes the momentum forcing term when imposing the no-slip boundary condition on the immersed boundary, and F represents the volumetric fraction between the air and water, which equals to 0 in air and 1 in water.

2.3 *The Morison equation*

The wave force, calculated by Morison's equation, consists of two components: the drag force and the inertia force. Considering the relative motion of the structure to the water, the expression is as follows:

$$f_i = C_d \frac{\rho_w}{2} D(u_i - \dot{\xi}_i)\left|u_i - \dot{\xi}_i\right| + \rho_w \frac{\pi D^2}{4}\frac{\partial u_i}{\partial t} + C_{m0}\rho_w \frac{\pi D^2}{4}\left(\frac{\partial u_i}{\partial t} - \ddot{\xi}_i\right) \tag{5}$$

where f_i is the wave force acting on the cylinder with unit length; ρ_w is the density of water; D is the diameter of the cylinder; u_i is the velocity of the water parcel; C_d is the drag coefficient, C_{m0} is the additional mass coefficient, and C_m=1+C_{m0} is the coefficient of inertia force coefficient. There are no suitable reference specifications and formulas yet for hydrodynamic coefficients of elliptical cross-sections, so C_d and C_m are calculated by a three-dimensional FDM-VBF-VOF hydrodynamic model that captures the effects of cross-sectional shape.

3 NUMERICAL SIMULATION SETUP

Considering the influence of wave nonlinearity and structural nonlinearity, the numerical calculations were conducted to analyze the motion response characteristics of the SFT under the action of different incident wave periods and wave heights (T=6s-26s, H=9m). The main simulation parameters are listed in Table 1. The damping ratio of the structure is set to 0.8%.

Since Ansys does not provide elliptical pipe elements, and the hollow beam elements are unable to differentiate between internal and external media (which leads to a change in the buoyancy/weight ratio and hydrodynamic force), we propose a composite beam modeling method in which the interior of an elliptical cross-section hollow beam is filled with another elliptical cross-section beam without mass and stiffness, as shown in Figure 1.

Give the structure an initial displacement, and let it vibrate freely in the water, after the free decay test, we can get the horizontal first-order natural frequency is 0.154 Hz, and vertical first-order natural frequency is 0.295 Hz. The vertical natural frequency is about 2 times the horizontal natural frequency.

Table 1. Test parameters.

Parameter	Symbols	Value	Unit
Water depth	h	100	m
Submergence depth	d_m	45	m
Buoyancy to weight ratio	BWR	1.3	/
Length	l	13000	m
Cross-section dimension of external beam	$a_1 \times b_1$	40×15	m
Density of the external beam	ρ_1	4354	kg/m^3
Young's modulus of external beam	E_1	4.20E+10	Pa
Cross-section dimension of internal beam	$a_2 \times b_2$	38×13	m
Density of the internal beam	ρ_2	0	kg/m^3
Young's modulus of internal beam	E_2	10	Pa
Inclination angle of mooring line	α	60	°
Installation angle of mooring line	β	60	°
Stiffness of mooring line	k	3.5E+8	N/m
Spacing of mooring lines	s	100	m

4 RESULTS AND DISCUSSION

4.1 *The hydrodynamic coefficient*

The hydrodynamic coefficient is calculated as follows:

(1) When the structure is fixed, the Equation (5) is simplified as:

$$f_i = C_d \frac{\rho_w}{2} D u_i |u_i| + C_m \rho_w \frac{\pi D^2}{4} \frac{\partial u_i}{\partial t} \tag{6}$$

(2) The theoretical wave force $f_c(i)$ is obtained by the Morrison equation, where the expressions for velocity and acceleration are from linear wave theory. The equations for velocity and acceleration in the horizontal and vertical directions are given below:

$$\begin{aligned} u_y &= \frac{\partial \phi}{\partial y} = \frac{gkA}{\omega} \frac{\cosh k(z+d)}{\cosh kd} \text{ and } \frac{\partial u_y}{\partial t} = gkA \frac{\cosh k(z+d)}{\cosh kd} \\ u_z &= \frac{\partial \phi}{\partial z} = \frac{gkA}{\omega} \frac{\sinh k(z+d)}{\cosh kd} \text{ and } \frac{\partial u_z}{\partial t} = gkA \frac{\sinh k(z+d)}{\cosh kd} \end{aligned} \tag{7}$$

(3) The sum of error squares between the wave force $f_m(i)$ and $f_c(i)$ calculated by the FDM-VBF-VOF numerical model is:

$$Q = \sum_{i=1}^{n} [f_c(i) - f_m(i)]^2 \tag{8}$$

(4) By the least square method, the hydrodynamic coefficients C_d and C_m can be obtained from $\frac{\partial Q}{\partial C_d} = \frac{\partial Q}{\partial C_m} = 0$.

Using the above method, the hydrodynamic coefficients of the elliptical cross-section under two wave conditions in this study are obtained, as shown in Table 2. It can be seen that the vertical inertia force coefficient is about 2.7 times that of the horizontal inertia force coefficient, which is consistent with the ratio of the elliptical long axis to short axis; the inertia force coefficients increase slightly with the increase of the period, C_{my}=1.2~1.3 and C_{mz}=3.2~3.5; Since the drag force accounts for the small percentage of the total wave force, the drag coefficient solution is poorly accurate, as shown in Figure 2. According to Kunisu (2010), inertial forces play a dominant role when the K_C number is less than 15 (K_C=$u_m T/D$, where u_m is the maximum velocity of the water parcel at the center of the model). The range of K_C numbers involved in this study is 0.012-2.17, so the effect of drag force is ignored in the subsequent study, and C_{my} took a mean value of 1.25 and C_{mz} took a mean value of 3.35.

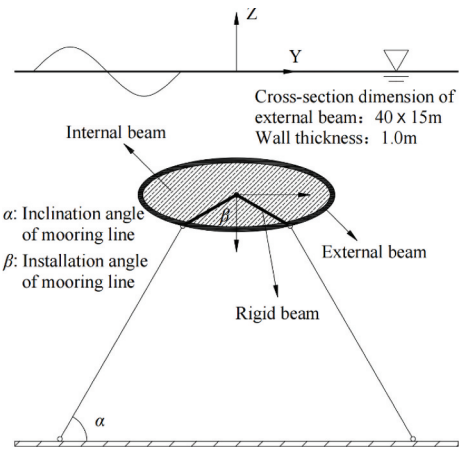


Figure 1. Schematic diagram of composite ellipse section.

Table 2. The hydrodynamic coefficient.

Wave condition	C_{my}	C_{mz}	C_{dy}	C_{dz}
H=9m, T=9s	1.2	3.2	/	19.8
H=9m, T=12s	1.3	3.5	/	7.7

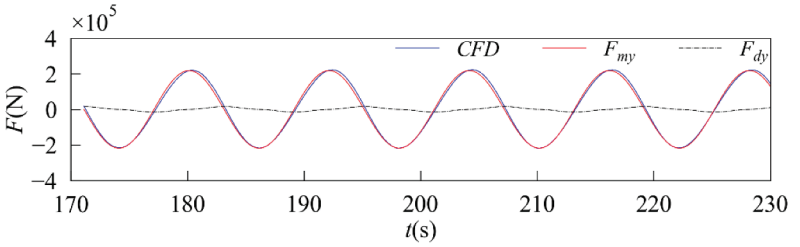


Figure 2. Comparison of total wave force, drag force and the inertia force at H=9m, T=12s.

4.2 *Response amplitude of the SFT*

Figure 3 and Figure 4 show the horizontal and vertical displacement distribution of the tunnel at H=9m, T=7.3s, respectively. It can be seen that the tunnel vibrates in a first order mode in both the horizontal and vertical directions, with the maximum displacement in the midspan.

Figure 5 and Figure 6 depict the time histories of horizontal and vertical displacement in the quarter span and midspan of the tunnel at H=9m, T=7.3s, respectively. It can be seen that the horizontal and vertical displacement amplitudes gradually increase to a fixed value with time. In addition, all other cases in this study also vibrate in first order mode, so in the following analysis, we focus on the displacement in the midspan of the tunnel.

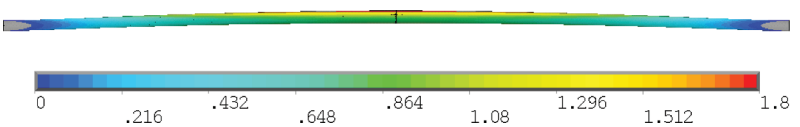


Figure 3. Horizontal displacement distribution of the tunnel at H=9m, T=7.3s (magnified 20 times).

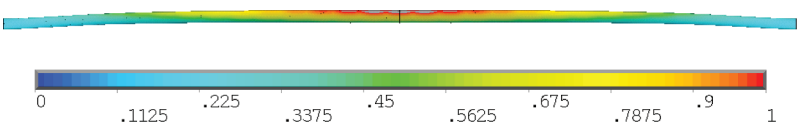


Figure 4. Vertical displacement distribution of the tunnel at H=9m, T=7.3s (magnified 100 times).

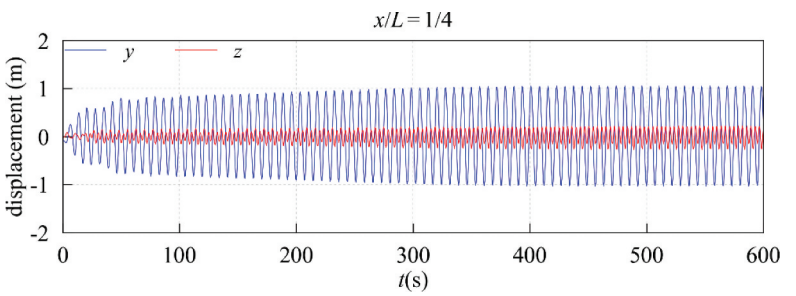


Figure 5. Time history of horizontal and vertical displacement in the quarter span of the tunnel at H=9m, T=7.3s.

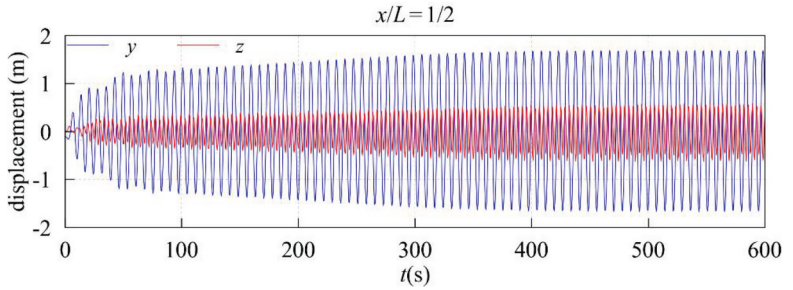


Figure 6. Time history of horizontal and vertical displacement in the midspan of the tunnel at H=9m, T=7.3s.

Figure 7 shows the variation of maximum horizontal and vertical displacements of the SFT with dimensionless wave frequency. It can be found that when the incident wave frequency is close to the horizontal natural frequency of the SFT, the horizontal resonance motion of the tunnel is excited, and the horizontal and vertical displacements of the SFT reach the maximum values of 1.68m and 0.6m, respectively; when the incident wave frequency is close to half of the horizontal natural frequency of the SFT, the parametric resonance of the tunnel is excited, and the horizontal and vertical displacements of the SFT reach the peak values of 0.93m and 0.2m, respectively.

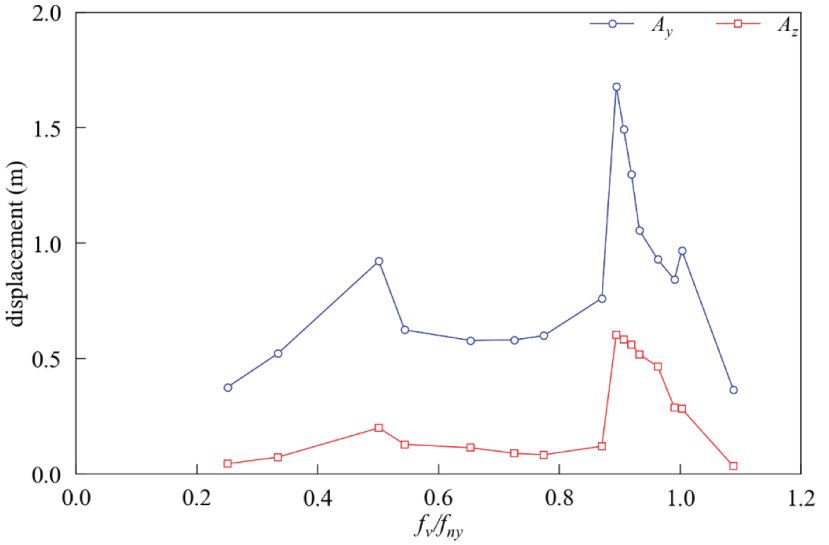


Figure 7. Variation of maximum horizontal and vertical displacements of the SFT with wave frequency.

4.3 *Response frequency of SFT*

Figure 8 demonstrates the variation of the horizontal and vertical response frequencies of the SFT with dimensionless wave frequency. It can be seen that the main horizontal response frequency of the SFT is consistent with the wave frequency. The vertical response frequency of the SFT is twice the wave frequency in the range of f_v/f_{ny}=0.87-1.0 (T=6.5s-7.5), while outside of this range, the main vertical response frequency of the SFT is consistent with the wave frequency. It is also worth noting that the structure does not have a single response frequency and that only the frequency with the largest amplitude is shown in the figure.

Figure 9 shows the horizontal and vertical response frequency amplitude spectrum at two cases. It can be seen that the movement of the structure has many frequency components, including wave frequency and multiple wave frequency. This is because both the nonlinearity of waves and the nonlinearity of structures are considered.

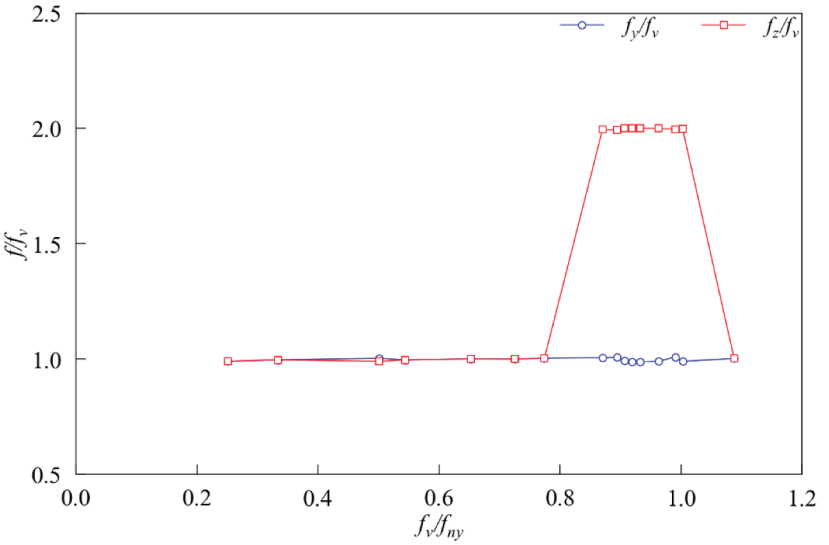


Figure 8. Variation of SFT response frequency with wave frequency.

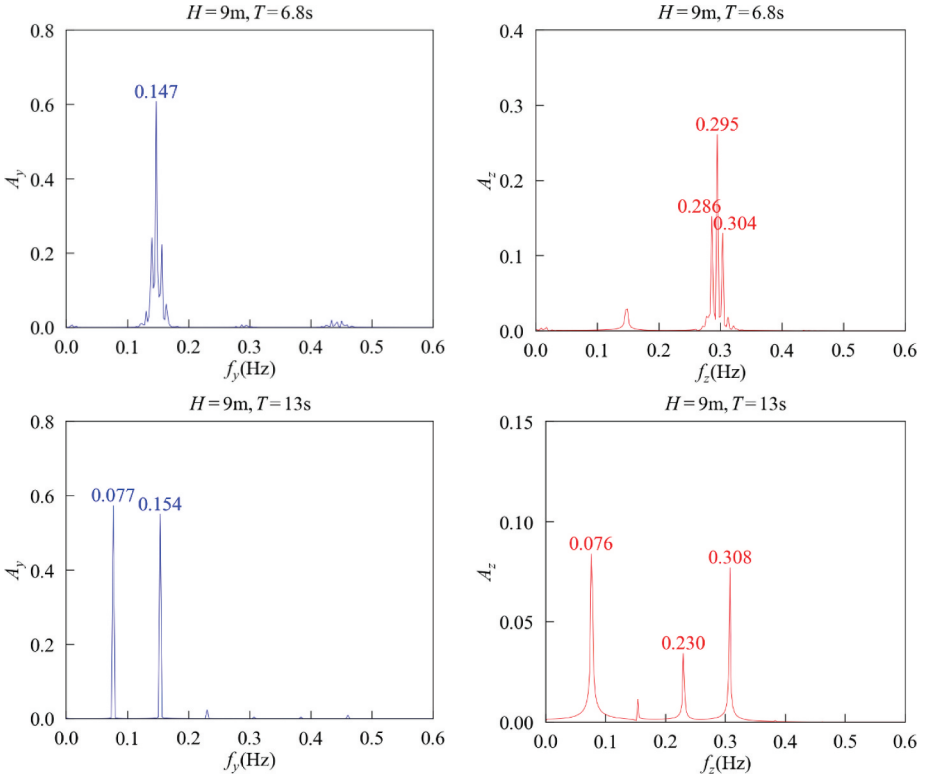


Figure 9. Horizontal and vertical response frequency amplitude spectrum.

5 CONCLUSION

Considering the influence of wave nonlinearity and structural nonlinearity, numerical calculations were conducted to analyze the motion response characteristics of the SFT under the action of different incident wave periods and wave heights. The main findings are summarized as follows:

(1) When the incident wave frequency is close to the horizontal natural frequency of the SFT, the horizontal resonance motion of the SFT is excited, and the horizontal and vertical displacements of the SFT reach the maximum values of 1.68m and 0.6m, respectively.
(2) When the incident wave frequency is close to half of the horizontal natural frequency of the SFT, the parametric resonance of the SFT is excited, and the horizontal and vertical displacements of the SFT reach the peak values of 0.93m and 0.2m, respectively.
(3) The main horizontal response frequency of the SFT is consistent with the wave frequency. The vertical response frequency of the SFT is twice the wave frequency in the range of f_v/f_{ny}=0.87-1.0 (T=6.5s-7.5), while outside of this range, the main frequency of the vertical response of the SFT is consistent with the wave frequency.

ACKNOWLEDGMENTS

This work was funded by the National Natural Science Foundation of China. [Grant Number 52031002 and Number 51979028].

REFERENCES

Chen, W., Wang, C., Ren, B. & Lin, P., 2023. Experimental study of the motion characteristics of a twin-circular submerged floating tunnel under wave actions. Ocean Eng. 288, 116114.

Iovane, G., Mazzolani, F.M., Landolfo, R., Begovic, E., Bilotta, E. & Faggiano, B., 2023. Assessment of experimental tests on SFT small scale specimen. Appl. Ocean Res. 138, 103656.

Li, Q., Jiang, S. & Chen, X., 2018. Experiment on pressure characteristics of submerged floating tunnel with different section types under wave condition. Pol Marit Res. 25(s3), 54–60.

Lin, P., Cheng, L. & Liu, D., 2016. A two-phase flow model for wave–structure interaction using a virtual boundary force method. Comput. Fluids. 129, 101–110.

Mandara, A., Russo, E., Faggiano, B. & Mazzolani, F.M., 2016. Analysis of fluid-structure interaction for a submerged floating tunnel. Procedia Engineering. 166, 397–404.

Wang, C., Ren, B. & Lin, P., 2022. A coupled flow and beam model for fluid–slender body interaction. J. Fluid. Struct. 115, 103781.

Wang, C., Lin, P. & Ren, B., A numerical model for simulation of two-phase flows interaction with flexible slender bodies, Phys. Fluids 35(12) (2023).

Xu, W., Ma, Y., Liu, G., Li, M., Li, A., Jia, M., He, Z. & Du, Z., 2023. A review of research on tether-type submerged floating tunnels. Appl. Ocean Res. 134, 103525.

Zhang, H., Yang, Z., Li, J., Yuan, C., Xie, M., Yang, H. & Yin, H., 2021. A global review for the hydrodynamic response investigation method of submerged floating tunnels. Ocean Eng. 225, 108825.

Zhao, H., Ding, H., Wang, C., Li, K., Wang, G. & Ren, B., 2023. Vortex-induced vibration at low Reynolds numbers: vortex shedding modes transitions. Ocean Eng. 288, 115931.

Zou, P., Bricker, J., Uijttewaal & W., 2020. Optimization of submerged floating tunnel cross-section based on parametric bézier curves and hybrid backpropagation - genetic algorithm. Mar. Struct. 74, 102807.

Bridge Maintenance, Safety, Management, Digitalization and Sustainability – Jensen, Frangopol & Schmidt (eds)
© 2024 The Author(s), ISBN 978-1-032-77040-6
Open Access: www.taylorfrancis.com, CC BY-NC-ND 4.0 license

Modeling of two-dimensional water motion field during a seaquake

V. Maugeri, L. Martinelli & F. Perotti
Department of Civil and Environmental Engineering, Politecnico di Milano, Milan, Italy

ABSTRACT: This study investigates seaquake phenomena, analyzing the role of P-waves in generating seismic waves in water. Different modeling approaches for understanding the dynamic water motion during seaquake are addressed and one-dimensional P-wave propagation in the frequency domain is compared to two dimensional propagation models in frequency and time domain. The comparison is specifically carried out for structures like Submerged Floating Tunnels focusing on the effect of water depth, self-damping and resonance on the water motion field. The two dimensional propagation model in frequency domain is extended to account for a non-flat seabed. The results obtained are critically compared to the ones delivered by a time domain approach utilizing a Finite Element discretization and exploiting the Domain Reduction Method for soil-structure interaction analysis.

1 INTRODUCTION

Seaquake phenomena are associated to seismic events that occur beneath the oceanic Earth's crust. These can generate significant energy release, resulting in the propagation of seismic waves throughout the surrounding water.

Among the various types of seismic waves, P-waves (primary, or compressional, waves) play an essential role in seawater propagation. Understanding their behavior and characteristics is crucial for various applications, since the derived motion field is fundamental to assess the potential impact on submerged and floating structures.

The present work aims to offer a first contribution concerning the knowledge of the dynamic water motion field during a seaquake, comparing different modelling methodologies. The problem is tackled in two dimensions, both in time and frequency domain, and compared to one-dimensional vertical propagation of P waves in frequency domain, i.e. to the most frequent approach adopted in practical applications. This comparison is of great interest for long structures, as Submerged Floating Tunnels are.

The frequency domain solution is further updated by removing the hypothesis of flat seabed, assuming that the soil-water interface follows a piece-wise constant profile.

The resulting water motion field is first examined for resonance phenomena, observing the dependence on water depth and self damping. Then, the results are critically compared against those coming from the time domain approach, which are based on the use of Finite Elements and implementation in ABAQUS (Dassault Systèmes Simulia Corp. 2022) of the soil-structure interaction analysis technique called Domain Reduction Method (Bielak et al. 2003).

2 TWO DIMENSIONAL FREQUENCY-DOMAIN MODEL

The model developed in this chapter aims to reproduce, in two dimensions, the water motion field due to seaquake events. The equations used to represent compressive waves propagation are based on (Wang et al 2004) theory; this model is here used to analyze the effects of porous seabed on dynamic pressures of ideal fluid under the action of P waves, deriving the water motion field in terms of a displacement potential. In the present study, the porous medium

DOI: 10.1201/9781003483755-124

(which represents the overlying sediment to the seabed) considered by (Wang et al. 2004) is neglected and an ideal fluid (water) is directly in contact with the underlying elastic bedrock.

The model accounts for both the inclination of the incident wave at the water-bedrock interface, and the contribution provided by S waves propagation into the soil medium. The ground motion is expressed through its vertical and horizontal components.

The formulation can address the case of multiple layers, each with its own governing equations.

The first layer, representing the linear elastic bedrock, uses Lamé-Navier's equation derived from elastodynamics equilibrium. The second layer, ideal compressible water, assumes compressible seismic wave propagation, neglecting S-waves due to an ideal fluid assumption. Water damping, crucial for realistic motion outcomes, is assumed as linear hysteretic damping; in such model dissipation is independent of excitation frequency and affects the P-wave velocity in seawater by introducing an imaginary part proportional to the non-dimensional damping coefficient.

2.1 *Flat seabed model*

In the simplest case, the water is directly in contact with the flat semi-infinite elastic bedrock. A plane P-wave hits the interface between the bedrock and the water with an incidence angle θ and an angular frequency ω. A transmitted P wave propagates initially upward through water, while reflected P and S wave propagate downward in the elastic half-space. The P waves which propagate upward are then reflected on the free surface, generating a downward propagating P wave.

The wave number k_x in x direction is the same due to Snell's Law in all layers, while k_{wz}, in z direction, changes depending on the layer properties.

Starting from the scalar and vector displacement potentials, φ_s and ψ_s, for the elastic bedrock ($z<0$), and the scalar displacement potential φ_w for the water ($z>0$) defined as in Wang et al., the following vertical and horizontal components of the water motion field are obtained:

$$\xi_{wz}(x,z,t,\omega) = ik_{wz}\left[-A_{lP1}e^{i(\omega t-k_x x-k_{wz}z)} + A_{lP2}e^{i(\omega t-k_x x+k_{wz}z)}\right] \tag{1}$$

$$v_{wz}(x,z,t,\omega) = \omega k_{wz}\left[A_{lP1}e^{i(\omega t-k_x x-k_{wz}z)} - A_{lP2}e^{i(\omega t-k_x x+k_{wz}z)}\right] \tag{2}$$

$$a_{wz}(x,z,t,\omega) = i\omega^2 k_{wz}\left[A_{lP1}e^{i(\omega t-k_x x-k_{wz}z)} - A_{lP2}e^{i(\omega t-k_x x+k_{wz}z)}\right] \tag{3}$$

$$\xi_{wx}(x,z,t,\omega) = -ik_x\left[A_{lP1}e^{i(\omega t-k_x x-k_{wz}z)} + A_{lP2}e^{i(\omega t-k_x x+k_{wz}z)}\right] \tag{4}$$

$$v_{wx}(x,z,t,\omega) = \omega k_x\left[A_{lP1}e^{i(\omega t-k_x x-k_{wz}z)} + A_{lP2}e^{i(\omega t-k_x x+k_{wz}z)}\right] \tag{5}$$

$$a_{wx}(x,z,t,\omega) = i\omega^2 k_x\left[A_{lP1}e^{i(\omega t-k_x x-k_{wz}z)} + A_{lP2}e^{i(\omega t-k_x x+k_{wz}z)}\right] \tag{6}$$

In Equations 1-6 ξ_w, v_w, a_w denote the displacement, velocity and acceleration in water, ω is the angular frequency of the incident wave, i is the imaginary unit, t is the time, while A_{lP1}, A_{lP2} are unknown constant coefficients representing waves amplitude, respectively related to transmitted and reflected P waves in the water. Wave numbers k, with their components along x and z directions, depend on wave propagation velocities in each medium. The unknown amplitudes are determined through the imposition of the following boundary conditions: equilibrium of fluid pressure at the water free surface, compatibility of normal displacements at bedrock-water interface, equilibrium of normal and tangential stresses at the bedrock-water interface.

2.2 *Rising bedrock model*

The model can be further improved, varying the water depth through a piece-wise constant function, which approximates the water depth to a constant value in each finite length in which the domain is subdivided. In this way, the system is solved for each portion of the

domain, calculating the contribution of that portion to the adjacent water columns, which can show different depths.

In this case, the unknown amplitudes A_{lP1}, A_{lP2} are functions of the global coordinate x, defining the location of P-wave source along the longitudinal domain of the bedrock. In fact, these parameters are evaluated by solving the system for each water depth in which the specific ground portion is defined, leading to different results.

2.3 *Two-dimensional development of the problem*

Integration of the results in Equation 1-6 along the entire longitudinal dimension x of the problem is necessary to recover the overall motion field across the entire water domain, considering that each portion of the water-seabed interface represents a source of spherically propagating P-waves, which gives its contribution in terms of motion field in a generic point P of the water domain.

At each seabed point the earthquake motion can be expressed starting from the direct PSD of the ground motion components. The spatial variability of the ground motion is introduced through a coherency function, allowing to define the Cross Power Spectral Densities (CPSD). Once the ground motion is known at each ground site in terms of PSDs and CPSDs, it is possible to superimpose the results. The contributions in the generic point P provided by each infinitesimal source having x_p and z_p as horizontal and vertical distance respectively from the point P is obtained, simplifying the problem, subdividing the horizontal domain into N_P portions having δ_x length. In addition, each portion is assumed to be characterized by a constant value in x of the PSDs and CPSDs (the average value). For example, the overall water vertical velocity is given by

$$v_{wz,tot}(x_P, z_P, \omega) = \sum_{i=1}^{N_P} \left\{ \omega k_{wz} \left[A_{lP1} e^{i\left(-k_x x_P^i - k_{wz} z_P\right)} - A_{lP2} e^{i\left(-k_x x_P^i + k_{wz} z_P\right)} \right] \right\} \delta_x \tag{7}$$

3 2D TIME-DOMAIN MODEL

As explained in Chapter 2.2, introducing a varying water depth by means of a frequency-domain formulation results to be a complex task. An alternative way to model the wave propagation phenomenon in a two-dimensional domain is to study it in time-domain. In the following a two-dimensional seaquake model developed in the ABAQUS Finite Element (Dassault Systèmes Simulia Corp. 2022) code is proposed, characterized by the implementation of a state-of-the-art method to perform soil-structure interaction analyses. A comparison with the results coming from frequency-domain model is then performed.

3.1 *Semi-unbounded medium and seismic force definition*

Two main aspects need to be investigated to well represent wave propagation in Finite Elements in a semi-unbounded medium: the identification of the domain in which the soil-structure interaction (SSI) analysis has to be performed, and the selection of proper boundary conditions for the selected domain. Wave propagation between soil and seawater is a fluid-structure interaction problem, in which the soil must be elsewhere truncated. In fact, the model should be able to simulate the dissipation of energy occurring when an outgoing wave approaches the infinitely extending boundaries of the modeled domain, preventing any spurious reflection towards the domain of interest. This fluid-structure interaction system can be interpreted as a soil-structure-interaction problem, in which the water behaves like a structure.

There are different methodologies to perform soil-structure interaction analyses. In general terms, these methods differ for the extension of the modeled domain, the necessity of employing specific boundary conditions, and the way in which input forces are included in the model.

In (Lysmer and Kuhlemeyer 1969) viscous boundaries are introduced to absorb outgoing incident waves. This boundary condition is the one selected to develop the following analyses. Note that, on practical grounds, the required elements are already implemented in ABAQUS under the name of infinite elements (4 nodes CINPE4). It is also worth noting that many studies, such as the one of (Kontoe et al. 2007), demonstrated that their functionality highly depends on the SSI

technique used for the analysis. In fact, when they are used alone on the side boundaries of a simple direct method, they fail to reproduce free-field response and lead to serious inaccuracy of the response in the near field. By contrast, the same study shows that, when these standard viscous boundaries are combined with an innovative SSI scheme such as the Domain Reduction Method (DRM), originally formulated in (Bielak et al. 2003), and implemented in the present work, their efficiency significantly improves. This is because the DRM procedure allows the dashpots to be located at a sufficient distance from the excitation source, thus reducing the energy to be transmitted to the scattered energy only, deriving from the structure.

The DRM allows to define the seismic forces in the model through a set of effective nodal forces P^{eff}. These forces are defined in two layers of nodes: ${P_b}^{eff}$ corresponds to nodal forces on an inner boundary Γ, while ${P_e}^{eff}$ are defined in Γ_e, which is the surface (boundary) externally adjacent to Γ:

$$P^{eff} = \begin{bmatrix} {P_i}^{eff} \\ {P_b}^{eff} \\ {P_e}^{eff} \end{bmatrix} = \begin{bmatrix} 0 \\ -M_{be}^{\Omega^+} \ddot{u}_e^0 - K_{be}^{\Omega^+} u_e^0 \\ M_{eb}^{\Omega^+} \ddot{u}_b^0 - K_{eb}^{\Omega^+} u_b^0 \end{bmatrix} \tag{8}$$

where M and K denote mass and stiffness matrices, the subscripts e, and b, refer to nodes in either the exterior boundary Γ_e or on the inner boundary Γ, respectively. The superscripts Ω and Ω^+ refer to the domains over which the various matrices are defined. Specifically, Ω is the inner domain containing the geological feature of interest (i.e. water), which is separated by Γ from Ω^+ that represents the truncated semi-infinite exterior domain. Finally, u^0 and $\ddot{u}^0$ represent the free-field within motion in terms of displacement and acceleration respectively.

The developed time-domain model relies on a fully automated implementation of the DRM in ABAQUS. This implementation technique relies on an additional hypothesis on the evaluation of free-field motion, that is evaluated assuming vertical propagating waves. Thanks to this assumption, free-field motion determination is performed by a deconvolution analysis, which is provided by the software STRATA (Kottke et al 2009). These motion components are automatically extracted, read, and manipulated through a MATLAB (The MathWorks, Inc. 2022) preprocessing module, where effective nodal forces are evaluated through Equations 8, using structural matrices directly exported from ABAQUS. Once the effective earthquake forces are evaluated, they are included in the ABAQUS main model through a further manipulation of the input file, where parts of the input script, defining amplitude and location of each nodal force, are directly written by another MATLAB code.

3.2 *Soil modeling*

The soil part is defined as a 2D planar deformable body, and the material is modeled as homogeneous, isotropic, linear elastic and composed by only one infinite layer, extending in vertical and horizontal directions. The identified parameters to model the soil are listed in Table 1:

Table 1. Mechanical parameters of soil in ABAQUS.

E	ν	λ	μ	ρ	v_p	v_S
Pa	-	*Pa*	*Pa*	*kg/m³*	*m/s*	*m/s*
1.1489e+09	0.3	6.6283e+08	4.4189e+08	1000	902.25	482.26

Regarding the criteria for meshing the domain, two types of elements are used in the model. The ones inside the domain's boundaries are linear plane strain elements with reduced integration (CPE4R), belonging to the family of solid continuum elements. The elements on the boundaries are 4-node infinite elements (CINPE4) reproducing the unlimited extension of the domain. Regarding the interaction between soil and fluid, the applied modeling technique is the surface-based tie constraint, which links the relative motion between the two parts by simply defining a master-slave surface pair.

3.3 *Water modeling*

In general, to model water material, two requirements are necessary: first, the material must have zero or negligible shear stiffness, such that the propagation of shear waves is prevented; second, the material must be characterized by a volumetric module such that the propagation speed of compressive waves is comparable to the real one. In this model, two options are employed and compared. The first alternative is represented by equation of state (EOS) materials, which are specific type of materials available in Abaqus/Explicit (Dassault Systèmes Simulia Corp. 2006a). They provide a hydrodynamic material in which the pressure is defined as a function of the density and the internal energy, whereas its volumetric strength is determined by an equation of state. The parameters s, c_0, and Γ_0 are the input constants to define the material behavior in ABAQUS. The literature offers enough information about the selection of these parameters. In ABAQUS benchmarks (Dassault Systèmes Simulia Corp. 2006b, 2006c) the constants s and Γ_0 are set to zero whereas c_0 is selected such that the elastic bulk modulus ($K = \rho_0 c_0^2$) is reduced to well represent sloshing phenomenon, with a value c_0 = 30 ÷ 50 *m/s*. However, since the task of this study is to properly represent the wave propagation problem, the elastic wave velocity is set to the real one (c_0 = 1483 *m/s*), therefore the volumetric stiffness is 2.2 *GPa*. Concerning the dynamic shear viscosity, a value of $\eta_v = 13e^{-4}$ $Pa \cdot s$ is chosen to be consistent with the values suggested in ABAQUS benchmarks. Finally, the mass density is set to 1000 kg/m^3.

The second method arises from Kuznetsov works (Shugan et al 2021), in which the author proposes to model water by quasi-elastic medium with small Young's modulus and large Poisson's ratio. In fact, by setting a very high value for the Poisson's ratio close to the limit 0.5, and accordingly reducing the Young's modulus, it is possible to obtain a material with the same volumetric stiffness of the water and a negligible shear modulus.

Regarding the identification of meshing elements, in all the mentioned modeling techniques, the water is composed by first order plain strain elements CPE4R, as the soil. However, as suggested by ABAQUS Manual (Dassault Systèmes Simulia Corp. 2006b, 2006c), the hourglass scaling factor is set to 25.

3.4 *Meshing techniques and mesh size selection*

To properly capture the wave propagation behavior in a discretized domain, the domain discretization must comply with the Courant-Friedrichs-Lewy (CFL) (Moura et al 2013) limitation. In the present case, assuming a maximum excitation frequency of 25 *Hz*, and considering the maximum and minimum wave velocities associated to water and soil respectively, the largest allowed mesh size is about 2.4 m. However, to be conservative and to guarantee a proper resolution even when higher frequencies occur, the mesh size is furtherly reduced to have a uniform value of Δx = 1 m.

Finally, it is important to mention that the techniques used to model the water material must be supported by a specific ABAQUS remeshing function called Arbitrary Lagrangian-Eulerian adaptive meshing (ALE) in order to maintaining a high-quality mesh throughout an analysis, even when large deformation or loss of material occur. The developed FE model follows the indications coming from Abaqus manual (Dassault Systèmes Simulia Corp. 2006b, 2006c) and Buccino's work (Buccino 2019) in this respect.

4 NUMERICAL RESULTS

Numerical results are first analyzed for the frequency-domain models, where the flat seabed and the rising bedrock models are compared with the one-dimensional analytical model provided by Hamamoto (Hamamoto 1995). Eventually, the proposed frequency-domain flat seabed model is then compared to the time-domain ones for both water modeling techniques, under the simplifying assumption of vertical propagating waves, which actually makes the frequency-domain model one-dimensional ($\theta = 0°$).

The bedrock depth assumed in this analysis starts from 40 *m* for x = 0 *m*, it increases by 28.5 *m* every δ_x = 100 *m*, reaching the maximum value of 325 *m* in correspondence of x =

1000 m, and it remains constant along the following 3000 m; finally, the seabed arises symmetrically to the other bank for the remaining kilometer. Overall, the horizontal length is 5000 m. The geometry is schematically represented in Figure 1.

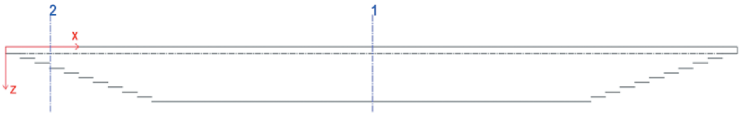


Figure 1. Reference sections for the comparison of frequency-domain models.

Bedrock elastic parameters are defined by Lamè constants λ = 76 983.35 $10^6 Pa$ and μ = 51 750 $10^6 Pa$, whereas material density is ρ = 2200 kg/m^3. To define the earthquake motion at a single point, Kanai-Tajimi PSD modified by Clough and Penzien (Clough and Penzien 1995) has been adopted. In addition, the parameters characterizing the PSD are the ones evaluated by Martinelli (Martinelli et al 2011) to minimize the difference between the consequent pseudo-acceleration response spectrum RS_a and the one prescribed by Eurocodes . The adopted coherency function is the one by Luco and Wong one (Luco and Wong 1987).

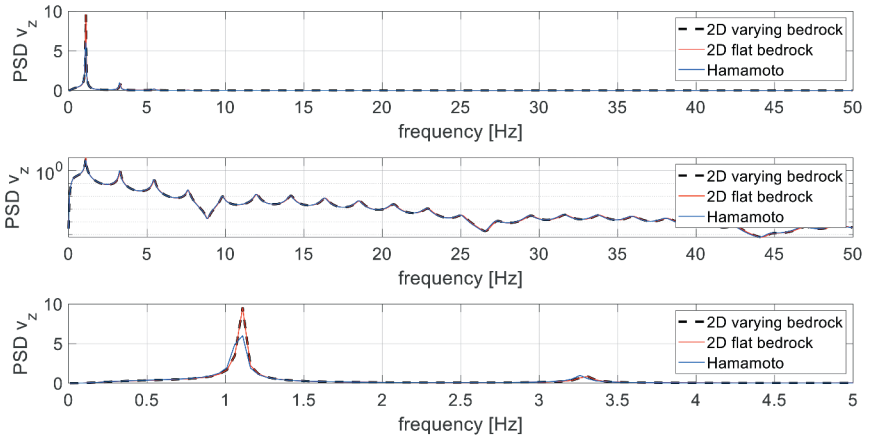


Figure 2. Section 1, 40m depth from water free surface. Comparison of the three frequency-domain models, in terms of vertical velocity PSD.

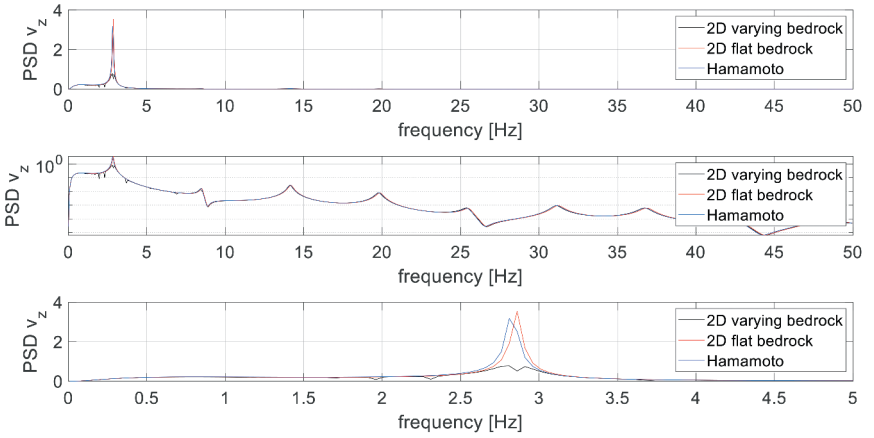


Figure 3. Section 2, 40m depth from water free surface. Comparison of the three frequency-domain models, in terms of vertical velocity PSD.

The results are reported in terms of vertical velocity power spectral densities at 40 m below the water free surface, for two sample sections (Figure 2 and Figure 3).

As it can be observed, for Section 1 both the two-dimensional models are characterized by a slightly amplified response with respect to the one-dimensional Hamamoto model, especially at the water resonance frequency 1.1 *Hz*. Furthermore, as it was expected in this case, flat-seabed and varying-seabed cases lead to the same results, since the Section 1 is located on the symmetry axis of the system, which is characterized by a large portion of flat seabed.

By contrast, for Section 2 the two-dimensional models diverge in their outcomes, especially at frequencies below 5 *Hz*. In fact, while the flat-seabed model is characterized by a slightly amplified response with respect to the one-dimensional Hamamoto model at the first water resonance frequency, the varying-seabed model leads to much less pronounced amplitudes, with relevant reduction of the response at the first water resonance frequency. This kind of destructive interference occurring in the varying seabed case can be appreciated by looking at the small-scale plot of Figure 3. This behavior can be attributed to the space discretization of the system. In fact, by analyzing the frequencies at which those rifts occur, it can be recognized that they correspond to the natural frequencies of the adjacent discretized water columns.

Concerning the horizontal velocity component, which is not reported in the figures, it is characterized by the same resonance frequencies of the vertical component, with an amplitude that is about 20% of the vertical one.

For models in time domain, the reference ground motion supplied to STRATA for obtaining the "within" free-field motion is an outcrop sinusoidal vertical acceleration with an amplitude of 1 m/s^2, frequency of 7.5 *Hz* and duration of 20 *s*. Furthermore, a baseline correction is performed throughout the whole 20 seconds of simulation, to guarantee null residual displacements at the end of the analysis. The geometry is the one depicted in Figure 4 with $\beta = 45°$, and the resulting vertical acceleration is reported for the set D of nodes above the inclined seabed portion in Figure 5.

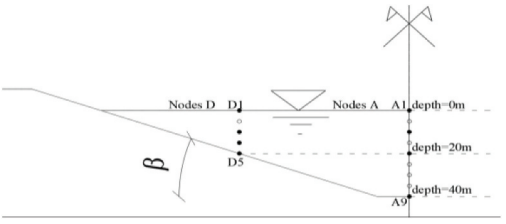


Figure 4. Nodes for motion evaluation in time-domain models.

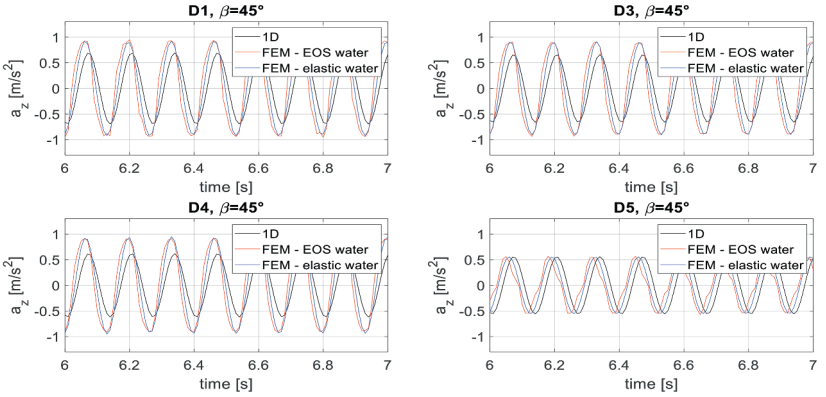


Figure 5. Nodes D: vertical acceleration from t=6s to t=7s, seismic force at 7.5Hz, β=45°.

As it can be noticed, results provided by frequency-domain analysis at corresponding depths have some common aspects to the ones given by ABAQUS models. When the water is

modeled as EOS material, small scale plots highlight high frequency components appearing in the solution, while large scale plots show modulation in time. Nodes located above the inclined portion of the seabed, present some relevant differences in the results with respect to the one-dimensional case, for both water modelling techniques. Nodes located above the flat portion of the seabed (not shown in this work), present results very similar to the frequency-domain case for both water modelling techniques. Regarding horizontal components, which are not reported in the figures, they present the same high frequency components and modulation in time; in addition, higher horizontal accelerations are observed in the vicinity of the coast.

5 CONCLUSIONS

The present research work analyzes the dynamic water motion field during a seaquake using different modelling methodologies. The problem is tackled in two dimensions, both in time and frequency domain, and compared to one-dimensional vertical propagation of P waves in frequency domain.

The results presented show the effect of using a 2D propagation model versus a 1D one and of removing the hypothesis of flat seabed, assuming that the soil-water interface follows a piece-wise constant function.

Comparison of results obtained in time domain from a FE model point out how all the frequency domain models can be used for prediction of the water motion if the seabed is substantially flat; the results, however, substantially differ near the shore where the FE modeling approach highlights the occurrence of higher horizontal accelerations.

REFERENCES

Bielak, J. Loukatis, K. Hisada, Y & Yoshimura. C. 2003. Domain Reduction Method for Three-Dimensional Earthquake Modeling in Localized Regions, Part I: Theory. *Bulletin of the Seismological Society of America* 93: 817–824.

Buccino, G. Guerini, C. & Perotti, F. 2019. A case study for sloshing phenomenon in a cylindrical tank under seismic events: numerical modeling and comparison with current regulations. *Advances in Engineering Materials. Structures and Systems*.

Clough, R. W. & Penzien, J. 1995. *Dynamics of Structures*. Computers & Structures.

Dassault Systèmes Simulia Corp. 2006a. 17.9.1 Equation of State. *ABAQUS Analysis User's Manual*.

Dassault Systèmes Simulia Corp. 2006b. 1.11.7 Water sloshing in a pitching tank. *ABAQUS Benchmark's Manual*.

Dassault Systèmes Simulia Corp. 2006c. 12.1.14 Water sloshing in a baffled tank. *ABAQUS Benchmark's Manual*.

Dassault Systèmes Simulia Corp. 2022. *ABAQUS/CAE 2022.*

Hamamoto, T. 1995. Stochastic fluid-structure interaction of large circular floating islands during wind waves and seaquakes. *Probabilistic Engineering Mechanics*.

Kontoe, S. Zdravkovic, L. Potts, D. M. & Salandy, N. E. 2007. The use of absorbing boundaries in dynamic analysis of soil-structure interaction problems. *4th International Conference on Earthquake Geotechnical Engineering*.

Kottke, A. R. & Rathje E. M. 2009. *Technical Manual for Strata*. PEER Report 2008/10 Pacific Earthquake Engineering Research Center College of Engineering University of California, Berkeley.

Shugan, I. Kuznetsov, S. Saprykina, Y. & Chen Y. 2021. Physics of Traveling Waves in Shallow Water Environment. *Water* 13(21).

Lysmer, J. & Kuhlemeyer, R. L. 1969. Finite Dynamic Model for Infinite Media. *Journal of the Engineering Mechanics Division of the ASCE* 859–877.

Luco, J. E. & Wong, H. L. 1987. Seismic response of foundations embedded in layered half-space. *Earthquake Engineering & Structural Dynamics* 15: 233–247.

Martinelli, L. Barbella, G. & Feriani, A. 2011. A numerical procedure for simulating the multi-support seismic response of submerged floating tunnels anchored by cables. *Engineering Structures* 33 2850–2860.

Moura, C. A. d. & Kubrusly, C. S. 2013. *The Courant–Friedrichs–Lewy (CFL) Condition*. Birkhauser.

The MathWorks, Inc. 2022. *MATLAB R2022a and Statistics Toolbox*. Natick.

Wang, J. Zhang, C. & Jin, F. 2004. Analytical solutions for dynamic pressures of coupling fluid-soil-porous medium due to P wave incidence. *Earthquake engineering and engineering vibration* 3.

Bridge Maintenance, Safety, Management, Digitalization and Sustainability – Jensen, Frangopol & Schmidt (eds)
© 2024 The Author(s), ISBN 978-1-032-77040-6
Open Access: www.taylorfrancis.com, CC BY-NC-ND 4.0 license

Analysis of hydroelastic response of a SFT based on the Discrete-Module-Beam method

C. Ji, Y.Q. Chen, X.T. Zhang & X. Li
State Key Laboratory of Ocean Engineering, Shanghai Jiao Tong University, Shanghai, China
SJTU Sanya Yazhou Bay Institute of Deepsea Technology, Sanya, China

K. Li, D. Zhong & Zhou
China Merchants Chongqing Communications Technology Research & Design Institute Co., Ltd., Chongqing, China

ABSTRACT: SFT is a super large floating structure with huge horizontal scale and low structural stiffness, the dynamic response of which can not be calculated according to the rigid body hypothesis. Under the framework of the Discrete-Module-Beam (DMB) method, the hydroelastic behavior of a fixed horizontal hollow tube body that is completely submerged under the action of different regular waves is investigated. In the DMB method, the floating elastic structure is divided into a sufficient number of rigid bodies connected by beam elements. These bodies are equivalent to mass nodes with mass concentrated at the center of gravity and bearing all the loads acting on the submodules. The hydroelastic response of the SFT is obtained based on the potential flow theory and the Morison equation, respectively. The results show that the two modeling methods can both accurately calculate the hydroelastic response of the underwater suspended tunnel in their applicable ranges.

1 INTRODUCTION

Submerged floating tunnels (SFTs), also known as Archimedes Bridges, are new structures designed to cross long distances in deep water. Compared with bridges or immersed tube tunnels, SFTs have better environmental adaptability, greater crossing capacity, lower construction costs, and do not block water traffic. For this reason, they are attractive to academic and engineering circles. SFT is one type of very large floating structure, whose horizontal size is on the order of kilometers, and is much larger than the vertical size, therefore the deformation of the tunnel under wave excitation cannot be ignored. Therefore, the hydroelastic method, which takes into account the coupling effect of fluid and structural deformation, is used to analyze the dynamic response of SFTs under the action of waves (Price et al, 1985).

Several methods were proposed for the hydroelastic analysis of very large floating structures, among which the mode superposition method (Newman, 1994) and the direct coupling method (Das et al, 2012) are the most widely used. The mode superposition method analyzes all necessary elastic modes and superimposes all modes together to obtain the hydroelastic response (Fu et al, 2007). The three-dimensional finite element (FEM) method is usually used to determine the mode and natural frequency. When the structure has complex geometry and connection features, it is slightly difficult to determine the best mode combination. Another method is to combine finite element structural dynamics simulation with 3D hydrodynamic time-domain tools, called the direct coupling method. Its advantages are that it does not need to calculate mode characteristics in advance, can introduce nonlinearity in the time domain, and can simulate complex structural shapes. However, this method is very time-consuming.

DOI: 10.1201/9781003483755-125

In recent years, Lu et al. have proposed a simpler hydroelastic theory called the Discrete Module Beam (DMB) method (Lu et al, 2019). The method divides the elastic body into multiple rigid bodies connected by beam elements. With a sufficient number of elastic-connected rigid bodies being divided, the DMB method can solve the hydroelastic problem without predetermining the elastic mode of the structure and is more suitable for solving the dynamic response of very large floating structures with complex connection forms. Compared with the direct coupling method, the computational efficiency of the DMB method is greatly improved. In addition, Zhang et al. extended its application to complex structural shapes through finite element simulation, where the stiffness of the complex structure is converted to the stiffness of the equivalent beam (Zhang et al, 2019). Jin et al. established a time-domain coupled simulation model to study the hydroelastic behavior of SFT under the random wave and earthquake excitation (Jin et al, 2021).

The purpose of this paper is to extend the DMB method to the hydroelastic analysis of SFTs and to verify this method by comparing it with Jin's research work (Jin, 2022). In the framework of the DMB method, potential flow theory and the Morison method are used respectively to solve the hydroelastic response of an underwater suspended tunnel with fixed ends.

2 BASIC THEORY

2.1 *Potential flow theory*

The DMB method is used to predict the hydroelastic response of the suspended tunnel model, as shown in Figure 1. First, the whole structure is simplified into a hollow cylinder structure and divided into several sub-modules along the length direction. The mass matrix $\mathbf{M}$, the hydrostatic restoring force matrix $\mathbf{C}$, the additional mass matrix $A(\omega)$, the damping matrix $\mathbf{B}(\omega)$, and the wave exciting force matrix $\mathbf{F}_E$ of the multi-body structure are further solved. With the finite element method, the stiffness matrix of the whole structure is assembled according to the structural stiffness matrix of each beam element, and the external load is fully defined on the center of mass of each submodule. Euler-Bernoulli beams and Saint-Venant distortion theory interpret the elastic behavior of beam elements. According to the force balance of nodes, the motion equation in the frequency domain is constructed to calculate the displacement of each mass node:

$$\left[-\omega^2(\mathbf{M}+\mathbf{A}(\omega))-i\omega\mathbf{B}(\omega)+(\mathbf{C}+\mathbf{K}_{st})\right]\xi=\mathbf{F}_E \tag{1}$$

where $\mathbf{M}$ is the mass matrix of concentrated masses, $\mathbf{K}_{st}$ is the stiffness matrix of the total structure and ξ is the displacement matrix of concentrated masses.

The two ends of the SFT model are set as fixed boundary conditions by modifying the stiffness matrix of the beam elements at both ends. If both ends of beam element e are connected to the concentrated mass i and j, then the relationship between the structural deformation forces $\mathbf{F}_{st}^{i}$ and $\mathbf{F}_{st}^{j}$ at both ends of the beam element and the displacements ξ_i and ξ_j of the two concentrated masses is:

$$\begin{bmatrix}\mathbf{F}_{st}^{i}\\ \mathbf{F}_{st}^{j}\end{bmatrix}=-\begin{bmatrix}\mathbf{k}_e^{(i,i)} & \mathbf{k}_e^{(i,j)}\\ \mathbf{k}_e^{(j,i)} & \mathbf{k}_e^{(j,j)}\end{bmatrix}\begin{bmatrix}\xi_i\\ \xi_j\end{bmatrix} \tag{2}$$

where $\mathbf{k}_e^{(i,i)}$, $\mathbf{k}_e^{(i,j)}$, $\mathbf{k}_e^{(j,i)}$and $\mathbf{k}_e^{(j,j)}$ are the submatrices of the structural stiffness matrix $\mathbf{k}_e$ of beam element e. It is worth noting that for the beam elements located at both ends, the structural deformation force at the endpoints is zero.

After restoring the displacement of the mass node, a subelement f between the node r at any position and its adjacent concentrated mass node i is established on each beam element, and the stiffness matrix of the subelement is solved. The structural force and displacement of any node are restored by solving equations (3)-(5):

$$\begin{bmatrix} \mathbf{F}_{st}^{i} \\ \mathbf{F}_{st}^{j} \end{bmatrix} = -\begin{bmatrix} \mathbf{k}_{e,f}^{(i,i)} & \mathbf{k}_{e,f}^{(i,r)} \\ \mathbf{k}_{e,f}^{(r,i)} & \mathbf{k}_{e,f}^{(r,r)} \end{bmatrix} \begin{bmatrix} \xi_i \\ \xi_r \end{bmatrix} \tag{3}$$

$$\xi_r = \left(\mathbf{k}_{e,f}^{(i,r)}\right)^{-1} (\mathbf{F}_{st}^{i} - \mathbf{k}_{e,f}^{(i,i)} \xi_i) \tag{4}$$

$$\mathbf{F}_{st}^{r} = \mathbf{k}_{e,f}^{(r,i)} \xi_i + \mathbf{k}_{e,f}^{(r,r)} \left(\mathbf{k}_{e,f}^{(i,r)}\right)^{-1} (\mathbf{F}_{st}^{i} - \mathbf{k}_{e,f}^{(i,i)} \xi_i) \tag{5}$$

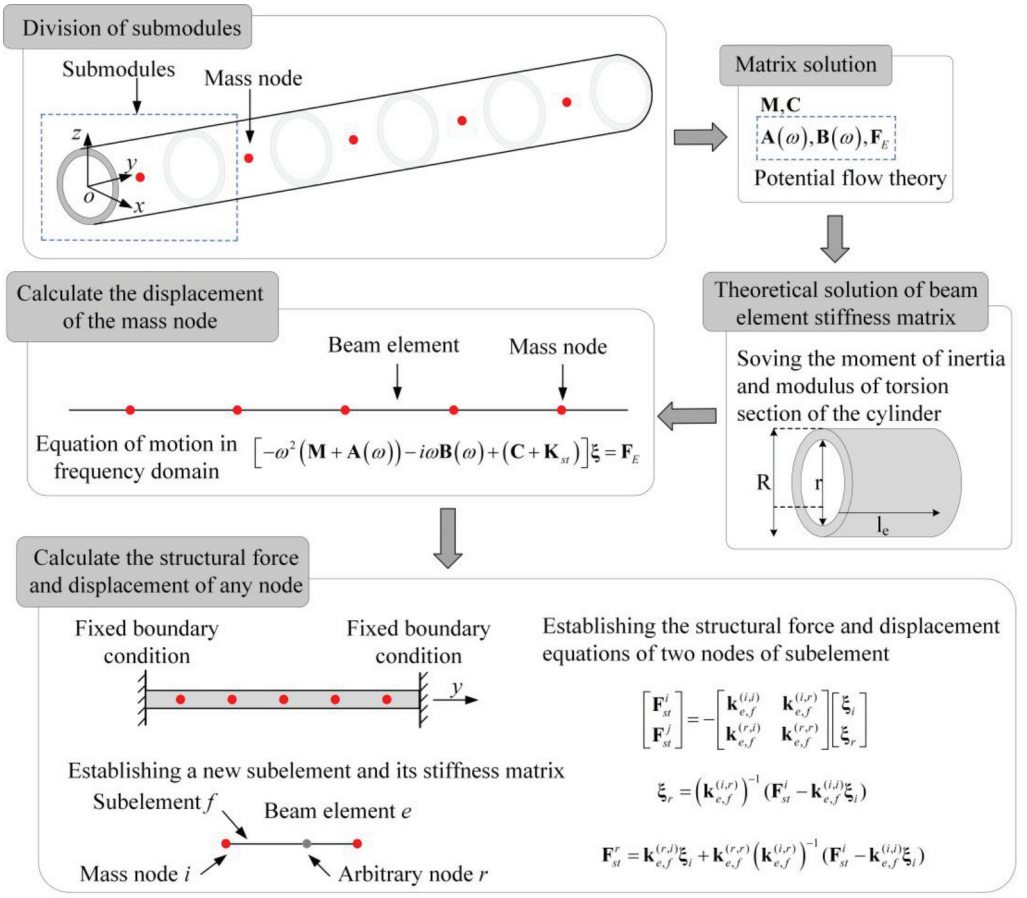


Figure 1. The steps of calculating the hydroelastic response by the DMB-potential flow method.

2.2 *Morison method*

The diameter D of the tube body of SFTs is generally not more than 25m, and the wavelength L of the design wave is about 160 m. When D/L is less than 0.2, the effect of wave diffraction can be ignored and the Morison equation, which only considers the viscosity and inertia of water, is adopted. In this paper, the method combined with DMB and Morison formula is used to predict the hydroelastic response of the suspended tunnel model, as shown in Figure 2:

The velocity of water particle in the horizontal and vertical directions:

$$u = \frac{\pi H}{T}\frac{\cosh(k(z+d))}{\sinh(kd)}\cos(kx-\omega t)$$
$$v = \frac{\pi H}{T}\frac{\sinh(k(z+d))}{\sinh(kd)}\sin(kx-\omega t) \tag{6}$$

Acceleration of water particle in horizontal and vertical directions:

$$\dot{u} = \frac{2\pi^2 H}{T^2}\frac{\cosh(k(z+d))}{\sinh(kd)}\sin(kx-\omega t)$$
$$\dot{v} = \frac{2\pi^2 H}{T^2}\frac{\sinh(k(z+d))}{\sinh(kd)}\cos(kx-\omega t) \tag{7}$$

where H is the wave height, T is the wave period, d is the water depth, k is the wave number, ω is the wave frequency and y is the coordinate of SFT along the axis.

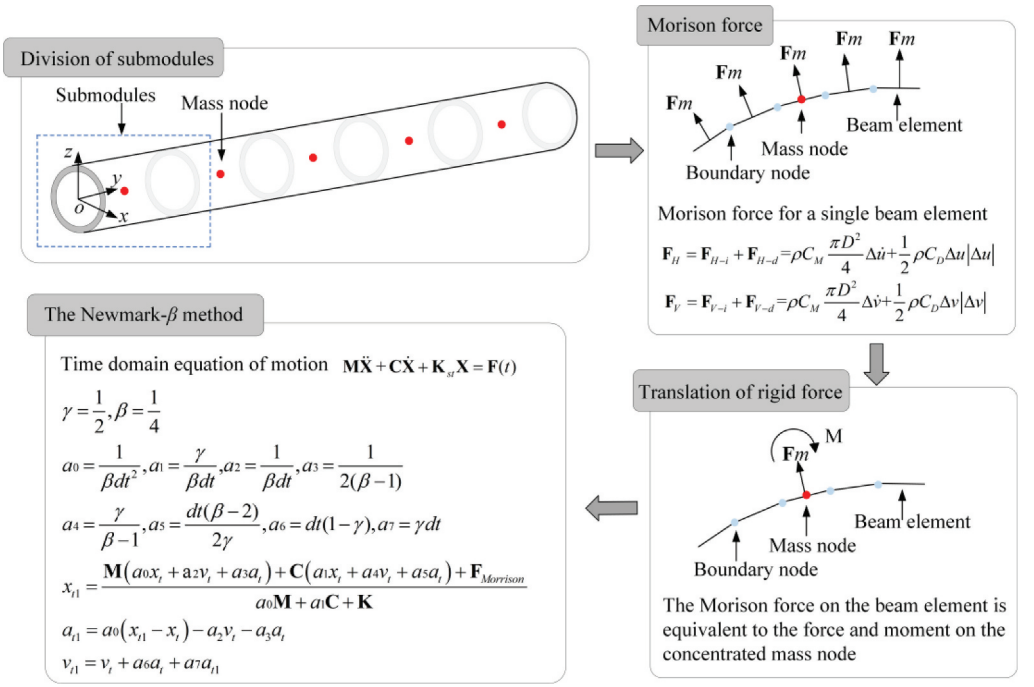


Figure 2. The steps of calculating the hydroelastic response by the DMB-Morison method.

The Morison force on the beam element is calculated by the velocity and acceleration of the water quality point at the midpoint of the axis of each beam element:

$$\mathbf{F}_{H-d} = \frac{1}{2}\rho C_D D u|u| = \frac{\rho C_D D\pi^2 H^2}{2T^2} e^{\frac{4\pi z}{L}}\left(\frac{\cosh(k(z+d))}{\sinh(kd)}\right)^2 \cos(kx-\omega t)|\cos(kx-\omega t)| \tag{8}$$

$$\mathbf{F}_{H-i} = \rho C_M \frac{\pi D^2}{4}\dot{u} = \frac{\rho C_M D^2\pi^3 H}{2T^2} e^{\frac{2\pi z}{L}}\left(\frac{\cosh(k(z+d))}{\sinh(kd)}\right)\sin(kx-\omega t) \tag{9}$$

$$\mathbf{F}_H = \mathbf{F}_{H-i} + \mathbf{F}_{H-d} \tag{10}$$

$$\mathbf{F}_{V-d} = \frac{1}{2}\rho C_D D v|v| = \frac{\rho C_D D\pi^2 H^2}{2T^2} e^{\frac{4\pi z}{L}}\left(\frac{\cosh(k(z+d))}{\sinh(kd)}\right)^2 \sin(kx-\omega t)|\sin(kx-\omega t)| \tag{11}$$

$$\mathbf{F}_{V-i} = \rho C_M \frac{\pi D^2}{4} \dot{v} = \frac{\rho C_M D^2 \pi^3 H}{2T^2} e^{\frac{2\pi z}{L}} \left(\frac{\cosh(k(z+d))}{\sinh(kd)}\right) \cos(kx - \omega t) \tag{12}$$

$$\mathbf{F}_V = \mathbf{F}_{V-i} + \mathbf{F}_{V-d} \tag{13}$$

Each submodule is divided into several beam elements and the force and moment of each are calculated by the Morison equation, which are equivalent to those on the concentrated mass of the corresponding submodule according to the translation theorem of rigid force.

The dynamic response of the structure is calculated by solving the structural dynamic balance differential equation:

$$\mathbf{M}\ddot{\boldsymbol{X}} + C\dot{\boldsymbol{X}} + \mathbf{K}_{st}\mathbf{X} = \mathbf{F}(t) \tag{14}$$

The Newmark-β method was used to iteratively solve displacement, velocity and acceleration, as shown in Figure 2.

3 MODEL LAYOUT AND VALIDATION

3.1 *Model layout*

Jin (2022) explored the hydroelastic characteristics of a completely submerged horizontal hollow cylinder under different regular waves with the DMB method and compared the settlement results of the potential flow theory method with the frequency domain and the Morison method based on the time domain.

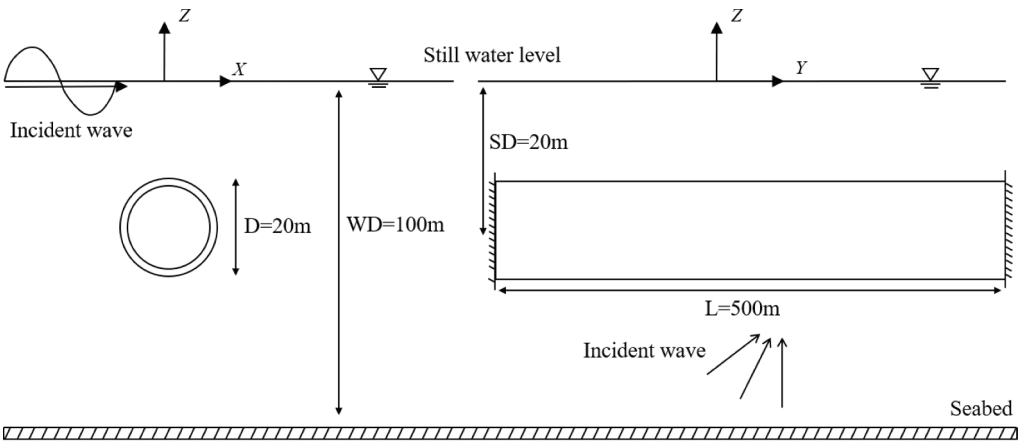


Figure 3. Configuration of a hollow cylinder with fixed-fixed boundary condition.

The same calculation model is established in this paper, and the model configuration and the dimensions of the hollow cylinder are shown in Figure 3 and Table 1. The model is a concrete structure with a density and Young's modulus of 2300 kg/m^3 and 30GPa, respectively. The length of the concrete cylinder is fixed at 500m, the outer diameter is 20m, the submerged depth is 20m, the water depth is 100m, and the angles between the wave incident direction and the length direction of the cylinder are 30°, 60°, and 90°. The two ends of the cylinder are set as fixed boundary conditions, that is, the displacement and angles remain unchanged. The buoyant weight ratio of the cylinder is set to 1.0, that is, the buoyancy of the cylinder is the same as the dry weight. The wave height is 1m.

Table 1. Geometric dimensions and mechanical properties of the hollow cylinder.

Parameter	Unit	Value
Length	m	500
Diameter	m	20
Density	kg/m^3	2300
Submerged depth	m	20
Young's modulus	Pa	3e10
Buoyancy-weight ratio		1

3.2 *Validation*

The vertical displacement response of the center position of the model when regular waves are vertically incident and inclined incident at different frequencies is shown in Figures 4-6. It can be seen that the calculated results of of Morison equation in this paper are in good agreement with those calculated by Orcaflex and Jin, which proves the accuracy of this method.

In the high-frequency range of waves, the calculated results with the Morison equation have a large deviation compared with those by Orcaflex, which may be because the wavelength decreases and the influence of wave diffraction cannot be ignored, so the Morison equation is no longer applicable.

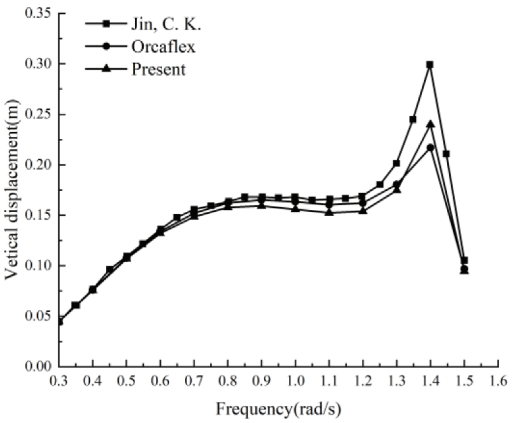


Figure 4. The vertical displacement response of the center position of the model when the regular wave is vertically incident.

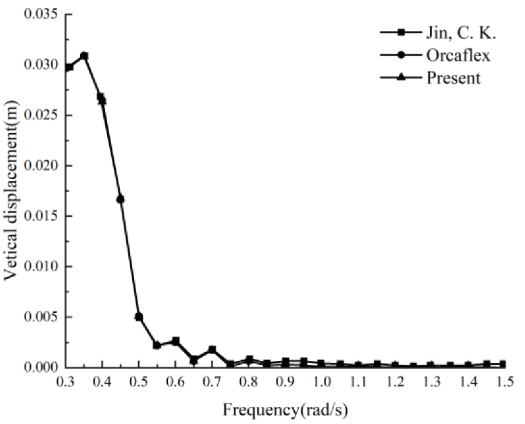


Figure 5. The vertical displacement response of the center position of the model when the regular wave is incident along 30°.

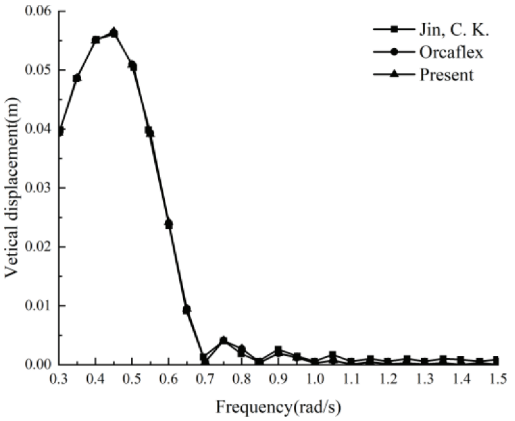


Figure 6. The vertical displacement response of the center position of the model when the regular wave is incident along 60°.

The bending moment along the length direction of the model under the action of the vertically incident regular wave (ω=1rad/s) is shown in Figure 7. It can be seen that the calculated result of the DMB method are in good agreement with that of Orcaflex.

At present, the bending moment is restored by cubic spline curve interpolation, that is, the bending moment value at the adjacent node is used for interpolation. This method is only suitable for structures with simple shapes. Complex geometrics requires a new interpolation method to reduce structural forces.

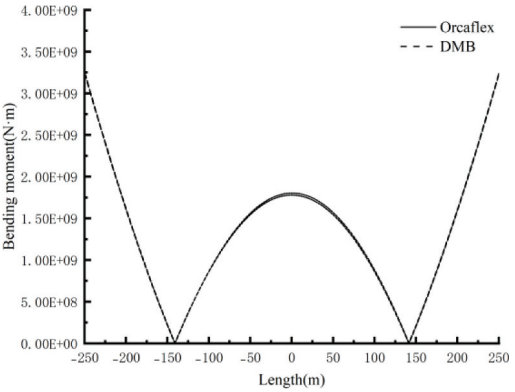


Figure 7. Bending moment along tunnel length when ω=1rad/s.

4 CONCLUSIONS

Under the framework of the DMB hydroelasticity theory, this paper proposes a method to calculate the elastic response of SFTs under wave action in both frequency and time domains, and the numerical model was validated by comparing the numerical results with those of related paper and commercial software.

The results show that the DMB method can accurately calculate the displacement response and structural force response of the fixed suspension tunnel at both ends, and the Morison method can accurately estimate the displacement response of the submerged hollow cylinder within its applicable frequency range. The application range of the DMB method is expanded.

It is worth mentioning that the equivalent displacement response of the tunnel can be calculated by equivalent hydrodynamic pressure distribution along the length direction of the tunnel through the DMB method. Still, it cannot be considered that the equivalent

displacement is the same as the displacement under the real hydrodynamic pressure distribution. In the future, it is necessary to find a new method to restore the pressure distribution by equivalent displacement, that is, to find a hydrodynamic distribution under which the displacement response is consistent with that calculated by the DMB method. In addition, the problem of coupling response between the mooring lines and tube body will be solved in future research, and the influence of different buoyancy-weight ratios (BWRs) on the overall motion response of the SFT will be further considered.

ACKNOWLEDGEMENT

This work is supported by the Natural Science Foundation of Chongqing, China (No. CSTB2023NSCQ-MSX0432), National Natural Science Foundation of China (No. 42206227), Hainan Provincial Natural Science Foundation of China (No. 520QN290), the Oceanic Interdisciplinary Program of Shanghai Jiao Tong University (No. SL2022PT103) and the Hainan Provincial Science and Technology Plan—Sanya Yazhou Bay Science and Technology City Natural Science Foundation Joint Project, China (No. 2021JJLH0062).

REFERENCES

Das, S. & Cheung, K. F. 2012. Hydroelasticity of marine vessels advancing in a seaway. *Journal of Fluids and Structures* 34: 271–290.

Fu, S. X. & Moan, T. & Chen, X. J. & Cui, W. C. 2007. Hydroelastic Analysis of Flexible Floating Interconnected Structures. *Ocean Engineering* 34(11): 1516–531.

Jin, C. K. & Kim M. H. 2021. The Effect of Key Design Parameters on the Global Performance of Submerged Floating Tunnel under Target Wave and Earthquake Excitations. Computer Modeling in Engineering & Sciences 128(1): 315–37.

Jin, C. K. 2022. Comparison of Potential Theory and Morison Equation for Deformable Horizontal Cylinders. *Sustainable Marine Structures* 4(2).

Lu, D. & Fu, S. X. & Zhang, X. T. & Guo, F. & Gao, Y. 2019. A Method to Estimate the Hydroelastic Behaviour of VLFS Based on Multi-rigid-body Dynamics and Beam Bending. *Ships and Offshore Structures* 14(4): 354–62.

Newman, J. N. 1994. Wave effects on deformable bodies. *Applied Ocean Research* 16(1): 47–59.

Price, W. G. & Wu, Y. S. 1985. Hydroelasticity of Marine Structures. In Theoretical and Applied Mechanics: *Proceedings of the XVIth International Congress of Theoretical and Applied Mechanics held in Lyngby Denmark* 19–25 August 1984. IUTAM.

Zhang, X. T. & Lu D. 2018. An Extension of a Discrete-module-beam-bending-based Hydroelasticity Method for a Flexible Structure with Complex Geometric Features. *Ocean Engineering* 163: 22–28.

Bridge Maintenance, Safety, Management, Digitalization and Sustainability – Jensen, Frangopol & Schmidt (eds)
© 2024 The Author(s), ISBN 978-1-032-77040-6
Open Access: www.taylorfrancis.com, CC BY-NC-ND 4.0 license

Main issues of the structural analysis of SFT against environmental loads

G. Iovane, F.M. Mazzolani, R. Landolfo, E. Begovic, E. Bilotta & B. Faggiano
University of Naples Federico II, Napoli, Italy

ABSTRACT: The Submerged Floating Tunnel (SFT) is an innovative concept for crossing waterways. It is a tube, submerged at a specific depth, fixed in position through anchorage systems, providing opportune restraints and stiffness against service and environmental loads. Numerous feasibility studies and preliminary designs have been carried out up to today, but no SFT has been realized yet. However the SFT solution attracts more and more attention, having several advantages with respect to traditional structures. The focus of this paper is on the fundamental aspects related to the structural analysis of the behavior of SFT against environmental loads, such as hydrodynamic and seismic actions, based on a literature review. In particular, theoretical evaluations and numerical analyses on SFTs solutions adopting different cross-sections, structural materials, support systems, joints, under diverse imposed loads, are presented and discussed.

1 INTRODUCTION

The Submerged Floating Tunnel (SFT) consists of a tubular structure immersed in the water at an appropriate depth, compatible with the free navigation at the surface, fixed in position through anchoring cables systems. The structure should be designed to achieve a positive residual buoyancy (i.e. the buoyancy overcomes the weight of the tunnel), so that anchorages are always in tension, providing an effective restraint condition both in vertical and horizontal planes.

Even though not yet exploited in engineering applications, the concept of SFT has gained interest in recent years from both theoretical and practical points of view. As a demonstration of this, a great amount of proposals have been presented all around the world, like in China, Indonesia, Italy, Japan, Mexico, Norway, South Korea, Switzerland, USA, concerning a number of possible implementations of the SFT concept (Iovane et al., 2023).

Compared to traditional structural systems for long span waterway crossings, such as suspension and stayed bridges, as well as immersed and underground tunnels, the SFT shows many advantages, among others low influence of weather conditions, great adaptability to site morphology, low environmental impact. Research studies extensively deal with the analysis of the SFT structural response against wave, current and seism-induced dynamic loads in combination with the residual buoyancy, giving rise to an hydrodynamic interaction between water and structure (Mazzolani et al., 2008; Martire et al., 2010; Faggiano et al., 2019). Researches are also devoted to catch and model the state of the water, as well as the kinematics of water particles due to currents and waves, since it is crucial for the safety of offshore structures. Thus, a wealth of observed data and theories exists (Sorensen, 1993; Hedges, 1995).

In this context, the main purpose of the paper is to collate and summarize the research achievements on the hydrodynamic behaviour of tethered SFT under environmental and seismic actions, highlighting the main issues of the analytical formulations, the physical and numerical models, as well as of the structural response.

DOI: 10.1201/9781003483755-126

2 HYDRODYNAMIC ACTION MODEL

The determination of the hydrodynamic forces generated by the relative motion between the water and the SFT structure is a complex problem since it involves many variables. When an immersed body is invested by a fluid flow, it is subjected by a force, which depends on the fluid-structure acceleration and velocity. The contribution due to velocity can be split in two components: the drag and the lift forces, which are parallel and perpendicular to the flow direction.

The most used methods to model hydrodynamic actions are: Morison equation, Diffraction theory by boundary element method (or potential theory) and Navier–Stokes (N–S) models.

In the field of the design of offshore structures, the Morison equation (Morison et al, 1950) is the most widespread and simple way to calculate the hydrodynamic forces F_h per unit length. It was developed for slender cylindrical components. Based on an empirical approach, it considers the effects of water viscosity and inertia through the following equation (1), where ρ_w is the water density, D is the external diameter of the structural element (i.e. tunnel or cable), C_I is the inertial coefficient, C_M is the added mass coefficient, C_D is the drag coefficient, a_w, a_s and v_w, v_s are the water and structure acceleration and velocity, respectively:

$$F_h = \rho_w \frac{\pi D^2}{4} [(C_I - C_M)(a_w - a_s) + C_M a_w] + \frac{1}{2}\rho_w C_D D(v_w - v_s)|v_w - v_s| \quad (1)$$

The first addend is the inertial contribution, given by the sum of the diffraction effects, due to the presence of the structure, proportional to the relative acceleration between the water and the structure (the motion of the water particles is deviated by the presence of the marine structure), and the Froude-Krilov force, related to the undisturbed flow of water. The first contribution is the additional inertia force needed to accelerate a structure immersed in a fluid. The second contribution is due to the dynamic pressure field that accelerates the amount of water moved by the body.

The second addend is the drag force or resistance, produced by the separation of the water flow from the body surface due to the viscosity of the fluid. The separation of the fluid generates a turbulent wake, occurring mainly below the downstream portion of the body, thus entailing a difference between the pressures acting on the upstream and downstream part of the body, whose resultant is the drag force. Flow separation and resulting turbulence is the key phenomenon influencing the dynamic pressure field occurring at the water structure interface. It strongly depends on the Reynolds number, which is defined as the ratio between the product of the water velocity V and the cylinder diameter D (or the cross-section projection of the body in a direction orthogonal to the flow) and the kinematic viscosity of the water ν (equal to approximately 10-6 m^2/s).

Note that the lift force, perpendicular to the flow direction, is not covered by the Morison equation, which is only for the inline forces in an oscillatory flow (inertia and drag). Therefore the lift force has been addressed separately by Strouhal (1878) similarly to the drag force, by using the following equation (2), in function of the water density ρ_w, the external diameter of the tunnel D, the lift coefficient C_L and the water velocity v_w:

$$F_L = \frac{1}{2}\rho_w C_L D v_w^2 \quad (2)$$

Many authors have used Morison equation in SFT studies (i.e.Faggiano et al., 2001; Di Pilato et al., 2008; Martire et al., 2010; Wahyuni et al., 2009; Kunisu et al., 2010; Cantero et al., 2016; Jin and Kim, 2018; Won et al., 2019). The equation can be used also to roughly estimate hydrodynamic loadings during seismic events, once the water velocities and accelerations due to seaquake are determined (Martire et al., 2010).

The Diffraction Theory proposed by MacCamy and Fuchs (1954) can be also used for hydrodynamic force computation. This method assumes that the fluid is inviscid and incompressible, with an irrotational motion. The velocity potential generated by wave field and SFT is assumed to be divided into the incident and the diffraction potentials. The velocity potential can be evaluated through the boundary element method (BEM), then the pressure distribution acting on the

tunnel surface can be obtained using the Bernoulli's equation. Based on the pressure distribution, the force and moment acting on the tunnel can be determined. Jin et al. (2020) calculated the wave force of SFT based on the diffraction theory through the BEM, while Guerber et al. (2012), Hannan et al. (2014), Bai et al. (2014), Teng et al. (2019) through the Fully Non-Linear Potential Flow Theory (FNPT), demonstrating the accuracy and convergence. Nevertheless, since the convection potential flow method assumes an irrotational flow, the nonlinear interactions of waves with submerged constructions, the flow separation, the vortex generation and shedding are difficult to be evaluated satisfactorily. Besides, this type of model is not able to predict the pitch motion of an SFT structure caused by viscous damping around the structure.

In general, the diffraction theory is mostly used when the wave force acts on a large size structure, such as ships and floating platforms, for which the inertial force is dominant for the wave force evaluation, while the Morison equation is used when the structural size is rather small, for which both the inertial and drag forces are non-negligible. Comparison of these two methods by Kunisu (2010) for the hydrodynamic computation of SFTs highlighted that for common construction conditions (like water depth 100m, submerged water depth 30m, tube diameter 23m), both drag and inertial forces are significant. When larger tube diameters are considered, the inertial force would dominate. Moreover, both Morison equation and diffraction theory was found to provide accurate hydrodynamic calculations.

With the development of computer technology, it has been possible to carry out a direct numerical simulation of the wave-structure interaction based on the *Navier-Stokes (N-S) models*, by implementing different theoretical relationships. Long (2009) used simultaneously fifth-order Stokes wave theory and Morison formula to evaluate the dynamic response of an SFT. Many other researchers have applied high-precision numerical models in addition to empirical formulas (Muhammad et al., 2017; Chen et al., 2020). With regards to the numerical modelling techniques to solve Reynolds Averaged Navier-Stokes (RANS) equation, Marker-And-Cell (MAC) and Volume Of Fluid (VOF) (Hirt and Nichols, 1981) are often used for the simulation of the free surface wave generation. The MAC method calculates the free surface by recording movement of each of the fluid particles, requiring huge amount of both computational space for storage and time for computation. The VOF method overcomes this shortcoming (Rahman et al., 2006). Peng et al. (2013) applied the Immersed Boundary Method (IBM) to deal with the movable SFT under waves, with a numerical model based on Eulerian grid methods (fluid Eulerian and Lagrangian domain). Ren et al. (2017) applied a Smoothed Particle Hydrodynamics (SPH) model, a meshless method with simple mathematical formulation and high computational efficiency, to simulate the nonlinear interaction between waves and the SFT, gaining a good agreement between numerical results and experimental data.

3 STRUCTURAL MODEL

In the last decades, several studies have focused on the analyses of the structural performance of SFT under real environmental conditions through numerical semi-empirical models (Chen et al., 2018) and experimental investigations (Iovane et al., 2023).

From the analysis of the scientific literature, it is possible to distinguish three different structural modeling approaches: (1) cables and tunnel are studied separately; (2) simplified coupled tunnel-cable model with one-dimensional elements (beam elements); (3) advanced coupled tunnel-cable model with 2D elements (shell elements) or 3D elements (solid elements).

With regards to the first approach, Kunisu (2010) analyzed an SFT with elliptical cross-section for investigating the influence of diameter and installation depth on the hydrodynamic force. The model considered only the tube with hinge end restraints. The hydrodynamic force was evaluated based on the diffraction theory by Boundary Element Method (Figure 1). Zou et al. (2021), Xu et al. (2022) and Liu et al. (2023) modeled two tunnels as separate cylinders, restrained through springs with specific stiffness, with the purpose to evaluate the effects of Vortex Induced Vibration (VIV) as a function of distance and diameter between tubes. Other authors (Lin et al., 2016; Cantero et al., 2016; Wu and Mei, 2017; Figure 1) studied the behavior of the only anchor-cable under parametric axial excitation, modeling the cable as beam element

in tension with the base end hinge restraint, while the tunnel as a simple lumped mass block equipped with springs having stiffness, damping and vibration directions along the cable-axes.

With regards to the simplified coupled tunnel-cable model (Figure 2), Xie et al. (2023) modelled both the tunnel and the anchor-cables as one-dimensional beam elements with bending and axial stiffnesses equivalent to those of the SFT and anchor cables, respectively, opportunely supported at the ends, where either transverse displacements or torsional rotations are restrained. Similarly, Di Pilato et al. (2008) modelled the tunnel by means of geometrically non-linear beam finite elements, neglecting axial deformation and torsional behavior, with a cross section having area and moment of inertia equivalent to the studied SFT. The tube masse is lumped at each connection-to-anchoring section. As the same the anchoring system is modelled by beam elements having equivalent total area and slenderness of the real cables. The soil–structure interaction effects are taken into account by considering three springs at the bottom of each anchor element and at the tunnel end sections.

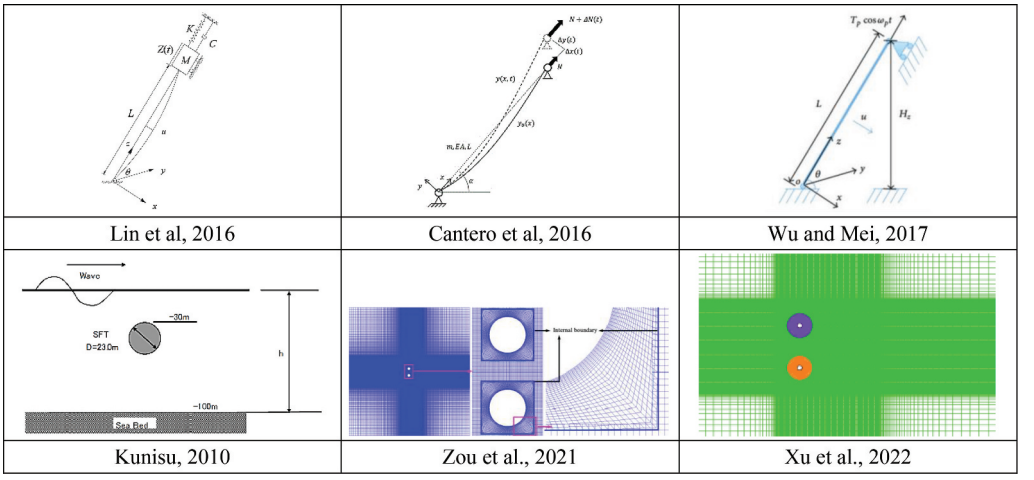


Figure 1. Literature review of the SFT structural models: Separate tunnel and cable system.

Also Martire et al. (2010) set up a FE numerical model of a SFT structure with an elliptical cross section, by varying either the cable system configurations in the transversal plane or the crossing lengths, corresponding to pedestrian crossings, railway and motorway crossings. The tunnel is modeled by means of quadratic beam elements, with masses lumped at the connection-to-anchoring sections, while cables through quadratic beam hybrid elements, with predominant axial stiffness, geometric non-linearity, negligible inertia moments of the cross-section. The connection between the cable anchoring systems and the tunnel is modelled through a rigid body constraint, so that the actual dimensions of SFT cross-sections are taken into account. Spherical hinge are considered at both ends of each cables.

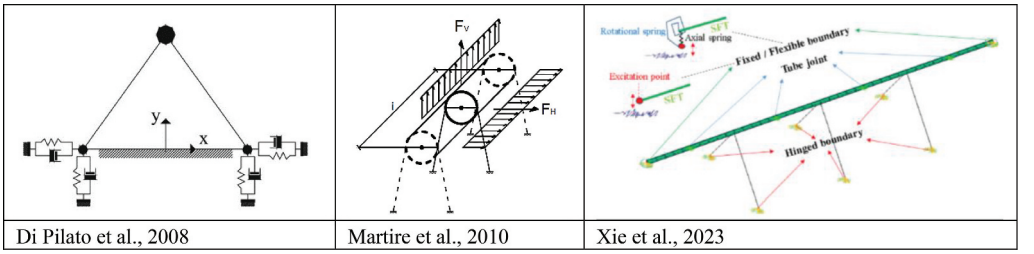


Figure 2. Literature review of the SFT structural models: Simplified coupled tunnel-cable model.

In the context of advanced coupled tube-anchoring system modelling, the global vibration behavior of the SFT tube and the local oscillations of the cables are coupled under realistic environmental conditions. The tunnel and cables are modeled in a more refined way, considering the real geometry and shape of the cross-section with 2D or 3D elements appropriately scaled (Figure 3).

In particular, the SFT end restraints are usually modeled through springs in both vertical and horizontal transverse directions that prevent rotations. Axial displacements are prevented too. The anchoring cables are connected to the tunnel and at the foundation through spherical hinges. In more refined models, the tunnel is characterized by a sandwich cross-section, so that the contacts between the layers are modeled through a simple contact interaction, defining a friction coefficient, while the tunnel-water contact is modeled through a general interaction, in which all relative displacements and rotations are allowed (Wahyuni et al., 2009; Long et al., 2009; Muhammad et al., 2017; Won et al., 2019; Chen et al., 2020; Kim and Kwak, 2021). Moreover, to simulate the response of solids and fluids in high dynamic conditions, as in case of explosions and impacts, the coupled Eulerian-Lagrangian (CEL) hydro code is used (Faggiano et al., 2019). The global behavior, the vibrations induced by the hydrodynamic loads, the influence of the oscillation of the cables on the tunnel behavior, the corresponding pressures and stresses of the coupled tunnel-anchor cable system are thus evaluated with higher accuracy, however at the expense of high computational time of analysis (Figure 3).

Lastly, it is worth noticing that experimental investigations play a key role for the insight of the SFT structural behavior and for the development of the construction technologies, with the special task to calibrate numerical models aimed at the parametric study of the hydrodynamic response of SFTs. During the last 10 years, several scale model tests of SFTs under wave loads have been carried out for several different purposes by different authors. Details can be found in Iovane et al. (2023).

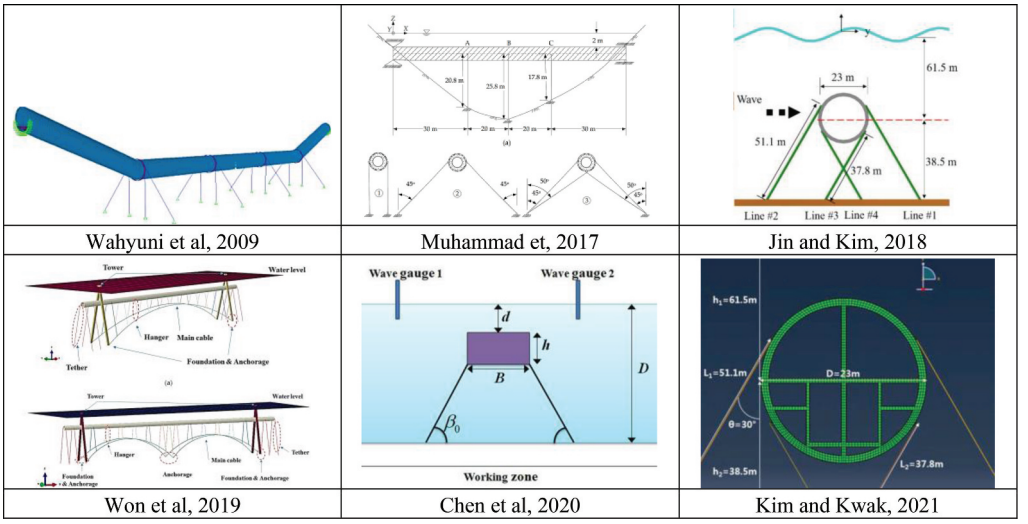


Figure 3. Literature review of the SFT structural models: Advanced coupled tunnel-cable model.

4 COMMON TYPE OF ANALYSIS AND GENERAL OUTPUTS

With regards to the evaluation of the hydrodynamic behavior of SFT models in terms of internal forces, deformation and displacements, most studies concern numerical analysis with regular and irregular wave-induced dynamic loads, by varying the conditions of wave, such as height and period. Moreover, the influences of several structural factors, like the mooring lines configuration, the immersion depth of the SFT, the shape of the tunnel cross-section, the SFT configuration with single cylinder or two cylinders (tandem configuration), the buoyancy

to weight ratio (BWR), on the global dynamic response of SFTs are investigated, in order to provide suitable and reliable criteria for the structural design.

Generally, dynamic time history analyses are carried out. Among these, many authors (Martire et al., 2010; Wahyuni et al., 2009; Muhammad et al., 2017; Jin and Kim, 2018; Won et al., 2019; Chen et al., 2020; Kim and Kwak, 2021) studied SFT with a single tube and different cable system configurations, through non-linear dynamic analyses, by using advanced structural calculation programs. The numerical results show that the mooring systems type and inclination play a significant role on either the tunnel deformation and displacement or on the tensile forces in the anchoring cables under hydrodynamic loads. Specifically, the vertical cables counteract the buoyancy induced by the water, while the inclined cables stabilize the tunnel under hydrodynamic actions. Moreover, by increasing the inclination of the anchoring system, the tension in the cables and the transversal displacements of the tube are reduced.

As concerns the shape of the tube cross section, it greatly affects the fluid-structure interaction (Kunisu, 2010). Elliptical and circular cross-section shapes provide smaller oscillations of the tube as respect to rectangular and polygonal cross-section shapes, resulting in lower anchor cables tension, in a more uniform distribution of pressure on the tunnel, as well as minimizing the drag force due to hydrodynamic forces and the vortex shedding induced vibrations (Jin and Kim, 2018). With this regards, the spacing between two tubes in a tandem configuration has important effects on the vortex shedding induced vibrations, which decreases by increasing the spacing (Zou et al., 2021; Xu et al., 2022).

Also the immersion depth of tunnel and the BWR affect the global response of SFT, with particular reference to the stress in the cables and along the tube. In fact, as the immersion depth increases, the drag and lift forces decrease, wave effects are damped, the effects of hydrodynamic actions due to the currents increase, while effects induced by the seism remain almost unchanged (Faggiano et al., 2001). Furthermore, the length of the mooring lines decreases, leading to greater lateral stiffness under transverse loads and lower vibration of the mooring lines. These results were also confirmed by studies conducted on only anchor cables by Lin et al. (2016) and Cantero et al. (2016), who specifically analyzed the tension in the mooring lines during a dynamic cyclic parametric axial excitation. Moreover they highlighted that as the BWR increases, the cable axial force also increases, leading to a reduction of the probability of tethers slacking, ensuring permanent tension in the tethers and reducing the displacement amplitudes. However, this implies higher bending moments on the tube that can be critical at the landfalls (Iovane et al., 2023).

With regards to analysis of the seismic behaviour of SFT, Martire et al. (2010) proved that the multi-support excitation due the seism significantly influence the SFT response. This is specially true in case of long SFT, for which a large number of vibration modes is involved in the oscillations, being higher modes contribution being more relevant. Moreover when the vertical water motion is considered, it strongly affects the frequency content of vertical vibrations, moving it in the high frequency range. It is also shown that short SFTs are subjected to great bending moments in the tunnel, with maximum values close to the middle section, while in long SFTs the critical issue is related to the axial force stressing the anchorages, mainly near the shore where cables are shorter and therefore more rigid. The performed analyses show that stresses induced in the tunnel and in the anchorages generally reduce due to vertical water motion.

5 CONCLUSIVE REMARKS

In this paper, the state of the art on scientific literature focused on the evaluation of the response of the SFT under hydrodynamic loads is summarized. In particular, the models of the actions and of the structure, most frequently adopted, as well as the common type of analysis and the main general outputs are presented.

With regards to the environmental actions, wave and currents are defined according to consolidated models, taking into account the specificities of the site of construction, as well as the ensuing hydrodynamic forces can be generally determined by means of the consolidated Morison equation. As concerns the seismic actions, the seismic input energy

can be transferred to the tunnel through the shore connections and anchoring foundations, but the vertical seismic component can be also transferred through the layer of water. Moreover, for short-span SFT it is reasonable to consider a single excitation of the ground motion, but for long and large-span structures connected to the seabed with multi-supports, the spatial features of the ground motion are significant for the seismic response of the system and the ground motion of multi-supports are often different. Therefore the most suitable model for the seismic actions is a set of time histories of the ground motion, which adequately take into account the spatial variability, introduced in a three-dimensional dynamic analysis. The effect on the SFT structure of the vertical seismic component through the water should be accounted for.

The structural models used for the analysis of the SFT behaviour can be mainly of three types, depending on the degree of the numerical approximation: separate models for the anchoring systems and the tunnel, when the local response is to be studied, or the coupled model for anchor cable-tunnel system, when the global response is to be studied. In the latter case, the FE model can be simplified, using one-dimensional beam elements for cables and tunnel, or it can be advanced, using 2D or 3D elements, with opportune interaction models between parts. The use of advanced models allows to deepen the fluid-structure interaction and provide the complete pressure and stress distribution within the tube cross-section, at the cost of longer computational times of structural analysis.

Main general outcomes evidence that design criteria should include the shape of the tunnel cross section, the inclination of the anchoring system, the SFT immersion depth, taking into account that tunnel rectangular and polygonal cross-section shapes involve greater water flows turbulence and thus larger oscillations of the tube as respect to elliptical and circular cross-section shapes, larger inclination of the anchor cables result in lower tension in the cables and greater transversal stiffness of the tube, larger SFT immersion depth entails shorter anchor cables, therefore greater cable axial stiffness and tunnel lateral stiffness.

It is worth noticing that the number of studies and the involved countries on the SFT technology has increased in recent years, also evidencing the sustainability of the structural solution. Further to numerical investigations also experimental campaigns in tanks on small scale specimens have been carried out, especially in Europe and in Asia. Outcomes demonstrate the suitability of the SFT. The preparation of SFT design guidelines, collecting the requirements ensuing from the acquired knowledge is compulsory. Nevertheless in order to overcome the mistrust of a new technology, the construction of a full scale SFT will be surely encouraging.

ACKNOWLEDGEMENTS

The project FRA2020 (Sub-Float - Submerged Floating Tunnels for waterway crossings) funded by the University of Naples Federico II is acknowledged.

REFERENCES

Bai, W., Hannan, M.A., Ang, K.K. 2014. Numerical simulation of fully nonlinear wave interaction with submerged structures: Fixed or subjected to constrained motion, Journal of Fluids and Structures, 49 (2014) 534–553. http://dx.doi.org/10.1016/j.jfluidstructs.2014.05.011.

Cantero, D., Ronnquist, A., Naess, A. 2016. Recent Studies of Parametrically Excited Mooring Cables for Submerged Floating Tunnels, Procedia Engineering, 166 (2016) 99–106.

Chen, X., Chen, Z., Cai S., Xu W., Zhuo X., Lv J., Zhao J. 2020. Numerical investigation of dynamic re-sponses and mooring forces of submerged floating tunnel driven by surface waves, Scientific Reports – NatureResearch, 10:18836. https://doi.org/10.1038/s41598-020-75907-8.

Chen, Z., Xiang, Y., Lin, H., Yang, Y. 2018. Coupled Vibration Analysis of Submerged Floating Tunnel System in Wave and Current, Appl. Sci., 2018, 8, 1311. doi:10.3390/app8081311.

Di Pilato, M., Feriani, A., Perotti, F. 2008. Numerical models for the dynamic response of submerged floating tunnels under seismic loading, Earthquake Engineering and Structural Dynamics, Vol. 37, pp. 1203–1222.

Faggiano, B., Iovane, G., Toscano, I., Mazzolani, F.M., Landolfo R. 2019. Preliminary study on the behaviour of the SFT Qiandao prototype against explosions and impacts, Proceedings of the 14th International Conference on Vibration Problems (ICOVP 2019), 1–4 september, Crete, Greece, E. J. Sa-pountzakis et al. (eds.), Lecture Notes in Mechanical Engineering, SPRINGER NATURE Singapore Pte Ltd. 2021 https://doi.org/10.1007/978-981-15-8049-9_50.

Faggiano, B., Mazzolani, F.M., Landolfo, R. 2001. Design and modelling aspects concerning the submerged floating tunnels: an application to the Messina Strait crossing, 4th Symposium on Strait Crossing, Bergen, Norway, Sep 02-05, 2001, Ed. Krokeborg, J, 511–519.

Guerber, E., Benoit, M., Grilli, S.T., Buvat, C. 2012. A fully nonlinear implicit model for wave interactions with submerged structures in forced or free motion, Eng Anal Bound Elem, 2012;36 (7):1151–63.

Hannan, M.A., Bai, W., Ang, K.K. 2014. Modeling of Fully Nonlinear Wave Radiation by Submerged Moving Structures Using the Higher Order Boundary Element Method, J. Marine Sci. Appl., (2014) 13: 1–10. DOI: 10.1007/s11804-014-1226-1.

Hedges, T.S. 1995. Regions of validity of analytical wave theories, Proc. Inst. Civ. Eng., Wat., Marit., & Energy, 112, June, 111–114.

Hirt, C.W. & Nichols, B.D. 1981. Volume of fluid (VOF) method for the dynamics of free boundaries, Journal of Computational Physics, Volume 39, Issue 1, January 1981, Pages 201–225.

Iovane, G., Mazzolani, F.M., Landolfo R., Begovic E., Bilotta, E., Faggiano, B. 2023. Assessment of experimental tests on SFT small scale specimen, Applied Ocean Research, Volume 138, September 2023, Article number 103656. Publisher: Elsevier Ltd. ISSN: 01411187. DOI: 10.1016/j.apor.2023.103656.

Jin, C. & Kim, M.H. 2018. Time-Domain Hydro-Elastic Analysis of a SFT (Submerged Floating Tunnel) with Mooring Lines under Extreme Wave and Seismic Excitations, Appl. Sci. 2018, 8, 2386; doi:10.3390/app8122386.

Jin, R., Gou, Y., Geng, B., Zhang, H., Liu, Y. 2020. Coupled dynamic analysis for wave action on a tension leg-type submerged floating tunnel in time domain, Ocean Engineering, 212 (2020) 107600.

Kim, G.J. & Kwal, H.G. 2021. Investigation of tensile force on mooring line for a submerged floating tunnel, Bridge Maintenance, Safety, Management, Life-Cycle Sustainability and Innovations, 1st Edition. ISBN9780429279119. https://doi.org/10.1201/9780429279119-113.

Kunisu, H. 2010. Evaluation of wave force acting on Submerged Floating Tunnels, Procedia Engineering, 4, 99–105. © 2010 Published by Elsevier Ltd.

Lin, K., Xiang, Y., Yang, Y. 2016. Coupled vibration analysis of CFRP cable-tube system under parametric excitation in submerged floating tunnel, 2nd International Symposium on Submerged Floating Tunnels and Underwater Tunnel Structures. Procedia Engineering 166 (2016) 288–295. doi: 10.1016/j.proeng.2016.11.551.

Liu, G., Song, Z., Xu, W., Sha, M. 2023. Numerical study on the VIVs of two side-by-side elastically coupled cylinders under different Re and natural frequencies, Ocean Engineering, 284 (2023) 115261. https://doi.org/10.1016/j.oceaneng.2023.115261.

Long, X., Ge, F., Wang, L., Hong, Y. 2009. Effects of fundamental structure parameters on dynamic responses of submerged floating tunnel under hydrodynamic loads, Acta Mech Sin, (2009) 25:335–344. DOI 10.1007/s10409-009-0233-y.

MacCamy, R.C. & Fuchs, R.A. 1954. Wave Forces on Piles: A Diffraction Theory, Tech Memo, No. 69, U.S. Army Corps of Engineers, Beach Erosion Board.

Martire, G., Faggiano, B., Esposto, M., Mazzolani, F.M., Zollo, A., Stabile, T.A. 2010. Seismic analysis of a SFT solution for the Messina Strait crossing, Procedia Engineering, 4 (2010) 303–310. doi:10.1016/j.proeng.2010.08.034.

Mazzolani, F.M., Landolfo, R., Faggiano, B., Esposto, M., Perotti, F., Barbella, G. 2008. Structural analyses of the Submerged Floating Tunnel prototype in Qiandao Lake (PR of China), International Journal Advances in Structural Engineering, 11, 4, 2008, 439–454.

Morison, J. R., O'Brien, M. P., Johnson, J. W., Schaaf, S. A. 1950. The force exerted by surface waves on piles, Petroleum Transactions, American Institute of Mining Engineers, 189: 149–154, doi:10.2118/950149-G.

Muhammad, N., Ullah, Z., Choi, D.H. 2017. Performance Evaluation of Submerged Floating Tunnel Subjected to Hydrodynamic and Seismic Excitations, Appl. Sci., 2017, 7, 1122; doi:10.3390/app7111122.

Peng, W., Lee, K., Shin, S., Mizutani, N. 2013. Numerical simulation of interactions between water waves and inclined-moored submerged floating breakwaters, Coastal Engineering, 82 (2013) 76–87.

Rahman, A., Mizutami, N., Kawasaki, K. 2006. Numerical modeling of dynamic responses and mooring forces of submerged floating breakwater, Coastal Engineering, 53 (2006) 799–815. doi:10.1016/j.coastaleng.2006.04.001.

Ren, B., He, M., Li, Y., Dong, P. 2017. Application of smoothed particle hydrodynamics for modeling the wave-moored floating breakwater interaction, Applied Ocean Research, 67 (2017) 277–290. http://dx.doi.org/10.1016/j.apor.2017.07.011.

Sorensen, R.M. 1993. Basic Wave Mechanics for Coastal and Ocean Engineers, John Wiley & Sons, New York.

Strouhal, V. 1878. Ueber eine besondere Art der Tonerregung (On an unusual sort of sound excitation), Annalen der Physik und Chemie, 3rd series, 5 (10): 216–251.

Teng, B., Mao, H., Ning, D., Zhang, C. 2019. Viscous numerical examination of hydrodynamic forces on a submerged horizontal circular cylinder undergoing forced oscillation, Journal of Hydrodynamics, 2019, 31(5): 887–899. https://doi.org/10.1007/s42241-018-0082-x.

Wahyuni, E., Raka, G.P., Budiman, E. 2009. Structural behaviour of Submerged Floating Tunnels with different cable configurations under environmental loading Dinamika TEKNIK SIPIL, Akreditasi BAN DIKTI No: 110/DIKTI/Kep/2009.

Won, D., Seo, J., Kim S., Parl, W.S. 2019. Hydrodynamic Behavior of Submerged Floating Tunnels with Suspension Cables and Towers under Irregular Waves, Appl. Sci., 2019, 9, 5494; doi:10.3390/app9245494.

Wu, Z. & Mei, G. 2017. Dynamic Response Analysis of Cable of Submerged Floating Tunnel under Hydrodynamic Force and Earthquake, Hindawi, Shock and Vibration, Volume 2017, Article ID 3670769, 14 pages. https://doi.org/10.1155/2017/3670769.

Xie, J., Li, J., Chen, J., Xu, Q. 2023. Seismic response analysis of submerged floating tunnel considering non-uniform excitation and flexible-support boundary effect, Ocean Engineering, 286 (2023) 115468. https://doi.org/10.1016/j.oceaneng.2023.115468.

Xu, W., Wu, H., Sha, M., Wang, E. 2022. Numerical study on the flow-induced vibrations of two elastically mounted side-by-side cylinders at subcritical Reynolds numbers, Applied Ocean Research, Volume 124, July 2022, 103191. https://doi.org/10.1016/j.apor.2022.103191.

Zou, Q., Ding, L., Zou, R., Kong, H., Wang, H., Zhang, L. 2021. Two-degree-of-freedom flow-induced vibration of two circular cylinders with constraint for different arrangements, Ocean Engineering, 225 (2021) 108806. https://doi.org/10.1016/j.oceaneng.2021.108806.


Taylor & Francis
Taylor & Francis Group
http://taylorandfrancis.com

MS12: Decision-making in bridge management - Gaps between research and practice and recommendations for the future

Organizers: P. Linneberg & A. Strauss


Taylor & Francis
Taylor & Francis Group
http://taylorandfrancis.com

Bridge Maintenance, Safety, Management, Digitalization and Sustainability – Jensen, Frangopol & Schmidt (eds)
© 2024 The Author(s), ISBN 978-1-032-77040-6
Open Access: www.taylorfrancis.com, CC BY-NC-ND 4.0 license

Current and future decision-making in Danish and Austrian bridge management

P. Linneberg
COWI A/S, Kongens Lyngby, Denmark

A. Strauss
University of Natural Resources and Life Sciences, Vienna, Austria

ABSTRACT: Infrastructure systems, such as bridges, are a driver for economic growth and development of countries. Similarly, development of operation and maintenance strategies for infrastructure systems may aim at optimal management using Key Performance Indicators (KPIs) such as reliability, redundancy, availability, safety, economy, environmental performance, and resilience. With a background in Danish consultancy and Austrian research this paper discusses how KPIs are accounted for in current bridge management. New technologies, such as structural health monitoring, artificial intelligence supported virtual/immersive inspections and reliability-based structural assessments, push for quantitative rather than qualitative decisions regarding interventions on element or structural level. Combined with risk-based decision-making based on multiple KPIs should allow bridge managers to make more objective, transparent and better decisions. This paper provides examples of some of the gaps between research-based decision-making models and technologies and thereby also the gap between current and future decision-making practice in Denmark and Austria.

1 INTRODUCTION

Infrastructure systems, such as bridges, are a driver for economic growth and development of countries. Every single day infrastructure operators and owners strive to make decisions that allow for optimal operation and maintenance (O&M) whether on bridge element, system or portfolio level. Decision-making is made on all levels within an owner/operator organization and often many years before the interventions. As a basis for decision making, infrastructure managers rely on data as well as systems/tools developed and operated internally within their organization or by external companies. The quality of information and the knowledge of the structures with their local peculiarities, damage processes as well as associated intervention costs and methods are crucial for good decision-making.

The project COST TU1402 on quantifying the Value of structural health Information (VoI) for decision support prepared a Guide for practicing engineers (COST TU1402, 2019) that summarized that the knowledge about the decision context is the fundamental factor for optimal decision-making and is generally in association with:

- decision maker (private or public authority),
- decision scenario (future use of the structure)
- decision time horizon and other time constraints,
- technical constraints such as code requirements or safety targets,
- complexity of the 'case study',
- socio-economic or political preferences,

DOI: 10.1201/9781003483755-127

Decisions are made using one or several Key Performance Indicators (KPIs) such as reliability, redundancy, availability, safety, economy, environmental performance, and resilience. Top level or executive asset management policies often address some or all the KPIs. How these policies are translated within the owner/operator organization into daily operation is not always transparent, and for a good reason - because this translation is not straightforward. However, decisions need to be transparent as infrastructure operators and owners are accountable towards various stakeholders (public at large, government, concession contract provider etc.). With a background in Danish consultancy and Austrian research this paper discusses how KPIs are accounted for in current bridge management.

New technologies, such as structural health monitoring, artificial intelligence supported virtual/immersive inspections and reliability-based structural assessments, push for quantitative rather than qualitative decisions regarding interventions on element, structural or portfolio level. Combined with risk-based decision-making based on multiple KPIs should allow bridge managers to make more objective, transparent and better decisions.

Based on experience from consultancy and research this paper discussed scope, ambitions and prioritization incl. KPIs related to bridge management in Denmark and Austria. Likewise, new trends in Danish and Austrian bridge management such as UAV-based immersive inspections and the revival of proof-loading for existing structures is debated. Last, gaps between current and future decision-making in bridge management whether technical (e.g. lack of data), educational (e.g. communication and training) and/or economic/contractual are also debated.

The paper is structured to present Key Performance Indicators (KPIs) in bridge management (chapter 2), supporting technologies (chapter 3) followed by a discussion of the general status, new trends and gap between current and future decision-making in bridge management in Denmark (chapter 4) and Austria (chapter 5). The conclusion provides a comparison and an outlook for the future.

2 KEY PERFORMANCE INDICATORS (KPI) IN BRIDGE MANAGEMENT

The performance-based evaluation of engineering structures is becoming increasingly important and allows maintenance management and long-term planning to be carried out according to the needs of the user and owner. Often, performance evaluations make use of the term Performance Indicator (PI), which stems from economics and measures the success of an organization or of a particular activity (such as projects) with which it engages. The application of this term to physical objects is coupled to their fitness for purpose. The PI measures the fitness for purpose of a physical object such as a route (portfolio of bridges), a bridge or one of its elements.

Since the fitness for purpose can change over time, so does the value of a PI. Maintenance interventions can also change the value of PI. Generally, there is no clear distinction between PIs and KPIs. In this article, like the COST TU1406 project WG3 report (COST TU1406, 2018), KPIs relate to a whole bridge and are in terms of Reliability, Availability, Safety, Economy, and Environment (RASEE) defined as follows:

Reliability is the probability that abridge will be fit for purpose during its service life. It is the complement of the probability of structural failure (structural safety), operational failure (serviceability) or any other failure mode chosen by the infrastructure manager or required by other stakeholders.

Availability is the proportion of time a structure is open for service. It does not include failure-related service outages, but those due to expected maintenance interventions. Alternatively, Availability can for instance include additional travel time due to an imposed traffic regime on a bridge.

Safety is the situation of life and limb being protected from harm during the service life of a bridge. Loss of life and limb due to structural failure is not included by this definition (since it would overlap with the Reliability).

Economy is related to minimizing the long-term cost of maintenance activities over the service life of a structure. Herein the user costs for instance for bridges incurred due to detours and delays are not included.

Environment is related to minimizing the harm to environment during the service life of a structure.

Furthermore, in recent years, *Resilience* as a KPI has been addressed by some infrastructure managers. Resilience is associated with the ability of a structural system to deliver a certain service level even after the occurrence of an extreme event or series of events, and to recover the desired functionality as fast as possible. One can see that Resilience may be seen as a combination of the above listed KPIs as a function of time.

Often the KPIs will be evaluated for different maintenance scenarios looking for the most feasible one. Here, it must be underlined that the KPIs Reliability and Safety can be evaluated based on inspection and/or investigation at a point in time (i.e. static quality assessment) but can also be predicted over time (i.e. dynamic quality assessment). The KPIs Availability, Economy and Environment can only be reasonably applied as a function of time and are very strongly linked to political and social constraints and needs.

3 SUPPORTING TECHNOLOGIES

In order to evaluate KPI's and subsequent for the infrastructure managers to make decisions, detailed information on structural performance is required. In recent years several supporting technologies have been applied in the field of bridge management.

Structural Heath Monitoring (SHM) of bridges using sensor technologies and Bayesian updating has gained significant momentum. One application is loading response versification often applied to major bridges. Loads could be environmental as well as traffic. Such monitoring is often launched as campaigns which is beneficial for the bridge operator as sensors have a limited service life compared to the service life of the bridge. Another 'campaign' monitoring example is proof -loading of 'ordinary bridges', which has also gained momentum during recent years, see section 4.2. Most bridge degradation processes are slow under 'normal' environmental exposure. This is part of the motivation for launching long term monitoring related to bridge resistance such as monitoring the level of corrosion in different depths within a concrete structure to provide data for service life updating. Long term monitoring comes with a (semi-)continuous O&M cost that needs to be considered. Furthermore, it must be acknowledged that SHM provide data that must be processed to provide information. This information needs to be visualized and possibly integrated into existing management systems. In addition, the infrastructure manager also needs to decide where to store, process and visualize data and information for decision-making.

Immersive (virtual) inspection is another technology that has made it possible to have a better view and understanding of existing conditions. The use of Unmanned Aircraft Systems (UAS) and Photogrammetry to create photorealistic reality models have yielded significant benefits by allowing inspectors, bridge maintenance personnel, and engineers to have a clearer view of what is happening on critical infrastructure and to also perform many of the tasks virtually that would have previously required expensive travel, access equipment, and manual labor. Not to mention the impact on the normal operations of a transportation infrastructure asset (reduced availability and safety). Infrastructure owners and engineering firms are starting to apply them on projects to see tangible benefits in terms of costs, time, environmental impact, and safety. Artificial Intelligence can also aid the inspectors. Some examples have appeared with machine vision technology that lets inspectors get a more consistent and objective understanding of issues, such as cracking, spalling, or corrosion. The AI-ML detector can go through all the 2D images to detect and then mark the cracks in the photos and display the result in the 3D reality model. A post-processing cleaning step can find and remove known false positives.

Reliability-based assessment of existing bridges started many decades ago. In Denmark the Danish Road Directorate published their first guideline on this matter in 2004, ref. (DRD,

2004). In 2023 effort have been made in order to update the 2004 version which is soon to be published. It is fair to say that the guideline has not been used extensively in practice but when it has been used significant repair and replacement savings have been obtained. It is expected that the sustainability agenda promote refined analysis for prolonged service lives and hence reliability-based methods. In popular terms money should be spend on calculations rather than materials.

Reliability-based assessment pave the way for detailed quantitative rather than qualitative decisions on element and structure level. Combined with assessment of consequences the infrastructure manager can make quantitative risk-based decisions based on one or multiple KPI's. Today, many infrastructure owners make qualitative risk-based decisions as an individual or within a sector, a department, or an asset type but if they want to align decisions across asset types as a start, they need to be quantitative. Infrastructure managers strive to make objective and transparent decisions – and risk-based methods could support this process. Similarly, risk-based methodologies also pave the way for portfolio management in a network related context.

4 BRIDGE MANAGEMENT IN DENMARK

The following sections provide a general status and highlight some new trends from bridge management in Denmark with special focus on roadway bridges on the state network. Furthermore, gaps between current and future decision-making have been summarized – all seen from the perspective of a consultant.

4.1 *General status*

According to [Ebbesen, 2022] asset management at the Danish Road Directorate (DRD) is defined as "...Asset Management includes methods, processes, procedures, data and IT systems that together ensure the implementation and documentation of the long-term economically most optimum operation and maintenance or reinvestment of the non-current assets with the given economic framework and the expectations of the society".

Asset management support the objective of providing safe, functional and economic optimized maintained roads (incl. bridges) in conformity with the politically defined needs and priorities including sustainability. Economic optimized maintained roads is controlled using Net Present Value Life Cycle Costs (LCC) benchmark of maintenance strategies. In case of scarce financial resources, the owner must be able to prioritize safety and functionality and account for the consequences for condition as technical KPI and financial aspects of omitting economic optimum (minimal LCC) operation and maintenance, ref. [Ebbesen, 20222].

According to [Ebbesen, 2022] the ambition of the DRD is "By means of transverse Asset Management for the operation and maintenance of the roads, the Danish Road Directorate will achieve high quality and transparency in the underlying data for decisions, execution and implementation as well as reporting. At the same time, the given resources and skills are utilized optimally across the Danish Road Directorate. Within the given framework, the aim is to minimize the total life cycle cost of the road network, while agreed service level is maintained."

According to the above, the following list of decision-making objectives can be highlighted:

- Safety and functionality are always given highest priority,
- Condition assessment provides the basis for the estimation of maintenance needs,
- Operational activities (cleaning, minor repair jobs etc.) are linked to service level which is balanced politically in line with the appropriate funds,
- Prioritization of O&M tasks is based on technical and economic assessment of likelihood and consequences. This assessment is most often conducted as an implicit risk assessment, where technical and economic KPIs, ref. section 2, incl. social and traffic-related importance are evaluated and quantified to an extend where unambiguous and transparent

decisions on maintenance or reinvestment strategy can be made. It is clear that data are in demand in order to be quantitative rather than qualitative in this assessment,
- The above decisions are logged on an ongoing basis in order to be able to explain development of grants spending, technical progress and actual production.

4.2 *New trends*

In Denmark it is common to use of a traditional hierarchy of inspections, comprising routine, principal, and special inspections. In recent years, the Danish Road Directorate has with success implemented a UAV-based immersive inspection workflow on some of their major bridges.

Major bridges are often difficult to reach (at arms-length), typically because they span from coast to coast. This implies that inspections shall be performed by rope access and/or moveable underbridge inspection gantries on trucks. Performing such inspections comes with a risk to the bridge users (due to traffic restrictions) as well as the inspection personnel working at heights and/or near water. Furthermore, this inspection type is labor-intensive and costly. The immersive inspection workflow comprises a drone flight where RGB and often also thermal pictures are obtained with 70-80% overlay. From these pictures a reality model is established. Thermal images obtained during e.g. temperature rise provides excellent data on delamination of concrete structures that otherwise only could be obtained using hammer tapping or by use of NDT equipment at the concrete surface.

Using the reality capture model an immersive inspection can be performed at the office. This allows for collaboration between the inspector and various experts, the inspector can be well rested and go back-and forth between locations of interest. Defects and be annotated on the reality capture model for easy communication between consultant, owner and contractor and all data are stored for easy reuse – maybe in connection with defect prognosis at the next principal inspection.

Furthermore, several trained artificial intelligence (AI) models for defect detection are being used. They assist the inspector during virtual inspection especially at vulnerable zones (could be that a crack-overlay highlight flow of forces at half-joints or beneath bearings).

The use of proof-load testing for documentation of allowable traffic load on roadway bridges are performed by the Danish Road Directorate (DRD) during recent years. This is an example, where the DRD as owner has been very active with interaction and financial support to research. Proof-loading in Denmark has proven technical and economic attractive. Furthermore, it supports the sustainability agenda – keeping the portfolio of bridges fit for society demands regarding traffic loads. As highlighted by [Straus et al, 2022], it is important that owners and consultants are in close contact with universities, so that decision-support models developed by research are easy to implement and respond to the exact needs of the owner. This owner-interaction also motivates standardization and development of guidelines, so that the research-outcome can be used by the industry at large.

Maintenance activities in Denmark are preventive rather than reactive. With the increased use of Artificial Intelligence throughout the industry the concept of cognitive learning or cognitive maintenance activities has also found the way to selected Danish owners. It seems to be an area where the technology needs to mature or prove itself robust for a portfolio of O&M scenarios. Again, interaction between owners, consultants and research is needed for easy implementation and exploration of the full potential of this interesting area of research.

4.3 *Gaps between current and future decision-making*

Seen from the perspective of Danish consultancy, some gaps between current and future decision-making has been divided into the following clusters: technical, educational and economic/contractual:

Technical

- With increased complexity of quantitative decision-models, valid data are in demand. Research, owners and consultants should work close together, so that decision-models are based on data that can be obtain with reasonable efforts.
- Owners strive to digitalize existing data and make these readily available. This should allow for better prognosis, pattern recognition not yet known utilizing AI, attaching data to digital twins incl. reality capture models.
- 'Alignment' of asset management across asset types. Owners would like to make objective and transparent decisions across asset type incl. aligned budget allocation.
- Transition from a defragmented IT landscape to integrated IT solutions is a constant strive.
- Asset management is often based on implicit risk-based assessment. There is a strive to make these decisions more quantitative. One such initiative is to perform reliability-based load capacity assessment of existing bridge.
- Sustainability is high on the owner agenda. This fosters new materials, new technologies and new ways of working.

Educational:

- O&M is a broad technical area comprising many different technical disciplines. This may be part of the reason why universities struggle to make tailormade courses in asset management.
- Danish owners support and run industry courses such as 'principal bridge inspection'. Such courses, where hands on experience is required, are better suited as industry courses rather than university courses.

Economic/contractual:

- Contracts shall support innovation. This is one of the most powerful instruments to make industry ready research.

5 BRIDGE MANAGEMENT IN AUSTRIA

5.1 *General status*

All the relevant infrastructure operators in Austria have built up valuable database systems. The common understanding is that database maintenance is essential for inventory evaluation and for work with the inventory. On the one hand, an accurately maintained database is necessary; on the other hand, the effort required for data maintenance must not be neglected. Operators of infrastructure assets have clearly defined data fields which must be updated after every bridge inspection, ref. (RVS 13.04.11).

With regard to condition assessment and evaluation, the operators have established clearly defined processes based on experience and expert knowledge. The regular survey of the state of maintenance serves to identify and rectify defects and possible damage in a timely manner. Condition is determined by three types of inspection (surveillance, control and main inspection) which differ in terms of effort and time intervals.

The guidelines for carrying out a Surveillance and/or Controlling represent the minimum standard in accordance with RVS and operator internal standards. The aim is to ensure a uniform and efficient procedure. This should ensure the best possible availability and traffic safety, the utilization of life cycles and thus an economical approach, ref. RVS 13.03.11.

The procedure for the Main Inspections (RVS 13.03.11) is also regulated in RVS 13.03.11 and is to be regarded as a minimum standard. The examination is associated with 5 condition classes and inspection intervals of up to 5 years, in which a condition grade and a maintenance measure are determined with a near-hand examination. Most operators also have additional standards to raise the level of quality and ensure a uniform approach to asset management.

Monitoring, in particular Structural Health Monitoring (SHM), is to be seen as a special case in Austria and does not replace conventional inspections such as ongoing surveillance, controlling or main inspections. The data collected in this way are provided for both the action side and the resistance side. Sensors are installed temporarily or permanently on the structures. Depending on the task, the sensors can be used to measure different physical parameters statically and/or dynamically. In Austria there is a distinction made between global and local monitoring methods. According to RVS 13.03.01, the following objectives can be pursued with monitoring of engineering structures: (a) Measurement-based documentation of construction conditions, (b) Monitoring of condition development during operation, (c) Early detection of critical structural conditions, (d) Comparative values for structural calculations, (e) Influence of boundary conditions (e.g. temperature) on load-bearing behavior, (f) Recording of real variables on the action and resistance side as a basis for updating, (g) Monitoring of structural areas that cannot be visually inspected, (h) Recording of the real behavior of structures even under exceptional loads (e.g. special transports) or test loads. The monitoring must be adapted to the existing situation and the importance of the structure as well as the hazard potential and the complexity of the task.

For the component Assessment, condition grades from 1 to 5 are assigned for the individual elements in accordance with Annex 5 of RVS 13.03.11 and, based on this, for the overall structure. The condition classes in accordance with RVS 13.03.11 essentially assess the urgency of the rehabilitation based on the structural condition. Structures with relevant deficits on element level would therefore not necessarily be classified as being in a structurally defective condition. In order to prevent misunderstandings in management about the urgency of measures, it is standard practice that for bridges with relevant deficits according to the standards on which the planning is based, these deficits should be included in the overall assessment of the structural condition. Depending on the engineering assessment and requirements, special inspections can be initiated in accordance with RVS 13.03.11 due to the prevailing state of preservation or if the extent of damage cannot be determined with sufficient accuracy using simple testing equipment. In addition to the triggering measure, all other assets that match the main measure (e.g. Intervention on a bridge in urgent need of repair) in terms of space and time are also reported. This already considers what the next measure in this area will be. The outcome may be that components have to be repaired before the theoretical standard life cycle expires in order to ensure that the section in question remains free of construction sites for the following years. The aim is to move from a purely condition-based maintenance of the individual assets to an overall maintenance project.

Measures are prioritized in the following order: Structural capacity, Road safety, Availability. If the above-mentioned characteristics cannot be used to adequately prioritize measures, a robustness index can be used as defined in internal guidelines of the infrastructure operators. If it is also not possible to prioritize the measures using this, the impact on the customer must be taken into account.

Based on the historical component classifications maintained in the database, an ageing model of the individual components is determined using Markov chains. These ageing models are also the basis for the prognosis calculations of the condition development that will be calculated using the dTIMS software tool. It is worth noting that this is a standard deterioration model, which may deviate from the actual deterioration of the individual components of the asset. A grade of 3 indicates that the structure can still be used to its full extent, but also creates a certain awareness that this structure will need to be repaired in the foreseeable future. Up to a score of 3, the data is very valid; from a grade less than 3, there is a lack of available data due to the relatively good condition of the bridge structures in the network, which means that a greater variation must be assumed here.

A probabilistic life cycle model is used to determine the long-term budget requirements for the bridge structures of some operators. Based on the year of construction of the structure, the standard life cycle with the corresponding cost estimates is used to determine the theoretical maintenance requirements. This procedure provides an estimate of the resources to be expected if the portfolio behaves in accordance with the previous pre-scribed assumptions made. The current condition is only taken into account indirectly by adjusting the Markov chain models.

5.2 *New trends*

As described in 5.1, a clearly defined inspection and assessment procedure has also been established in Austria, which comprising routine, principal, and special inspections and allows to include innovative monitoring concepts.

For special cases, such as structures with high piers, but also for very long and inaccessible structures, video and innovative monitoring systems (UAV or Satellite Systems) have also been trialled and used as a supplement for some time. In connection with this, there are also developments as to how such monitoring information can be made available to maintenance managers and decisions makers in the future in the form of BIM concepts, for example, and in what form this BIM information can possibly supplement the established databases in a data-based assessment strategy.

In Austria, there are similar developments and considerations for reality capture models on certain structures, although the implementation incl. AI technology has not yet found its way into daily practice. However, a number of research projects supported by infrastructure operators are being conducted on the topics of BIM, AI and IoT as well as reality capture models and digital twin topics.

5.3 *Gaps between current and future decision-making*

On the basis of the above-mentioned gaps between the current and future decision-making of our Danish partners, the following can be mentioned for the Austrian side in addition to the above-mentioned gaps

Technical

- Data safety/security and also the verifiability of the data and decision processes by engineering experts
- Transparency of the decision-making processes, which refers not only to a structure but also to the network level
- Avoidance of small errors with major consequences in the decision-making processes and the associated automation
- Implementation of scientific methods in practical processes and their verifiability - the impossibility of installing a living laboratory due to large economic effects

Educational:

- The professions in the field of infrastructure inspection and asset management require a high level of expertise in engineering, digitalization techniques, understanding of time-dependent processes and economic as well as political and environmental processes.

Economic/contractual:

- Digitalization, especially the digital transformation of inspections and asset management, will require investments in digital systems and their maintenance and servicing, as well as the training of personnel on these media, in addition to investments in the classic maintenance of structures. These investments must be accepted

6 CONCLUSION

Many of the issues presented in this article were also investigated and discussed as part of IABSE TG5.4 (Strauss et al, 2022) and can be summarised as follows:

- Most of the infrastructure operators have very well-developed systems for assessing the condition of their infrastructure assets.
- Inventory and asset management databases and their importance for an objective assessment as well as future planning of refurbishments and interventions is indisputable

- The use of monitoring systems and SHM concepts for the performance assessment is only commissioned for specific reasons in the countries analysed and must not replace traditional engineering-based inspections, however, a freer interpretation can already be seen, e.g. in areas that are difficult to access or for very long-span structures.
- The methods, some of which are highly digitalised by scientists, are only used to a limited extent in daily practice, as their validation and plausibility checks are only possible to a limited extent in short periods of time and long-term planning is usually also influenced by many unforeseeable factors.
- With increasing academic training at universities and in praxis in the areas of asset management, confidence in scientific methods is growing and the number of experts and methods are finding more and more their way into practice.
- AI and IoT techniques are increasingly being used by some of the operators and owners combined with engineering survey methods.
- Data-driven assessment or risk-based assessment in general is only partially implemented in daily practice, as it is often limited by political barriers and regulations.
- The merging of asset management systems with performance indicator systems paired with testing procedures is still in its beginnings and requires more communication and training.

Overall, the survey results of TG5.4, especially for the two countries presented in this article, show that operators are taking powerful steps towards digitalization and digital transformation, while maintaining proven, reliable engineering methods.

REFERENCES

COST TU1402, COST Action TU1402 Quantifying the Value of Structural Health Monitoring, Quantifying the Value of Structural Health Information for Decision Support, Guide for practicing engineers (Diamantidis, D., Sykora, M., Sousa, H.), May 2019

COST TU1406, WG3 technical report, Establishment of a quality control plan. ISBN: 978-86-7518-200-9. boutik.pt, Braga, Portugal.

DRD 2004. Reliability-based classification of the load carrying capacity of existing bridges. Danish Road Directorate (DRD), 2004, Denmark

Ebbesen, M. 2022. Data-driven Asset Management of bridges and structures on the state roads of Denmark; *Proc. IABMAS 2022*, *Barcelona*, 11-15 July 2022. London: CRC Press.

Linneberg, P. 2020. From condition to performance assessment of bridges – The challenge; *Proc. IABMAS 2020*, *Sapporo*, 11-18 April 2021. London: CRC Press.

Strauss, A., Orcesi, A., Lampropoulos, A., Briseghella, B., Frangopol, D. M., Sousa, H., Casas, J., Matos, J. C., Schellenberg, K., Valenzuela, M., Akiyama, M., Linneberg, P., Hajdin, R., Moser, T., IABSE Survey of Implemented Decision-making Models used by Public and Private Owners/Operators of Road- and Railway Infrastructures, *Structural Engineering International*, DOI: 10.1080/10168664.2022.2154731 RVS 13.04.11, Brückenbauwerke, FSV, August 2009.

Bridge Maintenance, Safety, Management, Digitalization and Sustainability – Jensen, Frangopol & Schmidt (eds)
© 2024 The Author(s), ISBN 978-1-032-77040-6
Open Access: www.taylorfrancis.com, CC BY-NC-ND 4.0 license

Comparison of ranking frameworks for specification of bridge scour monitoring systems using a case study database

W. Yaqoobi, G. Gavriel, T. Tryfonas & P.J. Vardanega
University of Bristol, Bristol, UK

M. Pregnolato
University of Bristol, Bristol, UK
Delft University of Technology (TU Delft), Delft, The Netherlands

ABSTRACT: Hydraulic actions resulting in scour are a major cause of bridge failures worldwide. The development of scour is affected by various factors including structural geometry, river morphology and weather conditions. Detection of scour is often carried out using visual inspection-based methods. Visual inspection requires the expertise of divers which incurs high levels of risk, especially during times of high-water flow. Therefore, sensing technologies are becoming increasingly popular with the aim to supplement or replace higher risk visual inspection approaches. Specification of Structural Health Monitoring (SHM) systems is an important activity for bridge engineers and asset managers. This activity can be assisted by SHM rating frameworks, the use of which gives evidence to support specification of monitoring systems for individual bridges. In this paper, three previously published scour rating frameworks are compared using a bridge case study database.

1 INTRODUCTION

1.1 *Background*

Bridge scour is the erosion of material around bridge piers, abutments, and foundations (e.g. Kirby *et al.* 2015). Scour accounts for approximately 60% of bridge failures, including pier scour incidents (Lagasse *et al.* 1997). As a result of scouring actions, the foundations of a bridge may become unstable potentially resulting in collapse (e.g. Maddison 2012). About 60,000 highway and railway bridges span watercourses in the UK, many of which are over 150 years old with unknown foundations (especially unknown foundation depths) (e.g. Clubley *et al.* 2015).

Scour is a challenge for engineers due to the complex soil-water-structure interactions (cf. Kirby *et al.* 2015, Pregnolato *et al.* 2022). Empirical scour depth prediction methods show considerable scatter (cf. Gavriel *et al*. 2023, Shahriar *et al*. 2023). Hence it is important to monitor scour in the field and if possible, employ real time monitoring (cf. Prendergast & Gavin 2014, Vardanega *et al.* 2021). It is also desirable to develop efficient and durable scour monitoring systems (e.g. Pizarro *et al.* 2020, Vardanega *et al.* 2021). These systems are important for evaluating the scour process and for providing early warnings for hazard mitigation (Prendergast & Gavin 2014). Scour monitoring systems should possess key characteristics such as accuracy, longevity, ease of installation, non-obstructiveness to bridge owners or users, cost-effectiveness, and the ability to withstand a range of environmental conditions (cf. Vardanega *et al.* 2021, Pregnolato *et al.* 2022).

The impact of scour on bridges is becoming more serious every year due to climate change (Sasidharan *et al.* 2023). The increase in frequency and severity of flood incidents

DOI: 10.1201/9781003483755-128

(due to the effects of climate change) heightens the risk of scour to bridges (Foley 2021). A bridge collapse is considered a socio economical problem as it is associated with loss of life, high economic losses, and disruptions to traffic (Pregnolato *et al.* 2021, Dawson *et al*. 2018). It is therefore necessary for engineers to ensure that the effects of scour are mitigated and managed.

1.2 *Scour monitoring*

Prendergast & Gavin (2014) and Vardanega *et al.* (2021) present reviews on various scour monitoring devices. Numerous monitoring techniques have been developed which are able to detect scour occurrence: these techniques can be broadly categorized into 'direct' and 'indirect' technologies (see Pregnolato *et al.* 2022). Direct technologies involve the use of sensors near the bridge foundations, while indirect technologies rely on approaches such as remote sensing or modelling (Pregnolato *et al.* 2022). For instance, two direct technologies are the mechanical sounding rod and the sliding magnetic collar (SMC); devices that are simple to install and produce data which are easy to interpret (cf. Lu *et al.* 2008). Sonar, another direct technology, although easy to use, is prone to the effects of turbulent flow, turbidity, and debris (cf. Fisher *et al.* 2013, Hong *et al.* 2016).

Indirect technologies usually measure the structural response and performance over time to estimate scour depth (Pregnolato *et al.* 2022). These technologies include float-out devices which have high operational capacity in harsh flow conditions enabling their use during times of flooding when scour holes are more likely to develop (Prendergast & Gavin 2014, Pregnolato *et al.* 2022). One downside of float-out devices is that their power supply and reliability cannot be checked once deployed (Prendergast & Gavin 2014). Float out devices are placed in the riverbed and will activate when released during scouring, by floating above the surface (Prendergast & Gavin 2014, Tola *et al.* 2023). Numbered bricks are robust during flood events and are useful for measuring scour (Lu *et al*. 2008). Smart magnetic rocks can monitor scour depth, but they are also susceptible to being washed away during high flows (Jiang *et al.* 2022).

Visual inspection, which is typically carried out by divers, is still a common scour monitoring technique (e.g. Clubley *et al.* 2015, Kirby *et al.* 2015, Selvakumaran *et al.* 2018). Operations cannot however take place during flood events due to the high risk involved for the divers. Divers are only able to inspect a bridge for scour holes after the flood event is over (e.g. Larrarte *et al.* 2020). Visual inspection sometimes may give inaccurate information about the current scour situation due to the presence of debris and lack of clear visibility (e.g. Clubley *et al.* 2015). An example of false inspection is the collapse of the Mayou bridge in France back in 2009 (Larrarte *et al.* 2020). Despite a visual inspection carried out two years prior to the incident, the inspectors failed to detect any scour hole (Larrarte *et al.* 2020). The use of scour monitoring devices can result in less reliance on visual inspections. To decide on the best combination of scour devices for the monitoring of a specific bridge SHM scour assessment frameworks may be used.

1.3 *Study aims*

In this paper, three scour assessment frameworks (Vardanega *et al*. 2021, Pregnolato *et al*. 2022, Lueker *et al*. 2010a, b) are applied to nine bridge case studies reported in the literature (Hayden & Puleo 2011, Wang *et al.* 2012, Zarafshan *et al.* 2012, Topczewski *et al.* 2016, Peng 2020, Lin *et al.* 2021, Weissmann *et al.* 2021, Zhan *et al.* 2022, San Martin *et al.* 2023). This paper aims to provide guidance for those seeking to select an appropriate framework for use during the specification of scour monitoring systems. This aim is accomplished by: (a) applying nine case studies to the three aforementioned frameworks (b) comparing the results from the nine case studies and (c) evaluating the capabilities of each framework to provide guidance as to which is the most suitable framework depending on the situation.

2 SCOUR RATING FRAMEWORKS

2.1 *Framework 1 - Vardanega et al. (2021)*

Framework 1 has been developed by Vardanega *et al.* (2021) based on preliminary work by Gavriel (2019). Framework 1 evaluates the suitability of scour monitoring devices based on five criteria given in Table 1. For each of the five criteria a device can score between 1 to 5 (5 being the highest). The score from each category is summed up to give the total score. This process is repeated for all devices under consideration. The devices are then ranked from highest to lowest score. Framework 1 also provides an indication of the relative applicability of each device depending on the score ranges given in Table 2.

Table 1. Criteria for sensor-rating methodology (taken from Vardanega *et al.* 2021).

Criterion	Description
Q1	Ease of installation
Q2	Ease of operation
Q3	Ease of data logging/capture
Q4	Ease of data interpretation
Q5	Measurement frequency

Table 2. Sensor-rating category (taken from Vardanega *et al.* 2021).

Total score	Applicability for scour detection and monitoring
23-25	Very high applicability
18-22	High applicability
13-17	Moderate applicability
8-12	Low applicability
5-7	Very low applicability

2.2 *Framework 2 - Pregnolato et al. (2022)*

Framework 2 by Pregnolato *et al.* (2022) is a further development of the approach by Vardanega *et al.* (2021). This approach was used to evaluate the feasibility of various monitoring technologies for scour detection and monitoring on three railway bridges in the UK (Pregnolato *et al.* 2022). The study follows a three-stage evaluation process. In Stage 1, available technologies are assessed against the requirements of the CIRIA manual (Kirby *et al.* 2015) and those of Network Rail (see Table 3 for the Stage 1 criteria). Technologies that do not satisfy all the requirements of Table 3 are disregarded and do not pass to Stage 2. In Stage 2, sensors are assessed over nine criteria listed in Table 4. The main difference to Framework 1 is the introduction of heuristically assigned weights on each category. The category score is between 1 to 5 as in Vardanega *et al.* (2021). In the final stage the scores from each category are multiplied by the weight of that category and they are then summed up. The devices are then ranked from highest to lowest score and assessed in a similar way to that shown in Table 2 (see Pregnolato *et al.* 2022 for further details).

2.3 *Framework 3 – Scour Monitoring Decision Framework (SMDF) Lueker et al. (2010a, b)*

Framework 3 is the Scour Monitoring Decision Framework (SMDF) proposed by Lueker *et al.* (2010a, b). Framework 3 was developed for the evaluation and selection of scour monitoring devices on river bridges in Minnesota (USA). Framework 3 can evaluate one bridge at a time and can consider multiple piers or abutments of that bridge. Framework 3 requires

site-specific information about the assessed bridge. The required information includes details about the bridge location and dimensions, flow conditions, bridge conditions, structural elements, and environmental factors. Based on these inputs the framework compares the various types of fixed scour monitoring equipment. By entering sufficient information about the site and the bridge, Framework 3 can rank instruments by suitability for the specific bridge site. Framework 3 is also able to show the effect each of the site/bridge characteristics inputted has on each score for each device. A data file for each bridge containing the structural and environmental information about the specific site is prepared i.e. the input data. The workbook compares the structural and environmental information inputted to the ideal structural and environmental conditions as indicated by the worksheet. The two are illustrated on a bar chart for which a score in the form of a percentage is shown (see Lueker *et al.* 2010a, b for further details). In this framework, each case study can only be assessed against the devices available in the SMDF.

Table 3. Mandatory criteria for Stage 1 (based on Pregnolato *et al*. 2022).

Criteria	Description
R1	Suitability for use at a remote site
R2	Capability of installation on or near a bridge pier or abutment
R3	Capability of obtaining readings from above the water surface (transmitting data without need for underwater access)
R4	Operation capability during storm and flood conditions
R5	Ability to operate from battery, solar power or fuel cell
R6	Ability to operate without the need to mobilize personnel during flood condition
R7	Industry-ready in a related application and/or laboratory-proof for scour assessment

Table 4. Stage 2 Criteria (Q) and Weights for Framework 2 (based on Pregnolato *et al.* 2022).

Criteria	Description	Weight
Q1	Purchase Cost	0.8
Q2	Expected Lifespan	1.1
Q3	Environmental Limitations	1.2
Q4	Robustness	1.2
Q5	Maintenance Requirements	1
Q6	Whole-life Cost	0.8
Q7	Accuracy, Repeatability, Reliability	1
Q8	Ease of Installation (access)	0.7
Q9	Power Consumption	0.8

3 CASE STUDIES

In this section, an assessment is conducted using Frameworks 1 to 3 which are applied to nine different case studies. Table 5 shows the results of the scour rating framework comparison conducted. When using Framework 3 if additional information concerning the location and dimension of the bridge was not available and required, Google Earth was used to estimate this information.

4 DISCUSSION

The comparison of the frameworks as applied to the nine-case studies are given in Table 5. For CS1 from Lin *et al.* (2021), MEMS sensor (which is the device installed on the bridge at

the time of the case study) scored very high for both Frameworks 1 and 2. For Framework 3, evaluating MEMS was not an option as this device is not included in Framework 3. Nevertheless, the case study was tested over the nine already available SHM devices which showed that TA/V device (79%) was the best option followed by the FO device (66%). Framework 1 and 2 can be easily used on already reported case studies to test the suitability of a known device but this may not be an option when using Framework 3 unless the device of interest is available in Framework 3. In the case of a bridge where the user wants a recommendation of a monitoring approach Framework 3 is more suitable.

For CS2, from Zarafshan *et al.* (2012), FBG device (which is the device installed on the bridge at the time of the case study) was ranked as more suitable by Framework 1 (19/25, High Applicability) compared to Framework 2 (27.6/43, Moderate Applicability). The device (which is similar to that reported in the case study of Lin *et al.* 2021) was not one of the nine available devices. However, Framework 3 shows that the TA/V device scored the highest (69%) followed by the FO device (68%). For CS2 the FO device although ranked second, scored higher compared to CS1. The TA/V device only scored 1% more than the FO device.

For CS3, PF was available as one of the nine devices in Framework 3. The PF device scored higher in Framework 1 (20/25, High Applicability) compared to Framework 2 (27.9/43, Moderate Applicability). Framework 3 listed the device fifth best, indicating that there may be more suitable devices. The device scored 59% according to Framework 3, providing similar results to Framework 2.

For CS4, from Zhan *et al.* (2022), the device installed on the bridge at the time of the case study was an accelerometer. Framework 1 scored the device as being of low applicability (11/25, Low Applicability) compared to Framework 2 for which the device did not pass to Stage 2 as it did not meet the criteria in Table 3. For Framework 3 the TA/V device (70%) scored the highest followed by the FO device (67%).

For CS5, from Weissmann *et al.* (2021), the approaches evaluated were US (sonar) and MSC. The US and MSC are highly applicable according to Framework 1 (21/25) and moderately applicable (32.1/43) according to Framework 2. Framework 3, once again, lists TA/V (78%) and FO (67%) as the top two devices. The MSC scored 48% while SN scored 49% according to Framework 3.

CS6, 7 and 8 all test a version of sonar (SN) which is also one of the nine devices available in Framework 3. SN was ranked as Moderately Applicable for CS6 (17/25) and Highly Applicable for CS7 (20/25) and CS8 (21/25). The device was ranked as Moderately Applicable for all three case studies when Framework 2 is applied. When Framework 3 was applied, SN scored 56%, 48% and 52% for case studies 6,7 and 8 respectively. The top two devices according to Framework 3 are the TA/V and FO device for all three case studies. Frameworks 1 and 2 give similar results for SN in all three case studies. For case studies 6 and 8, the score of SN by Framework 3 is slightly higher than 50%.

For CS9, the Limnimeter (LNM), the device installed on the bridge at the time of the case study (San Martin *et al.* 2023), scored very low with Framework 1 (9/25) and did not pass to the next stage for Framework 2. The LNM requires the intervention of a human operator during times of high flow to take the reading, making it a riskier device to deploy. The LNM is not one of the nine available devices in Framework 3. The results from Framework 3 show TA/V (68%) and FO (64%) as the top two devices for CS9 followed by ASC (62%).

5 SUMMARY AND CONCLUSIONS

Frameworks 1 and 2 provide similar results for the reviewed case studies with Framework 2 generally indicating lower applicability. According to Framework 3, the most suitable devices, for the nine case studies, are the TA/V and FO devices. In the cases where comparison between all three Frameworks could be done, the three Frameworks tended to agree. To allow a better comparison between the three Frameworks, as a next step, the nine devices available in Framework 3 should be tested for the nine case studies and ranked. A larger database could also be assembled for future calibration efforts of these (and possibly other) frameworks.

Table 5. The application of Frameworks 1 to 3 to previously published case studies.

CS	Bridge Name	Location	References	Device(s)	Framework 1	Framework 2	Framework 3
#1	Da-Chia Bridge	Taiwan	Lin *et al.* (2021)	MEMS	Score: 22/25 High Applicability	Score: 33.5/43 High Applicability	TA/V: 79%, FO: 66%, ASC: 63%, PF: 62%, SR: 59%, SN: 52%, TDR: 51%, MSC: 46%, PSDS: 45%.
#2	Salt Creek River Bridge	Chicago (USA)	Zarafshan *et al.* (2012)	FBG	Score: 19/25 High Applicability	Score: 27.6/43 Moderate Applicability	TA/V: 69%, FO: 68%, ASC: 57%, TDR: 56%, PF: 54%, SN: 48%, SR: 45%, PSDS: 42%, MSC: 32
#3	Sibin Bridge	Taiwan	Wang *et al.* (2012)	PF	Score: 20/25 High Applicability	Score: 27.9/43 Moderate Applicability	TA/V: 77%, FO: 69%, ASC: 63%, SR: 59%, PF: 59%, TDR: 47%, MSC: 47%, SN: 46%, PSDS: 41%
#4	Jigezhuang Bridge	Beijing (China)	Zhan *et al.* (2022)	ACC	Score: 11/25 Low Applicability	Table 3 criteria not met.	TA/V: 70%, FO: 67%, ASC: 58%, TDR: 57%, PF: 55%, SN: 51%, SR: 48%, PSDS: 42%, MSC: 34%
#5	Mustang Creek Bridge	Texas (USA)	Weissmann *et al.* (2021)	US and MSC	Score: 21/25 High Applicability	Total: 32.1/43 Moderate Applicability	TA/V: 78%, FO: 67%, ASC: 64%, SR: 61%, PF: 59%, SN: 49%,TDR: 48%, MSC: 48%, PSDS: 44%.
#6	Hangzhou Bay Sea Crossing Bridge	China	Peng (2020)	DS	Score: 17/25 Moderate Applicability	Total: 30.30/43 Moderate Applicability	TA/V: 70%, FO: 62%, TDR: 60%, ASC: 59%, PF: 57%, SN: 56%, SR: 49%, PSDS: 45%, MSC: 36%
#7	Góra Kalwaria	Poland	Topczewski *et al.* (2016)	3-D SN	Score: 20/25 High Applicability	Total: 30.2/43 Moderate Applicability	TA/V: 77%, FO: 68%, ASC: 63%, PF: 59%, SR: 58%, SN: 48%, TDR: 48%, MSC: 46%, PSDS: 43%
#8	The Indian River Inlet Bridge	Delaware (USA)	Hayden & Puleo (2011)	3-D PS	Score: 21/25 High Applicability	Total: 27.10/43 Moderate Applicability	TA/V: 81%, FO: 67%, ASC: 63%, PF: 62%, SR: 58%, SN: 52%, TDR: 51%, MSC: 46%, PSDS: 43%
#9	Rucúe Bridge	Chile	San Martin *et al.* (2023)	LNM	Score: 9/25 Low Applicability	Table 3 criteria not met.	TA/V: 68%, FO: 64%, ASC: 62%, TDR: 60%, PF: 56%, SN: 54%, SR: 47%, PSDS: 45%, MSC: 37%

[Note: Case Study = CS; MEMS = Vibration based Micro Electro Mechanical Accelerometer System Sensor; FBG = Fiber-optic Bragg Grating; ACC = Accelerometer; US = Ultrasonic Sensors (sonar); DS = Dual-axis Sonar; PS = Profiling Sonar; LNM = Limnimeter; TA/V = Tilt Angle/Vibration; ASC = Automatic Sliding Collar; PF = Piezoelectric Film; SR = Sounding Rod; SN = Sonar; TDR = Time Domain Reflectometry; MSC = Magnetic Sliding Collar; PSDS = Pneumatic Scour Detection System and FO = Float Out].

This paper has compared three scour rating frameworks using a selection of case studies from the literature. Frameworks 1 and 2 can evaluate monitoring devices and their accompanying instruments, offering insights into their applicability for specific scenarios. However, a-priori knowledge of possible sensing technologies is needed to effectively employ these frameworks. Framework 3 can yield results for nine monitoring devices, but it does require some updating especially with respect to the cost information.

ACKNOWLEDGMENTS

Special thanks to Matthew Lueker, University of Minnesota for sharing the SMDF spreadsheet and case study data. The work has been also funded in part by the Horizon Europe project ELABORATOR (Grant agreement ID: 101103772).

REFERENCES

Clubley, S. Manes, C. & Richards, D. 2015. High-resolution sonars set to revolutionise bridge scour inspections. *Proceedings of the Institution of Civil Engineers – Civil Engineering*, 168(1): 35–42. https://doi.org/10.1680/cien.14.00033

Dawson, R.J., Thompson, D., Johns, D., Wood, R., Darch, G., Chapman, L. & Hall, J.W. 2018. A systems framework for national assessment of climate risks to infrastructure. *Philosophical Transactions of the Royal Society A: Mathematical, Physical and Engineering Sciences*, 376(2121): [20170298]. https://doi.org/10.1098/rsta.2017.0298

Fisher, M., Chowdhury, M.N., Khan, A.A. & Atamturktur, S. 2013. An evaluation of scour measurement devices. *Flow Measurement and Instrumentation*, 33: 55–67. https://doi.org/10.1016/j.flowmeasinst.2013.05.001

Foley J. 2021. Managing flood risk in the face of a changing climate. Environment Agency, London, UK. Available from: <https://environmentagency.blog.gov.uk/2021/07/20/managing-flood-risk-in-the-face-of-a-changing-climate/> [04/03/2024]

Gavriel, G. 2019. An innovating rating system for assessing scour monitoring devices. Undergraduate Research, *Report No. 181RP009*, Department of Civil Engineering, University of Bristol, Bristol, UK

Gavriel, G., Vardanega, P.J. & Pregnolato, M. 2023. Comparison of maximum scour estimations using the HEC-18 method with field data from the USGS database. In: I. Lungu, I-B. Teodoru, & L. Batali (eds.)) *European Geotechnical Engineering - Unity and Diversity: Proceedings of the 17th Danube–European Conference on Geotechnical Engineering*, 7-9 June 2023, *Bucharest*, *Romania*. Politehnium Publishing House, Işai, România, vol. 2, pp. 631–638.

Hayden, J.T. & Puleo, J.A. 2011. Near Real-Time Scour Monitoring System: Application to Indian River Inlet, Delaware. *Journal of Hydraulic Engineering (ASCE)*, 137(9): 1037–1046. https://doi.org/10.1061/(ASCE)HY.1943-7900.0000399

Hong, J.H., Guo, W.D. Chiew, Y.M. & Chen, C.H. 2016. A new practical method to simulate flood-induced bridge pier scour—A case study of Mingchu bridge piers on the Cho-Shui River. *Water*, 8(6): [238]. https://doi.org/10.3390/w8060238

Jiang, S., Wang, Q., Sun, W. & Tan, Y. 2022. Bridge scour monitoring using smart magnetic rock. *Measurement*, 205: [112175]. https://doi.org/10.1016/j.measurement.2022.112175

Kirby, A.M., Roca. M., Kitchen A., Escarameia, M. & Chesterton, O.J. 2015. Manual on scour at bridges and other hydraulic structures, second edition. *Report no. CIRIA C742*, Department of Transport, London, UK.

Lagasse, P.F. Richardson, E.V. Schall, J.D. & Price, G.R. 1997. NCHRP report 396: instrumentation for measuring scour at bridge piers and abutments. Transportation Research Board, National Research Council, Washington, DC. Available from:; https://onlinepubs.trb.org/Onlinepubs/nchrp/nchrp_rpt_396.pdf; [04/03/2024].

Larrarte, F. Chevalier, C., Battist, L. & Chollet, H. 2020. Hydraulics and bridges: A French case study of monitoring of a bridge affected by scour. *Flow Measurement and Instrumentation*, 74: [101783]. https://doi.org/10.1016/j.flowmeasinst.2020.101783

Lin, Y.B. Lee, F.Z. Chang, K.C. Lai, J.S. Lo, S.W. Wu, J.H. & Lin, T.K. 2021. The artificial intelligence of things sensing system of real-time bridge scour monitoring for early warning during floods. *Sensors*, 21(14): [4942]. https://doi.org/10.3390/s21144942

Lu, J.Y., Hong, J.H. Su, C.C. Wang, C.Y. & Lai, J.S. 2008. Field Measurements and Simulation of Bridge Scour Depth Variations during Floods. *Journal of Hydraulic Engineering (ASCE)*, 134(6): 810–821. https://doi.org/10.1061/(ASCE)0733-9429(2008)134:6(810)

Lueker, M., Marr, J., Ellis, C., Hendrickson, A., Winsted, V. 2010a. Bridge Scour Monitoring Technologies: Development of Evaluation and Selection Protocols for Application on River Bridges in Minnesota. In: S.E. Burns *et al.* (eds.), *Proceedings 5th International Conference on Scour and Erosion (ICSE-5), November 7-10, 2010, San Francisco*, American Society of Civil Engineers, Reston, VA, USA, 949–957. https://doi.org/10.1061/41147(392)95

Lueker, M., Marr J., Ellis, C., Winsted, V. & Akula, S.R. 2010b. Bridge Scour Monitoring Technologies: Development of Evaluation and Selection Protocols for Application on River Bridges in Minnesota, *Report No. MN/RC 2010-14*. Research Services Section, Minnesota Department of Transportation, St. Paul, MN, USA. Available from:; https://rosap.ntl.bts.gov/view/dot/17886> [04/03/2024].

Maddison, B. 2012. Scour failure of bridges. *Proceedings of the Institution of Civil Engineers - Forensic Engineering*, 165(1): 39–52. https://doi.org/10.1680/feng.2012.165.1.39

Peng, L. 2020. Design and Implementation of Realtime Scour Monitoring of Hangzhou Bay Sea-Crossing Bridge Pier Based on Dual-Axis Scanning Sonar. *IOP Conference Series: Earth and Environmental Science*, 527: [012003]. https://doi.org/10.1088/1755-1315/527/1/012003

Pregnolato, M., Vardanega, P.J., Limongelli, M.P., Giordano, P.F. & Prendergast, L.J. 2021. Risk-based bridge scour management: a survey. In: H. Yokota & D.M. Frangopol (eds.) *Proceedings of the 10th International Conference on Bridge Maintenance, Safety and Management (IABMAS 2020)*, April 11-15, 2021, *Sapporo, Japan*, CRC Press/Balkema, Taylor & Francis Group, pp. 693–701. https://doi.org/10.1201/9780429279119-91

Pregnolato, M., Gavriel, G., Thompson, D. Anderson, M. Fox, I. & Giles, K. 2022. Scour monitoring for railway assets (UK). In: J.R. Casas, D.M. Frangopol & J. Turmo, (eds.), *Bridge Safety, Maintenance, Management, Life-Cycle, Resilience and Sustainability*, CRC Press, pp. 879–884. https://doi.org/10.1201/9781003322641-105

Prendergast, L.J. & Gavin, K. 2014. A review of bridge scour monitoring techniques. *Journal of Rock Mechanics and Geotechnical Engineering*, 6(2):138–149. https://doi.org/10.1016/j.jrmge.2014.01.007

Pizarro, A., Manfreda, S. & Tubaldi, E. 2020. The Science behind Scour at Bridge Foundations: A Review. *Water*, 12(2): [374]. https://doi.org/10.3390/w12020374

San Martin, C. Rifo, C. Guerra, M. Ettmer, B. & Link, O. 2023. Monitoring Scour at Bridge Piers in Rivers with Supercritical Flows. *Hydrology*, 10(7): [147]. http://dx.doi.org/10.3390/hydrology10070147

Sasidharan, M., Parlikad, A.K. Schooling, J. Hadjidemetriou, G.M. Hamer, M. Kirwan, A. & Roffe, S. 2023. A bridge scour risk management approach to deal with uncertain climate future. *Transportation Research Part D: Transport and Environment*, 114: [103567]. https://doi.org/10.1016/j.trd.2022.103567

Selvakumaran, S., Plank, S., Geiß, C., Rossi, C. & Middleton, C. 2018. Remote monitoring to predict bridge scour failure using Interferometric Synthetic Aperture Radar (InSAR) stacking techniques. *International Journal of Applied Earth Observation and Geoinformation*, 74: 463–470. https://doi.org/10.1016/j.jag.2018.07.004

Shahriar, A.R. Gabr, M.A. Montoya, B.M. & Ortiz, A.C. 2023. Local scour around bridge abutments: Assessment of accuracy and conservatism. *Journal of Hydrology*, 619: [129280]. https://doi.org/10.1016/j.jhydrol.2023.129280

Tola, S., Tinoco, J. Matos, J.C. & Obrien, E. 2023. Scour Detection with Monitoring Methods and Machine Learning Algorithms—A Critical Review. *Applied Sciences*, 13(3): [1661]. https://doi.org/10.3390/app13031661

Topczewski, Ł. Cieśla, J. Mikołajewski, P. Adamski, P. & Markowski, Z. 2016. Monitoring of scour around bridge piers and abutments. *Transportation Research Procedia*, 14: 3963–3971. https://doi.org/10.1016/j.trpro.2016.05.493

Vardanega, P.J. Gavriel, G. & Pregnolato, M. 2021. Assessing the suitability of bridge-scour-monitoring devices. *Proceedings of the Institution of Civil Engineers – Forensic Engineering*, 174(4): 105–117. https://doi.org/10.1680/jfoen.20.00022

Wang, C-Y. Wang, H-L. & Ho, C-C. 2012. A piezoelectric film type scour monitoring system for bridge pier. *Advances in Structural Engineering*, 15(6): 897–905. https://doi.org/10.1260/1369-4332.15.6.897

Weissmann, J. Chun, H.T. & Haas, C. 2021. Pilot installation of a bridge scour monitoring site. *Transportation Research Record*, 1749(1): 68–72. https://doi.org/10.3141/1749-11

Zarafshan, A. Iranmanesh, A. & Ansari, F. 2012. Vibration-Based Method and Sensor for Monitoring of Bridge Scour. *Journal of Bridge Engineering (ASCE)*, 17(6): 829–838. https://doi.org/10.1061/(ASCE)BE.1943-5592.0000362

Zhan, J. Wang, Y. Zhang, F. An, Y. & Liu, K. 2022. Scour depth evaluation of highway bridge piers using vibration measurements and finite element model updating. *Engineering Structures*, 253: [113815]. https://doi.org/10.1016/j.engstruct.2021.113815

Bridge Maintenance, Safety, Management, Digitalization and Sustainability – Jensen, Frangopol & Schmidt (eds)
© 2024 The Author(s), ISBN 978-1-032-77040-6
Open Access: www.taylorfrancis.com, CC BY-NC-ND 4.0 license

Next generation risks challenge bridge maintenance and management in Finland

J. Wuorenjuuri
Sweco Finland Oy

ABSTRACT: The Finnish bridges have been traditionally well kept. However, there are many significant findings of new types of technical challenges in bridge maintenance that will cause significant funding and innovative needs soon in the future. The environment, load management and aging of structures have been in focus earlier, but traditional bridge inspections are not sufficient to find these new structural risks. New generations of risks cannot be managed by only traditional inspections. Also, a new generation of bridge management is needed. Finland is not alone with these challenges.

1 INTRODUCTION

The merger of the road, railway and maritime authorities and the establishment of the Finnish Transport Infrastructure Agency in 2011 was a significant step forward in bridge management and maintenance in Finland. In the case of bridges, this has been significant in the improvement of resources and the quality and coverage of design, construction, and maintenance procedures. Although railway bridges and road bridges differ in many ways in terms of maintenance, there are also similarities. In particular, the procedures were unified by comparing and selecting the best operating methods from the practices of all engineering structures.

In Finland, the national road network is divided into 79 maintenance areas and the rail network is divided into maintenance areas. The basic maintenance actions are given to private companies that are supervised by the Agency officials. The maintenance company performs the basic maintenance and annual inspections. The Finnish Transport Infrastructure Agency conducts research, repair programing and commissions bridge inspections. Repairs are separate tasks for companies specialized in the field of bridge repairs. The repair debt program has increased bridge repairs in recent years.

2 THE TRADITIONAL CHALLENGES

In addition to aging, the traditional challenges of bridges in Finland have been related to heavier traffic, changes in load conditions and identifying special structural solutions. These challenges have been well managed, but there has also been development of new challenges in the recent years. Repair activities have often been not only slowing the aging process or modernizing the bridge, but also new innovations.

The starting point of all bridge management and maintenance is safety everywhere. Maintenance tasks must be planned and performed under the conditions of road and train traffic. Safety always involves both work and train/vehicle safety aspects, and often also electrical safety near electrified tracks. During repair and maintenance measures, it is usually not possible to interrupt traffic for a very long time, so work methods in the infra environment are

DOI: 10.1201/9781003483755-129

always chosen according to how traffic can be organized. There has been an improvement in this planning in Finland in recent years.

In Finland, the actual loads on bridges have developed significantly over the years. Older bridges are designed for much lower loads than the traffic that crosses them now. Old railway bridges also have many load accumulations, which is a fatigue issue. Although today's bridges are designed for fatigue, older bridges are usually not designed for fatigue at all. Older bridges may have fatigue-related damage, although these are not always recognized as fatigue-related problems.

Railroad bridges often also have special structures that must be considered in maintenance and upkeep. These include for example riveted steel structures in significant joints, different edge structure solutions, fall protection deficiencies of old bridges and diverse track structures. Road bridges have joints that need attention. Old railings on bridges do not meet the requirements of safety, especially when aged and damaged.

Of course, railway bridges have also practical challenges compared to road bridges. Access to structures is often difficult in Finland or at least requires special arrangements. Railroad bridges may be at the end of non-road access routes, and the transport of repair materials or equipment to the site sometimes requires ingenuity. The electric track makes lifting work more difficult, limits the use of large work tools in treatment procedures. There is a great number of large road bridges that need special arrangements just to get to get access to details.

3 THE TRADITIONAL CHALLENGES

3.1 *Riveted bridges*

In 2009, serious damage was found in the riveted steel bridge joints. It was found that the joints of the beams supporting the tracks were swaying under the traffic. In worst cases the rail had suffered serious local wear. When the rivets were examined, it was possible to find with ultrasound that some of the rivets were broken and the movement in the joint was at worst visible with the naked eye. In this case, the 60-meter span steel truss bridge was repaired by strengthening the joints. The following years, similar joint damage was observed in many bridges, which also needed to be urgently repaired.

The Finnish Transport Agency carried out a risk mapping based on the calculation of the bearing capacity of all steel bridges and the assessment of the consequences, based on which joint inspections of steel bridges were systematically carried out. 91 bridges were selected for the steel bridge program. In addition to the special inspections, the maintenance companies were given instructions for an enhanced inspection. Especially significant were the cases where track measurement errors cannot be explained on the track itself in the track structure. In on-going projects, it was re-evaluated whether risky bridges should be replaced instead of repaired.

Today, most of the steel bridges of main line tracks have been renovated into modern bridges. In addition, quick joint repairs have been made to a dozen bridges on other track sections to extend their life cycle. All riveted bridges are examined with ultrasound every 10 years. Monitoring of these structures has been tested, but it has been a challenge to monitor all joints. Also, studies have been made how critical these movements are. A new question is whether a fixed bolted joint has the same behavior than the original riveted joint.

Several studies of joints and rivets have been carried out, and repair methods of these joints have been introduced in a way that does not disturb traffic. Most of the costs of the repair work are scaffolding costs when the scaffolding is hung from the bridge. There are probably several reasons for the damage, but the most damaged joints have been found in those bridges where the load accumulations have been the greatest. In certain cases, it has been possible to show that the secondary structures participate in carrying the load more than what was considered in the old calculations. The dimensional accuracy of the joints and manufacturing defects have also been a factor in the progression of damage.

Old railways bridges of steel without a without the ballast layers also have other maintenance challenges. Wooden sleepers, track structures, rail movement joints and transition zones are special structures, for which special expertise should also be focused on. Since most bridge

maintenance activities focus on concrete bridges, the number of available experts of these structures has been minimized. The experts need and understanding of these structures and is essential for any old structure. The challenges and problems are so diverse that the owners have not been able to highlight the problems in the contracts, and so the maintenance companies have not been able to offer the expertise. This leads to the maintenance of steel bridges being only light actions and running after possible faults.

3.2 *Aesthetics or lifetime durability*

In the design and construction of bridges, the 1960s-70s seemed to be a period in which wonderful slender bridge structures were designed, built, and admired. It was seen professionally talented if all capacity of materials could be used in design. Some of the bridges were new innovations, where the lifetime of the bridge was not prioritized very highly. Not all bridges were made this way, but many significant bridges were. However, this design approach has had its downside, as many bridges from that era now have problems that require constant maintenance and monitoring. A traditional special inspection does not necessarily provide an answer to problems. The problems cannot be detected in one inspection. With these bridges, it is important to know how to maintain and understand the history of the bridge structure and the overall behavior.

Bridges, which are still aesthetically stunning, are the most valuable structures in the rail and road network. The aging network and its structures are a challenge for maintenance anyway. It's good that life cycle aspects and easy maintainability in the design of new bridges have increased the value in the railway bridge industry.

3.3 *Post-tensioned structures*

In 2012, a water tower collapsed in Jyväskylä early in the morning. Fortunately, there were no personal injuries, but the collapse has had significant effects. One of the main reasons for the collapse of the prefabricated and tensioned water tower was the corrosion of the tension cables. The steel of post tensioning was rusted on the surface, but the most important were the cracks, which had significantly weakened some of the steels. According to the research, it was a so-called delayed hydrogen fracture, which is possible with older, stronger permanently stressed steels.

The Finnish Transport Infrastructure Agency immediately studied whether road and railway bridges have been made with excessively strong post tension steel of the same type and from the same era. Several bridges were found. Completely similar cases and a dozen other suspicious cases were found on bridges. Special inspections were targeted at all these bridges with risk spans. There were some closures to road bridges, and they were built again. On the railways it was not possible close train traffic, so these bridges are also heavily monitored and managed. Perhaps the most significant bridge that was renewed because of this is the long road bridge crossing the Ilmala railway yard rails in Helsinki, which was found to be tensioned with corresponding steels. The bridge was closed to car traffic almost immediately. The bridge has since been rebuilt.

Bridge structures under tension also have other challenges. Tensioned trough bridges, which were built before frost-resistant concrete was developed, are challenging due to frost cracking. Large concrete surfaces are susceptible to weathering. Although they can be coated and processed afterwards, the weather stress is so severe that the concrete has already been found to be deeply damaged on several bridges. This requires a very extensive special inspection program for bridges and, of course, the repair measures are technically more difficult than just repairing the surface. Of course, worst case scenario is the aging that influences load bearing capacity and the functioning of the tendons.

3.4 *Quality of concrete*

Defects in the quality of concrete occur in other bridges as well. Of course, most of the concrete damage in concrete structures is caused by aging, but in recent years, because of special

inspection efforts, it has also been possible to find other types of concrete quality problems, both in new and older railway bridges. In surprisingly many bridges, there is reason to suspect the presence of alkaline aggregate in the concrete.

In newer bridges, strength deficiencies have now been observed in the concrete, which are thought to be due to over-optimization of the concrete manufacturing processes. Concrete and cement quality issues have come up. In some cases, concrete has had too much air, and this causes losses in strength and lifetime behavior. Transporting concrete from longer distances has been aided by adding air to it. New codes and testing of concrete have been introduced.

3.5 *Consequences*

In Finland, there has been a situation for a long time where the number of bridges in poor condition has been growing. Thanks go to a good management system and the efficient and successful allocation of repair funds. But these new generations problems also have meant that many of these bridges are rebuilt well before their planned design life is over.

The funding needs greater estimates for repairs. Unfortunately, there are still large bridges in the repair programs, which are both technically challenging and expensive to renew or repair. In addition, the repair works are difficult to coordinate in terms of road and train traffic, and exceptional arrangements for train traffic must be agreed upon several years in advance. Even though the number of bridge repairs is under control; it can be argued that all the easy bridge repairs have been done and the difficult and expensive bridge repairs remain.

When the speeds of traffic and the weight of freight vehicles have increased, it has been necessary to think about installing speed and weight limits on older bridges, if there is a doubt that the behavior of the bridge is no longer controllable due to damage or otherwise. The Finnish Transport Infrastructure Agency maintains information about traffic restrictions caused by bridges in the management systems. The number of traffic restrictions has increased significantly in the past years.

Some of the bridges are clearly weight-restricted as old bridges, when calculations do not make the bridge withstand the new load requirements. But there are also cases where the damage to the bridge has progressed so far that the installation of a traffic limitations has been a necessary measure. In addition, these bridges cause pressure on daily maintenance. They must be monitored daily and possibly organized monitoring so that safety can be guaranteed.

Aging and deteriorating infrastructure, including bridges, are an even bigger challenge for basic maintenance. At its most effective, daily maintenance is the best medicine to ensure the safety and condition of bridges. The maintenance person must have enough activity and understanding to take care of the condition of the bridges. It is very valuable information for the owner of the bridge and the owner's experts when the maintenance personnel reports that he does not understand why there is a problem on a certain bridge that the problem cannot be removed by his own efforts. This automatically leads to additional studies of bridge experts.

Daily maintenance is also the most cost-effective way to maintain bridges. By making small repairs in maintenance, the owner can extend the repair interval of bridges by up to several tens of years. Active maintenance personnel should be given better opportunities to take care of the bridges. It would also reduce the owners work by reducing the bureaucracy associated with the tendering of repair works and the collection of initial data. If the owner does not know how to define bridge maintenance in tender documents and contracts, it also leads to the fact that contractors do not know how to resource enough skilled personnel for bridge maintenance.

4 MEETING THE CHALLENGES

4.1 *Bridge management system*

At the beginning of 2017, the Finnish Transport Agency introduced a register of engineering structures, which includes bridges and all other structures related to roads, railway, and maritime infrastructure. The register has been developed for several years and almost the entire

industry has been involved in doing this in some way. This is a big step towards more effective maintenance management. There is a lot of information on repairs related to bridge repairs in the register. All bridges decisions are now in the same process of making decisions as other engineering structures.

Of course, data maintenance processes play an important role in ensuring that the register contains high quality information in the future. The Finnish Transport Infrastructure Agency has great goals that all data from maintenance and inspections to planning and construction is gathered into the system. The challenge is to get all implementation information up to date in the register, especially when the processes and delays in the delivery of implementation information vary almost from contract to contract. The delivery and collection of register data is also expert work, which is not so simple for all operators who come to infrastructure projects as new designers or contractors.

4.2 *Bridge inspections*

Since the beginning of the Finnish Transport Infrastructure Agency, a lot has been invested in bridge inspections, and the information and benefits obtained from them are great. All bridges undergo a general expert inspection every five years. Carrying out general inspections requires a bridge inspection qualification. Bridges with known faults, are listed and inspected more thoroughly.

The number of special inspections of bridges has been increased considerably. The number of special inspections in a year has doubled or tripled. Also, most of the repair design is now based on special inspections. With the special inspections, maintenance programming has become more detailed, and repairs have been able to be optimized even better. There has been better starting information for repair planning than before.

Bridge monitoring has also been increased. In 2016, the Finnish Transport Agency completed a Monitoring Guide to improve the operations of subscribers and a Monitoring Handbook as a tool for planners. As the possibilities of monitoring increase and the costs become more reasonable, it is important that the clients know how to define the contents and requirements of the monitoring assignments well. Different monitoring projects, monitoring project phases and actors are identified in the instructions, and the instructions have already been used successfully in several orders.

The Finnish Transport Infrastructure Agency also renewed the annual maintenance inspections for railway bridges. With the new instruction, the inspections involved not only renewing the forms, but also defining the reporting requirements. The maintenance person is now also required to have an annual inspection qualification. This has been reflected in the improvement of the quality of the inspections and in the improvement of the possibilities of utilizing the inspection results.

4.3 *Knowing the weak points*

As mentioned above, there are numerous new challenges in the bridges that cannot be detected by traditional inspections. In Finland a continuous improvement in inspection methods and data quality in the database are crucial. Of course, there will be new challenges in the future also, but it is a success story how these problems of bridges have been handled in the management systems.

It is known, where the week points are, why they are named as monitored structures and how to manage them, keeping the bridges safe for the users. These hidden defects are part of the complete management and maintenance systems.

5 CONCLUSIONS

Although the maintenance of bridges in Finland has always been done very professionally, there has been a significant shift in bridge maintenance. More resources have been obtained both in terms of know-how and money. Road and track projects and bridge repairs are better

defined, which can be seen in the fact that bridge repairs are better included and managed in large road and rail projects. Competent people are needed now and certainly more in the future, but the development of railway bridges is now of interest to a wide range of professionals, from professionals to decision-makers. And even though bridges are replaced with new bridges, old bridges are still valued by keeping them in good condition.

REFERENCES

Finnish Transport Infrastructure Agency. Manual for Railway Bridges *RATATEKNISET OHJEET (RATO) osa 8, Rautatiesillat, 2020*. Helsinki

Finnish Transport Infrastructure Agency. Bridge managements system, Helsinki

Tampere Technical University, Fatigue Testing of Riveted Joints of the Kruunukylänjoki Bridge, Tuomo Siitonen, Masters Thesis, 2015

Finnish Transport Infrastructure Agency. Väyläviraston sillat 31.12.2022, Sillaston rakenne, palvelutaso ja kunto Osa 1: Tiesillat Osa 2: Rautatiesillat

Bridge Maintenance, Safety, Management, Digitalization and Sustainability – Jensen, Frangopol & Schmidt (eds)
© 2024 The Author(s), ISBN 978-1-032-77040-6
Open Access: www.taylorfrancis.com, CC BY-NC-ND 4.0 license

The effect of conceptualization on bridge maintenance prioritization

K. Zangpo, A. Amir & M. Henry
Shibaura Institute of Technology, Tokyo, Japan

ABSTRACT: The safety and operability of bridges are key elements for ensuring the functionality of highway networks. However, in Bhutan, road bridges are aging and deteriorating faster than they are maintained. This may be due to the current practice of bridge prioritization for periodic maintenance by ranking based on bridge inventory data and bridge structure condition data, as the ranking is affected not only by the actual condition of the bridges but also by bridge characteristics unrelated to the condition. Therefore, the statistical effect of indicator selection on the ranking of bridges for maintenance prioritization needs to be examined. This research explores the effect of different conceptualizations of maintenance prioritizations by analyzing how the rankings of the bridges change depending on what combination of bridge data are used for calculating the maintenance priority. This study will clarify how uncertainties in the subjective choice of conceptualization affects the bridge ranking for maintenance prioritization.

1 INTRODUCTION

Bridges are a crucial component of road infrastructure. While they are constructed to serve the purpose of connecting roads, inadequate maintenance can impose a significant burden on a country's economy (Mansour et al., 2019). This is particularly evident in Bhutan, where many bridges are ageing and need prioritization for maintenance. However, in Bhutan, due to budget constraints in the road sector, funds have often been reallocated to constructing new bridges, neglecting the maintenance of existing ones. This lack of attention to bridge maintenance is partly attributed to the absence of a systematic maintenance strategy within the Department of Surface Transport (DoST) and the lack of a decisive tool for prioritizing bridge maintenance.

The Japan International Cooperation Agency (JICA) supported the "Construction and Maintenance of Bridge" (CAMBRIDGE) project in Bhutan from 2016 to 2022. This project aimed to develop a comprehensive Bridge Management System (BMS) to facilitate decision-making in prioritizing bridge maintenance within the country. The BMS in Bhutan prioritizes maintenance by ranking bridges based on inventory data and their structural condition. Ranking and prioritizing provide the insight needed for the decision-making process (Dabous & Alkass, UK). Different departments of transportation widely employ various ranking and prioritization procedures to evaluate and select bridge projects. However, the conceptualization behind ranking bridges for maintenance prioritization is an essential aspect of bridge management. Conceptualization is the source of uncertainty (Henry & Opon, 2022) and in the BMS, it can potentially lead to alterations in the prioritization ranks of bridges depending on the chosen conceptualizations. Various approaches or models based on different conceptualizations have been developed to prioritize bridge maintenance, with each approach emphasizing distinct factors. Zhang & Wang (2017) underscore the importance of considering bridges' rankings at the network level, the condition of structural elements, and conducting risk analyses for selected maintenance strategies to effectively prioritize within budget constraints. Similarly, Contreras et al. (2019) focused on factors like aggregated ratings, average daily traffic, safety, resilience, serviceability, and comfort, determining

DOI: 10.1201/9781003483755-130

weights for these factors to enable systematic maintenance prioritization under budget constraints. Echaveguren & Dechent (2019) proposed a prioritization index considering structural condition, hydraulic vulnerability, seismic risk, and the bridge's significance in the road network to prioritize maintenance at the network level. Correspondingly, Whealan et al. (2019) introduced an approach that assesses factors such as bridge condition, maintenance urgency, traffic impact, costs associated with failure, and natural disaster risk to rank bridges for maintenance. While the development of these objective and transparent prioritization formulas is crucial for effective bridge maintenance management, it is also important to assess and understand the impact of various conceptualizations on bridge ranking, as conceptualization can introduce uncertainty into the prioritization of bridges for maintenance planning.

Hence, this study explores the effect of different conceptualizations on bridge maintenance prioritization by analyzing data obtained from the DoST. This data includes bridge inventory (characteristics of the bridges), condition data of the entire bridge, superstructure, and substructure, as well as the condition of secondary facilities such as bearings, ancillary facilities, expansion joints, and drainages. Three conceptualization scenarios were analyzed: firstly, ranking bridges based solely on bridge structure condition data; secondly, considering both bridge structure and secondary facilities condition data; and thirdly, a comprehensive approach that includes all data combinations, namely bridge inventory, structure condition, and secondary facilities condition. The results of these scenarios were compared with the baseline scenario to determine the impact of different conceptualization approaches on bridge ranking for maintenance prioritization. Comprehending the impact of conceptualization on prioritization is crucial for the roads department in any country facing similar uncertainties in the prioritization process. This understanding helps in carefully defining a strategy for ranking bridges and facilitates the development of an effective maintenance plan.

2 RESEARCH METHODOLOGY

2.1 *Data acquisition*

The Bridge Management System (BMS) data were obtained from the Department of Surface Transport (DoST) under the Ministry of Infrastructure and Transport in Bhutan. The BMS data included inventory data for 235 bridges, along with bridge inspection data for the year 2023. These bridges are located along national highways, Dzongkhag Roads (connecting each district to the Local Government Centre), and Access Roads under the administration of DoST. During the data cleaning process, it was noted that the construction year for 9 bridges (approximately 3.8% of the total) was missing. Consequently, the analysis was conducted on the remaining 226 bridges. The BMS database, developed as part of the JICA Project "CAMBRIDGE," comprises both inventory and inspection data for each bridge. It's important to note that the inventory data, which includes detailed bridge characteristics as illustrated in Table 1 below, is collected and updated only for newly constructed bridges and is not updated unless there is a change in the bridge characteristics.

Table 1. Bridge inventory data.

Inventory	Type
Bridge classification	Concrete, steel, composite, bailey bridge
Road classification	Primary NH*, Secondary NH, Dzongkhag Road, Access Road
Loading capacity of bridge (tonne)	8, 12, 18, 24, 40, 70
Average Daily Traffic (ADT)	<50, 50-100, 100<
Age of bridge (years)	0-10, 11-20, 21-30, 31-40, 41-50, 50<
Abutment type	Reinforced Cement Concrete, Random Rubble Masonry
Rainfall conditions	Light, Moderate, High
Alternate route	Yes, No

* NH: National Highway

The bridges are usually inspected twice a year, and, for maintenance prioritization, the bridges are ranked based on the scores calculated from bridge inventory data and the inspection data. The bridge inspection data consists of damage rating criteria for individual bridge elements such as the overall condition of the bridge, superstructure (deck and girder), and the substructure of the bridge. Each damage rating criterion has its respective damage score points. This damage rating criteria and distribution of damage score points for each bridge element were framed during the CAMBRIDGE project. Table 2 shows the sum of the maximum damage scores for each bridge element.

Table 2. Bridge damage criteria with the sum of the maximum score for each bridge element.

Bridge elements	Maximum score
Overall condition	60
Superstructure (concrete deck)	55
Superstructure (steel deck)	25
Superstructure (concrete girder)	70
Superstructure (Steel girder)	65
Substructure (Masonry)	40
Substructure (Masonry)	10

2.2 *Conceptualizations of maintenance prioritization*

In the present context, the bridges are ranked based on the calculated scores from the inventory data and the inspection data, and based on this rank the bridges are prioritized for periodic maintenance. However, it is important to note that the inclusion of inventory data, such as road categories, bridge types, and other factors, may lead to changes in ranks even though they may not directly impact the structural condition of the bridge. This leads to the exploration of the effect of different conceptualization scenarios on the prioritization of bridges to see the effect of choice in the conceptualization approach by analyzing how the rank of the bridge changes depending on each method of conceptualization scenario. In this research, the current

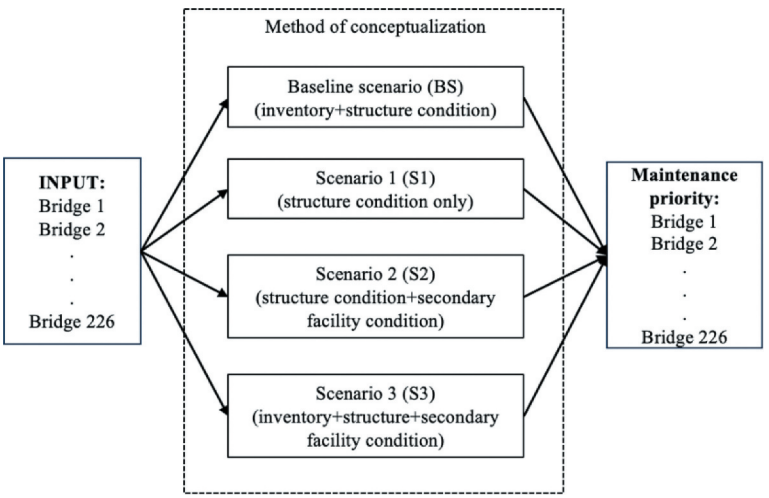


Figure 1. Analytical framework for examining the effect of conceptualization on maintenance prioritization.

practice of bridge prioritization by ranking based on inventory data and structure condition data was considered as the baseline scenario (BS) and further explored three different conceptualizations to study the statistical effect on the conceptualizations for bridge ranking. The first scenario (S1) considered only the structural condition of the bridge, the second scenario (S2) considers the structure condition, as well as the secondary facility condition of the bridge, and the third scenario (S3), includes not only the structure and secondary facility condition but also the inventory of the bridge. The analytical framework used for this study is shown in Figure 1.

The difference in each conceptualization scenario is reflected based on the inclusion or exclusion of either bridge inventory or the secondary facility condition while computing the prioritization ranking. The baseline scenario includes inventory data and the structure condition data whereas scenario S1 excludes the inventory data. Scenario S2 differentiates from S1 with the inclusion of the secondary facility condition of the bridge. While S3 and baseline scenarios have common inventory and structure conditions, S3 has an additional secondary facility condition that distinguishes it from the baseline scenarios as shown in Table 3.

Table 3. Distinguishing feature of each conceptualization scenario.

	Are secondary facility conditions included?		
		Yes	No
Inventory included?	Yes	S3	Baseline
	No	S2	S1

The propagation of uncertainty from the choice of conceptualization can be analyzed using sensitivity analysis to quantify the average rank and standard deviation of the ranks of all bridges across the four conceptualization scenarios. This shift in the rank of a particular bridge will infer the sensitivity of the bridge rank concerning the choice of the conceptualizations for maintenance prioritization.

2.3 *Assigning damage score points for the secondary facility conditions*

The secondary facility conditions of the bridges, such as bearing, railing, expansion joints, and drainage facilities, are also inspected together with the structural condition of the bridge. Since they are not considered in the prioritization of the bridge in the current prioritization method, they do not have any distribution of scores against their damage scales. However, based on the importance of the facility members and the similar point allocations from existing bridge elements, suitable scores were also assigned to the secondary facility conditions. The score of zero applies to the excellent condition without any defect to the secondary facilities and higher scores denote the high level of defects/damages observed. These scores were assigned specifically for this research to analyze the role of conceptualizations in ranking the bridges for prioritization.

2.4 *Data normalization and priority ranking*

The bridges with different abutment types get different scores from the observed damage criterion during the inspection. The Reinforced Cement Concrete (RCC) abutment bridges get a maximum score of 40 while Random Rubble Masonry (RRM) abutment bridges get only 10 points. Therefore, the RCC bridge scores were normalized from 40 to a maximum of 10 points so that the ranking comparisons can be done regardless of abutment type.

The total score for each bridge was then computed based on the damage criterion and the distributed scores for each damage scale observed in the bridge elements and with these scores, the rank of the bridge was generated for all the bridges in all four scenarios. However, due to the different calculation processes used during the conceptualizations, the rank of the bridges was inconsistent within these four scenarios and the range of the ranks is also different

for each scenario. Hence, the ranks in all four scenarios were normalized from 0 to 1 with the highest normalized priority of 1.0 for the highest rank bridge and similarly, lowest rank bridges get the normalized priority of 0.0, and the normalized priority of the bridges falling between the highest and lowest ranks is linearly calculated between 0.0 and 1.0. This process was repeated for all scenarios and each bridge obtained four priority ranks based on the four different conceptualization scenarios adopted. The correlation matrix was also developed to check the relationship between different conceptualization approaches to see how the introduction of different categories of criteria influences the prioritization ranking of bridges. The normalized priority ranks of BS, S1, S2, and S3 were used to calculate the average normalized priority rank to represent the average priority across the four different scenarios. The standard deviation was also calculated, which shows the variability in the priority of the bridges due to the choice of conceptualizations.

3 RESULT AND DISCUSSION

3.1 *Priority ranks in each scenario*

Table 4 shows the five highest, and five lowest normalized priority ranks of the bridges obtained in each conceptual scenario. Since there are 226 bridges in total, all the bridges' rankings are not displayed, rather the top and bottom five are to see the consistency in the ranking for these bridges regarding the choice of conceptualization methods. For baseline and Scenario 3, bridge B151 exhibits the highest priority rank whereas Bridge B129 is the highest for Scenario 1 and Scenario 2. While the baseline scenario and Scenario 3 maintain a consistent priority rank for up to the second highest priority rank, Scenario 1 and Scenario 2 are consistent up to the third highest priority rank. Similar patterns are observed for the bottom 3 priority rank for the baseline scenario and Scenario 3. However, Scenario 1 and Scenario 2 have 100 bridges with the same rank at the bottom of the prioritization.

Table 4. Priority rank in each scenario.

	Baseline Scenario		Scenario 1		Scenario 2		Scenario 3	
Rank	Bridge No.	Priority rank	Bridge No.	Priority rank	Bridge No	Priority rank	Bridge No	Priority rank
1	B151	1.000	B129	1.000	B129	1.000	B151	1000
2	B184	0.996	B151	0.988	B151.	0.992	B184	0.996
3	B136	0.991	B136	0.975	B136	0.984	B129	0.991
4	B135	0.987	B127	0.963	B115	0.976	B136	0.987
5	B18	0.982	B115	0.950	B184	0.968	B115	0.982
222	B134	0.022	B222	0.000	B222	0.000	B8	0.022
223	B1	0.013	B223	0.000	B223	0.000	B138	0.022
224	B6	0.009	B224	0.000	B224	0.000	B6	0.009
225	B180	0.004	B225	0.000	B225	0.000	B180	0.004
226	B14	0.000	B226	0.000	B226	0.000	B1	0.000

Overall, the rank of the bridges is inconsistent across each scenario, but some scenarios exhibit a similar rank of the bridges when they have common categories of criteria for prioritization used for the conceptualization. The correlation matrix in Table 5 shows how the introduction of different categories of criteria for prioritization influences the ranking for prioritization. In a correlation matrix, variables with correlation coefficient values close to −1.0 or 1.0 are highly correlated, whereas variables having correlation values close to 0 are regarded as non-correlated (Amir & Henry, 2023). It was observed that the correlation coefficient of the baseline scenario and S3 was found to be 0.97, highly showing a correlation between these two

scenarios. While this strong correlation is due to the common inventory data, the inclusion of secondary facility condition data in scenario 3 does not affect the overall ranking of the bridge compared to the baseline scenario. Similarly, the correlation coefficient between S1 and S2 was found to be 0.87 showing these two scenarios also correlated due to common structure condition data. Correspondingly, the inclusion of secondary facility condition data in scenario 2 does not affect much the overall rank of the bridges compared to scenario 1.

Table 5. Correlation matrix in each conceptualization scenario.

	Baseline	S1	S2
S1	0.55		
S2	0.47	0.87	
S3	0.97	0.58	0.58

3.2 *Relationship between the average priorities and their standard deviations*

The normalized priority ranks from the four scenarios were used to compute the average normalized priority rank of each bridge to represent a single priority rank across all four scenarios. The standard deviation of the four normalized priority ranks was also calculated for each bridge to quantify the variability in the bridge's ranks, which indicates the sensitivity in the rank of the bridge due to the uncertainty that arises from the choice of conceptualization.

From Figure 2 which shows variability in the rank of 226 bridges against their average normalized priority, it can be observed that certain bridges are highly sensitive to the choice of conceptualization while certain bridges are not regardless of what prioritization

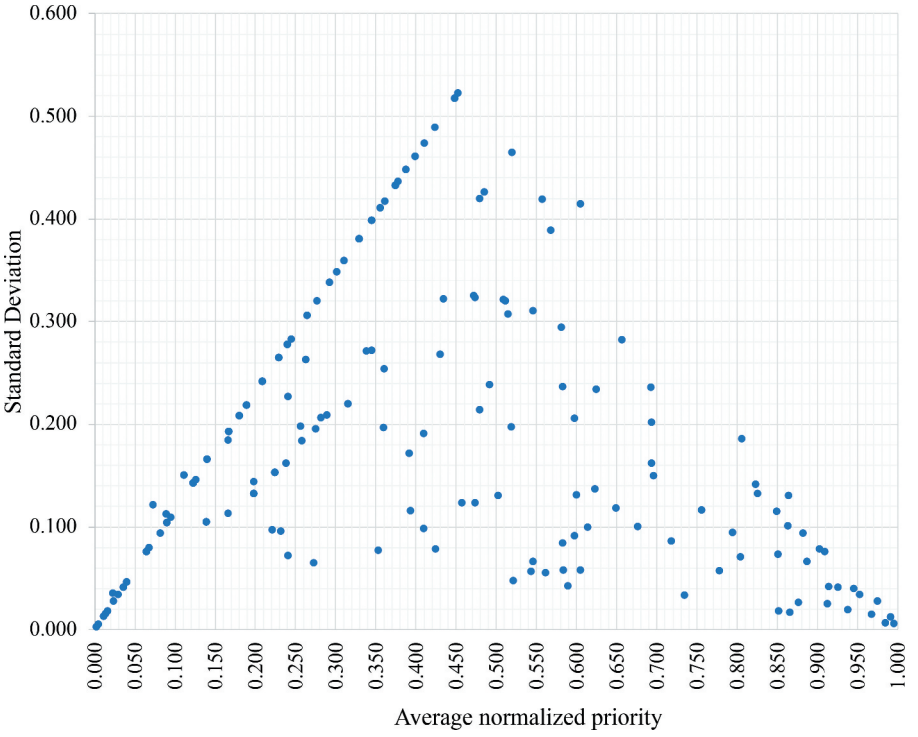


Figure 2. Average normalized priority of bridges against standard deviation.

conceptualizations are used. Bridges with extreme (very high or very low) average priority are consistent in their rank regardless of what conceptualization is used. The bridges with high average priority tend to have a low standard deviation, which suggests that regardless of what conceptualization is used these bridges have high normalized priority. It can be ascertained that there is little uncertainty about their priority and their rank is not very affected by the choice of conceptualization. The bridges with the low average priority also tend to have low standard deviation, so it can be surmised that they are consistently a low priority regardless of how the priority is conceptualized.

It is observed that the high-average priority bridges have a higher level of damage in the bridge structure conditions and thus they have high scores in the structure conditions. These bridges are located along higher classifications of road, have medium to high loading capacity of bridge, and have high average daily traffic volume, and the older age of the bridge contributes higher to the inventory scores. With these two high scores, the average score remains high with a less standard deviation. On the other hand, low-average priority bridges have lower levels of damage, and they score the least in the bridge structure conditions. These bridges are located along the lower classifications of roads with less average daily traffic and younger ages of the bridge which contributes least to the inventory scores. With these two low scores, the average score remains low with less standard deviation. Hence, the bridges with both high and low average normalized priority are insensitive to the selection of conceptualizations.

In Scenario 1 and Scenario 2, many bridges have the same normalized priority of 0. However, normalized priority in the baseline scenario and Scenario 3 are highly linearly correlated with almost the same value. With the same normalized priority in the two scenarios in S1 and S2, their average normalized priority is a linear function of a change of just one variable since the normalized priority of baseline and S3 are almost the same. This results in the linear change of the standard deviation with the average normalized priority, which can be observed on the left side of Figure 2. Since the average normalized priority will be just the function of the baseline scenario and Scenario 3, and when those values increase, the average normalized priority will also increase. Similarly, the standard deviation also increases at an equivalent rate. When these average normalized priority increases, the standard deviation shifts by the same amount since standard deviation is a function of how far the values in baseline and S3 are from S1 and S2. Hence, a linear straight line is observed for the standard deviation with the increase in average normalized priority.

The bridges in the middle range of average normalized priority exhibit absolute more uncertainty since they have low priority in one or two conceptualization scenarios but have high priority in the remaining scenarios. These bridges are highly sensitive to the choice of conceptualizations due to zero scores in the structure condition of the bridge, but the inventory scores are higher. These bridges have good structural condition but their location in a higher classification of roads, high traffic volume, classification of bridge types, and the age of the bridge contributes to high scores in conceptualizations that include inventory, which creates a large gap from the structure conditions. The average of these two scores depends entirely upon the inventory condition of the bridge and accordingly, the standard deviation varies. There arises an ambiguous situation as to whether they can be low priority or high priority. These bridges are highly sensitive to the choice of conceptualization which can result in the alteration of its priority ranking depending upon the choice of conceptualizations.

4 CONCLUSION

This paper examined the statistical effect of conceptualization on the maintenance prioritization of bridges based on four different conceptual scenarios. The bridges were ranked in each scenario and these ranks were compared with the average normalized rank to see how the ranks change depending on the choice of conceptualizations.

The introduction of different categories of criteria for the prioritizations in different conceptualizations influences the ranking of the bridges for prioritizations. Two categories of criteria such as inventory data and secondary facility condition data were introduced in two scenarios to see how the rank changes. The baseline scenario and Scenario 3 show a strong correlation

due to the common inventory data, whereas the baseline scenario and Scenario 1 show a high difference in rank due to the difference in inventory data. However, the introduction of secondary facility condition data in Scenario 2 does not influence much the prioritization ranks from Scenario 1. This concludes that, even if the secondary facility condition data are included in the prioritization, the prioritization ranks are not sensitive to the inclusion of this data.

The bridges with high average normalized priority are consistently high priority regardless of the conceptualizations. There is little uncertainty in the fact that they are high-priority bridges. Similarly, the bridges with low average normalized priority are consistently low priority regardless of the conceptualizations for they don't need prioritizations. The high and low average normalized priority bridges have low certainty in the context of decision-making and can be confident in terms of budget allocations that high-priority bridges are always higher priority regardless of how the prioritization is conceptualized. However, the bridges in the middle range of the average normalized priority are highly sensitive to the choice of conceptualization. While these bridges are low priority when considering only the structure condition of the bridge, the same bridges are high priority when the inventory condition data is introduced. This leads to ambiguity in setting the priority into either low or high priority for those bridges.

This study delved into the understanding of how conceptualization can impact the prioritization of bridges for maintenance planning. Therefore, the road department should carefully define strategies for effective prioritization in bridge maintenance planning.

ACKNOWLEDGMENTS

The authors would like to thank the Japan International Cooperation Agency (JICA) for the support through the Road Asset Management Platform (RAMP) at Shibaura Institute of Technology (SIT) and the Department of Surface Transport (DoST) for providing the BMS data without which this research would not be possible.

REFERENCES

Amir, A. and Henry, M., 2023. Reverse Engineering of Maintenance Budget Allocation Using Decision Tree Analysis for Data-Driven Highway Network Management. *Sustainability*, *15*(13), p.10467.

Contreras-Nieto, C., Shan, Y., Lewis, P. and Hartell, J.A., 2019. Bridge maintenance prioritization using analytic hierarchy process and fusion tables. *Automation in Construction*, *101*, pp.99–110.

Dabous, S.A. and Alkass, S., A ranking and prioritizing method for bridge management.

Echaveguren, T. and Dechent, P., 2019. Allocation of bridge maintenance costs based on prioritization indexes. *Revista de la construcción*, *18*(3), pp.568–578.

Henry, M. and Opon, J. (2022) "The role of conceptualization in the evaluation of sustainable concrete", *Acta Polytechnica CTU Proceedings*, 33, pp. 219–225. doi: 10.14311/APP.2022.33.0219.

Mansour, D.M.M., Moustafa, I.M., Khalil, A.H. and Mahdi, H.A., 2019. An assessment model for identifying maintenance priorities strategy for bridges. *Ain Shams Engineering Journal*, *10*(4), pp.695–704.

Whelan, M.J., Cavalline, T.L., Alar, A. and Lane, K., 2019. *Guidelines for Prioritization of Bridge Replacement, Rehabilitation, and Preservation Projects* (No. FHWA/NC/2016-05). North Carolina. Dept. of Transportation.

Zhang, W. and Wang, N., 2017. Bridge network maintenance prioritization under budget constraint. *Structural safety*, *67*, pp.96–104.

Bridge Maintenance, Safety, Management, Digitalization and Sustainability – Jensen, Frangopol & Schmidt (eds)
© 2024 The Author(s), ISBN 978-1-032-77040-6
Open Access: www.taylorfrancis.com, CC BY-NC-ND 4.0 license

Bridge condition index: A review of methodologies used in Bridge Management Systems

A. Agredo Chávez, J. Gonzalez-Libreros, C. Wang & G. Sas
Luleå University of Technology, Luleå, Sweden

ABSTRACT: The transport infrastructure consists of roads, bridges, and tunnel networks. Among these, bridges, viaducts, and tunnels are particularly vulnerable due to structural degradation caused by environmental conditions, overloading, and other factors. Ensuring the safety of these assets, especially at the network level, is a significant challenge. The emergence of Bridge Management Systems (BMS) addresses the need for comprehensive information in managing inspections, condition assessments, and optimizing investments in bridge maintenance. Despite the benefits, many countries face challenges in identifying high-risk bridges. Issues include the lack of high-quality data, mixed ownership of assets, diverse management system platforms, varying condition rating schemes, and the absence of a risk-based assessment. This review aims to highlight current practices and research efforts in evaluating bridge condition indices/ratings (BCI) for existing bridges. The identified knowledge gaps emphasize the need for national authorities to develop policies leading to a unified and functional approach for condition rating.

1 INTRODUCTION

Since the late 1980s the structural health assessment and monitoring of bridges represented a critical topic in the field of civil infrastructure management (Thompson et al., 1998). Transportation agencies face the challenge of balancing limited resources with the growing demands of an aging highway system, particularly in addressing the diverse needs of numerous bridges. While deciding what is more optimal for each bridge is crucial, it is important to realize that the ideal choice for one bridge may not match the overall priorities of the entire bridge system, especially when dealing with financial limitations.(Rashidi and Gibson, 2012). Acknowledging this complexity, bridge engineers, bridge managers and owners, and public officials understand the necessity for established methods and procedures. These methods are essential not only to assess the current and future conditions of bridges but also to determine the most effective allocation of funds within a broader system of bridges. The objective is to make informed choices regarding various types of bridge maintenance, repair, rehabilitation, and replacement options. Currently, municipalities face considerable financial strain due to their underperforming aging infrastructure. This escalates the risk of service disruptions compelling decision-makers to undertake immediate interventions (Soliman and Frangopol, 2015)

The emergence of Bridge Management Systems (BMS) addresses the growing demand for effective management of bridge-related information. BMS employs a comprehensive set of methodologies and procedures to oversee data throughout a bridge's entire life cycle, encompassing project design, construction, monitoring, maintenance, and eventual decommissioning as defined by Rogulj and Kilić Pamuković (2023). BMS is a response to the heightened awareness of bridge collapse incidents (Arismendi et al., 2020) particularly in forecasting the degradation of bridges influenced by changing climate conditions (Nasr et al., 2020). Some countries, such as The United States, France, and Italy (AASHTO, 2018, CEREMA, 2019, CSLP, 2020), have introduced national guidelines to provide detailed instructions for the

DOI: 10.1201/9781003483755-131

development and adoption of multi-risk BMS, aiming to optimize the management of bridges at both national and regional levels.

Within the complex framework that encompasses BMS, condition assessment and bridge health rating stand out as one of the most critical parts in assessing bridge damage for future allocation of budget. Currently, national authorities address the condition rating scales in the guidelines with different approaches, which makes them not easily comparable (Iacovino et al., 2022). These differences in approaches could yield to different conclusions related to the management of the target asset within the road network. Establishing a standardized rating system offers numerous benefits, notably facilitating an objective comparison of the health status of infrastructures. This contributes to the allocation of economic funds for the rehabilitation and modernization of these infrastructural assets (Matos et al., 2023).

This study compares how different countries rate the condition of existing bridges and their methodologies used. A review was conducted on their standards, guidelines, and practices. The objectives of the study are: (1) to examine different ways countries evaluate bridge condition index (BCI), (2) to identify variations in the factors influencing these condition ratings, and (3) to explore emerging trends that could lead to a more comprehensive approach in evaluating and scoring bridges for budget allocation.

2 BRIDGE MANAGEMENT SYSTEMS

2.1 *Components*

According to (Omar and Nehdi, 2018), a fully developed BMS should include four main components for the implementation of a functional BMS.

2.1.1 *Data inventory*

Information related to each stage in the life cycle of bridges must be gathered and stored. Typically, the inventory comprises technical drawings of the initial project design and as built condition, written reports from regular on-site inspections, data series obtained from monitoring sensors, and geographically referenced information pertaining to the structure's location (FHA, 2022).

2.1.2 *Bridge condition rating*

Bridge condition rating (BCR) consists of condition assessment and a rating system. The efficacy of a bridge management system relies on the precision and on the extent of the condition data collected. Condition assessment involves comparing the as-designed, as-built, and as-is states of structures, alongside an evaluation of their current load-bearing capacity. The evaluation of the as-is state involves various tools for field and site inspections. While various bridge owners and managers employ distinct strategies for condition rating (see Table 1 and Table 2), the element-based inspection is widely recognized as the most commonly used technique for assessing conditions (Rashidi and Gibson, 2012). Given that bridge inspection involves inherent imprecision, the bridge condition rating naturally incorporates uncertainty, especially when local authorities lack specific guidelines for damage assessment and condition rating (Dabous, 2017).

2.1.3 *Deterioration prediction and cost models.*

A deterioration model (usually Markov-chain theory for bridge deterioration (Liu and Frangopol, 2006)) is used to predict the future condition of the bridge and its components by means of mathematical models and numerical simulations using finite element method. This scenario becomes particularly beneficial when detailed data from in-depth inspections or load tests are accessible. Cost models associated with maintenance, rehabilitation and replacement is also presented.

2.1.4 *Maintenance planning*

The outputs from condition rating and simulations, collectively function as input for executing intervention prioritization, a pivotal element within the maintenance planning component of a BMS framework. The prioritization of interventions, whether on individual elements or the entire structure, is determined through a multi-criteria approach that considers the risk of

defects or collapse. Specialized methods, such as the Analytic Hierarchy Process (AHP), have been developed to streamline and automate this type of management (Santarsiero et al., 2021).

Current Bridge Management Systems (BMS) vary in terms of the number of modules they possess. Some function solely as data management systems without the capability to forecast deterioration. Meanwhile, other systems allow for deterioration predictions, employing either deterministic or more or less complex probabilistic deterioration models (Lukas and Borrmann, 2012). Some BMS apply multi-risk methodologies for prioritization of maintenance and/or rehabilitation of a bridge within a given network, which can provide information of the likelihood of occurrence of adverse events and their associated consequences (Saydam et al., 2013). Nevertheless, current literature on applying probabilistic risk methodologies to BMS is limited. Many transportation agencies predominantly use only the risk towards structural deficiency to allocate funding for deficient bridges (Yang and Frangopol, 2018). Therefore, the respective practices of BMS's modules vary from agency to agency.

3 REVIEW OF EXISTING BRIDGE CONDITION INDICES

Current practices in BMS are reviewed with the aim to map out the main parameters involved in the assessment of bridge health condition rating worldwide. BCI, also known as: Bridge Health Index (BHI), Bridge Condition Rating (BCR), or Attention Class (CdA), between others, is the term used in literature to define rating systems for bridges. These performance ratings serve to show how vulnerable bridges are to structural or operational hazards, such as hurricanes, earthquakes, or overloaded trucks, and to assess their effectiveness in handling these scenarios (Adu-Gyamfi et al., 2016).

Table 1 displays the BCI employed by BMS in different countries along with the corresponding guidelines applied for the calculation of condition ratings within the BMS. Additionally, it is shown if the guidelines consider a multi-risk assessment in the calculation of the condition rating and the frequency of inspection dictated by the standard.

Table 1. Bridge Management System's BCI and guidelines per country.

Country	BMS	Guidelines	Multi-risk	Risk type	Inspection freq. R* /D**
Slovenia	MOST	MOST guidelines			5 y.
USA	AASHTOware	NBI AASHTO	✓	Seismic, Floods, scour	2 y.
Sweden	BaTMan	BaTMan Teknisk Handbok			6 months 6 years
Finland	HiBris, HankeSiha	Finnra Guidelines			1 year 6 years
Norway	BRUTUS	HB129, HB136,147			1 year. 5 years
Italy	INBEE	MIT 2020	✓	Str.-found, Seismic, Hydraulic, Landslide	2 years
Portugal	GOA	IP			6 years
Slovakia	-	SSC			1 year. 4 years.
France	LAGORA	IQOA	✓	Scour	1 year 6 years
Denmark	DANBRO+				6 months 6 years
UK	SMIS	CS469 2021	✓	Scour Hydraulic	1 year 6 years

* Regular inspection
** Detailed inspection

In Table 1, it is possible to identify significant variations in condition ratings depending on the country. Ranging from qualitative to quantitative approaches and featuring a considerable gap between BCI values, the assessment considers the worst condition in either an ascending or descending manner. Nevertheless, when there is an increase in the number of levels or categories within a system used to rate the condition of bridges, it becomes more difficult to express clear differences between the various states of structural condition (Matos et al., 2023). The challenge arises because the boundaries that separate one level from another become less distinct or harder to define. As the complexity of the rating system increases, it becomes harder to clearly distinguish between the different conditions or states of the structure being assessed.

Moreover, it is possible to notice how new guidelines are incorporating the use of multi-risk assessment. For instance, after the events of the collapse of the Morandi Bridge, Italian Ministry of Transport and Infrastructure worked on improvements in the reliability of existing Italian bridges (Sano et al., 2023). The new Guidelines for the classification and management of risk, the evaluation of safety and the monitoring of existing bridges was published in 2020 (CSLP, 2020), determining risk classification based on hazard, exposure, and vulnerability (see Figure 1).

The concept of risk in BMS comprises two key elements: the probability of failure and the consequences. The probability of failure is associated with the forces acting on the structure

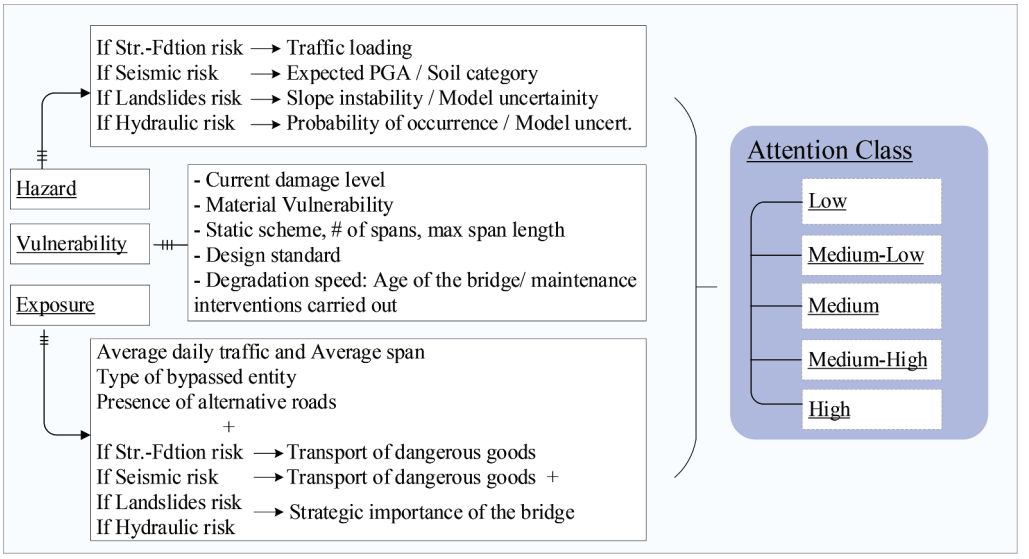


Figure 1. Scheme for Italian guidelines for attention class (CdA) classification (CSLP, 2020).

due to specific events. The consequences encompass user costs, social costs, and the expenses associated with repairs or reconstruction. In this regard, in the context of seismic assessment, the probability of failure is linked to seismic forces, while the consequences are tied to the damage incurred by the bridge (Valenzuela et al., 2009). The assessment of risk depends on the specific hazards associated with each country. For example, seismic activity is a significant consideration in Italy and the USA, but not as much in England or France. This distinction becomes crucial if European codes aim for unification, as certain hazards, like earthquakes, would carry greater weight in calculations compared to others, such as hurricanes.

On this matter, it is important to analyze how BCI is calculated in every country. By doing this, it is possible to capture the parameters of influence that govern the rating of bridges. Currently, most BMSs rely on element-level information for calculating BCIs, indices vary primarily based on the type of information and the quantity of data used in their calculation. According to literature (Adu-Gyamfi et al., 2016, Casas and Bien, 2007, Iacovino et al., 2022, Pregnolato et al., 2024), the different approaches used by the guidelines to calculate the condition index are:

- Ratio-Based Methods: These methods involve assigning a Bridge Condition Number (BCN) based on the ratio of the current condition to the condition when the bridge was new.
- Weighted Averaging Approach: This approach is suitable for planning maintenance and rehabilitation activities. It estimates the overall structure condition by combining condition ratings of individual bridge elements identified during inspection, with weights based on their significance or contribution to structural integrity. The urgency of intervention depends on the probability of structure or element failure.
- Worst-Conditioned Component Approach: Common in systems inspecting key bridge components, this method identifies critical defects by approximating the BCI to the rating of the worst-conditioned component. The German and Japanese BCIs are the examples of this approach.
- Qualitative Methods: Qualitative methods describe a bridge's condition as "Poor," "Fair," or "Good" capturing information about the critical defects in bridge components. For example, in Sweden, repair priorities are scheduled based on severity, functional, and economic condition (related to the extent of damage).
- Risk-based Prioritization: Thie method is focus on prioritization of bridge repair and replacement works in a system. The aim of the proposed method is to offer bridge owners and managers, a transparent and objective scheme for bridge evaluation and project prioritization through a risk-based strategy.

Table 2 depicts a summary of the approaches utilized by the previously mentioned countries.

Table 2. Bridge Management System's BCI approach.

Country	Condition Definition	Original Language	BCR approach	BCI	Worst condition
Slovenia	Condition Rating	(R)	Weighted average	0-40	>25
USA	BHI	Bridge Health Index	Ratio-based /Risk-based	0-9	0
Sweden	Alllowed Classes	Tillståndsklasser (TK)	Qualatitive/ Weighted average	Good (0) Bad (3)	Bad (3)
Finland	Condition Index	KTI	Weighted average	0-4	4
Norway	Condition Number	Skadegrad	Qualitative	1-4	4
Italy	Attention Class	Classe di Attenzione (CdA)	Weighted average/ Risk-based	Low-High	high
Portugal	Condition State	(EC)	Qualitative	0-5	5
Slovakia	Condition Index	Index stavebno-technického stavu	Weighted average	I-VII	VII
France	Condition Class	Classe d'état	Qualitative	1-3U	3U
Denmark	Condition Rating	Tilstandskarakter	Qualitative	0-5	5
UK	BCI	Bridge Condition Index	Weighted average	0-100	(<65)

Some agencies could incorporate two methods to evaluate a BCI, for instance, BaTMan in Sweden incorporates the qualitative method only if specified important structural elements (such as supports, primary load-bearing elements, foundation, etc.) are assigned to a condition class 3. If they are assigned a lower condition class, the determination of the overall condition class relies on the weighting factors outlined in the guidelines. Certain organizations that have adopted risk-based methodologies still depend on the inspector's judgment to determine severity of deterioration elements. For example, the Italian guidelines (CSLP, 2020) use an attention class to assess the structure's vulnerability through visual inspection. In this approach, the inspector assigns defect severity and extent, and the process involves a weighted average.

A significant drawback of the examined methods for calculating the BCI is the absence of entirely objective data. This limitation stems from the prevalent use of visual inspection, which relies on the inspector's expertise and judgment. Consequently, the assignment of weights can vary, resulting in different ratings for the same bridge by different inspectors. Autonomous damage detection is arising as a tool to overcome this problem. Some road agencies (i.e., New Jersey Department of Transportation) incorporate a value of uncertainty in the calculation of the perceived risk to account for a factor to account for the level of uncertainty associated with the selected assessment approach, including the quality control measures employed. Table 3 describes a summary the advantages and limitations associated with each approach aimed to estimate the BCI.

Table 3. Advantages and limitation for the calculation approach of Bridge Condition Indices (BCI).

Ratio-based approach	Weighted Average approach	Worst-Conditioned approach	Qualitative Approach	Risk-based approach
Advantages				
Useful in resource allocation for bridge networks.	Index combines all defects identified at the element level.	Correlates the bridge condition to the weakest link in the structure.	Straightforward and representation of the bridge condition without relying on a numerical scale.	More transparent and objective method for assessing bridges and prioritizing projects.
Can be integrated into prioritization models for allocating funds.		Useful for assessing the vulnerability of a bridge in case of extreme events.		
Limitations				
Could be inconsistent if no standardized guidelines for bridge element inspection are available.	Difficulties in assessing how the condition of an element impacts the overall structure of the bridge	Does not provide a comprehensive view of the distribution of deterioration across the bridge.	Inefficient for prioritizing and planning maintenance as it lacks a quantitative scale for ranking bridges in a network.	The ranking is frequently determined by individual owner/agency-defined criteria or perceptions of risk.

4 IDENTIFICATION OF PARAMETERS OF INFLUENCE

Apart from the variation in the calculation methods, most of the parameters used in determining the BCI are similar. Each country considers various damage characteristics: extent (how widespread the damage is), severity (intensity of the damage), and intervention urgency (recommended repair time for safety, usability, and durability). Additionally, structural type, material vulnerabilities, degradation level, the structural element under assessment, traffic load, environmental exposure, and the type of bypassed entity (if a bridge spans over a river, a major highway, a railway line, etc.) are other parameter commonly found within the methodologies assessed. However, certain parameters are not frequently considered in these calculations.

4.1 *Design standard*

Numerous bridges constructed during the '50s and '60s exhibit structural and technological shortcomings inherently associated with the construction era. These deficiencies stem from the absence of seismic design codes and limitations tied to the technologies and materials available during that period, rendering them "afflicted by design" (Cutrone et al., 2022). Furthermore, in order to be able to estimate the level of vulnerability of the works, it is important to know the hypotheses underlying their creation and, among these, the loads foreseen in the design phases.

4.2 *Static scheme*

The vulnerability of structures is closely tied to their structural characteristics, encompassing static scheme and response to external forces. Parameters such as redundancy in the static scheme (greater hyperstaticity indicates lower vulnerability), susceptibility to brittle failures (e.g., shear failures for Gerber beams), are important factors when assessing vulnerability in structures with varying static schemes, materials, and spans.

4.3 *Age of the structure/Last inspection performed*

Comparing bridges based on their year of construction is particularly relevant when there have not been significant maintenance interventions. However, if well-documented maintenance has effectively reduced degradation, returning the structure to its initial condition, the focus should shift to the year of the last maintenance intervention. In such cases, a special concern should be assigned to bridges with more recent interventions, even if their current degradation level matches that of structures with less recent maintenance.

4.4 *Environmental exposure*

Climate influences on the rate of bridge deterioration. A study lead by (Šelih, 2014) found that structural decay is slowest in the Mediterranean climate, moderately slow in the Alpine climate (likely due to fewer annual freeze-thaw cycles), and notably faster in the continental climate, characterized by numerous freeze/thaw cycles during winter.

4.5 *Road alternatives*

In areas with insufficient infrastructure, the collapse of a road bridge could have catastrophic consequences for road traffic, particularly in emergency situations, as there may be a lack of alternative routes. Some agencies, like the North Carolina Department of Transportation (NCDOT) consider this on the calculation of the ranking criteria for Priority Replacement Index (PRI).

Some guidelines include additional factors like the transportation of dangerous goods, military significance, or serving as an evacuation route for nuclear incidents. Assessing exposure involves analyzing traffic data, including vehicle frequency, and considering the network's resilience to unexpected situations.

5 CONCLUSIONS

The aim of this paper was to provide an overview of different methodologies within the field of bridge condition rating. The methodologies employed for bridge condition rating differ from country to country, and the parameters considered in the assessment could also vary. The variations in these approaches may lead to different conclusions regarding the management of the specific asset within the road network, especially when analyzing the road infrastructure at border crossings. In essence, the methods used to assess or address issues at these border-related road structures may differ, potentially leading to divergent recommendations or management decisions. A comprehensive approach for bridge condition index is essential, it should not only evaluate bridge health by identifying its degree of degradation but also all potential hazards to encompass risks. New guidelines incorporate concepts of risk and bridge prioritization indexes to account for hazards, societal, environmental, political, and military consequences to provide a more objective classification of the bridge when funds for maintenance need to be allocated.

Recommendations for a unified condition rating system is imperative. This system should address the diverse needs and challenges, including those posed by climate changes. However, to limit the number of such levels to ensure that engineers can easily classify bridges without encountering unnecessary complications.

ACKNOWLEDGMENTS

The authors gratefully acknowledge financial support from INTERREG AURORA as part of the Sustainable Construction And Build Environment in Arctic Climate project.

REFERENCES

AASHTO 2018. Manual for Bridge Evaluation, 3rd Edition (with 2020 and 2022 Interim Revisions). Washington, DC: American Association of State Highway and Transportation Officials.

Adu-Gyamfi, Y., Chase, S., Aktan, A. & Minaie 2016. *Synthesis of National and International Methodologies Used for Bridge Health Indices*.

Arismendi, R., Barros, A., Vatn, J. & Grall, A. Prognostics and maintenance optimization in bridge management. *In*: Beer, M. & Zio, E., eds. 29th European Safety and Reliability Conference, ESREL 2019, 2020. Research Publishing Services, 653–660.

Casas, J. R. & Bien, J. 2007. Updated inventory on condition assessment procedures for bridges: Sustainble Bridges SB D3.2- Including an Appendix on Methods of railway bridge testing and evaluation in Poland.

CEREMA, C. F. S. A. E. O. R. T. E. M. A. U. P. 2019. Analyse de risque des ponts en site affouillable.

Cslp, C. S. D. P. 2020. Linee Guida Per La Classificazione e Gestione Del Rischio, La Valutazione Della Sicurezza Ed Il Monitoraggio Dei Ponti Esistenti Rome, Italy: Ministero delle Infrastrutture e dei Trasporti MIT.

Cutrone, B., Salvatore, W., Renzi, E. & Tamasi, G. "Guidelines for the classification and management of risk, for the evaluation of safety and for the monitoring of existing bridges". Critical analysis and identification of innovative methods to improve the classification of landslide risk. *In*: FERRO, G. a. & Restuccia, L., eds. 19th ANIDIS Conference, Seismic Engineering in Italy, 2022. Elsevier B.V., 713–720.

Dabous, S. A. 2017. Assessing transition probability of bridge deterioration using Dempster-Shafer theory of evidence. *Bridge Structures*, 12, 97–106.

Fha, U. S. D. O. T.-F. H. A. 2022. Specifications for the National Bridge Inventory.

Iacovino, C., Turksezer, Z. I., Giordano, P. F. & Limongelli, M. P. 2022. A Survey of Bridge Condition Rating Systems. *In*: Pellegrino, C., Faleschini, F., Zanini, M. A., Matos, J. C., Casas, J. R. & Strauss, A. (eds.) *1st Conference of the European Association on Quality Control of Bridges and Structures, EUROSTRUCT 2021.* Springer Science and Business Media Deutschland GmbH.

Liu, M. & Frangopol, D. M. 2006. Probability-based bridge network performance evaluation. *Journal of Bridge Engineering*, 11, 633–641.

Lukas, K. & Borrmann, A. 2012. Integrated bridge management from 3D-model to network level.

Matos, J. C., Nicoletti, V., Kralovanec, J., Sousa, H. S., Gara, F., Moravcik, M. & Morais, M. J. 2023. Comparison of Condition Rating Systems for Bridges in Three European Countries. *Applied Sciences* [Online], 13.

Nasr, A., Kjellström, E., Björnsson, I., Honfi, D., Ivanov, O. L. & Johansson, J. 2020. Bridges in a changing climate: a study of the potential impacts of climate change on bridges and their possible adaptations. *Structure and Infrastructure Engineering*, 16, 738–749.

Omar, T. & Nehdi, M. 2018. Condition Assessment of Reinforced Concrete Bridges: Current Practice and Research Challenges. *Infrastructures*, 3, 1–23.

Pregnolato, M., Giordano, P. F., Panici, D., Prendergast, L. J. & Pina, Limongelli, M. 2024. A comparison of the UK and Italian national risk-based guidelines for assessing hydraulic actions on bridges. *Structure and Infrastructure Engineering*, 20, 117–130.

Rashidi, M. & Gibson, P. 2012. A methodology for bridge condition evaluation. *Journal of Civil Engineering and Architecture*, 6, 1149–1157.

Rogulj, K. & KiliĆ Pamuković, J. 2023. Sustainable planning based decision-making approach for the restoration of historic road bridges. *Structure and Infrastructure Engineering*.

Sano, S., Costa, G., Giordano, P. F., Pregnolato, M. & Limongelli, M. P. 2023. Multi-risk assessment for bridges: the application of the Italian Guidelines. *ce/papers*, 6, 772–779.

Santarsiero, G., Masi, A., Picciano, V. & Digrisolo, A. 2021. The Italian Guidelines on Risk Classification and Management of Bridges: Applications and Remarks on Large Scale Risk Assessments. *Infrastructures*, 6, 111.

Saydam, D., Frangopol, D. & Dong, Y. 2013. Assessment of Risk Using Bridge Element Condition Ratings. *Journal of Infrastructure Systems*, 19, 252–265.

Šelih, J. 2014. Analysis of bridge condition on state network in Slovenia. *Gradevinar*, 66, 811–822.

Soliman, M. & Frangopol, D. M. 2015. Life-cycle cost evaluation of conventional and corrosion-resistant steel for bridges. *Journal of Bridge Engineering*, 20.

Thompson, P. D., Small, E. P., Johnson, M. & Marshall, A. R. 1998. The Pontis Bridge Management System. *Structural Engineering International*, 8, 303–308.

Valenzuela, S., Solminihac, H. & Echaveguren, T. 2009. Proposal of an Integrated Index for Prioritization of Bridge Maintenance. *Journal of Bridge Engineering*, 15, 337.

Yang, D. Y. & Frangopol, D. M. 2018. Risk-informed bridge ranking at project and network levels. *Journal of Infrastructure Systems*, 24.


Taylor & Francis
Taylor & Francis Group
http://taylorandfrancis.com

MS13: Bridge loading – measurement and modelling

Organizers: C. Caprani, A. Nowak, E. O'Brien & X. Ruan


Taylor & Francis
Taylor & Francis Group
http://taylorandfrancis.com

Bridge Maintenance, Safety, Management, Digitalization and Sustainability – Jensen, Frangopol & Schmidt (eds)
© 2024 The Author(s), ISBN 978-1-032-77040-6
Open Access: www.taylorfrancis.com, CC BY-NC-ND 4.0 license

Braking effects on vehicle-bridge interaction

A. Aloisio
Department of Civil, Construction-Architectural and Environmental Engineering, University of L'Aquila, L'Aquila, Italy

G. Quaranta
Department of Structural and Geotechnical Engineering, Sapienza University of Rome, Rome, Italy

A. Contento
College of Civil Engineering, Fuzhou University, Fuzhou, China

M.M. Rosso
Dipartimento di Ingegneria Strutturale, Edile e Geotecnica, Politecnico di Torino, Torino, Italy

ABSTRACT: When analyzing the impact of vehicle braking on a bridge, it becomes evident that the bridge's deflection increases significantly compared to when a vehicle is in constant motion. The magnitude of this deflection is influenced by the Vehicle-Bridge Interaction (VBI) phenomena, which is significantly activated by road roughness. This road roughness instigates specific dynamics in the vehicle, accentuating the VBI. Our study introduces a probabilistic model to quantify this amplification factor due to a vehicle's hard braking at the bridge's mid-span across various road roughness categories. The amplification factor is defined as the ratio between maximum deflections during vehicle braking and those when the vehicle is at a consistent speed. It's estimated considering parameters like the vehicle's mass, velocity, natural frequency, and damping. For our VBI model, we utilized the finite difference method to discretize the coupled governing equations. Here, the vehicle is represented as a two-degree-of-freedom system, accounting for both its bouncing and pitching motions. The model's computational efficiency facilitated extensive analyses where parameters were chosen via the Latin Hypercube sampling method. Ultimately, we validated our model outputs against real-world bridge displacement measurements under varied conditions.

1 INTRODUCTION

The displacement impact factor IF is commonly considered in order to quantify the effects of braking on bridge dynamics under traffic loads. It is defined as follows:

$$\mathrm{IF} = \frac{w_{b,braking}}{w_{b,constant}}, \tag{1}$$

where $w_{b,braking}$ and $w_{b,constant}$ are the maximum bridge deflection under braking conditions and the value corresponding to a vehicle that moves at a constant speed, respectively.

The thorough examination of vehicle-bridge dynamic interactions necessitates considering a multitude of factors. However, many research works employ analogous, oversimplified models. This trend, coupled with the paucity of studies comparing these various modeling techniques, hinders understanding the significance of all elements and parameters related to braking in estimating its impact on bridge dynamics. It's pivotal not only to assess alternative

DOI: 10.1201/9781003483755-132

modeling methodologies based on their intricacy, precision, and computational implications but also to gauge their utility in real-world applications, including sensitivity and reliability assessments. Consequently, this research delves into two distinct modeling strategies to explore the dynamics of vehicle-bridge interactions during braking scenarios. The initial category encompasses models rooted in foundational physics principles. Notably, six such models, distinguished by varying degrees of complexity and precision, are incorporated into this study. A detailed outline of these models, along with their inherent assumptions, is presented in Table 1.

Table 1. Considered physics-based models of the vehicle-bridge interaction in braking conditions.

Model assumptions					
Model label	IF label	Roughness	Vehicle model	Inertial effects	Braking friction
1dof-hb-st	$IF_{1,hb,st}$	Stationary	1 degree-of-freedom	No	No
1dof-hb-st	$IF_{1,bl,st}$	Stationary	1 degree-of-freedom	No	Yes
1dof-sb-nst	$IF_{1,bl,nst}$	Nonstationary	1 degree-of-freedom	No	Yes
2dof-hb-st	$IF_{2,hb,st}$	Stationary	2 degrees-of-freedom	Yes	No
2dof-sb-st	$IF_{2,bl,st}$	Stationary	2 degrees-of-freedom	Yes	Yes
2dof-sb-nst	$IF_{2,bl,nst}$	Nonstationary	2 degrees-of-freedom	Yes	Yes

Physics-based models, governed by differential equations, can be computationally intensive when executed repeatedly. Metamodels present an effective solution for such computational demands. The objective is to craft an efficient, data-driven model of vehicle-bridge dynamics during braking to swiftly estimate outcomes, such as the bridge's IF response, based on key parameters. Crafting these metamodels demands both the identification of an apt function and its numeric coefficients. Machine learning has emerged as a potent tool for this purpose across various domains. This research delves into the potential of two primary supervised learning methods:

1. Neural Networks: They are utilized due to their renowned capability as comprehensive function approximators for vehicle-bridge dynamics.
2. Genetic Programming: This evolutionary computing technique searches for an optimal symbolic model function that closely mirrors the intended outcome.

2 METHODS

2.1 *Road roughness model*

The randomness of the road surface roughness can be represented by means of a periodic modulated random process. Within the ISO 8608 specifications (ISO/TC, 1995), the road surface roughness depends on the vehicle Fspeed through a formulation that relates the velocity power spectral density (PSD) and the displacement PSD. The general expression for the displacement PSD of the road surface roughness S_d is the following:

$$S_d(n) = S_d(n_0) \cdot \left(\frac{n}{n_0}\right)^{-a}, \tag{2}$$

where n is the spatial frequency (cycles/m), $n_0 = 0.1$ cycles/m is the reference value of the spatial frequency, and a is a suitable exponent. Equation 2 gives an estimate of the actual road roughness level $S_d(n)$ as function of the corresponding reference value $S_d(n_0)$. Note that the classification of the road roughness according to the ISO 8608 specifications is based on a constant vehicle velocity PSD by taking $a = 2$. The road roughness r can be generated as function of the spatial coordinate x through the following equation:

$$r(x) = \sum_{p=1}^{Q} d_p \cos(n_p x + \varphi_p), \tag{3}$$

where n_p is the pth spatial frequency and φ_p is the pth random phase angle, being Q the total number of harmonics assumed to generate the road roughness profile. Moreover, d_p is the pth amplitude, which is computed as follows:

$$d_p = \sqrt{2S_d(n)\Delta n}, \tag{4}$$

where Δn denotes the sampling interval of the spatial frequency. The nonstationary road roughess has been defined based on the paper by (Yin, Fang, Cai, & Deng, 2010).

2.2 *Vehicle-bridge interaction model*

Translation and rotational dynamic equilibrium equations of the vehicle mass can be written as follows:

$$m_v\left[\ddot{w}_v + \left(\frac{\ddot{r}(x_r) + \ddot{r}(x_f)}{2}\right) + \left(\frac{\ddot{w}_b(x_r,t) + \ddot{w}_b(x_f,t)}{2}\right)\right] + 2c_v\dot{w}_v + 2k_v w_v = 0, \tag{5}$$

$$I_v\left[\ddot{\theta}_v + \left(\frac{\ddot{r}(x_r) - \ddot{r}(x_f)}{B}\right) + \left(\frac{\ddot{w}_b(x_r,t) - \ddot{w}_b(x_f,t)}{B}\right)\right] + m_v h\ddot{x}_v + \frac{B^2}{2}c_v\dot{\theta}_v + \frac{B^2}{2}k_v\theta_v = 0, \tag{6}$$

where m_v, I_v, c_v,k_v are mass, inertia, damping coefficient and sprung stiffness of the vehicle, respectively. Moreover, h is the height of the vehicle centre of mass distance from the road surface and B is the distance between the contact points of the two wheels. The absolute vertical displacement of the vehicle mass is given by three terms, namely w_v (i.e., relative displacement between the road surface and the center of gravity of the vehicle mass), r (i.e., road roughness, that is the distance between the road surface and the averaged road surface), and w_b (i.e., deflection measured from the line axis of the bridge). Similarly, the absolute rotation of the vehicle is given by three contributions, namely θ_v (i.e., relative rotation between the vehicle and road surface), r, and w_b. The coupling between the bridge and the vehicle is due to the inertial terms in Eq. 5 and Eq. 6, whereas damping and elastic term are only affected by the relative displacement between the vehicle and the road surface. The contact force of the rear wheel $f_{c,\,r}$ can be derived from the equilibrium equation:

$$m_w[\ddot{r}(x_r) + \ddot{w}_b(x_r,t)] + f_{c,r} - c_v\left(\dot{w}_v + \dot{\theta}_v\frac{B}{2}\right) - k_v\left(w_v + \theta_v\frac{B}{2}\right) = 0, \tag{7}$$

where m_w is the mass of the wheel. So doing, it is obtained:

$$f_{c,r} = -m_w[\ddot{r}(x_r) + \ddot{w}_b(x_r,t)] + c_v\left(\dot{w}_v + \dot{\theta}_v\frac{B}{2}\right) + k_v\left(w_v + \theta_v\frac{B}{2}\right). \tag{8}$$

Similarly, the contact force for the front wheel $f_{c,\,f}$ is:

$$f_{c,f} = -m_w\left[\ddot{r}(x_f) + \ddot{w}_b(x_f,t)\right] + c_v\left(\dot{w}_v - \dot{\theta}_v\frac{B}{2}\right) + k_v\left(w_v - \theta_v\frac{B}{2}\right). \tag{9}$$

The contact force due to the vehicle oscillation does not include the weight of the sprung-mass system $m_w g$ + $m_v g$. Horizontal friction forces arise between the tyres and the bridge

surface during braking. If the width of the contact area between the tyre and the bridge is T, then the bending moment induced by the friction forces is:

$$\begin{aligned} m(x) &= \frac{\mu m_v y_s}{T}\left[H\left(x_r - \dot{x}_v t - \frac{T}{2}\right) - H\left(x_r - \dot{x}_v t + \frac{T}{2}\right)\right] + \\ &+ \frac{\mu m_v y_s}{T}\left[H\left(x_f - \dot{x}_v t - \frac{T}{2}\right) - H\left(x_f - \dot{x}_v t + \frac{T}{2}\right)\right] \approx \\ &\approx \frac{\mu m_v y_s}{B}\left[H\left(x_v - \dot{x}_v t - \frac{B}{2}\right) - H\left(x_v - \dot{x}_v t + \frac{B}{2}\right)\right], \end{aligned} \tag{10}$$

where y_s is the distance between the beam center of mass and the road surface while H is the Heaviside step function. Equation 10 approximates the two distributed bending moments induced by friction forces corresponding to the two tyres with a single distributed bending moment that extends over the wheelbase.

The partial derivative of the approximated expression for the distributed bending moment can be written as:

$$\begin{aligned} \frac{\partial m(x)}{\partial x} &= \frac{\mu m_v y_s}{B}\left[\delta_r\left(x_v - \dot{x}_v t - \frac{B}{2}\right) - \delta_f\left(x_v - \dot{x}_v t + \frac{B}{2}\right)\right] = \\ &= F\left[\delta_r\left(x_v - \dot{x}_v t - \frac{B}{2}\right) - \delta_f\left(x_v - \dot{x}_v t + \frac{B}{2}\right)\right], \end{aligned} \tag{11}$$

where δ_r and δ_f are the Dirac delta corresponding to the rear and front wheels, respectively.

The bridge is modeled as linear elastic Euler–Bernoulli beam with constant mass per unit length ρA (where ρ is the specific mass and A is the cross-section area of the beam) and constant bending stiffness EJ (where E is the elastic modulus and J the cross-section inertia of the beam). The continuous vertical displacement $w_b(x, t)$ of the bridge is governed by the following partial differential equation (Fryba, 2013):

$$\begin{aligned} &\rho A \ddot{w}_b(x,t) + EJ w_{r,xxxx}(x,t) = \delta_r(x_r - \dot{x}_v t)\left(f_{c,r} + m_w g + \frac{1}{2} m_v g\right) + \\ &\delta_f(x_f - \dot{x}_v t)\left(f_{c,f} + m_w g + \frac{1}{2} m_v g\right) + \frac{(x)}{\partial x}, \end{aligned} \tag{12}$$

The following boundary conditions apply on the left and on the right for a pinned-pinned beam:

$$w_b(0,t) = 0,\ w_{b,xx}(0,t) = 0, \tag{13}$$

$$w_b(L,t) = 0,\ w_{b,xx}(L,t) = 0, \tag{14}$$

respectively.

2.3 *Machine-learning*

This study employs a layered feed-forward neural network. Optimizing the design of the neural network is vital for enhancing its precision and forecasting abilities for fresh data. While various methods exist for network layout optimization (Quaranta, Lacarbonara, & Masri, 2020), this research adopts a method rooted in genetic algorithms (Azimi, Khoshrou, & Osanloo, 2019). These algorithms use a computational model that symbolically integrates variables, constants, and operators. Beginning with an arbitrary set of potential solutions, the model undergoes modifications via genetic processes until specific criteria are met. To address

the issue of bloat in genetic programming, our approach views model precision and intricacy as competing factors, aligning with the insights of Ekart & Nemeth, 2001.

3 RESULTS

The study focuses on a pre-stressed concrete girder bridge with simple support, part of Italy's highway system (Aloisio, Pasca, Alaggio, & Fragiacomo, 2020). The section is trapezoidal, 2.3 m tall, and features two cantilevered extensions each 3.85 m in width, strengthened with bonded post-tensioned cables. Every bridge section rests on a pair of pillars spaced roughly 40 m apart. Montecarlo analyses indicate that braking effects largely hinge on road conditions and vehicle's starting speed (Aloisio, Contento, Alaggio, & Quaranta, 2023). Figure 1 illustrates the IF against starting speed, drawing from experimental findings and both physics-based and surrogate models.

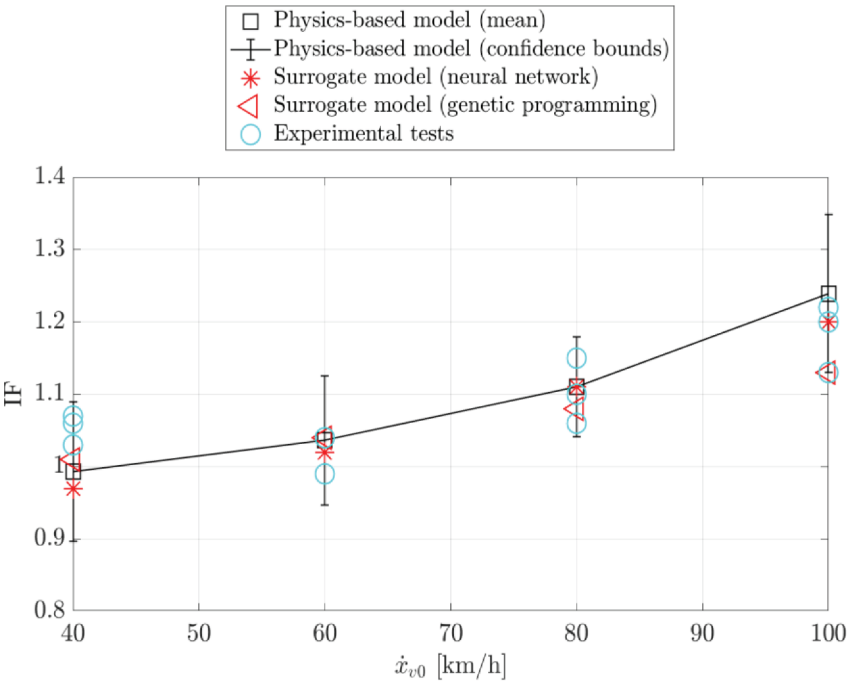


Figure 1. Variation of the IF as a function of the vehicle velocity: confidence bounds estimated using the physics-based model, nominal values carried out through surrogate modelling, and experimental data.

The symbolic form of the final surrogate models for IF and $w_{b,braking}$ obtained via genetic programming is the following:

$$\begin{aligned} \mathrm{IF} = \theta_{IF1} + \theta_{IF2} f_{v,p} h^2 + \theta_{IF3} B \dot{x}_{v0}^2 + \theta_{IF4} B f_{v,p} h + \\ \frac{1}{m_v}\left(\theta_{IF5} \dot{x}_{v0}^2 f_{v,p} h + \theta_{IF6} B f_{v,p} h + \theta_{IF7} B^2 h\right), \end{aligned} \tag{15}$$

$$\begin{aligned} w_{b,braking} = \theta_{w_b 1} + \theta_{w_b 2} B + \theta_{w_b 3} \dot{x}_{v0} + \frac{\theta_{w_b 4} h + \theta_{w_b 5} m_v}{f_{v,b}} + \\ \frac{\theta_{w_b 6} f_{v,p} + \theta_{w_b 7} h + \theta_{w_b 8} m_v}{B^{\theta_{w_b 9}}} (in[m]), \end{aligned} \tag{16}$$

respectively. The involved sets of coefficients, $\boldsymbol{\Theta}_{IF}$ and $\boldsymbol{\Theta}_{w_b}$, are listed in Tab 2.

Table 2. Coefficients of the genetic programming-derived surrogate models for IF and $w_{braking}$ in Eq. 15 and Eq. 16, respectively.

IF (Θ_{IF})	$w_{braking}$ (Θ_{w_b})
$\theta_{IF1} = 1.009$	$\theta_{w_b1} = 2.8268\text{E} - 04$
$\theta_{IF2} = 0.0024$	$\theta_{w_b2} = 9.9309\text{E} - 06$
$\theta_{IF3} = -1.6712\text{E} - 07$	$\theta_{w_b3} = -2.4731\text{E} - 06$
$\theta_{IF4} = -0.0013$	$\theta_{w_b4} = -4.9481\text{E} - 07$
$\theta_{IF5} = 2.0845\text{E} - 05$	$\theta_{w_b5} = -7.2693\text{E} - 06$
$\theta_{IF6} = -0.0042$	$\theta_{w_b6} = -8.9722\text{E} - 05$
$\theta_{IF7} = -6.7429\text{E} - 04$	$\theta_{w_b7} = -6.7173\text{E} - 05$
	$\theta_{w_b8} = -2.1517\text{E} - 04$
	$\theta_{w_b9} = 0.0833$

These surrogate models for IF and $w_{b,braking}$ involve the same parameters except for $f_{v,b}$, which is missing within the symbolic expression for IF. The results demonstrate that genetic programming is also able to produce good surrogate models. Considering the compact form of the final symbolic expressions, the accuracy of the genetic programming is still deemed satisfactory. However, the surrogate model for the IF carried out via genetic programming is slightly less accurate than those produced via artificial neural networks, being R^2 between 80% and 85%. The surrogate models for $w_{b,braking}$ obtained by means of genetic programming and artificial neural networks display almost the same accuracy level, being R^2 around 99% for both machine learning techniques.

4 CONCLUSIONS

This paper's primary conclusions include:

- The most intense dynamic load arises from hard braking, which typically produces Impact Factor (IF) values at or above one. To get the most conservative bridge response estimates during this condition, a precise two degree-of-freedom vehicle model is crucial.
- For hard braking, a two degrees-of-freedom model results in higher IF values. However, for softer braking, a single degree-of-freedom model often provides more conservative bridge movement estimations.
- Soft braking effects on bridge behavior vary based on the road's surface quality model. Using a nonstationary model generally results in higher IFs than a stationary one. This relationship shifts with increased surface irregularity. For intense braking, greater road roughness leads to decreased average IFs.
- IF value variability mainly arises from braking types and the vehicle model. Soft braking with a two degrees-of-freedom model shows notable IF dispersion. IF variability also has some dependence on surface quality during hard braking, with smoother roads causing greater IF dispersion.

REFERENCES

Aloisio, A., Contento, A., Alaggio, R., & Quaranta, G. 2023. *Physics-based models, surrogate models and experimental assessment of the vehicle–bridge interaction in braking conditions*. Mechanical Systems and Signal Processing, 194: 110276.

Aloisio, A., Pasca, D.P., Alaggio, R., & Fragiacomo, M. 2020. *Bayesian estimate of the elastic modulus of concrete box girders from dynamic identification: A statistical framework for the a24 motorway in Italy*. Structure and Infrastructure Engineering, 1–13.

Azimi, Y., Khoshrou, S.H., & Osanloo, M. 2019. *Prediction of blast induced ground vibration (bigv) of quarry mining using hybrid genetic algorithm optimized artificial neural network*. Measurement, 147: 106874.

Ekart, A., & Nemeth, S.Z. 2001. *Selection based on the pareto nondomination criterion for controlling code growth in genetic programming*. Genetic Programming and Evolvable Machines, 2(1): 61–73.

Fr`yba, L. 2013. *Vibration of solids and structures under moving loads*. Springer Science & Business Media, 1.

ISO/TC, T.C., Vibration, M., Measurement, S.S.S., Vibration, E.of Mechanical, & Machines, S. as Applied to. 1995. *Mechanical Vibration–Road Surface Profiles–Reporting of Measured Data*. International Organization for Standardization, 8608.

Quaranta, G., Lacarbonara, W., & Masri, S.F. 2020. *A review on computational intelligence for identification of nonlinear dynamical systems*. Nonlinear Dynamics, 99(2): 1709–1761.

Yin, X., Fang, Z., Cai, C., & Deng, L. 2010. *Non-stationary random vibration of bridges under vehicles with variable speed*. Engineering Structures, 32(8): 2166–2174.

Bridge Maintenance, Safety, Management, Digitalization and Sustainability – Jensen, Frangopol & Schmidt (eds)
© 2024 The Author(s), ISBN 978-1-032-77040-6
Open Access: www.taylorfrancis.com, CC BY-NC-ND 4.0 license

Distributed fiber optic sensing during static and dynamic bridge loading

L. Strasser & W. Lienhart
Institute of Engineering Geodesy and Measurement Systems, Graz University of Technology

ABSTRACT: In order to ensure a safe operation of bridges and other civil infrastructure, efficient methods for condition assessment are necessary. Distributed Fiber Optic Sensing (DFOS) offers highly accurate monitoring and provides significant advantages over point-wise sensors.

In order to assess the condition of an Austrian highway bridge, static and dynamic load tests have been performed. Two spans have been equipped with fiber optic cables and point-wise sensors. Through the use of Optical Backscatter Reflectometry (OBR), the strain distribution of the bridge spans under static load was measured. Additionally, the use of Distributed Acoustic Sensing (DAS) enabled the measurement of vibrations along the bridge spans under dynamic load.

In this paper we demonstrate that through the use of complementary DFOS techniques, a more comprehensive analysis of the bridge's behavior can be achieved. The resulting measurements are verified not only by the bridge's numerical model, but also by co-located point-wise reference sensors.

1 INTRODUCTION

In order to assure a safe operation of bridges, many of them have to be placed under observation. This applies especially to bridges which by now are coming to the end of their design lifetime. As shown in Figure 1, this affects the majority of bridges, since the main construction activity in many parts of the world has taken place during the 1960s and 1970s.

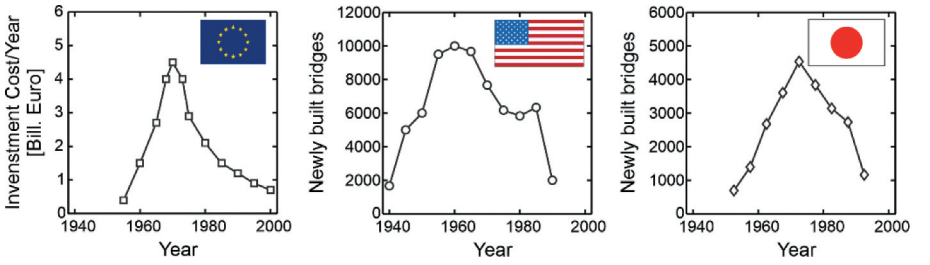


Figure 1. Investment costs in Europe (Geier & Wenzel 2002) and bridge construction activity in USA (Chase & Washer 1997) and Japan (Fujino & Abe 2004).

Different monitoring techniques can be applied for bridge monitoring to assess the current health state of the bridge, to enable condition-based and predictive maintenance and to extend the lifetime of the structure. Generally, monitoring systems can be classified into surface mounted/embeddable sensors and remote sensing techniques, where a line of sight to the object is required. Another distinction can be made between point-wise and distributed

DOI: 10.1201/9781003483755-133

sensors. Point-wise sensors suitable for bridge monitoring are e.g. accelerometers (Xu & Xia 2012), which can give an insight into the bridge's vibrations and provide data for point-wise frequency analysis. Furthermore, modern Robotic Total Stations (RTS) can also serve for the determination of point-wise frequency behavior as they can measure absolute displacements in 3 directions, although with a limited frequency range (Psimoulis & Stiros 2013, Lienhart et al. 2023). Another possibility is the usage of tilt sensors, which can –when placed correctly – give an insight into the temperature- and load-induced deformation of the bridge. Additionally, GNSS sensors (Schönberger et al. 2022) and high-speed cameras (Ehrhart & Lienhart 2015, Yoneyama & Ueda 2012) have successfully been applied for bridge monitoring. The drawback of all these sensors is that they only provide information related to the designated position. In order to obtain a bigger picture, multiple sensors would be needed. This is where distributed sensors show their potential. Ranging from profile laser scanners (Schill et al. 2022) and interferometric radars to Distributed Fiber Optic Sensing (DFOS), these methods enable the seamless monitoring of entire bridge spans. Whereas laser scanners and radars can deliver only line-of-sight measurements, DFOS can give an insight into the bridge's behavior at any time with the use of only a single sensing fiber. Different DFOS techniques enable the measurement of long- and short-term deformations and can even be used for frequency analysis (Strasser et al. 2023). The methods are described in more detail in the following section.

2 BRIDGE MONITORING WITH DFOS

In recent years, civil infrastructure monitoring with DFOS has become more popular, especially for bridges (Pannese et al. 2020, Barker et al. 2022). The principle of DFOS is light coupled into a glass fiber, in which the entire fiber serves as a sensing element. By propagating through the fiber, the light captures information along it. Due to natural impurities inside the fiber, parts of the light are backscattered to the interrogation unit from every point along the fiber. Figure 2 schematically demonstrates the generic working principle of DFOS.

If temperature and/or strain changes affect the fiber, the backscatter also changes and the information can be measured with high accuracy. As the velocity of the light inside the glass fiber is known, the impact position along the fiber can be determined. The accuracy of this position can reach from µm to several meters and is dependent on the gauge length, which describes the length considered for the calculation of the strain along the fiber (Hartog 2017).

Different DFOS techniques make use of different backscattering effects. These are depicted in Figure 2 and are dependent on strain and temperature changes.

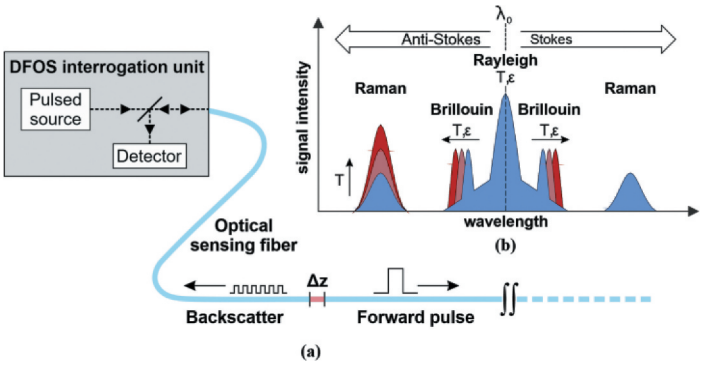


Figure 2. Schematic representation of distributed fiber optic sensors (a) and different backscattering effects (b). (Monsberger & Lienhart 2021).

This article focuses on the use of Optical Backscatter Reflectometry (OBR) and Distributed Acoustic Sensing (DAS) measurements, both of which make use of the Rayleigh backscatter,

although they deliver different results. OBR provides highly accurate strain information along the entire fiber with a local resolution in the range of a few millimeters. The measurement principle utilizes the unique 'fingerprint' of each fiber, caused by the production process. Every subsequent measurement is compared to a zero-measurement from which long-term changes can be derived. In principle, in OBR measurements the scatter amplitude is a random but static property and can be modelled as a continuous weak Fiber Bragg Grating (FBG) with a random period (Luna 2013). In contrast, DAS is able to deliver a seamless frequency profile along the entire fiber by sending high frequency light pulses into it (Owen et al. 2012). Vibrations can be measured and even single vehicles crossing the bridge can be identified. The combination of both techniques can give a valuable insight in the short- and long-term behavior of the bridge. Table 1 demonstrates the main characteristics of both measurement techniques.

Table 1. Overview on used DFOS techniques.

	DAS (Febus 2021)	OBR (Luna 2013)
Backscatter component	Rayleigh	Rayleigh
Absolute measurements	No	Yes
Measurand	Strain (rate)	Strain, Temperature
Spatial resolution	≥ 1 m	≥20 µm
Sensing range	Up to 50 km	Up to 2 km
Measurement rate	Up to several kHz	Static (<1Hz)

3 LOAD TEST OF A HIGHWAY BRIDGE

The results shown in this paper are derived from measurements on a highway bridge in the Austrian Alps (Figure 3). The steel-concrete composite bridge was built in the late 1960s and consists of 7 spans with a total length of 560 m. Although they share the same pillars with heights up to 80 m, the two carriageways are vibration-decoupled from each other. The bridge is exposed to high traffic volume, since it is the main route crossing the Alps from northern Europe to southern Europe. Therefore, its operability is of high interest and a safe operation has to be ensured.

In order to assess the condition of the bridge and perform regular monitoring, two out of the seven spans have been equipped with different monitoring systems. For DFOS measurements, two fiber loops have been installed along the steel bridge beam on the top and the bottom. Additionally, several prisms for Robotic Total Station measurements have been installed, as well as accelerometers in the middle of span 7. Laser scans have additionally been performed on this span. The different monitoring techniques complement one another and although this paper focuses only on the DFOS measurements, the point-wise sensors can be used as a reference. More information on the RTS measurements can be found in Lienhart et al. (2023). Figure 4 demonstrates the installed monitoring systems on the bridge spans.

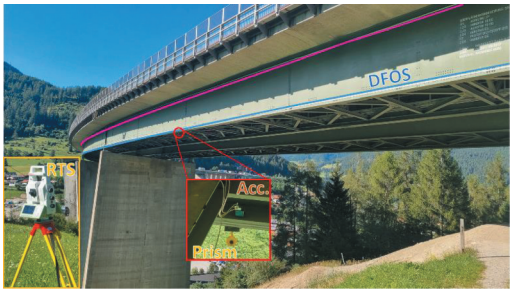


Figure 3. Monitored highway bridge in the Austrian Alps.

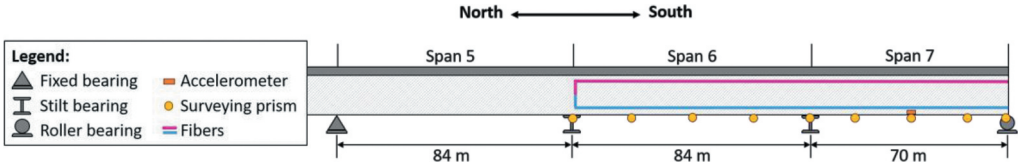


Figure 4. Schematic representation of installed monitoring systems.

In addition to epoch-wise monitoring, a load test was carried out in order to assess the condition of the bridge and to compare it to numerical models calculated in advance. For the load test, one carriageway was closed for normal traffic. Two trucks with a weight of 55 tons each were used for the load test. Several runs of the trucks crossing the bridge at a defined distance and a defined speed were carried out. Additionally, the trucks stopped at several predefined positions on the bridge in order to carry out static measurements. The following sections show the results of the static and dynamic load scenarios.

4 STATIC LOAD TEST

For a complete assessment of the bridge condition, both the behavior under static and dynamic load are of interest. First, the results of the static OBR measurements are discussed. As previously mentioned, there have been different scenarios on where the trucks stopped at the bridge. Either both trucks stop in the middle of span 6, or both in the middle of span 7, or one each. In order to measure the absolute displacements of the bridge deck, RTS measurements were carried out. Figure 5 (left) shows the displacement of the deck on several positions for the load scenario of both trucks being placed in the middle of span 6. The downward movement of span 6 results in a simultaneous uplift in span 7. These absolute displacement measurements can also be converted into strain readings between those few points, since the load causes not only a sag but also a length change between those points. This result can be compared to the strain distribution obtained by the OBR measurements. In order to compare displacement to strain, it has to be mentioned that the downward movement of the deck caused by a vertical load leads to positive strain on the lower part and negative strain on the upper part, as depicted in Figure 5 (right).

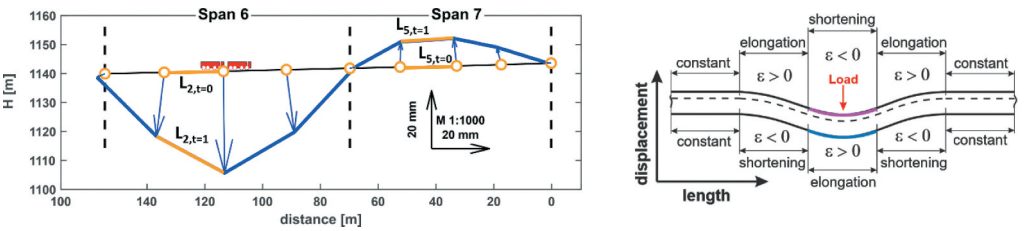


Figure 5. Left: Displacement and strain measured with RTS. Right: Schematic representation of the relation between displacement and strain.

The comparison with the OBR measurements shown in Figure 6 (left) shows a very good agreement for both data series. The low level of detail for the RTS measurements due to the small amount of measurement points outlines the main benefit of the DFOS measurements, which provide a seamless strain profile along the entire fiber for the upper and lower bridge beam. The high spatial resolution strain measurements show a sawtooth pattern with peaks along the bridge spans.

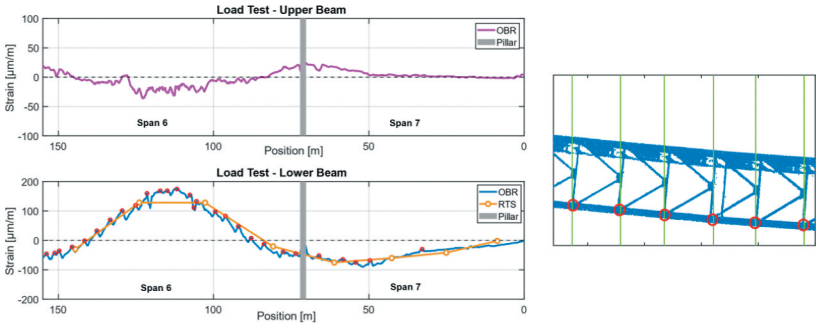


Figure 6. Left: Comparison of RTS and OBR measurements. Right: Comparison of peak locations with laser scan data.

After comparing the peak locations to the laser scan of span 7, it was discovered that the positions of the peaks match the locations of the girder connectors (Figure 6, right). Figure 7 shows the measured strain for all load scenarios for both the upper and lower fiber at the beam. The strain behavior of the upper and lower part differs significantly, which can be explained by the high vertical location of the neutral axis of the bridge beam (Figure 5, right). Furthermore, the same load results in less strain in span 7, which can be explained by its shorter length.

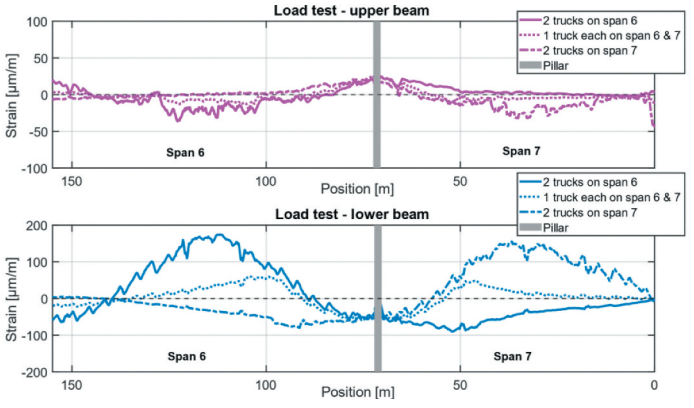


Figure 7. OBR measurements for all load scenarios for upper and lower fiber.

For all load scenarios, numerical models have been used to predict the absolute displacements and strain, which were then compared with the actual measurement. Figure 8 shows the comparison for the load scenario of both trucks being positioned in span 6. The data shows a very good agreement with a little higher strain in the numerical model, caused by more pessimistic assumptions made in its calculation. Furthermore, it should be noticed that the peaks in the strain distribution are also present in the numerical model.

5 DYNAMIC LOAD TEST

As described in the previous sections, the OBR measurements can only be used for the determination of a static load scenario. To also analyze the dynamic behavior of the bridge through the passing of the trucks, DAS measurements can be performed. Although the spatial resolution amounts to only a few meters, the measurements benefit from the high temporal

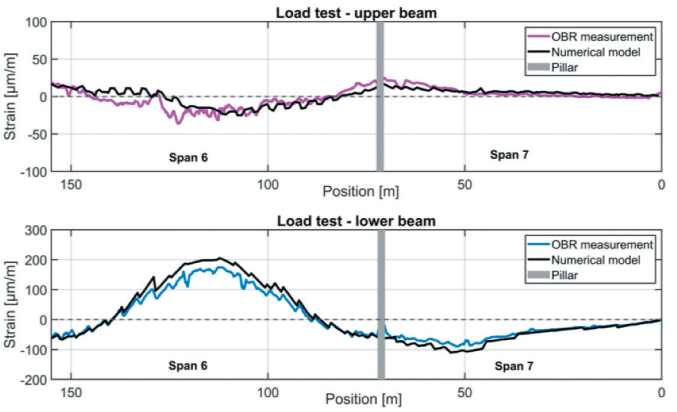


Figure 8. Comparison of OBR measurements and the numerical model.

resolution with a sampling rate of 1 kHz. This enables a seamless frequency analysis along the entire bridge spans. Furthermore, the passing of the trucks can be visualized in the data, and even their velocity can be estimated. Figure 9 shows a waterfall plot of the trucks passing on the bridge and after that driving back to position themselves on span 6.

In order to obtain the frequency behavior of the bridge at the time the trucks are passing, a frequency analysis can be performed. Figure 10 shows the frequency distribution for a location in the middle of span 7. At the same position, an accelerometer was additionally mounted, which can be used as a reference. The data series show very good agreement, both displaying a peak at 2.5 Hz.

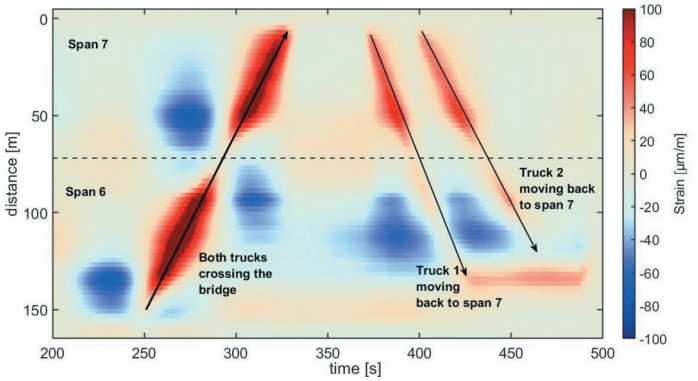


Figure 9. Waterfall plot of DAS measurements showing the movement of the trucks.

As previously mentioned, the main advantage of DFOS is the seamless monitoring along the entire fiber. Therefore, the frequency behavior can be evaluated on several points along the bridge spans. Figure 11 shows the frequency analysis on different points along span 7 for the upper and lower fiber line. First, a difference between locations along span 7 can be noticed with the peak frequency components decreasing at the end of span 7, which is also the end of the entire bridge. The amplitudes derived from the upper fiber are much lower, although the main frequencies remain unchanged, staying between 2 and 3 Hz. The lower amplitudes can once more be explained by the high neutral axis and consequently less movement in the upper part. Taking a look at the frequency behavior above the pillar between the spans, the amplitudes are rather low compared to the spans (Figure 12). Furthermore, the frequencies show a wider range by decreasing under 2 Hz.

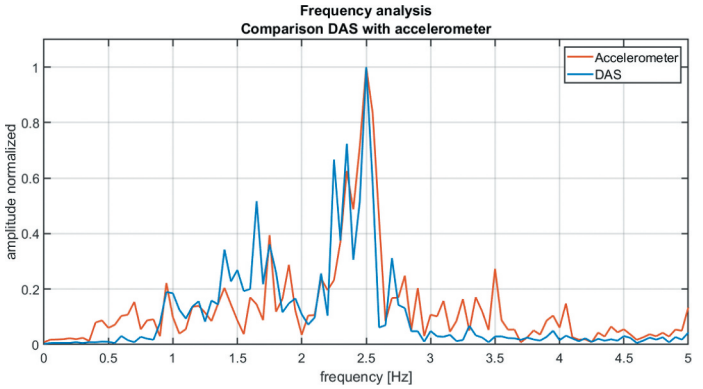


Figure 10. Comparison of frequency spectra from DAS and accelerometer measurements at the same location.

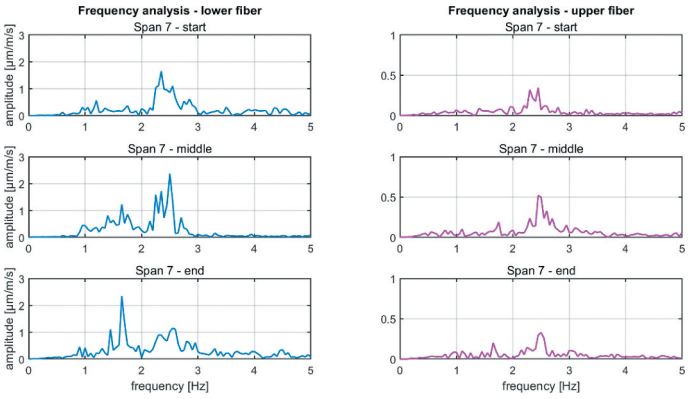


Figure 11. Frequency analysis at different fiber locations for upper and lower fiber on the bridge beam.

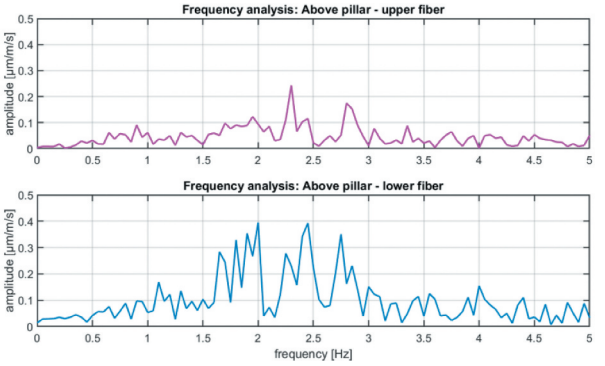


Figure 12. Frequency analysis above pillar for upper and lower fiber on the bridge beam.

6 SUMMARY AND OUTLOOK

This analysis outlines the advantages of using DFOS for bridge monitoring. The one-time installation of a fiber at the bridge enables the usage of different DFOS techniques, each providing different information. The same fiber can be used for both static and dynamic

measurements by connecting different interrogation units to it. The information obtained includes not only a detailed and highly accurate strain distribution, but also a seamless frequency analysis along the entire bridge spans. The gapless information has significant advantages compared to point-wise techniques. Nevertheless, the simultaneous point-wise measurements are a reasonable complement and can also serve as a reference to DFOS measurements. The comparison with the precalculated numerical model of the bridge showed very positive results with high agreement. The small difference in the strain values proves a better condition of the bridge than indicated by the numerical model.

ACKNOWLEDGEMENTS

We want to acknowledge the support of the Austrian Highway Agency (ASFINAG), especially Peter Augschöll for the possibility of performing a load test on the bridge. Further, we want to appreciate the cooperation with Patrick Huber from Fritsch, Chiari & Partner (FCP) and acknowledge the calculation of the numerical models.

REFERENCES

Barker, C., Woods, J., Hoult, N. A., Le, H. & Tolikonda, V. 2022. Pre- and Post-Rehabilitation Monitoring of a Steel Railway Bridge with Distributed and Discrete Sensors. *Journal of Bridge Engineering*, Vol.27, Issue 4.

Chase, S. B. & Washer, G. 1997. Nondestructive Evaluation for Bridge Management in the Next Century. Federal Highway Administration.

Ehrhart, M. & Lienhart, W. 2015. Monitoring of Civil Engineering Structures using a State-of-the-art Image Assisted Total Station. *Journal of Applied Geodesy*, Vol. 9, No. 3: 174–182.

Febus Optics SAS. 2021. Febus A1-R: Technical Datasheet. *Technical Datasheet*. Pau, France.

Fujino, Y. & Abe, M. 2004. Structural Health Monitoring – Current Status and Future. *Proc. 2nd European Workshop on Structural Health Monitoring*, *Lancaster, USA*: 3–10.

Geier, R. & Wenzel, H. 2002. Bridge Classification Based Upon Ambient Vibration Monitoring. *Proc. 1st European Workshop on Structural Health Monitoring*, *Lancaster, USA*: 981–988.

Hartog, A. H. 2017. *An Introduction to Distributed Optical Fibre Sensors*. CRC Press, Taylor & Francis Group.

Lienhart, W., Schill, F. & Moser, T. 2023: Dynamic Bridge Monitoring with Remote Sensing Techniques. In *Proceedings of the 14th International Workshop on Structural Health Monitoring (IWSHM)*, *Stanford, USA*: 140–147.

Luna Technologies. 2013. Optical Backscatter Reflectometer 4600. *User Guide*. Blacksburg, USA.

Monsberger, C. & Lienhart, W. 2021. Distributed Fiber Optic Shape Sensing of Concrete Structures. *Sensors 2021*, 21, 6098.

Owen, A., Duckworth, G., Worsley, J. 2012: Fibre Optic Distributed Acoustic Sensing for Border Monitoring. *European Intelligence and Security Informatics Conference*: 362–364.

Pannese, E. M., Take, W. A, Hoult, N. A., Yan, R. & Le, H. 2020. Bridge transition monitoring: Interpretation of track defects using digital image correlation and distributed fiber optic strain sensing. *Journal of Rail and Rapid Transit*, Vol. 234(6): 616–637.

Psimoulis, P. & Stiros C. 2013. Measuring Deflections of a Short-Span Railway Bridge Using a Robotic Total Station, *Journal of Bridge Engineering* 18(2): 182–185.

Schill, F., Michel, C. & Firus, A. 2022. Contactless Deformation Monitoring of Bridges with Spatio-Temporal Resolution: Profile Scanning and Microwave Interferometry. *Sensors*, 22, 9562.

Schönberger, C., Lienhart, W. & Moser, T. 2022. Dynamic monitoring of civil infrastructures with geodetic sensors. In *Proceedings 5th Joint International Symposium on Deformation Monitoring (JISDM), Valencia, Spain*: 537–543.

Strasser, L., Lienhart, W. & Winkler, M. 2023: Static and Dynamic Bridge Monitoring with Distributed Fiber Optic Sensing. In *Proceedings of the 14th International Workshop on Structural Health Monitoring (IWSHM), Stanford, USA*: 1745–1752.

Xu, Y. & Xia, Y. 2012. *Structural Health Monitoring of Long-Span Suspension Bridges*. New York: Spon Press.

Yoneyama, S. & Ueda, H. 2012. Bridge Deflection Measurement Using Digital Image Correlation with Camera Movement Correction. *Materials Transactions*, Vol. 53, Issue 2: 285–290.

Bridge Maintenance, Safety, Management, Digitalization and Sustainability – Jensen, Frangopol & Schmidt (eds)
© 2024 The Author(s), ISBN 978-1-032-77040-6
Open Access: www.taylorfrancis.com, CC BY-NC-ND 4.0 license

Structural load modelling of walking humans with gait cycle-dependent model parameters

M.J.A. Fritzsche, S.R. Lorenzen & C. Hübler
Institute of Structural Mechanics and Design, Technical University of Darmstadt, Darmstadt, Germany

A. Firus
ISEA Tec GmbH, Friedrichshafen, Baden-Württemberg, Germany

M.A. Stasica & A. Seyfarth
Lauflabor Locomotion Laboratory, Institute of Sports Science and Centre for Cognitive Science, Technical University of Darmstadt, Darmstadt, Germany

ABSTRACT: In recent years, research on human-induced vibrations has developed several advanced modelling approaches aimed at achieving a more accurate description of human-structure interaction (HSI). The prevailing method involves using the load function from walking individuals on rigid ground as a starting point, considering the deviation when walking on vibrating structures, and incorporating the person as a single degree of freedom (SDOF) model coupled with the structure. However, this approach suffers from the need for case-by-case consideration, as the load model parameters are not universally applicable for each HSI model. To overcome these limitations, this study presents a modelling approach that strives to capture the HSI by accounting for the gait cycle dependency of the SDOF parameters. To apply the proposed model, measurement data collected on an experimental pedestrian bridge were analysed. The results show that further analyses and more data processing are required to evaluate whether the model is a good approach to account for human-induced vibrations including HSI.

1 INTRODUCTION

Various load models have been developed in recent years to describe the interaction between humans and structures (HSI) caused by pedestrians walking on vibration-prone structures Caprani & Ahmadi (2016). These models vary in complexity, with some approaches assuming the human-induced load by using a moving force (MF), a moving mass (MM), and a single-degree-of-freedom oscillator (SDOF) model. Most studies to date have focused on numerical analysis, assuming lumped biomechanical parameters based on existing literature (Archbold (2004), Caprani et al. (2011), da Silva et al. (2013), Qin et al. (2013), Shahabpoor et. al. (2013)) or using optimized model parameters (Czwikla & Kasperski (2017), Fanning et al. (2005), Zhang et al. (2015), Zivanović (2015)). In most cases, however, there is still a lack of experimental validation of these models.

It should be noted that all previously published models calculate new parameters for each human-structure interaction case, meaning that the values cannot be generally applied. Therefore, this paper proposes a modelling approach that differs slightly but essentially from previous SDOF models. The main difference lies in the consideration of changes in spring-damper values of the SDOF model that are dependent on both gait cycle, as shown by Firus et al. (2017), and vibration, as shown by Zivanović (2015).

DOI: 10.1201/9781003483755-134

First, the experimental setup is described briefly, including the measurement technology used to determine the load model parameters based on real test runs with walking pedestrians. The new load modelling approach and the methodology used to calculate the SDOF model parameters are then presented. Finally, exemplary calculation results of a single run of a walking individual emphasise the need for further analyses.

2 METHODS

2.1 *Experimental setup*

The experimental investigations were carried out on the HUMVIB bridge, which was developed and built on the Lichtwiese campus of TU Darmstadt to investigate the vertical HSI effects (see Figure 1). The bridge consists of two longitudinal, load-bearing steel girders HEA 240 (structural steel S235JR), on which 13 concrete slabs form the bridge deck. Without a movable centre support, the bridge is a single-span system with a span of 13.24 m and a natural frequency of 2.02 Hz. As the natural frequency of the structure is in the typical human cadence range, the system is susceptible to human-induced vibrations. By adding the optional centre column, the single-span beam system becomes a much stiffer double-span system, increasing the natural frequency to 7.71 Hz and making the system no longer susceptible to human-induced vibrations. For further details regarding the HUMVIB bridge, it is referred to Fritzsche et al. (2023).

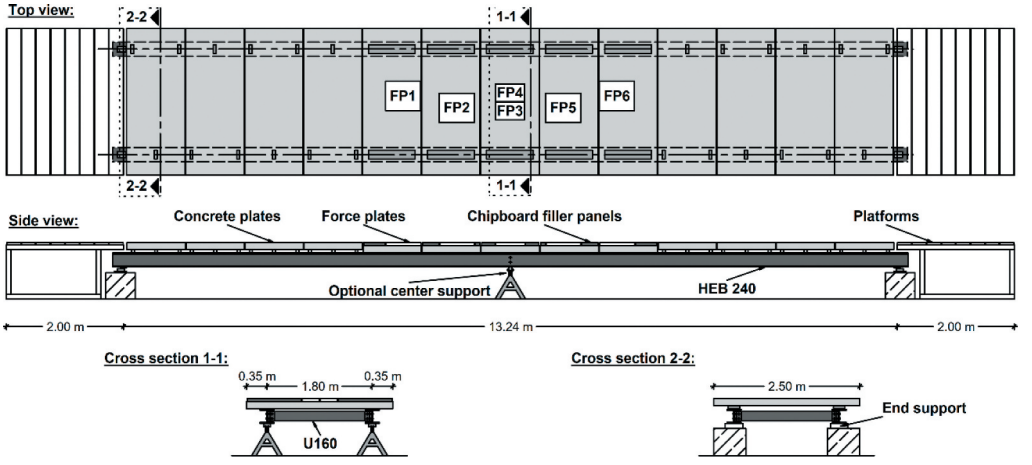


Figure 1. HUMVIB bridge with six portable 3D force plates (FP) mounted on the bridge deck.

To measure the structural response due to human-induced vibrations, the steel girders of the HUMVIB bridge have been equipped with acceleration, displacement, and strain sensors arranged according to the positions shown in Figure 2. Using the structural response measured at discrete points, the bridge response is estimated at each time t for discrete locations x in the longitudinal direction of the bridge. The accelerations of the bridge can thus be used

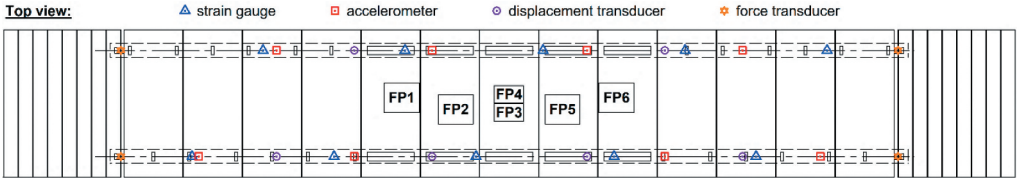


Figure 2. Sensor setup for the structural response measurement.

to extract the inertial forces from the measured ground reaction forces (GRF) of the force plates and to determine the relative displacement of the pedestrian with respect to the bridge deck. The GRF of the participants are measured using six mobile force plates type 9260AA6/AA3 from Kistler Instrumente AG. The force plates are arranged in such a way that five individual steps are recorded for each run. The force plates measure at a sampling rate of 1,000 Hz and can determine the centre of pressure in addition to horizontal and vertical GRF.

2.2 *Load model approach*

Figure 3 shows the proposed modelling approach for a structural load model of walking individuals. The key aspect of this model compared to other SDOF modelling approaches is the structural independence of the model parameters. Therefore, the unknown model parameters k_p and d_p are determined on a rigid ground as shown in Figure 3a assuming that they are not constant but variable over the gait cycle T. The mass of the person is given as M_p and corresponds to the dead load of the pedestrian.

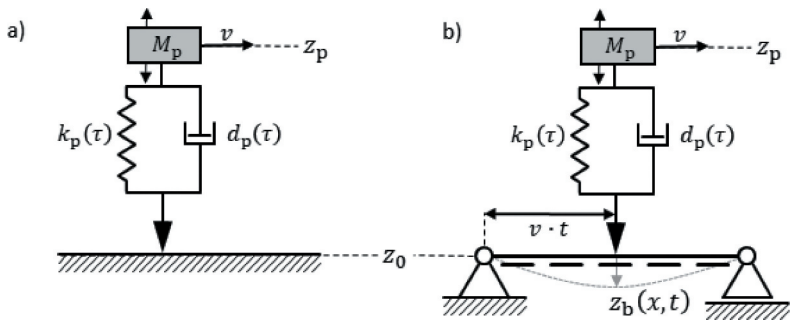


Figure 3. SDOF model for walking persons with model parameters depending on the gait cycle.

The normal gait cycle is shown in Table 1 and consists of a stance phase (STP) and swing phase (SWP) of each leg. Since we measured the total GRF of both legs, as we assume that the walking person is an SDOF, the model parameters reflect the combined behaviour of both legs and not the behaviour of the walking person for each individual leg. The process of walking can be divided in several subphases of the gait cycle. In most cases and according to Hartmann et al. (2010) we have eight phases within a gait cycle with the loading response phase covering the first 10% of the gait cycle.

Table 1. Normal gait cycle with approximated event timings (according to Hartmann et al. (2010)).

gait cycle 100%							
stance phase (STP) ≈ 60 %					swing phase (SWP) ≈ 40 %		
initial contact	loading response	Mid STP	terminal STP	pre-SWP	initial SWP	Mid SWP	terminal SWP
0 %	0 to 10 %	10 to 30 %	30 to 50 %	50 to 60 %	60 to 73 %	73 to 87 %	87 to 100 %

$$F_z(t) = -M_p \cdot \left(g + \ddot{z}_p(t)\right) = k_p(\tau) \cdot (z_0 + z_{rel}(t)) + d_p(\tau) \cdot \dot{z}_{rel}(t) \tag{1}$$

$$z_{rel}(t) = z_p(t) - z_b(t) \tag{2}$$

To determine the unknown and time-variant load model parameters k_p and d_p, we first consider the dynamic equilibrium for Figure 3. The measured vertical ground reaction force (GRF) F_z results from the acceleration of the point mass. This must be equal to the sum of the

spring and damper force on the ground. The static component of the acceleration due to gravity or the mass displacement z_0 of the spring as a static component are reduced, which means that only the dynamic force can be used to determine the spring-damper parameters k_p and d_p over time. Motion capture (MoCap) data are used to calculate the centre of mass (COM) and determine the coordinate z_p. For a more detailed description of the COM calculation, see Section 2.3.

The velocity $\dot{z}_{\mathrm{rel}}$ and acceleration $\ddot{z}_{rel}$ at any time t are obtained by single or double derivation of the displacement z_{rel}. Assuming rigid ground conditions, z_{b} and its derivatives are zero, so that $z_{\mathrm{p}} = z_{\mathrm{rel}}$. Hence, the unknowns are reduced to the model parameters k_p and d_{p}. Since there are two unknowns per time step, the equation system is underdetermined for each time step. By setting up several systems of equations for several time steps t_{n}, a definite or, for more than two equations, an overdetermined linear system of equations can be created for time intervals t_1 to t_{n}. Within the selected time interval, the SDOF parameters are constant and the more equations or time steps in the time interval are used to determine them, the more robust they are. For the overdetermined system of equations, the unconstrained least-squares method is used to identify the corresponding stiffness k_{p} and damping coefficient d_{p}.

Once the model parameters are calculated on rigid ground, the load model can be applied to a structure as shown in Figure 3b, resulting in a combined HSI model. If the displacement z_{b} of a structure is not zero, the calculation of z_{rel} must take this into account. This can be done using structural response sensors and is explained in more detail within Section 2.4.

It should be noted that the spring-damper values are not related to the time t but to the gait cycle of each double step of the period T or time step in the gait cycle τ. The model considers the influence of the spring-damper mass of the SDOF of the pedestrians on the structural response but defined independently of the structural model. In this case, the HSI is considered solely through the interaction of the person's point mass with the gait cycle depending on the spring/damper values with the structure.

2.3 *Calculation of the centre of mass*

The COM of the test person is calculated according to Equation 3, in which the COM of the total body is calculated depending on the COM of the individual body segments. Here, m_i is the segment mass, z_{i} is the COM coordinate of segment i, which results in the COM coordinate z_{p} in z-direction. For the other spatial directions in x- and y-direction the calculation is identical using x_i and y_i to calculate x_{p} and y_{p} respectively. The segmentation was limited to 14 segments (segments of arms/hands and legs/feet double, head and trunk single) with segment masses and COM according to Table 2.

$$z_{\mathrm{p}} = \frac{\sum_{i=1}^{14} m_i \cdot z_i}{\sum_{i=1}^{14} m_i} \tag{3}$$

The segment lengths of the legs, arms and torso are calculated directly from the relative marker positions of the motion capture system. The joint node of the elbow is formed from the mean value of markers 12 and 13, as shown in Figure 4. In this way, the segment lengths, labelled A to E according to Figure 4, can be clearly determined. The other segment lengths for hands, feet, head, and neck are calculated according to Winter (2009). The reason for this is the fact that the marker set used does not allow a direct calculation of the segment lengths, as the segment length does not have a start or end point for the calculation.

2.4 *Determination of bridge displacement*

To form the dynamic equilibrium according to Equation 1, considering the displacement of the bridge, local sensors for the structural response can be used. In this case, a signal z_1 from a displacement sensor attached to one of the main beams of the HUMVIB bridge is used (see Figure 2). For all time steps t, the corresponding displacement for any location x on the bridge with the bridge length L can be determined based on the value of x_1 according to

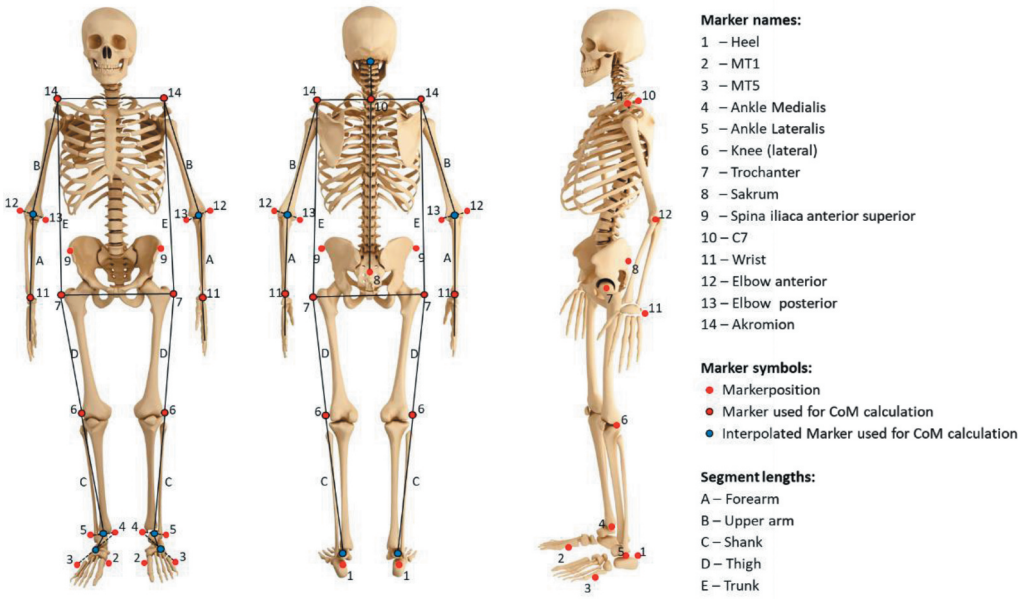


Figure 4. Positions of the passive markers on the participants and visualization of the segment lengths.

Table 2. Segment weights according to Winter (2009).

Index	Segment	Segment weight/ Total weight	COM/segment length (proximal)
1	Hand	0.006	0.506
2	Forearm	0.016	0.430
3	Upper arm	0.028	0.436
4	Foot	0.0145	0.500
5	Shank	0.0465	0.433
6	Thigh	0.100	0.433
7	Trunk	0.497	0.500
8	Head and neck	0.081	1.000

Equation 4. Here, the similarity of the bending curve to the main vibration is considered. Accordingly, higher natural modes or lateral and torsional vibrations are neglected.

$$z_b(t) = z_1(t) \cdot \frac{\sin\left(\frac{\pi}{\mathrm{L}} \cdot x(t)\right)}{\sin\left(\frac{\pi}{\mathrm{L}} \cdot x_1\right)} = z_1(t) \cdot \frac{\sin\left(\frac{\pi}{\mathrm{L}} \cdot l_s \cdot f_p \cdot t\right)}{\sin\left(\frac{\pi}{\mathrm{L}} \cdot x_1\right)} \tag{4}$$

The position x of the walking pedestrian can either be tracked by the MoCap or calculated by deriving the step length l_s and the cadence f_p from the force plate (FP) data, assuming a constant velocity v_p during the run. Since the MoCap data are also used to calculate the vertical displacement of the SDOF model, these are also favoured here.

In Figure 5, the displacement assumed from the bending curve affinity of the vibration at the position x_2=2.65 m of the displacement sensor D_01 has been calculated on the basis of the displacement sensor D02 at the position x_1=5.30 m of the 13.24 m long HUMVIB bridge. The dotted line shows the residual of the measurement signal of sensor D01 compared to the calculated values of the virtual sensor at the same position, which is approximately zero. Thus, the displacement at each time step can be calculated for each location x_i at which the walking pedestrian is located so that the dynamic equilibrium of the SDOF model can be calculated according to Equation 1 for the relative displacement z_{rel}.

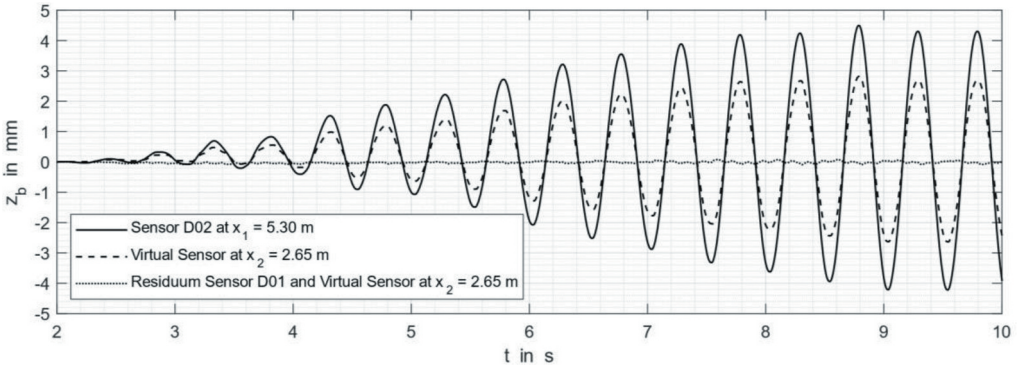


Figure 5. Measured displacement of the HUMVIB Bridge for sensor D02 at location x_1 = 5.30 m (solid line) compared to the approximated displacement of a virtual sensor at location x_2 = 2.65 m (dashed line) and the difference curve between the virtual sensor and a physical sensor D01 at the same location (dotted line) under pedestrian load with approx. 2.0 Hz walking frequency.

3 RESULTS

Figure 6 shows the application of the load model approach mentioned in Section 2.2 exemplarily on one single run of one pedestrian walking across the HUMVIB bridge. Since the spring-damper values of the SDOF model are to be determined for rigid ground, the overruns are carried out on the two-span system configuration. The processed sum curve of the vertical GRFs F_z of the subject is shown at the very top graph followed by the COM displacement z_p below. The signals from the MoCap and the force plates were filtered with a low-pass filter (Butterworth 4th order) with a cut-off frequency of 10 Hz.

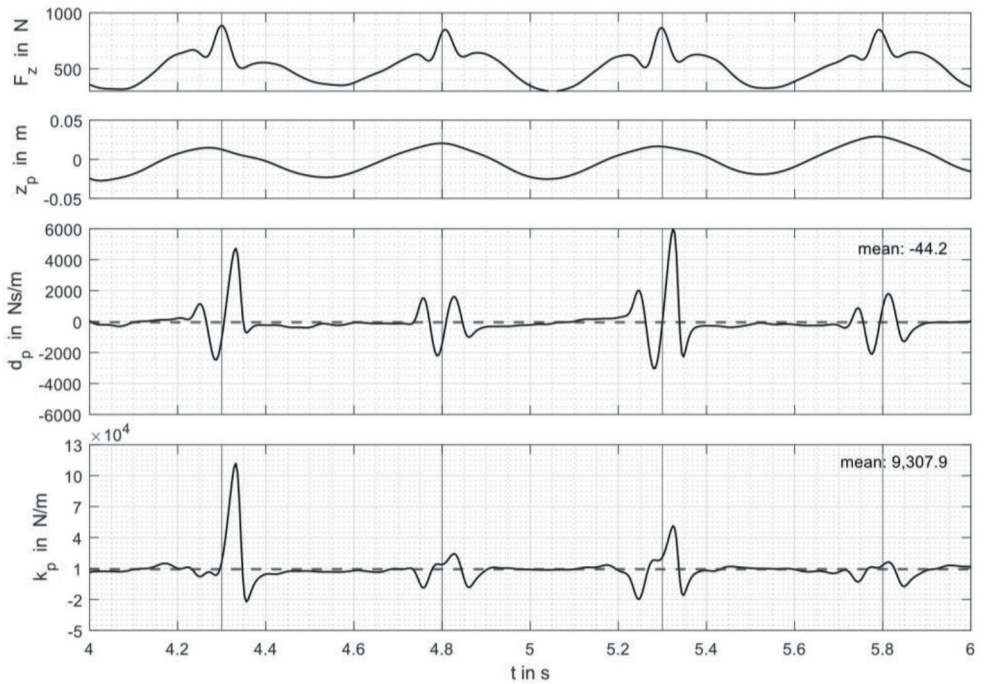


Figure 6. Vertical GRF F_z (top) and the vertical COM coordinates z_p (second graph) at walking with 2 Hz for rigid ground conditions. The lower two graphs show the calculated model parameters d_p and k_p (solid line) and the mean values for the time range between 4 and 6 seconds (dashed line).

The least squares optimisation problem was then solved for each time window, which was chosen here with four samples and thus two times overdetermined linear systems of equations. The window size was chosen small to emphasise the change in spring-damper values depending on the gait cycle. Further investigation regarding optimal time window sizes are definitely necessary. While a clear harmonic progression can be derived for the COM displacement, this is not a justified simplification for the SDOF model parameters. However, the extreme variations in the SDOF model parameters only occur in the area after the initial contact phase of the gait cycle according to Figure 4, which is caused by the sudden change in vertical GRF. Before and after the loading response phase, the spring-damper values are almost constant relative to the extreme change within this phase.

The four consecutive gait cycles shown in Figure 6 clearly demonstrate the intra-variability even within a single overrun. Accordingly, it is necessary to analyse many different steps to determine the subject dependency of the spring-damper values. Similarly, only the curves for walking on a rigid surface with a cadence of 2.0 Hz are shown here. The influence of the cadence on the SDOF model parameters must be analysed.

In Figure 7, the vertical GRF for one of double steps of Figure 6 is focused. In addition to the reference measurement of the 3D force plate, the vertical GRFs were calculated based on the COM for a moving mass (MM) without taking spring-damper values into account. Since in this case the force results solely from the COM acceleration and the mass of the person, the same forces should result for both curves (MM and 3D force plate).

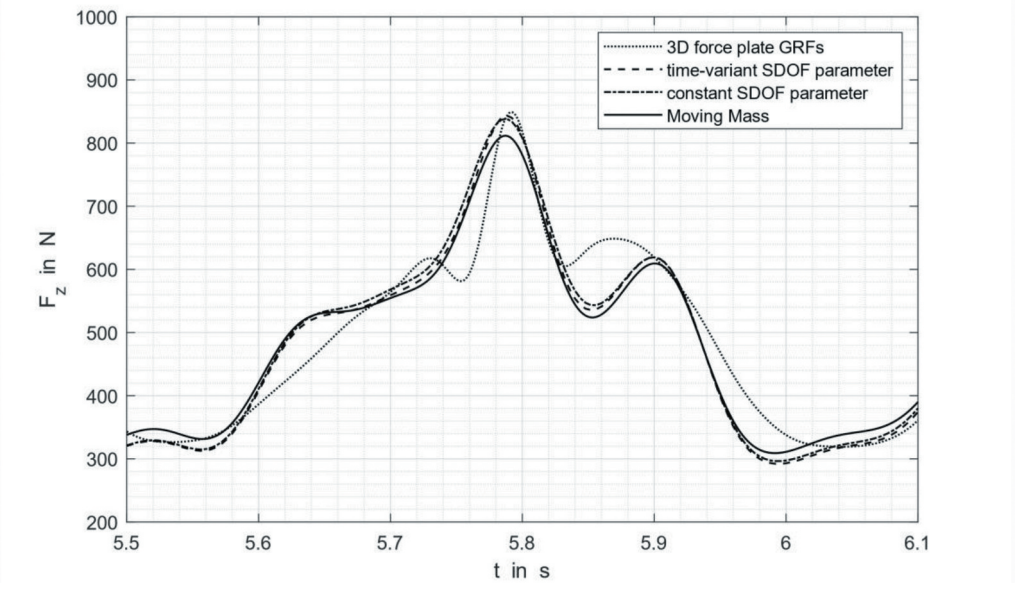


Figure 7. Vertical GRF for double step three of Figure 6.

However, there are clear differences, which are due to uncertainties in the calculation of the COM, errors in the coordinate transformation and orientation of the local coordinate systems transferred to the global coordinate system of the HUMVIB bridge, as well as measurement deviations (due to measurement technology, weight of the person, distribution of the segment masses, etc.). Further optimisation of the post-processing of MoCap data and COM calculation should reduce this deviation. However, as the deviations are quite high, the vertical GRF calculated according to Newton's second law of motion and not the 3D force plate GRFs is used as a reference value for comparison with the results of the SDOF model.

In addition, the vertical GRFs calculated with the SDOF model are shown in Figure 7. The previously determined SDOF model parameters are shown once with the time-variant (dashed line) and the time-invariant mean value (dashed-dotted line). Both approaches show

deviations compared to the MM model. In comparison, the reference values of the MM model are very close to the two SDOF model parameter assumptions. It can be observed that the time variant SDOF parameters map better than for constant values.

4 CONCLUSION

Within this contribution, a new load model approach was presented, which introduces the modelling of walking individuals as an SDOF model with gait cycle-dependent model parameters. The advantage of this modelling approach is the independence of the HSI model parameters regarding the explicit human structure configuration. However, the results presented so far only show the model used for the HUMVIB bridge as the only structure and only the application for the two-span configuration.

The processing of the measurement data required to solve the dynamic equilibrium was presented to determine the initially unknown SDOF model parameters (spring-damper values). The time-varying spring-damper values determined using the method of least squares exhibit fewer errors than those determined using the assumption of constant model parameters, as assumed in existing modelling approaches.

The results show that the methodology must first be improved before the transfer to other structures or the single-span configuration as a vibration-prone structure and thus the consideration of HSI effects on the spring-damper values. Due to the intra-variability of the individual stages, the deviations from the GRF calculated with the MM model are many times greater than the change caused by the different system configurations or HSI effects. Without analysing many individual steps, no significant deviation or well-founded statement can therefore be made.

By analysing many individual steps, the SDOF parameters for individuals as well as for a large sample of people are to be considered in further investigations. This will reduce the scattering due to inter- and intra-variability of the gait data and provide more robust SDOF model parameters. The cadence dependence and HSI-effect-related influences for other system configurations and structures on the SDOF parameters must also be determined. Furthermore, additional post-processing of the data is required to minimise the deviations of the calculation using COM compared to directly measured GRFs using force plates.

ACKNOWLEDGMENTS

The authors gratefully acknowledge the support of the DFG (German Research Foundation), whose funding of the project HUMVIB - HUMan-structure interaction and gait adaptation during locomotion on VIBrating structures (project number 446124066) made it possible to carry out this research.

REFERENCES

Archbold, P. 2004. *Interactive Load Models for Pedestrian Footbridges*. Dublin: National University of Ireland, Department of Civil Engineering.

Caprani, C. C. & Ahmadi, E. 2016. Formulation of human–structure interaction system models for vertical vibration. *Journal of Sound and Vibration* 377: 346–367.

Caprani, C. C., Keogh, J., Archbold, P. & Fanning, P. 2011. Characteristic vertical response of a footbridge due to crowd loading. *Proceedings of the 8th International Conference on Structural Dynamics*: 978–985.

Czwikla, B. & Kasperski, M. 2017. Perceptibility of Vibrations by Pedestrians. *Proceedings of the Footbridge 2017 Berlin - Tell A Story Conference*.

Da Silva, F. T., Brito, H. M. B. F. & Pimentel, R. L. 2013. Modeling of crowd load in vertical direction using biodynamic model for pedestrians crossing footbridges. *Canadian Journal of Civil Engineering* 40 (12): 1196–1204.

Fanning, P., Archbold, P. & Pavic, A. 2005. A novel interactive pedestrian load model for flexible footbridges. *Proceeding of the 2005 society for experimental mechanics annual conference on experimental and applied mecanics*: 7–9.

Firus, A., Schneider, J., Seyfarth, A. & Schumacher, C. 2017. Investigation of the Human-Structure Interaction on a Full-Scale Experimental Footbridge. *Proceedings of the Footbridge 2017 Berlin - Tell A Story Conference*.

Fritzsche, M. J. A., Stasica, M. A., Lorenzen, S. R., Seyfarth, A., Schneider, J. & Hübler, C. 2023. A Study on the Influence of Vibration-Prone Structures on Ground Reaction Forces and Gait Adaptation of Walking Individuals. *SSRN (Preprint)*.

Hartmann, M., Kreuzpointner, F., Haefner, R., Michels, H., Schwirtz, A. & Haas, J. P. 2010. Effects of Juvenile Idiopathic Arthritis on Kinematics and Kinetics of the Lower Extremities Call for Consequences in Physical Activities Recommendations. *International Journal of Pediatrics* 2010: Article ID 835984.

Qin, J. W., Law, S. S., Yang, Q. S. & Yang, N. 2013. Pedestrian–bridge dynamic interaction, including human participation. *Journal of Sound and Vibration* 332(4): 1107–1124.

Shahabpoor, E., Pavic, A., & Racic, V. 2013. Using MSD Model to Simulate Human-Structure Interaction During Walking. In *Topics in Dynamics of Civil Structures*, *Volume 4* as part of the *Conference Proceedings of the Society for Experimental Mechanics Series (CPSEMS)*: 357–364.

Winter, D. A. 2009. *Biomechanics and Motor Control of Human Movement*. Hoboken, New Jersey, United States: John Wiley & Sons, Inc.

Zhang, M., Georgakis, C. T., Qu, W., & Chen, J. 2015. SMD Model Parameters of Pedestrians for Vertical Human-Structure Interaction. In *Dynamics of Civil Structures, Volume 2* as part of the *Conference Proceedings of the Society for Experimental Mechanics Series (CPSEMS)*: 311–317.

Zivanović, S. 2015. Modelling human actions on lightweight structures: Experimental and numerical developments. In *MATEC Web of Conferences, volume 24* as part of the *Conference Proceedings of EVACES'15, 6th International Conference on Experimental Vibration Analysis for Civil Engineering Structures*: 19–21.

Bridge Maintenance, Safety, Management, Digitalization and Sustainability – Jensen, Frangopol & Schmidt (eds)
© 2024 The Author(s), ISBN 978-1-032-77040-6
Open Access: www.taylorfrancis.com, CC BY-NC-ND 4.0 license

CFD analyses for wind load assessment of the new Bomarsund arch bridge

F. El Azrak, S. Sadrizadeh, J. Leander & R. Karoumi
K.T.H. Royal Institute of Technology, Stockholm, Sweden

ABSTRACT: The trend in recent years to build longer and slender bridges has created new challenges in terms of safety and structural integrity. This study focuses on the effects of wind-induced vibrations on the hangers of the Bomarsund Bridge in Åland, Finland. Those close to the mid-span have exhibited significant vibrations, requiring a thorough investigation to understand the response of the bridge to wind action. Computational Fluid Dynamics (CFD) simulations were performed using ANSYS Fluent to calculate the aerodynamic coefficients characterizing the given section (i.e. Strouhal number, drag, shedding frequencies, etc.) and to investigate the vortex-induced vibration (VIV) phenomena at different wind speeds. The results showed inconsistent drag coefficients at varying wind speeds and lower drag for geometries with rounded edges. The study highlighted the significant dependence of the Strouhal number on wind speed, challenging traditional geometry-based estimations. These findings can be used to implement effective measures to mitigate wind-induced vibrations.

1 INTRODUCTION

The examination of vortex-induced vibrations (VIV) is essential when analyzing components of slender metal bridges exposed to significant gusts of wind. This aeroelastic phenomenon arises due to a complex interaction between the wind flow and the structure and can lead to a compromise of the structural integrity of the whole system. In-depth analyses and comprehensive explorations of various aspects related to VIV have been studied by, e.g., William and Roshko (1988), Dahl et al. (2006), Mao et al. (2016), and Wang et al. (2017). Bluff bodies with rectangular sections in particular, as for the bridge hangers, have been studied by Dey and Das (2015) and Yuce and Kareem (2016). The loss of streamlined flow significantly increases the body's resistance to the impact. These VIVs result from the development of a shedding street wake behind the bluff body. The oscillations are characterized by two fundamental frequencies, one in the direction of the wind and one perpendicular to it. The latter is the one that is consequential as it defines a fundamental dimensionless parameter such as the Strouhal number. This parameter categorizes the type of vortex shedding, ranging from viscous to quasi-steady state dominancy.

2 CASE STUDY

The Bomarsund Bridge, Figure 1, is a newly built bridge connecting Bomarsund and the island of Prästö in the municipality of Sund, in Åland, an area affected by strong wind gusts. Its main load-bearing structure is of steel designed by the Swedish company WSP in 2023. This bridge has attracted a lot of attention, particularly for its interesting structural and dynamic challenges, such as the high vibrations of the hangers, especially the longer ones close to the midspan of the bridge. These excessive vibrations are of critical importance because of their potential to cause structural fatigue problems, particularly in the hanger section, thus threatening the overall integrity of the bridge. Using the Abaqus software, the first two

DOI: 10.1201/9781003483755-135

natural frequencies of the hanger were defined: the first natural frequency of transverse vibration at 6.6 Hz and the first in the longitudinal direction at 14.1 Hz. These vibrations are compared with the lift and drag frequencies for the model implemented in ANSYS Fluent.



Figure 1. New constructed Bomarsund Bridge.

3 METHODOLOGY

Using ANSYS Fluent for CFD, it was possible to simulate the airflow around the hanger section and study the flow patterns, velocity distributions, pressure profiles and extract the aerodynamic quantities. The simulations were performed in two-dimensional (2D) space, which allows efficient yet accurate representation of the primary aerodynamic characteristics while minimizing computational cost. Both steady and transient state analyses were performed, the latter was required for this study to capture the shedding frequency and calculate the Strouhal number. For the steady analysis the solution was run for 6000-12000 iterations, while for the transient solution the convergence was reached with a time step of 0.01s for a total of 60s of flow simulation Convergence criteria, including absolute thresholds set at 0.001 for continuity, related to mass balance, x-y velocity components for a stabilized velocity distribution, k (turbulence kinetic energy) and ϵ (dissipation rate of kinetic energy) to ensure that the turbulence model has reached a stable solution. The processing workflow used in ANSYS is presented in Figure 2.

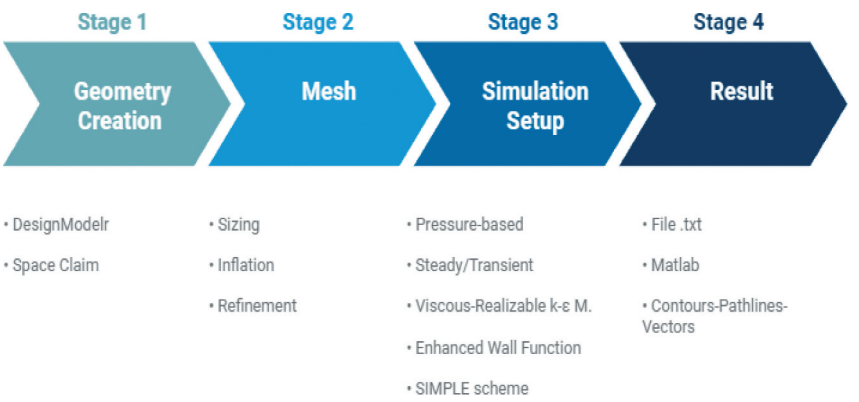


Figure 2. Processing workflow for ANSYS fluent simulations.

3.1 *Computational wind domain and mesh*

The wind domain was sized based on the characteristic dimension of the hanger d = 25.38 cm, see Figure 3. The final size of the wind domain was set to 20d from the inlet and far-field, and 40d from the outlet. The mesh was generated based on the need to find a compromise between cell fineness and computational cost. Local meshing refinements were used to obtain a denser cell zone around the cross-section and a high mesh quality. There are several parameters to evaluate, the most important being skewness, minimum orthogonal quality, and aspect ratio. The skewness is the percentage difference between the optimal cell size and the actual cell size (<1), the average value was kept below or at a maximum of 0.33. A good orthogonal quality (≈1) was maintained for a high percentage of cells, with an average value above 0.2. While the aspect ratio is the ratio of the base to the height of the cell, a value less than 35 indicates a good mesh, for the current model it was kept below 10.

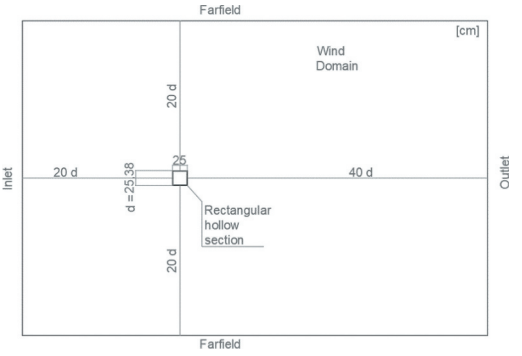


Figure 3. Computational wind domain.

3.2 *Simulation settings*

To accurately model the turbulent flow pattern around the steel section, the Realisable k- ϵ model was chosen with Enhanced Wall Treatments. These allow to model near-wall flow with higher accuracy by considering the effects of turbulence and resolving boundary layer phenomena. All the simulations were performed using a Pressure-Based Solver with a SIMPLE coupled algorithm. This is the most widely used algorithm, both for transient and steady solutions, and uses a relationship between velocity and pressure correction to enforce the conservation of mass and obtain the pressure field.

4 RESULTS

The following results summarize the extracted data of several simulations, each designed to meet a specific purpose. There is a macro division between steady-state and transient simulations, the difference between the two being that the latter allows time-dependent data to be obtained and is essential to capture the shedding frequency, which is of considerable importance for the purpose of the research.

4.1 *Steady-state solution*

The steady-state simulations were carried out primarily to verify the model on which to run a transient simulation, but also to assess the differences between the aerodynamic values in the two different state analyses. The range of wind speeds investigated for steady-state analysis varies between 2.5 m/s and 10 m/s, and two different geometries were considered, one of rectangular cross-section with no rounded edges, and the other with rounded edges.

Table 1. Aerodynamic coefficients for the steady solution: no rounded edges.

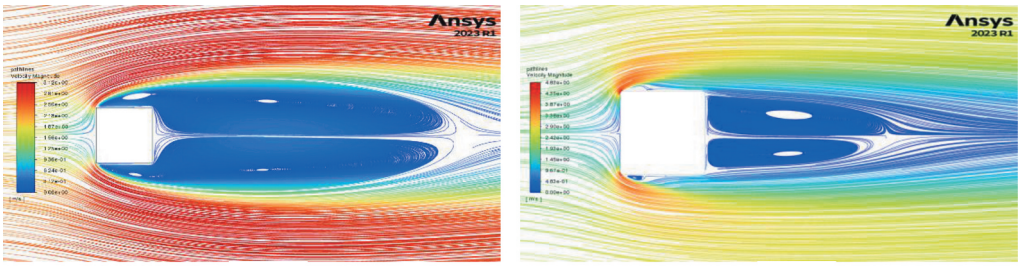
Wind speed [m/s]	2.5	5.0	7.5	10
Drag Coeff. C_D	1.379	1.397	1.398	1.402
Lift Coeff. C_L	0.000	0.002	0.001	0.001
Moment Coeff. C_M	-5.345	-5.410	-5.414	-5.432

The drag coefficient, denoted by C_D, represents the resistance of a cross-section in the direction of the wind flow. The increasing CD with wind speed, as shown in Table 1, is consistent with the fact that the drag force is proportional to the square of the flow velocity. However, it should be noted that this relationship cannot be extended to all speeds, as the drag force also depends on other factors. This issue will be covered in the following sections. An intriguing outcome is achieved for the lift coefficient C_L, which gauges the force perpendicular to the flow. Since the wind force acts without any angle of attack, it is expected that the coefficient fluctuates around zero. This implies that, on average, the hanger division undergoes negligible lift, suggesting that the structure does not create considerable transversal forces, a desirable trait for maintaining the structural stability. The moment coefficient C_M denotes the hanger section's inclination to rotate in response to fluid forces. Negative values signify the section's orientation of rotation. As with the C_D, C_M increases with wind speed, denoting that the section encounters amplified rotational forces at higher wind speeds.

Table 2. Aerodynamic coefficients for the steady solution: rounded edges r = 1 cm.

Wind speed [m/s]	2.5	5.0	7.5	10
Drag Coeff. C_D	0.889	1.096	1.144	1.145
Lift Coeff. C_L	0.059	0.019	0.000	-0.011
Moment Coeff. C_M	-3.249	-4.155	-4.390	-4.426

Table 2 displays the outcomes of the model with rounded edges. The presence of the radius in the wall section undoubtedly affects the aerodynamic coefficients. As the edge radius is introduced, the drag coefficient is reduced. A notable decline in C_D was evident. Smoothing and increasing the size of the radii of the edges generally decreases drag, following a common principle of aerodynamics. The reduction in drag is linked to an improvement in the flow characteristics around the section. The edge that was not rounded generated a significant negative moment, demonstrating a strong inclination to rotate under the influence of fluid forces. The negative moment magnitude decreased with rounded edges, which implies a reduced tendency to rotate. Rounded shapes generally result in greater stability due to the reduction of moments that might cause rotation. By analyzing the pathlines shown in Figure 4, of the two different sections, it becomes clear that the radius significantly influences the fluid flow behavior. In particular, the streamlines and vortexes are notably impacted by the presence of a radius. Sections with radii exhibit significantly shorter vortices waves compared to the sections without rounded edges. This phenomenon suggests that the vortexes generated by rounded sections are more confined and compact. The velocity of the fluid flow near the rounded section is significantly lower. The presence of radii seems to reduce the turbulence effects with a consequent increase in the velocity of the fluid flow. These observations lead to an important conclusion: the resistance encountered by the wind flow is reduced when a section contains radii. The formation of two perfectly symmetrical vortexes behind the section. It is a peculiarity of a steady flow simulation. The introduction of rounded edges alters the flow patterns, limiting the development of vortices and reducing the flow velocities in the vicinity of the section. In practical terms, this means that it is essential to consider the actual radii of the section edges to achieve accurate and realistic simulations. However, for a conservative approach, it may be advantageous to ignore the radius in the simulation.



(a) (b)

Figure 4. Velocity magnitude pathlines for not rounded (a) vs rounded (b) edges of rectangular cross section.

This effectively overestimates the drag of the section and provides a safety margin. This conservative approach ensures that the verification process accounts for higher aerodynamic forces, thereby increasing the safety and reliability of the structure.

4.2 *Transient-state solution*

The transient simulation brings to a solution that allows the extraction of time-dependent data, capturing aerodynamic effects over different temporal scales. Shedding frequencies and related parameters, including the Strouhal number, can be obtained through this process. This type of analysis provides a possibility to investigate the phenomenon of Vortex Induced Vibrations (VIV). The range of wind speeds investigated, ranging from 2.5 m/s to 30 m/s, is wider than the one for the steady solution, as the focus is shifted towards high speeds and Reynold number. The graphs in Figure 5 depict aerodynamic coefficients for a rectangular cross-section that was derived from a transient state solution at varying wind speeds. There is a tendency for the drag coefficient (C_D) to decrease as wind speed increases, reaching a minimum at v = 30 m/s. However, until a speed of 10 m/s is reached, the drag coefficient increases, following the same trend as observed in the steady solution. Nevertheless, for the remaining speed range, the behavior aligns as expected with the results reported from the literature, (Hoerner, 1965; Yuce & Kareem, 2016) see Figure 6, in which the drag coefficient values are plotted as a function of the Reynold number instead of the wind speed.

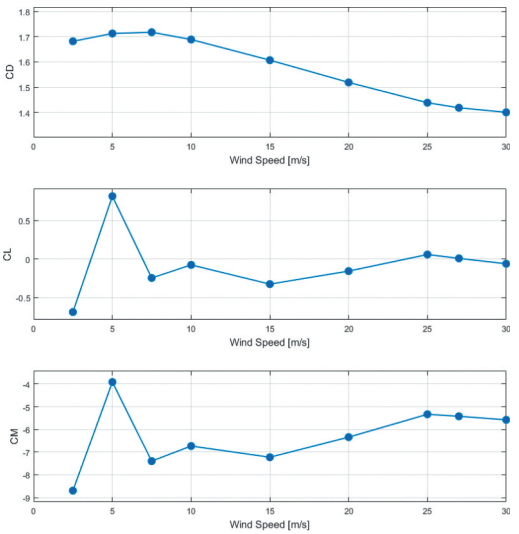


Figure 5. Aerodynamic coefficients at different wind speeds.

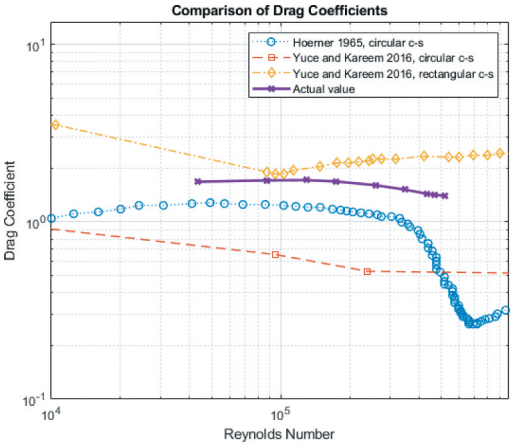
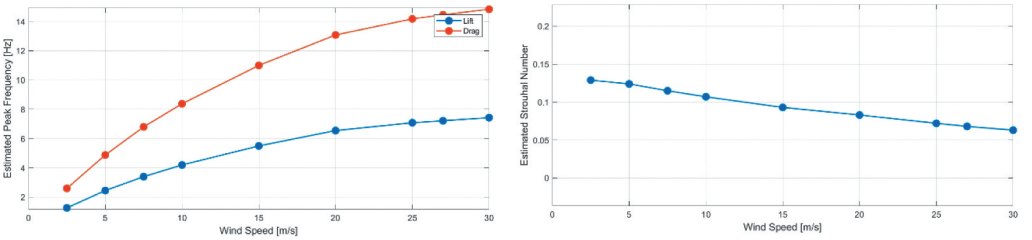


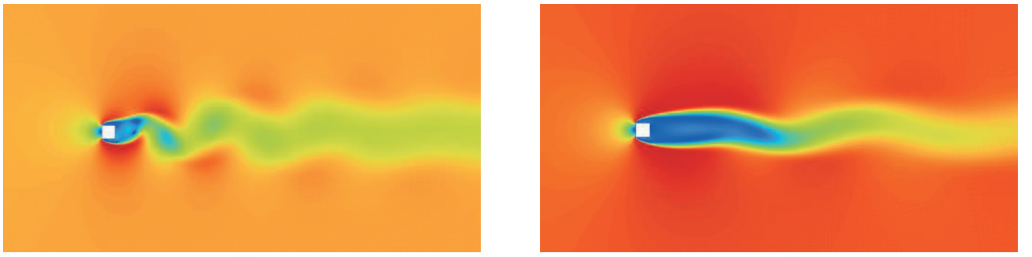
Figure 6. Aerodynamic coefficients vs Reynolds.

This is since at a higher Reynold number, flow around the structure becomes more streamlined, due to the high wind speed intensity, thereby reducing drag. For 2D simulations, the coefficient of lift (C_L) is of little significance as its value is small and oscillates around zero. Therefore, it is not possible to define a specific trend for the lift, which changes randomly in magnitude and sign due to the oscillating value around zero. The moment coefficient gradually decreases at higher speeds, following the trend of the drag coefficient. The values in Figure 5 are punctual values at time t = 60 s, which represents the end of the simulated time. The peak value in the lift at 5 m/s is not relevant because the mean value of the lift for the simulation at 5 m/s and all other simulations tends to zero. The estimated peak frequencies of drag and lift, Figure 7, were calculated using Fast Fourier Transformation (FFT) of their respective signals, and related amplitudes were subsequently extrapolated. This allowed for the calculation of the Strouhal number S_t, based on the estimated peak frequency of lift. An intriguing observation pertains to the drag frequency magnitude, which fluctuates between 5.5 Hz and 8 Hz for wind speeds ranging from 5 m/s to 10 m/s. According to the Abaqus frequency analysis, the first natural frequency of the structure is approximately 6 Hz, while the others vary within a range of up to 14 Hz. The fundamental natural frequency's vibration is out of plane. As a result, it can be concluded that the critical wind speed for the hangar ranges from 5 to 8 m/s. This wind speed range falls within reasonable values for the geographical location of the Bomarsund Bridge. The calculation of the Strouhal number, a significant parameter that signifies the shedding of vortexes surrounding the structure, considers the lift peak frequency. A decreasing trend of Strouhal numbers with increasing wind speed is observed, indicating that a shift from regular to more irregular vortex shedding patterns is occurring. A characteristic phenomenon of vortex shedding was observed, with the peak frequency of drag being twice the one for lift in the frequency domain spectra. Two vortexes of equal strength and opposite signs are shed during each oscillation period in the wake of a structure, such as a rectangular cross-section. It is important to note that the sign of the vortex has no impact on the experienced drag force. This distinctive feature results in a period-doubling effect. Regarding the wind flow configuration, it is interesting to observe how it changes above the range of wind speed simulated. At low speeds behind the bluff body, the Von Karman vortex street forms, allowing the identification of zones where the flow changes direction and local eddies form. As wind speeds increase, the vortex shedding tail becomes more elongated and less turbulent, resulting in a more streamlined flow. This explains the reduction in the magnitude of the drag coefficient. In Figure 8, two contour images are presented as examples of the vortex shedding tail for low and high wind speeds - one at 7.5 m/s and the other at 27 m/s.



(a) (b)

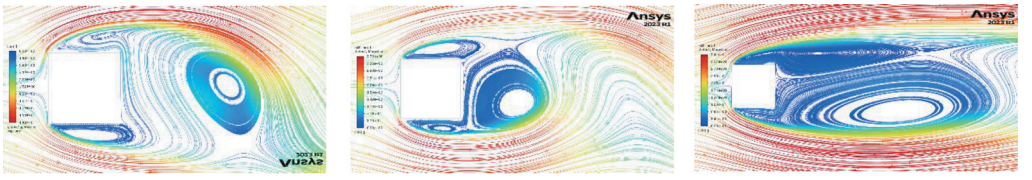
Figure 7. Lift and drag frequencies (a) and Strouhal number (b) at different wind speeds.



(a) (b)

Figure 8. Transient solution: Velocity contour at different wind speeds at t = 60 s.

It is also noteworthy to examine the form of the shedding vortex located at the rear of the cross-section. For the steady solution, the two vortexes were symmetric, but with a transient state analysis representing the effect of turbulence over time, it is apparent that this symmetry is lost. Additionally, lower wind speeds result in larger eddies that are also distributed laterally to the section. At high velocities, the vortex tail becomes more streamlined, and a second vortex forms above the first one. Some examples are reported in Figure 9, for different speeds that cover the whole range of wind speeds simulated.



(a) v = 2.5 m/s (b) v = 10 m/s (c) v = 27 m/s

Figure 9. Transient solution: Velocity pathlines at different wind speeds at t = 60 s.

5 CONCLUSIONS

The aerodynamic performance of a bridge hanger was investigated using CFD analysis. The distinction between steady-state and transient simulations allowed the detection of time-dependent phenomena such as shedding frequencies and related parameters. However, the steady-state solution overestimates the magnitude of the aerodynamic coefficients compared to the transient analyses and does not provide information on the shedding frequency and the time-dependent response of the cross-section. This type of simulation remains a valid

technique for obtaining an overview of the aerodynamic properties of the fluid around a bluff body and for investigating different factors that could influence the dynamic behavior of the structure, such as geometry influences. By increasing the wind speed from 2.5 m/s to 10 m/s for both geometries analysed, the drag coefficient increases, but the presence of rounded edges results in lower values compared to the rectangular cross-section with sharp edges, highlighting an improvement in vortex shedding stability for more rounded geometries. Moving to transient solutions, it was accurately characterized VIV by investigating a single rectangular cross-section with sharp edges at varying wind speeds. The aerodynamic coefficients, such as drag and Strouhal number (St), showed significant variability within the wind velocity range of 2.5 m/s to 30 m/s. This emphasizes the sensitivity of aerodynamic parameters to different magnitudes of wind speeds. For wind speeds below 7.5 m/s, an increasing trend in drag was observed, while for wind speeds above 30 m/s, drag coefficients decreased, indicating the effect of vortex street confinement due to high-speed flow. Additionally, the Strouhal number (S_t) shows a decreased trend across the investigated wind speed range, revealing its dependence on wind speed rather than solely on the geometry of the bluff body analyzed. The S_t value is typically determined based on the geometry, as per the Eurocode Standards. Specifically, for a rectangular cross-section without rounded edges, the S_t value is 0.12. However, this simulation has shown that the S_t value varies with wind speed, ranging from 0.129 for a wind speed of 2.5 m/s to 0.063 for a wind speed of 30 m/s. The comparison of the aerodynamic frequencies and the fundamental frequencies of the structure demonstrates the significance of assessing both crosswind and headwind response in identifying the direction that is more susceptible to resonance phenomena under vortex shedding phenomena.

REFERENCES

Dahl, J. M., Hover, F. S., & Triantafyllou, M. S. (2006). Two-degree-of-freedom vortex-induced vibrations using a force assisted apparatus. *Journal of Fluids and Structures*, *22*(6–7), 807–818.

Dey, P., & Das, A. Kr. (2015). Numerical analysis of drag and lift reduction of square cylinder. *Engineering Science and Technology, an International Journal*, *18*(4), 758–768.

Hoerner. (1965). *Fluid Dynamic Drag*.

Mao, L., Liu, Q., Wang, G., & Zhou, S. (2016). Lift force, drag force, and tension response in vortex-induced vibration for marine risers under shear flow. *Journal of Vibro engineering*, *18*(2), 1187–1197.

Wang, E., Xiao, Q., & Incecik, A. (2017). Three-dimensional numerical simulation of two-degree-of-freedom VIV of a circular cylinder with varying natural frequency ratios at *Re* = 500. *Journal of Fluids and Structures*, *73*, 162–182.

Williamson, C. H. K., & Roshko, A. (1988). Vortex formation in the wake of an oscillating cylinder. *Journal of Fluids and Structures*, *2*(4), 355–381.

Yuce, M. I., & Kareem, D. A. (2016). A Numerical Analysis of Fluid Flow Around Circular and Square Cylinders. *Journal AWWA*, *108*(10).

Bridge Maintenance, Safety, Management, Digitalization and Sustainability – Jensen, Frangopol & Schmidt (eds)
© 2024 The Author(s), ISBN 978-1-032-77040-6
Open Access: www.taylorfrancis.com, CC BY-NC-ND 4.0 license

Bridge damage evaluation model based on vehicle excitation and ML

Zhihua Xiong
Northwest A&F University, Yangling, China
RWTH Aachen University, Aachen, Germany

Tuotuo Cong, Wenhao Zhang & Zhuoxi Liang
Northwest A&F University, Yangling, China

ABSTRACT: To realize rapid damage assessment of old bridges in remote areas, this paper proposes a rapid damage evaluation platform based on the combination of dynamic response of bridges and Machine Learning (ML). Selecting several typical old bridges, the acceleration signals of these superstructures under different vehicle loads were collected. The damage indicator defines the health status of superstructure, which is developed from the wavelet packet theory. Finally, a set of damage recognition models with universal applicability is established according to the optimized algorithms derived from ML training. The results shows that the proposed approach provides a rapid and economic damage identification of bridges. The approach is a prospective solution for rapid structural evaluation of similar girder bridges.

Keywords: Old bridge, Structural health, Wavelet packet, Machine learning

1 INTRODUCTION

Bridge structures are prone to damage during the operational stage due to vehicle overloads and performance degradation. Structural damage can significantly influence the safety of bridges, which makes the Structural Health Monitoring (SHM) of great significance (He et al 2022, Svendsen et al 2022). Considerable progress has been made in the field of damage identification, which serves as a core role in bridge SHM (Bao & Li 2021, Malekloo et al 2022). In this regard, the accuracy of damage identification methods has been extensively validated on bridge structures (Wang & Shi 2018; Pan et al 2019; Machorro-Lopez et al 2021). These methods involve constructing various damage indicators to identify structural damage. With the continued advancement of research in the field of ML, the integration of ML techniques into structural damage identification has gained significant attention. Khodabandehlou et al. (2019) proposed a structural damage identification method based on Convolution Neural Network (CNN). Mousavi et al. (2021) combined Empirical Wavelet Transforms (EWT) and Artificial Neural Network (ANN) to identify the damage of steel truss bridge models. The damage identification method combining wavelet packet theory and machine learning has been verified on bridges in remote region (She et al 2023; Liang et al 2023).

For the numerous small and medium-span bridges in remote region, it is challenging to conduct or to install individual inspections due to remote geographical locations and tight maintenance cost. In this paper, wavelet packet analysis of SHM methods based on vehicle excitation together with optimized ML algorithm, the damage database was established. A fast identification platform was developed.

DOI: 10.1201/9781003483755-136

2 CONSTRUCTION OF DAMAGE IDENTIFICATION INDEX BASED ON WAVELET PACKET ANALYSIS

The wavelet packet is a set of wavelet basis functions, which has the advantage of characterizing the local features of the signal in the time-frequency domain and overcomes the disadvantage of poor high-frequency resolution in the decomposition of the low-frequency part due to the fixed sub band taken by the resolution of each layer. By using wavelet packet analysis, the response signal of bridge structure under vehicle excitation is decomposed into different frequency bands, and the energy characteristic values of each frequency band are obtained. In the response signal of the damaged structure, the energy of different nodes contains the damage information of the structure, and the damage information can be extracted by wavelet packet decomposition to obtain the damage state of the structure.

For the dynamic response signal x(t), the total energy under the J-layer decomposition can be defined as:

$$E_\chi = \int_{-\infty}^{\infty} \chi^2(t)dt = \sum_{m=0}^{2^j-1}\sum_{n=0}^{2^j-1}\int_{-\infty}^{+\infty} \chi_j^m(t)\chi_j^n(t)dt \tag{1}$$

By using the orthogonality relationship, the total signal energy of each frequency band can be obtained:

$$E_\chi = \sum_{i=0}^{2^j-1} E_{\chi_j^i} \tag{2}$$

In the above equation, $E_{x_j^i} = \int_{-\infty}^{+\infty} [X_j^i(t)]^2 dt$ is the signal energy in band *i*.

When bridge is damaged, the dynamic response signal of the bridge will fluctuate, and the energy of the corresponding frequency band will increase or decrease after the wavelet packet is decomposed. Based on the above principle, the response signal of the superstructure under vehicle excitation and the wavelet packet analysis are adopted. The Wavelet Packet Energy change Rate Sum Square (WPERSS) is defined as (Zhu & Sun 2015.):

$$WPERSS = \sum_{j=0}^{2^i-1}\left[\frac{(E_{f_i^j})_b - (E_{f_i^j})_a}{(E_{f_i^j})_a}\right]^2 = \sum_{i=1}^{m}\left[\frac{(E_{f_i^j})_b}{(E_{f_i^j})_a} - 1\right]^2 \tag{3}$$

Among them, $(E_{f_j^i})_b$ represents the signal energy of the response of the healthy bridge structure, $(E_{f_j^i})_a$ represents the signal energy of the response of the damaged bridge structure, *i* represents the scale, which is the number of decomposition layers, $m=2^i-1$ represents the total number of wavelet packet decomposition frequency bands.

3 PROJECT OVERVIEW

3.1 *Profile of Hou River Bridge*

The Hou River Bridge was completed and opened to traffic in 1997. With a total length of 15 meters, the bridge has a span arrangement of (3x5) meters and a width of 6 meters. The bridge deck is designed to accommodate a net width of 0.25 meters for guardrails, 5.5 meters for the driving lane, and an additional 0.25 meters for guardrails. The superstructure of the bridge consists of reinforced concrete beams, with each span comprised of six beams and each beam having a width of 1.0 meter. The hollow concrete slab and the cast-in-place deck, which are key components of the bridge, are constructed using C40 concrete. The overall arrangement of the bridge is shown in Figure 1

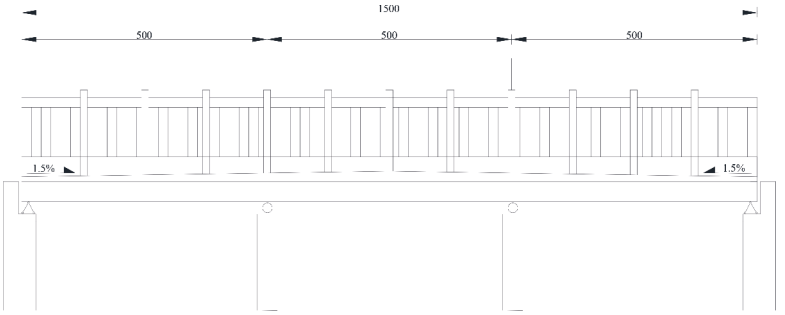


Figure 1. Bridge elevation view.

3.2 *Numerical modelling*

The engineering structure is discretized into 43,656 C3D8R elements using the finite element software Abaqus. The elastic modulus of each span of concrete is obtained using interpolation as follows: 29.8 GPa, 30.84 GPa, and 30.48 GPa. The density of the entire bridge is uniformly set at 2460 kg/m³, and the Poisson's ratio is uniformly set at 0.2. Based on the actual construction conditions, the structure is a continuous simply supported structure with the bridge deck cast as a whole. Therefore, tie contacts are established between the decks of each span. Fixed constraints are applied at both ends of the bridge abutments and the bottom of the bridge piers.

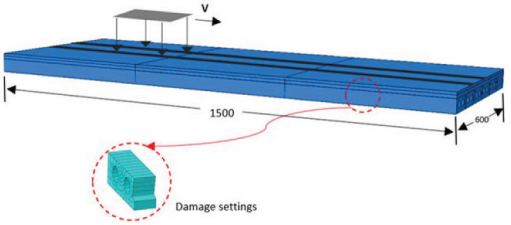


Figure 2. FE model.

3.3 *Identification of damage case*

Selecting the Hou River Bridge in Figure 2 as a case, the damage position is accurately simulated by setting the damage on different beams, and there are 9 measuring points with an equal distance of 0.5m on each beam. The local damage conditions of the structure are corresponded to by stiffness reduction, and there are three damage conditions of 10%, 20%, and 30%. There are six beams in the whole span, and the cross-section and load are symmetrical. It is assumed to be sufficient to analyze the three beams in the structure. The damage settings are shown in Figure 3.

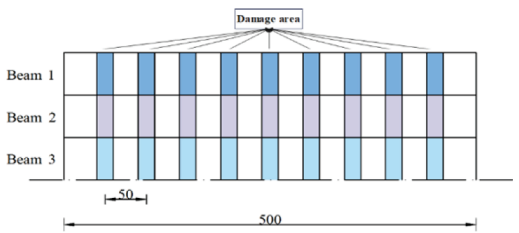


Figure 3. The damage cases of the structure.

Based on previous research (Liang et al 2023), we have selected the db20 wavelet basis function with a decomposition level of 5 to decompose the unit acceleration signal's free attenuation segment. This decomposition evenly divides the signal frequency band into 32 frequency bands. Additionally, at the same measuring point, three deliberate damage conditions of 10%, 20%, and 30% were introduced. The obtained WPERSS values, as shown in Figure 4, clearly indicate that the WPERSS value accurately identifies the location of damage while maintaining a positive correlation with the severity of damage at the measuring point.

Furthermore, three different levels of damage reduction were applied to each measuring point, as depicted in Figure 3. The corresponding damage index values were then derived, as displayed in Figures 5, 6, and 7. It was observed that the WPERSS value increased as the reduction degree of measuring points intensified. This observation confirms the excellent quantification capability of the WPERSS value as a damage indicator.

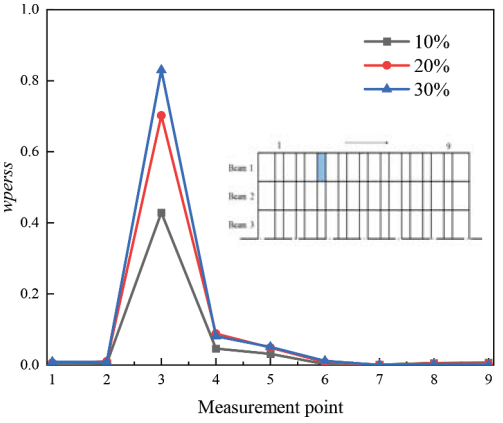


Figure 4. WPERSS values of different damage degrees at the same measurement point.

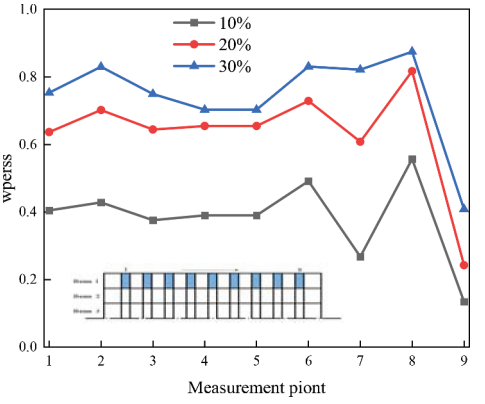


Figure 5. WPERSS values of different damage degrees at each measurement point of Beam1.

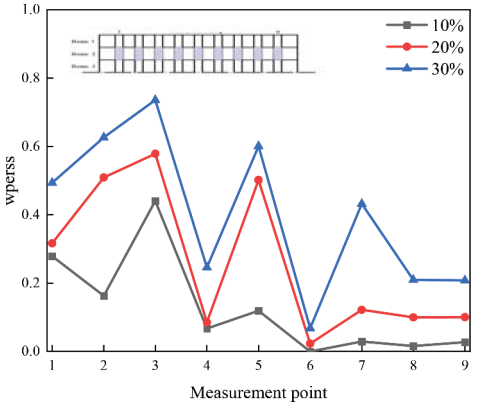


Figure 6. WPERSS values of different damage degrees at each measurement point of Beam2.

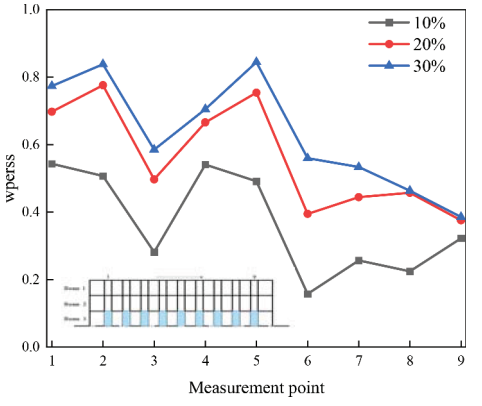
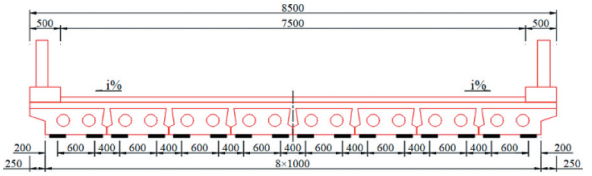
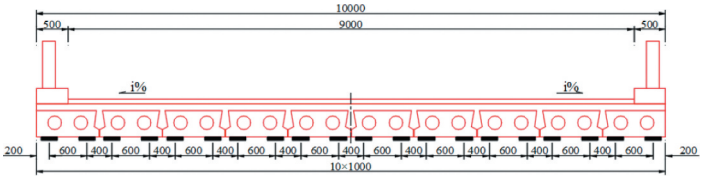


Figure 7. WPERSS values of different damage degrees at each measurement point of Beam3.

4 DEVELOPMENT OF RAPID EVALUATION PLATFORM

Various bridge numeric models with different width-to-span ratios were developed through on-site investigations, reflecting actual bridge in remote region. The prototype of bridges utilized general hollow slab bridge drawings issued by the Transportation authorities. The cross-

Table 1. Basic information of the bridge.

Model	Span lengh (m)	Bridge width (m)	Section
1	6.0	8.5	
2	8.0		
3	6.0	10.0	
4	8.0		

sectional arrangements and bridge span designs for single-span bridges are summarized in Table 1.

According to the cross-sectional arrangements and span of bridge, acceleration measurement points were spaced at equidistance on each beam. Parametric analysis was then conducted to calculate the corresponding damage index values for each damage scenario.

4.1 *BPNN optimization algorithm selection*

Back Propagation Neural Network (BPNN) has a strong ability to perform nonlinear mapping and self-learning, allowing it to accurately predict outputs based on input data (Ma et al. 2023). However, due to improper selection of initial weights and thresholds, BPNN may suffer from local convergence and slow convergence speed. To address this issue, this study utilizes Particle Swarm Optimization (PSO) algorithm to optimize BPNN.

For the BP neural network damage identification model, a three-layer BP neural network structure is selected in this study, as shown in Figure 8. The model consists of an output layer that represents the output event (bridge damage index denoted as y), a hidden layer, and an input layer that includes four input variables: lateral displacement $x1$, longitudinal displacement $x2$, damage identification index value $x3$, and aspect ratio $x4$.

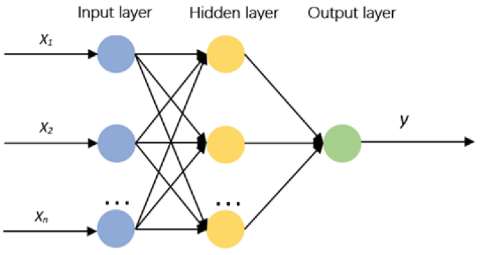


Figure 8. 3-Layer BPNN model.

To determine the optimal number of nodes in the hidden layer, this study utilized multiple simulation data sets as the training set and 9 sets of data from 9 measuring points in field tests

as the prediction set. The entire dataset was divided into 70% for training and 30% for testing. Multiple machine learning models were constructed when n=3, 4, 5, 6, 7, 8, 9, 10, 11, 12, 13, and the model with the smallest error was selected as the optimal machine learning model to evaluate the extent of damage in the target bridge. To demonstrate the training accuracy of the machine learning model, two metrics were introduced: Root Mean Square Error (RMSE) and Pearson correlation coefficient (R).

In Figure 9, it can be concluded that when the number of nodes in the hidden layer is set to 8, the PSO-BPNN algorithm achieves the smallest RMSE and the maximum correlation coefficient R. This indicates that the training effect is the best with this configuration. Consequently, a BPNN neural network model with 8 hidden layer nodes and PSO optimization was selected to evaluate the damage degree of the target bridge.

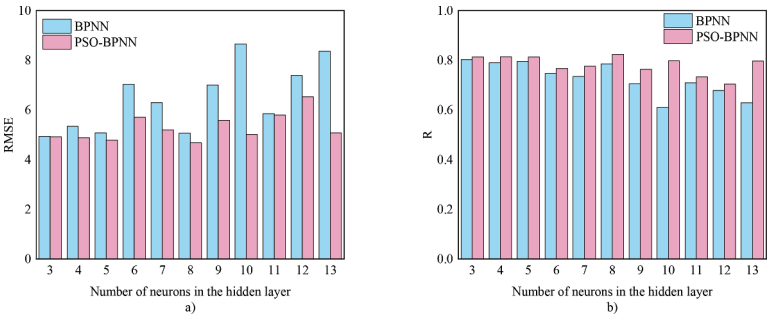


Figure 9. a) RMSE of BPNN models. b) R of BPNN models.

4.2 *Rapid identification platform development*

The structural signals collected from bridge dynamic loading experiments may not directly reflect the structural damage of the bridge. To address this, a bridge state rapid assessment software package was developed using a Python code editor, it is named RAAB, RAAB integrates evaluation methods to quickly process the collected structural signals and derive information about the bridge damage. RAAB consists of three modules: bridge basic information, bridge mechanics information, and bridge assessment and maintenance. The interface is shown in Figure 10. Figure 11 is the software flow diagram.

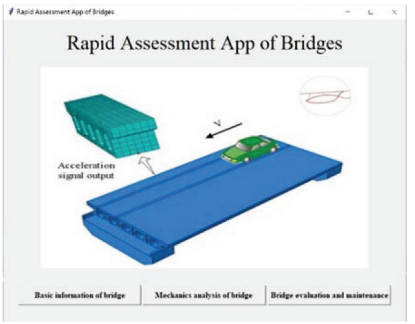


Figure 10. RAAB interface.

4.3 *Verification of RAAB*

To verify the function of RAAB, a bridge model with a length of 6.0 m and a width of 8.5 m was created as shown in Figure 12. Single-damage and multi-damage conditions were set respectively, as shown in Table 2. By inputting the acceleration signal into RAAB, we obtained the specific damage degree index value of each measuring point. The final damage

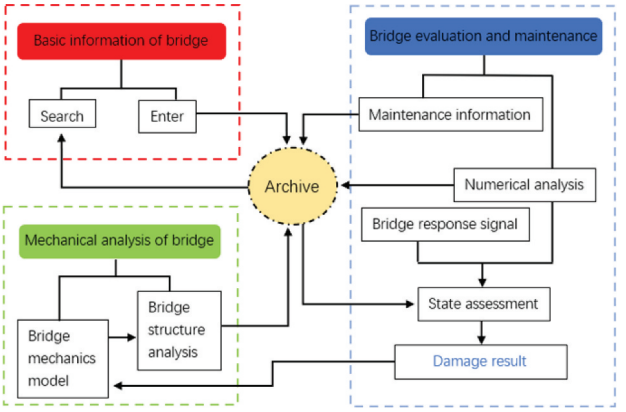


Figure 11. Flowchart of RAAB.

degree prediction results are shown in Figure 13. The results show that the damage results generated by RAAB are highly consistent with the actual model damage setting.

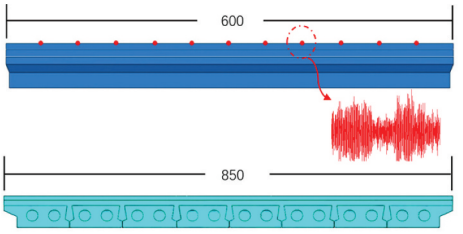


Figure 12. Validation of the numeric model.

Table 2. Damage condition.

Damage Cases	Number	Damage section	Damage degree
Single damage	K1、K2	Section 2	15%;25%
Single damage	K3、K4	Section 4	15%;25%
Single damage	K5、K6	Section 10	15%;25%
Multi-damage	K7	Section 3&5	15%
Multi-damage	K8	Section 7&8	25%

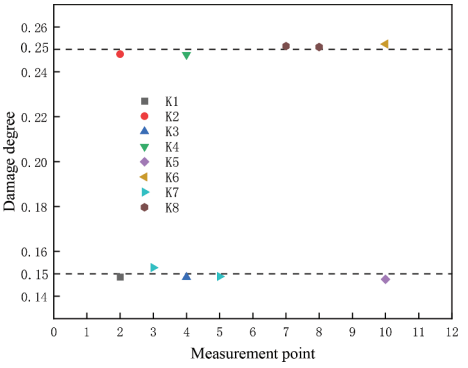


Figure 13. Damage degree of each working condition.

5 CONCLUSIONS

In this paper, a fast and feasible detection method is proposed to identify the damage of old bridges in remote areas. Comparing the two BP neural network algorithms, the error results show that the prediction accuracy of PSO-BP algorithm is better than BP. At the same time, the damage database is established, and the software platform RAAB is developed. Through the actual engineering verification matched with the database, RAAB can accurately identify the damage location, and the error of the damage quantization value is less than 5%. The platform could hopefully provide a solution for bridge structural evaluation in remote areas.

ACKNOWLEDGEMENTS

The authors are grateful for the financial support of Science and Technology Project of Department of Transport of Shaanxi Province (22-23K).

REFERENCES

Bao, Y., & Li, H. (2021). Machine learning paradigm for structural health monitoring. *Structural Health Monitoring*, 20(4), 1353–1372.

He, Z., Li, W., Salehi, H., Zhang, H., Zhou, H., & Jiao, P. (2022). Integrated structural health monitoring in bridge engineering. *Automation in Construction*, 136, 104168.

Khodabandehlou, H., et al. 2019. Vibration-based structural condition assessment using convolution neural networks. *Structural Control and Health Monitoring* 26(2): e2308.

Liang, Z. X., et al. 2023. Damage identification of Chi River bridge based on vehicle excitation and WPEVCR. *Advances in Bridge Engineering* 4(1): 21.

Ma, X., et al. 2023. Investigation of changing SARA and fatigue properties of asphalt bitumen under ageing and analysis of their relation based upon the BP neural network. *Construction and Building Materials* 394: 132163.

Machorro-Lopez, J. M. et al. 2021. Wavelet energy accumulation method applied on the Rio Papaloapan Bridge for damage identification. *Mathematics* 9(4): 422.

Malekloo, A., Ozer, E., AlHamaydeh, M., & Girolami, M. (2022). Machine learning and structural health monitoring overview with emerging technology and high-dimensional data source highlights. *Structural Health Monitoring*, 21(4), 1906–1955.

Mousavi, A. A., et al. 2021. Damage detection and localization of a steel truss bridge model subjected to impact and white noise excitations using empirical wavelet transform neural network approach. *Measurement* 185: 110060.

Pan, Y., et al. 2019. Structural health monitoring and assessment using wavelet packet energy spectrum. *Safety Science* 120: 652–665.

She, J. C., et al. 2023. Structural health evaluation of arch bridge by field test and optimized BPNN algorithm. *Frattura Ed Integrità Strutturale* 65: 160–177.

Svendsen, B. T., Frøseth, G. T., Øiseth, O., & Rønnquist, A. (2022). A data-based structural health monitoring approach for damage detection in steel bridges using experimental data. *Journal of Civil Structural Health Monitoring*, 1–15.

Wang, P. B. & Shi, Q. H. 2018. Damage Identification in Structures Based on Energy Curvature Difference of Wavelet Packet Transform. *Shock and Vibration*: 1–13.

Zhu, J. S. & Sun, Y. D. 2015. Bridge Damage Identification Index Based on Wavelet Packet Energy. *Journal of Vibration,Measurement & Diagnosis* 35(04). 715-721+800. (in Chinese)

Bridge Maintenance, Safety, Management, Digitalization and Sustainability – Jensen, Frangopol & Schmidt (eds)
© 2024 The Author(s), ISBN 978-1-032-77040-6
Open Access: www.taylorfrancis.com, CC BY-NC-ND 4.0 license

Experimental determination of trough bridges pressure distribution

S. Sarmiento, J. González-Libreros & G. Sas
Luleå University of Technology, Sweden

O. Enoksson & T. Höjsten
Trafikverket, Sweden

ABSTRACT: The IronOre line between Narvik in Norway and Luleå in Sweden faces challenges with aging bridges and an increase in allowable axle loads. In this line, reinforced concrete trough bridges constitute about 50% of the bridge population; therefore, they are crucial for the country's economy. An essential factor of trough bridge design is how traffic loads are distributed on the concrete surface. Thus, in this study, a laboratory campaign was implemented by monitoring the pressure on the slab and beams of a new full-scale trough bridge. The monitoring was made using load cells placed on the slab and beam surfaces at points of interest. The pressure was measured for different axle load levels and static and cycling loads. This study belongs to a more extensive experimental campaign where further tests on load distribution are planned. The results show how the loads are distributed among the sleepers and the final transversal and longitudinal distribution shapes on the bridge.

1 INTRODUCTION

In Sweden, there are approximately 21,000 bridges connected to the rail and road network, with 4,000 dedicated to railways (Trafikverket 2022). Among these, roughly 83% are reinforced concrete bridges (BaTMan 2021). Specifically, of the 4,000 railway bridges, 1,000 (23%) fall into the category of trough bridges (Sarmiento Nova et al. 2021). A typical reinforced concrete trough bridge is constituted by two longitudinal beams that support a slab forming a U-shape, which functions as a container for the ballast and railway track.

Many of the trough bridges in Sweden are approaching their intended lifespans, raising concerns about their current capacity and safety. Despite their age, previous studies (Elfgren et al. 1996) have shown that these bridges do not exhibit visible damage, suggesting a potentially hidden capacity that should be accounted for when assessing their current performance. Previous bridge designs were grounded in conventional assumptions, potentially leading to a conservative estimation of their strength capacity.

Understanding the stresses transferred through the track and support is crucial for developing design practices that ensure adequate track performance, especially for railway trough bridges (Unluoglu et al. 2023). Significant differences exist in pressure distribution when comparing various codes and experimental studies. Eurocode 1 (CEN-1991 2003) and the Swedish standard, TDOK 2013:0267 (Trafikverket 2019), assume a uniform distribution, contrary to experimental tests revealing a double parabolic shape (Andersson 2020, Sadeghi 2005, Navaratnarajah et al. 2018, Piaxâo et al. 2018). Multiple factors contribute to these differences, including sleeper seating, ballast compaction, sleeper spacing, rail bending stiffness, and the presence of additional layers for load distribution (Esen et al. 2022).

Current literature emphasizes the need for more experimental investigation into sleeper-ballast contact pressure and stress distribution along and across the ballast (Sadeghi 2005). Therefore, this paper aims to contribute to research on traffic load distribution for typical

DOI: 10.1201/9781003483755-137

concrete trough bridges in Sweden. The goal is to enhance our understanding of their actual load-bearing capacity and behavior. To achieve this, an experimental study on a full-scale reinforced concrete trough bridge was conducted, measuring load distribution in a laboratory setting. Load plates were fabricated and strategically placed on the concrete slab surface to measure load magnitudes. The study involved static and cyclic loading, and the obtained pressure profiles were compared with current standards.

2 BACKGROUND

Determining and field-testing the stress distribution pattern along and across the ballast has proven to be a complex task. Through both experimental and numerical analyses, existing literature has revealed that the assumption of uniformly distributed pressures does not accurately reflect reality.

Early investigations into this matter were conducted by Talbot (1980), who proposed various hypothetical distributions of the bearing pressure at the ballast-tie interface. These hypotheses were formulated based on the variability of the contact area from one tie to another. Given the inherent difficulty in precisely predicting pressure distribution between the sleeper and the ballast, Sadeghi (2005) further presented hypothetical contact pressure data gathered from various theoretical and field test studies, illustrating at least six distribution types.

In contrast to these findings, Eurocode 1 (CEN-1991 2003) assumes a transversally uniformly distributed load on the slab. It employs a trapezoidal transition from the sleeper's bottom through the ballast to the slab's surface, with an inclined ratio of 4:1 (Figure 1a). The Swedish administration's TRV (Trafikverket 2019) also assumes a uniform distribution but with a steeper slope of 2:1 (Figure 1b). Additionally, from Figure 1, it is possible to observe that the Swedish standard assumes a shorter distance under the sleeper (2.25m), whereas the CEN-1991 2003 considers the entire length of the sleeper.

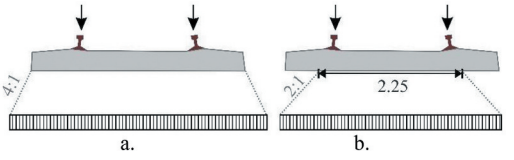


Figure 1. Load distribution through the ballast according to a. Eurocode 1 (CEN-1991 2003) and b. the Swedish standard (Trafikverket 2019). measurements in meters. (measures in meters).

The American Railway Engineering Maintenance-of-way Association (AREMA) assumes a pressure distribution according to Figure 2a (AREMA 2010). The pressure distribution has a double parabolic shape simplified with a uniformly distributed load with the length L_{eff}. L_{eff} is calculated as 1/3 of the length of the sleeper and is acting at the ends of the sleeper, where the load is assumed to be the largest. Standards Australia (2003) takes a load that is partially uniformly distributed under the rail seats of the sleeper and no load in the middle of the sleeper, as presented in Figure 2b.

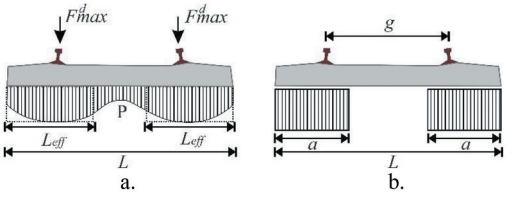


Figure 2. Load distribution assumption according to a. AREMA (2010), where F^d_{max} Is the load from the rails on the sleeper and b. the australian standards (Standard Australia 2003).

The load distribution in the longitudinal direction for one axle load can, according CEN-1991 (2003), can be assumed to be distributed between the three sleepers, according to Figure 3a. Half of the axle load is considered to be distributed to the sleeper directly below the axle load and one-quarter of the load to the two adjacent sleepers. The distance 'a' in the figure is between sleepers, 'b' is the length distribution of the load, and Q_{vi} is the load from one axle load. The slope for the transmission of the load to the slab is 4:1. The TDOK 2013:0267 makes the same assumptions; however, the slope is the same as the transversal (2:1) and establishes two additional cases for the distribution of loads among sleepers (see Figure 3b).

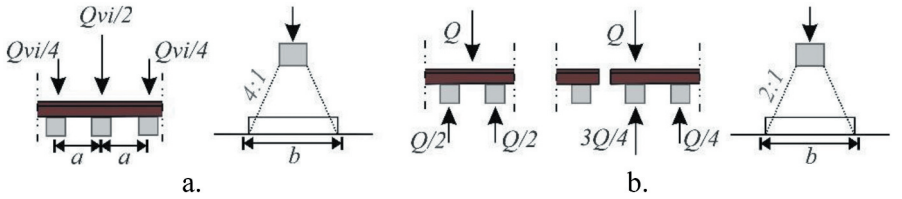


Figure 3. Longitudinal aoad distribution according to a. Eurocode 1 (CEN-1991, 2003) and b. TDOK 2013:0267 with additional cases of axle load (Q) distribution between sleepers. (Trafikverket, 2019).

According to the U.S. Army Corps of Engineers (2000), the longitudinal load between sleepers can be assumed to be distributed according to Figure 4a. This case is valid when the axle load is placed directly on top of a sleeper. U.S. Army Corps of Engineers (2000) underlined some essential aspects that affect the load distribution, such as the size of the axle load, track design, and track condition. Profillidis (2006) suggests that the load can instead be assumed to be distributed across five sleepers, with the distribution being 7 %, 23 %, 40 %, 23 %, and 7 % of the total axle load according to Figure 4b. Lichtberger (2005) suggested a load distribution that is very close to this and a distribution according to Figure 4c.

Experimental tests have shown that the load distribution is more of a double parabolic shape instead, where the stresses are more concentrated directly under the section in which the train wheels are in contact with the rails and underlying sleepers (rail seating) (Esmaeili et al. 2019, Andersson 2020, Sadeghi 2005, Zakeri & Sadeghi 2007, Navaratnarajah et al. 2018, Piaxâo et al. 2018).

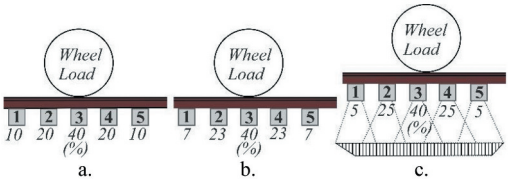


Figure 4. Pressure distribution according to a. (U.S. Army Corps of Engineers, 2000) b. Profillidis (2006) and c. Lichrberger (2005).

Finite Element (FE) modeling has been broadly implemented to understand the behavior of railway track structures. Sadeghi (2005), for instance, employed FE modeling to analyze track structure responses under static and transient loads. In this investigation, the deflection was considered proportional to the pressure beneath the sleeper, resulting in a deflection pattern composed of two parabolas—a model akin to that proposed by Talbot (1980) and ORE (1968). Zakeri & Sadeghi (2007) and Aursudkij (2007) further affirmed the existence of non-uniform contact pressure between the ballast and the sleeper, describing a parabolic pressure distribution diminishing with depth.

Navaratnarajah et al. (2018) explored the impact of Under Sleeper Pads (USPs) on track behavior, revealing higher stresses in the ballast directly under the rail seat where the wheel load is applied, with pressure decreasing on average with ballast depth.

Andersson (2020) conducted an FE analysis investigating load distribution through the ballast on a 4.0 m reinforced concrete trough bridge. Results indicated a more uniform distribution for a thicker ballast layer, affirming a double parabolic shape for a 0.6 m ballast layer. Conversely, load distribution peaks were lower for a 1.0 m thick ballast layer, reflecting a more even load distribution.

Sarmiento et al. (2021) developed an FE model of a trough bridge employing different pressure distributions to assess their impact on bridge performance. A parametric study and reliability analysis were conducted under various boundary conditions, revealing that assumptions about support conditions and pressure patterns significantly influence this type of structure's capacity, failure mode, and probability of failure. Failure modes could range from flexure at the support to shear, depending on the pressure pattern.

Other numerical approaches have been presented, such as Kaewunruen & Mirza (2017), who used a combination of Discrete Element (DEM) and Finite Element Methodology (FEM) to analyze ballast behavior under dynamic loading. They reported high ballast stresses directly below the outer rail during yielding. Additionally, Eriksson et al. (2023) compared FEM and DEM results on load distribution, noting that FEM exhibits a smoother and more even load distribution compared to the unique patterns observed in the DE model.

3 DESCRIPTION CASE STUDY

An analysis of the bridge population in Sweden concluded that a typical single-span trough bridge has, on average, a span length of 6.8 m and a width of 5.4 m. Therefore, the geometry and available design of a trough bridge close to the average was used as a base for building two reinforced concrete trough bridges at the Luleå University of Technology. The geometry is displayed in Figure 5. It used a concrete quality C40 and reinforcement bars class Ks40. The railway track used rails type UIC60, a ballast class I with a height of 27 cm from the concrete slab top surface to the bottom sleeper surface, and sleepers with fast clippers.

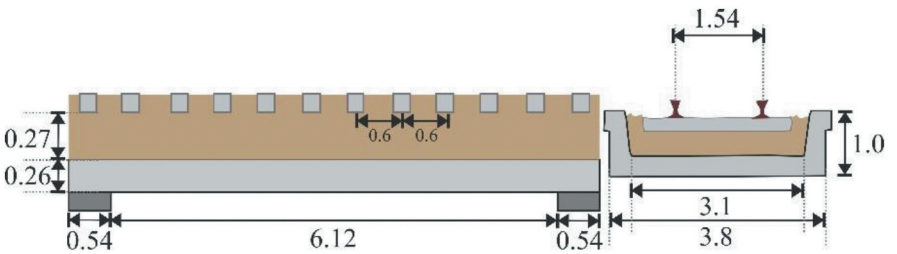


Figure 5. Geometry of the two casted trough bridges at LTU.

4 DESCRIPTION EXPERIMENTS

4.1 *Instrumentation*

To measure how the pressure is distributed on the concrete surface, 12 load plates consisting of two steel plates and four (4) force transducers were built. A force transducer, also known as a load cell, is a sensor that measures the force or load applied to it. These devices are widely used in various applications, from industrial settings to scientific research, where the accurate measurement of force or weight is necessary. The range of applications includes load testing, materials testing, industrial weighing scales, and force feedback in robotics and haptic devices.

A force transducer typically operates on the principle of strain gauges. When a force is applied to the transducer, it deforms slightly, causing the strain gauge to stretch or compress. This change in strain causes a difference in the gauge's electrical resistance. Force transducers need to be carefully calibrated to ensure accurate and consistent measurements. Calibration involves applying known forces to the transducer and recording the corresponding output signals.

For this study, force transducer type C9C, which is a compact design compressive force transducer with accuracy class 0.2, was chosen. The force transducers can measure forces from 50 N to 50 kN, and they are considered to have high rigidity and are particularly suited for dynamic measurement tasks. Figure 6a shows an example of a force transducer C9C.

The steel plates were designed to support the expected load during the test and serve as a box for the force transducers. Therefore, the steel plates have an area of 25x25 cm and thickness of 2.1 and 1.1 for the bottom and top plates, respectively. Once the steel plates were designed and fabricated, the force transducers were placed on the bottom steel plate and then closed with the top steel plate, as shown in Figure 6b-c.

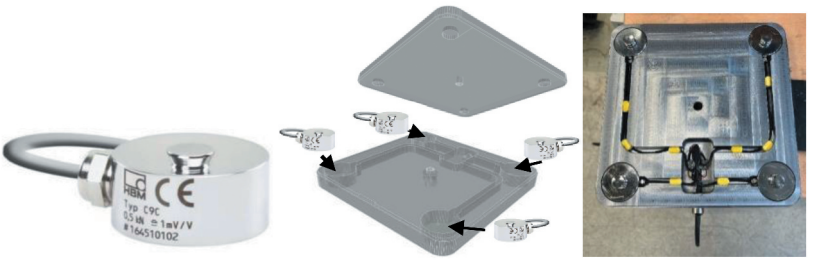


Figure 6. A. Example of a force transducer type C9C steel plates of pressure cells b. 3D model of steel plates and transducers' position and b. picture of the assembling.

4.2 *Test protocol and set-up*

The test protocol consisted of two main stages: static and cyclic loads. A load rate of 0.6 kN/s was used for the static stage, and for the cycles, a frequency of 1 Hz was used. The load ranges and the number of cycles is illustrated in Figure 7. The test set-up consisted of one load applied with a hydraulic jack, equally distributed into two beams (see Figure 8a). During the test, stops were established to inspect the bridge for crack development control and to perform photogrammetry. The moments of inspection are also illustrated in Figure 7.

It was considered the test set-up to position the load plates, which consisted of one axle load at 0.9 meters from the mid-span. Therefore, the plates were distributed transversally and longitudinally above the axle position (see Figure 8a-b). Also, two plates were located on the surface of the longitudinal beam to control the transference of pressure to the beam.

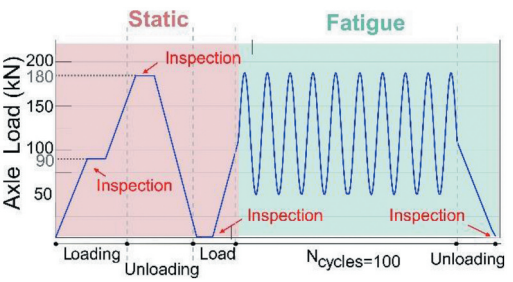


Figure 7. Sketch of the test protocol.

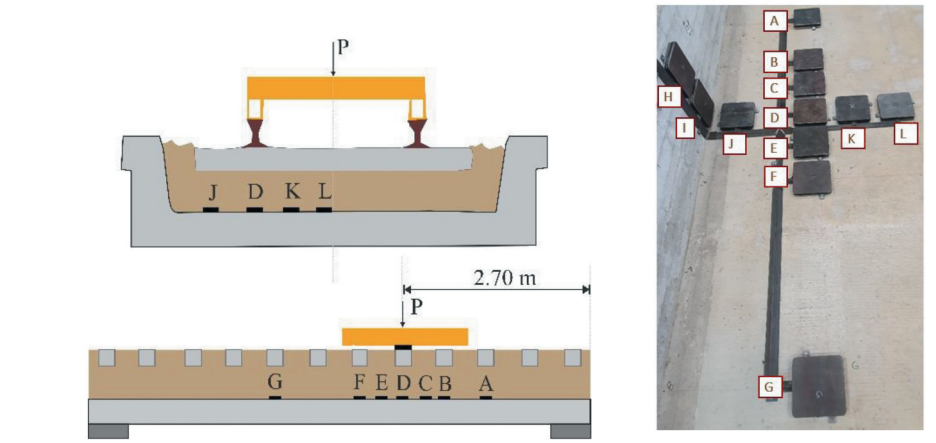


Figure 8. A. Position of the load plates and test set-up and b. picture after instalation.

Plates A-G were placed to obtain the pressure profiles of the force along one of the axle longitudinal edges. The idea was to capture the load transmitted above the closest sleepers and in between them. Transversally, plates D, J, K, and L provide the shape of the wheel load distribution. It is assumed that because of symmetry in load position and structure, the distribution is symmetric as well.

5 RESULTS AND DISCUSSION

The transversal and longitudinal pressure profiles obtained for different load levels (90, 120, 150, and 180 kN) are displayed in Figure 9, which show the applied load, the position of the plates, and the respective load value.

The transversal pressure profile displays a higher load on Plate K, a similar load magnitude on Plates D and L, and a lower magnitude on Plate J. The obtained pressure pattern describes a parabola with a peak at 32.25 cm from the rail edge. The bridge's symmetrical behavior was checked by measuring the displacements under the load application in each railway position. Therefore, it can be affirmed that the pressure in the transversal direction describes a double-parabola shape (or w-shape).

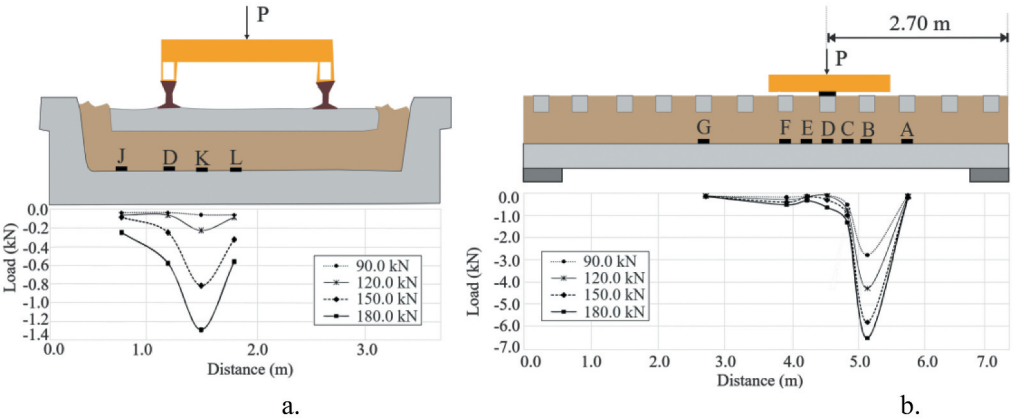


Figure 9. a. transversal pressure profile b. longitudinal pressure profile.

The longitudinal pressure distribution obtained exhibits a high peak on Plate B, which significantly drops on Plate C, continues to decrease on Plate D-E, and experiences a slight increase on Plate F compared with Plate E (0.19 kN for an axle load of 180 kN). Given the position of the axle load, Plate G did not receive any load, and Plate A only received a small percentage.

The obtained results show that the axle load was highly concentrated at the sleeper behind the axle load application. This result might be the influence of parameters such as the level of compaction of the ballast and how the sleepers were sitting. When the ballast was placed, it was carefully sorted and leveled so that all the sleepers were aligned; however, there still exists the possibility of existing voids underneath some sleepers, such as the sleeper above Plate D, where the load was applied. This made the load to be transferred to the sleeper behind. Also, since the compaction after a few cycles has been shown to affect the distribution of loads, it can be affirmed that it is necessary to have a stage of 'compaction' before applying the static load. Nevertheless, the results showed that the pressure is not uniformly distributed on the entire concrete surface, as design standards assume, in any of the directions (transversal and longitudinal).

The pressure profile was also calculated following TRV and Eurocode standards (based on Figs. 2-3), and the values were compared with the experimental results presented above. Figure 11a-b compare transversal and longitudinal profiles, respectively. The peak load was higher in the experiments than the standards, which can be because the ballast was not compacted, and a small number of cycles was applied. However, the pressure on the remaining points of the slabs was much smaller in the tests than in the standards, indicating a smaller load spread (load distribution length). The Eurocode shows the same distribution as TRV, transversally and longitudinally; however, Eurocode showed more pronounced peaks and higher-pressure values given that the distribution length was shorter, and the loads were more concentrated near the load application.

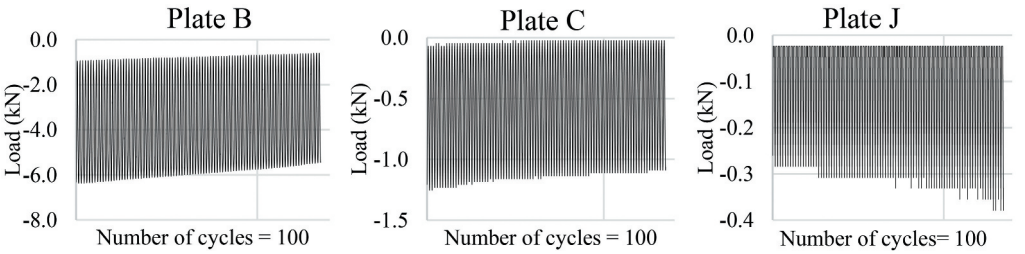


Figure 10. Loads in plates B, C, and J during the fatigue test.

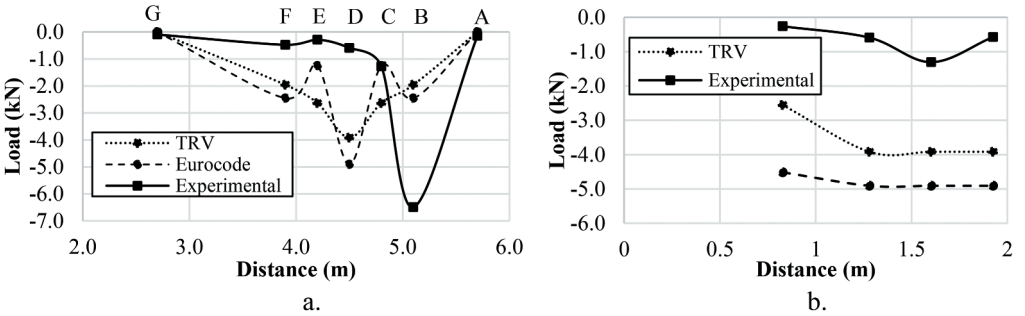


Figure 11. Comparison of load distribution among TRV, Eurocode (CEN-1991 2003), and Experimental results a. longitudinally and b. transversally.

6 CONCLUSIONS

Given the results obtained and analysis carried out, the following conclusions can be drawn:

- Experimental results showed that the transversal pressure distribution of loads on the concrete slab is not uniform for the entire surface, but it follows a w-shape distribution. The results showed that given the configuration of ballast particles, some concentration of loads would be expected near the load application.
- The ballast compaction influences the pressure distribution. A non-compacted ballast, such as the one used in the test, tends to concentrate the loads in smaller slab areas. For a total of 100 cycles applied, a re-distribution of loads was observed.
- It is necessary to check the sleeper's contact area to certify that the highest load is transmitted to the sleeper where the axle load is applied. Techniques such as tamping can ensure a more uniform contact area between ballast-sleepers.
- Significant differences in pressure profiles between the experiments and Eurocode and TRV standards were obtained. The assumption of a more uniformly distributed load might lead to either an underestimation or overestimation of the concentration of stresses in different critical points of the structure.
- Further experiments should be conducted by considering more compacted ballast and additional load plates that can eliminate the uncertainties regarding contact between the sleeper-ballast and uniform distribution of ballast aggregates.

ACKNOWLEDGEMENTS

We would like to thank to the Industry program for research and innovation of Construction for the Transport sector (BBT) and the European Horizon 2020 Joint Technology Initiative Shift2Rail through contract no. 101012456 (IN2TRACK3) for financing this research.

REFERENCES

Andersson, A. 2020. Load distribution on railway slab bridges. *Stockholm*: *KTH Royale Institute of Technology*.

AREMA. 2010. Manual for railway engineering. *American Railway Engineering Maintenance-of way Association*.

Aursudkij, B. 2007. A laboratory study of railway ballast behavior under traffic loading and tamping maintenance. *PhD dissertation. Nottingham Trent University*.

BaTMan. 2021. BaTMan – Bro och Tunnel Management. *BaTMan Extern Portal (trafikverket.se)*

CEN-1991. 2003. Eurocode 1: Actions on structures – Part 2: Traffic loads on bridges. *Brussels: European Committee for Standardization*.

Elfgren, L., Ohlsson, U., Danielsson, G., Åström, L., Johansson, H., Paulsson, B., & Töyrä, B. 1996. 30 ton på Malmbanan. Rapport 3.3 Infrastruktur.: Forsknings-och utvecklingsprojekt avseende betongbroars bärighet. Banverket.

Eriksson, A, Ullrich, A, Wang, C, Gonzalez-Libreros, J, Johansson, J, Enoksson, O, Quist, J & Sas, G. 2023. Numerical and Analytical Evaluation of Load Distribution Patterns on Ballasted Concrete Railway Bridges. *In International Symposium of the International Federation for Structural Concrete* (pp. 109–118). Cham: Springer Nature Switzerland.

Esen, A. F, Woodward, P. K, Laghrouche, O, & Connolly, D. P. 2022. Stress distribution in reinforced railway structures. Transportation Geotechnics, 32, 100699.

Esmaeili, M., Yousefian, K. & Nouri, R. 2019. Vertical load distribution in ballasted railway tracks with steel slag and limestone ballasts. *International Journal of Pavement Engineering*, 20(9): 1065–1072.

Kaewunruen, S. & Mirza,O.2017.Hybrid discrete element: finite element simulation for railway bridge-track interaction.*IOP Conference Series. Materials Science and Engineering*.

Lichtberger, B. 2005. Track Compendium. *Hamburg: Eurail press*.

Navaratnarajah, S. K., Indraratna, B., & Ngo, N. T. 2018. Influence of under sleeper pads on ballast behavior under cyclic loading: experimental and numerical studies. *Journal of Geotechnical and Geoenvironmental Engineering*, 140.

ORE. 1968. Stresses in concrete sleepers: Stress in the rails. U. *Report D71/RP/E*.
Paixão, A., Varandas, J.N., Fortunato, E. & Calçada, R. 2018. Numerical simulations to improve the use of under sleeper pads at transition zones to railway bridges. *Engineering Structures*, 164: 169–182.
Profillidis, V.A. 2014. Railway management and engineering. *Fourth edition . Farnham, Surrey, Eng-land*: *Ashgate Publishing Limited. Railway management and engineering. Ashgate Publishing Ltd*.
Sadeghi, J. 2005. Investigation on the accuracy of the current practices in analysis of railway track concrete sleepers. *International Journal of Civil Engineering*, 3(1): 31–45.
Sarmiento Nova, S.J., Gustafsson, J., Åkergren, D., Gonzalez-Libreros, J.H., Sas, G. & Elfgren, L. 2021. Pressure Distribution Patterns Between the Ballast and the Concrete Slab in Railway Trough Bridges. *In Proceedings of the 31st European Safety and Reliability Conference (ESREL 2021). Research Publishing Services*, 1093–1100.
Standard Australia. 2003. Australian Standard – Railway track material, part 14: Prestressed Concrete Sleepers. *(AS1085.14.). Sydney, NSW, Australia.*
Talbot, A. N. 1980. Stresses in railroad track: the Talbot reports. *AREA*.
Trafikverket. 2019. TDOK 2013:0267 – Bärighetsberäkning av broar. *Borlänge*.
Trafikverket. 2022. Så sköter vi broar och tunnlar. Available at: https://www.trafikverket.se/resa-ochtrafik/underhall/sa-skoter-vi-broar-och-tunnlar/ (Accessed: 22 08 2022).
Unluoglu, H. A., Bryson, L. S., & Rose, J. G. 2023. Stress Distribution in a Railroad Track at the Crosstie–Ballast Interface. *Journal of Transportation Engineering*, Part A: Systems, 149(8), 04023074.
U.S. Army Corps of Engineers. 2000. Railroad Design and Rehabilitation. Washinton DC: Engineering and Construction Division.
Zakeri, J. A., & Sadeghi, J. 2007. Field investigation on load distribution and deflections of railway track sleepers. *Journal of Mechanical Science and Technology*, 21(12): 1948–1956.

Bridge Maintenance, Safety, Management, Digitalization and Sustainability – Jensen, Frangopol & Schmidt (eds)
© 2024 The Author(s), ISBN 978-1-032-77040-6
Open Access: www.taylorfrancis.com, CC BY-NC-ND 4.0 license

FE model and verification as digital twin of structural behavior for infrastructure management

H. Shirahata
Department of Urban and Civil Engineering Tokyo City University, Tokyo, Japan

T. Kawai
Department of Design and Data Science Tokyo City University, Yokohama, Japan

M. Tai
Department of Civil Engineering University of the Ryukyus, Okinawa, Japan

T. Aoki & H. Hara
Civil Aviation Bureau, Ministry of Land, Infrastructure, Transport and Tourism, Tokyo, Japan

ABSTRACT: This study aims at the development of digital twin that consists of two parts. One is data storage of inspection data. The other is numerical model to evaluate the performance of the structure. The objective of the numerical model is to predict the influence of the deterioration, when the deterioration gets worse. A bridge was picked up and the finite element model was built. Reproduction of the actual behavior is very important to estimate the influence of deterioration. The field loading test was conducted for the verification. A heavy vehicle of 40 tons was loaded. By considering the reinforced concrete sidewalk and steel fences of sidewalks, the agreement between the actual structure and numerical model could be improved up to 92 %. After the loading test, continuous monitoring of bridge weigh-in-motion was carried out. The result showed that the traffic condition of the bridge was not serious very much.

1 INTRODUCTION

Deterioration of infrastructure has become one of the most serious problems. Appropriate maintenance works are necessary. From 2014 in Japan, periodical inspections have been started. The inspection should be a close visual inspection, for example, within 1m. The results of inspection are open to the public on the web by the administrator of infrastructure such as bridges and tunnels. Because the period of the inspection is 5 years, the second cycle is coming to the end in the fiscal year of 2023.

Even though the guideline of the inspection was published, the results are not always consistent by the administrators. This problem usually comes from the recordability of the inspection data. In order to improve the recordability, some studies have investigated the application of a bridge in a computer space with data storage.

In recent years, digital twin has been applied in many fields (Nakabo 2022, Thelen 2023, Zhang 2022). Digital twin is a counterpart usually in the computer space and plays important roles such as simulation, monitoring, data storage, and maintenance. This study aims at developing a digital twin, as shown in Figure 1. We will develop two types of digital models in a computer space. One is used for data storage of periodical maintenance work in every five years. The model can also work as a simulator of inspection prior to the actual work. The other model is related to structural behavior (Fujikubo 2021). It

DOI: 10.1201/9781003483755-138

is easy to accelerate a deterioration such as corrosion in the virtual space, while it actually takes long time to reduce the thickness of the member. The numerical model predicts the performance of the structure such as ultimate strength. Based on the results of the numerical analyses, it is possible to know the weak point in advance. In the next maintenance works, inspection of the weak points can avoid the fatal failure of the structure (Sugisaki 2023).

In this study, as a prototype of modeling the digital twin of a structural behavior, an existing bridge was chosen and the verification was conducted by the field test. This paper describes the details of the field test.

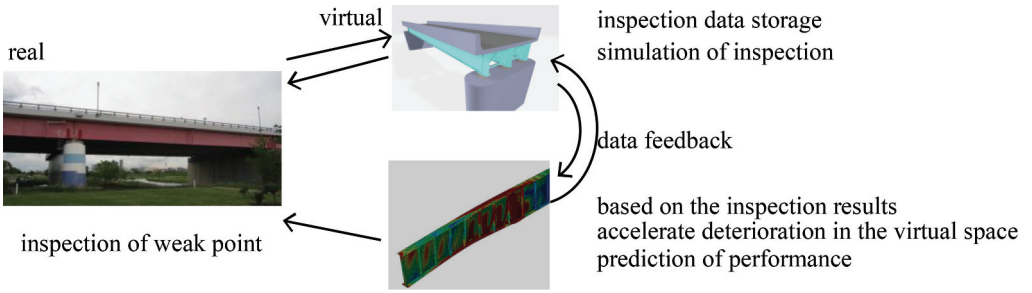


Figure 1. Concept of digital twin in this study.

2 BRIDGE OF INVESTIGATION

A real bridge in Tokyo area was chosen. Figure 2 shows the bridge. The bridge is a three span continuous bridge of 150 m long. The bridge is about 15 m wide and consists of two lanes of two ways and pedestrian deck on both sides. It consists of two steel box girders. An orthotropic steel deck system was applied. The bridge was completed in the late 1980s.

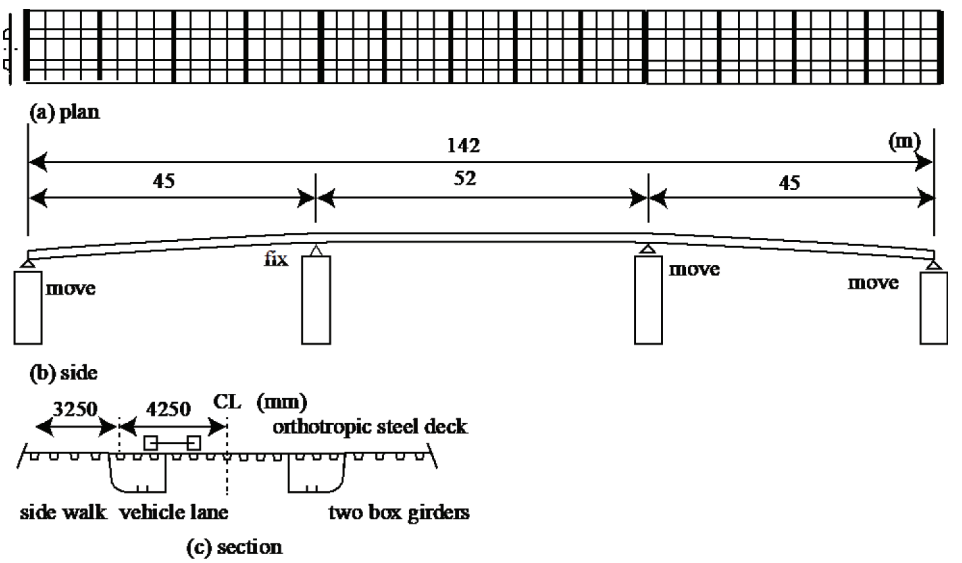


Figure 2. Bridge of investigation.

2.1 *Finite element model*

Prior to the field measurement, numerical model by the finite element method was constructed. It was possible to find the complete drawings of the bridge. Based on the drawings, the numerical model could be established. Shell elements were employed for the box girder and deck system. Solid elements were applied for the pavement, asphalt concrete. At first, reinforced concrete of pedestrian deck, to cover the side block, and fences were not modeled.

The size of the elements was not bigger than 20 cm by 20 cm. A commercial software of Marc was used. As the pre- and post- processor, Mentat was used. The total number of nodes and elements were 435000 and 455000, respectively.

2.2 *Field measurement*

Field loading test was carried out. Figure 3 summarizes the items of measurements. There were five items. One was strains at the center of each span. The second was displacement of roller bearings. The third was temperature at the center of the bridge both inside and outside of the girder.

Figure 4(a) shows the placement of strain gauges. Dots in Figure 4 correspond to nodes of finite element analysis. Strains were measured almost at the center of the three spans about 60 cm away from the diaphragm.

Figure 4(b) shows the details of bearings. A spherical type was used. At each bearing location, two laser sensors were used in the bridge axis and lateral directions.

Figure 4(c) shows the placement of thermo sensor around the center of the bridge. Two thermo sensors were put inside of the girder at the upper and lower flanges, respectively. One thermo sensor was also put outside of the girder.

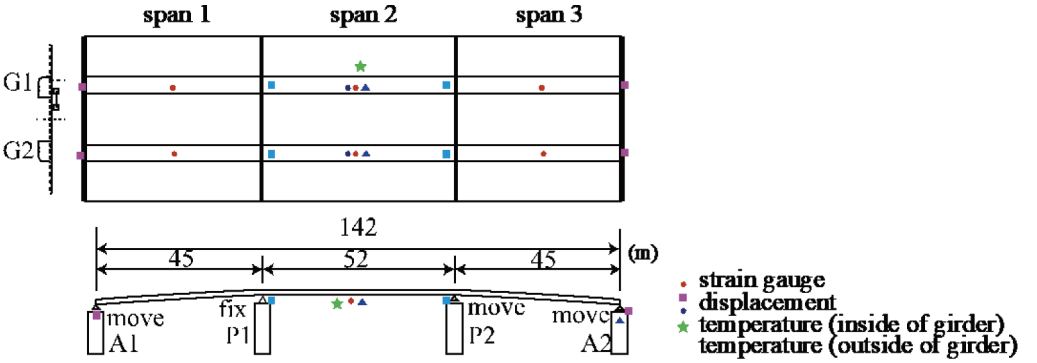


Figure 3. Items of measurement of field load test.

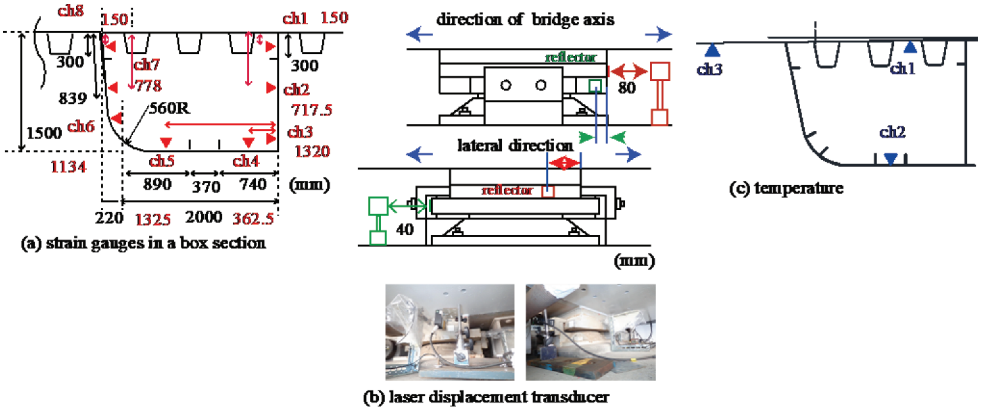


Figure 4. Strain gauges in a box girder section.

3 FIELD LOADING TEST

3.1 *Vehicle*

A truck of about 45 tons were used by the field loading test as shown in Figure 5. The truck consists of 5 axles and the axial loads are shown in Figure 6. Generally, in Japan, a truck of over 25 tons requires the permission for driving.

Two types of loading were performed. One was static and the other was dynamic. In case of static loading, the vehicle took positions along the bridge axis as many as 30 patterns. Considering the probable local maximum strains at axle position and the vehicle had 5 axles, strain data was recorded at 5 axle positions adding to the center of the vehicle. At each location of strain gauge, the vehicle was placed corresponding to axles 1 through 5 and the center. Especially in the center span, at two more points of quarter of the center span length, the vehicle was placed. Regarding the lateral direction, the center of the vehicle was the same as the center of the lane.

In case of dynamic loading, vehicle moved at the speed of about 30 km/hour. The driver tried to keep the center of the lane.

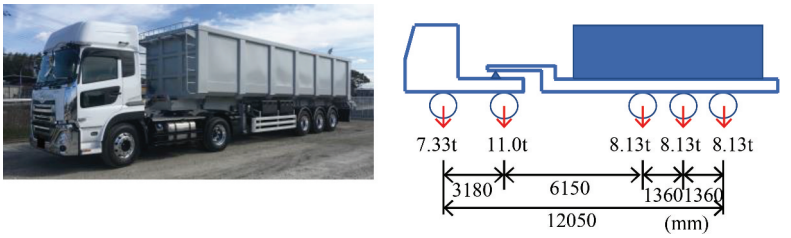


Figure 5. Truck ofcfield loading test.

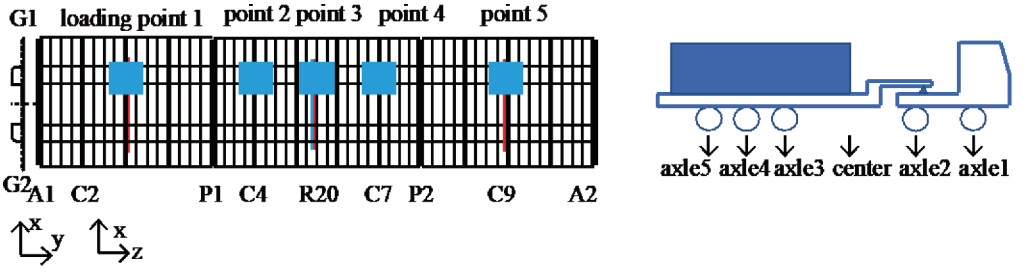


Figure 6. Main five loading points and axles.

3.2 *Verification of the numerical model*

Influence line of the bridge was obtained. The boundary conditions were applied by the analyses, considering the loading points by the field test. By comparing between the analysis and field test, the results of analyses were verified.

Strains were compared at the maximum point that is the center of the second span. The results are shown in Table 1. The strain was 66 μ by the field measurement. Only steel girder and pavement were modeled in the first numerical model. The value was 87.2 μ. This result implies that the stiffness of other components was not negligible. As shown in Table 1, the influences of sidewalk made by reinforced concrete (RC), steel plate covering the RC sidewalk,

and fences on the curb and between sidewalk and traffic lane. Finally, the strain was reduced up to 71.6 μ that was 92.7 % of the actual measurement.

There still existed the error. The possible reason was the stiffness of the asphalt pavement. The field test was carried out in the winter night. The stiff ness used was the highest value of 2000 MPa. That still could be higher. Another reason could be the low functionality of the moving bearings. That would be shown later. Hereafter, the results of numerical analyses were shown by the stiffest case.

3.3 *Results of numerical analyses and loading test*

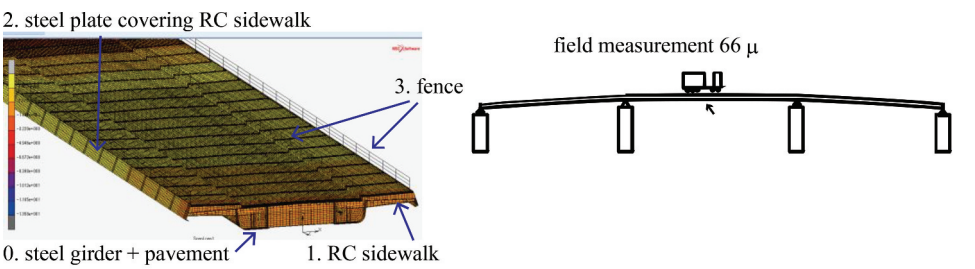
Figure 7 shows the comparison between the numerical analyses and the loading test. These are the influence lines of strain at the center of the bridge. Figures 7 (a) through (h) represent channels 1 through 8, respectively. Strains of bottom flange were almost the same by comparison between channels 4 and 5. Strain of channel 8 did not change very much. Neutral axis should be located around the channel. All of the strains were not completely the same, but relatively good agreement could be seen.

Figure 8 shows the influence lines of displacement of the bearings. Figures 8 (a), (b) and (c) show those of G1 girder A1 support G1 girder A2 support, and G2 girder A1 support, respectively. All of the influence lines correspond to the displacement in the axis direction. As shown in Figure 8 (a), the maximum dis- placement could be seen in span 1. Result by numerical analysis was about 1.5 mm, in contrast, that by field test was 0.6 mm. Field test result also shows almost no displacement in span 2. It is possible that the bearing does not work as a movable support.

To reproduce the behavior precisely, agreement of 100 % is preferable. Except for the functionality of the movable bearing, the field test and numerical analysis were in good agreement. However, at the same time, simplicity of linear calculation is also important. Although the nonlinearity of the numerical model is still the subject to be resolved, linear analyses would be done in this study.

In addition to the static loading test described previously, dynamic loading test was also carried out. The main objective was to confirm the movement of bearing even under dynamic loading. The result is shown in Figure 9. The vehicle was traveling on girder 1 (G1) from span 1 through 3. Displacement of lateral direction did not change very much. Displacement in the axis direction showed smooth move. However, the maximum displacement was about 0.33 mm that was much smaller than the numerical analysis of about 1.5 mm. For both static and dynamic loading tests, the bearing did not move smoothly.

Table 1. Accuracy of models.



model	strain (μ)	ratio (field/analysis)
girder + pavement	87.2	76.1%
girder + pavement + RC pedestrian deck	79.4	83.6%
girder + pavement + RC ped. deck + steel plate for RC ped. deck	73.7	90.1%
girder + pavement + RC ped. deck + steel plate for RC ped. deck + fence	71.6	92.7%

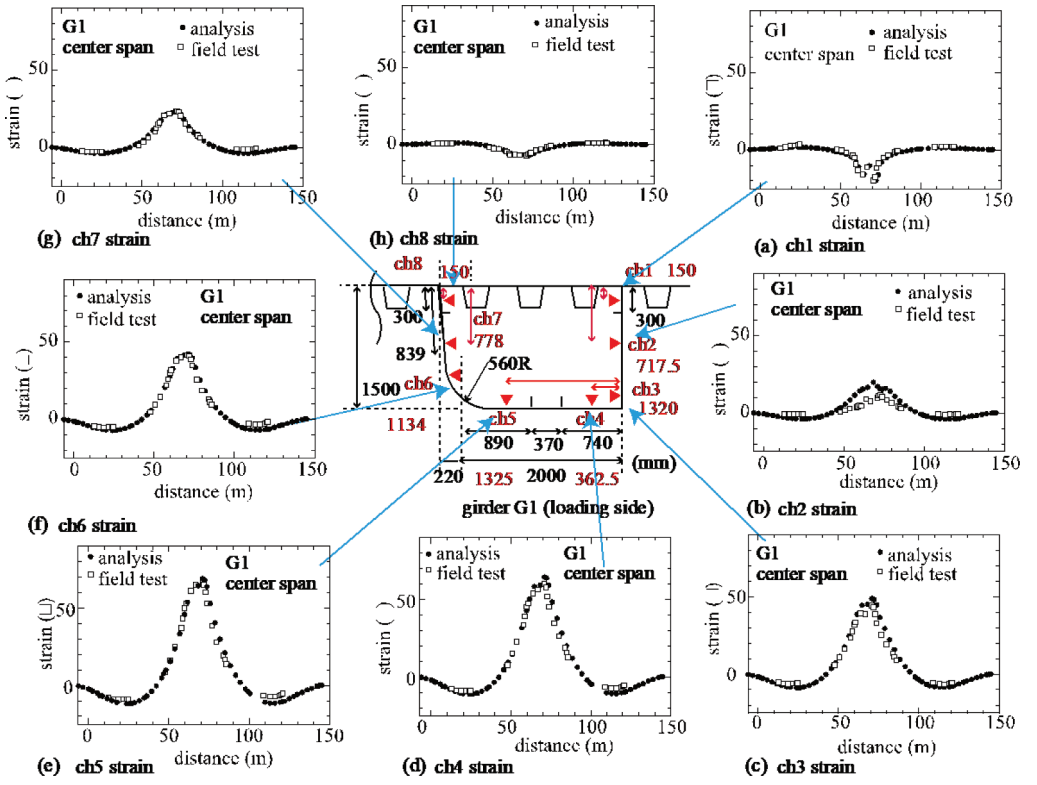


Figure 7. Strain distribution of main girder at the center of the bridge.

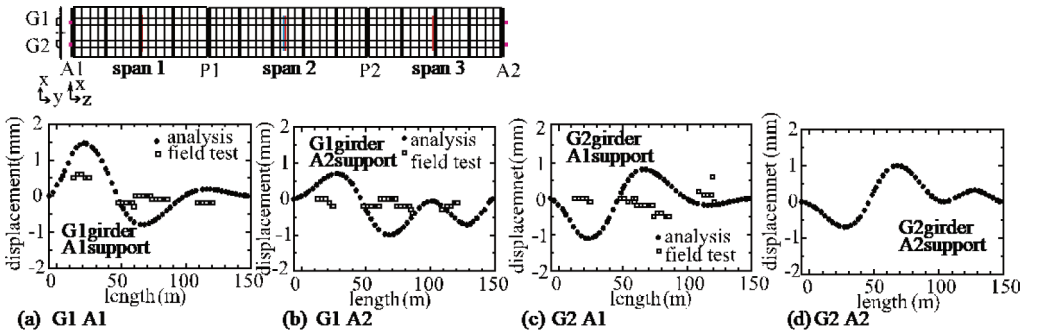


Figure 8. Displacement of bearings.

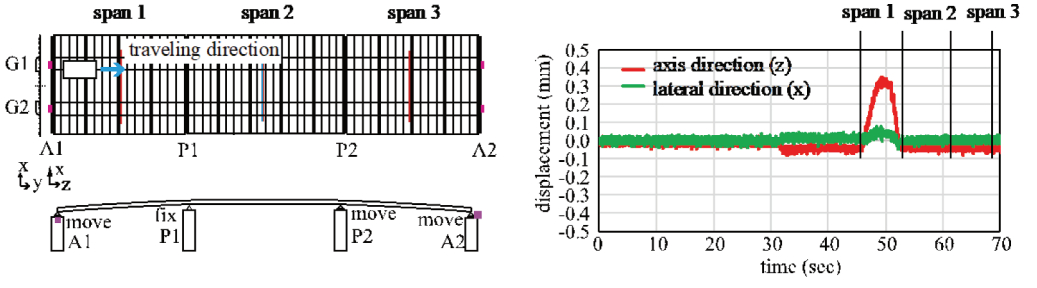


Figure 9. Displacement of bearing by the field loading test (dynamic).

4 BRIDGE WEIGH IN MOTION

Bridge weigh in motion (BWIM) was conducted (Zolghadri 2016). BWIM has been applied to estimate axle loads of vehicles with relatively simple instrumentation such as strain gauge, displacement transducer, or accelerometer (Sekiya 2018). Figure 10 shows the items measured in the BWIM. Those were almost the same as the field test, including strain, temperature, and displacement. The test was carried out in a week of February, 2022.

Figure 11 shows an example of daily transition. Figures 11 (a), (b), (c), and (d) show strain of the bot- tom flange, displacements of bearings of support A1 and A2, and temperature, respectively. The date was 15th February. It was a fine day.

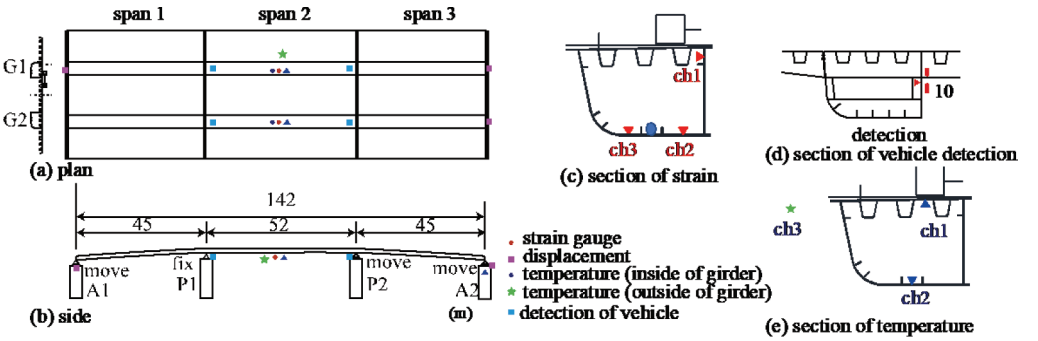


Figure 10. Setup of Bridge-Weigh-In-Motion (BWIM).

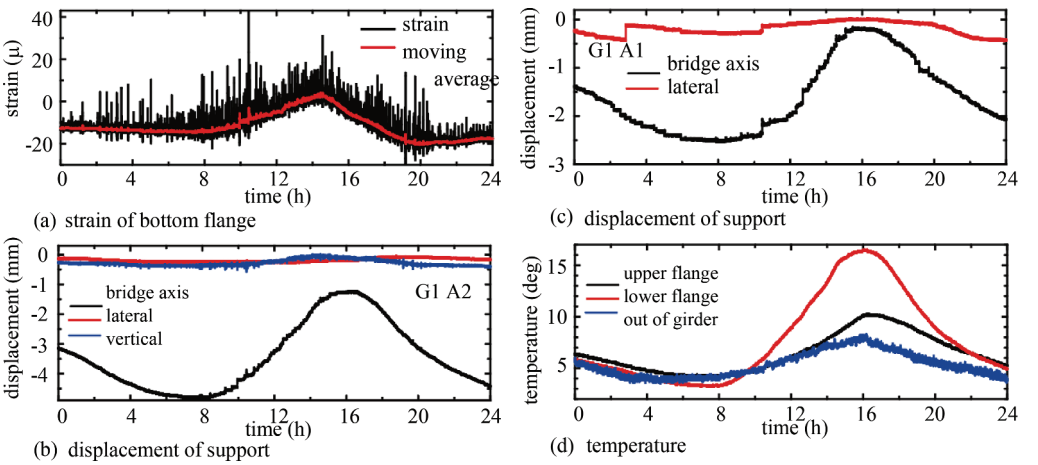


Figure 11. Data by BWIM.

Many spikes can be seen in Figure 11 (a). That rep- resents passage of vehicles. All of the items showed similar tendency as the temperature, higher values in daytime and lower values in night. As shown in Figure 11 (d), temperatures of the upper flange and out of girder took almost the same values. In contrast, that of the lower flange got much higher value. The upper flange was underneath of the deck system of which heat capacity is much higher.

As shown in Figures 11 (b) and (c), displacements in lateral and vertical directions did not change in comparison with the bridge axis direction. Displacements in the axis direction also showed the trend of daily temperature. Some step wise behaviors could be seen. That came from the nonlinearity of the bridge bearings.

For the estimation of axle loads, acquisition of influence lines is necessary. The dynamic response was decomposed by the known axle loads in the loading test described in the previous section.

Usually, dynamic response of a bridge $w(x,t)$ can be represented by equation (1).

$$w(x,t) = \sum_{i=1}^{n} p_i h(t-\tau_i) \tag{1}$$

where, p_i is the axle load of the i-th axle. $h(t)$ is an influence line. τ_i is a time when the axle gets in the bridge, n is the number of axles.

By the Fourier transformation, we obtain equation (2).

$$F(w(\omega)) = \int_{-\infty}^{\infty} e^{-i\omega t} w(x,t)dt \tag{2}$$

Substituting equation (2) into (1).

$$\begin{aligned} F(w(\omega)) &= F\left(\sum_{i=1}^{n} p_i h(t-\tau_i)\right) \\ &= \sum_{i=1}^{n} \left(p_i F(h(t-\tau_i))\right) \\ &= \sum_{i=1}^{n} \left(p_i e^{i\omega t_i} F(h(t))\right) \end{aligned} \tag{3}$$

By Fourier transformation of $w(x,t)$ of the loading test, equations with respect to $F(h(t))$ are obtained. After solving the equations about $F(h(t))$, inverse Fourier transformation gives the influence line of $h(t)$.

In case of BWIM, axle load p_i is unknown variable. Assume that $w^m(x,t)$ is an obtained waveform by BWIM. Error E can be represented by equation (4). Where T is the total time, k is the number of time steps. For the optimization of axle loads, error E should be minimized.

$$E = \sum_{k=1}^{T} (w^m - w)^2 \tag{4}$$

$$\frac{\partial E}{\partial p_i} = 2\sum_{k=1}^{T} (w^m - w)\frac{\partial (w^m - w)}{\partial p_i} \tag{5}$$

Table 2. Results of BWIM of one week.

Load(kN)	Tue	Wed	Thu	Fri	Sat	Sun	Mon	Totla
400~	0	0	1	0	0	0	1	2
300~400	0	1	2	1	1	0	1	6
250~300	0	0	1	1	0	0	1	3
200~250	3	4	6	2	4	0	7	26
150~200	13	13	6	15	11	11	12	81
120~150	25	25	24	19	18	16	15	142
100~120	20	19	24	17	5	0	25	110
90~100	34	36	30	35	6	1	34	176
80~90	46	32	31	29	12	8	29	187
70~80	21	27	20	25	8	6	18	125
60~70	64	54	64	64	25	28	56	355
50~60	71	84	73	72	57	54	70	481
40~50	112	99	108	99	59	55	98	630
30~40	117	127	126	13264	43	11	27	21
20~30	462	464	414	464	328	282	44	52859
10~20	515	512	541	518	329	314	52	03249

Equation (5) is a simultaneous equation about p_i. We can obtain unknown p_i.

Table 2 shows the traffic volume of vehicle weights of one week. The heaviest vehicle was as much as 400 kN. A video camera was installed at the site. Al- though the camera was not always working during the week, the results of BWIM and the camera showed good agreement.

5 SUMMARY AND FUTURE WORK

Conclusions obtained in this study are as follows.

A numerical model of a bridge was established in the computer space. As structural point of view, this model was used as the digital twin. Field measurement was carried out to verify the numerical model. The stiffness of the secondary component such as covering plate of side-walk, fence was not negligible to achieve actual behavior. In comparison with the strain at the bottom flange of the center span, 96% of agreement was obtained.

Monitoring by bridge-weigh-in-motion was con- ducted. Comparison with the video camera, the number of vehicles could be estimated relatively precisely. Phenomenon caused by the nonlinearity of movable supports were observed. It is necessary to con- sider the nonlinearity and get in the model. As the second step of the infrastructure management, we will find the weak points of the structure, in particular, seismic behavior.

ACKNOWLEDGMENT

This study was supported by Tokyo City University Prioritized Studies. The authors would express our gratitude to the financial support.

REFERENCES

Fujikubo, M. 2021. Concept of ship structure of digital twin. *Bulletin of The Japan Society of Naval Architects and Ocean Engineers* 94, 14–18.

Nakabo, Y. 2022. Digital twin and safety. *Journal of the Robotics Society of Japan* 40 (7), 585–588.

Sekiya, H, Kubota, K, and Miki, C 2018. Simplified portable bridge weigh in motion system using accelerometers. *Journal of Bridge Engineering* 23 (1).

Sugisaki, K., Chun, P-J., and Abe, M. 2023. Basic concept of digital twin and application to civil engineer ing. *Artificial Intelligence and Data Science, JSCE* 4, 13–20.

Thelen, A., Zhang, X., Fink, O., Lu, Y., Ghosh, S., Youn, B.D.,Todd, M.D., Mahadevan, S., Hu, C., and Hu, Z. 2023. A comprehensive review of digital twin part-2: roles of uncertainty quantification and optimization, a battery digital twin, and perspectives. *Structural and Multidisciplinary Optimization* 66 (1).

Zhang, R., Wang, F., Cai, J., Wang, Y., Guo, H. and Zheng, J. 2022. Digital twin and its applications: A survey. *The International Journal of Advanced Manufacturing Technology* 123, 4123—4136.

Zolghadri, N., Halling, M.W., Johnson, N., and Barr, P.J. 2016. Field verification of simplified bridge weigh-in-motion techniques. *Journal of Bridge Engineering* 21 (2).

Bridge Maintenance, Safety, Management, Digitalization and Sustainability – Jensen, Frangopol & Schmidt (eds)
© 2024 The Author(s), ISBN 978-1-032-77040-6
Open Access: www.taylorfrancis.com, CC BY-NC-ND 4.0 license

On the assessment of the vibrational response of highly-skewed high-speed railway bridges

M.D. Martínez-Rodrigo, J.C. Sánchez-Quesada & E. Moliner
Mechanical Engineering and Construction Department, Universitat Jaume I, Spain

A. Romero & P. Galvín
E.T.S. de Ingeniería, Universidad de Sevilla, Spain
ENGREEN Laboratory of Engineering for Energy and Environmental Sustainability, Spain

ABSTRACT: The aim of this study is to evaluate the vertical vibrational response of simply-supported (SS) highly-skewed railway bridges. Configurations of interest are pre-stressed concrete girder deck bridges with and without end transverse diaphragms from conventional and High-Speed (HS) lines. Two detailed 3D Finite Element (FE) numerical models including the ballast track are implemented and updated from experimental modal data from two real bridges of approximately 15 and 25 m of span lengths. The evolution of modal parameters and maximum acceleration under passing trains is investigated for several variants of the reference models. Conclusions regarding the effect of skewness correlated with the execution procedure of the transverse diaphragms are finally extracted.

1 INTRODUCTION

The accurate assessment of train running safety on railway bridges has become an issue of major importance in the last decades. The European Union Agency for Railways (ERA) recently published a technical note on the investigations needed for closing the Technical Specifications for Interoperability open points on railway bridge dynamics (ERA 2022). Therefore, the train-track-bridge interaction problem is a matter of concern and investigation, still up-to-date, and far to be closed.

Since the opening of the first HS railway lines worldwide it has become clear that, at certain speeds, railway bridges may experience excessive vertical accelerations at the platform, leading to premature deconsolidation of the ballast layer, the consequent loss of track stability, fatigue problems in steel bridges or strand breakage in pre-stressed concrete ones in the long term, an increase in the operating costs of the lines, deterioration of passenger comfort, etc. (Ishibashi 2004) Research in the past showed that single-track bridges composed of SS short-to-medium spans (12-25 m) are especially critical, due to their low mass and typical natural frequencies (Frýba 2008) The problem of the excessive vibrations of railway bridges and viaducts is aggravated by resonance (Yang et al. 1997). A convoy causes resonance of a bridge when the passing time between groups of axles with a certain repetition pattern is a multiple of one of the natural periods of the structure. Because of the problems detected in several HS railway bridges, and to ensure traffic safety, the maximum vertical acceleration in these structures is limited to 3.5 m/s^2 in ballast tracks, and to 5 m/s^2 in slab tracks (CEN 2002). This constitutes one of the most restrictive Serviceability Limit States (SLS) in the design of new structures.

This work is devoted to oblique SS girder bridges, as those shown in Figure 1. In Spain, in the 80's several bridges were built with pre-stressed concrete double-T girders and upper slabs for spans in the range 10-25 m, both in HS and in conventional lines, despite their low torsional stiffness, some of them being oblique in plan. Oblique or skewed bridges are built

DOI: 10.1201/9781003483755-139

when, for topographical reasons, the superstructure cannot be perpendicular to the abutments and piers. Skewed bridges experience an inherently coupled 3D dynamic response when traversed by trains (Nguyen et al. 2014), especially in multi-track decks due to the eccentricity of the track, different from that of straight bridges, for which the dynamic response under moving trains may be assimilated to that of a beam-type structure mostly deforming under longitudinal bending. Several methods in the design codes for dynamic analysis of railway bridges are based on this premise. The actual relevance of the participation of 3D modes in the case of skewed bridges when traversed by trains at high speeds is still not well known.

The aim of this work is to analyse the influence of skewness on the dynamic response of railway bridges composed by SS pre-stressed concrete multi-girder decks. The correlation with the stiffening effect of transverse diaphragms for different span lengths will be evaluated through a sensitivity analysis over a wide catalogue of bridges. Conclusions regarding the evolution of the maximum vertical acceleration and its distribution over the platform depending on the actual speed window considered will be finally presented.

2 GIRDER BRIDGES UNDER STUDY

Two existing railway bridges, constitute the starting point for this investigation: the bridges over Arroyo Bracea and Jabalón watercourses, from now on Arroyo Bracea and Jabalón bridges (see Figure 1). Both belong to the Madrid-Sevilla High-Speed railway line, which in 2022 completed 30 years of service, and are approximately 100 km separated along the track.

Arroyo Bracea Bridge is composed by two identical 15.25 m SS spans and presents a skew angle of β=135º. The deck is composed by a 25 cm thick, 11.6 m wide cast-in-place concrete slab resting over five 1.05 m high pre-stressed concrete I girders. The girders lean on two external abutments and an intermediate pier through laminated rubber bearings. Two transverse concrete diaphragms link the girders at the supports. The slab carries two ballast tracks with an equal eccentricity of 2.15 m, two sidewalks and handrails. The rails present a UIC60 cross section and are continuously welded. The rails are supported by rail pads and fixed with clips on monoblock concrete sleepers with a regular spacing d=0.60 m.

Jabalón Bridge, is also a SS bridge with three equal spans of 24.9 m and crosses Jabalón River with similar obliqueness. The longer spans justify the difference in the girders height and slab thickness but, apart from this, both bridges are of the same typology. The ballast track layout and components are identical in both cases.



Figure 1. (a) Jabalón HS railway Bridge; (ii) detail of transverse diaphragm at the support.

In July 2016 and in May 2019 two experimental programs were carried out by the authors to identify Arroyo Bracea and Jabalón bridges dynamic properties. On the bridges the vertical response underneath the longitudinal girders was measured under ambient vibration and under operating conditions, for several train passages in both directions. The natural frequencies and corresponding mode-shapes were identified from ambient vibration by Stochastic Subspace Identification (Reynders 2012). Modal damping was obtained from the free vibrations left by the train passages, as it is considered to be more representative of the structures response under moving trains than that associated to ambient excitation. In Figure 2 the natural frequencies, mode-shapes and modal damping ratios identified for the first four modes are included for both

(a)-(d) Arroyo Bracea and (e)-(h) Jabalón bridges. This information is used in what follows to update 3D finite element (FE) numerical models from both structures.

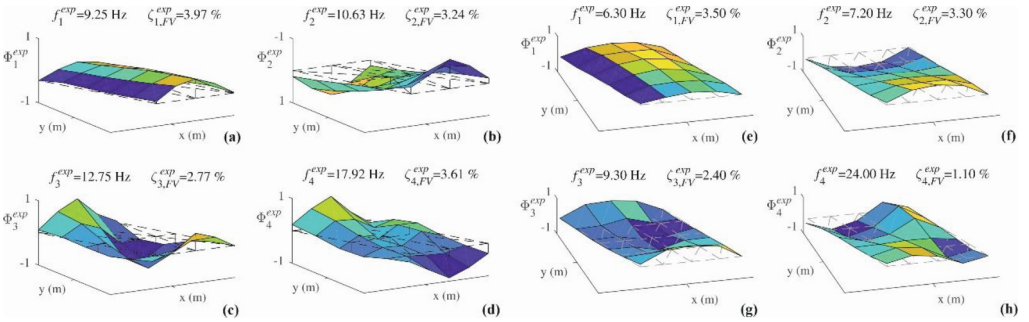


Figure 2. Natural frequencies, mode-shapes and modal damping ratios identified experimentally in (a)-(d) Arroyo Bracea and (e)-(h) Jabalón bridges.

3 NUMERICAL MODELS AND MODAL UPDATING

A 3D FE model is implemented in ANSYS(R)2020R2 for dynamic analysis of the track-bridge systems of interest (Figure 3). As for the deck, the longitudinal girders, the slab, and the transverse diaphragms are meshed with isotropic Kirchoff shell FE (SHELL181) with 6 degrees of freedom (DOFs) per node. The laminated rubber bearings, located under each girder at the supports, are modelled with solid elements (SOLID185) with 3 DOFs per node, considering their real dimensions. The vertical displacement of all the nodes at the bottom surface of the bearings is restrained, therefore ideal fixed boundary conditions are assumed and the flexibility of the piers, abutments and any interaction with the soil is neglected. Transverse bearings restraining the horizontal movement of the girders with respect to the pier cap lateral walls, present in Jabalón Bridge, are modelled as discrete elastic springs (COMBIN14).

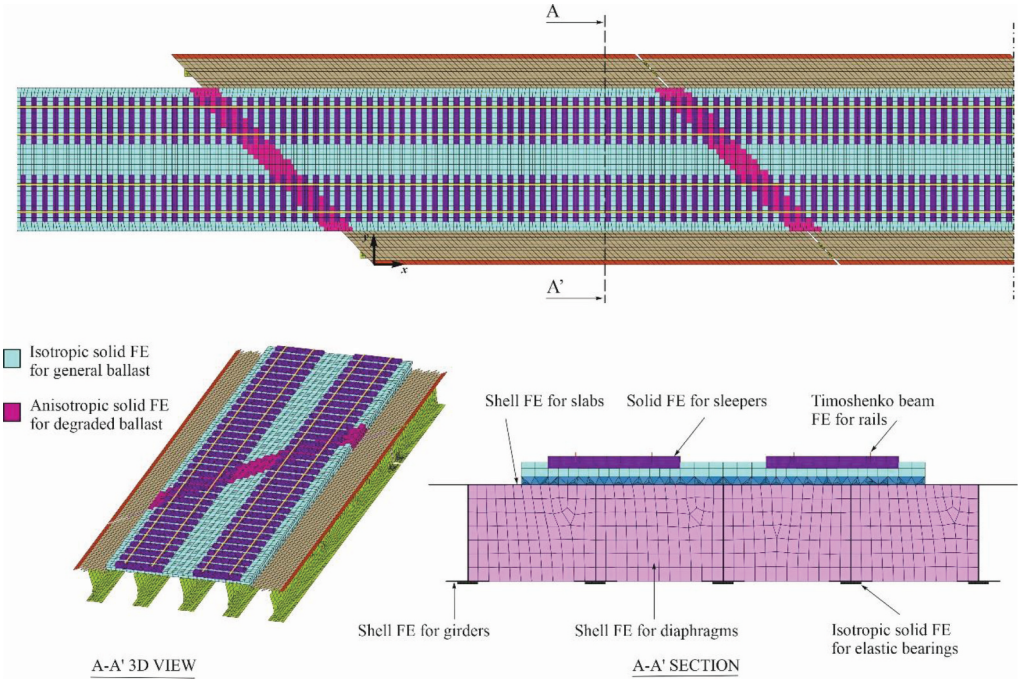


Figure 3. FE numerical model.

The ballast bed is discretised with solid FE (SOLID185). Two constitutive models are adopted over the platform: the volume of ballast along the transverse joint between adjacent spans or degraded ballast, shaded in purple in Figure 2, is represented as transversely isotropic, to consider the possible loss of stiffness due to the relative movement caused by passing trains. This effect is accomplished by reducing the vertical elastic modulus with respect to that associated to the remaining ballast, an approach also adopted in previous research works (Ticona Melo 2020). Additionally, this type of material permits the representation of different interlocking mechanisms of the ballast granules in the out-of-plane (vertical) and in the in-plane (horizontal) directions. For the non-degraded ballast region (marked in blue in Figure 3), a linear isotropic material behaviour is considered. The sleepers are meshed into SOLID185 elements with elastic isotropic behaviour, while Timoshenko beam elements with 6 DOFs per node (BEAM188) are adopted for the rails. Finally, the rail-pads are simulated as discrete spring-dashpot elements (COMBIN14) with constant vertical stiffness and viscous damping connecting the relative vertical displacements and velocities between the rails and the sleepers through kinematic constraints applied over the contact area between both elements.

To simulate the continuity of the railway track along the adjacent embankment, the ballast track model is extended 15 m from the abutments on both sides, which is equivalent to 25 times the sleeper spacing and adequate according to convergence tests performed on the modal parameters. At these extensions, the ballast mesh rests on a subgrade layer, also discretised with SOLID185 isotropic elastic elements. The three translations of the nodes at the horizontal lower plane of this layer are fully restrained. The self-weight of non-structural elements such as the handrails is included as additional lumped masses (MASS21) uniformly distributed along the two external borders. Additional density is also considered in the sidewalks areas.

The FE model is first updated to accurately reproduce the modal parameters experimentally identified of Arroyo Bracea and Jabalón bridges. The calibration procedure comprises two steps: a sensitivity analysis and an optimisation by means of a Genetic Algorithm, involving the use of ANSYS(R)2020R2 and MATLAB.2018b. The purpose of the first step is the selection of the model parameters that influence the most the prediction of the natural frequencies and mode shapes to be included in the optimisation procedure.

The correspondence between the first four experimentally identified modal parameters and those predicted by the calibrated numerical models is provided in Table 1, in terms of frequency differences and MAC numbers.

Table 1. Natural frequencies, frequency differences and MAC values between experimental and numerical first four paired modes.

Structure	Arroyo Bracea Bridge				Jabalón Bridge			
Mode	1	2	3	4	1	2	3	4
$f_{i,exp}$ (Hz)	9.25	10.63	12.75	17.92	6.30	7.20	9.30	24.00
$f_{j,num}$ (Hz)	9.22	11.04	12.67	17.86	6.09	7.41	9.88	19.07
e_{ij} (%)	0.28	-3.87	0.61	0.34	3.40	-2.86	-6.29	20.52
MAC_{ij} (-)	0.96	0.94	0.95	0.98	0.93	0.95	0.95	0.68

4 SENSITIVITY ANALYSES

In this section a sensitivity analysis on the bridges modal parameters and maximum dynamic response under passing trains is presented. The main goal is to evaluate the influence of the deck obliqueness and diaphragm configuration on the modal properties (section 4.1) and dynamic response under moving loads (section 4.2) of the bridge typology of study. For the aforementioned tasks, variations of Arroyo Bracea and Jabalón bridge models are considered. Arroyo Bracea derived models represent girder bridges with a span length of approximately 15 m while Jabalón derived models present a longer span in the vicinity of 25 m. In what follows all the bridge models are limited to just one span and include the track extensions.

4.1 *Evolution of the modal parameters*

In Figure 4 the evolution of the first, second and third natural frequencies, which correspond to the first longitudinal bending, first torsion and first transverse bending modes, is represented for variations of the deck obliquity β and for three diaphragm realistic configurations. FD stands for full diaphragms. This implies that the diaphragms are connected to the girders web, the upper flange and the slab between adjacent girders. In the numerical model both displacements and rotations of the diaphragms, girders and slab shell elements are fully connected in this case. PD stands for partially connected diaphragms. In this case the diaphragms are connected only to the girders vertical web, as it happens in some bridges to simplify the construction process. Finally, ND stands for no diaphragms or total absence of these elements. 12 levels of obliquity are considered for each length and diaphragm configuration. Therefore, modal analyses are performed over 72 different bridges.

In the first row of plots in Figure 4 the evolution of the natural frequencies is represented vs. the skewness of the deck. Notice that the natural frequency is expressed relative to the straight (not-skewed) case for the same diaphragm configuration (FD, PD or ND). Solid and dashed traces distinguish Arroyo Bracea and Jabalón bridges derived models, respectively. In general, the obliqueness of the deck leads to a raise of the natural frequencies. The fundamental frequency is especially affected, increasing approximately 10% for the shortest bridges and highest obliquity considered. The effect of the skewness on the bridges with spans close to 25 m is lower, with a maximum increase of approximately 6%. The first torsion natural frequency also increases with the skew angle but to a lesser extent. In this case, the difference between shorter and longer bridges is smaller. The third frequency is almost unaffected by the skew angle, at least for moderate skew levels. In the second row of plots the natural frequencies are expressed relative to decks with full diaphragms and the same obliqueness, to highlight the influence of the diaphragm configuration. The second and third frequencies reduce when the diaphragms are not fully connected (PD) and further reduce in the total absence of these stiffening elements. This does not happen for the fundamental frequency, which makes sense as the deformation of the cross-section is negligible in this case, and it is especially visible in the case of the third transverse bending mode, with an important transverse deformation of the cross-section. This reduction is in general higher for shorter bridges and is approximately constant with the level of skewness.

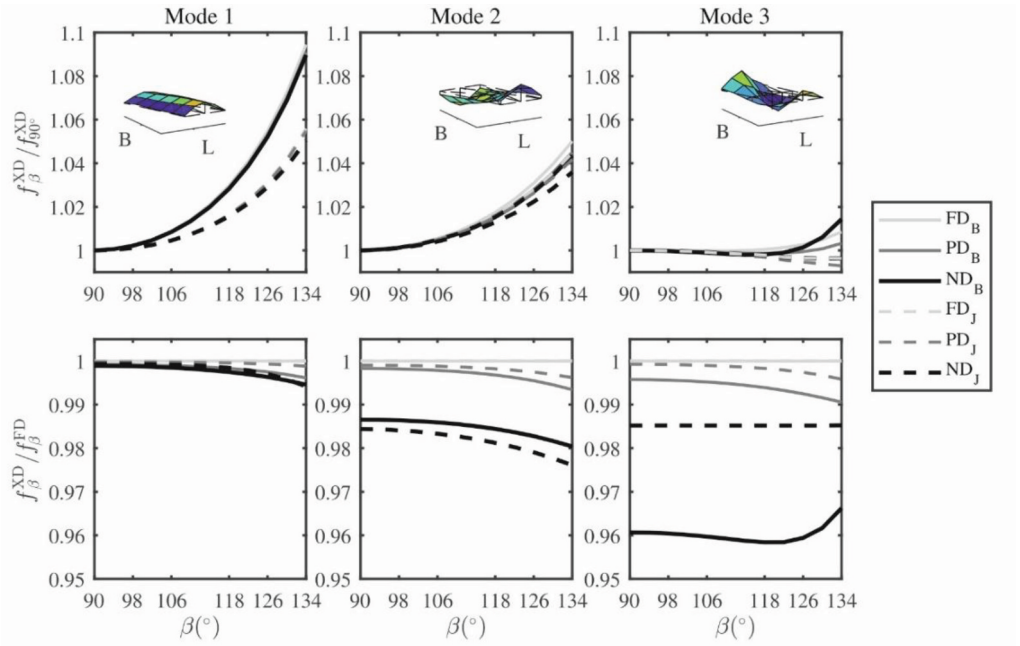


Figure 4. Frequency evolution with skew angle for different diaphragm configurations (FD, PD and ND) for Arroyo Bracea (B) and Jabalón (J) bridges derived models.

4.2 *Evolution of the maximum acceleration under moving trains*

In this section the vertical acceleration over the platform for the same catalogue of bridges is evaluated in terms of the bridge obliqueness and diaphragm configuration. To this end, the bridge acceleration is obtained at the 25 points of post-process shown in Figure 4 where Ai, Bi, Ci, Di and E_i are points under the girders lower flange along the left support, one quarter, mid-span, three-quarters of the span and right support, respectively.

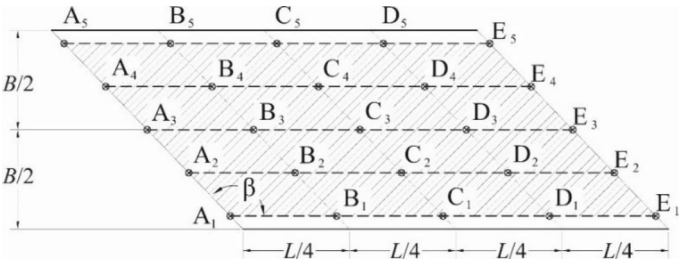


Figure 5. Post-process points.

The vertical response of the bridges is obtained under the circulation of the ten trains from the moving load model HSLM-A from Eurocode 1 (CEN 2022) in the speed range [144, V_{lim}] km/h every 3.6 km/h. The equations are solved in the time domain admitting modal superposition of the normal modes, including the contributions of modes with natural frequency lower than 30 Hz. In Figure 6 envelopes of maximum acceleration for the ten trains are represented at each postprocess point considering a progressively increasing upper limit V_{lim} from 200 km/h to 420 km/h. Only acceleration values higher than 3.5 m/s^2 are shown in colour in Figure 6. Each representation corresponds to the 90º straight case with full diaphragms for the Arroyo Bracea (left) and the Jabalón (right) bridges, respectively.

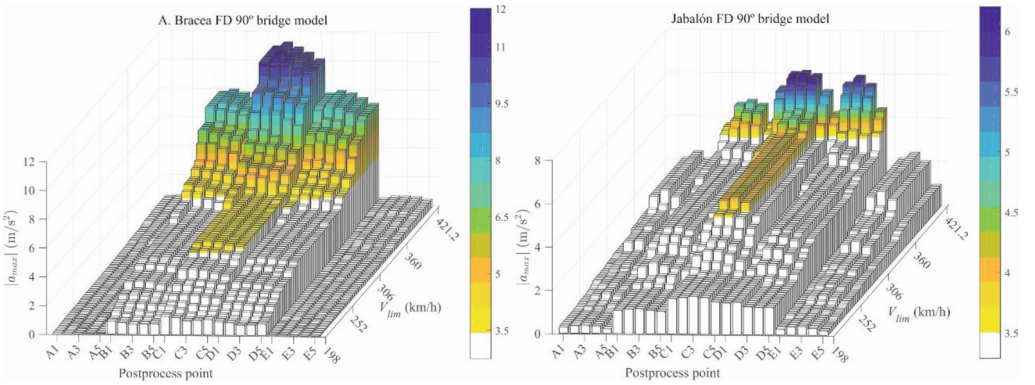


Figure 6. Maximum vertical acceleration at the 25 post-process points for different speed windows [200, V_{lim}] km/h for Arroyo Bracea and Jabalón bridges derived models (β=90º and FD configuration).

From the figures it can be observed that in Arroyo Bracea Bridge the maximum response takes place at the central section and at point C2, which corresponds to the second girder, underneath to the loaded track. In the case of Jabalón Bridge something similar happens but the acceleration at three-quarters of the span is more relevant. In both cases the maximum response increases as the upper speed limit considered does, following a stepped pattern as the speed window progressively accommodates the appearance of new resonances associated to the characteristic distances of the HSLM-A model. The maximum acceleration starts to exceed 3.5 m/s^2 for speeds higher than 255.60 km/h in the case or Arroyo Bracea and higher than 270 km/h in the case of Jabalón Bridge.

Next, in Figures 7 and 8 plan views of the previous 3D representations are shown, for Arroyo Bracea and for Jabalón derived models, for three levels of obliqueness and the three diaphragm configurations envisaged. In general, the maximum acceleration reduces with the skew angle. This is due to the increase of the fundamental frequency and associated resonant speeds, and their exceedance of the upper speed limit in the most skewed cases. On the other hand, there is not significant difference in the response between the FD and PD models. This implies that the effect fully connecting the transverse diaphragms is negligible, both in the shortest and longest bridges. The total absence of diaphragms does lead to moderately higher accelerations in the case of prominent skewness, especially in the shortest bridges.

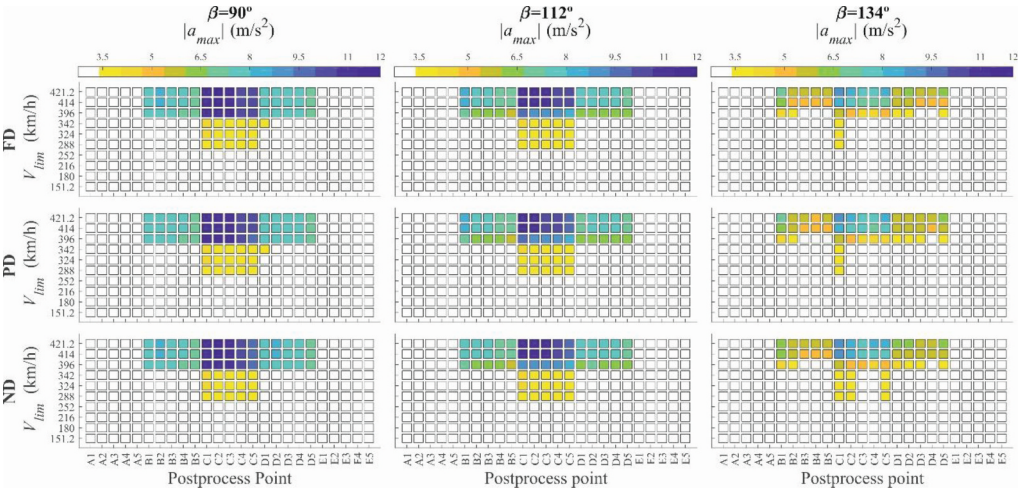


Figure 7. a_{max} at the 25 post-process points for different speed windows [200, V_{lim}] km/h for Arroyo Bracea Bridge derived models for β=[90º,112º,134º] and three diaphragm configurations.

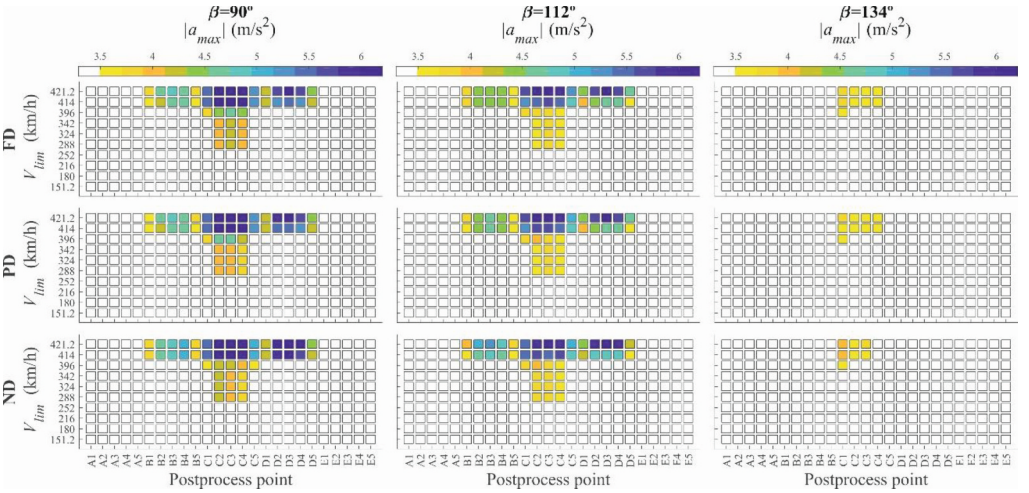


Figure 8. a_{max} at the 25 post-process points for different speed windows [200, V_{lim}] km/h for Jabalón Bridge derived models for β=[90º,112º,134º] and three diaphragm configurations.

5 CONCLUSIONS

Oblique girder railway bridges present a complex dynamic behaviour under railway traffic, due to the contribution to the vertical response of 3D modes of vibration. Transverse diaphragms at the end sections of SS girder decks are generally installed to

stiffen the cross-section, but on some occasions these elements are poorly built or do not exist. In this investigation the evolution of the lowest modal properties is investigated with the level of deck obliqueness for different diaphragm configurations and span lengths. Regarding the evolution of the first natural frequencies, the following is concluded:

- The fundamental frequency increases approximately 10% with obliqueness for the shortest bridges and highest obliquities considered. The effect of the skewness on the bridges with spans close to 25 m is lower (6%). The first torsion natural frequency also increases with the skew angle but to a lesser extent, the difference between shorter and longer bridges being smaller. The third frequency is almost unaffected by skewness.
- The second and third frequencies reduce when the diaphragms are not fully connected and further reduce in the total absence of these elements. This does not happen for the fundamental frequency, and it is especially visible in the case of the third transverse bending mode. This reduction is in general higher for shorter bridges and is approximately constant with the level of skewness.

Also, the maximum response in terms of vertical accelerations over the platform area is analysed in terms of these same parameters. The main conclusions extracted are the following:

- The maximum response increases as the upper speed limit considered does, following a stepped pattern as the speed window progressively accommodates the appearance of new resonances associated to the characteristic distances of the HSLM-A trains.
- The maximum acceleration reduces with the skew angle. This is due to the increase of the fundamental frequency and associated resonant speeds, and their exceedance of the upper speed limit in the most skewed cases.
- There is not significant difference in the response between the FD and PD models. This implies that the effect of fully connecting the transverse diaphragms to the slab is negligible, both in the shortest and longest bridges. The total absence of diaphragms does lead to a higher response in the case of prominent skewness in the shortest bridges.

ACKNOWLEDGEMENTS

The authors would like to acknowledge the financial support provided by the Spanish Ministry of Science and Innovation under the research project PID2022-138674OB-C2; PROYEXCEL 00659 funded by Regional Ministry of Economic Transformation, Industry, Knowledge and Universities of Andalusia; Generalitat Valenciana under the research project AICO/2021/200, and the Andalusian Scientific Computing Centre (CICA).

REFERENCES

CEN 2002a. EN 1990 Basis of structural design. Annex A2: Application for bridges. European Committee for Standardization, Brussels.

CEN 2002b. EN 1991-2, Eurocode 1: Actions on Structures - Part 2: Traffic loads on bridges. European Committee for Standardization, Brussels.

ERA 2022. ERA technical note on work needed for closing TSI open points on bridge dynamics. ERA1193-TD-01-2022.

Frýba, L. 2008. Dynamic behaviour of bridges due to high speed trains. *Bridges for High-Speed railways: Revised papers from the Workshop*. Boca Ratón, CRC Press.

Ishibashi, T. 2004. Shinkansen structures in japan. *Workshop on bridges for High-Speed railways*.

Nguyen, K., Goicolea, J.M., Galbadón, F. 2014. Comparison of dynamic effects of high-speed traffic load on ballasted track using a simplified two-dimensional and full three-dimensional model. *Proceedings of the Institution of Mechanical Engineers, Part F: Journal of Rail and Rapid Transit* 228(2):128–142.

Reynders, E. 2012. System identification methods for (operational) modal analysis: review and comparison. *Archives of Computational Methods in Engineering* 19:51–124.

Ticona Melo, L.R.T., Ribeiro, D., Calçada, R., Bittencourt, T.N. 2020. Validation of a vertical train-trackbridge dynamic interaction model based on limited experimental data. *Structure and Infrastructure Engineering* 16(1):181–201.

Yang, Y., Yau, J., Hsu, L. 1997. Vibration of simple beams due to trains moving at high speeds. *Engineering Structures* 2(4):257–271.

Bridge Maintenance, Safety, Management, Digitalization and Sustainability – Jensen, Frangopol & Schmidt (eds)
© 2024 The Author(s), ISBN 978-1-032-77040-6
Open Access: www.taylorfrancis.com, CC BY-NC-ND 4.0 license

Modal identification and soil-structure interaction analysis of a portal frame railway bridge

J. Chordà-Monsonís, J.C. Sánchez-Quesada, E. Moliner & M.D. Martínez-Rodrigo
Universitat Jaume I, Castelló de la Plana, Spain

A. Romero & P. Galvín
Universidad de Sevilla, Sevilla, Spain

ABSTRACT: The dynamic response of portal frame bridges is influenced by soil-structure interaction. Due to the complexity of the phenomenon, predicting its dynamic behaviour is difficult and time-consuming. For this reason, this interaction is rarely considered in the numerical analyses. However, recent research is providing further evidence about the importance of considering it to avoid discrepancies between numerical and experimental results. In this contribution, a study on an existing portal frame railway bridge is carried out. First, the determination of its modal parameters is addressed. Then, a 3D finite-element numerical model of the bridge is implemented considering the track, track-bridge-soil system. Perfectly matched layers are considered at the model boundaries. The results obtained with this model are employed to implement a simplified version on which the soil is substituted by a series of spring-dashpots. After calibration, a comparison is carried out with the experimental and numerical modes of the bridge.

1 INTRODUCTION

The need of transition to a more sustainable means of transportation is leading to an expansion in railway networks in a number of European countries. As part of the rail infrastructure, a typical solution to allow its adequate implementation are the portal frame underpasses. This type of bridge consists of a reinforced concrete rigid frame flanked by integral wing walls surrounded by an embankment. As could be expected, due to their integration within the soil, the dynamic response of portal frame bridges is strongly influenced by Soil-Structure Interaction (SSI) (Zangeneh 2018). However, simulating this complex interaction mechanism entails a high computational cost. For this reason, SSI is not always included in the numerical analyses dedicated to predicting the dynamic behaviour of railway bridges (Galvín 2022). In the case of portal frames, the large soil-structure contact area provides the bridge an additional capacity to dissipate energy that affects in a significant way its modal characteristics and response under passing trains. Therefore, neglecting the dynamic stiffness of the surrounding soil in the numerical models may be the source of the divergences found between numerical and experimentally measured modal parameters (Zangeneh 2021). This could lead to incoherencies in the optimisation design process and misinterpretations of the Serviceability Limit States of such structures, given that the mathematical modelling is not performed with sufficient precision. As including the effect of SSI tends to reduce the fundamental frequency (Martínez-Rodrigo 2018) and increase the modal damping, the corresponding resonant train velocity could be also minor than expected without SSI. Besides, due to the additional damping, the dynamic response of the bridges in resonance could be overestimated, leading to inefficient structural solutions (Salcher 2020). It is then essential to consider SSI in the dynamic analyses of portal frame bridges to predict their dynamic behaviour in an accurate manner. In this matter, as previous research has found, the effects of SSI on portal frames are not yet well

DOI: 10.1201/9781003483755-140

known. A key factor contributing to this aspect might be the lack of reliable simple models to simulate the SSI. In consequence, experimental-numerical validation of results on portal frames are seldom found in the literature (Zangeneh 2018).

In this contribution, a study on an existing portal frame is carried out with the following objectives: (i) to experimentally identify the modal parameters of the bridge and (ii) to implement a numerical model to simulate the modal behaviour of the structure with a reasonable computational cost. To this end, a 3D Finite Element (FE) model of the structure considering the track, the bridge and the surrounding soil is implemented and padded with Perfectly Matched Layers (PML) acting as absorbing boundaries to reduce the extension of the soil domain and reproduce the radiation of incident waves through the soil layers. This model is used to obtain impedance functions that will simulate the soil-bridge interaction in a subsequent simplified model. Finally, the calibration of the track and bridge parameters is carried out and a numerical-experimental comparison of the bridge modes is conducted. The work herein presented is organised as follows. In Section 2, the portal frame under study and the modal identification process are described in detail. In Section 3, the implementation of the numerical models of the bridge is explained. Section 4 addresses how SSI is implemented on the simplified model. In Section 5, the performance of this model is assessed, and in Section 6, the main conclusions of the contribution are summarised.

2 BRIDGE UNDER STUDY AND MODAL IDENTIFICATION

2.1 *The bridge*

The portal frame under study is located on the high-speed (HS) line Madrid-Sevilla, in the section between Ciudad Real and Brazatortas. A total number of three tracks pass over the bridge: two for HS traffic and one for conventional services. The underpass consists of a reinforced concrete rectangular box integral section. The most distinctive characteristic of this bridge is that it is divided along its width in two sections by means of a longitudinal joint. In this way, two coupled structures are found: one under the HS tracks, and another under the conventional traffic track. Figure 1 shows an image of the bridge. The dimensions of the structure can be found on Figure 2, where L = 8 m, H = 5.7 m, W_1 = 13.3 m, W_2 = 8.8 m, S_1 = 1.1 m and S_2 = 1 m. The dashed line represents the longitudinal joint.



Figure 1. The underpass object of study.

2.2 *Modal identification*

An experimental campaign was carried out in September 2022 with the intention to characterise the modal parameters of the bridge. The dynamic response of the structure was recorded using 27 piezoelectric accelerometers with a nominal sensitivity of 10V/g. The sensors were distributed on the inner face of the bridge slab as indicated in Figure 3: 18 on the top slab (shown in red); 6 at the walls at a height of 2.6 m (shown in yellow); and 3 on the floor (shown in blue). The dynamic response of the structure was recorded under the passage of 27 trains

and from the ambient vibration. This latter recording, acquired at a sampling frequency of 4096 Hz and of 3600 s of duration, was then used to determine the modal parameters of the bridge. The signal was decimated to 256 Hz and a high-pass Chebyshev filter of 1 Hz was applied. Then, an Operational Modal Analysis (OMA) was carried out.

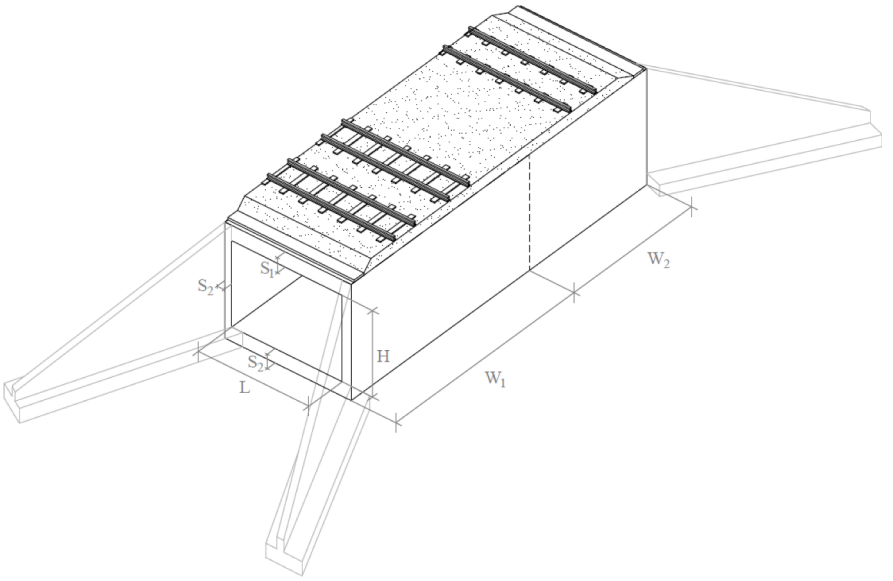


Figure 2. General view of the portal frame.

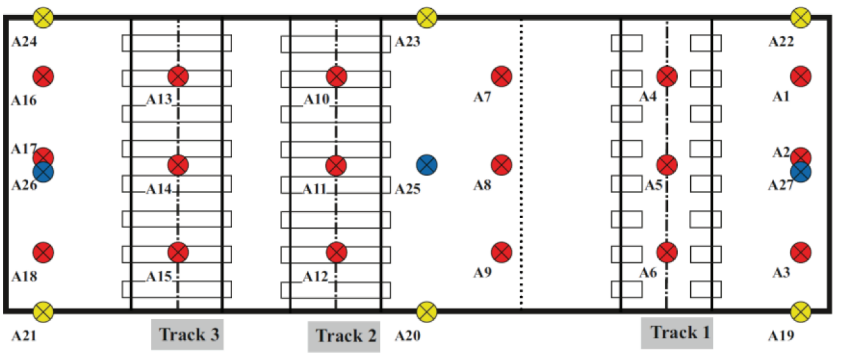
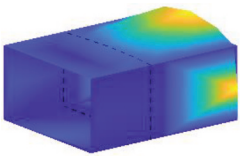
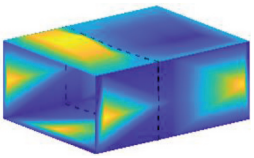
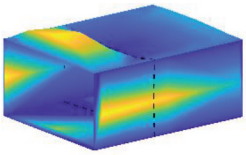
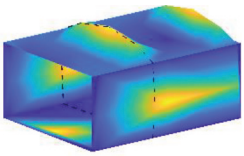


Figure 3. Schematic representation of the accelerometer layout.

The Enhanced Frequency Domain Decomposition (EFDD) method was used to identify the modes of the structure. The identification process presented several difficulties because of two factors. In the first place, the Singular Value Decomposition (SVD) plot generated with the ambient vibration data from the underpass led to unclear results, as the graphic representation lacked prominent discernible peaks that would typically indicate the presence of a structural mode of vibration in certain frequency ranges, notably in the interval between 20 and 30 Hz. For this reason, the bridge response recorded under the passage of 27 trains was also analysed. After a careful study of the Frequency Response Functions (FRF) from each accelerometer, two different trends were detected among the sensors on the top slab of the HS

section (A7 to A18) and those on top of the conventional one (A1 to A6). Specifically, the data drawn a clear pattern on which maximum acceleration peaks on the range from 20 to 30 Hz tended to occur near 24 Hz on the accelerometers located in the HS section, whereas maximum peaks were mostly detected around 27 Hz on the accelerometers on the conventional one. This confirmed what was previously obtained in the OMA. The reasons why this analysis was at first unclear were: (i) the soil interference in the measures probably incremented the noise captured by the sensors, and (ii) the partially uncoupled response of the two structures resulted into an unequal participation of the bridge sections in several modes. Due to this circumstance, the bridge has coupled or mixed modes, on which both the HS and the conventional sections have a noticeable deformation. However, in some cases, uncoupled modes, on which the participation of a single of the bridge sections (HS or conventional) is predominant are also detected. For that reason, the ambient vibration signals were also subjected to OMA and postprocess from three points of view, considering: (i) all the accelerometers (A1 to A27); (ii) those on the HS section (A7 to A18, A20, A21 and A23 to A26); and (iii) those on the conventional section (A1 to A6, A19, A22 and A27). This procedure allowed to ensure the identification of several uncoupled modes that were also noticeable when considering the signal with all the accelerometers. Table 1 lists the identified modes of the bridge. The first mode corresponds to the longitudinal bending of the HS section. In this case, the participation of the conventional part is negligible. In the second and third modes, the deformation on the conventional section is predominant. This situation is more accentuated in the third mode that, properly speaking, constitutes the fundamental bending mode of this bridge section. The fourth mode represents a transverse bending mode of the structure, on which both sections of the bridge participate.

Table 1. Modes identified with the OMA.

Mode 1	Mode 2	Mode 3	Mode 4
			
f_1 = 22.407 Hz	f_2 = 25.440 Hz	f_3 = 26.802 Hz	f_4 = 44.266 Hz

3 NUMERICAL PROCEDURE

The numerical procedure proposed is intended to assess the viability of reproducing the modal behaviour of the bridge with an admissible computational cost. To achieve this, first, a numerical model considering the track, bridge and the surrounding soil is implemented. In this step, the SSI is analysed and the results are used to configure a simplified version of the previous model.

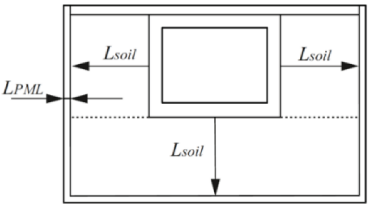


Figure 4. Dimensions of the soil and PML domains in the complete numerical model.

3.1 *Complete soil-bridge-track numerical model*

To begin with, a 3D numerical model of the bridge is implemented considering the tracks, the bridge, and the surrounding soil by means of the FE method. To avoid spurious wave reflections at the boundaries of the model, solid PML elements are implemented to absorb propagating waves. This allows the reduction of the soil domain and enables a faster computation. Sufficient soil and PML dimensions have been determined to ensure the adequacy and stability of the results, as L_{soil} = 6 m and L_{PML} = 0.5 m. Figure 4 shows the layout of the model.

Three layers of PML elements are considered. The mesh sizing in the PML region is discretised based on the frequency, as it is generally recommended to fit between 5 and 20 elements per wave length $\lambda = 2\pi \cdot c_s/\omega$ (Coronado 2016) being ω the highest detected natural frequency of the bridge. A homogeneous soil stratum is considered with C_s = 350 m/s, as at that propagation speed, the experimental modes were numerically predicted at their corresponding frequencies. The main characteristics of the model are listed on Table 2. A view of the model is available on Figure 6 (left). The soil volume under the bridge and the backfill forms a rectangular prism of dimensions 24 m × 49.1 m × 7.5 m. This model has 1,340,132 Degrees of Freedom (DOF).

Table 2. Mechanical properties of the model.

Entity	Part	Property	Symbol	Value	Unit
Track	Rail	Elastic modulus	E_r	$2.10 \cdot 10^{11}$	Pa
		Moment of inertia	I_r	$3\,038 \cdot 10^{-8}$	m^4
		Linear mass	m_r	60.34	kg/m
	Rail pad	Stiffness	K_d	$1.00 \cdot 10^8$	N/m
		Damping	C_d	$7.50 \cdot 10^4$	Ns/m
	Sleepers	Elastic modulus	E_p	$3.60 \cdot 10^{10}$	Pa
		Poisson's ratio	v_p	0.2	[–]
		Mass	m_p	320	kg
	Ballast	Elastic modulus	E_b	$1.10 \cdot 10^8$	Pa
		Poisson's ratio	v_b	0.2	[–]
		Density	ρ_b	1950	kg/m^3
		Height	h_b	0.728	m
Bridge	Slab	Elastic modulus	E_l	$35.71 \cdot 10^9$	Pa
		Poisson's ratio	v_l	0.2	[–]
		Density	ρ_l	2500	kg/m^3
	Joint	Elastic modulus	E_j	9522.50	Pa
		Poisson's ratio	v_j	0.2	[–]
		Density	ρ_j	2500	kg/m^3
Soil		Shear wave speed	c_s	350	m/s
		Poisson's ratio	v_s	0.2	[–]
		Density	ρ_s	1950	kg/m^3

3.2 *Simplified model*

A simplified version of the previously described model is implemented. The key point of this approach is the inertial decoupling of the bridge-track system from the surrounding soil. Thus, in the simplified model, the soil is substituted by a series of linear spring-dashpots that simulate the dynamic interaction of the soil with the portal frame. A total number of 65 spring-dashpots are uniformly distributed over the whole area of the bridge-soil interface at the bridge walls and the bottom face of the box slab. At each point, they are arranged in the three spatial directions (X, Y and Z): one perpendicular and two tangential to the contact surface, as shown in Figure 5. Below, an image of the simplified model is shown in Figure 6 (right). This model has a total of 175,904 DOF, which is an important reduction in comparison with the complete version.

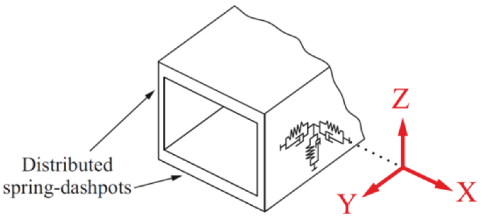


Figure 5. Distribution and orientation of the spring-dashpots.

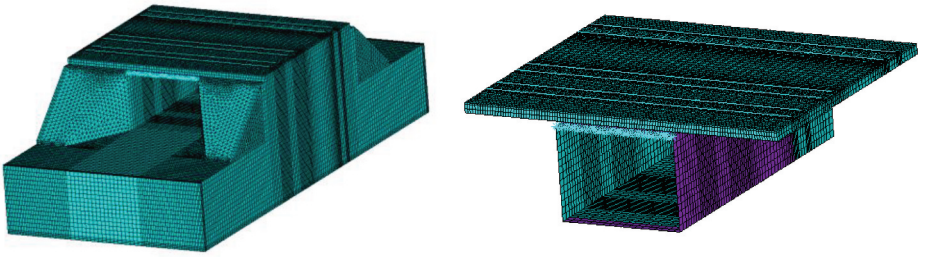


Figure 6. Views of the complete model (left) and the simplified one (right).

4 SSI ON THE SIMPLIFIED MODEL

The calibration process herein described is aimed to configure the simplified model to reproduce the experimental modes of vibration of the portal frame seen in Section 2. With this objective, the first point to consider is to determine the properties of the spring-dashpots. Based on that, two different approaches are defined. The first one combines the SSI results obtained with the complete model with mathematical formulation provided in the literature to obtain the values for different sets of spring-dashpots. Instead, in the second approach, the totality of these elements are calibrated from the SSI data extracted from the complete model. In both cases, a final calibration is carried out on the mechanical properties of the portal frame to ensure a good approximation to the real modal bridge behaviour. Later in Section 5, an experimental-numerical comparison of the bridge modes is shown.

4.1 *Two different approaches*

The first approach follows a similar methodology to that described in (Zangeneh 2018). Accordingly, the procedure required to assign values to the spring-dashpots varies depending on the zone of the bridge in question. Hence, for the elements at the bridge walls, stiffness and damping properties are calculated with the expressions provided in the previous reference. Still, a different method is used for the spring-dashpots located at the soil-bridge interface of the bottom slab. As it is well known, it is possible to model the interaction between a plate and the surrounding soil by means of frequency-dependent lumped impedances. Thus, the dynamic stiffness can be obtained based on a harmonic analysis performed on the complete model. In this line, a continuous distributed vertical harmonic force $F_s\ (\omega)$ is applied covering the span length of the frame on both rails of Track 2 (the centre track on Figure 3). Then, the displacement at each spring-dashpot location in the three spatial directions is obtained. Subsequently, the dynamic stiffness can be defined according to (Galvín 2022) as $K_{v,d}\ (\omega) = F_s\ (\omega)/U_s(\omega)$, where $U_s\ (\omega)$ is the displacement of the slab at each point, yielding the following properties of stiffness $K_v\ (\omega) = \mathrm{Re}\{K_{v,d}\ (\omega)\}$ and damping $C_v\ (\omega) = \mathrm{Im}\{K_{v,d}\ (\omega)\}/\omega$ on the system.

In the second approach, the method described above consisting in the harmonic analysis on the complete model is used to assign the properties to all the spring-dashpots, regardless of their location. In both approaches, the spring-dashpots are tuned to the fundamental frequency of the bridge (f_1, see Table 1).

5 RESULTS

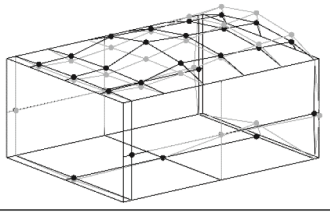
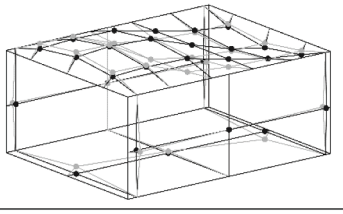
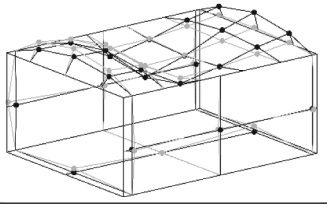
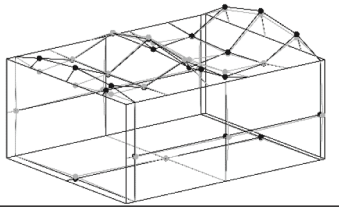
A final calibration is conducted on the mechanical properties of the simplified model, particularly, on the ballast density and on the elastic modulus of the bridge slab. However, as previously seen, the structure presents an asymmetric modal behaviour: the participation of both bridge sections (HS and conventional) is unequal, leading to a predominant deformation of a section with respect to the other in certain modes. In light of that, the authors have found that differentiating the main properties of the slab and the ballast from both bridge sections is necessary to replicate in an accurate manner the experimental modal parameters of the structure. Thus, the final calibration is performed based on the two approaches proposed: the first one, that combines mathematical expressions and the SSI results of the complete model to assign the values to the spring-dashpots and the second one, that it is based entirely on the SSI results. The calibration process led to the results given in Table 3.

Table 3. Mechanical properties of the bridge before and after calibration.

Approach	Parameter	Bridge section	Nominal	Updated	Variation
Approach 1	Ballast density (kg/m^3)	Conventional	1950	1560	-20%
		High Speed	1950	1950	0%
	Slab elastic modulus (GPa)	Conventional	35.71	35.71	0%
		High Speed	35.71	27.50	-23%
Approach 2	Ballast density (kg/m^3)	Conventional	1950	1560	-20%
		High Speed	1950	2340	20%
	Slab elastic modulus (GPa)	Conventional	35.71	30.35	-15%
		High Speed	35.71	26.07	-27%

A modal analysis is performed to compare the modes calculated numerically and those identified experimentally. Table 4 shows the modal shapes in both cases. The numerical modes are represented in black, whereas the experimental ones are depicted in grey. For the sake of brevity, the images correspond only to the Approach 2, as the results from Approach 1 are similar.

Table 4. Comparison of the numerical and experimental modes of the frame, considering Approach 2.

Mode 1	Mode 2
	
Mode 3	**Mode 4**
	

The complete results regarding the frequency obtained with the two approaches are listed on Table 5. The Modal Assurance Criterion (MAC) calculated considering the accelerometers on the top slab (A1 to A18) is used to assess the relationship between the numerical and the experimental modes.

Table 5. Frequencies and MACs of the numerical modes computed with the two approaches considered.

Results	f_1	f_2	f_3	f_4	MAC_1	MAC_2	MAC_3	MAC_4
Experimental	22.407	25.440	26.802	44.266	-	-	-	-
Approach 1	22.459	25.561	27.490	39.445	0.675	0.716	0.455	0.778
Approach 2	22.492	25.432	27.011	37.515	0.629	0.563	0.628	0.767

6 CONCLUSIONS

In this work, the modal identification of an existing portal frame railway bridge is carried out. Then, a 3D FE numerical model is implemented considering the track, the bridge, and the soil. The complete model is padded with PML layers to reduce the computational cost. The SSI data obtained with this model is later used to configure a simplified version of it, in which the effect of the soil is simulated with distributed linear frequency-dependent spring-dashpots at the bridge-soil interfaces. Two alternative approaches are conducted to determine the properties of the spring-dashpots. In the first one, those located at the walls are calculated according to expressions given in the literature, and those located on the lower slab are computed from the SSI data obtained numerically with the complete model. In the second approach, the properties of the totality of the spring-dashpots are computed with this last method. Finally, a modal analysis is carried out on the simplified model considering both approaches. In summary, the next can be concluded:

- The combined analysis of the OMA results with the FRF data of the train passages led to a better understanding of the modal behaviour of the structure, heavily influenced by the effect of the soil and the division on two separated structures.
- The use of the simplified model led to satisfactory results, as, after final calibration, the numerical-experimental comparison resulted in a good approximation of the experimental modes of the bridge based on the two approaches considered.

These outcomes could be useful in future research devoted to predicting the dynamic behaviour of partially buried structures such as portal frames, and to assess the integrity, safety and sustainability of the railway infrastructure.

ACKNOWLEDGEMENTS

The authors acknowledge: Universitat Jaume I (PREDOC/2022/26); Spanish Ministry of Science and Innovation (PID2022-138674OB-C2); Regional Ministry of Economic Transformation, Industry, Knowledge and Universities of Andalusia (PROYEXCEL 00659); Generalitat Valenciana (AICO/2021/200) and the Andalusian Scientific Computing Centre (CICA).

REFERENCES

Coronado, C. & Gidwani, N., 2016. *Calculation of dynamic impedance foundations using finite element procedures*. San Francisco: Bechtel Power Corporation Nuclear security & Environmental

Galvín, P., Romero, A., Moliner, E., Connolly, D. P. & Martínez-Rodrigo, M.D. 2022. Fast simulation of railway bridge dynamics accounting for soil-structure interaction. *Bulletin of Earthquake Engineering* 23: 3195–3213

Martínez-Rodrigo, M.D., Galvín, P., Doménech, A. & Romero, A., 2018. Effect of soil properties on the dynamic response of simply-supported bridges under railway traffic through coupled boundary element-finite element analyises. *Engineering Structures* 170: 78–90

Salcher, P. 2020. Effect of soil-structure interaction on the dynamics of portal frame railway bridges. *Bautechnik* 97(7): 490–498

Zangeneh, A., Svedholm, C., Andersson, A.C. & Pacoste, C. 2018. Identification of soil-structure interaction effect in a portal frame railway bridge through full-scale dynamic testing. *Engineering Structures* 159: 299–309

Zangeneh, A., François, S., Lombaert C. & Pacoste, C. 2021. Modal analysis of coupled soil-structure systems. *Soil Dynamics and Earthquake Engineering* 144: 106645

Bridge Maintenance, Safety, Management, Digitalization and Sustainability – Jensen, Frangopol & Schmidt (eds)
© 2024 The Author(s), ISBN 978-1-032-77040-6
Open Access: www.taylorfrancis.com, CC BY-NC-ND 4.0 license

Enhancing structural performance prediction through Bayesian updating with considering load and speed uncertainty

F. Shaker
Graduate Student, Department of Civil Engineering, Monash University, Melbourne, Australia

C. Caprani
Associate Professor, Department of Civil Engineering, Monash University, Melbourne, Australia

ABSTRACT: Finite-Element (FE) models, crucial for predicting structural responses, often rely on oversimplified assumptions, contrasting sharply with real-world data obtained through Structural Health Monitoring (SHM). To enhance the accuracy of these predictions, Bayesian updating techniques are employed, underscoring the significance of integrating comprehensive knowledge, including uncertainties in load and speed. These techniques refine structural models by merging prior engineering insights with SHM data. This paper delves into the latest advancements in Bayesian updating and their practical application for engineers. A case study featuring a simple beam model under a moving load showcases these methods' applicability, highlighting the importance of updating structural parameters by incorporating all available prior knowledge, especially regarding load and speed conditions. Our findings bolster ongoing efforts to ensure the reliability and safety of bridge structures amid evolving transportation demands.

1 INTRODUCTION

1.1 *Overview*

Bridges are integral to transportation networks, functioning as critical links that support communities and economies. Ensuring their safety and efficient operation is a paramount concern, particularly in light of the dynamic and often unpredictable nature of transportation demands. Traditional FE models, commonly employed for predicting structural responses, are often based on oversimplified assumptions about structural behavior. This discrepancy between theoretical models and real-world performance highlights the importance of SHM, which provides empirical data that often significantly deviates from FE model predictions (Ni & Chen, 2021).

1.2 *State-of-the-art in Bayesian updating*

SHM data is utilized to improve numerical models through the use of Bayesian model updating, which is becoming more and more common in structural engineering (Fang et al., 2022; Zhou et al., 2022). Although bridge designs can be effectively assessed using conventional techniques such as conjugate priors (Ni et al., 2020), the field is currently shifting towards more flexible methods that combine engineering knowledge with empirical data. Overcoming the drawbacks of the Metropolis-Hastings (MH) algorithm, the Hamiltonian Monte Carlo (HMC) approach has proven to be more effective for high-dimensional spaces and intricate parameter connections in structural models (Betancourt, 2019). The application of HMC in structural engineering has to be enhanced, according to recent research, which also emphasizes the significance of using suitable sampling techniques and taking parameter correlations and prior knowledge into account (Bouzas et al., 2022).

DOI: 10.1201/9781003483755-141

1.3 *Considering load uncertainties*

A critical aspect of this investigation is the consideration of parameter correlations and external factors that significantly influence structural performance. Bridge infrastructure deterioration modeling using Bayesian methods, as discussed in works by Mueller & Stewart (2011) often assumes independence between model parameters. However, as identified by Enright & Frangopol (1998) significant correlations between bridge deterioration parameters exist and should be addressed (Mueller & Stewart, 2011; Enright & Frangopol, 1998).

Research on bridge deterioration has also explored the impact of external factors such as traffic loading and environmental conditions on the deterioration process, highlighted the influence of external factors on bridge deterioration (Calvert et al., 2020). Moreover, efforts have been made to integrate these factors into deterioration modeling through multivariate regression modeling and seismic fragility methods. While the existing literature has made significant strides in understanding the multivariate dependencies and deterioration modeling of bridges, there is still a need for comprehensive studies that address the combined impacts of inherent and external correlations on Bayesian updating performance (Al-Rashed et al., 2023; Fujiu et al., 2022).

Studies show that vehicle loads, especially heavy vehicles, significantly accelerate pavement deterioration. This highlights the importance of accounting for these effects in predictive models (Bhandari et al., 2023). In addition, traffic loads influence the time-dependent bridge reliability, as evidenced by research on prestressed row box girder bridges (Biondini & Frangopol, 2016). Complex interactions of load, mass, construction type, materials, and environmental conditions all contribute to the overall structural integrity and performance of bridges, necessitating a comprehensive approach to modeling and analysis (Yang et al., 2018). Thus, when Bayesian updating is used for infrastructure modeling, an appropriate representation of load and speed uncertainty is needed to increase model accuracy and reliability. Considering these key factors, the updating process can enhance prediction accuracy.

1.4 *Contribution*

This study aims to fill the gaps in Bayesian updating of structural models by using non-conjugate priors to better represent multivariate correlations, as well as adding key explanatory variables such as load and speed to account for externalities and effects well. We illustrate the practical application of these techniques by performing a case study on a basic beam model under a moving point load, and highlight the importance of a thorough understanding of prior knowledge, especially for load and velocity conditions. Diving deeper into state-of-the-art Bayesian models, this review focuses primarily on HMC methods to address uncertainties in structural modeling. These uncertainties, when incorporated into Bayesian models, not only lead to an increase in the accuracy and applicability of predictions but also facilitate an investigation into the capacity of the HMC method to span complex parameter spaces. The complexity posed by this uncertainty is effectively navigated, providing valuable insights into the usefulness and effectiveness of advanced Bayesian sampling techniques in real-world design situations.

2 METHOD

2.1 *Bayes' theorem*

Finite element model updating (FEMU) can be considered a statistical problem. Using Bayes' theorem, measured data (D) are used to update the prior knowledge of parameters that take uncertainty into account:

$$P(\theta|D) = \frac{P(D|\theta)P(\theta)}{P(D)} \tag{1}$$

where, θ and $P(\theta)$ represent uncertain parameters, and the prior PDF for θ, respectively. D is the measurement or data, and the term $P(D|\theta)$ is the likelihood function that introduces the probability of the observed data (D) for specified model parameters (θ). $P(\theta|D)$ represents the posterior function. $P(D)$ is the normalization factor.

To gather prior information, experts can provide assessments and conduct experiments on a smaller scale in laboratories. This helps to quantify uncertainties associated with relevant parameters before any data is collected. To establish the likelihood function, we consider the equation that governs probabilistic model measurements and accounts for errors in model outputs. The focus on determining the likelihood function highlights the importance of accurately modeling the chances of observing the data given the model parameters, including how errors in the model's outputs are accounted for. This process is crucial for effectively updating the model parameters based on new data. Sampling methods are used to calculate the PDF of the posterior distribution (Ereiz et al., 2022). It can be difficult to obtain analytical solutions that accurately characterize the PDF of uncertain parameters. Thus, sampling methods are frequently employed in Bayesian model updating.

2.2 *Sampling method*

The HMC algorithm is a technique within the Markov Chain Monte Carlo (MCMC) framework, designed to improve sampling efficiency compared to methods like the MH algorithm. HMC uses gradient information to navigate the parameter space, allowing for informed steps and a higher acceptance rate with larger step sizes. This leads to samples with reduced interdependence and hence fewer samples are needed for accurate approximations. HMC is particularly effective in Bayesian analysis due to its ability to cover long distances in parameter space smoothly, despite requiring careful tuning of steps and step size for accurate approximations. (Duane et al., 1987; Baisthakur & Chakraborty, 2020).

The No-U-Turn Sampler (NUTS) addresses hyperparameter tuning challenges in HMC by dynamically selecting the number of leapfrog steps for each sample, enhancing the flexibility and efficiency of Bayesian model updating. As just one of the modern Probabilistic Programming Languages, *PyMC* facilitates the development of probabilistic models that incorporate real-world data from SHM. (Hoffman & Gelman, 2014; Fang et al., 2022).

2.3 *Convergence test and effective sample size*

In this study, the Gelman-Rubin statistic ($\hat{R}$) was employed to evaluate the convergence of the Markov chain algorithm (Gelman & Rubin, 1992). When the value of $\hat{R}$ approaches 1, it indicates convergence. Values greater than 1 suggest a lack of convergence (Gelman & Rubin, 1992).

The effective sample size (ESS) is a measure of the number of independent samples that provide information equivalent to truly correlated samples. An increased ESS denotes a more accurate and efficient parameter estimate. The effective sample size is influenced by the correlation between samples. When the samples in the MCMC series are correlated, the effective sample size is smaller.

In a system modeled using the MCMC method, introducing more uncertainties and complex relationships between priors can affect $\hat{R}$ and ESS. When more uncertain parameters are incorporated into a system that has been MCMC modeled, it introduces more complexity and variability into the simulation, which could lead to correlated samples in the MCMC chain.

In the context of the present study, the inclusion of load and speed uncertainty results in a higher correlation between subsequent samples because random variations in system

parameters make the subsequent state more reliant on the previous one. Despite the introduction of more complexity and variability into the simulation, we leverage state-of-the-art NUTS techniques to achieve high ESS and acceptable $\hat{R}$ values. This demonstrates the robustness of the approach in handling increased uncertainty while maintaining reliable parameter estimates. We thus provide a meaningful comparison between traditional MCMC and HMC for a typical structural engineering problem.

3 APPLICATION

We focus on a practical example in structural engineering with a beam being subjected to a moving point load, the goal is to assess how considering load uncertainties can affect updating uncertain parameters. Consider a 20 m long beam that is exposed to a moving point load (P = 100 kN) and has a flexural rigidity (EI = 200 MNm^2), shown in Figure 1. A closed-form function (Equation 2) using Macaulay's method calculates deflection at each desired point when the point load crosses the beam.

$$\delta = \frac{P\,L^3}{6EI}\left[a^3(1-x) - \langle a-x\rangle^3 + a(1-x)^3 - a(1-x)\right] \tag{2}$$

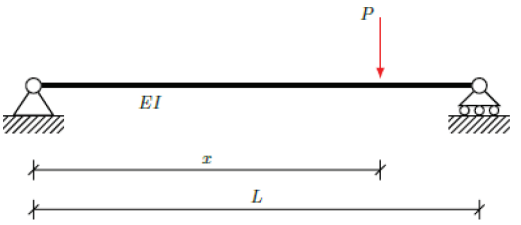


Figure 1. Beam and moving point load.

The Macaulay bracket symbol is represented by the notation $\langle a-x\rangle$. This mathematical notation is made to produce particular results depending on the sign of the phrase included within it. The term enclosed in the Macaulay bracket evaluates to zero when it is negative and to its true value when it is positive (Caprani, 2009). P stands for the point load's magnitude, a for the point on the beam where the deflection is important, and x for the place where the point load is traveling along
the length of the beam.

3.1 *Incorporating load magnitude and speed as uncertain parameters*

To understand how the beam behaves structurally, two additional factors that introduce uncertainty will be considered - the load's magnitude (P) and its speed (v). To model the deflection (δ), we use Equation 3 that takes into account these uncertain parameters:

In this equation, we use t to represent the time points when the deflection is measured. P stands
for the uncertain magnitude of the load, and v represents the uncertain speed at which the load is applied.

$$\delta = \frac{PL^3}{6EI}\left[a^3\left(1-\frac{vt}{L}\right) - \left\langle a-\frac{vt}{L}\right\rangle^3 + a\left(1-\frac{vt}{L}\right)^3 - a\left(1-\frac{vt}{L}\right)\right] \tag{3}$$

We acknowledge the importance of considering both the uncertainty in load and speed when analyzing how prior parameters correlate with sampling techniques. By incorporating these uncertainties into our analysis, we can thoroughly examine the structural behavior across various scenarios and provide a more precise representation of real-world conditions. We consider the uncertainty in P and v and compare the efficiency and accuracy of HMC sampling technique.

3.2 *Generating data*

For this application, simulated deflection data will be generated for five virtual sensors positioned along the beam from the known model. These virtual sensors are located at $0.25L$, $0.4L$, $0.5L$, $0.6L$, and $0.75L$ on the beam. At specific time intervals of 0.05 seconds, these sensors record the deflection (δ_m) of the beam. Artificial Gaussian noise was added to the deflections to reflect realistic measurement conditions as follows:

$$\delta_m = \delta + \varepsilon \tag{4}$$

where $\varepsilon \sim \mathcal{N}(0.0, 0.005)$ is a random variable with a normal distribution, indicating unbiased noise with a standard deviation of 5 mm.

To generate the simulated data, a point load is applied to move along the beam completely. During the traverse, 200 deflection values are simulated and recorded. This controlled virtual sensing provides the necessary data to accurately update the uncertain parameters of the beam using HMC-NUTS sampling. Figure 2 illustrates the theoretical and simulated measurements.

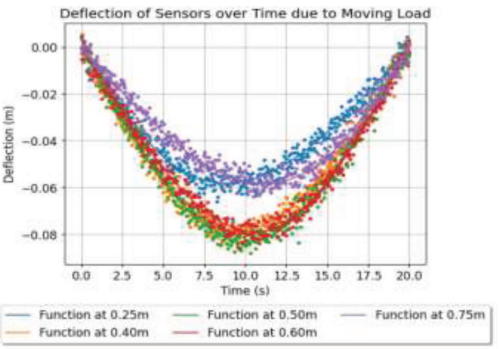


Figure 2. Function and data results plot.

3.3 *Priors and likelihood*

In engineering problems, using previous knowledge helps in establishing reasonable assumptions for uncertain parameters.

The case study models uncertain variables, EI and L, using a Beta distribution and a Normal distribution respectively. A non-conjugate prior for EI is used to account for engineering bounds. Reasonable limits are established through a Beta-distributed parameter, η. In the second phase, two additional load parameters, P and v, are introduced. P is modeled as a Normal distribution, while v is modeled as a Uniform distribution.

Table 1 summarizes prior distributions, including parameters, modes, and support. The likelihood function is a Normal distribution with a mean of zero and a Half-Normal distribution for modeling the standard deviation, ensuring non-negative values.

Table 1. The prior distributions.

Parameter	Distribution	Parameters	Mode	Support
EI (kNm^2)	Beta	$\alpha = 2$, $\beta = 3$	183300	(150000, 250000)
L (m)	Normal	$\mu = 20$, $\sigma = 0.01$	20	$(-\infty, +\infty)$
P (kN)	Normal	$\mu = 100$, $\sigma = 20$	100	$(-\infty, +\infty)$
v (m/s)	Uniform	$v_{min} = 0.75$, $v_{max} = 1.25$		(0.75, 0.125)

4 RESULTS

4.1 *Statistical results*

When load and speed uncertainty are introduced into the Bayesian updating process through NUTS, the convergence metrics $\hat{R}$ and ESS should be considered to make sure that the model works effectively. Parameter estimates are provided in Table 2. The $\hat{R}$ values are consistently close to 1 when load and speed uncertainty are taken into account. This suggests that even with these extra complications, NUTS is still able to successfully attain convergence. The durability of NUTS in managing complex scenarios with extra uncertain factors is demonstrated by the stability of $\hat{R}$ values, even with the increasing complexity of the model.

When load and speed uncertainties are taken into account, the effective sample size metrics, ESS-bulk and ESS-tail continue to have high values. This implies that NUTS can explore the parameter space efficiently. The preservation of high ESS values highlights the effectiveness of NUTS in sampling a wide range of the posterior distribution, even in a more complex model because of load and speed uncertainties.

Table 2. Comparison of parameter estimates without and with load uncertainties.

Parameter	Method	Mean	ESS Bulk	ESS Tail	$\hat{R}$
EI (kNm^2)	Phase 1*	200081.931	1759.0	2176.0	1.0
EI (kNm^2)	Phase 2**	190274.286	1589.0	2133.0	1.0
L (m)	Phase 1	20.009	1763.0	2279.0	1.0
L (m)	Phase 2	20.000	2503.0	2456.0	1.0
P (kN)	Phase 2	95.041	1635.0	2029.0	1.0
v (m/s)	Phase 2	1.000	2107.0	2327.0	1.0

* Without load uncertainties. ** With load uncertainties.

4.2 *Pair plots*

Pair plots of the NUTS sampling points offer a powerful visual depiction of the posterior distributions for important structural parameters, highlighting the effects of different situations. As shown in Figure 3, The data points for EI and L are closely clustered when load uncertainty is absent, demonstrating NUTS's ability to effectively sample from high probability density regions and provide accurate parameter estimations. Nevertheless, the data distribution within the pair plots noticeably widens with the introduction of load and speed uncertainty. The wider distribution of sample points that characterizes the phenomena does not imply a decline in sampling efficiency. Rather, it emphasizes how flexible the algorithm is in accommodating the growing unpredictability of the system, encompassing a broader range of potential results. This broader scope is especially important for structural engineering, where

it is crucial to evaluate the performance of structures realistically under a variety of unpredictable circumstances in order to guarantee resilience and safety.

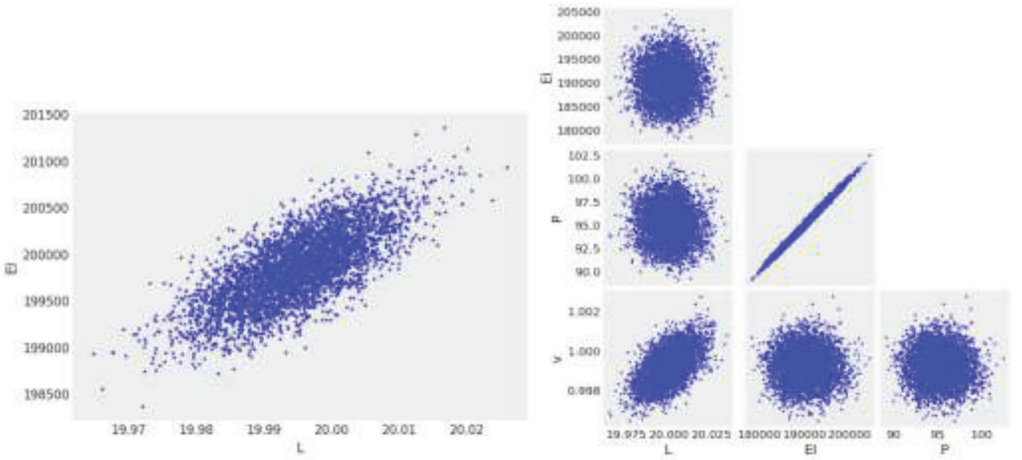


Figure 3. Pair Plots: (a) Without; (b) With load uncertainties.

4.3 *Posterior probability density functions*

Figure 4 shows the resulting posterior density and trace plots for uncertain prior parameters. The dotted or dashed lines in the trace plots represent individual traces of the sampling chains. In the presence of uncertain loads, NUTS has shown stability and strong convergence properties in producing reliable chains. All the trace plots show good convergence. This consistency suggests that the NUTS method is capable of managing the complexities inherent in these posterior distributions. The model updates that take into account deeper knowledge of load dynamics and actual condition are well-founded, and the resulting parameter estimations are reliable and representative of the underlying physical processes.

In our Bayesian analysis, as depicted in Figure 5, the findings underscore a broader methodological insight: sometimes, more complex models can yield better sampling results. This is exemplified in the posterior distributions for parameters such as L and EI. The observed variations in these distributions, particularly for EI are not so much about the specifics of load and speed uncertainties, but rather about how increased model complexity can lead to significant changes in parameter estimations. For instance, the noticeable broadening in the posterior distribution of EI, which implies a larger standard deviation and the shift in its mean value from 190,274 kNm² to 200,082 kNm² suggest a heightened sensitivity to model nuances and indicates increased uncertainty or variability in EI. This could imply a broader range of plausible stiffness characteristics than previously considered, a finding that is crucial for understanding the robustness of structural designs. The long tails of the distribution, indicating a non-negligible likelihood of extreme values, further exemplify how complex Bayesian models can reveal crucial insights into parameter behaviors that simpler models might not capture. Due to the function within the structural system under study, L has less sensitive to changes in load, as indicated by the relative stability of the mean. The HDI's wider distribution, however, highlights the necessity of taking a wider range of possible outcomes into consideration even for parameters that seem to be stable. This is especially relevant for structural engineering applications, where accurate load-bearing capacity calculations are critical to guaranteeing safety and adhering to design guidelines.

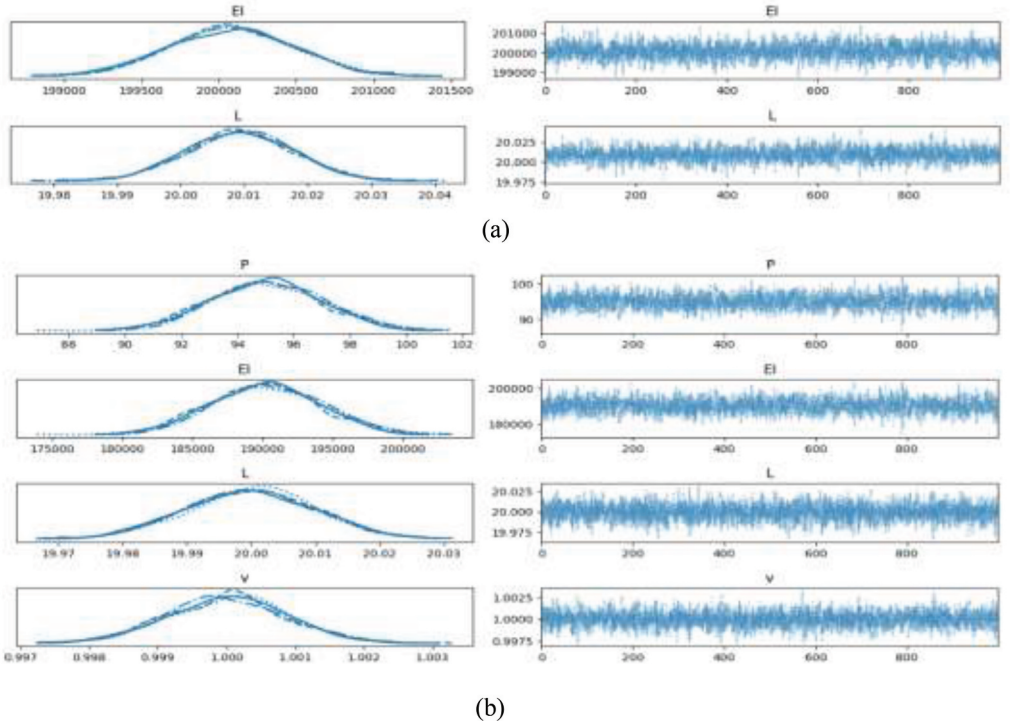


Figure 4. Comparison of posterior density and trace plots: (a) without, and; (b) with load uncertainties.

5 CONCLUSION

This study demonstrates the effectiveness of updating Bayesian models in bridge infrastructure evaluation by combining engineering ideas with data from structural health monitoring in a sophisticated way. By employing sophisticated MCMC methods, such as the NUTS, it enhances Bayesian inference by providing adaptable uncertainty representations via non-conjugate priors.

Our results demonstrate the importance of considering a wide range of uncertainties and complexities in the evaluation of structural parameters. The impact of various uncertain

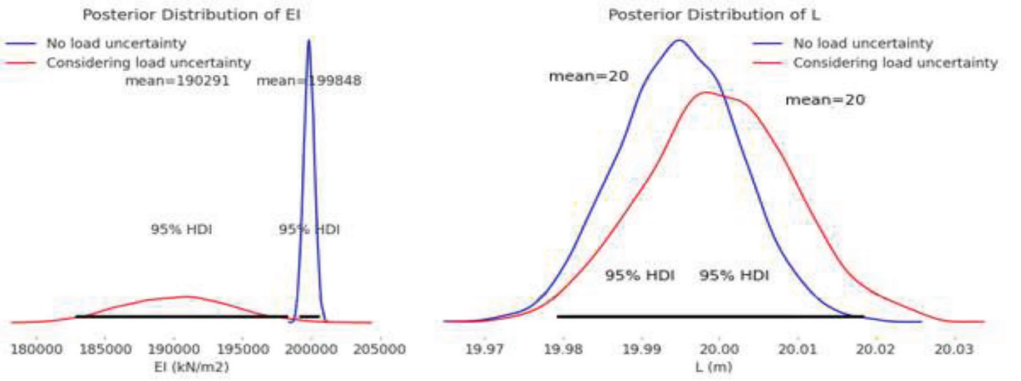


Figure 5. Posterior results comparison.

factors on the posterior distributions of key parameters illustrates the necessity of a comprehensive approach in modeling. This inclusive modeling strategy not only provides a more accurate representation of real-world conditions but also enhances the reliability of our predictions and assessments in structural engineering.

We illustrate how these Bayesian approaches improve uncertainty quantification and preserve strong convergence diagnostics using a case study of a beam subject to varying stresses. This emphasizes the necessity of contemporary, cohesive analytical frameworks in structural engineering that combine theoretical concepts, empirical data, and prior knowledge.

REFERENCES

Baisthakur, S. & Chakraborty, A. 2020. Modified Hamiltonian Monte Carlo-based Bayesian finite element model updating of steel truss bridge. *Structural Control and Health Monitoring*, 27(8): e2556.

Betancourt, M. 2019. The Convergence of Markov Chain Monte Carlo Methods: From the Metropolis Method to Hamiltonian Monte Carlo. *Annalen der Physik*, 531(3): 1700214.

Bhandari, S., Luo, X. & Wang, F. 2023. Understanding the effects of structural factors and traffic loading on flexible pavement performance. *International Journal of Transportation Science and Technology*, 12(1): 258–272.

Biondini, F. & Frangopol, D.M. 2016. Life-Cycle Performance of Deteriorating Structural Systems under Uncertainty: Review. *Journal of Structural Engineering*, 142(9): F4016001.

Bouzas, O., Conde, B., Cabaleiro, M. & Riveiro, B. 2022. A holistic methodology for the non-destructive experimental characterization and reliability-based structural assessment of historical steel bridges. *Engineering Structures*, 270: 114867.

Caprani, C. 2009. Deflection of Flexural Members - Macaulay's Method 3rd Year Structural Engineering. https://www.academia.edu/4409785/Deflection_of_Flexural_Members_Macaulays_Method_3rd_Year_Structural_Engineering 17 December 2022.

Duane, S., Kennedy, A.D., Pendleton, B.J. & Roweth, D. 1987. Hybrid Monte Carlo. *Physics Letters B*, 195(2): 216–222.

Enright, M.P. & Frangopol, D.M. 1998. Service-Life Prediction of Deteriorating Concrete Bridges. *Journal of Structural Engineering*, 124(3): 309–317.

Ereiz, S., Duvnjak, I. & Fernando Jiménez-Alonso, J. 2022. Review of finite element model updating methods for structural applications. *Structures*, 41: 684–723.

Fang, C., Liu, H.-J., Lam, H.-F., Adeagbo, M.O. & Peng, H.-Y. 2022. Practical model updating of the Ting Kau Bridge through the MCMC-based Bayesian algorithm utilizing measured modal parameters. *Engineering Structures*, 254: 113839.

Gelman, A. & Rubin, D.B. 1992. Inference from Iterative Simulation Using Multiple Sequences. *Statistical Science*, 7(4): 457–472.

Hoffman, M.D. & Gelman, A. 2014. The No-U-Turn Sampler: Adaptively Setting Path Lengths in Hamiltonian Monte Carlo. http://arxiv.org/abs/1111.4246 27 January 2023.

Mueller, J. & Stewart, M.G. 2011. Balancing the Risks, Benefits, and Costs of Homeland Security., 7.

Ni, Y.Q., Wang, Y.W. & Zhang, C. 2020. A Bayesian approach for condition assessment and damage alarm of bridge expansion joints using long-term structural health monitoring data. *Engineering Structures*, 212: 110520.

Ni, Y.Q., Wong, K.Y. & Xia, Y. 2011. Health Checks through Landmark Bridges to Sky-High Structures. *Advances in Structural Engineering*, 14(1): 103–119.

Yang, X., Dong, Y., Sun, S., Zhang, F., Sun, J. & Wang, Z. 2018. Mesozoic-Cenozoic deformation characteristics of the Zhuozishan Mountain in the northern Helanshan tectonic belt. *Scientia Geologica Sinica*, 53: 799–818.

Zhou, X., Kim, C.-W., Zhang, F.-L. & Chang, K.-C. 2022. Vibration-based Bayesian model updating of an actual steel truss bridge subjected to incremental damage. *Engineering Structures*, 260: 114226.

Bridge Maintenance, Safety, Management, Digitalization and Sustainability – Jensen, Frangopol & Schmidt (eds)
© 2024 The Author(s), ISBN 978-1-032-77040-6
Open Access: www.taylorfrancis.com, CC BY-NC-ND 4.0 license

Utilizing bWIM-data to calibrate new traffic load models on embankment

H. Lilja
Heikki Lilja Consulting Oy, Finland

J. Qvisen
Proxion Oy, Finland

A. O'Connor
Department of Civil, Structural & Environmental Engineering Trinity College, Ireland

ABSTRACT: This study introduces an innovative methodology for calibrating road traffic load models on embankments using bridge weigh-in-motion (bWIM) data, focusing on developing a rapid and reproducible calibration technique, targeting the calibration of new geotechnical load models introduced in the second generation of the Eurocode standard prEN 1991-2. While the study does not aim for final model calibration, it lays the foundation for future extensive calibrations using a broader dataset and advanced reliability-based data analysis. The study is a part of the ongoing efforts of the IABSE Task Group 1.10, established in January 2023, to integrate road traffic data into bridge research, design, and assessment.

1 INTRODUCTION

This article presents a novel methodology utilizing Bridge Weigh-in-Motion (bWIM) measurements to evaluate and assess load levels on road embankments. This approach facilitates the initial calibration of newly proposed load models for geotechnical structures as outlined in the second generation of the Eurocode standard, prEN 1991-2.

While this study does not aim to achieve the final calibration of the load models, it introduces a rapid and reproducible method for preliminary calibration. Comprehensive and final calibrations will incorporate a broader data selection and employ more sophisticated, reliability-based data analysis techniques.

This publication is the inaugural article in a series representing the work of IABSE Task Group 1.10, established in January 2023. The project's primary goal is to foster a platform for exchanging knowledge and enhancing the understanding of the benefits of applying road traffic data in bridge research, design, and evaluation.

2 TRAFFIC LOAD MODELS IN 1ST GENERATION OF EUROCODE

2.1 *Traffic load model for bridge design*

The primary road traffic load model for bridge design in the Eurocode is Load Model 1 (LM1), comprising tandem loads (TS) and uniformly distributed loads (UDL). Specifically, the tandem load is 600 kN on lane one and 400 kN on lane two, while the UDL is 9 kPa for lane one and 2.5 kPa for lane two, as specified in EN 1991-2.

Additionally, the Eurocode introduces a frequent load model with a one-week return period. This model is derived by adjusting tandem loads with a factor of α_Q = 0,75 and ULD with α_q = 0,4., given in EN 1990 Annex A.2.

DOI: 10.1201/9781003483755-142

Initially calibrated using beam elements for bridge structures, LM1 has, over a decade of application, shown to represent actual traffic loads effectively, particularly when values are tailored in the National Annex to reflect local traffic conditions. However, LM1 might overestimate static traffic loads for short influence lines, offset by greater dynamic amplification under traffic flow. Conversely, it may underestimate the negative moments in small to medium-length continuous bridges under heavy special transportations. These limitations can be addressed by Load Model 3 (LM3), as delineated in Annex A of EN 1991-2. LM1 tends to be overly conservative for very long spans compared to simulated traffic flows.

2.2 *Traffic load model for geotechnical structures*

The same LM1 is currently employed for geotechnical structures, such as embankments and retaining walls, as per the Eurocode. The highly concentrated nature of this load model, characterized by two 300 kN axles with 1.2 m axle spacing, has drawn criticism, particularly in regions with soft soil conditions. Additionally, some member nations have opted not to apply LM1 for embankments, choosing instead to retain their national load models.

3 TRAFFIC LOAD MODELS IN 2ND GENERATION OF EUROCODES

3.1 *Traffic load model for bridge design*

In the second generation of the Eurocodes, the Load Model 1 (LM1) remains unchanged for bridge design. This decision reflects the consensus on LM1's adequacy and flexibility to accommodate national calibrations through the National Annex, ensuring it meets specific local requirements.

3.2 *Traffic load model for geotechnical structures*

The second generation of the Eurocode, specifically prEN 1991-2, introduces two new load models for geotechnical structures. The first model, designated for the area behind bridge abutments, applies a patch load of 600 kN over a 5m x 3m area (mirroring the Tandem System of LM1 on lane 1) combined with a uniform load of 9 kPa on the remaining embankment areas.

A simplified load model is proposed for geotechnical structures capable of redistributing loads, such as retaining walls. This model comprises a 20 kPa load on one lane (3m wide) and 9 kPa on the additional lanes. Both models offer the flexibility of adjustment in the National Annex of prEN 1991-2, allowing customization to local conditions.

This study analyses these new geotechnical load models against traffic loads measured on select Finnish roads. The analysis utilizes three sets of week-long traffic data collected via Bridge Weigh-in-Motion (bWIM) systems. The datasets represent diverse traffic scenarios: Traffic 1 embodies one of the heaviest traffic flows observed in the Finnish road network, Traffic 2 represents typical traffic conditions, and Traffic 3 highlights a road section regularly used by special transportation vehicles. Traffic 1 was measured in the year 2018, and Traffic 2 and Traffic 3 were measured in the year 2014.

4 MEASURED TRAFFIC LOADS

4.1 *The program developed for the study*

This study employs a novel program to analyze two-lane traffic over influence lines of varying lengths. This analysis method effectively captures the weight-time history of traffic over specific lane lengths. Utilizing this approach, the program determines and records the maximum weights observed during the measurement period for single-lane and simultaneous two-lane scenarios. These data points are documented in an Excel file for detailed subsequent analysis.

Additionally, the program tracks and records the axle configurations of vehicles that contribute to the most significant loading effects. This feature is precious in identifying the impact of various vehicle types on traffic load patterns.

The traffic data are imported into the program in a standardized format, which makes it easier to analyze and compare different datasets. The development of this standardized data format is a collaborative effort led by IABSE TG1.10, which is committed to creating tools that utilize WIM data effectively in the design and assessment of bridges.

4.2 *Limitations of the study*

The authors recognize that further work is essential to refine the calibration of load models for inclusion in the National Annex. This study provides only a snapshot of traffic load scenarios, capturing the most extreme loading conditions observed during the one-week measurement period. These results must be extrapolated using probabilistic methods for a more extended return period to achieve a comprehensive understanding.

In this analysis, real-time traffic data were utilized for both lanes. Future studies are planned to introduce elements of randomness into the one-week bWIM data to simulate varied traffic conditions more accurately. It is important to note that this study does not encompass exceptional design scenarios, such as those involving accidents leading to stationary heavy vehicles on a lane. Such scenarios require separate consideration due to their unique impact on load distributions.

4.3 *Hidden safety in the load models*

This study reveals that the heaviest measured loads typically originate from vehicles operating under special permits, a trend particularly noticeable in the Traffic 3 dataset. It is essential to recognize that the load variation from special transportation is generally limited, as these vehicles tend to adhere strictly to the load limits specified in their permits. Additionally, the routes for the heaviest special transportations are often carefully planned, avoiding the most adversely impacted travel lines on roads and bridges. In design load models, the load is uniformly spread across the entire width of the carriageway and hard shoulders, enhancing the model's reliability.

4.4 *Results for the example data*

Figures 1 to 3 illustrate the highest, mean, and 20th highest measured weights for Traffic 1, Traffic 2, and Traffic 3, respectively. The measurement period for the traffics were one week and only heavy vehicles weighing over 10 tons were included in the measurements. In these graphs, red represents data for lane A, blue for lane B, and black indicates the weights for both lanes combined. Figures 4, 5, and 6 focus on the highest 20 loads for loaded lengths up to 30 meters.

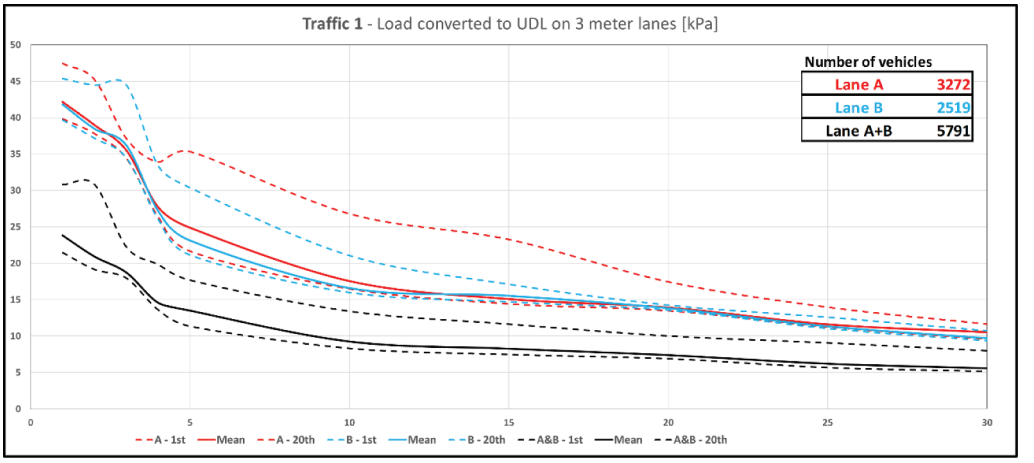


Figure 1. Traffic 1: Measured loads [kN/m^2] for 1 m. . .30 m loaded length.

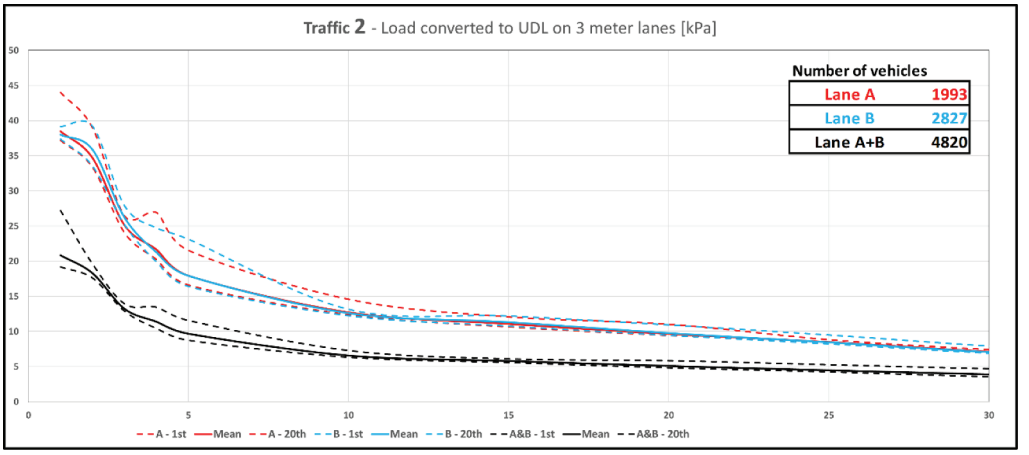


Figure 2. Traffic 2: Measured loads [kN/m^2] for up to 1 m. . .30 m loaded length.

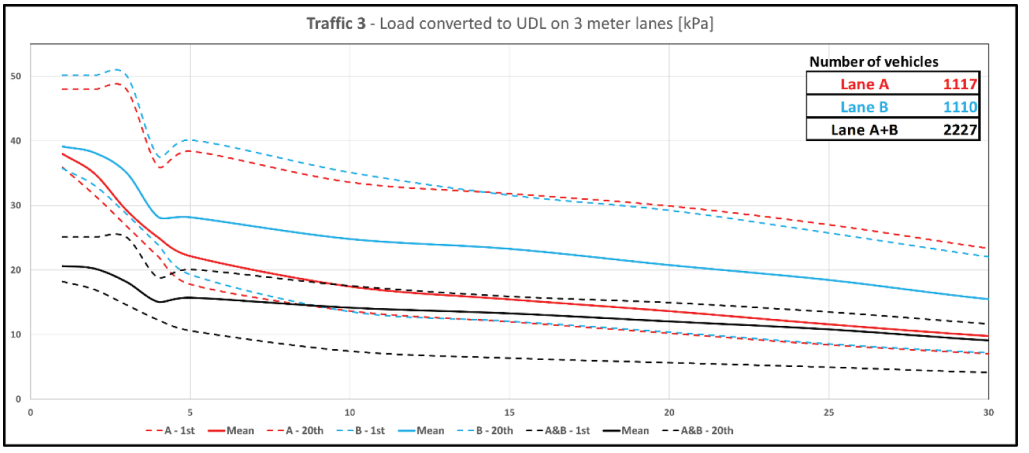


Figure 3. Traffic 3: Measured loads [kN/m^2] for up to 1 m. . .30 m loaded length.

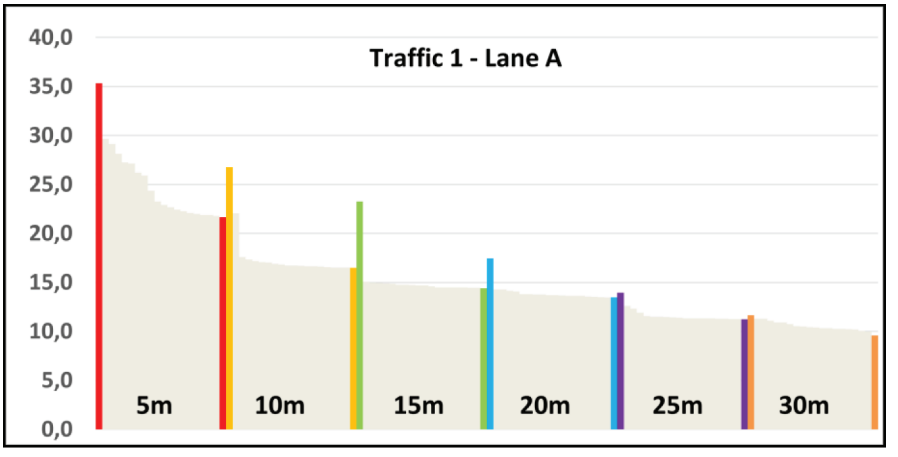


Figure 4. Traffic 1 (lane A): Top 20 measured loads [kN/m^2] for loaded lengths 5 to 30m.

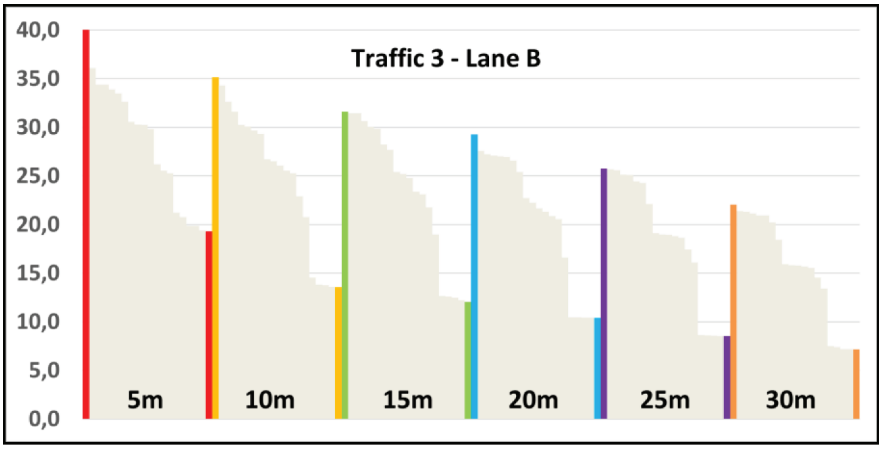


Figure 5. Traffic 2 (lane B): Top 20 measured loads [kN/m^2] for loaded lengths 5 to 30m.

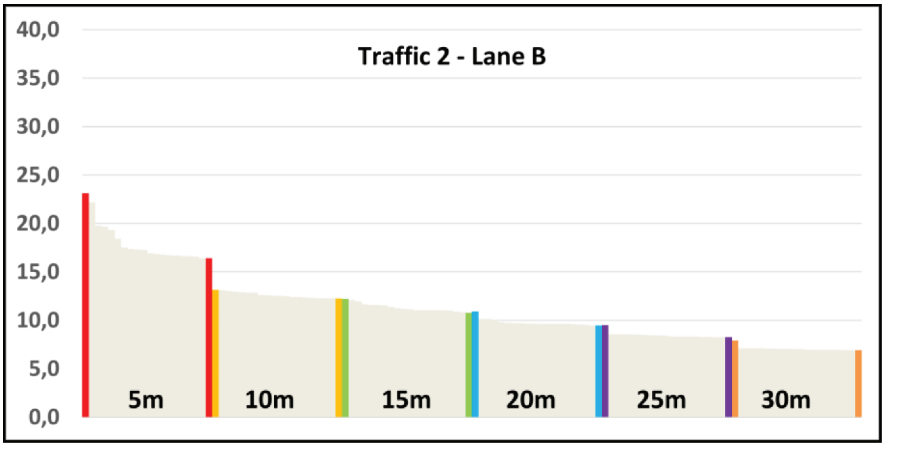


Figure 6. Traffic 3 (lane B): Top 20 measured loads [kN/m^2] for loaded lengths 5 to 30m.

Figures 7, 8, and 9 are included to draw a direct comparison between bWIM data and the Eurocode's frequent load model, which plays a significant role in the serviceability design of bridges. This comparison is beneficial because the time frame of our measurements matches the expected return period of this frequent load model. The axle configurations of vehicles that result in the highest loads are illustrated in Table 1, giving insights into vehicles that produce the most significant load impacts.

4.5 *Notes from the preliminary results*

4.5.1 *Figures 1 to 3*

The new 40 kPa load model for a 5-meter lane section in geotechnical structures is likely sufficient for even the most severe special transportation conditions. This assessment is based on the stable load magnitude and relatively consistent axle variation in these transportations. An increase in the load magnitude is not currently projected, as the existing bridges' load capacities tend to dictate these limits.

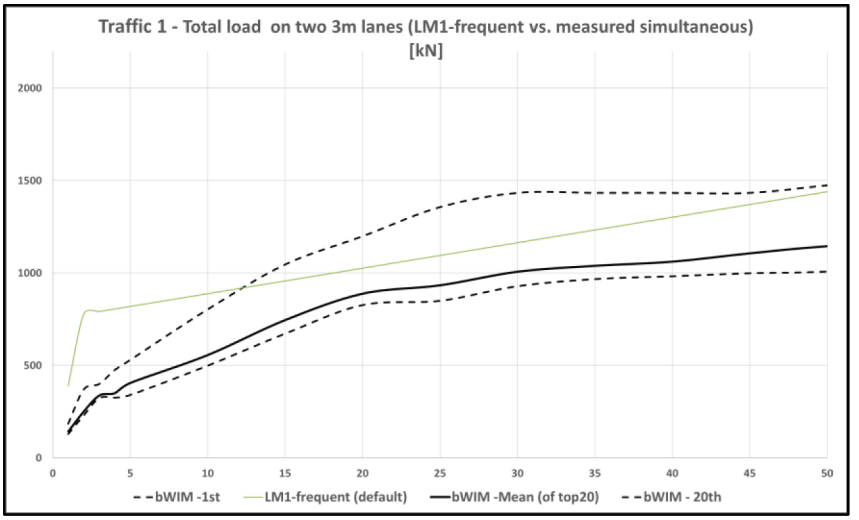


Figure 7. Traffic 1 (two lanes): comparison to LM1-frequent.

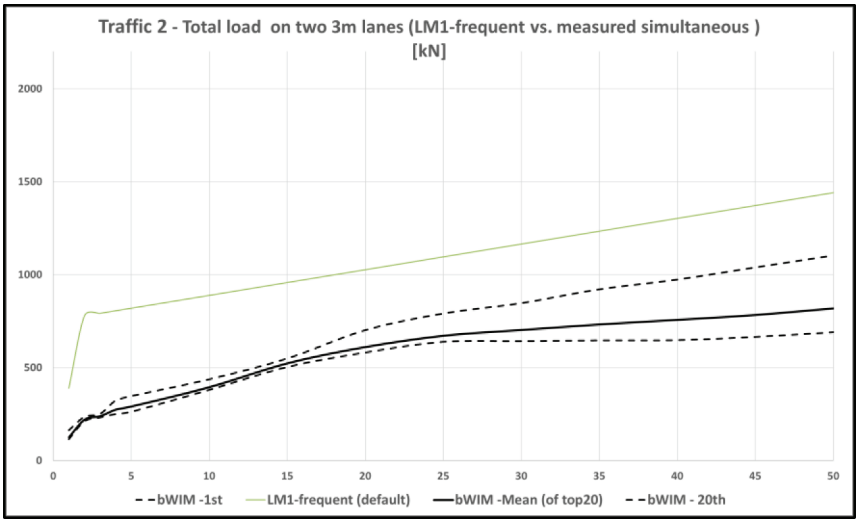


Figure 8. Traffic 2 (two lanes): comparison to LM1-frequent.

The simplified 20 kPa (one lane) and 9 kPa (other lanes) model appears appropriate for regular traffic. However, it may need adjustment for special transportations depending on the severity of their line of travel.

4.5.2 *Figures 4 to 6*

Traffic 1 reveals several high-load occurrences, yet they remain below the 40 kPa level (for 5 meters) of the newly introduced geotechnical load model, suggesting its adequacy. In contrast, Traffic 2 exhibits lighter loads, easily accommodated by the new models. Traffic 3, however, with its significant special transportation presence, frequently exceeds the bounds of the simplified model over distances up to 30 meters.

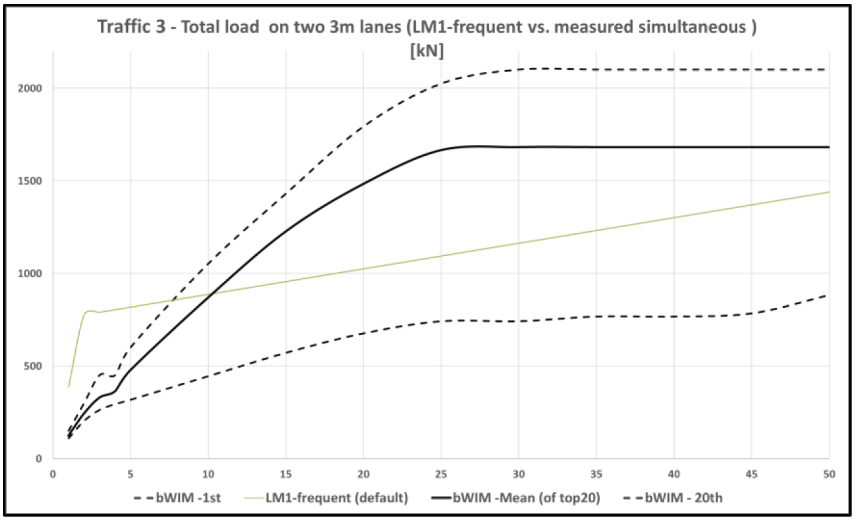


Figure 9. Traffic 3 (two lanes): comparison to LM1-frequent.

Table 1. Axle configurations causing the most adverse loads.

Traffic 1 – Lane A		Traffic 2 – Lane B		Traffic 3 – Lane B	
Interval [m]	Axle configuration	Interval [m]	Axle configuration	Interval [m]	Axle configuration
0-1	o--o	0-2	o--oo--o--o--o	0-15	o--o--oo--ooo--oooooooo
2	ooo--oo--oo--o	3	o--o--ooo	20	o--ooo--oooooooooooo
3	o--ooo--oo--ooo	4	o--ooo	25-120	o--o--oo--oooooooooooo
4	ooo--oo--oo--o	5	o--o--oooo	130-150	o--ooo--oooooooooo
5	o--oooo	10	o--ooo--oo--oo		o--ooo--oooooooooooo
10-40	ooo--oo--oo--o	15	o--ooo--oooo	160-200	o--o--oo--oooooooooooo
45-50	o--ooo--ooo--ooooo	20-45	o--ooo--oo--oooooo		o--ooo--oooooooooooo
60-70	o--oooo--oooo	50-80	o--o--ooo		
	o--oo--oo--ooo		o--ooo--oo--oooooo		
80-130	o--ooo--oo--ooo	90-130	o--oo--oo--oo		
	o--ooo--oo--o--o		o--oo--oo--o--o		
140-190	ooo--oo--oo--o	140-200	o--oo--oo--oo		
	o--ooo--oo--oo		o--oo--oo--o--o		
200	o--ooo--oo--o--oo--ooo		o--oo--ooo--o--o		
	o--o--o--o				
	o--ooo--oo--ooo				

4.5.3 *Figures 7 to 9*

These figures compare measured traffic weights with the Eurocodes' frequent load model based on a one-week return period. For regular traffic flows (Traffic 1 and 2), the measured peak loads may occasionally be slightly above the usual design load model with specific measured lengths but without significant cause for alarm. Special transportation, however, might require additional measures, such as integrating special vehicle types mentioned in Annex A of EN 1991-2.

4.5.4 *Table 1*

As shown in Table 1, Traffic 1 and Traffic 2 mainly comprise standard vehicles commonly used in Finland, known for being heavier than those in Central Europe. Traffic 3, however, is

marked by a range of special transports, including extremely heavy vehicles with up to 16 axles and weights surpassing 200 tons.

4.5.5 *Final calibration of new load models*

For the calibration of the new load models to be accurate, a broader array of bWIM data should be examined. The introduction of suitable probabilistic methods is also necessary to ensure the models align with the return periods of the structures being designed.

Given that Finnish traffic presented in this study is often heavier than in other European countries, some countries might need to modify the default values in the National Annexes to suit their specific traffic profiles.

5 OTHER USE CASES FOR THE WIM-DATA

The developed program can be tailored to examine more complex influence lines, which is crucial for accurately calibrating the static load model LM1, facilitating comparisons between bridge responses and the LM1 bridge design load model across a diverse range of bridge types and spans.

Additionally, the program can be expanded to perform comprehensive fatigue assessments, incorporating methods like the reservoir technique and Miner's linear summarization, which would allow the calibration of fatigue load models as per Eurocode and the development of fatigue models based on measured traffic data (FLM 5 in EN 1991-2).

6 IABSE TG 1.10

The initiatives of IABSE TG1.10 are expected to make substantial contributions to bridge engineering. While part of this effort involves enhancing load models, the broader goal is to create advanced tools for quick and accurate calibration of bridge loads using WIM data. This advancement will undoubtedly enrich the practice of bridge engineering, making WIM measurements a more integral part of the process.

7 CONCLUSIONS

The study outlined in this article gives a good starting point for more comprehensive research aiming to calibrate the new load models in prEN 1991-2.

It is important to note that Eurocode load models are specifically derived with certain traffic conditions, such as the heavy traffic in Auxerre, which influenced the ENV models. These models may not be entirely suitable for other road networks, possibly too conservative or not conservative enough in some (rare) instances. Proper calibration of these models is crucial for improving the reliability of bridges and the sustainability of infrastructure projects. The 2nd generation Eurocodes, replacing the 1st generation by 2028, provide a good opportunity for this calibration.

ACKNOWLEDGEMENTS

This research project was carried out under the funding of the Finnish Transport Infrastructure Agency. The Bridge weight in motion – monitoring and data extraction – was performed by Trafikia Ab and the Finnish Transport Infrastructure Agency.

REFERENCES

European Committee for Standardization. EN 1990. Basis of structural design.

European Committee for Standardization. EN 1991-2. Actions on structures. Part 2: Traffic loads on bridges.

Bridge Maintenance, Safety, Management, Digitalization and Sustainability – Jensen, Frangopol & Schmidt (eds)
© 2024 The Author(s), ISBN 978-1-032-77040-6
Open Access: www.taylorfrancis.com, CC BY-NC-ND 4.0 license

Torsion effects in Super-T girder grillage analysis

J.W. Ngan & C.C. Caprani
Monash University, Clayton, Melbourne, Australia

M. Melhem
The Department of Transport and Planning, Melbourne, Australia

ABSTRACT: In a grillage analysis of Super-T girder bridge decks, linear-elastic analysis considering full torsion stiffness may not be appropriate for ultimate limit states. For members subjected to compatibility torsion, typically in Super-T girder bridge decks, the onset of cracking at the torsion cracking moment (T_{cr}) results in reduced stiffness as loads increase towards the ultimate limit case. Consequently, the section experiences lower torsion moments (non-linear behavior) that redistribute through greater bending moments. Therefore, as an alternative, a linear-elastic grillage analysis model considering a reduced proportion of torsion stiffness can help avoid this phenomenon of overestimating torsion and underestimating moments in grillage models. This study evaluates the effect of varying torsion considerations in grillage analysis. To represent the complete range of designs possible for a Super-T PSC member, it is necessary to analyze bridge decks with feasible lower and upper spans of a standard Super-T section. For the range of feasible spans, the section cracking torsion moment is first quantified, noting the amount of beneficial prestress force present. Following, grillage analysis is performed - each with increasing proportions of torsion stiffness from 0 to 100% of torsion constant, J for longitudinal members (Super-T girders). Torsion cracking resistance is then quantified for each feasible span. The results showed that most proportions of torsion stiffness did not lead to the torsion moment exceeding the torsion cracking moment. Overall, the results show that a range of 10 - 40 % of torsion constant J would allow bridge designers a good balance between the need for torsion design - minimizing conservatism in longitudinal bending moments.

1 INTRODUCTION

Torsion in structural members can redistribute when torsional stiffness of members is reduced from onset of excessive torsion cracking. This phenomenon is typically described as torsion compatibility where the torsion can be distributed to moments in the longitudinal direction of structural members (Wyche, 2000). Like many bridge decks, Super-T girder bridge decks are subjected to torsion compatibility and must consider torsion designs.

In a grillage analysis of Super-T girder bridge decks, linear elasticity considering full torsion stiffness may not be appropriate for ultimate limit states. For members subjected to compatibility torsion, typical in Super-T girder bridge decks, the onset of cracking at the torsion cracking moment T_{cr} results in a reducing stiffness as loads increase towards ultimate (Collins and Mitchell, 1997). Consequently, the section experiences lower torsion moments (non-linear behavior) that redistribute through greater bending moments.

As an alternative, linear elasticity considering a reduced proportion of torsion stiffness could be done in a grillage analysis to emulate this phenomenon shown in Figure 1. Previous work of Wyche (2000) suggests that 20% of the torsion constant, J could replicate a torsional moment of $0.25\phi T_{cr}$. However, this work considered the results from only one 34 m spanning

DOI: 10.1201/9781003483755-143

bridge with 1.5 m deep Super-T girders designed for T44 and HLP320 loading (Austroads, 1992). Therefore, it remains to find the appropriate proportion of torsion stiffness that achieves this goal for the entire suite of Super-T girders designs to M1600 loading for ultimate limit state.

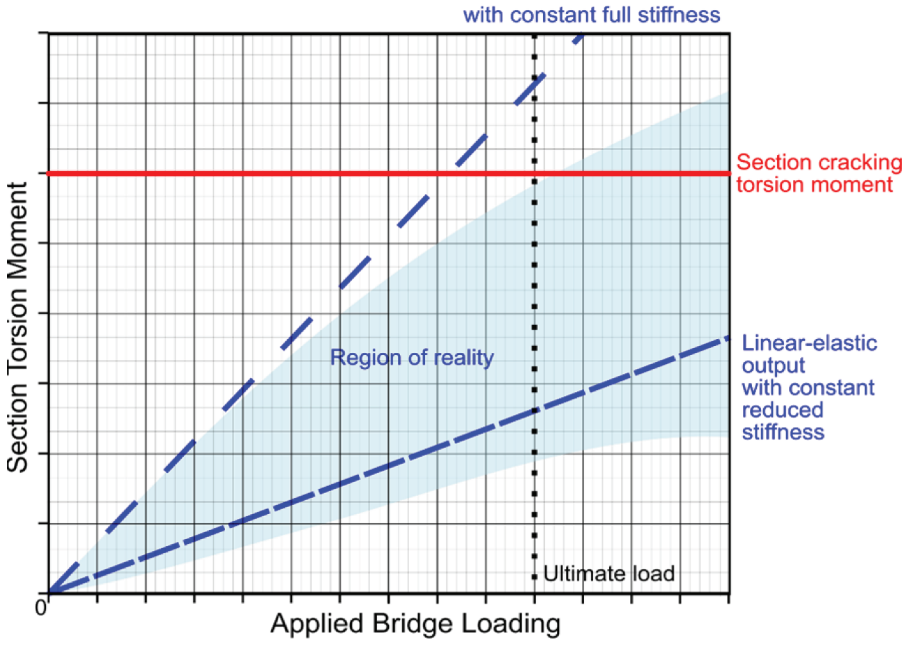


Figure 1. Section torsion moment vs. applied bridge loading in concrete bridge decks is a non-linear phenomenon at ultimate loads (adapted from Collins & Mitchell, 1997).

2 METHODOLOGY

To represent the complete range of designs possible for a standard Super-T girder section, it is necessary to analyze bridge decks with the feasible lower and upper spans of a standard section (Melhem et al., 2019). To investigate the maximum appropriate proportion of torsion stiffness that emulates the non-linear behavior (Figure 1), for each of these $5 \times 2 = 10$ spans:

- Quantify the section cracking torsion moment, T_{cr}, noting the amount of beneficial prestress present.
- Run multiple grillage analysis, each with increasing proportions of torsion stiffness from 0 to 100% of J for the longitudinal members (Super-T girders), for a representative bridge deck and ultimate design loading.

For this, the use of scripting languages (Python) and packages enabled the grillage analysis to be completed quickly and efficiently. The work of this paper feeds of existing freely available open-source packages such as *OpenSeesPy* (Zhu et al., 2018) and *sectionproperties*.

2.1 *Super-T properties*

The Super-T girder properties were directly obtained using *sectionproperties* package. An example stress analysis (principal stresses) output using the packages is shown in Figure 2. The geometry of Super-T sections was chosen as per designations (T1 to T5) with 2.1 m flange width, 75 mm flange depth, and 180 mm overlay slab. The materials chosen for concrete of beam and slab are 65 MPa and 40 MPa respectively.

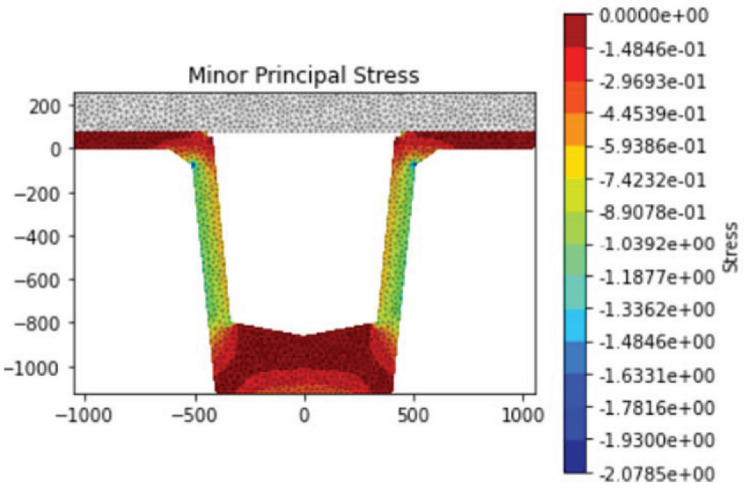


Figure 2. Example output of principal tensile stresses in Super-T girders. (Units in mm and MPa).

2.2 *Torsion cracking resistance*

To quantify the section cracking torsion moment, T_{cr}, an axial load is applied representing prestress following designs by Melhem et al. (2019). 15.2 mm diameter strands are used. Both cases of no debonding and an extreme of 50 % debonding are considered.

Optimization problem is solved to determine the maximum torsion that can be applied to the section under the prestress forces before principal tensile (minor) stresses in the beam reaches the limit of 0.33 $\sqrt{f'_c}$. A total of 10 sections (5 × 2) section cracking torsion moments were calculated.

2.3 *Grillage analysis*

The bridge deck is modelled typically with one carriageway of a dual carriageway road bridge as shown in Figure 3. The bridge deck has zero support skew angle. Super-T girders properties are considered in Section 2.1. The ultimate loading includes dead load – self weight of beams; superimposed dead loads – barrier and asphalt surfacing; and live load of M1600 with dynamic load amplification (DLA) on three design lanes arranged transversely such that Beam 1 (Figure 3) is the most heavily loaded lane.

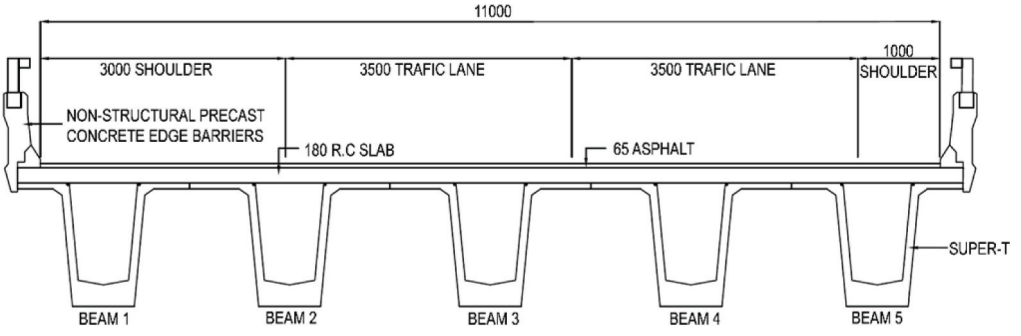


Figure 3. Section torsion moment vs. applied bridge loading in concrete bridge decks is a non-linear phenomenon at ultimate loads (adapted from Collins & Mitchell, 1997).

The torsion constants for the Super-T girders are increased from 0 to 100% at 10% increments – which in turn gives 11 grillage analysis for each of the 10 grillage models. For all grillage analysis, the maximum torsion moment from ultimate loading, T^*, is extracted.

3 RESULTS AND DISCUSSIONS

3.1 *Torsion cracking moments*

Figure 4 and Figure 5 show the torsion moment identified from the grillage analysis of Section 2.3, with the y-axis as ratio of torsion moment, T, for the different torsion constant proportions with the factored cracking torsion moment (ϕ = 0.7). Each figure represents different reductions (extreme cases) in prestress to mimic the likely debonding present in the cracked section. These figures also highlight the suggested locations according to different codes and references where torsion moment should be limited to the cracking moment. These locations are:

- $0.25\phi T_{cr}$ (seen in AS5100.5,2017)
- $0.67\phi T_{cr}$ (seen in Collins & Mitchell, 1997 and Canadian Standards)
- $1.0\phi Tcr$ (seen in ACI Report 445.1R-12)

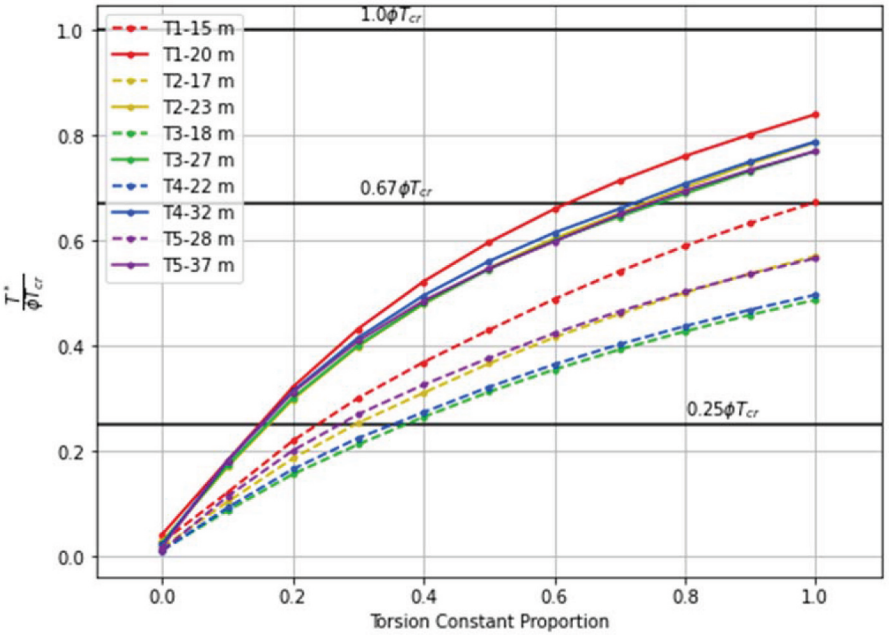


Figure 4. Effect of torsion constant on resulting torsion moments, the full design prestress is applied.

Lastly, the effect of torsion constant variation on maximum bending moment and shear forces are shown in Figure 6 and Figure 7 respectively. The increase in both load effect due to proportional torsion constant, J, is evident and expected since lower torsion constants result in redistribution of torsion moments to longitudinal bending moments and subsequently increases in shear forces.

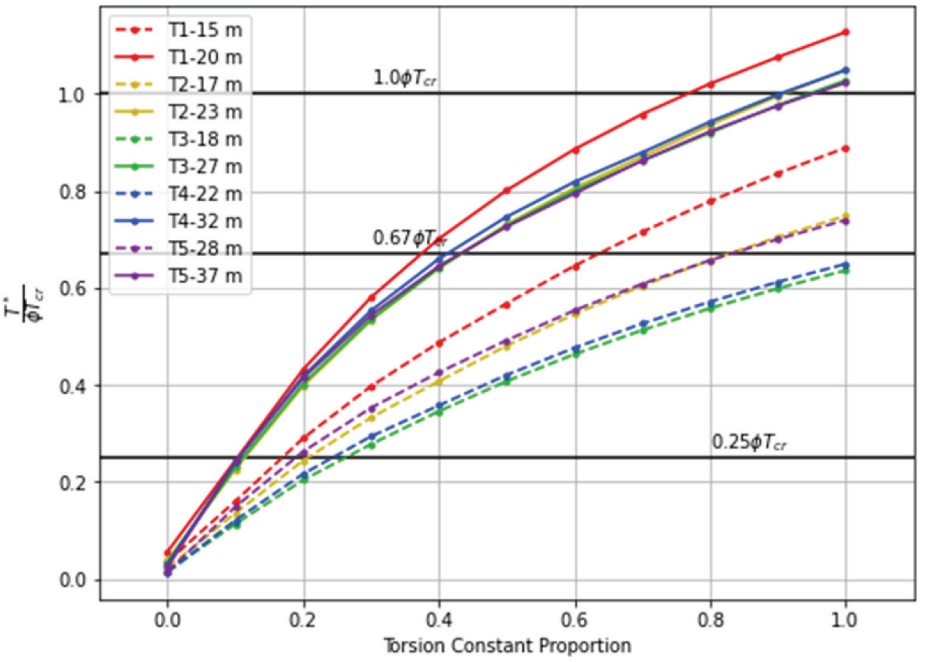


Figure 5. Effect of torsion constant on resulting torsion moments, using an extreme case of 50% prestress debonding.

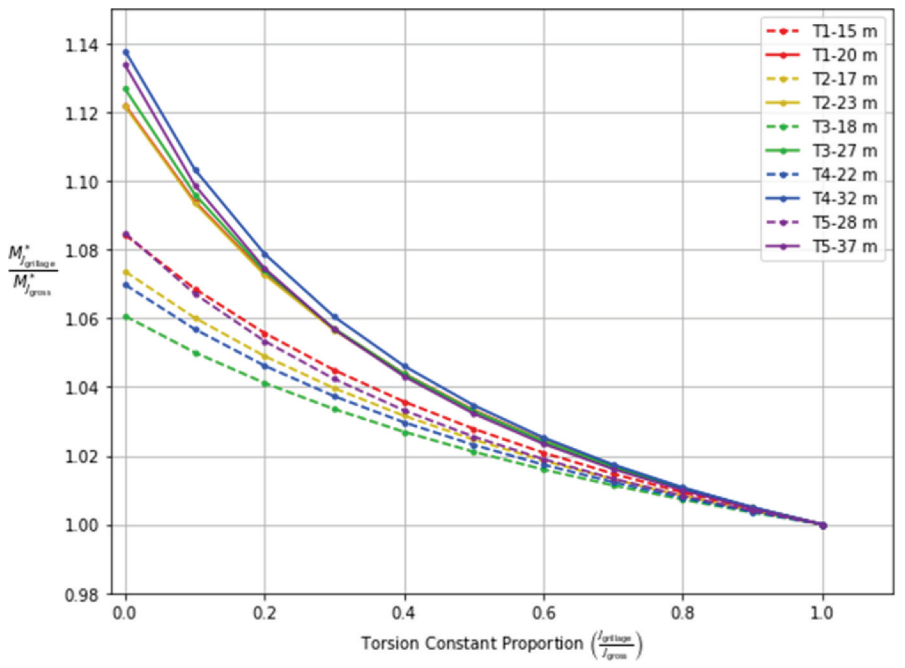


Figure 6. Effect of torsion constant on resulting bending moments.

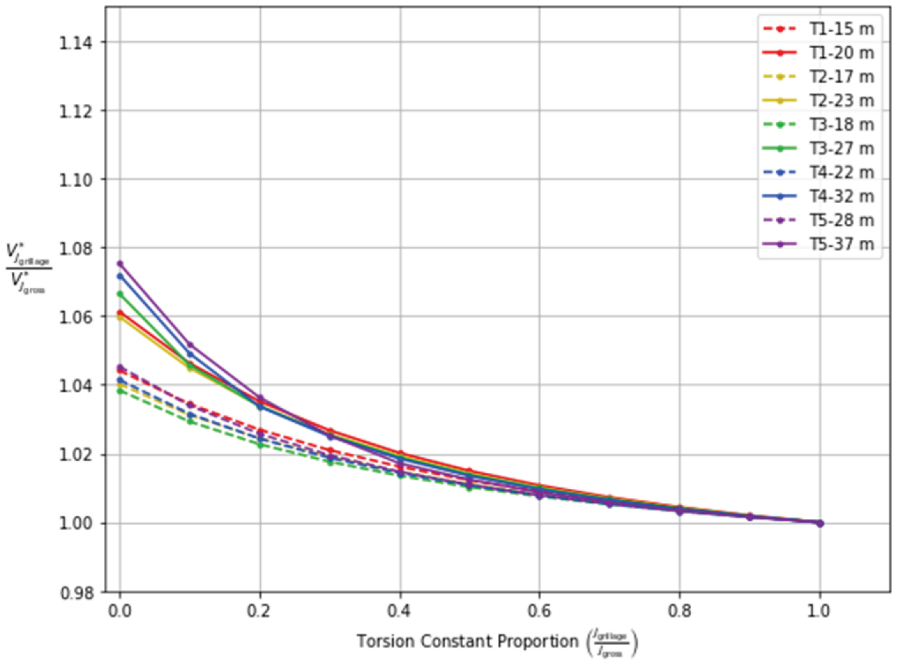


Figure 7. Effect of torsion constant on resulting shear forces.

3.2 *Discussion*

The selection of the appropriate fraction of ϕT_{cr} that should be targeted in selection the proportion of J is not clear. Indeed, the current code seems to target $0.67\phi T_{cr}$, which is simply an empirical limit below which torsion effects can be neglected. It was developed from a study on spandrel beams ultimate (Collins and Mitchell, 1997) and although it has found its way into several codes of practice, its applicability to bridge decks is questionable.

As can be seen from the results, most combinations do not exceed the ϕT_{cr} even for the extreme case of prestress debonding and so redistribution will not occur in most cases. For the 50% prestress debonding case, the limit of $0.67\phi T_{cr}$ is another recommendation that appears, and again the justification is unclear.

If the goal of the torsion constant recommendation is to reduce the need for designers to consider torsion, and the 0.25 limit remains, then a range of 10-40% torsion constant, J, would allow designers find a good balance between the need to design for torsion (based on the redistribution of loads), and minimizing conservatism in longitudinal bending moments. Indeed, as shown in Figure 6, the increases in bending moment for the recommended range of torsion constant proportions is reasonable with a maximum of 10 % increase bending moments.

4 CONCLUSIONS

The onset of cracking at the torsion cracking moment (T_{cr}) limit in Super-T girder bridge decks results in reduced stiffness as loads increase towards the ultimate limit case. In most cases, linear elastic analysis considering full torsion stiffness may not be appropriate for ultimate limit state. In this work, linear-elastic grillage analysis considering a reduced proportion of torsion stiffness is considered to evaluate this phenomenon of overestimating torsion and underestimating moments in grillage models. Based on extensive grillage analysis and Super-T girder combinations, the torsion moment in most Super-T girders considered do not exceed

the torsion cracking moment limit of ϕT_{cr} with $\phi = 0.7$. The results also highlight the questionability of current code limits for torsion cracking moment – future work in needed to re-evaluate these limits. A recommendation of 10-40% proportion of torsion constant, J, will allow designers freedom in torsion design as well as minimizing conservatism in longitudinal bending moments.

REFERENCES

ACI REPORT 445.1 R-12 2013. Report on Torsion in Structural Concrete. Joint ACI-ASCE Committee 445.

AUSTROADS 1992. Austroads Bridge Design Code. Sydney: Austroads.

Collins, M. P. & Mitchell, D. 1997. *Prestressed Concrete Structures*, Response Publications.

Melhem, M. M., Caprani, C. C. & Stewart, M. G. 2019. Reliability of Super-T PSC girders at serviceability limit state stresses across all span ranges. *Structure and Infrastructure Engineering*, 15, 812–821.

STANDARDS AUSTRALIA 2017. Bridge design, Part 5: Concrete. *AS5100.5:2017*

Wyche, J. Shear and Torsion - A Look at Super Ts. 4th Austroad Bridge Conference, 2000 Adelaide, South Australia.

Zhu, M., Mckenna, F. & Scott, M. H. 2018. OpenSeesPy: Python library for the OpenSees finite element framework. *SoftwareX*, 7, 6–11.

Bridge Maintenance, Safety, Management, Digitalization and Sustainability – Jensen, Frangopol & Schmidt (eds)
© 2024 The Author(s), ISBN 978-1-032-77040-6
Open Access: www.taylorfrancis.com, CC BY-NC-ND 4.0 license

Reliability calibration of load factors for the Australian rail traffic load model

Colin C. Caprani & M. Shihabuddin Khan
Monash University, Melbourne, Australia

ABSTRACT: Rail traffic loads in Australia are based on AS5100 Part 2, which stipulates a number of simulated axle groups, including a simulated locomotive, called the 300LA load model. The nominal axle loads and spacings are intended to replicate a heavy-haul rail line. As a result, for light rail, metro rail, and other forms of rail, the nominal axle loads are scaled, e.g. 150LA for light rail. However, the live load factor applied to these different load models remains 1.6 for all cases. It is hypothesized that the application of the same load factor to these different forms of rail live loading will result in inconsistent reliabilities being achieved by designs to AS5100. Therefore this paper examines the achieved reliabilities under current design practice for precast concrete bridges. From these results a revised set of load factors for the different forms of loading will be determined using reliability calibration. These load factors will ensure a more consistent reliability is achieved for designs using scaled versions of the 300LA load model. As such, this work should find use in the next revision of AS5100.

1 INTRODUCTION

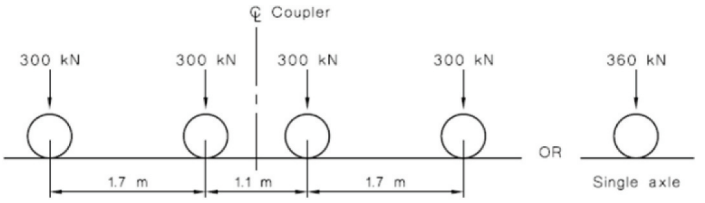
1.1 *Background*

The Australian rail bridge live load model over recent decades is briefly reviewed. From 1974 until 1996, the Cooper M250 load was used. However, in 1996 a Railway Supplement was added to the 1992 Australian Bridge Design Code, developed by the Australasian Railway Association. This addition specified the 300-A-12 rail live load model, shown in Figure 1.

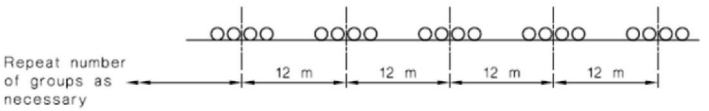
O'Connor and Shaw (2000) outline the background to the development of the 300-A-12 load. In particular it is worth noting that a study by Brameld (1995) examined heavy haul data from major mines in Queensland which had wagons of 90 tonne nominal gross mass. The data shows that the axle loads have a mean of 225 kN and 2% coefficient of variation. From this, Brameld examined the structural reliability of 3 bridges of spans 10, 15, and 25 m in order to determine a suitable live load factor. Three cases were considered, in which the capacity reduction factors and dead load factors were set at 0.8 and 1.2 respectively. The superimposed dead load factor was varied as 2.0, 1.2, and 1.2, and the live load factor varied as 1.6, 1.6, and 1.4, for each of the three cases respectively. In all cases the reliability incidences exceed 6.00, and so Brameld concludes that the live load factor can be 1.4. Indeed, Appendix C of the Stage 4 Final Report By Selby-Smith and Bowman recommends that the 1.4 factor is adequate and even conservative. However, inexplicably, a live load factor of 1.6 was adopted for the 1996 Railway Supplement.

A further development of the 300-A-12 live load model was proposed by Marcer (2002) in recognition that the loading was inadequate for spans around 20 m. In particular, it was proposed to add the 360 kN to simulate coupled six axle locomotives on spans around 15-22 m. The resulting bending moment envelope is stated to better match existing trains. Interestingly, Marcer (2002) notes that this proposal maintains a "20% reserve" to existing trains. That is, it is recognized that the live load model is 20% more onerous than the heaviest (NSW) train. Nevertheless, this model

DOI: 10.1201/9781003483755-144

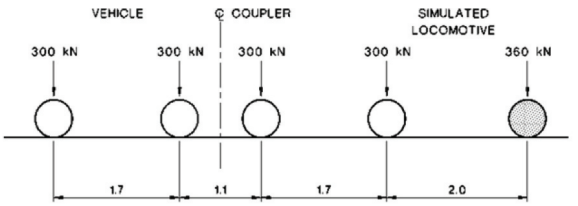


(a) Axle loads;

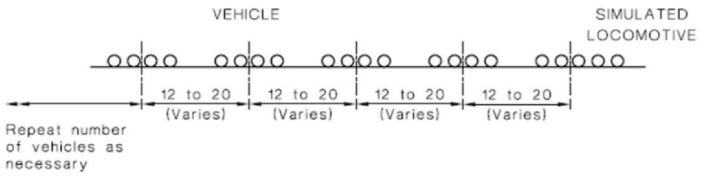


(b) Axle group spacings;

Figure 1. The 1996 300-A-12 rail live load model.



(a) axle loads;



(b) axle group spacings;

Figure 2. The current AS51100.2 300LA load model.

was adopted into the 2004 edition of AS5100 – the Australasian bridge design code, and termed the 300LA load model, shown in Figure 2.

1.2 *Motivation, contribution, and limitations*

Although not included in the 2004 edition of AS5100 Part 2, the 2017 edition added a 150LA load model for light rail, obtained by scaling all axle weights in the 300LA load model by a factor of 0.5. Further, in mid-2023, Amendment 1 of AS5100.2 was published for Public Comment, and also included a 200LA load model for passenger lines. Indeed, the 300LA load model is routinely scaled to achieve designs for railway lines other than heavy haul. For example:

- Metropolitan Trains Melbourne (MTM) specify a 245LA load model for some sections of the broad gauge network in Melbourne (Salandanan et al 2023).
- Metronet in Perth specify a 220LA load model, as suggested by a public comment in response to the proposed Amendment 1 of AS5100.2.

In spite of this scaling of the load model, the live load partial factor remains 1.6 in all cases between 150LA and 300LA. Thus, the question arises as to whether or not consistent safety is achieved for all designs to a scaled version of the 300LA load model.

It is worth noting here an intriguing observation by Brameld (1995): he notes that the live load factor has been established for the heaviest rail loadings but which have much less variability than lighter rail loadings. Consequently he suggests that a sliding load which increases as the basic design load decreases could be suitable. Thus, this work examines the current level of safety achieved by the current Australian railway live lode model specified in AS5100.2. More recent material statistics and probabilistic models are adopted. Based on this, partial factors to achieve a more consistent level of safety are proposed.

In this paper we consider just the ultimate limit states for bending and shear. Furthermore, we consider only precast concrete quality resistance models, as this is a very common form of bridge construction in Australia.

2 METHODOLOGY

2.1 *Design model*

A generic design equation is defined. The equation is normalized, and includes adjustments for the relative contributions of self-weight, G, to total self weight and permanent loads, P, $a_g = G/(G+P)$, and the relative contribution of live, Q, to total load, $a_q = Q/(G+P+Q)$. In particular, $a_g = 1$ means there is no permanent load, and $a_q = 1$ represents the extreme case where there is only live load.

The generic normalized design equation is:

$$\phi z r_k = \left(1 - a_q\right)\left[a_g \gamma_g g_k + \left(1 - a_g\right)\gamma_p p_k\right] + a_q \gamma_q q_k \tag{1}$$

from which the design variable z is found as a multiplier of the normalized characteristic resistance, r_k, for the normalized characteristic self-weight g_k, other permanent loads, p_k, and variable loads, q_k, using the set of partial factors under examination, ϕ for resistance, γ_g for self-weight, γ_p for other permanent loads, and γ_q for variable loads. The partial factors used in the design are taken from those in AS5100 and are shown in Table 1 below.

Table 1. Partial factors used in the designs from AS5100.

Variable	Symbol	Partial Factor
Self-weight	γ_g	1.2
Permanent loads	γ_p	1.7
Variable loads	γ_q	1.6

2.2 *Limit state function*

The limit state function from which the reliability index of the generic design conducted in accordance with Equation (1) can be determined is given by:

$$g(z) = \omega_R z R - \omega_S\left[\left(1 - a_q\right)\left(a_g G + \left(1 - a_g\right)P\right) + a_q Q\right] \tag{2}$$

in which ω_R and ω_S are the model uncertainties for resistance and load effects respectively, and the random variables R, G, P, and Q, correspond to their characteristic values in Equation (1). The First Order Reliability Method (FORM) is used to establish the reliability indices.

2.3 *Probabilistic models*

The probabilistic models used in this work as shown in Table 2. Each of the probabilistic models is described as follows, by their index:

1. As recommended for structural frameworks by JCSS (2000), and so is somewhat conservative for simpler structural forms like simply-supported or continuous beams.
2. As used in Rakoczy and Nowak (2013) for precast components.
3. Per Köhler et al (2023) for low COV permanent load forms (e.g. services).
4. From Brameld (1995): based on a mean axle load of 225 kN and a CoV of 2%.
5. Per Tb. 10 of Foster et al (2016) for the AS3600 moment capacity model.
6. Conservatively based on the relative difference between the "old" and "new" material data in Tb. 6 of Stewart et al (2016) (about 0.03 for bias and 0.05 for CoV) as applied to the results from Melhem et al (2022).
7. Using the Super-T results from Tb. 1-2 of Melhem et al (2020) which used response surfaces from the MCFT software Response2000 to compare with the predictions from the simplified MCFT in AS5100 and AS3600.
8. Based on the AS3600 model but adapted for the relative difference between the "old" and "new" material. data as described in Stewart et al (2016); these are far lower (conservative) than those reported in Agarwal et al (2021).

Table 2. Probabilistic models of the normalized variables parametrized by the bias and coefficient of variation. Note that values are based on a normalized mean of 1.0 for the random variables; i.e. $x_k = 1.0/\lambda$.

No.	Random Variable	Symbol	Distribution	Bias, λ	COV, V	Char. Value, x_k
	Load Models					
1	Actions model	ω_S	Lognormal	1.00	0.10	-
2	Self-weight (precast)	G	Normal	1.03	0.08	0.97
3	Permanent	P	Normal	1.00	0.10	1.00
4	Rail (300LA)	Q	Normal	0.75	0.02	1.33
	Bending					
5	Resistance model	ω_R	Normal	1.06	0.05	-
6	AS5100 Precast	R	Lognormal	1.08	0.08	0.93
	Shear					
7	Resistance model	ω_R	Normal	1.06	0.07	-
8	AS5100	R	Lognormal	1.08	0.07	0.93

2.4 *Models for scaled 300LA loading*

Table 2 (No. 4) shows the statistics for the 300LA model derived from Brameld's background work. However, for scaled versions of the load model, these statistics ought to be amended to reflect that lighter loadings have both more variability (i.e. higher COV) and actual values closer to the nominal (i.e. a small bias). In lieu of more detailed data, the values assumed for this work as shown in Table 3.

Table 3. Probabilistic models of scaled 300LA load models.

Load model	Bias	COV
300LA	0.75	2%
250LA	0.80	4%
200LA	0.85	6%
150LA	0.90	8%

3 RESULTS

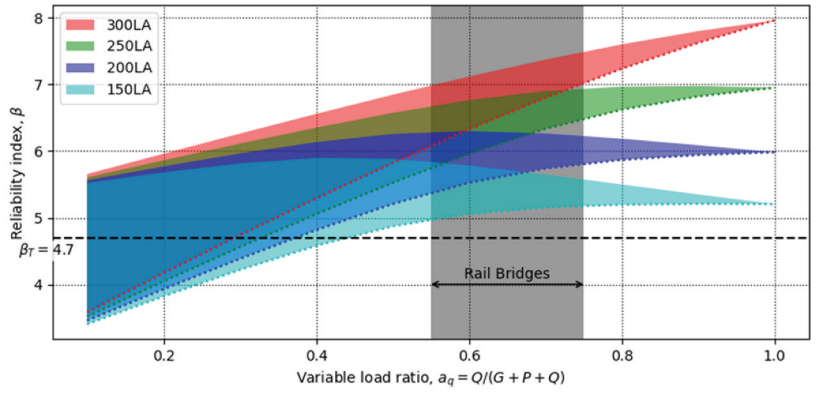
3.1 *Overview*

The actions bending, shear, and axial compression are examined under different load cases across the full range of a_g, and the feasible range of a_q. The typical range of a_q for some bridge types are indicated. The value of a_g = 1 is indicated by a dotted line, and typically occurs at the bottom of the region due to the added safety from the permanent load partial factor.

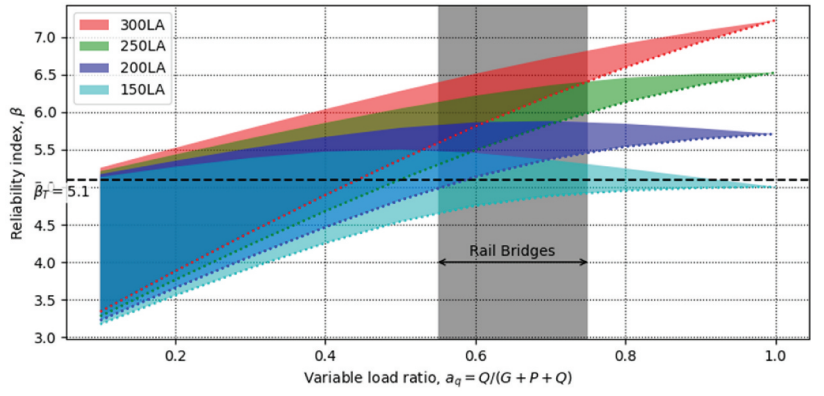
The reliability indices shown are for an annual basis. The targets shown are β_T = 4.7 for ductile failures and β_T = 5.1 for brittle failures. These values were used in the calibration of AS3600 (Foster et al 2016, Stewart et al 2016) and are high by international standards (ISO2394).

3.2 *Current safety*

The current levels of safety achieved by designs to AS5100 for different scalings of the 300LA load model are shown in Figure 3.



(a) Bending;



(b) Shear

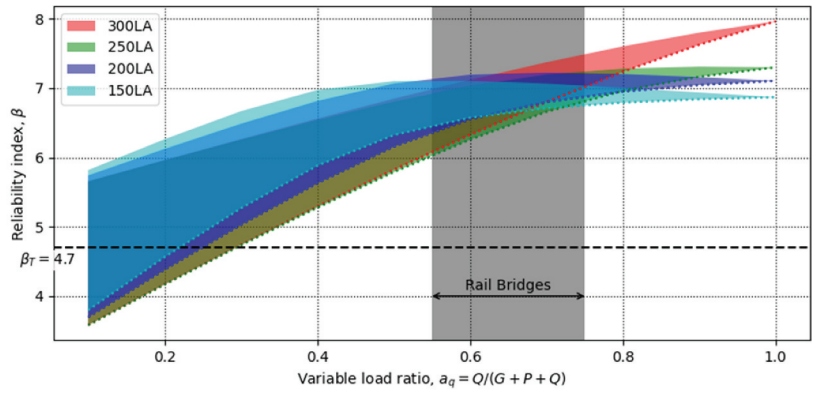
Figure 3. Current levels of safety achieved by precast concrete rail bridge designs to AS5100.

It can be seen from the figure that the different load models achieve very different levels of safety. Notably the safety achieved under ULS bending is extremely high, while that for shear is mostly high. However, there is a proportion of 150LA bridges with relatively low live and dead load ratios ($a_q \approx 0.5$, $a_g > 0.5$) for which the shear design safety is less than the highest international target.

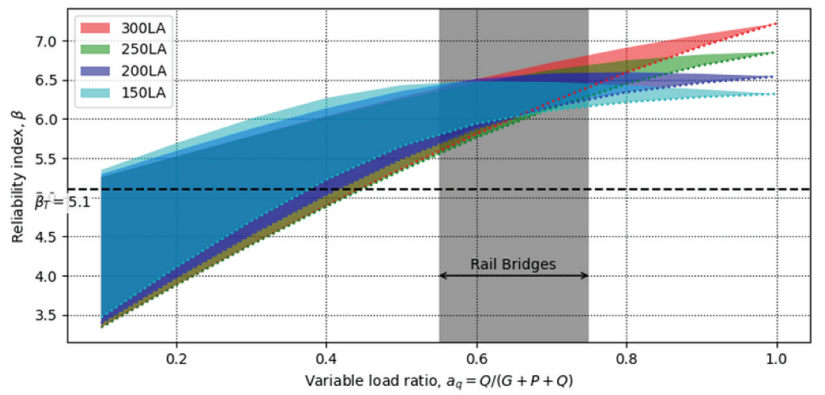
From these results, it is clear that precast concrete rail bridge designs to AS5100 achieve inconsistent levels of safety, depending on the scaling of the 300LA load model.

3.3 *Safety consistent with 300LA*

Considering the results from Figure 3, we postulate that the level of safety achieved by 300LA designs is the implicit target (or acceptable) level of safety for AS5100. Consequently, alternative partial factors are considered to achieve safety consistent with designs to 300LA for the other scaled versions of the load model. These alternative partial factors are given later. This presumes that the 300LA safety is the level sought in the specification of AS5100. The partial factors are adjusted such that in the typical variable load ratio region for rail bridges, each load model mostly exceeds that of the target region. The results are shown in Figure 4.



(a) Bending;



(b) Shear;

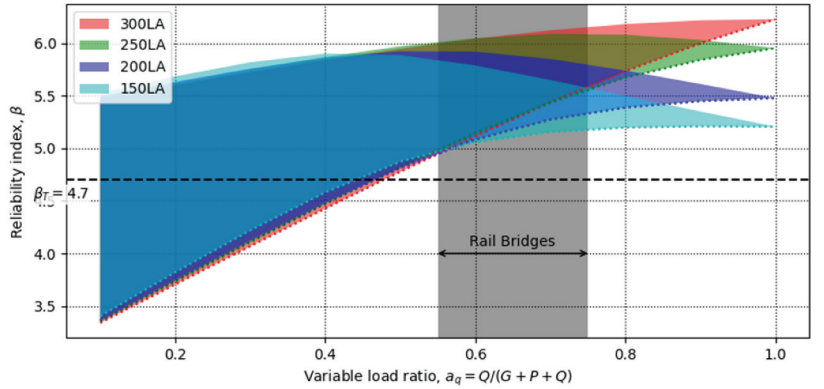
Figure 4. Levels of safety achieved by designs with adjusted partial factors to match 300LA safety.

3.4 *Safety consistent wth 150LA*

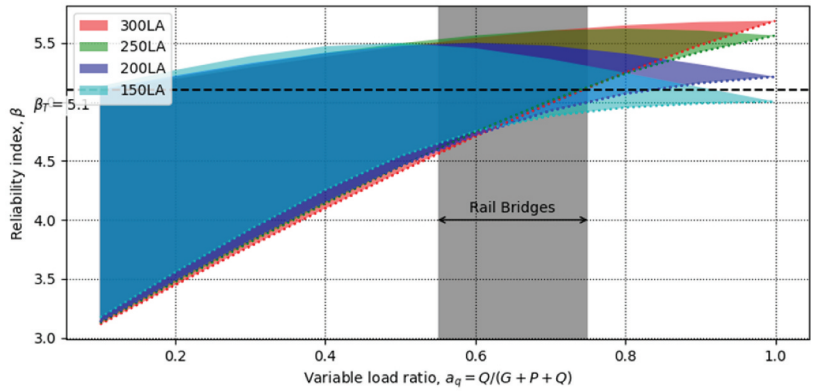
In contrast to Figure 4, and referring to Figure 3 we postulate that alternatively the 150LA safety is that which is implicitly deemed satisfactory by AS5100 (even though there is a portion of shear designs with low permanent load are lower than $\beta_T = 5.1$ as mentioned earlier). Thus, proposing another set of partial factors to match this level of safety yields the results shown in Figure 5.

3.5 *Adjusted partial factors*

The adjusted partial factors found to achieve consistent safety in Figures 4 and 5 are shown in Table 4. The match was achieved through trial and error and visual assessment, ensuring that achieved safeties were typically at least that of the 300LA or 150LA target region.



(a) Bending;



(b) Shear;

Figure 5. Levels of safety achieved by designs with adjusted partial factors to match 150LA safety.

Table 4. Live load partial factors for consistent safety.

	Safety to 300LA		Safety to 150LA	
Load model	Bending	Shear	Bending	Shear
300LA	1.60	1.60	1.25	1.25
250LA	1.70	1.70	1.35	1.35
200LA	2.00	1.90	1.45	1.45
150LA	2.30	2.15	1.60	1.60

4 DISCUSSION AND CONCLUSIONS

4.1 *Discussion*

Although current practice for the design of rail bridges in Australia scales the 300LA load model, the results here show that this results in inconsistent safety being achieved. Indeed, the levels of safety being achieved are extraordinarily high against international standards, but this is to be somewhat expected, as was noted in the background studies to the load model in 1995. Nevertheless, it is not reasonable that public safety should differ depending on the load model, and so a set of partial factors to achieve consistent safety for bending and shear designs are explored. However, the target level of safety could be international practice, the safety achieved

by designs to 300LA, or those for 150LA. Presuming Australasian societal acceptance is that of 300LA or 150LA, these are examined in detail. Perversely, the resulting partial factors for 300LA-consistent safety are either very high (indicating that 300LA safety is too high); or 150LA-consistent safety are too low (indicating that 150LA designs are relatively less safe and more in line with international practice, save for designs with low permanent load, $a_g > 0.5$).

4.2 *Conclusions*

Precast concrete designs to AS5100 achieve very high levels of safety for ULS bending and shear. These designs are not consistent, depending on the scaling of the 300LA load model. The live load partial factor is more reasonably described as a linear scaling akin to:

$$\gamma_q = 1.25 + 0.35(300 - Q)/150 \tag{3}$$

based on the shear and bending results for 150LA-consistent safety in Table 4 and where 300LA ≥ Q ≥ 150LA is the scaled magnitude of the 300LA load model. Nevertheless, more work is required to confirmed this finding for other actions and bridge forms.

REFERENCES

Agarwal, A., Foster, S.J., and Stewart M.G. (2021), "Model Error and Reliability of Reinforced Concrete Beams in Shear Designed According to the Modified Compression Field Theory". Structural Concrete 22, pp. 3711–3726.

Brameld, G. (1995), Austroads/ROA Bridge Design Code: Load Factors and Rating, Report addendum to Appendix C of Stage 4 Final Report to Railways of Australia: Bridge Design Code. Maunsell Pty Ltd Consulting Engineers.

Foster, S.J. et al. "Calibration of Australian Standard AS3600 Concrete Structures: Part I StatisticalAnalysis of Material Properties and Model Error". In: Australian Journal of Structural Engineering 17.4 (2016), pp. 242–253. doi: 10.1080/13287982.2016.1246793.

JCSS. 2001) Probabilistic Model Code – Part 3. Joint Committee on Structural Safety.

Köhler, J., Hingorani, R., and Sørensen, J.D. "Reliability Level of the Second Generation of the Eurocodes – Status and Potential". In: 14th International Conference on Applications of Statistics and Probability in Civil Engineering, ICASP14. Dublin, Ireland, July 2023.

Marcer, J.R. (2002), 'Revised railway provisions of the new bridge design standard', Proceedings of Conference on Railway Engineering, Wollongong, 10-13 November, pp. 281–9.

Melhem, M.M., Caprani, C.C., and Stewart, M.G. (2022), "Reliability updating of partial factors for empirical codes: Application to Super-T PSC girders designs at the ultimate limit state in bending". In: Structures 35, pp. 233–242.

Melhem, M.M. et al. (2020), Bridge Assessment Beyond the AS5100 Deterministic Methodology. Tech. rep. AP-R617-20. ISBN 978-1-925854-95-4. Austroads.

O'Connor, C., Shaw, P. (2000), Bridge Loads: An International Perspective, CRC Press, Boca Raton.

Rakoczy, A.M. and Nowak, A.S. (2013) "Reliability-Based Sensitivity Analysis for Prestressed Concrete Girder Bridges". In: PCI Journal 58.4, pp. 81–92.

Salandanan, J., Slaim, S., Zabihi, A. (2023), 'Rail bridges renewal program', Proceedings of the 11th Australian Small Bridges Conference, 16-7 May, pp. 758–64.

Stewart, M.G. et al. (2016), "Calibration of Australian Standard AS3600 Concrete Structures Part II: Reliability Indices and Changes to Capacity Reduction Factors". In: Australian Journal of Structural Engineering 17.4, pp. 254–266.

Bridge Maintenance, Safety, Management, Digitalization and Sustainability – Jensen, Frangopol & Schmidt (eds)
© 2024 The Author(s), ISBN 978-1-032-77040-6
Open Access: www.taylorfrancis.com, CC BY-NC-ND 4.0 license

Probabilistic updating of characteristic train load for the Little Belt Bridge anno 1935

J.H. Roldsgaard, C. Pedersen & S.T. Nielsen
Monitoring & Analysis of Existing Structures, Transport, Ramboll DK A/S, Denmark

A. O'Connor
Trinity College Dublin, Dublin, Ireland

S.E. Gaardmand
Bridges and Structures, Banedanmark, Denmark

ABSTRACT: This contribution aims to present the application of a probabilistic methodology to update the characteristic train load for the Little Belt Bridge (Lillebæltsbroen), constructed in 1935, in Denmark. On the basis of measurements near the bridge between March 2016 and December 2021 the characteristic train load is updated based upon actual train passages on the structure. This paper presents the basis for this probabilistic analysis which concluded that (i) the theoretical train load determined in 1996 based on the background studies carried out in the 1980s for the Great Belt fixed link was still appropriate and (ii) that the load reduction factor which reflects the joint probability of occurrence of two heavy trains on the bridge also still is appropriate and might even be reduced slightly. The paper presents the basis for the analysis of characteristic loads for an existing structure where recorded loading data is available. It serves as a valuable contribution for bridge owners tasked with the management of existing landmark structures.

1 INTRODUCTION

The Little Belt Bridge, or Lillebæltsbroen in Danish, is a renowned landmark in Denmark, elegantly spanning the Little Belt strait to connect the mainland of Jutland with the island of Funen. The bridge, officially opened in 1935, features a distinctive design, encompassing a graceful arched structure that stretches approximately 1,178 meters across the vibrant waters of the Little Belt. The bridge has undergone renovations and enhancements over the years to adapt to evolving engineering standards and increased traffic demands, ensuring its continued significance as a vital transportation link on the Danish transportation network. In 1996, a comprehensive study was conducted to assess the train load on the bridge. The study focused on analyzing the dynamic effects and forces exerted by trains traversing the bridge, taking into account factors such as speed, weight distribution, and the frequency of train crossings. Instrumentation and monitoring systems were employed to collect data on the actual loads experienced by the bridge during train movements. Being almost 30 years since this study was conducted, it was considered appropriate to assess if the developed loads against which the structure was assessed were still relevant in current conditions. As a result, Ramboll were commissioned by Banedanmark to establish the 'current' characteristic uniform distributed load (UDL) by using up-to-date measurement and registering of actual trains, and subsequently employing stochastic modeling techniques. This paper presents the results of this analysis detailing (i) the collection and statistical assessment of train data, (ii) determination of the characteristic load on the bridge, for single and multiple passages, based upon this data,

DOI: 10.1201/9781003483755-145

(iii) the development of a theoretical model to emulate this load and (iv) finally comparison of the results of the analysis with those of the 1996 study.



Figure 1. Photo of the Little Belt Bridge anno 1935 and layout of the road and rails on the bridge.

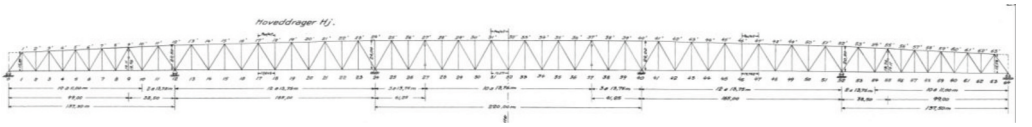


Figure 2. Extract from original drawing of the Little Belt Bridge anno 1935 showing the plan view.

1.1 *Characteristics of the Little Belt Bridge anno 1935*

The Little Belt Bridge anno 1935 as shown in Figure 1 is a riveted truss bridge carrying both two lanes of road traffic, sidewalk for pedestrians and two tracks for railway traffic. The total length of the bridge is 1,178m and with a width of 20.5m, The main steel structure has a total length of 825m divided into 5 spans as shown in Figure 2. The main span is 220m and the clearance 34m. The bridge is the only railway connection between Funen and Jutland, whereas the main road traffic is carried by the nearby cable supported Little Belt Bridge anno 1970. The global statical system of the Little Belt Bridge anno 1935 is described in Schaper (1935).

1.2 *Scope*

This paper presents the main results of a project initialized by Banedanmark, where the overall scope was a re-assessment of the load carrying capacity of the Little Belt Bridge anno 1935. This included determination of the characteristic uniform distributed load (UDL) from measurements/registration of actual trains through stochastic modelling. The stochastic determined characteristic UDL was to be applied instead of the Eurocode load scheme for the re-assessment of the bridge.

For the global system, the critical loading scenario is the uniformly distributed load (UDL) applied over the onerous part of the influence line, while the individual axle loads affect secondary elements.

A representative influence line for the global system is shown in Figure 3. From the figure it can be seen that the influence line is approximately 500m and that the onerous part is approx. 170m, which is approx. the same as the length of the span of 165m (see Figure 2), as positive

values indicates relieving part of the influence line and negative values indicate the onerous part. Hence, a conservative train length of 165m is assumed for the statistical analysis of the characteristic UDL to be used for design checks of the Little Belt Bridge anno 1935.

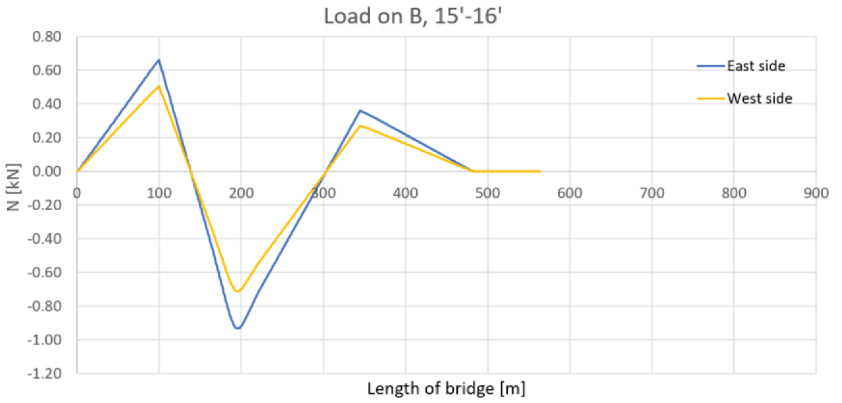


Figure 3. Global influence line of a critical section in the main girder system.

2 DATA

Banedanmark and the Danish Road Directorate are the owner of the Danish Rail Network and serves as the administrator of the Little Belt Bridge from 1935. Banedanmark has put approx. 6 years of rail traffic data for disposal, which contain the following information for all trains passing the measurement station at the city Bred on Funen, see Figure 4.

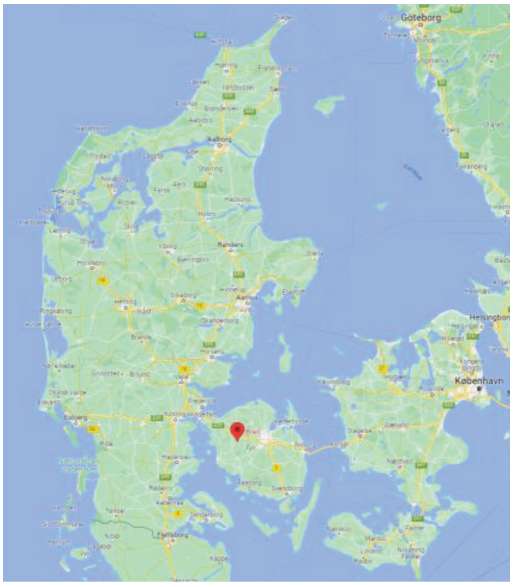


Figure 4. Map of Denmark, where the measurement station Bred on Funen is marked with red.

All trains passing Bred on Funen will also pass the Little Belt Bridge from 1935 hence it is assumed that the data obtained at Bred is directly transferrable for assessment of the Little Belt Bridge from 1935.

The following information is given in the data:

- Unique Train ID
- Timestamp per axle
- Number of axles per wagon
- Weight of each axle
- Speed of the axles (calculated based on timestamp of the axles)
- Direction (Funen-Jutland or Jutland-Funen)
- Average load on the right and left wheel
- Peak load on the right and left wheel
- For some wagons more detailed information is given such as IC3 or IC4 and others are named unknown

The raw data was assessed qualitatively to ensure that the data was applicable, and all the relevant information included.

2.1 *Data assessment*

The UDL for each train is calculated based on the fictive train length of 165m. For trains shorter than 165m it means that the total load of the given train is increased according by dividing with L_{train}/165m. For trains longer than 165m the maximum of a moving average of the UDL is used in the further analyses. Table 1 shows some characteristics of the available data together with the average and the standard deviation of the UDL for a given year and also for the average and standard deviation of the heaviest 730 trains for a given year.

Table 1. Overview of some of the characteristics of the measured/registered train data.

	Year		2016	2017	2018	2019	2020	2021
	Days with data	No.	292	365	365	365	366	365
Eastbound	Trains	No.	25,061	32,763	32,213	30,246	32,358	32,683
	Axles	No.	793,510	1,007,274	978,519	869,130	920,380	857,202
	Average UDL (165 m)	[t/m]	1.55	1.55	1.57	1.54	1.48	1.45
	std. UDL (165 m)	[t/m]	0.94	0.93	0.92	0.91	0.88	0.83
	Average UDL of the 730 heaviest trains (165 m)	[t/m]	4.66	4.94	4.95	4.81	4.58	4.07
	std. UDL of the 730 heaviest trains (165 m)	[t/m]	0.51	0.53	0.55	0.68	0.58	0.43
Westbound	Trains	No.	25,295	33,206	32,974	30,755	18,328*	
	Axles	No.	791,443	1,003,406	977,794	869,615	529,364	
	Average UDL (165 m)	[t/m]	1.55	1.56	1.56	1.54	1.52	
	std. UDL (165 m)	[t/m]	0.95	0.95	0.95	0.82	0.97	
	Average UDL of the 730 heaviest trains (165 m)	[t/m]	4.86	5.33	5.31	5.01	4.66	
	std. UDL of the 730 heaviest trains (165 m)	[t/m]	0.70	0.76	0.82	0.80	0.83	

* Data towards the end of year 2020 for the westbound direction is suspicious, however, it is assessed not to influence the overall conclusions in Rambøll (2023a).

3 CHARACTERISTIC TRAIN LOAD

The characteristic train load for one and two tracks is assessed in the following sections based on the data presented in Section 2. As the load effect is a linear function of the load the two expressions are exchanged without further introduction.

3.1 *Train on one track*

Assuming that the arrival of a train on the bridge follows a Poisson process with an arrival rate of ν_i (number of trains i per year) the annual extreme value distribution of the load effect can be described as (Ditlevsen & Madsen, 1994):

$$F_{max}(x) = \exp(-\nu T(1 - F_s(x)))$$

where T = 1 year and $F_s(x)$ is the cumulative distribution function of the load effect. The characteristic UDL is taken as the 98%-fractile of the annual extreme value distribution.

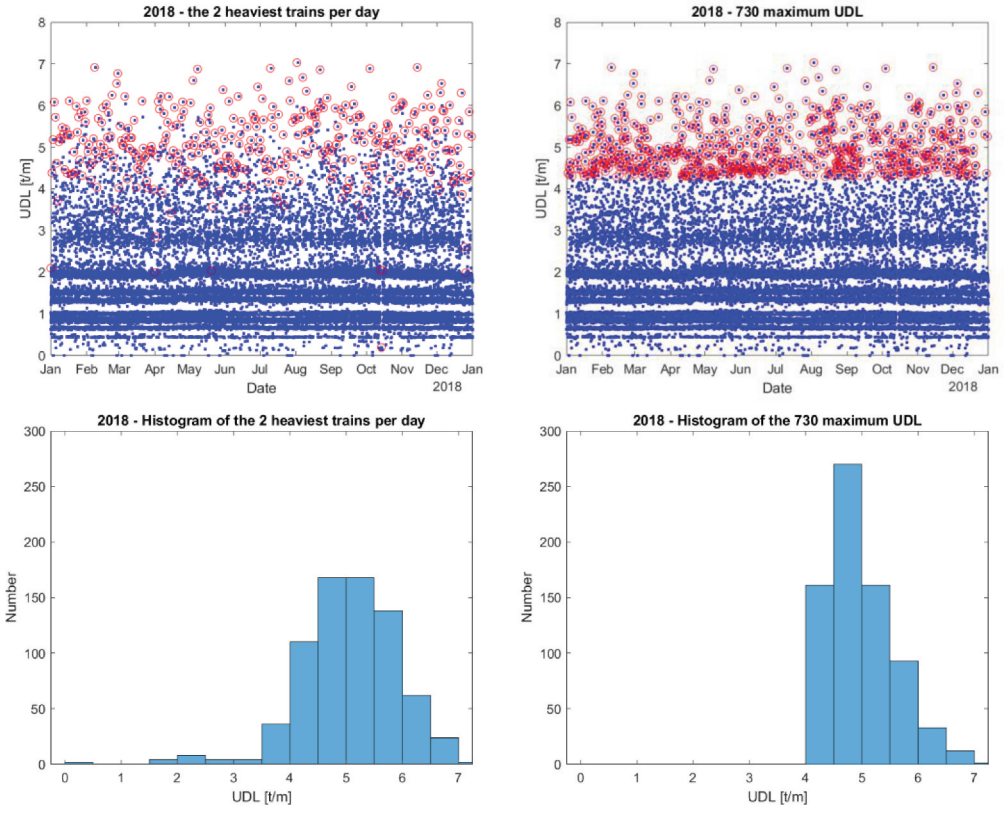


Figure 5. The two figures at the top show the two daily maxima of the UDL (marked with red) and the 730 heaviest train (marked with red) based on UDL independent of the date to the left and right respectively. Below are the associated histograms shown.

For selection of the trains to use for estimation of the extreme value distribution a daily maxima and peak-over-threshold method is used. Figure 5 to the left shows the 2 heaviest (UDL 165m) daily trains and associated histogram, whereas to the right the 730 heaviest train for year 2018 is shown together with the associated histogram. The average UDL changes from 4.68 t/m to 4.95 t/m and the standard deviation of the UDL from 0.89 t/m to 0.55 t/m between the two methods of peak selection. Hence, the characteristic value is larger when choosing the 2 daily maxima as the standard deviation is higher, however, since the load of the bridge in the ultimate limit state is independent on the load history it is assessed to be more appropriate to select the peaks as the 730 heaviest trains per year.

Figures 6 and 7 show the characteristic UDL as function of the number of yearly number of trains accounted for in the extreme value analysis for east- and westbound direction

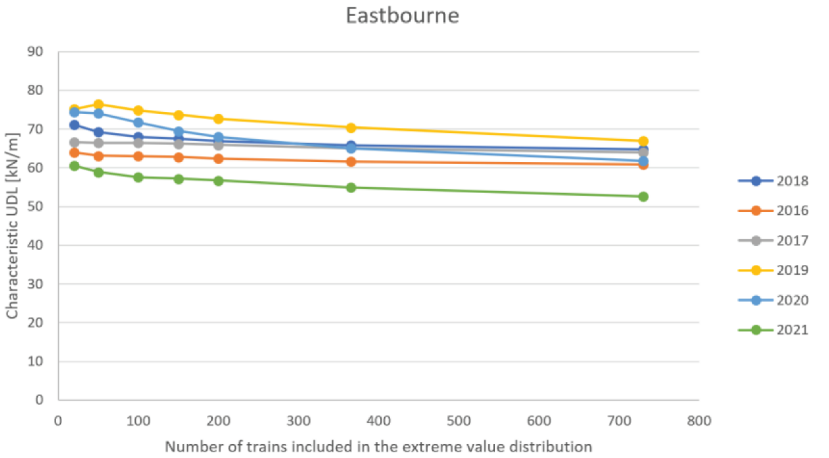


Figure 6. Characteristic UDL based on approx. 6 years of Eastbourne train data for different numbers of maxima included in the extreme value analysis.

respectively. For the eastbound direction a small tendency for the characteristic UDL to decrease with increase of the number of trains included in the extreme value analysis. The characteristic UDL used for earlier re-assessment of the Little Belt Bridge anno 1935 is 72.6 kN/m, hence comparing the values found in Figure 6 with this the characteristic UDL found from the actual measured/registered trains as presented in Section 2 is in general lower.

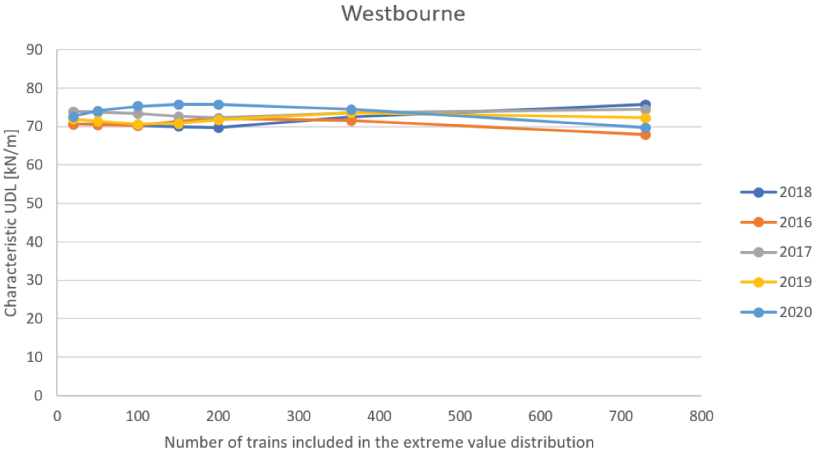


Figure 7. Characteristic UDL based on approx. 5 years of Westbourne train data.

For the westbound direction the same tendency as seen in the eastbound direction is not found. Here it is found that the characteristic UDL is reasonable constant with the number of number of trains selected for the extreme value analysis. In general, the characteristic UDL is higher for the westbound direction than for the eastbound direction. However, overall for the years between 2018-2020 for the westbound direction the characteristic UDL based on measured/registered trains is fairly comparable with the 72.6 kN/m as used in earlier re-assessment – spanning between 69.7 kN/m to 75.8 kN/m.

3.2 *Trains on two tracks*

Again, it is assumed that the arrival of one train follows a Poisson process, it is furthermore assumed that arrival of two trains simultaneously follows a Poisson process. This is seen as

a reasonable assumption as the passage of a train on the bridge is below 1 minute, which blurry the effect from timetables.

The annual extreme value distribution of the load effect of two trains simultaneously on the bridge can be given as (Ditlevsen & Madsen, 1994):

$$F_{max}(x) = \exp(-\nu_{12} T(1 - F_s(x)))$$

where ν_{12} is the yearly arrival rate of two heavy trains on the bridge simultaneously determined by:

$$\nu_{12} = \nu_1 \nu_2 (d_1 + d_2) \frac{24}{12}$$

where ν_1 and ν_2 is the speed of the train in the east- and westbound direction and the d_1 and d_2 is the duration of the load effect from passage of a train in track one and two respectively.

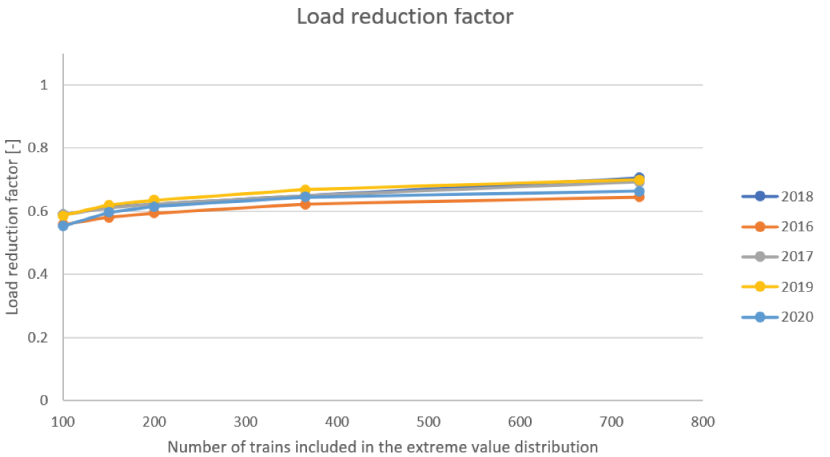


Figure 8. Load reduction factor as function of number of trains included in the extreme value distribution.

The load reduction factor with simultaneously trains on both tracks used in the re-assessment of the global load effects is determined based on measured/registered data and shown in Figure 7. Here it is seen that for between 200 to 730 heavy trains per year in the extreme value distribution that the load reduction factor is about 0.60-0.71, which is comparable with the 0,77 used in earlier re-assessment by Rambøll, however, still lower. Reading Figure 5 and 7 together it seen that the characteristic load decreases with the number of trains accounted for the in the extreme value analysis, whereas the reduction factor increases, hence the total load is approximately constant and independent on the number of trains used for the extreme value analysis.

4 THEORETICAL MODEL

In 1996 the Little Belt Bridge anno 1935 was re-assessed in both ultimate and fatigue limit state (ULS and FLS) (COWI 1996). In association with this re-assessment the characteristic UDL was assessed based on a theoretical train load model created for the Great Belt Link, the basis for the train load model is given in Table 2. The Great Belt Link is located on the same stretch as the Little Belt Bridge anno 1935. Some of the freight trains passing the measuring station at Bred on Funen might unload or load at Funen, hence not fully representative of the train load passing the Great Belt Link. However, this is assessed to be a minor change in the train load and the measured/registered data is assessed to be fairly representative for trains passing the Great Belt Link as well.

The characteristic UDL and load reduction factor on the basis of the data shown in Table 2 is calculated as described in Section 3. The results are shown in Table 3.

Table 2. Background parameters for the train load model used for the design of the Great Belt Link.

	Average Axle Weight [t]	Std. Axle Weight [t]	Average UDL [t/m]	Std. UDL [t/m]
Eastbound	19.4	2.1	6.45	0.20
Westbound	19.4	2.1	6.45	0.20

Table 3. Results based on the theoretical model for the Great Belt Link.

Trains per track per day	Characteristic UDL [kN/m]	Load reduction factor
2	72.6	0.77
4	72.9	0.81
10	73.3	0.83

The results of above presented theoretical analysis is comparable with the results of the analysis of the characteristic UDL and load reduction factor based on measured/registered data of trains passing the Little Belt Bridge anno 1935. This means that the theoretical model established for the design of the Great Belt Link to a large extent is representative for global load effects with same order of magnitude as for the Little Belt Bridge anno 1935 and the West Bridge of the Great Belt passing.

5 CONCLUSIONS

Based on measured/registered data of actual trains at Bred on Funen in Denmark close to the Little Belt Bridge anno 1935 the characteristic uniform distributed load (UDL) is found in the above analysis. The results of the analysis are comparable with the results of the theoretical train load model based on train characteristics made for the design of the Great Belt Bridge. The approach for reaching this result was a qualitative rough assessment of the raw data to ensure applicability of the data. The assumptions around the stochastic modelling of the train load from previously re-assessment were re-visited and found applicable hence, also used in the most recent re-assessment of the Little Belt Bridge anno 1935. This included modelling of the global influence length, moving average evaluation of all train passage together with extreme value selection and comparison of the effect on the characteristic values by choosing 2 daily maxima or the 730 heaviest trains per year.

This means that the characteristic UDL of 72.6 kN/m and a load reduction factor of 0.77 for simultaneously trains on two tracks are still applicable and have been used in the most recent re-assessment of the Little Belt Bridge anno 1935, proving that the theoretical train load model developed for the design of the Great Belt Bridge was a close approximation of the future train load.

REFERENCES

COWI, 1996. Bæreevne- og levetidsvurdering af Lillebæltsbroen af 1935. Revision 0.

Ditlevsen, O. & Madsen, H.O. 1994, Stochastic vehicle-queue-load model for large brigdes, Journal of Engineering Mechanics 120 (9): 1829–1847

Ditlevsen, O. & Madsen, H.O. 2007. Structural reliability Methods. Internet edition 2 3..7, http://www.od-website.dk//index-2.html/books.htm.

Rambøll, 2023a. Lillebæltsbroen af 1935 sandsynlighedsbaseret opdatering af ULS. Revision 0.

Schaper, G. 1935. Die Brücke über den Kleinen Belt. In zeitschrift des vereines deutscher ingenieure, Nr. 19, page 563–568 11. Mai 1935.

Bridge Maintenance, Safety, Management, Digitalization and Sustainability – Jensen, Frangopol & Schmidt (eds)
© 2024 The Author(s), ISBN 978-1-032-77040-6
Open Access: www.taylorfrancis.com, CC BY-NC-ND 4.0 license

Influence of the correlation of GVWs in the simulation of vehicle spatial distribution of extreme effects in long-span bridges

X. Wang
Department of Bridge Engineering, Tongji University, Shanghai, China
Department of Civil and Environmental Engineering, Universitat Politècnica de Catalunya (UPC-BarcelonaTech), Barcelona, Spain

X. Ruan
Department of Bridge Engineering, Tongji University, Shanghai, China

J.R. Casas
Department of Civil and Environmental Engineering, Universitat Politècnica de Catalunya (UPC-BarcelonaTech), Barcelona, Spain

M. Zhang
College of Civil and Transportation Engineering, Shenzhen University, Shenzhen, China

ABSTRACT: Compared to small and medium-span bridges, long-span bridges have longer loading spaces and more complex extreme response value scenarios. It is shown that the phenomena of heavy vehicle aggregation and heavy vehicle queuing are important factors affecting the response extremes of long-span bridges both in congested and free flow traffic situations. Therefore, is necessary to study the correlation between heavy vehicle weights for extreme response value scenarios in long-span bridges. Based on previous studies, this paper analyzes and demonstrates in detail the necessity to account for the correlation between vehicle weights when considering extreme response value scenarios, and proposes a methodology for its modeling. It is concluded that a correlation length of 100 meters is recommended, and that for the most extreme response scenarios involving long-span bridges, it is necessary to re-evaluate the correlation between GVWs.

1 INTRODUCTION

The traffic load is one of the most important variable actions for the accurate design and assessment of existing bridges. Due to the spatial and temporal high randomness and variability on the weights of vehicles, there are massive feasible loading scenarios during bridge operation. Therefore, it is challenging to model all of the actual values of traffic load on bridges in a deterministic way. Probabilistic concepts should be employed to consider the numerous sources of uncertainty in the traffic modeling.

Numerous studies have been already devoted to the study of traffic load effects in long-span bridges. Because the corresponding dominating traffic distribution scenarios are notably distinct, the responses to the traffic load of bridges with long-loaded lengths are different from those with medium or small-loaded lengths (Caprani 2013, O'Brien et al. 2012, Caprani et al. 2008, Chen & Cai 2007). The traffic load of long-span bridges is governed by high-volume traffic or congestion. Because the span is long and there are numerous vehicles on several lanes, the influence of groups of trucks is important for their structural assessment (Chen & Wu 2011, Xu et al. 2012). Due to the characteristics of influence lines of short and medium-span bridges, the

DOI: 10.1201/9781003483755-146

maximum response of multi-lane bridges with spans less than 60 m is determined by a single heavy truck, two trucks side-by-side, or two trucks following in the same lane for continuous spans (Soriano et al. 2017). Meanwhile, the research of Caprani et al. (2008) shows that it is not realistic to believe that two truck events drive the design of short to medium-span bridges. Clearly, four truck events play an important role (Caprani et al. 2008). Comparatively, long-span bridges have more diverse and complicated extreme response scenarios.

Based on the long-term WIM data and congestion situation, Hwang & Kim (2019) proposed a multi-lane load model for long-span bridges and found that the load effect by the proposed congested model shows comparable values to AASHTO LRFD or Honshu-Shikoku bridge design code. Guo & Caprani (2019) focused on load patterning on long-span bridges and proposed a rational and practical load patterning method based on both congested and free-flow traffic. They suggested that the design traffic load model for long-span bridges can be obtained by reducing traffic load levels currently specified in the codes. However, the above studies are mainly concerned with the extreme load effects for long-span bridges, while the vehicle scenarios that cause these extreme response values are also of interest.

Indeed, previous traffic load models have shortcomings when it comes to representing the complicated spatial distribution of traffic loads on the bridge deck quantitatively. Actually, the probability of the spatial distribution pattern of vehicles on a bridge deck with long-span provoking maximum load effects is vital for assessing bridge safety and also helps to understand the performance of bridges under vehicle loads. During the period of operation, the formation of platoons, which is the grouping of heavy vehicles, may pose a significant threat to the safety of long-span bridges. The proportion of heavy vehicles in the traffic flow is more critical to the structural effect than the traffic flow itself (Lipari et al. 2017). Various spatial patterns of vehicle distribution will induce varying load effects, according to the influence line/surface of the considered effect. At the same time, the traditional simulation method only focuses on simulating traffic flow and ignores extreme response scenarios. This makes it a low efficient and highly costly method, particularly when calculating extreme responses over long reference periods.

Considering the limitation of traditional vehicle load models in spatial distribution modeling, Chen et al. (2019) proposed a probabilistic approach for modeling the spatial distribution of heavy vehicles for long-span bridges by utilizing an undirected graphical method. Wang et al. (2024) proposed a probabilistic model to describe the heavy vehicle distribution on the bridge deck when extreme response is obtained. In the presented model, the heavy vehicle concentration phenomenon was described by considering the correlation relationship between the adjacent gross vehicle weights (GVWs).

In this paper, based on the probabilistic model for vehicle scenarios leading to extreme load effects proposed in the research of Wang et al. (2024), the necessity and methodology of considering the correlation of GVWs in the simulation of vehicle spatial distribution is further discussed. The paper is structured as follows: Chapter 2 presents discussions on the reason for assuming a correlation between GVWs and the method to consider its level. Chapter 3 gives the results and discussions obtained by different levels of correlation for some selected load effects. The main conclusions of this study are summarized in Chapter 4.

2 CORRELATION BETWEEN ADJACENT GVWS

2.1 *The reason for assuming a correlation between GVWs*

According to previous research, it is accepted that there is a correlation between GVWs of the same lane and adjacent lanes in a multi-lane highway. Nowak (1993, 1995) investigated three values of GVW correlation for trucks in the same lane and adjacent lanes: $\rho = 0$ (no correlation), $\rho = 0.5$ (partial correlation), and $\rho = 1$ (full correlation), where ρ is the Pearson correlation coefficient. Based on simulations, the full correlation of truck GVWs was concluded to govern two-lane traffic loading and was also validated through site observations in the US. More recently, in a comprehensive traffic loading study, O'Brien & Enright (2011) found there were correlations between the GVWs of successive

trucks from WIM data in the EU and the inter-lane truck GVWs were also correlated based on the inter-lane gap. These correlations resulted in an increase of up to 8% in lifetime maximum loading. Zhou et al. (2018) found that the GVW of successive trucks is correlated and that the autocorrelation coefficient for two accompanying trucks with a time gap below 5 seconds is 5%.

Based on the above research, a correlation length in the autocorrelation function for GVWs is assumed in the proposed model. It should be noted that the proposed model is seeking scenarios that can produce extreme load responses, therefore, the correlation between the GVWs within a certain range must be more pronounced (i.e., scenarios with high correlations are more likely to produce extreme responses).

The maximum response of bridges with spans less than 60 m is determined by a single heavy truck, two trucks side-by-side, or two trucks following in the same lane for continuous spans (Chen & Wu 2011). Comparatively, long-span bridges have more diverse extreme response scenarios, and the influence of platooning becomes more important (Soriano et al. 2017, Hwang & Kim 2019). Thus, as the length of the loaded part contributing to the structural response (the so-called load length) increases, the governing scenario necessarily contains more heavy vehicles (e.g., all heavy vehicles within 200 meters make a non-negligible contribution to the extremes). In summary, the correlation between several GVWs must be reconsidered for the extreme response scenarios for long-span bridges.

Meanwhile, the gap assumption in traffic flow, especially in congested traffic, is very important and can make a huge difference to the result (Micu et al. 2019). To develop a model for scenarios of extreme LE, it is necessary to develop a spatial distribution model of heavy vehicles on the bridge deck. To resolve the modeling of vehicle location on the bridge deck, the bridge deck is divided into several cells according to the lane and specific constant cell length, dl. dl is determined according to the statistical data of the length of heavy vehicles. According to Chen et al. (2019), the average length of large vehicles is 15.13 m. Based on the measured WIM data, the total wheelbase (i.e., the distance from the first axle to the last axle) of the multi-axle vehicle shows a peak value of 17.5 m. Considering the influences of the front and rear overhang of the heavy vehicle, and the gap between the vehicles while driving, the length of the cell should be slightly longer than the wheelbase. Therefore, the length of the cells is taken as 20 m.

2.2 *How to consider the correlation level*

Several consecutive trucks in one lane or side-by-side trucks in adjacent lanes are the critical scenarios causing the extreme load effect, threatening the safety of bridge structures. The governing loading combination for long-loading length is always several groups of trucks and numerous on-bridge vehicles, not several side-by-side trucks or several following trucks. Therefore, in the proposed model it is assumed that there is a two-by-two correlation between the GVWs of all vehicles within a certain length of the same lane for scenarios of maximum-response-per-day event, rather than simply assuming a correlation between the GVWs of two key heavy vehicles. However, GVWs in vehicle sequences generated merely by Monte-Carlo simulation are independent of each other (Zhou et al. 2018). Therefore, Nataf transformation was employed to consider the correlation between GVWs as explained below.

The objective of setting the correlation parameters is to describe the correlation between GVWs within a certain length in the same lane for the proposed scenarios, which is reflected by the correlation function. The Pearson coefficient of correlation is adopted to characterize the correlation of GVW as expressed in Equation (1):

$$\rho_{j,k} = \frac{\alpha_{j,k}}{\lambda_j \cdot \lambda_k}, \tag{1}$$

where $\rho_{j,\,k}$ represents the coefficient of correlation between the GVW of locations l_j and l_k (i.e., the distance between j and k is short), $\alpha_{j,\,k}$ corresponds to the covariance between the GVWs, λ_j

and λ_k indicate the standard deviations of the GVWs at l_j and l_k, respectively. It is common sense that the correlation coefficient $\rho_{j,\ k}$ between two GVWs becomes weaker with increasing distance lag, $|\ l_j - l_k\ |$. Referring to engineering cases in related research, the following exponential correlation function is employed (Li & Zhang 2016, Mahadevan & Haldar 1991):

$$\rho_{j,k}\ = \exp\left(-\frac{\left|l_j - l_k\right|}{D}\right), \tag{2}$$

where D represents the scale factor reflecting the correlation length. Considering a cell the space occupied by a heavy truck (a value of 20 m is considered here), for instance, if $|\ l_j - l_k\ |$ takes the value of one centroid interval of adjacent cells (which means $|\ l_j - l_k\ | = 20$ m), then, $\rho_{j,\ k} = 0.3679$, 0.6703, and 0.8187 when D is 20 m, 50 m, and 100 m respectively (i.e., $\rho_{j,k}\ = \exp\left(-\frac{20}{20}\right) = 0.3679, \quad \rho_{j,k}\ = \exp\left(-\frac{20}{50}\right) = 0.6703, \quad \rho_{j,k}\ = \exp\left(-\frac{20}{100}\right) = 0.8187$).

Nataf transformation can be used to transfer any random variables into standard Gaussian distribution (Zhao et al. 2020). The marginal cumulative density functions (CDF) of an n-dimensional correlated random vector $\vec{\beta} = [\beta_1,\ \beta_2, \ldots, \beta_n]$ is $F_j(\beta_j)$, and the correlation coefficient matrix $K = \left[\mathrm{K}_{j,k} = \kappa_{j,k}\right]$. By Nataf transformation, $\vec{\beta}$ can be transferred into independent standard normal variables $\vec{\zeta} = \left[\zeta_j\right]$. The procedure of Nataf transformation is as follows (Der Kiureghian & Liu 1986):

Correlated standard normal variables $\vec{\xi} = \left[\xi_j\right]$ are transferred from $\vec{\beta}$ by Equation (3).

$$\xi_j = \Phi^{-1}\left(F_j\left(\beta_j\right)\right) \tag{3}$$

where $\Phi^{-\ 1}(\cdot)$ is the inverse CDF of standard Gaussian distribution. The correlation coefficient matrix of $\vec{\xi}$ is supposed as $K' = \left[\kappa'_{j,k}\right]$. Then the relationship between $\kappa_{j,k}$ and $\kappa'_{j,k}$ is shown as Equation (4).

$$\kappa_{j,k} = \int_{-\infty}^{\infty}\int_{-\infty}^{\infty}\frac{F_j^{-1}\left(\Phi\left(\beta_j\right)\right) - E\left(\beta_j\right)}{SD\left(\beta_j\right)}\cdot\frac{F_k^{-1}(\Phi(\beta_k)) - E(\beta_k)}{SD(\beta_k)}\omega\left(\beta_j,\beta_k;\kappa'_{j,k}\right)d\beta_j d\beta_k \tag{4}$$

where $\omega\left(\beta_j,\beta_k;\kappa'_{j,k}\right)$ is given by Equation (5), $E(\cdot)$ and $SD(\cdot)$ are the mean and standard deviation of variables, respectively.

$$\omega\left(\beta_j,\beta_k;\kappa'_{j,k}\right) = \frac{1}{2\pi\sqrt{1-\kappa'^2_{j,k}}}exp\left\{-\frac{\beta_j^2 - 2\kappa'_{j,k}\beta_j\beta_k + \beta_k^2}{2\left(1-\kappa'^2_{j,k}\right)}\right\} \tag{5}$$

According to Equations (4) and (5), $\kappa'_{j,k}$ can be calculated by $\kappa_{j,k}$. The relationship between $\kappa_{j,k}$ and $\kappa'_{j,k}$ can be simplified as Equation (6). $P_{j,k}$ can be approximately estimated by a polynomial as Equation (7).

$$\kappa'_{j,k} = P_{j,k}\cdot\kappa_{j,k} \tag{6}$$

$$P_{j,k} = \frac{\kappa'_{j,k}}{\kappa_{j,k}} = p_1\kappa_{j,k}^3 + p_2\kappa_{j,k}^2 + p_3\kappa_{j,k} + p_4 \tag{7}$$

where the parameters p_1 to p_4 can be calculated by the Monte Carlo method.

Since the covariance matrix of $\vec{\xi}$ is positive definite, $\mathbf{K}'$ can be decomposed into a lower and an upper triangular matrix via Cholesky factorization as shown in Equation (8):

$$\mathrm{K}' = \mathrm{A}\cdot\mathrm{A}^{\mathrm{T}} = \begin{bmatrix} a_{11} & 0 & \cdots & 0 \\ a_{12} & a_{22} & \cdots & 0 \\ \vdots & \vdots & & \vdots \\ a_{1n} & a_{2n} & \cdots & a_{nn} \end{bmatrix}\begin{bmatrix} a_{11} & a_{12} & \cdots & a_{1n} \\ 0 & a_{22} & \cdots & a_{2n} \\ \vdots & \vdots & & \vdots \\ 0 & 0 & \cdots & a_{nn} \end{bmatrix} = \begin{bmatrix} 1 & \kappa'_{12} & \cdots & \kappa'_{1n} \\ \kappa'_{12} & 1 & \cdots & \kappa'_{2n} \\ \vdots & \vdots & \ddots & \vdots \\ \kappa'_{1n} & \kappa'_{2n} & \cdots & 1 \end{bmatrix} \tag{8}$$

where **A** is a lower triangular matrix. Therefore, the variables $\vec{\xi}$ can be expressed as the product of **A** and the independent standard normal variables $\vec{\zeta}$, as shown in Equation (9):

$$\vec{\xi} = \mathbf{A} \cdot \vec{\zeta} \tag{9}$$

Then the relationship of the independent standard normal variables $\vec{\zeta}$ and the original correlated variables $\vec{\beta}$ can be established as Equation (10):

$$\begin{aligned} \beta_1 &= F_1^{-1}(\Phi(a_{11}\zeta_1)) \\ \beta_2 &= F_2^{-1}(\Phi(a_{21}\zeta_1 + a_{22}\zeta_2)) \\ &\vdots \\ \beta_n &= F_n^{-1}(\Phi(a_{n1}\zeta_1 + a_{n2}\zeta_2 + \cdots + a_{nn}\zeta_n)) \end{aligned} \tag{10}$$

where $\Phi(\cdot)$ is the CDF of standard Gaussian distribution. Then, the Monte Carlo method is used to analyze the scenarios of extreme load effect, in which the correlated GVWs are simulated according to Equation (10).

2.3 *The immeasurability of the correlation parameters*

Taking a correlation length of 100 m as an example, Figure 1 depicts the GVW correlation between the first heavy vehicle (the red one) and other simulated heavy vehicles with a possible presence in the same lane. In the figure, it can be seen that the correlation between simulated GVWs based on the Nataf method becomes smaller as the distance increases. In Figure 1, the correlation length in the Nataf simulation is 100 m and it can be seen that when the distance between the trucks is 100 m, the correlation between the GVWs of the two vehicles is 0.3679. When the distance is greater than 120 m, the correlation between the GVWs of the two vehicles is basically less than 0.3 (i.e., a weaker correlation).

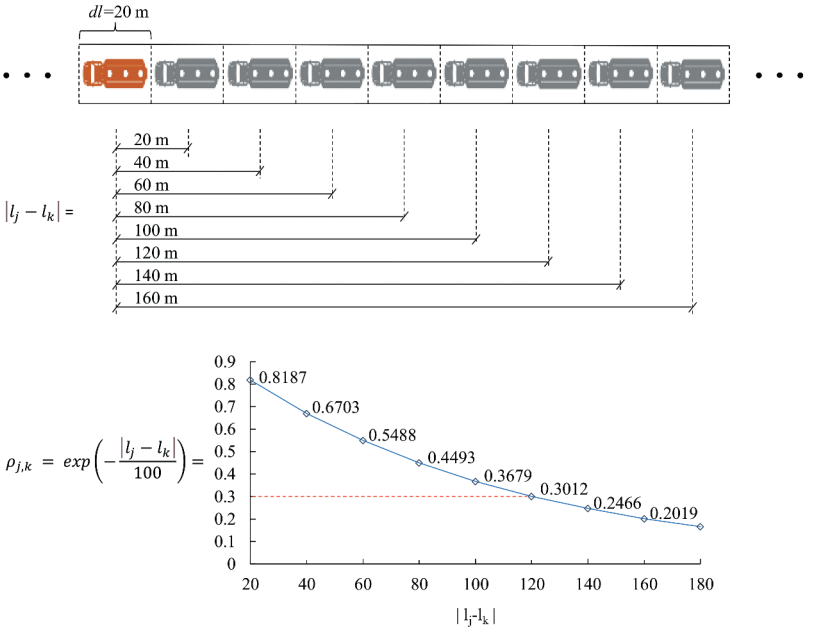


Figure 1. The correlation between the GVWs of simulated heavy vehicles for D=100 m.

Based on the above description, the larger the correlation length D, the higher the level of correlation of GVWs between heavy vehicles in the lane. Therefore, the value of D has an important influence in the correlation between GVWs and, at the end, in the loading effects.

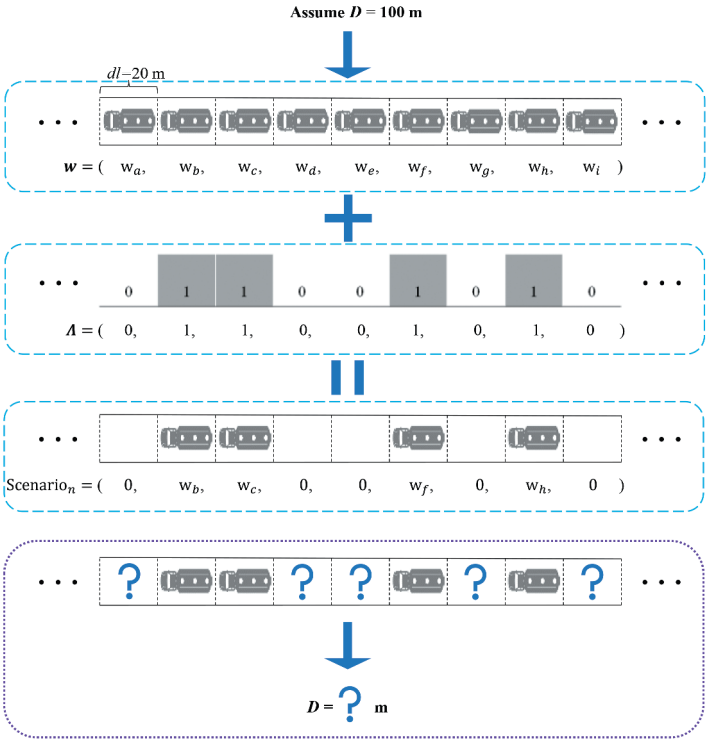


Figure 2. The process of simulation of correlated GVWs and its immeasurability.

However, the value of D is not measurable according to the simulation of maximum response scenarios as presented in (Wang et al. 2024). In fact, as shown in Figure 2, where the simulation process is presented, if only the extreme response scenarios are available and the GVWs in the blank cells are not known, the correlation lengths cannot be calculated. It also should be noted that the Kriging interpolation method, which is very popular in the field of geotechnical engineering, can be used to solve this problem, which will be the subject of future work. As the actual value of D cannot be known, in the present study the aim is to see which is the sensitivity of the maximum load effects to its value. Just reasonable assumptions are made on the correlation lengths, i.e., 20 m, 50 m, and 100 m. and their effect on the obtained results are analyzed and discussed. The process is as follows: Firstly, the GVW correlation length of multi-vehicle events is assumed (i.e., 20 m, 50 m, 100 m); Secondly, the GVW simulation with correlation is performed based on the Nataf method; Thirdly, the presence or absence of heavy vehicles in each cell is simulated based on the Poisson method (Wang et al. 2024); Finally, the simulated vehicle scenario is obtained and the load effect calculated.

3 RESULTS AND DISCUSSION

The method has been applied to two kinds of effects of a cable-stayed bridge, first is the axial force of the longest cable at mid-span; second is the vertical deflection of main girder at mid-span of the main span. The elevation of the cable-stayed bridge and the influence lines of the effects are shown in Figure 3, meanwhile, the cable of the first effect is marked with the green dot-dash line in the figure. Figure 4 displays the differences between the CDF of the effects for different correlation levels. Figure 4 (a) shows the CDF of the extremum of vertical deflection, and Figure 4 (b) shows the CDF of the extremum of axial cable force. The subfigures are the partial magnification.

For low response values, it becomes evident that the influence of the correlation length is negligible. However, in the calculation of the maximum load effects, the higher extreme values are of interest. It can be seen that when the CDF value is more than 0.9, the influence of D is evident and the exceeding probability is larger for the extreme effect simulated with a higher correlation length. Assuming no correlation at all provides results on the unsafe side in the order of 10% when compared with the results for D = 100m, which is a reasonable guess. The extreme value increases with the increase of the correlation in the GVWs, as a result of the assumption of the value of the correlation length. This is because the distribution of the effect extremum of simulated scenarios has longer tail behavior for a larger correlation. At a high CDF value as shown in subfigures in Figure 4, the effect extremum increases significantly with increasing correlation coefficient of GVWs. This follows the physical meaning that a larger probability of heavy vehicle queuing will lead to a larger probability of occurrence of extreme response values. An obvious fact is that the correlation coefficient of GVWs has a direct relationship with the probability of heavy vehicle queuing. It can also be seen that, with a sufficient number of Monte Carlo simulations, statistical differences in the simulation results under different correlations can be manifested.

4 CONCLUSIONS

Due to the fact that a greater variety of extreme response scenarios are present in long-span bridges, and the impact of truck groups is significant, in this paper a simulation approach of on-bridge deck vehicle distribution considering the correlation level of vehicles is concerned to evaluate the influence of the correlation length in the extreme values of the response. The

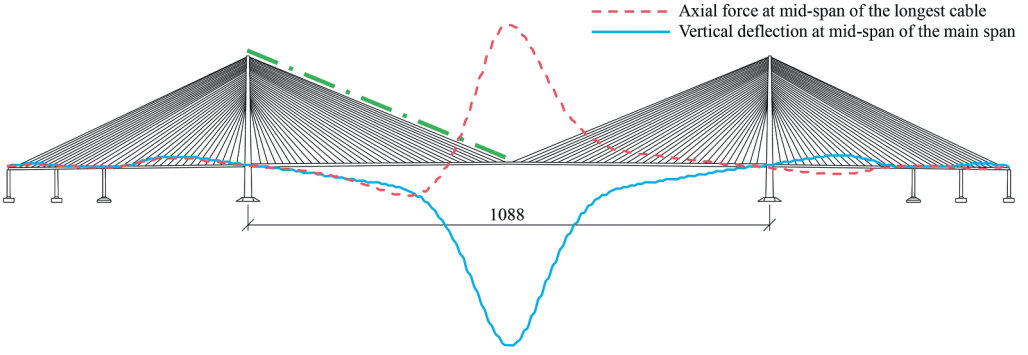


Figure 3. The elevation of the investigated cable-stayed bridge and the effects' influence lines.

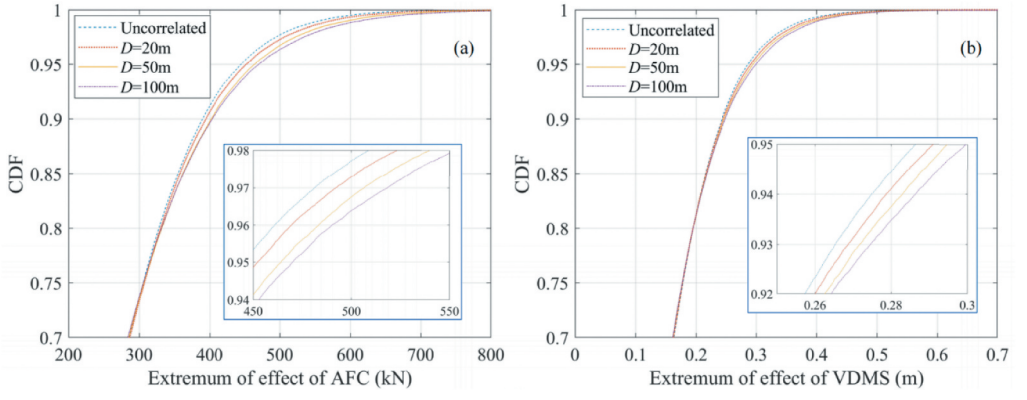


Figure 4. Response results (CDF) of two effects under different correlation levels: (a) axial force at mid-span of the longest cable; (b) vertical deflection at mid-span of the main span.

necessity and methodology of considering the correlation of GVWs are carefully discussed. It is found that with the increase of correlation level of neighboring GVWs, the simulated load effects are more prone to get extreme values, which means an increasing probability of the most unfavorable spatial arrangement of on-bridge vehicles. The correlation model is based on the concept of a correlation length. Due to the impossibility of calculating this length, several values are assumed and their influence on the simulated results analyzed. Based on the results obtained for several correlation lengths, it is recommended that the correlation level should be chosen as 100 meters. Meanwhile, it is necessary to reevaluate the association between GVWs for the most extreme response scenarios involving long-span bridges.

REFERENCES

Caprani, C.C. O'Brien, E.J. & McLachlan, G.J. 2008. Characteristic traffic load effects from a mixture of loading events on short to medium span bridges. *Structural Safety* 30(5): 394–404.

Caprani, C.C. 2013. Lifetime highway bridge traffic load effect from a combination of traffic states allowing for dynamic amplification. *Journal of Bridge Engineering* 18(9): 901–909.

Chen, S.R. & Cai, C.S. 2007. Equivalent wheel load approach for slender cable-stayed bridge fatigue assessment under traffic and wind: Feasibility study. *Journal of Bridge Engineering* 12(6): 755–764.

Chen, S.R. & Wu, J. 2011. Modeling stochastic live load for long-span bridge based on microscopic traffic flow simulation. *Computers & Structures* 89(9–10): 813–824.

Chen, Z. Bao, Y. Chen, J. & Li, H. 2019. Modelling the spatial distribution of heavy vehicle loads on long-span bridges based on undirected graphical model. *Structure and Infrastructure Engineering* 15(11): 1485–1499.

Der Kiureghian, A. & Liu, P.L. 1986. Structural reliability under incomplete probability information. *Journal of Engineering Mechanics* 112(1): 85–104.

Guo, D. & Caprani, C.C. 2019. Traffic load patterning on long span bridges: A rational approach. *Structural Safety* 77: 18–29.

Hwang, E.S. & Kim, D.Y. 2019. Live load model for long span steel cable bridges considering traffic congestion scenarios. *International Journal of Steel Structures* 19(6): 1996–2009.

Lipari, A. Caprani, C.C. & O'Brien, E.J. 2017. A methodology for calculating congested traffic characteristic loading on long-span bridges using site-specific data. *Computers & Structures* 190: 1–12.

Li, Q. Wang, C. & Zhang, H. 2016. A probabilistic framework for hurricane damage assessment considering non-stationarity and correlation in hurricane actions. *Structural Safety* 59: 108–117.

Mahadevan, S. & Haldar, A. 1991. Practical random field discretization in stochastic finite element analysis. *Structural Safety* 9(4): 283–304.

Micu, E.A. Malekjafarian, A. O'Brien, E.J. Quilligan, M. McKinstray, R. Angus, E. Lydon, M. & Catbas, F.N. 2019. Evaluation of the extreme traffic load effects on the Forth Road Bridge using image analysis of traffic data. *Advances in Engineering Software* 137: 102711.

Nowak, A.S. 1993. Live load model for highway bridges. *Structural Safety* 13: 53–66.

Nowak, A.S. 1995. Calibration of LRFD bridge design code. *Journal of Structural Engineering, ASCE* 121(8): 1245–1251.

O'Brien, E.J. & Enright, B. 2011. Modeling same-direction two-lane traffic for bridge loading. *Structural Safety* 33(4): 296–304.

O'Brien, E.J. Hayrapetova, A. & Walsh, C. 2012. The use of micro-simulation for congested traffic load modeling of medium-and long-span bridges. *Structure and Infrastructure Engineering* 8(3): 269–276.

Soriano, M. Casas, J.R. & Ghosn, M. 2017. Simplified probabilistic model for maximum traffic load from Weigh-in-Motion data. *Structure and Infrastructure Engineering* 13(4): 454–467.

Wang, X. Ruan, X. Casas, J.R. & Zhang, M. 2024. Probabilistic model of traffic scenarios for extreme load effects in long-span bridges. *Structural Safety* 106: 102382.

Xu, Y.L. Chen, Z.W. & Xia, Y. 2012. Fatigue assessment of multi-loading suspension bridges using continuum damage model. *International Journal of Fatigue* 40: 27–35.

Zhao, L.F. Zhou, Z.F. Song, Y.Q. Meng, M.Z. & Huang, Q.A. 2020. Uncertainty quantification of MEMS devices with correlated random parameters. *Microsystem Technologies* 26(5): 1689–1696.

Zhou, J. Shi, X. Caprani, C.C. & Xin, R. 2018. Multi-lane factor for bridge traffic load from extreme events of coincident lane load effects. *Structural Safety* 72: 17–29.

Bridge Maintenance, Safety, Management, Digitalization and Sustainability – Jensen, Frangopol & Schmidt (eds)
© 2024 The Author(s), ISBN 978-1-032-77040-6
Open Access: www.taylorfrancis.com, CC BY-NC-ND 4.0 license

PyBTLS: A Python package for traffic load simulation on short-to-medium bridges

Z. Zhou
Ph.D. Candidate, Monash University, Melbourne, VIC, Australia

C. Caprani
Associate Professor, Monash University, Melbourne, VIC, Australia

ABSTRACT: PyBTLS is an open-source Python package developed for the efficient simulation of traffic loads on short-to-medium-span bridges, under a GPLv3 license. This tool addresses the gap in the bridge research field regarding generating new bridge structure load effect data with its corresponding traffic record from a known traffic condition. With the benefit of bridge structure load effect data, bridge traffic load models can be more comprehensive; therefore, the precision of bridge design and assessments can be enhanced. PyBTLS is based on C++ fundamentally but offers a user-friendly Python application programming interface (API). Users can easily generate diverse traffic scenarios and conduct load effect calculations with integrated or customized influence lines for long time periods. This paper introduces PyBTLS's basis and functionalities broadly, along with a real-world application case to indicate its workflow. Beyond its current capabilities, under the open-source license, contributions from bridge engineering researchers are welcomed. It is hoped that the release of this software will help accelerate research and practice.

1 INTRODUCTION

Economic development accompanied by freight growth is leading to higher traffic loads on bridges. Concurrently, the capacity of bridges is dropping due to structural ageing. Thus, to ensure safety, the assessment of existing bridges becomes increasingly significant. According to reliability theory, assessment results rely on the collected bridge information, and the information characterised by greater randomness is most significant (OBrien et al., 2015). Traffic, as one of the most variable sources of load on bridges, has been a focal point of research in recent decades. To acquire more comprehensive traffic data for more precise traffic load models, bridge engineers have employed technologies such as strain-sensor networks and Weigh-in-Motion (WIM) systems (Moses, 1979).

Although traffic and structure monitoring technologies have significantly enhanced the accuracy of traffic load models, their installations, due to budget constraints, are mostly limited to long-span bridges serving as major traffic infrastructures, such as Melbourne's West Gate Bridge (Roadsys, 2022). For the most common short-to-medium-span road bridges, there is a notable gap in the efficient acquisition of traffic load data. A category of research, exemplified by Zhang and Au (2017), generates traffic load data by manually adjusting their simplified traffic, which is inefficient and could potentially lead to biases.

The newly-released Python package PyBTLS (i.e., bridge traffic load simulation) addresses the research and practice gaps by facilitating state-of-the-art traffic simulations on any short-to-medium-span bridges; typically for spans are less than about 50 metres. The traffic in these simulations can be generated from known traffic conditions, where a known traffic condition

DOI: 10.1201/9781003483755-147

is defined by its vehicle characteristics (e.g., number of axles, axle spacings, axle weights, etc.) and traffic flow characteristics (e.g., traffic volume, traffic composition, etc.). The vehicle characteristics can be obtained through WIM systems installed in that region; The traffic flow characteristics can be acquired via relatively inexpensive methods, such as loop detectors or computer-vision-based vehicle counting and classification. With the benefit of bridge traffic load data from the simulations, more precise traffic load models can be proposed for bridge design standards worldwide, or the distributions of load effect can be used in the reliability assessment of an existing bridge.

In this paper, the general information of PyBTLS and its functionalities is introduced broadly first. Then, PyBTLS's classes and their interrelations are presented. Finally, the workflow of a PyBTLS simulation is introduced via a real-world bridge assessment project.

2 GENERAL INFORMATION AND FUNCTIONALITIES

PyBTLS is wrapped from a Windows-only C++ program BTLS (Caprani, 2021) via pybind11 (Schreiner et al., 2023), a Python-C++ wrapping library. This wrapping makes PyBTLS cross-platform, and it also simultaneously benefits from both the convenience of Python and the efficiency of C++. PyBTLS follows the GPLv3 open-source license (Free Software Foundation, 2007).

The software implements the calculation and evolution methodologies described in Chapter 3 of OBrien et al. (2021).

2.1 *Assumptions*

The main assumptions of PyBTLS, suitable for short-to-medium span bridges are:

- The vehicles do not have lane-change behaviours; such behaviour is not included in the traffic evolution model.
- The vehicles are at constant velocities when crossing the bridge.

2.2 *Functionalities*

The key functionalities of PyBTLS are:

- PyBTLS can conduct the following pre-processing:
  - Classify vehicles based on a vehicle classification scheme.
  - Classify vehicles based on common vehicle properties, such as the number of axles, gross vehicle weight, etc.
  - Get statistical information from a WIM database (e.g., quantiles, standard deviation, etc.).
  - Divide a WIM database into several sub-databases.
  - Assemble a new WIM database from the provided sub-databases.
- PyBTLS has four basic simulating modes:
  - Calculate load effects caused by a single vehicle, which is useful for validations.
  - Generate traffic according to a traffic generation model and calculate its load effects. This can be done in memory, and so extremely long-run simulations are possible (1000s of years of traffic).
  - Calculate load effects caused by recorded traffic read in from a WIM file.
  - Generate traffic according to one of the traffic generation models and output to file.
- For the output, PyBTLS can:
  - Extract statistical information from recorded or generated traffic.
  - Record time-history data of the load effects.
  - Indicate the amplitudes of the load effects of each event (i.e., number of vehicles on bridge changes).

  - Conduct block-maximum or peak-over-threshold analysis on the generated traffic load effect data to derive extreme load events (OBrien et al., 2015).
  - Conduct rainflow-counting analysis (Lee and Tjhung, 2011) on the generated traffic load data to derive fatigue load events.
- PyBTLS can conduct the following post-processing:
  - Plot the load effect simulation outputs.

3 CLASS MAP

PyBTLS is written in an object-oriented style. This means that the common functionalities of certain classes are abstracted into base classes, while the details of each implementation are in derived classes. In particular, this makes it relatively easy to add new vehicle generators, and new traffic generators as shown below.

The simulation-relevant classes in PyBTLS and their interrelationships are elucidated in Figure 1. The classes are as follows:

- `Vehicle`: This class is designed for the customization of vehicles. A vehicle instance requires the following fundamental attributes: number of axles, axle spacings, axle weights, and axle widths.
- `Bridge`: This class is pivotal for traffic load calculation. In PyBTLS, the essence of a load effect on a bridge is conceptualized as a series of influence lines (each corresponding to a lane) or an influence surface. Although most influence lines or surfaces have complex shapes and should be defined by discrete data points calculated from the structure analysis packages such as PyCBA (Caprani, 2023) and ospgrillage (Ngan and Caprani, 2022), PyBTLS still incorporates nine built-in influence lines according to their mathematical expressions, as depicted in Table 1. A bridge instance can be set with multiple load effects for different bridge components.

Table 1. The built-in influence lines in PyBTLS.

PyBTLS Index	Influence Line	Number of Spans
1	Sagging moment at mid span	1
2	Hogging moment at mid support	2
3	Shear force at left support	1
4	Shear force at right support	1
5	Shear force at right support	2
6	Shear force at left support	2
7	Total amount of loads on the bridge (i.e., a unit IL)	Any
8	Hogging moment at the second support	3
9	Hogging moment at the third support	3

- `TrafficGenerator`: This is the class for traffic generation, and each lane should have a generator. A `TrafficGenerator` instance requires the following inputs: a vehicle generator (which creates the physical vehicle), a headway generator for creating the haps between vehicles, and a lane flow composition, for managing flow rates and vehicle occurrences. The lane flow composition includes hourly average speed information of the traffic flow and the hourly traffic composition.
  - PyBTLS currently contains three types of vehicle generators:
    - `VehicleGenGrave`: Utilizes statistical distributions of common trucks based on several European site data (Grave, 2002). The VehicleGenGrave is not readily applicable outside Europe due to varying legal truck configurations by region.
    - `VehicleGenGarage`: Generates vehicles through random sampling based on the collected WIM database.

  - `VehicleGenNominal`: Generates identical vehicles based on a user-defined vehicle, which is very useful for validations or similar studies.
- PyBTLS currently offers four types of headway generators:
  - `HeadwayGenNHM`: Based on a truck-only headway distribution concluded from the highway on Auxerre (Grave, 2002).
  - `HeadwayGenConstant`: Sets identical headway and speed for all vehicles.
  - `HeadwayGenCongested`: It adopts an input nominal axle gap, representing the average spacing between vehicles in traffic congestion, along with a coefficient of variation for the gap to ensure randomness (Blacoe et al., 2012).
  - `HeadwayGenFreeflow`: It uses a Poisson arrival assumption based on the normalized headway model (Crespo-Minguillon and Casas, 1997).

- `TrafficLoader`: This class is used for loading a recorded traffic flow. Users can also customize a traffic flow by creating and assembling each Vehicle instance.
- `OutputConfig`: This class determines the output of the simulation.
- `Simulation`: Depending on the input argument, this class automatically runs the corresponding simulating mode.

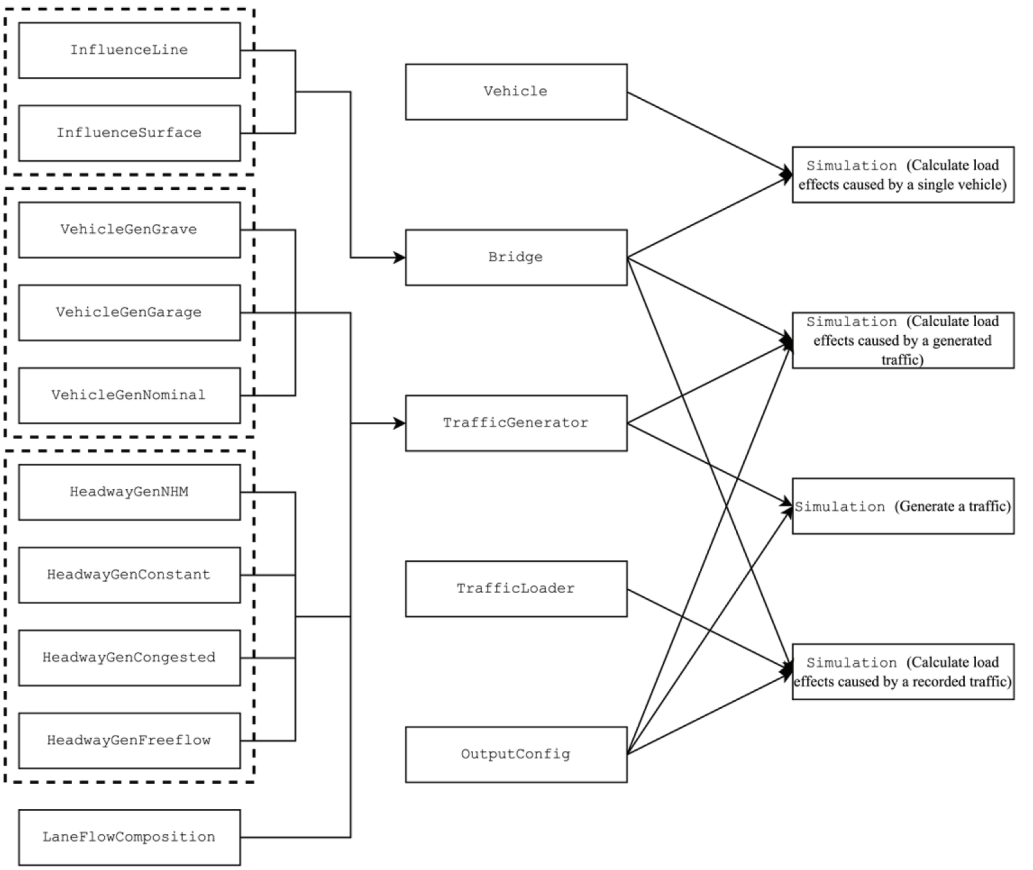


Figure 1. Class map of PyBTLS.

4 EXAMPLE

To demonstrate how PyBTLS can be applied, an example from a past Austroads-sponsored (Australian road research agencies) project in which BTLS was used is introduced here to illustrate the general workflow of PyBTLS. The project focused on integrating the

probability-based bridge assessment (PBBA) framework into existing Australian road bridges' assessment procedures (Melhem and Caprani, 2022). The selected bridges were representative, but they were not equipped with sensor networks for monitoring. Therefore, within the constraints of a limited budget and project timeline, employing BTLS to generate artificial traffic load data emerged as a good option. The following part shows the fundamental code for conducting the simulation for one of the bridges in the project, with explanations.

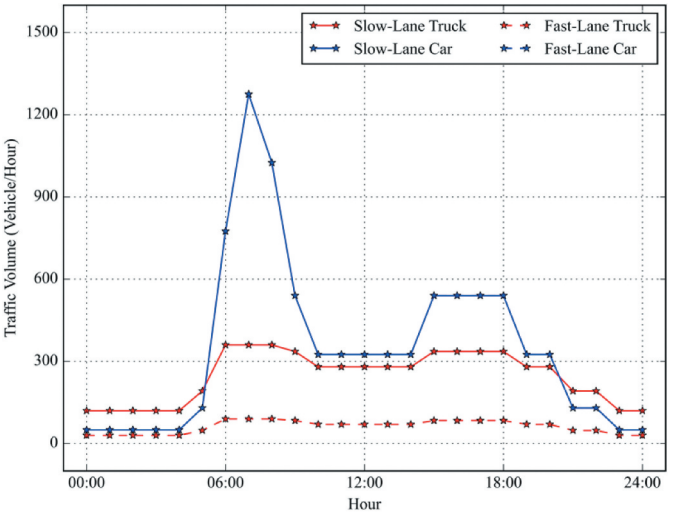


Figure 2. The traffic flow for demonstration.

Here, we consider a 20-metre single-span bridge with two lanes of unidirectional traffic. The hourly traffic flow rates are shown in Figure 2 (Lipari, 2013). The midspan bending moment is sought. In the project, 100 years of traffic data was generated, but in the demonstration, we only generated 1 year (250 working days). The steps are shown in Figure 3 below.

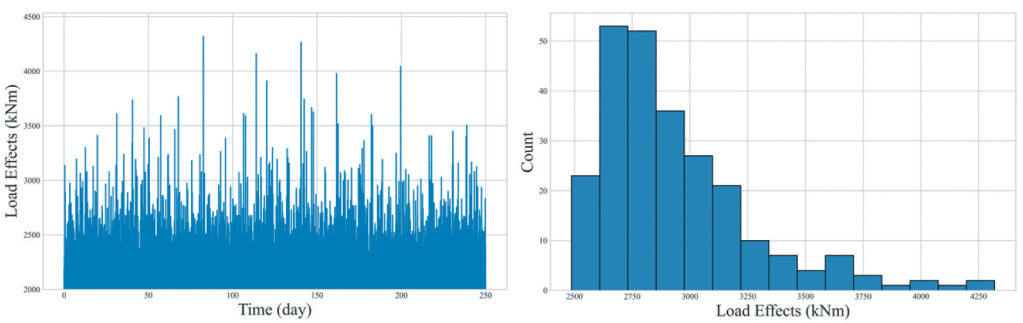
A description of each line of the source code is given:

- Line 1: Import the package.
- Line 2 – 9: Regard the bridge as simply supported, and the midspan bending moment for a simply supported bridge is built-in to PyBTLS (see Table 1). Then, the influence line shapes are the same for both two lanes but with different weights according to transverse distribution of the load across the bridge deck.
- Line 10 – 17: The `VehicleGenGarage` is selected as the vehicle generator. The busiest bridge in Melbourne, West Gate Bridge, had installed a pavement WIM system, which recorded millions of vehicles. Thus, a truck garage file from the WGB is taken to represent Australian freight. The kernel ensures the randomness of the trucks during the sampling instead of just repeating the garage. The kernel is made by bias and standard deviation values for gross vehicle weight, axle group weights and axle group spacings.
- Line 18: The `HeadwayGenFreeflow` is selected as the headway generator with a minimum vehicle gap of 0.1 second and minimum vehicle spacing of 1 metre. This approach is conservative according to Chapter 3 of OBrien et al. (2021).
- Line 19 – 38: The lane flow compositions of the two lanes are defined based on the data in Figure 2.
- Line 39 – 41: Establish a traffic generator.
- Line 42 – 44: Set an output configuration to obtain time history and block maximum data. The block size is set to 1 day.
- Line 45 – 53: Use the bridge, traffic generator, and output configuration objects to create a simulation task. In practice, by repeating Line 2 – 44 with corresponding input arguments, more than one simulation task can be created.

Line	Code
1	`import PyBTLS`
2	`load_effect_1 = Py-BTLS.InfluenceLine("built-in")`
3	`load_effect_1 = PyBTLS.InfluenceLine("built-in")`
4	`load_effect_1.set_IL(type = 1, length = 20.0)`
5	`bridge_20m = PyBTLS.Bridge(length = 20.0, no_lane = 2)`
6	`bridge_20m.add_load_effect(`
7	`inf_line_surf = load_effect_1,`
8	`inf_weight = [1.3*1.0, 1.3*0.8]`
9	`)`
10	`WGB_garage = PyBTLS.GarageProcessing.load_garage_file(`
11	`"WGB_garage.txt"`
12	`)`
13	`kernel = [[1.0,0.08], [1.0,0.05], [1.0,0.02]]`
14	`vehicle_gen = PyBTLS.VehicleGenGarage(`
15	`garage = WGB_garage,`
16	`kernel = kernel`
17	`)`
18	`headway_gen = PyBTLS.HeadwayGenFreeflow()`
19	`lfc_slow_lane = PyBTLS.LaneFlowComposition(`
20	`lane_index = 1,`
21	`lane_dir = 1`
22	`)`
23	`lfc_slow_lane.assign_lane_data(`
24	`hourly_truck_flow = [120, 120, …, 120],`
25	`hourly_car_percentage = [29.41, 29.41, …, 29.41],`
26	`hourly_speed_mean = [80/3.6*10]*24,`
27	`hourly_speed_std = [10]*24`
28	`)`
29	`lfc_fast_lane = PyBTLS.LaneFlowComposition(`
30	`lane_index = 2,`
31	`lane_dir = 1`
32	`)`
33	`lfc_fast_lane.assign_lane_data(`

```
            hourly_truck_flow = [30, 30, …, 30],
            hourly_car_percentage = [62.50, 62.50, …, 62.50],
            hourly_speed_mean = [100/3.6*10]*24,
            hourly_speed_std = [10]*24
            )
traffic_gen = PyBTLS.TrafficGenerator(no_lane = 2)
traffic_gen.add_lane(vehicle_gen, headway_gen, lfc_slow_lane)
traffic_gen.add_lane(vehicle_gen, headway_gen, lfc_fast_lane)
output_config = PyBTLS.OutputConfig()
output_config.set_output_general(write_time_history = True)
output_config.set_output_BM(block_size_days = 1)
sim_task = PyBTLS.Simulation()
sim_task.add_sim(
            bridge = bridge_20m,
            traffic_generator = traffic_gen,
            no_day = 250,
            output_config = output_config,
            time_step = 0.01,
            tag = "SimBridge20m"
            )
sim_task.run()
PyBTLS.Plot.plot_TH("SimBridge20m/TH_20.txt")
PyBTLS.Plot.plot_BM("SimBridge20m/BM_S_20_Eff_1.txt")
```

Figure 3. Example code for simulation of loading on a 20m bridge.



(a) Time history (b) Block Maximum histogram

Figure 4. The outputs from the demonstration.

- Line 54: After all simulation tasks are created, they are suspended until users call the `run()` method to start running. When there is more than one simulation task being created, PyBTLS uses multiprocessing to run these simulations simultaneously. In this demonstration, only one simulation task was created, and it occupied one minute runtime on a core of an Apple M1Pro chip.
- Line 55 – 56: Plot the time-history and block-maximum result by the PyBTLS post-processing module, Figure 4.

5 CONCLUSION

In summary, PyBTLS has the capability to expand the traffic load database for short and medium-span bridges, thereby greatly enhancing the accuracy of bridge traffic models. It facilitates studies leading to new traffic load models for codes; and also facilitates the development of load effect distributions for the structural reliability assessment of existing bridges. Such an approach helps to extend the utility of existing WIM stations.

The traffic and load effect data generated by PyBTLS can be used in studies related to bridge strength and fatigue. As an open-source package, interested researchers and practitioners can contribute to PyBTLS to expand its capabilities as required for application in different countries and contexts.

For more details about PyBTLS, please refer to the repository https://github.com/ccaprani/btls.

REFERENCES

Blacoe, S., Caprani, C. C., O'brien, E. J. & Lipari, A. Determination of minimum gap in congested traffic. Bridge & Concrete Research in Ireland, Dublin, Ireland, 6-7 September, 2012, 2012.

Caprani, C. C. 2021. *Bridge Traffic Load Simulation* [Online]. Available: https://github.com/ccaprani/btls/tree/v1.3.5 [Accessed 2023].

Caprani, C. C. 2023. *Python continuous beam analysis* [Online]. Available: https://github.com/ccaprani/pycba/ [Accessed 2023].

Crespo-Minguillon, C. & Casas, J. R. 1997. A comprehensive traffic load model for bridge safety checking. *Structural safety*, 19, 339–359.

FREE SOFTWARE FOUNDATION, I. 2007. *GNU General Public License* [Online]. Available:https://www.gnu.org/licenses/gpl-.0.html[Accessed2023].

Grave, S. 2002. *Modelling of site-specific traffic loading on short to medium span bridges*. Trinity College Dublin.

Lee, Y.-L. & Tjhung, T. 2011. Rainflow cycle counting techniques. *Metal Fatigue Analysis Handbook: Practical Problem-solving Techniques for Computer-aided Engineering*, 89.

Lipari, A. 2013. *Micro-simulation modelling of traffic loading on long-span bridges*. University College Dublin.

Melhem, M. M. & Caprani, C. C. 2022. Promoting probability-based bridge assessment in engineering practice: an Australian case study. *Structure and Infrastructure Engineering*, 18, 1472–1486.

Moses, F. 1979. Weigh-in-motion system using instrumented bridges. *Transportation Engineering Journal of ASCE*, 105, 233–249.

Ngan, J. & Caprani, C. 2022. ospgrillage: A bridge deck grillage analysis preprocessor forOpenSeesPy. *Journal of Open Source Software*, 7, 4404.

Obrien, E., Nowak, A. & Caprani, C. 2021. *Bridge traffic loading: From research to practice*, CRC Press.

Obrien, E. J., Schmidt, F., Hajializadeh, D., Zhou, X.-Y., Enright, B., Caprani, C. C., Wilson, S. & Sheils, E. 2015. A review of probabilistic methods of assessment of load effects in bridges. *Structural safety*, 53, 44–56.

Roadsys, I. 2022. *West Gate Bridge Weigh-in-Motion System* [Online]. Available: https://roadsysllc.com/data-collection/west-gate-bridge-weigh-in-motion-system/ [Accessed 2023].

Schreiner, H., Moldovan, D., Rhinelander, J.,Grosse, R., W., & JAKOB, W. 2023. Available: https://github.com/pybind/pybind11[Accessed2023].

Zhang, J. & Au, F. 2017. Fatigue reliability assessment considering traffic flow variation based on weigh-in-motion data. *Advances in Structural Engineering*, 20, 125–138.

SPECIAL SESSIONS

SS01: Short-span bridges and culverts: Analysis, evaluation, durability, and rehabilitation

Organizers: D. Beben, H. Sezen, J. Vaslestad & T. Maleska


Taylor & Francis
Taylor & Francis Group
http://taylorandfrancis.com

Bridge Maintenance, Safety, Management, Digitalization and Sustainability – Jensen, Frangopol & Schmidt (eds)
© 2024 The Author(s), ISBN 978-1-032-77040-6
Open Access: www.taylorfrancis.com, CC BY-NC-ND 4.0 license

Restoration of the Rochers Noirs Viaduct

E. Combescure
Chief Engineer, Setec tpi, Paris, France

S. Doussau
Architect, RL&A, Lyon, France

C. Lacipiere
Project Engineer, Baudin Chateauneuf, Neyron, France

N. Aubree
Project Manager, Setec Diades, Bordeaux, France

L. Pace
Site Engineer, Setec Diades, Bordeaux, France

ABSTRACT: The diagnosis of the Rochers Noirs Viaduct, listed as a Heritage Building in 2000 and closed to traffic since 2006, revealed some significant defects in the suspension cables that shall be completely renewed. Furthermore, the upper steel decking, only designed to support personnel maintaining the original railway line, is unfit for future use and shall also be fully replaced to enable the re-opening of the viaduct for soft mobilities. Some rehabilitation works also need to be undertaken on the masonry and ironworking. As of November 2023, the deck is supported by a temporary suspension, the old suspension has been dismantled, the new suspension has been installed, and the load transfer from temporary to new suspension is about to take place, while the painting works are ongoing.

1 PRESENTATION OF THE BRIDGE

The Rochers Noirs Viaduct was built between 1911 and 1913, between the rural cities of Soursac and Lapleau in the Correze department in France. Its originality lies in a hybrid suspension (Figure 1) made of two fans, comprising inclined stay cables linked to two half parabolic cables, the whole being assembled as a triangulated mesh. Each cable mesh is connected to an upper catenary cable, called an Ordish, through vertical hangers. This type of rigid suspension system was developed in order to allow trains of the Transcorrézien line to cross the bridge.

At deck level, the crossbeams connected to the suspension cables by vertical hangers are spaced at 11.80m intervals with a main span of 140m. The deck is 5.0m wide and is made of two longitudinal inner I girders under the rails at 1m spacing and two external I girders, made of riveted assembled plates. The deck is elevated at 90m above the Luzege river. The masonry pylons reach respective heights of 55m on the Soursac side and 43m on the Lapleau side.

The Tramway line was closed in 1959, and the viaduct was then transformed into a road bridge in 1963. The viaduct has been closed to traffic since 2006, following evidence of severe defects on the suspension cables. The bridge is now being restored to enable reopening to public for soft mobilities at the end of 2024.

DOI: 10.1201/9781003483755-148

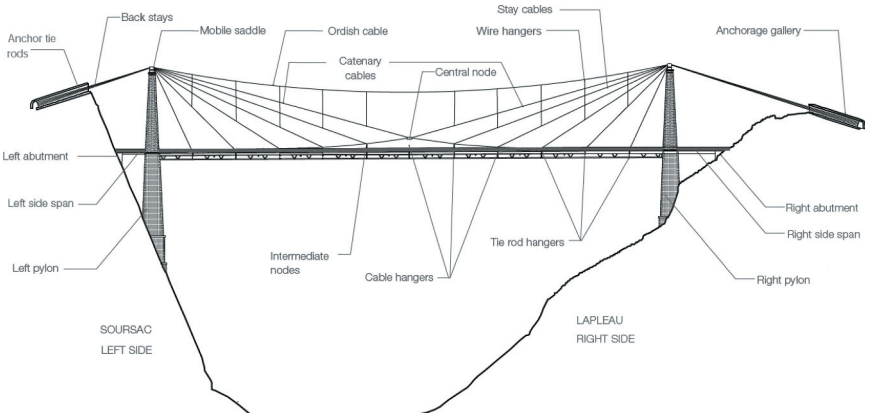


Figure 1. Glossary of the viaduct of the Rochers Noirs (© RL&A).

2 HERITAGE CONTEXT

2.1 *A local network amongst the national networks*

At the time of the industrial revolution in the mid-19th century, passenger lines connected the first railways intended to transport coal. The national network developed rapidly, but large companies were not interested in regional railways considered as unprofitable. In order to enhance the development of railway lines in the rest of the territory, the State regulates the development of the network and wants to provide Corrèze with a secondary network, the Paris-Orléans-Corrèze. Since large population areas are not serviced by this line, the General Council opts for the creation of a complementary tram network in Corrèze. The Rochers Noirs viaduct constitutes the strong point of the Tulle-Ussel line.

2.2 *Invention of the Gisclard suspension system*

Albert Gisclard was born in 1844. After entering the Ecole Polytechnique at the age of 20, he joined military engineering where he designed many types of bridges, with the aim of quickly and efficiently replacing those destroyed during conflicts. In 1900, he filed a patent for a suspension bridge allowing the passage of much heavier loads than on traditional suspension bridges which were invented and built by Marc Seguin, then improved by Ferdinand Arnodin. "The cables are arranged in a very particular and complex pattern, casting sockets are placed at their ends and at their intersections, to form a rigid system of triangles and polygons which can be calculated from the rules of static and which gives to the structural system a great rigidity which was lacking in medium- and long-span suspension bridges". To test the feasibility and effectiveness of the system, he gave the construction license to the Arnodin company.

2.3 *Adopting the Gisclard system for the Rochers Noirs Viaduct*

The configuration of the land, the curves to be respected on the Lapleau side, the tunnel on te Soursac side and the depth of the ravine encouraged the Tramways Company of Corrèze to rule out ordinary metal bridges due to the financial cost. The solution of a suspension bridge was chosen and a comparative study between several systems was performed. These preliminary studies were carried out in 1909, when the Gisclard suspension bridge at La Cassagne in France had just been completed and gave interesting results during the load test. The technical and economic advantages of this new type of bridge were thus recognized, and the Gisclard system was adopted for the crossing of the Luzège. The bridge was inaugurated in 1913 (Figure 2).

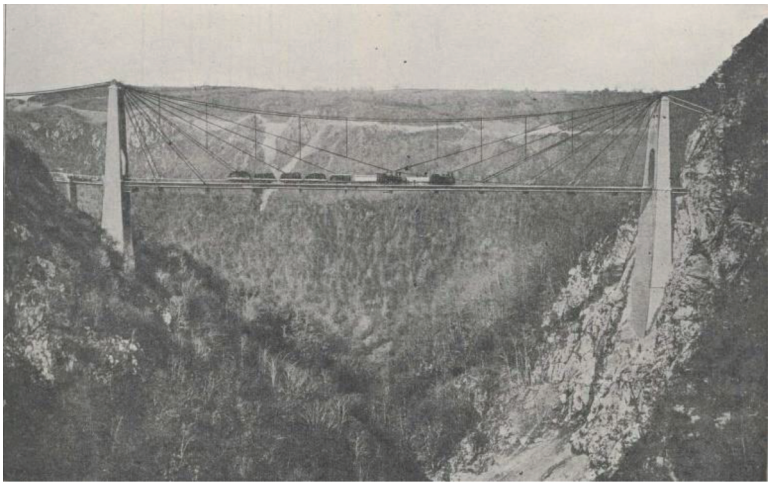


Figure 2. Load testing during bridge opening [1].

2.4 *Content of the work permit on listed Heritage Building*

The bridge was listed as a Heritage Building in 2000 due to its unique features as an exceptional work of art, testimony to avant-garde technology and emblematic of the research for theoretical and constructive innovations in the early 1900s. It is one of the only remaining examples of a Gisclard bridge still preserved today. The restoration project, presented as part of the work permit on a/the Listed Heritage Building, was necessary to rediscover the use of the Rochers Noirs Viaduct, an essential condition for the transmission of this heritage. Its new function as a bridge for soft mobilities will guarantee its maintenance and therefore its long-term conservation. The main challenge is to find a compromise which allows both the preservation and highlighting of the historical building, while respecting the authenticity of the form and material and ensuring the safety of users.

3 DETAILED INSPECTION AND BRIDGE DIAGNOSIS

The purpose of the diagnosis carried out in 2020 at the start of the project was to update the health condition of the viaduct. The Setec Diades inspectors did not observe significant development of defects since the last bridge inspection in 2005. However, the viaduct is still subject to ageing and climatic hazards.

The suspension components show signs of widespread external corrosion, due to the deterioration of the existing anti-corrosion coating. Putty defects are systematically observed at the cable ends at socket entry level.

These visual findings on the condition of the cables are supplemented by the results of auscultation campaigns conducted by the Owner to assess the internal condition of the cables. In fact, three electromagnetic inspection campaigns were previously carried out, in 1979, 1982 and 2004. Considering evidence of multiple internal wire breaks, the condition of the cables was considered to be severely deteriorated. The result of the 1982 inspection of cables was the main trigger for the road traffic closure on the bridge. Finally, hardness tests on the tie rods of the suspension carried out in 2004 concluded that all the tie rods were fragile at cold temperature such that the bridge was totally closed to public in 2005.

The mobile saddles at the top of the pylons were first considered to be in good visual condition. However, the endoscopy inspection carried out subsequently revealed a general state of rusting between the rollers and the base plates (Figure 3). Hence, the mobile saddles were considered to be blocked and not functional since they could not move freely at pylon tops, a condition for the proper structural behaviour of the masonry pylons.



Figure 3. Mobile saddle and rolling cylinders at pylon top (© setec diades).

The steel beams of the deck have a deteriorated anti-corrosion coating. However, the general structural condition of the beams is considered satisfactory. Some occasional repairs are to be expected for the most significant defects, in particular due to the poor water drainage details of the deck with the installation in 1960 of drainage tubes directly above the cross beams.

The decking shows significant deformations, and even some localized tears. Its drainage is almost non-existent, and the corrosion is widespread (Figure 4).

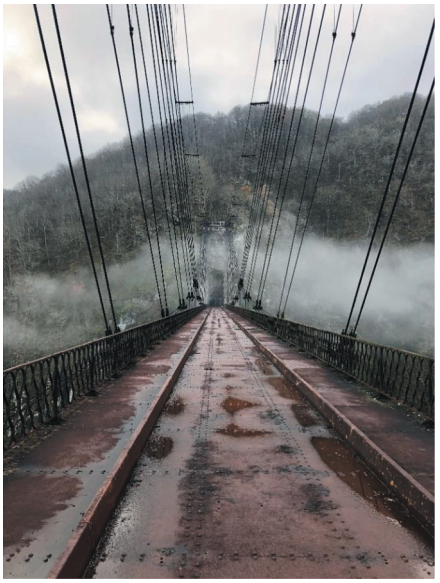


Figure 4. State of steel decking before replacement works (© setec diades).

The handrails do not meet current standard requirements but have notable heritage value. They will be restored and strengthened (Figure 5).

The anchorage galleries, directly dug into the rock cliffs with a horseshoe shape, are also a specific feature of this bridge. They are subject to constant ambient humidity and significant water stagnation at their low point, due to the absence of drainage. The resulting condition of the tie rods anchoring the back stays is very poor, with advanced corrosion and significant section losses, even though they were renewed in 1985.

The state of conservation of the masonry of the pylons is very good. The inspection was carried out by drone by establishing orthophotographs. However, some areas are hidden, either by heavy covers of vegetation or, at the top of the pylon, by drippings of coal pitch used as cable coating.



Figure 5. In situ test for the new handrail (© setec diades).

4 DESIGN STUDIES OF THE RESTORATION PROJECT

4.1 *Structural assessment of the viaduct*

The bridge was modelled and recalculated in the future configuration using a large displacement finite element model with the Pythagore© software developed by Setec tpi. It was also fully modelled in 3D on Tekla (Figure 6).

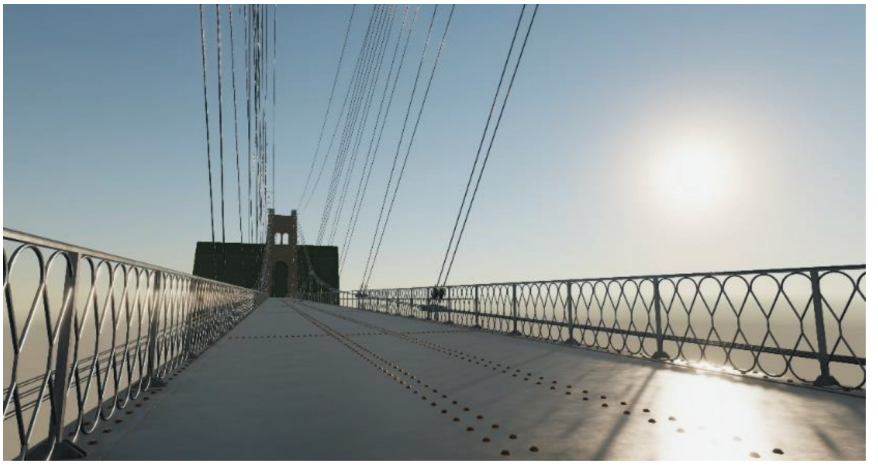


Figure 6. Tekla model of the bridge (© Setec tpi).

The original test train weighed 137.5t, while the Eurocode pedestrian load represents 190t distributed over the entire main span. In addition, the decking must be able to support at all points the loads of isolated wheels from the accidental 12t vehicle prescribed by the Eurocode for pedestrian bridges, while the wheels of the train could only be located onto the inner longitudinal girders of the deck under the rails. The existing decking, made up of an unstiffened 6mm steel sheet designed only for railway maintenance personnel loads, is therefore unsuitable for future use and must be replaced entirely. The new decking will be made up of a 10mm steel plate fitted with 10mm x 100mm transversal stiffeners spaced every 250mm. The verifications in the future situation also include the comfort criteria for pedestrian bridges, the verification of the temporary stages during cable replacement works, and the finite element verification of the retained elements of the suspension, namely the mobile saddles, the steel cylinders at intermediates nodes and the central node.

4.2 *Suspension replacement*

The existing cables are replaced by cables of identical technology, namely Open Spiral Strand (OSS) cables with wires having a rope grade of 1770 MPa. Despite the increase of the rope grade compared to the existing one, the diameter of the new cables is set at 85% of the existing

diameter by the Works Permit on Heritage Building, for the sake of cost-efficiency. The tie rods connecting the cables together are replaced by high resilience steel tie rods. The existing base plates and rollers of the mobile saddle, which were heavily corroded, are replaced by identical stainless-steel elements. The iron cylinders located at the intersection nodes of the triangulated cable mesh, the central nodes, and the mobile saddles, are preserved due to their high heritage value and their satisfactory health condition, after ultrasonic inspection and structural assessment my modelling are carried out.

4.3 *Masonry works*

The project also includes a regeneration of the masonry which includes cleaning the facings, removing the vegetation covering the masonry of the piers and abutments, removing backfill material accumulated behind the piers, dismantling and then reassembling the disorganized masonry, general repointing of the exterior facings, and finally the application of aqua fortis to the facings. Suitability tests on the colour of the joint relining material were carried out in the presence of the DRAC Région Nouvelle Aquitaine and the Architect.

4.4 *Paint works*

The decking will be painted with an ACQPA C4H ANV complex, covered with a non-slip waterproofing complex and fitted with drain tubes that are long enough to purge rainwater without splashing on the beams. All metal beams will be repainted under confinement with a black ACQPA C4H AMV complex in accordance with the original colour of the bridge. The cables will be provided with double protection by the mean of hot dip galvanisation plus paint protection according to ITSEOA recommendations. The tie rods in the anchorage galleries will also be coated with double protection galvanization plus painting, due to the humid environment in the anchor galleries. Additional drains are to be core-drilled at the low points of the anchor galleries down to road level to continuously evacuate infiltration water from the galleries, reducing the ambient humidity and therefore the development of the corrosion of the tie rods in the anchorage galleries.

5 RESTORATION WORKS

5.1 *General methodology*

Suspension replacement is the first task to be carried out for obvious safety reasons. Once complete, the decking can then be replaced safely. The repair works on the pylons, the restoration and strengthening of the handrails, and paint works are carried out after the load transfer onto the temporary suspension and in parallel with other suspension tasks and decking replacement.

5.2 *Detailed design*

The detailed design is based on a complete topographical survey of the viaduct by a scanner, supplemented by manual on site measurements. Three general calculation models were used:

- a calculation model for assessing the existing situation before works on site to determine the allowable loads during construction,
- a calculation model of the bridge in the temporary stages, to assess the suspension replacement works,
- a calculation model of the bridge to verify the bridge after it is re-opened to public for soft mobilities.

These calculation models were carried out with SCIA finite element models in 3D (Figure 7), in non-linear and large displacements analysis. These models are also used for load transfer calculations and to design the large number of temporary works required on site. In terms of drawings, a complete 3D CAD model of the bridge in the different phases of work and in its environment enabled the design of new elements and numerous temporary works. In total, 97 drawings and 41 calculation notes will have been produced.

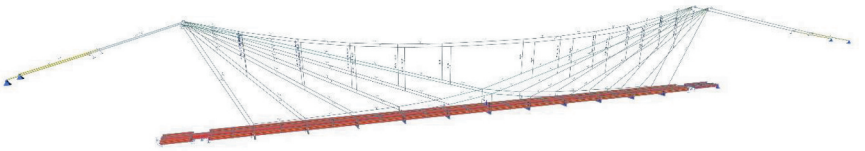


Figure 7. Detailed design structural model (© Baudin Châteauneuf).

5.3 *Temporary suspension principles*

The temporary suspension is made of typical parabolic suspension cables placed above the existing suspension. To facilitate the connection of the vertical hangers to the deck, the spacing between the two fans of the temporary suspension is reduced in the main span part by a set of strut and tie.



Figure 8. Temporary suspension cables and steel frame at pylon tops (© Jean-Dominique Lamy).

At the top of each pylon leg, the temporary suspension rests on a metal frame (Figure 8) supported on two reinforced concrete anchor blocks placed on either side of the leg. The loads are transferred to the masonry by friction through to six pre-stressed horizontal bars clamped to the masonry. The geometry of these frames has been designed to facilitate the disassembly and assembly of the cables, the mobile saddle refurbishment, and the replacement of the rollers.

The temporary cables are anchored in the existing horseshoe anchorage galleries following the same principle as the existing cables. The position of these cables has been carefully studied to allow the cohabitation of the two suspension systems and the handling of all the anchoring elements (plates, tie rods, deflectors).

Due to restricted accessibility on site, the studies included strong assembly constraints. Indeed, the design of the temporary frames placed at pylon tops allowed assembly and dismantling in assemblies of less than 1t, which made it possible to carry out the helicopter transport of these structures (2 times 10t after assembly).

The existing state of the deck also limited access and equipment on the structure. Accordingly, the suspension was designed to be assembled almost entirely on the ground before erection. The suspension was erected with portable traction.

5.4 *Manufacturing for heritage listed Bridge*

The new cables of the bridge were manufactured in the Châteauneuf sur Loire workshop with a stranding machine allowing the manufacture of Open Spiral Strand cables identical in appearance and technology to the existing cables (Figure 9).

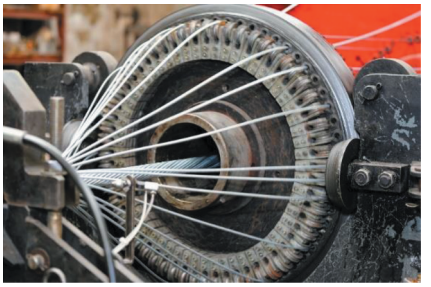


Figure 9. Stranding machine in operation (© Jean-Dominique Lamy).

The new cable sockets were manufactured with a shape very similar to that of the existing sockets. The diversity of cable diameters, and shapes and types of sockets led to the creation of 27 different pieces. The heaviest socket is a massive piece of steel weighing 93kg.

The new decking will be connected to the bridge beams using the arrangement of existing holes. The existing rivets holes will be reused, and the use of rounded head bolts will preserve the aesthetics of the riveted structures, while being more economic than traditional rivets installed at a high temperature with furnace on site.

5.5 *Load transfer*

After the installation of the temporary suspension, the last step of securing the structure was carried out: the load transfer n°1. 101 hydraulic jacks with a capacity of 10 tonnes to 100 tonnes are being used for the load transfer. The jacks are positioned on the temporary vertical hangers and the back stays of the two suspensions. These operations are carried out in stages whose order and jacking strokes have been studied to limit the movement of the saddles, considering that the existing saddles are blocked. At the end of each stage, an analysis of the geometry and pressure measurements are carried out to validate the conformity of the phase and to continue the load transfer. As of October 2023, the bridge is supported by the temporary suspension and the existing Gisclard suspension has been removed (Figure 10).



Figure 10. Bridge configuration in Octobre 2023 with temporary suspension (© Baudin Châteauneuf).

REFERENCES

[1] Le génie Civil du Samedi 31 mai 1913. Revue Hebdomadaire des industries françaises et étrangères - Travaux publics: Pont suspendu fixe, système Gisclard sur la Luzège

Bridge Maintenance, Safety, Management, Digitalization and Sustainability – Jensen, Frangopol & Schmidt (eds)
© 2024 The Author(s), ISBN 978-1-032-77040-6
Open Access: www.taylorfrancis.com, CC BY-NC-ND 4.0 license

Load rating of cast-in-place reinforced concrete box culverts based on load testing

A. Peiris, C. Hutchinson & I. Harik
Department of Civil Engineering, University of Kentucky, Lexington, KY, USA

A. Cole
HDR, Lexington, KY, USA

E. Russell
U.S. Army Engineer Research and Development Center, Vicksburg, MS, USA

ABSTRACT: Many in-service Reinforced concrete box culverts (RCBCs), designed according to older design codes using lighter design truck weights, may require restrictive load posting when rated for current design and permit loads although no structural distress is observed. Most load rating engineers typically utilize 2 dimensional (2D) structural frame software, which leads to fast but highly conservative results. The ratings are negatively affected by the conservative live-load attenuation through soil fill, along with the inability of the 2D method to account for any lateral load distribution. The present study aimed to load rate RCBCs based on strains obtained from field testing. The testing evaluated strains induced by live-load distribution through soil fill when load rating eighteen (18) cast-in-place RCBCs in Kentucky. RCBCs with one-, two-, three-, and four-cells were load tested and the effects of truck live loads analyzed. Fill heights varied from 0 m to 3.6 m, cell spans from 3.0 m to 6.7 m, and culvert spans from 6.7 m to 18.6 m. Strain gauges were attached to the interior surfaces of culverts and the data recorded corresponding to known truck loads and positions. Irrespective of the number of cells in the RCBC, strain variations in the top slab were similar with change in fill height. Maximum strains in the top slabs measured less than 10 microstrain, a value at which live-load effects could be considered negligible, at fill heights greater than 3.05 m. The load rating based on field tests improved both Inventory and Operating rating factors for all tested RCBCs.

1 INTRODUCTION

1.1 *Culvert load rating*

Guidelines from the Federal Highway Administration (FHWA) in the United States categorize structures with a span equal to or greater than 6.1 m as bridges. Culverts meeting this criterion are designated as bridge-size culverts. The majority of bridge-sized culverts take the form of Reinforced Concrete Box Culverts (RCBCs). In Kentucky, more than 90% of these culverts are RCBCs, and of that percentage, over 98% are of the cast-in-place (CIP) variety. A significant portion, exceeding 90%, of Kentucky's RCBCs were constructed before the introduction of Load and Resistance Factor Design (LRFD) Specifications by American Association of State Highway and Transportation Officials (AASHTO) in 1994. Despite having been in service for decades with no apparent structural deterioration, many of these pre-LRFD RCBCs may require load posting when assessed for current design and permit vehicles, particularly those designed according to older codes and for lighter truck weights.

DOI: 10.1201/9781003483755-149

This discrepancy between field inspections and calculated load rating results for culverts has been observed by highway officials at both state and federal levels (Wood et al. 2016).

The prevailing method involves load rating the different components within a RCBC, assuming a unit width for the culvert, as per AASHTO's Manual for Bridge Evaluation (MBE 2018). The capacity of the load rated RCBC member (e.g. top slab, walls, bottom slab) is determined based on material and sectional properties, as well as the rating level. Additional information for capacity calculation may be obtained from field inspections of the culvert condition. Flexure, shear, and axial stresses constitute the dead- and live-load effects used for analytical load ratings.

Computer programs like BRASS-CULVERT (WYDOT, 2013) efficiently conduct analyses using plane 2D frame elements. While load rating through 3D finite element analysis (FEA) offers advantages such as accounting for soil-structure interaction and improved load distribution, this approach can be expensive, time-intensive, and challenging to develop due to the frequently unknown properties of backfill soil. In a standard analytical load rating, calculating dead load effects attributable to self-weight, soil fill, and pavement is relatively straightforward based on material unit weights. The assessment of live-load effects on various reinforced concrete elements of a RCBC is a more intricate process, involving several parameters (AASHTO 2018). These parameters encompass live-load attenuation through the soil fill in both longitudinal and transverse directions, estimated dynamic effects, live-load surcharge, and the consideration of multiple presence effects when more than one traffic lane is loaded. AASHTO LRFD Specifications (2020) provide guidance on deriving live-load effects for RCBCs based on fill height. Live-load effects determined in adherence to these specifications can sometimes be overly conservative, as noted by Okeil et al. (2018) and Orton (2015). According to Wood et al. (2016), older in-service RCBCs often exhibit minimal structural damage, yet calculated load ratings suggest inadequate capacity for the rating truck, necessitating load posting or potentially replacement.

1.2 *Research on culvert testing*

Tadros et al. (1989) conducted experimental assessments of pressures induced by live loads on RCBCs, comparing them with theoretical outcomes and prior AASHTO Standard Specifications. Abdel-Karim et al. (1990) suggested that live-load effects can be disregarded when they constitute less than 5% of the total load effect. They also noted that rigid pavements and the two-way action in the top slab can assist in distributing the effects of wheel loads onto culverts. The influence of pavement stiffness was experimentally assessed by Acharya et al. (2016), revealing that three times less deflection occurred when the truck was positioned over concrete pavement compared to an unsurfaced area. Evaluation of the AASHTO LRFD Specification load distribution for culverts with low fill (fill depth < 0.6 m) using finite element analysis was carried out by McGrath et al. (2005). It was concluded that these low fill culverts should be designed ignoring the live load attenuation through the fill depth. McGrath et al. (2005) also found shear failure rarely controlled the failure in RCBCs and determined that the load distribution width parallel to the span should be increased in the AASHTO LRFD Specifications to account for two-way action in the top slab.

Orton et al. (2015) conducted load tests on ten bridge-size RCBCs in Missouri, featuring fill depths ranging from 0.8 m to 4.0 m. Among these, two had 3-cells, while the rest had 2-cells. The study revealed that live load effects decreased with increasing fill depth, concluding that the AASHTO LRFD Specifications are more conservative at lower fill depths compared to greater fill depths. In a separate study, Okeil et al. (2018) conducted load tests on eight bridge-size RCBCs in Louisiana. This included one 2-cell culvert, while the remaining culverts were 3-, 4-, or 5-cell structures with cell spans ranging from 1.5 m to 2.4 m. Calibrated finite element models of the RCBCs indicated that the rating factor increased with the fill-height to span-length ratio.

2 LOAD TESTING OF CULVERTS

2.1 *The need for load tests*

The culvert load testing was a component of a broader study aimed at assessing and load rating 1,169 bridge sized RCBCs in Kentucky. After a thorough review of methods and software,

BRASS-CULVERT, developed by the Wyoming Department of Transportation (WYDOT, 2013), was selected due to its rapid analysis capabilities using plane frame elements. This software, incorporating the latest AASHTO Specifications and standard truck types, serves as an efficient and user-friendly load rating tool. In the analysis of a culvert, axle live loads are distributed through the fill depth based on relevant AASHTO guidance. However, the software does not account for the transverse load distribution by the culvert top slab, or the distribution of axle loads due to asphalt pavement. Load rating results indicated that 64.8% of the culverts have an Inventory Rating Factor less than 1, with 94.5% of the failures occurring within the top slab (74.3% in flexure and 20.2% in shear). Given that over 60% of the RCBCs had been in service for at least 60 years (constructed prior to 1959) without observable structural degradation, the results from BRASS-CULVERT were deemed excessively conservative. Load testing was identified as (1) a way of identifying the actual load distribution of RCBCs through compacted backfill under truck live loads; (2) a method of load rating RCBCs in general, provided the necessary range of spans and fill heights were included in the test matrix; and (3) a load rating tool for culverts that lack plans or have incomplete plans.

2.2 *Test outline*

Field load testing used loaded trucks, with scale-measured axle weights, and strain gauges attached to the interior surfaces of culverts. Most data came from design plans, although fill

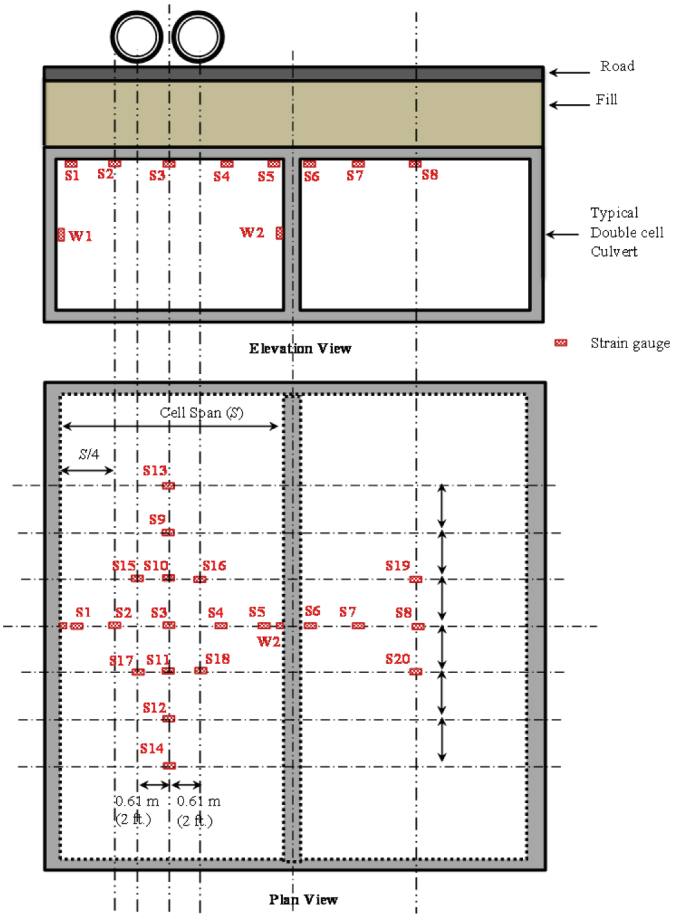


Figure 1. Typical strain gauge layout for a 2-cell culvert.

heights were field measured using a survey level. This was a result of design values in plans being inaccurate, possibly due to changes in roadway elevations over time. Eighteen (18) RCBCs in Kentucky with one-, two-, three-, and four-cells were load tested and the effects of truck live loads analyzed. Fill heights varied from 0 m to 3.6 m, cell spans from 3.0 m to 6.7 m, and culvert spans from 6.7 m to 18.6 m. The principal instrumentation utilized were reusable strain gauges affixed to the concrete surface through two metal tabs attached with adhesive. Figure 1 illustrates a typical strain gauge layout on the top slab and walls for a 2-cell RCBC.

These gauges were attached to nodes that wirelessly transmitted strain data to a laptop. Strain gauges were laid out in a cruciform pattern centered at midspan of the primary cell. This cell was evaluated in detail and hence more extensively gauged. For 3-cell culverts only two cells were instrumented; the interior cell was considered the primary cell. A typical gauge setup in the primary cell of a low-fill RCBC is shown in Figure 2. The truck load applied on a 4-cell RCBC, along with the data acquisition carried out from the creek bank, is seen in Figure 3. Both single rear axle and tandem rear axle trucks were used for the live-load application. Truck weights were measured before testing on a certified load scale. Multiple load cases, along different wheel paths, were used in the testing. Prior to testing, tire positions were pre-marked on the road surface to accurately position the axles.



Figure 2. Strain gauges on a primary cell.



Figure 3. Truck loading and data acquisition.

3 LOAD TEST RESULTS

3.1 *Normalizing truck weights*

Various trucks were employed for testing, each with different axle weights. The recorded strains underwent normalization to equivalent AASHTO truck weights, specifically the HS20 loading (145 kN rear axles). It was assumed that the strains fell within the linear response region. The normalization of strains relied on the ratio between positive moments induced on the top slab by the rear axle weights of the test truck and those of the AASHTO truck. This normalization was feasible since maximum positive strains consistently occurred when the rear axle(s) were positioned at the midspan of the culvert cell, with the front axle either off the culvert or situated on an adjacent cell. The AASHTO LRFD Specifications load distribution was assumed when attenuating live-load pressure through the fill depth. In the FEA software SAP2000 (CSI, 2018), the top slab was modeled as a continuous beam, and corresponding moments were calculated for both the test truck and AASHTO truck. Assuming an uncracked concrete section was critical for obtaining the most conservative load rating results. The moments generated by the rear axle of the test truck ranged from 81.2% to 110.7% of the moments produced by the AASHTO truck.

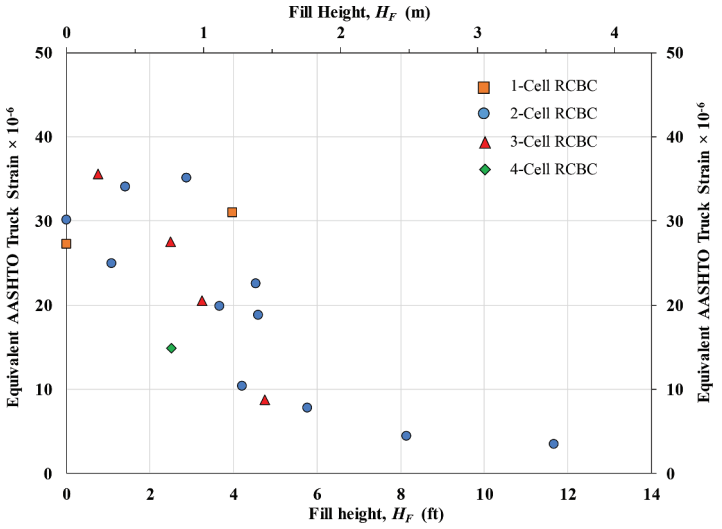


Figure 4. Maximum positive strain variation with fill height.

3.2 *Maximum strain variation with fill height*

In Figure 4, equivalent AASHTO truck strains, derived from the maximum positive strains observed during the load tests for all tested culverts, are plotted against the measured fill heights. The figure also indicates the number of cells in each culvert. The data presented in Figure 4 reveals that as the fill height increased, the maximum positive strain in the top slab declined. This trend is consistent for both 2- and 3-cell culverts, and the strain data for the lone 4-cell culvert tested also aligns with this pattern. Beyond a fill height of 1.8 m, strains are less than 10×10^{-6}. The data suggests, contrary to the AASHTO guidelines, that live-load effects become negligible beyond a specific fill height, regardless of the number of cells in the culvert.

3.3 *Load rating based on load tests*

Field-measured strains were utilized to perform load rating on the RCBC top slabs for flexure in accordance with MBE guidelines for diagnostic load testing. Ratings derived from field measurements were adjusted by considering the analytical load rating factor and accounting

for observed benefits in the load testing. Maximum positive strains, and in the case of multi-cell culverts, negative strains 150 mm from the interior wall, were taken into consideration and updated using the MBE relationship in Equation (1):

$$RF_T = RF_c K \tag{1}$$

where

RF_T = load-rating factor for the live-load capacity based on the load test result

RF_c = rating factor based on calculations prior to incorporating test results

K = adjustment factor resulting from the comparison of measured test behavior with the analytical model

Inventory and operating rating factors for an AASHTO truck based on LRFR that were calculated are provided in Table 1 along with the corresponding rating from BRASS-CULVERT (WYDOT, 2013) for positive bending of the top slab. BRASS-CULVERT analyzes RCBCs as plane frame elements and allows easy and quick development of the culvert model, specifying the size of the reinforcement within the slabs and walls as well as the material properties of the steel and concrete for each culvert. While effects such as lateral earth and water pressure are considered, since soil structure interaction is not considered, only the unit weight of soil is required as an input. But as seen in Table 1, the load rating based on the 2D software provides very highly conservative rating factors. The load rating based on field tests improved both Inventory and Operating rating factors for all tested RCBCs. Similar results were observed for other load rating vehicles as well.

Table 1. Load rating of tested culverts.

	LRFR AASHTO Truck Inventory Rating Factor		LRFR AASHTO Truck Operating Rating Factor	
Culvert ID	BRASS CULVERT	Load Test	BRASS CULVERT	Load Test
025B00043N	1.15	3.31	1.49	4.28
011B00058N	1.54	7.60	2.00	9.85
040C00052N	0.89	4.23	1.16	5.49
034B00005N	0.98	3.19	1.28	4.14
034B00109N	2.29	17.44	2.96	22.61
104B00017N	0.52	5.86	0.68	7.59
104B00018N	0.67	3.94	0.87	5.10
088C00072N	0.97	4.09	1.25	5.31
099B00064N	1.65	9.82	2.14	12.73
097B00059N	1.07	4.30	1.39	5.57
097B00060N	0.78	4.60	1.01	5.96
097B00061N	0.8	2.90	1.04	3.76
097B00062N	1.09	6.36	1.41	8.25
099B00054N	0.87	3.98	1.13	5.16
099B00055N	0.69	2.81	0.89	3.64
096B00023N	4.67	17.20	6.05	22.30
094B00011N	1.33	7.56	1.72	9.80
120B00037N	2.04	6.68	2.64	8.66

4 CONCLUSIONS

The effect of truck live loads was investigated for the top slab of eighteen (18) cast-in-place (CIP) reinforced concrete bridge-size culverts (RCBCs). These RCBCs included configurations with one-, two-, three-, and four-cells, featuring fill heights (H_F) ranging from 0 m to 3.6 m, clear cell spans (S) spanning from 3.0 m to 6.7 m, and culvert spans varying between

6.7 m and 18.6 m. Reusable strain gauges affixed to the interior surfaces of the culverts was used to investigate the effects, and trucks with known axle weights served as the live load. Positive strains measured in the top slab were converted to equivalent AASHTO truck strains for comparison. The load rating based on the load test results improved the rating for all culverts tested. The study supports the following conclusions:

- With increasing fill height, the maximum positive live-load strain, ε_{LL}^{+}, in the top slab under the AASHTO truck load becomes negligible ($\varepsilon_{LL}^{+} < 10\times10^{-6}$) for fill heights $H_F > 3.05$ m.
- In contrast to AASHTO guidelines for multicell culverts, fill height does not need to surpass the clear distance between end walls for live-load effects to be considered negligible.

REFERENCES

AASHTO. (2020). LRFD Bridge Design Specifications, 9th Ed., American Association of State Highway and Transportation Officials, Washington, DC.

AASHTO. (2018). The Manual for Bridge Evaluation, 3rd Ed., American Association of State Highway and Transportation Officials, Washington, DC.

Abdel-Karim, A.M., Tadros, M.K., and Benak, J.V. (1990). "Live Load Distribution on Concrete Box Culverts." *Transportation Research Record 1288*, 136–151.

Acharya, R., Han, H., Brennan, J.J., Parsons, R.L., and Khatri, D.K. (2016). "Structural Response of a Low-Fill Box Culvert under Static and Traffic Loading." *J. Perform. Contr. Facil.*, 30(1):04014184.

CSI. (2018). SAP2000 Structural Analysis and Design, Version 22.1. Computers & Structures, Inc.

McGrath, T.J., Liepins, A.A., and Beaver, J.L. (2005). "Live load distribution widths for reinforced concrete box sections." *Transportation Research Record: Journal of the Transportation Research Board*, CD 11-S, Transportation Research Board of the National Academies, Washington, DC, 99–108.

Okeil, A. M., Ulger, T., and Elshoura, A. (2018) "Live load rating of cast-in-place concrete box culverts." Rep. No. *FHWA/LA.17/593*, Louisiana Dept. of Transportation and Development, Baton Rouge, LA.

Orton, S.L., Loehr, J.E., Boeckmann, A. and Havens, G. (2015). "Live-load Effect in Reinforced Concrete Box Culverts under Soil Fill." *J. Bridge Eng.*, 20(11):04015003.

Tadros, M.K., Benak, J.V., Abdel-Karim, A.M., and Bexten, K.A. (1989). "Field Testing of a Concrete Box Culvert." *Journal of the Transportation Research Board*, 1231, 49–55.

Wood, T.A., Lawson, W.D., Surles, J.G., Jayawickrama, P.W. and Seo, H. (2016). "Improved Load Rating of Reinforced-Concrete Box Culverts Using Depth-Calibrated Live-Load Attenuation." J. Bridge Eng., 21(12): 04016095.

WYDOT. (2013). Analysis, Design and Rating of Reinforced Concrete Box Culverts, BRASS-CULVERT™, Version 2.3.5. Wyoming Department of Transportation.

Bridge Maintenance, Safety, Management, Digitalization and Sustainability – Jensen, Frangopol & Schmidt (eds)
© 2024 The Author(s), ISBN 978-1-032-77040-6
Open Access: www.taylorfrancis.com, CC BY-NC-ND 4.0 license

Seismic finite element method simulation of a soil-steel bridge with a gravel-rubber mix

T. Maleska, D. Beben & J. Nowacka
Faculty of Civil Engineering and Architecture, Opole University of Technology, Opole, Poland

A. Fiamingo & M.R. Massimino
Department of Civil Engineering and Architecture, University of Catania, Catania, Italy

ABSTRACT: Soil–steel complex bridges have been applied for many years in transport infra- structure. They are widely used in North America, Europe and Australia. The design codes and calculation methods related to soil–steel complex bridges and culverts specify, among others, the re- quirements for backfill. The typical backfill should be well-granulated sands and well-compacted gravels of harsh, coarse, or round grains. The behaviour of these bridges under static loads is relatively well understood. However, the response of these bridges to dynamic loads, especially seismic loads, is not fully known. Examples from the United States and Australia show that earthquakes damaged such bridges. Therefore, new solutions for the backfill are currently being sought to increase damping properties to minimize dynamic influences. The present study deals with a numerical simulation of a soil-steel complex bridge using a gravel-rubber mixture from end-of-life tire recycling as the backfill. A nonlinear model with El Centro records and the time history method was used. Using the DIANA program, numerical calculations were performed for two cases, i.e., the bridge shell covered with a traditional backfill and the gravel-rubber mix. The bridge has two closed pipe arches in its cross-sec- tion. The load-carrying structure was constructed as two shells assembled from corrugated steel plate sheets (depth = 0.05 m, pitch = 0.15 m, plate thickness = 0.003 m, shell span = 4.40 m, shell height = 2.80 m). The results suggest that the gravel-rubber mix can be used in soil-steel complex bridges as an alternative to traditional backfill. This results in better absorption of the seismic energy by the gravel-rubber mix than the conventional granular backfill. An indirect effect is the use of tire recycling, which is part of the sustainable development of the construction industry.

1 INTRODUCTION

Soil-steel complex bridges are becoming increasingly common in our landscape (Figure 1). This state of affairs is influenced by the numerous advantages of these structures, i.e., primarily the speed of construction and construction costs of this type of object (Beben 2020). The economic aspect is essential nowadays, and in the case of soil-steel bridges, there is a chance to reduce construction costs by up to 60% compared to traditional bridges made of steel or concrete. How- ever, due to their construction (a thin corrugated shell covered with soil), buried steel structures (pipelines, bridges, culverts, pipes, and tunnels) seem sensitive to seismic shocks, as shown in Figure 2. Therefore, searching for a backfill material that would reduce seismic excitation is nec- essary.

In earthquake engineering, recent studies Tsang (2009) show that Geotechnical Seismic Isola- tion (GSI) is a potential and emerging technique to mitigate the seismic effects on structural sys- tems involving Dynamic Soil Structure Interaction (DSSI). The main idea is to

DOI: 10.1201/9781003483755-150

improve the foun- dation soil and, therefore, to reduce the accelerations and the seismic energy that reach the foundations (Forcellini, 2017, Tsang 2022). Different geo-materials can be adopted as GSI (Somma et al. 2022, Tsiavos et al. 2022), among which the Gravel Rubber Mixtures (GRMs). GRMs represent an eco-sustainable solution because the rubber grains are obtained from ELTs (End of Life Tires), whose disposal is an environmental problem. The sustainability and ad- vantages of the GRMs have been investigated by laboratory and in-situ tests (Anastasiadis et al. 2012, Senetakis & Anastasiadis 2015, Pitilakis et al. 2021), but only a few numerical analyses on structures and infrastructures have been performed (Chiaro et al. 2023, Abate et al. 2023). Thanks to the lower shear stiffness and high-damping material, the GRMs are a promising GSI system, ensuring high-energy dissipation due to the rubber inclusions.



Figure 1. Example of the soil-steel bridge in Opole (Poland).

The analysis of soil-steel bridges/culverts subjected to seismic excitation has already been un- dertaken. It is concerned with the determination of the impact of (i) boundary conditions (Maleska & Beben 2023a), (ii) soil cover height (Maleska & Beben 2022, 2023b, Lee et al. 2006), (iii) assessment of the effectiveness of the use of additional longitudinal ribs to strengthen the shell (Maleska et al. 2021), (iv) EPS relieving elements (Maleska et al. 2019, Santos et al. 2020). Mah- goub & El Naggar (2021) presented some aspects of the seismic design of soil-steel culverts.

Thus, the impact of the backfill type on the seismic response of soil-steel bridges has yet to be studied. Therefore, this study aimed to determine the reaction of the soil-steel bridge under seis- mic load, in which a backfill mixed with granulated rubber from ELTs was used. In soil-steel bridges, the backfill is the essential element of the structure, where, in combination with the cor- rugated steel shell, it creates a load-bearing quasi-composite structure. The study analysed dis- placements and accelerations for two bridge models (Model I – standard backfill and Model II – GRM backfill) under seismic excitation using a finite element code.

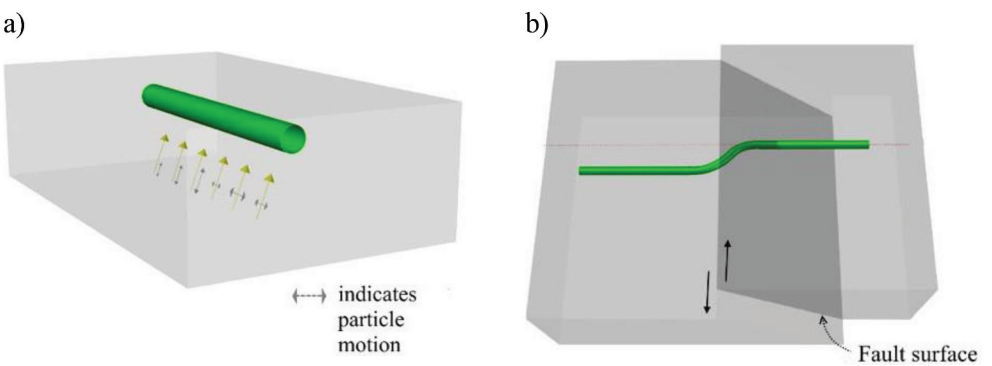


Figure 2. Mechanism of the behaviour of buried steel structures during earthquakes: a) seismic wave propagation, b) pipeline deformation (Psyrras & Sextos 2018).

2 DESCRIPTION OF RESEARCH APPROACH

2.1 *Description of the investigated real bridge*

The analysed structure is a railway soil–steel complex bridge located in Krosnowice in the Lower Silesian Voivodeship, Poland. This structure consists of two shells (Figure 3). The steel shells of this object have a pipe-arch section and are constructed of corrugated steel plates (CSP) with a thickness of t = 3 mm and dimensions of 50 × 150 mm. The shells in the bridge structure have a span of L1 = L2 = 4.4 m and are erected directly on the ground (Figure 3b). The clear height of the shells is 2.8 m. The individual sheets of the CSPs are fixed with M20 high-strength bolts. The backfill height above the CSP shells is equal to 2.4 m. The length of the bridge in the steel shell crown is 16.0 m and 21.8 m at the base.

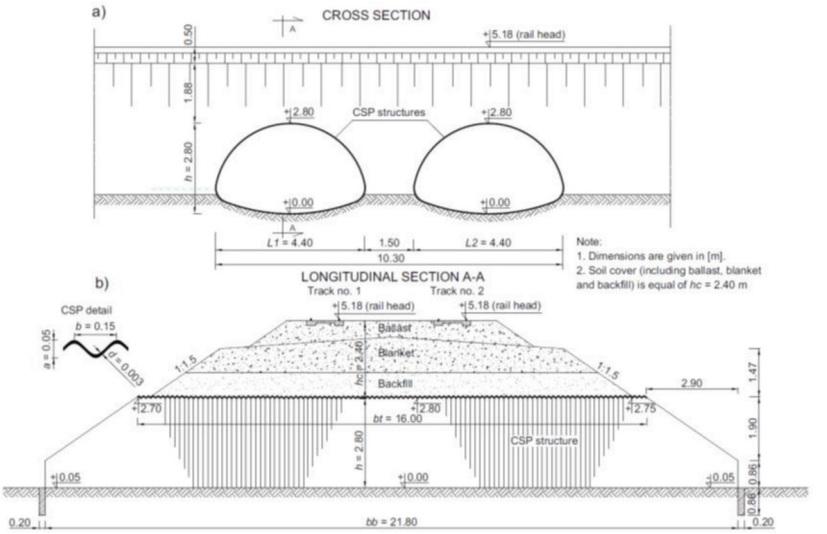


Figure 3. Analysed bridge: a) cross-section and b) longitudinal section.

2.2 *Description of the developed numerical model*

2.2.1 *Steel shell*

As mentioned, these shells are characterized by a pipe-arch cross-section and are constructed of CSPs with dimensions of 50 × 150 mm and a thickness of t = 3 mm. Considering the corrugation parameters, the area cross-section was 3.77 mm^2/mm, and the moment of inertia was 1176.60 mm^4/mm. The following properties of steel were used in the DIANA FEA: Young modulus 205 GPa, density 7850 kg/m^3, Poisson ratio of 0.3 and strength yield of 235 MPa.

2.2.2 *Backfill*

Two types of backfill were considered in the study: (i) standard backfill (Model I) and (ii) GRM backfill (Model II). In the case of the standard backfill (Model I), the nonlinear hyperbolic Dun- can-Chang constitutive model was used (Table 1). The GRM (Model II) had the following prop- erties: a content of rubber equal to 45% and a content of gravel equal to 55% (for the total volume of the mixture), Gs=2.07 (specific gravity), D50,R/D50,G =1.2 (ratio between the mean diameter of the rubber grain and that of the gravel grain), Dr = 50% (relative density), (v) γ =20.3 kN/m^3 (density). GRM was modelled using the Hardening Soil with small strains constitutive model with the parameters included in Table 1.

2.2.3 *Boundary conditions*

The boundary conditions were used as pinned support, shown in Figure 4a. A detailed description of these boundary conditions was presented in the paper by Maleska & Beben (2023a).

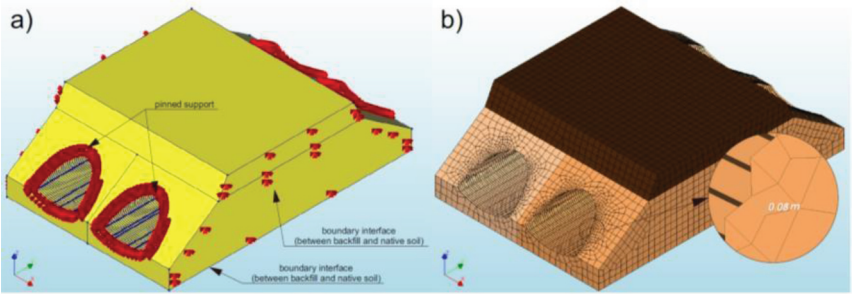


Figure 4. Numerical model of the bridge: a) boundary conditions, b) mesh of finite elements.

Table 1. Properties of the backfills used for the numerical analysis.

Duncan-Chang constitutive model – standard backfill (Model I)	
parameter	value
Density [kN/m^3]	20.5
Young modulus [MPa]	100
Poisson ratio [-]	0.2
Friction angle [°]	39
Dilatation angle [°]	5
Cohesion [kPa]	3.0
Failure ratio [-]	0.7
Unloading-reloading stiffness [kPa]	1
Reference pressure [kPa]	101.35
unloading-reloading curve [-]	0.25
Backbone curve [-]	1.1
Minimum compressive stress [kPa]	0.35
Minimum tangential stiffness of the backbone curve [kPa]	1.2
Hardening Soil with small strains constitutive model – GRM backfill (Model II)	
Density [kN/m^3]	20.3
Reference secant stiffness in standard drained triaxial test [kPa]	2183
Reference tangent stiffness for primary oedometer loading [kPa]	2183
Reference unloading/reloading stiffness [kPa]	6550
Failure Ratio [-]	0.9
Reference pressure [kPa]	100
Power for stress-level dependency of stiffness [-]	0.77
Friction angle [°]	38
Dilatancy angle [°]	0
Cohesion [kPa]	0.00
Poisson Ratio [-]	0.3
Reference initial shear modulus [kPa]	1221.688
The shear strain level at which the secant shear modulus was reduced by about 70% of the initial shear modulus [-]	8.49E-05

2.2.4 *Seismic excitation*

El Centro records from the USA were used as seismic excitation in the DIANA FEA numerical program (Figure 5). This record dates from May 18, 1940, and is considered destructive. Intensity X characterizes it on the Mercalli scale (6.9 on the Richter scale). This excitation is irregular (strongly stochastic). In addition, it should be added that this record is characterized by an ex- tended zone of high intensity, which translates into a significant impact on structures. Most engi- neering structures cannot cope with such a strong excitation, so it was decided to use it in this study.

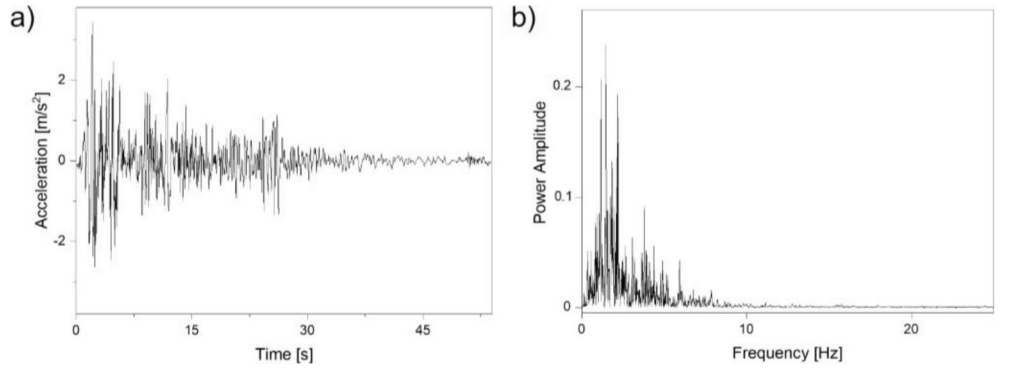


Figure 5. El Centro time-history for the direction of a) X (NS), b) spectrum response of X (NS).

2.2.5 *Interface*

The interaction between the backfill and the steel shell has been considered by applying an auto- matic interface with the "Coulomb friction" function. In this function, the angle of internal friction of 39°, the dilation angle of 5°, the stiffness of 100000 kN/m^3, and the cohesion of 3 kPa were assumed.

3 RESULTS OF NUMERICAL SIMULATIONS

3.1 *General remarks*

The DIANA FEA numerical program based on the finite element method using the time history method, which is recommended by the design standards (AASHTO 2017, CHBDC 2017 or CEN 2005), was used to assess the impact of seismic excitation on the tested object. The time history method analyses the response and behaviour of the structure in individual time steps throughout the duration of the given seismic excitation as a result of the numerical analysis obtained displace- ment and acceleration results for two models (Model I – standard backfill and Model II – GRM).

3.2 *Displacements*

The numerical analysis shows that the largest displacements in the soil-steel bridge shell were recorded in Model II, where the GRM was used. In this model, the maximum displacement due to seismic excitation was –4.89 × 10^{-3} m (Figure 6b). Whereas Model I had a smaller displacement than Model II by 80% and was –9.65 × 10^{-4} m (Figure 6a).

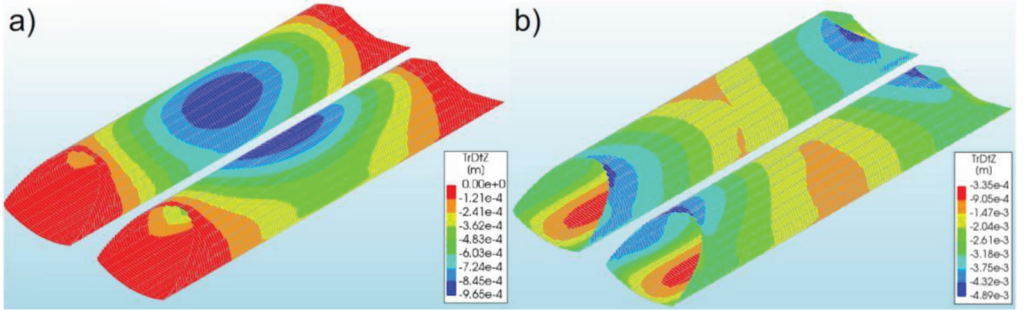


Figure 6. Maps of maximal vertical displacements in the CSP shells of models: a) I and b) II.

Different places of occurrence of maximum displacements in both models were also noticed. In Model I with standard backfill, the maximum displacements were recorded in the middle of the length of the CSP shells in their crown (Figure 6a). The maximum displacements in Model I are concentrated over a larger area of shells, while in Model II, the maximum displacements are dis- persed (Figure 6b). In Model II, the maximum displacements were recorded on small fragments of the inlet and outlet in both shells.

It should be added that in both models at the inlet and outlet of the bridge, the use of RC collars was simulated (as the pinned supports), which is consistent with the general practice in construct- ing this type of bridge. The obtained results show that in the case of the GRM (Model II), there are small concentrations of displacements in the area of the RC collars, and for a typical backfill (Model I), they are shifted to the centre of the shell near the crown.

In addition, it can be seen that the maximum displacements in Model II (Figure 7b) occurred around 50 seconds of the earthquake duration, while in Model I (Figure 7a), the maximum displace- ments were recorded around 6-7 seconds of the excitation duration. It can be seen that the struc- tures are excited differently, so they have different dynamic characteristics.

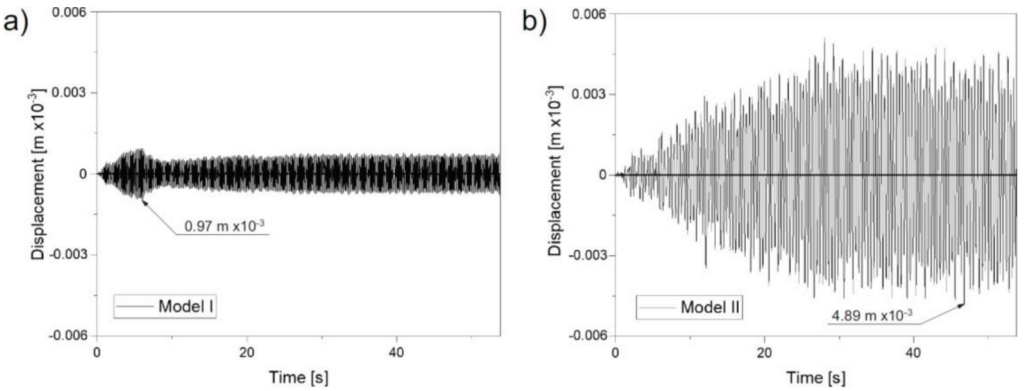


Figure 7. Time History of vertical displacements of bridge models: a) I and b) II.

3.3 *Accelerations*

The highest accelerations of 6.04 m/s^2 (Figure 8b) were recorded in Model II (gravel-rubber mix). On the other hand, in Model I (standard backfill), accelerations were lower by 38% compared to Model II and amounted to 3.74 m/s^2 (Figure 8a).

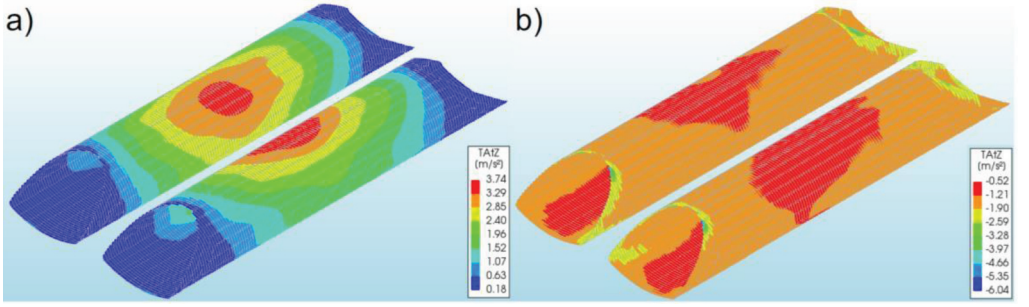


Figure 8. Maps of maximal accelerations of CSP shell of models: a) I and b) II.

The places of maximum accelerations were analogous to displacements, i.e. in Model I (stand- ard backfill), they were noted in the middle of the length of the shells, in their crown (Figure 8a). The places of maximum accelerations in Model I were concentrated, while in

Model II, the max- imum accelerations were dispersed over a larger area. In Model II (Figure 8b), maximum accelera- tions were recorded at the inlet and outlet in both shells. Moreover, these accelerations were local, covering a small area of steel shells.

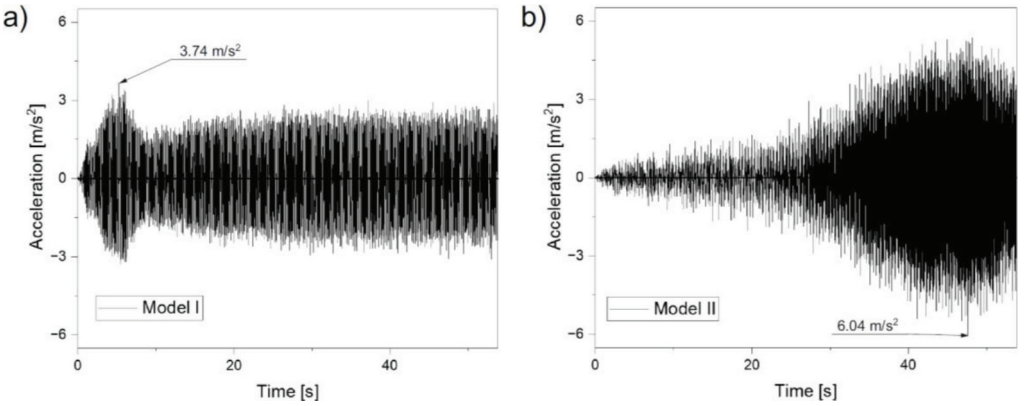


Figure 9. Time history of accelerations of bridge models: a) I and b) II.

It should also be emphasized that the maximum accelerations in Models I and II were recorded at a similar time as in the case of displacements. In Model I (Figure 9a), the maximum accelerations were recorded around 6-7 seconds of the excitation duration, while in Model II (Figure 9b), around 50 seconds of the seismic excitation duration.

4 CONCLUSIONS

As a result of the numerical analysis, it can be concluded that using a backfill mixed with 45% by volume of granulated rubber from ELTs in its composition does not reduce displacements and accelerations in the analysed soil-steel bridge. However, it should be noted that the bridge built using GRM (Model II) has a much better ability to distribute the seismic load over a larger area (no load concentration). In addition, after the analysis, it can be concluded that:

- displacements of the soil-steel bridge caused by seismic excitation are small, but various types of backfills reveal different bridge behaviour. The question arises: shouldn't slightly larger dis- placements be allowed at the expense of a more favourable distribution of loads over a larger area?
- maximum displacements and accelerations in Model II (GRM) occur much later than in Model I (standard backfill). This proves the higher seismic resistance of Model II,
- the obtained results prove the great possibilities of using backfill with the addition of used tires as an alternative to traditional backfill in constructing soil-steel bridges in seismic areas.

In conclusion, further research is needed to determine the effect of GRM in soil-steel bridges/culverts under different types of loads. In the future, it is planned to conduct experimental tests of the soil-steel bridge using a GRM under static and cyclic loads caused by the simulation of passing vehicles. In addition, it is planned to carry out tests for a varied composition of the backfill, assuming a variable ratio of pieces of used tires to the soil.

REFERENCES

AASHTO 2017. *Bridge LRFD Design Specifications*. Washington: American Association of State Highway and Transportation Officials.

Abate, G., Fiamingo, A., Massimino, M.R. & Pitilakis, D. 2023. FEM investigation of full-scale tests on DSSI, including gravel-rubber mixtures as geotechnical seismic isolation. *Soil Dynamics and Earthquake Engineering* 172: 108033.

Anastasiadis, A., Senetakis, K., Pitilakis, K., Gargala, C., Karakasi, I., Edil, T. & Dean, S.W. 2012. Dynamic behavior of sand/rubber mixtures. Part I: Effect of rubber content and duration of confinement on small-strain shear modulus and damping ratio. *Journal of ASTM International* 9(2): 103680.

Beben, D. 2020. *Soil-Steel Bridges. Design*, *Maintenance and Durability*. Cham: Springer.

CHBDC 2017. *Canadian Highway Bridge Design Code CAN/CSA-S6-17*. Mississauga: Canadian Standards Association International. Ontario.

CEN 2005. *Eurocode 8*, *Actions Design of structures for earthquake resistance*. Brussels: European Committee for Standardization.

Chiaro, G., Palermo, A., Banasiak, L., Tasalloti, A., Granello, G. & Hernandez, E. 2023. Seismic response of low-rise buildings with eco-rubber geotechnical seismic isolation (ERGSI) foundation system: nu- merical investigation. *Bulletin of Earthquake Engineering* 21(8): 3797–3821.

Forcellini, D. 2017. Assessment on geotechnical seismic isolation (GSI) on bridge configurations. *Innovative Infrastructure Solutions* 2: 760.

Lee, S., Chung, H., Chun, B., Ahn, B. & Rhee, J. 2006. Dynamic behaviours of corrugated steel plate structures in open-cut tunnels. *Tunneling and Underground Space Technology* 21(3–4): 385.

Mahgoub, A. & El Naggar, H. 2021. Seismic Design of Metal Arch Culverts: Design Codes vs. Full Dynamic Analysis. *Journal of Earthquake Engineering* 25(11): 2231–2268.

Maleska, T. & Beben, D. 2023. Behaviour of soil-steel composite bridges under strong seismic excitation with various boundary conditions. *Materials* 16(2): 650.

Maleska, T. & Beben, D. 2023. Effect of the soil cover depth on the seismic response in a large-span thin-walled corrugated steel plate bridge. *Soil Dynamics and Earthquake Engineering* 166: 107744.

Maleska, T. & Beben, D., Nowacka, J. 2021. Seismic vulnerability of a soil-steel composite tunnel – Norway Tolpinrud Railway Tunnel Case Study. *Tunnelling and Underground Space Technology* 110: 103808.

Maleska, T. & Beben, D. 2022. Behaviour of soil-steel composite bridge with various cover depths under seismic excitation. *Steel and Composite Structures* 42(6): 747–764.

Maleska, T., Nowacka, J. & Beben, D. 2019. Application of EPS Geofoam to a Soil–Steel Bridge to Reduce Seismic Excitations. *Geosciences* 9(10).

Psyrras, N. & Sextos, A. 2018. Safety of buried steel natural *gas pipelines under earthquake-induced ground shaking: A review*. *Soil* Dynamics and Earthquake Engineering 106: 254–277.

Pitilakis, D., Anastasiadis, A., Vratsikidis, A., Kapouniaris, A., Massimino, M.R., Abate, G. & Corsico, S. 2021. Large-scale field testing of geotechnical seismic isolation of structures using gravel-rubber mix- tures. *Earthquake Engineering & Structural Dynamics* 50(10): 2712–2731.

Santos, R.R.V., Kang, J. & Park, J.S. 2020. Effects of embedded trench installations using expanded poly- styrene geofoam applied to buried corrugated steel arch structures. *Tunnelling and Underground Space Technology* 98: 103323.

Senetakis, K. & Anastasiadis, A. 2015. Effects of state of test sample, specimen geometry and sample preparation on dynamic properties of rubber–sand mixtures. *Geosynthetics International* 22(4): 301–310.

Somma, F., Bilotta, E., Flora, A. & Viggiani, G.M.B. 2022. Centrifuge modeling of shallow foundation lateral disconnection to reduce seismic vulnerability. *Journal of Geotechnical and Geoenvironmental Engineering* 148(2): 04021187.

Tsang, H.H. 2009. Geotechnical Seismic Isolation. In Miuraand Takumi & Yuuki Ikeda (eds.), *Earthquake Engineering: New Research*; New York: Nova Science Publishers, Inc., pp. 55–87.

Tsang, H.H. 2022. Analytical design models for geotechnical seismic isolation systems. *Bulletin of Earthquake Engineering* 21: 3881–3904.

Tsiavos, A., Kolyfetis, D., Panzarasa, G., Burgert, I. & Stojadinovic, B. 2022. Shaking table investigation of a low-cost and sustainable timber-based energy dissipation system with recentering ability. *Bulletin of Earthquake Engineering* 21(8): 3949–3968

Bridge Maintenance, Safety, Management, Digitalization and Sustainability – Jensen, Frangopol & Schmidt (eds)
© 2024 The Author(s), ISBN 978-1-032-77040-6
Open Access: www.taylorfrancis.com, CC BY-NC-ND 4.0 license

Long-term monitoring of earth pressure in a soil-steel composite railway tunnel

T. Maleska & D. Beben
Faculty of Civil Engineering and Architecture, Opole University of Technology, Katowicka, Opole, Poland

J. Vaslestad
Norwegian University of Life Sciences/Norwegian Public Roads Administration, Operations and Maintenance, Moss, Norway

ABSTRACT: Objects in transport infrastructure, such as bridges, tunnels and culverts, are usually built using reinforced concrete structures. However, since the 1970s, many structures have been constructed with corrugated steel plates and surrounding backfill to form soil-steel composite structures. The paper analyses the soil-steel composite railway tunnel located in Tolpinrud, Norway. The analysed tunnel has a cross-section in the form of a pipe arch with a 7.81 m span and a 6.92 m rise. The tunnel is constructed of steel plates with a 200 mm corrugation pitch, 55 mm depth and 6.8 mm plate thickness. The depth of the soil cover over the steel shell crown varied from 1.1 to 1.6 m. The study's main aim is to show the long-term behaviour of the soil-steel tunnel as well as earth pressure, which has been monitored for 25 years. Experimental studies of the soil-steel railway tunnel were compared with the results of finite element analyses (FEA) performed in the numerical program DIANA FEA. The numerical analysis took into account subsidence and earth pressure during the operation of the tunnel. The long-term behaviour of the soil-steel tunnel demonstrates that there are changes in earth pressure distribution and structural response over time after construction. The numerical analysis performed can be helpful in the design of new soil-steel tunnels and bridges situated on roads and railways. In addition, the study results may help assess the technical condition of the existing soil-steel composite structures.

1 INTRODUCTION

Over the last two decades, a significant increase in the construction of soil-steel structures (bridges, culverts and tunnels) has been observed (Beben, 2020). The increasing interest in these structures is mainly influenced by their advantages, such as (i) speed of assembly, (ii) low construction costs, (iii) continuity of construction, (iv) possibility of off-site construction, and (v) inclusion of sustainable development concepts. Many such structures can be found in the USA, Canada and Europe (Figure 1).

The study of soil-steel bridges has been conducted for many years. Many aspects and work conditions of soil-steel structures under various loads have been analysed. The tests were carried out mainly under static and dynamic loads. In the case of static tests, the influence of the soil pressure on the shell during the backfilling process was analysed by Koruszewicz & Kunecki (2011) and Maleska & Beben (2019), among others. The impact of live loads from vehicles on the soil-steel bridge was presented by, for example, Yea et al. (2014), Wadi et al. (2018) or in laboratory conditions by Mai et al. (2014), Garcia et al. (2015). In terms of dynamic loads, analyses of these objects concerned the impact of passing trucks or trains (Beben, 2013, Flener & Karoumi, 2009). Structures with spans up to 6 m are most often considered. Only a few studies have been conducted on soil-steel tunnels (Vaslestad, 1989,

DOI: 10.1201/9781003483755-151

Kunecki et al. 2007). Analysing the seismic impact on these structures is particularly rare (Mahgoub & El Naggar, 2021, Maleska & Beben, 2021). In seismic design practice for bridges, the loads caused by earthquakes in a seismically active region are often several times more severe than those arising from other causes. The long-term monitoring of the RC tunnel was presented by Maleska et al. (2022).



Figure 1. Example of soil-steel composite tunnel.

As can be seen, most of the analyses and tests concerned soil-steel structure behaviour under specific short-term loads. Therefore, long-term studies are needed to consider these structures' behaviour over time. The primary purpose of this paper is to show the long-term earth pressure (monitoring for 25 years) on the soil-steel tunnel.

2 DESCRIPTION OF EXPERIMENTAL TESTING AND NUMERICAL MODELLING

2.1 *Tunnel description and experimental testing*

The analysed soil-steel tunnel is located at Hønefoss, about 60 km north of Oslo in Norway and completed in 1982. The structure serves as a railroad tunnel under the main road. The shell structure consists of a pipe arch with a 7.81 m span and a 6.92 m rise (Figure 2). The total length of the tunnel is 106 m.

The tunnel is constructed of corrugation steel plates (CSP) with a 200 mm pitch, 55 mm depth and 6.8 mm plate thickness. The shell structure of the tunnel was strengthened using two longitudinal RC beams (0.7×0.7 m). These beams were situated at the quarter points of the shell (Figure 2). It should be added that the analysed tunnel was designed based on static calculations, the contractor's experience and the literature available at that time. The tunnel shell was backfilled using gravel and sand compacted to a minimum 97% Standard Proctor. The backfill was placed in 0.20 m thick layers and adequately compacted using a vibratory roller and bulldozer. The depth of the soil cover over the shell crown varied from 1.1 to 1.6 m (1.1 m was adopted in numerical analysis (Figure 2)). The in-situ soil is a medium-stiff clay with undrained shear strength from 40 to 80 kN/m^2. RC front walls were used to strengthen the tunnel's inlet and outlet. The savings compared to a typical RC tunnel cost were about 25% (Vaslestad, 1989).

During experimental testing, earth pressure cells of the Glotzl type were mounted on the structure 25 m from the northern end and 50 m from the north end (Figure 3). Four earth pressure cells were used in each section. Using specially constructed brackets, four earth pressure cells (measurement points) were bolted onto the steel structure. The brackets have the same corrugation and radius as the

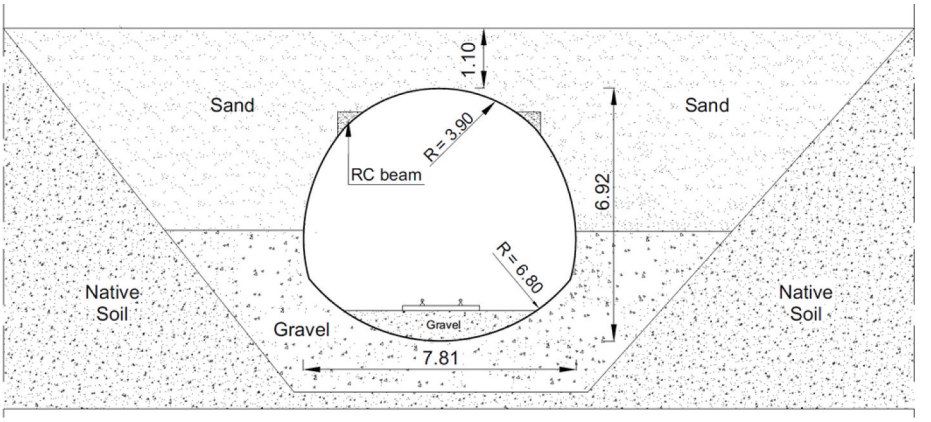


Figure 2. Cross-section of the analysed soil-steel composite tunnel (dimensions are given in [m]).

culvert structure. The earth pressure on the tunnel structure was tested in the steel shell crown (point #1), at the bottom of the tunnel (point #2), on the side walls on the left (point #3) and on the right (point #4). The earth pressure cells are 0.30 m × 0.40 m × 0.005 m. The brackets are 0.60 m × 0.80 m. Calibration of the cells was performed by the manufacturer and was found to agree well with calibration checks in the laboratory. Calibration of the cells with temperature variations from +20°C to –30°C was also performed in the laboratory. Thermistors were placed near each earth pressure cell and in the backfill to give data for temperature corrections and freezing depths (Vaslestad, 1989).

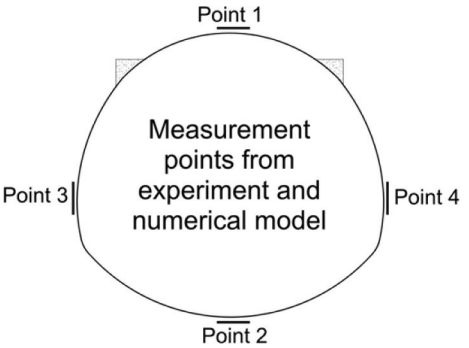


Figure 3. Location of measurement points from earth pressure cells for Tolpinrud tunnel.

2.2 *Description of the FEM model*

The computational analysis used DIANA FEA software based on the finite element method (FEM). This software is dedicated to analysing soil behaviour, where advanced study of the impact of soil on structures is required, e.g., over time. The backfill (gravel and sand) was modelled using a Duncan-ßChang non-linear elastic hyperbolic model (Duncan & Chang, 1970) (solid elements of HX24L type) with Young's moduli of 100 MPa (gravel) and 38.42 MPa (sand), a Poisson ratio of 0.2, densities of 2050 kg/m^3 (gravel) and 2010 kg/m^3 (sand), 3 kPa cohesion, dilation angles of 5° (gravel) and 5.6° (sand), internal friction angles of 39° (gravel) and 34.6° (sand), a failure ratio of 0.7, a 1000 N/m^2 unloading-reloading stiffness, a 0.25 exponent for the unloading reloading curve, a 101350 N/m^2 reference pressure, 350 N/m^2 minimum compressive stress and a 1.1 exponent for the backbone curve.

The shell was modelled as a real object using corrugation profiles with RC beams. The CSP was modelled as an elastic-plastic model (shell curved elements – Q24IF) with a 205 GPa Young's modulus, a 7850 kg/m^3 density, a 0.3 Poisson ratio and a 235 MPa yield strength for

the steel. An 8.29 mm^2/mm cross-sectional area, a 3213.20 mm^4/mm moment of inertia and a 103.65 mm^3/mm elastic section modulus were also used.

The RC beams were modelled using enhanced truss elements according to Eurocode (EC 1992-1-1, 2008). The C30/37 concrete had the following parameters: 0.2 Poisson ratio, 30 MPa characteristic cylinder compressive strength, 38 MPa mean compressive strength, 2.90 MPa mean tensile strength, 32837 MPa elastic modulus, 20 MPa design compressive strength (for αcc = 1.00), 17 MPa design compressive strength (for αcc = 0.85), 1.35 MPa design tensile strength (for αct = 1.00), 0.151% minimum longitudinal tension reinforcement ratio and 0.088% minimum shear reinforcement ratio.

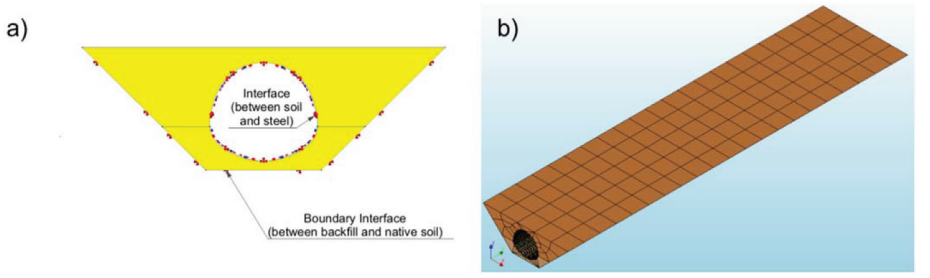


Figure 4. A numerical model of the soil-steel tunnel: a) boundary conditions and b) finite element mesh.

The soil-structure interaction was modelled using an automatic interface. The properties of the interface were a "Coulomb friction" function with a 39° internal friction angle, 3 kPa cohesion, 5° dilation angle and 100000 kN/m^3 rigidity.

The boundary conditions were modelled as hinged support at the inlet and outlet of the tunnel (Figure 4a). This approach simulates the RC front walls like in a real tunnel. In addition, the base and sidewalls of the numerical model were also restricted using hinged supports using the special function ("boundary interface" – Figure 4a) in the DIANA FEA program. This function allows the correct interaction between the backfill and boundary edge (native soil).

Obviously, the impact on the obtained results has the density of the finite element mesh (Figure 4b). Therefore, in the initial stage of numerical calculations, the influence of finite element mesh density in the tested soil-steel tunnel was analysed. It was found that finite elements did not exceed 5.0 m for the backfill and 1.0 m for the steel shell. These dimensions of finite elements can allow a compromise between the result's accuracy and the duration of calculations to be obtained. However, the discretisation of the backfill near the steel shell was much denser. The soil mesh size was only a few centimetres near the shell curves.

3 ANALYSIS OF FEM AND MEASUREMENT RESULTS

3.1 *General remarks*

In engineering practice, it is rare for the monitoring period of objects to be as long as, in this case, 25 years. The presented experimental research lasted from 1981 to 2006. Another important aspect is that an object made of corrugated sheets was used for the study. It is a complex structure that, combined with the soil, creates a composite structure whose properties, e.g., soil stiffness, may change over time. The analysis of such a structure is complicated and ambiguous, as shown in this study.

3.2 *Earth pressure*

As presented earlier, a structure located in Norway was used to analyse the impact of earth pressure on the structure of a soil-steel tunnel. The earth pressure was recorded at 4 points shown in Figure 3, where the values from the FEM numerical analysis were also read.

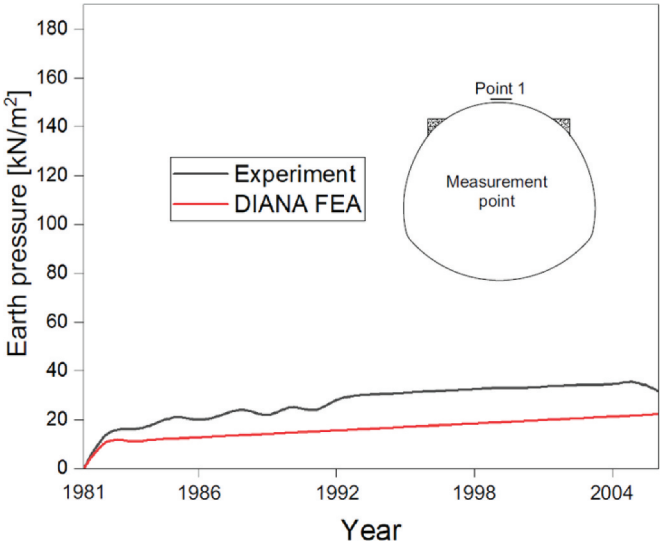


Figure 5. Earth pressure at tunnel crown (measurement point #1) for experiment and FEM model.

Analysing the earth pressure near the tunnel crown (point #1 – Figure 5), it can be seen that the earth pressure increases with the period of tunnel operation. In the case of experimental studies and FEM calculations, it was reported that the maximum values were obtained in a similar period, i.e. near 24 (experimental test) and 25 years (FEM analysis). The maximum measured earth pressure was approximately 35 kN/m^2, while from the numerical analysis in this place, it was about 22 kN/m^2, so they were 37% lower than the measured values. Moreover, it can be seen that after the first year of monitoring, the measured earth pressure was 14 kN/m^2, and the FEM model obtained 11 kN/m^2. The difference was about 20%. It should be added that the earth pressure course was almost linear in the case of the experiment and linear in the case of the FEM analysis.

In the case of point #2, located under the bottom of the steel tunnel (Figure 6), a different trend can be observed than in the case of earth pressure at the level of the tunnel crown. At point #2, in the period of approximately 6 years from the beginning of the measurements, the earth pressure in the case of the experiment was higher than in the remaining years. In the second year of monitoring, the maximum earth pressure was approximately 37 kN/m^2. Moreover, it can be seen that in the period from 1992 to 2005, the earth pressure had an approximately constant value of about 24 kN/m^2. However, in the case of FEM analysis, it was noted that during the first two years, the earth pressure increased (to approximately 140 kN/m^2) and then began to decrease (to about 132 kN/m^2). Only after roughly the 4th year of tunnel operation did the earth pressure gradually increase linearly to reach the maximum value, i.e. 153 kN/m^2. Comparing the maximum results from numerical and experimental tests, it can be seen that the difference is more significant than in the case of the earth pressure in the tunnel crown (point #1). This may be because the soil located under the bottom of the tunnel probably changes its parameters due to soil compaction related to the operation of the railway tunnel. This may increase the stiffness of the soil under the tunnel and thus stabilise the earth pressure at a lower level than indicated by numerical calculations because such phenomena are difficult to reproduce in the FEM model.

In the case of the analysis of the earth pressure near the side wall of the tunnel (point #3 – Figure 7), it can be seen that the values in the case of both the experiment and the FEM analysis increase from the moment the tunnel operation began. They reached the maximum value in the final monitoring period, i.e. after 25 years, and amounted to a maximum of 125 kN/m^2 in the case of experimental tests, while in the FEM analysis it was 178 kN/m^2. Therefore, the difference between the experiment and the calculations was 42%. It should be noted that after

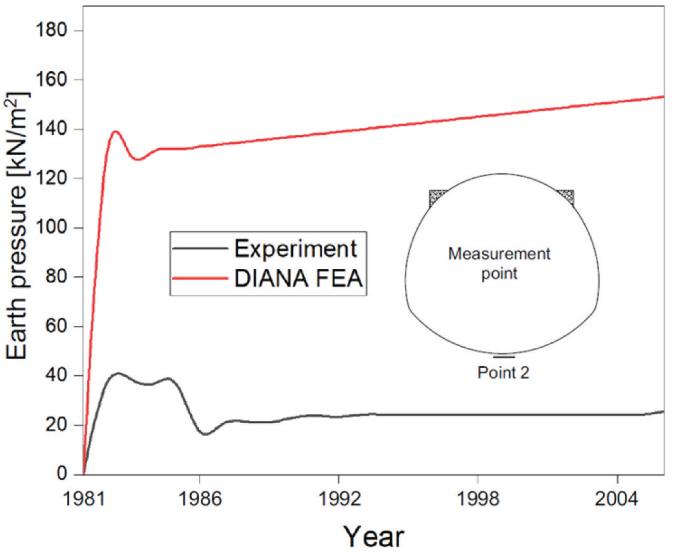


Figure 6. Earth pressure below the tunnel (point #2) obtained from the experiment and FEM analysis.

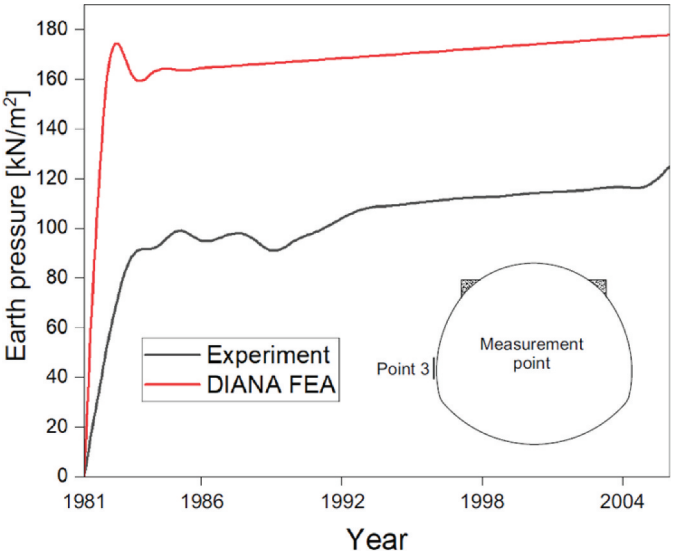


Figure 7. Earth pressures near the side wall (point #3) obtained from tests and the FEM model.

the first year of analysis, in the case of the numerical model, the earth pressure reached approximately 175 kN/m^2, then decreased to about 160 kN/m^2, and then gradually increased, reaching a maximum in the last year of monitoring (178 kN/m^2). In the case of experimental tests, the earth pressure increased from the 3rd year (99 kN/m^2) and then decreased slightly until 1989 (91 kN/m^2). Then, from 1990, the earth pressure gradually increased, reaching a maximum (125 kN/m^2) in the last year of monitoring (25th year of measurements – 2006).

In the last of the tested points (location near the side wall of the tunnel – point #4 (Figure 8)), it can be observed that the earth pressures obtained from experimental tests were more linear than in point #3, located on the other side of the tunnel, also nearby side wall. It was noticed that the earth pressure gradually increased until it reached a maximum value of 125 kN/m^2 (the same as in point #3). However, in the case of the FEM analysis,

the trend was the same as in the case of point #3, i.e. at the beginning, the earth pressure reached 175 kN/m^2, then decreased to approximately 160 kN/m^2, and then increased linearly again, reaching a maximum in the last year of the analysis (178 kN/m^2).

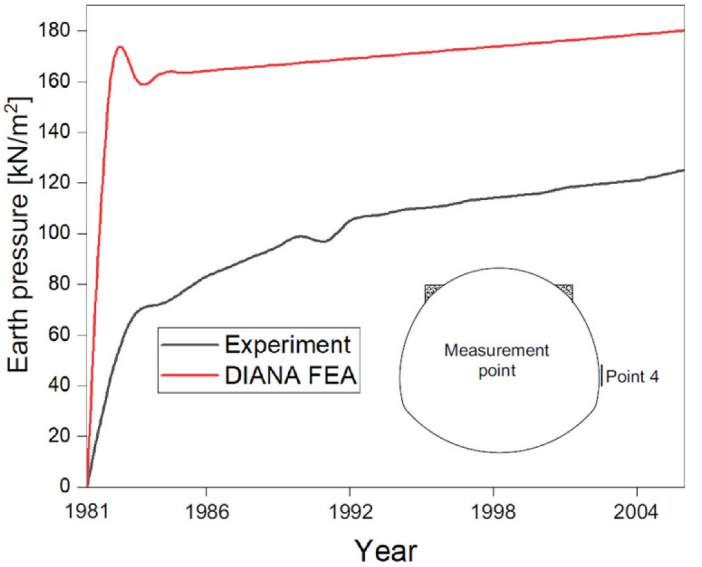


Figure 8. Earth pressure at the side wall of the tunnel (point #4) received from experiment and model FEM.

In the case of both analysed points located near the side walls of the tunnel (#3 and 4), such significant differences between the experimental and numerical results indicate that it is difficult to take into account in the FEM model the phenomena occurring in the soil over time. Similarly to point #2 located under the tunnel. Additionally, taking into account the phenomenon of arching, i.e. the redistribution of loads around a flexible steel shell, in the FEA model is also difficult. These parameters are selected based more on the researcher's experience than the actual conditions in a given structure.

Moreover, the existing differences between experimental and numerical results may be caused by many reasons, such as the estimation of the soil constitutive model parameters and boundary locations (maybe too close to the tunnel). In addition, the soil constitutive model does not consider soil plasticity, which may play a valuable role in the examined case history.

4 CONCLUSION

As a result of monitoring carried out over 25 years, a constant increase in earth pressure around the soil-steel tunnel was observed. Additionally, as a result of the experimental tests and FEM analysis, the following conclusions can be drawn:

- The most significant increase in earth pressure occurs until the first year of monitoring, then the pressure stabilises with a gradual, linear increase.
- The highest earth pressures were recorded at points #3 and 4, which were located near the tunnel's side walls. However, the lowest earth pressures occurred near the crown of the steel shell.
- The most significant agreement between the experiment and FEM analysis was obtained for the case at point #1 (steel shell crown) in the first year of monitoring, which was approximately 20%. However, after 25 years of measurement, this difference was already

37%. A much larger discrepancy (from about 40% to over 300%) from the results was noticed at the remaining measurement points (#2–4). This is due to the difficulty in taking into account the soil behaviour over time and the arching phenomenon in the FEM model.

In summary, further research is necessary to estimate the correct behaviour of the soil-steel tunnel structure over time. The discrepancies between the numerical values may also be influenced by the fact that there is railway traffic in the tunnel, causing vibrations that were not considered in the numerical analysis. Vibrations emitted by passing trains may affect soil compaction other than that described in the available literature and implemented in the FEM software. Additionally, the size of the FE model (i.e. the extent of the soil around the steel tunnel structure included in the model construction), estimation of the soil constitutive model parameters, and boundary locations of the FE model may also be important. In the future, it is planned to perform additional FEM calculations taking into account the aspects mentioned above.

REFERENCES

Beben, D. 2013. Field performance of corrugated steel plate road culvert under normal live load conditions. *Journal of Performance Constructed Facilities* 27(6): 807–817.

Beben, D. 2020. *Soil-Steel Bridges. Design, Maintenance and Durability*. Cham: Springer.

EC 1992-1-1. 2008. *Design of concrete structures. General rules and rules for buildings*. Brussels: European Committee for Standardization.

Flener, E.B. & Karoumi, R. 2009. Dynamic testing of a soil-steel composite railway bridge. *Engineering Structures* 31: 2803–2811.

Garcia, D.B. & Moore, I.D. 2015. Performance of deteriorated corrugated steel culverts rehabilitated with sprayed-on cementitious liners subjected to surface load. *Tunnelling and Underground Space Technology* 47: 222–232.

Koruszewicz, L. & Kunecki, B. 2011. Behaviour of the steel box-type culvert during backfilling. *Archives of Civil and Mechanical Engineering* 1(3): 637–650.

Kunecki, B., Vaslestad, J. & Emdal, A. 2007. Long term earth pressure measurements of two large-span flexible culverts in Norway. In Lark Robert (ed.), *Bridge design, construction and maintenance; Proceeding of Fifth International Conference on Current and Future Trends in Bridge Design. Construction and Maintenance. Beijing. China, 2007; pp.* 122-131. Leeds: Emerald Publishing.

Kunecki, B., Vaslestad, J. & Janusz, L. 2007. The example of form the road infrastructure using the flexible structures – Polish and Norwegian experiences. *Archives of Institution of Civil Engineering* 4: 301–306.

Mahgoub, A. & El Naggar, H. 2021. Seismic Design of Metal Arch Culverts: Design Codes vs. Full Dynamic Analysis. *Journal of Earthquake Engineering* 25(11): 2231–2268.

Mai, V.T., Moore, I.D. & Hoult, N.A. 2014. Performance of two-dimensional analysis: Deteriorated metal culverts under surface live load. *Tunnelling and Underground Space Technology* 42: 152–160.

Maleska T., Beben D. & Nowacka J. 2021. Seismic vulnerability of a soil-steel composite tunnel – Norway Tolpinrud Railway Tunnel Case Study. *Tunnelling and Underground Space Technology* 110: 103808.

Maleska, T. & Beben, D. 2019. Numerical analysis of a soil-steel bridge during backfilling using various shell models. *Engineering Structures* 196(1): 1–12.

Maleska, T., Nowacka, J., Beben, D. & Vaslestad, J. 2022. Long-term behaviour of instrumented RC culvert with high soil cover using EPS for load reduction. In Joan Ramon Casas, Dan M. Frangopol & Jose Turmo (eds.), *Bridge Safety, Maintenance, Management, Life-Cycle, Resilience and Sustainability*; *Proceedings of 11th International Conference on Bridge Maintenance, Safety & Management (IABMAS 2022)*, *Barcelona, Spain*, July 11-15, 2022. London: CRC Press.

Vaslestad, J. 1989. Long-term behavior of flexible large-span culverts. Transp. Res. Rec. 1231: 14–24.

Wadi,A., Pettersson, L. & Karoumi, R. 2018. FEM simulation of a full-scale loading-to-failure test of a corrugated steel culvert. *Steel and Composite Structures* 27(2): 217–227.

Yea, K.Y., Sezen, H. & Fox, P.J. 2014. Simulation of Behavior of In-Service Metal Culverts. *Journal of Pipeline Systems and Engineering Practice* 5: 1–8.

Bridge Maintenance, Safety, Management, Digitalization and Sustainability – Jensen, Frangopol & Schmidt (eds)
© 2024 The Author(s), ISBN 978-1-032-77040-6
Open Access: www.taylorfrancis.com, CC BY-NC-ND 4.0 license

Experimental tests of a soil-steel culvert with a shallow soil cover under static loading

T. Maleska, D. Beben, P. Bobra & B. Jedraszak
Faculty of Civil Engineering and Architecture, Opole University of Technology, Opole, Poland

ABSTRACT: Soil-steel culverts and bridges are more and more often an element of road and railway infrastructure in Poland and the world. In many cases, using an appropriate soil cover depth over such structures is impossible, which is necessary to operate these objects safely. Therefore, the paper's primary purpose is to assess the behaviour of the soil-steel culvert with a soil cover height of 0.20 m above the steel shell. This height of soil cover of structures is extremely low, below the requirements of standards (e.g., Canadian Standards). The tested soil-steel culvert has the following dimensions: (i) span 2.1 m, (ii) height 1.45 m, (iii) length 2.32 m, (iv) sheet thickness 2.5 mm, and the wave profile is 68×13 mm. Experimental tests were carried out in a laboratory in a specially constructed test box with dimensions of 2.32 m × 4.34 m × 2.49 m. As a result of the tests, the behaviour of this structure under static load was observed. A standardised static road load was used in the model tests of the soil-steel culvert. During the tests, the vehicle load was simulated by concentrated force (loading speed was 1 kN/s, and the maximum load duration was 600 seconds). The tests measured displacements and strains of the corrugated steel shell under a given load. The obtained results are of great cognitive importance, as similar studies have not been performed so far.

1 INTRODUTION

Steel culverts made of corrugated sheets are increasingly an element of road and railway infrastructure in Poland and worldwide (Beben 2020). Figure 1 shows an example of a soil-steel bridge. In many cases, applying appropriate soil cover over such structures is impossible, which is necessary to operate these objects safely. Moreover, the minimum soil cover height is required by standards or design recommendations (CHBDC 2017, Rowinska et al. 2004).

So far, there are studies on the influence of the height of soil cover above soil-steel structures. In the paper by Flener (2010), the results obtained using the Canadian standard (CHBDC 2017) were compared with the FEM results. In this case, the height of the soil cover above the steel shell was from 2.5 to 4.08 m. Significant discrepancies were observed between the standard results and those obtained from FEM, which reached over 50%. In the work of Elshimi et al. (2011), soil cover heights in the range of 0.45–1.5 m were analysed. The effect of backfill pressure on the steel coating was determined. An increase in internal forces and displacements was observed in objects with increased soil above the shell structure. The influence of the backfill height with different methods of foundation of the steel shell was analysed in the work of Wysokowski et al. (2007). The analysed arch structure was founded on two types of foundations, i.e., a rigid foundation (reinforced concrete foundation strip) and a flexible foundation (corrugated steel plate). It was found that the type of foundation used did not matter much for the displacements in the crown. The obtained results were compared for seven heights of backfill layers. The displacements from the experiment and FEM analysis were at a comparable level, and the differences between them did not exceed a few percent. Regarding the influence of the soil cover height, Maleska & Beben (2022 and 2023)

DOI: 10.1201/9781003483755-152

investigated the response of a soil-steel bridge using seismic excitations. It was found that the effect of backfill is noticeable and depends on many factors, i.e. boundary conditions, structure span, etc. Moreover, it was found that further research is necessary on the impact of the backfill height on the soil-steel structure.

It should be added that the analysis of soil-steel bridges under static load is primarily a search for an answer to the question: what will be the deformations of the steel shell caused by the placement and compaction of the backfill (construction stage), and what will be the impact of static loads from vehicles? Analyses of the impact of backfill compaction on soil-steel bridges were undertaken, among others, by Taleb & Moore (1999), Manko & Beben (2005), Pittino & Gosler (2006), Beben (2012), Kunecki (2014), Maleska & Beben (2019). It was found that during backfilling, displacement and bending moments in the shell are quite high, especially in the initial backfill layers.



Figure 1. View of soil-steel bridge from Norway.

The primary purpose of the research carried out in this study was to assess the behaviour of a soil-steel culvert with a shallow soil cover of 0.20 m above the steel shell. This made it possible to determine the object's behaviour under the tested static load. This research is of great innovative importance due to the analysis of a quasi-composite bridge structure and the possibility of using lower soil cover than the relevant standards require. The study analysed the course of strains and displacements over time for a steel corrugated shell for applied loads in the 0–37.5 kN range.

2 DESCRIPTION OF LABORATORY TEST

2.1 *Culvert shape and dimension of steel box*

The problem in this type of laboratory testing is to test the largest possible object without scaling or other simplifications. Therefore, the experimental tests were carried out in the laboratory in a specially constructed research box (Figure 2) with dimensions of 2.32 m × 4.34 m × 2.49 m. The tested steel culvert made of corrugated sheets had the following sizes: (i) span 2.1 m, (ii) height 1.45 m, (iii) length 2.32 m, (iv) thickness of the sheets was 2.5 mm.

The tested corrugated sheet culvert is made of S250 steel. The backfill consisted of a gravel mix. The backfill was placed in layers every 0.20 m to a height of 2.00 m. The backfill used in the experimental tests is a standard aggregate used to construct this type of facility. As part of these tests, the following loading forces were performed: (i) 5 kN (weight of a typical passenger car,

approximately 2 tons), (ii) 10 kN (car with a curb weight of up to 4 tons), (iii) 25 kN (weight of a small truck up to 10 tons), (iv) 30 kN (truck weight up to 12 tons), (v) 35 kN (truck weight up to 14 tons) and (vi) 37.5 kN (truck weight up to 15 tons - maximum load).

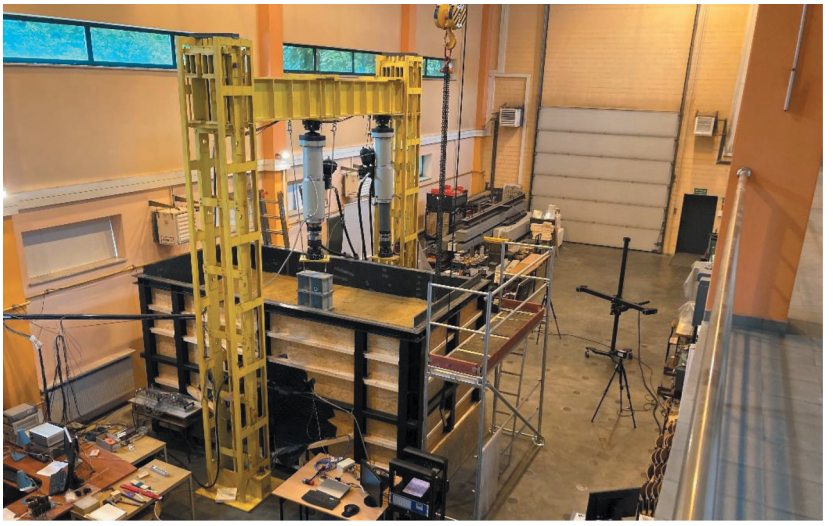


Figure 2. View of the experimental test in a laboratory.

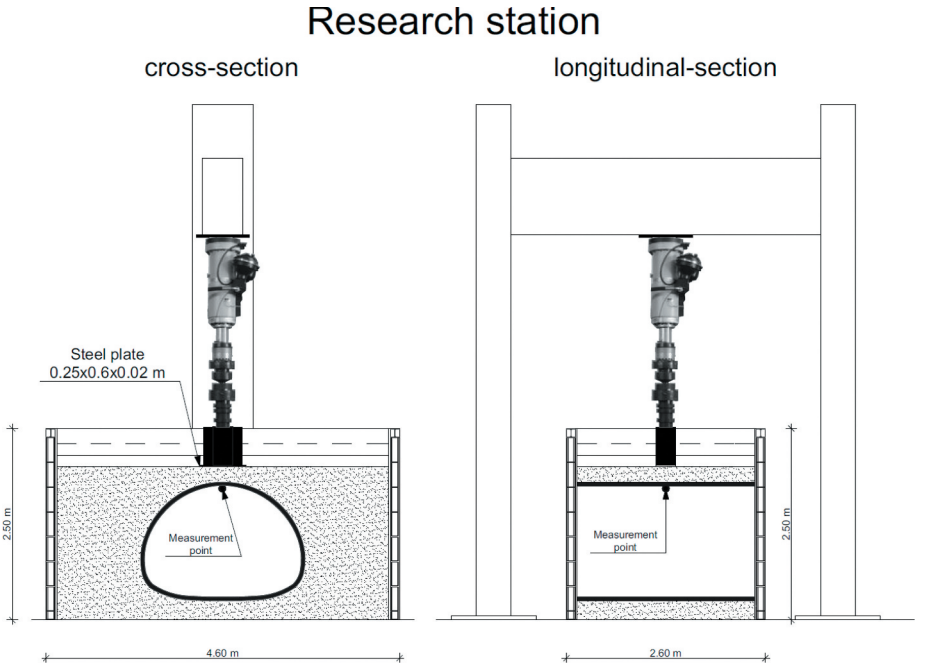


Figure 3. View of the experimental research site.

2.2 *Description of the experiment*

For model tests of the culvert, static load from concentrated force was simulated. It was applied to the soil from a hydraulic cylinder via a steel sheet with dimensions of 0.25×0.6×0.02 m and other transition elements (Figure 3). The force was applied exactly at the centre of the culvert's

span and length. The set static force increased at a rate of 1 kN/s (t_1) (Figure 4) from 0 kN to a maximum value of 37.5 kN. The increase in static load from 0 kN to the maximum value (F_{max} = 37.5 kN) lasted 10 minutes (t_1), and then the maximum load was maintained for 10 minutes (t_2). Subsequently, the set load decreased from the maximum value until the culvert was completely relieved at a speed of 1 kN/s (t_3). After unloading the tested structure, the measurement was maintained for the next 10 minutes to observe how the steel shell returned to its initial state (t_4).

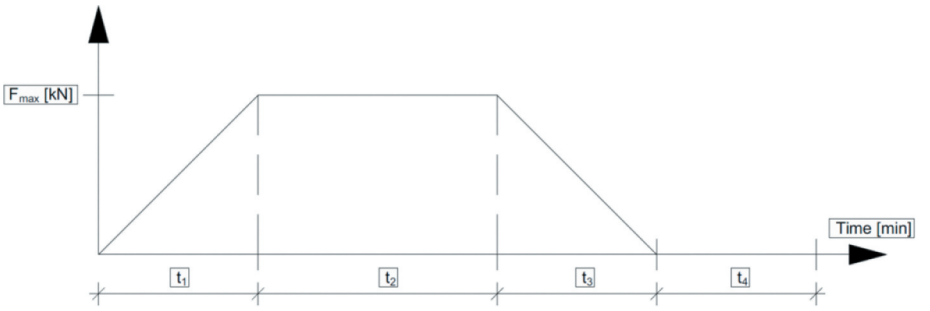


Figure 4. A time period of applied loads from the experiment.

In order to generate the required force, a steel frame was used with a hydraulic actuator placed on it, the operating range of which ranged from 0 to 250 kN. Strain gauges (TFs-10/120 (K)) were used to record the strains of the steel shell. The registration of displacements was made using LVDT sensors. The arrangement of measurement sensors (strain gauges and LVDTs) is shown in Figure 5, but in this paper, it is limited to presenting displacements and strains in the shell crown (cross-section B-B and point $4C_{lg}$), where the maximum values usually occur. A static force was also applied directly above the sensors (Figure 3).

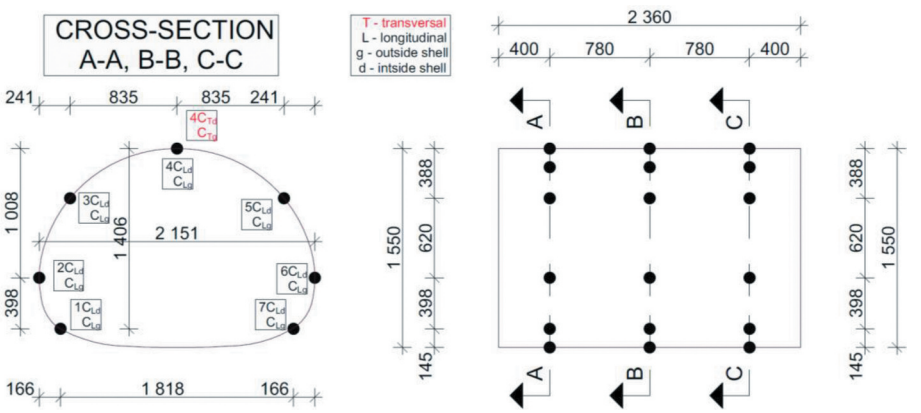


Figure 5. View of the measurement points.

3 RESULTS

3.1 *General remarks*

During the research, it was necessary to determine the parameter that would be the limit for the maximum load-bearing capacity of the tested structure. It should be added that the purpose of the tests was not to destroy the structure but only to assess its behaviour under a given load and

to determine the impact of deformations of the culvert shell under a given load. It was decided that this parameter would be the maximum deformation of the steel shell and, therefore, the maximum effort of the steel shell. Knowing the deformation of the steel shell and the strength parameters, it is possible to determine the effort of the steel shell by the maximum stress (yield strength). For the tested steel shell, the yield strength was 250 MPa. Therefore, in the tests carried out, attempts were made to obtain the maximum external load without exceeding the yield strength of steel. The value of the tested experimental model with a soil cover of 0.20 m was 37.5 kN. It should be noted that the soil cover of 0.20 m is shallow and unacceptable by standards (CHBDC 2017).

3.2 *Strains*

After conducting the experimental tests, it can be seen that in the experimental model with a soil cover height of only 0.20 m (below the CHBDC 2017 recommendations), a maximum load of only 37.5 kN was obtained from the concentrated static force. At this load, deformations of –1150 μm/m were recorded (Figure 6), equating to a stress of approximately 230 MPa in the steel shell of the bridge. This stress was considered limiting because the yield stress declared by the manufacturer was 250 MPa. Therefore, higher external load values were not chosen to avoid the destruction of the model.

However, in the remaining cases, smaller strains of the steel shell were achieved. The strain values ranged from –46 μm/m to –979 μm/m; therefore, the steel strain ranged from 9.2 MPa to 195.8 MPa. It can be seen that for loads in the range of 5–10 kN, the strain values were 4% (–46 μm/m) and 8% (–94 μm/m) of the maximum deformation values of the force of 37.5 kN, respectively. However, from a load value of 25 kN, a significant increase in strains in the steel shell can be observed. For a load of 25 kN (43% of the maximum given load), the strain value was –498 μm/m, and for a force of 30 kN (55% of the maximum load), the strain was equal to –634 μm/m. However, for a force of 35 kN (85% of the value from a force of 37.5 kN), a strain of –979 μm/m was recorded.

It is also worth paying attention to the time histories of strains presented in Figure 6. They show that as a result of applying a load, the shell immediately absorbed the given external load, and therefore, the steel shell was strained. In the case of unloading, the maximum strain values were quickly reduced and reached near the initial state. The recorded permanent strains did not exceed 27%. The noticeable relationship increases as the applied load increases. Therefore, the structure is flexible, probably due to the shallow soil cover.

3.3 *Displacements*

In the case of maximum displacements (Figure 7), similar relationships and trends were observed as in the case of strains (Figure 6). In the tested experimental model (soil cover height equal to 0.20 m), the maximum displacements for a concentrated force of 37.5 kN were 8.45 mm. In the remaining load cases tested (5–35 kN), it was noticed that the displacements were lower and ranged from 0.31 mm to 7.73 mm. A displacement of 0.31 mm was recorded for a load of 5 kN (4% of the maximum displacement of 37.5 kN) and a displacement of 7.73 mm for a load of 35 kN (94% of 37.5 kN). In other load cases, the following values of vertical displacements in the shell crown were obtained: (i) 5.46 mm - from a force of 30 kN (65% of the load 37.5 kN), (ii) 4.75 mm - from a force of 25 kN (56% of the load 37.5 kN) and (iii) 0.80 mm – from a force of 10 kN (9% of the load of 37.5 kN).

Moreover, by analysing Figure 7, one can notice a similarity to strains with a rapid increase in displacements immediately after applying a specific load. However, in the case of unloading, there is a quick return to the initial state (permanent displacements observed not exceeding 37%). This behaviour of displacements also proves the correctness of the results because the tendency of their appearance in the steel is closely related to the effort of the shell and, therefore, to their strains.

In addition, it is essential to determine whether the tested soil-steel culvert does not exceed the permissible displacement levels provided for in the standards and recommendations. The

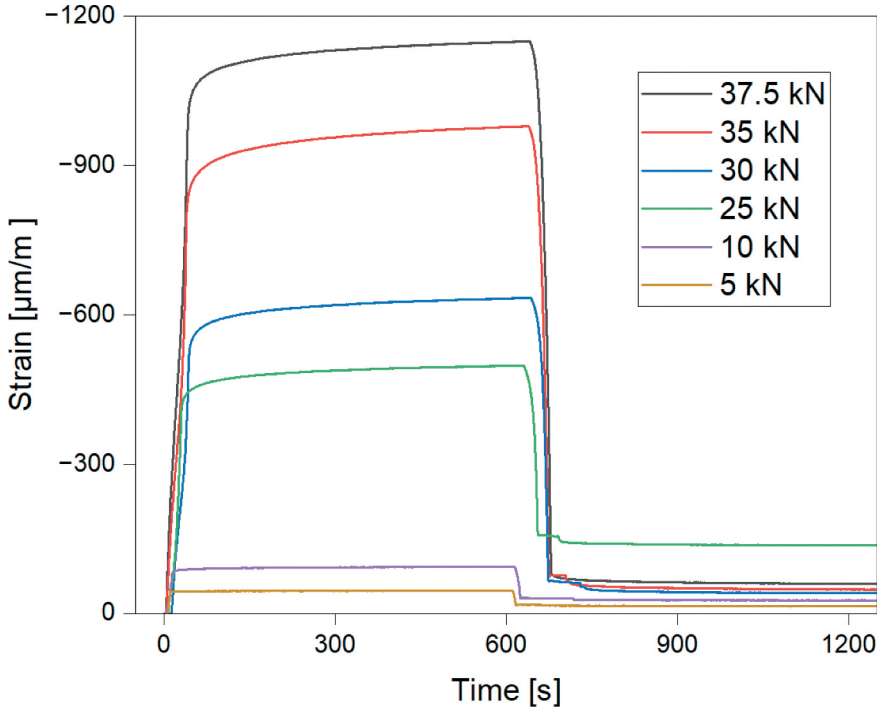


Figure 6. Maximum strains from an experiment in the time domain.

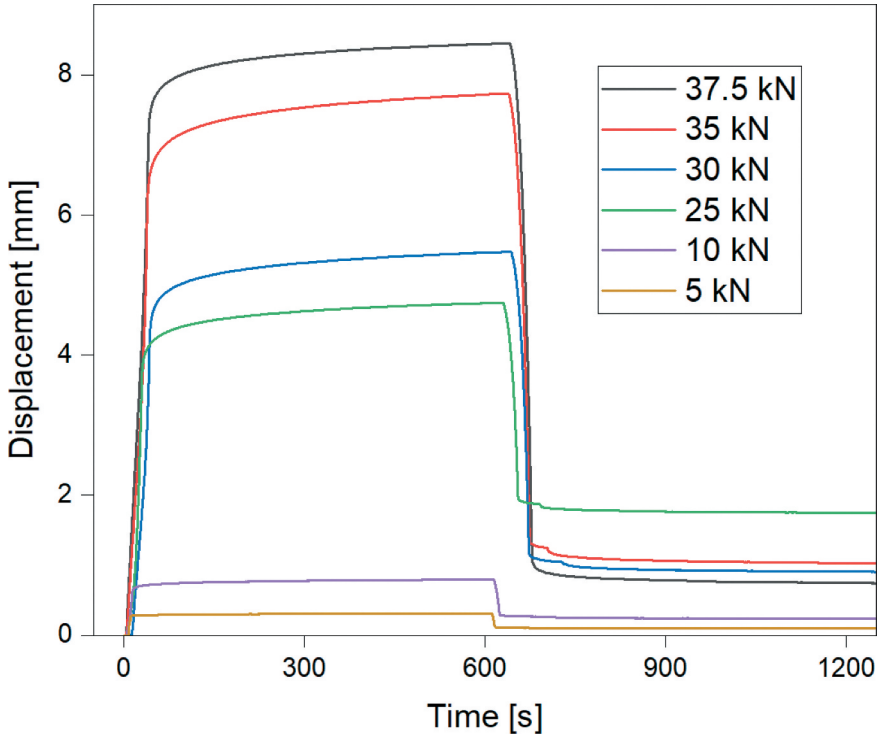


Figure 7. Maximum displacements from an experiment in the time domain.

maximum design displacement is determined as the allowable deflection of the buried bridges/culverts, which should not exceed the value calculated based on the following conditions, namely:

(i) 5% of the span, i.e. 105 mm (AASHTO 2017),
(ii) 0.5% of the span, i.e. 10.5 mm (CHBDC 2017),
(iii) 2% of the span, i.e. 42 mm (CSPI 2007),
(iv) 10% of the rise, i.e. 145 mm (NCSPA 2018).

It is clearly visible that the conditions resulting from the NCSPA (2018), AASHTO (2017) and CSPI (2007) recommendations are less restrictive than the requirements proposed by CHBDC (2017) for the buried bridges/culverts. As shown in the study, the maximum displacement of the culvert was 8.45 mm is smaller than the permissible values calculated under the above four conditions. The above conditions are caused by a conservative approach to determining the limit values (not considering the soil-structure interaction phenomenon and increased safety factors).

4 CONCLUSION

After preliminary tests, it can be concluded that the structure of the soil-steel culvert, despite the extremely low level (lower than the recommendations of standards and guidelines), is able to transfer a load equal to the wheel pressure of a truck weighing 15 tons. Moreover, after the research carried out, it can be concluded that:

- The displacements and strains of the shell increased with the load, but two main increases in the tested values are visible, i.e. after applying a load of 25 kN and 35 kN. For loads above 25 kN, displacements and strains increased slowly over time.
- The structure of the culvert with a low soil cover behaved elastically under a given load, which was manifested by a quick response to the given loads and unloading of the structure. Permanent displacements and strains of the steel culvert were recorded as 37% and 27% (approximately 10 minutes after unloading), respectively.
- According to various standards and recommendations, the permissible displacements of the tested soil-steel culvert were not exceeded. However, the CHBDC standard (2017) approach is closest to the maximum measured displacement.

To sum up, further research is necessary to assess the behaviour of soil-steel structures with low soil cover, as there are many practical cases where the use of such shallow cover is necessary. It makes sense to strengthen soil-steel bridges with various types of geogrids and geotextiles because this may bring significant benefits in the form of increased load-bearing capacity of the structure. As a result, this may translate into lower material consumption and workload of people and equipment, resulting in lower costs of building a new facility or cheaper modernisation of an existing facility. Therefore, further research will examine materials that strengthen the soil above the steel shell or stress-relieving materials that cause the redistribution of stresses in the soil and shell resulting from external loads.

ACKNOWLEDGEMENTS

The authors would like to thank ViaCon Polska from Rydzyna for providing the steel culvert for experimental tests and ROLMEX from Dobrodzień for helping construct the steel box. The research was carried out as part of the MINIATURA project financed by the National Science Centre.

REFERENCES

AASHTO. 2017. AASHTO LRFD bridge design specifications. 8th Ed. Washington: American Association of State Highway and Transportation Officials, DC.

Beben, D. 2012. Numerical study of performance of soil-steel bridge during soil backfilling. *Structural Engineering and Mechanics* 42(4): 571–587.
Beben, D. 2020. *Soil-Steel Bridges. Design, Maintenance and Durability*. Cham: Springer.
Canadian Highway Bridge Design Code (CHBDC) S6-14 (11th Edition). 2017. Ontario: Canadian Standards Association, Canada.
CSPI. 2007. Handbook of Steel Drainage & Highway Products, Canadian Edition. Cambridge: Corrugated Steel Pipe Institute, Ontario, Canada.
Elshimi, T.M., Mak, A.C., Brachman, R.W.I. & Moore, I.D. 2011. Behaviour of a deep-corrugated large-span box culvert during backfilling. In: *Gibson Group Association Management. Pan-American Conference on Teaching and Learning of Geotechnical Engineering*. Toronto, Canada.
Flener, B.E. 2010. Soil-steel interaction of long-span box culverts-performance during backfilling. *Journal of Geotechnical and Geoenvironmental Engineering* 136(6): 823–32.
Kunecki, B. 2014. Field test and three-dimensional numerical analysis of soil-steel tunnel during backfilling. *Transportation Research Record, Journal of the Transportation Research Board* 2462(1): 55–60.
Maleska, T. & Beben, D. 2019. Numerical analysis of a soil-steel bridge during backfilling using various shell models. *Engineering Structures* 196: 1–12.
Maleska, T. & Beben, D. 2022. Behaviour of soil-steel composite bridge with various cover depths under seismic excitation. *Steel Composite Structures* 42(6): 747–764.
Maleska, T. & Beben, D. 2023. Effect of the soil cover depth on the seismic response in a large-span thin-walled corrugated steel plate bridge. *Soil Dynamics and Earthquake Engineering* 166, 107744.
Manko, Z. & Beben, D. 2005. Research on steel shell of a road bridge made of corrugated plates during backfilling. *Journal of Bridge Engineering* 10(5): 592–603.
NCSPA. 2018. Corrugated Steel Pipe Design Manual. Dallas: National Corrugated Steel Pipe Association, TX.
Pittino, G. & Gosler, J. 2006. Structural plate steel underpasses during backfilling – how to minimize the bending moment. *The 4th International FLAC Symposium on Numerical Modeling in Geomechanics*, Madrid, Spain.
Rowinska, W., Wysokowski, A. & Pryga, A. 2004. Design and technological recommendations for flexible engineering structures made of corrugated sheets. Zmigrod: *GDDKiA*, IBDiM.
Taleb, B. & Moore, I.D. 1999. Metal culvert response to earth loading. Performance of two-dimensional analysis. *Transportation Research Record: Journal of the Transportation Research Board* 1656(1): 25–36.
Wysokowski, A., Gorna, J., Monka, M. & Tomala, P. 2007. Comparative full scale test of behaviour of corrugated steel arch structure placed on corrugated flexible foundations and rigid concrete foundations. *Archives of Institute of Civil Engineering* 1: 261–272.

Bridge Maintenance, Safety, Management, Digitalization and Sustainability – Jensen, Frangopol & Schmidt (eds)
© 2024 The Author(s), ISBN 978-1-032-77040-6
Open Access: www.taylorfrancis.com, CC BY-NC-ND 4.0 license

Maximum shear strength of prestressed concrete deep beams

X. Duanmu & D. Xu
Tongji University, Shanghai, China

K. Hu
Anhui Transportation Holding Group Co., Ltd., Hefei, China

ABSTRACT: The shear performance of prestressed deep girders is pivotal for accelerated bridge construction. There are few tests on prestressed deep girders and even fewer discussions on their upper shear limits. This study introduces four full-scale post-tensioned bonded prestressed concrete T-beam tests and the upper limit value provisions are summarized. The four T-beam shear tests and comparative analysis of other test results reveal that the upper limit value of prestressed concrete deep beams is influenced by reinforcement and shear span ratio. Longitudinal prestress enhances cracking and ultimate loading, while the effect of the vertical component of prestressing is controversial and requires further investigation. The AASHTO method was found to be more appropriate for the upper limit values of T-beams, compared with the ACI 318-19 specification. Struct and Tie Model (STM) underestimated the shear strength.

1 INTRODUCTION

In recent years, with the rapid advancement of China's bridge design and construction technology, particularly in the industrialized construction of assembled bridges such as small box girders and T girders, the study of shear resistance in prestressed concrete deep beam components has become a crucial research problem.

Shear tests on prestressed I-beams with a/h ratios less than 2.0 were conducted by Arthur (1965), Mahgoub (1975), Kang (1989), Shahawy (1996), Tan (1999a), and Laskar (2010), encompassing pre-tensioning tests. Teng(1998), Tan(1999b), Wang(2009) and Yang(2020) carried out tests on unbonded post-tensioned rectangular beams with short shear spans. Wang (2009) conducted tests on bonded post-tensioned prestressed rectangular beams. However, to the best of the author's knowledge, no tests have been performed on bonded post-tensioned concrete T-beams with short shear spans, and there is a scarcity of experiments on post-tensioning, especially those involving bonded post-tensioning.

As a typical method for fast prefabricated bridge construction, post-tensioning is in high demand. Full-scale tests are essential for a more accurate reflection of structural responses. To advance the understanding of shear resistance in prestressed concrete deep beams, this paper presents the findings from laboratory tests conducted on four full-scale prestressed concrete T-beam tests.

Simultaneously, the upper limit of concrete bridge shear strength, also known as minimum web thickness requirements, constitutes a significant aspect of concrete design specifications. The stipulation of shear strength upper limit values can influence the design of web thickness. In many countries, due to these regulations, webs are typically variable in thickness, posing challenges to industrial development. Currently, there is limited discussion on the shear strength upper limit values for prestressed concrete deep beams. This paper discuss the parameters which have influence on the shear strength of prestressed deep beam. The primary methods for designing deep beams are empirical formulae or STM models. This paper reviews

DOI: 10.1201/9781003483755-153

upper limit value methods in ACI 318-19 (ACI Committee 318, 2019) and LRFD bridge design specifications (AASHTO, 2020), compares them with collected experimental data. Then the authors will discuss the specifications on STM models in ACI 318-19 and AASHTO, points out current research deficiencies.

2 GENERAL METHODS

2.1 *Upper limit of the deep beam*

The AASHTO code employs the Modified Compression-Field Theory (MCFT) for design, and the maximum load capacity of a pure shear concrete member is $0.5\nu f_c^{'}$ (AASHTO, 2020). In the code, the $\tau/f_c^{'}$ is given according to MCFT, that is, the reasonable range of values of 0.5ν is from 0.05 to 0.25, with 0.25 as the upper limit value, i.e. 0.5ν=0.5, thus:

$$V \leq 0.25 f_c^{'} b_v d_v + V_P \tag{1}$$

where $f_c^{'}$ denotes the compressive strength of the concrete cylinder, b_v is the width of the web, and d_v is the effective height, which can be taken as $0.9h_0$. V_P is the vertical component of the prestressing force.

ACI's Committee 326 (1962) analyzed the test data and found that with higher stirrup ratios, the compression zone would break down before the web reinforcement yielded, thus requiring a limit on its maximum value (ACI Committee 318, 2019). The following formula is used for the current ACI 318-19 code upper limit for shear design:

$$V \leq 10\sqrt{f_c^{'}} b_v d_v \tag{2}$$

The symbols' significance aligns with those in the AASHTO code. The code considers crack resistance during design to ensure the structure's crack width remains within a defined range under service loads.

2.2 *STM of the deep beam*

An increasing number of deep beam designs are adopting the Strut-and-Tie Method (STM), derived from the plasticity lower bound theorem. This method necessitates the concrete to be fully plasticity developed, along with a specific arrangement of reinforcement in the web. In instances where the web lacks sufficient reinforcement, the concrete strength is discounted. Therefore, when the stirrup ratio is appropriately provided, it can be regarded as the upper limit of shear for deep beams.

In the context of deep beams reinforced with minimal web reinforcement adhering to Equation 4, the code does not explicitly delineate the contribution of prestress to shear capacity.

$$\theta = \tan^{-1}\left(\frac{0.9d}{a}\right) \tag{3}$$

$$\sum \frac{A_{si}}{b_s s_i} \sin^2 \alpha_i \geq 0.0025 \tag{4}$$

$$V_{c,cal} = 0.85\nu(l_b \sin\theta + w_t \cos\theta) b_w f_c^{'} \tag{5}$$

where θ represents the strut angle, d denotes the effective depth, a signifies the shear span, s_i represents the spacing between layers of reinforcement. Each layer has a reinforcement area denoted as A_{si} and crosses the inclined strut at an angle α_i with respect to its axis. b_s is the width of the strut. The recommended value for ν in the code is 0.75; otherwise, it defaults to ν = 0.4. l_b

refers to the width of the bearing, w_t represents the effective height of concrete concentric with a tie, and b_w denotes the web width.

In the AASHTO specification, the Strut-and-Tie Method (STM) closely resembles that of ACI's. The primary difference lies in the coefficient of effective concrete strength, denoted as ν, determined by Equation 8. This computation relies on the satisfaction of Equations 7 and 8, with a specified value of 0.45 assigned for structures lacking crack control reinforcement.

$$\frac{A_h}{b_w s_h} \geq 0.003 \tag{6}$$

$$\frac{A_v}{b_w s_v} \geq 0.003 \tag{7}$$

$$v = 0.85 - \frac{f'_c}{20(\text{ksi})} (0.45 \leq v \leq 0.65) \tag{8}$$

where, s_h and s_v represent the spacing between layers of horizontal or vertical reinforcement, respectively. Each layer is characterized by a reinforcement area denoted as A_h or A_v. When adequately reinforced, STM's maximum shear capacity closely aligns. The discount factor for ACI is 0.85 × 0.75 = 0.64, and for AASHTO, it is 0.65.

3 TEST RESULTS

3.1 *Test setup*

Two prestressed deep beams, as illustrated in Figure 1, were fabricated and subjected to failure testing. The design was derived from a prestressed concrete lightweight T-beam bridge with a 25 m span. The bridge features a width of 12.75 m, a girder height of 1.605 m, and is composed of four T-beams arranged transversely, each with a single girder width of 2 m.

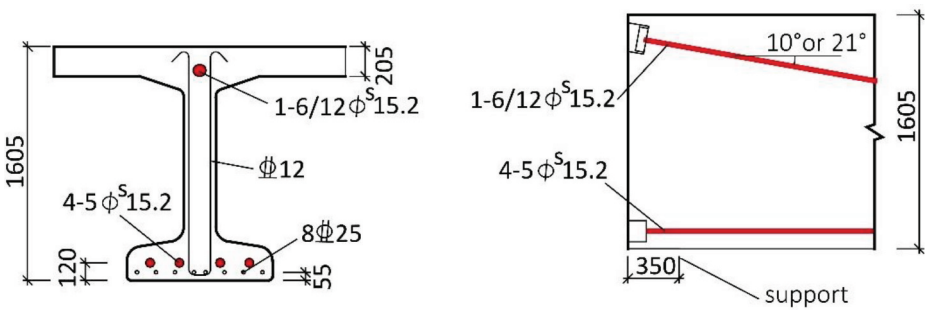


Figure 1. End sections of test beams (Unit: mm).

The web plate has a thickness of 0.22 m, the flange plate has a thickness of 0.2 m, the bottom flange width is 1.0 m, and the entire bridge adopts an equal cross-section arrangement. The girder's bottom is equipped with 8 HRB400 bars of φ25 mm, and the stirrup reinforcement ratio is 1.03%. In the bottom flange, 4 bundles of 5-φs15.2 mm prestressing tendons are arranged, while in the web plate, 1 bundle of 12-φs15.2 mm or 6-φs15.2 mm prestressing tendon is arranged, with bending angles of 10° or 21°, respectively. The cross-sectional form of the test beam and its end reinforcement are depicted in Figure 2. For clarity, Table 1 provides a summary of the main parameters in the test beams.

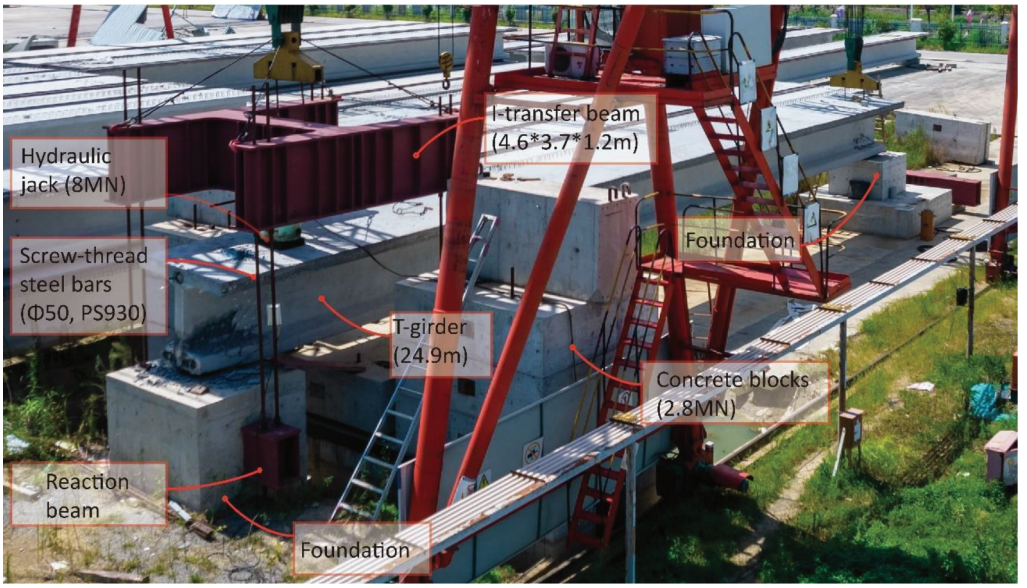


Figure 2. Layout of Light-Weight T-Beam test.

3.2 *Test results*

The experiment employed a three-point loading method, as illustrated in Figure 2. An elastic rubber bearing with dimensions of 0.5 * 0.5m was positioned at the bottom, and another rubber bearing of dimensions 0.5 * 0.6m was placed 1.6m away from the center of the bottom bearing. Loading was conducted incrementally (F1 to F4), reaching cracking loads of 1930kN, 2120kN, 2120kN, 2490kN, respectively. As loading progressed, inclined cracks emanated from the loading point towards the support, gradually intensifying. Simultaneously, localized spalling of concrete occurred at the top or bottom. The shear damage patterns of the four sets of lightweight T-beam specimens are depicted in Figure 3. The beams achieved their maximum load-bearing capacity at loads of 4890kN, 4800kN, 4960kN, and 5140kN, respectively. This resulted in a reduction in the applied load, signifying the occurrence of web shear damage.

Table 1. Key parameters of the tests.

Beam	Top prestressing (angle)	f_{cu}(MPa)	Failure shear(kN)
F1	6ϕ15.2 (10◦)	55.3	4890
F2	12ϕ15.2 (10◦)	66.7	4800
F3	6ϕ15.2 (21◦)	55.3	4960
F4	12ϕ15.2 (21◦)	66.7	5140

4 INFLUENCE PARAMETERS

This paper compiles prestressed concrete deep beam tests, encompassing diverse cross-section forms (rectangular, T-shaped), varied prestressing methods (bonded post-tensioning, unbonded post-tensioning, and pre-tensioning), and a range of parameter variations including shear-to-span ratios, prestressing amounts, prestressing inclinations, and stirrup reinforcement ratios. The impact of these diverse parameters on structural shear capacity is systematically analyzed by normalizing shear stress with $\sqrt{f'_c}$, enabling a comparative assessment of structural capacity.



Figure 3. Shear failure mode of Light-Weight T-Beam specimens.

4.1 *Web reinforcement*

The upper limit on shear capacity is attributed to excessive stirrup reinforcement, where additional stirrup reinforcement fails to enhance shear capacity. This requirement is typically applicable to slender beams, as stirrup reinforcement exerts a more pronounced influence on them. In Figure 4, it is observed that for a small shear span ratio, the load-carrying capacity of the beam increases with the reinforcement ratio. The figure directly compares test beams with identical web reinforcement ratios. The Shahawy test indicates that when stirrup reinforcement $\rho_v f_y$ > 400MPa, the increase in load-carrying capacity with an increase in reinforcement ratio is insignificant, occurring at a corresponding stirrup reinforcement rate of approximately 1%. While the stirrup reinforcement rate in other tests is not extensively varied, it is evident that the beam's capacity increases until the reinforcement rate reaches $\rho_v f_y$ = 400MPa. Hence, it is evident that considering the quantity of web reinforcement is essential for assessing the shear capacity of prestressed concrete deep beams.

In both ACI 318-19 and AASHTO codes, the shear capacity of deep beams is predominantly modeled using STM, with minimum reinforcement ratio requirements, such as 0.25% or 0.3%. These values are notably smaller than the findings in the tests. Simultaneously, in

Table 2. Collected test specimens.

Parameter	Specimens
$\rho_v f_y$	Shahawy (1996) (B1-00-0R-S, B1-00-R-S, B1-00-2R-S, B1-00-3R-S, B1-00-2R2-S); Shahawy (1996) (B1-00-0R-N, B1-00-R-N, B1-00-2R-N, B1-00-3R-N, B1-00-2R2-N); Teng(1998) (P1-1-0-WO, P1-1-0-WV); Teng 1998 (P1-1-5-WO, P1-1-5-WV); Kang (1989) (YA6-4E, YA6-4W, YB6-5E,YB6-5W,YC6-7E, YC6-7W); Laskar (2010) (B1-N, B1-S, B2-N, B2-S)
a/h	Shahawy (1996) (A4-00-0R(2)-N, A4-00-0R(2)-S, B1-00-0R-N, B1-00-0R-S); Tan(1999b) (1P-500/0.50, 1P-500/0.75, 1P-500/1.00); Arthur (1965) (B4, B6-1, B7-1, B10-3, B12-1, C1-2, C2-1, C4,C5-1, C6-1, C6-2, C7-1, C7-3, C8-1, C8-3, C8-4); Mahgoub (1975) (B3, B6, C1, C9, D1, D2)
σ_P	Teng(1998) (P-1a, P-1b, P-1b(2),P1-1-5-WO); Mahgoub (1975) (A5, C1, E2, E3); Kang (1989) (YB6-6E, YB6-6W, YB8-1E, YB8-1W,YB10-1E)
$V_P/\sqrt{f_c'}$	Wang(2009) (P1,P3, P4); Yang(2020) (BP2, BP3, BP4); Teng(1998) (P-1c(2), P-1d(2), P-1e(2)); Laskar (2010) (B2-S, B3-N); Author (F1, F2, F3, F4)

instances where the stirrup reinforcement strength is comparatively weak, there are limitations on restricting the reinforcement rate of the hoop reinforcement. Therefore, when imposing limits on reinforcement rates, it is crucial to consider both the value of the reinforcement rate and the yield strength of the stirrup reinforcement.

4.2 *Shear span ratio*

The shear span ratio consistently exerts a significant influence on shear resistance, evident in the Figure 4 as the shear capacity of the structure diminishes with an increasing shear span ratio. The above effects can be considered in the different models. For instance, in STM, the alteration in the inclination of the inclined compression column reflects this effect. Some models may explicitly incorporate a law inversely proportional to the shear span ratio, such as (a/d) or $(a/d)^{0.7}$. The provisions of the code, utilizing the traditional formulas (1) and (2) as upper limits, do not consider the influence of the shear span ratio. Consequently, in such cases, the model is constrained by design limitations for small shear span ratios, proving unfavorable and evidently uneconomical.

4.3 *Initial prestress*

In slender beams, various codes account for the influence of horizontal prestressing, but they do so in different ways. These considerations include the increase in cracking loads due to prestressing, reduction of horizontal strains, and reduction of the compressive strength of the concrete. In deep beams, such effects are typically not taken into consideration. However, the test results indicate that horizontal prestressing does have some influence on shear resistance.

4.4 *Vertical prestressing force*

In the AASHTO code, the vertical component of prestressing force is considered to enhance shear capacity, a consideration absent in the ACI 318-19. STM also necessitates the consideration of the external load effect of prestressing, although this is not explicitly specified. The authors of this paper conducted tests revealing that the vertical component of prestressing can indeed increase the shear capacity of deep beams. However, results from other tests, such as those by Wang, show the opposite effect. Wang's tests on unbonded rectangular beams differ from this paper's investigation on bonded T-beams. Moreover, when compared to Wang's results, this paper's tests incorporated a significantly higher arrangement of stirrup reinforcement (1% compared to Wang's 0.2%). Wang attributes the lower stirrup reinforcement performance to excessively large prestressing inclinations, hindering prestressing development. In contrast, this paper observes that, the majority of stirrup reinforcement remains below the yield strength. Overall, the tests in this paper suggest that the contribution of prestressing to the load-carrying capacity of prestressed deep beams is comparatively small.

5 DISCUSSIONS

The experimental design in this paper employed specimens with a shear span ratio (a/h) of 1, achieving a stirrup reinforcement ratio of 1.03%. This meets the minimum reinforcement ratio requirements outlined in the Strut-and-Tie Models (STMs) of ACI 318-19 and AASHTO, making it eligible for calculation as the upper limit value of shear resistance. Analyzing the results from Equations 1 and 2 alongside the two STMs, it is evident that the calculated value from Equation 1 closely aligns with the experimental values. Selecting Equation 1 as the upper limit value is considered reasonable and leans toward safety. In contrast, the value stipulated in the ACI 318-19 code is conservative, suggesting that the upper limit value for STM is somewhat biased towards safety. The primary factors influencing the small upper limit value for STM include (1) the issue of the width of the support versus the width of the tie, where

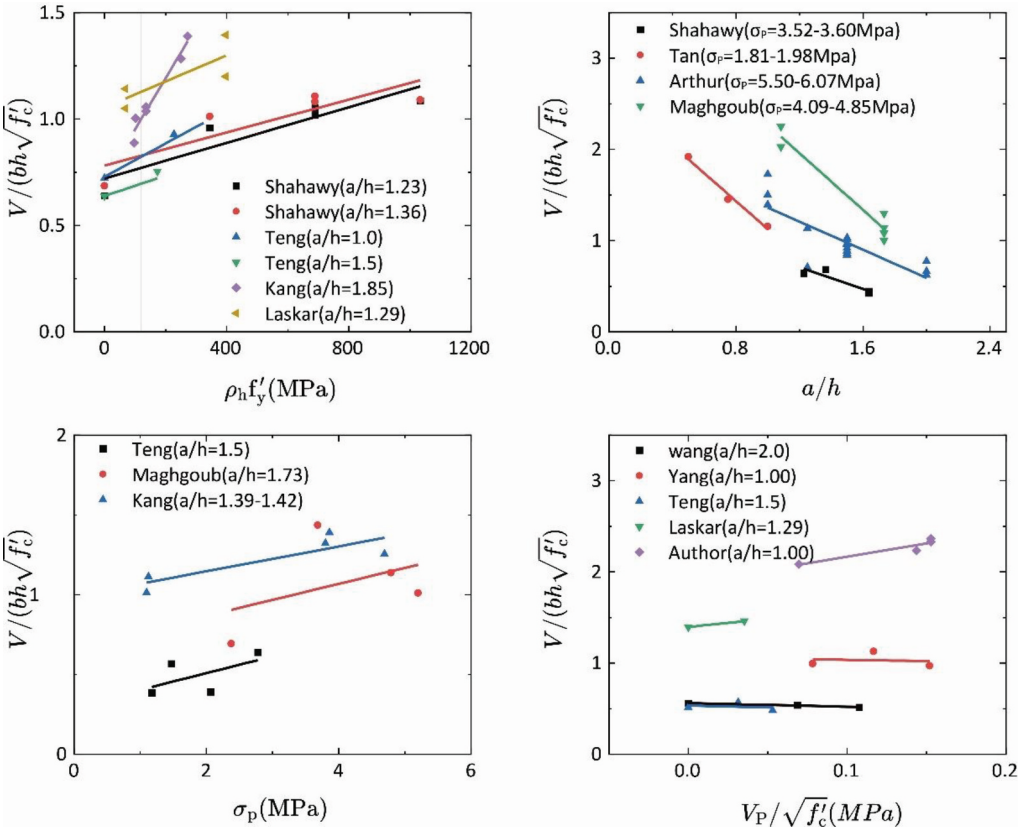


Figure 4. Influence of parameters on shear strength.

T-beams with flanges distribute the width of the support without causing localized damage, and (2) distinguishing only the effect brought by the minimum reinforcement rate, without considering the impact of concrete strength under high reinforcement rates.

Currently, this paper has concluded full-scale post-tensioning tests on bonded prestressed concrete, limiting the range of shear span ratios. Subsequent research should conduct additional tests with varying shear span ratios. Furthermore, addressing the limitations of the current STM model, specifically related to the influence of lower reinforcement ratios and improving calculations for the widening effect at the support, is essential. Investigating the impact of web width in post-tensioned prestressing requires further study, as does exploring the effects of grouting and the material of the pipe on the compressive strength of concrete. The influence of the vertical component of prestressing also necessitates more tests to discuss the effects of unbonded and bonded prestressing methods.

Table 3. Comparasion of different models.

		AASHTO				ACI 318-19			
Beam	Failure shear V_{exp}(kN)	Eq. (1)	Eq.(1)/ V_{exp}	STM	STM/ V_{exp}	Eq.(2)	Eq.(2)/ V_{exp}	STM	STM/ V_{exp}
F1	4890	3723	0.76	1221	0.25	1740	0.36	1693	0.35
F2	4800	4245	0.88	1306	0.27	1911	0.40	2024	0.42
F3	4960	3723	0.75	1221	0.25	1740	0.35	1693	0.34
F4	5140	4430	0.86	1306	0.25	1911	0.37	2022	0.39
Average			0.81		0.26		0.37		0.38

6 CONCLUSIONS

In conclusion, this study has provided a thorough examination of methodologies for determining the upper shear limit value of prestressed concrete deep girders. Through the four T-beam shear tests and collection of experimental data, the following conclusions have been achieved:

(1) The upper limit value of prestressed concrete deep beams is influenced by both the reinforcement ratio and shear span ratio. Longitudinal prestress has been observed to improve cracking and ultimate load capacities.
(2) AASHTO code is more suitable for determining the upper limit value for T-beams, in contrast to the ACI 318-19 code. Strut-and-Tie Model (STM) were found to underestimate the upper limit of shear strength.
(3) The influence of the vertical component of prestress necessitating further investigation.

ACKNOWLEDGEMENTS

The authors acknowledge the financial supports from National Natural Science Foundation of China (Grant numbers [52078363])and Science and Technology Project of Anhui Transportation Holding Group Co., Ltd (Grant numbers[JKKJ-2020-40]).

REFERENCES

AASHTO. 2020. *LRFD bridge design specifications*. American Association of State Highway and Transportation Officials.

ACI Committee 318. 2019. Building Code Requirements for Structural Concrete and Commentary.

ACI-ASCE Committee 326. 1962. Shear and Diagonal Tension. *ACI JOURNAL*, 11(3): 352–396.

Arthur, P.D. 1965. The shear strength of pre-tensioned I beams with unreinforced webs. *Magazine of Concrete Research*, 17(53): 199–210.

Kang, G.Y., Wu, Z.M., Wang, L.Y. & Xue, B.H. 1989. Ultimate Shear Tests of Prestressed Concrete I-Beams. *Proceedings of the Institution of Civil Engineers*, 87(3): 401–414.

Laskar, A., Hsu, T. & Mo, Y.L. 2010. Shear Strengths of Prestressed Concrete Beams Part 1: Experiments and Shear Design Equations. *ACI Structural Journal*, 107(3): 330–339.

Mahgoub, M.O. 1975. Shear strength of prestressed concrete beams without web reinforcement. *Magazine of Concrete Research*, 27(93).

Shahawy, M.A. & Batchelor, B. deV. 1996. Shear Behavior of Full-Scale Prestressed Concrete Girders: Comparison Between AASHTO Specifications and LRFD Code. *PCI Journal*, 41(3): 48–62.

Tan, K.H. 1999a. Shear Behaviour and Analysis of Partially Prestressed I-Girders. *Structural Engineer*, 77(23 & 24).

Tan, K.H., Lu, H.Y. & Teng, S. 1999b. Size effect in large prestressed concrete deep beams. *ACI Structural Journal*, 96(6): 937–946.

Teng, S., Kong, F.K. & Poh, S.P. 1998. Shear Strength of Reinforced and Prestressed Concrete Deep Beams. Part II: The Supporting Evidence. *Proceedings of the Institution of Civil Engineers - Structures and Buildings*, 128(2): 124–143.

Wang, G.-L. 2009. *Experimental and Theoretical Research on Shear Behavior of Prestressed Concrete Beams*. PhD Thesis. Southeast University.

Yang, T.Y., Amani Dashlejeh, A., Arabzadeh, A. & Hizaji, R. 2020. New model for prediction of ultimate load of prestressed RC deep beams. *Structures*, 23: 509–517.

Bridge Maintenance, Safety, Management, Digitalization and Sustainability – Jensen, Frangopol & Schmidt (eds)
© 2024 The Author(s), ISBN 978-1-032-77040-6
Open Access: www.taylorfrancis.com, CC BY-NC-ND 4.0 license

Low carbon solution for short-span bridges: Soil-steel composite bridges versus concrete bridges

Guangli Du
Department of the Built Environment, Aalborg University Copenhagen, Denmark

Adam Czerepak
ViaCon Group, Product & Solutions Director - Bridges & Culverts, Wroclaw, Poland

ABSTRACT: soil-steel composite bridges (SSCB) are extensively utilized for constructing culverts and small-span bridges in numerous countries worldwide, particularly in Europe and North America. The widespread adoption of SSCBs is attributed to their various advantages, such as swift construction, easy installation, low maintenance, straightforward renovations or extensions, and high geometric flexibility, enabling seamless adaptation to terrain conditions and functional requirements. An alternative solution for such structures is the use of reinforced concrete bridges (RCB), including concrete boxes, slabs, frames, or beams bridges. Under the global shift towards a low-carbon strategy and reduction of greenhouse emissions from the transport sector, assessing potential solutions for culverts or small bridges, it is essential to consider their environmental impact. And this is a practice increasingly common across various economic sectors, including engineering.

This paper aims to compare the environmental impact of SSCBs and RCBs by analyzing selected 29 equivalent case studies from several European countries using the cradle-to-gate Life Cycle Assessment (LCA) methodology. Two key environmental impact indicators are selected for evaluation: global warming potential and energy consumption. Data for the analysis of these indicators are derived from Environmental Product Declarations (EPD) and the environmental database Ecoinvent v.3.8.

The case studies demonstrate the advantages of soil-steel bridges over reinforced concrete bridges in the chosen environmental indicators. The main reason for the superior performance of SSCBs lies in their highly efficient use of material mass to ensure the same functionality and load capacity comparing to the concrete solutions. The main load-bearing component of SSCBs is a thin and lightweight corrugated steel plate, which acts as a flexible shell interacting effectively with the surrounding compacted soil. This solution significantly reduces overall resource consumption and carbon emissions.

1 INTRODUCTION

Bridge construction contributes to a substantial share of carbon emissions and resource consumptions. Under the global shift towards a low-carbon strategy, the European Union requests a further reduction of CO2 emissions from the construction sector. Seeking sustainable practices in bridge construction is a key step towards resilient bridge structures with lower carbon emissions. For short span bridges, steel-soil composite bridge (SSCB) is widely adopted and functionally equivalent to the traditional reinforced concrete bridges (RCB). Comparing to RCB, SSCB is easy in construction, low maintenance and competitive cost. By replacing the on-site activities with off-site machines in prefabrication, SSCB can substantially reduce the construction waste by up to 40%. This is because RCBs require the on-site

DOI: 10.1201/9781003483755-154

formwork and reinforcement installations, while the main structure element of SSCB is prefabricated in the factory and bolted on-site, with very minimum equipment needed, and the use of the steel materials is 100% recyclable without loss in quality.

Several studies have conducted mechanical analyses on SSCB bridges; see Mellat et al. (2014), Flener and Karoumi (2009), Pettersson et al. (2015), and Wadi et al. (2020). However, there is a lack of study performed on environmental performance of these two types of bridge designs (Du et al., 2018). This study investigates the environmental performance of SSCB comparing with RCB using cradle-to-gate life cycle assessment (LCA) method associated with 29 equivalent case studies from several European countries. The analysis evaluates the indicator of global warming potential (GWP) in ton CO_2 equivalent and total primary energy demand in GJ, following the technical standards EN15804 for construction products. The indicator of GWP takes account of all substances that contribute to the climate change (IPCC 2013), while the indicator of total primary energy considers energy consumption including both non-renewable energy (e.g. fossil and nuclear) and the renewable energy (e.g. solar, wind, biomass, geothermal, hydro) sources. The functional unit in this study is defined as the entire bridge including all of the structural components during the design life span of 100 years. The analysis is carried out using the LCA calculator developed by ITB Poland Building Research Institute. The dominant structural components, key activities and materials that contribute to the most environmental impacts are tracked. Due to a significant reduction in self-weight, SSCB shows the comparatively low environmental impact over RCB solutions among all considered impact categories.

2 LCA METHODOLOGY

As defined in the ISO 14040 and ISO 14044 standards, Life Cycle Assessment (LCA) is a standardized and internationally recognized approach for quantifying the resource consumption, environmental impacts, emissions as well as the health impacts linked to a product or service through its whole life cycle. The LCA analysis of covers 7 modules, including material manufacture and transportation (A1-3), replacement of building components (B4), operational energy (B6), and waste processing (C3-4), as shown in Figure 1. Among those modules, the material manufacturing phase is the most dominant contributor to the total environmental impact throughout the entire life cycle. Although including B, C and D stages are in favor of SSCB, this study focuses on "cradle-to-gate" analysis covering modules A1-A3 quantifying the impacts associated with upstream material manufacturing. The declared modules are shown in Figure 1.

The material manufacture phase encompasses all the upstream processes of materials used to construct the bridge, from the extraction of raw materials until products are ready for use at the factory gate. To model the impact from this phase, the Ecoinvent database and EPDs containing the unit environmental profiles for each relevant material is applied. Each of the

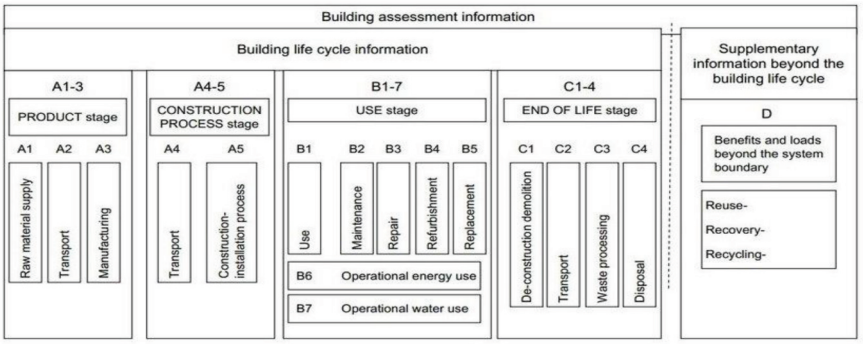


Figure 1. Life cycle modules.

unit environmental impact for the material or process is associated with air, solid and liquid releases linked to the material production, and then aggregated into the mid-point environmental impact categories. The summarized bills of material quantities of the selected bridge are obtained from the drawings and bills of material quantities.

Life Cycle Inventory data (LCI) is a key phase in the LCA that involves the detailed collection and quantification of data associated with the product. The data covers the inputs (energy, resources) and outputs (emissions, waste, etc). LCI databases as Ecoinvent, GaBi and Ökobau are widely used in LCA analysis and contain data for generic and average construction products. Besides, there are also a large number of environmental product declarations (EPD) data owned by the individual producers for a specific product or product groups. For this paper LCA analysis have been done for SSCB with environmental indicators taken from EPD and compared to RCB where the environmental indicators have been taken from Ecoinvent v.3.8. The EPDs are prepared based on data collected from the actual production site in accordance with European standards EN15804. The environmental impact of each process and material type is adopted to quantify the carbon emissions and energy consumption related to the bridge material manufacture scenarios.

3 SOIL-STEEL COMPOSITE BRIDGE (SSCB) AND REINFORCED CONCRETE BRIDGE (RCB)

The environmental performance throughout the life cycle of a bridge can be significantly influenced by the type of bridge chosen. Two commonly employed solutions for short-span bridges are the SSCB and the RCB, both serving the same purpose and often designed with a lifespan of 100 years.

The RCB typically comprises a reinforced concrete frame, concrete slab, or beams placed on bridge abutments, forming the load-carrying structure, see Figure 2. The construction of RCB takes about 3 - 4 months for a small RCB, including concrete foundations. In contrast to the SSCB, the construction of RCB involves scaffolding, formwork, reinforcing, and concrete pouring, considerably extending the construction time and, consequently, increasing environmental burdens.

On the other hand, SSCB is a simpler and functionally equivalent structure to RCB. It consists of a corrugated steel shell, usually protected against corrosion by hot deep galvanization and paint layers, surrounded by compacted frictional soil, see Figure 3. Depending on the bridge span, SSCB can be designed with different corrugation sizes and steel plate thicknesses. The steel plates are often divided into several corrugated and curved sections for easier transportation, bolting together on-site. After bolting, the conduit is backfilled with carefully compacted frictional soil. The shorter construction time of SSCB, compared to RCB (typically 3 - 4 weeks for a small bridge), significantly reduces traffic disturbances and mitigates associated environmental impacts, especially in cases of replacing old bridges. SSCB is primarily designed for short-span bridges, ranging from 3 to 20 meters. Recent advancements in deep

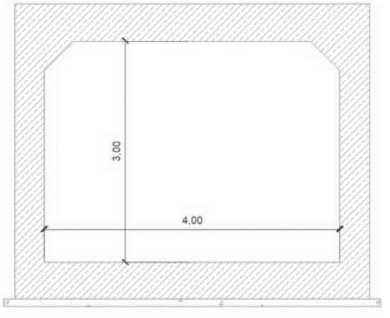


Figure 2. The example of RCB cross section.

corrugations and improved steel qualities have enabled relatively large spans, with a record documented in the Guinness Book of Records showcasing a maximum span of approximately 33 meters, built in United Arab Emirates in 2019.

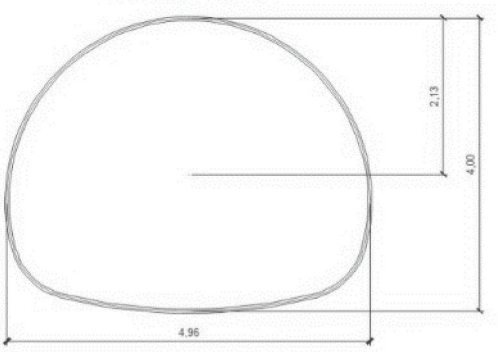


Figure 3. The example soil-steel composite bridge/culvert solution as an equivalent replacement for the RCB structure of Figure 2.

The rise in the popularity of SSCBs can be attributed largely to advancements in designing, manufacturing, and anti-corrosion protection techniques that allow to prolong life time up to 100 years which is usually required for bridges. This has effectively eliminated potential operational issues. SSCBs offer numerous advantages, including efficient use of material mass for desired bearing capacity, swift construction, easy installation, uncomplicated renovations or expansions, and exceptional geometric adaptability, allowing seamless adjustment to terrain conditions and functional requirements.

Due to the current emphasis on sustainable development in every sector of the economy, SSCBs are also being examined for their environmental impact. This is confirmed by LCA analyzes that will be presented in the following sections of this paper.

4 LCA OF SSCB AND RCB

The LCA was carried out on the basis of 29 projects from various European countries, where two solutions, SSCB and RCB, were proposed in each of these projects, equivalent in terms of load capacity and functionality.

These were culverts and bridges ranging from several to a dozen or so meters span (in cross-section). The comparative analysis was carried out for modules A1, A2 and A3 and for following environmental indicators:

- Global warming potential
- Total primary energy

The environmental indicators for each item were calculated using the LCA calculator developed by the "Instytut Techniki Budowlanej" in Warsaw, Poland (Figure 3). The calculation results are presented in Table 1.

The results presented in Table 1 were obtained by calculating the material mass multiplied by the environmental indicator given per ton. Designers derived the mass from drawings or Bill of Quantities (BOQ) tables. For RCB, the mass includes concrete, reinforcement bars, and backfilling, while for SSCB, it comprises steel plates, concrete foundations (for arches), and backfilling.

The backfilling material for both solutions was considered within the range necessary to complete each solution. For SSCB, the range is larger because the backfilling material is a part of the soil-steel solution contributing to the bearing capacity calculation.

Designers individually define this range, typically as span/2 for the left side and span/2 for the right side from the steel shell. Below, a few drawings of bridge cross sections (Figure 5-7) are presented as examples from the 29 analyzed projects.

Table 1. The values of environmental indicators for the SSCB and RCA solution from selected projects.

Item	SSCB		RCB	
	Global Warming Potential [eq. ton Co_2]	Total primary energy [GJ]	Global Warming Potential [eq. ton Co_2]	Total primary energy [GJ]
1	138	1 547	197	1 705
2	34	326	46	379
3	145	1 622	299	2 595
4	170	2 014	662	5 758
5	138	1 598	310	2 989
6	19	206	41	411
7	83	940	229	1 926
8	32	375	53	499
9	35	427	75	708
10	551	5 903	1 063	9 493
11	95	957	188	1 797
12	103	1 078	129	1 300
13	39	459	94	915
14	32	305	56	591
15	115	1 134	223	2 156
16	198	1 907	294	2 752
17	65	793	94	842
18	178	1 928	273	2 458
19	56	585	144	1 261
20	63	686	103	1 069
21	263	2 704	798	7 439
22	32	368	61	552
23	731	9 678	1 632	16 301
24	70	829	273	2 407
25	9 758	105 167	18 310	174 344
26	2 630	26 994	3 337	30 782
27	3 040	39 585	3 552	42 313
28	220	2 427	452	4 214
29	9 311	99 982	16 927	153 586

5 RESULTS

In all 29 cases studied, the use of SSCB resulted in more favorable environmental indicators. The reduction in environmental indicators when using SSCB compared to RCB is presented in Table 2. On average, there is a 47% reduction in GWP and a 34% reduction in energy consumption when using SSCB as opposed to RCB.

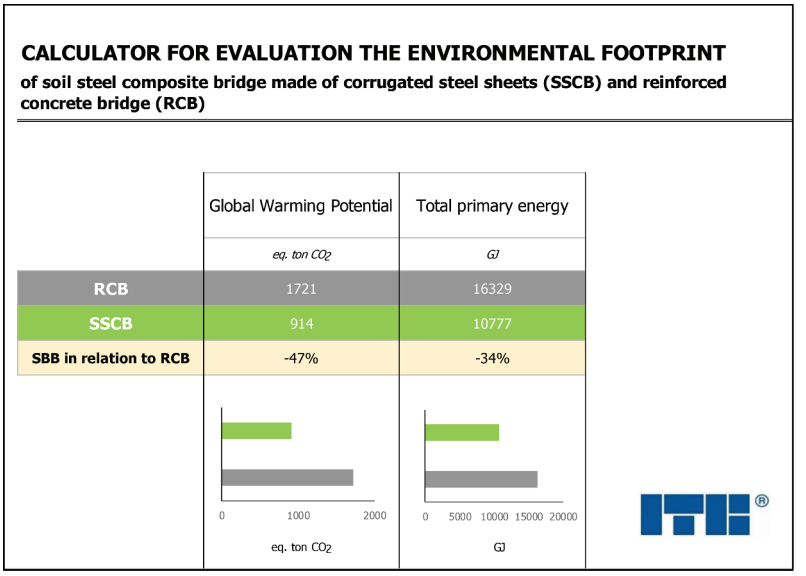


Figure 4. LCA calculator prepared by "Instytut Techniki Budowlanej" Warsaw, Poland, used for analysis presented in this paper.

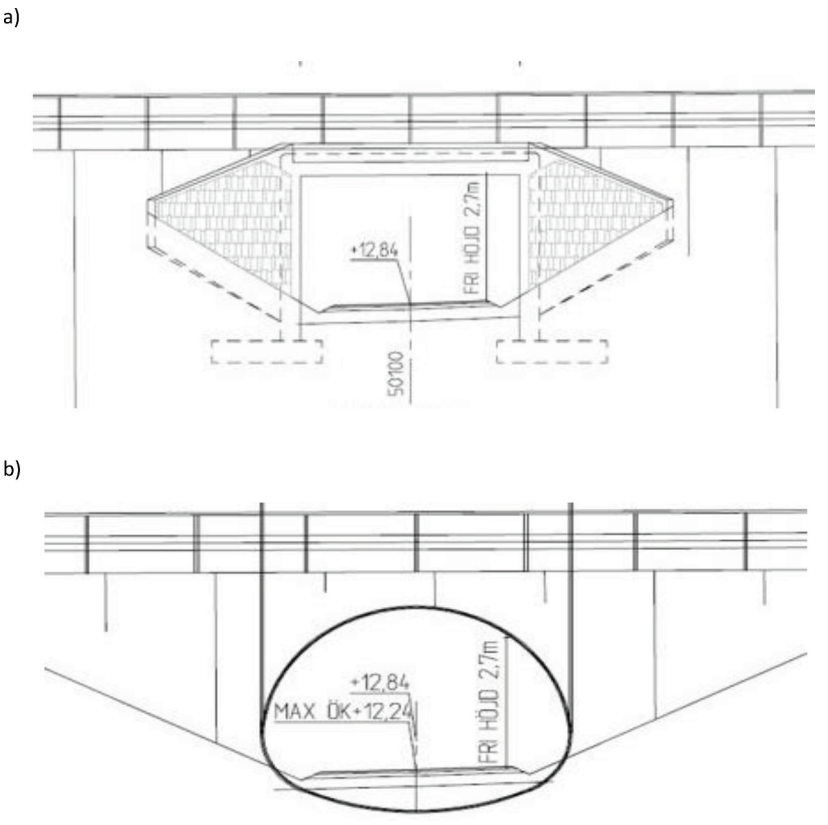


Figure 5. The example of short-span bridge cross section from selected projects - equivalent alternatives in terms of load capacity and functionality: a) RCB, b) SSCB.

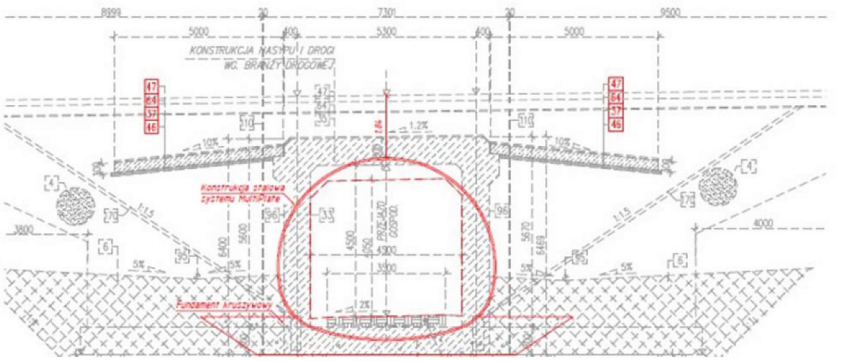


Figure 6. The example of short-span bridge cross section from selected projects - equivalent SSCB round shape (in red color) as an alternative to RCB bridge (in grey color).

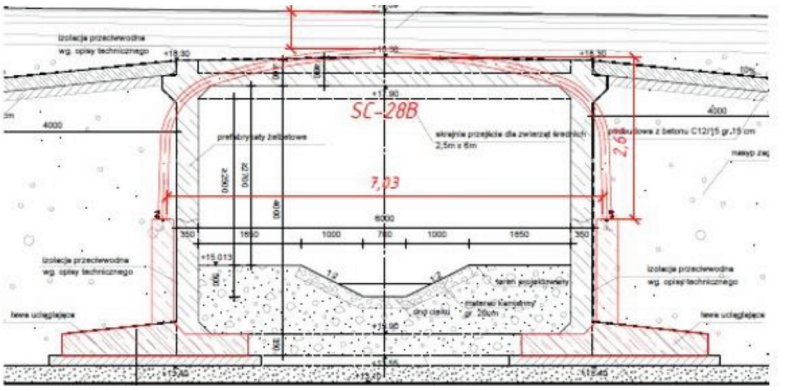


Figure 7. The example of short-span bridge cross section from selected projects - equivalent SSCB low arch shape (in red color) as an alternative to RCB bridge (in grey color).

6 CONCLUSIONS

In the past, soil-steel composite bridges (SSCB) might have been considered a specialized or innovative approach. However, in the current era, SSCBs employing corrugated bolted plates or helically corrugated pipes have become widely popular for constructing culverts and small-span bridges across almost every European country, as well as in other continents, gaining global recognition for their significant potential.

This paper compared two types of commonly used short-span bridges SSCB and RCB. The SSCBs show advantages over the RCBs in A1, A2 and A3 phases, which is up to 74% less in the indicator of GWP and 66% in total primary energy. The main reason for the superior performance of SSCB lies in their highly efficient use of material mass to ensure the same functionality and load capacity comparing to the RCB solutions. The main load-bearing component of SSCBs is a thin and lightweight corrugated steel plate, which acts as a flexible shell interacting effectively with the surrounding compacted soil. This corrugated steel plate can be engineered to have a high strength-to-weight ratio, allowing for lighter bridge designs, compared to concrete bridges or other steel beam or grid bridges. A high strength-to-weight ratio and other advantages like fast construction and potential for recyclability makes this kind of solution more beneficial for the environment. This solution significantly reduces overall resource consumption

Table 2. Comparison of environmental indicators between SSCB and RCB.

Item	SSCB v RCB - Global Warming Potential	SSCB v RCB - Total primary energy
1	-30%	-9%
2	-26%	-14%
3	-51%	-37%
4	-74%	-65%
5	-55%	-47%
6	-52%	-50%
7	-64%	-51%
8	-39%	-25%
9	-54%	-40%
10	-48%	-38%
11	-50%	-47%
12	-20%	-17%
13	-58%	-50%
14	-44%	-48%
15	-48%	-47%
16	-32%	-31%
17	-31%	-6%
18	-35%	-22%
19	-61%	-54%
20	-39%	-36%
21	-67%	-64%
22	-48%	-33%
23	-55%	-41%
24	-74%	-66%
25	**-47%**	-40%
26	-21%	-12%
27	-14%	-6%
28	-51%	-42%
29	-45%	-35%
AVE.	-47%	-34%

and carbon emissions. There are also other studies where more LCA phases (A, B, C, D) have been analyzed, comparing the SSCB and RCB solution. The results are in line with the thesis presented in this paper.

REFERENCES

Du, G., Pettersson, L. and Karoumi, R., 2018. Soil-steel composite bridge: An alternative design solution for short spans considering LCA. *Journal of Cleaner Production*, *189*, pp.647–661.EN 15804 Sustainability of construction works - Environmental product declarations - Core rules for the product category of construction products.

EN 15978:2011 Sustainability of construction works - Assessment of environmental performance of buildings - Calculation method.

Ecoinvent database version 3.8
Flener EB, Karoumi R. Dynamic testing of a soil–steel composite railway bridge. Engineering structures. 2009 Dec 1;31(12):2803–11.
GaBi Sphera's Life Cycle Assessment Database
Ökobau database - https://www.oekobaudat.de/en.html
ISO 14040:2008 – "Environmental management – Life cycle assessment – Principles and framework"
ISO 14044:2008 – "Environmental management – Life cycle assessment – Requirements and guidelines"
Environmental Product Declaration Type III ITB No.127/2020, Steel structures MultiPlate,SuperCor and UltraCor (2021-2025) Instytut Techniki Budowlanej (ITB).
LCA calculator of SSCB developed by the "Instytut Techniki Budowlanej" in Warsaw, Poland
Mellat P, Andersson A, Pettersson L, Karoumi R. Dynamic behaviour of a short span soil–steel composite bridge for high-speed railways–Field measurements and FE-analysis. Engineering Structures. 2014 Jun 15; 69:49–61.
Pettersson, L., Flener, E.B. and Sundquist, H., 2015. Design of soil–steel composite bridges. *Structural Engineering International*, *25*(2), pp.159–172.
Mellat P, Andersson A, Pettersson L, Karoumi R. Dynamic behaviour of a short span soil–steel composite bridge for high-speed railways–Field measurements and FE-analysis. Engineering Structures. 2014 Jun 15; 69:49–61.
Pettersson, L., Flener, E.B. and Sundquist, H., 2015. Design of soil–steel composite bridges. *Structural Engineering International*, *25*(2), pp.159–172.

Bridge Maintenance, Safety, Management, Digitalization and Sustainability – Jensen, Frangopol & Schmidt (eds)
© 2024 The Author(s), ISBN 978-1-032-77040-6
Open Access: www.taylorfrancis.com, CC BY-NC-ND 4.0 license

Soil-steel composite bridges, advantages – based on case studies

Baturalp Şentürk
ViaCon Turkey, Design Engineer, Istanbul, Turkey

Michael Nygaard Nonbo
ViaCon Denmark, Technical Sales Representative Business Unit Bridges & Culverts, Naestved, Denmark

ABSTRACT: Until a decade or two ago, soil-steel composite bridges (SSCB) could have been described as a niche or innovative approach. However, in present times, SSCBs utilizing corrugated bolted plates or helically corrugated pipes have gained widespread popularity for constructing culverts and small-span bridges across nearly every European country and have earned global recognition for their remarkable potential.

The surge in popularity of SSCBs can be attributed to the mastery and refinement of designing, manufacturing, and anti-corrosion protection techniques to a significant degree. As a result, potential operational issues have been effectively eliminated.

Several benefits of SSCB can be highlighted, including highly efficient use of material mass to achieve desired bearing-capacity, rapid construction, effortless installation, simple renovations or expansions, and excellent geometric adaptability, allowing seamless adjustment to both terrain conditions and functional needs.

SSCBs find their most frequent application as culverts, ranging from 1 meter to over 20 meters in span, serving as both culverts and small bridges. An impressive feat was documented in the Guinness Book of Records, showcasing the maximum span achieved, reaching approximately 33 meters.

The objective of this paper is to showcase a selected case studies, from different European countries, and from road and railway projects, to underscore the remarkable capacity of SCCB in overcoming challenging construction obstacles, leading to substantial cost savings and significantly shortened installation timelines.

1 ESKISEHIR ECOLOGICAL BRIDGE CASE STUDY

1.1 *General information*

The bridges made to protect wild animals' living areas purposes have been named ecological bridges in the market. The Eskisehir Ecological Bridge is the first ecological bridge constructed over the high-speed railway line in Türkiye. The main reason for constructing an ecological bridge for this site on Mihaliccik in Eskisehir was local wild animals. Before the construction, there were too many wild animals wasted by train crashes. These crashes brought the effect of decreasing the number of special wild species. The decrease in these numbers was disrupting the balance of nature's wildlife. In addition, it was difficult for the animals to access their nests on the opposite side of the road due to the train line, which blocked the roads that the animals used in their daily lives. On the other hand, these crashes also brought economic disfavors.

To eliminate these problems, biologists and engineers conducted many investigations before starting the project stage like following the animal traces and excrement at the construction site, to setting up the structure to the correct transition point for local animals like wild boar, wolves, red deer, etc. (see Figure 1).

DOI: 10.1201/9781003483755-155



Figure 1. a) The final situation of the bridge; b) The captures from the camera trap.

The structure is made from two segments of corrugated steel plates. The thicknesses of the plates were 7mm for the main part and 5.5mm for the ribbed part. Even though there was a rib plate, the plate did not cover all of the structure; the implementation was made one in two plates. The thicknesses were determined by finite element analyses (Plaxis was used as software for this project's design) (see Figure 2). For the live load analyses, the AASHTO HL93 truckload was taken into account in terms of emergency passings. The structure has 18.55m span, 9.65m rise, and 1.50m cover height parameter. The total top length is 46.55m and the total bottom length is 74.15m which were specified according to the wild animals' needs and the project site requirements such as electrical works. The steel plates were produced as S420 steel class and the total weight of the structure is 230 tones. The plates were connected by M20 class 8.8 bolts. While the use of FEM analysis, the AASHTO approaches have been used in terms of load factors. According to the results, the design was governed by combined utilization with M_{max} and N_{max} which caused the structure 99% of utilization.

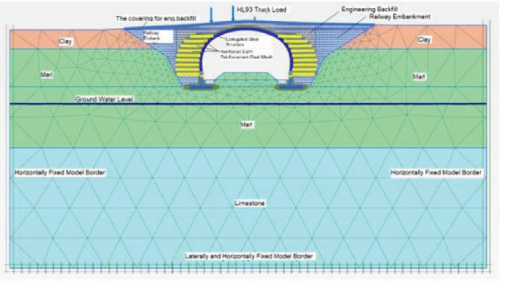


Figure 2. FEM model.

1.2 *Application and construction site challenges*

The designing and construction stage of the project was extremely challenging in terms of being included in the railway institution's budget and also the application site. This project would be applied on the high-speed railway line and the railway authority did not want to cut off railway traffic during the construction. All construction processes were performed during the nighttime zone when the railway is not actively working, generally between 10 pm and 5 am. Also, the weather conditions were tough during construction and concrete casting for foundations. To use the time efficiently, during the project application on the site, plates were assembled to create a ring at the assembly platform near the foundations, and lifting operations of assembled rings were managed overnight (see Figure 3). The structure installation

was finished in 23 days. All the construction stage including foundations, soil works, corrugated steel structure, etc. was completed in 2.5 months.



Figure 3. The construction site during the implementation.

Throughout the construction process, all the electrical current was cut off by the institution during the ring installation on the foundations. The electric current in the wire is 27000 Volt, and to select the cross-section of the project, this current is also taken into account. This means that the minimum distance between the structure plates and the electric line had to be 1.30m to prevent electrical jumping according to the engineer's suggestion. So, the structure dimensions were chosen due to not only railway heights, but also the electrical current line.

One of the main challenges for the analysis process by Plaxis is the huge peaking deflection during the engineering backfill construction stages. To decrease this deflection, the steel meshes around the structure have been applied every 1m in the engineering backfilling (see Figure 4). Also, the engineering backfilling has been applied on 0.3m layers and each layer compacted up to 95%.



Figure 4. Steel mesh application during construction.

After the construction stage of the project was finished, polyurea coating application was made on the inside structural plate face to obtain full waterproofing to prevent any electrical problems during the project's lifetime, also, umbrella water protection was applied over the structure. All the design details of the project were prepared by the ViaCon Türkiye design team including structural control, foundation dimensions, foundation control and layout of reinforced concrete rebar, and others. The design site model of the project was defined in Plaxis depending on the site soil investigation report which was prepared under the control of ViaCon Türkiye. Then, all stages of the project were modeled and analyzed to see the exact behavior of the system.

2 GEOMETRICAL ADAPTABILITY - THE SYRINGE IN GLADSAXE

The background for this project was that the capital city in Denmark, Copenhagen wanted to promote the interest in cycling. They decided to make it safe for the cyclists so they created a program as part of which municipalities within the capital could apply for funding of projects that would promote the use of bicycles as means transportation.

The design should include the connection from the MultiPlate structure to the sheet pile wall. The result was a traditional concrete headwall around the tunnel in one end (see Figure 5 a), at the other end of the underpass the idea was to make a beveled end with a slope of 1:3 (see Figure 5 b).



Figure 5. a) Concrete "portal" in one end; b) Long wing and slope at the other end.

Table 1. Profile data.

Profile	Year	Location	Span	Rise	Bottom length	Skew angle
VR9	2013	Gladsaxe, Denmark	4,77 m	3,83 m	49,85m	28°

As shown in the figure and in Table 1 with the skew angle of 28° the beveled end reached a length of approx. 15 meters. This almost syringe-like shape introduces a challenge when it comes to the soil pressure on the beveled end.

To stabilize this long beveled end the engineers of ViaCon made a combination of a concrete collar and a soil reinforcement using 7 layers of geogrids. The geogrid had a strength of 20 kN/m and was fastened to the side of the MultiPlate with L-shaped steel profiles. The grid was supplied in 1 meter width and the design consisted of 7 layers with a distance of 190 mm to 460 mm.

In order to ensure sufficient anchorage capacity, the length of the geogrid is min. 4 meters from the MP side plates. The contractor installed compacted gravel on top of each geogrid layer and the geogrids were stretched before backfilling.

The concrete collar was designed to be minimum 400 mm wide and cover the steel plates of 600 mm.

The design of this MultiPlate-structure shows the versatility in shaping the material fit the visual expression you want.

3 SIMPLE RENOVATION – PARTIAL RELINING

In 1983 this pedestrian/bicycle underpass was installed in the Municipality of Odense. The profile is a WB6/VR6 made from MultiPlate in the MP200 corrugation.

Sometime during this tunnels life and cycles of the asphalt repair work, the asphalt has been poured out in the full available width leaving cavities along the corrugated steel in which road salt was collected. This eventually created corrosion with local corrosion holes.

The road crossing the tunnel is a subjected to heavy traffic since it connects to one of the main roads to Odense. Hence, it would be of great inconvenience to demolish the old tunnel and reestablish a new one.

It was assessed that due to the low utilization in the bottom part of the tunnel the load carrying capacity of the existing structure was still sufficient. However, the corroded area needed to be sealed off.

In this case a partial relining with the bottom half of the slightly smaller WB4/VR4-profile was chosen (see Figure 6 a) and Table 2).



Figure 6. a) New bottom of WB4/VR4-profile placed inside an existing WB6-profile; b) Final result with wooden handrail in transition between old and new construction.

Table 2. Profile data.

Profile	Year	Location	Span	Rise	Bottom length
VR4-bottom	2021	Odense, Denmark	3,64 m	1,19 m	28,1m

When the new bottom is pulled/assembled in the existing tunnel, the gap between the profiles is filled with concrete. To prevent the new bottom floating upwards, Z-profiles bolted to its sides caught brackets welded to the existing structure.

To finish off the filled gap between the existing tunnel and the new bottom, and wooden handrail was made (see Figure 6 b)). Moreover, the asphalt was reestablished with an inwards slope along the steel bottom.

The process of partially relining the existing tunnel was both less inconvenienced and cheaper than replacing the tunnel.

4 RAPID CONSTRUCTION – THE FLYING TUNNEL

One of the advantages of the SSCB is their relatively low weight. This feature was utilized during the installation of this pedestrian underpass.

The pedestrian underpass is a part of a new bike path project stretching from Stenholt to Nørre Knudstrup along route 13 in Silkeborg Municipality.

Along this path a new underpass crossing Route 13 had to be made, and since this road is a main road with very heavy traffic the time it needed to be closed, should be reduced to an absolute minimum.

The closure time was decided to be in an extended weekend in relation to a public holyday in May 2023 given the contractor a 3-days window to cut open the road, excavate for and installing a 30 m pedestrian tunnel, backfill and reestablish the road with asphalt.



Figure 7. Assembled tunnel swiftly craned in place.

Table 3. Profile data.

Profile	Year	Location	Span	Rise	Bottom length	Total weight
VR8	2023	Silkeborg, Denmark	4,63 m	3,64 m	31,3 m	20,2t

The solution was to assemble a VR8-profile (see Table 3) in the MP200 corrugation on a temporary, prepared jobsite parallel to the main road. This was done well ahead of the actual closure time of the road, and the tunnel was assembled within reach of a mobile crane.

To even the load, 8 lifting brackets were temporarily bolted to the VR8-tunnel a connected to lifting frame. The weight of ca. 20t for +30m of complete tunnel was an easy task for the mobile crane making it a fast job (see Figure 7).

Thereby the contractor planning of the most critical logistics was limited to:

- their own excavators, machines and crew
- an external mobile crane
- an external asphalt crew

In comparison 20 t would have been the approximate weight of only a couple of meters of a similar sized precast concrete tunnel. A precast concrete solution would have required a big

number of carefully planned element deliveries to keep the mobile crane running effectively. Hence, increasing the risk of the entire installation.

The SSCB-solution kept the logistic chain very simply making it less likely that anything could go wrong.

5 CONCLUSION

As the above examples show, SSCB-solution are not only a technically effective choice, but also flexible and adaptive, making them an ideal solution for a variety of site and design conditions.

Currently, the use of SSCB employing either corrugated bolted plates or helically corrugated pipes has become extensively favored for the construction of culverts and short-span bridges. This approach has garnered worldwide acclaim due to its impressive capabilities.

The initial hurdles related to achieving an optimal design, seamless construction, and implementing suitable anti-corrosion protection measures have been successfully overcome. This progress highlights the adaptability and advancements in the field, showcasing how SSCB have evolved to address and surmount these challenges. The widespread acceptance of these structures on a global scale is a testament to their effectiveness and the refined techniques applied to ensure durability and longevity.

REFERENCES

AASHTO LRFD bridge design specifications. 2017. Washington, D.C.: American Association of State Highway and Transportation Officials.

Larsen, E. S. et al. 2019. Håndbog, Projekteringsgrundlag for stålrørsbroer. Copenhagen: Vejdirektoratet

Petterson, L. & Sundquist, H. 2007. Design of soil steel composite bridges – Report 112, 5th Edition 2014. Stockholm: KTH.

Plaxis Material Models Manual. 2021. Exton, PA: Bentley Software Company.

Wadi, A. 2019. Soil Steel Composite Bridges. Stockholm: KTH.

Bridge Maintenance, Safety, Management, Digitalization and Sustainability – Jensen, Frangopol & Schmidt (eds)
© 2024 The Author(s), ISBN 978-1-032-77040-6
Open Access: www.taylorfrancis.com, CC BY-NC-ND 4.0 license

The corrosion of reinforced concrete bridge structures and its influence

Gerelt-Od Shijir
Ministry of Road and Transport Development of Mongolia, Ulaanbaatar

Duinkherjav Yagaanbuyant, Khasnavch Sambuu & Mungun Duinkherjav
Mongolian University of Science and Technology, Ulaanbaatar

Sugarjav Namsraijav
Ministry of Road and Transport Development of Mongolia, Ulaanbaatar

Anktsetseg Gantulga & Khorolsuren Tumur-Ochir
Road and Transport Development Center, Ulaanbaatar, Mongolia

Nyamjargal Bayasgalan
Bros property LLC, Ulaanbaatar, Mongolia

ABSTRACT: The physical and mechanical properties of structural materials depend on changes in natural factors, as well as changes in the structure of the surrounding environment caused by pollution of the environment, soil, and water as a result of human activity. The speed of movement of air and water, the penetration of moisture due to soil adhesion, as well as the spread and penetration of harmful substances create the risk of carbination of the concrete structures. These defects may seem innocuous initially, but in the long run can have deleterious effects on its lifecycle performance. Since the problem of determining the service life of a bridge is related to the durability of its elements, the article will consider the rate of carbonation of concrete and its effect on corrosion of reinforcementь as well as a study of the durability of the structure.

1 INTRODUCTION

Moisture penetration, air humidity, and the spread of harmful substances, salt, solar radiation, and temperature changes can lead to corrosion and carbonation of concrete, negatively impacting the performance of bridge structures. In many countries' regulatory documents, the service life of bridge structures is standardized to be between 70 and 100 years due to climatic conditions, regulatory requirements, and construction quality. The thickness of the protective layer of concrete and the duration of the concrete carbonation process are factors that influence the residual life of a bridge structure.

In Mongolia, due to inadequate waterproofing and delayed maintenance and repair work, bridge structures such as expansion joints, reinforced concrete spans, supports, and other components are constantly exposed to moisture, air humidity, and alternating freezing and thawing of water-saturated zones. This leads to surface carbonation of the reinforced concrete structure, the formation of cracks, and the onset of reinforcement corrosion, ultimately affecting the load-bearing capacity, strength, and durability of the bridge structure under constant load.

2 CONDITION AND OPERATION OF BRIDGES IN MONGOLIA

Mongolia's total road network is 112,893.8 km, and only 973 bridges are in use, according to a survey conducted in 2022. The survey results show that out of the total number of bridge structures in operation in Mongolia, there are 593 reinforced concrete bridges, 345 wooden bridges, 7 composite bridges, and 28 other types respectively (Table 1).

DOI: 10.1201/9781003483755-156

Table 1. Types of bridges.

Types	Number	Length	Percentage
		m	%
Concrete	593	32,527.71	60.88
Wooden	345	8,630.80	35.42
Composite	7	1,755.30	0.72
Other	28	1,419.00	2.88
Total	973	44,332.81	100

Approximately 60.88 percent of the existing bridges in Mongolia are reinforced concrete bridges. Issues such as investigating the technical conditions and load capacity of the bridges, determining the technical operational levels of bridge lifespan and damage of bridges, estimating the lifespan of bridge spans and other bridge-related facilities, repairing and reinforcing the bridge spans, and not reducing the load capacity of the bridges, increasing the load capacity, and increasing the road capacity/traffic capacity of the bridges have been severely raised. A pressing issue is the problem of predicting the service life of reinforced concrete structures and determining the durability of the bridge. (Khasnavch, et al., 2022)

According to the results of size studies: 231 bridges are less than 10 m long, 266 bridges are 10-20 m long, 270 bridges are 20-50 m long, 96 bridges are 50-100 m long, 63 bridges are 100-200 m long, and 47 bridges are more than 200 m long. By the time of construction of bridges in Mongolia: 5.65% were built before 1960, 36.38% in the period 1961-1990, 6.68% in the period 1991-2000, 16.44% in the period 2001-2010, 21.58% in the period 2010-2015, and 13.26% after 2015 (Figure 1).

As part of this study, 30 reinforced concrete bridges were selected from the bridges operating in the country, taking into account parameters such as year of construction, age, total length, type and length of foundations, supports and spans. The year of construction, survey of dimensions, service life and planning of the standard load capacity of the surveyed bridges, level of operation and risk assessment are shown graphically in Figures 2, 3 and 4. (JICA, 2015)

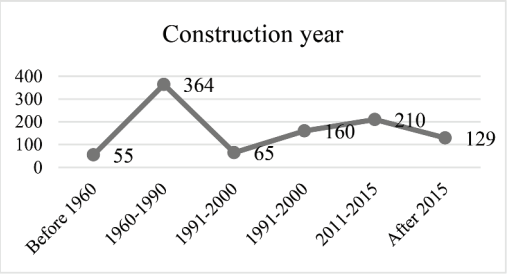


Figure 1. Construction year.

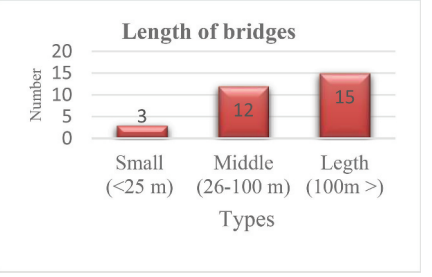


Figure 2. Length of bridges.

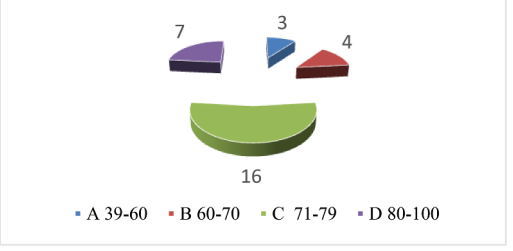


Figure 3. Bridge utilization rate.

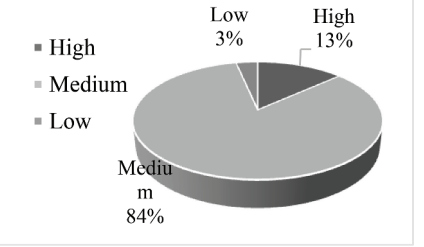


Figure 4. Bridge risk assessment.

3 CONCRETE CORROSION AND ITS INFLUENCE

The durability of concrete is usually understood as the ability to reliably maintain its original shape, dimensions, and physical and mechanical parameters when used under the influence of the environment. Concrete corrosion is a loss of quality caused by exposure to the environment without mechanical influence. Corrosion is a very dangerous phenomenon, since it occurs hidden for a long time and deteriorates the quality of concrete. This process has many reasons. (Dashjamts & Battsagaan, 2013)

Concrete corrosion is a complex physical and chemical process of interaction between the components of cement stone and the external environment and the resulting formation of undesirable compounds, sometimes their internal movement, which most often causes a decrease in the strength of concrete or its complete destruction. The main hazards for bridge structures are considered to be mineralized surface and groundwater containing various substances that differ in the degree of danger of substances dissolved in water, their content, temperature, and characteristics of concrete. Depending on the properties of the aggressive environment, corrosion can occur in the main directions, according to which the following types of concrete corrosion are distinguished. (Dvorkin & Dvorkin, 2006)

A. The first type of corrosion combines processes associated with the leaching of soluble parts of cement stone under the influence of water - the environment (water with low bicarbonate alkalinity, fresh water are especially dangerous). Leaching is understood as the process of dissolution and removal of calcium hydroxide Ca $(OH)_2$ (slaked lime) by water from the concrete body, and the graph of this process is shown in Figure 7. (Jiao, et al., 2016)

B. The second type of corrosion combines processes associated with exchange reactions between the components of the cement stone of concrete and an aggressive environment with the formation on the surface of concrete of amorphous, poorly soluble corrosion products that do not have astringent properties, as well as easily soluble compounds that are washed out with water. Corrosion occurs when water reacts with substances that accelerate the release of soluble compounds, such as lime (calcium oxide hydrate), that attack the concrete.

Components that contribute to the destruction of cement stone include carbonic acid and other water-soluble acids, such as sodium chloride and other chloride salts, as well as substances that increase the solubility of calcium oxide in water. (Larsen, 2020)

C. The third type of corrosion combines processes associated with an increase in the volume of the solid phase of cement stone minerals, deposition of corrosion products, freezing of water, or crystallization of salts in the pores. Crystallization corrosion is understood as the mechanical destruction of concrete and reinforced concrete structures from internal stresses that arise when the volume of constituent materials increases. This type of corrosion occurs when concrete is exposed to sulfuric acid salts (sulfates).

Under certain conditions, types of concrete corrosion can overlap with one another. In this case, it is necessary to identify the leading type of corrosion, the maximum speed of which determines the durability of the structure. For example, the second and third types of corrosion occur when concrete is exposed to water containing magnesium sulfate. Figure 5 shows a diagram of the types of corrosion of concrete under the influence of water and aqueous solutions. In addition to

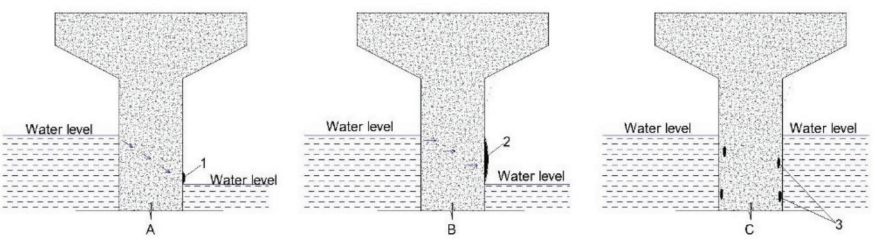


Figure 5. Types of corrosion and diagram of the formation mechanism.

the formation of concrete corrosion due to the action of aqueous solutions, reinforced concrete structures are also subject to other types of corrosion; in addition to concrete, corrosion of reinforcement is observed.

A. The first type of corrosion or leaching process; B. The second type of corrosion is a chemical effect on leaching; C. The third type of corrosion or the process of salt crystallization. 1-accumulation of lime and calcium carbonate, 2-occurrence of corrosion, 3-occurrence of corrosion inside the concrete body.

D. Corrosion due to freeze-thaw cycles In Mongolia, which has an extreme climate, bridge structures undergo repeated freeze-thaw cycles, leading to a deterioration in their quality. If there were no cracks in the concrete, water could not seep in and cause freezing. Cracks in concrete and reinforced concrete structures are common, and they are a leading indicator of damage. These cracks appear as a result of design errors and incorrect actions during concrete work. (Salmeron, et al., 2022)

According to the results of research by the Scientific Research Institute of Hydrometeorology for 2001-2010, when constructing a graph and taking into account the fluctuation of temperatures in April and October, it was found that the influence of zero temperature becomes borderline between freezing and thawing temperatures of concrete.

Immediately after concreting, due to the inability to create conditions for the normal process of cement consolidation, mass transfer occurs due to the evaporation of water, resulting in the formation of cracks on the exposed surface of the concrete. If the cement mortar begins to set, the cracks and pores formed on its surface will not close, and then water will seep in. The water inside will freeze and expand, forming a thin layer on the surface, resulting in cracks.

Concrete will crack to varying degrees due to repeated wetting and drying. It swells slightly when wet and contracts when cooled. As a result of shrinkage, cracks will appear, starting from the surface of the concrete. It will crumble, losing weight and structure, and strength is lost, leading to corrosion (Examples in Figures 6, 7 and 8). Essentially, this corrosion of concrete is not only the fault of moisture and water in the environment, but is also the result of improper actions by the contractor, who created the opportunity for water, moisture, and gas to enter the concrete structure during preparation and production.

If water could not penetrate the concrete, no matter how cold the environment, the concrete would not suffer structural failure due to volume expansion from freezing. Water in the pores of concrete does not freeze at a temperature of 0°C, and the freezing point of the very small amount of water that freezes in capillaries is well below 0°C. Therefore, the structure should be sealed to protect it from cold weather conditions. For example, reducing the water-cement ratio is a simple way to completely stop mass transfer in concrete at the first stage of compaction.



Figure 6. Concrete corrosion and defects on the reinforced concrete surface of a girder.



Figure 7. Concrete corrosion and defects on the reinforced concrete surface of an anchorage.



Figure 8. Concrete corrosion and defects on the reinforced concrete surface of a support.

When concrete is fully cured, less than 50% of the water in the composition reacts with the cement to form cement paste. Ordinary Portland cement absorbs 17-20% of its weight in water in 28 days and hardens. The residual water becomes excess water and eventually evaporates, forming capillaries. Scientists have confirmed that when concrete fully hardens, 23-25% of the cement by weight combines with water to form a solid.

According to the researchers, water seeping into 0.1-0.5 micron cracks and pores in concrete freezes and causes structural damage. However, it is believed that large pores will not be completely filled with water and will not be damaged by freezing. If air bubbles (closed pores) with a diameter of less than 0.2 mm are evenly distributed within the structure of the cement stone, researchers prove that the structure will not be destroyed during freezing. However, it can be seen that even if aeration additives are used only in the concrete of the bridge structure and methods are used to protect it from atmospheric exposure to cold, if the structure is washed with water due to insufficient drainage and the presence of capillary pores filled with water, cracks and damage will occur intensively.

The main condition for the destruction of concrete is the process of freezing and thawing. Repeated cycles of freezing and thawing lead to the gradual deterioration of concrete. This is due to the fact that during freezing, stresses arise that are close to the limit, which are destroyed during thawing. This failure mechanism is similar to the failure of a solid body as a result of repeated loading. Compacting the structure is considered the only reliable way to protect against physical corrosion, which reduces the quality of concrete due to wetting, drying, and freezing. Gibson in 1938 and Lerch in 1959 noted that the influence of the chemical activity of coarse and fine aggregates on the destruction of concrete is inevitable. Later, in 1964, Hadley studied the alkali-silicon reaction and believed that this reaction was a strange phenomenon.

4 DURABILITY STUDY

The strength of reinforced concrete structures is assessed by the corrosion of concrete and reinforcement. Corrosion of reinforced concrete structures occurs under the influence of O_2, Cl, and CO_2. Corrosion of reinforcement caused by Cl is more common in elements in contact with salt in bridge structures. To control the corrosion of reinforcement caused by Cl in concrete, it was carried out using a Proceq device from Resipod, Switzerland. The Resipod is a device that measures the electrical resistance of concrete surfaces. The electrical resistivity of concrete provides information about the state of reinforced concrete structures. The resistivity of concrete is directly related to the corrosion process and the corrosion rate of concrete. Figures 11 and 12 present the results of measuring the resistivity of the concrete surface of the structures of the studied reinforced concrete bridges using the Resipod device. (Hudson, et al., 2015)

For concrete and reinforced concrete structures with conventional Portland cement binders, with a specific resistance of less than 100 kΩcm, no corrosion of concrete reinforcement occurs, and with a specific resistance of 200-300 kΩcm, the process of corrosion of concrete reinforcement has begun. If the resistivity exceeds 300 kΩcm, it means that there is severe corrosion of the concrete reinforcement and additional measures must be taken to strengthen and protect the concrete. Although we conduct our research under the assumption that corrosion in reinforced concrete structures is primarily caused by carbonation of the concrete, we have observed evidence of galvanic corrosion due to the use of reinforcement in the grounding of the support.



Figure 9. Cracks arising due concrete supports.



Figure 10. Concrete strength of reinforced concrete structures.

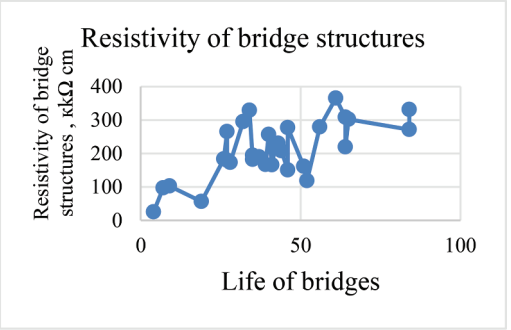


Figure 11. Comparison of resistivity of bridge structures.

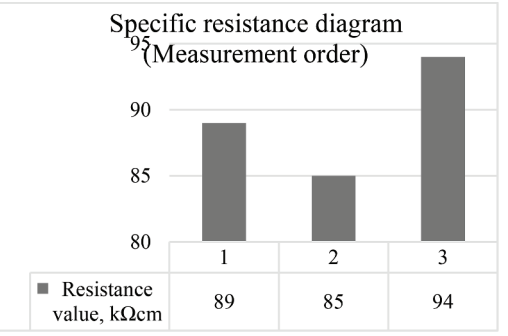


Figure 12. Results measured by Resipod.

4.1. *Experimental studies of bridge supports*

As part of the research, an examination and diagnostics of the operational condition of a - 162 m long reinforced concrete bridge across the Ongi River in Arvaikheer was carried out in August 2023. The bridge over the Ongi River is located on the Erdenesant-Arvaikheer road and has 9 spans with 5 beams 18 m long.

4.2. *Determination of the strength of concrete bridge structures (UPV test – Direct test method)*

The test results for the concrete strength of the Ongi River Bridge support structures were obtained using the UPV Direct test method and the Schmidt tool. The strength of the concrete of the main support was determined by direct ultrasound at 3-4 points, and the strength of the concrete of the edge support was determined by the echo method (UPV Indirect test method echo). In addition, the effect of carbonation of concrete was calculated when determining the strength of concrete using the Schmidt tool (Figure 10). The strength of concrete is checked by ultrasonic testing.

4.3. *Determination of the strength of concrete samples (Concrete Core Test)*

Using a HILTI 200 electric drill, a concrete sample with a diameter of 95 mm was taken from each support. After carbonation analysis, the sides were leveled and then pressed using a PSU-125 press machine (Figures 13 and 14). As part of the research, in August 2023, an examination and diagnostics of the operational condition of a 162 m long reinforced concrete bridge across the Ongi River in Arvaikheer was carried out. The bridge over the Ongi River is located on the Erdenesant-Arvaikheer road, has 9 spans with 5 beams 18 m long. (Kabashi, et al., 2015)



Figure 13. Removed from the supports cylindrical samples before the compression tests.



Figure 14. Removed from the supports cylindrical samples after the compression tests.

To check the progress of carbonation in concrete (CO_2), the depth of carbonation was measured by spraying a phenolphthalein solution onto samples taken from the bridge piers.

The carbonation depth of concrete ranges from 6-32 mm, with an average value of 15.9 mm. Table 2 shows the carbonation depth of drilled concrete samples (Figures 15 and 16).



Figure 15. Carbonation analysis of all samples taken from the support.



Figure 16. Carbonation measurement of samples taken from support P1.

4.4. *Corrosion of pole reinforcement (Half-cell potential test)*

In this experiment, we did not have Copper-Copper sulphate, so we used a Resipod device from Proceq, Switzerland. Table 2 presents the results of measuring the resistivity of the concrete surface of a reinforced concrete support with the Resipod device. The electrical resistivity of concrete is directly related to the corrosion process and the corrosion rate of the reinforcement. The electrical resistivity value of the bridge support concrete is 53.3-160 kΩcm.

Table 2. Degree of carbination, resistivity, strength of support's concrete.

No	Support	Carbination mm	Resistivity kΩcm	Strength of concrete mPa
1	A1	4	160	27.65
2	A2	8	125	29.78
3	P1	32	53.3	29.78
4	P2	13	70.5	27.65
5	P3	5	138	28.30
6	P4	20	57.8	28.30
7	P5	25	62	26.95
8	P4	20	98	26.95
9	P7		94	23.40
10	P8		94	28.30

4.5. *Corrosion of pole reinforcement (Half-cell potential test)*

In this experiment we did not have (Copper-Copper sulphate), so we used a Resipod device from Proceq, Switzerland. (Figures 17, 18). Table 2 presents the results of measuring the resistivity of the concrete surface of a reinforced concrete support with the Resipod tool. The electrical resistivity of concrete is directly related to the corrosion process and the corrosion rate of the reinforcement. The electrical resistivity value of the bridge support concrete is 53.3-160 kΩcm. (Hudson, et al., 2015)



Figure 17. The carbonation study of reinforced concrete supports using the Resipod device.



Figure 18. Measuring the resistivity of the concrete surface.

4.6. *Wear and damage to bridge supports*

Were observed, with no deep or wide cracks (structural or non-structural) in the 10 bridge supports. However, in the water contact area of some supports, the strength of the concrete was reduced due to the effects of freezing and thawing. This led to the exposure of some of the horizontal reinforced concrete reinforcement on P5, P6, and P7 supports (see Figures 19 and 20). No other damage or defects were observed in the reinforced concrete bridge supports.



Figure 19. Damage of freezing and thawing the concrete on P5 support.



Figure 20. Damage of freezing and thawing of of the concrete on P6 support.

5 CONCLUSIONS

1. With the development of the country, an urgent problem has arisen: the reduction in the performance of the structure and the acceleration of the degradation process, leading to the gradual "aging" of bridges and the loss of their operational qualities. This is manifested in the form of structural destruction, a decrease in the strength properties of concrete, and the formation of various kinds of cracks. Therefore, it is important to carry out inspection and diagnostic work on bridges, identify and analyze damage, and determine their preliminary service life.
2. According to the results of monitoring the bridge over the Ongi River, the strength of the concrete support is 20-32 MPa, the depth of carbonation of concrete is 6-32 mm with an average value of 15.9 mm, and the electrical resistivity of the concrete support is 53.3-160 kΩcm. The thickness of the concrete protective layer of reinforcement supports P5, P6, and P7 is less than designed, and therefore it is necessary to strengthen the bridge supports.

REFERENCES

Bajenov, 2002. *Concrete technology (in russian)*. s.l.:s.n.

Dashjamts & Battsagaan, 2013. *Theoretical and methodological basis of measures to protect concrete and reinforced concrete structures from weathering (in mongolian)*, Ulaanbaatar: Mongolian University of Science and Technology.

Dvorkin, L. & Dvorkin, O., 2006. *Basics of concrete science (in russian)*. 1nd ed. Sant Peterburg: Stroi-Beton.

Hudson, D., Kevern, J. & Halmen, C., 2015. *Evaluation of Resistivity Meters for Concrete Quality Assurance*, Kansas: University of Missouri.

Jiao, J., Diao, B. & Wang, C., 2016. *The Carbonation model of Concrete Structures and its application*. Guangzhou, Atlantis press, International conference on Civil, Transportation and Environment.

JICA, 2015. *Project for Capacity development on bridge maintenance and management, in Mongolia*. Ulaanbaatar, Minstry of Road and Transportation.

Kabashi, N., Krasniqi, C. & Dautaj, A., 2015. *Evaluation the Compressive Strength in Concrete Structures Using the Insitu Test Methods*. Prishtina, University of Prishtina, Kosovo.

Khasnavch, Tsas-Orgilmaa & Sugarjav, 2022. *Current status and maintenance system of bridges in Mongolia*. Barcelona, Bridge Safety, Maintenance, Management, Life-Cycle, Residence and Sustainability-Casas, Frangopol & Turmo (eds).

Larsen, R., 2020. *Corrosion effects on the durability of reinforced concrete structures*. Philadelphia, Materials performance.

Salmeron, Criner, Xin Zhang & Dyke, 2022. *Physics-based modelling of construction defects in concrete decks*. Barcelona, Bridge Safety, Maintenance, Management, Life-Cycle, Residence and Sustainability.


Taylor & Francis
Taylor & Francis Group
http://taylorandfrancis.com

SS02: Bridge Weigh-in-Motion: Recent experiences, technology developments, and new applications

Organizer: D. Cantero


Taylor & Francis
Taylor & Francis Group
http://taylorandfrancis.com

Bridge Maintenance, Safety, Management, Digitalization and Sustainability – Jensen, Frangopol & Schmidt (eds)
© 2024 The Author(s), ISBN 978-1-032-77040-6
Open Access: www.taylorfrancis.com, CC BY-NC-ND 4.0 license

New feature based on influence lines for anomaly detection in bridge monitoring

A. Döring & M. Vogelbacher
Institute for Automation and Applied Informatics, Karlsruhe Institute of Technology, Karlsruhe, Germany

O. Schneider & J. Müller
Büro für Strukturmechanik, Coburg, Germany

S. Hinz
Institute of Photogrammetry and Remote Sensing, Karlsruhe Institute of Technology, Karlsruhe, Germany

J. Matthes
Institute for Automation and Applied Informatics, Karlsruhe Institute of Technology, Karlsruhe, Germany

ABSTRACT: Bridge monitoring using displacement, strain, acceleration or rotation measurements during normal operation can be a good supplement to conventional manual bridge inspections. In order to detect damage from the measured signal, features must be extracted from the signal that are primarily damage-sensitive. In recent years, features based on the influence lines have been increasingly investigated. The influence line represents the simplified signal that can be measured with a sensor at a fixed position when a single vehicle crosses the bridge. In this paper, we present the new feature normalised integrated influence lines (niil). We show that niil is sensitive to damage, independent of vehicle geometry, velocity, sampling rate, deviation from ideal lane and robust against noise using the analytical bending beam and strain data from a real bridge that has been successively damaged. niil can be calculated based on the curvature, rotation or displacement influence lines.

1 INTRODUCTION

Bridges in Germany are usually designed for 100 years (Mehlhorn & Curbach 2014). Most bridges were built until 1980 and are prestressed concrete bridges (BASt 2023). Recently, prestressed concrete bridges from the 1960s to 1980s have suddenly started to fail or need to be replaced in the near future (Schlenga 2022). In Germany, the condition of a bridge is assessed by visual manual inspections every three years. Bridge monitoring can be an opportunity to observe old bridges between inspection intervals, especially bridges that have received a poor rating. In bridge monitoring, the condition of a bridge is assessed on the basis of the bridge movement which is measured via sensors. The most common sensors measure strain or acceleration. Strain can be measured with strain gauges or with fibre Bragg grating (FBG) sensors and acceleration with accelerometers (Zarate Garnica et al. 2021). The rotation can be determined using inclinometers or calculated from accelerometers (Hester et al. 2019). There are also non-contact solutions for measuring bridge movement, such as the displacement measured with the ground based radar (GBR) (Zarate Garnica et al. 2021).

The condition of the bridge cannot simply be deduced from the measured signal. Therefore, features are required for damage detection in bridge monitoring. The features must be damage-sensitive, robust against measurement noise and temperature changes and independent of the vehicle parameters, the vehicle velocity and the driving lane selection.

DOI: 10.1201/9781003483755-157

Further below in this section, we give a rough overview of some features for bridge monitoring. In section 2 we introduce the new feature normalised integrated influence lines (**niil**). In section 3 we analyse the new feature on the stepped Euler-Bernoulli bending beam and in section 4 on measurements of a real bridge. The paper is finalised with the conclusion.

1.1 *Related work and open questions*

Damage assessment using bridge monitoring is carried out in four stages (Rytter 1993). In the first stage, the presence of damage is recognised. The following stages can only be determined with a very accurate model of the real bridge which require a great effort to create. For this work, we assume that no sufficiently accurate model of the bridge is available and limit ourselves to damage detection (first stage). A monitoring system that does not use a model for damage detection belongs to the data-driven approaches. Furthermore, it is assumed that no data of damaged states are available, therefore only anomaly detection can be performed (Fugate et al. 2001). The vehicle parameters remain unknown during damage detection with the features.

The most frequently used features are based on the modal parameters. These include the natural frequencies, modes and curvatures of the modes. However, the modal parameters have some disadvantages, such as dependencies on the temperature, the lack of damage sensitivity or the use of derivatives (Brownjohn 2011, Cawley 2018). The calculation of derivatives is not trivial for real measurement data due to measurement noise. The determination of the modal parameters with the operational modal analysis is afflicted with further uncertainties.

An alternative to the modal parameters are features based on the influence line (IL). The IL can be the curvature, rotation or displacement IL. The curvature can be considered proportional to the strain if the deformations are small (Spura 2019). Some features based on the IL are not independent of the vehicle geometry. The transferability of some features that use the derivatives to real measurements with measurement noise can be doubted. There are only a few features available that are based on the displacement IL.

The most promising are the so-called *R* features. With the *R* feature, the ratio of two integrated ILs is used as a feature (Döring et al. 2022, Döring et al. 2023 and Jansen 2020). The ILs are determined at two different sensor positions. In Döring et al. (2023) we identified sensor positions for the curvature ILs that may have a high damage-sensitivity. For these sensor positions the integral of the ILs is zero and cannot be used for the *R* feature if the integral is in the denominator. Furthermore, the number of dimensions of the *R* features increases non-linearly with $(n_\mathrm{D} - 1)\, n_\mathrm{D}/2$ if n_D is the number of sensors. The visualisation of several *R* features is difficult and not easy interpretable. The features of Hong et al. 2016 and Wu et al. 2017 are similar to the feature niil presented here. These features are normalised to the integrated signal of one sensor. However, the sensor is not predefined and the integral of the selected sensor can become zero depending on the boundary condition and damage. Furthermore, these features are based on FBG sensors, which are expensive and cannot be easily attached to existing bridges.

2 NEW FEATURE

In this section we introduce the new feature normalised integrated influence lines (**niil**).

The integral

$$A(x_\mathrm{ref}) = A((s(x_\mathrm{ref}, d_F)) = \int_0^{L+a_\mathrm{T}} s\big(x_{ref}, x\big)\,\mathrm{d}d_F \approx \sum_{k=0}^{n_\mathrm{samples}} s(x_\mathrm{ref}, \Delta d_F \cdot k) \cdot \Delta d_F \tag{1}$$

of the superpositioned ILs $s(x_\mathrm{ref})$ in sensor position x_ref is formed from 0 to $L + a_\mathrm{T}$ as a function of the load position d_F, where a_T is the distance between the first and last axis. Assuming a constant velocity v, the load position d_F can be determined via the relationship

$$d_F = vt, \tag{2}$$

where t corresponds to the time. n_{samples} corresponds to the number of samples of a crossing, k is the sample number and d_F is the resulting step $\Delta d_F = (L + a_T) / n_{\text{samples}}$. The curvature, rotation or displacement IL can be used as the IL. The integrated signals (superpositioned ILs) are summarised in the vector

$$\boldsymbol{a} = [A(x_1)A(x_2)\cdots A(x_{n_{\text{sensors}}})]^{\mathrm{T}}. \tag{3}$$

Finally, the new feature

$$\mathbf{niil} = \frac{\boldsymbol{a}}{\sqrt{\boldsymbol{a}^{\mathrm{T}}\boldsymbol{a}}} \tag{4}$$

can be calculated by using normalisation. Normalisation is used to cancel out the influence of the load. The dimension of **niil** corresponds to the number of sensors n_{sensors} used and therefore does not grow exponentially, as with the R feature. We assume that feature **niil** has the same behaviour in terms of dependence on lane deviation and temperature as the R feature. We therefore recommend calculating the **niil** feature only for sensors within the same girder. This means that two **niil** features should be calculated for a bridge with two girders.

3 APPLICATION OF THE NEW FEATURE TO THE STEPPED EULER-BERNOULLI BENDING BEAM

In this section, we use the example of the analytical bending beam to show that the new feature **niil** is independent of the number of samples and thus independent of the sampling rate and velocity, as well as independent of the vehicle geometry. However, there must be a sufficient number of sampling points per vehicle crossing for damage detection. First, we present the setup in section 3.1. This is followed by the results in section 3.2, which are discussed in section 3.3.

3.1 *Setup*

We use the implementation of the stepped Euler-Bernoulli bending beam from Döring 2022a in Matlab, which we explained in detail in Döring et al. (2022). Figure 1 shows the bending beam with the main parameters. The beam in Figure 1 is a statically indeterminate system, since the beam consists of a continuous beam with three supports. The beam has the length L and the centre support is always located at $b_{\text{m}} = 1/2L$. The damage is modelled by a reduction in bending stiffness

$$\Delta EI = \frac{(EI)_1 - (EI)_2}{(EI)_1} \tag{5}$$

The bending stiffness $(EI)_2$ applies between b_1 and b_2 and $(EI)_1$ outside. To obtain the IL, the load F moves from 0 to L. We consider $n_{\text{sensors}} = 7$ sensors equidistantly distributed in the beam, which are represented by the magnifying glass symbol in Figure 1. The sensor positions were selected so that the potentially damage-sensitive sensor positions at $x_{\text{ref}} = 3/8L$ and $x_{\text{ref}} = 5/8L$ of the curvature ILs can be taken into account. These sensor positions are the positions where the integral of the IL for the undamaged beam becomes zero (Döring et al. 2023). Such sensor positions also exist for the integral of the rotation and the displacement ILs of the undamaged beam. The integrated displacement ILs for the undamaged beam become zero in $x_{\text{ref}} = \{0, 1/2L, L\}$ and the rotation ILs become zero in $x_{\text{ref}} = \{(1 + \sqrt{33})/32 \quad L, 1/2 \quad L, (31 - \sqrt{33})/32 \quad L\}$. The displacement is zero in the aforementioned sensor positions and is therefore useless. In contrast, the rotation is not equal to zero at the mentioned points. However, we only consider the potential damage-sensitive sensor positions for the curvature ILs.

For the following analysis, we consider the ten damage scenarios in Table 1. Damage scenario 0 is the undamaged beam. The damage scenarios with a 1 before the hyphen are scenarios in which the damage is in the centre of the field (between $b_1 = 0.2L$ and $b_2 = 0.3L$), in

scenarios with 2 before the hyphen the damage is above the centre support (between $b_1 = 0.45L$ and $b_2 = 0.55L$) and in the scenarios with 3 before the hyphen, the damage is such that no sensor is located in the damage location (between $b_1 = 0.2625L$ and $b_2 = 0.3625L$). The numbers after the hyphen show the reduction in bending stiffness ΔEI in percent.

To test the invariance of the new feature **niil** to the vehicle geometry, we consider six loadcases, whereby the load cases consisted of one to four loads. These represent the axes in simplified form. The distance between the loads and the amplitudes of the loads were selected at different values.

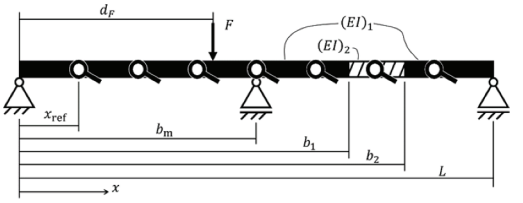


Figure 1. Drawing of the stepped Euler-Bernoulli bending beam with seven sensor positions (magnifying glass symbol) and the moving load F.

Table 1. Parameters for the damage scenarios. b_1 is the left limit of damage, b_2 the right limit of damage and ΔEI the reduction in bending stiffness.

Damage scenario	b_1	b_2	ΔEI
0	-	-	-
1-5	0.2 L	0.3L	5%
1-20	0.2 L	0.3 L	20%
1-35	0.2 L	0.3 L	35%
2-5	0.45 L	0.55 L	5%
2-20	0.45 L	0.55 L	20%
2-35	0.45 L	0.55 L	35%
3-5	0.2625 L	0.3625 L	5%
3-20	0.2625 L	0.3625 L	20%
3-35	0.2625 L	0.3625 L	35%

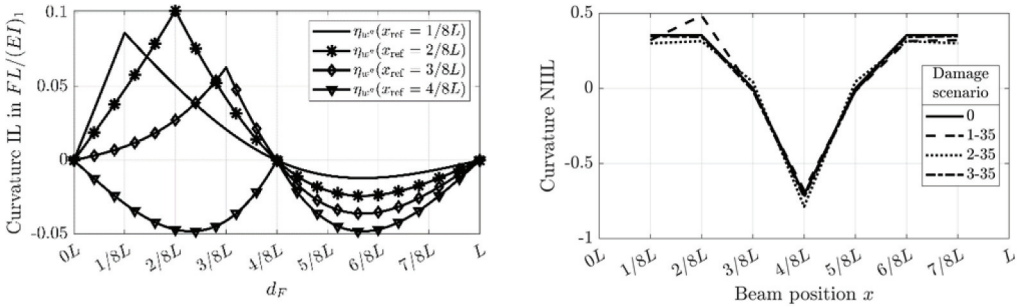
The different load cases lead to the same feature **niil**, therefore the configuration of the load cases is not presented. In addition, the resulting signals of the superpositioned ILs is analysed with 500, 1000 and 2000 samples. This determines whether **niil** is independent of the number of samples and the vehicle velocity.

3.2 *Results*

Figure 2a shows the curvature ILs with a unit load for the sensors in the left half of the beam. The course of the ILs for the undamaged beam for the mirrored sensors of the right field is mirrored in the centre support position b_{m}. After determining the superpositioned signals, the feature **niil** can be calculated for the seven sensors. These are visualised in Figure 2b based on the superpositioned curvature ILs for damage scenarios 0, 1-35, 2-35 and 3-35. The greatest deviation from damage scenario 0 can be observed for 1-35 in sensor position $x_{\mathrm{ref}} = 2/8L$, where also the centre of the damage is located. For damage scenario 2-35, there is also a greater deviation from scenario 0 for the sensor position which lies within the damage ($x_{\mathrm{ref}} = 4/8L$). No major deviation is noticeable for damage scenario 3-35. Here, as for the two other damage scenarios with damage, the value in the damage-sensitive sensor positions $x_{\mathrm{ref}} = 3/8L$ and $x_{\mathrm{ref}} = 5/8L$ is not equal to zero, which indicates the presence of damage. All curves for the different load cases and samples are superimposed. The feature **niil** based on the rotation and displacement IL shows a comparable behaviour. However, the **niil** courses based on

the rotation and displacement ILs visually show a higher deviation for damage scenario 3-35 compared to **niil** based on the curvature ILs.

Figure 3 shows the Euclidean distance of **niil** for the individual damage scenarios to damage scenario 0. The circle symbol represents the results for the feature **niil** based on the curvature ILs, the triangle symbol based on the rotation ILs and the square symbol based on the displacement ILs. First, it can be determined for all three variables that the Euclidean distance increases with increasing reduction in bending stiffness ΔEI for the respective damage position. If the sensor positions are within the damage – these are the cases with a 1 or 2 in front of the hyphen – then **niil** has the highest Euclidean distance based on the curvature IL compared to the rotation and displacement ILs. The highest Euclidean distance is observed for the damage scenario1-35. The Euclidean distance of **niil** based on the curvature ILs is second highest for damage scenario 2-35. Damage position 2 leads to the lowest Euclidean distance for **niil** based on the rotation and displacement influence lines. If the sensor is not located in the sensor position, **niil** performs comparatively worst based on the curvature ILs. For damage position 3, **niil** performs best based on the rotation ILs. Otherwise, **niil** based on the rotation ILs is the second best for damage positions 1 and 2.



a) Curvature ILs for different sensor positions the left beam half for an undamaged beam.

b) Feature **niil** based on the curvature influence lines for three damage scenarios.

Figure 2. Curvature influence lines and the corresponding feature niil.

3.3 *Discussion*

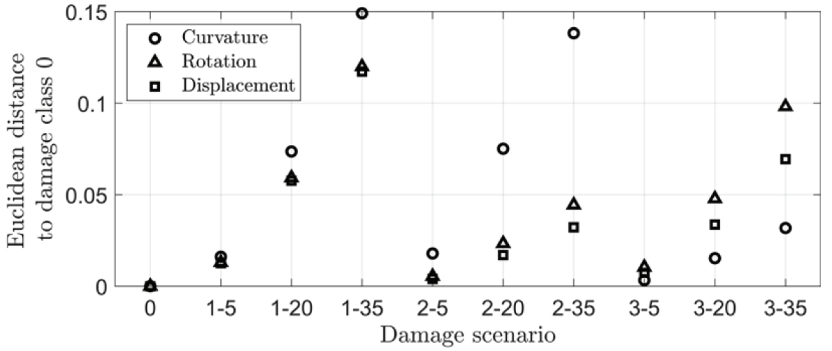


Figure 3. Euclidean distance of niil for the individual damage scenarios to the damage scenario 0. The results for niil based on the curvature ILs are represented by the circle symbols, those based on the rotation ILs by the triangle symbols and those based on the displacement ILs by the square symbols.

From the results, we can first conclude that the Euclidean distance with the feature **niil** can be used to detect damage in a bending beam based on the curvature, rotation and displacement

ILs. The Euclidean distance increases proportionally to the amount of the reduction in bending stiffness for a damage location. The feature **niil** is independent of the considered number of samples and thus independent of the velocity and sampling rate. Furthermore, **niil** is independent of the vehicle geometry, as the different load configurations lead to the same course of **niil**. Compared to the *R* feature, the new feature **niil** can be visualised and interpreted more easily. It can also be seen that **niil** based on curvature ILs shows a higher deviation from the undamaged beam for sensors located within the damage. A further investigation shows that the maximum, minimum or absolute maximum values of the signals are not independent of the vehicle geometry. This means that invariance to the vehicle geometry can only be achieved with the integral of the signals. The damage-sensitive sensor positions appear to have a smaller effect on the curvature IL, as the damage position 3 leads to a low Euclidean distance in comparison.

In the next section, the feature is analysed on measurement data of a real damaged bridge.

4 APPLICATION OF THE NEW FEATURE ON REAL DAMAGED BRIDGE

In this section, we present the feature **niil** using real measurement data from a damaged bridge. Firstly, we present the test setup in section 4.1. This is followed by the results in section 4.2 and the discussion in section 4.3.

4.1 *Setup*

The bridge BW 70 on the B279 federal road in Bavaria/Germany connects the towns Baunach and Breitengüßbach. We have already described this bridge in Döring et al. 2021. The bridge is a prestressed two-span bridge built as a continuous girder in 1962. Figure 4 shows the ground plan with the cross-section. The bridge has one lane in each direction and consists of two girders. One girder contains nine tension cables. During the construction of the replacement bridge, tests were carried out on the existing bridge. The bridge was successively damaged. 18 linear strain gauges were installed under the bridge. Figure 4 shows the approximate position of the sensors. An excavator with a total weight of 19.4 t was selected for the tests. For each damage scenario, the excavator made around 25 crossings per driving direction over the bridge. Due to the multiple crossings, the lane subsequently deviates between the crossings. For this reason, the feature is analysed for the independence of the lane deviation. One crossing consists of 3,800 to 4,000 samples. Firstly, six of the nine tension cables were successively cut in position C, represented by the square in Figure 4. This was followed by further cuts step by step through six tension cables in position D. While the letter of a damage scenario name hereinafter refers to the damage position, the number after the letter indicates the number of cut tension cables. The pre-processing consisted of removing the trend and extracting the time window in which the vehicle was on the bridge.

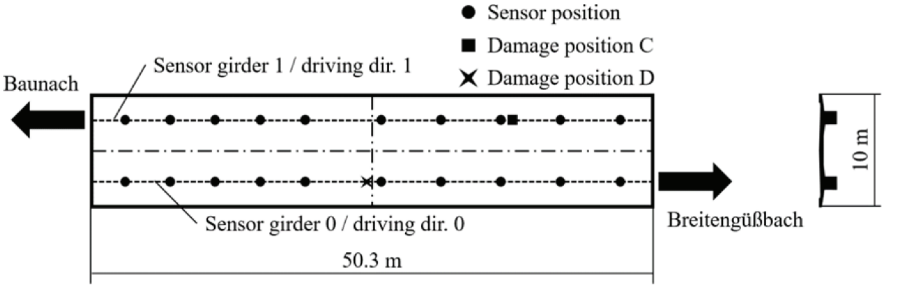


Figure 4. The left-hand side shows the floor plan of bridge BW 70 with the sensor positions and the damage positions. The cross-sectional area is shown on the right-hand side.

4.2 *Results*

In this section, we present the results of the feature **niil** based on the strain signals obtained from the strain gauges attached to the bridge. The mean value of the feature **niil** can be seen in

Figures 5a and 5b for three selected damage scenarios for the crossings in direction 1. The damage scenarios are the undamaged bridge B0 (solid curve) and the scenarios C6 (dashed curve) and D6 (dashed-dotted curve). Figure 5a shows **niil** for the damage scenarios for the sensors in girder 0 and Figure 5b for the sensors in girder 1. Surprisingly, the largest deviation in Figure 5a is for the sensors in the left field, although the damage is in the right field. A greater visual difference is visible in Figure 5b for girder 1. Here, the largest deviation in the sensors is above the centre support and the field where the field in which the damage C is located. While there is a large difference between the damage scenario B0 and C6, the visual deviation from D6 to C6 is small.

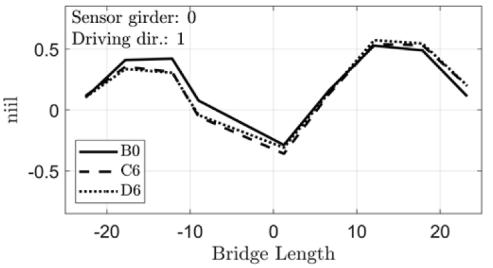
The Mahalanobis distance (MD) represents the distance from the case to be tested to the mean value normalised to the standard deviation of the reference state. Figures 5c and 5d show the MD to damage scenario B0 in the box plot for the individual damage scenarios. The lower edge of the box indicates the 25 % quantile, the centre line the median and the upper line the 75 % quantile. The whiskers show the outliers. If the outliers are too far from the box, they are represented by a plus sign. The outlier with the highest MD in girder 0 in Figure 5c for damage scenario B0 has a value of MD = 4.42, while the lowest outlier in damage scenario C1 has MD = 4.57. This means that there is no overlap between the two damage scenarios for any of the 25 crossings per damage scenario. We assume that **niil** is normally distributed within a damage scenario. Since **niil** has $n_D = 8$ dimensions in this example, 95.76 % of the crossings of the reference state are within MD ≤ 4 (Wang et al. 2015). The median for girder 0 for B0 in Figure 5c is MD = 2.83 and the median for C1 is MD = 7.75. In Figure 5d for **niil** based on the sensors of girder 1, the median for the damage scenario is MD = 2.83 and for the damage scenario C1 the median is MD = 8.41. In Figure 5d there is also no overlap between the scenarios B0 and C1. Here, the difference between the highest outlier of B0 and the lowest outlier of C1 is ΔMD = 2.33. The MD is higher for the other damage scenarios than for C1. In general, the MD in girder 1 is greater than in girder 0 for the individual damage scenarios. Girder 1 is the girder over which the vehicle drives and in which the damage is first introduced.

4.3 *Discussion*

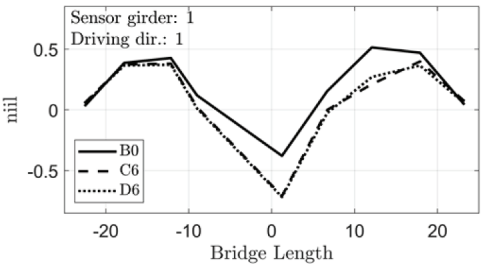
The behaviour of an artificially created crack may differ from that of a crack caused by several load cycles. By cutting the tension cables with a saw or drill, there is no contact in the cut area under pressure. The behaviour between the artificial crack and a crack caused by several load cycles should be the same if the vehicle is in the same field as the crack, as the crack opens under tension in both cases. However, if the vehicle is in the opposite field to the crack, the behaviour may be different, as the slowly formed crack is closed under pressure, whereas the artificially created crack remains open. However, the difference should be small, as on the one hand the load in the crack is significantly smaller because the vehicle is in the opposite field and on the other hand the concrete can take over the load transfer under pressure. A significant change in the MD to the undamaged bridge can already be observed after the first tensioning cable is cut. However, we cannot simply deduce the damage location from the comparison of the **niil** course. The MD increases proportionally to the damage up to damage scenario C6. After that, the MD decreases again slightly. However, from damage scenario C2 onwards, MD>20 already applies to all crossings of the other damage scenarios for both sensor girders. The MD is higher in the girder where the first damage position is located and over which the vehicle is driving. The outlier with the highest MD for damage scenario B0 is so low that there is no overlap with the other damage scenarios. From this, we conclude that the feature **niil** is sensitive to damage and that the influence of measurement noise is reduced and independence from lane selection in considered setup is achieved.

5 CONCLUSION

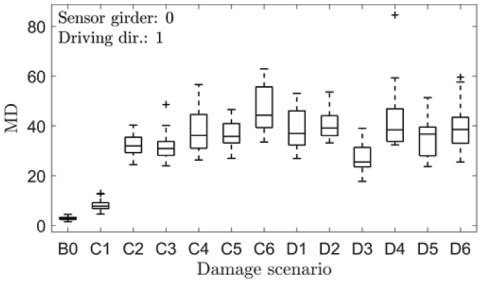
In this paper we introduce the new feature **niil**, which is based on the ILs. **niil** can be calculated for the curvature, rotation or displacement ILs. To calculate **niil**, the signal of a single crossing



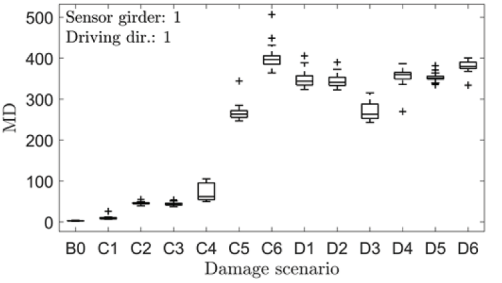
a) **niil** for sensors in girder 0 and crossings in driving direction 1. The course represent the average value of the 25 crossings.



b) **niil** for sensors in girder 1 and crossings in driving direction 1. The course represent the average value of the 25 crossings.



c) Mahalanobis distance (MD) for feature **niil** to damage scenario 0 for sensors in girder 0 and the crossings direction 1.



d) Mahalanobis distance (MD) for feature **niil** to damage scenario 0 for sensors in girder 1 and the crossings direction 1.

Figure 5. Results of the niil for the bridge BW70. The top two figures show the feature niil for crossings in driving direction 1 and the bottom two figures show the MD to damage scenario 0. The figures on the left show the results for girder 0 and those on the right for girder 1.

over the bridge is first integrated for all available sensors. Then the integrated signals are summarised in a vector and normalised to the Euclidean norm. The feature **niil** thus corresponds to the *R* feature, whereby **niil** is easier to visualise and thus easier to interpret. **niil** is invariant to vehicle geometry, velocity and the considered sampling rate and is robust against measurement noise as well as lane deviation to a certain extend. **niil** was investigated on the bending beam and on a real bridge that was successively damaged. On the real bridge, it can be shown that the new feature leads to a significant increase in the MD from just one cut through the tension cables. The feature **niil** still needs to be investigated with further damage scenarios. In addition, the question arises as to how far the number of sensors can be reduced and whether **niil** is independent of the temperature. The results in section 4.2 indicate that the feature **niil** is well suited for anomaly detection. Furthermore, the damage-sensitive sensor positions in the analytical bending beam can now be used, as it is no longer necessary to divide by zero for the undamaged beam. It still needs to be clarified to what extent the damage-sensitive sensor positions from the bending beam can be transferred to real structures and to what extent they are robust against measurement noise.

ACKNOWLEDGEMENT

This work was developed as part of the projects iBridge with the funding number 01IS13011C and ZEBBRA with the funding number 13N14709, which were funded by the Federal Ministry of Education and Research. We would like to thank the project partners ci-tec and the Institute of Sensor and Actuator Technology (ISAT) of the Coburg University of Applied Sciences and Arts as well as M. Arnold, H.B. Keller, S. Keller, C. Michel, O. Scherer and P. Waibel.

REFERENCES

Brownjohn, J.M.W. et al. 2011. Vibration-based monitoring of civil infrastructure: challenges and successes. *Journal of Civil Structural Health Monitoring*, vol. 1, no. 3-4, pp. 79–95.

Cawley, P. 2018. Structural health monitoring: Closing the gap between research and industrial deployment. *Structural Health Monitoring*, vol. 17, no. 5, pp. 1225–1244.

Döring, A. et al. 2021. Ratio-based features for data-driven bridge monitoring and damage detection. *10th IABMAS*, 2532–2541, CRC Press.

Döring, A. et al. 2022. Ratio-based features for bridge damage detection based on displacement influence line and curvature influence line. *11th IABMAS*, CRC Press.

Döring, A. 2022a. Stepped-Euler-Bernoulli-Beam for Matlab. *Zenodo*.

Döring, A. et al. 2023. Investigations on ratio-based integral features based on influencelines for bridge damage detection. *Infrastructures*, vol. 8, no. 12.

Federal Highway Research Institute (BASt) 2023. Brückenstatistik. Accessed on: October 2, 2023.

Fugate, M.L. et al. 2001. Vibration-based damage detection using statistical process control. *Mechanical Systems and Signal Processing*, vol. 15, no. 4, 707–721.

Hester, D., et al. 2019. Identifying damage in a bridge by analysing rotation response to a moving load. *Structure and Infrastructure Engineering*, vol. 16, no. 7, 1050–1065.

Hong, W. et al. 2016. Strain-based damage-assessment method for bridges under moving vehicular loads using Long-Gauge strain sensing. *Journal of Bridge Engineering*, vol. 21, no. 10.

Jansen, A. & Geißler, K. 2020. Ausreißererkennung zur Strukturüberwachung von Bestandsbrücken durch Bauwerksmonitoring mit vier Signalmerkmalen. *Brückenkolloquium*, vol. 4, no. 1, pp. 313–322.

Mehlhorn, G. & Curbach, M. 2014. Handbuch Brücken. Wiesbaden: Springer Fachmedien.

Schlenga, S., 2022. Autobahn Westfalen: Brückenneubau an der A45 läuft seit Jahren mit Hochdruck. *Autobahn GmbH*. Accessed on: May 1, 2022.

Spura, C. 2019. Technische Mechanik 2. Elastostatik. *Springer Fachmedien Wiesbaden*.

Rytter, A. 1993. Vibrational based inspection of civil engineering structures. PhD thesis. Aalborg University.

Wang, B. et al. 2015. Confidence analysis of standard deviational ellipse and its extension into higher dimensional euclidean space. *PLOS ONE*, vol. 10, no. 3.

Wu, B. et al 2017. Stiffness monitoring and damage assessment of bridges under moving vehicular loads using spatially-distributed optical fiber sensors. *Smart Materials and Structures*, vol. 26, no. 3.

Zarate Garnica, G. I. et al. 2021. Monitoring structural responses during proof load testing of reinforced concrete bridges: A review. *11th IABMAS*, CRC Press.

Bridge Maintenance, Safety, Management, Digitalization and Sustainability – Jensen, Frangopol & Schmidt (eds)
© 2024 The Author(s), ISBN 978-1-032-77040-6
Open Access: www.taylorfrancis.com, CC BY-NC-ND 4.0 license

Vehicle speed estimation in BWIM systems via convoluted reciprocity

D. Cantero
NTNU Norwegian University of Science and Technology, Trondheim, Norway

C.W. Kim
Kyoto University, Kyoto, Japan

ABSTRACT: The first step in a BWIM system is to obtain the speed of the vehicle to be weighted. There exist several possibilities to estimate the vehicle's velocity, being the most popular the method that calculates the correlation between signals from two separate sensors. In practice, this method is sufficiently accurate for most BWIM installations. However, it does not perform well in certain situations, most notably in the case of an ideal simply supported configuration or for systems with highly asymmetric influence lines. This paper introduces a new theoretically consistent method, termed convoluted reciprocity, that allows for accurate vehicle speed estimates for any structural configuration and shape of influence line. This document presents in detail the theoretical background of the novel approach complemented by numerical simulations. The performance in speed estimation of the new method is compared directly to the estimates obtained via the correlation method. In addition, these methods are compared empirically with the measured responses of a scaled bridge under controlled laboratory conditions. The results show that the convoluted reciprocity idea does provide very accurate results, while it relies on the same sensor configuration of standard BWIM systems.

1 INTRODUCTION

A Bridge Weigh-in-Motion (BWIM) is an installation to estimate the weight of vehicles as they traverse a bridge at regular traffic speeds. This process relies on analysing the structural responses recorded, which are then processed to deduce details such as vehicle speed, axle configuration, individual axle weights, and the overall gross vehicle weight. Typically, BWIM installations utilize strain signals, often detected using transducers or directly through strain gauges affixed to the bridge soffit (Žnidarič et al. 2017). The placement of the weighing sensors is usually at the point of maximum strain response, specifically at the mid-span in the longitudinal direction. In the transverse direction, these sensors are positioned at various points across the section, and their signals are combined for use in the standard BWIM algorithm.

In the early days of BWIM technology, speed and axle detectors were positioned on the pavement near the bridge ends, resulting in traffic disruptions and durability issues. However, this approach was later replaced by alternative solutions that rely solely on sensors installed on the bridge soffit. These alternatives, known as FAD (free of axle detectors) or NOR (nothing on the road) solutions, were introduced by the WAVE project (OBrien and Žnidarič 2001). The supplementary sensors needed for FAD and NOR are typically situated at one-quarter and three-quarters of the span or on secondary elements with relatively shorter influence lines and distinctive sharp peaks (Kalin et al. 2006).

DOI: 10.1201/9781003483755-158

In the BWIM system, determining the speed of a passing vehicle is the initial step before moving on to axle identification and the final weight calculation. Thus, accurate vehicle weighing relies heavily on the precision of speed estimation. However, deducing the vehicle's speed from global strain signals is challenging (Yu et al., 2016) because these measured responses typically lack distinct sharp features. Moreover, structural dynamic components and noise contribute to the complexity. Speed estimation must be accomplished without prior knowledge of the vehicle's properties and axle configuration. Ideally, the signals used for speed estimation should exhibit clear peaks corresponding to each axle. However, achieving this ideal scenario is not always feasible due to the structural configuration of the bridge.

Arguably, the most commonly used approach for speed estimation involves calculating the cross-correlation (or simply, correlation) between signals measured at two different sections in the longitudinal direction (Yu et al., 2016). The speed is estimated by dividing the distance between sensors by the time lag that maximizes the correlation. For optimal performance, both signals should ideally be time-shifted copies. In Bridge Weigh-in-Motion (BWIM) installations, achieving this ideal scenario requires identical influence lines at the two measured locations, a condition rarely met in practice. However, if the influence lines exhibit very sharp peaks, enabling individual axle detection, the correlation-based speed estimation has been found to provide sufficiently accurate results (Hajializadeh et al., 2020). The experimental campaign conducted by Zolghadri et al. in 2016, aimed at estimating speeds for various bridges and vehicle types, concluded that the correlation method is generally effective, reporting average errors of approximately 9%. Consequently, this method is widely implemented for speed estimation, as exemplified by a recent study by MacLeod and Arjomandi in 2022. Nevertheless, when the asymmetry of the influence lines is too pronounced, the correlation method may yield inaccurate speed estimates. This limitation is recognized, and correction strategies have been proposed. Kalin et al. in 2006 introduced a correction based on qualified maxima, reporting satisfactory results even for simply supported bridges.

Nevertheless, there is no universally applicable method for speed estimation in standard BWIM installations. Consequently, the objective is to introduce a generic approach that can be employed across various bridge typologies. This paper puts forth a novel concept termed convoluted reciprocity (CR), aiming to establish a theoretically consistent method for speed determination, which was originally introduced in (Cantero and Kim, 2024). The proposed method is theoretically formulated, numerically examined, and validated through results obtained from laboratory experiments. The study involves a comparative analysis of the performance in speed estimation using the standard correlation approach and the new method based on CR.

2 CONVOLUTED RECIPROCITY

The determination of a bridge's quasi-static response resulting from the passage of a vehicle can be computed by utilizing the influence line. Specifically, the response at position A is obtained through the convolution of the influence line at A with the loading function (Frøseth et al., 2017), as depicted in Equation (1). The loading function, denoted as $P(t)$, is composed of a series of impulse functions with magnitudes P_j, each corresponding to an axle j, and these functions are time-shifted based on the axle distances and the speed of the vehicle, denoted as v, while I_A represents the influence line for the measured load effect at location A on the bridge.

$$S_A(t) = P(t) * I_A(t) \tag{1}$$

The influence line at another location B is I_B. The convolution of Equation (1) by I_B is:

$$S_A(t) * I_B(t) = P(t) * I_A(t) * I_B(t) \tag{2}$$

Taking advantage of the commutative property of the convolution operator, Equation (2) can be rewritten, using the definition in Equation (1), as:

$$S_A(t) * I_B(t) = S_B(t) * I_A(t) \tag{3}$$

The relationship described in Equation (3) is referred to as Convoluted Reciprocity (CR). This expression demonstrates that the convolution of the response at location A by the influence line at location B equals the convolution of the response at B by the influence line at A. This straightforward yet powerful theoretical outcome can be exploited for speed estimation.

Furthermore, the expression in Equation (3) can be generalized to a broader scenario. When multiplied by the loading function $P_C(t)$ for a vehicle of known speed (referred to as the calibration vehicle), it yields Equation (4). This signifies that the convoluted reciprocity relationship also holds between two arbitrary bridge locations, A and B, for responses to two separate vehicle crossing events. Importantly, this relationship remains valid for the responses of any two vehicles, irrespective of their axle configuration.

$$S_A(t) * S_{B,C}(t) = S_B(t) * S_{A,C}(t) \tag{4}$$

2.1 *Speed estimation procedure*

This section illustrates the procedure to estimate speed utilizing the CR relationship. The following explanation explores the case of a simply supported beam traversed by a 2-axle vehicle. At first, only the quasi-static response is simulated numerically using the open-source software VBI-2D (Cantero, 2024).

The procedure requires information from two sensors, say at ¼ and ¾ of bridge span. The influence lines and the responses due to the passing vehicle of unknown speed at these to bridge locations are shown in Figure 1.

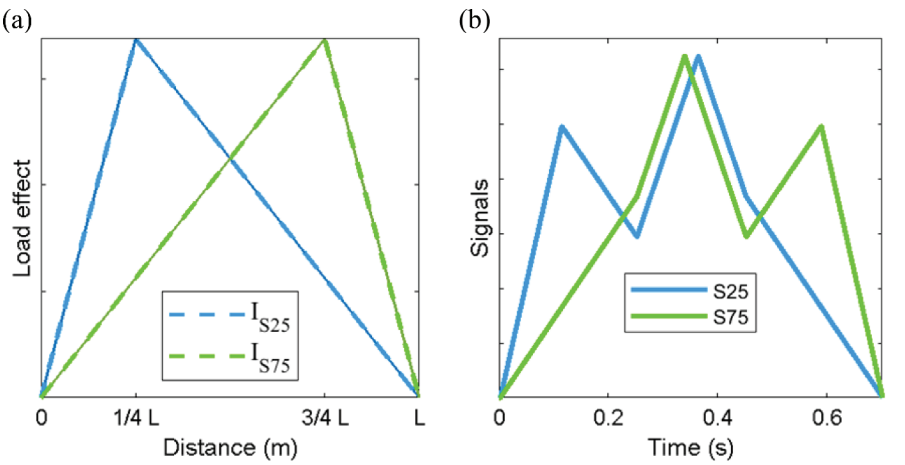


Figure 1. Available information for speed estimation; (a) Influence lines at two locations; (b) Measured signals during vehicle passage.

To estimate the speed the proposed method rescales the influence lines assuming different speeds and evaluates the validity of the convoluted reciprocity equality. While, by definition, an influence line is described in the space domain, the influence lines, $I_A(x)$ and $I_B(x)$, can be transformed into the time domain by knowing (or assuming) the vehicle's traversing speed,

denoted as v. The value of v that satisfies Equation (3) corresponds to the speed of the vehicle. For example, Figure 2 illustrates the outcomes of the left-hand side and right-hand side of Equation (3) for three different assumed speeds. In cases where the assumed speed does not align with the actual speed of the event, both sides of the convoluted reciprocity (CR) relationship (Figure 2(a) and (c)) manifest clear discrepancies. However, when the assumed speed matches the actual speed, then both results match (see Figure 2(b)).

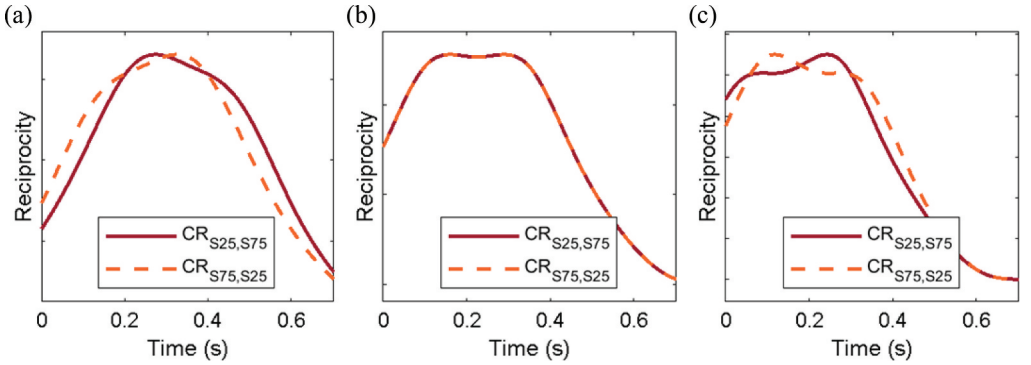


Figure 2. Convoluted reciprocity for a selection of assumed speeds: (a) v = 15 m/s; (b) v = 20 m/s; (c) v = 25 m/s.

For any given speed, the disparity between the right-hand side and the left-hand side of the equation is assessed using the norm of their difference. The value that minimizes this difference serves as the estimated speed of the crossing vehicle. To quantify the dissimilarity between both sides of the equation, this study recommends the use of the 2-norm. Figure 3(a) displays the norms for a range of guessed speeds, with the minimum value distinctly corresponding to the correct speed of the vehicle.

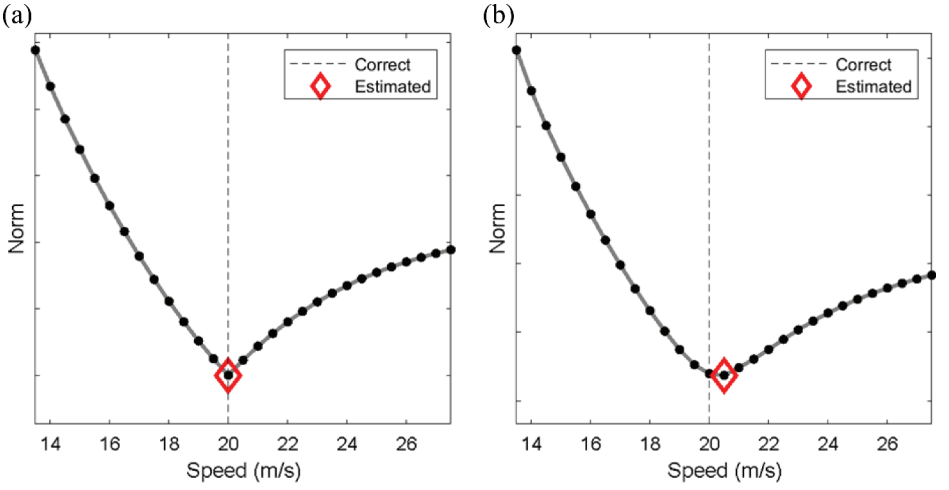


Figure 3. Norm of CR relationship for a range of speed guesses. (a) Ideal quasi-static response; (b) With dynamics.

The example depicted in Figure 3(a) utilized ideal quasi-static bridge responses, leading to a flawless speed estimation (20 m/s). However, when dynamic components of the bridge response are incorporated into the signals, the convoluted reciprocity procedure yields a speed

estimate of 20.41 m/s (2.06% error). For reference, Figure 3(b) displays the norms of the convoluted reciprocity for the range of speeds considered, highlighting the minor discrepancy attributed to the disturbances introduced by the dynamic components in the signals.

Therefore, the convoluted reciprocity (CR) relationship proves effective in deriving speed estimates. This has been demonstrated using the influence lines from each sensor. A comparable procedure can also be developed using the signals from a vehicle of known speed (referred to as the calibration vehicle), relying on the relationship provided in Equation 4. The speed estimation method based on influence lines is denoted as CRI, whereas the method utilizing signals from the calibration vehicle is called CRV.

3 SPEED ESTIMATION METHODS COMPARISON

This section examines the performance of speed estimation methods in the case of a simply supported beam. Initially, a numerical study is conducted, followed by the validation of results through an experimental study. Both CR methods, CRI and CRV, are employed and compared against the outcomes obtained using the standard correlation method.

3.1 *Numerical study*

A Monte Carlo simulation is executed, simulating 20,000 single vehicle events on five bridge spans crossed by 5-axle articulated trucks. The characteristics of the vehicles were randomly sampled, resulting in crossing events with varying geometries, axle loads, mass distributions, and suspension properties. For additional details regarding the adopted properties for the bridge models, vehicle models, and road profile, interested readers are directed to Cantero and Kim (2024). Additionally, the speeds of the vehicles were randomly sampled from a uniform distribution, with values ranging from 50 to 120 km/h (13.89 to 33.33 m/s).

Figure 4 quantifies the error in speed estimation statistically for the three methods under investigation. The findings distinctly reveal that the CR-based methods surpass speed estimation via correlation.

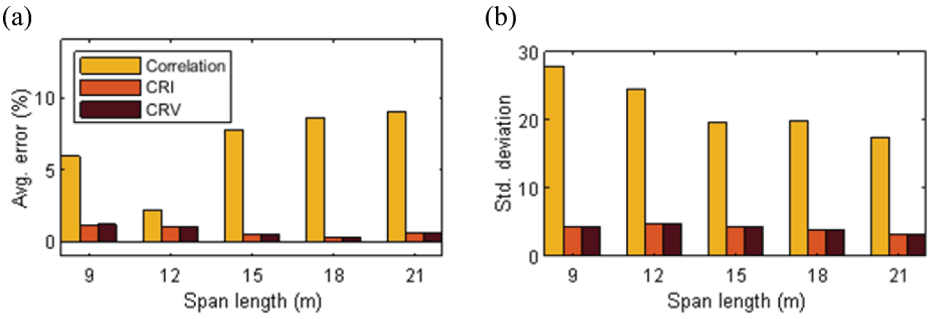


Figure 4. Speed estimation errors of simulated events. (a) Mean error (%); (b) Standard deviation.

3.2 *Experimental study*

A laboratory experiment was conducted to replicate the crossing of a vehicle on a bridge using a scaled setup of a beam traversed by a model vehicle. Figure 5 illustrates the 4-axle model vehicle employed in the experiment, which was moved across the access tracks and beam through a pulley system. The vehicle underwent back-and-forth movement across the beam 12 times, resulting in 24 crossing events. This loading sequence was carried out for two different constant speeds, specifically at V1 = 0.551 m/s and V2 = 1.048 m/s. The 5.6 m long steel beam was configured in a simply supported arrangement spanning 5.4 m. The beam was equipped

with strain gauges positioned at 25% (= ¼ L), 50% (= ½ L), and 75% (= ¾ L) of L, generating signals S_{25}, S_{50}, and S_{75}. The sampling frequency was 2048 Hz using the NI9237 data acquisition system. (For more details, refer to Cantero and Kim (2024)).

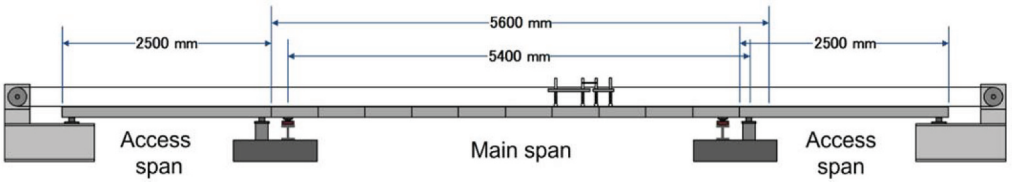


Figure 5. Experimental set-up.

Figure 6(a) presents a sample of the measured strain signals during the passage of a single vehicle traveling at speed V2. These signals underwent processing to eliminate noise using a zero-phase first-order Butterworth lowpass filter with a 1 Hz cut-off frequency. Utilizing known information about the vehicle and its traversing speed, the influence lines at each sensor location were determined through the matrix method (Obrien et al., 2006). The final influence lines considered in this study (depicted in Figure 6(b)) represent the average results extracted from multiple vehicle passages.

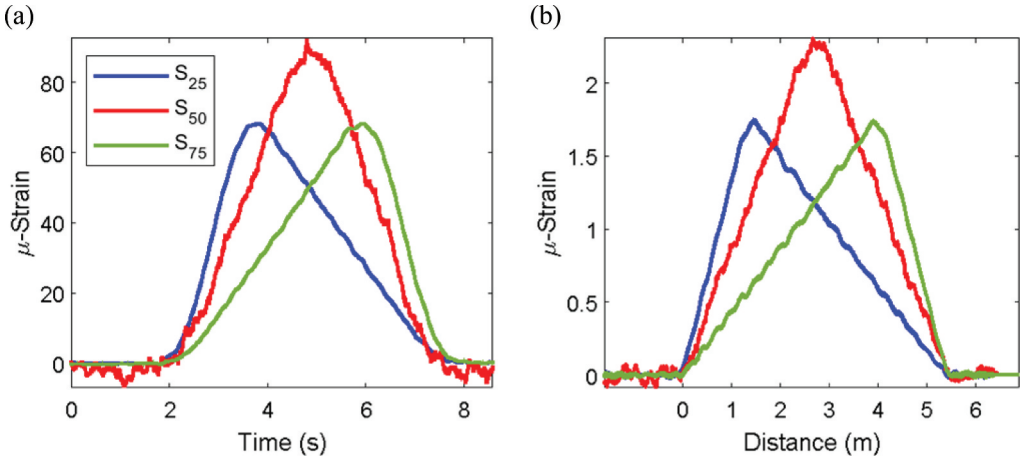


Figure 6. (a) Sample strain responses at 3 sensor locations; (b) Extracted influence lines.

Speed is estimated for all crossing events using the measured signals. The correlation method is computed, considering the correction strategy described by Kalin et al. (2006) based on qualified maxima. Additionally, both potential applications of the convoluted reciprocity approach were independently explored. The CRI method utilized the average influence lines depicted in Figure 6(b), while CRV employed the bridge responses from the initial event at speed V1. Figure 7 illustrates the estimated speeds for each method and event, facilitating a comparison with the actual speed value of the model vehicle. The results clearly demonstrate that for the novel speed estimation methods (CRI and CRV), the errors are significantly smaller than those based on correlation.

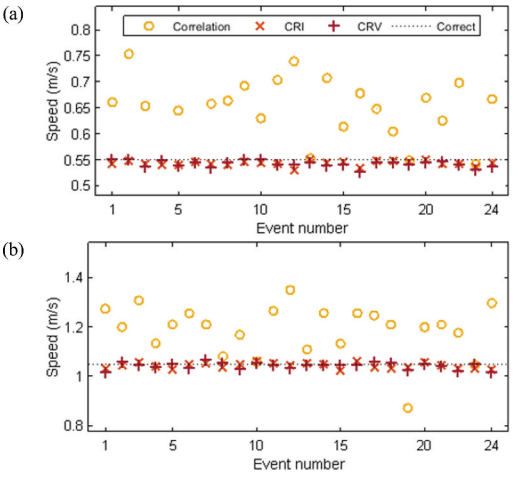


Figure 7. Speed estimation for various methods from experimental data, for speeds: (a) V1= 0.551 m/s; (b) V2 = 1.048 m/s.

4 CONCLUSION

This paper introduced a novel concept, convoluted reciprocity (CR), establishing a relationship between responses recorded at two distinct locations for two independent crossing events. This simple yet powerful idea was employed to propose a theoretically consistent method for determining the speed of passing vehicles. Two variations of the method were presented: CRI based on the sensors' influence lines and CRV based on the bridge response for a calibration vehicle. Their performance was numerically evaluated across a range of vehicle and bridge configurations, demonstrating that the newly proposed methods offer more accurate and robust speed estimates. To validate these findings, laboratory tests were conducted on a scaled bridge traversed by a model vehicle, and the analysis of the empirical data confirmed the results.

Therefore, this document has introduced and validated the concept of convoluted reciprocity. This theoretical discovery offers a novel approach to addressing the speed estimation problem. Its derivation relies solely on the properties of the convolution operation, making the result independent of the properties, configuration, or boundary conditions of the structure. In this regard, the outcome is universal, enabling the method's application with any two sensor locations in the longitudinal direction.

REFERENCES

Cantero, D. 2014. VBI-2D Vehicle-bridge interaction simulation and validation framework for Matlab. Submitted for publication.

Cantero, D. & Kim, C.W. 2024. Convoluted reciprocity and other methods for vehicle speed estimation in Bridge Weigh-in-Motion systems. *ASCE Journal of Bridge Engineering*. (In-Press). DOI: 10.1061/JBENF2.BEENG-6422

Frøseth, G.T. & Rønnquist, A. & Cantero, D. & Øiseth, O. 2017. Influence line extraction by deconvolution in the frequency domain. *Computers and Structures* 189: 31–30. DOI: 10.1016/j.compstruc.2017.04.014

Hajializadeh, D. & Žnidarič, A. & Kalin, J. & Obrien, E.J. 2020. Development and testing of a railway Bridge Weigh-in-Motion system. *Applied Sciences* 10: 4708. DOI: 10.3390/app10144708

Kalin, J. & Žnidarič, A. & and Lavrič, I. 2006. Practical implementation of Nothing-on-the-Road Bridge Weigh-in-Motion system. *Slovenian National Building and Civil Engineering Institute*; 207: 3–10.

MacLeod, E. & Arjomandi, K. 2022. Enhanced Bridge Weigh-in-Motion system using hybrid strain–acceleration sensor data. *ASCE Journal of Bridge Engineering* 27(9): 04022077. DOI: 10.1061/(ASCE)BE.1943-5592.0001924

OBrien, E.J. & Quilligan, M.J. & Karoumi, R. 2006. Calculating an influence line from direct measurements. *Proceedings of the Institution of Civil Engineers. Bridge Engineering* 159(BE1): 31–34. DOI: 10.1680/bren.2006.159.1.31

OBrien, E.J. & Žnidarič, A. 2001. *WAVE Weighing-in-motion of axles and vehicles for Europe. Report of Work Package 1.2*. Ljubljana, Slovenia: Zavod za gradbeništvo.

Yu, Y. & Cai, C.S. & Deng, Lu. 2016. State-of-the-art review on Bridge Weigh-in-Motion technology. *Advances in Structural Engineering* 19(9): 1514–1530. DOI: 10.1177/1369433216655922

Žnidarič, A. & Kalin, J. & Kreslin, M. 2017. Improved accuracy and robustness of Bridge Weigh-in-Motion systems, *Structure and Infrastructure Engineering* 14: 412–424. DOI: 10.1080/15732479.2017.1406958

Zolghadri, N. & Halling, M.W. & Johnson, N. & Barr, P.J. 2016. Field verification of simplified Bridge Weigh-in-Motion techniques. *ASCE Journal of Bridge Engineering* 21(10): 04016063. DOI: 10.1061/(ASCE)BE.1943-5592.0000930

Bridge Maintenance, Safety, Management, Digitalization and Sustainability – Jensen, Frangopol & Schmidt (eds)
© 2024 The Author(s), ISBN 978-1-032-77040-6
Open Access: www.taylorfrancis.com, CC BY-NC-ND 4.0 license

Strain-based FEM-aided bridge health monitoring: A case study

P. Rizzo & A. Enshaeian
Department of Civil and Environmental Engineering, University of Pittsburgh, Pittsburgh, PA

A. Ghahremani
Department of Mechanical Engineering and Materials Science, University of Pittsburgh, Pittsburgh, PA

ABSTRACT: This article presents a physics-based structural health monitoring (SHM) approach applied to a lenticular truss bridge to predict the deformations associated with the presence of transient loads. A detailed finite element model was generated using a commercial software to create an accurate model of the bridge. The presence of concentrated loads on the deck at different locations was simulated, and a static analysis was performed to quantify the deformations induced by the loads. Such deformations were then compared to the strains recorded by an array of wireless strain gages during a controlled truckload test performed by an independent third-party. The test consisted of several low-speed crossings at controlled distances from the bridge parapets using a truck with a certified load. The array was part of a SHM system that consisted of wireless strain gages, displacement sensors, and rotational gages. The results of the comparative analysis show that the proposed physics-based monitoring is capable of identifying sensor-related faults and of determining the load distributions across the bridge. In addition, the data relative to near four-years monitoring are presented and show the reliability of the SHM system as well as the challenges associated with environmental effects on the strain reading.

1 INTRODUCTION

There are over 600,000 highway bridges in the United States (Federal Highway Administration, 2019), each of which is assigned with a single-digit number (0 to 9) to describe the physical condition of its main parts (Pennsylvania Department of Transportation, 2023). If the lowest rating is greater than or equal to 7, the bridge is classified as good; if it is less than or equal to 4, the classification is poor. Bridges rated 5 or 6 are classified as fair (Federal Highway Administration, 2023). Currently, about 7.5% of bridges are labeled in "poor" condition (ASCE, 2021). In the U.S. each bridge must be inspected at least once every two years (U.S. Department of Transportation, 2023). However, periodic inspections may miss the onset of critical issues between two consecutive inspections. This is raising the attention towards cost-effective structural health monitoring (SHM) strategies that evolves the maintenance paradigm from time-based NDE in which a structure is inspected periodically, to permanent-based where sensors monitor 24/7 to flag, locate, and quantify damage as it happens. Strain is the most frequently monitored parameter in bridge health monitoring (Glisic, 2022).

In 2017, the Pennsylvania Department of Transportation (PennDOT) started a pilot bridge instrumentation program. Ten bridges across south and southwest Pennsylvania were instrumented during the period 2017-2019 with an array of commercial wireless sensors able to provide real-time information about static and (for some bridges) dynamic responses. The installations were completed by a company, hereinafter referred to as the Vendor, not

DOI: 10.1201/9781003483755-159

involved in the study presented here. One of the ten bridges is the iconic Smithfield Street Bridge, built nearly 140 years ago in the city of Pittsburgh (Figure 1).

In this paper, we present some results of a holistic study of the bridge. The study combined finite element (FE) modeling with the analysis of strain data. A high-fidelity FE model was developed using the commercial software ANSYS® to prove the reliability of the strain measurements, to determine the required sensitivity to detect subtle changes in the structure, and to simulate a few loading scenarios under pristine and simulated damage conditions. Specifically, the model was used first to predict the static deformation along two control members of the truss caused by the individual crossing of three AASHTO standard trucks. Three data-driven analyses were conducted. In the first analysis, the strains and the temperatures were examined to quantify the static response of the structure to thermal loading. Then, the effect of the temperature on the recorded strains was mitigated using a simple procedure to extract and isolate the effects of live loads, which indicates, in the context of this paper, the traffic load or any transient rapid event, such as impact, occurring on the bridge during normal operation. Finally, the live loads data were coupled to an unsupervised learning class based on outlier analysis (OA) to identify notable transient events. OA was chosen to leverage the experience of one of the authors (Lanza di Scalea, et. al., 2005; Rizzo, et. al., 2007; Bagheri, et. al., 2015; Zheng, et. al., 2020; Ghahremani, et. al., 2022). The study presented in this paper is part of a more comprehensive study that involve the analyses of several other bridges, which have been reported elsewhere (Rizzo and Enshaeian 2021, Ghahremani et al. 2022, Rizzo et al. 2023).

The scientific contribution of this paper lays on the holistic approach taken to monitor an old and iconic bridge. An extensive numerical analysis of the pristine bridge and of the bridge with a few simulated damage scenarios was completed using a high-fidelity model. The model was validated with the experimental measurements taken with an array of wireless sensors during a controlled truckload test. In addition, the measurements relative to three years of monitoring were examined using an ad hoc signal processing to successfully identify non-critical structural anomalies.

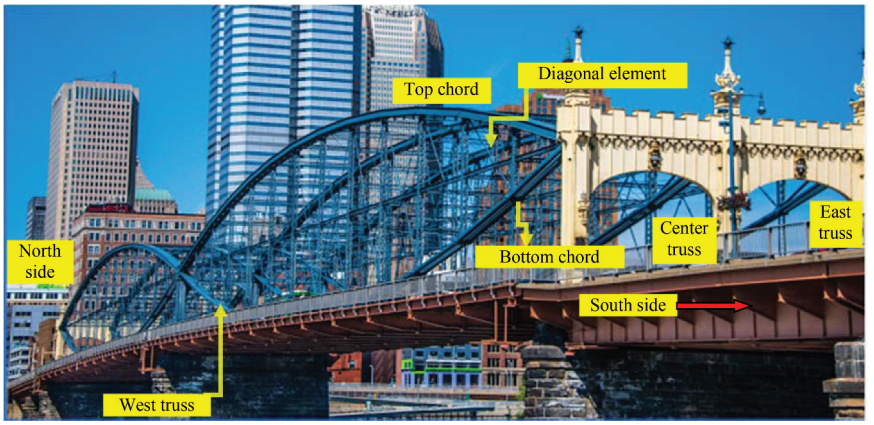


Figure 1. The Smithfield Street Bridge with directions and nomenclature.

2 THE BRIDGE AND THE NUMERICAL SETUP

The Smithfield Street Bridge is 542 m long and consists of seven spans. The iconic parts of the Bridge are Span 3, close to downtown, and Span 4, close to the South Side neighborhood. Span 4 is the subject of this study. The superstructure of spans 3 and 4 are made of riveted built-up lenticular through-trusses. For convenience, each lenticular truss is labeled as the west, center, and east trusses (Figure 1). Each truss is composed by three main parts: the top chord, the bottom chord, and the diagonal element. The top chord is formed by four I-shape

steel members riveted together. The bottom chord is formed by a variable number (six to eight) of bars pinned together. The diagonal element is instead a single bar. Table 1 lists the areas of the cross-section of those elements instrumented with the wireless strain gages.

In July 2019, the Vendor, which was not involved in the study presented here, instrumented the trusses of Span 4 with 18 wireless strain gages. Shortly after installation, a truckload test was performed using a 26,272 kg truck. The steer axle was 7,992 kg and the drive 'tandem' axles were 18,280 kg. First, the truck travelled northbound twice (Tests 1 and 2) crawling at about 8 km/h on the left lane. Then, the truck stopped at both ends of span 4. Tests 1 and 2 were repeated with the truck crawling northbound on the right lane (Tests 3 and 4). After that, the truck was directed southbound, and Tests 1 to 4 were replicated and are labeled as Tests 5 and 6 (right lane) and Tests 7 and 8 (left lane).

The high-fidelity FE model of the superstructure and the deck of Span 4 was created in ANSYS 2020 R2. To make the static analysis computationally manageable, the following simplifications were made: (1) the small longitudinal components found under the deck and the stiffeners of the floorbeams were not modeled; (2) the splice plates and a few other connection members were neglected; (3) the rebar of the concrete deck were replaced by a steel plate under the deck; (4) the portals were approximated; (5) the bottom chord was modeled as a single 203.2 x 254 mm2 (8" × 10") steel bar instead of the actual ten 203.2 x 25.4 mm2 (8"×1") bars; (6) the top chord became a rectangular element with the cross-section area equal to the total cross-sectional area of the true chord. A total of 880 structural components, more than 244,700 finite elements, and over 698,700 nodes constituted the final model. A screenshot of the FE model is shown in Figure 2. The Young modulus of structural steel (200 GPa, 29,000 ksi), and the typical type A concrete (24.1 GPa, 3,500 ksi) were considered.

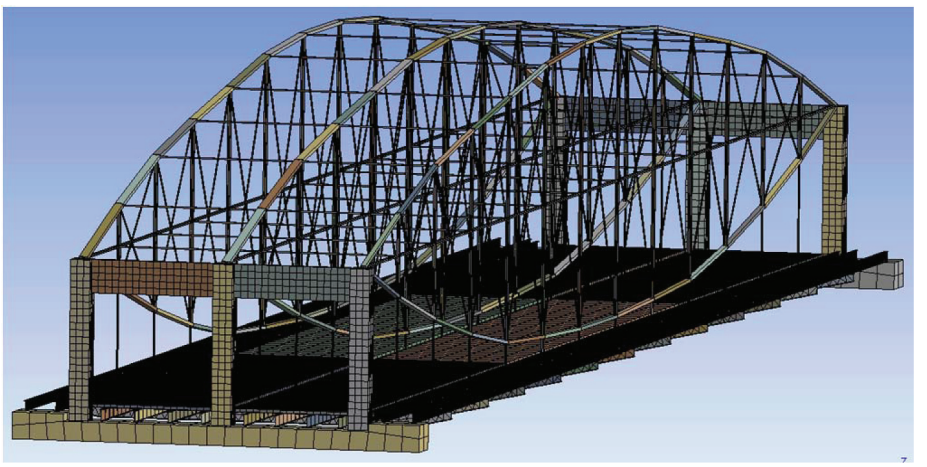


Figure 2. Screenshot of the FEM of the Smithfield Street Bridge.

3 NUMERICAL SIMULATIONS

Three AASHTO (American Association of State Highway and Transportation) trucks, namely the ML-80, the H20, and the HS20 were selected. A fourth truck, identical to the truck used to perform the load test, was considered. The static analyses calculated the deformation generated by each individual truck on the two diagonal members hereinafter labelled as L1U2 (Figure 3) and L1′U2′, monitored with two strain gages. These members are considered control members because they sustain the largest stress among the components being monitored. Each truck was placed on the northbound left lane. A few truck positions were considered to identify the location that maximizes the deformation of control members. Figure 3

provides a close-up view of the setup relative to the AASHTO ML-80 truck, near to member L1U2, i.e., close to the north end of span 4. The distance of the rear wheels from the north portal ranged between 7.620 m to 15.24 m at 1.27 m interval in order to find the largest numerical load and strain.

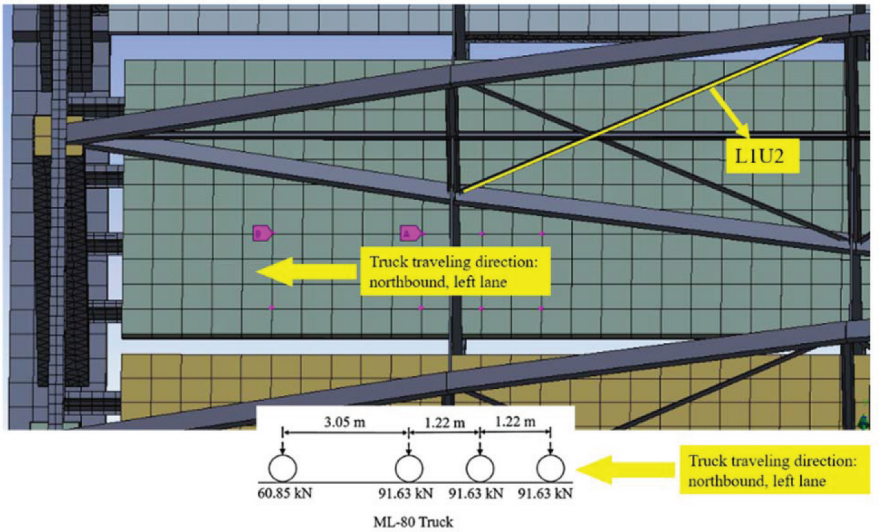


Figure 3. Numerical analysis of the ML-80 truck. The pink dots locate the position of the truck wheels.

The same approach was applied to calculate the largest values on the diagonal member close to the south side of the bridge. The same numerical analysis was applied using the other three trucks. The maximum calculated strains in the two diagonal members of the center truss are presented in Table 1. Owing to the linearity of the model, the numerical deformations are proportional to the weight of the truck. It must be noted though that the points of application of the forces, i.e. the position of the wheels, differ from truck to truck along the longitudinal direction but the distance of the right wheels from the parapet are the same.

Table 1. Numerical maximum strain at the two control diagonal members of the Span 4 center truss as a result of the presence of a single truck. Values expressed in με.

Truss member	Truck Type Company Truck	ML-80	H20	HS20
Member L_1U_2	80.89	114.1	62.28	98.95
Member $L'_1U'_2$	80.92	114.3	62.33	99.05

The FE results relative to the truck used in the field were compared to the experimental results reported by the Vendor. The case of crossing the northbound left lane twice is presented here. The strains measured by sensor S09, bonded to the diagonal member L1U2 (see Figure 3) were equal to 67.0 and 66.9 με. These values are about 17% lower than the calculated numerical deformation of 80.9 με listed in Table 1. The experimental values recorded by the sensor bonded to the diagonal member L'1U'2, were equal to 71.5 and 71.2 με, i.e. only 12.3% lower than the numerical prediction of 80.9 με. The difference between the numerical and the experimental value is likely due to a discrepancy between the numerical and the real (but unknown) lateral distance of the truck from the east parapet. To prove this hypothesis,

we considered the case of the same truck 1.91 m away from the centerline instead of the 0.89 m simulated location. The numerical strain of member L1U2 is now 69.2 με, just 3.3% higher than the experimental values recorded by the sensor. Similarly, when the numerical truck is 1.27 m (50 in.) from the center truss, the calculated strain of member L'1U'2 is equal to 77.09 με, just 7.8% higher than the recorded values from the corresponding sensor. The outcome of this analysis is that a direct comparison between the FE estimation and the experimental measurements suffers from the lack of knowledge about the exact lateral position of the truck. Nonetheless, the agreement between the numerical and the experimental results is quite good and prove the reliability of the model.

4 THE STRUCTURAL HEALTH MONITORING PARADIGM

The data from the 18 strain gages were processed using a general framework designed by the Authors and implemented in MATLAB®. For the sake of space, only a few results can be presented here. To minimize any bias attributable to the temperature, a simple procedure was implemented. The procedure was as follows. First, the raw strain data and the raw temperature data were synchronized by up-sampling and interpolating the temperature data. Then, the 15-minutes moving average for both parameters was calculated and the difference between the raw and the moving averaged strain was calculated to obtain what hereinafter is referred to as the "true strain".

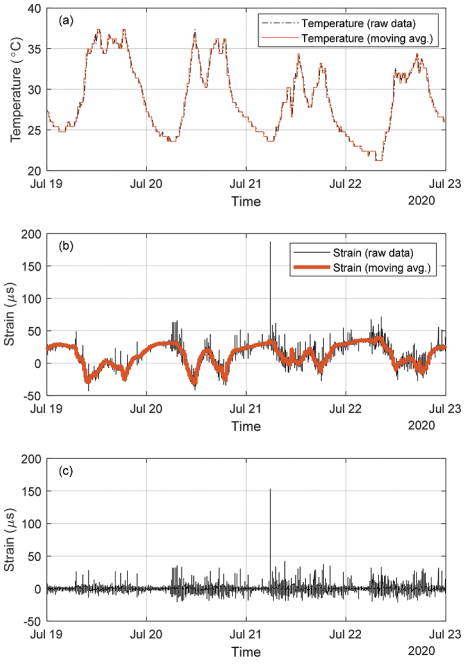


Figure 4. Mitigation strategy to isolate transient events. (a) Top. Raw and 15-minutes moving average of the temperature data. (b) Center. Raw and 15-minutes moving average of the strain data. (c) Bottom. Live load strain.

The effectiveness of the procedure is shown in described above was demonstrated further with Figure 4, which shows the data recorded by one sensor on July 19 – 23 of year 2020. The steel temperature and the corresponding moving average are presented in Figure 4a and they overlap because metal heating or cooling takes longer than 15 minutes. The raw strains and the corresponding moving average are presented instead in Figure 4b. The moving average is

clearly tied to the temperature trend. The decrease of the temperature increases the strain and vice versa. The raw strains are instead a combination of traffic and thermal load. The difference between the two, i.e. the true strain, is presented in Figure 4c. Besides the fact that the absence of traffic is seen in the early hours of each day, Figure 4c shows a peak (152 με) triggered by the crossing of a very heavy truck traveling southbound.

The data analysis was extended to include three years, 01 – August – 2019 to 31 – July – 2022. This included the analysis of the thermal effects. An example of raw strains and the corresponding raw temperatures from one of the 18 sensors is shown in Figure 4. The graph is bound the ±4σ interval and a linear regression whose equation and the corresponding R^2 are displayed.

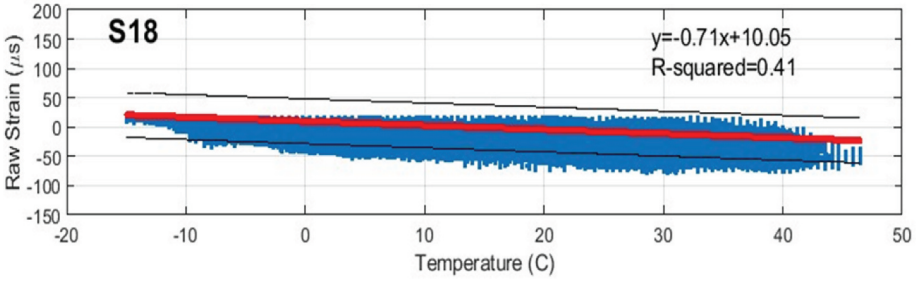


Figure 5. Raw strain vs raw temperature recorded by one of the 18 gages for three years.

The slope for each sensor is visualized on the bridge schematics of Figure 6. Consistent with the presence of an expansion joint at the south end of Span 4, eight of the nine slopes calculated from the sensors bonded on the south end of the bridge are higher than the corresponding slopes from the north end. The only exception is S12, for which the value of -0.34 με/°C is smaller than the slope calculated for gage S07 (-0.53 με/°C). The strain gradients across the nine monitored members located on the north end are nearly the same. The only relevant exception is the diagonal member of the center truss, i.e. gage S09. It is interesting to note that the slope at

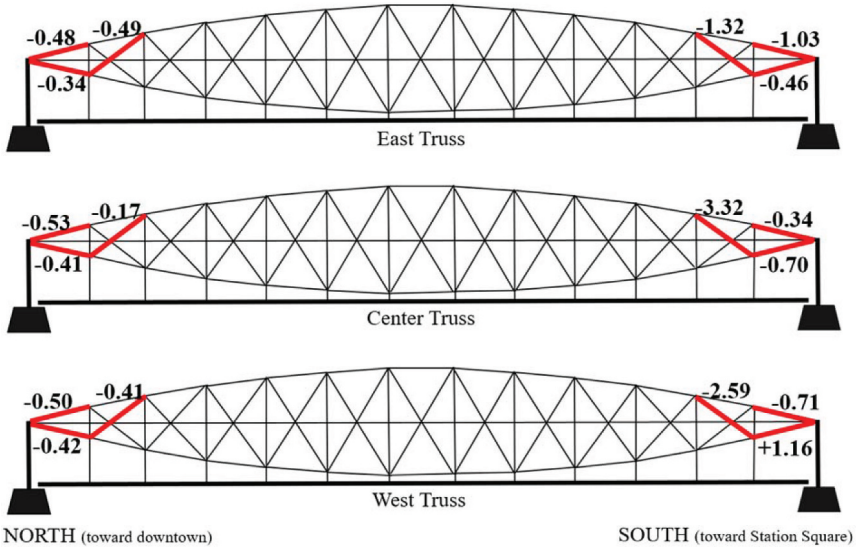


Figure 6. Drawings of the east, center and west truss with the members instrumented and the corrsponding strain rate expressed in με/°C.

S04 is 51% the value of S16 (-1.32 με/°C vs -2.59 με/°C), and 40% the value of S10 (-1.32 με/°C vs -3.32 με/°C). Notably, the slope associated with S10 (-3.32 με/°C) is nearly twenty-fold the value calculated for S09 (-0.17 με/°C). Such difference is not seen in any other pair. Finally, the cross comparison of the bottom south east and west chord suggests that the west chord expands more than its east counterpart, despite the cross-section of the latter is smaller.

Finally, the "true strains", which represent an accurate quantification of the deformation triggered by the live loads, were analyzed. For the sake of space, the results of the outlier analysis OA are presented. OA is a novelty detection method that establishes whether a new configuration of a given system is discordant or inconsistent from the baseline configuration, which consists of an existing set of data (or patterns) that describes the normal operative conditions. In this study multivariate OA was performed by computing the Mahalanobis squared distance (MSD) [Bagheri et al. 2015, Zheng et al. 2020, Rizzo et al. 2007] was used, and each truss was considered individually. As such, the input vector contains the true strains from six sensors. The baseline consisted of all the data collected during the month of August 2019. This relatively short interval was deemed to be representative of the baseline because the OA was applied to the true strains, and the true strains are unbiased by thermal effect. The threshold was instead set as the upper value of 4σ. The results of the OA relative to the west truss are presented in Figure 7. The figure shows the reliability of the analysis at identifying outliers of a certain significance.

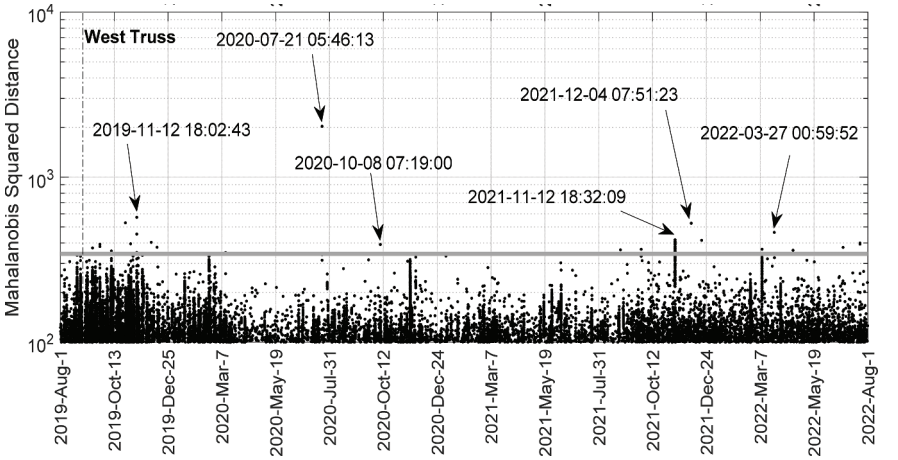


Figure 7. Mahalanobis squared distance applied to the strain gage data on the individual trusses. From top to botto, east, center, and west truss.

5 CONCLUSIONS

This paper presented some results of a fully comprehensive study about the Smithfield Street Bridge one of the oldest and most iconic bridge in the city of Pittsburgh. The study consisted of modeling the bridge with a commercial finite element software to predict the deformation of those members that are currently monitored with wireless strain sensors bonded to some of the members of the three lenticular trusses that represent the superstructure of Span 4. The deformation calculated from the numerical model were calculated under the assumption that the bridge is subjected to the load of a truck of with well-defined geometry and weight. One of these trucks was identical to the vehicle used by the private company to perform a truck load test. The results from this truck test were compared with the numerical results predicted with the FE model and they show very good agreement, despite uncertainties about the lateral distance of the truck from the centerline of the bridge. Then, the paper presents the experimental analyses of the strain data that were conducted to evaluate the effects of the temperature to identify any anomalous behavior of the

members being monitored, and to identify structural anomalies using a multivariate statistic based on outlier analysis. Overall, it was observed that the south side of the west truss exhibits slightly larger thermal deformations than its east counterpart. The outlier analysis revealed some isolated peaks that can be attributed to heavy traffic or a sudden transient event of different kind.

ACKNOWLEDGEMENTS

The authors acknowledge the support of the Pennsylvania Department of Transportation (PennDOT) under contract 4400018535, PIT WO 003 titled "Data Management, Mining, and Inference for Bridge Monitoring". The contents of this document are not meant to represent standards and are not intended for use as a reference in specifications, contracts, regulations, statutes, or any other legal document. The opinions and interpretations expressed are those of the authors and other duly referenced sources. The views and findings reported herein are solely those of the writers and not necessarily those of PennDOT. This paper does not constitute a standard, a specification, or regulations. The model presented here is based on drawings of the Bridge provided to the Authors and may not necessarily reflect any modifications made over the years to rehabilitate/retrofit the structure. The third author performed this research while working under the supervision of the first author. The finite element data may be made available upon reasonable requests. The availability of the raw strain data may require special permission from the research sponsor.

REFERENCES

ASCE Report Card 2021. https://infrastructurereportcard.org/wp-content/uploads/2020/12/Bridges-2021.pdf.

Bagheri, A., Pistone, E. & Rizzo, P. 2015. Outlier Analysis and Artificial Neural Network for the Non-contact Nondestructive Evaluation of Immersed Plates. *Research in Nondestructive Evaluation* 26(3): 154–173. https://doi.org/10.1080/09349847.2015.1022677.

Federal Highway Administration. 2019. https://www.fhwa.dot.gov/bridge/nbi/ascii.cfm.

Federal Highway Administration. (last date accessed November 20th, 2023). https://www.fhwa.dot.gov/bridge/britab.cfm.

Ghahremani, B., Enshaeian, A., and Rizzo, P. (2022). "Bridge Health Monitoring using Strain Data and High-Fidelity Finite Element Analysis," Sensors journal, Physical Sensors (A section of Sensors (ISSN 1424-8220), Special Issue "Sensor and Embedded System Applications in Structural Engineering and Engineering Seismology", 22(14), 5172; https://doi.org/10.3390/s22145172 (I.F. 3.847).

Glisic, B. 2022. Concise Historic Overview of Strain Sensors Used in the Monitoring of Civil Structures: The First One Hundred Years. *Sensors Journal* 22(6). https://doi.org/10.3390/s22062397.

Lanza di Scalea, F., Rizzo, P., Coccia, S., Bartoli, I., Fateh, M., Viola, E. & Pascale, G. 2005. Non-contact ultrasonic inspection of rails and signal processing for automatic defect detection and classification. *Insight: Non-Destructive Testing and Condition Monitoring* 47(6): 346–353. https://doi.org/10.1784/insi.47.6.346.66449.

Pennsylvania Department of Transportation. (last date accessed November 20th, 2023). https://www.penndot.pa.gov/ProjectAndPrograms/Bridges/Pages/Bridge-Inspection-Terminology.aspx.

Rizzo, P., Sorrivi, E., Lanza di Scalea, F. & Viola, E. 2007. Wavelet-based outlier analysis for guided wave structural monitoring: Application to multi-wire strands. *Journal of Sound and Vibration* 307(1–2): 52–68. https://doi.org/10.1016/j.jsv.2007.06.058.

Rizzo, P., and Enshaeian, A. (2021). "Bridge Health Monitoring in the United States: a Review," *Structural Monitoring and Maintenance*, *An International Journal*, 8(1), 1–50, DOI: https://doi.org/10.12989/smm.2021.8.1.001 .

Rizzo, P., Enshaeian, A., and Ghahremani, B. (2023). "Diagnostics of Concrete Box Beam Bridges using Wireless Sensors and Finite Element Analysis," ASME Journal of Nondestructive Evaluation, Diagnostics and Prognostics of Engineering Systems, accepted October 2nd 2023.

U.S. Department of Transportation. (last date accessed November 20th, 2023). https://www.transportation.gov/testimony/highway-bridge-inspections.

Zheng, B., Rizzo, P. & Nasrollahi, A. 2020. Outlier analysis of nonlinear solitary waves for health monitoring applications. *Structural Health Monitoring* 19(4): 1160–1174. https://doi.org/10.1177/1475921719876089.

Bridge Maintenance, Safety, Management, Digitalization and Sustainability – Jensen, Frangopol & Schmidt (eds)
© 2024 The Author(s), ISBN 978-1-032-77040-6
Open Access: www.taylorfrancis.com, CC BY-NC-ND 4.0 license

Actual bridge verification of monitoring technique using optical fiber sensors

S. Aoki
Shutoko Technology Center, Structural Technology Research Laboratory

T. Maeshima & I. Iwaki
Nihon University, College of Engineering

ABSTRACT: Japan's Metropolitan Expressway is an expressway network linking major cities around the capital, Tokyo. In legally-mandated inspections once each 5 years, the need to construct scaffolds and individual differences between inspectors were issues in close visual inspections of RC decks. The authors investigated a method for evaluating the deterioration of deck slabs by monitoring with optical fiber sensors (length: 1000 mm). To understand the relationship between actions and responses, the strain in RC deck slabs was monitored using 245 kN and 118 kN constant load vehicles. The strain on the underside of RC deck slabs with a crack density of 9.8 m/m^2 was 37 μ under the action of 245 kN and 19 μ under 118 kN. In a laboratory test under live loads similar to those in actual bridges, the strain immediately before punching shear failure was 500 μ or more, indicating that failure is not urgent at present.

1 INTRODUCTION

Japan's Metropolitan Expressway (Shuto-kosoku-doro) is a network of automotive expressways linking Yokohama, Saitama and other major cities in the Tokyo Metropolitan area, centering on the nation's capital, Tokyo. Although the Metropolitan Expressway was originally constructed in preparation for the opening of the 1964 Tokyo Olympics, fast-paced road construction was necessary at the time, and for this reason, much of the system was constructed above rivers and general roads, where land for construction could be secured easily. About 75 % (approximately 240 km) of the total service length of 330 km consists of elevated structures. Of the total length, about 40 % (approx. 145 km) of all routes have been in service for 40 years or longer, and deterioration with age has become a problem (Figure 1). The conditions of use have now become severe, as the average daily traffic volume of the entire Metropolitan Expressway system is 1 million vehicles/day, and in particular, the volume of large vehicles is about 5 times greater than on general roads.

The Route No. 3 Shibuya Line of the Metropolitan Expressway is an automotive expressway with a total length of 13.5 km, which is connected to a national expressway with a distance of approximately 350 km between the capital, Tokyo, with Nagoya, the largest city in the Chubu region. This route was opened to service in 1971 and has now been in use for 52 years, and the current daily spot traffic volume exceeds 130,000 vehicles.

As a monitoring method which makes it possible to grasp the overall state of a bridge, "Bridge-Weight-In-Motion (BWIM)" was proposed in a previous study [1], [2]. This method is used as a system for specifying vehicles and evaluating the soundness of the target bridge as a whole based on deflection (strain) measurements. However, because it is necessary to measure the weight of vehicles accurately, and it is essential to accurately acquire data on vehicle

DOI: 10.1201/9781003483755-160

traffic characteristics such as speed, course, wheel position, etc., and use multiple vehicle detection sensors, the challenges accompanying the enormous volume of data acquisition and data analysis have been mentioned. Moreover, the high cost of the various types of sensors and the time required in sensor installation are also issues.

In addition, the general method for quantitative evaluation of the condition of RC deck slabs is judgment based on the deflection or crack density of the bottom surface of the deck slab. However, the need to construct scaffolds for close work and variations in judgments of hammering tests and recording of the crack length by individual inspectors were issues.

Therefore, in this research, the authors investigated a monitoring technique for RC deck slabs utilizing optical fiber sensor (hereinafter, OFS) [3], [4], [5], which are used in long-term monitoring of social infrastructure, and studied an evaluation method that is different from the conventional techniques based on deflection and crack density.

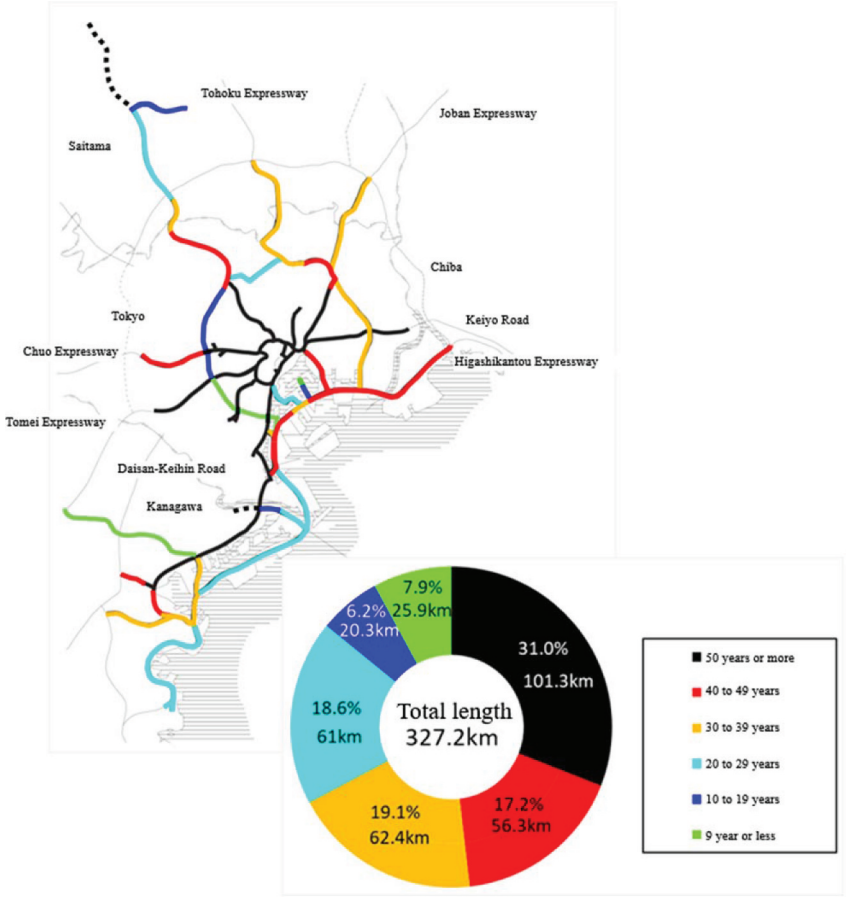


Figure 1. Routes of the Metropolitan Expressway by years in service and service length.

2 STRUCTURAL SPECIFICATIONS AND INSPECTION HISTORY OF RC DECK SLAB

2.1 *Structural specifications*

The RC deck slab used as the target of monitoring in this research is a steel I-girder bridge that was completed in 1971 and is a 4-girder structure with a span length of 30 m, deck slab span length of 3.2 m, and a deck slab thickness of 200 mm (Figure 2).

Because the deck slab was designed prior to 1972, decreased durability due the smaller number of reinforcing bars required at the time was a concern. Therefore, two stringers (longitudinal reinforcing members) were added between each pair of main girders in 1999. In addition, as an environmental measure for areas alongside the expressway, sound-absorbing panels were installed under the deck slab in 2000 to reduce the reverberation on general roads. These sound-absorbing panels are also used as scaffolding during close visual inspections.

2.2 *Inspection history*

The oldest inspection history of this section is a photographic record of the deck slab taken in 1990 (Figure 3a). In the inspection method used at that time, the condition of the underside of the deck slab was photographed in each trave (deck slab section enclosed between girders and cross beams), and the progress of deterioration was judged by comparing these photographs and the condition of the next time the bridge was photographed. However, because installation of the sound-absorbing panels made it impossible to photograph the underside of the deck slab, close visual inspection was adopted. After the sound-absorbing panels were installed, close visual inspections were conducted in 2008 and 2014, but in 2017, deterioration in the form of tortoise shell-like cracking, spalling of the cover concrete over the reinforcing bars, and an abnormal hollow sound in hammering tests were reported (Figure 3b).

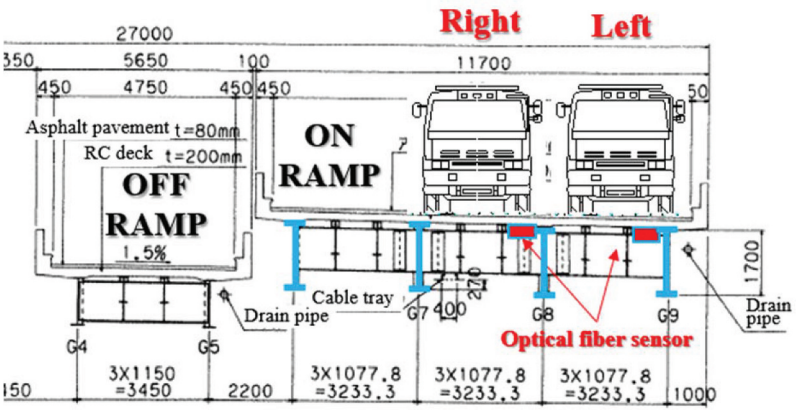
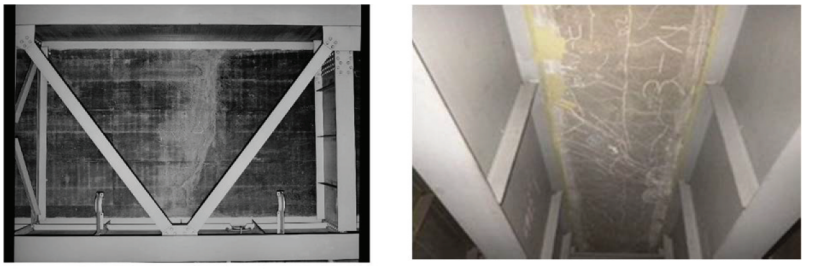


Figure 2. Sectional view showing monitoring positions.



(a) (b)

Figure 3. Photographic record of underside of RC deck slab.

3 CLOSE VISUAL INSPECTION OF RC DECK SLAB

3.1 *Inspection method*

To understand the current condition of the RC deck slab, a new visual inspection in close proximity to the underside of the deck slab was conducted, cracks that could be observed visually were traced with chalk, and a crack diagram was prepared. The total length of the cracks was calculated from this crack diagram, and the crack density[6], expressed as length per unit area (m/m^2), was arranged. Figure 4 shows the crack diagram and crack density.

3.2 *Inspection method*

As a result of the visual inspection, the crack density in the trave with the largest value was 9.8 m/m^2. Since the pavement had been replaced, and waterproofing work was also performed on upper side of the deck slab in November 2007, water leakage was not observed from the bottom surface. Significant deterioration was apparent in four traves, as shown in Figure 4. While cracks could also be seen in other traves, the progress of cracking was slight and the crack density was limited to about 3 m/m^2. No progress of the crack density was observed in close visual inspections carried out in the winter (February 2023) and summer (August 2023).

4 STRAIN MONITORING OF BOTTOM SIDE OF RC DECK SLAB

4.1 *Outline of OFS*

To evaluate the degree of deterioration of the RC deck slabs in which cracks had occurred, the strain under the action of live loading was monitored. As the sensors to be used in monitoring, OFS capable of measuring cracked concrete surfaces were selected. Conventionally, 60 mm foil-type gauges are used when measuring the strain of concrete structures, but because these gauges only measure a local range, it is not possible to measure the maximum strain due to opening/closing of cracks. However, OFS make it possible to monitor strain as the average strain including cracks in the optical fiber sensor by fixing the string-shaped sensor, with a length of 1 meter, to the bottom surface of the RC deck slab with screws. The sampling period was set at 100 Hz.

4.2 *Installation positions of OFS*

The installation positions of the OFS are shown in Figure 5. Two RC deck slabs with conspicuous cracking ("cracked RC decks") were selected and installed in the bridge axial direction, and adjacent deck slabs with only slight cracking ("sound RC decks") were also installed.

4.3 *Outline of load vehicle measurements*

In the actual bridge measurements, strain under the action of load vehicles was measured by driving the load vehicles on the left and right lanes, respectively. The gross weights of the load vehicles used here were 239 kN and 114 kN. The dynamic measurements were conducted at night-time, when the traffic volume was comparatively slight. The vehicle speed was 60 kph. The travel cases are shown in Figure 6.

4.4 *Monitoring results*

In the results of monitoring of the actual bridge (Figure 7) in Case 1, the strain on the left lane deck (load: 239 kN) was 37 μ, while that on the right lane deck (114 kN) was 24 μ. In Case 2, the strain on the right lane deck (239 kN) was 26 μ and that on the left lane deck (114 kN) was 19 μ. In all cases, the strain was small.

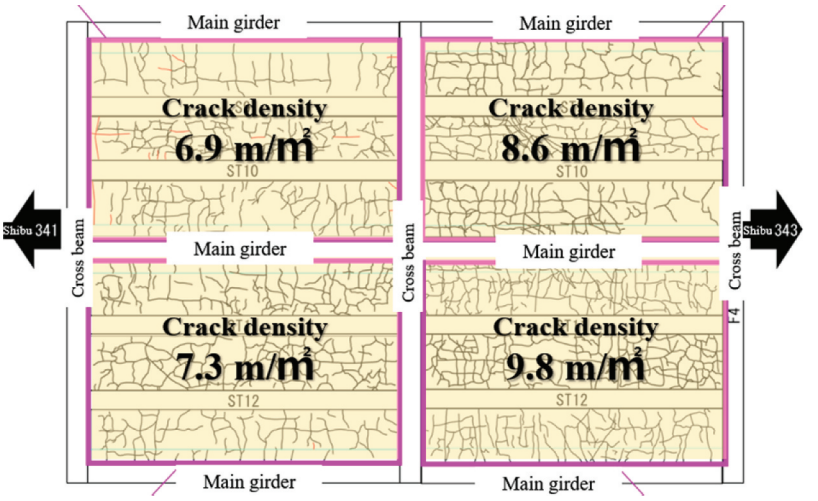


Figure 4. Result of close visual inspection (crack density).

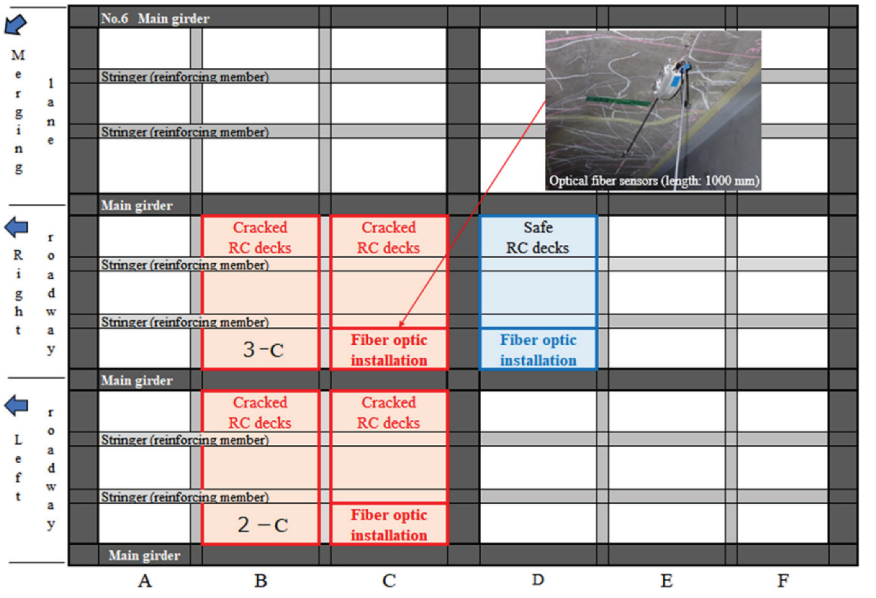


Figure 5. Installation positions of OFS installed on underside of RC deck slab.

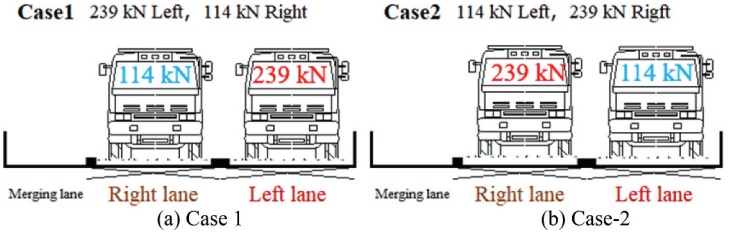


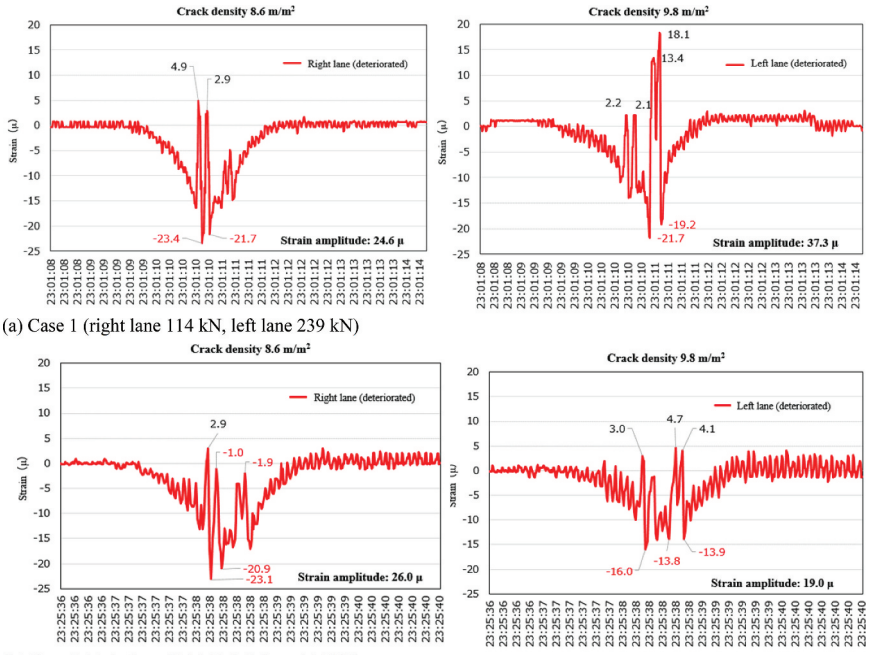
Figure 6. Travel cases in load vehicle measurements.

5 LABORATORY TEST

5.1 *Outline of laboratory test*

In addition to monitoring the RC deck slabs at the actual bridge, a laboratory test was conducted by preparing sample RC deck slabs and applying wheel loads similar to those that act on actual bridges by using a wheel load running test device[7], [8], which is used to evaluate the durability of RC deck slabs. This device cyclically loads a steel wheel set to the wheel load as the force of a hydraulic rotating crank, and can evaluate fatigue durability up to shear failure.

The loads applied in this test were increased in increments of 10 kN by running the load wheel 100 times at each 10 kN increment, assuming the wheel loads that act on actual bridges. Loading was carried out at 5 levels up to a maximum load of 98 kN, as shown in Figure 9. After reaching the maximum load of 98 kN, the maximum load was increased further, and the test was continued until shear failure occurred, assuming a targeted crack density of 10 m/m^2.



(a) Case 1 (right lane 114 kN, left lane 239 kN)

(b) Case 2 (right lane 239 kN, left lane 114 kN)

Figure 7. Strain during load vehicle travel; (top) (a) Case 1, bottom (b) Case 2).

5.2 *Test results*

Figure 10 shows the relationship between the crack density and the strain amplitude until punching shear failure occurs, which was obtained as a result of the wheel load running test. Strain of approximately 200 μ was generated at the crack density of 10 m/m^2, and the strain amplitude immediately before ultimate shear failure was approximately 500 μ (crack density: approx. 16 m/m^2). When these results were compared with the results of monitoring at the actual bridge, the strain of the actual bridge was 37 μ under loading of approximately 75 kN (= 149 kN/2 axles) and the crack density of 9.8 m/m^2. Because this is about 1/10 of the strain in the laboratory test, the current condition of the bridge was not urgent, and follow-up observation was considered to be an appropriate response.

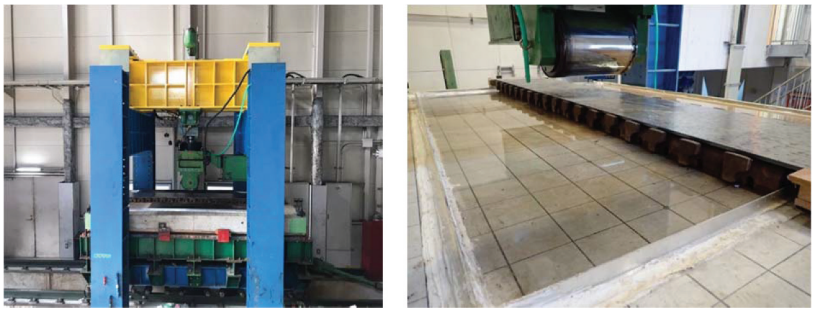


Figure 8. Wheel load running test device.

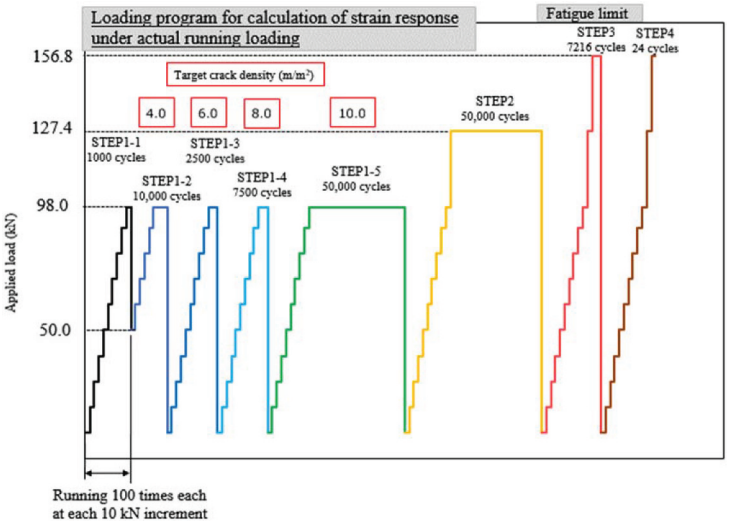


Figure 9. Loading steps in wheel load running test.

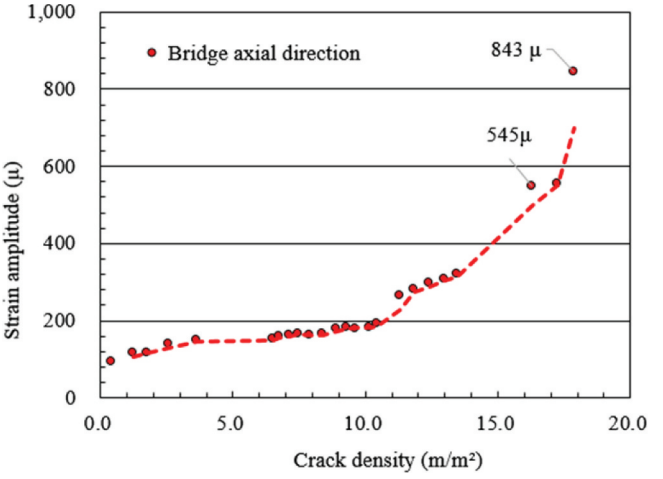


Figure 10. Relationship of strain amplitude and crack density.

6 CONCLUSIONS

Unlike the conventional method for evaluation of the degree of deterioration of RC deck slabs, in this study, the strain at the bottom side of the deck slab was measured using OFS, and the current state of the deck slab was evaluated from the relationship between the strain measured at the actual bridge and the strain obtained in a laboratory test. Because the changes in strain could be measured until ultimate shear failure occurred in the laboratory test, it is now considered possible to propose the timing of repairs of the RC deck slabs of actual bridges in a deteriorated condition based only on the strain obtained by monitoring.

However, because cracks progress rapidly if water penetrates from the pavement into the interior of an RC deck slab, the authors wish to conduct future research to clarify the conditions of the use for the proposed technique, including the timing of the start of monitoring, and the selection and assignment of the priority order of deck slabs that require monitoring.

ACKNOWLEDGMENTS

This research was conducted in collaboration with the Nihon University College of Engineering. We would like to thank the staff and students of the institutions to which the authors belong for their generous cooperation in investigating the health of RC deck slabs. We would like to take this opportunity to express our gratitude to all concerned for their invaluable assistance.

REFERENCES

[1] Kawakatsu, T. Aihara, K & Takasu, A. 2019. Deep Sensing Approach to Single-Sensor Vehicle Weighing System on Bridges. *IEEE Sensors Journal*, (vol.19), No.1

[2] Francis, B.C., Speedwell L.C., Jorge S., Bernard J., Franziska S., Alexandre, B & Alain, E. 2021. Real Condition Experiment on a New Bridge Weigh-In-Motion Solution for the Traffic Assessment on Road Bridges. IABSE Congress Ghent.

[3] X,W,Ye. Y, H, Su & J,P, Han. 2014. Structural Health Monitoring of Civil Infrastructure Using Optical Fiber Sensing Technology a Comprehensive Review. *The Scientific World Journal,vol.2014*.

[4] Kado, M.,Cartiaux, F,B. & Tajima, M. 2018. Study on Structural Monitoring Aimed At Detecting The Soundness of Nuclear Facilities after a Huge Disaster. Japan Society of Maintenology. ICMST-Tohoku. Sendai:Japan.

[5] Francis,B,C. Sofia,K. Georgios,A& Patrice,M,C. 2019. Bridge Monitoring & Assessment via OSMOS Optical Strands. 4th Joint International Symposium on Deformation Monitoring (JISDM). 15-17 May 2019. Athens:Greece.

[6] Matsui,S & Maeda,Y. 1986. A Rational Evaluation Method for Deterioration of Highway Bridge Decks. *Journal of structural mechanics and earthquake engineering. No. 374*/ I-6.

[7] Iwaki,I. 2016. Experimental Study on Fatigue Durability of Road Bridge Decks Subjected Chloride Induced Deterioration Or ASR. EASEC-14, Special Session3. Hochimin:Vletnam.

[8] Hisabe, N., Okada M., Miyama D., Matsui S., Onishi H., Kobayashi A. Fukunaga, H & Mimato, Y. 2003. Fatigue Life Extension of Damaged RC Slabs by Strengthening with Carbon Fiber Sheets Attaching Method. 19tf Us-Japan Bridge Engineering Workshop. Panel on Wind and Seismic Effects. UJNR, Tsukuba.

Bridge Maintenance, Safety, Management, Digitalization and Sustainability – Jensen, Frangopol & Schmidt (eds)
© 2024 The Author(s), ISBN 978-1-032-77040-6
Open Access: www.taylorfrancis.com, CC BY-NC-ND 4.0 license

Bridge Weigh-in-Motion applied to heritage iron truss bridges in France

F.-B. Cartiaux, V. Le Corvec & J. Semiao
OSMOS Group, Paris, France

B. Jacob
Université Gustave Eiffel, Champs-sur-Marne, France

ABSTRACT: Bridge Weigh-in-Motion (B-WIM) systems use the deck of a bridge as a scale for the estimation of the gross vehicle weight (GVW) and axle loads. Thus, the bridge design has a strong incidence on the performance, and even on the applicability of B-WIM. Usual bridge types for B-WIM are common beam girder concrete or composite bridges or concrete slabs, for which numerous application cases are described in the literature. In the frame of the "Ponts Connectés" (smart bridges) research program funded by the French government, two heritage iron truss bridges have been instrumented with sensors to monitor structural health issues, including B-WIM sensors. Both bridges are long continuous iron truss boxes spanning the Loire River, with respectively five and eleven 45-meter-long spans. This configuration, and the historical background of these nineteenth century assets initially designed for light local traffic, makes them a challenging case study for B-WIM application. The B-WIM system implemented is the WIM+D solution by OSMOS. Load tests on the bridges were carried out in April 2022, to adjust the B-WIM system and to assess its performance according to COST 323. One system was accepted in class C(15) and the second one in class B(10), which are very fair results for such B-WIM applications. This paper describes in detail the B-WIM system implemented, its adaptation to this particular type of bridges, and the results of the load test. Technical considerations to explain the different performance on the two bridges despite of their similarity are also discussed.

1 INTRODUCTION

Road infrastructure owners and managers can get significant benefit from an accurate knowledge of the real traffic level, in terms of asset management (Dolcemascolo et al., 2015), road and truck safety including overweight detection (Jacob et al., 2010), and assessment of the impact of the traffic in terms of damages to optimize the maintenance operations (Schmidt et al., 2013). To get this knowledge, Weigh-in-Motion (WIM) solutions allow estimating the gross vehicle weight (GVW) of each individual vehicle, sometimes along with its silhouette and load by axle, without interrupting the traffic flow.

Usual WIM systems use road sensors installed inside the pavement, which implies works with road closures, sensitivity to the pavement conditions, and inconvenience when the road must undergo pavement maintenance works. Bridge-WIM (B-WIM) solutions avoid these issues, by using a bridge located anywhere along the road as a scale. Sensors are installed on the bridge, either on a bottom flange of main girders, or under the deck, avoiding works on the road itself and allowing a high robustness of the WIM system, insensitive to pavement conditions.

DOI: 10.1201/9781003483755-161

As a counterpart, the accuracy of a B-WIM system for GVW and axle load strongly depends on the bridge design and may highly vary from one bridge to another. Classical applications of B-WIM use common reinforced or prestressed concrete bridges and are well documented (Cartiaux et al., 2021, 2023a). This contribution paper reports a particular case study on two historical iron-truss bridges, initially designed for light local traffic in the nineteenth century, over the Loire River in France.

This study takes place in the frame of the "GeRICO" research project, supported by the French government and steered by the Cerema as part of the "Programme National Ponts". The project lasted over two years from 2021 to 2023, including the continuous monitoring of the two bridges over 18 months, and a load test performed in April 2022. The accuracy test results of the B-WIM system are discussed in this paper.

2 BRIDGE-WIM SOLUTION

2.1 *The WIM+D solution*

The B-WIM solution called "WIM+D" was first released by OSMOS in 2018 (Cartiaux et al., 2019) and has been operational on at least 15 bridges as of 2022 (Cartiaux et al., 2023b). It relies on strain measurements on main girders and slabs by optical strands. Compared to previous B-WIM techniques, the novelty of the OSMOS WIM+D solution is to separate the estimation of GVW and axle loads.

GVW is obtained from sensors measuring global effects on main girders, where vibration effects are smooth and influence lines are accurate. Meanwhile, only one sensor per main girder is required, usually not more than two or four, to obtain an accurate GVW estimation whatever the transverse location of the vehicle.

The vehicle speed is derived from the time gap between peak measurements from the sensors dedicated to the GVW estimation and additional sensors located on a next span.

The axle load is obtained from additional sensors measuring local strain, like the bending of a short-span element (concrete slab or longitudinal stiffener on an orthotropic deck) under wheel loads. Only one axle load sensor is required for each traffic lane over the bridge, i.e., two sensors on common road bridges. The axle load is computed by distributing the previously estimated GVW on the several axles identified by the axle load sensors, with ratios deduced from the relative amplitude of the local effect for each axle.

2.2 *COST 323 methodology for the performance assessment*

Assessing the accuracy of an on-site WIM system requires a dedicated verification procedure, which implies to use a sample of vehicles as reference loads and let them drive on the bridge at various speeds, in all available traffic lanes (and even out of lane). The GVW of each test vehicle is measured on a certified weighbridge, before and after each test period. If needed, axle spacing and loads are measured at the same occasion to get their reference values.

The accuracy assessment is carried out by comparing the results given by the B-WIM as the vehicles are driven on the bridge to these reference values. A statistical analysis of the relative errors of GVW or axle load is carried out. Thus, a significant number of test vehicle passages is required. A usual accuracy assessment of the WIM+D system implies two or three different vehicles, each one of them running at least 10 to 20 times back-and-forward on the bridge. As a result of this statistical analysis, the system is eventually accepted into an accuracy class.

Such accuracy classes are defined according to the COST 323 methodology, taking into account the statistical uncertainty related to the number of measures, the environmental test conditions and the reproducibility or repeatability (Jacob et al., 2002, Brouste, 2021). The COST 323 defines accuracy classes ranking from A(5) to E(30): The best class A(5) means that a given proportion of the relative errors (depending on the test conditions, typically 95%) is less than 5% for GVW, while the worst class E(30) requires the same proportion of relative errors below 30%.

On an isostatic prestressed concrete deck in good conditions, with four main beam girders and 32 m long spans, the WIM+D system was accepted class A(5) (Cartiaux et al., 2023a).

3 IMPLEMENTATION ON IRON TRUSS BRIDGES

3.1 *Description of the bridges*

The Haut-Village and the Mauves bridges are two historical iron truss bridges spanning the Loire River upstream the city of Nantes, in western France (Figure 1). Both were built in 1882 for light local traffic of horse-drawn carts, and now supporting modern road traffic. They have a very similar design: a single box girder made of iron truss, with main spans of 45 m in length. The piers are made of masonry founded on timber piles in the riverbed. The Haut-Village bridge is 225 m long with five spans, and the Mauves bridge is 482 m long with eleven spans.

One main difference shall be noticed between the two bridges: the Mauves bridge underwent a refurbishment of the road slab and transverse beams in 2020, when the historical brick arches were replaced by a thin slab made of ultra-high performance fiber reinforced concrete (UHPFRC). The Haut-Village bridge keeps its historical brick arches on one span, while they were replaced by a reinforced concrete slab on the four other ones, which were rebuilt after World War II.



Figure 1. Haut-Village Bridge (left) and Mauves Bridge (right).

3.2 *Sensor installation*

Numerous sensors have been installed on both bridges in the frame of the GeRICO project, for different purposes beyond WIM, like operational modal analysis and model updating (Cartiaux et al., 2023c). They include many optical strands for strain measurement, accelerometers for vibration assessment and some extensometers. We only focus here on the few optical strands used for WIM: six of them for each bridge, among 26 in total on the Haut-Village bridge and 18 on the Mauves bridge.

The set of WIM-dedicated optical strand strain sensors is divided into three categories, according to the purpose of each measurement:

- Two "Gross Weight Sensors" are set on the lower flange of the main lateral truss beams at mid-span, to record strain due to the main bending of the deck structure,
- Two "Speed Sensors" are similarly set on the next span. The speed of the vehicle is estimated and then used to compute the GVW.
- Two "Axle Load Sensors" are measuring local strain while axles are crossing the bridge. On the Haut-Village bridge, they are set under the concrete slab, but unfortunately it appeared that the local bending was not significant enough in this case to give an acceptable result for the axle loads. Whereas, on the Mauves bridge, these sensors are set longitudinally under the UHPFRC slab and give very good results.

Figure 2 displays the sensor setup for the example of the Mauves bridge, on two consecutive spans ("T6" and "T7"). The setup for the Haut-Village bridge is similar.

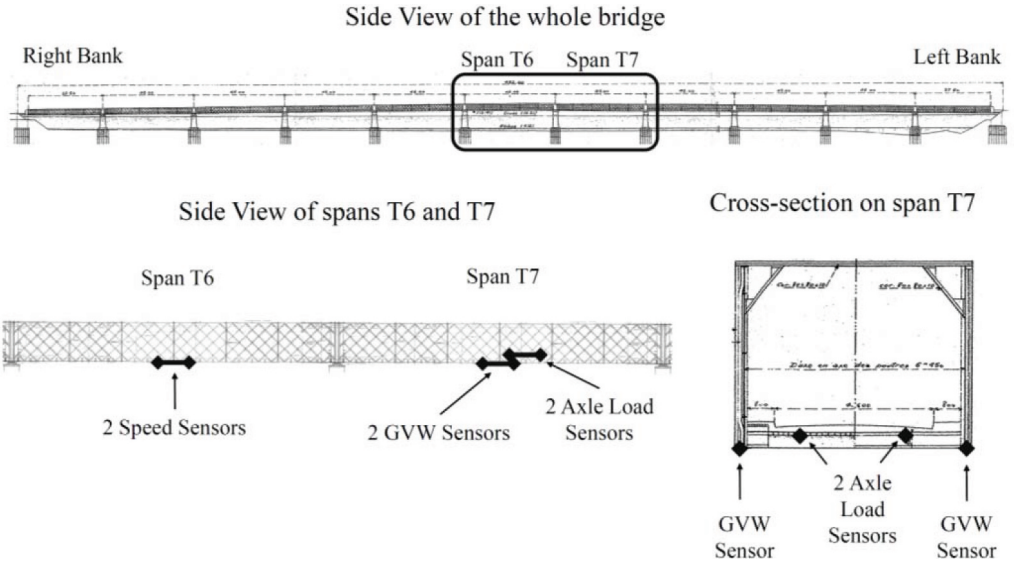


Figure 2. Sensor setup on the Mauves Bridge: only sensors used for the WIM.

3.3 *Load test for the adjustment and performance assessment*

In a B-WIM system, the bridge deck itself is a part of the measurement device. Its mechanical response to the traffic loads is used to deduce the GVW and axle loads. Thus, this response is learned by performing a load test for the adjustment of the B-WIM.

This load test consists in several passages of different vehicles at various speeds on the bridge. It can also be used to assess the performance of the system, provided that the passages used for the adjustment are separated from the ones used for this assessment. It is recommended to perform one test for the adjustment and a second test for the assessment (Cartiaux et al., 2023a). However, in the case of the two iron-truss bridges, the load tests took place on one single day for each bridge: April 20, 2022, for the Haut-Village and April 21, 2022, for Mauves. So, the same test was used for both adjustment and assessment, with two separated sets of passages in each test.

Table 1 reports the test conditions for adjustment and assessment of the WIM+D performance on both bridges.

Table 1. Summary of the load tests.

Bridge and vehicles	GVW (tons)	Passages (tons)	Passages for adjustment	Passages for adjustment
Haut-Village				
2-Axles lorry	9.3	24	4	19
Tractor	3.4	24	Not used: for information only (light weight)	
Mauves				
Heavy 2-Axles lorry	12.1	20	2	7
Light 2-Axles lorry	9.2	22	4	18
Tractor	6.9	9	Not used: for information only (light weight)	

Due to load limitations on the bridges, only vehicles up to 12 tons were used for the load test. However, the B-WIM relies on the flexibility of the bridge deck, thus it needs some

significant strain under the effect of the traffic. This is not the case with light vehicles. Indeed, the 2-axles lorries used for the load test induce strain levels with an order of magnitude of 0.015‰ in the iron truss elements, which is very low, but sufficient for being used as input data for the B-WIM. The tractor with a GVW less than 7 tons did not induce sufficient strain on the monitored elements to give a satisfactory performance. Thus, it was decided to assess the performance for vehicles over 9 tons only and to set this value as the lower limit of operation of the B-WIM for the case of these bridges.

Figure 3 displays the raw strain measurements obtained on the six sensors of the Mauves bridge for one passage of the 12-tons lorry: This strain is due to the bending of the two spans, one after the other, along with a light hyperstatic effect due to the continuity of the bridge deck (negative strain on span T6 when the vehicle is driven on span T7). Also, the strain measured by the axle load sensors (in blue) under the UHPFRC slab show very clear peaks which are correlated to the axle loads.

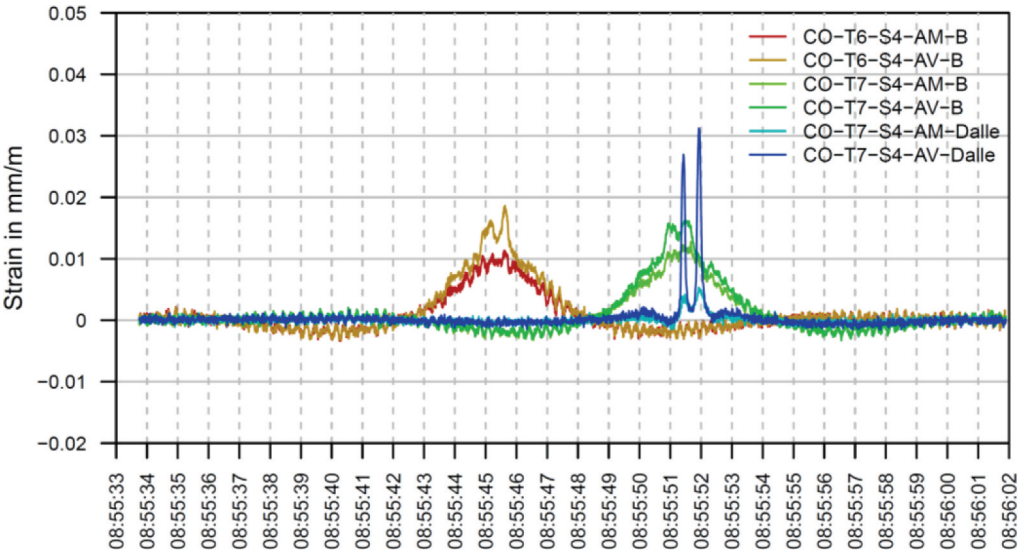


Figure 3. Strain data measured by the six sensors of the Mauves bridge under the 12-tons lorry.

4 PERFORMANCE ASSESSMENT

4.1 *Accuracy for the gross vehicle weight*

The Haut-Village and Mauves bridges are challenging for the application of B-WIM, compared to usual cases with shorter, less numerous, or even isostatic spans. Indeed, the B-WIM methodology relies on the strain of the bridge deck, which means that the whole influence line of the measured strain should theoretically be considered. In the case of such long continuous decks, highly hyperstatic, the length of this influence line is virtually of a few hundreds of meters, which induces issues for the distinction of consecutive vehicles. Moreover, the iron truss structure, aged of more than 140 years, increases uncertainties compared to more classical deck designs.

The issue of hyperstaticity is addressed by selecting a truncated part of the signal: only the short period when the vehicle is driven on the span where each sensor is set is used for the B-WIM, while hyperstatic effects measured before and after are neglected. This choice induces some risk for the accuracy of the GVW estimation, however, it has the advantages of a light pre-processing of the data and a good efficiency for the distinction of consecutive vehicles.

The accuracy of the B-WIM system is assessed according to the COST 323 action. Depending on the test conditions, i.e., reproducibility and repeatability, and of the sample sizes,

a minimum level of confidence π_0 is required to meet an accuracy class defined by a tolerance δ (in %). The probability (or frequency) of the error laying in the interval $[-\delta,\delta]$, must be above π_0. Accuracy classes are defined by the tolerance on GVW, from A(5) to D(25), the number in brackets being this tolerance. The tolerances for the other quantities (axle loads, group of axles loads...) are larger than for GVW (Jacob et al., 2002).

Table 2 releases the results of the performance assessment on both bridges, for the GVW, with the details of the analysis. π_0 is the minimum required level of confidence, which corresponds to the lowest acceptable tolerance δ_{min}, i.e. the interval $[-\delta_{min},\delta_{min}]$, for the test conditions and sample size. δ is the tolerance of the accepted class listed in the COST 323, with a higher confidence level π.

Table 2. Performance assessment of the B-WIM for the Gross Vehicle Weight (GVW).

Bridge and test set	π_0 (%)	δ (%)	δ_{min} (%)	π (%)	COST 323 Class	Max Error (%)	Min Error (%)
Haut-Village							
All passages (24), for info.	94.7	15	14.2	96.2	C(15)	6.8	-17.6
Assessment only (35)	94.0	15	12.2	98.5	C(15)	6.8	-9.0
Mauves							
All passages (42), for info.	93.5	10	8.0	98.1	B(10)	7.1	-12.6
Assessment only (35)	93.0	10	7.4	98.8	B(10)	7.1	-5.2

For each of the two bridges, one passage is neither used for adjustment nor for assessment, because it has been considered as an outlier regarding the statistical distribution of all other passages. For both bridges, it corresponds to the minimum (algebraic) error. However, we decided to include these two outliers in the "all passages" sets for both bridges, the result of which is given for information only.

The Haut-Village B-WIM is accepted in Class C(15) and the Mauves one in Class B(10) for the GVW. We notice that there is no difference on the result if we consider all passages (including outliers), or only the ones dedicated to the assessment. In the case of the Mauves Bridge, the value 7.4% for δ_{min} means that the system is very near to Class B+(7), which is a very good result for a B-WIM on this type of bridge deck.

4.2 *Accuracy for the axle load on the Mauves bridge*

The accuracy for the axle loads is relevant on the Mauves bridge only, where the UHPFRC slab enables a good detection of the axles. The results are classified according to the COST 323 methodology, with details as released in Table 3.

Table 3. Performance assessment of the B-WIM for the axle load, on the Mauves Bridge.

Test set	π_0 (%)	δ (%)	δ_{min} (%)	π (%)	COST 323 Class	Max Error	Min Error
All axles (84)	94.7	10.9	10.8	95.0	B+(7)	10.4	-13.4
9 tons 2-axles lorry (44)	96.0	15	11.0	99.5	B(10)	10.4	-11.1
12 tons 2-axles lorry (40)	95.9	15	13.1	98.2	B(10)	10.1	-13.4
Front axles (42)	93.5	8	5.4	99.5	A(5)	0.5	-2.9
Rear axles (42)	93.5	15	11.6	98.6	B(10)	10.4	-13.4

The results for the axle loads are very good, with a B-WIM system accepted in class B+(7). The better class assessed for the axle loads compared to the GVW is explained by the statistical methodology of the COST 323: the sample of axles is wider than the one of vehicles, and the accuracy classes for axle loads have a wider tolerance δ. We notice excellent results for the front axles with class A(5) and less than 3% relative error in absolute value.

By contrast, the strain measurements on the aged thick reinforced concrete slab of the Haut-Village bridge are not relevant for the axle load estimation. This illustrates the strong incidence of the secondary structures of the bridge deck used for axle load estimation by the WIM+D system: the local bending must be significant, which is not fulfilled on every type of bridge. The UHPFRC thin slab of the Mauves bridge appears as a perfect type of structure for this purpose.

5 DISCUSSION AND CONCLUSION

5.1 *Difference between the two bridges*

This case study is a unique opportunity to study the performance of B-WIM systems on two similar bridges unusual for this application, due to high hyperstaticity and historical age, yet with an interesting comparative study due to slight differences between the two bridges.

Indeed, the span length and the general design of the iron truss decks are the same, but the Mauves bridge did benefit from recent refurbishment works in 2020. These works include a complete rebuilding of the secondary transverse elements of the deck, with a new UHPFRC slab to carry the road, and the addition of a lateral way for cycles and pedestrians. The Haut-Village bridge still stands with secondary transverse elements dating back to its rebuilding after World War II, or even earlier for one of the five spans.

Despite of its larger number of spans which increases the uncertainty related to hyperstaticity (eleven spans versus five), the Mauves bridge gives better results for the application of B-WIM: It is accepted in class B(10) for the GVW and B+(7) for the axle loads, whereas the Haut-Village bridge is accepted in class C(15) for the GVW and is not conclusive (and not classified) for axle loads.

This result shows that the main structures of the bridge deck are not the only factor of efficiency for the B-WIM, and secondary structures have also some incidence, even indirectly, for the estimation of the GVW. Indeed, it is assumed that the new transverse beams and UHPFRC slab of the Mauves bridge have a mechanical behavior more repeatable and linear than the aged concrete slab and brick arches of the Haut-Village bridge. This reduces the uncertainty on the B-WIM result for the GVW, even if the latter is deduced from global bending of the main spans only: the participation of secondary structures to this bending cannot be neglected. We assume also that a significant part of the global bending rigidity of the Haut-Village bridge is due to these uncertain secondary elements, which is less the case for the Mauves bridge.

5.2 *Conclusion and perspectives*

The case study of both Haut-Village and Mauves bridges gives very encouraging results for the application of B-WIM to historical highly hyperstatic iron truss bridge decks. With a performance assessment in class B(10) for the Mauves bridge and C(15) for the Haut-Village bridge according to COST 323, the accuracy of the WIM+D system for the gross vehicle weight is convenient for the purposes of statistical analysis of the traffic loads and for the detection of large overweight.

The performance regarding the axle loads is strongly dependent of the secondary structures of the bridge decks, which are very different from one bridge to the other. The aged concrete slab and brick arches of the Haut-Village bridge appear unsuitable for the purpose of axle detection, whereas the new UHPFRC slab of the Mauves bridge is an ideal structure for axle load estimation. Thus, the WIM+D system has been accepted in class B+(7) for axle loads on the Mauves bridge. This is one of the best performances yet achieved for a B-WIM regarding the axle loads, and it is worth to note that this is achieved on a type of bridge deck which is unusual for B-WIM applications, compared to more common concrete or composite beam girders. This performance is also achieved despite of a high hyperstaticity of both bridges, with several continuous long spans of 45 m.

Such historical bridges, initially designed for light local traffic of horse-drawn carts and relying on aged iron truss deck structures, deserve a specific attention regarding the real traffic

loads and are often subject to load limitations. This case study shows that B-WIM with the WIM+D system is a suitable solution to assess the real level of traffic on the bridge and to detect overweight vehicles, with an accuracy comparable to the one obtained on more common bridge decks. The low quantity of strain sensors involved (six only for one bridge) and the light and portable setup makes it an economical solution compared to classical WIM systems inside the pavement. B-WIM could thus become a standard way to assess traffic conditions on historical iron-truss bridges.

ACKNOWLEDGMENTS

The authors wish to thank the Loire Atlantique Department for supporting this research by making the Haut-Village and Mauves bridges available for this study. They are grateful also to the partners of the GeRICO project: SCE, Strains, and the City of Angers. This research received a financial support from the French government in the frame of the "Programme National Ponts", steered by the Cerema.

REFERENCES

Brouste, A. 2021. Testing the accuracy of WIM systems: application to a B-WIM case. *Measurement, 185*.

Cartiaux, F.-B., Koutsonika, S., Andrikopoulos, G., Pelletier, P. 2019. Bridge Monitoring & Assessment via OSMOS Optical Strands. *Proceedings of the Fourth Joint International Symposium on Deformation Monitoring JISDM 2019*.

Cartiaux, F.-B., Le Corvec, V., Semiao, J., Jacob, B., Schmidt, F., Brouste, A., Ehrlacher, A. 2021. Real Condition Experiment on a new Bridge Weigh-in-Motion Solution for the Traffic Assessment on Road Bridges. *Proceedings of the IABSE Congress Ghent 2021 – Structural Engineering for Future Societal Needs*: 1242–1248. IABSE.

Cartiaux, F.-B., Fort, V., Pelletier, P.M., Jacob, B., Brouste, A. 2023a. Combined Bridge Weigh-In-Motion and Structural Health Monitoring on Road Bridges: Case Study on the Salso Viaduct (Italy). *In: Rizzo P., Milazzo A. (eds) European Workshop on Structural Health Monitoring. EWSHM 2022. Lecture Notes in Civil Engineering*, vol 254. Springer, Cham.

Cartiaux, F.-B., Le Corvec, V., Semiao, J., Brouste, A. 2023b. Bridge weigh-in-motion: Feedback on various types of bridges. *Life-Cycle of Structures and Infrastructure Systems*: 1911-1918. IALCCE.

Cartiaux, F.-B., Majoli, E., Menuet, C. 2023c. SHM et recalage de modèle numérique. *7e Journée SHM-France*, Bouguenais, March 14, 2023. https://www.shm-france.fr/wp-content/uploads/20230314-SHM-France-salle6-4-Osmos-SCE-Strains.pdf

Dolcemascolo V., Hornych P., Jacob B., Schmidt F., Klein E. 2015. Heavy Vehicle Traffic and Overload Monitoring in France and Applications. *Proceedings of the XXVth World Road Congress, Road and Mobility creating new Value from Transport*, Seoul, Nov. 2-6, 2015.

Jacob, B., O'Brien, E., Jehaes, S. 2002. COST 323, European Specification on Weigh-in-Motion of Road Vehicles. EUCOCOST/323/8/99.

Jacob B., Feypell de la Beaumelle V. 2010. Improving truck safety: Potential of weigh-in-motion technology. *IATSS Research*, 34, 2010: 9–15.

Schmidt F., Glaeser K.-P., Hornych P., Piau J.-M., Jacob B. 2013. Impacts from Truck Traffic on Road Infrastructure. *PIARC, Routes/Roads 358*, 2013: 74–83.

Bridge Maintenance, Safety, Management, Digitalization and Sustainability – Jensen, Frangopol & Schmidt (eds)
© 2024 The Author(s), ISBN 978-1-032-77040-6
Open Access: www.taylorfrancis.com, CC BY-NC-ND 4.0 license

Assessment of the accuracy of Bridge Weigh-In-Motion (B-WIM) system in Indonesia

W. Nugraha, S. Ramadhani & G. Sukmara
Directorate General of Highway, Ministry of Public Works and Housing, Republic of Indonesia

ABSTRACT: Bridge Weigh-in-Motion (B-WIM) systems have become increasingly popular in Indonesia due to their ability to measure the weight and axle load of vehicles without the need for them to stop at a weighbridge. As a permanent and reliable system, B-WIM has been installed in several locations throughout Indonesia for over three years. The purpose of this research is to assess the accuracy of the B-WIM system in various locations and identify the factors that influence its precision. The study utilizes the calibration procedure outlined in the COST 323 standard for accuracy assessment. Ten bridges were calibrated, with five of them undergoing recalibration after years of operation. The results show that B-WIM systems generally provide high accuracy in measuring gross vehicle weight (GVW). However, the accuracy of axle-specific weight measurements was found to be relatively lower. The relationship between bridge types and accuracy classes was explored, revealing that short-span girders, both steel and precast concrete girders, exhibited high accuracy levels when the pavement condition was well-maintained. Recalibration was found to improve accuracy, except for one site with a longer timespan between calibrations, possibly due to pavement deterioration. The findings highlight the importance of maintaining pavement conditions to minimize dynamic effects on B-WIM measurements. Managerially, this research provides valuable insights for transportation authorities in Indonesia to identify areas for improvement in the B-WIM system and ensure reliable and precise measurements for various purposes, including overloading law enforcement and bridge condition evaluation.

1 INTRODUCTION

Overloading vehicles pose significant challenges to the infrastructure of developing countries like Indonesia, causing extensive damage to bridges and roads. Such damages can result in catastrophic failures, road closures, and expensive repairs, necessitating urgent measures to address this issue (Jacob & Cottineau, 2016). One solution lies in enforcing laws against overloading vehicles, which requires the weighing of heavy vehicles. However, weighing vehicles on a weighbridge, which is the traditional method for determining vehicle weight and axle load, presents challenges. It requires vehicles to come to a complete stop, leading to traffic congestion and sometimes allowing heavily loaded vehicles to pass without being weighed at all (Karim et al., 2014). This approach is inefficient, particularly on roads with high traffic volume. In recent years, the emergence of Bridge Weigh-in-Motion (B-WIM) systems has provided an alternative solution. These systems enable vehicle weighing to be conducted as vehicles pass over a bridge, eliminating the need for them to stop (Nugraha et al., 2022). This method is more efficient and less disruptive to traffic flow, addressing the shortcomings of the traditional weighbridge approach (Gajda et al., 2018).

B-WIM is a Weigh-in-Motion (WIM) system that utilizes a bridge as the weighing medium, measuring the response of the bridge due to vehicle loading as vehicles pass over it (Nugraha & Sukmara, 2016). Various types of bridges, such as girder bridges and culvert bridges, can be

DOI: 10.1201/9781003483755-162

used for B-WIM (van Loo & Žnidarič, 2019). The bridge response is captured using a set of strain transducers connected to a data acquisition and processing system (Lydon et al., 2016). This system collects and processes the response data to provide essential information, including gross vehicle weight (GVW), axle load, axle distance, vehicle speed, and vehicle classification (Brouste, 2021). The Moses algorithm is employed to transform the transducer response into accurate weighing results (Moses, 1979). With the sensors installed beneath the bridge, the B-WIM system ensures long-term reliability without direct contact between the sensors and vehicle tires (Kalhori et al., 2018). B-WIM has been successfully implemented in multiple locations across Indonesia for over three years, providing valuable vehicle data for road authorities and supporting overloading law enforcement efforts.

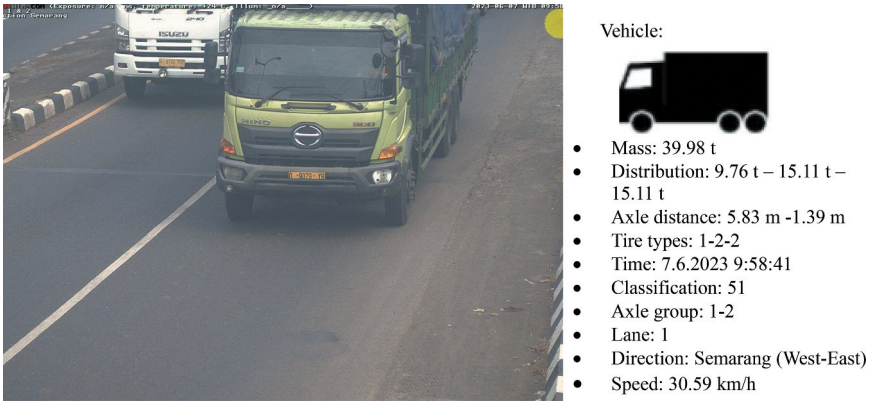


Figure 1. Example of B-WIM vehicle weighing measurement result.

Provides an example of B-WIM vehicle weighing measurement results, illustrating a 3-axle truck with a gross vehicle weight (GVW) of 39.98 tons. It is evident that this vehicle is significantly overloaded, with each axle load exceeding the legal maximum of 10 tons. Specifically, the first axle load measures 9.76 tons, while the second and third axles carry loads of 15.11 tons each. This means that the vehicle is overweight by more than 50%. Such overloading poses a significant risk as it accelerates the deterioration of roads and bridges beyond their designed lifespan. By employing B-WIM to instantaneously measure vehicle weights, road authorities can effectively enforce regulations by identifying license plates and measurement results. This proactive approach helps to address the problem of overloading, consequently mitigating the issues associated with road and bridge deterioration.

This research aims to evaluate the reliability and accuracy of B-WIM systems in Indonesia. It focuses on assessing their performance in measuring vehicle weights and axle loads, understanding factors affecting accuracy, and comparing B-WIM measurements with the COST323 standard (Laboratoire Central des Ponts et Chaussées, 2002). These evaluations are crucial for real traffic measurement, overloading control, and infrastructure assessment. The research employs the COST 323 calibration procedure to determine accuracy classes and provide valuable insights to transportation authorities. The goal is to identify areas for improvement, ensuring precise measurements for overloading control and infrastructure management, enhancing overall transportation efficiency in Indonesia.

2 METHODOLOGY

In this research, the evaluation of B-WIM measurement accuracy will be conducted using the calibration procedure outlined in the COST 323 standard (Laboratoire Central des Ponts et Chaussées, 2002). As part of the installation process, it is essential to perform an initial calibration of the WIM system. This procedure involves using a pre-weighed vehicle or truck,

which has been weighed using static weighbridge station, as shown in Figure 2. The static weighing measurements include data such as gross vehicle weight (GVW), single axle load, axle group load, and axle distance. The pre-weighed truck is then driven over each line of the WIM system, repeating the process a minimum of 10 times. To determine the accuracy class of the WIM system, Jacob (2000) proposed a method that calculates the confidence interval width (δ). This calculation incorporates the mean, standard deviation, and the number of vehicle passes per lane for the calibration vehicle weighing data. Finally, the obtained confidence interval width (δ) is compared to the accuracy class tolerances specified in the COST 323 standard, as illustrated in Table 1.



Figure 2. Pre-weighed truck for calibration.

Table 1. Tolerances of the accuracy classes (δ in %)(Laboratoire Central des Ponts et Chaussées, 2002).

Criteria (type of measurement)	Domain of use	Accuracy Classes:Confidence interval width δ (%)						
		A (5)	B+ (7)	B(10)	C (15)	D+ (20)	D (25)	E
1. Gross weight Axle load:	Gross weight > 3,5 t Axle load > 1 t	5	7	10	15	20	25	>25
2. group of axles		7	10	13	18	23	28	>28
3. single axle		8	11	15	20	25	30	>30
4. axle of a group		10	14	20	25	30	35	>35
Speed	V>30 km/h	2	3	4	6	8	10	>10
Inter-axle distance		2	3	4	6	8	10	>10

This research aims to classify and evaluate the accuracy class of each B-WIM site by employing the proposed method. In order to ensure precise measurements, several sites have undergone annual recalibration. This study also explores the relationship between accuracy class and time, shedding light on the long-term performance of B-WIM systems. Furthermore, the influence of paving conditions on the accuracy of B-WIM measurements is closely monitored and discussed. It is evident that the accuracy of B-WIM is highly dependent on the condition of the pavement on the bridge and its approach. Additionally, various types of bridges, including Steel Composite Girder, PCI Girder, Culvert, and Voided Slab bridges, have been

utilized for B-WIM systems in Indonesia as listed in Table 2. This research also investigates the relationship between bridge types and accuracy class, providing valuable insights into the performance and suitability of different bridge structures for B-WIM applications.

Table 2. B-WIM sites in Indonesia.

Site ID number	Bridge name	Bridge type	Location
ID001	Pawiro Baru A	Steel composite girder	Central Java National Road
	Pawiro Baru B	Prestressed concrete I-girder	Central Java National Road
ID002	Air Ibul Besar	Prestressed concrete I-girder	South Sumatera National Road
ID004	Kaligawe Railway Overpass	Prestressed concrete I-girder	Semarang City Toll Road
ID005	Ciliweut Nameng 3	Voided slab	Banten National Road
ID006	Surabaya KM 757+4	Prestressed concrete I-girder	Surabaya Sidoarjo Toll Road
ID007	Katulampah Bogor	Prestressed concrete I-girder	Jakarta Bogor Ciawi Toll Road
ID008	JNK KM 654+800	Prestressed concrete I-girder	Surabaya Madiun Toll Road
ID009	Padalarang Tollroad	Prestressed concrete I-girder	Padalarang Toll Road
ID010	JLJ KM 54+20 B	Prestressed concrete I-girder	Jakarta Outer Ring Toll Road

3 RESULTS AND DISCUSSION

In this research, a total of 10 bridges were calibrated, with 5 of them undergoing a second calibration after years of operation. As an example, the calibration run of ID010 for lane 1 in 2022 is presented in Table 3. Site ID010 is situated on Jalan Tol Lingkar Luar Jakarta KM 54 +20 B and features a precast concrete I-girder bridge with two lanes. For both Lane 1 and Lane 2, the calibration run was conducted with the vehicle passing 11 times. The calibration truck utilized was a 3-axle statically weighed truck, with a gross vehicle weight (GVW) of 21.62 tons as displayed on Figure 3. The axle weights for the first, second, and third axles were 6.54 tons, 7.64 tons, and 7.44 tons, respectively. Mean and standard deviation values were calculated for the differences between B-WIM measurements and static weighbridge measurements of the calibration truck, considering parameters such as GVW, single axle, and group axle. These mean and standard deviation results were utilized in calculating the width of the confidence interval (δ).



Figure 3. Static GVW measurement result of calibration truck.

Table 3. Calibration runs of site ID010 for lane 1 (2022).

	GVW Static Scale	GVW BWIM	Difference		W1	W2	W3	Diff W1	Diff W2	Diff W3	Diff Group
No	ton	ton	ton	%	ton	ton	ton	%	%	%	%
1	21.62	20.91	0.71	3.28%	6.42	7.25	7.25	-1.83%	-5.10%	-2.55%	-3.85%
2	21.62	21.77	-0.15	-0.69%	6.32	7.73	7.73	-3.36%	1.18%	3.90%	2.52%
3	21.62	21.61	0.01	0.05%	6.3	7.65	7.65	-3.67%	0.13%	2.82%	1.46%
4	21.62	21.27	0.35	1.62%	6.58	7.35	7.35	0.61%	-3.80%	-1.21%	-2.52%
5	21.62	21.74	-0.12	-0.56%	6.58	7.58	7.58	0.61%	-0.79%	1.88%	0.53%
6	21.62	21.69	-0.07	-0.32%	6.63	7.53	7.53	1.38%	-1.44%	1.21%	-0.13%
7	21.62	21.58	0.04	0.19%	6.57	7.5	7.5	0.46%	-1.83%	0.81%	-0.53%
8	21.62	21.52	0.1	0.46%	6.48	7.52	7.52	-0.92%	-1.57%	1.08%	-0.27%
9	21.62	21.37	0.25	1.16%	6.44	7.47	7.47	-1.53%	-2.23%	0.40%	-0.93%
10	21.62	21.58	0.04	0.19%	6.62	7.48	7.48	1.22%	-2.09%	0.54%	-0.80%
11	21.62	21.7	-0.08	-0.37%	6.56	7.57	7.57	0.31%	-0.92%	1.75%	0.40%

The determination of the delta class was performed using the method proposed by Jacob (2000), as specified in the COST323 standard, as displayed in Table 4. For Lane 1, the mean average difference in gross vehicle weight (GVW) was found to be 0.45% with a standard deviation of 1.12%. The mean average difference in axle 1 weight was -0.61% with a standard deviation of 1.70%. Similarly, the mean average difference in the group of axles, which refers to the combined weight of axle 2 and axle 3 of the truck, was 0.97% with a standard deviation of 1.68%. These calculations were then repeated for Lane 2 using the same method. It is noteworthy that all parameters, including GVW, group of axles, and single axle, obtained the highest accuracy class of A(5) for both Lane 1 and Lane 2. These results indicate that the B-WIM system on Site ID010 performed exceptionally well with the highest level of accuracy.

Table 4. Accuracy class determination for ID010 2022 calibration.

	Lane 1			Lane 2		
Parameters	GVW	Group	Single	GVW	Group	Single
Number of run	11	11	11	11	11	11
Mean	0.45	0.37	0.61	0.29	0.22	1.14
St Dev	1.12	1.66	1.70	1.03	1.39	2.03
Delta Critical, δ_{crit}	3.50	3.50	3.20	3.10	2.90	4.00
Delta Class, δ	5	5	5	5	5	5
Class	A(5)	A(5)	A(5)	A(5)	A(5)	A(5)

The accuracy class results obtained from the calibration of ten bridges are presented in Table 5. Among these bridges, five sites underwent calibration twice after years of operation. The repeated calibration allowed for an assessment of the accuracy class over time, providing insights into the system's performance and potential changes in accuracy. By conducting multiple calibrations, this research was able to explore the consistency and reliability of the B-WIM system's accuracy class across different sites and evaluate any variations that may arise. The findings from these repeated calibrations contribute to a comprehensive understanding of the long-term accuracy and performance of the B-WIM system in various bridge locations.

The analysis of Table 5 reveals that the B-WIM system generally achieves a high accuracy class for gross vehicle weight (GVW) measurements. Across the ten bridges, GVW measurements consistently obtained accuracy classes ranging from the lowest C(15) on two bridges to predominantly A(5) on seven bridges. This demonstrates the B-WIM system's capability to accurately measure the total weight of vehicles passing over the bridges. However, a closer examination of the accuracy classes for individual axle loads reveals a lower level of precision compared to the GVW measurements. Only three bridges achieved an accuracy class of A(5) for single axle measurements, while the majority exhibited accuracy classes ranging from B+(7), B(10), C(15), D(25),

Table 5. Accuracy class of All ID site calibration.

Site ID number	Bridge name	Calibration Time	Lane 1			Lane 2		
			GVW	Group	Single	GVW	Group	Single
ID001	Pawiro Baru A	2017	A(5)	A(5)	C(15)	A(5)	A(5)	A(5)
	Pawiro Baru B	2017	A(5)	A(5)	C(15)	A(5)	A(5)	A(5)
ID002	Air Ibul Besar	2017	C(15)	B(10)	E(30)	A(5)	A(5)	D +(20)
ID004	Kaligawe Railway Overpass	2018	A(5)	A(5)	B(10)	A(5)	A(5)	B(10)
		2022	B(10)	B+(7)	B(10)	B+(7)	B+(7)	C(15)
ID005	Ciliweut Nameng 3	2018	B(10)	C(15)	E(30)	B(10)	B(10)	E(35)
ID006	Surabaya KM 757+4	2019	B+(7)	B(10)	D(25)	A(5)	B+(7)	D(25)
ID007	Katulampah Bogor	2021	C(15)	E(30)	E(30)	B(10)	B(10)	E(35)
		2023	A(5)	A(5)	B(10)	B+(7)	B+(7)	C(15)
ID008	JNK KM 654+800	2022	B+(7)	A(5)	D+(20)	A(5)	A(5)	C(15)
		2023	A(5)	A(5)	C(15)	A(5)	A(5)	B(10)
ID009	Padalarang Tollroad	2022	A(5)	A(5)	B(10)	B+(7)	A(5)	A(5)
		2023	A(5)	A(5)	B(10)	A(5)	A(5)	B(10)
ID010	JLJ KM 54+20 B	2022	A(5)	A(5)	A(5)	A(5)	A(5)	A(5)
		2023	A(5)	A(5)	A(5)	A(5)	A(5)	A(5)

and even E(30) and E(35). These findings suggest that the B-WIM system may encounter challenges in accurately capturing axle-specific weight information. One possible explanation for this disparity could be the placement of the axle detection sensors below the bridge slab. Depending on the thickness of the slab and pavement, the sensors may not directly sense the axle response due to minimal generated signal. Consequently, this introduces greater uncertainty in the measurement of single axle loads compared to the GVW, leading to lower accuracy class ratings.

The impact of recalibration on B-WIM measurement accuracy was analyzed by plotting the critical confidence interval width, (δcrit), on the y-axis against the year of calibration on the

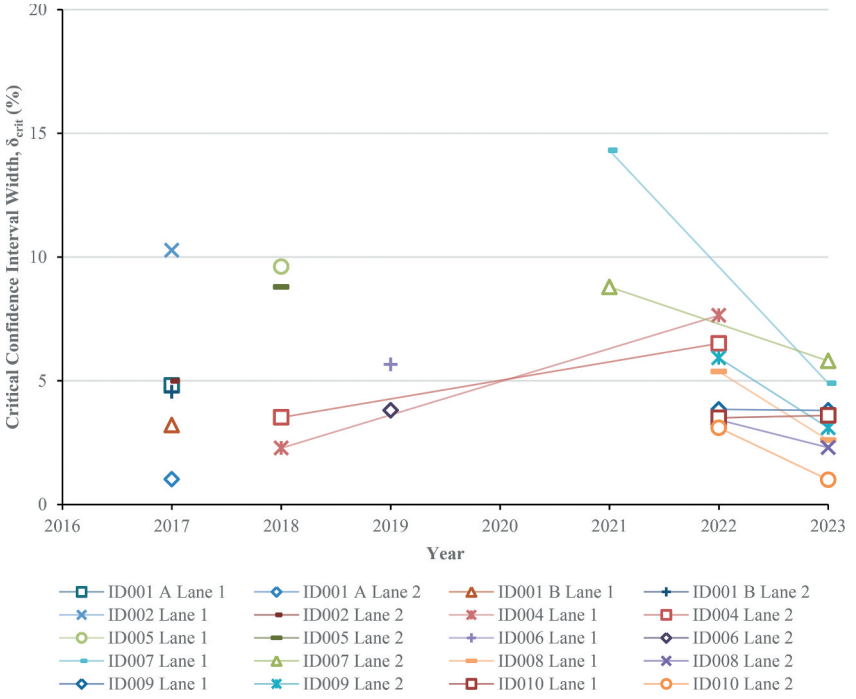


Figure 4. Critical confidence interval width (δcrit) of GVW measurements.

x-axis. In Figure 4, the critical confidence interval width for GVW measurements was specifically chosen to provide a clear analysis. The results indicated that the majority of recalibrations (four out of five sites) resulted in improved accuracy, as reflected by lower δcrit values compared to the initial calibration. This demonstrates that recalibration can enhance the accuracy of B-WIM measurements by determining new calibration factors and improving the measurement results. However, it is worth noting that Site ID004 exhibited lower accuracy after recalibration. This discrepancy may be attributed to the four-year interval between calibrations, which suggests possible pavement surface and approach deterioration on the bridge. To maintain measurement accuracy, recalibration at intervals of 1-2 years is recommended, as evidenced by the four sites that underwent recalibration within this timeframe after the initial calibration. Given that several sites installed between 2017 and 2019 have only been calibrated once, it is essential to prioritize their recalibration in the near future to ensure the sustained accuracy level.

Based on the findings presented in Table 5 and Figure 4, an investigation into the relationship between bridge types and accuracy class can be conducted. The majority of measurements classified as A(5) were obtained from PCI girder bridges. However, it should be noted that some of these bridges exhibited lower accuracy class due to poor pavement conditions on the bridge surface and approach. For instance, Site ID002, the Air Ibul Besar bridge located on Jalan Lintas Timur National Road in Palembang City, South Sumatera, demonstrated relatively low accuracy class on Lane 1. The GVW measurement had a class of C(15), the group of axles had a class of B(10), and the single axles had a class of E(30). Although the pavement on top of the bridge was in good condition, as it had recently been resurfaced during calibration, the steep incline of the approach, as shown in Figure 5, caused vehicles to de-accelerate before passing the bridge. This resulted in significant impacts and dynamic effects during the measurement process, ultimately lowering the accuracy class for this particular bridge.



Figure 5. Site ID002 pavement condition.

Among the evaluated bridge sites, only Site ID005 stood out as a non-girder bridge, specifically a voided slab bridge, which is not an ideal bridge type for B-WIM due to limited measurement route alternatives. As expected, this bridge demonstrated relatively low accuracy class. The weak lateral connection between the voided slab components had a significant impact on accuracy, even for GVW measurements, which generally exhibited high accuracy in

bridge WIM systems. Furthermore, single axle measurements showed the lowest accuracy compared to other bridge types. This was attributed to the installation of axle detection sensors on the bottom of the voided slab, as the bottom part of the top flange was inaccessible. Consequently, the measurement of axle responses from passing vehicles was weakened due to interference caused by the void between the two flanges of the voided slab. The results emphasize the importance of a well-maintained pavement surface and approach on bridge WIM systems to minimize the dynamic effects of vehicles passing over the bridge and ensure minimal differences between B-WIM measurements and static measurements. In line with the recommendations of COST323, short-span girders, both steel and PCI, offer high accuracy levels. However, it is crucial to maintain the pavement in good condition to ensure optimal measurement accuracy.

4 CONCLUSIONS

In conclusion, this research focused on the evaluation of B-WIM measurement accuracy in the context of bridge installations. By employing the calibration procedure outlined in the COST 323 standard, the accuracy classes of the B-WIM systems at various bridge sites were assessed. The findings revealed that while the gross vehicle weight (GVW) measurements generally exhibited high accuracy classes, the accuracy of axle-specific measurements was comparatively lower. The results highlighted the influence of bridge types, such as PCI girder bridges and voided slab bridges, on measurement accuracy, with the latter presenting challenges due to weak lateral connections and sensor placement. It was also observed that recalibration, when performed on a regular basis, led to improved accuracy. However, sites that underwent infrequent recalibration or experienced deteriorating pavement conditions exhibited lower accuracy levels. The implications of this research are significant for transportation authorities and bridge managers. The accurate measurement of vehicle weights plays a crucial role in enforcing overloading regulations and assessing the impact of heavy vehicles on bridge and road deterioration. By utilizing B-WIM systems, authorities can identify overloaded vehicles and implement targeted law enforcement measures to protect infrastructure and ensure road safety. Furthermore, the findings emphasize the importance of maintaining optimal pavement conditions and considering bridge types in B-WIM installations to enhance accuracy.

ACKNOWLEDGEMENTS

The authors would like to express their gratitude to the Ministry of Public Works and Housing, Republic of Indonesia for their invaluable support and provision of necessary facilities, which have been instrumental in the successful completion of this research. Additionally, we would like to extend our sincere thanks to PT Jasa Marga Tollroad for generously sharing the data required for this study, enabling us to conduct a comprehensive analysis. Special thanks are also due to Cestel d.o.o and its Indonesian counterpart, PT Bia Tekno Solusi, for providing the B-WIM system in Indonesia, as well as for their unwavering support and assistance throughout the research process. The contributions of these organizations have played a vital role in the realization of this study, and we are deeply grateful for their invaluable collaboration.

REFERENCES

Brouste, A. (2021). Testing the accuracy of WIM systems: Application to a B-WIM case. *Measurement: Journal of the International Measurement Confederation*, *185*, 1–16. https://doi.org/10.1016/j.measurement.2021.110068

Gajda, J., Burnos, P., & Sroka, R. (2018). Accuracy Assessment of Weigh-in-Motion Systems for Vehicle's Direct Enforcement. *IEEE Intelligent Transportation Systems Magazine*, *10*(1), 88–94. https://doi.org/10.1109/MITS.2017.2776111

Jacob, B. (2000). Assessment of the accuracy and classification of weigh-in-motion systems: Part 1. Statistical background. *Heavy Vehicle Systems*, *7*(2–3), 136–152. https://doi.org/10.1504/ijhvs.2000.004860

Jacob, B., & Cottineau, L. M. (2016). Weigh-in-motion for Direct Enforcement of Overloaded Commercial Vehicles. *Transportation Research Procedia*, *14*(0), 1413–1422. https://doi.org/10.1016/j.trpro.2016.05.214

Kalhori, H., Makki Alamdari, M., Zhu, X., & Samali, B. (2018). Nothing-on-Road Axle Detection Strategies in Bridge-Weigh-in-Motion for a Cable-Stayed Bridge: Case Study. *Journal of Bridge Engineering*, *23*(8). https://doi.org/10.1061/(ASCE)BE.1943-5592.0001259

Karim, M. R., Ibrahim, N. I., Saifizul, A. A., & Yamanaka, H. (2014). Effectiveness of vehicle weight enforcement in a developing country using weigh-in-motion sorting system considering vehicle by-pass and enforcement capability. *IATSS Research*, *37*(2), 124–129. https://doi.org/10.1016/j.iatssr.2013.06.004

Laboratoire Central des Ponts et Chaussées. (2002). *COST 323 Weigh-in-Motion of Road Vehicles*: *Final Report (1993-1998)*.

Lydon, M., Taylor, S. E., Robinson, D., Mufti, A., & Brien, E. J. O. (2016). Recent developments in bridge weigh in motion (B-WIM). *Journal of Civil Structural Health Monitoring*, *6*(1), 69–81. https://doi.org/10.1007/s13349-015-0119-6

Moses, F. (1979). Weigh-in-Motion System Using Instrumented Bridges. *Transportation Engineering Journal of ASCE*, *105*(3), 233–249.

Nugraha, W., Sidi, I. D., Suarjana, M., & Zulkifli, E. (2022). Reliability evaluation of steel truss bridge due to traffic load based on bridge weigh-in-motion measurement. *Structural Monitoring and Maintenance*, *9*(4), 323–336. http://www.techno-press.com/?page=container&journal=smm&volume=9&num=4

Nugraha, W., & Sukmara, G. (2016). *WIM Bridge: Ujicoba Model Fisik Teknologi Pengukuran Beban Kendaraan Bergerak menggunakan Jembatan Terinstrumentasi*. Puslitbang Jalan dan Jembatan, Kementerian Pekerjaan Umum dan Perumahan Rakyat.

van Loo, H., & Žnidarič, A. (2019). Guide for Users of Weigh-In-Motion.*Iswim, International Society for Weigh-in-Motion*.

Bridge Maintenance, Safety, Management, Digitalization and Sustainability – Jensen, Frangopol & Schmidt (eds)
© 2024 The Author(s), ISBN 978-1-032-77040-6
Open Access: www.taylorfrancis.com, CC BY-NC-ND 4.0 license

Bridge weigh-in-motion event detection using wavelet scattering features and unsupervised learning

Vahid Bokaeian, Jeremy Bowmaster & Kaveh Arjomandi
Department of Civil Engineering, University of New Brunswick, Fredericton, Canada

ABSTRACT: This study introduces an unsupervised approach to categorize the acceleration time history of a highway bridge into three distinct classes: vehicle events, the bridge's free vibration, and noise. We employ a combination of wavelet scattering networks and principal component analysis for extracting features, while the Gaussian mixture model is utilized for clustering the data segments into these classes. The results are compared to a manually adjusted database of events identified through computer vision, aligned with the acceleration data to define event intervals. The effectiveness of this method in identifying events from the bridge's acceleration data is evident. It successfully detected all events without omission and accurately separated the free vibrations.

1 INTRODUCTION

Bridge Weigh-in-Motion (BWIM) refers to methods for estimating vehicle weights as they cross a bridge at highway speeds. Unlike traditional weighing stations, BWIM systems do not require vehicles to stop, thus providing a non-intrusive means of collecting weight data. This technology is particularly useful for infrastructure management, allowing for the monitoring of overweight vehicles that may damage roadways and bridges, and for enforcing weight limits.

The roots of Bridge Weigh-In-Motion (BWIM) technology can be traced to the 1960s, gaining significant momentum in the mid-1970s due to the groundbreaking efforts of Fred Moses (Moses 1979). This technology is based on the concept of an 'influence line' (IL), a representation that illustrates the effect of a unit load at varying positions on a bridge on a specific response, such as strain or bending moment, at a designated point on the structure. Before deploying the algorithm, it's essential to calibrate the bridge, which involves establishing its IL. This calibration process generally requires driving vehicles with known weights over the bridge and recording the resultant responses. Moses' algorithm assumes that the total influence at any given moment is the cumulative effect of the individual axle weights at their respective locations on the bridge. Through the resolution of these equations, it becomes possible to approximate the weights of the separate axles.

Many researchers have used the concept of influence line to estimate axle weights and vehicle weights on bridges, and axle detection is a critical process in most of them, where the accuracy of the algorithm for weighing axles is highly dependent on two key parameters: vehicle speed and axle spacing (Algohi, Mufti, and Thomson 2018; He et al. 2021; Macleod and Arjomandi 2022; MacLeod and Arjomandi 2023). There have been different non-IL-based methods proposed by researchers, but most of them are limited to specific traffic scenarios (Yu, Cai, and Liu 2021), not verified by real traffic data (Chatterjee et al. 2006; Zhou et al. 2021), or are computationally expensive (Zhou et al. 2020; Zhu, Li, and Zhang 2022).

While these methods have served their purpose, they sometimes lack adaptability, computational efficiency, and precision. These shortcomings can lead to inaccurate

DOI: 10.1201/9781003483755-163

measurements, increased maintenance costs, and potential structural vulnerabilities. The integration of Artificial Intelligence (AI) into BWIM systems offers the potential to enhance adaptability and accuracy, paving the way for more resilient and efficient infrastructure monitoring. This study is part of a research project defined in the Smart Structures Research Group (SSRG), University of New Brunswick, that aims to develop an AI-integrated BWIM system that utilizes sensor data for precise event detection, classification and weight estimation on highway bridges. The system also implements computer vision techniques to adeptly categorize vehicles, focusing on their presence, axle count, and spacing.

2 METHODOLOGY

2.1 *Structure instrumentation*

The chosen structure for instrumentation is a single-span prestressed concrete girder bridge which functions as an overpass for Route 2 and is situated proximate to the town of Sackville, NB, Canada. The bridge was erected in the year 1994, and the specified speed limit on this bridge section of the highway is 110 kph. The bridge is identified as L930 by the New Brunswick Department of Transportation and Infrastructure (NBDTI).

The bridge's underside has been equipped with thirty sensors, as shown in Figure 1:

- Nine accelerometers, which record uniaxial vibrations, facilitate modal analysis, thereby yielding essential model data.
- Fifteen foil strain gauges are purposed to record the overall response, aiding in weight determination algorithms, while an additional four strain gauges are designed to measure localized strain in the deck, particularly to identify the axles of traversing vehicles.
- Furthermore, a Basler ace acA1440-73gc GigE camera has been installed to consistently capture visuals of the vehicular movement across the bridge, operating at a frequency of 10 Hz.

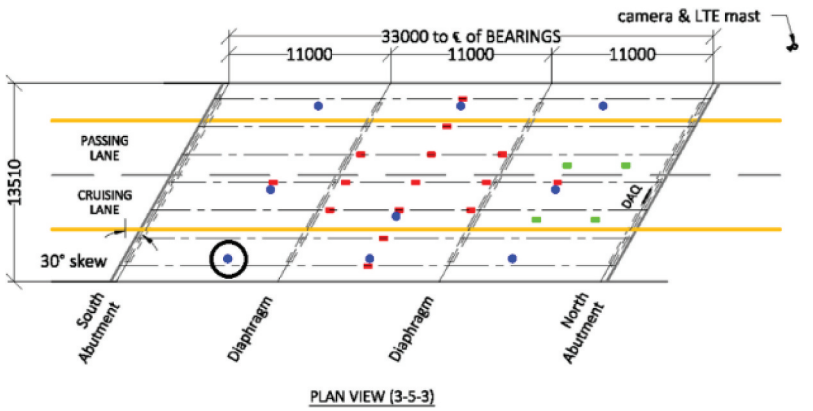


Figure 1. L930 sensor layout. This instrumentation plan is intended for general BWIM research and we only utilize acceleration data from a singlesensor (indicated by a black circle in Figure 1) for the current study.

2.2 *Dataset preparation*

In this study, the YOLOv8n model is specifically trained to detect vehicles in the region of interest (ROI) of the bridge images. By applying the YOLOv8n model to the preprocessed images, vehicles present in the ROI are detected and localized. These images are utilized to prepare an approximate start and end time for events that occurred on the bridge. After

observing acceleration data for the same period of time, a dataset of manually identified events (including time intervals in which there is vehicle(s) between the two expansion joints on the bridge) is prepared.

2.3 *Time series feature extraction*

2.3.1 *Data preprocessing*

The first step in the feature extraction process is to read and preprocess the acceleration data. The raw data is typically stored in TDMS (Technical Data Management Streaming) files, with a sampling frequency of 1280 Hz. The time and acceleration values are extracted from the raw data and organized into arrays for further processing.

After preprocessing the data, the acceleration data is windowed, which involves dividing the data into smaller windows of equal time duration (window size) 0.5 seconds, or 640 samples. Windowing allows for the analysis of the acceleration data in smaller segments, enabling the detection of events that occur within specific time intervals. By analyzing the acceleration data in these windows, it becomes possible to identify patterns associated with bridge events.

2.3.2 *Wavelet scattering features*

The foundational principle of the wavelet scattering transform is rooted in a technique known as the wavelet transform. This method involves utilizing wave-like oscillations, known as wavelets, which are adaptable in scale and position to closely match a given signal. By combining these wavelets linearly, a new representation of the signal is created. The application of the wavelet to the signal results in a series of coefficients. These coefficients illustrate the correlation between the wavelet and the signal, offering a new depiction of the original signal that encompasses both time and localized frequency information (Jean Effil and Rajeswari 2022). This characteristic makes the wavelet transform an effective tool for analyzing nonstationary signals, primarily due to its capacity for time-frequency localization. However, one limitation of this method is its lack of translation invariance (Liu et al. 2020).

Building upon the wavelet transform, the wavelet scattering transform aims to create representations that are invariant to translation and resilient to deformations. It achieves this through a combination of convolution, nonlinear processing, and scaling operations. The scattering transform extends the signal data across various decomposition paths, effectively delocalizing it (Jean Effil and Rajeswari 2022). This approach has been recognized for its efficacy in classification tasks, as pointed out by multiple studies (Andén and Mallat 2011; Bruna and Mallat 2011; Liu et al. 2020; Seydoux et al. 2020).

In this paper, the notations used in (Andén and Mallat 2011; Liu et al. 2020) are followed. Consider a signal denoted as $f(t)$ being analyzed. The construction of filters for capturing the full range of frequencies in this signal involves the use of a low-pass filter ϕ and a wavelet function Ψ. The low-pass filter, represented as $\phi_J(t)$, yields descriptions of f that are invariant to local translations at a predefined scale T. We use the notation Λ_k to describe a set of wavelet indices that offer an octave frequency resolution Q_k. By dilating the wavelet Ψ, we can create a multiscale high-pass filter bank $\{\Psi_{j_k}\}_{j_k \in \Lambda_k}$.

The implementation of a wavelet scattering transform is realized through a deep convolution network. This network iterates over a combination of traditional wavelet transform, nonlinear modulus, and averaging operations. The convolution process $S_0 f(t) = f * \phi_J(t)$ generates a feature of f that is locally translation invariant. However, this process also results in the loss of high-frequency information. The lost high-frequency details are recaptured using a wavelet modulus transform defined as Equation 1:

$$|W_1|f = \{S_0 f(t), |f * \Psi_{j1}(t)|\}_{j_1 \in \Lambda_1} \tag{1}$$

To obtain the first-order scattering coefficients, the wavelet modulus coefficients are averaged with ϕ_J, as shown in Equation 2:

$$S_1 f(t) = \left\{ \left| f * \Psi_{j1} \right| * \phi_J(t) \right\}_{j_1 \in \Lambda_1} \tag{2}$$

To retrieve the information lost in this averaging, we consider $S_1 f(t)$ as the low-frequency component of $\left| f * \Psi_{j_1} \right|$. The complementary high-frequency coefficients are then extracted through Equation 3:

$$|W_2| \left| f * \Psi_{j1} \right| = \left\{ S_1 f(t), \left| \left| f * \Psi_{j1} \right| * \Psi_{j2}(t) \right| \right\}_{j_2 \in \Lambda_2} \tag{3}$$

This leads to the definition of the second-order scattering coefficients, as shown in Equation 4:

$$S_2 f(t) = \left\{ \left| \left| f * \Psi_{j1} \right| * \Psi_{j2} \right| * \phi_J(t) \right\}_{j_i \in \Lambda_i}, \; i = 1, 2. \tag{4}$$

By iterating this process, we define wavelet modulus convolutions as Equation 5:

$$U_m f(t) = \left\{ \left| \left| \left| f * \Psi_{j1} \right| * \ldots * \left| \Psi_{j_m} \right| \right| \right\}_{j_i \in \Lambda_i}, \; i = 1, 2, \ldots, m. \tag{5}$$

Averaging $U_m f(t)$ with ϕ_J results in the m-th-order scattering coefficients, as shown in Equation 6:

$$S_m f(t) = \left\{ \left| \left| \left| f * \Psi_{j1} \right| * \ldots * \left| \Psi_{j_m} \right| * \phi_J(t) \right| \right\}_{j_i \in \Lambda_i}, \; i = 1, 2, \ldots, m. \tag{6}$$

The final scattering matrix, which is shown in Equation 7:

$$S_m f(t) = \left\{ \left| \left| \left| f * \Psi_{j1} \right| * \ldots * \left| \Psi_{j_m} \right| * \phi_J(t) \right| \right\}_{j_i \in \Lambda_i}, \; i = 1, 2, \ldots, m. \tag{7}$$

amalgamates all orders of scattering coefficients to describe the signal features, where l represents the maximum decomposition order.

The network's translation invariance is up to the scale determined by the averaging operation through the low-pass filter ϕ_J. As an inherent property of the wavelet transform, the features $Sf(t)$ exhibit stability against local deformations.

Despite its structural resemblance to conventional CNNs, the wavelet scattering network differs in two main aspects. Firstly, the filters are preset rather than learned. Secondly, the features extracted are not solely from the output of the last convolution layer but also from the combination of all layers (Liu et al. 2020).

In this research, a wavelet time scattering decomposition network using the Gabor (analytic Morlet) wavelet was created in Matlab. In the standard setup, the wavelet scattering network has two layers. This is based on the standard architecture of scattering networks, which are designed to capture both first-order and second-order scattering coefficients. The first layer captures the first-order coefficients, which are wavelet transforms of the signal. The second layer further processes the output of the first layer, capturing second-order coefficients.

2.3.3 *Dimensionality reduction*

With a sampling frequency set at 1280 Hz and a signal length of 640 samples, the output from the wavelet scattering network, following the specified configuration, results in an array of dimensions 5x105 for each window. These arrays are subsequently reshaped into single rows comprising 525 elements each. They are then vertically stacked, creating a dataset with dimensions 7198x525, which includes 525 variables and 7198 instances. In the process of conducting principal component analysis (PCA), the first 20 principal components were selected. These components account for over 95% of the variance in the data, and serve as features for the subsequent clustering algorithm.

2.4 *GMM*

In this study, we utilize features that have been dimensionally reduced via the PCA algorithm to group acceleration data. The clustering is achieved through the implementation of a Gaussian mixture model (Reynolds 2009). This model is centered around identifying a collection of K Gaussian distributions, each characterized by its mean μk and covariance Σk (for k = 1…K), which collectively provide the most accurate representation of the data set. Distinguished from the K-means clustering algorithm, the Gaussian mixture model offers a probabilistic framework, adding flexibility. This flexibility is evident in its ability to handle anisotropic covariances, accommodate clusters with differing internal variances, and apply a soft decision boundary for classification (Reynolds 2009; Seydoux et al. 2020).

Similar to the K-means algorithm, clustering based on the Gaussian mixture model is influenced by initial conditions and may result in convergence to a local rather than a global optimum. To address this issue, we performed the clustering with 100 random starting points. We then selected the clustering with the lowest Negative Log Likelihood (NLL). The NLL serves as a metric for evaluating the cost function within the optimization process. Utilizing this method aids in reducing the likelihood of converging to a local optimum, a notable risk given the iterative nature of the algorithm and its sensitivity to the initial conditions (You, Li, and Du 2023).

3 RESULTS AND DISCUSSION

As previously mentioned, 'events' in our context refer to the periods when one or more vehicles are present between the two expansion joints on the bridge. The rationale for choosing to cluster the acceleration data into three categories was to test the effectiveness of the current method in distinctly categorizing the three types of acceleration data, namely:

- Noise,
- Free vibration of the bridge,
- Vehicle-induced vibrations (referred to as 'events').

An example of how the final clustering compares with the actual recorded events is illustrated in Figure 2.

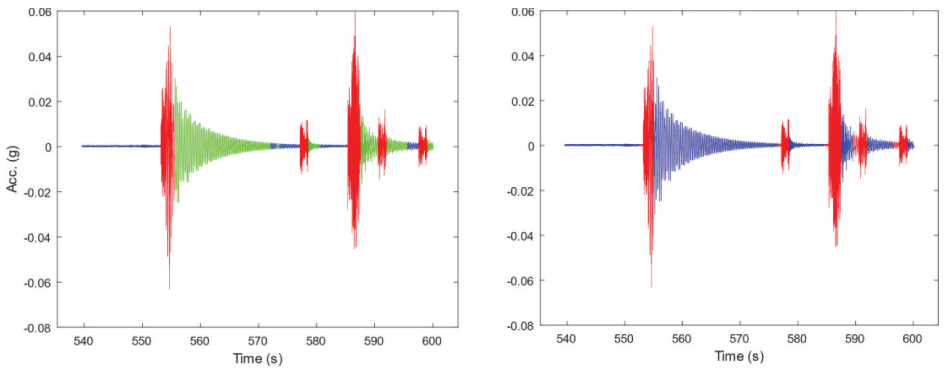


Figure 2. Sample result of event detection.

Upon reviewing the results from the entire dataset, it is obvious that the algorithm demonstrates proficiency in distinguishing event intervals within the acceleration history data. Nonetheless, a more detailed analysis is necessary to accurately assess the precision and reliability of this technique. In the next section, we will delve into an in-depth exploration of the confusion matrix, along with a thorough examination of both false negatives and false positives, to gain a more comprehensive understanding of the algorithm's robustness.

3.1 *Confusion matrix*

The confusion matrix serves as a tool for assessing the efficacy of classification algorithms. It can be structured as follows, according to (Fawcett 2006):

Table 1. Definition of confusion matrix.

Actual \ Predicted	Predicted Positive	Predicted Negative
Actual positive	True Positive (TP)	False Negative (FN)
Actual Negative	False Positive (FP)	True Negative (TN)

Typically, confusion matrices are utilized in supervised classification tasks. In these tasks, a model is trained on labeled data to learn specific patterns, which it then applies to predict labels for new, unlabeled inputs. However, our research employs an unsupervised method, as the classification model was developed without the use of manually identified events. Instead, we apply the concept of a confusion matrix to draw comparisons between manually identified events and the segments of data that have been clustered.

First, the noise and free vibration classes need to be merged into a "Non-event" class .Assuming that the current method is capable of accurately separate out the 3 classes of acceleration data, we made another assumption, and that is if we look at the mean absolute peak acceleration in all windows in a given class C (MAP_c), the "Event" class will have the highest MAP:

It is then necessary to combine the noise and free vibration classes into a single category, which we termed 'Non-event'. Operating under the assumption that this method could effectively segregate these three types of acceleration data, we introduced an additional hypothesis. This involves examining the mean absolute peak acceleration (MAP) across all data windows within a specific class C, denoted as (MAP_c). The formula for MAP_c, is given as Equation 8:

$$MAP_c = \frac{\sum_{i=1}^{n_c} max\left(abs\left(Seg_{i,c}\right)\right)}{n_c} \tag{8}$$

n_c: number of windows assigned to cluster C,

$Seg_{i,c}$: window i in cluster C.

Based on the MAP values, we ranked the classes and merged the two with the lowest MAP values into the 'Non-event' category. The confusion matrix can now be formed, as tabulated in Table 2.

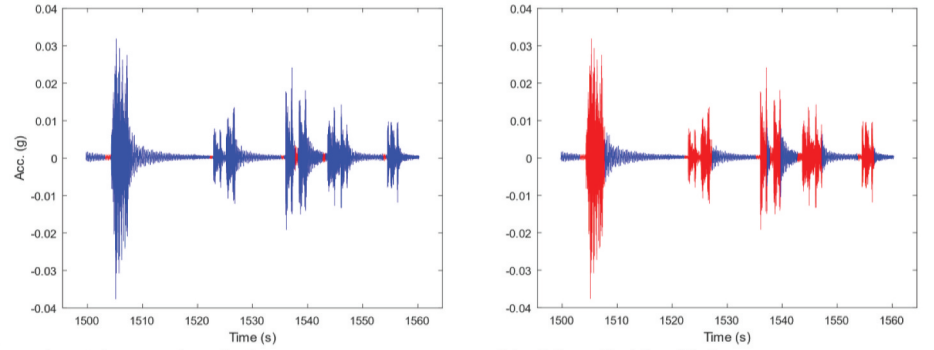
Table 2. Confusion matrix.

		Predicted Class	
		Event	Non-Event
Actual Class	Event	1899	491
	Non-Event	73	4735

Initial observations from the confusion matrix indicate a notable presence of false detections, particularly false negatives, which might initially suggest a risk of overlooking some events. However, this preliminary assessment requires a deeper analysis. In the next section we will look at these false classification in detail.

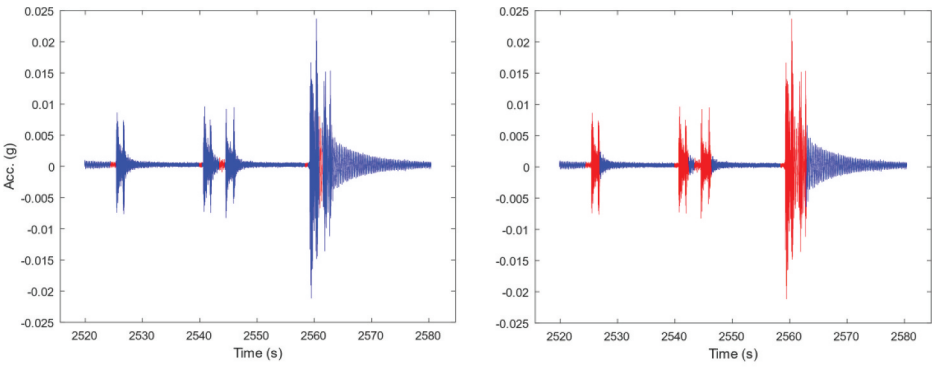
3.2 *False classifications*

Samples of false negatives and false positives event detection are illustrated in Figure 3 and Figure 4.



a) False negatives (red) b) Manually identified events

Figure 3. A sample of false negative detection.



a) False positives (red) b) Manually identified events

Figure 4. A sample of false positive detection.

An analysis of all misclassifications reveals two primary causes. Firstly, the manual identification of the dataset involves analyzing images at a rate of 10 frames per second and correlating these with acceleration time history indexes. This method may lead to some inaccuracies in event labeling. Secondly, for the purpose of comparing classification outcomes, it was necessary to assess the data windows individually. Events identified manually might start or end within these window intervals, necessitating the inclusion of entire windows as events, which can contribute to misclassifications.

Nevertheless, it's noteworthy that no actual events were missed by the algorithm. The majority of false detections occur immediately before or after actual events, typically lasting just 1-2 windows (0.5-1 seconds), a relatively brief duration. The proposed method is a reliable approach for differentiating between events, the bridge's free vibration, and noise. Our future research will focus on classifying these detected events (and correlated events from other sensors installed on the bridge) based on the number and types of vehicles involved and determining vehicle parameters for a new hybrid BWIM system.

4 CONCLUSION

In this study, an unsupervised approach was introduced to distinguish vehicle-induced vibrations (referred to as 'events') from bridge free vibrations and noise, using data from a single-channel accelerometer on a concrete highway bridge. This approach involved employing

a wavelet scattering network to derive stable features from acceleration data segments. Once the dimensionality of these initial scattering features was reduced, the refined features were input into a Gaussian mixture model (GMM) classifier. This classifier's objective was to optimally fit N normal distributions to the data, with N being a pre-set value of 3 in our study, corresponding to event, free vibration, and noise categories. The window classifications obtained were then cross-referenced against an event dataset, which was developed using an adapted YOLOv8n model and manually fine-tuned.

Based on our findings, the effectiveness of this method in identifying events from the bridge's acceleration data is evident. It successfully detected all events without omission and accurately separated the free vibrations. Consequently, this method proves to be sufficiently reliable for extracting an event dataset, paving the way for further enhancements and research in our Bridge Weigh-In-Motion (BWIM) system.

REFERENCES

Algohi, B., A. Mufti, and D. Thomson. 2018. "Detection of Speed and Axle Configuration of Moving Vehicles Using Acoustic Emission." *Journal of Civil Structural Health Monitoring* 8(3):353–62.

Andén, Joakim, and Stéphane Mallat. 2011. "Multiscale Scattering for Audio Classification." Pp. 657–62 in *ISMIR*. Miami, Florida.

Bruna, Joan, and Stéphane Mallat. 2011. "Classification with Scattering Operators." Pp. 1561–66 in *CVPR 2011*. IEEE.

Chatterjee, Pranesh, Eugene OBrien, Yingyan Li, and Arturo González. 2006. "Wavelet Domain Analysis for Identification of Vehicle Axles from Bridge Measurements." *Computers & Structures* 84 (28):1792–1801.

Fawcett, Tom. 2006. "An Introduction to ROC Analysis." *Pattern Recognition Letters* 27(8):861–74.

He, W., X. Liang, L. Deng, X. Kong, and H. Xie. 2021. "Axle Configuration and Weight Sensing for Moving Vehicles on Bridges Based on the Clustering and Gradient Method." *Remote Sensing* 13(17).

Jean Effil, N., and R. Rajeswari. 2022. "Wavelet Scattering Transform and Long Short-Term Memory Network-Based Noninvasive Blood Pressure Estimation from Photoplethysmograph Signals." *Signal, Image and Video Processing* 16(1):1–9.

Liu, Zhishuai, Guihua Yao, Qing Zhang, Junpu Zhang, and Xueying Zeng. 2020. "Wavelet Scattering Transform for ECG Beat Classification." *Computational and Mathematical Methods in Medicine* 2020.

Macleod, E., and K. Arjomandi. 2022. "Enhanced Bridge Weigh-in-Motion System Using Hybrid Strain-Acceleration Sensor Data." *Journal of Bridge Engineering* 27(9).

MacLeod, E., and K. Arjomandi. 2023. "Dynamic Bridge Weigh-in-Motion Using Estimated Modal Parameters from Ambient Vibration Tests." *Engineering Structures* 289.

Moses, Fred. 1979. "Weigh-in-Motion System Using Instrumented Bridges." *Transportation Engineering Journal of ASCE* 105(3):233–49.

Reynolds, Douglas A. 2009. "Gaussian Mixture Models." *Encyclopedia of Biometrics* 741(659–663).

Seydoux, Léonard, Randall Balestriero, Piero Poli, Maarten de Hoop, Michel Campillo, and Richard Baraniuk. 2020. "Clustering Earthquake Signals and Background Noises in Continuous Seismic Data with Unsupervised Deep Learning." *Nature Communications* 11(1):3972.

You, Jie, Zhaoxuan Li, and Junli Du. 2023. "A New Iterative Initialization of EM Algorithm for Gaussian Mixture Models." *Plos One* 18(4):e0284114.

Yu, Y., C. S. Cai, and Y. Liu. 2021. "Probabilistic Vehicle Weight Estimation Using Physics-Constrained Generative Adversarial Network." *Computer-Aided Civil and Infrastructure Engineering* 36(6):781–99.

Zhou, Y., Y. Pei, Z. Li, L. Fang, Y. Zhao, and W. Yi. 2020. "Vehicle Weight Identification System for Spatiotemporal Load Distribution on Bridges Based on Non-Contact Machine Vision Technology and Deep Learning Algorithms." *Measurement: Journal of the International Measurement Confederation* 159.

Zhou, Y., Y. Pei, S. Zhou, Y. Zhao, J. Hu, and W. Yi. 2021. "Novel Methodology for Identifying the Weight of Moving Vehicles on Bridges Using Structural Response Pattern Extraction and Deep Learning Algorithms." *Measurement: Journal of the International Measurement Confederation* 168.

Zhu, J., X. Li, and C. Zhang. 2022. "Fine-Grained Identification of Vehicle Loads on Bridges Based on Computer Vision." *Journal of Civil Structural Health Monitoring* 12(2):427–46.

Bridge Maintenance, Safety, Management, Digitalization and Sustainability – Jensen, Frangopol & Schmidt (eds)
© 2024 The Author(s), ISBN 978-1-032-77040-6
Open Access: www.taylorfrancis.com, CC BY-NC-ND 4.0 license

Machine-learning for analyzing bridge displacement using radar data

M. Arnold
ci-tec GmbH, Karlsruhe, Germany

S. Keller
Institute of Photogrammetry and Remote Sensing (IPF), Karlsruhe, Germany

ABSTRACT: This paper introduces a novel machine-learning approach based on non-invasive ground-based radar (GBR) time series data for classifying short-span bridge vehicle crossing events. GBR is used to remotely measure the bridge displacement, which is otherwise difficult to acquire but is an essential quantity for Structural Health Monitoring (SHM). For a comprehensive Bridge SHM, monitoring traffic is beneficial to gain knowledge about the actual loading situation. This can be challenging with global responses like displacement. This study indicates that it is possible to classify crossings as single- or multi-presence from displacement signals using tree-based learners and MiniRocket. Thus, our approach serves as a proof of concept to establish remote and data-driven displacement approaches in the context of BWIM. We rely on recordings of the bridge deck taken by an unmanned aerial vehicle as reference data. Despite a small, imbalanced, and biased dataset, we achieve a balanced accuracy of 90%.

1 INTRODUCTION

Bridges are an essential part of any transportation system. Failure can lead to fatalities, but even a gradual decline in loading capacity may already significantly impact freight traffic. Therefore, it is necessary to assess their condition regularly. In Germany, bridges are inspected periodically, frequently visually. These superficial inspections may detect external damage, including cracks, but they do not provide any information about the behavior of the bridge itself, like the load-bearing capacity. On the other hand, to apply adequate measures such as load restrictions, it is vital to have insights into the weight of vehicles to which the bridge is exposed.

So-called weigh-in-motion (WIM) systems are usually deployed to monitor traffic, but they typically require directly attached sensors, inflicting damage on the bridge (Paul & Roy 2023).

Pavement-based WIMs have direct contact with vehicles, simplifying traffic characterization, but the sensors are exposed to significant stress. Nothing-on-road (NOR) bridge WIMs (BWIM) try to avoid traffic exposure by only attaching sensors to the lower side of the bridge and using the bridge itself as a scale (Yu et al. 2016). To minimize interference, remote and non-invasive systems have been investigated (Ojio et al. 2016). While BWIM reduces both the system complexity, sensor exposure, and cost, signal analysis becomes more challenging. Accordingly, traffic characterization from vehicle crossings, henceforth called events, is still an active field of research. Many standard BWIM Structural Health Monitoring (SHM) methods cannot handle multiple-presence crossings and instead require single-vehicle events (OBrien et al. 2006; Ieng 2015). Such single-events must be detected automatically for a BWIM under normal traffic conditions. Moghadam et al. (2023) introduce a method for calculating a bridge influence line from multi-presence crossings. However, they recommend using a different approach for single crossings since it is more exact, making a differentiation between single and multi events desirable.

DOI: 10.1201/9781003483755-164

Kawakatsu et al. (2023) use Deep Learning (DL) for BWIM. They train Convolution Neural Networks (CNN) to classify traffic using equally long strain time series. According to their study, the CNNs can handle multi-presence events. However, they do not study the effects of several vehicles. Ground-based radars (GBR) have recently been investigated for monitoring bridges (Gentile & Bernardini 2010; Michel & Keller 2021a, b, 2022). Since they are easy to set up and require little maintenance, inspections can be performed on the fly. More importantly, GBR measures the bridge displacement. Displacement is highly relevant in SHM, reflecting bridge stiffness and bearing capability (Zhao et al. 2015). However, it is difficult to measure. With GBR, this data is accessible directly and accurately (Michel & Keller 2021a), making it a significant contender for NOR BWIM. Since deflection is challenging to measure, displacement-based BWIM has barely been studied. For instance, Ojio et al. (2016) have determined the bridge displacement with a camera. They use a second camera, not the displacement, to monitor the traffic and extract relevant features like the axle count. However, additional hardware increases the costs. Extracting traffic information from the displacement time series directly would be cheaper. Arnold & Keller (2020) and Arnold et al. (2021) show that Machine Learning (ML) based data-driven processing of bridge displacement signals is possible. They exploit a Random Forest (RF) and a CNN to detect and extract vehicle crossings successfully. As a next step, these events need to be analyzed regarding their potential for traffic characterization. Firstly, detected events should be differentiated between single- or multiple-presence events. One big challenge is that displacement, unlike strain, does not contain a localized bridge response. Furthermore, events and their corresponding time series are of varying length due to different vehicle numbers, speeds, and lengths. Varying-length time series classification is an active but insufficiently studied topic. One option is to extract features from a given time series (Bier et al. 2022). Other approaches like Random Convolutional Kernel Transform (ROCKET) (Dempster 2020) or MiniRocket (Dempster et al. 2021) achieve state-of-the-art results in public databases (Dau et al. 2019). In this paper, we will use a feature-based approach and MiniRocket to introduce an ML-based single-/multi-classification. More specifically, the main contributions of this paper are:

- a detailed description of the GBR data and the UAV dataset used in this study,
- a profound investigation of a varying-length bridge crossing classification in terms of single- versus multi-presence events using different ML approaches,
- an in-depth analysis of the potential of data augmentation for time series event classification,
- a comprehensive application of our approach to an entirely unknown dataset.

In Section 2, we will explain the setup for GBR measurements and describe the used dataset. Our methodology, including preprocessing, feature extraction and ML-models is detailed in Section 3. The results of our approach are laid out and discussed in Section 4. Finally, Section 5 summarizes the main findings of this study.

2 GBR MEASUREMENTS AND DATASET

In this section, we will briefly describe the GBR measurement setup. A more detailed explanation can be found in Michel & Keller (2021a), for example. Afterwards, we will introduce the UAV dataset for single-event classification.

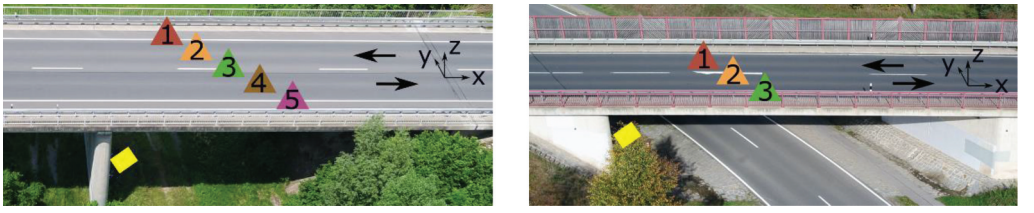


Figure 1. Overview of Bridge A (left) and Bridge B (right), including their reflectors.

2.1 *GBR measurement setup*

Measurements have been conducted at two bridges in Germany, henceforth referred to as Bridges A and B. To achieve a high signal-to-noise ratio five respectively three corner reflectors have been attached at the bottom of Bridge A and B. Both bridges and the approximate positions of the corner reflectors are shown in Figure 1. Bridge A has two fields, yet only one is monitored.

While Bridge A has undisturbed measurements, the vehicles using the street below Bridge B can cause significant disturbances in the time series data (Michel & Keller 2021a). On both infrastructures, one lane is present for each driving direction, as indicated by the black arrows. The yellow rectangle in Figure 1 represents the GBR. Its measuring principle is based on frequency modulation and interferometry (Gentile & Bernardini 2010). Modulation allows the GBR to measure multiple points along its line of sight (LOS). The maximum range resolution Δr amounts to 0.75m, according to

$$\Delta r = \frac{c}{2 \cdot B} = 0.75\ m, \tag{1}$$

with the speed of light $c = 3\times10^8$ ms^{-2} and a bandwidth B = 200 MHz. That is, every 0.75 m, the bridge displacement can be measured by summing up all reflected signals. For this purpose, all reflectors are spread along the x- and y-plane to make them distinguishable measurement points. The displacement is deducted using interferometry. With a sampling rate of 200 Hz, the phase shift $\Delta\varphi$ of each point is measured and then transformed to vertical displacement Δz using

$$\Delta z = \frac{\lambda}{4\pi}\frac{R}{\mathrm{h}} \cdot \Delta\varphi, \tag{2}$$

where h is the height difference between bridge and GRB, R is the distance of the GBR to a measurement point and λ is the GBR wavelength.

2.2 *Dataset*

To acquire ground truth data for the event classification, an unmanned aerial vehicle (UAV) has been deployed to film the bridge topside. During postprocessing, those videos have been synchronized with the radar data and used to build a database of vehicle crossings. Table 1 gives a general overview of the dataset for both bridges. As mentioned before, disturbances occur at Bridge B. We will only regard undisturbed events in this work. Overall, 1111 vehicles have been recorded for Bridge A and 730 for Bridge B. Since an event can contain several vehicles, the number of events is smaller, with 964 events for Bridge A and 500 for Bridge B, respectively. Besides the small dataset size, the imbalance of the dataset poses another challenge. This is true in two ways: Firstly, multi events are scarce compared to single events. Secondly, trucks appear less often than cars. Since trucks are inherently slower than cars and cars tend to cue behind a slow truck, trucks are underrepresented in single-events. In the case of Bridge A, for example, 241 trucks are single events, whereas 608 single events contain cars.

Table 1. Overview of the UAV-recorded events used for the event classification.

Bridge	Vehicles	Trucks	Cars	Events	Single Events	Multi Events
A	1110	341	769	962	849	112
B	491	114	377	343	271	72

While single events can differ significantly, multi-presence events come in an even greater variety: For instance, two heavy trucks might cross the bridge simultaneously in opposite directions. This scenario would be very relevant for SHM due to the significant stress induced on the bridge. Still, it is also challenging to visually differentiate from a single-event using only time series displacement data. To better understand, Figure 2 shows one single and one multi event for each bridge, although these examples do not cover the broad spectrum of traffic situations in the dataset. The corresponding time series data for all reflectors is drawn below each UAV

image. For each vehicle, its time on the monitored field is highlighted. Since there are overlapping areas in the lower plots, these are classified as multi events. Bridge A multi event shows a truck finishing its overtaking maneuver of another truck on the bridge field. The time series already resembles a single event of a very slow vehicle, e.g., when compared to the Bridge B single event. Thus, parallel crossings are barely distinguishable from single events. Attributing the maximum displacement or the maximum load of such an event falsely to one vehicle would lead to overestimating the bridge load and possibly to unnecessary reinforcements. A small car follows after the two trucks, but the vibration heavily masks the bridge bending the car causes. Finally, the Bridge B multi event shows a more straightforward example of two consecutive cars. The curious signal shape of RB3 in the Bridge B single event can be attributed to the fact that more than one displacement component is measured by the GBR (Michel & Keller 2021a).

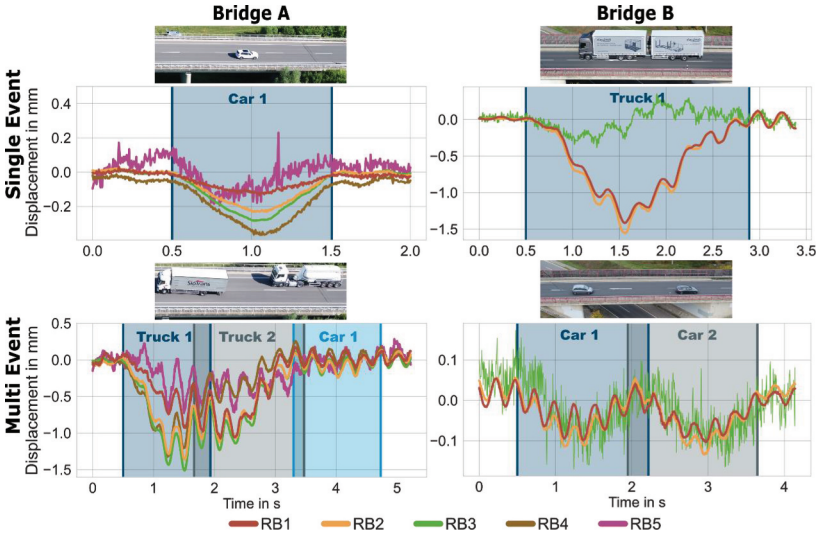


Figure 2. Example for a single (upper) and a multi event (lower) for Bridge A and Bridge B.

Figure 2 gives the impression that it could be sufficient to monitor the length of an event or its maximum displacement for one or two reflectors to classify it successfully. To illustrate that the distributions for both classes overlap significantly regarding such features, Figure 3 shows the duration of an event and the maximum displacement for reflector 3 of Bridge A and their corresponding Kernel Density Estimations (KDE). Although multi events tend to take longer, two consecutive cars are often faster than a single truck. And events of two trucks crossing the bridge in parallel on opposite lanes might last as long as a single truck event. On the other hand, most multi events have a higher deflection since slow and heavy trucks are involved, yet a clear decision boundary is not apparent. Although these two features alone are not enough to make a correct classification, additional features in combination with ML might be more successful.

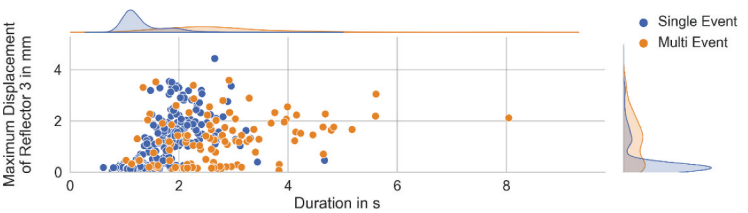


Figure 3. Maximum displacement and duration with normalized KDE.

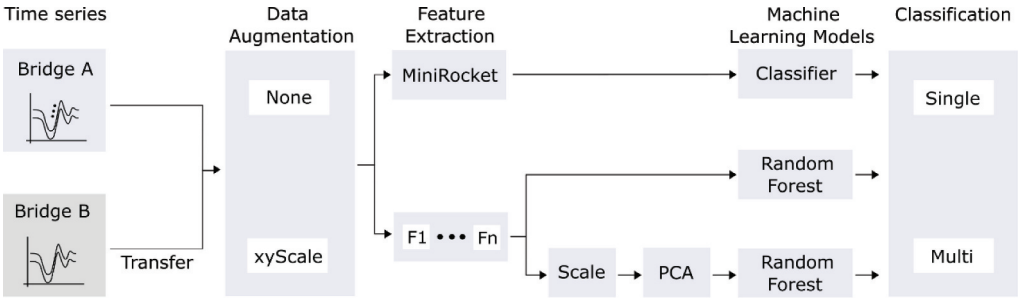


Figure 4. Schema of the methodological classification approach.

3 METHODOLOGY

In this chapter, we will shortly explain the methodology of the single- and multi-presence classification. Our proposed methodology consists of three steps: the data augmentation, the feature extraction and the ML models to classify the events. Figure 4 provides the schema of all steps.

3.1 *Preprocessing*

As evident from Section 2.1, bridges can have a varying amount of measurement points. For this study, we assume that at least two points are available at each bridge. Therefore, we use the two reflectors 2 and 4 for Bridge A and 1 and 3 for Bridge B, respectively. For comparison, we also train our models with all five reflectors of Bridge A. We split Bridge A data into training, validation, and test sets using a 70:15:15 ratio, with each subset mirroring the overall distribution of single and multi events. Finally, to investigate transferability, we did not train our models on the dataset of Bridge B.

In accordance with Ruiz et al. (2021), we try to minimize the amount of preprocessing, i.e., we did not normalize the time series. We ensure, that all time series start at a displacement of 0 mm by removing the offset. As described in Section 2.2, single events tend to have a smaller maximum deflection. To mitigate this bias, we apply data augmentation in the form of y-scaling. We choose five values in the range of -0.1 mm to -4.0 mm (see Figure 3) superimposed with random values, in which the maximum displacement of each event would be scaled. To tackle the bias in duration, we oversampled all single-events by factors 2 and 3 and downsampled all multi events accordingly. We combine both scalings (xyScale) and compare it to no augmentation (None).

3.2 *Feature extraction*

Both approaches are based on features extracted from the time series. The features of the RF classifiers are listed in Table 2, together with the functions to extract them. We have extracted every feature for each used reflector time series. With 14 features, this yields 28 features for two reflectors and 70 for five reflectors, respectively. We also train an RF after scaling the features and applying principal component analysis (PCA) to reduce the dimensionality. We use eight components since they explain over 95% of the variance for the None dataset.

Unlike manual feature selection, MiniRocket uses random convolutional kernels to extract 9,996 features itself. The properties and specifications of those kernels can be followed by Dempster et al. (2021). We use the sktime implementation (Löning et al. 2019), which can handle variable-length input. The final extracted feature of each convolution is the proportion of positive values (PPV). Theoretically, the number of kernels can be regarded as a hyperparameter. However, Dempster et al. (2021) recommend using 10000 kernels. Due to using the PPV and the bias from the convolution results, normalization is unnecessary.

Table 2. These 14 features have been extracted from the GBR time series data $\underline{x}$. For calculation, the Python-packages numpy and scipy have been used. All non-default values are stated.

Feature No.	Name of Feature	Basis of Calculation
1	Maximum	max($\underline{x}$)
2	Minimum	min($\underline{x}$)
3	Mean	mean($\underline{x}$)
4	Standard Dev.	min($\underline{x}$)
5	Skewness	skew($\underline{x}$)
6	Kurtosis	kurt($\underline{x}$)
7	Median	median($\underline{x}$)
8	Length	ken($\underline{x}$)
9	Quantile25	quantil($\underline{x}$, 0.25)
10	Quantile75	quantil($\underline{x}$, 0.75)
11	NbrPeaks	len(find_peaks($\underline{x}$, distance=4, width=5, rel_height=0.5))
12	xMinPosRatio	argmin($\underline{x}$)/len($\underline{x}$)
13	Power	sum($\underline{x}^2$)/len($\underline{x}$)
14	MAD	median_abs_deviation($\underline{x}$)

3.3 *Machine learning models*

Using the validation set, we apply grid search to the models in the second to last column in Figure 4 to find the optimal set of hyperparameters. Since the dataset is imbalanced, we use "balanced_accuracy" as the score for the grid search. Furthermore, we apply class weights during training. The features extracted from MiniRocket are passed to a classifier.

For small datasets with less than 10000 observations, like in the None case, a ridge classifier is recommended by Dempster et al. (2021). Otherwise, logistic regression, which we use for xyScale, is suggested. Since MiniRocket is independent of y-scaling, we might introduce overfitting to the classifier with our data augmentation approach.

4 RESULTS AND DISCUSSION

The study's objective is to investigate the potential of ML approaches to classify GBR variable-length time series vehicle crossings. Table 3 shows the results of the single vs. multi event classification concerning Overall Accuracy (OA), Precision (P), Recall (RC) and Balanced Accuracy (BA).

Concerning Bridge A with two reflectors, all models have an OA, P, and RC above 90%. However, these values are heavily skewed since single-events are much more present. Therefore, we included BA, the average of recall from each class. All BAs are close to each other, between 82% to 87%, with MiniRocket having the highest score. These results are deceptive, as there are correlations between duration and maximum displacement and event type, as described in Section 2.2. Figure 5 highlights this aspect. The decision boundary for MiniRocket in the left plot almost exclusively depends on the duration, with every event longer than 2.5 s classified as a multi event.

The boundary becomes more complex after applying xyScale data augmentation. Fewer long single-events are now misclassified as multi events, as seen in Figure 5 on the right. Conversely, MiniRocket has more difficulties with medium-length single-events. The effect of xyScale also shows in the BA of all three models. RF and PCA RF achieve a worse BA since they have to find more complex relationships. MiniRocket improves with data augmentation, achieving the best results for two reflectors on one bridge, with a BA of 90%. Considering the small size of the dataset and without providing any prior domain knowledge, these are very auspicious results. Figure 5 also shows that short multi events are still misclassified as single-events. Heavier augmentation in time might solve this issue. When using five reflectors, we did not expect any additional information in those time series, but on the contrary, to achieve worse results due to the higher complexity. Accordingly, RF and MiniRocket achieve equal or worse results. Interestingly enough, PCA RF has better results than with only two reflectors. One explanation could be that the driving side is more distinct with more data, which can help detect multiple events.

Finally, the tests on Bridge B show that a transfer to an unknown dataset can be successful to a certain degree. With None augmentation, all models suffer again under the correlation depicted in Figure 5. The BA is even 90% and above. This score is partially due to the more extensive dataset, where usual events, e.g., cars following a truck, are more prominent, whereas complex events, such as two trucks simultaneously, are rare. The transfer seems challenging for RF and MiniRocket trained with xyScale, since even OA and RC are around 50%. Only PCA RF has values of over 80% and even a BA of 74%. As with five reflectors for Bridge A, the PCA appears to extract robust features. Considering that both bridges have unequal numbers of fields and are of different size, this is a promising result regarding transferability.

Table 3. Test results for all classificators.

Bridge	Number of Reflectors	Data Augmentation	Model	OA	P	RC	BA
A	2	None	RF	0.91	0.97	0.93	0.85
			PCA RF	0.94	0.95	0.98	0.82
			MiniRocket	0.95	0.97	0.98	0.87
		xyScale	RF	0.90	0.94	0.93	0.76
			PCA RF	0.90	0.95	0.94	0.79
			MiniRocket	0.98	0.98	0.97	0.90
	5	xyScale	RF	0.94	0.94	0.99	0.76
			PCA RF	0.95	0.97	0.98	0.87
			MiniRocket	0.94	0.96	0.97	0.84
B		None	RF	0.96	0.97	0.98	0.94
			PCA RF	0.92	0.97	0.93	0.90
			MiniRocket	0.95	0.97	0.96	0.93
		xyScale	RF	0.59	0.92	0.57	0.69
			PCA RF	0.84	0.89	0.92	0.74
			MiniRocket	0.59	0.97	0.50	0.72

5 CONCLUSION

This paper introduced a data-driven ML approach to classifying multi-variate GBR time series from bridge vehicle crossings. The GBR data originates from two bridges in Germany, which a UAV also monitors as ground truth. One bridge has been used for training, validation, and testing, whereas the second bridge only served as a test set to evaluate transferability. We also investigated the effect of varying measurement points as input. The classification goal is to differentiate between single- and multi-presence events. Particularly challenging is the variable length of the time series and the correlation of the length with a class. For this purpose, we have examined the potential of data augmentation. Methodically, we implement and apply three different ML approaches. We use an RF with 14 hand-crafted features per reflector as input, an RF that uses the output of a PCA as input. Finally, we compare their performance to MiniRocket, a state-of-the-art ML model in time series classification. It shows that MiniRocket outperforms the other models when applying data augmentation to tackle biases. With a BA of 90%, it achieves satisfying results.

Concerning transferability to an utterly unknown bridge, MiniRocket needs to catch up in BA compared to PCA RF and has only a BA of 74%. Keeping the second bridge out of the training cycle allowed us to test the transferability and reduced the training size, making it more challenging for the models. In the future, we will monitor further bridges from which the models can more easily extrapolate to new structures. Also, pre-training in combination with DL could be exploited to widen our dataset.

In sum, we showed that a data-driven classification of GBR data is possible. These promising results can link an event detection, as described by Arnold et al. (2021), and a GBR-based BWIM, which focuses, in the first step, on single-events. With this, a non-invasive and remote BWIM and SHM would be possible.

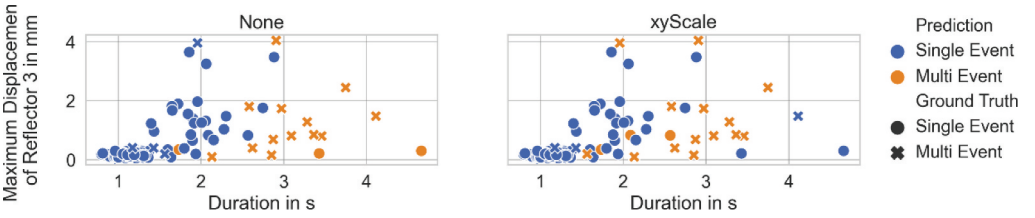


Figure 5. Test set classification results for MiniRocket with None and xyScale data augmentation.

REFERENCES

Arnold, M., Hoyer, M., & Keller, S. 2021. Convolutional Neural Networks for Detecting Bridge Crossing Events With Ground-Based Interferometric Radar Data. *ISPRS Annals of the Photogrammetry, Remote Sensing and Spatial Information Science*s 1-2021, 31–38.

Arnold, M. & Keller, S. 2020. Detection and Classification of Bridge Crossing Events With Ground Based Interferometric Radar Data and Machine Learning Approaches. *ISPRS Annals of the Photogrammetry, Remote Sensing and Spatial In formation Sciences* 12020, 109–116.

Bier, A., Jastrzebska, A., & Olszewski, P. 2022. Variable-Length Multivariate Time Series Classification Using ROCKET: A Case Study of Incident Detection. *IEEE Access* 10, 95701–95715.

Dau, H. A., Bagnall, A., Kamgar, K., Yeh, C.-C. M., Zhu, Y., Gharghabi, S., Ratanamahatana, C. A., & Keogh, E. 2019. The UCR Time Series Archive. *arXiv:1810.07758* [cs, stat].

Dempster, A. 2020. ROCKET: exceptionally fast and accurate time series classification using random convolutional kernels. *Data Mining and Knowledge Discovery* (34), 42.

Dempster, A., Schmidt, D. F., & Webb, G. I. 2021. MINIROCKET: A Very Fast (Almost) Deterministic Transform for Time Series Classification. *Proceedings of the 27th ACM SIGKDD conference on knowledge discovery & data mining* (pp. 248–257)

Gentile, C. & Bernardini, G. 2010. An interferometric radar for non-contact measurement of deflections on civil engineering structures: laboratory and full-scale tests. *Structure and Infrastructure Engineering* 6(5), 521–534.

Ieng, S.-S. 2015. Bridge Influence Line Estimation for Bridge Weigh-in-Motion System. *Journal of Computing in Civil Engineering* 29(1), 06014006.

Kawakatsu, T., Aihara, K., Takasu, A., Nagayama, T., & Adachi, J. 2023. Data-Driven Bridge Weigh-In-Motion. *IEEE Sensors Journal*, 1–1. Conference Name: IEEE Sensors Journal.

Löning, M., Bagnall, A., Ganesh, S., & Kazakov, V. 2019. sktime: A Unified Interface for Machine Learning with Time Series.

Michel, C. & Keller, S. 2021a. Advancing Ground-Based Radar Processing for Bridge Infrastructure Monitoring. *Sensors* 21(6), 2172. Number: 6 Publisher: Multidisciplinary Digital Publishing Institute.

Michel, C.& Keller, S. 2021b. Introducing a non-invasive monitoring approach for bridge infrastructure with ground-based interferometric radar. In EUSAR 2021; *13th European Conference on Synthetic Aperture Radar*, pp. 1–5.

Michel, C. & Keller, S. 2022. Determining and Investigating the Variability of Bridges' Natural Frequencies with Ground-Based Radar. *Applied Sciences* 12(11), 5354.

Moghadam, A., Al Hamaydeh, M., & Sarlo, R. 2023. Dual-purpose procedure for bridge health Monitoring and weigh-in-motion used for multiple-vehicle events. *Automation in Construction* 148.

OBrien, E. J., Quilligan, M. J., & Karoumi, R. 2006. Calculating an influence line from direct measurements. *Proceedings of the Institution of Civil Engineers - Bridge Engineering* 159(1), 31–34.

Ojio, T., Carey, C. H., OBrien, E. J., Doherty, C., & Taylor, S. E. 2016. Contactless Bridge Weigh-in-Motion. *Journal of Bridge Engineering* 21(7), 04016032.

Paul, D. & Roy, K. 2023. Application of bridge weigh-in-motion system in bridge health monitoring: a state-of-the-art review. *Structural Health Monitoring*, 147592172311544.

Ruiz, A. P., Flynn, M., Large, J., Middlehurst, M., & Bagnall, A. 2021. The great multivariate time series classification bake off: a review and experimental evaluation of recent algorithmic advances. *Data Mining and Knowledge Discovery* 35(2), 401–449.

Yu, Y., Cai, C., & Deng, L. 2016. State-of-the-art review on bridge weigh-in-motion technology. Advances in *Structural Engineering* 19(9), 1514–1530. Publisher: SAGE Publications Ltd STM.

Zhao, X., Liu, H., Yu, Y., Xu, X., Hu, W., Li, M., & Ou, J. 2015. Bridge Displacement Monitoring Method Based on Laser Projection-Sensing Technology. *Sensors* 15(4), 8444–8463.

Bridge Maintenance, Safety, Management, Digitalization and Sustainability – Jensen, Frangopol & Schmidt (eds)
© 2024 The Author(s), ISBN 978-1-032-77040-6
Open Access: www.taylorfrancis.com, CC BY-NC-ND 4.0 license

Accuracy of BWIM considering autocorrelation in bridge dynamic response

K. Maruyama, I. Yoshida & H. Sekiya
Tokyo City University, Setagaya-ku, Tokyo, Japan

ABSTRACT: Many researchers have developed the bridge weigh-in-motion (BWIM) techniques to estimate axle weight and gross vehicle weight (GVW) of the traveling vehicles. BWIM assumes that the bridge response due to traveling vehicles results from the influence line and the vehicle specification, such as the axle spacing and weight. However, traveling vehicles also cause dynamic responses. In this study, the dynamic response is considered in the observation error with autocorrelation in the time domain. Specifically, it is considered in the covariance matrix of the observation error. The accuracy of three methods, Mehtod-1A; ordinary least square method (OLS), Method-1B; OLS with low-pass filtering of displacement response, Method-2; proposed method considering autocorrelation in bridge dynamic response, are compared. Methods 1B and 2 contribute to enhanced estimation accuracy; however, it is worth noting that Method 1B introduces biases in the estimates due to filtering.

1 INTRODUCTION

In order to maintain the integrity of bridges, it is important to have a system that can efficiently and simply evaluate the current state of the loads acting on the bridge and utilize them for maintenance management. The causes of damage in steel bridges include corrosion and fatigue. In this study, we focus on fatigue, which is caused by repetitive stresses due to moving vehicles. In particular, high stresses caused by heavy vehicles have a significant impact on fatigue.

Gross vehicle weight (GVW) and axle weights are sometimes estimated by gauges installed at toll gates. However, these gauges have some problems such as the need for traffic control during installation and high cost. As a system for measuring traffic loads using bridges, Bridge weigh-in-motion (BWIM) was proposed by Moses in the 1970s (Moses, 1979). BWIM is a method of estimating the axle weights by considering the bridge as a weighting scale, measuring the strains or displacements of the bridge caused by the moving vehicle. Over the past several decades, BWIM technology has attracted attention as a promising tool for overweight enforcement, fatigue prediction and maintenance planning over the past few decades.

Throughout the past few decades, numerous BWIM algorithms have been developed, aiming either to estimate static axle weights or to identify the dynamic time history of axle forces in moving vehicles (Yu et al. 2016). The former methods are more straightforward, as they assume that the bridge response attributed to a moving load can be expressed as the product of the influence line and the axle weight (He et al. 2019, Lydon et al. 2016). Yoshida et al. (2021) proposed Bayesian BWIM (BBWIM). Within the BBWIM framework, conventional BWIM can be interpreted as assuming white noise for observation and modeling errors (Yoshida et al. 2023). In this paper, we investigate the accuracy of estimated weights using the conventional method with/without filtering, and BBWIM considering autocorrelation in bridge dynamic response. The study utilizes synthesized observation data of bridge displacement with colored noise.

DOI: 10.1201/9781003483755-165

2 ALGORITHM FOR BWIM

2.1 *Method-1, Conventional method*

Moses' proposed algorithm for static BWIM has gained widespread utilization. This algorithm employs the least-squares method to estimate axle weights by minimizing the sum of squared residuals between the measured and the predicted bridge response. The predicted bridge response is calculated based on influence line and information regarding the target vehicle. The predictive equation for the bridge response derived from the influence line is denoted by equation (1).

$$\boldsymbol{z}_D = \boldsymbol{H}_I \boldsymbol{x}_W + \boldsymbol{v} \tag{1}$$

where $\boldsymbol{z}_D$ denotes the measured bridge response (In this study, displacement response), $\boldsymbol{H}_I$ represents an influence line matrix, $\boldsymbol{x}_W$ represents a vector comprising axle weights, and $\boldsymbol{v}$ represents a vector of residual between the measured and predicted responses essentially, the observation and modeling error. The formation of $\boldsymbol{H}_I$ is contingent upon the axle information from vehicles in each data, with the number of columns aligning with the total axle count across all vehicles. For more details, refer to previous publication (Yoshida et al., 2023).

The conditional probability $P(\boldsymbol{x}_W|\boldsymbol{z}_D)$ for a given observation value $\boldsymbol{z}_D$ can be calculated from Bayes' formula.

$$\boldsymbol{P}(\boldsymbol{x}_W|\boldsymbol{z}_D) = \frac{P(\boldsymbol{z}_D|\boldsymbol{x}_W)P(\boldsymbol{x}_W)}{P(\boldsymbol{z}_D)} \tag{2}$$

The concept of maximum a posteriori (MAP) estimation is widely known in a Bayesian inverse problem. The MAP estimate for the optimal x value is obtained by maximizing the logarithm of the numerator, which is the product of the conditional probability $P(\boldsymbol{z}_D \mid \boldsymbol{x}_W)$ and the prior probability $P(\boldsymbol{x}_W)$. The solutions derived are dependent on the selection of prior information. To achieve solutions independent of this selection, non-informative priors can be employed, where axle weights are estimated solely from the measured bridge response induced by a passing vehicle. For a non-informative prior, a prior with a uniform distribution or a Gaussian distribution with a very large standard deviation can be assigned. In this case, the objective function is represented by the following residual sum of squares:

$$J = (\boldsymbol{z}_D - \boldsymbol{H}_I \ \boldsymbol{x}_W)^T \boldsymbol{R}^{-1} (\boldsymbol{z}_D - \boldsymbol{H}_I \ \boldsymbol{x}_W) \tag{3}$$

where $\boldsymbol{R}$ is the covariance matrix of $\boldsymbol{v}$. When the residual $\boldsymbol{v}$ is independent and identically distributed (i.i.d.), $\boldsymbol{R}$ is given by the following:

$$\boldsymbol{R} = \sigma_{\boldsymbol{R}^2} I \tag{4}$$

where $\sigma_{\boldsymbol{R}^2}$ is the variance of the residual, $\boldsymbol{I}$ is identity matrix. The MAP estimate that minimizes equation (3) is obtained by

$$\hat{\boldsymbol{x}}w = \left(\boldsymbol{H}_I^T \boldsymbol{H}_I\right)^{-1} \boldsymbol{H}_I^T z_D \tag{5}$$

2.2 *Method-2, BBWIM method considering autocorrelation in bridge dynamic response*

The underlying assumption posits that the bridge displacement response can be effectively decomposed into two distinctive components: a static component associated with the vehicle weight and a dynamic component arising from the first vibrational mode of the bridge. Equation (4) corresponds to assuming that the residual is uncorrelated noise in the time domain, i.e., white noise. However, as shown in Figure 1 which indicates an example of dynamic component of actually measured bridge response caused by a moving vehicle, the noise or residual $\boldsymbol{v}$ is clearly correlated and is not white noise. The proper modeling of the covariance matrix $\boldsymbol{R}$ necessitates the inclusion of non-diagonal components (Yoshida et al. 2023). The correlation

of the residual in the time domain is considered in the autocorrelation matrix $\boldsymbol{C}$. The autocorrelation function $cor(j\Delta t)$ for the dynamic component is calculated numerically using

$$cor(j\Delta t) = \frac{1}{m\sigma_{R^2}} \sum_{i=1}^{m-j} v(i\Delta t)v(i\Delta t + j\Delta t) \tag{6}$$

where Δt is the time increment, $t = i\Delta t$, $\tau = j\Delta t$, and m is the number of measured data points. The autocorrelation matrix $\boldsymbol{C}$ is calculated by the autocorrelation function. The autocovariance matrix $\boldsymbol{R}$ is derived by taking the product of the autocorrelation matrix $\boldsymbol{C}$ and the variance of the residuals σ_R^2.

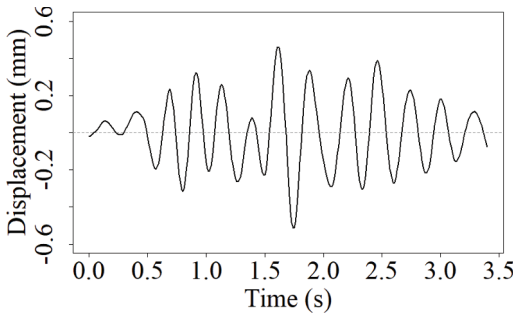


Figure 1. Dynamic component in measured data.

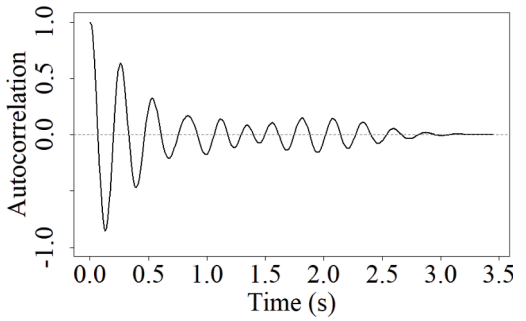


Figure 2. Autocorrelation function of dynamic component in measured data.

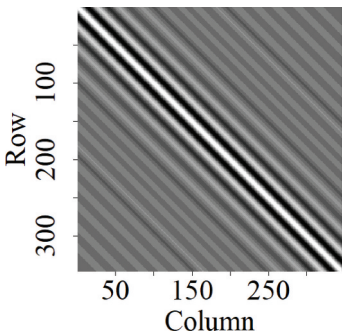


Figure 3. Contour map of autocorrelation matrix C of the dynamic component.

$$\boldsymbol{R} = \sigma_{\boldsymbol{R}^2 C} \tag{7}$$

The least-squares solution that minimizes equation (3) is obtained by

$$\hat{\boldsymbol{x}}_W = \boldsymbol{P}\boldsymbol{H}_I^T \boldsymbol{R}^{-1} z_D \tag{8}$$

$$\boldsymbol{P} = (\boldsymbol{H}_I^T \boldsymbol{R}^{-1} \boldsymbol{H}_I)^{-1} \tag{9}$$

where $\boldsymbol{P}$ is the posterior covariance matrix of the estimate $\hat{\boldsymbol{x}}_W$.

3 SIMULATED COLORED NOISE FOR SYNTHESIZED OBSERVATION DATA

The simulated colored noise is synthesized based on the dynamic components in an actual measured data, which is shown in Figure 1. The autocorrelation function of the dynamic component is calculated by applying equation (6). Figure 2 illustrates the autocorrelation function of the dynamic components (Figure 1) observed in the measured data. The contour map of the autocorrelation matrix $\boldsymbol{C}$ of the dynamic component is shown in Figure 3. When white noise is assumed, in other words, when using the conventional method (Method-1), the diagonal component of $\boldsymbol{C}$ takes a value of 1, and the others take a value of 0. For colored noise, it takes values between 0 and 1 dependent on the distance from the diagonal component (time lag). The simulated colored noise is generated based on the autocorrelation matrix $\boldsymbol{C}$ (Figure 3) of dynamic component in the measured displacement response. Ten generated colored noises are shown in Figure 4. The standard deviation of the simulated colored noise is assumed to be 5% of the maximum amplitude for static component. The dynamic component in the measured data displays non-stationarity, while the simulated noise conforms to a stationary pattern. Delving into the consideration of non-stationarity is recognized as a promising avenue for future research.

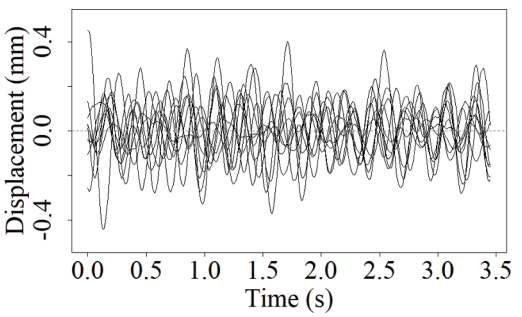


Figure 4. Generated 10 colored noises.

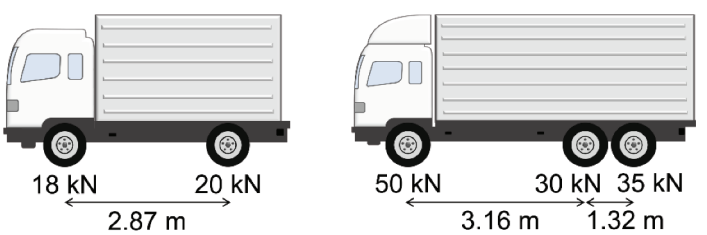
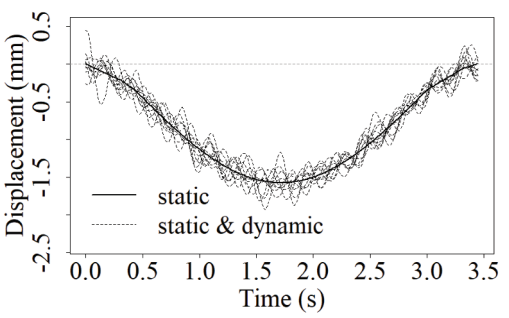
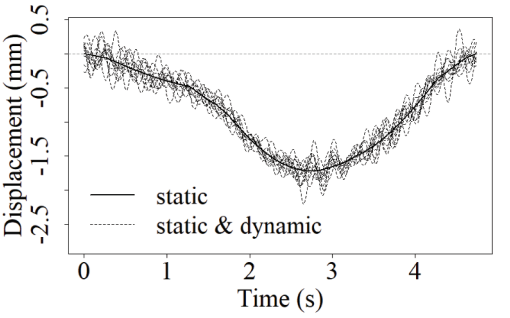


Figure 5. The axle weights and axle spacing of the vehicle used in the simulation.



(a) Single driving condition (Case-1).



(b) In-line driving condition (Case-2).

Figure 6. The simulated displacement response.

4 ESTIMATION OF AXLE WEIGHTS BY METHOD-1 AND -2

4.1 *Procedure for estimation of accuracy of the methods*

Monte Carlo simulation (MCS) of estimation of axle weights is performed by using the simulated displacement response with colored noise to investigate the validity of modeling the covariance matrix $\boldsymbol{R}$. In the MCS, 1000 response displacement time histories with autocorrelation are gane-rated, and then axle weight and GVW are estimated for each synthesized response data.

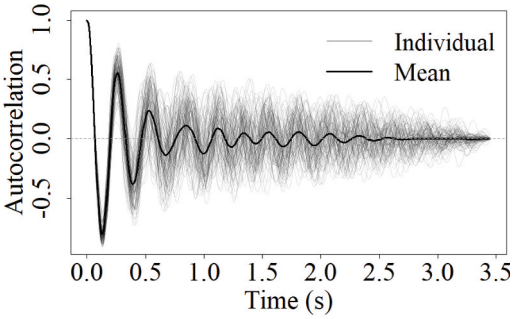
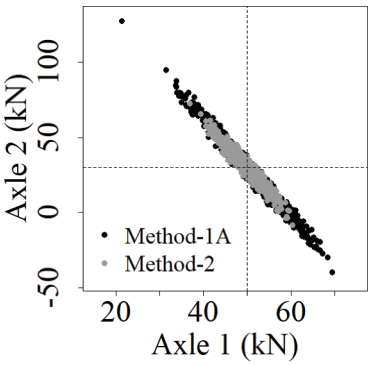
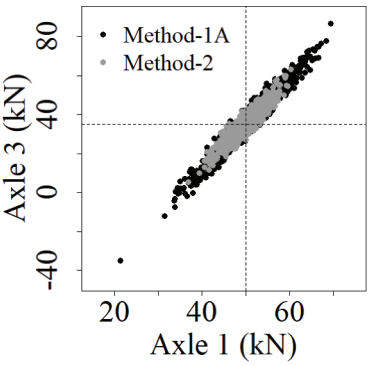


Figure 7. 100 autocorrelation functions calculated from the dynamic components of a three-axle vehicle single driving and their mean.



(a) Comparison of Axle 1 and 2



(b) Comparison of Axle 1 and 3

Figure 8. The scatter plot of estimated axle weights.

The moving vehicles are assumed to be two-axle and three-axle. The vehicle specifications are shown in Figure 5. The measurement section of the bridge is 30 m in length with two lanes, one for driving lane and the other for passing lane. It is assumed that the influence line is estimated by the displacement response measured at the center of middle girder. The influence line is used for both lanes because the cross section of the bridge is symmetrical.

In this study, two cases of driving conditions are assumed. Case-1 is single driving of three-axle vehicle, and Case-2 is in-line driving of two-axle and three-axle vehicle. In both cases, the vehicle speed is constant at 10 m/s (36km/h). Figure 6 shows examples of synthesized displacement responses including simulated colored noise for each case. The estimation accuracy of three methods is compared. Method-1A is ordinary least square method (OLS), which is conventional method, uses identity matrix for correlation matrix $\boldsymbol{C}$. Method-1B is also a conventional method, however it uses a 1 Hz low-pass filter to remove dynamic component from the observation data for BWIM. These two methods estimate the axle weight using equation (5). Method-2 considers the dynamic component in the covariance matrix $\boldsymbol{R}$ and uses equations (8) and (9).

Method-2 employs a correlation matrix $\boldsymbol{C}$, estimated as the mean of the autocorrelation functions derived from 1000 simulated colored noises. An example of the autocorrelation function $cor(j\Delta t)$ assuming single driving of a three-axle vehicle is shown in Fig. 7.

4.2 *Case-1, single driving case*

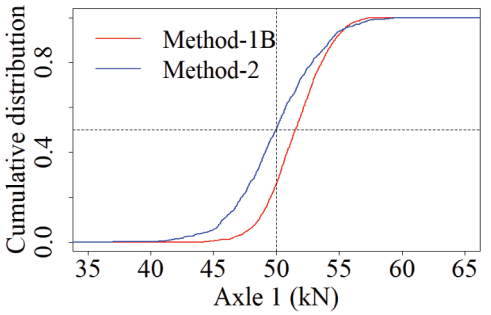
Single driving case of the three-axle vehicle namely, Case-1 is discussed in this section. The 1000 estimated weights of a three-axle vehicle for the 1000 synthesized observation data are shown in Figure 8. This figure compares estimated weights by Method-1A and Method-2. The dash lines in the figure show the actual weight of each axle. As can be seen in the figure, strong negative correlation is observed between adjacent axles, which means when the first axle weight estimate is larg.er (smaller) than the true value, the second axle estimate tends to be smaller (larger). The standard deviations of the estimated weights are summarized in Table 1. The standard deviations of the estimated axle weights using Method-1A are approximately twice those for Method-1B (with low pass filter) and Method-2.

Table 1. The standard deviations of the estimated axle weight by each method.

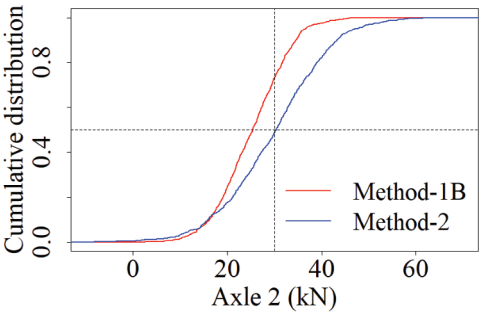
Method	Axle 1	Axle 2	Axle 3
1A	6.39	21.23	15.31
1B	2.35	7.26	5.20
2	3.35	10.87	7.80

Figure. 9 compares the cumulative distribution functions (CDFs) of each estimated axle associated with the Method-1B and Method-2. In the case of Method-2, the median values (i.e., the values for a cumulative probability of 0.5) of all three CDFs closely match the actual weights shown by the vertical dashed line. Method-1B has the smallest standard deviation among the three cases, however, it shows a bias (relative errors of the mean values). The bias of the first, second and third axle weight estimated by Method-1B are 3.1, -15.6, and 8.7 % respectively. The low pass filter (Method-1B) reduces the variability of the estimation results, however causes bias due to the distortion of the displacement response caused by the filtering.

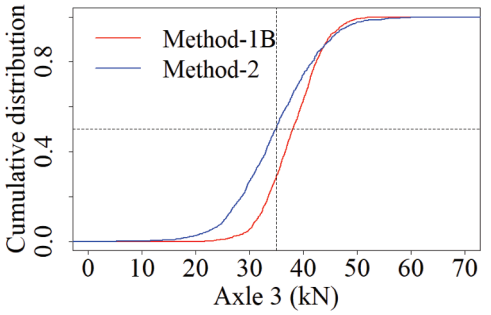
A histogram of the GVW estimated by each method is shown in Figure 10. The standard deviations of the estimated GVW by Method-1A, -1B, and -2 are 0.44, 0.22, and 0.22, respectively. Similar to the axle weight, Method-2 demonstrates an enhancement in estimation accuracy for GVW. The bias of the estimated GVW by Method-1A, -1B and -2 are 1.8×10^{-2}, 10.0×10^{-2}, 0.4×10^{-2} % respectively, which are extremely small by all methods. No significant bias is observed even with Method-1B. Conventional BWIM systems, employing Moses' method (Method-1) that overlooks dynamic components in the measured response, can



(a) Axle 1



(b) Axle 2



(c) Axle 3

Figure 9. The cumulative distribution function of axle weights estimated by Method-1B and -2.

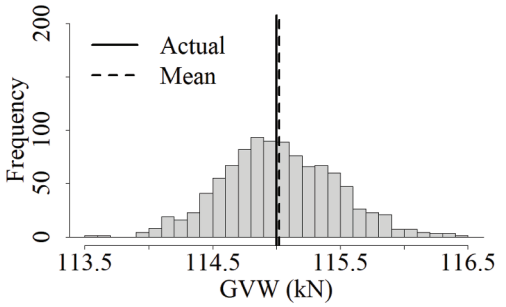
provide reasonably accurate estimates of GVW. However, in situations where precise axle weight information is crucial, such as in pavement maintenance applications (Pais et al., 2013), it is advisable to utilize Method-2 (BBWIM). This method, which considers the auto-correlation of observation noise, proves instrumental for the precise estimation of axle weights.

Table 2. The bias of measured gross vehicle weight in Case-2 [$\times 10^{-2}$ %].

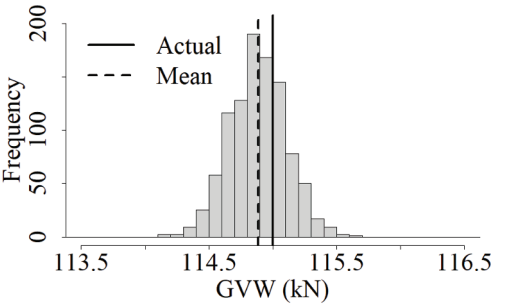
Test vehicle type	Method-1A	Method-1B	Method-2
Two-axle	0.2	12.9	3.2
Three-axle	3.6	-18.2	0.1

4.3 *Case-2, in-line driving case*

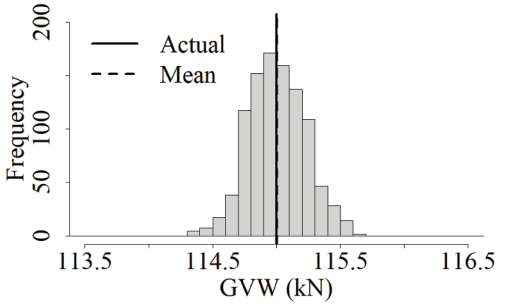
A case involving two vehicles, referred to as Case-2, is also studied. The distance between vehicles is assumed to be 10 m. Parameters such as the axle weight are the same as in Case-1. As in Case-1, 1000 synthesized responses were generated for the observation data to estimate axle weights and GVW. Figure 11(a) summarizes the standard deviations of the estimated axle weights by the three methods. As in Case-1, the standard deviations by Method-1B, -2 are much smaller than those by Method-1A. The improvement in estimation accuracy is more pronounced for three-axle vehicles than for two-axle vehicles. This suggests that Method-2 is more effective for vehicles with a larger number of axles and shorter axle spacing. The bias in the estimated axle weights, as shown in Figure 11(b), is significantly reduced, particularly for



(a) Method-1A

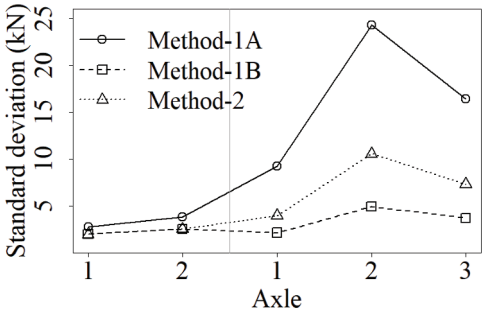


(b) Method-1B

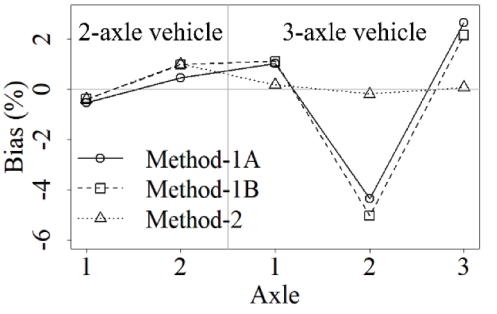


(c) Method-2

Figure 10. Comparison of estimated gross vehicle weight.



(a) Standard deviation of estimated each axle weight



(b) The bias of estimated each axle weight

Figure 11. Comparison of estimated axle weight in Case-2.

the second axle of a three-axle vehicle, when using Method-2. As shown in Table-2, the bias in GVW estimation is small as in Case-1.

5 CONCLUSION

In conventional BWIM, the residual, configured observation and modelling errors, is typically handled by presuming identical and independent noise within a probabilistic framework. In this study, a comparative accuracy analysis was carried out for three methods: conventional BWIM (Method-1A), conventional BWIM with low-pass filtering (Method-1B), and Bayesian

BWIM (Method-2). The evaluation was performed via a series of numerical simulations employing synthetic data. Method-2 specifically considers the autocorrelation of dynamic components within bridge responses using the covariance matrix $\boldsymbol{R}$. While both Method-1B and Method-2 result in a reduction of the standard deviation of the estimated weights, Method-1B shows biases in estimated weights due to the influence of filtering. Notably, the BBWIM method (Method-2) proves advantageous as it does not incur a significant computational cost, making it suitable for real-time vehicle monitoring.

In this study, the covariance matrix $\boldsymbol{R}$ is derived from the dynamic component, assuming stationary correlated observation noise. However, it is acknowledged that some measured data exhibit strong non-stationarity. The consideration of such non-stationarity is deferred for future exploration.

REFERENCES

He, W. Ling, T. O'Brien, e. J. & Deng, L. 2019. Virtual axle method for bridge weigh-in-motion systems requiring no axle detector, *J. Bridge Eng*. Vol.24, No.9: 04019086.

Lydon, M. Taylor, S. E. Robinson, D. Mufti A., & O'Brien, E. J. 2016. Recent developments in bridge weigh in motion (B-WIM). *J. Civ. Struct. Health Monit*. 6 (1): pp.69–81.

Moses, F. 1979. Weigh-in-motion system using instrumented bridge. *Transportation Eng. J. of ASCE*. Vol.105, No.TE3: pp.233–249.

Pais, J. C. Amorim, S. I. r. & Minhoto, M. J. C. 2013. Impact of Traffic Overload on Road Pavement Performance. *J. Transp. Eng*. 139(9): pp.873–879.

Yoshida, I. Sekiya, H. & Mustafa, S. 2021. Bayesian Bridge Weigh-In-Motion and Uncertainty Estimation. *ASCE-ASME J. Risk Uncertainty Eng. Syst., Part A, Civ. Eng*. 7(1): 04021001.

Yoshida, I. Mustafa, S. Maruyama, K. & Sekiya, H. 2023. Bridge weigh-in-motion considering dynamic response in observation noise with application to multiple driving conditions. *Structural Safety*. Vol.103: 102350.

Yu, Y. Cai, C. S. & Deng, L. 2016. State-of-the-art review on bridge weigh-in-motion technology. *Adv. Struct. Eng*. 19 (9): pp.1514–1530.

Bridge Maintenance, Safety, Management, Digitalization and Sustainability – Jensen, Frangopol & Schmidt (eds)
© 2024 The Author(s), ISBN 978-1-032-77040-6
Open Access: www.taylorfrancis.com, CC BY-NC-ND 4.0 license

Exploring Kriging metamodeling for applications in bridge Weigh-in-Motion prediction

P. Agüero-Barrantes
LanammeUCR, Universidad de Costa Rica, San Pedro, Costa Rica

S. Lobo-Aguilar
Escuela de Ingeniería Civil, Universidad de Costa Rica, San Pedro, Costa Rica

R.E. Christenson & A. Hain
Civil and Environmental Engineering Department, University of Connecticut, Storrs, USA

ABSTRACT: Bridge Weigh-In-Motion systems can be installed and serviced on highway bridges to provide measurements of truck traffic without interrupting traffic. This paper presents the application of Gaussian Process Modeling to BWIM. The Kriging metamodeling approach, allows for the strategic selection of training vehicles to generate a BWIM metamodel. The proposed approach extends the BWIM concept of influence area from response time histories to geometric input spaces from the strain response wave. The simulated dynamic response of simply supported bridges in the US Interstate Highway System were performed using Finite Element Modeling of moving loads, generating response waves. Geometric properties of the response waves are the input to train the Kriging metamodel of a predefined training truck group. The performance of the prediction of the GVW is evaluated with the ASTM WIM Standard.

1 INTRODUCTION

Cost effective solutions through Transportation Infrastructure Management approach can support decision making regarding the investment of limited resources. Managers collect high quality data to offer the best information to the stakeholders. Data regarding individual bridge structural conditions and the functional characteristics of the traffic continuously populate large databases to provide quality information for managers to aid in decision making. Examples of this data include the number of axles and the gross vehicle weight (GVW) of heavy truck traffic. This information can be used for the structural design of future bridges and assessment of the remaining service life of current infrastructure.

Weigh stations are the traditional way of obtaining such information with a very accurate result. However, weigh stations are costly and time-consuming to implement. In this context, the concept of smart infrastructure, specifically Weigh-In-Motion (WIM) technology, is an alternative tool that can provide valuable data. The original concept of WIM systems, called Pavement Weigh-In-Motion (PWIM), is to place sensors directly into the pavement, measuring vehicle properties while they cross over the sensors themselves. Although these systems are advantageous, their installation requires lane closures, putting workers in potentially dangerous situations adjacent to moving traffic; and damaging the pavement by cutting or excavating for sensor installation. Further, the dynamic interaction between the pavement and the truck can significantly affect the error in the results (Wall et al, 2009).

DOI: 10.1201/9781003483755-166

Another WIM approach, suggested initially by Moses in 1979 and known as Bridge Weigh-In-Motion (BWIM), is to instrument the structural members of a bridge and use the bridge itself as a calibrated sensor. This approach, installing relatively inexpensive sensors underneath the bridge, provides a cost-effective solution without the costs and risks to construction workers, and damage to the pavement associated with PWIM sensors. There are a variety of proposals for sensor types and locations, and methods for post-processing the raw data recorded by BWIM systems (Yu et al, 2016). For example, the Moses' proposal (1979) is based in minimization of the error between the predicted bending moment and the measured bending moment of a beam-slab bridge. Ojio and Yamada (Ojio & Yamada, 2002) introduced the influence area method, calculating the area under the strain response curve, adjusting for velocity, and using a calibration factor identified from a test calibration truck. Orthotropic algorithms use different optimization routines to minimize the error objective function. Some of these optimization methods are the conjugate direction method (Jacob et al, 2001), genetic algorithms (Jiang et al, 2004; Au et al, 2004; Deng & Cai, 2009), least-squares method and regularization technique (Law et al, 2006). The reaction force method (Ojio & Yamada, 2002; Muñoz et al, 2011) uses the influence line of the reaction force, which allows the axle detection. Other approaches like artificial neural networks (Kim et al, 2009; Hitchcock et al, 2012) offer similar accuracy with the traditional BWIM algorithm using the influence line concept without any knowledge of the bridge behavior. Lobo-Aguilar and Christenson (2019) proposed a simplified approach for shear strain data measured at one third of the span using the difference of magnitude at the discontinuity of record. These methods can be potentially improved using Artificial Intelligence. In this paper, the Kriging metamodeling technique is used as a data post-processing tool that provides a prediction of GVW. Various input parameters are considered to develop general rules for different scenarios, varying the length of the simulated bridges and simulated sensor location.

Kriging, also known as Gaussian process modeling or best linear unbiased prediction (BLUP), is a stochastic modeling algorithm used for generating a simpler model of a complex problem. Gaussian process prediction is used for interpolation, regression, and prediction (Rasmussen & Williams, 2006; Sacks et al, 1989). Applications in two- and three-dimensional input spaces can be found in geostatistics, environmental science, hydrogeology, environmental and climate models, among other specialties. Modern geographic information systems (GIS) include Kriging as an analysis tool. Broader research has demonstrated that Gaussian process prediction could be used in a general context. Sacks et al. (1989) described Gaussian Process Regression (GPR) in computer experiments, and Williams and Rasmussen (1996) described GPR in the machine-learning context. Additionally, Sakata et al. (2003) evaluated the applicability of Kriging metamodeling method to engineering structural optimization providing a stiffened cylinder example. Raponi et al. (2019) proposed the Kriging-Guided Level Set Method (KG-LSM) for the topology optimization of crash structures in both linear elastic and non-linear test cases, addressing the limitations of the state-of-the-art methods for crashworthiness due to strong nonlinearities and discontinuities characterizing the problem. Dang et al. (2020) approximated the dynamic responses of dynamic structures under seismic excitations with Kriging metamodels and then used them to construct fragility curves of the structures. Ligeikis and Christenson (2020) used Principal Component Analysis (PCA) and Ordinary Kriging to metamodel frequency response functions magnitude and phase vectors obtained in experimental structural dynamics tests.

This paper explores critical aspects needed to apply Kriging metamodeling to BWIM GVW prediction. Metamodels were trained with geometrical properties and PCA of the horizontal strain response waves as input space parameters and the GVW as metamodel output. The metamodels were used for GVW prediction and the results compared to the weight data generated in the simulation. Different bridge lengths, sensor locations, training groups, and pre-processing techniques were explored. General rules are identified to aid users in the application of Kriging metamodeling for BWIM of various bridges.

2 THERORETICAL AND EXPERIMENTAL BACKGROUND

2.1 *Kriging metamodeling*

Originally developed as a spatial interpolation tool in geo-statistics (Krige, 1951), Kriging was first proposed as a metamodeling method for computer experiments by Sacks et al. (1989). Metamodeling can reduce the associated computational costs by substituting an expensive computational model with a metamodel, a functional approximation of the original model that is much faster to evaluate.

Several variations of Kriging exist with varying levels of complexity (Christensen, 2001; Wackernagel, 2003; Santner et al, 2003). Ordinary Kriging (OK) is the most widely used Kriging method and was employed for this study. The correlation function (also called kernel or covariance function) relates the correlation between two input samples being crucial in the application of Kriging. There are many different correlation functions that can be used for metamodeling purposes (Lataniotis et al, 2020). Stein (1999) recommended the Matérn (1986) class kernel covariance for physical processes, which was utilized for this study.

2.2 *Geometric manipulation of response waves to generate input spaces*

All the theory behind the generation of Kriging input spaces from the RW can be found Agüero-Barrantes (2022). In these manipulations, the dimensionality of the strain waves is reduced by the calculation of the geometric properties under the curve (centroids and area) and its perimeter. Another proposed parameter is the first principal component of the application of PCA (Jolliffe, 2002). Subsequently, vectors of these new parameters are used as inputs to a Gaussian process model to approximate the weight of the passing vehicles.

2.3 *Experimental validation*

The experimental validation of this research was published in Agüero-Barrantes et al (2022) where the results of the application of this proposal were performed in a single-span simply supported steel bridge. The experimental results demonstrated that a comparable WIM performance for GVW prediction (ASTM, 2017) was obtained comparing the results are with other BWIM methodology (Agüero-Barrantes et al, 2021) with advances in terms of sensor reduction, installation ease, and data processing.

3 FINITE ELEMENT SIMULATION

In order to provide further insight into BWIM, simulations of the traffic stream and the RW are performed. The following general procedure is presented for every Kriging metamodel input space explored.

Finite element modeling (FEM) of a single-span simply supported bridge was developed. The structure was modeled with beam-type elements with vertical and rotational degrees-of-freedom to include displacements, velocities and accelerations. The vehicle axles were modeled as impulsive loads crossing over a beam at constant velocity, which does not interact dynamically with the bridge, which is reasonable assumption for the purpose of this paper purposes (Yang et al, 2004). The FEM simulation was verified using prior BWIM measurement in Connecticut and Costa Rica (Lobo-Aguilar, 2018; Agüero-Barrantes et al, 2021).

The chosen scenario for the BWIM simulation is the US Interstate Highway System. The simulated vehicle types where chosen based on the most representative vehicle classes moving across the United States according to USDOT (2000). The vehicles used for this study (FHWA classes 06, 08, 09, and 10) cover 84.1% of the truck fleet and 86.2% of the travels on US highways. After selecting the vehicle classes, the axle spacing criteria is based on AASHTO (2018) and Hallenbeck et al (2014). The traffic speed range is based on De Leonardis et al (2018).

Further detail of this simulation criteria can be found in Agüero-Barrantes (2022).

4 PREPROCESSING, METAMODELING AND PERFORMANCE CRITERIA

Ordinary Kriging was chosen to implement BWIM for this study. The MATLAB-based uncertainty quantification framework UQLab (Marelli & Sudret, 2014, Lataniotis et al, 2020) was used for the metamodeling generation. In this research, a gradient-based optimization was selected to maintain repeatability in the results. UQLab uses the MATLAB function fmicon() in the gradient-based optimization case. Homogeneous (homocedastic) noise variance was included in the metamodeling calculation, available through the UQLab's command SigmaNSQ.

The performance reported in this research is based on ASTM E1318 standard (2017), which defines the functional performance requirements for PWIM systems that predicts the GVW of vehicles. The ASTM E1318 standard specifies that 95% of the GVW values produced by the WIM system must be within the tolerance limit. The tolerance limit for GVW is ±10% for WIM Systems Type I and ±15% for WIM Systems Type II. For reference purposes, all GVW prediction results include these limits, however, in this research an ASTM E1318 calibration simulation was not performed since the calibration group specified in the standard does not work well the proposed Kriging methodology. The calibration truck criteria used here included three trucks, specifically one three-axle (class 06), one four-axle (class 08), and one five-axle truck (class 09) with variable loading conditions, as described in Agüero-Barrantes (2022). A comparable number of ASTM's calibration runs were proposed to train the Kriging metamodel with the geometric input approach.

In regards of preprocessing, the MATLAB's function cluster() using a Gaussian Mixture Model (GMM) as input was the clustering technique tested in this research. The GMM model was generated with the function fitgmdist(). When clustering is used, more than one metamodel is generated to predict the GVW of the traffic stream. The data clusters are assigned to the corresponding metamodel to improve the performance of the GVW prediction. Strain response wave data can be filtered to retain the static behavior of the bridge using a low-pass filter (LPF). In this study, the simulated response wave data was filtered with an eight-pole LPF with a cut-off frequency of 70% of the first natural frequency of the bridge, as an additional preprocessing tool to compare with non-filtered data results.

5 RESULTS FROM FEM SIMULATION

Three input spaces were explored after FEM simulation, data preprocessing, and geometric-based input space generation. The first input space to explore, tagged as IS1, is based on the area under the response wave A_{RW} and the centroid of this area in the time axis t_c (horizontal centroid); the second and third input spaces tagged as IS2 and IS3, are detailed in Agüero-Barrantes (2022).

Multiple bride lengths (S= 20.4 m, M= 41.1 m, L= 54.9 m), sensor positions (CE= close-to-end, MS=mid-span) and training groups were considered in the simulation. For example, Figure 1 shows the performance of the IS1 prediction based on 1000 vehicles using FEM simulation to generate RWs. The results are sorted by training group (tagged as group A and B) and after that by the highest percentage of compliance between the ±10% tolerance limit (Type I) represented by black bars, and finally by the highest percentage of compliance between the ±15% tolerance limit (Type II) represented by grey bars.

Type II performance is fulfilled (95% or higher compliance) in all length cases of CE sensor location with no preprocessing, with small influence of the training group. That means that preprocessing (clustering or filtering) does not improve the performance for CE sensor location. When the sensor is placed at MS and no preprocessing is performed, the Type II performance is fulfilled in three simulation cases, the clustered data results improved the performance, however the results from LPF data improve the performance from three to five compliant cases.

Regarding Type I performance fulfillment (95% or higher compliance), only two cases are compliant. The first case is the 27.3 m-long (90 ft) bridge with a close-to-end sensor location and GMM cluster preprocessing (tagged as S/CE/GMM in Figure 1a), trained with group A, where

the GMM clustering was able to improve the Type I performance from 89.5% between the ±10% tolerance limit (without clustering) to 95.8% with GMM clustering. The second case corresponds to the 54.9 m-long (180 ft) bridge with a close-to-end sensor location and LPF preprocessing (tagged as L/CE/LPF in Figure 2a), trained with group B, where the GMM clustering was able to improve the Type I performance from 68.7% between the ±10% tolerance limit (without clustering) to 95.3%.

Full performance results, including IS2 and IS3, can be found in Agüero-Barrantes (2022).

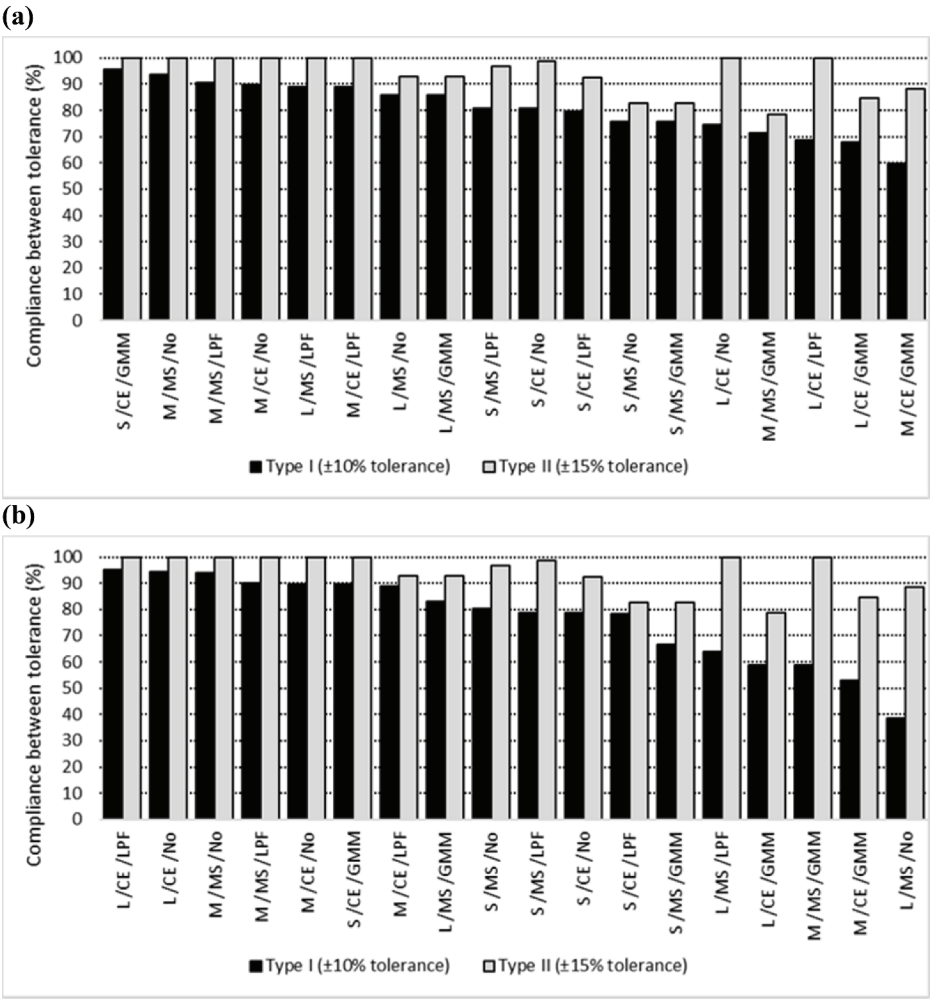


Figure 1. IS1 simulation performance analysis for (a) Group A, (b) Group B (CE= close-to-end, MS=mid-span, S= 20.4 m, M= 41.1 m, L= 54.9 m).

6 CONCLUSIONS

This paper presents a summary of the applied methodology to predict the GVW of moving trucks, based on simulated traffic data, and using Kriging metamodeling to ease the calculation process. This analysis provides insight of the artificial intelligence application to BWIM. Different geometric input spaces, bridge lengths, sensor locations, training groups, and preprocessing techniques were studied. This research demonstrates very promising results to use

Kriging metamodeling for the GVW prediction with a single sensor, without measurement or calculation of the vehicle velocity.

An example was presented, based on the ASTM E1318 performance requirements for WIM systems, Type II performance can be fulfilled for all analyzed bridge lengths with close-to-end sensor location and no preprocessing. Regarding satisfying the Type I WIM system performance, it is compliant in some cases involving Gaussian Mixture Model clustering and Low Pass Filtering. The upcoming challenge to investigate Kriging metamodeling for GVW prediction is to improve the performance to fulfill Type I WIM system requirements. It is recommended to analyze the spatial correlation of the input-output space data, developing BWIM specific covariance functions.

REFERENCES

AASHTO (2018). A Policy on Geometric Design of Highways and Streets. 7th Edition. American Association of State Highway and Transportation Officials.

Agüero-Barrantes, P., Lobo-Aguilar, S. & Christenson, R.E. 2021. Sparse Sensing Bridge Weigh-in-Motion for Single-Span Bridges. Métodos y Materiales. Vol. 11. 2215–4558.

Agüero-Barrantes, P., Christenson, R. E. & Lobo-Aguilar, S. 2022. Utilizing Kriging Metamodeling to provide Practical and Effective Bridge Weigh-In-Motion. Journal of Bridge Engineering, ASCE, 1084-0702. DOI: 10.1061/JBENF2.BEENG-5760.

Aguero-Barrantes, P. 2022. "Advanced Testing and Monitoring of Transportation Structures toward Sustainable Infrastructure". Doctoral Dissertation. University of Connecticut. http://hdl.handle.net/11134/20002:860706942

ASTM Standard E1318, 09. 2017. Standard Specification for Highway Weigh-In-Motion (WIM) Systems with User Requirements and Test Methods, ASTM International, West Conshohocken, PA, DOI: 10.1520/E1318-09R17, www.astm.org.

Au, F., R. Jiang & Y. Cheung. 2004. Parameter identification of vehicles moving on continuous bridges. Journal of Sound and Vibration. 269(1-2): 91–111.

Christensen, R. 2001. Advanced Linear Modeling. Multivariate, Time Series, and Spatial Data: Nonparametric Regression and Response Surface Maximization. Second Edition. Springer-Verlag, New York. DOI: 10.1007/978-1-4757-3847-6.

Dang, C. T., T. Tran, D. M. Nguyen, M. Pham & T. P. Le. 2020. Use of Kriging metamodels for seismic fragility analysis of structures. CIGOS 2019, Innovation for Sustainable Infrastructure. https://doi.org/10.1007/978-981-15-0802-8_45.

De Leonardis, D., Huey, R. & Green, J. 2018. National Traffic Speeds Survey III: 2015. Report No. DOT HS 812 485. National Highway Traffic Safety Administration. Washington, DC.

Deng, L. & C. S. Cai. 2009. Identification of parameters of vehicles moving on bridges. Engineering Structures. 31(10): 2474–2485.

Hallenbeck, M. E., O. I. Selezneva & R. Quinley. 2014. Publication No. FHWA-HRT-13-091: Verification, Refinement, and Applicability of Long-Term Pavement Performance Vehicle Classification Rules. Federal Highway Administration.

Hitchcock, W.A., N. Uddin, V. Sisiopiku, T. Salama, J. Kirby, H. Zhao H. Toutanji & J. Richardson. 2012. Report Number 07212: Bridge Weigh-In-Motion System Testing and Evaluation., University Transportation Center of Alabama.

Jacob, B., Cebon, D., O'Brien, E. J., Henny, R., de Vaulchier, G., Grandpré, D., Hallström, B., Jehaes, S., Baumgärtner, W., Huhtala, M., Znidaric, A. & Caprez, M. 2001. Weighing-in-Motion of axles and vehicles for Europe (WAVE). General Report. RTD project, RO-96-SC, 403. Laboratoire Central des Ponts et Chaussées.

Jiang, R., F. Au & Y. Cheung. 2004. Identification of vehicles moving on continuous bridges with rough surface. Journal of Sound and Vibration. 274(3-5): 1045–1063.

Jolliffe, I. T. 2002. The Principal Component Analysis. Second Edition. Springer-Verlag New York. 0-387-95442.

Kim, S., S. Lee & M. Park. 2009. Vehicle signal analysis using artificial neural networks for a bridge weigh-in-motion system. Sensors. 9(10): 7943–7956.

Krige, D. G. 1951. A statistical approach to some mine valuation and allied problems on the Witwatersrand. Master's Thesis, University of the Witwatersrand, South Africa.

Lataniotis, C., D. Wicaksono, S. Marelli & B. Sudret. 2022. UQLab user manual – Kriging (Gaussian process modeling). Report # UQlab-V2.0, Chair of Risk, Safety and Uncertainty Quantification, ETH Zurich, Switzerland.

Law, S. S., J. Q. Bu, X. Q. Zhu & S. L. Chan. 2006. Vehicle condition surveillance on continuous ridges based on response sensitivity. Journal of Engineering Mechanics. 132(Wall et al, 2009): 78–86.

Ligeikis, C. & R. E. Christenson. 2020. Identifying Stochastic Frequency Response Functions Using Real-Time Hybrid Substructuring, Principal Component Analysis, and Kriging Metamodeling. Experimental Techniques. The Society for Experimental Mechanics. https://doi.org/10.1007/s40799-020-00389-2

Lobo-Aguilar, S. 2018. Advances in Smart Structure Technologies for Civil Infrastructures. Doctoral Dissertations. No.1870, 2018. https://opencommons.uconn.edu/dissertations/1870

Lobo-Aguilar, S. & R. E. Christenson. 2019. A simplified shear-strain based Bridge Weigh-in-Motion Method for in-Service Highway Bridges. Métodos y Materiales. Vol. 8. 2215–4558.

Marelli, S. & B. Sudret. 2014. UQLab: A Framework for Uncertainty Quantification in MATLAB. In The 2nd International Conference on Vulnerability and Risk Analysis and Management (ICVRAM 2014), University of Liverpool, United Kingdom, July 13–16, pp. 2554–2563. DOI:10.1061/9780784413609.257.

Matérn, B. 1986. Spatial Variation. Second Edition. Springer-Verlag, Berlin.

Moses, F. 1979. Weigh-in-motion system using instrumented bridges. Transportation Engineering Journal of ASCE. 105(3): 233–249.

Muñoz, E., D. Gómez, F. Núñez & C. Florez. 2011. Determinación de Cargas Dinámicas de Camiones Pesados que Transitan en un Puente Basado en Algoritmos Genéticos e Instrumentación. Revista Ingeniería y Construcción. Vol. 26 pp. 321–352. http://dx.doi.org/10.4067/S0718-50732011000300005

Ojio, T. & K. Yamada. 2002. Bridge Weigh-In-Motion System Using Stringer of Plate Girder Bridges. Pre-proceedings of the 3rd International Conference on Weigh-In-Motion, Orlando, Florida, pp. 209–218.

Ojio, T. & K. Yamada. 2005. Bridge WIM by reaction force method. System Using Stringer of Plate Girder Bridges. Pre-proceedings of the 4th International Conference on Weigh-In-Motion, Taipei, Taiwan. pp. 209–218.

Raponi, E., M. Bujny, M. Olhofer, N. Aulig, S. Boria & F. Duddeck. 2019. Kriging-assisted topology optimization of crash structures. Computer Methods in Applied Mechanics and Engineering. 348 (2019) 730–752. https://doi.org/10.1016/j.cma.2019.02.002

Rasmussen, C. E. & C. K. I. Williams. 2006. Gaussian processes for Machine Learning. The MIT Press. Massachusetts Institute of Technology.

Sacks, J., W. J. Welch, T. J. Mitchell & H. P. Wynn. 1989. Design and analysis of computer experiments. Statistical science. 409–423.

Sakata, S., F. Ashida & M. Zako. 2003. Structural optimization using Kriging Approximation. Computer Methods in Applied Mechanics and Engineering. 192: 923–939.

Santner, T. J., B. J. Williams & W. I. Notz. 2003. The Design and Analysis of Computer Experiments. New York, NY: Springer-Verlag.

Stein, M. L. 1999. Interpolation of Spatial Data. Springer-Verlag. New York.

USDOT. 2000. Publication Number: FHWA-PL-00-29: Comprehensive Truck Size and Weight Study. The U.S. Department of Transportation's. fhwa.dot.gov/reports/tswstudy

Wackernagel, H. 2003. Multivariable Geostatistics. Third Edition. Springer-Verlag, Berlin. DOI: 10.1007/978-3-662-05294-5.

Wall, C. J., R.E. Christenson, A.H. McDonnell, & A. Jamalipour. 2009. Report No. CT-225-3-09-5: A Non-Intrusive Bridge Weigh-in-Motion System for a Single Span Steel Girder Bridge Using Only Strain Measurements. Office of Research and Materials. Bureau of Engineering and Construction. Connecticut Department of Transportation.

Williams, C. K. I. & C. E. Rasmussen. 1996. Gaussian Processes for Regression. In Advances in Neural Information Processing Systems 8 (Touretzky, D. S., M. C. Mozer, and M. E. Hasselmo, ed.), MIT Press, 1996. pp. 514–520.

Yang, Y. B., J. D. Yau & Y. S. Wu. 2004. Vehicle-Bridge Interaction Dynamics. With Applications to High-Speed Railways. World Scientific Publishing Co. .

Yu, Y., C. S. Cai & L. Deng. 2016. State-of-the-Art Review on Bridge Weigh-in-Motion Technology. Advances in Structural Engineering. Vol 19(9) 1514–1530. DOI: 10.1177/1369433216655922.

Bridge Maintenance, Safety, Management, Digitalization and Sustainability – Jensen, Frangopol & Schmidt (eds)
© 2024 The Author(s), ISBN 978-1-032-77040-6
Open Access: www.taylorfrancis.com, CC BY-NC-ND 4.0 license

Challenges of implementing bridge weigh-in-motion on a century-old steel-riveted railway bridge

D. Hekič, M. Kosič, J. Kalin, A. Žnidarič & A. Anžlin
Slovenian National Building and Civil Engineering Institute, Ljubljana, Slovenia

ABSTRACT: This study explores the challenges and methodologies involved in implementing bridge weigh-in-motion (B-WIM) system on a century-old steel riveted railway bridge. A unique aspect of this study, funded by the EU H2020 Shift2Rail Joint Undertaking, was the adaptation of B-WIM systems to the specific constraints of railway bridges since, traditionally, this technology is used to collect heavy gross vehicle loading data on road bridges. The paper details the experimental setup on an old steel-riveted railway bridge, including sensor placement and calibration processes. It highlights the complexities encountered, such as differences in bridge response due to passenger and other type of trains. It introduces the system calibration strategy using known axle loads from passenger locomotives. The study provides insights into the structural response of old steel bridges under traffic loads, contributing valuable data to the field of railway bridge monitoring and maintenance.

1 INTRODUCTION

With a few exceptions (Liljencrantz et al. 2007), the bridge weigh-in-motion (B-WIM) systems have been primarily used for road bridges. The BridgeMon project (Ni Choine et al. 2014) showed that the algorithms used for road bridges can be adapted for use on railway bridges, with some constraints related to vehicle design. At the same time, B-WIM measurements within the Assets4Rail project (Anžlin et al. 2020) exposed some new challenges, likely associated with the complex behaviour of old steel bridges (Lachinger et al. 2021).

This recently concluded project, which received funding from the Shift2Rail Joint Undertaking under the EU H2020 funding, aimed to contribute to the modal shift by developing new railway asset monitoring and maintenance technologies. Part of the project was the fatigue lifetime assessment of existing steel railway bridges, considering realistic traffic loads and structural response under actual traffic loads. Performing B-WIM measurements on a century-old steel riveted bridge and under all the traffic on the bridge required some simplifications of the applied procedures. One was the B-WIM system calibration procedure, which applies axle loads and distances of statically weighed calibration vehicles as a reference. In this case, the system was calibrated using axle loads and distances of a passenger train locomotive taken from the publicly available technical specifications.

The implemented strategy worked well for random passenger trains. However, deviations have been observed when correlating the B-WIM weights of the trains with the measured displacements near the mid-span of the bridge. This paper presents the calibration procedure and monitoring results and discusses possible reasons for the load-dependent phenomena and/or challenges at B-WIM weights estimation.

2 TEST BRIDGE DESCRIPTION

The tests were performed on a 100-year-old steel-riveted bridge, shown in Figure 1. The bridge consists of two parallel steel superstructures placed on masonry abutments, spaced

DOI: 10.1201/9781003483755-167

16 m from each other and positioned obliquely to the track alignment. The distance between the structural bearings is 18.5 m. Each superstructure is 5 m wide, and the height between the rolling surface and the road below is 4.8 m. The superstructure is designed as a grillage made of steel sections connected with rivets and no welds.



Figure 1. View from the top (left) and bottom (right) of the old steel riveted bridge.

The main (plate) girders are 210 cm high and 1.2 cm thick. Its upper and bottom flange are both 25 cm wide. Close to the bridge mid-span, the thickness of the bottom flange is increased to withstand the bending moments. The 75 cm high cross girders with 32 cm width flanges distribute the load between the two main girders. The stringers (secondary longitudinal beams), placed under the railway sleepers, distribute the load to the cross girders. They are 50 cm high with 25 cm wide flanges. 1.2 cm thick steel plates are used for all stringers. The track consists of UNI 60 rails and indirect and rigid fastening systems. The wooden sleepers are anchored to the structure with metal anchor bolts.

Besides structural elements whose primary purpose is to carry vertical loads, bracing below the deck, made primarily of riveted L steel sections, carries horizontal loads. It consists of wind bracing (WB) and lateral torsional buckling bracing (LTB) of longitudinal beams.

3 EXPERIMENTAL SETUP

The bridge measurement system considered various types of sensors. The 3-axial MEMS accelerometers (DEWESoft 2023) were labelled from A01x, A01y, A01z to A12x, A12y, A12z. Four inductive strain transducers, labelled e1 to e4, measured strain in micrometres per meter (μm/m). The setup also comprised two linear variable differential transformers, LVDT1 and LVDT2, for measuring displacement. The 12 foil-type strain gauges, labelled SG01 to SG10, SMP1 and SMP2, acquire the strains in μm/m. Sensors SG01 to SG10 were used to measure the structural response, while SMP1 and SMP2 captured strains in railway rail for B-WIM axle and velocity detection purposes. The disposition of the sensors in plain view is shown in Figure 2.

After on-site inspection, the initial sensor disposition had to be adjusted as some locations were unsuitable for the sensor installation. The geometry of the entire bridge was measured on-site, and a 3D model with final sensor disposition was created (Figure 3). This model served as geometry input for creating the BIM model and integrating the sensor data in the BIM model, which was a separate test of the EU project.

Strains from the SG07 sensor installed at the midspan of the S2_L element were used to calculate the axle loads of the ongoing traffic. SG06 sensor was installed parallel to the SG07 sensor at the S2_R element. E1 sensor was installed at the midspan of the WB diagonal, which connects the CG1 and CG2 elements. SG05 was installed at the top flange of the CG4 element, and SG06 was installed at the bottom flange. SG09, SG10, and E3 sensors were mounted on the S2_L element, as shown in Figure 4.

The accelerometers A09-A12 were installed on the top flange of the PG elements, and the A01-A08 on the bottom flange. Displacements were measured with LVDT1 and LVDT2 at the left and right PG midspan, respectively. SG03 and SG04 captured strains in PG at LVDT1 and LVDT2 locations, respectively. SMP1 and SMP2 sensors were glued on the bottom side of the

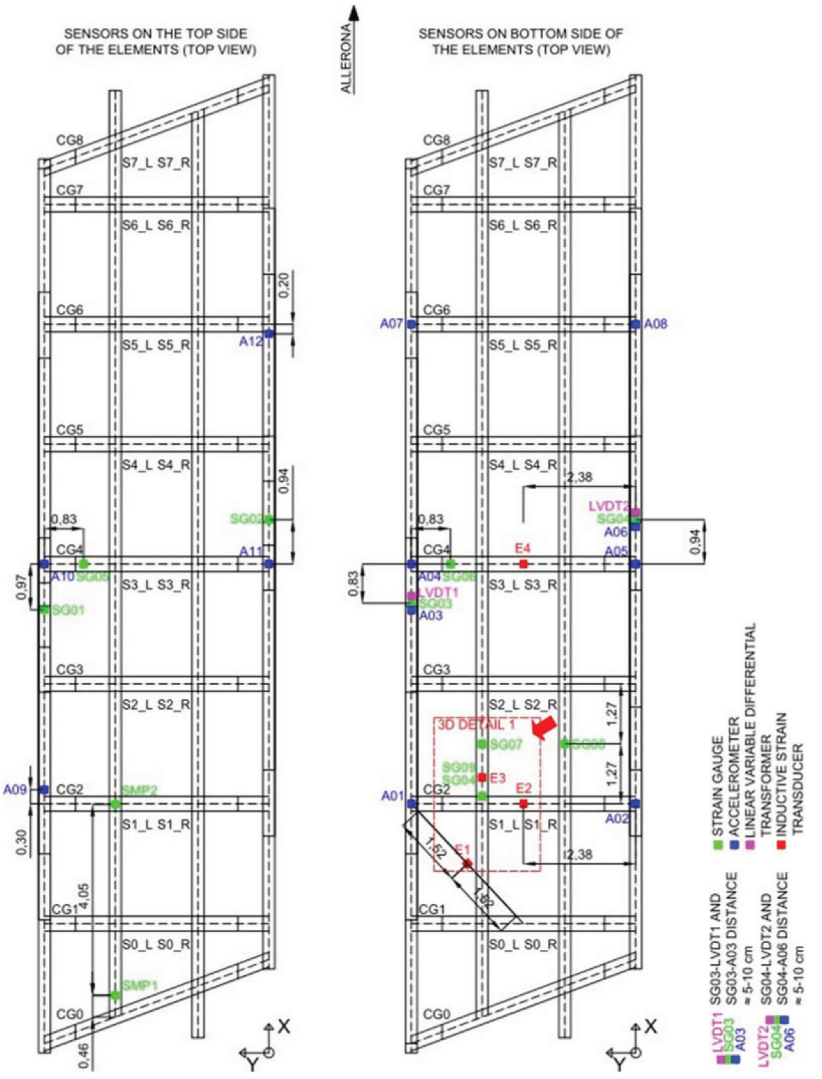


Figure 2. Disposition of the sensors in plain view on the upper (top) and lower side (bottom) of the elements.

rail to detect trains' axles and velocities for the B-WIM calculations. Finally, only SMP1 was used to detect axles. E2 and E4, installed at the midspan and the bottom flange of cross girders, provided inputs to calculate the speed of the crossing trains.

4 CALIBRATION OF THE B-WIM SYSTEM

B-WIM systems collect axle loads, axle distances and headways of all heavy freight vehicles crossing the instrumented bridge. This information is vital for optimised bridge safety analysis, which ensures structural integrity and safety of bridges and, at the same time, allows for optimal management of bridge stock. Calibration of any WIM system is essential to ensure the accuracy and reliability of measurements.

During the bridge testing, 23 train passages were recorded over 14 hours, most driving at approximately 90-100 km/h. This included seven passenger trains exhibiting similar responses and eight long freight trains. The remaining eight passages were unclassified.

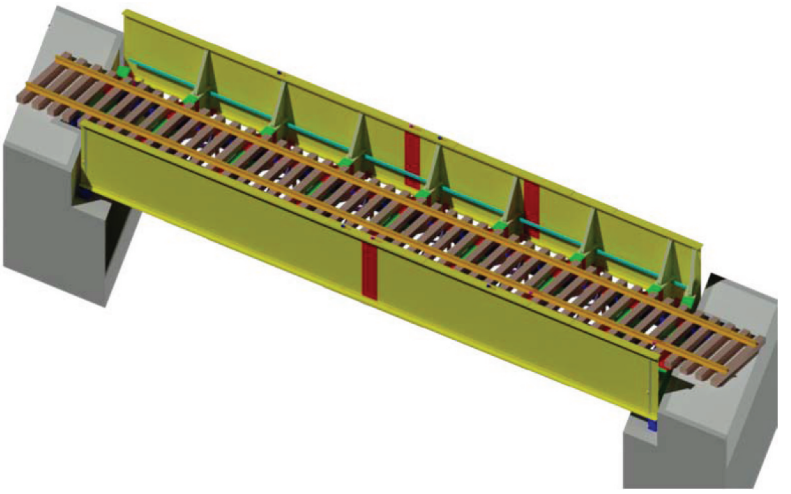


Figure 3. The 3D bridge model with sensor locations.

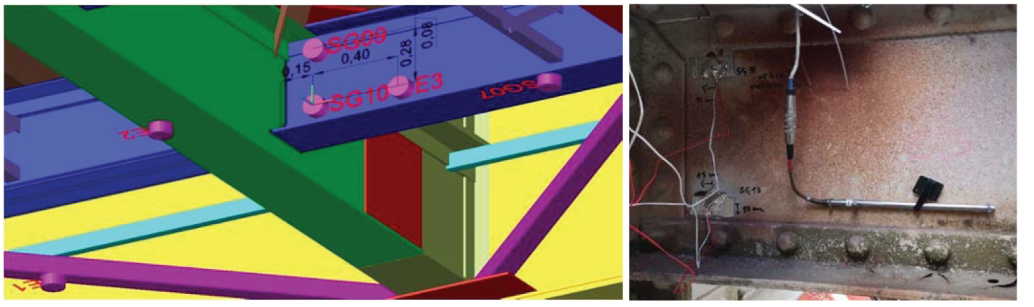


Figure 4. 3D view of the position of sensors SG07, SG09, SG10, E2, and E3 (left); installed sensors SG09, SG10 and E3 mounted on the bridge.

The B-WIM system calibration accounts for all bridge details, like concrete and steel thicknesses, which influence the relationship between the weights calculated by the B-WIM algorithm from the measured strains and the actual axle loads. For road-based B-WIM systems, calibration typically involves vehicles with statically weighed axle loads that cross the bridge multiple times. The mean value of the actual vs. measured weight ratios is taken as the calibration factor and is used to convert the strain-based results into kN.

Implementing this procedure on railway tracks is challenging as the weighing stations for trains are not always available. Furthermore, hiring a calibration train to perform multiple crossings is expensive and time-consuming. In our study, we had no information about the axle loads of the trains passing over the bridge. Nevertheless, it is beneficial for railway B-WIM applications that the weights of the locomotives are relatively consistent, especially of the electric passenger locomotives that do not carry fuel or passengers (Figure 5). The study revealed that the locomotives of these trains were of the type E.464, each with a gross weight of 72 tons (Locomotiva FS E.464. 2021).

Upon examining the signals from the B-WIM system, it was noted that the locomotives in all seven passenger train passages had almost identical axle distances and similar weights. Hence, it was assumed these were the same type of locomotives, suitable for use in calibration. The calibration factor was adjusted to align the mean Gross Vehicle Weight (GVW) of these locomotives (12 overall) to 72 tons. The standard deviation of the GVWs was 3.3% of the mean, placing the accuracy of the locomotives' GVWs in the accuracy class B(10) according to the European specifications for weigh-in-motion (Jacob et al. 2002).



Figure 5. Locomotive type E.464, captured during the test (left) and from Wikipedia (Incola 2021) (right).

5 INITIAL FE MODEL

The test bridge model was designed using the software package MIDAS Civil (2020). Its extruded 3D view is given in Figure 6.

All structural elements were formulated according to the Timoshenko beam theory, with the effect of shear deformations considered. The connections of all elements were assumed to be fixed at both ends, except for bracing elements, which were assumed to be pinned at both ends. The geometry, cross-sections and material properties were defined according to the original design documentation and on-site measurements. To model its exact geometry, rigid links were used to connect centroids of interconnected elements. While the cross-section of stringers and cross girders did not vary with length, the cross-section of the plate girder near the mid-span had more stiffening plates on the flanges. Therefore, five different cross-sections were defined only for modelling plate girders. Figure 7 compares the model with the actual structure, focusing on the cross–girder–plate detail. Rigid links were defined in the FE model to take into account the stiffening effects provided by the connection.

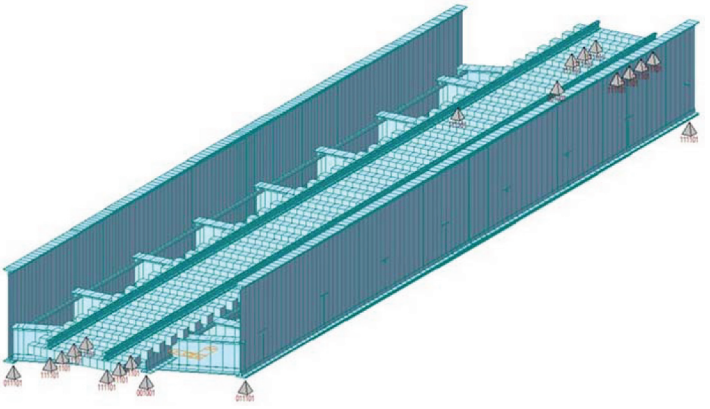


Figure 6. Extruded 3D view of the initial finite element (FE) model.

6 MANUALLY CALIBRATED FE MODEL

To more realistically estimate the remaining lifetime of the considered bridge, the initial FE model was manually calibrated to match the measured response. The calibrated FE model afterwards served to estimate the number of cycles for fatigue estimation in critical details. A series of measurements were performed for this purpose: accelerations (ambient vibrations), strains and displacements (under passing trains).



Figure 7. Cross girder – plate girder detail: structure (left) and FE model (right).

Table 1. Comparison of natural frequencies: Measurements, initial and calibrated FE model.

Frequency [Hz]	Measurements	Initial FE model	Calibrated FE model
1st bending	11.0 – 11.5	14.6	11.8
1st torsion	16.0	19.2	16.0

An enhanced frequency domain decomposition (EFDD) technique (Structural Vibration Solution 2023) was used to identify natural frequencies and mode shapes. Table 1 summarises the comparison of the measured natural frequencies with those obtained from the initial and calibrated FE model. 1st bending and 1st torsional natural frequencies were used to calibrate the FE model.

The close agreement between the measured and modelled frequencies for both bending and torsional modes was achieved mainly with additional mass, which was taken into account as a uniform increase of steel density for all steel structural elements by 11 %. This mass increase was identified by comparing the detailed 3D model (Figure 3), which included all the non-structural elements and connecting plates. While the overall mass of the initial FE model was 33 tons, the overall mass of the calibrated FE model was 37 tons (both masses exclude the mass of the sleepers and rails). Another essential modification of the initial FE model was the reduction of Young's elastic modulus of all structural elements by 5 % to globally take into account the weakened structural elements due to corrosion and loosened connections. While structural bearings, according to the design documentation, enabled the rotation of the supports both in longitudinal, transverse and vertical directions, it was observed on the site that due to corrosion of those bearings, the rotations in transverse and vertical directions might have been prevented. This was taken into account in the calibrated FE model.

Measured and modelled displacements and strains were primarily compared for passenger trains. Trains were simulated statically in the FE model, moving point forces (axles) step by step. Axle loads and distances needed to form the train in the FE model were obtained from the B-WIM.

Figure 8 compares displacements for measured response and responses of the initial and calibrated FE models during the train passage nr. 3 (passenger train). The first and last vehicles in this train were electric locomotives (Incola 2021), which were among 12 locomotives used for B-WIM calibration. GVWs of locomotives and wagons were estimated as 69.8 t, 37.1 t, 38.3 t, 36.9 t, 34.9 t, 36.7 t, 36.0 t, 37.0 t and 69.2 t. Note that although displacements capture the global response of the bridge, the number of valleys in the signals is not the same as the number of vehicles in the train. This is mainly due to the wheelbase of the wagons, which is greater than the span length.

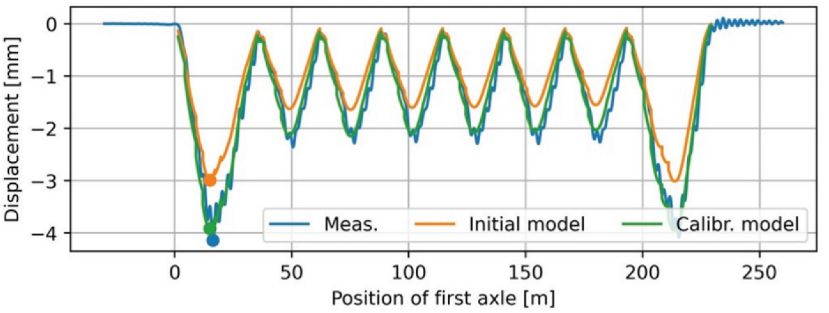


Figure 8. Comparison of measured and modelled displacements during train passage nr. 3 (passenger train) at LVDT1 sensor for the initial and manually calibrated FE model.

Comparing the FE model responses with the measurements in Figure 8, it is clear that the calibrated FE model agrees well with the actual structure. Minimum values of the measured, initial FE and calibrated FE model response are marked with blue, orange and green markers and amount to -4.1 mm, -3.0 mm and -3.9 mm, respectively.

Figure 9 compares the measured and modelled responses under the train passage nr. 9, which is a light train of unidentified type and does not contain the locomotive for B-WIM calibration. GVWs of locomotives and wagons were estimated as 49.2 t, 48.0 t and 50.3 t.

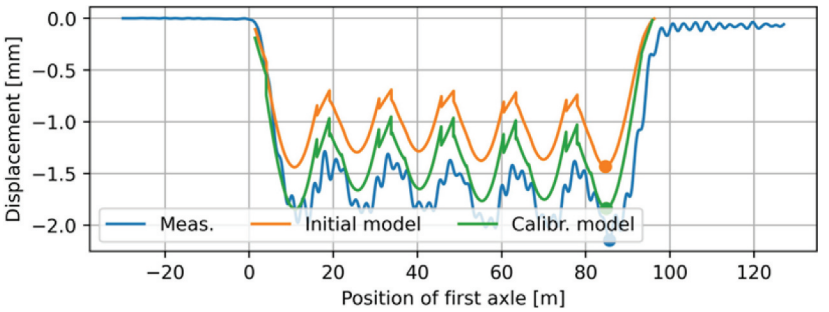


Figure 9. Comparison of measured and modelled displacements during train passage nr. 9 (light train, unidentified type) at LVDT1 sensor for the initial and manually calibrated FE model.

A comparison of the minimum measured and modelled responses of -2.1 mm, -1.4 mm and -1.8 mm (markers in Figure 9) indicates that a match of the calibrated FE model with the measurements is poorer than for the train passage nr. 3. Similar trend was observed for other train passages which are not shown in this paper, mainly for the ones which did not contain the calibration locomotives. This deviation might identify the load-dependant phenomena, such as flexibility of the connections or non-linear friction in the structural bearings. The deviation can also be viewed in the way that the weights of lighter trains were underestimated, resulting in the underestimated response of the FE model. Finally, the ratio of the mass of the calibration locomotive versus the mass of the bridge is high - approximately 2, suggesting that both the B-WIM algorithm and the FE model should be upgraded to account for the inertia effects of the passing trains, which are negligible for the roadway (concrete) bridges.

7 CONCLUSIONS

The B-WIM system application on a century-old steel-riveted railway bridge introduced challenges associated with its complex behaviour under train loading. The study demonstrated that the B-WIM system setup effectively monitored the bridge performance under the traffic

loading. The calibration procedure was adapted for railway B-WIM applications using passenger train locomotives with known and stable gross weights to calculate the calibration factors for B-WIM measurements. Those results were used to simulate the train passages in the FE model and compare the modelled and measured responses. Such a calibration process proved effective for railway B-WIM measurements but highlighted the need to extend the calibration to diverse train types.

The calibrated FE model provided an excellent match with the measured 1st bending and 1st torsional frequency. It also matched well with the measured displacements at the mid-span of the bridge, especially for the train passages that included the calibration locomotive. Deviations from the measurements were observed for trains that differed from the passage trains in terms of weights and axle configurations, indicating the possible load-dependent phenomena and/or inaccurately estimated B-WIM weights.

The results contributed to understanding the dynamic performance of old railway bridges under ambient vibrations and under train passages. Moreover, they highlighted the important contribution of the railway B-WIM systems, which provide the necessary data to calibrate the FE models on the response under train. Future research will focus on the calibration methods and explore the structural specifics and detailed modelling of various bridge designs to improve the accuracy and reliability of B-WIM measurements for railway applications. Moreover, B-WIM algorithms and the FE models should be improved to account for the dynamic response of the bridge and bridge-vehicle interaction, mostly due to large vehicle-to-bridge mass ratio.

REFERENCES

Anžlin, A., Hekič, D., Kalin, J., Kosič, M., Ralbovsky, M. & Lachinger, S. 2020. Assets4rail deliverable D3.3: Improved fatigue consumption assessment through structural and on-board monitoring.

DEWESoft, 2023. DEWESoft IOLITEi 3xMEMC-ACC [online]. Available from: https://downloads.dewesoft.com/brochures/dewesoft-iolitei-3xmems-acc-datasheet-en.pdf [Accessed 26 Dec 2023].

Incola, 2021. Locomotiva E.464.603 in sosta presso la stazione di Asti. [online]. Wikipedia. Available from: https://it.wikipedia.org/wiki/File:E.464.603_Asti.tif [Accessed 23 Sep 2021].

Jacob, B., OBrien, E.J. & Jehaes, S. (Eds.). 2002. Weigh-in-Motion of Road Vehicles: Final Report of the COST 323 Action.

Lachinger, S., Ralbovsky, M., Vorwagner, A., Hekič, D., Kosič, M. & Anžlin, A. 2021. Numerical calibration of railway bridge based on measurement data. In *Structural Engineering for Future Societal Needs; Proc. IABSE congress, Ghent 2021*: 1264–1272.

Liljencrantz, A., Karoumi, R., & Olofsson, P. 2007. Implementing bridge weigh-in-motion for railway traffic. *Computers & Structures*, 85 (1), 80–88.

Locomotiva FS E.464. [online], 2021. Wikipedia. Available from: https://it.wikipedia.org/wiki/Locomotiva_FS_E.464 [Accessed 4 Sep 2021].

MIDAS Information Technology Co., Ltd., MIDAS Civil, v1.2. [online], 2020. Available from: https://www.midasoft.com/bridge-library/civil/products/midascivil [Accessed 27 Jan 2023].

Ni Choine, M., Žnidarič, A., Corbally, R. & Kalin, J. 2014. Algorithm & Techical Specification for combined Railway Bridge WIM/SHM system.

Structural Vibration Solution. 2023. ARTeMIS Modal Pro [online]. Available from: https://www.svibs.com/artemis-modal-pro/ [Accessed 26 Dec 2023].

Bridge Maintenance, Safety, Management, Digitalization and Sustainability – Jensen, Frangopol & Schmidt (eds)
© 2024 The Author(s), ISBN 978-1-032-77040-6
Open Access: www.taylorfrancis.com, CC BY-NC-ND 4.0 license

Radio-interferometry based continuous bridge deformation monitoring – a case study

K. Leppänen, J. Salmi, M. Fattah, T. Heikkinen, M. Lehtinen, O. Leppänen & N. Väisänen
Koherent Oy, Vantaa, Finland

T. Tirkkonen & H. Raunio
Finnish Transport Infrastructure Agency, Helsinki, Finland

ABSTRACT: New technology for continuous and accurate monitoring of bridges is presented. The technology is based on radio interferometry and allows bridge deformation monitoring with down to sub-millimeter accuracy over spans of several hundreds of meters in all weather conditions. As the technology allows affordable 24/7 3D monitoring of both slow changes over years as well as accurate characterization of vibration modes, it is a suitable data source for digital twins and bridge condition evaluation through data analysis techniques including artificial intelligence. This paper presents a case study where the system has been installed on a 220-meter suspension bridge. The basic operation of the technology and the deployment configuration on the bridge are described. The performance of the system is analyzed and compared against an optical reference measurement system. Finally, the suitability of the new monitoring technology for different bridge types is discussed.

1 INTRODUCTION

With the aging bridge infrastructure there is a continuous need to improve structural health monitoring (SHM) technologies. Especially the ability to reliably, continuously, accurately and directly measure both slow and fast movements in bridges has been practically absent. Continuous 3D displacement data also opens new opportunities for sophisticated data analysis techniques for the estimation of the remaining structural lifetime.

In this paper we present a new radio based SHM technology that is designed exactly for this purpose. We analyze its performance in a case study where the technology was tested in a real bridge. The case study was arranged in co-operation between the Finnish Transport Infrastructure Agency and Koherent, a Finnish start-up company established in 2019 that has developed the technology. The bridge, an old suspension bridge with 220-meter span, was selected as it already has rich SHM instrumentation that can be used for measurement data comparison.

In Section 2 we describe the technology itself. Section 3 introduces the bridge and the reference instrumentation. Section 4 describes the installation and the running of the case study. The results are analyzed in Section 5. Finally, in Section 6 we give conclusions.

2 THE NEW MEASUREMENT TECHNOLOGY

2.1 *Measurement principle*

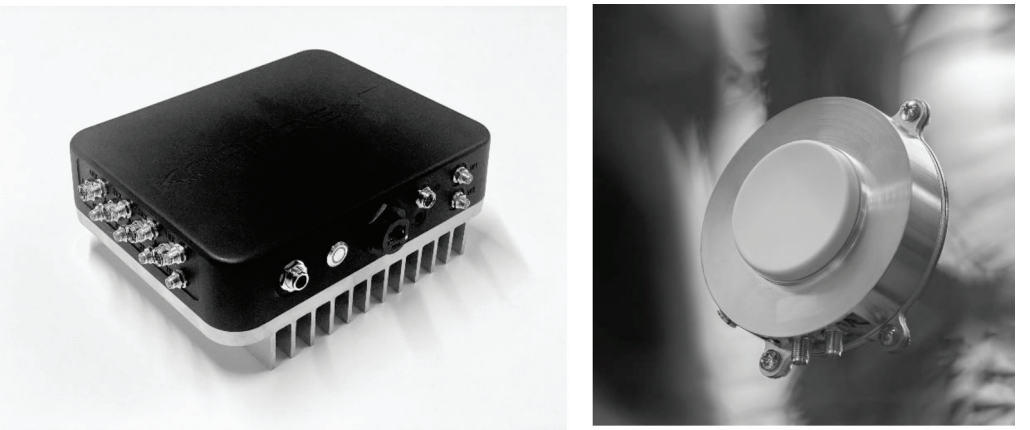
The main principle is the very accurate measurement of distance between the sensors. Radio signals in the 5 GHz Wi-Fi band are sent from sensor to sensor and the accurate distance between the reference points of the sensors is measured constantly. This is based on

DOI: 10.1201/9781003483755-168

interferometric measurement, i.e., measurement of the radio signal phase. The intrinsic accuracy of the phase measurements is good enough to reach a precision of a few tens of micrometers in the distance measurement. The system constantly measures the instrumental phase response which is removed from the data. This allows a high absolute accuracy for the measurement as well as eliminates any drift caused by hardware aging. The oscillator used as the time standard is accurate enough not to cause a noticeable distance error within the measurement precision.

2.2 *Hardware*

The hardware components are 1) the radio unit (RU); see Figure 1a, that forms the signals to be transmitted and processes the received signals; 2) the active sensor unit (SU), see Figure 1b, that actually transmits and receives the measurement signals. Up to four SUs can be connected to a single RU with coaxial signal cables. The reference point to which all the positions or distances refer to is a couple mm below the middle of the round plastic cover.



a) b)

Figure 1. a) Radio Unit (RU); b) Sensor unit (SU).

Figure 2 Illustrates the Koherent system architecture for SHM. The RU is connected to the computing cluster, e.g., through a 4G or 5G network. The computing cluster both controls the measurement hardware and computes the distances between the sensor reference points. The maximum supported position update rate is 200 Hz, allowing 3D measurement of vibrations in the structure up to 100 Hz frequency. In large structures, much lower measurement rates can be used. Also, long-term changes in the structures can be monitored by the same system, i.e., it covers time scales from 10 milliseconds to several years.

Deployment of the system requires power and communication for the radio units. The power requirement is 10 watts for continuous measurement. The power can be reduced significantly by using a low-duty-cycle mode where the measurements are conducted e.g. once per hour. In such usage a solar panel would suffice. In icy conditions it is possible to switch on heaters in the sensor units. This will increase the power consumption to almost 30 watts. The radio units are equipped with Wi-Fi and Ethernet that allow many different communication options to the computation cluster. The communication cluster can be in the cloud, edge cloud or on-premises. During installation, there is no need to measure the sensor positions: the system will measure the mutual geometry automatically upon start-up.

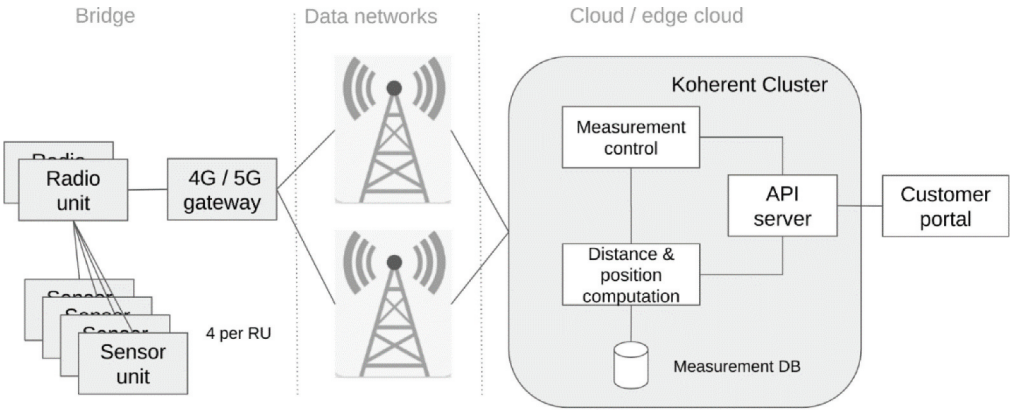


Figure 2. Koherent system architecture for structural health monitoring.

2.3 *Key features*

The main advantages of the new measurement technology are

1) the ability to measure distance changes accurately (within 0.1 millimeters) over distance of hundreds of meters when a clear line-of-sight is available between the sensors and the changes in air refractive index are compensated (point 5 in the limitations below);
2) low instrumental drift in the measurement over the years: the estimated distance remains within a few tenths of a millimeter regardless of the measurement distance;
3) insensitivity to weather: due to the low operation frequency, rain, snow, fog, dust etc. do not have significant impact;
4) significantly better tolerance to interference compared to RTK GNSS.

Only points 1 and 2 were validated with high confidence in this case study. Points 3 and 4 were validated to some extent. However, the conditions on the test bridge were not especially challenging in those respects.

Also, it should be possible to measure relative displacements through a wall, assuming the radio propagation characteristics of the wall (e.g., water content in the wall) do not change significantly. However, that has not been validated in practice.

The main limitations of the technology in its current form are

1) the need for clear line-of-sight for the highest accuracy;
2) the need for power (10W) and communication for each radio unit;
3) the need for cabling for each sensor unit;
4) sensitivity to nearby radio reflections when the highest accuracy is required (far-away reflections can be compensated);
5) need to compensate for the signal propagation speed in air when highest accuracy is required (this can be done e.g., with a fixed calibration link that is constantly monitored);
6) collection of snow and ice on the sensors will affect the measurement accuracy (if not removed by the heating in truly adverse conditions).

3 KIRJALANSALMI BRIDGE AND THE REFERENCE INSTRUMENTATION

Kirjalansalmi bridge, see Figure 3, is a suspension bridge situated in south-western part of Finland near the city of Turku. Road 180 where the bridge is situated, connects a vast archipelago to mainland. The bridge was built in 1963. The main span of the bridge is 220m and the effective width is 10 m. The deck structure consists of two steel truss girders, transversal truss girders, secondary beam girders and a concrete slab.

Kirjalansalmi bridge has an SHM system. The first monitoring system for the bridge was built in 2007. The system has been renewed step by step and some new sensors have been added. Today the monitoring system has strain gauges in main structures, temperature sensors, accelerometers, deflection sensors and a separate weather station. The system is used to provide continuous data about the behavior of the bridge structure due to traffic loads and temperature. The original monitoring system has a two-dimensional (X/Y) displacement sensor. The infra red transmitter is placed on the immovable concrete end support of the bridge and the reflector is placed on the maintenance walkway hanging from the bridge structure. This displacement sensor is also working as reference instrumentation to the Koherent measuring system.



Figure 3. Kirjalansalmi suspension bridge with 220-meter main span.

4 INSTALLING THE NEW SYSTEM AND RUNNING THE MEASUREMENTS

4.1 *Measurement configuration*

In order to compare the Koherent monitoring system against the existing laser-based system, the crossbeam with the laser reflector was chosen as the attachment point. This is about 46 meters from the northernmost pillar and roughly one fourth of the total span of the bridge. The sensor attachment points can be seen in Figure 4. This under-the-bridge deployment was seen as the easiest option as there was no need to install sensors on the pylons and on top of the deck (risk of vandalism). The downside was the sub-optimal measurement geometry as will be seen below.

Three sensors were attached to the cross-beam, one near the laser reflector and the others near the ends of the beam. The movements of these sensors were measured with reference to the three sensors attached to the north pillars. As the monitoring is based on the distance measurement between the sensors on the beam and the sensors on the pillars, the highest accuracy could be achieved in the direction of the bridge. The height difference of the upper and lower sensors in the pillars was about 6 meters. This meant that any up-down movement, or movement in the z-axis, of the bridge deck translated to distance differences in the measured links at a ratio of roughly 6/46 = 0.13. Therefore, to achieve an accuracy of 1 mm in the deck z-movements, an accuracy of 0.13 mm was required in the distance measurement. Similarly, the horizontal distance between the pillar reference sensors was about 12 meters, leading to somewhat better geometry for y-movements (transverse movements of the bridge deck).

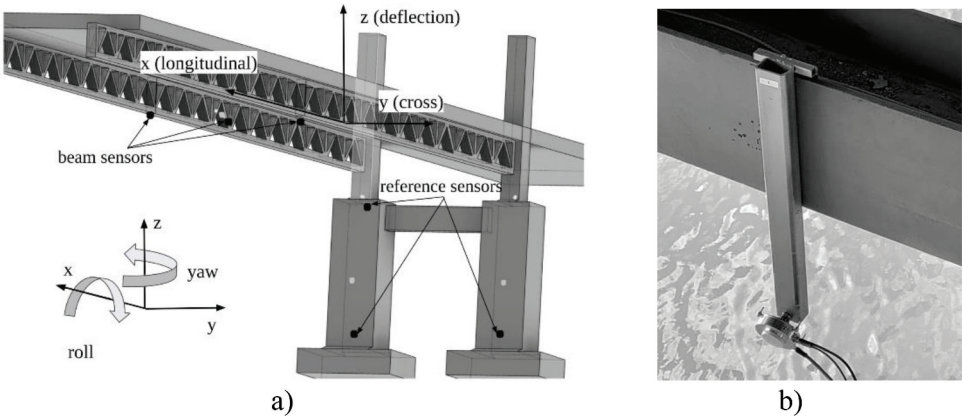


Figure 4. a) Installation plan, coordinate system and parameterization. b) Sensor installed on the cross-beam.

As we had three sensors attached to the beam, in addition to the translatory movement of the beam in x, y, and z, it was also possible to measure the changes in the beam's orientation. With this sensor geometry, two angles could be measured: the roll angle, i.e. the tilting of the deck, and the yaw angle (turning around the vertical z-axis).

4.2 *Installation*

Three radio units were used: one for the beam and one for each of the two northern pillars. These were connected to two 4G modems with Ethernet cables to send the data to cloud for processing in the computation cluster, see Figure 2. AC power from the bridge was available for both the radio units and the modems. The installation of the equipment took one full day. A harness had to be used for the pillar installations. The system was already operational during the same day.

After the system startup the geometry of the reference sensors was measured by using the distance measurement between the sensors. The actual measurement of the crossbeam movement ran continuously and autonomously for four weeks. All the crossbeam measurement parameters were stored in a cloud database 100 times per second.

5 MEASUREMENT RESULTS AND THEIR ANALYSIS

5.1 *Parametrization*

It would have been possible to measure and report the position of each individual sensor on the cross beam with respect to the reference sensors. However, it was decided to calculate five positional values for the beam that are more useful for interpretation of the bridge behavior: the linear movements of the beam center point in x, y, and z directions as well as the roll and yaw angles. These values were estimated by the cluster based on the continuous individual distance measurements between the sensors on the beam and the reference sensors on the pillars.

5.2 *Dynamic events*

Figure 5 Shows a typical bridge crossing by a heavy vehicle (a truck with a trailer) from the south. The dashed line is the Koherent measurement while dots represent the laser measurements. The third graph from top shows the vertical deflection of the cross beam. First, when the truck enters the bridge at the southern end, at approximately 05:28:45 UTC, the northern end starts moving upwards. When the truck crosses the measurement point, we can see a larger movement, about 240 mm, downwards. Lighter vehicles enter the bridge at the time when the truck leaves the bridge causing again an upwards movement. The fourth graph shows how the bridge deck tilts around 0.12 degrees towards east, reflecting the fact that the truck uses the

eastern lane. The first and the second graphs show x and y movement, respectively. One can see that the cross beam moves about 10 mm to north, which is natural as the truck bends the part of the bridge deck north of the cross beam downwards and therefore makes it shorter.

Comparing with the laser reference system measurement, we can see that the match is quite good for the vertical (z) deflection measurement. However, there is a clear deviation in the lateral (y) measurement. This could be related to the 1.5 meter vertical distance between the prism and the sensor combined with bridge deck tilt. However, the deviation does not match the tilt angle measurement and is most likely an unidentified problem in the laser measurement. This problem is even clearer in Figure 6 with the truck moving from north to south, as the laser system completely fails to record any lateral movement which is very clearly visible in the Koherent measurement data. Again, the observed bridge deck tilt is not sufficient to explain this behavior. Figure 7 shows a zoomed-in version of Figure 6 and illustrates good match in estimated movement in the deflection direction (z-coordinate).

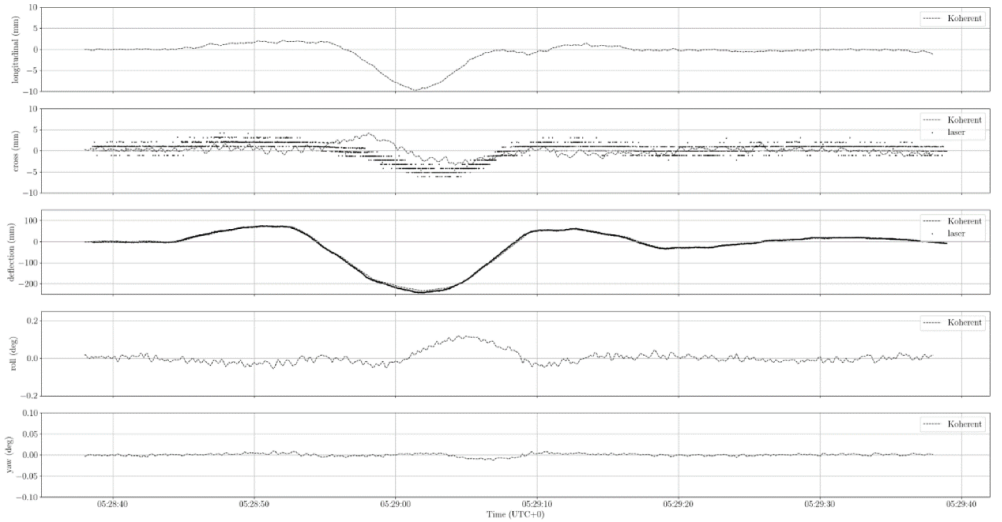


Figure 5. Large vehicle moving northbound.

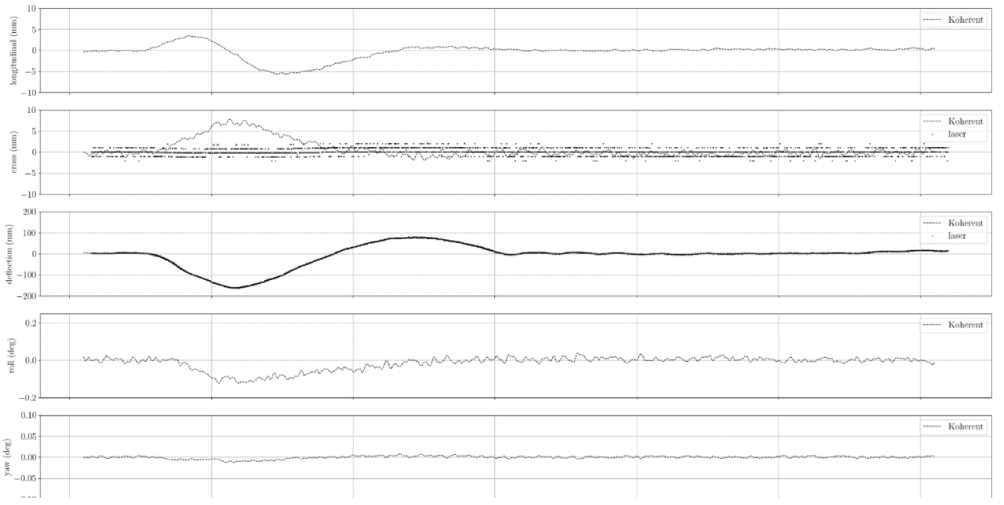


Figure 6. Large vehicle moving southbound.

5.3 *Long-term stability*

The drift in the Koherent measurement system during the four-week test project was studied by comparing it against the laser system. Fifteen-minute averages of the difference in z-coordinate were computed for the four-week period and shown in Figure 8. The two systems are in agreement within 1 mm. Because of the measurement geometry ratio 1:8, the drift in the distance measurement between the sensors over the 46 meters distance has drifted at most ~0.1mm over the four-week period. Figure 8a also nicely reveals the diurnal thermal cycles of the bridge.

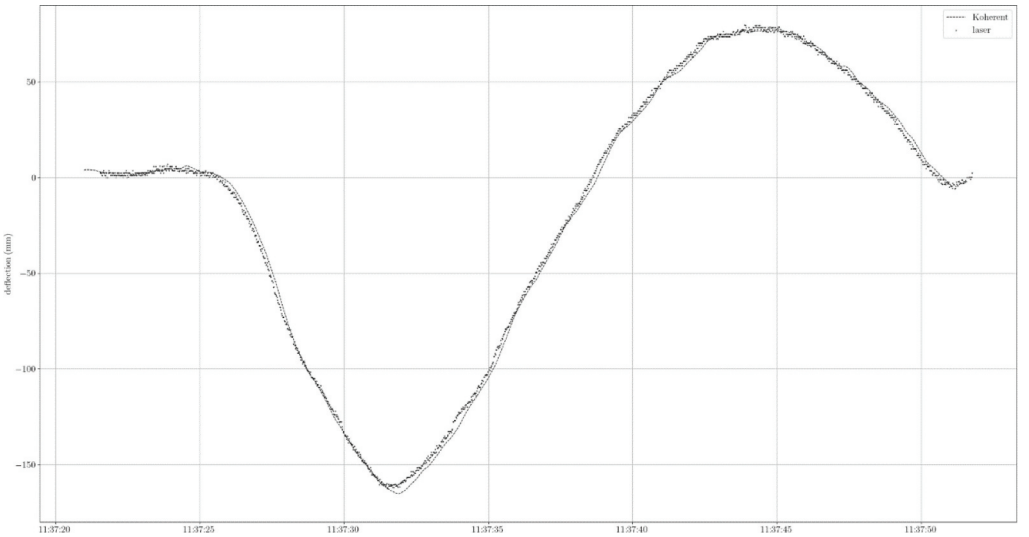


Figure 7. Zoomed in version of the deflection estimate (z) of the large vehicle moving southbound in Figure 6.

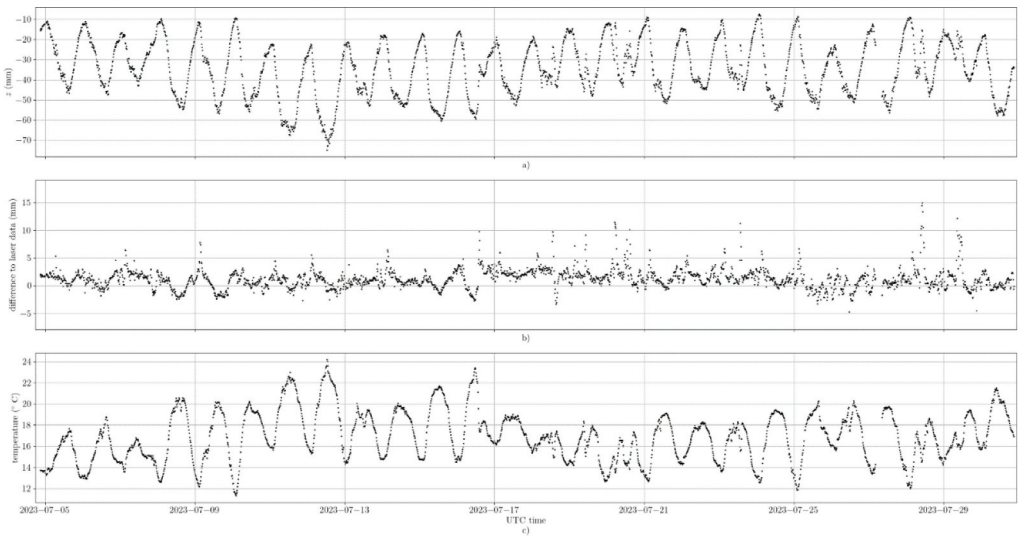


Figure 8. Each point represents a fifteen-minute average of a) z-coordinate (deflection), measured by Koherent; b) difference between Koherent and the laser measurement; c) temperature.

5.4 *Displacement measurement precision*

Figure 9 shows an event where a large vehicle crosses the bridge early in the morning while the bridge is otherwise silent. Figure 9a and 9b show the relative change in the estimated parameters. One can also observe how the bridge vibrates long after the vehicle has passed. Figure 9c shows a period of 10 s just before the vehicle enters the bridge. The measurement precision is on the order of 0.1 mm for the vertical movement and 20 micrometers for the longitudinal movement (relative distance precision). Because of the radio-interferometric measurement principle, this result does not depend on the distance until the distance increases to a point where the thermal noise in the received radio signal starts to dominate the result. With the current parameters this happens roughly at 300 meters distance and can be extended even further by increasing the signal integration time.

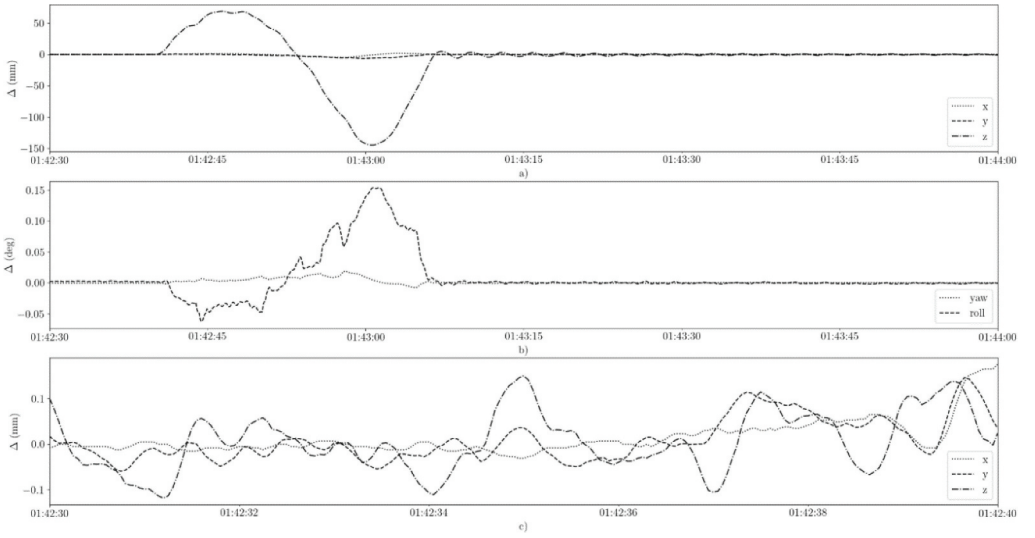


Figure 9. Estimates from a silent bridge at night with a single large vehicle crossing a) x-, y-, and z-coordinates; b) yaw and roll angles; c) zoomed in of x, y, z just before vehicle enters the bridge.

6 CONCLUSIONS

The presented case study shows the usability of the new technology for continuous bridge monitoring. Especially the dynamic and long-term accuracy were confirmed. Even with the non-optimal measurement geometry of 1:8, the vertical deck movements were still monitored with 1 mm accuracy. Also, the fast bridge movements were accurately monitored. The instrumental drift in distance measurement was found to be at most on the order of 0.1 mm. The intrinsic precision of the displacement measurement with the quiet bridge was found to be 20 micrometers. As the system is relatively easy and fast to install and offers a direct window to highly accurate and continuous bridge deformation data, we believe it can play a significant role in ascertaining the safety of old bridges.

ACKNOWLEDGEMENTS

This research received financial support from Business Finland.

REFERENCES

Koherent, Bridge Monitoring & Life Cycle Management, https://vimeo.com/891057411

Bridge Maintenance, Safety, Management, Digitalization and Sustainability – Jensen, Frangopol & Schmidt (eds)
© 2024 The Author(s), ISBN 978-1-032-77040-6
Open Access: www.taylorfrancis.com, CC BY-NC-ND 4.0 license

A regression based B-WIM method for railway bridges

S. Lachinger, J. Struhar & M. Ralbovsky
AIT – Austrian Institute of Technology GmbH

ABSTRACT: The Scope of the presented study is a Bridge-Weigh-in-Motion (B-WIM) method for the identification and quantification of train axles (loads and distances) using a regression-based machine learning model trained with synthetic generated train responses from trains passing over the bridge structure and data from structural health monitoring (SHM).

The B-WIM method uses synthetic train responses, generated with a calibrated numerical model of the bridge structure. Using a database with a large set of different generic train configurations (axle loads and distances) synthetic structural responses at different sensor positions are generated. The synthetic responses are downsampled and Peak-based features are derived and split into a training and a validation dataset for a regression-based machine learning model.

The trained machine learning model is used to calculate predicted axle loads and distances. Validation for synthetic data is then done by comparison with the known axle configurations for the generic train database. In upcoming steps of the ongoing research project, the trained machine learning model will then be used for identification of the axle loads and distances of the real trains passing over the bridge structure using features derived from the recorded monitoring data.

1 INTRODUCTION

Weigh-In-Motion (WIM) systems are generally used to measure traffic loads in road and railway networks during vehicle passage. Usually, these measurement systems are mainly designed for the detection of overloaded vehicles (e.g. trucks in road networks or freight wagons in train networks). Some operators use this data to line out overloaded wagons or trucks after passage to reduce damage to the rail or road infrastructure. The recorded data can also be used as base for statistical evaluation or for the derivation of load models for the assessment of structures (Sjaarda et.al., 2020). In this study the focus is on railway applications.

WIM systems, where the sensor reaction measured on a bridge is used to inversely calculate the traffic loads, are called Bridge Weigh-In-Motion (B-WIM) systems. These systems can be especially useful when no WIM system is installed in the area of interest in the traffic network and also, when the installation of a commercial WIM system would be too expensive or an installation on the track, as needed for approaches using measurements on the rail itself (Pau, Vestoni, 2021), would be not feasible due to limited access to the track, which can be a common problem especially in railway networks. (Žnidarič et.al. 2016) showed an application of a B-WIM method for a steel truss railway bridge based on the evaluation of influence lines. Another advantage of B-WIM is, that data from existing SHM installations can be used to calculate the traffic that generated the measured responses.

For railway applications not only the maximal load on a track is out of interest, but also the total sequence of axle loads is important, e.g. for the assessment of cumulative fatigue damage on steel structures within the network. Here the measured axle load sequences per train can be used to derive route specific fatigue load models, that are less conservative than fatigue load models from design codes. For the project DEEB-Infra two different B-WIM methods have been derived with the aim to get additional load data for the extrapolation of

DOI: 10.1201/9781003483755-169

valid fatigue load models for different parts of a railway network without permanently installed WIM-system. One B-WIM method, developed by the project-partner TU-Darmstadt (Riedel et.al. 2023) calibrates the axle loads based on the dynamic response of the bridge structure during train passage and tries to minimize the differences to a calibrated numerical model of the bridge. The advantage of this approach is, that it can handle resonance effects during train passage if they are also present in the numerical model. On the downside this approach does only calculate axle loads, the axle distances must be measured separately, e.g. with light barriers installed on the track. The second B-WIM method, which is introduced here, is developed by project partner AIT and uses an approach incorporating a regression-based machine learning model (MLM). It can derive axle loads and axles distances together with the downside that it is based on a static evaluation, so is not able to consider resonance effects within the measured response. As resonance effects should be avoided in generals and are much more likely to happen on high-speed railway lines this approach seems suitable for most tracks and bridge structures that are not excited in their resonance frequencies. The presented results are still intermediate at the time of writing this paper and cover the basic concept and results for synthetic (perfect) training and test data. The project is still ongoing and final validation of the method will be done in subsequent publications.

2 CONCEPT OF THE B-WIM METHOD

The presented B-WIM method is based on regression using a machine learning model (MLM) with the aim to predict the axle loads and distances of a train that passed the bridge structure. Figure 1 gives an overview over the approach for the B-WIM method.

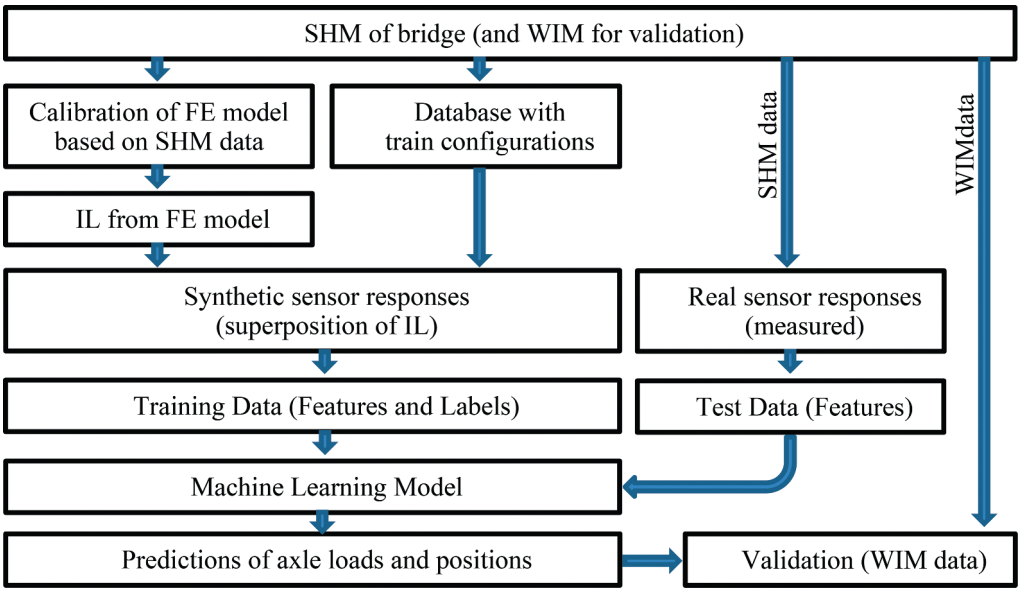


Figure 1. Basic approach used for B-WIM.

2.1 *Bridge structure*

For generation of the synthetic test data a real bridge structure is taken into consideration. The considered bridge, shown in Figure 2, for demonstration of the B-WIM method is a century old single span steel truss bridge located in Austria which is currently still under operation.



Figure 2. Steel railway bridge used for demonstration of B-WIM method.

The bridge has several signs of its age and defects, that initiated a large monitoring campaign and the development of a numerical model that was calibrated based on monitoring data. Also, a commercial WIM system is installed on the track providing the data for the validation of the B-WIM method. The bridge structure and the calibration of the numerical model is described in (Lachinger et.al., 2023). For the demonstration of the B-WIM method in this study influence lines (IL) of the calibrated model are used. As the quality of the predicted loads using B-WIM increases with sensors capturing the local response of the structure, i.e. directly show axles and/or bogie loads, the chosen IL represents sensor positions of a strain gauges at the longitudinal girder – which carries the sleepers – approximately in the middle of the bridge structure. Using sensor positions which represent more the global response of the structure, i.e. at the main truss, would lead to a decrease in the prediction quality.

2.2 *Training data*

In the first step a numerical model of the bridge structure is calibrated to give a good representation of the actual structure. Different approaches for the calibration of the model can be used, for the calibration of a FE-model an approach using least squares minimization of the difference of all sensor values was presented in (Lachinger et.al., 2023). From the calibrated numerical model, influence lines (IL) are derived for the considered sensor positions. Using an existing database with nearly 5000 train configurations (axle loads and axle distances) synthetic sensor responses for each of the train configurations are generated by superposition of the IL multiplicated with the respective axles loads, shifted by the absolute axle positions. This approach is valid for bridge structures where linear elastic behavior can be assumed (e.g. steel bridges). If no linear elastic behavior can be assumed, the total train responses can be calculated directly, which is numerically more expensive. Figure 3 shows an example of a generated synthetic sensor response and the corresponding axle loads of the train configuration. All sensor responses are evaluated in the distance domain. For sensor responses from actual monitoring the train speed can be used for the transformation.

The features are derived from the synthetic sensor responses. Therefore, the synthetic sensor reactions are down sampled into a Peak-Valley sequence using a peak finding algorithm. A set of features is calculated for each individual peak of the sensor reaction. Per peak the following features are calculated with reference to a set cut off limit, as shown in Figure 4:

- Peak amplitude (to cut off limit)
- Distances to adjacent valleys (left and right side)
- Peak-Valley amplitude (left and right side)

- Area under sensor reaction between left and right valley
- Absolute position of the peak and relative position (=0 if reference peak)

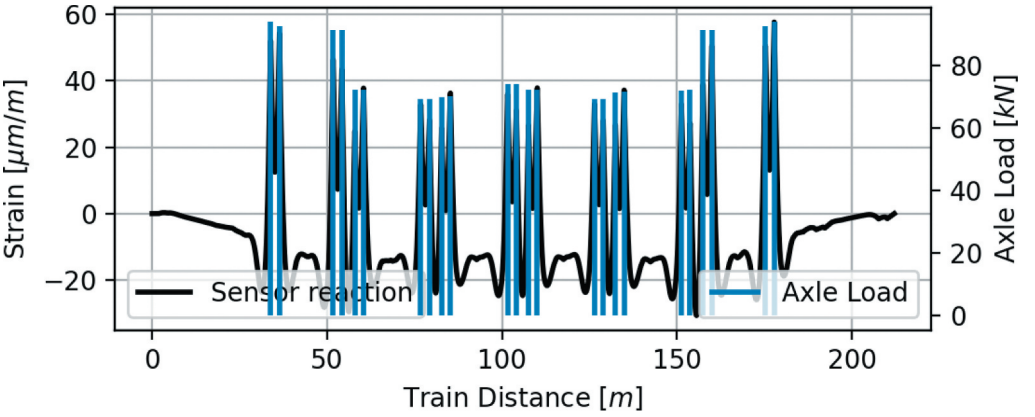


Figure 3. Example of synthetic sensor reaction and train axle loads.

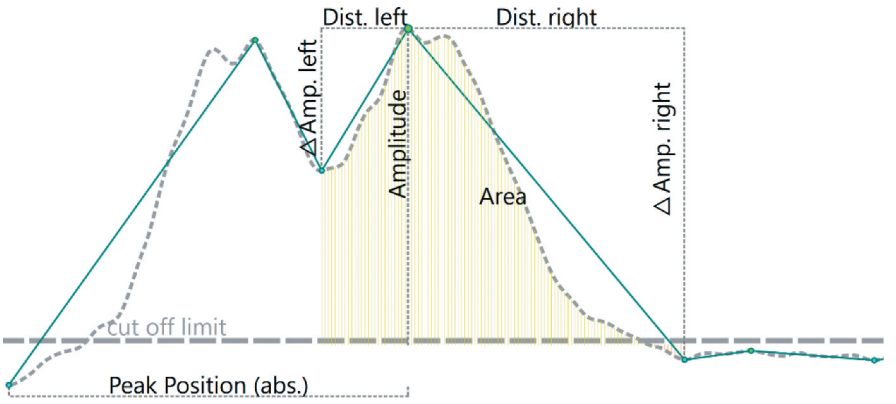


Figure 4. Features derived from individual peaks.

The complete feature set for each peak (when reference peak) must consider the influence of all axles that are at the bridge structure at once. Therefore, preceding and subsequent peaks to the reference peak are considered with their relative position, if they are within the scope of the IL before and after the considered sensor with the peak of the IL positioned at the sensor position. This also represents the sensor position on the bridge structure as the IL usually equals the bridge length. The labels for each peak are the axle loads and positions relative to the peak position of the axles in the scope (between the valleys) of the reference peak. The set of features and labels from the synthetic sensor reactions is used as training data for the MLM.

2.3 *Computational implementation of the MLM*

The Python toolkit scikit-learn was used for this study which provides an easy to implement set of different MLM that also can be exchanged easily to test different models. For the current study a Random Forest regressor was used, as it showed to give the best results after comparison of different MLM within the scikit-learn toolkit. It also has decent performance and some traceability of the results if necessary.

The primary challenge in the computational implementation was to prepare the data pre-processing pipeline in very flexible way, that enables to switch used sensor or used feature set very quickly in one spot and to evaluate the impact of a change. The pipeline stages de-construct the input train data into the feature set that can be predicted by the regressor. So, the pipeline needs to remember some information (e.g. absolute peak position) to enable the re-construction of predicted labels, i.e. axle loads and relative position to reference peak, into a complete train configuration.

- The first stage in the pipeline splits the signal from the selected sensor reaction into smaller pieces. The pipe stage hops over all signal peaks and cuts pieces with the length of the IL of the signal and within this cutout calculates the requested features, as described in Chapter 0.
- The second stage transforms the feature lists with variable length in a zero padded matrix of fixed shape (number-of-features, max-length-of-value-list).
- In the third stage each of the features will be normalized (scaled) to give equal weights to the individual feature types. This also makes the regression more robust against outliers.
- The fourth stage reshapes all the scaled values from one signal block to a 1-D value array that can be fed to the regressor.

Postprocessing involves the re-construction of the predicted label data into complete train configurations and extraction of additional information (e.g. peak-valley sequences) that can be used for calculation of metrics to validate the results against the measured train data from WIM measurements.

3 B-WIM METHOD FOR SYNTHETIC TRAIN DATA

The synthetic dataset was randomly split. 90% of the dataset formed the training dataset and 10% of the dataset the validation (or test) dataset for validation checks to see if the model can predict synthetic axle loads. Figure 5 shows an example for the data of one wagon within a train in the validation dataset. The solid black line shows the (synthetic) sensor response and the dashed blue line the down sampled data used for the calculation of the features. The magenta bar indicates position and amplitude of the (known) axle loads and the red circle markers show the predicted loads that should ideally match with the tip of the magenta bars. In the example in Figure 5 we see a pretty good match between label loads and predicted loads.

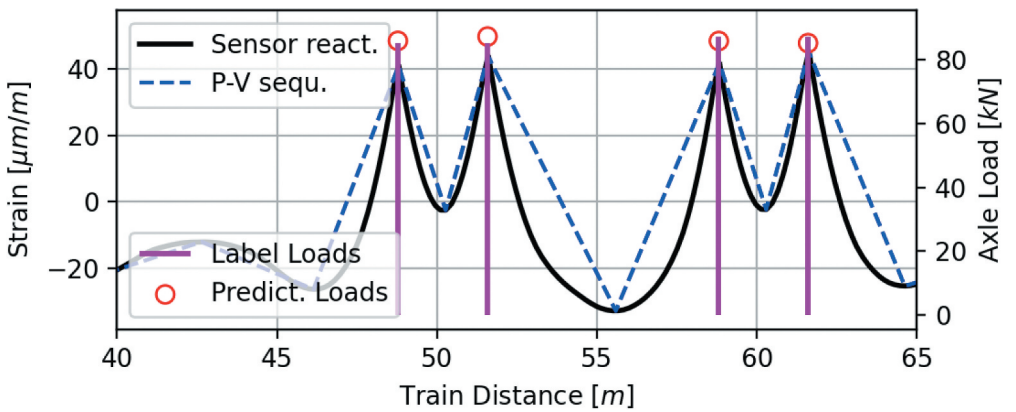


Figure 5. Example comparison of labels and prediction for a wagon of a sample train.

To get a good overview of the results the predicted loads are evaluated: (i) for the totals of the individual trains (total length and load sum) and (ii) peakwise by evaluation of the predicted loads between the preceding and successive valley for each peak. For the peakwise evaluation the following parameters are considered for the differences between label and predicted loads:

- Number of axles per peak
- Load sum per peak
- Center of gravity

Figure 6 shows histograms of these evaluation parameters for the synthetic test data of a chosen sensor considering data from 490 train responses. It can clearly be seen, that for the chosen sensor with the used parameters the synthetic data gives very good results, but individual outliers exist.

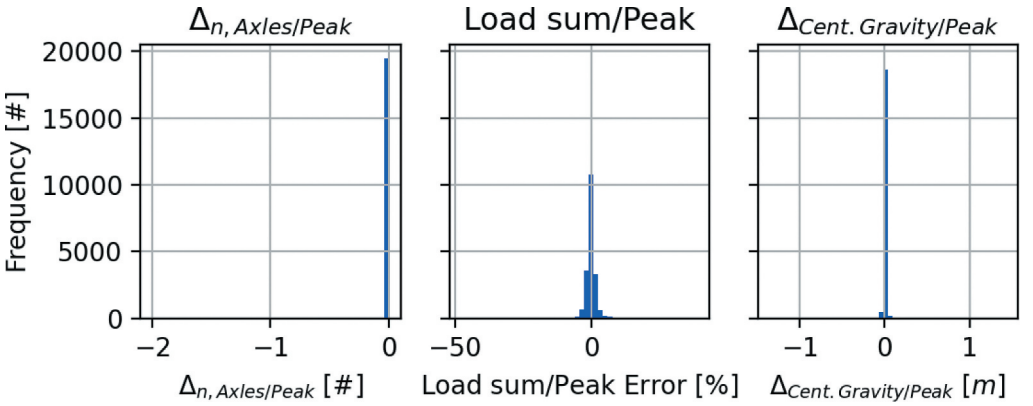


Figure 6. Peakwise evaluation of synthetic test data.

Table 1 sums up the metrics for total and peakwise evaluation of the predicted loads. Three different metrics are shown: (i) ME is the mean error of the prediction and shows the bias of the predicted results, (ii) MAE is the mean absolute error of the prediction and (iii) RMSE is the root mean squared error of the prediction which is the standard deviation of the prediction error. MAE is in general more robust against outliers than RMSE.

Table 1. Metrics for synthetic test data.

Evaluation	Paramter	Unit	ME (Bias)	MAE	RMSE
Total	Length	[m]	0,0034	0,0130	0,1098
	Load sum	[kN]	-0,3470	1,9798	7,0277
Peakwise	Nr. Axles	[#]	0,0028	0,0028	0,0540
	Load sum	[kN]	-0,0284	1,1027	2,2557
	Center of Gravity	[m]	0,0047	0,0095	0,0833

The metrics in Table 1 show very little bias and deviations. MAE and RMSE only indicate minor deviations around the true values. Only very few individual outliers exist. Concluding the proposed B-WIM method can predict the synthetic (and perfect) loads very good, which is prerequisite for the upcoming usage of the trained MLM for real data from SHM.

4 CONCLUSIONS AND OUTLOOK

A new Bridge-Weigh-in-Motion (B-WIM) method is introduced in this paper and a proof of concept is shown for synthetic structural responses. The B-WIM method uses a regression-based machine learning model which is trained on a dataset derived from synthetic structural responses of about 5000 train configurations calculated as passing over a (calibrated) numerical model. For this "perfect" data the method can predict the axle loads and distances of trains passing the bridge structure with a very small error.

In the ongoing work on the project, the machine learning model, trained with the synthetic dataset will be taken to predict real train passages by using a test dataset generated from data from structural health monitoring. Validation will be done against data from a commercial Weigh-In-Motion system installed at the same track the bridge structure is located. Results from these real testing will be presented in upcoming publications.

ACKNOWLEDGEMENTS

The work presented was done within the research project DEEB-Infra (www.deeb-infra.de) funded by the mFund promoted by the Federal Ministry of Transport and Digital Infrastructure in Germany. The project is carried out by the project partners Technical University Darmstadt, Deutsche Bahn AG, Revotec ZT GmbH, iSEA Tec GmbH and AIT – Austrian Institute of Technology GmbH.

REFERENCES

Lachinger, S. & Pissermayr, S & Ralbovsky, M. & Vorwagner, A. 2023. Case study: Impact of route specific loads and numerical model calibration on fatigue assessment of an existing railway bridge. In Papadrakiakis, M & Fragiadakis, M. (eds.), *COMPDYN 2023, 9th International Conference on Computational Methods in Structural Dynamics and Earthquake Engineering*, *Athens, 12-14 June 2023*. Pages 1321-1336. Athens: National Technical University of Athens

Pau A, Vestroni F. 2021. Weigh-in-motion of train loads based on measurements of rail strains. *Struct Control Health Monit. 28(11)*: e2818. https://doi.org/10.1002/stc.2818.

Riedel, H. & Firus, A. & Vospernig, M. & Apostolidi, E. & Schneider, J. (2023), QUICK-B-WIM: Large scale application of a moving force identification method on a railway bridge. *ce/papers*, *6*: 863-869. https://doi.org/10.1002/cepa.2119

Sjaarda, M., Meystre, T., Nussbaumer, A. and Hirt, M.A. (2020), A systematic approach to estimating traffic load effects on bridges using weigh-in-motion data. *Stahlbau*, *89*: 585-598. https://doi.org/10.1002/stab.202000048

Žnidarič, A. & Kalin, J. & Kreslin, M. & Favai, P. & Kolakowski, P. (2016) 'Railway Bridge Weigh-in-Motion System', *Transportation Research Procedia*, *14, pp.* 4010–4019. doi: https://doi.org/10.1016/j.trpro.2016.05.498

Bridge Maintenance, Safety, Management, Digitalization and Sustainability – Jensen, Frangopol & Schmidt (eds)
© 2024 The Author(s), ISBN 978-1-032-77040-6
Open Access: www.taylorfrancis.com, CC BY-NC-ND 4.0 license

A deep learning-based BWIM system of a cable-stayed bridge

B. Szinyéri & B. Kovari
Faculty of Electrical Engineering and Informatics, Department of Automation and Applied Informatics Budapest, University of Technology and Economics, Budapest, Hungary

I. Völgyi, D. Kollár & A.L. Joó
Faculty of Civil Engineering, Department of Structural Engineering, Budapest University of Technology and Economics, Budapest, Hungary

ABSTRACT: Multiple breakthroughs have emerged across various applications due to deep learning. These advancements can also be adapted for Bridge Weigh-In-Motion (BWIM) systems. A deep learning-based algorithm has been developed previously by the authors, which can be integrated into these systems. That algorithm shows promising results when compared to so-called static methods. One of the main contributions of our developments is handling the error of the preprocessing steps more efficiently. A developed axle load estimator is presented in this paper that builds on our previous solution, and which was tested in operation on a cable-stayed bridge. The algorithm handles multi-lane scenarios more efficiently when compared to our previous solution. The comparison of this novel algorithm and Moses' algorithm is also presented in this paper. Our solution achieves lower error rates both on a synthetic dataset, and a real measurement-based annotated dataset.

1 INTRODUCTION

Bridge Weigh-in-Motion (BWIM) systems monitor the traffic of a bridge. Not only detecting vehicle presences but also axle load estimation of vehicles is a vital task of these systems (Carraro et. al 2019). Civil engineers can perform advanced fatigue and damage analysis (Lee et al. 2022) of the bridge based on real traffic data. It helps predict the bridge life cycle and schedule maintenance.

A monitoring system has been already installed on the Monostor bridge on the Hungarian-Slovakian border, connecting Komárom and Komárno (Szinyéri et al. 2023a, Kollár et al. 2023). Uniaxial strain gauges are placed under the bridge deck. These strain gauges provide data for the BWIM system. Strain gauges are placed in two cross-sections of the bridge. Sensors can be grouped into two sensor arrays based on the cross-sections. The main sensor array consists of 16 strain gauges (named T1-T16), while the secondary sensor array consists of 10 strain gauges (named T201-T205, T212-T216). Their setup is also presented in Figures 1 and 2. Two lanes are present on the bridge: in the so-called HU→SVK lane, vehicles are traveling from the Hungarian side to the Slovakian side of the bridge, while vehicles are crossing the bridge in the opposite direction in the SVK→HU lane.

Our research group has previously investigated the aforementioned steel bridge with orthotropic deck and has created a deep learning-based axle load estimation approach (Szinyéri et al. 2023a). This axle load estimation solution assumes that speed and axle location information have already been calculated in the preprocessing steps. It has been already shown that this solution can handle errors of these preprocessing steps more efficiently when compared to traditional, Moses' algorithm-based static methods (Szinyéri & Kovari, 2023b). The most significant disadvantage of the system is that it performs worse when vehicles are present in multiple lanes. This paper aims to solve this issue and create an algorithm that is better than Moses' algorithm under these circumstances as well.

The paper is structured the following way: a literature review and a summary of the used dataset are presented in Section 2. The upgraded deep learning-based solution is discussed in

DOI: 10.1201/9781003483755-170

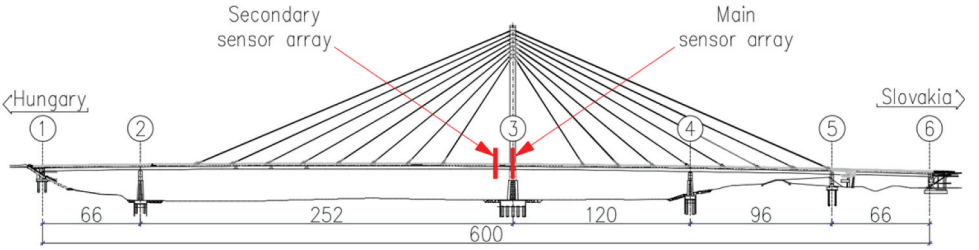


Figure 1. Side view of the bridge. The cross-section of the main and the secondary sensor array can be seen in this figure.

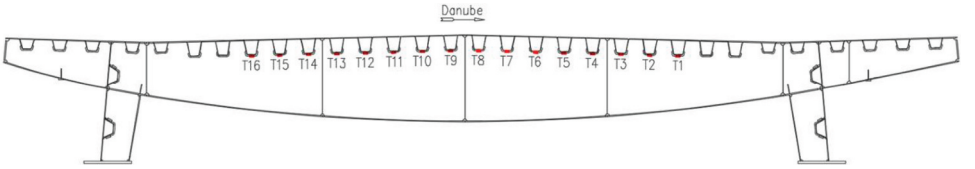


Figure 2. Cross-section with the main sensor array consisting of sixteen strain gauges.

Section 3. The solution is evaluated on a synthetic dataset in Section 4 and on a real measurement-based annotated dataset in Section 5. Finally, Section 6 gives a summary of this paper, states conclusions, and outlines the direction of further work.

2 LITERATURE REVIEW

First, the pipeline of the system and a brief introduction of preprocessing steps are presented. Then, the state-of-the-art axle load estimating methods are presented. Finally, the BME-Simulated I (BME-S1) synthetic dataset is presented which will be used for evaluation in Section 4.

A prerequisite of estimating axle loads is knowing the proper axle locations and speed of each vehicle; axle spacings can be also derived from this information. The pipeline of BWIM systems usually has four main steps: the first step is detecting vehicle time windows (Ma et al. 2020), thus a time interval, when each vehicle was crossing above the sensor arrays. The second step is estimating the speed of each detected vehicle (He et al. 2017). It can be done since sensors are installed in two cross-sections, and the measured strain responses of each vehicle in the two sensor arrays are very similar to each other. The next step is detecting axle locations (Chatterjee et al. 2006), while the last step is estimating axle loads (Carraro et al. 2019). Finally, the calculated axle loads and axle spacings can be used for extracting further information. This paper focuses on the last step, thus the problem of axle load estimation based on known speed and axle spacing information is to be solved.

Four axle load estimation algorithms are discussed in this section. Other axle load estimation algorithms are just modifications of these algorithms; therefore, they are not detailed in this paper, only mentioned.

The traditional algorithm of axle load estimation is the Moses' algorithm (Moses 1979). It was the first algorithm presented in the literature about 40 years ago. Several modified algorithms have been developed since the publication of this method which are based on this approach. Carraro et. al (2019) created a comparison of these static algorithms. These solutions are based on the simulation process. If we know the proper parameters of vehicles crossing the bridge, then we can simulate the strain response of the bridge. This simulation process uses the concept of influence line (Moses 1979) or influence surface (Szinyéri et al. 2023). It is assumed that the axle spacings and speed of each vehicle were calculated before using Moses' algorithm. The task is then to calculate axle loads that produce the most similar simulated strain signals when compared to measured signals.

The Virtual Axle Method (He et al. 2019) is a developed version of Moses' algorithm, leveraging the knowledge of each vehicle's speed. Axle locations and axle loads are calculated in the same module in this case.

There are several deep learning-based algorithms in this field as well, which can be used not only for axle load estimation but also for estimating speed or axle locations. Wu et. al (2020) presented BwimNet, which is a Physics Informed Neural Network (PINN) that calculates all important parameters of a vehicle in only one module. State-of-the-art of PINNs was presented by Cuomo et al. (2022).

Our research group has previously created the BME-Simulated I (BME-S1) dataset (Szinyéri et al. 2023a), which is a public dataset in this field. It is also suitable for deep learning-based supervised training of neural networks. It is a large synthetic dataset, which contains 96 012 training vehicle samples and 12 808 test vehicle samples. Several traffic scenarios are modeled in this dataset. Each scenario can be grouped by the aspect of whether vehicles are present in one lane or both lanes. A subset of scenarios contains close-range following vehicles, while others do not. These close-range following vehicles (Ma et al. 2020) are also called convoys. This dataset is also suitable for incremental development. A small, annotated dataset is also attached to this dataset to ensure that a solution working on the synthetic dataset also works on the measured signals.

If proper axle spacings and speed of each vehicle were known, then Moses' algorithm would be the best algorithm to fit the simulated signal to the measured signal and to calculate the most proper axle loads. Our deep learning-based solution achieves better results when compared to Moses' algorithm on one-lane scenarios when these errors are considered (Szinyéri & Kovari, 2023b). On multi-lane scenarios, they have achieved nearly the same error so far. In this paper, a developed version of this deep learning-based approach is presented, which solves the problem of multi-lane scenarios by achieving better results than Moses' algorithm.

3 CONTRIBUTION

The developed deep learning-based solution is presented in this section, which is trained for multi-lane scenarios as well. Only the modified algorithm is presented in this paper, the former version of the algorithm can be found in (Szinyéri et al. 2023a).

The algorithm still relies on knowing proper axle locations and speed. The solution continues to operate based on the application of a neural network. The neural network computes the axle loads of one vehicle, while it also takes other nearby vehicles into account. The neural network has four input parameters, four input tensors. The first tensor describes the axles of the examined vehicle by tensors derived from strain signals. The second tensor describes the other axles by the same computation. The third parameter describes the lane of each axle. The last parameter is a distance matrix. The algorithm has four substeps: the first substep creates the aforementioned tensors. The second substep creates a local descriptor vector for each axle. The third substep creates a global descriptor vector for each axle, considering the effect of other axles as well. Finally, axle loads are extracted from these global descriptor vectors. Each parameter and substep is detailed below.

First, the methodology of creating the input parameters is described. As mentioned before, time window of a vehicle, axle locations and speed of each vehicle are supposed to be known. First, new computed channels are derived from strain signals by summing some of the sensors. T1-T8, T1-T5, T9-T16 and T12-T16 sensors are summed in our solution. Then, these signals are dilated so that the mean of values inside the time window of the examined vehicle equals zero. Then, the tensors are extracted from these strain signals by the usage of axle time windows. An axle time window is derived from the axle location and speed for each axle. If the axle location is defined by the timestamp t, the vehicle speed is v, the required window size is T samples, and the required resampling distance is L, then $\Delta t = L/v$ defines the time difference between two samples, so the axle time window can be defined as extracting the strain value in the $[t-(T/2)*\Delta t;\ t-(T/2-1)*\Delta t,\ \ldots,\ t-\Delta t, t,\ t+\Delta t,\ \ldots, t+(T/2)*\Delta t\ ]$ moments. In our case, the resampling distance (L) was set to 200 mm and T was set to 73. The resampling is done by cubic interpolation. Figure 3 gives an illustration of this process.

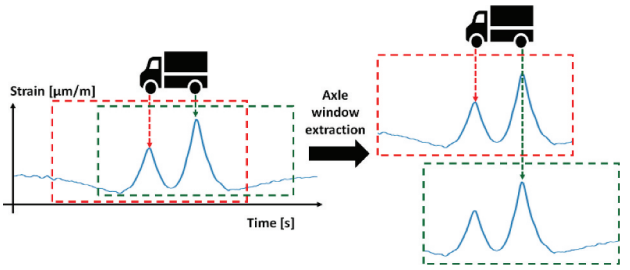


Figure 3. The step of extracting the time window of an axle. The strain signal represents a derived channel.

The lane information is only an index of the lane. The distance matrix is a $\mathbb{R}^{NxM}$ size matrix, where the $D[i,j]$ element describes the distance of the i-th and the j-th axle in the moment when the i-th axle is in the cross-section of the main sensor array. Figure 4 describes the calculation method. The examined vehicle has N axles and the nearby vehicles including the examined vehicle itself have M axles in total.

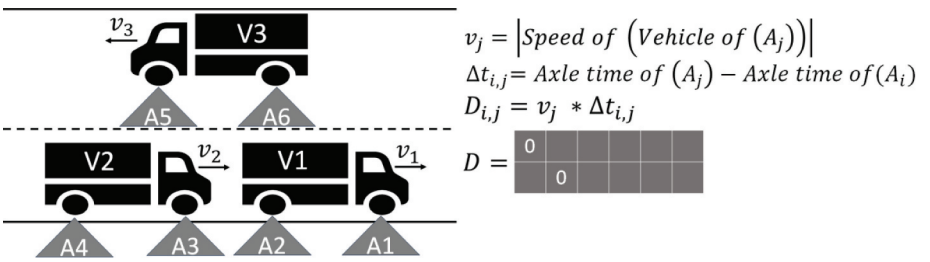


Figure 4. Illustration of extracting the distance matrix. Here $N = 2$ and $M = 6$ if vehicle *V1* is selected.

The neural network is a composition of three dense neural networks. Figures 5 and 6 describe the architecture of the neural network, while the algorithm is presented in Algorithm 1. The *SignalOfAxles* tensor in the algorithm represents a $\mathbb{R}^{NxChxT}$ sized tensor, it contains the preprocessed signal of each axle. The *SignalOfOther Axles* also contains these axles and the other axles nearby; it is a $\mathbb{R}^{MxChxT}$ sized tensor. The parameter *Ch* defines the number of channels which is four in our case. The first N elements of the *SignalOfOtherAxles* tensor equals the *SignalOfOtherAxles* tensor since they contain the axle information of the examined vehicle. The *Lane* tensor contains the index of each axle. The *D* matrix was described before. The *LocalNet* is a dense neural network that contains 256, 512, 128 and 24 neurons in each layer; thus, this network can be described as a $\mathbb{R}^{Ch*T} \rightarrow \mathbb{R}^{24}$ transformation. It encodes the window of each axle without knowing about other axles. *GlobalNet* is another dense neural network that contains a $\mathbb{R}^{24+24+1+1+1} \rightarrow \mathbb{R}^{48}$ transformation. The input of this net is the encoded vector of two axles, the lane index of each axle and the distance of them. *NxM* pairs of local descriptors are concatenated with lane and distance information, and then these results are summed for each axle of the examined vehicle. *RegNet* does the regression step; thus, it extracts the axle loads from each descriptor vector; it is a $\mathbb{R}^{48} \rightarrow \mathbb{R}^{1}$ transformation. It contains a residual connection (Szegedy et al 2017) that means concatenating the input and the output tensor, so it is like boosting in fact.

Data augmentation techniques are used during the training of the neural network. The goal is to prepare the neural network for several error types.

The first augmentation technique is used to prepare the network for the vehicle speed error given by the preprocessing steps. It is modeled by a Gaussian noise added to the ground-truth speed value.

The second augmentation technique is applied to prepare the network for the axle location error given by the axle detector. Gaussian noise is added to the timestamps of the axles. The

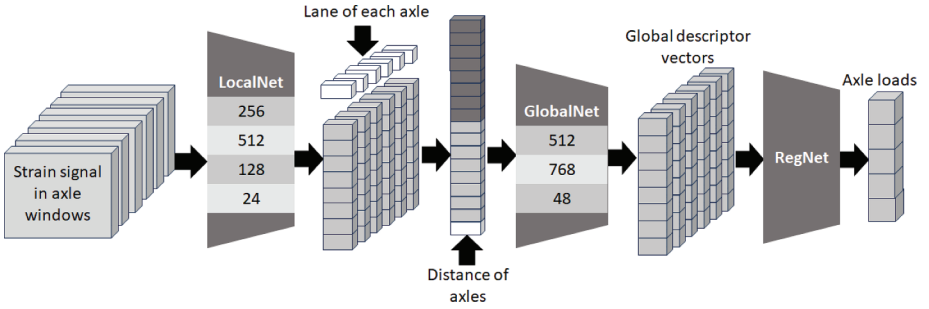


Figure 5. The architecture of the neural network.

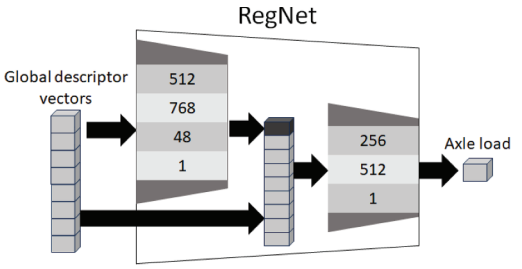


Figure 6. The architecture of the *RegNet* module. The residual connection is also shown.

Algorithm 1 . Computing axle loads from tensors.

Input: *SignalOfAxles[N, Ch, T], SignalOfOtherAxles[M, Ch, T], Lane[M], D[N, M]*
Output: *AxleLoads[N]*

1. *LocDescrOfAxles* ← [*LocalNet*(*Flatten*(*SignalOfAxles[i]*)) **for** *i* **in** *1..N*]
2. *LocDescrOfOtherAxles* ← [*LocalNet*(*Flatten*(*SignalOfOtherAxles[j]*)) **for** *j* **in** *1..M*]
3. **for** *i* **in** *1..N*
4. **Begin**
5. *AxleLoads[i]* ← *RegNet*(**Σ** [*GlobalNet*(
6. *Concat*(*LocDescrOfAxles[i], LocDescrOfOtherAxles[j], Lane[i], Lane[j], D[i, j]*))
7. **for** *j* **in** *1..M*])
8. **end_**

timestamp of an axle shows the time when a vehicle is crossing above the main sensor array. Therefore, a noisy D matrix is created for each case.

The third augmentation technique models the noise that can be observed in the signals. It is also modeled by adding Gaussian noise. The noise level is set differently in all cases. Other research (Wu et al. 2020) used similar techniques as well.

The Symmetric Weighted Mean Absolute Percentage Error (SWMAPE) is used as a loss function during training. It is used instead of Mean Absolute Percentage Error (MAPE), since it gives numerical stability during backpropagation. If the $y \in \mathbb{R}^N$ vector represents the expected axle loads and the $\hat{y} \in \mathbb{R}^N$ vector represents the calculated axle loads, then the SWMAPE error can be calculated the following way:

$$SWMAPE(\hat{y},\ y) = \frac{100\%}{N} \sum_{i=1}^{N} \frac{|y_i - \hat{y}_i|}{(|y_i| + |\hat{y}_i|)/2} \tag{1}$$

If we have several vehicles, then the accumulated SWMAPE error is the mean of SWMAPE errors for each vehicle.

4 EVALUATION

Evaluation of the deep learning-based solution is described in this section. The comparison of this method and Moses' algorithm is also included. First, the results achieved on the BME-S1 synthetic dataset are discussed; then, experimental tests on real measured data are provided.

Two types of error levels are described. Each error level describes the vehicle speed error and the axle location error of the preprocessing steps, and the noise observed in the signal. Data augmentation is handled the same way as in Section 3. The standard deviation of the Gaussian noise in each case is presented in Table 1.

Table 1. List of defined error levels. Standard deviations of vehicle speed, axle location and signal error are given for augmenting test data.

	Speed	Axle location	Signal
Error level	error [km/h]	error [1/100 s]	error [μm/m]
Ground-truth	0.0	0.0	0.0
Noisy	1.5	0.3	2.0

Table 2 describes the errors achieved when ground-truth data is provided. The gross vehicle weight (GVW) equals the sum of axle loads. Mean Absolute Percentage Error (MAPE) of calculated GVWs and given GVWs are computed. Mean Signed Percentage Error (MSPE) describes how each axle load estimator tends to underestimate or overestimate the GVW or axle loads of the vehicles (AW). The standard deviation of the percentage errors is also presented for axle weights and gross vehicle weight as well. It can be seen in the table, that our development achieves better results than Moses' algorithm on one-lane scenarios and multi-lane scenarios as well. The difference between the two axle load estimators is even higher when considering multi-lane scenarios.

Table 2. Error of the estimated axle weight (AW) and gross vehicle weight (GVW) for each axle load estimator on both one-lane and multi-lane scenarios when no noise is added.

Dataset	One-lane		Mutli-lane	
Metric	Proposed Method	Moses algorithm	Proposed method	Moses algorithm
GVW MAPE [%]	**1.51**	2.17	**2.43**	3.44
GVW MSPE [%]	-1.36	-2.01	0.14	-2.06
GVW σ[%]	**1.34**	2.32	**3.88**	5.82
AW MAPE [%]	**2.02**	2.40	**3.68**	5.30
AW MSPE [%]	-1.51	-2.12	0.36	-2.16
AW σ[%]	**2.33**	2.78	**6.16**	11.0

Table 3 describes the errors achieved when noise is added. It is shown in the table, that the neural network is still better than Moses' algorithm on one-lane scenarios, but the gap is not as large as in multi-lane scenarios. The developed neural network achieves better results than the Moses' algorithm on multi-lane scenarios. The gap is larger in this case than in one-lane scenarios.

Table 4 describes the results achieved on the multi-lane dataset. It can be seen that if only the heaviest vehicle is evaluated in every scenario, the errors are kept near as low as in one-

lane scenarios. Since only the heavy vehicles are important in most bridge engineering applications e.g. damage and fatigue analysis, it is a promising result.

Summarizing the results, it can be stated that our proposed method outperforms the traditional method, especially in the multi-lane scenarios.

Table 3. Error of the estimated axle weight (AW) and gross vehicle weight (GVW) for each axle load estimator on both one-lane and multi-lane scenarios when noise is added.

Dataset	One-lane		Mutli-lane	
Metric	Proposed method	Moses' algorithm	Proposed method	Moses' algorithm
GVW MAPE [%]	**2.37**	3.11	**3.32**	4.27
GVW MSPE [%]	-1.39	-2.44	0.18	-2.50
GVW σ[%]	**3.02**	3.28	**4.97**	6.39
AW MAPE [%]	**3.99**	4.42	**5.32**	6.91
AW MSPE [%]	-1.48	-2.60	0.42	-2.67
AW σ[%]	5.75	**5.51**	**8.19**	12.02

Table 4. Error of the estimated axle weight (AW) and gross vehicle weight (GVW) for each axle load estimator on multi-lane scenarios when noise is added.

Dataset	All vehicles		Only the heaviest vehicle	
Metric	Proposed method	Moses' algorithm	Proposed method	Moses' algorithm
GVW MAPE [%]	**3.32**	4.27	**2.35**	3.13
GVW MSPE [%]	0.18	-2.50	-0.16	-2.46
GVW σ[%]	**4.97**	6.39	**3.12**	3.36
AW MAPE [%]	**5.32**	6.91	**3.66**	4.61
AW MSPE [%]	0.42	-2.67	0.07	-2.56
AW σ[%]	**8.19**	12.02	**5.14**	5.95

5 EXPERIMENTAL RESULTS

End-to-end tests are also carried out. The pipeline contains a deep learning-based axle detector (Kawakatsu et. al 2020, Lorenzen et al. 2022) and a vehicle speed estimator using the peak-to-peak approach (He et al. 2017) in the current phase of development. A smaller set of real scenarios is available for us. The real annotated dataset contains 10 two-axle, 3 five-axle and 2 four-axle vehicles crossing the bridge. Only the heaviest axle and the gross vehicle weight of each vehicle are available for all vehicles. Results are presented in Table 5. One of these cases is a multi-lane scenario, others are one-lane scenarios.

It can be seen that the neural network achieves lower MAPE errors when estimating gross vehicle weight or the heaviest axle load of each vehicle. The Moses' algorithm tends to underestimate both the axle loads and the gross vehicle weight based on the MSPE metrics but even if axle loads were forced by scaling to set this error to be zero, the Moses' algorithm would still have worse or near the same performance since standard deviation of percentage errors is lower for neural networks.

6 CONCLUSION

The development of a deep learning-based solution is presented in this paper. It is tested on the BME-S1 dataset which is a large synthetic dataset. The new solution performs better when compared to the previous version of this algorithm or Moses' algorithm.

Table 5. The error of the estimated gross vehicle weight (GVW) and the error of the estimated heaviest axle weight (HAW) of each axle load estimator.

Metric	Proposed Method	Moses' algorithm
GVW MAPE [%]	**2.22**	3.88
GVW MSPE [%]	-0.09	-2.85
GVW σ[%]	**2.74**	3.95
HAW MAPE [%]	**3.32**	4.26
HAW MSPE [%]	-1.98	-3.31
HAW σ[%]	**3.47**	3.53

Both our algorithm and Moses' algorithm cannot handle failing sensors. Further work should focus on cases when one or more sensors do not work properly. Deep learning-based solutions can be effective in this field as well. Further work should also focus on camera-based BWIM systems as well to prepare the system for more complex traffic scenarios as well.

REFERENCES

Carraro, F., Gonçalves, M.S., Lopez, R.H., Miguel, L.F.F. & Valente, A.M. 2019. Weight estimation on static B-WIM algorithms: A comparative study. *Engineering Structures* 198, 109463. http://dx.doi.org/10.1016/j.engstruct.2019.109463

Chatterjee, P., OBrien, E., Li, Y. & González, A. 2006. Wavelet domain analysis for identification of vehicle axles from bridge measurements. *Computers & Structures* 84(28): 1792–1801. http://dx.doi.org/10.1016/j.compstruc.2006.04.013

Cuomo, S., Di Cola, V.S., Giampaolo, F., Rozza, G., Raissi, M. & Piccialli, F. 2022. Scientific Machine Learning Through Physics–Informed Neural Networks: Where we are and What's Next. *Journal of Scientific Computing* 92(3): 1–62. https://doi.org/10.1007/s10915-022-01939-z

He, W., Deng, L., Shi, H., Cai, C.S. & Yu, Y. 2017. Novel virtual simply supported beam method for detecting the speed and axles of moving vehicles on bridges. *Journal of Bridge Engineering* 22(4), 04016141. https://doi.org/10.1061/(asce)be.1943-5592.0001019

He, W., Ling, T., OBrien, E.J. & Deng, L. 2019. Virtual axle method for bridge weigh-in-motion systems requiring no axle detector. *Journal of Bridge Engineering* 24(9), 04019086. https://doi.org/10.1061/(asce)be.1943-5592.0001474

Lorenzen, S.R., Riedel, H., Rupp, M.M., Schmeiser, L., Berthold, H., Firus, A. & Schneider, J. 2022. Virtual axle detector based on analysis of bridge acceleration measurements by fully convolutional network. *Sensors* 22(22), 8963. https://doi.org/10.3390/s22228963

Kawakatsu, T., Aihara, K., Takasu, A. & Adachi, J. 2020. Fully-Neural approach to heavy vehicle detection on bridges using a single strain sensor. *ICASSP 2020 - 2020 IEEE International Conference on Acoustics, Speech and Signal Processing (ICASSP)*. http://dx.doi.org/10.1109/icassp40776.2020.9053137

Kollár, D., Völgyi, I. & Joó, A.L. 2023. Assessment of residual stresses in welded T-joints using contour method. *Thin-Walled Structures* 190, 110966. https://doi.org/10.1016/j.tws.2023.110966

Ma, R., Zhang, Z., Dong, Y. & Pan, Y. 2020. Deep learning based vehicle detection and classification methodology using strain sensors under bridge deck. *Sensors* 20(18), 5051. https://doi.org/10.3390/s20185051

Moses, F. 1979. Weigh-in-Motion system using instrumented bridges. *Transportation Engineering Journal of ASCE* 105(3): 233–249. https://doi.org/10.1061/tpejan.0000783

Szegedy, C., Ioffe, S., Vanhoucke, V. & Alemi, A. 2017. Inception-v4, inception-resnet and the impact of residual connections on learning. *Proceedings of the AAAI conference on artificial intelligence* 31(1): 4278–4284. https://doi.org/10.1609/aaai.v31i1.11231

Szinyéri, B., Kővári, B., Völgyi, I., Kollár, D. & Joó, A.L. 2023. A strain gauge-based Bridge Weigh-In-Motion system using deep learning. *Engineering Structures* 277, 115472. https://doi.org/10.1016/j.engstruct.2022.115472

Szinyéri, B. & Kovari, B. 2023. Comparison of a Deep Learning-based Axle Load Estimator and the Matrix Method in Strain Gauge-based Bridge Weigh-In-Motion Systems. *10th International Conference on Soft Computing & Machine Intelligence (ISCMI)*, in press

Wu, Y., Deng, L. & He, W. 2020. BwimNet: A novel method for identifying moving vehicles utilizing a modified encoder-decoder architecture. *Sensors* 20(24), 7170. https://doi.org/10.3390/s20247170

Bridge Maintenance, Safety, Management, Digitalization and Sustainability – Jensen, Frangopol & Schmidt (eds)
© 2024 The Author(s), ISBN 978-1-032-77040-6
Open Access: www.taylorfrancis.com, CC BY-NC-ND 4.0 license

Load estimation precision for moving forces with position uncertainties through AKF

C.Y. Zhou
College of Civil Engineering and Architecture, Zhejiang University, Hangzhou, Zhejiang, PR China
Zhejiang University - University of Illinois at Urbana-Champaign Institute, Zhejiang University, Haining, Zhejiang, PR China

C. Demartino
Zhejiang University - University of Illinois at Urbana-Champaign Institute, Zhejiang University, Haining, Zhejiang, PR China
Department of Civil and Environmental Engineering, University of Illinois at Urbana-Champaign, Urbana, IL, USA

ABSTRACT: This paper presents a quantitative analysis of load estimation through augmented Kalman filter (AKF) for dynamic systems subjected to moving forces with position uncertainties. AKF incorporates unknown inputs with estimated system states, enabling the filter to estimate unknown forces. Identification algorithms like AKF often necessitate knowledge of the position of a moving load; however, the uncertainty in force position is frequently overlooked in the analysis. These uncertainties may stem from a variety of factors, including sensor noise, measurement inaccuracies, or the inherent variability in the force's intended path. For example, vehicle position tracking can be achieved through straightforward methods like entry and exit sensors, assuming a constant velocity model. Alternatively, it can involve more sophisticated remote sensing techniques, such as computer vision or LiDAR-based systems, which provide a more accurate representation of the vehicle's position. In this context, this paper presents a pioneering effort to quantify the impact of load estimation precision in scenarios involving moving forces with position uncertainties under diverse conditions using AKF. The study focuses on a simply supported bridge case, with the tuning of AKF parameters accomplished through the L-curve method. Tests involving various position noise levels combined with different velocities of the applied forces were conducted.

1 INSTRUCTION

Moving loads are ubiquitous in mechanical and civil engineering within daily lives. In many instances, a comprehensive understanding of the moving loads applied to structures proves beneficial. Consider, for instance, the context of a bridge—a structure designed to bear moving loads, playing a critical role in supporting everyday urban activities. The precise knowledge of the moving forces on the bridges can be great helpful for structure maintenance and improving bridge design (Lydon 2016). Therefore, the identification of dynamic loads stands as a paramount undertaking.

Significant efforts have been dedicated to the field of moving force identification. Direct measurement methods, such as axle-level instrumentation (Cantieni 1992), have been proposed. More recently, attention has shifted towards indirect measurement methods, commonly referred to as Bridge Weigh-in-Motion (BWIM) (Yu 2016). Moses (Moses 1979) early proposed the BWIM method, employing influence lines and strain measurements. Law (Law 1999) proposed a frequency and time domain method to retrieve the dynamic load history. OBrien (OBrien

DOI: 10.1201/9781003483755-171

2006) applied Tikhonov regularization to reduce algorithm inaccuracies. Liu (Liu 2020) used compressed sensing theory to shorten the sample length of response data for identification.

In addition to analytical methods and the influence line method, the Kalman filter (KF) has become a potent and promising tool for moving load identification. The KF is a recursive optimal estimation algorithm that achieves precise estimation by integrating the model of the system and measurement data (Welch 1995). Lourens (Lourens 2012) introduced the augmented Kalman filter (AKF), which incorporates unknown inputs with estimated system states, enabling the filter to estimate unknown forces. Based on Lourens' work, Lai (Lai 2022) applied the AKF to moving load identification, assessing its accuracy through field tests. Lai's work presented the feasibility and effectiveness of utilizing the AKF in time-variant systems.

Following the literature review conducted above, existing research reveals certain limitations. Notably, identification algorithms frequently require knowledge of the position of a moving load, yet they often overlook positional noise (Feng 2015). Basic methods, like entry and exit sensors, assuming a constant velocity model, can accomplish this task (Lai 2022). Conversely, more advanced techniques, such as computer vision or LiDAR-based systems, offer a heightened precision in representing the vehicle's position. Regardless of the chosen method, it is crucial to recognize the inevitable presence of positional errors, which can impact the accuracy of identification.

Therefore, this paper investigates the effect of the load position noise on the moving force identification of the AKF. The study focuses on a simply supported Finite Element (FE) beam. The tuning of AKF parameters was accomplished using the L-curve method, and tests of various position noise levels along with different velocities of the forces were conducted. The subsequent sections of the paper are structured as follows: Section 2 provides the relevant equations, Section 3 presents the numerical tests, and finally, Section 4 comprises the conclusion and discussion.

2 MODELING

2.1 *Equation of motion*

The analysis incorporates a Finite Element Method (FEM) discretization to model the structural response under the influence of a dynamic load. This discretization employs one-dimensional beam elements within a two-dimensional space, each node having three Degrees of Freedom (DOFs). Figure 1 serves as an illustrative representation of the model, depicting a simply supported beam subjected to two moving forces, denoted as f_1 and f_2. These forces represent a singular vehicle with two axles in motion at a given velocity s and a fixed axle distance b_1.

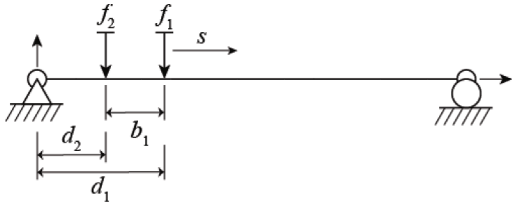


Figure 1. Diagram of a simply supported beam subjected to a two-axle vehicle.

The equation of motion of the FE model can be represented as:

$$M\ddot{u}(t) + C\dot{u}(t) + Ku(t) = S_f(t)f(t) \tag{1}$$

where $u(t) \in \mathbb{R}^{n_d}$ represents the displacement vector, n_d is the number of DOFs of the model. $M \in \mathbb{R}^{n_d \times n_d}$, $C \in \mathbb{R}^{n_d \times n_d}$, and $K \in \mathbb{R}^{n_d \times n_d}$ are the global mass matrix, damping matrix, and

stiffness matrix, respectively, $f(t) \in \mathbb{R}^{n_f}$ denotes the input load vector, n_f is the number of the input loads, $S_f(t) \in \mathbb{R}^{n_d \times n_f}$ represents the load distribution matrix indicating how moving loads apply to the system.

The damping is modeled through the famous Rayleigh damping i.e. C is a linear combination of the stiffness and mass matrices:

$$C = \alpha M + \beta K \tag{2}$$

where α and β are the Rayleigh damping coefficients of M and K, respectively.

2.2 *AKF modeling*

Suppose the discretization time step size is set to Δt. $\bullet_k$ denotes the current time is $k\Delta t$. The augmented stat vector $X_k \in \mathbb{R}^{2n_d+n_f}$ is defined as:

$$X_k = \begin{bmatrix} u_k \\ \dot{u}_k \\ f_k \end{bmatrix} \tag{3}$$

where $\boldsymbol{u}_k$ represents the displacement state vector, $\dot{u}_k$ represents the velocity state vector, and $\boldsymbol{f}_k$ is the force vector.

The augmented state-space representation of both the bridge and the vehicle is expressed as:

$$\begin{cases} X_k = A_{k-1} X_{k-1} + w_{k-1} \\ z_k = H_k X_k + v_k \end{cases} \tag{4}$$

where $A_{k-1} \in \mathbb{R}^{(2n_d+n_f)\times(2n_d+n_f)}$ is the augmented system matrix, defined as:

$$A_{k-1} = \begin{bmatrix} A_d & B_{d,k-1} \\ 0 & I \end{bmatrix} \tag{5}$$

where A_d and $B_{d,k-1}$ are obtained by discretizing the continuous system matrix A_c and B_c defined as:

$$A_c = \begin{bmatrix} 0 & I \\ -M^{-1}K & -M^{-1}C \end{bmatrix} \tag{6}$$

$$B_c(t) = \begin{bmatrix} 0 \\ M^{-1}S_f(t) \end{bmatrix} \tag{7}$$

The augmented output influence matrix $H_k \in \mathbb{R}^{n_z \times (2n_d+n_f)}$ is contingent upon the measured DOFs. $z_k \in \mathbb{R}^{n_z}$ represents the measured vector and n_z is the number of the measured points. The process noise w_{k-1} denotes the zero-mean noise in the state equation and is characterized by the associated covariance matrix $Q \in \mathbb{R}^{(2n_d+n_f)\times(2n_d+n_f)}$, and v_k is the zero-mean measurement noise with associated covariance matrix $R \in \mathbb{R}^{n_z \times n_z}$.

The covariance matrix $\boldsymbol{Q}$ is expressed as:

$$Q = \begin{bmatrix} Q_u & 0 \\ 0 & Q_f \end{bmatrix} \tag{8}$$

Where $Q_u = \mathrm{diag}\left(\sigma_u^2\right) \in \mathbb{R}^{2n_d \times 2n_d}$ is the covariance matrix of the displacement and velocity, and $Q_f = \mathrm{diag}\left(\sigma_f^2\right) \in \mathbb{R}^{n_f \times n_f}$ is the covariance matrix associated with the white force noise. Both σ_u^2 and σ_f^2 serve as tuning parameters in this study, influencing the system's response to uncertainties in the displacement, velocity, and external force components.

The equations of the Kalman filter are given as:

i. Measurement update

$$\begin{aligned} L_k &= P_k^- H_k^{\mathrm{T}} \left(H_k P_k^- H_k^{\mathrm{T}} + R\right)^{-1} \\ \hat{X}_k &= \hat{X}_k^- + L_k\left(z_k - H_k \hat{X}_k^-\right) \\ P_k &= (I - L_k H_k) P_k^- (I - L_k H_k)^{\mathrm{T}} + L_k R L_k^{\mathrm{T}} \end{aligned} \tag{9}$$

ii. Time update

$$\begin{aligned} \hat{X}_{k+1}^- &= A_k \hat{X}_k \\ P_{k+1}^- &= A_k P_k A_k^{\mathrm{T}} + Q \end{aligned} \tag{10}$$

where $\hat{X}_k^-$ and $\hat{X}_k$ are the prior and posterior estimation of the augmented state vector at k-th step respectively, P_k^- and P_k are the prior and posterior error covariance matrix at k-th step respectively, and L_k represents the well-known Kalman gain.

2.3 *AKF tuning*

For the covariance matrix Q, the tuning process from the L-curve method is selected. When employ the L-curve, σ_u^2 and σ_f^2 are assumed to share the same value. Initially, σ_u^2 is determined based on the minimum error norm $\left\|z_k - H_k \widehat{X}_k^-\right\|_2$. σ_u^2 is searched within the given range $\left[\min\left(\sigma_u^2\right), \max\left(\sigma_u^2\right)\right]$ with an exponential step size of $^{10}1$. For each value of σ_u^2 the range of σ_f^2 given by $\left[\min\left(\sigma_f^2\right), \max\left(\sigma_f^2\right)\right]$ is searched for the minimum error norm. σ_u^2 is then selected at the corner of the L-curve. Subsequently, σ_f^2 can be decided by the smooth error $\|f_k\|_2$ and the error norm $\left\|z_k - H_k \widehat{X}_k^-\right\|_2$ obtained given the fixed σ_u^2 and the same range $\left[\min\left(\sigma_f^2\right), \max\left(\sigma_f^2\right)\right]$. For further details, interested readers can refer to Lourens et al. (Lourens 2012); Lagerblad et al. (Lagerblad 2019).

3 NUMERICAL EXAMPLE

3.1 *FE model*

This section investigates a single span simply supported bridge model subjected to moving forces. The detailed parameters of the finite element (FE) model are outlined in Table 1. The model comprises 12 elastic-beam-column type elements, resulting in a total of 35 DOFs, as presented in Figure 2. Measurement channels were positioned at the vertical DOFs of five nodes within the model, as illustrated in Figure 2.

Table 1. FE model parameters.

Parameters	Value	Parameters	Value
Length (m)	30	Section inertial moment (m^4)	0.8
Element number	12	Elastic modulus (Pa)	3×10^{10}
Density (kg/m^3)	3000	Damping coefficient α	1.5×10^{-1}
Section area (m^2)	3	Damping coefficient β	5×10^{-5}

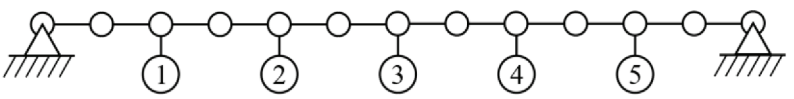


Figure 2. FE model and the measurement placement.

To introduce the model error, the elastic modulus and the damping coefficients were multiplied by a random number generated from a normal distribution with a mean of 1 and a standard deviation of 0.05. The mode properties after the introduction of the model error are shown in Figure 3.

Position noise is introduced to simulate the identification uncertainty of the tracking method, formulated as follows:

$$\mathrm{d}_{k+1}^{i} = \mathrm{d}_{k}^{i} + [s + \mathcal{N}(0, PNL \times s)] \times \Delta t \tag{11}$$

where d_{k}^{i} represents the location of the ith axle force of the vehicle at the kth time step, PNL denotes the position noise level, and s is the velocity of the vehicle.

To evaluate the accuracy of the identification, the error is computed as the norm of the difference between the true and estimated axle force vectors, expressed as:

$$E = \frac{\|f_{true} - f_i\|}{\|f_{true}\|} \times 100\% \tag{12}$$

where f_i represents the identified force vector over the crossing period and f_{true} is the true force vector of the same length.

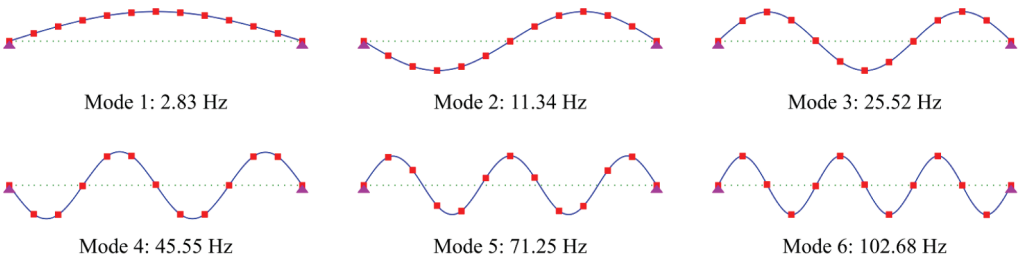


Figure 3. Mode shape and mode frequency of the adjusted FE model.

3.2 *Tuning results*

The following scenario is considered: a vehicle with two axles, specifically, the first axle (denoted as f_1) with a weight of 68.7 kN and the second axle (denoted as f_2) with a weight of 127.5 kN, is applied to a bridge at a constant velocity of 20 m/s. A white noise of 5% was introduced to the true response and the force position data. This scenario is analyzed in the presence of model errors. The sampling frequency is 200 Hz. The initial force variance $P_0^{f_i}$ is set as 4×10^{10} kN^2 and the rest initial state variance is set as 0 kN^2, indicating that the filter assumes the bridge to be static before the vehicle enters. For this study, σ_u^2 was searched

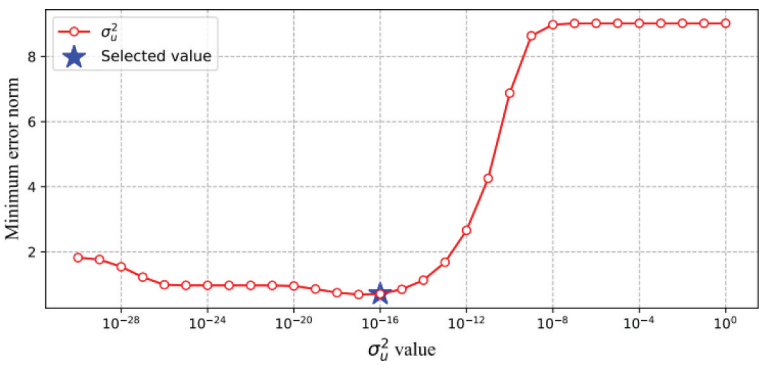


Figure 4. Tuning process of σ_u^2.

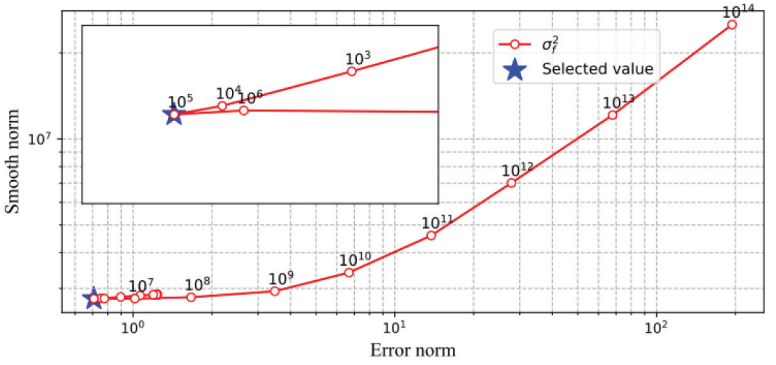


Figure 5. Tuning process of σ_f^2 given $\sigma_u^2 = 10^{-16}$.

within the range of $[10^{-30}, 10^{0}]$ with an exponential step size of 10^{1} while σ_f^2 was assigned the range of $[\sigma_u^2 \times 10^{0}, \sigma_u^2 \times 10^{30}]$ with an exponential step size of 10^{1}. The tuning process was plotted in Figure 4 and Figure 5 and the parameters were selected as $\sigma_u^2 = 10^{-16}$ and $\sigma_f^2 = 10^{5}$.

3.3 *AKF results*

This study examines the impact of varying noise levels on the precision of identification results for a two-axle vehicle at different velocities, using the same vehicle configuration as detailed in subsection 3.2. Four distinct levels of force position noise—1%, 2%, 5%, and 10%—have been chosen for analysis. Additionally, three different velocities—20 m/s, 30 m/s, and 40 m/s—are taken into consideration. Consequently, a total of 12 test combinations are investigated. For each combination, 50 tests are conducted to derive statistical measures of the identification accuracy. The sampling frequency is held constant at 200 Hz throughout this study. The parameters of the filter were chosen to be the same as those employed in the tuning process and aligned with the results obtained from the tuning phase.

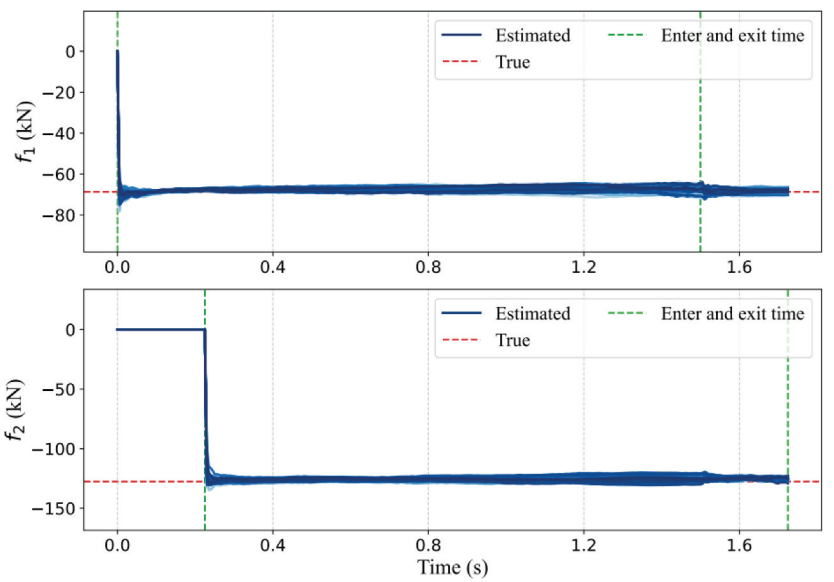


Figure 6. Estimation of axle force with the position noise of 1% for a velocity of 20 m/s.

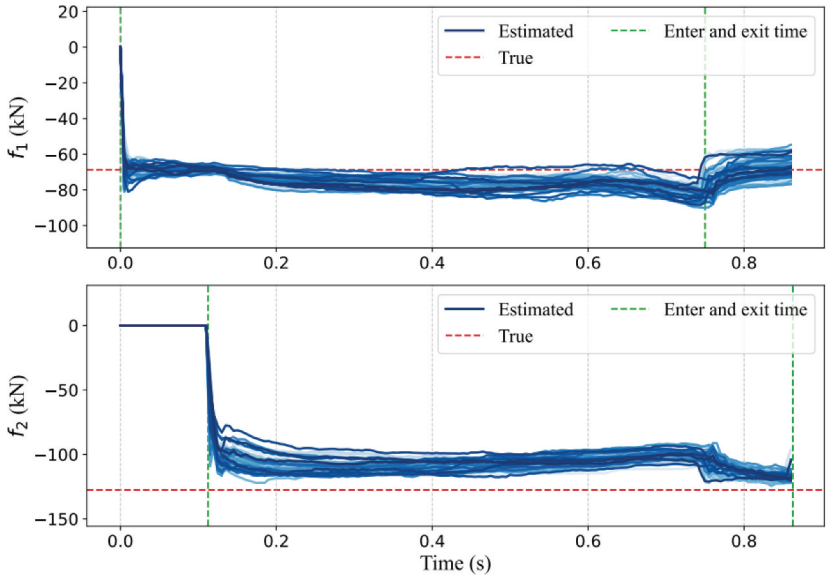


Figure 7. Estimation of axle force with the position noise of 10% for a velocity of 40 m/s.

Figure 6 and Figure 7 depict the time history of force estimation and uncertainty for two extreme cases: 1% position noise at 20 m/s and 10% position noise at 40 m/s, respectively. In scenarios with low noise levels, the estimated force values closely align with the true force values. Conversely, under conditions of high noise, the filter encounters challenges in accurately tracking the true value, yet it still produces results that are sufficiently accurate.

Table 2 presents detailed error values. The identification error for a single axle and the sum weight exhibit an increase with higher levels of position noise, as indicated in the table. The filter faces greater difficulty in accurately estimating the true force with heightened position noise. Additionally, at a velocity of 40 m/s, the identification errors are larger than those observed at lower velocities. Higher velocities result in a shortened crossing time, offering the estimation process less input information, and the presence of more axles introduces additional unknown states. Cases at 30 m/s exhibit better performance compared to those at

Table 2. Mean (standard deviation) of error of different combinations.

Velocity (m/s)	20				30			
PNL (%)	1	2	5	10	1	2	5	10
f_1 (%)	2.14 (±0.92)	2.12 (±1.02)	3.03 (±1.13)	9.47 (±3.33)	2.08 (±0.77)	1.95 (±0.89)	2.67 (±1.08)	7.59 (±2.68)
f_2 (%)	1.91 (±0.75)	2.24 (±0.76)	5.68 (±1.38)	16.03 (±2.67)	1.72 (±0.69)	2.23 (±0.80)	4.76 (±1.36)	12.77 (±1.98)
Sum (%)	1.68 (±0.62)	1.87 (±0.65)	3.03 (±0.84)	7.36 (±1.21)	1.58 (±0.60)	1.80 (±0.62)	2.66 (±0.79)	5.91 (±0.80)
Velocity (m/s)	40							
PNL (%)	1	2	5	10				
f_1 (%)	7.31 (±1.12)	7.92 (±1.36)	8.92 (±2.23)	11.03 (±2.87)				
f_2 (%)	11.35 (±0.81)	11.55 (±1.02)	12.78 (±1.80)	17.01 (±2.59)				
Sum (%)	5.96 (±0.47)	5.90 (±0.52)	6.26 (±0.73)	8.05 (±1.19)				

* PNL: position noise level.

20 m/s, which may be attributed to the tuned parameters being more suitable for scenarios with a velocity of 30 m/s.

4 CONCLUSIONS

In this study, we conducted an analysis of force identification using an AKF for structure subjected to moving forces with position uncertainties. The analysis took into account both model and response errors. The impact of position noise was investigated through numerical analyses on a simply supported bridge subjected to a two-axle vehicle. The vehicle was modeled as two constant concentrated forces moving with a fixed distance and a specified velocity. The results indicate that position noise leads to a decrease in identification accuracy across all velocity cases. This effect is particularly strong at lower velocities, while at higher velocities, the impact is less significant.

Certain limitations exist in the current framework, such as the omission of dynamic effects related to moving loads and a primary focus on scenarios involving a single two-axle vehicle. Ongoing research efforts are dedicated to addressing these limitations and enhancing the comprehensiveness of the proposed methodology.

REFERENCES

Cantieni, R. (1992). Dynamic behavior of highway bridges under the passage of heavy vehicles.

Feng, D., Sun, H., & Feng, M. Q. (2015). Simultaneous identification of bridge structural parameters and vehicle loads. Computers & Structures, 157, 76–88.

Lagerblad, U., Wentzel, H., & Kulachenko, A. (2019). Dynamic response identification based on state estimation and operational modal analysis. Mechanical Systems and Signal Processing, 129, 37–53.

Lai, X., Furkan, M., Bartoli, I., Aktan, A. E., & Grimmelsman, K. (2022). Bridge weigh-in-motion using augmented Kalman filter and model updating. Journal of Civil Structural Health Monitoring, 12(3), 593–610.

Law, S. S., Chan, T. H., & Zeng, Q. H. (1999). Moving force identification—a frequency and time domains analysis.

Liu, H., Yu, L., Luo, Z., & Pan, C. (2020). Compressed sensing for moving force identification using redundant dictionaries. Mechanical Systems and Signal Processing, 138, 106535.

Lourens, E., Reynders, E., De Roeck, G., Degrande, G., & Lombaert, G. (2012). An augmented Kalman filter for force identification in structural dynamics. Mechanical systems and signal processing, 27, 446–460.

Lydon, M., Taylor, S. E., Robinson, D., Mufti, A., & Brien, E. J. O. (2016). Recent developments in bridge weigh in motion (B-WIM). Journal of Civil Structural Health Monitoring, 6, 69–81.

Moses, F. (1979). Weigh-in-motion system using instrumented bridges. Transportation Engineering Journal of ASCE, 105(3), 233–249.

OBrien, E. J., Rowley, C. W., Gonzalez, A., & Green, M. F. (2009). A regularised solution to the bridge weigh-in-motion equations. International Journal of Heavy Vehicle Systems, 16(3), 310–327.

Welch, G., & Bishop, G. (1995). An introduction to the Kalman filter.

Yu, Y., Cai, C. S., & Deng, L. (2016). State-of-the-art review on bridge weigh-in-motion technology. Advances in Structural Engineering, 19(9), 1514–1530.


Taylor & Francis
Taylor & Francis Group
http://taylorandfrancis.com

SS03: Estimating future preventive bridge interventions

Organizers: B.T. Adey, H. Mehranfar & S. Chuo


Taylor & Francis
Taylor & Francis Group
http://taylorandfrancis.com

Bridge Maintenance, Safety, Management, Digitalization and Sustainability – Jensen, Frangopol & Schmidt (eds)
© 2024 The Author(s), ISBN 978-1-032-77040-6
Open Access: www.taylorfrancis.com, CC BY-NC-ND 4.0 license

Improvements in providing overviews of future bridge interventions, their possession windows, and costs

H. Mehranfar, B.T. Adey & S. Chuo
Chair of Infrastructure Management, Institute of Construction & Infrastructure Management ETH Zurich, Switzerland

ABSTRACT: Bridge managers estimate intervention requirements years in advance. They do this to help ensure that work that needs to be carried out can be planned appropriately in terms of quality and timing. These initial estimates must be done at least 10 years before an intervention is required and perhaps even up to 20 years. These large time periods are required so that detailed investigations can be carried out, decisions can be made as to what should be done, work sites can be planned that exploit synergies between multiple interventions, that intervals can be built into train schedules so that there is enough time to do the work, and then the construction sites can be planned in detail. This paper proposes a methodology to be used by bridge managers to obtain a consistent and complete overview of these future bridge interventions and give indications of the required possession windows required in train schedules, and the approximate costs. The methodology is an improvement on the existing bridge management system methodologies in that it uses nonhomogeneous transition probabilities, instead of homogeneous ones, and explicitly estimates the risks associated with different types of bridge failure as a function of the condition states of the different structural components. Existing methodologies do not explicitly consider failure risk in this manner. The methodology is demonstrated using a 100m-long steel truss bridge in Switzerland. The results are visualized using BIM, which allows bridge managers to better understand the algorithmic results and facilitates discussions between multiple stakeholders of the planning process to prioritize interventions. The use of the methodology is expected to improve both effectiveness and efficiency of the intervention planning process.

1 INTRODUCTION

In the current intervention planning process, the estimation of intervention requirements for bridges is often conducted in a somewhat iterative and qualitative manner. This usually involves discussing the findings of inspection reports by bridge managers with inspectors and engineers in order to ensure a shared understanding of bridge conditions to enable informed decision-making regarding the intervention requirements for bridges over future planning periods. This process is challenging and time-consuming due to the lack of a systematic and efficient methodology to generate an overview regarding all possible upcoming interventions. This lack not only makes it difficult to have a complete overview of the required possession times and financial requirements for executing interventions but it may also lead to deviations in scheduling of interventions to be executed at the ideal time. This will likely result in frequent service disruptions as well as excessive intervention costs. Consequently, a systematic methodology to efficiently estimate intervention requirements in a digital environment would help bridge managers reduce service disruptions and intervention costs by facilitating

DOI: 10.1201/9781003483755-172

a common understanding of intervention requirements, their required possession times and costs using available data on the condition of bridges. Such a methodology addresses the gap in the current intervention planning process.

There exist numerous methodologies aiming at helping bridge managers in their decision-making on estimating the required interventions. For example, (Adey and Hajdin 2011, Adey *et al.* 2015) proposed methodologies to determine the optimal intervention strategies for a bridge portfolio using asset-level information. These methodologies, although efficient and systematic, could not provide complete and detailed estimates of intervention requirements. Such details include conducting analyses on the component (or element) level, estimates of failure risks, required possession windows, and costs. Each of these gaps was addressed in different ways in several works. For example, (Martani *et al.* 2021, Kim *et al.* 2022) focused on making their estimates on the component level. (Adey *et al.* 2010, 2012) proposed methodologies to estimate the failure risks associated with the bridges. (Adey and Hajdin 2011, Burkhalter and Adey 2021, 2022) made estimates of intervention costs and required possession windows in their work. Despite some works such as (Mehranfar, Adey, *et al.* 2023b) proposed a methodology to cover all of these aspects for providing a detailed and complete overview of intervention requirements for aiding bridge managers in their decision-making, they were not being integrated into BIM.

This paper proposes a methodology to systematically generate a complete overview of intervention requirements, their required possession windows, costs, and associated failure risks over multiple planning periods. The methodology, furthermore, pipelines this information efficiently to be presented in BIM in a user-friendly manner.

2 METHODOLOGY

An overview of the steps for generating a complete overview of intervention requirements along with their visualisation in BIM over multiple planning periods is provided in Figure 1.

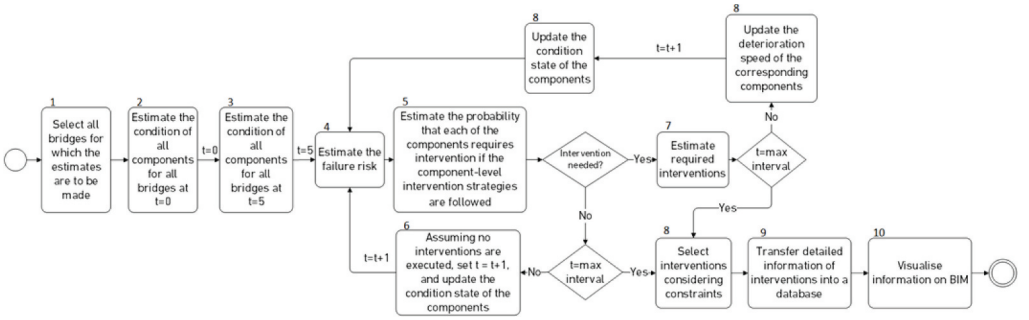


Figure 1. Steps to estimate and visualize component-level intervention requirements.

Step 1: Select all bridges for which the estimates are to be made. The bridges that are being investigated in detail do not need these estimates.

Step 2: Estimate the condition of all components for all bridges at t=0.

Step 3: Estimate the condition of all components for all bridges at the start of the planning period to be considered, for example, t=5.

Step 4: Estimate the failure risks at t=5.

Step 5: Estimate the probability that each of the components will require intervention if the component-level intervention strategies are followed.

Step 6: Assuming no interventions are executed, set t = t+1 and repeat Steps 3 to 6 until the probabilities of components requiring intervention and the failure risks have been estimated for each of the years in the planning period.

Step 7: Estimate the required interventions. If the probability of requiring an intervention on at least one of the components is higher than the threshold value set, or the sum of the failure risks in the planning period is higher than a specific threshold value, it is considered that an intervention is to be executed on the bridge in this period, and information is given on the possible intervention types and the one that has the most likelihood, the possible and most likely possessions window requirement, and the expected intervention costs as a function of the type of intervention and possession windows.

Step 8: Select intervention interventions considering the constraints, e.g., thresholds for triggering execution of interventions, and propose interventions to postpone if the execution of all interventions is not possible: If it is known that not all interventions are possible within the planning period, e.g., due to a restricted budget even at this early stage, the indicator of the risk of failure is used to prioritize the bridge interventions, i.e., the bridges exhibiting the highest risk are first on the list. The bridges lowest on the list are postponed until the costs of the interventions included in the list are below the allocated budget.

Step 9: Transfer the detailed information of interventions into a database. The details regarding the selected component-level intervention, along with the information regarding the required possession windows, expected costs, and associated failure risks are transferred into a database to be used for visualization.

Step 10: Visualize information on BIM. The information regarding the intervention requirements that exist on the database is pipelined into the BIM of bridges to generate a user-friendly and complete overview of component-intervention requirements on the bridges.

3 EXAMPLE BRIDGE

Figure 2 shows the BIM of the example steel truss bridges, which consists of multiple components. These components, as shown in Figure 2, are trusses, girders, bearings, abutments, foundations, and the pier. Five discrete condition states on a scale of one to five are used to describe the different damage severities of the components that include the specific details of each condition state. A Condition State of 1 (CS1) implies that the component is in perfect condition, while CS5 states that the component is at the end of its lifecycle. These are assumed for all components in the same way done in (Mehranfar, Adey, *et al.* 2023b).

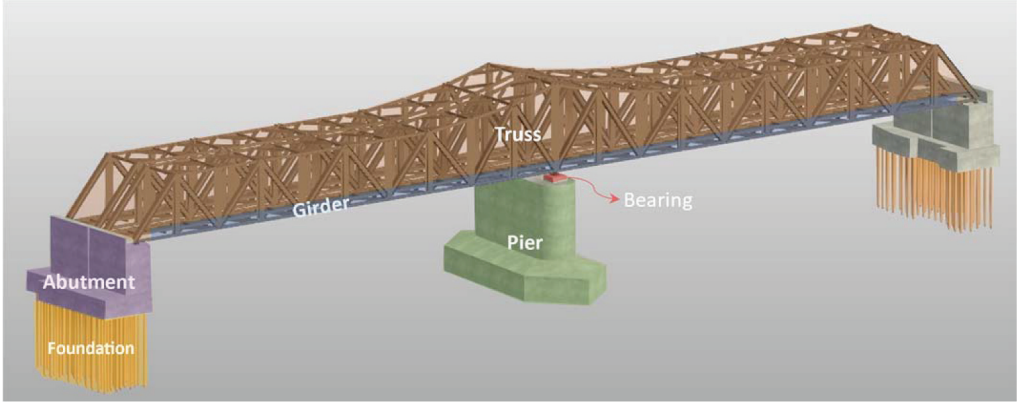


Figure 2. BIM of the example steel truss bridge.

3.1 *Condition of components at t=0 and t=5*

The current CS of the components is estimated by comparing the damage indicators mentioned in the inspection reports with the definition of CSs for the bridge components. For the

components that this information was not available, CSs were estimated using the method proposed by (Chuo *et al.* 2023). It is estimated that at t=0, foundations are in CS3, abutments are in CS2, the pier is in CS2, the bearings are in CS4, girders are in CS3, and the truss is in CS3.

The future CS of the components at t=5 was estimated using a probabilistic discrete state model with nonhomogeneous transition probabilities as done in (Mehranfar, Adey, *et al.* 2023b). In this model, the transition probabilities are for a one-year period as one year is usually the time between two consecutive routine inspections on the bridges. Additionally, the deterioration rates are assumed to accelerate by 2% as a function of the times maintenance interventions are executed on the components. The deterioration rates reset to default when the component is replaced.

A summary of the CS of the components at t=5 is provided in Table 1. It is seen that it is highly likely that the foundations are in CS3, abutments in CS2, the pier in CS2, bearings in CS5, girders in CS3, and trusses in CS3. These are estimated by multiplying the CS of the component in t=0 with the probability that their CS transits into the possible future CS within 5 years.

Table 1. A summary of the CS of components at t=5.

	CS				
Component	1	2	3	4	5
Foundations	0%	0%	63%	26%	12%
Abutments	0%	78%	18%	3%	1%
Pier	0%	75%	20%	4%	1%
Bearings	0%	0%	0%	33%	67%
Girders	0%	0%	47%	31%	22%
Trusses	0%	0%	47%	31%	21%

3.2 *Component-level intervention strategies*

There are multiple possibilities for the type of interventions that can be executed on each component. These are dependent on the severity of the observed damages. For example, in a planning period, one of three different intervention types including rehabilitation, renewal, and replacement can be executed on a damaged truss. These intervention types are defined to reflect the increasing effort and work required for interventions for all components in the same way discussed in (Mehranfar, Adey, *et al.* 2023b, 2023a).

Total costs of executing each intervention type on each component are estimated in terms of owner and user costs. The owner costs are roughly calculated using a reference pricing index (SFSO 2021). The user costs are approximately calculated with respect to the added travel time due to taking alternative connections during the possession windows required for the execution of interventions in the same way explained in (Mehranfar, Adey, *et al.* 2023a). An example of the intervention costs for the trusses is shown in Table 2. This table states that the more complex and intensive the work, the more expensive it becomes. These values are estimated for all components in the same manner.

Table 2. Example intervention costs for trusses.

Intervention type	Unit owner cost (mu/m^2)	Area (m^2)	Duration of the service disturbance (weeks)	Owner cost (mu)	Service disturbance costs (mu)
Rehabilitation	75	2'200	4	165'000	1'302'480
Renewal	150	2'200	10	330'000	3'256'200
Replacement	400	2'200	15	880'000	4'884'300

To account for the imperfection execution of interventions, the effectiveness of interventions for improving the condition of components to CS1 is assumed to be 85% for rehabilitation, 90% for renewal, and 100% for replacement. These values are illustrative, and they should be adjusted when implemented in a bridge management system.

The intervention strategies for the components are assumed to be:

- Execute no interventions when components are in CS1 or CS3.
- Rehabilitate when components are in CS3.
- Renew when components are in CS4.
- Replace when components are in CS5.

3.3 *Failure risks*

Failure risks need to be estimated in order to prioritise the initiation of a detailed investigation of the bridges recommended by the intervention strategies if not all of them can be initiated. Failure risks are estimated using fault tree analysis. Three fault trees are developed to estimate the probability and consequences associated with the failure of bridges to provide sufficient service, depending on the condition of the components. The top events of these fault trees are defined to cover the severity of the serviceability failure, which is a function of the severity of the component failures, i.e., "restricted service", "closure for up to two months" and "closure for more than two months". The occurrence of each top event results in the execution of different immediate interventions on the components.

The basic events include gradual and sudden deterioration events. These events occur due to a combination of different loads, e.g., excessive traffic loads, flooding, etc. More specific information regarding the use of failure risks for estimating the serviceability failure due to the execution of immediate interventions is found in (Mehranfar, Adey, *et al.* 2023b).

Connecting the estimates of failure risks to the condition of components allows setting a threshold on added total failure risks. Such thresholds can later be used to compare the level of failure risk with the predefined threshold to prioritise interventions. Figure 3 shows the evolution of the failure risks over time for the example steel truss bridge. Here, the threshold is considered as the value of failure risks if all components are in CS4. It is seen that the bridge manager can postpone the execution of interventions until t=11 as the failure risks meet their threshold at that time.

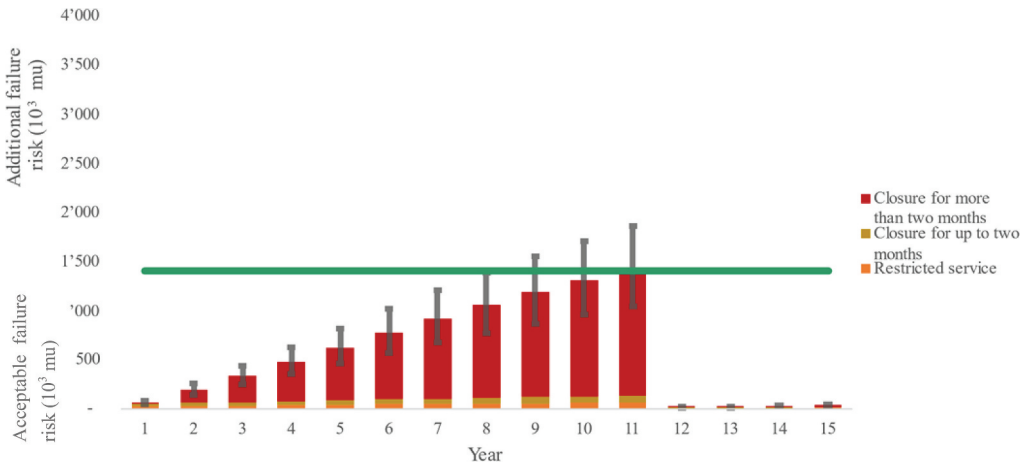


Figure 3. Evolution of failure risks considering a failure risks threshold.

4 ESTIMATES OF MOST LIKELY COMPONENT-LEVEL INTERVENTIONS

An overview of estimated most likely component-level interventions following consideration of component-level intervention strategies is provided in Table 3. This table serves as a starting point for discussing what activities will be precisely required for the bridge. It is assumed that the interventions are required to be executed on the components when the condition of bridge components meets the criteria mentioned in their intervention strategies. It is seen, for example, that the bridge abutments are highly likely to require rehabilitation in the period between t=6 and t=10 and if this intervention is executed on the abutments, it is likely that it will take 11 weeks to complete. Of this time, no service disturbance is needed for 6 weeks, and a service restriction is needed to be implemented for 4 weeks.

Table 3. The most likely intervention between t=6 and t=10 and between t=11 and t=15.

Planning period (expected year)	Component	Intervention type	Expected duration (weeks)	Expected required possessions (weeks) if done alone			Expected owner costs (10^3 mu)
				None	Restrictions on the traffic	Closure	
t=6 to t=10 (year 6)	Foundations	Rehabilitation	12	6	5	1	90
	Girders	Rehabilitation	6	2	4	-	330
	Trusses	Rehabilitation	8	5	3	-	165
	Bearings	Replacement	4	3	1	-	120
	Abutments	Rehabilitation	11	6	5	-	100
t=11 to t=15 (year 15)	Pier	Rehabilitation	10	6	4	-	480

5 VISUALISATIONS OF COMPONENT-LEVEL INTERVENTION ESTIMATES IN BIM

So that bridge managers have a better understanding of the component-level intervention estimates, BIM is used to visualise the evolution of CSs and the most likely intervention requirements over multiple planning periods. More detailed information regarding the use of BIM for infrastructure management is found in (Elshani 2023, Mehranfar, Chuo, *et al.* 2023, Chuo *et al.* in prep).

Figure 4 represents an example of the visualization of component-level CSs evolution and intervention estimates during multiple planning periods developed in the Autodesk Revit® environment. For example, it is seen in (a) that the CS of bridge foundations in t=5 is represented using a specific colour code. Further information regarding the CS of foundations, is also provided upon clicking on the foundation. As another example, an overview of intervention requirements in the planning period between t=6 and t=10 is shown in (b) for the example steel truss bridge.

6 CONCLUSION

This paper presents a systematic methodology for estimating a complete overview of component-level intervention requirements in the early phases of the intervention planning process. A demonstration was conducted on a steel truss bridge with a length of 100 m located in Switzerland, along with visualisations in BIM. The main novelty of the proposed methodology is in concentrating on the bridge components instead of bridges, the use of

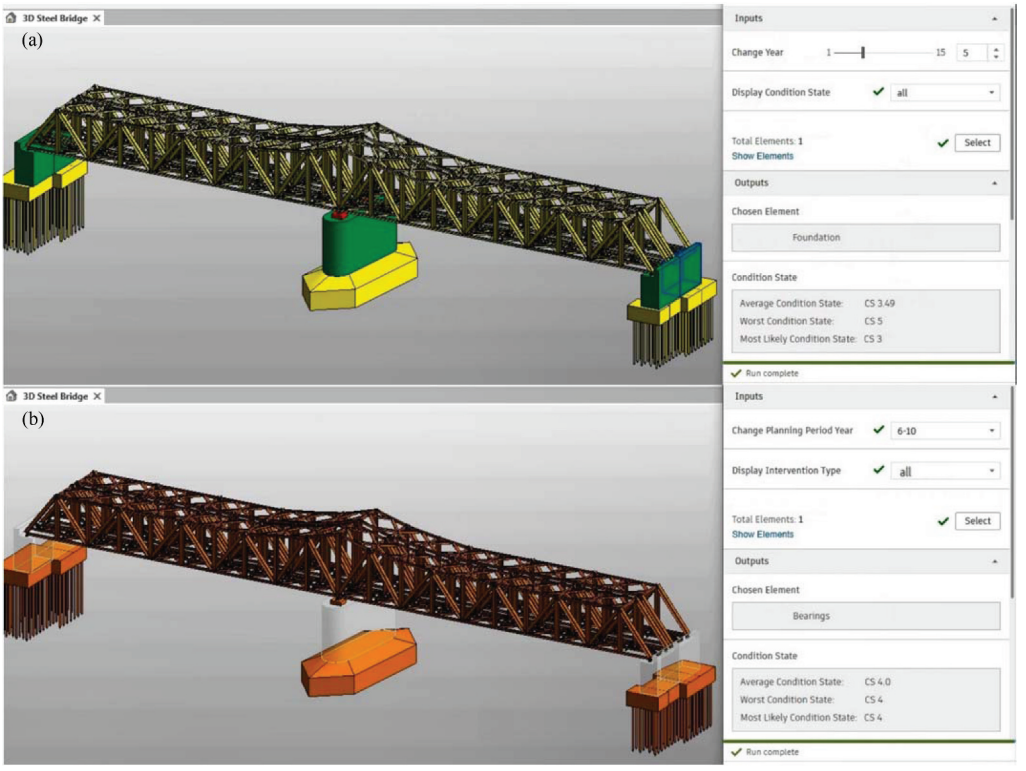


Figure 4. Example of illustrating the evolution of CSs (a), and the intervention requirements (b) over multiple planning periods using BIM.

nonhomogeneous transition probabilities connected to the number of times that a maintenance intervention is executed on the components and visualizing results in BIM.

The probabilistic modelling used in this paper considers a discrete scale of 1-5 in order to ensure compatibility with models used in the state-of-the-practice. The estimates of failure risks are made by developing tree fault trees with respect to the severity of the service disturbance. The consequences are estimated in terms of both user and owner costs associated with executing immediate interventions. The failure probabilities are estimated as a function of the CS of the components. The component-level intervention estimates are visualised in BIM to provide bridge managers with a new perspective that can help them make decisions and communicate with other stakeholders in the intervention planning process. Such visalisations are particularly beneficial when the component-level intervention estimates are generated for a portfolio of bridges within a transportation network.

Future research must focus on streamlining the connection between a complete overview of component-level intervention estimates and BIM in an efficient manner. This includes investigating how the BIM for bridges should be generated to ensure scalability and how the information should be exchanged.

ACKNOWLEDGEMENT

This work is part of the STABILITY research project that is supported by the ETH Mobility Initiative and the ETH Zurich Foundation. The authors would like to thank Dr. Saviz Moghtadernejad of the National Research Council Canada for her insights and feedback during the development of this work.

REFERENCES

Adey, B.T., Birdsall, J.D., and Hajdin, R., 2010. A methodology to estimate risk related to road links, due to latent processes. *In*: *Bridge Maintenance, Safety, Management and Life-Cycle Optimization*. Presented at the Fifth International Conference on Bridge Maintenance, Safety, Management, Philadelphia, Pennsylvania, USA: CRC, 221–221.

Adey, B.T. and Hajdin, R., 2011. Methodology for determination of financial needs of gradually deteriorating bridges with only structure level data. *Structure and Infrastructure Engineering*, 7 (7–8), 645–660.

Adey, B.T., Hajdin, R., and Brühwiler, E., 2015. Optimal intervention strategies for multiple bridges during catch-up periods using age equivalents. *In*: *Advances in Bridge Maintenance, Safety Management, and Life-Cycle Performance, Set of Book & CD-ROM*. CRC Press, 685–686.

Adey, B.T., Herrmann, T., Tsafatinos, K., Luking, J., Schindele, N., and Hajdin, R., 2012. Methodology and base cost models to determine the total benefits of preservation interventions on road sections in Switzerland. *Structure and Infrastructure Engineering*, 8 (7), 639–654.

Burkhalter, M. and Adey, B.T., 2021. Quantifying net benefits of intervention programmes to enable their digitalised generation. *Infrastructure Asset Management*, 8 (3), 141–154.

Burkhalter, M. and Adey, B.T., 2022. Digitalizing the Determination of Railway Infrastructure Intervention Programs: A Network Optimization Model. *Journal of Infrastructure Systems*, 28 (2), 04022012.

Chuo, S., Mehranfar, H., Elshani, G, Adey, B.T., and Hässig, S., in prep. Connecting predictive algorithms to BIM to improve the planning process. International Association for Bridge Maintenance And Safety, Copenhagen, Denmark.

Chuo, S., Moghtadernejad, S., Adey, B.T., and Mehranfar, H., 2023. Estimation of bridge component condition states with varying data availability. *In*: *Life-Cycle of Structures and Infrastructure Systems*. CRC Press.

Elshani, G., 2023. Connecting Future Predictions of Railway Assets to BIM. Master's Thesis. Technische Universität München.

Kim, S., Ge, B., and Frangopol, D.M., 2022. Probabilistic Optimum Bridge System Maintenance Management Considering Correlations of Deteriorating Components and Service Life Extensions. *ASCE-ASME Journal of Risk and Uncertainty in Engineering Systems, Part A: Civil Engineering*, 8 (3).

Martani, C., Adey, B.T., and Wenk, K., 2021. Determining optimal intervention strategies for bridges considering both gradual deterioration and sudden events. *In*: *Life-Cycle Civil Engineering: Innovation, Theory and Practice*. CRC Press, 1071–1076.

Mehranfar, H., Adey, B.T., Moghtadernejad, S., and Chuo, S., 2023a. Automated early estimation of bridge interventions, possession windows and costs. *Infrastructure Asset Management*, 1–13.

Mehranfar, H., Adey, B.T., Moghtadernejad, S., and Chuo, S.Y.-P., 2023b. Efficient early estimates of bridge interventions: Costs, required possession times and associated failure risks. *In*: *Life-Cycle of Structures and Infrastructure Systems*. Presented at the 8th International Symposium on Life-Cycle Civil Engineering (IALCCE 2023), CRC Press, 2112–2119.

Mehranfar, H., Chuo, S.Y.-P., Burkhalter, M., Moghtadernejad, S., and Adey, B.T., 2023. Digitally supported intervention planning process. Presented at the Center for Sustainable Future Mobility Symposium 2023 (CSFM 2023), ETH Zurich.

SFSO, 2021. Swiss Construction Price Index. XLSX.

Bridge Maintenance, Safety, Management, Digitalization and Sustainability – Jensen, Frangopol & Schmidt (eds)
© 2024 The Author(s), ISBN 978-1-032-77040-6
Open Access: www.taylorfrancis.com, CC BY-NC-ND 4.0 license

Connecting predictive algorithms to BIM to improve the planning process

S. Chuo, H. Mehranfar & B.T. Adey
Institute of Construction and Infrastructure Management, ETH Zürich, Zürich, Switzerland

G. Elshani
BPR Dr. Schäpertöns Consult GmbH, München, Germany

ABSTRACT: Bridge managers estimate the intervention requirements, and their associated costs, required possession times and failure risks in years advance. They communicate this information to multiple stakeholders involved in the intervention planning process using reports and tables. As it is difficult for stakeholders to process all the information in short periods of time this process can lead to misinterpretations, which in turn can lead to multiple iterations and discussions. With the rise of algorithms and BIMs to predict, plan, and manage future interventions, there is now an opportunity to use these tools to improve the efficiency of the planning process. This paper presents a methodology to do this, i.e., to demonstrate how predictive algorithms can be connected to BIM to facilitate discussions of the multiple stakeholders involved in the intervention planning process, and how the process can be improved. The methodology is demonstrated on a railway steel truss bridge in Switzerland.

1 INTRODUCTION

With the rapid advancement and ubiquitous use of information and communication technology, digital data and tools become increasingly pragmatic for the effective and efficient management of railway infrastructure. To that effect, European Commission's Sustainable and Smart Mobility Strategy calls for an action plan of 82 initiatives to bring European transport on track for the future, which includes issuing "recommendations for the transition to automation and digitalisation and their impact on the transport workforce" (European Commission, 2020). With digitalisation becoming a crucial driver to modernise infrastructure management, it has the potential to enable predictive maintenance to plan interventions in advance, with the goal of minimising disruption to traffic operation for the users. However, the digital transformation entails data availability, access, and exchange within an infrastructure management organisation, in order to support interlinked databases for asset data management solutions and big data for maintenance prediction (European Committee of the Regions et al., 2019). This requires reliable data collection, compatible tools and systems to facilitate data management and sharing across different entities, digital solutions to process data and support future intervention planning, as well as formulated coordination to mediate decision-making between entities.

The decisions on intervention planning are applied to a network of infrastructure assets and their components, and maintenance interventions that aim to sustain the existing level of service need to be estimated and communicated to other stakeholders who rely on that information for their own decision-making. With the requirement to plan and coordinate interventions years in advance, infrastructure managers need to have an express knowledge of the evolution of asset condition into the future, as well as the intervention requirements, including their associated costs, required possession times, and failure risks. As infrastructure management advances

DOI: 10.1201/9781003483755-173

towards digitalisation, such as the use of data-driven algorithms to determine the optimal intervention programs, their implementation will functionally evolve the decision-making process for infrastructure managers. This in turn enables objective, effective, and efficient decision-making for existing assets and future infrastructure expansion. The improvement to the intervention planning process through digitalisation is a complex challenge that requires an understanding of: (1) the current intervention planning process within different infrastructure management organisations, (2) digital tools available to facilitate the decision-making for intervention planning of infrastructure assets, and (3) coordination between these digital tools and interaction between these tools and the infrastructure managers. Therefore, this paper provides an overview of the railway intervention planning process, as well as demonstrates how digitals tools such as predictive algorithms and building information models (BIMs) can be connected to make intervention decisions.

2 INTERVENTION PLANNING PROCESS

Although academic research continues to develop state-of-the-art methodologies concerning intervention planning as well as life-cycle analysis and management, there lacks real-world application (Frangopol & Soliman, 2016). Consequently, for the railway transportation industry to accept and implement the proposed methodologies, it is necessary to prescribe guidelines for their adoption, and to evaluate the improvement in efficiency by comparing the current industry practice and any proposed changes to the intervention planning process. Schraven et al. (2011) outlined the decisions needed in infrastructure management, with regard to infrastructure objectives, technical and functional performance, and interventions. Jamali and Adey (2016) examined the effect of management decision processes to determine the optimal management strategy, where the processes were modeled using Business Process Model and Notation (BPMN) and they were compared to assess the impact. Adey (2019) defined a conceptually ideal road infrastructure management process at a high level, however, no differentiation was made between the management of a large network (e.g., national) and a small network (e.g., regional). There is currently no complete overview of the railway infrastructure management process in the literature, only some descriptions of specific subprocess exist, such as the estimation of the railway intervention program (Burkhalter & Adey, 2018).

To understand the typical railway intervention planning process, the planning activities are modeled based on firsthand experiences and interactions with railway companies. The model is inspired by their internal documents (e.g., guidelines or reports), and interviews were conducted

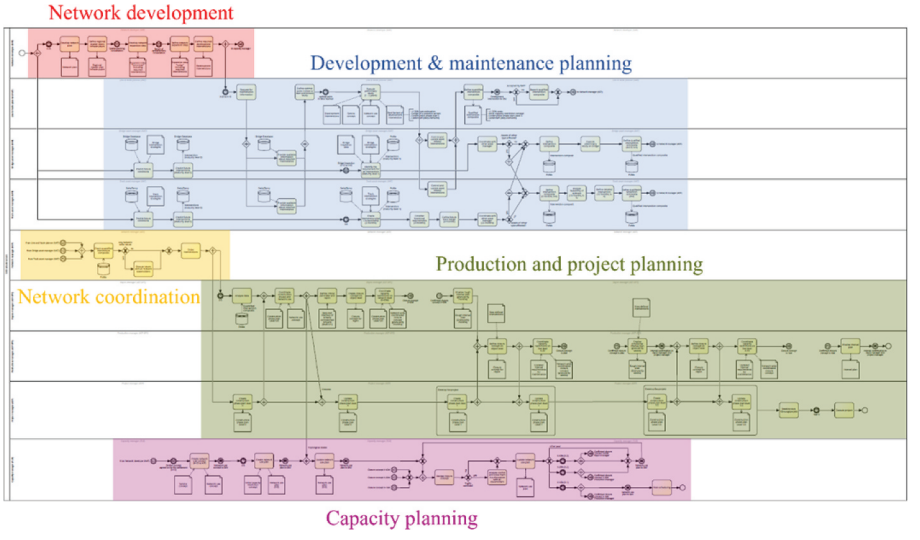


Figure 1. Main groups of railway intervention planning activities.

with the stakeholders who are involved within the process and make decision. The results are modeled using BPMN, so the planning activities are organised according to the actor. Figure 1 illustrates the main groups of intervention planning activities in the railway context.

To decide on the maintenance interventions on the assets, there needs first an overview of their condition states at present, and an understanding of how these conditions states will evolve (i.e., deteriorate) over time. With this information available, the intervention requirements are estimated, where the granularity can be based on the asset, component, or element level, in increasing level of detail. The interventions depend on the definition of intervention strategy, i.e., all interventions to be executed considering all possible condition states. The estimated intervention requirements are refined into intervention programs, i.e., the exact interventions to be executed considering the specific condition states. This typically means that the individual interventions are then clustered into projects, taking into consideration economical, topological, structural, and resource dependencies. The planning of project execution requires coordination between the intervention requirements and required service to be provided, e.g., a rehabilitation of a railway steel truss requires a weekend of possession time to set up and perform the work, therefore the railway service cannot be offered during that time due to closure of the corridor. This results in phased construction plans to detail the sequence, duration, and schedule of work activities, and in the railway context it also leads to an adjusted train schedule for the passengers and corridor availability for the freight trains, in terms of service cancellations or speed reduction.

The coordination between governments, agencies, and relevant stakeholders is an intricate and iterative process, where the collection, storage, distribution, and access of information and data form the foundation of decision-making on interventions. Therefore, digital solutions such as data-driven predictive algorithms offer an opportunity to streamline the required estimations and decisions throughout the intervention planning process, and BIM provide a collaborative platform to manage the digital information of infrastructure assets. These tools will become vital to the digitalisation of effective and efficient intervention planning in the future.

3 DIGITAL TOOLS IN INTERVENTION PLANNING

3.1 *Intervention planning predictive algorithms*

With an understanding of the current condition state, deterioration rate and future condition state, infrastructure managers are able to determine the optimal intervention programs using predictive algorithms, planning for what interventions need to be carried out on what infrastructure assets at what time in the next planning period taking into consideration the synergies between assets (Burkhalter & Adey, 2022; Mehranfar et al., 2023a, 2023b). These algorithms provide information on the component level, e.g., a railway bridge may consist of trusses, girders, bearings, abutments, foundations, piers, rails, sleepers, and ballast. This level of detail is important, especially in the railway context considering that most data are recorded only on the asset level, and the existing industry practices are usually qualitative and time-consuming. The quantitative and data-driven algorithms are therefore more effective and efficient, and the results allow infrastructure managers to be in the position to make systematic early estimates of future interventions on their portfolio of assets.

This is an improvement over the existing practice, where the provided information for intervention planning is often in the form of reports or tables, and although they contain all the necessary details with regards to a specific asset or a portfolio of assets, they often take more time to absorb and understand by other stakeholders. The difficulty to process all the information, coupled with the constraint to make decisions in a short amount of time, lead to multiple iterations and discussion to clarify intervention requirements, so everyone can agree on what should be done to maintain the assets. Therefore, the intervention planning predictive algorithms would help facilitate communication between the stakeholders in the planning process, particularly years in advance to help determine the timing of required detailed investigations by engineering offices.

3.2 *Building information modeling*

As the railway transportation industry prepares the shift towards digitalisation, BIM becomes increasingly relevant in infrastructure maintenance planning, as the digital representation of the physical asset and its functional characteristics facilitate a shared knowledge resource for information to support improved decision-making. While BIM applications for bridge maintenance have been developed extensively (Panah & Kioumarsi, 2021), there is limited BIM application for railway maintenance, where the focus has mostly been on design and construction, such as railway track alignment (Huang et al., 2011), code compliance checking (Häußler et al., 2021), and planning of construction process (Neves et al., 2019).

The difficulties are the result of interoperability issues between BIM tools, and the use of openBIM has been proposed, which enables collaboration, communication, and exchange of information without restricting solutions to a specific software. For example, Ciccone et al. (Ciccone et al., 2022) used openBIM to create a single digital model of an existing 47 km railway line in Italy. This is important because a railway line may consist of tracks, turnouts, stations, crossings, bridges, and tunnels, and the coordination of maintenance interventions relies on an understanding of the dependencies and impact between railway assets. However, the model created by Ciccone et al. does not include the visualisation of asset condition states and required interventions across time, which is critical to infrastructure managers in communicating with other stakeholders during the intervention planning process for decision-making.

4 DEVELOPMENT OF BIM FOR THE EXAMPLE RAILWAY BRIDGE

The methodology to demonstrate how predictive algorithms can be connected to BIM is described using a railway steel truss bridge in Switzerland spanning over a river, and it is 110 m in length and 11 m in width. There are two parallel steel trusses, where the upstream truss was built in the 1920s to replace the original bridge built in the 1870s, and the downstream truss was built in the 1960s. The bridge comprises one pier in the middle, two abutments on each end, 12 roller bearings on the pier and abutments, and two pairs of girders to support the two railway tracks.

The asset owner of this railway bridge does not have an existing digital model, therefore the original design drawings were requested and used as reference to model it in 3D using Autodesk Revit as the BIM authoring tool. The design drawings provide guidance in terms of the exact components that are part of the bridge, as well as the scale and location for each component relative to the rest of the bridge structure. Google Maps and Google Earth were also used as additional public sources of visual reference, so the satellite imagery, aerial photography, and street maps help model the railway bridge as realistic as possible.

To establish an efficient workflow, a family catalogue of railway bridge components was created to standardise asset modeling, as this methodology is expected to apply to a portfolio of bridges in the future. While creating these objects, the geometry that represent the 3D objects are considered so they can be modelled parametrically (e.g., length, width, height,

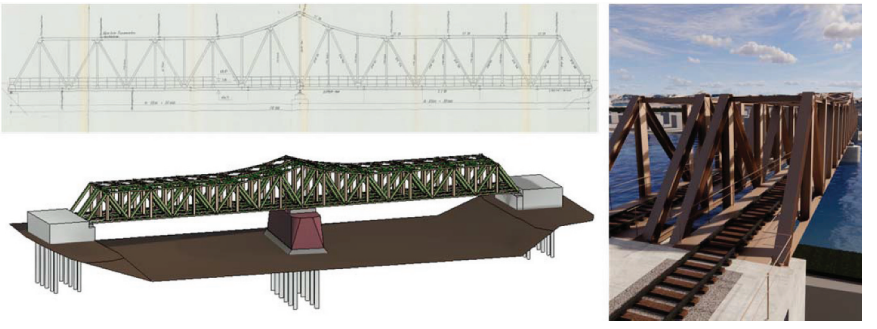


Figure 2. The example bridge represented by its cross section in 2D drawing and its 3D model.

etc.), as well as the information that underly them (e.g., construction year, materials, etc.). Additional considerations are also made, such as interoperability between different BIM authoring. This is important because it allows the models to potentially be used by other stakeholders using other software for decision-making. This results in the parametric modeling of bridge components in the Level of Development of 200, sufficient for the purpose of intervention planning which is early in the planning process. Figure 2 shows the cross section of the example railway bridge from 2D drawing, the 3D digital model of the bridge modeled using the family catalogue, and its 3D rendering.

Apart from the geometric models, other semantic data have also been included in the standard objects of the family catalogue in the form of parameters. This is especially relevant for the data exchange across different databases and digital systems, considering identity data that are unique to the internal referencing of the infrastructure management organisation, as well as open data schema specification such as the latest Industry Foundation Class (IFC) format IFC 4x3, which now includes rail and infrastructure components. This results in a Level of Information of 300.

5 CONNECTING PREDICTIVE ALGORITHMS TO BIM

5.1 *Setting up Revit project*

The connection of predictive algorithms on intervention planning to BIM leads to an intuitive understanding through the visualisation of asset component condition states and intervention requirements over time. Therefore, to efficiently use the family catalogue and to reach the proposed visualisation, a specific setup needs to be done on the Revit project containing the bridge assets. This setup includes the arrangement of the project parameters, global parameters, filter rules, filter overrides, and view settings.

The project parameters are needed to store information about the condition states, their deterioration, and different aspects of the planned interventions. These parameters have been assigned using the Revit category the components belong to. So, all components will automatically have the named parameters available in the instance information. This embedded information can then be used for the proposed visualisation, and any other use cases of the digital model to be expanded on in the rest of the intervention planning process (e.g., network coordination and construction planning).

To provide values as a basis to compare the user input with the calculated values for the condition states and interventions on the components, global parameters are also required in the BIM project setup. The assignment of these parameters works similarly to the project parameters mentioned earlier, using component categories as a basis for the assignment.

To visualise the information that the different components possess, view specific filter overrides are used. These filters follow defined rules, where two parameters are being compared. In the case of the values fulfilling the conditions, the filters will become active in the view, providing either one or multiple line, pattern, and transparency overrides of the bridge components. Using these filters provides a quick and straightforward visualisation of the given data on condition states and intervention requirements. It is important to note that these filter overrides apply only specific to a certain view in the Revit user interface, and this would leave the global visibility of the bridge components unaffected.

For the colour overrides provided by the view filters to become visible, the visual style of the active view should be set on either ‘Shaded’ or ‘Consistent Colours’. To set this up in Revit projects, view templates should be used, which can then be applied to the views as needed. Using a view template also generalises the view specific filter overrides, making the manual setup for every single view unnecessary.

All other parts of the project setup, including project parameters, global parameters, and filter rules can be transferred between projects using the ‘Transfer Project Standards’ tool. By utilising this transfer, the proposed methodology can also be applied to existing BIM models, empowering the infrastructure managers to exploit the potential of predictive algorithms for decision-making.

5.2 *Setting up dynamo*

After the railway bridge is modeled and the parameters of the project are established, the BIM is now ready to connect to the output from the intervention planning algorithms, and the data to be connected include the bridge component condition states and intervention requirements. The condition states are recorded from 1 to 5, with state 1 representing as good as new, and state 5 representing replacement should be immediate. Each condition state has a certain probability, and based on the expected gradual deterioration, these probabilities also change over time. The interventions include the attributes of planning period and intervention type. The planning period takes place on a 5-year interval, e.g., year 1 to 5 is planning period 1, and year 6 to 10 is planning period 2. This is consistent with the planning of intervention execution in a certain time window, especially when this is done years in advance. Intervention type depends on the definition of the intervention strategy, in terms of rehabilitation, renewal, or replacement. Each intervention type has its associated cost and possession requirement, and they are important for the clustering of interventions in the optimal intervention programs.

In the BIM authoring tool Revit, Dynamo is a preinstalled open-source plug-in, and it is a direction connection with the Revit interface, making it possible to easily access and export elements to and from it. A Dynamo script is developed to automate the dynamic assignment of condition states and interventions to the corresponding components in the model from the output of the predictive algorithms, as well as to provide visualisation using colour filters in the 3D model. Although there are many steps needed to make the connection work, the three main stages are: (1) data import, (2) value assignment, and (3) output visualisation. In addition to the built-in nodes provided in Dynamo that serve the standard functions and workflows, custom nodes were also created to fulfill the needs of specific tasks that are not included in the standard library. Figure 3 outlines an overview of the Dynamo script that was developed to connect the conditions states and interventions from the predictive algorithms to the BIM, i.e., importing the algorithm results and assigning them correctly to their associated components, and visualising the results based on defined filter rules for the colour overrides in the model.

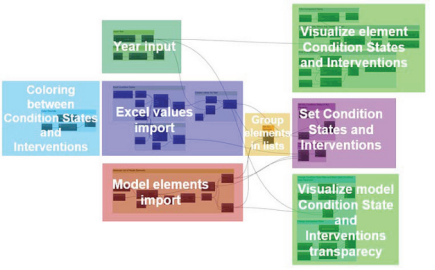


Figure 3. Overview of the Dynamo script.

5.3 *Using the digital tool for decision-making*

Finally, with the connection between the predictive algorithms and BIM established, Revit becomes the platform between the digital tools and the infrastructure managers who need to make decisions on the interventions. Instead of working with the 3D model itself and the complicated Dynamo script which could be intimidating for those not familiar with visual programming and coding, an interactive user interface is incorporated using the Dynamo Player in Revit. This graphic interface is used to provide more detailed information, apart from the colour overrides which can be seen in the 3D model itself, as well as a more intuitive way of handling the model and its parameters by introducing dropdown manus and action buttons. It supplies the users with input options, such as changing the evaluated year. Furthermore, it is separated into acquiring information on the component level, giving data about the condition states and interventions of one selected component of interest, as well as filtering out all components that are in one specific condition state or fulfil an intervention filter on the global scale. Figure 4 demonstrates the Dynamo Player user interface to the right, indicating the

inputs and outputs, as well as the resulting visualisation in the 3D model in the form of colour overrides on the railway bridge components.

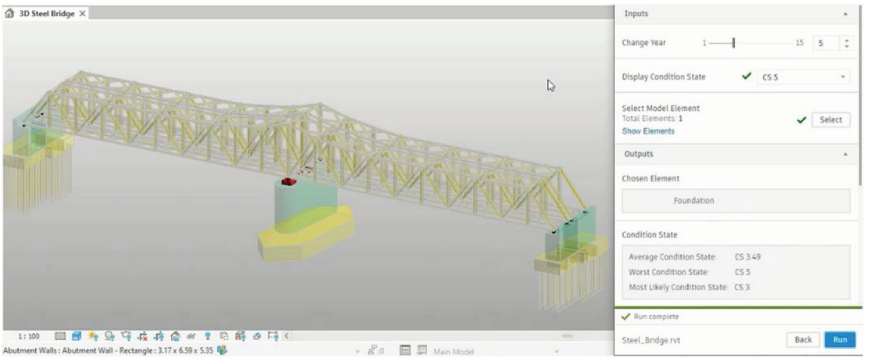


Figure 4. Demonstration of the user interface and connected results in Revit.

In the example, by selecting the global transparency for condition state 5 in year 5 in the input section of the Dynamo Player, it runs the Dynamo script as described earlier, and only components that satisfy the filter requirements would be visible. This allows the ability to see components even in a complex model where there are significantly more components, or the model is developed on the element level, so they might appear to be small in the 3D model. In addition to the visual representation of the condition states and interventions using colour overrides, the information about the selected component is also displayed in the output section of the Dynamo Player, such as the name of the selected component (referred to as element in Figure 4), the calculated condition states (i.e., average, worst, and most likely) based on the probabilities of the five states, as well as the five condition states and their probabilities (not shown in Figure 4).

6 CONCLUSIONS

In the intervention planning process, predictive algorithms and BIM have the potential to transform decision-making and how stakeholders interact with each other. The connection between these digital tools is demonstrated on an example railway bridge, where the results are visualised in BIM with colours, and an intuitive user interface is shown. However, it is important to note that this methodology is not meant to replace the existing process, but rather supplement infrastructure managers with a robust tool that takes advantage of the latest state-of-the-art technologies, which provides a general overview of the asset condition states and supports the decision-making process for the necessary interventions.

The methodology can also be applied to intervention planning of other infrastructure assets. For example, although there are some differences between the railway and road intervention planning process, especially in terms of how teams are defined and organised as well as the tools and methods used to make decisions throughout the process, the procedure to make intervention decisions is similar as described in Section 2. Also, even if the asset condition states are recorded on the element level, as is the case in most road asset management databases around the world, the method of the predictive algorithms can still be applied to that level of detail, and the results are expected to be very similar to that of the existing algorithms for railway interventions. Therefore, the connection between the predictive algorithms and BIMs would still be useful for road infrastructure managers to make and communicate their decisions with other stakeholders.

It is expected that the digital models will need to be continuously updated and enriched, to reflect the decisions and/or modifications made to the planned intervention on infrastructure assets. As part of the challenge to improve data quality over time, a single source of truth becomes an important anchor that connects the information that might exist in different models and different databases. This source would lay the foundation for a better

management of asset data. Nonetheless, the methodology allows stakeholders in the intervention planning process to collaborate more effectively. The 3D models would serve as a common visual platform for joint assessments, planning, and decision-making. With data integrated into these models, the interdependencies between components and between assets can be analysed, allowing for more informed and coordinated decisions on maintenance, repairs, and optimisations. This shared digital environment enhances communication between teams while enabling the railway networks to be managed with increased efficiency.

ACKNOWLEDGEMENTS

This research project is supported by the ETH Mobility Initiative and the ETH Zurich Foundation. The authors would like to acknowledge Prof. Dr. Qian Chen of the University of British Columbia and Mr. Andreas Stolz for their insights during the initial formulations and ensuing discussions of this research.

REFERENCES

Adey, B. T. (2019). A road infrastructure asset management process: Gains in efficiency and effectiveness. *Infrastructure Asset Management*, *6*(1), 2–14. https://doi.org/10.1680/jinam.17.00018

Burkhalter, M., & Adey, B. T. (2018). A Network Flow Model Approach to Determining Optimal Intervention Programs for Railway Infrastructure Networks. *Infrastructures*, *3*(3), Article 3. https://doi.org/10.3390/infrastructures3030031

Burkhalter, M., & Adey, B. T. (2022). Digitalizing the Determination of Railway Infrastructure Intervention Programs: A Network Optimization Model. *Journal of Infrastructure Systems*, *28*(2), 04022012. https://doi.org/10.1061/(ASCE)IS.1943-555X.0000681

Ciccone, A., Stasio, S. D., Asprone, D., Salzano, A., & Nicolella, M. (2022). Application of openBIM for the Management of Existing Railway Infrastructure: Case Study of the Cancello–Benevento Railway Line. *Sustainability*, *14*(4), Article 4. https://doi.org/10.3390/su14042283

European Commission. (2020). *Sustainable and Smart Mobility Strategy – putting European transport on track for the future*. https://eur-lex.europa.eu/legal-content/EN/TXT/?uri=CELEX%3A52020DC0789

European Committee of the Regions, Pucher, J., Schausberger, W., Werneck, T., & Weiss, J. (2019). *The contribution of the rail sector to delivering EU policy priorities at local and regional level*. Publications Office of the European Union. https://data.europa.eu/doi/10.2863/861794

Frangopol, D. M., & Soliman, M. (2016). Life-cycle of structural systems: Recent achievements and future directions. *Structure and Infrastructure Engineering*, *12*(1), 1–20. https://doi.org/10.1080/15732479.2014.999794

Häußler, M., Esser, S., & Borrmann, A. (2021). Code compliance checking of railway designs by integrating BIM, BPMN and DMN. *Automation in Construction*, *121*, 103427. https://doi.org/10.1016/j.autcon.2020.103427

Huang, S.-F., Chen, C.-S., & Dzeng, R.-J. (2011). Design of Track Alignment Using Building Information Modeling. *Journal of Transportation Engineering*, *137*(11), 823–830. https://doi.org/10.1061/(ASCE)TE.1943-5436.0000287

Jamali, A., & Adey, B. T. (2016). The effect of management decision processes on the management of bridges. *Journal of Civil Engineering and Management*, *22*(1), 92–104. https://doi.org/10.3846/13923730.2014.897967

Mehranfar, H., Adey, B. T., Moghtadernejad, S., & Chuo, S. (2023a). Automated early estimation of bridge interventions, possession windows and costs. *Infrastructure Asset Management*, 1–13. https://doi.org/10.1680/jinam.23.00038

Mehranfar, H., Adey, B. T., Moghtadernejad, S., & Chuo, S. (2023b). Efficient early estimates of bridge interventions: Costs, required possession times and associated failure risks. *Life-Cycle of Structures and Infrastructure Systems*.

Neves, J., Sampaio, Z., & Vilela, M. (2019). A Case Study of BIM Implementation in Rail Track Rehabilitation. *Infrastructures*, *4*(1), Article 1. https://doi.org/10.3390/infrastructures4010008

Panah, R. S., & Kioumarsi, M. (2021). Application of Building Information Modelling (BIM) in the Health Monitoring and Maintenance Process: A Systematic Review. *Sensors*, *21*(3), Article 3. https://doi.org/10.3390/s21030837

Schraven, D., Hartmann, A., & Dewulf, G. (2011). Effectiveness of infrastructure asset management: Challenges for public agencies. *Built Environment Project and Asset Management*, *1*(1), 61–74. https://doi.org/10.1108/20441241111143786

Bridge Maintenance, Safety, Management, Digitalization and Sustainability – Jensen, Frangopol & Schmidt (eds)
© 2024 The Author(s), ISBN 978-1-032-77040-6
Open Access: www.taylorfrancis.com, CC BY-NC-ND 4.0 license

Bridge deterioration modeling considering the climate change effects

S. Moghtadernejad, Z. Lounis & J. Zhang
National Research Council Canada, Ottawa, Canada

ABSTRACT: The effective management of bridge maintenance activities requires planning for necessary interventions in the future. Such planning is crucial to establish maintenance schedules with minimal life cycle costs and environmental impacts. Achieving this depends on reliable deterioration prediction models that consider key factors influencing deterioration and the associated uncertainties. Presently, predominant deterioration models in practice use inspection data and Markov models with the assumption of constant deterioration rates. However, factors like age, maintenance activities, traffic variations, and climate change can alter deterioration rates and transition probabilities of bridge elements over time. Climate change, particularly, with rising temperatures and extreme weather events, accelerates bridge deterioration. This study provides an overview of deterioration prediction models capable of accounting for temporal dynamics of bridge deterioration, where time-variant transition probabilities are modelled as functions of the factors influencing the deterioration process. Subsequently, it discusses their merits and challenges for practical implementation.

1 INTRODUCTION

Bridges are crucial components of transportation infrastructure, providing safe and efficient transport of people, goods, and services. However, they are subject to various factors that can cause deterioration, such as environmental exposure, traffic loads, and aging. With the increasing age of infrastructure and the need to ensure safe and efficient transportation networks, bridge deterioration modelling remains a critical tool for effective infrastructure maintenance and management. Bridge deterioration modelling is a process of estimating the rate at which a bridge's condition will degrade over time based on various factors such as material properties, design specifications, traffic loads, environmental conditions, and maintenance history. The objective of bridge deterioration modelling is to provide critical insights into the expected life cycle performance of bridges over time, estimate potential damage and the remaining service life of bridges, and help bridge owners and managers plan effective maintenance and repair strategies. It helps with improving safety, maximizing the service life of bridges, managing assets effectively, and optimizing decision-making.

Climate change is causing significant variations in temperature, precipitation patterns, and extreme weather events and its impacts on bridge infrastructure are becoming increasingly concerning. One of the most significant effects of climate change is the acceleration of bridge deterioration across various regions globally. As temperatures rise, adverse chemical reactions within construction materials accelerate, consequently the deterioration process is expedited (Shirkhani et al., 2023). Changes in weather patterns, such as increased precipitation in certain regions, can impact the corrosion speed of construction materials. More frequent and severe climate-induced events, such as floods, hurricanes, heavy rainfall, and storms, can pose risks

DOI: 10.1201/9781003483755-174

to bridge structures (Moghtadernejad et al., 2020). For example, intense precipitation can erode soil around bridge foundations and compromise their integrity. Floods impose immense pressure on piers and abutments, which can lead to scouring or even the collapse of bridges. Heatwaves contribute to the thermal expansion in bridge materials and cause cracks and deformations that weaken the structure. Moreover, climate change can result in more frequent freeze-thaw cycles in some regions which can affect materials like concrete. Coastal bridges face additional threats due to rising sea levels and saltwater intrusion. Saltwater corrodes reinforced concrete and steel bridges and accelerates the deterioration process. Storm surges and coastal erosion further compromise the integrity of these bridges. In regions with permafrost, rising temperatures trigger ground thawing that undermines the stability of bridge foundations, making them more susceptible to settling and erosion.

The climate-induced changes in bridge deterioration rates make existing predictive models less reliable. This may lead to unforeseen failure of bridges, long traffic disruption, high rehabilitation and replacement costs, and significant negative socio-economic impacts. It is therefore necessary to evaluate, maintain and manage bridges under the effects of future climatic loads and incorporate the potential impacts of increased temperature, precipitation and wind on the deterioration of bridge structures.

This paper investigates how one can incorporate climate change effects into deterioration models to allow for more accurate predictions and enable the development of optimal bridge maintenance plans. In the following section, a comprehensive overview of existing bridge deterioration models is provided based on their underlying methodology, along with a discussion of their limitations and merits for implementation in practice. Subsequently, promising deterioration models are further investigated to assess their flexibility for incorporating climate variations into the deterioration modeling process.

2 BRIDGE DETERIORATION MODELS

2.1 *Classification*

Bridge deterioration models include two primary classifications: mechanistic (also referred to as physical models) and empirical (also referred to as data-driven) models, which may exhibit either stochastic or deterministic characteristics. Mechanistic models are rooted in physical principles and aim to model the underlying mechanisms driving deterioration processes within bridges. They often involve complex physical laws, chemical reactions, and mathematical equations governing the deterioration process. These models are developed to predict the deterioration of various elements based on the triggering deterioration mechanism. For example, in the literature, several analytical models are developed for predicting deterioration of reinforced concrete decks, including models for predicting freeze-thaw damage (Bazant et al., 1988), carbonation damage (Isgor & Razaqpur, 2004) or chloride-induced damage (Zhang & Lounis, 2009). Nickless (2017) investigated the application of available mechanistic deterioration models to bridge management and design practice in Colorado.

Mechanistic models are a valuable tool in bridge deterioration prediction and can be highly effective when properly developed and validated. However, despite their potential benefits, there are some limitations to their use in bridge deterioration prediction. One challenge is the need for reliable data on the properties of the bridge materials and the environmental conditions. Additionally, the development of mechanistic models can be time-consuming and computationally intensive, making them more difficult to implement on a large scale or on a portfolio of bridges. Finally, these models may not capture all complex interactions that can contribute to bridge deterioration, which brings forward the importance of investigating other types of models.

Contrary to mechanistic models, empirical models rely on observed condition data without explicit consideration of underlying physical principles. These models utilize statistical methods to infer patterns from historical data and make predictions based on the observed trends. They are relatively simple to use and require fewer input parameters than mechanistic

models. Thus, these models have inherent limitations because they may not be able to capture the underlying physics and mechanics of the deterioration process as accurately as mechanistic models, and are limited by their assumptions and simplifications of the complex deterioration mechanisms of bridges. In addition, the accuracy and effectiveness of these models rely heavily on the availability and quality of data, which can be difficult to obtain. However, they can be continuously improved by collecting new data and refining the modeling techniques.

Both mechanistic and empirical models can have stochastic or deterministic attributes. Stochastic models incorporate random variables to include inherent uncertainties in the deterioration process and account for the variability in deterioration rates due to various influencing factors. On the other hand, deterministic models provide predictions without considering randomness and assume constant or predictable deterioration behavior based on fixed parameters and conditions.

An example of the application of empirical models includes the work done by (Ilbeigi & Ebrahimi Meimand, 2020) who used the historical data of bridges in Ohio to create an ordinal regression model to statistically examine the effects of bridge characteristics on variations in its conditions and predict the future bridge conditions. The outcomes of this study indicate that bridge characteristics such as age, average daily traffic, deck area, and structural material, are statistically significant variables that explain variations in bridge deterioration.

Machine learning methods, such as Artificial Neural Networks (ANN), also fall under the category of empirical models. These methods have gained popularity among researchers (Huang, 2010) due to their immense potential in handling vast datasets containing various variables, including age, temperature, precipitation, etc. However, the adaptation of these models in practice is slow due to their mathematical complexity, the requirement for more sophisticated software and the fact that the users cannot see what happens in the prediction process but are supposed to assume the results as appropriate.

In recent years researchers have combined different types of models and data sources to provide more accurate predictions of bridge deterioration over time (Lethanh et al., 2017; Li et al., 2023; Mizutani et al., 2017; Mohammed Abdelkader et al., 2019). These hybrid models typically incorporate structural analysis and environmental data, information on past maintenance and repair records, as well as other relevant data such as traffic patterns and weather conditions. Examples include combining Markov models with mechanistic deterioration models, ANNs, or Bayesian Networks (BNs), to improve the deterioration predictions.

2.2 *Models currently used in practice*

In practice, few agencies prefer predicting the deterioration of bridges using mechanistic models. These agencies determine bridge service life using the capacity of its elements to withstand different stresses and loss of strength reaching a specific threshold. Another approach involves predicting the expected service life of an asset based on the time until corrosion, determined by the material's resistance to chloride ions (Zhang & Lounis, 2009). However, applying these approaches at a network level can be challenging due to the need for extensive data on asset dimensions and conditions.

As inspection methods advanced and agencies started to collect and store inspection data more frequently and systematically, bridge deterioration prediction in practice shifted towards using the inspection data. According to the IABMAS survey of bridge management systems (Mirzaei et al., 2014) most existing bridge management systems and deterioration models around the world are based on element-level condition state inspection. Most bridge management systems use Markovian deterioration prediction models, which are suitable for dealing with the uncertainties in the deterioration process. Some use a combination of Markovian and Weibull models. These models are well suited to the "severity and extent" condition state inspection, such as in the Ontario Structure Inspection Manual (Ministry of Transportation Ontario, 2018). Few have more sophisticated deterioration prediction models that provide the ability to have different deterioration rates for a given element under differing environments (e.g., benign, moderate, and severe environments).

To the best of the authors' knowledge, current deterioration prediction models utilized in bridge management systems do not directly account for climate change or extreme weather events. According to a survey conducted by Stantec (Ellis, 2023), the current emphasis is on integrating the impacts of climate change in risk assessments related to factors such as flood risks, scour, permafrost effects, and similar concerns.

To propose a model for bridge deterioration that is capable of incorporating the effects of climate change, it is helpful to adapt the existing models that are already in use within the industry. This will facilitate its acceptance and implementation, since familiarity with established models reduces reluctance from practitioners and decision-makers, and offers a smoother transition toward incorporating the updated models. Moreover, adapting an existing model has the advantage of building upon a framework that has already undergone validation and scrutiny, which potentially requires fewer resources for implementation in standard practices. Consequently, in the subsequent section, a close examination of the most commonly used deterioration prediction models in practice will be conducted.

3 DETERIORATION MODELS TO INCORPORATE CLIMATE CHANGE EFFECTS

3.1 *Markovian models*

In a Markov model, the bridge component condition is assessed at regular intervals, e.g., annually. During each interval, the bridge component either stays in the same state or moves to a lower state (Parzen, 1962). In homogenous Markov models, the probability of transitioning between states remains constant, irrespective of the asset's age or past events, a principle known as the "memoryless assumption". Future condition predictions are calculated by multiplying the current state by the transition probability matrix.

$$y_k = \sum_j x_j P_{jk} \quad for\ all\ k \tag{1}$$

where j is the condition state in this period, x is the fraction in state j, and p is the transition probability from j to k. Roelfstra et al. (2004) noted that the coefficients of the probability matrix can be represented in two ways: 1) as the percentage of an element that changed from state j to state k after one inspection interval, or 2) the probability of an element to pass from condition state j to condition state k after one inspection interval.

These models are commonly employed in bridge management systems to predict the future condition of structures and plan maintenance activities. Most Markov models do not take into account the impacts of climate change and extreme weather events on the deterioration of bridge components. The conventional Markov model is simple and efficient at both project and network levels and can deal with the uncertainties in the deterioration process (Lounis, 2000; Madanat et al., 1995; Moghtadernejad et al., 2021; Setunge & Hasan, 2011). However, it has several limitations that are highlighted by, Thompson & Ford (2012) and Morcous (2006).

Markov models use data from inspections of the condition state of the infrastructure over time to estimate the deterioration curves. Hence, the quality of data plays a significant role in the accuracy of deterioration prediction and the resulting lifecycle cost estimations. Despite the recent progress towards more frequent and accurate monitoring of bridges, real-world data often do not exist in sufficient quantity, contain errors and discrepancies, and are not always suitable for estimating the transition probabilities. Roelfstra et al. (2004) compared Markov models to numerical simulations of corrosion damage. They noted that a lack of inspection data for the worst and second-worst condition states can lead to unreliable predictions made by Markov models.

Since transition probabilities are calculated for a constant period, inspection records should reflect this time interval to be accurate. However, inspections from the data do not necessarily occur at constant intervals (Morcous, 2006). Thompson & Ford (2012) highlight the inability

of the model to efficiently consider the interactive effects between deterioration mechanisms of different bridge elements, such as the interaction between deteriorating joints and the surrounding deck area. They claim these models are too basic for specific applications, especially due to their "memoryless assumption," i.e., the deterioration rate does not change with time.

To overcome the limitations of homogenous Markov models with respect to the stationarity of the transition probabilities, researchers have proposed various modifications and enhancements to the model. Some have compartmented the data based on factors, such as weather and traffic conditions, into the model to account for their impact on bridge deterioration. Other researchers have proposed using non-homogenous Markov models that allow for time-varying transition probabilities. For example, in a significant research paper published by Mizutani & Yuan (2023), the authors introduced a continuous-time Markov chain characterized by regime switches. Within these regimes, state transitions depend on an underlying, latent Markov chain that captures the overall aging pattern of an asset.

As more data on projections of future climatic conditions under different emission scenarios and their impacts on bridge deterioration become available, non-homogenous Markov models (NHMMs) are likely to become even more reliable, allowing transportation agencies to make informed decisions about when to conduct maintenance or rehabilitation activities considering the impacts of climate change (Pandey & Lounis, 2023). However, there are some challenges associated with the use of NHMMs in bridge deterioration prediction. One challenge is obtaining high-quality data, which is critical for accurately training and validating the model. A second challenge is selecting a relevant emission scenario and projecting future climatic data for temperature, precipitation and wind considering the non-stationarity of climate and modeling their impacts on bridge deterioration. Another challenge is identifying the most relevant variables to include in the model, since having too many variables can lead to overfitting, while excluding important variables can lead to inaccurate predictions.

3.2 *Weibull models*

The homogeneous Markov model described earlier, while simple, might be too basic for the prediction of deterioration rates, especially for assets with a long service life. The most prominent limitation is the "memoryless assumption," implying that the deterioration rate does not change with time. As Markov models are very adaptable, one can overcome this limitation by adding age dependency to them, and make it into a so-called "Weibull survival probability" model. The Weibull curve has the following functional form:

$$y_{1g} = \exp\left(-1.0 \times \left(\frac{g}{\alpha}\right)^{\beta}\right) \tag{2}$$

Where y_{1g} is the probability of the element not failing at age g, given no maintenance action is taken between year 0 and g; β is the shaping parameter, which determines the initial slowing effect on deterioration; and α is the scaling parameter, calculated as:

$$\alpha = \frac{\mathrm{t}}{(ln2)^{1/\beta}} \tag{3}$$

where t is the median service life expectancy from the model. A shaping parameter of 1 is mathematically equivalent to a Markov model, where the transition probability does not vary with time. Higher shaping parameters slow the initial rate of deterioration, which then accelerates as the asset gets older. It's important to note that the Weibull model does not alter the Markov median service life expectancy; however, it can assess the uncertainty in service life expectancy. As the shaping parameter increases, the range of uncertainty narrows. The shaping parameter in the Weibull model can be determined through a statistical method called "maximum likelihood estimation". This process involves systematically testing various values of the shaping parameter (β) until the best fit to the data is achieved.

One valuable use of the Weibull model is in capturing the start of deterioration, i.e., transitioning from the best to the second-best state. While the Markov model shows a rapid decline in condition, which is often unrealistic for new assets, the Weibull model can slow this onset, making the initial stages of deterioration more realistic. Additionally, it is beneficial in analyzing the transition from the second-worst condition state to the worst state. Unlike the Markov model, it refines this estimate and offers a measure of uncertainty in the time to failure. For assets already in the second-worst state, the Weibull model estimates what fraction will fail within a specified time period, which can help with more accurate budgeting for different intervals like a 2-year budget or a 10-year horizon. Hence, the pertinent inquiry is how to integrate climate change factors into bridge deterioration modeling using the Weibull model. Addressing this necessitates exploring an alternative to this approach akin to the Weibull model, yet one that accommodates additional explanatory variables beyond just age, called "Cox Survival Probability Model". The equation for the Cox model is:

$$y_{1g} = \exp\left(-1.0 \times \left(\frac{g}{\alpha}\right)^{\beta}\right) \times \exp(b_1 X_1 + b_2 X_2 + \ldots + b_n X_n) \tag{4}$$

where the variables X_n are explanatory variables such as traffic volume, environmental factors, etc. They can be continuous variables or binary values. The coefficients b_n are determined by linear regression or can be estimated in the same manner as the Weibull shaping parameter. The multiplier can shift the survival probability either upward or downward. If all explanatory variables are zero, then the multiplier will have no effect.

Despite the potential of this model in developing a deterioration model that fully accounts for influencing variables, the model requires analyzing individual state transitions independently and may demand extensive data collection and management. Moreover, researchers have found out that, it is unusual for more than three or four explanatory variables to have a beneficial effect on the Cox model (Thompson & Ford, 2012).

3.3 *Ordered probit models*

An alternative approach for agencies to predict asset deterioration considering influencing factors such as age, traffic, climate conditions, etc., is the Ordered Probit model (Thompson & Ford, 2012). This model is useful for assets with discrete, ordered condition states such as the National Bridge Inventory (NBI) or the Ontario Structure Inspection Manual (OSIM) rating systems. In this model, the likelihood of an asset being in a specific condition state at a given time (t) is determined by life expectancy factors and threshold parameters (μ).

These thresholds act as boundaries between condition states. For example, for a 1-4 rating scale, 1 being the best and 4 the worst, depending on the model sum ($\sum \beta x$) and threshold parameters (μ), the probability of being in a certain condition state follows a normal distribution. In this model, one can isolate the impact of one specific variable (e.g., temperature) on the predicted condition state of an asset while keeping all other factors constant. Mathematically, the exact probability of an asset being in any condition state follows the cumulative standard normal distribution with the variable X taking the following forms:

$$P(CS = 4) = \left[\sum \beta x\right] \sim N(0,1) \tag{5}$$

$$P(CS = 3) = \left[\mu_1 - \sum \beta x\right] \sim N(0,1) - \left[-\sum \beta x\right] \sim N(0,1) \tag{6}$$

$$P(CS = 2) = \left[\mu_2 - \sum \beta x\right] \sim N(0,1) - \left[\mu_1 - \sum \beta x\right] \sim N(0,1) \tag{7}$$

$$P(CS = 1) = 1 - \left[\mu_2 - \sum \beta x\right] \sim N(0,1) \tag{8}$$

where:

$P(CS = i)$ = Predicted probability of an asset being in condition state CS i;

x = set of independent variables, e.g., age, material type, environment/climate, etc.;

β = set of parameter estimates corresponding to independent variables;

μ = threshold parameters, which in comparison to parameter estimates and variable values, indicate the likelihood of being in a given condition state;

$[\mu_2 - \sum \beta x] = X$ value that can be used to calculate normal distribution test statistic;

$N(0,\ 1)$ = indicates the cumulative, standard normal distribution with mean = 0 and standard deviation = 1

4 DISCUSSIONS

It is established that accurate estimation of bridge condition states is crucial for effective planning of interventions. However, most deterioration models used in practice assume a constant deterioration rate over time, which does not reflect reality. Therefore, there is a need for a practical approach to account for diverse variables (e.g., age, environmental conditions, maintenance activities) that influence the deterioration rate of bridge elements.

After conducting a comprehensive review of existing literature and interviews with practitioners, certain methods have emerged as promising for further exploration. Integrated Markov/Weibull models, or Ordered Probit models offer the advantage of accommodating a wider range of explanatory variables, including age, climate change and extreme weather events. Due to their probabilistic nature, these models can incorporate uncertainties in input variables including different climate projections. To implement this approach effectively, historical data must be compartmentalized to represent different variables, e.g., climatic change observed over past years. By estimating transition probabilities for each compartment, the "variations" in the rate of deterioration concerning different or combinations of different explanatory variables can be examined. This analysis enables the forecasting of future deterioration rates, allowing for practical maintenance strategies aligned with changing climate patterns.

While these methods hold significant promise, there are several obstacles to extracting their full potential. This is mostly due to the need for comprehensive data collection efforts to obtain high-quality historical data across various climatic conditions. As a general guideline, the Weibull and Cox models need around 200 or more inspection pairs for a realistic prediction. If the model is partitioned, then each separate model needs to have around this sample size. Faster data collection can be achieved through the integration of real-time data streams and sensors into predictive models to have a nuanced understanding of bridge deterioration under changing environmental conditions. However, in the absence of comprehensive historical data, improving the accuracy of deterioration models becomes challenging. Even small variations in transition probability values can lead to significant fluctuations in the deterioration predictions. This sensitivity underscores the importance of reliable historical data. The absence of a long inspection history introduces substantial uncertainties, making it difficult to establish a precise correlation between climatic changes and the deterioration rate of bridge elements. Incorporating the effects of climate change into the deterioration model under such circumstances could introduce unnecessary complexity and potentially lead to unreliable predictions.

Additionally, as indicated in Figure 1, climate projections for the next 20 years, under the worst-case scenario SSP5-8.5, indicate an increase of around 0.6 °C. This increase is not expected to significantly alter the speed of deterioration for bridge elements (gradual deterioration). Hence, immediate concerns should focus on collecting sufficient data and considering the increasing occurrence and severity of climate-related hazards, such as floods, scour, and storms, which can lead to sudden deterioration. Understanding the potential implications of these events on bridge elements and incorporating this knowledge into risk mitigation strategies and improving the resilience of bridges, should be prioritized over attempting to incorporate small temperature variations into the deterioration model in the absence of sufficient

data to produce accurate results. By addressing these immediate threats in the risk analysis process, bridge management practices can be more effectively tailored to mitigate the impacts of climate change on bridge elements.

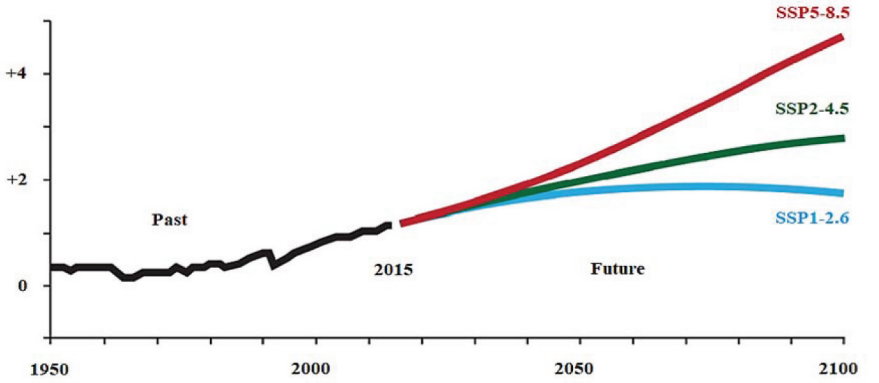


Figure 1. Global temperature change projections under the three SSP based emissions scenarios adapted from ClimateData.ca.

REFERENCES

Bazant, Z. P., Chern, J., Rosenberg, A. M., & Gaidis, J. M. (1988). Mathematical model for freeze-thaw durability of concrete. *Journal of the American Ceramic Society*, *71*(9), 776–783.

Ellis, R. M. (2023). *Review of state of practice of bridge management in Canada and USA in a changing climate*.

Huang, Y.-H. (2010). Artificial neural network model of bridge deterioration. *Journal of Performance of Constructed Facilities*, *24*(6), 597–602.

Ilbeigi, M., & Ebrahimi Meimand, M. (2020). Statistical forecasting of bridge deterioration conditions. *Journal of Performance of Constructed Facilities*, *34*(1), 04019104.

Isgor, O. B., & Razaqpur, A. G. (2004). Finite element modeling of coupled heat transfer, moisture transport and carbonation processes in concrete structures. *Cement and Concrete Composites*, *26*(1), 57–73.

Lethanh, N., Hackl, J., & Adey, B. T. (2017). Determination of Markov transition probabilities to be used in bridge management from mechanistic-empirical models. *Journal of Bridge Engineering*, *22*(10), 4017063.

Li, Z., Zhou, J., Nassif, H., Coit, D., & Bae, J. (2023). Fusing physics-inferred information from stochastic model with machine learning approaches for degradation prediction. *Reliability Engineering & System Safety*, *232*, 109078.

Lounis, Z. (2000). Reliability-based life prediction of aging concrete bridge decks. *Life Prediction and Aging Management of Concrete Structures*, 229–238.

Madanat, S. M., Mishalani, R., & Ibrahim, W. H. W. (1995). Estimation of infrastructure transition probabilities from condition rating data. *Journal of Infrastructure Systems*, *1*(2), 120–125.

Ministry of Transportation Ontario. (2018). *Ontario Structure Inspection Manual: (OSIM)*. Ministry of Transportation.

Mirzaei, Z., Adey, B. T., Klatter, L., & Thompson. P. (2014). *Overview of Existing Bridge Management Systems*.

Mizutani, D., Lethanh, N., Adey, B. T., & Kaito, K. (2017). Improving the Estimation of Markov Transition Probabilities Using Mechanistic-Empirical Models. *Frontiers in Built Environment*, *3*, 58.

Mizutani, D., & Yuan, X. (2023). Infrastructure deterioration modeling with an inhomogeneous continuous time Markov chain: A latent state approach with analytic transition probabilities. *Computer-Aided Civil and Infrastructure Engineering*.

Moghtadernejad, S., Adey, B. T., & Hackl, J. (2020). Determination of the Post-disaster Optimal Restoration Intervention Programs for Transportation Infrastructure. *Joint International Resilience Conference "Interconnected–Resilience Innovations for Sustainable Development Goals."*

Moghtadernejad, S., Huber, G., Hackl, J., & Adey, B. T. (2021). Data-driven estimation of deterioration curves: a railway supporting structures case study. *Infrastructure Asset Management*. https://doi.org/10.1680/jinam.21.00006

Mohammed Abdelkader, E., Zayed, T., & Marzouk, M. (2019). A computerized hybrid Bayesian-based approach for modelling the deterioration of concrete bridge decks. *Structure and Infrastructure Engineering*, *15*(9), 1178–1199. https://doi.org/10.1080/15732479.2019.1619782

Morcous, G. (2006). Performance prediction of bridge deck systems using Markov chains. *Journal of Performance of Constructed Facilities*, *20*(2), 146–155.

Nickless, K. (2017). *Investigation of mechanistic deterioration modeling for bridge design and management*. Colorado State University.

Pandey, M. D., & Lounis, Z. (2023). Stochastic modelling of non-stationary environmental loads for reliability analysis under the changing climate. *Structural Safety*, *103*, 102348.

Parzen, E. (1962). On estimation of a probability density function and mode. *The Annals of Mathematical Statistics*, *33*(3), 1065–1076.

Roelfstra, G., Hajdin, R., Adey, B. T., & Brühwiler, E. (2004). Condition evolution in bridge management systems and corrosion-induced deterioration. *Journal of Bridge Engineering*, *9*(3), 268–277.

Setunge, S., & Hasan, M. S. (2011). Concrete bridge deterioration prediction using Markov chain approach. *International Conference on Structural Engineering Construction and Management*. http://dl.lib.mrt.ac.lk/handle/123/9508

Shirkhani, H., Lounis, Z., & Zhang, J. (2023). Life-cycle design of concrete highway bridge decks under climate change. In *Life-Cycle of Structures and Infrastructure Systems* (pp. 1609–1616). CRC Press.

Thompson, P. D., & Ford, K. M. (2012). *Estimating life expectancies of highway assets: Guidebook* (Vol. 1). Transportation Research Board.

Zhang, J., & Lounis, Z. (2009). Nonlinear relationships between parameters of simplified diffusion-based model for service life design of concrete structures exposed to chlorides. *Cement and Concrete Composites*, *31*(8), 591–600.

Bridge Maintenance, Safety, Management, Digitalization and Sustainability – Jensen, Frangopol & Schmidt (eds)
© 2024 The Author(s), ISBN 978-1-032-77040-6
Open Access: www.taylorfrancis.com, CC BY-NC-ND 4.0 license

Application of open deep learning datasets for building vision-based bridge condition monitoring solutions

K. Tomaszkiewicz & T. Owerko
AGH University of Krakow, Krakow, Poland

ABSTRACT: The operational phase of bridges is the longest phase in the entire structure's life cycle. During this phase, defects occurring in earlier stages of the life cycle may become apparent. Structural condition monitoring and defect detection at an early stage of their formation make it possible to react faster, protect the damage and stop or delay the degradation process. To support the engineer's work, deep learning-based solutions are becoming popular. However, to make solutions based on such algorithms effective and helpful for the engineer, it is necessary to provide a good dataset to train them. This paper summarizes publicly available open datasets of bridge damage images that can be used to train DL algorithms for classification, object detection and segmentation. The presented approach refers to the usability of datasets from the point of view of training DL algorithms, as well as the usability of algorithms trained on their basis to support the bridge engineer's work.

1 INTRODUCTION

The operational phase is the longest phase in the bridge entire life cycle. This phase is strongly determined by factors occurring at earlier stages of the life cycle, which have a significant impact on the structure's future performance. Monitoring the structure's working and its response to environmental conditions and the loads, along with periodical inspections of the structure's technical condition, make it possible to detect defects at an early stage of their formation. This makes it possible to react more quickly, to protect the damage and to stop or delay the degradation process of the damaged element of the structure, and thus of the entire structure.

In most countries, a significant number of bridges are in the operational phase, and budgets for maintenance and repair of structures are increasing. More than 43,500 bridges in the U.S. are in poor condition and have been classified as "structurally deficient", 224,000 bridge spans need repair, and 78,800 bridges should be replaced - and it would take nearly 30 years to repair these structures at the current rate (A.R.& T.B. Association, 2022). Due to the important role of the operational phase, there is a need for methods that will improve the bridge monitoring process.

To support the engineer's work during monitoring the condition of structures and performing inspections, solutions using artificial intelligence algorithms, in particular deep learning (hereafter: DL), are becoming available. They are applied not only for image analysis, but also for analyzing video recordings, data from SHM systems, etc. (Dong & Catbas, 2021; Sabato et al., 2023; Zhang et al., 2022). In terms of detecting damage visible on images, these algorithms make it possible to quickly assess the technical condition of a bridge, and thus detect damage at an early stage. They are an important support for the engineer's work especially in those cases where the damage is not visible to the human eye and may be undetected during the engineer's inspection.

The basis for creating effective and robust DL algorithms which can be used to support the engineer's work is the datasets on which the algorithms are trained. Evaluation of the quality and effectiveness of a solution based on a trained DL algorithm for damage detection purposes

DOI: 10.1201/9781003483755-175

should be based not only on the analysis of metrics and evaluation tools characteristic for the machine learning domain. The solution's effectiveness should also be considered from the perspective of the domain knowledge of bridge engineering, and thus the quality and effectiveness of the solution should be evaluated in relation to domain requirements included in standards, manuals, or other documents. This form of evaluation is possible only if the basis for training the algorithm is a well-prepared and described dataset. Despite the quick development of DL algorithms, also in bridge damage detection on images, the availability of data on which algorithms can be trained is limited. There are papers summarizing the progress in the field of machine learning with a description of the used datasets, including for non-vision data (Bianchi & Hebdon, 2022b). However, these works provide only basic parameters of datasets, such as the dataset name, reference, type of presented damage, material of damaged element, size, availability, year of creation, or reference to the experiment in which the dataset was used. However, they do not address the fundamental issue, that is, the effectiveness of these datasets in relation to domain knowledge and the ability to meet the requirements of the bridge industry.

This paper summarizes open datasets in the form of bridge damage images that can be used to train DL algorithms for classification, object detection and damage segmentation. The presented approach addresses the usability of datasets from the point of view of training DL algorithms (type of dataset count, dataset balancing, etc.), as well as the usability of algorithms trained on their basis to support the bridge engineer's work (whether they describe the size of the damage, the cause of the damage, etc.). The paper is a discussion of the quality of creating, documenting, and sharing damage datasets.

Chapter 2 presents the key aspects addressed in the datasets analysis in terms of their usability for DL purposes and in relation to the bridge engineering domain knowledge aspects. A datasets description based on established criteria is presented in Chapter 3. Chapter 4 shows the practical application of DL-based solutions for vision-based bridge monitoring. Chapter 5 summarizes the work.

2 METHOD OF REVIEW

This paper is concentrated on the analysis of open bridge damage image datasets, which are dedicated to solving three basic groups of problems for which DL algorithms are used, i.e. classification, object detection and segmentation. Only datasets for which the dataset authors have declared that the dataset is used for bridge solutions (e.g. in the dataset name or description) are included. By "open datasets", the authors of this paper mean such data, the obtaining of which does not require contact with the author, and the data are available immediately for download. This paper excluded those datasets where, despite the authors' declared availability, references to the datasets did not work, showed an error, or returned information about planned future availability. Such datasets which are the result of merging other datasets are also not included. The review was conducted to consider the usefulness of the dataset with respect to aspects related to the training of DL algorithms and the ability to use algorithms trained on the considered datasets to solve bridge engineer problems.

Regarding the aspects related to the training of DL algorithms, attention has been given to:

- The size of each class in the dataset, and thus the balance of the dataset - which has a direct impact on what metrics should be applied to the dataset under consideration (Tomaszkiewicz & Owerko, 2022),
- The resolution of the images, including making the original images available for adaptation to the size of the input data for the selected neural network - which has an indirect effect on the class of algorithms that can be used in the solution,
- The data storage format, including the type of compression that affects the quality of the source data (Bouderbal et al., 2021; Dodge & Karam, 2016; Gandor & Nalepa, 2022),
- The way in which data is organized (folder structure, file name, clarity of class naming),
- Explanation of the meaning of labeling - when describing classes numerically as "0", "1", etc.

- The degree of complexity of the surface to be analyzed (resolution of the source information in the space of the problem domain) - e.g., different colors of concrete, different lighting conditions of the photo, the presence of noise in the photos, etc.

Regarding the aspects related to the evaluation of the ability to use algorithms trained on the considered datasets to solve bridge engineer's problem, attention has been given to:

- The type of damage represented in the dataset,
- How the images were acquired - including the type of equipment used, the conditions under which the images were acquired
- Explanation by the authors of the way in which the images were annotated - on what criteria the decision was made to assign a class to the damage, extract the damage area for object detection, or assign pixels as damaged for segmentation of the data. In particular, attention was paid to whether the authors created annotations based on guidelines, instructions, etc.
- Correctness of image annotations - whether the images received correct annotations,
- Description of the bridge elements to which damage images correspond (the name of the element, material, type of bridge object indicating the nature of the work of the structure),
- Size of the damage - e.g. width of the crack,
- Cause of damage - e.g. fatigue cracking.

3 REVIEW OF OPEN DEEP LEARNING DATASETS OF BRIDGE DAMAGE IMAGES

This chapter is organised in such a way that at the beginning, in tabular form (Table 1), it presents the classes that each of the datasets contains, their size and image, labels and masks parameters. A detailed overview of each dataset is presented below the table, providing a description of its characteristics and a discussion of its quality and usability.

Table 1. General Characteristics Of The Datasets.

Dataset name	Class	Number of images or damages	Images, labels, and masks parameters
"SDNET2018" (Dorafshan et al., 2018)	Bridge deck - C cracked	2025	Images:
	Bridge deck - U uncracked	11595	256x256px RGB (.jpg)
	Wall - C cracked	3851	
	Wall - U uncracked	14287	
	Pavement - C cracked	2608	
	Pavement - U uncracked	21726	
"crack-detection" (tjdxxhy)	0 - cracked	4055	Images:
	1 - noncracked	2014	224x224px RGB (.jpg)
			Labels: (.txt)
"Concrete-Bridge-Crack-Dataset" (MCBDD-ZRE)	Cracks	1050	Images:
	Background	2772	200x200px RGB (.jpg)
"CCNY Concrete Structure Spalling and Crack database (CSSC)" (CCNY Robotics Lab, n.d.)	Crack - accept	13448	Images:
	Crack - nonaccept	11652	100x100px RGB (.jpeg)
	Spalling - accept	7376	
	Spalling- nonaccept	11747	
	Crack - accept	12422	Images:
	Crack - nonaccept	11678	130x130px RGB (.jpeg)
	Spalling - accept	8574	
	Spalling- nonaccept	11350	

(*Continued*)

Table 1. (*Continued*)

Dataset name	Class	Number of images or damages	Images, labels, and masks parameters
"Multi-classifier for RC bridge defects" (Hüthwohl et al., 2019)	Corrosion - rust staining Corrosion - no rust staining ExposedReinforcement - exposed reinforcement ExposedReinforcement - no exposed reinforcement MultiClassifier - cracks MultiClassifier - spalling MultiClassifier - scaling MultiClassifier - no defect MultiClassifier - efflorescence	355 415 223 203 789 427 168 452 311	Images: various sizes RGB (.jpg)
"Cambridge Bridge Inspection Dataset" (Huethwohl, 2017)	Potentially unhealthy Healthy	691 337	Images: 299x299px RGB (.jpg)
"The COncrete DEfect BRidge IMage: CODEBRIM" (Mundt et al., 2019)	crack spallation exposed bars efflorescence corrosion stain	2507 1898 1507 833 1559	Images: various sizes, RGB (.png) Labels: (.xml)
"Bridge Crack Library" (Jin et al., 2022)	non-steel crack images steel crack images noise images	5769 2036 3195	Images: 256x256 px, RGB (.jpg) Masks: 256x256 px gray scale (png)
"Bridge Crack Library 2.0" (Jin & Li, 2022)	crack	23 400	Images: 256x256 px, RGB, (.jpg) Masks: 256x256 px gray scale (.png)
"Labeled Cracks in the Wild (LCW) Dataset" (Bianchi & Hebdon, 2021b)	Images with normal crack widths Images with dilated crack widths	3773 959	Images: original with diffrent sizes/ 512x512 px RGB (.jpeg) Masks: original with diffrent sizes/ 512x512 px gray scale (.png)
"Corrosion Condition State Semantic Segmentation Dataset" (Bianchi & Hebdon, 2021a)	corrosion	440	Images: 512x512px RGB (.jpeg) Masks: 512x512px RGB (.png)
"NCCD-PF - A pre-failure narrow concrete cracks dataset for engineering structures damage classification and semantic segmentation" (Tomaszkiewicz & Owerko, 2023)	classification dataset - cracked classification dataset - uncracked segmentation dataset	668 4720 5388	Images: 224x224px RGB (.jpg) Masks: 224x224px RGB (.png)

One of the largest datasets for the concrete crack classification in terms of size is the dataset ***"SDNET2018"*** (Dorafshan et al., 2018). It was built from 230 images of cracked and non-cracked concrete, including reinforced concrete (54 images of bridge decks and 72 images of walls) and unreinforced concrete (104 images of pavements), which were divided into sub-images. It should be noted that there is a large imbalance of images of cracked and uncracked concrete for each class. The images were taken using a 16-MP Nikon camera from a distance of 0.5m, without using the zoom. In addition, they contain obstructions including shadows,

surface debris, inclusions, scaling and also show different colors and textures of concrete surfaces. The damage is not always located in the central part of the image. What is interesting to note is that the set of non-cracked photos also includes photos of expansion joints, which makes the researcher's solution more robust. The images show cracks with widths ranging from 0.06mm to 25mm. The bridge piers for which the images were acquired were located at the Utah State University system, material, and structural health (SMASH) laboratory, the wall and pavement images came from USU campus. This shows that the images of walls and pavement are not representative of the operating conditions of bridges.

The ***"crack-detection"*** dataset (tjdxxhy) for concrete crack classification presented in the paper (Xu et al., 2019), was created by artificially expanding the dataset presented in (Wang et al., 2019). The original images (1024x1024px) were cropped to 512x512px images. From the resulting 8272 images, blurry images were removed, which gave a set of 6069 images. From this set of images, a training and validation set was randomly selected, and the images were cropped to 224x224px. The images are presented in .jpg format, and class assignments are presented in . txt files by assigning the digit "0" or "1" to the file name, but the dataset authors do not explicitly define these designations. The analysis conducted by the authors of this paper made it possible to specify the number of individual damages for each class. The dataset authors do not define the crack widths, but visual assessment allows to conclude that these are very large damages, probably out of limits. The dataset also includes images with shadow, strong exposure, with cracks only on the edges (which cover a small percentage of the image) or cracks where vegetation is present. Damage is found not only in the central part of the image, but also near the edges. There are also cracks with many branches and complex geometry.

The dataset for the concrete crack classification problem is also the ***"Concrete-Bridge-Crack-Dataset"*** (MCBDD-ZRE). The dataset contains very different concrete surfaces in terms of color, finishing quality, lighting of the photo. The authors do not define the crack widths values.

The ***"CCNY Concrete Structure Spalling and Crack database (CSSC)"*** dataset (CCNY Robotics Lab, n.d.) is a dataset dedicated to the problem of crack and spalling classification, which was developed with the help from Civil Engineers. It should be noted, however, that analyzing the "nonaccept" subset, it is possible to also find images that, in the opinion of the authors of this paper, should be classified as cracked into the "accept" set. It is not clear what damage classification criteria the dataset's authors adopted. The photos vary widely in terms of color, concrete surface finish. Some of the photos are zoom in on the damage, but some are shots of a larger section of the space. It should be noted the possible use of a part of the dataset, i.e. spalling photos for other applications. Most of the photos show very large damage, in which the reinforcement is clearly exposed. It is therefore possible to use the photos to build a dataset for detecting reinforcement in exposed concrete.

The ***"Cambridge Bridge Inspection Dataset"*** (Huethwohl, 2017) is a dataset of bridge inspections which, as defined by the authors, is used to classify concrete defects such as cracking, graffiti, vegetation, and blistering. However, all these defects are included as a common "Potentially unhealthy" class - the authors of the dataset did not divide this class into different types of damage in more detail, hence it is not possible to train an algorithm on such a prepared dataset to detect each type of damage. The other class is the "Healthy" class. The images contain different colors of concrete surfaces and cracks of large width, but there is no information about the width of the crack and its cause. Only for 18 photos, information about the element from which the damage occurred, i.e. concrete wall, is given in their name.

The ***"Multi-classifier for RC bridge defects"*** dataset (Hüthwohl et al., 2019) is dedicated for classification of concrete surface defects such as corrosion, exposed reinforcement, cracks, spalling, scaling, efflorescence. It was created based on self-collected image samples and Departments of Transportation inspection databases. The number of individual classes is shown in Table 1. It should be noted that it is not clear how to classify the images into the "general" category, since it also includes such damage that could be classified into the other listed classes. For the most part, the damage is very visible in the photos, taking up most of the image.

"The COncrete DEfect BRidge IMage: CODEBRIM" dataset (Mundt et al., 2019) is dedicated for classification and object detection of concrete surface defects such as crack, spallation, exposed bars, efflorescence, corrosion stain. The images were acquired under varying

weather conditions on 30 bridges. The bridges were characterized by varying technical condition, degree of damage and surface appearance. The dataset consists of 1590 images, in which 5354 bounding boxes (largely with overlapping defects) and 2506 nonoverlapping background bounding boxes were annotated. The dataset was prepared in several variants (original images in full resolution with bounding box annotations, images with the extracted crops/patches with class labels from the bounding boxes, images with the cropped patches with corresponding class labels, which were divided into training, validation and test sets for machine learning, the set balanced to reproduce the results of the authors' experiment (Mundt et al., 2019).

The ***„Bridge Crack Library"*** dataset (Jin et al., 2022) is a dataset for semantic segmentation of cracks which is based on 1180 raw images collected during inspections of in-service bridges. In addition, the ***„Bridge Crack Library 2.0"*** segmentation dataset (Jin & Li, 2022) is a dataset of crack images synthetically created based on the "Bridge Crack Library" dataset (Jin et al., 2022).

The ***„Labeled Cracks in the Wild (LCW) Dataset"*** (Bianchi & Hebdon, 2021b) is a dataset which is dedicsted for crack segmentation. It consists of real images extracted from structural inspection reports of the Virginia Department of Transportation (VDOT). A characteristic feature of the dataset is that it presents cracks in a global scene rather than a close-up of the damaged surface. The damage was annotated using GIMP software, and the authors also provide image annotation guidelines (Bianchi & Hebdon, 2022a). The authors also provide images scaled to 512x512px, used for training and testing the DeeplabV3+ model.

The ***"Corrosion Condition State Semantic Segmentation Dataset"*** (Bianchi & Hebdon, 2021a) is dedicated for segmentation of steel component corrosion, where the classes are four corrosion class categories: [good, fair, poor, severe]. Images were annotated according to the corrosion condition guidelines of the American Association of State Highway and Transportation Officials (AASHTO) and the Bridge Inspector's Reference Manual (BIRM). The data was collected from Virginia Department of Transportation (VDOT) bridge inspection reports. Guidelines for annotating photos in reference to the abovementioned documents and examples of annotation with explanation were also included with the dataset.

The **"NCCD-PF - A pre-failure narrow concrete cracks dataset for engineering structures damage classification and semantic segmentation"** dataset (Tomaszkiewicz & Owerko, 2023) is dedicated for classification and semantic segmentation of narrow cracks (with a width below the limiting value specified in EC 1992-1-1, i.e. 0.3mm). It contains images of cracks occurring on various elements of engineering structures (bridges, viaducts, tunnels) made of reinforced concrete (including abutments, tunnel walls, concrete barriers, pillars). The photos were taken during the construction and inspection of engineering structures, at various stages of the structure's operation. The damages are varied in terms of the causes of damage.

4 PRACTICAL USE

The use of open datasets for building vision-based bridge condition monitoring solutions is important for several reasons. DL-based solutions allow to analyse large data sets and that can detect very small damages that may not be visible to the human eye. Such structural damage can be an indication of an on-going material degradation process, and early detection of such damages can help optimise the bridge operating costs by avoiding costly repairs and extending the life of bridges. Images acquired using, for example, UAV imagery, particularly for areas that are difficult to access, can help to diagnose these areas more effectively. However, to make an informed decision about the risk to the structure caused by the occurrence of a particular type of damage, it is necessary to make a connection between this damage and aspects such as the time of the damage and the location of the damage.

One example of this is concrete surface damage in the form of shrinkage cracks. These appear after the concrete has been poured and are closely linked to the concrete hardening process. Their appearance on the concrete surface may occur within the first few hours or days after concrete pouring (depending on factors such as the size of the element, environmental conditions, type of concrete surface curing). By detecting and inventorying such damages, including consideration of the time when the photograph was taken, it is possible to make assumptions about

the probable cause of the damage by relating the time when the damage occurred to the structure's construction schedule. For example, the detection of cracks in the lower part of the abutment just after pouring may suggest that they were caused by concrete shrinkage, while their occurrence after placing the load on the structure, or at the stage of test loading, may indicate that the element is not working properly or that there is a structural defect. For this reason, it is important that in creating the dataset it is also important to fill it with information such as, among other things, the type of element damaged and the cause of the damage.

By linking the information about the damage detected on the image with the Digital Twin of the bridge, it can also be used to verify the cause of the damage, e.g. by analysing the stress state of the element. On the other hand, machine learning algorithms can be supported by information from the Digital Twin of the bridge about the assignment of image data to a specific structural element. Providing such information as input for DL algorithms can help to identify regions of interest for which further diagnostics will be carried out.

5 CONCLUSION

The conducted analysis indicated that despite the increasing interest in the use of deep learning-based algorithms for bridge damage detection, there is significantly limited access to open datasets of bridge damage images. There is also no standardized way to create datasets of structure damage. In particular, the authors of datasets do not address aspects that are important for a bridge engineer during the description of datasets, such as the size of the damage, the cause of the damage, the relation of the damage to the element's work, among others. In many cases, the method of class assignment, bounding boxes or pixel classification is not described by the authors. There are also such datasets where, despite defining the possibility of detecting with them several types of damage, all images are grouped into a single class, which makes it impossible to accurately detect a specific type of damage, and thus to use such a dataset. Therefore, it is important to focus on the careful preparation of data for training machine learning algorithms, and the selection of metrics and ways to verify the correctness of the obtained solutions in the perspective of the bridge engineers' domain knowledge. Such an approach can allow the creation of more robust algorithms that not only achieve good results from the perspective of deep learning metrics, but also provide important support for the bridge engineer's work.

ACKNOWLEDGMENTS

The authors would like to acknowledge the support from the project Europe's Rail Flagship Project 4 - Sustainable and green rail systems that has received cofounding from the Horizon Europe Framework Programme (HORIZON) under grant agreement number 101101917 and Ministry of Education and Science in Poland under grant agreement number MEiN 5337/HE/2023/2. The project is being implemented at the AGH University of Krakow in 2022-2026.

REFERENCES

A.R.& T.B. Association. (2022). *2022 Bridge Report*. https://artbabridgereport.org/reports/2022-ARTBA-Bridge-Report.pdf

Bianchi, E., & Hebdon, M. (2021a). *Corrosion Condition State Semantic Segmentation Dataset*.

Bianchi, E., & Hebdon, M. (2021b). *Labeled Cracks in the Wild (LCW) Dataset*.

Bianchi, E., & Hebdon, M. (2022a). Development of Extendable Open-Source Structural Inspection Datasets. *Journal of Computing in Civil Engineering*, *36*(6), 04022039.

Bianchi, E., & Hebdon, M. (2022b). Visual structural inspection datasets. *Automation in Construction*, *139*, 104299

Bouderbal, I., Amamra, A., & Benatia, M. A. (2021). How Would Image Down-Sampling and Compression Impact Object Detection in the Context of Self-driving Vehicles ? *Lecture Notes in Networks and Systems*, *199 LNNS*, 25–37.

CCNY Robotics Lab. (n.d.). *CCNYRoboticsLab/pytorch_Concrete_Inspection: The Pytorch Implementation of Our Concrete Crack and Spall Detection*. https://github.com/CCNYRoboticsLab/pytorch_Concrete_Inspection

Dodge, S., & Karam, L. (2016). Understanding how image quality affects deep neural networks. *2016 8th International Conference on Quality of Multimedia Experience, QoMEX 2016*.

Dong, C. Z., & Catbas, F. N. (2021). A review of computer vision–based structural health monitoring at local and global levels. *Structural Health Monitoring*, *20*(2), 692–743.

Dorafshan, S., Thomas, R. J., & Maguire, M. (2018). SDNET2018: An annotated image dataset for non-contact concrete crack detection using deep convolutional neural networks. *Data in Brief*, *21*, 1664.

Gandor, T., & Nalepa, J. (2022). First Gradually, Then Suddenly: Understanding the Impact of Image Compression on Object Detection Using Deep Learning. *Sensors 2022, Vol. 22, Page 1104*, *22*(3), 1104.

Huethwohl, P. (2017). *Cambridge Bridge Inspection Dataset*.

Hüthwohl, P., Lu, R., & Brilakis, I. (2019). *Multi-classifier for RC bridge defects*.

Jin, T., & Li, Z. (2022). *Bridge Crack Library 2.0*. Harvard Dataverse.

Jin, T., Li, Z., Ding, Y., Ma, S., & Ou, Y. (2022). *Bridge Crack Library*.

MCBDD-ZRE. (n.d.). *MCBDD-ZRE/Concrete-Bridge-Crack-Dataset-*. https://github.com/MCBDD-ZRE/Concrete-Bridge-Crack-Dataset-

Mundt, M., Majumder, S., Murali, S., Panetsos, P., & Ramesh, V. (2019a). *CODEBRIM: COncrete DEfect BRidge IMage Dataset*. Zenodo.

Mundt, M., Majumder, S., Murali, S., Panetsos, P., & Ramesh, V. (2019b). *Meta-learning Convolutional Neural Architectures for Multi-target Concrete Defect Classification with the COncrete DEfect BRidge IMage Dataset*.

Sabato, A., Dabetwar, S., Kulkarni, N. N., & Fortino, G. (2023). Noncontact Sensing Techniques for AI-Aided Structural Health Monitoring: A Systematic Review. *IEEE Sensors Journal*, *23*(5), 4672–4684.

tjdxxhy. (n.d.). *tjdxxhy/crack-detection*. https://github.com/tjdxxhy/crack-detection

Tomaszkiewicz, K., & Owerko, T. (2022, June 20). Deep machine learning in bridge structures durability analysis. *Proceedings of the 5th Joint International Symposium on Deformation Monitoring - JISDM 2022*.

Tomaszkiewicz, K., & Owerko, T. (2023). *NCCD-PF - A pre-failure narrow concrete cracks dataset for engineering structures damage classification and semantic segmentation*. Zenodo.

Wang, Y., Zhang, J. Y., Liu, J. X., Zhang, Y., Chen, Z. P., Li, C. G., He, K., & Yan, R. Bin. (2019). Research on Crack Detection Algorithm of the Concrete Bridge Based on Image Processing. *Procedia Computer Science*, *154*, 610–616.

Xu, H., Su, X., Wang, Y., Cai, H., Cui, K., & Chen, X. (2019). Automatic Bridge Crack Detection Using a Convolutional Neural Network. *Applied Sciences 2019,Vol. 9, Page 2867*, *9*(14), 2867.

Zhang, G. Q., Wang, B., Li, J., & Xu, Y. L. (2022). The application of deep learning in bridge health monitoring: a literature review. *Advances in Bridge Engineering 2022 3:1*, *3*(1), 1–27.

Bridge Maintenance, Safety, Management, Digitalization and Sustainability – Jensen, Frangopol & Schmidt (eds)
© 2024 The Author(s), ISBN 978-1-032-77040-6
Open Access: www.taylorfrancis.com, CC BY-NC-ND 4.0 license

Influence of the pavement conditions on the bridge response

M.G. Mulas, M. Riso & A. Sgambati
Department of Civil and Environmental Engineering (DICA), Politecnico di Milano, Milano, Italy

F. Basone & M. Longo
SACERTIS Ingegneria S.r.l., Torino, Italy

ABSTRACT: This work investigates the influence of pavement conditions on the bridge response. When monitoring is available for the bridge at study, a correlation between the response, usually in terms of acceleration, and the roughness level can point out the need for a maintenance intervention. This paper focuses on the preliminary numerical work devoted to the study of vehicle-bridge interaction, taking advantage of a combined usage of a commercial and of a research code. The case study is a 4-span 60m long highway viaduct in the Northern Italy. Static and dynamic tests were performed after the installation of the SHM system (MEMS clinometers and accelerometers) and its dynamic behavior was continuously monitored in conditions of pre- and post-paving. A FE model was established with SAP2000 and updated to account for the experimental results. As a positive novelty of this work, the analysis of bridge-vehicle interaction is tackled by exploiting the capabilities of the commercial code and of a previously developed research code, named INTER. The structural matrices and the relevant tables of nodes are extracted from SAP2000 and, after some manipulations, adopted as input data to INTER. The interaction analysis accounts for roughness and adopts an ad-hoc developed 13-DOFs vehicle model, representing the one adopted in tests. Preliminary results show the influence of the roughness on the acceleration of selected points, investigating the variability of results tied to the generation of roughness profiles from the PSD function in Eurocode1.

1 INTRODUCTION

In the last two centuries, the progress of technology, materials and industrial world have led to a massive construction of bridges for roads and railroads. Nowadays, the civil engineering community tackles the need for the assessment and maintenance of bridges designed with obsolete codes for less intensive traffic, while, in conjunction with the evolution of structural schemes and the adoption of advanced materials, it faces the challenge of a design accounting for several extreme environmental load conditions. Within this framework, the dynamic interaction between a bridge and a travelling vehicle (VBI, Vehicle-Bridge Interaction) plays a fundamental role in a wide range of issues, as an analysis of the recent literature shows. VBI accounting for the effects of pavement roughness conditions the fatigue life analysis (Bhetuwal et al, 2022) and introduces an additional damping to the bridge (Stoura & Dimitrakopoulos, 2020). VBI allows for indirect bridge monitoring, since modal identification and damage detection are possible through the analysis of the dynamic response of an instrumented vehicle crossing the bridge. The topic, investigated since the pioneering work of YB Yang et al (2004), has generated wide research efforts both on the theoretical aspects (Yang & Yang, 2018) and on the structural health monitoring techniques based on vibration measurements (Zhu & Law, 2015) that is still ongoing (Yang et al, 2022). The contemporary presence of VBI and seismic excitation is accounted for (Paraskeva et al, 2017). The dynamic response of a new type of structure that is still at the proposal level, the submerged floating tunnel, is

DOI: 10.1201/9781003483755-176

investigated under the coupled effect of hydrodynamic loads and crossing vehicles (Mulas et al, 2018; Lin et al, 2022).

Pavement roughness is one of the factors affecting the bridge response under vehicle traffic. Due to the repeated passage of vehicles, roughness generally increases, worsening the quality of the generic roughness profile that can be detected on the bridge at study. Inspection is necessary to establish the degradation level, and usually a threshold is introduced for the need of maintenance. Aim of this work is investigating the effect of the roughness on the bridge response, both from an experimental and a numerical point of view, to verify whether the bridge response can be assumed as an indicator of pavement degradation. The case study is a 4-span reinforced concrete (RC) highway viaduct, instrumented for structural health monitoring (SHM) purposes and subjected to both static and dynamic tests, under a passing truck. Numerical analyses adopt a complete 3D model of the structure, generated with SAP2000, an ad-hoc developed 13 DOF (degrees of freedom) vehicle model and roughness profiles generated from the PSD function of Eurocode 1. Coupled equations of motion of the VBI problem are integrated following the work of Feriani et al. (2008, 2010), as last implemented in the research code named INTER (Maneo, 2016). This paper presents selected experimental and numerical results of the research work just described.

2 THE CASE STUDY

The structure at study is a highway RC bridge built in the late 1960s and located in Northern Italy (see Figure 1). The 4-span bridge is approximately symmetric about mid-span. The overall length of approximately 60 m is subdivided into 9m-long end spans and two 20m-long central spans. All the spans are simply supported at the ends, with abutments at the two ends and intermediate piles in the central zone. The supports of each span are devices made of multipurpose reinforced neoprene rubber sheets and strips. Joints between adjacent spans are placed below the pavement. Each deck girder is composed of six beams with reinforced concrete slabs having a constant height equal to 20cm (see Figure 2). The beams at the end spans have constant height while the two central ones have variable height (1.20m ÷ 1.70m).

2.1 *SHM system*

The reference structure was instrumented by clinometers and accelerometers for SHM purposes. In 2019, a set of 58 MEMS bi-axial clinometers and 42 tri-axial accelerometers was

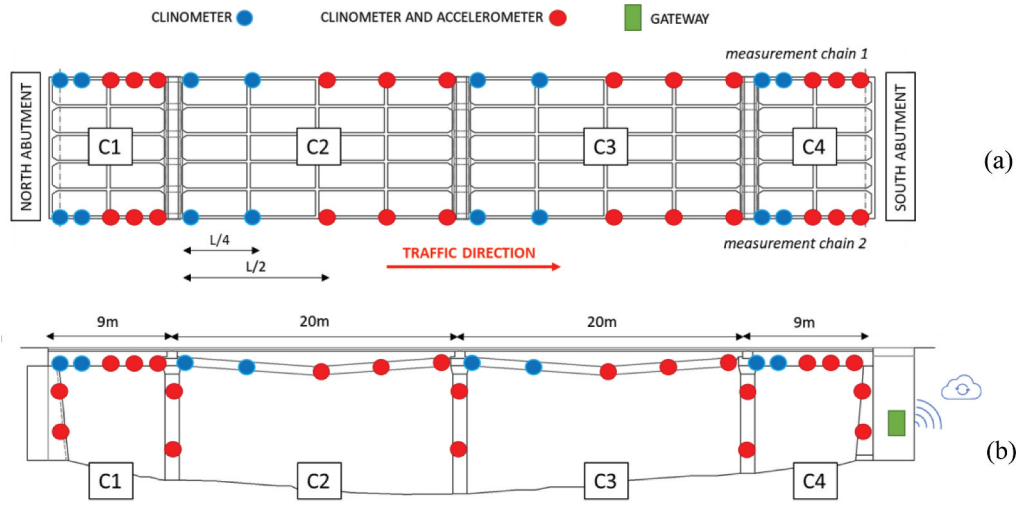


Figure 1. Plan view (a) and lateral view (b) of the bridge with the sensors positioning.

placed on the bridge, and one IoT Gateway was installed on one of the abutments. The biaxial MEMS clinometers measure along two axes, i.e. x and y, aligned to the transversal and longitudinal directions of the bridge respectively, whilst the triaxial MEMS accelerometers have the additional z-axis oriented along the vertical direction. Both accelerometers and clinometers are equipped with a 32-bit microcontroller, humidity and temperature sensors.

The precabled SHM system is made of two chains of clinometers and accelerometers placed along the two external beams of the deck. In all spans, each chain is made of 5 sensors (2 clinometers and 3 accelerometers), placed approximately at midspan, at ¼ of span and near the bearings**.** Figure 1 shows a plan and lateral view with the sensors positioning. Static (clinometers) and dynamic (accelerometers) MEMS sensors measure residual deformations and vibrations due to traffic. Each clinometer provides synthetic statistical parameters (mean value, standard deviation, maximum and minimum rotation), internal temperature and relative humidity, with a sampling frequency of 208 Hz. Tri-axial accelerometers provide continuous data along 3 axes, with a range of ±2 g and a bandwidth of 100 Hz. Acquisition parameters are tunable with remote control.

The continuous monitoring system promptly notifies anomalies due to two alerting systems. The first one detects rapidly growing anomalies; algorithms at the gateway level notifies in semi real-time short-term phenomena. The second performs long-term controls at the cloud level, to detect slow changes in the structure behaviour (long-term phenomena). In both cases, a degree of robustness is provided through multi-parameter cross-checks among sensors in space and in time.

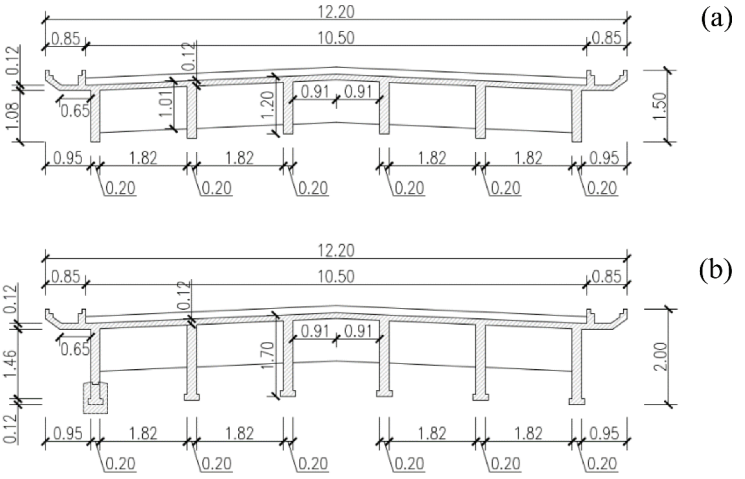


Figure 2. Cross-section of the bridge: (a) end spans; (b) central spans.

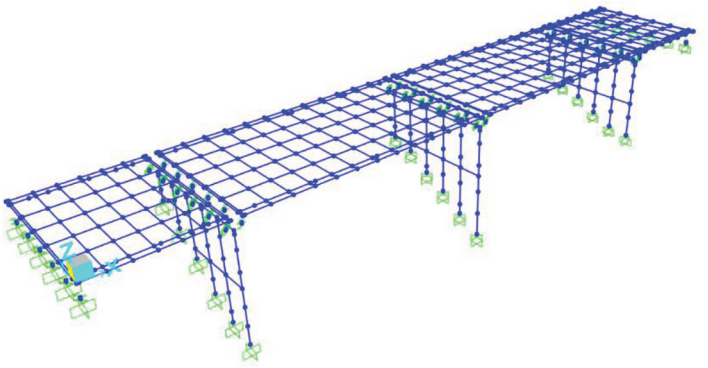


Figure 3. Three-dimensional view of FE model.

2.2 *FE modeling of structure*

The 3D finite element (FE) model of the structure, developed within the SAP2000 software platform, is based on the bridge cross-section, different for end spans (Figure 2a) and for central spans (Figure 2b), and is shown in Figure 3. Each span has been discretized through 6 DOFs beam elements in both the longitudinal and transversal direction, having proper mechanical and geometric characteristics. To take into account the stiffening behavior of the slab in transverse direction, fictitious transverse elements have been added ad deck level. Elastomeric supports are modelled by *links elements* that simulate the device stiffness in three mutually orthogonal directions.

2.3 *Description of experimental tests*

Experimental tests under a moving truck were carried out in absence of traffic, to avoid that the accelerometer signals are contaminated by the transit of other unknown vehicles. Figure 4 shows the adopted vehicle, the heaviest (44 tons) that can circulate on the viaduct without special authorizations. The vehicle moved with three different speeds (i.e. 20, 40 and 60 km/h), on a known trajectory, either on driving or on overtaking lanes. Seven months after the tests, the viaduct was re-paved, suggesting the existence of degraded pavement conditions during the tests.

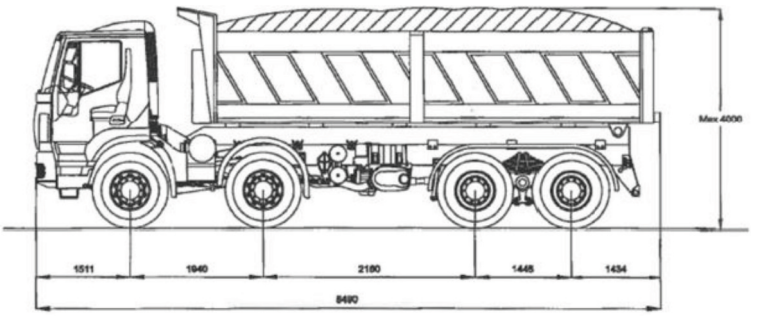


Figure 4. Geometric characteristics of the vehicle (units: cm).

Figure 5 shows the time history of the vertical acceleration of two sensors at the second span midspan, on the right beam (Figure 5a, b) and on the left beam (Figure 5c, d). The first two plots refer to the transit of the truck on the driving lane; for the last two, the truck is moving on the overtaking lane. In both cases, the signal refers to the sensor closer to the moving vehicle. The vehicle travels at 40km/h for cases (a) and (c) and at 60 km/h for cases (b) and (d). Even though the magnitude of the max acceleration appears independent on the vehicle speed, a different shape is found for the two speeds. The response of the left beam during the overtaking test (Figure 5c,d) is remarkably smaller than the one of the right beam during the driving test (Figure 5 a, b).

3 NUMERICAL MODELLING: ROUGHNESS AND VEHICLE

Experimental profiles provide a more realistic and smoother description of the road surface roughness, while numerical ones, generated by assigning random phases to amplitudes respecting a given Power Spectral Density (PSD) function of the roughness, describe different situations with a variation of the PSD parameters. This work adopts the PSD function G_d proposed by Eurocode1:

$$G_d(n) = G_d(n_0)\left(\frac{n}{n_0}\right)^{-w} \tag{1}$$

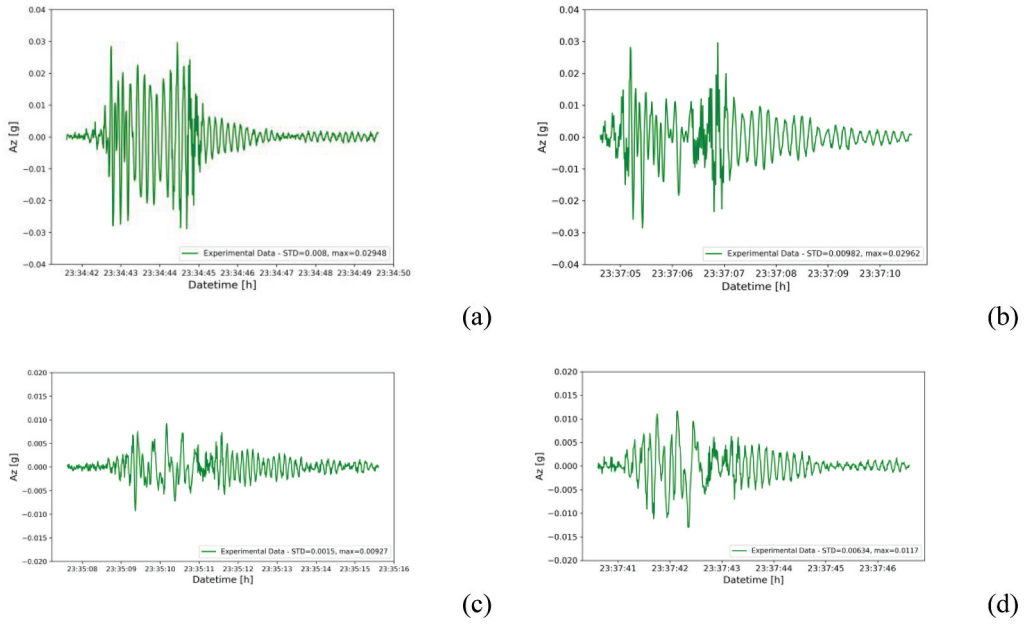


Figure 5. Vertical acceleration at 2nd span midspan for a vehicle moving on the driving lane at (a) v=40 km/h; (b) v=60km/h and for a vehicle moving on overtaking lane at (c), v=40 km/h; (d) v=60 km/h.

where n_0 = 0.1 cycles m^{-1} is the reference spatial frequency, $G_d(n_0)$ is the corresponding value of the spectrum, and w is an exponent equal to 2. EC1 provides parameters value for roughness classes. In this work, only the first five (from A to E) are considered, listing very good, good, medium, poor and very poor pavement roughness. Class A pavements correspond to a newly paved highway, while the B-C values can be considered as a lower limit for main roads. Figure 6a shows four profiles at the border between classes A and B, B and C, C and D and D and E. Figure 6b shows three class B profiles generated with different seeds. Class C is not allowed by standard codes for the paving of bridges and highways, but is still acceptable for main classes of roads; the lower limit for the case study is hence the class B.

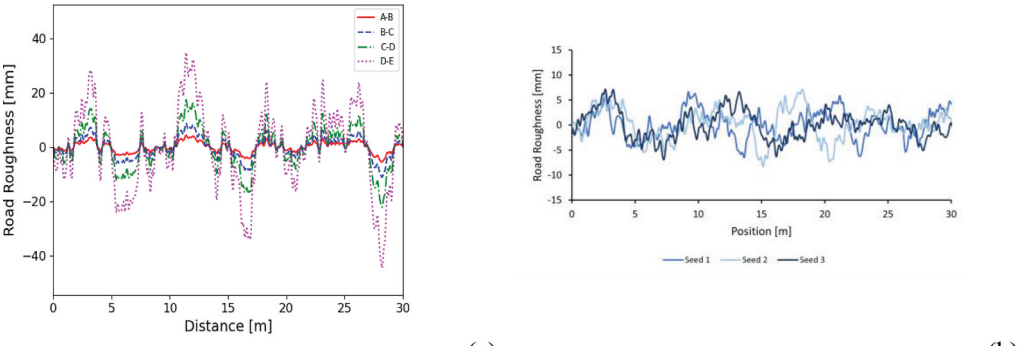


Figure 6. Roughness profiles: (a) different classes, same seed; (b) class B, three different seeds.

A 3-D mechanical system with 13 DOFs (Figure 7) was developed in this work, to simulate the truck adopted in the dynamic tests (Gou et al, 2001). The model has four independent axes and two rigid masses, the engine and the trailer, connected through a 3D hinge. Each body is connected, through the suspension system (a spring/dashpot device), to four unsprung

masses that in turn are connected to the ground through another spring/dashpot device representing the tires.

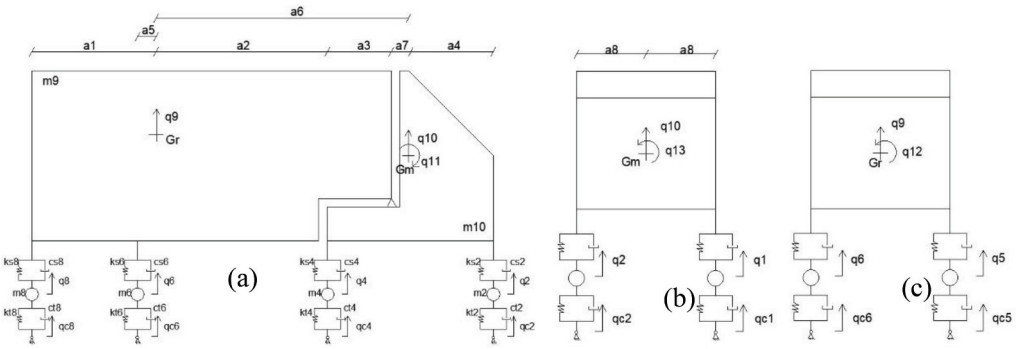


Figure 7. 13-DOF model of the truck: (a) lateral view; (b) front view; (c) rear view.

Each tire has a vertical DOF that is constrained to move as the corresponding contact point on the bridge. The equation of motion of the system is derived under the following assumptions: (a) the vehicle travels at a constant speed along a straight line parallel to the bridge axis; (b) horizontal and vertical motion are uncoupled; (c) a perfect contact takes place at massless points; (d) only vertical contact forces are transmitted at contact points.

4 NUMERICAL SIMULATION OF INTERACTION

In this work, the VBI coupled problem is solved by deriving the coupled equation of motion and subsequently devising an uncoupled iterative solution procedure. In this way, bridge and crossing vehicle are analyzed separately: the vehicle is subjected, on its wheels, to roughness and bridge motion and the bridge is subjected to vehicle's contact forces. Under the assumptions listed at the end of the previous paragraph, Lagrange's equations allows to define mathematically the problem of vehicle-structure interaction with a system of ordinary differential equations:

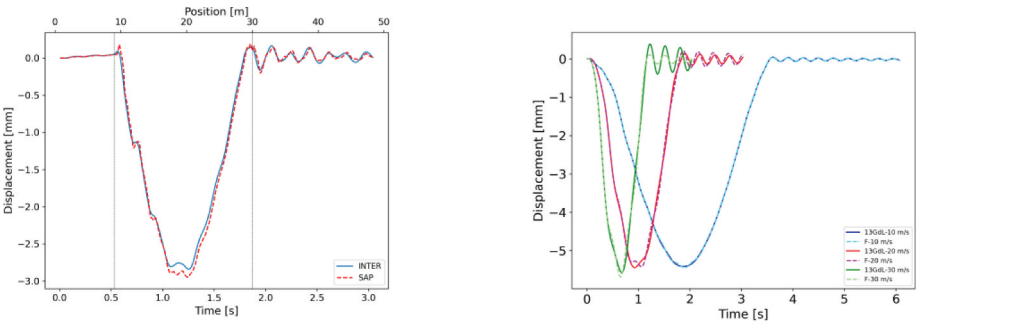
$$\frac{d}{dt}\left(\frac{\partial T}{\partial \dot{q}_k}\right)+\frac{\partial V}{\partial q_k}+\frac{\partial D}{\partial \dot{q}_k}=0 \;\; k=1,\ldots,n_{dof} \tag{2}$$

In Equation (2), T is the total kinetic energy of the system composed of bridge and crossing vehicles, V is the potential energy of the same system and D is the dissipation function that accounts for energy dissipation due to both the bridge and the vehicle masses motion. The equation of motion obtained in this way describes the coupled vehicle-structure behavior. The assumption of massless contact points uncouples the mass matrix of the coupled system. The system of equations is solved through a forced decoupling of the equations (obtained by moving to the right-hand side both coupling and time-dependent terms) associated to an iterative procedure, established at each step of the time history. Convergence is achieved when, at two subsequent iterations, the value of contact forces at the system interface is within a prefixed tolerance (Feriani et al. 2008, 2010). This work adopts a recent version of the code INTER (Maneo, 2016).

In this work, the potential of the iterative procedure is fully exploited through a numerical interface in MATLAB© between SAP2000 and INTER. The MATLAB© code reads the relevant data of the SAP2000 FE model and, after same manipulation, writes them in a format compatible with the code INTER. Data includes the structural matrices, the coordinates of nodes and the numbers of equation associated to each DOF of each node. An extensive

validation has been performed on the transfer procedure, by adopting several FE models. As an example, Figure 8a reports the time history of the vertical displacement at midspan of the 2nd span, due to a vertical force of 400kN travelling along the bridge axis at a speed of 60 km/h. The two vertical dashed lines mark the time instants when the travelling force enters and exits the span. The agreement between the numerical response of the two codes is excellent: the small discrepancies can be tied to the different algorithm adopted by the two codes to subdivide (and to transfer) the applied force to the mesh nodes, that are generally different from the contact point.

The 13-DOF vehicle validation is performed on the FE model of a 30m long bridge (Feriani et al 2008, 2010). The vehicle travels along the bridge axis, at three different speeds, namely 10, 20 and 30 m/s, and over a smooth profile (no roughness). Figure 8b shows the results for the time history of the midspan displacement: at each speed, results are practically coincident with those generated by a set of forces equal to the static values of contact forces transmitted by each wheel, thus validating the derivation and implementation of the new vehicle model.



(a) (b)

Figure 8. Validation of the research code, time history of midspan displacement: (a) INTER vs. SAP: force travelling along the bridge axis; (b) 13-DOF vehicle and static forces transmitted by the vehicle travelling along the bridge (Feriani et al. 2008, 2010) axis.

5 RESULTS

The dynamic analysis aiming to detect the roughness effect on the response has been tackled by means of a probabilistic approach, not having any knowledge beforehand of profile measurements in site. The focus of the analysis is to determine a plausible roughness class from the direct comparison of the experimental vertical acceleration time-history and its numerical counterpart, which combines the structural responses due to twenty separate analyses for each roughness class. The code INTER allows the user to account for the variations of roughness in the longitudinal direction, with the adoption of semi-random profiles, as well as in the transverse direction, by assigning a different profile to the vehicle's left and right wheels. Hence, each analysis is characterized by the adoption of different profiles, while remaining in the same roughness class.

In this work only the analyses referring to the tests at 60 km/h are considered, as this is the speed that resembles the most the actual service conditions of the structure. In fact, the other four tests have been exploited mostly as validation of the obtained results and are not shown here for the sake of brevity. In addition, separate analyses are carried out for the dynamic tests on the two lanes, which form the deck of the bridge, due to the different level of acceleration recorded.

Figures 9a, b shows (in dark green) the experimental vertical accelerations, recorded at the 2nd span midspan, due to the truck moving over the driving lane and the overtaking lane, respectively. Each signal is recorded by the sensor closer to the moving vehicle. The results indicate that the roughness conditions on the two lanes differ quite noticeably. The numerical counterpart of the test is obtained by extracting, at each time instant, the maximum and

minimum values of the results of the twenty analyses adopting profiles belonging to the same class. Hence, a numerical "fuse" (in light green) is obtained, and the fuse that better matches the experimental results is chosen. For the driving lane, numerical and experimental accelerations are in agreement if the selected profiles belong to the geometric mean of the regularity class B, while for the overtaking lane the target has been set to the geometric mean of class A. This outcome may be explained with the different traffic conditions on the two lanes, as the majority of heavy vehicles stays on the right side of the deck, causing a more concentrated and extended decay of the regularity conditions of the road surface.

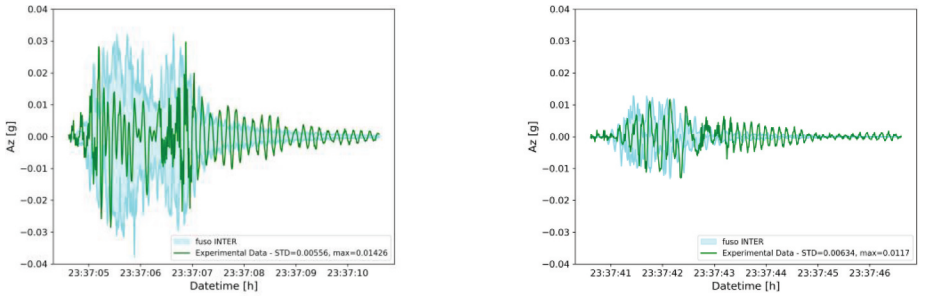


Figure 9. Vertical acceleration at the 2nd span midspan, truck traveling at v=60km/h: (a) on the driving lane, numerical fuse due to geometric mean of roughness class B; (b) on the overtaking lane, numerical fuse due to geometric mean of class A.

6 CONCLUSIONS

Aim of this work was to investigate the effect of the pavement roughness on the experimental response of a highway bridge, a relevant issue from the maintenance point of view. The preliminary work here shown was focused on the numerical simulation of experimental tests, where a truck crosses the bridge. The results have shown that, even though the experimental results cannot be reproduced exactly, due to the lack of knowledge of the real roughness profile and the imperfect knowledge of the truck mechanical properties and trajectory, it is possible to identify the roughness class of the pavement from the bridge response. This result validates the numerical procedure and suggests further developments, based on the continuous monitoring data available.

As shown here, recorded accelerations can differ considerably based on the pavement conditions. As a final aim of this research work, the SHM data analysis should first individuate a set of synthetic parameters able to classify the level of recorded acceleration. Second, the parameters values should be connected to a roughness class. While a poor quality of roughness reduces the safety of passing vehicles, denoting the need for maintenance, care must be taken in the data analysis, since road roughness represents a further confounding effect in the evaluation of structural response, in addition to thermal conditions (Darò et al, 2023). The reason for any variation of the dynamic behavior should be investigated, to avoid erroneous interpretations. In this respect, the analysis of data in the frequency domain should always be performed.

Further studies will focus on the analysis of data of the continuous SHM system. Even though not shown here for the sake of brevity, a preliminary comparison of accelerations recorded before and after a re-paving intervention was performed. Synthetic but significant parameters that can be easily extracted from the records, as peak values, standard deviation and RMS, were able to catch the different pavement quality, showing the feasibility of the procedure just suggested.

CREDITS

This paper stems from the work performed by M. Riso and A. Sgambati during their MS thesis in Civil Engineering at Politecnico di Milano, under the guidance of M.G. Mulas. Data

on the bridge (FE model and experimental data) are due to Francesco Basone and Monica Longo of Sacertis Srl, where M. Riso and A. Sgambati performed a stage period. The contribution of former students R. Pantalena, T. Carta and L. Candido in developing the code INTER is gratefully acknowledged.

REFERENCES

Bhetuwal, U & Shrestha, JK & Pradhananga, R. 2022. *Fatigue life analysis of steel–concrete composite bridge considering road surface conditions*. Innovative Infrastructure Solutions, 7:124, https://doi.org/10.1007/s41062-021-00730-7.

Eurocode 1. 2003. *Actions of structures. Part 2. Traffic loads on bridges*, EN 1991-2, Annex B3.

Darò, P & De Cicco, B & La Mazza, D & Longo, M & Chiariotti, P & Manzoni, S & Cigada, A & Mancini, G. (2023). *Thermal effects on bridges dynamic behaviour*. EVACES 2023, LNCE 432, 748–757, 2023.

Feriani, A.& Mulas, MG & Lucchini, G. 2008. *Vehicle-bridge dynamic interaction: an uncoupled approach*, in Proc. of ISMA 2008, Editors P. Sas, M. De Munck, 609–624, Paper ID 142.

Feriani, A & Mulas, M. G.& Candido, L. 2010. *Iterative procedures for the uncoupled analysis of vehicle-bridge dynamic interaction*, Proc. of ISMA 2010, Editors P. Sas, B. Bergen, 1371-1386, Paper ID 576.

Guo, WH & Xu, YL. 2001. *Fully computerized approach to study cable-stayed bridge-vehicle interaction*, Journal of Sound and Vibration, 248(4), 745–761.

Lin, H & Xiang, Y & Yang Y & Gao, C. 2022. *Fluid-vehicle-tunnel coupled vibration analysis of a submerged floating tunnel based on wake oscillator model*. ASCE J of Waterway, Port, Coastal, and Ocean Engineering, 148(1): 04021037. https://doi.org/10.1061/(ASCE)WW.1943-5460.0000677.

Maneo, A. 2016. *Procedure di integrazione iterative nell'analisi dell'interazione veicolo-struttura*, MS Thesis, Politecnico di Milano, Italy (in Italian).

Mulas, MG & Martinelli, L & Palamà, G. 2018. *Dynamic interaction with travelling vehicles in a submerged floating tunnel*. IABMAS 2018. CRC Press, Taylor & Francis Group, 838–844.

Paraskeva, TS & Dimitrakopoulos, EG & Zeng, Q. 2017. *Dynamic vehicle–bridge interaction under simultaneous vertical earthquake excitation*. Bull Earthquake Eng. 15:71–95. DOI 10.1007/s10518-016-9954-z.

Stoura, CD & Dimitrakopoulos. EG. 2020. *Additional damping effect on bridges because of vehicle-bridge interaction*, J of Sound and Vibration, Volume 476, 115294.

Yang, D & Zhan, Y & Zhang, J & Au FTK. 2022. *Iterative reference-driven S-transform time-varying parameter identification for bridges under moving vehicle*. J of Sound and Vibration 517, 116477.

Yang, YB & Lin, CW & Yau, JD. 2004. *Extracting bridge frequencies from the dynamic response of a passing vehicle*, J. of Sound and Vibration, 272, 471–493.

Yang, YB & Yang, JP. 2018. *State-of-the-Art Review on Modal Identification and Damage Detection of Bridges by Moving Test Vehicles*. Intl J of Structural Stability and Dynamics, 18 (2), 1850025 (31). DOI: 10.1142/S0219455418500256.

Zhu, XQ & Law, SS. 2015. *Structural health monitoring based on vehicle-bridge interaction: Accomplishments and challenges*, Advances in Structural Engineering, 18(12), 1999–2015.

SS04: Advances in machine learning and data-driven system identification techniques for structural health monitoring

Organizers: J. Diaz-Rozo, C. Bielza, C. Ocampo-Martinez & P. Larrañaga


Taylor & Francis
Taylor & Francis Group
http://taylorandfrancis.com

Bridge Maintenance, Safety, Management, Digitalization and Sustainability – Jensen, Frangopol & Schmidt (eds)
© 2024 The Author(s), ISBN 978-1-032-77040-6
Open Access: www.taylorfrancis.com, CC BY-NC-ND 4.0 license

Long-term performance evaluation of low-cost sensors using AI-driven tools

F. Lozano-Galant, S. Emadi & S. Komarizadehasl
Universitat Politècnica de Catalunya BarcelonaTech, Barcelona, Spain

J. González-Arteaga
Universidad de Castilla-La Mancha, Cuenca, Spain

Y. Xia
Tongji University, Shanghai, China

J.A. Lozano-Galant
Universidad de Castilla-La Mancha, Ciudad Real, Spain

ABSTRACT: In civil engineering and architectural applications, Micro Electro-Mechanical System (MEMS) accelerometer-based inclinometers are widely used due to their cost-effectiveness. However, a major challenge associated with these devices is their long-term durability and reliability. Typically, commercial inclinometers are employed to calibrate low-cost solutions over time, which ultimately increases monitoring costs and significantly reduces their economic advantages. To address this limitation, this paper presents a novel approach based on Artificial Intelligence (AI) to evaluate the long-term performance of the low-cost inclinometer called LARA (Low-Cost Adaptable Reliable Anglemeter). This AI-driven tool utilizes a Multilayer Perceptron to predict the inclination of a monitored steel structure under real environmental conditions. By comparing the predicted results with actual on-site measurements, potential inaccuracies in the low-cost inclinometer can be automatically detected, indicating the need for recalibration. The effectiveness and applicability of the proposed tool are demonstrated through a study conducted on a real steel frame located in Spain. This study demonstrates how the AI-based approach can enhance the assessment of the low-cost inclinometer's performance and its suitability for long-term monitoring of real structures.

1 INTRODUCTION

In the midst of the fourth industrial revolution, often referred to as Industry 4.0, civil engineering and architecture are experiencing profound changes (Alaloul et al. (20202)). These disciplines are being reshaped by the digital era, altering traditional methodologies for planning, designing, constructing, and maintaining infrastructures and buildings. Leading this paradigm shift are sophisticated technologies like Artificial Intelligence (AI), which have the capability to perform tasks traditionally dependent on human intelligence. AI tools include a wide range of applications.

Structural health monitoring (SHM) stands as a highly promising area of research within civil engineering and architecture, aimed at enhancing the safety and reliability of structures. Traditionally, SHM techniques rely on sensors and physical inspections to evaluate the health of the infrastructures. However, the development of AI technologies is transforming SHM into a more dynamic and anticipatory field. A review of the application of AI tools in bridge SHM applications was presented in Sun et al. (2020).

DOI: 10.1201/9781003483755-177

Sensors play a key role in SHM applications by enabling the collection of real-time data on-site. Among the most common sensor types are structural sensors like accelerometers and inclinometers, and environmental sensors for measuring the environmental temperature. Nevertheless, the high costs of traditional commercial monitoring solutions often restrict their use in conventional structures, where most structural pathologies are found. To tackle this challenge, a variety of low-cost monitoring solutions have been developed over the past decade. In addition to their reduced cost, these devices are also traditionally distinguished by their versatility and adaptability. Among the wide array of low-cost monitoring devices, inclinometers, also known as tilt sensors, deserve special attention for their widespread application across structural SHM applications.

A cost-effective method for measuring inclinations documented in the literature, involves the use of Micro-Electro-Mechanical Systems (MEMS) accelerometers. Nevertheless, this monitoring approach also comes with certain inherent technological challenges. Primarily, these devices necessitate periodic calibration to ensure precision and are prone to drift, which can compromise the reliability of their readings without consistent recalibration. Additionally, their sensitivity to environmental factors like temperature and humidity may adversely affect their accuracy. Moreover, low-cost sensors typically have a reduced operational lifespan, leading to greater maintenance and replacement expenditures over time. To mitigate these issues, various artificial intelligence applications have been explored in a number of works. For example, Podder et al. (2023), proposed an artificial intelligence application for MEMS-Based Sensors and manufacturing process optimization, Guo et al. (2023), studied the temperature drift compensation of a MEMS accelerometers, Pan et al. (2010), used neural network to compensate a quartz accelerometer, and Hoang et al. (2020) applied an AI tool to improve the inclination measurement of a MEMS accelerometer.

A principal challenge associated with low-cost inclinometers is to assure their long-term durability. For accurate and consistent operation over extended periods, it is often necessary to validate their precision against more expensive commercial alternatives. This requirement for on-site validation leads to an increase in the monitoring expenses, thus diminishing the cost-benefit of utilizing low-cost devices. To address this issue, the present study introduces an AI-based methodology designed to validate the long-term performance of low-cost inclinometers. This methodology correlates the historically predicted responses for different environmental conditions, to autonomously detect inaccuracies in the inclinometer readings. This approach eliminates the need for expensive monitoring instruments by leveraging exclusively on structural and environmental data, specifically humidity and temperature, collected through low-cost sensors. The application of the proposed methodology is applied to the low-cost inclinometer Low-Cost Adaptable Reliable Anglemeter (LARA) (Komarizadehasl et al. 2022) and it is validated through the long-term monitoring of a real steel frame located in Spain.

The structure of this paper is as follows: Section 2 reviews the main features of the low-cost inclinometer LARA, detailing its design and essential components. Section 3 introduces a new AI tool designed to assess the impact of environmental factors, namely temperature and humidity, on the inclination measurements provided by LARA. The implementation of this methodology is demonstrated in Section 4 through the analysis of a real steel frame. Finally, the main conclusions are drawn in Section 5.

2 LOW-COST ADAPTABLE RELIABLE ANGLEMETER (LARA)

LARA (Figure 1), acronym for Low-cost Adaptable Reliable Anglemeter, refers to a monitoring device designed to measure structural parameters (accelerations or inclinations). Unlike most low-cost accelerometers in the literature, LARA possesses a distinctive feature: it can be remotely configured to operate as either a triaxial accelerometer or inclinometer (Komarizadehasl et al. 2022). When functioning as an inclinometer, LARA utilizes the gyroscopes within its accelerometers along the X, Y, and Z axes to determine the orientation with respect to the gravitational force. LARA working as inclinometer can reach a precision of up to 0.002º working in the static mode for a measurement range between 0º and 4°.

LARA consists of five precisely aligned and synchronized MPU9250 chipsets, complemented by a multiplexer. Each MPU9250 chipset is equipped with an accelerometer, gyroscope, and magnetometer, enabling comprehensive data collection and analysis. LARA employs a strategy to enhance its performance by averaging measurements from the five MPU9250 sensors, all operating together with a multiplexer TCA9548A. This approach effectively improves the accuracy of the reference low-cost sensor, MPU9250, from 0.055° to 0.002°. These sensors are connected to an Arduino Due board microcontroller functioning as a data conditioner, and to a Raspberry Pi single-board computer.

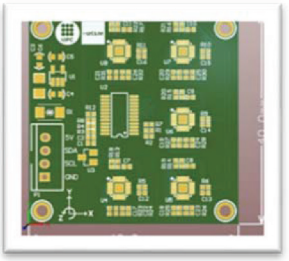


Figure 1. LARA monitoring system.

This monitoring solution is designed as a user-friendly Internet of Things (IoT)-based sensor, simplifying the setup process. Once the sensor is installed on a structure, it only requires connection to a 5V, 2.5A battery or a power source through the Raspberry Pi adapter to send wirelessly throught the internet the measured information according to programmed settings.

3 ARTIFICIAL INTELLIGENCE TOOL

In this section, a novel Artificial Intelligence (AI) tool, designed to analyze the impact of environmental factors such as temperature and humidity on inclination measurements is introduced. The subsequent sub-sections provide detailed descriptions of the tool's principal features, its architecture, and the methodology employed in its training.

3.1 *Multilayer perceptron architecture*

The developed AI tool is based on a Multilayer Perceptron (MLP), a class of artificial neural network characterized by its sequential multi-layered arrangement of neurons. MLPs are defined by their feedforward structure, wherein data moves unidirectionally from input to output layers, without any loops or cycles within the network. With an adequate number of hidden neurons and properly curated training data, MLPs have the capability to approximate any continuous function with the desired accuracy.

The MLP was based on the scikit-learn package Pedregosa et al. (2011), a comprehensive open-source machine learning library. This tool includes a powerful data preprocessing algorithm, which include but are not limited to, feature scaling, categorical variable encoding, missing values imputation, and feature selection. Furthermore, its compatibility with other Python libraries facilitates efficient data handling and visualization, which is crucial during the model development and deployment stages.

The designed MLP models aim to forecast X-axis inclinations of LARA by analyzing LARA's Y-axis rotations, along with temperature and humidity readings from low-cost environmental sensors. Once trained, the model can be applied to detect irregular measurements through a comparison between its predictions and the actual X-axis rotations recorded by LARA. A discrepancy between these predicted and observed rotations may signal an error (such as calibration errors, unaccounted external loads, or potential structural damages).

Future work will focus on enhancing the method's capability to distinguish between these errors.

The configuration of the input layer, hidden layers, activation functions, output layer, and solver in the MLP proposed for this study are outlined below:

- Input Layer: The input layer is composed of three neurons that process the normalized data for on-site Y-axis rotations, temperature, and relative humidity. The Y-axis rotations are recorded by LARA, while temperature and humidity are monitored using the low-cost sensor SHT22, which is widely used in a variety of research applications (see e.g. Mobaraki et al. (2022)).
- Activation Functions: The rectified linear activation function (ReLU), obtained from the scikit-learn library, is the chosen activation function for the neurons.
- Output Layer: The output layer is comprised of a single neuron that outputs the LARA-measured X-axis rotations.
- Solver: The 'adam' solver from the scikit-learn library is selected.

A typical architecture of the proposed MLP is summarized in Figure 2. This architecture includes two hidden layers, denoted as i and j, with m and n hidden neurons, respectively.

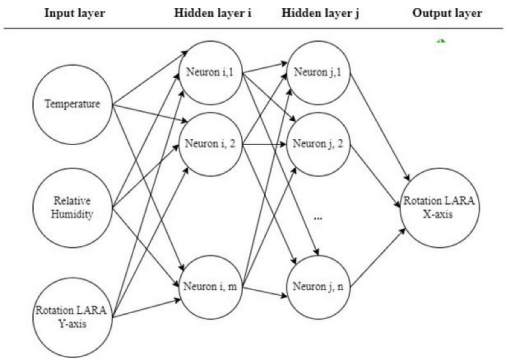


Figure 2. Typical architecture of the proposed MLP.

The following section describes how the network's architecture is customized and trained specifically for the analyzed case study.

4 CASE STUDY

In this section, the main characteristics of case study and the main aspects of its monitoring program, are first described. Then, the developed AI tool is customized for the analysis to check the long-term performance of LARA in this structure. Finally, obtained results are analyzed.

4.1 *Description of the structure and monitoring program*

The case study corresponds with a steel gable frame (Figure 3.a) located at the Institute of Technology at the University of Castilla-La Mancha in Cuenca, Spain. Its dimensions include a length of 11.5 meters and a height of 6 meters. This frame is constructed using HEB 300 columns and IPE 400 beams.

The selection of this building was influenced by its beneficial features for reducing wind impacts. This is due to its ideal placement and the wind-shielding barriers on its roof. Additionally, the roof is mostly subject to sporadic live loads during maintenance, minimizing their effect. Therefore, the main changes in the building's structure are driven by environmental elements like temperature and humidity.

The structures have been under continuous monitoring since it was built in 2008 to assess the effects of differential settlements. The monitoring strategy includes monitoring soil moisture at 27 locations, 4 inclinometers and 4 thermometers. A detailed explanation of the results of the monitoring program is presented in González-Arteaga et al. (2019). The gable frame under study was monitored with an inclinometer model EL Tiltmeter SC. This device provides measurements of both one-axle inclinations and temperatures with 1 arc second and 30×10-5°C resolutions. This inclinometer, as shown in Figure 3.b, was positioned at the connection between the beam and the column, and it records readings at 15-minute intervals.

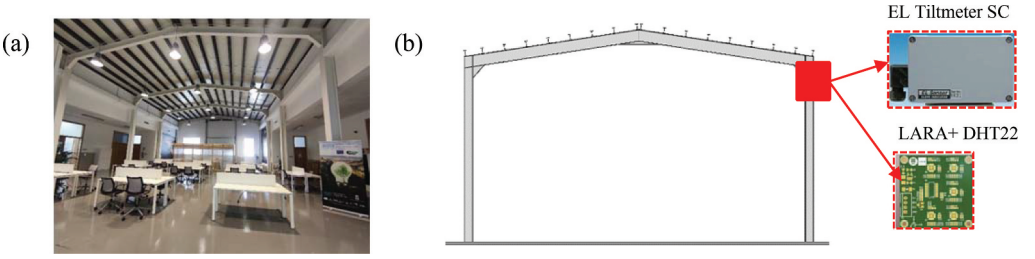


Figure 3. Monitored steel gable frame and inclinometer location.

The low-cost monitoring solution incorporated in this structure consisted of two sensors: (1) LARA, which measures inclinations in three axes, and (2) DHT22, which measures environmental temperature and humidity. Both sensors were installed at the same location as the commercial inclinometer as indicated in Figure 3.b. The reading interval for both sensors is set at 15 minutes to facilitate comparison with the commercial inclinometer. Additionally, both sensors were connected to the electrical power supply of the building.

To illustrate, Figure 4 presents the inclinations and temperatures measured by the commercial inclinometer on February 20th, 2023. The analysis of this figure highlights the significant influence of temperature on the rotations of the structure.

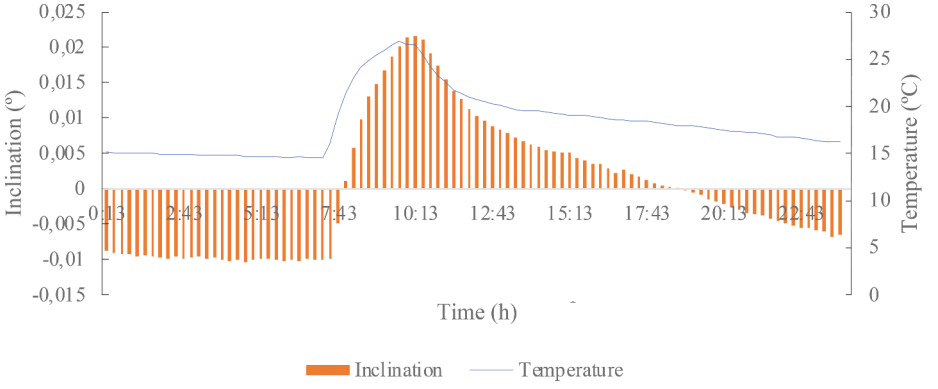


Figure 4. Evolution of temperature and inclination in one day (February 20th 2023).

Figure 5 Presents a comparison of the inclination data recorded by a commercial sensor versus the data from LARA during a monitoring period of three days, from the 20th to the 22nd of February 2023. The examination of this data reveals that while LARA has a relatively lower precision, both sensors display comparable patterns in detecting the influence of environmental factors over time. It is important to highlight that in this research, the commercial inclinometer's function is strictly to confirm the accuracy of LARA's measurements, facilitating the calibration process for the MPL developed in the next section. The Standard Deviation, SD and the Mean Square Error, MSE, obtained from the comparison of LARA and the commercial sensor are 0.02408 and 0.00058, respectively.



Figure 5. Comparison of the inclinations between EL Tiltmeter SC and LARA From February 20th to February 22nd, 2023.

4.2 *AI Tool*

After empirical analyses, the MLP was designed with a consistent structure of three hidden layers, each layer housing 5 neurons. Additionally, the learning rate was set at 0.0001 to enhance the efficiency of the model's training process. The training of this architecture was exclusively based on the information from the low-cost sensors from January 10th till May 17th, 2023, with an interval of 15 minutes. Over this period, a total of 5790 data points, including temperature, humidity, and rotations in X and Y axes, were recorded, and analyzed. This data was randomly divided into the three following sets: (1) a training dataset, which included 70% of the total data; (2) a cross-validation dataset, comprising 15% of the data; and (3) a testing dataset, also making up 15% of the data.

4.3 *Results*

Displays a comparison of the X-axis rotational predictions made by the MLP tool against the actual readings recorded by LARA from the test dataset.

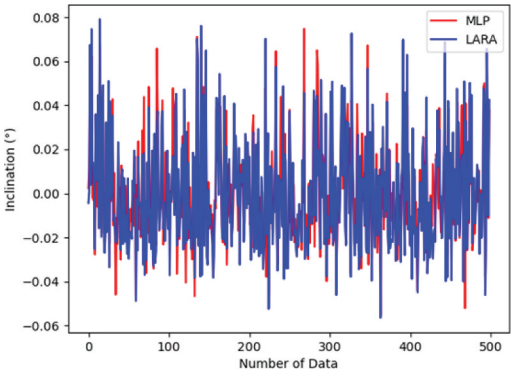


Figure 6. Comparison of the X-axis rotations predicted by the MLP (red) tool and those obtained by LARA (blue) from January 21st to April 1st 2023.

Based on the comparison of the predicted results and those obtained by LARA for the same analyzed period, the Mean Squared Error (MSE), and the Standard Deviation (SD) were calculated. The obtained values were MSE 0.0004, and SD 0.0187.

The probability density of errors with the fitted normal distribution is characterized by a mean of 0.00037 and a SD of 0.0187. This function is presented in Figure 7.

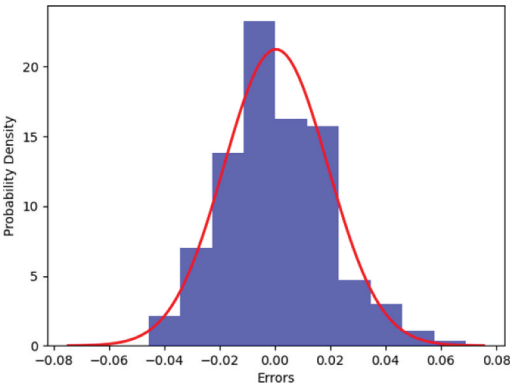


Figure 7. Probability density of errors with fitted normal distribution in the test set.

The calculated MSE values over a predetermined environmental cycle (such as a day) can serve as indicators for the potential necessity of LARA recalibration. This need arises when the acquired values surpass those obtained through a comparison of LARA with a commercial inclinometer.

In Figure 8, the MSE of 10 specific day of March 2023 are displayed. The analysis of this figure shows the reliability of the results obtained as the threshold from the comparison with the commercial inclinometer (MSE of 0.00058) is not exceeded. Exceeding this MSE threshold in the future might indicate the need of recalibration of the low-cost sensor.

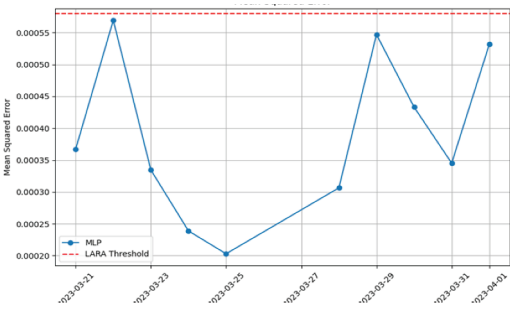


Figure 8. Example of the MSE Of MLP model result from April 21st To 1st Of May 2023.

5 CONCLUSIONS

While Micro Electro-Mechanical System (MEMS) accelerometer-based inclinometers offer cost-effective solutions for civil engineering and architectural applications, their long-term durability and reliability have been a challenge. To address this limitation and avoid the costly calibration with commercial inclinometers, we proposed an innovative Artificial Intelligence (AI)-based approach. The AI-driven tool utilizes a Multilayer Perceptron Neural Network to predict the inclination of a monitored steel structure under real environmental conditions. By comparing the predicted responses with actual on-site measurements, we can automatically

identify potential inaccuracies in the low-cost inclinometer, thus indicating the need for recalibration.

The application of our proposed AI tool is specifically designed for the low-cost inclinometer LARA (Low-Cost Adaptable Reliable Anglemeter) and was demonstrated through a study on a real steel frame. The results highlighted the effectiveness and applicability of the proposed approach, showing its ability to accurately evaluate the long-term performance of LARA under real-world conditions. This innovative approach provides a reliable and cost-efficient solution for monitoring structural inclinations, ensuring the structural health and safety of buildings without compromising on accuracy and reliability. In future works, the application of the developed AI-tool in bridges will be studied.

ACKNOWLEDGEMENTS

The authors are indebted to the projects PID2021-126405OB-C31 and PID2021-126405OB-C32 funded by FEDER funds—A Way to Make Europe and Spanish Ministry of Economy and Competitiveness MICIN/AEI/10.13039/501100011033/, and National Natural Science Foundation of China (52278313).

REFERENCES

Alaloul, W. S. Liew, M. S. Zawawi, a N. A. & Kennedy, I. B. 2020. Industrial revolution 4.0 in the construction industry: challenges and opportunities for stakeholders, *Ain Shams Engineering Journal*, 11(1): 225–230.

González-Arteaga, J. Alonso, J. Moya, M. Merlo, O. Navarro, V. & Yustres, A. 2019. Long-term monitoring of the distribution of a building's settlements: sectorization and study of the underlying factors, *Eng Struct*, 205: 110111.

Guo, G. Chai, B. Cheng, R. & Wang, Y. 2023 Temperature drift compensation of a MEMS accelerometer based on DLSTM and ISSA, *Sensors*, 23(4): 1809.

Hoang M. L. & Pietrosanto, A. 2022. New artificial intelligence approach to inclination measurement based on MEMS accelerometer, IEEE Transactions on Artificial Intelligence, 3(1), 67–77.

Komarizadehasl, S. Komary, M. Alahmad, A. Lozano-GalantJ., A. Ramos, G. & Turmo, J. 2022 A novel wireless low-cost inclinometer made from combining the measurements of multiple MEMS gyroscopes and accelerometers, *Sensors*, 22(15): 5605.

Mobaraki, B. Komarizadehasl, S. Castilla Pascual, F.J. & Lozano-Galant, J. A. 2022. Application of low-cost sensors for accurate ambient temperature monitoring, *Buildings 2022, 12*, 1411.

Pan, Y, Li, Y. Ren, C. & Luo, H. 2010. Study on the compensation for a quartz accelerometer based on a wavelet neural network, *Meas Sci Technol*, 21(10): 105202.

Pedregosa, F., Varoquaux, G., Gramfort, A., Michel, V., Thirion, B., Grisel, O., Blondel, M., Prettenhofer, P., Weiss, R., Dubourg, V., Vanderplas, J., Passos, A., Cournapeau, D., Brucher, M., Perrot, M., Duchesnay, E.: 2011. Scikit-learn: machine learning in Python. J. Mach. Learn. Res. 12, 2825–2830.

Podder, I. Fischl, T. & Bub, U. 2023. Artificial Intelligence Applications for MEMS-Based Sensors and Manufacturing Process Optimization, *Telecom*, 4(1): 165–197.

Sun, L. Shang, Z. Xia, Y. Bhowmick, S. & Nagarajaiah, S. 2020. Review of bridge structural health monitoring aided by big data and artificial intelligence: From Condition Assessment to Damage Detection, *Journal of Structural Engineering*, 146 (5).

Bridge Maintenance, Safety, Management, Digitalization and Sustainability – Jensen, Frangopol & Schmidt (eds)
© 2024 The Author(s), ISBN 978-1-032-77040-6
Open Access: www.taylorfrancis.com, CC BY-NC-ND 4.0 license

Fast bridge health monitoring deployment with transferable expertise

R. Sojo-García
Universidad Politécnica de Madrid, Madrid, Spain
Aingura IIoT, Donostia-San Sebastian, Spain

P. Larrañaga & C. Bielza
Universidad Politécnica de Madrid, Madrid, Spain

J. Díaz-Rozo
Aingura IIoT, Donostia-San Sebastian, Spain

ABSTRACT: Machine learning stands out as one of the most widely researched fields in the industry, where it has demonstrated great abilities to model complex system dynamics. This paper takes advantage of one of those models, Bayesian networks (BNs), for analyzing such dynamics in the infrastructure field. Specifically, bridge health monitoring tasks, which are crucial to prevent from dangerous changes within the structure's behavior and ensure the durability of the bridge. However, such modeling requires to capture a substantial amount of data, which can be time-consuming. Considering this challenge, this work aims to accelerate the deployment of these models through related transferable expertise. This involves leveraging data from similar systems to facilitate the learning process of the network. Specifically, two methods, PC-MAX-TL and DBLogLP, are proposed for estimating the structure and parameters, respectively, of the BN under such settings. PC-MAX-TL is an adaptation of the PC-MAX method (a well-known constrained-based structural learning algorithm) tailored to incorporate auxiliary knowledge, while DBLogLP is based on log-linear pooling principles. To demonstrate the reliability of PC-MAX-TL and DBLogLP, an empirical evaluation will be conducted using data from a real scenario: the San Mamés bridge in Bilbao (Spain). This bridge is composed of six different spans that are evaluated independently, and therefore, can be used to address the data scarcity of a certain target span. Then, the results will be compared against the model estimated just with PC-MAX from two perspectives: graphically, looking at the conditional dependencies found in the BNs; and quantitatively, analyzing (1) the network's mean log-likelihood, and (2) the log-likelihood variance. Thus, we demonstrate the proposed methodology's effectiveness, and justify for this bridge that we can accelerate in some days the deployment of the machine learning-based monitoring system.

1 INTRODUCTION

The construction of infrastructures is one of the ancient fields of human development, for which nowadays there are different devices designed to monitor their health evolution along time. Either in industrial environments or for the daily use of people, these systems are thought to withstand extremely variable loads. Therefore, it is important to carefully sensorize them to avoid changes that could affect the endurance of the structure. Since it is impossible to prevent from all kinds of hazards, the usual way of proceeding is to model the behavior of the system and use machine learning techniques to detect deteriorations, thus performing anomaly detection. When these anomalies are spread over time, the infrastructure's model can experience concept drifts, causing it to no longer behave as it used to. One way of modeling that behavior is through BNs, which allow to represent the dependencies of variables

DOI: 10.1201/9781003483755-178

according to the dynamic response of the system and return a measure of how well the model fits the incoming data. However, a correct analysis depends on the collection of sufficient data, something that could require days or even weeks. This problem can be addressed fusing networks of similar characteristics to accelerate the deployment of the model during the earliest stages of data acquisition. Nevertheless, this solution does not consider the particularities of the new data that, indeed, affects the dynamic response. Two methods, PC-MAX-TL and DBLogLP, are proposed for estimating the structure and parameters of the model that represents the incoming data through transferable expertise based on the similarity of other infrastructures with respect to the model of interest. Then, the proposed methodology will be tested with data from a real scenario, the San Mamés bridge in Bilbao (Spain), and evaluated through different analyses against a model obtained with conventional methods.

The paper is organized as follows. Section 2 provides the necessary knowledge about the different types of BNs covered throughout this paper. Section 3 reviews relevant state-of-the-art approaches related to the fusion and construction of networks as well as other transfer learning techniques. Section 4 details the proposed methodology. Section 5 describes the data, and analyzes the results obtained. Finally, Section 6 concludes the paper.

2 THEORETICAL FRAMEWORK

A BN is a machine learning model denoted as $\mathcal{B} = (\mathcal{G}, \theta)$ that comprises a direct acyclic graph (DAG) $\mathcal{G}$ and a set of parameters θ for which $\mathcal{G} = (V, A)$ is defined as a set of nodes V, and a set of arcs $A \subseteq V \times V$ between these nodes. When these arcs are not oriented, they are called edges E. For learning $\mathcal{B}$ we have a dataset $\mathcal{D}$ with n different variables $\mathcal{X} = \{X_1, \ldots, X_n\}$ and N instances $\mathcal{D} = \{x^{(1)}, \ldots, x^{(N)}\}$. Each arc in A represents a probabilistic dependence between variables, therefore, for each DAG there is a set of conditional dependences and independences embedded in the parameters θ for the conditional probability distribution (CPD) associated to each variable. Then, the joint probability distribution (JPD) of $X_1, \ldots, X_n$ can be factorized using these CPDs. For continuous variables each CPD can be seen as a conditional probability density function (PDF), that can be defined such that:

$$f(X) = \Pi_{i=1}^{n} f(x_i | X_{Pa(i)}) \tag{1}$$

where $\boldsymbol{Pa}(i)$ denotes the parents of X_i in $\mathcal{G}$. We can classify continuous BNs into three main types depending on the assumptions made about the data distribution. These types are parametric, non-parametric and semiparametric BNs.

Parametric BNs assume that the BN can be modeled using a finite number of parameters, where the most popular is the linear Gaussian Bayesian network (LGBN) (Shachter & Kenley, 1989). This type of model assumes that each conditional PDF can be modeled using a Gaussian distribution, for which the mean is a linear combination of some regression coefficients β associated to each node and its parents, and a variance σ^2. On the other hand, non-parametric BNs do not assume any specific distribution for the data. Consequently, there is an unknown, potentially infinite number of parameters in the model. Considering this scenario, Hofmann & Tresp (1996) introduced a non-parametric type based on kernel density estimation (KDE) called KDE BNs. Here, the PDF is estimated taking into account the contribution of each individual instance, becoming a more flexible, but demanding solution, that depends on the training data size and the correct selection of the bandwidth matrix, which acts as a smoothing parameter. Finally, the semiparametric BNs (SPBNs) (Atienza, et al., 2022) encompass both types using Linear Gaussian (LG) CPDs to model parametric relationships, and conditional KDEs (CKDEs) to model the non-parametric ones.

Similarly, there are also different ways of estimating a BN, for which the structure of the data and its corresponding parameters are learnt. There are three main structural learning approaches: constrained-based, which perform conditional independence (CI) tests to assess whether two subsets of variables are conditionally independent given another subset, for instance the PC family methods (PC (Spirtes & Glymour, 1991, PC-Stable (Colombo & Maathuis, 2014) or PC-MAX

(Ramsey, 2016); scored-based, where the best structure is found through an optimization algorithm such as in hill-climbing (HC) (Bouckaert, 1994; and hybrid, where usually the skeleton of the graph is first found through constrained-based methods, and then a scored-based algorithm is used to orientate the edges. Then, depending on whether the CPDs of the nodes are Gausssian or not, the parameters can be obtained through different methods. For this work, we will use the standard maximum likelihood estimate (MLE) or the normal reference rule extended to the multivariate case (Wand, 1992) for bandwidth estimation, respectively.

3 RELATED WORK

Transferring expertise from related problems can be helpful for addressing challenges such as data scarcity or time constraints. This way, we can facilitate the learning process of a new BN taking advantage of the acquired knowledge. However, before exploring the different technologies related to the use of transferable expertise, it is crucial to have some knowledge about the fusion of networks within a specific domain. This process involves the fusion of structures and parameters during the construction of the new network.

Two popular techniques for the fusion of parameters are the *linear pooling* (Stone, 1961) and the *log-linear pooling* (Genest, 1984), for which a weighted arithmetic average and a geometric average are used, respectively, to aggregate the parameters of k models. In terms of structures, the first approach was made in Matzkevich & Abramson (1992) with FUSE_-DAGS. Here, given two DAGs $\mathcal{G}_1$ and $\mathcal{G}_2$, the fusion of structures is performed as the union of their nodes and intersection of their arcs, i.e., $\mathcal{G}_3 = (V_1 \cup V_2, A_1 \cap A_2)$. On the other hand, since the structural fusion usually requires a common topological order among the nodes, two methods for transforming a DAG $\mathcal{G}$ into another given a topological order of nodes were introduced in Matzkevich & Abramson (1993). However, Peña (2011) later critiqued these methods and proposed a set of corrections as well as a complexity analysis. Alternatively, Puerta, et al. (2021) proposed a transformation algorithm and a heuristic search to identify and establish the optimal order, whereas Feng, et al. (2014) introduced a set of desirable properties to any DAG, like avoiding cycles and preserving the conditional independencies. Considering these properties, they proposed a set of addition and deletion rules for the structure learning together with a fuzzy fusion (Liu & Song, 2001) for the parameter aggregation.

Moving to the transferable expertise, we will refer to the model of interest as the target $\mathcal{G}_0$, and the K models for which we have enough data as the auxiliary tasks $\mathcal{G} = \{\mathcal{G}_1, \ldots, \mathcal{G}_K\}$. One of the most important contributions to the state of the art is the work conducted in Luis et al. (2010), where they proposed a modification of the PC algorithm, PC-TL, that linearly combines the information provided by different tasks with the target. This combination is performed considering just the most similar task on each iteration of the learning process. Additionally, they proposed two methodologies for aggregating the parameters, the distance based linear pool (DBLP) and the local linear pool (LoLP). Jia et al. (2010) extended this approach to a soil fertility grading issue by considering, not only the similarity, but also the geographical position of land squares, where it adjusts the weight factors of the linear combination based on the geographical position. Recent contributions such as Hou, et al. (2022) introduce a varying coefficient for parameter learning that adjusts the dependence on the target as the available data increases, whereas Hao et al. (2021) proposed an updating BN model for virtual machines performance estimation, where the structure and parameters are updated according to a re-weighting of the data based on the model performance.

4 METHODOLOGY

The structure learning process of this method is mainly constrained-based although it additionally uses HC to eliminate possible cycles and orient the remaining edges. We refer to it as the PC-MAX-TL algorithm. PC-MAX-TL has been adapted to work without any constraint with both Gaussian and non-Gaussian variables, for which LGBNs and the Fisher's Z test are used in the Gaussian case, and SPBNs and the conditional correlation independence (CCI)

test (Ramsey, 2014) in the non-Gaussian. In addition, we present the distance-based log-linear pooling (DBLogLP), which is an aggregation method based on DBLP for the fusion of parameters. This novel aggregation method has the advantage of preserving the conditional independencies and addresses the fusion of PDFs for both Gaussian and non-Gaussian domains. The steps that describe the complete learning process are the following:

1. PC-MAX phase.
   a. Global similarity estimation.
   b. PC-Stable adjacency phase.
   c. Max p-value orientation.
2. HC phase.
   a. Generation of a new fused dataset $\mathcal{D}_f$ for the edge orientation.
   b. Cycle detection. If no cycle is detected use HC to orient the edges, otherwise handle the conflicting arcs and then orient.
   c. Return the best DAG.
3. MLE and DBLogLP for aggregating the target and the auxiliary tasks parameters.

4.1 *PC-MAX-TL*

PC-MAX-TL can be seen as a hybrid learning method with strong constraints into the search space of HC. First, it uses a constrained-based approach that takes advantage of the proposed methodology for PC-TL and one of the algorithms from the PC family, PC-MAX, to analyze the conditional dependencies of the graph. Then, a second phase uses the score and search method HC to address typical problems of this kind of algorithms.

Among the contributions proposed by PC-TL to find a better $\mathcal{G}_0$, there is a metric to measure the similarity S_k between a given auxiliary task and the target. This metric is calculated as the product of a global S_{g_k} and a local S_{l_k} similarities, and used to get the task with the highest value, i.e. the closest task, during the PC adjacency phase. These similarities are defined as:

$$S_{g_k} = dep_k + ind_k, S_{l_k}(X, Y|S) = \begin{cases} 1 \; if \; I_0(X, Y|S) = I_k(X, Y|S) \\ 0.5 \; if \; I_0(X, Y|S) \neq I_k(X, Y|S) \end{cases} \tag{2}$$

$$S_k(X, Y|S) = S_{g_k} \cdot S_{l_k}(X, Y|S) \tag{3}$$

where dep_k and ind_k are respectively, the number of common conditional dependencies and independencies between $\mathcal{G}_k$ and $\mathcal{G}_0$, and $I_0(X, Y|S)$ and $I_k(X, Y|S)$ are the statistics of their CI tests for each pair of X and Y variables conditional on a subset S. Bearing this in mind, $I_F(X, Y|S)$ is defined as the linear combination of the target with its closest auxiliary task:

$$I_F(X, Y|S) = \alpha_0(X, Y|S) \cdot abs(I_0(X, Y|S)) + \alpha_k(X, Y|S) \cdot abs(I_k(X, Y|S)) \tag{4}$$

where *abs(I)* denotes the absolute value of the statistic, and α refers to its confidence factor.

4.1.1 *PC-MAX phase*

The similarity evaluation from PC-TL remains the same for PC-MAX-TL (step 1a). However, to evaluate the edge removals and arc orientations during our PC-Stable adjacency phase (step 1b), it is needed a suitable metric to assess the confidence of each continuous CI test in the combined independence measure. To do so, we kept the reasoning used for the confidence factor α in the original PC-TL, and defined a new confidence factor α_0 such that:

$$\alpha_0 = \frac{N_0}{N_0 + N_k} \tag{5}$$

where N_0 is the size of the target dataset $\mathcal{D}_0$ and N_k the size of the most similar auxiliary dataset $\mathcal{D}_k$. This way, the trust on the target test increases proportionally to N_0, resulting in better independence assessments during the earliest stages of the data acquisition and ensuring

future convergences. On the other hand, we reformulated Equation (4) to use the p-value of the statistic during the arc evaluation such that:

$$p_F(X,\ Y|S) = \alpha_0 p_0(X,\ Y|S) + (1-\alpha_0)p_k(X,\ Y|S) \tag{6}$$

where $p_F(X,\ Y|S)$denotes the combined p-value for each pair of X and Y variables conditional on a subset S. Then, the remaining edges are oriented as possible according to PC-MAX with the combined independence measure (step 1c).

4.1.2 *HC phase*

The result of the PC-MAX phase can be a DAG, although most of the times we end up with a partially directed graph (PDG) that occasionally has cycles. To deal with those situations, we defined the algorithm presented in step 2, where the final orientation is conducted using HC with the k-fold cross-validation log-likelihood score function described in Atienza, et al. (2022). Here, it is important to note that the search space of HC is constrained to the undirected edges that were retained from step 1. Consequently, HC is forced to preserve the arcs of $\mathcal{G}_0$. The cycles are handled by removing one combination of conflicting arcs at a time and adding it into the search space of HC, thereby leaving the decision of either reversing or removing the conflicting arc to the algorithm. However, when $\mathcal{D}_0$ does not contain enough instances the results of the final orientation might be poor due to the lack of information. Therefore, we decided to include a 10% data from the two most similar auxiliary tasks selected throughout the previous phase to address this issue. The result is a new fused dataset $\mathcal{D}_f$ that improves the orientation process leading to better arcs. From this loop, we end with a list of possible DAGs of which the most suitable is selected using the mean of the log-likelihood as a measure of the structure goodness.

4.2 *DBLogLP*

After the structure estimation, the parameters are obtained integrating the knowledge from the target and all the auxiliary tasks. To do so, we obtain a set of initial parameters for each dataset using MLE with the estimated DAG from PC-MAX-TL. This way, it is ensured that the parameters of both target and auxiliary tasks come from the same set of parents, otherwise the aggregation with DBLogLP (step 3) would not be possible. The procedure of DBLogLP first calculates a geometric average of auxiliary parameters that are later combined with those of the target, thereby preserving the conditional independencies. The mean PDF for node i is defined as:

$$\bar{f}(X_i) = \prod_{k=1}^{K} f_k(X_i)^{w_{ki}} \tag{7}$$

where w_{ki} is the weight associated to the auxiliary task k for the PDF of node i. This weight is calculated as the normalized inverse of the maximum Kullback-Leibler divergence (KL) between the auxiliary conditional PDF $f_k(X_i)$ and the target conditional PDF $f_0(X_i)$ (Koliander et al., 2022). Then, the resulting parameters from Equation (7) are integrated with those of the target in the following way:

$$f_0^{'}(X_i) = f_0(X_i)^{c_N}\bar{f}(X_i)^{1-c_N} \tag{8}$$

where c_N is the confidence coefficient that indicates how much to trust the estimations of the target. Similarly to α_0 in Equation (5), this coefficient depends on the number of instances from the target. Therefore, it is obtained as:

$$c_N = \frac{N_0 - N_{min}}{N_{max} - N_{min}},\ 0.25 \leq c_N \leq 0.75 \tag{9}$$

where N_{min} and N_{max} are the normalization factors that must be defined at the beginning of the algorithm. Here, we decided to limit the values of the confidence coefficient c_N to keep the trust in the target parameters between the 25% and 75%. Thus, neither the target is completely ignored, nor the auxiliary tasks. It must be noted that depending on the type of BN, the parameters to be combined are different. For Gaussian nodes, we will have to aggregate LG

CPDs whose parameters are the variance σ^2 and the regression coefficients β, while for non-Gaussian nodes we have CKDEs and the bandwidth matrix.

5 EXPERIMENTS

We will use data from our Aingura Insights Edge device deployed at the San Mamés bridge in Bilbao, Spain. The bridge incorporates a mixed metallic structure with V-shaped supports and consists of six different spans whose characteristics are slightly different, allowing us to categorize them as different structures within a common system (the bridge). The total length of the bridge encompasses 323 m, but each span has a specific length. These lengths are 53 m for spans 1 and 5, 60 m for spans 2, 3 and 4, and 37 m for span 6. Each span has its corresponding dataset, which is composed by different pairs of natural frequencies and damping factors estimated from accelerometers readings by proprietary algorithms deployed at the edge device. These variables capture the dynamic response of the bridge, expressed through natural frequencies characterized by mixtures of Gaussians and damping factors following Gamma distributions. Anyhow, we will evaluate the methodology under both Gaussian and non-Gaussian circumstances. The data used for this purpose was collected between the 23rd of March and the 3rd of May 2023, which represents approximately 1000 vehicles per day. We run one experiment per target span, while the five remaining spans are use as auxiliary data. With respect to the configuration of the experiments, we have selected different significance level for each CI test associated to each BN. In the case of LGBNs and the Fisher's Z test, we use a 0.05 significance level, however, experimentally we found that this level was too restrictive for the CCI test. Hence, in that case, we incremented the value from 0.05 to 0.08. Additionally, N_{min} and N_{max} are set to 20 and 1500 in both LGBNs and SPBNs. Finally, we have selected the first 3000 instances for the training sets of the auxiliary data, whereas the target sample is gradually incremented in batches of 40, starting in 20 until 2000. The remaining data is saved for testing.

That said, the first thing we can notice when we draw the DAG of the standard PC-MAX (Figure 1), is the inability of the algorithm to find relationships between the nodes at the earliest stages of the data acquisition. Besides, the SPBN is unable to correctly assess the type of the nodes in the DAG, where the white nodes are LG CPDs and the grey nodes CKDEs. Here, the natural frequencies 3 and 5, and the damping factors 2 and 4, were set as Gaussian nodes, when as we mentioned earlier they look like mixtures of Gaussians and Gamma distributions, respectively. On the contrary, it can be seen from Figure 2 that PC-MAX-TL is able to address this issue quite effectively. In fact, it correctly captures the dependencies of the natural frequencies establishing arcs from the first two to the third, fourth and fifth, while each of them is paired with its damping factor both in LGBNs and SPBNs (NAT_FREQ and DAMP in the graph).

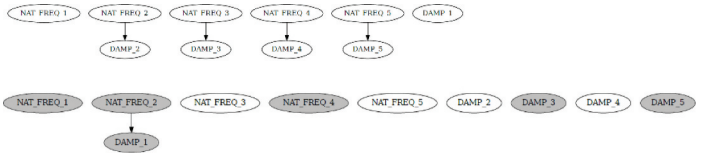


Figure 1. PC-MAX DAG from span 1 with 20 instances. Top: LGBN. Bottom: SPBN.

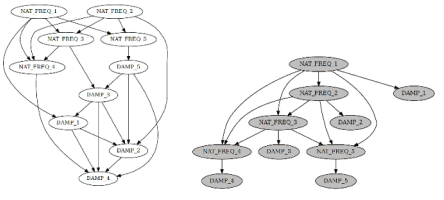


Figure 2. PC-MAX-TL DAG from span 1 with 20 instances. Left: LGBN. Right: SPBN.

As regards the quality assessment of the network in terms of mean log-likelihood (Figure 3), the PC-MAX-TL models (blue lines) exhibit better starting points in general. Then, they maintain the score within a small range of variation, whereas the network alone (PC-MAX) needs some time to reach such level. The convergence of both systems depends on the model, for instance, in span 1 it happens around 1000 and in span 6 it is almost immediately, but around 500 instances most of them have converged or reduced significantly the difference. However, we also see some drops in the means of spans 1 and 5 within the SPBN, as well as span 6 in both LGBN and SPBN. In this case, the issue may lie within the training set. The inclusion of certain portions of noisy data during experiments could be contributing to an increase in the system's variability, consequently resulting in a drop in the score. On the other hand, the SPBNs seem to be more sensitive to this noise than the LGBNs due to their parameter aggregation methodology, which requires the fusion of bandwidth matrices, thereby affecting to the smoothing of PDFs in the CKDE nodes.

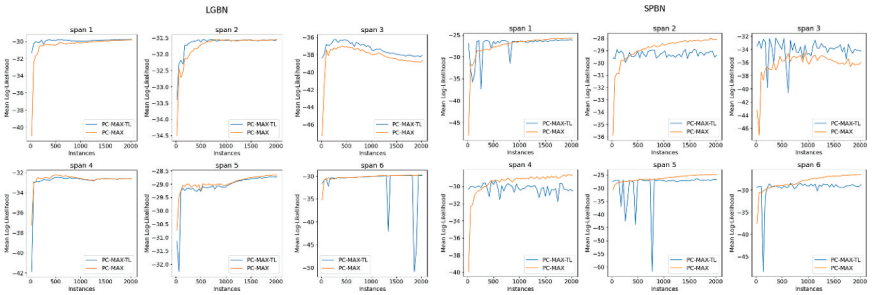


Figure 3. Networks mean log-likelihood. Left: LGBN. Right: SPBN.

Finally, the stability analysis (Figure 4) shows that the deviations of the PC-MAX-TL models (blue lines) exhibit very few variations from the very beginning, returning more stable measures with lower deviations in practically all cases from both LGBNs and SPBNs. In fact, even in the scenarios where the deviation of PC-MAX is lower, the stability tends to converge to the level of PC-MAX-TL, that is the case of spans 2 and 4. Additionally, it can be seen that the drops in the means detailed in the previous paragraph match the peaks in the deviations, which as mentioned, is caused by an increase in the variability of the data. However, even under the presence of noise their stability levels are higher than in PC-MAX. For instance, the deviations of spans 1 and 3 in the SPBN are 10 to 20 units lower.

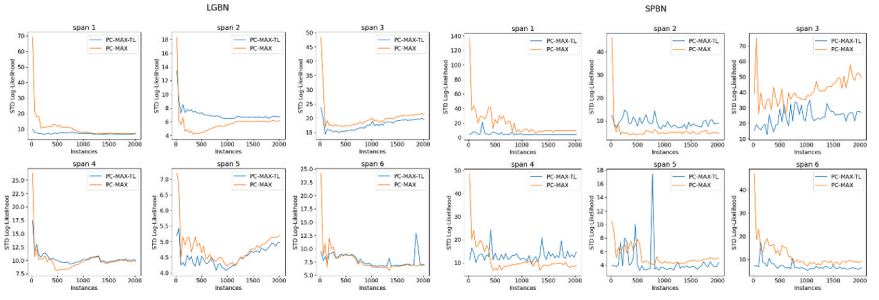


Figure 4. Networks stability. Left: LGBN. Right: SPBN.

6 CONCLUSION

The use of transferable expertise has been the basis of our methodology composed by two novel procedures, PC-MAX-TL and DBLogLP, for which we have reviewed all the aspects involved in the network construction and justify their reliability for building and aggregating models in presence of data scarcity. PC-MAX-TL returns DAGs with much better conditional

dependencies compared to PC-MAX at the earliest stages of data acquisition, and its combination with DBLogLP ensures a much more stable model despite the noise, which is crucial for its application in the industry. The convergences achieved in terms of mean log-likelihood are around 500 instances, while the stability returns better scores throughout the whole experiment. Therefore, considering that on average the San Mamés bridge gets 1000 impulses per day, the most important impact is that the required time for the bridge health monitoring systems could be reduced by one or two days.

ACKNOWLEDGEMENTS

This work has been partially supported by the Spanish Ministry of Science and Innovation through the RTC2019-006871-7 DSTREAMS project, the PID2022-139977NB-I00 and TED2021-131310B-I00 projects, and by the grant to the ELLIS Unit Madrid by the Autonomous Region of Madrid.

REFERENCES

Atienza, D., Bielza, C., & Larrañaga, P. (2022). Semiparametric Bayesian networks. *Information Sciences*, 564–582.

Bouckaert, R. R. (1994). Properties of Bayesian belief network learning algorithms. *Proceedings of the Tenth Conference on Uncertainty in Artificial Intelligence*, 102–109.

Colombo, D., & Maathuis, M. H. (2014). Order-independent constraint-based causal structure learning. *Journal of Machine Learning Research*, 3921–3962.

Feng, G., Zhang, J.-D., & Liao, S. S. (2014). A novel method for combining Bayesian networks, theoretical analysis, and its applications. *Pattern Recognition*, 2057–2069.

Genest, C. (1984). A characterization theorem for externally Bayesian groups. *The Annals of Statistics*, 1100–1105.

Hao, J., Gan, J., Zhou, J., & Wang, J. (2021). Performance prediction of virtual machines via transfer learning of Bayesian network. *2021 IEEE 6th International Conference on Computer and Communication Systems*, 217–222.

Hofmann, R., & Tresp, V. (1996). Discovering structure in continuous variables using Bayesian networks. *Advances in Neural Information Processing Systems 8*.

Hou, Y., Yang, A., Guo, W., Zheng, E., Xiao, Q., Guo, Z., & Huang, Z. (2022). Bearing fault diagnosis under small data set condition: A Bayesian network method with transfer learning for parameter estimation. *IEEE Access*, 35768–35783.

Jia, H.-Y., Chen, J., Yu, H.-L., & Liu, D.-Y. (2010). Soil fertility grading with Bayesian network transfer learning. *2010 International Conference on Machine Learning and Cybernetics*, 1159–1163.

Koliander, G., El-Laham, Y., Djurić, P. M., & Hlawatsch, F. (2022). Fusion of probability density functions. *Proceedings of the IEEE*, 404–453.

Liu, W.-Y., & Song, N. (2001). The fuzzy association degree in semantic data models. *Fuzzy Sets and Systems*, 203–208.

Luis, R., Sucar, L., & Morales, E. (2010). Inductive transfer for learning Bayesian networks. *Machine Learning*, 227–255.

Matzkevich, I., & Abramson, B. (1992). The topological fusion of Bayes nets. *Uncertainty in Artificial Intelligence*, 191–198.

Matzkevich, I., & Abramson, B. (1993). Deriving a minimal I-map of a belief network. *Uncertainty in Artificial Intelligence*, 159–165.

Peña, J. M. (2011). Finding consensus Bayesian network structures. *Journal of Artificial Intelligence Research*, 661–687.

Puerta, J. M., Aledo, J. A., Gámez, J. A., & Laborda, J. D. (2021). Efficient and accurate structural fusion of Bayesian networks. *Information Fusion*, 155–169.

Ramsey, J. D. (2014). A scalable conditional independence test for nonlinear, non-Gaussian data.

Ramsey, J. D. (2016). Improving accuracy and scalability of the PC algorithm by maximizing p-value.

Shachter, R. D., & Kenley, C. R. (1989). Gaussian influence diagrams. *Management Science*, 527–550.

Spirtes, P., & Glymour, C. (1991). An algorithm for fast recovery of sparse causal graphs. *Social Science Computer Review*, 62–72.

Stone, M. (1961). The opinion pool. *The Annals of Mathematical Statistics*, 32(4) 1339–1342.

Wand, M. P. (1992). Error analysis for general multivariate kernel estimators. *Journal of Nonparametric Statistics*, 1–15.

Bridge Maintenance, Safety, Management, Digitalization and Sustainability – Jensen, Frangopol & Schmidt (eds)
© 2024 The Author(s), ISBN 978-1-032-77040-6
Open Access: www.taylorfrancis.com, CC BY-NC-ND 4.0 license

Anomaly detection with switching Kalman filter and imitation learning

Zhanwen Xin & James-A. Goulet
Polytechnique Montreal, Montreal, Canada

ABSTRACT: The detection of anomalies in structural health monitoring (SHM) time-series is notoriously difficult, because one needs to separate reversible patterns caused by the environmental factors and loading, from the baseline irreversible degradation, whereas anomalies typically consist in long-term drifts that have an effect that is orders of magnitude smaller than the reversible patterns. The switching Kalman filter (SKF) has been shown to be an effective tool to address these challenges by quantifying the probability of a switch between different regimes corresponding to normal stationary conditions and abnormal non-stationary ones. Current applications of the SKF have relied on the probability of regime switch as a proxy for detecting anomalies. Despite its capacity to outperform threshold-based detection approaches, it remains prone to (1) missed alarms when the reversible and irreversible pattern separation fails, and (2) false alarms when the predictive capacity of the stationary model is too limited. Previous works have shown that these issues can be mitigated by replacing an alarm triggering policy based solely on the probability of regime switch, with imitation learning (IL) agents that build policies based on the probability of regime switch as well as the trend hidden state. This study further enhances the IL agents by including high-dimensional hidden states vectors as well as by leveraging multiple time steps from the data history. The IL agents that have learnt the underlying dependencies between the high-dimensional hidden state estimates and the labeled actions, which in our context, are whether to trigger an alarm or not, are tested on time series including synthetic and real ones collected on a bridge located in Canada. The results show that the new method provides anomaly detection agents that improve the detectability of anomalies, and are self-adaptive to new stationary conditions.

1 INTRODUCTION

Detecting anomalies in time series is an effective way to identify infrastructures' deterioration before they can be visually observed (Pimentel et al, 2014). Time series anomaly detection methods have the potential to be scaled to infrastructure networks because they do not require a physics-based model of the structure's behaviour (Hamida & Goulet, 2022). Schmidl et al. (2022) categorized the methodologies for time-series anomaly detection as distance, forecasting, and reconstruction-based methods. Among them, the distance and forecasting methods were shown to be effective (Sarmadi & Karamodin, 2020; Willm, 1967) in identifying outliers, yet prone to missed and false alarms in SHM anomaly detection, where the anomalies typically consist in long-term drifts of baselines overlapped by reversible patterns with much bigger magnitude.

The switching Kalman filter (SKF) is a good fit for the detection of baseline changes in structural health monitoring (SHM). Compared to the Hidden Markov Models (HMM) which often model hidden states as discrete variable (Coraça et al., 2023), the state space of the hidden variables in SKF is continuous. Previous studies have shown its effectiveness in baseline extraction (Goulet, 2017), estimation of periodic patterns (Nguyen & Goulet, 2018b), and detection of non-stationary regime quantified by probability values (Nguyen & Goulet, 2018a). However, the probability of the non-stationary

DOI: 10.1201/9781003483755-179

regime sometimes fails to identify regime switches, has delays, or triggers undesirable false alarms, especially when the triggering threshold is not well calibrated. This issue has been partially mitigated by an imitation learning (IL) decision-making framework, that triggers alarms by considering not only the probability of non-stationary regime, but also the baseline estimation of local trend (Khazaeli, 2022). The framework removes the necessity of setting a threshold on the probability of regime switch, and is capable to detect anomalies with lower magnitudes and longer durations compared to only using the probability of non-stationary regime. Yet, it is limited to low-dimensional features and time series with a single anomaly, which prevents it from being used in practice where multiple anomalies might happen during the life of an infrastructure.

The IL task in the decision-making framework typically employs neural networks, which are suitable for the problems having large dimensionalities. This allows us to further leverage the hidden states estimated by the SKF through the inclusion of higher dimensional features and history data in the input of neural networks instead of being limited to the two-dimensional features for the existing decision-making framework. On the other hand, the existing framework is not compatible with time series including multiple anomalies because the model is not able to adapt to new stationary regimes after a non-stationary one. In this paper, we proposed a reference regime, with which the models can be reset during a new stationary regime, and thus continuously detect anomalies.

The objectives of this paper are twofold: (1) it is to include high-dimensional features in the decision-making framework, and (2) to develop a detection method that can handle multiple subsequent anomalies. The structure of this paper is the following: Section 2 reviews the SKF and IL methods, Section 3 presents the methodology of this study, Section 4 presents experiments on a synthetic time series and a real one measured on a bridge, comparing the performance of the SKF and the new framework.

2 BACKGROUND

In this section, the principles behind the switching Kalman filter and imitation learning, as well as their limitations are introduced.

2.1 *Switching Kalman filter*

The Kalman filter is used for decomposing the signal of a stationary linear dynamic system by recursively estimating the moments of hidden states between pairs of consecutive time steps (Welch & Bishop, 2001). By denoting $\boldsymbol{X}$ as the vector including all the hidden states, $\boldsymbol{y}$ as the observed signal, $\mathbf{A}$, $\mathbf{F}$, $\mathbf{Q}$ and $\mathbf{R}$ as the model matrices, and $\mathscr{L}$ as the likelihood of observing $\boldsymbol{y}$ given the model prediction, the Kalman filter from time step $t-1$ to t is summarized by

$$\left(\mu^X_{t/t}, \Sigma^X_{t/t}, L_{t/t}\right) = \text{Filter}\left(\mu^X_{t-1/t-1}, \Sigma^X_{t-1/t-1}, y_t; A, F, Q, R\right) \tag{1}$$

where the subscript t/t denotes the updated estimate at time t using all the observations up to t. In Bayesian dynamic linear models (BDLM), the model matrices, $\mathbf{A}$, $\mathbf{F}$, $\mathbf{Q}$ and $\mathbf{R}$, can be built modularly using various generic components (Goulet, 2020) such as (a) baseline components that describe the local level (LL), trend(LT), and acceleration (LA) of time series; (b) periodic components that capture the harmonic periodic (PD) or non-harmonic kernel regression (KR) patterns, and (c) a residual component which represents the model errors that cannot fit in any other explainable components.

The switching Kalman filter (SKF) is an extension of the Kalman filter that allows modeling non-stationary signals, made of multiple stationary regimes (Murphy, 1998). The Kalman filter transiting from regime i at time $t-1$ to regime j at t is represented by

$$\left(\mu^{i,j}_{t/t}, \Sigma^{i,j}_{t/t}, L^{i,j}_{t/t}\right) = \text{Filter}\left(\mu^i_{t-1/t-1}, \Sigma^i_{t-1/t-1}, y_t; A^j, F^j, Q^j, R^j\right) \tag{2}$$

Given the hidden states estimation in regime i at time $t-1$, it estimates the moments of the hidden states at time t by using model j, as well as the likelihood of the regime transition from i to j by comparing the observed signal $\boldsymbol{y}$ and the model prediction. By denoting $\pi^{l}_{t-1|t-1}$ as the probability of regime i at time $t-1$, and $Z^{i,j}$ as the pre-defined transition probability from $s_{t-1} = i$ to $s_t = j$, the probability of the regime j at time t is computed by

$$\pi^{j}_{t/t} = \sum_{i=1}^{S} M^{i,j}_{t-1,t/t}, \tag{3}$$

$$M^{i,j}_{t-1,t/t} = \frac{L^{i,j}_{t/t} \cdot z^{i,j} \cdot \pi^{i}_{t-1|t-1}}{\sum_{i}\sum_{j} L^{i,j}_{t/t} \cdot z^{i,j} \cdot \pi^{i}_{t-1|t-1}} \tag{4}$$

The hidden states estimated in different transitions can then be merged with $L^{i,j}_{t/t}$ and $\pi^{j}_{t/t}$ by using Gaussian mixture reduction (Runnalls, 2007). With the closed-form solution to estimate the probability of different regimes, SKF was shown to be effective in detecting anomalies in real time series by relying on the probability of the non-stationary regime as a criterion for triggering alarms (Nguyen & Goulet, 2018a). However, this probability may fail to capture the regime switches when time series are affected by unobserved external factors, or when it is subject to high level of noise. Figure 1 showcases a time series affected by a high level of noise, where the stationary regime is defined by a constant local trend. The non-stationary regime's probability, simply denoted as π, remains around zero at all times, yet the local trend hidden state (x^{LT}) switches to a new range after the regime change, indicated by the vertical dot-dashed lines. In such a case, an anomaly detection policy relying solely on the non-stationary regime's probability without considering other hidden states would be prone to missing alarms.

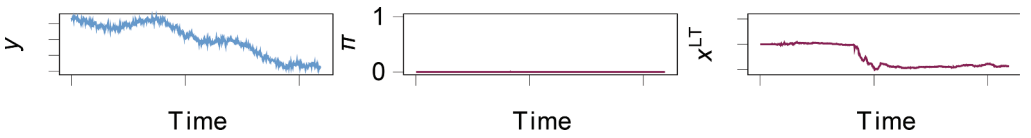


Figure 1. Limitation of the switching Kalman filter. The stationary regime in the time series y has a constant speed. The vertical dot-dashed lines indicate the time step when the speed changes. The non-stationary regime's probability π fails to capture the regime change. Yet, the local trend hidden state (x^{LT}) correctly estimates the speed change with a time delay.

2.2 *Imitation learning*

Imitation learning (IL), also known as behaviour cloning and learning from demonstration, maps a given state directly to an action without considering the long-term sequential effects (Zheng et al, 2022). The objective of an IL agent is to reproduce experts' demonstrations on how to act as a function of states. The expert's demonstration set consisting $\boldsymbol{D}$ instances is defined as $D = \{D_1, D_2, \ldots, D_D\}$, where each demonstration D_i is a state-action pair, i.e., $D_i = \left(s_i, a_i^{\mathrm{expert}}\right)$. For the anomaly detection in SHM, Khazaeli (2022) employed IL algorithms to determine whether a structure is in a normal or abnormal state given the monitoring data at time t. The state space at each time step t was defined by $s_t \in S = \left\{\mu^{LT}_{t|t}, \pi_{t|t}\right\}$, where $\mu^{LT}_{t|t}$ is the expected value of local trend hidden state, and $\pi_{t/t}$ is the probability of the non-stationary regime estimated by the switching Kalman filter. The actions are whether to trigger an alarm or not, $a_t^{expert} \in A = \left\{a^0 : \text{trigger an alarm}, a^1 : \text{not trigger an alarm}\right\}$, which are labeled from synthetic anomalies. His results showed that IL agents are capable to detect anomalies with lower magnitudes and longer durations compared to only using the probability of regime switch. However, the framework in this study is limited to low-dimensional features and deterministic setups. Time series with multiple anomalies, each defined by a regime switch, are not

compatible with the existing method because the local trend used in the state space cannot adapt to new stationary regimes. In the next section, we will introduce a new methodology, in order to overcome their limitations.

3 METHODOLOGY

This section presents a decision-making framework that leverages the high-dimensional hidden states from SKF, and a reset mechanism for the local trend in order to allow decision-making agents to adapt to different trend-stationary regimes.

3.1 *State-action pairs as the input and output of decision-making agents*

Decision-making agents for SHM must be able to handle high-dimensional states as the input for the reasons that (1) multiple hidden states other than the local trend and the probability of the non-stationary regime in SKF might contain useful patterns that contribute to the anomaly detection as shown in Figure 1; (2) patterns are typically time-dependant as anomaly develops with time, so the hidden state estimates not only at the current time step, but also at previous ones should be considered in the decision making. By using neural networks as the supervised imitation learning model, the state space can be expanded to higher dimensions simply by increasing the number of input nodes.

The action output of triggering an alarm or not is labeled according to the non-stationary (**ns**) and stationary (**s**) regimes in time series. Figure 2 depicts the labeling of the two regimes partitioned by different range of the synthetic anomaly's local trend, which gradually shifts from 0 to a negative value $-m$ following a Gaussian cumulative distributed function with random mean and variance scaled by $-m$. The anomaly duration is defined by the 95% confidence interval bounded by $-0.025m$ and $-0.975m$. The non-stationary regime begins with the anomaly, and ends when the SKF detects it and returns again to the new stationary regime. The pairs of the high dimensional input state and the output action defined above form the demonstration set D to train the IL decision-making agents.

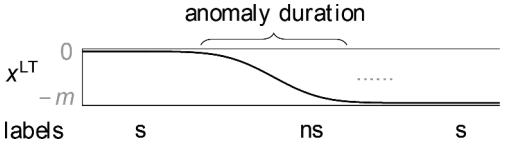


Figure 2. Labeling of non-stationary (ns) and stationary (s) regimes, which corresponds to the action of triggering an alarm or not respectively, according to the anomaly local trend(x^{LT}).

3.2 *Reset mechanism for the local trend*

As presented in Figure 1, the local trend hidden state X^{LT} is a key feature in our imitation learning decision making framework. The departure of X^{LT} from the trend baseline of the stationary regime contributes to the anomaly detection policy. However, when the time series is in a new stationary regime, where the X^{LT} baseline changes to a new level, the model trained on the previous baseline will no longer be valid and will fail to continuously detect anomalies unless it is retrained on the new regime. This causes issues in practice because SHM time series typically spans from years to decades, during which multiple anomalies may happen. To avoid retraining models in each stationary regime and to have a continuous anomaly detecting system, it is more effective to reset X^{LT} to a fixed baseline for different stationary regimes.

In order to develop such a reset mechanism and adapt X^{LT} to new trend-stationary regimes, we propose two new hidden states namely the local-trend reference $\boldsymbol{X}^{LTr}$ and the local trend in agent's vision X^{LTa}, where $X^{LTa} = X^{LT} - X^{LTr}$. The agent makes decisions based on the difference between the actual local trend estimated by the SKF, and the reference value, which is estimated by the Kalman smoother (Murphy, 1999). The stages to determine X^{LTr} are

illustrated in Figure 3, along with time-series observations (y) and the probability of regime switch (π). At the initialization stage of the analysis, $\boldsymbol{X}^{\mathrm{LTr}}$ is defined as the smoothed local trend at time step t_0 using all the future observations until the end of the initialization stage corresponding to the time t_1 when the standard deviation of the smoothed estimation $\sigma^{LT}_{t_0|t_1}$ is smaller than a pre-defined threshold $\tilde{\sigma}^{\mathrm{LT}}$. After the initialization, $\boldsymbol{X}^{\mathrm{LTr}}$ remains constant in the stationary stage. The non-stationary stage begins when π is bigger than a threshold $\tilde{\pi}$ corresponding to the time t_2, when the model realizes that a new $\boldsymbol{X}^{\mathrm{LTr}}$ is needed, but cannot be estimated yet, because the local trend estimate is not stable enough to be used as a reference for the new regime. Hidden states are considered as stable at the time step t_4, $\tilde{n}_w$ steps away from t_3, when $\pi < \tilde{\pi}$. $\tilde{n}_w$ is a pre-defined number of waiting steps. The Kalman smoother is employed to estimate the local trend at t_4 using all the future observations until time t_5, where $\sigma^{\mathrm{LT}}_{t_4|t_5} < \tilde{\sigma}^{\mathrm{LT}}$. Eventually, $\boldsymbol{X}^{\mathrm{LTr}}$ stays constant for the remaining of the new stationary stage.

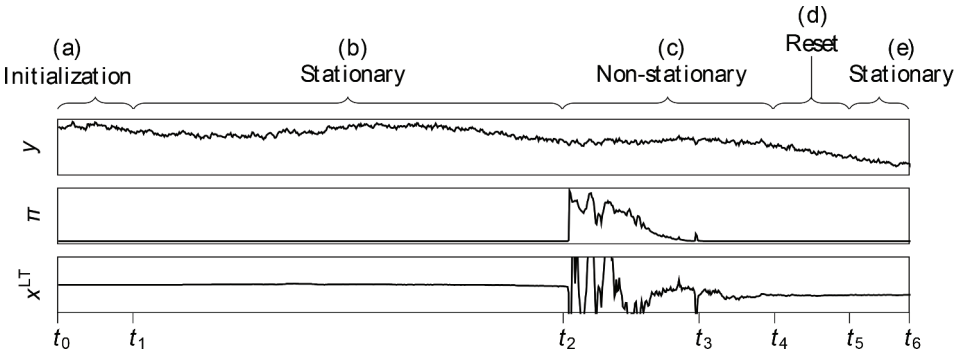


Figure 3. Reset mechanism for x^{LT} in one time series including five stages.

Figure 4 presents an example estimating the $\boldsymbol{X}^{\mathrm{LTr}}$ and $\boldsymbol{X}^{\mathrm{LTa}}$ in a time series including three regimes with reset hyperparameters $\tilde{\sigma}^{\mathrm{LT}} = 0.01$, $\tilde{\pi} = 0.1$ and $\tilde{n}_{\mathrm{w}} = 50$. The local-trend reference for the first regime converges quickly to the true value thanks to the accurate prior knowledge. As the time series enter the second regime, the x^{LT} estimate fluctuates, and the reset process for x^{LTr} and x^{LTa} is triggered. When x^{LT} becomes stable again, x^{LTr} is estimated using the Kalman smoother, and converges gradually to the true value. It is reset again when the time series is in the third regime, after which x^{LTr} is estimated and converges again. The reset local trend $\boldsymbol{X}^{\mathrm{LTa}}$ has a baseline around zero in different regimes, as required by the continuous IL agents.

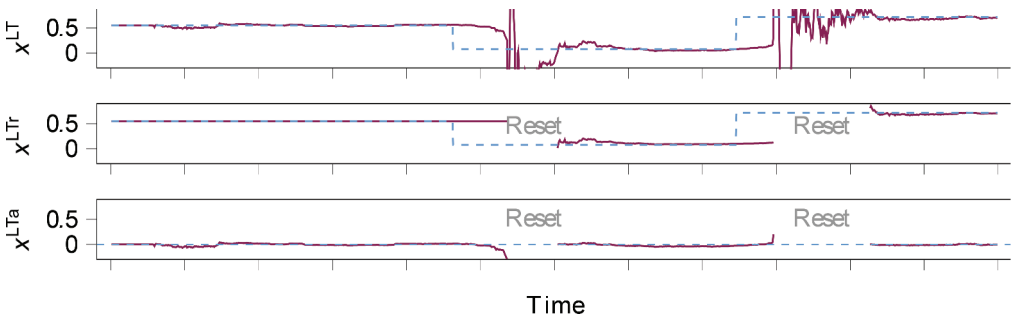


Figure 4. Estimation of local-trend reference x^{LTr} and local trend in agent's vision X^{LTa} in one time-series having three regimes with different local trends.

3.3 *SKF-IL framework for anomaly detection*

The proposed anomaly detection framework for coupling SKF and IL is designed for online operation on cases presenting small changes in the irreversible baseline, which are developing over long periods, such as corrosion, crack-opening, foundation settlements, etc. The IL agents

are trained using synthetic time series where the true labels are available as defined in Section 3.1. The pretrained agents then operate on real time series where labels are unavailable. The input hidden states of the IL agents in the training and testing process are estimated by the SKF presented in Section 2.1 and the reset mechanism in Section 3.2. Figure 5 shows a flow chart of the above-mentioned process.

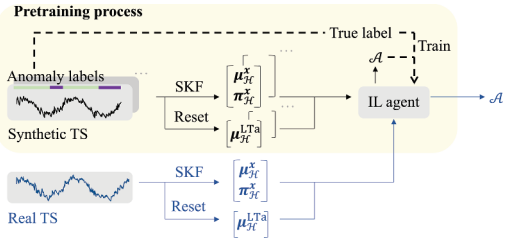


Figure 5. The training and testing process of the SKF-IL anomaly detection framework. μ_H^x represents the mean values of hidden states over time history H, π_H^x is the probability of the non-stationary regime.

4 EXPERIMENTS

An IL decision-making agent modeled by a neural network with two fully connected hidden layers of 64 hidden units, is trained with 900,000 demonstrations, $D_t = \left(s_t, a_t^{\text{expert}}\right)$, pulled out from 1,000 synthetic time series. The state space consists of the non-stationary regime's probability (π), the expected value of the local trend in the agent's vision (μ^{LTa}), as well as the expected value of the residual component (μ^{res}), at previous time steps with a logarithmic spacing from t to $t-128$, i.e., $S_t = \left\{\pi_{t-128,t-64,\ldots t-1,t}, \mu^{\text{LTa}}_{t-128,t-64,\ldots t-1,t}, \mu^{\text{res.}}_{t-128,t-64,\ldots t-1,t}\right\}$. The activation function is the rectified linear unit, and the objective function is defined by the cross-entropy loss. The pre-trained agent is tested on unseen synthetic time series in Section 4.1, and on real time series measured on a bridge in Section 4.2.

4.1 *Synthetic data*

This section verifies the anomaly detectability of the IL agent and the effectiveness of the reset mechanism for handling multiple anomalies. A synthetic time series (y) spanning 20 years is

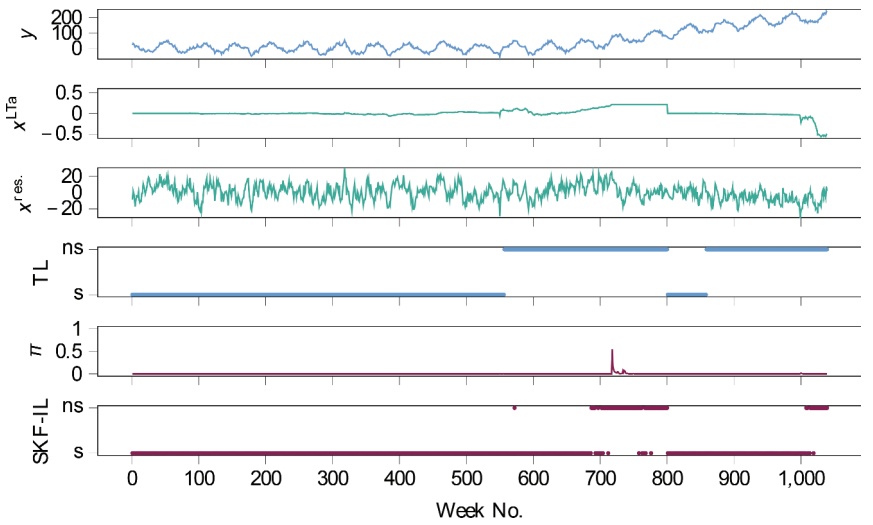


Figure 6. Testing the IL decision-making agent on a synthetic time series with two anomalies.

generated with BDLM as displayed in Figure 6. Two anomalies that shift the local trend are randomly introduced in the 557th and 859th week as indicated by the dot-dashed lines. The pre-processed hidden states x^{LTa}, x^{res}, the true labels (TL) of anomalies, the regime-switching probability π, and the decisions made by the SKF-IL agent are plotted along with y. The SKF relying only on π is capable to identify the first anomaly in the 718th week, and misses the second one with a threshold of 0.1 as in the reset mechanism. By contrast, the SKF-IL agent triggers one alarm much earlier in the 572nd week and again continues from the 687th week during the first anomaly. In addition, it detects the second anomaly missed by π in the 1008th week.

4.2 *Bridge data*

In this section, the performance of the pre-trained agent is tested on a time series measuring the elongation on a bridge. The elongation measurements are dependent on the temperature, which can be modeled by using the observation matrix $\mathbf{F}$ in the Kalman filter. The data is continuous, and the raw time series, covering the period between 2019/08/16 and 2021/11/16 is aggregated during a preprocessing step to a unified time step interval of two data points per week. It is assumed to have a zero local trend, given that no structural anomalies were observed during this period. A synthetic anomaly that shifts the zero local trend to 0.023 mm/year is introduced on 2020/11/12, as indicated by the dot-dashed lines in Figure 7, whereas the changes in the dashed local level baseline is difficult to be visually identified in the y-plot.

The hidden states of x^{LTa}, x^{res}, the true anomaly labels (TL), the probability of the non-stationary regime π estimated using the SKF, the anomalies detected by the forecasting method Prophet (Taylor & Letham, 2018), as well as the anomalies identified by our SKF-IL agent, are plotted following the elongation measurements y. The estimation of x^{LTa} remains around zero, but has fluctuations after the anomaly is introduced. The values of π gradually drifts from 0 to 1 in July 2021. Following the threshold that defines a non-stationary regime in the reset mechanism, $\tilde{\pi} = 0.1$, the SKF detects the anomaly on 2021/07/16 with a delay of more than eight months, which will be even longer if the threshold is set higher. The Prophet algorithm fails to detect the anomalies, and provides two false alarms that are triggered before the anomaly is introduced with an interval width threshold of 99%. Without the need of

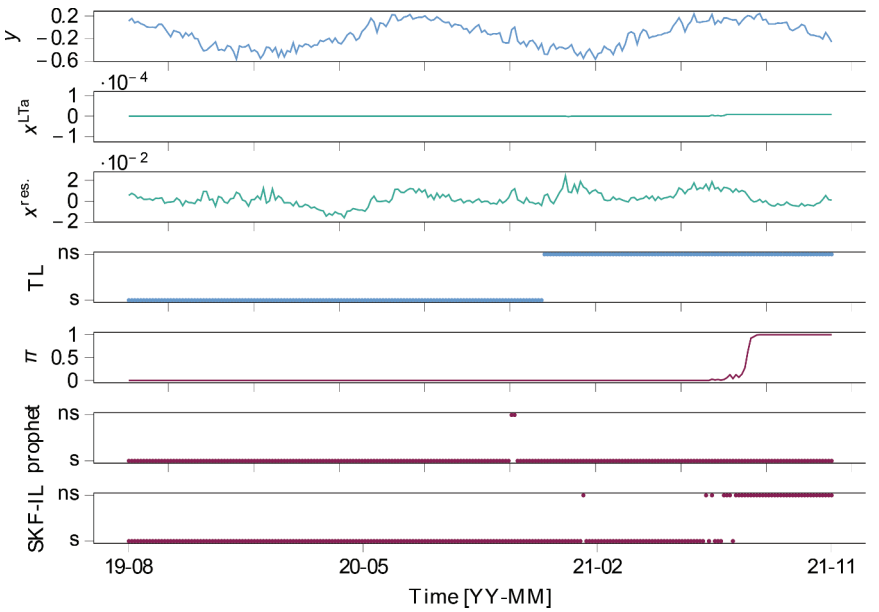


Figure 7. Testing the IL decision-making agent on a real time series measured on a bridge with one anomaly that shift the zero local trend to 0.023 mm/year.

defining a triggering threshold for the non-stationary regime's probability, the pre-trained agent detects the anomaly firstly on 2021/01/01 with a delay of less than two months, and continuously triggers more alarms after 2021/07/05. Results obtained from the real data validate our experiment on the synthetic one, where the hidden state estimates' history contributes to a decision-making policy that is capable to detect anomalies earlier than the one relying only on the non-stationary regime's probability.

5 CONCLUSION

This paper introduces a decision-making framework that detects the regime switches in time series, which is commonly encountered when anomalies develop in infrastructures. The existing switching Kalman filter identifies the regime switch by defining a threshold for the non-stationary regime's probability, which is prone to missed or delayed alarms. The imitation learning (IL) agent presented in this paper leverages hidden states in addition to the non-stationary regime's probability, as well as the history data in the decision-making process. Experiments on a synthetic time series and a real one measuring the elongation of a bridge have shown that the proposed agent can detect the regime switches earlier, reduce missed alarms, and self-adapt to new stationary regime, which allows it to continuously detect anomalies. Although much work remains to be done to probabilistically evaluate the agents' performance in big datasets, its reliability showcased in this paper makes it a promising anomaly detection framework for structural health monitoring.

REFERENCES

Coraça, E. M. & Ferreira, J. V. & Nóbrega, E. G.O. 2023. An unsupervised structural health monitoring framework based on Variational Autoencoders and Hidden Markov Models. *Reliability Engineering & System Safety* 231:109025.

Goulet, J.-A. 2017. Bayesian Dynamic Linear Models for Structural Health Monitoring. *Structural Control and Health Monitoring* 24: 1545–2263.

Goulet, J.-A. 2020. *Probabilistic Machine Learning for Civil Engineers*. Cambridge: MIT Press.

Hamida, Z. & Goulet, J.-A. 2022. A stochastic model for estimating the network-scale deterioration and effect of interventions on bridges. *Structural Control and Health Monitoring* 29: e2916.

Khazaeli, S. 2022. *Damage Detection for Structural Health Monitoring Using Reinforcement and Imitation Learning*. Montreal: Polytechnique Montréal.

Murphy, K.P. 1998. *Switching Kalman filters*. Vancouver: The University of British Columbia.

Murphy, K.P. 1999. *Filtering, smoothing and the junction tree algorithm*. Berkeley: University of California, Berkeley.

Nguyen, L.H. & Goulet, J.-A. 2018a. Anomaly Detection with the Switching Kalman Filter for Structural Health Monitoring. *Structural Control and Health Monitoring* 25: e2136.

Nguyen, L.H. & Goulet, J.-A. 2018b. Structural Health Monitoring with dependence on non-harmonic periodic hidden covariates. *Engineering Structures* 166: 187–194.

Pimentel, M.A.F. & Clifton, D.A. & Clifton, L. & Tarassenko, L. 2014. A review of novelty detection. *Signal Processing* 99: 215–249.

Runnalls, A. 2007. Kullback-Leibler approach to Gaussian mixture reduction. *IEEE Transactions on Aerospace and Electronic Systems* 43: 989–999.

Sarmadi, H. & Karamodin A. 2020. A novel anomaly detection method based on adaptive Mahalanobis-squared distance and one-class kNN rule for structural health monitoring un- der environmental effects. *Mechanical Systems and Signal Processing* 40: 106495.

Schmidl, S. & Wenig, P. & Papenbrock T. 2022. Anomaly detection in time series: A comprehensive evaluation. *Proceedings of the VLDB Endowment*.

Taylor, S. J. & Letham, B. 2018. Forecasting at scale. *The American Statistician* 72: 37–45.

Willm, N. B. G. 1967. Les méthodes de surveillance des barrages au service de la production hydraulique d'electricité de france-problèmes ancients et solutions nouvelles. *Proceedings of 9th ICOLD Congres*.

Welch, G. & Bishop, G. 2001. *An introduction to the Kalman filter*. Chapel Hill: University of North Carolina.

Zheng, B. & Verma, S. & Zhou, J. & Tsang, I. & Chen, F. 2022. Imitation learning: Progress, taxonomies and challenges. *IEEE Transactions on Neural Networks and Learning Systems*.

Bridge Maintenance, Safety, Management, Digitalization and Sustainability – Jensen, Frangopol & Schmidt (eds)
© 2024 The Author(s), ISBN 978-1-032-77040-6
Open Access: www.taylorfrancis.com, CC BY-NC-ND 4.0 license

Improving frequency-features by parametric study of data-driven SHM schemes

C. Puerto-Santana
Automatic Control Department, Universitat Politècnica de Catalunya, Barcelona, Spain
Aingura IIoT, San Sebastian, Spain

J. Diaz-Rozo
Aingura IIoT, San Sebastian, Spain

C. Ocampo-Martinez
Automatic Control Department, Universitat Politècnica de Catalunya, Barcelona, Spain

ABSTRACT: In recent years, structural health monitoring (SHM) has advanced significantly, providing insights about structures with the integration of Big Data and Machine Learning tools. Modern SHM involves extracting features to capture structural behavior, providing valuable insights. The Random Decrement Technique (RDT) is crucial in estimating free responses and frequency-features through System Identification (SID) techniques. Despite the effectiveness of RDT and SID in SHM, a comprehensive sensitivity analysis of parameters and resulting frequency-features is still a topic of research. This article analyses the parameters for RDT and Hankel alternative view of Koopman (HAVOK) approach in extracting modal parameters from a real structural bridge in Andoain, Spain. The study reveals that extending the Hankel horizon minimizes damping factor variance, and increasing averaged segments or the time duration of these segments ensures stable numerical values of the estimated modal parameters. Ultimately, the algorithm parametrization depends on the resource constraints in desired monitoring deployments.

1 INTRODUCTION

In the last decades, standards, and regulations like those described in Gatti (2019) have been created to ensure the safety and correct operation of mechanical structures. These standards help to prevent catastrophic failures that could lead to loss of lives and resources. Furthermore, these regulations contain guidelines regarding materials, structural design, modal analysis, static and dynamic testing, among others. SHM has emerged as a vital component for structural maintenance by using technological innovations, such as sensors and embedded systems, to revolutionize monitoring in mechanical structures. These developments provide real-time actionable insights into the well-being of structures, enabling to predict, prevent, and respond to potential failures with precision.

The accuracy and reliability of SHM systems are fundamentally dependent on the calibration of the parameters that are used for their algorithms. Furthermore, ensuring that these parameters are correctly set is the basis of the proper operation of SHM algorithms as shown in Sirin-goringo et al. (2008), Górski (2015) and Reynolds et al. (2016). Without accurate calibration, the effectiveness of SHM systems diminishes, and the vital decisions based on the collected data become prone to error. Therefore, parameter calibration is an essential step in SHM systems to prevent structure failures and, by extension, to protect the lives of those who depend on them.

In this article, the relation between the input parameters for a proposed data driven SHM scheme and the resulting frequency-features of this scheme is studied. A systematic parameter sweeping

DOI: 10.1201/9781003483755-180

approach is employed to evaluate the influence of input variables on the resulting modal parameters. The studied SHM scheme involves generating the random decrement signature of the studied structure using mechanical vibration signals and generating a state-space model these signatures. This approach uses the Hankel alternative view of the Koopman operator method, known as HAVOK, to extract the natural frequencies and damping factors of the studied structure.

2 RELATED WORK

2.1 *Structural health monitoring schemes*

SHM was initially described by Houser et al. (1997) as using sensors and structural analysis to identify failures or changes in structures. It was also defined by Aktan (1996) as a conditional assessment tool where raw data from sensors are used to analyze existing changes in the behavior of an analyzed structure over time.

Data driven SHM approaches employ sensors data to create stochastic models as tools to detect structural abnormal behavior. The deployment of these methodologies is computationally less expensive than model-based methods, furthermore, these methods can be scalable to online operation for several structures without the dependence of any physical model. Nevertheless, data-driven SHM methods have some challenges and limitations regarding physical interpretation, calibration, and assumptions over the data as exposed by Sun et al. (2020). With the arrival of Big data, advanced embedded systems, and Machine Learning methods, some of these challenges have been tackle, providing more reliable SHM methods and successful deployments such as the presented by Tidriri et al. (2016) and Magalhaes (2009).

Recent machine-learning-based and big-data-based SHM methods typically consist of four stages. Firstly, the data are acquired and preprocessed to extract the information related to the structure. Then, mathematical models are built using model-based or data-based methods. Subsequently, features that contain meaningful information from the structure are extracted. Finally, these features are used to create a baseline of the bridge as a way of identifying anomalies or faults within the structure.

2.1 *Frequency-features for structural health monitoring*

Frequency-features stand out as the foundation of vibration-based damage detection in structures. Regarding SHM, natural frequencies and damping factors are frequency-features that are closely connected with structural stiffness, mass, and damping parameters as exposed by Sun et al. (2020). However, their estimation is highly sensible to external loads, noise, and sometimes is not suitable for detecting minor faults in real deployments.

In recent years, several authors presented methodologies for frequency-feature extraction that tackle some challenges regarding structural fault detection. Some of the most recent frequency-feature extraction approaches are depicted in Table 1. These approaches are mainly focused on creating signal-based models from an approximation of the structural free response using System Identification techniques and variations from existing model structures. Moreover, the estimation of the impulse responses of the structures is mainly performed using the RDT which stands as a proper signal processing technique to estimate the free response of structures subjected to random excitations.

Table 1. SHM methods for frequency-feature extraction in the literature.

Reference	Description of the SHM method
Magalhães et al. (2009)	Stochastic subspace identification and stabilization diagrams.
He et al. (2011)	RDT SID. and singular value decomposition.
Roveri et al. (2012)	Hilbert transformation and instant frequency estimation.
Kim et al. (2012)	SID for vehicle-structure interaction.
Zhang et al. (2016)	Variations of RDT and parameter identification schemes.
Tomaszkiewicz et al. (2022)	Variations of the RDT combined with exponential regression.

3 CONCEPTUAL FRAMEWORK

This section presents an overview of the key concepts and principles that underlie the used SHM scheme for the presented approach.

3.1 *Random decrement technique*

The RDT is a signal processing tool that has been used in recent years for vibration-based-SHM. This method aims to extract an approximation of the structural free responses when the analyzed structure is subjected to random zero-mean excitations.

This method consists of three phases. Firstly, a threshold for the amplitude s_{th} and slope of the vibration signal $s(t)$ are selected. Then, the time segments that match the initial conditions are extracted, and finally these segments are averaged to cancel the effect of random excitations and preserve the deterministic response of the structure. Some variations of the RTD using several triggering conditions are presented by Brincker et al. (1992), Cioara et al. (2000), Alampalli et al. (2005) and Amador et al. (2022). The resulting signal of the RDT is commonly called random decrement signature (RDS) which can be written as

$$s_{rds}(t_\tau) = E[s(t_\tau)|s_{th}] \approx \frac{1}{l_{rds}} \sum_{k=0}^{l_{rds}-1} s(\tau_k), \tau_k \in (t_{thk}, t_{thk} + \tau), \tag{1}$$

where $E[\,\cdot\,]$ is the expected value, $t_{thk}, \quad k \in \mathbb{Z}_+$ is the time where $s(t)$ crosses s_{th} and $t_\tau \in (0, \tau)$, whereas $\tau \in \mathbb{R}$ is the duration of the free responses and l_{rds} is the number of segments used for the computation of the RDS.

3.2 *Hankel alternative view of Koopman operator*

System Identification techniques are data-driven tools used to fit data from dynamic systems to mathematical model structures as an approximation of said system. HAVOK is a recent SID technique that creates and approximation of the Koopman operator of non-forced dynamic systems by using time embedding and singular value decomposition tools. The HAVOK model structure can be written as

$$v(n) = Av(n-1) + Bv_{\eta+1}(n), \tag{2}$$

with $A \in \mathbb{R}^{\eta \times \eta}$ and $B \in \mathbb{R}^{\eta \times 1}$, where as η is the model's order. The HAVOK model is computed from the truncated matrix $V_{\eta+1} \in \mathbb{R}^{\eta+1 \times \eta+1}$, which contains the $\eta + 1$ principal components of observed sensors. The model in Equation (2) uses the last principal component of $V_{\eta+1}$ as an artificial force that excites the system. This representation allows to identify and compensate non-linear behavior that can introduce noise in the estimation of natural frequencies of the studied dynamical system. Simulated validation of several non-linear systems illustrates the effectiveness of HAVOK method as shown in Brunton et al. (2017).

4 PROPOSED ANALYSIS

The following assumptions are stated for the proposed analysis:

a. The data is acquired at a constant sample frequency f_s, ensuring that the signals remain free from aliasing.
b. The sensors data $s(t)$ contain the information about the spectrum of the studied structure within its frequency range.
c. The model order η of the HAVOK SID model can be estimated by using eigen realization information criterion or stability diagrams as shown in Bakir (2011) and Bauer (2001).
d. The set of eigenvalues Λ used for extracting the natural frequencies and damping factors have a stable-underdamped characteristic.

4.1 *Frequency feature extraction*

The proposed feature extraction scheme for vibration based SHM is presented in Figure 1. This SHM scheme has been implemented in several applications using different SID techniques such as the described by He et al. (2011). On the other hand, some variations of the RDT such as the presented by Vesterholm et al. (2020) have been used to extract frequency-features. The proposed enhancement of this SHM scheme and its description is next explained.

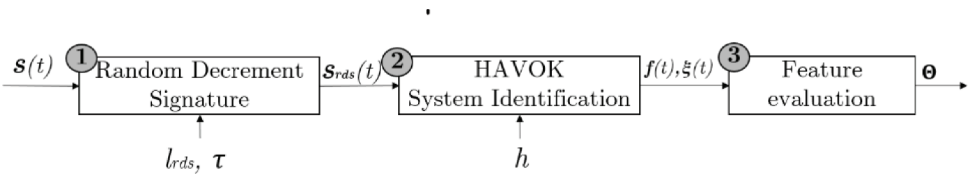


Figure 1. Proposed data-driven SHM scheme using RDS and SID for feature-feature extraction.

1. The input vibration signals $s(t)$ that monitor the structure are used to compute the RDS of each channel using a time duration per segment τ and averaging every l_{rds} segments. The triggering condition for this scheme is defined as

$$C_s := \left\{ (m\sigma_s(1-b) < s(t)\sigma_s(1+b)) \& \left(\frac{ds(t)}{dt} < 0 \right) \right\} \tag{3}$$

   where $m\sigma_s$, $m \in R$ is a multiple of the standard deviation σ_s of the raw signals, while b is a regulator variable between 0 and 1 that allows to identify the initial condition of the RDS into a band of search for numerical purposes. Furthermore, since the time derivative must be less than zero for the triggering condition, only decreasing impulses are considered for the RDS generation. The use of a multiple of the standard deviation $m\sigma_s$ in Equation (3) is intended to set a statistical threshold for anomaly detection. Events or responses that deviate from the normal behavior by a specified number of standard deviations are correlated with the random excitation across the structure. Furthermore, this criterion has found application in various deployments, presented by Xu et al. (2015) and Zhang et al. (2016). Moreover, the used of a range band of search for the initial conditions was presented in Vesterholm et al. (2020), such a band gives flexibility to the search of the initial condition amplitude of the RDS for numerical data. Finally, the RDS can be computed averaging $s(t)$ at the times $t_{C_s k}$ that meet the C_s condition as

$$s_{rds}(t_\tau) = E[s(t_\tau)|C_s] \approx \frac{1}{l_{rds}} \sum_{k=0}^{l_{rds}-1} s(\tau_k), \tau_k \in (t_{C_s k}, t_{C_s k} + \tau) \tag{4}$$

   For multivariate analysis, Equation (3) must be applied to the principal component of the vibration signals and the RDS of each channel can be extracted independently based on this criterion with Equation (4). The principal component of the signals can be obtained using SVD techniques as reported by Shlens (2014).
2. Once the RDS signal $s_{rds}(t)$ of each channel is extracted, the HAVOK model is computated using the RDS of all channels as input data for the algorithm. A model in the form of Equation (2) is obtained for each group of RDSs. Following *Assumption (a)* and *Assumption (d)*, if the sampling frequency of the raw data f_s is constant, then the natural frequencies f_n and damping factors ξ_n can be computed with the discrete model matrix A and f_s as

$$f_n := \left\{ \frac{f_s}{2\pi} \left(\log(\rho)^2 + \beta^2 \right)^{\frac{1}{2}}, \lambda = \rho e^{\mp i\beta} \in \Lambda \right\} \tag{5.1}$$

$$\xi_n := \left\{ -\frac{\log(\rho)}{\left((\log(\rho))^2 + \beta^2 \right)^{\frac{1}{2}}}, \lambda = \rho\ e^{\mp i\beta} \in \Lambda \right\} \tag{5.2}$$

$$\Lambda := \{\lambda \in C | \|I - A\lambda\| = 0\} \tag{5.3}$$

with $\rho \leq 1$ and $\beta \neq [-\pi, 0, \pi]$. Furthermore, based on *Assumption (b)*, if the sensors are properly preprocessed, then, the modal parameters of Equations (5.1), (5.2) and (5.3) represent the physical behavior of the studied bridge.

3. The set of natural frequencies and damping factors are stored and evaluated through the sample mean and standard deviation statistical measurements.

Based on the SHM scheme previously discussed, the frequency-features were generated for several numerical values of l_{rds}, τ and h. Finally, the set of sample means, and standard deviations of the modal parameters were computed for each group of input parameters.

5 VALIDATION ASSESSMENT

5.1 *Experimental set-up*

The 12-th Andoain St is a prestressed concrete slab bridge with an urban major arterial functionality class. The monitoring of the infrastructure was led by the company Aingura IIoT, who instrumented the bridge beams with piezoelectric accelerometers. A general view of the bridge and its sensors scheme are shown in Figure 2.

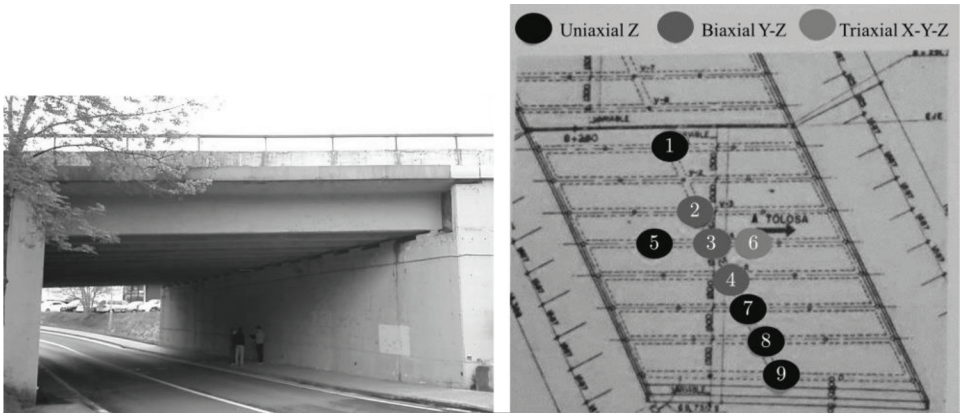


Figure 2. 12 Andoain St bridge location and sensor placement specifications.

The sensors data were collected by an embedded system at a sample frequency of 350 Hz. A subset of data collected between 05/06/2023 and 12/06/2023 was used to validate the proposed methodology. The parameters used in the evaluation of this methodology are shown in Table 2.

Table 2. Parameters used for the implementation of the proposed methodology.

Description	Parameter	Value
Amplitude for RDS	s_{th} [-]	$1.6\sigma_s$
Sample frequency	f_s [Hz]	350.0
Sensors used for the analysis	s(t) [-]	$[s_1(t), s_3(t), s_5(t), s_9(t)]$
Bandwidth for triggering condition	b [-]	0.2
Model order for HAVOK model	η [-]	8
Time interval of transient segments	τ [s]	[0.5, 1.0, 1.5, 2.0, 2.5, 3.0, 3.5, 4.0, 4.5, 5.0, 5.5, 6.0, 8.0, 10.0]
Number of segments for RDS computation	l_{rds} [-]	[5, 10, 20, 30, 40, 50, 100, 150, 200, 350, 500, 750, 1000, 1500, 2000]
Horizon for Hankel time embedding	h [-]	[9, 10, 11, 12, 13, 18, 20, 22, 23, 28, 33, 38]

The selection of the input parameter sets was made based on the parameters used in SHM deployments within the literature as reported by Xu et al. (2015) and He et al. (2011). For the selected study period, 64583 segments were extracted using the criteria of Equation (3). In total, 2520 experiments were carried out in which 1000 samples of frequency-features were extracted for each experiment. In addition, the computational time necessary to extract the frequency-features was calculated for each set of input parameters.

5.2 *Frequency-features results*

The impact of increasing the numerical value of the input parameters on the sample mean of the frequency-features is depicted in Figure 3. In general, the value of the computed natural frequencies decreases as the input parameters increase. Furthermore, the numerical value of the natural frequency only converges to a numerical value with the increase of l_{rds}. Specifically, the modal parameters exhibit convergence in their sample means when more than 700 segments (input param tested=10 for l_{rds}). On the other hand, the damping factors increase their numerical value with l_{rds} and decrease with τ and h. Moreover, the rate of change of the damping factors is high for all the Hankel horizon tested while the damping factors rate of change seems to have a smaller variation as τ and l_{rds} increase.

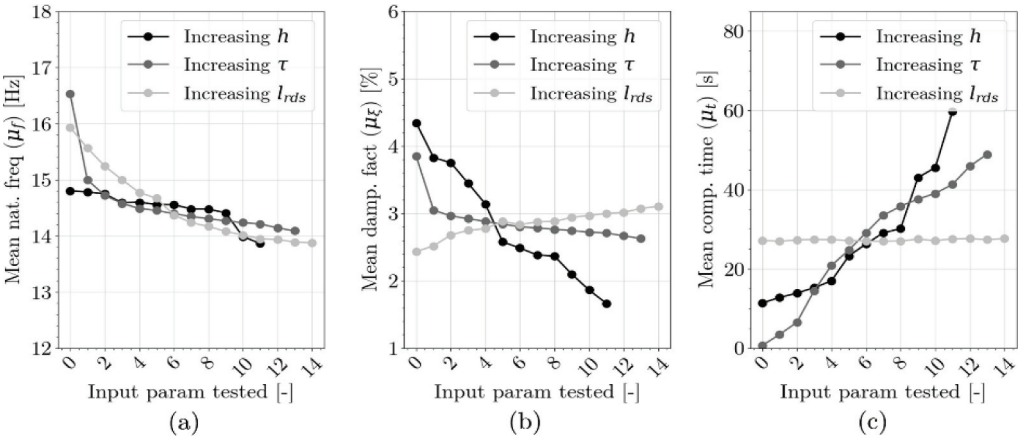


Figure 3. Sample mean of the frequency features and computing time for the tested experiments as a function of the input parameters. (a) Natural frequencies. (b) Damping factors. (c) Computational time.

The Hankel horizon has the highest impact in the computational time of the frequency-features for the tested experiments, while the number of averaged segments does not seem to have a significant impact on computational costs compared to the other two evaluated parameters, as it is shown in Figure 3.

Figure 4 depicts the variation of the frequency-features as a function of l_{rds}, h and τ. The standard deviation of the natural frequencies follows a similar pattern to the mean sample values. Increasing l_{rds} minimizes the standard deviation of the natural frequencies. Likewise, as all input values increase, the standard deviation of damping factors decreases. The experiments with highest h have the lowest standard deviation in the computed damping factors.

Since h and τ have the most significant impact on the computing time, a comprehensive sensitivity analysis was conducted to observe the behavior of the frequency-features when these parameters are fixed. Figure 5 provides a comprehensive joint sensitivity analysis by fixing h and τ to common values used in the literature such as the presented by Górski (2015) and Farhey (2005).

Figure 5 demonstrates that, by fixing h, the frequency-features converge to a stable mean and standard deviation as l_{rds} increases. Additionally, increasing τ accelerates the convergence rate. On the other hand, increasing h has no effect on the convergence rate of the numerical value of the frequency-features sample mean and standard deviation. Nevertheless, the value of h generates

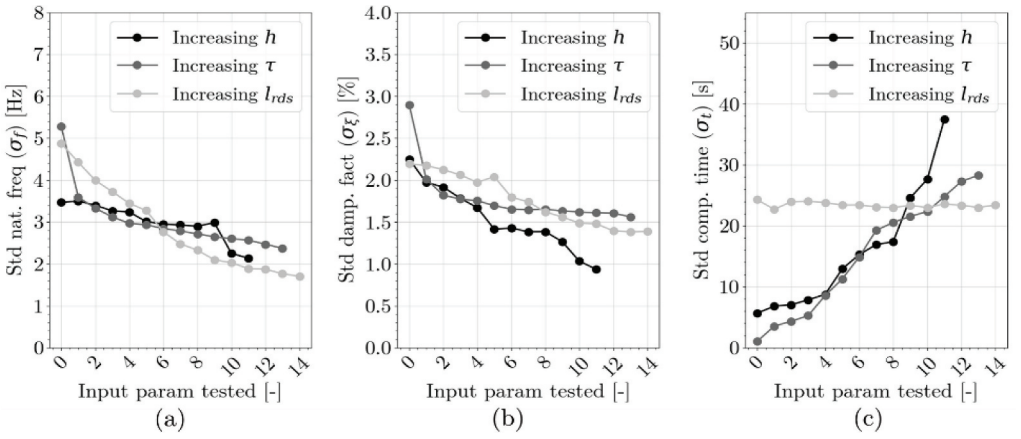


Figure 4. Sample standard deviation of the frequency features and computing time for the tested experiments as a function of the input parameters. (a) Natural frequencies. (b) Damping factors. (c) Computational time.

a change in the convergence value of the natural frequencies in such a way that a higher h generates a higher natural frequencies sample mean and a lower damping factors sample mean.

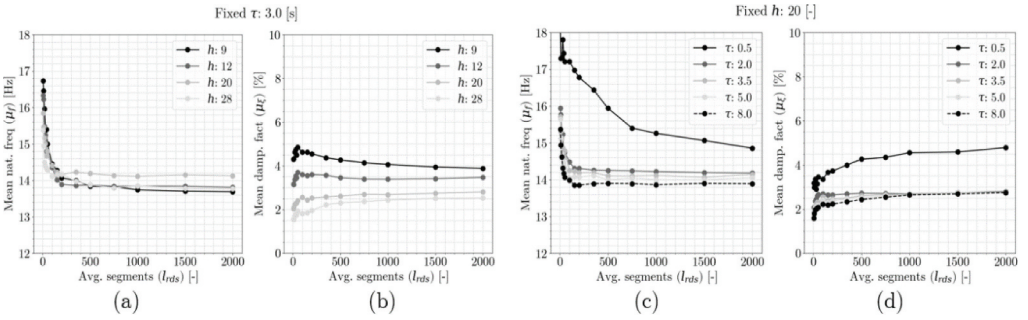


Figure 5. Sample mean and standard deviation of the frequency features as a function of the number of averaged segments. (a) Natural frequencies for several Hankel horizons fixing τ = 3[s]. (b) Damping factors for several Hankel horizons fixing τ = 3[s]. (c) Natural frequencies for several segments durations fixing h=20[-]. (d) Damping factors for several segments durations fixing h=20[-].

6 CONCLUSION

This study introduces a sensitivity analysis of frequency variables in SHM methods. The evaluation assessment showed that employing different input parameters for a structural health monitoring scheme can lead to variations in the obtained frequency-features when using the same mechanical vibration dataset. To compute a low variance set of frequency-features at a low computational cost, one approach involves increasing the number of segments used to calculate the random decrement signal. Another method consists in extending the duration of pulses while maintaining a constant number of segments and increasing the horizon of the Hankel matrices, leading to similar convergence of modal parameters. However, it is noted that increasing the duration of segments and the horizon of the Hankel matrix also achieves convergence but at a higher computational cost. Choosing the correct parameters for structure monitoring ensures that the obtained frequency-features reflect genuine changes in the monitored structure over time. This approach minimizes the influence of random variations that may occur when applying the necessary algorithms for feature computation. Regarding real deployments, it is concluded that obtaining comparable modal

characteristics of the RDS is feasible by adjusting the segments duration based on in situ resource constraints.

REFERENCES

Aktan, A. E., Farhey, D. N., Brown, D. L., Dalal, V., Helmicki, A. J., Hunt, V. J., & Shelley, S. J. (1996). Condition assessment for bridge management. *Journal of Infrastructure Systems*, *2*, 108–117.

Alampalli, S., & Cioara, T. G. (2000). Selective random decrement technique for processing bridge vibration data. *Proceedings of Conference on Structural Materials Technology IV, Technomic Publishers: Lancaster*, (pp. 75–80).

Alampalli, S., & Cioara, T. G. (2005). Selective random decrement techniques for bridge monitoring systems. *Bridge structures*, *1*, 397–404.

Bakir, P. G. (2011). Automation of the stabilization diagrams for subspace based system identification. *Expert Systems with Applications*, *38*, 14390–14397.

Bauer, D. (2001). Order estimation for subspace methods. *Automatica*, *37*, 1561–1573.

Brincker, R., & Amador, S. (2022). On the theory of random decrement. *Mechanical Systems and Signal Processing*, *173*, 109060.

Brincker, R., Krenk, S., Kirkegaard, P. H., & Rytter, A. (1992). Identification of dynamical properties from correlation function estimates. *Danish Society for Structural Science and Engineering*.

Brunton, S. L., Brunton, B. W., Proctor, J. L., Kaiser, E., & Kutz, J. N. (2017). Chaos as an intermittently forced linear system. *Nature Communications*, *8*, 19.

Cioara, T. G., & Alampalli, S. (2000). Particular Methods in Signal Processing for Remote Bridge Monitoring Systems. In *Advanced Technology in Structural Engineering* (pp. 1–8).

Farhey, D. N. (2005). Bridge instrumentation and monitoring for structural diagnostics. *Structural Health Monitoring*, *4*, 301–318.

Gatti, M. (2019). Structural health monitoring of an operational bridge: A case study. *Engineering Structures*, *195*, 200–209.

Górski, P. (2015). Investigation of dynamic characteristics of tall industrial chimney based on GPS measurements using Random Decrement Method. *Engineering Structures*, *83*, 30–49.

He, X. H., Hua, X. G., Chen, Z. Q., & Huang, F. L. (2011). EMD-based random decrement technique for modal parameter identification of an existing railway bridge. *Engineering Structures*, *33*, 1348–1356.

Housner, G., Bergman, L. A., Caughey, T. K., Chassiakos, A. G., Claus, R. O., Masri, S. F., Yao, J. T. (1997). Structural control: past, present, and future. *Journal of Engineering Mechanics*, *123*, 897–971.

Kim, J., & Lynch, J. P. (2012). Experimental analysis of vehicle–bridge interaction using a wireless monitoring system and a two-stage system identification technique. *Mechanical Systems and Signal Processing*, *28*, 3–19.

Magalhães, F., Cunha, A., & Caetano, E. (2009). Online automatic identification of the modal parameters of a long span arch bridge. *Mechanical Systems and Signal Processing*, *23*, 316–329.

Reynolds, T., Casagrande, D., & Tomasi, R. (2016). Comparison of multi-storey cross-laminated timber and timber frame buildings by in situ modal analysis. *Construction and Building Materials*, *102*, 1009–1017.

Roveri, N., & Carcaterra, A. (2012). Damage detection in structures under traveling loads by Hilbert–Huang transform. *Mechanical Systems and Signal Processing*, *28*, 128–144.

Shlens, J. (2014). A tutorial on principal component analysis. *arXiv preprint arXiv:1404.1100*.

Siringoringo, D. M., & Fujino, Y. (2008). System identification of suspension bridge from ambient vibration response. *Engineering Structures*, *30*, 462–477.

Sun, L., Shang, Z., Xia, Y., Bhowmick, S., & Nagarajaiah, S. (2020). Review of bridge structural health monitoring aided by big data and artificial intelligence: From condition assessment to damage detection. *Journal of Structural Engineering*, *146*, 04020073.

Tidriri, K., Chatti, N., Verron, S., & Tiplica, T. (2016). Bridging data-driven and model-based approaches for process fault diagnosis and health monitoring: A review of researches and future challenges. *Annual reviews in control*, *42*, 63–81.

Tomaszkiewicz, K., & Owerko, T. (2022). Estimation of the bridge damping decrement for in-situ recorded signal with unusual features. In *Bridge Safety, Maintenance, Management, Life-Cycle, Resilience and Sustainability*. CRC Press.

Vesterholm, K. K., Brincker, R., & Brandt, A. (2020). Random decrement technique for detection and characterization of nonlinear behavior. *Mechanical Systems and Signal Processing*, *143*, 106841.

Xu, A. N., Xie, Z. N., Gu, M., & Wu, J. (2015). Amplitude dependency of damping of tall structures by the random decrement technique. *Wind and Structures*, *21*, 159–182.

Zhang, Y., & Song, H. W. (2016). Non-overlapped random decrement technique for parameter identification in operational modal analysis. *Journal of Sound and Vibration*, *366*, 528–543.

Bridge Maintenance, Safety, Management, Digitalization and Sustainability – Jensen, Frangopol & Schmidt (eds)
© 2024 The Author(s), ISBN 978-1-032-77040-6
Open Access: www.taylorfrancis.com, CC BY-NC-ND 4.0 license

Robust modal identification of a large-span bridge with the new SpCF technique

S.D.R. Amador
Technical University of Denmark (DTU), Kgs. Lyngby, Denmark

L. Gaile
Riga Technical University, Riga, Latvia

R. Brincker
Brincker Monitoring ApS, Copenhagen, Denmark

C.E. Ventura
The University of British Columbia (UBC), British Columbia, Canada

ABSTRACT: When performing vibration tests on bridges, engineers face the challenge of extracting the global dynamic properties of these structures from the vibration responses measured at several degrees of freedom. In this paper, the new subspace-based poly-Reference Complex Frequency (SpCF) technique is applied to the vibration measurements of a large span bridge. The advantage of the SpCF with regard to other modal or system identification techniques is that it provides robust estimates for the modal properties, which leads to very clear stabilization diagrams. In order to assess the performance of the new SpCF, its estimates for the modal properties of the aforementioned bridge are compared to those of the poly-reference Least Squares Complex Frequency (pLSCF, also known by its commercial name polymax), which is deemed as a standard technique in experimental and operational modal analysis.

1 INTRODUCTION

When performing output-only modal identification engineers face the challenge of extracting the modal properties of the tested structures from the vibration data in an accurate and robust fashion. Several time-domain system identification techniques exist for this purpose as, for instance the Ibrahim Time Domain (ITD) (Ibrahim & Milkulcik 1997, Ibrahim 1984 & Fukozono 1986), the Poly-reference Least Squares Complex Exponential (pLSCE) (Vold et al. 1982), the Eigen-system Realization Algorithm (Juang & Pappa 1985) and the Stochastic Subspace Identification (SSI) (Peeters, B. & De-Roeck 1999).

Alternatively, identification methods formulated in the frequency-domain such as the Poly-reference Least Squares Complex Frequency (pLSCF) (Peeters et al. 2007) and poly-reference Complex Frequency (pCF) (Amador & Brincker 2023a, b & c) can also be utilized to estimate the modal properties from vibration data. Whilst the former are applied to a time-domain function like the impulse response or the correlation function, the latter operates on a frequency-domain function such as the Frequency Response Function (FRF) or the Half Spectrum (HS).

The advantages of using subspace driven time-domain methods like the ERA and the SSI with regards to their Least Squares counterparts such as the ITD and pLSCE, is that former tend to provide clearer stabilization diagrams, facilitating the extraction of the physical modal properties from the numerical ones and, in turn, leading to a more robust modal parameter estimation.

DOI: 10.1201/9781003483755-181

Another benefit of utilizing subspace driven identification methods is related to the fact that they can provide very robust and accurate estimates even when applied to vibration data containing the measurement of several sensors.

The idea of using subspaces of the system matrices in the identification process is widely used in time domain system identification. Recently, this idea was extended to the frequency domain in the formulation of the Subspace-based pCF (SpCF) described in Amador & Brincker 2023d. In this paper, the performance of the recently introduced SpCF method is assessed by means of the Operational Modal Analysis (OMA) of a large span bridge, namely the Port Mann stay cable bridge located in Vancouver, British Columbia, Canada. The bridge has been continuously monitored since it was opened to traffic in 2012 by means of 54 accelerometers. In order to assess the performance of the SpCF, its estimates for the modal properties of the Port Mann bridge are compared to those of the pLSCF, which is regarded by many as standard in frequency-domain modal analysis.

2 BACKGROUND THEORY: THE SPCF APPROACH

The FRF matrix of a structural system with general viscous damping containing the information of N_i inputs, N_i outputs and n vibration modes, and sampled with a time step, Δt, can be modeled by the so-called frequency-domain state-space model with an arbitrary forward time shift, as (Amador & Brincker 2023a, b & c)

$$z^r \boldsymbol{H}(z) = \boldsymbol{C}(\boldsymbol{I}z - A)^{-1} B \tag{1}$$

where r denotes a discrete-time forward shift or a time delay ($\tau = r\Delta t$) and $\boldsymbol{H}$(z) stands for the FRF in z-domain; $\boldsymbol{A}$, $\boldsymbol{B}$ and $\boldsymbol{C}$ are the discrete-time state matrix, the input matrix and the output matrix, respectively; $\boldsymbol{I}$ denotes the identity matrix and $z = e^{j\omega\Delta t}$ is the z-domain variable expressed as a function of the imaginary unity, $j = \sqrt{-1}$, and the angular frequency, ω (in rads/sec). From the eigenvalue decomposition of the discrete-time state matrix

$$\boldsymbol{A} = \boldsymbol{\Psi}\boldsymbol{\Lambda}\boldsymbol{\Psi}^{-1} \tag{2}$$

it can be proven that relations between the eigenvectors $\boldsymbol{\Psi}$ and eigenvalues $\boldsymbol{\Lambda}$, and the invariants of the classic modal model is given by (Amador 2015)

$$\boldsymbol{\Psi} = \begin{bmatrix} \boldsymbol{\Phi} \\ \boldsymbol{\Phi\Lambda} \end{bmatrix}, \ \boldsymbol{\Phi} = C\boldsymbol{\Psi}, \boldsymbol{\Gamma}^T = \boldsymbol{\Psi}^{-1} B \tag{3}$$

where $\boldsymbol{\Phi}$ denotes the mode shape matrix, $\boldsymbol{\Gamma}$ the modal participation matrix, and $(\cdot)^T$ stands for the matrix transpose. Writing down Eq (1) for r ranging from 0 to a maximum time shift n and combining the resulting equations in single matrix expression, gives

$$\boldsymbol{H}_0(z) = \boldsymbol{O}(\boldsymbol{I}z - \boldsymbol{A})^{-1}\boldsymbol{B} \tag{4}$$

with

$$\boldsymbol{H}_i(z) = \begin{bmatrix} z^i \boldsymbol{H}(z) \\ z^{i+1}\boldsymbol{H}(z) \\ \vdots \\ z^{i+n}\boldsymbol{H}(z) \end{bmatrix} \tag{5}$$

and

$$\boldsymbol{O} = \begin{bmatrix} \boldsymbol{C} \\ \boldsymbol{CA} \\ \vdots \\ \boldsymbol{CA}^n \end{bmatrix} \tag{6}$$

standing for the so-called *Observability* matrix. Eq. (4) can be written for two discrete consecutive frequency lines ω_a and ω_b ($\forall \omega_a > \omega_b$) spaced from each other by a single discrete frequency step $\Delta\omega$, giving

$$\boldsymbol{O}^{-1}\boldsymbol{H}_1(z_a) - \boldsymbol{A}\boldsymbol{O}^{-1}\boldsymbol{H}_0(z_a) = \boldsymbol{B} \tag{7}$$

$$\boldsymbol{O}^{-1}\boldsymbol{H}_1(z_b) - \boldsymbol{A}\boldsymbol{O}^{-1}\boldsymbol{H}_0(z_b) = \boldsymbol{B} \tag{8}$$

Combining Eqs. (7) and (8), and writing the resulting expression for all frequencies lines in the range of 0 (DC) to N_v (Nyquist frequency), gives

$$\boldsymbol{O}^{-1}\boldsymbol{Q} = \boldsymbol{A}\boldsymbol{O}^{-1}\boldsymbol{P} \tag{9}$$

where the system matrices Q and P are given by

$$\boldsymbol{P} = \left[\left(\begin{Bmatrix} z_1^0 \\ \vdots \\ z_1^n \end{Bmatrix} \otimes \boldsymbol{H}(z_1) - \begin{Bmatrix} z_0^0 \\ \vdots \\ z_0^n \end{Bmatrix} \otimes \boldsymbol{H}(z_1) \right) \quad \cdots \right.$$

$$\left. \left(\begin{Bmatrix} z_{N_v}^0 \\ \vdots \\ z_{N_v}^n \end{Bmatrix} \otimes \boldsymbol{H}(z_{N_v}) - \begin{Bmatrix} z_{N_v-1}^0 \\ \vdots \\ z_{N_v-1}^n \end{Bmatrix} \otimes \boldsymbol{H}(z_{N_v-1}) \right) \right] \tag{10}$$

$$\boldsymbol{Q} = \left[\left(\begin{Bmatrix} z_1^1 \\ \vdots \\ z_1^{n+1} \end{Bmatrix} \otimes \boldsymbol{H}(z_1) - \begin{Bmatrix} z_0^1 \\ \vdots \\ z_0^{n+1} \end{Bmatrix} \otimes \boldsymbol{H}(z_1) \right) \quad \cdots \right.$$

$$\left. \left(\begin{Bmatrix} z_{N_v}^1 \\ \vdots \\ z_{N_v}^{n+1} \end{Bmatrix} \otimes \boldsymbol{H}\left(z_{N_f}\right) - \begin{Bmatrix} z_{N_v-1}^1 \\ \vdots \\ z_{N_v-1}^{n+1} \end{Bmatrix} \otimes \boldsymbol{H}(z_{N_v-1}) \right) \right] \tag{11}$$

with $\otimes$ denoting the *Kronecker product*. The derivation of the SpCF technique (Amador & Brincker 2023d) is accomplished by factoring the Q matrix as follows

$$\boldsymbol{Q}_{\mathrm{RE}} = [\,\mathbf{Re}(Q) \quad \mathbf{Im}(Q)\,] = O\Upsilon \tag{12}$$

with $\boldsymbol{Y}$ standing for the *Frequency-domain Controllability* matrix (Amador & Brincker 2023d). Replacing $\boldsymbol{Q}$ by $\boldsymbol{Q}_{\mathrm{RE}}$ and $\boldsymbol{P}$ by $P_{\mathrm{RE}} = [\,\mathbf{Re}(P) \quad \mathbf{Im}(P)\,]$ in Eq. (9), gives

$$P_{\mathrm{RE}} = OA\Upsilon \tag{13}$$

The key step towards the derivation of the SpCF is to estimate matrices $\boldsymbol{O}$ and $\boldsymbol{Y}$. This is accomplished by taking the SVD of $\boldsymbol{Q}_{\mathrm{RE}}$, giving

$$Q_{\mathrm{RE}} = USV^H \tag{14}$$

where $\boldsymbol{U}$ and $\boldsymbol{V}$ are orthogonal matrices containing the singular vectors and $\boldsymbol{S}$ is diagonal matrix containing the singular values of $\boldsymbol{Q}_{\mathrm{RE}}$, with $(\cdot)^H$ denoting the complex conjugate transpose (Hermitian) of a complex matrix. From Eq. (14), estimates for $\boldsymbol{O}$ and $\boldsymbol{Y}$ can be computed using the i^{th} subspace of $\boldsymbol{Q}_{\mathrm{RE}}$ as

$$\begin{aligned} \hat{\boldsymbol{O}}_i &= U_i S_i^{1/2} \\ \hat{\Upsilon}_i &= S_i^{1/2} V_i^H \end{aligned} \tag{15}$$

where $U_i = [u_1 \quad \cdots \quad u_i]$, $V_i = [v_1 \quad \cdots \quad v_i]$, and $S_i = \mathbf{diag}([s_1 \quad \cdots \quad s_i])$, with $\mathbf{diag}(\cdot)$ denoting the diagonal matrix operator, $\boldsymbol{u}_{\mathrm{k}}$ and v_k the column vectors of $\boldsymbol{U}$ and $\boldsymbol{V}$, and s_k designating the diagonal elements of $\boldsymbol{S}$. Once the estimates $\widehat{O}_i$ and $\widehat{\Upsilon}_i$ are computed from Eq. (15), the estimate for the discrete-time state matrix is computed from i^{th} subspace of $\boldsymbol{Q}_{\mathrm{RE}}$, as

$$\widehat{A}_i = \widehat{O}_i^{+} P_{\mathrm{RE}} \widehat{\Upsilon}_i^{+} = S_i^{-1/2} U_i^H P_{\mathrm{RE}} V_i S_i^{-1/2} \tag{16}$$

with $(\cdot)^+$ denoting the pseudo-inverse of a matrix. The estimate for the output matrix $\widehat{C}_i$, on the other hand, is found by retrieving the first N_o rows of $\widehat{O}_i$. Next, the estimates for the modal properties can be computed, firstly, by taking the eigenvalue decomposition of $\widehat{A}_i = \widehat{\boldsymbol{\Psi}}_i \widehat{\boldsymbol{\Lambda}}_i \widehat{\boldsymbol{\Psi}}_i^{-1}$. Then, by making use of relations (3), the mode shape matrix is estimated as

$$\widehat{\boldsymbol{\Phi}}_i = \widehat{C}_i \widehat{\boldsymbol{\Psi}}_i \tag{17}$$

Finally, the continuous-time poles can be retrieved from the main diagonal of $\widehat{\boldsymbol{\Lambda}}_i$ as described, for instance, in (Brincker, R. & Ventura 2015).

3 APPLICATION EXAMPLE: OMA OF THE PORT MANN STAY CABLE BRIDGE

In addition to providing clear stabilization diagrams, the subspace driven system identification techniques possess the ability of handling the information of several sensors at once. This follows from the fact that the SVD condenses and reduces physical information in the big system matrices in a much smaller subspace, leading to very robust identification and, thereby, to very clear stabilization diagrams. In order to assess this characteristic, the SpCF is applied to the vibration responses of the Port Mann bridge depicted in Figure 1, which has been continuously monitored since 2012 by means of 54 acceleration sensors placed on the footing, pylons and floating decks, as indicated in Figure 2.

The Port Mann Bridge is a 10-lane large span cable-stayed bridge spanning the Fraser River in Vancouver, British Columbia. The cable-stayed central span is one of the longest in the world measuring 850-meter-long. The North and South main span superstructure consists of steel field sections, pre-cast deck panels and stay cables. The North and South approaches are both span-by-span superstructures with pre-cast segment decks. 144 cable stays extend from each 535-foot-tall tower. The vibration responses of the bridge are continuously acquired by a vibration monitoring system with a sampling rate of 200 Hz. The vibration responses of the bridge are stored in datasets containing 40min worth of data. The dataset utilized to assess the performance of the SpCF technique was acquired on the 9$^{\mathrm{th}}$ of April 2015. For this purpose, the acceleration response histories in such a dataset were de-trended, filtered with an 8th order lowpass Chebyshev Type I filter and resampled with a sampling frequency of 2 Hz.

Finally, the HS matrix was estimated with a frequency resolution of 513 frequency lines by taking the Fourier Transform of the positive part of a Correlation Function matrix previously computed from the filtered response histories with 1024 time lags. The estimation of the HS



Figure 1. Port Mann Cable-stayed bridge spanning the Fraser River in Vancouver, British Columbia, Canada.

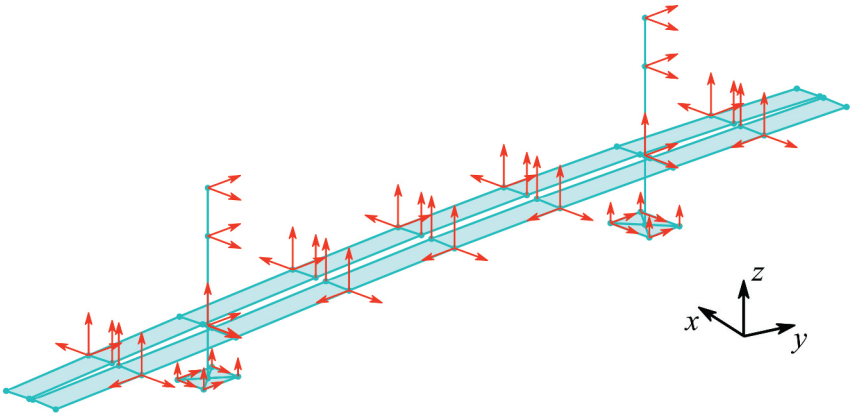


Figure 2. Sensors' locations and measurement directions adopted in the continuous vibration monitoring of the Port Mann bridge in Vancouver, British Columbia, Canada.

matrix was carried out by applying an exponential window with a decay rate of 99,9999% to the positive part of the CF function to minimize the leakage effects and the spurious influence of the higher correlation lags on the estimated frequency function.

Once estimated, the HS matrix with dimension 54 x 35 x 513 was used as primary data both by the pCF and the pLSCF algorithm. The identification of the modal properties of the Port Mann bridge was carried out with a HS matrix with only 35 columns conveniently chosen to be related to the responses of the floating deck and pylons, which possess higher amplitudes of vibrations. This allowed, on the one hand, to reduce the size of the HS matrix and, thereby, the computational time needed to run the pLSCF and SpCF algorithms, and on the other hand, to improve the accuracy of their estimates for the global modal properties of the bridge.

Next, the pLSCF and SpCF methods were applied to estimated HS matrix. The pLSCF technique, also known by its commercial name PolyMAX (Peeters et al. 2007), is known for being a very accurate and robust frequency domain identification algorithm, and therefore, it is regarded as a standard modal identification approach by the modal analysis community and is commercialized in several modal identification software.

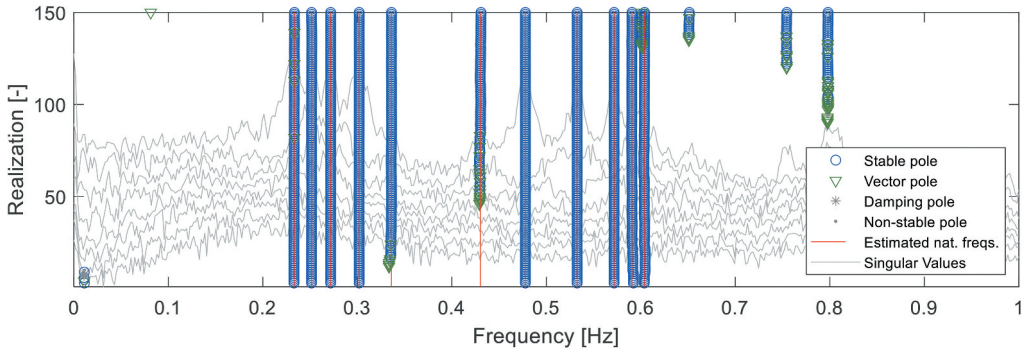


Figure 3. Stabilization diagram constructed with the SpCF technique from the vibration responses of the Port Mann bridge by performing 150 realizations of the system matrices constructed with a maximum model order $n = 4$. The vertical solid lines indicate the identified vibration modes and the background gray lines (plotted solely for validation purposes) are the singular values obtained from the SVD of the full spectral matrix at each frequency line.

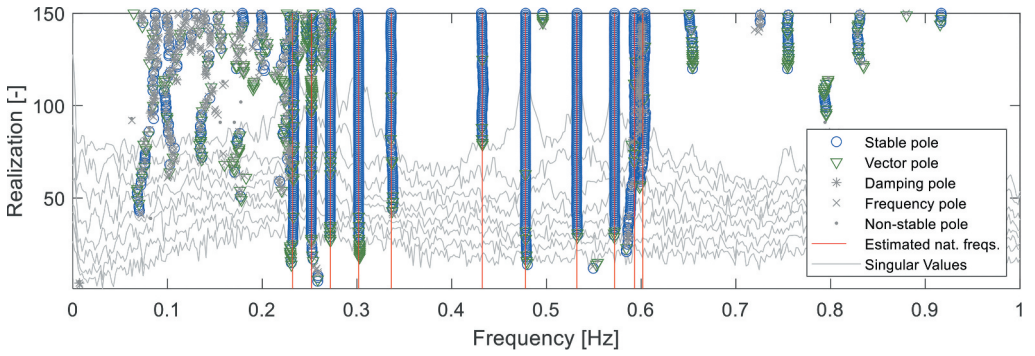
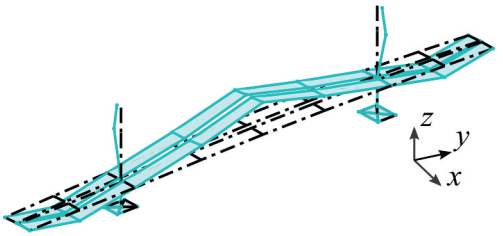


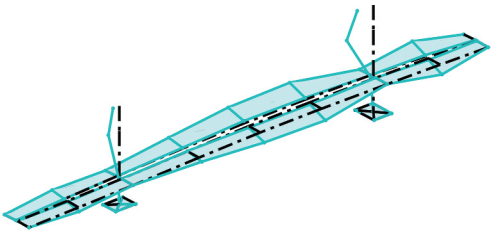
Figure 4. Stabilization diagram constructed with the pLSCF technique from the vibration responses of the Port Mann bridge by performing 150 realizations of the system matrices constructed with a maximum model order $n = 4$. The vertical solid lines indicate the identified vibration modes and the background gray lines (plotted solely for validation purposes) are the singular values obtained from the SVD of the full spectral matrix at each frequency line.

Table 1. Identification results obtained from the SpCF and pLSCF techniques for the Port Mann bridge.

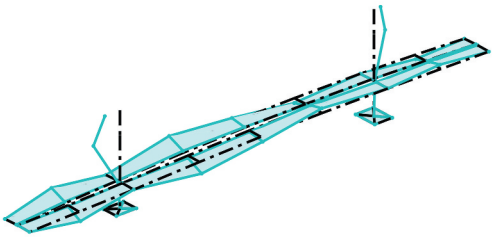
	SpCF		pLSCF	
Mode	Natural Frequency (Hz)	Damping Ratio (%)	Natural Frequency (Hz)	Damping Ratio (%)
1	0.2332	0.495	0.2320	1.074
2	0.2516	0.666	0.2520	0.523
3	0.2718	0.509	0.2719	0.362
4	0.3020	0.693	0.3017	0.662
5	0.3361	0.924	0.3363	1.639
6	0.4302	0.637	0.4322	1.147
7	0.4779	0.517	0.4779	0.521
8	0.5326	0.504	0.5321	0.459
9	0.5717	0.412	0.5719	0.402
10	0.5906	1.357	0.5931	1.301



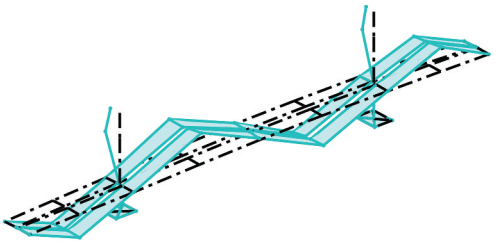
$f_1 = 0.233\ Hz, \xi_1 = 0.495\ \%$



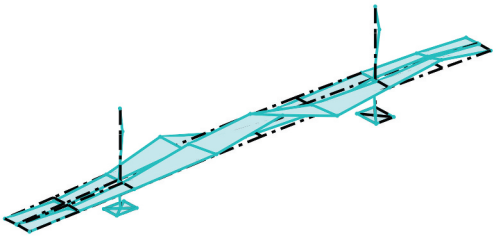
$f_2 = 0.252\ Hz, \xi_2 = 0.666\ \%$



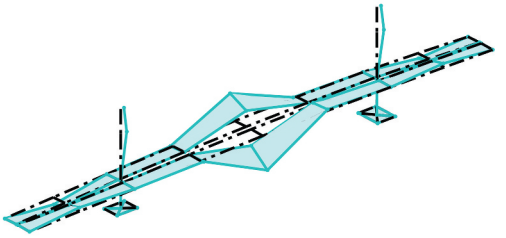
$f_3 = 0.272\ Hz, \xi_3 = 0.509\ \%$



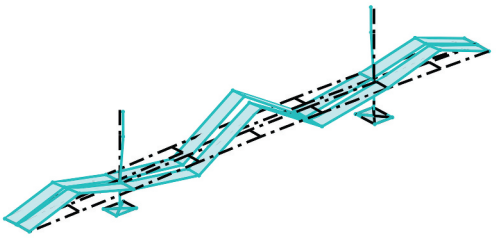
$f_4 = 0.302\ Hz, \xi_4 = 0.693\ \%$



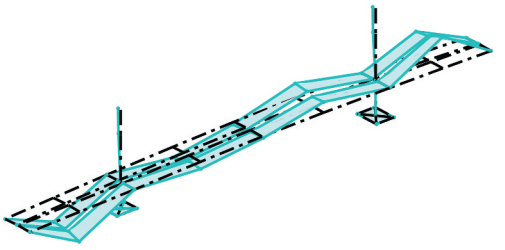
$f_5 = 0.336\ Hz, \xi_5 = 0.924\ \%$



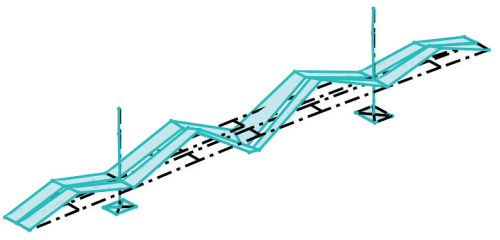
$f_6 = 0.430\ Hz, \xi_6 = 0.637\ \%$



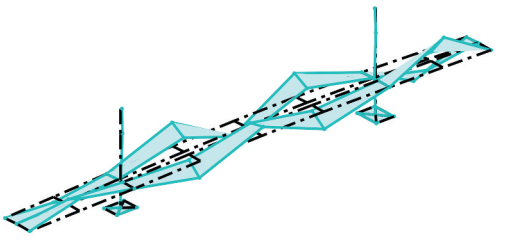
$f_7 = 0.478\ Hz, \xi_7 = 0.517\ \%$



$f_8 = 0.533\ Hz, \xi_8 = 0.504\ \%$



$f_9 = 0.572\ Hz, \xi_9 = 0.412\ \%$



$f_{10} = 0.591\ Hz, \xi_{10} = 1.357\ \%$

Figure 5. First ten vibration mode shapes identified with the SpCF technique.

Thus, the pLSCF algorithm is used as reference in the application example presented in this paper to assess the performance, robustness and accuracy of the SpCF approach. Aiming at sorting the physical modal properties from the numerical ones, stabilization diagrams were constructed by performing 150 realizations of the system matrices of both techniques which were assembled with a maximum model order $n = 4$. The stabilization diagrams constructed with the pLSCF and SpCF techniques are shown in Figures 3 and 4, respectively, wherein the vertical solid red lines indicate the natural frequencies automatically identified with the Hierarchical Clustering Algorithm (HCA) described in Amador 2015.

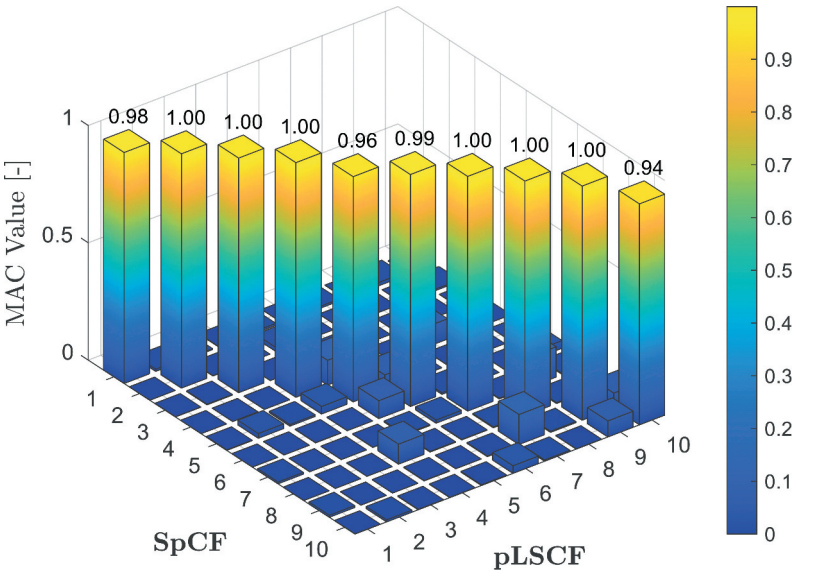


Figure 6. Modal Assurance Criterion (MAC) between the mode vectors estimated with the pLSCF and SpCF techniques.

By comparing the plots shown in such figures, it becomes clear that the SpCF provided clearer stabilization diagrams, which facilitated the identification of the first eleven vibration modes of the Port Mann bridge. The estimates for the natural frequencies and damping ratios of the first ten vibration modes obtained with both techniques are shown in Table 1. The results presented in this table show that the SpCF method provided estimates for the modal properties of Port Mann bridge that match fairly well those obtained with the pLSCF algorithm. The first ten vibration mode shapes automatically identified with SpCF approach by means of the stabilization diagram depicted in Figure 3 are shown in Figure 5.

The results presented in Figure 5 illustrate the ability of the SpCF method of providing accurate estimates for the mode shapes, even when it is applied to the vibration responses of a high number of sensors. The mode shape vectors estimated with the SpCF approach are compared to their counterparts estimated with the pLSCF technique in Figure 6. Similar to the other modal properties, this figure shows that the mode shapes estimated with the SpCF technique are very well correlated with those estimated with the pLSCF approach.

4 CONCLUSION

This paper assesses the performance of the new SpCF system identification technique in handling the vibration responses of a high number of sensors at once. For this purpose, the SpCF algorithm was applied to the vibration data of a large span stay cable bridge containing the responses measured with 54 accelerometers. In order to assess its performance, the SpCF

identification results were compared, in terms of stabilization diagrams and MAC, to those of the pLSCF algorithm, which is deemed as a standard system identification method due to its ability of providing clear stabilization diagrams. By comparing the diagrams constructed with both techniques, it became clear that the SpCF approach provided clearer stabilization diagram than that of the pLSCF approach, which in turn, led to a robust identification of the first ten vibration modes of the Port Mann bridge. In addition to this robustness, the SpCF approach also provided estimates for the modal properties of the Port Mann bridge which are very well correlated with the estimates obtained with the pLSCF method.

ACKNOWLEDGMENTS

The author acknowledges the funding received from DTU Offshore - Danish Offshore Technology Centre (DOTC) - to develop, formulate and implement the SpCF technique.

REFERENCES

Ibrahim, S. R. & Milkulcik, E. C. 1997. A Method for Direct Identification of Vibration Parameters from Free Response. *Shock and Vibration Bulletin*, 47: 83–196.

Ibrahim, S. R. 1984. A Modal Identification Algorithm for Higher Accuracy Requirements. *AIAA Paper , in*: *Proceedings of the 25th Structures, Structural Dynamics and Materials Conference*, Palm Springs, California, No. 84-0928: 117–122.

Fukozono, K. 1986. Investigation of Multiple-reference Ibrahim Time Domain Modal Parameters Estimation Technique. *MSc. Thesis*, *Department of Mechanical and Industrial Engineering, University of Cincinnati*.

Vold, H., Kundrat, J., Rocklin, G. T. & Russel, R. 1982. A Multi-input Modal Estimation Algorithm for Mini-computers. *SAE Technical Paper Number 820194* .

Peeters, B. & De-Roeck, G. 1999. Reference-based Stochastic Subspace Identification for Output-only Modal Analysis. *Mechanical Systems and Signal Processing*. 13(6): 855–878.

Peeters, B., Van-Der-Auweraera, H., Vanhollebeck, F. & Guillaume, P. 2007. Operational Modal Analysis for Estimating the Dynamic Properties of a Stadium Structure During a Football Game. *Shock and Vibration*, 14(1): 283–303.

Amador, S.D.R.& Brincker, R. 2023a. The New Poly-reference Complex Frequency Formulated in Modal Model (pCF-MM): A New Trend in Experimental Modal Analysis? *In*: *Proceedings of the 41st Int. Modal Analysis Conference (IMAC2023)*, *Austin, TX, USA*.

Amador, S.D.R. & Brincker, R. 2023b. OMA of a High-rise TV Tower Using the Novel Poly-reference Complex Frequency Modal Identification Technique Formulated in Modal Model. *In*: *Proceedings of the 41st Int. Modal Analysis Conference (IMAC2023)*, *Austin, TX, USA*.

Amador, S.D.R. & Brincker, R. 2023c. A robust poly-reference frequency-domain identification method to extract dynamic properties from vibration data. *Communications Engineering*. 2, 73.

Amador, S.D.R. & Brincker, R. 2023d. Modal Identification of a Steel Platform Specimen with a Subspace Implementation of the Poly-reference Complex Frequency Method Formulated in Modal Model (pCF-MM). *In*: *Proceedings of the 12th Int. Conference on Structural Dynamics (EURODYN 2023)*, *Delft*, *The Netherlands*.

Juang, J. N. & Pappa, R. S. 1985. An Eigensystem Realization Algorithm for Modal Parameter Identification and Modal Reduction. *Journal of Guidance, Control and Dynamics*. 8(5): 620–627.

Amador, S.D.R. 2015. Uncertainty Quantification in Operational Modal Analysis and Continuous Monitoring of Special Structures. *PhD thesis. Department of Civil Engineering, Faculty of Engineering of University of Porto, Porto, Portugal*.

Brincker, R. & Ventura, C. 2015. Introduction To Operational Modal Analysis. *Wiley, 1st ed.*


Taylor & Francis
Taylor & Francis Group
http://taylorandfrancis.com

SS05: Underground and above-ground infrastructure resilience and sustainability

Organizers: M. Domaneschi, B. Chiaia, G.C. Marano, V. Villa & S. Argyroudis


Taylor & Francis
Taylor & Francis Group
http://taylorandfrancis.com

Bridge Maintenance, Safety, Management, Digitalization and Sustainability – Jensen, Frangopol & Schmidt (eds)
© 2024 The Author(s), ISBN 978-1-032-77040-6
Open Access: www.taylorfrancis.com, CC BY-NC-ND 4.0 license

Development of a novel bridge deck-to-pier connection for improved tsunami resilience

R.K. Pagel
University of Canterbury, Christchurch, New Zealand

A. Palermo
University of California, San Diego, USA

I.N. Robertson
University of Hawaii at Manoa, Honolulu, USA

G.De Francesco
California Polytechnic State University, San Luis Obispo, USA

ABSTRACT: Tsunami events have caused significant coastal damage in the past two decades, including the widespread failure of bridges. The 2011 East Japan tsunami revealed a common bridge failure mode: superstructures disconnecting from piers due to weak deck-to-pier connections unable to withstand uplift forces. This study proposes a novel deck-to-pier connection to enhance bridge resilience to tsunami. The connection consists of a mechanical bar that increases vertical displacement capacity, dissipates tsunami energy through material hysteresis, and yields before damage to critical bridge elements. By concentrating tsunami damage into a replaceable element, the post-event repairs are quick and economical to undertake, reducing bridge downtime. A series of experimental tests, conducted on a 1/3 scale pier cap and bridge deck specimen, investigate the connection and bridge system response. This study validates the design philosophy, and investigates bar materials suitable for coastal environments, including mild steel, stainless steel and glass fibre reinforced polymer.

1 INTRODUCTION

Bridges frequently serve as vital connections between coastal communities, particularly for isolated areas with limited transportation networks. The functionality of these structures is essential for recovery efforts during and in the immediate aftermath of a natural hazard, as demonstrated by the 2004 and 2011 tsunami events.

Reconnaissance conducted after the 2011 East Japan tsunami found that over 300 bridges were significantly damaged in this event (Akiyama et al. 2012). Many of these bridges were found with damage consistent with large uplift forces acting on the superstructure: damage to the connection between the bridge deck and pier, decks found flipped upstream or next to the piers and damage to the top of the shear keys on the piers (Kawashima 2012; Shoji, Hiraki & Ezura 2012; Unjoh 2012).

Subsequent research highlighted the large forces acting on bridge sub- and superstructures during tsunami inundation (e.g. Azadbakht & Yim 2015). Researchers identified that the magnitude of these actions depends on several parameters, including the wave height and velocity (Istrati et al. 2018), the wave type and how it breaks (Araki, Ishino & Deguchi 2010) and amplification from local bathymetry and topography (Yeh, Robertson & Preuss 2005). Similarly,

DOI: 10.1201/9781003483755-182

many factors were found to influence how the bridge responds, such as the substructure and span arrangement, which affect load distribution (Motley et al. 2016) and the type of girders used, due to the air entrapment effect, which can generate additional buoyancy forces (Azadbakht & Yim 2016; Istrati & Buckle 2019; Seiffert, Ertekin & Robertson 2015).

Bridges typically have different force-resisting mechanisms for lateral and vertical actions, so the relative magnitude of these actions can significantly affect the response and the level of damage induced on the structure. An investigation by Robertson et al. (2007) revealed that bridges are often inadequately designed for the uplift forces generated by wave loading. Furthermore, Yeh, Sato and Tajima (2013) identified that the initial wave loading can weaken critical force-resisting components, resulting in significant damage during the return wave loading.

In response to the evident scale of damage caused by these waves, solutions have been proposed to mitigate the effects of tsunami inundation on bridge structures. Researchers have investigated including perforations in the superstructure to allow the air and water to move vertically through the deck. An experimental study by Cuomo, Shimosako and Takahashi (2009) found that air relief slots in the bridge deck could reduce the uplift forces for small wave amplitudes. However, these slots were found to be inadequate for larger waves. Additionally, an experimental study by Lukkunaprasit et al. (2011) on a 1:100 scale bridge indicated that the peak uplift force could be reduced by up to 25%.

Another approach proposed to mitigate tsunami damage involved optimising the bridge superstructure for hydrodynamic loads. Zhang, Hoshikuma and Usui (2012) proposed installing a fairing on the side of the bridge deck to improve the hydrodynamic flow during tsunami inundation. Their experimental testing concluded that this could minimise the horizontal force but would increase the uplift force for some fairing geometries. Both proposed solutions require further experimental validation and development to verify their practicality in the design of bridges.

However, these solutions do not fully address the inability of a bridge system to resist the large uplift forces induced by tsunami inundation. Therefore, this research proposes a novel deck-to-pier connection to accommodate these tsunami forces. This paper presents an overview of the development of this novel connection and experimental testing conducted to verify the design and detailing of this connection.

2 NOVEL BRIDGE DECK-TO-PIER CONNECTION

This research proposed a novel bridge deck-to-pier connection. The connection consists of mechanical bars designed to elongate under tsunami uplift actions, allowing the bridge deck to displace vertically and rotate. This design philosophy aims to limit forces induced onto the bridge substructure, dissipate tsunami wave energy, and delay the washout failure of the deck. While these bars are designed for uplift forces, the lateral component of the tsunami force will be resisted by concrete or steel shear keys.

The bars are not constrained vertically, so once the tsunami flow has subsided, the stabilising effect of the deck's weight will provide re-centring force, and the bridge deck will return to its initial position. Due to the large lever arm between the mechanical bars and the deck's centre of rotation, the bars will yield at low rotations. Therefore, any significant deck rotation due to tsunami inundation will result in residual deformations, requiring the bars to be replaced. However, when the superstructure is appropriately designed for rotations, the post-event repairs will likely be limited to bar replacement and minor concrete repairs.

Three bar materials were investigated for their feasibility to be used in this connection: galvanised mild carbon steel, stainless steel and glass fibre reinforced polymer (GFRP). These materials were chosen based on their material properties and suitability for coastal environments. Both carbon and stainless steel exhibit ductile post-yield behaviour with large displacement capacities, while GFRP is elastic until rupture. The use of glass fibres means the bar is lightweight and non-corrosive, and the longitudinal arrangement of these fibres results in a low shear capacity and a brittle failure mechanism.

3 LARGE SCALE EXPERIMENTAL TESTING

3.1 *Prototype and specimen design*

The chosen prototype bridge configuration represents a typical medium-span New Zealand bridge, as depicted in Figure 1. The prototype comprises a cast in-situ reinforced concrete substructure and a precast, post-tensioned concrete superstructure. Two 30m spans are simply supported on a 1.5m diameter circular pier and pier cap beam. The bridge deck comprised five standard super-tee beams in accordance with details outlined in Research Report 364 (New Zealand Transport Agency 2008).

Wave heights for the coastal Christchurch location were obtained from Power (2013) and were used in conjunction with the AASHTO Guide Specifications (AASHTO 2022), to determine the tsunami forces. All concrete elements were designed for these forces in accordance with NZS 3101 (Standards New Zealand 2006).

A 1/3 scale model of the prototype structure was used in the experimental testing phases. This structure consisted of a deck unit with three tee beams cast integrally. A precast pier cap and foundation, which supported the deck, were post-tensioned to the strong floor to minimise unintended displacements of these elements.

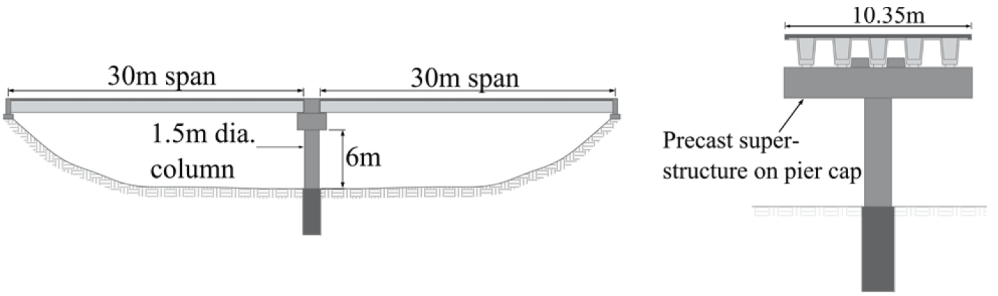


Figure 1. Prototype bridge structure: (left) Longitudinal profile, (right) Elevation profile.

3.2 *Connection detailing*

The bars were debonded within Drossbach ducts located within the pier cap and deck, as shown in Figure 2. The positioning of these ducts within the flange of the tee beam was selected to avoid clashes with the heavily reinforced and typically post-tensioned base of the beam web; however, the ducts could be moved for different geometries. Additionally, positioning the ducts within the flange of the beam was viable due to the diaphragm spanning between adjacent webs, which provided additional transverse stiffness to the bridge deck.

Anchorages were located at the top of the deck and the base of the pier cap. These consisted of flange nuts and washers installed snug-tight for the carbon steel and stainless steel bars and a 300mm sleeve anchorage, which the GFRP was epoxied into (Figure 3). The anchorages were designed to be easily accessible, facilitate the replacement of the bars, and enable corrosion monitoring. For this experimental testing, the washers and nuts were positioned flush with the base of the pier cap (and the top of the deck). For future application, it is recommended to embed these into a grout pocket to minimise the effect on the roadway.

3.3 *Design recommendations for countering tsunami demands*

Design changes should be considered to minimise the damage induced on bridge structures due to tsunami inundation and to effectively integrate the proposed connection alongside standard bridge details.

Unlike typical bridge design, which primarily considers downward forces, tsunami inundation applies upward forces on the bridge deck and, therefore, can induce tension along the top of the deck. This tension force will typically require additional steel reinforcement to be included within the beam flange to satisfy design requirements.

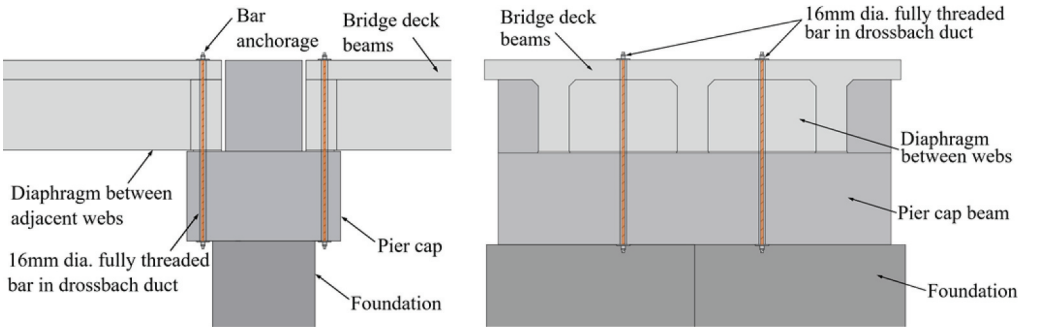


Figure 2. Schematic of the bars anchorage detailing within the deck and pier cap of the specimen structure (left) side view (right) cross-sectional view at pier.



Figure 3. Bar anchorages below the pier cap: installed washer and nut/flange nut (left) the carbon steel bar, (middle) the stainless steel bar and (right) internal sleeve with the epoxied GFRP bar before installation.

The mechanical bars should be designed considering both uplift loads and overturning moments. A capacity design process should be used to ensure that the bars yield before the superstructure and the substructure elements. It is recommended to check a minimum of three critical cases:

1. The start of the initial wave inundation, when uplift force acts on the offshore edge of the bridge deck, creating an overturning moment about the onshore elements. Downward force should be considered if the wave height exceeds the superstructure height for all three cases.
2. Halfway through of the initial wave inundation, when uplift force is distributed across the entire underside of the bridge deck, creating an upwards deck motion.
3. The start of the return wave inundation, when uplift force acts on the onshore edge of the bridge deck, creating an overturning moment about the offshore elements.

It is advisable to consider the duct size relative to the size of the bar. A large duct allows for large deck rotations and lateral displacements before the bar is engaged, while a small duct may be easier to implement alongside existing reinforcing. Depending on the positioning of the ducts, additional reinforcing (U-bars or similar) may be required to tie the ducts into the main reinforcing cage in both the pier cap and the deck diaphragm.

The shear keys and diaphragm should be designed to the maximum lateral demands induced by the tsunami while also considering seismic lateral demands if applicable. In addition, the shear keys should be of sufficient height considering the maximum expected superstructure uplift. A shear key with angled sides in the transverse direction will allow more rotation and potentially be damaged less than a shear key with straight sides. The gap between the shear key and the edge of the bridge beam influences how much the deck can translate under tsunami inundation and, thus, how much shear load is transferred to the structural fuse bars.

3.4 *Experimental test set-up*

This experimental study was set up to simulate both the vertical and horizontal force components of the tsunami force. Four hydraulic actuators positioned beneath the bridge deck were used to simulate the vertical component of the force, while two actuators attached to the strong wall simulated the horizontal force (Figure 4). The vertical actuators were positioned offset from the centreline of the deck to induce an overturning moment and associated rotation on the bridge deck. The two east vertical actuators were connected to the deck to apply the initial wave loading, and to simulate an anticlockwise rotation of the bridge deck. The return wave loading was applied using the west set of actuators, via a clockwise rotation. Potentiometers were positioned on the deck to measure displacements, while load cells and strain gauges were attached to the bars to capture the applied loads and strains.

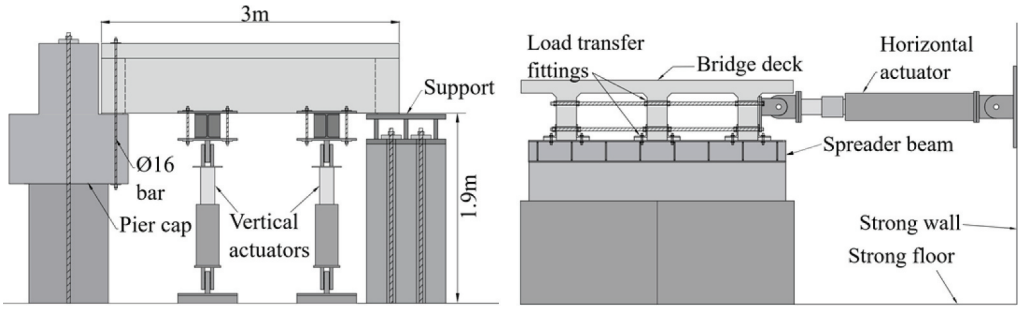


Figure 4. (Left) Schematic of the side view of the testing set up from the west, showing vertical actuators only (right) Schematic of the cross-sectional view of the testing set up, showing horizontal actuators only.

3.5 *Experimental testing programme*

The testing programme aimed to validate the predictions of the bridge deck-to-pier connections response under tsunami loading. Given the potential variation in the ratio of the vertical and horizontal force component magnitudes, as Istrati et al. (2016) noted, the angle of incidence of tsunami waves can vary significantly. This variability can lead to differences in the bridge structural performance, so an envelope of loading cases was developed to capture all likely actions. The envelope consisted of horizontal-only actions (0°) to vertical-only actions (90°) and included an intermediate case consisting of combined horizontal and vertical actions (45°), as shown in Table 1.

The vertical loading was applied so as to initiate rotation of the deck. A design ultimate limit state rotation of 0.02 radians was selected for the loading protocol. This rotation exceeded the yield rotation capacity for the steel and stainless steel bars and was less than the rupture rotation capacity of the GFRP bars.

The horizontal loading was applied, assuming that the shear key would allow lateral displacement of the deck before it was engaged. The applied lateral displacement resulted in a small amount of shear load applied to the bars.

One loading protocol was developed for each test phase and considered the initial and return wave loading. Figure 5 outlines the loading protocol displacement history for the uplift loading case.

4 EXPERIMENTAL RESULTS

An experimental study was undertaken to validate the theoretical predictions and assess the system response under representative tsunami loads. This section outlines the findings from eight tests conducted in Phases 1 – 3 (refer to Table 1). The bridge deck-to-pier connection response, in terms of overturning moment versus rotation, is presented for all three bar

Table 1. Summary of the testing programme (loading direction is taken from the horizontal)

Phase	Direction	Test ID	Test
1:Uplift loading	90°	P1-1	Carbon steel
		P1-2	Stainless steel
		P1-3	GFRP
2:Lateral loading	0°	P2-1	Carbon steel
		P2-2	Carbon steel
3:Combined loading	45°	P3-1	Carbon steel
		P3-2	Stainless steel
		P3-3	GFRP

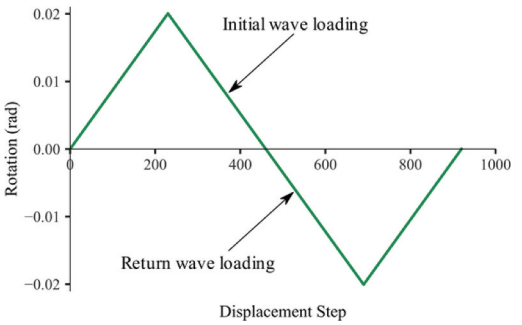


Figure 5. Loading protocol displacement history for uplift loading.

materials investigated in Figure 6. As expected, minimal damage was observed to the pier cap or deck for these eight tests, indicating that damage was effectively concentrated into the bars.

Under the overturning-only loading scenario, the carbon steel and stainless steel bars were subjected to displacements that exceeded their yield limit, resulting in large energy dissipations and residual deformations. The plastic deformation induced on the bars from the initial wave loading meant larger rotations were required to engage the bars under the return wave loading. As such, less bar capacity was activated under the return wave loading for the same rotation (Table 2), which was particularly significant for the carbon steel bars.

On the contrary, the glass fibre reinforced polymer bars (GFRP) exhibited primarily linear elastic behaviour for the overturning only loading scenario. The elastic behaviour of these bars resulted in lower residual displacements and a more optimum return wave response (3.1% degradation compared with 25% and 13.2% for carbon steel and stainless steel, respectively). Additionally, a small amount of slip (0.1-0.2%) was observed in the anchorage.

Applying shear load to the carbon steel and stainless steel bars effectively created a post-tensioning force, activating more bar capacity than the overturning-only loading scenario. However, the shear load weakened the GFRP bars, and one bar prematurely ruptured in the

Table 2. Maximum overturning moment capacity achieved for each loading case.

	Carbon Steel		Stainless Steel		GFRP	
	UP*	LAT/UP	UP	LAT/UP	UP	LAT/UP
Initial wave capacity (kNm)	225.5	229.1	320.8	345.6	222.5	211.5
Return wave capacity (kNm)	169.2	166.9	278.3	276.7	218.2	184.8
Degradation (%)	*25.0*	*27.1*	*13.2*	*19.9*	*3.1*	*12.6*

*Note: UP refers to the uplift-only loading, and LAT/UP refers to the combined lateral and uplift loading. Degradation refers to the reduction in load obtained in the return wave loading compared with the initial wave loading when both are limited to 0.02 radian rotation.

initial wave loading. This bar rupture reduced the total overturning moment capacity by 5.0% for the initial wave loading and 15.3% for the return wave loading, compared with the scenario with no lateral loading. These results have highlighted the need to design shear keys to limit the maximum lateral displacement of the deck. Implementing a well-designed shear key will minimise the shear forces induced on the bars, which is particularly important when utilising the GFRP bars.

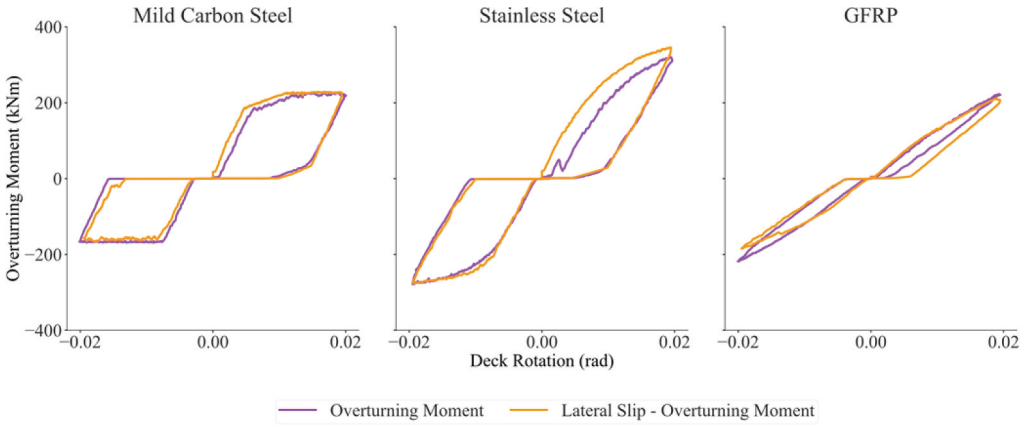


Figure 6. Comparison of the moment-rotation response for all three bar materials investigated.

5 CONCLUSION

The 2011 East Japan tsunami highlighted the vulnerability of bridges to the uplift forces induced by tsunami waves. Reconnaissance indicated that the connection between the deck and the pier was susceptible to uplift forces, and, in many cases, these connections failed, causing the bridge deck to wash out in the tsunami flow.

This research proposes a novel bridge deck-to-pier connection to increase resilience against tsunami inundation. The connection utilises mechanical bars that elongate under tsunami loading, allowing the deck to displace vertically and rotate. By designing the bars properly, damage can be concentrated into these elements, to minimise damage to critical bridge components, including the bridge substructure. Following a tsunami event, repairs are likely limited to replacing the bars and minor concrete repairs.

An experimental study was conducted to validate the theoretical predictions and assess the bar response under typical tsunami loads. Three loading protocols, considering a range of likely tsunami wave angles of incidence, were proposed in this experimental study and could be used for future large-scale experimental programmes. This study highlighted that carbon steel and stainless steel bars effectively dissipated tsunami wave energy but exhibited residual deformations in the initial wave loading resulting in a different return wave loading behaviour. In contrast, the glass fibre reinforced polymer (GFRP) bars had minimal residual deformations and thus had a more similar response under both the initial and return wave loading. However, one of the bars ruptured when shear force was induced on the bars via lateral displacements of the bridge deck. This bar rupture resulted in a reduced capacity for the return wave loading, highlighting the importance of the shear key being designed to limit lateral displacements of the deck.

These tests confirmed that tsunami force could effectively be concentrated into the bar and limit the damage induced on the bridge deck and pier. Based on this, it is anticipated that this proposed bridge deck-to-pier connection could minimise the bridge downtime following a tsunami event. Lastly, the experimental testing highlighted the need to consider the full effects of tsunami forces on a bridge and adapt the structure design accordingly.

ACKNOWLEDGEMENTS

The authors extend their gratitude to Precast NZ for their partial funding of the specimen and to Ramset Reid, BBR Contech, Pultron Composites, GPIl and Freysinnet for their material contributions. Special appreciation is directed to Busck Prestressed Concrete Ltd for precasting the specimens. Additionally, the authors acknowledge the invaluable support and assistance provided by the University of Canterbury's Structural Engineering Laboratory technicians.

REFERENCES

AASHTO 2022, *Draft Guide Specification for Bridges Subjected to Tsunami*.

Akiyama, M, Frangopol, DM, Arai, M & Koshimura, S 2012, 'Probabilistic assessment of structural performance of bridges under tsunami hazard', *Structures Congress 2012*, pp. 1919–1928.

Araki, S, Ishino, K & Deguchi, I 2010, 'Stability of girder bridge against tsunami fluid force', *Coastal Engineering Proceedings*, pp. 1–12.

Azadbakht, M & Yim, S 2016, 'Effect of trapped air on wave forces on coastal bridge superstructures', *Journal of Ocean Engineering and Marine Energy*, vol. 2, pp. 139–158.

Azadbakht, M & Yim, SC 2015, 'Simulation and estimation of tsunami loads on bridge superstructures', *Journal of Waterway, Port, Coastal, and Ocean Engineering*, vol. 141, no. 2, American Society of Civil Engineers (ASCE), p. 04014031.

Cuomo, G, Shimosako, K & Takahashi, S 2009, 'Wave-in-deck loads on coastal bridges and the role of air', *Coastal Engineering*, vol. 56, pp. 793–809.

Istrati, D & Buckle, I 2019, 'Role of trapped air on the tsunami-induced transient loads and response of coastal bridges', *Geosciences*, vol. 9, no. 4, p. 191.

Istrati, D, Buckle, I, Lomonaco, P & Yim, S 2018, 'Deciphering the tsunami wave impact and associated connection forces in open-girder coastal bridges', *Journal of Marine Science and Engineering*, vol. 6, p. 148.

Kawashima, K 2012, 'Damage of bridges due to the 2011 Great East Japan earthquake', *Journal of Japan Association for Earthquake Engineering*, vol. 12, no. 4, pp. 319–338.

Kosa, K, Nii, S, Miyahara, K & Shoji, M 2010, 'Experimental study for estimating tsunami forces acting on bridge girders', *Proceedings of the 27th US-Japan Bridge Engineering Workshop*, Tsukuna, pp. 1–14.

Lukkunaprasit, P, Lau, TL, Ruangrassamee, A & Ohmachi, T 2011, 'Tsunami wave loading on a bridge deck with perforations', *Science of Tsunami Hazards*, vol. 30, no. 4, pp. 244–252.

Motley, M, Wong, HK, Qin, X, Winter, A & Eberhard, M 2016, 'Tsunami-induced forces on skewed bridges', *Journal of Waterway, Port, Coastal, and Ocean Engineering*, vol. 142, no. 3, p. 4015025.

New Zealand Transport Agency 2008, *Research Report 364 Standard precast concrete bridge beams*.

Power, W 2013, *Review of tsunami hazard in New Zealand*, Lower Hutt.

Robertson, I, Riggs, HR, Yim, SC & Young, YL 2007, 'Lessons from Hurricane Katrina storm surge on bridges and buildings', *Journal of Waterway, Port, Coastal, and Ocean Engineering*, vol. 133, no. 6, American Society of Civil Engineers (ASCE), pp. 463–483.

Seiffert, BR, Ertekin, RC & Robertson, I 2015, 'Wave loads on a coastal bridge deck and the role of entrapped air', *Applied Ocean Research*, vol. 53, Elsevier B.V., pp. 91–106.

Shoji, G, Hiraki, Y & Ezura, Y 2012, 'Evaluation of tsunami fluid force acting on the bridge deck damaged by the 2011 of the Pacific coast of Tohoku earthquake tsunami', *9th International Conference on Urban Earthquake Engineering*, pp. 2049–2054.

Standards New Zealand 2006, *NZ S3101 Concrete structures standard: Part 1 - The design of concrete structures*.

Unjoh, S 2012, 'Tsunami damage to bridge structures in Rikuzen-Takada City and the emergency road network recovery actions', *Proceedings of the International Symposium on Engineering Lessons Learned from the 2011 Great East Japan Earthquake*, pp. 1429–1438.

Yeh, H, Robertson, I & Preuss, J 2005, 'Development of design guidelines for structures that serve as tsunami vertical evacuation sites', *Open File Report 2005-4*, no. November 2005, p. 42.

Yeh, H, Sato, S & Tajima, Y 2013, 'The 11 March 2011 East Japan earthquake and tsunami: tsunami effects on coastal infrastructure and buildings', *Pure and Applied Geophysics*, vol. 170, no. 6–8, pp. 1019–1031.

Zhang, G, Hoshikuma, J & Usui, T 2012, 'An experimental study on countermeasure for mitigating tsunami effect on highway bridge', *15th World Conference on Earthquake Engineering*.

Bridge Maintenance, Safety, Management, Digitalization and Sustainability – Jensen, Frangopol & Schmidt (eds)
© 2024 The Author(s), ISBN 978-1-032-77040-6
Open Access: www.taylorfrancis.com, CC BY-NC-ND 4.0 license

The seismic response and resilience of nearby underground infrastructures

M. Dalmasso, M. Civera & B. Chiaia
Department of Structural, Geotechnical and Building Engineering, Politecnico di Torino, Turin, Italy

ABSTRACT: To assess the seismic resilience of civil structures and infrastructures, a detailed investigation of their response to strong motions is required. However, while the effects of major and minor earthquakes on above-ground infrastructures (e.g. road bridges) are relatively well-known, fewer studies have addressed underground ones (e.g. shallow or deep tunnels). In fact, while many bridges are heavily instrumented, few tunnels are equipped with the sensor networks needed for proper structural health monitoring. On the one hand, it is well-expected that both underwater and mountain tunnels will suffer much less significant structural damage than bridges. Nevertheless, research works on their respective responses, analysing comparatively different kinds of tunnels under the same seismic input, are lacking. This is even more true for studies involving recorded data and quantitative measurements. Here, the dynamic responses of one shallow underwater tunnel, built using the immersed tube technique in soft soil, and one deep tunnel, excavated in sandstone and shale rock, are directly compared. These two infrastructures are located close to each other in the San Francisco Bay Area and endured a very close near-fault earthquake. The results show that the tunnel in hard rock guaranteed a higher seismic resilience than the underwater tunnel dug in soft soil.

1 INTRODUCTION

Underground structures and infrastructures have strong robustness to sustain seismic events; nevertheless, they are not immune to them. Depending on the nature of the surrounding soil, several damaging mechanisms may be caused by strong motions.

In loose, water-saturated granular soils such as sand, silt, or gravel, seismic liquefaction can occur. In this scenario, due to the intense shaking of the ground, the surroundings of the tunnel temporarily lose their strength and behave like a liquid. In turn, without external constrictions, the tunnels may suffer uplifting due to their buoyancy in the liquified soil. This is a typical issue of underwater tunnels. Instead, based on the current reports found in the scientific literature, the direct effects of the strong motion on the tunnel structural elements themselves seem to be very limited. Hence, soil-structure interactions seem to be the main cause of potential damage and/or collapse.

The main failure causes are different for what concerns deep tunnels, excavated in rocks or hard soil. Based on the aftermaths of the Mw=7.6 Chi-Chi Earthquake of 21 September 1999 on 57 investigated cases, post-earthquake surveys (Wang et al., 2001) evidenced structural damage in 49 of them. Differently from their underwater counterparts in soft soils, both direct and indirect failure mechanisms were found to be involved. The systematic investigation highlighted the nine most common failure mechanisms as: sheared-off lining, crack development near the opening, bottom cracks, slope failure induced by tunnel collapse, inclined cracks, longitudinal cracks, transverse cracks, extended cross cracks, and wall deformation. Thus, not only site conditions (such as active fault displacement, rock rupture, weathering and decompression) and slope failures at the tunnel openings but also direct damage can be encountered. In this latter case, the tunnel shaking-induced damage is directly dependent on the structural form and building materials, such as e.g. the quality of the reinforced concrete tunnel linings

DOI: 10.1201/9781003483755-183

(Fantilli et al., 2023). Similar effects were observed in Japan (Asakura & Sato, 1996) and the rest of the world (Sharma & Judd, 1991).

To assess the seismic fragility of underground infrastructures some methods have been introduced. For instance, one is based on fragility curves for existing structures, adopting a stochastic approach exploiting the Hazus database (Marano et al., 2011). Another is based on the results of the 3D Incremental Dynamic Analysis (IDA), which takes into consideration bi-directional ground motions and coefficients of the structural components pertinent to the infrastructure (Ma et al., 2024).

However, despite all the scientific literature available on the topic, a side-by-side experimental comparison of the seismic response of deep and shallow tunnels does not seem to have been reported yet. To this aim, this short study directly compares two case studies, located in the San Francisco Bay Area, during the same near-fault seismic event.

2 CASE STUDIES

The two case studies analysed here are the Transbay Tube, also known as the Bay Area Rapid Transit (BART) Transbay Tunnel, and the Caldecott Tunnels (specifically, the third and fourth bores). These infrastructures are all instrumented with permanent Structural Health Monitoring (SHM) systems. They have been chosen based on their proximity, both to each other and to the epicentre of the seismic event of interest, the Mw=4.4 Berkeley Earthquake of 04 January 2018. Their respective locations are reported in Figure 1; considering the position as per the longitude and latitude assigned to the respective stations in the Centre for Engineering Strong Motion Data (CESMD) database[1] (CE58580 for the Transbay Tube, CE58359 and CE58540 for the Caldecott Tunnels), the distances are only 10.78 km and 3.71 km. Hence, the two infrastructures are expected to be highly excited by the very near-fault earthquake.



Figure 1. Locations of the epicentre (Berkeley Earthquake of 04 Jan 2018, Mw=4.4, 02:39:37 PST, 37.8552N 122.2568W Depth 12.3 km), indicated by ☆, and the two infrastructures, highlighted in red, with shakemap MMI contours superimposed in green. Modified from https://earthquake.usgs.gov/earthquakes/eventpage/nc72948801/map.

2.1 *The Transbay Tube*

The Transbay Tube is used here as an example of an underwater tunnel. It connects Oakland (on its East end) to San Francisco (West side), running beneath the waters of the San Francisco Bay. This infrastructure became operational in 1974, operating alongside the San Francisco-Oakland Bay Bridge, which instead opened in 1936. The construction of the tunnel employed an innovative immersion tube technique. Initially, a trench was dug into the bay's

1. https://www.strongmotioncenter.org/

seabed, and then tubular steel and reinforced concrete segments were submerged and subsequently covered with layers of rocks, sand, and gravel.

The tunnel reaches a maximum depth of -41 meters below sea level and spans a distance of 5.8 kilometres. At its terminus, it connects through two boring tunnels. Importantly, this connection is engineered with robust joints designed to allow the tunnel to withstand significant seismic activity without breaking, ensuring safety during earthquakes. In between, the tunnel consists of 57 segments, each averaging 100 meters in length, 7.3 meters in height, and 15 meters in width. Each segment comprises two separate train tunnels, with a pedestrian gallery in the centre intended for emergency purposes.

In the early 2000s, the Transbay Tube underwent seismic retrofitting to reduce movement in case of liquefaction of the surrounding sand and gravel. This retrofitting involved compacting the sand and gravel and utilising concrete-encased supports. Regarding the geological conditions of the infrastructures, Figure 2 reports the official stratigraphy as obtained by soil characterization tests. Generally speaking, the bay soil stratigraphy includes an uppermost layer of marine clay denominated as Young Bay Mud (YBM), overlying Old Bay Clay (OBC) or alluvial sands (Metropolitan Transportation Commission, 2015).

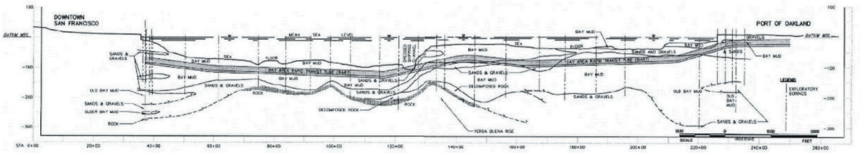


Figure 2. Interpreted geotechnical cross-sections of the Transbay tube alignment across San Francisco Bay. modified from (Parsons Brinckerhoff Quade & Douglas, 1965).

Table 1. Description of the output channels deployed on the bart transbay tunnel. the selected channels are marked in bold letters and indicated by *. 'trans': transversal; 'long': longitudinal; 'n.a.': not available in the CESMD database (CE58580).

Channel	Direction	Position	Channel	Direction	Position
01	up	W of Sliding Joint (539+78)	21	up	Tube 26: East End (624+00)
02	**trans**	**W of Sliding Joint (539+78)***	**22**	**trans**	**Tube 26: East End (624+00)***
03	long	W of Sliding Joint (539+78)	23	long	Tube 26: East End (624+00)
04	n.a.	n.a.	24	up	Tube 30: Near West QtrPt (635 +13)
05	n.a.	n.a.	25	trans	Tube 30: Near West QtrPt (635 +13)
06	n.a.	n.a	26	long	Tube 30: Near West QtrPt (635 +13)
07	up	E of Sliding Joint (539+97)	27	up	Tube 37: Mid-Length (659+18)
08	**trans**	**E of Sliding Joint (539+97)***	28	trans	Tube 37: Mid-Length (659+18)
09	long	E of Sliding Joint (539+97)	29	long	Tube 37: Mid-Length (659+18)
10	n.a.	n.a.	30	up	Tube 46: Mid-Length (690+72)
11	n.a.	n.a.	31	trans	Tube 46: Mid-Length (690+72)
12	up	Tube 7: West End (559+06)	32	long	Tube 46: Mid-Length (690+72)
13	trans	Tube 7: West End (559+06)	33	up	Tube 50: West End (703+32)
14	long	Tube 7: West End (559+06)	34	trans	Tube 50: West End (703+32)
15	up	Tube 11: East End (575+15)	35	long	Tube 50: West End (703+32)
16	trans	Tube 11: East End (575+15)	36	n.a.	n.a.
17	long	Tube 11: East End (575+15)	37	n.a.	n.a.
18	up	Tube 19: Mid-Length (599 +93)	38	up	Tube 53: West End (713+96)
19	trans	Tube 19: Mid-Length (599 +93)	**39**	**trans**	**Tube 53: West End (713+96)***
20	long	Tube 19: Mid-Length (599 +93)	40	long	Tube 53: West End (713+96)

The sensor setup is the one of the CE58580 station, reported in full detail in Table 1. The * symbol indicates the sensors considered for the following analysis.

In this regard, to keep this analysis brief yet as complete as possible, it was decided to consider a subset of four other output channels, deemed as the most interesting ones, and focusing only on the transversal response of the infrastructure.

From other ongoing studies (Dalmasso et al., 2024), it was assessed that channel 22, due to its minimal proximity to the (underwater) surface, suffered the largest transverse maximum acceleration. Hence, this channel was selected as representative of the most critical subsection. Channels 2 and 8 are included to account for the behavior of the San Francisco end, before and after the sliding seismic joint. Finally, channel 39 is also included as representative of the opposite end (Oakland side).

2.2 *The Caldecott Tunnels*

The third and fourth bores of the Caldecott Tunnels serve here as examples of deep tunnels. In detail, they belong to the State Route 24 tract that crosses the Berkeley Hills, East of Oakland. The fourth bore was initiated in 2010, finished in late 2012, and opened to traffic on November 16, 2013. It added two 3.7 m traffic lanes to the already-existing three bores. It was excavated with the innovative New Austrian Tunneling Method (NATM). Its typical cross-section is 15.2 m wide, for a total length of 1036 m. Following the standard procedure observed by Caltrans for "critical" structures along vital transportation routes such as SR 24, the seismic design of the Bore 4 relied on the Safety Evaluation Earthquake (SEE), considering a 1,500-year return period seismic event for the design, as well as a less severe Functional Evaluation Earthquake (FEE), considering a 300-year return period seismic event (Thapa et al., 2013). The requirements were set such that the fourth bore should remain fully operational (no or minimal damage) in case of the FEE event and can be reopened within 72 hours in case of the SEE event. These are discussed in more detail in (Yang et al., 2008). Regarding the other three pre-existing tunnels, Bore 3 were built in the early 1960s and instrumented since 1979.

The geologic profile of the mountain is reported in Figure 3. As can be seen, the tunnels intersect four major and three minor faults (all of them inactive) (Jacobs Associates, 2009), which may represent the most critical points. Overall, all strata represent weak, highly fractured, and sheared sedimentary rock formations.

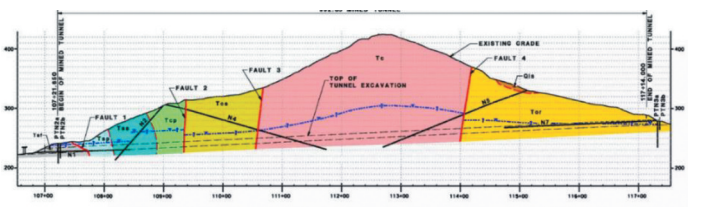
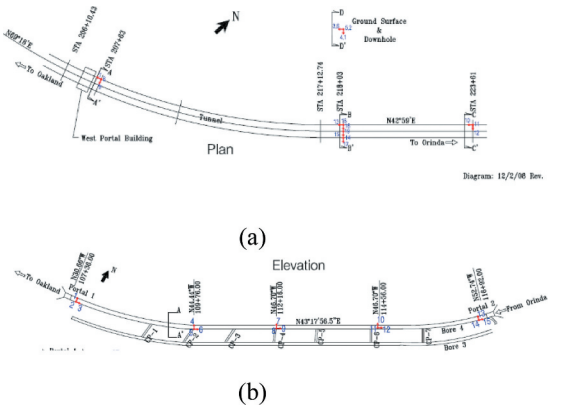


Figure 3. Geologic profile of the Caldecott Tunnels fourth bore. Retrieved from (Jacobs Associates, 2009).

Regarding the sensor layouts, the infrastructure presents two CESMD stations, CE58359 and CE58540, deployed respectively in the older Bore 3 and the newer Bore 4. These include 19 and 21 output channels respectively, shown in Figure 4. In both cases, again for conciseness' sake, it was decided to consider only a subset of accelerometers, located at different cross-sections and oriented in the direction transversal to the tunnel direction. For CE58359, due to the limited number of instrumented cross-sections (only three), all of them were analysed, thus considering channels 9, 12, and 16 (for better comparability with respect to the other options, channels 15 and 17).

For CE58540, it was considered that numerical and, especially, experimental evidence found in the scientific literature highlights two majorly at-risk locations for deep tunnels: the intersections with (active) faults and the portals at both ends. These aspects are confirmed by

the specific structural design considered for Bore 4 (Wilson et al., 2014). Applying these general considerations to the specific case under investigation, channels 1 and 13, located at the two ends of Bore 4, were selected for in-depth analysis. Instead, no channel is exactly located at any fault; furthermore, from the geological recordings mentioned above, they are all considered to be inactive. Thus, channel 7 was considered, due to its mid-length position.



(a)

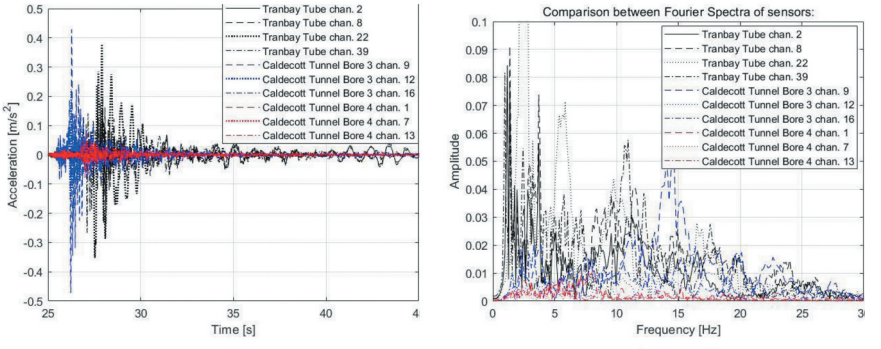
(b)

Figure 4. Top view of (a) Bore 3 with the three instrumented cross-sections, (b) Bore 4 with the five instrumented cross-sections marked.

3 RESULTS

In this section, the seismic responses of the selected case studies to the Berkely 2018 event are reported and discussed. These are reported as a side-by-side comparison to better highlight similarities and differences.

More specifically, Figures 5.a and 5.b report the seismic response at the selected output channels in the time and frequency domain. Notably, the accelerograms of stations CE58359, CE58540, and CE58580 have been time-synchronized, thus showing the different times of arrival. Finally, the Arias Intensity build-up curves, also known as Husid diagrams, are portrayed in Figure 6.



(a) (b)

Figure 5. Comparison of the acceleration time series (a) and Fourier spectra (b) at the selected output channels for the shallow underwater and deep underground tunnels.

The record length of the Transbay Tunnel is 65.835 seconds, composed of 6584 points equally spaced by $\Delta t = 0.01$ seconds. On the other hand, the signals recorded for Bore 3 span 58.0 seconds and are composed of 11600 points, while for Bore 4 there are 12255 for a recorded length of 61.275 seconds. Both cases are equally spaced by $\Delta t = 0.005$ seconds.

A key observation from Figure 5.a is the smaller amplitude of accelerograms for Caldecott Tunnel Bore 4 (maximum acceleration registered 0.08 m/s^2) compared with the other two cases (maximum acceleration registered 0.47 m/s^2 and 0.37 m/s^2 for Transbay Tube and Bore 3, respectively). Additionally, the acceleration peaks occur at different times for the three infrastructures. Indeed, the first structure that experiences the maximum acceleration is the Caldecott tunnel Bore 3, then Bore 4 and lastly the Transbay Tube. However, this is consistent with the distances from the epicentre; the delay between the peak acceleration between Caldecott Tunnel Bore 3 and the Transbay Tube is 2 seconds, while it is only 0.7 seconds between the two bores of the mountain tunnels. Interestingly, the seismically-induced oscillation of the Caldecott Tunnel Bore 4 becomes depleted in a much shorter time than the other two infrastructures.

In the frequency domain, signal spectra are analyzed for specific intervals corresponding to the seismic motion of each structure. For the Transbay Tube, it has been considered recorded signals between 28.3 and 43.0 seconds, for Bore 3 it has been considered the signals included between 25.0 and 34.0 seconds and lastly for Bore 4 signals comprehended between 27.5 and 39.5 seconds. Of course, also, in this case, the amplitudes of the Fourier spectra of the Bore 4 are smaller compared with the ones of the other two cases. Aside from a few general observations regarding the energy distribution in the lowest frequencies (below 5 Hz), this visualization of the recorded outputs doesn't provide any immediately discernible specific insights.

The analysis in the time-frequency domain, not fully reported here due to space constraints, enables to see more clearly how the duration of the recording in all the Transbay Tube and the Caldecott Tunnel number 4 is included in the range between 30 and 45 seconds. For the Bore 3, the duration is contained in the range between the 20 and 30 seconds. On the other hand, the frequency content is variable, considering the three different structures, but also considering different channels of the same structure. However, in all cases, this is always mainly contained under 10 Hz. Another distinction between the cases is the amplitude behaviours. For instance, the amplitude of channel 2 of the Transbay Tube decreases much faster than the one recorded at channel 39 of the same infrastructure.

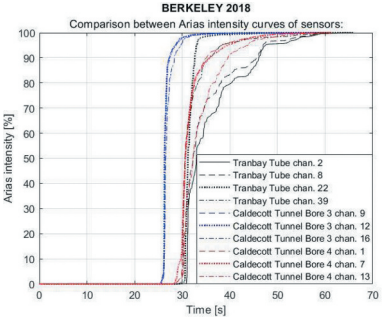


Figure 6. Comparison of the Husid diagrams for all the available transverse output channels of the shallow underwater and deep underground tunnels.

The Husid diagrams offer some interesting perspectives. In fact, they allow us to visualise how the Arias intensity (AI), defined by (Arias, 1970) as

$$\mathrm{AI} = \frac{\pi}{2g}\int_{o}^{t_{max}} a(t)^2 dt \tag{1}$$

cumulates over time. In turn, the AI is a well-known index of the seismic energy, related to the squared ground acceleration at time t, the total duration t_{max}, and the gravitational acceleration g. In this sense, Husid diagrams are extensively employed to estimate the seismic significant duration, as generally done in terms of D_{S595} (Trifunac & Brady, 1975) as the time elapsed between the two instants when 5% and 95% of the total energy is reached. From Figure 6, it can be seen how the D_{S595} duration of the event increases with the distance from the epicentre (it must be remarked that the Caldecott tunnel number 3 is much shorter than the BART Transbay Tube, hence, these effects are much less evident).

However, even considering this geometric attenuation due to the increased distance travelled by the seismic waves, the Husid diagrams offer some hints about the expected dynamic behaviour of the two underground infrastructures.

First, in both cases, the behaviour is similar to the dynamic response induced by an impulsive force since the earthquake epicentre is very close to the two infrastructures, which are both well confined by the surrounding ground. That does not allow for large free vibrations after the initial shock. From Figure 6, this is particularly noticeable for the Caldecott Tunnel bore 3 (in dark blue) at all cross-sections.

In general terms, the response of the Transbay Tube is overall in line with the expected dynamic behaviour of long submerged tunnels under strong motions of similar magnitude - see e.g (Dikmen, 2016) - as also reported in other recent works (Dalmasso et al., 2024).

Conversely, the two bores excavated in the hard rock show, as expected, a lower total duration, which is significant and more evident in the case of Bore 3.

These small yet noticeable differences, fully detailed in Table 2, could explain the different seismic robustness of underwater and mountainous tunnels, excavated (respectively) in soft and hard soils. Please note that all channels are reported, from the top down, in order of increasing distance from the epicenter.

Table 2. Significant duration and Arias Intensity of the selected output channels, ordered from the end closer to the epicentre to the one farther away.

Channel (BART)	D_{S595} [s]	AI [m/s]	Ch. (Bore3)	D_{S595} [s]	AI [m/s]	Channel (Bore4)	D_{S595} [s]	AI [m/s]
39	8.250	0.0021	9	2.355	0.0049	1	8.405	2.93e-4
22	2.370	0.0094	16	3.620	9.84e-4	7	10.410	1.02e-4
8	15.940	0.0029	12	2.575	6.17e-4	13	13.460	6.95e-5
2	16.440	0.0017						

The seismic durations of the channels related to the Transbay Tube are generally (with a few exceptions at specific locations) longer than those of the two bores of the Caldecott Tunnel. On the one hand, this could be a negative aspect since, as it is well-known, a longer seismic event results in more structural damage, all other things being equal (Jeong & Iwan, 1988).

Furthermore, one should consider that, since the infrastructure is considerably long, the seismic duration is higher than 10 seconds for channels 2 and 8, located farther from the epicentre, and lower than 10 seconds for channels 22 and 39, situated closer. Interestingly, for channel 22, there is an outstanding small value, likely due to its minimal proximity to the underwater surface. In a surprising turn, the Caldecott Tunnel exhibits different seismic durations between Bore 3 and 4. Nevertheless, there is a consistent trend within channels of the same bore, due to their much shorter length.

The two bores of the Caldecott tunnel, in general, are subjected to an Arias Intensity one order of magnitude lower than that of the Transbay Tube. This aspect, combined with the Transbay Tube's longer significant duration, can be seen as an explanation of why the deep mountain tunnels can be expected to be at a much lower risk. However, the dissimilarities between the two bores of the Caldecott Tunnel, despite their very close proximity, do not allow us to ascertain which one should be considered at major risk.

All these observations, however, are limited to one strong motion of a particularly close seismic event; thus, their generalization to other (near-fault or not) earthquakes will require further studies on a larger dataset.

4 CONCLUSIONS

This brief contribution reported a comparative analysis of the recorded seismic response of two deep and one shallow tunnels, recorded during the same near-fault seismic event. This side-by-side comparison was made possible by the recent seismic event of Berkeley 2018, which was recorded by the three nearby stations. This study highlighted some major aspects, namely:

- The Caldecott Tunnel Bore 4 experienced an acceleration that is an order of magnitude lower than the one of the Transbay Tube and, most interestingly, the nearby Bore 3.
- The seismic duration of the Transbay Tube is variable in its length, differently from the bores which have almost constant seismic duration. The arias intensity in the Transbay Tube is also higher than the cases of the bore tunnels.
- Therefore, in conclusion, the seismic resilience of the two bores excavated in hard rock can be guaranteed to be higher than that of the underwater tunnel dug in soft soil. This well-known aspect can be explained, at least partially, by their shorter significant duration and lower Arias Intensity, even when accounting for the slightly different distances for near-fault earthquakes.

These preliminary investigations will serve as a basis for future studies in the field of tunnel vibration-based monitoring under strong seismic motions.

ACKNOWLEDGEMENTS

This work is part of the research activity developed by the authors within the framework of the 'PNRR': SPOKE 7 "CCAM, Connected Networks, and Smart Infrastructure" - WP4.

REFERENCES

Arias, A. (1970). A measure of earthquake intensity. *Seismic Design for Nuclear Power Plants*, 438–483.

Asakura, T., & Sato, Y. (1996). Damage to Mountain Tunnels in Hazard Area. *Soils and Foundations*, 36 (Special), 301–310. https://doi.org/10.3208/SANDF.36.SPECIAL_301

Dalmasso, M., Civera, M., De Biagi, V., Surace, C., & Chiaia, B. (2024). A Comparative Analysis of the Seismic Response of a Nearby Tunnel and Bridge. *Proceedings of the 18th World Conference on Earthquake Engineering (*WCEE2024*)*.

Dikmen, S. U. (2016). Response of Marmaray Submerged Tunnel during 2014 Northern Aegean Earthquake (Mw=6.9). *Soil Dynamics and Earthquake Engineering*, *90*, 15–31. https://doi.org/10.1016/J.SOILDYN.2016.08.006

Fantilli, A. P., Chiaia, B., & Giordano, M. (2023). The strength of concrete in existing Italian tunnels. In *Expanding Underground - Knowledge and Passion to Make a Positive Impact on the World* (pp. 3057–3064).

Jacobs Associates. (2009). *Caldecott Improvement Project - Geotechnical Baseline Report*.

Jeong, G. D., & Iwan, W. D. (1988). The effect of earthquake duration on the damage of structures. *Earthquake Engineering & Structural Dynamics*, *16*(8), 1201–1211. https://doi.org/10.1002/EQE.4290160808

Ma, C., Li, K., Lu, D., Li, X., Liu, Z., & Du, X. (2024). Seismic fragility analysis of underground structures subjected to bi-directional ground motions based on the damage weight coefficients of components. *Soil Dynamics and Earthquake Engineering*, *178*, 108437. https://doi.org/10.1016/j.soildyn.2023.108437

Marano, G. C., Greco, R., & Morrone, E. (2011). Analytical evaluation of essential facilities fragility curves by using a stochastic approach. *Engineering Structures*, *33*(1), 191–201. https://doi.org/10.1016/j.engstruct.2010.10.005

Metropolitan Transportation Commission. (2015). *Core Capacity Transit Study (CCTS) Initial Engineering Study, Appendix A – Engineering Methodology, Environmental Engineering, and Permitting*.

Parsons Brinckerhoff Quade & Douglas. (1965). *Geologic Cross Section along the BART Transbay Tunnel*, *Engineering Geology of the Bay Area Rapid Transit (BART) System*.

Sharma, S., & Judd, W. R. (1991). Underground opening damage from earthquakes. *Engineering Geology*, *30*(3–4), 263–276. https://doi.org/10.1016/0013-7952(91)90063-Q

Thapa, B., Nitschke, A., Ramirez, I., McRae, M., & Gall, V. (2013). *Lessons Learned from NATM Design and Construction of the Caldecott Fourth Bore*.

Trifunac, M. D., & Brady, A. G. (1975). A study on the duration of strong earthquake ground motion. *Bulletin of the Seismological Society of America*, *65*(3), 581–626. https://doi.org/10.1785/BSSA0650030581

Wang, W. L., Wang, T. T., Su, J. J., Lin, C. H., Seng, C. R., & Huang, T. H. (2001). Assessment of damage in mountain tunnels due to the Taiwan Chi-Chi Earthquake. *Tunnelling and Underground Space Technology*, *16*(3), 133–150. https://doi.org/10.1016/S0886-7798(01)00047-5

Wilson, P., Shamsabadi, A., & Law, H. (2014, July). Site-Specific Seismic Coefficients for Retaining Wall/Slope Design: Fourth Bore Caldecott Tunnel. *Tenth U.S. Conference on Earthquake Engineering*.

Yang, C.-T., Law, H., & Shamsabadi, A. (2008). *Seismic Analyses for the Fourth Bore of Caldecott Tunnel*. 1–10. https://doi.org/10.1061/40975(318)208

Bridge Maintenance, Safety, Management, Digitalization and Sustainability – Jensen, Frangopol & Schmidt (eds)
© 2024 The Author(s), ISBN 978-1-032-77040-6
Open Access: www.taylorfrancis.com, CC BY-NC-ND 4.0 license

Blockchain technology conception in digital data collection for damage assessment and L.C.A.

L. Gioberti, M. Domaneschi, V. Villa & B. Chiaia
Politecnico di Torino, Torino, Italy

N. Catbas
University of Central Florida, Orlando, Florida, USA

ABSTRACT: In the modern transportation networks, such as metropolitan infrastructures, advanced technologies play a crucial role in enhancing efficiency. Infrastructure management is paramount for safety and sustainability. The integration of IoT and digital technologies in smart infrastructures poses challenges in the evolving digital landscape, particularly in ensuring the security and integrity of monitoring data. This study explores the potential applications of blockchain technology to enhance data authenticity and security in real-time subways monitoring. By leveraging blockchain, the study aims to establish a secure digital twin, ensuring the accuracy and integrity of acquired data. The technology's decentralized and tamper-resistant nature makes it well-suited for safeguarding critical monitoring data, offering a reliable foundation for proactive maintenance strategies. The findings indicate a promising avenue for blockchain in fortifying data management and information security in infrastructure assessment. For these reasons, blockchain could represent a valid solution to the modern challenges involved in the lifecycle management of infrastructure such as subways.

1 INTRODUCTION

In recent years, the development of our cities has increasingly focused on maximizing the use of existing built space. In this perspective, the creation of ever-expanding and efficient metropolitan networks allows us to harness technological advancements while respecting environmental criteria and the demand for effective and rapid transportation means.

Similarly, one of the significant challenges of this century is related to the adaptability of our infrastructure to the ongoing climate changes. The application of Internet of Things (IoT) technologies in recent years has resulted in the generation of numerous data, the analysis of which is crucial for the management and implementation of smart cities (Xiaoming, 2022). It becomes indispensable to acquire data with the absolute certainty of its accuracy and security, a necessary objective given the strategic and economic importance that infrastructures such as subways have demonstrated for our cities and societies.

Blockchain technology, originally arising from the financial sector, has recently exhibited such versatility that its application has extended to various fields. Currently, there are three types of blockchains (Swan, 2015):

Type 1.0 associated with cryptocurrencies;

Type 2.0 typically linked to economic, marketing, and financial applications;

Type 3.0 associated with other applications.

The proliferation of IoT devices has ushered in an era of unparalleled connectivity, enabling seamless communication and data exchange. However, this interconnectedness also amplifies concerns related to data security, integrity, and authenticity. Blockchain technology,

DOI: 10.1201/9781003483755-184

characterized by its decentralized, distributed ledger system, provides an innovative framework to address these challenges. IoT systems simplify a real-time data collection and provide automatic and remote control mechanisms, for this they generate massive volumes of data that require network connectivity and power, processing and storage resources to transform these data into information. (Lokshina et al, 2019).

The proliferation of increasingly widespread IoT sensors has led to the generation of large amounts of data that not only need to be protected but also properly managed, maintained, and archived. In the perspective of a vision of interconnected structures and infrastructures aimed at implementing the resilience of our cities, the so-called smart cities (A. R. Javed et al., 2022).

With this scenario in mind, the need to track and certify data becomes indispensable. For this reason, it is crucial to envision consent systems, typical of blockchain technology, that can seamlessly integrate with Big Data management. We can speak about Big Data when the quantities are on the order of petabytes (Al Nuaimi et al., 2015).

Moreover, the application of blockchain technology would not only certify data related to structural monitoring but can also be extended to the broader concept of project monitoring, encompassing cost management and maintenance planning. This would result in the creation of a system characterized by a high level of traceability of actions and transparency, enabling the reduction of the complex bureaucratic processes that typically characterize the management of such infrastructure projects.

The study has therefore set the ambitious goal of identifying a possible architecture that not only ensures data security but also enables its transparent and efficient use at all levels and throughout the entire lifecycle of the infrastructure.

2 BLOCKCHAIN TODAY

Today, blockchain technology has found substantial application in both financial realms, with established projects like Bitcoin and Ethereum, and in the industrial sector. Several companies utilize blockchain for data security and traceability. The strength of this technology lies in its versatility, allowing seamless integration and ensuring interoperability with various data types, especially evident in applications related to Digital Twins used by industries for product development (Götz et al., 2020).

Numerous works in the literature explore the possibility of developing models that integrate blockchain frameworks for applications in Digital Twins and IoT sensors. In the construction industry, the adoption of blockchain has been slower, with many potential applications yet to be explored and evaluated. Certainly, integration with Building Information Modeling (BIM) models has allowed for optimal utilization of BIM methodology, originally designed to facilitate collaboration and information transmission among different processes and stakeholders in the design phase (Krämer et al., 2018).It is noteworthy that for BIM methodology to achieve its maximum potential, data sharing and processing are required by both technicians and stakeholders, who play distinct roles and have different data needs. The success of decision-making processes is precisely determined by the quality of data and the type of communication established. Consequently, over the years, models have been developed that involve the integration of blockchain technology, ensuring the security and traceability, and providing tracking throughout the project's lifecycle, which extends beyond its construction phase.

One of the less-explored applications, which will be examined in the following paragraphs, is the possibility of tracking the various stages that data undergoes. When referring to data, it encompasses not only physical data but any type of information, such as the occurrence of maintenance processes, the entities involved, quantities, and materials utilized.

With the development of new sensors and connected technologies such as 5G, the implementation of Information and Communication Technology (ICT) in Building Information Modeling (BIM) processes has become feasible. Similar to industrial processes, frameworks have been initiated to facilitate integration not only with BIM models but also with sensors that enable real-time data collection from the structure, enhancing decision-making processes

in emergency situations or refining maintenance procedures in consideration of the real-time evolution of the structure. (Pasini et al., 2016).

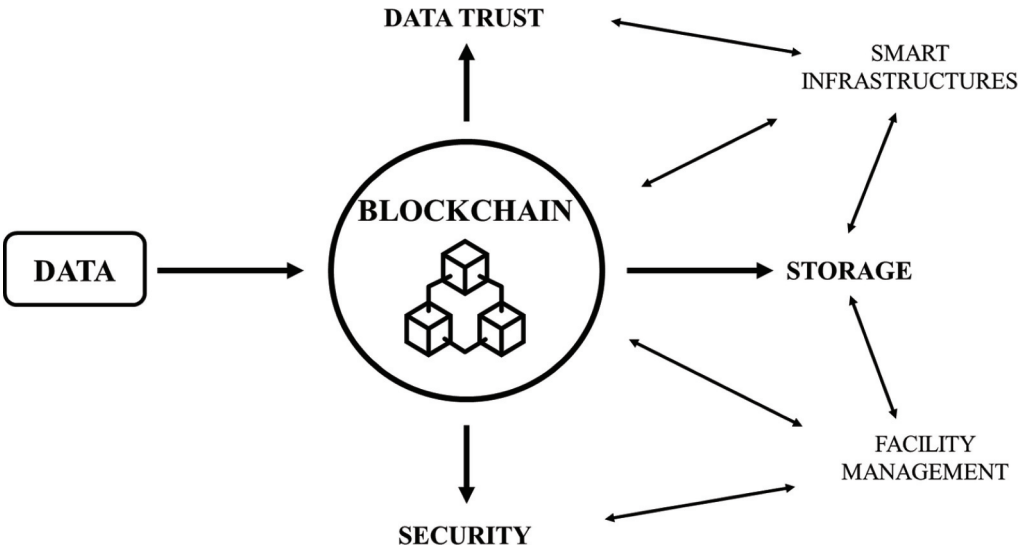


Figure 1. Potential uses of blockchain for data management.

In this context, various authors concur in asserting that blockchain technology presents undeniable advantages when applied to the construction sector.

Consider, for instance, a system combining Cloud computing, IoT, and BIM, which not only requires ensuring data interoperability but also its integrity and accuracy. Tracking the various stages that the data undergoes throughout the project is crucial, along with addressing the significant issue of security, especially concerning critical structures and infrastructure like subways. Such challenges could be effectively tackled with the utilization of blockchain technology would serve as an immutable method to store data and information and use and reuse it at different times. (Kshetri, 2017).

Otherway some of these applications may be affected by one of the still partially unresolved issues of blockchain related to scalability. The term scalability refers to the ability to handle a growing number of transactions without compromising performance. Factors influencing this capacity can be identified by the consensus mechanism used, the block sizes representing the amount of exchanged data, and the number of nodes. That is, the extent, also understood as the physical extension, of the network; each node corresponds to a computer.

Next-generation blockchains have partially addressed these challenges by adopting solutions such as sharding. Sharding is a technique that allows the subdivision into smaller and more easily manageable parts (Zamani et al., 2018).

Alongside sharding, complementary solutions are usually implemented, involving the creation of secondary blockchains alongside the main one with specific tasks; in this case, they are referred to as sidechains (Lohachab et al., 2022).

In any case, it is evident that blockchain technology and the applications arising from it require the resolution of what is defined in the literature as the 'blockchain trilemma,' which involves scalability, decentralization, and security. The trilemma highlights how it is currently impossible to simultaneously implement all three aforementioned characteristics, each of which in turn affects the consensus system (Buterin, 2015), as highlighted by Figure 2.

The trilemma underscores how the implementation of one of the three fundamental characteristics can impact one or even both of the remaining features. Over the years, various solutions have been developed to address this ongoing and evolving trilemma.

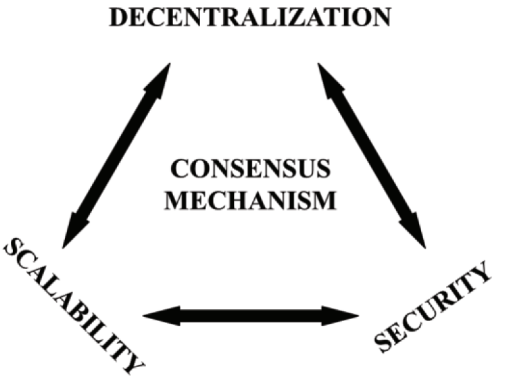


Figure 2. Blockchain's trilemma.

In this regard, the development of new blockchain architectures has significantly improved scalability without excessively sacrificing security or decentralization (Bano et al., 2017).

In the end blockchain could ensure the possibility of access to individual data without the interlocutor gaining access to the entire database. This capability has made the development of blockchain for structure management throughout its lifecycle.

Methodology

The work has focused on defining a potential architecture for implementing a framework that maximizes the benefits of IoT sensors, integrated into a digital twin benefiting from blockchain technology. This study stems from the authors' belief that a digital twin, to be considered as such, not only needs to provide an effective view of the studied infrastructure based on well-defined physical and environmental parameters but also must allow the implementation of functions for efficient facility management while ensuring data management, whether related to a physical-mechanical or economic parameter.

The work has been based on two specific questions:

How is the state of the art of blockchain technology and the level of application it has reached in the construction industry.

What possible architecture to adopt to perform optimally according to the needs presented by such infrastructures?

The work involved an extensive review of existing literature and a deep exploration of blockchain technology-related literature. This enabled an understanding of potential positive aspects while simultaneously identifying possible implementations to address some challenges in applying this technology.

In the Figure 3, you can observe the workflow followed by the team. It is evident how the requirements of these infrastructures have been connected with the characteristics expected of

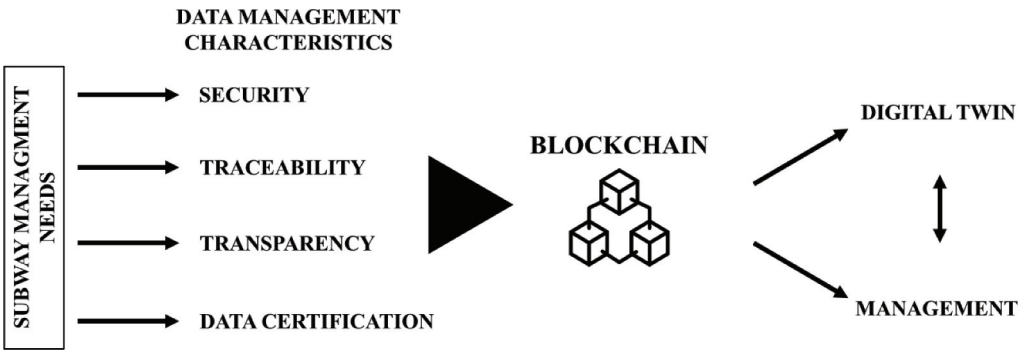


Figure 3. The correlation between the needs of a subway infrastructure and the utilization of blockchain for its management.

a system to be considered efficient from a data management perspective. Starting from data management, the application of blockchain technology has been initiated, with the ultimate focus being the potential implementation in digital twin and LCA systems.

3 APPLICATION

The application of Blockchain technology in the management of subway monitoring systems, as well as in the management and scheduling of maintenance procedures, and handling relationships with various suppliers, presents an innovative approach. The creation of a blockchain framework leveraging recent developments, such as technologies that do not require mining, is a significant step forward. Traditional mining procedures have been associated with substantial computational efforts, resulting in both economic and environmental burdens, particularly in early applications.

Recent advancements have given rise to blockchains like IOTA (Alshaikhli et al., 2022), specifically designed for managing and transmitting data from IoT sensors. The entire infrastructure could be equipped with structural or environmental sensors, collecting data on various parameters under investigation. In this scenario, the operator could decide between two strategies.

The first strategy involves acquiring data from sensors and certifying it. This can occur immediately or by setting a specific delta time to collect data packets that are then certified together.

The second strategy involves connecting, using technologies like 5G, to obtain a digital twin containing the collected data and certifying the final result only afterwards.

As shown in the diagram in Figure 4, the two strategies diverge on the subject of certification. The first proposed solution suggests certifying raw data, allowing not only for archiving but also for safeguarding them from potential tampering. On the other hand, the second strategy involves certifying the digital twin.

Certifying the model not only provides the ability to validate the current state of the infrastructure but also validates various post-processing operations to which the data are subjected.

Both strategies can be executed through manual or automated certification operations.

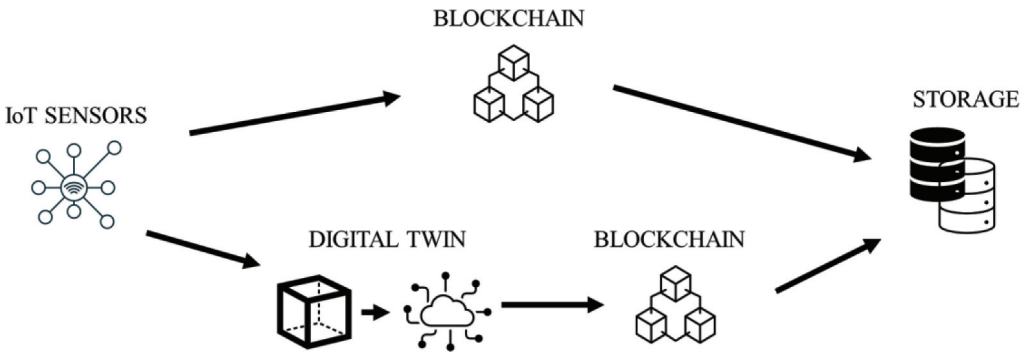


Figure 4. Two possible application of blockchain for data security.

Subsequently, the protected and certified data could be shared with all parties involved in various operations. The framework architecture allows data owners to share data with selected entities, ensuring data compartmentalization among individual users. This procedure ensures traceability and confidentiality levels among different users that the current BIM methodology may not completely guarantee.

Simultaneously, creating a blockchain linked to the structure enables the transmission of useful information for various processes. With a single cryptocurrency, it becomes possible to make payments for services and transmit technical instructions, materials, quantities, and more, all in one transaction, this possibility is provided by smart contracts. (Ghiani, 2021).

To create a smart contract the first step is the parties define the corresponding objectives for each party and agree on the expected outcomes.

In the next step all specifications and contract clauses are written in computer logic language and coded in a programmatic way.

All specifications and contract clauses are then written with computer logic and coded in a programmatic way. Then the smart contract will be sent to the Blockchain, that will be executed on its own when specific criteria are activated. When a consensus is achieved from the majority, the transaction will be added to the ledger, the smart contract will be executed, and the results will be registered (Cachin et al. 2017).

Through the consensus mechanism, it is possible to guarantee the transparency of operations, which is typical of blockchain technology. The application of this procedure allows administrations to establish economic and operational relationships based on a dedicated cryptocurrency. This cryptocurrency acts as a guarantor of a broader system involving operating companies, infrastructure managers, and technicians.

POSSIBILE SMART CONTRACT SCHEME	
Contract ID	XXXXXX
From	Client ID
To	Contractor ID
Time	gg/mm/aa - hh:mm:ss
INPUT	BIM File
	Work Size [mq, t, ecc…]
	Material
	Work of time
	Cost
	Notes
	Ecc.
Signature	

Figure 5. Example of smart contract.

In a way, the cryptocurrency takes on the role of a digital certification for adhering to specific technical, economic, and environmental characteristics. This ensures a quality system among the involved companies, allowing them to demonstrate compliance and adherence to established standards.

In the end with this solution it is possible obtain a system with different characteristics:

Strong security;

Data trust;

Traceability;

Transparency;
Quality control.

The diagram below (Figure6) illustrates the identified architecture intended for use in implementing a framework that can ensure multiple functionalities, proving to be both dynamic and efficient across different territorial and managerial contexts.

The diagram shows how the solutions involve using blockchain in two different time steps. This is because it is believed that the optimal solution should not only have the certification of pristine data, which could also be used in legal disputes, but also utilize the blockchain to certify and protect the digital twin. This solution allows for the creation of a data background and provides a mechanism to have an always updated and verified digital twin that can be used to track various events and interventions that the structure has undergone over the years.

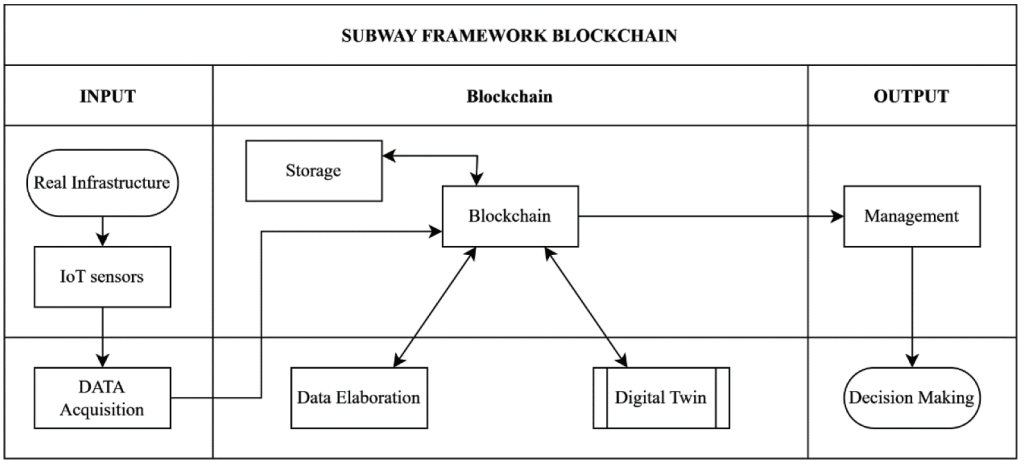


Figure 6. Framework's architecture to use blockchain for subway infrastructures.

The use of a certified model containing all the information, verified and transparent, related to the entire life of the structure is not to be underestimated. In this way, the life cycle analysis process could benefit from it, including the verification of any environmental criteria introduced in the years following the construction and commissioning of the subway.

4 CONCLUSION

This work has allowed for a clear definition of milestones and requirements necessary for the development of a framework aimed at the optimal combination of blockchain technologies with the capabilities of IoT. The obtained results and the defined architecture of the framework will lead to developments, through the use of an open-source ecosystem, resulting in a blockchain that is usable and adaptable to all the needs involved in the physical and economic management of infrastructures such as subways.

It is believed that the use of blockchain can maximize the utilization of existing tools, still underutilized to date, provided by the BIM methodology. Additionally, it serves as a valuable tool to ensure the security and transparency of all operations, both during the construction phase and management phase throughout the entire lifecycle.

REFERENCES

Al Nuaimi, E., Al Neyadi, H., Mohamed, N. et al. Applications of big data to smart cities. J Internet Serv Appl 6, 25 (2015). https://doi.org/10.1186/s13174-015-0041-5.

Alshaikhli, M., Elfouly, T., Elharrouss, O., Mohamed, A., Ottakath, N. 2022. Evolution of Internet of Things From Blockchain to IOTA: A Survey, in IEEE Access, vol. 10, pp. 844–866, doi: https://doi.org/10.1109/ACCESS.2021.3138353.

Bano, S., Sonnino, A., Al-Bassam, M., Azouvi, S., McCorry, P., Meiklejohn, S., & Danezis, G. 2017. Consensus in the age of blockchains. *arXiv preprint arXiv:1711.03936*.

Cachin, C., Vukolić, M. 2017. Blockchain Consensus Protocols in the Wild. IBM Research - Zurich. arXiv:1707.01873.

Celik, Y., Petri, I., Barati, M., 2023. Blockchain supported BIM data provenance for construction projects, *Computers in Industry*, Volume 144, 103768, ISSN 0166–3615, https://doi.org/10.1016/j.compind.2022.103768.

Ethereum. Sharding faq. https://github.com/ethereum/wiki/wiki/Sharding-FAQ. [Online, Accessed: Dec/01/2023].

Ghiani, A. *2021. Blockchain*: *Linee guida.* Giappichelli.

Götz, C.S., Karlsson, P. and Yitmen, I. 2022, "Exploring applicability, interoperability and integrability of Blockchain-based digital twins for asset life cycle management", *Smart and Sustainable Built Environment*, Vol. 11 No. 3, pp. 532–558. https://doi.org/10.1108/SASBE-08-2020-0115.

Javed, A. R., Shahzad, F., Rehman, S., U., Zikria, Y.B., Razzak, I., Jalil, Z., Xu, G., Future smart cities: requirements, emerging technologies, applications, challenges, and future aspects, *Cities*, Volume 129, 2022, 103794, 0264-2751, https://doi.org/10.1016/j.cities.2022.103794.

Krämer, M., Besenyői, Z., 2018. Towards digitalization of building operations with BIM. IOP Conf. Ser.: Mater. Sci. Eng. 365, 022067. http://dx.doi.org/10.1088/1757-899X/365/2/022067.

Kshetri, N. 2017. Blockchain's roles in strengthening cybersecurity and protecting privacy, Telecommunications Policy, Volume 41, 10, 2017, 1027–1038, 0308-5961, https://doi.org/10.1016/j.telpol.2017.09.003.

Lohachab, A., Garg, S., Kang, B., Amin, M. B., Lee, J., Chen, S., Xu. X. 2022. Towards Interconnected Blockchains: A Comprehensive Review of the Role of Interoperability among Disparate Blockchains. *ACM Comput. Survey*. 54, 7, 135, 39 https://doi.org/10.1145/3460287.

Lokshina, I. V., Greguš, M., Thomas, W. L. 2019. Application of Integrated Building Information Modeling, IoT and Blockchain Technologies in System Design of a Smart Building, *Procedia Computer Science*, Volume 160, 497–502, 1877-0509, https://doi.org/10.1016/j.procs.2019.11.058.

Pasini, D., Ventura, S. M., Rinaldi, S., Bellagente, P., Flammini, A., Ciribini, A. L. C. "Exploiting Internet of Things and building information modeling framework for management of cognitive buildings," *2016 IEEE International Smart Cities Conference (ISC2)*, Trento, Italy, 2016, pp. 1–6, doi: https://doi.org/10.1109/ISC2.2016.7580817.

Swan, M. 2015. *Blockchain: Blueprint for a new economy*. O'Reilly Media, Inc.

Xiaoming, L., Hao, L., Weixi, W., Ye Zheng, Haibin, L., Zhihan, L. 2022. Big data analysis of the Internet of Things in the digital twins of smart city based on deep learning, *Future Generation Computer Systems*, Volume 128, 167–177, 0167-739X, https://doi.org/10.1016/j.future.2021.10.006.

Zamani, M., Movahedi, M., Raykova, M. 2018. RapidChain: Scaling Blockchain via Full Sharding. In Proceedings of the 2018 ACM SIGSAC Conference on Computer and Communications Security (CCS '18). Association for Computing Machinery, New York, NY, USA, 931–948. https://doi.org/10.1145/3243734.3243853

Bridge Maintenance, Safety, Management, Digitalization and Sustainability – Jensen, Frangopol & Schmidt (eds)
© 2024 The Author(s), ISBN 978-1-032-77040-6
Open Access: www.taylorfrancis.com, CC BY-NC-ND 4.0 license

Analytical seismic resilience identifiers of bridges

F. Soleimani
Department of Civil and Construction Engineering, Oregon State University, Corvallis, USA

D. Hajializadeh
School of Sustainability, Civil and Environmental Engineering, University of Surrey, Guildford, Surrey, UK

ABSTRACT: This paper introduces a novel probabilistic framework for assessing the resilience of highway bridges using a machine learning (ML) algorithm, specifically an ensemble learning tree-based model. By leveraging ML's computational power, the study explores the impact of various parameters on the resilience of concrete box-girder bridges under extreme events, with a particular focus on seismic hazards. Sixteen input variables, including ground motion intensity, concrete and steel strengths, and deck width, are investigated for their influence on the bridge's resilience. Results highlight the importance of features such as peak ground acceleration and the number of bridge columns per bent, offering valuable insights for informed decision-making in the resilience assessment of bridges. The study pioneers an embedded feature identification technique to identify key structural-based resilience identifiers, providing a comprehensive understanding of the resilience drivers in bridge infrastructure.

1 INTRODUCTION

Highway bridges, as integral components of transportation infrastructure, play a pivotal role in ensuring communication efficiency and traffic flow across various regions. However, their vulnerability to catastrophic events poses a significant threat to network functionality, impacting emergency responses and socio-economic recovery. Past seismic events underscored the susceptibility of bridges to severe seismically-induced damages, leading to disruptions in vital transportation routes and, in some cases, catastrophic consequences (Kawashima et al. 2011, Schanack et al. 2012). As urbanization and population growth continue, the need to enhance the seismic resilience of bridges becomes increasingly paramount. The seismic performance of bridges is a multifaceted indicator, involving complex interactions between structural engineering, geotechnical considerations, and regional seismic hazards. Analyzing and understanding the seismic resilience of bridges requires a comprehensive approach that goes beyond traditional structural assessments. This paper delves into the realm of analytical seismic resilience identifiers for bridges, aiming to establish a framework that enables a holistic understanding of a bridge's ability to withstand and recover from seismic events. The outcomes offer insights for targeted optimization of resilient design, rapid recovery processes and sustainable retrofit decisions.

Resilience, defined as the transport network's ability to withstand extreme events, operate during such conditions, and promptly recover upon a disruption, is a paramount consideration in the context of extreme events (Department for Transport 2014, Henry & Emmanuel Ramirez-Marquez 2012, Hajializadeh & Imani 2020). Yet, resilience's complexity and varying definitions pose challenges for decision-making. In the engineering sector, resilience often focuses on post-event rebound capability, quantified by recovery rates or area metrics. Existing models, however, lack flexibility and may overlook uncertainties.

DOI: 10.1201/9781003483755-185

In recent years, advancements in structural engineering, materials science, and data analytics have provided new opportunities to assess and improve the seismic resilience of bridges. This paper explores these developments and seeks to identify key analytical parameters that can serve as resilience indicators for bridges. By doing so, we aim to contribute to the ongoing discourse on enhancing the earthquake resistance of critical infrastructure and mitigating the societal impacts of seismic events.

This study introduces a novel ensemble learning-based resilience model, leveraging machine learning's computational power to discern the impact of structural features on bridge resilience. Unlike classical models, ensemble learning accommodates complex relationships without predetermined functional forms or parameter distributions. By incorporating uncertain configurational features, this research enhances the realism and reliability of resilience estimations, providing a pioneering framework for seismic resilience identification in bridge engineering. Through this exploration, we aspire to offer valuable insights that contribute to the ongoing efforts to enhance the seismic resilience of bridges and, consequently, the overall resilience of transportation networks in earthquake-prone regions.

2 ANALYTICAL SEISMIC RESILIENCE OF BRIDGES

The presented research in this study focuses on the seismic behavior of two-span continuous concrete box-girder (2SCC-BG) highway bridges to build a cohort of case study bridges. The analysis encompasses three distinct design periods: pre-1971, 1971–1990, and post-1990, considering two bridge configurations with rigid diaphragm and seat abutments.

Analytical finite element models are developed for this bridge type across the specified design eras. Box-girder bridges feature integral diaphragms at the bents, serving as solid connections. Bridges constructed before 1971 exclusively transmit negative moments, whereas those built between 1971 and 1990, as well as those constructed after 1990, transfer both positive and negative moments across the interface of the deck and bent columns. Multi-span continuous concrete box-girder bridges incorporate circular columns, their diameter and reinforcement dependent on the number of columns per bent, influenced by the bridge width. Longitudinal and transverse reinforcement ratios dictate the number and spacing of #11 longitudinal reinforcing bars and #4 stirrups in the finite element models. Girders are generally sized according to acceptable depth-to-span ratios, specifically 0.055 for cast-in-place reinforced concrete boxes and 0.04 for prestressed concrete boxes. The superstructure integrates with the diaphragm abutment, transferring all forces and moments. Seat abutments utilize 14 in. x 14 in. elastomeric bearing pads, introducing a 2.5 in. gap at the abutment seat. Single column bents feature a moment transfer connection and are upheld by a pile cap, supported by a cluster of piles beneath it. Abutments consist of a 6 ft tall backwall, supported by Class 70 cast-in-driven-hole piles spaced at 7 ft intervals. The adopted values for concrete compressive strength and reinforcing steel yield strength are 4860 psi and 67.4 ksi, respectively.

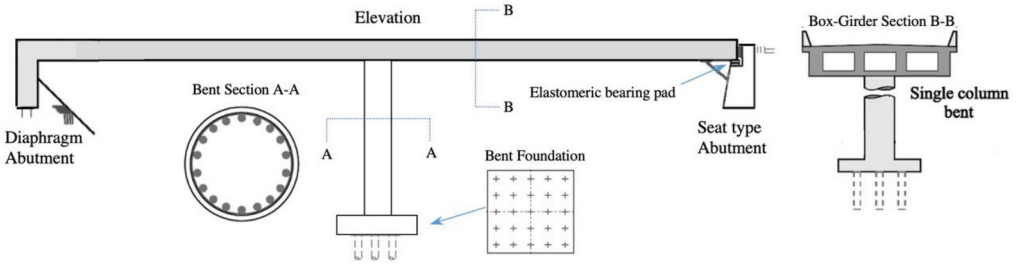


Figure 1. General layout of 2SCC-BG bridges.

The bridges are numerically modeled and analyzed using OpenSEES (McKenna et al., 2000). Figure 1 and Tables 1-2 present the details and characteristics of the modeled 2SCC-

BG bridges. The superstructure is simulated employing elastic beam-column elements with concentrated mass along the centerline, as these elements typically maintain elasticity during seismic events. Composite section properties are utilized in the calculation of deck element characteristics to account for the inclusion of box-girders.

Columns employ displacement-based beam-column elements with rigid links for moment and force transfer within the bent. Rigid links are employed to establish a connection between the column's top and the solid diaphragm. Modeling columns involves the use of discretized fiber-defined cross-sections, offering the distinct advantage of specifying material properties tailored to different locations within a member's cross-section. As an example, unconfined concrete properties are allocated to the cover concrete, while confined concrete properties are designated for the core fibers. Additionally, the exact positioning of longitudinal reinforcing bars and pre-stressing strands can be specified, with corresponding material properties assigned to each.

Transverse rigid elements and displacement beam-column elements model the solid diaphragm and columns, respectively. Translation and rotational springs at the column base represent foundation behavior. Longitudinal response of the abutment considers passive and active resistance, modeled with a hyperbolic soil model. These are represented through linear springs as zero-length elements positioned at the base of the column.

Earth pressures acting on the abutment may arise from the longitudinal response of the bridge deck, and these pressures are further heightened by the impact of the deck against the abutment backwall, particularly in the case of seat abutments. The abutment's reaction in the longitudinal direction differs from that in the transverse direction. Moreover, the longitudinal response encompasses two forms of resistance: passive resistance, occurring when the abutment wall compresses the backfill soil, and active resistance, arising when the abutment backwall moves away from the backfill soil. Passive resistance is contributed by both the backfill soil and the piles, while active resistance is solely provided by the piles. To capture the abutment's response, the hyperbolic soil model proposed by Shamsabadi and Yan (2008) is employed in this study. Zero-length springs, characterized by nonlinear soil behavior, are employed to depict the response of the abutment soil. The HyperbolicGapMaterial feature in OpenSEES is utilized to simulate the response of the backfill soil, based on the model proposed by Shamsabadi and Yan (2008).

For diaphragm abutments, there is no gap between the deck and the abutment backwall, while a gap is present in the case of seat-type abutments. The response of the piles is modeled using a trilinear approach based on the recommendations of Choi (2002). The reaction of elastomeric bearing pads in seat-type abutments is simulated by assigning an elastic perfectly plastic material to zero-length elements, capturing its force deformation response. In continuous bridge superstructures, the control of relative transverse movement between the deck and abutments is crucial, and this is achieved through the utilization of zero-length elements. These elements are defined by the nonlinear force deformation response proposed by Megally et al. (2002), effectively capturing the behavior of shear keys. This study employs the contact element approach proposed by Muthukumar and DesRoches (2006) to model the impact between the deck and abutment backwall, specifically in the case of seat-type abutments. A 4.5% Rayleigh damping is implemented in the time history analysis conducted on the bridge model subjected to a pair of ground motion records.

This study addresses excitations' uncertainty by utilizing Baker's suite of ground motions, which comprises 160 motions compiled by Baker et al. (2011) for the PEER Transportation Research Program. The motions, sourced from the PEER Next Generation Attenuation Project ground motion library (Chiou, et al. 2008), are representative of shallow crustal earthquakes with magnitudes ranging from 4.3 to 7.9. The Baker set includes two sets of 120 broad-band ground motions, reflecting response spectra distribution for moderately large earthquakes at small distances. Additionally, it encompasses a set of 40 ground motions characterized by strong velocity pulses, indicative of sites experiencing near-fault directivity effects.

This study encompasses uncertainties in structural geometric and material parameters, alongside uncertainties associated with ground motions. Parameters susceptible to variation, capturing uncertainties across three significant design eras for the bridge class, are identified. Employing Latin Hypercube Sampling, a set of statistically significant yet nominally identical 3D bridge models is developed by sampling across the parameter range. In total, one hundred

and sixty analytical bridge models are generated to match the number of ground motions in the Baker suite, and these models are then randomly paired to establish bridge model-ground motion pairs. For each scenario, a non-linear time history analysis is executed, and the peak component demands are documented to ascertain the correlation between the peak demands and the ground motion intensity measure.

In this investigation, the susceptibility of various bridge components is examined. Employing finite element models for bridges, pertinent peak demand measures like column curvature ductility, bearing and abutment deformations are documented. Subsequently, probabilistic seismic demand models are formulated, and the fragility analysis procedure is applied to generate analytical fragility curves for both individual bridge components and the entire system (Figure 2).

Table 1. Properties of bridge modelling.

Bridge parameters	Distribution	Units	Distribution Parameters
Concrete compressive strength	Normal	ksi	μ=5.0, σ=0.63
Reinforcing steel yield strength	Lognormal	ksi	μ=4.21, σ=0.08
Span length	Empirical	ft	μ=114.8, σ=40.5
Deck width	Empirical	ft	μ=67.2, σ=42.2
Vertical under clearance	Empirical	ft	μ=18, σ=3.7
Abutment concrete pile effective stiffness	Lognormal	kip/in	μ=80 σ=00.3
Damping ratio	Normal	-	μ=0.045, σ=0.0125
Shear modulus of elastomeric bearing pads	Uniform	ksi	[80-250]
Abutment backwall height	Uniform	ft	[3.5-8.5]
Gap between deck and seat type abutment backwall	Uniform	in	[0-1.5]
Restrainer cable length	Uniform	ft	[8-20]
Mass factor	Uniform	-	[1.1-1.4]

Table 2. Component capacities adopted in this study.

Engineering demand parameter	Eras	Units	DS1	DS2	DS3	DS4
Column curvature ductility	Pre 1971	NA	0.8	0.9	1.0	1.2
	1971-1990	NA	1.0	2.0	3.5	5.0
	Post 1990	NA	1.0	4.0	8.0	12.0
Deck displacement	All	Inches	1.0	3.0	10.0	15.0
Foundation rotation	All	Radian	1.5	6.0	NA	NA
Foundation displacement	All	Inches	1.0	4.0	NA	NA
Bearing displacement	All	Inches	1.0	4.0	NA	NA
Abutment passive displacement	All	Inches	3.0	10.0	NA	NA
Abutment active displacement	All	Inches	1.5	4.0	NA	NA
Abutment transverse displacement	All	Inches	1.0	4.0	NA	NA

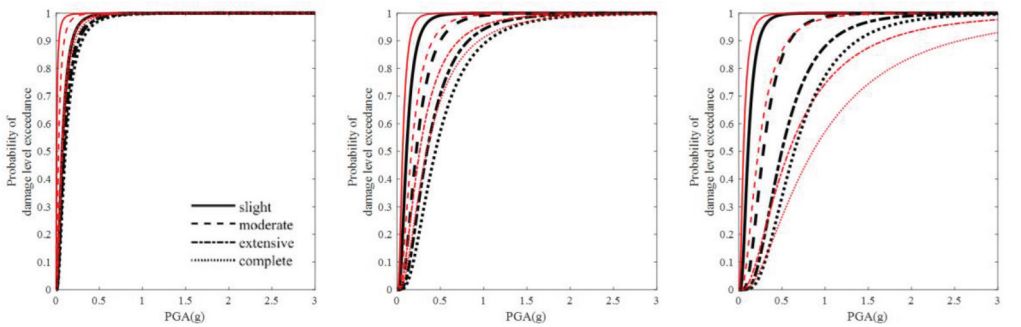


Figure 2. Fragility curves of the investigated bridges – black and red lines correspond to rigid and seat abutment accordingly.

The probabilistic seismic analysis of structures involves the development of seismic demand models, often presented as probability distributions describing structural responses contingent on a seismic intensity measure. These demand models represent the likelihood of structural demand given the intensity measure and are referred to as probabilistic seismic demand models.

Fragility curves are the most common approach considered in bridge risk assessment for diverse bridge components, depicting engineering demand parameters (EDPs) such as column curvature ductility as a function of intensity measures for diverse hazard scenarios (e.g. fatigue (Aloisio et al., 2023) and flooding (Pucci et al., 2023)). In the seismic risk assessment context, often modeled through a single-variable linear regression (Equation 1), fragility curves estimate median values with variability expressed through dispersion (β_{DM}) (Equation 2), a methodology introduced by Shome et al. (1998) and applied extensively in bridge performance analyses (Gardoni et al., 2003; Padgett and DesRoches, 2008; Zhong et al., 2008; Ramanathan, 2012; Soleimani et al., 2017a). Modified seismic demand models tailored to specific bridge characteristics have also been proposed (Soleimani, 2017; Soleimani et al., 2017b; Soleimani & Liu, 2021).

$$\ln(\mu_{DM}) = \ln(a) + b\ln(IM) \tag{1}$$

$$\beta_{DM} = \sqrt{\frac{\sum_{i=1}^{n} [\ln(DM_i) - (\ln(a) + b\ ln(IM_i))]^2}{n-2}} \tag{2}$$

Seismic fragility involves convolution of demand and capacity models, with analytical fragility curves expressing the probability (Equation 3) for a bridge component's performance given seismic intensity. To estimate bridge system fragilities, a joint probabilistic approach and Monte Carlo simulations are often employed (Nielson and DesRoches, 2007). Limit states are characterized by mean (S_C) and dispersion (β_C) values, assumed to be lognormal, akin to Probabilistic Seismic Demand Models (PSDMs). However, this lognormal assumption may not universally apply, prompting the need for a more generalized machine learning (ML)-based framework.

$$P[S_D \geq S_C|IM] = \Phi\left(\frac{\ln(\mu_{DM}/S_C)}{\sqrt{\beta_{DM}^2 + \beta_C^2}}\right) \tag{3}$$

In this study, $P[S_D \geq S_C|IM]$ is used to formulate normalized bridge performance indicator ($\bar{Q}(t)$) as shown in Equation 4, which in turn used to quantify resilience. A performance indicator represents bridge following a seismic event, in which structural capacity decreases, depending on the failure absorption patterns, varying intensity of hazard and structural specifications. Typically, failure absorption patters are simplified as a sudden drop in performance, categorized as slight, moderate, extensive, and complete damage states (FEMA, 2009). Upon duration of stabilization following full failure absorption and depending on the recovery resources available, the performance indicator is restored to a new/original level. For the purpose of this study, the asset's behavior is formulated post-failure absorption with sudden drop in performance, corresponding to four damage states of slight, moderate, extensive and completed. Whilst acknowledging a wide range of possible recovery trajectories for different types of bridges and context, for the purpose of demonstration of the concept, recovery trajectories as recommended by (HAZUS-MH, 2011) with mean recovery times ($m_{t,d}$) and standard deviations ($\sigma_{t,d}$) for each damage state are used in this research. The area of remaining performance indicator is used as resilience indicator in this study.

$$\bar{Q}(t) = \sum_{d=1}^{nDs} (1 - P[S_D \geq S_C|IM]) \times \Phi\left(\frac{t - m_{t,d}}{\sigma_{t,d}}\right) \tag{4}$$

3 ENSEMBLE LEARNING-BASED METHODOLOGY

In recent years, the field of structural engineering has increasingly turned to machine learning as a powerful tool for predicting and evaluating the seismic response of structures. The emergence of ensemble learning as a promising paradigm has added a new dimension to this

approach (Yang et al. 2010, Harrou et al. 2019, Li et al. 2019), leveraging the strengths of multiple individual models to enhance predictive performance and generalization. This study explores the application of ensemble learning methods, particularly focusing on the widely used Random Forest algorithm, in the analysis of seismic resilience identifiers for bridges.

Ensemble learning methods, introduced by Dietterich (2000), are recognized for their unbiased nature and their ability to capture complex relationships between input and response variables. Their popularity stems from the reduction of model variance with low bias, making them effective in addressing challenges such as weak predictors, small sample size, and overfitting of training data. The unique approach of ensemble learning in combining multiple individual learners contributes to enhanced prediction quality relative to single regression models, thereby reducing overall prediction error.

A cornerstone of the ensemble learning methodology is the decision tree algorithm proposed by Breiman et al. (1984), which efficiently addresses large datasets, complicated data structures, and missing values. While individual decision trees provide intuitive insights into the relationships between input variables and outputs, they are sensitive to minor changes in the training dataset. The ensemble method, encompassing multiple decision trees generated in parallel or sequentially, overcomes this sensitivity and prevents overfitting, improving accuracy and generalization ability (Ishwaran and Kogalure 2010, Yang et al. 2010, Zhou 2021).

Random Forest, a prominent ensemble learning technique, constructs multiple regression trees in parallel, with no interaction between them (Liu et al. 2012). This technique is particularly well-suited for the complex and multidimensional nature of seismic resilience assessment in bridge engineering. By aggregating predictions from diverse individual trees, Random Forest enhances robustness, reduces overfitting, and provides valuable insights into the intricate interplay of factors contributing to the seismic resilience of a bridge (Hastie et al., 2009).

Our methodology employs Random Forest to analyze a comprehensive set of seismic resilience indicators for bridges, encompassing structural characteristics, material parameters, and seismic data. The ensemble learning approach allows the integration of information from various sources, extracting nuanced patterns not apparent through traditional analytical methods.

The interpretability of Random Forest enables the identification of influential factors contributing to the seismic resilience of bridges. This understanding allows engineers and policymakers to prioritize interventions and design strategies, ultimately enhancing the overall resilience of bridge structures in seismic-prone regions.

In this study, a random allocation of 80% to training and 20% to testing is employed. Sixteen input variables are selected to encompass material, geometric, and structural properties, along with PGA, for predicting bridge resilience. Subsequently, the seismic resilience is estimated for the testing dataset using the models trained with Random Forest.

4 SEISMIC RESILIENCE INDICATORS

This section presents the critical evaluation of the impact of input bridge characteristics on predicting the resilience index. Beyond gaining insights into the most influential parameters in

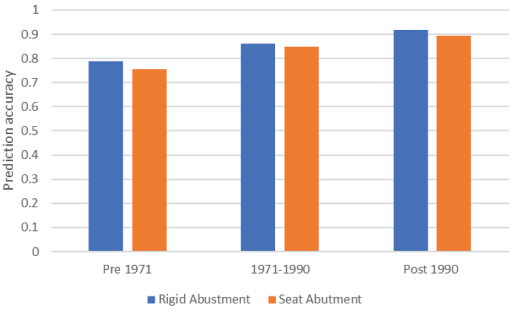


Figure 3. Evaluation of the predictive model (prediction accuracy).

defined bridge resilience indicator, identifying input variables with minimal relevance allows for their exclusion, reducing model complexity and optimizing efficiency. Figure 3 presents the prediction accuracy of the developed predictive model for all three eras and two groups of rigid and seat abutment cases.

To gauge variable importance, the EL algorithm, a random forest, permutes variables to track averaged changes in prediction errors and node impurities throughout the tree-splitting process. Figure 2 illustrates variable importance measured using EL algorithms (logarithmic scale). These scores indicate the contribution level of each variable to outcome prediction, with higher scores indicating more significant contributions.

As can be seen from Figure 4, overall, the most predictive parameters are Peak Ground Acceleration (PGA) and the number of column bents, whereas soil type (sand or clay), girder type (prestressed or reinforced concrete) and column diameter are less predictive. The impact of PGA is attributed to fragility curves' importance in resilience index calculation. While both PGA and structural parameters influence fragility curve shapes, structural characteristics exhibit a more gradual impact compared to the pronounced effect of PGA. Additionally, the recovery projection patterns used in this study are solely a function of damage state, which could be enhanced by formulating recovery projections based on diverse structural forms and characteristics, albeit beyond this study's scope.

Further examination in Figure 4 reveals that reinforcement ratio and superstructure depth consistently rank among the top five influential features. Foundation translational stiffness is prominent for bridges from the pre-1971 and 1971-1990 eras. Column height significantly influences bridges with rigid diaphragm abutments, particularly those designed in earlier eras, while bridges with seat abutments showcase greater sensitivity of column height in earlier era designs. Conversely, deck width holds more influence for bridges with seat abutments compared to those with rigid diaphragms.

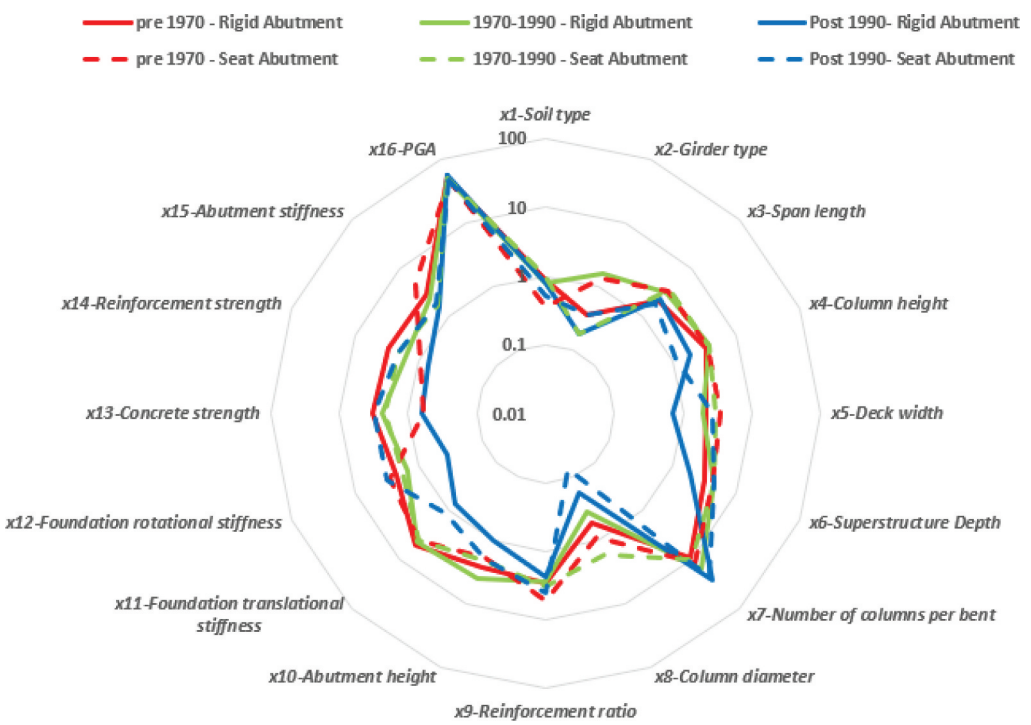


Figure 4. Features ranking based on their level of importance measures in predicting bridge resilience.

These observed distinctions may be linked to increased vulnerability, particularly of columns, in bridges designed in earlier eras compared to more recent, seismically advanced structures. Differences in results between bridges with seat and rigid abutments may be attributed to their structural performance under seismic excitation, with rigid abutments moving synchronously with the superstructure, while seat abutments and superstructures move independently.

5 SUMMARY AND CONCLUSIONS

This research delved into the potential utilization of ensemble learning (EL)-based machine learning (ML) algorithm using random forest, to predict the seismic resilience of bridges reliably. Sixteen parameters were scrutinized as input variables for developing EL-based models, which play a crucial role in the analytical development of probabilistic seismic demand and fragility curves used to quantify bridge seismic resilience.

To assess the predictive performance of the EL-based model, the accuracy is presented showing a consistent level of good accuracy for different bridge groups.

Furthermore, the study measured the feature importance of the considered variables and provided a ranking based on their contribution to predicting seismic resilience. Ground motion intensity (PGA) and the number of bridge columns per bent emerged as the most influential features in all scenarios, while the type of superstructure girder and soil had the least impact on predictions. This insights into influential parameters can inform decisions in bridge resilience assessment and aid in developing concise models.

The research presented EL-based methodology, shedding light on the application of ML algorithms in seismic resilience assessments of bridges. Future studies can address limitations by testing the generalization of findings to other bridge types, such as I- and T-girder bridges, and exploring the sensitivity of bridge resilience to different ground motion characteristics beyond the considered PGA in this study.

REFERENCES

Aloisio, A., Rosso, M.M., Fragiacomo, M. and Alaggio, R., 2023, March. Fragility estimate of railway bridges due to concrete fatigue. In Structures (Vol. 49, pp. 70–87). Elsevier.

Baker, J.W., Lin, T., Shahi, S.K. and Jayaram, N., 2011. New ground motion selection procedures and selected motions for the PEER transportation research program. PEER report, 3.

Breiman, L., Friedman, J., Stone, C. J., & Olshen, R. A. (1984). Classification and regression trees. CRC press.

Chiou, B., Darragh, R., Gregor, N., & Silva, W. (2008). NGA project strong-motion database. Earthquake Spectra, 24(1), 23–44.

Choi, E., 2002. Seismic analysis and retrofit of mid-America bridges. Georgia Institute of Technology.

Department for Transport. (2014). Transport Resilience Review: A review of the resilience of the transport network to extreme weather events. Available online: https://assets.publishing.service.gov.uk/government/uploads/system/uploads/attachment_data/file/335115/transport-resilience-review-web.pdf.

Decò, A., Bocchini, P., & Frangopol, D. M. (2013). A probabilistic approach for the prediction of seismic resilience of bridges. Earthquake Engineering & Structural Dynamics, 42(10), 1469–1487.

Dietterich, T. G. (2000). Ensemble methods in machine learning. In International workshop on multiple classifier systems (pp. 1–15). Springer, Berlin, Heidelberg.

FEMA. (2009). HAZUS-MH MR4–Earthquake Model User Manual.

Gardoni, P., Mosalam, K. M., & Der Kiureghian, A. (2003). Probabilistic seismic demand models and fragility estimates for RC bridges. Journal of earthquake engineering, 7(spec01), 79–106.

Hajializadeh, D., & Imani, M. (2020). RV-DSS: Towards a resilience and vulnerability-informed decision support system framework for interdependent infrastructure systems. Computers and Industrial Engineering, 156, p.107276.

Harrou, F., Saidi, A., & Sun, Y. (2019). Wind power prediction using bootstrap aggregating trees approach to enabling sustainable wind power integration in a smart grid. Energy Conversion and Management, 201, 112077.

Hastie, T., Tibshirani, R., & Friedman, J. (2009). Random forests. In The elements of statistical learning (pp. 587–604). Springer, New York, NY.
HAZUS-MH. (2011). Multi-hazard loss estimation methodology: Earthquake model Hazus-MH MR5 technical manual.
Henry, D., & Ramirez-Marquez, J. E. (2012). Generic metrics and quantitative approaches for system resilience as a function of time. Reliability Engineering & System Safety, 99, 114–122.
Ishwaran, H., & Kogalur, U. B. (2010). Consistency of random survival forests. Statistics & probability letters, 80(13-14), 1056–1064.
Kawashima, K., Unjoh, S., Hoshikuma, J.-I., and Kosa, K. (2011). "Damage of bridges due to the 2010 Maule, Chile, earthquake." J. Earthquake Eng., 15(7), 1036–1068.
Li, Z., Goebel, K., & Wu, D. (2019). Degradation modeling and remaining useful life prediction of aircraft engines using ensemble learning. Journal of Engineering for Gas Turbines and Power, 141(4).
Liu, Y., Wang, Y., & Zhang, J. (2012, September). New machine learning algorithm: Random forest. In International Conference on Information Computing and Applications (pp. 246–252). Springer, Berlin, Heidelberg.
McKenna, F., Fenves, G.L. and Scott, M.H., 2000. Open system for earthquake engineering simulation. University of California, Berkeley, CA.
Megally, S. H., Silva, F. P. & Seible, F., 2002. Seismic Response of Sacrificial Shear Keys in Bridge Abutments.
Muthukumar, S. & DesRoches, R., 2006. A Hertz contact model with non-linear damping for pounding simulation. Earthquake Engineering & Structural Dynamics, 35(7), pp. 811–828.
Nielson, B. G., & DesRoches, R. (2007). Seismic fragility methodology for highway bridges using a component level approach. Earthquake Engineering & Structural Dynamics, 36(6), 823–839.
Padgett, J. E., Nielson, B. G., & DesRoches, R. (2008). Selection of optimal intensity measures in probabilistic seismic demand models of highway bridge portfolios. Earthquake engineering & structural dynamics, 37(5), 711–725.
Pucci, A., Eickmeier, D., Sousa, H.S., Giresini, L., Matos, J.C. and Holst, R., 2023. Fragility analysis based on damaged bridges during the 2021 flood in Germany. Applied Sciences, 13(18), p.10454.
Ramanathan, K. N. (2012). Next generation seismic fragility curves for California bridges incorporating the evolution in seismic design philosophy (Doctoral dissertation, Georgia Institute of Technology).
Shamsabadi, A. and Yan, L., 2008. Closed-form force-displacement backbone curves for bridge abutment-backfill systems. In Geotechnical earthquake engineering and soil dynamics IV (pp. 1–10).
Schanack, F., Valdebenito, G., and Alvial, J. (2012). "Seismic damage to bridges during the 27 February 2010 magnitude 8.8 Chile earthquake." Earthquake Spectra, 28(1), 301–315.
Shome, N., Cornell, C. A., Bazzurro, P., & Carballo, J. E. (1998). Earthquakes, records, and nonlinear responses. Earthquake Spectra, 14(3), 469–500.
Soleimani, F., Mangalathu, S., & DesRoches, R. (2017a). A comparative analytical study on the fragility assessment of box-girder bridges with various column shapes. Engineering Structures, 153, 460–478.
Soleimani, F., Vidakovic, B., DesRoches, R., & Padgett, J. E. (2017b). Identification of the significant uncertain parameters in the seismic response of irregular bridges. Engineering Structures, 141, 356–372.
Soleimani, F. (2017). Fragility of California bridges-development of modification factors (Doctoral dissertation, Georgia Institute of Technology).
Soleimani, F., & Liu, X. (2021). Artificial neural network application in predicting probabilistic seismic demands of bridge components. Earthquake Engineering & Structural Dynamics.
Yang, P., Hwa Yang, Y., B Zhou, B., & Y Zomaya, A. (2010). A review of ensemble methods in bioinformatics. Current Bioinformatics, 5(4), 296–308.
Zhong, J., Gardoni, P., Rosowsky, D., & Haukaas, T. (2008). Probabilistic seismic demand models and fragility estimates for reinforced concrete bridges with two-column bents. Journal of engineering mechanics, 134(6), 495-
Zhou, Z. H. (2021). Ensemble learning. In Machine Learning (pp. 181–210). Springer, Singapore.

Bridge Maintenance, Safety, Management, Digitalization and Sustainability – Jensen, Frangopol & Schmidt (eds)
© 2024 The Author(s), ISBN 978-1-032-77040-6
Open Access: www.taylorfrancis.com, CC BY-NC-ND 4.0 license

Dynamic measurements for assessing bridge response to foundation scour

M. Aimar, M. Civera, B. Chiaia, S. Foti, A. Quattrone & D. Sabia
Department of Structural, Geotechnical and Building Engineering, Politecnico di Torino, Turin, Italy

ABSTRACT: Hydraulic actions are considered one of the main causes of bridge collapse worldwide. Among them, foundation scour plays an important relevant role. However, the assessment of foundation conditions is a difficult task, especially for existing bridges. Indeed, a complete characterization is often hindered by the limited accessibility and, in some cases, by the lack of available information on both the structural and the geotechnical design. On the other hand, an effective identification of foundation scour can be crucial for an accurate prediction of the long-term bridge performance, also for the planning of possible retrofit interventions. This paper presents the results of an experimental study carried out on a road bridge in Piedmont, severely affected by foundation scour and under strict surveillance by the Metropolitan City of Turin. Dynamic measurements were collected on the superstructure and the foundations. This enables to get an insight into the modal response of the deck and to detect asymmetries in the foundation behavior due to the presence of scour. This study demonstrates the potential of in situ measurements as a tool for the characterization of scour conditions of existing bridges and thus for the improvement of the resilience of transportation infrastructures.

1 INTRODUCTION: FOUNDATION SCOUR IN RIVER BRIDGES

The particular case study of interest, which will be detailed in the remainder of this paper, regards a riverside tract of a long road bridge. Indeed, even when bridges and viaducts just run alongside the river bank, without crossing it, they can be heavily affected by the time-varying conditions of the water-soil-foundation interactions.

In this regard, foundation scour is, by far, the most common cause of collapse for river bridges (Borlenghi et al., 2022) Recent examples of severely scoured bridges in Italy can be found in (Pizarro et al., 2020) and (Aimar et al., 2024).

Therefore, the scour phenomenon requires particular attention from geotechnical, structural, and hydraulic engineers, especially since its complex dynamics are not yet totally understood and easily predictable (Borlenghi et al., 2022; Ciancimino et al., 2021, 2022; Foti et al., 2023).

To this aim, this short contribution presents some preliminary results from dynamic identifications carried out on the deck and foundation caps of one segment of a very long road bridge, located in Inverso Pinasca (Piedmont, Northwestern Italy) and subject to heavy scour due to an ongoing change in the Chisone river course.

2 THE INVERSO PINASCA BRIDGE

The Inverso Pinasca bridge is part of a large set of renewal works performed between 2004 and 2005 to improve the road connection between Turin (the 2006 Winter Olympic Games host city) and Séstriere (a main ski resort) on the SP 166 road through the Chisone Valley. This route is inserted in an Alpine environment, with most of the traffic occurring during the winter season due to the influx of ski and mountain tourists. In

DOI: 10.1201/9781003483755-186

particular, the small village of Inverso Pinasca (circa 600 inhabitants), as the Italian name *Inverso* (inverse) suggests, lies on the southern side of the valley, shadowed by the mountains. The majority of the other villages are situated on the northern (sunnier) side of the Chisone River. The bridge object of this study follows this southern bank before crossing the river after the village.



Figure 1. Side view of the Inverso Pinasca bridge in its full length, as captured during preliminary in situ surveys (February 3rd, 2023).

2.1 *Details of the tract of interest: Foundations and superstructure.*

The whole bridge (left side of Figure 2) measures 1849.90 m from end to end. The superstructure consists of four continuous decks, divided by expansion joints (that make all segments act as detached, independent units) and lying on 45 piers. the deck width is constantly 14.6 m, with one lane per direction.

The tract of interest is highlighted in red in Figure 2. It has a mixed profile, with rectilinear and curvilinear sections. These are located (as mentioned earlier) between the Chisone River on their East side and the small town of Inverso Pinasca on the West side.

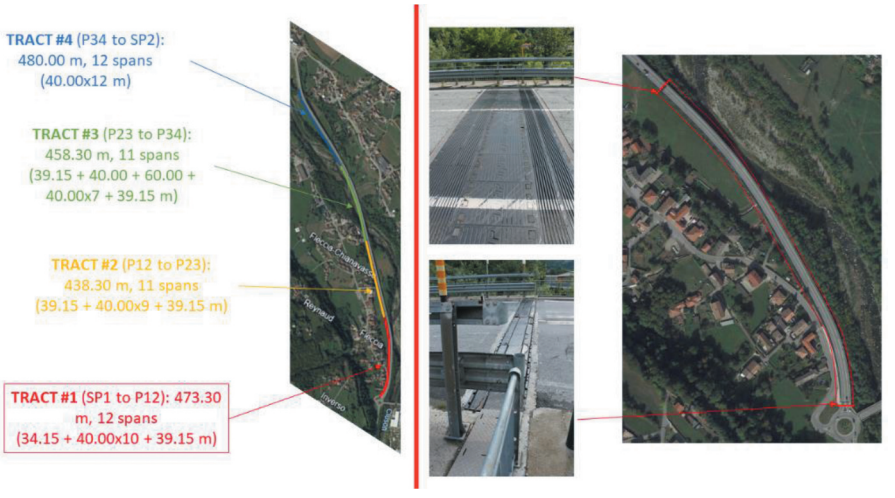


Figure 2. The four segments of the bridge continuous deck, with the one of interest (tract #1) highlighted in red and zoomed in on the right side. The two joints at its South and North ends are also portrayed.

The superstructure lies on deep foundations, with 8 piles per pile cap. These piles are particularly large (1.5 m in diameter), with a depth varying at each pier but included in a minimum of 14 m (pier P1, corresponding to the Southern abutments) and a maximum of 33 m (P24, out of the tract of interest here).

2.2 *Site-specific risks*

The area where the bridge lies is relatively seismically active, if compared to the rest of the Piedmont region. However, in absolute terms, it is classified as a low seismic hazard area, with an expected Peak Ground Acceleration (PGA) of 0.133 g (class 3S according to the local implementation of the Chapter 7 of the Italian NTC 2018 (Ministero delle Infrastrutture e dei Trasporti, 2018), considering a 10% probability of exceedance in 50 years). It is also worth noting the state-of-the-art seismic design of the bridge, where all bearings rest on seismic isolators.

From a hydrogeologic perspective, the area is free from landslide hazards, with only some slow ground movements on the north bank (hence, on the opposite side of the Chisone River) and no avalanche hazard due to the relatively warm climate year-round at the valley bottom.

Instead, the whole length of the infrastructure is classified by the Istituto Superiore per la Protezione e la Ricerca Ambientale (ISPRA)[1] as a high flood hazard area. The last major flood (October 2000, when the bridge of interest was yet to be constructed) caused the collapse of a nearby river crossing. Therefore, from a multi-risk assessment point of view, the potential scouring of the bridge piers can be identified as the main potential source of danger.

2.3 *Current scouring state*

The repeated alluvial events that affected the Chisone valley since the construction year (for instance, in 2010 and 2016) induced a migration of the main channel of the river, which has gradually shifted towards the orographic right, in correspondence with the bridge piers. The migration has resulted in strong undermining of the pier foundations in correspondence with a portion of the bridge, namely the one between P8 and P11. The modified shape of the streambed resulted in the exposure of the top part of foundation piles and general scour of piers, with depths up to 3.8 m for pier P9 (computed from the bottom surface of the pier cap) and 3.5 m for pier P10. It has to be remarked that the scour hole is not symmetrical because of the presence of a scarp more or less around the longitudinal axis of the bridge. Therefore, only half of the foundation is exposed. Furthermore, the scour hole below pier P8 has been partially refilled with coarse soil to prevent further erosion in this portion.

A map of the surveyed piers is reported in Figure 3, with the respective photo documentation of the scouring state as of mid-2023.

3 THE DYNAMIC IDENTIFICATION CAMPAIGN

The aim of the dynamic identification campaign was two-fold. On the one hand, it focused on the estimation of the modal parameters of the superstructure. Furthermore, it targeted peculiarities in the soil-structure system response to have an indirect insight into the influence of scour on the dynamic response, in terms of asymmetric features in the behavior. For this purpose, the survey focused on a portion of the bridge including parts affected and not affected by scouring. Indeed, the relative response can directly provide indications about the scour influence.

The setup included 13 PCB 3701G3FA3G uniaxial capacitive sensors, mainly located along the external longitudinal beams of the deck (Figure 4). The asymmetric location was mainly dictated by the accessibility of the beams on the river side, due to the presence of the scarp. In

1. https://idrogeo.isprambiente.it/app/pir

addition, 5 PCB 356B18 triaxial capacitive sensors were located on the longitudinal beams, in correspondence with the piers, to track the complete motion and to capture the influence of the seismic bearings.

Furthermore, high-sensitivity (10 V/g) PCB 393B04 piezoelectric sensors were located on the top of the foundation pad, both in uniaxial vertical or multiaxial configuration, to track the motion of the pier. The considered piers were P7, P8 and P9, each characterized by a different scour magnitude (Figure 5). For all the piers, a minimum sensor layout was adopted, consisting of four vertical sensors on the corners plus one/two horizontals, to track the relative asymmetries in both the vertical response and the horizontal response. However, being P9 the most deteriorated pier, a dense layout was adopted for this.

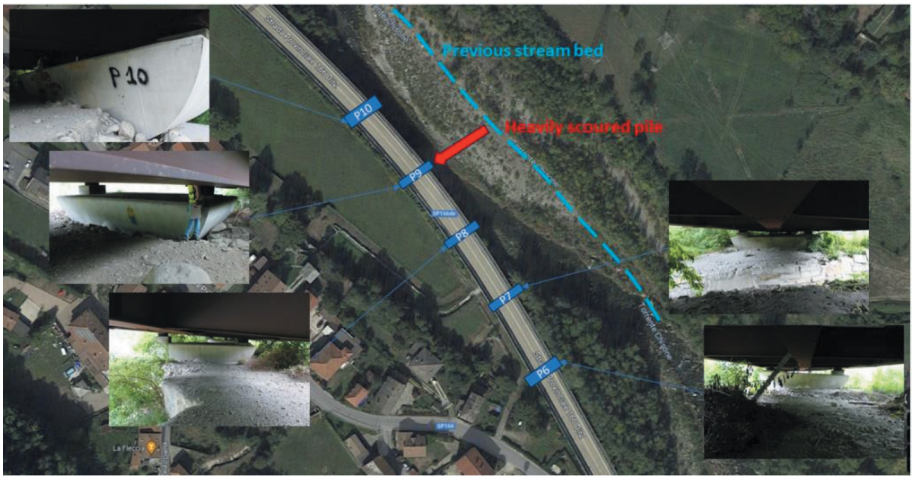


Figure 3. The current (mid-2023) scouring state at the pier foundations of interest. The most critical one (P9) is indicated by the red arrow. The blue dashed line represents the river course as of 2004 (during construction).

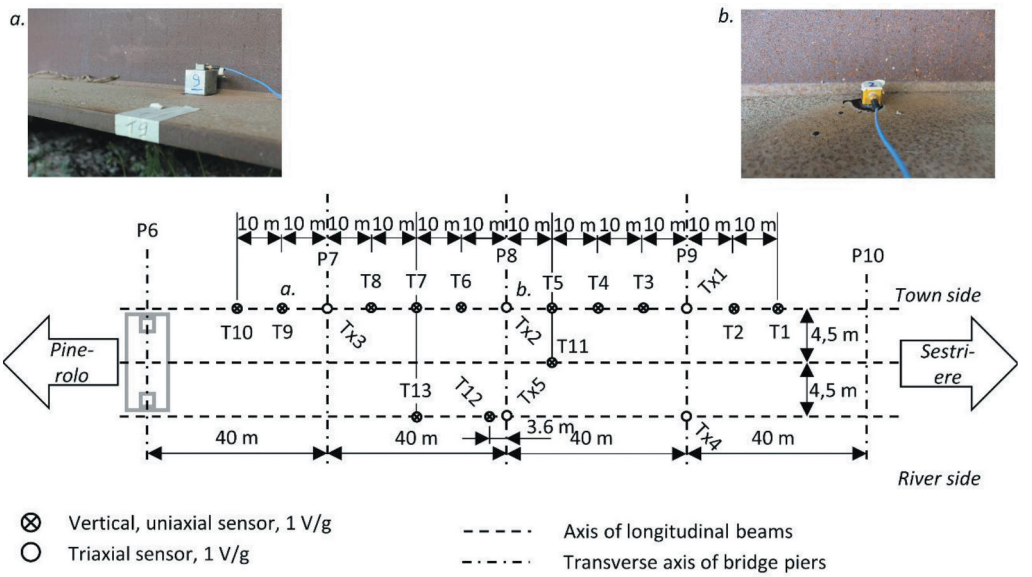


Figure 4. The sensor layout for the bridge deck, including a picture of the capacitive uniaxial (a) and piezoelectric triaxial (b) Accelerometers.

The acquisition was carried out through a 40-channel, LMS Siemens SCADAS acquisition device, using a 256-Hz sampling rate.

The limited number of channels and of high-sensitivity sensors compared to the inspected locations forced to perform the measurements through multiple setups. In all the setups, the

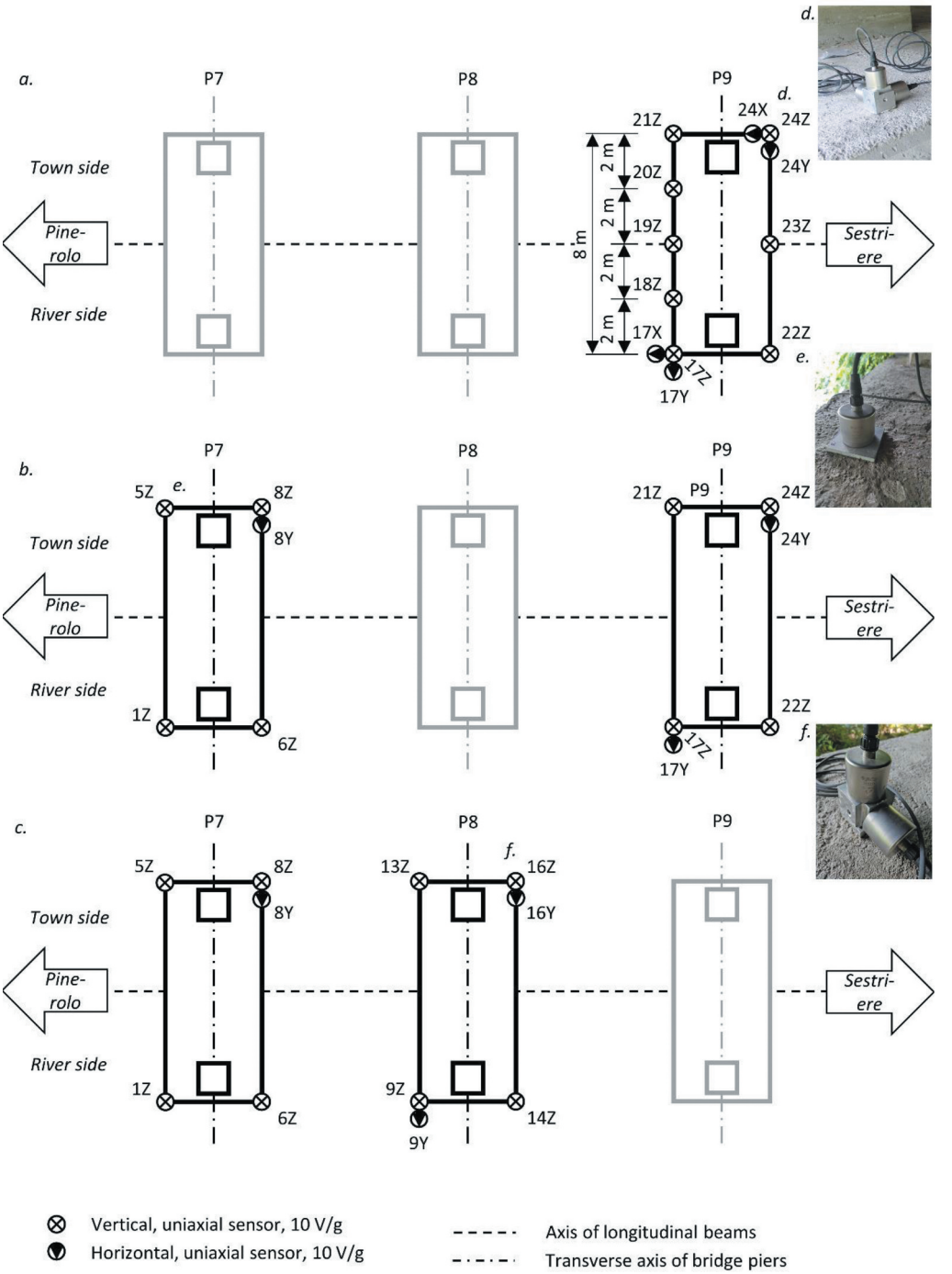


Figure 5. The first (a), second (b) and third (c) sensor layouts for the pier caps, including a picture of the high-sensitivity accelerometers in uniaxial (e), biaxial (f), and triaxial (d) configuration.

sensors on the deck and part of those installed on pier P9 were kept unchanged, also to provide a reference for the normalization and harmonization of measurements, whereas the high-sensitivity sensors were located to measure each couple of piers (i.e., P7-P9, P7-P8 and P9 only; see Figure 5). The rationale behind this strategy is to address the relative response of each couple of piers, with different scour conditions, to have an insight into the effect of scour.

4 PRELIMINARY RESULTS

The results described in this section refer to the first insights gained from a preliminary analysis of the gathered acquisitions, in terms of the response of the bridge deck and pier foundations.

4.1 *Insights from the bridge deck*

From a preliminary analysis of some of the signals acquired from the sensors deployed on the bridge deck, the main vibrational modes of the bridge deck in the tract under investigation seem to be a first vertical flexural mode at circa 2.20 Hz and a torsional one at 2.44 Hz. These values are averaged over six different ambient vibration acquisitions, analysed with the Automated Operational Modal Analysis code described in (Civera et al., 2022; Mugnaini et al., 2022). Both modes appear to have a relatively high damping, with the damping ratio ξ being larger than 2.5% in both cases. This is most likely due to the presence of seismic isolators at all bearings.

Furthermore, the detailed analysis of all modes highlights an asymmetry between the town- and the river-side. That is to say, the peak relative displacement (corresponding e.g. to the antinode at midspan for mode #1; see Figure 6.a) was found to be higher on the side of Inverso Pinasca, in all acquisitions. Considering six signals and the first mode shape, this difference in peak amplitude can be estimated at 28.51 ± 2.08 % ($\mu \pm \sigma$), thus, almost a third. Considering that all the sensors start from their zero, the slight transverse inclination of the deck should not have a direct influence. However, some numerical simulations of the uncalibrated FE model of the deck only (Figure 6.c) show that the leftward curvature of the deck naturally induces some higher vibration amplitudes on the riverside, as was also well expected. Nevertheless, these asymmetries could be (at least partially) also exacerbated by the absence of the scoured ground on the riverside (due to the loss of stiffness). Therefore, these aspects will need further studies to be properly investigated and understood.

4.2 *Insights from the pier caps*

For a quick assessment of the foundation response, this study estimated the RMS vertical acceleration (here, labelled as a_z) recorded at the vertices of each pier cap, consistently with the approach adopted in (Foti & Sabia, 2010). For a more reliable estimate, a_z was computed from 10-s long time windows extracted from the recorded data, each corresponding to the passage of a vehicle on the bridge deck. Figure 7 shows the estimated a_z for piers P7 and P9, that is, the ones with the least and the most scoured foundations. Results are clustered according to the side of the load application. Furthermore, they highlight the trend on the upstream side and the downstream side, to investigate asymmetries both in the town-river direction and along the longitudinal axis of the bridge. Finally, for each pulse considered, a_z data are normalized with respect to their average value, to remove the influence of the load entity on their magnitude.

In all the cases, a larger a_z is observed at the side corresponding to the load application, as expected. However, some relevant differences can be observed when comparing the dynamic behavior of P9 and P7. On the one hand, the spatial distribution of a_z is similar when vehicles pass on the town side, in terms of asymmetry. Instead, for loads

on the riverside, a_z is quasi-uniform in P7 (as the normalized value is almost close to the unit) whereas larger variations are observed for P9. This means that, for the same loads, the vibration levels in P9 are highly asymmetric compared to P7, due to the stiffness variations induced by foundation scour. On the other hand, in P9, a_z is significantly larger downstream than upstream. Notably, this is observed both on the town side and on the river side, for all the considered load pulses and application locations. Instead, this discrepancy is smaller in P8 (not reported here) and almost negligible in P7. This result was somewhat unexpected, as the erosion mostly acts along the longitudinal axis of the bridge and should not produce relevant differences in the response between upstream and downstream. Instead, this evidence may indicate that stiffness variations in the soil-structure system due to scour also occur along the flow direction of the river – and not only in the transverse direction, as it may be expected from the available information. This may be a consequence of the curvature of the main river channel, which results in a complex morphology of the scour hole.

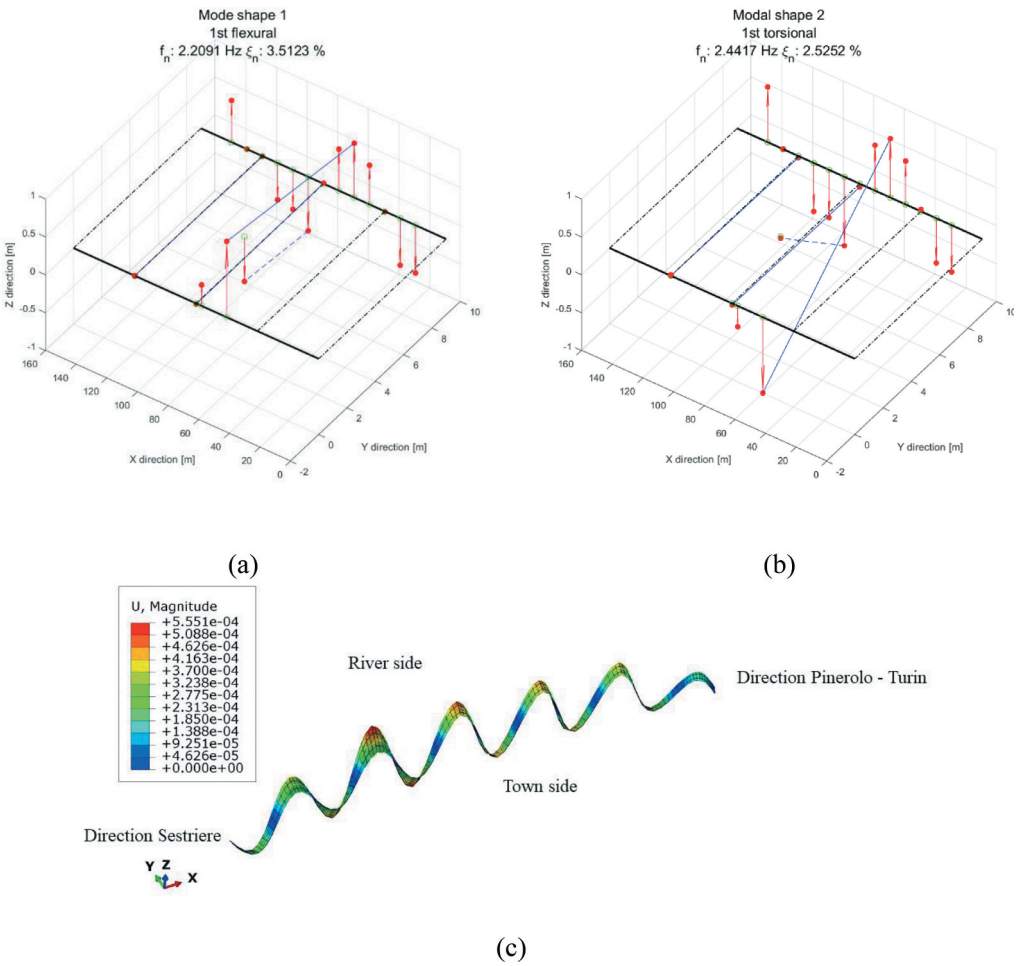


Figure 6. (a-b) The mode shapes identified from the deck bridge dynamic response (example taken from the ninth acquisition). The blue lines connect the modal displacements captured by the accelerometers located on the town side of the deck with their counterparts on the other side (or at mid-width for T5-T11). The black lines represent the deck layout in its undeformed shape. (c) First flexural mode, according to a preliminary simulation (uncalibrated, deck only) run on Abaqus 2019.

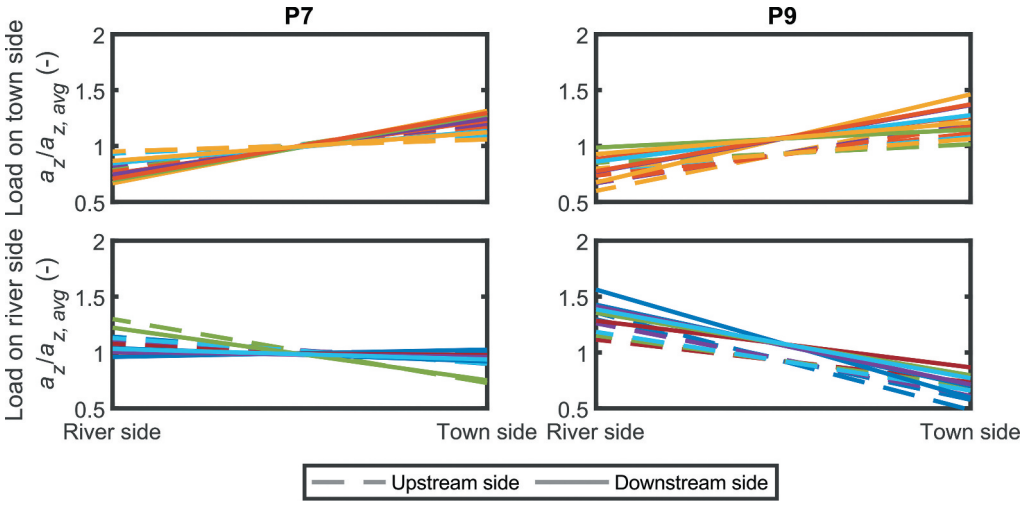


Figure 7. Estimated normalized acceleration RMS at the pier caps, for P7 and P9 and for loads applied on the town side or the river side. Results are clustered according to the considered side of the pier cap (i.e., downstream and upstream). Each color corresponds to a specific load (i.e., vehicle moving on the deck), with the continuous line representing the vibration level observed downstream and the dashed line representing the response on the upstream side.

5 CONCLUSIONS AND FUTURE WORKS

This study described the experimental campaign carried out to investigate the dynamic response of a multi-span bridge near to Turin, which is affected by foundation scour. The survey addressed both the deck and the foundation response over a portion of the bridge, which includes scoured and unscoured piers. The rationale behind this strategy is to address the relative response of nearby portions of the bridge, with different scour conditions, to have an insight into the effect of scour. Preliminary results from the processing of experimental data demonstrated the presence of asymmetric behavior on both the deck modal shapes and the piers vibration magnitude, which can be attributed to the inhomogeneity of the distribution of soil stiffness due to scour. Ongoing studies, to be reported in the near future, are focusing on more detailed assessment of scour effects on the bridge pier caps and deck. As the local administrative entity (Città Metropolitana di Torino) is currently planning for hydraulic and geotechnical countermeasures, future works will report as well the dynamic behaviour of the target infrastructure before and after interventions.

ACKNOWLEDGEMENTS

This work is part of the research activity developed by the authors within the framework of the 'PNRR': SPOKE 7 "CCAM, Connected Networks, and Smart Infrastructure" - WP4. The Authors would like to thank the institution of Città Metropolitana di Torino, especially Marco Benso, Matteo Tizzani, and Giovanni Luca Zagardo, for their precious help and support.

REFERENCES

Aimar, M., Civera, M., Foti, S., & Chiaia, B. (2024). Preliminary Insights from Surveys of Bridges at High Scouring Risk in West Piedmont. *II Fabre Conference – Existing Bridges, Viaducts and Tunnels: Research, Innovation and Applications (FABRE24)*.

Borlenghi, P., D'Angelo, M., Ballio, F., & Gentile, C. (2022). Continuous Monitoring of Masonry Arch Bridges to Evaluate the Scour Action. *Lecture Notes in Civil Engineering*, *200 LNCE*, 400–408. https://doi.org/10.1007/978-3-030-91877-4_46

Ciancimino, A., Anastasopoulos, I., Foti, S., & Gajo, A. (2022). Numerical modelling of the effects of foundation scour on the response of a bridge pier. *Acta Geotechnica*, *17*(9), 3697–3717. https://doi.org/10.1007/S11440-022-01591-9

Ciancimino, A., Jones, L., Sakellariadis, L., Anastasopoulos, I., & Foti, S. (2021). Experimental assessment of the performance of a bridge pier subjected to flood-induced foundation scour. Https://Doi.Org/10.1680/Jgeot.20.P.230, *72*(11), 998–1015. https://doi.org/10.1680/JGEOT.20.P.230

Civera, M., Mugnaini, V., & Zanotti Fragonara, L. (2022). Machine Learning-Based Automatic Operational Modal Analysis: A Structural Health Monitoring Application to Masonry Arch Bridges. *Structural Control and Health Monitoring*, *29*(10), e3028. https://doi.org/https://doi.org/10.1002/stc.3028

Foti, S., Aimar, M., & Ciancimino, A. (2023). Influence of scour of foundations on the seismic performance of bridges. *SECED 2023* .

Foti, S., & Sabia, D. (2010). Influence of Foundation Scour on the Dynamic Response of an Existing Bridge. *Journal of Bridge Engineering*, *16*(2), 295–304. https://doi.org/10.1061/(ASCE)BE.1943-5592.0000146

Ministero delle Infrastrutture e dei Trasporti. (2018). *Norme Tecniche per le Costruzioni 2018 (NTC 2018)*.

Mugnaini, V., Zanotti Fragonara, L., & Civera, M. (2022). A Machine Learning Approach for Automatic Operational Modal Analysis. *Mechanical Systems and Signal Processing*, *170*. https://doi.org/https://doi.org/10.1016/j.ymssp.2022.108813

Pizarro, A., Manfreda, S., & Tubaldi, E. (2020). The Science behind Scour at Bridge Foundations: A Review. *Water 2020, Vol. 12, Page 374*,*12*(2), 374.https://doi.org/10.3390/W12020374

SS06: Forensic engineering and damaged structures. Critical cases studies and lesson learned of LATAM road bridges

Organizers: M.A. Valenzuela, M. Marquez, F. Cerda & G. Valdebenito


Taylor & Francis
Taylor & Francis Group
http://taylorandfrancis.com

Bridge Maintenance, Safety, Management, Digitalization and Sustainability – Jensen, Frangopol & Schmidt (eds)
© 2024 The Author(s), ISBN 978-1-032-77040-6
Open Access: www.taylorfrancis.com, CC BY-NC-ND 4.0 license

Seismic design modifications for damage prevention in skewed bridges

T. Amaya & H. Santa María
Department of Structural and Geotechnical Engineering, Pontificia Universidad Católica de Chile, Santiago, Chile
CIGIDEN, Research Center for Integrated Disaster Risk Management, Macul, Santiago, Chile

ABSTRACT: The seismic design of bridges is vital for safety and functionality, especially for skewed bridges with asymmetrical geometry. This study assesses the impact of seismic design criteria on the seismic performance of Chilean skewed bridges. Fragility curves for bridges designed under the current design criteria are compared with those prior to 2010. Nonlinear analytical models, of typical Chilean bridges are subjected to ground motions records to obtain the damage probabilities of the bridges. The fragility assessment reveals that changes in design criteria alter component damage probabilities, with a more pronounced effect observed for skewed bridges compared to straight bridges. Additionally, current seismic design criteria reduce superstructure displacement and rotation but increase substructure stresses. Insights from this study contribute to the evaluation of seismic performance and offer recommendations for reinforcing vulnerable bridges.

Keywords: seismic fragility, bridge seismic design, seismic fragility curves, skewed bridges

1 INTRODUCTION

The seismic design of bridges is crucial to ensuring their safety and functionality. A comprehensive understanding of how seismic design requirements impact the bridge seismic response is essential for accurate analysis and successful design. This is particularly important when dealing with skewed bridge structures, in which their asymmetrical geometry may alter their seismic performance. The 2010 Mw 8.8 Maule Earthquake in Chile caused extensive damage to many bridges across the country (Kawashima et al., 2011) with the most common types of damage resulting from large displacements of the superstructure, a phenomenon particularly observed in skewed bridges. In response to the observed bridge damage, new seismic design criteria were introduced (MOP, 2020). These changes include the extension of seat support lengths, addition of diaphragms, higher design forces for vertical seismic bars, adjustments to interior and exterior shear key specifications, as well as modifications in the anchorage of elastomeric bearings. Notably, for skewed bridges, there are specific considerations that require a greater number of connecting elements between the superstructure and substructure, depending on the geometry of the bridge deck (MOP, 2020). While several authors (Aldea et al., 2021; Wilches et al., 2019, 2021) have explored the impact of seismic design on the behavior, damage mechanisms, and fragility of Chilean bridges, there is not enough research analyzing how seismic vulnerability varies with the skew angle. Particularly, there is a lack of studies on how changes in seismic design requirements influence the response of skewed bridges under different conditions of bridge deck geometry.

The objective of this study is to assess the impact of changes in the seismic design criteria on the seismic vulnerability of Chilean skewed bridges. For that aim, a typical Chilean bridge is

DOI: 10.1201/9781003483755-187

considered as a case study. The benchmark bridge is analyzed considering different values of the skew angle (0, 15 and 30 degrees) and two seismic design conditions: seismic designs before 2010 and those adopted afterward. The influence of the seismic design criteria is evaluated by comparing fragility curves and the nonlinear seismic response of the different cases of bridges.

2 METHODOLOGY

2.1 *Case study*

This study considers the typical bridge structure obtained after a statistical analysis (Wilches et al., 2019) of available information on Chilean bridges, which corresponds to a simply supported bridge with prestressed concrete girders. The bridge comprises two spans with a continuous slab, each measuring 27 meters in length and 13 meters in width. The superstructure consists of four prestressed concrete girders, supported by elastomeric bearings on a central pier of three columns and seat-type abutments at each end. For this bridge, three skew angle cases were considered: the scenario of a straight bridge (0 degrees) and angles of 15 and 30 degrees. For these bridges, two different design conditions were analyzed: one using the design requirements enforced before 2010 (Ministerio de Obras Públicas, 2002) (referred to as Seismic design 1) and another with the design requirements after 2010 (MOP, 2020) (referred to as Seismic design 2). The bridges with Seismic design 1 are equipped with exterior shear keys and unbonded elastomeric bearings under the main girders. In contrast, the bridges with Seismic design 2 incorporate both interior and exterior shear keys, alongside bonded elastomeric bearings. Additionally, in Seismic design 2, the design forces of shear keys and seismic bars, as well as the length of the seat support increase. Furthermore, for skewed bridges, Seismic design 2 mandates a larger number of interior shear keys when the specified condition of excessive displacements is met. This condition, depicted in Figure 1, relates the aspect ratio of the bridge deck to the skew angle of the bridge.

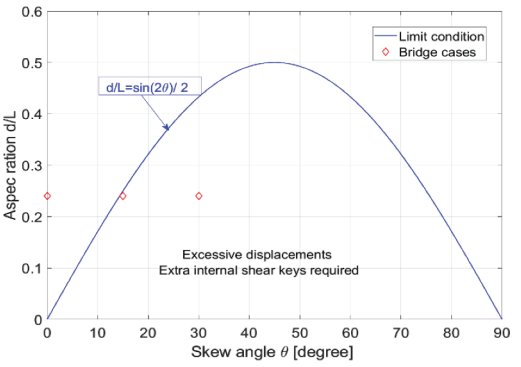


Figure 1. Aspect ratio (d/L) vs skew angle.

2.2 *Numerical models*

Three-dimensional analytical models were developed for the bridges using OpenSees (McKenna, 2011). Figure 2 shows the modelling approach of the bridges. The superstructure was modeled using elastic beam-column elements. The columns were modeled using displacement-based beam-column elements with fibers sections. The foundations of piers and abutments were modeled using linear springs. Unbonded elastomeric bearings were modeled using Flat Slider Bearing elements (McKenna, 2011); and bonded elastomeric bearings were modeled using Elastomeric Bearing (Bouc-Wen) elements (McKenna, 2011). The interaction between the deck and abutments was simulated by incorporating nonlinear springs. The passive soil pressure was modeled using a hyperbolic backbone curve (Shamsabadi et al., 2009),

while pounding between the deck and abutments was simulated using an impact material (McKenna, 2011). Interior and exterior shear keys were modeled using a trilinear constitutive following (Silva et al., 2003). The properties of reinforced concrete were represented using the Hysteretic material (McKenna, 2011), while the gap between shear keys and girders was simulated with the ElasticPPGap material (McKenna, 2011).

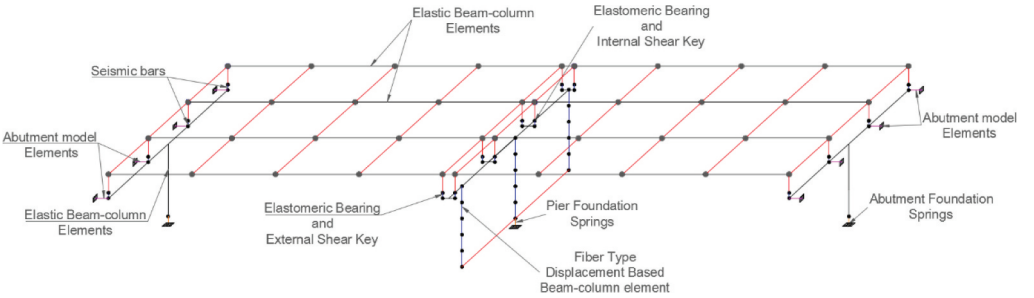


Figure 2. Nonlinear numerical model.

In this study, we obtain fragility curves for the bridges employing the Multiple Stripe Analysis method (Baker, 2015). The chosen intensity measure (IM) corresponds to the spectral acceleration at a period of 0.6 seconds, which represents the average of the fundamental periods of the bridges. To obtain the fragility curves, seismic records were carefully selected through a probabilistic seismic hazard assessment (PSHA). In this study, the bridges are assumed to be located at site latitude 33.097◦S, longitude 71.547◦W. The seismic hazard curve at the site is estimated through PSHA using the SeismicHazard platform (Candia et al., 2019). A total of 11 pairs of seismic records were selected across 8 intensity levels, covering return periods ranging from 72 to 4975 years. The seismic hazard curve, along with the corresponding intensity levels, is shown in Figure 3. The seismic records were selected from the Siberrisk database (Castro et al., 2022). The record selection process was guided by the conditioned spectrum (Baker & Asce, 2011) corresponding to each intensity level.

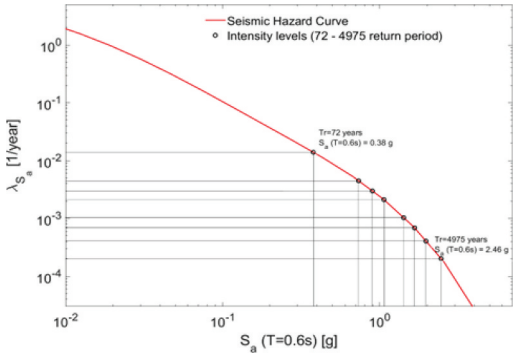


Figure 3. Seismic hazard curve.

2.2.1 *Damage states*

This study uses different engineering demand parameters (EDPs) for superstructure and substructure elements in constructing the fragility curves. Three damage states (DS) are considered, each with specific numerical values detailed in Table 1.

For bridges equipped with unbonded elastomeric bearings (Seismic design 1), DS1 is reached when the residual displacement of the elastomeric bearings exceeds 50 mm. DS2 occurs when the maximum displacement of the bearings surpasses the displacement corresponding to the maximum capacity of the shear keys, set at 160 mm. DS3 is defined by transversal displacement exceeding the length of the seat support in the transverse direction. For bridges equipped with bonded bearings (Seismic design 2), two damage states, DS1 and DS2, are associated with the shear strain of the bearings. These damage states are reached when the shear strain exceeds 150% and 200%, respectively. These numerical values were adopted based in previous research studies (Alam et al., 2012; Zhang & Huo, 2009). The third damage state is defined by the transverse collapse of the superstructure.

For the substructure, the EDP relies on the displacement ductility of the columns. The thresholds for damage states related to column displacement are established using values derived from Billah & Allam (Muntasir Billah & Shahria Alam, 2015). In addition, we considered an extra damage state associated with the potential collapse of the bridge in the longitudinal direction.

In this study, we develop fragility curves individually for superstructure and substructure damage. Additionally, we establish fragility curves representing bridge damage as a system, where both substructure and superstructure damage contribute to the overall system damage. The damage probabilities of the bridge as a system are calculated using Equation 1. Where P_{sys} is the probability of damage of the entire bridge and P_{EDP} is the probability of damage of the superstructure or substructure of the bridge.

$$P_{sys}(DS_i|IM) = 1 - \prod_{EDP_j}\left(1 - P_{EDP_j}[DS_i|IM]\right) \quad (1)$$

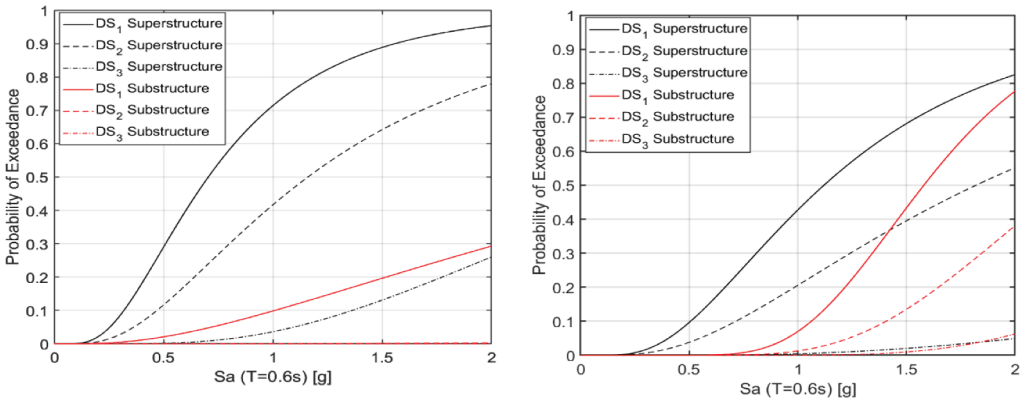
Table 1. Bridge EDP and damage state values.

Bridge elements	EDP	Damage state 1 (DS1)	Damage state 2 (DS2)	Damage state 3 (DS3)
Superstructure	Unbonded elastomeric bearing	50 mm (RD)	160 mm (MD)	Transversal collapse *
Superstructure	Bonded elastomeric bearing	150 % (SS)	200 % (SS)	Transversal collapse *
Superstructure	Unseating	—-	—-	Longitudinal collapse *
Substructure	Column (μ_d)	1.22	1.78	4.8

RD: Residual displacement
MD: Maximum displacement
SS: Shear strain
μd: Displacement ductility
*: Numerical value variable depending on bridge and seismic design.

3 RESULTS

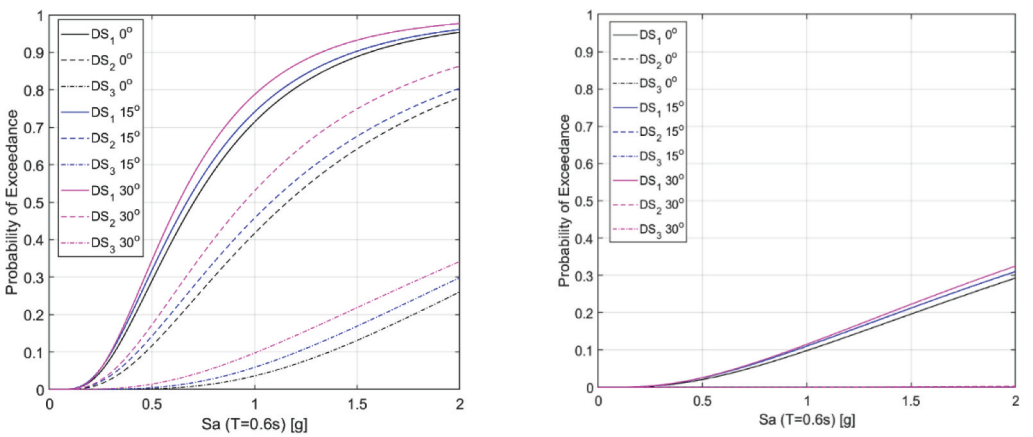
In order to compare the effect of the changes of the seismic design criteria on the damage probabilities of the bridges, Figure 4 depicts the superstructure – substructure fragility curves of the straight bridge (0 degrees) designed with the two seismic design configurations. Figure 4a and 4b present the fragility curves related to Seismic design 1 and Seismic design 2, respectively. These fragility curves illustrate changes in the bridge's damage mechanisms in response to the altered design requirements. In the bridge designed under Seismic design 1 (see Figure 4a), there is a notable prevalence of high probabilities of superstructure damage, while the probabilities of substructure damage are relatively low. In contrast, in the case of the bridge designed with Seismic design 2 (see Figure 4b), the probabilities of superstructure damage decrease, compared to Seismic design 1, but there is a noticeable increase in the probabilities of substructure damage.



a) Seismic design 1 b) Seismic design 2

Figure 4. Superstructure – substructure fragility curves for straight bridge.

Figure 5 compares the fragility curves for the superstructure and substructure for bridges employing Seismic design 1 and the three skew angles. As the skew angle increases, the probabilities of superstructure damage also increase. For instance, in Figure 5a, at an intensity of 1.5 g and considering DS2, the superstructure damage probabilities are 64%, 68%, and 75% for skew angles of 0◦, 15◦, and 30◦, respectively. Consistent patterns are observed across all three damage states. Notably, the increasing skew angle enhances the tendency for planar rotation in the bridge deck, ultimately amplifying superstructure displacement. This underlines the crucial role of skew angle in influencing superstructure response under seismic conditions. For substructure damage (see Figure 5b), the fragility curves remain similar for all skew angles. As mentioned before, under Seismic design 1, substructure damage is minimal, emphasizing the predominant impact of skew angle on the superstructure.

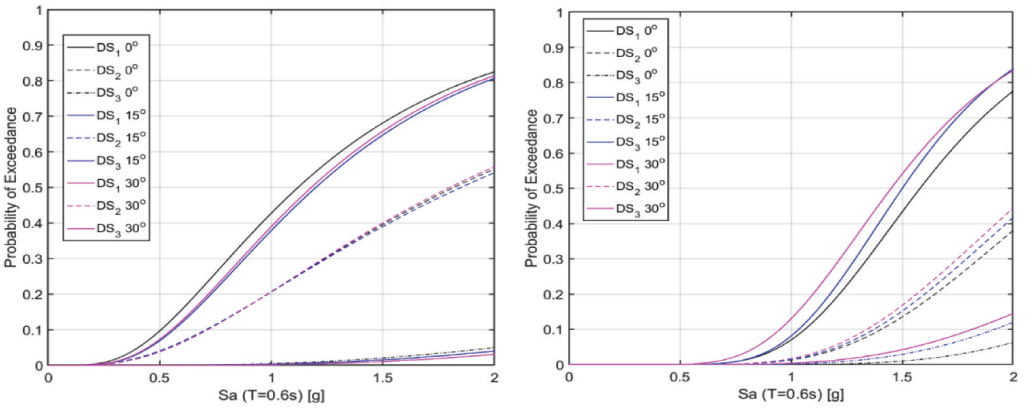


a) Superstructure b) Substructure

Figure 5. Superstructure – substructure fragility curves, Seismic design 1.

Figure 6 shows the superstructure – substructure fragility curves for the bridges with Seismic design 2 and the three skew angles. For this design condition, two primary observations emerge. Firstly, the probabilities of superstructure damage (see Figure 6a) are lower compared to the Seismic design 1 condition and remain consistent across all three skew angles. The introduction of additional internal shear keys, as a design requirement, effectively restricts the

displacement and rotation of the bridge deck, consequently reducing the superstructure damage probability. On the other hand, in Figure 6b, it is observed that as the skew angle increases, the probabilities of substructure damage also increase. For instance, at an intensity of 1.5g and considering DS1, the damage probabilities are 43%, 50%, and 54% for skew angles of 0◦, 15◦, and 30◦, respectively. Similar trends are noted for all three damage states. This phenomenon arises because, while the inclusion of additional interior shear keys limits superstructure displacements, it concurrently enhances the transmission of forces from the deck to the substructure, thereby escalating the probabilities of substructure damage.



a) Superstructure b) Substructure

Figure 6. Superstructure – substructure fragility curves, Seismic design 2.

Figure 7 illustrates the system fragility curves for the bridges designed with the two seismic design configurations. For the Seismic design 1 condition (see Figure 7a), as the skew angle increases, the probabilities of damage also increase. For instance, in Figure 7a, at an intensity of 1.5g and considering DS3, the damage probabilities are 13%, 17%, and 22% for skew angles of 0◦, 15◦, and 30◦, respectively. In contrast, under the Seismic design 2 condition (see Figure 7b), the probabilities for all three damage states are lower compared to the Seismic design 1 case, and there are smaller differences among the various skew angle cases. For example, in Figure 7b, at an intensity of 1.5g and considering DS3, the damage probabilities are 3%, 4%, and 5% for skew angles of 0◦, 15◦, and 30◦, respectively.

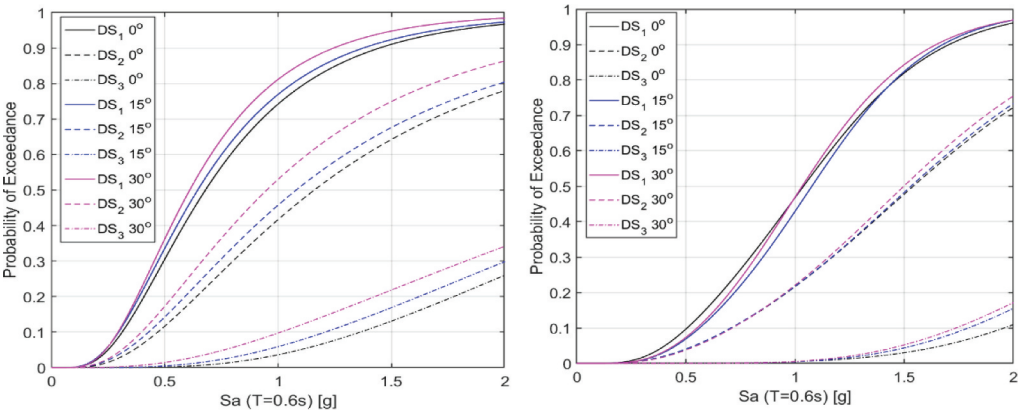
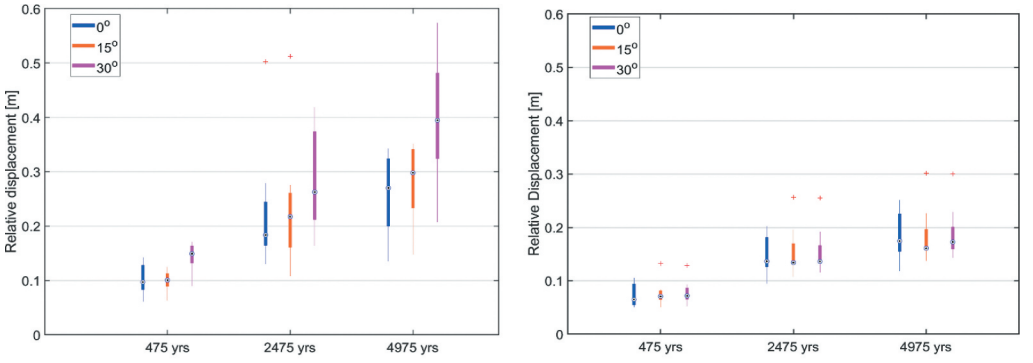


Figure 7. System fragility curves, Seismic design 1 and Seismic design 2.

To analyze the effect of both design conditions on the rotational response of the bridge decks, Figure 8 compares the maximum relative transverse displacement response. Box plot graphs are presented depicting responses to seismic records corresponding to three return periods. Under the Seismic design 1 condition, a clear effect of the skew angle is observed, where higher angles exhibit a greater tendency for rotation. In contrast, for the Seismic design 2 condition, rotations are lower and more controlled with the increase in the skew angle. These results, along with the previously presented fragility curves, indicate that the current seismic design criteria are effective in controlling the skew angle effect. They effectively limit the displacement and rotation of the superstructure, resulting in lower probabilities of damage for the bridges.



a) Seismic design1 b) Seismic design 2

Figure 8. System fragility curves, Seismic design 1 and Seismic design 2.

4 CONCLUSIONS

The analysis presented in this study examines the impact of changes in the seismic design criteria on the seismic fragility of Chilean skewed bridges, using a representative Chilean bridge as a case study. Three skew angle scenarios (0, 15, and 30 degrees) were considered, and seismic design provisions before and after the 2010 Maule Earthquake were evaluated. Nonlinear three-dimensional models were developed in the OpenSees software, and fragility curves were generated using the Multiple Stripes Analysis method. The results indicate that the change in the design criteria reduces superstructure damage but increases substructure damage. In the Seismic design 1 condition, skew angle primarily influences superstructure damage probabilities, whereas in the Seismic design 2 condition, the influence is more pronounced in substructure damage probabilities. The system fragility curves demonstrate that the revised seismic design criteria effectively decrease overall bridge damage probabilities and mitigate the skew angle effect. Additionally, the current design requirements were found to reduce deck rotation effects in the bridges.

ACKNOWLEDGMENTS

The authors wish to acknowledge the funding provided by ANID through project FONDECYT #1231824 and Research Center for Integrated Disaster Risk Management (CIGIDEN) ANID/FONDAP 1522A0005. Teodoro Amaya thanks funding from ANID (Chilean National Agency for Research and Development) through the ANID Doctorate Scholarship No21211554.

REFERENCES

Alam, M. S., Bhuiyan, M. A. R., & Billah, A. H. M. M. (2012). Seismic fragility assessment of SMA-bar restrained multi-span continuous highway bridge isolated by different laminated rubber bearings in medium to strong seismic risk zones. *Bulletin of Earthquake Engineering*, *10*(6), 1885–1909. https://doi.org/10.1007/S10518-012-9381-8/METRICS

Aldea, S., Bazaez, R., Astroza, R., & Hernandez, F. (2021). Seismic fragility assessment of Chilean skewed highway bridges. *Engineering Structures*, *249*, 113300. https://doi.org/10.1016/J.ENGSTRUCT.2021.113300

Baker, J. W. (2015). Efficient analytical fragility function fitting using dynamic structural analysis. *Earthquake Spectra*, *31*(1), 579–599. https://doi.org/10.1193/021113EQS025M/ASSET/IMAGES/LARGE/10.1193_021113EQS025M-FIG8.JPEG

Baker, J. W., & Asce, A. M. (2011). *Conditional Mean Spectrum: Tool for Ground-Motion Selection*. https://doi.org/10.1061/(ASCE)ST.1943-541X.0000215

Candia, G., Macedo, J., Jaimes, M. A., & Magna-Verdugo, C. (2019). A New State-of-the-Art Platform for Probabilistic and Deterministic Seismic Hazard Assessment. *Seismological Research Letters*, *90*(6), 2262–2275. https://doi.org/10.1785/0220190025

Kawashima, K., Unjoh, S., Hoshikuma, J.-I., & Kosa, K. (2011). Damage of bridges due to the 2010 Maule, Chile, earthquake. *Journal of Earthquake Engineering*, *15*(7), 1036–1068.

McKenna, F. (2011). OpenSees: a framework for earthquake engineering simulation. *Computing in Science & Engineering*, *13*(4), 58–66.

Ministerio de Obras Públicas. (2002). *Manual de carreteras - Volumen No 3 - Instruccions y criterios de diseño. Chile*.

Mop, M. de O. Públicas. (2020). *Manual de Carreteras, Vol 3.*

Muntasir Billah, A. H. M., & Shahria Alam, M. (2015). *Seismic Fragility Assessment of Concrete Bridge Pier Reinforced with Superelastic Shape Memory Alloy*. https://doi.org/10.1193/112512EQS337M

Shamsabadi, A., Khalili-Tehrani, P., Stewart, J. P., & Taciroglu, E. (2009). Validated simulation models for lateral response of bridge abutments with typical backfills. *Journal of Bridge Engineering*, *15*(3), 302–311.

Silva, P. F., Megally, S., & Seible, F. (2003). Seismic performance of sacrificial interior shear keys. *Structural Journal*, *100*(2), 177–187.

Wilches, J., Santa Maria, H., Leon, R., Riddell, R., Hube, M., Arrate, C., & Via, C. E. (2021). Engineering Practice Paper Evolution of seismic design codes of highway bridges in Chile. *Earthquake Spectra*, *37*(3), 2174–2204. https://doi.org/10.1177/8755293020988011

Wilches, J., Santa María, H., Riddell, R., & Arrate, C. (2019). Effects of changes in seismic design criteria in the transverse and vertical response of Chilean highway bridges. *Engineering Structures*, *191*, 370–385.

Zhang, J., & Huo, Y. (2009). Evaluating effectiveness and optimum design of isolation devices for highway bridges using the fragility function method. *Engineering Structures*, *31*(8), 1648–1660. https://doi.org/10.1016/J.ENGSTRUCT.2009.02.017.

Bridge Maintenance, Safety, Management, Digitalization and Sustainability – Jensen, Frangopol & Schmidt (eds)
© 2024 The Author(s), ISBN 978-1-032-77040-6
Open Access: www.taylorfrancis.com, CC BY-NC-ND 4.0 license

Collapse of Cau Cau Bridge: Forensic engineering study

M.A. Valenzuela
Pontificia Universidad Católica de Valparaíso, Valparaíso, Chile

M. Márquez
Dirección de Vialidad, Ministerio de Obras Públicas, Santiago, Chile

ABSTRACT: The city of Valdivia is located in the Los Rìos Region, in southern Chile, crossed by several rivers, among which is the navigable Cau Cau river, which divides Isla Teja from the Las Ánimas sector. The Ministry of Public Works tendered the design and construction of the Cau Cau Bridge, which provides a new road alternative to access both the city and the coast of the region and allows the passage of boats, including towards the city shipyard. The awarded proposal consists of three structures: a 110-meter-long northern access viaduct, the main bascule bridge, 165 meters in total and a 70-meter main span, and the 88-meter southern access viaduct. The Cau Cau Bridge is the first mobile structure built in Chile. On February 24, 2015, during the startup stage of the construction phase, and while the lifting operation of the decks is being carried out, one of the hydraulic lifting devices in the southern sector fails, finally generating that the bridge was not opened to service. This paper provides the forensic engineering study carried out by the principal after the failure produced in one of the deck leaves, with a critical analysis of the management protocol carried out, the hypotheses of the causes, analysis of the manufacturing process, assembly and construction process of the deck, study of the oleo hydraulic and mechanical systems and the modeling of the structural system, in order to determine the origin of the failure. The conclusions of the investigation and the lessons learned for the process of design and construction of singular bridges in Chile and their application in other projects are delivered.

1 INTRODUCTION

The Construction of the Cau Cau Bridge and Access Project aims to design a new road connection to optimize traffic in the road network of the city of Valdivia, located in the Valdivia Province, Los Ríos Region.

Specifically, for the traffic coming from the northern sector of the city heading west, which previously had to circulate through the center of the city of Valdivia.

With this new road connection, the volume of vehicular traffic through the center of Valdivia is reduced, utilizing existing roadways.

Due to the city of Valdivia being surrounded by a network of watercourses (Valdivia, Cruces, and Cau Cau rivers to the west, Calle Calle river to the north, and Angachillas, Tornagaleones, and Futa rivers to the south), the construction of bridges is necessary to provide connectivity to different areas through existing roads.

Therefore, to connect the Las Ánimas sector, i.e., the northern side of Valdivia, with Isla Teja and provide feasibility for this new road connection, a bascule-type bridge over the Cau Cau River was designed, considering it is a navigable river.

The Cau Cau River is a natural barrier that prevents the integration of both riverbanks (Las Ánimas and Isla Teja), as well as the development of both sectors, due to the lack of road connectivity (Figure 1). Therefore, within the Communal and Regional Development, the project, in addition to improving the connection of productive sectors to and from Niebla

DOI: 10.1201/9781003483755-188

and reducing congestion in downtown Valdivia, enables the development of the Las Ánimas sector, which has proposals for urban expansion in both housing and facilities, sectors awaiting this new project.

The New Regulatory Plan for Valdivia establishes a new urban boundary and incorporates some changes in land use for sectors located both north and south of the river. Areas for housing development, facilities, productive activities, and harmless industry are designated. The previous point will generate increased use of the road to be developed, as the densification of the area could increase.

This development respects the wetland areas of the zone as a tourist attraction. Additionally, the bridge itself will be another tourist attraction due to its bascule operation, increasing pedestrian demand and walks in the northwest sector of Valdivia, as it is the first bascule bridge designed and built in Chile. Furthermore, the New Regulatory Plan leaves a reserve for a road strip that would directly connect Route 205 with the Cau Cau Bridge in the future, providing an even more direct connection to Isla Teja and Niebla.

The characteristic of the Cau-Cau Bridge being a movable bridge also considers communal and regional development regarding the anticipated growth in future fluvial activities since there is no height restriction for vessel passage, unlike existing bridges Pedro de Valdivia and Calle Calle, which limit the height to 10 m. The Cau Cau Bridge is the only option for the passage of vessels with a height greater than 10 m.

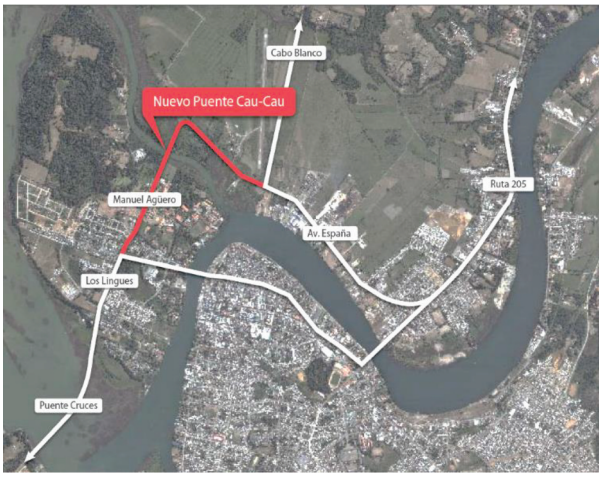


Figure 1. Cau Cau bridge location.

2 DESCRIPTION

The project involves the construction of a bascule bridge over the Cau Cau River and the improvement and paving of the accesses (NSM, 2011) (MOP, 2011).

The bridge consists of a movable span with a length of 70 m and a clearance of 7 m, composed of a bascule bridge with two leaves of 35 m each and two spans of 15.5 m, including 10 m counterweight spans (Figure 2).

The movable structure to be built over the Cau Cau River is of the bascule type. This bridge type allows the movement of the deck by rotation about a horizontal axis through a hinge and hydraulic lifting systems. The crossing conditions at the Cau Cau River require the use of a bascule bridge with two leaves.

In the proposed arrangement, the hinge joints have been placed, spanning the strict 70 m width of the riverbed, to minimize the required structure. This design integrates the bridge pier and abutment into a single element accessible from the shore for the installation of lifting machinery.

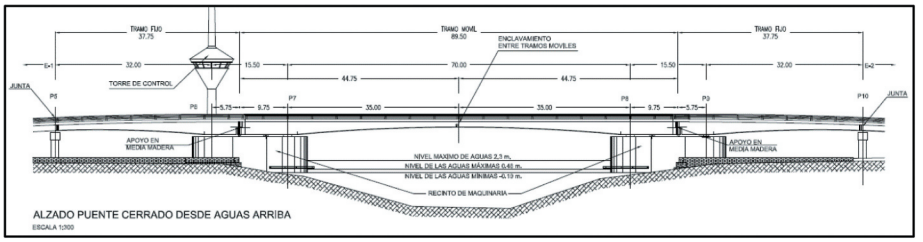


Figure 2. Bascule section view.

The cross-section of the span is metallic and consists of two main beams with a double "T" section, spaced 6.5 m apart, and a deck with a metallic orthotropic slab formed by transverse beams spaced 3.5 m apart, extending into lateral cantilevers of 3.84 m. The main beams have a variable depth, with 3.0 m at the supports and 1.5 m at the center of the span, with a parabolic variation between them (Figure 3).

The cross-section of the movable bridge and viaducts has two roadways, each 4.0 m wide, and sidewalks, 1.77 m and 3.27 m wide on each side. At the ends, there is space for the accommodation of corresponding safety barriers, resulting in a total deck width of 14.20 m. The deck has a 2.5% camber from the centerline of the roadways, and the two side sidewalks have a 20% camber towards the roadways.

The pavement surface of the movable span consists of a 6.0 mm thick epoxy resin-based coating, sprinkled with fine aggregate to enhance vehicle adherence, with significantly lower weight compared to a standard asphalt pavement layer.

Additionally, the project includes two fixed spans (north and south viaducts). The north viaduct is 142 m long, with one span of 32 m and five spans of 22 m each, all simply supported. The south viaduct is 120 m long, with one span of 32 m and four spans of 22 m each, all simply supported.

The superstructure of the viaducts is structured with 3 steel beams, a variable thickness in situ reinforced concrete upper slab, and a 5 cm thick asphalt riding surface. The deck is supported on the infrastructure through neoprene plates, located at the ends of each beam, and is anchored to it through anchor bars.

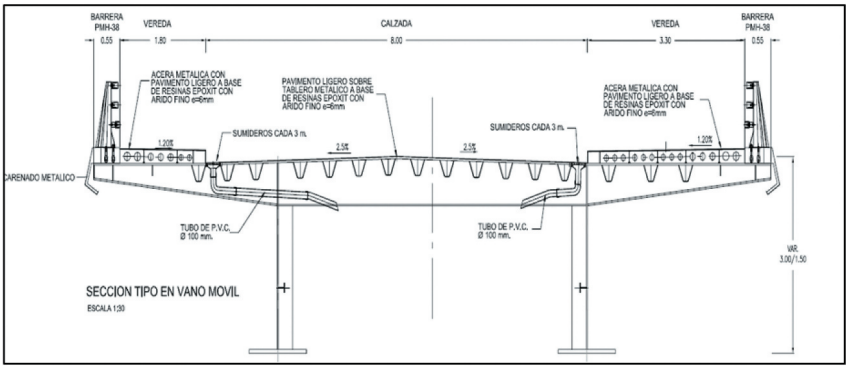


Figure 3. Cross-sectional profile of the bascule section.

The infrastructure of the viaducts comprises 2 abutments and 7 piers. The abutments are of the solid wall type with wings parallel to the roadway and foundation through in-situ pre-excavated and concrete-filled piles of 35 m, while the piers consist of 3 pile-piles, where the piles are pre-excavated and concrete-filled in situ with an average length of 35 m.

The bascule bridge is designed with a double system of mechanical devices (Figure 4). On one hand, the main machinery applies the necessary force to ensure movement around the

pivot axis and secure stability during the opening phase. On the other hand, there are interlocking systems between both movable spans and between the movable span and the access viaduct. These elements must be released to allow the opening movement and must be reactivated once the structure is closed.

The main machinery consists of hydraulic jacks (each with a capacity of 750 tons) capable of producing a moment around the pivot axis by applying forces against the compensation span and the foundation of the abutment-pier to complete the imbalance pair not covered by the counterweights. The entire bridge movement and interlocking system are hydraulic, including pumps, valves, filters, and systems with smooth braking at the end of both opening and closing movements.

Two hydraulic jacks are employed on each side, connected to the deck on the inner side of the beams where the counterweights are located. In the closed bridge position, they extend to 12.40 m, and in the open bridge position, they contract to 7.0 m.

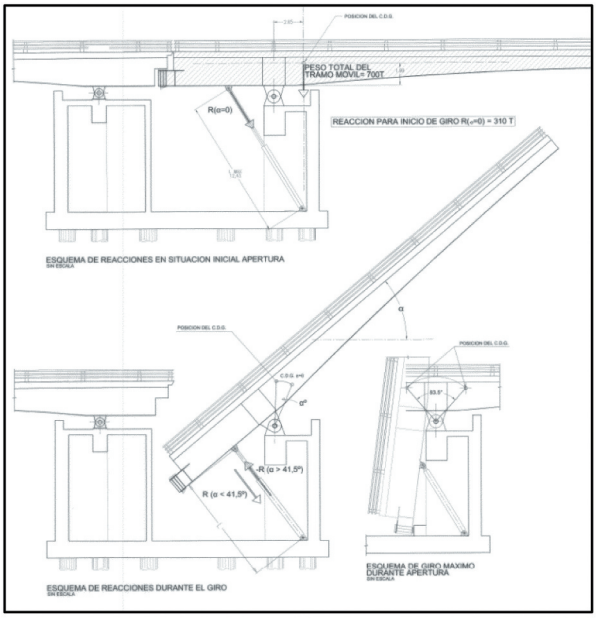


Figure 4. General overview of the tilting system.

Finally, the project includes access works, sanitation, road safety, landscaping, lighting, river defenses, and a control tower.

3 EVENT

The overall failure of the Cau Cau Bridge occurred on February 24, 2015, during the testing process to prepare the bridge for operation. It happened while the south leave was being raised slightly, which needed to be lifted first to subsequently lift the north leave of the bridge.

The failure occurred particularly in the southeast leave of the bridge, and it unfolded chronologically as follows:

The startup test began with the lifting of the south leave to 11°, intending to open it and then proceed to lift the north leave to its maximum angle of 82°.

The lift of the south leave started at 12:07:10 hrs. with an initial pressure of 372 psi at 0°, then, after 6 seconds, reaching a pressure of 2420.5 psi at 11.08°. This position was maintained while awaiting the start of the lift of the north leave.

After 10 seconds, a first sharp sound emanated from the south leave compartment. Five seconds later, a second noise occurred, followed by a strong impact of the southeast cylinder against the concrete support base 1 second later.

Over the next 4 seconds, there was a transverse oscillation of the bridge deck, during which the weight of the bridge deck was fully taken by the west cylinder of the south leave, stabilizing the leave's opening at 10°.

The descent of the south leave, according to the information available, was manually performed from the V12 valve of the safety system until reaching the resting position at 0°. The descent of the leave was completed at 12:26:28 hrs.



Figure 5. Final position of leaves after the collapse.

4 FORENSIC ENGINEERING

In light of the previously described event, the Highway Directorate of the Ministry of Public Works has decided to contract technical consulting services for forensic investigation. In this regard, the consultancy services were awarded to SECON, a firm with an interdisciplinary team encompassing structural, mechanical, and metallurgical areas, supervised by the Inspection Office of the Highway Directorate. The contract's objectives included: Determining the causes and origin of the failure; Reviewing the temporary lifting project; Proposing solutions to the detected failures; Following the engineering forensic protocol, a final diagnostic report on the failures and proposed solutions was requested.

In 2010, Chile experienced its most intense earthquake, and referencing this event until 2020, several structures failed, many due to extreme events (Valenzuela et al., 2020), with the collapse of the Cau Cau Bridge being part of this category. From these experiences, the Highway Directorate of the Ministry of Public Works developed a program of protocols and a methodology for forensic investigation. Thus, the investigation activities on the Cau Cau Bridge have been integrated into current protocols (Valenzuela & Márquez, 2023), (PIARC, 2023).

In particular, the investigation on the Cau Cau Bridge included the review of information gathered from records provided by the Highway Directorate, on-site inspection visits, laboratory sample evaluations, and the examination of all other pertinent volatile and non-volatile data.

The methodology employed for this study consisted of three phases.

Review and evaluation of background Information.

This involved the examination of the following: Documents from the project bidding phase (specifications, blueprints, studies, and schematics); Documents from the construction phase (projects, blueprints, schematics, photographs); Documents related to previous bridge failures; Information regarding the failure on February 24, 2015; Documents related to the temporary lifting system of the bridge.

On-Site Inspection

Multiple on-site visits were conducted to verify the current state of the bridge structure, its operational conditions, and the state of the failed component (rod-cylinder-fork joint). Additionally, a detailed inspection and dimensional verification of the piece were performed during its transportation for study. Samples of the failed component were extracted by certified laboratories for material testing, and inspections of southeast arm cylinder pieces were carried out at the supplier's facility.

Failure Analysis

The analysis and study of the bridge failure were conducted, considering three areas of focus:

Evaluation and Analysis of the Oleo Hydraulic System: This encompassed an assessment of the oleo hydraulic system, spanning from the proposal stage during project and bidding phases to its construction and utilization in the lifting system.

Mechanical System Evaluation (Metallurgical): This involved assessing the quality of materials used in the manufacturing of the lifting cylinders, along with their respective forks. Laboratory tests and microscopic examinations of the material involved in the failure were conducted, in conjunction with a review of blueprints and quality documents related to the lifting cylinders.

Structural Analysis: This phase entailed the modeling and analysis of components with failures using Ansys for mechanical elements and Sofistik for structural analysis. These tools were employed to verify hypothetical failure scenarios prior to the results of the metallographic analyses performed on the failed components.

5 FORENSIC STUDY RESULTS

The SECON team (Contreras, 2015) and the Inspection Office concluded, based on the review of records and results of the technical inspection, the following relevant aspects concerning the failure:

5.1 *Background analysis*

As part of the supplementary background information, failures or issues preceding the collapse of the bascule system were considered. Among the most relevant are:

Bascule Mechanism and Modification of the Locking System between the Fixed and Mobile Systems.

The bascule mechanism operates through two hydraulic jacks acting in parallel. In the initial closed configuration (0°), the hydraulic jacks start pulling (i.e., in tension) with maximum force until, at an intermediate position (approx. 41.5°) when the center of gravity is located above the fixed hinge, the jacks begin pushing (i.e., in compression) until the final open position (83°). The locking mechanism in the center of the bridge consists of two hydraulic latches that are activated once the bridge is in the closed position. Initially, a similar locking system with a hydraulic latch for the rear span, at the junction with the fixed section, was considered in the project but was eliminated during the bidding stage. Although this rear latch system is not necessary for the structure's balance, it is customary to have this system to prevent issues at the joint between the fixed and mobile spans, which could later impact service conditions.

Modifications During Construction

Several structural adjustments were necessary during construction due to construction errors and/or modifications.

- Incorrect Assembly of the North and South Bascule Spans
  Due to errors during execution, the North and South bascule spans were mistakenly installed interchangeably. Since the deck is not symmetrical (i.e., the structure's axis does not align with the roadway axis), structural adjustments were required to avoid disassembling both spans and placing them in their correct positions. The adopted solution involved continuously welding

longitudinal stiffeners with a thickness of 8 mm and variable height, onto which an 8 mm upper plate was welded. This resulted in noticeable upward vertical deformation at the center of the mobile span and appreciable differential deformation between both ends of the deck (transversely). These deformations at the central joint (interlocking between mobile spans) affect the behavior of the hydraulic latch interlocking system due to the misalignment of both spans. All solutions adopted to adjust the deck's geometry led to an increase in the deck's self-weight and a shift in the center of gravity position of the structure.

- Cutting of Fixed Support Lugs
  The construction procedure adopted for the assembly of each bascule span involved lateral positioning parallel to the river and subsequent vertical axis rotation to its final position. To achieve this, the decision was made to cut the lugs of the fixed supports, subsequently welding them once the deck span was in its final position. The full-penetration welding during the cooling process resulted in the loss of verticality of the lugs. The non-verticality of the anchor lugs affected the proper functioning of the fixed hinge (e.g., wear due to friction, pin and hinge binding, etc.).

Adjustment in the Position of the Mobile Hinge

Interference points between the pistons and the fixed structure of the chamber and deck were identified. To address these interferences, it was decided to shift the pull point of the lifting system (upper hinge of the cylinder) to a position closer to the fixed hinge. This involves a modification in the forces to be applied by the lifting system, consequently affecting the stresses/strains in the deck and the rotation angle corresponding to the indifferent equilibrium position, in relation to the original project.

5.2 *Metallographic and structural analyses*

The following observations were carried out:

- The stresses generated in the failure zone are well below the yield values of the materials.
- Based on the results from three structural models subject to loads from their self-weight, imbalanced loads on the cylinders, and lateral displacements of the deck, it was concluded that the stresses that could have occurred in the failure zone are well below the specified material yield stress.

The rupture occurred due to inadequate and defective execution of secondary welding. Conclusions from metallographic studies include:

- The material specified for the fork, AISI-SAE 1045, does not comply with ASTM A29 standards, as the steel's microstructure indicates that it was cast and not shaped as required by the standard.
- Quality procedures in the welding of the stem-fork joint were not followed (Figure 6), and the failure initiated in the Heat-Affected Zone (ZAC).
- Filler welding was performed on the fork before thread manufacturing and machining.



Figure 6. Sample of the welding applied on the fork – lug.

6 FINAL COMMENTS

Upon completing the forensic engineering work, the Directorate of Highways of the Ministry of Public Works establishes the following lessons learned:

- Specific Bidding Projects for Unique Bridges: Before tendering unique bridge projects, especially when dealing with first-time experiences in certain structural typologies or their magnitude, it is necessary to enhance the capabilities of the professionals involved in the process. This involves forming technical-legal teams for their development, starting from the pre-investment phase and throughout the investment phase (design, construction, and operation/maintenance). This consideration extends not only to the capacities of the client but also to those of the contractors and consulting services for the Inspection Fiscal.
- The work carried out around Forensic Engineering on the Cau Cau Bridge allowed obtaining information crucial for decision-making regarding projects developed after the failure event, ultimately leading to the bridge's operational status.
- Among the elements contemplated for repair or modification based on the consultant's recommendations are:

  a) Orthotropic Deck - The deck has deformations due to the metallic overlay installed because of the incorrect assembly of the bridge leaves.
  b) Fixed Joint - The fixed joints exhibited significant damage due to errors in project execution.
  c) Cylinder - It recommends removing the remaining three cylinders and replacing them to avoid the risk of failure.
  d) Hydraulic-Oil System - The cylinders should be replaced, and the hydraulic-oil system should be improved.
  e) PLC (Programmable Logic Controller) - The control and emergency system must be reinforced.
  f) Central Latch - The central latch underwent modifications compared to its original design

- Comparative Review with Other Bascule Structures in Specialized Disciplines:

Based on visits conducted to various European bascule bridges, certain elements subject to updating due to advancements in the state of the art in the field were identified. The visited bridges include: Porta D'Europa Bridge, Barcelona, Spain; Leixoes Bridge, Porto, Portugal and Estacio Bridge, Murcia, Spain. Main issue to improve in Cau Cau Bridge are: bearing, dumpers, interlocking, control ITS – monitoring and instrumentation, sidewalks and stock.

ACKNOWLEDGMENT

The authors acknowledge the contribution and research of SECON Consultancy and P.E. Sergio Contreras; P.E. Metallurgy MSc. Manuel Cabrera and Dr. Eng. Fernando Sima

REFERENCES

MOP - Dirección de Vialidad, (2011) Bases Construcción Puente Cau Cau y accesos Provincia de Valdivia, Región de los Ríos, Fecha: Abril 2011, Santiago.

Contreras, S. (2015), Informe Final Obra Puente Cau Cau – Valdvia. Materia: Estudio de falla y diagnostico estructural. Fecha 10.08.2015

NSM Ingenieros Ltda. Nelson San Martín S., (2011) Proyecto: Puente Cau Cau.

Valenzuela, M.A. & Pinto, H. Marquez, M. Seguel, J.L. (2020) State of the Art of Chilean bridge collapse. Proposal of Actions in Chilean Bridge Engineering, IABMAS.

Valenzuela, M.A & Marquez, M. (2023) Forensic Engineering Procedures Applied to the Old Cancura Bridge, Los Lagos Region, Chile, XXVII° Congreso Mundial de la Carretera, Prague

PIARC, (2023) Report Forensic Engineering For Structural Failures. 2023R8EN - TECHNICAL COMMITTEE 4.2 BRIDGES. ISBN 978-2-84060-790-8, France.

Bridge Maintenance, Safety, Management, Digitalization and Sustainability – Jensen, Frangopol & Schmidt (eds)
© 2024 The Author(s), ISBN 978-1-032-77040-6
Open Access: www.taylorfrancis.com, CC BY-NC-ND 4.0 license

Use of advanced non-destructive methods for the structural diagnosis of the Cau-Cau Bridge, Chile

G. Valdebenito
Faculty of Engineering, Universidad Austral de Chile

M. Marquez
Ministery of Public Works, Chile

M. Valenzuela
Faculty of Engineering, Pontificia Universidad Católica de Valparaíso, Chile

J.L. Seguel
JLS Engineers, Chile

ABSTRACT: As a consequence of the failures experienced by the Cau Cau Bridge, Chile, the Ministry of Public Works of Chile entrusted the performance of a series of tests to this structure, which included invasive and non-invasive tests, load tests and various experimental and numerical analyzes to generate a detailed structural diagnosis.

This paper reports the main results of non-invasive tests carried out on the reinforced concrete elements of this structure. Special geophysical tests using high-frequency Ground Penetration Radar, the use of traditional non-invasive methods, as well as the use of remote sensing methods based on high-range Terrestrial Laser Scanning for 3D modeling in conditions with and without loading are highlighted and detailed.

Results show the advantages related to the great precision, speed and reliability of the use of these non-invasive methods as support for an opportune structural diagnosis of bridges.

1 INTRODUCTION

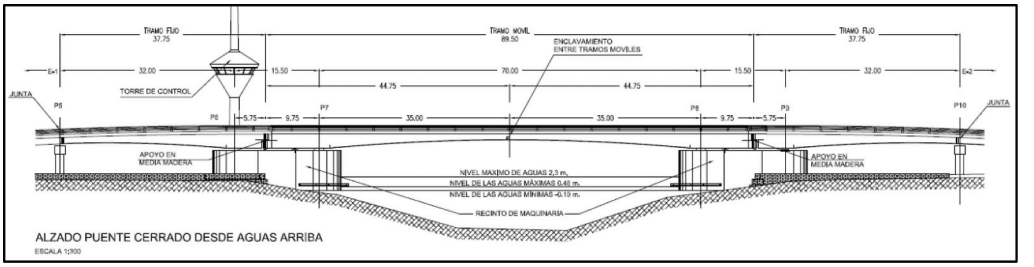
The Cau Cau bridge is located in the city of Valdivia, Chile. This structure is movable and is located over the Cau Cau River, connecting the Las Ánimas sector with the Isla Teja sector (See Figure1). It was built by the company AZVI CHILE S.A. between 2012 and 2015.



Figure 1. Location of Cau Cau Bridge, in the city of Valdivia, southern Chile.

DOI: 10.1201/9781003483755-189

The bridge consists of a movable span with a length of 70 m and a clearance of 7 m, composed of a bascule bridge with two leaves of 35 m each and two spans of 15.5 m, including 10 m counterweight spans (Figure 2). The movable structure to be built over the Cau Cau River is of the bascule type. This bridge type allows the movement of the deck by rotation about a horizontal axis through a hinge and hydraulic lifting systems. The crossing conditions at the Cau Cau River require the use of a bascule bridge with two leaves. Figure 3 shows the cross section of the structure (MOP, 2011).



Figur 2. Bascule section view.

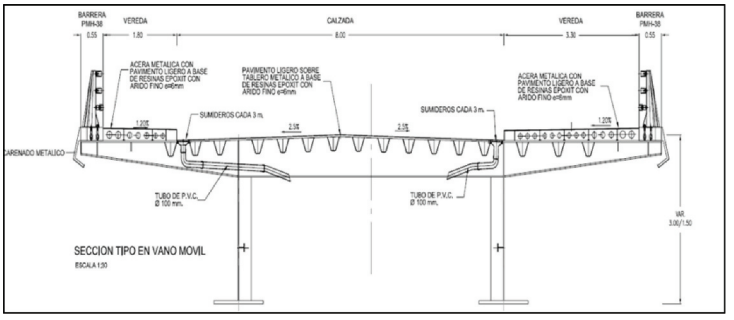


Figure 3. Cross-sectional profile of the bascule section.

The overall failure of the Cau Cau Bridge occurred on February 24, 2015, during the testing process to prepare the bridge for operation. It happened while the south leave was being raised slightly, which needed to be lifted first to subsequently lift the north leave of the bridge. A strong impact of the southeast cylinder against the concrete support base occurred, originating a stop in the process and the subsequent problems. The failure is well described in several studies and documents (Contreras, 2015; VMB Ingeniería Estructural, 2016; RiNA, 2018).

This paper exposes the non-invasive structural auscultations carried out on the Cau Cau bridge, as well as tele-detection strategies applied by means of terrestrial LiDAR for the precise geometric definition of the bridge including load testings and measurements with this 3D technique. The main objective is to determine the homogeneity of the concrete and its mechanical properties, in addition to the identification and checking of the arrangement of the reinforcement with respect to the project plans. Specifically, it is of interest for repairing strategies, the evaluation of the resistance and homogeneity of the concrete in the different elements monitored, based on the results of the compression tests carried out on concrete and results obtained from ultrasound and sclerometric testings. On the other hand, the distribution of the reinforcing is characterized based on high frequency Ground Penetrating Radar (GPR) results, and comparing these surveys with the project specifications (RiNA, 2018).

2 LIGHTLY INVASIVE AND NON-INVASIVE SURVEYS PERFORMED AND RESULTS

2.1 *Lightly invasive auscultation. Assessment of resistance and homogeneity of concrete*

Reinforced bars scanner was used for the identification of in situ concrete test tubes. Those tubes were tested at Materials Laboratory in Universidad Austral de Chile. In the particular case of extracting tubes at height, an articulated man-lift platform was used. Prior to lifting the platform, the system is fixed in a horizontal position, ensuring that it will not move at the time of extraction (Figure 4).



Figure 4. Extracting concrete tubes for compressive testing.

Additionally, ultrasonic and sclerometric tests were applied to the tubes, in order to calibrate results with obtained compressive resistances. With this, it is possible to explore other areas of the structure and to obtain mechanical properties without excessive lightly invasive tests (Figures 5a b).





Figure 5. (a) Ultrasonic testings for the tubes at laboratory. (b) Ultrasonic testings in the structure.

Sclerometric tests were carried out at 136 points in different structural elements of the bridge. It should be noted that according to the NCh1565 standard (INN, 1979), this procedure is not applicable to the determination of concrete resistance, so in this case it was applied

only to estimate levels of homogeneity in concrete. It is indicated in the regulations that the errors of the method range around 20 to 25%.

Strengths obtained in laboratory are above the project specifications for all the auscultation areas (H-30 concrete), obtaining the maximum resistances in the approach slabs and viaducts, while the minimum resistances were obtained in the piers. The above could indicate that the quality of the concrete used in the piers is comparatively lower than those used in the other areas.

Regarding the ultrasound results, it was observed that the average values obtained in the northern and southern sectors are similar to each other. In the case of the southern sector, the deviation exceeds 10% of the average for this element. Average time values for the viaduct are in the order of 2700 m/microsec), for indirect tests.

Sclerometric tests showed average values of 702 kg/cm2 for the viaduct, with dispersions up to 50 kg/cm2, that can be excessive.

2.2 *Non-invasive geophysical surveys. Reinforcement identification and detection of pathologies*

To characterize the arrangement of reinforcement in the defined areas of the bridge, two complementary non-invasive methods were used: reinforcement scanner and Ground Penetrating Radar.

The reinforcement scanner or pacometer was used to characterize the presence of reinforcing steel in the structure, mainly determining the spacing and direction of the reinforcing bars, managing to estimate in certain areas the thickness of the mechanical recover of the concrete. It should be noted that one of the main limitations of this device is that as the mechanical recover increases, precision can be poor in determining its thickness, also making it difficult to detect the diameters and location of the reinforcing bars. On the other hand, in cases where the mechanical recover very low and/or the reinforcement is very dense, the identification of individual bars can be difficult or non-precise.

To solve difficulties related with penetration capacity and resolution, medium and high frequency Ground Penetrating Radar (GPR) was used to identify with more precision the location, spatial distribution and recovering of the reinforcement. This technique constitutes the state-of-the art for the non-invasive auscultation in reinforced concrete structures. For the bridge, two frequencies (antennas) were used: 800 MHz and 2700 MHz. The first for the identification of deep reinforced bars and deep detection of cavities and concrete pathologies (up to 1,2 m). The second, for detailed shallow identification of bars and detailed pathologies (up to 60 cm). When executing field surveys, the main considerations that must be taken into account are related with the calibration of acquisition and visualization parameters, which must be adjusted based on the characteristics of the element to be explored. Considering that the penetration capacity of the emitted electromagnetic wave varies depending on the characteristics of the medium, it is necessary to carry out previous tests to calibrate the speed of wave propagation in the medium to be explored (or the dielectric parameter). This calibration was carried out on the interior wall of the south engine room, which has a thickness of 50 cm. (see Figure 6a). Based on this, the propagation velocity of radar waves in the medium (reinforced concrete) was adjusted in such a way that the reflection associated with the opposite face of the wall coincides with the known thickness of the element. Based on this, the propagation speed of the medium obtained was 90 m/microsec. This value is absolutely consistent with typical velocities in concrete with similar humidity conditions.

Post-processing involves, in general terms, the application of 1D filters, 2D filters, static correction, migrations and gain adjustments. Obviously, the application of these post-processing tools will be particular for each radargram (2D image obtained with GPR), and will be applied depending on the objective of the study. It should be noted that unlike the reinforcement scanner, GPR allows the generation of a continuous survey of the element (2D image), determining in the same profile the general distribution of the mechanical recover and the distribution of the steel bars. In some cases, despite the application of different filters, corrections and gains, it is not possible to visualize the object(s) of interest, which indicates that the raw radargram does not contain the necessary information due to the unfavorable conditions of the exploration medium. The results obtained are conditional on the correct interpretation of the reflections or anomalies that are displayed in a post-processed radargram.



Figure 6. (a) Calibration of the GPR. (b) Field surveys with high frequency GPR.

Results of the radargrams post-processed showed adequate distribution of the reinforcement, as well as bar recover, without evidence of pathologies inside the analyzed concrete areas. Figures 7a b show typical radargrams obtained, in this case, for piers and walls of the engine area respectively.

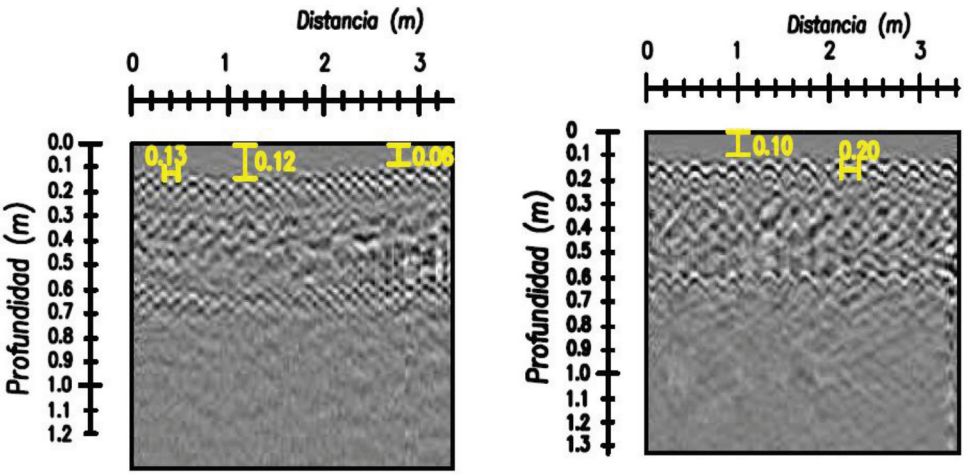


Figure 7. (a) Radargram showing a 2D postprocessed image of the northern pier. (b) Radargram showing a 2D postprocessed image of the engine walls.

2.3 *Remote-sensing techniques*

Remote sensing field surveys were carried out with the objective of generating a high-definition point clouds of the northern and southern sectors of the bridge. For this, a RIEGL VZ-2000 high range Terrestrial Laser Scanner (TLS) was used. The survey was organized in several field campaigns, which consisted of a differentiated survey for each sector of the bridge (North and South). In addition, two campaigns were considered to raise each of the engine rooms associated with the bridge. This technique, permits the generation of high definition complete 3D geometric models of the bridge, including difficult access areas. The georeferenced and multi-adjust post-processing for each position, permits the generation of the complete model, including the engine areas, permitting and adequate link of the interior and exterior areas. This point clouds, constitutes 3D DEMs (Digital Elevation Models) of the structure in detail, permitting load test verifications by means of DoD

(differences of DEMs) as well subsequent generation of structural modellings. Figures 8a b illustrates the TLS field surveys.



Figure 8. (a) Field survey with TLS of the access. (b) Capturing the 3D geometry of the bridge.

As a result, it was possible to obtain calibrated 3D models. Figure 9 shows part of the complete 3D model of the bridge, as well as Figure 10 shows a DEM obtained for calibration model with real load tests. The three control points are observed for the vertical deflection measurements for each loading condition.

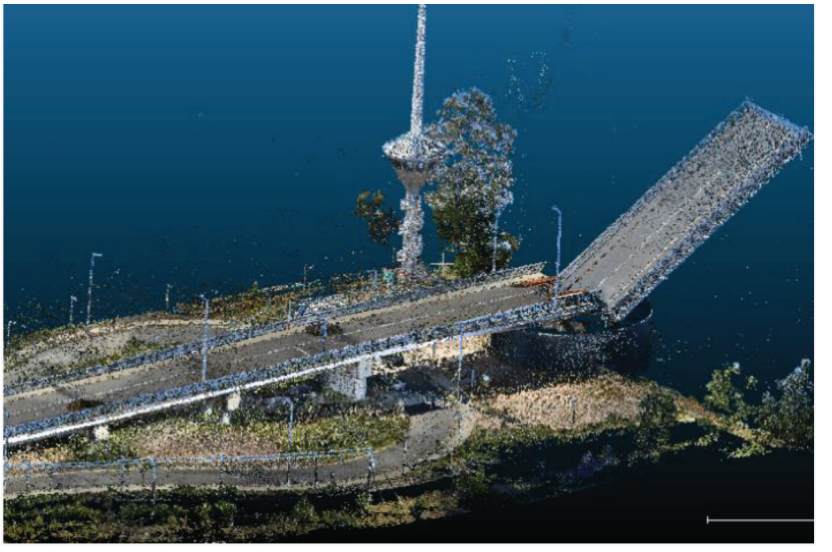


Figure 9. 3D model of the obtained with a high resolution high range terrestrial laser scanner. Real colors of the point cloud were generated with a high definition camera installed in the TLS.

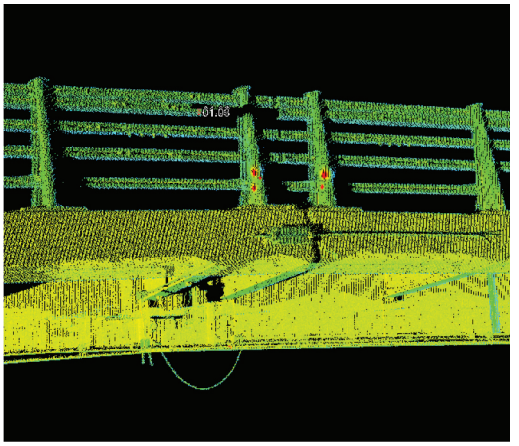


Figure 10. DEM for the measured deflections obtained with real load cases.

3 CONCLUSIONS

Several lightly invasive and non-invasive auscultation surveys were performed in the Cau Cau bridge. Main conclusions are:

- The use of lightly invasive testings are mandatory for calibration of models, especially for the definition of mechanical properties. For the bridge, results of resistance are above the specifications of the original project.
- Non-invasive surveys were highly useful for identification of real distribution of steel bars. GPR technique is fast and economical technique that permits generation of 2D images inside the concrete with a high definition and precision. The bar spacings and related information obtained are consistent with results obtained with pacometer, and also tend to be consistent with what is indicated in the planimetry and technical specifications.
- 3D modelling by means of remote sensing by means of TLS permits the generation of complete geometric 3D models of the structure, as well as calibration with real load tests, resulting in a fast and more precise technique compared with traditional topographic methods.

ACKNOWLEDGMENTS

Authors of this work thank to Ministry of Public Work, Chilean Government. Also, our acknowledges to Natural and Anthropogenic Risks Research Center (RiNA) at Universidad Austral de Chile, for providing their help and support.

REFERENCES

MOP - Dirección de Vialidad, (2011) Bases Construcción Puente Cau Cau y accesos Provincia de Valdivia, Región de los Ríos, Fecha: Abril 2011, Santiago.

Contreras, S. (2015), Informe Final Obra Puente Cau Cau – Valdvia. Materia: Estudio de falla y diagnostico estructural. Fecha 10.08.2015

VMB Ingeniería Estructural (2016), "Consultoría para la Puesta en Servicio del Puente Cau Cau, Región de Los Ríos" Informe de Reparación. Santiago, Chile.

RiNA Natural and Anthropogenics Risks Research Center (2018), "Estudios de Auscultación Estructural y Modelación Geométrica 3D Mediante Escaner Laser Terrestre. Informe de Resultados". Universidad Austral de Chile, Valdivia, Chile.

Instituto Nacional de Normalización (INN) (1979), "Hormigón – Determinación del Indice Esclerométrico". Santiago, Chile.

Bridge Maintenance, Safety, Management, Digitalization and Sustainability – Jensen, Frangopol & Schmidt (eds)
© 2024 The Author(s), ISBN 978-1-032-77040-6
Open Access: www.taylorfrancis.com, CC BY-NC-ND 4.0 license

A study on machine learning for creating crack images of RC columns

H. Yasukawa & H. Naito
Tohoku University, Sendai, Miyagi, Japan

H. Fujioka & S. Fujikura
Utsunomiya University, Utsunomiya, Tochigi, Japan

ABSTRACT: A reversed cyclic loading test was conducted on a RC column specimen to examine the effectiveness of vibration measuring and machine learning for damage evaluation of RC columns. In the loading test, 11 acceleration sensors were placed on the surface of the column to obtain frequency responses at concrete cracking and spalling of the cover concrete. It was determined that an unsupervised learning model can evaluate the damage levels and locations, based on intact data measured before the loading test. Moreover, a following supervised learning method indicated the possibility of creating crack images on RC columns, from frequency responses measured with sensors.

1 INTRODUCTION

Civil structures (e.g. roads, railways, power plants, dams) are essential for modern living. However, a lot of civil structures are aging in Japan. In addition, some structures have serious damage resulting from natural disasters, such as large earthquakes, floods, landslides, avalanches. Non-destructive inspection and evaluation of civil structures are needed to detect damages and evaluate their safety performance.

Many studies on non-destructive testing and structural health monitoring have been conducted. These methods are useful to detect invisible damages (e.g. cracks, voids, delamination) within concrete structures (Maccan et al., 2001). The effectiveness of an impact echo method for detecting damage in concrete structures has been demonstrated (Cheng and Sansalone, 1993). Moreover, the possibility of an impact echo method for evaluating not only the damage location but also the damage sizes has been researched (Huang et al., 2010). In addition, it has been determined that electromagnetic wave methods are also useful to detect cracks, voids, and delamination near the surface of concrete structures (Barreira et al., 2007).

Deep learning (DL) has been used in non-destructive evaluation of structures (Avci et al., 2021). Its merits include accurate diagnosis and reducing inspection duration and labor. However, it has difficulty in collecting a large amount of training data, since civil structures might have various damage depending on the situation. Anomaly detection methods based on an autoencoder have been useful to evaluate damage levels and locations without labeled training data (Chow et al., 2020, Fujisaku et al., 2023). Furthermore, generative AI has created the possibility of creating crack images in concrete structures. Dung et al. (2019) has performed a crack image classification task with a convolutional neural network. Engineers can discuss reasonable maintenance plans from the evaluated damage conditions and structural performances based on the created crack images. Generative AI crack images provide innovative inspection and maintenance of civil structures, though experimental data and further examinations are needed.

In this study, a reversed cyclic loading test was conducted on a RC column specimen. In the test, 11 acceleration sensors were placed on the surface of the column for obtaining vibration

DOI: 10.1201/9781003483755-190

characteristic data at each loading step. An unsupervised learning method for evaluating damage levels and locations was examined. Moreover, a supervised learning method was also used for creating crack images in the RC column.

2 REVERSED CYCLIC LOADING TEST

A reversed cyclic loading test was conducted on a RC column specimen. The details of the specimen are shown in Figure 1. Diameters of the longitudinal and transverse bars were 16 mm and 6 mm, respectively. The transverse bars were arranged at an interval of 60 mm. The design yield

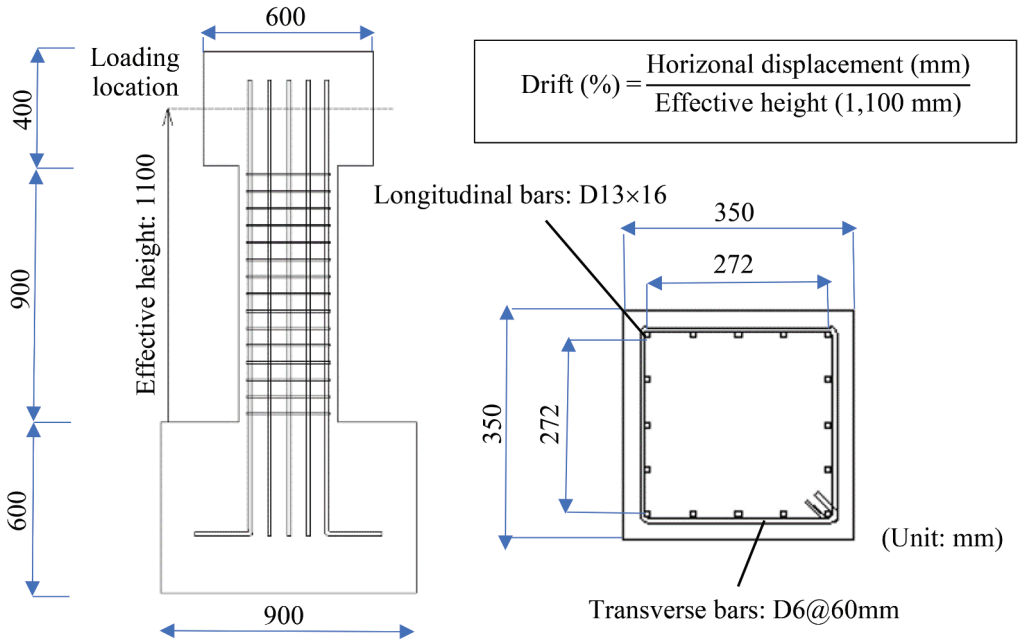


Figure 1. Details of the RC column.

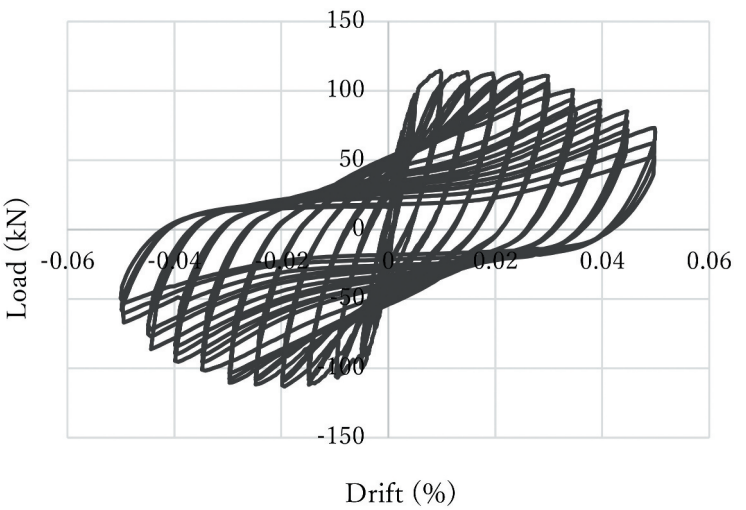


Figure 2. Load-drift relationship.

strength of bars was 295 N/mm^2. Material properties of concrete were obtained from test cylinders with a diameter of 100 mm and a height of 200 mm. The compressive strength and elastic modulus of the concrete were 35.3 N/mm^2 and 28,500 N/mm^2, respectively.

An axial force of 122 kN was applied to the top of the column. A lateral load was applied at the height of 1100 mm from the bottom of the column, as shown in Figure 1. The loading steps were set to drifts of +/–0.25 %, +/–0.5 %, +/–1.0 %, +/–1.5 %, . . ., and +/– 5.0%, where the drift was defined as the horizontal displacement divided by the effective height of 1100 mm. The number of cycles were three at each loading step.

Figure 2 shows the relationship between load and drift obtained in the loading test. In addition, crack images observed at the drift of 3.0 % are shown in Section 4, Figures 8, and 9. The column failed in flexural mode. In particular, the horizontal load decreased over the drift of 3.5 %, when the cover concrete spalled.

3 ANOMALY DETECTION USING UNSUPERVISED LEARNING

3.1 *Vibration monitoring*

In this section, the effectiveness of vibration monitoring and unsupervised learning for damage detection was examined. Forced vibration testing with a portal electric-magnetic vibrator was conducted on the column at each loading step (Naito et al., 2019). The excitation and measurement locations with acceleration sensors are shown in Figure 3. The sensors were placed on the south surface (S200 to S850) and the north surface (N225 to N675) for obtaining frequency response functions in the loading test.

The vibrator had a mass of 1.8 kg, a diameter of 95 mm, a height of 62 mm, the maximum excitation force of 50 N, and a frequency range of 100 to 20,000 Hz. Using the vibrator, white noise force was applied at the height of 850 mm from the bottom of the column. The excitation force was controlled at a power spectral density (PSD) of 0.5 $(m/s^2)^2$ /Hz over a frequency range of 1,000 to 20,000 Hz. The root mean square of acceleration amplitude (RMS) was 97.6 m/s^2.

Frequency response functions were obtained from the acceleration records with the sensors, using a Fast Fourier transform (FFT). The frequency responses had the range of 1,000 to 20,000 Hz with a resolution of 97.7 Hz. As a result, the deep learning models, described in a later section, used 194 parameters of one-dimensional data as features.

3.2 *Anomaly detection*

An autoencoder based on a neural network was used for damage evaluation. The structure of the autoencoder is shown in Figure 4. The model was built and trained with Keras and TensorFlow in Python. The input data f_i (i = 1 to 194) was given from the frequency responses and compressed through three hidden layers. Decoding was carried out in the same process. A Rectified Linear Unit (ReLU) was used as activation functions of the hidden layers. Sigmoid function was used in the output layer. The optimizer was Adam. The model was trained with a batch size of 16. Early stopping was employed in the training process. The training was terminated when the validation loss did not improve for three epochs.

The autoencoder was trained on frequency responses obtained from the intact column before loading. The autoencoder can reconstruct test data well when it is similar to the training data. However, the autoencoder cannot reconstruct test data from the damaged column since the data is different from the training data. Damage evaluation was based on anomaly scores calculated from the reconstruction error with an additional process. Moving averages of the input f_i (i = 1 to 194) and the output g_i (i = 1 to 194) with a width of 10 parameters were taken (Fujisaku et al., 2023). The anomaly score e was defined as,

$$e = \frac{\sum_{i=1}^{194} |f_i - g_i|}{\sum_{i=1}^{194} f_i} \tag{1}$$

3.3 *Results and discussions*

396 intact frequency responses were obtained from each sensor before the loading test. Moreover, 5 frequency responses were obtained from each sensor at each loading step. The autoencoder was trained on the intact data for each sensor location. As an example, Figure 5 shows comparisons between input and reconstructed output data of S200. The intact data before loading was reconstructed well, whereas the test data obtained at the drift of 3.0 % was not reconstructed.

Figure 6 shows the relationships between anomaly score and drift for the 11 sensor locations. Where, the anomaly score was normalized by the threshold determined as the average of anomaly score of the intact data. The anomaly scores were evaluated from averaging 5 measurement trials at each loading step.

From the results, the anomaly scores of S200 increased as the drift increased, as large flexural cracks occurred around the bottom of the column. Moreover, the cover concrete spalled over the drift of 3.5 %, resulting in high anomaly scores of S200.

The anomaly scores of S300 and S400 were also increased during the negative loading rather than the positive loading. This indicates that large cracks on the tensile/south surface during the negative loading increased the anomaly scores of S300 and S400. On the other hand, the anomaly scores were lower when the cracks were closed during the positive loading.

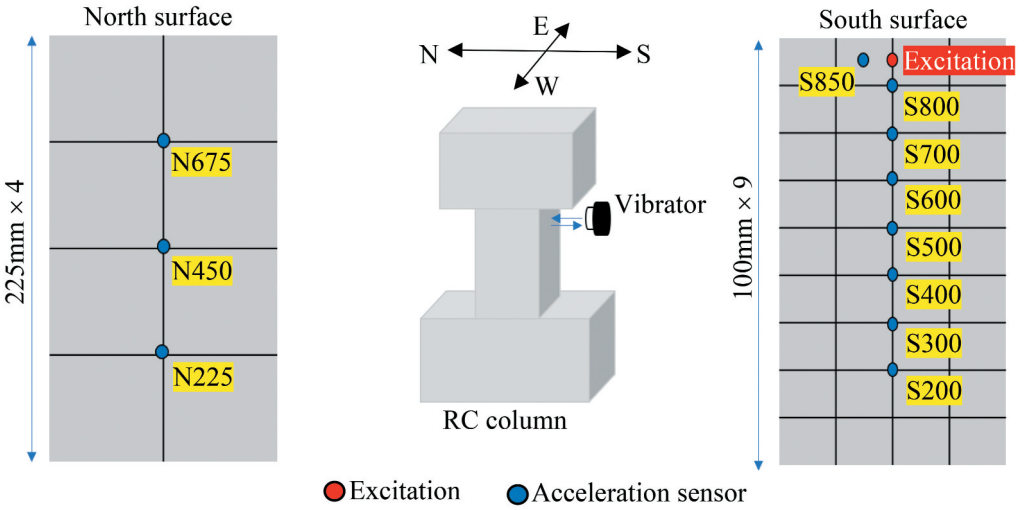


Figure 3. Excitation and measurement locations.

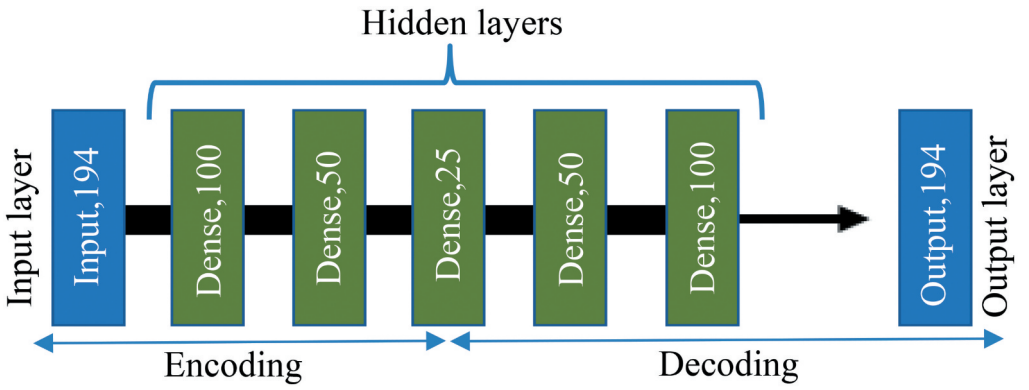


Figure 4. The structure of the autoencoder.

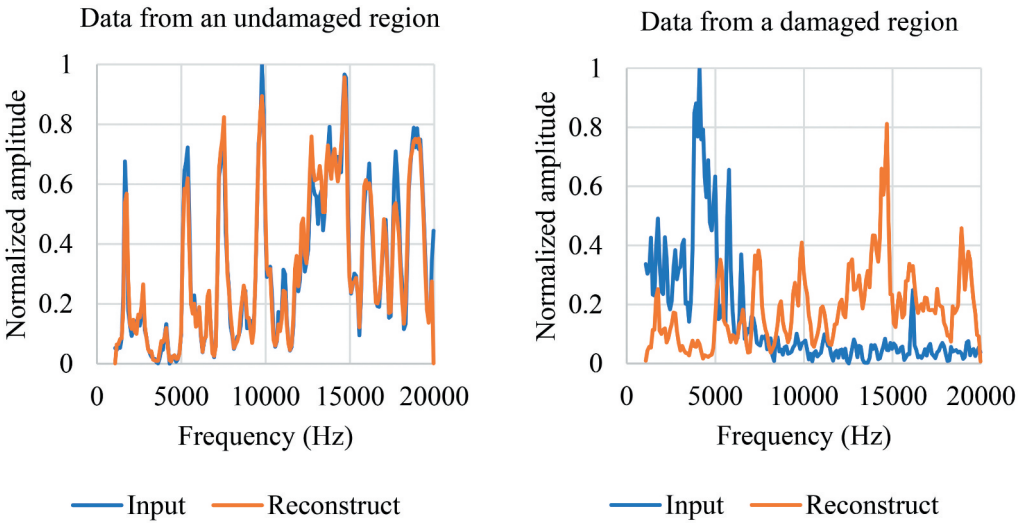


Figure 5. Comparisons between input and reconstructed data through the autoencoder.

Around the top of the column, the anomaly scores of S600-S850 were low. Slight cracks appeared around the sensor locations through visual observation. This indicates the autoencoder cannot detect slight flexural cracks.

From the results, the anomaly detection method based on an autoencoder is useful to detect damage (e. g. large flexural cracks, spalling of cover concrete) in RC columns. The proposed method detects serious damages but does not register slight cracks that do not affect structural performance.

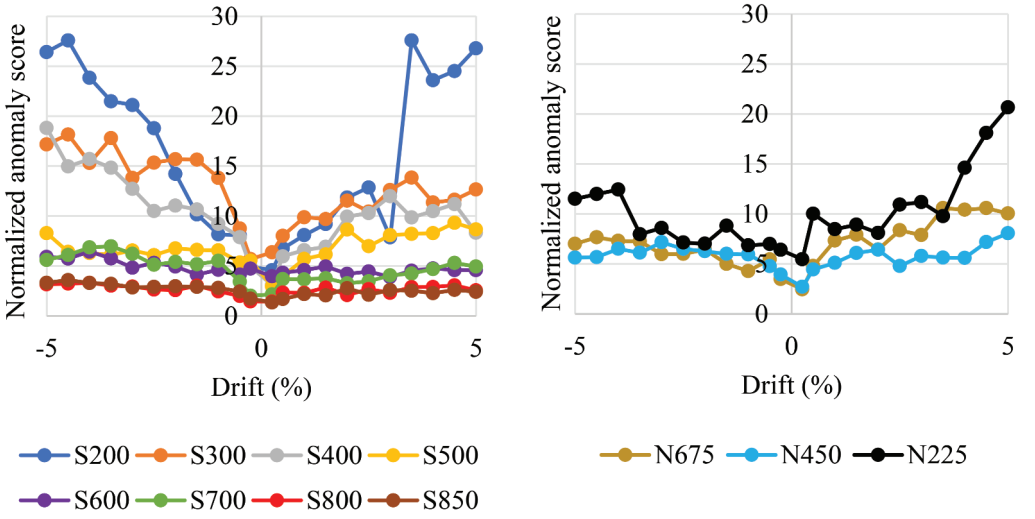


Figure 6. Relationship between anomaly score and drift of the column.

4 CREATING CRACK IMAGES USING SUPERVISED LEARNING

4.1 *Convolutional neural network*

The effectiveness of anomaly detection based on an autoencoder was shown in Section 3. However, the method does not provide detailed information on the cracks (e. g. crack widths,

lengths, angles, and crack density). In response, supervised learning was used for creating crack images in the damaged RC column.

The structure of a convolutional neural network (CNN) is shown in Figure 7. The model was built and trained with Keras and TensorFlow in Python. The one-dimensional data of frequency responses were also given in the input. The input with 194 neurons was broken down into one-dimensional convolutional layers through 10 filters with a kernel size of 3 and a stride of 2. In all layers except the output layer, batch normalization was applied between convolutional layers and activation functions, where Exponential Linear Unit (ELU) was used as the activation function. In the output layer, Sigmoid function was used as the activation function. The optimizer was Adam, with a learning rate of 0.0001 to 0.001. The model was trained for 200 epochs with a batch size of 16.

For labeling the data in the supervised learning, 2-dimensional crack images observed on the south and north surfaces at each drift were given in another input layer, as shown in Figure 7. The crack images observed around the sensor locations were converted to the sizes of 175 × 150 pixels. The crack images obtained at the drifts of 0.5 to 3.0 % were used in the training process, since the cover concrete spalled at the drift of 3.5 %. In addition, the data obtained from the sensor S850 was not used in the examination.

The datasets of two cases were compared. In the case of A, all frequency responses and crack images obtained in the loading test were given to train the CNN. In the case of B, the data obtained at the tested drift was removed from the dataset of Case A. These datasets contained the frequency responses and crack images from all sensor locations, except for S850. The amount of training data of Cases A and B were 580 and 550, respectively.

4.2 *Results and discussions*

Figures 8 and 9 illustrate the crack images at the drift of 3.0 % using the trained CNN. In Case A, the created images agreed with the experimental images. This result indicates the possibility of creating crack images based on vibration monitoring and supervised learning subject to a large amount of training data.

On the other hand, the created images in Case B were unclear around the bottom of the column, due to lack of training data at the tested drift. In particular, the data obtained at the drift of 3.0 % were very different from those of the drift of 0.5 to 2.5 %, since large cracks occurred at the drift of 3.0 % in the loading test. However, the trained model in Case B provided fine images around the middle and top of the column, even with limited training data.

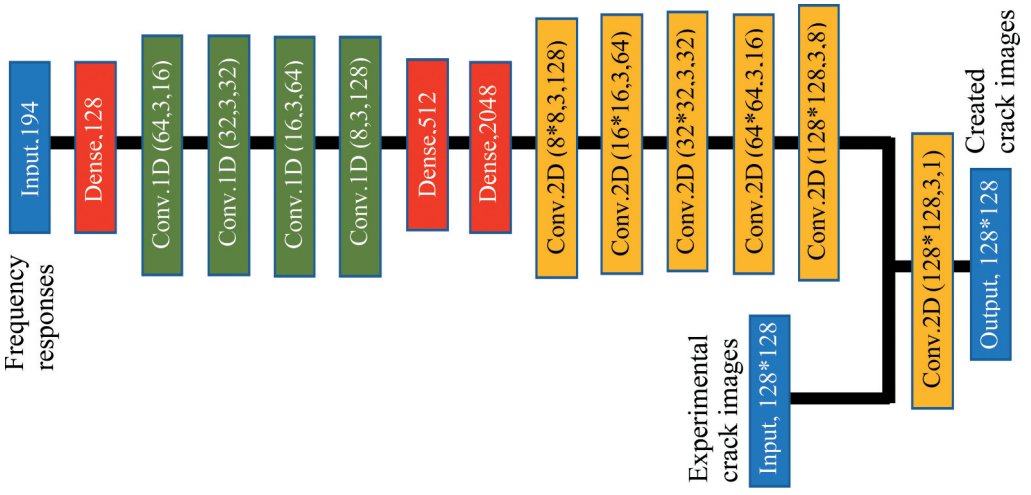


Figure 7. The structure of the convolutional neural network.

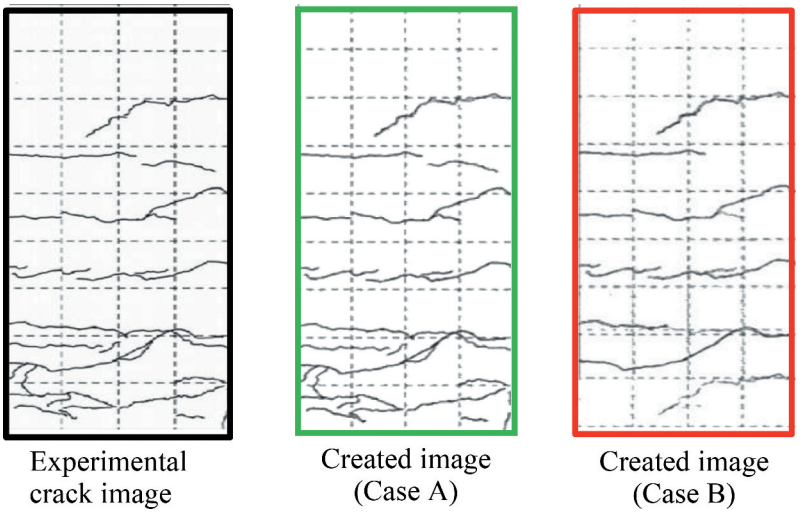


Figure 8. Created crack images on the south surface.

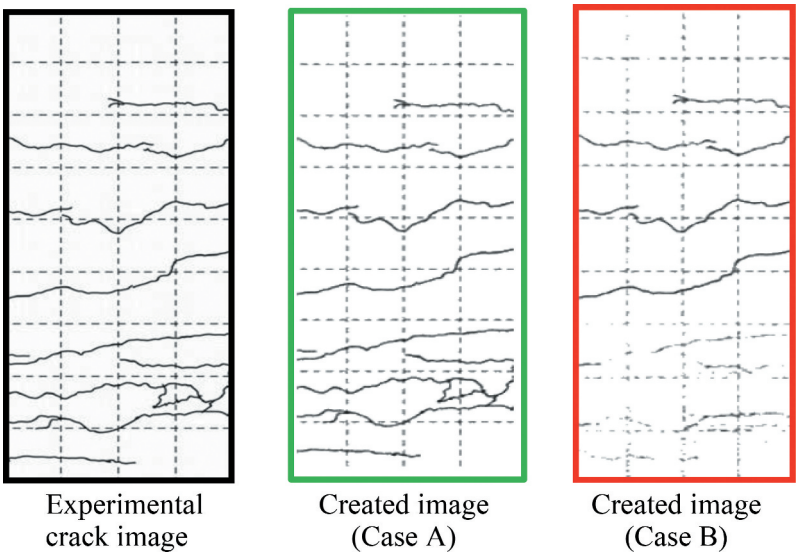


Figure 9. Created crack image on the north surface.

5 CONCLUSIONS

In this study, the effectiveness of vibration monitoring and machine learning for detecting damage of RC columns was examined. Anomaly detection (unsupervised learning) and creation of crack images (supervised learning) were conducted on a RC column specimen subjected to a reversed cyclic loading. From these examinations, findings were observed as indicated:

(1) A damage detection method using an autoencoder was proposed. Anomaly scores were evaluated on the RC column specimen before and after the loading. From the results, the anomaly scores decreased when large flexural cracks and spalling of cover concrete occurred in the column. Moreover, the anomaly score was not sensitive to a slight crack.

(2) A convolutional neural network was built for creating crack images in the RC column. The trained model created crack images accurately. The possibility of machine learning for creating crack images was shown, though requires a large amount of training data.

These findings were obtained from the loading test and vibration monitoring on the RC column specimen. Additional experiments and calculations are needed to improve the methods for damage detection and creating crack images. Moreover, numerical simulations (e.g. concrete cracking analyses, wave propagation analyses) would be useful to obtain a large dataset for training deep learning models. The authors are considering the use of simulation tools and transfer learning in a further study.

In addition, these supervised and unsupervised machine learning were examined for each sensor independently. This means the machine learning methods can be used not only for structural health monitoring with multiple sensors but also for conventional non-destructive inspection (e.g. hammering testing, impact echo method) with using a single sensor. In particular, the unsupervised method is thought to be helpful for improving non-destructive inspection of concrete structures in site.

ACKNOWLEDGEMENTS

A part of this research was conducted by JST FOREST Program (Grant Number JPMJFR2150, Japan), and Japan Society for the Promotion of Science (Grant Number 22H01568). In addition, we thank students of Utsunomiya University for their help in the column loading test.

REFERENCES

McCann, D. M. & Forde, M.C. 2001. Review of NDT methods in the assessment of concrete and masonry structures, *NDT&E International* 34: 71–84.

Cheng, C. & Sansalone, M. 1993. The impact-echo response of concrete plates containing delaminations: numerical, experimental and field studies, *Materials and Structures* 26: 274–285.

Huang, Y. H., Ni, S. H., Lo, K. F. & Charng, J. J. 2010. Assessment of identifiable defect size in a drilled shaft using sonic echo method: Numerical simulation, *Computers and Geotechnics* 37: 757–768.

Barreira, E., Vasco, P. & Freitas. 2007. Evaluation of building materials using infrared thermography, *Construction and Building Materials* 21: 218–224.

Avci, O., Abdeljaber, O., Kiranyaz, S., Hussein, M., Gabbouj, M. & Inman, D. J. 2021. A review of vibration-based damage detection in civil structures: From traditional methods to machine learning and deep learning applications, *Mechanical Systems and Signal Processing* 147: 107077.

Chow, J. K., Su, Z., Wu, J., Tan, P. S., Mao, X. & Wang, Y. H. 2020. Anomaly detection of defects on concrete structures with the convolutional autoencoder, *Advanced Engineering Informatics* 45: 101105.

Fujisaku, Y., Naito, H., Kimoto, T., Matsumura, M., Takeshima, N., Okada, S. & Ono, K. 2023. A study on damage evaluation method for box section steel columns using Autoencoder, *Proceedings of the 33rd International Ocean and Polar Engineering Conference*, 3215–3221.

Dung, C. V. & Anh, L. D. 2019. Autonomous concrete crack detection using deep fully convolutional neural network, *Automation in Construction* 99: 52–58.

Naito, H. & Bolander, J. E. 2019. Damage detection method for RC members using local vibration testing, *Engineering Structures* 178: 361–374.


Taylor & Francis
Taylor & Francis Group
http://taylorandfrancis.com

SS07: Vehicle-based sensing solutions for indirect bridge condition monitoring

Organizers: R. Corbally, A. Malekjafarian, S.R. Lorenzen & C.-H. Kim


Taylor & Francis
Taylor & Francis Group
http://taylorandfrancis.com

Bridge Maintenance, Safety, Management, Digitalization and Sustainability – Jensen, Frangopol & Schmidt (eds)
© 2024 The Author(s), ISBN 978-1-032-77040-6
Open Access: www.taylorfrancis.com, CC BY-NC-ND 4.0 license

Mitigation of unwanted effects in drive-by acceleration data for bridge monitoring

M. Casero & A. González
University College Dublin, Dublin, Ireland

K. Feng
Queen's University Belfast, Belfast, UK

ABSTRACT: Drive-by bridge health monitoring is hindered by the adverse effects of the road surface. In this paper, noisy accelerations are simulated for the unsprung mass of a quarter-car crossing a beam with a rough road profile at two different speeds. The fast Fourier transform, and the transfer function are applied to extract real and imaginary parts of the response of the contact point with the bridge, thus mitigating the impact of vehicle-related factors. The responses for the two speeds are subtracted in the spatial domain to isolate the bridge component within the resulting power spectral density, effectively removing the influence of the road profile. Damage is characterized by comparison with a database of power spectral densities derived from the contact point response of a moving constant force. The methodology exhibits great accuracy in identifying the damage caused by a localized crack of size 10% to 30% of the beam depth.

1 INTRODUCTION

Road vehicles can be equipped with devices that measure the response of underlying road and bridge infrastructure to evaluate its structural condition as they travel along. While their use in monitoring road condition, particularly roughness, is widespread, their application to bridges is limited. Existing proposals for applying drive-by to bridge monitoring heavily rely on theoretical tests, lacking substantial support from field campaigns (Malekjafarian et al., 2022). Often, experiments are confined to laboratory results using scaled models of vehicles and bridges, which fail to accurately replicate real-world conditions and tend to result in quasi-static scenarios. Field implementations are rare, and they primarily involve simple means to extract bridge frequencies from vehicle accelerations, such as the fast Fourier transform (FFT) or power spectral density (PSD). This information is then used to detect potential changes in bridge behavior. The following paragraph reviews successful instances of drive-by systems tested on bridges in the field and their outcomes.

Lin and Yang (2005) successfully estimated the 1st bridge frequency from trailer accelerations for vehicle speeds up to 35 km/h. Yang and Chang (2009) employed empirical mode decomposition on the acceleration data from a tractor-trailer vehicle driving at 10 km/h to enhance the visibility of bridge frequencies, including higher modes. Elhattab et al. (2018) utilized frequency-independent underdamped pining stochastic resonance to identify the 1st bridge frequency from measurements taken from a three-axle truck driving at up to 53 km/h. Singh and Sadhu (2022) proposed a time-frequency method based on a Wavelet packet transform of the vehicle measurements to decouple vehicle-bridge interactions. Yang et al. (2022) suggested parking the monitoring vehicle on the bridge, excited by random traffic, to obtain the first four bridge frequencies of the bridge while avoiding the impact of the road profile. With the advancement of smartphone technology, the use of smartphones for measuring

DOI: 10.1201/9781003483755-191

accelerations in drive-by systems is gaining popularity (Shirzad-Ghaleroudkhani and Gul, 2021). In contrast, Liu et al. (2023) measured tire pressure and related it to the relative displacement between the axle and contact point, as the latter is more sensitive to bridge frequencies and less influenced by vehicle dynamics.

The literature review underscores acceleration as the preferred response in field implementations due to the simplicity and affordability of its collection, but successful results are typically limited to detecting frequency changes in medium and long-span bridges (Li et al., 2023). The goal of this paper is to expand on the current capabilities of drive-by technology, by using acceleration data to detect, locate, and quantify damage in the form of an equivalent stiffness loss in a short-span bridge. Here, the main challenge lies in separating the bridge component from the usually larger vehicle and road components, which heavily influence the measured acceleration, even more so in shorter bridges. The methodology section outlines a five-step damage detection algorithm that mitigates road and vehicle components in drive-by measurements. The results section demonstrates the accuracy of the algorithm across 1800 different damage scenarios and measurements contaminated with two noise levels (1% and 5% noise). Finally, the conclusions section highlights the main findings of this work and suggests avenues for future research.

2 METHODOLOGY

2.1 *Vehicle-bridge interaction model*

The algorithm's functionality is illustrated using a quarter-car (QC) vehicle model. The sprung and unsprung masses are assumed to be 8900 and 1100 kg respectively, therefore the gross vehicle weight (GVW) equals 98 kN (Cebon, 1999). The suspension and tire stiffness are specified as 2×10^3 and 3.5×10^3 kN/m, respectively, with adopted viscous damping of 40 kNs/m for the suspension and 4 kNs/m for the tire. These properties yield vehicle frequencies of 1.89 and 11.35 Hz. The QC traverses a planar simply supported discretized bridge model featuring a -15 m span length and a 0.75 m depth. The bridge model consists of 150 discretized beam elements, each with a length of 0.1 m, cross-sectional area of 11.25 m^2, and a uniform 2nd moment of area (I) of 0.5273 m^4. Typical properties of reinforced concrete are assumed for the bridge material, with a modulus of elasticity of 35 GPa and a unit weight of 2500 kg/m^3. The road profile is characterized as class 'A' per ISO standards, with a geometrical spatial mean equal to 0.1×10^{-6} m^3/cycle. In its healthy state, the first two longitudinal modes of vibration of the bridge correspond to frequencies of 5.66 and 22.62 Hz. Bridge damage is introduced following the stiffness loss model proposed by Sinha et al. (2002) for a crack. The reduction in the 2nd moment of area is maximum at the crack location where $I = (1 - (1 - \lambda)^3) \times 0.5273$ m^4, with λ representing the ratio of the crack depth to the cross-section height. The value of I increases linearly up to 0.5273 m^4 at a distance of 1.125 m on either side of the crack.

2.2 *Drive-by algorithm for locating and quantifying reductions in bridge stiffness*

The five-step damage detection algorithm proposed in this paper capitalizes on the sensitivity of the PSD of the bridge response to the location and severity of the damage. To successfully isolate the bridge component contained within the axle acceleration, it is crucial to consider the transfer function (TF) between the vehicle and the contact point with the bridge, together with the spatial invariant nature of the road profile.

2.2.1 *Steps 1 and 2: Acceleration measurement at two speeds, and conversion to frequency domain*

First, the vehicle traverses the bridge at two different constant speeds, and the vertical acceleration at the QC is recorded. Two potential measurement locations, namely the unsprung and the sprung masses of the QC model, are initially considered. Speeds of v_1 = 5 m/s and v_2 = 10 m/s are used to illustrate the proposed methodology. The FFT is applied to the acceleration time history to calculate the real and imaginary parts of the signal in the frequency domain.

2.2.2 *Step 3: Removal of PSD content associated with vehicular components*

In Step 3, the TF is applied to estimate the contact point response from the measurements at the vehicle. In general, the TF is the ratio between two responses, i.e. the acceleration of the unsprung mass and the acceleration of the contact point in the frequency domain. Consequently, the contact point response can be calculated using the TF without direct measurement. Practical challenges in directly measuring the contact point response make the use of the TF a viable solution. The TF can be obtained by driving the vehicle over a stretch of road with a known profile. For the simulations in this paper, the theoretical TF between the QC and the contact point is utilized.

The PSD of the contact point is reconstructed from the real and imaginary parts resulting from the application of the TF to the vehicle acceleration. It is anticipated that the PSD of the contact point will alleviate the impact of the vehicle component contained in the original measured/simulated signal. The effectiveness of the TF in removing the vehicle content from the PSD can be visualized in Figure 1 for the vehicle moving at 5 m/s over smooth (Figure 1a, b) and class 'A' (Figure 1c, d) road profiles. Figure 1a, c and Figure 1b, d use the acceleration of the sprung and unsprung masses respectively, as the measurement location in the vehicle. Figure 1a, b illustrates the amplification of the amplitude of the PSD around the 1st bridge frequency (5.66 Hz) after applying the TF in the absence of a road profile. The plots also show a good match between the PSDs of the estimated and true contact point responses. In Figure 1a, b, the estimated contact point PSD contains only the bridge component in the absence of the road profile. When the rough road profile is introduced (Figure 1c, d), the estimated contact point PSD contains both the bridge and road components. The unsprung mass is preferred over the sprung mass due to its easier accessibility in a vehicle; hence, the following steps will exclusively focus on the unsprung mass response.

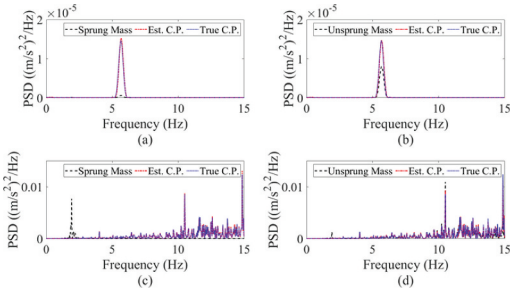


Figure 1. True vs estimated contact point PSDs via sprung mass and unsprung mass acceleration with: (a, b) a smooth road, (c, d) a class 'A' road, at 5 m/s.

2.2.3 *Step 4: Removal of the PSD content associated with road frequencies*

The real and imaginary parts of the FFT of the acceleration signal of the unsprung mass of the QC traveling over the bridge at 5 and 10 m/s are given in Figure 2 for reference. The real ($a_{CP}(f)$) and imaginary ($b_{CP}(f)$) parts at the contact point resulting from the application of the TF in Step 3 are also shown in Figure 2.

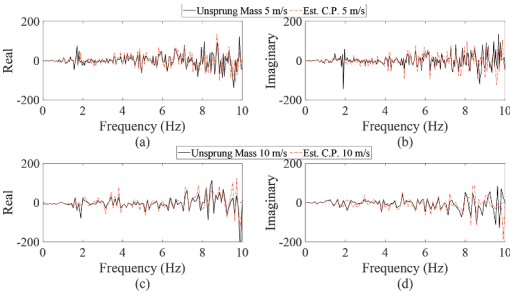


Figure 2. Real (a, c) and imaginary parts (b, d) of the unsprung mass and contact point responses at 5 m/s (a, b) and 10 m/s (c, d) in the frequency domain.

The real and imaginary parts presented in Figure 2 are expressed in the temporal frequency domain, preventing direct comparisons at different vehicle speeds (Figure 2a, c). To facilitate comparison in the spatial frequency domain (cycle/m), the values in the temporal frequency domain are normalized by the vehicle speed, and the amplitudes of the real and imaginary parts are multiplied by $1/v^4$, where v is the vehicle speed in m/s. Regardless of the vehicle speed, the representation of the road profile in the spatial frequency domain should be the same. Therefore, subtracting the real and imaginary parts of the contact point at two different speeds in the spatial frequency domain is expected to eliminate or significantly mitigate the road component. The outcome of this subtraction is depicted in Figure 3a, b for the real and imaginary parts. The subtracted real and imaginary parts are then transformed back into the frequency domain to improve the visualization of the relevant peak frequencies (Figure 3c, d). The peak corresponding to the 1st bridge frequency is marked with vertical dashed lines in Figure 3a, b (1.13 cycle/m) and Figure 3c, d (5.66 Hz).

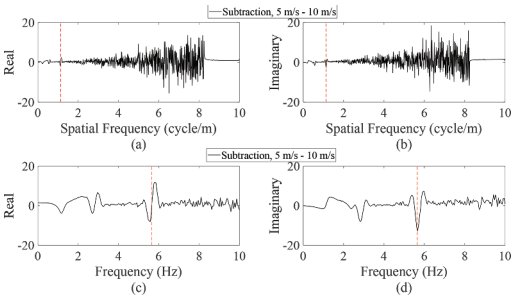


Figure 3. Subtracted real (a, c) and imaginary parts (b, d) of the contact point in the spatial frequency (a, b) and frequency (c, d) domains.

To enhance the visibility of the 1st bridge frequency, the PSD associated with the real and imaginary parts shown in Figure 3c, d is calculated. When carrying out this calculation, it is possible to use either vehicle speed as reference (v_i), i.e., $i = 1, 2$ and $j \neq i$ in Equation 1.

$$PSD_{bridge}(f) = \left(a_{CP}(f)|_{v_i} - \frac{v_i^2 \times a_{CP}(f)|_{v_j}}{v_j^2} \right)^2 + \left(b_{CP}(f)|_{v_i} - \frac{v_i^2 \times b_{CP}(f)|_{v_j}}{v_j^2} \right)^2 \quad (1)$$

Figure 4 displays the final estimated PSD, labeled as "Est. Bridge", which contains solely the estimated bridge component of the contact point acceleration. This is juxtaposed with the estimated PSD associated with the total acceleration of the contact point, labeled as "Est. C. P.", which includes both bridge and road components, as directly obtained via the TF. Additionally, the figure incorporates the PSD of the unsprung mass acceleration ("Unsprung mass"), the true PSD linked to the irregularities of the road profile ("True R.P.") and the true PSD associated with the bridge component of the contact point acceleration ("True Bridge") for comparative analysis. Figure 4a showcases an estimated 1st bridge frequency of 5.76 Hz using v_1 = 5 m/s as a reference, indicating an error of 1.77%. The estimated amplitude of the peak is 1.59×10^{-5} g^2/Hz with a relative error of –2.45% compared to its true amplitude of 1.63×10^{-5} g^2/Hz. The "Est. Bridge" curve in Figure 4b uses v_2 = 10 m/s as reference, yielding a bridge frequency of 5.71 Hz and amplitude of 5.17×10^{-5} g^2/Hz, with relative errors of 0.88% and 46.88% respectively. Even though the bridge frequency is slightly more accurate in the last instance, the zoom-in windows in Figure 4 reveal that the overall shape of the PSD is closer to the true one in Figure 4a, suggesting more accurate results are obtained when making the conversion using the lower of the two speeds. Figure 4 demonstrates that the proposed approach, involving the TF and subtraction at two speeds, estimates a PSD containing peaks associated with the bridge frequencies only. Therefore, this estimated PSD should closely resemble the PSD extracted from a P-load model with the same GVW as the vehicle

and traveling over a numerical model of the bridge at the same speeds. Here, P-load model refers to a constant force traversing the bridge, where vehicle dynamics and the road profile are disregarded, and there is no interaction between the vehicle and the bridge.

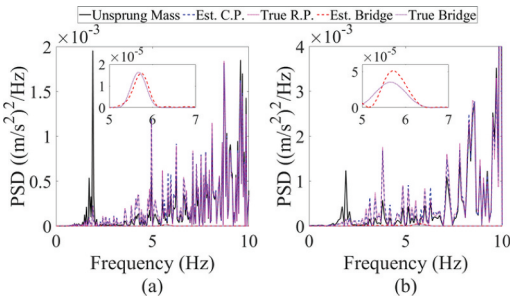


Figure 4. Estimated PSD of acceleration of the contact point, estimated and true PSD of bridge component, and true PSD of road irregularities, for speeds of: (a) 5 m/s, (b) 10 m/s.

2.2.4 *Step 5: Damage detection through comparison with P-load database*

Steps 1 to 4 encompass the manipulations necessary to extract pertinent information from the acceleration signals measured in the field (or numerically simulated in this paper). After completing these steps, the algorithm compares the estimated PSD of the bridge, as shown in Figure 4, with a database of PSDs derived from a numerical model of the bridge subjected to a P-load with the same GVW as the vehicle. To enable a comparison between the P-load and the estimated PSD from Step 4, the database must be built by subtracting the PSD from P-load crossings at the same vehicle speeds used in Steps 1 to 4. The use of a P-load model offers a dual advantage: (1) only the static weight of the vehicle needs to be known (dynamic parameters are unnecessary), and (2) the computational time required is significantly reduced compared to the use of a full vehicle model. In the numerical model, the location and severity of the damage are varied to cover a broad spectrum of scenarios. In particular, the severity varies from $\lambda = 10\%$ to $\lambda = 30\%$ in 1% increments, while the location ranges from 0 to 15 m in 0.1 m increments. By comparing the estimated PSD of the bridge component of the contact point (referred to as "Est. Bridge") in Figure 4 to each of the PSDs in the database, it is possible to determine the damage location and severity of the optimal solution. The latter is given by the PSD from the P-load database resulting in the minimum least squares difference with respect to the "Est. Bridge" curve. The least squares are calculated for a portion of the PSD covering ±0.5 Hz around the peak frequency.

3 RESULTS

The algorithm undergoes testing for 1800 different damage scenarios using the bridge, QC vehicle, and road models described in the preceding section. These scenarios are randomly generated by sampling locations between 0 and 15 m and severities (λ) ranging from 10% to 30% with millimetric precision. Understandably, the algorithm's sensitivity diminishes as the damage gets smaller, and scenarios with severity λ below 10% are excluded. Given that field measurements will be affected by noise, the simulated acceleration signals are contaminated with an additive noise model. This involves randomly sampling values from a normal distribution with a zero mean and a standard deviation equal to a percentage (i.e. 1% or 5% in this test) of the standard deviation of the noise-free acceleration, which are then added to the noise-free acceleration response. Subsequently, Steps 2 to 4 of the proposed methodology are applied to the noisy acceleration to estimate the PSD of the bridge component of the contact point. A database of PSDs is established based on a P-load and a bridge model containing the severity and location range under investigation to select the optimal solution as per Step 5. It

is acknowledged that there is an inherent error as a result of the discretization selected for the solution space to be explored by the P-load model. In this paper, PSDs due to a P-load model are obtained in increments of damage severity with 0.75 cm steps and increments of damage location with 0.1 m steps.

The errors in the estimation of the damage location and severity are depicted in Figure 5a, b for 1% noise, and in Figure 5c, d for 5% noise. In these plots, the true location and severity of the tested damage are represented along horizontal and vertical axes, respectively. The color scheme indicates the error magnitude in terms of severity (in cm) and localization (in m). Errors are computed as the estimated value of the location (or severity) of the damage minus the true values.

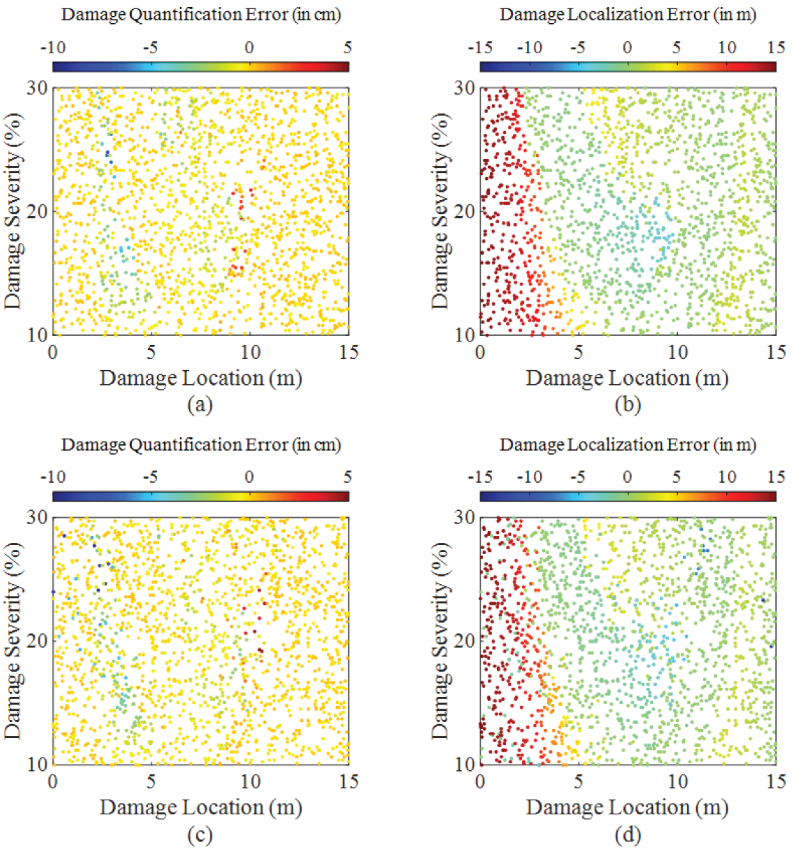


Figure 5. Algorithm prediction errors: with 1% noise: (a) severity and (b) localization; and 5% noise: (c) severity and (d) localization.

The algorithm demonstrates a high level of accuracy in predicting damage severity under both levels of noise (Figure 5a, c). The similar distribution of errors across both noise levels attests to the robustness of the algorithm. For example, when grouping the 1800 random damage scenarios into two severity ranges (10% to 20% and 20% to 30%) and three location ranges (0-5 m, 5-10 m, and 10-15 m), each group consisting of approximately 300 simulations, the largest average error for severity prediction is observed in the group defined by the 0-5 m location range and 10% to 20% severity range. These errors are –0.69 cm (with a standard deviation σ of 1.15 cm) and –0.76 cm (σ = 1.18 cm) for the 1% and 5% noise levels, respectively.

The performance worsens for smaller damage severities and locations closer to the left-hand support, indicated by dark-colored markers in Figure 5b, d. Figure 6a shows the histogram of the localization errors for the two noise levels. While most of the localization errors cluster

around zero, the histogram reveals a right-hand side tail with large errors, corresponding to the observations in Figure 5b, d. When the damage is situated near the left-hand support, the algorithm occasionally chooses a location close to the right-hand support as the optimal solution. In a few isolated cases with 5% noise, the opposite scenario arises, where damage on the right-hand side of the bridge is incorrectly identified at the left-hand side. Figure 6b plots the localization error versus the true location, highlighting a distinctive linear pattern for damage scenarios near the supports. For both noise levels, several points are distributed along the top dashed line, meaning that they share the same damage location estimated as 15 m, i.e. the location of the right-hand support of the bridge. Hence, scenarios on the left-hand side of the dashed line correspond to those at the right-hand side tail of the histogram in Figure 6a. A similar pattern starts to emerge for the 5% level of noise, with two values at the left-hand side of the histogram that can be seen on the bottom right-hand side corner of Figure 6b. Broadly speaking, when the damage is located within the first and last quarters of the span, the algorithm may misidentify the damage location significantly. On the other hand, when the damage is closer to the midspan, the magnitude of the localization error tends to decrease.

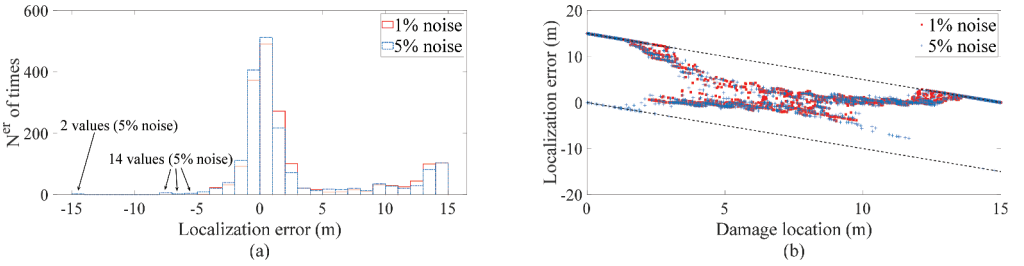


Figure 6. (a) Histogram of damage localization errors, (b) Pattern of localization errors.

The error pattern in damage localization is primarily attributed to two factors: (1) the estimated PSD from the QC tends to exhibit a smaller amplitude than the PSD for the P-load case corresponding to the same damage location and severity, and (2) the amplitude of the PSD in the P-load database for damage near the left-hand support is marginally greater than the PSD in the P-load database for a damage scenario with the same severity, but located near the right-hand support. Figure 7 illustrates an instance of this situation. The estimated PSD of the bridge component of the contact point using the QC is represented for two damage scenarios: (D1) a crack with severity of λ = 10.27% (7.7 cm crack) positioned at 2.267 m from the left-hand support (labelled '7.7 cm @ 2.267 m Est. Bridge'), and (D2) a crack with severity of λ = 10.27% (7.7 cm crack) located at 14.583 m from the left-hand support (labelled '7.7 cm @ 14.583 m Est. Bridge'). Several PSDs

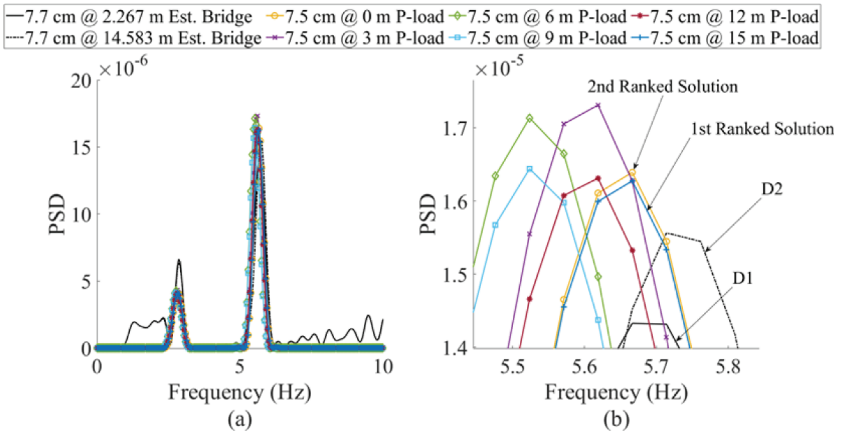


Figure 7. (a) Estimated PSDs for two damage locations vs PSDs from P-load database, (b) zoom-in plot.

from the P-load database for a similar severity (7.5 cm) but different locations (0, 3, 6, 9, 12, and 15 m) are also represented (i.e. '7.5 cm @ 0 m P-load', '7.5 cm @ 3 m P-load', . . ., '7.5 cm @ 15 m P-load'). In the zoom-in window, Figure 7b, it is evident that the PSD of the P-load database for the damage located at 15 m (i.e. '7.5 cm @ 15 m P-load'), or the 1st ranked solution, closely resembles both D1 and D2, even when these two damages are located in opposite ends of the span. The curve '7.5 cm @ 0 m P-load' bears a strong resemblance to '7.5 cm @ 15 m P-load', but has a slightly higher amplitude than the 1st ranked solution for the 15 m location (i.e. the right-hand support). Differences between P-load curves with the same severity, but symmetric locations with respect to midspan (i.e. 0 and 15 m, 3 and 12 m, or 6 and 9 m), become more pronounced for damages located farther from the supports.

4 CONCLUSIONS

The dynamic response of a point that is part of a vehicle-bridge dynamic interaction system can stem from three potential sources: the bridge, the vehicle, and the road surface. Vibrations directly measured on the bridge typically reflect the bridge component, while vibrations measured on the vehicle mainly contain vehicle and road components. Existing literature presents experimental evidence highlighting the successful extraction of bridge frequencies from vehicle accelerations. However, effective field tests are restricted to medium and long-span bridges with good road profiles. In essence, the amplitude of the bridge vibrations within drive-by measurements must be sufficiently high to avoid being overshadowed by vehicle and road components. Also, longer bridges result in lengthier drive-by records, enhancing frequency resolution. Hence, short-span bridges are less conducive to drive-by assessments, a major downside considering the prevalence of these spans in the bridge inventory. To address this limitation, this paper has proposed a methodology that not only extends the applicability of drive-by technology to a broader span range, but also facilitates the localization and quantification of damage. The methodology relies on the accurate removal of vehicle and road components before extracting the PSD associated with the bridge frequency. Successful numerical testing has been conducted for a 15 m bridge span with 1800 different simulated damage scenarios under two noise levels (1% and 5%). The best results have been achieved for the quantification of damage, with a mean error of –0.32 cm (σ = 0.83 cm) for the 1% level of noise and –0.37 cm (σ = 1.04 cm) for the 5% level of noise, taking all 1800 simulations into account. However, some difficulties have been identified regarding the localization of the damage near the supports. This issue arises from the fact that cracks of the same severity in symmetrical locations relative to midspan produce similar effects. Therefore, if the algorithm predicts damage close to either support, the bridge owner would be advised to inspect both. Experimental testing on a real bridge is imperative to comprehend additional potential challenges stemming from the implementation of this novel drive-by methodology in the field.

ACKNOWLEDGEMENTS

This research has received funding from Science Foundation Ireland (SFI)'s US-Ireland R&D Partnership Programme under the proposal id. 16/US/I3277 titled MARS-Fly.

REFERENCES

Cebon, D. 1999. *Handbook of vehicle-road interaction*, Boca Raton, FL, USA, CRC Press.

Elhattab, A., Uddin, N. & e, O. B. 2018. Drive-By Bridge Frequency Identification under Operational Roadway Speeds Employing Frequency Independent Underdamped Pinning Stochastic Resonance (FI-UPSR). *Sensors (Basel)*, 18, 4207.

Li, Z., lin, W. & Zhang, Y. 2023. Drive-by bridge damage detection using Mel-frequency cepstral coefficients and support vector machine. *Structural Health Monitoring*, 14759217221150932.

Lin, C. W. & Yang, Y. B. 2005. Use of a passing vehicle to scan the fundamental bridge frequencies: An experimental verification. *Engineering Structures*, 27, 1865–1878.
Liu, C. Y., Zhu, Y. P. & Ye, H. 2023. Bridge frequency identification based on relative displacement of axle and contact point using tire pressure monitoring. *Mechanical Systems and Signal Processing*, 183, 109613.
Malekjafarian, A., Corbally, R. & Gong, W. J. 2022. A review of mobile sensing of bridges using moving vehicles: Progress to date, challenges and future trends. *Structures*, 44, 1466–1489.
Shirzad-Ghaleroudkhani, N. & Gul, M. 2021. An Enhanced Inverse Filtering Methodology for Drive-By Frequency Identification of Bridges Using Smartphones in Real-Life Conditions. *Smart Cities*, 4, 499–513.
Singh, P. & Sadhu, A. 2022. A hybrid time-frequency method for robust drive-by modal identification of bridges. *Engineering Structures*, 266, 114624.
Sinha, J. K., Friswell, M. I. & Edwards, S. 2002. Simplified models for the location of cracks in beam structures using measured vibration data. *Journal of Sound and Vibration*, 251, 13–38.
Yang, Y. B. & Chang, K. C. 2009. Extraction of bridge frequencies from the dynamic response of a passing vehicle enhanced by the EMD technique. *Journal of Sound and Vibration*, 322, 718–739.
Yang, Y. B., Li, Z., Wang, Z. L., Shi, K., Xu, H., Qiu, F. Q. & Zhu, J. F. 2022. A novel frequency-free movable test vehicle for retrieving modal parameters of bridges: Theory and experiment. *Mechanical Systems and Signal Processing*, 170, 108854.

Bridge Maintenance, Safety, Management, Digitalization and Sustainability – Jensen, Frangopol & Schmidt (eds)
© 2024 The Author(s), ISBN 978-1-032-77040-6
Open Access: www.taylorfrancis.com, CC BY-NC-ND 4.0 license

Smartphone-based monitoring: Improving the bridges braking force model

M. Breveglieri & G. Feltrin
Empa -Swiss Federal Laboratories for Materials Science and Technology, Dübendorf, CH

ABSTRACT: Smartphones can be used to collect real-world information to address the lack of data on the frequency and magnitude of heavy vehicle braking events which was encountered during project AGB 2011/003 (Updated Braking Forces for Road Bridges). The current research aims to obtain a large database of deceleration profiles and to accurately estimate the frequency of braking events per road type by instrumenting a fleet of heavy vehicles in order to improve the previously developed model. For this purpose, Android applications have been developed to collect acceleration, gyroscope and GPS data. Preliminary tests were conducted to validate the use of smartphones against a high-precision system to ensure the accuracy of both acceleration and GPS measurements. The results of a pilot test, conducted by instrumenting one heavy vehicle before the start of the 22-vehicle test campaign, are presented here. This pilot test demonstrates that the smartphone can provide accurate results, resulting in a significant cost reduction compared to traditional measurement systems.

1 INTRODUCTION

While in modern design standards vertical traffic force models are based on probabilistic evaluations targeting a predefined reference return period, braking force models are still derived from a deterministic ad-hoc characterization of the braking process with simplified vehicle configurations. As a consequence, the return period of the braking force is unknown and probably not consistent with that of the vertical load model. The research project AGB 2011/003, entitled "Updated Braking Forces for Road Bridges" (Martins et al., 2016), aimed to improve the assessment of braking forces on road bridges through the development of a novel stochastic procedure.

As long as direct experimental validation is not possible one must rely on computational prediction with "realistic" models. The accuracy of the results of a stochastic model depends on the assumptions made by the model and the reliability of the input data. The model developed in AGB 2011/003 relies on three main types of data: traffic data, the braking deceleration profiles to be assigned to each vehicle, and the frequency of heavy braking events on the motorway.

The traffic data on Swiss highways provided by the Federal Road office are very extensive and of good quality, therefore traffic configurations were extracted starting from the automatic road traffic count station, and the Weight in Motion station located at two locations on the highway (Sjaarda et al., 2000). A key challenge was the limited availability of data on the frequency and magnitude of heavy vehicle braking events. The frequency of heavy braking events on motorways, primary roads and secondary roads was determined mainly based on data from a Dutch field test - AOS Field Operational Test, (FOT-Net partners, 2016) with instrumented vehicles. The system originally gathered for testing electronic accident prevention systems, recorded the most significant positive and negative acceleration peaks in the direction of travel within a 2-minute interval, furthermore, the vehicle's position was only recorded via GPS every 2 minutes. However, these data partially fulfilled the requirements for

DOI: 10.1201/9781003483755-192

determining the frequency of heavy braking events. The braking deceleration profiles (magnitude of the braking) were extracted from field tests with instrumented passenger cars in the USA - 100-Car Naturalistic Driving study, NDS, (Dingus et al., 2006). Nevertheless, these data are not optimal for accurately representing the deceleration profiles of heavy truck braking events (Martins et al., 2016).

Since the conclusion of project AGB 2011/003 (Martins et al., 2016) the UDRIVE project (Bärgman et al., 2017; Barnard et al., 2016) focused, among other issues, on the frequency of heavy braking events per road category (urban, interurban and motorway). On motorways, one event per 5,500 km was recorded, increasing to approximately one event per 200 km on interurban roads and one event per 50 km on urban roads. Comparisons with a study of long-distance drivers in the USA (Hickman & Hanowski, 2011) reveal similar frequencies on motorways (1 event per 8,000 km), considering only safety-relevant events with a braking deceleration limit of 5.0 m/s². Adjusting the UDRIVE data to a 4.0 m/s² limit would reduce the highway frequency to approximately one event per 8,000 km, a sevenfold deviation from the AGB 2011/003 project. This reduction in frequency has a direct effect on the characteristic value of the braking force, decreasing it by around 20 % for a return period of 1,000 years (Eurocode reference period for loads on road bridges). Despite enhancements to the database from international field tests, notable disparities between the AOS and UDRIVE project evaluations highlight the limited data and substantial uncertainty surrounding the frequency of severe braking events, necessitating further investigation. In addition, results from countries such as the USA, Canada, or Australia cannot be directly extrapolated to Swiss conditions.

2 AIM OF THE RESEARCH

The research aims to improve the knowledge of the frequency and magnitude of braking events of heavy vehicles in order to improve the results of the model developed in (Martins et al., 2016) for the assessment of braking forces on road bridges. This includes the use of smartphones for data collection, specifically acceleration, gyroscope and GPS data. The present work also demonstrates how smartphones can be used as monitoring devices as an alternative to high-quality measurement systems to address existing gaps in the field of evaluation of braking forces on road bridges. Smartphones were chosen for their cost-effectiveness. While the characteristics of sensors embedded in smartphones may not be comparable to those of high-precision professional instruments, for this study, such high-quality features are deemed unnecessary, as explained in (Feltrin & Breveglieri, 2024). In the present work, the preliminary results of a pilot project conducted before the test campaign with 22 heavy vehicles are presented.

3 METHODS

3.1 *Instrumentation*

Modern mid-range smartphones are equipped with a three-axis accelerometer, a three-axis gyroscope and a GPS receiver. As part of this research, three different Android apps were developed. The first app was programmed to collect data from the GPS receiver to locate the truck's position on its daily route and therefore the location of braking events. The data acquisition rate was set to 1 second. For each acquisition, a time stamp, longitude, latitude, and elevation of the vehicle position, a measure of the position inaccuracy, speed, and bearing angle of the vehicle were recorded. The speed and direction of travel are determined directly from the GPS sensor. The second app was programmed to collect data from the accelerometer sensor. The recording of an event was triggered and stopped as soon as the acceleration in the direction of travel exceeded a threshold of 2 m/s^2. Data acquisition was extended to include readings taken before and after the thresholds were crossed, i.e. buffer both before and after the event.

In order to minimize false triggering, the acceleration in the direction of travel was first filtered with a digital low-pass filter to trigger the measurement. The upper cut-off frequency of the filter was 2 Hz. The filtered acceleration was only used to trigger the measurement. The unfiltered acceleration, i.e. the direct reading from the sensor, was recorded.

A time stamp, the sensor time and the accelerations in three mutually perpendicular directions were recorded. The time stamp is provided by the smartphone's internal clock and is used for synchronization with the data from the other recording programs. The sensor time corresponds to the time of the accelerometer's internal clock and was recorded to avoid time jumps due to periodical clock synchronizations of the smartphones, which would lead to a time distortion of the braking deceleration. The sampling rate was set to 50 Hz.

The recording program calibrates to zero by recording accelerations on the three axes for 10 seconds, calculating average values, and storing them as calibration values. These values are then subtracted from recorded accelerations to compensate for gravity and sensor inaccuracies. Calibration assumes a flat surface, with tilt verified by observing the calibration vector. The angular rotation (gyroscope data) is continuously recorded in three mutually perpendicular axes with a third application. As the rotation rate is primarily used to correct the direction of travel from the position measurement and this has a sampling rate of 1 Hz, the sampling rate of the angle measurement is 10 Hz. The timestamp, like in the acceleration app, is provided by the smartphone's internal clock, and by the sensor time.

3.2 *Validation of the measuring system*

As part of the ongoing project, several tests have been carried out to assess the quality of the data provided by the smartphone's sensor. These tests typically included comparing the data recorded by the phone with a high-quality measurement system in different driving and laboratory conditions as further explained in (Feltrin & Breveglieri, 2024). The investigation was not limited to checking the quality of the acceleration time histories but was also extended to the GPS receiver data. Figure 1 shows the setup of the last performed validation test carried out by instrumenting a Volvo school tractor from Planzer AG (Dietikon, CH). The tractor was equipped with two pairs of capacitive uniaxial accelerometers (PCB), strategically placed to measure both vertical and horizontal (along the main axis) accelerations. Two PCB accelerometers connected to a HBM amplifier and data acquisition system, were used as reference measurements in all the verification tests. The first pair was fixed to the chassis between the tractor axles, while the second pair was mounted inside the side box of the tractor, attached to a heavy steel plate (Figure 1). The smartphone was mounted on the same plate. The MEMS sensor installed in the phone is a 6-axis motion sensor from TDK, specifically the ICM42605M. This sensor is capable of recording both acceleration and angular velocity (gyroscope data) in all three axes. A GPS receiver, linked to the same recording system that records deceleration, was positioned on top of the cab to ensure good GPS signal reception and to be used as a reference measurement.

The test consisted of driving 29 km and intentionally braking to trigger the accelerometer measurement. The driver was instructed to vary the braking strength during the test. 32 braking events were recorded during the test. From the test results it was observed that there was a consistent difference in acceleration variance between the frame and the side box, attributed to the driver compartment suspension system. The difference could be minimized by applying a transfer function calibrated using the side box as input and the frame as output. Figure 2 shows an acceleration comparison between the reference system measurement at different position and the phone for an illustrative deceleration profile. The deceleration profile of the phone after applying the identified transfer function (PhoneCorr) is also shown. To reduce acceleration noise, all signals were filtered with a Chebyshev Type II low-pass filter with a stopband frequency of 4 Hz. Figure 2 clearly illustrates the disparity between the frame and side box measurements, regardless of whether the data is from the phone or the reference system. It also highlights the similarity between the reference system and phone profiles when installed in the same location, and finally, the effectiveness of applying a transfer function to

correct for the phone acceleration trajectory. In terms of frequency content, no significant difference was observed between the sensors used for frequencies below 4 Hz. A direct comparison of the peak values for all braking events reveals that the error attributed to the phone, when compared to the frame measurement, can be around 0.8 m/s² for braking events exceeding 7 m/s². For braking events in the range of 2 m/s², the error is approximately 0.4 m/s², corresponding to percentage errors of approximately 10 % and 20 %, for hard and soft braking respectively. When comparing the phone to the accelerometer located at the same position in the side box, the absolute error is within the range of 0.1 m/s², with percentage errors below 2 % for accelerations greater than 4 m/s², and is not influenced by the magnitude of braking. This test demonstrates that the phone can provide reliable results, and the source of error can be mainly related to the installation position. Figure 3 presents the measurement comparison between the phone and the GPS receiver of the measurement system.

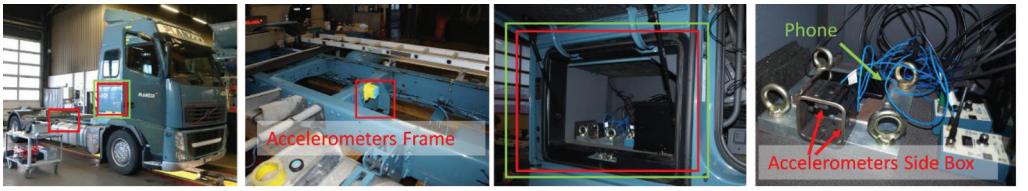


Figure 1. Validation test setup.

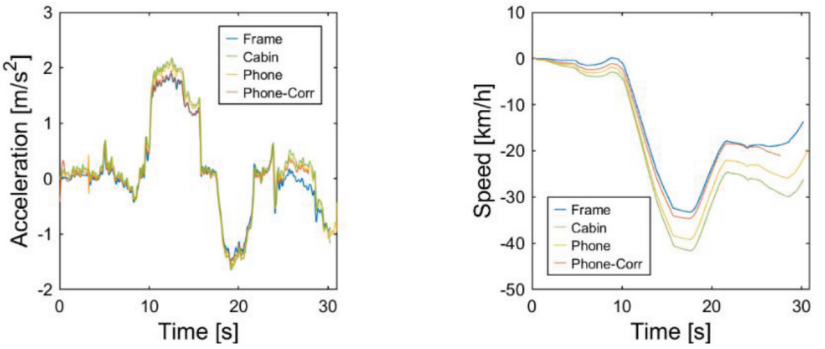


Figure 2. Acceleration data comparison during a braking event.

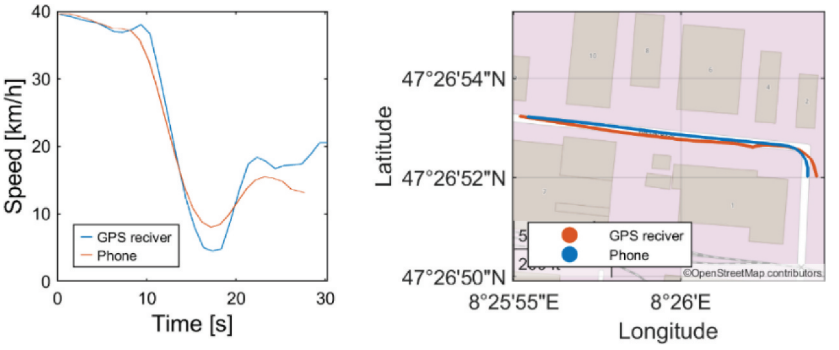


Figure 3. GPS receiver data comparison during a braking event.

4 PILOT TEST

4.1 *Aim of the test*

Before starting the test campaign, which involved 22 heavy vehicles (launched in June 2023) a preliminary pilot test was conducted. This aimed to assess the device's performance over an extended duration, identify potential measurement challenges inherent in such systems, and refine both data collection and analysis processes. To this end, a 5-axle articulated truck was instrumented. After sharing preliminary results with the logistics company, was decided to install the phone directly on the chassis frame, housed in a protective box (Figure 4). This approach eliminated the need for dynamic characterization for each vehicle used in the monitoring program and ultimately could provide better data. The collected data were transmitted at the end of each day to an SFTP server. Remote access software (TeamViewer GmbH) was installed on the phone facilitating phone management and addressing any potential system issues. To avoid drift accumulation in accelerometer and gyroscope measurements, and to reduce the possibility of missing data measurements due to application crashes, all applications were restarted and recalibrated at the beginning of each work week. For the present pilot study, a SAMSUNG Galaxy XCover Pro, a phone released in Q1/2020, with 8 GB RAM, and an 8-core Exynos 9611 chipset, running Android 13 SDK 31, was used. The same phone was used during the test presented in section 3.2.



Figure 4. Smartphone installation.

5 DATA ANALYSIS

5.1 *Raw data fusion and preparation*

The collected files are processed daily to systematically minimize potential errors. The first step is to merge the files containing the respective raw route data (GPS), and gyroscope angular velocities (gyroscope) and organize them according to the time stamp, to correct the traveling direction, i.e. bearing. At higher vehicle speeds, the accuracy of the bearing information is typically good. As the speed of the vehicle decreases, the accuracy of the direction of travel also decreases as the effect of the geolocalisation error increases. When the vehicle is stationary, the GPS latitude and longitude readings may inaccurately indicate movement, resulting in a characteristic loop-like wandering in confined spaces that produces inaccuracies leading to sudden sharp changes in direction. Despite the small relative distance between points, the loop-like wandering over time accumulates and affects also the calculation of the distance traveled. It is therefore essential to correct not only the bearing, which is relevant to determine the road category, but also the latitude, longitude and speed inaccuracies in such cases. The two files containing the data of the route and angular velocities are then merged into a single file. The direction correction algorithm isolates segments with speeds below 12 km/h, detects abrupt direction changes, and iteratively refines the route by approximating the points to be corrected with spline polynomials until a better approximation of the direction is achieved. The distance traveled is also calculated from the corrected coordinates (latitude and altitude) and height above sea level. An additional column is added with the average acceleration calculated from the changes in speed.

Braking event periods are indicated by assigning a number in a new column based on the lexicographical order of the files containing the raw data for the braking events. This "marking" is used to make a first approximate assignment of the braking event to the geographic position of the vehicle. An additional column is introduced to indicate whether the vehicle is stationary. A speed of less than 5 km/h and an angular change of less than 0.5° is chosen as the standstill criterion. In addition, the standstill criterion must be maintained continuously for at least 5 seconds.

The timestamp in GPS data makes it possible to identify the acceleration file corresponding to a braking event. All acceleration files undergo signal filtering using the low-pass filter mentioned above and synchronization with GPS data. This synchronization aligns the GPS-derived speed with the speed calculated by integrating the accelerometer signal in the direction of travel. While acceleration integration provides only the change in speed and lacks pre-braking speed information, synchronization allows estimation of both the initial and final post-braking speeds. To address potential inaccuracies associated with accelerometer zero (constant acceleration not equal to zero when the vehicle is stationary), an objective function is applied. This function shifts the acceleration signal in the vertical plane to minimize the error between the speed calculated by the accelerometer and the speed measured by GPS, thereby aiming to reduce small biases in the accelerometer measurement.

5.2 *Evaluation of the distance traveled according to road classes*

The assessment of driven kilometers for each road class type relies on the OpenStreetMap (OSM) geographic database. The OSM database primarily comprises geometric objects with attributes consisting of a key and a value assigned to each object. The road classes selected for the project include "Class 1- Motorway" (key: Motorway /_link, Trunk /_link), Class 2- Main Roads (key: Primary /_link), Secondary /_link), Class 3- Local Roads (key: Tertiary, Residential and Class 4-Other (key: Unclassified, Service and Living street). The road category is determined based on the current geodetic coordinates of the vehicle, by sending a query to the OSM server requesting road segments in the immediate vicinity. Due to positional inaccuracies, a single distance criterion can lead to errors. To address this, the road category determination is extended to include direction of travel, vehicle speed, and perpendicular distance in a unified objective function. The direction of travel narrows the selection to road sections that are aligned with the direction of the vehicle, while the vehicle speed helps to exclude inappropriate road categories.

The most accurate method is to determine the road class for each vehicle coordinate and calculate the distance traveled per road class accordingly, but this approach suffers from significant computation times that are hardly feasible. However, not all waypoints need to be evaluated suggesting the use of a larger sampling period and then identifying the point where the change occurred within that sampling interval, nevertheless this approach was also to be found computationally inefficient, as explained in (Feltrin & Breveglieri, 2024). In the same study, it was shown that incorporating additional trip information into the computational procedure to identify potential road class changes is the most convenient strategy in terms of computational efficiency. For this reason, an algorithm has been developed that checks the speed and direction of the vehicle over the distance traveled to identify the point of possible class change. A significant decrease in speed or a major change in the direction of a vehicle could indicate a change in road. On the other hand, if no slowdown or major change in direction is observed, it is possible to skip to the next point. Therefore, starting from a waypoint with known road class, the algorithm selects a new waypoint according to the sampling period and checks for speed and direction changes at the current waypoint to determine if the vehicle may have changed road class. If the check is negative, the algorithm proceeds to a new waypoint. If positive, the road class of the current waypoint is determined. If the road class of the current waypoint matches the road class of the last waypoint, the waypoints in between are marked with the current road class and the algorithm proceeds to a new waypoint. If the road class of the current waypoint does not match the road class of the last waypoint, a binary

search is used to find the waypoint with the road class change. Accordingly, the waypoints between the last waypoint and the current waypoint are marked with the initial road class and the waypoints after the current waypoint are marked with the new road class. This procedure greatly reduces the number of queries to the OSM database.

6 RESULTS

The pilot test lasted three months, during which the trucks traveled 21,317 kilometers across Switzerland in Figure 5 (left). The roads traveled during the 56 days of monitoring, taking into account the interruption of the system. An analysis of the kilometers traveled by road class showed that 16,938 km were on motorways (Class-1), 3,456 km on main roads (Class-2), 905 km on local roads (Class-2) and 18 km on other roads (Class-4). In percentage terms, these constitute 79 %, 16 %, 4 %, and 1 %, respectively, highlighting the majority of kilometers driven on motorways. Figure 5(right) shows a daily journey of 618 kilometers, with the motorway in purple, major roads in cyan, and local roads in red. Colored dots mark the locations of braking events (deceleration greater than 2 m/s^2), using the same color code as the road classification. A closer look at the figure reveals that the majority of braking events occur on local and major roads, with a limited number on the motorway. For example, on Road Class 1 ("Motorway"), the average speed over 478 km was 73.3 km and 6 braking events were recorded (1 event every 80 km). In comparison, on Road Class 2 ("Main Roads"), although only 105 km were covered, a higher number of braking events occurred: 29 (1 event every 4 km).

Figure 6 Provides a summary of the key data recorded during a braking event, including acceleration, speed calculated from acceleration integration (blue), and GPS data (yellow). The event shown is geolocated within the same figure and occurred on a main road. The green triangle marker indicates the direction of travel, and the green section highlights the point of higher acceleration. The highest recorded deceleration peak reached 6.3 m/s² and was observed on a main road. When plotting the distribution of acceleration peaks for each road class in Figure 7, it becomes evident that despite the maximum value, the majority of accelerations are close to the selected threshold value and barely exceed the 4 m/s² threshold used in AGB 2011/003.

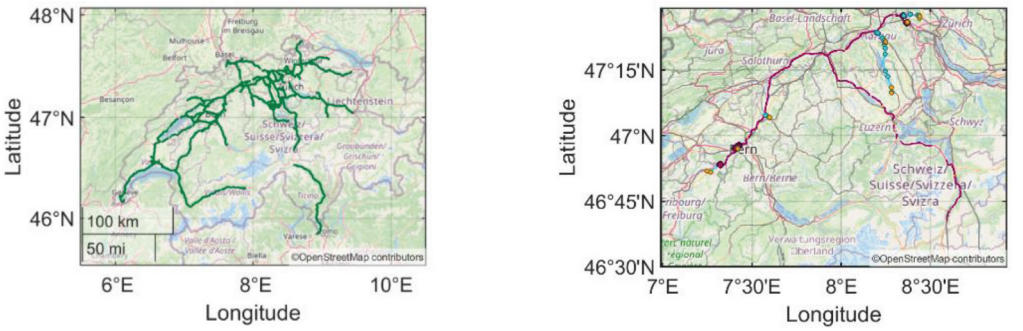


Figure 5. Route traveled by truck during the pilot test (left), explanatory daily route (right).

This suggests a lower magnitude than initially considered in the completed project (Martins et al., 2016). In addition, the braking rate from the pilot study is significantly lower, with no recorded braking events exceeding 4 m/s² on a motorway. Therefore, a direct comparison with AGB 2011/003 is not possible. Using a threshold of 3 m/s², the braking rate is one event per 1540 km, which is more in line with the UDrive project than AGB 2011/003. However, more data is needed to draw conclusions on both braking rate and braking magnitudes. The magnitude or intensity of braking events is not determined solely by the value of the maximum deceleration. Other factors, such as the duration of the braking and a plateau value of the

acceleration representing its average, among other parameters, are representative of the magnitude of the event, as discussed in (Feltrin & Breveglieri, 2024). A lower magnitude affects the forces acting on the bridge, which are calculated by multiplying the mass of each truck by its deceleration profiles assigned during the definition of the braking kinematics (Martins et al., 2016). Therefore, it affects the empirical probability distribution of the forces generated by the simulations. The frequency of braking events, on the other hand, influences the estimation of parameters. As described in Martins et al., 2016), the frequency of braking events allows the quantile of the probability distribution of the braking force in terms of the order statistic to be estimated as the k^{th} order realization of the braking force. It also allows to associate the characteristic value of the braking force with a given return period.

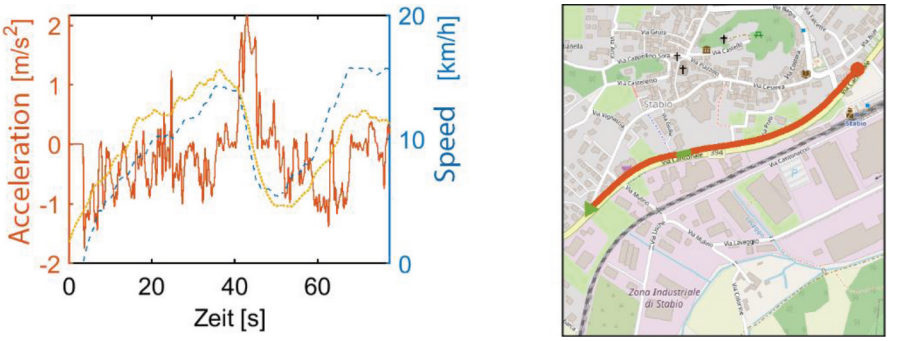


Figure 6. Example of data representing a braking event.

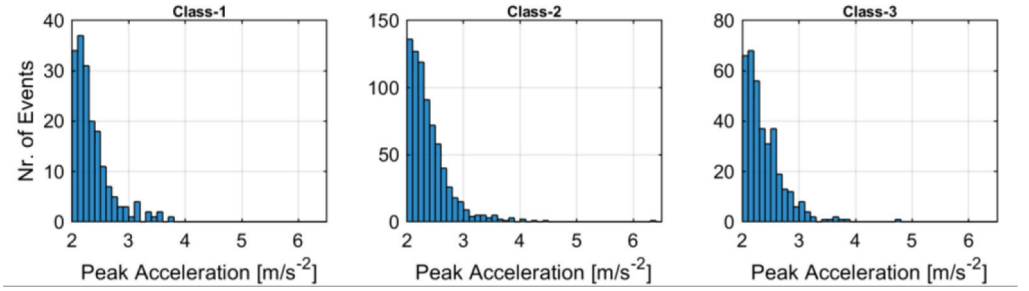


Figure 7. Number of braking events by road class.

7 CONCLUSIONS

This paper provides an overview of the Android smartphone-based monitoring system developed to record braking events along with their geolocation data. The system is designed to collect data from a fleet of heavy vehicles operating on Swiss roads for about nine months, with the scope to improve the model developed by (Martins et al., 2016) to calculate the braking forces on road bridges. The aim is to address the lack of knowledge on braking frequency (defined as braking events per kilometer driven on different road classes) and braking deceleration characteristics. The paper describes the monitoring strategy, data processing methods and relevant preliminary tests.

The validation test performed to compare the phone measurements with a high-precision reference system showed that the accuracy provided by the smartphone is appropriate for the purpose of this research. In terms of acceleration, the deviations are mainly related to the installation of the phone rather than the accuracy of the phone's accelerometer. The GPS data provided, although not as good as in the case of the reference system, do not adversely affect the data processing procedure for the calculation of the distance traveled and the geolocalisation of the braking event.

The phone's GPS receiver has been enhanced with information from the OSM database to identify road classes and morphology. The use of OSM was fundamental to assess the truck's travel distance on different road classes, taking into account expected variations in braking rates for different road types.

A pilot study was carried out to test the monitoring system and data processing over several months before the start of the monitoring campaign, demonstrating the long-term stability of the smartphone and the feasibility and efficiency of the data processing procedure. The results of the pilot study showed a braking rate significantly lower than assumed in (Martins et al., 2016) and braking magnitudes hardly exceeding 4 m/s². If these results are validated during the fleet monitoring campaign, it is expected to have a significant impact on the calculated braking forces, resulting in lower values compared to the original stochastic model calculations and the current Eurocode standards.

ACKNOWLEDGMENTS

The authors would like to thank the Swiss Federal Roads Office for their financial support and the logistics company Planzer AG (Dietikon, Switzerland) for its extraordinary personal and technical support during the monitoring campaign.

REFERENCES

Bärgman, J., van Nes, N., Christoph, M., Janssen, R., Heijne, V., Carsten, O., Dotzauer, M., Utesch, F., Svanberg, E., & Pereira Cocron, M. 2017. The UDrive dataset and key analysis results. *EU FP7 Project UDRIVE Consortium*.

Barnard, Y., Utesch, F., van Nes, N., Eenink, R., & Baumann, M. 2016. The study design of UDRIVE: the naturalistic driving study across Europe for cars, trucks and scooters. *European Transport Research Review*, 8(2).

Dingus, T. A., Klauer, S. G., Neale, V. L., Petersen, A., Lee, S. E., Sudweeks, J., & others. 2006. The 100-Car Naturalistic Driving Study, Phase II – Results of the 100-Car Field Experiment (DOT HS 810 593). *National Highway Traffic Safety Administration*.

Feltrin, G., & Breveglieri, M. 2024. Monitoring von Bremsereignissen schwerer Fahrzeuge zur Bestimmung der Bremskräfte auf Strassenbrücken - BGT-20-02D. *Forschungsprojekt - Bundesamt Für Strassen ASTRA*.

FOT-Net partners. 2016. FOT-Net WIKI: AOS. http://wiki.fot-net.eu/index.php?title=AOS. Last accessed February 2016.

Hickman, J., & Hanowski, R. 2011. Use of a video monitoring approach to reduce at-risk driving behaviors in commercial vehicle operations. *Transportation Research Part F: Traffic Psychology and Behaviour*, 14(3), 189–198.

Martins, J., Feltrin, G., & Beyer, K. 2016. Updated braking forces for the assessment of road bridges - AGB 2011/003). *Forschungsprojekt - Bundesamt Für Strassen ASTRA*.

Sjaarda, M., Nussbaumer, A., Breveglieri, M., & Feltin, G. 2022. Impact of heavy vehicles platooning of Swiss bridges - AGB2017/004. *Forschungsprojekt -Bundesamt Für Strassen ASTRA*.

Bridge Maintenance, Safety, Management, Digitalization and Sustainability – Jensen, Frangopol & Schmidt (eds)
© 2024 The Author(s), ISBN 978-1-032-77040-6
Open Access: www.taylorfrancis.com, CC BY-NC-ND 4.0 license

Bridge damage classification using multiple responses of vehicles and 1-D convolutional neural networks

Z. Li, Y. Lan & W. Lin
Department of Civil Engineering, Aalto University, Espoo, Finland

ABSTRACT: Bridges exposed to extreme environmental conditions are susceptible to damage and even failure during service life. Traditional monitoring techniques may necessitate the installation of numerous sensors on the bridge, which can be time-consuming and costly. Instead, the indirect method typically employs several accelerometers attached to the passing vehicle, which is more economical and more accessible to operate. To promote the development of the indirect method, this paper proposes a novel vehicle vibration-based method for classifying bridge damage of varying severity using cutting-edge deep learning techniques. Initially, the framework for damage classification based on the responses of a single vehicle and 1-dimensional convolutional neural networks (1-D CNNs) is appropriately designed and introduced. Then, the proposed approach is evaluated using a steel continuous beam and a model truck in the laboratory, which is utilized to simulate a vehicle-bridge interaction (VBI) system in engineering applications. The experimental results indicate that the bridge's damage severity can be predicted by the CNN with high accuracy, thereby validating the inclusion of bridge damage information in the passing vehicle's responses. Furthermore, it is determined that employing multiple responses from the vehicle facilitates the improvement of damage classification accuracy. Heavier vehicles are conducive to the transfer of more bridge-damaged information and are therefore recommended in engineering.

1 INTRODUCTION

Bridge structures play a vital role in European transportation systems, yet their aging and deterioration pose significant challenges. Over the past decades, the need for structural health monitoring (SHM) of bridges has become increasingly apparent. Traditional monitoring heavily relies on visual inspections by experienced engineers, but this approach becomes impractical for newly constructed bridges spanning tens or even hundreds of meters. In the 21st century, a promising and expedient solution to bridge health monitoring has emerged through the vibration-based approach (Hou and Xia, 2021). This method involves monitoring the modal parameters throughout the bridge's service life, offering insights into potential damage occurrences. However, the conventional approach mandates the installation of a large number of sensors, including temperature sensors, accelerometers, strain gauges, etc. directly on the bridge (referred to as the direct method) to establish a sensing network. Undoubtedly, this solution incurs a high cost and is typically reserved for significant projects rather than short- and mid-span bridges.

Over the past two decades, researchers worldwide have developed the indirect method, involving the installation of sensors on passing vehicles rather than directly on bridges (Malekjafarian et al., 2022; Wang et al., 2022; Xu et al., 2024; Yang et al., 2024). This approach is characterized for its economic efficiency and convenient applications. Numerous numerical simulations and experiments have demonstrated the viability of extracting bridge modal parameters from vehicle responses (Feng et al., 2023; Li et al., 2023a). However, practical

DOI: 10.1201/9781003483755-193

engineering observations reveal that modal parameters of bridges may not be highly sensitive to damage due to the influence of operational conditions, such as temperature effects and ongoing traffic. Consequently, bridge health monitoring based on changes in modal parameters may face essential challenges.

In recent years, artificial intelligence (AI) has made significant strides across various domains, notably enhancing bridge health monitoring. Traditional direct methods initially employed intelligent techniques such as supervised deep learning (DL) and transfer learning (TL), yielding robust results in bridge health monitoring. When applying the indirect method, vehicle responses typically include vehicular information, road roughness, and bridge vibrations, with the latter being particularly challenging to identify (González et al., 2023). DL techniques are good at extracting essential features, making them valuable for identifying bridge information from passing vehicle responses. Malekjafarian et al. (2019) developed a machine learning approach using vehicle accelerations to detect and quantify bridge damage. Two strategies, involving time-domain or frequency-domain responses from multiple vehicle runs, successfully identified damage occurrences and provided references for damage severity. Corbally and Malekjafarian (2022) improved this method by incorporating contact-point (CP) frequency responses into artificial neural networks (ANNs), demonstrating superior performance in identifying bridge damage. The proposed method underwent robust testing with variations in vehicle speeds, ambient temperatures, and road roughness levels. In 2023, Li et al. (2023b) emphasized the importance of considering both low and high-frequency responses of passing vehicles for extracting bridge damage-sensitive features. Furthermore, their findings verified that short-time vibrations during vehicular passage contain valuable information for determining the bridge's health state (Li et al., 2023c). To overcome the challenges that DL techniques typically require a large number of samples, a physics-guided framework was proposed by Lan et al. The results verified the effectiveness of the proposed method in damage indication, quantification, and localization (Lan et al., 2024). Despite these advancements, most studies have simplified vehicles into a quarter-car model during training (Corbally and Malekjafarian, 2023). The vehicle's response along with one degree of freedom (DOF) is considered. In practice, vehicles have multiple DOFs, and each can contain bridge-related information (Li et al., 2023d). Therefore, for improved accuracy in the training process, responses from multiple positions of the vehicle need to be considered.

This paper introduces an innovative approach to damage classification using 1-dimensional convolutional neural networks (1-D CNNs) to advance the monitoring process. Sensors are strategically positioned on various locations of a passing vehicle, collecting its accelerations as it traverses the bridge. Subsequently, the time-domain vehicular accelerations obtained from multiple positions are transformed into the frequency domain. These frequency-domain responses are then employed as inputs across different channels of the 1-D CNN for damage severity classification. To illustrate the effectiveness of the proposed method, an experimental study involving a U-shape beam and a scaled truck is conducted. The subsequent sections of this paper are structured as follows: Section 2 delves into the theoretical foundation of employing 1-D CNNs for damage classification within the indirect method. Section 3 outlines the laboratory experimental setups for the vehicle-bridge interaction (VBI) system and introduces artificial damage cases. Results and discussions are offered in Section 4. Finally, Section 5 provides the conclusion of this paper, summarizing the key findings and potential avenues for future research.

2 THEORY FOUDATION

2.1 *Vehicle's multiple responses*

This paper introduces a novel approach using multiple responses of the vehicle, distinguishing itself from existing studies. Assuming a vehicle equipped with N accelerometers, denoted as $\ddot{z}_i$ for the accelerations measured by the ith sensor, this study advocates optimal sensor placement aligning with the 3-D vehicle's seven degrees of freedom, as detailed in the reference (Li

et al., 2023d). However, practical challenges arise in accurately localizing the vehicle body's gravity center and capturing vibrations from the vehicular wheels, particularly given the intricate suspension systems. As an initial study, this paper employs a pragmatic solution, utilizing only two accelerometers strategically placed on the front and rear axles, denoted as $N = 2$.

Further, in order to remove the influence of unrelated information about the bridge, only when the vehicle is on the bridge will the vehicle's accelerations be recorded. This can typically be achieved by installing GPS sensors on the passing vehicle (Lan et al., 2023). Signals collected by the vehicle could be truncated according to location information. Assume that the vehicle's rear wheels enter the bridge at T_{in} and its front wheels leave the bridge at T_{out}, and only the vehicle's accelerations within T_p will be utilized, where T_p is the vehicle's passing time and is shown in Eq. (1),

$$T_p = T_{out} - T_{in} \tag{1}$$

2.2 *1-D CNNs*

In contrast to traditional 2-D CNNs tailored for image analysis, 1-D CNNs specialize in handling single-dimensional inputs. While standard images possess three channels—R, G, and B—the proposed method incorporates multiple signal channels derived from diverse positions on the moving vehicle. The architecture of 1-D CNNs encompasses convolutional layers, 1-D max-pooling/average pooling layers, and fully connected layers. The computations within the convolutional layers can be expressed by Eqs. (2) and (3) (Abdeljaber et al., 2018),

$$x_k^l = b_k^l + \sum_{i=1}^{N_{l-1}} \mathrm{CONV}\left(w_{ik}^{l-1}, s_i^{l-1}\right) \tag{2}$$

$$y_k^l = f\left(x_k^l\right) \tag{3}$$

where x_k^l means the input of the lth layer. b_k^l represents the bias of the kth neuron at layer l. CONV $(\cdot)$ denotes the 1-D convolution without zero padding. w_{ik}^{l-1} is the 1-D kernel from the ith neuron at layer $l-1$ to the kth neuron at layer l. f means the activation function. Typical activation functions include rectified linear unit (ReLU), Sigmoid, and Tanh.

1-D max-pooling/average-pooling layers efficiently down-sample the data by selecting the maximum/average value within a defined neighborhood. Interested readers can find further details in the reference (Murray and Perronnin, 2014). The resulting output is flattened into one dimension before being connected to fully connected layers. The ultimate output of the fully connected layer corresponds to the different damage severities in this paper.

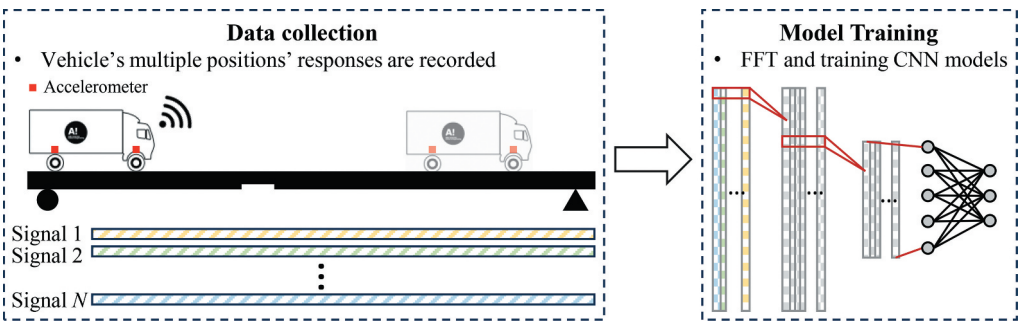


Figure 1. Data collection and model training.

3 LABORATORY EXPERIMENTS

3.1 *Vehicle models*

This paper employs a meticulously scaled model truck to simulate real-world engineering vehicles. Figures 2 and 3 illustrate the truck, its system and installed accelerometers. The employed truck model is the Tamiya Mercedes-Benz 1850L, with a scale ratio of 1:14. The truck's self-mass, denoted as T0, is 4.305 kg, and to simulate heavy vehicles, an additional mass of 5.157 kg is added (referred to as T5). A guide-wire system ensures the truck follows a straight path without colliding with the beam's flange. The bottom view of the scaled truck is depicted in Figure 3, showcasing its scaled suspension system, engine, connecting shaft, and more. Driven by a 540-brushed electric motor powered by a Tamiya Ni-MH 7.2 V–3000 mAh battery, the vehicle introduces engine noise that inevitably affects acceleration data collection in engineering. Two Brüel & Kjær accelerometers (type 4371) are attached to the front and rear axles (Figure 3), with a sampling frequency set at 10 kHz. The vehicle, remotely controlled, exhibits slight speed variations across runs due to battery constraints. However, to allow for optimal vibrations, the wire tension is deliberately kept loose, resulting in slightly varied passing traces during multiple beam crossings.

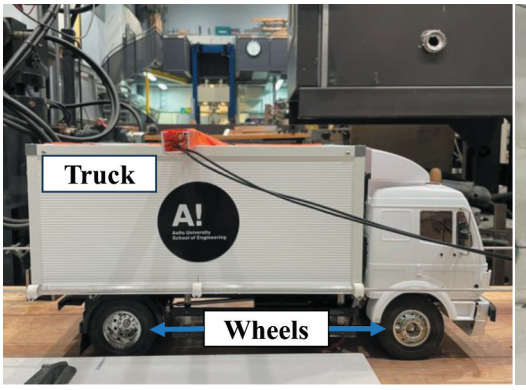


Figure 2. Model truck (lateral).

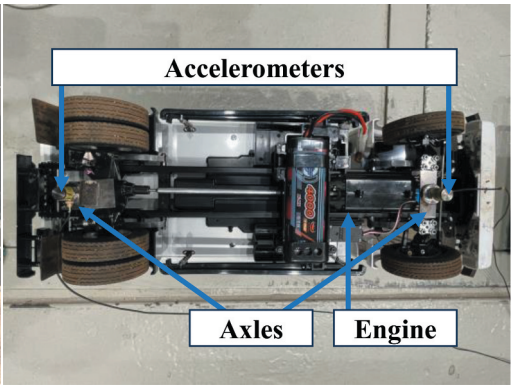


Figure 3. Model truck (bottom).

3.2 *Bridge model*

In this experiment, a single continuous beam with three supports is employed for the bridge configuration, as shown in Figure 4. The utilized beam is a UPE 300 with a cross-sectional area of 5660 mm^2, a span length of 5.7 m, a support length of 0.15 m, and a mass of 248.64 kg. To maintain a relatively constant speed as the truck traverses the beams, acceleration and deceleration runways are positioned at the beam ends. For comparison purposes, accelerometers are also installed at the bottom of the beam to capture its vibrations concurrently with the truck's passage. Additionally, to clearly identify the beam's modal frequencies, impulse excitation using an impact hammer is applied. Employing FFT analysis, the natural frequencies of the beam are obtained, as illustrated in Figure 5, revealing the first two frequencies as 30.75 and 42.53 Hz.

3.3 *Damage scenarios*

In practical engineering, the occurrence of damage can lead to a decrease in a bridge's natural frequencies. An effective experimental method for simulating damage involves adding mass to the bridge, a process known to cause a reduction in natural frequencies (Cerda et al., 2014).



Figure 4. Bridge model.

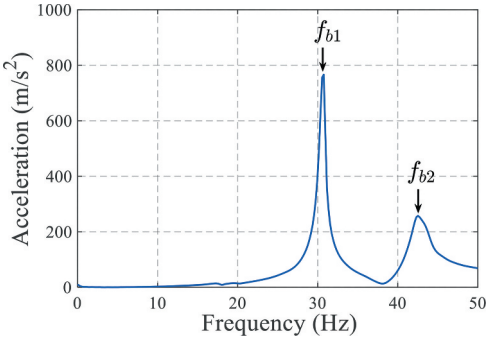


Figure 5. Bridge frequency spectrum.

This approach offers the advantage of easy recovery, allowing the beam to return to an undamaged state when necessary. In this study, various masses are applied to the bridge to simulate different artificial damage scenarios. Damage degrees are represented by the ratios of added masses to the beam's mass. For example, when there are two 5 kg masses and two hooks (4 kg) added to the beam's two spans, the damage degree is (5+5+4)/248.64 =5.6%. Table 1 summarizes all scenarios (S0-S6), where S0 means an undamaged bridge, while scenarios S1-S6 represent varying degrees of damage.

Table 1. Damage scenarios.

Scenarios	S0	S1	S2	S3	S4	S5	S6
Added mass/kg	0	5	10	15	20	25	30
Damage degree	0	5.6%	9.6%	13.7%	17.7%	21.7%	25.7%
T0 runs	50	49	50	42	51	51	47
T5 runs	57	56	57	56	57	56	57

4 RESULTS AND DISCUSSIONS

4.1 *Model training and testing*

In this study, runs of T0 or T5 are divided into two groups. 70% of runs are utilized for training and the rest are for testing. As outlined in Section 2, the vehicle's time-domain signals on the bridge are transformed into the frequency domain. To mitigate contamination from environmental noises, only vehicle frequency-domain responses within 100 Hz are utilized for training, as validated in previous work (Li et al., 2023c). Zeros padding is applied to align input time-domain signals, resulting in an FFT frequency resolution of 0.0763 Hz, yielding 1310 response points within the 0-100 Hz range. The training is conducted on an Aalto University workstation equipped with Intel Core i7-9750 CPUs, 16 GB RAM, and an NVIDIA GTX 1650 graphic card for tensor computation acceleration. All code is implemented in Python 3.9 with the PyTorch package. The model architecture, detailed in Table 2, employs hyperparameters including a learning rate of $1e^{-4}$, Adam optimizer, cross-entropy loss, batch size of 16, and 200 epochs.

4.2 *Damage classification using 1-D CNNs*

When utilizing the vehicle's frequency-domain responses within 0-100 Hz for training, loss curves for T0 and T5 vehicles have been plotted in Figures 6 and 7. Notably, for both T0 and T5 vehicles, employing responses from two axles yields smaller losses compared to using responses from only one axle. The difference is relatively minor for T0, as the lighter vehicle

Table 2. Architecture of the 1-D CNNs.

Layer	Pooling	Output shape	Batch normal	Activation
Conv1d	–	1310×20	Yes	ReLU
Conv1d	–	1310×20	Yes	ReLU
Conv1d	Max	655×20	Yes	ReLU
Conv1d	–	655×40	Yes	ReLU
Conv1d	–	655×40	Yes	ReLU
Conv1d	Max	327×40	Yes	ReLU
Conv1d	–	325×60	Yes	ReLU
Conv1d	–	325×40	Yes	ReLU
Conv1d	Avg	65×20	Yes	ReLU
Flattened	–	1300	No	–
Fully Connected	–	7	No	–

* Conv1d: 1-dimenasional convolutional layer, ReLU: Rectified linear unit

may not induce strong vehicle-bridge interaction responses, resulting in less bridge information transferred to the vehicle. Despite including responses from another axle in the training, the model's ability shows marginal improvement. In contrast, for the heavier T5 vehicle, the inclusion of responses from two axles significantly reduces the loss. This is attributed to the incorporation of valuable bridge damage information in the vehicle's axles' responses, enhancing the model's damage classification capabilities.

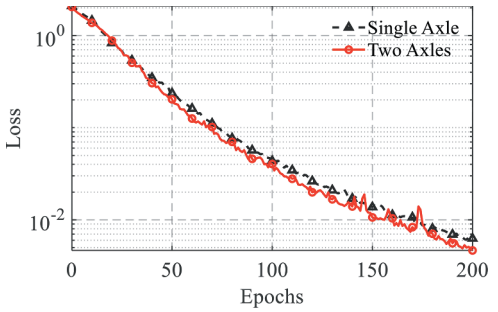


Figure 6. Loss curve using T0 vehicle.

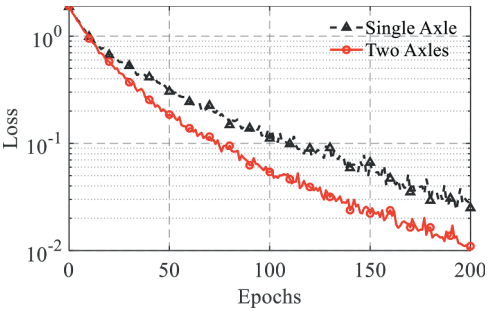


Figure 7. Loss curve using T5 vehicle.

To evaluate the capability of the trained model, some criteria listed in Eq. (4) are utilized,

$$Accuracy = \frac{TP + TN}{TP + FP + TN + FN}, Precision = \frac{TP}{TP + FP}, Recall = \frac{TP}{TP + FN} \tag{4}$$

where True Positive (TP) refers to a sample belonging to the positive class being classified correctly; True Negative (TN) refers to a sample belonging to the negative class being classified correctly; False Positive (FP) refers to a sample belonging to the negative class but being classified wrongly as belonging to the positive class; False Negative (FN) refers to a sample belonging to the positive class but being classified wrongly as belonging to the negative class. The damage classification accuracy using T0 and T5 are plotted in Figures 8 and 9.

We can see that for both T0 and T5 vehicles, employing responses from both axles yields higher accuracy compared to using responses from a single axle. Notably, with T0, accuracy stabilizes below 80% after 50 epochs. Conversely, Figure 9 illustrates that when a heavier vehicle is employed, accuracy consistently exceeds 95%. Consequently, in practical engineering

applications, it is advisable to recommend the use of heavier vehicles, as they can gather more damage-related information about the bridge.

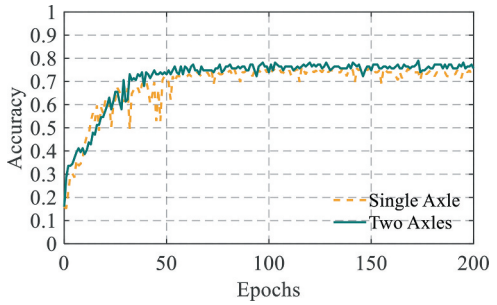


Figure 8. Damage classification accuracy (T0).

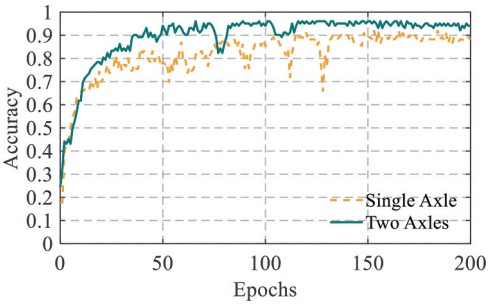


Figure 9. Damage classification accuracy (T5).

To assess the predictive capabilities of the trained DL model for damage severity classification, we employ the confusion matrix (CM), a widely used tool, to show the best bridge damage classification results. Figures 10 and 11 illustrate the CMs for T0 and T5, respectively.

From Figure 10, we can see that with the use of a light vehicle, the overall damage classification accuracy reaches 79%. Across most damage scenarios, ***Recall*** values range between 50% and 95%, though certain instances, such as S3, exhibit low ***Recall***, indicating inaccuracies in predicting damage severity. Contrastingly, when employing a heavier vehicle, as shown in Figure 11, ***Recall*** values can consistently approach or exceed 90%, with some cases achieving 100% ***Precision*** and ***Recall*** values. The overall accuracy of damage classification across all scenarios increases significantly to 96.1%. Therefore, we can conclude that in practical engineering, heavier vehicles are recommended for the indirect bridge health monitoring using responses of passing vehicles.

4.3 *Further discussions*

In this study, we employ a scaled truck and a U-shaped beam to simulate real VBI scenarios. The road roughness, primarily caused by the wheels' tread, is relatively good compared to practical engineering cases. To alleviate the influence of road roughness, various techniques, such as CP responses and residual CP responses between wheels or connected vehicles, can be

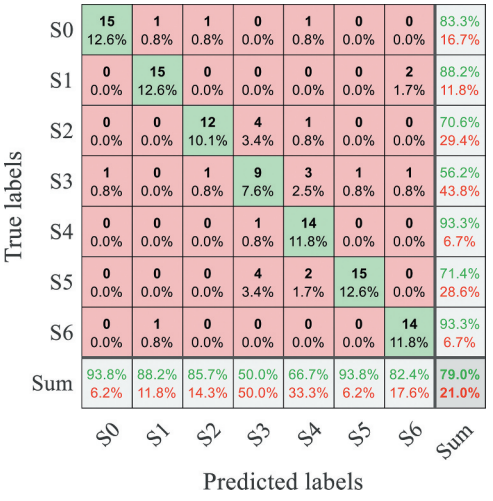


Figure 10. Damage classification results (T0).

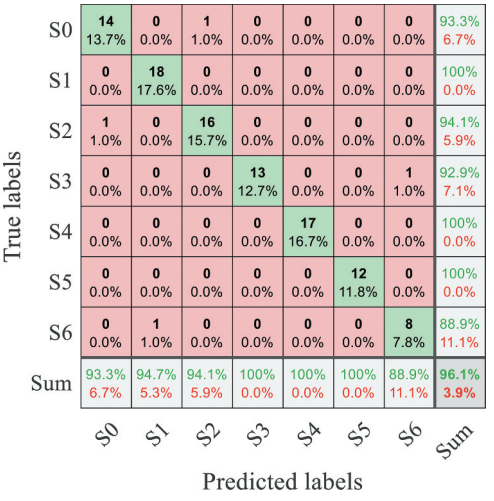


Figure 11. Damage classification results (T5).

examined. Furthermore, it is noted that as an initial investigation, this paper mainly explored the superior capability when responses of multiple positions of the vehicle are utilized. To overcome the challenges that labeled damaged data are difficult to obtain in engineering, semi-supervised or unsupervised DL techniques deserve further studies.

5 CONCLUSIONS

This paper proposed a bridge damage classification strategy using responses of the passing vehicle's multiple positions and 1-D CNNs. Firstly, the fundamental theories about CNNs are introduced. Then, the proposed method was verified via a scaled truck and continuous beam in laboratory experiments. The experimental results indicate that the bridge's damage severity can be predicted by the CNN with high accuracy, and some concluding remarks are drawn below:

(1) The passing vehicle's responses on multiple positions can contain bridge damage information. Therefore, in the DL model training process, the responses from more DOFs are supposed to be included to increase its damage classification capability.
(2) Heavier vehicles can make the VBI interaction responses stronger. Through this, more bridge damage-related information can be transferred to the passing vehicles' vibrations, resulting in boosted damage classification accuracy.

Even though there are some key findings, some important influence factors, such as ongoing traffic and very poor road roughness, have not been checked. Our future studies will include these factors and further unsupervised DL models before engineering applications.

ACKNOWLEDGEMENT

This research was fully sponsored by the Jane and Aatos Erkko Foundation in Finland (Grant No. 210018). The support for the vibration tests provided by the staff of the laboratories in the Department of Civil Engineering and the Department of Mechanical Engineering at Aalto University was greatly appreciated.

REFERENCES

Abdeljaber, O., Avci, O., Kiranyaz, M.S., Boashash, B., Sodano, H., & Inman, D.J. 2018. 1-D CNNs for structural damage detection: Verification on a structural health monitoring benchmark data. *Neurocomputing* 275, 1308–1317.

Cerda, F., Chen, S., Bielak, J., Garrett, J.H., Rizzo, P., & Kovacevic, J. 2014. Indirect structural health monitoring of a simplified laboratory-scale bridge model. *Smart Structures and Systems* 13, 849–868.

Corbally, R., & Malekjafarian, A. 2023. A deep-learning framework for classifying the type, location, and severity of bridge damage using drive-by measurements. *Computer-Aided Civil and Infrastructure Engineering*

Corbally, R., & Malekjafarian, A. 2022. A data-driven approach for drive-by damage detection in bridges considering the influence of temperature change. *Engineering Structures* 253, 113783.

Feng, K., Casero, M., & González, A. 2023. Characterization of the road profile and the rotational stiffness of supports in a bridge based on axle accelerations of a crossing vehicle. *Computer-Aided Civil and Infrastructure Engineering* 38, 1935–1954.

González, A., Feng, K., & Casero, M. 2023. Effective separation of vehicle, road and bridge information from drive-by acceleration data via the power spectral density resulting from crossings at various speeds. *Developments in the Built Environment* 14, 100162.

Hou, R., & Xia, Y. 2021. Review on the new development of vibration-based damage identification for civil engineering structures: 2010–2019. *Journal of Sound and Vibration* 491, 115741.

Lan, Y., Li, Z., Koski, K., Fülöp, L., Tirkkonen, T., & Lin, W. 2023. Bridge frequency identification in city bus monitoring: A coherence-PPI algorithm. *Engineering Structures* 296, 116913.
Lan, Y., Li, Z., & Lin, W. 2024. Physics-guided diagnosis framework for bridge health monitoring using raw vehicle accelerations. *Mechanical Systems and Signal Processing* 206, 110899.
Li, Z., Lan, Y., & Lin, W. 2023a. Indirect damage detection for bridges using sensing and temporarily parked vehicles. *Engineering Structures* 291, 116459.
Li, Z., Lin, W., & Zhang, Y. 2023b. Drive-by bridge damage detection using Mel-frequency cepstral coefficients and support vector machine. *Structural Health Monitoring* 22, 3302–3319.
Li, Z., Lin, W., & Zhang, Y. 2023c. Real-time drive-by bridge damage detection using deep auto-encoder. *Structures* 47, 1167–1181.
Li, Z., Lin, W., & Zhang, Y. 2023d. Bridge Frequency Scanning Using the Contact-Point Response of an Instrumented 3D Vehicle: Theory and Numerical Simulation. *Structural Control and Health Monitoring* 2023, 3924349.
Malekjafarian, A., Corbally, R., & Gong, W. 2022. A review of mobile sensing of bridges using moving vehicles: Progress to date, challenges and future trends. *Structures* 44, 1466–1489.
Malekjafarian, A., Golpayegani, F., Moloney, C., & Clarke, S. 2019. A Machine Learning Approach to Bridge-Damage Detection Using Responses Measured on a Passing Vehicle. *Sensors* 19, 4035.
Murray, N., & Perronnin, F. 2014. Generalized max pooling, in: Proceedings of the IEEE Conference on Computer Vision and Pattern Recognition. pp. 2473–2480
Wang, Z.L., Yang, J.P., Shi, K., Xu, H., Qiu, F.Q., & Yang, Y.B. 2022. Recent Advances in Researches on Vehicle Scanning Method for Bridges. *International Journal of Structural Stability and Dynamics* 22, 2230005.
Xu, H., Liu, Y.H., Chen, J., Yang, D.S., & Yang, Y.B. 2024. Novel formula for determining bridge damping ratio from two wheels of a scanning vehicle by wavelet transform. *Mechanical Systems and Signal Processing* 208, 111026.
Yang, Y.B., Chen, J., & Xu, H. 2024. Normalized formula for removing damping effect in recovering bridge mode shapes using a moving and a stationary vehicle. *Journal of Sound and Vibration* 573, 118219.

Bridge Maintenance, Safety, Management, Digitalization and Sustainability – Jensen, Frangopol & Schmidt (eds)
© 2024 The Author(s), ISBN 978-1-032-77040-6
Open Access: www.taylorfrancis.com, CC BY-NC-ND 4.0 license

Crowdsensing and indirect structural health monitoring in HE FUTURAL

D. Garcia-Sanchez, D. Zamora & I. Arakistain
TECNALIA Basque Research and Technology Alliance "BRTA", Derio, Spain

T. Katika
Institute of Communication & Computer Systems (ICCS), Athens, Greece

ABSTRACT: In this paper, a crowdsensing and Indirect Structural Health Monitoring (iSHM) strategy is presented within the framework of the FUTURAL project. This development was based on the hypothesis that regular "health" inspections are not a realistic option in terms of cost and time. This iSHM strategy takes advantage of the dynamic responses of instrumented vehicles that monitor the "health" of roads or bridges as they pass, based on data collected by on-board IoT sensors or smartphones, which can be temporarily installed on shared mobility vehicles according to user preferences or permanently installed in inspection vehicles covering a specific route. For other structures, with an extra focus on building health assessments, visual input/feedback will be collected from users' smartphones. The proposed solution will allow monitoring of multiple buildings at a territorial level.

The solution will be verified in rural areas in Spain (Durangaldea) and Austria (Pongau).

1 INTRODUCTION

In European Union, the architecture, engineering, construction, and operation (AECO) sector is a significant industry. It contributes up to 9% of the EU's gross domestic product (GDP) and 18 million direct jobs, i.e., more than 6% of all employment in Europe. However, this crucial sector for the global economy is lagging in the adoption of Information and Communication Technology (ICT) and digital transformation when compared to other industries such as telecoms or the manufacturing sector.

New ICT technologies can help the AECO sector catch up with other sectors and the adoption of digital technologies can significantly improve effectiveness and efficiency. In particular, considering the construction operation and maintenance procedures, the implementation of automatic processes through sensors and monitoring systems, along with the development of algorithms for predictive maintenance and the identification of critical events, can greatly improve the performance in the sector contributing to the implementation of better maintenance and intervention strategies.

In the past, monitoring was meant to provide information to support condition assessment and check the safety of the structure. Currently, the objective of monitoring is not only to assess the current condition, but also to forecast the future performance to optimize in terms of cost-effectiveness the allocation of available resources, all by taking advantage of today's technological capabilities provided by IoT sensors and connected environments.

2 QUICK ASSESSMENT OF THE STRUCTURAL CONDITION AFTER EVENTS

As explained in Gkoumas et al. 2023, technologies and their applications for measuring and managing civil structure full-scale performance are targeted at serviceability -in respect of

DOI: 10.1201/9781003483755-194

vibrations, resilience -in respect of structural health monitoring and sustainability -in respect of optimised design.

Some traditional SHM technologies are piezoelectric impedance transducers, magnetoelastic stress sensors, and synthetic aperture radar. Traditional discrete monitoring sensors are still relevant in monitoring bridges at critical locations, where the development of cracks or large stresses are expected. Moreover, despite some of these technologies being considered obsolete, modern iterations of the same devices might be found in the market, offering high performance.

On the other hand, distributed sensing technologies, such as fiber optics and smart sensing materials, represents one of the latest evolutions in the SHM field. Although large companies have been somewhat reluctant to use new technologies, fiber optics have many advantages, such as geometric adaptability, the possibility of being embedded in concrete, capability of measuring a variety of perturbations (e.g., strain, acceleration, temperature, etc.), high signal-to-noise ratio, and resistance to harsh environments. They are probably the best option to monitor long structures, such as tunnels, and some of the most recent sensors can be easily installed on existing structures with tape or glue.

Other recent innovations are related to noncontact sensing, which is particularly useful in situations where traditional human inspection operations are complex or unsafe. Examples are: (1) digital image correlation, where cameras are used to detect displacement, deformations, stresses, and crack propagation; (2) infrared, where the variation in the surface temperature of the material is used to identify phenomena such as delamination, detachment, and cracks; (3) Light Detection and Ranging (LiDAR) sensors that can be mounted on vehicles or drones to scan the infrastructure even under low light conditions to identify deformations/displacements that may have occurred; and (4) indirect structural health monitoring (iSHM).

3 ISHM AS NEW PARADIGM SHIFT

iSHM (Fan et al. 2024) (Calderon Hurtado et al. 2024), in its current state, still deals with several challenges that need to be overcome to bring it into practice. It represents a paradigm shift, from the current situation where most monitoring is by human inspection to the time when most monitoring will be indirect, with all the instrumentation in passing vehicles (i.e., for bridge and road applications). Gkoumas et al. 2023 identified three main points: (i) iSHM with a single vehicle is difficult; (ii) direct monitoring with a fleet of vehicles is feasible, and (iii) iSHM with a fleet of vehicles is the future. In this regard, OBrien proposed mining data from a fleet of instrumented passing vehicles. He described a 3-step process, as follows: (a) processing of accelerations measured on the vehicles using an inverse Newmark-beta method to determine moving reference deflections under vehicle axles, as explained in Keenahan et al., 2020; (b) using off-bridge deflection data to calibrate the vehicles of the fleet, exploiting the fact that they all pass over the same road profile; (c) using on-bridge data to determine a moving-reference influence line, that is, deflection at a (moving) point on the bridge due to a unit (moving) load. He showed, through simulations, that the moving reference influence line was damage-sensitive and was an effective way of aggregating data from a wide variety of uncontrolled passing vehicles from the general traffic. They concluded that a fleet-based approach has great potential as an effective means of iSHM in the future. The next step was to prove this concept by instrumenting vehicles in full-scale field trials. Other approaches, also reported in Gkoumas et al. 2023, such as the one presented by Dr. Cantero (Sarwar et al. 2021), rely on a data-driven approach. They proposed a deep autoencoder ML model to process signals from passing vehicles and obtain a damage indicator that allowed the detection of bridge damage. In summary, experience shows that it is feasible to detect changes in structural behavior indirectly by analyzing signals from accelerometers embedded in specialized vehicles crossing bridges at low speeds. They also concluded that numerous vehicle passages are required to obtain robust results. In other words, Machine Learning (ML) techniques can be used to process indirect measurement signals and identify significant deviations in vehicle responses that could indicate severe infrastructure damage processes, which can be applied relatively easily across the entire road network to support existing bridge maintenance strategies.

We can conclude that iSHM appears to have potential if vehicles can be instrumented at a low cost and the massive amount of data generated is collected centrally. Algorithms also need to be developed to make a practical application feasible, for which the combination of data methods with numerical models, as well as indirect measurement data on cars with some direct measurement data on the bridge, does not seem to have been exploited to its full potential in a way that can fill the gaps that separate approaches inevitably have.

4 RECENT RELEVANT PROJECTS

4.1 *Mitica project*

The European Commission Joint Research Centre (JRC) established an exploratory research project MITICA (Monitoring Transport Infrastructures with Connected and Automated vehicles) to investigate the opportunity to use novel methods for infrastructure motoring, aiming at the efficient maintenance of the European aging road infrastructure.

The discussions taken during the workshop held at the JRC in Ispra (Italy) on 6&7 of June, 2022 highlight the high interest within the academic and technical community to developing vehicle assisted iSHM. During the workshop, a special focus was placed on innovative indirect structural health-monitoring approaches. These rely on vehicle-bridge interactions and the deployment of sensor-equipped vehicles to monitor existing bridge infrastructure, including results from the JRC MITICA Project.

This report aims to serve as a reference document in the area of iSHM using passing vehicles, for both scholars and policymakers.

4.2 *Good vibration project*

Good Vibration project aims to implement a modal-based indirect structural health monitoring of bridges through opportunistic data coming from smartphones placed in vehicles crossing the bridge. The project is being studied at the MIT Senseable City Lab, whose mission is to study the interactions between the physical and digital layer of cities, seeking opportunities that could bring benefits to communities.

The project specifically focuses on bridge structural health monitoring and the possibility of applying the paradigm of crowdsensing to the monitoring of bridge infrastructure worldwide.

The research then focused on mode shape estimation and semi-controlled data acquisition, realized within a three-year partnership with Anas S.p.A., the Italian national road maintenance and construction company. In particular, this methodology involves transforming each time history into a space-frequency map. Such reshaping is realized by applying the so-called synchrosqueezed wavelet transform, which guarantees better performance than other wavelets in terms of frequency smearing, as explained by Daubechies et al. 2011. Synchrosqueezing transforms single-bridge trips into maps containing bridge dynamics, vehicle dynamics, and noise. All maps were combined to obtain a final average map. Averaging allows us to highlight bridge structural behavior, reducing the effects of noise and vehicle dynamics. All trips, indeed, share the same bridge dynamics content, while the vehicle and noise are different for every trip. This methodology explains the power of big data in this application: the more maps are averaged together, the less noisy the final map will be. After synchrosqueezing is applied, the Most Probable Modal Frequencies algorithm is exploited to estimate a bridge's natural frequencies, which appear on the space-frequency map under the form of statistical wavelet ridges. Mode shape reconstruction is based on a similar concept: cutting the map in correspondence of the modal frequency and the intensity of the statistical ridges, which represents the amplitude of the bridge motion at each spatial location. Because the data acquisition is not synchronous, only the absolute mode shapes can be estimated.

The app, installed on the smartphones of a pilot group of Anas road operators (the Italian Autonomous Roads Corporation), requires no interaction with the user and acquires data in an autonomous manner. The minimization of battery consumption and data transmission has been achieved thanks to a geofencing algorithm, which densifies data collection when the smartphone

is localized in the proximity of a bridge of interest. According to the data pipeline, the Anas fleet collects data, transfers them to an Anas database, and then transfers them to MIT for processing.

The case studies involved in the campaign are all located in Italy, three near Rome, and one in the Dolomites, close to Cortina. The latter, called "Ponte Cadore," was the object of further experiments. A 272 m single span bridge, built as a hyperstatic structure with two pins and two diagonal supports, in 2013 Anas performed a monitoring campaign that involved a dynamic testing. In 2021, another experimental campaign was deployed to study the effects of vehicle dynamics, sensor performance, and GPS accuracy on the effectiveness of drive-by monitoring. The campaign consisted of Ambient Vibration Testing (AVT), to verify the dynamic properties of the bridge, and data collection was performed via two e-scooters on which both a smartphone and a professional wireless accelerometer were installed. Such a rich dataset, combined with more than 1000 passages recorded through the app by Anas personnel in 2022, allowed us to test the performance of drive-by monitoring according to the choice of sensor diagnostic vehicles. The first analyses pointed out outstanding results from e-scooters, which were able to identify more mode shapes than cars. This outcome opens interesting horizons for the use of micro-mobility in urban environments to scan the health of bridge infrastructure.

4.3 *Im-safe*

IM-SAFE EU project[1] supports the preparation of the mandate for CEN which aims at improving standardisation of the assessment of structural performance and of the proactive maintenance practices for the European transport infrastructure so that optimal use is made of information from inspection, monitoring and testing. The project focuses on bridges, tunnels, and other large infrastructures in road and railway networks.

The rapid growth of large-scale civil infrastructure and increasing dependence of society on the availability of transport networks has driven political and societal pressure to keep transport infrastructure available and to provide the required service level without unforeseen investments to maintain the desired performance. There is a general consensus that effective and cost-optimal maintenance is only possible with appropriate policies and rational decisions. Such policies and decisions should be considered and supported by timely, available, meaningful, and accurate information. In this respect, the monitoring of structures is expected to become a key enabler of proactive maintenance strategies to ensure the safety of the transport infrastructure during its entire service life.

One of the most interesting outputs of the IM-SAFE project is the online knowledge database, which contains a large number of examples in which data-informed approaches that involve monitoring of structures have been implemented at various stages of the maintenance decision-making[2].

5 FUTURAL PROJECT

Within the FUTURAL project, which held its Kick-off Meeting in Athens last June 2023, and in particular within the developments leading to the Smart Solution for Resilience to Shocks, the indirect measurement from vehicles in pilot cases of bridges in the rural areas of Durangaldea (Spain) and Pongau (Austria) is currently proposed.

In December 2023, work started on the pilot structure in Durangaldea, a 3-span road bridge with high piers, and a central span resting on half-joint (or dapped-end) supports, which require repair. This bridge is also vulnerable in its foundation because of torrential runoff under the structure, as well as being located in an area prone to a violent natural phe-

1. IM-SAFE-Project. European Union's Horizon 2020 research and innovation programme under grant agreement No 958171.
2. IM-SAFE Knowledge Base. IM-SAFE-Project. European Union's Horizon 2020 research and innovation programme under grant agreement No 958171.

nomenon called debris flow. Thus, because this structure is a critical node of the transport network of Durangaldea, providing access to the main communication routes, and is particularly vulnerable to climatic and natural phenomena, it was chosen as a pilot case for the development of ISHM algorithms for its control before, during, and after significant events.

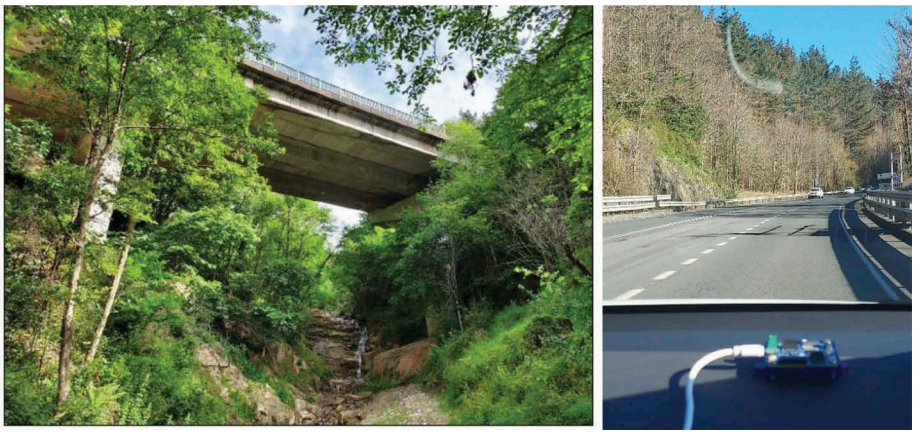


Figure 1. Image of the bridge on BI-633 road in Berriz (rural area of Durangaldea, Bizkaia, Spain) and image of the accelerometer onboard the car, attached to the dashboard, crossing the BI-633 road bridge in Berriz (rural area of Durangaldea, Bizkaia, Spain).

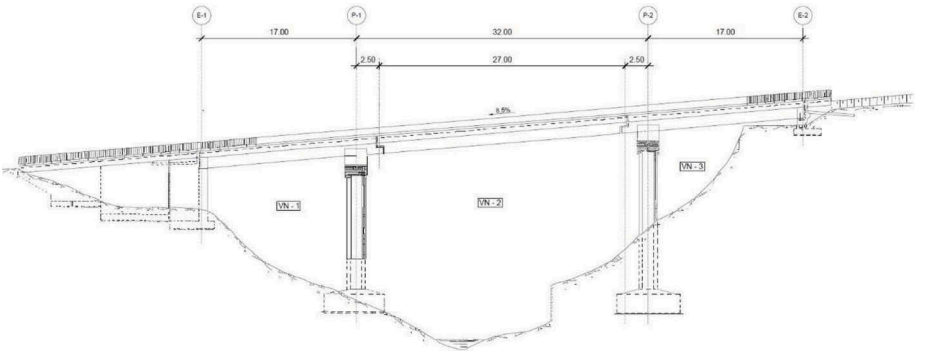


Figure 2. Elevation view of the bridge with the length of its spans. Image courtesy of the Provincial Council of Bizkaia.

For in-vehicle measurements, we chose to use "Steval-stwinkt1b" development kit from ST Microelectronics, which includes a IIS3DWB ultra-wide bandwidth (up to 6 kHz), low-noise, 3-axis digital MEMS accelerometer. ARM Cortex-M4 based STM32 microcontrollers allow us to train and run embedded extrapolation and outliers algorithms for low power microcontrollers (Later in the project, we will test other algorithms running on a cloud system, which will enable the processing of large amounts of data coming from other types of devices, such as smartphones or sensors without advanced local processing capabilities). In any case, low-cost and low-power edge computing, devices are considered an advance towards a low latency distributed processing with lower remote communication data rate requirements.

In this first phase of development, we are working with promising results on an anomaly detection system on the same signals recorded by the on-board accelerometer. To perform the first analyses, 6 measurements have been carried out with IIS3DWB vibrometer from ST Microelectronics at a 26KHz high sampling rate (so that a high number of analysis points are ensured even if the recordings are of short duration) with the vehicle crossing the bridge in the downward

sense and 6 measurements with the vehicle crossing the bridge in the upward sense (all of them with controlled speed between 70-75Km/h).Then, after duly cutting the signals between the acceleration peaks generated by the vehicle hitting the expansion joint at the entrance and exit of the bridge, a Machine Learning algorithm (Nanoedge Studio software is used to train an Edge Computing algorithm for STM32 microcontroller) is trained on the time series (with 4 signals in the downward sense and an anomalous record, just to define a "normal" class) obtaining that:

1. When comparing (asking the trained algorithm) with another record in the downward sense (of the two reserved for testing) it turns out that it is practically equal to the "normal" one (99% match).
2. When comparing (asking the trained algorithm as in the previous case) with a record in the upward sense, it turns out to be 90% similar (going down the car goes slightly faster, with the entrance and exit strokes stronger due to defects in that area of the expansion joint, which is to be replaced in 2024). This is expected to improve, or simply become more uniform, by training with more signals and/or without distinguishing between going up and down.

3 & 4. When asking for two anomalous records, it detects that both are 100% anomalous.

No bridge damage has been synthetically recreated in this early phase of FUTURAL, so in this first test the anomalous records are a passage of the car over another bridge and the passage of the vehicle over the road (without a bridge). In a more advanced stage of the developments, the sensitivity to damage will be tested after affecting the signals by a damage ratio obtained from computational models.

As example, Figure 3 includes some results with 99% of coincidence when asking the algorithm, trained with signals in the downward direction of car traffic, for another signal (not used in the training) in the same direction (all at about 72-75Km/h car speed). Similar results when asking the algorithm trained with signals in the downward direction of car traffic for a signal in the opposite direction (at about 70 km/h car speed; asking for an anomalous record (car driving on the road without a bridge); and asking for an anomalous record (car crossing another bridge). This are preliminary tests (feasible damage scenario will be generated at a later stage of development).

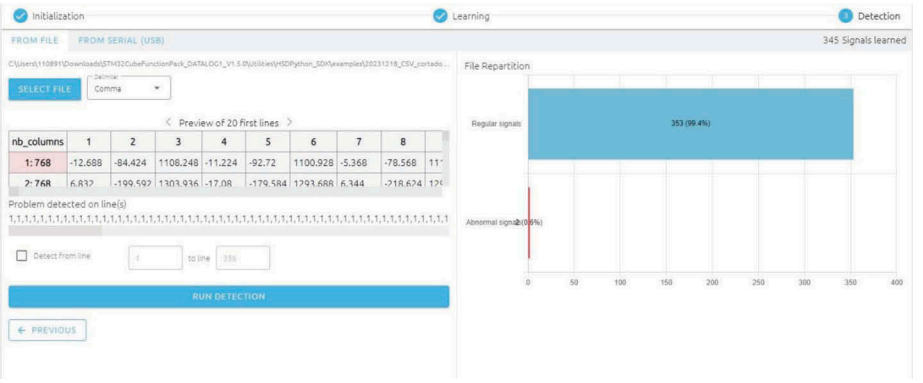


Figure 3. Image of the result for point 1 above.

It is important to note that not all processing is currently done on-chip. For this, it needs to be modified with an accelerometer to allow for less sampling and regulation of consumption, which will be studied further as knowledge of the pilot case improves.

Further work leading to a Smart Solution for Resilience to Shocks in FUTURAL, which will not be completed until the end of 2025, in addition to the study of the sensitivity of this application to a reasonable damage scenario, will comprise the development of other algorithms for off-chip processing, which would be usable for other types of devices without the capability to incorporate complex algorithms at the edge, such as self-developed Internet of

Things (IoT) sensors or smartphones, among others. For this, an alternative to be studied could be the future implementation of a deep autoencoder model for damage assessment of road bridges using vehicle responses as discussed in Gkoumas et al. 2023, along the lines of the work by Sarwar et al. 2021, cited above.

As concluded by other works, already referred to, another key step in the process will be to collect a good database of car crossings. This data can also be enriched with in-situ sensor measurements (permanent or temporary) on the bridge, with one of the focal points of the FUTURAL Smart Solution for Resilience to Shocks being to rely on multi-sensor information, combining both accelerations measured by onboard sensors with different bridge and weather event measurements to drive a cost-effective and connected solution for structural assessment before, during and after significant natural events.

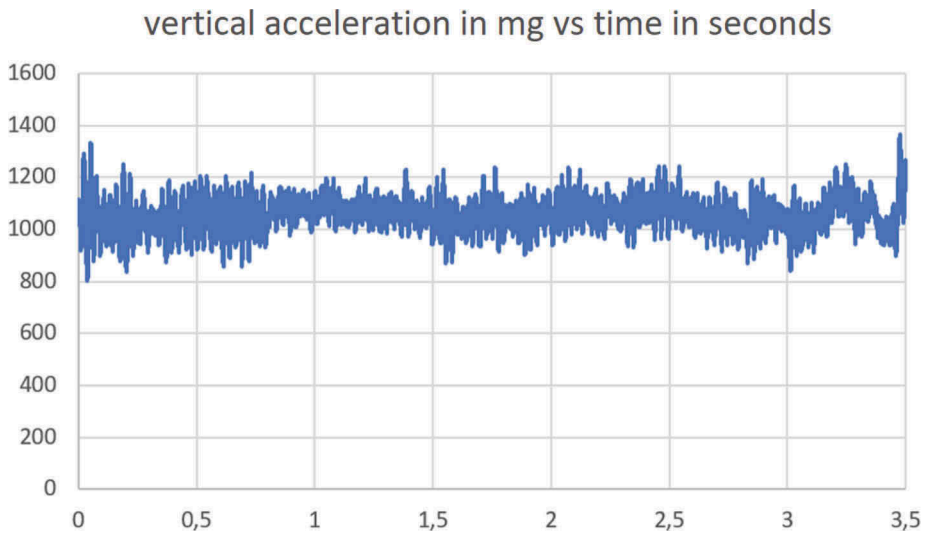


Figure 4. Image of a sample acceleration record from the tests described above.

Last but not least, it will be necessary to automate the cutting of the signal, leaving only the part corresponding to the bridge for local analysis (preprocessing) or server (postprocessing), for which the most desirable option would be the incorporation of a GPS to the onboard sensor, whatever it may be. Likewise, it is necessary to enable data communication from the sensor to the Cloud, being the GPS metadata also crucial to locate each bridge measurement in the transport network (here a GIS-based platform could be of support for a contextualization of the data and results).

6 CONCLUSIONS

Current challenges in this field are:

- Short duration of signals
- Interference from the pavement-induced vibration
- Accounting for Environmental and Operational Influences
- Quantification of Damage
- Experimental Verification of Drive-by Concepts

Enablers of iSHM are:

- vehicle communication
- on-board sensing and computing

– the management of big data, the integration with existing infrastructures monitoring (providing additional reference signals for better indirect assessment)
– the implementation of advanced algorithms and machine learning data processing

Moreover, standardization of both hardware, communication protocols and data, just like in the other environments adopting new digital technologies (e.g. smart cities), can ensure the iSHM future development with effective integration and interoperability of components and processes from different developers. However, acceleration measurements are the standard, and the processing can be derived to a device-independent Cloud system, this the device only must ensure sufficient quality of the measurement and its communication. Nevertheless, the inclusion of devices with complex processing capabilities, such as the ST development kit tested in this initial phase of FUTURAL, are considered a great advantage (reducing the processing and storage requirements for a crowdsensing platform).

In the future, local monitoring systems will possibly be integrated into smart cities digital platforms. This would allow the interaction with smart infrastructures that collect and process physical measurements and data, and then transfer relevant information to centralized systems, contributing to the functioning of urban system as a whole.

When talking about digital twins (DT) of the entire critical infrastructure or even the entire city, the consequences regarding resources for data elaboration, maintenance or storage, could in the end, affect the sustainability of the system. Also, the cost in terms of CO_2 emissions for maintaining a DT for many years at the level of system of systems. This cost maybe needs to be measured with the advantages the digital transformation is bringing. The only answer at this moment is to promote different scales for different needs (i) regarding local and global, these could be relevant at different scales, local at the bridge scale, global at network scale; (ii) regarding the amount of data collected nowadays, it is huge, and we should reflect on what data are actually needed before collecting them; (iii) the use of DT is often downscaled to the integration of a FEM and/or BIM model: considering DTs as a tool for optimizing future management rather than a tool used to perform damage detection.

ACKNOWLEDGEMENTS

Authors would like to acknowledge the Horizon Europe (HE) program within FUTURAL project (GA 101083958).

REFERENCES

Calderon Hurtado, A., Makki Alamdari, M., Atroshchenko, E., Chang, K.C., Kim, C.W. (2024). A data-driven methodology for bridge indirect health monitoring using unsupervised computer vision, Mechanical Systems and Signal Processing, Volume 210, 2024, 111109, ISSN 0888-3270.

Daubechies, I., Lu, J., Wu, H.T. (2011). Synchrosqueezed Wavelet Transforms: an Empirical Mode Decomposition like Tool, Applied and Computational Harmonic Analysis, 30(2), 243–261. https://doi.org/10.1016/j.acha.2010.08.002.

Fan, Z., Tang, X., Chen, Y. et al. (2024). Review of anomaly detection in large span bridges: available methods, recent advancements and future trends. ABEN 5, 2. https://doi.org/10.1186/s43251-024-00113-9.

Gkoumas, K., Galassi, M., Allaix, D. et al. (2023). Indirect structural health monitoring (iSHM) of transport infrastructure in the digital age – MITICA (Monitoring Transport Infrastructures with Connected and Automated vehicles) workshop report, Publications Office of the European Union, 2023, https://data.europa.eu/doi/10.2760/364830.

Keenahan, J., Ren, Y., and OBrien, E.J. (2020). Determination of Road Profile Using Multiple Passing Vehicle Measurements, Structure and Infrastructure Engineering, 16(9), 1262–1275. doi: 10.1080/15732479.2019.1703757.

Sarwar, M.Z., Cantero, D. (2021). Deep autoencoder architecture for bridge damage assessment using responses from several vehicles, Engineering Structures, Volume 246. https://doi.org/10.1016/j.engstruct.2021.113064.

Singh, P., Sadhu, A. (2023). Contact point response-based indirect bridge health monitoring using robust empirical mode decompostion, Journal of Sound and Vibration, Volume 567.

Bridge Maintenance, Safety, Management, Digitalization and Sustainability – Jensen, Frangopol & Schmidt (eds)
© 2024 The Author(s), ISBN 978-1-032-77040-6
Open Access: www.taylorfrancis.com, CC BY-NC-ND 4.0 license

Fleet monitoring using a Bayesian approach to detect bridge bearing damage

E.J. OBrien
School of Civil Engineering, University College Dublin, Dublin, Ireland

Y. Ren
Research Institute of Highway, Ministry of Transport, China

T.T.X. Tran & E. Ozer
School of Civil Engineering, University College Dublin, Dublin, Ireland

V. Pakrashi
School of Mechanical and Materials Engineering, University College Dublin, Dublin, Ireland

ABSTRACT: This paper proposes the use of a Bayesian approach to detect bridge bearing damage using simulated acceleration measurements collected from a fleet of notional instrumented vehicles. On-bridge vehicle accelerations are used to update bridge and vehicle properties. Four different bridge damage states are considered with different bearing damage conditions. The results show that bridge properties, i.e., second moment of area and bearing stiffnesses, can be inferred accurately from the acceleration measurements using a Bayesian updating approach. The fleet monitoring concept with the Bayesian approach is computationally efficient when a large quantity of measurement is involved.

1 INTRODUCTION

An increasing number of road bridges, particularly in Europe, are aging and deteriorating which has resulted in a number of recent failures, e.g., Malahide Estuary bridge collapse in 2009; Genoa bridge collapse in 2019. The safety of these pieces of critical infrastructure is important to prevent future fatal collapses or operational interruptions. Regular bridge condition monitoring, ensuring timely maintenance or repair, is necessary to achieve this goal. Recent practice heavily relies on visual inspection, which tends to be infrequent, expensive, disruptive to traffic and potentially unsafe for those involved. Electronic monitoring using sensors installed on bridges can be costly and time-consuming. This method is often applied on longer bridges. However, for large numbers of medium and short-span bridges, it becomes infeasible due to the high cost of set-up, operation and maintenance. An alternative solution is 'drive-by' or 'indirect' monitoring, which uses sensors installed in passing vehicles. This is potentially much more cost effective and becomes accurate when data from a large fleet of passing vehicles is combined. So called 'fleet' monitoring has the potential to generate the paradigm shift from visual to electronic monitoring of bridges, enhancing the capability for early damage detection and effectively extending infrastructure life.

'Drive-by' monitoring has been generating increasing interest in recent years (Malekjafarian et al. 2022). The concept was first proposed by Yang et al. 2004, 2005 and validated by passing an instrumented vehicle over a real bridge (Lin et al. 2005). It is expected to be time efficient, scalable, and hence to greatly reduce cost as sensors are mounted on in-service vehicles passing over bridges on a daily basis. It has the potential to monitor a large stock of bridges as

DOI: 10.1201/9781003483755-195

vehicles pass through the network. Dynamic data collected from instrumented vehicles can provide information on bridge condition via vehicle/bridge dynamic interaction mechanisms. However, drive-by monitoring also involves a number of significant challenges (Malekjafarian et al. 2022): (1) extracting bridge information from vehicle vibration is difficult as the signal is dominated by the influence of road roughness, (2) high vehicle speed on short-span bridges results in very small segments of data (1 or 2 seconds), (3) light vehicles induce insufficient bridge excitation, and (4) environmental effects and variation in vehicle configuration significantly influence the measurements. These challenges can be overcome if a sufficiently large quantity of data is collected from a fleet of in-service vehicles passing over the target bridge.

'Drive-by' damage detection relies on the extraction of bridge damage-sensitive features from measurements containing information on the vehicle and the road profile, as well as the bridge properties. The bridge features can be dynamic properties, such as natural frequency, mode shape or damping, or other pseudo-static features, such as deflection under load. Key frequencies in the data include bridge and vehicle natural frequencies, moving vehicle pseudo-frequencies, and road profile frequencies, as first identified by Yang et al. 2004. The method has now been validated by Yang and others (McGetrick et al. 2010, Kim et al. 2011), including some limited field experiments (Siringoringo et al., 2012). Siringoringo et al., 2012 identifies the first natural frequency, at a driving velocity below 30 km/h, with a maximum estimation error of 11.4% – insufficient to detect low levels of damage. Changes in estimated mode shapes can also indicate bridge damage but it works only with low-speed data (Yang et al. 2014, Malekjafarian et al. 2014) and has not been validated in the field.

Apart from modal-based detection, OBrien et al. 2014 measure dynamic axle force using the Moving Force Identification method and use the inferred force signals to identify global bridge stiffness loss. The results show good potential to use this low-cost method to detect global damage in short to medium span bridges. OBrien et al. 2015 simulate the time-shifted difference in inferred apparent profile from Traffic Speed Deflectometer data and use Cross Entropy optimization to detect damage effectively. Keenahan et al. 2020 introduce the fleet monitoring concept to calculate road profile from vehicle acceleration without prior knowledge of vehicle properties. OBrien et al. 2023 detect bridge bearing damage using measurements from a fleet of vehicles through a moving reference influence function. The above studies show that increasing data collected from many vehicles can significantly improve the accuracy of drive-by and fleet bridge condition monitoring.

An alternative approach to infer vehicle/bridge properties is Bayesian updating, using data collected from sensors mounted on passing vehicles. While the accuracy of drive-by monitoring is sensitive to vehicle speed, pavement roughness, vehicle weight and environment-induced bridge property variation, the Bayesian approach is robust. It results in probabilistic estimations which are updated as data is added continuously. For this reason, fleet monitoring following the Bayesian approach is effective and computationally efficient relative to deterministic methods such as optimisation. Wilson et al. 2006 predict patterns of statistical spatial repeatability using a fleet of truck models inferred from dynamic tyre force measurements. That study shows that the fitted models inferred from the Bayesian framework agree well with the 'true' distributions. Kumar et al. 2021 use Bayesian inference to estimate tyre model parameters and then uses these parameters as inputs to reconstruct vehicle bridge interaction forces that can indicate bridge damage.

The latest Bayesian approaches expressed above focus on calibration of multiple parameters of a fleet using tyre force/pressure measurements. Changes on Vehicle-Bridge-Interaction forces can indicate changes in bridge condition. The Bayesian updating can be done both as vehicle and bridge properties simultaneously using inertial on-board measurements, eventually providing bridge condition information. This paper explores the fleet monitoring concept using the Bayesian approach for bridge damage detection. Vehicle sprung mass and bridge properties such as spring stiffness of the bearings, are updated probabilistically using data simulated by a fleet of vehicle models. The method can quantify bridge bearing damage at different levels.

2 NUMERICAL MODELING

2.1 *Vehicle-bridge interaction model*

A coupled vehicle and bridge model is used in this paper. A fleet of quarter car models is simulated passing over a 20 m simply supported finite element (FE) beam, with a smooth profile, as shown in Figure 1. This vehicle–bridge interaction model has been used by many other authors (Elhattab et al. 2016, Malekjafarian et al. 2019). The bridge has a modulus of elasticity of $E = 35\times10^9$ N/m^2, density, ρ = 37,500 kg/m^3, second moment of area, I_{bridge}=1.259 m^4 and a bridge damping ratio of 3%. Rotational springs are added at each beam support to represent the bridge bearing stiffnesses, $K_{rot,1}$ and $K_{rot,2}$ (Kliewer et al. 2017, OBrien et al. 2023). A fleet of vehicles is generated based on the mean and standard deviation of vehicle properties presented in Table 1.

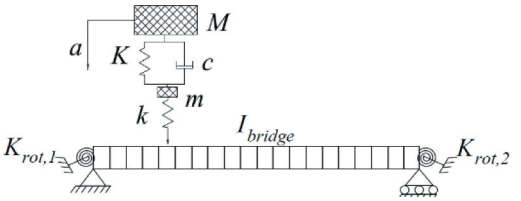


Figure 1. Quarter-car and bridge model.

Table 1. Vehicle properties.

Parameter	Symbol	Unit	Mean	St. dev.
Sprung mass	M	kg	4,450	445
Unsprung mass	m	kg	420	42
Suspension stiffness	K	N/m	500,000	50,000
Tyre stiffness	k	N/m	1,950,000	195,000
Suspension damping	c	Ns/m	20,000	2000

Bearing damage is deemed to be in the form of a loss of bearing spring stiffness. The values of K_{rot} ranges from zero (free to rotate) to infinity (fully fixed). To test the bearing damage level of the bridge model, one vehicle is simulated crossing this bridge with different values of $K_{rot,1}$ and $K_{rot,2}$. Then, the area under the deflection curve of the bridge is used to verify changes

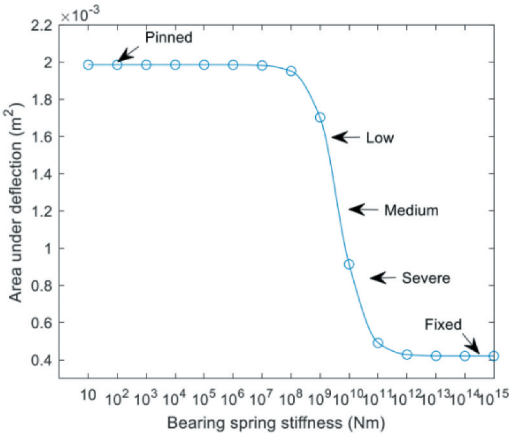


Figure 2. Area under the deflection curve with different values for K_{rot}.

in the bridge condition. The parameters, $K_{rot,1}$ and $K_{rot,2}$ start from 0 Nm/rad and increase to 10^{15} Nm/rad, where the supports behave as effectively fully fixed. The area under the deflection curve with different stiffness values are shown in Figure 2. Here, $K_{rot,1}$ is equal to $K_{rot,2}$ and represented by K_{rot}. It shows that there is no obvious change in the area under the deflection curve if K_{rot} is less than 10^7 Nm/rad. After 10^7 Nm/rad, the area starts to reduce. For higher values (over 10^{11} Nm/rad), the areas do not show significant further change.

3 DETECTION OF BRIDGE BEARING DAMAGE USING BAYESIAN UPDATING

3.1 *Bearing damage*

A Bayesian updating method is introduced in this section to detect bridge bearing damage. Four different bearing damage states are considered and corresponding vehicle accelerations are generated: $K_{rot,1} = K_{rot,2} = \{0, \ 10^9, \ 10^{10}, \ 10^{12}\}$ Nm/rad. All the vehicle properties can be found using data from the approach (off-bridge) section except vehicle sprung mass (Keenahan et al. 2020). The vehicle sprung mass, bridge 2nd moment of area, I_{bridge} and bridge bearing stiffnesses $K_{rot,\ 1}$ and $K_{rot,\ 2}$, are inferred from these 'measured' accelerations using the Bayesian approach. Here, it is assumed that all 20 elements of the bridge have the same 2nd moment of area, equal to I_{bridge}.

3.2 *Data likelihood*

A simple independent Gaussian error model is used to calculate the deviations of the observed bridge deflections from the true values. The Gaussian error model is formulated in terms of the probability of a specific deflection (Wilson et al. 2006, Obrien et al. 2023):

$$\begin{aligned} p(\boldsymbol{w_n}|M_n, I_{bridge}, K_{rot,1}\ , K_{rot,2}\ ) &= \prod_{i=1}^{P} p\big(w_n(y_i; M_n)|W_n(y_i; M_n, I_{bridge}, K_{rot,1}\ , K_{rot,2}\ )\big) \\ &= \prod_{i=1}^{P} \frac{1}{\sqrt{2\pi\sigma_2^2}} \exp\left(-\frac{1}{2\sigma_2^2}\big(w_n(y_i; M_n) - W_n(y_i; M_n, I_{bridge}, K_{rot,1}\ , K_{rot,2})\big)^2\right) \\ &= \big(2\pi\sigma_2^2\big)^{-0.5P} \exp\left(-\frac{1}{2\sigma_2^2}\sum_{i=1}^{P}\big(w_n(y_i; M_n) - W_n\big(y_i; M_n, I_{bridge}, K_{rot,1}\ , K_{rot,2}\big)\big)^2\right) \end{aligned} \tag{1}$$

where $W_n(y_i\ ;\ M_n,\ I_{bridge},\ K_{rot,1},\ K_{rot,2}\ )$ is the expected bridge deflection observed from the n^{th} vehicle with M_n crossing the bridge with true properties, I_{bridge}, $K_{rot,1}$, $K_{rot,2}$. The term, $w_n(y_i\ ;\ M_n)$ is the observed bridge deflection signal which is calculated from the 'measured' accelerations using the Inverse Newmark-beta method. The Inverse Newmark-beta method to calculate the apparent profile directly from 'measured' accelerations was proposed by Keenahan et al. 2020. It is assumed that each vehicle's observations are independent:

$$\begin{aligned} p\big(\boldsymbol{w}|\boldsymbol{M_{1:N}}, I_{bridge}, K_{rot,1}\ , K_{rot,2}\ \big) &= \prod_{n=1}^{N} p\big(\boldsymbol{w_n}|M_n, I_{bridge}, K_{rot,1}\ , K_{rot,2}\ \big) \\ &= \big(2\pi\sigma_2^2\big)^{-0.5NP} \exp\Big(-\frac{1}{2\sigma_2^2}\sum_{n=1}^{N}\sum_{i=1}^{P}\big(w_n(y_i; M_n) - W_n\big(y_i; M_n, I_{bridge}, K_{rot,1}\ , K_{rot,2}\big)\big)^2 \end{aligned} \tag{2}$$

3.3 *Priors*

A prior distribution, $p(M_n|\varphi_M)$, is introduced for each vehicle mass. It is the distribution of vehicle masses across the population of vehicles. For each vehicle class, the mass distribution is assumed to be the same – histograms of vehicle weights have been shown to be repeatable at a given site. This distribution is taken to be normal and φ_M is its mean and variance. It is

assumed that these priors are independent for each vehicle, so the prior for all masses $\boldsymbol{M}_{1:N} = (M_1, \ldots M_N)$ is:

$$p(\boldsymbol{M_{1:N}}|\varphi_M) = \prod_{n=1}^{N} p((M_n|\varphi_M)). \tag{3}$$

Bridge properties, such as I_{bridge}, $K_{rot,1}$ and $K_{rot,2}$ are constant values across an interval. Their distribution is assumed to be uniform over an interval $(a,\ b)$, with density:

$$p(x) = \frac{1}{b-a}, a \le x \le b. \tag{4}$$

3.4 *Posterior distribution*

A posterior distribution for the bridge section is introduced. By Bayes' Law, this is given in terms of the likelihood and prior terms by:

$$\begin{aligned} &p\left(\boldsymbol{M_{1:N}}, I_{bridge}, K_{rot,1}\ , K_{rot,2}|\boldsymbol{w}\right) \\ &\propto p\left(\boldsymbol{w}|\boldsymbol{M_{1:N}}, I_{bridge}, K_{rot,1}\ , K_{rot,2}\ \right)\left(\prod_{i=1}^{N} p((M_n|\varphi_M))\right)p\left(I_{bridge}\right)p\left(K_{rot,1}\right)p\left(K_{rot,2}\right) \end{aligned} \tag{5}$$

3.5 *MCMC algorithm and calculation results*

The question now is the issue of computing Equation (5). The proposal here is to do it by Monte Carlo sampling, specifically Markov Chain Monte Carlo (MCMC) which is suitable for complex and high dimensional distributions. A fleet with 30 different vehicles is simulated crossing the bridge and sprung mass accelerations of these vehicles are generated as 'true' accelerations. Additive White Gaussian Noise of 2% is added to the measurements to allow for inaccuracy. Then these accelerations are used as input into the MCMC algorithm to back-calculate the bridge and vehicle properties. The MCMC process can determine the bridge second moment of area, I_{bridge}, the bearing damage levels $K_{rot,1}$, $K_{rot,2}$ and vehicle sprung mass value, M at the same time.

The calculated K_{rot} and I_{bridge} of the four damage states considered, are shown in Table 2. For the second and third state, both the bearing spring stiffness values, K_{rot} and bridge property, I_{bridge} can be calculated with good accuracy. However, for the first and fourth damage state, only the bridge property, I_{bridge} can be calculated. The calculated bearing spring stiffness values are different to the true ones. As shown in Figure 2, if the value of K_{rot} is less than 10^8, the bearing damage condition is low, and it is very close to the healthy state. It is also worth noting that the areas under the deflection curves are almost the same. Similarly, for higher values of K_{rot}, the bearings are approaching being fully fixed and the areas under the deflection curves will not change as the value of K_{rot} increases. The calculated sprung masses values for the second damage state are shown in Figure 3 and the calculated sprung masses are very close to the true masses.

Table 2. Calculated bridge properties by MCMC.

Damage states		1	2	3	4
$K_{rot,1}$ (Nm/rad)	True	0	10^9	10^{10}	10^{12}
	Calculated	4.3×10^7	1.28×10^9	1.06×10^{10}	6.0×10^{12}
$K_{rot,2}$ (Nm/rad)	True	0	10^9	10^{10}	10^{12}
	Calculated	1.0×10^7	1.01×10^9	1.00×10^{10}	1.8×10^{12}
I_{bridge}(m^4)	True	1.26	1.26	1.26	1.26
	Calculated	1.22	1.22	1.24	1.23

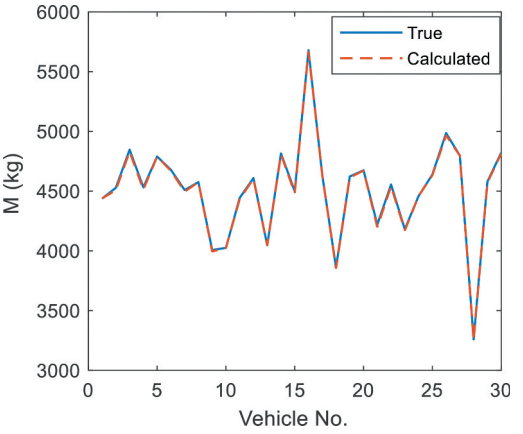


Figure 3. True and calculated sprung masses of the 30 vehicles, from MCMC for damage state 2.

4 CONCLUSION AND FUTURE WORK

This paper uses a Bayesian approach to detect bridge damage using a fleet of instrumented vehicles. Here, the on-bridge vehicle accelerations collected from a fleet of simulated vehicles are used to determine the bridge properties, vehicle sprung masses and the spring stiffnesses of the bearings. Four different bridge damage states are considered with different bearing damage conditions. The results show that the bridge properties and spring stiffnesses can be calculated with good accuracy using this Bayesian approach. The calculated bearing spring stiffnesses can be used to determine the bearing damage condition.

It is acknowledged that the road surface profile on the bridge, assumed to be smooth in this paper, may have a significant effect. It would be desirable to demonstrate the ability to detect lower levels of damage. For future work, bridges with non-smooth profiles will be investigated. The results in this research are based on simple numerical models and there will be challenges for real vehicles in the field. Accuracy will be improved by considering larger fleets of vehicles.

ACKNOWLEDGEMENT

Dr. Thanh T.X. Tran acknowledges funding from the Irish Research Council under Project ID: GOIPD/2023/1040. Vikram Pakrashi acknowledges Science Foundation Ireland TRaIN project 22-NCF-FD-10995 and NexSys 21/SPP/3756.

REFERENCES

Elhattab, A., Uddin, N. and OBrien, E., 2016. Drive-by bridge damage monitoring using Bridge Displacement Profile Difference. *Journal of Civil Structural Health Monitoring*, *6*, pp.839–850.

Keenahan, J., Ren, Y. and OBrien, E.J., 2020. Determination of road profile using multiple pass using vehicle measurements. *Structure and Infrastructure Engineering*, *16*(9), pp.1262–1275.

Kim, C.W., Isemoto, R., Toshinami, T., Kawatani, M., McGetrick, P. and OBrien, E.J., 2011. Experimental investigation of drive-by bridge inspection. In *5th International Conference on Structural Health Monitoring of Intelligent Infrastructure (SHMII-5)*, *Cancun, Mexico*, 11-15 December, 2011. Instituto de Ingeniería, UNAM.

Kliewer, K. and Glisic, B., 2017. Normalized curvature ratio for damage detection in beam-like structures. *Frontiers in Built Environment*, *3*, p.50.

Kumar, G.S., Krishnanunni, C.G. and Rao, B.N., 2021. Indirect damage identification in bridges based on dynamic tyre pressure monitoring. *International Journal of Structural Stability and Dynamics*, *21* (04), p.2150056.

Lin, C.W. and Yang, Y.B., 2005. Use of a passing vehicle to scan the fundamental bridge frequencies: An experimental verification. *Engineering Structures*, *27*(13), pp.1865–1878.

Malekjafarian, A. and OBrien, E.J., 2014. Identification of bridge mode shapes using short time frequency domain decomposition of the responses measured in a passing vehicle. *Engineering Structures*, *81*, pp.386–397.

Malekjafarian, A., Corbally, R. and Gong, W., 2022, October. A review of mobile sensing of bridges using moving vehicles: Progress to date, challenges and future trends. In *Structures* (Vol. 44, pp. 1466–1489). Elsevier.

Malekjafarian, A., Golpayegani, F., Moloney, C. and Clarke, S., 2019. A machine learning approach to bridge-damage detection using responses measured on a passing vehicle. *Sensors*, *19*(18), p.4035.

McGetrick, P., Kim, C.W. and OBrien, E.J., 2010, November. Experimental investigation of the detection of bridge dynamic parameters using a moving vehicle. In *Proceedings of the 23rd KKCNN Symposium on Civil Engineering*.

OBrien, E.J. and Keenahan, J., 2015. Drive-by damage detection in bridges using the apparent profile. *Structural Control and Health Monitoring*, *22*(5), pp.813–825.

OBrien, E.J., McCrum, D.P. and Wang, S., 2023. Drive-By Fleet Monitoring to Detect Bearing Damage in Bridges Using a Moving Reference Influence Function. *International Journal of Structural Stability and Dynamics*, p.2340003.

OBrien, E.J., McGetrick, P.J. and González, A., 2014. A drive-by inspection system via vehicle moving force identification. *Smart Structures and Systems*, *13*(5), pp.821–848.

OBrien, E.J., Wilson, S., Keenahan, J. and Ren, Y., 2023. A Bayesian Approach to the Estimation of Road Profile and Bridge Damage from a Fleet Passing Vehicle Measurements. International Journal of Structural Stability and Dynamics.

Siringoringo, D.M. and Fujino, Y., 2012. Estimating bridge fundamental frequency from vibration response of instrumented passing vehicle: analytical and experimental study. *Advances in Structural Engineering*, *15*(3), pp.417–433.

Wilson, S.P., Harris, N.K. and OBrien, E.J., 2006. The use of Bayesian statistics to predict patterns of spatial repeatability. *Transportation Research Part C: Emerging Technologies*, 14(5), pp.303–315.

Yang, Y.B. and Lin, C.W., 2005. Vehicle–bridge interaction dynamics and potential applications. *Journal of sound and vibration*, *284*(1-2), pp.205–226.

Yang, Y.B., Li, Y.C. and Chang, K.C., 2014. Constructing the mode shapes of a bridge from a passing vehicle: a theoretical study. *Smart Structures and Systems*, *13*(5), pp.797–819.

Yang, Y.B., Lin, C.W. and Yau, J.D., 2004. Extracting bridge frequencies from the dynamic response of a passing vehicle. *Journal of Sound and Vibration*, *272*(3-5), pp.471–493.

Bridge Maintenance, Safety, Management, Digitalization and Sustainability – Jensen, Frangopol & Schmidt (eds)
© 2024 The Author(s), ISBN 978-1-032-77040-6
Open Access: www.taylorfrancis.com, CC BY-NC-ND 4.0 license

Indirect bridge condition monitoring using feature selection strategy

R. Ghiasi, R. Corbally & A. Malekjafarian
Structural Dynamics and Assessment Laboratory, School of Civil Engineering, University College Dublin, Dublin, Ireland

ABSTRACT: Bridge damage detection (BDD) techniques have been widely explored over the last years driven by the advances of computational intelligence technologies. Drive-by monitoring approaches, using sensors in a vehicle, provide a promising framework for BDD. In this context, the aim of this paper is to present a novel automated methodology for damage detection based on the extraction of features from the vibration responses measured on a passing vehicle using filter-type feature selection scheme. Feature extraction is performed in the time domain and then feature selection (FS) is applied to increase the relevance of the feature set by choosing the most important features based on their ability to discriminate between different classes of data. Finally, a cascade forward neural network (CFNN) is used to classify damage severity. The method was tested using a finite element (FE) model of concrete beam-and-slab bridge by considering vehicle bridge interaction (VBI). Results show that when the Pearson correlation coefficient (PCC) is used as a feature selection algorithm and an CFNN as a classifier, 94% accuracy can be achieved for identifying the level of cracking in bridge.

1 INTRODUCTION

Transportation networks require ongoing inspection and maintenance of their physical infrastructure assets to ensure that they remain functional. Bridges are critical components, and it is essential that they are inspected and maintained appropriately to ensure that vehicles can travel in a safe and efficient manner. As transport networks age and the infrastructure deteriorates over time, inspection of large bridge stocks and prioritization of maintenance budgets towards specific structures becomes more and more challenging. For this reason, there is a clear need for quick and efficient techniques for ongoing monitoring and inspection of bridges.

Drive-by bridge monitoring approaches utilize in-vehicle sensors to monitor bridge condition based on measurements taken as the vehicle traverses the bridge. The drive-by concept was initially proposed by Yang et al. (2004) where it was theoretically demonstrated that the fundamental frequency of a bridge can be extracted from the vibration of the traversing vehicle. Given that bridge frequency is sensitive to damage, this represented a method of monitoring changes in bridge condition over time, without the need to install sensors on the bridge, or the need for manual visual inspections. Since the concept was initially proposed, there have been numerous developments in the use of drive-by bridge inspection techniques. Different damage mechanisms can affect bridge vibrations in different ways so there have been various efforts to examine how drive-by techniques can be used to identify these changes, e.g. for scour (Fitzgerald et al., 2019), cracking in the deck (McGetrick & Kim, 2013, Malekjafarian et al., 2018) or changes in boundary conditions (Mei & Gül, 2019, Cerda, 2014) amongst others. Drive-by techniques have also been used for different applications, including calculation of bridge modes shapes (Corbally & Malekjafarian, 2022a), bridge damping (Keenahan et al., 2014), estimation of vehicle properties and investigation of pavement characteristics (McGetrick et al., 2017, McGetrick et al., 2013).

DOI: 10.1201/9781003483755-196

More recently there have been a number of developments where researchers have explored the use of Machine Learning approaches to account for environmental or operational factors which may influence the measured bridge properties during any given vehicle passage (Sarwar & Cantero, 2021, Li et al., 2023, Corbally & Malekjafarian, 2023). The adoption of machine learning techniques for drive-by bridge monitoring is becoming more prominent, as discussed by Malekjafarian et al. (2022). The advantage of utilizing machine learning approaches lies primarily in their ability to identify and learn trends in the measured signals which can be attributed to different bridge conditions, and also to external influences such as temperature or vehicle speed (Locke et al., 2020, Corbally & Malekjafarian, 2022b). This paper presents a new approach which adopts a cascade forward neural network (CFNN) to classify the severity of bridge damage based on measured vibrations from a vehicle passing over a bridge. Damage-sensitive features are automatically extracted from the measured vibrations, and those with the greatest importance are selected to differentiate between different classes of damage, before the CFNN is adopted to classify the damage severity. The methodology is demonstrated using a finite element (FE) model of concrete beam-and-slab bridge, where the ability of the algorithm to identify cracking is tested.

2 METHODOLOGY

The proposed framework comprises five stages, elaborated in detail in Figure 1. The framework starts with data collection and signal processing, and then sensitive features are extracted and selected in steps 3 and 4. Finally the damage state is predicted in step 5. The detail of each step is explained in the below paragraphs.

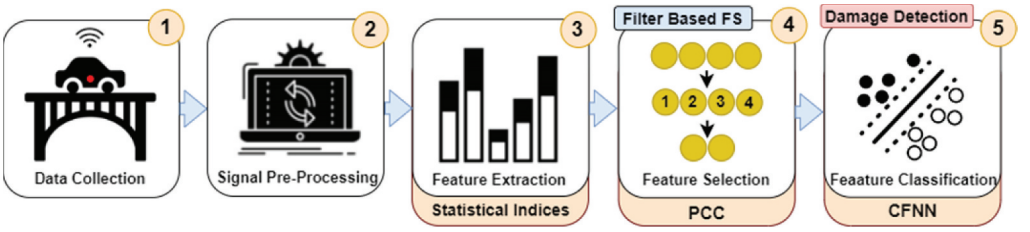


Figure 1. Proposed framework for indirect monitoring of bridge.

After collecting acceleration responses on the vehicle's axle and the body, in Step 2, the recorded sensor acceleration responses undergo a cleansing and filtering process. For this purpose, a band-pass filter (BPF) is used to reduce the effect of noise and environmental variables on the response (Corbally & Malekjafarian, 2022b). In this study, a 3rd order Butterworth BPF (5–25 Hz) is applied to all data channels prior to feature extraction step. The chosen band retains the frequencies of primary interest, removes drift/error, the influence of pavement and other unwanted noise (Corbally & Malekjafarian, 2022b).

In the third step (Features Extraction), to reduce the length of the data and extract meaningful information from the responses, statistical features of signals are extracted from the raw acceleration signal measured on the vehicle. These features (such as Root mean square, Variance, Mean, Shape factor, Crest factor, etc.) are computed in the time domain and provide a summary of the statistics of the signal over a time window with a specified number of sample points (Buckley et al., 2023).

When the feature set is extracted, a filter-based feature selection method called Pearson correlation coefficient (PCC) (Saidi et al., 2019) is used to reduce the dimensionality of the problem. The PCC quantifies the linear relationship between a feature and the target variable. Ranging from -1 to 1, a high absolute PCC indicates strong correlation, guiding the selection of informative features for enhanced model performance (Saidi et al., 2019). It's important to note that the target variable in this work represents the specific damage classes. This metric

offers a concise and interpretable means of optimizing feature subsets that are used as the input vector to the damage classification algorithm.

In the final step (Features Classification), the classification algorithm using a CFNN (Fathnejat et al., 2014) is trained based on 80% of the data. CFNN is a robust classification algorithm that leverages a series of interconnected layers to extract hierarchical representations from input data (Fathnejat et al., 2014). By systematically forwarding information through hidden layers to an output layer, the CFNN excels at discerning intricate patterns and relationships within features (Torkzadeh et al., 2016). In this paper, the output of CFNN is damaged states of the desired bridge.

The evaluation metric used to reflect the overall performance of the classification model is balanced accuracy classification score (Ritto et al., 2022), which is measures the average accuracy obtained from both the minority and majority classes.

3 NUMERICAL MODELING

The methodology is tested using a quarter-car vehicle model, passing over a finite element representation of bridge. The quarter car model, as shown in Figure 2, consists of two degrees of freedom, with two lumped masses, representing the vertical motion of the (i) vehicle body (M_v=8,900 kg) and (ii) the axle (including the wheel) (M_w=1,100 kg). The two masses are connected using a spring and dashpot representing the stiffness (k_v=2x10^6 N/m) and damping (c_v=40,000 Ns/m) properties of the vehicle suspension and the axle degree of freedom is connected to the bridge using a spring to represent the tire stiffness (k_T=3.5x10^6 N/m). While the quarter-car is a simplified representation of the actual behavior of a vehicle, it has been widely adopted to represent the two primary modes of vibration of a vehicle, i.e. 'bounce' of the vehicle body and axle 'hop'.

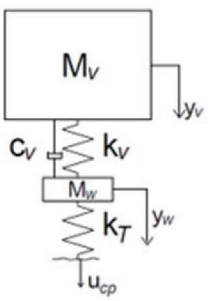


Figure 2. Quarter-car vehicle model.

A typical beam-and-slab bridge, as shown in Figure 3, was modelled with a 'Class A' pavement representing a smooth road surface in good condition. The FE model of the bridge consisted of 25 no. beam elements, with the second moment of area ($I_0 = 1.156$ m^4) and mass per unit length ($m = 17,384$ kg/m) of the cross section shown in Figure 3 assigned to each element along with a Young's modulus of $E_0 = 35$ GPa. Rayleigh damping of 2%. Damage to the bridge was modelled as cracking at a single location longitudinally along the bridge, following the method proposed by Sinha et al. (2002), whereby a localized reduction of stiffness is introduced at the crack location, and propagates away from the crack longitudinally across the affected zone.

A series of vehicle passages across the bridge were simulated, with the speeds were randomly generated for each passage by sampling from a normal distribution with a mean value of 20 m/s and a standard deviation of 1.7 m/s. 200 passages across the healthy bridge were simulated, and the acceleration response (without any artificial noise) on the vehicle's axle, and on the body of the vehicle were saved for each passage. Similarly, 100 passages were simulated across the bridge in each of three different damage cases, representing (i) 10%, (ii), 20% and (iii) 30% cracking at midspan.

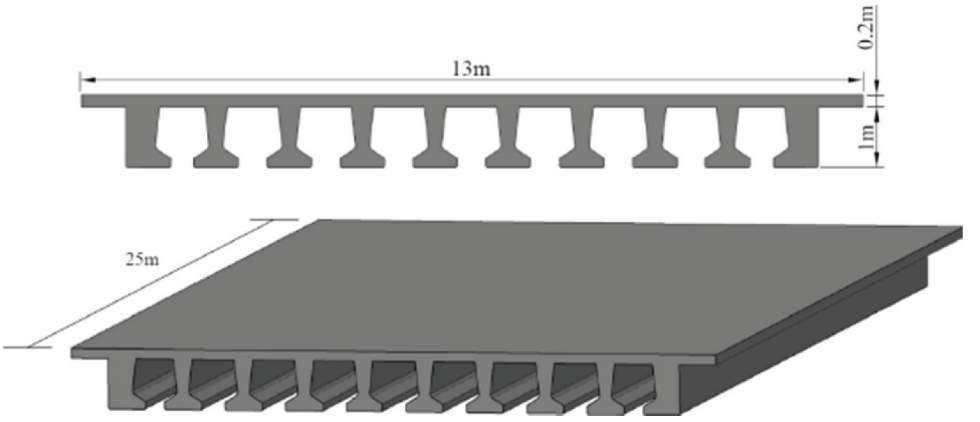


Figure 3. Cross section and 3D view of bridge deck.

4 RESULTS

4.1 *Feature extraction and features selection*

After acquisition of the acceleration response of the vehicle over the bridge and applying BPF, the third step of the proposed framework is to extract the damage-sensitive features from the raw data. According to the number of accelerometer sensors considered for the vehicle (3) and the number of features extracted from each response (10), the final features matrix has 30 columns. This matrix is input of the feature selection step.

Figure 4 shows the ranking of the top 10 features based on the PCC algorithm. In this diagram, the horizontal axis shows PCC values for different features. As can be seen in the figure, the response recorded by both sensors is necessary to achieve the desired accuracy, meanwhile, most of the selected features (7/10) are from the sensor that is installed on the body. This shows that the use of this sensor is necessary to detect damage in the bridge. In

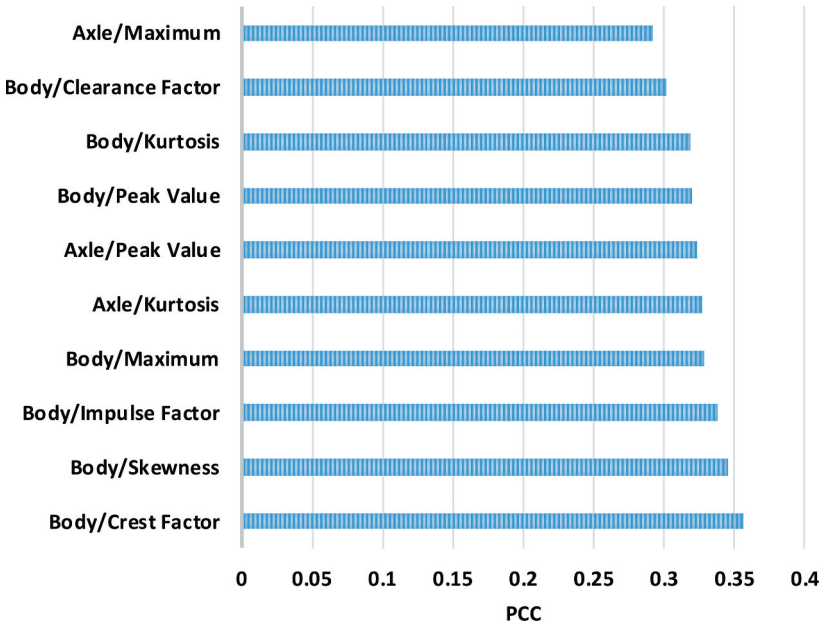


Figure 4. Feature subset selection using PCC.

order to check the selected features, the scatter plot of two pair of them are shown in Figure 5 and Figure 6 which are grouped by damage state of bridge.

It is apparent from Figure 5 and Figure 6 that the selected features in different damage classes have different distribution intervals, and they can be used as features which are sensitive to structural damage in the bridge. However, the sensor placed on the body of the car, exhibits the changes of different damage modes within a more specific range. One possible explanation for this is the filtering out of minor changes in acceleration response induced by pavement roughness through the use of a suspension system.

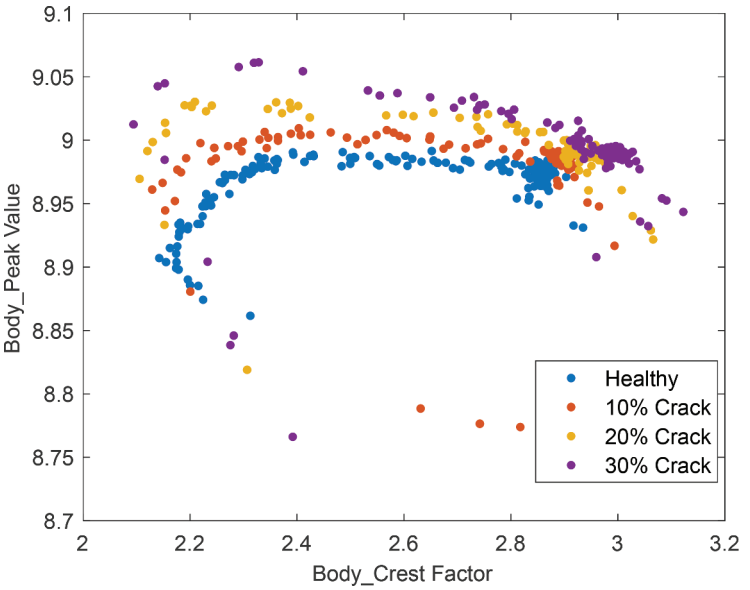


Figure 5. Scatter plot of crest factor and peak value of body sensor grouped by damage state.

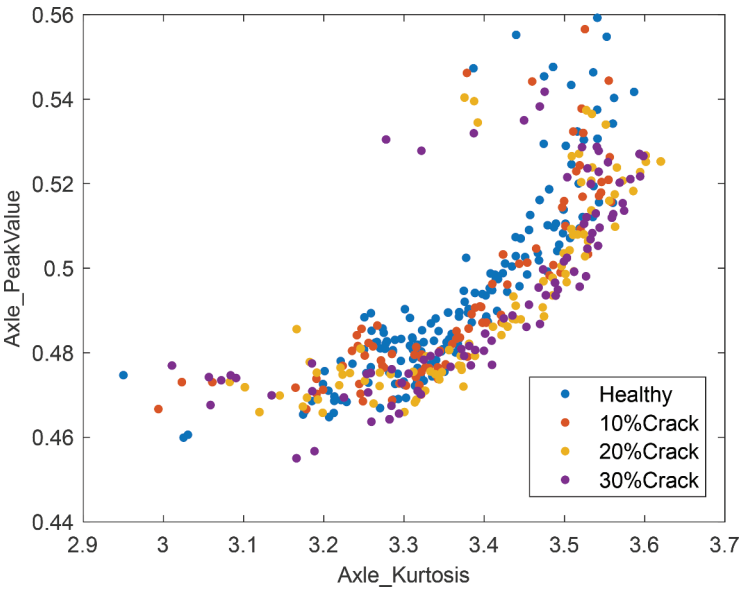


Figure 6. Scatter plot of kurtosis and peak value of axle sensor grouped by damage state.

4.2 *Feature classification*

In the last step, the top 10 features selected in the previous step are used as input to the classification algorithm. CFNN is trained on 80% of the dataset and tested on the remaining 20% of the data. In addition, 2 hidden layers, each with 10 neurons, are considered as inner layers of the network. The maximum epoch is set to 50, and Levenberg-Marquardt is chosen as the training function. The classification results are shown in Figure 7. The overall classification accuracy of the algorithm is 94% and the true positive rates (TPR) is above 92% in all classes. Furthermore, the false negative rates (FNR) in all classes are below 7.1% that shows reliability of the proposed framework. These results have been obtained by considering only 10 selected features and this indicates a 66% reduction in the dimension of the input data to the CFNN algorithm.

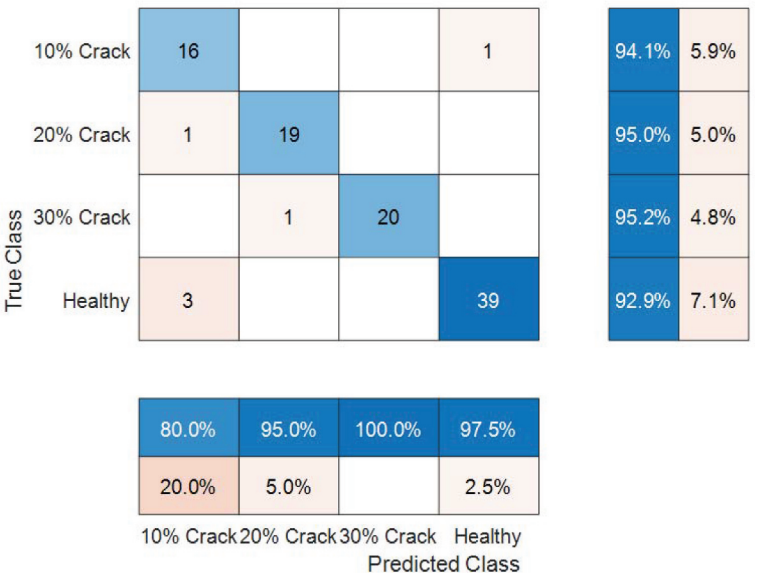


Figure 7. Confusion matrix for CFNN.

The performance progress of CFNN is displayed in Figure 8. This figure does not indicate any major problems with the training. The validation and test curves are very similar, and overfitting has not occurred.

According to the results shown, it can be concluded that the proposed data-driven framework has a high accuracy when detecting damage in a bridge using the responses collected by the moving vehicle. Drive-by monitoring scheme significantly reduces the number of sensors and the overall cost required for the SHM of bridges.

5 CONCLUSIONS

In this paper, a data-driven framework for structural health monitoring of bridges using drive-by monitoring was presented. After recording the acceleration response simulated from a numerical of vehicle-bridge interaction model using the sensors mounted on the moving vehicle, statistic indicators were extracted from the raw data and then sorted based on their ability to distinguish between different damage states.

The results showed that the sensor placed on the body of the vehicle has a clear sensitivity to bridge damage. In addition, by using a subset of features as input to the CFNN algorithm, 94% classification accuracy was achieved. Also, the PCC that was used as the feature selection method in this paper, has reduced the number of input data to the classification algorithm by 66%.

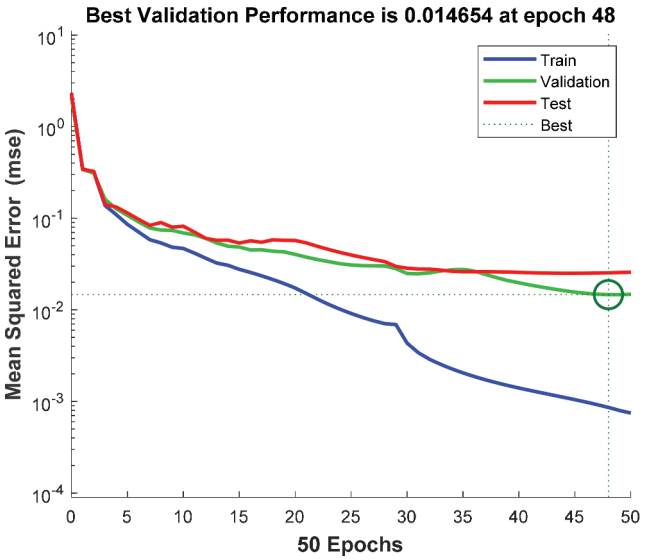


Figure 8. Performance progress for CFNN.

The results of the implementation of the proposed framework on the numerical model of a real concrete bridge indicate that the drive-by monitoring scheme can be implemented on real structures, although the effect of environmental variables on the accuracy of the algorithm should be investigated.

ACKNOWLEDGEMENT

This publication has emanated from research conducted with the financial support of Science Foundation Ireland under Grant number 20/FFP-P/8706. The authors also wish to express their gratitude for the financial support received from the Irish Research Council (IRC) GOIPD/2023/1588.

REFERENCES

Buckley, T., Ghosh, B. & Pakrashi, V. 2023. A feature extraction & selection benchmark for structural health monitoring. *Structural Health Monitoring*, 22(3): 2082–2127.

Cerda, F., Chen, S., Bielak, J., Garrett, J. H., Rizzo, P., & Kovacevic, J. 2014. Indirect structural health monitoring of a simplified laboratory-scale bridge model. *Smart Structures and Systems*, 13(5): 849–868.

Corbally, R. & Malekjafarian, A. 2022a. Bridge damage detection using operating deflection shape ratios obtained from a passing vehicle. *Journal of Sound and Vibration*: 117225.

Corbally, R. & Malekjafarian, A. 2022b. A data-driven approach for drive-by damage detection in bridges considering the influence of temperature change. *Engineering Structures*, 253.

Corbally, R. & Malekjafarian, A. 2023. A deep-learning framework for classifying the type, location, and severity of bridge damage using drive-by measurements. *Computer-Aided Civil and Infrastructure Engineering*.

Fathnejat, H., Torkzadeh, P., Salajegheh, E. & Ghiasi, R. 2014. Structural damage detection by model updating method based on cascade feed-forward neural network as an efficient approximation mechanism. *Int J Optim Civil Eng*, 4(4): 451–72.

Fitzgerald, P. C., Malekjafarian, A., Cantero, D., Obrien, E. J. & Prendergast, L. J. 2019. Drive-by scour monitoring of railway bridges using a wavelet-based approach. *Engineering Structures*, 191: 1–11.

Keenahan, J., Obrien, E. J., Mcgetrick, P. J. & Gonzalez, A. 2014. The use of a dynamic truck–trailer drive-by system to monitor bridge damping. *Structural Health Monitoring: An International Journal*, 13(2): 143–157.

Li, Z., Lin, W. & Zhang, Y. 2023. Real-time drive-by bridge damage detection using deep auto-encoder. *Structures*, 47: 1167–1181.
Locke, W., Sybrandt, J., Redmond, L., Safro, I. & Atamturktur, S. 2020. Using drive-by health monitoring to detect bridge damage considering environmental and operational effects. *Journal of Sound and Vibration*, 468.
Malekjafarian, A., Corbally, R. & Gong, W. 2022. A review of mobile sensing of bridges using moving vehicles: Progress to date, challenges and future trends. *Structures*, 44: 1466–1489.
Malekjafarian, A., Martinez, D. & Obrien, E. J. 2018. The feasibility of using laser doppler vibrometer measurements from a passing vehicle for bridge damage detection. *Shock and Vibration*, 2018: 1–10.
Mcgetrick, P. J., Hester, D. & Taylor, S. E. 2017. Implementation of a drive-by monitoring system for transport infrastructure utilising smartphone technology and gnss. *Journal of Civil Structural Health Monitoring*, 7(2): 175–189.
Mcgetrick, P. J., Kim, C.-W., Gonzalez, A. & Obrien, E. J. 2013. Dynamic axle force and road profile identification using a moving vehicle. *International Journal of Architecture, Engineering and Construction*, 2(1): 1–16.
Mcgetrick, P. J. & Kim, C. W. 2013. A parametric study of a drive by bridge inspection system based on the morlet wavelet. *Key Engineering Materials*, 569-570: 262–269.
Mei, Q. & Gül, M. 2019. A crowdsourcing-based methodology using smartphones for bridge health monitoring. *Structural Health Monitoring*, 18(5-6): 1602–1619.
Ritto, T., Worden, K., Wagg, D., Rochinha, F. & Gardner, P. 2022. A transfer learning-based digital twin for detecting localised torsional friction in deviated wells. *Mechanical Systems and Signal Processing*, 173: 109000.
Saidi, R., Bouaguel, W. & Essoussi, N. 2019. Hybrid feature selection method based on the genetic algorithm and pearson correlation coefficient. *Machine learning paradigms: theory and application*: 3–24.
Sarwar, M. Z. & Cantero, D. 2021. Deep autoencoder architecture for bridge damage assessment using responses from several vehicles. *Engineering Structures*, 246.
Sinha, J. K., Friswell, M. I. & Edwards, S. 2002. Simplified models for the location of cracks in beam structures using measured vibration data. *Journal of Sound and Vibration*, 251(1): 13–38.
Torkzadeh, P., Fathnejat, H. & Ghiasi, R. 2016. Damage detection of plate-like structures using intelligent surrogate model. *Smart Struct. Syst*, 18(6): 1233–1250.
Yang, Y. B., Lin, C. W. & Yau, J. D. 2004. Extracting bridge frequencies from the dynamic response of a passing vehicle. *Journal of Sound and Vibration*, 272(3-5): 471–493.

Bridge Maintenance, Safety, Management, Digitalization and Sustainability – Jensen, Frangopol & Schmidt (eds)
© 2024 The Author(s), ISBN 978-1-032-77040-6
Open Access: www.taylorfrancis.com, CC BY-NC-ND 4.0 license

Crowd-sensing drive-by monitoring for bridge frequency identification

Yifu Lan, Zhenkun Li & Weiwei Lin
Aalto University, Espoo, Finland

ABSTRACT: The drive-by inspection methods have garnered significant attention in recent years, owing to their advantages in mobility, cost-effectiveness, and efficiency. However, in practical applications, even simple extraction of bridge frequencies from an ordinary/commercial vehicle proves to be challenging; components associated with road roughness and vehicle dynamics typically dominate the vehicle vibration response. Current research typically attempts to alleviate these influences by minimizing variability (e.g., driving in the same lane, using the same speed, etc.), and by employing custom vehicles, though such practices are often difficult to implement. Recent advancements have pivoted towards "crowd-sensing" or "fleet monitoring" approaches, which undoubtedly introduce greater variability, thus potentially making the aforementioned strategies less preferable. In light of this, this paper presents a novel coherence-based approach applied to crowd-sensing drive-by monitoring systems which leverage data from multiple vehicles. The fundamental idea is to identify bridge frequencies as common vibrational components across a variety of vehicles driving over it. It encourages the introduction of variability in drive-by measurements to filter bridge frequencies. The proposed method is explored through numerical experiments, incorporating Monte Carlo methods. The results highlight the method's efficacy in eliminating the influences of road roughness, environmental noise, and vehicle parameter variations, with accurate identification of bridge frequencies. From the perspective of the method, this paper also illustrates the advantages of crowd-sensing drive-by monitoring and its practical feasibility in engineering problems.

1 INSTRUCTION

Bridge frequency plays a vital role in understanding essential characteristics of bridges (Nagayama et al. 2017). However, traditional methods of frequency measurement, which typically involve installing sensors directly on bridges, are fraught with challenges. These include substantial labor costs, risks related to onsite work, disruptions to traffic flow, and the expenses associated with sensor upkeep (Abdulkarem et al. 2020). An alternative is the drive-by method, which has seen a surge in interest and research activity recently. This technique utilizes vehicles as moving sensors, gathering dynamic data of bridges through the vehicle-bridge interaction (VBI) (Yang et al. 2004). It necessitates minimal equipment on the vehicle, presenting an effective and cost-efficient means of obtaining critical information about bridges (Lan et al. 2023, 2024).

However, in practice, even the seemingly simple task of extracting bridge frequencies can be quite challenging. Current research on drive-by monitoring mostly focuses on developing and validating methodologies in numerical studies, controlled laboratory environments, and small-scale structures using specialized vehicles (Malekjafarian et al. 2022). Drive-by measurements using ordinary/commercial vehicles on normal bridge structures are prone to large uncertainties (Nagayama et al. 2017). The amplitude of spectral peaks related to bridge frequencies may be low, and interference signals caused by road roughness components or

DOI: 10.1201/9781003483755-197

vehicle dynamics could mask the signals of interest. Non-bridge frequency peaks often combine with weak bridge frequency peaks (or are entirely absent), leading to misleading frequency identification (Lan et al. 2022). Therefore, discerning bridge information from the complex and variable signal components in vehicle responses is a key issue.

In light of this, considerable research has been conducted to eliminate the vibration components of the interference and extract the bridge frequency from the vehicle response. For instance, Yang et al. (2021) proposed to utilize the contact point (CP) response between the bridge and the vehicle to measure the bridge frequency; it was found to be independent of the vehicle frequency. This approach then removes the influence of surface irregularities by deducting the CP responses from two adjacent axles or trailers, allowing the bridge frequency to be deduced from the residual response. Nevertheless, practical implementation of such techniques often requires axles or trailers to follow identical trajectories and may necessitate the use of specialized vehicles or additional equipment like shakers (Yang et al. 2020, 2021, 2022). Unfortunately, these are not always available, and integrating such methods into commercial vehicles for daily monitoring proves even more challenging.

On the other hand, recent advancements have pivoted towards "crowd-sensing" or "fleet monitoring" approaches. Such methods can significantly reduce maintenance costs, as they do not require special arrangements for monitoring, including the custom vehicles (Mei & Gül 2019). Vibrational data of bridges can be automatically collected as vehicles pass over them, enabling the regular monitoring of numerous bridges within a region. Furthermore, due to its crowdsourcing nature, this technique offers robustness against operational effects and human errors. However, the crowd-sensing measurements will inevitably introduce greater variability (Mei et al. 2019; Mei & Gül 2019), potentially making the above strategies less desirable. There is a need to propose algorithms for crowd-sensing drive-by monitoring.

One idea is the application of cross-spectral estimation. Nagayama et al. (2017) utilized cross-spectral density function estimation techniques to extract bridge frequencies as common vibrational components in the responses of two ordinary vehicles. The effectiveness of this method was validated through field tests. Lan et al. (2023) obtained bridge frequencies as common signals among different sensors mounted on a truck model through laboratory experiments. In the cross-spectra obtained using these methods, peaks unrelated to the bridge frequencies were weakened. However, their performance is influenced by factors such as speed, road roughness, and vehicle weight; they are not always successful. In this regard, Lan et al. (2023) proposed a Coherence-PPI (Prominent Peak Identification) algorithm, a method that uses a Bayesian framework to further filter bridge-related peaks from a large number of coherences, allowing the identification of bridge frequencies under uncertainties such as road roughness. They verified the method by using multiple drive-by measurements of a city bus. The algorithm results demonstrate that more diverse vehicle parameters and more passing measurements are beneficial for filtering bridge frequencies. This also inspires the application of the algorithm to multi-vehicle tasks (i.e., crowd-sensing drive-by monitoring).

This study introduces a crowd-sensing drive-by monitoring algorithm for extracting bridge frequencies based on coherence and a Bayesian framework, which is a modification of the previously proposed Coherence-PPI algorithm by the authors. The underlying idea is to identify bridge frequencies as common vibrational components among different vehicles. Instead of using multiple runs of a single vehicle as input in previous studies, it utilizes runs by different vehicles as input (crowd-sensing measurements). To validate the proposed algorithm, a numerical study was conducted. The crowd-sensing measurements were simulated using vehicles with random parameters, and the effectiveness and robustness of them under various conditions (e.g., road roughness and environmental noise) were investigated using methods that include the Monte Carlo approach.

2 ALGORITHM

This algorithm is a revision of the previously proposed Coherence-PPI algorithm by the authors (Lan et al. 2023), modified for crowd-sensing measurements. It comprises three parts, namely coherence computation, threshold determination, and selection of prominent peaks

(PPs) and frequency identification. It is worth noting that some contents of the algorithm are simplified here. For a detailed description, one can refer to the original text.

2.1 *Coherence computation*

This step presents the methodology used for calculating coherence in crowd-sensing measurements. Generally, there are four main contributors to vehicle vibration: bridge vibration, road roughness, vehicle dynamics, and environmental noise. In the frequency spectrum, the peaks that correspond to bridge vibrations often appear less distinct in comparison to others. Yet, to some extent, they are deemed to exhibit a commonality across different passages. Peaks related to road roughness and vehicle dynamics tended to vary with different trajectory, speed, etc. Environmental noise is random. The coherence between the two signals is mathematically expressed as (Bendat & Piersol 2011):

$$C_{xy}(f) = \frac{\left|G_{xy}(f)\right|^2}{G_{xx}(f)G_{yy}(f)} \tag{1}$$

where $G_{xy}(f)$ is the cross-spectral density of signals x and y, $G_{xx}(f)$ is the power spectral density of signal x, and $G_{yy}(f)$ is the power spectral density of signal y.

For multi-vehicle passages on the same bridge, coherences are calculated for every possible pairing of them (see Figure 1). If there are n vehicle passages, then the total number of coherences is $N = C_n^2 = \frac{n(n-1)}{2}$. The coherence for any two runs, denoted as $\{X_i\}$, is computed using Equation 1. In this context, $\{X_i\}$ is a vector, and $[X]$ is a matrix consisting of N coherence vectors. It should be noted that due to varying speeds of different vehicles, their time-domain lengths differ. Thus, it is necessary to ensure that the input signals for algorithm are of equal length. In this regard, a 3-second time segment is selected from each signal to ensure they have equal frequency domain resolution.

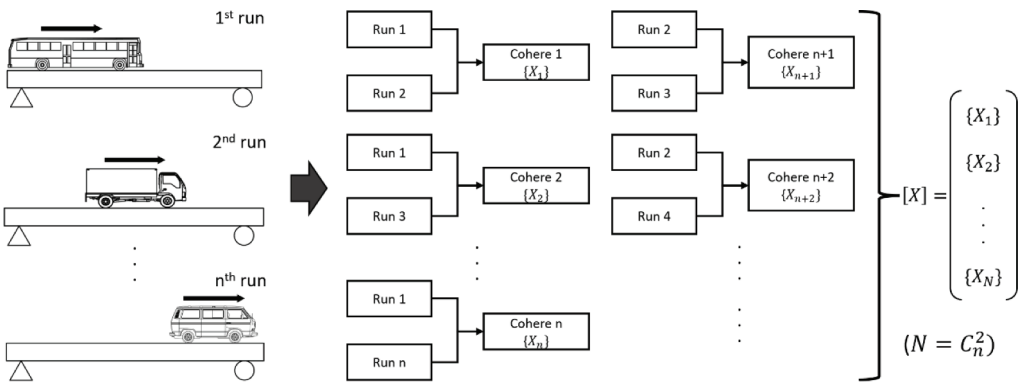


Figure 1. Coherence computation process.

2.2 *Threshold determination*

This step aims to determine the threshold that maximizes the occurrence of bridge-related frequencies. The Bayesian theorem (Bernardo & Smith 2009) provides a mathematical framework. Event B is defined as the attainment of the target frequency, and event H represents the occurrence when the coherence value is greater than or equal to a certain value (i.e., the threshold). The likelihood $P(H \mid B)$ signifies the probability that, when the target frequency is known, its corresponding coherence value is greater than the threshold. The prior $P(B)$ is the probability of attaining the target frequency in the absence of a threshold, whereas the evidence $P(H)$, is the probability that the coherence value is greater than the threshold. The

posterior $P(B \mid H)$, that is, the probability that the target frequency can be obtained when the threshold is given, can be calculated as:

$$P(B|H) = \frac{P(H|B) \cdot P(B)}{P(H)} \tag{2}$$

Building on earlier studies (Nagayama et al. 2017; Lan et al. 2023a, 2023b), bridge-related peaks are more likely to correspond to high percentile coherence values; that is, given the bridge frequency θ, it is more likely to correspond to a high percentile of coherence value t_0:

$$P[H(t_0)|B_\theta] > E(P) \tag{3}$$

The distribution of all coherence values may approximate a normal distribution. Considering that $P(B)$ is a constant, it suggests that choosing a larger threshold value for coherence is reasonable (Lan et al. 2023).

According to the 3-sigma rule in statistics, in a normal distribution, approximately 68% of observations fall within one standard deviation of the mean ($\tau = 0.84$), 95% within two standard deviations ($\tau = 0.975$), and 99.7% within three standard deviations ($\tau = 0.9985$). In this study, a threshold of $\tau = 0.84$ can be chosen.

2.3 *Selection of PPs and frequency identification*

This step counts the probability of each frequency interval above the threshold. The frequency range from 0 to 50Hz is divided into 100 intervals (θ_1,θ_2...,θ_{100}), with each representing a 0.5Hz interval. The interval, θ, containing the bridge frequency will exhibit the maximum probability value. During the procedure, the peaks in coherence that exceed the threshold, denoted as P_i, along with their corresponding frequencies F_i, are recorded. They are used to form a new matrix, [P], which can be thought of as a prominent peak matrix:

$$\begin{bmatrix} P_1 P_2 \dots P_n \\ F_1\ F_2 \dots F_n \end{bmatrix} = [P] \tag{4}$$

Then, the occurrence of these prominent peaks (PP) within each frequency interval is counted. The interval of the maximum occurrences is indicative of the bridge's fundamental frequency.

3 VBI MODEL

To validate the algorithm and to study the impact of various factors, a numerical study will be conducted. The following presents the construction of the VBI model used for the simulations in this work. A 2-DOF quarter-car model is utilized to simulate the rear axle system of a vehicle, and at the same time, an Euler-Bernoulli beam model is used to represent the simply supported bridge, as shown in Figure 2. This simplification aligns with that used in the study by Liu et al. (2023), who demonstrated that overlooking the impact of front suspension vibrations on the rear axle system is akin to introducing a certain level of noise into the results, which they deemed acceptable. This study adopts an unusually high noise level (10%), contrasting with previous studies that often considered 5% as a high noise level (Li et al. 2023). The adoption of the 2-DOF quarter-car model offers a compromise between model complexity and computational efficiency. This is particularly beneficial for implementing computationally intensive methods such as Monte Carlo simulations. For the bridge, each node in this finite element (FE) beam model is characterized by 2 DOFs: vertical translation and rotation. The beam model comprises n elements and $n + 1$ nodes, resulting in a total of $2n$ DOFs, not including the vertical constraints at the ends of the bridge. The bridge has a total length of L, and it features uniform flexural rigidity, denoted as EI, and a consistent mass per unit length, represented by m. Additionally, the damping characteristics of the bridge are approximated using mass-stiffness proportional Rayleigh damping.

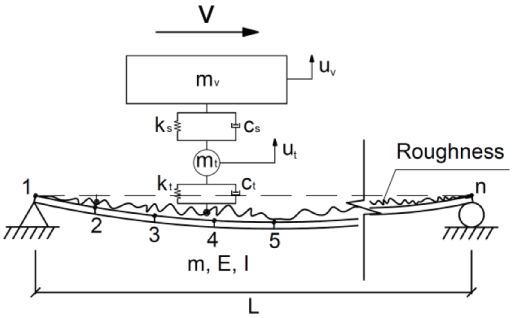


Figure 2. VBI model.

The fundamental equations governing the VBI system are as follows:

$$[M_v]\{\ddot{y}_v\} + [C_v]\{\dot{y}_v\} + [K_v]\{y_v\} = \{F_{cv}\} \tag{5}$$

$$[M_b]\{\ddot{y}_b\} + [C_b]\{\dot{y}_b\} + [K_b]\{y_b\} = \{F_{cb}\} \tag{6}$$

For the vehicle, $[M_v]$, $[C_v]$, and $[K_v]$ signify the vehicle's mass, damping, and stiffness matrices, respectively, and $\{y_v\}$ is the displacement vector. The time-varying interaction force on the vehicle is $\{F_{cv}\}$. For the bridge, $[M_b]$, $[C_b]$, and $[K_b]$ denote the bridge's mass, damping, and stiffness matrices, respectively, and $\{y_b\}$ is the bridge's nodal displacement vector. The force acting on the bridge is represented by $\{F_{cb}\}$.

The subsystem matrices and response vector for the vehicle model are as follows, where the body and axle masses are denoted by m_v and m_t, the suspension and tire damping by c_s and c_t, and the suspension and tire stiffness by k_s and k_t, respectively. The vertical displacements of the vehicle body and axle are denoted u_v and u_t, respectively.

$$[M_v] = \begin{bmatrix} m_v & \\ & m_t \end{bmatrix} \tag{7}$$

$$[C_v] = \begin{bmatrix} c_s & -c_s \\ -c_s & c_s + c_t \end{bmatrix} \tag{8}$$

$$[K_v] = \begin{bmatrix} k_s & -k_s \\ -k_s & k_s + k_t \end{bmatrix} \tag{9}$$

$$\{y_v\} = \begin{bmatrix} u_v & u_t \end{bmatrix}^T \tag{10}$$

The Newmark-Beta method is used to obtain the dynamic responses of the vehicle through the VBI process. The parameters β and γ of the Newmark-Beta method are selected as 0.25 and 0.5, respectively.

In this study, road roughness is simulated according to ISO 8608 (Múčka 2018), using a Power Spectral Density (PSD) function that characterizes roughness for different classes. Five roughness classes are defined, with coefficients: Class A ($0 - 2^5$), B ($2^5 - 2^7$), C ($2^7 - 2^9$), D ($2^9 - 2^{11}$), and E ($2^{11} - 2^{13}$) in units of $10^{-6}m^3$. A standard zero-mean real-valued stationary Gaussian process simulates the surface roughness profile, summing harmonic waves with specific spatial frequencies and random phase angles to construct the profile.

This noise is introduced into the signal using the formula given in Equation 11 (Xu et al. 2022). In this equation, $\ddot{u}_p$ represents the acceleration data of the vehicle that has been polluted. The term E_p denotes the level of environmental noise, N_s is a variable following the standard normal distribution, and $\sigma_{\ddot{u}_v}$is the standard deviation of the vehicle's acceleration response, denoted by $\ddot{u}_v$. In this study, noise is set to be 10%.

$$\ddot{u}_p = \ddot{u}_v + E_p N_s \sigma_{\ddot{u}_v} \tag{11}$$

4 NUMERICAL STUDY

4.1 *Simulations and algorithm results*

In this section, the simulation of crowd-sensing measurements over a bridge will be demonstrated using vehicles with random parameters. The bridge parameters are: m = 2000 kg/m, $EI = 6.06 \times 10^{1\circ}$ N·m^2, L = 45 m. The random parameters will be selected within a normal distribution based on the rear axle parameters of a bus. For example, the parameters of a bus can be: $m_v = 1.0 \times 10^4$ kg, $m_t = 1.0 \times 10^3$ kg, $c_s = 1.0 \times 10^4$ N·s/m, $c_t = 0$, $k_s = 4.0 \times 10^5$ N/m, $k_t = 3.5 \times 10^6$ N/m, and v = 7.5 m/s. The randomly generated vehicle parameters for the $i-th$ passage can be represented as follows:

$$Para_i^* = normrnd(Para, \sigma) \tag{12}$$

where *normrnd* is the normal distribution function, *Para* denotes the baseline bus parameters, which is the above-mentioned m_v, c_s, etc., and σ is the standard deviation of the normal distribution. In this study, it is taken as one-quarter of the original parameter (i.e., *Para*/4).

Under Grade "E" road conditions (poorest), it is evident from the responses obtained using vehicles with baseline parameters (see Figure 3a) that, although some peaks in the spectrum appear to be related to the bridge frequency, it is challenging to determine the bridge frequency. By contrast, in the algorithm results obtained from 100 random vehicle measurements (see Figure 3b), the bridge frequency can be clearly identified as the most prominent peak even under the poorest road roughness. Measurements obtained from multiple vehicles can filter the bridge-related components in the signal, because the distinct characteristics of each vehicle infuse variability into the non-bridge components of the signals. This proves the effectiveness of the proposed algorithm. It is noteworthy that this work only considered the scenario of a single vehicle on the bridge at a time. The case of multiple vehicles simultaneously on the bridge merits further exploration in future research.

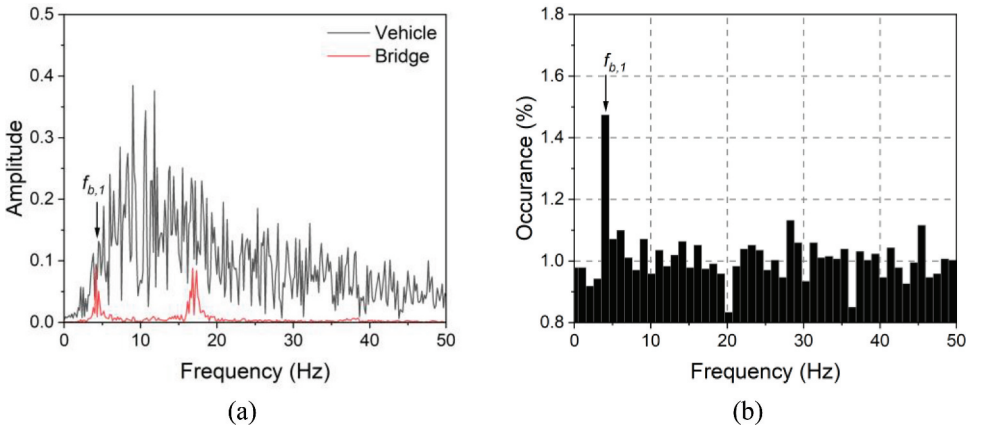


Figure 3. Frequency identification results: (a) frequency spectrum; (b) algorithm output.

4.2 *Effect of vehicle runs and Monte Carlo simulations*

This study also explored the effect of the number of vehicle passages on the results. Under the same conditions and using random functions as above, the algorithm results for different vehicle passages are illustrated in Figure 4. When results are obtained from a smaller number of vehicle passes, the peaks associated with the bridge frequency may not be well identified. Therefore, an adequate number of runs should be ensured to achieve statistical significance in the results; in this study, 50 passages were found to be sufficient.

This section also employs Monte Carlo simulations to validate the robustness of the proposed algorithm. The fundamental concept of Monte Carlo simulations is to utilize randomness to solve problems that could, in principle, be deterministic (Z.Mooney 1997). Utilizing

VBI simulations, random samples are produced, where each set of 50 samples (equating to 50 vehicle passages) is used as a single algorithm input, denoted as $[X]q$ (q=1, 2, 3…), with the corresponding output being $P_q(B_\theta \mid H_\tau)$. When the algorithm is run 2000 times for each road roughness, the Monte Carlo result for that roughness level should be $\frac{1}{2000}\sum_{q=1}^{2000} P_q(B_\theta \mid H_\tau)$. From Figure 5, it is evident that the algorithm performs effectively and similarly across various road roughness. This demonstrates the robustness of the proposed algorithm and its insensitivity to road surface conditions, which is considered one of the most critical factors affecting drive-by methods.

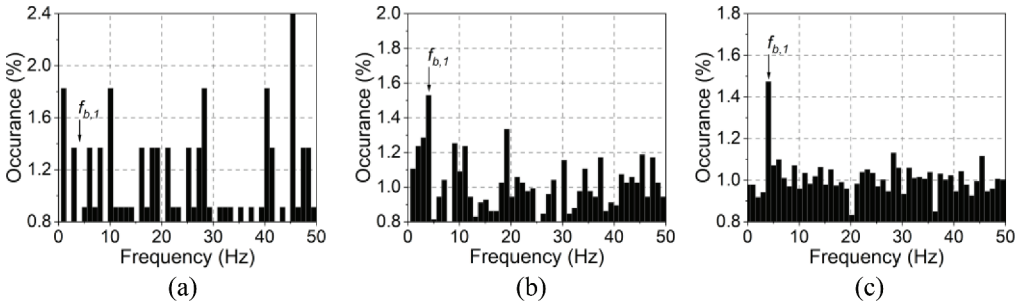


Figure 4. Algorithm outputs for different vehicle runs: (a) runs = 10; (b) runs = 50; (c) runs = 100.

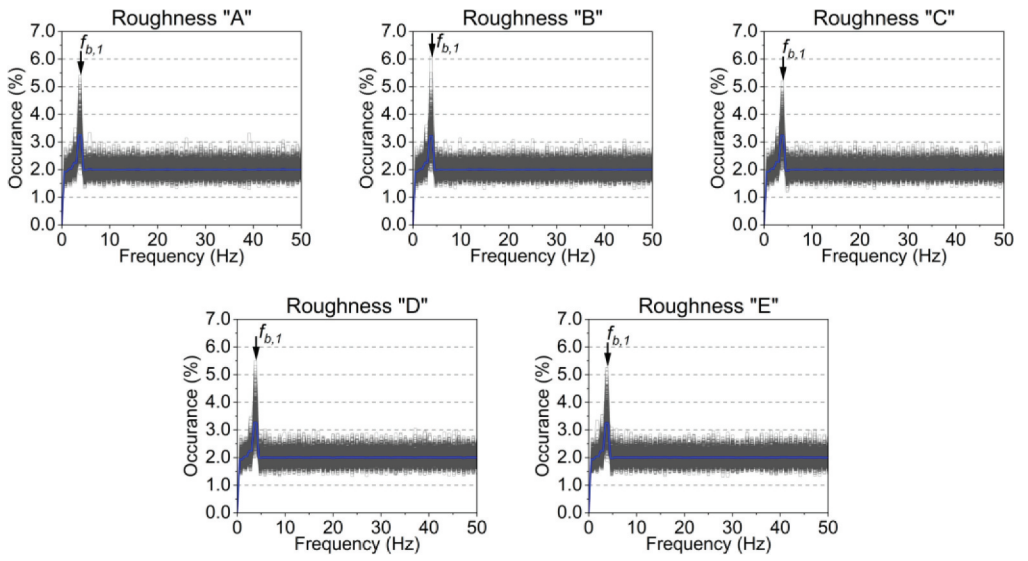


Figure 5. Monte Carlo results.

5 CONCLUSION

This study presents a crowd-sensing drive-by monitoring algorithm for extracting bridge frequencies. It is a modification of the Coherence-PPI algorithm previously proposed by the authors, adapted for multi-vehicle measurements. To validate the proposed algorithm, a numerical study was conducted, where the crowd-sensing measurements were simulated using vehicles with random parameters. According to numerical studies, several conclusions can be drawn:

(1) Under the influence of road roughness and environmental noise, the algorithm based on crowd-sensing measurements successfully identifies the bridge's fundamental frequency.

(2) The frequencies identified by the algorithm are statistical results, where numerous measurements enhance clarity and ensure reliability in frequency estimation.
(3) The robustness of this method has been examined using the Monte Carlo approach. The algorithm's outcomes are unaffected by the level of road roughness.

Despite the findings summarized above, field tests are required to assess the performance of this method in practice.

ACKNOWLEDGMENT

This research is sponsored by the Jane and Aatos Erkko Foundation in Finland (Grant No. 210018). Any findings, opinions, conclusions, and recommendations of this paper are those of the authors and do not necessarily reflect the views of the research sponsor.

REFERENCES

Nagayama, T., Reksowardojo, A.P., Su, D. & Mizutani, T.2017. Bridge natural frequency estimation by extracting the common vibration component from the responses of two vehicles. *Engineering Structures* 150: 821–829.

Abdulkarem, M., Samsudin, K., Rokhani, F.Z. & A Rasid, M.F. 2020. Wireless sensor network for structural health monitoring: A contemporary review of technologies, challenges, and future direction. *Structural Health Monitoring* 19(3): 693–735.

Yang, Y.B., Lin, C.W. & Yau, J.D. 2004. Extracting bridge frequencies from the dynamic response of a passing vehicle. *Journal of Sound and Vibration* 272(3): 471–493.

Lan, Y., Zhang, Y. & Lin, W. 2023. Diagnosis algorithms for indirect bridge health monitoring via an optimized AdaBoost-linear SVM. *Engineering Structures* 275: 115239.

Lan, Y., Li, Z. & Lin, W. 2024. Physics-guided diagnosis framework for bridge health monitoring using raw vehicle accelerations. *Mechanical Systems and Signal Processing* 206: 110899.

Malekjafarian, A., Corbally, R. & Gong, W. 2022. A review of mobile sensing of bridges using moving vehicles: Progress to date, challenges and future trends. *Structures* 44: 1466–1489.

Lan, Y., Lin, W. & Zhang, Y. 2022. Bridge frequency identification using vibration responses from sensors on a passing vehicle. *Bridge Safety, Maintenance, Management, Life-Cycle, Resilience and Sustainability*. CRC Press.

Yang, Y.B., Mo, X.Q., Shi, K., Wang, Z.L., Xu, H. & Wu, Y.T. 2021. Contact Residue for Simultaneous Removal of Vehicle's Frequency and Surface Roughness in Scanning Bridge Frequencies Using Two Connected Vehicles. *International Journal of Structural Stability and Dynamics* 21(13): 2171006.

Yang, Y.B., Xu, H., Zhang, B., Xiong, F. & Wang, Z.L. 2020. Measuring bridge frequencies by a test vehicle in non-moving and moving states. *Engineering Structures* 203: 109859.

Yang, Y.B., Huang, C.C., Xu, H., Wang, M.H., Wang, Z.L. & Shi, K. 2022. Frequency extraction for bridges with rough surface by a moving test vehicle enhanced by a shaker. *Engineering Structures* 266: 114598.

Mei, Q. & Gül, M. 2019. A crowdsourcing-based methodology using smartphones for bridge health monitoring. *Structural Health Monitoring* 18(5–6): 1602–1619.

Mei, Q., Gül, M. & Boay, M. 2019. Indirect health monitoring of bridges using Mel-frequency cepstral coefficients and principal component analysis. *Mechanical Systems and Signal Processing* 119: 523–546.

Lan, Y., Lin, W. & Zhang, Y. 2023. Bridge Frequency Identification Using Multiple Sensor Responses of an Ordinary Vehicle. *International Journal of Structural Stability and Dynamics* 23(05): 2350056.

Lan, Y., Li, Z., Koski, K., Fülöp, L., Tirkkonen, T. & Lin, W. 2023. Bridge frequency identification in city bus monitoring: A coherence-PPI algorithm. *Engineering Structures* 296: 116913.

Bendat, J.S. & Piersol, A.G. 2011. *Random data: analysis and measurement procedures*. John Wiley & Sons.

Bernardo, J.M. & Smith, A.F. 2009. *Bayesian theory*. John Wiley & Sons.

Liu, C., Zhu, Y. & Ye, H. 2023. Bridge frequency identification based on relative displacement of axle and contact point using tire pressure monitoring. *Mechanical Systems and Signal Processing* 183: 109613.

Li, Z., Lan, Y. & Lin, W. 2023. Indirect damage detection for bridges using sensing and temporarily parked vehicles. *Engineering Structures* 291: 116459.

Múčka, P. 2018. Simulated Road Profiles According to ISO 8608 in Vibration Analysis. *Journal of Testing and Evaluation* 46: 20160265.

Xu, H., Liu, Y.H., Wang, Z.L., Shi, K., Zhang, B. & Yang, Y.B. 2022. General contact response of single-axle two-mass test vehicles for scanning bridge frequencies considering suspension effect. *Engineering Structures* 270: 114880.

Z.Mooney, C. 1997. *Monte Carlo Simulation*. SAGE Publications, Inc.

Bridge Maintenance, Safety, Management, Digitalization and Sustainability – Jensen, Frangopol & Schmidt (eds)
© 2024 The Author(s), ISBN 978-1-032-77040-6
Open Access: www.taylorfrancis.com, CC BY-NC-ND 4.0 license

Bridge low-frequency displacement estimation using bridge acceleration for a VBI system

X. Lu, L. Sun & Y. Xia
Department of Bridge Engineering, College of Civil Engineering, Tongji University, China

C.W. Kim, K.C. Chang & Z. Han
Department of Civil & Earth Resources Engineering, Graduate School of Engineering, Kyoto University, Japan

ABSTRACT: Bridge displacement provides valuable information for bridge health monitoring. However, direct displacement measurement techniques are always costly to apply to large numbers of short and medium span bridges. To overcome these difficulties, indirect displacement estimation approaches have been developed as an alternative. Such indirect approaches use bridge acceleration, which can reduce the cost and be more convenient. However, the direct double integration of bridge acceleration can lead to low-frequency drift in the estimated bridge displacement caused by the unknown initial condition and measurement noise. This study focuses on the bridge displacement induced by the vehicle load in a simple vehicle-bridge interaction (VBI) system. The bridge displacement, which has been shown to have a non-zero mean and is mainly contributed by the low-frequency bridge vibration, is estimated using the bridge acceleration combined with the bridge mode shape. Tikhonov regularization is used to suppress the negative influence of the measurement noise. The proposed method is validated by a laboratory experiment.

1 INTRODUCTION

The health monitoring of common short- and medium-span bridges is a critical issue in civil engineering (Sofi et al. 2022). As reported by the American Society of Civil Engineers (ASCE) infrastructure maps in 2021 (ASCE 2021), more than 46,000 bridges in the United States are considered structurally deficient. In China, more than 1 million bridges will have been built by 2023 (China Govern Report, 2022), and a large number of them have been in service for more than 50 years with rapidly increasing traffic. Excessive deterioration of these bridges would cause potential risks to the normal operation of transportation systems (Milillo et al. 2019). Therefore, it is necessary to obtain monitoring data to reduce these risks.

Among various types of monitoring indicators, bridge displacement under vehicle load is an important indicator for bridge weight-in-motion (WIM) (Kim et al. 2022) and damage detection (Ge et al. 2023). To measure bridge displacement, scholars have proposed many methods, which can be generally classified into two categories: direct and indirect. The direct method directly measures bridge displacement using advanced instruments such as the linear variable differential transformer (LVDT) (Peddle et al. 2011), the laser Doppler vibrometer (LDV) (Garg et al. 2019), and the millimeter wave radar (Michel et al. 2021). While these instruments can provide an accurate measurement, they are always expensive. For example, a set of industrial millimeter wave radars can cost more than $0.2 million. Considering the large number of short and medium span bridges, the expected cost is unacceptable (Li et al. 2023).

DOI: 10.1201/9781003483755-198

In contrast to direct measurement, indirect measurement can be more economical, where the bridge displacement is estimated indirectly from the monitoring data of common monitoring sensors. A common method is to use an accelerometer (Gindy et al. 2007). The time history of the bridge displacement can be obtained by double integrations of the acceleration. However, in real engineering, the measured bridge acceleration signal contains unknown environmental and measurement noise (Gindy et al. 2008; Nagayama & Zhang 2017). In addition, the initial state of the bridge is also unknown. Therefore, the direct double integration would produce an unrealistic drifting displacement.

To solve this problem, an optional method is proposed by Park et al. (Park et al. 2005) to estimate the high-frequency displacement using the bridge acceleration processed by the Tikhonov regularization (Golub et al. 1999). Essentially, this study assumes that the high-frequency displacement should be a stationary zero-mean time series signal. The zero mean was then set as the regularization element to remove the potential interference from noise. In addition, the zero-mean assumption can solve the unknown initial condition problem through the regularization process. However, for medium and short span bridges, the vehicle load-induced bridge displacement is mainly contributed by low frequency rather than high-frequency displacement. As Biggs verified in (Biggs, 1964), for a simple vehicle-bridge interaction (VBI) system (Kim et al. 2005), the low-frequency displacement of an observation point on the bridge approximates the corresponding static deflection curve under the moving vehicle gravity (Frýba 2013) and is non-zero mean.

To estimate the non-zero low-frequency bridge displacement, Shin et al (Shin et al. 2012) used the measured strain and theoretical mode shapes. Park combined the methods proposed in (Park et al. 2005) and (Shin et al. 2012) and proposed a new regularization element (Park et al. 2013) as a data fusion method. This regularization item is a non-zero mean and is essentially the sum of the displacements that are estimated from the mode shapes. Similar to the method proposed in (Park et al. 2005), the new regularization element provides a baseline of the target displacement and helps to remove the negative influence of measurement noise.

A shortcoming of the method proposed in (Park et al. 2013) is that the vertical distance between the observation point and the neutral axis in the cross-section, as a key parameter, is unknown. Considering that in actual engineering, the cross-section is not homogeneous, the distance is difficult to estimate.

In this study, a new method was proposed to estimate the low-frequency bridge displacement from the noisy low-frequency bridge acceleration in VBI systems. In this study, we theoretically analyzed the characteristics of low-frequency and high-frequency bridge acceleration in a VBI system. Then, based on these characteristics, the Tikhonov regularization method in (Park et al. 2013) was modified to estimate the bridge displacement from low-frequency acceleration. Instead of strain gauges, accelerometers were used to obtain the mode shapes of a target bridge and to build the regularization item. Moreover, instead of measuring the distance between the observation point and the neutral axis, the new method switches to measuring the vehicle speed, which can be obtained cheaply and easily with a common radar. Then the low-frequency bridge displacement is estimated. The proposed method was validated through a laboratory experiment. Compared with the methods in the above research, the new method inherits the advantage of indirect measurement methods and solves the difficulties in application.

In Sec. 2, characteristics of the bridge dynamics in the VBI system were illustrated. The algorithm of the Tikhonov Regularization was also introduced. In Sec. 3, the proposed method was validated with laboratory experiments.

2 METHODOLOGY

2.1 *Dynamics of a simple VBI system*

A typical VBI system consists of a moving vehicle, a bridge, and the interaction between the tire and the surface of the bridge. The dynamic equations of a simple VBI system with

a single-degree-of-freedom sprung mass and a simply supported beam are listed as follows. For the vehicle (Yang & Lin 2005),

$$m_v\ddot{u}_v(t) + k_v[u_v(t) - u_w(t)] = 0 \tag{1}$$

where, $u_v(t)$ and $\ddot{u}_v(t)$ are vertical displacement and the acceleration of the vehicle. $u_w(t)$ is the vertical displacement of the contact point. The model does not include road roughness, considering its limited influence on bridge dynamics (Chang et al. 2010).

For the bridge,

$$\bar{m}\ddot{u}_b(x,t) + EIu_b''''(x,t) = \{k_v[u_v(t) - u_w(t)] - m_v g\}\delta(x - vt) \tag{2}$$

where, $u_b(x, t)$ denotes the vertical displacement of the bridge at x at time point t. $\bar{m}$ is the unit mass, E is the elastic modulus, I is the moment of inertia. g is the acceleration of gravity, a prime denotes differentiation to coordinate x.

When the vehicle mass is much smaller than the bridge mass, Eq. (2) can be simplified as Eq. (3), in which the interaction force is simplified as a moving force.

$$\bar{m}\ddot{u}_b(x,t) + EIu_b''''(x,t) = -m_v g\delta(x - vt) \tag{3}$$

The solution to Eq. (3) is shown as Eq. (4. a),

$$u_b(x,t) = \sum n\frac{\Delta_{st,n}}{1 - S_n^2}\left\{sin\frac{n\pi x}{L}\left[sin\frac{n\pi vt}{L} - S_n sin\omega_{b,n}t\right]\right\} \tag{4.a}$$

where S_n denotes the non-dimensional speed parameter, and $\omega_{b,n}$ is the bridge natural frequency, and can be formulated as follows.

$$\Delta_{st,n} = \frac{-2m_v gL^3}{n^4\pi^4 EI} \tag{4.b}$$

$$S_n = \frac{n\pi v}{L\omega_{b,n}} \tag{4.c}$$

$$\omega_{b,n} = \frac{n^2\pi^2}{L^2}\sqrt{\frac{EI}{\bar{m}}} \tag{4.d}$$

The bridge displacement $u_b(x, t)$ in Eq. (4.a) can be divided into $u_{b,N}(x, t)$ (shown as Eq. 5 (a)) and $u_{b,D}(x, t)$ (shown as Eq. 5(b)).

$$u_{b,N}(x,t) = \sum n\frac{\Delta_{st,n}}{1 - S_n^2} sin\frac{n\pi x}{L}\left(-S_n sin\omega_{b,n}t\right) \tag{5.a}$$

$$u_{b,D}(x,t) = \sum n\frac{\Delta_{st,n}}{1 - S_n^2} sin\frac{n\pi x}{L} sin\frac{n\pi vt}{L} \tag{5.b}$$

$u_{b,N}(x, t)$ is a summation of multiple sinusoid waves whose frequencies are the bridge natural frequency $\omega_{b,n}$. Similarly, $u_{b,D}(x, t)$ consists of multiple sinusoid waves whose frequencies are the driving-force frequencies $\omega_n = \frac{n\pi v}{L}$.

This study focuses on the $u_{b,D}(x, t)$. As Paultre et al. presented in (Paultre et al. 1992), for the general cases of highway system, the ratio between ω_1 and $\omega_{b,1}$ is always smaller than 0.15. Therefore, ω_n is always much smaller than $\omega_{b,n}$. Then, the $u_{b,N}(x, t)$ is defined as the high-frequency part and the $u_{b,D}(x, t)$ is defined as the low-frequency part. Yang and Lin illustrated in

(Yang & Lin 2005) that the contribution of the low-frequency displacement $u_{b,D}(x, t)$ to the whole displacement $u_b(x, t)$ is much higher than the contribution of the high-frequency components $u_{b,N}(x, t)$.

2.2 *Application of Tikhonov regularization in displacement estimation*

To estimate high-frequency vibration of the bridge, Park et al (Park et al. 2005) used the Tikhonov regularization method. Bridge displacement is estimated from measured bridge acceleration following Eq. (6):

$$\min_u \prod = \frac{1}{2}\left\| L_a\left(L_c u - (\Delta t)^2 \bar{a}\right)\right\|_2^2 + \frac{\lambda^2}{2}\|u\|_2^2 \tag{6}$$

where L_a is a diagonal weighting matrix with all diagonal entries of 1 except the first and last entries, which are equal to $\frac{1}{\sqrt{2}}$. L_c is the second-order differential operator matrix of the discretized trapezoidal rule. u here denotes the high-frequency bridge displacement $u_{b,N}(x, t)$. Δt is the sampling time interval. $\bar{a}$ is the vector of the measured bridge acceleration at x.

However, for the low-frequency displacement $u_{b,D}(x, t)$, the first driving-force component contributes the most (He et al. 2017). Unlike the high-frequency vibration, as derived from Eq. (5. b), $u_{b,D,1}(x, t)$ is a half-period sinusoid curve which has a non-zero mean. Therefore, Park et al (Park et al. 2013) modified Eq. (6) as

$$\min_u \prod = \frac{1}{2}||L_a(L_c u_i - (\Delta t)^2 \bar{a}_i||_2^2 + \frac{\lambda^2}{2}||u_i - D_i\{\bar{\varepsilon}\}||_2^2 \tag{7}$$

where u_i is the displacement vector at the i-th measuring point on the bridge, $\bar{a}_i$ is the bridge acceleration, D_i is the transfer matrix from multiple strain vectors to the u_i. $\{\bar{\varepsilon}\}$ is the strain responses at all of the measuring points. $D_i\{\bar{\varepsilon}\}$ denotes the estimated displacement from measured strain which is non-zero-mean vector.

2.3 *Low-frequency displacement estimation from low-frequency acceleration*

To make an estimation of the non-zero mean low-frequency bridge displacement, bridge low-frequency acceleration was utilized. It can be inferred from Eq. (5. b) that,

$$\{\bar{a}_{low}\} = -\frac{\pi^2 v^2}{L^2}\begin{bmatrix} sin\frac{\pi x_1}{L} & \cdots & n^2 sin\frac{n\pi x_1}{L} \\ \vdots & \ddots & \vdots \\ sin\frac{\pi x_r}{L} & \cdots & n^2 sin\frac{n\pi x_r}{L} \end{bmatrix}\begin{Bmatrix} \frac{\Delta_{st,1}}{1-S_1^2} sin\frac{\pi v t}{L} \\ \vdots \\ \frac{\Delta_{st,n}}{1-S_n^2} sin\frac{n\pi v t}{L} \end{Bmatrix} \tag{8}$$

and

$$\{u_{b,D}(t)\} = \begin{bmatrix} sin\frac{\pi x_1}{L} & \cdots & sin\frac{n\pi x_1}{L} \\ \vdots & \ddots & \vdots \\ sin\frac{\pi x_r}{L} & \cdots & sin\frac{n\pi x_r}{L} \end{bmatrix}\begin{Bmatrix} \frac{\Delta_{st,1}}{1-S_1^2} sin\frac{\pi v t}{L} \\ \vdots \\ \frac{\Delta_{st,m}}{1-S_m^2} sin\frac{m\pi v t}{L} \end{Bmatrix} \tag{9}$$

Therefore, by assuming that,

$$\{u_{b,D}(t)\} = T\{\bar{a}_{low}\} \tag{10}$$

Where T is the transfer matrix from multiple acceleration vectors to the u_i. Substituting Eq. (8) and (9) into Eq. (10), one can obtain that

$$T = -\frac{L^2}{\pi^2 v^2}\begin{bmatrix} sin\frac{\pi x_1}{L} & \cdots & sin\frac{n\pi x_1}{L} \\ \vdots & \ddots & \vdots \\ sin\frac{\pi x_r}{L} & \cdots & sin\frac{n\pi x_r}{L} \end{bmatrix}\begin{bmatrix} sin\frac{\pi x_1}{L} & \cdots & n^2 sin\frac{n\pi x_1}{L} \\ \vdots & \ddots & \vdots \\ sin\frac{\pi x_r}{L} & \cdots & n^2 sin\frac{n\pi x_r}{L} \end{bmatrix}^{+} \tag{11}$$

where + denotes the transfer of a generalized inverse matrix. The new objective optimization function is proposed as Eq. (12).

$$\min_{u_{i,b-low-Fre}} \prod = \frac{1}{2}||L_a\left(L_c u_{i,b,D} - (\Delta t)^2 \bar{a}_{i-low}\right)||_2^2 + \frac{\lambda^2}{2}||u_{i,b,D} - T_i\{\bar{a}_{low}\}||_2^2 \tag{12}$$

where $\bar{a}_{i-low}$ is the low-frequency bridge acceleration at the i-th monitoring point, $\{\bar{a}_{low}\}$ is the acceleration vector of multiple monitoring points, T_i is the i-th row of the transformer matrix T. The solution of (12) is

$$u_{i,b,D} = \left({L_{ac}}^T L_{ac} + \lambda^2 I\right)^{-1}\left({L_{ac}}^T L_a \bar{a}_{i-low}(\Delta t)^2 + \lambda^2 T_i\{\bar{a}_{low}\}\right) \tag{13}$$

where

$$L_{ac} = L_a L_c \tag{14}$$

Instead of measuring the distance between the observation point and the central axis, the new regularization formulation measures the moving vehicle's speed, which is supposed can be easily obtained with an inexpensive speed radar. In addition, we assumed that vibration mode shapes in Eq. (8) can also be measured with the multiple accelerometers. In this study, we only consider the simple scenario of a single vehicle traveling on the bridge. More complex scenarios, such as multiple lanes with multiple vehicles, or the potential bending torsional coupling effect of some bridges, are not considered.

3 EXPERIMENT VALIDATION

The VBI system used for the experiment consists of three beams for the bridge and a vehicle model. These three beams are simply supported steel beams (Figure 1) with a constant H-section. The span length of the center beam is 5.4 m. The remaining two spans are designed as acceleration and deceleration spans to keep the vehicle moving at a constant speed on the center beam. Figure 2 shows the vehicle as a sprung mass system moving along a pair of tracks installed on the bridge. The track surface has a very good road roughness condition



Figure 1. Experimental beams.

(ISO 8608:2016). A servomotor and a fixed pulley were installed at each end of the bridge. To form a driving system, the motor was connected to the vehicle with a nylon cable. The sprung mass of the vehicle was 11.83 kg.

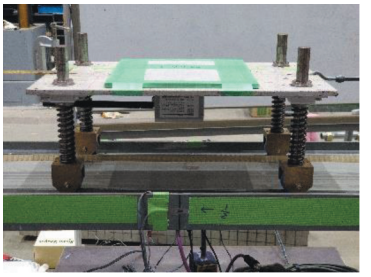
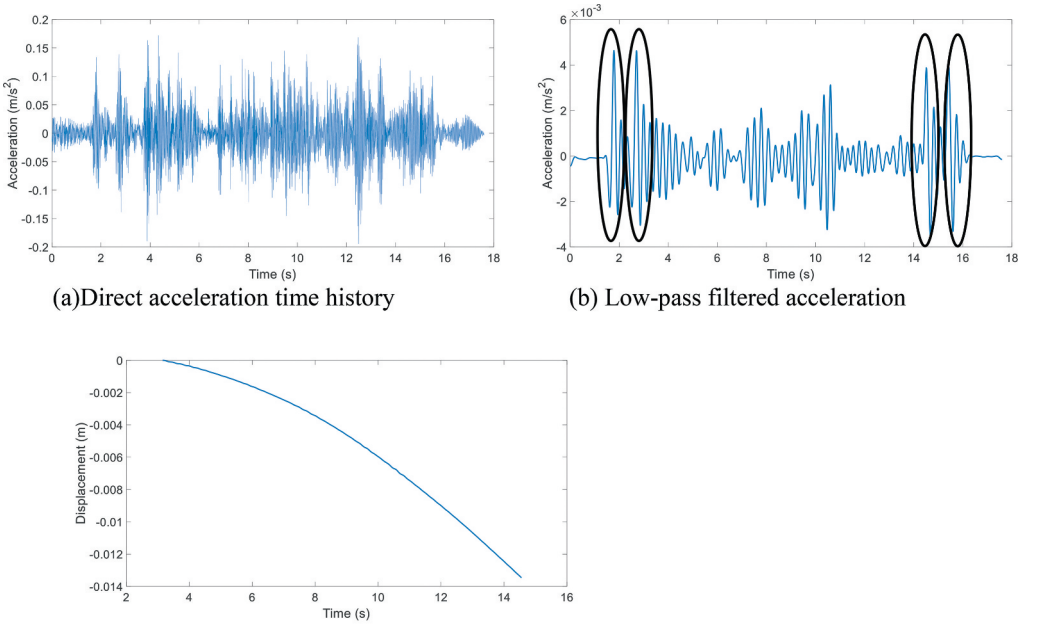


Figure 2. Moving vehicle model.



(a)Direct acceleration time history

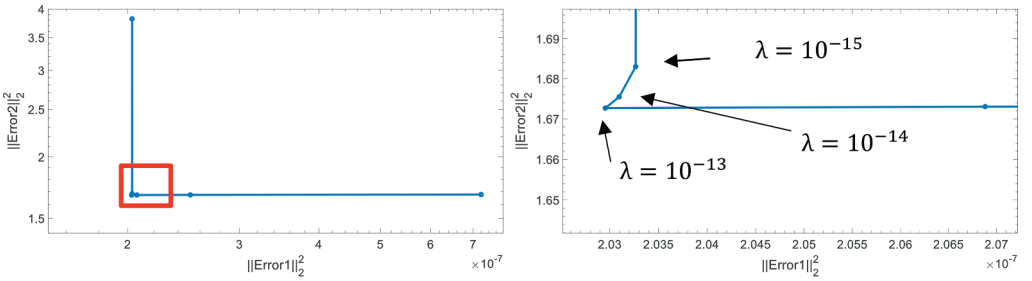
(b) Low-pass filtered acceleration

(c) Displacement obtained from double integration of low-frequency acceleration.

Figure 3. Dynamic responses of the mid-span bridge with the speed of 0.43 m/s.

The proposed displacement estimation method was verified by an experiment with 0.43 m/s. The direct time histories of the mid-span bridge acceleration and the low-frequency acceleration (extract with a l-Hz low-pass filter) are shown in Figure 3 (a) and (b), respectively. In Figure 3 (b), four instants involving the entry and exit of the beam are marked. The vertical displacement of the mid-span, which is calculated through double integration of the direct beam acceleration, is shown in Figure 3(c). An apparent drift occurs for the obtained displacement.

Since the displacement corresponding to the second driving force mode is zero for the mid-span, and the amplitude of the third driving force mode is 1.2% of the amplitude of the first driving force mode according to Eq. (5. b), only the first driving force mode was included in the displacement estimation. Consequently, only the first bending mode was included in the construction of the relevant matrices from Eq. (8) to Eq (11).



(a) L-curve (b) Zoomed L-curve at the turning point

Figure 4. Determination of the λ with L-curve method. (The rectangle-marked L-curve is zoomed and illustrated in (b)).

The L-curve method is used to determine the value of λ. As shown in Figure 4 (a) and 4 (b), it is supposed that the most appropriate would lies within the range from 1×10^{-14} to 1×10^{-13}. Therefore, the ridge trace (Friendly 2013) figure is used. The minimum value of λ was set to 1×10^{-14} and linearly increased to 1×10^{-13} with the step of 1×10^{-14}. The directly estimated bridge displacement was shown in Figure 5. Then, the estimated displacements at 1, 2, … 10 seconds were selected as multiple targets. Figure 6 illustrates the change of these displacements with the ten values (from 1×10-14 to 1×10-13) of λ. It should be noted that the slope of these curves shows a notable change when λ is equal to 2×10^{-14}, which means that when λ is close to 2×10^{-14}, the estimated target tends to become stable. The final validation was done by comparing the detrend-ed (with MATLAB (Mathworks 2021)) estimated low-frequency displacement with the measured displacement. It can be seen that among all these λ values, the estimated displacement with 2×10^{-14} best matches the measured displacement (shown in

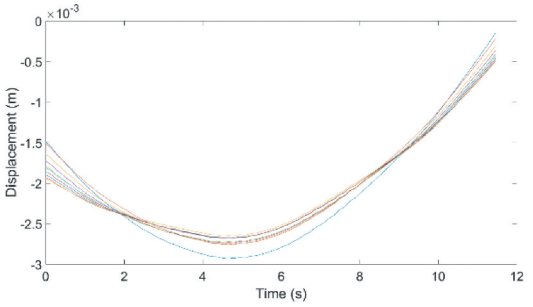


Figure 5. Directly estimated bridge displacement at mid-span for different λ ranges from 1×10^{-14} to from 1×10^{-13}. (Each curve denotes an estimated displacement corresponding to a λ.).

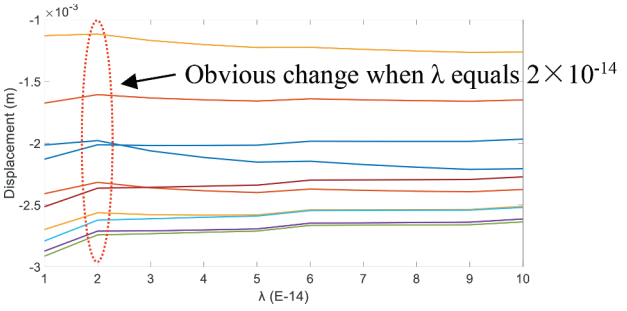


Figure 6. Ridge trace figure corresponding to different values of λ. (Each curve denotes an estimated displacement corresponding to a λ. It should be noted that all these displacement curve has an obvious change when λ equals 2×10^{-14}, marked with an ellipse).

Figure 7). Therefore, the proposed method has been validated for low-frequency bridge displacement estimation.

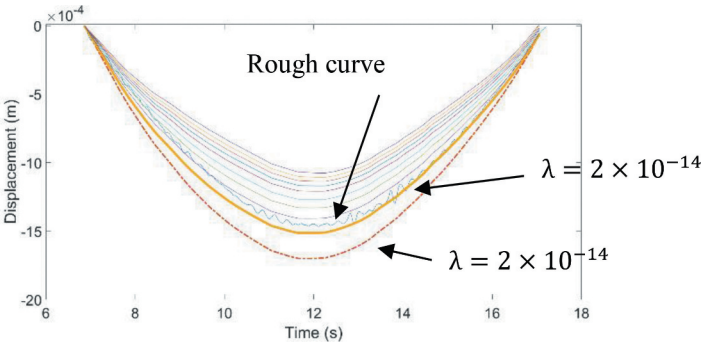


Figure 7. De-trend estimated bridge displacement at mid-span for different λ. (The dash-dot curve is corresponding to 1×10^{-14}, and the 2×10^{-14} curve has the largest width. The rough curve is the measured low-frequency displacement, and the first curve above the rough curve is corresponding to 3×10^{-14}).

4 CONCLUSIONS

This study proposed a novel method to estimate low-frequency bridge displacement from measured noisy low-frequency acceleration. In this study, the characteristics of low-frequency and high-frequency bridge vibrations in a simple VBI system were analyzed. Based on these characteristics, Tikhonov regularization was used to estimate the non-zero mean low-frequency bridge displacement under a moving vehicle. A laboratory experiments were then performed to validate the proposed method. The detailed conclusions are summarized as follows:

(1) The dynamic bridge responses in the simple VBI system consist of bridge frequency-related responses and driving force-related responses. The former is high frequency with zero mean displacement, and the latter is low frequency with non-zero mean displacement.

(2) The low-frequency bridge acceleration can be separated from the directly measured bridge acceleration with a low-pass filter. For the laboratory experiment, low-frequency bridge acceleration contains noise and it is hard to obtain the accurate displacement through double integrations.

(4) The key regularization parameter λ can be determined with the L-curve method, if necessary, combined with the ridge trace figure. The laboratory experiment results show good results for low-frequency bridge displacement estimation with the proposed method.

Compared with the direct methods in previous study, the proposed method inherits the low-cost advantage of the indirect method. Moreover, in comparison to the existing indirect method, this method uses the low-frequency acceleration, which not only streamlines the monitoring system, but also overcomes the difficulty of estimating the neutral axis distance. Therefore, this method is expected to be more applicable in actual engineering.

REFERENCES

[1] Sofi, A., Regita, J. J., Rane, B., & Lau, H. H. (2022). Structural health monitoring using wireless smart sensor network–An overview. Mechanical Systems and Signal Processing, 163, 108113.

[2] ASCE. Report card for America's infrastructure, https://infrastructurereportcard.org/cat-item/bridges/ (2021, accessed September 20, 2023).

[3] Govern Report for infrastructures in China. (2022) https://www.gov.cn/lianbo/bumen/202306/content_6887539.htm (2023, accessed September 20, 2023).

[4] Milillo P, Giardina G, Perissin D, et al. Pre-collapse space geodetic observations of critical infrastructure: the morandi bridge, genoa, italy. Remote Sens 2019; 11: 1403.
[5] Kim, S. W., Yun, D. W., Park, D. U., Chang, S. J., & Park, J. B. (2022). Vehicle load estimation using the reaction force of a vertical displacement sensor based on fiber Bragg grating. Sensors, 22(4), 1572.
[6] Ge, L., Koo, K. Y., Wang, M., Brownjohn, J., & Dan, D. (2023). Bridge damage detection using precise vision-based displacement influence lines and weigh-in-motion devices: Experimental validation. Engineering Structures, 288, 116185.
[7] Peddle, J., Goudreau, A., Carlson, E., & Santini-Bell, E. (2011). Bridge displacement measurement through digital image correlation. Bridge Structures, 7(4), 165–173.
[8] Garg, P., Moreu, F., Ozdagli, A., Taha, M. R., & Mascareñas, D. (2019). Noncontact dynamic displacement measurement of structures using a moving laser Doppler vibrometer. Journal of Bridge Engineering, 24(9), 04019089.
[9] Michel, C., & Keller, S. (2021). Advancing ground-based radar processing for bridge infrastructure monitoring. Sensors, 21(6), 2172.
[10] Li, Shengli, Zhenzhen Liang, and Pan Guo. A FBG pull-wire vertical displacement sensor for health monitoring of medium-small span bridges. Measurement 211 (2023): 112613.
[11] Gindy, M., Nassif, H. H., & Velde, J. (2007). Bridge displacement estimates from measured acceleration records. Transportation research record, 2028(1), 136–145.
[12] Gindy, M., Vaccaro, R., Nassif, H., & Velde, J. (2008). A state-space approach for deriving bridge displacement from acceleration. Computer-Aided Civil and Infrastructure Engineering, 23(4), 281–290.
[13] Nagayama, T., & Zhang, C. (2017). Deflection estimation of a steel box girder bridge using multi-channel acceleration measurement. In IABSE Symposium: Engineering the Future, Vancouver, Canada, 21-23 September 2017, 1667–1674.
[14] Park, K. T., Kim, S. H., Park, H. S., & Lee, K. W. (2005). The determination of bridge displacement using measured acceleration. Engineering Structures, 27(3), 371–378.
[15] Golub, G. H., Hansen, P. C., & O'Leary, D. P. (1999). Tikhonov regularization and total least squares. SIAM journal on matrix analysis and applications, 21(1), 185–194.
[16] Biggs J. M. Introduction to structural dynamics. New York:McGraw-Hill;1964.
[17] Kim, C. W., Kawatani, M., & Kim, K. B. (2005). Three-dimensional dynamic analysis for bridge–vehicle interaction with roadway roughness. Computers & structures, 83(19-20), 1627–1645.
[18] Frýba L. Vibration of solids and structures under moving loads. Heidelberg: Springer; 2013.
[19] Shin, S., Lee, S. U., Kim, Y., & Kim, N. S. (2012). Estimation of bridge displacement responses using FBG sensors and theoretical mode shapes. Structural engineering and mechanics: An international journal, 42(2), 229–245.
[20] Park, J. W., Sim, S. H., & Jung, H. J. (2013). Displacement estimation using multimetric data fusion. IEEE/ASME Transactions On Mechatronics, 18(6), 1675–1682.
[21] Yang, Y. B., & Lin, C. W. (2005). Vehicle–bridge interaction dynamics and potential applications. Journal of sound and vibration, 284(1-2), 205–226.
[22] Chang, K. C., Wu, F. B., & Yang, Y. B. (2010). Effect of road surface roughness on indirect approach for measuring bridge frequencies from a passing vehicle. Interaction and multiscale mechanics, 3(4), 299–308.
[23] Paultre, P., Chaallal, O., & Proulx, J. (1992). Bridge dynamics and dynamic amplification factors—a review of analytical and experimental findings. Canadian Journal of Civil Engineering, 19(2), 260–278.
[24] He, W. Y., Ren, W. X., & Zhu, S. (2017). Damage detection of beam structures using quasi-static moving load induced displacement response. Engineering Structures, 145, 70–82.
[25] ISO 8608: 2016. Mechanical vibration – Road surface profiles – Reporting of measured data.
[26] Friendly, M. (2013). The generalized ridge trace plot: Visualizing bias and precision. Journal of Computational and Graphical Statistics, 22(1), 50–68.
[27] Mathworks Inc, 2021.

Bridge Maintenance, Safety, Management, Digitalization and Sustainability – Jensen, Frangopol & Schmidt (eds)
© 2024 The Author(s), ISBN 978-1-032-77040-6
Open Access: www.taylorfrancis.com, CC BY-NC-ND 4.0 license

Automated analysis of drive-by monitoring data

J. Brötzmann, Y. Yang & U. Rüppel
Institute of Numerical Methods and Informatics in Civil Engineering (IIB)
Technical University of Darmstadt, Darmstadt, Germany

M.M. Rupp & S.R. Lorenzen
Institute of Structural Mechanics and Design (ISM+D)
Technical University of Darmstadt, Darmstadt, Germany

ABSTRACT: In the coming years, numerous bridges in Germany are reaching the end of their designed service life of over hundred years. However, due to diverse factors, it is crucial to extend their lifespan. Hence, a cost-effective and scalable solution is necessary to monitor and evaluate their condition. Drive-by Monitoring, which employs sensors on the passing vehicle to assess the bridge properties or condition, is one potential approach. Two extensive drive-by measurement campaigns have been carried out by the Institute of Structural Mechanics and Design (ISM+D), resulting in data for over 3000 kilometres of railway and numerous bridge crossings. The objective of this work is to construct and apply a framework for the automated analysis, management, and storage of this data. Attaining a high degree of automation for the application is crucial, which is why an application using various algorithms has been developed.

1 INTRODUCTION

DB InfraGO AG, a subsidiary of Deutsche Bahn AG (DB AG), operates over 25,000 bridges in Germany (Knapp 2019). With a service life of around 120 years, 40% of the railway bridges are over 80 years old (Knapp 2019, Geißler et al. 2019). This age structure shows that the structural condition of many railway bridges is affected by the challenges associated with the naturally ageing infrastructure. Combined with increasing traffic loads, additional challenges arise. Furthermore, bridges are neuralgic and important points for a robust and continuous transport of goods. Network-wide, continuous monitoring will therefore play an important role in the future to prioritise the renewal process.

Structural Health Monitoring generally addresses this issue. Due to the large number of bridges in combination with poor accessibility or required track closure permits and limited financial, human and time resources, the application of conventional methods, in particular direct monitoring where sensors are installed on the structure, is difficult (Geißler et al. 2019, Yang & Yang 2018). Alternative methods, such as indirect or drive-by monitoring, where sensors on the passing vehicle are used to monitor the bridges, can provide a solution (Malekjafarian et al. 2022). Drive-by Monitoring is a cost-effective and efficient method that can be scaled up across the network, especially if the equipped trains are used for regular services (Yang & Yang 2018, Malekjafarian et al. 2022). For example, DB AG already uses such an indirect system on 14,000 kilometres to monitor track geometry (Lorenzen et al. 2023).

However, the amount of data generated by network-wide continuous drive-by monitoring is enormous and needs to be managed and analysed. So, the main objective of this paper is to develop a tool that facilitates the management and analysis of drive-by monitoring data with a user-friendly graphical interface. Two drive-by measurement campaigns have been carried out by the authors. As a result, data are available for more than 3000 kilometres of railway and many bridge crossings. With the help of these two measurement campaigns a framework for the management and automatic analysis of this data is developed and implemented.

DOI: 10.1201/9781003483755-199

A high to complete degree of automation of the application is important. To be accessible from anywhere and with any device, a browser-based solution using a web framework is preferred. Python was chosen as the programming language as several data analyses are required.

As the data is generated by sensors installed on a train, location is a key element and therefore a map visualising the line travelled will be highly valuable. So, automatic mapping of the line on the railway network is required. The sensors record continuously, and their data is divided into predefined time intervals. New algorithms are needed to divide the data into specific data packages. In the scope of this work the focus lies on monitoring of railway bridges, so the data should be cut accordingly and assigned automatically to the bridge crossed. There are several possible solutions. If GPS is also recorded, it can be used to track the train on the railway network. Another possibility is to use the starting point of the measurement campaign, detect the first bridge crossing and then use the known network to assign the bridges. As described above, further bridge characteristics should be derived for (predictive) monitoring purposes.

The initiation for this work is design and development centred since a highly automated application is desired. To demonstrate the relevance of this topic, a motivation was provided in this Section 1. The next section outlines the available data, its structure and description. Section 3 then presents the concept of the proposed solution. With that in mind, the following section details the implications of the concept. This is followed by the evaluation and implementation of the concept, finishing with a conclusion and outlook in the last section.

2 DATA SETS

2.1 *Field measurements*

As reported by Rupp et al. (Rupp 2023), the ISM+D collected drive-by monitoring data as part of the ZEKISS research project (ZEKISS 2023), funded by the German Federal Ministry for Digital and Transport. The ISM+D, supported by German Federal Railways (DB), used the advanced TrainLab (aTL) to collect data while travelling on the German rail network.

The aTL is a laboratory train used by DB to test new technologies for the railway sector. Two trains have been deployed for this purpose. The technical basis for these trains is the ICE-TD, which was used for passenger transport until 2017. The trains consist of two middle and two end carriages and have a total length of 107 metres. The four carriages have conventional bogies, resulting in 16 axles and therefore 32 wheels (Advanced TrainLab 2023).

In the measurement campaign, a uniaxial acceleration sensor was mounted on each axle box using specially designed brackets (see Figure 2), giving a total of 32 sensors (Rupp 2023). Uniaxial piezoelectric accelerometers of the type PCB-(M)622B01 (manufactured by PCB Synotech GmbH, located in Hückelhoven, Germany) with a sensitivity of 100 mV/g (±5 %), a broadband resolution of 0.00005 g, a measuring range of ±50 g and a frequency range of 0.58 - 6,000 Hz (±5 %) were used. The sensor cables were installed under the car bodies and routed through specific doors via the windows to Quantum MX1601B amplifiers (manufactured by Hottinger Brüel & Kjaer GmbH, located in Darmstadt, Germany) (Rupp 2023). Figure 1 shows the placements of the sensors. The sensors were used to record the vertical accelerations of the wheelset. The sampling frequency was 5000 Hz. This high frequency was chosen to ensure one data point per centimetre as the train can travel at speeds of up to 200 km/h. The contact time between the train and the bridges is therefore extremely short (Rupp 2023).

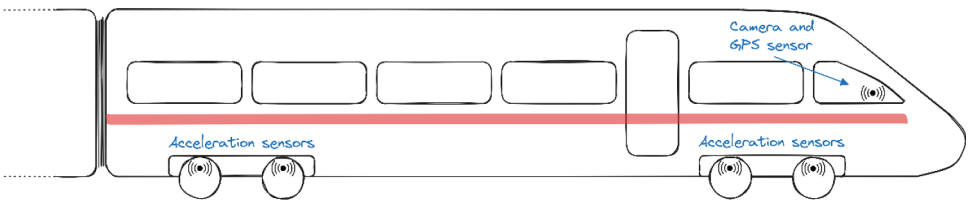


Figure 1. Sketch of the train with the locations of the sensors.

Additionally, two GPS sensors were installed to record the GPS position and speed of the train. The GPS antenna was also used to synchronise the train measurements with the monitoring system installed on the bridges. One sensor was placed in one of the middle carriages and the other in the front, as shown in Figure 1. The sampling frequency of the sensors was 1 Hz. The GPS signals allow the train to be located on the railway network. With the localisation of the train, the acceleration signals are also positioned, so that relevant bridge crossings can be assigned to specific measurement packages. In addition, a camera was placed in the driver's cab. The camera captured 30 frames per second enabling the recording of external influences as well. The camera was synchronised with the GPS sensors (Rupp 2023).



Figure 2. Acceleration sensor mounted on the axle box.

With the high sampling frequency of the acceleration sensors and other data collected such as GPS and images, a lot of data needs to be stored. The following section shows the structure of the drive-by monitoring data. The continuous measurement of the acceleration sensors is sliced into pre-defined data packages of 30 seconds with a file size of 120 megabytes. The measurement points MP1xx and MP2xx contain the acceleration signals from the axle boxes of both sides.

```
[...]
Channel "MP103" (155383 Entries) 46
Channel "MP104" (155383 Entries) 47
Channel "MP203" (155383 Entries) 50
Channel "MP204" (155383 Entries) 51
[...]
Channel "GNSS_Latitude" (155383 Entries) 54
Channel "GNSS_Longitude" (155383 Entries) 55
Channel "GNSS_Altitude" (155383 Entries) 56
Channel "GNSS_Speed" (155383 Entries) 57
[...]
```

2.2 *Open data of Deutsche Bahn*

As stated in section 1, the objective is to facilitate and automate the management and analyses of collected drive-by monitoring data. A crucial aspect of this entails the mapping of the travelled line and the corresponding measurement data to the existing lines within the rail network, including any crossed bridges. For this task, the DB's accessible open data (Deutsche

Bahn 2023) of the rail network can be used. The data packages of interest are the coordinates of the different lines and bridges. The following two tables show the data description.

Table 1. Data description of the shapefile "lines" inside the data set "Geo-Line-Network".

Field	Description	Type	Format (example)
LINE_NO	Four-digit line number of DB	Number	2650
[. . .]	[. . .]	[. . .]	[. . .]
GEOMETRY	List of points of a polygon line consisting of longitude and latitude; WGS 84 (EPSG: 4326)	Number	9.383436, 54.743787

The data is stored in the shapefile format, which is widely used for vector-based geodata due to its simplicity. To extract the coordinates, the GeoPandas package (GeoPandas 2023) in Python can be used. The bridge information is retained in a csv file, which can be easily managed using Python.

Table 2. Data description of the table "bridges" inside the data set "Geo-Bridge".

Field	Description	Type	Format (example)
LINE_NO	Four-digit line number of DB	Number	2650
[. . .]	[. . .]	[. . .]	[. . .]
GEOGR_LAT	Geographical coordinates: Latitude ETRS 89 (EPSG: 4258)	Number	54.77366638
GEOGR_LON	Geographical coordinates: longitude ETRS 89 (EPSG: 4258)	Number	9.43702642
[. . .]	[. . .]	[. . .]	[. . .]

Both tables contain coordinates used as reference when mapping and assigning measurement data to lines and bridges. To make this comparison possible, this data must be stored in a framework. Consequently, an algorithm needs to be developed to perform this task.

3 CONCEPTUAL OVERVIEW

The user interface should be simple and straightforward as shown in Figure 3. The only action required from the user is to upload the data or reference the corresponding folder. The application processes the data for management and storage as well provides a visual output for the user. Since geolocation of the data plays a key role, a map visualises where the data has been collected and which bridges have been crossed. This is shown in section 5.

4 IMPLEMENTATION

To effectively implement the above concept, a general architecture illustrated in Figure 4 has been formulated. This design facilitates the separation of distinct tasks into different services. For example, the graphical user interface (GUI) acts as the frontend, which can be separated from the storage and management of data in the backend. Additionally, as the application is intended to be browser-based, the selection of a web framework is necessary. Therefore, Django (Django 2023) was chosen due to its fast and easy configuration process, together with the variety of built-in features. Django uses built-in models and default databases (DB1, . . .) to handle incoming data, with a clear separation of GUI and business logic, as intended in the architecture in Figure 4. There are several well-known companies that also use Django, such as Instagram, Spotify, YouTube, or Dropbox (GeeksforGeeks 2023).

Besides the general architecture, the matching of the measured line with existing lines and bridges is a very important step. This can be implemented through algorithms that compare

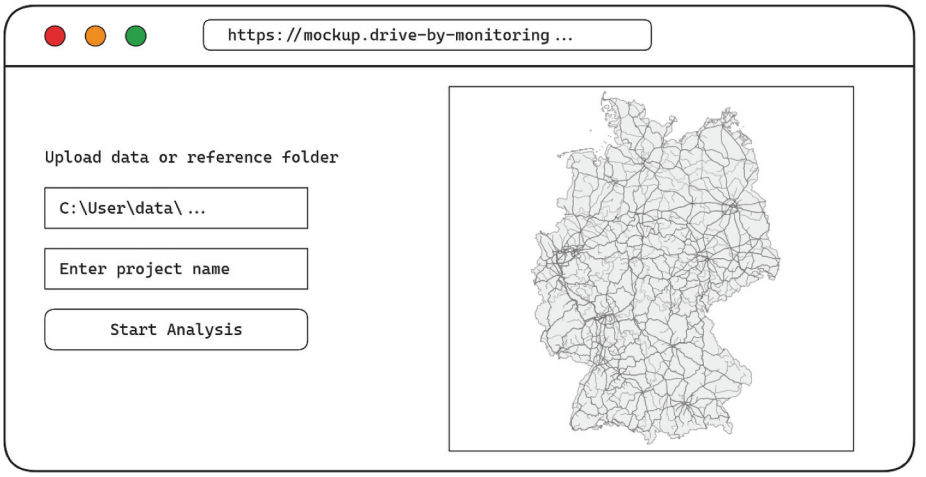


Figure 3. Mockup of the user interface of the application. Source of the railway network: Hbf878 2020.

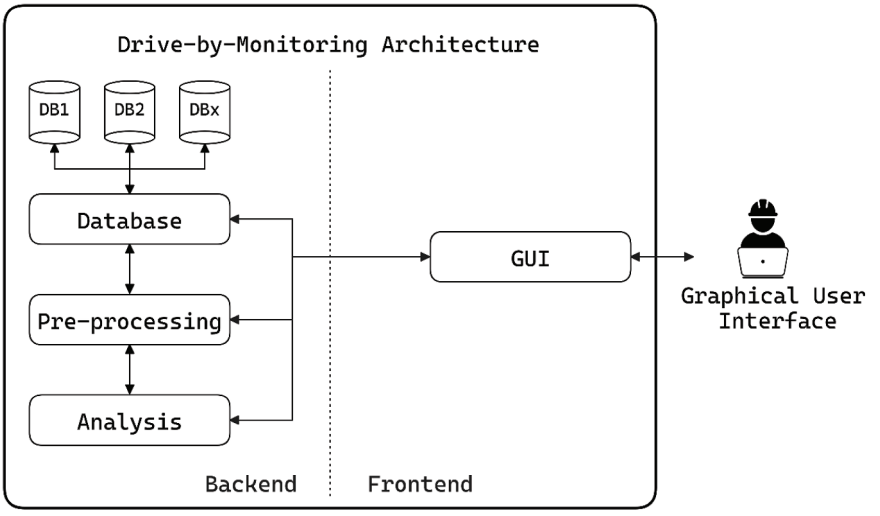


Figure 4. General architecture of the developed application.

coordinates. All signals were recorded using the catmanAP software and stored in a binary file. The Python package AP reader (Bohmann 2023) is used to extract data and features. A plausibility check of the GPS sensor is performed to rule out any malfunctions. The consecutive coordinates are checked for proximity and a general geographical location in Germany. The next step is to compare the coordinates of the measured line with those of existing lines and bridges in the open data of DB, as explained in subsection 2.2.

The travelled line of the measurement campaign is number 2650. It starts in Cologne and ends in Dusseldorf. Opening the shapefile provided by Deutsche Bahn and searching for the line number delivers the coordinates as follows.

```
LINESTRING Z (6.974548 50.940881 0, 6.97595 50.940729 0,
6.977346 50.940555 0, 6.980121 50.940159 0, 6.982896
50.939762 0, [...]

2650
```

Extracting the data from the very first measurement package gives the first coordinates as follows.

```
GNSS_Latitude 50.9407245
GNSS_Longitude 6.9748565
```

As directly visible, the coordinates appear to be close to each other. However, this is only the case if the line number of the trip is already known or provided as input. Requiring minimal user input while analysing the data independently is the main aim of this application. Therefore, when a new measurement package is entered as input, the algorithm must perform a thorough search of the entire open data set and make comparisons between each coordinate. This is achieved using the Euclidean distance metric (2) and searching for the minimum distance. The two points m (measured coordinates) and e (existing coordinates) are defined through their coordinates consisting of latitude and longitude (1). Note, that the coordinates in the open data set of DB are swapped.

$$m = (m_{lat}, m_{lon}) \; and \; e = (e_{lat}, e_{lon}) \tag{1}$$

$$d(m,e) = \sqrt{(e_{lat} - m_{lat})^2 + (e_{lon} - m_{lon})^2} \tag{2}$$

In Python, this can be implemented with the 'spatial algorithms' package of SciPy (SciPy 2023) which provides many fundamental distance computation algorithms. The function 'cdist' computes the distance between each pair of the two inputs. Based on these calculations the minimum distance can be determined and each measured coordinate can be associated with a line number. In this way, the measured line can be matched with existing line numbers of the railway network.

Nevertheless, the acceleration sensors generate 75,000 coordinate points at a minimum sampling frequency of 2500 Hz. Given the presence of latitude and longitude, there are 150,000 data points to check. However, the GPS sensor operates at only 1 Hz, so the remaining data points are repeated to match the acceleration data. Reducing the data set to just these unique coordinates significantly reduces the data set to just 31 coordinates. Despite this, it is still necessary to compare these 31 coordinates with every coordinate in the open data set of DB.

Another crucial objective is to identify the bridges that have been crossed and link them to a respective measurement package of the bridges. This will help the user to analyse measurements of specific bridges (e.g., in the context of Structural Health Monitoring). The DB csv file (see subsection 2.2) contains relevant data that can be easily used in Python. Since the line number is already known from the previous analysis, only the bridges belonging to this line are compared with the measured GPS signals. This process is analogous to comparing lines. However, it is not beneficial to search for the smallest Euclidean distance since a measurement package may include crossings of several bridges. Therefore, the distance in metres is calculated using the Haversine formula. The Haversine formula computes the distance on the surface of a sphere between two points based on their latitude and longitude (Chopde 2013). Using a threshold of 30 metres, bridges within a radius of 30 metres of the measured coordinates can be identified and assigned to the corresponding measurement package. The threshold of 30 metres has initially been chosen due to the train's maximum velocity of approximately 200 km/h or 55.56 m/s. This means that at this speed, a GPS signal (sampling frequency 1 Hz) is recorded every 56 metres. So, the set threshold makes sure that no bridge is left out. This can be verified by counting the number of bridges on the existing line and comparing it with the overall number of identified crossed bridges through the implemented algorithm. The evaluation has shown that the minimal

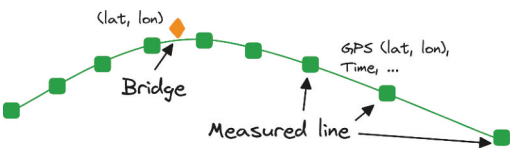


Figure 5. Identifying bridge crossings.

distances between the measured coordinates and the bridges is in average around 10 metres, confirming that the threshold is sufficient.

Figure 5 displays a location of a bridge and the measured line. The exact time of a crossing can be calculated using the train's velocity that is recorded as well.

5 EVALUATION

As there is sufficient data collected from the measurement campaign, the framework and the algorithms can be extensively tested. Figure 6 shows a specific measurement package on a map. The algorithm overall derived the line number 2650 from the measured GPS signal. In the first few measurements, line numbers 2660, 2654, or 2652 were calculated. Since the trip started in Cologne and there are different lines branching out, it is possible that other lines are closer to the measured GPS signals. Nevertheless, also different lines can be travelled during one measurement. A visual based verification of the algorithm is possible by displaying the measured line on a map (Figure 6).

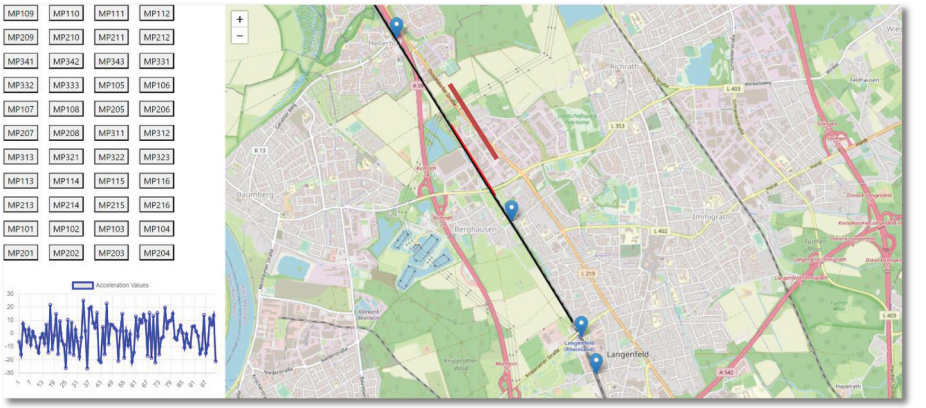


Figure 6. Browser-based visualisation of one measurement package (dark red) on a map and its acceleration measurements (MP. . .). The markers are the bridges on the line.

Bridges or bridge crossings can also be assigned to packages. For example, for the ninth measurement package the algorithm found two bridges, that were crossed during the time frame of this package. It's the eighth and ninth bridge on the line 2650 with the coordinates (50.95305818, 7.00128504) and (50.95377379, 7.00427725) respectively. The bridges in the provided open csv file have neither names nor IDs. The first coordinate of the ninth package is (50.95294117, 7.00122367) and the last (50.95391750, 7.00740033). A comparison shows that the algorithm correctly assigned the bridges to the ninth package. A visualization in a map makes a comparison even simpler. However, it is visible that the eighth bridge is near the first coordinate of the current package. Therefore, it will also be close to the last coordinate of the previous package. Due to the limited accuracy of the GPS signal and other uncertainties, the bridge is assigned to both packages. Furthermore, a sufficient distance before and after the bridge is required for subsequent analysis of the measured acceleration signals of the bridge crossing.

6 CONCLUSION AND OUTLOOK

As demonstrated in the previous section, the use of a browser-based map visualisation is a very efficient way of displaying location-based data. The algorithms used to calculate the line travelled and identify bridges crossed are also effective.

However, matching the line and then deriving the line number is a computationally expensive process, taking approximately four minutes to complete. This could be optimised by locating the first measured GPS signal in the railway network, then comparing the subsequent

measured coordinates with the coordinates of lines near the initial location. Alternatively, an input field could be included for the user to specify the line travelled. This would result in a slightly different user interface. However, if such measurement campaigns were to be carried out nationwide and on a daily basis, a fully automated solution would be required.

Furthermore, it is important to note that a browser-based solution would require the data to be uploaded or sent to the framework. Since file sizes are relatively large, the process may take some time depending on the internet connection. Local software applications could address this issue, or the presented algorithms could be carried out directly on the edge device collecting the measurement data. The derived information could be stored as meta data and referenced to measurement packages.

Additionally, further analysis services, such as those presented in Rupp et al. (Rupp 2023), can be smoothly and easily integrated. Furthermore, the proposed solution can be integrated into the digital twin framework developed within the ZEKISS research project, see e.g., Brötzmann et al. (Brötzmann 2022).

REFERENCES

Advanced TrainLab 2023. The fastest lab on rails. https://www.deutschebahn.com/en/Digitalization/The-fastest-lab-on-rails-6935126, accessed 21. Nov. 2023.

Bohmann 2023. leonbohmann/APReader: v1.1.2. https://github.com/leonbohmann/APReader, accessed 22. Nov. 2023.

Brötzmann, J., Thiele, C. D., Rüppel, U., Lorenzen, S. R., Berthold, H. & Schneider, J. 2022. A review of the digital twin in the AEC sector in the context of application. Bridge Safety, Maintenance, Management, Life-Cycle, Resilience and Sustainability, 855–862. DOI: 10.1201/9781003322641-102.

Chopde, N. R. & Nichat, M. 2013. Landmark based shortest path detection by using A* and Haversine formula. International Journal of Innovative Research in Computer and Communication Engineering, 1(2), 298–302.

Deutsche Bahn 2023. Open-Data-Portal. Das Datenportal der Deutschen Bahn AG. https://data.deutschebahn.com/, accessed 24. Nov. 2023.

Django 2023. The web framework for perfectionists with deadlines. https://www.djangoproject.com/, accessed 24. Nov. 2023.

GeeksforGeeks 2023. Python Web Development - Django Tutorial, 2021. URL https://www.geeksforgeeks.org/python-web-development-django-tutorial/, accessed 20. Nov. 2023.

Geißler, K., Steffens, N. & Stein R. 2019. Grundlagen der sicherheitsäquivalenten Bewertung von Brücken mit Bauwerksmonitoring. *Stahlbau 88(4)*, 338–353.

GeoPandas 2023. GeoPandas is an open-source project to make working with geospatial data in python easier. https://geopandas.org/en/stable/, accessed 24. Nov. 2023.

Hbf878 2020. Map of German rail network. https://commons.wikimedia.org/w/index.php?curid=-89862775, accessed 21. Nov. 2023.

Knapp, N. 2019. *Faktenblatt – Eisenbahnbrücken bei der Deutschen Bahn*. https://www.deutschebahn.com/resource/blob/6860076/452fa9432001be62ac986886a2e60dd2/MP-Bruecken-Faktenblatt-875-Bruecken-data.pdf.

Lorenzen S. R., Wolter K. U., Rupp M.M., Grunert G. Apostolidi E. & Schneider J. 2023. Indirect monitoring of Railway Bridges using the Continuous Track Monitoring System CTM2.0. In *9th International Conference on Computational Methods in Structural Dynamics and Earthquake Engineering*. DOI: 10.7712/120123.10477.20349.

Malekjafarian A., Corbally R. & Gong W. 2022. *A review of mobile sensing of bridges using moving vehicles: Progress to date, challenges and future trends*, Structures, vol. 44, no. August, pp. 1466–1489, 2022. DOI: 10.1016/j.istruc.2022.08.075.

Rupp, M.M., Lorenzen, S.R., Fritzsche, M.A., Riedel, H., Kohl, A., Apostolidi, E. & Schneider, J. 2023. High-speed drive-by monitoring: field testing with an intercity express train (ICE). ce/papers, 6: 854–862. DOI: 10.1002/cepa.2045.

SciPy 2023. Fundamental algorithms for scientific computing in Python. https://scipy.org/, accessed 22. Nov. 2023.

Yang, Y. B. & J. P. Yang. 2018. *State-of-the-Art Review on Modal Identification and Damage Detection of Bridges by Moving Test Vehicles*, Volume 18.

ZEKISS 2023. Zustandsbewertung von Eisenbahnbrücken und Fahrzeugen mit KI-Methoden zur Auswertung von Sensordaten und strukturdynamischen Modellen. https://zekiss.de/, accessed 22. Nov. 2023.

Bridge Maintenance, Safety, Management, Digitalization and Sustainability – Jensen, Frangopol & Schmidt (eds)
© 2024 The Author(s), ISBN 978-1-032-77040-6
Open Access: www.taylorfrancis.com, CC BY-NC-ND 4.0 license

OMA-driven structural assessment to prevent fatigue-induced failure in steel bridges

Guangli Du
Department of the Built Environment, Aalborg University, Denmark

Rune Brincker
Brincker Monitoring ApS, Denmark

Sandro Amador
Department of Civil Engineering and Mechanical Engineering, Technical University of Denmark

Umberto Alibrandi
Department of Civil and Architectural Engineering, Aarhus University, Denmark

ABSTRACT: Fatigue cracks in steel bridges can lead to catastrophic failure and cause significant risks to public safety. These cracks can grow, propagate, reduce the structure maximum design capacity, and ultimately lead to a sudden failure. Fatigue cracks in steel bridges are primarily induced by the cyclic loading from constant traffic loads over time. Therefore, monitoring fatigue on steel bridges is essential to ensure structural safety. Operational modal analysis (OMA) is a non-destructive testing technique that can be used to monitor fatigue-induced damage through changes in modal parameters. When the fatigue crack grows the stiffness of the beam will reduce. This study implements OMA on a simply supported steel beam with changing stiffness. The natural frequencies and mode shapes of the beam are obtained through OMA, and combined with a model to predict the stress/strains at any point of the structure. The case study shows how maximum stresses and the natural frequencies that are affected by the crack growth are varying due to changes in stiffness. The result demonstrates that by combining OMA with fatigue assessment, the risk of fatigue failure in steel bridges can be significantly reduced.

1 INTRODUCTION

Fatigue crack is a critical issue for metallic structures. Especially for steel bridges that are subjected to the cyclic loading from constant traffic over time. Fatigue can reduce structure load-bearing capacity and overall service life (Azaïs et al., 2019; Kirkegaard et al.,1991; Leander, 2013; Avci et al., 2021). Also, weld imperfections often increase stress concentration that serve as potential initiators for fatigue cracking. If an initiated crack is subjected to cyclic loads, the crack will grow for each load cycle even if the stress level is far below the yield stress. When the crack has propagated beyond a threshold level, early failure may occur.

Recently growing attention has been obtained by Operational Modal Analysis (OMA) (Brincker and Vantura, 2015; Amador and Brincker, 2021, Alibrandi et al. 2023) and vibration based SHM (Lysgaard et al., 2020; Diord et al., 2017; Peeters De-Roeck, 2001; Alibrandi, 2022;). The underlying idea of these technologies is to enable engineers to assess the structural condition of different structural systems by simply extracting the system's physical properties - which are intrinsically related to the stiffness or strength of the system - from the vibration responses continuously acquired in a vibration-based monitoring campaign. Due to

DOI: 10.1201/9781003483755-200

the non-destructive character of these structural assessment techniques, they have become very popular amongst the structural engineering community and have increasingly been used in damage and structural condition assessment of modern society's civil infrastructure. This paper aims to illustrate the detectability on a case where the total fatigue life was seriously reduced due to un-expected stress concentration. It explores how a crack in a large steel bridge can be detected from the drop of the natural frequency. Additionally, it examines the timeframe available to the bridge owner for reaction when the natural frequency decline reaches a magnitude detectable through operational modal analysis (OMA).

2 FATIGUE ASSESSMENT

2.1 *Considered structure*

A support beam in a large bridge structure is illustrated in this study. As shown in Figure 1, the force F is applied on the bridge super structure, and as a result the dominating mass of this problem is not the mass of the beam, but the mass m of the part of the structure that is introducing the force F. As illustrated in Figure 1, a crack with the length a is introduced at the bottom of the beam, so that when vibrations occur on the bridge the associated fatigue will make the crack grow to a point that the crack growth might lead to a final failure.

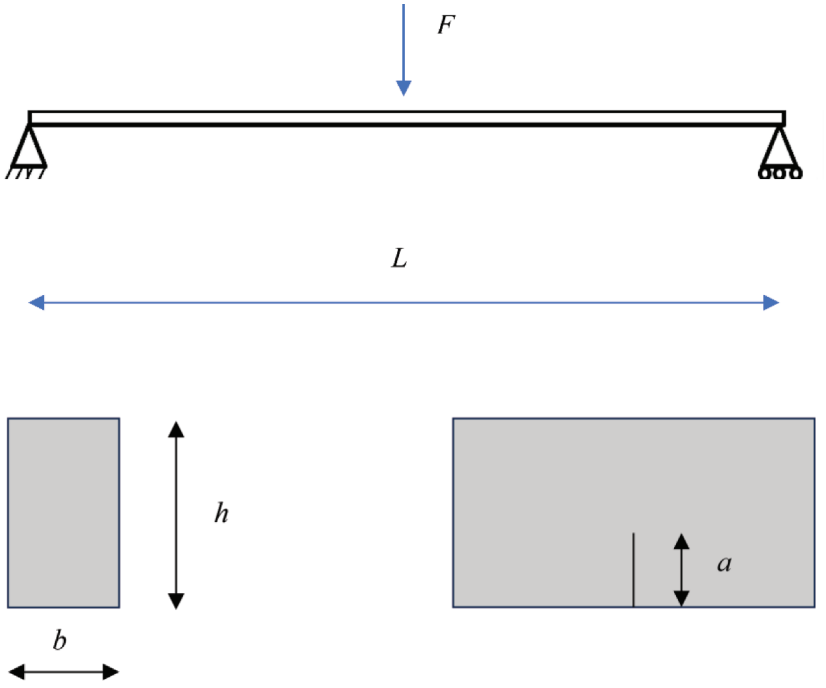


Figure 1. Top: Beam structure with a beam length L loaded with a point load F in the middle. Bottom: beam depth h,beam width $b$and a crack with length a in the middle of tension side of the beam.

2.2 *Stress and deformation*

Ignoring the crack, the stress in the beam is described by the bending moment that is given by

$$M = \frac{1}{4}FL \tag{1}$$

And the maximum stress at the bottom of the beam is then obtained dividing Eq. (1) by the resistant moment $W = \frac{1}{6}bh^2$

$$\sigma_0 = \frac{M}{W} = \frac{3}{2}\frac{FL}{bh^2} \tag{2}$$

The deformation in the middle of the considered beam is

$$u = \frac{FL^3}{48EI} \tag{3}$$

where EI is the bending stiffness, E is the Youngs Modulus and I is the geometrical moment of inertia. This defines the compliance for the crack length equal to zero

$$C_b = u/F = \frac{L^3}{48EI} \tag{4}$$

2.2 *Stress intensity*

The stress distribution around the crack is described by the stress intensity factor

$$K_I(a) = \sigma_0\sqrt{\pi a\, f(a/h)} \tag{5}$$

where the function $f(a/h)$ is given by

$$f\left(\frac{a}{h}\right) = 1.12 - 1.39\frac{a}{h} + 7.3\left(\frac{a}{h}\right)^2 - 13\left(\frac{a}{h}\right)^3 + 14\left(\frac{a}{h}\right)^4 \tag{6}$$

see Kåre Hellan (1984). In Figure 2 this solution is shown as a function of the crack length comparing with a similar solution from the reference Engineering Library.

2.3 *Fatigue crack growth*

The approach of the fracture mechanics describes the functional relationship between the crack depth a with the size and number of load cycles, where linear elastic behavior of the material is assumed. The fatigue crack growth is generally divided into three regions: (A) the crack growth process is governed by a threshold below which no crack growth occurs, (B) the crack growth is described by a linear relationship between log (ΔK) and log (da/dN), (C) fatigue crack growth interferes with fracture. The Paris law describes the second region. By assuming constant load amplitude, region (B) becomes

$$\frac{da}{dN} = A(\Delta K)^m \tag{7}$$

where ΔK is the intensity factor range, m, A are the Paris constants, and da is the extension of the crack over N load cycles. The intensity factor range is the difference of the maximum and the minimum of the stress intensity factor in one single stress cycle. For simplicity we will assume a constant stress cycle with amplitude σ_1, so that the intensity factor range is given by

$$\Delta K(a) = 2\sigma_1\sqrt{\pi a\, f\ (a/h)} \tag{8}$$

The number of load cycles extending the crack from a to + da is then given by

$$dN = \frac{da}{A\Delta K(a)^m} \tag{9}$$

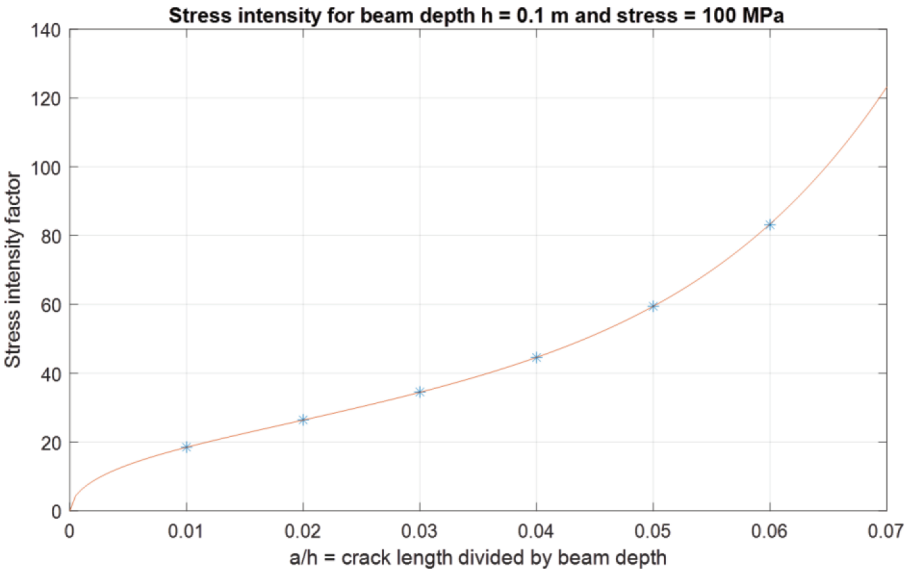


Figure 2. Stress intensity factor as a function of the crack length. The solution given by reference Kåre (1984) (red curve) is compared to solution from reference Engineering Library (blue asterisks).

2.4 *Fatigue failure*

When the fatigue crack grows, the stress intensity factor increase correspondingly until a critical crack length is reached where

$$K_I(a_c) = K_c \tag{10}$$

with K denoting the critical stress intensity factor, and where for the final failure, the stress intensity factor $K_I(a_c)$ is the sum of the stress intensity factor for the mean stress given by Eq. (5) and the half of the intensity range $\Delta K(a_c)$ given by Eq. (8)

The number of cycles N to fracture can then be obtained from the integration of Eq. (9) to yield

$$N = 2A \int_{a=a_0}^{a=a_c} K_t(a) - m_{da} \tag{11}$$

where a_0 is the initial crack length.

2.5 *Time To React (TTR)*

When the fatigue crack grows the stiffness of the beam will reduce, i.e. we will see an increasing compliance. It can be shown that the added compliance can be calculated as (Rincker, 2022)

$$\Delta C = \frac{2}{F^2} \int_{a_0}^{a+\Delta a} K_I^2/E \, da = \frac{\pi}{2Eh^2} \int_{a_0}^{a+\Delta a} a f(a/h)^2 \, da \tag{12}$$

As mentioned, we assume the beam to be a smaller part of bridge carrying the load F from the main structure, but also the main structure will introduce an associated mass m to move together with the mid point of the beam. Thus, neglecting the beam mass by assuming that it is small compared to m we have the following expression for the natural frequency f_b of the beam before a crack is introduced

$$f_b = \frac{1}{\sqrt{C_b m}} \tag{13}$$

After introducing the crack the natural frequency is

$$f_a = \frac{1}{\sqrt{(C_b + \Delta C)m}} \tag{14}$$

and we can define the dimensionless frequency ratio

$$\frac{f_a}{f_b} = \sqrt{\frac{C_b m}{(C_b + \Delta C)m}} = (1 + \Delta C / C_b)^{-1/2} \tag{15}$$

3 CONSIDERED CRACK EXTENSION CASES

For the illustrative purpose, we assume a beam case with the following material properties:

- Yeilding stress: 250 MPa
- Youngs modulus: 210 GPa
- Critical intensity factor: 50 MPa x $m^{1/2}$, see Wikipedia
- Paris constants: m = 3 and A = 10^{-8} mm/cycle, see Milović et al (2011)
- Initial crack lengths: a_0 = 2, 1, 0.5, 0.25 and 0.125 mm
- geometry of the considered beam: h = 1 m, b = 0.1 m and L = 10 m

Two cases are considered: one where the mean stress σ_0 is zero or close to zero, so it can be neglected, and one where the mean stress σ_0 is 10 % of the yielding stress. In both cases we focus on studying the errors occurred in the design process or fabrication, which has reduced

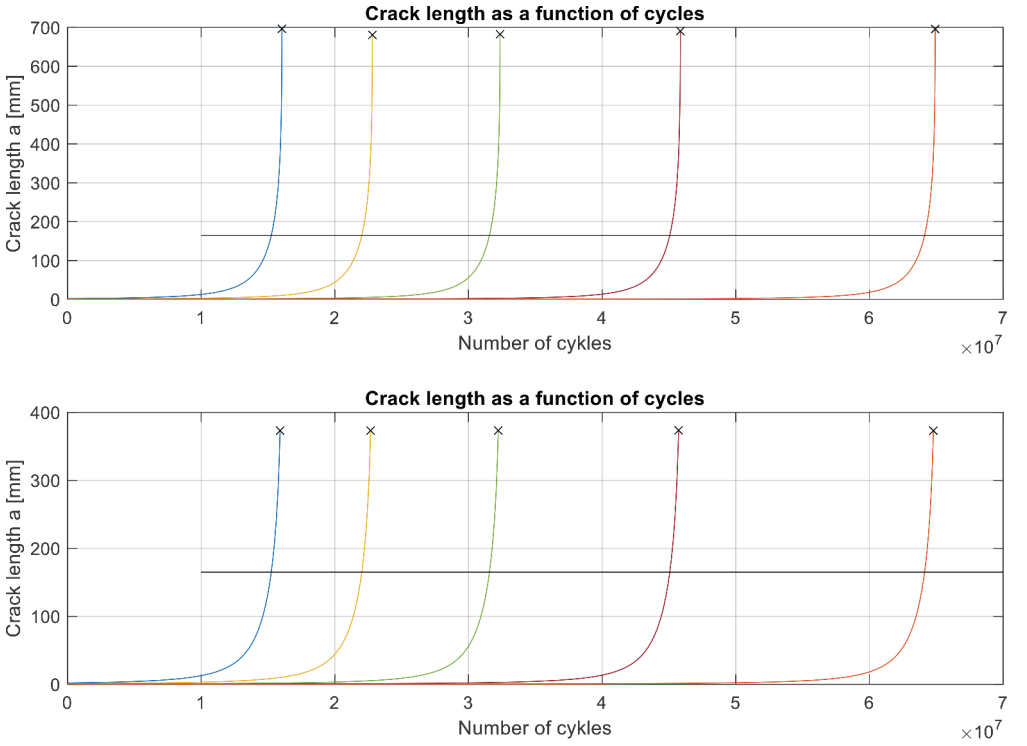


Figure 3. Crack length as a function of cycles for different initial crack length's (from the left) a_0 = 2, 1, 0.5, 0.25 and 0.125 mm. Top plot gives the results for zero mean stress, and the bottom plot for a means stress that is 10 % of the yielding stress. The horizontal line in both plots indicates the crack length for which the natural frequency of the beam has dropped 0.1 %.

the fatigue life to 10 % of the target life-time that is set to 20 years. The natural frequency of the beam including the mass from the structure loading the beam is set to 1 Hz.

Figure 3 Shows the crack propagation for different crack lengths, top plot for the zero mean stress and bottom plot for the mean stress equal to 10 % of the yielding stress. The horizontal line in both plots indicates the crack length for which the natural frequency of the beam has dropped 0.1 %, that is a = 165 mm.

From the theory of the crack extension, we see that the curves are the same for the two mean stress cases. The only difference is when the mean stress is large, which causes the final failure to happen earlier. This is due a higher value of the mean stress intensity factor.

We can now read the values of the curves, and calculate the number of cycles it takes to propagate the crack from a =165 mm to a_c. The results are given in Table 1 and 2 where results are also given for a frequency drop of 0.2 %, 0.5 % and 1 %.

Table 1. Time to react (TTR) for different frequency drop for the case of zero mean stress.

Freq. drop [%]	Crack [mm]	TTR [h]	TTR [days]
0.10	165	221.1	9.2
0.20	238	120.8	5.0
0.50	357	43.9	1.8
1.00	470	14.4	0.6

Table 2. Time to react (TTR) for different frequency drop for the case of a mean stress = 10 % of the yielding stress.

Freq. drop [%]	Crack [mm]	TTR [h]	TTR [days]
0.10	165	183.3	7.6
0.20	238	83.1	3.5
0.50	357	6.1	0.3
1.00	470	0.0	0.0

4 DISCUSSIONS

To detect a frequency drop of 0.1 %, we would need at least an uncertainty on the estimated natural frequency of that range. A frequency uncertainty of 0.1 % is normally difficult to achieve using classical OMA. However, in this case we have many test instruments, and thus, it is natural to assume that averaging these tests, we might easily reduce uncertainty to 0.1 %.

In addition to the uncertainties on the estimates for the natural frequencies, over time, changes in the environmental conditions may easily increase the uncertainty to something like 1 %. That is why we have considered four values in Tables 1 and 2 for the frequency drop in the range from 0.1 % to 1 %.

As shown in Table 1, in case when the mean stress is small, we will have time to react for all the considered frequency drops. For the smallest drop, we have plenty of time to react – about a week. For biggest drop we still have time to react – about 7 hours.

Similarly, as shown in Table 2, if we can detect reasonable small frequency drops, then we still have time to react for a larger mean stress – in case of a frequency drop of 0.5 % we have 6 hours to react. That is still a reasonable time, and it should be considered realistic to achieve an uncertainty smaller than 0.5 % for real life OMA.

REFERENCES

Avci, O., Abdeljaber, O., Kiranyaz, S., Hussein, M., Gabbouj, M. and Inman, D.J., 2021. A review of vibration-based damage detection in civil structures: From traditional methods to Machine Learning and Deep Learning applications. Mechanical systems and signal processing, 147, p.107077.

Azaïs, R., Gégout-petit, A., Greciet, F., Azaïs, R., Gégout-petit, A., Greciet, F., 2019. Rupture detection in fatigue crack propagation To cite this version : HAL Id : hal–01862267.

Alibrandi U, Du G, Diord R. A. S, Brinker R. 2022. Utility of Information (UoI) for probabilistic fatigue monitoring. In Beer M, Zio E, Phoon K-K, Ayyub BM, editors, Proc. of the 8th Intl. Symp. on Reliability Engineering and Risk Management (ISRERM). Research Publishing, Singapore. 2022. p. 662–666.

Alibrandi, U. 2022. Risk-Informed Digital Twin of Buildings and Infrastructures for Sustainable and Resilient urban communities, *ASCE-ASME Journal of Risk and Uncertainty in Engineering Systems, Part A: Civil Engineering*

B. Peeters and G. De-Roeck, One-year monitoring of the z24-bridge: Environmental effects versus damage events.

U. Alibrandi, L. He, A. Contento, I K-T Pang, K.M. Mosalam and B. Briseghella, Risk-informed Digital Twin of a butterfly-arch stress-ribbon pedestrian bridge, *ARCH23, 10th International Conference on arch bridges* Fuzhou, China, October 25-27, 2023

R. Brincker, *Note on energy release and stiffness reduction* V1-7. Internal note, Department of Civil engineering, Technical University of Denmark 2022.

R. Brincker and C. Ventura, Introduction to Operational Modal Analysis. John Wiley & Sons, Chicester, UK, 2015.

S. A. Diord, F. Magalhães, A. Cunha, E. Caetano, and N. Martins, Automated modal tracking in a football stadium suspension roof for detection of structural changes, Control and Health Monitoring, vol. 24, no. 11, e2006, 2017.

Engineering Library: *Stress Intensity Factor*. https://engineeringlibrary.org/reference/fracture-mechanics-stress-intensity-factor

P. Lysgaard, S. Amador, S. Nielsen, E. Katsanos, and R. Brincker, Vibration-based damage detection using input output and output-only environmental models: A comparison, Proceedings of the International Modal Analysis Conference (IMAC), Houston, TX, USA, 2020.

A. D. R Sandro; R. Brincker. Robust multi-dataset identification with frequency domain decomposition, Journal of Sound and Vibration, vol. 508, p. 116 207, 2021.

Milović et al: *Determination of fatigue crack growth parameters in welded joint of HSLA steel*. Paper presented at the Eleventh Meeting "New Trends in Fatigue and Fracture" (NT2F11), Polignano a Mare, Italy, 3–6 July, 2011.

Kåre Hellan: *Introduction to fracture mechanics*. McGraw-Hill 1984.

Kirkegaard, P.H., Sørensen, J.D., Brincker, R., 1991. Fatigue reliability analysis of a mono-tower platform. Mar. Struct. 4, 413–434. https://doi.org/10.1016/0951-8339(91)90035-A

ADDIN Mendeley Bibliography CSL_BIBLIOGRAPHY Leander, J., 2013. Refining the fatigue assessment procedure of existing steel bridges 124.

Wikipedia: https://en.wikipedia.org/wiki/Fracture_toughness

Earthquake engineering structural dynamics, vol. 30, no. 2, pp. 149–171, 2001.

Bridge Maintenance, Safety, Management, Digitalization and Sustainability – Jensen, Frangopol & Schmidt (eds)
© 2024 The Author(s), ISBN 978-1-032-77040-6
Open Access: www.taylorfrancis.com, CC BY-NC-ND 4.0 license

SHM for railway bridges: Real time analysis of the train transit and thermal data

G. Ascari, A. Dalle Fratte & A. Terraneo
Akron srl, Bovisio-Masciago, Italy

P. Scali
Euroferroviaria, Roma, Italy

ABSTRACT: Fundamental aspects in railway bridges are the extreme stiffness and the relative influence of the impact of the train transits as compared to the variations resulting from the thermal phenomena. Within the framework of structural monitoring of railway bridges, an innovative approach in the monitoring techniques for the measurement of the relevant parameters of the structures is presented. This method allows to separate the effects of the train transit alone from the measurement of the parameters in certain rest conditions (environmental noise and thermal effects), already during the acquisition phase (edge computing) in near-real time. This approach enables to create two distinct datasets in terms of stresses, strains and displacements. Those, together with the measurement of the mass and speed of the trains transiting on the bridge, and considering the high frequency of train transit, allow the immediate use of the monitoring data for the construction of a dedicated dataset in terms of cause-effect (e. g. curvatures, bending moment, shear stresses), which can be used to verify the behavior of the structure comparing it with what expected. The differentiated measurement and the innovative calculation processes allow detailed analysis of a single-track deck or, in the case of double-track decks, the distinction of the transit direction (with evaluation of torsional phenomena) or of simultaneous transit on both tracks (greater flexural effects). The presented monitoring solution (hw & sw) allows to extract engineering parameters directly during the acquisition phase, assimilating and effectively treating each train transit as a single load test.

1 INTRODUCTION

In the context of the study of the health and maintenance of railway bridges, a fundamental issue concerns the difference in the analysis approach of the variation of the measured parameters due to thermals effects and caused by external forcing.

The main attention is generally focused on how the external forcing affect the structure behavior, not considering that the effect that the thermal variation has on the same parameters is generally an order of magnitude higher.

Therefore, it becomes fundamental the separation of the acquired dataset in the data related to the rest conditions of the structure (thermal variations and environmental noise effects) and related to the effects of the forcing alone (e.g. train transits, but also applicable to wind gusts, earthquakes, other).

The topic presented in the article addresses an in-depth analysis of the thermal effects and the critical issues related to the correction of the acquired data from the thermal component, and suggests a monitoring system solution that separates the two datasets (rest conditions and external forcing) in real time during the acquisition phase, using advanced edge computing functions.

DOI: 10.1201/9781003483755-201

2 THERMAL EFFECT ON THE STRUCTURES

The analyses on several databases acquired for different monitored structures on an annual basis, led to the observation that the variation of the parameters such as deformation, displacement measure at the bearings and tilt due to the thermal effect alone is generally an order of magnitude higher than the variation of the same parameters due to the effect of an external forcing, such as the train transit.

In order to correctly evaluate how the external forcing alone affects the structure, a procedure that corrects the data from the thermal effect is necessary. During the short-term daily cycle and within the long-term seasonal cycle, the parameter being measured is at different values depending on the temperature and thermal inertia. There are different common methods to correct the data from the thermal component, such as linear and multivariate regression methods.

However, there are some critical issues that affect the correction and the results. In fact, in the analysis of the temperature effects it cannot be avoided to take into consideration the effects of the possible different insolation determined by the position and the geometry of the structure.

3 CRITICAL ISSUES

The main critical issues concerning the correction of the acquired data from the thermal component are the thermal shift, the thermal inertia, the oversampling and the overfitting.

3.1 *Thermal shift*

The thermal shift consists in the presence of a temporal shift between the daily absolute maximum/minimum peak values of the temperature with the absolute maximum/minimum values of the parameter being measured. The parameters such as deformation, displacement at the bearings, tilt, respond differently depending on the increasing (heating) or decreasing (cooling) temperature of the temperature gradient during the daily heating and cooling phases.

This phenomenon is not only referable to a shift in the deformation response with respect to the temperature variation, but also to different ways of heating of the structure. The thermal shift value is variable during the year and during the individual heating and cooling phases in a single daily cycle (Figure 1).

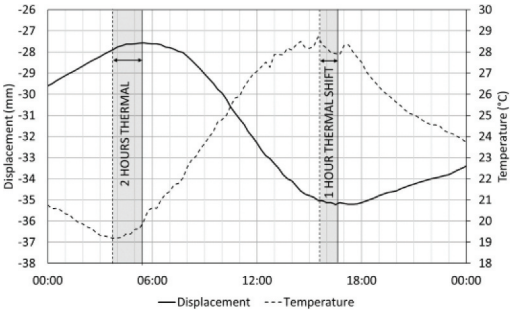
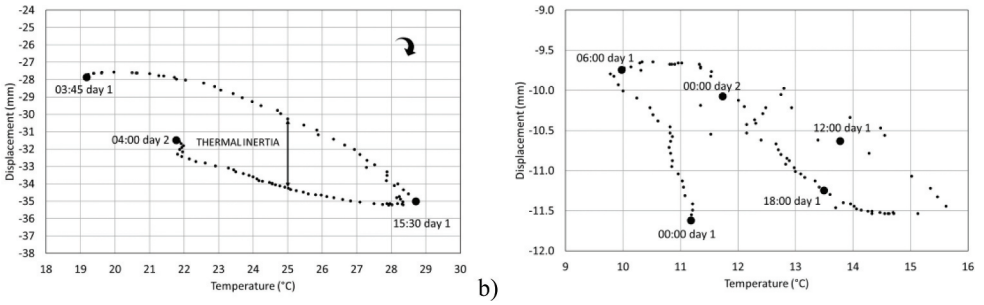


Figure 1. Thermal shift during the heating and the cooling phases in a daily cycle for a displacement sensor. The graph shows a displacement curve and a temperature curve. It is possible to notice the difference in the width of the shift during the heating and the cooling phases. The shift value is calculated between the minimum value of the temperature and the maximum value of the displacement for the heating phase and the maximum value of the temperature and the minimum value of the displacement for the cooling phase.

3.2 *Thermal inertia*

The phenomenon of thermal inertia, or the different heating/cooling rates of the structure, determines a non-linearity of the measured parameter in relation to the temperature variation during a daily cycle. The relationship between the parameter being measured (e.g. deformation or displacement) and the temperature outlines a single or double ring "elliptical" path during the daily thermal cycle. In this cycle, at a same temperature value, the corresponding measured parameter is different depending on whether it is measuring during the heating phase or the cooling phase (Figures 2a).



a) b)

Figure 2. a) thermal inertia in a thermal daily cycle (minimum – maximum – minimum); b) thermal inertia in the 24 hours, for an irregular daily cycle.

However, the daily cycle doesn't outline a regular sinusoidal trend. On days in which sudden temperature variations occur or in which the temperature variation does not follow the normal hysteresis daily cycle of minimum-maximum-minimum, the resulting correlation curve (temperature-parameter) may have a highly irregular trend. In these cases, the issue of thermal inertia becomes more complicated, also impacting on the methods chosen to correct the thermal curves. Therefore, the simple regression methods (linear or multivariate) for the correction of the thermal component may not be enough nor effective (Figure 2b).

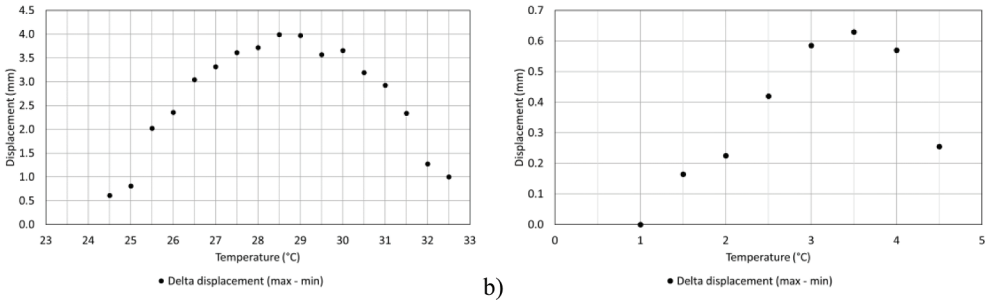
3.3 *Variation of the inertia during a thermal cycle*

Thermal inertia is one of the main factors that make the correction with a simple linear regression method ineffective. The thermal inertia value varies over the daily cycle, depending on the average daily temperature. Therefore, its effect has repercussions both in the short term and in the long term, complicating the mathematical laws that describe the phenomenon. An in-depth analysis of the maximum daily values of thermal inertia is proposed.

A sufficiently high number of daily thermal cycles (minimum – maximum – minimum) were consider, in order to confirm the observations. The temperature values (acquired up to the second decimal) has been rounded to 0.5 °C. For each half degree of temperature, the maximum value and minimum value of the parameter being measured (displacement) were considered and the delta (maximum value minus minimum value) was performed (Figures 3a, b).

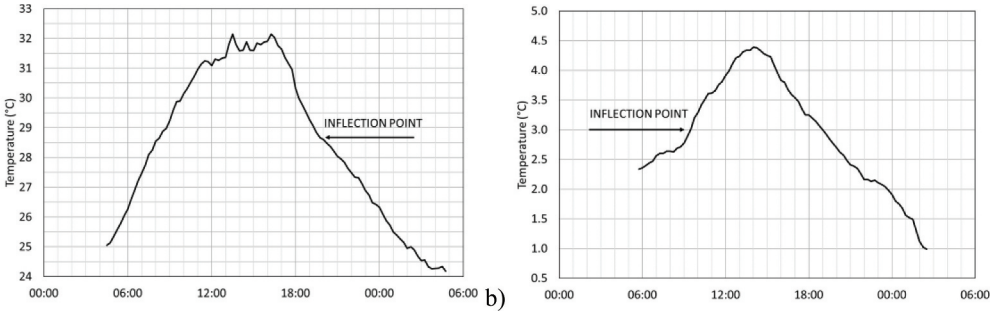
It is shown that the maximum value of delta has a correspondence with the average temperature of a thermal cycle (minimum – maximum – minimum) and with the inflection point of the temperature curve, assimilated to a sinusoid curve (Figures 4a, b).

The analysis was performed for warm and cold periods. The validity of the observation is confirmed, although for lower average temperatures the thermal inertia values are lower (due to the daily temperature range, which is generally more limited in cold periods).



a) b)

Figure 3. Delta (maximum displacement value minus minimum displacement value) for each value of temperature (rounded to a step equal to 0.5 °C) during an entire thermal cycle during a) the warm period and b) the cold period.



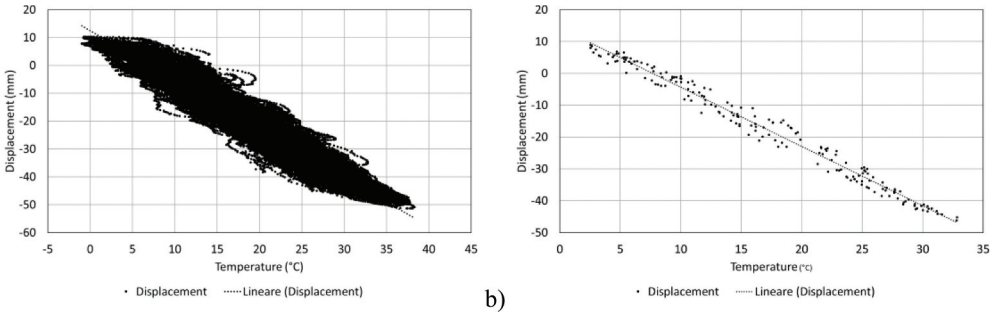
a) b)

Figure 4. a) temperature curve used for the analysis shown in Figure 4a, and inflection point at about 28.5 °C, corresponding to the average daily temperature; b) temperature curve used for the analysis shown in Figure 4b, and inflection point at about 3.0 °C, corresponding to the average daily temperature.

3.4 *Oversampling and overfitting*

Regardless of the method used for thermal correction, it is necessary to analyze the phenomena related to oversampling. By averaging the data acquired over different time intervals (1, 6, 12, 18, 24, 48, 96 hours) it can be noticed that the dispersion of the data is decreased (Figures 5a, b), and consequently, also the correlation index (Table 1, Figure 6).

The use of a large amount of data in static structural monitoring (e.g. sampling rate equal to 15 minutes) leads to a low usability of "simplified" thermal models. Consequently, it is easy to incur into overfitting problems, i.e. a high forecast error caused by the complexity of the model. Overfitting occurs when the model cannot be generalized and overfits the training dataset.



a) b)

Figure 5. Cross correlation graphs between the temperature and the displacement values for a) a two years database and sampling frequency of 15 min and b) for a two years database and averaging on 96 hours.

The graph in Figure 6 represents the variation of the correlation coefficient between temperature and displacement (for two different sensors) as the time grouping changes (from sampling rate equal to 15 minutes up to data averaged over 96 hours). A two-year database was considered for the analyses.

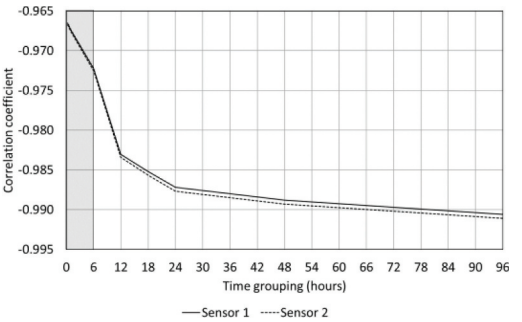


Figure 6. Variation of the cross-correlation values (Table 1), for increasing time averaging.

Table 1. Correlation coefficient variation for different degree (time) of data averaging.

Averaging degree	Correlation	coefficient
	Sensor 1	Sensor 2
15 min	-0.967	-0.967
1 hour	-0.967	-0.968
6 hours	-0.972	-0.973
12 hours	-0.983	-0.983
18 hours	-0.985	-0.986
24 hours	-0.987	-0.988
48 hours	-0.989	-0.989
96 hours	-0.991	-0.991

The improvement of the correlation coefficient using a database averaged over longer periods depends on the elimination of the thermal shift (after the first 6 hours, as the shift is generally shorter) and on the smoothing of the peculiar effects of each individual daily cycle.

In order to better fit the data by grouping the data on a time basis, a sufficiently long acquisition period is necessary, in order to perform a correct analysis of seasonal thermal cycles and to have a significant quantity of points to validate the observations. It is also necessary to correctly estimate the appropriate reactivity period to obtain the precision of the expected data.

4 REAL-TIME MEASUREMENT AND CALCULATION OF THE TRAIN TRANSITS EFFECTS ON THE BRIDGE

4.1 *Separation of train transit effects from thermal effects*

Given the critical issues for the correction of the effect of the thermal component in the post-processing phase, the best solution is to operate directly during the acquisition phase, using advanced edge computing functions that are performed directly on the field computer. The particular acquisition and processing mode functions developed for the monitoring system allows the separation of the acquired dataset in the data related to the rest conditions of the

structure (thermal variations and environmental noise effects) and related to the effects of the forcing alone (e.g. train transits, but also applicable to wind gusts, earthquakes, other).

In Figures 7, 8a and 8b it is shown an example of separation of the two datasets acquired on a pre-compressed concrete railway double track bridge. The acquired data are from two different strain gage installed on the same beam, one in the intrados position and the other in the extrados position. In Figures 9a e 9b it is shown the analysis on a daily curvature, calculated as difference in modulus between the intrados and extrados strain values measured on the same beam, divided by the distance between the two installed sensors.

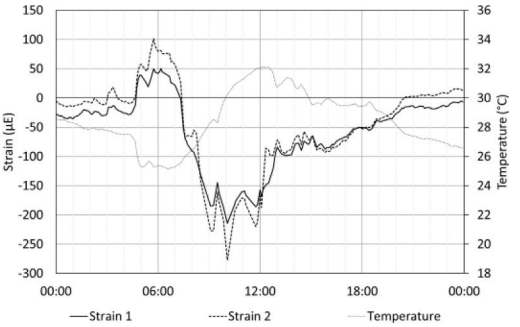


Figure 7. Daily variation of the value of two different strain sensors and temperature in rest conditions.

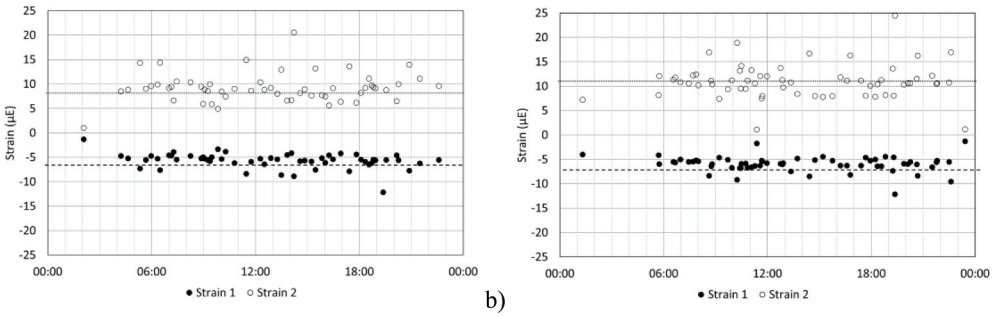


Figure 8. Daily variation of the value of two different strain sensors in forcing conditions. The graph on the left is related to the train transit on track 1 (a), the graph on the right to the train transit on track 2 (b).

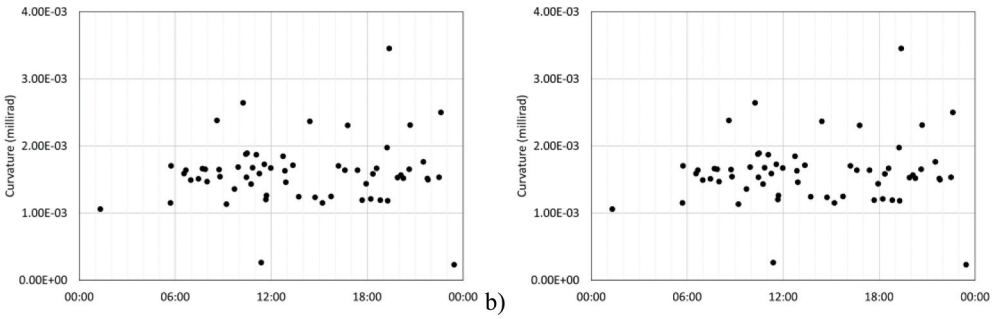


Figure 9. Daily value of curvature, calculated as difference in modulus between the intrados and extrados strain values measured on the same beam, divided by the distance between the two installed sensors. The graph on the left is related to the train transit on track 1 (a), the graph on the right to the train transit on track 2 (b).

4.2 *Value occurrence analysis*

From the dataset relating to the thermal component and from the dataset relating to the effects of the train transit component, it is useful to perform an analysis of the recurrence of the values, in particular the maximum daily values, in order to identify a "threshold" level for the identification of an evolution in the behavior of the structure in response to both the thermal and the forcing effects (e.g. railway trains in transit).

Regarding the variation of the parameter due to the thermal effect, it is necessary to have an entire annual monitoring cycle, to outline the upper and the lower limits of the variation range. Regarding the variation of the parameter due to the sole effect of the forcing (train transit), a population of a few hundred trains will be enough to validate the upper limit.

It is therefore possible to use this analysis to outline the thresholds for a diagnosis of the occurrence of an anomaly in the behavior of the bridge, in terms of variation in the distribution of the maximum daily recurrence peak values and use this parameter as a possible indicator to monitor the health of the monitored structure.

4.2.1 *Analysis for the thermal effect*

In this paragraph it is presented the analysis of the occurrences of the values during rest conditions, as effect of thermal variation and environmental noise (Figure 10a), and the range of variability of the monitored parameter during an entire seasonal cycle (Figure 10b), obtained as maximum and minimum daily values.

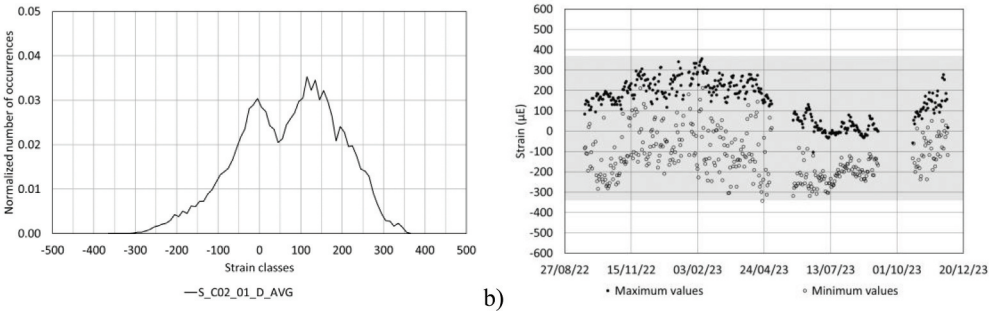


Figure 10. a) analysis of the occurrences of the values (strain) during rest conditions; b) range of variability of the monitored parameter during an entire seasonal cycle (rest conditions), obtained as maximum and minimum daily values.

4.2.2 *Analysis for the external forcing: Train transits*

Below, it is presented the analysis of the occurrences of the values during forcing conditions, as effect of train transit. Important information is already available from the acquisitions

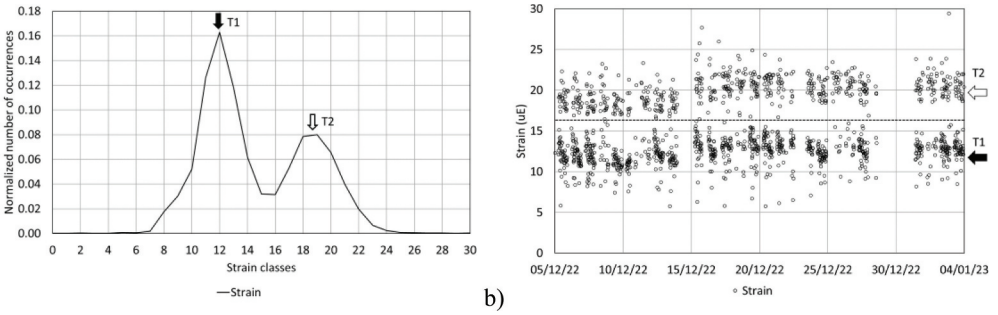


Figure 11. Analysis of the occurrences of the values (strain) during train transits (a). It can be noticed the presence of two defined picks related to the transit of two different type of train (b).

dedicated to train transits regarding the presence of two distinct families of behavioral response effects, due to two different types of trains, T1 and T2, characterized by different masses (Figures 11a, b).

The analysis of the variations in the maximum daily peak values on a database of one year of acquisition for a strain parameter is presented below (Figure 12a), with the separation of the analysis for the two families of values related to the transits of the two different types of trains. From the graph obtained, a trend can be outlined, which seems to have a link with the variations of the parameter with the thermal variation, albeit on a very small scale (around approximately ± 1 uE for the first family of trains and approximately ± 1.5 uE for the second family of trains). The same type of analysis was carried out using the curvature value, calculated as difference in modulus between the intrados and extrados strain values measured on the same beam, divided by the distance between the two installed sensors (Figure 12b).

Considering that the correlations between the calculated peak values and the average temperature and the correlation between the peak values and the daily averaged variation of the parameter in rest conditions are very low, it is assumed that the variation of the pick values and of the pick of curvature values during the train transits is affected by a variation in the elastic modulus of the constituent material (concrete) with the variation of the average daily temperature during the seasonal cycle.

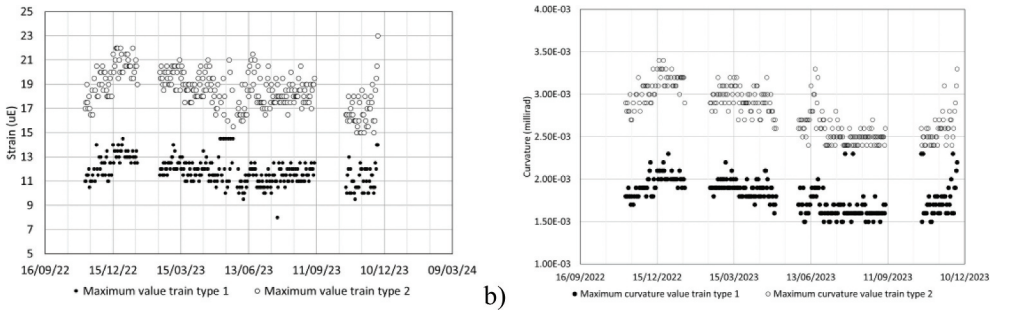


Figure 12. a) variations in the maximum daily peak values on a database of one year of acquisition for a strain; b) variations in the maximum daily peak values of the curvature on a database of one year of acquisition.

5 CONCLUSIONS

This work presents a monitoring system solution that allows the real-time separation of thermal effects from the effects of forcing agents on a structure. The variation of parameters such as deformation, displacement at the bearings and at the joints and tilt, due to the thermal effect alone is generally an order of magnitude higher than the variation of the same parameters due to the effect of external forcing, such as the train transits. Therefore, the analysis of the behavior of a bridge in terms of prediction of the parameters being measured and analysis of possible damage requires a considerable training period (generally in the order of at least 2 seasons).

The monitoring solution presented allows the separation of the the measurements of the structure parameters in rest conditions from the measurements related to the transit of trains. With this method it is possible to use the transits of railway trains of an operating railway line as a continuous series of load tests. The system also provides the possibility to calculate the transit speed of the trains and, using a dynamic weight in motion system, the dynamic force-effects correlation. The use of hardware and software solutions that allow real-time analysis not only of the parameters being measured, but also of calculated parameters (e.g. curvature), also allow the consolidation of measurement information in engineering parameters.

Given the generally high frequency of transits on railway lines, it is possible, directly from the monitoring acquired data, to classify the type of trains in transit, to determine the cause-effect relationship both on measured parameters and directly on engineering parameters (virtual channels obtained from algorithms applied to the acquired data), to calculate the repetitiveness of the effects on the bridge structures through the analysis of the occurrences (Gaussian curves) and to verify the coherence of the forcing/effects relationship over time.

The information thus calculated and analyzed allows, in a short period of time from the activation of the SHM system, the definition of more efficient alert or alarm thresholds, definable based on the behavioral models (FEM) of the structure.

REFERENCES

UNI21015343_EIT - UNI/TR 11634 (2016). "Linee guida per il monitoraggio strutturale" – UNI Ente Italiano di Normazione.

Ministero delle Infrastrutture e dei Trasporti, Consiglio Superiore dei Lavori Pubblici (2020) "Linee guida per la classificazione e gestione del rischio, la valutazione della sicurezza ed il monitoraggio dei ponti esistenti".

Mills T. (2019). Applied Time Series Analysis – Academic Press.

Green J.R. & Margerison D. (1978). Statistical treatment of experimental data – Elsevier.

G.Ascari et al.(2022). Monitoring the San Michele Railway Bridge after the refurbishing works – IABMAS2022, 11th International Conference on Bridge Maintenance, Safety and Management.

Bridge Maintenance, Safety, Management, Digitalization and Sustainability – Jensen, Frangopol & Schmidt (eds)
© 2024 The Author(s), ISBN 978-1-032-77040-6
Open Access: www.taylorfrancis.com, CC BY-NC-ND 4.0 license

A deep-autoencoder-based drive-by methodology for high-speed railway bridge damage detection

E.F. Souza
Civil Engineering Department – UTFPR, Guarapuava, Brazil
Department of Structural and Geotechnical Engineering – USP, São Paulo, Brazil

C. Bragança & T.N. Bittencourt
Department of Structural and Geotechnical Engineering – USP, São Paulo, Brazil

D. Ribeiro
School of Engineering Polytechnic of Porto – ISEP/ Construct–LESE, Porto, Portugal

H. Carvalho
Department of Structural Engineering – UFMG, Belo Horizonte, Minas Gerais, Brazil

ABSTRACT: Drive-by methodologies have emerged as a feasible and cost-effective monitoring solution for accurately and early detect damage on railway bridges while minimizing train operation interruptions. This study presents a novel approach for drive-by damage detection in high-speed railway (HSR) bridges. The methodology relies on acceleration records collected from multiple bridge crossings by an operational train equipped with onboard sensors. Log-Mel spectrogram features derived from the acceleration records are used together with sparse autoencoders for computing statistical distribution-based damage indexes. Numerical simulations were performed on a 3D vehicle-track-bridge interaction system (VTBI) model implemented in Matlab® to evaluate the robustness and effectiveness of the proposed approach. The model considers several damage scenarios, vehicle speeds, and environmental and operational variations (EOVs), such as multiple track irregularities and varying measurement noise. The results showed that the proposed approach can successfully detect and localize damages, as well as characterize their severity, especially for very early-stage damages.

1 INTRODUCTION

The significant technological advancement in railways regarding increased train speeds has enabled a rapid, safe, and environmentally friendly alternative to air transport for connecting various cities worldwide. In comparison to conventional railway lines, high-speed lines present more strict requirements concerning track geometry, not permitting sharp curves or steep gradients. As a result, bridges and viaducts occupy a substantial percentage of the railway network, allowing trains to overcome topographical obstacles more smoothly (Kang *et al.*, 2018). With this rise in the number of bridges and the higher demands in terms of train safety operation, there is an urgent need for implementing SHM systems capable of identifying damages in these structures. Nonetheless, implementing such systems represents a high and prohibitive cost for smaller-scale structures, rendering comprehensive railway monitoring infeasible. In the face of this reality, researchers have been exploring the possibility of implementing monitoring systems and using vehicles that regularly travel on tracks as mobile sensors able to detect damage in structures (Malekjafarian *et al.*, 2015, 2022). These monitoring strategies are called drive-by monitoring and represent a significant advancement in cost compared to traditional SHM techniques, since, in theory, a single instrumented vehicle would be capable of monitoring the entire extension of a railway (Locke *et al.*, 2020).

DOI: 10.1201/9781003483755-202

Aiming the accurate damage detection, studies have been conducted using various non-modal techniques for feature extraction, mainly based on signal processing and optimization-based parameter identification. Cepstral analysis has recently gathered interest among researchers and recent studies (Li, Morgantini, *et al.*, 2023) indicate the significant potential of these features on structural damage detection, particularly the Mel-frequency cepstrum (MFC). Despite the significant amount of research on damage detection investigating the application of cepstrum features, most of the studies are still focused on wayside applications (Zhang *et al.*, 2011) or in areas other than bridge SHM (Abdul & Al-Talabani, 2022). Therefore, the use of Mel-frequency damage features in drive-by monitoring is relatively recent. Pioneering work in this direction was conducted by Mei et al. (2019), where MFCC extracted from acceleration measured onboard of road vehicles were used as indicators for damage detection on bridges. Souza et al. (2022) first introduced the use of MFCC as damage features in a high-speed railway context, successfully demonstrating the sensitivity to damage, noise robustness, and capability of MFCC-derived damage indexes to offer reliable insights into damage location and severity under distinct track conditions and speeds.

Studies that include the use of AE in conjunction with drive-by methods are rare and all are related to road vehicles. To the best of the authors' knowledge, only three papers have been published regarding this approach (Calderon Hurtado *et al.*, 2023; Li, Lin, *et al.*, 2023; Liu *et al.*, 2020). The application of AE associated with MFSC in the context of drive-by monitoring of railway bridges is still, to the best of the found knowledge, unreported in the literature. Given this evident gap, this study introduces a novel drive-by damage detection method for HSR bridges, considering the analysis of multiple instances of train crossings over a bridge, during which onboard sensors are installed on the carbodies and bogies of a service train. The vehicle dynamic responses were evaluated on a 3D vehicle-track-bridge interaction system (VTBI) model implemented in Matlab®. The acceleration records are transformed into the time-frequency domain using Log-Mel spectrogram features extracted via a proposed adapted Mel-frequency scale. Then, these 2D image-like processed data are leveraged to compute statistical distribution-based damage indexes through the application of a deep learning algorithm, specifically a sparse autoencoder. The proposed numerical methodology considers several damage scenarios, vehicle running speeds, and EOVs, particularly distinct track irregularity conditions and varying levels of measurement noise. The main original contributions of this research work are:

- The development of a drive-by damage detection methodology to assess the presence of localized damage in high-speed railway bridges, capable of identifying its localization, type, and severity, with robustness regarding EOVs.
- The use of adapted Mel-frequency damage-sensitive features in association with a deep learning technique (sparse autoencoders) constituting a statistical distribution-based damage index.

2 PROPOSED DRIVE-BY DAMAGE DETECTION METHOD

The railway bridge damage detection methodology presented in this paper consists of a four-step process. In this process the sensitive damage features extracted from a indirect SHM system and its derived damage index are able to provide consistent and robust information regarding of the damage detection, localization and severity. Figure 1 depicts an overview of the proposed method, whose stages are discussed in detail on the following subsections.

2.1 *Data acquisiton*

The proposed method for detecting damage is numerically assessed through simulated data representing the dynamic responses of the vehicle components. These responses were derived from dynamic analyses performed using the 3D VTBI model implemented in Matlab®. For each baseline and damage scenario, the dataset is generated under batches of crossing events of the same train over the bridge. All carbodies and bogies of the train are instrumented, and therefore the datasets consist of their vertical acceleration responses associated with the train speed (v), as well as the damage location and irregularity profile characteristics.

2.2 *Feature extraction*

The feature extraction process is of paramount importance in damage detection systems. It must eliminate the influence of environmental and operational factors from the dynamic responses to enable the conversion of raw time series data into alternative damage-sensitive information. This section details the steps to derive the cepstral features from the sampled signals acquired from the drive-by monitoring system.

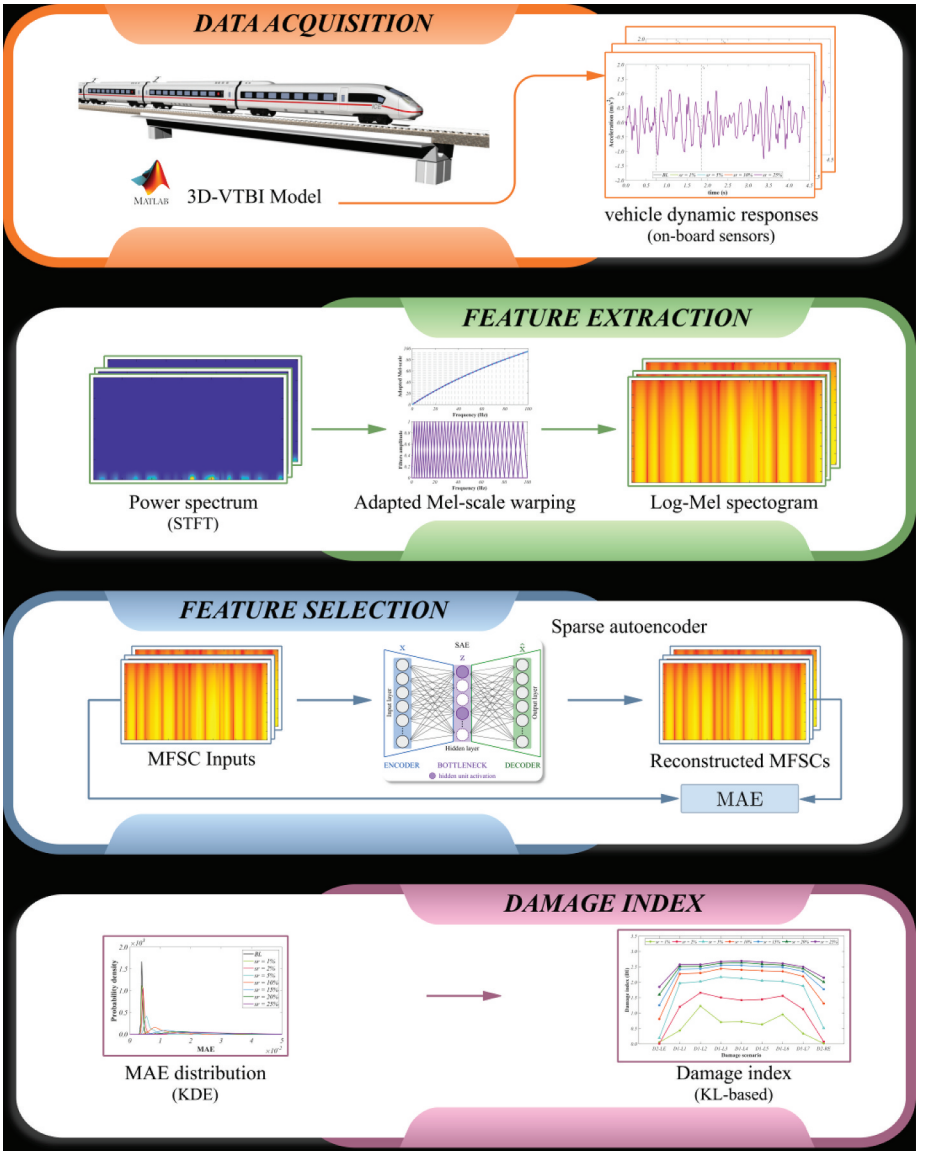


Figure 1. Flowchart of the proposed drive-by damage detection methodology for railway bridges.

2.2.1 *Short-time Fourier transform*

The STFT is used to preprocess the vehicle acceleration responses and to manage non-linear factors within the railway environment. This technique allows performing time-frequency analysis and involves applying the Discrete Fourier Transform (at b equally spaced frequency

bins) to each of the N overlapped short-time frames of a sampled signal $x[n]$. As a result, a power spectrum matrix $\mathbf{P}$ of size $b \times N$ is accomplished, which captures the signal's magnitude spectra over time.

2.2.2 *Log-Mel spectrogram features*

Spatiotemporal content of MFSC is used to train deep sparse autoencoder architectures tailored for railway bridge damage detection rather than time-series representations or linear frequency spectrograms. After evaluating the power spectrum $\mathbf{P}$, frequency warping is employed to enhance the signal's characteristics in the Mel-frequency scale by triangular filters whose centers are equally spaced into the Mel-scale. To make the Mel warping suitable for cepstral feature extraction in the context of SHM applications, the authors propose adapting the Mel warping approach. Instead of the frequency warping used in speech analysis, a linear weighting procedure is taken, using a scale that emulates the Mel scale trend up to a cutoff frequency f_c. In this study, it was adopted a uniform distribution of the triangular filter centers along the adapted Mel-frequency scale $\widetilde{m}$ given by:

$$m = 2595log(1 + f/700) \tag{1}$$

2.2.3 *Feature selection*

Several SHM approaches have been developed using Deep Learning (DL) for its ability to process and successfully analyze large amounts of data. These models involve the use of complex abstractions to represent data information, employing both linear and nonlinear mapping techniques across multiple processing layers. Among the available DL algorithms, Sparse Autoencoder (SAE) stands out as a promising alternative in bridge SHM systems. In this work, the SAE models are trained by inputs generated from the carbodies' and bogies' responses while crossing the target bridge under healthy conditions, i.e., baseline scenarios. Therefore, the model is not expected to reconstruct unseen data referring to damage scenarios since it has not learned them. To leverage this aspect, mean absolute error (MAE) is used to measure the reconstructed error, which can be expressed by

$$MAE = \frac{1}{n}\sum\nolimits_{i=1}^{n} |x_i - \widehat{x}_i| \tag{2}$$

where x_i and $\hat{x}_i$ are the corresponding ith components of the SAE input and output vectors, respectively.

2.2.4 *Damage index*

In cases where batches of crossing instances are considered, MAE exhibits substantial variation due to the varying sensor positions and train speeds. Nevertheless, MAE distributions can be used for damage diagnosis by assessing the dissimilarity between those obtained from a series of passages over a healthy bridge (baseline) and over it under a damaged.

The probability density distributions of MAE values for each damage scenario are determined using kernel density estimation (KDE) in this study. A KDE presents a smooth curve, enhancing the visualization of probability density function details while incorporating the locations of all sample points. A Damage Index (DI) is then calculated based on the KL divergence to measure the dissimilarity between two KDE for damage identification and severity assessment. The KL divergence is a metric rooted in information theory that quantifies the loss of information while approximating a probability distribution $p(r)$ with another distribution $p'(r)$, both with the same set χ of outcomes and is given by

$$KL(p'|p) = \sum\nolimits_{r\in\chi} p'(r) log\left(\frac{p'(r)}{p(r)}\right) \tag{3}$$

From Eq. (2) and Eq. (3), the adopted DI in this work can be written as follows:

$$DI = log\left(KL\left(KDE^{(u)}|KDE^{(d)}\right) + 10\right) - 1 \tag{4}$$

where $KDE^{(u)}$ and $KDE^{(d)}$ are the MAE estimated distributions for a baseline scenario and for a damage scenario, respectively. To derive Eq.(4), a log-linearized relationship is taken as the KL divergence provides either a nonnegative real value or infinity.

3 RESULTS AND DISCUSSION

3.1 *Case study*

Figure 2 shows the case study used in the present work for performing the dynamic analyses. The bridge deck consists of an idealized prestressed box-girder with a span of L_B =50.4 m, and the instrumented vehicle considered is the third-generation German high-speed train, the ICE3 Velaro, composed of eight cars. The total length of the ballasted track was assumed to be 497.4 m, consisting of the section over the bridge extended by the entry and exit lengths, each 223.5 m long. Therefore, the running distance for the vehicle is 303.9 m.

The bridge deck is modeled as a simply supported Euler-Bernoulli beam using 3D finite elements (FE), with bearing supports modeled using linear springs. In the ballasted track model, left and right rails (subscript *Lr* and *Rr*, respectively) are also modeled using 3D beams FE discretely supported at rail-sleeper junctions. The model incorporates three layers of spring-dashpot assemblies, which characterize the elasticity and damping of rail pads and fastenings, ballast, and subgrade.



Figure 2. Case study used in the present work for the numerical simulations.

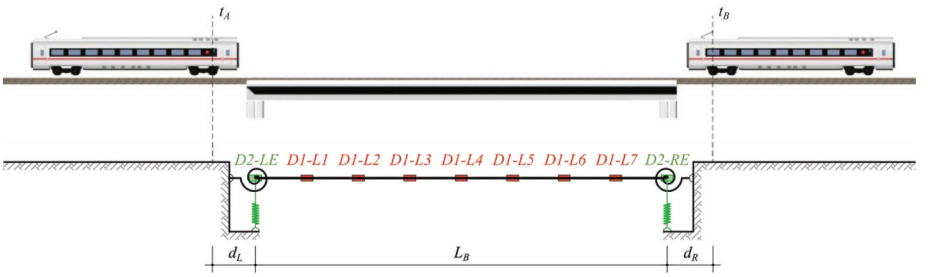


Figure 3. Types of damages and their location on the application case.

3.2 *Simulated scenarios*

Baseline (healthy condition) and damage scenarios were simulated to evaluate the proposed damage detection methodology, considering a wide range of train speeds (for the consideration of batches of crossing events) and three different track irregularity profiles to

verify the robustness of the proposal regarding track conditions. The damage scenarios were chosen based on two of the several possible failure states in a HSR bridge infrastructure: i) Type D1, characterized by a local reduction of the bridge deck flexural stiffness ($E_B I_{By}$)

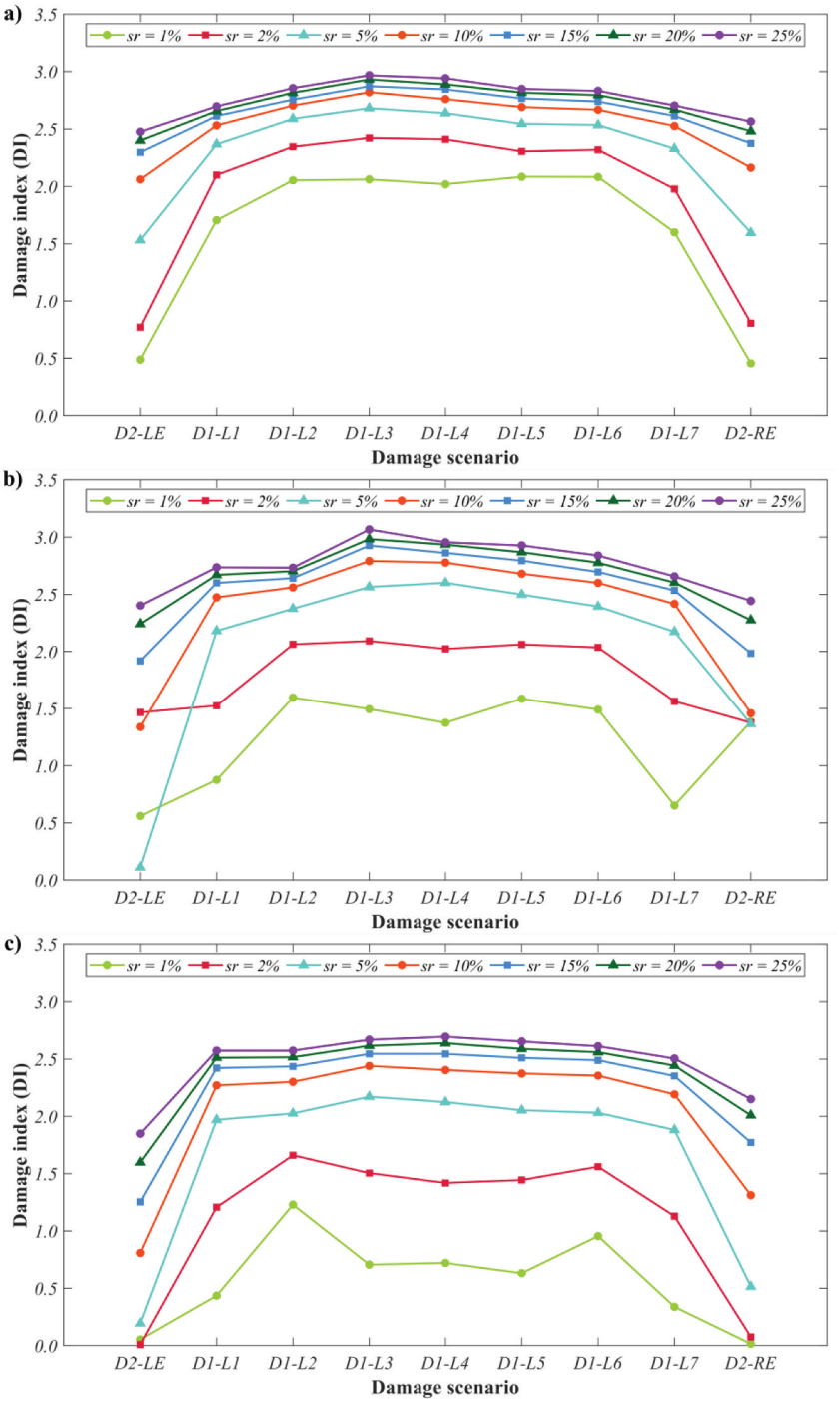


Figure 4. Damage index based on the bogie responses for the different damage scenarios considered in this study, and for different track conditions: a) NC, b) LD, and c) HD.

at a cross-section of the structure, and ii) Type D2, related to a loss of the vertical stiffness in a bearing device (K_{Bz}).

All the simulated damage scenarios consider only one damage location; nevertheless, different locations of damage were evaluated as illustrated in Figure 3. Damages type D1 were assessed at sections with a length of 1.5 m located at the first, second, third, …, seventh eighths of the span and labeled as D1-L1, D1-L2, …, D1-L7, respectively. The damage scenarios designated by D2-LE and D2-RE refer to those where the vertical stiffness reduction was considered in the bearing devices of the bridge located at its left and right ends, respectively. The stiffness reduction (sr) levels assumed for all damage scenarios were sr =1 %, 2 %, 5 %, 10 %,15 %, 20 % and 25 %.

A total of 45 simulations were conducted for baseline states, combining the range of 15 train speeds (v =180, 190, 200, …, 320 km/h) with three types of track conditions: track irregularities not considered (NC) and track irregularity profiles of quality low disturbance (LD) and high disturbance (HD), generated according to German track irregularity PSDs. For the damage scenarios, 1029 simulations were carried out for the damages type D1 and 294 for the damages type D2, combining the same three types of track conditions as for the baseline scenarios with the range of 7 train speeds (v =190, 210, 230, …, 310 km/h) and the damage location and severity.

3.3 *Damage index performance*

This section presents the efficiency of the proposed drive-by damage detection methodology by using a DI (Eq.(4)) based on the KL divergence between KDE distributions for baseline and damage scenarios fitted on the vehicle responses from batches of crossing events of the same train.

Figure 4 illustrates how the DI values vary significantly for various bridge conditions, as calculated from signal records of onboard sensors on the bogies, regardless of the track operational conditions. For the baseline, the magnitude of DI is highly near zero and, therefore, omitted. The robustness of the proposed method is displayed by the sensitivity of DI magnitude in distinguishing different damage severity, even and mainly for the lower levels. This aspect is particularly appealing when it comes to early-stage damage identification. The reason why the difference in the magnitude of the damage indices between cases with greater severity becomes less distinct is explained by the KDE of the MAE distribution. As the severity of the damage increases, the KDE curves of the MAE distributions tend to assume a similar shape, resulting in divergence values with respect to the baseline scenario that are less discrepant.

The results demonstrate the ability of MFSC to highlight the most significant energy content observable (here by the adapted Mel-frequency scale). In addition, in combination with the temporal-spatial resolution of the STFT, MFSC-based features successfully address the well-documented challenge of identifying damage in regions close to the bridge's supports under operational conditions. Similar results were obtained for the DI values calculated from signal records of onboard sensors on the carbodies.

4 CONCLUSIONS

The present work introduced a novel approach for HSR drive-by bridge damage detection utilizing adapted Mel-frequency damage-sensitive features in association with deep learning algorithms (sparse autoencoders) to produce a statistical distribution-based damage index. The suggested methodology for indirect SHM in the railway field uses vehicle responses from multiple instances of a service train crossing the target bridge, which were simulated using a 3D VTBI model implemented in Matlab®.

The trained SAE models can effectively and accurately represent the feature space related to vehicle responses for healthy conditions and generate reconstructed Log-Mel spectrogram with error distributions whose KL divergences display sensitivity to the damage in the bridge. Mel-spectrogram features, in turn, can convert the temporal representation of the vehicle acceleration signals into a comprehensive representation of frequency, time, and intensity (power) in higher dimensions. This characteristic renders Mel-frequency cepstral features very compatible with autoencoder architectures. The results indicate that the proposed approach

provides a damage index that can successfully identify the presence of localized damage along the span and at their ends. It can also distinguish its severity (mainly for early-stage damages), regardless of train speed, sensor position, and environmental and operational variations such as track irregularities and artificial noise. Such results suggest the potential of applying Mel-frequency damage-sensitive features associated with machine learning algorithms in the drive-by assessment of high-speed railway bridges based on their existing conditions.

REFERENCES

Abdul, Z.K. and Al-Talabani, A.K. (2022), "Mel Frequency Cepstral Coefficient and its Applications: A Review", *IEEE Access*, doi: 10.1109/ACCESS.2022.3223444.

Balsamo, L., Betti, R. and Beigi, H. (2014), "A structural health monitoring strategy using cepstral features", *Journal of Sound and Vibration*, Vol. 333 No. 19, pp. 4526–4542, doi: 10.1016/j.jsv.2014.04.062.

Bochud, N., Gomez, A.M., Rus, G., Carmona, J.L. and Peinado, A.M. (2011), "Robust parametrization for non-destructive evaluation of composites using ultrasonic signals", *ICASSP, IEEE International Conference on Acoustics, Speech and Signal Processing - Proceedings*, IEEE, pp. 1789–1792, doi: 10.1109/ICASSP.2011.5946850.

Calderon Hurtado, A., Kaur, K., Makki Alamdari, M., Atroshchenko, E., Chang, K.C. and Kim, C.W. (2023), "Unsupervised learning-based framework for indirect structural health monitoring using adversarial autoencoder", *Journal of Sound and Vibration*, Vol. 550, p. 117598, doi: 10.1016/j.jsv.2023.117598.

Dackermann, U., Smith, W.A. and Randall, R.B. (2014), "Damage identification based on response-only measurements using cepstrum analysis and artificial neural networks", *Structural Health Monitoring*, Vol. 13 No. 4, pp. 430–444, doi: 10.1177/1475921714542890.

Joseph, G.V. and Pakrashi, V. (2022), "Spiking Neural Networks for Structural Health Monitoring", *Sensors*, Vol. 22 No. 23, p. 9245, doi: 10.3390/s22239245.

Kang, C., Schneider, S., Wenner, M. and Marx, S. (2018), "Development of design and construction of high-speed railway bridges in Germany", *Engineering Structures*, Vol. 163 No. February, pp. 184–196, doi: 10.1016/j.engstruct.2018.02.059.

Lee, J., Choi, H., Park, D., Chung, Y., Kim, H.Y. and Yoon, S. (2016), "Fault detection and diagnosis of railway point machines by sound analysis", *Sensors (Switzerland)*, Vol. 16 No. 4, p. 549, doi: 10.3390/s16040549.

Li, L., Morgantini, M. and Betti, R. (2023), "Structural damage assessment through a new generalized autoencoder with features in the quefrency domain", *Mechanical Systems and Signal Processing*, Vol. 184, doi: 10.1016/J.YMSSP.2022.109713.

Li, Z., Lin, W. and Zhang, Y. (2023), "Real-time drive-by bridge damage detection using deep auto-encoder", *Structures*, Elsevier Ltd, Vol. 47 No. December 2022, pp. 1167–1181, doi: 10.1016/j.istruc.2022.11.094.

Liu, J., Chen, S., Berges, M., Bielak, J., Garrett, J.H., Kovacevic, J. and Noh, H.Y. (2020), "Diagnosis algorithms for indirect structural health monitoring of a bridge model via dimensionality reduction", *Mechanical Systems and Signal Processing*, doi: 10.1016/J.YMSSP.2019.106454.

Locke, W., Sybrandt, J., Redmond, L., Safro, I. and Atamturktur, S. (2020), "Using drive-by health monitoring to detect bridge damage considering environmental and operational effects", *JOURNAL OF SOUND AND VIBRATION*, ACADEMIC PRESS LTD- ELSEVIER SCIENCE LTD, 24-28 OVAL RD, LONDON NW1 7DX, ENGLAND, Vol. 468, doi: 10.1016/j.jsv.2019.115088.

Malekjafarian, A., Corbally, R. and Gong, W. (2022), "A review of mobile sensing of bridges using moving vehicles: Progress to date, challenges and future trends", *Structures*, Elsevier Ltd, Vol. 44, pp. 1466–1489, doi: 10.1016/j.istruc.2022.08.075.

Malekjafarian, A., McGetrick, P.J. and OBrien, E.J. (2015), "A Review of Indirect Bridge Monitoring Using Passing Vehicles", edited by Lallart, M.*Shock and Vibration*, Hindawi Publishing Corporation, Vol. 2015, p. 286139, doi: 10.1155/2015/286139.

Mei, Q., Gül, M. and Boay, M. (2019), "Indirect health monitoring of bridges using Mel-frequency cepstral coefficients and principal component analysis", *Mechanical Systems and Signal Processing*, Vol. 119, pp. 523–546, doi: 10.1016/j.ymssp.2018.10.006.

de Souza, E.F., Bittencourt, T.N., Ribeiro, D. and Carvalho, H. (2022), "Feasibility of Applying Mel-Frequency Cepstral Coefficients in a Drive-by Damage Detection Methodology for High-Speed Railway Bridges", *Sustainability*, Vol. 14 No. 20, doi: 10.3390/su142013290.

Zhang, G., Harichandran, R.S. and Ramuhalli, P. (2011), "Application of noise cancelling and damage detection algorithms in NDE of concrete bridge decks using impact signals", *Journal of Nondestructive Evaluation*, Vol. 30 No. 4, pp. 259–272, doi: 10.1007/s10921-011-0114-8.

Bridge Maintenance, Safety, Management, Digitalization and Sustainability – Jensen, Frangopol & Schmidt (eds)
© 2024 The Author(s), ISBN 978-1-032-77040-6
Open Access: www.taylorfrancis.com, CC BY-NC-ND 4.0 license

Indirect continuous monitoring of bridge transitions using the CTM 2.0

M.M. Rupp, S.R. Lorenzen & C. Hübler
TU Darmstadt – Institute of Structural Mechanics and Design, Darmstadt, Germany

K.U. Wolter
DB Systemtechnik GmbH, München, Germany

G. Grunert
DB Netz AG, Berlin, Germany

R. Stein
GMG Ingenieurgesellschaft mbH, Dresden, Germany

ABSTRACT: Bridges are a neuralgic point for robust rail transport. Increasing rail traffic over the next years, combined with new vehicle developments, will lead to increased loads, especially in bridge transition areas. This requires regular network-wide monitoring to ensure safety standards and is associated with high maintenance costs.

DB Systemtechnik GmbH has successfully deployed the Continuous Track Monitoring (CTM) system, which uses sensors on scheduled trains to monitor indirectly and continuously railway tracks. This paper uses a case study to analyse how this concept can be extended to the monitoring of bridge transitions without modifying the CTM. By comparison with sleeper responses measured directly in the transition area of a tied arch bridge, it is shown that the CTM can reliably capture both the magnitude and time span of recurrent changes in track bedding or ballast deterioration, allowing optimised maintenance planning, thereby reducing costs and increasing reliability.

1 INTRODUCTION

The development of trains, marked by increasing speeds and new innovative axle configurations intensifies the demands on railway infrastructure (Karimi 2020). This challenge is acute in the transition zones of railway bridges, where abrupt stiffness changes and differential track settlements result in amplified dynamic wheel loads. These forces accelerate the deterioration of ballast and track settlements (Pannese et al. 2020, Wang & Markine 2019). This deterioration often manifests as white spots, indicating a need for frequent maintenance interventions to maintain track geometry (Lichtberger 2005). The transition between soft embankment and very stiff abutments and bridges with interruption of the ballast bed, as found in bridges with open decks, are particularly affected.

The ballast layer, a crucial element for track geometry and maintenance costs, can account for up to 30 % of total superstructure maintenance costs (Lichtberger 2005). In the Netherlands, the frequency of maintenance in transition zones is up to eight times higher compared to open tracks (Wang & Markine 2019, Wang et al. 2018). As a result, maintaining these transition zones represents a significant financial effort, with annual costs reaching approximately $ 200 million USD in the USA in 2012 and $ 110 million USD in Europe in 1999 (Pannese et al. 2020, Wang et al. 2018). Infrastructure managers are responding to this situation in new

DOI: 10.1201/9781003483755-203

bridges by designing the transition zones accordingly (no inclined support structure terminations, cement wedges, drag plates), but for a large number of existing transition zones, major interventions are associated with large investments. Despite its critical importance, the majority of differential track settlements at bridge transitions are currently assessed through visual inspection, which may be ineffective in the early stages (Pannese et al. 2020).

The increased rail traffic on our current infrastructure intensifies existing challenges, particularly limiting the time available for crucial inspections and maintenance (Lorenzen et al. 2023). This situation underscores the importance of regular monitoring to control track alignment and prevent potential disruptions or derailments (Falamarzi et al. 2019). Addressing this need, the Continuous Track Monitoring System 2.0 (CTM 2.0), developed by DB Systemtechnik GmbH, has been a key innovation. This system, which has been in operation for more than two decades and has been installed on regular trains, enables continuous monitoring of railway infrastructure. It plays a key role in early fault detection and improves maintenance planning (Lorenzen et al. 2023).

As already mentioned, the CTM system has been in use successfully for a long time, but only for the originally developed case of track geometry monitoring. The objective of this paper is to extend the scope of the measurement system. Therefore, it will be investigated whether and how the measurement data of the CTM 2.0 system can be used to monitor bridge transitions and in particular white spots throughout the network during regular train operations. By analysing the track geometry as determined by the CTM 2.0 together with sleeper responses directly measured and recorded by a long-term monitoring system.

2 CONTINUOUS TRACK MONITORING SYSTEM 2.0

The CTM is an indirect measurement system that uses acceleration sensors on axle boxes to continuously monitor track quality. The system consists of sensor boxes with sensors, measuring amplifiers, data recorders, positioning systems and data transmission devices (see Figure 1). The modular design and the use of standard industrial components ensures that the components can be easily replaced or improved individually. The system is also designed to be installed on regular scheduled trains. In this way, regular traffic is not interrupted for monitoring purposes and maintenance costs of CTM are kept to a minimum.

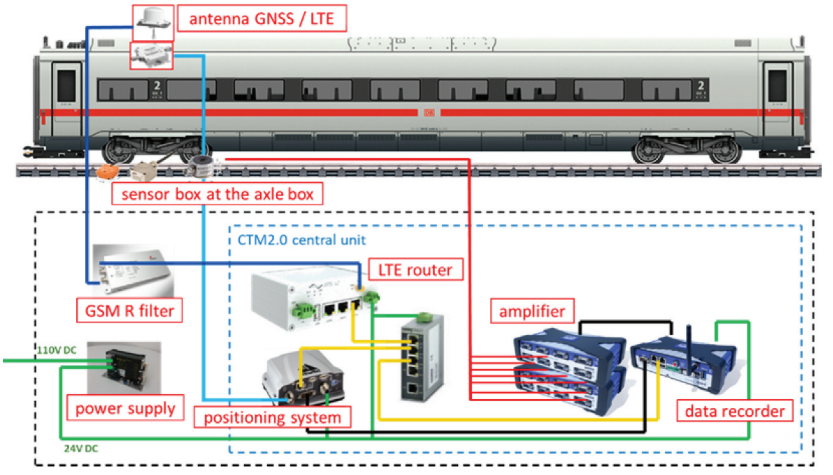


Figure 1. Principle of the CTM 2.0 measuring system.

Unlike the first generation CTM 1.0, the second generation CTM 2.0 transmits all acceleration data directly from the vehicle to the office. In addition, the position and speed are continuously recorded to determine the location of each measurement point and to match the

results to the corresponding tracks. Longitudinal track irregularities are calculated in the office by analysing the accelerations measured at the axle boxes within the wavelength limits of the European standard EN13848 (DIN EN 13848 2019). Finally, the results can be compared with those of other inspection vehicles. The validation of the CTM 2.0 shows an exact match with other inspection vehicles. Furthermore, the CTM measurement uncertainty of the vertical track geometry is less than 0.5 mm considering 20 test drives (Wolter 2021).

This system (see Figure 1), developed by DB Systemtechnik GmbH, has now been in use for more than two decades for the assessment of the track geometry of the superstructure. During this time, it has been continuously improved on the basis of operational experience and feedback from infrastructure managers. This has resulted in the ability to meet the wide range of requirements of vehicle owners, measuring system operators, and infrastructure managers. Ensuring that the system does not affect vehicle operation or require additional maintenance is essential for vehicle owners. For system operators, the system must be self-sufficient and fully autonomous. Automated monitoring reports and results must be provided for integration into existing maintenance databases. Infrastructure managers need to have valid and comparable results that can be evaluated against infrastructure operator standards (Wolter & Liu 2021).

DB Netz AG currently has a fleet of CTM measurement systems of different generations in operation, which are used by DB Systemtechnik GmbH to continuously monitor more than 14,000 kilometres of track in Germany on behalf of DB Netz AG. The results obtained are regularly made available to DB Netz AG to improve track maintenance. The monitoring data make it possible to detect faults at an early stage, facilitate the specific planning of repair work and allow the quality and sustainability of repairs to be checked. Figure 2 shows the lines operated by DB Netz AG on which the CTM track measurement systems are used for continuous monitoring.



Figure 2. Map of lines that are continuously monitored with CTM track measurement systems.

3 CASE STUDY: TIED-ARCH STEEL BRIDGE

3.1 *The tied-arch steel bridge*

The structure (see Figure 3) in this case study is a double-track tied-arch steel bridge with a span of 77.5 m. As part of the ZEKISS research project, this bridge was instrumented with various acceleration and strain sensors and monitored for over a year from January 2022 to March 2023. The CTM 2.0 monitoring area also includes this bridge.

During an on-site visit at the beginning of May 2021, a white spot was detected in the superstructure of the bridge transition (see Figure 3a). Strong pumping of the sleepers in this area was also observed during train crossings. This white spot is the result of a defective drainage in the backfill area, which can be noticed as well by vegetation in the superstructure (see Figure 3a). The defect was rectified during a maintenance operation (see Figure 3b). Another relevant maintenance operation was the ballast tamping of the analysed line section in Sept./ Oct. 2021.

For these reasons, the investigation of the temporal evolution of this spot was a monitoring task. So, an acceleration sensor was instrumented on a sleeper (see Figures 3c). A capacitive accelerometer from PJM was used, which has a measurement range of ±10 g and can record accelerations in the low frequency range. The position of the acceleration sensor can be obtained from the blueprint of the bridge (see Figure 4). The white spot is located behind the bridge in direction of travel 2. The position of the bridge on the line is marked for comparison with the indirect monitoring.

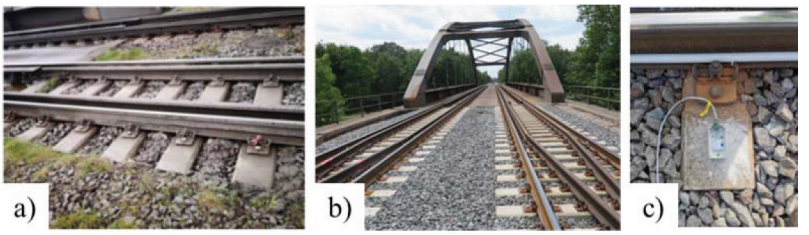


Figure 3. a) white spot in the transition area with vegetation, b) same spot after repairing the drainage, c) installation of the acceleration sensor on the sleeper.

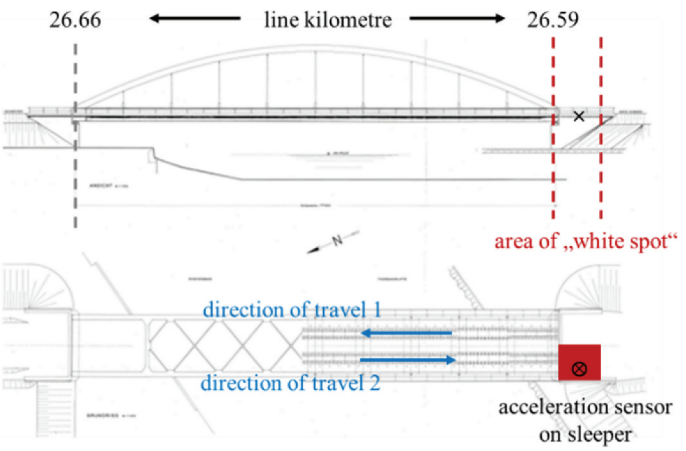


Figure 4. Blueprint of the bridge; red: area of white spot, blue: direction of travel, black circle: position of the acceleration sensor.

Over 85,000 crossings were recorded and analysed. Figure 5 shows the max.-min.-spans of the measured accelerations (range between minimum and maximum acceleration values) of all crossings for each month in a violin plot. The edges indicate a kernel density function fitted to the data. A temporal trend over time is visible. The mean value of the max.-min.-spans which is marked by a dash increases while the outliers of the max.-min.-spans (see dots in Figure 5) have no particular pattern. These values probably result from hard impacts due to non-round wheels. This tendency can be clearly seen by comparing the empirical probability distributions

of the max.-min.-spans for different time periods (see Figure 6). A significant increase in the empirical probability of large max.-min.-spans can be seen towards the end of the measurement campaign.

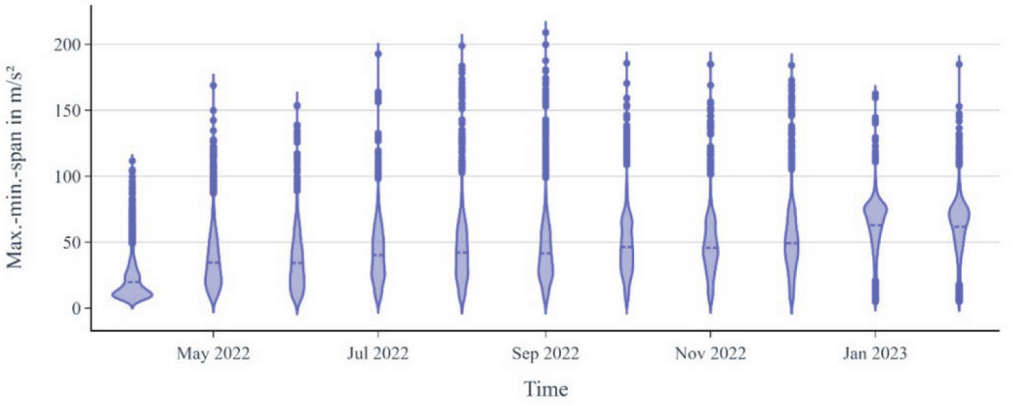


Figure 5. Max.-min.-spans of sleeper acceleration (measured with sensor on sleeper) plotted over time (85,188 train crossings).

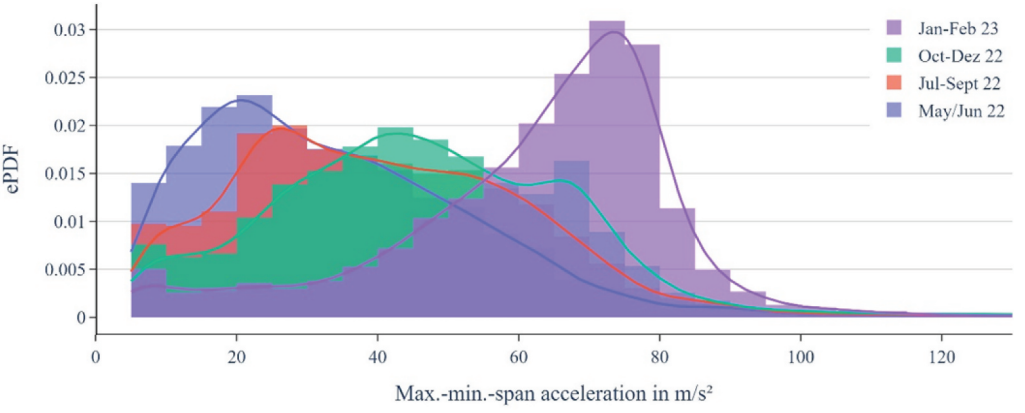


Figure 6. Empirical probability density function (ePDF) of the max.-min.-spans for four time periods.

This observation is analysed below by directly comparing the signal of vertical accelerations of the sleeper from the period May 2022 with March 2023 under the passenger train BR4010 (axle loads approx. 12 t). This vehicle is in May 2022 actually faster (approx. 180 km/h) than in March 2023 (approx. 140 km/h). However, the accelerations in March 2023 are about 3 times higher (compare Figures 7, 8) The displacement signals integrated from the accelerations also increase from about 1.0 mm (May 2022) to about 2.4 mm (March 2023). The detailed view shows a small peak in the displacement curve, which probably occurs when the sleeper touches the bottom of the void (Sysyn et al. 2020). This peak is about 0.2 mm in May 2022 and about 1.5 mm in March 2023.

3.2 *Evaluation of the CTM 2.0 measurements*

A total of 71 crossings in direction 2 are available for analysis of the white spot in the period from August 2020 to March 2022. As an example, the vertical track geometry according to DIN EN 13848 (DIN EN 13848 2019) of the left axle box can be plotted for all available

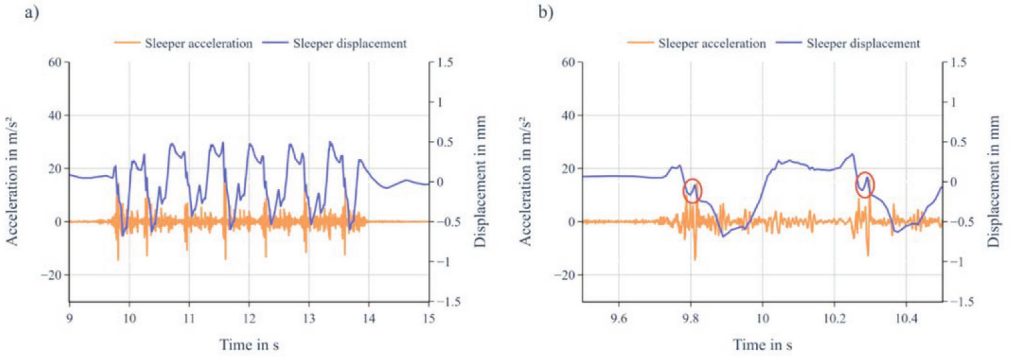


Figure 7. a) acceleration and displacement signal of sleeper (BR4010, 180 km/h, May 22), b) detailed view.

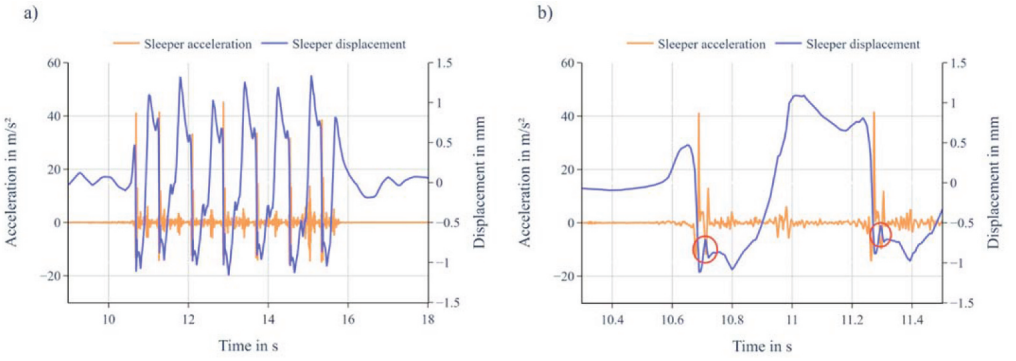


Figure 8. a) acceleration and displacement signal of sleeper (BR4010, 140 km/h, Mar 23), b) detailed view.

crossings over the line kilometre (see Figure 9). The vertical track geometry is the z-direction of a cartesian coordinate system, where the x-direction indicates the direction of travel of the train. It therefore indicates the deviation perpendicular to the running surface (height of rail running surface from smoothed vertical position) (DIN EN 13848 2019). The blue colour indicates the crossings between August 2020 and October 2021, and green shows the crossings between November 2021 and March 2022. With the CTM's positioning system, the bridge (see Section 3.1) can be located in the grey area. The white spot is hatched in red (see also Figure 4). Figure 9 reveals that the vertical track geometry is highest in the transition areas. The most prominent peak is in the area of the white spot. Large variations in the track geometry can as well be observed there.

In direction 1 in total 80 crossings are available, which can be visualised in an equivalent manner for comparison purposes (see Figure 10). Looking at the bridge transitions in this direction of travel (1), there are also peaks visible indicating increased stresses. However, the variation and magnitude of the peaks is much smaller compared to the white spot in opposite direction (2).

In both directions, two characteristic profiles of the vertical track geometry with different peak values are visible. In the following the different profiles can be explained by tamping operations in Sept./Oct. 2021.

In order to analyse the white spot, the area highlighted in red (see Figure 9) is extracted for further investigations. The max.-min.-spans of the vertical track geometry are derived in a similar way to the evaluation in Section 3.1, but now for the CTM system and no longer for the accelerometer on the sleeper. In addition, the corresponding max.-min.-spans of the

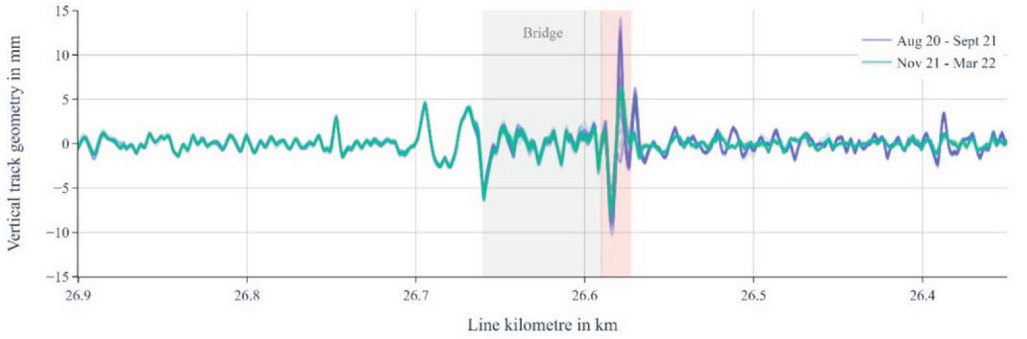


Figure 9. Vertical track geometry (measured with CTM's left axle box) according to DIN EN 13848 of all available 71 crossings plotted over the line kilometre (direction of travel 2); grey: location of the bridge, red: area of white spot.



Figure 10. Vertical track geometry (measured with CTM's left axle box) according to DIN EN 13848 of all available 80 crossings plotted over the line kilometre (direction of travel 1); grey: location of the bridge.

opposite direction (1) are extracted for comparison as well. All of these max.-min.-spans can be plotted over time (see Figure11). The colours in Figure 11 are chosen according to Figures 9 & 10 to emphasise the respective changes in the vertical track geometry. A clear increase in the max.-min.-spans over time can be seen, interrupted in form of steps. These steps are caused by tamping operations, which initially leads to an improvement in the bedding of the track. The bedding is then reduced over time due to the stresses on the track bed in the transition areas, which is reflected in an increase of the max.-min.-spans. The different colours chosen, as in Figures 9 & 10, now allow the different characteristic track geometry profiles to be associated with the tamping operations. This is plausible as tamping significantly and permanently changes the track geometry, which must be reflected in the measurement. In direction 2, the profiles only differ from the white spot onwards. This can probably be explained by the partial tamping of the fault with a single fault tamping machine, as the white spot was already known to DB Netz AG.

It can be observed that a change in the track bedding or a deterioration of the superstructure in areas of bridge transitions leads to an increase of peaks in track geometry profiles, so that the different extreme values can be interpreted as strong indication of a changed bedding behaviour. This change is particularly evident in white spots and can be seen in the measurement data in the much stronger increase in the extreme values compared to the opposite direction (1) without a white spot. The max-min-spans of the vertical track geometry is therefore well suited for monitoring changes in bridge transition areas.

The day of the on-site visit (see Section 3.1) is also marked (dashed black line in Figure 11) and is relatively close to the next tamping operation. The values in this period are high, indicating that the observations on the bridge (strong pumping of the sleepers) are consistent with the evaluation of the CTM. The period that overlaps with the monitoring of the tied arch bridge is marked in grey. The start of the bridge monitoring is therefore shortly after a tamping operation. This is also consistent with the analysis of the sleeper acceleration measurements in the white spot. Thereby it was found that the accelerations and displacements of the sleeper were low at the beginning and increased monotonically during the measurement campaign. The time between tamping operations could be recorded and the deterioration of the bedding be determined, as with the CTM one cycle before. Both the time span (slightly more than 1 year) and the magnitude of the changes (about a factor of 3) correspond between the indirect monitoring (CTM) and the measurement on the sleeper. A more detailed comparison of the two measurements was not conducted because the overlap of the measurement periods is small.

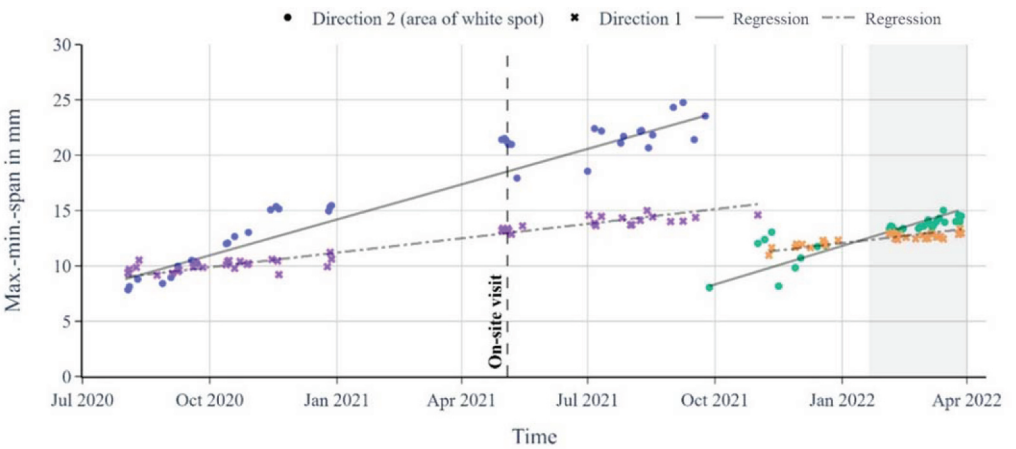


Figure 11. Max.-min.-spans of the vertical track geometry (left axle box) over time; colours chosen according to Figure 9 & 10, grey: period which overlaps with the tied-arch steel bridge monitoring.

4 CONCLUSION

In this paper, the CTM 2.0 system from DB Systemtechnik GmbH, which can be installed on regular scheduled trains, has been investigated to show its potential for monitoring bridge transitions. Using a case study of a transition zone of a tied-arch steel bridge, it was shown for the first time that the CTM 2.0 system can effectively monitor ballast deterioration in bridge transition areas, which had not been evaluated yet. No adjustments to the system are required as the track geometry measurement that is conducted anyway was used. The paper proposed the use of max.-min. spans for monitoring, which made it possible to reliably capture the changes that occur over time. The comparison with a direct measurement on a sleeper shows that both the magnitude and the time span of the recurrent changes in track bedding can be consistently obtained.

In future it could be possible to optimise tamping operations or maintenance with indirect measurements, by defining limit values based on metrics such as empirical variance, gradients, etc. White spots or voids could be detected in the form of outlier detection, as the changes here are much more significant. However, further measurements or a larger data set are required to make a more detailed comparison between the direct sleeper monitoring in the area of the white spot and the indirect monitoring (CTM), as the overlap of the measurement periods in this case is very small. Especially for the definition of the limit values an analysis

with a data set representative for the rail network must be carried out. At the same time, this data set can be used to create possible prediction models for the optimisation of the planning of tamping operations.

It can be concluded that the CTM system has the potential to monitor bridge transitions and in particular white spots throughout the network during regular train operations in a cost-saving manner, thereby increasing the safety and reliability of train operations.

ACKNOWLEDGEMENTS

The authors would like to acknowledge the financial support of the research project ZEKISS ("Condition assessment of railroad bridges and vehicles with AI methods for the evaluation of sensor data and structural dynamic models"), funded by mFund awarded by the Federal Ministry of Transport and Digital Infrastructure of Germany. Research in ZEKISS is carried out in collaboration with the German railway company DB Netz AG, the Wolfel Engineering GmbH and the GMG Ingenieurgesellschaft mbH (www.zekiss.de).

REFERENCES

DIN EN 13848-1:2019-06. Bahnanwendungen – Oberbau – Gleislagequalität – Teil 1: Beschreibung der Gleisgeometrie. Deutsche Fassung EN 13848:2019.

Falamarzi S., Moridpour S. & Nazem M. 2019. A review of rail track degradation prediction models. In *Australian Journal of Civil Engineering*. DOI:10.1080/14488353.2019.1667710

Karimi, S. 2020. *Experimentelle und numerische Untersuchung der Wechselwirkung zwischen Tragwerk und Gleis*. Wien: Universität für Bodenkultur.

Lichtberger, B. 2005. *Track compendium: formation, permanent way, maintenance, economics*. Hamburg: Eurail Press.

Lorenzen S. et al. 2023. Indirect monitoring of Railway Bridges using the Continuous Track Monitoring System CTM2.0. In *9th International Conference on Computational Methods in Structural Dynamics and Earthquake Engineering*. DOI: 10.7712/120123.10477.20349.

Sysyn M., Nabochenko O. & Kavolchuk V. 2020. Experimental investigation of the dynamic behavior of railway track with sleeper voids. In *Railway Engineering Science* Bd. 28: S. 290–304. DOI 10.1007/s40534-020-00217-8.

Pannese E.M., Take W.A., Hoult A. H., Yan R. & Le H. 2019. Bridge transition monitoring: Interpretation of track defects using digital image correlation and distributed fiber optic strain sensing. In *Proc. Inst. Mech. Eng. Part F: J. Rail Rapid Transit* vol. 234: pp. 616–637. DOI: 10.1177/0954409719851626.

Wang H., Chang L. & Markine V. 2018. Structural health monitoring of railway transition zones using satellite radar data. In *Sensors* vol. 18 (no. 2): pp. 8–11. DOI: 10.3390/s18020413.

Wang H. & Markine V. 2019. Dynamic behaviour of the track in transitions zones considering the differential settlement. In *J. Sound Vib*. vol. 459. DOI: 10.1016/j.jsv.2019.114863.

Wolter, K.U. & Liu, X. 2021. Vehicle-track-interaction measurements as a basis for continuous infrastructure monitoring (CIM) and for the development of digital twins. In *3rd International Workshop on Structural Health Monitoring for Railway System*, DOI: 10.12783/iwshm-rs2021/36023

Wolter, K. U. 2021. Erfahrungen mit Onboard Track Monitoring. In *ÖVG Fachtagung 2021 – Tagungsband*.

Bridge Maintenance, Safety, Management, Digitalization and Sustainability – Jensen, Frangopol & Schmidt (eds)
© 2024 The Author(s), ISBN 978-1-032-77040-6
Open Access: www.taylorfrancis.com, CC BY-NC-ND 4.0 license

Drive-by monitoring to assess railway bridge accelerations

S.R. Lorenzen, M.M. Rupp & C. Hübler
TU Darmstadt – Institute of Structural Mechanics and Design, Darmstadt, Germany

ABSTRACT: This study explores the use of drive-by monitoring as an alternative to conventional bridge-mounted sensors for monitoring maximum accelerations in railway bridge structures, a key factor in maintaining track ballast stability. Given the extensive rail network and the ongoing development of railway vehicles, traditional methods using bridge sensors require considerable effort, highlighting the need for a more efficient approach. This work analyses data from two field tests, using an ICE 4 train on a bridge with a 19.5 metre span and an ICE TD on a 16.4 metre span bridge, with synchronised acceleration measurements taken from both the train's axle boxes and the bridge's main girders. This allows for a direct comparison between the new drive-by approach and a conventional bridge sensor-based approach. Results indicate that axle box acceleration sensors in a drive-by approach are effective in monitoring bridge accelerations.

1 INTRODUCTION

Railway bridges have a considerable service life, with the average lifespan in Germany reaching 122 years (Knapp 2019). During this time, railway vehicles undergo numerous evolutionary stages, resulting in significant increases in axle loads and speeds (Karimi 2020). These changes pose challenges to these bridge structures beyond the original design expectations. Particularly problematic situations occur when changes in axle spacing and speed induce resonances in the bridge structures where no resonant excitations were expected (Firus *et al.* 2018, Matsuoka *et al.* 2021). This scenario can cause substantial accelerations and deflections in the structures. To ensure the stability of the track ballast, the maximum vertical acceleration of ballasted bridge structures is limited to 3.5 m/s² by the Eurocode (German Institute for Standardisation Registered Association 2021). However, Austrian regulations also allow accelerations of 6 m/s² for existing ballasted bridges (Austrian Standard Institute 2014).

Due to the large number of bridges in the network, combined with the continuous development of vehicles, conventional monitoring methods using sensors on the bridge structure would require a tremendous amount of work. A cost-effective alternative for monitoring acceleration limits could be the implementation of drive-by monitoring. The concept of drive-by monitoring was proposed about 20 years ago (Yang *et al.* 2004). Since then there has been a lot of research and development. An overview of the research conducted in this area can be found in (Yang and Yang 2018, Malekjafarian *et al.* 2022 and Souza *et al.* 2023). However, to the best of our knowledge, despite its practical importance, the topic of acceleration assessment has not yet become a focus of the community.

This paper analyses data from two field tests, where synchronised acceleration measurements were conducted on the main girders of the bridge and the axle boxes of the train. An ICE 4 was used on a bridge with a 19.5 metre span, and an ICE TD on a bridge spanning 16.4 metres.

DOI: 10.1201/9781003483755-204

2 FIELD MEASUREMENTS

2.1 *ICE 4 on Schmutter Bridge*

The first measurement campaign was initiated during the introduction of the ICE 4 in 2017. A comprehensive background, detailed description and analyses of the measurement data can be found in Firus *et al.* 2018, Firus 2021 and Lorenzen 2023. The Schmutter Bridge (see Figure 1) is a single-span, double-track, simply supported structure, with a span of 19.5 metre, consisting of two separate steel box girders coupled via track ballast. It was equipped with 44 accelerometers, positioned at 1.95 metre intervals along 11 structural axes (see Figure 2). Seven accelerometers were not available for all crossings; these are marked in white, while all others are marked in red. For this study, we focused on the four acceleration sensors located on axis 6 (labelled as A6, B6, C6, & D6), each with a measurement range of ± 5 g. These sensors were connected to HBM MX840B amplifiers and recorded data at a frequency of 1200 Hz.

The test train, a 12-car ICE 4, was equipped with 8 accelerometers on the axle boxes of cars 8 and 9 (labelled T_1 to T_8), each with a range of ± 100 g (see Figure 3). These sensors were connected to HBM 1-ML801B amplifiers to acquire data at 2400 Hz.

During the campaign, a total of 52 crossings were performed, 26 in each direction. Axles were detected by photoelectric sensors positioned at both ends of the bridge, to facilitate tracking of average speed (see Figure 4). A constant speed was a valid assumption considering the train driver's adherence to the set speed instructions and the minimal speed variations in the area. Axle spacing, axle loads and the traveled speeds are detailed in Firus 2021.

To synchronise the data between bridge and train, coils and magnets were attached to the rails and the train. This setup triggered the measurement system whenever the magnets passed over the coils.

The first bending frequency of the bridge structure, identified with covariance-driven stochastic subspace identification (SSI-COV) using free decay signals, showed significant amplitude dependence, fluctuating between approximately 5.1 Hz and 5.8 Hz (Lorenzen *et al.* 2022a and Lorenzen 2023). To ensure a consistent comparison of the frequency content and to retain the dominant vibration mode, while eliminating transient signals, both the train acceleration data and the bridge measurements were filtered using a 4th order Butterworth filter with a cut-off frequency of 8 Hz.



Figure 1. Schmutter bridge with a crossing ICE 4.

2.2 *ICE TD on Garather Bach Bridge*

In 2022, the second measurement campaign analysed in this study involved the ICE TD train on the Garather Bach bridge (see Figure 5). This bridge was equipped with a permanent monitoring system as part of the ZEKISS research project. Detailed discussions of these measurements and data analyses from the bridge are available in Lorenzen *et al.* 2022b, Lorenzen 2023 and Lorenzen *et al.* 2023 with specific focus on the ICE TD measurements in Lorenzen 2023 and Rupp *et al.* 2023.

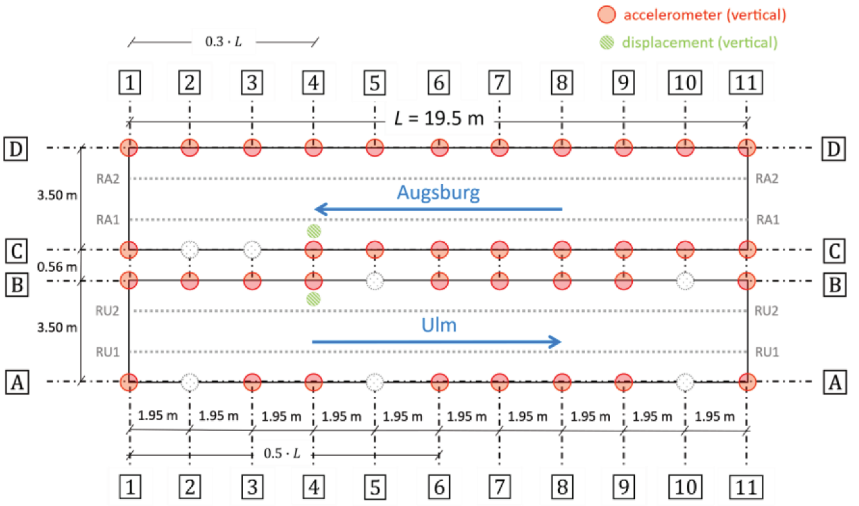


Figure 2. Sensor setup installed on the schmutter bridge.

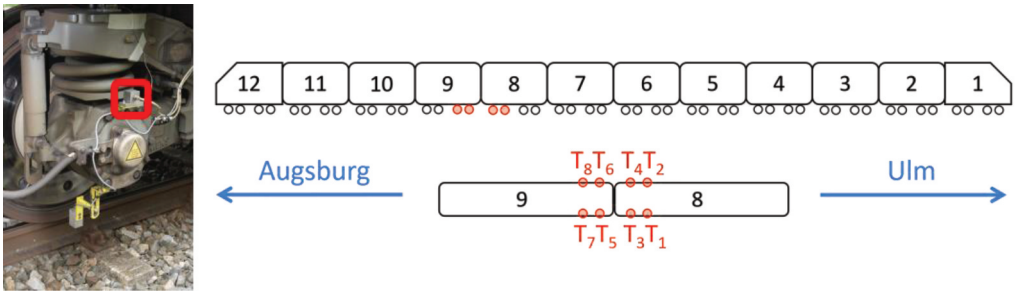


Figure 3. Sensor setup installed on the ICE 4.

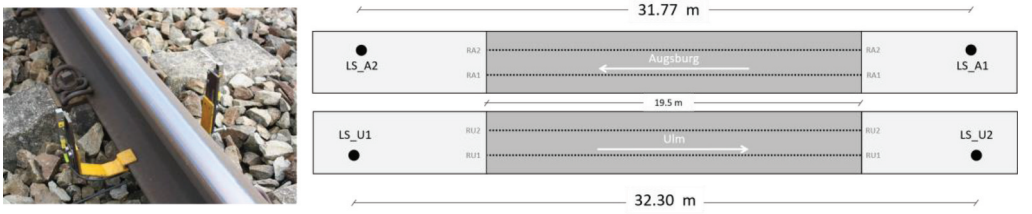


Figure 4. Photoelectric sensors for axle detection.

The Garather Bach bridge is a single span, single-track, simply supported steel trough bridge with a ballasted superstructure and has a span of 16.4 metres. Our study focused on two acceleration sensors (A2 & A7; see Figure 6) each with a measurement range of ± 5 g. These sensors, connected to HBK MX1601B measuring amplifiers, recorded data at a frequency of 1000 Hz. To track the train's axles, strain gauges G1 and G5 were used on the rails, also connected to HBK MX1601B amplifiers. The signals were sampled at 5000 Hz.

In addition to the bridge instrumentation, the 4-car ICE TD train was equipped with 32 accelerometers (labelled as T_{1L} to T_{16L} & T_{1R} to T_{16R}), each with a ± 100 g range, mounted on the axle boxes as shown in Figure 7. These devices were connected to a HBK QuantumX MX1601B and 3 QuantumX MX840B amplifiers, with a sampling rate of 5000 Hz. Five accelerometers failed during the test; they are marked in grey and were excluded from the analysis (see Figure 7).



Figure 5. Garather Bach bridge with a crossing ICE TD.

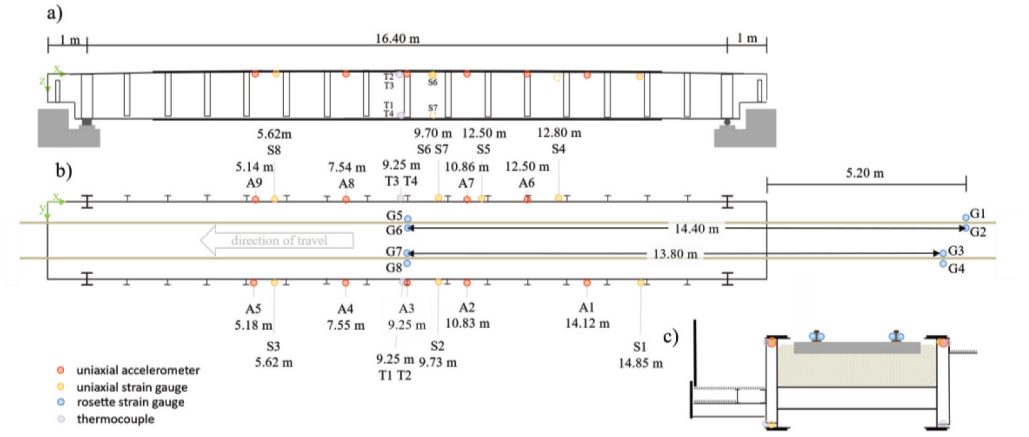


Figure 6. Permanent monitoring setup installed on the Garather Bach bridge. a) side view b) top view c) cross section.

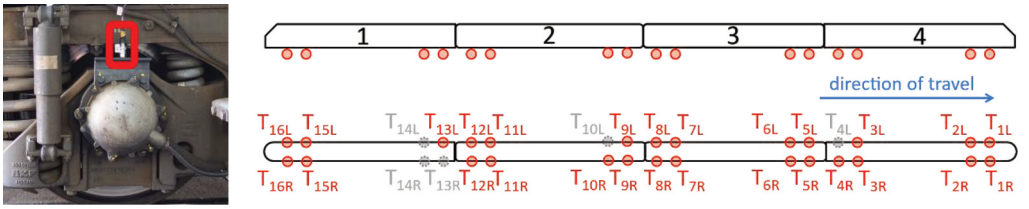


Figure 7. Sensor setup installed on the ICE TD.

During the measurement campaign, 13 crossings were recorded. However, one crossing was carried out at less than 10 km/h and the bridge accelerations are extremely low, so only 12 crossings were analysed.

To determine the train's position, two 1-GPS-USB-18Hz (HBK) Multi-GNSS receivers were connected to the measurement computer. A GPS module of the same type was installed on the bridge. By using the satellite timing from these GPS receivers, we synchronised the data from the train and bridge systems.

Like the Schmutter bridge findings, the first bending frequency of the Garather Bach bridge, identified with SSI-COV using free decay signals, showed significant amplitude dependency, ranging between approximately 5.6 Hz and 6.5 Hz (Lorenzen *et al.* 2022b and Lorenzen 2023). As in the previous section, we applied the same methodology for data consistency. Both the train and the bridge accelerations were filtered using a 4th order Butterworth filter with a cut-off frequency of 8.5 Hz. The cutoff frequency is therefore 0.5 Hz higher than before, the reason for this is that the bending frequencies are slightly higher for this bridge. This approach was chosen to ensure a uniform comparison of frequency content, while preserving the dominant vibration mode and eliminating transient signals.

3 METHOD FOR COMPARISON OF AXLE BOX WITH BRIDGE ACCELERATIONS

Due to track irregularities, the data collected by the acceleration sensors on the axle boxes is speed dependent. Owing to the brief contact period, it is reasonable to assume that the train's speed remains approximately constant during these intervals. Consequently, each sensor is subject to identical speed-dependent effects. The solution to this issue is to use the residual signal, which is obtained by subtracting the phase-shifted signal of a preceding axle from the signal of the current axle (see Figure 8).

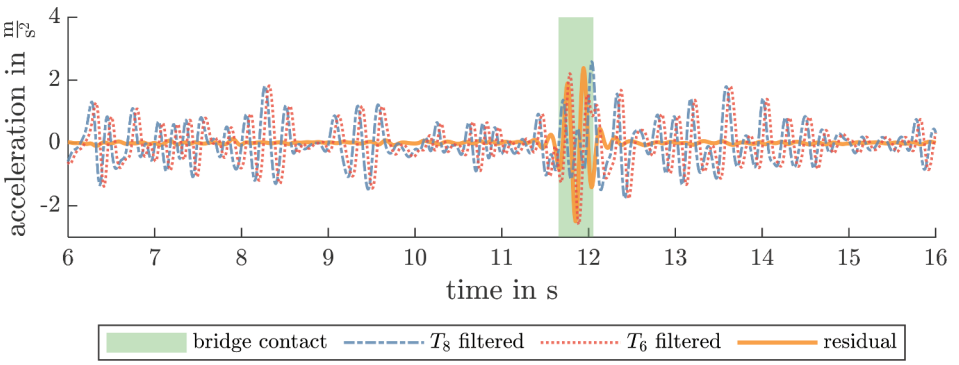


Figure 8. Filtered signals T_8 and T_6 (ICE 4), along with the residual signal, showing the contact time on the bridge during a crossing towards Augsburg.

In the first field test (see Section 2.1), only four axles were instrumented, and the residual was always calculated with respect to the axle immediately in front in direction of travel. In the second field test (see Section 2.2), the first axle was also instrumented, so the first axle residual was always used. The first axle residual is advantageous as the bridge vibration is still minimal.

To compare the accelerations, the maximum absolute value of the accelerations of the residual signals is compared with the maximum absolute value of the bridge accelerations during the contact period of each axle.

For a quantitative evaluation, we calculated the percentage error between the residual signal from the acceleration measurements on the train and the measured bridge accelerations. Denoting the maximum absolute acceleration on the train as $\max(|a_{\text{train}}|)$ and on the bridge as $\max(|a_{\text{bridge}}|)$, both being positive real numbers, the percentage error $E_{\%}$ is defined as:

$$E_{\%} = \frac{\max(|a_{\text{train}}|) - \max(|a_{\text{bridge}}|)}{\max(|a_{\text{bridge}}|)} \cdot 100\% \tag{1}$$

We consider $\max(|a_{\text{bridge}}|)$ to be the true or target value. We did not use the absolute value of the difference to preserve the sign, thereby indicating whether the values are overestimated or underestimated. For the summary of all crossings, the absolute values of the percentage errors were also calculated as follows:

$$|E_{\%}| = \frac{|\max(|a_{\text{train}}|) - \max(|a_{\text{bridge}}|)|}{\max(|a_{\text{bridge}}|)} \cdot 100\% \tag{2}$$

Before presenting the results, it should be noted that, due to the characteristics of the sensors, a larger relative error is to be expected at lower accelerations. In addition, the determination is based on the residual signal. This means that, depending on the phase shift of the signals, which in turn depends on the axle spacing and the speed travelled, the bridge vibration is either amplified (with opposite sign) or attenuated (with the same sign). Furthermore, if the ratio of travel speed to bridge frequency is too high, it is no longer guaranteed that the sensor will be close to the centre when the maximum amplitude occurs, and will therefore not detect the maximum acceleration, but only a fraction of it.

4 RESULTS

4.1 *ICE 4 on Schmutter Bridge*

In our analysis of the ICE 4 passages over the Schmutter Bridge, we found that it was not possible to derive valid residual signals for the pairings of T_5 with T_7 and T_4 with T_6. This issue arose due to the high dissimilarity between the signals, which prevented effective cancellation of accelerations when subtracting the phase-shifted signals. However, for all other residual signals, we calculated the percentage error $E_{\%}$ according to Equation (1). The errors were compared with the sensor on the same side as the corresponding train sensor. For crossings towards Ulm, this includes T_3 - T_1 and T_5 - T_3 paired with A6, and T_4 - T_2 and T_8 - T_6 paired with B6. For crossings towards Augsburg, this involves T_6 - T_8 and T_2 - T_4 with D6, and T_1 - T_3 and T_3 - T_5 with C6. The results are separated for the directions towards Ulm and Augsburg. Figure 9 shows how the results relate to both train speed and bridge acceleration (see Figure 9).

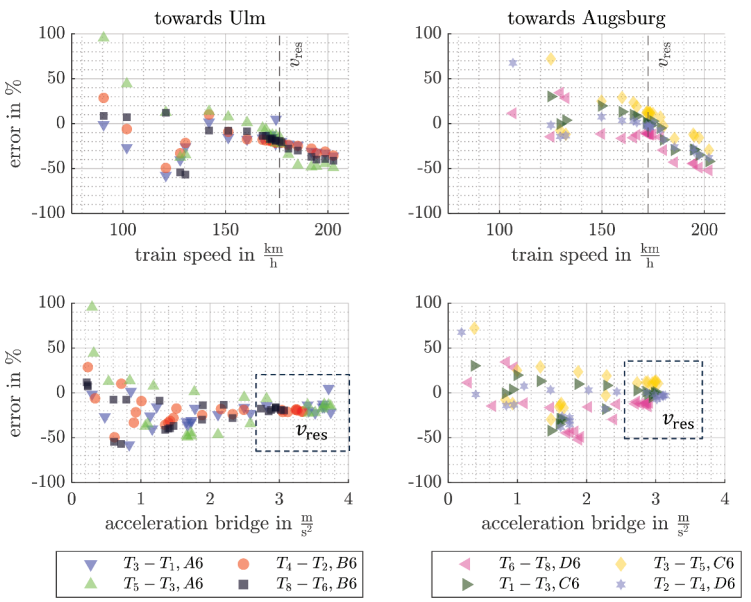


Figure 9. Percentage error in acceleration at the Schmutter bridge, separated by direction of travel.

For both directions, our analysis revealed a negative correlation between the percentage error and the train speed. The train resonance speed, indicated by a dashed line labelled as v_{res}, shows that the error is small near the resonance condition. The minimal errors observed at resonance inducing speeds correspond to high accelerations where small errors are also prevalent. Crucially, in the context of our study, the small errors at high accelerations, close to the threshold, are of primary importance, whereas larger errors at lower accelerations are considered less relevant.

The results are summarised quantitatively in Table 1. The mean values and standard deviations of the percentage error (see Eq. (1)) and the absolute values of the percentage error (see Eq. (2)) are displayed separately for the direction towards Ulm and towards Augsburg.

Table 1. Summary of mean and standard deviation of percentage errors and absolute values of percentage errors from residual signals of axle box accelerations on ICE 4 in comparison to sensor readings on Schmutter bridge.

	Ulm		Augsburg	
	mean in %	std. in %	mean in %	std. in %
percentage error	-18.6	21.2	0.4	40.9
absolute values percentage error	23.8	15.1	21.7	34.6

4.2 *ICE TD on Garather Bach Bridge*

For the second measurement campaign, the percentage error for all axles was determined for the 12 crossings according to Equation (1). The sensors on the left side in direction of travel (T_{iL}) were compared with the bridge sensor A2 and the sensors on the right side in direction of travel (T_{iR}) with the bridge sensor A7. The results are plotted separately for each axle as a function of bridge acceleration (see Figure 10). The plots are arranged line by line according to the coaches, i.e., the first column corresponds to the first axles, the second column to the second axles and so on.

It can be seen that the bridge accelerations tend to be underestimated by the sensors of the first bogie axles (columns 1 and 3) and overestimated by those of the second bogie axles (columns 2 and 4). For high amplitudes, the best results are obtained with the second bogie axles. As the amplitudes of the bridge vibration during the passage of the first and second axle of a bogie are very similar, this behaviour is probably caused by the phase shift relative to the bridge vibration.

The results are summarised quantitatively in Table 2. The mean values and standard deviations of the percentage errors and the absolute values of the percentage errors are displayed separately for the left and right sides.

5 CONCLUSION

To ensure ballast stability, allowable accelerations on bridge structures are regulated by technical standards. However, monitoring actual accelerations using bridge instrumentation is labourious. A more economical approach is the use of sensors on trains. This study aimed to explore, for the first time, the extent to which bridge accelerations can be estimated using train-mounted sensors. Our investigation involved field tests with two different bridges and trains. Both structures could be resonantly excited by the trains, leading to particularly high structural responses potentially critical for ballast stability. However, the tests have shown that there is no destabilisation of the ballast in the supporting structure.

The study of the percentage error between accelerations measured with sensors on the bridge and on the train showed that the error decreases with increasing amplitude. Therefore, in resonance scenarios, our findings indicate that estimating bridge acceleration based on axle

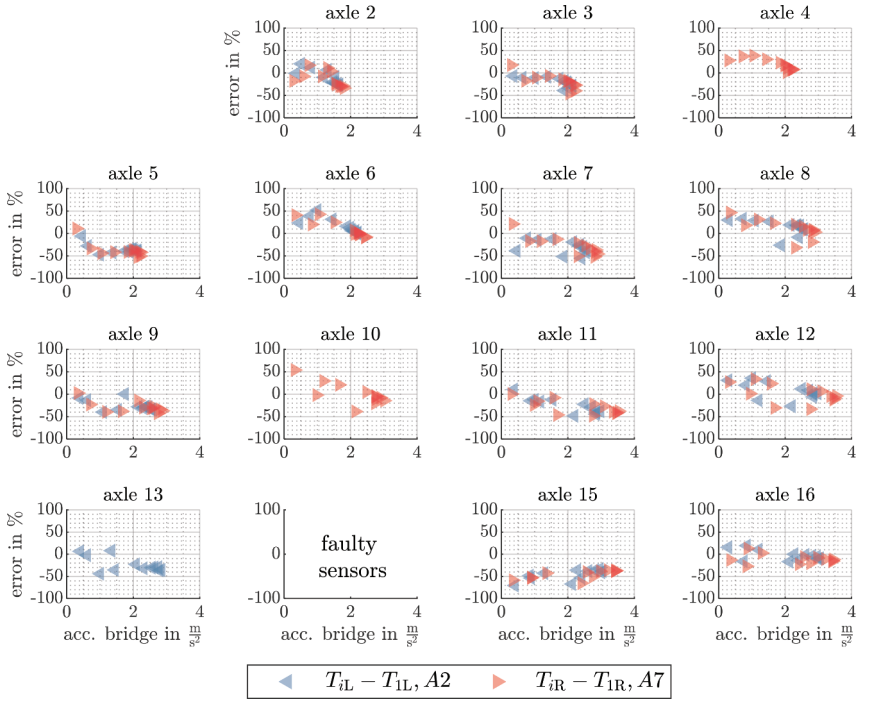


Figure 10. Percentage error for the left and right sensors compared to the bridge sensors separately for each axle.

Table 2. Summary of mean and standard deviation of percentage errors and absolute values of percentage errors from residual signals of axle box accelerations on ICE TD in comparison to sensor readings on Garather Bach bridge.

	left		right	
	mean in %	std. in %	mean in %	std. in %
percentage error	-15.0	24.2	-15.0	25.5
absolute values percentage error	24.2	15.0	24.3	15.4

box accelerations is within an acceptable range for assessing the bridge's accelerations. This holds significant practical value, as it encompasses critical states.

For future studies, it would be beneficial to examine the influence of the relationship between the periods of bridge vibrations and contact times.

ACKNOWLEDGEMENTS

The authors would like to acknowledge the financial support of the research project ZEKISS ("Condition assessment of railroad bridges and vehicles with AI methods for the evaluation of sensor data and structural dynamic models"), funded by mFund (mFund, 2020) awarded by the Federal Ministry of Transport and Digital Infrastructure of Germany. Research in ZEKISS is carried out in collaboration with the German railway company DB Netz AG, the Wolfel Engineering GmbH and the GMG Ingenieurgesellschaft mbH (www.zekiss.de)

REFERENCES

Austrian Standard Institute (2014) *ONR 24008 - Bewertung der Tragfähigkeit bestehender Eisenbahn- und Straßenbrücken*.

German Institute for Standardisation Registered Association (2021) *Eurocode: Grundlagen der Tragwerksplanung*: *Deutsche Fassung EN 1990:2002* + A1:2005 + A1:2005/AC:2010.

Firus, A. *et al.* (2018) 'Untersuchungen zum Dynamischen Verhalten einer Eisenbahnbrücke bei Anregung durch den neuen ICE 4', *VDI Berichte*, 2018(2321), pp. 233–248. doi: 10.51202/9783181023211-233.

Firus, A. (2021) *A contribution to moving force identification in bridge dynamics*. doi: 10.26083/tuprints-00020293.

Karimi, S. (2020) *Experimentelle und numerische Untersuchung der Wechselwirkung zwischen Tragwerk und Gleis*. Universität für Bodenkultur Wien.

Knapp, N. (2019) *Faktenblatt Eisenbahnbrücken bei der Deutschen Bahn Faktenblatt*. Available at: https://www.deutschebahn.com/resource/blob/6860076/452fa9432001be62ac986886a2e60dd2/MP-Bruecken-Faktenblatt-875-Bruecken-data.pdf.

Lorenzen, S. R., Berthold, H., *et al.* (2022a) 'Deep learning based indirect monitoring to identify bridge natural frequencies using sensors on a passing train', in *BARCELONA IABMAS 2022: 11th International Conference on Bridge Maintenance, Safety and Management*. Barcelona.

Lorenzen, S. R., Riedel, H., *et al.* (2022b) 'Virtual Axle Detector Based on Analysis of Bridge Acceleration Measurements by Fully Convolutional Network', *Sensors*, 22(22), pp. 1–17. doi: 10.3390/s22228963.

Lorenzen, S. R. (2023) *Railway Bridge Monitoring with Minimal Sensor Deployment : Virtual Sensing and Resonance Curve-Based Drive-by Monitoring*. Technical University of Darmstadt.

Lorenzen, Steven Robert *et al.* (2023) 'Long-term validation of virtual sensing of a railway bridge with ballasted superstructure', 6(5), pp. 725–733. doi: 10.1002/cepa.2126.

Malekjafarian, A., Corbally, R. and Gong, W. (2022) 'A review of mobile sensing of bridges using moving vehicles: Progress to date, challenges and future trends', *Structures*. Elsevier Ltd, 44(August), pp. 1466–1489. doi: 10.1016/j.istruc.2022.08.075.

Matsuoka, K. *et al.* (2021) 'Drive-by methodology to identify resonant bridges using track irregularity measured by high-speed trains', *Mechanical Systems and Signal Processing*. The Author(s), 158, p. 107667. doi: 10.1016/j.ymssp.2021.107667.

Rupp, M. M. *et al.* (2023) 'High-speed drive-by monitoring: field testing with an intercity express train (ICE)', *Eurostruct*, 6(5), pp. 854–862. doi: 10.1002/cepa.2045.

Souza, E. F. *et al.* (2023) 'Drive-by Methodologies Applied to Railway Infrastructure Subsystems: A Literature Review—Part I: Bridges and Viaducts', *Applied Sciences (Switzerland)*, 13(12). doi: 10.3390/app13126940.

Yang, Y. B., Lin, C. W. and Yau, J. D. (2004) 'Extracting bridge frequencies from the dynamic response of a passing vehicle', *Journal of Sound and Vibration*, 272(3–5), pp. 471–493. doi: 10.1016/S0022-460X(03)00378-X.

Yang, Y. B. and Yang, J. P. (2018) 'State-of-the-Art Review on Modal Identification and Damage Detection of Bridges by Moving Test Vehicles', *International Journal of Structural Stability and Dynamics*, 18(2). doi: 10.1142/S0219455418500256.

Bridge Maintenance, Safety, Management, Digitalization and Sustainability – Jensen, Frangopol & Schmidt (eds)
© 2024 The Author(s), ISBN 978-1-032-77040-6
Open Access: www.taylorfrancis.com, CC BY-NC-ND 4.0 license

Empirical study on smartphone-vehicle trip metadata and bridge modal property estimates

T.J. Matarazzo
United States Military Academy, New York, USA
Massachusetts Institute of Technology, Massachusetts, USA

L. Cronin, G. Marasco, I. Dabbaghchian & S.N. Pakzad
Lehigh University, Pennsylvania, USA

S.S. Eshkevari
Uber Technologies Inc., California, USA
Massachusetts Institute of Technology, Massachusetts, USA

D. Sen
Southern Illinois University, Carbondale, USA

P. Santi & C. Ratti
Massachusetts Institute of Technology, Massachusetts, USA

ABSTRACT: Bridge dynamic properties can be extracted through the analyses of crowdsourced smartphone-vehicle trip (SVT) data collected during routine trips over bridges. The key advantage of crowdsourced SVT data is the ease in generating large volumes of data at very low costs compared to modern structural health monitoring (SHM) systems. By default, these SVT datasets generally contain measurements from over a dozen sensors embedded within the smartphone. Such SVT metadata are presumed to capture important variables that influence the inherent quality of the vibration data and the resulting accuracy of dynamical property estimates. However, the quantitative relationships between key metadata variables such as vehicle speed or trip direction are not well understood in real-world scenarios. This paper studies how the estimates of the absolute valued mode shapes (AMS) are affected by metadata variables of smartphone-vehicle trip (SVT) datasets. This study considers SVT data collected on two bridges (i) the Golden Gate Bridge in California, and (ii) the Gene Hartzell Memorial Bridge in Pennsylvania and focuses on the influence of vehicle speed and vehicle travel direction. A better understanding how such variables impact the estimation of bridge dynamic properties is critical to the future design and implementation of effective crowdsourcing campaigns.

1 INTRODUCTION

Over the past two decades, researchers have studied methods using sensors in moving vehicles to monitor bridge dynamical properties (Yang and Chang, 2009). The motivation for these "indirect bridge monitoring" methods are rooted in their potential advantages over traditional structural health monitoring (SHM) systems that consist of a distributed sensor network installed directly on the structure (Brownjohn et al., 1992; Smyth et al., 2003; Lynch and Loh, 2006). Indirect modal identification methods for bridges have been developed to determine bridge modal properties by analyzing measurements from sensors that are not installed on the

DOI: 10.1201/9781003483755-205

structure, instead, the sensors are attached to a moving vehicle (Yang et al., 2004; Lin and Yang, 2005).

Early successes were primarily demonstrated in controlled experimental tests or synthetic data, which does not fully represent real-world conditions. Additionally, the integration of mobile sensor networks, particularly leveraging ubiquitous devices like smartphones, has become a focal point in this research field (McGetrick et al., 2015; Yang et al., 2020; Gonzalez et al., 2012; Eshke-´ vari et al., 2019; Eshkevari and Pakzad, 2019; Eshkevari et al., 2020, 2022; Gkoumas et al., 2023; Malekjafarian et al., 2022; McGetrick et al., 2017; Matarazzo et al., 2018; ?; Yang et al., 2020). Although smartphones possess less accurate sensors overall, studies have shown their successful application in SHM.

Recent investigations into indirect methods using smartphone sensors in real-world scenarios, considering factors like operational traffic loading and typical bridge trips, have yielded promising results. Notably, accurate estimates of bridge modal frequencies have been obtained from data crowdsourced during smartphone-vehicle trips (SVT) (Matarazzo et al., 2022). However, crowdsourced SVT data fall into three classes—controlled, partially-controlled, and uncontrolled—based on the analysts' oversight and influence on data collection. The impact of SVT data quality variations, considering trip metadata such as vehicle speed or smartphone model, remains unclear.

In some instances, crowdsourced SVT metadata may signal poor data quality, and including such datasets could adversely affect SHM results. This becomes particularly crucial when dealing with large data volumes, reaching tens of thousands of datasets. For example, crowdsensing platforms with monthly data streams on this scale could greatly benefit from preprocessing tools that filter out noisy or less impactful datasets. This study aims to assess the quality of individual datasets in relation to the overall population, exploring their classification to develop tools that enhance the accuracy of estimation results in SHM.

This paper studies how the absolute mode shapes (AMS) estimates are affected by metadata variables of smartphone-vehicle trip (SVT) datasets. This study considers SVT data collected on two bridges (i) the Golden Gate Bridge in California, and (ii) the Gene Hartzell Memorial Bridge in Pennsylvania. This study focuses on the influence of vehicle speed and vehicle travel direction.

2 SMARTPHONE-VEHICLE TRIP (SVT) DATA COLLECTION

This study analyzes smartphone-vehicle trip (SVT) data collected on the Golden Gate Bridge in California and the Gene Hartzell Memorial Bridge in Pennsylvania. The Golden Gate Bridge (GGB) is located in San Francisco is amongst the world most renowned bridges. It is a suspension bridge with total length of 2740 meters and its main span spans a length of 1280 meters. The GGB accommodates an annual average daily traffic (AADT) volume exceeding 100,000 vehicles. This means even a low rate contribution to the crowdsourced data from vehicles would yield an abundance of SVT data per day. In total 152 SVT datasets were collected in two batches as part of the *Good Vibrations* project Lab (2023). The first batch includes 102 trips collected in a controlled environment, which means variables such as vehicle speed and orientation of smartphone is controlled. The other part was provided by UBER from its ride-hailing fleet, which consists of 50 trips made by a diverse set of drivers and vehicles therefore it is considered as uncontrolled dataset.

The Gene Hartzell Memorial bridge (GHMB) is located in Pennsylvania. This bridge was built in 2001 and is a steel truss bridge with overal lenth of 540 meters and main span length of 180 meters. GHMB is on the PA route 33 and has an AADT of around 59,000 vehicles. For the GHMB 332 SVT datasets were three different batches. 102 trips are collected with vehicles passing with an average speed of 19.6 m/s with little deviation. Another batch of 98 trips are collected with vehicle velocity of 22.2 to 36.1 m/s. With the aid of Pennsylvania department of transportation, another data collection batch was conducted to collect 132 more trips with lower vehicle velocity ranges. The trips are collected using seven different vehicles of the research team. The GHMB has two lane on each travel direction and during

the data collection, the right lane of the northbound was closed by officials and was only used by the research team's vehicles. The rest of the bridge stayed open to normal daily traffic. For this campaign the vehicle speed of the trips ranges between 4.5 to 13.5 m/s.

Each SVT dataset contains over a dozen measurement channels such as acceleration in three directions, vehicle speed, GPS, GPS accuracy, etc. The accelerometer triaxial accelerometer measurements (X,Y, and Z-directions) were sampled at 100 Hz and GPS (latitude, longitude) were sampled at a rate of 1 Hz.This study focuses on vehicle speed and GPS channels and their influence on the estimation of the absolute value mode shapes (AMS) of the bridge.

3 EXTRACTION OF ABSOLUTE MODE SHAPES

The bridge modal properties of interest in this study are the mode shapes. It is assumed that bridge modal frequencies have already been identified. It is important to note that the collected SVT datasets are asynchronous. A methodology proposed in Cronin et al. (2022) is implemented to estimate the *absolute value mode shapes* (AMS) – it is not yet possible to extract mode shape phase information from asynchronous sensor measurements – hence the *absolute value*. The methodology builds an aggregated frequency-space map using wavelet transforms and determines AMS from frequency-banded portions of this map.

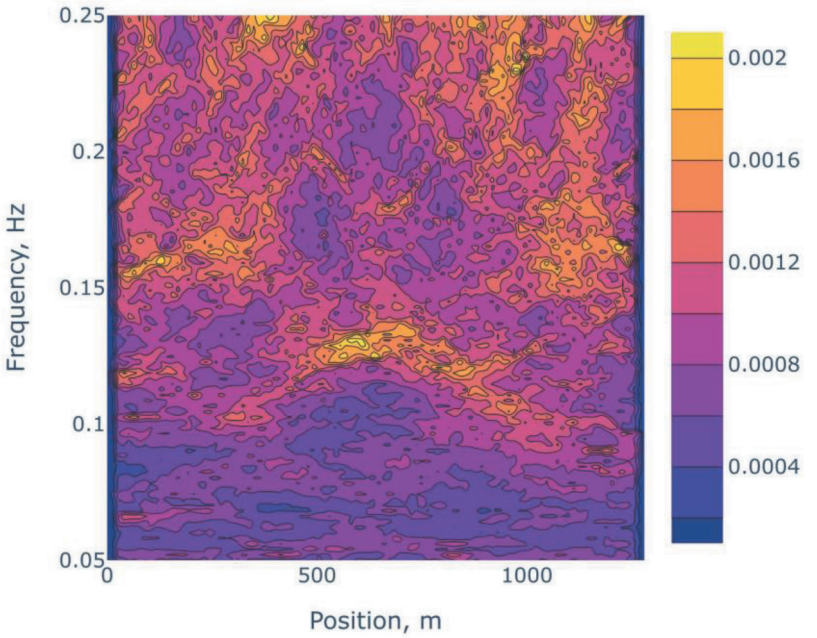


Figure 1. Aggregated frequency-space map for the GGB SVT data. Lighter colors (yellows) indicate a larger power (magnitude) in the frequency spectrum.

The overall idea behind the methodology is to aggregate the magnitude of the acceleration signal's frequency contents spatially. This is achieved using the synchrosqueezed wavelet transform to break down the collected acceleration time series into their time-frequency components. Using the GPS data from the phones, the vehicle's position is known at each time step. With these two pieces of information, magnitude and position, the aggreagtion process can begin. The signal magnitude at each position and frequency is aggregated across the entire SVT dataset, yielding a map of the frequency, position, and magnitude. Figure 1 shows an aggregated frequency-space map for the controlled GGB dataset collected by the research

team (102 trips). The first three modes are prominent in the collected dataset, and the ridges can be seen at frequencies 0.106, 0.132, and 0.169 Hz.

Cronin et al. (2022) recovers the absolute mode shapes for the first three modes from this dataset with all MAC values above 0.95, indicating high accuracy. With respect to Figure 1, the absolute modes shapes would be the section slices of the space-frequency map at the natural frequencies of the bridge. Figure 1 also highlights an imperfection in localizing time-frequency components and separating closely spaced frequencies. For example, the first and second modes are closely spaced, leading to smearing between the frequency bands and the"U" shaped ridge at the center span. This smearing artifact is not exclusive to wavelet transforms, but is an overall difficulty across all time-frequency transforms.

4 OBSERVATIONS ON THE INFLUENCE OF SPEED AND TRAVEL DIRECTION

This study empirically observes how the absolute mode shape estimates can vary based on two key variables: vehicle speed and direction of travel. The influence of vehicle speed on modal frequency estimation have been studied, e.g., peak shift in the power spectral density of the signal. Formal relationships between vehicle speed and mode shapes are not yet known. The direction of travel is an important variable whose effect on modal property estimates has not been well studied. As crowdsourcing campaigns continue, the bridges studied will include those with more complex, unsymmetric geometries and it is in these cases where such direction may be most pronounced. Interaction effects or other latent variables are not considered in this study.

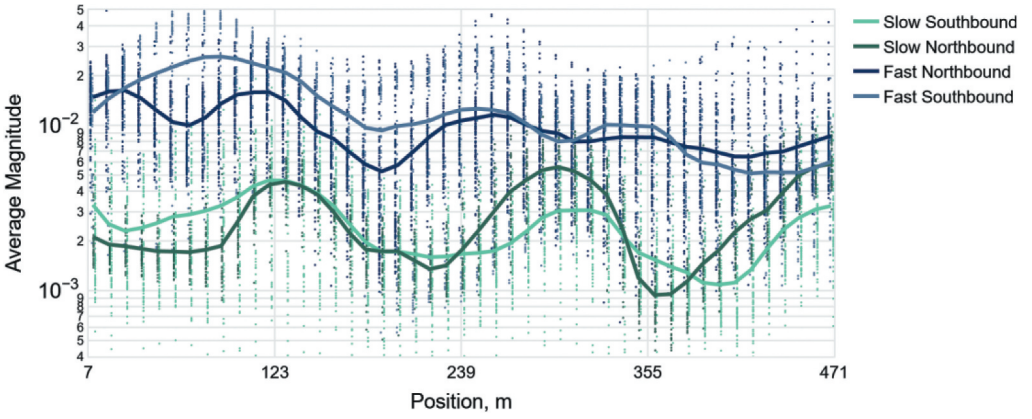


Figure 2. Absolute mode shape of the third vertical mode of the Gene Hartzell Memorial Bridge (GHMB) considering individual trips. Individual points are color-coded into four categories: 1) slow southbound (light green), 2) slow northbound (dark green), 3) fast northbound (dark blue), and 4) fast southbound (light blue).

First, the GHMB dataset is considered. Figure 2 shows a few scatter plots corresponding to the absolute mode shape for the third vertical mode of the bridge. The magnitudes of these scatter plots are unscaled and come directly from the aggregated frequency-space map. Nonetheless, the average of all the points (all trips in a dataset) is the average absolute mode shape, i.e., AMS estimate. Each individual point represents the magnitude of one trip at that location on the bridge, and at any one location, there is a distribution of magnitudes. The solid lines represent the average of the respective direction-speed subset. Figure 2 shows that the faster speeds (in either direction) are associated with larger mode shape magnitudes, and the slower speeds are associated with smaller magnitudes. One possible explanation is that faster vehicle

speeds are correlated with higher amplitude signals recorded by the smartphone accelerometers, yet it is inconclusive whether this is an apparent result for all modes. There are no clear visual trends with regard to southbound versus northbound trips.

Figure 3 attempts to expose general trends with respect to speed for multiple bridges and modes (different colors). Due to variations in the scale and mean of each estimate, the MAC value would not be able to accurately assess consistency in mode shapes. Instead, the cosine similarity between the AMS of of a single trip and the true AMS based on fixed sensor reference data is calculated and used as a proxy metric for quality. Finally, cosine similarities equal to one indicate a good match (like MAC value).

The trendlines in the plot show simple linear regression fits to highlight potential trends and relationships between AMS accuracy and speed. Most of these fits show lines with decreasing slopes, which suggest a decline in cosine similarity with increases in speed. The exception is the first horizontal mode for the GGB (GGB-C-H1). The GHMB dataset, red scatter in Figure 3, spans the widest range of speeds and the most samples of the controlled datasets; the regression line was highly significant ($F = 80.15$, $p < .0001$), suggesting a negative dependency of sample quality on speed. While maintaining an inverse relationship, the fits for the GGB modes are not significant ($p > .05$). The fit for the horizontal GGB mode has a positive slope, suggesting that mode shape accuracy improves with vehicle speed, which is inconsistent the hypothesis of faster speeds reducing quality of mode shape estimates. Overall, these results are preliminary and provide limited quantification on how vehicle speed can affect quality of some specific mode shapes. Complications arise from large difference in the range of vehicle speeds considered in the GGB and GHMB applications, 20-70 km/hr vs. 20-120 km/hr, as well as the nonuniform sampling of the speeds.

In summary, while we can confirm speed is a quality predictor, this observation is not statistically significant for GGB modes. The quality of an individual SVT is affected by a wide range of features including bridge length, traffic speed, length ratio, road profile roughness, expansion joints, to name a few. In our analysis, we found evidence of speed affecting a metric

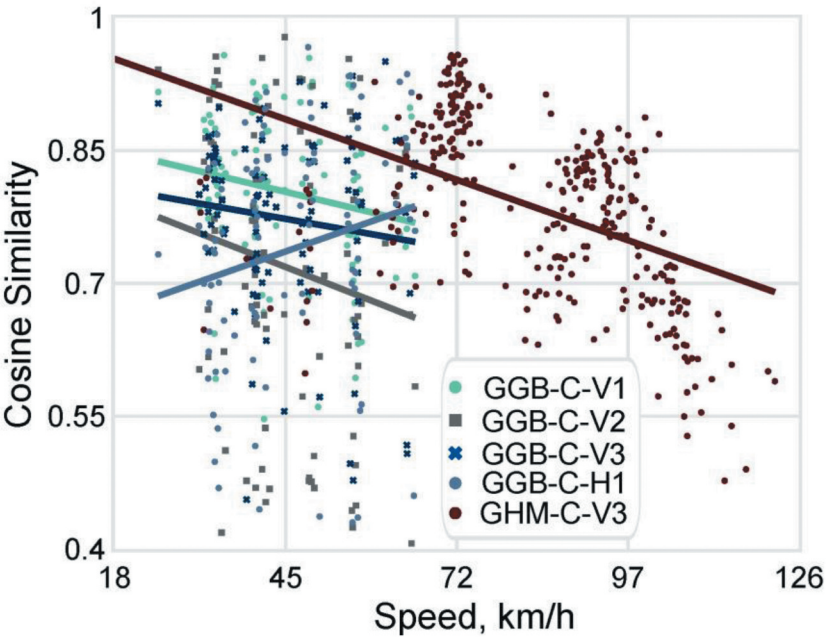


Figure 3. An analysis of the effect of speed of each SVT from GGB and GHMB case studies. Cosine similarity is a distance metric comparing the relative error between a fixed sensor reference and the AMS estimate from a single pass of over the bridge.

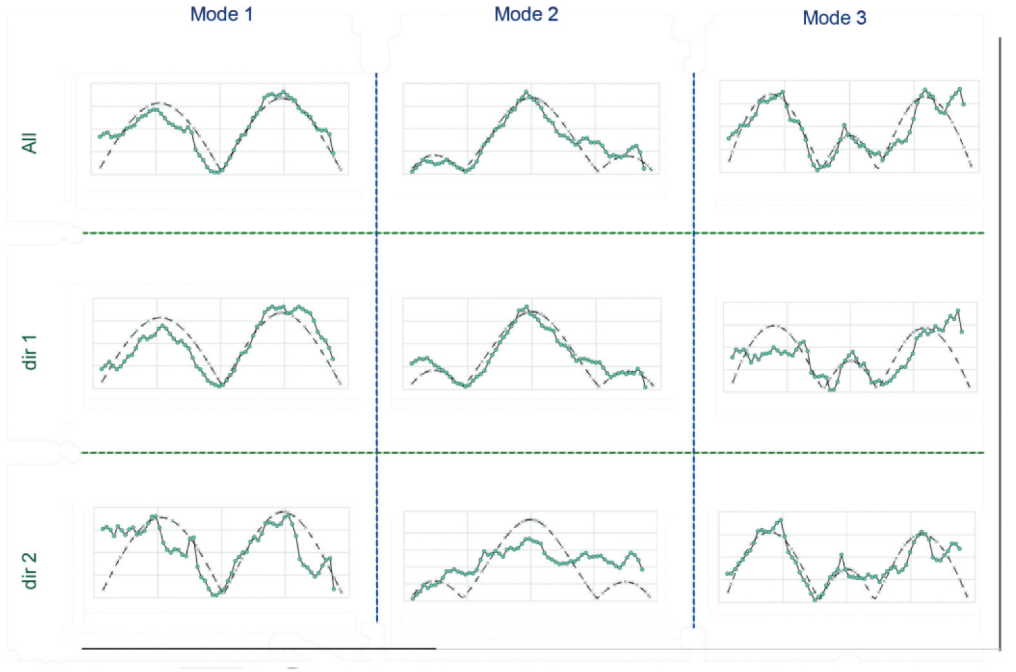


Figure 4. The effect of direction of travel on the GGB identified modes. Row 1 uses all of the data (102 trips). Row 2 presents the aggregation from only the northbound trips (dir 1), and Row 3 is the aggregation of only southbound trips (dir 2).

of mode shape quality, yet further investigation is needed to establish empirical rules for predicting the quality of individual SVT data based on trip metadata and features.

Figure 4 presents the first three vertical modes of the Golden Gate Bridge from the controlled dataset split by direction ("dir 1" = Northbound and "dir 2" = Southbound). Additionally, the full dataset aggregated mode shape is presented as a dashed line. While there do not appear to be any observable trends, significant differences between the datasets are apparent. For the first two modes, traveling in direction 1 appears to produce AMS that is closer to the overall result. For the 3rd mode, traveling southbound results in closer AMS.

5 CONCLUSION

This work analyzed over 400 crowdsourced smartphone-vehicle trip data collected on two bridges, the Golden Gate Bridge (GGB) and the Gene Hartzell Memorial Bridge (GHMB), to observe potential relationships between vehicle speed, travel direction, and the accuracy of absolute value mode shapes (AMS). Interaction effects were not considered. In analyses of the GHMB data, higher speeds were associated with larger AMS magnitudes, and the slower speeds were associated with smaller AMS magnitudes. While notable and consistent, these amplitudes did not appear to have an effect on AMS quality. In-depth analyses considering five modes identified on both bridges attempted to quantify trends between AMS quality and speed. Significant linear regressions on four modes (third vertical mode from GHMB and first three vertical modes from GGB) suggested a negative dependency of quality on speed. Importantly, the opposite relationship was observed for the horizontal mode from GGB – increasing speeds generally improved AMS accuracy. Finally, analyses of the first three vertical modes of the GGB showed significant visual differences between northbound trips and southbound trips.

In summary, these analyses identified notable differences between datasets collected at slow speeds versus high speeds. While there was some evidence to suggest AMS estimate quality decreases with speed, further analyses are needed to better establish generalized empirical laws. Differences due to travel direction were observed; however explicit trends could not be identified. Furthermore, it is possible such differences are caused by a different variable that was not controlled in this study.

REFERENCES

Brownjohn, J., A. Dumanoglu, and R. Severn (1992). Ambient vibration survey of the fatih sultan mehmet (second bosporus) suspension bridge. *Earthquake engineering & structural dynamics 21*(10), 907–924.

Cronin, L., S. S. Eshkevari, T. J. Matarazzo, S. Milardo, I. Dabbaghchian, P. Santi, S. N. Pakzad, and C. Ratti (2022). Identifying damage-sensitive spatial vibration characteristics of bridges from widespread smartphone data. *arXiv Preprint*.

Eshkevari, S. S., L. Cronin, T. J. Matarazzo, and S. N. Pakzad (2022). Bridge modal property identification based on asynchronous mobile sensing data. *Structural Health Monitoring 0*(0), 14759217221109014.

Eshkevari, S. S., T. J. Matarazzo, and S. N. Pakzad (2020). Bridge modal identification using acceleration measurements within moving vehicles. *Mechanical Systems and Signal Processing 141*, 106733.

Eshkevari, S. S. and S. Pakzad (2019). Bridge structural identification using moving vehicle acceleration measurements. In *Dynamics of Civil Structures, Volume 2*, pp. 251–261. Springer.

Eshkevari, S. S., S. N. Pakzad, M. Takac, and T. J. Matarazzo (2019). Modal identification of a bridge with sparse vibration data. *Journal of engineering mechanics DOI: 10.1061/(ASCE)EM. 1943-7889.0001733*.

Gkoumas, K., M. C. Galassi, D. Allaix, A. Anthoine, S. Argyroudis, G. Baldini, L. Benedetti, F. Bono, J. Brownjohn, E. Caetano, et al. (2023). Indirect structural health monitoring (ishm) of transport infrastructure in the digital age. Technical report, Luxembourg: Publications Office of the European Union.

Gonzalez, A., E. J. OBrien, and P. McGetrick (2012). Identification of damping in a bridge using′ a moving instrumented vehicle. *Journal of Sound and Vibration 331*(18), 4115–4131.

Lab, S. C. (2023). Mit senseable city lab good vibrations project website. https://senseable.mit.edu/good vibrations/.Accessed: 2023 − 01 − 03.

Lynch, J. P. and K. J. Loh (2006). A summary review of wireless sensors and sensor networks for structural health monitoring. *Shock and vibration digest 38*(2), 91–130.

Malekjafarian, A., R. Corbally, and W. Gong (2022). A review of mobile sensing of bridges using moving vehicles: Progress to date, challenges and future trends. *Structures 44*, 1466–1489.

Matarazzo, T. J., D. Kondor, S. Milardo, S. S. Eshkevari, P. Santi, S. N. Pakzad, M. J. Buehler, and C. Ratti (2022). Crowdsourcing bridge dynamic monitoring with smartphone vehicle trips. *Communications engineering 1*(1), 29.

Matarazzo, T. J., P. Santi, S. N. Pakzad, K. Carter, C. Ratti, B. Moaveni, C. Osgood, and N. Jacob (2018). Crowdsensing framework for monitoring bridge vibrations using moving smartphones. *Proceedings of the IEEE 106*(4), 577–593.

McGetrick, P., D. Hester, and S. Taylor (2017). Implementation of a drive-by monitoring system for transport infrastructure utilising smartphone technology and gnss. *Journal of Civil Structural Health Monitoring 7*(2), 175–189.

McGetrick, P. J., C.-W. Kim, A. Gonzalez, and E. J. Brien (2015).′ Experimental validation of a drive-by stiffness identification method for bridge monitoring. *Structural Health Monitoring 14*(4), 317–331.

Smyth, A. W., J.-S. Pei, and S. F. Masri (2003). System identification of the vincent thomas suspension bridge using earthquake records. *Earthquake Engineering & Structural Dynamics 32*(3), 339–367.

Yang, Y. and K. Chang (2009). Extracting the bridge frequencies indirectly from a passing vehicle: Parametric study. *Engineering Structures 31*(10), 2448–2459.

Yang, Y.-B., J. P. Yang, B. Zhang, and Y. Wu (2020). *Vehicle Scanning Method for Bridges*. Wiley Online Library.

SS08: Posttension analysis, design, and assessment in bridge construction

Organizers: U. Attanayake, H. Aktan, M. LaViolette & C. Rogers


Taylor & Francis
Taylor & Francis Group
http://taylorandfrancis.com

Bridge Maintenance, Safety, Management, Digitalization and Sustainability – Jensen, Frangopol & Schmidt (eds)
© 2024 The Author(s), ISBN 978-1-032-77040-6
Open Access: www.taylorfrancis.com, CC BY-NC-ND 4.0 license

Simplified stage construction and creep analysis of a segmental precast concrete bridge

A. Guarnieri, F. Bontempi & F. Petrini
University of Rome La Sapienza, Italy

ABSTRACT: In this work, a simplified methodology is developed for evaluating the evolution of strain/stresses or forces/deflections during the construction process of a segmental concrete precast bridge erected using a balanced cantilever method. The focus of the study is on modeling the entire construction process in stages (most significant) and the prestressing system, considering creep effects in a finite element model. During construction, the superstructure adopts a cantilever static scheme that change into a supported continuous beam upon the last stage. An original method for calculating creep phenomena has been implemented, involving the definition of a 'weighted' creep factor, which allows bypassing the limitations of the more common commercial codes in modeling such phenomena. Once the conceptual framework of the problem modeling is defined, it becomes possible to transfer all the acquired knowledge to more sophisticated models that use 2D or 3D elements and can address more complex local issues.

1 INTRODUCTION

For concrete bridges, the partition of the deck into segments becomes necessary for spans exceeding 50m, and the use of segments prefabrication proves to be a cost-effective solution in terms of launching equipment costs for long extensions and spans up to 120m. The construction methodology adopted in this work is well known as "Balanced Cantilever Method (BCM)" where the structure is erected by cantilevering through the initial construction of two cantilevers supported by an adequate prestressing system Barras et al. (2003). The typical cross – sections used in this type of construction are single-cell or multi-cell box girder, appropriately equipped with upper and lower ducts for prestressing tendons and eventually deviators in the case of external post - tensioning *Suntharavadivel (2005)*. The static scheme can vary (with continuous beam or frames static schemes) depending on economic, environmental, and construction needs, but reference will be made here to the case of a continuous deck on multiple supports with a parabolic tapering (a suitable solution for spans greater than 70m). The BCM involves constructing the deck starting from the piers and symmetrically progressing cantilever-wise from both sides, progressively placing various segments (each ranging from 3 to 6 meters in length) until they meet in the midspan where closure occurs through the installation of a cast-in-place stitch segment (this process is applied to all central spans). The portion of the deck coming from the abutment, of shorter length, can be erected either using an asymmetric cantilever technique or can be temporarily supported by a provisional structure until the structural continuity of the bridge is restored. In prefabrication, the placement of segment pairs generally occurs every 7 days, and in the work presented here, prefabricated segments positioned using ground cranes will be considered: their use does not impose additional load on the structure during the segment placement phase, and the weight of the segment does not bear on it until they are fixed through temporary prestressing bars. Post - tension in the cantilever construction phase is applied to the top slab with a strong eccentricity to generate a bottom positive moment that counteracts the upper negative moment induced by the self-weight in the cantilever diagram. At the end of construction, after the casting of the stitch segment, structural continuity will be restored by using post - tensioned continuity

DOI: 10.1201/9781003483755-206

tendons, which can be placed either inside the bottom slab or internally within the box girder through external prestress. These tendons will be tasked with making the entire deck integral and providing a moment opposing that generated by permanent nonstructural and service loads. The use of segments also needs the restoration of shear continuity through "dry" joints Petrangeli (1996) that exploit the presence of "shear keys" between two successive segments. The use of shear keys is combined with the use of epoxy resins applied to the face of one of the two segments before temporary anchorage and, in addition to serving as a waterproofing function, can offer decent tensile strength during the construction stage Shamass et al. (2016). In conclusion of this brief introduction, it is important to emphasize that one of the most significant aspects of this construction method concerns geometric issues Petrangeli (1996), as cantilever lengths of different spans will have different vertical displacements. The investigation of differential displacements between the ends of the two cantilevers (the one from the abutment and the one from the pier) is crucial for designing initial elevations and any altimetric calibrations of the various segments to avoid misalignments during the casting of the stitch segment.

2 CASE STUDY

The proposed deck is sized from the beginning with reference to the spans that typically characterize this design solution, emphasizing that the focus of the study is not so much on the correct sizing of all structural elements and the search for the most economically advantageous solution but on the simplified procedure that can be implemented in many commercial and non-specific bridge finite elements software.

2.1 *Bridge description*

The structure consists of a continuous beam with three spans on four supports, featuring single-cell box girder with variable height, ranging from 5.0 m at the central support on piers to 2.0 m at the mid-spans (Figure 1) through parabolic tapering. The initial construction stage involves erecting two symmetrical central cantilevers each of length 90.0 m and two side cantilevers each of length 18.0 m, employing cantilever diagram during construction stages (Figure 1, left side). Subsequently, structural continuity will be restored through the casting of three stitch segments, each with a length of 0.60 m, and the insertion and prestressing of continuity tendons (Figure 1, right side). The materials assumed involve the use of C40/50 class concrete and low-relaxation 7-wire stabilized strands with a diameter of 15.7mm (0.6") and Young's modulus E=201.000 MPa. In the conception of the cross sections Florida Department of Trasportation (2002), consideration has been given to the space occupied by the strands, their respective anchorage plates *Tensa (2023),* and the possible tendon layout, in order to consider sections that could be as closely adherent to reality as possible. This is because the space requirements of the prestressing elements involve appropriate thickening that significantly increases the self-weight of each segment that must be considered.

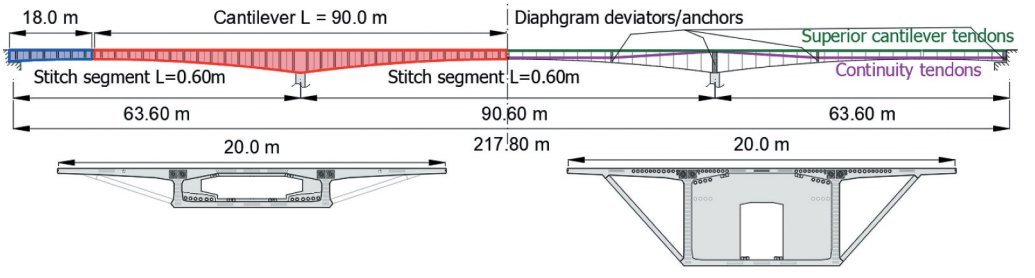


Figure 1. Longitudinal section of the bridge above, with the dimension of cantilever beams on the left and the disposition of tendons on the right. below, the cross-section of the box girder, with the midspan section on the left (2.0 m deep) and the section on the piers on the right (5.0 m deep).

2.2 *Stage construction process*

Leaving aside the prefabrication phase, construction begins when the first segment is transported to the construction site, and lifting operations commence from below, placing it at the top of the piers using a crane or mobile crane. After positioning, altimetric calibration of the supports of the pier head segment is carried out, previously arranged on the pier, and a temporary fixed support is created using prestressed loop tendons to provide a certain rotational stiffness in case of load asymmetries. Successive pairs of segments are transported to the site, and before proceeding with the placement, an epoxy resin layer (with a working time of 1-2 hours and a drying time of about 1 hour) is applied to one of the two faces of each pair of conjugate segments (there are two pairs). Its purpose is to lubricate, waterproof, and possibly, with the use of specific resins, provide tensile capacity for the joints Shamass et. al (2016). At this point, the pair of segments is positioned symmetrically on both sides of the structure. Using positioning bars passed through specific anchorage blisters, a temporary centered prestressing is applied to obtain a uniform compression of 0.2 – 0.3 MPa and allow the resin to take hold. After tensioning the positioning bars, the segment can support itself on the already constructed part of the structure, and the launching equipment can be released, allowing workers to proceed with the tendon placement operations. Once the resin has set, stressing of the upper prestressing tendons, previously inserted into the dedicated ducts in the upper slab, is carried out. If the resin used allows it, any tensile forces on the joint induced by the upper prestressing can be permitted during the construction stages, provided that the tensile strength of the concrete $\sigma_{t,limc}= 0.25 \cdot f_{ck}^{0.5}$ *Ministero delle Infrastrutture e dei Trasporti (2018)* is not exceeded. Once prestressing is complete, the positioning bars can be removed. If the resin does not allow for tensile stresses, temporary prestressing can be maintained until the lower continuity tendons are prestressed. This process is repeated for all subsequent segments to be inserted. Upon reaching the midspan of the span, it is necessary to create the closing segment that joins the decks coming from the two cantilevers (or from the abutments), making the bridge continuous. This is done by initially leaving a space of about 0.6 – 1.0 m between the last two segments and performing a cast-in-place pour. To connect the cantilever from the abutment with that from the pier, an altimetric correction of the supports must be provided before casting the stitch segment since, given the two different lengths, the displacements at the ends will be different. The last operation to be carried out in the construction stage is related to the stressing of the continuity tendons. These tendons will be positioned as the construction progresses and can be either internal (in which case they pass within the lower slab) or external (in which case they are placed inside the box and pass through deviators created with thickenings or actual diaphragms with variable thickness, usually from 0.4 to 1.0 m). Of these two configurations, modern construction techniques prefer the second because external post - tension (with tendons passing inside the box girder) allows for a complete inspection and repair in case of degradation, a critical aspect in post-tension with injected tendons *Suntharavadivel (2005)*. External post - tension also has the advantage of negligible friction losses, with the possibility of covering long distances with continuous tendons, as well as significant economic benefits in case of errors. It is advisable, during the prefabrication phase, to provide additional ducts in various deviators so that additional prestressing can be supplied over time if needed. During the construction, the bridge has fixed supports on piers and abutments, and at the end of the construction, a continuous beam over four support is reached with removal of temporary rotational constraints realized with the loop tendons mentioned above. In the upcoming analysis, the mentioned stages have been reproduced adopting appropriate simplifying assumptions:

1. Frictional phenomena are neglected, and bilateral tendons stressing is assumed
2. Relaxation and shrinkage effects are disregarded due to the use of stabilized strands and controlled 28-day curing (they can, however, be implemented in the procedure to be illustrated)
3. It is assumed that low tensile stresses are allowed during the construction stages
4. The effect of injecting the upper cables is neglected

5. A construction time of 98 days is considered (7 days for each pair of segments) for a total of 14 pairs, excluding the first one at the top of the piers
6. Each segment undergoes the initial loading step at an age of 28 days

Point 1 is considered plausible since the only tendons subject to friction are the upper ones. However, by introducing double side stressing, it ensures that both ends of the i-th pair of segments are subjected to the same compressive force. The occurrence of internal friction within the tendon does not affect the state of stress since the cable is pseudo-straight and does not have to transfer loads based on its curvature. Point 4 is considered plausible because the upper tendons primarily work during assembly to support the self-weight of the segments. The injection of these ducts, which occurs after the release of the beam's weight, does not provide substantial contributions to bearing additional loads, as these will be entirely supported by the continuity tendon.

3 FINITE ELEMENT MODEL AND ANALYSIS SETUP

The software used in this work is STRAND7©, which is not specific for bridge analysis. This paper aims to assist owners of this code or similar ones in the study of these types of bridges or similar structures, considering the possibly similar software limitations shown below. In STRAND7©, it is not possible to implement the evolution of creep phenomena (quasi static solver) simultaneously with the "assembly" of various elements in the non linear stage construction solver. Typically, what is done is taking the output of the stage construction solver and using it as an initial step for the creep analysis of the solver at each step. However, this approach tends to overestimate the effects of creep, as the load would be applied entirely in the initial step without considering the actual aging of concrete loaded at 7-day intervals. Importantly, it also does not account for the variation of boundary conditions after the first 98 days of assembly. This approach affects the initial tensile force to be given to the various tendons in the bridge design. An alternative procedure will be proposed to address these issues with good approximation while maintaining an acceptable solution accuracy.

3.1 *Phase 1 – Non linear construction stage analysis*

In the construction stage analysis Zucca et al. (2018), *Geethu (2016)* with STRAUS7©, it is possible to insert and/or remove elements and modify internal (link elements) or external constraint conditions during various construction stages, considering both geometric and material nonlinearities. The model used for this purpose involves the use of Beam-type elements (with flexural stiffness) for various segments and Truss-type elements (with only axial stiffness) to simulate the tendons. Since the tendons are eccentric, they are connected to the centroid of the Beam elements using rigid links. The tapering of segment elements and the behavior of sliding filaments in the tendons are achieved through the specific command now present in the majority of FEA software. Regarding the support conditions, a distinction is made between side cantilevers and central cantilevers. Side cantilevers lies directly on the abutment, and the support conditions will be simulated with a fixed support preventing vertical translation, horizontal translation, and rotation in the plane during the construction stage. Subsequently, after entering service, the external constraints on rotation and horizontal translation will be removed, simulating a roller support. It should be noted that the operation of removing external constraints can be performed on both solvers. For the central cantilevers, there is greater complexity due to the necessary presence of internal constraints (connection between pier and superstructure) that cannot be removed when transitioning from one solver to another. This modeling issue is addressed by using master-slave link elements for internal connections that do not change from the construction stage to service conditions. These link elements enforce the selected degrees of freedom to have the same displacements. In the case of the first pier-superstructure connection (chosen as a fixed point of the structure), relative horizontal and vertical translational displacements are fixed (hinge support). In the second connection, only

the relative vertical displacement between abutment and superstructure is fixed (roller support). The simulation of the temporary rotational constraint during construction is introduced by inserting an external constraint that blocks rotation in the plane. In the real case, any bending moment generated by potential load asymmetries is countered by the flexural stiffness of the pier. In the assumed modeling, the rotational constraint is external and does not transmit bending actions to the pier. However, if the construction is executed correctly, these actions

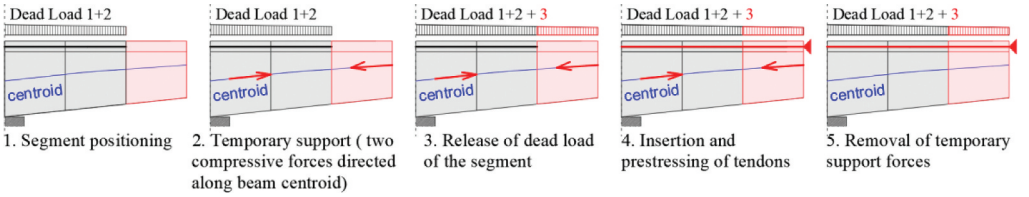


Figure 2. Modeling of the process from segment positioning to tendon stressing.

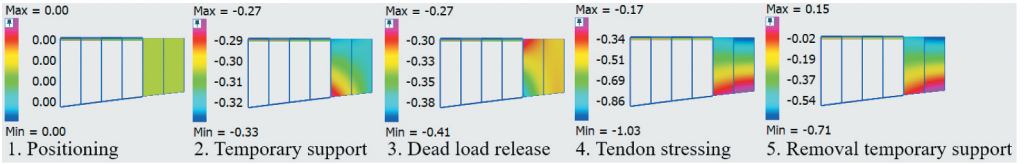


Figure 3. Example of stage construction analysis for segment number three, stresses in MPa.

are not significant enough in this stage to explicitly require rotational continuity between the pier and the superstructure. The adopted simplification is deemed appropriate, and in service, the rotational constraint will be removed, restoring the hinge and roller behavior ensured by internal constraints. Having defined the boundary conditions, the next step was to define the construction stages that would be most critical for the controls on compressive and especially tensile stresses limits. Except for the first segment, a sequence of identical actions was defined for all subsequent segments until the casting of the stitch segment. The construction stages analysis begins with the placement of the first segment (beam element), assumed to be attached to the crane until prestressing occurs (resulting in zero self-weight on the structure). The upper prestressed tendon (truss element) is inserted, stressing is applied to the segment through an assigned pre-stress load on the tendon, and the crane is released (applying the self-weight to the structure). At this point, the first segment is positioned at the top of the pier (or abutment) and temporarily clamped with a fixed support. The placement of subsequent segments occurs similarly but with some additional steps. After placing the initial elements in stage zero, all subsequent ones will need to be placed on a deformed configuration compared to the initial modeling, with nodes of the model having undergone mutual displacements due to initial loads. This implies that, upon inserting additional elements in subsequent stages, these will be pre-deformed compared to the initially modeled configuration, introducing states of stress that are not real. To avoid this behavior, various software options provide more or less complex solutions. In the case of STRAUS7©, the morphing and rotate cluster options have allowed the insertion of elements into the deformed configuration with an initial rigid rotation equal to the rotation of the node to which the new element is attached, without introducing states of pre-stress. From the second segment onwards, the construction stages involve placing the segment on the structure (self-weight not yet acting), inserting temporary anchorages (this phase occurs immediately after applying epoxy resins, ensuring minimal compression and the ability to release the cranes), simulated by a load centered on the centroid of the newly inserted and the preceding element, releasing the self-weight, inserting and tensioning the upper prestressing tendons (Figure 2). The process is repeated until the insertion of the

stitch segment and the insertion of the continuity tendons, which, at the end of the staged analysis, will be inserted but unloaded. It is useful to repeat the analysis twice to evaluate the elastic differential vertical displacement that occurs between the ends of the cantilevers and assign this value as a positive vertical settlement of the hinge on the abutments, thus reproducing the altimetric calibration of the supports before the closure casting. Figure 3 illustrates the evolution of the stress state for the third segment.

3.2 *Phase 2 – Analysis of creep phenomena and long-term behavior*

The study of creep phenomena with STRAND7© Tahmasebinia et al. (2019) occurs by using the solution obtained from the staged solver as the initial input for the time-stepping analysis. Two issues need to be addressed: the first involves the variability of boundary conditions affected by creep, starting with a cantilever scheme and eventually transitioning to a continuous beam scheme. The second arises from the solver constraint in which all loads from construction stages are applied from the initial step *Geethu (2016)*. The first problem is circumvented by observing that during the first 98 days of construction, creep phenomena tend to move the ends of the cantilevers away from those of the side spans with elongations of the stitch segment and the continuity tendon (this occurs only in the model since creep phenomena are introduced downstream of the construction and not during). As a result, a no-tension constitutive relationship is assigned to the three stitch segments, while the continuity tendon is assigned a zero elastic modulus, which will activate after 98 days along with its respective prestressing load. Once the time-stepping analysis is launched, in the first 98 days, the stitch segments will be non-reactive (concrete in tension); creep will act on the cantilever scheme. However, after 98 days, the entire elastic modulus, along with its corresponding tension load, is assigned to the continuity tendon. Temporary external constraints are removed by releasing rotations, resulting in the entire deck being compressed, just like the stitch segments, which, working in compression, contribute stiffness to the structural system. From this point onwards, all creep deformations and additional loads (permanent non-structural and service loads) will develop on the static scheme of a continuous beam over multiple supports. The second problem involves a significant overestimation of creep deformations. This aspect has led to the adoption of a methodology that will be explored in the following section, aiming to find a solution that still overestimates creep effects (underestimating them poses a significant challenge in older bridges) but minimizes the difference with the real solution as much as possible.

3.2.1 *Creep analysis*

The creep model used for the analysis is that of UNI EN 1992-1-1 Appendix B. The creep coefficient is defined as:

$$\Phi(t_f, t_i) = \beta(t_f, t_i)\beta(t_i)\beta(f_{cm})\Phi_{RH} = \left(\frac{t_f - t_i}{\beta_H + (t_f - t_i)}\right)^{0.3} \cdot \frac{1}{0.1 + t_i^{0.2}} .\beta(f_{cm})\Phi_{RH} \tag{1}$$

where $\beta(t_f, t_i)$ represents the time development function starting from $t_f = t_i$ varying between 0 and approximately 1, while the remaining terms that depend on various factors (Relative Humidity %, mean compressive strength of concrete at 28 days f_{cm}, concrete age at the time of loading t_i, effective thickness h_0) provide the modulus of the creep function. The time and age dependence of the concrete at the time of loading are regulated by the first two terms. In nowadays software creep analysis is generally conducted through step-by-step analysis Petrangeli (1996), which, for concrete matured for at least 28 days, is such that:

$$\varepsilon(t_f, t_i) = \frac{\sigma_0}{E_{28}}[1 + \Phi(t_f, t_0)] + \sum_i \frac{\Delta\sigma_i}{E_{28}} 1 + \Phi(t_f, t_i)] \tag{2}$$

The search for the exact solution through step-by-step integration requires that the various load steps $\Delta\sigma$ be introduced stage by stage with different concrete ages t_i for each element. However, using the already assembled superstructure as the initial step, the load is applied integrally and instantaneously. For instance, considering the first element, at the end of construction, the concrete age t_f will be 98 days + 28 days with $t_f - t_i = 98$ days. For the last element, t_f will be 0 days + 28 days with $t_f - t_i = 0$ days (construction is completed at the installation of the last element), while in this case, all elements will be evaluated at $t_f = 98$ days. To mitigate the overestimation of deformations resulting from such software limitations, the following approach is proposed:

$$\varepsilon(t_f, t_i) = \sum_i \frac{\Delta\sigma_i}{E_{28}}(1 + \Phi(t_f, t_i)) = \frac{\Delta\sigma_{tot}}{E_{28}}\left(1 + c \cdot \Phi\left(t_f, t_i^*, \beta_H^*\right)\right) \tag{3}$$

Setting aside the parameter 'c' (that is introduced only to scale creep coefficient Φ) for now, which will be used later, fictitious values for the age of the concrete at the first load 't_i' and the parameter 'β_H' are sought for each concrete element. These values are assigned to the various concrete elements during the analysis phase to enforce the equality of deformations (of the chosen control fibre) between the real curve that represent the correct strain evolution of the chosen control fibre according with (2) and the approximated one according with (3) at the point 't_f.' If equality is assumed at infinite time, it is easily demonstrated that the influence of 'β_H' is null (and therefore the real value will be used). The only parameter to be identified is 't_i^*', which can be obtained simply by reversing the expression for $\beta(t_i^*)$, as follows:

$$\beta(t^*) = \frac{\sum_i \beta(t_i)\Delta\sigma_i}{\Delta\sigma_{tot}} = \frac{1}{0.1 + t^{*0.2}} \tag{4}$$

The use of this formulation, however, still leads to a certain overestimation of creep deformations compared to the real solution, coinciding with the approximate one only at infinite time.

A more complex approach involves applying (3) while varying the three parameters t_i, β_H and c, imposing a condition: the sum of the absolute percentage errors on deformations between the approximate curve and the real curve, evaluated at $t_{fc} = 98$ days, $t_\infty = 10{,}000$ days, t_a, and t_b, where the latter two are arbitrarily chosen points such that the first is close to t_{fc} and the second is a long-term value (>1000 days), is minimized. Through a target search using a simple spreadsheet, the point of minimum of the target function sum of errors $f_{\%}(t_i, \beta H, c, t_a, t_b)$ is sought, resulting in a curve that is closer to the real one. There is another possibility, not considered here as it strongly underestimates deformation compared to the real one, which involves imposing equality between the real and approximating functions at the end of the construction point t_{fc} as a function of the sole variable t^*. Although intuitive, it is essential to emphasize that the evolution of the stress state in terms of $\Delta\sigma_i$ is obtained from the stage analysis by choosing a control fiber (whose correct strain evolution is showed in Figure 4 according with (2)) for each element, where the stress variation is acquired for use in equation (3). In addition, although the approximate solution is entirely incorrect from 0 to 98 days, this is of little importance since the critical conditions to be verified are the short-term ones (maximum stresses check) and the long-term ones (decompression). If these two conditions are verified, all those in between will also be satisfied. Figure 3-4 illustrate the real strain-time curves and those obtained through the three types of approximations seen earlier. With the defining curves for each element of the structure, it is possible to start the stepwise analysis, introduce permanent actions following the installation of the stitch segments and the tensioning of the continuity tendons, and study their effects over time. In this study, the creep coefficient weighted at infinite time was employed (Figure 4 - 5 red curve), obtaining a response that overestimates creep deformations but was still considered plausible, having neglected the effects of steel relaxation and residual shrinkage after the 28-day curing

period for each element. Figure 6 shows the evolution of vertical displacements and bending moments over time on the bridge in question. The purple arrows in Figure 6 (above) represent the differential displacement between the ends of the cantilevers and are zeroed by imposing a vertical settlement on the supports of the abutments, reproducing the previously mentioned altimetric calibration.

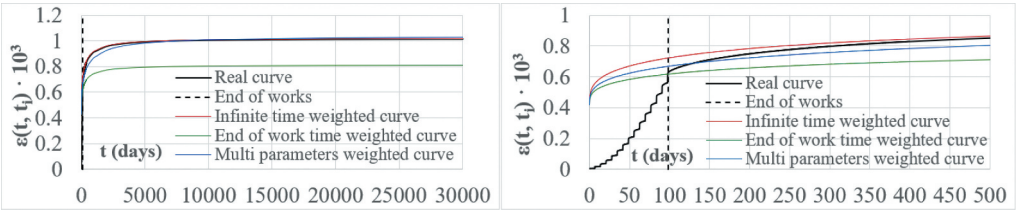


Figure 4. Strain – time curve comparison for segment 1, the multi parameter weighted curve was obtained with c = 0.985, t* = 85 days, β_H = 5628, t_a = 128 days, t_b = 5628 days.

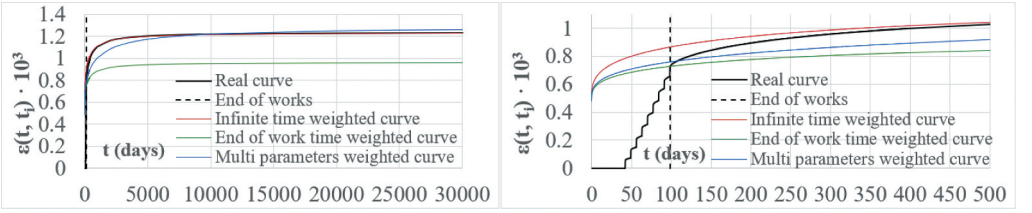


Figure 5. Strain – time curve comparison for segment 7, the multi parameter weighted curve was obtained with c = 0.967, t* = 41 days, β_H = 3245, t_a = 113 days, t_b = 7000 days.

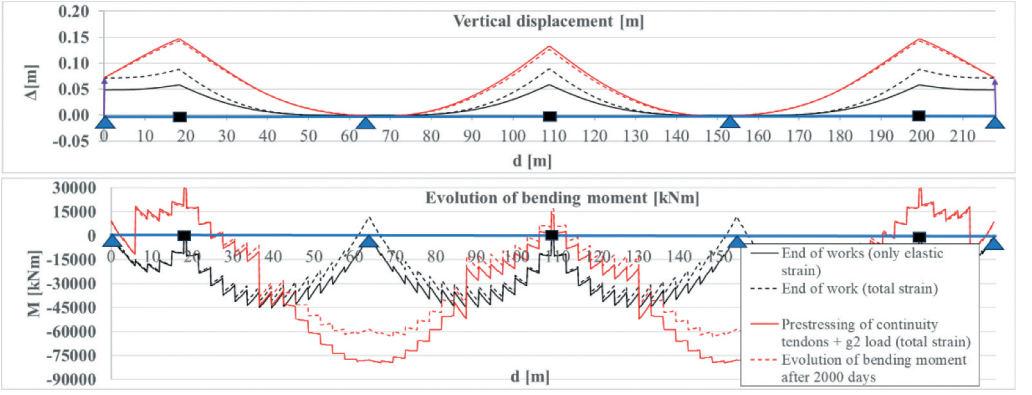


Figure 6. Evolution of vertical displacement (above) and bending moments (bottom) from 98d to 2000d.

4 CONCLUSION

Through the adopted computational model for the study of this bridge, the global quantities involved in the construction of the deck during all construction stages were

analyzed and evaluated. The purpose of the entire work was to understand the construction process of the specific bridge, distinguishing between negligible operations and those that must be considered and consequently analyzed. The next step was to translate these stages from reality to the FEA model, where an attempt was made to reproduce a sequence of actions and conditions that approached the real behavior as closely as possible. It is essential to understand how this work aims to lay the groundwork for a simplified modeling of bridge structures subject to non-negligible construction stages with creep effects. This allows for a good approximation of the evolution over time of bending moments and displacements (Figure 6) even with non-specialized software. Although phenomena such as shrinkage and relaxation have been neglected in the model, there is nothing preventing their addition to the analysis, given the model's setup. Once the workflow is understood, it will be possible to transfer all the acquired concepts to more sophisticated models that use 2D or 3D elements, enabling the analysis of more complex issues such as local statics and kinematics, D-Regions, etc.

ACKNOWLEDGEMENT

This paper is derived from the master's thesis work of the first author under the supervision of the second and third authors.

REFERENCES

Barras, P., De Matteis, D., Derais, J., Duviard, M., Guillot, D., Lacombe, J., Lacoste, G., Lecointre, D., Ojeda, V., Paillusseau, P. & Reinhard, J. 2003. *Prestressed concrete bridges built using the cantilever method, Design guide*. Bagneux: Sétra

Florida Department of Trasportation 2002. *New Directions for Florida Post-Tensioned Bridges*. Tallahassee: Corven Engineering

Geethu, G. & Praseeda 2016. Comparison of Conventional and Construction Stage Analysis of a RCC Building. *International Journal of Science Technology & Engineering* 3(03)Ministero delle Infrastrutture e dei Trasporti, CSLLPP 2018. *Norme tecniche italiane per le costruzioni*.

Petrangeli, M. 1996. *Progettazione e costruzione di ponti con cenni di patologia e diagnostica dei ponti esistenti, IV Edizione*. Milano: Casa Editrice Ambrosiana

Shamass, R., Zhou, X., Ph.D., M.Asce & Wu, Z. 2016. Numerical Analysis of Shear-off Failure of Keyed Epoxied Joints in Precast Concrete Segmental Bridges. *Journal of Bridge Engineering* 22(1)

Suntharavadivel, T.G. & Aravinthan, T. 2005. Overview of external post-tensioning in bridge. *Proceedings of the 2005 Southern Region Engineering Conference (SREC 2005)*. Toowoomba, Australia

Tahmasebinia, F., Fogerty, D., Wu, L., Li, Z., Sepasgozar, S., Zhang, K., Sepasgozar, S. & Marroquin, F. 2019. Numerical Analysis of the Creep and Shrinkage Experienced in the Sydney Opera House and the Rise of Digital Twin as Future Monitoring Technology. *Journal of buildings* 9(6)

Tensa Gruppo de Eccher, *Post-Tensioning datasheet*. Milano: Tensa

Zucca, M., Longarini, N., De Socio, F. & Migliori, I. 2018. Construction Stage Analysis for a New Mixed Structure Building in Milan. *International Journal of Structural Glass and Advanced Materials Research* 2(1): 66–72

Zucca, M., Longarini, N., De Socio, F. & Migliori, I. 2018. Construction Stage Analysis for a New Mixed Structure Building in Milan. *International Journal of Structural Glass and Advanced Materials Research* 2(1): 66–72

Bridge Maintenance, Safety, Management, Digitalization and Sustainability – Jensen, Frangopol & Schmidt (eds)
© 2024 The Author(s), ISBN 978-1-032-77040-6
Open Access: www.taylorfrancis.com, CC BY-NC-ND 4.0 license

NDE for pre-stressing systems condition: Metrological validation

S. Zorzi
University of Trento, Trento, Italy

F. Rossi
University of Strathclyde, Glasgow, UK

D. Tonelli
University of Trento, Trento, Italy

E. Tubaldi
University of Strathclyde, Glasgow, UK

D. Zonta
University of Trento, Trento, Italy

ABSTRACT: The rise in prestressed reinforced concrete bridges surpassing their projected lifespan has spurred increased attention from infrastructure managers and authorities toward monitoring and maintenance. Accurate understanding of bridge degradation is pivotal for efficient planning and prioritizing maintenance. According to several guidelines, the prestressing system, central in risk assessment and maintenance, demands careful evaluation. Said guidelines also suggest employing non-destructive, semi-destructive, and destructive tests to assess this system's condition. Though numerous innovative investigation techniques exist, their efficacy remains debated, necessitating further exploration. This study focuses on validating the efficacy of three non-destructive tests (NDTs): Digital Radiography, Ground Penetration Radar, and Reflectometric Impulse Measurement Test, conducted on the Alveo Vecchio viaduct—a decommissioned bridge repurposed as a testing site. Classification analyses between NDTs results and observed defect intensity during controlled beam demolition offer insights into their accuracy. This research contributes substantially to understanding the precision of non-destructive tests.

1 INTRODUCTION

The growing concern among infrastructure managers and control authorities revolves around the increasing number of prestressed concrete bridges surpassing their lifespan. Ensuring the safety of these bridges requires accurate monitoring and assessment of their prestressing systems (Bonopera et al., 2020). To this end, Non-Destructive Evaluation (NDEs) are commonly employed to inspect the prestressing systems of post-tensioned PC bridges. However, the validation of the accuracy of those commonly deployed Non-Destructive Tests (NDTs) continues to pose unresolved challenges within the scientific community.

This study conducts a metrological validation of Digital Radiography (DR), Ground Penetration Radar (GPR), and Reflectometric Impulse Measurement Test (RIMT) (Kashif Ur Rehman et al., 2016), assessing their efficacy in detecting defects within the prestressing system of a PC bridge's girders (Innocenzi et al., 2022). Specifically, this NDTs theoretically allows to identify grouting voids in ducts, assess the integrity of steel wires, and determine their positioning along the girders (Lim & Cao, 2013).

The metrological validation was conducted on the Alveo Vecchio Viaduct, which was repurposed as an open-air laboratory following its decommissioning. Four beams of the viaduct

DOI: 10.1201/9781003483755-207

were subjected to NDTs, after which they were demolished for defect survey. This operation involved: (i) extracting the prestressing system, (ii) opening metallic ducts, and directly (iii) examining duct, grout, and strand defects along the prestressing cables. A metrological validation of the NDTs was carried out by using a classifier based on the Bayesian network (BN) (Thulasiraman & Swamy, 1992) and calculating proper metrics related to the confusion matrices (CMs) obtained by the classification (Murphy, 2013).

2 CASE STUDY

Previously part of the Italian A16 highway, in 2005 the Alveo Vecchio viaduct was decommissioned due to a landslide that caused a pier's displacement and a span's collapse. In 2019, the viaduct was readapted as an outdoor research laboratory within the research agreement between the Ministry of Infrastructure, Autostrade per l'Italia S.p.A., and the University of Trento. This collaboration aims to develop inspection protocols, validate NDT techniques, and evaluate monitoring systems to ensure the performance and safety of existing highway bridges. Further details on the outdoor laboratory and the ongoing experimental activities are provided by Tonelli et al. (2020, 2023).

Specifically, the Alveo Vecchio viaduct consists of two decks, each consisting of three 32.5-meter spans made of prestressed reinforced concrete. Four prestressed concrete beams connected by a reinforced concrete slab characterized each deck. Every prestressed beam is realized with 14 post-tensioned cables of 12-Ø7mm steel wires. Figure 1 shows a detailed graphical representation of the viaduct.

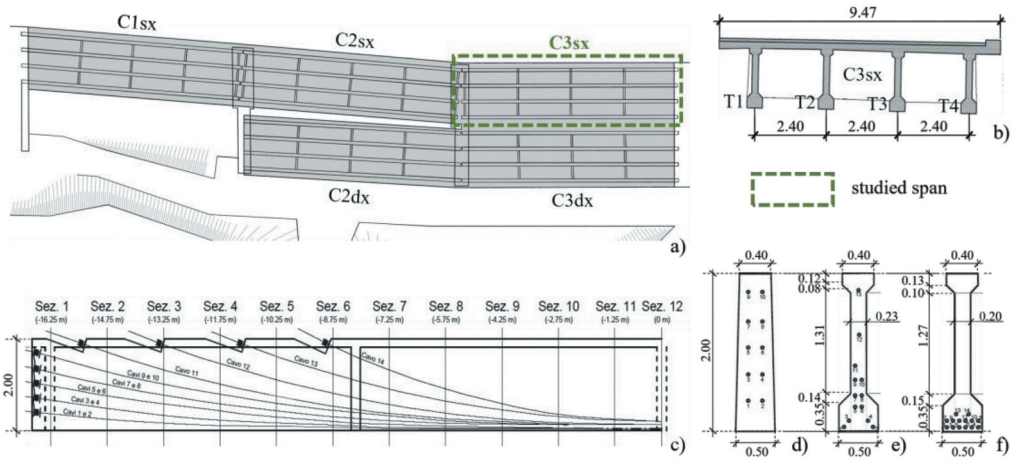


Figure 1. Alveo Vecchio viaduct. (a) Top view, (b) cross-section, (c) cables layout longitudinal section, (d) cross section 1, (e) cross section n. 6, (f) cross section n. 12. All measurements are expressed in meters.

3 METHODOLOGY

This research aims to validate Digital Radiography, Ground Penetrating Radar, and Reflectometric Impulsive Measurement Tests through an in-depth evaluation of their efficiency in identifying defects in prestressing systems of concrete bridge beams. The validation process is organized as follows: (i) performing NDTs on the C3sx span of the Alveo Vecchio Viaduct, (ii) demolition of the prestressing system to identify the actual defects in the cables, and finally, (iii) using a classifier to analyze the ability of NDTs to predict the actual state of the prestressing system.

During the state demolition and surveying phase, steel duct defects (voids, perforations, and lack of integrity), injected grout defects (fracturing and injection voids), and steel wire

defects (corrosion, section reduction, and breaks) were classified. This paper focuses on the defects of grout injection voids (G.V) and steel wire corrosion (S.C). In fact, among the most related defects concerning the considered NDTs, G.V and S.C are the most significant defects in prestressing systems.

To perform the metrological validation of NDTs, each cable was segmented into 10 cm-long sections, and both NDT results and observed defects were classified according to intensity. This segmentation facilitates organizing the experimental results into ordered vectors, creating categorical ordinal variables suitable for analysis by classification methods. Those variables are categorical variables with a logical order.

Table 1 outlines the ascending classes based on the intensity of NDT results, classifying DR into three levels of defects and RIMT into two types of defects with different intensity classes. GPR intensity is defined in three classes. Table 2 shows the classes for cable defects, defining 6 classes for G.V and 13 classes for steel strand corrosion. To allow more reliable classification, these classes were later made binary: 0 for no defect and 1 for the presence of a defect, as highlighted in Table 2.

Table 1. Classes of NDT outcomes and relative quantitative intensity scale.

Test ID	Description	Intensity scale
RIMT.V	Reflectometric Impulse Measurement Test for injection voids identification	0-1, 1-2, 2-3, 3-4, 4-5
RIMT.C	Reflectometric Impulse Measurement Test for strands corrosion identification	0-1, 1-2, 2-3, 3-4, 4-5
RD.V	Digital Radiography	0, 1, 2
GPR.C	Ground Penetration Radar	0, 1, 2

Table 2. Classes of cable defects and relative quantitative intensity scale.

State ID	Description	Intensity scale
G.V	Percentage of grouting voids	**0** := [=0%]; **1** := [<25%, <50%, <5%, <100%, =100%];
S.C	Corrosion of steel strands	**0** := [0/12]; **1** := [1/12, 2/12, 3/12, . . ., 12/12];

This paper focused on the analysis of NDT performance in predicting defect conditions in cables using a BN-based classification method, as represented in Figure 2.

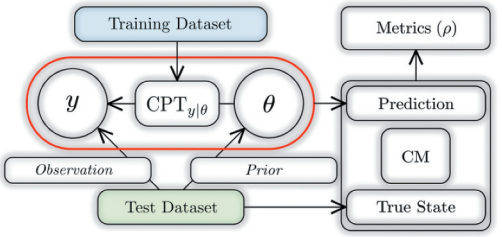


Figure 2. BN-based classifier framework.

The proposed framework is similar to the Naïve Bayes classification method (James et al., 2021). Unlike Naïve Bayes, the proposed BN-based classifier involves training on the likelihood ($y|\theta$) rather than directly on the a posteriori distribution ($\theta|y$), which also considers the prior condition of the dataset. Note that y denotes the NDT outcomes, and θ represents the defect classes of the cable; both are classified as categorical ordinal variables. The BN-based classifier was trained on the 75% of the total dataset. Within this phase, the conditional probability table ($\mathbf{CPT}_{y|\theta}$), which represent the likelihood term, was obtained by normalizing the

contingency table concerning the NDT outcomes, y. Therefore, each column reports the conditional probability of y given the knowledge of θ.

Next, moving to the testing phase, the prediction of the defect state for each element in the test dataset was performed using the Bayes theorem considering the sample's prior distribution. A matrix form of this expression is

$$\mathbf{CPT}_{\theta|y} = [\mathrm{diag}\{\mathbf{CPT}_{y|\theta}\,\boldsymbol{p}_\theta\}]^{-1}\,[\mathbf{CPT}_{y|\theta}\,\mathrm{diag}\{\boldsymbol{p}_\theta\}], \tag{1}$$

where $\mathbf{CPT}_{\theta|y}$ is the posterior conditional probability table, $\mathbf{CPT}_{y|\theta}$ is the classifier likelihood and $\boldsymbol{p}_\theta$ is the sample prior probability mass vector.

The prediction of the defect state, θ_P, was determined as the maximum a-posteriori, θ_{MAP}, as per Equation (2).

$$\theta_P(y_j) = \theta_{MAP}(y_j) = \underset{\theta_i}{\mathrm{Argmax}}\{[\boldsymbol{CPT}_{\theta|y}]_{i,j}\}\ \forall y_j \tag{2}$$

Subsequently, for each element in the dataset, the cable defect prediction, θ_P, was compared with the actual cable defect, θ_T. As a result of this, the confusion matrix was computed (Murphy, 2013). The evaluation of classification performance, based on CMs, involved the accuracy metric ACC, (Fawcett, 2006), the positive predictive value PPV, (Powers, 2008), the negative predictive value NPV, (Powers, 2008), and Matthews correlation coefficient MCC, (Matthews, 1975). Specifically, ACC is defined as the percentage of correct predictions out of the total number of predictions. PPV and NPV measure the performance of NDTs in identifying cable defects (true positive) and no defects (false positive), respectively. Finally, the MCC measures the overall prediction quality of NDTs. The values of the metrics considered are between 0 and 1. A high value means that NDTs perform well.

4 RESULTS

This section presents the results of the metrological validation analysis. First, the state defect prior distribution is defined on the grounds of the following parameters: (i) beam type (external or internal), (ii) cable type (anchored in the head of the beam or anchored in the slab), (iii) location of the segment along the longitudinal axis of the beam (within 2.5 m of the anchorage, within 2.5 m of the spacing, or outside the above regions). The selected parameters represent the intrinsic factors of the prestressing system that influence cable defects. Therefore, all cable segments were divided into 12 groups based on the above definitions, characterized by a specific prior distribution. The prior distribution is calculated on the total dataset.

The results are gathered in confusion (CM) and normalized confusion matrix (nCM). Note that nCM reports the false negative rate and false positive rate of the classification. CM and nCM are graphically described in Figure 3.

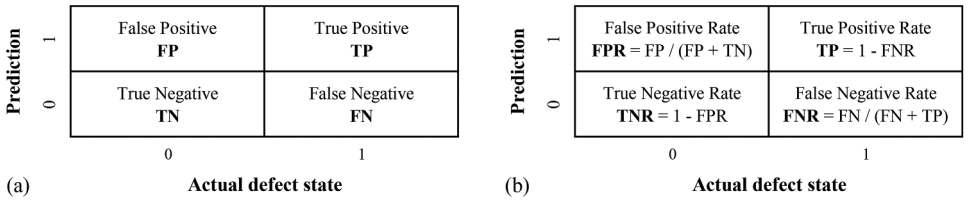


Figure 3. Binary confusion matrix definition. (a) confusion matrix; (b) normalized confusion matrix.

Based on CMs, the ACC, PPV, NPV, and MCC are discussed. The results are presented in two different forms: (i) a single elaboration with fixed dataset subsets for the training and the test phases; (ii) a statistical analysis resulting from 1000 elaboration with different training

datasets and test datasets. This latter result is presented in the form $\mu \pm \sigma$, where μ and σ are the mean and the standard deviation, respectively.

4.1 *Injection voids defects*

The present subsection reports the results of the metrological validation analysis on the injected void defects. As for the defects related to injected grout, our focus was mainly on NDT outcomes with DR.V (Figures 4 and 5), RIMT.V (Figures 6 and 7), and GPR.C (Figures 8 and 9) described in Table 1.

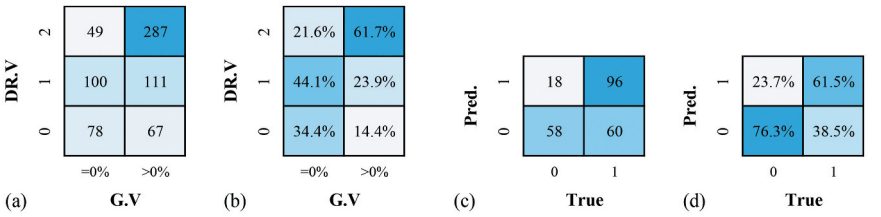


Figure 4. DR.V performance with respect to G.V detection. (a) CT; (b) $\boldsymbol{CPT}_{y|\theta}$; (c) CM; (d) nCM. ACC = 0.664, PPV = 0.842, NPV =0.492, MCC = 0.355.

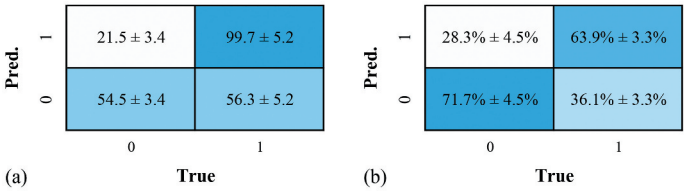


Figure 5. Statistical analysis of DR.V performance with respect to G.V detection. (a) CM; (b) nCM. ACC = 0.665 ± 0.026, PPV = 0.823 ± 0.024, NPV = 0.493 ± 0.028, MCC = 0.335 ± 0.052.

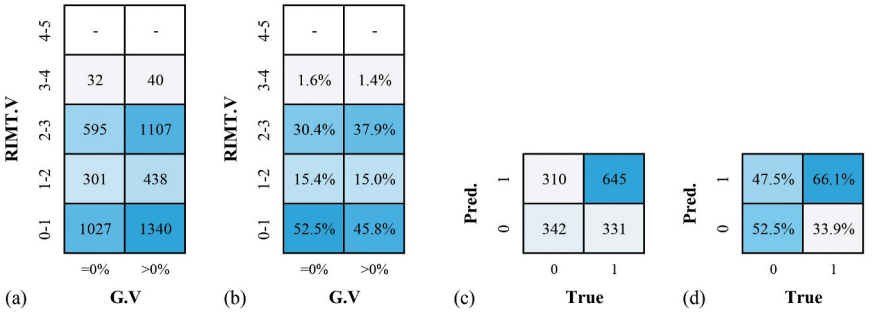


Figure 6. RIMT.V performance with respect to G.V detection. (a) CT; (b) $\boldsymbol{CPT}_{y|\theta}$; (c) CM; (d) nCM. ACC = 0.606, PPV = 0.675, NPV =0.508, MCC = 0.184.

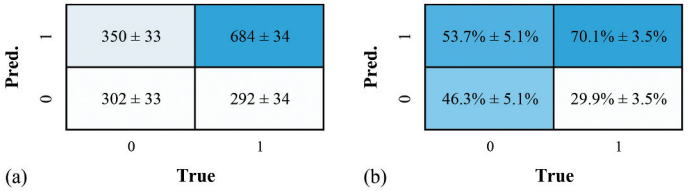


Figure 7. Statistical analysis of RIMT.V performance with respect to G.V detection. (a) CM; (b) nCM. ACC = 0.606 ± 0.010, PPV = 0.662 ± 0.013, NPV = 0.509 ± 0.014, MCC = 0.168 ± 0.025.

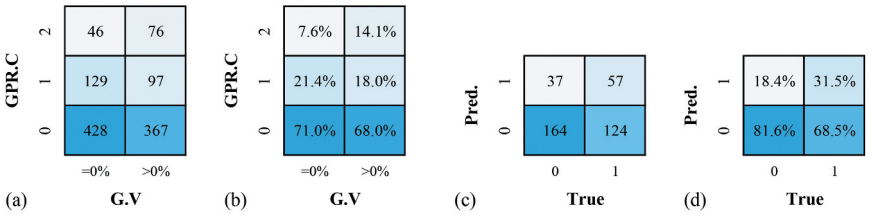


Figure 8. GPR.C performance with respect to G.V detection. (a) CT; (b) $\boldsymbol{CPT}_{y|\theta}$; (c) CM; (d) nCM. ACC = 0.575, PPV = 0.606, NPV =0.569, MCC = 0.152.

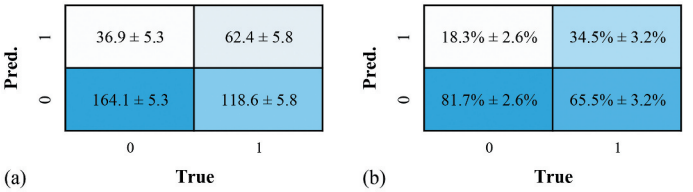


Figure 9. Statistical analysis of GPR.C performance with respect to G.V detection. (a) CM; (b) nCM. ACC = 0.593 ± 0.019, PPV = 0.629 ± 0.038, NPV = 0.581 ± 0.014, MCC = 0.184 ± 0.044.

4.2 *Steel wires corrosion defects*

The present subsection reports the results of the metrological validation analysis on the steel corrosion defects (S.C). As reported in the previous subsection, the same procedure used for injected grout defects is adopted. The analyses on steel corrosion defects focus exclusively on RIMT.C (Figures 10 and 11) and GPR.C (Figures 12 and 13).

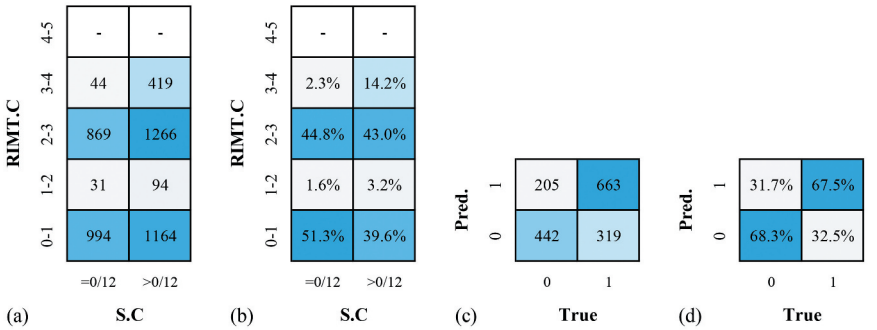


Figure 10. RIMT.C performance with respect to S.C detection. (a) CT; (b) $\boldsymbol{CPT}_{y|\theta}$; (c) CM; (d) nCM. ACC = 0.678, PPV = 0.764, NPV =0.581, MCC = 0.351.

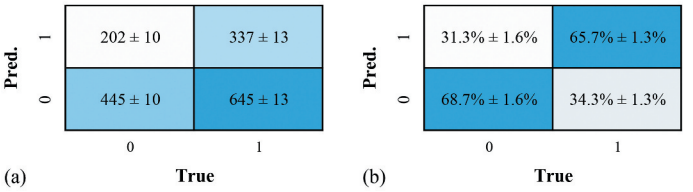


Figure 11. Statistical analysis of RIMT.C performance with respect to S.C detection. (a) CM; (b) nCM. ACC = 0.669 ± 0.010, PPV = 0.761 ± 0.010, NPV = 0.569 ± 0.011, MCC = 0.337 ± 0.021.

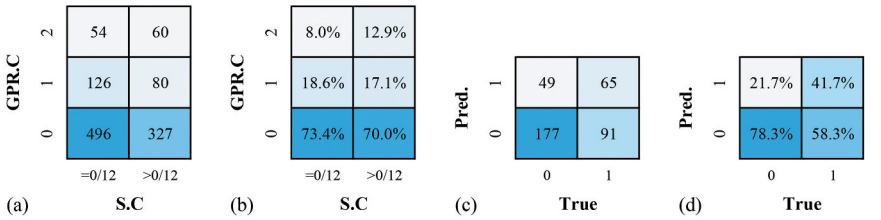


Figure 12. RIMT.C performance with respect to S.C detection. (a) CT; (b) $\boldsymbol{CPT}_{y|\theta}$; (c) CM; (d) nCM. ACC = 0.634, PPV = 0.570, NPV =0.660, MCC = 0.215.

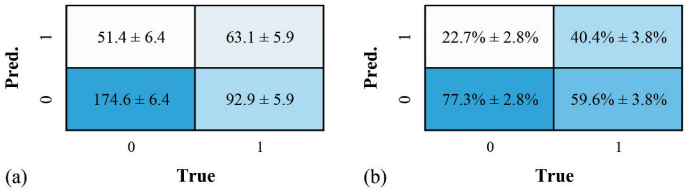


Figure 13. Statistical analysis of GPR.C performance with respect to S.C detection. (a) CM; (b) nCM. ACC = 0.622 ± 0.020, PPV = 0.552 ± 0.034, NPV = 0.653 ± 0.015, MCC = 0.190 ± 0.044.

5 DISCUSSION

The proposed metrological validation analysis results reveal a moderate efficacy of DR in detecting grout defects (ACC = 0.665 ± 0.026, MCC = 0.335 ± 0.052). The performance significantly improves (ACC = 0.714 ± 0.032, PPV = 0.808 ± 0.031, NPV = 0.604 ± 0.037, MCC = 0.423 ± 0.064) when excluding overlapped cables, specifically those anchored in the beam header. However, due to the inherent challenge of interpreting radiographic images for each overlapping cable, decoupling is not possible, impacting the overall performance of DR. RIMTs and GPR tests exhibit limited ability in predicting grout defects (MCC values less than 0.2).

Nevertheless, accounting for the a priori state distribution, RIMTs demonstrate a moderate capability in detecting steel corrosion defects (ACC = 0.669 ± 0.010, MCC = 0.337 ± 0.021). In contrast, the GPR can not predict corrosion defects (MCC = 0.190 ± 0.044).

Generally, the considered NDTs display relatively low Negative Predictive Values (NPV) (less than 0.6), indicating limited predictive ability when the test result is negative. Furthermore, given the relatively high false-negative rate values (greater than 30 percent), the prediction of the state appears moderately unreliable.

It is crucial to note that the results presented in this paper arise from the binary discretization of the classes shown in Table 2.

6 CONCLUSION

This study proposes a metrological validation of Digital Radiography tests, Ground Penetration Radar tests, and Reflectometric Impulse Measurement Tests in identifying defects within the system of prestressed concrete bridges. The metrological validation is based on the Alveo Vecchio viaduct outdoor research laboratory.

To perform the metrological validation, the NDT outcomes are compared in terms of observed defects along the cables after the bridge demolition. The investigation focuses on injected grout void defects and steel wire corrosion defects. The metrological validation of

NDTs is conducted employing a BN-based classification method, assessing informative performance metrics derived from confusion matrices.

The results indicate a moderate performance for DR in predicting injected grout defects and for RIMT in detecting steel corrosion defects. Conversely, GPR demonstrated poor performance for both considered defect states. Overall, the NDT methods under consideration exhibited a notable false-negative rate exceeding 30 percent, underscoring their limited capability in detecting cable defects.

ACKNOWLEDGEMENT

The studies presented here were carried out as part of the activities envisaged by a research agreement between the University of Trento and Autostrade per l'Italia SpA, and supported by Fondazione CARITRO Cassa di Risparmio di Trento e Rovereto (grant number 2021.0224), MIUR PON RI 2014-2020 Program (Project MITIGO, ARS01_00964), the Agreement between the High Council of Public Works (CSLLPP) and the ReLUIS Consortium implementing Ministerial Decree 578/2020 and Ministerial Decree 240/2022, and the Agreement between the Italian Department of Civil Protection (DPC) and the ReLUIS Consortium. The contents of this paper represent the authors' ideas and do not necessarily correspond to the official opinion and policies of CSLLPP and DPC.

REFERENCES

Bonopera, M., Chang, K.-C., & Lee, Z.-K. 2020. State-of-the-Art Review on Determining Prestress Losses in Prestressed Concrete Girders. *Applied Sciences*, 10(20), 7257.

Fawcett, T. 2006. An introduction to ROC analysis. *Pattern Recognition Letters*, 27(8), 861–874.

Innocenzi, R. D., Pigliapoco, G., Carbonari, S., Gara, F., & Dezi, L. 2022. Damage Detection of Post-tensioned Cables in Existing Bridges with Digital Radiography. *Proceedings of the 1st Conference of the European Association on Quality Control of Bridges and Structures* (Vol. 200, pp. 662–669). Springer International Publishing.

James, G., Witten, D., Hastie, T., & Tibshirani, R. 2021. An introduction to statistical learning with applications in R. *Springer Science and Business Media*.

Kashif Ur Rehman, S., Ibrahim, Z., Memon, S. A., & Jameel, M. 2016. Nondestructive test methods for concrete bridges: A review. *Construction and Building Materials*, 107, 58–86.

Lim, M. K., & Cao, H. 2013. Combining multiple NDT methods to improve testing effectiveness. *Construction and Building Materials*, 38, 1310–1315.

Matthews, B. W. 1975. Comparison of the predicted and observed secondary structure of T4 phage lysozyme. *Biochimica et Biophysica Acta (BBA) - Protein Structure*, 405(2), 442–451.

Murphy, K. P. 2013. Machine learning: A probabilistic perspective. *MIT Press*.

Powers, D. 2008. Evaluation: From Precision, Recall and F-Factor to ROC, Informedness, Markedness & Correlation. *Mach. Learn. Technol.*, 2.

Thulasiraman, K., & Swamy, M. N. S. 1992. Graphs: Theory and algorithms. *Wiley*.

Tonelli, D., Luchetta, M., Rossi, F., Migliorino, P., & Zonta, D. 2020. Structural Health Monitoring Based on Acoustic Emissions: Validation on a Prestressed Concrete Bridge Tested to Failure. *Sensors*, 20(24), 7272.

Tonelli, D., Rossi, F., Brighenti, F., Verzobio, A., Bonelli, A., & Zonta, D. 2023. Prestressed concrete bridge tested to failure: The Alveo Vecchio viaduct case study. *Journal of Civil Structural Health Monitoring*, 13(4–5), 873–899.

Bridge Maintenance, Safety, Management, Digitalization and Sustainability – Jensen, Frangopol & Schmidt (eds)
© 2024 The Author(s), ISBN 978-1-032-77040-6
Open Access: www.taylorfrancis.com, CC BY-NC-ND 4.0 license

The impact of post-tension modeling techniques on calculated concrete member stresses

K. Basnayake
Parsons Corporation, East Hartford, CT, USA

U. Attanayake
Department of Civil and Construction Engineering, Center for Structural Durability, Western Michigan University, Kalamazoo, MI, USA

ABSTRACT: Post-tensioning is a form of prestressing of concrete members to increase its tensile load capacity. The process includes (i) installing tendons inside plastic or steel ducts embedded in concrete, (ii) pulling tendons from one or both ends up to a predefined force after concrete attains a specified strength for the operation, and (c) anchoring the ends to maintain the required force in the tendons. Ducts are typically grouted to enhance durability and establish strain compatibility between tendons and the surrounding concrete. Due to wobbling effect and friction, the force along the tendon decreases during the jacking operation. Further, the force in the tendon is slightly reduced during anchoring. Different modeling techniques are used to represent the stress state in post-tensioned concrete members. One such technique is to embed the tendons in 2D or 3D structural elements representing the concrete member by excluding the influence of the ducts. This modeling techniques utilizes the gross cross-section area of the concrete member to calculate stresses. This can be a concern when empty ducts are present during multi-stage post-tensioning. A common technique implemented in commercial software is to model the concrete member using 1D line elements with the post-tensioning force applied as member loads. As a more precise technique, a refined 3D finite element model can be used to represent the geometry with empty ducts and the sequence of post-tensioning and grouting. However, this technique also presents several challenges including the simulation of tendon force variation along its length. Strain measurements recorded during post-tensioning of an instrumented tie girder of a tied network arch bridge are used to evaluate the impact of different modeling techniques on girder stresses. The paper describes different post-tension modeling techniques and their capabilities and limitations to represent the stress state of concrete members.

1 INTRODUCTION

Post-tensioning (PT) is a form of prestressing of concrete members to increase its tensile load capacity. During post-tensioning, the tendons are stressed and anchored at the ends of the concrete member after concrete attains the required compressive strength to withstand the applied force. The PT ducts are typically grouted to maintain strain compatibility between the surrounding concrete and the tendons, as well as to improve durability. The stresses in a post-tensioned member are calculated using the effective prestressing force after accounting for all the losses. Immediate losses (short-term losses) and time-dependent losses (long-term losses) are considered in the design of post-tensioned members. Immediate losses are recorded between the time of tendon stressing and the time when the prestressing force is transferred to the concrete at the anchorages. Friction between the tendon-duct interface, anchorage set, and elastic shortening of the concrete member contribute to immediate losses. The subsequent losses due to concrete shrinkage, concrete creep, and steel relaxation are considered as the time-dependent losses (PTI 2006).

DOI: 10.1201/9781003483755-208

In the structural analysis of post-tensioned members, the tendon is modeled using two approaches: (1) as an applied loading or (2) as a load resisting element. The load balancing method, primary moment method, and equivalent load through discretization of the tendon force method are three methods used when the tendon is modeled as an applied loading (Lin 1961, Aalami 1990, and Aalami 2000). Under these methods, the tendon is removed from its housing member and is replaced with the force it exerts on the housing member (PTI 2006). Even though the load balancing method is commonly used for the hand calculation of stresses in post-tensioned members, the method fails to account for the variation of prestressing force along the length of tendon (Aalami 2000). When the tendon is modeled as a load resisting element, the tendon is modeled as a distinct element linked to its housing member and an initial prestress force, after friction and anchorage set losses, is applied as a loading to the tendon. Any deformation in the concrete member due to long-term losses and elastic shortening are implicitly accounted for by the corresponding displacement in the tendon element.

2 POST-TENSION MODELING TECHNIQUES IN COMMERCIAL FINITE ELEMENT SOFTWARE

The beam, truss, plane stress, or solid elements can be used to model tendons as load resisting elements in refined finite models (Ellobody and Bailey 2008, Bažant et al. 2012. Huang 2012, and French et al. 2014). This technique can be implemented in commercial finite element software such as ABAQUS, ANSYS, SAP 2000, MIDAS FEA, and MIDAS Civil. The two primary challenges of modeling post-tensioning in refined finite element models are (1) modeling the interaction between concrete and tendon at various stages of post-tensioning, and (2) modeling the varying prestress force along the length of the tendon.

2.1 *Modeling concrete and tendon interaction*

During post-tensioning, the tendons remain unbonded to the surrounding concrete until the ducts are grouted. The unbonded tendon force is transferred to concrete through the end anchorages. Once grouted, any change in the tendon force is transferred from the tendon to the concrete through strain compatibility. Therefore, the contact interaction defined between the tendon and the concrete should reflect the bonded and unbonded stages. Several studies simulated post-tensioning procedures by defining a perfect bond between the tendon and the concrete member (Bažant et al. 2012, French et al. 2014, and Mohammed et al. 2017). This technique is valid once the ducts are grouted, but significantly misrepresents the force transfer mechanism between concrete and the tendon before grouting and does not represent the effective section area of the concrete member (concrete gross cross-section area minus the empty post-tensioned duct area). The following are the three techniques implemented in literature to model the behavior of a post-tensioned member with unbonded tendons:

a) The first technique uses surface-to-surface contact between the tendon and the concrete member (Ellobody and Bailey 2008, Huang et al. 2010, Huang 2012, Kang and Huang 2012, French et al. 2014, and Kang et al. 2015). A frictionless contact is defined in the tangential direction to define the interaction during post-tensioning. The tangential contact behavior is changed from frictionless to hard contact at the grouting stage to represent a perfect bond.
b) The second technique uses tube-to-tube contact elements (ITT21 and ITT31 elements) in the Abaqus element library (Huang et al. 2010, Huang 2012, and Kang and Huang 2012). The tube-to-tube contact elements are used to model the relative motion of two tubes representing the tendon and the duct along the line defined by the axis of one of the tubes (slide line). The post-tensioned duct embedded in concrete is modeled as the outer tube. The tendon is modeled as the inner tube. The slide line is defined for the inner tube. Frictional characteristics can be assigned to define the surface interaction between the inner and outer tube surfaces (Abaqus 2018).
c) The third technique uses springs to model the interaction between an unbonded tendon and the concrete member (Huang et al. 2010). The unbonded tendon is connected to

a virtual tendon embedded in the concrete member using spring elements at discrete locations to maintain the tendon profile. The virtual tendon is similar to the real tendon but is assigned with a very low elasticity modulus. The springs are assumed to be rigid with no axial and bending deformations.

2.2 *Modeling the varying prestress force*

The variation of the prestressing force with time due to concrete creep, concrete shrinkage, and elastic shortening is captured implicitly by the finite element model when the tendons are modeled as load resisting elements. However, modeling the variation of the prestressing force along the tendon length after friction and anchorage set losses is challenging, particularly in 3D refined finite element modeling. A few studies have modeled the friction and anchorage set losses in 2D finite element modeling (Vecchio et al. 2006, Huang 2012, and Huang and Kang 2018). Vecchio et al. (2006) used bond link elements to model the friction losses in an unbonded tendon in a 2D reinforced concrete beam. Huang (2012) and Huang and Kang (2018) proposed a two-dimensional nonlinear finite element formulation to model the prestress force variation along the length of a post-tensioned tendon after friction and anchorage set losses. In contrast to 2D finite element modeling, there are no methods implemented in literature to model the varying prestress force in 3D finite element modeling when solid elements are used to model the surrounding concrete and beam, truss, or solid elements are used to model the tendons. Even though a friction model can be used in the tube-to-tube contact elements to represent the interaction between the tendon and the duct, the activation of the friction in the tangential direction requires a contact between the inner and outer tubes to generate a normal force (Abaqus 2018). The common approach in 3D finite element modeling is to represent the prestressing force as a uniform force. Studies have followed different approaches to calculate the magnitude of this uniform force. For example, French et al. (2014) applied a stress equivalent to the jacking stress minus the friction losses averaged over the tendon length. Huang et al. (2010) applied an average stress after accounting for the prestress losses due to friction and anchorage set but the calculation method of the effective prestress and the average stress is not given in detail. The ADAPT-FELT program, a calculation tool used to compute losses in prestressed tendons, calculates an average initial stress which is the average of the stress distribution after friction and anchorage set losses (ADAPT 2017). Once the magnitude of the uniform force is established, the uniform force is applied as a predefined field of stress (Ellobody and Bailey 2008, French et al. 2014, Huang 2010, Bažant et al. 2012, and Mohammed et al. 2017) or a temperature range with an appropriate thermal expansion coefficient is defined to generate an equivalent prestressing force (Huang 2012 and Brenkus 2016).

3 ASSESSING STRESSES IN A POST-TENSIONED TIE GIRDER

3.1 *Instrumented post-tensioned tie girder*

The west tie girder of the network tied arch bridge in Michigan, USA, commonly known as the 2nd Avenue Bridge, shown in Figure 1, was selected for this study. The skeleton of the bridge was built off site in a staging area. The completed skeleton was transported using self-propelled modular transporters (SPMTs) and placed at the final alignment to complete the construction. As shown in Figure 1, the uniform prismatic portion of the tie girder is 188 ft long. The girder cross-section is 3.25 ft wide and 4 ft tall and has 12 PT tendons (TT01 to TT12). Each tendon has 19 - 0.6 in. Grade 270 Low-relaxation 7-wire strands. Corrugated plastic ducts with a 4.6 in. diameter were used as PT ducts. The tie girder was longitudinally post-tensioned in two stages (PT Stage 1 and PT Stage 2). The tendons for PT Stage 1 were stressed in two steps (PT Stage 1-1 and PT Stage 1-2) at the staging area prior to the bridge move. During PT Stage 1-1, only TT08 was stressed. During PT Stage 1-2, five tendons in the order of TT05, TT04, TT09, TT06, and TT07 were stressed. During PT Stage 2, the remaining six tendons in the order of TT03, TT10, TT12, TT01, TT02, and TT11 were stressed. The jacking force per tendon was 780 kips and the tendons

were stressed from the southwest (SW) end. The age of the west tie girder at PT Stage 1-1, PT Stage 1-2, and PT Stage 2 was 60, 167, and 280 days, respectively. The scope of this study is limited to evaluating the state of stress in the west tie girder until bridge move; i.e., only PT Stage 1-1 and 1-2 were considered.

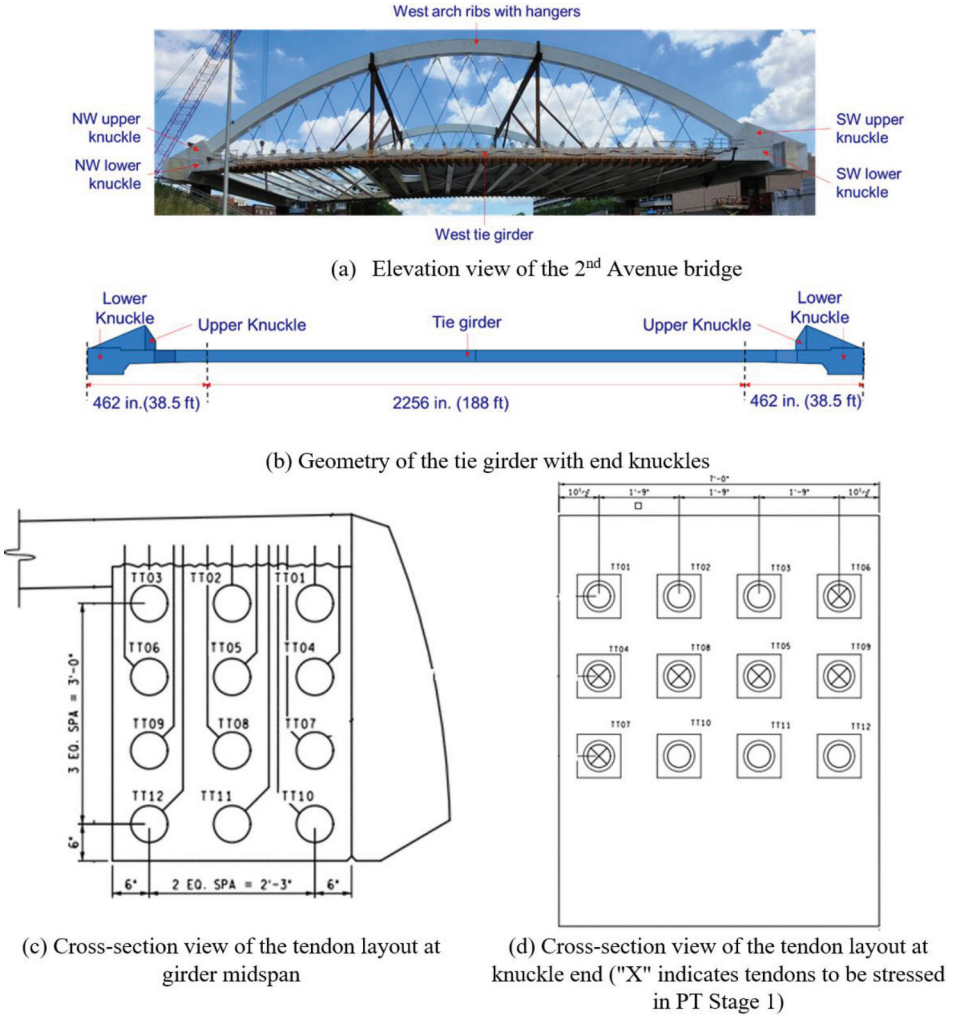


Figure 1. Details of the tie girder; (a) Elevation view of the bridge, (b) Geometry of the tie girder with end knuckles, (c) Cross-section view of the tendon layout at girder midspan, (d) Cross-section view of the tendon layout at knuckle end.

The typical practice is to use the gross cross-sectional area of tie girder to calculate stresses during post-tension application. However, this approach results in lower stresses since the space due to empty ducts are not included in calculations. Table 1 shows the difference between the stresses calculated at the tie girder midspan during PT Stage 1-1 and PT Stage 1-2 with gross and net cross-sectional areas. The stresses calculated using gross cross-sectional area resulted in 33% lower stresses at girder top and 5% lower stresses at girder bottom, at PT Stage 1-1. Compared to PT Stage 1-1, the stresses calculated using gross cross-sectional area resulted in 7% lower stresses in the girder at PT Stage 1-2. During the service life of the girder, the use of gross cross-sectional area has a less impact on the stresses calculated. However,

during the construction (such as during the PT Stage 1-1), the use of gross cross-sectional area to calculate the stresses in the girder can underestimate the actual stress developed at certain locations in the girder. Therefore, the correct representation of the effective cross-sectional area is important for calculating stresses during post-tensioning.

Table 1. Tie girder stresses considering the gross and net cross-sectional areas.

At Girder Section	PT Stage 1-1 Stresses			PT Stage 1-2 Stresses		
	Gross Area (psi)	Net Area (psi)	Deviation with Respect to Gross Area (%)	Gross Area (psi)	Net Area (psi)	Deviation with Respect to Gross Area (%)
Top	-75	-111	33	-2327	-2513	7
Middle	-399	-435	8			
Bottom	-723	-760	5			

3.2 *Finite element model description*

A three-dimensional finite element model of the west tie girder with the end knuckles was developed using Abaqus Standard 2023 incorporating time-dependent concrete properties. The tendons were modeled using 1D elements with an equivalent circular cross-section to represent all the nineteen strands in a single duct. The tendon layout was maintained along the duct profile. Wedge plates were modeled at the end anchorages to transfer the force from the tendons to the concrete girder. The geometry of the grouted PT ducts were circular cylinders with a diameter of 4.6 inches. Mild steel reinforcement in concrete members was not modeled. The lower knuckles with the empty PT ducts and the upper knuckles were modeled with 10-node three-dimensional quadratic tetrahedral elements (C3D10). The tie girder, grouted PT ducts, and wedge plates were modeled using 8-node three-dimensional quadratic linear brick (hexahedral) elements with incompatible modes (C3D8I). The tendons were modeled with 3-node quadratic beam (B32) elements. Surface-to-surface tie constraints were used to connect incompatible mesh configurations. The time-dependent material properties were defined for concrete assuming material isotropy. The time-dependent variation of the concrete elasticity modulus and Poisson's ratio was defined using measured data and the field variables option in Abaqus.

3.3 *Post-tension modeling*

For accurate representation of the stress due to post-tensioning, the correct girder sectional geometry (area and section modulus), tendon eccentricity, and the tendon forces needs to be correctly modeled. The eccentricity of tendons along the plan and elevation profiles were controlled using spring elements, as proposed by Huang (2012) and shown in Figure 2.

In the finite element model developed in this study, the net area of the girder was modeled. The grouting sequence was modeled by activating the corresponding grout elements in parallel to the grouting operations. After grouting the ducts, both the concrete and the tendons contribute to the stiffness. Strain compatibility takes effect between tendons and the concrete

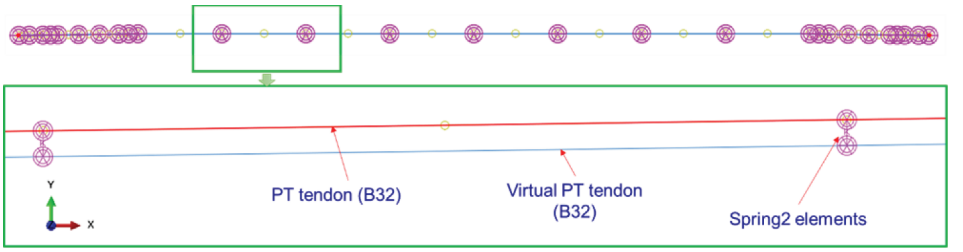


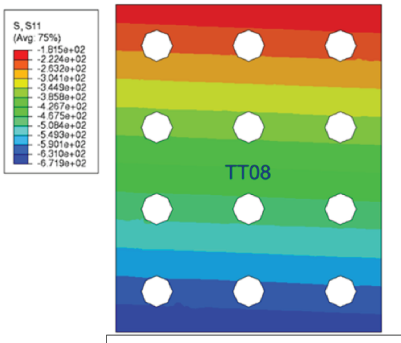
Figure 2. The modeling approach used to maintain the tendon eccentricity.

girder sections. Once the mesh representing the grout was activated, the virtual tendon was deactivated and tie constraints were used between the center nodes of the mesh representing the grout and the nodes along the tendon. Surface-to-surface interaction with tie constraints was used between the outer surface of the grout and concrete to represent the bonding between the grout and girder concrete.

The variation of the tendon force along the profile due to friction and anchorage set losses cannot be explicitly modeled in Abaqus. Therefore, the average force in each tendon after friction and anchorage set losses was used. Predefined temperature fields were assigned for each tendon such that the resultant force/stress in the tendon is equal to the average force/stress after friction and anchorage set losses. Anisotropic thermal expansion was assumed for prestressing steel. Since the elastic shortening of the girder took place when the average stress is applied to the tendon, the tendon force/stress decreased. Since this elastic shortening did not reflect the elastic shortening from the jacking operation, the exact value of the stress to be applied as a predefined field was decided after performing several iterations to achieve the expected average prestress in the tendon. The time-dependent concrete creep and shrinkage in the tie girder was modeled using the UEXPAN user subroutine with the creep and shrinkage behaviors defined as per CEB-FIP 2010 model. The stresses in the tendons were automatically calculated for elastic shortening due to sequential stressing of the tendons and long-term losses due to concrete creep and shrinkage. After grouting, strain compatibility exists between the tendon and the surrounding concrete. Any change in stress (due to creep, shrinkage, and stressing sequence) is directly transferred to the tendon from the concrete.

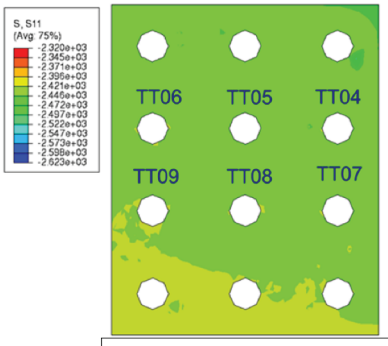
3.4 *Finite element model verification with theoretical values*

The model accuracy was verified using the stresses at the midspan of the tie girder due to PT Stage 1-1 and PT Stage 1-2. Figure 3 shows the midspan stress distribution at the end of PT Stage 1-1 and PT Stage 1-2. As shown in Figure 3(a), at the end of stressing TT08 for PT Stage 1-1, tensile and compressive stresses are observed at the top and bottom of the section, respectively. At the end of stressing TT04, TT05, TT09, TT06, and TT07 for PT Stage 1-2, uniform compressive stresses are observed at the midspan. The stresses were calculated manually at the end of each post-tensioning stage by considering tendon forces and eccentricities. The simulation results agreed with the theoretical calculations with zero or negligible deviations at the middle of the section and reasonable deviations at the top and bottom of the



	Average stress (psi) at the section		
	Top	**Middle**	**Bottom**
Calculated	-216	-426	-635
ABAQUS	-189	-426	-664
Deviation	-28	0	29

(a) At the end of PT Stage 1-1



	Average stress (psi) at the section		
	Top	**Middle**	**Bottom**
Calculated	-2427	-2425	-2422
ABAQUS	-2443	-2427	-2416
Deviation	16	2	-6

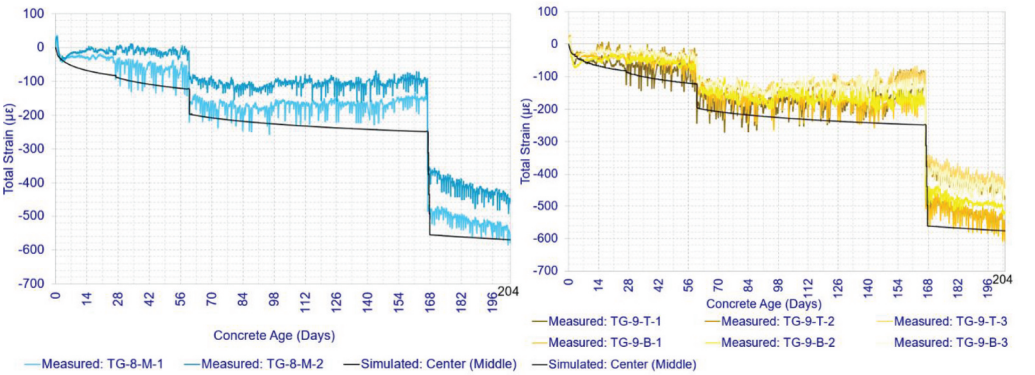
(b) At the end of PT Stage 1-2

Figure 3. Tie girder midspan stress at the end of (a) PT Stage 1-1 and (b) PT Stage 1-2 (Note: compressive stresses are negative).

section. The deviation of stress at the top and bottom of the section could be due to slight difference in the tendon force eccentricity in the model.

3.5 *Comparison of the finite element model results with the measured data*

Time-dependent strains were extracted from the vibrating wire gage (VWG) sensors at the mid span and at the north end of the west tie girder. The measured strains were compared with the results from the finite element analysis until the bridge move. Figure 4 shows the measured and simulated total strain in the west tie girder. The simulated strains at TG-8 and TG-9 match with the measured strains, with the simulated strains showing a slight overestimation.



(a) At tie girder midspan (TG-8) (b) At tie girder north end (TG-9)

Figure 4. Measured and the simulated total strain in the west tie girder at (a) TG-8 and (b) TG-9.

4 SUMMARY AND CONCLUSIONS

The stress state of a post-tensioned member is governed by the magnitude of the effective prestressing force in the tendons and the concrete elasticity modulus at the time of load application. The effective prestress force is the remaining force after total prestress loss. Friction between tendon and duct, anchorage set, and elastic shortening due to sequential tendon stressing cause the immediate prestress losses that occur during the stressing and prestress transfer operations. Concrete creep, concrete shrinkage, and steel relaxation cause the time-dependent losses that occur throughout the service life.

In this study, the strains in a post-tensioned concrete tie girder in a network tied arch bridge was numerically simulated and the results were validated using the strain data collected from the girder during the bridge construction. The concrete elements and anchorage wedge plates were modeled with solid (hexahedral or tetrahedral) elements. The tendons were modeled with beam elements. The average tendon stress after short-term prestress losses due to the effects of tendon curvature, wobble effects, and anchorage set was applied as the initial prestress force. This initial prestress force was applied by defining predefined fields of temperature to cool down the tendon. The elastic shortening losses due to sequential tendon stressing and the concrete creep and shrinkage were captured in the model with the concrete deformation. The tendon eccentricity within the tie girder prior to grouting the PT ducts was maintained by connecting the PT tendon to a virtual tendon that was embedded in the concrete. This virtual tendon profile was similar in geometry to the real tendon but was assigned a lower elasticity modulus. The real and virtual tendons were connected at discrete locations along the tendon length using Spring2 elements that were assigned with higher stiffnesses in the perpendicular and transverse directions to the tendon. After grouting the PT ducts, the tendons were connected to the grouted PT ducts using tie constraints to maintain strain compatibility. The simulated strains were approximate to the measured strains in the tie girder, but with an upper bound.

The simulation techniques followed in this study can be used to model the stresses in a post-tensioned member and thereby overcome the drawbacks in typical post-tension modeling techniques of embedding the PT tendon in the concrete and using gross-section properties of the post-tensioned member without accounting for the presence of empty PT ducts. However, the techniques are applicable only for determinate structures which can deform and generate an average stress distribution along the member.

ACKNOWLEDGEMENT

This project was funded by the Michigan Department of Transportation (MDOT) through the Center of Excellence for Structural Durability at Western Michigan University. The authors would like to acknowledge the support of MDOT engineers and the members of the Z-Contractors. Authors appreciate the contribution of Harsha Amunugama, Srikanth Vemula, Sanjoy Bhowmik, Naveen Ranasinghe, and Uresh Wijesinghe for instrumentation and data collection.

REFERENCES

1. Aalami, B. O. (1990) "Load Balancing - A Comprehensive Solution to Post-Tensioning." *ACI Struct. J.*, 87(6): 662–670.
2. Aalami, B. O. (2000). "Structural Modeling of Posttensioned Members". *Journal of Structural Engineering*, 126 (2).
3. Abaqus. (2018). Abaqus/CAE User's Guide. SIMULIA User Assistance 2018.
4. ADAPT Corporation. (2017). *ADAPT-FELT 2017 User Manual*. ADAPT Corporation, Redwood City, California.
5. Bažant, Z. K. P., Qiang, Y., and Guang-Hua, L. (2012). "Excessive Long-Time Deflections of Prestressed Box Girders. II: Numerical Analysis and Lessons Learned". *Journal of Structural Engineering*, 138 (6): 687–696.
6. Brenkus, N. R. (2016). "Ultimate Strength of Post-tensioned Girders with Mixed Bonded and Unbonded Prestressing". PhD. Dissertation, University of Florida, Florida.
7. Ellobody, E. and Bailey, C. G. (2008). "Behavior of Unbonded Post-Tensioned One-way Concrete Slabs". *Advances in Structural Engineering*, 11(1): 107–120.
8. French, C. E. W., Shield, C. K., and Hedegaard, B. D. (2014). "Modeling and Monitoring the Long-Term Behavior of Post-Tensioned Concrete Bridges". Report no MN/RC 2014-39, Minnesota Department of Transportation, Research Services & Library, St. Paul, Minnesota.
9. Huang, Y., Kang, T. H., K., Ramseyer, C., and Rha, C. (2010). "Background to Multi-Scale Modelling of Unbonded Post-Tensioned Concrete Structures." *International Journal of Theoretical and Applied Multiscale Mechanics*, 1 (3): 219–235.
10. Huang, Y. (2012). Finite Element Method for Posttensioned Prestressed Concrete Structures. PhD. Thesis, University of Oklahoma, Oklahoma.
11. Huang, Y. and Kang, T. H. K. (2018). "Modeling of Sliding Behavior of Unbonded Tendons in Post-Tensioned Concrete Members". *ACI Structural Journal*, 115 (4): 1153–1164.
12. Kang, T. and Huang, Y. (2012). "Computer Modeling of Post-Tensioned Structures". *4th International Conference on Computer Modeling and Simulation (ICCMS 2012)*, IPCSIT 22 (2012), Singapore.
13. Kang, T. H. K., Huang, Y., Shin, M., Lee, J. D., and Chor, A. S. (2015). "Experimental and Numerical Assessment of Bonded and Unbonded Post-Tensioned Concrete Members". *ACI Structural Journal*, 112 (6): 735–757.
14. Lin T. Y. and Burns, N. (1991). *Design of Prestressed Concrete Structures*. 3rd Edition, John Wiley & Sons, New York.
15. Mohammed, A. H., Tayşi, N., Nassani, D. E., and Hussein, A. K. (2017). "Finite Element Analysis and Optimization of Bonded Post-Tensioned Concrete Slabs". *Cogent Engineering*, 4(1).
16. Post-Tensioning Institute (PTI). (2006). Post-Tensioning Manual. 6th Edition, Phoenix, Arizona.
17. Vecchio, F. J., Gauvreau, P., and Liu, L. (2006). "Modeling of Unbonded Post-Tensioned Concrete Beams Critical in Shear". *ACI Structural Journal*, 103(1): 57–64.

Bridge Maintenance, Safety, Management, Digitalization and Sustainability – Jensen, Frangopol & Schmidt (eds)
© 2024 The Author(s), ISBN 978-1-032-77040-6
Open Access: www.taylorfrancis.com, CC BY-NC-ND 4.0 license

Service life determination of post-tensioned hanger rods

A.P Ranasinghe & H.T Al-Khateeb
Jacobs Engineering, New Jersey, USA

ABSTRACT: Post Tensioned Hanger Rods are used in Cable Stayed and Tied Arch Bridges. As these bridges become old, it is important to have an idea of the service life of these Hanger Rods. This will enable a proper maintenance plan to be implemented in a timely manner. For new designs, provisions can be incorporated to enhance the service life of the Hanger Rods. The biggest challenge for the hanger rods is corrosion. The corrosion rate of metals will depend on the atmosphere of the rod and how well it is protected from moisture and other chemicals. Hot dip galvanizing of the rods is common. Such organizations like the American Galvanizers Association have published corrosion rates of Zinc and other metals. Their Zinc Coating Life Predictor can be used to predict the service life of the rods. Encasing the rods in steel pipes can increase the service life. Sealing the pipes or filling them with grout can further enhance it. This paper describes how the service life of hanger rods were calculate for a bridge in the California High Speed Rail Project.

1 INTRODUCTION

1.1 *Project information*

The California High Speed Rail (CAHSR) is the pioneer high-speed rail program in the nation, connecting San Francisco to Los Angeles in less than three hours at speeds over 200 miles (320 km) per hour. The second and third Construction Packages (CP 2-3) of the First Construction Segment include 65 miles (104 km) of rail through several counties. The project includes at-grade and aerial structures in addition to local and state route under-passes and overhead structures.

The State Route - 43 Underpass is a Network Tied Arch Bridge in this project. It has post-tensioned hanger rods, and their service life is an important parameter in preparing a maintenance manual for the bridge.

Post-tensioned hanger rods find application in Cable-Stayed and Tied Arch Bridges. As these bridges age, understanding the service life of these hanger rods becomes crucial. This knowledge facilitates the timely implementation of an effective maintenance plan. Moreover, in new designs, provisions can be integrated to improve the service life of the hanger rods.

The design life of the bridge structures in CAHSR Project is 100 years. The Post Tension Institute (PTI) arbitrarily assigns 75 years for the design life of hanger cables and rods. The above project required to determine the service life of the hanger rods using a more rational method. Hence the procedures presented in this paper were used to estimate the service life of the hanger rods of the above tied arch bridge in the (CAHSR) Project.

1.2 *Needs for galvanizing*

One of the biggest challenges for the hanger rods is corrosion. Corrosion of metals is a chemical process rooted in science. After the metals are processed, they tend to revert into their natural and low energy state of ore. The energy used to transform ore into metal is reversed if the metal

DOI: 10.1201/9781003483755-209

is exposed to oxygen and water. As the metal is exposed to these elements, the corrosion process begins, and oxides and other compounds are formed on the steel surface.

Steel is an efficient and durable construction material. It is readily available, cost effective, aesthetically pleasing, sustainable, and strong as a construction material. Like all metals, steel corrodes when exposed to the atmosphere. Therefore, it is important to consider corrosion protection. There are several corrosion protection methods including: Hot-Dip Galvanizing (HDG), Duplex Systems, Zinc Coatings, Protective Coatings, Special Steels, and Sacrificial Anodes.

The American Post Tension Institute (PTI) recommends the use of High Strength Steel Grade 150 deformed thread bars meeting ASTM A 722 "Standard Specification for High-Strength Steel Bars for Prestressed Concrete" Type 2 and Hot Dip Galvanized per ASTM A 123. In addition to its inherent corrosion resistance, HDG has other superior qualities such as lowest initial cost, durability, longevity, availability, versatility, sustainability, and aesthetics compared to other corrosion protection methods. Therefore, HDG of the hanger rods is common.

The corrosion rate of metals will depend on the atmosphere of the rod and how well it is protected from moisture and other chemicals. According to the American Galvanizers Association, the corrosion rate of metals will increase going from Rural, Suburban, Temperate Marine, Tropical Marine to Industrial environments. They have published corrosion rates of Zinc and other metals. This data can be used to predict the service life of the rods.

Encasing the rods in steel pipes offers an initial boost to their service life, while sealing the pipes or utilizing grout can further extend this duration. Within this paper, strategies aimed at bolstering the overall durability of these hanger rods are also presented.

2 STATE-OF-THE ART OF HOT DIP GALVANIZING

2.1 *Hot dip galvanizing process*

As per the American Galvanizers Association, Hot Dip Galvanizing is the process of dipping fabricated steel (i.e., steel hanger rods in this case) into a kettle containing molten zinc. While the steel fabrication is in the kettle, the Iron in the steel metallurgically reacts with the molten zinc to form a tightly bonded alloy coating that provides superior corrosion protection to steel.

(Weisenberger, 2014) has provided an excellent photo tour of a galvanizing plant in Arizona, USA that explains the HDG process quite well. Steel comes to the facility at various states of cleanliness and is sandblasted if necessary. Then all steel batches go through a series of tanks or "baths". The first bath is a caustic dip with Sodium Hydroxide that will remove oil, grease, and dirt. In order to neutralize the batch, it is soaked in water. The third tank is an acid bath which removes any oxidation. Sulfuric or Hydrochloric Acid is used for this "pickling" process. From the pickling tank the batch goes to rinse off the acid. The next and final bath before the actual zinc dip is a zinc ammonium chloride mixture, which acts as a fluxing agent. It also contains a chlorine salt that encapsulates the metal and prevents it from oxidizing again.

Following the flux, the batch is dipped in a kettle. The Zinc in the kettle is at 835 ^{O} F (446^{O} C) for 3.5 minutes. The batches are raised and lowered into the kettle to make sure the zinc gets into all the nukes and crannies, tapping them as necessary to remove excess zinc and skimming the top of the tank to make sure that no detritus adheres to the steel as it is removed from the top.

3 SERVICE LIFE PREDICTION OF POST-TENSION HANGER RODS

3.1 *Corrosion rate of zinc coating – Use of ZCLP*

If the corrosion rate of the zinc coating and its thickness is known, then the time to corrode the coating can be calculated. An updated tool now makes it easier for engineers to estimate the service life of zinc coatings and predict their performance (Krzywicki, 2024). The Zinc

Coating Life Predictor (ZCLP) is available on the American Galvanizers Association's website (zclp.galvanizeit.org). It can be used to predict the service life of hanger rods. The web-based ZLCP requires numerical input of six yearly average atmospheric parameters: annual precipitation, sulfur dioxide deposition rate, relative humidity, airborne salinity, air temperature, and sheltering condition (open air, rain-sheltered or indoor). The 'Resources" tab at the top of the website contains links to this data. The corrosion prediction calculations are based on models that were developed using statistical methods, neural network technology, and an extensive worldwide corrosion database.

3.2 *Limitations of available tools*

The ZLCP cannot be applied to coatings containing alloying elements larger than 1% or painted products. Additionally, yearly average wind direction can significantly affect corrosion rates for structure within one mile of the coastline. The tool does not incorporate data from accelerate corrosion tests such as salt spray tests due to the absence of real-world wet-dry circles. It assumes that the zinc coating is not subjected to significant damage or defects, which could accelerate corrosion and reduce performance.

3.3 *Corrosion rate of zinc coating using charts*

If the corrosion rate of the zinc coating and its thickness is known, then the time to corrode the coating can be calculated.

The challenge is to use an appropriate value for the corrosion rate of the zinc layer. It depends on many environmental and other factors as discussed earlier in this paper.

American Galvanizers Association has provided Service Life Charts based on decades of corrosion data collected from galvanized steel samples exposed to five defined environments in cities all over the world. The five defined environmental conditions are Rural, Suburban, Temperate Marine, Tropical Marine, and Industrial. Figure 1 shows the service life for different zinc coating thicknesses, in various environmental conditions and coating thicknesses.

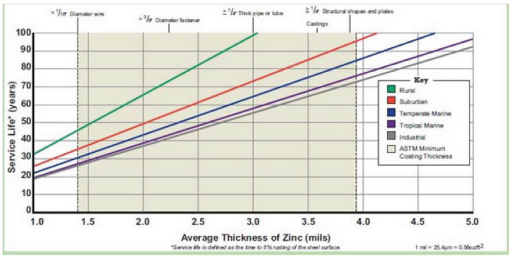


Figure 1. Service life chart for hot dip galvanized coatings.

The 9ASM Handbook, Corrosion,1987), provides corrosion rates of structural steel in various environments. One needs to select a location with similar environmental conditions where the hanger rods are used, and utilize the charts and tables provided for the service life calculations.

It should be noted that the corrosion rate provided in the charts generally assume that the hanger rods are in an open area. However, if they are enclosed by steel pipes, the enclosed hanger rods will be protected by the pipes provided there is no frequent condensation. In that case the hanger rods will be first protected by the steel pipes. However, if there is frequent condensation on the surface of the hanger cables, then the pipes cannot provide proper protection and that should be considered in the calculations. One conservative method of compensation is to ignore the protection provided by the pipes.

4 DESIGN EXAMPLE

4.1 *Bridge application details*

The hanger rods of the tied arch bridge consist of High Strength Steel Grade 150 deformed thread bars meeting ASTM A 722 and Hot Dip Galvanized per ASTM A 123. The 3" (75 mm) diameter hanger cables are encased in Schedule 40, 8" (200mm) diameter steel pipes. Steel pipes are not galvanized, and the bridge is located in an urban environment. There is minimal condensation inside the casing pipe. Minimum diameter of the hanger cables required for stress and fatigue is 2.975" (74mm). Estimate the service life of the hanger cables.

4.2 *Calculations*

From ASTM 123 the zinc coating for a 2.975" rod is 3.9 mils

From Figure 1, Service Life of a zinc coating 3.9 mils thick in an industrial environment = {95 Years}

Extra diameter of hanger cables = 0.5x(3"-2.975")
= 0.0125" (12.5mils)

From Table 2 of ASM Handbook, the corrosion thickness of steel in an industrial environment in 15.5 years = 5.3 mils

Number of years for the extra steel in the hanger able to corrode = (15.5x12.5/5.3) = {36 Years}

Thickness of Sch. 40 casing pipe = 0.322" (322 mils)

Number of years for the Sch. 40 casing pipe to corrode = (15.5x322/5.3) = {941 Years}

Service Life with no heavy condensation or moisture in the casing pipe = (95 + 36+ 941) = 1,072 Years

Service Life with heavy condensation or moisture in the casing pipe = (95 + 36+ 0) = 131 Years

4.3 *Important considerations for HDG*

The following are important considerations when HDG hanger rods are utilized:

a) Hydrogen embrittlement is of concern for steels of ultimate tensile strength of 150 ksi (1100 MPa). During the chemical reaction between steel, rust and the chemicals used in the pickling stages of the galvanizing process, hydrogen is produced and absorbed by the steel. The very small grain structure of high strength steel prevents the hydrogen from being expelled during immersion in the molten zinc. When placed under stress in use, the steel may become brittle and fracture. To prevent hydrogen embrittlement from occurring the hanger rods should be blast cleaned before they are sent to the galvanizer. Only mechanical pre-cleaning is allowed, and acid wash or acid pickling is not allowed.
b) Hanger rods should meet the requirements of PTI Recommendations Section 3.2.4 and be tested after galvanizing for, corrosion, ductility, strength, and fatigue as per Section 3.2.4.1.
c) Threads should be made after galvanizing. It is important to maintain correct zinc layer thickness. Less than the specified thickness will reduce the life span of the hanger rods. Larger than specified thickness can affect the tolerances. Though robust and difficult to damage, large galvanize coating thicknesses can be damaged during handling and installation. Also, very thick coatings are subject to damage during transportation. Galvanizing a trial batch of the hanger rods is recommended to ensure that the correct thickness is achieved.
d) Depending on the size of the molten zinc kettle, some hanger rods may need to be dipped one half at a time. This procedure is known as progressive dipping (Double Dipping). Uneven heating and cooling may cause warpage or distortion of the hanger rods.

e) Where the galvanized pipes are in contact with wet concrete, there will be an initial reaction of the galvanizing layer due to the reaction of the zinc with the wet concrete. The reaction will stop after the initial curing stages of the concrete. If the pipe is not galvanized, and comes in contact with the galvanized rod, and if wetted, a bimetallic corrosion may follow, and the zinc layer will be lost sacrificially. These possibilities might need to be considered as part of the overall design and durability.

4.4 *Testing of HDG hanger rods and anchorages*

The following tests should be done on the hanger rods and anchorages as per PTI Recommendations:

a) Quality control tests for hanger rods as per Section 3.2.4.1
b) Tests for steel pipes as per Section 3.5.2
c) Salt Fog Tests as per 4.1.4.1 and 4.1.4.2
d) Temporary corrosion protection as per Section 4.1.5
e) Anchorage Leak Test as per Section 4.1.6
f) Anchorage Fatigue Test as per Section 4.2

5 CONCLUSIONS

This paper presents a systematic approach to estimate the service life of hot dip galvanized steel hanger rods. It also provides some recommendations to properly galvanize hanger rods:

1) In order to prevent Hydrogen Embrittlement, blast cleaning or other mechanical cleaning of the hanger rods should be performed before they are immersed in the molten zinc kettle. Acid pickling or chemical cleaning normally associated with preparations prior to the galvanizing is not recommended.
2) The thickness of the rods will also affect the tolerance of the galvanized layer. Further there may be variations in the thickness of zinc over the length of the rod. Galvanizing a trial batch of rods is recommended to check thickness attained.
3) The rods should be first galvanized and then threaded.
4) The length of the rod will also require a check with the galvaniser in that the length of rod can be dipped in the bath, as there will be a limit to the size that can be immersed.
5) Do not allow the pipe casing to come in contact with wet concrete or the hanger rods.

REFERENCES

AASHTO LRFD Specifications for bridges, Seventh Edition, 2014, AASHTO, Washington, DC, USA.
America Galvanizers Association, 6881 South Holy Circle, Suite 108 Centennial, Colorado 80112, USA.
ASM Handbook, Corrosion, Volume 13, Table 2, 1987, American Society of Metals International, Materials Park, Ohio, USA.
ASTM A123/A123M Specification for zinc (Hot dip galvanized) coatings on iron and steel products, USA.
Krzywicki, J. 2024, Crafting a coat, modern steel construction, AISC, 130 E Randolf Street, Suite 2000, Chicago, Illinois 60609.
Post Tension Institute, 2014, Recommendations for stay cable design, testing, and installation, Seventh Edition, Post Tension Institute, Michigan, USA.
Weisenberger, G, 2014, Galvanizing illustrated, modern steel construction, AISC, 130 E Randolf Street, Suite 2000, Chicago, Illinois 60609.

Bridge Maintenance, Safety, Management, Digitalization and Sustainability – Jensen, Frangopol & Schmidt (eds)
© 2024 The Author(s), ISBN 978-1-032-77040-6
Open Access: www.taylorfrancis.com, CC BY-NC-ND 4.0 license

The comparative analysis of post-tensioned tendons in ultra-high-performance box girders

M. Tsas-Orgilmaa
Mongolian University of Science and Technology, Ulaanbaatar, Mongolia

Han Sang Mook
Kumoh, National Institute of Technology, Gumi, South Korea

ABSTRACT: The UHPC (ultra-high-performance concrete) composite box girder consists of three segments of UHPC U-shaped girder, 50 mm UHPC depth deck plate and reinforced high-strength concrete (HSC) slab with 240 mm depth. The steel fiber 1.5% of volume fraction was added to the UHPC mixture to induce ductile behavior in the girder. The webs and deck plate of the box girder are not reinforced in the longitudinal direction and no stirrups. Totally 146 tendons inserted in upper and lower flanges of girder to induce flexural strength of composite box girder. Moreover, FBG (fiber bragg grating) sensors are used in lower flange to monitor stress-strain relationship of tendons. The objective of this study is to calculate the instantaneous prestress loss and compare it to the results of experiment and finite element analysis of 50 m UHPC post-tensioned composite box girder. The finite element analysis was used as a strong analytical tool for modeling of UHPC composite box girder. The commercial version of MIDAS FEA was used. The difference in instantaneous loss of tendons between analytical calculation and experimental result are 2-9%. The analytical calculation and FEA show good agreement with experimental result.

1 INTRODUCTION

There are two stages of stress loss considered in prestressed concrete structures. It includes instantaneous prestress loss which occurs during construction stage, time-dependent prestress loss which occurs during the service stage of the structure. The instantaneous prestress loss consists of loss due to elastic shortening, loss due to anchorage seating and loss due to friction. Time-dependent loss consists of loss due to creep, loss due to shrinkage, loss due to temperature effects and loss due to relaxation. The evaluation of final stress force of the prestressed strand is not easy after completion of the structure on site. Therefore, to overcome this drawback, several researchers developed a smart strand which was embedded fiber bragg grating (FBG) sensor in core of wire of the prestressing strand. It gives an opportunity to control the stress-strain relationship of presstressing strand for long term.

In 2015, (Kim, et al., 2015) adopted carbon fiber as the material for the core wire for the sensing strand. That kind of carbon fiber core wire is fabricated by adjusting its diameter to 5.3 mm so as to achieve a diameter of about 5.4-5.5 mm when the external nylon cover fiber is included. Moreover, the volume fraction of the carbon fiber is adjusted to be larger than 65%. The corresponding stiffness of the actually as-fabrictaed carbon core wire is approximately 163 GPa. The tensile test of core wire and strand verified that this smart strand demonstrates structural performance equivalent or superior to the traditional prestressed concrete wire strand. The measuring performance of the sensing strand was also verified to be capable of measuring strain up to a range of 13000-14000 microstrain. The sensing strand developed in this study exhibits consistent structural performance that allow it replace the traditional prestressed concrete wire strand, constitutes the most adequate method to measure the axial strain of the strand, and secures the reliability of the measured data.

DOI: 10.1201/9781003483755-210

In 2016, (Keunhee, et al., 2016) conducted a research on the distribution of prestressing forces for 24 types of 49 girders by using multi-strands in girders. In this study, a special device was conceived to deposit electromagnetic sensors onto each strand so as to measure the prestress force in each individual strand of the multi-strand system.The distribution of the mean prestress force per anchor head have means ranging between 164 KN and 200 KN, and standard deviations ranging between 5.1 KN and 8.4 KN. The prestress force per strand ranging between 144 KN and 220 KN is seen to cover a wider range than the mean of the prestress force per anchor head.

In accordance above studies, the FBG sensors are capable tool to measure the prestress force of prestressed concrete structures. The objective of this study is to calculate the instantaneous prestress loss and compare it to the experimental result and finite element analysis of UHPC post-tensioned composite box girder.

2 CALCULATION OF INSTANTANEOUS PRESTRESS LOSS

2.1 *Design 50 m UHPC composite box girder*

The 50 m span UHPC Composite box girder consists of UHPFRC U-shaped girder, UHPC deck slab 50x2500x50000 (thickness, width, and length) mm and HSC reinforced slab 240x2500x50000 (thickness, width, and length) mm. The 50 m span UHPFRC U-shaped girder consists of three segments, which were integrated at two joint sections such as scheme (17+16 +17) m. The 50 m span UHPC U-shaped girder is designed with prestressing tendons 2x7 and 6x22 tendons in the upper and lower flanges respectively. Lower tendons were indicated T1, T2, T3, T4, T5, T6 and upper tendons were indicated left T7 and right T7. After post-tensioning of tendons grouting was injected into sheaths and cured with heat treatment. The steel fiber 1.5% of volume fraction was added to UHPC to induce a ductile behavior in the girder.

The feature of the U-girder is not reinforced longitudinal and transverse direction except from 0 m to 4 m reinforcement of anchoring zone. The U-shaped girder was connected to the UHPC deck plate and high-strength concrete (HSC) slab by shear key and bar connectors.

2.2 *Cross section properties of U-shaped girder*

The properties of a cross-section such as an area, a first moment of area, a moment of inertia, coordinates of centroid and eccentricities of tendons were calculated for determining prestress loss caused in post-tensioned tendons. Figure 1 shows cross-section and simple cross-section and positions of tendons of U-shaped girder.

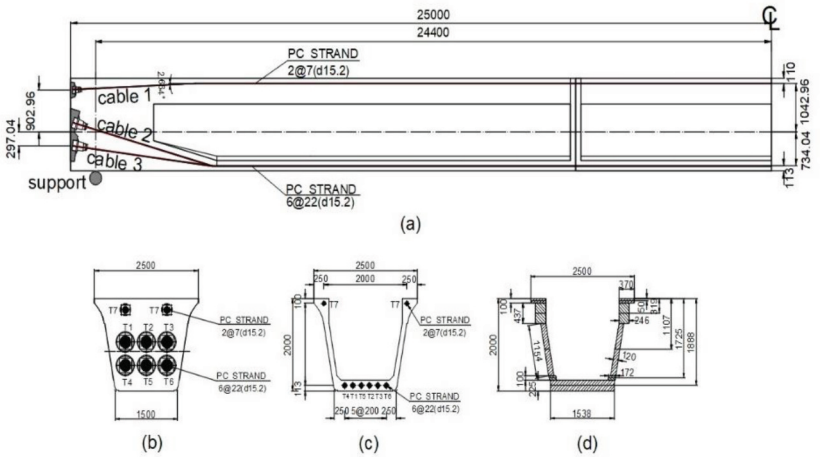


Figure 1. U girder profile and cross sections: (a) girder profile, (b) at support, (c) at midspan (d) transformed cross section at midspan (all dimensions in mm).

Calculated cross-section properties are:
Area of cross section: $A_{c,\,u} = 0.947 \cdot 10^6$ mm^2
First moment of area: $S_y = 1.092 \cdot 10^9$ mm^3
Moment of inertia: $I_{c,\,u} = 3.575 \cdot 10^{10}$ mm^4
Squared radius of gyration: $r^2 = 3.275 \cdot 10^4$ mm^2
Coordinates of centroid: $x_{c,\,u} = 0$; $y_{c,\,u} = 1152.96$ mm
Distance from the centroid to extreme top/bottom edge of U-girder: $y_1 = y_c = 1152.96$ mm, $y_2 = 847.04$ mm

2.3 *Calculation of instantaneous prestress loss of UHPC box girder*

The analytical computation of instantaneous loss of prestress is followed by the KCI Structural Concrete Design Code (KCI, 2012). The instantaneous loss of prestress comprises of loss due to elastic shortening loss, anchorage seating loss and loss due to friction as expressed in Equation 1.

$$\Delta f_{pim} = \Delta f_{fr} + \Delta f_{an} + \Delta f_{el} \tag{1}$$

Where, Δf_{pim}= instantaneous loss of prestress; Δf_{fr} = prestress loss due to friction; Δf_{an} = prestress loss due to anchorage seating; Δf_{el}= prestress loss due to elastic shortening.

2.3.1 *Friction loss*

The values of the curvature and wobble effect are $K = 0.0016$, $\mu = 0.18$ given respectively in (KCI, 2012).

The friction loss is determined by the Equation.2. It should be noted that the maximum frictional loss would be at the far end of the girder if jacking is from one end (KCI, 2012).

$$\Delta f_{fr} = f_{f0}(\mu\alpha + KL) \tag{2}$$

Where f_{f0} = transferring stress, N/mm^2; L = whole length of tendon, mm; α = inclination of tendon, in radians; μ = curvature effect; K = wobble effect.

According to the material property of seven wire strand yield strength of SWPC 7A (15.2mm) tendon is determined as $f_{py} = 1471$ N/mm^2 and the tensile strength is $f_{pu} = 1730$ N/mm^2. Based on (KCI, 2012) the transferring stress must not exceed maximum permissible stress in the strand immediately after transfer. The maximum permissible stresses are $0.82 \cdot f_{py} = 1206$ N/mm2 or $0.74 \cdot f_{pu} = 1280$ N/mm^2. Therefore, in this case $0.82 \cdot f_{py} = 1206$ N/mm^2 is assumed for transferring stress.

Jacking force for a tendon is determined by Equation 3.

$$P_j = f_{f0} \times A_p \tag{3}$$

Where: P_j= jacking force, KN; f_{f0}= transferring stress, N/mm^2; A_p – cross sectional area of a tendon, mm^2.

A summary of loss due to friction is shown in Table 1.

Table 1. Prestress loss due to friction.

	Unit	Tendon T7	T1, T2, T3	T4, T5, T6
Number of tendons (for a bundle)		7	22	22
Cross sectional area	mm^2	970.9	3051.4	3051.4
Inclination of tendon, α	degree	2.764	15.492	7.459
Curvature effect, μ	-	0.18	0.18	0.18
Wobble effect, K	-	0.0016	0.0016	0.0016
Length of tendon, L	m	50.07	50.252	50.058
Jacking force for a tendon, P_j	KN	1171.1	3680.7	3680.7
Loss due to friction - Δf_{fr},				
At prestressing section	N/mm^2	0	0	0
At midspan	N/mm^2	53.3	77.83	62.43
At right	N/mm^2	106.6	155.66	124.86

2.3.2 *Anchorage seating loss*

The loss due to anchorage seating is influenced by anchorage setting length l_{set}, and friction loss per length of tendon p.

Loss due to anchorage seating is determined by Equation 4.

$$\Delta P = 2p \times l_{set} \tag{4}$$

Where, ΔP = anchorage loss force in tendon, KN; p = friction loss per length of tendon, N/mm; l_{set} = anchorage setting length, mm.

$$p = \frac{P_j - P_i}{L} \tag{5}$$

Where, p = friction loss per length of tendon, N/mm; P_j = jacking force at prestressing section, KN; P_i = tendon force at midspan after friction, KN; L = whole length of tendon, mm.

Anchorage setting length is determined by Equation 6

$$l_{set} = \sqrt{\frac{\Delta l A_p E_p}{p}} \tag{6}$$

$$\Delta P = 2p \times l_{set} \tag{7}$$

Where, Δl = anchorage slip, mm; A_p = cross sectional area of tendon, mm2; E_p = elasticity modulus of tendon, N/mm^2.

A summary of loss due to anchorage seating is shown in Table 2.

Table 2. Prestress loss due to anchorage seating.

Characteristic	Unit	Tendon T7	T1, T2, T3	T4, T5, T6
Friction loss per length of tendon, p	N/mm	2.07	9.45	7.61
Anchorage setting length, l_{set}	mm	23726	19682	21934
Anchorage loss force in tendon, ΔP	KN	98.21	372.08	333.88
Tendon force at midspan after friction, P_i	KH	1072.91	3308.58	3346.78
Prestress f_{pi}, N/mm^2				
At prestressing section	N/mm^2	1105.07	1084.28	1096.80
At midspan	N/mm^2	1155.64	1145.25	1151.51
At right	N/mm^2	0	0	0
Loss due to anchorage seating Δf_{an},				
At prestressing section	N/mm^2	101.15	121.94	109.42
At midspan	N/mm^2	0	0	0
At right	N/mm^2	0	0	0

2.3.3 *Elastic shortening of post-tensioned elements*

In this case of study, composite box girder has eight bundles of tendons. As each tendon is tensioned, there will be a loss of prestress in the previously tensioned tendons due to elastic shortening of the member. The elastic shortening is determined by Equation 8.

$$\Delta f_{el} = \frac{1}{2} \times n \times f_{cir} \tag{8}$$

Where, n = modular ratio, n = 4.48; f_{cir} = average compressive stress in the concrete along the length of the girder at the center of gravity of the tendon immediately after the prestress transfer.

Average compressive stress in the concrete along the length of the girder at the center of gravity of the tendon immediately after the prestress transfer is determined by Equation 9

$$f_{cir} = \frac{f_{cs}(\text{midspan}) + f_{cs}(\text{PS section})}{2} \tag{9}$$

Compressive stress of tendons after post-tensioning

$$f_{cs} = \frac{P_i}{A_c} + \frac{P_i}{I_c} e_p^2 - \frac{M_d}{I_c} e_p \tag{10}$$

Where, P_i = initial prestressing force (after anchorage seating loss); A_c = area of gross section of concrete, $^{mm}2$ $A_c = 0.947 \times {}^{10}6$ $^{mm}2$; M_d = bending moment due to self-weight, Nmm; I_c = moment of inertia of gross section of concrete, $^{mm}4$; $I_c = 3.575 \times {}^{1010}$ $^{mm}4$; e_p = eccentricity of center of gravity of tendons with respect to center, of gravity of concrete, mm.

Eccentricities of tendons are calculated in followings:

At support

e_{et} = 902.96 mm – for T7 tendons in top flange

e_{eb1} = 202.96 mm – for T1,T2,T3 tendons in bottom flange

e_{eb2} = 297.04 mm – for T4,T5,T6 tendons in bottom flange

At midspan

e_{ct} = 1042.96 mm – for T7 tendons in top flange

e_{cb1} = 734.04 mm – for T1,T2,T3, T4,T5,T6 tendons in bottom flange

A summary of loss due to elastic shortening is shown in Table 3.

Table 3. Prestress loss due to elastic shortening.

		Tendon		
Characteristic	Unit	T7	T1, T2, T3	T4, T5, T6
Jacking force for a tendon, P_j				
At prestressing section	KN	1171.1	3680.7	3680.7
At midspan	KN	1119.4	3443.2	3490.2
At right	KN	1119.4	3443.2	3490.2
Prestress, f_{cs}				
At prestressing section	N/mm^2	27.95	8.13	12.97
At midspan	N/mm^2	166.20	86.24	85.49
At right	N/mm^2	166.20	86.24	85.49
Bending moment due to self-weight, M_d, Nmm				
At prestressing section	N/mm	0	0	0
At midspan	N/mm	$6.9 \cdot 10^9$	$6.9 \cdot 10^9$	$6.9 \cdot 10^9$
At right	N/mm	$6.9 \cdot 10^9$	$6. \cdot 10^9$	$6.9 \cdot 10^9$
Average compressive stress, f_{cir}, N/mm^2				
At prestressing section	N/mm^2			
At midspan	N/mm^2	97.07	47.19	49.23
At right	N/mm^2	97.07	47.19	49.23
Loss due to elastic shortening, Δf_{el}				
At prestressing section	N/mm^2	217.57	105.76	110.34
At midspan	N/mm^2	217.57	105.76	110.34
At right	N/mm^2	217.57	105.76	110.34

Instantaneous loss of prestress is summarized in Table 4

At the end of the calculation of the instantaneous prestress loss, the total percent of prestress loss is shown at prestressing section, at midspan and at right end of girder respectively in Table 5. The maximum instantaneous loss was 26% for at prestressing section and the minimum

Table 4. A summary of instantaneous loss.

Characteristic	Unit	Tendon		
		T7	T1, T2, T3	T4, T5, T6
Total instantaneous prestress loss, Δf_{pim}				
At prestressing section	N/mm^2	318.72	227.70	219.76
At midspan	N/mm^2	270.87	183.59	172.77
At right	N/mm^2	324.17	261.42	235.20
Jacking force for a bundle, P_i				
At prestressing section	KN	861.46	2985.2	3009.42
At midspan	KN	912.55	3119.78	3152.81
At right	KN	856.17	2882.29	2962.31
Jacking force for a tendon, Pi				
At prestressing section	N/mm^2	123.07	135.69	136.79
At midspan	N/mm^2	130.36	141.81	143.31
At right	N/mm^2	122.31	131.01	134.65

Table 5. Total percent of instantaneous prestress loss.

Characteristic	Unit	Total percent of instantaneous prestress loss, %		
		T7	T1, T2, T3	T4, T5, T6
At prestressing section	KN	26	19	18
At midspan	KN	22	15	14
At right	KN	18	22	19

instantaneous loss was 18% at right for T7. In the case of lower tendons, the maximum instantaneous loss was 22% at right and the minimum instantaneous loss was 14% at midspan.

3 EXPERIMENTAL STUDY OF 50 M UHPC COMPOSITE BOX GIRDER

The composite box girder was instrumented by embedded FBG optical wires for analyzing post-tensioned tendons which were inserted in lower flanges T2 and T5.

When applied load was increased over 5000 KN, the experiment was stopped due to actuator hydro pump capacity (Tsas-Orgilmaa.M, et al., 2018b). The final step of applied load was 5048.19 KN. The UHPC composite box girder was not occurred to failure. At transfer of

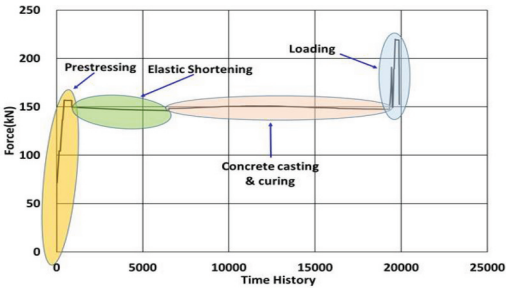


Figure 2. Force versus time history analysis of FBG (Kim, et al., 2018).

prestress force to tendons 184.5 KN jacking force was given for each tendon. The Figure 2 shows force versus time history analysis result. According to this record, 152 KN prestress force was given and decreased to 144 KN in T2 and T5 tendons due to instantaneous prestress loss. After prestress loss the force increased over 150 KN due to the placement of the UHPC deck plate and casting of HSC slab. During the four-point bending test, the force in the prestressing tendon increased to 220 KN and showed little flat values and dropped slightly to 151 KN.

The Figure 3 illustrated applied load versus strain analysis result of embedded FBG optical wires which were inserted in tendons T2 and T5. According to the applied load versus strain analysis the strain values were gradually increased until 2850 microstrain under 5048.19 KN load.

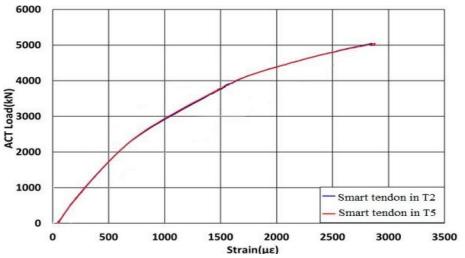


Figure 3. Applied load versus strain of tendon (Kim, et al., 2018).

4 THE NONLINEAR MODEL OF TENDONS

The MIDAS FEA was used to model UHPC composite box girder. Tendons of UHPC composite box girder were modeled as two node bar element. To achieve accurate results, the hexahedron element was used to create a 3D model of UHPC composite box girder. One hexahedron element must contain one bar element. Therefore, the dimension of mesh is 125 mm for tendons and solid UHPC.

The model assumed that the 2-node bar element is perfectly bonded in a solid 3D element. Post-tensioning force is given to both ends of tendons by jacking force. The value of given jacking force for each tendon is 152 KN. The model solved with 40 steps increments, 30 iterations in each increment by Newton Raphson method. The convergence criteria were such as energy norm -0.001. The nonlinearity of tendons was assumed as perfect elastic-plastic model under Von Mises yield criteria to describe the stress-strain relationship.

As a result of FEA solution by MIDAS FEA post-processing was done based on applied load on composite box girder, and strain and stress of tendons. Figure 4 (Tsas-Orgilmaa.M, 2019) shows curves of applied load versus strain/stress of tendons at midspan of girder. According to

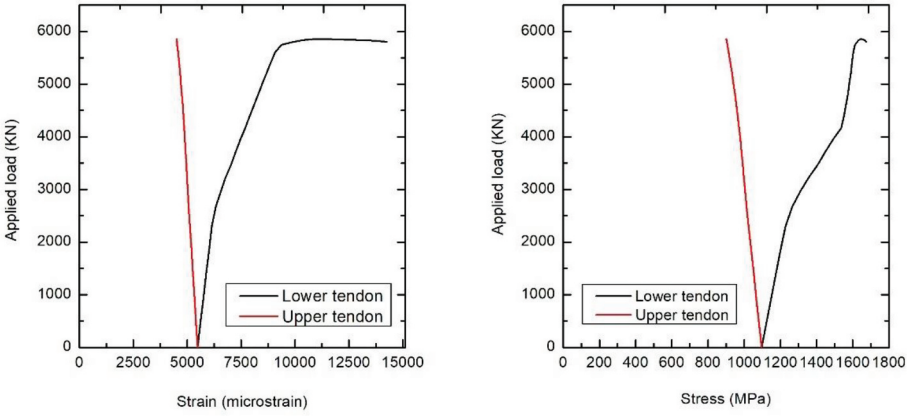


Figure 4. Applied load versus strain/stress of tendons at midspan (Tsas-Orgilmaa.M, 2019).

the applied load versus strain curve, the lower tendons work in tension. The ultimate point of applied load 5855.02 KN and strain reached 11434 microstrain. The failure point of model is determined at the point of 5807.69 KN applied load, strain reached 14238 microstrain.

5 DISCUSSION

Before applying external load to the composite box girder, the prestressing tendons has been tensioned with 152 KN jacking force. Thus each tendon has been previously given 5479 microstrain before the four-point bending test. After applying 5048.19 KN load, the strain of tendons reached 2850 microstrain. The total strain after sum up increase to 8329 microstrain. According to the finite element analysis, the strain of lower tendons under 5048.19 KN load reached 8529 microstrain. The standard deviation of finite element analysis an experimental result is 1.07 and the coefficient of variation is 10.2%. It shows very good result in strain of tendons.

According to the calculation of instantaneous prestress loss the jacking forces were at prestressing section 135.69 KN, at midspan 141.81 KN, at right 131.01 KN for T1, T2, T3 tendons and at prestressing section 136.79 KN, at midspan 143.31 KN, at right 134.65 KN for T4, T5, T6 tendons, respectively.

In the case of experiment, the jacking force was 144 KN. Based on the experiment and calculation of jacking force for a tendon, the difference between the experiment and calculation ranges 2-9% based on Table 4.

6 CONCLUSION

In the frame of the study, the instantaneous prestress loss was determined for 8 tendons of composite box girder, and the post-processing of finite element analysis of composite box girder was done in stress-strain applied load versus strain/stress of tendons and compared to the experimental results. The prestress loss after instantaneous prestress loss was determined from 14% to 26% at prestressing, at midspan, and at right for 8 tendons.

Based on the records of FBG optical wires, the difference of strain between finite element analysis and experimental result was determined as 2-9%. The standard deviation of finite element analysis for an experimental result is 1.07 and the coefficient of variation is 10.2%. It shows very good agreement in strain of tendons.

ACKNOWLEDGEMENT

The experimental part of this study was carried out at the Structural Engineering Laboratory of KICT, and the finite element analysis of 50 m UHPC composite box girder was done at UHPC Laboratory, as part of Ph.D candidate thesis at the Civil Engineering Department, Kumoh National Institute of Technology, Gumi, Korea. I would like to express my gratitude to my supervisor Professor Han Sang Mook and my colleagues who jointly conducted the experimental research.

REFERENCES

KCI, 2012. *Structural Concrete Design Code*, Seoul, Korea: Korea Concrete Institute (KCI), bookstore .kci.or.kr/kci/Book/bookdetail?Pid=103 KCI 9.4.2.1.

Keunhee, C. et al., 2016. Estimation of prestress force distribution in multi-strand system of prestressed concrete structures using field data measured by electromagnetic sensor. *Sensors*, 16, 1317(8), pp. 1–14.

Kim, S. et al., 2018. *Measurement performance of smart strand applied to UHPC girder bridges*. Jeju-do, Korea Concrete Society, pp. 81–82.

Kim, S. T. et al., 2015. A Sensor-type PC strand with an embedded FBG sensor for monitoring prestress forces. *Sensors*, Volume 15, pp. 1060–1070.

Tsas-Orgilmaa. M, 2019. *Thesis for a doctor of philosophy Flexural behavior of 50 m span UHPC composite box girder*, Gumi, Korea: Kumoh National Institute of Technology.

Tsas-Orgilmaa. M, Han, S. M., Kim, D. H. & Jeong, M. S., 2018b. *Flexural behavior of ultra high performance fiber reinforced concrete 50m composite box girder*. Fuzhou, China, RILEM publications, pp. 801–814.

Bridge Maintenance, Safety, Management, Digitalization and Sustainability – Jensen, Frangopol & Schmidt (eds)
© 2024 The Author(s), ISBN 978-1-032-77040-6
Open Access: www.taylorfrancis.com, CC BY-NC-ND 4.0 license

Finite element analysis of over-height vehicle collisions on prestressed girder bridges

A. Samadzad, S. Cathey, M. Whelan, N. Braxtan & S. Chen
University of North Carolina at Charlotte, Charlotte, N.C., U.S.A

ABSTRACT: The accidental collision of over-height vehicles, especially construction equipment hauled on trailers and dump trucks with unintentionally raised beds, with bridge girders is an event that often occurs multiple times a year in many states within the U.S. The evaluation of bridges subjected to over-height impacts is typically informed by visual inspection, however some damage mechanisms having significant effects on the strength and durability of prestressed concrete girders may not be visually apparent and therefore can be difficult to assess. Furthermore, the damages resulting from an over-height vehicle collision, and subsequent repair and replacement implications, are dependent on the nature and speed of the offending vehicle and the characteristics of the bridge subjected to the impact force. In this paper, a framework for high fidelity finite element analysis of over-height vehicle collisions with prestressed concrete girder bridges is developed to provide a physics-based approach for predicting the damages from over-height vehicle impacts and the influence of the damage on the residual capacity. When coupled with field observations, high fidelity finite element analysis can provide a means for improving post-impact damage assessments and avoiding unnecessary repair and replacement actions while mitigating potential safety risks. The paper details the modeling strategies and constitutive models adopted to create finite element models of conventional prestressed concrete girder bridges, demonstrates the automatic generation of finite element models from key parameters of bridge plans, and presents simulation results for a representative bridge to examine the influence of over-height vehicle characteristics and speed on the predicted extent of damage.

1 INTRODUCTION

According to a recent analysis of a regional database of bridge failures in the United States, collisions are the second most common cause of bridge failures, with the failure typically occurring as a partial collapse (Cook et al. 2015). However, the majority of collisions of over-height vehicles and carried freight with bridges result in minor or moderate damage that can be repaired (Feldman et al. 1996), although often at significant cost and with potentially lengthy disruption to service. In 2020 alone, 14,630 vehicle collisions with bridges were reported throughout the United States (National Center for Statistics and Analysis 2022). Statistical analysis of a large database of bridge collision incidents in New York State indicated that over-height vehicle collisions are significantly more prevalent than vehicle collisions with abutments or piers. Furthermore, the majority of over-height collisions were attributed to trucks and trailers carrying construction equipment, materials, and other objects (Agrawal et al. 2011).

Experimental insight on the behavior of prestressed concrete girder bridges under lateral impacts has been extremely limited. The few exceptions include laboratory testing of model-scale partial width bridge spans to investigate the effect of intermediate diaphragm type and location (Abendroth et al. 1995) and a single experimental test of a full-scale girder subjected to lateral impact from a large concrete mass carried by a cart (Jing et al. 2016). The latter experiment was conducted with an independent girder and therefore does not reflect the contributions that end diaphragms, intermediate diaphragms, additional girders, and a complete deck would provide in an actual bridge, while the former experiment relied on quasistatic loading as a substitute to

DOI: 10.1201/9781003483755-211

impact loading. Due to technical and logistical challenges, risks, and significant costs associated with impact testing of full-scale bridge girders, finite element (FE) analysis has been the predominant tool for investigating the behavior of bridges under impact loads and understanding the effect of design features and impactor characteristics on the resulting severity of damage.

A significant portion of earlier research on the response of prestressed concrete girder bridges to over-height collisions centered on the role of intermediate diaphragms and effect of the diaphragm design on the lateral resistance of the bridge (Abendroth et al. 1995, Qiao et al. 2008). However, FE analysis that served as the basis for this early research was hindered by the technological capabilities of the time as reflected by coarse meshes, simplified constitutive models, idealized boundary conditions, absence of strain-rate effects, neglect of bent diaphragms and other bridge components that may contribute to the girder resistance, and simplified modeling of the impact through prescribed force time histories rather than explicitly modeling the impacting object with a contact model. A critical review prepared subsequent to much of this early research classified the effect of diaphragms during lateral impacts as "not fully addressed" and recommended that high-fidelity modeling be pursued to overcome the limitations of imposed by the computational simplifications (Cai et al. 2007).

Recently, the investigation of over-height vehicle impacts to bridge girders has experienced renewed interest with the support of high-fidelity FE analysis with advanced constitutive models. Xu et al. (2013) developed FE models for container, tipper, and tank trucks and simulated the collision of these vehicles with a prestressed concrete girder bridge model to investigate damage mechanisms and impact force characteristics as well as to develop a simplified model to predict the collision force time history. Oppong et al. (2021a) conducted parametric analysis of the collision of several construction objects as well as a tractor-semitrailer with reinforced concrete bridge girders to investigate variations in impact forces and girder damage. Simplified equations were developed to predict the impact force characteristics for concrete pipe and steel tank collisions. This work was extended to reinforced concrete bridge girders constructed with high-strength concrete and ultrahigh-performance concrete (Oppong et al. 2021b). The numerical simulations suggest that the mean impact force is greater for collisions with ultrahigh-performance concrete girders, but the lateral displacement and resulting damage is reduced.

2 AUTOMATED MODEL GENERATION AND MODELING APPROACH

This paper discusses the development of high-fidelity FE models of complete bridge superstructures to investigate the influence of bridge and impacting object characteristics on the severity of damage to prestressed concrete girders. LS-DYNA was selected by the authors as the FE analysis software package for the research and all simulations disclosed in this paper are conducted using the explicit time integration scheme.

2.1 *Automated model generation*

The construction of large, detailed FE models can be a time-consuming exercise and ensuring consistency in the modeling technique and assignment of model parameters is extremely challenging when a set of FE models are created manually. To address this challenge and to facilitate rapid development of parametric models, the authors have written an extensive library of MATLAB scripts to automatically prepare LS-DYNA keyword files using a defined structure of geometric and material properties that can be extracted from bridge plans. The library is capable of automatically generating keyword files for highly detailed FE models of prestressed concrete girder bridges, implementing the modeling approach and staged analysis sequence described in the subsequent sections, with no manual intervention or manipulation of the keyword files prior to the analysis.

2.2 *Description of finite element modeling approach*

The concrete in the girders is modeled using constant stress hexahedral solid elements with the Continuous Surface Cap Model (CSCM) used for constitutive modeling of the nonlinear, inelastic, and strain-rate dependent behavior of the concrete. CSCM has been found to provide realistic predictions for the behavior of reinforced concrete members subjected to impact loading (Adhikary

et al. 2005, Saini and Shafei, 2019). Automatic parameter generation for this constitutive model is available in LS-DYNA requiring only the mass density, maximum aggregate size, and unconfined compressive strength of the concrete. A database of 2D meshes for standard girder cross sections has been developed by the authors using HyperMesh to ensure high element quality while constraining the minimum edge size to prevent a small number of elements from establishing an unnecessarily small time step. These 2D meshes are then used to create the 3D meshes for the girders by replicating the node set and connectivity at uniform increments along the length of each girder. Prestressing strands are modeled using truss elements with a plastic kinematic material model implemented with yielding and isotropic hardening. Mild reinforcement is similarly modeled as a plastic kinematic material, although Hughes-Liu beam elements are used to ensure stability of shear reinforcement that is not fully embedded in concrete prior to the introduction of the deck. Both the prestressing strand and the mild reinforcement include strain-rate effects using the Cowper and Symonds model. The constrained beam in solid constraint is used to couple the strands and reinforcement to the concrete in the model. Sole plates at the bearing surfaces are modeled with shell elements assigned to shared nodes with the concrete elements in the girder. This effectively permits the ability to prescribe both translational and rotational boundary conditions using a single node at the bearing location.

The reinforced concrete deck is modeled with constant stress hexahedral solid elements. Shared nodes are used to couple the girders to the deck. End and continuous bent diaphragms are also modeled with constant stress hexahedral solid elements. Given the difficulty in generating a mesh for the bent diaphragms that would share nodes with the girder elements without introducing small or highly distorted elements, tied nodes to surface contact was used to couple the bent diaphragms to the girders. A similar approach is used to model cast-in-place reinforced concrete diaphragms. For simplicity, the authors adopt an elastic material model for the deck and bent diaphragms under an assumption that the bridge deck and bent diaphragms will experience little to no damage from lateral impact to the girder. For bridges with steel intermediate diaphragms, the channel member and connecting plates are modeled with shell elements. For bridges with X-brace with strut intermediate diaphragms, Hughes-Liu beam elements are used to model the individual members of each diaphragm. Steel intermediate diaphragms are modeled with the plastic kinematic material model and include yielding, isotropic hardening, and strain-rate dependency.

2.3 *Description of analysis sequence*

To accurately initialize the internal state of stress and initial camber in the complete bridge model, a staged development of the FE models that replicates aspects of the construction sequence is required. Specifically, prestressed concrete girder bridges are constructed of girders that are prestressed prior to placement at the site and then the diaphragms, deck, and remaining bridge components are placed or cast. Consequently, it is necessary to introduce the effects of prestressing in a model that initially consists of just the girders so that the bridge deck does not act compositely with the girders during the introduction of prestressing, as the contribution of the deck would significantly affect the stress, neutral axis location, and camber in the model. A schematic representation of the staged development of the FE model is presented in Figure 1. The staged initialization of the full bridge model is accomplished by using the full restart capability of LS-DYNA. Advantageously, the full restart feature only requires initialization of the bridge model once. Multiple impact analyses can be performed on the initialized model by consistently restarting from the d3dump file created at the conclusion of Step 2.

The introduction of prestressing force in this study was based on applying an equivalent temperature-induced shrinkage in the elements representing the prestressing strands. This general approach was detailed in Jiang and Chorzepa (2015), however the equation provided for the temperature change in this source does not account for elastic shortening. When elastic shortening is included in the strain compatibility, the temperature change, ΔT, associated with a desired prestressing force, f, in the model is:

$$\Delta T = \frac{f}{\alpha}\left(\frac{1}{E_s A_s} + \frac{1}{E_c A_c} + \frac{e^2}{E_c I_c}\right) \tag{1}$$

where α is the temperature coefficient, E_s is the modulus of elasticity for the strands, E_c is the modulus of elasticity for the concrete, A_s is the cross sectional area of the strands, A_s is the cross sectional area of the concrete, I_c is the moment of inertia of the concrete, and e is the eccentricity of the strands. The desired prestressing force introduced into the model can account for typical prestress losses, which can be estimated specifically for the age of the structure at the time of the simulated impact. The application of the prestress in the model is applied simultaneously with the introduction of body forces due to gravitational acceleration during a transient analysis with explicit time integration. This analysis extends over a multiple of the natural period of the girder associated with the fundamental mode for major axis flexure. Mass proportional damping is applied at this stage to suppress resonance of the vibrational modes during the application of the static loads. During the introduction of the prestress force, idealized boundary conditions are assigned at the bearing locations.

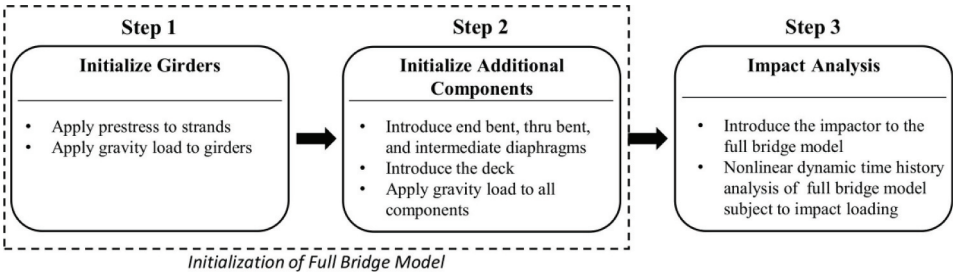


Figure 1. Staged development and analysis of prestressed concrete girder bridge models.

Following the initialization of the individual girders, the remaining bridge components are introduced to the model. During this second step of the initialization of the bridge model, the idealized boundary conditions are replaced with linear elastic translational and rotational springs to approximate the behavior of the elastomeric bearings. The springs are introduced in LS-DYNA using the linear elastic discrete beam material model and the spring stiffnesses are calculated for compressive, shear, flexural, and torsional behavior of the steel-reinforced elastomeric bearings using AASHTO-based guidance outlined in Whelan & Janoyan (2011). The second step of the model initialization introduces the body forces in the added components due to gravitation acceleration as well as establishes equilibrium of the model with the elastic boundary conditions. At the conclusion of this step, mass proportional damping is removed from the model, the impacting object and associated contact model are introduced, and transient analysis is conducted to simulate the damage to the bridge resulting from the collision.

2.4 *Details of bridge span used as a case study*

As detailed above, the developed library of scripts automates the development of high-fidelity models of prestressed concrete bridges, which will ultimately facilitate parametric analysis of the effect of bridge and impacting object characteristics on the severity of damage to prestressed concrete girder bridges. In this paper, a case study of a FE of a single bridge span created by the developed library of scripts is presented and preliminary results from impact simulations are discussed. The bridge span modeled in this paper is a representation of an actual design from the bridge inventory of the State of North Carolina with all geometric and material properties sourced from bridge plans.

The bridge span consists of six AASHTO Type IV girders spaced 2.46 m on-center and spanning 23.72 m. The span has a 10° skew, a crown point at the center of the cross section with symmetric 2% slope on each side of the crown point, and an out-to-out width of 14.5 m. The reinforced concrete deck is 210 mm thick. Each girder is prestressed with a total of 26 low relaxation grade 1860 (270) strands of 15.24 mm diameter. All strands in the girders are straight and bonded over the full length of the span. The compressive strength of the concrete in the girders is 41.4 MPa and the maximum aggregate size is 8 mm. The girders include additional longitudinal reinforcing steel at the ends and near the connection to intermediate diaphragms as well as shear

reinforcement along the span. The girders are supported by rectangular steel reinforced elastomeric bearings with one bearing being designed as an expansion bearing to accommodate thermal expansion. Intermediate diaphragms comprised of steel channels bolted to angle connector plates are present at the midspan of the girders. The span includes reinforced concrete partial depth end bent diaphragms and full depth continuous bent diaphragms. The mass density of all concrete materials in the model was taken as 2,400 kg/m^3, while the mass density of all steel materials in the model was taken as 8,000 kg/m^3. An edge size of 50 mm was used to develop the mesh for the FE model of this bridge span.

Figure 2 presents the bridge model as well as the vertical displacement in the model after the staged initialization. The positive displacement at the midspan of the girder predicted by the FE analysis was verified through comparison with the calculated camber as well as estimates provided on the bridge plans. It is noted that the negative displacements throughout the bridge deck are generated due to the introduction of the deck to the model after the introduction of prestressing to the girders, consistent with the construction sequence. The downward displacement reflects the deflection resulting from the self-weight of the deck and intermediate diaphragms.

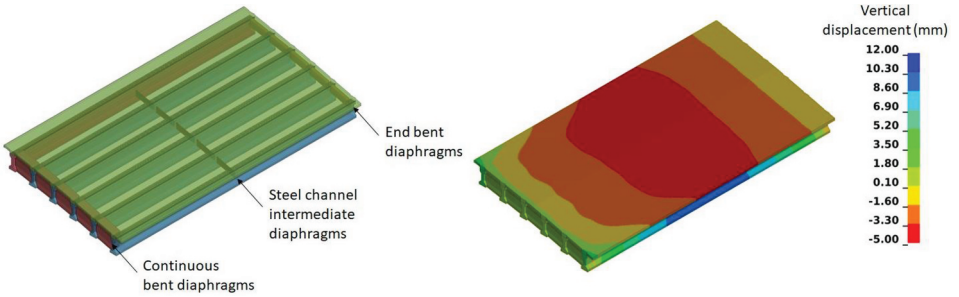


Figure 2. FE model of prestressed concrete bridge: a) rendering of components in model; b) vertical displacement after staged initialization of the model.

3 IMPACT SIMULATIONS

A recently published study utilized high-fidelity FE analysis to examine the variation in impact forces and develop simplified equations to predict the peak and mean force of the impactor (Oppong et al. 2021a). In the authors' opinion, this study established a benchmark for high fidelity modeling of overheight collisions to bridge girders. However, the study was limited to reinforced concrete girders and, furthermore, the database of simulations used to develop the simplified equations was based on a single span length. Prior to conducting the current study, the authors replicated the results in the referenced paper to ensure that the modeling approach, assumptions, and parameters used were consistent with those used by the other authors. In the current study, the authors adopt the geometry and modeling strategies for the steel tank and concrete pipe impacting objects detailed in this referenced publication. The steel tank model is a closed ended hollow cylinder with an outer diameter of 2.19 m, a wall thickness of 15 mm, and a length of 2.29 m that is modeled with shell elements. The same plastic kinematic material model developed for the mild reinforcement in the bridge was assigned to the steel tank. The concrete pipe model is an open ended hollow cylinder with a wall thickness of 178 mm and the same outside diameter and length as the steel tank. Solid elements were used to model the concrete pipe with the CSCM constitutive model. Erosion settings for the concrete of the impactor and the girders were established such that erosion occurs when the damage exceeds 0.99 and the maximum principal strain exceeds 0.1. The automatic surface-to-surface contact card was used to model contact between the respective impactor and girder.

A set of simulations were performed with each impactor model to preliminarily investigate the variation in the impact force characteristics and damage to the girder with the impact location and impactor velocity. For each impactor, nonlinear transient analysis was conducted for impacts occurring at the quarter point, third point, and midspan of the bridge. The midspan location is

coincident with the location of the intermediate diaphragm. For each impact location, simulations were performed for impactor velocities of 72.4 km/h, 88.5 km/h, 104.6 km/h, and 120.7 km/h. All simulations were performed for a termination time of 300 ms to ensure that all significant dynamics were completed by the end of the analysis. Time histories for the lateral displacements at the respective impact location were used to confirm this. For all cases investigated, the top of the tank or pipe was located 330 mm above the base of the bottom flange of the girder. The total mass of the steel tank model is 2795 kg and the estimated contact area associated with the impact to the bottom flange of the girder is 2622 cm^2. The total mass of the concrete pipe model is 6171 kg and the estimated contact area associated with the impact to the bottom flange of the girder is 1690 cm^2. The output time interval for the contact force time histories was $1x10^{-5}$ s.

The typical variation in impact force time history across the impactor velocities is presented in Figure 3. The duration of the time histories plotted in this figure is truncated to 6 ms, as this is the time window over which the magnitudes of the impact forces are significant. The FE results presented in this figure were obtained with the steel tank model, but similar observations were made with the simulation data obtained with the concrete pipe model. As expected, the peak force and impulse increases as the velocity of the impactor increases. Figure 4 presents impact force time histories for collisions of the concrete pipe with a velocity of 104.6 km/h at the three different locations in the span. The results suggest that neither the peak force nor the impulse are sensitive to the location of the impact in the bridge span. Similar results were obtained for the other velocities as well as for the simulations performed with the steel tank model. The duration of the impact is also approximately twice as long as that presented in Oppong et al. (2021a). The longer contact duration may be the result of a more flexible girder, which is the result of the significantly longer span length of the bridge modeled in the current paper as well as the complete modeling of the superstructure.

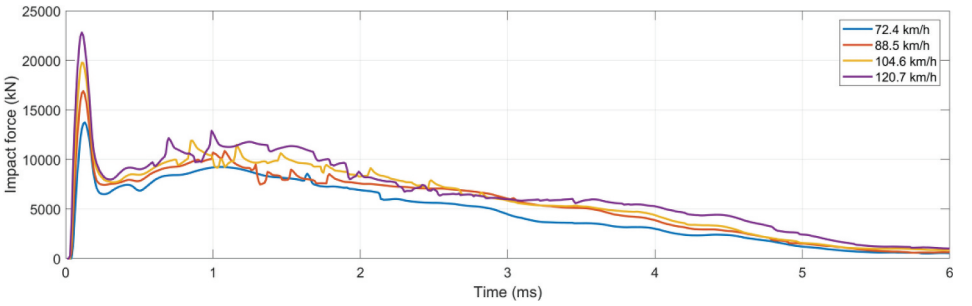


Figure 3. Impact force time histories for steel tank collision at midspan of the bridge.

As previously mentioned, Oppong et al. 2021a developed a set of prediction equations for the peak and mean impact forces developed by collisions of steel tanks and concrete pipes based on parametric analysis conducted with a reinforced concrete girder model. In this referenced paper, the mean impact force was defined as the impulse divided by the duration of the impact. In the current study, the peak impact forces were extracted from the force time histories and the mean impact forces were calculated by numerical integration. Figure 5 presents a comparison between the results from the 24 FE simulations and the predictions developed with the simplified equations. These preliminary results suggest that the prediction equation significantly overpredicts the peak forces from the steel tank when extended to this case study. However, the peak impact forces developed for the concrete pipe exhibit reasonably strong agreement with the prediction equation. Conversely, the mean impact forces, or impulse, developed by the FE simulations with the steel tank agree well with the prediction equation, while the mean impact forces from the simulations with the concrete pipe are significantly lower than the anticipated by the prediction equation.

Figure 6 presents the condition of the exterior girder at the end of the simulation for the four different velocities of the steel tank collision at the quarter point and the midspan. The fringe pattern depicted in the figure and indicated in the legend is the maximum principal strain. Some

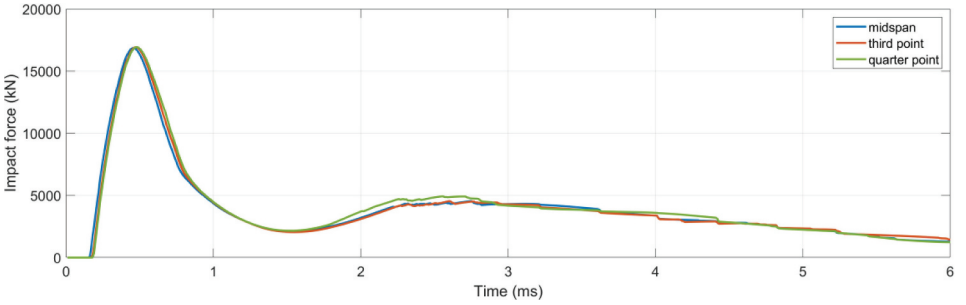


Figure 4. Impact force time histories for concrete pipe collisions with velocity of 104.6 km/h.

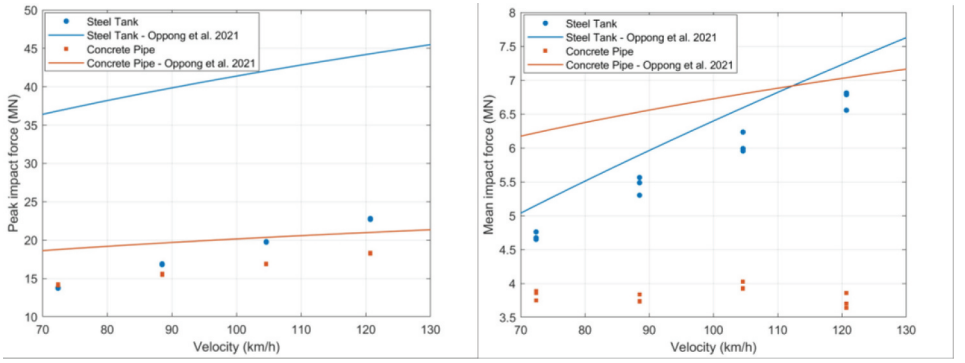


Figure 5. Comparison between FE results from high-fidelity bridge model and prediction equations: a) peak impact force; b) mean impact force.

erosion of elements can be observed for the greater levels of damage severity. The simulations predict damage in the form of spalling and loss of side cover at the contact area, lateral and torsional deformation of the impacted girder, localized loss of prestress and a significant crack extending up to the top of the web of the girder. In general, the damage patterns are consistent with expectations based on documented field observations (Feldman et al. 1996). While some differences are apparent in the damage produced at different impact locations, the FE results suggest that the velocity of the impactor has a more significant influence on the severity of damage than the impact location. In this limited preliminary study, the authors found that the presence of the steel intermediate diaphragm reduced the extent of lateral displacement for impacts at the midspan. Lastly, it is noted that the degree of damage apparent in the FE simulations is significant, however Oppong et al. (2021a) pointed out that the steel tank and concrete pipe impactor models generated significantly greater impact forces and greater damage than their other models of construction objects or the tractor semi-trailer model. Future extension of this work will expand the simulation database to include additional impactors as well as additional bridge models.

4 CONCLUSION

This paper presented a high-fidelity approach to modeling prestressed concrete girder bridges and simulating the collision of vehicles and construction objects. Preliminary results obtained from a set of 24 simulations performed with two different impactors, three different impact locations, and four different speeds suggest that the characteristics of the impact force time history are not affected by the location of the impact. Comparison of the impact force time histories with a set of prediction equations from the literature developed with a reinforced concrete beam model yielded mixed results. Based on this limited preliminary investigation, the severity of damage to the girder appears to be affected more significantly by the velocity of the impactor

than the location of the impact. Early evidence from the study indicates that steel intermediate diaphragms result in reduced lateral deformation for impacts occurring near the diaphragm.



Figure 6. Damage pattern across exterior girder for steel tank with velocity of 72.4 km/h, 88.5 km/h, 104.6 km/h, and 120.7 km/h: (a) impact at quarter point of span; (b) impact at midspan.

REFERENCES

Abendroth, R., Klaiber, F., & Shafer, M. 1995. Diaphragm effectiveness in prestressed-concrete girder bridges. *Journal of Structural Engineering* 121(9): 1362–1369.

Adhikary, S., Li, B., & Fujikake, K. 2015. Low Velocity Impact Response of Reinforced Concrete Beams: Experimental and Numerical Investigation. *International Journal of Protective Structures*, 6 (1): 81–111. SAGE Publications. https://doi.org/10.1260/2041-4196.6.1.81.

Agrawal, A., Xu, X. & Chen, Z. 2011. *Bridge-vehicle impact assessment*. Final report number C-07-10, University Transportation Research Center, New York State Department of Transportation (UTRC/NYSDOT).

Cai, C., Araujo, M., Chandolu, A., Avent, R., & Alaywan, W. 2007. Diaphragm effects of prestressed concrete girder bridges: review and discussion. *Practice Periodical on Structural Design and Construction* 12(3): 161–167.

Cook, W., Barr, P., & Halling, M. 2015. Bridge failure rate. *Journal of Performance of Constructed Facilities* 29(3): 04014080–1.

Feldman, L., Jirsa, J., Fowler, D., & Carrasquillo, R. 1996. *Current Practice in the Repair of Prestressed Bridge Girders*. Center for Transportation Research, The University of Texas at Austin, FHWA/TX-96/ 1370-1.

Jiang, H. & Chorzepa. 2015. An effective numerical simulation methodology to predict the impact response of pre-stressed concrete members. *Engineering Failure Analysis* 55: 63–78.

Jing, Y., Ma, Z., & Clarke, D. 2016. Full-scale lateral impact testing of prestressed concrete girder. *Structural Concrete*. 17(6): 947–958.

National Center for Statistics and Analysis. 2022. *Traffic Safety Facts 2020: A Compilation of Motor Vehicle Crash Data*. 242. National Highway Traffic Safety Administration.

Oppong, K., Saini, D. & Shafei, B. 2021a. Characterization of impact-induced forces and damage to bridge superstructures due to over-height collision. *Engineering Structures* 236: 112014

Oppong, K., Saini, D. & Shafei, B. 2021b. Ultrahigh-performance concrete for improving impact resistance of bridge superstructures to overheight collision. *Journal of Bridge Engineering* 26(9): 04021060

Qiao, P., Yang, M., & McLean, D. 2008. *Effect of Intermediate Diaphragms to Prestressed Concrete Bridge Girders in Over-Height Truck Impacts*. Washington State Transportation Center (TRAC).

Saini, D. & Shafei, B. 2019. Concrete constitutive models for low velocity impact simulations. *International Journal of Impact Engineering* 132: 103329.

Whelan, M. & Janoyan, K. 2012. Assessment of simplified linear dynamic analysis of a multispan skew bridge on steel-reinforced elastomeric bearings. *Journal of Bridge Engineering* 17(1): 151–160.

Xu, L., Lu, X., Guan, H., & Zhang, Y. 2013. Finite-element and simplified models for collision simulation between overheight trucks and bridge superstructures. *Journal of Bridge Engineering* 18(11): 1140–1151.

Bridge Maintenance, Safety, Management, Digitalization and Sustainability – Jensen, Frangopol & Schmidt (eds)
© 2024 The Author(s), ISBN 978-1-032-77040-6
Open Access: www.taylorfrancis.com, CC BY-NC-ND 4.0 license

Assessment of internal condition of a post-tensioned tie girder during construction

U. Attanayake, H. Amunugama, K. Basnayake & H. Aktan
Center for Structural Durability, Department of Civil and Construction Engineering, Western Michigan University, Kalamazoo, MI, USA

E. Niederleithinger
Division 8.2 NDT Methods for Civil Engineering, Bundesanstalt für Materialforschung und -prüfung (BAM), Berlin, Germany

ABSTRACT: A 265 ft (80.8 m) long post-tensioned concrete tie girder was being fabricated as a cast-in-place girder at an off-site location. The 3.25 ft (1.0 m) wide and 4 ft (1.2 m) deep section included 12 empty post-tensioning ducts and a congested reinforcement cage. A lack of workability was noticed during the placement of concrete delivered by one of the trucks. This necessitated a nondestructive investigation of the girder interior for indications of insufficient consolidation. Ultrasonic tomography was selected as a suitable technique. Wave signal propagation through the reinforced concrete section (with and without ducts) was simulated to evaluate the likelihood of detecting backwall reflections. Backwall reflection detection was required for the calibration of phase values for the classification of reflector types (i.e., the internal details and voids). The simulation showed the likelihood of visualizing only the empty ducts and longitudinal reinforcement located near the scanned surface with very light reflections from the empty ducts at the 2nd column located at a distance of 19.5 in. (495.3 mm) from the vertical surface. Based on the simulation results and the understating of girder details, data collection protocols were developed and executed. This paper describes structural details of the post-tensioned concrete tie girder, simulation results, data collection plan, findings, and the capabilities and limitations of the state-of-the-art technology for visualizing the interior of concrete sections with complicated details.

1 INTRODUCTION

An unbraced network tied arch bridge was constructed in Detroit, Michigan, as a replacement of the 2nd Avenue Bridge over Interstate (I) 94 freeway. This 265 ft (80.8 m) long and 96.5 ft (29.4 m) wide bridge has a skew of eighteen degrees (18°) making it a unique structure among the network arch bridges in the U.S. Figure 1 shows the structural components of the bridge. The structural assembly consists of two trapezoidal steel arch ribs connected at each end to post-tensioned concrete tie girders through the knuckles, post-tensioned concrete end diaphragms, steel floorbeams, lateral bracings, floorbeam diaphragm, and hangers. The bridge structure was assembled in a staging area near the bridge site. Subsequently, the assembled structure was moved into alignment by self-propelled modular transporters (SPMTs). Following the SPMT move and placement of the assembled structure on permanent bearings, the remaining construction activities were completed.

The east tie girder was fabricated on Thursday January 13, 2022, using a concrete mix with a maximum aggregate size of ¾ in. (19 mm). The concrete delivered in Truck #3 indicated a lack of workability during placement. Visula and photographic evidence of poor concrete workability was documented. In response, a nondestructive testing was initiated to investigate girder interior for indications of insufficient consolidation, if any. The placement of concrete delivered by Truck #3 extends from a location in between floorbeams L and M to floorbeam Q. The Truck #3

DOI: 10.1201/9781003483755-212

concrete filled the entire girder width and about ⅔rd of the girder height from the bottom (i.e. about 2.7 ft; 0.823 m). The floorbeam spacing is 14 ft (4.2 m), and the length of the specific girder segment is about 50 ft (15.2 m). The tie girder reinforcement detail is shown in Figure 2.

Since the deck and the sacrificial nose had not been completed at the time of tie girder condition evaluation, the girder top surface was roughened with exposed slab ties, as shown in Figure 3. The girder surface was accessible from all four sides for measurements, except at the floorbeam connections. The typical section depth and width of the completed girder is 4 ft (1.2 m) and 3.25 ft (1.0 m), as shown in Figure 3. The cross-sections T-T and V-V shown in Figure 3 represent tie girder details between and at the floorbeams, respectively. The plastic corrugated post-tensioning ducts in the tie girder have an internal diameter of 3.93 in. (100 mm).

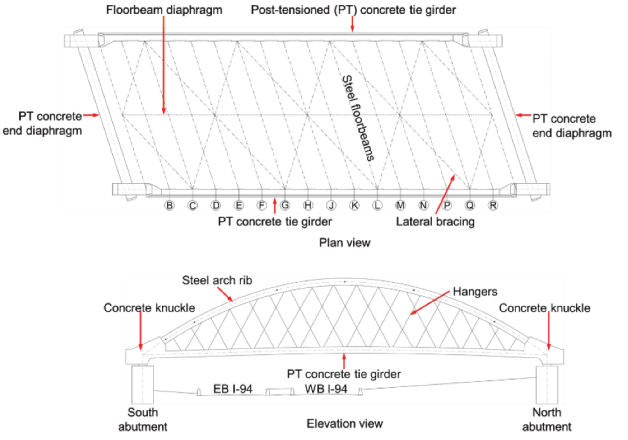


Figure 1. Major components of bridge superstructure.

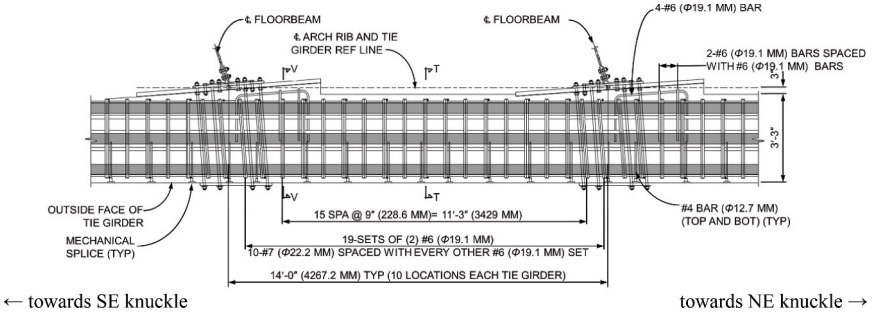
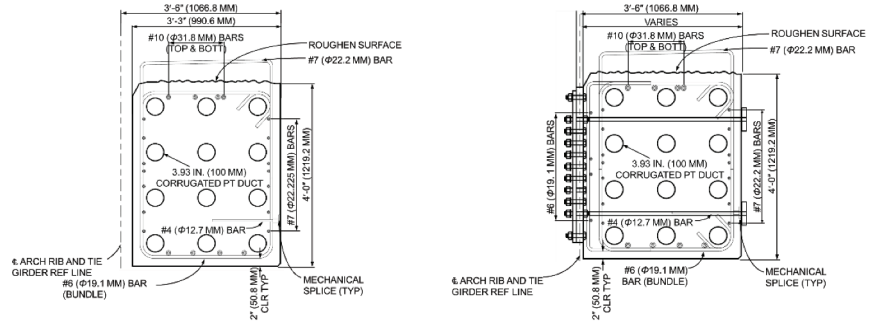


Figure 2. Typical tie girder reinforcement detail (plan view).



Section T-T: Section in between floor beams

Section V-V: Section at the floor beam

Figure 3. East tie girder sections T-T and V-V as of 01/26/2022 (from SE knuckle towards NE knuckle).

2 TECHNOLOGY FOR VISUALIZING THE INTERIOR OF THE TIE GIRDER

A group of authorities representing the bridge owner, contractor, designer, consultants, and nondestructive testing experts deliberated on available technologies to visualize the internal condition of the tie girder segment and detect any potential voids or lack of consolidation with a dense reinforcement cage and 12 empty ducts. The consensus was to try the A1040 MIRA (an ultrasonic pulse-echo device designed for imaging of the internal structure of concrete) to visualize the girder's interior. The device has an array of 48 dry-point-contact shear wave transducers (12 columns and 4 rows). Shear wave transducers are favorable due to lower signal attenuation and backscattering compared to longitudinal wave transducers. The data collected with different transmitter-receiver distances (aperture) in a single position results in better resolution and image accuracy. The principle approach for identifying and locating a defect is to inspect the reflected signal amplitude through the device data display. The data collected on a grid can be postprocessed using a special software to generate C and D scans in addition to A and B scans (Basnayake et al. 2021).

The device functionality was evaluated by calibrating and collecting data from two reference specimens. Also, the raw data (signals) were evaluated using a specialized software to verify the proper functioning of each channel and the equipment.

3 PLANNING FOR DATA COLLECTION AND ANALYSIS

3.1 *Simulations to evaluate data collection procedure*

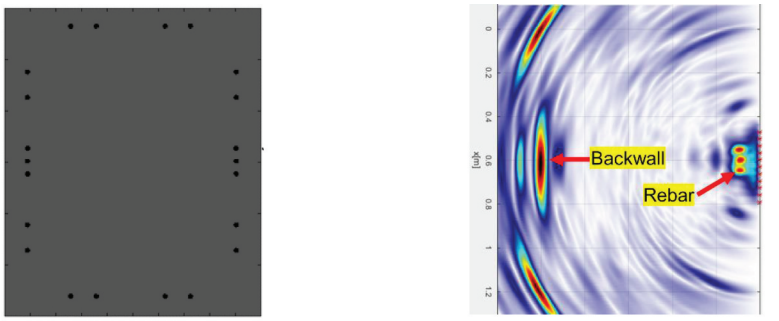
Prior to data collection, the measurement process was numerically simulated to verify the ultrasonic wave propagation and wave rebound within a concrete specimen. The measurement refinement and direction was decided based on the simulations of the concrete volume with obstacles. Since the quality of concrete in this model was assumed satisfactory, the obstacles impacting wave propagation in this case included rebars and empty post-tensioning ducts.

Signal propagation was simulated through a 3.25 ft (1.0 m) wide and 4 ft (1.2 m) deep reinforced concrete section (with and without ducts) to evaluate the likelihood of detecting backwall reflections. Backwall reflection detection is required for the calibration of phase values for the classification of reflector types (i.e., the internal details and voids). The simulation emulates a single MIRA scan on the right side vertical surface and at a depth of 23.6 in. (600 mm) from the top surface. The unit was placed with the excitation direction parallel to the ducts. The following observations were made from the simulation of three different cases:

(1) Reinforced concrete section: As shown in Figure 4(a), strong reflections are clearly visible from the longitudinal reinforcement located closer to the right-side vertical surface and directly in front of the unit. Also, a strong backwall reflection is visible at a distance of 3.25 ft (1.0 m) from the right-side vertical surface of the reinforced concrete section.
(2) Reinforced concrete section with 12 empty ducts: As shown in Figure 4(b), out of the 12 empty ducts, only the ducts and longitudinal reinforcement located near the scanned surface are visible. Very light reflections appear from the 2nd column of the empty ducts, which are located at a depth of 19.5 in. (495.3 mm) from the scanned surface.
(3) Reinforced concrete section with 12 grouted ducts containing post-tensioning strands: As shown in Figure 4(c), simulation shows backwall reflection only when the ducts are grouted. Light reflections appear from the grouted ducts closer to the scanned surface. Similar to the two previous simulations, longitudinal reinforcement located closer to the scanned surface shows strong reflections.

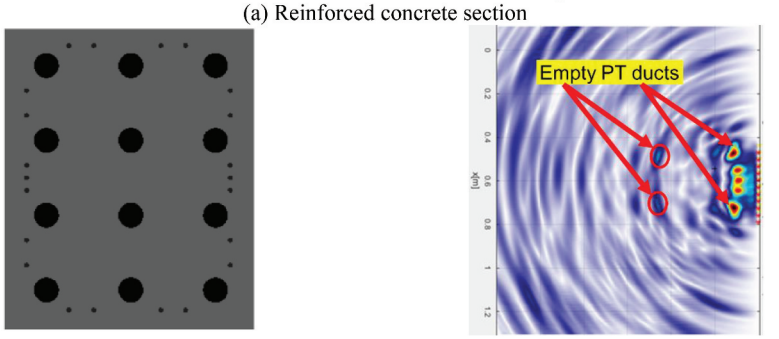
3.2 *Evaluation of data analysis procedure*

As shown in Figure 4(b), strong reflections were expected from longitudinal reinforcement and empty ducts located nearest the scanned surface when the unit was placed with the excitation direction parallel to the ducts. Weak reflections were observed from the second column of



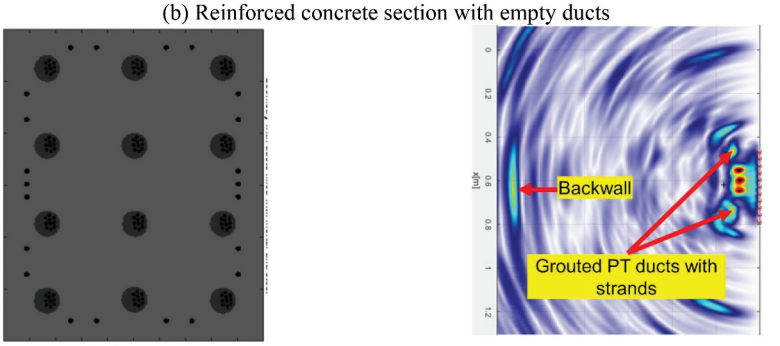
Section detail Signal reflections

(a) Reinforced concrete section



Section details Signal reflections

(b) Reinforced concrete section with empty ducts



Section details Signal reflections

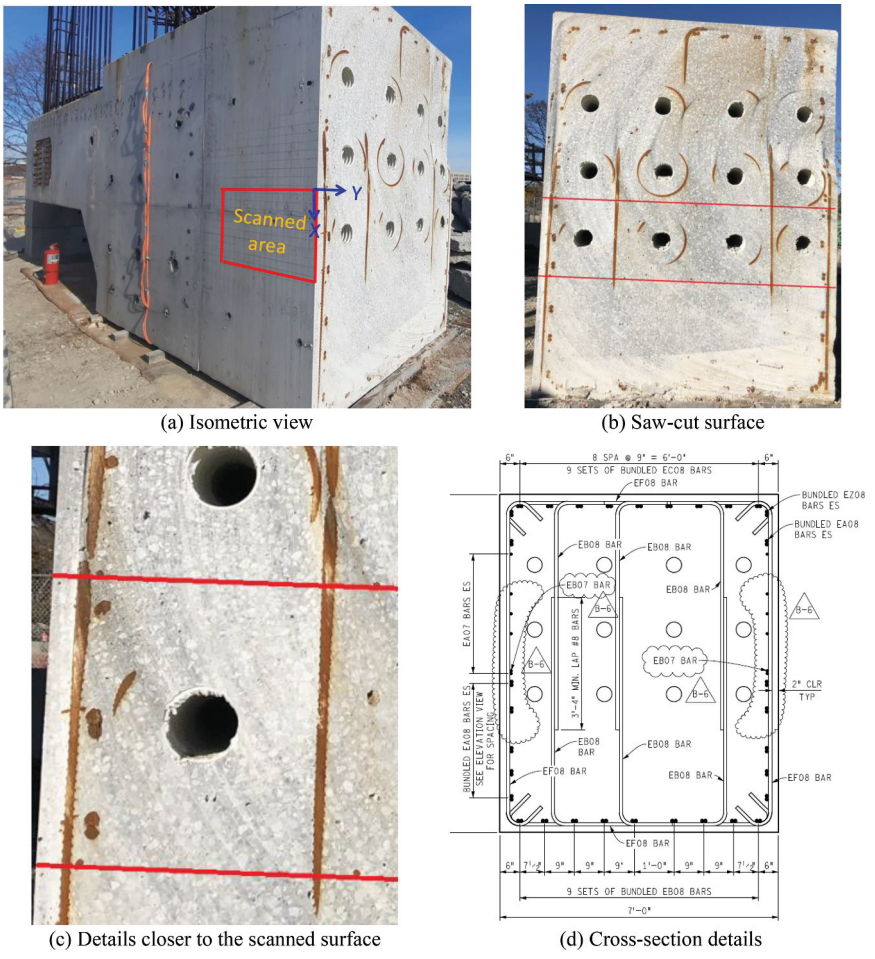
(c)Reinforced concrete section with grouted ducts containing post-tensioning strands

Figure 4. Simulation results showing limitations of the depth of observation.

empty ducts that were located at a depth of 19.5 in. (495.3 mm) from the vertical surface. Since the simulation models did not include voids or anomalies, no other reflections were observed.

To further validate the simulation observations, measurements were performed on the mock-up knuckle. The mock-up knuckle was fabricated to evaluate the possible challenges in meeting the required construction quality. The details of the knuckle were known, and the concrete condition was visible over the saw cut surface. Figure 5 shows an isometric view, saw-cut surface, details closer to the scanned surface, and cross-section details of the lower portion of the knuckle.

Figures 6(a) and (b) show the reconstructed data at sections in between the stirrups and at a stirrup. As shown in Figure 6(a) (i) and (ii), the reflections are evident from three longitudinal reinforcement bundles and the duct nearest the scanned surface. The three reinforcement bundles include two bundles of #8 (25.4 mm) bars and one bundle of #7 (22.2 mm) bars, which were the primary reasons for strong reflections. As shown in Figure 6(b), signals are disturbed and shielded by vertical stirrups producing multiple reflections. As shown in Figure 6(a) (iii) and 6(b) (iii),



(a) Isometric view

(b) Saw-cut surface

(c) Details closer to the scanned surface

(d) Cross-section details

Figure 5. Lower part of the mock-up knuckle.

phase distribution is disturbed insignificantly away from the stirrups. Since the backwall reflection was not visible, phase values of the empty post-tensioning duct were used to calibrate the phase diagram after carefully evaluating the reflection of the duct at sections away from the stirrups.

3.3 *Planning for tie girder data collection*

Based on the observations made from the numerical simulations and mock-up data analysis, it was decided that data collection will be performed from the two sides and the bottom of the tie girder segments between two floorbeams. At the floor beam connections, however, data was collected only from the outside and bottom surfaces of the tie girder. Since shear waves have uncertain sensitivity to elongated objects (such as rebars or post-tensioning ducts), the recommendation is to survey twice with different orientations ("polarizations") of the device if objects in all directions are of importance. If and only if there is a preferred orientation of the objects, or if an object is sufficiently large with an upper side more or less parallel to the subsurface, one survey is deemed sufficient. Since the investigation involved unknown interior conditions, data collection refinement was decided to be at a 2 in. (50 mm) spacing parallel to the excitation direction and at a 4 in. (100 mm) spacing perpendicular to the excitation direction. A detailed plan for data collection and recording was developed. The plan included measurement grids, device orientation, starting position on the grid, and the sequence of data collection.

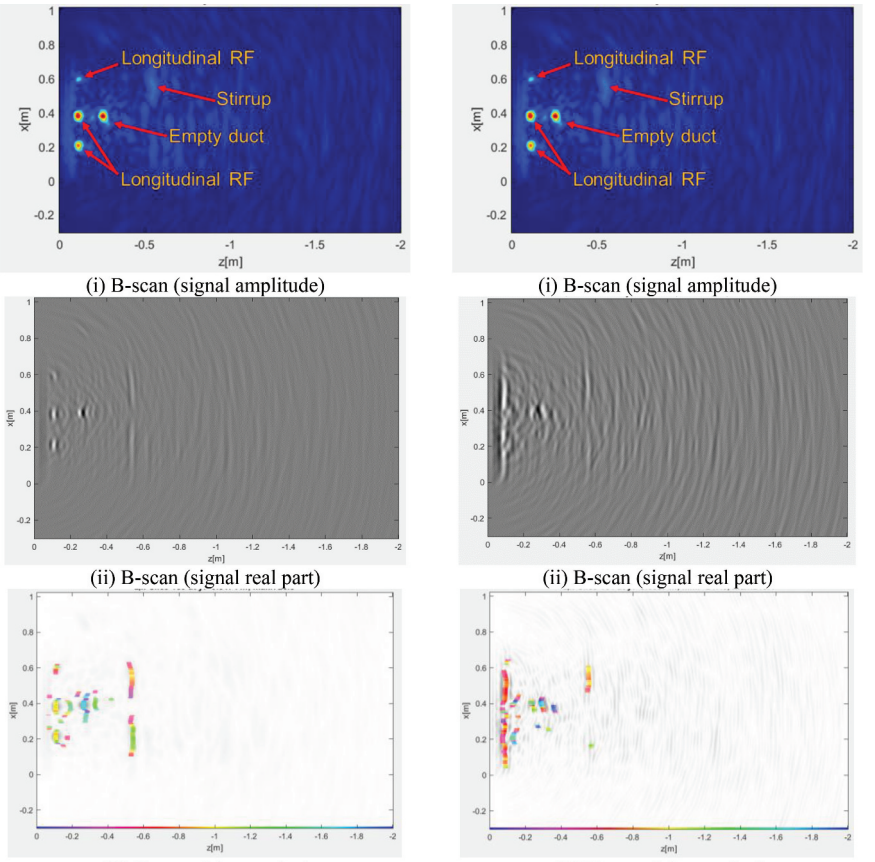


Figure 6. B-scans at a section (a) between vertical stirrups and (b) at a vertical stirrup showing signal strength, real part, and phase value distribution.

4 RESULTS AND CONCLUSIONS

The data from three sections, (i) the reference section between floorbeams C and D, (ii) Section 3 between floorbeams N and P, and (iii) Section 5 between floorbeams P and Q, were analyzed to develop signal strength and phase value plots. Data was collected with the excitation direction parallel and perpendicular to the ducts. Interior of the tie girder was characterized using 3D reconstructions. Observations at a large number of sections were documented and evaluated by comparing results from multiple sections with similar details. Figure 7 presents one of the formats used for documenting the analysis results.

The following conclusions are developed from this study:

- Simulation of shear wave propagation through this complicated and congested section demonstrated the capabilities and limitations of the tomography technology for visualizing the interior conditions of the tie girder.
- Data collection and analysis of the mock-up knuckle and the simulation of shear wave propagation through the tie girder helped to realize the challenges and advance the confidence on the nondestructive evaluation results.
- More reflections are observed from the outside surface scans. This could indicate voids closer to the outside surface. While drawing the 2-in. (50 mm) grid, many bugholes were

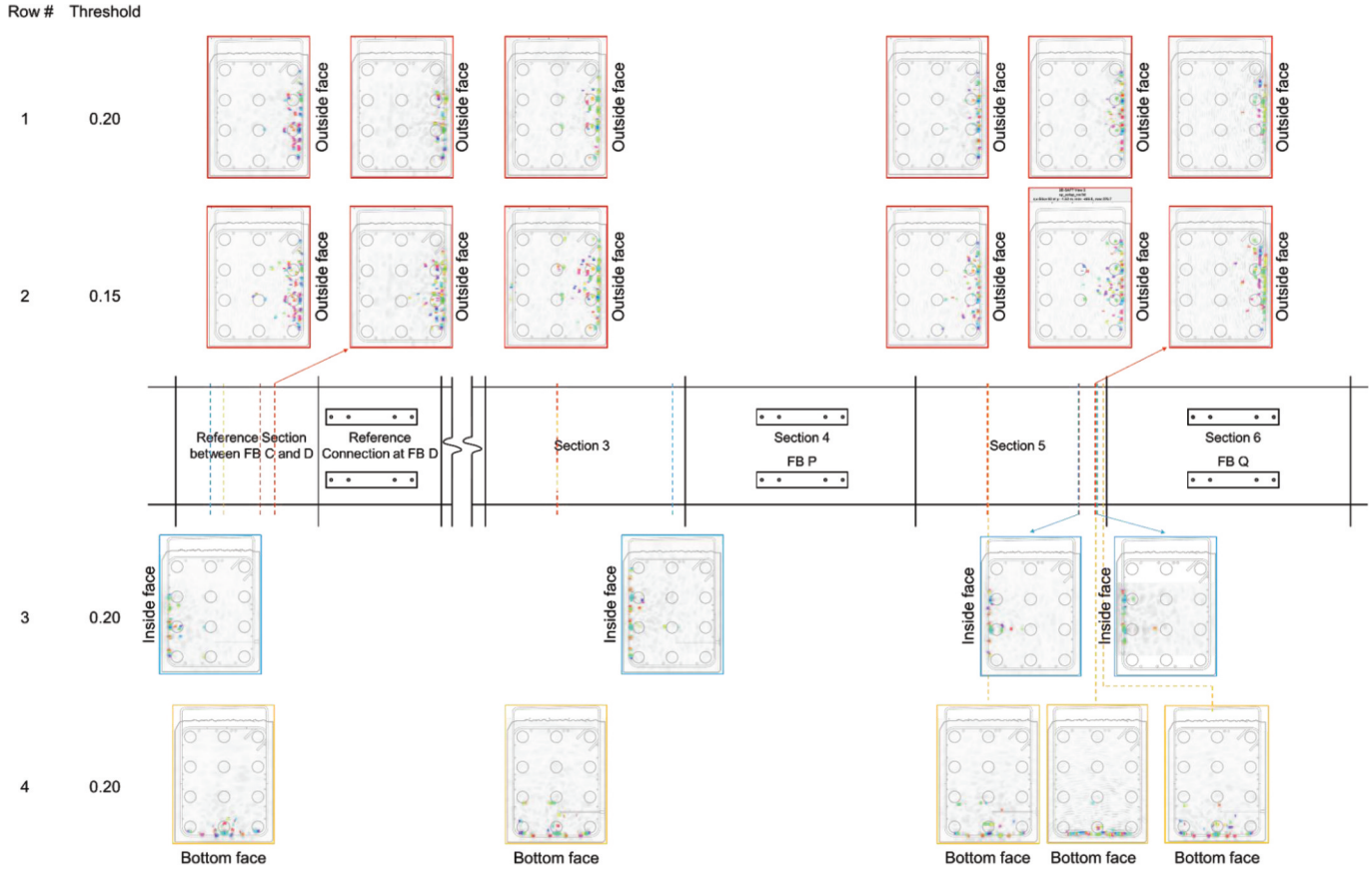


Figure 7. Summary of findings at the sections located between floor beams.

observed on the outside surface. Certain bugholes on Section 5 were as deep as 1 in. (25.4 mm). Compared to the outside surface, the inside and bottom surface quality of Section 5 is significantly better. Similar conditions are observed at the other cross-sections of the girder.

- Inside and bottom surface scans show strong reflections from the ducts and reinforcement nearest the scanned surface and weak reflections from the empty ducts at the second layer. This indicates that the concrete quality towards the inside and bottom surfaces is superior to the quality of concrete near the outside surface.
- After comparing all scans from outside surfaces and reducing the phase value threshold to 0.15, a section within Section 5 showed few additional reflections. One of the reflections is located at about 42.5 in. (107.95 mm) south of the south end of the floor beam Q anchor plates. These reflections are observed at only 15% signal strength: typically, an indication of weak reflections (small voids). In this case, however, this assessment might not be valid since weak reflections are also observed at the 4 in. (100 mm) diameter second column empty ducts. Since the length of the reflector is only about 3 in. (75 mm) along the tie girder length, its significance was considered to be minimal when compared to the overall section quality.
- After careful evaluation of all the observations and considering the meticulous process implemented for visualizing the interior of the girder, it was decided to move forward with construction. The project was successfully completed in 2023.

ACKNOWLEDGEMENT

This project was funded by the Michigan Department of Transportation (MDOT) through the Center of Excellence for Structural Durability at Western Michigan University. The authors would like to acknowledge the support of MDOT engineers and the members of the Z-Contractors. The authors would like to thank Dr. Klaus Mayer for simulating stress wave propagation through the tie girder cross-section to identify condition assessment limitations, sharing necessary tools, expertise, and time to address the project needs. A special thank is due to Eng. Jens Wöstmann (BAM) for performing analysis of a selected number of datasets and providing results to evaluate the data analysis process and assumptions. Authors appreciate the contribution of Srikanth Vemula, Sanjoy Bhowmik, and Uresh Wijesinghe for data collection.

REFERENCES

1. Basnayake, K., Amunugama, H., and Attanayake, U. (2021). "Detection of Concrete Surface Cracks Using Ultrasonic Pulse Velocity (UPV) Methods," the 11th International Conference on Structural Engineering and Construction Management 2021, December 17-19, 2021.

Bridge Maintenance, Safety, Management, Digitalization and Sustainability – Jensen, Frangopol & Schmidt (eds)
© 2024 The Author(s), ISBN 978-1-032-77040-6
Open Access: www.taylorfrancis.com, CC BY-NC-ND 4.0 license

Reliability analysis of end cracking in continuous prestressed concrete girders

A.M. Okeil
Department of Civil and Environmental Engineering, Louisiana State University, Baton Rouge, LA, USA

S. Ghimire
Enbridge, Inc., Houston, Texas, USA

ABSTRACT: Constructing bridges using precast prestressed concrete girders is extremely popular because of their durability and ease of construction. Establishing continuity between precast girders has its advantages and has been employed in many projects. It causes the development of positive restraint moments at intermediate supports as a result of long-term effects such as creep, shrinkage and thermal gradients. Prestressed concrete girder end cracking occurs if the positive restraint moments exceed the girder's cracking moment. In this study, the probability of girder end cracking in continuous prestressed concrete bridges is assessed using structural reliability concepts. This study focuses on two bridge configurations with different lengths and girder cross sections, which were assumed to be continuous over two spans. Design parameters such as dimensions, modulus of elasticity, modulus of rupture, area of prestressing steel and temperature gradient are first defined as random variables. A limit state function to assess the probability of girder end cracking is established based on the identified random variables for the serviceability limit state. The effects of creep, shrinkage, prestress, and temperature gradient were considered in the analyses. Monte Carlo simulations were then used to assess the probability of girder end cracking for an assumed girder age of 28 days. Results show that for this girder age, the probability of girder end cracking is high (68.2% – 91.8%); highlighting the vulnerability of prestressed concrete girder end cracking when used in continuous bridge spans as has been observed in the field. The vulnerability of girder ends to cracking is exacerbated by the fact that not the entire section is yet engaged in resisting restraint moments due to St. Venant's principal.

1 INTRODUCTION

Assessing the vulnerability of concrete girders to cracking is typically done deterministically. Practice has shown that cracking still occurs in situations where it is not expected (Hossain et al. 2020). Like other structural design quantities, many of the parameters involved in determining the cracking moment, M_{cr}, are not deterministic, which is a source of uncertainty in the assessed M_{cr} values. This implies that absolute safety or zero probability of failure cannot be achieved (Nowak and Collins 2000). Therefore, it is crucial to produce structural designs with an acceptable low probability of failure which translates into a reasonable safety level. Acceptable safety levels must meet societal expectations, which are achieved by strictly following code requirements that set minimum design requirements that must be met (e.g. minimum flexural capacity to meet gravity/wind/seismic load demands for strength limit states or allowable deflections for serviceability). Modern design codes such as the American Concrete Institute's (ACI) *Building Code Requirements for Structural Concrete – ACI 318-19* (ACI 2019) and American Association of State Highway and Transportation Officials (AASHTO) *Bridge Design Specifications (BDS)* (AASHTO 2020) are developed by considering the sources of uncertainty involved in design based on structural reliability concepts (Nowak and Collins 2000).

DOI: 10.1201/9781003483755-213

Many factors need to be considered in the design and construction of continuous bridges compared to simply supported bridges. One of these factors is the development of positive restraining moments at intermediate supports. Positive restraining moments are caused by time dependent factors such as creep, shrinkage, and thermal gradient, and are one of the main causes of girder bottom flange, or continuity diaphragm, cracking near the supports (Okeil et al. 2013). Cambering of girders due to long-term effects causes the bottom flanges of the girders to translate away from each other at the continuous supports. Positive moment reinforcement restrains this movement, which leads to tension, and hence the development of a positive moment. Creep is a time dependent physical property of concrete that leads to deformations under sustained loads (Hossain et al. 2014). Shrinkage is also a time dependent physical property that occurs due to the drying up of water molecules from the concrete mix in concrete structures in the absence of sustained. Thermal stresses are caused by changes in the ambient temperatures surrounding the structure, which is typically not uniform. Consequently, some structural components that are not free to expand or contract experience additional stresses due to these temperature changes.

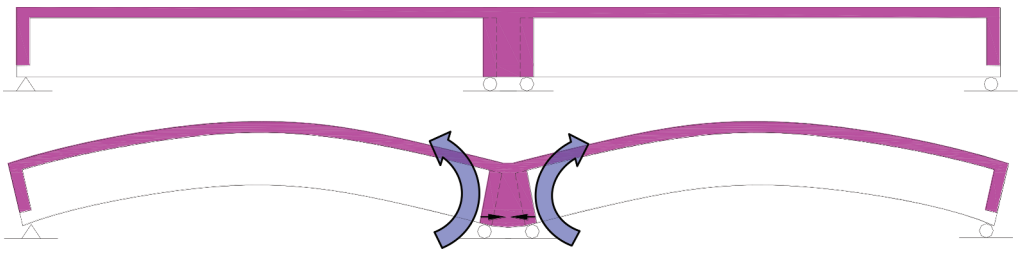


Figure 1. Positive restraint moment caused by long-term effects.

In this study, two continuous slab-on-prestressed concrete (PSC) girder bridge configurations with different lengths and girder cross sections are studied for the purpose of assessing the probability of cracking at girder ends due to positive restraint moments. A probabilistic limit state function is established based on random variables (dimensions, material properties, . . .etc.) for the serviceability limit state. The effects of creep, shrinkage, prestress, and temperature gradient were considered in the analyses. The probability of girder end cracking in continuous prestressed concrete bridges for an assumed girder age of 28 days is assessed using theory of structural reliability using Monte Carlo Simulations (MCS).

2 MOTIVATION

Slab-on-PSC girder bridges are considered one of the most popular alternatives for bridge construction in the United States and many other parts of the world. Ease of construction and superior durability due to their uncracked nature are only a couple of the reasons often sighted for their appeal to designers and bridge owners. Cracking, therefore, is not a welcome behavior for PSC bridges. In addition to loosing stiffness, cracked PSC girders are prone to rapid deterioration as a result of the exposure of internal reinforcement to the environment. This study is motivated by the need to understand the cracking vulnerability of PSC continuous bridges for the purpose of building new bridges with construction details that achieve the end goal of building longer span bridges that are safe and durable. The effect of thermal changes on PSC continuous bridges have been overlooked for a long time (Elbadry and Ghali 1986), but as recent studies have shown (Hossain et al. 2020), it has been found that temperature field changes result in thermal stresses that can be critical and cause cracking of PSC girders in bridges. Hence, it is crucial to develop a better understanding of the behavior of this popular bridge alternative by studying behavior under temperature gradient effects to reduce the probability of cracking, which may lead to shorter design life.

3 METHODOLOGY

Two continuous slab-on-PSC girder bridges with different lengths and girder cross sections are selected for this study. The bridges are first analyzed to obtain the internal force demands that typically develop in such bridge configurations. The RESTRAINT program (Mirmiran et al. 2001) that was developed as part of the National Cooperative Highway Research Program (NCHRP) project on establishing positive moment continuity (Miller et al. 2004) was modified to add the capability to account for temperature gradient effects on restraint moments in what will be referred to as mRESTRAINT-TG. mRESTRAINT-TG is capable of calculating the restraint moments caused by creep, shrinkage, and temperature gradients for a continuous slab-on-girder prestressed concrete bridges with various geometric configurations. Uncertainties inherent in the variables involved in these demands are then introduced. The resulting random variables are then introduced to a limit state function to assess the probability of cracking.

A random variable can be defined as a variable whose value can vary because of epistemic or aleatory uncertainties; i.e., not deterministic. Random variables are important for estimating the reliability of structures because there are many factors in the design and construction of structures whose outcomes are not deterministic. Random variables can be modeled as continuous or discrete random variables. For this study, all parameters such as concrete elastic modulus and modulus of rupture, area of prestressing steel and temperature gradient are modeled as continuous random variables. A limit state function mathematically defines the boundary of a desired and undesired performance of any structure (Nowak and Collins 2000). These boundaries are represented by an equation that in its simplest form is the difference between the structure's capacity to resist applied loads (R) and the applied load effects (L):

$$g(R, L) = R - L \tag{1}$$

where, $g(R, L)$ is the limit state function. If $g(\ )$ is greater than zero, it can be said that the structure did not fail, where failure is simply defined as not meeting design requirements. Conversely, if $g(\ )$ is less than zero it can be said that the structure failed at meeting the design requirements since it its capacity is less than the load demands it is subjected to. Since the aim of this study is to assess the probability of cracking due by positive restraint moments that develop due to thermal gradients in continuous PSC girder bridges, the limit state function for this study is taken as follows:

$$g(\ ) = M_{cr}\ - M_{TG} \tag{2}$$

where M_{cr} is cracking moment of the girder, and M_{TG} is restraint moment due to thermal gradient. In addition to M_{TG}, continuous beams are also subjected to thermally induced primary stresses (Priestley 1985). Since primary stresses occur due to the temperature gradient as a result of maintaining that structural sections remain plane, it does not generate additional moments and should be accounted for in this study. This primary stress effect occurs even in simply supported bridges. Creep and shrinkage also cause secondary restraint moments in continuous bridges. It should be noted that prestressing effects were ignored in this study since the sections at the girder ends are subjected to minimal compressive stresses because of the transfer length. After adding these effects, the limit state function becomes

$$g(\ ) = M_{cr} - M_{TG} - \text{primary stress effect} - M_{(\text{CR+SH})} \tag{3}$$

Monte Carlo simulation was used for calculating the probability of cracking due to positive restraint moments developed by thermal gradient. For the study, the probability of cracking was calculated for two scenarios. First, the cross-sectional properties were calculated using the gross section as is typically done. Another case was considered where the web of the cross section was ignored. The second case was considered in this study because finite element analyses showed that the cold joint does not fully engage the web of the girder. As can be seen in Figure 2, a gap develops between the continuity diaphragm and the girders' webs above the

bottom flange after the forces exceed the friction at the cold joint. Consequently, the stress distribution was found to be concentrated around the bottom flange positive moment reinforcement at the girder ends rather than the entire cross section (Hossain and Okeil 2014). This observation confirms St. Venant's principal (von Mises 1945). In other words, the web can only be engaged in resisting the restrain moments after a distance typically taken equal to the member's depth. Therefore, it was deemed necessary to assess the probability of failure for both assumptions, i.e. with and without the considerations of web. Figure 3 shows the cases described above that were considered in this study.

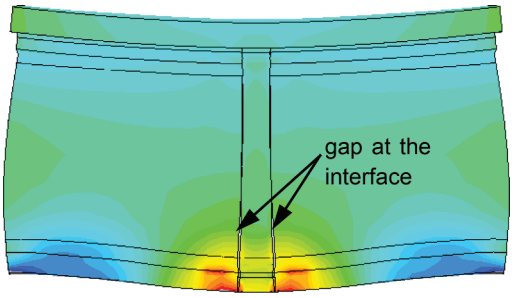


Figure 2. Gap between continuity diaphragm and girder webs at the cold joint interface.

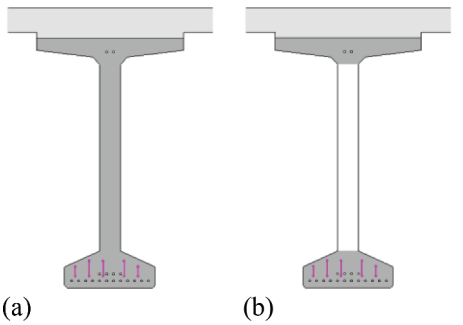


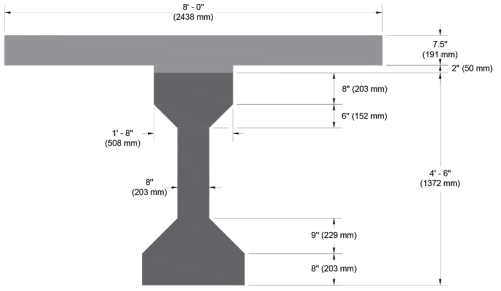
Figure 3. Cross sections considered in this study, (a) full composite section, (b) reduced composite section.

3.1 *Details of case study bridges*

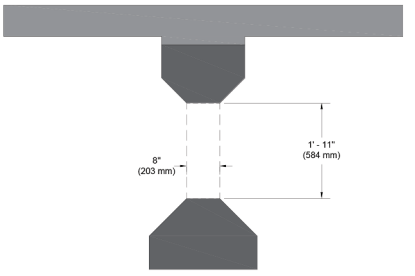
The bridges selected for this study were assumed to be continuous over two spans with equal span lengths. A deck slab with an 8-in. (203 mm) thickness was considered in this study and the girders were placed at a spacing equal to 8 ft (2.44 m). To accommodate girder camber due to prestressing, a 1.0-in. (25 mm) haunch was also considered. A standard AASHTO Type-IV section was chosen for the first bridge to meet design requirements for a 100 ft (30.48 m) span length. Figure 4-(a) and (b) show the dimensions of AASHTO Type-IV girder with and without the web part respectively. The span length for the second bridge was taken equal to 120 ft (36.58 m), which required a larger standard section, namely AASHTO BT-72. As stated earlier, both bridges were analyzed twice, once with the full gross section properties and the other after eliminating the web contribution of the cross-sectional properties. Figure 4-(c) and (d) show the dimensions of the girder with and without web parts, respectively.

The analysis using mRESTRAINT-TG dissects the cross section into a sufficient number of layers, or fibers, for calculations of composite area, moment of inertia, non-composite area and temperature variations. The nominal values taken for modulus of elasticity of girder and deck were 5,422 ksi (37.4 MPa) and 3,834 ksi (26.4 MPa), respectively. The nominal value

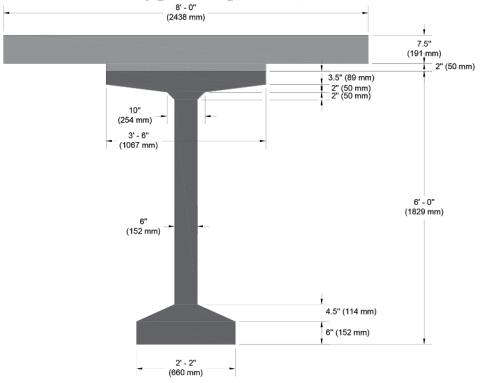
taken for modulus of rupture is 0.678 ksi (4.7 MPa), and the nominal value of area of pre-stressing strand was 0.217 in^2 (140 mm^2). Figure 5 shows the temperature gradient model used in this study is based on AASHTO BDS for Zone 2.



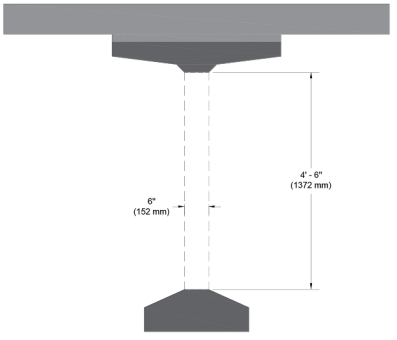
(a) AASHTO Type IV girder (with web)



(b) AASHTO Type IV girder (without web)



(c) AASHTO BT-72 girder (with web)



(d) AASHTO BT-72 girder (without web)

Figure 4. Bridge girders considered in this study.

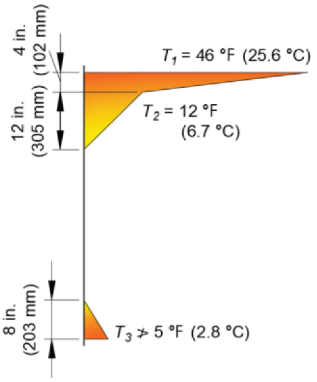


Figure 5. Temperature gradient model in this study.

4.2 *Calculation of probability of cracking*

The commercially available software MATLAB was used to generate random variables with the appropriate distribution types (e.g. normal or lognormal) for all random variables in the limit state function. More details about the statistical characteristics of the random variables can be found elsewhere (Ghimire 2014). Monte Carlo simulation was then conducted using

the generated random values to calculate probability of cracking of the girder based on the limit state function. The flowchart of the MCS used in this study is shown in Figure 6.

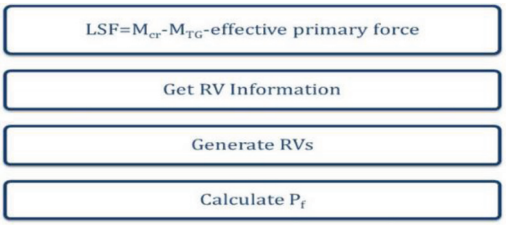


Figure 6. Flow-Chart for Monte-Carlo Simulation.

The probability of girder end cracking was first calculated for moment developed due to the temperature gradient only and later restraint moment developed due to creep and shrinkage was also added to probability of cracking. The girder's size and properties were all same for both cases. The nominal values of the restraint moment due to creep and shrinkage was taken from the mRESTRAINT-TG program for the 2 span bridge cases with AASHTO Type-IV and AASHTO BT-72 girders. The magnitude of the restraining moment due to creep and shrinkage is affect by the girder age at time of establishing continuity. Accordingly, it was assumed that girder age was 28 days when the continuity was established. As with all simulation methods, a sensitivity study was first conducted to determine a suitable number of simulations. Five different numbers of simulations were used to calculate the probabilities of cracking. The number of simulations used were 1,000, 10,000, 100,000 and 1,000,000.

4 RESULTS

The results presented in this section were obtained following the methodology described in the previous section. Table 1 and Table 2 list the results of the probability of cracking considering the restraint moment due thermal gradient, M_{TG}, only as a least critical scenario. It can be seen that the probability of cracking almost stabilizes at 1,000,000 simulations. For the 1st Bridge case (TYPE IV, L =100 ft), the probability of cracking when the web is considered is around 16.0%. When the web is not considered for the same bridge, the probability of cracking increases to about 29.0%. The difference in these results is because of the reduced girder section, and its geometric properties (e.g. area and moment of inertia), and hence the cracking moment, M_{cr}. The corresponding values for the 2nd Bridge (BT-72, L =120 ft), the probability of cracking increases when the web is considered is about 23.9% when the web is included in the analysis and 48% when the web is not considered.

It should be noted that these probabilities are higher than what is typically expected for strength limit states, which typically corresponds to a reliability index, β, equal to 3.5 (P_f = 0.0023). This is expected since the consequences of exceeding serviceability limit states are not as consequential as exceeding strength limit states that can lead to jeopardizing safety and economic losses (Wassef et al. 2014). As stated earlier, the results presented in Table 1

Table 1. Results from Monte-Carlo Simulations for 1st Bridge (TYPE IV, L =100 ft).

Number of simulations	Probability of Cracking (with Web)	Probability of Cracking (without Web)
1,000	14.5 %	26.6 %
10,000	14.6 %	26.7 %
100,000	15.1 %	27.5 %
1,000,000	15.9 %	28.5 %

Table 2. Results from Monte-Carlo Simulations for 2nd Bridge (BT-72, L =120 ft).

Number of simulations	Probability of Cracking (with Web)	Probability of Cracking (without Web)
1,000	22.9 %	47.4 %
10,000	23.5 %	47.4 %
100,000	23.8 %	47.9 %
1,000000	23.9 %	48.0 %

and Table 2 list the probability of girder end cracking when only restraint moment developed due to the temperature gradient is considered. Subsequent analyses were performed for the complete limit state function including the effects of creep and shrinkage. As a result of the increase of the restraint moment, the probability of girder end cracking will be even higher. The probability of cracking calculated for these cases increases to about 68.2% for the 1st Bridge case (TYPE IV, L =100 ft) and 79.0% for the 2nd Bridge case (BT-72, L =120 ft) if the web is considered and 77.7% and 91.8% for both cases, respectively, when the web is not considered. These probabilities are extremely high (β equal to –0.47 and –1.39) and exceed any values acceptable to code committees even for the less stringent serviceability limit states. These results confirm the aforementioned field observations of cracks at girder ends in a monitored bridge that used the positive continuity detail (see Figure 7). These bottom flange cracks can propagate into diagonal shear cracks in the web over time as they open and close on a daily basis with thermal cycles.

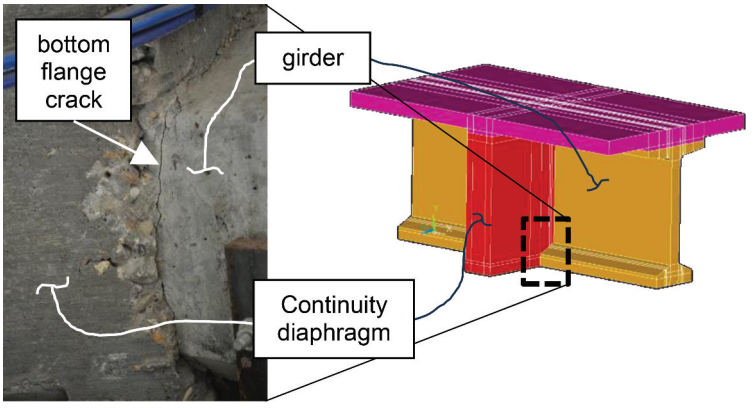


Figure 7. Bottom flange cracking in monitored bridge.

5 CONCLUSION

The following conclusions can be drawn from the results presented in this paper:

1. Temperature gradients can cause large restraint moments in continuous bridges and should be considered in the design of continuous slab-on-PSC girder bridges. Temperature gradients exacerbate the effect of creep and shrinkage leading to even larger restraint moments in continuous slab-on-PSC girder bridges.
2. Positive restraint moments may cause cracking at the girder ends. Results show that the probability of cracking that is more likely than not (>50%).
3. The study showed that the probability of cracking is affected by girder size as it was noted that the number increased with increase in size of girder. This may be because larger girders are more susceptible to temperature gradient effects.

4. In checking the cracking of the girder ends, it is recommended that the web portion be ignored as it not engaged in the moment resistance of the cross section due to the disturbed stress state as a result of lumping the force transfer in the bottom positive moment reinforcement in the bottom flanges (St. Venant's principal).

Accordingly, thermal gradients effects should be considered in the design of continuous slab-on-PSC girder bridges. A full parametric study is needed to study the probability of cracking over a wider range of parameters (span lengths, number of spans, temperature gradient models). Cracking mitigation measures should also be investigated to reduce the probability of cracking.

REFERENCES

AASHTO (2020). *LRFD Bridge Design Specifications*, 9th Ed., American Association of State Highway and Transportation Officials, Washington, D.C.

ACI (2019). *Building Code Requirements for Structural Concrete – ACI 318-19*, American Concrete Institute, Farmington Hills, MI.

Elbadry, M., and Ghali, A. (1986). "Thermal Stresses and Cracking of Concrete Bridges." *Journal of the American Concrete Institute*, 83(6), pp. 1001–1009.

Ghimire, S. (2014). "Restraint Moments due to Thermal Gradients in Continuous Prestressed Concrete Girder Bridges." M.S. Thesis, Department of Civil and Environmental Engineering, Louisiana State University.

Hossain, T., and Okeil, A. M. (2014). "Force transfer mechanism in positive moment continuity details for prestressed concrete girder bridges." *Computers and Concrete*, 14(2), pp. 109–125. doi:10.12989/cac.2014.14.2.109.

Hossain, T., Okeil, A. M., and Cai, C. S. (2014). "Calibrated Finite Element Modeling of Creep Behavior of Prestressed Concrete Bridge Girders." *ACI Structural Journal*, 111(6).

Hossain, T., Segura, S., and Okeil, A. (2020). "Structural effects of temperature gradient on a continuous prestressed concrete girder bridge: Analysis and field measurements." *Structure and Infrastructure Engineering*, 16(11), pp. 1539–1550. doi:10.1080/15732479.2020.1713167.

Miller, R. A., Castrodale, R., Mirmiran, A., and Hastak, M. (2004). "Connection of Simple-Span Precast Concrete Girders for Continuity." NCHRP Report 519, T. R. Board, Washington, D.C., p. 191.

Mirmiran, A., Kulkarni, S., Castrodale, R., Miller, R., and Hastak, M. (2001). "Nonlinear continuity analysis of precast, prestressed concrete girders with cast-in-place decks and diaphragms." *PCI Journal*, 46(5), pp. 60–80.

Nowak, A. S., and Collins, K. R. (2000). *Reliability of Structures*, McGraw Hill, USA.

Okeil, A. M., Hossain, T., and Cai, C. S. (2013). "Field Monitoring Of Positive Moment Continuity Detail In A Skewed Prestressed Concrete Bulb-T Girder Bridge." *PCI Journal*, SPR 2013, pp. 80–90.

Priestley, M. J. N. (1985). "Long Term Observations of Concrete Structures. Analysis of Temperature Gradient Effects." *Materials and Structures/Materiaux et Constructions*, (106), pp. 309–316.

von Mises, R. (1945). "On Saint-Venant's Principle." *Bulletin of the American Mathematical Society*, 51, pp. 555–562.

Wassef, W. G., Kulicki, J. M., Nassif, H., Mertz, D., and Nowak, A. S. (2014). "Calibration of AASHTO LRFD Concrete Bridge Design Specifications for Serviciability ", Web-Only Document 201, National Cooperative Highway Research Program, Transportation Research Board, Washington, DC, p. 151.

Bridge Maintenance, Safety, Management, Digitalization and Sustainability – Jensen, Frangopol & Schmidt (eds)
© 2024 The Author(s), ISBN 978-1-032-77040-6
Open Access: www.taylorfrancis.com, CC BY-NC-ND 4.0 license

Selection of post-tensioned tie girders for the 2nd Avenue network tied arch bridge

M. LaViolette
HDR, Omaha, NE, USA

U. Attanayake
Center for Structural Durability, Department of Civil and Construction Engineering, Western Michigan University, Kalamazoo, MI, USA

B. Wagner
Michigan Department of Transportation, Lansing, MI, USA

ABSTRACT: A unique network tied-arch bridge with free-standing, unbraced arch ribs was designed to carry the 2nd Avenue traffic over the Interstate Highway (I-94) in Detroit, Michigan. This 96.5 ft wide and 18° skew bridge with a 245 ft span is the first unbraced network arch bridge in Michigan, the fourth in the U.S., and the only unbraced and skewed network tied-arch bridge in the world. The bridge superstructure was assembled at a nearby staging area and moved into place on the permanent abutments using Self-Propelled Modular Transporters (SPMTs) and launching techniques. This design and construction method was selected for this site to minimize traffic disruption, improve safety, and allow 2nd Avenue to completely span over I-94 without intermediate supports to facilitate future widening and alignment shift of I-94 freeway and the adjacent interchange. Several alternative designs were considered; a) the use of post-tensioned concrete tie girders, (b) the use of internally redundant steel tie girders and (c) a multi-span bridge with a movable pier. During preconstruction planning, the contractor submitted a Value Engineering Change Proposal to erect the bridge in place by using a combination of cast-in-place concrete and spliced precast segmental tie girders. The paper describes the project and the technical basis for the selection and implementation of the post-tensioned concrete tie girders.

1 INTRODUCTION

The interstate highway (I-94 freeway) segment between the east of I-96/I-94 interchange to the east of Conner Avenue in the Metro Detroit area, shown in Figure 1, is being upgraded to eliminate safety concerns associated with the presence of narrow median shoulders, inadequate capacity with three driving lanes in each direction, and inadequate clearance for freeway entrance/exit ramps. In 1994, the Michigan Department of Transportation (MDOT) initiated an Environmental Impact Study (EIS) to evaluate possible ramifications due to this corridor improvement project. In December 2004, the Federal Highway Administration (FHWA) approved the Final Environmental Impact Statement (FEIS) for modernizing this freeway segment.

In December 2005, a Record of Decision (ROD) was issued allowing MDOT to proceed with the final design, property acquisition, and construction operations in support of modernizing the I-94 corridor. A detailed engineering report was completed by fall 2010 incorporating the critical information for moving the project forward. At the time of the ROD, it was anticipated that the full buildout could take 20 to 30 years due to funding constraints. However, numerous bridges carrying traffic over I-94 were beyond their original design life and had deteriorated to the point that they needed to be reconstructed prior to the corridor project. As a result, MDOT prioritized the worst condition bridges and began designing and constructing them as part of

DOI: 10.1201/9781003483755-214



Figure 1. I-94 corridor segments selected for improvements (courtesy: MDOT).

the I-94 Advanced Bridges program while still conducting stakeholder engagements to provide a platform to discuss potential approaches to enhance local connectivity and mobility across the freeway as well as potential bridge aesthetic criteria that could enhance the local communities.

The scope of the corridor modernization project includes upgrades to 6.7 miles of the freeway, service roads, bridges, and interchanges considering safety, capacity, local connection, and condition. The following are the specific activities included in the project to improve safety and mobility:

- Address existing traffic congestion while considering future travel demand.
- Address poor pavement and bridge conditions.
- Connect important routes in an effective and efficient manner.
- Improve neighborhood connectivity across I-94 and along service drives to enhance traffic circulation through the local road system.
- Provide improvements supporting multimodal transportation.
- Upgrade infrastructure to meet current design standards.

The freeway upgrade includes addition of a fourth lane in each direction; widening the median shoulders to better accommodate disabled vehicles and emergency responders; and



Figure 2. I-94 Freeway current and proposed designs (courtesy: MDOT).



Figure 3. Constellation pattern on abutment walls.

lengthening freeway entrance/exist ramps to improve safety, capacity, and travel time reliability. Figure 2 shows the generalized 1-94 current and proposed designs.

The modernization project includes upgrades to 67 bridge structures, including 6 railroad overpasses, 11 of which were reconstructed in advance of the freeway reconstruction. Figure 1 shows the locations of these advanced bridges with each bridge featuring one vehicle lane in each direction, wide sidewalks or shared use paths with protective barriers and ornamental railings, pedestrian lighting, bridge piers representing the barrel arch design, and abutment walls with constellation patterns (as shown in Figure 3).

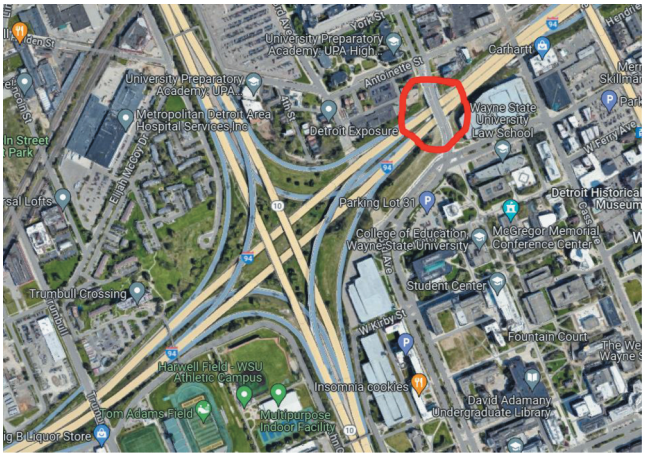


Figure 4. The location of the 2nd Avenue over I-94 freeway (courtesy: Google maps).

2 THE 2ND AVENUE BRIDGE OVER I-94

2.1 *Site constraints*

The proximity of the site to M-10 and I-94 interchange, as shown in Figure 4, required a bridge without intermediate supports and adequate underclearance to span over eight traffic lanes, four wide shoulders, and two entrance/exit ramps. Also, the proposed future alignment of the I-94 freeway will not only be widened, but will be shifted approximately 40 feet to the north of the current alignment. Since the construction of this portion of the freeway will not be completed for several years, the bridge selected for this site is expected to accommodate not only the current alignment that will remain in place for some time, but also a future widened and shifted alignment.

The new alignment of the I-94 freeway and the 2nd Avenue had an impact on three properties in the area, as shown in Figure 5. The FEIS provided detailed information on the impacts of the project on these properties. The ROD outlined the decision-making process and the specific measures to be taken to mitigate the impacts of the project on the affected properties. Overall, these measures were designed to minimize the negative impacts of the 2nd Avenue bridge construction and the I-94 modernization project on the surrounding area.

Property No. 1 is the United Sound Systems Recording Studio (USSRS) building located at 5840 Second Avenue. It was a historically significant recording studio that was founded by James V. Siracuse in 1933. Due to its association with some of the most influential musical artists of the 20th century, particularly the earliest beginnings of the world-famous Motown Music, the USSRS was eligible for inclusion in the National Register of Historic Places (NRHP). To maintain the building and prevent its demolition, MDOT and the State Historic Preservation Officer (SHPO) discussed the possibility of relocating the USSRS. Ultimately, it was decided to move the property further north and take protective measures during the construction phase of the bridge. Property No. 2 is a two-story Prairie Style house at 5832 Second



Figure 5. Three properties impacted by the new bridge construction.

Avenue. This building was constructed in 1916 as a two-family dwelling. Upon reevaluation, it was determined that this house was also eligible for inclusion in the NRHP. However, due to changes in the I-94/M-10 interchange ramp, the 0.10-acre site was acquired and the house was demolished. Similarly, the 0.28-acre site located at 5821 Second Avenue, labeled as Property No. 3 in the figure, was also acquired by MDOT. Since this site was found to be an imminent public safety hazard, the house on the property was demolished earlier than anticipated. As a result, it was no longer eligible for listing in the NRHP.

From a bridge design standpoint, the presence of the USSRS required a revision to the proposed bridge alignment and more importantly, the use of a skewed bridge. Even though a skew less than 20 degrees normally requires a minor adjustment to the design detail of a conventional girder bridge, the need for a skew became a significant factor in the design of an arch bridge.

2.2 *Bridge configuration and construction methods*

The 2nd Avenue bridge is one of the advanced bridges with non-motorized facilities (i.e. wide shared use paths with protective barriers and ornamental railings), one vehicle lane in each direction, and pedestrian lighting. A network tied arch bridge was selected as a replacement of the 2nd Avenue Bridge over I-94 freeway. This 265 ft long and 96.5 ft wide bridge has a skew of 18° making it a unique structure among the network arch bridges in the U.S. Figure 6 shows the structural components of the bridge. The structural assembly consists of two trapezoidal steel arch ribs connected at each end to post-tensioned tie girders through the knuckles, post-tensioned end diaphragms, steel floor beams, lateral bracings, and hangers. The lateral bracings between the arches were excluded since the use of lateral bracings in a skewed arch bridge is not aesthetically pleasing because the entire bridge appears significantly warped when viewed from the driver's perspective. The Naruse Okumatsushima bridge in Japan is an example of a skewed network arch bridge with lateral bracings. The 2nd Avenue bridge is also equipped with color-changing and energy-efficient LED aesthetic lighting to provide a visual centerpiece for the entire corridor.

At the start of the project, MDOT and the design team identified the prime objective of constructing this signature bridge without impacting I-94 traffic for more than a few days – perhaps as short as a weekend closure (e.g. from 10 p.m. Friday to 5 a.m. Monday) to completely avoid rush hour traffic. MDOT and the design team held a series of confidential meetings with several industry-leading specialty contractors to solicit input on feasible means of moving the bridge into its final position. The design team evaluated several construction alternatives and ultimately selected one in which the bridge skeleton – essentially the entire arch span except the concrete deck – would be constructed in a nearby parking lot and moved into place using self-propelled modular transporters (SPMTs). An SPMT is a flatbed trailer with a large array of wheels used for transporting massive objects big or heavy for conventional trucks. Following the SPMT move and placement of the assembled structure on permanent bearings, the remaining construction activities were completed.

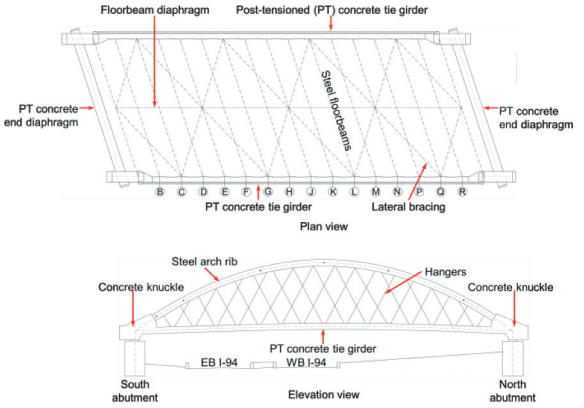


Figure 6. Major components of bridge superstructure.

3 SELECTION OF POST-TENSIONED CONCRETE TIE GIRDERS

For complex bridges such as this network tied arch span, the method and sequence of construction is extremely important to the design of the permanent bridge. The structure must be able to withstand any forces applied during construction and thus the designer must anticipate the most reasonable sequence of installation.

First and foremost, the design of the permanent structure must ensure adequate strength and stiffness, in accordance with the design codes and criteria, to resist gravity loads and environmental effects such as wind, temperature, and seismic ground motions. Initially, the bridge was designed as it will exist during in-service conditions without addressing the method of construction in fine detail. Following the selection of the most feasible construction sequence, the bridge was again analyzed and designed based on the assumed location of temporary supports and the order in which bridge components are added or made composite in the overall structure. The permanent bridge members were analyzed at each step of the assumed construction sequence to confirm that the bridge could resist the applied loads without creating overstress conditions or unacceptable deflections that could create fit-up problems at a future step.

Traditionally, tied arch superstructures have used steel members, typically box sections, to resist the thrust of the loaded arch rib. Modern tied arches utilizing steel tie girders have done so by using heavily bolted box sections which require holes and hatches to inspect the interior. These box sections typically consist of four plates that are bolted together at the corners with internal angles so that a crack forming in a single plate cannot propagate to the adjacent plate and lead to failure of the box. The need for redundancy of the box means that extra material is required beyond what is needed to carry design loads.

The clear-span options for the I-94 Advanced Bridges face an unusually difficult challenge in coping with a reduced vertical clearance beneath the bridge – a challenge that is especially acute at the 2nd Avenue bridge site due to the close proximity to the M-10/John Lodge freeway. The likelihood of over-height vehicle strikes makes it vital that a robust and redundant tie system be provided for the bridge. The increased depth of a steel tie girder and the potential for severe damage or plate failure due to a vehicle impact, made the steel tie girder undesirable for this project.

At the complex bridge meeting held on February 9, 2016, it was agreed among the design team, and MDOT that a traditional fracture-critical steel girder would be eliminated from consideration on the project and that only post-tensioned concrete tie girders would be considered for the arch bridges. Further discussions with MDOT, after the type studies were submitted, re-affirmed the selection of a post-tensioned concrete tie girder for the final design.

The tie girder reinforcement detail is shown in Figure 7. The plastic corrugated ducts in the tie girder have an internal diameter of 3.93 in. In addition, cross-section T-T and V-V details are shown in Figure 8, which illustrate the overall dimensions and number of ducts in each tie girder.

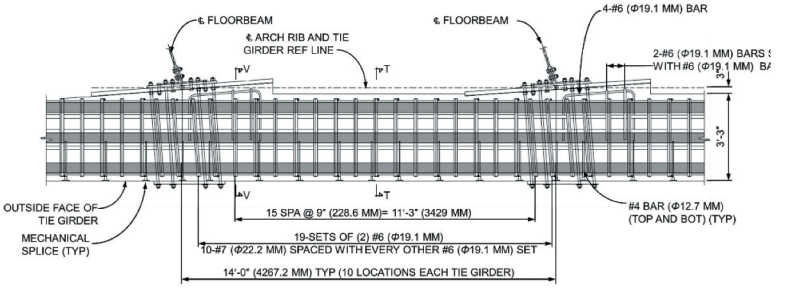
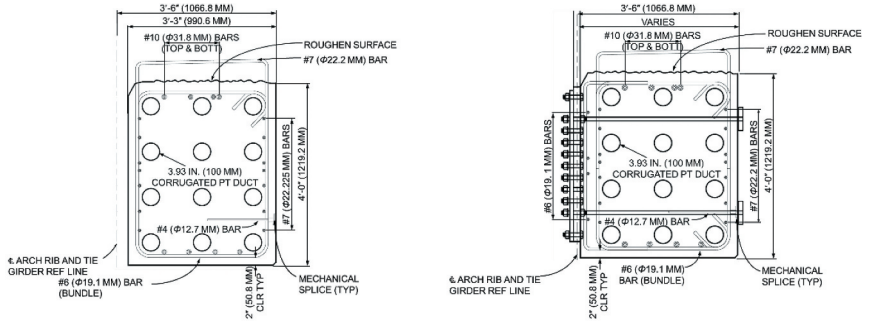


Figure 7. Typical tie girder reinforcement detail (plan view).



Section T-T: Section in between floor beams

Section V-V: Section at the floor beam

Figure 8. East tie girder section T-T and V-V as of 01/26/2022 (from SE knuckle towards NE knuckle).

A summary of the perceived advantages and disadvantages of the post-tensioned concrete and steel tie girder options includes the following:

Post-tensioned Concrete Tie Girders – Advantages:

- Post-tensioning keeps concrete in compression to reduce cracking, increase durability and extend service life.
- Internal redundancy is provided by using 12 ducts with 19 multi-strand post-tensioning tendons in each duct.
- May be constructed of precast, pre-tensioned concrete and spliced in the field or site cast.
- Post-tensioning can be performed in stages to balance applied loads during construction.
- Additional "empty" ducts can be provided for future use or replacement if desired.
- Damaged concrete and broken strands can be repaired in the event of a vehicle impact.

Post-tensioned Concrete Tie Girders – Disadvantages:

- Heavier lifting weight than steel – an important consideration for bridges built using ABC methods.
- Requires post-tensioning equipment and experience – somewhat limited in Michigan, but specialized assistance is available through the chosen supplier.

Steel Tie Girder – Advantages:

- Internally redundant steel box section can be designed using four separate plates bolted together at the corners.
- Lighter weight than a concrete tie girder.

Steel Tie Girder – Disadvantages:

- Member size is too small to provide internal access for inspection.
- Extra material beyond that needed by design is required to provide redundancy.
- Inspection handholes provide opportunity for moisture/debris accumulation and corrosion.

- Requires future re-painting.
- Repairs to steel are feasible, but difficult to recover loads that have been shed to other plates in the box section.

The design team also identified two feasible methods for constructing a concrete tie girder prior to moving the member into position spanning I-94. These methods are described in the following sections.

3.1 *Site cast concrete tie girder*

The term "cast in place" may be something of a misnomer in this case and perhaps a more accurate description of the two casting methods is site-cast and plant-cast concrete tie girder.

The site cast tie girder option consists of building conventional concrete forms on the available hard-surfaced parking lots near the bridge site and casting the tie girders using contractor forces. The advantages and disadvantages of site casting are as follows:

Site Cast Concrete Tie Girders – Advantages:

- Conventional casting that can be self-performed by contractor allows better control of project schedule and risk.
- Contractor can utilize forms for both tie girders in the same location.

Site Cast Concrete Tie Girders – Disadvantages:

- Requires additional field inspection due to the accurate geometry control required for fit-up of the floor system later in the process.
- Requires tighter than normal construction tolerances for use with ABC assembly.
- Any waviness or surface imperfections of tie girder would be highly visible in final product.

3.2 *Plant cast concrete tie girder*

The tie girders could be cast in smaller sections in a Precast/Prestressed Concrete Institute (PCI)-certified plant and then delivered and spliced in the field to complete the assembly of the tie girder. Possible splice details include either cast-in-place joints or match-cast shear key joints at the mating faces of the tie girder sections. The advantages and disadvantages of plant casting are as follows:

Plant Cast Concrete Tie Girder – Advantages:

- Concrete casting is performed by a PCI-certified plant using existing casting beds.
- Pretensioning of the precast sections would reduce shrinkage and handling stresses prior to assembly in the field.
- Smooth, reusable steel casting beds maximize visual quality of concrete.
- Plant cast operations can be conducted during cold weather.
- Tie girder can be cast in shorter sub-assemblies and spliced once they arrive onsite to form the complete member.

Plant Cast Tie Girder – Disadvantages:

- Plant cast knuckle section will be very heavy and awkward to ship to the site.
- Splicing of precast sections in the field would require connection details.
- Construction method is not typical for Michigan-based contractors.

4 SUMMARY AND CONCLUSIONS

After considering the advantages and disadvantages described in the previous sections of this document, the designers recommended the following structural details for the network tied arch bridges at 2nd Avenue over I-94:

- Arch Ribs: Unbraced, trapezoidal steel box section

- Floorbeams: Fabricated steel plate girders with steel wide flange stringers (as needed)
- Tie Girder: Site cast, post-tensioned concrete with section to provide accurate geometry control and floorbeam/hanger connection points.

The designers were confident that this combination of details would provide the best combination of constructability, reduced material lead times, shortened construction schedule, long-term durability and aesthetic appeal.

Assembly of the bridge skeleton was performed on temporary supports in a parking lot approximately 500 feet from the final location of the bridge. The assembly work faced many challenges, not the least of which was the COVID pandemic and related work delays and supply chain shortages. The bridge skeleton, weighing more than 2500 tons and nearly the size of a football field was ready to be moved into place by the start of July 2022. Nearly 70 truckloads of SPMTs and support equipment arrived onsite beginning on July 6 and the weight of the bridge was lifted by SPMTs approximately 10 days later. After some final adjustments, the bridge was driven from the staging area on July 19th and positioned directly behind the south abutment. Following the closure of I-94 and some final preparations, the bridge was launched over the top of the abutment on skid tracks and transferred to another set of SPMTs positioned down on I-94 on July 23rd. On Sunday, July 24th, the arch span was slowly driven across I-94 and landed safely on the other side by the end of the day. Figure 9 presents two views of the bridge move operation.



(a) (b)

Figure 9. Images of the skeleton supported on SPMTs during the move (a) at the staging area (July 19, 2022) and (b) during the move across I-94 (July 24, 2022).

The bridge move proceeded without an incident. The move was interrupted intermittently for a few minor elevation adjustments at one corner of the bridge or another during the



Figure 10. The 2nd Avenue network tied arch bridge in Detroit, MI, USA.

operation to maintain four corners of the bridge in the same plane at which they were cast to avoid damage to concrete or undue stresses on the bridge. Following completion of the bridge move and the transfer of the bridge to the permanent bearings, the structure received a thorough inspection by the designer and MDOT staff to ensure that it was safe to reopen I-94 traffic. The concrete bridge deck was placed and final adjustments made to the bridge prior to opening 2nd Avenue to traffic in mid-December, 2022. The completed bridge is shown in Figure 10.

ACKNOWLEDGEMENT

This project was constructed by the Michigan Department of Transportation and their support of innovative design and construction practices is very much appreciated. Z-Contractors of Shelby Township, MI, was the general contractor for the bridge and their willingness to expand their normal construction practices for a highly unusual bridge is highly commendable. The entire team would agree that this project could not have been completed without teamwork and collaboration.

Bridge Maintenance, Safety, Management, Digitalization and Sustainability – Jensen, Frangopol & Schmidt (eds)
© 2024 The Author(s), ISBN 978-1-032-77040-6
Open Access: www.taylorfrancis.com, CC BY-NC-ND 4.0 license

Post-tensioning tendons under strand breakages: Modelling approach for bonded tendons

B. Vecino, C.M.C. Renedo, J. Naranjo-Pérez, I.M. Díaz & J.H. García-Palacios
E.T.S.I. Caminos, Canales y Puertos, Universidad Politécnica de Madrid, Madrid, Spain

ABSTRACT: Recently, numerous failures have been detected in external post-tensioning tendons due to brittle fracture in stress corrosion situations. Non-destructive testing (NDT) techniques related to vibration-based structural health monitoring (SHM) can be used to detect anomalies and the grade of damage in these structural elements and thus, prevent their collapse. This paper aims to propose and validate a modelling strategy of taut short external post-tensioning tendons. The authors have carried out a detailed finite element (FE) model of the tendon to be used on an evolutionary analysis of the breakage process. The model is validated comparing the degradation curves measured in an experimental test previously carried out in the literature, in which accelerated corrosion was induced on a real posttensioning tendon. This work has been developed in an attempt to stablish realistic Performance Indicators (PIs) that could serve as an effective alarm for predicting the tendon breakage. The steel has been modelled as a non-linear elastoplastic material.

1 INTRODUCTION

Recently, several failures have been detected in external post-tensioning tendons due to brittle breakage in stress corrosion cracking situations (interaction of corrosion and mechanical stress) (Texas Transportation Institute 2009). Two examples of bridge collapses are: Viaducto O Castro A-6 (Lugo), 2022 and Morandi bridge, Genova (Italy), 2018. In the case of bonded tendons (strands are protected directly by cement grout), when breakage occurs the grout prevents the strands from sliding inside due to the self-anchoring, so there is a transference of the stressing force from the broken strand to the healthy strands. Therefore, global stressing force in the tendon does not decrease proportionally to the steel section lose despite the breakage of a strand, this complicates the detection of damage, especially through the use of modal properties. The self-anchoring phenomena affects the sensibility of global performance indicators (PIs) and should be taken into account in the design of structural health monitoring (SHM) systems.

The use of non-destructive testing (NDT) techniques to detect potential tendon deterioration is essential to plan the tendon maintenance and anticipate damage. A vibration-based NDT technique can be used in intermittent and continuous monitoring for damage detection. This NDT technique relies on the sensitivity of some structural PIs to damage, such as: the natural frequencies and the ratios between them, the modal shape and even the damping ratios. Structural damage can be represented by deviations of these indicator's normal values during the monitoring process.

The main objective is to propose a modelling strategy of taut short external post-tensioning tendons and validate it using experimental results previously published. Thus, this strategy can be adopted for: i) creating a digital twin to be used within model based SHM systems, ii) assessing performance indicator sensitivity to the grade of degradation, and iii) setting effective alarms when implementing SHM systems.

In the Section 2, a finite element (FE) model-based numerically modelling strategy of taut bonded tendons is presented and contrasted (in Section 3) with experimental results carried out by Lee and Kang (2019).

DOI: 10.1201/9781003483755-215

2 FE MODEL

A detailed FE model of a seven-strand tendon is developed. The experiment carried out by Lee & Kang (2019) is used as reference in order to compare their experimental results and the numerical results obtained in this investigation. The purpose is to determine de sensitivity of de PIs studied and to reproduce as accurately as possible the degradation curves obtained by Lee & Kang.

2.1 *FE model description*

The Lee & Kang experiment consists of stressing a 10 m tendon in two independent cases: at 40% and 70% of the minimum ultimate load of a prestressing strand. Then, five strands are broken successively by accelerated corrosion in 24 hours. To carry out the breakage of the strands, the grout is retired in the 30 cm central section, leaving the strands exposed (Figure 1).

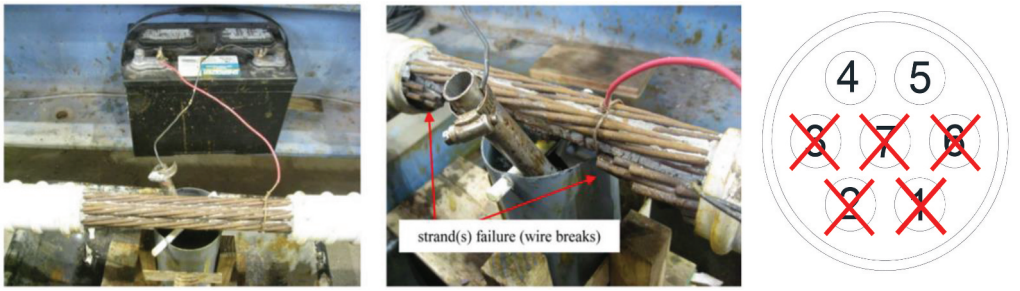


Figure 1. Strand breakage procedure. Lee & Kang (2019).

Therefore, the FE model represents a 10 m tendon of seven steel strands surrounded by grout. The 30 cm central section is modelled without grout to reproduce de Lee & Kang experiment. The strands are designed with a split element in their central section to simulate strand breakages by deactivating the contact between the two sides of the strand (strand-strand contact), which initially are modelled with a bonded contact to guarantee its continuity before breakage. 3D Solid elements are used for the strands and grout in this model. Sweep meshing method has been used so that the positions of the nodes match with those of the grout in each section. Both ends of the seven strands are modelled with fixed support, that is rotation and translation are restrained at both supports.

The stress state reached by the stressing of the strands are modelled by a thermal load. The two stressing states reached by Lee & Kang are considered: 40% and 70% of the minimum ultimate load of a prestressing strand, so the forces considered are 775 kN and 1241 kN, respectively.

A lineal elastic surface-to-surface contact model between the grout and the strands is assumed. Considering the severe self-anchoring observed experimentally and the 30 cm transfer length (Russell & Burns 1993), the contact stiffness adopted is $k = 1 \cdot 10^{15}$ N/m/m^2.

Plasticity of steel strands is considered. The elastoplastic model used presents the following characteristics: i) Bilinear isotropic hardening law (Figure 2), ii) Von Mises yield criterion, iii) Associated flow rule.

2.2 *FE analysis description*

A non-linear analysis by load steps is then performed. A sparse direct solver and the Newton-Raphson algorithm with convergence in forces and displacements are used. The non-linearity is caused by the activation and deactivation of contacts, which is solved by the "Pure Penalty" methodology, in which the contact stiffness is updated during each iteration to ensure minimum penetration between the contact surfaces. Additionally, the influence of plasticity on the

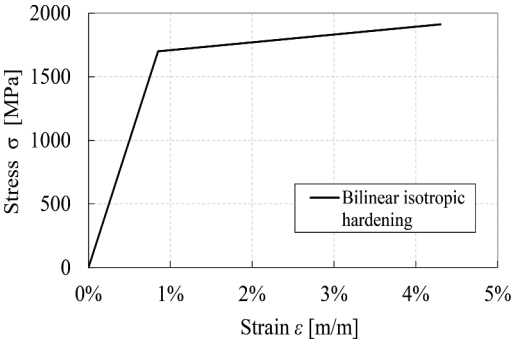


Figure 2. Bilinear isotropic stress-strain behaviour for the strands.

FE model is studied by carrying out two analyses, one where the materials are kept elastic and another where the plasticity of the steel strands is considered (Figure 2).

The FE analysis follows these steps: i) Stressing of strands by applying a thermal load, ii) Activation of strand-grout contacts to simulate the grout injection, and iii) Successive breakage of strands by deactivating the strand-strand contacts (Figure 3).

A modal analysis is carried out following each strand breakage step to evaluate the progressive degradation of the tendon natural frequencies (as PI). The characteristic stress state of the load step in which this modal analysis is carried out has been considered by means of a preload state. To include this preload prior to the modal analysis, the program performs a linear perturbation analysis on the structure, where the tangent matrix $[K_i^T]$ is used to obtain the effect of the preload.

$$[K_i^T] = [K_i^M] + [S_i] \tag{1}$$

where $[K_i^T]$ = global tangent matrix; $[K_i^M]$ = part of the tangent stiffness contributed from the material property; and $[S_i]$ = stress stiffening matrix introduced by non-zero stresses from the structure.

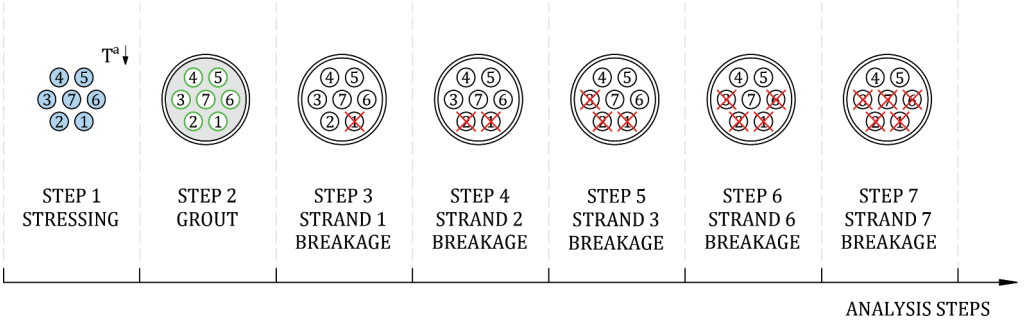


Figure 3. FE analysis steps (crosses indicate the broken strands).

2.3 *Model validation*

The model can be validated by comparing the stressing force in the anchorage obtained with the FE model considering plasticity and the experimental results obtained by Lee & Kang (Figure 4). It can be observed that the results trend is very similar although slight differences arise between both results, probably due to the plasticity model used or to the high stiffness contact between the grout and the strands considered. However, the comparison of results is satisfactory, and the model is validated.

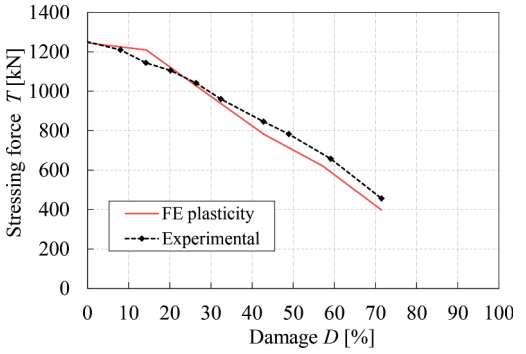


Figure 4. Model validation by stressing force in anchorage comparison.

3 RESULTS DISCUSSION

3.1 *Normal stresses along strand*

The normal stresses along the strands with successive strand breakages are obtained. Three different cases are studied to observe the stress state achieved in each type of strand: i) an outer strand that breaks, ii) an inner strand that does not break and iii) the central strand that breaks. Plasticity has not been initially considered. Subsequently, the normal stresses along the central strand without plasticity will be compared with the case where plasticity is considered.

The sequence of strand breaks is shown in Figure 3: strand 1, strand 2, strand 3, strand 6 and finally, the central strand 7. Strands 4 and 5 are not broken in the analysis. Damage (D) is defined as the ratio of the number of broken strands (N_B) to the total number of strands (N_T):

$$D = \frac{N_B}{N_T} \tag{2}$$

3.1.1 *No plasticity*

Strand 2 is an outer strand that breaks at some point in the analysis. The results show that stresses of a strand increases when a neighbour strand breaks. When breakage occurs, the broken strand normal stress is only lost in the surroundings of the broken section because of

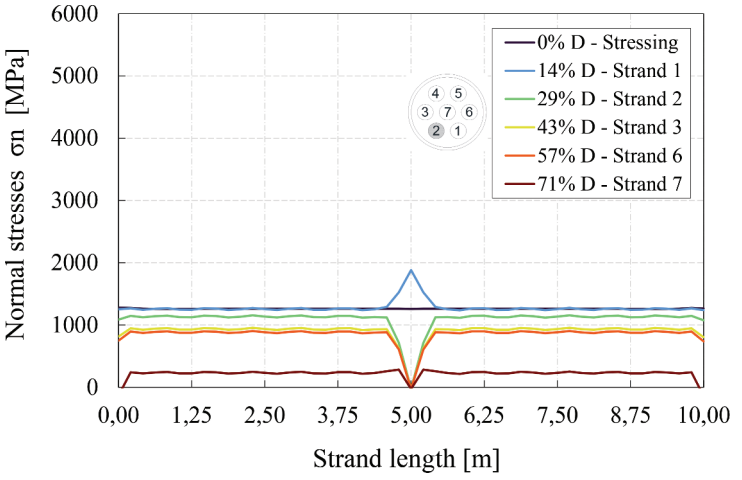


Figure 5. Normal stresses along strand 2 length, no plasticity considered, for different level of damage.

the self-anchorage phenomena. Due to the high stiffness of the elastic grout-strand contact assumed, the relative sliding only takes place in the transfer length, the remaining length approximately keeps its stresses (Figure 5).

Strand 4 is an outer strand that does not break in the analysis (Figure 6). As with strand 2, when strands close to strand 4 break, there is an increase in the stresses. This strand does not break during the analysis; however, a decrease of stresses can be observed in the central section due to the eccentric breakage. This implies the appearance of bending stresses in the tendon, which cause traction of the strands near the broken one and compression of the strands opposite the broken one (Figure 7).

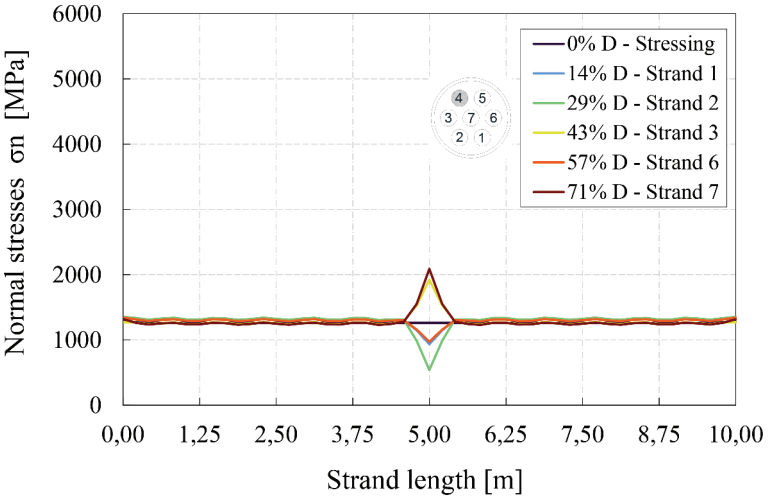


Figure 6. Normal stresses along strand 4 length, no plasticity considered, for different level of damage.

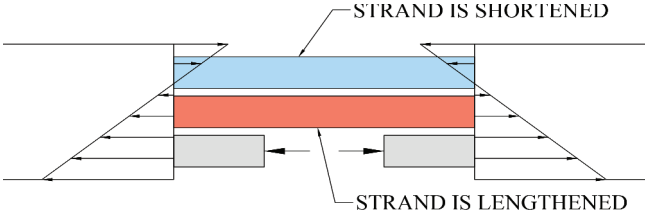


Figure 7. Conceptual illustration of the eccentric breakage in the tendon.

Strand 7 presents a particular situation as it is the central strand (Figure 8). It supports most of the stresses during each successive break because it is located next to all the strands that break. It reaches an excessively high stress in its central section, it should be noted that these values could not be supported in reality by the steel, but in this case a purely elastic behaviour of the steel has been assumed.

3.1.2 *Plasticity*

In Figure 9, the normal stresses along strand 7 considering plasticity are shown. The evolution of stress transference due to successive strand breakage is conceptually similar in the two cases: with and without plasticity. However, the maximum stresses reached are very different. The stresses obtained with plasticity are much lower (and actually, more realistic), demonstrating that the consideration of plasticity is crucial for modelling correctly the breakage strand phenomenon.

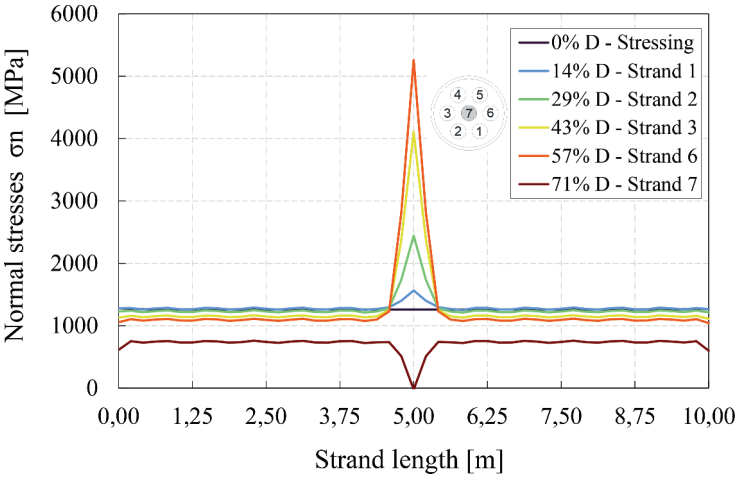


Figure 8. Normal stresses along strand 7 length, no plasticity considered, for different level of damage.

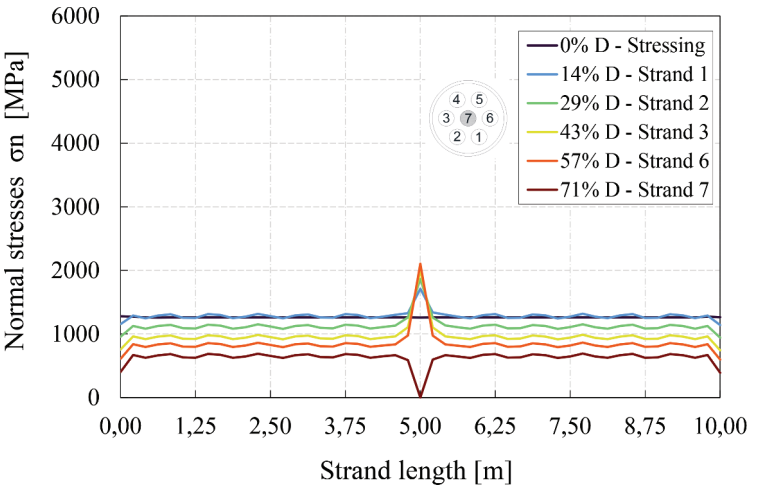


Figure 9. Normal stresses along strand 7, plasticity considered, for different level of damage.

3.2 *Frequencies*

The frequencies are compared with the experimental results obtained by Lee & Kang (2019) (Figure 10). The influence of the plasticity is also studied by comparing the numerical results obtained considering and not considering plasticity.

The experimental and numerical results not considering plasticity follow similar trends; however, differences arise mainly due to the high stiffness contact and the purely elastic materials assumed. When plasticity is considered, the experimental and numerical results are much more similar, this highlights the influence of plasticity on the results.

The results show that a tendon anomaly can be detected, as the frequencies are lower as the damage increases. Generally, tendon damage may be considered noticeable enough when the frequencies register values of 95% of the frequency obtained for healthy tendons (D=0% (Saluwu 1997)). Taking this into account, Lee & Kang's experimental results show that from approximately 20% damage the frequencies can be considered a sufficiently sensitive indicator. Also, the degradation curve is more pronounced for higher frequencies, therefore this indicator is more sensitive as the modal order increases.

Anyway, temperature dependency of the frequencies should be also analysed to confirm that this frequency variation is not marked by temperature variation (Chillitupa et al. 2023).

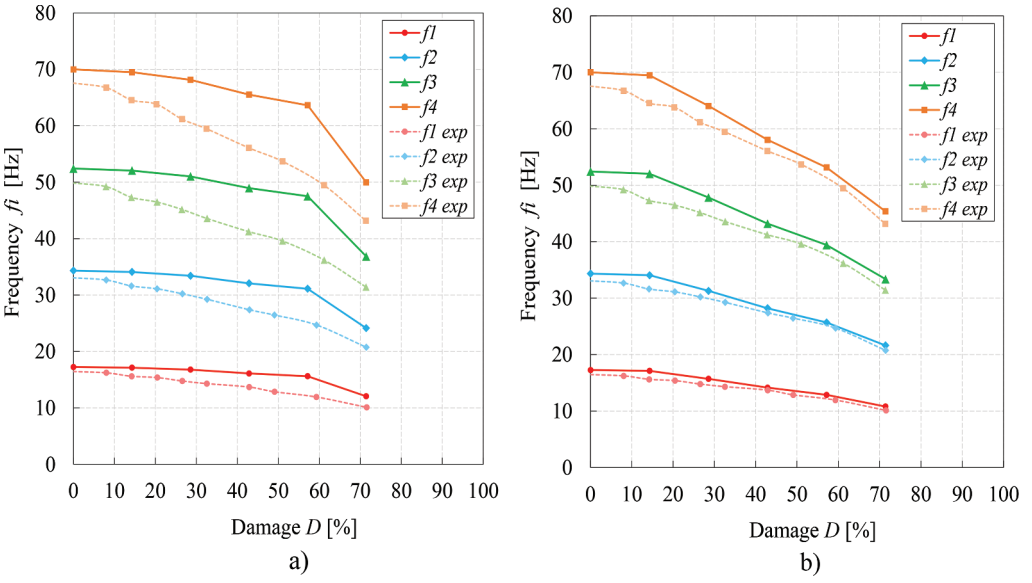


Figure 10. Evolution of the frequencies with the level of damage. a) No plasticity considered b) Plasticity considered.

3.3 *Stressing force in anchorage*

Stressing effective force in anchorage is the resultant of the stresses in the boundaries. Numerical results are also compared with the experimental results obtained by Lee & Kang (2019), as well as the numerical results with and without considering plasticity (Figure 11).

The same situation occurs with the stressing force as with the frequencies, the experimental and numerical results follow similar trends. The main differences are obtained when plasticity is not considered. Its great influence is again proved when it comes to detailed modelling in order to match realistic results. Figure 11 also show the degradation curve of the stressing force in the case where no self-anchorage is present, the curve is lineal. This is the case of non-adherent (unbounded) external post-tensioning tendons, where grout is replaced by a grease and the strands slide inside when the breakage occurs with minimum friction. The self-anchoring explains why the increase in damage is not proportional to the loss of steel cross-section.

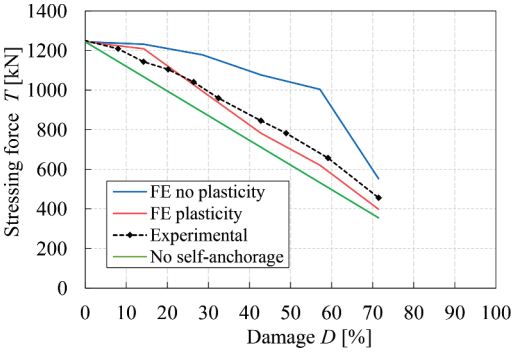


Figure 11. Stressing force in anchorage.

4 CONCLUSIONS

The proposed FE modelling approach reproduces quite well the mechanical behaviour of a prestressed bounded tendon under successive breakages. In this case, self-anchoring of strands in the grout is fundamental to understanding why stressing forces do not decrease proportionally with the area of steel lost in the strand, the FE model is able to successfully reproduce this phenomenon. Additionally, plasticity of strands plays an important role on the modelling accuracy.

The non-consideration of plasticity causes the stress redistribution when a strand breaks to be non-uniform, which seems to conclude that the stress redistribution in the strand is governed by the plastic nature of the steel. The consideration of this factor allows a more uniform distribution of the stresses in the healthy strands in the vicinity of the breakage and a greater deformation of this zone. Both elements are key to achieve a better adjustment of the model with the experimental results.

The high stiffness contact might not be the most suitable, leading to some small discrepancies of the results compared to reality. Once it has been demonstrated that plasticity is essential to obtain a more accurate FE model, as a subsequent modelling enhancement, it is necessary to refine a more realistic contact model to remove the remaining slight differences between numerical and experimental results.

As for the structural PI, the frequencies have been found to be the most sensitive indicator of damage detection, especially in the case of the higher frequencies.

ACKNOWLEDGEMENTS

Research project PID2021-127627OB-I00 funded by MCIN/AEI/10.13039/501100011033/ FEDER, EU. Belén Vecino acknowledges the Fundación Agustín de Betancourt for the financial support provided for the development of her doctoral thesis.

REFERENCES

Fib Model Code for Concrete Structures (2010). doi: https://doi.org/10.1002/9783433604090.

Lee, J. K., & Kang, J. W. (2019). Experimental Evaluation of Vibration Response of External Post-Tensioned Tendons with Corrosion. *KSCE Journal of Civil Engineering*, Volume 23, 2561–2572. doi: https://doi.org/10.1007/s12205-019-0735-5

Chillitupa-Palomino, L., Soria, J.M., Díaz, I.M., García-Palacios, J.H., & Naranjo-Pérez, J. (2023). Elimination of temperature effects on the modal properties on external post-tensioning tendons. A case of study. CMMoST Proceedings, 79–82.

Russell, B., & Burns, N. (1993). *Design guidelines for transfer, development and debonding of large diameter seven wire strands in pretensioned concrete girders*. Austin, Texas.

Salawu, O. (1997). Detection of structural damage through changes in frequency: a review. *Engineering Structures*, 19(9), 718–723.

Texas Transportation Institute (2009). Effect of voids in grouted, post-tensioned concrete bridge construction: Volume 1 – Electrochemical testing and reliability assessment. College Station, Texas.


Taylor & Francis
Taylor & Francis Group
http://taylorandfrancis.com

SS09: New Concepts and approaches in bridge management – BIM based bridge management, artificial intelligence, and other new concepts influencing future BMS

Organizers: R.M. Ellis, R. Hajdin & B. Baktas


Taylor & Francis
Taylor & Francis Group
http://taylorandfrancis.com

Bridge Maintenance, Safety, Management, Digitalization and Sustainability – Jensen, Frangopol & Schmidt (eds)
© 2024 The Author(s), ISBN 978-1-032-77040-6
Open Access: www.taylorfrancis.com, CC BY-NC-ND 4.0 license

Digital twin, BIM and asset management systems implementation

E. Spallarossa
Archimede srl

A. Bonicelli
Sina Spa

ABSTRACT: This paper describes a specific Inventory and Inspection System development with BIM (Building Information Modeling) applications for visual inspection data management and BMS (Bridge Management System) strategies development within a Bridge and Asset Management System implementation process. The specific Inventory and Inspection System is SINA ASTM company inspection system and its integration is developed within a collaboration with Archimede srl company, performing BIM and digital transformation. The paper focuses on a methodology for the dynamic management of infrastructures, ordinary maintenance and predictive maintenance, with a view to Asset Management development. Bim implementation, with the specific BIM use identification, other than design and construction, focused on inventory and inspection data organization, management, and capitalization. Typical Asset management KPIs are defined and business intelligence dashboards are implemented, also connected to BIM models. Asset Management System processes are developed developing scenarios and maintenance optimization processes towards network safety assurance.

1 INTRODUCTION

BIM (Building Information Modeling) is widely recognized for its application as a new design methodology. However, one of its significant added values lies in its application for infrastructure asset management, a concept reinforced by the recently published ISO 19650 standard, which focuses on managing information related to built assets throughout their entire lifecycle.

The adoption of BIM processes and procedures involves the utilization of intelligent parametric multi-dimensional modeling, essentially creating a virtual model of assets, to record and share information. This encompasses design data, information management, and maintenance asset information. With this approach, BIM transforms into a valuable and strategic digitalization tool that facilitates information sharing and management, especially in the context of asset preservation programming. In this scenario, the core of a systematic preservation approach revolves around the recording of inventory and inspection data. [14]

From this perspective, modern digital technologies can be employed not only to visually represent attributes such as position, geometry, and element types (e.g., masonry, concrete, steel structures) and record condition states but also to establish a standardized mechanism for cyclic data recording. These condition states can be aggregated at various application levels, including individual elements, structures (assets), and the entire network. The overarching concept is to transition from "National Bridge Elements" to

DOI: 10.1201/9781003483755-216

"BIM National Bridge Elements," complete with coded information and parameters. Additionally, this data can be translated into 3D models, capitalizing on emerging technologies and the adoption of the "Digital Twin" concept.

BIM delivers value by underpinning the creation, federation and exchange of shared models and corresponding structured data. While BIM development and its application to date has largely focused on the design and construction phases of assets, the most important BIM application is across the entire life cycle of assets as a key enabler of improved asset management within the recognized ISO55000[1].

The Business Value of BIM for Infrastructure' [6] highlights BIM's benefits:

- Conflict reduction through better interoperability.
- Enhanced project quality.
- Reduced rework.
- Improved productivity

BIM centers on an asset's needs, minimizing information loss during management changes. Evolving from CAD and 2D/3D drawings, BIM tools create detailed data files, forming an integrated system for managing construction and asset lifecycle, thus boosting efficiencies and the value of the asset and of the network.

This paper shows different steps of a BMS and BIM implementation towards and asset management system implementation. [10], [11], [12], [13].

2 BRIDGE ASSET MANAGEMENT AND BIM

BIM (Building Information Modeling) [4], [5] and asset/bridge management share a mutually supportive relationship. Both are technologies that empower owners, agencies, public administrations, and the entire supply chain to develop and implement processes, tools, and collaborative practices. These technologies optimize the costs, performance, and safety of infrastructure assets throughout their entire lifecycle. Having accurate and reliable information about assets is crucial for effective asset/bridge management as it underpins decision-making, planning, and the execution of activities. BIM provides a structured framework for the creation, collation, and exchange of asset information, thereby supporting effective asset management. BIM Management Systems (BMS) and BIM can support managers, technicians, and administrations with data recording processes, efficient information retrieval and organization procedures optimization. The ability to record conditions and the extent of deterioration at an infrastructural level (e.g., bridges, networks, etc.) can be accelerated and automated with new technologies and sensors. However, the initial step for consistent data is the organization of a structured data model [6]. A fundamental concept in the implementation of BIM and BMS should be the use of a standard for representing bridge information in a digital format. This standard should be easily adopted by software tools, minimize ambiguity, allow for diverse model applications, and ensure numerous advantages. BIM must provide the right information at the right time and with the correct Level of Information Need, particularly crucial for developing BIM models for inspection and bridge management systems support. Fine-tuning the Level of development needs is essential for maximizing the benefits of BIM, bridge, and asset management integration. This requires technicians and experts to share knowledge, experience, and information. In recognition of this, new standards like ISO 19650 parts 1, 2, and 3 are being developed to extend BIM to cover every phase of asset management. Consequently, new inspection and management approaches are leaning towards BIM technology, giving rise to several innovative techniques, already in use in various SINA and Archimede projects, such as:

1. Asset management — Overview, principles and terminology.

- Automated defect scanning and identification, leading to computer-aided inspection systems.
- Use of 3D digital bridge models, employing laser scanning surveys and 3D point clouds.
- Object-oriented bridge model development, using Building Information Modeling techniques for the design of new structures and the inspection, maintenance, rehabilitation, and repair of existing structures.
- Streamlined procedures for creating BIM Models of bridges and tunnels, aiding visual inspection recordings and management as decision-making tools in asset management."

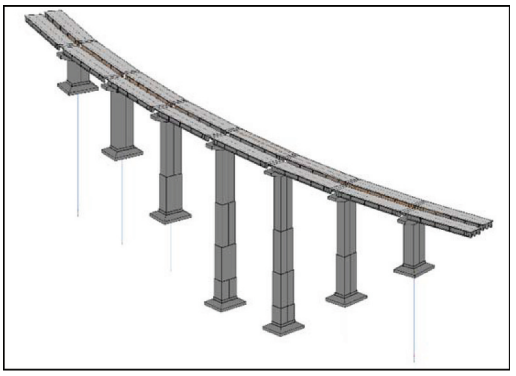


Figure 1. An example of a bridge BIM model to support visual inspection recording and management and business intelligence tools within a pilot project.

BIM and BMS development has been based on:

- Defining reference guidelines comprising definition of BIM modeling Level of information Needs;
- Defining structured data that make up the inventory and inspection databases;
- Optimizing the resources available for maintenance, based on forecasting and/or statistical models;
- Identification and use of the most suitable IT tool for the application area.

3 THE PILOT PROJECT SCOPE AND ITS IMPORTANCE

The pilot project showcased two applications of the Sina methodology Digital Twin, integrating BIM models with business intelligence dashboards:

- Inspection and Technical Approach: This method visualizes digitized deterioration of viaduct components, aiding in identifying deterioration locations, supporting maintenance, and optimizing sensor placement.
- Bridge Management Approach: This focuses on visualizing element condition states within a decision support system for the entire asset.

Asset management dashboards, as digital twins, enable dynamic, real-time navigation, allowing users to interact based on selected elements or deterioration types. Key to this is managing geolocated information, tested through a specialized dashboard that geolocates work and links to data sheets connected to the bridge's digital twin.



Figure 2. Business intelligence dashboard from the pilot project of bridge digital twin. On the geometrical reconstruction of the viaduct, is visible the different structural elements conditions.

The simpler integration systems for models, data, and maps, was tested, exploring alternatives to existing Sina solutions to meet the needs of technical users and operators. The goal was to expand the user base, targeting technicians and decision-makers. Archimede's solution integrates Business Intelligence tools with Sina's structure. This multi-application approach allows dynamic interaction with the BIM model using the Work Breakdown Structure (WBS). Users can view BIM model parameters for essential data, both geometric and inspection-related, graphically and descriptively. Inspection data specifically identifies anomalies and condition states of each structural element. The Business Intelligence tool, essential for creating Dashboards, allows for swift and dynamic information access, catering to different user roles. For instance:

- Inspection teams focus on the condition of structural elements.
- Teams assessing structural health look at service status distribution.

This integration, reflecting the anomaly digitization process, constitutes the 'Digital Twin' for inspection. It involves:

- Displaying elements by service status for targeted model searches and anomaly documentation.
- A comprehensive digitization strategy for anomalies, updating and browsing in real-time based on selected elements or anomalies.

Users can access shared information via a web portal without specific applications. For database and inventory management, we created a sheet that geolocates structures and provides links to technical sheets, all connected to the 3D model.

4 MAINTENANCE SCHEDULE BASED ON BRIDGE MANAGEMENT SYSTEM (BMS) PROGRAMMING

The FHWA's 'Bridge Preservation Guide' underscores the global challenge of cost-effectively maintaining bridges with limited funds. A balanced approach in bridge management, steering clear of the inefficient 'worst-first' strategy, is crucial. This can be achieved through Bridge Management Systems (BMS), which offer decision support across all bridge lifecycle phases and enhance management efficiency by using deterioration models and forecasting tools.

SINA's Inspection and Operational System (SIOS) is progressing towards a BMS, incorporating features such as:

- Inventory and Inspection data records.
- Bridge elements catalogue and condition ratings.
- Defined common actions based on bridge element condition states, including costs and impacts.

The goal is to develop a preservation policy to prolong service life and minimize maintenance costs, with BIM models and dashboards integrated into SIOS.The primary goal of developing SIOS as a BMS is to establish a preservation policy. This policy aims to slow the deterioration of bridge elements and extend their service life. A longer service life implies lower annual costs for rehabilitation and replacement. The integration of BIM models and dashboards within the evolving SIOS will be discussed in the subsequent chapters.

4.1 *Sios BMS home page*

The SIOS BMS homepage efficiently guides users through selecting bridges for analysis. It features bar graphs for a quick overview of the Health Index and Service States of viaduct elements, including a map view and a detailed table of attributes at the bottom for more specific analysis.



Figure 3. SIOS BMS homepage.

The first bar graph gives an immediate overview of the Health Index [1] [2] of the selected viaducts while the graph below shows the deterioration distribution of the last year (or the selected year) visual inspection data. A combined observation of the two graphs allows the user of the software to have an immediate information on the condition of the infrastructure. The table in the lower part of the page summarizes some significant attributes of the selected viaducts, for example the vulnerability class (according to MIMS Guidelines [9]), as well as the possibility of inserting further filters applied to the attributes of the viaducts.

4.2 *SIOS BMS dashboards*

Starting from SIOS BMS homepage it is possible to access dashboards both for in-depth analysis of the conditions of the structural elements [3], [7], [8],of each viaduct and for planning maintenance interventions. The detailed structural condition is presented explaining the state of service of the various constituent elements of the structure according to the last inspection results with particular attention to the analysis of the evolution of the condition during time. For this reason, in this method, it is of great value to have an inventory system of inspection results over time.



Figure 4. SIOS BMS dashboard of the detailed characteristic of a selected viaduct according with visual inspection results.

In the 'maintenance' section, users can plan interventions using a catalogue that outlines the costs and benefits of each action.

5 SIOS DATA FLOW FOR MAINTENANCE PROGRAMMING

This flowchart graphically illustrates the new process, showcasing how manual maintenance planning by the user and automatic planning by the optimizer are developed.

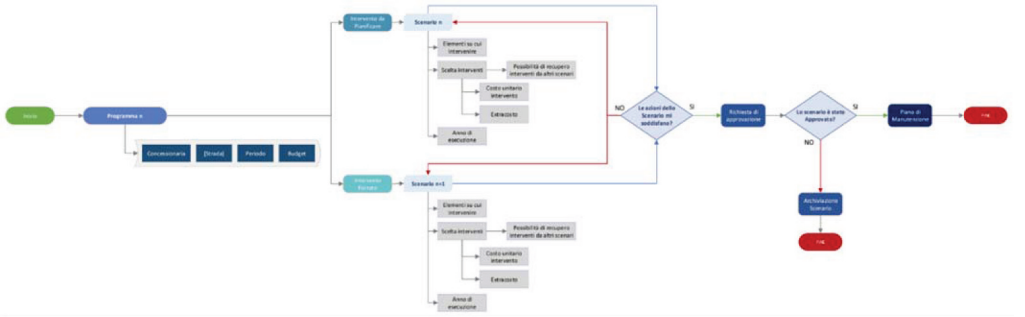


Figure 5. SIOS BMS maintenance programming data flow.

The process unfolds as follows:

- Creation of a Program: This step involves assigning an identifying name to the program and specifying the main properties that will be common to all the different Scenarios developed within it.
- Development of Different Scenarios: Within the program, various scenarios are created, each outlining the proposed maintenance interventions for the examined viaduct.
- Optimization: Within these scenarios, different kind of optimization cycles can be employed to recommend the most appropriate interventions for the viaducts

- Approval of Interventions: The proposed interventions within each scenario are then subject to review and approval.
- Finalization as a 'Maintenance Plan': Once the interventions are approved, the scenario is formalized into an official 'Maintenance Plan'.

6 TUNNELS DIGITAL TWINS PILOT PROJECT DEVELOPMENT

Parallel to the initiatives for bridges, a pilot project is also underway for tunnels. The objective of this project is to streamline the process of creating digital twins for tunnels and to establish the necessary data framework to support the integration of the SINA Inspection and Operational System (SIOS). This integration aims to facilitate comprehensive recording and management of inventory, inspection results, BIM models, and relevant data within an asset management system. During this pilot project, specific BIM models for tunnels have been developed, and SIOS has been adapted to effectively manage tunnel data, contributing to an efficient tunnel management system.

7 TEAM AND TECHNIICAL SKILL

The project was executed by a joint venture team comprising technical staff from both Sina and Archimede. The team involved different technical skills, such as: Project Managers, Bim Managers, Bim Coordinators, CDE specialists, Bim experts, stuctural engineers, Geothecnical Engineers, software developers, technical directors.

8 FUTURE DEVELOPMENT

Building upon the success of geolocating bridges, developing databases, and creating "digital twins" using 3D BIM software suites, SINA's research program aims to enhance asset inspection activities by incorporating virtual reality (VR) and augmented reality (AR). Specific applications of these technologies include: a) Training Inspectors: Using BIM technologies and VR simulations to create an instructional environment. b) Enhanced Inspection Surveys: SINA plans to test an immersive reality tool and software environment, providing real-time technical information to inspectors. This includes superimposing the "digital twin" with inspection data over the actual bridge. c) Remote Inspection Services: SINA is exploring two objectives: i) supporting field inspections with specialized back-office engineering expertise, and ii) pioneering advanced remote inspection services using devices such as drones, scanners, autonomous vehicles, and remote video surveillance. The anticipated benefits of these technologies include increased training effectiveness and efficiency with reduced costs, enhanced safety for trainee inspectors, reduced on-site costs (including indirect costs for infrastructure users), minimized post-processing activities, and improved quality of observations.

The next steps in the project involve:

- Fine-tuning bridge and asset management decision criteria and maintenance work costs.
- Setting up and refining the appropriate Level of Information Need (LOIN) for the BIM Models.
- Utilizing a calibrated photo dataset or high-resolution laser scanner survey to accurately replicate real deterioration in the BIM Model.
- Creating a simulated environment and developing a VR app for instructional use with the "digital twin."
- Analyzing the current database to prepare the necessary information for AR applications.
- Developing asset management software and tools for database updates
- Creating tools to compare, in real-time, the "3D digital twin" with the actual bridge, aiming to contrast the current situation with a previous one, such as deterioration maps from earlier inspections.

- Developing software tools to facilitate remote inspections, allowing on-site inspectors to share observations and exchange information with back-office engineers. Innovating new technologies and specialized sensors for use with AR software, enhancing human capabilities. The ultimate goal is to develop remote technologies capable of replacing the physical presence of inspectors.

REFERENCES

[1] FHWA. May 2016. *Synthesis of National and International Methodologies Used for Bridge Health Indices* PUBLICATION NO. FHWA-HRT-15-081.

[2] Inkoom, Sylvester. January 2017. Florida State University *Bridge Health Index: Study of Element Condition States and Importance Weights*, Transportation Research Record Journal of the Transportation Research Board 2612(1):67–75

[3] Weseman, W.A. 1995. *Recording and Coding Guide for the Structure Inventory and Appraisal of the Nation's Bridges*. FHWA, U.S. Department of Transportation.

[4] BUILDINGSMART. *The buildingSMART community is committed to creating and developing open digital ways of working for built asset environment*.

[5] U.S Department of Transportation Federal Highway Administration. April 2016. *Bridge Information Modeling Standardization*.

[6] Sacks, Rafael & Eastman, Chuck & Lee, Ghang & Teicholz, Paul. 2018. *BIM Handbook: A Guide to Building Information Modeling for Owners, Designers, Engineers, Contractors, and Facility Managers*. Wiley.

[7] AASHTO. (3d ed.) 2018. *The Manual for Bridge Evaluation*.

[8] AASHTO. (2d ed.) 2019. *Manual for Bridge Element Inspection*.

[9] MIMS - Ministry of Infrastructure and Transport Superior Council of Public Works. August 2022. *GUIDELINES FOR RISK CLASSIFICATION AND MANAGEMENT, SAFETY ASSESSMENT AND MONITORING OF EXISTING BRIDGES*

[10] Spallarossa, E. October 2004. *Evaluation Of Candidate Bridge Management Systems for Use with Italian Highway Bridges. IABMAS '04 (Second International Conference on Bridge Maintenance, Safety and Management)*. Kyoto, Japan.

[11] Spallarossa, E. June 2005. *Pontis® BMS Deterioration Models National Application. 9th International Conference on Structural Safety and Reliability (ICOSSAR'05)*. Rome.

[12] Spallarossa, E. July 2006. *The First Regional Level Bridge Management System Application in Italy. IABMAS '06 (Third International Conference on Bridge Maintenance, Safety and Management)*. Oporto, Portugal.

[13] Spallarossa, E. July 2012. *Bridge Management System implementation in Italy: Pontis® and other BMS application in Italy. IABMAS 2012, 6th International Conference on Bridge Maintenance, Safety and Management Politecnico di Milano*. Stresa, Lake Maggiore.

[14] Isailović, Dušan & Petronijević, Marija & Hajdin, Rade. The future of BIM and Bridge Management Systems. Faculty of Civil Engineering, University of Belgrade, Serbia. IABSE Symposium 2019 Guimarães Towards a Resilient Built Environment - Risk and Asset Management At: Guimarães, Portugal.

Bridge Maintenance, Safety, Management, Digitalization and Sustainability – Jensen, Frangopol & Schmidt (eds)
© 2024 The Author(s), ISBN 978-1-032-77040-6
Open Access: www.taylorfrancis.com, CC BY-NC-ND 4.0 license

Establishing data-driven life cycle benefits of bridge maintenance

B. Bektaş
Minnesota State University, Mankato, USA

ABSTRACT: Bridge maintenance and preservation activities are widely accepted to slow bridge deterioration rates and extend service life. In order to reflect the quantitative impact of bridge maintenance and preservation on bridge performance, State Departments of Transportation (DOTs) typically have utilized deterioration models or service life extension values that are based on expert elicitation in the United States. Research on quantifying the benefits of bridge preservation and maintenance, based on actual bridge data has been limited, if any. Consistently, the variables used for quantifying the impact of preservation in past research studies have either been assigned by expert elicitation, or the service life of treatments, as provided for specific bridge preservation products. Also, performance of bridge preservation treatments and their impact on bridge condition is highly dependent on bridge characteristics and external factors (e.g. traffic volume, climate, bridge condition). Therefore, there is imminent research need to quantify the impact of bridge preservation based on actual data sets for state DOTs. This paper presents preliminary research findings from an ongoing project in Minnesota. To date, the maintenance history data gathered by the Minnesota Department of Transportation (MnDOT) has undergone comprehensive review and evaluation. This data has been integrated with pertinent historical bridge condition information, and a preliminary modeling process has been conducted to forecast the extension of service life for deck components. Minnesota bridge decks were partitioned into four clusters using K-Means clustering analysis technique. Markov transition times for deck component ratings were computed separately for these clusters. Decks with recorded repair and maintenance had significantly higher transition times for ratings 7, 6, and 5 which correspond to good and fair conditions. The findings indicate that deck repair and maintenance extend the service life of bridge decks and significantly delay expensive bridge replacements. Future research steps include computation of Markov transition times for select bridge components and elements, bridge-, component- and element-level life cycle cost analysis and development of decision trees.

1 INTRODUCTION

1.1 *Research scope*

The proposal for this ongoing project outlined the imminent need for transportation agencies to quantify the impact of bridge maintenance and preservation activities. In this project, maintenance and preservation activities refer to bridge treatments that may be cyclical, proactive, or reactive, which may not necessarily improve condition but are aimed to slow bridge deterioration rates and extend service life. Existence of and confidence in data-driven deterioration and treatment efficiency models have been an obstacle in properly quantifying the life cycle cost impacts of bridge maintenance and preservation activities and consequently an obstacle to guiding decisions and resource allocation for these activities.

The expected research benefits from this research are interrelated and twofold. The first expected benefit is improved lifecycle costs for Minnesota bridges through development of models and decision trees that will feed into agency decision making framework and allow selection of appropriate bridge maintenance activities to extend/maintain bridge life in a cost-

DOI: 10.1201/9781003483755-217

efficient manner. The second expected research benefit is operations and maintenance fund savings by increasing the efficient use of funding for bridge maintenance based on the information developed from the research.

1.2 *Progress*

The research premise involves the utilization of agency data, which includes bridge inventory information such as design characteristics, material type, traffic volume carried, age, and environmental factors, along with construction history data regarding timing and cost, as well as historic condition data. The primary objective of this research is to identify the actual treatments applied to the bridge network and model their impacts on bridge condition. Initially, the research will focus on studying both bridge component and element condition data to assess the effects of past treatments on the time it takes for component condition ratings to change or element condition states to transition.

Previous tasks investigated the bridge inventory data with the goal of identifying bridge clusters within the Minnesota network that exhibit different historical behavior or deterioration patterns or have distinct decision-making dynamics, necessitating the development of separate decision trees. Past research in this field has often failed to provide customized research outcomes that offer specific parameters and model values for an agency, rather than just presenting variations in models. The project database is a relational database that includes following data on Minnesota bridges:

- Bridge design and material type
- Construction history, including cost
- Maintenance history
- Condition history of the various bridge components and elements
- Traffic
- Other relevant bridge inventory items

Recent work focused on preliminary Markov transition models for bridge component (deck, superstructure, and substructure) and element conditions. This paper presents and discusses initial models for bridge deck components.

2 DATA

The National Bridge Inspection Standards (NBIS), implemented by the Federal Highway Administration (FHWA) in 1968 (Lichtenstein, 1993), form the basis of bridge inspection and bridge management in the United States today. Typically, all bridges located on public roads with lengths more than 20 feet are inspected at least once every two years. Data on 116 NBI (National Bridge Inventory) items are reported annually to FHWA by the state transportation agencies. The data are compiled into the NBI by the FHWA, and Condition and Performance Reports based on the NBI data are prepared and submitted to Congress (FHWA, 2009). NBI items 58 through 66 in FHWA's Recording and Coding Guide (FHWA, 1995) constitute the NBI condition ratings. Three of them are especially important since they constitute the federal condition performance measures for National Highway System (NHS) bridges. Assigned to the three major parts in a bridge structure, these NBI condition ratings are deck, superstructure, and substructure condition ratings (items 58, 59, and 60 respectively) and are collected on a 9-0 scale (Table 1).

Initial efforts to define and collect bridge element data in the United States started in the late 1990s, with the development and implementation of bridge management systems (BMSs). Commonly Recognized (CoRe) Structural Elements Guide (AASHTO, 1997) was published by the American Association of State Highway and Transportation Officials (AASHTO) to define and standardize bridge element data inspection and collection. In 2011, the AASHTO Subcommittee on Bridges and Structures approved a new element-level bridge inspection manual (AASHTO, 2011), which was later updated in 2013 (AASHTO, 2013).

Table 1. NBI General Condition Rating (GCR) descriptions.

Number	Description
9	EXCELLENT CONDITION
8	VERY GOOD CONDITION
7	GOOD CONDITION
6	SATISFACTORY CONDITION
5	FAIR CONDITION
4	POOR CONDITION
3	SERIOUS CONDITION
2	CRITICAL CONDITION
1	"IMMINENT" FAILURE CONDITION
0	FAILED CONDITION

The new AASHTO Manual for Bridge Element Inspection (MBEI) replaced the Commonly Recognized Structural Elements. The new element inspection methodology incorporated the experience of inspecting elements by the state DOTs over twenty years and improved the guidelines. The bridge elements in the new manual are classified into three categories as National Bridge Elements (NBEs), Bridge Management Elements (BMEs) and Agency Developed Elements (ADEs). The number of condition states (CSs) are standardized as four, whereas CoRe elements had three, four or five CSs. Also, the new manual introduces a new, defect-based inspection methodology and separates wearing surfaces and protection systems from structural elements.

MnDOT has consistently collected both NBI GCR and element condition data over the years and stores both within their Structures Inspection Management System (SIMS). In 2023 NBI data, Minnesota had a total of 13,502 bridges, and 3,682 of these bridges were state-owned. The priority for this research is state-owned structures. Data on maintenance activities have also been consistently collected and stored in SIMS since 2008. The maintenance activity data used in this study covers 2008-2022 duration. In addition to the records in SIMS, MnDOT StateWide Integrated Financial Tools (SWIFT) also archives cost data on maintenance activities. The MnDOT Bridge Office has supplied the research team with two datasets containing maintenance activities: the Structure Information Management System (SIMS) data and the SIMS + SWIFT Bridge Cost Records (BCR) Data. The latter dataset also includes additional financial information, significantly expanding the available maintenance records beyond what is found in the SIMS data alone. Analysis of the datasets showed that SIMS records combined with SWIFT records (SIMS+SWIFT) contain more than five times the number of distinct bridge and year records compared to SIMS data. Figure 1 gives a visual summary of the maintenance acitivity data, categories under different resources. Local agencies (District 8 and counties) also have separate records that will be explored in later stages of the research. One challenge encountered with the SIMS+SWIFT data is the absence of element number associations for certain activities. Nevertheless, the timing of acitivities alongwith the work descriptions and work codes were utilized to create suitable associations to use SWIFT data.

The initial analysis of the dataset primarily centered around establishing connections between bridge components and elements with the recorded maintenance activities. This effort aimed to pinpoint the maintenance activities that had been consistently and comprehensively documented within the network. It's important to note that not all maintenance activities stored in the system held relevance for preservation or service life extension; for instance, activities like graffiti removal or tree maintenance had no impact. MnDOT engineers subsequently reviewed a suggested list of the most prevalent maintenance activities, based on their frequency in the dataset and their potential significance for preservation purposes.

It is important to emphasize that the determination of whether the observed data for a maintenance activity is adequate for the creation of statistically significant models will depend on several factors. These include the generation of inspection pairs involving subsequent element and General Condition Rating (GCR) inspections for calculating Markovian transition probabilities, along with the subsequent model estimation process.

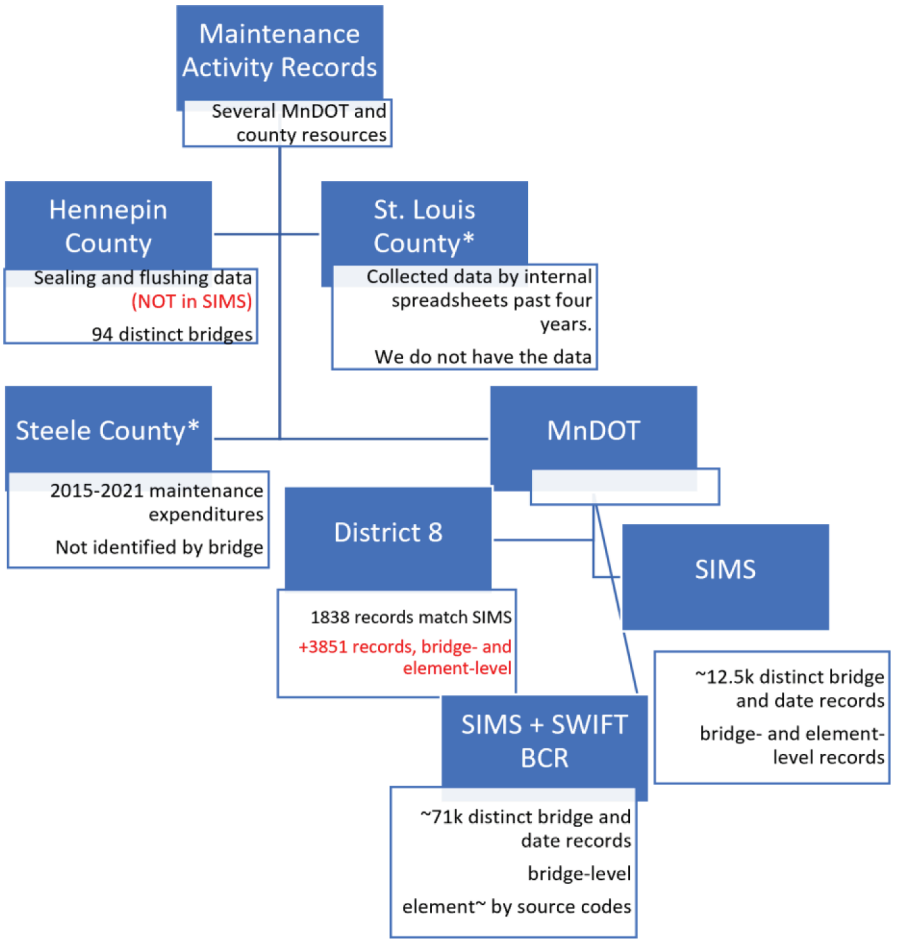


Figure 1. Maintenance data sources.

The list we have provided reflects an optimistic and comprehensive approach taken by our research team. Our intention was to ensure inclusivity and avoid excluding any potential models that could be valuable. Activities with more than fifty observations in the SIMS data were deliberately incorporated into this list. We anticipate that additional instances may be discovered when we leverage the SIMS+SWIFT dataset. The current threshold is informed by our previous experiences and has been set deliberately low to maintain inclusivity at this stage of our analysis.

3 ANALYSIS

3.1 *Approach*

In the initial modeling phase, we calculated Markov transition probabilities for the state-owned bridge decks in Minnesota. These bridge decks were categorized into four distinct groups, determined by the extent of available maintenance activity data spanning from 2011 to 2021. Out of a total of 3,682 state-owned bridges, 3,079 exhibited some level of bridge deck maintenance or repair activity. Descriptions of the bridge deck maintenance activities can be found in Table 3, and Table 4 provides a breakdown of the maintenance records' frequency for each activity across different years.

Table 2. Potential models by work description.

Work Description	Potential Element Models	Potential NBI GCR Models
Bridge poured/ relief joint seal	Poured Seal Joint 301, Approach Relief Joint 816	
Bridge approach panel	Concrete Approach Slab 321	
Bridge bearing assemblies	Elastomeric Bearing 310, Expansion Bearing 311	Superstructure
Bridge conc barrier/rail seal	Concrete Bridge Railing 331	
Bridge culvert maintenance	Concrete Culvert 241	Culvert
Bridge deck	Reinforced Concrete Deck 12, Wearing Surface 510	Deck
Bridge deck crack sealing	Concrete Wearing Surface - Cracking and Sealing 810 & RC Deck 12, 510, 521	Deck
Bridge deck sealing fixed	Concrete Deck Cracking Element 810, & RC Deck 12, 510	Deck
Bridge expansion, relief joints	Strip Seal Joint 300, Approach Relief Joint 816	Super/Sub
Bridge flushing	One to two bridge flushing records. 762 structures that were not flushed. Decks, Joints, Bearings (under joints).	Deck, Superstructure, Substructure
Bridge prep & painting	Steel Protective Coatings 515, steel elements (frequent superstructure elements)	Superstructure
Bridge slope protection	Scour 885, Slopes & Slope Protection 892, Deck & Approach Drainage 894	Substructure
Bridge substructure	Most frequent substructure elements (Concrete Column 205, Reinforced Concrete Abutment 215)	Substructure
Bridge superstructure	Most frequent superstructure elements (Prestressed Concrete Girder or Beam 109) Steel Girder	Superstructure
Joint reestablishment	Strip Seal Expansion Joint 300, Poured Seal Joint 301, Approach Relief Joint 816 underlying super/sub? Deck?	
Protection straps/curb plates	Plow Fingers 815, Strip Seal Expansion Joint 300	
Waterway maintenance	Deck & Approach Drainage 894 might fit better with element 899, 885, or 892. In a lot of cases, this is removing debris from the channel for flow or rip rap placement.	Channel
Maintenance Activity by Bridge	GCR Models for bridges that have low, medium, high levels of maintenance. The levels will be defined in the next task.	Deck, Superstructure, Substructure

The NBI GCR condition data span from 1992 to 2022, encompassing a more extensive timeframe than the available maintenance data. The assumption is that the available maintenance data is representative of the typical levels of maintenance for individual structures and the maintenance clusters sufficiently categorized maintenance levels for the deck sample.

Table 3. MnDOT bridge deck maintenance activities.

Activity Code	Activity Name	Description
2820	Bridge Deck Repair	Bridge deck repair, overlays, replacements, and underside deck delamination.
2836	Bridge Deck Sealing	Flood sealing bridge decks, approaches, and sidewalks.
2837	Bridge Flushing	Flushing bearings, superstructure elements, joints, railings, and decks.
2838	Bridge Deck Crack Sealing	Crack sealing decks, approaches, and sidewalks.

Table 4. Frequency of bridge deck maintenance activities by year.

Years	Repair 2820	Flood Sealing 2836	Crack Sealing 2838	Flushing 2837	Grand Total
2011	176	181	52	16	425
2012	258	265	32	1058	1613
2013	226	247	50	1011	1534
2014	227	250	62	1127	1666
2015	246	239	60	1171	1716
2016	256	191	63	1094	1604
2017	289	210	71	1258	1828
2018	239	208	83	1403	1933
2019	245	298	79	1041	1663
2020	347	302	130	1298	2077
2021	256	333	146	1255	1990

3.2 *K-Means clustering for deck maintenance*

Clustering involves grouping similar data objects into distinct clusters while ensuring differences between data in different clusters. Clustering techniques are widely utilized across various domains such as artificial intelligence, biology, customer relationship management, data compression, data mining, information retrieval, image processing, machine learning, marketing, medicine, pattern recognition, psychology, and statistics due to the increasing need for organizing and extracting valuable insights from vast amounts of data (Na et al., 2010).

K-Means is a straightforward unsupervised learning algorithm used for solving clustering problems. It classifies a dataset into a predetermined number of clusters (k clusters) in a simple manner. The key idea is to define k centroids, one for each cluster, strategically positioned to yield optimal results. These centroids should be as far apart as possible to minimize ambiguity (Kodinariya and Makwana, 2013). The algorithm then associates each data point with its nearest centroid, completing one iteration or group. Subsequently, new centroids are calculated as the centers of the clusters formed in the previous step. This process is repeated, with data points reassigned to the nearest new centroid, creating a loop. Through this loop, it becomes evident that the k centroids gradually change their positions until they no longer shift, signifying convergence. In other words, the centroids reach a stable position, and the clustering process is complete.

To conduct the clustering analysis, we compiled a dataset that documented the record count for each activity listed in Table 3, specifically covering the period from 2011 to 2021. This dataset was organized on a per-bridge basis, with each bridge identified by its unique bridge number. The frequencies of the four maintenance activities were selected as the parameters for the clustering analysis. We experimented with cluster numbers ranging from two to six, ultimately determining that four clusters yielded the most meaningful and coherent groupings. Table 5 summarizes the cluster means (by number of activity) and indicates the number of observations in each cluster. Figure 2 is a visual representation of the cluster means. The groupings are summarized as follows:

- Cluster 1 - “Minimal Repairs with Flushing”: This cluster has low deck repair and flood seal values but relatively high flushing and crack seal values.
- Cluster 2 - “Moderate Repairs with Balanced Maintenance”: Cluster 2 appears to have a balance between deck repairs, flood seal, flushing, and crack seal values.
- Cluster 3 - “Low Repairs with High Maintenance”: Cluster 3 has low deck repair values but relatively high flood seal, flushing, and crack seal values.
- Cluster 4 - “Low Repairs with High Maintenance and Flood Seal”: Cluster 4 has low deck repair values, high flood seal, flushing, and crack seal values, similar to Cluster 3 but with a higher focus on flood sealing.

Table 5. K-Means cluster means.

Cluster	Deck Repair	Flood Seal	Flushing	Crack Seal	Number of observations
1	0.47	0.08	2.80	0.31	1807
2	4.13	0.16	4.34	1.01	306
3	0.67	0.37	5.41	1.95	807
4	0.74	2.14	6.13	1.81	159

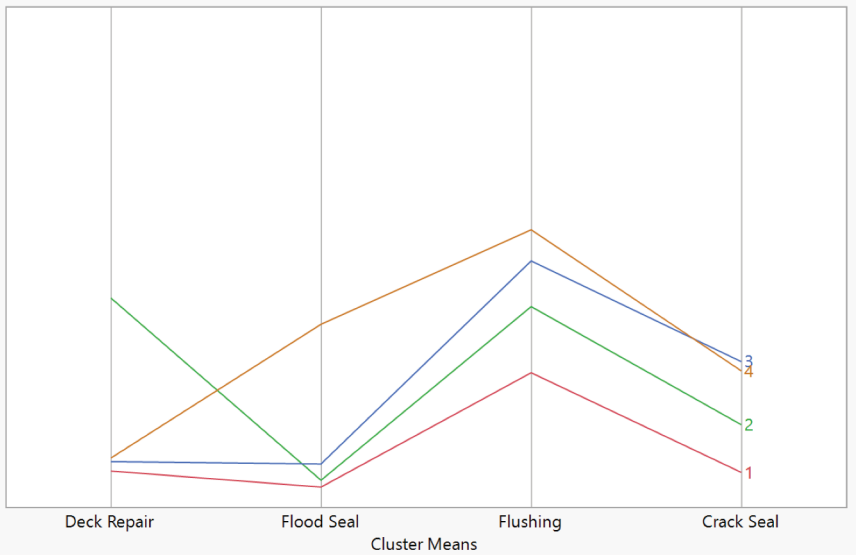


Figure 2. Parallel coordinate plot of cluster means.

3.3 *Markov transition probabilities*

To calculate the Markov transition probabilities, we adopted the methodology outlined in the recent collaborative deterioration model study for Midwest state DOTs conducted by Boadi et al. (Boadi et al., 2022). A specialized Minnesota database was prepared, and the data was updated to incorporate the most recent condition data. Subsequently, deck GCR models were computed for the previously identified bridge maintenance clusters. For conciseness, we have omitted the intricate modeling specifics, which can be found in the report titled "TPF-5(432): Bridge Element Deterioration for Midwest States" (Boadi et al., 2022).

In Table 6, we present computed Markov transition times for 3,711 Minnesota decks for NBI GCRs 9 through 5 for varying levels of maintenance activity. Cluster 0 bridges represent the group of structures with minimal amount of maintenance. Empty cells in the table present the GCRs for which the population size was too small to perform the algebraic computations and obtain a valid transition time. The same situation was valid for GCRs that were smaller than 5. However, GCRs values of 4 and below present poor conditions and bridges that are candidates for replacements and are therefore not of interest for this effort.

For high GCRs of 9 and 8, with the exception of Cluster 4 (Low Repairs with High Maintenance and Flood Seal) the transition times are higher for Cluster 0 (minimal maintenance). However, for GCRs of 7, 6 and 5, the transition times with valid computations for decks with maintenance and repair are consistently and considerably higher. These GCRs are also the GCR levels where most of the deck life cycle is realized. While further refinement and element-level analysis are crucial for the latter stages of the research, the findings quantify the life cycle extension for Minnesota bridge decks, presenting a strong case for data-driven value of bridge maintenance.

Table 6. Markov transition times by deck GCR rating and by maintenance clusters.

Deck GCR	9	8	7	6	5	Number of Observations
Cluster 0	3.29	6.46	9.67	7.83	11.32	2823
Cluster 1	1.07	2.49	16.85	31.33	18.36	487
Cluster 2		3.00	8.33	33.68		112
Cluster 3	1.78	3.40	16.47	44.29		243
Cluster 4	0.92	8.92	20.72			46

4 CONCLUSION

In this paper, we introduce a straightforward framework designed to classify maintenance levels for bridges and quantify the associated extension of their service life. Our research findings, based on consistent record-keeping by MnDOT, demonstrate that the effect of maintenance on extending bridge service life can be effectively measured. We share initial results from an ongoing study in Minnesota, aiming to predict the service life extension of deck components. Through K-Means clustering analysis, Minnesota bridge decks were categorized into four distinct groups. We calculated Markov transition times for deck component ratings within each cluster. It was observed that decks undergoing regular repair and maintenance exhibited notably higher transition times in ratings 7, 6, and 5, representing good to fair conditions. This suggests that timely deck repair and maintenance not only prolong the service life of bridge decks but also significantly postpone the need for costly bridge replacements. Data-driven estimates for bridge service life extension, derived from our findings, can be applied in various aspects of bridge management systems. This includes use in deterioration models, benefit calculations, or performance metric assessments. By relying on data-driven estimates rather than solely on expert elicitations, transportation agencies can gain greater confidence in their Bridge Management Systems (BMS) and the underlying modeling frameworks, reducing ambiguity and enhancing decision-making processes.

REFERENCES

AASHTO 1997. AASHTO Guide for Commonly Recognized (CoRe) Structural Elements. Standing Committee on Highways Washington, DC.

AASHTO 2011. AASHTO Guide Manual for Bridge Element Inspection, 1st Edition.

AASHTO 2013. *Manual for Bridge Element Inspection*.

Boadi, R., Thompson, P. D., Serigos, P., Bektas, B. & Xu, G. 2022. TPF-5(432): Bridge Element Deterioration for Midwest States, Final Report Wisconsin DOT.

FHWA 1995. *Recording and Coding Guide for the Structure Inventory and Appraisal of the Nations Bridges*, Washington D.C.

FHWA 2009. 2008 Status of the Nation's Highways, Bridges, and Transit: Condition and Performance, Report to the Congress. Washington D.C.

Kodinariya, T. M. & Makwana, P. R. 2013. Review on determining number of Cluster in K-Means Clustering. *International Journal*, 1, 90–95.

Lichtenstein, A. G. 1993. The Silver Bridge Collapse Recounted. *Journal of Performance of Constructed Facilities*, 7, 249–261.

Na, S., Xumin, L. & Yong, G. Research on k-means clustering algorithm: An improved k-means clustering algorithm. 2010 Third International Symposium on intelligent information technology and security informatics, 2010. Ieee, 63–67.

Bridge Maintenance, Safety, Management, Digitalization and Sustainability – Jensen, Frangopol & Schmidt (eds)
© 2024 The Author(s), ISBN 978-1-032-77040-6
Open Access: www.taylorfrancis.com, CC BY-NC-ND 4.0 license

Sensitivity analysis of bridge structural vulnerability class based on Italian Guidelines

S. Bianchi
Research Fellow, Department of Architecture, Building & Construction, Politecnico di Milano, Milano, Italy

L. Capacci
Assistant Professor, Department of Civil and Environmental Engineering, Politecnico di Milano, Milano, Italy

ABSTRACT: Optimal management of existing bridges over their service life is critical for infrastructure owners and practitioners who are called to guarantee adequate structural and functional performance of the transportation network they administrate. Documental analysis and visual inspections are valuable data supporting the decision-making process. A valuable support in the Italian context is provided by the "Guidelines for risk classification and management, safety assessment and monitoring of existing bridges" introduced in 2020. The guidelines promote a multi-hazard approach based on Attention Classes (ACs) defined from the combination of risk indicators regarding operating conditions from different perspectives, such as structural, seismic, hydraulic, and geological. This paper is aimed at providing a sensitivity analysis regarding the Structural Vulnerability Class (VC) defined by the Guidelines, with the aim of investigating the impact of epistemic uncertainties inherently biasing the bridge assessment, such as expert judgement subjectivity and missing historical data and as-built documentation.

1 INTRODUCTION

The urgent need to prioritize maintenance and repair for many bridges approaching the end of their service life is a common challenge faced by most developed countries worldwide (ASCE 2021, Biondini & Frangopol 2019). The adoption of expert-based methodologies and soft-computing tools (Bianchi & Biondini 2022a, b) can help bridge owners and public administrations to identify priorities. Furthermore, optimal allocation of limited resources for maintenance and repair interventions is essential across the entire transportation network considering risk-based bridge prioritization procedures (Yang & Frangopol 2018) and resilience-based management strategies (Capacci and Biondini 2020, Capacci et al. 2020, 2022). To support various road managers in implementing a standardized procedure for creating a uniform classification system of bridges, the Italian Government has adopted the "Guidelines for risk classification and management, safety assessment and monitoring of existing bridges" (Ministry of Infrastructure and Transportation 2022, Buratti et al. 2022), proposing a multi-hazard approach to prioritize maintenance and rehabilitation of the bridges in the Italian transportation network. The methodology defines rules for the evaluation an overall "Attention Class" (AC) for each bridge. The final AC is a comprehensive risk indicator combining four risk-specific AC: (I) Structural and Foundational, (II) Seismic, (III) Hydraulic, (IV) Geological.

This paper focuses on the assessment of the Structural Vulnerability Class (VC) as defined by Italian Guidelines. The procedure involves data collected through document research and

DOI: 10.1201/9781003483755-218

visual inspection. The steps in the approach rely on the engineering judgment of experts in charge of visual inspection process, introducing epistemic uncertainties based on their expertise. Other relevant sources of uncertainty can be related to the lack of design and as-built documentation. Case studies are proposed in this paper to investigate the influence of such epistemic uncertainties on the reliability of Structural VC estimates.

2 STRUCTURAL AND FOUNDATIONAL VULNERABILITY CLASS

According to Italian Guidelines, structural and foundational VC can assume the following values: LOW, MEDIUM-LOW, MEDIUM, MEDIUM-HIGH, HIGH. Four assessment steps are identified based on the logic workflow presented in Figure 1:

1. Identification of the level of Damage (*d*)
2. Evaluation of the effect of "Year of Construction" (VC_1).
3. Evaluation of the effect of "Design Standard" informing design loads (VC_2)
4. Combination of VC_2 with the initial bridge vulnerability VC_0 to obtain final VC.

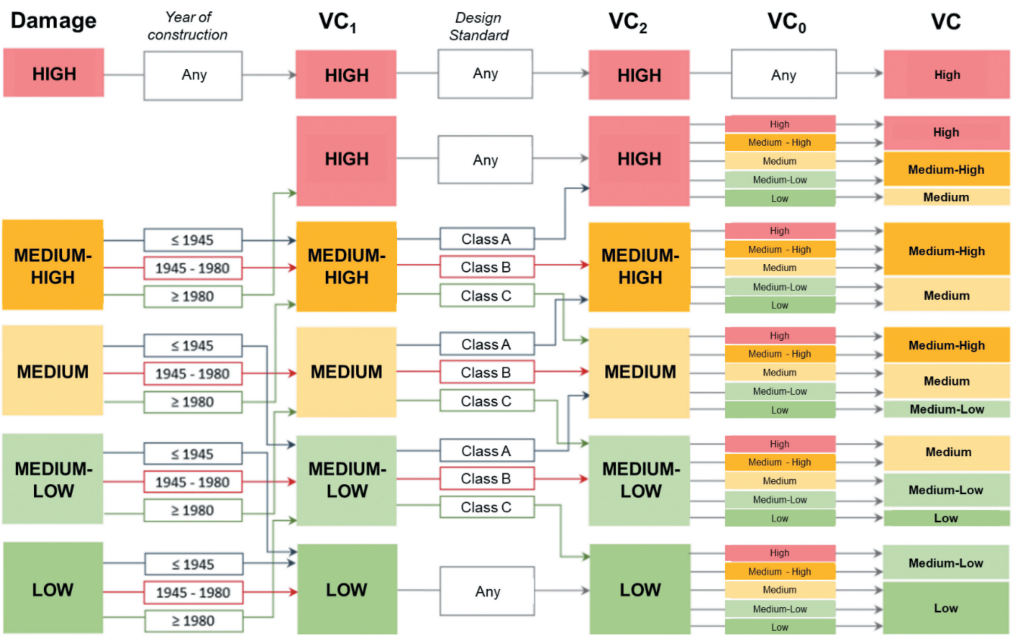


Figure 1. Logic workflow of structural and foundational VC (adapted from Ministry of Infrastructure and Transportation 2022).

2.1 *Step 1: Identification of the Level of Damage (d)*

The determination of damage level *d* relies on bridge visual inspections based on standardized forms filled by technicians during on site activities. These forms list various structural deficiencies categorized based on construction materials and structural members. Each deficiency is associated to a severity level and technicians can grade by predefined indices reflecting its extent and intensity. Value of indices is decided by expert inspectors on the base of engineering judgment. Finally, the damage level *d* is estimated by processing the collected data according to Table 1 based on damage severity and intensity as well as damage relevance in structural members eventually compromising the bridge safety.

2.2 *Step 2: Evaluation of the effect of "Year of Construction" (VC_1)*

Structural and foundational vulnerability can be also related to the year of construction. It represents the time required for the structure to reach the current Damage Level d. The damage level can be adjusted to obtain the Vulnerability Classification VC_1 according to the rules represented in Figure 1 which also depend on the construction periods identified by the Italian Guidelines: ≤1945, 1945–1980, ≥1980. Bridge exposure to chlorides effect, due to the aggressive action of marine wind currents de-icing salts, may result in more rapid evolution of degradation. In this case, value of VC_1 is increased.

Table 1. Damage level (*d*) for the evaluation of structural and foundational VC (adapted from Ministry of Infrastructure and Transportation 2022).

d_1	LOW	Small number of Medium and Low severity; any intensity; any element.
d_2	MEDIUM-LOW	(1) High number of Medium-High severity; Medium-Low intensity; any element. (2) Medium and Low severity; any intensity; any element.
d_3	MEDIUM	(1) High/Medium-High severity; High intensity; non-critical elements. (2) High severity; Medium-Low intensity; any element.
d_4	MEDIUM-HIGH	High or Medium-High severity; High intensity. Damage do not compromise structural safety
d_5	HIGH	High or Medium-High severity; any intensity; critical elements (e.g., Gerber joints, bearing, prestressing cables. . .) or identification of critical condition state (extensive cracks frameworks, foundation scour. . .)

2.3 *Step 3: Evaluation of the effect of "Design Standard" (VC_2)*

The understanding of the assumptions underlying their construction is essential in assessing the vulnerability classification of structures. A pivotal aspect among these considerations is the loading conditions considered during the design phases. The evolution of the historical Italian regulatory landscape has resulted in several updates to the definition of traffic loads (Buratti et al., 2019). Five design time intervals can be identified for bridge classification, along with the previously identified three construction time intervals associated to damage evolution rate informing VC_1. The intersection between such intervals leads to seven reference times t_i with i=1,..7 graphically represented in the timeline in Figure 2.

In this context, it is important to distinguish between bridges designed for both civil and military loads (1st category) and those designed for civil loads (2nd category). The impact of traffic loads also depends on their arrangement on the deck, i.e. on the total bridge span (L). Based on these characteristics, Italian Guidelines identifies three design classes as shown in Table 2. VC_1 is adjusted to obtain VC_2 according to rules represented in Figure 1.

Table 2. Identification of the design class.

	1st Category		2nd Category	
	L≤10 m	L>10m	L≤10 m	L>10m
Prior to 1933	Class A	Class A	Class A	Class A
Normale N.8 1933	Class A	Class A	Class A	Class A
Circ. 6018/1945	Class A	Class A	Class A	Class A
Circ. 772/1946	Class A	Class A	Class A	Class A
Circ. 820/1952	Class B	Class B	Class A	Class A
Circ. 384/1962	Class B	Class B	Class A	Class A
D.M. 1980	Class B	Class B	Class A	Class A
D.M. 1990	Class B	Class B	Class B	Class B
NTC 2005	Class C	Class B	Class C	Class B
NTC 2008	Class C	Class C	Class C	Class C
NTC 2018	Class C	Class C	Class C	Class C

It is worth noting that, the combination of the year of construction and design class can have either a beneficial, neutral, or detrimental effect on the computation of VC_2 (Figure 1), depending on the values they assume within each identified time interval. Table 3 lists the combination of these parameters for total length L<10m and design category I, while also pointing out their overall impact on VC_2 with respect to the level of damage (d). Similar table can be provided for the remaining combinations of total length and category.

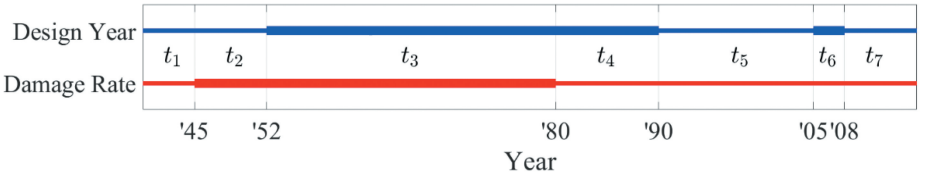


Figure 2. Timeline representing classification regarding damage evolution rate and design category.

Table 3. Year of construction and design class combinations for L<10m and design category I over time with the indication of the overall effect of the combination with respect to level of damage.

Time interval	Year of construction	Design class	Effect				
			d=1	d=2	d=3	d=4	d=5
t_1	≤1945	Class A	=	↑	=	↓	=
t_2	1945–1980	Class A	=	↓	↓	↓	=
t_3	1945–1980	Class B	=	=	=	=	=
t_4	≥1980	Class B	↓	↓	↓	↓	=
t_5	≥1980	Class B	↓	↓	↓	↓	=
t_6	≥1980	Class C	=	=	=	↓	=
t_7	≥1980	Class C	=	=	=	↓	=

Legend: (↑) Improvement; (=) No effect; (↓) Worsening with respect to the level of damage.

2.4 *Step 4: Evaluation of the effect of initial bridge vulnerability (VC)*

The vulnerability of bridges is also associated to their characteristics, including structural typology, maximum span length, number of spans and construction material. Based on combinations of these parameters, the Guidelines identify values of initial vulnerability classification (VC_0). The actual vulnerability class VC is identified based on the combination of classes VC_0 and VC_2 by means of the combination matrix resumed in Table 4.

Table 4. Combination matrix to obtain final VC.

		VC_0				
		LOW	**MEDIUM-LOW**	**MEDIUM**	**MEDIUM-HIGH**	**HIGH**
VC_2	**LOW**	LOW	LOW	LOW	MEDIUM-LOW	MEDIUM-LOW
	MEDIUM-LOW	LOW	MEDIUM-LOW	MEDIUM-LOW	MEDIUM	MEDIUM
	MEDIUM	MEDIUM-LOW	MEDIUM	MEDIUM	MEDIUM-HIGH	MEDIUM-HIGH
	MEDIUM-HIGH	MEDIUM	MEDIUM	MEDIUM-HIGH	MEDIUM-HIGH	MEDIUM-HIGH
	HIGH	MEDIUM	MEDIUM-HIGH	MEDIUM-HIGH	HIGH	HIGH

3 CASE STUDY ON PROBABILISTIC ASSESSMENT OF VULNERABILITY CLASS

3.1 *Epistemic uncertainties regarding engineering judgment*

The reliability of the expert judgment in correctly identifying the damage level d depends on the expertise of technical inspectors, who could overestimate (i.e., false positive) or underestimate (i.e., false negative) the actual bridge conditions. To account for realistic inspector's experiences, three expertise indices e_i are defined:

1. Complete lack of knowledge e_1. This scenario is representative of situations where bridge managers are prevented from conducting a detailed visual inspection to evaluate the extent and intensity of damage and identify specific vulnerability parameters.
2. Low inspector expertise e_2. Damage assessment is carried out via hasty visual inspections or by inadequately trained professionals leading to relevant potential biases.
3. High inspector expertise e_3. Damage assessment is thoroughly carried out highly trained professionals, reducing inaccuracies that may arise in scenario e_2.

The bias matrices in Tables 5–7 represent the epistemic uncertainties in the expert-based judgment. Each numerical value refers to the column-to-row conditional probability that the bridge is in the actual damage level (i.e., along the reference column) given the expert-based judgment of such damage level (i.e., along the reference row).

Table 5. Bias matrix for each expertise scenario e_1.

Actual Judgment	Low	Medium-Low	Medium	Medium-High	High
Low	0.20	0.20	0.20	0.20	0.20
Medium-Low	0.20	0.20	0.20	0.20	0.20
Medium	0.20	0.20	0.20	0.20	0.20
Medium-High	0.20	0.20	0.20	0.20	0.20
High	0.20	0.20	0.20	0.20	0.20

Table 6. Bias matrix for each expertise scenario e_2

Actual Judgment	Low	Medium-Low	Medium	Medium-High	High
Low	0.45	0.25	0.15	0.10	0.05
Medium-Low	0.20	0.40	0.20	0.12	0.08
Medium	0.10	0.20	0.40	0.20	0.10
Medium-High	0.08	0.12	0.20	0.40	0.20
High	0.05	0.10	0.15	0.25	0.45

Table 7. Bias matrix for each expertise scenario e_3

Actual Judgment	Low	Medium-Low	Medium	Medium-High	High
Low	0.80	0.12	0.06	0.02	0.00
Medium-Low	0.10	0.70	0.10	0.08	0.02
Medium	0.05	0.10	0.70	0.10	0.05
Medium-High	0.02	0.08	0.10	0.70	0.10
High	0.00	0.02	0.06	0.12	0.80

3.2 *Structural typologies*

The methodology for the evaluation of structural and foundational VC is applied to five bridges associated to five levels of VC_0. A brief description of structural typologies is provided in Table 8 aligned with the reference cases collected in Figure 3.

Table 8. Structural typologies identified by VC_0.

Bridge	Description	VC_0
Structural Typology 1 Figure 2a	Single span RC arch bridge with length lower than or equal to 5 m	0-LOW
Structural Typology 2 Figure 2b	Single RC arch bridge with length ranging 5 to 15 m	1-MEDIUM-LOW
Structural Typology 3 Figure 2c	Multi-span PC simply supported bridge with a maximum span length ranging 5 to 15 m	2-MEDIUM
Structural Typology 4 Figure 2d	Multi-span PC simply supported bridge with a maximum span length ranging 15 to 25 m	3-MEDIUM-HIGH
Structural Typology 5 Figure 2e	Multi-span PC simply supported bridge with Gerber joints with a maximum span length greater than 15 m	4-HIGH

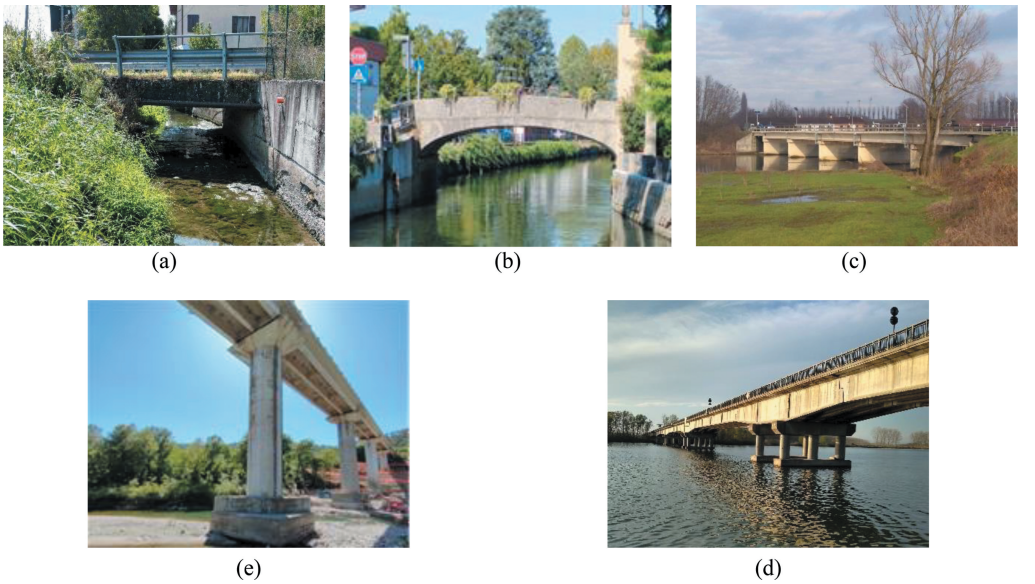


Figure 3. Examples of reference bridges: (a) Typology 1, (b) Typology 2, (c) Typology 3, (d) Typology 4 and (e) Typology 5.

3.3 *Impact of expertise in probabilistic vulnerability class VC*

The bridge is assumed to be designed in 1970 with total length L<10m, design category I, and not exposed to chlorides. The results can be extended to other combinations of input data. Each stacked bar chart collected in Figure 4 shows the statistical representation of the discrete random variable associated to the structural and foundational VC. Each bar represents the marginal probability for all five classes identified by the colors of each stacked bin consistently with the color palette shown in Figure 1. Then, each stack represents the results for a given scenario e_i related to the inspector's expertise. Finally, the results for a selected structural typology and damage level assigned by the inspector are collected over rows and columns, respectively.

The epistemic uncertainties related to different expertise scenarios result in an increase of the dispersion of the results about the central value. It is also worth highlighting that damage level of any investigated structural typology tend to exacerbate the expected value of the random variable VC. Consistently with the process, VC is not dependent on structural

typology for the highest level of damage. Therefore, if VC_0 is greater than or equal to 4, VC is not affected by the structural typology. Furthermore, graphs associated to VC_0 lower than 2 and damage level equal to 5 highlight the importance of the technicians' expertise in correctly assessing the level of damage. In these cases, a slight underestimation of the damage level (i.e. d=4) leads to a significant underestimation of VC, finally resulting as MEDIUM.

3.4 *Impact of bridge age in probabilistic vulnerability class VC*

Figure 5 Represents the time-variant probabilistic VC consistently with the seven intervals for design class and damage evolution identified in the timeline in Figure 2. For damage level 5, VC is not dependent either on design class or damage evolution, consistently with the workflow presented in Figure 1. For all other damage levels, graphs exhibit a pattern of alternating improvements and deteriorations of VC over time. This phenomenon can be primarily attributed to the combined effect of construction year and design class: Table 8 provides an overview of the overall effect for different combinations in this case study. Pairs of temporal intervals t_4–t_5, as well as t_6–t_7 share the same parameter combinations. This consistency is illustrated in Figure 5, where bars associated to these pairs of temporal periods are identical. It is worth noting that charts corresponding to d=2 deserves attention, as they reveal a negative difference of two VC between time instants t_1 and t_2 for VC_0 greater than 2. This is due to the fact that for d=2, there is an overall improvement effect at t_1 followed by a worsening effect at t_2.

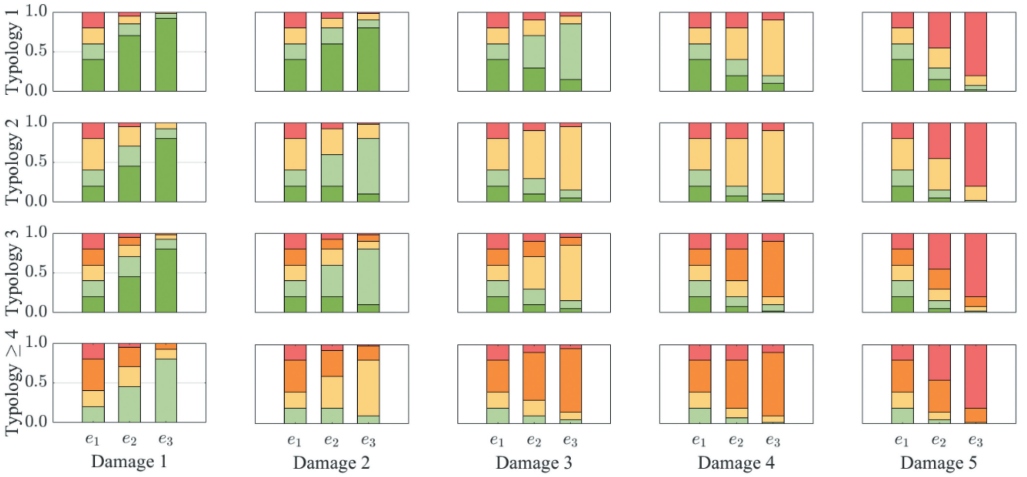


Figure 4. Probabilistic structural and foundational VC for all bridge typologies and observed damage levels considering total length L<10m, design category I, no exposure to chlorides, and design year 1970.

4 CONCLUSION

The prioritization of investments for maintenance and retrofit interventions over large bridge stocks is a crucial task for public administrations. The optimization of bridge management is aided by automated procedures implemented in BMSs exploiting logical workflows and numerical indicators computed on documental information and expert evaluations. This paper focuses on the assessment of the Structural Vulnerability Class (VC) as defined by Italian Guidelines and introduces a probabilistic perspective, introducing epistemic uncertainties related to bridge data collection process.

The results highlight the impact of the expert evaluations for the damage level on the final VC and point out the need of improving the quality of the data through an appropriate training of technicians. Expanding the proposed approach to other risk components such as the

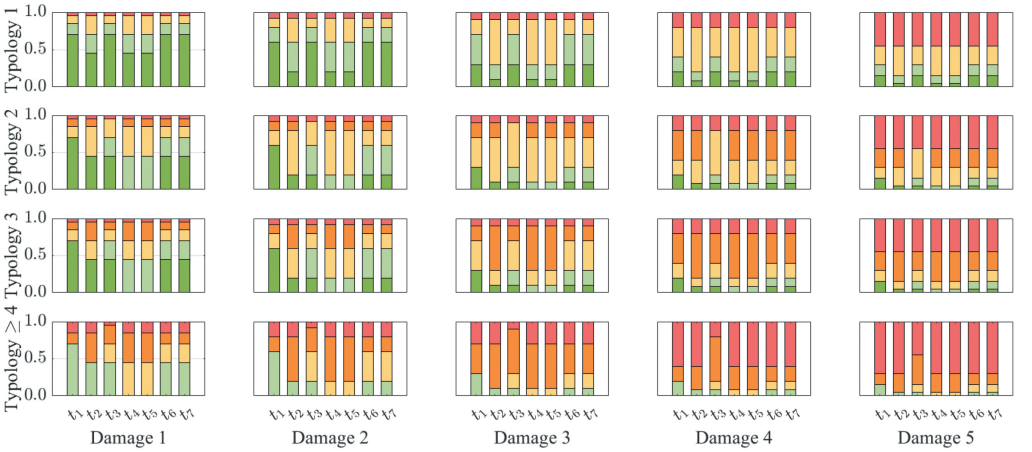


Figure 5. Probabilistic structural and foundational VC for all bridge typologies and observed damage levels considering total length L<10m, design category I, no exposure to chlorides, and expertise e_2.

seismic vulnerability (Capacci and Bianchi 2024) would allow to scale the impact of epistemic uncertainties up to the bridge Attention Class with a fully risk-based probabilistic approach.

REFERENCES

ASCE (2021). Report card for America's infrastructure.

Bianchi, S., & Biondini, F. (2022a). Bridge Condition Assessment Using Supervised Decision Trees. *1st Conference of the European Association on Quality Control of Bridges and Structures* (EUROSTRUCT 2021). Padova, August 29 – September 1.

Bianchi, S., & Biondini, F. (2022b). Life-Cycle Assessment of Deteriorating RC Bridges Using Artificial Neural Networks. *Journal of Infrastructure Systems*, 28(2), 04022005.

Biondini, F., Frangopol, D.M. (2019). *Life-cycle design, assessment and maintenance of structures and infrastructure systems*, ASCE, Reston, VA, USA.

Buratti, G., Cosentino, A., Morelli, F., Salvatore, W., Bencivenga, P., Zizi, M., De Matteis, G. (2019). Alcune considerazioni sull'evoluzione normativa dei carichi da traffico nella progettazione dei ponti stradali in Italia. *XIII Convegno ANIDIS*. Ascoli Piceno, September 15-19, 2019.

Buratti, G., Celati, S., Cosentino, A., Gaudioso, D., Mazzatura, I., Morelli, F., & Salvatore, W. (2022). The new guidelines of Italian Ministry of Infrastructures for the structural risk classification of existing bridges: genesis, examples of application and practical considerations. *1st Conference of the European Association on Quality Control of Bridges and Structures* (EUROSTRUCT 2021). Padova, August 29 – September 1.

Capacci, L., & Biondini, F. (2020). Probabilistic life-cycle seismic resilience assessment of aging bridge networks considering infrastructure upgrading. *Structure and Infrastructure Engineering*, *16*(4), 659–675.

Capacci, L. & Bianchi, S. (2024). Sensitivity analysis of seismic vulnerability class assessment under uncertainty. *18th World Conference on Earthquake Engineering (WCEE 2024)*, Milano, July 1-5, 2024.

Capacci, L., Biondini, F., & Titi, A. (2020). Lifetime seismic resilience of aging bridges and road networks. *Structure and Infrastructure Engineering*, *16*(2), 266–286.

Capacci, L., Biondini, F., & Frangopol, D. M. (2022). Resilience of aging structures and infrastructure systems with emphasis on seismic resilience of bridges and road networks. *Resilient Cities and Structures*, 1(2): 23–41.

Ministry of Infrastructure and Transport (2022). *Ministerial Decree 204 on 01.07.2022. Adoption of Guidelines for risk classification and management, safety assessment and monitoring of existing bridges.*

Yang, D.Y., Frangopol, D.M. (2018). Risk-informed bridge ranking at project and network levels. *Journal of Infrastructure System*. 24(3): 04018018.

Bridge Maintenance, Safety, Management, Digitalization and Sustainability – Jensen, Frangopol & Schmidt (eds)
© 2024 The Author(s), ISBN 978-1-032-77040-6
Open Access: www.taylorfrancis.com, CC BY-NC-ND 4.0 license

Automated construction of BIM models from point clouds to digitalise bridge assets

Rade Hajdin, Lazar Rakic & Holger Diederich
Infrastructure Management Consultants, Zürich, Switzerland

Rico Richter, Justus Hildebrand, Sebastian Schulz & Jürgen Döllner
Digital Engineering Faculty, Hasso Plattner Institute, University of Potsdam, Potsdam, Germany

Jennifer Bednorz
Federal Highway Research Institute (BASt), Bergisch Gladbach, Germany

ABSTRACT: The application of BIM in infrastructure asset management is intended to facilitate current management practices. For this purpose, existing bridges must be digitalised, which is challenging due to the related workload. Recent advancements in 3D surveying and artificial intelligence offer new possibilities for digitalisation. This paper presents a novel, modular framework for an automated construction of BIM models from bridge point clouds. The framework is based on a fusion of artificial intelligence and heuristic algorithms. Machine learning and geometric processing systems are utilised to segment bridge elements in point clouds and transform them into solid models. The final result is an as-is BIM model of a bridge, enriched with semantic information from databases, in the standardised IFC file format. The proposed framework could become a part of an expert system for interactive, machine-assisted construction of BIM models that will enable large-scale bridge asset digitalisation campaigns.

1 INTRODUCTION

The use of building information modelling (BIM) models (Sacks et al., 2018) in new construction projects is already included in the German implementation strategy (BMDV, 2021). These digital asset models can be then also used for more efficient asset management in operation and maintenance lifecycle phases. The benefit of the digitalisation in the later lifecycle phases will be fully exploited only when BIM models are available for most of the existing infrastructure assets. Depending on the quality of the information in the available 2D plans and infrastructure databases, the manual digitalisation of 2D plans could be labour-intensive or infeasible. BIM models derived in this manner may also represent the as-planned and not the wanted as-is state of an asset. Recent advancements in 3D surveying and artificial intelligence have unlocked new possibilities for an automated generation of BIM models from point cloud scans.

The objective of this work is to establish a BIM model generation procedure that is well-suited for bridge asset management. A novel, modular framework is presented, designed for the automated provision of as-is bridge BIM models from 3D point clouds (a process also known as Scan2BIM) for existing road bridges. This work can serve as the starting point for a comprehensive digitalisation campaign of the whole bridge inventory. The potential of artificial intelligence (AI) methods for the segmentation of bridge elements in point clouds is tested. Segmented point clusters of bridge elements are then algorithmically transformed into 3D solid models. Finally, a methodology for enriching geometric representations of bridge elements data from structure databases and geographical information systems (GIS) is developed.

DOI: 10.1201/9781003483755-219

2 BACKGROUND

The reconstruction of geometric data and associated semantics based on 3D survey is a key aspect of the digital representation of the built environment. The Scan2BIM process for bridge infrastructure assets typically consists of a collection of procedures that start with captured, raw point clouds and result in semantically enriched point clouds with clusters that correspond to bridge elements. The use of bridge element properties and parameters as well as geometry reconstruction methods are necessary to construct solid geometries and save them, e.g., in standardised Industry Foundation Classes (IFC) format. Most authors in the research field of bridge Scan2BIM process are showing efforts to obtain semantically meaningful bridge models in an automated way (Lu et al., 2019, Qin et al., 2019). They recursively decompose the bridge into parallel equidistant slices and then describe the bridge elements by analysing their 2D cross-section parameters and extrusion paths. Acquired bridge BIM models can then be linked with structure databases, GIS systems and bridge management systems (BMS). BMS (Lauridsen et al., 1998, Ryall, 2009) are used to manage the bridge assets more efficiently, e.g., with inventory organisation, maintenance planning and bridge inspection with condition assessment.

3 METHODOLOGY AND RESULTS

The methodology and results shown in this paper stem from the research project (Hajdin et al., in prep.), where a typical Scan2BIM process was enhanced by several significant features. These features are summarised in the following, as procedures that are split into two main parts.

3.1 *The learning part*

The learning part consists of the preparation of bridge data set, neural network training, design of procedures for point processing and transformation into solid models, as shown in Figure 1.

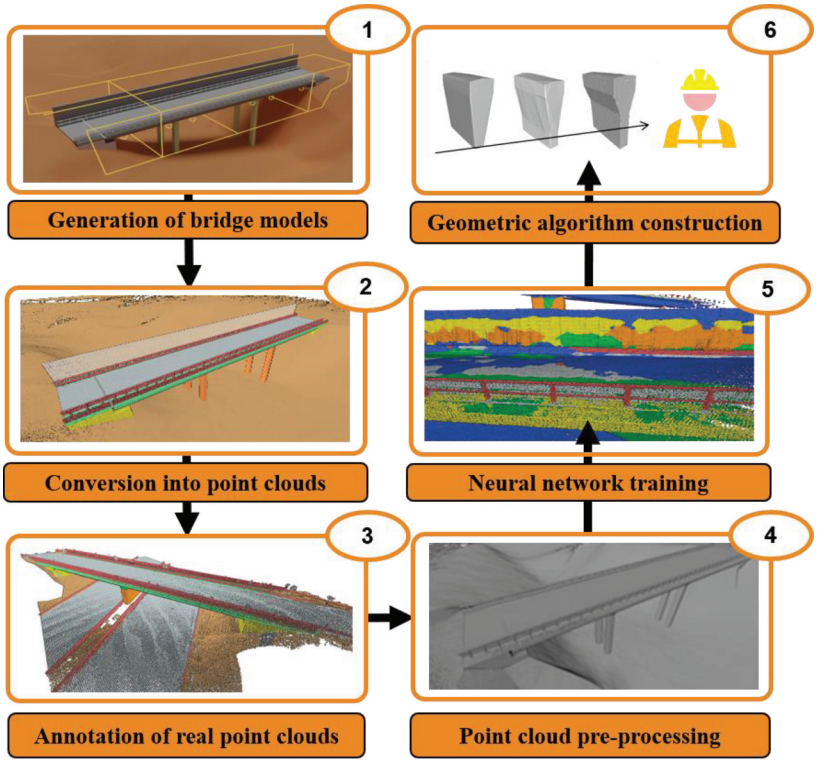


Figure 1. The learning part and its procedures.

3.1.1 *Procedure 1: Generation of bridge models as training data set*
Since the manual preparation of training data by 3D surveying is work intensive, another approach was chosen. 3D bridge models with semantics for each bridge element were generated in software and used to construct a training data set. The bridge models were generated by combining typical bridge elements from the specially developed bridge element database. The construction of this training data set was not a single step, but rather an iterative procedure, where the results of AI-based segmentation and processing were repeatedly evaluated, and new bridge and element models were added to the data set to mitigate the observed deficiencies.

3.1.2 *Procedure 2: Conversion into annotated point clouds*
Training data that are fed to the neural networks must resemble as far as possible the real-world scan data. The generated bridge models are therefore virtually scanned in software and converted into annotated bridge point clouds, as visualised in Figure 2. Both scans along virtual flight routes (mimicking drone scans) and scans on predefined static points (alike terrestrial scans) are simulated in this procedure, designed to mimic real scans and obtained point clouds.

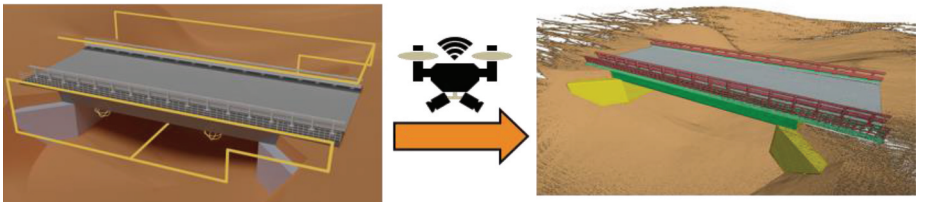


Figure 2. Bridge models and virtual scanning paths to obtain annotated bridge point clouds.

3.1.3 *Procedure 3: Annotation of real-world point clouds*
The training data set must also contain at least several real-world bridge point clouds, which ensures that all specific structural features are included. The training data was generated by annotating real-world bridge point clouds manually in software so that each point possesses in the end the semantics of the corresponding bridge element. This procedure is depicted in Figure 3.

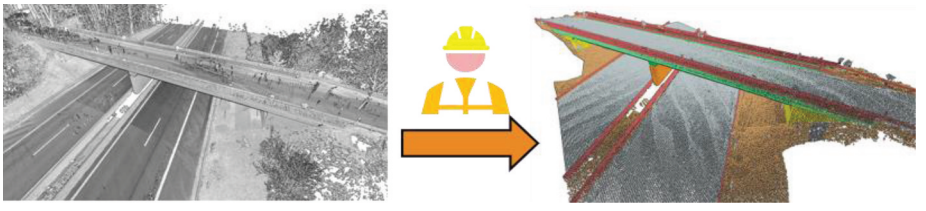


Figure 3. Manual annotation of real-world bridge point clouds for training data.

3.1.4 *Procedure 4: Point cloud pre-processing*
Point clouds are large data that can vary in point resolution and accuracy. Therefore, filtering procedures are required to bring point clouds in an adequate form for further processing. The data quality is improved by removing unwanted points and objects, as can be seen in Figure 4.

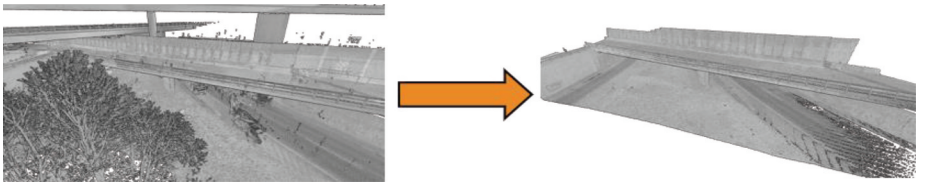


Figure 4. Point cloud pre-processing to improve the data quality for further procedures.

3.1.5 *Procedure 5: Neural network training*

Neural networks are trained with the training data consisting of generated and real-world annotated point clouds, as seen in the previous procedures. Trained neural networks can assign a bridge element class to every point of the point cloud with good accuracy, as shown in Figure 5.

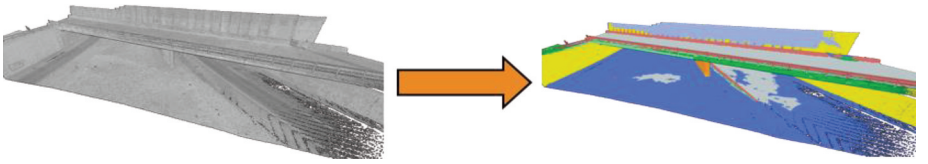


Figure 5. Neural networks add semantics to bridge point cloud points.

3.1.6 *Procedure 6: Geometric algorithm construction*

Geometric rule-based algorithms are developed to transform point clouds in higher-order geometric representations, surface and solid models, which are better suited for bridge representation in BIM. This is done by analysing different bridge element types and describing cross-sections and extrusion parameters, based on the established bridge property knowledge base.

3.2 *The application part*

The application part involves the processing of raw real-world bridge point clouds and the automated construction of BIM models from them, using trained neural networks and established geometric algorithms from the learning part. These procedures are overviewed in Figure 6.

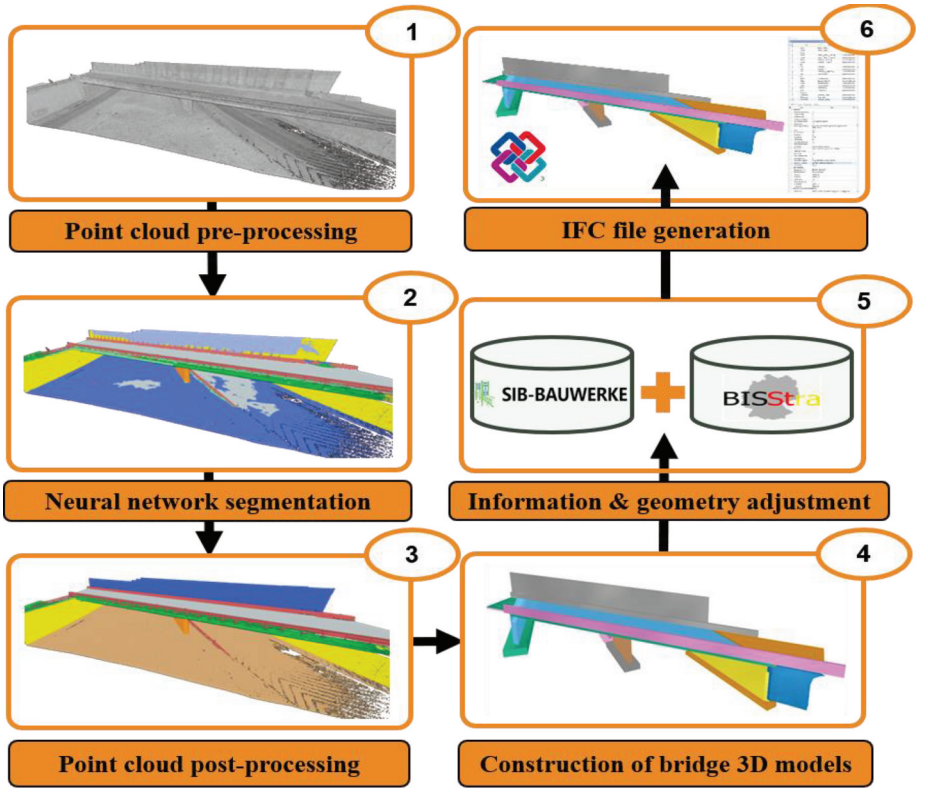


Figure 6. The application part and its procedures.

3.2.1 *Procedure 1: Point cloud pre-processing*
The pre-processing techniques already explained in the learning part are applied to raw real-world bridge point cloud scans to bring them in a suitable form for the upcoming procedures.

3.2.2 *Procedure 2: Neural network segmentation*
The trained neural network analyses points of the point cloud, where each point and its neighbours are processed and the most likely bridge element class is assigned to them. As a result, the bridge point cloud is segmented into point clusters belonging to different bridge element classes, based on what the neural network learned in the learning part. This segmentation is not perfect and post-processing steps are applied next to improve the bridge element assignment accuracy.

3.2.3 *Procedure 3: Point cloud post-processing*
Post-processing of segmented point clouds is necessary because AI-based segmentation can incorrectly classify individual points, especially on bridge elements' boundaries. By applying different analysis methods (e.g., region growing, clustering, majority voting), points are checked for their plausibility for the classes assigned by the AI-based segmentation and corrected as necessary. The resulting segmented point cloud of a real-world bridge is then given in Figure 7.

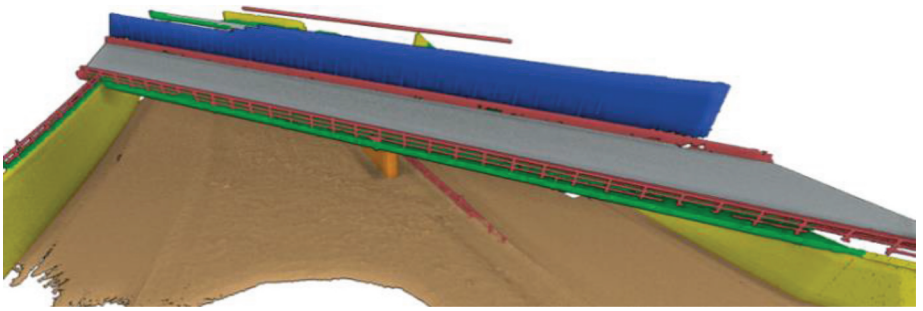


Figure 7. The result of AI-based segmented bridge point cloud showing different bridge elements.

3.2.4 *Procedure 4: Construction of bridge 3D models*
Methods for the cross-section recognition and extrusion direction of bridge elements have been implemented to generate 3D bridge element solid geometries. There are different cross-section characteristics and possibilities for parameterisation: predefined template, bounding box, convex envelope etc. The most suitable cross-section parametrisation and extrusion direction variants are chosen for each bridge element, generating solid bridge element geometries in Figure 8.

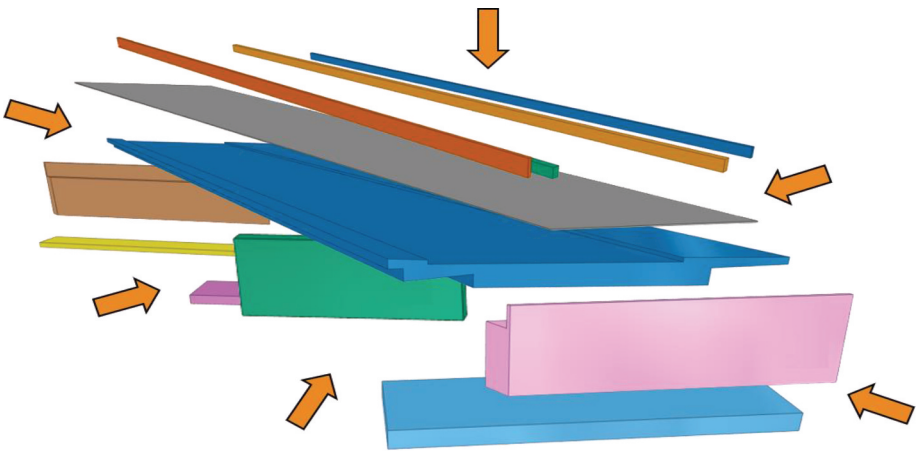


Figure 8. Bridge 3D model reconstruction with solid geometries for each element.

3.2.5 *Procedure 5: Information enrichment and geometry adjustment*
Bridge elements are enumerated based on the algorithmically determined bridge axis using the alignment data from the German Federal Road Information System (BISStra, 2024). Data from structure database of the German Building Database from the Federal and State Governments (SIB-Bauwerke, 2024) can be afterwards linked to the corresponding bridge elements and occluded bridge elements in scans, such as pavement layers, footings, expansion joints, bearings, abutment parts can be added and improved. Typical bridge properties and default values from the established knowledge base are used to generate realistic geometries where the information in point clouds or databases is lacking. The result of this step are improved and informationally enriched bridge elements and their merging into a single bridge model, shown in Figure 9.

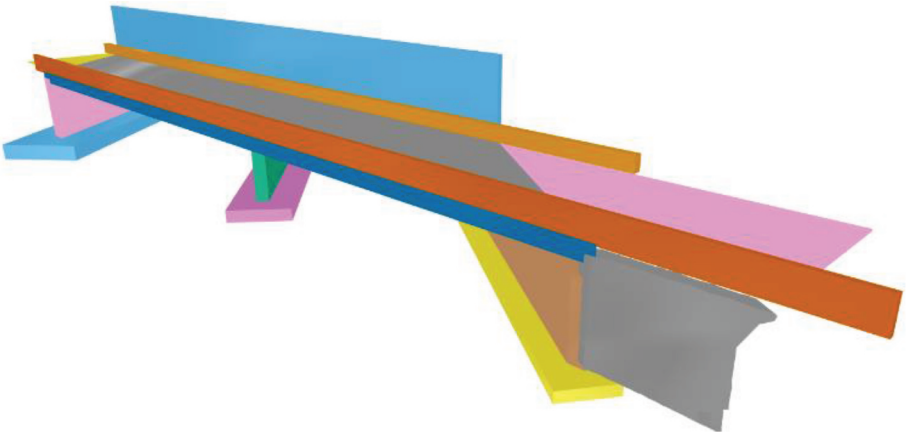


Figure 9. Resulting complete bridge model with reconstructed geometries of bridge elements.

3.2.6 *Procedure 6: IFC file generation*
The IFC format is an open file exchange format, intended to improve the data flow and file exchange between different disciplines. It captures the geometric, spatial, and semantic relationships between the individual elements of a structure (Liebich, 2009). The developed procedure in this work contains the conversion of the geometric representation and linked information from databases from the previous procedure into one IFC file, where a dedicated programming script has been implemented to automate this procedure. The IFC hierarchy corresponding to bridges with individual IFC entities for different bridge elements is established (e.g., IFC entities for beams, bearings, railings, slabs, columns) and additional information from structure databases and GIS systems (in the form of IFC property sets) is linked to these IFC entities.

3.3 *Results*

The final result of a processing procedure is a BIM model representing the as-is state of an existing bridge. Bridge elements are represented with solid geometries, enriched with information from structure and road databases in the standardised, open IFC file exchange format. The entire procedural chain from raw point cloud scan data to the final BIM model was implemented and tested on real bridges to demonstrate that the automated derivation of BIM models from point clouds is attainable. The used data formats ranging from point clouds to 3D solid models are all standardised. Different framework procedures are implemented modularly so that a further enhancement of the individual procedures is easily achievable. An example of the generated BIM model starting from the raw point cloud of a real bridge of the German Federal Highway Network is given. The raw, input point cloud to the framework is shown on the left, and the framework output, an IFC model with bridge geometry, is on the right in Figure 10.

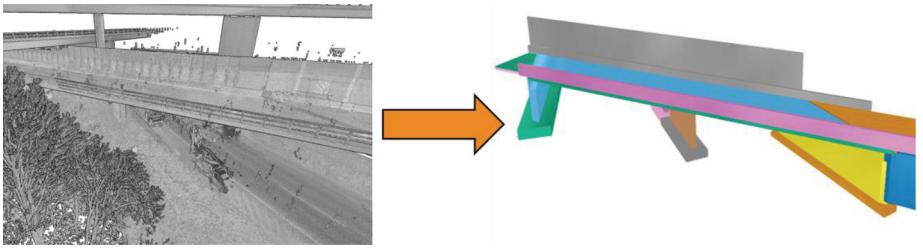


Figure 10. Transformation of raw bridge point cloud into IFC model with complete bridge geometry.

4 CONCLUSION

The developed procedure uses a blend of artificial intelligence and heuristic algorithms to process bridge point clouds into BIM models. By automating a rather strenuous Scan2BIM process, this work addresses the needs of bridge owners to have updated bridge asset data in their inventories. The developed methods exhibit robustness and prove the practical applicability that is needed for further development and a large-scale asset digitalisation campaign. Technological challenges such as large data volumes, varying acquisition data properties and distinct, complex geometry and bridge elements could be addressed and solved. The results and findings may accelerate digital transformation in the bridge infrastructure sector and improve asset management processes. The applicability of the developed procedures was tested on several existing road concrete bridges of the German Federal Highway Network System.

A significant potential lies in the complete digitalisation of structural inspection and maintenance planning. All findings, structural inspections and changes can be traced in the BIM model and processed over the entire lifecycle of a structure. This helps not only in decision-making on the individual structure, but also in providing valuable information strategically for the management of the entire structure inventory. Digital bridge models could also be embedded into 3D terrain models, which would enable a simulation of negative environmental impacts and the calculation of community resilience. It is evident in summary that these models are well-suited for use in asset management.

Obtained 3D element geometries can be also manually refined in modelling software to achieve a higher level of detail, add elements that are missing in scans, or record structural changes incurred during maintenance interventions. This means that the BIM model would stay up-to-date through the whole structure lifecycle, and such a model is also referred to as the digital twin (DT). The model may be even used for structural reassessment with some further post-processing steps, bringing it in a form suitable for finite element modelling (FEM) and structural analysis.

Lines of future work would include the construction of a more comprehensive 3D bridge element database. Neural networks trained on that exhaustive data collection and further geometric algorithms capturing more bridge properties would increase automation levels and the quality of results. An extended knowledge base of bridge properties will further aid in generating more detailed bridge geometric representations and better model proxies for bridge elements not visible to scanning devices and not properly recorded in the available databases.

ACKNOWLEDGEMENT

The presented work was funded by the Federal Highway Research Institute (BASt), Germany, through a research project Nr. FE 02.0436/2020/ARB “Development of procedures for the semi-automated construction of BIM models for existing road bridges”. The presented work was also partially funded by the Federal Ministry of Education and Research, Germany, through grant 01IS22062 “AI research group FFS-AI”.

REFERENCES

Sacks, R., Eastman, C., Lee, G., & Teicholz, P. 2018. *BIM Handbook: A Guide to Building Information modeling for Owners, Designers, Engineers, Contractors, and Facility Managers* (3rd ed.). Hoboken: John Wiley & Sons.

Federal Ministry for Digital and Transport (BMDV). 2021. Master Plan BIM Federal Highways (Masterplan BIM Bundesfernstraßen). [Internet]. 2021. [Accessed on 2024 January 25]. Available via: https://bmdv.bund.de/SharedDocs/DE/Anlage/StB/bim-rd-masterplan-bundesfernstrassen.pdf?__blob=publicationFile

Lu, R., Brilakis, I., & Middleton, C.R. 2019. Detection of Structural Components in Point Clouds of Existing RC Bridges: Detection of bridge components in point clouds. *Computer-Aided Civil and Infrastructure Engineering* 34(3): 191–212.

Qin, G., Zhou, Y., Hu, K., Han, D., & Ying, C. 2021. Automated Reconstruction of Parametric BIM for Bridge Based on Terrestrial Laser Scanning Data. *Advances in Civil Engineering* 7(1): 1–17.

Lauridsen, J., Bjerrum, J., Hutzen, A.N., & Lassen, B. 1998. Creating a Bridge Management System. *Structural Engineering International* 8(3): 216–220.

Ryall, M.J. 2009. *Bridge Management*. Oxford: Elsevier.

Hajdin, R., Richter, R., Rakic, L., Diederich, H., Hildebrand, J., Schulz, S., & Tanasic, N. Development of procedures for the semi-automated construction of BIM models for existing road bridges (Entwicklung von Verfahren zur (teil-)automatisierten Erstellung von BIM-Modellen für Straßenbrücken im Bestand). Bergisch Gladbach: Federal Highway Research Institute (BASt). Report in preparation.

Liebich, T. 2009. IFC 2x Edition 3 Model Implementation Guidance. [Internet]. [Accessed on 2024 January 25]. Available via: https://standards.buildingsmart.org/documents/Implementation/IFC2x_Model_Implementation_Guide_V2-0b.pdf

Federal Highway Research Institute (BASt). Bundesinformationssystem Straße (BISStra). [Internet]. [Accessed on 2024 January 25]. Available via: https://www.bast.de/DE/Verkehrstechnik/Fachthemen/v2-bisstra.html

Federal Highway Research Institute (BASt). Bauwerksdaten (SIB-Bauwerke). [Internet]. [Accessed on 2024 January 25]. Available via: https://www.bast.de/DE/Ingenieurbau/Fachthemen/b4-bauwerksdaten.html

Bridge Maintenance, Safety, Management, Digitalization and Sustainability – Jensen, Frangopol & Schmidt (eds)
© 2024 The Author(s), ISBN 978-1-032-77040-6
Open Access: www.taylorfrancis.com, CC BY-NC-ND 4.0 license

Leveraging digital twin tools for the Minnesota DOT Robert Street Bridge inspection

S. Becher
Bentley Systems, Neptune Beach, Florida, USA

B. Lovelace
Collins Engineers, St. Paul, Minnesota, USA

ABSTRACT: Many organizations who are responsible for inspecting, monitoring, and maintaining bridge infrastructure are faced with the challenges of workforce shortages and an increasing backlog of aging bridges. Addressing these challenges requires a multi-faceted solution from the owner/operators, the engineering consultants they rely on as well as the entire infrastructure industry. Leveraging the latest technology to improve the current workflows should be a significant component of the comprehensive solution. The collection of reality data with a UAS and creation of a digital twin has proven to be a valuable tool in augmenting traditional inspections by utilizing remote visualization. As the technology matures, there continues to be advances in the tools that can be used along with the digital twin to assist inspectors. This paper will highlight how Collins Engineers used these tools to augment their existing workflows as a consultant to the Minnesota Department of Transportation in a detailed inspection and rehabilitation plan for the Robert Street Bridge. This includes the use of photo navigation alongside the 3D model, inspection forms with georeferenced issues, and mobile tools used in the field. The technology and associated workflow utilized by Collins saved over 30% in inspection hours and the improved quality of the data collection will generate a 20% savings in construction costs.

In addition to highlighting the tools used in the case study, the paper will cover other tools that can be used within a digital twin including artificial intelligence crack and spall detection, augmented reality model visualization and internet of things (IoT) sensors for structural health monitoring. Other AI detectors that are currently under development will be discussed and how these innovations will continue to transform traditional workflows. The transformation from traditional inspection workflows has the potential to enhance safety, reduce costs and improve the accuracy of inspection results.

1 INTRODUCTION

Many organizations who are responsible for inspecting, monitoring, and maintaining bridge infrastructure are faced with the challenges of workforce shortages and an increasing backlog of aging bridges. Addressing these challenges requires a multi-faceted solution from the owner/operators, the engineering consultants they rely on as well as the entire infrastructure industry. Leveraging the latest technology to improve the current workflows should be a significant component of the comprehensive solution. The collection of reality data with a UAS and creation of a digital twin has proven to be a valuable tool in augmenting traditional inspections by utilizing remote visualization. As technology matures, there continues to be advances in the tools that can be used along with the digital twin to assist inspectors. These tools include georeferenced annotations of a 3D reality model, AI/ML assisted defect detection, AR/VR visualization, and IoT assisted structural health monitoring.

DOI: 10.1201/9781003483755-220

An effective way to demonstrate the benefits of the technology is to highlight a project where the tools were used to augment existing workflows. Collins Engineers worked closely with Bentley to implement the software to provide a completed inspection to Minnesota Department of Transportation on the Robert Street Bridge Rehabilitation project.



Figure 1. Robert Street Bridge.

2 PROJECT OVERVIEW

The Robert Street Bridge is an eight-span reinforced concrete arch bridge with the main span consisting of massive rainbow arch ribs that define its modern architectural style. The bridge is located in downtown St. Paul, MN and was constructed in 1926. The Robert Street Bridge is on the National Register of Historic Places and is an important vehicular and pedestrian connection crossing the Mississippi River. The bridge is owned by the Minnesota Department of Transportation and in addition to crossing the river it also crosses two railways and a local roadway for a total length of 1429 feet (436 meters).

The bridge was rehabilitated in 1989 but significant deterioration has occurred since then and the project includes a detailed inspection to support a bridge management plan to facilitate another rehabilitation project in the future.

Collins Engineers Inc. teamed with Michael Baker on this important project and our role included creating a digital twin of the structure, performing the detailed inspection and documenting, and communicating the condition of the bridge.

A key objective of this project includes collecting detailed information on the condition of the bridge through inspection and testing. Another objective is to calculate a load rating of the bridge based on the condition information to determine the current load carrying capacity

of the bridge. The last objectives include a bridge management plan and service life analysis that will inform the rehabilitation efforts.

The main challenge of this project is the difficulty in efficiently and accurately collecting detailed inspection information for such a large structure with so many defects and deficiencies. Using traditional inspection data collection methods would be very tedious and expensive so the team had to find innovative ways to not only be more efficient but also to provide a higher quality deliverable for the Minnesota Department of Transportation.

Workforce shortages are another challenge we needed to address. With traditional inspection methods highly trained and educated engineers spent much of their time doing mundane tasks such as measuring and sketching defects. The project team proposed using these new technologies and workflows to make data collection easier and ensure engineers were spending their time making decisions versus collecting data.



Figure 2. Field inspection.

3 PROJECT PLAN

In order to meet the challenges of this project, Collins' team proposed using UAS to collect data in order to create a detailed digital twin of the bridge. It was imperative to use a digital twin visualization tool that could be shared across the team, and would become the central repository for the inspection, inventory, and testing information. The team proposed collecting all the inspection information in the field using internet connected tablet computers using a custom form built by the project team to address the key observations relevant to the structure. Using this form would ensure consistent data and the ability to quickly input inspection information. The scope of work for the project included the following:

- Collected data using drones equipped with artificial intelligence to autonomously collect all images.
- Post process the images and ground control points to build digital twins of each span. Both automatic ground control points and semi-permanent QR codes were used to aid in the processing. The high-resolution images, georeferencing aids and software tool produced high quality models that were used to pre-inspect the bridge in the office.
- The models were uploaded into an online digital twin sharing service. The entire bridge could be viewed at one time or by individual span.
- The engineers on the team performed a pre-inspection in the office using the digital twin visualization tool along with the custom forms. Additionally, the team used artificial intelligence defect detection to automatically find and document concrete cracks and spalls.
- The fieldwork was performed, and all previously input inspection results were verified. Additional inspection information was input in the field using internet connected tablet computers.
- The digital twin with annotated inspection information was shared with the entire team and all team members had the ability to review and add information to the models.

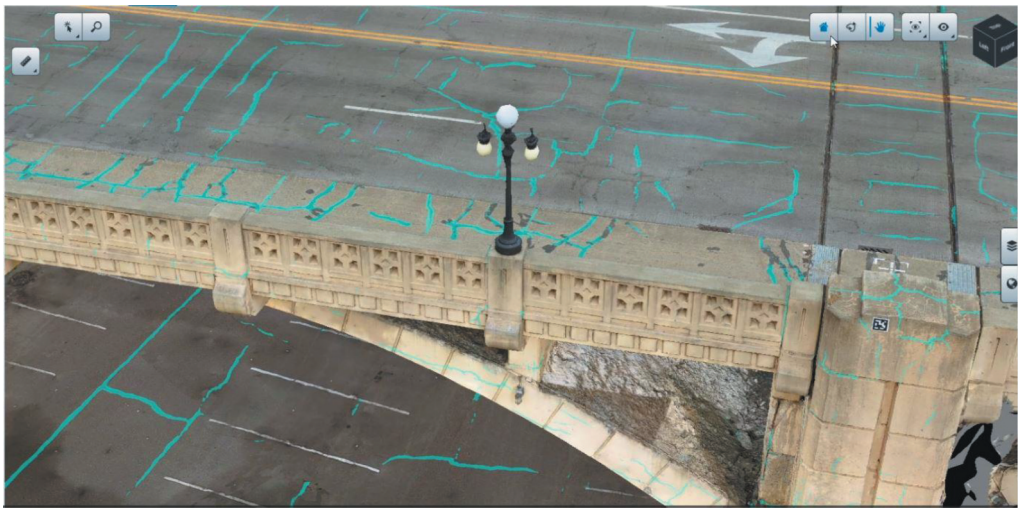


Figure 3. AI/ML crack detection.

One of the largest breakthroughs of our team approach included the ability to pre-inspect the bridge by using the digital twin in the office prior to starting field work. This method allows engineers to validate defects instead of recording detailed information in the field. Another significant breakthrough was the ability to use artificial intelligence to automatically find, quantify and communicate concrete crack information. This workflow using the tools is revolutionary and is a large leap forward in the bridge inspection industry. With our workforce shortages, applying these technologies will provide the industry with a way to deliver improved inspection results.

Another significant breakthrough is the ability to perform quality control based around the digital twin and photo navigation feature in the digital twin visualization tool. Previously, if an inspector missed a defect, the only way to verify was by performing an independent inspection. Using the digital twin, another inspector can easily and remotely check the field inspectors work for accuracy.

4 RESULTS

By using digital twins for the inspection our team saved over 30% on inspection hours and fees with a very significant improvement in the quantity and quality of the deliverables.

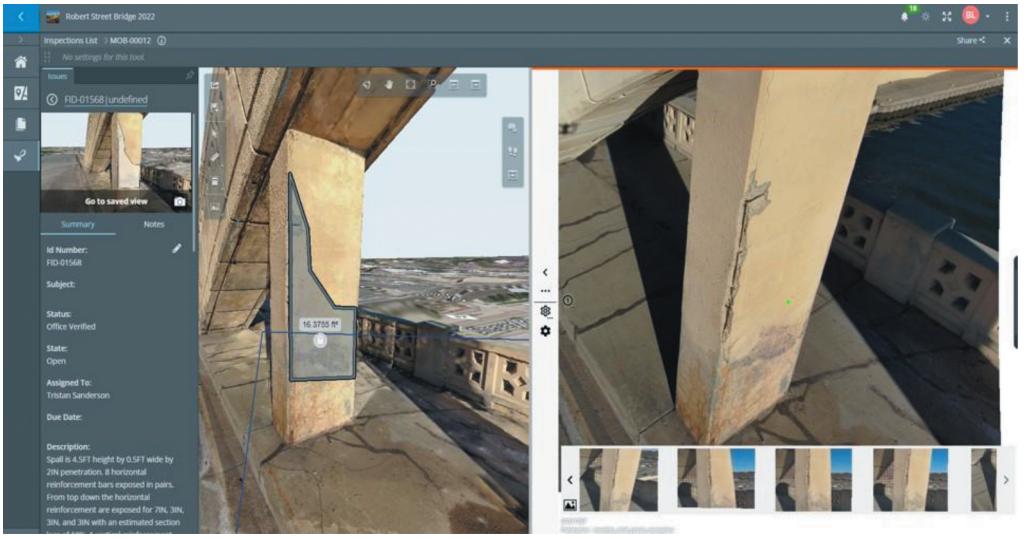


Figure 4. Office pre-inspection using digital twin.

As our team works through bridge rehabilitation process, we expect to see a minimum of 20% construction savings stemming from the improvements in the quality of inspection data since better decisions can be made with more complete information.

Our innovative workflow is impacting the local community by reducing the amount of time our teams need to spend in the field, which in turn reduces traffic control and lane closures. This not only reduces traffic impacts that the public is affected by but also reduces safety risks associated with lane closures and traffic control.

Implementing these tools into the workflows not only reduces safety risks for the public and inspectors, but it also reduces risk for the project team and MnDOT. Better data leads to better decisions, thereby reducing the risk of design errors or applying the wrong repair and rehabilitation solutions. The digital twin visualization tool provided a means to ensure that everyone on the project team had easy access to all the relevant information regarding the bridge. Team members also had the ability to contribute data to the model to further enhance collaboration from all stakeholders and used across disciplines. Due to the technology implemented, The Robert Street Bridge Rehabilitation Project has more quality data accessible to all team members than any other similar bridge inspection project.

Quantitative Summary of Results:

- 30% Reduction in inspection hours which is over $90,000 USD in savings.
- 20% Estimated future construction savings which could translate to up to $15M in savings.
- 20% fuel reduction.
- 10% reduction in material production during future construction.
- 1000x increase in the amount of quantifiable data available to decision makers.

5 FUTURE OUTLOOK

The Robert Street Bridge Project utilized tools to augment a workflow that generated significant benefits, despite being one of the first projects where the Collins team had used these tools. Future projects will undoubtedly use these tools faster and more easily to further improve the benefits. Additionally, the reliability and power of the tools will continue to be enhanced.

The Collins team effectively used the AI/ML concrete crack detector to streamline a tedious task of identifying a specific defect, however bridge inspections required identification of other defects such as spalling, corrosion, and delamination. AI/ML defect detection is still in early stages and the quality and types of the detectors will continuously be improved as the amount of data is inputted into the models.

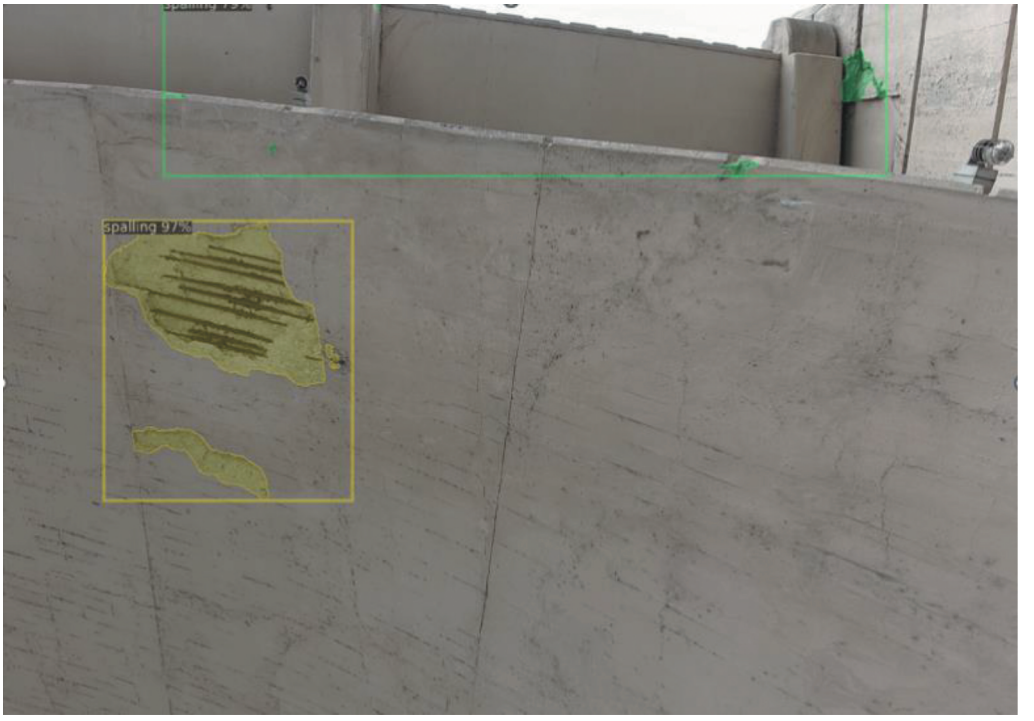


Figure 5. AI/ML spalling detection.

The visualization of 3D models also presents an opportunity for further enhancement of bridge inspection workflows. Extended reality (XR) offers many potential benefits including remote worker collaboration and bridge inspector training programs. The ability to easily navigate an accurate reality model at 1:1 scale, make annotations and have access to all relevant information at the touch of a hand, will further transform bridge inspection workflows. Essentially, workers will have the benefits of being onsite, with the convenience of a computer for documentation and reduce many of the inherent risk factors associated with bridge inspection.

Although IoT sensors were not used in the Robert Street Bridge, the integration of sensors into a monitoring program has the potential to further supplement the technology discussed earlier. While IoT sensors are not necessarily new, the data feeds they provide can be visualized in the same model created for remote inspections, giving owner/operators a more complete picture of the health and performance of the bridge in one environment.

The digital twins created, and the inspection data collected were targeted for our specific rehabilitation project, however it is expected that it will be used to manage this important bridge for many years to come. While the Robert Street Bridge is a large, multi-faceted project, this workflow can be adapted and streamlined for almost any kind of structure including smaller bridges, retaining walls and sign structures, among others. This type of technology will only continue to grow within the inspection and construction field. Collins and Bentley anticipate this new workflow will be adopted for many projects of this type in the next few years since the benefits are so compelling.

6 CONCLUSION

The Robert Street Bridge project serves as a compelling case study, showcasing the effectiveness of digital twins in augmenting traditional inspections through remote visualization. The challenges posed by workforce shortages and the complexity of inspecting aging structures were met with an innovative approach, resulting in substantial benefits, and paving the way for future advancements in the industry. The collaboration between Collins Engineers and Bentley Systems has demonstrated the transformative impact of leveraging the latest technology to streamline workflows and enhance the quality of inspection data. The project's success is evident in the significant reduction in inspection hours. The innovative workflow not only improved efficiency, but also had a positive impact on the local community by reducing the time spent in the field, minimizing traffic disruptions, and enhancing safety for both the public and inspectors. The outlook is promising, with continuous enhancements anticipated in AI/ML defect detection, extended reality (XR) applications, and the integration of IoT sensors.

While the digital twins and inspection data collected were tailored for the specific rehabilitation project of the Robert Street Bridge, the adaptability of this workflow for various structures, from smaller bridges to retaining walls, signifies a broader industry transformation. In essence, the Robert Street Bridge project marks a significant leap forward in the bridge inspection and maintenance field, setting a precedent for the industry to embrace and integrate advanced technologies that not only address current challenges but also pave the way for a more efficient, data-driven, and future-ready approach to infrastructure management.


Taylor & Francis
Taylor & Francis Group
http://taylorandfrancis.com

SS10: Artificial Intelligence for uncertainty, risk, and reliability assessment of bridge infrastructure

Organizers: D. Choe & M. Roohi


Taylor & Francis
Taylor & Francis Group
http://taylorandfrancis.com

Bridge Maintenance, Safety, Management, Digitalization and Sustainability – Jensen, Frangopol & Schmidt (eds)
© 2024 The Author(s), ISBN 978-1-032-77040-6
Open Access: www.taylorfrancis.com, CC BY-NC-ND 4.0 license

A chain-based construction method for bridges monitored within one cluster

Kaitian Wang & Xinteng Ma
School of Transportation Science and Engineering, Harbin Institute of Technology, Harbin, China

Zaiyang Jiang
Heilongjiang Highway Construction and Investment Center, Harbin, China
School of Transportation Science and Engineering, Harbin Institute of Technology, Harbin, China

Yang Liu
School of Transportation Science and Engineering, Harbin Institute of Technology, Harbin, China

ABSTRACT: The bridges monitored within one cluster is characterized by multiple device nodes, wide coverage, and dispersed locations. In order to improve the efficiency of system data transmission, this study proposes a monitoring method for wireless chain networking using device nodes. It not only reduces system construction costs, but also fully utilizes the characteristics of the monitoring system. Firstly, device nodes obtain information about neighboring nodes through channel detection and signal strength detection. Secondly, with the help of wireless data transmission methods, device nodes construct a data transmission protocol and extract a list of device nodes. Finally, a calculation method for optimal path of nodes is proposed to calculate the chain network path that includes all device nodes. This method effectively expands the data transmission distance of the monitoring system, improves data transmission efficiency and reduces the number of system device nodes used. This method fully meets the current and future needs for safety monitoring of bridge cluster structures.

1 INTRODUCTION

With the rapid and mature evolution of wireless technology, wireless sensing technology has attained a significant level of advancement. Presently, numerous monitoring solutions leverage wireless technology for communication. Wireless sensing technology offers distinct advantages over traditional wired sensing approaches. Firstly, Wireless sensors are flexible to use and easy to deploy, obviating the necessity for wired connections and mitigating safety hazards associated with intricate wiring. Secondly, the construction of wireless sensors is characterized by simplicity, as the collection and transmission modules are integrated on a single mainboard, leading to heightened hardware integration and obviating the requirement for expensive collection devices, consequently reducing overall system costs. Additionally, the wireless communication method facilitates the seamless addition and replacement of nodes within the network.

2 WIRELESS NETWORKING TECHNOLOGY OVERVIEW

The deployment of wireless sensors is contingent upon wireless networking technologies, with prevalent options encompassing mesh networks, clustered tree networks, and star topology networks such as Mesh networks, ZigBee networks, and LoRa networks. Mesh networks and clustered tree networks prove efficacious for extensive coverage of wireless sensing points. Nevertheless, when applied to structures like bridge clusters with elongated configurations, these network structures become unduly intricate, posing challenges in capitalizing on their advantages

DOI: 10.1201/9781003483755-221

and escalating network configuration expenses. The star topology network distinguishes itself through its uncomplicated structure, enabling direct communication between each terminal sensor device and a gateway device in a one-to-one fashion, thereby facilitating straightforward command transmission and reception. However, its limitation lies in the constrained transmission distance, necessitating terminal sensor devices and gateway devices to be confined within a fixed area for effective communication. In scenarios involving a high number of terminal sensor devices or an expansive coverage area, the requirement for multiple gateway devices often arises for zone-based management, resulting in a substantial escalation of system costs.

2.1 *Mesh wireless networks*

Mesh[1] wireless networks adopt a mesh pattern wherein nodes establish network connections. Depending on the method of connection between nodes, Mesh networks can be categorized as fully connected or partially connected. In a fully connected Mesh network, illustrated in Figure 1, direct communication is facilitated between any two terminal nodes. The connections between nodes constitute fixed routes, minimizing the occurrence of "multihop".

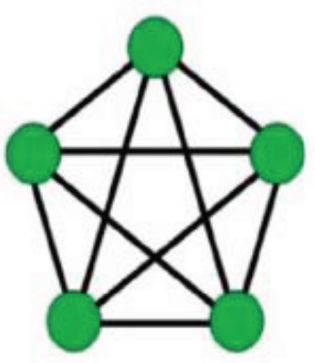


Figure 1. Fully connected Mesh network.

Fully connected networks [2] are typically only viable when the network scale is very small, as the complexity of such networks escalates with the increasing number of nodes. In the case of wired Mesh networks, the substantial and intricate number of cables interconnecting nodes renders fully connected Mesh networks nearly impractical in real-world scenarios. In contrast, partially connected Mesh networks feature nodes with routing capabilities, while others exclusively serve as terminals without routing abilities. Consequently, in practical engineering applications, partially connected Mesh networks are more commonly employed.

2.2 *ZigBee networks*

ZigBee networks[3] utilize a clustered tree routing structure comprising a coordinator, routers, and terminals. While each cluster includes only one coordinator, there can be multiple routers along with their corresponding terminals, as depicted in Figure 2. The cluster head node (router) in each cluster primarily manages routing discovery and maintenance. Communication between terminal nodes necessitates routing through routers and cannot occur directly, thereby reducing routing maintenance overhead but concurrently increasing the demand for routers in the network. Routing between routers is facilitated by the AODV[4] algorithm.

Within the ZigBee network architecture, low power consumption is achieved by allocating networking responsibilities exclusively to non-terminal nodes. Furthermore, the adoption of a clustered tree structure significantly diminishes the number of routing paths between nodes, thereby enhancing routing efficiency.

Notwithstanding these advantages, ZigBee networks exhibit certain drawbacks. Firstly, routers and coordinators within the network are unable to enter a sleep mode, resulting in network



Figure 2. Clustered tree network.

paralysis during the discovery or maintenance of new routes. Secondly, the efficiency of routing links between nodes is suboptimal, leading to diminished network throughput, especially in scenarios with substantial data volumes where message collisions may occur, potentially resulting in data loss. Lastly, there exists a notable dependency on coordinators. Given that the entire network relies on the coordinator for initiation and management, any malfunction of the coordinator can impede the addition of new nodes or even result in network paralysis.

2.3 *LoRa networks*

LoRa networks[5] embrace a star topology network architecture predominantly employed for low-power, multi-node communication, comprising terminal nodes, gateways, and servers, as depicted in Figure 3.

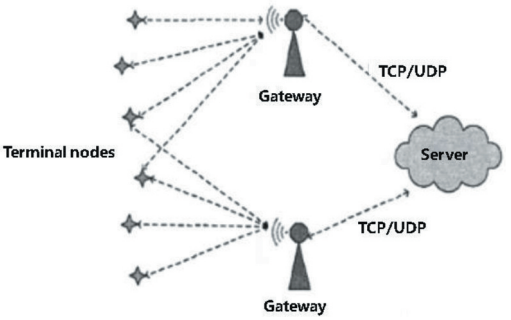


Figure 3. LoRa network.

1. Terminal Nodes: These nodes are responsible for data collection utilizing various sensors based on specific application requirements. In the uplink, terminal nodes transmit collected data to gateways through LoRa radio frequency signals. In the downlink, terminal nodes can receive messages from the gateways.
2. Gateways (Base Stations): Gateways handle the modulation and demodulation of LoRa signals. In the uplink, they encapsulate received data packets and establish connections to the server through standard IP. In the downlink, gateways receive data packets from the server and, based on the packet, determine transmission power, frequency, data rate, and specific transmission time.
3. Server: The server controls and processes messages. Network servers perform multiple functions, including extracting, storing, and analyzing payload data from terminal data packets according to the LoRa protocol. They manage terminal node registration and adjust physical layer parameters for terminal nodes in the network, such as transmission power, transmission rate, and encoding rate.

To mitigate concurrent conflicts in LoRa networks, it is crucial to ensure that only one node can send data at a given time. Traditional star network communication management employs a master node polling and slave nodes responding approach for data communication.

However, this method has drawbacks: if a node continuously sends data, other nodes may be unable to communicate with the master; slave nodes cannot actively send data and must wait for the master's query, jeopardizing real-time functionality; as the number of nodes in the network increases, the time used for each polling cycle and network latency also increase.

3 WIRELESS CHAIN NETWORK CONSTRUCTION METHOD

3.1 *Construction principle*

For the safety monitoring system of a bridge cluster structure, traditional network structures face limitations in fully harnessing the network's capabilities, leading to increased system costs and network configuration challenges. In response to the shortcomings of existing wireless networking technologies, this paper introduces a wireless chain networking method.

The wireless chain sensing network comprises a master device and multiple slave devices, with each node serving as both a terminal sensing device and a data forwarding router. Slave devices are equipped with functions for sensing data collection and data forwarding. The master device consolidates and summarizes data collected by each slave device, transmitting it to a designated server through cellular mobile networks or wired networks. This method optimally exploits the system's inherent characteristics, effectively extending the transmission distance, reducing the number of digital collection devices in use, and significantly lowering system costs and configuration complexities. The wireless chain network structure is illustrated in Figure 4.

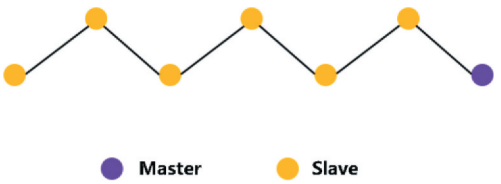


Figure 4. Wireless chain network structure diagram.

The construction principle of wireless chain network is as follows:

1. Sensor Node Deployment:
   Sensor nodes are strategically deployed in accordance with specific guidelines, considering factors such as geographical location, coverage range, and communication distance. The distance and arrangement of nodes play a crucial role in influencing network performance and coverage.
2. Network Detection and Connection:
   Following node deployment, sensor nodes initiate the establishment of communication links with neighboring nodes. The primary device broadcasts a network detection command, which includes its wireless address. Unconnected slave devices respond to this command, incorporating their wireless addresses. The primary device selects the closest slave device based on signal strength as the initial contact node.
3. Network Confirmation and State Transition:
   The primary device dispatches a network confirmation command to the chosen slave device, transitioning it to a connected state, signifying successful network formation. The slave device responds with a confirmation, and the primary device records the wireless address of the slave device, establishing a predecessor/successor relationship.
4. Chain Expansion:
   The first slave device temporarily assumes the role of the primary device, autonomously transmitting network detection commands. Devices not yet part of the network can respond to this command, including their wireless addresses. Through signal strength detection and the exchange of network confirmation commands, the first and second slave devices establish contact, recording each other's wireless addresses in their predecessor/successor tables.

5. Completion of Network Formation:
   This process continues until a slave device sends a network detection command but receives no reply, indicating that all devices have formed a chain network. At this juncture, each device, excluding the main and last slave devices, possesses both a predecessor and a successor. Adjacent nodes can freely communicate using wireless address identifiers. The wireless chain network offers an extended transmission distance, with each device functioning not only as a terminal but also as a relay. This network maximizes system and network characteristics, achieving long-distance data transmission.

In a chain sensor network, nodes typically transmit data along the chain's direction. The source node generates or collects data and transmits it to the next node. This sequential process continues until the data reaches the target node. To ensure reliable transmission, chain networks often implement data transfer protocols such as packet retransmission, error detection, and correction mechanisms. These measures address issues like signal interference, packet loss, and transmission errors that may occur in wireless environments.

3.2 *Time synchronization solution in wireless chain network*

In a sensor network, maintaining time synchronization is paramount as it ensures a consistent time reference for data collection across various sensors within the network[6]. This synchronization coordinates their actions and promotes data accuracy. The absence of time synchronization may result in disparate data, posing challenges in effectively coordinating information among sensors. For instance, in applications like structural safety monitoring for a cluster of bridges, if the timestamps of sensor data are not synchronized, accurate analysis of the sequence and duration of events becomes challenging. Moreover, time synchronization contributes to energy conservation. Through collaborative operation at specific time points and subsequent entry into sleep mode [7], sensors can collectively enhance overall efficiency. Consequently, achieving precise time synchronization stands as an indispensable step in constructing a resilient and efficient sensor network. The method to address time synchronization in wireless chain network is outlined as follows:

The master device first connects to the network and calibrates its own time. Once calibrated successfully, the clock synchronization program retrieves the current time t of the device, encapsulates it into a time synchronization signal frame, searches its successor table, identifies the master device's successor node, and sends the clock synchronization signal frame point-to-point to its successor node.

After the successor node receives the clock synchronization signal frame, it updates its own time to t based on the time information in the data frame. Assuming the transmission delay between the two devices is Δt_{11}, the time taken to encapsulate the frame, send data, receive data, and parse the data frame is Δt_{12}. Therefore, the total delay during the signal frame transmission process is given by:

$$\Delta t_1 = \Delta t_{11} + \Delta t_{12} \tag{1}$$

At this point, the time at the master device is $t + \Delta t_1$, and the time at the first subordinate device is t. After the first subordinate device receives the data, updates its own time to t, and continues to look up its successor table to find the successor node, it forwards the data frame to its successor node. The successor node, upon receiving the clock synchronization data frame, updates its time to t based on the time information in the signal frame and continues forwarding until it reaches the final node.

Assuming this wireless chain network has one main node and n subordinate nodes, when the data frame is transmitted to the j-th node ($1 \leq j \leq n$), the time at the j-th node is updated to t. At this moment, the time at the master device remains:

$$T_0 = t + \sum_{i=1}^{j} \Delta t_i \tag{2}$$

For the k-th node($1 \leq k \leq j$), its time is updated to

$$T_k = t + \sum_{i=k+1}^{n} \Delta t_i \tag{3}$$

When the data frame is transmitted to the last device, the time of the main device is

$$T_0 = t + \sum_{i=1}^{n} \Delta t_i \tag{4}$$

For the k-th node($1 \leq k \leq n$), its time is updated to

$$T_k = t + \sum_{i=k+1}^{n} \Delta t_i \tag{5}$$

When the last node in a wireless chain network receives the clock synchronization frame from the preceding node and adjusts its own time to t, it first checks its successor table. If no successor nodes are found, it indicates that the signal frame has reached the last node in the chained network. At this point, the node device searches the pseudorandom table, introduces a random delay timet_r, and inserts its current time $t + t_r$, into the time synchronization response frame. It then looks up the predecessor table, identifies its own predecessor node, and sends the clock synchronization signal response frame to its predecessor node.

Upon receiving the data, the predecessor node subtracts its own time $t + t_r + 2\Delta t_n$. from the time in the signal frame $t + t_r$. The average of this difference is taken as the offset for the time $t + t_r$ in the signal frame. The predecessor node updates its own time to $t + t_r + \Delta t_n$ and continues forwarding the data frame to its own predecessor node. This process continues until the final data frame is transmitted back to the main device.

During the process of the time synchronization response frame returning, when the data frame is transmitted back to the k-th node, the time at the k-th node is:

$$T_k = t + 2 \times \sum_{i=k+1}^{n} \Delta t_i + t_r \tag{6}$$

Taking the difference between the encapsulated time in the signal frame and the actual time, averaging this difference to obtain the time offset, and adding it to the time $t + t_r$, update the current device's time to:

$$T = t + \sum_{i=k+1}^{n} \Delta t_i + t_r \tag{7}$$

At this point, the time for the j-th device to the n-th device is:

$$T_k = t + \sum_{i=k+1}^{n} \Delta t_i + t_r \tag{8}$$

The time synchronization response frame is sent back to the main device node, and at this point, the time for all subordinate devices has been synchronized. However, there still exists a time difference with the baseline time of the main device, and the size of the time difference is:

$$\Delta T = \sum_{i=1}^{n} \Delta t_i \tag{9}$$

The time difference is equal to the current time at the main device minus the encapsulated time in the signal frame $t + t_r$, and the average of this difference is calculated. This time

difference is then used as the time offset, and it is placed in a clock offset frame, which is sent to each subordinate device. Upon receiving the offset frame, each subordinate device adds the time offset to its own time and forwards the offset frame to its successor node. This process continues until the last node completes the offset synchronization. At this point, the clock synchronization in the wireless chain network is completed, and the times of master and all subordinate devices are synchronized and aligned with the current standard time.

4 CONCLUSION

This paper addresses prevailing challenges in wireless networking technology by proposing a wireless chain networking method specifically tailored for the safety monitoring system of bridge cluster structures. The method offers several advantages:

1. The construction of a wireless chain sensor network ensures that each node serves dual functions as a terminal sensing device and a data forwarding router, thereby fully maximizing the node's performance.
2. Investigation into clock synchronization methods within the wireless chain sensor network guarantees uniform time benchmarks for data collection across all sensors. This synchronization coordinates their actions, ensuring precision in data accuracy.
3. In the context of safety monitoring systems for elongated structures such as bridge clusters, this method capitalizes on the inherent characteristics of the network structure. It effectively extends transmission distances, enhances data transmission efficiency, reduces the number of digital acquisition devices, and substantially diminishes system costs and configuration complexities.
4. In the future, through the integration of machine learning and intelligent algorithms[8], the wireless chain sensor network can autonomously adjust configurations, optimize resource allocation, and dynamically adapt its operating mode based on environmental changes. This integration enhances overall performance and adaptability. Through intelligent decision-making and collaboration within the network, higher levels of self-organization and coordination can be achieved, thereby augmenting overall performance and robustness.

ACKNOWLEDGMENTS

This study is supported by the Science and Technology Project of the Heilongjiang Provincial Department of Transportation (Grant No: HJK2023B020).

REFERENCES

[1] Yong L Y, Long F L. Collection tree-oriented mesh routing optimization for extending the lifetime of wireless sensor networks[J]. International Journal of Distributed Sensor Networks, 2022, 18(3):
[2] Mohsin K S, Mohammed A M, Yassien M H. Developing of Bluetooth mesh flooding between source-destination linking of nodes in wireless sensor networks[J]. Eastern-European Journal of Enterprise Technologies,2021, 6(9): 6–14.
[3] Meka S, Fonseca B. Improving Route Selections in ZigBee Wireless Sensor Networks [J]. Sensors, 2019, 20 (1): 164–164.
[4] Gupta V. Comparative Perpormance Analysis of AODV, DSR, DSDV, LARI and WRP Routing Protocols in MANET using GloMoSim 2.0.3 Simulator[J]. International Journal of Computer Applications, 2012.52(20).
[5] Truong V, Nayyar A, 2, et al. System Performance of Wireless Sensor Network Using LoRa–Zigbee Hybrid Communication [J]. Computers, Materials & Continua, 2021, 68 (2): 1615–1635.
[6] Zhendong R, Ying Z, Hongmian W, et al. Clock synchronization method for micro-power wireless networks based on LoRa ranging [J]. Journal of Physics: Conference Series, 2022, 2306 (1):
[7] Michael A, Kok-Yiu P W, C. P. J C. Battery lifespan enhancement strategies for edge computing-enabled wireless Bluetooth mesh sensor network for structural health monitoring[J]. Automation in Construction, 2022, 140
[8] Yajuan Z, Ru J, Xiang J, et al. Application of wireless sensor network technology based on artificial intelligence in security monitoring system [J]. Open Computer Science, 2023, 13 (1):

Bridge Maintenance, Safety, Management, Digitalization and Sustainability – Jensen, Frangopol & Schmidt (eds)
© 2024 The Author(s), ISBN 978-1-032-77040-6
Open Access: www.taylorfrancis.com, CC BY-NC-ND 4.0 license

Deep learning of smart aggregate's impedance signal for damage monitoring

Q.B. Ta, N.L. Pham & J.T. Kim
Department of Ocean Engineering, Pukyong National University, Busan, Korea

Q.Q. Pham
Department of Bridge and Road, Danang Architecture University, Danang, Vietnam

ABSTRACT: Damage monitoring is an essential step to ensure the safety of concrete structures. Smart aggregate technique has been proven for its advantage to detect early-stage internal cracks in concrete. In this study, a 1-D CNN-based method is developed for autonomously classifying the damage feature in a concrete anchorage zone using the raw impedance signatures of the embedded SA sensor. An overview of the developed method is presented. A 1-D CNN classification model using the impedance signals is constructed. The experiment on the SA-embedded concrete anchorage zone is carried out, and the impedance signals of the SA sensor are recorded under different applied force levels. The feasibility of the developed 1-D CNN model is examined to classify concrete damage features via noise-contaminated signals. The results show that the developed method can accurately classify the damaged features in the concrete anchorage zone.

1 INTRODUCTION

In demand for real-time SHM monitoring, the electromechanical impedance (EMI) technique has attracted significant attention from researchers due to its advantages, such as sensing and driving functionalities, fast response speed, stable performance, and low price (Na et al. 2018). The technique utilizes the coupling interaction between a PZT (lead zirconated titanate) transducer and the monitored structure to provide information about the local structural characteristics of the examined region (Liang et al. 1994). The technique has been extensively implemented for monitoring stress in concrete structures (Ai et al. 2019, Pham et al. 2021). Many studies propose using PZT sensors placed on the surface of concrete structures to detect changes in impedance response induced by local damage near the surface (Ai et al. 2019, Pham et al. 2021). However, those surface-mounted PZT sensors are found to be less sensitive to changes in internal concrete stress. The so-called smart aggregate (SA) sensor (Gu et al. 2006), which was embedded into a monitored concrete structure, has recently emerged as an alternative internal stress monitoring method. The change in internal concrete stresses and the occurrence of damage events can directly reflect on the impedance response (Wu et al. 2022).

In recent years, convolutional neural network (CNN)-based deep learning algorithms have emerged as efficient approaches for assessing structural conditions of civil infrastructures (Sony et al. 2021). While the traditional damage detection method consists of two main steps: (i) feature extraction and (2) dam-age identification (Yuan et al. 2020), a CNN-based method combines them in a single procedure (Abdeljaber et al. 2018). The network can directly process raw signals and autonomously learn optimal features for a damage identification task, considerably reducing the initial processing workload. Several studies explored the combination of the CNN and the impedance-based technique for damage assessment. Nguyen et al.

DOI: 10.1201/9781003483755-222

(2021) proposed a 1-D CNN model that learned impedance signatures for classifying different health conditions of a smart PZT interface. Recently, Nguyen et al. (2022) explored the ability of the 1-D CNN for autonomous features extraction for impedance-based prestress force prediction. Ai et al. (2022) proposed a 2-D CNN model to classify compressive stress and damage in concrete samples based on the admittance responses obtained from the PZT sensors surface-mounted on a concrete block. The above studies have demonstrated the applicability of CNN as an innovative algorithm for impedance-based damage detections with minimal signal preprocessing.

Despite the previous research attempts (Nguyen et al. 2021, Nguyen et al. 2022, Ai et al. 2022), the 1D CNN algorithm with the SA technique has not been investigated for damage classification of concrete anchorage zone. In this study, a 1-D CNN-based method is developed for autonomously classifying the damage feature in a concrete anchorage zone using the raw impedance signatures of the embedded SA sensor. Firstly, an overview of the developed method is presented. A 1-D CNN classification model using the impedance signals is constructed. Secondly, the experiment on the SA-embedded concrete anchorage zone is carried out, and the impedance signals of the SA sensors are recorded under different applied force levels. Finally, the feasibility of the developed 1-D CNN model is examined for classifying concrete damage features with noise-contaminated signals.

2 OVERVIEW OF METHOD

The overview of a method for automated concrete damage classification is illustrated in Figure 1. The key idea is to combine the smart aggregate-based impedance monitoring technique and the 1-D CNN-based damage classification model to classify concrete damage features induced by compression forces automatically. The proposed method combines feature extraction and damage classification tasks into a single architecture, enabling direct processing and automatic learning of optimal features from the raw impedance signals. This approach allows for streamlined and efficient analysis of the signal. As shown in Figure 1, the schematic of the proposed method includes two main stages: impedance measurement (stage 1) and damage features classification (stage 2).

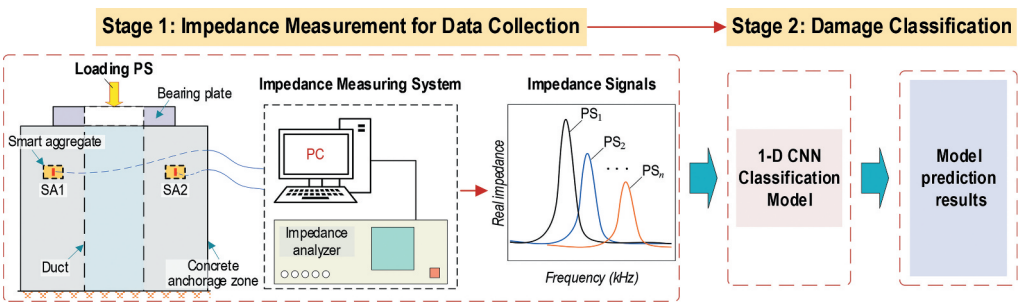


Figure 1. Schematic of methodology.

Figure 2 shows the architecture of the 1-D CNN classification model using SA's raw impedance signals. The model started with one Input layer, four Conv (Convolutional) layers, four ReLU (Rectified Linear Unit) layers, four Maxpool layers, three Fc (Fully Connected) layers, and finally, a Classification layer. The 1-D CNN model takes the 1×251 series raw impedance signal as the input, then returns the output, which can be used for classifying damage features in the anchorage zone.

The Conv layer comprises a set of trainable filters or kernels that slide over each element of the input data. The filters multiply the corresponding entries of the filters and data and then add them up. Each filter generates a frame of the feature map in the next subsampling layer,

and the depth of the convolution layer equals the number of frames. The ReLU layer replaces negative values from the output of the preceding layer with zero while keeping all positive values. The Maxpool layer slides filters over the output of the preceding layer and ex-tracts the element with the highest value. The purpose of the Maxpool layer is to reduce the computational cost by decreasing the size of the convolved feature. The Fc layers establish all possible connections between layers, meaning every input from the preceding layer influences every element of the output layer. The Fc layers combine and transform learned features into lower-dimensional representations suitable for the Classification layer.

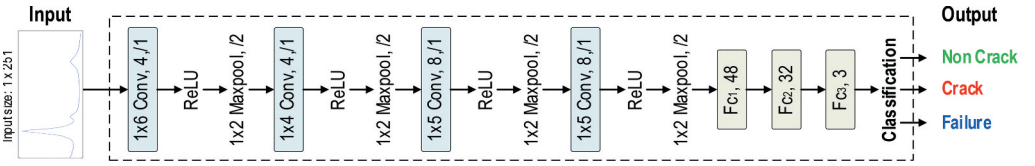


Figure 2. The architecture of the 1-D CNN classification model using SA's raw impedance signals.

3 EXPERIMENT

3.1 *Impedance monitoring of anchorage zone under compression*

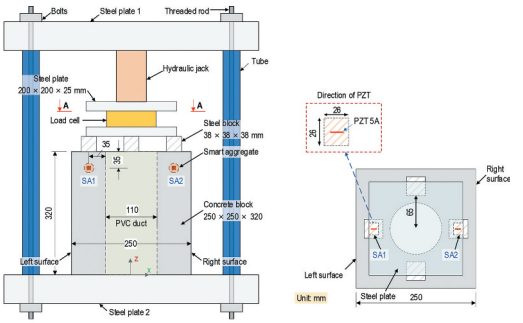
Figure 3 shows the schematic of an experiment on a lab-scale concrete anchorage zone embedded with smart aggregates under compression. The experiment was performed to obtain impedance responses of smart aggregates under the loading process. These impedance signals will be employed for data generation and fed to the 1-D CNN classification model. For impedance monitoring, two smart aggregate sensors SA1 and SA2 were installed in the concrete anchorage zone (see Figure 3a,b). The distance between the centers of these SA sensors to the concrete surface was set at about 35 mm. Note that SA1 was embedded in the left side of the anchorage zone, and SA2 was embedded in the right one. For the compression test, the anchorage zone was put on a supporting steel frame, which included two thick steel plates connected using four steel tubes and bolt connections (see Figure 3a). The steel frame was designed to resist tension induced by the anchorage zone. The compression force was generated via a hydraulic jack, and a combination of a load cell and indicator was utilized to monitor the actual compressive forces.

The impedance signals of the smart aggregates were measured using a wired impedance analyzer, specifically the HIOKI 3532. The analyzer excited a harmonic voltage of 1 V and recorded the impedance signals of the smart aggregates within a frequency range of 100-600 kHz (251 points). For each loading case, impedance signals were obtained four times or four ensembles. The laboratory temperature was kept constant at approximately 22°C to minimize the influence of temperature changes on the impedance responses. Eleven loading cases were assigned for impedance measurement in the anchorage zone. The compressive force P1 was set as the baseline at 100 kN, and the forces were gradually increased for the first six loading cases (P1-P6) from 100 to 200 kN with an increment of 20 kN. The applied forces were then raised from 200 to 230 kN for the next three loading scenarios (P7-P9) with an interval of 10 kN. Following that, during the P10 loading case, the compression force was increased to 235 kN, resulting in a partial collapse of the concrete. Finally, the applied force decreased to P11, set at 102 kN.

3.2 *Impedance signal of smart aggregates*

Figure 4 shows the impedance signals of SA1 under loading cases P1-P11, which were used to feed to the 1-D CNN classification model. It can be noted that the impedance signals are more sensitive to the applied forces at the highest peaks around 210 kHz. The impedance signatures of SA1 were slightly changed under forces P1-P6. Then a sudden change occurred

under force P7, thus showing a transformation of the concrete domain surrounding SA1 (e.g., inner concrete damage (Kocherla et al. 2020)). The signals were constantly varied under force P8, and another abrupt variation appeared under loading case P9 (the pristine crack close to SA1). The impedance signatures changed under force P10 (crack propagation), and the most variation in signals of SA1 occurred under force P11 (concrete failure). The impedance signatures of SA1 were matched to the crack appearances to make the following observations. First, when cracks occurred, significant changes in impedance signals were observed in SA1. Second, early incipient cracks and concrete damage appeared on the anchorage zone's left side, possibly due to unequally applied force (via four steel blocks) and the concrete structure's inelastic nature.



a) Side view b) View A-A

Figure 3. Schematic of the testing setup of impedance monitoring for anchorage zone under compression.

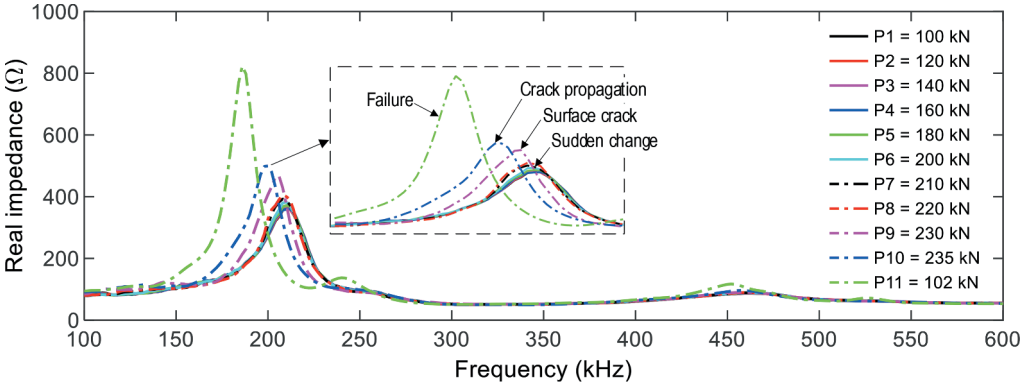


Figure 4. Real impedance signals of SA1 under compression forces.

4 DAMAGE CLASSIFICATION RESULTS

4.1 *Databank generation*

The signals of SA1, which were measured for eleven force levels (i.e., P1-P11), were used to construct the databank for the 1-D CNN model. The noise was injected considering the uncertainty of the measurement situation under the premise that the measured impedance signal data is insufficient for deep learning training, validation, and testing. The noise was injected into the impedance signal using Gaussian noise with several signal-to-noise ratio (SNR) levels. The following formula calculates the SNR level in decibels (dB) (Johnson 2006).

$$SNR = 10\log^{10}\left(\frac{P^{signal}}{P^{noise}}\right) \quad (1)$$

Since 1-D CNN models require data and corresponding annotated labels to train, a process called data labeling is needed. This process is to form a representation of what class of data signals belong to. The SA1 sensor during the experiment's loading of the eleven cases (i.e., P1-P11) is observed. Each observed status is assigned and grouped under the three labels "Non Crack", "Crack", and "Failure". The "Non Crack" label includes force cases ranging from P1 to P5, corresponding with the observed status "No crack". The "Crack" label includes force cases ranging from P6 to P10, which correspond to the observed status "Inner crack", "Inner crack + surface crack + crack propagation", and "Crack propagation". The "Failure" label is used for force case P11 corresponding to the observed status "Failure". Figure 5 shows the impedance signals classified under these assigned labels.

The 1-D CNN model requires a massive dataset for training and validation to achieve a reasonable generalization capability. In the experiment, the impedance signals of SA1 were recorded with four ensembles for each force case. Three groups, "Non Crack" (for P1-P5), "Crack" (for P6-P10), and "Failure" (for P11), have 20, 20, and 4 impedance signals, respectively. Table 1 shows the training and validating data for the 1-D CNN model. With each SNR level, 20, 20, and 18 impedance signals were generated in three groups "Non Crack", "Crack", and "Failure", respectively. Thus, a total of 160 samples were collected from the measured signals and the noise-contaminated generated signals. 80% of the total samples were used for training, and 20% were used for validating the 1-D CNN model.

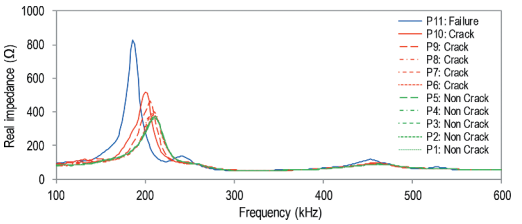


Figure 5. Impedance signals classified under three assigned labels.

With the same measured impedance signals, the larger the SNR, the smaller the noise is added. As a result, the impedance signal changes when adding noise with an SNR of 35 dB are smaller than that of 30 dB. It can be seen that noise with SNRs of 35 dB and 30 dB induces an insignificant effect on the general shape of the measured signals while it can simulate the realistic situations of noise contamination. The measured signals were injected by different SNR levels ranging from 20 to 16 dB with an interval of 2 dB. As shown in Table 2, in each noise level, there were 60, 60, and 40 new signals were generated in three groups "Non Crack", "Crack", and "Failure", respectively. A total of 480 signals were utilized for testing the 1-D CNN model. The noise-contaminated signals in three groups corresponding to SNR of 16 dB are illustrated in Figure 6.

Table 1. Training and validating data.

Assigned label	Current sample	Generated sample via SNR		Total sample	Ratio (Train/Validation)
		35 (dB)	30 (dB)		
Non Crack	20	20	20	60	80/20
Crack	20	20	20	60	
Failure	4	18	18	40	

Table 2. Number of testing data sets for evaluating trained model.

	Generated sample via SNR		
Assigned label	20 (dB)	18 (dB)	16 (dB)
Non Crack	60	60	60
Crack	60	60	60
Failure	40	40	40

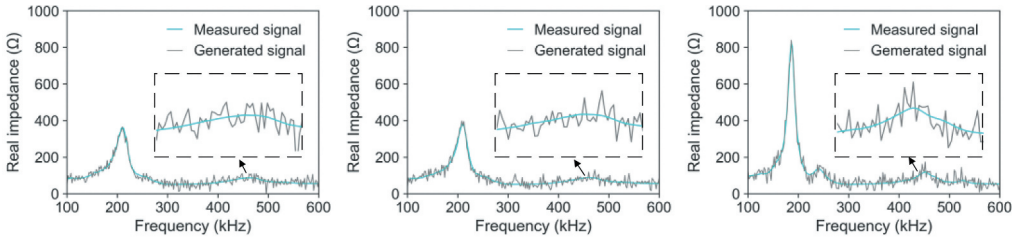


Figure 6. Adding noise to impedance signal with SNR = 16 (dB).

4.2 *Training results*

All experiments were performed on a desktop computer (GPU: GTX 2080 Ti 11G, CPU: Intel i9-9000KF 3.6 GHz, RAM: 64 GB). The 1-D CNN model was programmed using Python programing language (version 3.8). The designed 1-D CNN model was trained using the Adam training algorithm (Kingma and Ba 2014) with a mini-batch size of 1 and a learning rate of 0.001. Figure 7 shows the accuracy and loss value during the training and validation process of the 1-D CNN model. The training and validation accuracy of the 1-D CNN model gradually increased and reached over 95% at the 20th epoch. At the same time, the training and validation losses sharply reduce in a few first epochs and continue to converge at the end of the learning process. At the 20th epoch, the training and validation losses are recorded at approximately 0.1, suggesting the high accuracy of the trained 1-D CNN model.

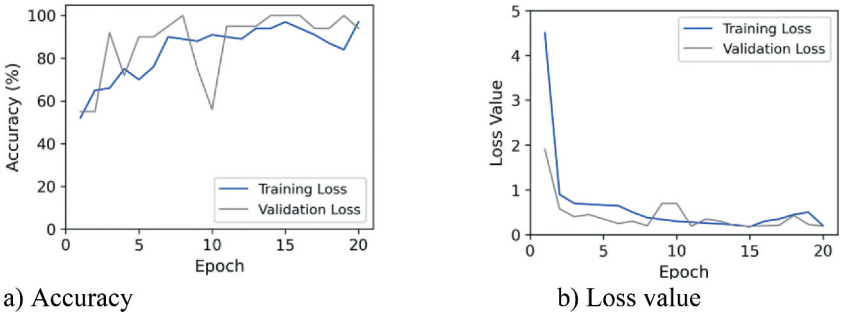


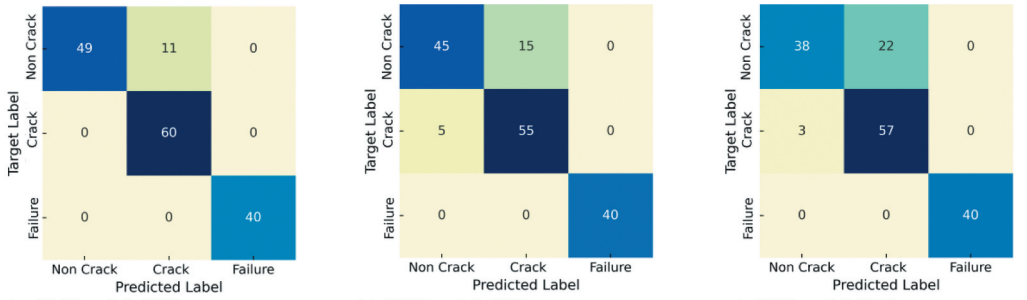
Figure 7. Accuracy and loss value during training and validating.

4.3 *Performance under noise levels*

Figure 8 illustrates the results of the damage feature classification of the trained model utilizing confusion matrixes without normalization. The confusion matrixes were plotted to show the number of correctly classified signals reflected in Table 2. Using absolute values in the confusion matrix to highlight correct classifications of investigated sample numbers has been utilized in some previous research studies (Mei et al. 2020, Yang et al. 2022). As shown in this

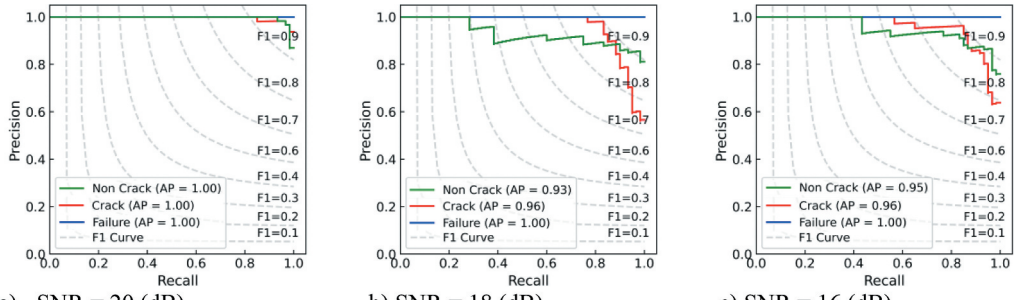
figure, in each SNR level, a total of 160 data samples in testing datasets are used to evaluate the performance of the model. With the SNR value of 20 dB, there are 11 samples that are misclassified between "Crack" and "Non Crack" conditions. The misclassified samples increased to 20 and 25, corresponding to SNR levels of 18 and 16 dB, respectively. It can be concluded that as the SNR level decreases, the accuracy of prediction labels tends to decrease.

As evaluation indicators, precision, recall, false negative rate, and false positive rate, which are calculated from four basic evaluation factors: true positive, true negative, false positive, and false negative, are applied. Figure 9 illustrates the performance of the trained 1-D CNN classification model, which is evaluated using precision/recall (P-R) and fusion (F1) curves. Higher precision means that the 1-D CNN model returns more relevant results than irrelevant ones, and high recall means that the 1-D CNN model returns most of the relevant results. The integration of the area under the P-R curve is called average precision (AP) and indicates the classification ability of the 1-D CNN model. The F1 curve measured the similarity between the predicted and target labels. In Figure 9, the AP indices reached 1.00, and the F1 score was larger than 0.9 in all three groups, indicating the high accuracy and reliability of the detector at SNR = 20 dB. In Figure 9b-c, when decreasing the SNR, the results show that the 1-D CNN maintained its classification performance as the AP indices are larger than 0.90.



a) SNR = 20 (dB) b) SNR = 18 (dB) c) SNR = 16 (dB)

Figure 8. Confusion matrix.



a) SNR = 20 (dB) b) SNR = 18 (dB) c) SNR = 16 (dB)

Figure 9. P-R curve and F1 curve.

5 CONCLUDING REMARKS

In this study, the 1-D CNN-based method was developed for autonomously classifying the damage feature in the concrete anchorage zone using the raw impedance signatures of the embedded SA sensor. Firstly, the overview of the developed method was presented. The 1-D CNN classification model learned the impedance signals for classifying the damage feature induced by compression was constructed. Secondly, the compression experiment on the SA-embedded concrete anchorage zone was carried out, and the impedance signals of the SA sensors were recorded under different applied

force levels. Finally, the feasibility of the developed 1-D CNN model for classifying concrete damage features with noise-contaminated signals was examined. The results revealed that the developed method could accurately classify the damaged features in the concrete anchorage zone.

Based on the analyzed results, the following remarks could be drawn: (1) the proposed classification model implicitly processes the raw impedance signals obtained from smart aggregates and autonomously outputs the concrete damage features; (2) the accuracy of the 1-D CNN model was significantly influenced by noises in the impedance signal, and the classification accuracy decreased with the increased of noise level; (3) the proposed 1-D CNN model was able to classify damage features even if from impedance signals having contaminated noises larger than noises in impedance signals used to train the model.

ACKNOWLEDGMENT

This work was supported by the Basic Science Research Program through the National Research Foundation of Korea (2022R1A2C1003889116178206434010 1).

REFERENCES

Abdeljaber, O.A.O., Kiranyaz, M.S., Boashash, B., Sodano, H., & Inman, D.J. 2018. 1-D CNNs for structural damage detection: Verification on a structural health monitoring benchmark data. *Neurocomputing* 275:1308–1317.

Ai, D., Luo, H., & Zhu, H. 2019. Numerical and experimental investigation of flexural performance on prestressed concrete structures using electromechanical admittance. *Mech. Syst. Signal Process*. 128: 244–265.

Ai, D., Mo, F., Han, Y., & Wen, J. 2022. Automated identification of compressive stress and damage in concrete specimen using convolutional neural network learned electromechanical admittance. *Eng. Struct*. 259:114176.

Gu, H., Song, G., Dhonde, H., Mo, Y.L. & Yan, S., 2006. Concrete early-age strength monitoring using embedded piezoelectric transducers. *Smart materials and structures* 15(6):1837.

Johnson, D.H. 2006. Signal-to-noise ratio. *Scholarpedia* 1(12):2088.

Kingma, D.P. & Ba, J., 2014. Adam: A method for stochastic optimization. *arXiv preprint arXiv:1412.6980*.

Kocherla, A., & Subramaniam, K.V.L. 2020. Embedded smart PZT-based sensor for internal damage detection in concrete under applied compression. *Measurement* 163:108018.

Liang, C., Sun, F.P., & Rogers, C.A. 1994. Coupled electromechanical analysis of adaptive material systems-determination of the actuator power consumption and system energy transfer. *J. Intell. Mater. Syst. Struct*. 8(4):335–343.

Mei, Z., Ivanov, K., Zhao, G., Wu, Y., Liu, M. & Wang, L., 2020. Foot type classification using sensor-enabled footwear and 1D-CNN. *Measurement* 165:108184.

Na, W.S., & Baek, J. 2018. A review of the piezoelectric electromechanical impedance based structural health monitoring technique for engineering structures. *Sensors* 18(5):1307.

Nguyen, T.T., Ta, Q.B., Ho, D.D., Kim, J.T., & Huynh, T.C. 2021. Deep learning-based functional assessment of piezoelectric-based smart interface under various degradations. *Smart Struct. Syst*. 28(1):69–87.

Nguyen, T.T., Phan,T.T.V., Ho, D.D., Man Singh Pradhan, A., & Huynh, T.C. 2022. Deep learning-based autonomous damage-sensitive feature extraction for impedance-based prestress monitoring. *Eng. Struct*. 259:114172.

Pham, Q.Q., Dang, N.L., & Kim, J.T. 2021. Piezoelectric sensor-embedded smart rock for damage monitoring in a prestressed anchorage zone. *Sensors* 21(2):353.

Sony, S., Dunphy, K., Sadhu, A., & Capretz, M. 2021. A systematic review of convolutional neural network-based structural condition assessment techniques. *Eng. Struct*. 226:111347.

Wu, C., Xiang, H., Jiang, S., & Ma, S. 2022. Stress monitoring of concrete via uniaxial piezoelectric sensor. *Sensors* 22(11):4041.

Yang, Z., Gao, W., Chen, L., Yuan, C., Chen, Q. & Kong, Q., 2022. A novel electromechanical impedance-based method for non-destructive evaluation of concrete fiber content. *Construction and Building Materials* 351:128972.

Yuan, F.G., Zargar, S.A., Chen, Q., Wang, S., Zonta, D., & Sohn, H., 2020. Machine learning for structural health monitoring: challenges and opportunities. *Proceedings of Sensors and Smart Structures Technologies for Civil, Mechanical, and Aerospace Systems 2020.*

Bridge Maintenance, Safety, Management, Digitalization and Sustainability – Jensen, Frangopol & Schmidt (eds)
© 2024 The Author(s), ISBN 978-1-032-77040-6
Open Access: www.taylorfrancis.com, CC BY-NC-ND 4.0 license

Neural network-based connectivity reliability analysis for bridge networks

Jie Wang
School of Transportation Science and Engineering, Harbin Institute of Technology, Harbin, China

Shunlong Li
School of Transportation Science and Engineering, Harbin Institute of Technology, Harbin, China
Key Laboratory of Intelligent Disaster Prevention for Civil Infrastructure, Ministry of Industry and Information Technology, China

ABSTRACT: The connectivity reliability analysis of bridge networks has been the focus of research in this field and is also a difficult problem because of NP-hard problem. In particular, when performing network strategy or optimization, it is very time-consuming as the network connectivity probabilities need to be solved hundreds of times. This study finds that neural network with fewer neurons and layers can quickly and efficiently solve the all-terminal connectivity reliability for large-scale bridge networks. Firstly, for the same network benchmark model, based on real bridge inspection data, the state probability samples of each edge in the network are extracted by data fitting, and Monte Carlo simulation is applied to approximate the all-terminal connectivity reliability of each network model under each sample. Secondly, multiple neural network models containing one, two and three layers with different neurons are proposed and 5-fold cross-validation is applied to obtain the hyperparameters of each model. Finally, in conjunction with appropriate optimizers and hyperparameters, it can be shown that simple single-layer network models can find sufficiently accurate all-terminal connectivity reliability for large-scale bridge network. The accuracy and efficiency of the pro-posed method is verified based on a real bridge network containing 216 directed edges with 63 nodes.

1 INTRODUCTION

Under the influence of combined effects, the service performance of bridges in bridge network will inevitably deteriorate or even fail (Yang & Frangopol, 2019). In recent years, bridge network connectivity reliability (reliability) analysis has gradually become the focus and difficulty of bridge network assessment. It mainly considers the safety of hardware facilities in the assessment, which refers to the probability that the nodes of the network will remain connected due to the degradation or failure of the hardware facilities (bridges), and therefore can also be called "hard connectivity performance" (Estes, 1997; Saydam et al., 2013). At the same time, the connectivity reliability is proved to be an NP-hard problem. At present, based on the number of relevant nodes, connectivity probabilities of bridge networks can be classified into 3 categories: two-terminal, *k*-terminal and all-terminal connectivity probabilities (Reed et al., 2019). Among them, the 2-terminal connectivity reliability calculates the probability of connectivity between 2 specified nodes (origin and destination points) without caring about the other nodes; the *k*-terminal and all-terminal are concerned with whether the selected *k* nodes and all nodes are connected or not, respectively. Currently, most studies have focused on evaluating two-terminal connectivity probabilities for small-scale bridge networks (Bai et al., 2020; Bocchini et al., 2011; Kang et al., 2008; Liu & Frangopol, 2006; Yang & Frangopol, 2020).

There are many well-established and easy-to-implement methods for 2-terminal connectivity reliability for small-scale networks (Yeh et al., 2022). The commonly used methods can be

DOI: 10.1201/9781003483755-223

classified into exact methods and approximate methods (Bai et al., 2016). Exact methods mainly refer to enumeration methods, which can be further classified into state-based enumeration methods and cut/path set-based enumeration methods. Meanwhile, researchers have proposed a variety of methods for approximating network connectivity probabilities, mainly including improved algorithms for exact methods (Wang et al., 2020), simulation algorithms (Claudio & Zio, 2005) and deep learning based methods (Lei et al., 2022). The evaluation of bridge networks based on deep learning algorithms is the result of the combination of artificial intelligence and traditional complex networks in recent years, showing good time-efficiency advantages (Davila-Frias et al., 2023; Nabian & Meidani, 2018). Therefore, this paper proposes a neural network-based all-terminal connectivity reliability analysis method for bridge networks.

Specifically, this paper applies the fully connected neural network (FCNN) to calculate the all-terminal connectivity reliability of the bridge network. Firstly, based on the limited real bridge inspection samples in the directed urban bridge network proposed in our previous work (Wang et al., 2024), the number of samples is expanded by data fitting, so as to fully ensure the amount of data required for neural network computation. Secondly, combining the experience of domestic and foreign research scholars, several FCNN model structures are designed, and 5-fold cross-validation is applied to obtain the computational error of each model. And the model with the highest accuracy is selected as the method for the all-terminal connectivity reliability of bridge network in this paper. The final results show that a simple single-layer fully connected neural network model can be used to derive the all-terminal connectivity reliability of a large bridge network with sufficient accuracy if coupled with appropriate optimizers and hyperparameters.

The rest of the paper is organized as follows: Section 2 briefly introduces the directed urban bridge network. Section 3 describes the data expansion method for finite number of samples. Section 4 presents the processing of FCNN hyperparameter selection based on 5-fold cross-validation. Section 5 concludes this paper.

2 GENERAL INTRODUCTION OF THE DIRECTED URBAN BRIDGE NETWORK

In this paper, a city located in the southern part of the Yangtze River Delta in China is used as an example. Based on the inspection information of 299 actual bridges in the city,

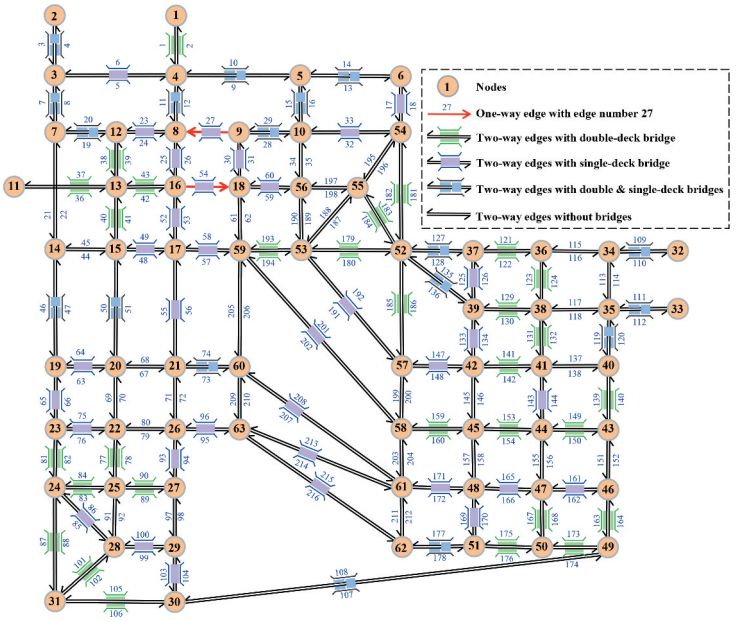


Figure 1. Topological model of the investigated urban bridge network (Wang et al., 2024).

a directed bridge network topology model is built according to the rules described in our previous work (Wang et al., 2024), which is designed to simulate the actual service state of the network to the maximum extent on the basis of the road directions and bridge types between all the nodes in the city, as shown in Figure 1. The topological model contains 63 nodes and 216 directed edges, including 107 two-way edge pairs and 2 one-way edges. Meanwhile, it has derived the failure probabilities of all bridges in the network, as well as the state probabilities of all edges or edge pairs for the period 2014-2018, and our goal of this paper is to efficiently derive the all-terminal connectivity reliability of the network based on neural network.

3 DATA EXPANSION METHOD FOR FINITE NUMBER OF SAMPLES

Before solving the all-terminal connectivity reliability of a bridge network based on neural networks, a sufficient number of data sets need to be prepared for processes such as training of the neural network. When analyzing the connectivity reliability of the directed urban bridge network, the state probabilities of the 216 directed edges in the network need to be used as 1 set of input data, while the connectivity reliability of the network needs to be used as the output of the model. However, only the state probabilities of each edge (pair) for 5 consecutive years from 2014-2018 and the network connectivity probabilities for the 5 years in (Wang et al., 2024) are available as input and output data, respectively, which is far from sufficient for the number of samples to perform the neural network training. Therefore, this section achieves data expansion through data fitting based on only existing real data.

As shown in Figure 2, the probability of being in the connected state (1 or (1, 1)) is high (greater than 0.99) for both the one-way edge containing 2 states and the two-way edge pair containing 4 states. By observation and fitting, it is found that the state probability distribution fits well with the power law distribution ($y = a \times x^b$). where a and b are the coefficients of this power law distribution, and for this research problem, x is the probability that an edge or edge pair is in the connected state (1 or (1, 1)).

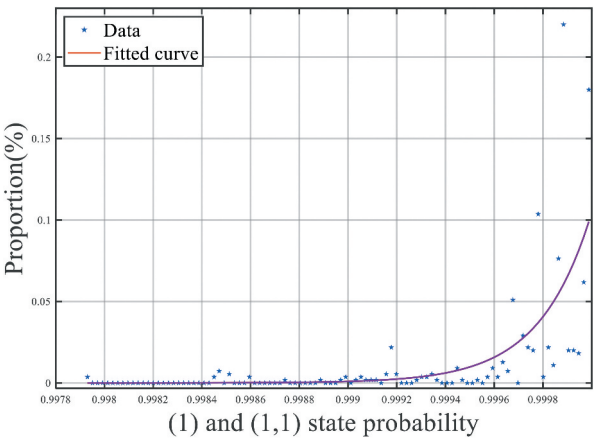


Figure 2. Fitting results of (1) and (1, 1) state probability.

Therefore, as shown in Figure 2, fitting based on the samples of 107 groups of two-way edge pairs and 2 one-way edges in the directed urban bridge network was calculated as a = 0.1046 and b = 4733.7955, and the root mean square error of the fitting result was 0.0234, which indicates that the fitting is good. Therefore, the probability of the connectivity state of each edge or edge pair in the newly extended sample can be generated based on the fitted power law distribution.

For a two-way edge containing 4 states, when the probability of the (1,1) state is known, it is necessary to determine the probabilities of the other three states ((1,0), (0,1), and (0,0)) separately. From a statistical point of view, 2 random numbers can be randomly selected based on the uniform distribution shown in Equation 1, and the third random number can be derived based on the probability of summing to one. Since the probability of the (0, 0) state is minimized. Therefore, the smallest of the 3 random numbers generated is assigned to (0, 0) as its state probability, and the remaining 2 random numbers are assigned as the state probabilities of (0, 1) and (1, 0), respectively.

$$U\left(\frac{1-P\left(\bar{e}_{i\to j},e_{j\to i}\right)}{3}\times(1-0.8),\frac{1-P\left(\bar{e}_{i\to j},e_{j\to i}\right)}{3}\times(1+0.8)\right) \tag{1}$$

Finally, the different state probabilities of each edge in the extended samples will be used as input data for the training, validation and testing process of the neural network, while the Monte Carlo simulation presented in (Wang et al., 2024) is used to compute the network connectivity reliability corresponding to the state probabilities of the edges or edge pairs obtained as the output dataset of the neural network. Eventually, a total of 1000 datasets were extended for subsequent studies.

4 FCNN HYPERPARAMETER SELECTION BASED ON 5-FOLD CROSS-VALIDATION

Fully-connected neural network is a multi-layer perceptual machine structure, which is designed based on the signal propagation process between animal nerves in biology (as shown in Figure 3), i.e., neuron receives the signal and distributes and passes it to each neuron in the next layer, which receives the input signals and calculates to generate the output command signals. And finally, aggregating neurons aggregate information for signal transmission, recognition, judgement, classification and control.

.

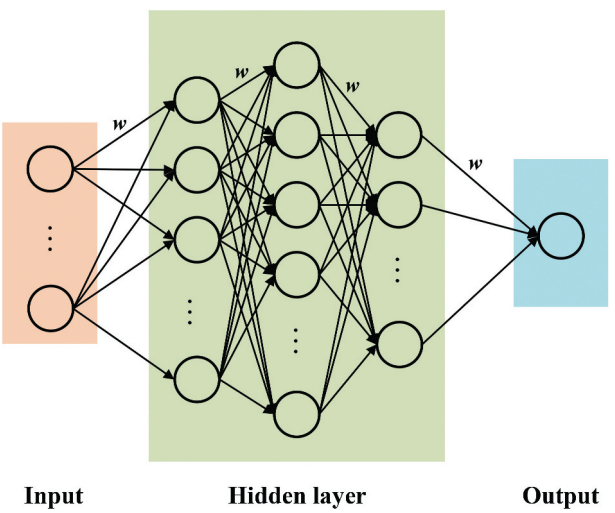


Figure 3. Schematic diagram of a FCNN model.

However, there are multiple neural network models that can be applied to the same problem. Parameters related to the model framework, such as the number of hidden layers, the number of neurons per layer, etc., are "hyperparameters" of the model. In order to determine the specific performance of the selected models on the target problem, a cross-validation

approach can be used for evaluation. Therefore, 5-fold cross-validation is used in this paper, i.e., the training set is divided into 5 parts, 4 groups are selected as the training set each time, and the remaining 1 group is used as the validation set. After completing the training and validation process and calculating the loss function value 5 times, the error of the 5 validation sets is averaged as the performance of the model.

Therefore. In this section, based on the existing research experience, several FCNN models are constructed, and the different parameters involved in the models are the number of hidden layers (NoHL), the number of neurons in the hidden layer (NoN), the value of droupout layer, the adjustment method of learning rate (lr_scheduler). And finally, the mean square error (MSE) of each model is calculated by applying 5-fold cross validation, which is used for evaluating the performance of the models in calculating the probability of all-terminal connectivity of the bridged network, and the final comparison results are shown in Table 1.

Table 1. Comparison of MSE of different models.

NO.	NoHL	NoN	lr_scheduler	Droupout	Min(MSE)
1-8	1	32	StepLR/CosineAnnealingLR	0/0.3/0.6/0.9	0.00014270
9-16	1	64	StepLR/CosineAnnealingLR	0/0.3/0.6/0.9	0.00015169
17-24	1	128	StepLR/CosineAnnealingLR	0/0.3/0.6/0.9	0.00018043
25-32	1	256	StepLR/CosineAnnealingLR	0/0.3/0.6/0.9	0.00023664
33-40	2	256×128	StepLR/CosineAnnealingLR	0/0.3/0.6/0.9	0.00036135
41-48	2	128×64	StepLR/CosineAnnealingLR	0/0.3/0.6/0.9	0.00015240
49-56	2	64×32	StepLR/CosineAnnealingLR	0/0.3/0.6/0.9	0.00021468
57-64	3	256×128×64	StepLR/CosineAnnealingLR	0/0.3/0.6/0.9	0.00023207
64-72	3	128×64×32	StepLR/CosineAnnealingLR	0/0.3/0.6/0.9	0.00019780

As shown in Table 1, when the number of hidden layers is 1, the number of neurons in the layer is 32, the Droupout value is 0.6, and the cosine annealing is selected for the learning rate decay method, the model has the lowest MSE value, and finally it is also selected as the final FCNN for solving the required connected probability of the directed urban bridge network. Meanwhile, the selected neural network model was validated on the test set and the results are shown in Figure 4 as shown below. The results show that the selected FCNN model is able to complete the problem of solving the connectivity reliability of the directed urban bridge network very well, and also the algorithm is computationally efficient.

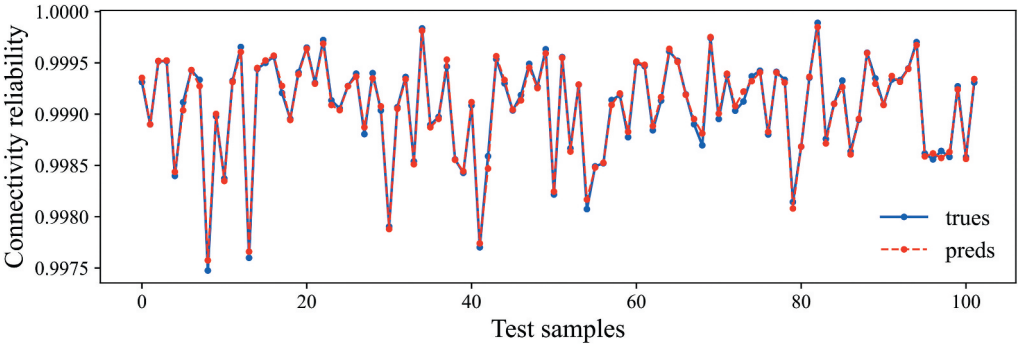


Figure 4. Comparison of computational results of selected FCNNs on the test set.

5 CONCLUSION

This paper implements a fast and efficient solution for the all-terminal connectivity reliability of bridge networks based on the fully connected neural network with fewer neurons and layers. Firstly, for the same network benchmark model, based on real bridge inspection data,

the state probability samples of each edge in the network are extracted and expended by data fitting to fulfill the data volume requirements. Secondly, several FCNN models containing one, two and three layers with different neurons are proposed and compared by the 5-fold cross-validation to obtain the hyperparameters. Finally, it has be proved that simple single-layer network models with 32 neurons can efficiently solved the all-terminal connectivity reliability problem of large-scale bridge network. The method accuracy and efficiency are by the real directed urban bridge network containing 216 directed edges with 63 nodes.

REFERENCES

Bai, G., Liu, T., Zhang, Y. A., & Tao, J. (2020). An Improved Method for Reliability Evaluation of Two-Terminal Multistate Networks Based on State Space Decomposition. *IEEE Transactions on Reliability*, *PP*(99), 1–12.

Bai, G., Tian, Z., & Ming, J. Z. (2016). An Improved Algorithm for Finding All Minimal Paths in a Network. *Reliability Engineering [?] System Safety*, *150*, 1–10.

Bocchini, P., Frangopol, D. M., & Deodatis, G. (2011). A random field based technique for the efficiency enhancement of bridge network life-cycle analysis under uncertainty. *Engineering Structures*, *33*(12), 3208–3217. http://dx.doi.org/10.1016/j.engstruct.2011.08.024

Claudio, M., & Zio, E. (2005). Solving advanced network reliability problems by means of cellular automata and Monte Carlo sampling. *Reliability Engineering & System Safety*, *89*(2), 219–226.

Davila-Frias, A., Yodo, N., Le, T., & Yadav, O. P. (2023). A deep neural network and Bayesian method based framework for all-terminal network reliability estimation considering degradation. *Reliability Engineering & System Safety*, *229*, 108881. http://dx.doi.org/http://dx.doi.org/10.1016/j.ress.2022.108881

Estes, A. C. (1997). *A system reliability approach to the lifetime optimization of inspection and repair of highway bridges*.

Kang, W.-H., Song, J., & Gardoni, P. (2008). Matrix-based system reliability method and applications to bridge networks. *Reliability Engineering & System Safety*, *93*(11), 1584–1593. http://dx.doi.org/10.1016/j.ress.2008.02.011

Lei, X., Xia, Y., Dong, Y., & Sun, L. (2022). Multi-level time-variant vulnerability assessment of deteriorating bridge networks with structural condition records. *Engineering Structures*, *266*, 114581. http://dx.doi.org/http://dx.doi.org/10.1016/j.engstruct.2022.114581

Liu, M., & Frangopol, D. M. (2006). Probability-Based Bridge Network Performance Evaluation. *Journal of Bridge Engineering*, *11*(5), 633–641.

Nabian, M. A., & Meidani, H. (2018). Deep Learning for Accelerated Seismic Reliability Analysis of Transportation Networks. *Computer-Aided Civil and Infrastructure Engineering*, *33*(6), 443–458.

Reed, S., Löfstrand, M., & Andrews, J. (2019). An efficient algorithm for computing exact system and survival signatures of K-terminal network reliability. *Reliability Engineering & System Safety*, *185*, 429–439. http://dx.doi.org/http://dx.doi.org/10.1016/j.ress.2019.01.011

Saydam, D., Bocchini, P., & Dan, M. F. (2013). Time-dependent risk associated with deterioration of highway bridge networks. *Engineering Structures*, *54*(3), 221–233.

Wang, J., Fang, K., Li, S., & He, S. (2020). Bayesian network-based vulnerability assessment of a large-scale bridge network using improved ORDER-II-Dijkstra algorithm. *Structure and Infrastructure Engineering*(17), 1–12.

Wang, J., Zhang, Y., Li, S., Xu, W., & Jin, Y. (2024). Directed network-based connectivity reliability evaluation for urban bridges. *Reliability Engineering & System Safety*, *241*, 109622. http://dx.doi.org/http://dx.doi.org/10.1016/j.ress.2023.109622

Yang, D. Y., & Frangopol, D. M. (2019). Societal risk assessment of transportation networks under uncertainties due to climate change and population growth. *Structural Safety*, *78*, 33–47.

Yang, D. Y., & Frangopol, D. M. (2020). Life-cycle management of deteriorating bridge networks with network-level risk bounds and system reliability analysis. *Structural Safety*, *83*. http://dx.doi.org/10.1016/j.strusafe.2019.101911

Yeh, W.-C., Tan, S.-Y., Forghani-elahabad, M., Khadiri, M. E., Jiang, Y., & Lin, C.-S. (2022). New binary-addition tree algorithm for the all-multiterminal binary-state network reliability problem. *Reliability Engineering & System Safety*, *224*. http://dx.doi.org/10.1016/j.ress.2022.108557

Bridge Maintenance, Safety, Management, Digitalization and Sustainability – Jensen, Frangopol & Schmidt (eds)
© 2024 The Author(s), ISBN 978-1-032-77040-6
Open Access: www.taylorfrancis.com, CC BY-NC-ND 4.0 license

Forward UQ based on Bayes-informed mixture distribution

Y. Zhang, Y. Dong & R.W. Feng
Department of Civil and Environmental Engineering, The Hong Kong Polytechnic University, Hong Kong, China

ABSTRACT: Assessing the reliability of bridge infrastructures under seismic excitations is of great importance for structural design and maintenance, where uncertainties of both structural parameters and loadings should be taken into account. However, evaluating the first-passage failure probability of bridge infrastructures subjected to stochastic seismic excitations efficiently and accurately is still a challenging problem. The first-passage failure probability can be estimated through the extreme value distribution (EVD) of structural responses. To obtain the underlying EVD of interest, three candidate distributions are first selected, i.e., two inverse Gaussian distributions and one Gamma distribution. The mixture of these three distributions is conducted from Bayesian perspective. First, a moment-generating function-guided likelihood function is employed for Bayesian inference, where the benchmark data can be obtained by Latin partially stratified sampling technique and the predicted data can be yielded by the mixture distribution. Then, the transitional Markov chain Monte Carlo can be employed to detect the posterior distributions of unknown parameters of the mixture distribution. Finally, the calibrated mixture distribution can be an explicit representation of the underlying unknown EVD and the failure probability can be easily obtained.

1 INTRODUCTION

Uncertainties are inevitable and widely exist in engineering problems, which significantly affect the structural response of interest. It is of paramount importance to assess the safety of engineering structures under the influence of these uncertainties. Various approaches have been developed for structural reliability analysis in the past few decades. Monte Carlo simulation (MCS) is regarded as a benchmark method for estimating the failure probability (Rubinstein & Kroese, 2016). MCS requires too many calls to the original physical model so many advanced simulation-based methods are further developed such as the importance sampling (Dai et al., 2016, Engelund & Rackwitz, 1993, Melchers, 1989), directional sampling (Ditlevsen et al., 1988) and subset sampling (Au & Beck, 2001). To circumvent substantial number of calls to the physical model, surrogate model or metamodel is widely employed to replace the original time-consuming physical model. Commonly used surrogate models include the polynomial chaos expansion (Blatman & Sudret, 2011, Zhang & Xu, 2021), Kriging model (Echard et al., 2011, Echard et al., 2013), artificial neural networks (Chojaczyk et al., 2015) and so on.

However, these methods may not efficient for the reliability analysis of stochastic dynamic systems. Commonly, a stochastic system, for instance, a random structure subjected to the fully non-stationary stochastic seismic excitation, is a high-dimensional system. The number of involved random variables is usually larger than 1000. The high-dimensional problem is caused by the process of simulating stochastic excitation. For example, the spectral representation method can be adopted to simulate the stochastic seismic excitation (Rice, 1944, Shinozuka, 1971). To ensure the accuracy of the simulation, thousands of random phases are required to simulate the random process, which leads to a high-dimensional forward

DOI: 10.1201/9781003483755-224

uncertainty propagation problem. Since the extreme structural response is of interest, so many researchers focus on the extreme value distribution of the response and the first passage failure probability (Chen & Li, 2007). Various moments-based approaches have been developed to fit the underlying EVD. To address the high-dimensional problem, sampling-based methods are adopted to assess the statistical moments of the structural response. Then, the possible distribution models such as the maximum entropy method and the mixture distribution are employed to reconstruct the unknown EVD by fitting a series estimated statistical moments (Dang et al., 2021, Dang & Xu, 2020).

Nevertheless, it is still hard to determine which kind of distribution model should be adopted and the estimation of the hyper parameters of the distribution model should be further investigated. In this paper, Bayesian inference is employed to infer the unknown hyper parameters of a mixture distribution. Two inverse Gaussian distributions and a Gamma distribution are utilized to fit the unknown EVD. The values of moment generating function related to the unknown EVD are employed for the likelihood function of Bayes' theorem. The transitional Markov chain Monte Carlo is utilized to determine the posterior distribution of hyper parameters of the mixture distribution. To validate the accuracy and efficiency of the proposed method, a continuous concrete highway bridge subjected to the fully non-stationary stochastic seismic excitation is investigated.

2 EXTREME VALUE DISTRIBUTION OF THE STOCHASTIC DYNAMIC SYSTEMS

2.1 *Structures subjected to the seismic excitation*

The governing equation of motion of a dynamic system subjected to the seismic excitation can be given as:

$$\mathbf{M}(\mathbf{X}_S)\ddot{U} + \mathbf{C}(\mathbf{X}_S)\dot{U} + F(U, \mathbf{X}_S) = -\mathbf{M}(\mathbf{X}_S)A(\mathbf{X}_L, t) \tag{1}$$

where **M, C** are mass and damping matrix, respectively. **F** represents the vector of restoring force. U, $\dot{U}$and U represent the displacement, velocity and acceleration, respectively. $\mathbf{X}_S$ and $\mathbf{X}_L$ denote n_1 random structural parameters and n_2 random variables related to the loading, i.e., the stochastic seismic excitation. Denote $\mathbf{X} = (\mathbf{X}_S, \mathbf{X}_L)$ as a n-dimensional random variable and $n = n_1 + n_2$.

The time-series structural response of interest can be denoted as:

$$Z(t) = H(\mathbf{X}, t) \tag{2}$$

where H is a physical operator. Then, the maximum absolute structural response can be given as:

$$Y = \max|Z(t)| = G(\mathbf{X}) \tag{3}$$

where Y is the extreme value of the time-series structural response over a time duration [0, T].

Given a threshold b, the so-called first passage failure probability can be calculated as (Chen & Li, 2007):

$$P_f = \Pr(Y > b) \tag{4}$$

It can be readily obtained from the extreme value distribution of the structural response:

$$P_f = \int_b^{+\infty} f_Y(y)\mathrm{d}y \tag{5}$$

Hence, it is of great importance to obtain the extreme value distribution of a stochastic dynamic system. However, it is usually hard to estimate the extreme value distribution since the stochastic dynamic system is commonly a high-dimensional system (n>1000). Assessing

the statistical moments of responses or estimating the failure probability is tricky for such a high-dimensional dynamic system.

2.2 *Spectral representation method for generating the stochastic seismic excitation*

Spectral representation method is employed to simulating the fully non-stationary stochastic seismic excitation in this paper. The ground acceleration can be expressed by (Shinozuka & Deodatis, 1991):

$$A(t) = \sqrt{2}\sum_{k=0}^{n_2-1}\sqrt{2S_A(w_k,t)\Delta w}[w_k t + \phi_k] \tag{6}$$

where $S_A(w, t)$ is the double-sided evolutionary power spectral density function:

$$S_A(w,t) = |M(w,t)|^2 S(w) \tag{7}$$

in which $M(w, t)$is a modulating function defined by:

$$M(w,t) = \exp\left(-\eta_0 \frac{wt}{w_a t_a}\right)\cdot\left[\frac{t}{c}\exp\left(1-\frac{t}{c}\right)\right]^2 \tag{8}$$

and $S(w)$ is the one-sided power spectral density function given by:

$$S(w) = \frac{w_g^4 + 4\zeta_g^2 w_g^2 w^2}{\left(w^2 - w_g^2\right)^2 + 4\zeta_g^2 w_g^2 w^2}\cdot\frac{w^4}{\left(w^2 - w_f^2\right)^2 + 4\zeta_f^2 w_f^2 w^2} S_0 \tag{9}$$

The relevant parameters can be specified as follows: Δt = 0.02s, T=30s, η_0 = 0.15,w_a = 5π rad/s, t_a = 30s, c=9, $w_g = w_a$, $w_f = 0.1w_g$, $\zeta_g = \zeta_f = 0.60$ and S_0 = 48.9332cm^2/s. To ensure the accuracy of the simulated stochastic seismic excitation, the number of random phases ϕ_k is set to n_2 = 1001 and $w_k = k\Delta w$, k = 0, 1, .., n_2 − 1. Hence, the stochastic dynamic system is a high-dimensional system with more than 1000 random variables.

3 BAYES-INFORMED MIXTURE DISTRIBUTION FOR EVD ESTIMATION

3.1 *Bayesian inference for unknown parameters estimation*

Bayesian inference is a core step for model calibration in Bayesian model updating. Let $\theta = (\theta_1, \theta_2, \ldots, \theta_m)$ be the unknown parameters that characterize a model $\mathcal{M}$. The basic idea of model calibration is to determine the posterior distributions over unknown parameters according to the observed data $\mathcal{D}$ and prior knowledge of θ. The posterior PDF of θ based on the Bayes' theorem gives:

$$p(\theta|\mathcal{D},\mathcal{M}) \propto p(\mathcal{D}|\theta,\mathcal{M})p(\theta|\mathcal{M}) \tag{10}$$

where $p(\mathcal{D}|\theta,\mathcal{M})$ is the likelihood function and $p(\theta|\mathcal{M})$ is the prior distribution of unknown parameters θ. To find the posterior distribution of θ, simulation-based method such as the transitional Markov chain Monte Carlo can be employed.

3.2 *Mixture distribution for constructing the unknown EVD*

The shape of the EVD of the response of a stochastic system is hard to be understood since the involved high-dimensional problem and complex dynamics. Moments-based method provides a possible way to deal with the high-dimensional uncertainty propagation problem, that is, the unknown distribution can be reconstructed by a distribution model via fitting a series

of estimated statistical moments. Herein, we assume a mixture distribution $\bar{\mathcal{M}}$ includes different kinds of candidate distributions:

$$\bar{\mathcal{M}} = \omega_1 C_1 + \omega_2 C_2 + \cdots + \omega_p C_p \tag{11}$$

where ω_i ($0 \le \omega_i \le 1$) is the i-th weight of the i-th candidate distribution C_i. Denote the unknown parameters of these candidate distributions as $\theta = (\theta_1, \theta_2, \ldots, \theta_m)$. According to the Bayes' theorem, the posterior distribution of θ can be expressed as (Zhang et al., 2023):

$$p(\theta, \omega | \mathcal{D}, \bar{\mathcal{M}}) \propto p(\mathcal{D} | \theta, \omega, \bar{\mathcal{M}}) p(\theta, \omega | \bar{\mathcal{M}}) \tag{12}$$

Hence, the distribution parameters and the weights are required to be calibrated through the observed dataset $\mathcal{D}$ and prior knowledge. Once the hyper parameters can be determined, the mixture distribution can be an explicit expression of the underlying EVD.

3.3 *Moment generating function-based likelihood function*

To determine the posterior distribution of hyper parameters of the mixture distribution, the observed data is of great importance. Different from the conventional engineering model calibration, the observed data is usually the structural response of interest. Herein, the hyper parameters of a distribution model are of interest so the probability densities should be the "response" instead. However, it is hard to use the probability densities directly from a limited number of samples. In this paper, the moment generating function is employed to construct the likelihood function since it can be regarded as an alternative specification of the probability density function. The moment generating function can be defined by (Dang et al., 2021):

$$M_Y(\alpha) = E[\exp(\alpha Y)] = \int_0^{+\infty} \exp(\alpha Y) f_Y(y) \mathrm{d}y, \ \alpha \in R \tag{13}$$

Thus, the problem of finding the PDF of Y is equivalent to finding the MGF. Equation (13) can be reformulated as:

$$M_Y(\alpha) = \int_{\Omega_{\mathbf{X}}} \exp(\alpha G(\mathbf{X})) f_{\mathbf{X}}(\mathbf{x}) \mathrm{d}\mathbf{x} \tag{14}$$

Nevertheless, it is hard to calculate the integral shown in Equation (14) directly. Simulation-based methods can be employed to estimate the integral. Herein, a so-called Latinized partially stratified sampling (LPSS) technique is adopted, which can be expressed by:

$$d^{(i)} = \frac{1}{N} \sum_{j=1}^{N} \exp\left(\alpha_i G\left(\mathbf{x}^{(j)}\right)\right), \ i = 1, 2, \ldots, N_d \tag{15}$$

where d is the value of moment generating function and N is the number of LPSS samples used for calculating d and N_d is the number of observed data used for Bayesian inference. These N_d samples can be seen as the "true" value of the moment generating function of Y, and the predicted one can be calculated by the mixture distribution:

$$\hat{d}^{(i)} = \omega_1 F_1(\alpha_i) + \omega_2 F_2(\alpha_i) + \cdots + \omega_p F_p(\alpha_i) \tag{16}$$

where F_i, $i = 1, 2, \ldots, p$ denotes the moment generating function of i-th candidate distribution.

Once we get the "true" and "predicted" data of the moment generating function, the MGF-based likelihood function can be taken as a Gaussian distribution with zero mean and equal variance σ^2 (Zhang et al., 2023):

$$p(\mathcal{D} | \theta, \omega, \bar{\mathcal{M}}) = \frac{1}{(2\pi\sigma^2)^{\frac{N_d}{2}}} \exp\left[-\frac{1}{2\sigma^2} \sum_{i=1}^{N_d} \left(d^{(i)} - \hat{d}^{(i)} \right) \right] \tag{17}$$

3.4 *Candidate distributions for the mixture distribution*

We can hardly know the shape of the extreme value distribution of the structural response so we select several candidate distributions to fit the underlying EVD. Two inverse Gaussian distributions and one Gamma distribution serve as the candidate distributions.

The first one is the inverse Gaussian (IG) distribution, which is a two-parameter distribution with support on (0, + ∞):

$$f(x;\theta_1,\theta_2)=\sqrt{\frac{\theta_2}{2\pi x^3}}\exp\left(-\frac{\theta_2(x-\theta_1)^2}{2\theta_1^2 x}\right) \tag{18}$$

and the MGF of inverse Gaussian distribution gives:

$$M_x(\alpha,\theta_1,\theta_2)=\exp\left[\frac{\theta_2}{\theta_1}\left(1-\sqrt{1-\frac{2\theta_1^2\alpha}{\theta_2}}\right)\right] \tag{19}$$

The first-four central moments of IG are listed as follows:

$$\mu_{\mathrm{IG}}=\theta_1,\sigma_{\mathrm{IG}}=\sqrt{\frac{\theta_1^3}{\theta_2}},\gamma_{\mathrm{IG}}=3\sqrt{\frac{\theta_1}{\theta_2}},\kappa_{\mathrm{IG}}=15\frac{\theta_1}{\theta_2} \tag{20}$$

Note that the second distribution is also an IG distribution characterized by parameters θ_3 and θ_4.

The third one is a Gamma distribution, which is also a two-parameter distribution on (0, + ∞). Its PDF is given by:

$$f(x;\theta_5,\theta_6)=\frac{1}{\Gamma(\theta_5)\theta_6^{\theta_5}}x^{\theta_5-1}\exp\left(-\frac{x}{\theta_6}\right) \tag{21}$$

The MGF of Gamma distribution gives:

$$M_x(\alpha,\theta_5,\theta_6)=(1-\theta_6\alpha)^{-\theta_5} \tag{22}$$

and the first-four central moments are:

$$\mu_{\mathrm{Gamma}}=\theta_5\theta_6,\sigma_{\mathrm{Gamma}}=\sqrt{\theta_5\theta_6^2},\gamma_{\mathrm{Gamma}}=\frac{2}{\sqrt{\theta_5}},\kappa_{\mathrm{Gamma}}=\frac{6}{\theta_5} \tag{23}$$

Based on Equation (16), the MGF of the mixture distribution can be calculated by:

$$\begin{aligned}\hat{d}^{(i)}&=\omega_1 M_x(\alpha_i,\varphi_1,\varphi_2)+\omega_2 M_x(\alpha_i,\varphi_3,\varphi_4)+\omega_3 M_x(\alpha_i,\varphi_5,\varphi_6)\\&=\omega_1\exp\left[\frac{\theta_2}{\theta_1}\left(1-\sqrt{1-\frac{2\theta_1^2\alpha}{\theta_2}}\right)\right]+\omega_2\exp\left[\frac{\theta_4}{\theta_3}\left(1-\sqrt{1-\frac{2\theta_3^2\alpha_i}{\theta_4}}\right)\right]+\omega_3(1-\theta_6\alpha_i)^{-\theta_5}\end{aligned} \tag{24}$$

To implement the TMCMC, the prior distributions of all hyper parameters follow uniform distributions, the parameters of uniform distributions are given by (Zhang et al., 2023):

$$\Omega_\theta=[0.9\theta_0,\ 1.1\theta_0],\ \Omega_\omega=[0,\ 1]^p \tag{25}$$

Herein p=3 and θ_0 can be calculated by the following:

$$\theta_1^0=\mu_{\mathrm{IG}},\ \theta_2^0=\frac{\mu_{\mathrm{IG}}^3}{\sigma_{\mathrm{IG}}^2},\theta_3^0=\mu_{\mathrm{IG}},\ \theta_4^0=\frac{\mu_{\mathrm{IG}}^3}{\sigma_{\mathrm{IG}}^2},\theta_5^0=\frac{\mu_{\mathrm{Gamma}}^2}{\sigma_{\mathrm{Gamma}}^2},\ \theta_6^0=\frac{\sigma_{\mathrm{Gamma}}^2}{\mu_{\mathrm{Gamma}}} \tag{26}$$

and α_i, i = 1, 2, .., $N_d$are $N_d$uniformly distributed discrete points over the interval [− 2, 0]. In this paper, N_d = 100 is adopted.

Once the posterior distribution over hyper parameters θ is determined, then the mixture distribution for representing the unknown EVD can be calculated through the mean values of θ:

$$\hat{f}_Y(y) = \omega_1 \sqrt{\frac{\theta_2}{2\pi y^3}} \exp\left(-\frac{\theta_2 (y-\theta_1)^2}{2\theta_1^2 y}\right) + \omega_2 \sqrt{\frac{\varphi_4}{2\pi y^3}} \exp\left(-\frac{\varphi_4 (y-\varphi_3)^2}{2\varphi_3^2 y}\right) + \omega_3 \frac{1}{\Gamma(\varphi_5)\varphi_6^{\varphi_5}} y^{\varphi_5 - 1} \exp\left(-\frac{y}{\varphi_6}\right) \tag{27}$$

4 NUMERICAL EXAMPLE

In this section, a practical continuous concrete highway bridge is investigated and the detail of the finite element model and involved random variables can refer to references (Wang et al., 2022, Zhang et al., 2023). The maximum pier drift ratio is of interest:

$$y = \max_{1 \le i \le 7} \left(\Delta_i^{\text{Pier top}} / h \right) \tag{28}$$

where $\Delta_i^{\text{Pier top}}$ denotes the top displacement of the i-th pier and h represents the height of the pier. There are 8 random structural parameters and 1001 random phases for simulating the stochastic seismic excitation are involved so it is a 1009-dimensional dynamic system.

To estimate the underlying EVD of the pier drift ratio, 900 samples generated by LPSS are employed to calculate the reference data of the moment generating function and 100 reference points are obtained by Equation (15). The predicted data is calculated by Equation (24). Once we get the reference and predicted data, the likelihood function expressed by Equation (17) can be constructed and then the posterior distribution of hyper parameters θ can be found by TMCMC. Table 1 shows the mean value and the coefficient of variation (CoV) of the hyper parameters. It can be seen that the CoV of all hyper parameters are very small, which indicates the margin posterior distributions of hyper parameters are highly peaked. Therefore, we can use the mean value of these hyper parameters to estimate the EVD.

Table 1. Mean and CoV of the hyper parameters.

Hyper parameter	ω_1	ω_2	ω_3	θ_1	θ_2	θ_3	θ_4	θ_5	θ_6
Mean	0.182	0.483	0.336	1.024	12.073	1.035	11.816	13.531	0.078
CoV	0.013	0.013	0.015	0.001	0.002	0.0003	0.003	0.003	0.004

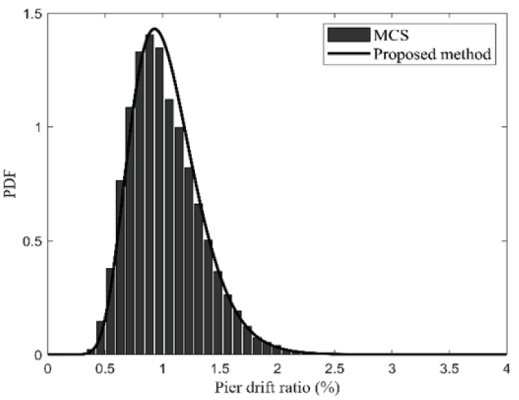


Figure 1. PDF of the maximum pier drift ratio.

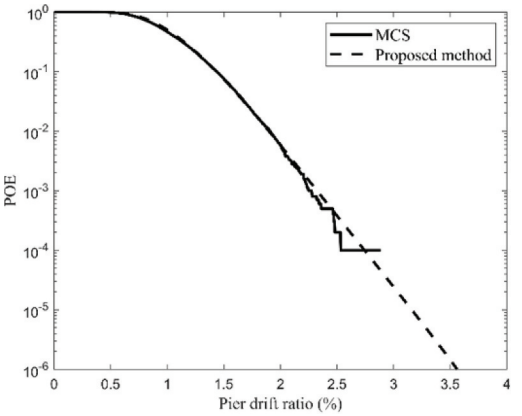


Figure 2. POE of the maximum pier drift ratio.

The PDF of the maximum pier drift ratio is depicted in Figure 1. The reference result is provided by 10^4 MCS and it can be found that the PDF by the proposed method is in accordance with the benchmark one. Note that the proposed method only consumes 900 calls to the finite element model. The probability of exceedance (POE) is of interest and POE in logarithmic scale is shown in Figure 2. The reliability analysis focuses more on the tail distribution. It can be found that the proposed method can also achieve fairly good accuracy in the tail of the distribution.

5 CONCLUSION

In this paper, a Bayes-informed mixture distribution is developed for fitting the extreme distribution of a high-dimensional stochastic system. The mixture distribution is composed of two inverse Gaussian distributions and a Gamma distribution. The unknown hyper parameters of the mixture distribution are calibrated by the Bayesian inference with the transitional Markov chain Monte Carlo. The reference data for likelihood function is the values of moment generating function, which can be calculated by a sampling method called LPSS. The predicted data can be easily calculated by the mixed moment generating function. Therefore, the hyper parameters can be easily found by Bayesian inference and the calibrated mixture distribution can be an explicit representation of the unknown EVD. A continuous concrete highway bridge subjected to the stochastic seismic excitation is investigated in this paper and the results show that the proposed method can ensure the efficiency and accuracy of the EVD estimation for a high-dimensional stochastic dynamic system.

REFERENCES

Au, S.-K. & Beck, J. L. 2001. Estimation of small failure probabilities in high dimensions by subset simulation. *Probabilistic Engineering Mechanics*, 16, 263–277.

Blatman, G. & Sudret, B. 2011. Adaptive sparse polynomial chaos expansion based on least angle regression. *Journal Of Computational Physics*, 230, 2345–2367.

Chen, J.-B. & Li, J. 2007. The extreme value distribution and dynamic reliability analysis of nonlinear structures with uncertain parameters. *Structural Safety*, 29, 77–93.

Chojaczyk, A. A., Teixeira, A. P., Neves, L. C., Cardoso, J. B. & Soares, C. G. 2015. Review and application of artificial neural networks models in reliability analysis of steel structures. *Structural Safety*, 52, 78–89.

Dai, H., Zhang, H. & Wang, W. 2016. A new maximum entropy-based importance sampling for reliability analysis. *Structural Safety*, 63, 71–80.

Dang, C., Wei, P. & Beer, M. 2021. An approach to evaluation of evd and small failure probabilities of uncertain nonlinear structures under stochastic seismic excitations. *Mechanical Systems And Signal Processing*, 152, 107468.
Dang, C. & Xu, J. 2020. A mixture distribution with fractional moments for efficient seismic reliability analysis of nonlinear structures. *Engineering Structures*, 208, 109912.
Ditlevsen, O., Bjerager, P., Olesen, R. & Hasofer, A. 1988. Directional simulation in gaussian processes. *Probabilistic Engineering Mechanics*, 3, 207–217.
Echard, B., Gayton, N. & Lemaire, M. 2011. Ak-Mcs: An active learning reliability method combining kriging and monte carlo simulation. *Structural Safety*, 33, 145–154.
Echard, B., Gayton, N., Lemaire, M. & Relun, N. 2013. A combined importance sampling and kriging reliability method for small failure probabilities with time-demanding numerical models. *Reliability Engineering & System Safety*, 111, 232–240.
Engelund, S. & Rackwitz, R. 1993. A benchmark study on importance sampling techniques in structural reliability. *Structural Safety*, 12, 255–276.
Melchers, R. 1989. Importance sampling in structural systems. *Structural Safety*, 6, 3–10.
Rice, S. O. 1944. Mathematical analysis of random noise. *The Bell System Technical Journal*, 23, 282–332.
Rubinstein, R. Y. & Kroese, D. P. 2016. *Simulation And The Monte Carlo Method*, John Wiley & Sons.
Shinozuka, M. 1971. Simulation of multivariate and multidimensional random processes. *The Journal Of The Acoustical Society Of America*, 49, 357–368.
Shinozuka, M. & Deodatis, G. 1991. Simulation of stochastic processes by spectral representation.
Wang, X., Yuan, X., Feng, R. & Dong, Y. 2022. Data-Driven probabilistic curvature capacity modeling of circular rc columns facilitating seismic fragility analyses of highway bridges. *Earthquake Engineering And Resilience*, 1, 211–224.
Zhang, Y., Dong, Y. & Feng, R. 2023. Bayes-informed mixture distribution for the evd estimation and dynamic reliability analysis. *Mechanical Systems And Signal Processing*, 197, 110352.
Zhang, Y. & Xu, J. 2021. Efficient reliability analysis with a Cda-Based dimension-reduction model and polynomial chaos expansion. *Computer Methods In Applied Mechanics And Engineering*, 373, 113467.

Bridge Maintenance, Safety, Management, Digitalization and Sustainability – Jensen, Frangopol & Schmidt (eds)
© 2024 The Author(s), ISBN 978-1-032-77040-6
Open Access: www.taylorfrancis.com, CC BY-NC-ND 4.0 license

Connectivity analysis of transportation networks incorporating bridges and pavements under uncertainty

Jiyu Xin
Harbin Institute of Technology, Harbin, China

Dan M. Frangopol
Lehigh University, Bethlehem, Pennsylvania, USA

Mitsuyoshi Akiyama
Waseda University, Tokyo, Japan

Xu Han
Texas A&M University, College Station, USA

ABSTRACT: Currently, a comprehensive management system for transportation networks incorporating bridges and pavements is still missing. In this study, both bridges and asphalt pavements are considered critical components in the connection among all nodes in the network. A framework for estimating the probabilistic life-cycle connectivity of transportation networks is proposed. Specifically, flexural and shear failure modes are considered for bridges. Four failure modes, including international roughness index, rut depth, alligator cracking, and transverse cracking, are considered for asphalt pavement using a neural network-based deep learning (DL) model trained by the Long-Term Pavement Performance (LTPP) database. In the case study of an existing transportation network located in Chester, Pennsylvania, the matrix-based system reliability method is applied to investigate the life-cycle connectivity and component importance based on the obtained reliability associated with individual bridges and asphalt pavement segments. The results show that both bridges and asphalt pavements make a significant contribution to the probability of network connectivity.

1 INTRODUCTION

A transportation network comprises several components such as roads, bridges, tunnels, and roadside features. Traditionally, bridges have been emphasized as critical components, often considered bottlenecks (Akgül & Frangopol 2003; Shinozuka et al. 2006). However, it is essential to recognize that pavements are equally significant components which are integral to a transportation network, by providing mobility and access to a diverse range of users. Illustratively, the United States has over 617,000 bridges, of which approximately 46,154 (i.e., 7.5%) are classified as structurally deficient, and more than 6 million kilometers of roadways, of which about 40% of pavements are in poor condition (ASCE, 2021). Therefore, prioritizing strategic investments in enhancing and preserving the conditions of bridges and pavements is imperative to prevent severe traffic disruptions, hindered post-event activities, and negative impacts on the economy, environment, and society (Akiyama et al. 2020; Frangopol 2011; Frangopol & Bocchini 2012).

In the assessment and prediction of the network performance, the associated indicators should take into account network connectivity since transportation networks involve multiple origin-destination pairs and numerous paths (Xin et al. 2023b; Firdaus et al. 2023). Meanwhile, the connectivity of each Origin-Destination (O-D) pair is inherently probabilistic due to uncertainties involved in the modeling of loading and structural resistance, characteristics of

DOI: 10.1201/9781003483755-225

hazards, and variations in operating conditions (Sabatino et al., 2016). To the best knowledge of the authors, however, there is currently no comprehensive probabilistic management system for transportation networks that integrates both bridges and pavements.

This paper introduces a framework for estimating the connectivity probability of transportation networks by incorporating both bridges and asphalt pavements through neural network-based deep learning models. The methodology involves evaluating the time-variant performance of bridges and asphalt pavements, considering the time-variant probability that captures the propagation of uncertainties throughout their life-cycle. The reliability analysis of individual bridges takes into account flexural and shear failure modes, considering corrosion hazards and traffic loads. For asphalt pavements, a bidirectional LSTM neural network (referred to as the BiLSTM model) is trained using data from the Long-Term Pavement Program (LTPP) (LTPP 2023). Subsequently, the pavement reliability is calculated, incorporating uncertainties related to pavement structure and property variables, climatic and traffic conditions, BiLSTM model predictions, and performance indicator measurements.

In a case study utilizing the matrix-based system reliability (MSR) method proposed by (Kang et al., 2008), the time-variant transportation network performance indicator is explored. This includes the probability of disconnection and importance measures for bridges, pavements, and bridge-pavement groups within an existing transportation network comprising seven bridges and five asphalt pavement segments located in Chester County, Pennsylvania.

2 PROCEDURE OF ESTIMATING THE CONNECTIVITY PROBABILITY OF TRANSPORTATION NETWORKS

2.1 *General procedure*

Figure 1 presents the flowchart of connectivity probability estimation of transportation networks containing bridges and asphalt pavements, which consists of three main parts:

(1) Bridge system analysis, including the reliability calculation considering two failure modes of flexural and shear.
(2) Pavement system analysis, including deep learning model training and the associated reliability analysis based on four performance indicators.
(3) Transportation network analysis, including connectivity reliability and importance measure using matrix-based system reliability method.

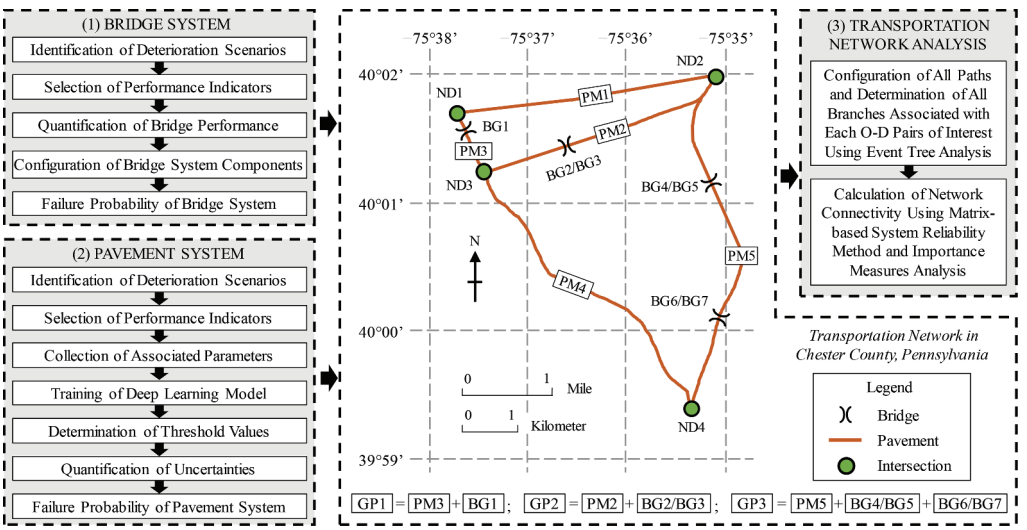


Figure 1. Flowchart of connectivity analysis of transportation network integrating bridges and pavements.

2.2 *Bridge analysis*

The failure analysis of a bridge involves treating it as a series-parallel system, where adjacent girders form parallel subsystems. Correlations between the load effects and resistances among different bridges are considered to assess the system reliability of an individual bridge. The number of girders in each parallel subsystem is related to factors such as the maximum live load effects generated by parallel trucks and the redundancy of the bridge superstructure (Han & Frangopol 2022). The equivalent component method, introduced by Gollwitzer & Rackwitz (1983), is employed to transform the series-parallel system model into a series system model. Then, the reliability of this series system is computed using the sequential compounding method, as detailed by Gong & Zhou (2017). More detailed information and reliability results are provided by Xin et al. (2023b).

2.3 *Pavement analysis*

Deep learning excels at handling large datasets by automatically and efficiently learning the complex relationship between inputs and outputs (Chollet 2021). In this study, a deep learning model comprising BiLSTM neural networks (Greff et al. 2016) was developed and trained to predict the performance indicators of asphalt pavement based on relevant operating conditions, including climate, traffic, and pavement property and structure (Xin et al. 2021a, b, 2022). The data used for model training are obtained from the LTPP database (Standard Data Release 37) published in August 2023 (FHWA 2017; LTPP 2023). The asphalt pavement is conceptualized as a series system encompassing four failure modes associated with indicators of (a) International Roughness Index (*IRI*), (b) rut depth (D_{rut}), (c) alligator cracking (C_{gator}), and (d) transverse cracking (C_{trans}) (AASHTO 2020; Ang and Tang 2007). The system failure probability is then calculated through the Monte Carlo simulation method. Additional details and reliability results are available in Xin et al. (2023a, 2023b).

2.4 *Transportation network analysis*

In this study, the matrix-based system reliability (MSR) method, introduced by Kang et al. (2008), is employed. This method is selected for its capability to efficiently estimate the probabilities of complex system events through simple matrix calculations. The network failure probability can be calculated as:

$$P(E_{DIS}) = \sum_{c:e_c \subseteq E_{DIS}} p_c = \mathbf{c}^{\mathrm{T}}\mathbf{p}, c = 1,\ 2,\ \ldots,\ Nev \tag{1}$$

where E_{DIS} = disconnection of the network; e_c (c = 1, …, *Nev*) = basic mutually exclusive and collectively exhaustive events with the total number of *Nev*; p_c = probability of e_c; $\mathbf{c}$ = event vector that represents the network event whose cth element is 1 if e_c belongs to the network event and 0 otherwise; and $\mathbf{p}$ = probability vector that contains p_c's. Details associated with the construction of event $\mathbf{c}$ and probability $\mathbf{p}$ vectors are provided by Kang et al. (2008).

Importance measures (IM) are helpful when identifying the bridges or pavements whose preservation and maintenance would most efficiently enhance the network connectivity (Song & Der Kiureghian 2005). Based on the Equation (1), the $\mathrm{IM_c}$ associated with component c can be calculated as:

$$\mathrm{IM}_c = P(E_c E_{sys} = E'_{sys})/P(E_{sys}) = (\mathbf{c}'^{\mathrm{T}}\mathbf{p})/(\mathbf{c}^{\mathrm{T}}\mathbf{p}) \tag{2}$$

$$\mathrm{NIM}_c = \mathrm{IM}_c / \sum_{c=1}^{Nc} \mathrm{IM}_c \tag{3}$$

where E_c = c component event; $\mathbf{c}'$ = event vector of E'_{sys}; NIM_c = normalized IM_c; and *Nc* = number of components in the network.

3 CASE STUDY

3.1 *Network connectivity*

The transportation network selected in the case study is shown in Figure 1, which contains seven bridges (i.e., BG1, BG2, BG3, BG4, BG5, BG6, and BG7), five pavement segments (i.e., PM1, PM2, PM3, PM4, and PM5) and four nodes (i.e., ND1, ND2, ND3, and ND4). Note that BG1 and PM 3 in series are lumped as group GP1; BG2, BG3, and PM2 in series are lumped as group GP2; BG4, BG5, BG6, BG7, and PM5 in series are lumped as GP3. Based on the reliability results obtained in sections 2.2 and 2.3, the network connectivity results considering at least 3 and 5 O-D pairs disconnected are shown in Figure 2 using Equations (1). Specifically, Figure 2(a) shows that the probability of disconnection associated with at least 3 and 5 O-D pairs increases with time. Figure 2(b) shows the comparison of the probability of disconnection associated with at least 3 O-D pairs using a base-10 logarithmic scale among three cases: C, C1, and C2. C is the base case in which both bridges and pavements are considered. PM1 and PM4 are assumed to never fail in the case of C1, and C2 only considers the bridges as vulnerable elements. It can be seen that the probability of disconnection is underestimated if the pavements are not taken into account in the connectivity analysis of a transportation network.

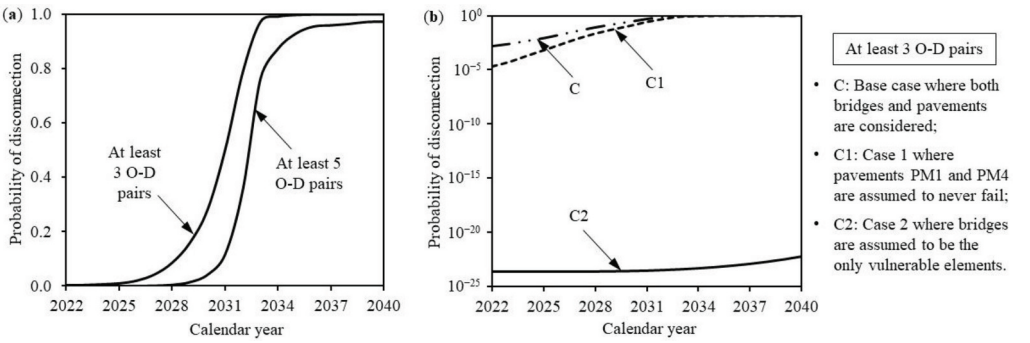


Figure 2. Probability of disconnection associated with (a) at least 3 and 5 O-D pairs and (b) a base-10 logarithmic scale for at least three O-D pairs that are disconnected under cases of C, C1, and C2.

3.2 *Importance measures of components*

Figure 3 shows the normalized importance measures of five components (i.e., PM1, PM4, GP1, GP2, and GP3) in the transportation network associated with the disconnection of at least 3 and 5 O-D pairs using Equations (2) and (3). For example, the importance associated with GP2 increases significantly from 2022 to 2031 for the case of at least 3 O-D pairs disconnected. Therefore, GP2 is expected to effectively reduce the network failure probability if retrofitted during this period.

4 CONCLUSIONS

A probabilistic framework for connectivity analysis of transportation networks incorporating bridges and asphalt pavements is proposed in this paper. The network connectivity and component importance measures associated with different O-D pairs are calculated using the matrix-based system reliability method.

Both bridges and asphalt pavements significantly influence the connectivity of the transportation network. Consequently, a traditional bridge network analysis that neglects pavement performance leads to an overestimation of network connectivity.

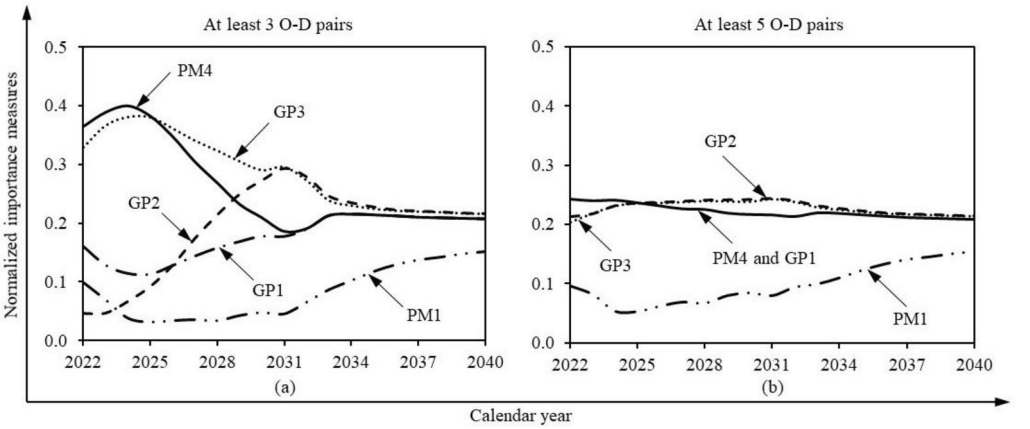


Figure 3. Normalized importance measures of bridge, pavements, and bridge-pavement groups associated with the disconnection of (a) at least 3 O-D pairs and (b) at least 5 O-D pairs.

Asphalt pavement generally offers a shorter service life of 15 to 25 years compared to bridges. Therefore, it is crucial to extend the service life of asphalt pavement to maintain network connectivity and to cope with postevent interventions.

REFERENCES

Akgül, F. & Frangopol, D.M. 2003. Rating and reliability of existing bridges in a network. *Journal of Bridge Engineering*, 8(6): 383–392.

Akiyama, M., Frangopol, D.M., & Ishibashi, H. 2020. Toward life-cycle reliability-, risk-and resilience-based design and assessment of bridges and bridge networks under independent and interacting hazards: emphasis on earthquake, tsunami and corrosion. *Structure and Infrastructure Engineering*, 16(1), 26–50.

American Association of State Highway and Transportation Officials (AASHTO). 2020. *Mechanistic-empirical pavement design guide* (3rd ed.). Washington, DC: AASHTO.

American Society of Civil Engineers (ASCE). 2021. *2021 Report Card for America's Infrastructure*. Reston, VA.

Ang, A. H.S. & Tang, W.H. 2007. *Probability concepts in engineering planning and design*. 2nd ed. New York: Wiley.

Chollet, F. 2021. *Deep learning with Python*. Simon and Schuster.

Federal Highway Administration (FHWA) - Office of Research, Development, and Technology: Infrastructure R&D. 2017. *The long-term pavement performance program* (FHWA-HRT-15-049). McLean, VA: FHWA.

Firdaus, P.S., Matsuzaki, H., Akiyama, M., Aoki, K. & Frangopol, D.M. Probabilistic connectivity assessment of bridge networks considering spatial correlations associated with flood and seismic hazards. *Structure and Infrastructure Engineering*, 2023. https://doi.org/10.1080/15732479.2023.2276373

Frangopol, D.M. 2011. Life-cycle performance, management, and optimisation of structural systems under uncertainty: accomplishments and challenges. *Structure and Infrastructure Engineering*, 7(6), 389–413.

Frangopol, D.M. & Bocchini, P. 2012. Bridge network performance, maintenance and optimisation under uncertainty: Accomplishments and challenges. *Structure and Infrastructure Engineering*, 8(4): 341–356

Gollwitzer, S. & Rackwitz, R. 1983. Equivalent components in first-order system reliability. *Reliability Engineering*, 5(2): 99–115.

Gong, C., & Zhou, W. 2017. Improvement of equivalent component approach for reliability analyses of series systems. *Structural Safety*, 68: 65–72.

Greff, K., Srivastava, R.K., Koutník, J., Steunebrink, B.R. & Schmidhuber, J. 2016. LSTM: A search space odyssey. *IEEE Transactions on Neural Networks and Learning Systems*, 28(10): 2222–2232.

Han, X. & Frangopol, D. M. 2022. Life-cycle connectivity-based maintenance strategy for bridge networks subjected to corrosion considering correlation of bridge resistances. *Structure and Infrastructure Engineering*, 18(12): 1614–1637.

Kang, W.-H., Song, J. & Gardoni, P. 2008. Matrix-based system reliability method and applications to bridge networks. *Reliability Engineering & System Safety*, 93(11): 1584–1593.

Long-Term Pavement Performance (LTPP). 2023. *Data from*: *LTPP DataPave online* [Dataset]. Retrieved from https://infopave.fhwa.dot.gov/Data/DataSelection

Sabatino, S., Frangopol, D. M. & Dong, Y. 2016. Life cycle utility-informed maintenance planning based on lifetime functions: Optimum balancing of cost, failure consequences and performance benefit. *Structure and Infrastructure Engineering*, 12(7): 830–847

Shinozuka, M., Zhou, Y., Banerjee, S. & Murachi, Y. 2006. Cost-effectiveness of seismic bridge retrofit. In *Proceeding of 3rd International Conference on Bridge Maintenance, Safety and Management*, 16–19. London: Taylor & Francis.

Xin, J., Akiyama, M., & Frangopol, D.M. 2023a. Sustainability-informed management optimization of asphalt pavement considering risk evaluated by multiple performance indicators using deep neural networks. *Reliability Engineering and System Safety*, 238, 109448.

Xin, J., Akiyama, M., Frangopol, D.M., Zhang, M., Pei, J. & Zhang, J. 2021a. Reliability-based life-cycle cost design of asphalt pavement using artificial neural networks. *Structure and Infrastructure Engineering*, 17(6), 872–886.

Xin, J., Akiyama, M., Frangopol, D.M. & Zhang, M. 2022. Multi-objective optimisation of in-service asphalt pavement maintenance schedule considering system reliability estimated via LSTM neural networks. *Structure and Infrastructure Engineering*, 18(7), 1002–1019.

Xin, J., Frangopol, D.M., Akiyama, M. & Han X. 2023b. Probabilistic life-cycle connectivity assessment of transportation network using deep learning. *ASCE's Journal of Bridge Engineering*, 28(9), 04023066.

Xin, J., Zhang, M., Akiyama, M., Frangopol, D.M. & Pei, J. 2021b. Life-cycle reliability estimation of asphalt pavement based on machine learning approach. *Life-Cycle Civil Engineering: Innovation, Theory and Practice*, A. Chen, X. Ruan, and D.M. Frangopol, eds., CRC Press/Balkema, Taylor & Francis Group plc, London, 246–251.

Bridge Maintenance, Safety, Management, Digitalization and Sustainability – Jensen, Frangopol & Schmidt (eds)
© 2024 The Author(s), ISBN 978-1-032-77040-6
Open Access: www.taylorfrancis.com, CC BY-NC-ND 4.0 license

U-Net model-based XCT images segmentation for steel corrosion in concrete

M. Zhang & W. Wang
College of Civil and Transportation Engineering, Shenzhen University, Shenzhen, China

ABSTRACT: The corrosion of reinforcing bar in concrete has been regarded as one of the most predominant factors for the degradation of reinforced concrete (RC) bridges. The accurate predictions of corrosion damages are the basis for the safety assessment of in-service bridges and the enhancement of new bridge designs. X-ray computed tomography (XCT) has been widely utilized to understand the corrosion process inside the concrete, offering three-dimensional (3D) visualization of steel corrosion. This study uses U-net model to detect various phases of steel corrosion evolution in concrete. The developed U-net model has shown superior segmentation performance on XCT images relating to steel corrosion in concrete. This significant advancement has automated the process of visualizing and 3D reconstructing the steel corrosion process inside the concrete. It enables the quantification of the volumetric expansion ratio of corrosion products.

1 INTRODUCTION

Steel corrosion in concrete is a major durability and maintenance issue for reinforced concrete (RC) bridges, particularly those in marine environments where chloride ion penetration often triggers steel corrosion. The depassivation of rebar occurs directly when a threshold concentration of chloride ions is reached in the concrete near the rebar surface, which finally results in the initiation of the rebar corrosion (de Vera et al. 2017, Alonso et al. 2000). The corrosion products occupy more volume than the original steel, causing volumetric expansion that induces tensile stresses in the surrounding concrete, resulting in cracks and eventually spalling of the concrete cover. This exposes the rebar to aggressive agents, further accelerating corrosion. Proper maintenance planning is crucial for ensuring the safety of aging RC bridges, especially under seismic loads (Akiyama et al. 2017, 2020, Zucca et al. 2023). Accurate corrosion damage prediction is fundamental for the safety assessment of in-service RC bridges and for improving designs of new bridges. In modeling corrosion-induced concrete cracking, the volumetric expansion coefficient is vital. Commonly, it is assumed constant, however, this approach overlooks the complexity of the corrosion process and can lead to imprecise predictions, as the actual boundaries of corrosion products do not always align with those estimated using a constant expansion coefficient (Du et al. 2014, Chen & Leung 2015).

X-ray computed tomography (XCT) offers a non-destructive method to acquire data for prediction models of corrosion damage. XCT has proven effective in providing detailed insights into steel corrosion in concrete, aiding in the durability assessment of RC structures (Jiang et al. 2023, Robuschi et al. 2021, Sun et al. 2021). XCT enables the capture of interior concrete images, showing the progression of reinforcement corrosion and allowing for the creation of three-dimensional images. However, processing XCT images for accurate analysis and reliable results is labor-intensive, often referred to as image segmentation. Multi Otsu's method, a popular segmentation approach, uses thresholding to segment phases in XCT images based on varying gray values (Bernachy-Barbe et al. 2020). However, this method

DOI: 10.1201/9781003483755-226

faces challenges in distinguishing features like cracks and pores in steel corrosion cases, and it struggles with image quality issues, impacting accuracy and performance. Moreover, its applicability is limited to specific specimen parameters.

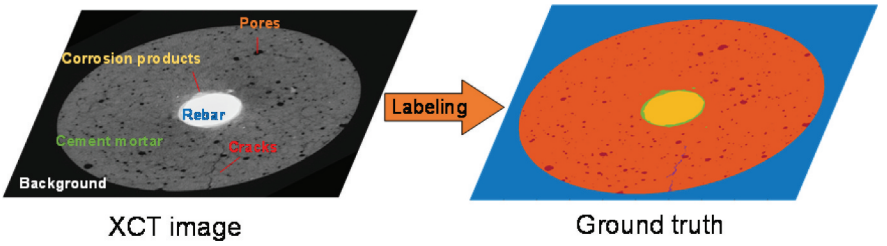


Figure 1. XCT image for steel corrosion in concrete and image labeling.

To address these limitations, deep learning (DL) algorithms should be proposed for automating the analysis of steel corrosion in concrete.

This study evaluates the effectiveness of a DL model (i.e., U-Net model) in processing XCT images of steel corrosion in concrete. The model, trained on XCT images showing rebar corrosion, is used to quantify the evolution of corrosion products, enhancing understanding of the corrosion process.

2 U-NET MODEL

2.1 *X-ray computed tomography and image labeling*

The obtained XCT images (image resolution: 2048 × 2048) for the specimen display a multi-phase system that includes cement mortar, pores, steel, corrosion products, and corrosion-induced cracking, as illustrated in Figure 1. To automatically distinguish the different phases in the XCT images, initial labeling is essential. This process is to establish the training dataset for the U-Net model. For the labeling process, it is necessary to associate each pixel in the XCT image with its respective phase. Before labeling, the XCT image has a pixel value ranging from 0 to 255. Once labeled, these values are transformed to a scale of 0 to 5, representing the different phases: cement mortar, pores, steel, corrosion products, and corrosion-induced cracking. It is worth noting that distinguishing between the pores and cracks is a challenging task, requiring increased manual effort. Considering the computational load and the learning ability of the U-Net model, the XCT images with 256 × 256 image resolution are obtained by automatic clipping, serving as the final inputting image.

2.2 *U-Net model structure*

Figure 2 displays the structure of the U-Net model, where its encoder path includes four contraction blocks. Each block typically contains two 3×3 convolutional layers, followed by a rectified linear unit (ReLU) activation function. The convolutional layers extract features from an image, beginning with padding to maintain consistent matrix size. A 3×3 sliding window moves across the image, using a stride of one, with convolutional operations applied via a kernel matrix to produce a numerical output. The output of this process is a feature map, a new matrix that serves as a condensed representation of the original image's specific features. Additionally, the ReLU activation function is used due to its efficiency in model training and reducing computational demands compared to other activation functions.

In the U-Net model, each convolutional block is followed by a 2×2 max-pooling layer, reducing the image's spatial dimensions by half and increasing its depth. With each

max-pooling layer, the number of feature channels typically doubles, allowing for the capture of more complex features. A 2×2 filter with a stride of 2 extracts the maximum value from each region of a 4×4 input sample, reducing the dimensions of a 256×256 matrix to 128×128.

The deepest layer serves as a bridge between contracting and expanding paths, consisting of two 3×3 convolutions with ReLU activations. The expansion path then employs up-convolution layers, doubling the image size at each step while halving the depth. Each up-convolution output is combined with a corresponding feature map from the contracting path, integrating high-resolution features. This process involves two 3×3 convolutions with ReLU activations after each up-sampling, culminating in an image size of 256×256×64. The final layer, a 1×1 convolution, maps feature vectors to the desired number of classes, producing a segmentation map with the same spatial dimensions as the original input.

2.3 *Model training*

A total of 2032 images were used during the training process of the U-Net model. These images are obtained from different positions of the specimens. The network was trained by using Adam optimizer with a learning rate of 1e-3 and batch size of 32. The training process was implemented in MATLAB on a system with 64GB RAM, a 13th gen Intel Core i9-13900KF CPU, and an NVIDIA GeForce RTX 4070Ti GPU. The training comprised a total of 1770 iterations. The entire training duration was about 1 hour. Figure 3(a) shows the loss function for both training and validation sets. The U-Net model's loss function stabilized after approximately 500 iterations. Figure 3(b) displays a rise in accuracy for both training and validation, which eventually plateau.

2.4 *Model evaluation*

Segmentation tasks aim to distinguish and label different objects, effectively classifying separate entities. Evaluating the effectiveness of a trained segmentation model necessitates testing its performance on a designated dataset. Key metrics for semantic segmentation models include precision, recall, F1 score, and intersection over union (IoU).

The precision metric quantifies the accuracy of positive predictions, calculated as the ratio of true positives (TP, correctly identified object pixels) to the sum of true and false positives (FP, incorrectly identified object pixels). It is defined as:

$$\text{Precision} = \text{TP}/(\text{TP} + \text{FP}) \tag{1}$$

Recall measures the proportion of actual positives that are correctly identified. It is defined as:

$$\text{Recall} = \text{TP}/(\text{TP} + \text{FN}) \tag{2}$$

where FN is false negatives (i.e. pixels of the object of interest that the model failed to identify).

The F1 score offers a balanced mean between precision and recall, accounting for both false positives and false negatives. It is the harmonic mean of precision and recall:

$$\text{F1 score} = (2 \times \text{Recall} \times \text{Precision})/(\text{Recall} + \text{Precision}) \tag{3}$$

IoU assesses the overlap between the model's predicted segmentation and the actual ground truth. It is the ratio of the intersecting area to the union area of the predicted and true segments, with scores ranging from 0 (no overlap) to 1 (perfect overlap):

$$\text{IoU} = \text{TP}/(\text{TP} + \text{FP} + \text{FN}) \tag{4}$$

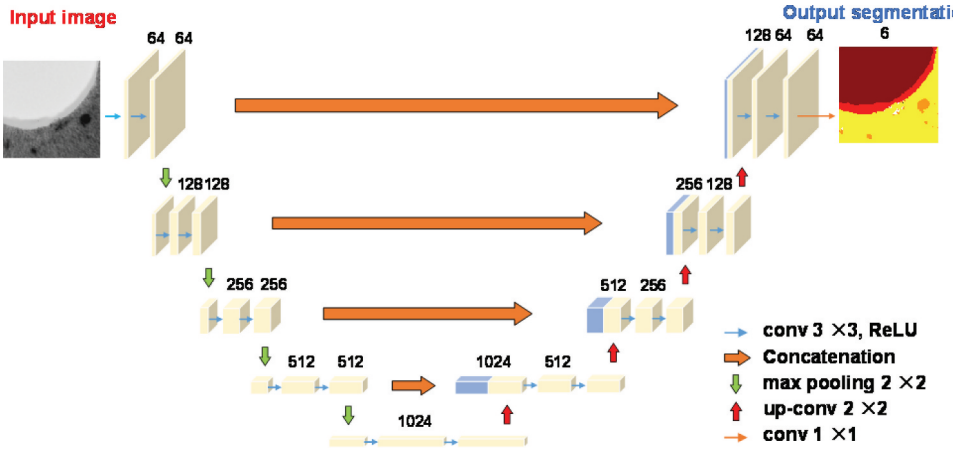


Figure 2. U-Net model structures.

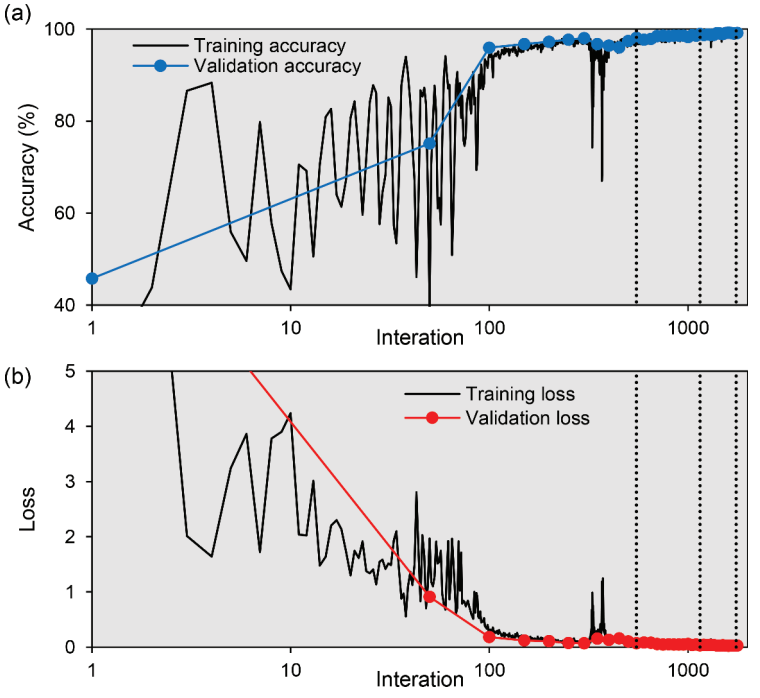


Figure 3. The accuracy and loss curves for U-Net model.

3 RESULTS AND DISCUSSIONS

3.1 *Performance on testing data*

Table 1 provides the results of the U-Net model's segmentation efficacy across various phases, showing its exceptional proficiency in categorizing both steel and cement mortar, as evidenced by F1 scores and IoU metrics. Table 1 also presents a comparative assessment with another deep learning model, specifically the Fully Convolutional Network (FCN) (Long et al. 2015), both trained on the same dataset. In contrast, the FCN model fails in accurately segmenting

cracks. Meanwhile, FCN demonstrates low results in F1 score (0.502) and IoU (0.339) for recognizing the corrosion products. These are lower than the results of the U-Net model. The U-Net model exhibits its lowest performance in crack segmentation, achieving an F1 score of 0.733 and an IoU of 0.603, possibly due to the structural similarity and segmentation complexities inherent in XCT images. Specifically, thin and irregular characteristics of the cracks, often merging with pores, pose significant segmentation challenges. Meanwhile, manual labeling of cracks in XCT images further complicates this task. Nevertheless, an IoU of 0.603 for crack segmentation is considered effective. Overall, the U-Net model demonstrates a robust mean IoU of 0.821 and an average F1 score of 0.891 on the test dataset, outperforming the FCN model in segmenting steel corrosion in concrete XCT images into different categories.

Table 1. Averages of the evaluation indicators for DL models.

Deep learning model	U-Net model		FCN model	
Category	F1 score	IoU	F1 score	IoU
Steel	0.995	0.990	0.960	0.924
Corrosion products	0.869	0.753	0.502	0.339
Pore	0.872	0.785	0.728	0.599
Cement mortar	0.986	0.976	0.979	0.962
Cracks	0.733	0.603	-	-

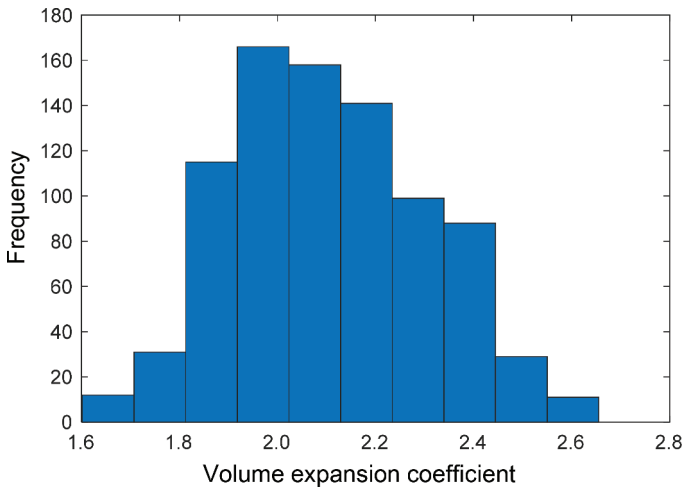


Figure 4. Histogram of volume expansion coefficient.

3.2 *Volume expansion coefficient of corrosion products*

The volume of corrosion products significantly impacts concrete damage, directly influencing structural performance modeling and service life prediction. Corrosion product accumulation causes volumetric expansions in steel, which is a critical factor in concrete cracking models, especially for predicting the time of surface cracking due to rebar corrosion. Previous research (Zhao et al. 2011) indicates a range of 2–4 for the expansion coefficient of corrosion products, with many models adopting a value of 3 (Zhang et al. 2021, Fang et al. 2023). However, there is a lack of consensus on the exact value, and most studies assume this coefficient to be constant, ignoring its variability and uncertainty.

Based on the acquired XCT images for the corroded RC specimens, the volume expansion coefficient can be derived for each cross-section by using U-Net model to recognize the

volumes of corrosion products and corroded rebar. As illustrated in Figure 4, the histogram of the volume expansion coefficient is obtained by a specimen corroded by the galvanostatic method. The average steel weight loss is 6.43%. The expansion ratio ranges from 1.60 to 2.66, with a mean of 2.11 and a standard deviation of 0.2. The result suggests that the expansion coefficient varies spatially. For more accurate modeling of corrosion-induced concrete cover cracking, it is recommended to consider the expansion coefficient as a probabilistic variable, accounting for its inherent uncertainty. The current practice of using a constant value oversimplifies the issue by not accounting for its spatial variations. Therefore, adopting mathematical frameworks that incorporate uncertainties, including the representation of ignorance, is crucial for more realistic and comprehensive modeling.

4 CONCLUSIONS

Over the last decade, XCT technology has significantly progressed in the field of durability analysis of RC bridges. Despite this, there has not been an introduction of a semantic segmentation model specifically for distinguishing different phases in XCT images associated with steel corrosion in concrete. This study presents a deep learning-based image segmentation model designed to automatically detect various phases of steel corrosion in concrete. The results show the efficacy and efficiency of the proposed U-Net model.

The volume expansion coefficient for corrosion products demonstrates spatial variability and uncertainty. Considering this coefficient as a constant in calculations might result in imprecise predictions. Due to the complexity of the corrosion process, it is crucial to treat this parameter as a random variable in a probabilistic approach to analyze concrete damage caused by corrosion. To accurately characterize this random variable, its statistical properties, including probability distribution, mean, and standard deviation, need to be established through additional experimental research.

REFERENCES

Akiyama, M., Frangopol, D. M., & Ishibashi, H. 2020. Toward life-cycle reliability-, risk- and resilience-based design and assessment of bridges and bridge networks under independent and interacting hazards: emphasis on earthquake, tsunami, and corrosion. *Structural and Infrastructure Engineering*, 16, 26–50.

Akiyama, M., Frangopol, D. M., & Takenaka, K. 2017. Reliability-based durability design and service life assessment of reinforced concrete deck slab of jetty structures. *Structural and Infrastructure Engineering*, 13, 468–477.

Alonso, C., Andrade, C., Castellote, M., & Castro, P. 2000. Chloride threshold values to depassivate reinforcing bars embedded in a standardized OPC mortar. *Cement and Concrete Research*, 30, 1047–1055.

Bernachy-Barbe, F., Sayari, T., Dewynter-Marty, V., & L'Hostis, V. 2020. Using X-ray microtomography to study the initiation of chloride-induced reinforcement corrosion in cracked concrete. *Construction and Building Materials*, 259, 119574.

Chen, E., & Leung, C. K. Y. 2015. Finite element modeling of concrete cover cracking due to non-uniform steel corrosion. Engineering Fracture Mechanics, 134, 61–78.

de Vera, G., Antón, C., López, M. P., & Climent, M. A. 2017. Depassivation time estimation in reinforced concrete structures exposed to chloride ingress: A probabilistic approach. *Cement and Concrete Composites*, 79, 21–33.

Du, X., Jin, L., & Zhang, R. 2014. Modeling the cracking of cover concrete due to non-uniform corrosion of reinforcement. *Corrosion Science*, 89, 189–202.

Fang, X., Pan, Z., Chen, A., Tian, H., & Ma, R. 2023. Phase-field method for modeling non-uniform corrosion-induced cracking in concrete. *Engineering Fracture Mechanics*, 281, 109131.

Jiang, C., Zhang, X., Lun, P., Memon, S. A., Luo, Q., Sun, H., Wang, W., Wang, X., & Wang, X. 2023. Quantitative characterization of reinforcement cross-sectional roughness and prediction of cover cracking based on machine learning under the influence of pitting corrosion. *Measurement*, 220, 113322.

Long, J., Shelhamer, E., & Darrell, T. 2015. Fully convolutional networks for semantic segmentation. In *2015 IEEE Conference on Computer Vision and Pattern Recognition* (pp. 3431–3440).

Robuschi, S., Tengattini, A., Dijkstra, J., Fernandez, I., & Lundgren, K. 2021. A closer look at corrosion of steel reinforcement bars in concrete using 3D neutron and X-ray computed tomography. *Cement and Concrete Research*, 144, 106439.

Sun, H., Jiang, C., Cao, K., Yu, D., Liu, W., Zhang, X., Xing, F., & Zhao, D. 2021. Monitoring of steel corrosion and cracking in cement paste exposed to combined sulfate–chloride attack with X-ray microtomography. *Construction and Building Materials*, 302, 124345.

Zhang, M., Akiyama, M., Shintani, M., Xin, J., & Frangopol, D. M. 2021. Probabilistic estimation of flexural loading capacity of existing RC structures based on observational corrosion-induced crack width distribution using machine learning. *Structural Safety*, 91, 102098.

Zhao, Y., Ren, H., Dai, H., & Jin, W. (2011). Composition and expansion coefficient of rust based on X-ray diffraction and thermal analysis. *Corrosion Science*, 53, 1646–1658.

Zucca, M., Crespi, P., Stochino, F., Puppio, M. L., & Coni, M. 2023. Maintenance interventions period of existing RC motorway viaducts located in moderate/high seismicity zones. *Structures*, 47, 976–990.

Bridge Maintenance, Safety, Management, Digitalization and Sustainability – Jensen, Frangopol & Schmidt (eds)
© 2024 The Author(s), ISBN 978-1-032-77040-6
Open Access: www.taylorfrancis.com, CC BY-NC-ND 4.0 license

Fragility interval predictions in non-seismically designed bridges

H. Neduri & J. Ghosh
Indian Institute of Technology Bombay, Mumbai, Maharashtra, India

ABSTRACT: Seismic fragility analysis of highway bridges remains a widely used technique to assess the structural damage and subsequent disruption to transportation networks during a seismic event. While modern bridge seismic design codes prescribe enhanced seismic detailing of bridges located in moderate to high seismic zones, a significant percentage of bridges are still non-seismically designed in these regions. Moreover, in addition to ground motion characteristics, a multitude of potentially uncertain parameters affect the seismic fragility of bridges leading to considerable variations in fragility predictions. In such cases, although a statistical screening may help in pruning down a large set of initial variables, the uncertainty in the significant parameters needs to be propagated through low-discrepancy sampling techniques to effectively cover the sample space. The samples can then be utilized for nonlinear fine element simulations of bridge models to determine the confidence intervals of seismic fragility predictions.

1 INTRODUCTION

In regions characterized by moderate seismicity, earthquakes, albeit infrequent, can have devastating consequences. The misconception of the risk associated with infrequent seismic events resulted in the delayed onset of seismic detailing requirements in these regions. The Central and Southeastern United States (CSUS), which is taken as the test bed for this study, is regarded as a typical moderate seismic zone. It is only after 1990, highway bridge design is shifted from conventional non-seismic design to seismic design practices in this region (Chen & Duan, 2014; Ramanathan et al., 2012). This delayed adoption of seismic design practices resulted in significant percentage of bridges being non-seismic till date (Nielson, 2005).

Although, considerable amount of literature exists on the seismic vulnerability assessment of these non-seismically designed highway bridges in CSUS (Choi et al., 2004; Nielson & DesRoches, 2007; Padgett et al., 2007), little research prevails on the seismic vulnerability assessment through parameterized fragility functions that may also aid in visualizing the fragility confidence intervals. Unlike "classical" fragility curves, these parameterized fragility functions are conditioned not only on the ground motion intensity measure (IM) but also on other critical bridge modelling parameters (Ghosh et al., 2013; Rokneddin et al., 2015). This helps in reassessing the bridge condition using instrumentation data (obtained from structural health monitoring techniques) without running time-intensive nonlinear time history analysis.

This study adopts a novel gradient-based ensemble learning metamodel for approximating the relationships between critical bridge modelling parameters (obtained from sensitivity analysis) and bridge component responses. Unlike traditional regression techniques, this method employs multiple weak learners (regression models) and follows the *wisdom of the crowd* principle, i.e. the collective opinion of the group is considered more accurate than any of the individual weak learner. Seismic vulnerability assessment of the bridge is realized by using the metamodel predictions of different bridge components and the parameterized fragility functions. This study takes it a step further and uses these parameterized fragility functions for uncertainty quantification of critical bridge modelling parameters using statistical linearization technique.

DOI: 10.1201/9781003483755-227

The paper begins by providing a brief overview of the ensemble-learning based metamodel framework adopted for seismic fragility assessment. The following sections elaborate the methodology involved in the development of parameterized fragility functions and the input parameter uncertainty quantification. Next, the application of the proposed framework is demonstrated using a case study example of Multi-Span Simply Supported (MSSS) steel girder bridge, describing each step of the framework in great detail. Finally, the paper concludes by highlighting the key insights from ensemble learning framework and parameterized fragility functions.

2 METAMODEL FRAMEWORK

This study adopts gradient-based least square boosting (GLS Boost) regression technique to fit the data. The data consists of predictor variables $\{IM, x_1,\ldots,x_n\}$, where IM is the intensity measure of ground motion and $x_1,\ldots,x_n$ are other bridge modelling parameters, and the predicted seismic response (y) of the selected bridge components.

GLS Boost is an ensemble learning technique that involves sequentially combining weak learners, like decision trees, into a strong predictive learner while minimizing a least square loss function. This works in a stage-wise approach by adding a new weak learner to correct the residuals (errors) made by the preceding learners. The ensemble technique also scales each weak learner appropriately to minimize overfitting and determine a generalized strong learner with low variance (Friedman, 2002; Hastie et al., 2009).

The goal of the GLS Boost algorithm is to find a function $F^*(IM, \mathbf{x})$ which maps $(IM, \mathbf{x})$ to y, such that the expected value of some specified loss function $\Psi[y, F(IM, \mathbf{x})]=0.5[y-F(IM, \mathbf{x})]^2$ is minimized.

$$F^*(IM,\mathbf{x}) = \underset{F(IM,\mathbf{x})}{\arg\min}\, E_{y,(IM,\mathbf{x})}\Psi(y, F(IM,\mathbf{x})) \tag{1}$$

Boosting approximates $F^*(IM, \mathbf{x})$ by an additive expansion of each weak learner as

$$F(IM,\mathbf{x}) = \sum_{m=0}^{M} \gamma_m h[(IM,\mathbf{x});\alpha_m] \tag{2}$$

where, $h[(IM, \mathbf{x});\alpha_m]$ is the base learner (typically a decision tree) with $\boldsymbol{\alpha}=\{\alpha_1,\alpha_2,\ldots,\alpha_M\}$as parameters and $\boldsymbol{\gamma}=\{\gamma_1,\gamma_2,\ldots,\gamma_M\}$as expansion coefficients. These coefficients are determined using gradient boosting algorithm (Friedman, 1999) to fit the training data in a forward stage-wise manner, that is coefficients for m^{th} weak learner $\{\alpha_m,\gamma_m\}$ are obtained only after $\{\alpha_i,\gamma_i\}$ $(i=0,1,\ldots,m-1)$ are trained. Furthermore, each successive weak learner tries to correct the residuals from all the previous learners thus promoting better fit to the data.

$$F_m(IM,\mathbf{x}) = F_{m-1}(IM,\mathbf{x}) + \nu\cdot\gamma_m h[(IM,\mathbf{x});\alpha_m] \tag{3}$$

Each successive weak learner is added to the existing prediction $F_{m-1}(IM, \mathbf{x})$ with a shrinkage parameter $0<\nu\leq 1$ as shown in Equation (3), that controls the learning rate of the algorithm. Small values of learning rate (<0.1) have been found to prevent overfitting and improve the generalization of the model (Friedman, 1999).

3 PARAMETERIZED FRAGILITY FUNCTIONS

Traditional fragility curves are conditioned only on the uncertainty of ground motion intensity measure (IM), even though it is well understood that a single parameter cannot adequately determine seismic response of a structure. To consider any number of uncertainty parameters in predicting the probability of structural damage, a popular statistical learning technique called logistic regression is proposed (Koutsourelakis, 2010). This technique is widely used where predictions of binary outcomes such as success or failure are sought. In bridge fragility, the binary outcomes imply whether or not a particular limits state is exceeded.

The logistic regression model is based on the logistic function, also known as the sigmoid function, which transforms the linear equation into a probability between 0 and 1. The logistic regression model estimates the coefficients of the predictor variables that maximize the likelihood of the observed data. LOGistic unIT is the natural log of the odds of binary (Bernoulli) function. It maps the probability values to real number range (0, ∞).

If d is the output binary variable (1 for failure and 0 for success) and $\boldsymbol{x_i}$ are the predictor variables then the probability p that $d=1$ for given $\boldsymbol{x_i}$ is represented by the logistic regression as:

$$logit(p) = \ln\left(\frac{p}{1-p}\right) = \sum_i \theta_i x_i \tag{4}$$

where θ_i are the regression coefficients for predictor variables $\boldsymbol{x_i}$ and the above equation can be manipulated to get the probability p as:

$$p = P[d = 1|x, \theta] = \frac{e^{\sum_i \theta_i x_i}}{1 + e^{\sum_i \theta_i x_i}} \tag{5}$$

The implementation of logistic regression to generate parameterized fragility functions is discussed in the subsequent sections.

4 STATISTICAL LINEARISATION

To quantify the modelling parameter uncertainty at the fragility level, a popular technique called statistical linearization is proposed (Lei & Schilling, 1994). This technique works by fitting a multi-linear regression model between the input parameters and the output response by minimizing the mean square error and then the variance of output is quantified using the obtained regression coefficients and intrinsic input parameter variances.

Consider n-independent input parameters ($U_1, U_2, U_3, \ldots, U_n$) with their respective means and variances as ($\mu_1, \mu_2, \mu_3, \ldots, \mu_n$) and ($\sigma_1^2, \sigma_2^2, \ldots, \sigma_n^2$) and V is the model output with mean μ_V. Model output and input parameters can be related using statistical linearization as follows:

$$V \approx \mu_V + \omega_1(U_1 - \mu_1) + \ldots + \omega_n(U_n - \mu_n) \tag{6}$$

The coefficients ω_i's and μ_V are obtained from multi-linear regression analysis. The variance of model output can be obtained from variance of input parameters as follows:

$$\sigma_Y^2 = \sum_{i=1}^{n} \omega_i^2 \sigma_i^2 \tag{7}$$

The variance in the output can be quantified from each input parameter separately by varying only single input variable and keeping others at their means using Equation (7).

Statistical linearization is well suited for seismic fragility development since input parameters in fragility are largely uncorrelated and relation between output response and input parameters is mostly linear (in the log-transformed space). However, it may not be well suited if the system is significantly nonlinear in nature. In those cases, nonlinear regression techniques should be considered (Lei & Schilling, 1994).

5 CASE STUDY EXAMPLE

Even with the advent of seismic design provisions emphasizing on the seismic design of bridges in moderate seismic zones like CSUS, significant number of bridges that stand till date are non-seismically designed. Among these non-seismically designed bridges, multi-span simply supported (MSSS) and multi-span continuous (MSC) type bridges of concrete and steel

girders are most prevalent. This study considers non-seismically designed MSSS steel girder bridge as a case study. A brief description of the selected bridge is given below.

The 3-D finite-element models for the case study bridge are developed using OpenSees (McKenna et al., 2000). The bridge superstructure consists of a set of steel girders with thin concrete deck on top. The super structure is modelled as elastic beam-column elements since it is expected to remain elastic during seismic loading. Since the superstructure is simply supported, gaps are present between adjacent decks as well as between abutment walls and decks, which significantly impacts the severity of pounding during a seismic event. Fixed and expansion type steel bearings are prevalently used for this bridge type. Past studies show that these types of bearings are a vulnerable component of this bridge type (Choi, 2002). The columns and bent beams (pier caps) are modelled using nonlinear displacement-based beam-column elements with fiber-defined cross-sections. This helps to model outer cover concrete, core concrete and steel reinforcement discretely with their appropriate stress-strain curves. One potential difference between column and bent beams models is the type of cross section, while the columns have circular cross section, the bent beams involve rectangular sections. The behavior of the bearings and abutments is modelled using nonlinear springs in both longitudinal and transverse directions. The pile foundations are modelled using simplified linear translational and rotational springs at the bases of the columns. Impact elements are modelled between the abutments and deck as well as between adjacent decks to capture the pounding effect during earthquake shaking using a contact element as proposed by (Muthukumar, 2003).

The bridge modelling discussed above is essential for performing nonlinear time history analysis with given ground motion data to predict seismic responses which can further be used for fragility predictions. While ground motion is a critical factor influencing these responses, other bridge parameters can also introduce significant uncertainties.

Table 1. Modelling parameters considered for preliminary screening (Nielson, 2005).

Sl. No.	Parameter name	Variable (units)	Lower bound (−)	Upper bound (+)
1	Concrete strength	f_{ck} (MPa)	26.70	40.80
2	Steel strength	f_y (MPa)	403.50	524.30
3	Steel fixed bearing coefficient of friction (multiplicative factor)	COF_fxd	0.5	1.5
4	Steel expansion bearing coefficient of friction (multiplicative factor)	COF_exp	0.5	1.5
5	Abutment passive stiffness	K_{abp} (kN/mm/m)	12.36	27.94
6	Abutment active stiffness	K_{aba} (kN/mm/pile)	3.85	10.15
7	Foundation translational stiffness	K_{ft} (kN/mm)	30.80	81.20
8	Foundation rotational stiffness	K_{fr} (kN/mm)	96.42	253.92
9	Mass	M (%)	91.00	109.00
10	Damping ratio	ζ	0.025	0.066
11	Initial stiffness of steel fixed bearing (multiplicative factor)	$mult_{brg}$	0.85	1.20
12	Adjacent decks gap (hinge gap)	h_{gap} (mm)	18	33
13	Abutment—deck gap	a_{gap} (cm)	3.09	4.52
14	Earthquake direction	Dir (deg)	0	360

Preliminary screening can be carried out on these bridge parameters to identify significant parameters that impact the bridge responses under seismic loading. Nielson (2005) considered these modelling parameters as shown in Table 1, for preliminary screening and performed an analysis of variance (ANOVA) to screen the important parameters. These parameters are shown in Table 2 and subsequently adopted for uncertainty propagation in this study.

Table 2. Significant parameters after preliminary screening (Nielson, 2005).

Significant parameters	
Initial stiffness of steel fixed bearing (multiplicative factor)	Steel fixed bearing coefficient of friction (multiplicative factor)
Abutment passive stiffness	Abutment active stiffness
Foundation translational stiffness	Foundation rotational stiffness
Mass	Damping ratio
Steel strength	Adjacent decks gap (hinge gap)
Abutment—deck gap	Earthquake direction

5.1 *Metamodel fitting*

For metamodel fitting, the above parameters have to be sampled randomly to have uniform representation of the whole sample space, in order to achieve this Sobol sequence (Hellekalek et al., 1998), one of the low-discrepancy quasi-random sequences, is adopted. As a general thumb rule, number of design runs (a design run is a nonlinear time history analysis of a particular bridge model in *OpenSees*) have to be $10\times n$ or higher for a good model fit, where n is the number of input parameters. In this study, 5 replicates of 96 available ground motions are made and are randomly paired with 480 random samples of all critical bridge parameters through Sobol sampling. This results in 480 design runs which far exceeds the general thumb rule by a considerable margin. The ground motion data used in this study is obtained from (Wen & Wu, 2001), (Rix & Fernandez, 2004) who developed synthetic ground motion based on the site-specific characteristics relevant to moderate seismic zone of CSUS.

As discussed earlier, this study adopts GLS Boost metamodel to fit analysis results, with significant parameters and peak ground acceleration (PGA) as predictor variables and the bridge component responses as outputs. While gradient boosting algorithms are generally better than other ensemble learning techniques like random forests (Caruana & Niculescu-Mizil, 2006),(Caruana et al., 2008) it should be tuned appropriately to the available data using several hyperparameters like number of trees, minimum leaf size (number of observations per each node) and learning rate. Along with tuning these hyperparameters, a 10-fold cross-validation is adopted to minimize the chance of overfitting. GLS Boost has been fitted to the 480 design runs and the goodness of fit is assessed across all the component responses using different measures like Root Mean Squared Error (RMSE) and Adjusted Rsquared (Adj. R^2). The adjusted R^2 for all the component responses is above 0.75 along with very low RMSE values, implying that GLS Boost fits the data adequately, as shown in Figure 1.

5.2 *Seismic fragility assessment*

The capacity limit states for MSSS steel bridge are adopted from (Nielson & DesRoches, 2007). By making use of the earlier discussed logistic regression technique, parameterized fragility curves can be developed for each bridge component (Ghosh et al., 2013) and the failure surface can be represented as Equation (8).

$$PF_{k|PGA,x_1.....x_n} = \frac{e^{\theta_{k,0}+\theta_{k,PGA}\ln(PGA)+\sum\theta_{k,i}x_i}}{1+e^{\theta_{k,0}+\theta_{k,PGA}\ln(PGA)+\sum\theta_{k,i}x_i}} \tag{8}$$

where $\theta_{k,0}$, $\theta_{k,PGA}$ and $\theta_{k,i}$ are the logistic regression coefficients for kth bridge component. The component level logistic regression can be upgraded to a system level logistic regression resulting in the development of parameterized fragility for the whole bridge. The logistic regression coefficients of the bridge system level at all damage states are shown in Table 3. It is important to note that although some parameter coefficients are very small compared to others, the values of each parameter coefficients are relative to the units of each parameter, hence parameters with typically large values may have small coefficients but still significantly affect the fragility function.

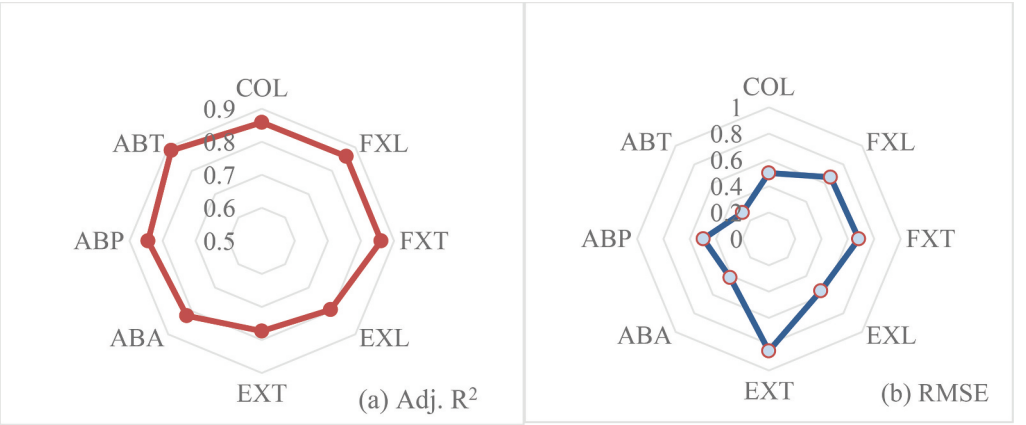


Figure 1. Radial charts showing adjusted R2 and RMSE estimates for column (COL), fixed bearing (FXL, FXT), expansion bearing (EXL, EXT) and abutment responses (ABA, ABP, ABT) for GLS Boost algorithm.

Table 3. Logistic regression coefficients at the bridge system level for all damage states.

Parameter	Slight	Moderate	Extensive	Complete
constant	7.775	5.682	2.945	1.155
$ln(PGA)$	3.799	4.327	4.051	3.752
f_y	-0.013	-0.009	-0.004	-0.003
COF_fxd	0.493	-0.591	1.107	1.484
$mult_{brg}$	-0.145	-0.106	0.150	0.158
K_{abp}	-0.019	-0.073	-0.071	-0.016
K_{aba}	-0.011	0.006	0.009	0.013
K_{fr}	0.000	0.000	0.000	0.000
K_{ft}	0.000	-0.001	0.003	-0.003
M	0.386	0.410	1.034	0.727
ζ	-4.701	-8.006	-6.468	-3.230
a_{gap}	0.047	0.293	-0.032	0.092
h_{gap}	-0.317	-0.446	-0.554	-0.269
Dir	0.000	-0.001	0.000	0.000

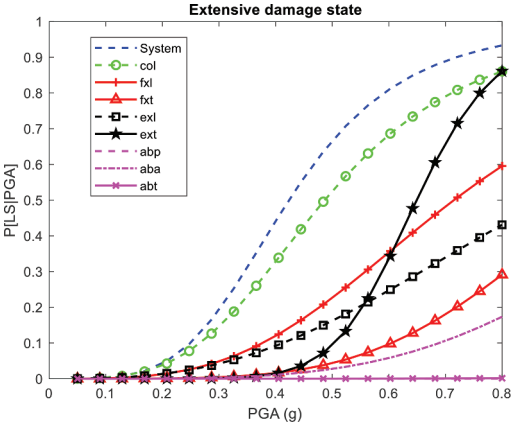


Figure 2. "Classical" component and system level fragility curves obtained after reducing the parameterized fragility functions for extensive limit state.

From these parameterized functions, "classical" fragility curve conditioned only on intensity measure (IM) can also be obtained by keeping all the other modelling parameters at their median values as shown in Figure 2. These multi-dimensional fragility curves are superior to the "classical" fragility curves, primarily in their capacity for uncertainty quantification of modelling parameters.

5.3 *Parameter uncertainty quantification*

Although parameter uncertainty propagation is very well integrated in seismic fragility assessment of bridges, quantification of that uncertainty at the system fragility level remains underexplored. This uncertainty quantification can be achieved by integrating parameterized fragility functions with statistical linearization technique. Statistical linearization can be applied to Equation (4), leveraging logistic regression coefficients previously evaluated using the survival-failure binary vector of the bridge at the system level. Through the utilization of the intrinsic variance of each modelling parameter's uncertainty, in conjunction with Equation (7), the variance in failure probability of the bridge can be computed. This makes it feasible to develop 95% confidence bounds around the mean fragility curve as illustrated in

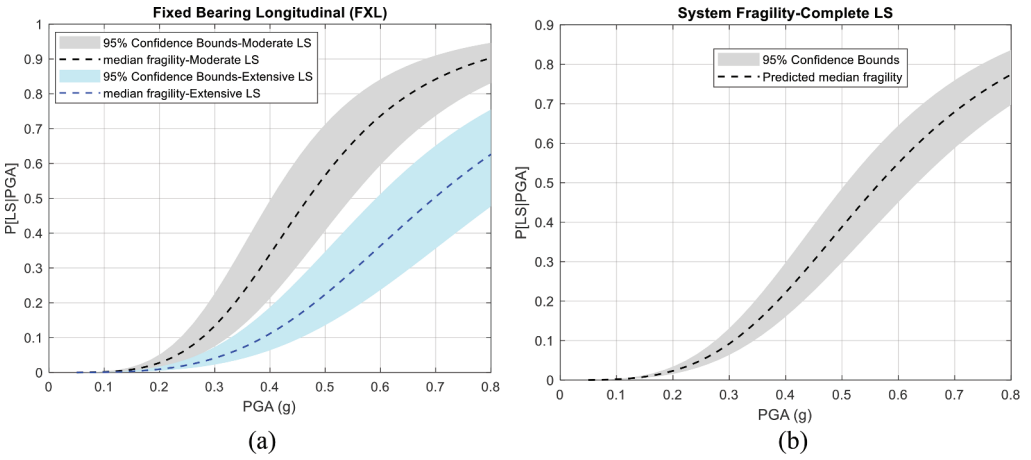


Figure 3. Predicted median fragility with 95% confidence bounds due to parameter uncertainty for: (a) fixed bearings in longitudinal direction (FXL) at moderate and extensive limit states; and (b) overall bridge system at complete limit state.

6 CONCLUSIONS

This study proposes a framework for parameter uncertainty quantification at the system fragility level which is little explored in the past literature. The framework involves a three-fold approach, using a novel ensemble learning-based metamodel for capturing the relationship between modelling parameters and component demand responses. Next, the development of parameterized fragility functions using logistic regression and the trained metamodel which are conditioned on all the critical bridge modelling parameters along with ground motion intensity measure (IM). Finally, statistical linearization technique is adopted for parameter uncertainty quantification and the 95% confidence bounds are developed to visualize this quantification using "classical" fragility curve at all damage states. This study recommends quantification of critical parameter uncertainty for reliable seismic fragility predictions of all bridge types both seismically and non-seismically designed variants.

REFERENCES

Caruana, R., Karampatziakis, N., & Yessenalina, A. (2008). An empirical evaluation of supervised learning in high dimensions. *Proceedings of the 25th International Conference on Machine Learning*.

Caruana, R., & Niculescu-Mizil, A. (2006). An Empirical Comparison of Supervised Learning Algorithms Using Different Performance Metrics. *Proceedings of the 23rd International Conference on Machine Learning*.

Chen, W. F., & Duan, L. (2014). Bridge engineering handbook: Seismic design, second edition. In *Bridge Engineering Handbook: Seismic Design*, *Second Edition*.

Choi, E. (2002). Seismic analysis and retrofit of mid-America bridges. *PhD. Thesis*, *School of Civil and Environmental Engineering, Georgia Institute of Technology*.

Choi, E., DesRoches, R., & Nielson, B. (2004). Seismic fragility of typical bridges in moderate seismic zones. *Engineering Structures*, *26*(2), 187–199.

Friedman, J. H. (1999). *Greedy Function Approximation: A Gradient Boosting Machine* (Vol. 29, Issue 5).

Friedman, J. H. (2002). Stochastic gradient boosting. In *Computational Statistics & Data Analysis* (Vol. 38).

Ghosh, J., Padgett, J. E., & Dueñas-Osorio, L. (2013). Surrogate modeling and failure surface visualization for efficient seismic vulnerability assessment of highway bridges. *Probabilistic Engineering Mechanics*, *34*, 189–199.

Hastie, T., Tibshirani, R., & Friedman, J. (2009). The Elements of Statistical Learning, Second Edition. *Springer New York, NY*, *27*(2).

Hellekalek, P., Larcher, G., & Beck, J. (1998). *Random and quasi-random point sets* (Vol. 138). Springer Science & Business Media.

Koutsourelakis, P. S. (2010). Assessing structural vulnerability against earthquakes using multi-dimensional fragility surfaces: A Bayesian framework. *Probabilistic Engineering Mechanics*, *25*(1), 49–60.

Lei, L., & Schilling, W. (1994). PARAMETER UNCERTAINTY PROPAGATION ANALYSIS FOR URBAN RAINFALL RUNOFF MODELLING. In *Pergamon Wat. Sci. Tech* (Vol. 29, Issue 2).

McKenna, F., Fenves, G. L., Scott, M. H., & others. (2000). Open system for earthquake engineering simulation. *University of California*, *Berkeley, CA*.

Muthukumar, S. (2003). *A contact element approach with hysteresis damping for the analysis and design of pounding in bridges*. Georgia Institute of Technology.

Nielson, B. G. (2005). *Analytical Fragility Curves for Highway Bridges in Moderate Seismic Zones*.

Nielson, B. G., & DesRoches, R. (2007). Analytical seismic fragility curves for typical bridges in the central and southeastern United States. *Earthquake Spectra*, *23*(3), 615–633.

Padgett, J. E., Asce, M., & Desroches, R. (2007). *Sensitivity of Seismic Response and Fragility to Parameter Uncertainty*.

Ramanathan, K., DesRoches, R., & Padgett, J. E. (2012). A comparison of pre-and post-seismic design considerations in moderate seismic zones through the fragility assessment of multispan bridge classes. *Engineering Structures*, *45*, 559–573.

Rix, G. J., & Fernandez, J. A. (2004). Earthquake ground motion simulation.

Rokneddin, K., Ghosh, J., Dueñas-Osorio, L., & Padgett, J. E. (2015). Uncertainty propagation in seismic reliability evaluation of aging transportation networks. *12th International Conference on Applications of Statistics and Probability in Civil Engineering, ICASP 2015*.

Wen, Y. K., & Wu, C.-L. (2001). Uniform hazard ground motions for mid-America cities. *Earthquake Spectra*, *17*(2), 359–384.

Bridge Maintenance, Safety, Management, Digitalization and Sustainability – Jensen, Frangopol & Schmidt (eds)
© 2024 The Author(s), ISBN 978-1-032-77040-6
Open Access: www.taylorfrancis.com, CC BY-NC-ND 4.0 license

Damage evaluation of steel columns using vibration testing and transfer learning

K. Watanabe & H. Naito
Tohoku University, Sendai, Miyagi, Japan

T. Kimoto
National Institute of Technology, Oita College, Oita, Japan

M. Matsumura
Kumamoto University, Kumamoto, Japan

N. Takeshima & S. Okada
IHI Infrastructure Systems Co., Ltd., Tokyo, Japan

K. Ono
Waseda University, Tokyo, Japan

ABSTRACT: An axial loading test was conducted on a steel column specimen with a box-shaped cross section, for improving structural health monitoring and non-destructive evaluation using machine learning. In the loading test, 8 acceleration sensors were placed on the surface of the column to obtain vibration characteristics at each loading step. A standard autoencoder was trained on intact frequency responses obtained before the loading test. From the results, anomaly scores calculated from the autoencoder were high around the local buckling regions. Furthermore, another autoencoder model trained on data measured from another specimen using applied transfer learning agreed with the results from the standard autoencoder. The effectiveness of coupling an autoencoder-based anomaly detection method and transfer learning when there is a lack of training data was shown.

1 INTRODUCTION

Many civil structures are aging in Japan. In addition, some structures have serious damage from accidental loads, such as large earthquakes, tsunamis, floods, landslides, and avalanches). To maintain safety performance and functions of the existing structures, it is needed to evaluate the conditions and structural performance of the structures. Non-destructive evaluation and structural health monitoring are useful for the reasonable maintenance of civil structures. The population of construction workers is decreasing, particularly in Japan, resulting in a serious shortage of human resources for the inspection and maintenance of civil structures. To address this issue, innovative technologies (e.g. inspection robots, sensing, monitoring, machine learning) have been investigated around the world.

In the previous study (Fujisaku et al., 2023), an axial loading test was conducted on a steel column specimen (Specimen No.0) with a box-shaped cross section. Moreover, an autoencoder-based anomaly detection method was built for damage evaluation of the column. Results had indicated the possibility of damage detection, though, it was only possible to compare data before and after loading with a single column specimen No.0. Deep learning should be available to detect damages for individual structures, using pre-trained models by capturing

DOI: 10.1201/9781003483755-228

similar data features. The use of machine learning is thought to be effective for improving inspection and evaluation of various civil structures.

In this study, an additional column specimen (Specimen No.1) was installed for improving the autoencoder-based damage detection method for individual structures. An axial loading test was conducted on the additional column specimen No.1. In the loading test, 8 acceleration sensors were placed on the surface of the column, to obtain vibration characteristics at each loading step. Moreover, unsupervised learning and transfer learning were examined to detect damage to the column. In particular, a trained model on the previous specimen No.0 was applied to the damage evaluation of the additional specimen No.1, through transfer learning.

2 AXIAL LOADING TEST ON A STEEL COLUMN

A steel column specimen (No.1) was installed. The details and material properties are shown in Figure 1 and Table 1. The column had a length of 900 mm and a box-shaped cross section with a sectional height of 450 mm and a sectional width of 450 mm. The column consisted of four-sided panels (2 flanges and 2 webs) and eight longitudinal ribs (stiffeners). Four ribs were welded on the outside of the flanges. Other ribs were welded on the inside of the webs. The design tensile strengths of the panels and ribs were 400 MPa and 700 MPa, respectively.

The test setup is shown in Figure 2. The column specimen had upper and lower loading plates on both sides. The panels were welded to the loading plates and subjected to the axial load. Whereas the ribs were not welded to the loading plates and not subjected to the axial load directly. Loading speed was set at 0.005 mm/s.

Figure 3 shows the load and displacement relationship in the loading test, where the displacement was obtained from averaging displacements using gauges at four corners. Figure 4 shows a buckling deformation diagram, where the buckling deformation was measured using mold gauges after the loading test. The flanges and webs buckled toward the outside and inside of the cross section, respectively. The buckling deformation increased in the post peak region in Figure 3, however, the load decreased slightly.

3 VIBRATION TEST ON THE COLUMN

Forced vibration testing with a portable electric-magnetic vibrator was conducted. Figures 3 and 4 show the measurement steps of vibration testing and deformation of the column. The excitation and measurement locations with acceleration sensors are shown in Figure 5. The

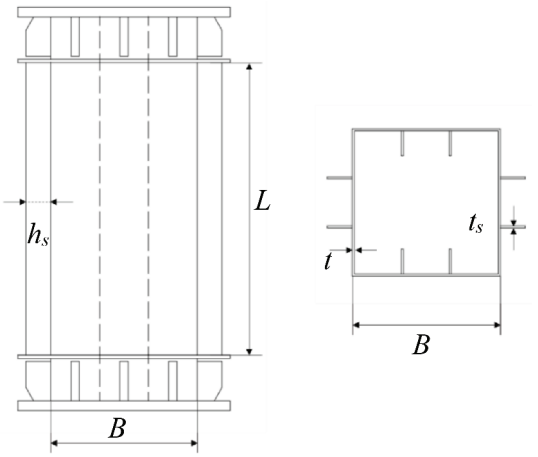


Figure 1. Details of the columns.

Table 1. Material properties of the column.

Webs and Flanges	Design strength	400 MPa
	Thickness t	6.5 mm
	Width B	450 mm
Longitu-dinal ribs	Design strength	700 MPa
	Thickness t_s	6.3 mm
	Width h_s	76 mm
Column length $\boldsymbol{L}$		900 mm

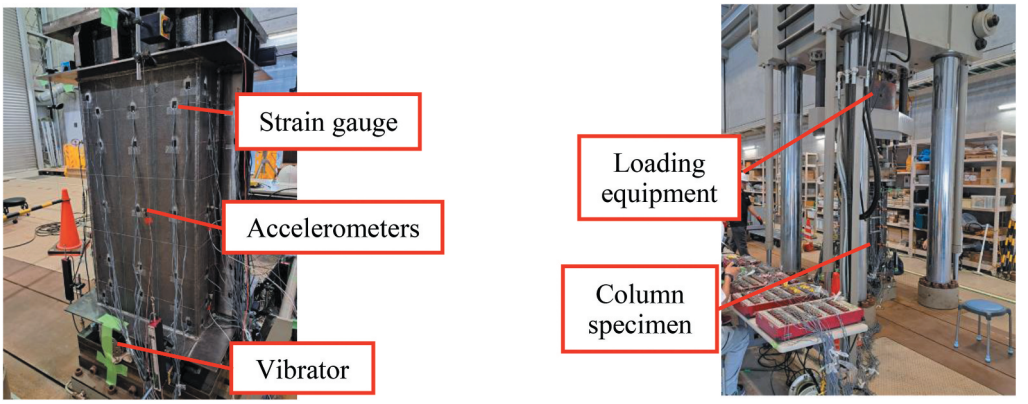


Figure 2. Axial loading test on the column.

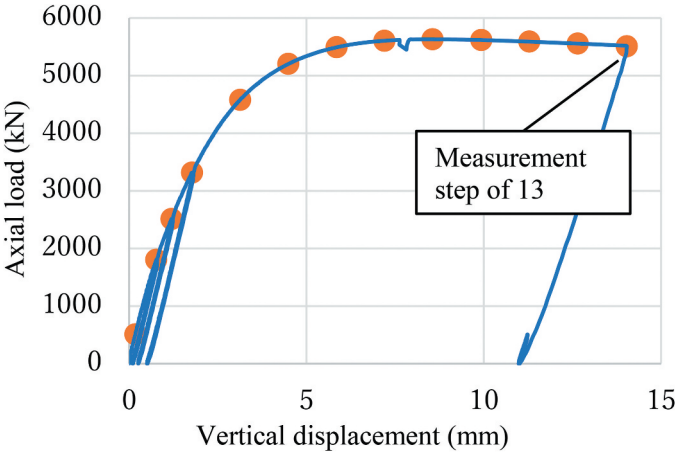


Figure 3. Load-displacement relationship.

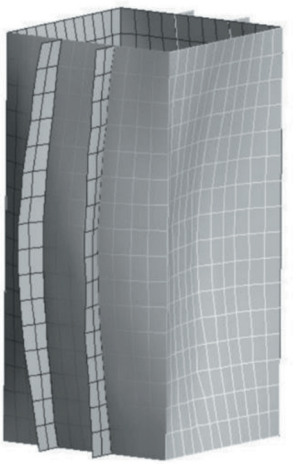


Figure 4. Buckling deformation.

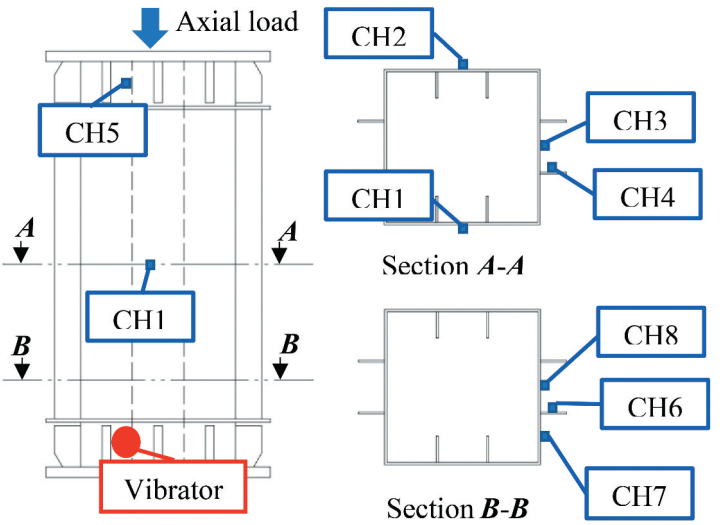


Figure 5. Excitation and measurement locations.

sensors were placed on the panels and ribs at the top (CH 5), middle (CHs 1-4), and bottom (CHs 6-8) of the column. The locations were the same as those of Specimen No.0 (Fujisaku et al., 2023).

The vibrator had a mass of 1.8 kg, a diameter of 95 mm, a height of 62 mm, the maximum excitation force of 50 N, and a frequency range of 100 to 20,000 Hz. Using the vibrator, white noise force was applied to the bottom of the column, as shown in Figures 2 and 5. The excitation force was controlled at a power spectral density (PSD) of 0.5 $(m/s^2)^2$/Hz over a frequency range of 1000 to 20,000 Hz. The root mean square of acceleration amplitude (RMS) was 97.6 m/s^2.

Frequency response functions were obtained from acceleration records using a fast Fourier transform. The frequency responses had a range of 1000 to 20,000 Hz with a resolution of 97.7 Hz. The amplitude was normalized by the maximum amplitude for each frequency response. Deep learning used 256 parameters of one-dimensional data as features, as described in a later section.

4 DAMAGE DETECTION

4.1 *Standard autoencoder*

4.1.1 *Model and evaluation method*

A conventional standard autoencoder based on a neural network (standard AE) was used for damage detection. The structure of the standard AE is shown in Figure 6. The model was built and trained with Tensorflow2 (tf.keras) in Python. The input data f_i (i = 1 to 256) was given from the frequency responses. The input data was compressed through three hidden layers, and decoding was applied to the compressed data in the same process. Rectified Linear Unit (ReLU) was used as activation functions of the hidden layers. Sigmoid function was used in the output

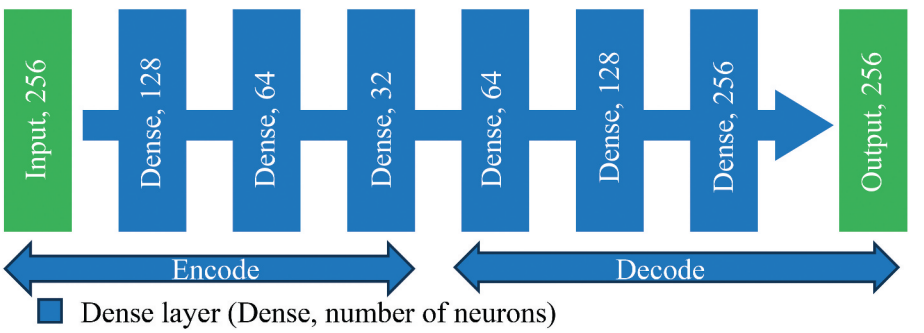


Figure 6. The structure of the autoencoder.

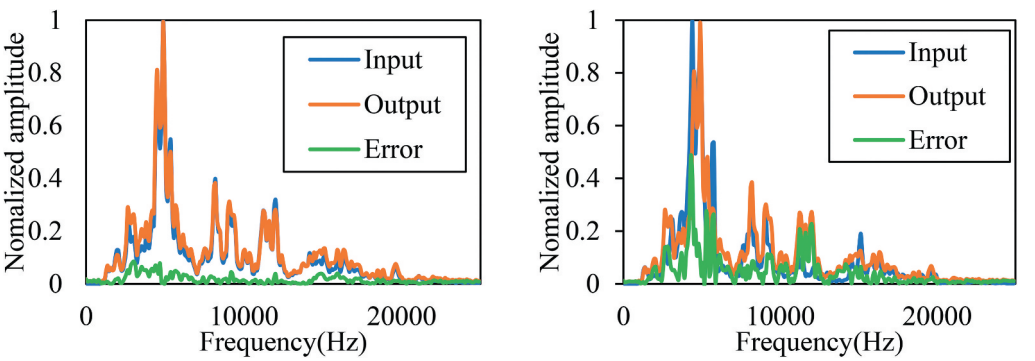


Figure 7. Comparisons between input and output (CH5, left: intact, right: damaged region).

layer. Adam optimization was used in the training process, with a batch size of 16 and a learning ratio of 0.001. Early stopping was applied during the training process to prevent over fitting.

The standard AE was trained on frequency responses obtained from the intact column before loading. The standard AE can reconstruct data of frequency responses well when they are similar to the training data. Whereas data from the damaged column cannot reconstruct, as the data is different from the intact training data. Damages could be evaluated with anomaly scores calculated from the reconstruction errors. In calculating the anomaly scores, two processes were conducted. First, averages of the input f_i (i = 1 to 256) and the output g_i (i = 1 to 256) with a width of 10 parameters were taken. Second, the error of $f_i - g_i$ (i = 1 to 256) was set to zero when the error was below 0.2, to reduce the influence of noise. The anomaly score was defined as,

$$e = \frac{\sum_{i=1}^{256} |f_i - g_i|}{\sum_{i=1}^{256} f_i} \tag{1}$$

4.1.2 *Anomaly scores from the standard autoencoder*

The standard AE was trained on approximately 250 frequency response functions for each sensor location, where the training data was measured before the loading test. Moreover, five test data of frequency responses were obtained at each measurement step and sensor location. Anomaly scores were evaluated for the test data using the trained standard AE.

As an example, Figure 7 shows frequency responses of CH5 obtained before loading and at measurement step 13. The trained model was able to successfully reconstruct the data

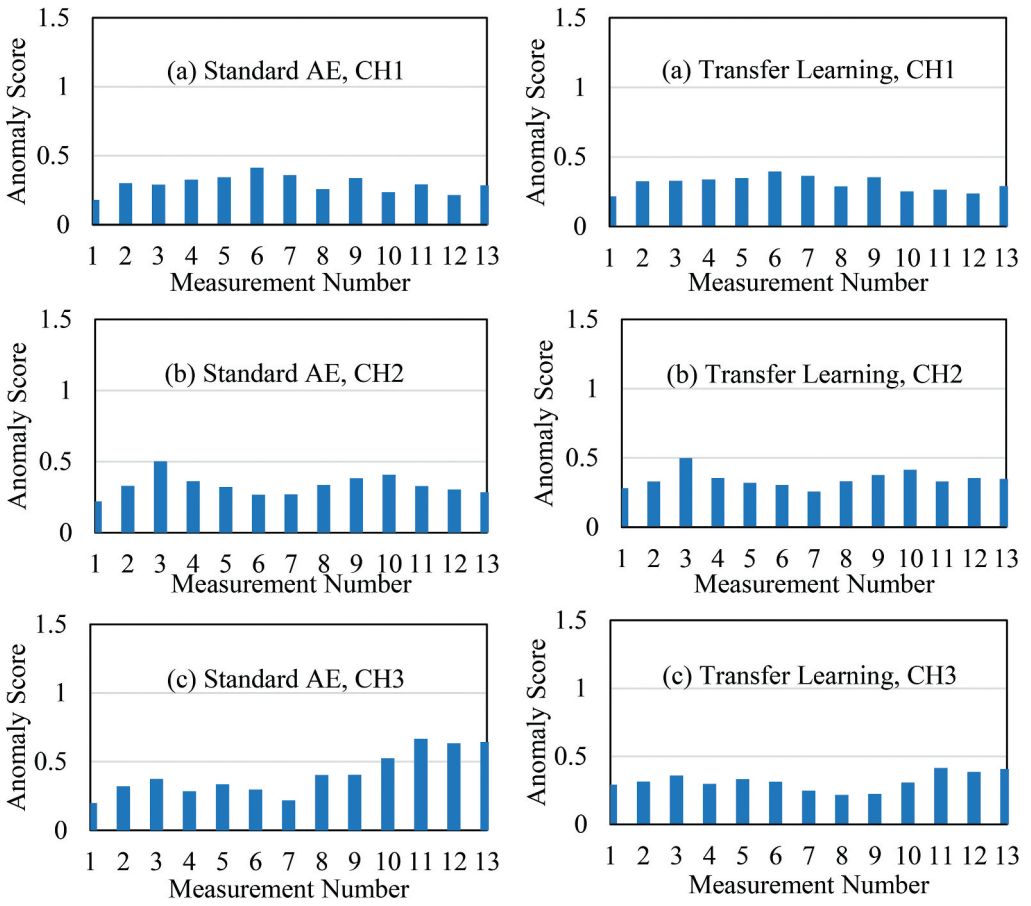


Figure 8. Anomaly scores using the standard AE and transfer learning (CHs 1-3).

obtained before loading, whereas the frequency response obtained from the damaged column did not reconstruct. The reconstruction error is used to evaluate anomaly scores in Eq. (1).

The left column in Figures 8 and 9 show the relationships between anomaly scores and measurement steps. Where, the mean of anomaly scores of the intact data was 0.186. As shown in Figure 9 (b), the anomaly score of CH5 increased as the measurement step increased. It is thought that the anomaly score of CH5 indicated the global damage level of the column, since the location of sensor CH5 was placed far from the excitation location, as shown in Figure 5.

In Figure 9, CHs 6-8 at the bottom of the column had high anomaly scores in the loading test. In particular, the score of CH6 placed on the rib was higher. In addition, the anomaly score of CH4 was similar to that of CH6, where CHs 4 and 6 were placed on the same rib. It is thought that local buckling deformation of the rib affects the anomaly score sensitively, compared to the panels. It is recommended to place sensors on ribs for health monitoring of steel columns.

In Figure 8, CHs 1-4 placed at the middle of the column had lower anomaly scores. This indicates that the boundary condition at the bottom affected the anomaly scores strongly.

As described above, the results show that: i) a sensor placed far from an excitation source is useful to evaluate the global damage level of columns, ii) it is recommended to place a sensor on a rib around the bottom for monitoring local buckling of steel columns. These results i) and ii) were also observed in the previous study with Specimen No.0 (Fujisaku et al., 2023), even though the buckling modes of Specimens Nos. 0 and 1 were quite different.

4.2 *Transfer learning on the autoencoder*

4.2.1 *Model and evaluation method*

In Section 4.1, the standard AE was trained on the intact data of Specimen No.1. In this section, a model was trained on data from Specimen No.0, that was installed in the previous study (Fujisaku et al. 2023). The differences between Nos. 0 and 1 were the rib width (No.0: 94 mm, No.1: 76 mm), the rib thickness (No.0: 8.3 mm, No.1: 6.3 mm), and the welding condition to the loading plates (No.0: welded, No.1: no weld).

Model-0 was trained on the intact data obtained before the loading test of Specimen No.0, through the autoencoder. Figure 10 shows the anomaly scores of CH5 in Specimen No.1, using Model-0. The anomaly scores did not change, since the training and test data were given from Specimens No.0 and No.1, respectively. This indicates that the standard AE is useful for monitoring structures with known initial conditions. However, the method has difficulty in detecting damage when there is a lack of the initial data, such as for aged structures.

In this section, transfer learning was examined for detecting damage of Specimen No.1 using Model-0. Transfer learning retains most of the weights of feature parameters in a model, for applying to another model through retraining with a few data. Figure 11 shows the structure of the transfer learning.

For retraining during transfer leaning, 9 frequency responses were taken randomly from each sensor location from the 250 intact data of No.1. The output and one hidden layer were retrained on the 9 frequency responses, where the weights of feature parameters in other layers were not changed. The retraining conditions were the same as described in Section 4.1.

4.2.2 *Anomaly scores from the transfer learning*

The right column in Figures 8 and 9 show the anomaly scores using the transfer learning. The scores agreed with those of the standard AE, except for CH6. Transfer learning improved damage evaluation using Model-0 and 9 retraining data. Results indicated the effectiveness of coupling unsupervised learning (autoencoder) and transfer learning. The proposed method is useful for non-destructive evaluation and structural health monitoring when initial inspection/monitoring data of structures are unavailable.

The reason for the differences in scores of CH6 was not clear. The sensor CH6 was placed on the rib at the bottom of No.1. It was sensitive to the deformation of the column with increases in loading step. It is thought that the amount of retraining data (9 frequency responses) was too small for the transfer learning of CH6.

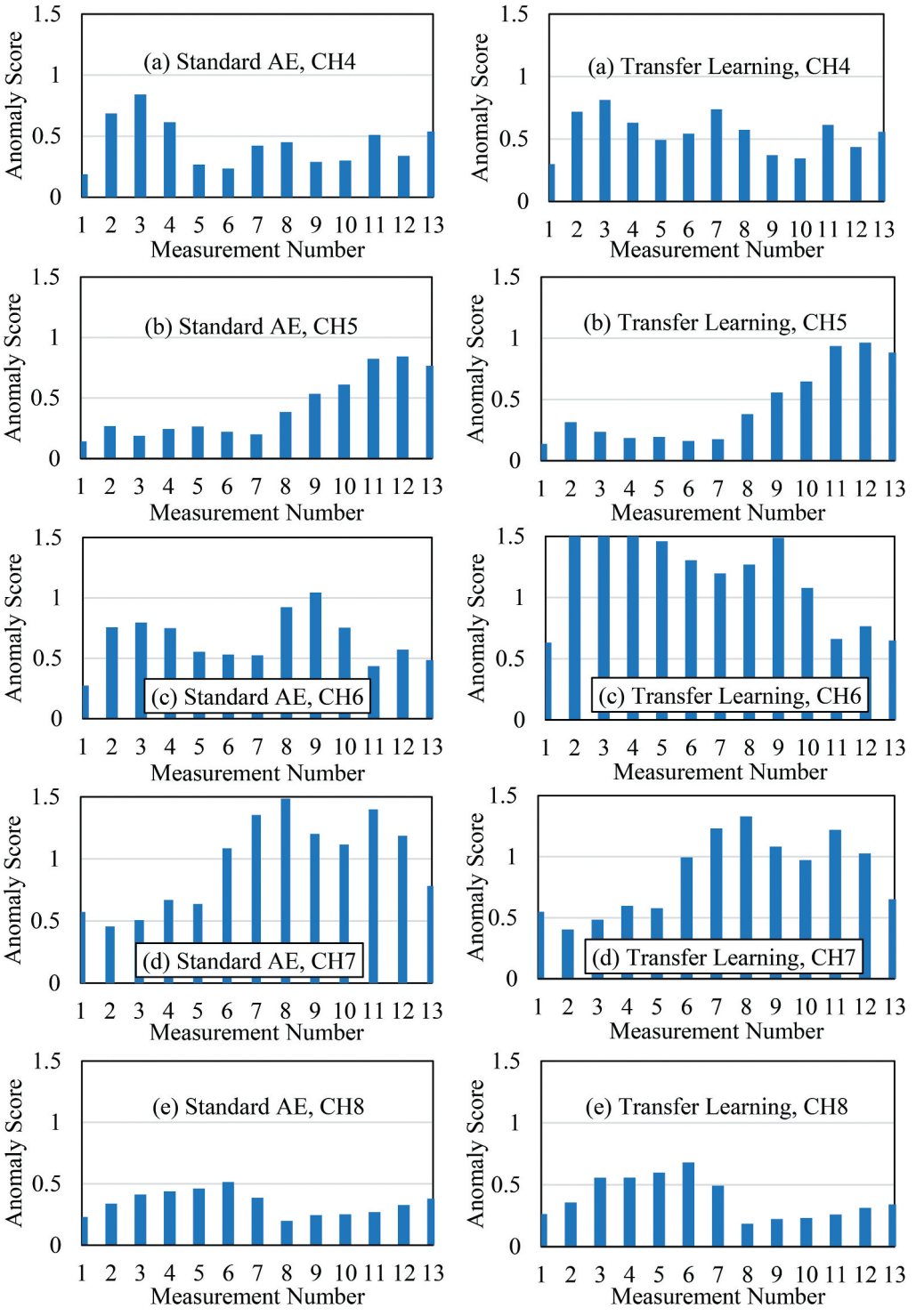


Figure 9. Anomaly scores using the standard AE and transfer learning (CHs 4-8).

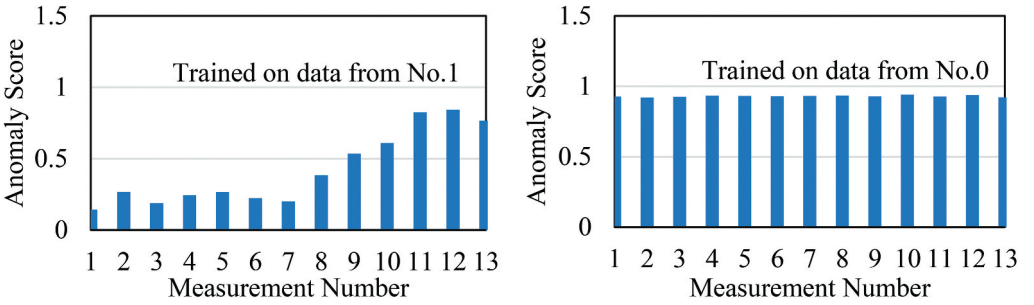


Figure 10. Anomaly scores of CH5 in Specimen No.1 using the standard AE.

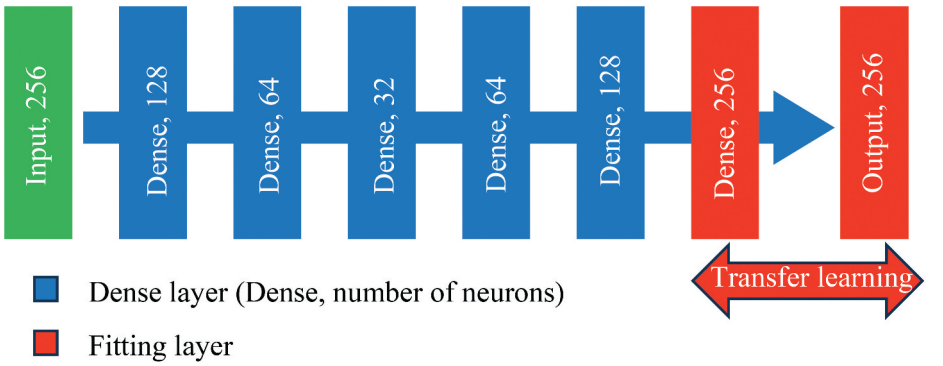


Figure 11. The structure of the transfer learning.

5 CONCLUSIONS

In this study, an axial loading test was conducted on a steel column with a box-shaped cross section, for examining damage detection using machine learning and vibration characteristics. In particular, the effectiveness of coupling unsupervised learning and transfer learning was examined. From the experimental results, the following findings were observed:

1) A standard autoencoder model was trained on 250 intact frequency responses measured before the loading test. The effectiveness of anomaly detection using an autoencoder was shown through the damage evaluation of a column containing local buckling of panels and ribs. In particular, the results indicated that: i) a sensor placed far from an excitation source is useful to evaluate the global damage level of columns, ii) it is recommended to place a sensor on a rib around the bottom for monitoring local buckling in steel columns.
2) An autoencoder model was trained on data measured from another column specimen. The trained model was retrained on 9 frequency responses through transfer learning. Anomaly scores from the transfer learning agreed well with those from the standard autoencoder trained on 250 intact data.

Coupling unsupervised learning (autoencoder) and transfer learning was effective for improving non-destructive evaluation and health monitoring of structures, even when initial inspection/monitoring data is lacking. However, these findings were obtained from a column specimen. Further experimentation and calculations are needed before applying the proposed method to actual civil structures.

ACKNOWLEDGEMENTS

A part of this research was conducted by the support of Steel Structure Research and Education Assistance Project, The Japan Iron and Steel Federation, JST FOREST Program (Grant

Number JPMJFR2150, Japan), and Japan Society for the Promotion of Science (Grant Number 22H01568). In addition, we thank students of Waseda University, Ryosuke Yamazaki, Rintaro Taguchi, and Haruhisa Kobayashi, for their help in the loading test on the column.

REFERENCES

Fujisaku, Y., Naito, H., Kimoto, T., Matsumura, M., Takeshima, N., Okada S. & Ono, K. 2023. A study on damage evaluation method for box section steel columns using autoencoder, *Proceedings of the International Ocean and Polar Engineering Conference* 33, 3215–3221.

Naito, H. & Bolander, J. E. 2019. Damage detection method for RC members using local vibration testing, *Engineering Structures* 178: 361–374.

Tan, C., Sun, F., Kong, T., Zhang, W., Yang, C. & Liu, C. 2018. A survey on deep transfer learning, *Artificial Neural Networks and Machine Learning*, ICANN 2018: 270–279.

Pan, S. J. & Yang, Q. 2010. A survey on transfer learning, *IEEE Transactions on Knowledge and Data Engineering* 22 (10): 1345–1359.

Breysse, D. 2012. Nondestructive evaluation of concrete strength: An historical review and a new perspective by combining NDT methods, *Construction and Building Materials* 33: 139–163.

Cnudde, V. & Boone, M. N. 2013. High-resolution X-ray computed tomography in geosciences: A review of the current technology and applications, *Earth-Science Reviews* 123: 1–17.

Li, H.-N., Li, D.-S. & Song, G.-B. 2004. Recent applications of fiber optic sensors to health monitoring in civil engineering, *Engineering Structures* 26: 1647–1657.

Zhao, R., Yan, R., Chen, Z., Mao, K., Wang, P. & Gao, R. X. 2019. Deep learning and its applications to machine health monitoring, *Mechanical Systems and Signal Processing* 115: 213–237.

Hu, K., Sivaraman, V., Luxan, B. G. & Rahman, A. 2016. Design and evaluation of a metropolitan air pollution sensing system, *IEEE Sensors Journal* 16:

Fawad, M., Koris, K., Salamak, M., Gerges, M., Bednarski, L. & Sienko, R. 2022. Nonlinear modelling of a bridge: A case study-based damage evaluation and proposal of Structural Health Monitoring (SHM) system, *Archives of Civil Engineering*: 569–584.

Bridge Maintenance, Safety, Management, Digitalization and Sustainability – Jensen, Frangopol & Schmidt (eds)
© 2024 The Author(s), ISBN 978-1-032-77040-6
Open Access: www.taylorfrancis.com, CC BY-NC-ND 4.0 license

Probabilistic modeling of bridge deterioration due to earthquakes

Leandro Iannacone
University College London, London, UK

Paolo Gardoni
University of Illinois at Urbana-Champaign, Champaign IL, USA

ABSTRACT: The physical state of a structure can be modeled as a function of its state variables (e.g., material and geometric properties). Deterioration processes cause changes in the state variables that in turn modify its ability to sustain given demands over time. Typically, deterioration processes are divided into gradual processes, where the deterioration evolves continuously over time, and shock processes, where the deterioration is modeled as discrete jumps. The damage accumulation within shock events is usually disregarded in simplified procedures that only model the total effect of the shock and use aggregated measures to quantify the shock intensity. However, this simplification can produce inaccurate estimates of the structure's reliability. As a result, it is important to account for the specific evolution of the damage also in such processes. This paper models shock deterioration as a rapidly evolving but still gradual process. We use the formulation based on Stochastic Differential Equations proposed by Iannacone & Gardoni (2023) to model the effect of the time history of ground motion sequences on the deterioration of a bridge. This formulation allows obtaining the state variables together with their associated uncertainties during the shock, which in turn can be used to obtain the time-varying reliability of the system. The models are calibrated based on the results of advanced Finite-Element Models which record the state of the system in real time. We combine the proposed formulation with available methods for generating spectrum-compatible seismic excitations for a site of interest to predict the deterioration over time and the time-varying reliability of the bridge during the occurrence of the shock.

1 INTRODUCTION

The long-lasting effect of ground motions on the condition of existing bridges has been of interest over the past few decades (e.g., Cui et al. 2019, Torti et al. 2022). Apart from exerting direct stress, for which assessing the probability of failure is crucial, these events also serve as one among various ongoing processes that deteriorate the system. In other words, even if a bridge is able to withstand an initial shock, its deteriorated conditions will affect its ability to sustain subsequent events (in particular, aftershocks). In fact, most bridges go through multiple earthquakes during their lifecycle, and aftershocks become problematic mainly due to the weakened state of the structure after the main shock, rather than the intensity of the aftershocks themselves (Li & Ellingwood 2007, Kumar & Gardoni 2014, and Iervolino et al. 2020). Multiple authors have addressed the estimation of the state of a bridge following the occurrence of a seismic event (e.g. Jeon et al. 2015, Raghunandan et al. 2015), with most recent works addressing the interactions between multiple processes (Jia et al. 2017). Building on the state-dependent framework proposed by Jia & Gardoni (2018), Iannacone & Gardoni (2019, 2023) proposed the use of Stochastic Differential Equations (SDEs) to model the time-varying evolution of the state variables of the system, i.e., a set of important properties (e.g., geometric properties, material properties) that determine its conditions. In Iannacone & Gardoni (2019,

DOI: 10.1201/9781003483755-229

2023), shocks are incorporated into the formulation using SDEs driven by a semimartingale driving noise (Grigoriu 2013). The discontinuous part of the semimartingales creates jumps in the evolution of the state variables which can be interpreted as the effects of shocks. An alternative approach to shock deterioration modeling is proposed by Iannacone & Gardoni (2021), also using SDEs as the basis. In this interpretation, the shocks are interpreted as short-time, continuous gradual deterioration processes. Ordinary Brownian motions (Grigoriu 2013) are used as the driving noise (as there is no need to have discontinuities in the processes), streamlining the calibration of the SDEs based on available data. In addition, this interpretation allows us to account for the specific ground motion characteristics (time-histories) for prediction purposes, rather than aggregated measures such as Peak Ground Acceleration and spectral acceleration. It also allows us to make full use of recent tools developed for the simulation of synthetic ground motions, both for mainshocks (Rezaeian & Der Kiureghian 2008) and mainshock-after shock sequences (Hu et al. 2018).

Iannacone & Gardoni (2021) observed that using the entire set of available ground motions (unrelated and coming from different locations around the world) to perform the calibration of a single deterioration process did not produce satisfactory results in terms of accuracy with the Finite Element Models (FEMs). As such, the results presented in Iannacone & Gardoni (2021) are based on calibrations performed on individual ground motions. While the results show high similarities with the FEM results, calibration performed on individual ground motions may limit the prediction capability of the models, as the synthetic ground motions used for future events may not share the same characteristics as the one used for calibration.

In this paper, we perform the calibration based on a set of spectrum-compatible ground motions (Choi & Lee 2003). We investigate the degree of accuracy of the calibrated model compared with the results from the Finite Element Models (FEMs) and compare it with similar results obtained by calibrating the models based on a set of unrelated ground motions. The deterioration models produced in this paper can be used for prediction purposes at the location of interest, as future earthquake events are realistically going to share the spectrum characteristics as the ones used for calibration.

The paper will be organized as follows: in Section 2 we will provide a brief overview of the SDE formulation introduced by Iannacone & Gardoni (2019, 2023) and of how it can be used to interpret shock occurrences as short-time gradual deterioration processes (Iannacone & Gardoni 2021); in Section 3 we will show the limitations of the calibration methods proposed in the aforementioned works when dealing with seismic excitations that are not spectrum-compatible; in Section 4 we will show how using spectrum-compatible excitations greatly improves the accuracy of the model and makes it suitable for prediction purposes; finally, in Section 5 we will present the conclusions of the work.

2 FORMULATION

Following the formulation by Jia & Gardoni (2018), we can define the vector of external conditions, $\mathbf{Z}(t)$, as a collection of the variables affecting the time-varying performance of the system, that are not related to the system itself. Subsets of this vector are the environmental conditions $\mathbf{E}(t)$, typically affecting gradual deterioration processes (e.g. atmospheric pressure, relative humidity and temperature), and the shock measures $\mathbf{IM}(t)$, typically affecting the shock deterioration processes. The vector $\mathbf{Z}(t)$ can hence be expressed as

$$\mathbf{Z}(t) = [\mathbf{E}(t), \mathbf{IM}(t)] \tag{1}$$

Jia & Gardoni (2018) proposed to investigate the evolution of a system subject to deterioration by looking at a set of state variables $\mathbf{X}(t) = [X_i(t), \ldots, X_n(t)]$, defined as the variables of the system that might be subject to change over time (e.g. material and geometric properties). In other words, the value of the state variables at any time t can be expressed as

$$\mathbf{X}(t) = \mathbf{X}[t, \mathbf{X}_0, \{\mathbf{Z}(t)\}; \Theta_{\mathbf{X}}] \tag{2}$$

where $\mathbf{X}_0$ is the value of the state variables at time $t = 0$, $\{\mathbf{Z}(t)\}$ is the sequence of external conditions up to time t, and $\boldsymbol{\Theta}_{\mathbf{X}}$ is a set of unknown parameters. Different forms have been proposed in the literature for the model in Eq. (2). In particular, Iannacone & Gardoni (2019, 2023), proposed to describe the evolution of the state variables using a set of Stochastic Differential Equations (SDEs). According to this formulation, the infinitesimal change in the state variables at time t, $\mathrm{d}\mathbf{X}(t)$, can be defined with the following formula:

$$\mathrm{d}\mathbf{X}(t;\boldsymbol{\Theta}_{\mathbf{X}}) = \boldsymbol{\mu}\left[t, \mathbf{X}(t), \{\mathbf{Z}(t)\}; \boldsymbol{\Theta}_{\boldsymbol{\mu}}\right]\mathrm{d}t + \boldsymbol{\sigma}[t, \mathbf{X}(t), \{\mathbf{Z}(t)\}; \boldsymbol{\Theta}_{\sigma}]\mathrm{d}\mathbf{S}(t;\boldsymbol{\Theta}_{\mathbf{S}}) \tag{3}$$

where $\boldsymbol{\mu}[\cdot]$ is a vector of drift coefficients, quantifying the deterministic change in $\mathbf{X}(t)$ over time, $\boldsymbol{\sigma}[\cdot]$ is a vector of diffusion coefficients, quantifying the uncertainties in the change of $\mathbf{X}(t)$ over time, and $\mathrm{d}\mathbf{S}(\cdot)$ is a driving noise term that defines the shape and behavior of the process (Grigoriu 2013). These terms are characterized by vectors of unknown parameters $\boldsymbol{\Theta}_{\boldsymbol{\mu}}$, $\boldsymbol{\Theta}_{\sigma}$ and $\boldsymbol{\Theta}_{\mathbf{S}}$, respectively. As highlighted by Iannacone & Gardoni (2019, 2023), the choice of the driving noise term $\mathrm{d}\mathbf{S}(\cdot)$ is key in determining the behavior of the stochastic process that is solution to the SDE in Eq. (3). Semimartingales have proven to be a suitable option, as they are able to incorporate both continuous changes in time (via a Brownian motion component) and discrete jumps at selected times (via a compensated Poisson process component). However, semimartingales, while extremely flexible, can come with limitations related to their mathematical tractability (Itô 1973). The interpretation for shock processes proposed in Iannacone & Gardoni (2021) allows us to select a continuous driving noise for Eq. (3) (such as a standard Brownian motion/Wiener process), which might facilitate the use of this framework in practice. In addition, an SDE-based formulation allows us to use of semi-closed form solutions that are available in the literature (Itô 1973, Grigoriu 2013).

The vector of shock measures $\mathbf{IM}(t)$ typically depends on the problem under analysis. In the case of earthquakes, it is generally composed of aggregated measures for the intensity of the shocks (e.g., Peak Ground Acceleration). To capture the effect of the time history of the shock, Iannacone & Gardoni (2021) defined the vector of shock measures as a set of functions of the instantaneous acceleration $a(t)$ of the earthquake, $\mathbf{h}[a(t)]$.

$$\mathbf{Z}(t) = \{\mathbf{E}(t), \mathbf{h}[a(t)]\} \tag{4}$$

where $\mathbf{h}[a(t)] = \{h_1[a(t)], \ldots, h_n[a(t)]\}$ is a set of n explanatory functions that relate the evolution of $\mathbf{X}(t)$ to the instantaneous ground acceleration $a(t)$. If this relationship is assumed to be linear, drift and diffusion terms in Eq. (3) can be rewritten as ($\cdot$ denotes the scalar product)

$$\boldsymbol{\mu}[\cdot] = \boldsymbol{\theta}_{\boldsymbol{\mu}\boldsymbol{h}} \cdot \mathbf{h}[a(t)] + f\left[t, \mathbf{X}(t), \mathbf{E}(t); \boldsymbol{\theta}_{\boldsymbol{\mu}\mathbf{x}}\right] \tag{5}$$

$$\boldsymbol{\sigma}[\cdot] = \boldsymbol{\theta}_{\boldsymbol{\sigma}\mathbf{h}} \cdot \mathbf{h}[a(t)] + f[t, \mathbf{X}(t), \mathbf{E}(t); \boldsymbol{\theta}_{\boldsymbol{\sigma}\mathbf{x}}] \tag{6}$$

where $\boldsymbol{\theta}_{\boldsymbol{\mu}h}$ and $\boldsymbol{\theta}_{\boldsymbol{\sigma}\mathbf{h}}$ are the sets of parameters that relate $\mathbf{X}(t)$ to $h[a(t)]$, and are subsets of $\boldsymbol{\Theta}_{\mu}$ and $\boldsymbol{\Theta}_{\sigma}$, respectively. $\boldsymbol{\theta}_{\boldsymbol{\mu}\mathbf{x}}$ and $\boldsymbol{\theta}_{\boldsymbol{\sigma}\mathbf{x}}$ can be defined as $\boldsymbol{\Theta}_{\mu} \backslash \boldsymbol{\theta}_{\boldsymbol{\mu}\boldsymbol{h}}$ and $\boldsymbol{\Theta}_{\sigma} \backslash \boldsymbol{\theta}_{\boldsymbol{\sigma}\mathbf{h}}$, respectively, and represent the subsets of unknown parameters that relate $\mathbf{X}(t)$ to aspects not directly related to the seismic excitation. The set of explanatory functions $h[a(t)]$ depends on the problem under consideration and can be selected based on engineering judgement and/or variable selection methods available in the literature, such as Lasso (Tibshirani 1996), or the stepwise deletion method proposed by Gardoni et al. (2002). The set of unknown parameters $\boldsymbol{\Theta}_{\mathbf{X}}$ in Eq. (3) can be calibrated based on available observations of the state variables, either coming from field observations or Finite Element Models (FEMs). When the semimartingale driving noise $\mathrm{d}\mathbf{S}(t;\boldsymbol{\Theta}_{\mathbf{S}})$ is replaced by an ordinary Brownian motion $\mathrm{d}\mathbf{B}$, the classical Euler-Maruyama approach for SDEs calibration can be used. The method is not reported here, but we refer the reader to Iannacone & Gardoni (2021) for a detailed explanation of the method and how it can be applied to models for the real-time deterioration of bridges during earthquakes.

3 CALIBRATION OF DETERIORATION MODELS BASED ON UNRELATED EARTHQUAKE EVENTS

This section analyzes the effect of a set of unrelated ground motions on a bridge using a FEM, and we calibrate a deterioration model in the form of Eq. (3) using the FEM results. The analyzed bridge is the two-span reinforced concrete bridge reported in Figure 1. We also report the value of important quantities (such as geometric and material properties) in Table 1.

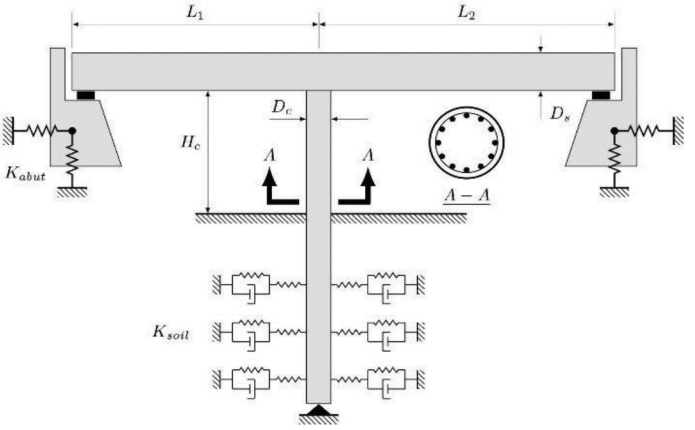


Figure 1. Layout for the bridge under analysis (adapted from Jia et al., 2017).

Table 1. Important quantities of the bridge under analysis.

Parameter	Symbol	Value
Shorter span length	L_1	25 m
Column Height	H	8.5 m
Column Diameter	D_c	1.54 m
Reinforcement Nominal Yield Strength	f_y	475 MPa
Concrete Nominal Strength	f_c'	40.55 MPa
FRP Composite Nominal Strength	f_{FRP}	1302 MPa
Tensile Modulus of FRP Composite	E_{FRP}	12400 MPa
Longitudinal Reinforcement Ratio	ρ_l	0.022
FRP Composite Volumetric Ratio	ρ_{FRP}	0.0334
Additional Bridge Dead Load	w_t	0.7
Long-to-Short Span Ratio	L_2/L_1	1.4
Lap Splice Length	L_S	0.86 m
Soil Type		C
Abutment Type		Roller

The analyses are performed using the software OpenSees (McKenna et al. 2006). The ground motions used for calibration present similar aggregated measures but wildly different time-histories. Namely, we use time-histories coming from the following earthquakes: Loma Prieta (California 1989), Tabas (Iran 1978), L'Aquila (Italy 2009), and Kobe (Japan 1995). Contrary to the analyses performed by Iannacone & Gardoni (2021), we calibrate a single deterioration model using the entire set of ground motions, and we show the limitations of the calibration in terms of accuracy for prediction purposes.

We use the FEM to record the variation of the first natural period of the structure T_n, which is expected to increase over time due to the reduction in stiffness caused by the incremental damage on the bridge. A stochastic model for the evolution of T_n (in the form of Eq. 3) is then calibrated based on the FEM results. Namely, the drift term in Eq. (3) is assumed to have the following form:

$$\boldsymbol{\mu}[\cdot] = \boldsymbol{\Theta}_{\boldsymbol{\mu}} \cdot \mathbf{h}[a(t)] = \sum_{i=1}^{7} \theta_i h_i[a(t)] \tag{7}$$

while the diffusion term is assumed to be a constant of value $\theta_\sigma = \theta_8$. The set of explanatory functions that are selected for the problem is shown in Table 2.

Table 2. Explanatory functions for the drift coefficient.

Explanatory function	Value
$h_1(t)$	$a(t)$
$h_2(t)$	$[a(t)]^2$
$h_3(t)$	$[a(t)]^3$
$h_4(t)$	$[a(t)]^4$
$h_5(t)$	$T_n[a(t)]^2$
$h_6(t)$	$\max_{(t-1)<\tau<t} [a(\tau)]^2$
$h_7(t)$	$\max_{(t-10)<\tau<t} [a(\tau)]^2$

The explanatory functions $h_1(t)$, $h_2(t)$, $h_3(t)$ and $h_4(t)$ investigate the direct effect of the instantaneous spectral acceleration $a(t)$ on the evolution of the first natural period of the structure. The explanatory function $h_5(t)$ investigates the effects of the possible interaction between the instantaneous spectral acceleration $a(t)$ and the value of the first natural period T_n itself, hence making the formulation state dependent. The explanatory functions $h_6(t)$ and $h_7(t)$ are included to capture the effects of the inertia of the system during the seismic excitation. In particular, $h_6(t)$ accounts for the presence of peaks in the seismic excitation in the last second before t, while $h_7(t)$ accounts for the presence of peaks in last 10 seconds before t.

Table 3. Estimates for the unknown parameters (unrelated ground motion records).

Unknown parameter	Mean	Standard Deviation
θ_1	0.0269	0.0613
θ_2	1.3609	0.8013
θ_3	−0.1473	0.4432
θ_4	0.4187	1.0876
θ_5	−0.8030	0.4456
θ_6	0.3630	0.1009
θ_7	−0.0130	0.0258
θ_8	0.0500	0.0014

Table 3 reports the statistics for the calibrated values for the set of parameters $\boldsymbol{\Theta}_{\boldsymbol{\mu}}$.

Figure 2 shows a comparison between the results from the FEM and the expected prediction from the SDE model.

To quantify the discrepancy between the two models, we provide in the figure the Root Mean Square Error for the ground motion *gm* (RMSE_{gm}), computed as follows:

$$\mathrm{RMSE}_{gm} = \frac{1}{N_{data,gm}} \sum_{i=1}^{N_{data,gm}} \left(x_{FEM,gm,i} - x_{SDE,gm,i}\right)^2 \tag{8}$$

where $x_{FEM,gm,i}$ is the data from the FEM model and $x_{SDE,gm,i}$ is the data from the SDE model. The RMSE is computed across the $N_{data,gm}$ datapoints included between the beginning of the ground motion (defined for this paper as the point where $h_2(t)$ exceeds 0.001 cm^2/s^4 for the first time) and the end of the ground motion (defined for this paper as the point where $h_6(t)$ falls below 0.001 cm^2/s^4 for the first time). The thresholds were selected based on engineering judgment to capture the start and the end of the portion of the ground motion record

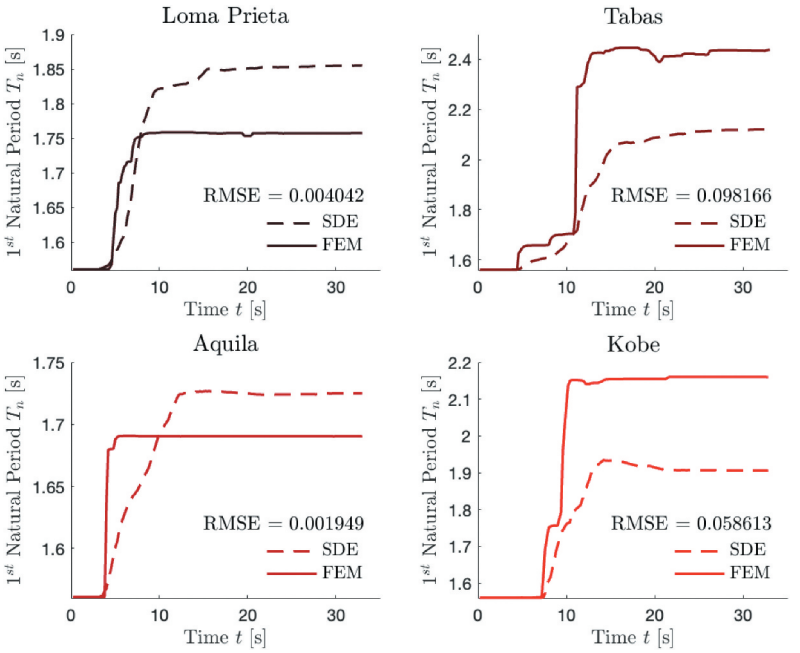


Figure 2. Predictions using the model calibrated based on unrelated ground motion records.

that effectively causes changes to the value of T_n. The average RMSE across the prediction for the four ground motions used for this example is 0.0407 s^2.

4 CALIBRATION OF DETERIORATION MODELS BASED ON SPECTRUM-COMPATIBLE EARTHQUAKE EVENTS

The same bridge as in Section 3 is now subject to a set of 6 spectrum-compatible ground motions. Time histories are spectrum-compatible when they exhibit similar characteristics in the frequency domain. In design practices, several codes require the selection of ground motion records that have response spectra similar to a pre-specified design spectrum (e.g., CEN 2004). Using spectrum-compatible ground motions also reduces the dispersion of the structural response of the structure. For this paper, we selected 6 spectrum-compatible ground motions using the software REXEL (Smerzini et al. 2014) and REXELweb (Sgobba et al. 2021). Figure 3 shows the target spectrum used for the selection along with the spectra of the selected records. The average spectrum of the selected records closely resembles the target spectrum.

The selected ground motions belong to the following earthquake sequences that occurred in Italy over the past few decades: Friuli (1976), Umbria-Marche (1997), Emilia (2012), and Central Italy (2016). A model in the same form as Section 3 is calibrated based on the results from the spectrum-compatible ground motions. Table 4 reports the statistics for the calibrated values of the unknown parameters.

Finally, Figure 4 shows the results of the prediction using the new model, for each of the 6 ground motions used for the calibration. The RMSE is also reported for each of the ground motions, computed as in Section 3. The predictions display a much higher level of accuracy compared with the case with unrelated ground motions. The average RMSE in this case is 0.0016 s^2, which is 96% lower than in Section 3 (even though the model now must adapt to 6 different ground motions compared to the 4 ground motions in the previous case).

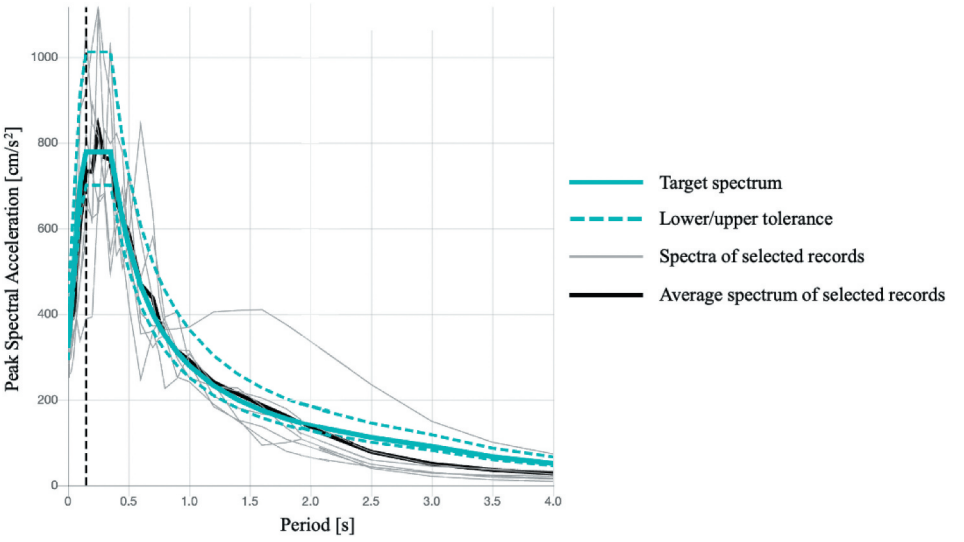


Figure 3. Target spectrum and spectra of the ground motion records selected for this example.

Table 4. Estimates for the unknown parameters (spectrum-compatible ground motion records).

Unknown parameter	Mean	Standard Deviation
θ_1	0.0353	0.0167
θ_2	7.3573	2.8564
θ_3	−2.2709	0.6207
θ_4	−24.2917	2.6009
θ_5	−3.3049	1.7516
θ_6	0.1564	0.0309
θ_7	−0.0191	0.0115
θ_8	0.0053	0.0001

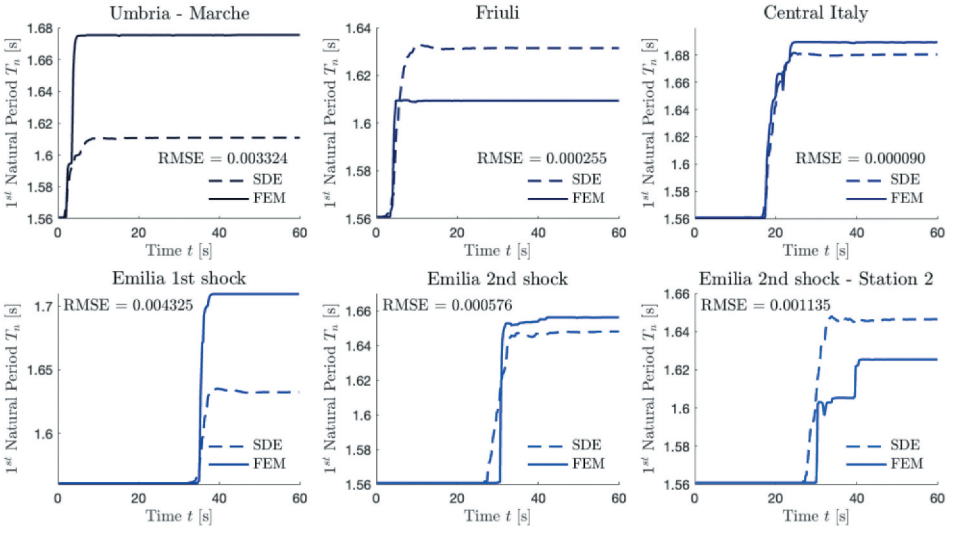


Figure 4. Predictions using the model calibrated based on spectrum-compatible ground motions.

5 CONCLUSIONS

In this paper, we calibrated Stochastic Differential Equation (SDE) models for the real-time deterioration of bridges during earthquake events. The data used for the model calibration was obtained by simulating the response of the bridge to multiple ground motion records through the Finite Element software OpenSees. Namely, we investigated the evolution of the first natural period of the structure as a direct effect of the ground motion. The selected SDE models allow to capture the effects of the instantaneous ground acceleration on the natural period, whereas typically used methods use aggregated measures of the shock (such as Peak Ground Acceleration or Spectral Acceleration) to predict the response of the structure and its deteriorated state at the end of the shock. In particular, the paper investigated how the selection of spectrum-compatible ground motion records can help reduce the scatter in the system response and can facilitate the calibration of a single SDE model for the deterioration of the structure. The results show that calibrating a single model on unrelated ground motion records can produce highly uncertain results that only reflect the original data in an average sense. When the calibration is based on spectrum-compatible records, the uncertainty is reduced, and a single calibrated model can capture the evolution of the system subject to multiple ground motions more accurately. The calibrated model can then be used to predict the response of the bridge to the occurrence of future earthquake events at the location of interest. While the models calibrated in this paper were tailored to the evolution of the first natural period of the structure, the same procedure can be used to calibrate models for the evolution of any of the state variables that are relevant to the system's capacity and demand. In particular, the calibrated SDEs can be incorporated into the recently proposed frameworks for computing the time-varying reliability of complex engineering systems, which use state-dependent models of the state variables (such as the proposed SDEs). Future works include the investigation of possible additional quantities to be included as regressors (and explanatory functions) in the proposed stochastic formulation, to improve the prediction capabilities of the models.

REFERENCES

CEN. 2004. Eurocode 8: Design of structures for earthquake resistance, Part 1: General rules, seismic actions and rules for buildings. *Brussels*: *European Committee for Standardization*.

Choi, D. H., & Lee, S. H. 2003. Multi-damping earthquake design spectra-compatible motion histories. *Nuclear engineering and design* 226(3), 221–230.

Cui, Z., Alipour, A., & Shafei, B. 2019. Structural performance of deteriorating reinforced concrete columns under multiple earthquake events. *Engineering Structures* 191, 460–468.

Gardoni, P., Der Kiureghian, A., & Mosalam, K. M. 2002. Probabilistic capacity models and fragility estimates for reinforced concrete columns based on experimental observations. *Journal of Engineering Mechanics* 128(10): 1024–1038.

Grigoriu, M. 2013. *Stochastic calculus: applications in science and engineering*. Springer Science & Business Media.

Hu, S., Gardoni, P., & Xu, L. 2018. Stochastic procedure for the simulation of synthetic main shock-aftershock ground motion sequences. *Earthquake Engineering & Structural Dynamics* 47(11): 2275–2296.

Iannacone, L., & Gardoni, P. 2019. Stochastic Differential Equations for the Deterioration Processes of Engineering Systems. In *Proceedings of the 13th International Conference on Applications of Statistics and Probability in Civil Engineering*, *Seoul, South Korea.*

Iannacone L., & Gardoni P. 2021. Time-varying Fragility Functions for Bridges subject to Main Shock-Aftershock Sequences Including Damage Accumulation during the Events and Calibration based on Available Data. *Proceedings of the 10th International Conference on Bridge Maintenance, Safety and Management (IABMAS2020)*, *Sapporo, Japan*

Iannacone L., & Gardoni P. 2023. Modeling Deterioration and Predicting Remaining Useful Life using Stochastic Differential Equations and Limited Data. *Reliability Engineering and System Safety (under review)*

Itô, K. 1973. Stochastic integration. *Vector and Operator Valued Measures and Applications*: 141–148.

Jeon, J. S., DesRoches, R., Lowes, L. N., & Brilakis, I. 2015. Framework of aftershock fragility assessment–case studies: older California reinforced concrete building frames. *Earthquake Engineering & Structural Dynamics* 44(15): 2617–2636.

Jia, G., Tabandeh, A., & Gardoni, P. 2017. Life-cycle analysis of engineering systems: Modeling deterioration, instantaneous reliability, and resilience. In *Risk and reliability analysis: Theory and applications*. Springer, Cham.

Jia, G., & Gardoni, P. 2018. Simulation-based approach for estimation of stochastic performances of deteriorating engineering systems. *Probabilistic Engineering Mechanics* 52: 28–39.

Kumar, R., & Gardoni, P. 2014. Effect of seismic degradation on the fragility of reinforced concrete bridges. *Engineering Structures* 79: 267–275.

Iervolino, I., Chioccarelli, E., & Suzuki, A. 2020. Seismic damage accumulation in multiple mainshock–aftershock sequences. *Earthquake Engineering & Structural Dynamics* 49(10): 1007–1027.

Li, Q., & Ellingwood, B. R. 2007. Performance evaluation and damage assessment of steel frame buildings under main shock–aftershock earthquake sequences. *Earthquake engineering & structural dynamics* 36(3): 405–427.

McKenna, F., Fenves, G. L., & Scott, M. H. 2006. OpenSees: Open system for earthquake engineering simulation. Pacific Earthquake Engineering Research Center, University of California, Berkeley, CA. http://opensees.berkeley.edu.

Raghunandan, M., Liel, A. B., & Luco, N. 2015. Aftershock collapse vulnerability assessment of reinforced concrete frame structures. *Earthquake Engineering & Structural Dynamics*, 44(3): 419–439.

Rezaeian, S., & Der Kiureghian, A. 2008. A stochastic ground motion model with separable temporal and spectral nonstationarities. *Earthquake Engineering & Structural Dynamics* 37(13): 1565–1584.

Sgobba, S., Felicetta, C., Russo, E., D'Amico, M., Lanzano, G., Pacor, F., Luzi, L., Baraschino, R., Baltzopoulos, G., & Iervolino, I. 2021. The online graphical user interface of REXELweb for the selection of accelerograms from the engineering strong motion database (ESM). In *39° Convegno nazionale Gruppo Nazionale di Geofisica della Terra Solida*, 22–24 giugno 2021.

Smerzini, C., Galasso, C., Iervolino, I., & Paolucci, R. 2014. Ground motion record selection based on broadband spectral compatibility. *Earthquake Spectra* 30(4): 1427–1448.

Tibshirani, R. 1996. Regression shrinkage and selection via the lasso. Journal of the Royal Statistical Society: Series B (Methodological) 58(1): 267–288.

Torti, M., Sacconi, S., Venanzi, I., & Ubertini, F. 2022. Monitoring-informed life-cycle cost analysis of deteriorating RC bridges under repeated earthquake loading. *Journal of Structural Engineering* 148(9), 04022145.

Bridge Maintenance, Safety, Management, Digitalization and Sustainability – Jensen, Frangopol & Schmidt (eds)
© 2024 The Author(s), ISBN 978-1-032-77040-6
Open Access: www.taylorfrancis.com, CC BY-NC-ND 4.0 license

A data-driven approach for quantifying reliability and resilience of transportation network

Saeid Ghasemi
Ph.D. Student, Durham School of Architectural Engineering and Construction, University of Nebraska-Lincoln, Omaha, NE, USA

Vahid Aghaeidoost
Ph.D. Candidate, Department of Civil Engineering, University of Calgary, Alberta, Canada

Milad Roohi
Assistant Professor, Durham School of Architectural Engineering and Construction, University of Nebraska-Lincoln, Omaha, NE, USA

ABSTRACT: Bridges are critical transportation infrastructure components, serving as vital links for mobility and evacuation during and after hazard occurrences. Ensuring their reliability and safety is of paramount importance. Traditional reliability assessment methods for bridge networks rely on complex mathematical models, often resulting in time-consuming processes. This paper leverages the power of data-driven algorithms to streamline and enhance the reliability and resilience evaluation of this infrastructure. A novel data-driven method of approach is developed to quantify the resilience of a transportation network within a community to facilitate proactive maintenance and decision-making processes. An ensemble of machine learning algorithms is used to train the predictive model and test its prediction accuracy to mitigate the risk of overfitting. Feature engineering techniques are employed to extract relevant information from the dataset, further enhancing the model's performance. Subsequently, the estimated reliability indices of bridges are used to perform network analysis and quantify the resilience of the network and its components by accounting for dependency between network components and the degree of centrality of each component for the mobility of the network. The proposed method is illustrated using real-world data for bridges and transportation infrastructure from a US community. The results show that the proposed approach possesses several features. Firstly, its capability to identify vulnerabilities in the transportation network helps inform decisions about prioritizing maintenance efforts during the life cycle of bridges (i.e., prior to extreme hazards) and prioritizing recovery following damaging events. Secondly, its flexibility to adapt to changing environmental conditions and evolving structural characteristics underscores its potential to be integrated into existing bridge management systems, providing a valuable tool for infrastructure stakeholders to make data-driven decisions and allocate resources efficiently.

1 INTRODUCTION

The seismic resilience of transportation networks, particularly bridges, is a critical factor in maintaining their integrity and safety. These structures are integral to the transportation of individuals and commodities, especially during seismic catastrophes. Investigations in this domain enable a thorough assessment of the susceptibilities within these networks, pinpoint areas of potential frailty, and devise methodologies to bolster their robustness. Comprehending the possible damages that might transpire during seismic incidents empowers engineers and policymakers to judiciously allocate resources for retrofitting, maintenance, and disaster preparedness initiatives (Farahani et al., 2023).

DOI: 10.1201/9781003483755-230

Network connectivity must be considered for evaluating network reliability and resilience, as a transportation network consists of multiple origin-destination pairs and paths. Over the past few decades, significant research has been undertaken on simulation-based metrics for transportation networks. Chang & Nojima (1998) suggested measures based on topology for evaluating the seismic performance of entire highway networks. Ng & Efstathiou (2006) defined network disconnectedness based on the number of unreachable node pairs and the maximum possible number of links. Liu & Frangopol (2006) expanded this disconnectedness concept to include uncertainties in network performance evaluation. Bocchini & Frangopol (2011) introduced the probabilistic full connected ratio, which is the ratio of the number of samples where all nodes are reachable to the total number of samples.

Transportation networks can face disruptions due to various factors that impact bridges, including their strength and the likelihood and severity of hazards (Sabatino et al., 2016). Different stakeholders have different concerns regarding the impacts of bridge failures. Therefore, it is crucial to consider all uncertainties related to the probability of bridge failures and their consequences when evaluating and making decisions about the performance of transportation networks. In recent years, researchers have studied how bridge networks respond to extreme events such as earthquakes (Capacci & Biondini, 2020), scour caused by floods (Liu et al., 2020), corrosion risk (Han & Frangopol, 2022), and the life-cycle performance of bridge parts and systems, considering the best actions, checks, monitoring, maintenance, and repairs (Dong & Frangopol, 2019).

Resilience assessment assists practitioners in measuring the physical, social and economic effects of transportation infrastructure investments quantitatively (Gardoni & Murphy, 2020). To perform resilience assessment, three steps are required (Bocchini & Frangopol, 2012): i) develop fragility curves for different damage levels to determine the probability of damage and functionality loss of structures, ii) link structural damage to the recovery patterns to determine the recovery functions for different damage levels, and iii) calculate the recovery time and resilience curves using recovery functions and the damage likelihood from fragility curves. The literature on the resilience of transportation networks has been very limited due to the high computational complexity, data limitations, and lack of relevant methodologies. Traditional reliability assessment methods for bridge networks rely on complex mathematical models, often resulting in time-consuming processes.

Recent advancements in Machine Learning (ML) have led to the integration of ML algorithms in the field of structural and earthquake engineering for taking advantage of their quick prediction and classification capabilities, among others. ML algorithms can detect and identify patterns in data, allowing engineers to better understand the behavior of transportation networks. This knowledge can be used to develop more accurate models for predicting network reliability and resiliency. Xie et al. (2020) studied the significance of different ML techniques, such as seismic hazard analysis, system identification and damage detection, seismic fragility assessment, and structural control for earthquake-related simulation. Wang et al. (2022) provided a comprehensive review of ML methods for risk and resilience assessment of bridge networks.

This paper aims to leverage the power of data-driven algorithms to streamline and enhance the reliability and resilience evaluation of transportation infrastructure. A novel data-driven methodology is developed to quantify the resilience of a transportation network within a community to facilitate proactive maintenance and decision-making processes. The proposed methodology is illustrated using real-world data for bridges and transportation infrastructure from a US community.

2 NETWORK RELIABILITY AND RESILIENCE ASSESSMENT

2.1 *Network reliability*

To make optimal decisions on investment for maintaining and updating the transportation network, including bridges, it is required to assess the network-level performance probabilistically (Frangopol, 1985). However, measuring the network performance under different uncertainties is often expensive or impossible because of its complexity, such as the connections, interactions, and dependencies among its parts (Frangopol & Bocchini, 2012a). This study uses the matrix-based

system reliability method suggested by Kang et al. (2008) because it can calculate the probabilities of complex system events efficiently using simple matrix operations. The network failure probability (i.e., $E_{Network}$= probability of disconnection) can be obtained as follows:

$$P(E_{Network}) = \sum_{j:e_j \subseteq E_{Network}} p_j = P(e_j) = c^T p, \quad j = 1, 2, \ldots, m \tag{1}$$

where e_j represents basic mutually exclusive and collectively exhaustive events with m total events, in which m is the number of distinct states for the ith bridge in the network, the probability of e_j is demonstrated by p_j. The network event vector is demonstrated by c, which for the jth element is 1 if e_j belongs to the network event and 0 otherwise.

2.2 *Resilience assessment*

Resilience is the capacity to reduce the impact of hazards and restore functionality after an event (Bruneau et al., 2003). The resilience of each bridge can be measured by the post-event functionality Q(t) of the bridge over a certain time period, as shown by the shaded area in Figure 1. The formula for resilience R is given by Frangopol & Bocchini (2012b):

$$\mathrm{R} = \frac{1}{\mathrm{t_h} - \mathrm{t_0}} \int_{\mathrm{t_0}}^{\mathrm{t_h}} \mathrm{Q(t)dt} \tag{2}$$

The hazard happened at time $\mathrm{t_0}$, and the recovery process was checked at time $\mathrm{t_h}$. The network resilience can be obtained as follows:

$$R_{Network} = c^T r \tag{3}$$

where c is the event vector, and r represents the component resilience index vector.

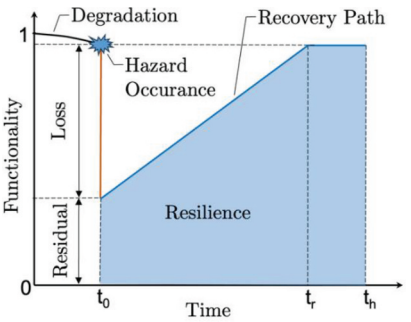


Figure 1. Schematic representation of the resilience of a system. The plot shows the functionality evolution before, during, and following the occurrence of a hazard.

3 PROPOSED METHODOLOGY FOR DATA-DRIVEN NETWORK RELIABILITY AND RESILIENCE PREDICTION

This section presents a proposed data-driven methodology to predict the reliability and resilience of a transportation network within a community. Figure 2 provides an overview of the methodology, which begins with characterizing the transportation infrastructure network. The next step involves implementing seismic reliability and resilience modeling of the networked infrastructure. This is done by i) developing a network connectivity/disconnectivity model and ii) implementing a fragility-based network resilience model using the IN-CORE platform (van de Lindt et al., 2023). The model can quantify the probability of exceeding different damage states for each component under different seismic events. Afterward, the IN-CORE model is used to generate an ensemble of earthquake scenarios by varying the magnitude and epicenter of the earthquakes. Seismic resilience modeling is performed for individual components within the network, and the connectivity/disconnectivity model is used to quantify network reliability and resilience indices.

The outputs of this analysis are then used as input to train reliability and resilience predictive models using an ensemble of ML algorithms that take earthquake event characteristics (such as earthquake magnitude and latitude and longitude of the epicenter) as input and predict reliability and resilience indices. The labeled data is divided into a training set and a testing set, with a ratio of 80% and 20%, respectively. The performance of different ML models is evaluated using two metrics: i) Pearson's r correlation coefficient and ii) coefficient of determination (R2). Pearson's r coefficient is a measure of the statistical relationship between two continuous variables. Its value ranges between -1 and 1, with higher value nearing 1 signifying a perfect linear correlation between the two variables. The R2 quantifies model goodness-of-fit based on the sum of squares method, where values closer to 1 indicate better performance. Conversely, values below zero signify performance that is worse than fitting the values to their median. The scores for each configuration are normalized in ascending or descending order. Models with strong predictive capabilities are evaluated based on a high goodness-of-fit, as indicated by Pearson's r and R2 values. The ML algorithms used in this study are K-nearest neighbors' regression (KNN), Decision trees (DT), Random forest (RF), Artificial Neural Network (ANN), Adaptive boosting (AdaBoost), and Support vector regression (SVR). The prediction accuracy is tested to mitigate the risk of overfitting. To enhance the model's performance, feature engineering techniques are employed to extract relevant information from the dataset.

As shown on the left side of Figure 2, the trained predictive model can ultimately be used by users (e.g., planners and decision-makers) to simulate the effects of an earthquake scenario before it occurs. This can aid in planning and mitigation efforts. Furthermore, the predictive simulation can also be utilized by emergency managers for post-earthquake planning and running scenarios to quantify the impacts.

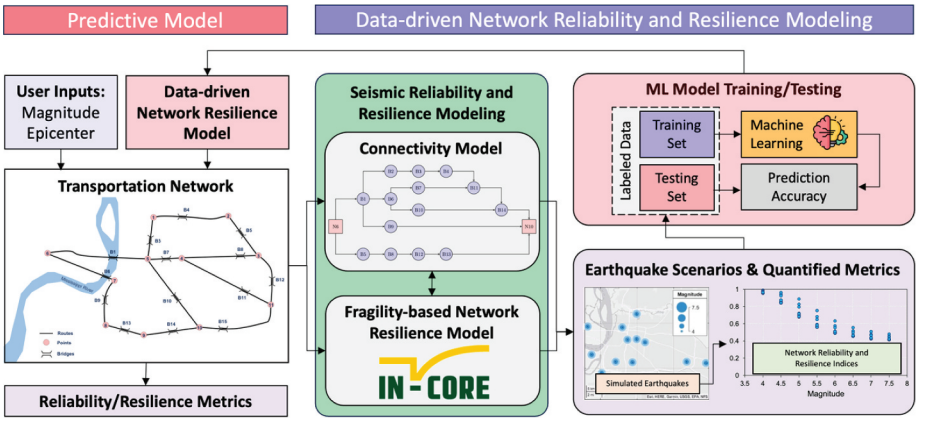


Figure 2. Data-driven framework of quantifying reliability and resilience of transportation network.

4 CASE STUDY

4.1 *Shelby county, memphis, TN, transportation network*

In this study, a simplified transportation network of Shelby County, Memphis, TN, has been employed to demonstrate the proposed approach. For this purpose, routes with bridges are considered and close nodes are merged to each other to show the access point to important centers. As shown in Figure 3, this network includes 11 important access points known as Nodes (1, 2, …, 11) in terms of access to temporary accommodation points, city evacuation, hospitals, and an airport; each route includes a bridge, and a total of 14 bridges are studied in this network. These bridges, which connect critical access points within the city of Memphis, have been selected from the city's bridge network. The bridges are categorized into five different types based on their structural systems, as shown in in Table 1. The geographic location of these bridges is shown in Figure 3 labeled as (B1, B2, …, B14). To calculate the damage probabilities of mentioned bridge types for different

damage states, 104 seismic events were simulated, with magnitudes from 4 to 7.5 on the Richter scale at different network locations, as shown in Figure 3. Various events with different magnitudes occurred at the same location, sharing the same epicenter. The larger earthquakes are represented with bigger circles, while the smaller earthquakes are shown with smaller circles.

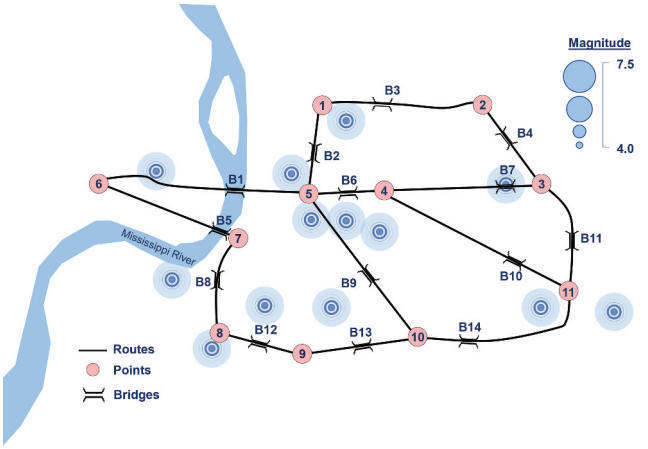


Figure 3. Bridge network representation for the Memphis area and seismic events location.

Table 1. Bridge information in the network.

ID	Classification	Definition	Material
B1, B10, B12, B14, B15	MSSS	Multiple Span, Simply Supported	Concrete
B3, B8, B9	MSC	Multiple Span, Continues	Concrete
B4, B7, B11	MSSS	Multiple Span, Simply Supported	Steel
B5	SS	Single Span	Concrete
B6, B13	MSC	Multiple Span, Continues	Steel

4.2 *Network connectivity/disconnectivity*

The matrix-based system reliability method (Kang et al., 2008) is used to find the network connectivity/disconnectivity between nodes. As an example, Figure 4 shows all the different paths between N10 and N6 that are used to find network reliability and resiliency. To represent any system event, an event vector c can be used, where the jth element is 1 if e_j is part of the system event and 0 if not. Based on the probability rules, the event vector is calculated as follows:

$$c[1] = \begin{bmatrix} 1 \\ 0 \end{bmatrix}, \; c[i] = \begin{bmatrix} c[i-1] & \mathbf{1} \\ c[i-1] & \mathbf{0} \end{bmatrix}, \; for \; i = 2, 3, \ldots, n \tag{4}$$

Let $\mathbf{0}$ and $\mathbf{1}$ be the column vectors of 2^{i-1} zeros and ones, respectively. Then, the event vector $c[n]$ has n columns, where the ith column is the event vector of the ith component event E_i, for $i = 1, \ldots, n$. For this example, the event vector can be calculated as follows:

$$C^{N10\to6} = C^{N10\to5\to6} .* C^{N10\to9\to8\to7\to6} .* C^{N10\to11\to4\to5\to6} .* C^{N10\to11\to4\to3\to2\to1\to5\to6} .* C^{N10\to11\to3\to4\to5\to6} .* C^{N10\to11\to3\to2\to1\to5\to6} \tag{5}$$

For example, the event vector for $N10 \to 5 \to 6$ path is calculated as follows:

$$C^{N10\to5\to6} = 1 - \left(1 - C^{E_{B10}}\right) .* \left(1 - C^{E_{B1}}\right) \tag{6}$$

Also, the probability vector is calculated as follows:

$$p[i+1] = \begin{bmatrix} p[i].p_{i+1} \\ p[i].\bar{p}_{i+1} \end{bmatrix} \tag{7}$$

in which $\bar{p} = 1 - p$.

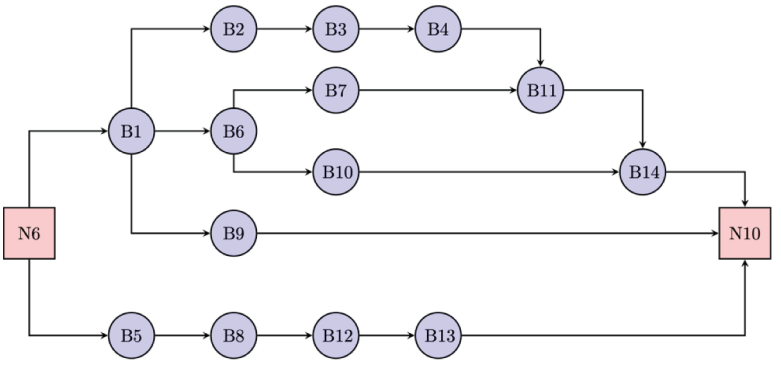


Figure 4. Network connectivity/disconnectivity block for paths from node 10 to node 6.

5 RESULTS AND DISCUSSION

The ML regression methods were applied to the input dataset for the regression of network system reliability and resilience indices. The magnitude, latitude, and longitude of 104 simulated seismic scenarios, as shown in Figure 3, are used as input parameters. Figure 5 represents the calculated actual values of (a) network reliability and (b) network resilience indices based on different seismic scenarios. As the magnitude of the simulated earthquake increases, the network reliability and resilience indices decrease. Furthermore, plot (a) shows a relatively broad range of network reliability index values for each magnitude, implying that an earthquake's location significantly affects network reliability, highlighting the importance of geographic factors in network design. In plot (b), the data points appear to cluster more tightly, particularly at higher magnitudes. This suggests that the network's resilience might be more consistent across different locations when subjected to larger earthquakes. However, there is still some variability, indicating that geographic location affects resilience, but to a lesser extent than it affects reliability. For example, at a Magnitude of 6.0, the reliability and resilience indices vary between 0.18-0.29 and 0.51-0.63 according to the location of earthquake occurrences, respectively. An illustrative example of how the network's resilience can be affected by epicenter is a seismic event that takes place near two routes that converge at a single access point. In this situation, the network's resilience would be compromised for accessing the point that is dependent on these two routes. A hypothetical example of a situation that impacts the network's resilience is a seismic event that happens near B1 and B5, which jeopardizes the movement and escape to access point 6 (N6). This can have consequences for the network's reliability and resilience.

Figure 6 demonstrates the result of ML models using radar plots. The Pearson's r and R2 values for each ML algorithm are calculated. The R2 values are represented by a dashed blue line with circle markers, while the Pearson's r coefficients are represented by a dashed green line with triangular markers. Each ML model on the radar plot is normalized a number between 0 and 1, where a value closer to 1 indicates a more accurate model. The results show that the SVR model is more accurate than other models for predicting the network reliability and resilience indices. Both R2 and Pearson's r values are 1 for SVR algorithm, which indicate it has the best performance in terms of explaining the variance and the strength of the linear relationship with the actual values. Moreover, the ANN algorithm has the subsequent best set of R2 and Pearson's r value after the SVR model. DT, on the other hand, is ranked lowest because it got the lowest reference index, especially in Pearson's r value in both system network (a) reliability and (b) resilience, as shown in

Figure 6. Overall, it is evident that SVR and ANN models achieve some of the highest performance among ML models for predicting the actual values of network system reliability and resilience. For example, for the network system reliability, SVR and ANN achieve maximum R2 scores of 1 and 0.97, and Pearson's r scores of 1 and 0.85, respectively. Moreover, in terms of network system resilience, SVR and ANN achieve maximum R2 scores of 1 and 0.94, and Pearson's r scores of 1 and 0.77, respectively. In contrast, DT algorithm has the poorest performance among ML models for predicting the network system reliability and resilience according to Pearson's r reference index. For the network system reliability and resilience, DT achieves a low Pearson's r score of 0.36 and 0.39, respectively, which indicate that the model has a weak linear relationship with the actual values. These low reference indices suggest that the DT model cannot fit the data well and has a high prediction error. Therefore, DT is not a suitable model for estimating the network system reliability and resilience.

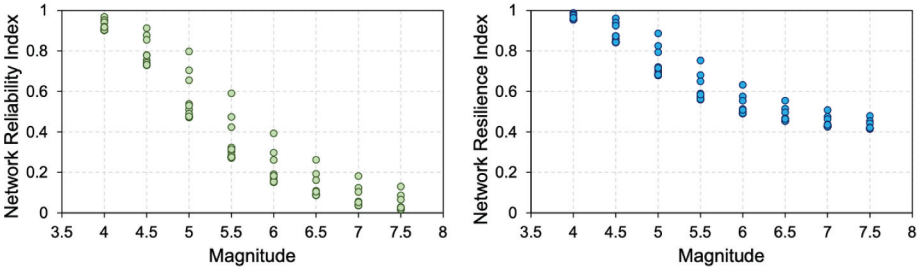


Figure 5. Actual values of network (left) reliability and (right) resilience index for different magnitudes.

The best-tuned model results are presented in Figure 7, where the x-axis represents the actual value of system network (a) reliability and (b) resilience, while the y-axis represents the predicted values by different ML models. The vertical distance of a point from the reference line (1:1 red line) is the error of the specific prediction made by the proposed model's predictions. Various ML models are shown with different colors and markers. Linear regression lines are fitted for a set of actual values to predict the value for network system (a) reliability and (b) resilience across different ML models. The color of each regression line matches the color of the corresponding ML model. As the SVR has the best model performance, its regression line coincides with the reference line, represented by the 1:1 red line. The ideal ML model is the model that the predictive value is exactly equal to actual values, where SVR model nearly demonstrates this case for network system (a) reliability and (b) resilience. The mean square error for the system network reliability and resiliency in the best model (SVR) is 2% and 1%, respectively. Conversely, the DT model, which has the lowest R2 and Pearson's r score, presents a mean square error of 7% for reliability and 4% for resiliency. For both the network system reliability and resilience, SVR regression shows nearly similar slopes to the reference line. Based on this, the predictions made by the proposed models for the network system reliability and resilience are expected to perform well. The data range for the network system reliability is between 0 and 1, while the network system resilience range is from 0.4 to 1. This could be why machine learning (ML) models predict the system network resilience slightly better. However, the predictions for system network reliability seem to follow the same trend as the system network resilience, as indicated by various ML models. Therefore, the proposed models are expected to make adequate predictions for both the network system reliability and network system resilience.

6 CONCLUSIONS

This paper presents a data-driven methodology for predicting the reliability and resilience of a transportation network using seismic reliability/resilience modeling and machine learning (ML) algorithms. The methodology involves characterizing the network, implementing seismic

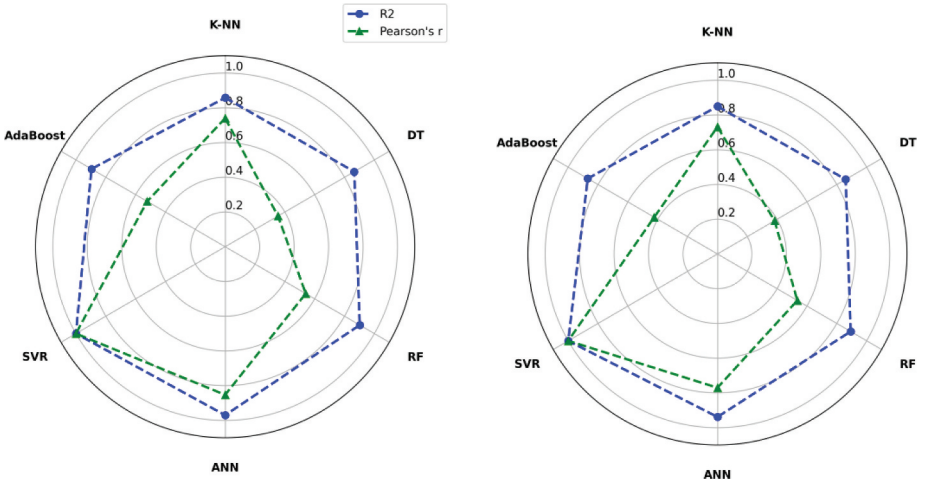


Figure 6. Reference index of network system (left) reliability and (right) resilience for various ML models.

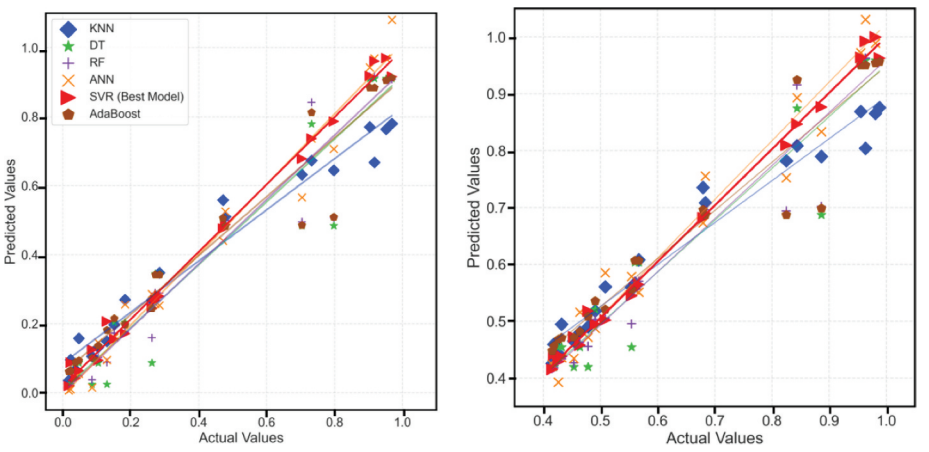


Figure 7. Testing results of proposed ML-based network system (left) reliability and (right) resilience models.

modeling, generating earthquake scenarios, and training predictive models using ML algorithms. The performance of the models is evaluated using Pearson's r coefficient and coefficient of determination (R2). The ML algorithms used include K-nearest neighbors' regression, Decision trees, Random forest, Artificial Neural Network, Adaptive boosting, and Support vector regression. Feature engineering techniques are employed to enhance the model's performance. The models demonstrated the significant impact of an earthquake's magnitude and epicenter location on the network's reliability and resilience. This prediction aids in the recovery of community services by establishing a theoretical calculation of the reliability and resilience of a bridge network.

The proposed framework has been illustrated using a simplified bridge network of Shelby County, TN. The results show that as earthquake magnitude increases, the network system reliability and resilience decrease, with variations attributed to earthquake location. The SVR and ANN models exhibit high performance in predicting the actual values of the network system reliability and resilience, as indicated by their high R2 and Pearson's r scores. The models' predictions for the network system reliability and resilience indices are reliable, as they align closely with the reference line. The mean of the residuals being close to zero suggests an even distribution and absence of systematic bias.

REFERENCES

Bocchini, P., & Frangopol, D. M. (2011). A stochastic computational framework for the joint transportation network fragility analysis and traffic flow distribution under extreme events. Probabilistic Engineering Mechanics, 26(2), 182–193. https://doi.org/10.1016/j.probengmech.2010.11.007

Bocchini, P., & Frangopol, D. M. (2012). Restoration of Bridge Networks after an Earthquake: Multicriteria Intervention Optimization. Earthquake Spectra, 28(2), 427–455. https://doi.org/10.1193/1.4000019

Bruneau, M., Chang, S. E., Eguchi, R. T., Lee, G. C., O'Rourke, T. D., Reinhorn, A. M., Shinozuka, M., Tierney, K., Wallace, W. A., & von Winterfeldt, D. (2003). A Framework to Quantitatively Assess and Enhance the Seismic Resilience of Communities. Earthquake Spectra, 19(4), 733–752. https://doi.org/10.1193/1.1623497

Capacci, L., & Biondini, F. (2020). Probabilistic life-cycle seismic resilience assessment of aging bridge networks considering infrastructure upgrading. Structure and Infrastructure Engineering, 16(4), 659–675. https://doi.org/10.1080/15732479.2020.1716258

Chang, S. E., & Nojima, N. (1998). Measuring lifeline system performance: Highway transportation systems in recent earthquakes. 6th National Earthquake Conference on Earthquake Engineering.

Dong, Y., & Frangopol, D. M. (2019). Life-Cycle Performance of Infrastructure Networks. In Life-Cycle Design, Assessment, and Maintenance of Structures and Infrastructure Systems (pp. 65–94). American Society of Civil Engineers (ASCE). https://doi.org/10.1061/9780784415467.ch03

Farahani, S., Shojaeian, A., Behnam, B., & Roohi, M. (2023). Probabilistic Seismic Multi-hazard Risk and Restoration Modeling for Resilience-informed Decision Making in Railway Networks. Sustainable and Resilient Infrastructure, 1–22.

Frangopol, D. M. (1985). Sensitivity of Reliability-Based Optimum Design. Journal of Structural Engineering, 111(8), 1703–1721. https://doi.org/10.1061/(ASCE)0733-9445(1985)111:8(1703)

Frangopol, D. M., & Bocchini, P. (2012a). Bridge network performance, maintenance and optimisation under uncertainty: Accomplishments and challenges. Structure and Infrastructure Engineering, 8(4), 341–356. https://doi.org/10.1080/15732479.2011.563089

Frangopol, D. M., & Bocchini, P. (2012b). Resilience As Optimization Criterion for the Rehabilitation of Bridges Belonging to a Transportation Network Subject to Earthquake. 2044–2055. https://doi.org/10.1061/41171(401)178

Gardoni, P., & Murphy, C. (2020). Society-based design: Promoting societal well-being by designing sustainable and resilient infrastructure. Sustainable and Resilient Infrastructure, 5(1–2), 4–19. https://doi.org/10.1080/23789689.2018.1448667

Han, X., & Frangopol, D. M. (2022). Life-cycle connectivity-based maintenance strategy for bridge networks subjected to corrosion considering correlation of bridge resistances. Structure and Infrastructure Engineering, 18(12), 1614–1637. https://doi.org/10.1080/15732479.2021.2023590

Kang, W.-H., Song, J., & Gardoni, P. (2008). Matrix-based system reliability method and applications to bridge networks. Reliability Engineering & System Safety, 93(11), 1584–1593. https://doi.org/10.1016/j.ress.2008.02.011

Liu, L., Yang, D. Y., & Frangopol, D. M. (2020). Network-Level Risk-Based Framework for Optimal Bridge Adaptation Management Considering Scour and Climate Change. Journal of Infrastructure Systems, 26(1), 04019037. https://doi.org/10.1061/(ASCE)IS.1943-555X.0000516

Liu, M., & Frangopol, D. M. (2006). Probability-Based Bridge Network Performance Evaluation. Journal of Bridge Engineering, 11(5), 633–641. https://doi.org/10.1061/(ASCE)1084-0702(2006)11:5(633)

Ng, A. K. S., & Efstathiou, J. (2006). Structural robustness of complex network. International Workshop and Conference on Network Science.

Sabatino, S., Frangopol, D. M., & Dong, Y. (2016). Life cycle utility-informed maintenance planning based on lifetime functions: Optimum balancing of cost, failure consequences and performance benefit. Structure and Infrastructure Engineering, 12(7), 830–847. https://doi.org/10.1080/15732479.2015.1064968

Van De Lindt, J. W., Kruse, J., Cox, D. T., Gardoni, P., Lee, J. S., Padgett, J., McAllister, T. P., Barbosa, A., Cutler, H., Van Zandt, S., Rosenheim, N., Navarro, C. M., Sutley, E., & Hamideh, S. (2023). The interdependent networked community resilience modeling environment (IN-CORE). Resilient Cities and Structures, 2(2), 57–66. https://doi.org/10.1016/j.rcns.2023.07.004

Wang, X., Mazumder, R. K., Salarieh, B., Salman, A. M., Shafieezadeh, A., & Li, Y. (2022). Machine Learning for Risk and Resilience Assessment in Structural Engineering: Progress and Future Trends. Journal of Structural Engineering, 148(8), 03122003. https://doi.org/10.1061/(ASCE)ST.1943-541X.0003392

Xie, Y., Ebad Sichani, M., Padgett, J. E., & DesRoches, R. (2020). The promise of implementing machine learning in earthquake engineering: A state-of-the-art review. Earthquake Spectra, 36(4), 1769–1801. https://doi.org/10.1177/8755293020919419


Taylor & Francis
Taylor & Francis Group
http://taylorandfrancis.com

SS11: Approaches to bridge management/bridge management systems in response to today's challenges

Organizers: R.M. Ellis & R. Hajdin


Taylor & Francis
Taylor & Francis Group
http://taylorandfrancis.com

Bridge Maintenance, Safety, Management, Digitalization and Sustainability – Jensen, Frangopol & Schmidt (eds)
© 2024 The Author(s), ISBN 978-1-032-77040-6
Open Access: www.taylorfrancis.com, CC BY-NC-ND 4.0 license

Forecasting the condition of British railway bridges via a hindcast

M.J. Hamer & G.S. Calvert
Network Rail, Milton Keynes, UK

ABSTRACT: Bridges are critical assets for the safe, reliable, and functional operation of transportation networks. Estimating future safety and reliability measures through predicting changes to asset condition, forecasting required interventions, and developing equitable resource allocations from limited budgets is a challenging task. Network Rail (NR) is the infrastructure manager for the railway in Great Britain and is responsible for the management of over 26,000 bridges. NR uses a strategic model (Bridges Forecasting Model) to forecast the work volumes, expenditure, and condition outputs for its bridge portfolio in different funding scenarios. In this paper a 'hindcast' exercise is presented. A hindcast has been employed to refine model parameters by calibrating the modelled bridge condition against the portfolio's observed condition profile between 2010 and 2023. This has enabled key decision makers (Government, regulators, central and regional asset engineers in NR) to have greater confidence in the outputs of the forecasting model.

1 INTRODUCTION

Operational railways are complex systems that are reliant on the dependable performance of a large quantity of different assets across several asset disciplines including track, signalling and civil infrastructure. For the civil infrastructure, bridge management and maintenance command a sizeable demand on resources to ensure the continued provision of safe service, with the Structures portfolio at Network Rail having £2.305 billion (~75% for bridges) allocated for renewal activities in Control Period 7 (CP7) (April 2024 – March 2029) (Office of Rail and Road, 2023).

The structural assessment and reliability analysis of bridges is well documented in the literature (Frangopol, Dong, & Sabatino, 2017). As part of the asset management strategy for bridges, decision support tools known as Bridge Management Systems (BMS) have been developed to support infrastructure managers in their decision making (Mirzaei, Adey, Klatter, & Thompson, 2014).

Network Rail (NR) has the Bridges Forecasting Model (Hamer, Calvert, & Neves, 2022), which predicts the condition of the portfolio of bridges in different funding scenarios. The purpose of this paper is to outline a hindcasting exercise, i.e. test the model by comparing its results over a historical period to real observations. The aim of which was to calibrate the model's parameters and hence improve the model's accuracy in terms of its ability to forecast future condition. Section 2 provides contextual information about NR and its Structures portfolio and asset management strategies. Section 3 outlines the Bridges Forecasting Model including its purpose, how it degrades assets and performs interventions. The hindcast itself is set out in Section 4, starting with the set-up, laying out different intervention effectiveness options, a comparison to the observed condition history of the bridges, and the applications of the findings.

DOI: 10.1201/9781003483755-231

2 BACKGROUND INFORMATION

2.1 *Network rail*

NR owns and operates the railway infrastructure in England, Wales and Scotland on behalf of the nation. That is over 30,000 km of track, over 26,000 bridges, 16,000 km of earthworks and thousands of signals, level crossings and points. It is also responsible for maintenance at 2,500 train stations, fully managing 18 of the largest. The network provides a vital service for passengers and freight users. It is of great strategic importance, both in terms of economic stimulation and within the low carbon agenda, it is a green mode of transport, but secondary it also reduces road usage. Hence, the importance for the railway service to be safe, reliable, and good value for money.

NR is financed by the UK government and paying customers (passengers and freight services). The infrastructure is managed in a devolved structure with decisions on which assets to renew/maintain made at region and route level. Here are regions (bold) and routes: (**Eastern**: Anglia, East Midlands, North East, and East Coast. **North West & Central**: North West, Central and West Coast. **Scotland**. **Southern**: Kent, Sussex and Wessex. **Wales & Western**: Wales and Western). Every five years, NR must apply for funds to maintain the asset portfolio. As part of that submission, NR must demonstrate that it understands the expected changes in portfolio asset condition over a 35-year horizon for different funding scenarios, hence a model is required.

2.2 *Structures portfolio*

The structures portfolio at NR is responsible for underline bridges (rail-over-road), overline bridges (road-over-rail), footbridges, tunnels, retaining walls, culverts, and coastal, estuarine and river defences. There are over 26,000 underline and overline bridges (60,000 decks) and they dominate the repair investment, and consequently the modelling focuses on those assets. The UK has some of the oldest rail bridges in the world; the majority of the NR portfolio was built in the 19th century. There are a wide variety of materials employed, typically classified into concrete, masonry, metallic, and timber, with many bridges composed of mixed materials. However, there are significant differences within each of those broad material types, for instance, the metallic category ranges from cast iron to modern steel. Some bridges are in benign rural environments, others are close to the coast (high salinity) or within highly corrosive urban environments. Whilst underline bridges receive greater loading than overline bridges, there are great differences between train traffic on different lines. Perhaps most problematic is that it is very difficult to even guess the usage, loading and maintenance history of a bridge that has been in service for well over 100 years. All this uncertainty and variability makes it a huge challenge to model the future condition and performance of these assets.

2.3 *Condition measurements*

Bridges are subject to three types of examination. There are yearly visual examinations that are brief and are principally to check if there have been any significant changes from the previous year. Detailed examinations produce a full report that summarises the condition of all the minor elements on the bridge, however, these occur with less frequency. The scheduling of detailed examinations are risk-based and range from an interval of one year for bridges in very poor condition to every eighteen years for good bridges; on average, bridges are examined every seven years. Digital records began at around the year 2000, typically bridges have 2-3 detailed examinations at present. Finally, capability examinations assess the strength of the bridge against its loading requirements, these are far less frequent and as a result typically each bridge has only had one performed. They are undertaken to quantify the relevance in changes in condition to understand the asset's capability for the existing or future loading requirements.

During a detailed examination, the two most significant defects on each minor element receive a score based on the severity and extent. The scores are alpha-numeric with severity (alpha component) defined by the seriousness of the defect and extent (numeric component) determined by how wide-spread the defect is on the element. For the bridges model, the scoring system is simplified onto a one-dimensional scale (0 (bad) – 100 (perfect)). The quasi-linear conversion between the alpha-numeric scale and the one-dimensional scale is derived from engineering judgement, the conversion is also irreversible because it is a many-to-one mapping. See (Hamer, Calvert, & Neves, 2022) for full details.

Using the detailed examination's minor element scores, a weighted average calculation can be performed to find the BCMI (Bridge Condition Marking Index) of an individual deck or an entire bridge. This is scored on the same 0-100 scale with 100 being perfect condition. Some minor elements are more important than others, the structurally important elements are denoted as Principal Load Bearing Elements (PLBEs), e.g., main girders. Finally, the definition of poor condition is important because that is typically the trigger to intervene with repair work, for masonry and concrete minor elements that is defined as elements with a BCMI less than or equal to 50, whereas for metallic and timber elements the poor threshold is 40. At portfolio level, two measures are typically calculated and monitored: BCMI which is a measure of the average condition, and the fraction of PLBEs in poor averaged per deck which relates to risk and is a measure of the size of the tail of the distribution.

2.4 *Interventions*

There are numerous ways that bridges are worked on, with vast differences in their scale, cost, and impact. At NR, there is a Cost and Volume handbook, which defines how to categorise and report the cost, scale and type of works. There is a large variance in the size of bridges, Work Volumes are reported in terms of the area (m^2) worked on. In CapEx Renewals, bridge interventions are reported within:

- Replacement
- Strengthening
- Repair
- Preventative
- Waterproofing

There is still a large degree of variance within those categories, and it is not uncommon for multiple work types to be performed on the same deck. Replacement and Strengthening interventions are usually to combat insufficient capability. Replacement is typically installing a new bridge deck but not all of the original bridge will necessarily be replaced, the supports for example could remain. Strengthening activities insert additional support to the structures (e.g. metallic beams) or modify the existing elements. Repair work is usually fixing defects relating to the condition of the elements. Preventative work refers to improving the surface protection, for example, the paintwork for metallic elements. Waterproofing is activity related to protecting the bridge from water ingress and would not be expected to vastly improve condition. Bridges also receive Minor and Reactive repair works; these are typically cheap activities but are still highly variable and it is difficult to assess the benefit to BCMI condition.

3 FORECASTING MODEL METHODOLOGY

3.1 *Modelling purpose*

Forecasting the impact of projected spend on asset condition is a management and regulatory necessity. The regional businesses themselves decide how much maintenance to perform and

to which assets, the modelling provides 'guidance' and 'assurance'. Typically, there are three broad questions that a forecasting model needs to address:

- How much work volume/spend is required to maintain a long-term steady state condition distribution for an asset portfolio?
- What is the long-term impact on condition for different scenarios of work volumes/ funding?
- How should funding be split at regional and route levels?

To attempt to answer those questions, mathematical models have been employed. For bridges, the methodology is 'bottom-up' and models each of its 26,000 bridges individually using a probabilistic simulation with all events (asset degradation, intervention selection and effectiveness, prioritisation) simulated stochastically.

This paper is largely concentrated on modelling large asset portfolios. NR has historically used modelling for different purposes as well. Previously, the focus of activity was more on asset level modelling. This modelling was applied to find answers to the following questions for a typical asset, for example, a generic metallic bridge: How often to inspect? What condition thresholds should be applied to trigger interventions? What type of interventions should be performed in different circumstances? These results have helped to define Asset Policy, which is a set of engineering rules regarding what interventions to perform in different conditions and those are the basis of the model's rules, even at the portfolio level.

The Bridges Forecasting Model is hosted on an Asset Investment Planning platform developed by Copperleaf Technologies alongside other NR asset models (e.g. Track and Signalling). However, the model is bespoke and the intellectual property is developed and owned by NR.

3.2 *Asset degradation*

In order to understand how bridge condition degrades with time in the future, it is crucial to look at the records of the past. NR has about 20 years of examination data, however that is still only a small fraction of most bridge's lifetime. On average, each bridge has received two or three detailed examinations on record.

The model degrades condition at minor element level because this is the most detailed level at which examinations record condition. To model one minor element's future condition, historical behaviour is the best source of understanding, however rather than using just information from its past, it is more useful to amalgamate the records of all similar elements together to produce greater intelligence. The model uses condition states, defined by the one-dimensional scores described in Section 2.3. It operates in yearly timesteps and hence each minor element has a probability of moving from each condition state to all possible output condition states.

The calculation of these probability matrices used a frequency approach and required several assumptions. The frequency approach requires that the interval between examinations is fixed and at NR the interval between examinations is variable, thus a normalisation procedure was performed to calculate probabilities for a five-year interval.

Additional assumptions were required on which records to exclude. Records were excluded from analysis because an element's condition improved, i.e. suspected maintenance work performed. Alternatively, records could be excluded because of extreme deterioration, which potentially could be due to an external factor, such as vehicle incursion.

Environmental factors such as being close to the coast (high salinity) or in an area of high corrosivity can significantly affect the degradation of bridge elements, particularly metallic elements (Calvert, Hamer, Neves, & Andrews, 2023). The model adjusts the probabilities in the degradation matrix to either accelerate or decelerate the expected degradation profile.

Correlated degradation of bridge elements is little understood and requires significant research. However, the model does implement a crude form of correlated degradation if two

minor elements of the same type and material are in similar condition then there is a probability that they degrade in a correlated manner.

Finally, capability information is held at deck level and is a large driver of work both in the model and reality. The current methodology is crude and degrades capability with time, dependent on the condition of the deck's minor elements. A greater understanding of capability degradation is a clear requirement to improve the model.

3.3 *Interventions – candidate selection and prioritisation*

To ensure the model replicates reality as much as possible and since examinations are infrequent. First the model must perform its own examinations and hence store two condition values: 'Actual' and 'Revealed', the former updates every year, while the latter only updates after a modelled examination. Then intervention decisions can only be made using the 'Revealed' condition information.

The logical framework for how invention candidates are suggested in the model was detailed in (Hamer, Calvert, & Neves, 2022). In summary, it is based on Asset Policy, with the model responding to either poor capability or condition with appropriate activities on an appropriate timescale. Replacements and Strengthening work address poor capability. Repair and Preventative schemes are driven by poor condition. Large works can either be performed to a group of minor elements on a deck (CapEx Renewals) or smaller works target single minor elements (Minor or Reactive Works). There are also opportunities to do Secondary or Tertiary works to elements of a different material or adjacent supports on the back of a large Primary works.

A critical function of the Bridges Forecasting Model is its ability to constrain and prioritise the suggested candidate interventions, this is how different funding scenarios can be assessed. The model has the functionality to constrain on cost and work volume with each model year potentially having a different constraint. These constraints are typically applied to portfolios at either national, regional, or route level.

To fit within constraints, the model must prioritise its assets to decide which receives work first. The model prioritises at deck level with a flexible formulation that includes asset condition, capability, and criticality (some bridges are on busier lines and are therefore more critical than others). However, if the model was to apply this prioritisation rigorously, then only the very worst decks would receive work and huge benefits to asset condition would be witnessed. In reality, engineers consider a multitude of sources of information before judging which intervention activities to prioritise and the information the model holds is only a small part of the picture. Hence the model has the ability to apply random 'noise' to the priority score, calibrating that functionality is challenging.

3.4 *Intervention effectiveness*

In practice, bridges interventions vary significantly, even within the broad categories of Replacement, Strengthening, Repair, Preventative, Waterproofing, and Minor Works. Hence, the resultant condition post-intervention varies too. The works might only be able to fix certain types of defects or cover a small area of the deck and miss other less severe defects. Therefore, it is crucial the model has the functionality to vary the effectiveness, i.e. amount of benefit to asset condition, of interventions. Replacement works are expected to deliver a new deck and hence perfect condition. Strengthening works and Repair interventions provide some condition benefit but vary hugely and therefore are difficult to quantify. Minor works might only benefit one element and so have minimal effect on the whole deck. Preventative and Waterproofing are expected to have minimal direct condition benefit, but they could slow future degradation.

These post-intervention condition distributions can be defined by intervention type and the material targeted. However, defining intervention effectiveness is challenging, a mixture of data analysis and engineering judgement is required.

4 HINDCASTING THE BRIDGES PORTFOLIO

Hindcasting is testing a mathematical model by comparing its results over a historical period to real observations. The intention of performing a hindcast on the Bridges Forecasting Model is to improve its accuracy by calibrating the model parameters so starting from some historical point in time, the model accurately matches present day condition. The steps required to execute the hindcast are:

- Identify a set of bridges with at least two examinations between some historical point and present day.
- Estimate the amount of CapEx renewals and Minor and Reactive work that has been performed to those bridges.
- Execute the Bridges Forecasting Model with that sample of bridges and compare modelled output condition to observed condition measures.
- Adjust the intervention effectiveness parameters (both in terms of asset selection and condition benefit) with the aim being to match observed condition. (At present the degradation behaviour in the model is fixed)

4.1 *Setting up the sample portfolio*

Due to NR's 5-year Control Periods (CP) and reporting mechanisms, the earliest reliable estimates of CapEx Renewals work performed are from 2010 onwards, so that is a logical point to begin the hindcast. In CP5 (2015-2019) reported work volumes in our Annual Return includes work type detail, but in CP4 (2010-2014) the work volumes are total only, hence the work type mix must be inferred from engineering judgement.

For an asset to be useful in a hindcast it must have had at least two examinations. Given that examinations are risk-based, and some bridges are on long intervals, the number of bridges with at least two examinations from 2010 onwards is about 60% of the portfolio. However, that 60% is a biased sample because on average these bridges are in a worse condition than the full portfolio. Moreover, the material distribution is skewed towards metallic because they are typically on shorter examination intervals. Hence the sample of bridges was modified by removing bridges at random, such that the average condition (BCMI) and the distribution and condition of the different material types aligned to the full portfolio. As a result, roughly 50% of the portfolio was utilised within the hindcast, which was deemed a sufficient sample.

4.2 *Intervention effectiveness options*

The effectiveness or the quantity of condition benefit from interventions is probably the largest source of uncertainty within the Bridges Forecasting Model. The effectiveness of interventions is difficult to accurately quantify because as discussed in Section 2.4 interventions are highly variable. Also records of completed works are sparse; applicable records were only available for 5 years (2015-2019) from roughly 50% of regions. The whole sample was less than 1000 work descriptions. Additionally, records are labelled at bridge level which, for multi-deck bridges, it then becomes difficult to judge which decks received work. The final problem is that, for the intervention record to be useful, ideally there would be an examination immediately before the works and another immediately afterwards. In practice however, examinations tend to be many years before the works and also many years after the works or even not performed yet, hence any impact of degradation needs to be assumed and accounted for.

To understand the effectiveness of interventions, two aspects need to be considered. The first is how well targeted the intervention was, hence analysing the asset's BCMI score before the works, in order to help calibrate the efficiency of the prioritisation in the model. The second is the improvement in BCMI score produced by the works. There are many ways to analyse the work history data, Table 1 sets out three options for estimating intervention

effectiveness depending on how the work records are filtered and analysed. Note that that the impact of degradation has been assumed within these results.

- The **'Lower'** option includes all activities that improve a single minor element score by 5 or more, this allows the whole deck to get worse. This filter is likely to be too lenient because Minor and Reactive Works to decks adjacent to workbank decks are potentially included.
- The **'Middle'** option focuses on the most improved deck on each bridge listed, with the idea being to inhibit the multi-deck reporting problem. Hence, this set neglects multi-deck schemes and with no minimum improvement criteria, data errors where no actual work takes place are also included.
- The final **'Upper'** option includes all works where the whole deck improves by more than 2.5 BCMI points. This option does neglect any works with minimal benefit to condition.

Based on reported Work Items and engineering judgement, Minor and Reactive works have been modelled by performing a set number of Single Element Works in each of the three effectiveness options. In terms of the number of Single Element Works for the full portfolio, the Upper, Middle and Lower scenarios are given 3,300, 1,700 and 1,100 respectively per year. Summarising in simple terms, so that only one Single Element Works can apply per deck then those activities equate to 5.6%, 2.9% and 1.9% of the decks for each scenario.

Table 1. Intervention effectiveness quantification options.

Scenario Options (Sample Size)	Criteria	Average BCMI before Works	Average BCMI Improvement	Comments
Lower (966)	All decks, any element improvement by >= 5	46.9	14.3	Likely includes Minor and Reactive Works
Middle (517)	Most improved deck on each bridge	43.9	18.0	Neglects multi-deck schemes
Upper (690)	All decks, deck Improvement by > 2.5	42.9	23.5	Neglects any work with minimal BCMI improvement

4.3 *Comparison to the observed history of bridge condition*

The hindcast model runs begin with each bridge in the condition from their first examination from 2010 onwards, that is declared Year 0. The model run includes all bridge decks in the sample and proceeds for 13 years (the maximum gap between first and last examinations for a single deck). Asset degradation is applied each year as well as appropriate levels of CapEx Renewals and Minor and Reactive work activities. The model outputs that are relevant for comparison to the real history are the condition outputs at the year of each deck's last examination, after that the condition is irrelevant because the real history is unknown. Hence, each deck is considered 'active' within the hindcast up until the year of its last examination and this ranges from 1 to 13 years. 6 years is the most populous interval and the average time spent in the model is 7.1 years.

Figure 1 displays the condition outputs (average BCMI and PLBEs in Poor) of the hindcast modelling for the underline bridge decks with a 6-year examination interval. Selecting different interval slices (e.g. 12-year) show similar results as well as grouping all decks together. Alternatively, investigating the Mean Squared Error (MSE) of the model runs against the real history also produces similar results. Both in terms of average values and MSE the 'Upper' intervention effectiveness option fits well for BCMI but the 'Middle' option works better for PLBEs in poor.

In order to produce a better fit with the real history, the model's intervention effectiveness settings were modified. The prioritisation efficiency was lowered, and the intervention effectiveness distributions were modified such that the BCMI improvement was similar to the

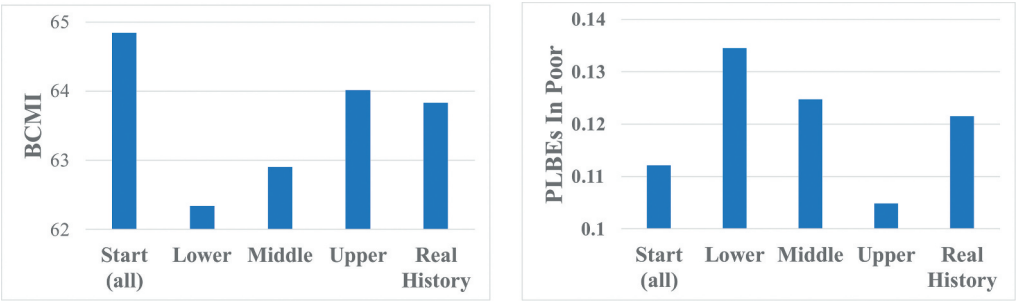


Figure 1. Average condition (BCMI and fraction of PLBEs in Poor) of Underline bridge decks on a 6-year examination interval at the start (first examination), then after 6 years in the model with the three intervention effectiveness options (Upper, Middle, and Lower) as well as the real history (last examination).

'Upper' option, but the distributions were stretched so that more elements remain in poor condition after works as per the 'Middle' option. Compared to the model parameters used in previous planning rounds this change weakened the effectiveness of modelled interventions. Effectively making the Steady State (hold portfolio condition static) scenario more expensive as a greater amount of work is required for the same condition benefit.

4.4 *Application of hindcast findings*

NR's internal and external stakeholders require confidence in the Bridges Forecasting Model's methodology and assumptions but ultimately it needs to be accurate, as the model influences decisions made around the levels of investment provisioned for bridges. This study demonstrates how the forecasted outputs from the model are likely to be more accurate as they have been calibrated on real world portfolio behaviour. Specifically, for planning the next five years (CP7), hindcasting has provided the justification for weakening the intervention effectiveness and hence increasing the required work volumes/funding for the same desired condition outputs in comparison to previous planning rounds. The model and its outputs have become critical evidence in the business planning process supporting the basis for greater funding if the bridges portfolio is going to be held at current condition.

5 CONCLUSIONS

This paper has presented a hindcasting methodology that has been utilised to calibrate NR's Bridge Forecasting Model. The method takes a sample of bridges and models, using degradation and interventions, forward in time from a set of examinations in the recent past with the aim of meeting present day condition. The model has many uncertainties, but the motivation behind hindcasting is that the inaccuracies in asset degradation and intervention selection and effectiveness would somewhat cancel out.

The limitations of the available data and model methodology are explained in greater detail in Hamer, Calvert and Neves (2022); however, it is worth restating the key sources of uncertainty. Bridge examinations are sparse and prone to the subjectivity of examiners. Currently the defects are not tracked and consequently assumptions are required to relate condition across successive examinations. Additionally, there is no engineering context with the condition data, i.e. a low BCMI score does not necessarily mean a repair is required. For hindcasting, accurate and extensive intervention records are crucial, without which it is difficult to know which decks have received work from bridge-level records. Minor and Reactive work records are very crude, especially quantifying condition improvements, so there is a large uncertainty in the quantity of those types of work. The model also has documented weaknesses, implementing asset degradation via a maximum likelihood approach with defect

dependencies would be a vast improvement (Calvert, Neves, Andrews, & Hamer, 2021). Further work would also be beneficial in the areas of environmental factors, correlated degradation of neighbouring elements and capability degradation.

As the existing funding environment is constrained, regions and routes must compete harder for government investment against other NR assets, within the transport sector and with other public spending obligations. It becomes imperative that spending plans are fully justified. Hence it is now even more critical that the Bridges Forecasting Model has been through a comprehensive validation process so that all stakeholders can have high confidence in the model outputs and the likely performance of the Bridges portfolio. This was the first attempt at hindcast analysis for bridges modelling at NR. It will no doubt be an iterative process which will need to be built upon year-on-year as more information is produced.

ACKNOWLEDGEMENTS

Matthew Hamer is a Principal Mathematical Modeller (matthew.hamer@networkrail.co.uk) and Gareth Calvert is a Whole Lifecycle Costing Manager (gareth.calvert@networkrail.co.uk), at Network Rail. Comment and collaboration opportunities from infrastructure asset managers involved with bridge management and modelling are welcome.

REFERENCES

Calvert, G., Hamer, M., Neves, L., & Andrews, J. (2023). Analysing the impact of local factors on the life-cycle of metallic bridge girders. *Life-Cycle of Structures and Infrastructure Systems* (pp. 453–460). Milan, Italy: CRC Press.

Calvert, G., Neves, L., Andrews, J., & Hamer, M. (2021). Incorporating defect specific condition indicators in a bridge life cycle analysis. *Engineering Structures*, *246*, 113003.

Frangopol, D. M., Dong, Y., & Sabatino, S. (2017). Bridge life-cycle performance and cost: analysis, prediction, optimisation and decision-making. *Structure and Infrastructure Engineering*, *13*(10), 1239–1257.

Hamer, M. J., Calvert, G. S., & Neves, L. C. (2022). An Overview Of Strategic Bridge Life Cycle Modelling On The British Railway. *Bridge Safety, Maintenance, Management, Life-Cycle, Resilience and Sustainability*. Barcelona, Spain: CRC Press.

Mirzaei, Z., Adey, B. T., Klatter, L., & Thompson, P. D. (2014). *The IABMAS Bridge Management Committee Overview of Existing Bridge Management Systems*. IABMAS.

Office of Rail and Road. (2023). PR23 final determination: Supporting document - sustainable and efficient costs. ORR.

Bridge Maintenance, Safety, Management, Digitalization and Sustainability – Jensen, Frangopol & Schmidt (eds)
© 2024 The Author(s), ISBN 978-1-032-77040-6
Open Access: www.taylorfrancis.com, CC BY-NC-ND 4.0 license

Vulnerability of network infrastructure due to potential extreme weather in PEI, Canada

D.J. Evans*
Prince Edward Island Department of Transportation and Infrastructure Charlottetown, Prince Edward Island, Canada

R.M. Ellis*
Stantec Consulting Ltd. Edmonton, Alberta, Canada

ABSTRACT: The Prince Edward Island Department of Transportation and Infrastructure (DTI) is responsible for the densest network of roadway and bridges per capita of any of the Canadian Provinces. DTI own and manage a variety of structures, with about 99.5% of which cross some sort of waterway (a creek, stream or river). Of the water crossing structures, approximately 11% of these are coastal in nature.

Over the last 16 years, DTI has adopted bridge management processes including implementing an advanced bridge management system (BMS). This has enabled the department to make significant improvements in the management of inventory and inspection data, the inspection process, tracking and reporting condition through a standard condition index, performing asset valuation, and in handling of inspection photos, videos, plans and other documents.

Recently, as a result of increased extreme weather events, there have been growing concerns related to the risks to our infrastructure and infrastructure resiliency. Rising sea levels are affecting the PEI coastline with estimated erosion of 30 cm per year and potentially affecting tidal flow in coastal rivers. Storm intensities are increasing; PEI was battered by Post Tropical Storm Fiona in September of 2022, which, among other destruction, downed several hundred hectares of woods in our province which still lays there today. In Spring 2023, wildfires occurred in many provinces across Canada, including several thousands of hectares in neighboring Nova Scotia.

DTI, in conjunction with Stantec, are implementing appraisal indices to include the effects of extreme events on flooding, scour, wildfires and other vulnerabilities and providing useful risk analysis and a measure of resiliency. This paper will highlight how the province is adapting our BMS to account for potential extreme weather-related events, such as flooding, scour, and wildfires. The paper will be of interest to other jurisdictions who manage bridges and culverts.

1 INTRODUCTION

1.1 *Prince Edward Island, Canada*

The Province of Prince Edward Island (PEI) is situated on the east coast of Canada and is the smallest of all the Canadian Provinces. The province has 5660 km of natural waterways throughout its land mass and is crossed at various locations by 5600 km of roadway network with over 1400 structures. It sits anywhere between a low elevation 0.00 m to a peak elevation of 142 m. Its geology is founded on weak to moderate sandstone bedrock overlaid with variations of glacial till, marine sediment deposit, silty sands and silty clays.

The primary industries, agriculture, and aquaculture, rely heavily on the surrounding environment and also rely heavily on the transportation network to get their products to market.

*Corresponding author: djevans@gov.pe.ca, Reed.Ellis@stantec.com

DOI: 10.1201/9781003483755-232

The department has spent the last 16 years developing and maintaining a Bridge Management System (BMS) for the provincial network of structures. Of the 1400 structures, only 289 are inspected on a biennial basis (i.e. once every two years). As of the end of 2023, the department completed its ninth full round of biennial inspections. The remaining structures (buried culverts) are being inspected and input into the system; however, reports on the first full cycle of these structure inspections will not be complete until 2024.

Recently, due to increased extreme weather events, there have been growing concerns related to the risks to our infrastructure and infrastructure resiliency. Rising sea levels are affecting the PEI coastline with estimated erosion of 30 cm per year and potentially affecting tidal flow in coastal rivers.

This paper will highlight how the province is adapting our BMS to account for potential extreme weather-related events, such as flood, scour, and wildfires. The paper will be of interest to other jurisdictions who manage bridges and culverts.

2 BRIDGE INSPECTION

2.1 *Inventory*

Like most jurisdictions across Canada, PEI's bridge inventory is a product of the construction boom from the late 50's to the early 90's. A good portion of the department's inventory is at or very near its intended design life and many structures are nearing the end of service life.

Like many other jurisdictions, the department continues to struggle with the condition of the inventory and the available capital dollars which are available to address these issues.

More information regarding the evolution of bridge inspections and bridge management in Prince Edward Island can be found in Evans et.al, 2014 and Evans, et.al, 2012.

3 BRIDGE MANAGEMENT SYSTEM

3.1 *Evolution of BMS on PEI*

DTI have historically relied on hard paper copies of our safety inspections with a rudimentary spreadsheet for asset management data. This housed such information as structure ID, structure type, material, span length, age (if known), location, route number, and other basic information.

After a literature review, the department decided on the best fit BMS for our inspection program, which was Ontario Bridge Management System (OBMS) (Thompson et.al, 2003). The BMS was compatible with the adopted inspection methodology of the Ontario Structure Inspection Manual (OSIM) (MTO 2000). This methodology is adopted by the majority of provinces in Canada and is based on element level, condition state inspection which is the most common inspection methodology used in bridge management systems today (Mirzaei et al. 2014). There are four (4) condition states Excellent, Good, Fair, and Poor and the inspection manual provides detailed descriptions of the defects for common bridge materials and how to rate the severity and extent of defects.

The department's consultant had been working on significant improvements to the OBMS and in 2010 the department licensed and implemented the new Stantec BMS platform as the new PEI BMS (Evans et.al, 2010).

3.2 *Stantec BMS*

The PEI BMS is compatible with inspection data in the OSIM format and calculates the Bridge Condition Index (BCI) (MTO 2009). There are many built-in reports that support the department in better managing bridge and culvert assets. The BMS meets or exceeds all the requirements of documents such as the AASHTO Guide to Bridge Management (AASHTO, 1994) and Bridge Management in Europe (BRIME 2002).

STANTEC BMS offers the following capabilities that were of interest to the department:

1. Improved photo, video, document management including search capabilities,
2. Automated project scoping and treatment selection using engineering models and benefit-cost analysis,
3. Element, project and network level risk analysis,
4. Network-level priority programming and budgeting,
5. Network and individual bridge target performance analysis,
6. Risk-based decision making,
7. Risk-based setting of inspection frequencies.
8. Bridge asset valuation
9. Tracking Critical Findings
10. Automated reporting of key performance indicators (KPI)

For further information regarding the capabilities of STANTEC BMS and other features, please refer to Evans et.al, 2014, Evans et.al, 2012, Ellis et.al, 2012 and Dalziel et.al, 2012.

4 VULNERABILITIES AND CONSEQUENCES

Being a province with highly erodible soil and being very close (or at) sea level poses some challenges with respect to flooding and scour.

Since 2002, the province has been subjected to increased storm frequency and intensities, which are described in Table 1.

Table 1. Significant weather events by year.

Year	Event	DTI Repair costs ($CDN)
2000	Storm surge event	$ 500 k
2003	Post Tropical Storm Juan	$ 2.8 M
2008	Post Tropical Storm Hanna	$ 1.8 M
2010	Rainfall/Wind event	$ 850 k
2014	Rainfall Event	$ 7.9 M
2019	Post Tropical Storm Dorian	$ 1.5 M
2022	Post Tropical Storm Fiona	$ 4.1 M

These events caused a variety of damage to our infrastructure, including that to roadways, culverts and bridge structures alike; however, there has historically been no method to account for the increased likelihood of a weather event impacting our infrastructure nor the consequences associated with these events.

4.1 *Flooding and scour*

As noted, the province is highly susceptible to flood and scour, be it by overland flooding due to significant rainfall events or by coastal flooding due to storm surges and wave run-up. These events have impacted how our transportation network functions and have been the cause of serious delays and loss of property.

Several locations have been damaged due to the storm events listed in Table 1. As expected, repairs and enhancements to these structures were a reactionary response to an environmental issue; however, this is not always the case.

In 2010, we replaced a structure in Darnley PEI. The former structure was a sixteen span, timber piled bridge structure with a vertical clearance of 4.06 m from HHWMT to the underside of the structure, with the top of the structure at 4.66 m above HHWMT. The new structure has a vertical clearance of 4.66 m above HHWMT with the top of the bridge deck being 6.865 m above HHWMT. The minimum bearing seat elevation on the north end of the



Photo 1. Scour due to overland flooding.



Photo 2. Erosion due to coastal effects.

structure is given at 3.044 m PEI Geodetic, NAD 83 (Hatch Mott MacDonald), which converts to Elev. 2.673 m CGVD2013.

In 2022, Hurricane Fiona introduced a tide elevation of 3.12 m CGVD2013 at the Darnley Tide Gauge, with a peak wind speed of 127.4 km/hr (Jardine, 2023). While this severely impacted the causeway approaches, it did not affect the structure in any measurable means. Had DTI not replaced the structure in 2010 and proactively raised the roadway profile, it would have undoubtedly resulted in a catastrophic loss of the structure. See photos 3 and 4.



Photo 3. Darnley Bridge During Fiona.



Photo 4. Darnley Bridge Post Fiona.

It's interesting to note that the average erosion rate for PEI prior to Fiona was in the 30 cm/ year range. The erosion loss due to Fiona was between 10.0 m in several locations and up to 25 metres in one location, roughly 30 to 80 years-worth of erosion in a single event. See photos 5 and 6.

4.2 *Wildfires*

While significant wildfires in the province of PEI are rare, they do occur. Between 1958 and 2012 (inclusive) there have been 107 wildfires recorded, with the most significant wildfire in 1960, destroying 6880 acres (2800 Ha) of wooded areas and countless properties. There are no records of any damage to any transportation structures.

However, 2023 has set a record in Canada, with over 18 million hectares lost to wildfires this year alone. In May of 2023, there was a wildfire in Crowbush PEI, which was fueled by downed trees due to Fiona and unusually dry conditions. It ravaged trough 7 acres (3 Ha) of woodland and was dangerously close to a propane fuel storage tank before it was brought under control by local fire departments.



Photo 5. Satellite Imagery of PEI before Fiona.



Photo 6. Satellite Imagery of PEI post Fiona.

Our neighboring province, Nova Scotia, also experienced devastating wildfires in 2023, loosing over 25,000 hectares and 200 homes; however, no reports of any transportation network losses.

While the risk of wildfires affecting our transportation network appears low, it doesn't suggest that DTI needs to be complacent about the issue.

5 IDENTIFYING APPRAISAL AND RISK INDICES

As indicated above, the province (for the most part) has taken a reactionary approach to the replacement and enhancement of our transportation structure network post events. Continuing research using BMS tools can enhance DTI's decision-making process with respect to identifying our vulnerabilities and consequences and the applying these to determine a risk profile for climate change and wildfires. For further information regarding these parameters and the science behind them, please refer to Ellis, 2023.

5.1 *Identifying vulnerabilities related to flood and scour*

The department has populated several of our coastal network structures in terms of structure, foundation type, AADT, detour lengths, streambed elevation, mean and high-water elevation

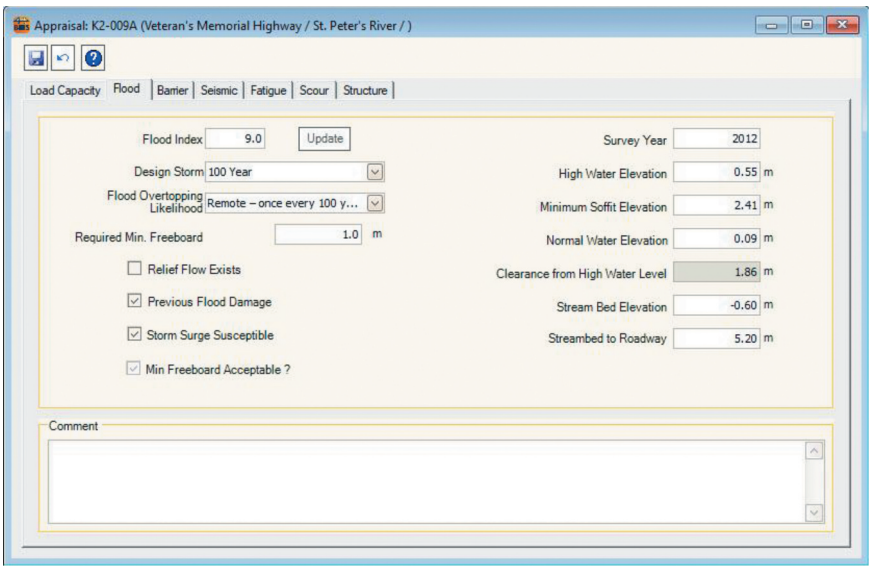


Figure 1. Survey information.

and underside of soffit elevation. There are also fields to include historic flooding or overtopping, the likelihood of overtopping, whether-or-not the structure has an acceptable minimum freeboard available and any relief flow that may be available and traffic delay consequences. See Figures 1, 2 and 3.

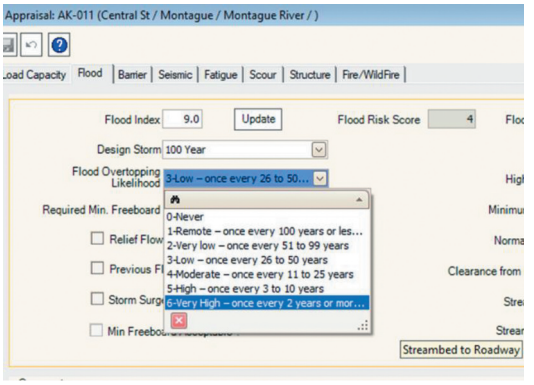


Figure 2. Flood overtopping likelihood.

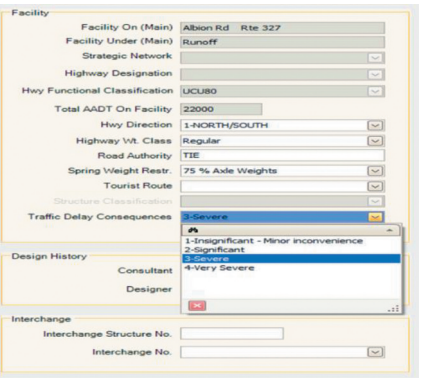


Figure 3. Traffic consequences.

As can be seen, the user will provide input for the pertinent fields and are given a weight with respect to their overall vulnerability and consequence. These are used to produce a risk matrix based on weather related events and can give the province some valuable information regarding their capital programming in any given cycle. See Figure 4 below.

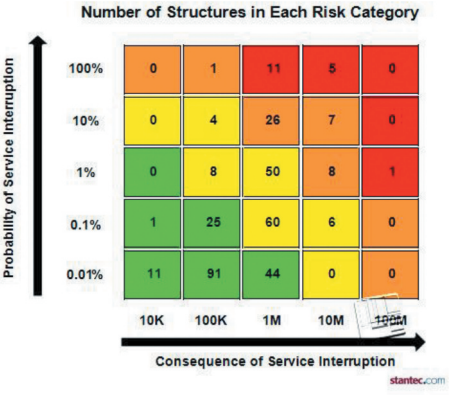


Figure 4. Example risk profile.

5.2 *Wildfires*

In a similar manner, the Department is looking to include the vulnerabilities and consequences associated with wildfire risks. The State of Florida in the U.S. has done some works in relation to structure type and proximity to fuel as it relates to wildfires (Sobanjo & Thompson, 2013).

The province of British Columbia makes provisions for the design of wildfire resistant structures, which includes vegetation management, as well as evaluation of existing structures subsequent to wildfires (BC Ministry of Forestry, 2023).

The province of Alberta, while no official documentation exists, relies on a vegetation management plan, which limits the amount of potential fuel that encroaches their Right-of-Way (ROW). While this is a noble goal to be achieved, it represents a significant cost to the

province of PEI, as land is a valued asset to private owners and vegetation management is an afterthought.

To further compound the issue, there are several structures that are on our highway network which are vulnerable not only due to their proximity of potential fuel, but as well due to their composition (timber superstructures). Of the 1488 structures, over one-third are timber. See Photos 7 and 8.



Photo 7. Upstream vegetation.



Photo 8. Up chainage vegetation.

Based on this, the department has chosen to begin applying pertinent vulnerability values based on main structure material type and proximity to vegetation. This will provide another risk profile for the network which will provide further information to the decision makers with respect to the risk for potential wildfires. More information on these risk profiles can be found in Ellis, 2023.

6 CONCLUSIONS AND RECOMMENDATIONS

The province uses the BMS forecasting models to report to senior management on the possible outcomes of the condition based on different possible budget scenarios (Evans et.al 2018). Considering various environmental factors, the focus is shifting towards a risk-based approach and managing those risks in a calculated manner.

These updated vulnerability and consequence factors will enhance our already robust bridge management system by providing additional information which will guide our policies and decision making.

The department plans to field test these new indices against actual weather-related events in the future, as it's not a matter of if an event will occur, it's when and with what intensity and duration. The department, in conjunction with the software developer, plans to continue to test these indices further to determine the threshold bounds for structure type, composition, and boundary conditions as they relate to weather events.

REFERENCES

Evans, D.J. & Ellis, R.M., 2018. Utilizing BMS to Develop Programs and Report for PEI Transportation. 9th International Conference on Bridge Maintenance, Safety and Management, IABMAS 2018, Melbourne, Australia

Evans, D.J. & Ellis, R.M., 2016. Tracking bridge conditions versus budgets using bridge management system tools in Prince Edward Island Department of Transportation and Infrastructure Renewal. 8th International Conference on Bridge Maintenance, Safety and Management, IABMAS 2016, Foz do Iguaçu, Brazil

Evans, D.J. & Ellis, R.M., 2014. Use of Advanced Bridge Management System Analytical Tools in Prince Edward Island Department of Transportation and Infrastructure Renewal. 7th International Conference on Bridge Maintenance, Safety and Management, IABMAS 2014, Shanghai, China.

Dalziel et al (2012) Application of bridge management system to determine preservation and improvement budgets, meet condition targets, and manage risk for the City of Hamilton. 6th International Conference on Bridge Maintenance, Safety and Management, IABMAS 2012, Stresa, Lake Maggiore, Italy.

Ellis, R.M., et al, 2012. Incorporating Risk and Criticality in Bridge Management Decision Making and Project Prioritization. 6th International Conference on Bridge Maintenance, Safety and Management, IABMAS 2012, Stresa, Lake Maggiore, Italy.

Evans, D.J.& Ellis, R.M., 2012. Development, implementation and application of Bridge Management Systems in Prince Edward Island. 6th Inter-national Conference on Bridge Maintenance, Safety and Management, IABMAS 2012, Stresa, Lake Maggiore, Italy.

Evans, D.J. & Ellis, R.M., 2010. Development, implementation and application of Bridge Management in Prince Edward Island, Canada. International Short and Medium Span Bridge Conference, Niagara Falls, Canada.

Ministry of Transportation of Ontario (MTO). 2003. Ontario Structure Inspection Manual. Queen's Printer for Ontario, Toronto, Canada.

Ministry of Transportation of Ontario (MTO). 2009. Bridge Condition Index (BCI) - An Overall Measure of Bridge Condition. Ministry of Transportation Engineering Standards Branch, St. Catharines, Ontario.

Mirzaei, Z., B.T. Adey, L. Klatter, & P.D. Thompson 2014. Overview of Existing Bridge Management Systems. International Association of Bridge Maintenance and Safety, Bridge Management Committee.

Thompson, P.D. & Ellis, R.M. 2010. Updating Bridge Deterioration Models with Irregular Inspection Intervals. 5th International Conference on Bridge Maintenance, Safety and Management, IABMAS 2010, Philadelphia, USA. https://www.princeedwardisland.ca/en/publication/annual-statistical-review-data-tables-2022

https://www.princeedwardisland.ca/en/information/environment-energy-and-climate-action/pei-forestry-commission

https://www.princeedwardisland.ca/en/service/hurricane-fiona-forestry-recovery-program

Jardine, D.E. 2023. Post Tropical Storm Fiona Highwater Mark and Shoreline Erosion, Field Notes with Photos. Prepared for the Government of Prince Edward Island, by D.E. Jardine Consulting. https://www.cbc.ca/news/canada/prince-edward-island/pei-rodd-crowbush-fire-woods-1.6825683

BC Ministry of Forests, 2023. Bridge Standards Manual.

Ellis, R.M. & Kamranian, Z., 2023. Considerations for Vulnerability and Risk of Bridges Considering Extreme Weather Events, 12th International Conference on Bridge Maintenance, Safety and Management, IABMAS 2024. Copenhagen, Denmark.

Sobanjo, J.O & Thompson, P.D. 2013. Development of Risk Models for Florida's Bridge Management System, Prepared for the State Maintenance Office, Florida Department of Transportation

Bridge Maintenance, Safety, Management, Digitalization and Sustainability – Jensen, Frangopol & Schmidt (eds)
© 2024 The Author(s), ISBN 978-1-032-77040-6
Open Access: www.taylorfrancis.com, CC BY-NC-ND 4.0 license

Considerations for vulnerability and risk assessment of bridges and culverts including extreme weather events

Reed M. Ellis & Zahra Kamranian
Stantec Consulting Ltd., Edmonton, Canada

ABSTRACT: As a result of increased extreme weather events in many parts of the world, there have been growing concerns related to the risks to transportation infrastructure and infrastructure resiliency. Recently, a national survey was completed which included, amongst other topics, how provincial and municipal bridge departments across Canada are responding to these challenges. In conjunction with several transportation agencies, Stantec has been developing appraisal indices to include the effects of extreme events on flooding, scour, wildfires and other vulnerabilities such as fatigue, seismic, and load carrying capacity. The appraisal ratings are being implemented in a Bridge Management System to provide input into risk analysis and resiliency assessment and assist agencies in decision making regarding these challenges. This paper will highlight how agencies can consider in a practical way the effects of potential extreme weather related events, such as flooding, scour, and wildfires. The results of this research as well as the findings of the recent national survey will be shared. Parameters that can be used as input into each appraisal are discussed e.g. for flooding, factors such as flood frequency, risk of overtopping, freeboard, traffic delay consequences can be considered. The paper will be of interest to other jurisdictions who manage bridges and culverts who may be developing responses to these challenges.

1 INTRODUCTION

Canada's bridges are aging and deteriorating due to exposure to aggressive environments, heavier traffic loads, inadequate maintenance and rehabilitation, and limited funding. Nearly 40% of Canada's bridges are in fair, poor, or very poor condition, thus requiring maintenance and rehabilitation, according to the 2019 Canadian Infrastructure Report Card (CIRC-Blue Plan 2019). Values of Canada's infrastructure deficit or gap have been estimated to range from $50 billion to $570 billion (INFC 2018). The situation is similar in many other countries.

The changing climate and increase in average temperature across Canada, as well as the increase in precipitation and wind in some Canadian regions (Cannon et al. 2020) will induce higher loads on bridges and can lead to accelerated aging and deterioration. In addition, extreme weather events, such as flooding, scour, thawing permafrost, etc., can lead to the deterioration, damage and failure of bridges. It has been estimated that climate change could cost Canada $21-$43 billion per year by 2050 (NRTEE 2011). Hence, highway bridges in Canada are at a higher risk if actions are not taken related to climate change adaptation. The consequences of the failure of highway bridges can be quite catastrophic, including fatalities, injuries, and traffic disruptions that impact personal mobility and the transport of goods, which in turn can have serious impacts on society, the economy, and the environment.

In a recent survey and study commissioned by the National Research Council of Canada (NRC), Stantec determined that most of the advanced bridge owner agencies are aware of the challenges surrounding climate change and extreme weather (NRC, 2023). All Provincial government agencies responded that the effects of climate change and extreme weather events are being considered in the design of new structures. Most are using guidance from hydraulic

DOI: 10.1201/9781003483755-233

studies, Environment Canada and other climatic data, and new Intensity-Duration-Frequency (IDF) curves to determine design flows and flood events, increases in scour potential, temperature range etc. In response to these challenges most have internal policies related to design requirements for increased freeboard, deck drainage, more stringent permafrost considerations, erosion and sediment control, river protection works, etc.

The situation is different for the assessment of existing structures when considering the impacts of climate change and extreme weather. These structures are generally designed to older standards. Most indicated that they consider increased design storm events or temperature ranges obtained using updated climatic data. This generally translates into remediation such as increased freeboard, river protection or training works, improved deck drainage etc.. Sometimes, hydraulic capacity can also be increased including constructing relief flow culverts beside existing structures. Beyond the design parameters, the main challenge for agencies is to determine which structures should be prioritised due to which vulnerability.

Agencies identified that guidance would be useful in concepts such as:

(a) what are the vulnerabilities to consider? (e.g., types of extreme weather events, flooding, scour, seismic, wildfire)
(b) what analytical tools are needed to help determine and plan for resiliency?

Vulnerabilities and risks need to be identified and the need for remediation should be considered and prioritised over the transportation network, corridor, etc.. It was concluded that with respect to the impacts of climate change and extreme weather, agencies would benefit from guidance in applying bridge management practices such as lifecycle cost analysis, benefit-cost analysis, risk analysis, determining and reporting of performance measures.

In the following, results of a research and development study into rating systems for structure flooding, scour, fatigue/fracture, load carrying capacity, and wildfire are described. We will specifically consider Flood Appraisal and Wildfire Appraisal as examples where appraisal tools have been developed and implemented in a bridge management system to help bridge owners deal with these challenges.

Application of these appraisal and risk analysis tools is covered in a companion paper by Evans, Darrell J. and Ellis, Reed M. (2023).

2 BRIDGE APPRAISALS, VULNERABILITIES, AND RISK

2.1 *Bridge Condition vs. Appraisal*

Similar to many other countries, in Canada the most common type of bridge inspection is element-level, condition state, severity and extent inspection wherein the structure is inspected by element (e.g. girder, bearing, deck wearing surface etc.) and specific defects are recorded for each element (Ontario Structures Inspection Manual (OSIM), Ministry of Transportation of Ontario, 2018). The resulting element condition state is descriptive of the element condition and the defects can be conveniently tracked over subsequent inspections. Advantages of this type of inspection method include ease of training, consistent and repeatable results, is it lends itself nicely to probabilistic deterioration model development. In addition, a condition index can be readily developed from this type of inspection method. The Bridge Condition Index (BCI) represents the condition of a structure on a 0 to 100 scale where 100 is best (like new) (MTO 2009). The condition index reflects the condition state of each element of the structure, weighted according to the value or replacement cost of the element (i.e. some measure of importance). Not only do these indices reflect condition of the structure, but they also provide a proxy for the current value of the structure wherein 100 represents full economic value of the structure but a deteriorated (lower) value represents a loss of economic value (valuation). Provided that the weighting of the elements that comprise the structure is determined with some consideration of replacement cost of each element, then the index can be taken to represent a measure of valuation (Ellis and Thompson, 2007.) For reference, the AASTHO element

level inspection used in USA (AASHTO 2019) is similar to the OSIM methodology and the BCI is similar to Bridge Health Index (Shepard & Johnson, 2001).

While condition is the most important consideration in determining need for maintenance and repair, strengthening, reporting performance measures, forecasting deterioration etc, it does not by itself reflect to what extent the structure meets level of service and other standards when compared to a structure built to current standards. Bridge Appraisals can be developed to rate many different types of standards such as Load Carrying Capacity, Waterway Adequacy (flooding), Deck Geometry, Roadway Alignment, and others (FHWA 1995). In general, ratings range from 9 to 1 having values such as 'Superior to', 'Equal to', or 'Below present desirable criteria'. Having such a rating system is useful in determining structures that do not meet standards and can therefore compete for funds for improvement. Functional adequacy or inadequacy is a determining factor in the reasons for bridge replacement at the end of service life. These factors are used in bridge management systems to help make decisions on recommended work and priorities.

2.2 *Appraisal, Vulnerability, and Risk*

In this paper, the following generally accepted definitions are being followed as applied to managing transportation structures:

a) Appraisal: an assessment and rating of the degree to which the structure meets current standards or level of service.
b) Vulnerability: the degree to which a system is susceptible to, or unable to cope with, a particular hazard
c) Risk: the potential for damage or loss as defined by probability times consequences.

To assist bridge managers in evaluating common levels of service, appraisals were previously developed and are available in the bridge management system (BMS) and are used to calculate an overall Sufficiency Index (Ellis, Reed M., Evans, Darrell J, 2019). The following appraisals contribute to the Sufficiency Index (SI):

- Load Carrying Capacity
- **Flooding** (most susceptible to climate change and extreme weather)
- **Scour** (most susceptible to climate change and extreme weather)
- Seismic
- Fatigue/Fracture
- Barriers
- Deck/Approach Geometrics

The concept of SI is similar to the Sufficiency Rating (SR) (FHWA 1995) except that for condition it uses the bridge condition index (BCI) instead of the more subjective component (9-1) ratings, it includes a few additional appraisals, and it includes the criticality and urgency of maintenance and repair actions (Ellis, Reed M., Hong, Kang, 2012)

The NRC research and survey indicated in particular agencies would benefit by being able to assess and make decisions regarding the vulnerabilities affected by climate change and extreme weather. In the list above, the two underlined, **Flood Appraisal** and **Scour Appraisal** are the most susceptible and potentially affected by climate change and extreme weather. It was desired that the appraisals be expanded to readily accept input based on updated (changing) climatic data and standards/levels of service. It was also desired to calculate vulnerabilities so that decision makers could more proactively respond in the form of remediation, designate alternate routes, or make other preparations. In addition, to assess probabilities and consequences and further aid in decision-making, a risk analysis and risk profile matrix was desired.

An additional goal was added following increased wildfire activity in several Canadian provinces in recent years. According to the Government of Canada, 2023 was the most destructive wildfire season in Canada on record (Government of Canada, Natural Resources 2023). See Figure 1. This was due to a combination of record high temperatures and

widespread drought across the country. Natural Resources reported that by September 5, more than 6,132 fires had torched a staggering 16.5 million hectares of land. This is more than double the 1989 record and significantly larger than the average of 2.5 million hectares of land that are consumed in Canada every year. For reference the combined area of Denmark and Germany is approximately 16.2 million hectares.

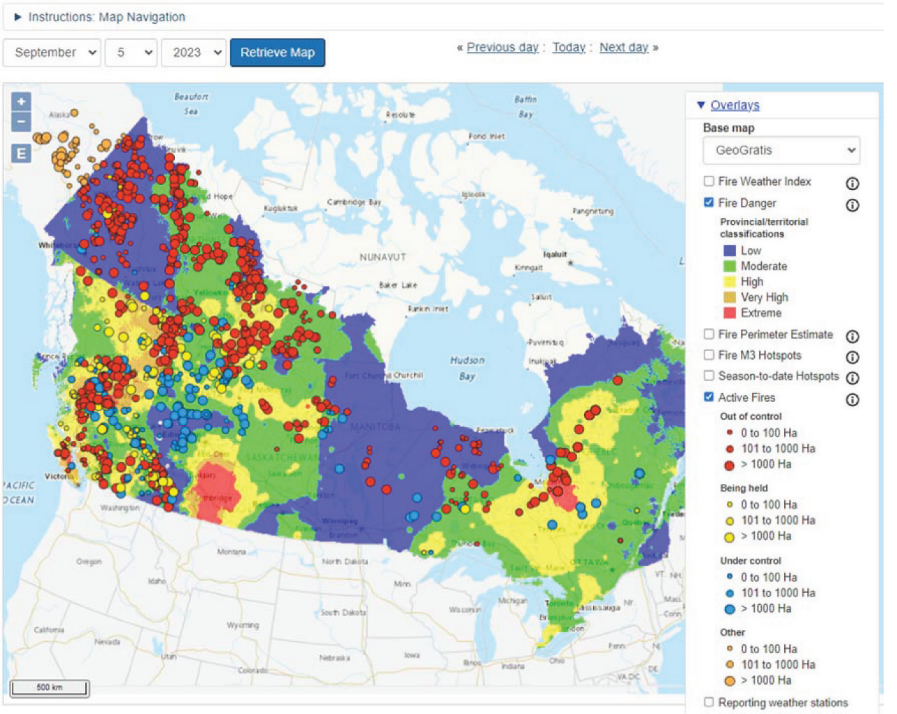


Figure 1. Active Wildfires as of September 5, 2023 (National Resources Canada).

It was therefore decided to research the relevant parameters and develop an appraisal for wildfire and bridge interaction and apply this to a provincial inventory to assess effectiveness of the algorithm. This is described further in Section 2.4.

2.3 *Flood Appraisal, Vulnerability, and Risk*

For bridges crossing watercourses and for culverts, the hydraulic capacity of the opening is an important design consideration. If the hydraulic capacity is inadequate, flooding will occur which can cause negative effects such as traffic delay, washout, or collapse.

Not surprisingly, flood appraisal is one of the more common appraisals and various approaches are used. Based on the results from the NRC report (NRC (2023)), our own design experience, literature review, and technical discussions with various agencies the most common factors considered for appraising flood are:

a) Expected flood level or design flood event
b) Freeboard (available clearance between high water and structure)
c) Desired Freeboard
d) Evidence of previous flood damage
e) Traffic delay consequences (e.g. AADT, highway functional class)
f) Flood overtopping likelihood (frequency)

With these parameters, bridge managers can determine an appraisal, as well as calculate flood vulnerability and risk.

2.3.1 *Flood appraisal*

The approach adopted in the bridge management system is described as follows:

$$Flood\ Appraisal = f(desired\ vs.\ actual\ freeboard,\ previous\ flood\ damage,\ overtopping\ likelihood) \quad (1)$$

where Flood Appraisal varies 10 (best) to 1.

In this case the desired freeboard and the desired level of overtopping likelihood are set as standards. For example, we can set desired freeboard of 1.5m for particular flood event and specify overtopping likelihood of 1/ 50 years and the user can experiment to see the results of these inputs. This allows the bridge owner to identify structures that do not meet current standards but also explore which structures would not meet future higher standards for example due to extreme weather.

The values for flood overtopping likelihood different levels were considered such as those defined by FHWA (FHWA 1995), (FHWA 2022) and others. We elected to use the following as most appropriate for our purposes and to be consistent with FHWA 2022:

Table 1. Likelihood of flood overtopping.

Remote	once every 100 years or less frequently
Very low	once every 51 to 99 years
Low	once every 26 to 50 years
Moderate	once every 11 to 25 years
High	once every 3 to 10 years
Very High	once every 2 years or more frequently

Table 2. Traffic delay consequences.

Insignificant - Minor inconvenience
Significant
Severe
Very Severe

2.3.2 *Flood vulnerability*

For vulnerability, the same inputs used for appraisal are used with the addition of traffic delays as a measure of the inability to cope with the hazard. Since the expected flood level and frequency are variables, vulnerability and risk can be determined for different levels of expected flood level and likelihood. This is ideal for evaluating different extreme weather assumptions. A vulnerability score can be calculated based on the following factors:

$$Flood\ Vulnerability = f\ (desired\ vs.\ actual\ freeboard,\ previous\ flood\ damage,\ overtopping\ likelihood, traffic\ delays\ linked\ to\ flood\ event) \quad (2)$$

where traffic delay consequences are described in Table 2.

2.3.3 *Flood risk and risk profile matrix*

A risk analysis consists of estimating probability and consequences of a particular event and defines risk as the product of probability and consequences. In the case of bridge and culvert flooding, overtopping likelihood is taken as the probability and for consequences we consider traffic delays together with a measure of economic loss of the structure as given by structure replacement cost.

$$\begin{aligned} Flood\ Risk &= Overtopping\ likelihood\ x\ Consequences \\ &= Overtopping\ likelihood\ x\ (traffic\ delay\ consequences + replacement\ cost) \end{aligned} \quad (3)$$

If the risk calculation is performed for the network of structures or highway corridor, the values can be displayed in the classic risk profile matrix as shown in Figure 2. If we define levels of risk as High, Medium-High, Medium, and Low, we can display the number of structures in the highest risk category corresponding to the top right 5 boxes, the next highest risk (medium-high) are shown in the middle band of 7 boxes, followed by Medium 7 boxes, and Low 6 boxes in the lower left.

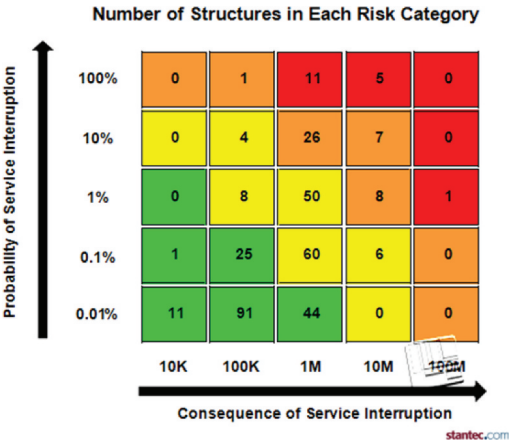


Figure 2. Flood risk profile matrix.

This approach is commonly applied in managing transportation infrastructure and is well suited to application in BMS. In the BMS used by PEI DTI, it was first developed for condition risk as described by Ellis et al 2012.

2.3.4 *Evaluation of the approach*

To evaluate the efficacy of the flood appraisal, vulnerability and risk analysis, a sample inventory was assessed with assistance from the Prince Edward Island Department of Transportation and Infrastructure (DTI). More details are provided in Evans & Ellis, 2023. Based on inputs of desired and available freeboard, previous flood damage, and flood overtopping likelihood (frequency) appraisals were calculated based on Eqn. 1. Vulnerabilities were calculated based on these inputs together with the potential traffic delays linked to the specified flood likelihood as described in Eqn. 2. A risk analysis was performed using the approach described in Eqn. 3. The resulting values provided a list of several structures that were the highest vulnerabilities which were consistent with the opinion of DTI and thus enabled decisions to be made regarding remediation. The priorities for remediation were arrived at using the results of the risk analysis.

In this way DTI could avoid chasing structures with the lowest flood appraisal or the highest vulnerability, even though this information is very useful. Instead, it is possible to focus on the highest risk first. The lowest appraisal or highest vulnerability structures may not represent the highest risk to the Department.

2.4 *Wildfire Appraisal, Vulnerability, and Risk*

For many parts of Canada and indeed many other countries around the world, bridges can be exposed to potential wildfires. As described earlier in this paper, it was desired to develop an appraisal for wildfire and bridge interaction and extend this to wildfire vulnerability and risk profiles. Although most agencies surveyed in the NRC study were keenly aware of wildfire risks, there was no available means to assess. A literature review revealed that very little work has been done. Florida DOT included wildfire as one of the risk models developed for use in

their bridge management system (Sobanjo & Thompson, 2013). The researchers assumed that damage to the structure is dependent on the structure material type and that road closures constitute the largest threat to roadways and bridges rather than physical member damage. Risk models were developed based on historical wildfire data. A risk index was calculated, and the 20 highest risk structures were identified.

The Government of British Columbia, Ministry of Forests, Lands, Natural Resource Operations and Rural Development (FLNRORD) commissioned a study in 2020 to identify information gaps in bridge protection with respect to wildfire events. The study reported that there has been very limited research done on bridge protection against wildfire events. Several knowledge gaps were identified with the main ones being that there is a lack of codes and standards related to fire protection of bridges and the limited number of empirical tests that have been performed to understand the performance of bridges exposed to wildfire. It was proposed that testing be carried out on bridge protection products such as intumescent paints and meshes, fire protective blankets, and insulation boards. Fire protection blankets and insulation boards can be deployed when high fire risk is identified for a given structure(s). Intumescent paints are a type of reactive paint which swells up or 'intumesces' to many times its original thickness when exposed to high temperatures, such as in the event of a fire. In addition, vegetative fuels and water management options should be considered as a hazard reduction practice around bridges.

For bridges in a potential wildfire environment, the following factors are proposed as inputs to the proposed wildfire appraisal:

a) Structure material (e.g. timber, steel, concrete)
b) Wildfire exposure factor (structure setback/clearances, forest fuel ratio, extent of protection provided)
c) Traffic delay consequences (e.g. AADT, highway functional class)
d) Wildfire likelihood (frequency)

With these parameters, bridge managers can determine wildfire appraisal, as well as calculate wildfire vulnerability and risk.

2.4.1 *Wildfire Appraisal*

The approach proposed for a new appraisal for wildfire is described as follows:

$$\begin{aligned} \textit{Wildfire Appraisal} &= f(\textit{structure material},\ \textit{wildfire likelihood},\ \textit{exposure factor}) \\ &= \textit{varies } 10\ (\textit{best})\ \textit{to } 1 \end{aligned} \tag{4}$$

Table 3. Wildfire Likelihood.

Remote
Very low
Low
Moderate
High
Very High

2.4.2 *Wildfire Vulnerability*

For wildfire vulnerability, the same inputs used for appraisal are used with the addition of traffic delays as a measure of the inability to cope with the hazard. Since wildfire likelihood and wildfire expose are variables, vulnerability and risk can be determined for different levels of assumptions. This is ideal for evaluating the future effects of climate change in increased temperature and drought. A vulnerability score can be calculated based on the following factors:

$$Wildfire\ Vulnerability = f\,(structure\ material,\ wildfire\ exposure\ factor\ wildfire\ likelihood,\ traffic\ delays\ linked\ to\ wildfire\ event) \quad (5)$$

where traffic delay consequences are described in Table 2 and wildfire likelihood is given in Table 3.

2.4.3 *Wildfire Risk and Risk Profile Matrix*
In the case of bridge exposure to wildfire, wildfire likelihood is taken as the probability and for consequences we consider traffic delays together with a measure of economic loss of the structure as given by structure replacement cost.

$$\begin{aligned} Wildfire\ Risk &= Wildfire\ likelihood\ x\ Consequences \\ &= Wildfire\ likelihood\ x\ (traffic\ delay\ consequences + replacement\ cost) \end{aligned} \quad (6)$$

A risk profile can be prepared similar to Figure 2.

2.4.4 *Evaluation of the Approach*
To evaluate the efficacy of the new wildfire appraisal, vulnerability and risk analysis, a sample inventory was assessed with assistance from the Prince Edward Island Department of Transportation and Infrastructure (DTI). More details are provided in Evans & Ellis, 2023. A sampling of structures in forested areas were selected having different material types, wildfire likelihood, wildfire exposure factors and traffic delay consequences. Wildfire appraisals were calculated based on Eqn. 4. Vulnerabilities were calculated based on Eqn. 5. A risk analysis was performed using the approach described in Eqn. 6. The resulting values provided a list of several structures that had higher vulnerabilities and thus enabled decisions to make plans for wildfire remediation such as site clearing, setback. Based on the risk analysis none of the structures were found to be high risk but some in medium risk category were identified.

3 FUTURE WORK

As the algorithms used in these appraisal, vulnerability, and risk calculations are new, a level of calibration is being carried out. The wildfire appraisal is entirely new, and it would also be beneficial to test on a larger inventory of wildfire hazard bridges. Nonetheless, the results are promising and already proving useful.

The next stage of work includes completing the similar appraisal, vulnerability and risk calculations for the other appraisals referred to in Section 2.2. Once this is done, it will be possible to create an overall vulnerability score comprising all of the appraisal hazards. Together with the already implemented condition risk profile, bridge managers will have a complete picture for the most common bridge vulnerabilities.

4 CONCLUSIONS

As a result of increased extreme weather events in many parts of the world, there have been growing concerns related to the risks to transportation infrastructure and infrastructure resiliency. Recently, a national survey was completed which included how provincial and municipal bridge departments across Canada are responding to these challenges. In conjunction with several transportation agencies, Stantec has been developing appraisal indices to include the effects of extreme events on flooding, scour, wildfires and other vulnerabilities such as fatigue, seismic, and load carrying capacity. The appraisal ratings are being implemented in a Bridge Management System to provide input into risk analysis to assist agencies in decision making regarding these challenges.

This paper has described how agencies can consider in a practical way the effects of potential extreme weather related events, such as flooding and wildfires. Parameters that can be used as

input into these appraisals were described. For flooding this includes actual vs desired freeboard, previous flood damage, likelihood of overtopping, and traffic delay consequences. A new appraisal was described for wildfires which is based on structure material, wildfire exposure factor, wildfire likelihood, and traffic delays linked to wildfire event. A methodology for risk profiles was described for the flood and wildfire appraisal examples. For a preliminary assessment, the methodologies were applied to the PEI DTI bridge inventory and the results were used to make decisions regarding flood remediation and wildfire preparedness.

ACKNOWLEDGMENTS

The authors would like to acknowledge the assistance of the Prince Edward Island Department of Transportation and Infrastructure (DTI), in particular Mr. Darrell Evans, A/Director for supporting and supplying the test inventory. The support of the National Research Council as part of the national survey and report on bridge management practices across Canada is also gratefully acknowledged.

REFERENCES

American Association of State Highway and Transportation Officials (AASHTO), 2019. Manual for Bridge Element Inspection.

Ellis, R.M., et al, 2012. Incorporating Risk and Criticality in Bridge Management Decision Making and Project Prioritization. 6th International Conference on Bridge Maintenance, Safety and Management, IABMAS 2012, Stresa, Italy.

Ellis, Reed M., Evans, Darrell J. A Canadian Bridge Sufficiency Index. 2019 TAC-ITS Canada Joint Conference, Halifax, NS.

Evans, Darrell J. and Ellis, Reed M. (2023) Vulnerability of Network Infrastructure due to potential extreme weather in PEI, Canada. 12th International Conference on Bridge Maintenance, Safety and Management, IABMAS 2024. Copenhagen, Denmark.

CIRC-Blue Plan 2019. Canadian Infrastructure Report Card 2019. http://canadianinfrastructure.ca/en/index.html

Cannon, A., et al., 2020. Climate-Resilient Buildings and Core Public Infrastructure: An Assessment of the Impacts of Climate Change on Climatic Design Data in Canada. https://publications.gc.ca/collections/collection_2021/eccc/En4-415-2020-eng.pdf

Federal Highway Administration (FHWA) 1995. Recording and Coding Guide for the Structure Inventory and Appraisal of the Nation's Bridges. Washington: US Federal Highway Administration. Report FHWA-PD-96-001.

Federal Highway Administration (FHWA) 2022. Specifications for the National Bridge Inventory. Washington: US Federal Highway Administration. Publication No. FHWA-HIF-22-017.

Government of Canada, Natural Resources, 2023. https://natural-resources.canada.ca/simply-science/canadas-record-breaking-wildfires-2023-fiery-wake-call/25303

Infrastructure Canada, 2018. About Infrastructure Canada. https://www.infrastructure.gc.ca/about-apropos/index-eng.html#1 (accessed Nov. 7, 2018)

Ministry of Transportation of Ontario (MTO). 2009. Ontario Structure Inspection Manual. Queen's Printer for Ontario, Toronto, Canada.

Ministry of Transportation of Ontario (MTO). 2008. Bridge Condition Index (BCI) - An Overall Measure of Bridge Condition. Queen's Printer for Ontario, Toronto, Canada.

Ministry of Forests, Lands, Natural Resource Operations and Rural Development (FLNRORD), BRIDGES & WILDFIRE EVENTS - Identifying Information Gaps in Bridge Protection in the Context of Resistance to Wildland Fire Events. Government of British Columbia, 2020.

National Research Council of Canada (2023). Review of State of Practice of Bridge Management in Canada and USA in a Changing Climate. A report prepared by Stantec Consulting Inc.

NRTEE 2011.Climate Prosperity - Paying the Price: The Economic Impacts of Climate Change for Canada. National Round Table on the Environment and the Economy.

Shepard, R.W., & Johnson, M.B., 2001. California Bridge Health Index: A Diagnostic Tool to Maximize Bridge Longevity, Investment. *TR News* 215: 6–11.

Sobanjo, John O, and Thompson, Paul D., 2013. Development of Risk Models for Florida's Bridge Management System. Report prepared for Florida Department of Transportation.

Bridge Maintenance, Safety, Management, Digitalization and Sustainability – Jensen, Frangopol & Schmidt (eds)
© 2024 The Author(s), ISBN 978-1-032-77040-6
Open Access: www.taylorfrancis.com, CC BY-NC-ND 4.0 license

Province of New Brunswick Bridge Management System

Zahra Kamranian M.Eng, P.Eng. & Reed M. Ellis Ph.D., P.Eng.
Stantec Consulting Ltd., Edmonton, Canada

ABSTRACT: The New Brunswick Department of Transportation and Infrastructure (NBDTI) has recently completed the implementation of their bridge management system (BMS). The system is an advanced customized-off-the-shelf (COTS) BMS that is designed to manage the assets thoroughly, including inventory, inspection, modelling, forecasting, prioritizing, and budgeting. The BMS will be used to manage over 6,100 structures consisting of bridges, bridge-sized culverts, retaining walls, wharfs, sea walls, sign structures, and minor culverts. A massive amount of legacy data had to be loaded, and several existing Department processes were added as links in the new BMS. Province-specific customization was required for deterioration, treatment, and cost models appropriate for local conditions, structure elements, materials, environment, and repair practices. This paper should be of interest to agencies considering implementing a bridge management system.

1 INTRODUCTION

The New Brunswick Department of Transportation and Infrastructure (NBDTI) is responsible for constructing and maintaining approximately 6,100 bridges, bridge-sized culverts, retaining walls, wharves, sea walls, sign structures and minor culverts. This comprehensive and diverse inventory is one of the largest provincial inventories in Canada.

NBDTI aims to make well-informed decisions that can be effectively presented to other departments, elected officials, and the public. It is crucial that NBDTI maintain their capital programs for structures on a firm and justified financial footing that allows a sustainable level of service over the long term and quickly demonstrates how changes to budgets can influence the condition of the network.

In NBDTI's legacy Bridge Management System (BMS), the structures modeling for bridges and large culverts had not been sufficient to assist in developing the capital program. It lacked the functionality to assess how the deterioration of one element may influence the deterioration of one or more other elements in the same structure. This legacy BMS was also not integrated with the inspection report database, forcing NBDTI staff to manually extract the data into a format the model could read. Moreover, it did not consider criteria such as the average annual daily traffic (AADT) and weight restrictions. The system was also approaching end of life due to a number of legacy tools that could become incompatible and inoperative as time progressed.

Therefore, NBDTI sought a mature commercial off-the-shelf (COTS) software system that could be customized to suit department requirements. COTS systems also have the advantage of providing known solutions in minimal time and much lower cost than new development. NBDTI had sophisticated requirements for analysis capabilities, including deterioration and cost modelling, lifecycle cost analysis, and benefit-cost analysis. Risk analysis and risk-based decision-making capabilities were also required for bridges and structures.

In line with NBDTI's vision for a more disciplined, integrated, and structured approach to managing its transportation infrastructure, NBDTI selected Stantec BMS as their COTS system

DOI: 10.1201/9781003483755-234

to implement. Stantec's bridge management system application was implemented between 2020 and 2022 to maximize the benefits of available transportation structures' funding, as well as build support for increased funding levels. The new BMS is an advanced engineering bridge management system designed to manage the assets' entire life cycle, including inventory, inspection data, modelling, forecasting, prioritizing, budgeting, and program development. The BMS fully meets the requirements for BMS as described by AASHTO (AASHTO, 1992) or ISO 55000 Standards for Asset Management (ISO 55000, 2014). The system is reported extensively by other Agencies in Canada in the IABMAS Report on Bridge Management Systems (Mirzaei et al, 2012.)

This paper focuses on NBDTI's first steps in implementing this robust transportation asset management system, how existing data/systems were leveraged, and how NBDTI's practices/ experience were combined with sound engineering models and comprehensive analysis tools to produce a complete management system.

2 OVERVIEW AND BENEFITS OF ASSET MANAGEMENT SYSTEMS

Structures typically represents one of the larger and significant investments transportation agencies manage. To efficiently manage asset information in an easy-to-use, accessible platform, and carry out asset management using industry-standard practices, transportation agencies need to be able to answer the following questions efficiently:

1. What assets do I own?
2. What is the current condition of these assets?
3. What are the current replacement costs and valuation of these assets?
4. What maintenance, repair, and rehabilitation actions are needed for these assets?
5. When do we need to do these actions?
6. How much budget is needed over the budgeting cycle?

Other questions are often raised, such as the tradeoff between budget and condition, what happens if the required budget needs cannot be met, and what risks and vulnerabilities may be present.

Thus, the bridge management system must enable the users to effectively manage the whole structure program, including inspection and data collection, needs identification, and decision-making. The asset management systems must also include the ability to calculate and report Key Performance Indicators (KPI) and performance measures and forecast these for different budget levels.

To achieve the above, it is desirable to follow a bottom-up approach, wherein the systems are data-driven from accepted field inspection and data collection processes. COTS systems tend to model the bottom-up approach, provided that they can be customized to suit an agency's specific practices. 'Enterprise' asset management system tends to work from the top-down and often force agency's to simplify their analysis to be consistent with other assets.

Stantec BMS is based on a 'bottom-up' approach and utilizes inventory data and inspection to produce a set of Element and Project-Level analysis results. These results are then used at the Network-Level (Thompson et al, 1999, Ellis et al (2008)). Stantec BMS produces results at three (3) levels of analysis: The Element-Level, the Project-Level and the Network-Level. Stantec BMS combines Element-Alternatives at the Element-Level into Project-Alternatives, each of which represent a possible multi-year strategic action plan to maintain the serviceability of the structure at a desired level. The analytical framework of Stantec BMS maintains consistency between the Element-Level, the Project-Level and the Network Level. Results at Element and Project Levels are used at the Network-Level. This means that any decisions made at one level can serve to constrain results at another level.

The analyses are organized into three levels of detail, as shown in Figure 1. The levels are:

1. Element level, which focuses on a selected structural element of one bridge. This tool uses a Markovian deterioration model and a set of feasible treatments to produce multiple Element Alternatives, each of which is a possible corrective action to respond to deteriorated conditions. Functional improvements are also included at this level.

2. Project level, which combines Element Alternatives into Project Alternatives, each of which represents a possible multi-year strategy to maintain service. The tool uses models of initial costs and life cycle costs to evaluate the Project Alternatives.
3. Network level, which combines the Project Alternatives on multiple bridges into Program Alternatives, each of which is a multi-year plan for work on all or part of a bridge inventory, designed to satisfy budget constraints and performance targets while minimizing life cycle costs.

Each level of analysis in this framework provides a set of evaluated alternatives to feed the broader-scale tool to its left. All three levels are designed to stay consistent with each other, so if a change is made at one level, the remaining levels will adjust appropriately.

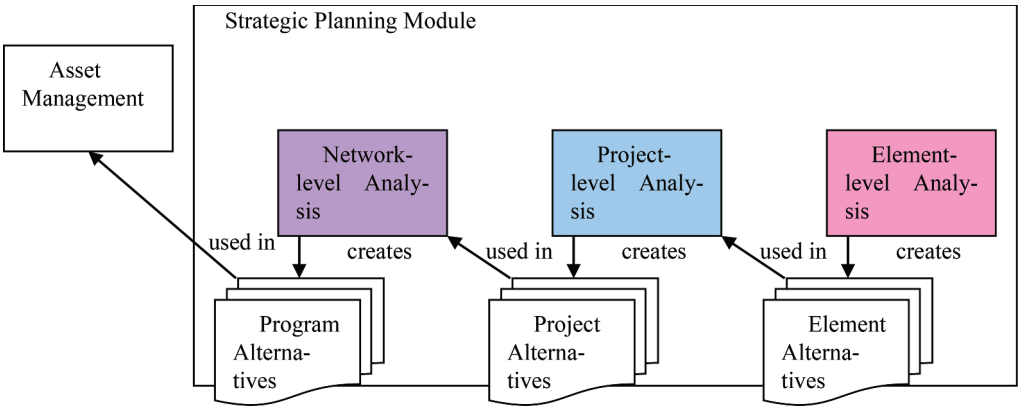


Figure 1. Levels of analysis.

On the other hand, in going from left to right in Figure 1, network-level analysis provides a context for the project level, because the network-level budget constraint affects which Project Alternatives can be programmed. For example, in a very constrained funding scenario many bridges will have to select the Do-Nothing alternative.

Similarly, the project-level analysis provides a context for the element level, influencing the cost-effectiveness of individual element treatments such as in the case when element treatments are combined at the same time to minimize traffic control costs, Ellis et al (2008).

3 OVERVIEW OF NBDTI'S BRIDGE MANAGEMENT SYSTEM (BMS) REQUIREMENTS

Specific requirements for NBDTI's BMS for structures are summarized below. Using their new BMS, the NBDTI desired to be able to:

1. Utilize the widely accepted bridge and culvert inspection methodology used in other provinces of Canada, OSIM (MTO 2018).
2. Standardize and centralize structures inventory information so it is easily accessible for users with different access levels across various departments.
3. Operate a multi-window user interface for all inventory, inspection, multimedia and analysis results while having context sensitive help.
4. Integrate with Department GIS and other internal systems.
5. Adopt an accepted and rational bridge condition index (BCI) that could be used to compare conditions between individual structures and as a network average performance measure to set performance targets. MTO, 2008).
6. Provide measures of criticality and risk that could be used in decision-making.
7. Develop of NBDTI-specific structure deterioration and cost models.

8. Establish prioritized work programs for their highway network using a lifecycle cost analysis and benefit-cost (B/C) framework.
9. Implement enhanced multi-media document management in the BMS.
10. Receive training in bridge management and the use of BMS.

4 IMPLEMENTATION AND CUSTOMIZATION OF BRIDGE MANAGEMENT SYSTEM

The system was able to be customized off-the-shelf to suit NBDTI practices and much of the implementation consisted of this customization process.

Inventory data and Department drop-down lists were customized for the BMS. A large number of screen labels and drop-down changes were required to match NBDTI terminology. Since NBDTI had been using a legacy bridge inventory and inspection system for many years, there were several legacy features that the Department wished to be added to the BMS. These features included a document management tool (Figure 2) which enables users of the BMS to track legacy documents such as microfilm, manage load rating file information, and record current location of these key frequently used documents. This tool supplements the existing document tools in the BMS which handle documents and all multimedia associated with inspections. A NBDTI-specific capital planning screen was added, and links within the BMS to internal legacy tools such as a photo management application, internal network folders, and the department GIS were added. Several complex reports were also added to the system to match those produced by the legacy system(s).

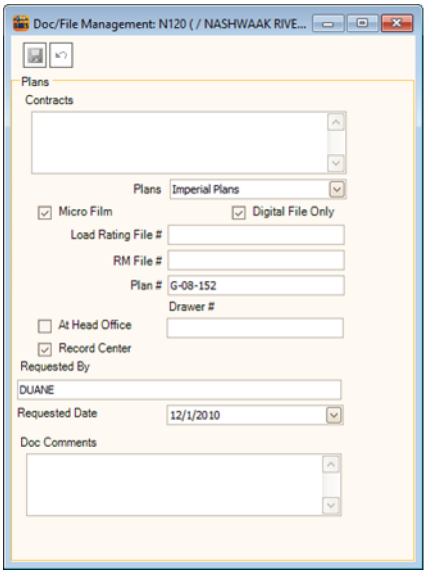


Figure 2. Document administration screen.

As is standard with a BMS implementation, Department-specific deterioration models (Figure 3), cost models, and analysis parameters were developed using expert elicitation and experience from the project team and knowledge from other similar jurisdictions in Canada that use the BMS.

A risk analysis module was included with the BMS (Figure 4 and Table 1), which required new structure level and element level engineering inputs. A new element level criticality rating was introduced Ellis et al (2012). Training on collecting the inputs required for this new analysis was provided as part of the two-week inspection training course provided to NBDTI staff during the project.

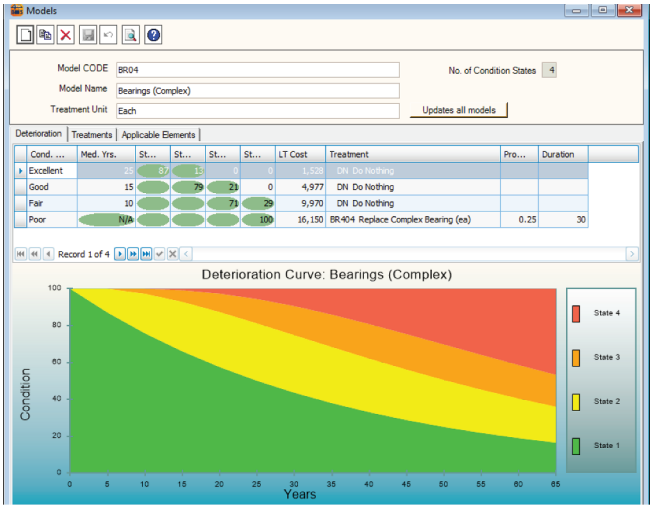


Figure 3. A sample deterioration model.

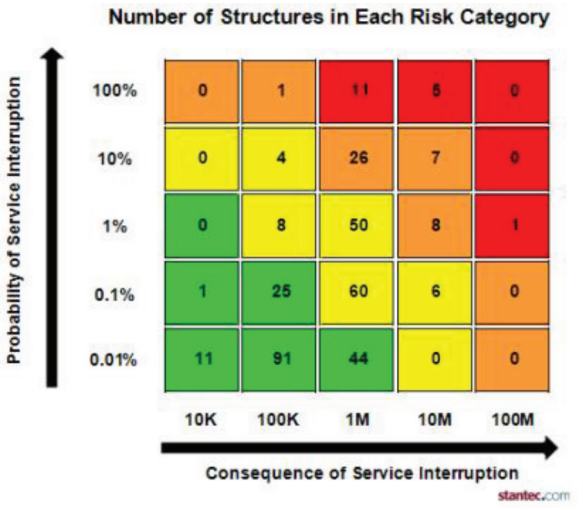


Figure 4. Network risk profile (number of structures).

Table 1. Network risk distribution (Deck Area).

Risk Level	Deck Area (sq.m.)	%
High	7,352	5.45%
Medium-High	22,782	16.89%
Medium	75,464	55.94%
Low	29,307	21.72%
Total	134,906	100.00%

5 CHALLENGES AND LESSONS LEARNED DURING THE IMPLEMENTATION

5.1 *Challenges*

In striving to meet NBDTI's goals, challenges were encountered during the BMS implementations. Overall, implementing two large complex asset management systems (structures and pavements) in parallel challenged resources for the consultant and department project team. The award time of the project (early 2020) was just a few weeks before the province and country went into pandemic lockdown. The project team had to accomplish nearly all tasks remotely, lacking the opportunity to have in-person workshops. Understandably this presented extenuating challenges, which were ultimately overcome due to the dedication of the project team.

Some specific challenges are listed below:

1. NBDTI has a long history of bridge management, including a legacy inventory and inspection system that had been in use for decades; there were features and functionality that NBDTI wished to customize in the new BMS, which increased the level of customization.
2. NBDTI had been using the specified (Ontario Structure Inspection Manual) OSIM inspection methodology, but it was a modified approach which meant that existing element and inspection information was not directly applicable to the new system.
3. Using the bridge management system to migrate inventory data and accept new inspection data while developing the customized system to suit NBDTI practice challenged the software development team to provide a constantly changing but usable system.
4. In developing BMS cost and deterioration models, it was found that the Department did not have deterioration data in an OSIM compatible format.
5. NBDTI wished to establish links to existing integrated systems from within the new BMS so the users could seamlessly use BMS with internal applications.

5.2 *Lessons learned*

In general, an effective communication plan among the project team proved essential to ensure project success, especially having to work remotely. This included regularly scheduled meetings and progress documentation and sign-off/approvals at various stages. The communication plan helped to communicate the expectations, changes needed, and scheduling restrictions, to ensure timely deliverables.

Every agency has specific customization needs. This is especially so if there is a long history of legacy systems usage. It is essential that knowledgeable working level staff be available from department and consultant to make the necessary conversions, and this was achieved provided throughout the project.

Due to the flexibility of the BMS interface, it was possible to provide users with different access levels across various departments depending on user needs, achieving one of the Department requirements.

Preferably, compatible inspection data is available at the start of the project but if not, it is better to wait until the system is implemented before inputting inspection data. It was challenging to collect over 2,000 inspections and enter this data while the system was being finalized. While this approach is possible, it consumes resources.

6 SUMMARY

NBDTI recently implemented a bridge management system for their bridges and other type of transportation structures. The new BMS was implemented as a COTS system.

As a result of the successful customization and implementation, the BMS can assist NBDTI in:

1. Providing capabilities to model future structural deterioration and recommend appropriate maintenance and rehabilitation.
2. Ensuring effective use of financial resources.
3. Extending management philosophies into short-term and long-term planning.
4. Helping manage network data and information.
5. Effectively communicating management requests.
6. Each year NBDTI is responsible for allocating the capital budgets to support its programs and fulfill its long-term strategic goals. Using the new systems will allow NBDTI to invest wisely and justify allocating funds needed for their assets.

ACKNOWLEDGEMENTS

This project was sponsored by the New Brunswick Department of Transportation and Infrastructure (NBDTI). Sincere thanks are extended to NBDTI staff Glen MacDonald, Sheldon Smith, and Tracy MacDonald for their invaluable contributions and support throughout the BMS implementation. The authors recognize and appreciate the assistance provided by Katie Lawlor, Joshua Fox, Joyce Brown, and Veronica Pelkey also with NBDTI.

REFERENCES

AASHTO, 1992. Guidelines for Bridge Management Systems.

Ellis, Reed M., Thompson, Paul D., Gagnon, Rene and Richard, Guy. 2008. Design and Implementation of a New Bridge Management System for the Ministry of Transport of Québec. 4th International Bridge Management Conference, IABMAS, Seoul, Korea.

Ellis, Reed M. and Hong, K. 2012. Incorporating Risk and Criticality in Bridge Management Decision Making and Project Prioritization. 6th International Conference on Bridge Maintenance, Safety and Management, IABMAS, Stresa, Italy.

Ministry of Transportation of Ontario (MTO). 2008. Bridge Condition Index (BCI) - An Over-all Measure of Bridge Condition. Queen's Printer for Ontario, Toronto, Canada.

Ministry of Transportation of Ontario (MTO). 2018. Ontario Structure Inspection Manual. Queen's Printer for Ontario, Toronto, Canada.

Mirzaei, Z., Adey, B. T., Klatter, L., & Thompson, P. D. 2014. The IABMAS Bridge Management Committee Overview of Existing Bridge Management Systems. IABMAS.

Thompson, P. D., Merlo, T., Kerr, B., Cheetham, A., Ellis, R. 1999. The New Ontario Bridge Management System. Proceedings 8th International Bridge Management Conference, Denver, CO.

ISO 55000. 2014. Standards for Asset Management. International Organization for Standardization

Bridge Maintenance, Safety, Management, Digitalization and Sustainability – Jensen, Frangopol & Schmidt (eds)
© 2024 The Author(s), ISBN 978-1-032-77040-6
Open Access: www.taylorfrancis.com, CC BY-NC-ND 4.0 license

Bridge deterioration prediction models: A review of management systems in the world

C.A.F. Souza, J.M.F Carvalho, A.C.P. Martins, F.G. Bellon, M.S. Andrade, D.S. Oliveira, J.C.L. Ribeiro, K.M.L. Cesar, B.S. Borges & G.P. Teixeira
Universidade Federal de Viçosa (UFV), Viçosa, Brasil

ABSTRACT: Predicting bridge deterioration is essential to an effective bridge management. Understanding the evolution of bridge performance in specific periods is fundamental to anticipating future needs and planning appropriate interventions. In this context, this paper aims to analyze Bridge Management Systems (BMS) that use deterioration prediction models and the methods employed. To perform this analysis, 12 BMSs from 12 countries were selected, considering the number of publications and citations related to the subject of "Bridge Management System" in each country. When examining the information from these systems, the significant importance of predictive models is evident. More than half of the systems (67%) use some type of deterioration prediction model, 25% do not use prediction models, and 8% did not obtain any information. Moreover, it is common to observe the countries that collaborate the most in BMS research adopt these models in their systems. Among the systems that employ deterioration prediction models, three main types were identified: physical, deterministic, and probabilistic models. In analyzing the bridge prediction models, it was found that 67% of them are based on probabilistic approaches using Markov chains, 11% are deterministic, 11% are physical models, and in 11% of the cases it was impossible to obtain information. These results highlight the preference for probabilistic approaches in modeling bridge deterioration, considering the uncertainty associated with the process. Such predictive models perform a crucial role in effectively managing bridges, enabling the anticipation of maintenance needs and the proper allocation of resources. In summary, the implementation of bridge deterioration prediction models is widely adopted in management systems worldwide, with probabilistic models based on Markov matrices being the most widely used. Understanding these models and their application can provide valuable insights for developing efficient and sustainable management strategies for bridge maintenance.

Keywords: Bridge, Deterioration Prediction Model, Bridge Management System, Physical Model, Deterministic Model, Probabilistic Model

1 INTRODUCTION

Effective bridge management plays a crucial role in maintaining the long-term performance, safety, and operational efficiency of these structures. Achieving this involves meticulous planning and execution of interventions. The core goal of bridge management is to optimize these interventions, seeking to attain optimal performance while minimizing associated risks. This process forms a solid foundation for informed investment choices. A fundamental component of this procedure involves the capability to forecast bridge deterioration as time progresses. Gaining insights into how the performance of structures evolves within specific timeframes is vital for enhancing the efficiency of intervention planning. Aiming to understand the processes underlying deterioration prediction and to identify the methods prevalent in bridge

DOI: 10.1201/9781003483755-235

management systems globally, this paper conducts a review covering a detailed analysis of the models employed to predict bridge degradation in management systems worldwide.

2 METHOD

To perform the bibliometric review, we used the Scopus database platform. The search was carried out in August 2023, using the term "Bridge Management System" in "Titles, Abstracts and Keywords". Only documents in English published in the 21st century (2001-2023) were considered. A total of 686 documents were found and analyzed. VOSViewer, Bibliometrics, and the Scopus platform tools were used in the analysis. After a thorough review of existing methods to predict deterioration in BMS, the three methods employed by the selected systems were chosen for the analytical review of this paper.

The bibliometric review identified the main countries producing studies on BMS and the most relevant areas of concentration in the academic products. The selection of the countries analyzed was based on two clearly defined criteria: the presence of at least twelve documents and a minimum of 200 citations for each country. Based on this analysis, the twelve countries with the highest academic outputs and citations were chosen for a more detailed analysis. For this review, selection criteria for the BMSs were established based on the following aspects: the current use of the system, and the choice of only one system per country (giving priority to the first system developed and the number of structures).

3 BIBLIOMETRIC REVIEW

Table 1 lists, the 12 largest most collaborative countries regarding scientific production in the area, considering the minimum criterion of 12 documents and 200 citations.

Table 1. List of selected countries, number of documents and citations.

Country	Nº documents	Citations
Australia	42	406
Canada	79	654
Germany	12	223
Ireland	13	323
Italy	33	303
Japan	57	337
Portugal	36	297
South Korea	44	474
Switzerland	24	294
Taiwan	25	237
United Kingdom	28	324
United States of America	157	2501

Figure 1(a) illustrates the substantial impact of the United States in this domain, evidenced by its extensive document count and network connections. This dominance can also be attributed to its pioneering role in spearheading research in this field. Upon analyzing the keywords, we extract the primary research domains within BMS, with two focal points emerging in relation to deterioration prediction: "Life Cycle" and "Deterioration," as depicted in Figure 1(b).

During the early 21st century, research within the realm of bridge management systems underwent a substantial surge. This upswing can be attributed primarily to the establishment of numerous systems in the 1990s and 2000s (Adey et al., 2014). While the output of related documents has since reached a steady state, the topic remains pertinent on a global scale. The annual distribution of research papers is illustrated in Figure 2.

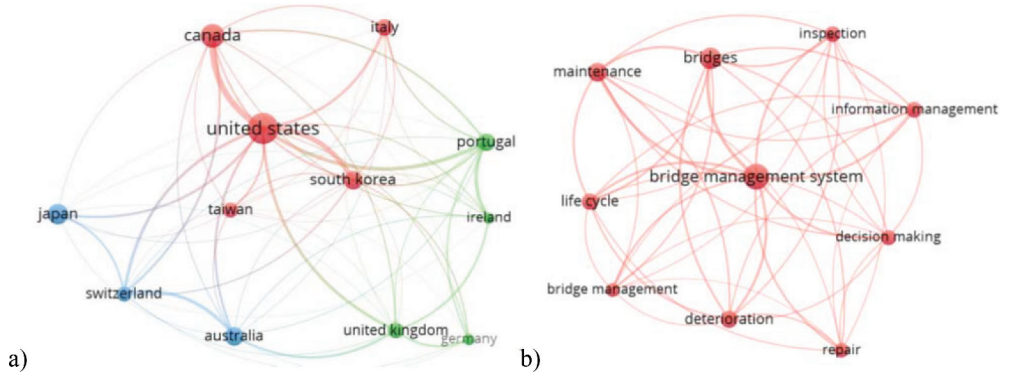


Figure 1. a) Connection between the selected countries; b) Keywords Analysis.

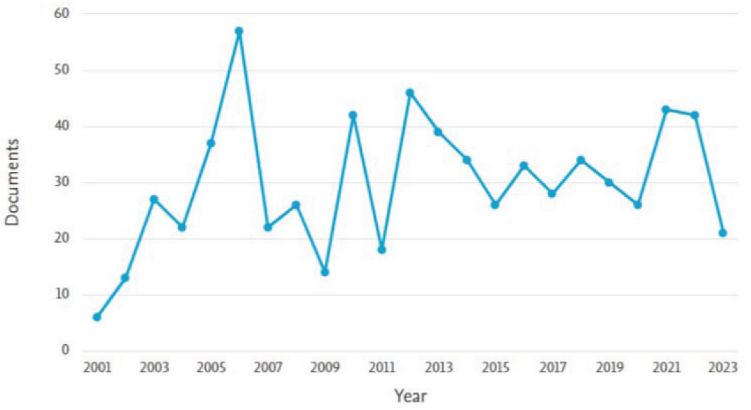


Figure 2. Documents by year.

In 2006, Figure 2 displays a pronounced peak, which can be ascribed to the occurrence of the 3rd International Conference on Bridge Maintenance, Safety, and Management (IABMAS). This event encompassed 34 publications dedicated to BMS, thus emerging as the primary contributor of papers for that year and century. Furthermore, it's noteworthy that the IABMAS congress, taking place biennially, instigated several publication spikes during even-numbered years such as 2006, 2010, and 2012.

In the realm of journals, notable contributions within the BMS domain encompass the Journal of Bridge Engineering, Journal of Infrastructure Systems, Structure and Infrastructure Engineering, and Transportation Research Record, as delineated in Table 2. Among these, the Structure and Infrastructure Engineering journal stands out with the highest number of publications (32), while the Journal of Bridge Engineering takes the lead in terms of citations (805).

Table 2. Journals with more publications.

Journal	Doc.	Citations
Journal of bridge engineering	22	805
Journal of infrastructure systems	15	357
Structure and infrastructure engineering	32	687
Transportation research record	30	291

4 ANALYTICAL REVIEW

4.1 *Bridge management system*

The foundation for a bridge to maintain its performance over its lifespan, ensuring a specific degree of safety and functionality, lies in how interventions are meticulously planned and executed. Bridge management seeks to optimize these interventions, aiming to ensure optimal performance while minimizing associated risks. This approach significantly contributes to the foundation of investment decisions (Oliveira, 2019).

A Bridge Management System (BMS) is structured into three primary categories: database management, data analysis, and decision support. The initial category pertains to data encompassing inventory details, evaluations of the bridge through inspections, cost-related information, and records of enhancement and preservation activities. These evaluations form a fundamental bedrock for data analysis, supplying vital inputs required for efficient information processing. Following this processing stage, the definition of analysis parameters follows, wherein each system must process and prioritize the most pertinent factors. Deterioration prediction and cost models constitute the most employed factors within this context (Adey et al., 2014). Lastly, decision support amalgamates insights derived from data analysis to serve as a bedrock and assist in making decisions and carrying out tasks, in a consistent and technically proficient manner.

Among the systems under scrutiny, the pioneering development and implementation transpired with KUBA, the Swiss Bridge Management System, in 1989. Shortly thereafter, in 1992, the USA introduced Pontis, which is currently known as AASHTOWare BrM. Subsequent instances emerged between 1996 and 2006 for the remaining systems, as detailed in Table 3.

Table 3. Selected BMS from each country (Adey et al., 2014; Habeenzu et al., 2021; Hsien-Ke et al., 2017; Mendonça et al., 2016).

Country	BMS	First Version
Australia	NSW	1996
Canada	OBMS	2002
Germany	GBMS	-
Ireland	EIRSPAN	2001
Italy	APTBMS	2004
Japan	RPIBMS	2006
Portugal	GOA	1999
South Korea	KRMBS	2005
Switzerland	KUBA	1989
Taiwan	TBMS	1999
United Kingdom	SMIS	1999
United States of America	AASHTOWare BrM	1992

Among the systems examined, AASHTOWare BrM in the United States is particularly noteworthy, covering a total of 750,908 structures, show in Figure 3. This predominance is justified by the adoption of this system by most states for the management of their structures. In 2021, 41 of the 50 asset management agencies in the United States used AASHTOWare BrM as part of their operations (AASHTOWare Bridge Management, 2021).

4.2 *Bridge deterioration prediction models*

The ability to anticipate the progressive decline of bridges over time plays a crucial role in the effective management of these structures. Understanding the performance trajectory of these constructions at defined intervals is essential to anticipate future requirements and plan appropriate medium to long-term interventions.

When examining the data from the twelve BMSs covered in this study, the significant importance of predictive models becomes evident. Over half of the systems (67%) employ some form of

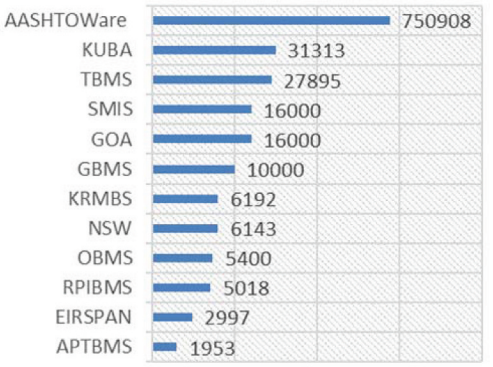


Figure 3. Number of structures in the selected BMSs (Adey et al., 2014; Habeenzu et al., 2021; Hsien-Ke et al., 2017; Mendonça et al., 2016).[1]

deterioration prediction model. These models are particularly prevalent in countries that stand out for their advanced research in BMS. Notably, the five countries leading in research in the field of bridge management systems generally incorporate deterioration prediction models in their respective systems. Of the systems investigated, eight BMSs adopt some form of deterioration prediction model (67%), while three do not make use of this feature (25%). For one of the systems, no information on the presence of such models was accessible (8%), as illustrated in Figure 4(a). All data collected are thoroughly presented in Table 4.

Table 4. Predicting deterioration in BMSs (Adey et al., 2014; Liao & Yau, 2011; Mendonça & Brito, 2014; Roelfstra et al., 2004).

BMS	Deterioration prediction models
NSW	Probabilistic deterioration prediction model in a system separates from the BMS
OBMS	Probabilistic deterioration prediction models by Markov chains
GBMS	Physical models for predicting deterioration (chlorides, carbonation and corrosion)
EIRSPAN	No deterioration prediction model
APTBMS	Probabilistic deterioration prediction models by Markov chains
RPIBMS	Probabilistic deterioration prediction models by Markov chains
GOA	No deterioration prediction model
KRMBS	Deterministic deterioration prediction model
KUBA	Probabilistic deterioration prediction models by Markov chains
TBMS	No deterioration prediction model
SMIS	-
AASHTOWare BrM	Probabilistic deterioration prediction models by Markov chains

Among the systems that adopt deterioration prediction models, three main models developed for integration into management systems are identified: physical models, deterministic models and, finally, probabilistic models that make use of Markov chains. In the examination of the prediction models applied to bridges, it is evident that 67% of them adopt a probabilistic approach based on Markov matrices, 11% are deterministic in nature, 11% are physical modeling and in 11% of the cases it was not possible to access detailed information on the elaboration of the model, as illustrated in Figure 4(b).

1. Data taken from the references may not correspond to the actual number of bridges in each system.

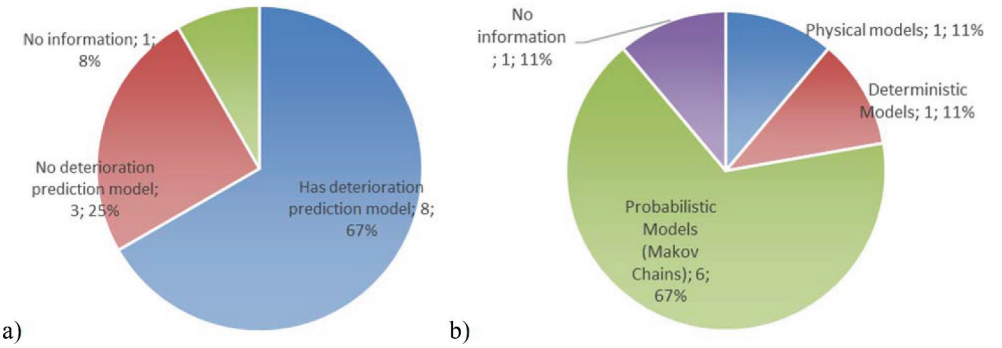


Figure 4. a) Predicting deterioration in BMSs; b) Type of deterioration prediction models used in BMSs.

4.2.1 *Physical models*

The deterioration of a structure emerges from the complex interaction of several physical processes within the system, interrelated with the materials used and the specific environmental conditions. To represent these degradation processes, either in the mechanical or chemical aspect, physical models have been developed to depict structure deterioration (Papadakis, 2013; Santamaria et al., 2019; Zambon et al., 2018).

Physical models addressing corrosion and carbonation are often preferred as they can clearly identify the main causes of deterioration in transportation infrastructure (Papadakis, 2013; Zambon et al., 2018). There are several models available for predicting the service life of reinforced concrete structures, considering factors such as chloride depassivation of reinforcement. The predominant formulations assume that the process is governed by diffusion (Andrade et al., 2019).

Some physical models that have not been implemented in the studied management systems can be explored in more detail in works such as Vieira et al. (2018) and Zambon et al. (2018). It is noteworthy that only the German GBMS system adopts physical models, which include chloride-induced corrosion and carbonation, for degradation prediction purposes.

4.2.2 *Deterministic models*

Based on mathematical or statistical equations, deterministic models establish connections between historical condition states and the service life of bridges. These structures may also incorporate additional factors that influence degradation. The main methods employed for the formulation of these models comprise projection curve fits, regressions, and the linear approach (García-Sánchez, 2016; Moscoso, 2017; Souza et al., 2023).

Among the most elaborate deterministic models today are regressions, which include both linear and non-linear regressions. In this context, the aim is to establish an empirical relationship between one or more variables, in which one of the variables is considered dependent on the others, which act as independent variables, if they are relevant. Regression analysis, in its essence, explores the interdependence between a variable of interest Y_i and one or multiple explanatory or predictor variables $X^{(j)}$.

Numerous researchers have been actively involved in crafting deterministic methodologies utilizing regression analyses to appraise the deterioration of bridges. Illustratively, notable references include the works of Jeong et al. (2017); Kim et al. (2019); Lu et al. (2019) and Souza et al. (2023). The KRMBS originating in South Korea stands as the singular management system that adopts a deterministic approach for the prediction of deterioration.

4.2.3 *Probabilistic models*

The process of deterioration in bridges, a synergistic interplay of multiple agents occurs, rendering the analysis of their individual influence rates unfeasible, as such, the phenomenon of deterioration takes on a probabilistic bias, where probabilistic deterioration models consider that deterioration over time is unknown, but there exists a probability for deterioration to unfold according to a certain law (Almeida, 2013; Oliveira, 2019).

The probabilistic degradation forecasting model predominantly employs Markov matrices, formed, for instance, by annual transition probabilities between different levels of condition states. This approach enables the prediction of the evolution of this performance parameter over time. This model finds common use in contemporary bridge management systems, primarily due to the relative ease in assembling data that allows for the identification of transition probabilities between different levels of this performance parameter.

Predicting bridge deterioration through Markov matrices involves stochastic processes, implying random processes that govern the behavior of a system over time, based on probabilistic considerations. These processes are categorized according to both Condition State and time, into discrete or continuous (Mishalani & Madanat, 2002).

Models classified by their state as discrete can be further divided into time-based or Condition State-based models. According to Mishalani & Madanat (2002), time-based models predict the probability of the time interval required for a change in the condition state of a bridge to occur. On the other hand, state-based models are models of deterioration that, within a chain Markovian process, predict the probability of a given bridge maintaining its condition state or changing its state within a fixed time span. State-based models can still consider the timing between discrete-time Markov processes and continuous-time Markov processes.

Various authors also have developed other models, including Calvert et al. (2020); L. Li et al. (2014); Manafpour et al. (2018); Santos et al. (2022) and Wellalage et al. (2015).

Eight management systems employ probabilistic models based on Markov matrices, as detailed in Table 4. Roelfstra et al. (2004) proposed a Condition State (CS) prediction of reinforced concrete highway bridges, using matrices calculated from simulated data, based on a model of chloride-induced reinforcement corrosion, to implement it in the Swiss KUBA system.

5 DISCUSSION AND CONCLUSION

In a comprehensive examination centered on a New York bridge, the work conducted by Xu & Azhari (2022) harnessed a predictive deterioration model to forge a bridge management strategy founded upon risk assessment. The findings revealed a substantial reduction in annual and overall costs when juxtaposed with conventional management methodologies, boasting an impressive 29% decrease in total expenses compared to the standard protocol. This underscores the effectiveness of a model-driven approach to bridge management. This aspect substantiates the adoption of bridge prediction models within the majority of analyzed systems, thereby enhancing safety, cost efficiency, and efficacy in managing these transportation infrastructures.

The most basic model is the physical one, but its applicability is often limited by the complex interaction of deterioration processes on bridges. This model is characterized by high uncertainty, stemming from a phenomenon-based approach rather than inspection data, which in turn restricts its capacity for updates. Both deterministic and probabilistic methods seek to strike a balance between the intricacies of development and the quality of the resulting model. While the deterministic model is easier to construct, it lacks precision and usefulness without complete information. For example, the absence of construction year data affects the accuracy of condition-age relationships. On the other hand, the probabilistic model requires more data but can have this data simulated, offering flexibility and precision. Unlike the deterministic approach, it's not bound by construction year or interventions. The deterioration curve in this model is anchored in time, not age, which makes it more dependable with an increased dataset.

These considerations steer bridge management systems toward the development of probabilistic models, particularly those rooted in Markov processes. It is worth noting that while not yet widely adopted in bridge management systems, deterioration prediction models utilizing artificial intelligence are steadily gaining ground and proving to be a viable alternative. This is evidenced by studies conducted by researchers such as Carvalho et al. (2019); Li et al. (2023); Miao et al. (2022); Santamaria Ariza et al. (2020) and Santos et al. (2022).

REFERENCES

AASHTOWare Bridge Management. (2021). 2021 Annual Bridge Management User Group Meeting – Opening Session. *2021 Annual Bridge Management User Group Meeting*.

Adey, Z., Klatter, L., & Thompson, P. (2014). *The iabmas bridge management committee overview of existing bridge management systems 2014*.

Almeida, J. (2013). *Sistema de Gestão de Pontes com Base em Custos de Ciclo de Vida*. Universidade do Porto.

Andrade, J., Possan, E., & Dal Molin DCC. (2019). Considerations about the service life prediction of reinforced concrete structures inserted in chloride environments. *J Build Pathol Rehabil*.

Calvert, G., Neves, L., Andrews, J., & Hamer, M. (2020). Multi-defect modelling of bridge deterioration using truncated inspection records. *Reliability Engineering and System Safety*, *200*. https://doi.org/10.1016/j.ress.2020.106962

Carvalho, T. P., Soares, F. A. A. M. N., Vita, R., Francisco, R. da P., Basto, J. P., & Alcalá, S. G. S. (2019). A systematic literature review of machine learning methods applied to predictive maintenance. *Computers & Industrial Engineering*, *137*, 106024. https://doi.org/10.1016/j.cie.2019.106024

García-Sánchez, D. (2016). *Control estadístico y modelos de regresión lineal. Una forma práctica de control de puentes*.

Habeenzu, H., McGetrick, P. J., Hester, D., & Taylor, S. E. (2021). Bridge management systems - A review of the state of the art and recommendations for future practice. *Bridge Maintenance, Safety, Management, Life-Cycle Sustainability and Innovations - Proceedings of the 10th International Conference on Bridge Maintenance, Safety and Management, IABMAS 2020*, 926–933. https://doi.org/10.1201/9780429279119-124

Hsien-Ke, L., Jallow, M., Nie-Jia, Y., Ming-Yi, J., Jyun-Hao, H., Cheng-Wei, S., & Po-Yuan, C. (2017). Comparison of bridge inspection methodologies and evaluation criteria in Taiwan and foreign practices. *ISARC 2017 - Proceedings of the 34th International Symposium on Automation and Robotics in Construction*, 317–324. https://doi.org/10.22260/isarc2017/0043

Jeong, Y., Kim, W., Lee, I., & Lee, J. (2017). Bridge service life estimation considering inspection reliability. *KSCE Journal of Civil Engineering*, *21*(5), 1882–1893. https://doi.org/10.1007/s12205-016-1042-z

Kim, J., Gucunski, N., & Dinh, K. (2019). Deterioration and Predictive Condition Modeling of Concrete Bridge Decks Based on Data from Periodic NDE Surveys. *Journal of Infrastructure Systems*, *25*(2). https://doi.org/10.1061/(ASCE)IS.1943-555X.0000483

Liao, H.-K., & Yau, N.-J. (2011). *DEVELOPMENT OF VARIOUS BRIDGE CONDITION INDICES FOR TAIWAN BRIDGE MANAGEMENT SYSTEM*.

Li, L., Sun, L., & Ning, G. (2014). Deterioration Prediction of Urban Bridges on Network Level Using Markov-Chain Model. *Mathematical Problems in Engineering*, *2014*, 1–10. https://doi.org/10.1155/2014/728107

Li, Z., Zhou, J., Nassif, H., Coit, D., & Bae, J. (2023). Fusing physics-inferred information from stochastic model with machine learning approaches for degradation prediction. *Reliability Engineering and System Safety*, *232*. https://doi.org/10.1016/j.ress.2022.109078

Lu, P., Wang, H., & Tolliver, D. (2019). Prediction of Bridge Component Ratings Using Ordinal Logistic Regression Model. *Mathematical Problems in Engineering*, *2019*, 1–11. https://doi.org/10.1155/2019/9797584

Manafpour, A., Guler, I., Radlińska, A., Rajabipour, F., & Warn, G. (2018). Stochastic Analysis and Time-Based Modeling of Concrete Bridge Deck Deterioration. *Journal of Bridge Engineering*, *23*(9). https://doi.org/10.1061/(ASCE)BE.1943-5592.0001285

Mendonça, T., & Brito, V. (2014). Bridge management in Portugal The past, the present, and the future. In *Bridge Maintenance, Safety, Management and Life extension*.

Mendonça, T., Brito, V., & Costa, S. (2016). APLICAÇÃO DE GESTÃO DE OBRAS DE ARTE – GOA –GESTÃO INTEGRADA DE ACTIVOS. In IEEES-3.

Miao, P., Yokota, H., & Zhang, Y. (2022). Deterioration prediction of existing concrete bridges using a LSTM recurrent neural network. *Structure and Infrastructure Engineering*.

Mishalani, R. G., & Madanat, S. M. (2002). *Computation of Infrastructure Transition Probabilities Using Stochastic Duration Models*. https://doi.org/10.1061/ASCE1076-034220028:4139

Moscoso, Y. F. M. (2017). *Modelos De Degradação Para Aplicação Em Sistemas De Gerenciamento De Obras De Arte Especiais - Oaes*. 210.

Oliveira, C. (2019). *Determinação e análise de taxas de deterioração de pontes rodoviárias do Brasil*. Universidade Federal de Minas Gerais.

Papadakis, V. G. (2013). Service life prediction of a reinforced concrete bridge exposed to chloride induced deterioration. *Advances in Concrete Construction*, *1*(3), 201–213. https://doi.org/10.12989/acc2013.1.3.201

Roelfstra, G., Hajdin, R., Adey, B., & Brü Hwiler, E. (2004). Condition Evolution in Bridge Management Systems and Corrosion-Induced Deterioration. *Journal of Bridge Engineering*. https://doi.org/10.1061/ASCE1084-070220049:3268

Santamaria Ariza, M., Zambon, I., S. Sousa, H., Campose Matos, J. A., & Strauss, A. (2020). Comparison of forecasting models to predict concrete bridge decks performance. *Structural Concrete*, *21*(4), 1240–1253. https://doi.org/10.1002/suco.201900434

Santamaria, M., Fernandes, J., & Matos, J. C. (2019). Overview on performance predictive models – Application to bridge management systems. *IABSE Symposium, Guimaraes 2019: Towards a Resilient Built Environment Risk and Asset Management - Report*, 1222–1229. https://doi.org/10.2749/guimaraes.2019.1222

Santos, A. F., Bonatte, M. S., Sousa, H. S., Bittencourt, T. N., & Matos, J. C. (2022). Improvement of the Inspection Interval of Highway Bridges through Predictive Models of Deterioration. *Buildings*, *12* (2). https://doi.org/10.3390/buildings12020124

Souza, C., Carvalho, J., Martins, A., Bellon, F., Alvarenga, M., Coelho, A., Andrade, M., Oliveira, D., Ribeiro, J., & Cesar Jr, K. (2023). Modelos determinísticos de previsão de degradação de pontes por regressão polinomial de 3ª ordem. *XIV Congresso Brasileiro de Pontes e Estruturas*.

Vieira, D. R., Moreira, A. L. R., Calmon, J. L., & Dominicini, W. K. (2018). Service life modeling of a bridge in a tropical marine environment for durable design. *Construction and Building Materials*, *163*, 315–325. https://doi.org/10.1016/j.conbuildmat.2017.12.080

Wellalage, N. K. W., Zhang, T., & Dwight, R. (2015). Calibrating Markov Chain–Based Deterioration Models for Predicting Future Conditions of Railway Bridge Elements. *Journal of Bridge Engineering*, *20*(2). https://doi.org/10.1061/(ASCE)BE.1943-5592.0000640

Xu, G., & Azhari, F. (2022). Data-driven optimization of repair schemes and inspection intervals for highway bridges. *Reliability Engineering and System Safety*, *228*. https://doi.org/10.1016/j.ress.2022.108779

Zambon, I., Vidocic, A., Strauss, A., Matos, J., & Friedl, N. (2018). Prediction of the remaining service life of existing concrete bridges in infrastructural networks based on carbonation and chloride ingress. *Smart Structures and Systems*.

Bridge Maintenance, Safety, Management, Digitalization and Sustainability – Jensen, Frangopol & Schmidt (eds)
© 2024 The Author(s), ISBN 978-1-032-77040-6
Open Access: www.taylorfrancis.com, CC BY-NC-ND 4.0 license

Developing a guideline for structural health monitoring of road bridges in Germany

F. Hille, R. Herrmann & R. Schneider
Bundesanstalt für Materialforschung und -prüfung (BAM), Berlin, Germany

S. Pitters & F. Wedel
Marx Krontal Partner MKP GmbH, Hannover, Germany

I. Hindersmann
Bundesanstalt für Straßenwesen (BASt), Bergisch Gladbach, Germany

ABSTRACT: In recent years, Structural Health Monitoring (SHM) has become a useful and increasingly widely used tool for supporting lifetime extensions of existing bridges with known structural deficiencies or indications of potentially critical damages or damage processes. At the same time, methods and tools are emerging, which enable monitoring-informed predictive maintenance of new and existing bridges based on digital twins. The monitoring process – starting from the definition of monitoring actions and ending with decisions based on monitoring outcomes – is complex and requires expertise in structural engineering, operation and maintenance of bridges, metrology, and data analytics. To support German road authorities, engineering consultancies, building contractors and other stakeholders of the bridge management, the Federal Highway Research Institute (BASt) has initiated the development of a new guideline for applying SHM as part of the management of road bridges. The guideline will present various use cases and for each identified use case, it will propose a proven monitoring scheme. In addition, the guideline will provide guidance on assessing the benefits of SHM as well as a common approach to managing monitoring data as a systematic basis for integrating monitoring data in the bridge management. This contribution discusses the motivation, objectives, and scope of the guideline, describes its use case centric structure and outlines the proposed data management.

1 INTRODUCTION

Germany's road infrastructure is facing several challenges, including a significant increase in traffic and a high average age of bridge structures. The maintenance management of bridges is currently based on standardized inspections, which largely assess the condition of the structure visually and manually. At the same time, the development of procedures and technical requirements for Structural Health Monitoring (hereinafter referred to as "monitoring" for short) has progressed to the point where it is one of the most widely used tools for reliably determining the structural condition of bridges and, if necessary, predicting developments. Monitoring describes the process of recording and processing measured values over a representative period of time and combines all the necessary tasks from the installation of sensors to the evaluation of the analyzed data. At present, the use of monitoring is largely limited to event-related (reactive) measures. However, the great potential of monitoring lies in the future support of predictive maintenance.

DOI: 10.1201/9781003483755-236

A survey conducted in 2020 among experts of federal and state road authorities found that the use of monitoring is limited to existing damage and deficiencies (Hindersmann, 2021). According to the survey, barriers include a lack of knowledge about the applications and benefits of monitoring, the procurement process of monitoring services as well as the handling of data storage.

Within the framework of the coordination committees for the maintenance of engineering structures, it was decided to promote the targeted use of monitoring. This approach is to ensure that the structures can be operated safely over the long term. The aim is to contribute to a reliable, safe, and sustainable infrastructure. The operators of the structures are to be supported by best practice examples, training and standardized procedures for the use of monitoring. This objective will additionally be emphasized by the fact that the German standard which regulates bridge inspections is currently revised and the next version will include monitoring as a standard inspection routine (Marzahn et al., 2023). Further, two guidelines regarding monitoring of bridges and other engineering structures have been developed recently in Germany (DBV, 2018), (DGZfP, 2022).

Against this background, the specific objective of a research project founded by the German Federal Highway Research Institute (BASt) is to produce a brochure-type guide for the practical application of monitoring of road bridge structures. Since a brochure will not cover all issues or questions that may arise in the context of a monitoring application in detail, an additional compendium-type report will be published. This report will not only cover technical issues but will specifically and additionally address issues such as the assessment of the monitoring's economic feasibility, how to tender and award monitoring installation and operation services, and what peculiarities should be considered when drafting contracts.

A variety of typical and executed monitoring applications on road bridges has also been described within the guideline. Ordered in monitoring use cases, their typical utilizations as well as their typical benefits are described, supplemented by model cases. The collection primarily compiles use cases that are already frequently used, though they are complimented by some rare cases.

Typically, measurement data and partially processed data too are currently held by the operator of the monitoring system. There is no principal data transfer from the specialist service provider to the client, mostly only reports. As more and more monitoring applications are implemented for the various use cases, standardization of procedures and the establishment of data management systems for the resulting data is of central importance. In addition to the reported and visually displayed results, the road administration also has the task of storing the processed measurement data in a machine-processable form, with the aim of using this data as a basis for a renewed evaluation, but also as a data basis for future interval-based evaluations. Within the project the basics for the design of suitable data management systems will be extracted as well as the question will be processed, how the inclusion of user agreements can be anchored in the contracts that govern how the data is to be described and how it is to be transferred.

This paper presents a procedure to obtain information on the current state of the art of the use of monitoring on road bridges in the federal and state road authorities in Germany. Based on this state of the art, a guideline for the application of SHM and a report are developed. The content of this paper is determined by the focus of the guideline, which is based on the best possible applicability to the use of monitoring within the maintenance process.

2 THE GUIDELINE DEVELOPMENT PROCESS

In preparation of the guideline an expert workshop with representatives of the state road and the federal highway authorities was planned to acquire the specific requirements and particularities. The workshop is supposed to be a key component of the project, as the project results and the guideline brochure can only be tailored to the administrations requirements through contact with the addressees. The workshop was carried out in two stages. The first stage involves as many stakeholders as possible, who are surveyed in order to get a feeling for the concerns of the addressees. An online tool was used to conduct the structured survey. Depending on the attendees' roles, alternative or additional questions were asked. The results of this survey were used to prepare for an expert workshop, where as the second stage they were presented and discussed.

2.1 *Online survey*

In an online survey, which was aimed at road bridge management authorities, monitoring system providers and bridge monitoring companies, we sought to understand the challenges hindering the implementation of monitoring. With 137 participants (35 persons from road bridge authorities), key findings include:

- Common Challenges: 43% reported that they had issues before, related to data handling and evaluation, procurement processes or vandalism/measurement faults.
- Guideline Awareness: While guidelines like DBV-guideline (DBV, 2018) or DGZfP- guideline (DGZfP, 2022) are recognized, full utilization is not yet established.

Figure 1 shows where the most frequent problems occurred related to monitoring.

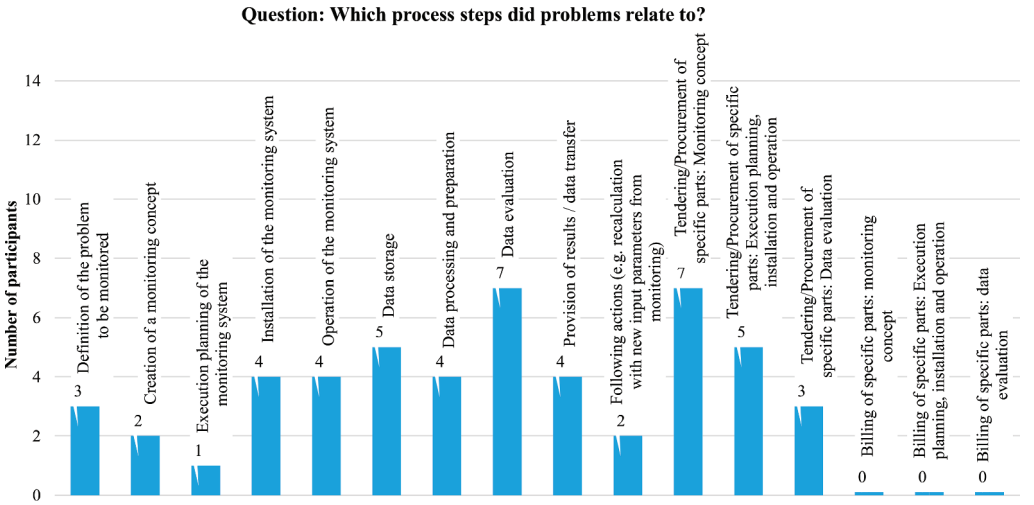


Figure 1. Results of the online survey on the topic: Which process steps did any problems relate to?.

2.2 *Expert workshop*

To get more detailed information and to be able to ask further questions, an expert workshop was conducted, involving representatives from the state road and the federal highway authorities, as well as the inviting BASt, BAM and MKP GmbH. The workshop addressed key issues raised in the earlier online survey. A key outcome of the workshop was the realization of the insufficient acceptance of the monitoring topic, as well as the associated guidelines. The following reasons were identified:

- Lack of a standardized process for guideline implementation in road authorities.
- Importance of active involvement of road authorities in guideline creation.
- Existing guidelines being fee-based, leading to administrative challenges.

To boost acceptance of the guideline created within this project and its brochure within the infrastructure sector, key strategies have been outlined. Firstly, there is an exploration of official introduction methods to establish credibility. Secondly, active involvement of states and recipients is emphasized, including a review process and acknowledgment of contributors. Thirdly, BASt commits to free publication to alleviate financial barriers. Lastly, a comprehensive publicity plan involves a BASt webinar, conference presentations, and potential post-project seminars for broader dissemination. These strategies collectively aim to ensure the guidelines' official, collaborative, and cost-free nature, fostering increased recognition and utilization within the infrastructure community.

3 SCOPE OF THE GUIDLINE

3.1 *Monitoring use cases*

The various possible uses of monitoring are summarized in the following section in the form of monitoring use cases. The project-specific use cases can be derived from project objectives and represent processes that contribute to the achievement of the defined objectives (BMDV, 2019).

Several use cases have already been identified in Hindersmann (2021), Hindersmann et al. (2023) and Nieborowski et al. (2023). These are use cases that are already frequently used in practice or which will have potential for future application. Currently, the use of monitoring is largely limited to event-related (reactive) measures (monitoring of known damage, monitoring of deficits from recalculation or construction). However, the great potential of monitoring also lies in supporting predictive maintenance.

The cases are structured within the guideline based on the template of the sample cover letter and the use case profile from BIM Deutschland (BIM = building information modeling) (BMDV, 2019). The preparation in the form of fact sheets is intended to achieve a clear and plausible presentation of the comprehensive possibilities for the use of monitoring in order to reduce barriers. For each use case, the initial task, the implementation and the benefits are described and concrete examples are used to illustrate the application in practice.

The following list summarizes the various use cases, described in the guideline:

- Known localized damages,
- known deficits from recalculation or construction,
- determination of effects,
- support for regular inspection procedure,
- accompaniment for major buildings,
- maintenance and reinforcement measures,
- load tests,
- predictive life cycle management,
- birth certificate,
- measures during the construction period,
- protection of buildings during neighboring construction work.

3.2 *Economic feasibility studies*

Before implementing a monitoring scheme, bridge owners and operators are concerned with determining its benefit-cost ratio. To evaluate this ratio, the expected costs associated with the future usage of a road bridge with and without monitoring have to be estimated. This is an intricate task since these expected costs depend on:

- the future development of the condition and performance of the bridge,
- the quality of the monitoring system and data processing,
- the possible monitoring outcomes,
- the future decisions associated with those monitoring outcomes (i.e., decisions on actions such as traffic restrictions, inspection, maintenance, bridge replacement etc.) and
- the direct and indirect costs associated with those actions as well as the costs of installing, operating, and maintaining a monitoring system.

The difference between the expected costs of operating a bridge without and with monitoring is the net value of information (VoI) provided by a monitoring system (Kamariotis, et al., 2022). If this metric is positive, the costs of a monitoring system are justified by its benefit.

A generic framework for quantifying the VoI of SHM systems is outlined in Straub, et al. (2017) and a practical concept for determining the VoI of threshold monitoring systems for road bridges and its implementation in a software tool is presented in Schubert, et al. (2020). Based on the existing (scientific) literature and the expertise provided by the German road authorities, the planned guideline will (a) highlight similarities and differences between

existing procedures for assessing the economic feasibility of maintenance actions and analyses for evaluating the benefit-cost ratio of monitoring systems and (b) provide practical advice on evaluating this ratio. It will also discuss situations in which such analyses are less relevant.

3.3 *Procurement process*

As described in Section 2 and also as shown in Figure 1, one of the most challenging areas for the bridge authorities when introducing monitoring into their daily work is the implementation of tendering, awarding and contracting activities. This is due to the novelty of monitoring as a technique to determine bridge safety measures. The lack of knowledge mostly regards the following points:

- What are the required services to be tendered and provided?
- Who are the players and which specifications and expertise potential bidders must provide?
- What are appropriate award criteria?
- What constraints need to be considered when drafting the contract?
- How liability claims need to be regulated and formulated?

Based on the authors' experience with the use of monitoring on road bridges, suggestions are made for the procedure. With regard to tendering, parts of the overall service can be tendered separately, depending on the requirements. There are also different types of tenders, depending on whether specific service points or the entire service is functionally tendered. The right choice is influenced by a number of factors. The brochure will provide suggestions for choosing the right type and scope of tender. The brochure also recommends criteria that should be considered when negotiating contracts. In addition to price, these include quality assurance criteria such as the qualifications of the bidders. This is particularly important in view of the fact that from time-to-time vendors "promise the moon". When drafting contracts, there are a number of special issues that need to be addressed and are not part of a classic bridge inspection. For example, how to deal with a temporary outage of parts the measurement equipment, e.g., due to vandalism. Minimum response times may need to be defined. Rules may also need to be established for very long measurements, to take into account the additional costs of aging measurement equipment that may need to be replaced. Liability issues also need to be addressed.

3.4 *Measurement technology*

In general, instrumentation combines all technical components of a monitoring system. This includes not only the actual sensors, but also components for signal transmission and data processing and storage. A classical monitoring system consists of sensors, sensor connection components, data acquisition systems, and a measurement computer, where further external components can be connected. To assist in the best practice application of monitoring in bridge condition assessment, the guideline lists and presents the various aspects that influence the selection of measurement technology. The selection of the measurement technology needs to be based on the monitoring concept. This concept takes into account all aspects of the technical implementation of a monitoring task in the monitoring system. Besides the actual monitoring objective this includes further aspects such as the type and size of the structure to be monitored, requirements for long-term stability or, if necessary, interchangeability, taking into account economic criteria. In addition, important requirements for the selection of the sensor technology such as measurement range, measurement accuracy, sensitivity, measurement resolution and sampling frequency must be defined. Last but not least, possible technical and environmental influences must also be taken into account. The guideline also describes the various technical components of conventional monitoring systems. In addition, new types of IoT monitoring systems (IoT= internet of things), usually organized in sensor network structures, are briefly discussed. The relationship between the measurement task and the measurement technology is presented to assist road bridge authorities. For each of the 15 different measurement tasks, the intent and the measurement task are shown, and possible measurement methods and sensor technologies are assigned.

In the final section, the best known and most commonly used sensors are summarized. For the sensors mentioned, typical applications, measurement and target variables are described. Further, the measurement principle is presented and, if necessary, comments on advantages and disadvantages or special notes on application limitations are given.

3.5 *Data management*

From the perspective of road authorities, managing the data generated by SHM applications is challenging, but it can be very valuable for future inspections and new methods that are offered by manufacturer and the SHM community. The current way of dealing with monitoring data, which typically includes time-series data from sensors and images in a variety of formats, quantities, and qualities, is that most of the data handling is done by the specialist service provider for structural measurements (SSPSM). Some very advanced road authorities in the field of SHM also fulfill the role as a SSPSM and specialist planner for SHM, already. In addition to services such as continuous monitoring of anomalies and exceeded limits, the SSPSM typically provides a report at defined points in time or at the end of the monitoring project, where the measurements are evaluated in detail and combined with various types of numerical analysis, modal analysis, structural assessment, and prognosis using models and data from external sources. This report is a document that includes plots and other visualizations of the data and the statements of the structural assessment at one point in time. The data management on the SSPSMs side is addressed in national, see e.g. (Empelmann, et al., 2023) and international literature, see e.g. (Rigotti, et al., 2022). The focus of this contribution is to solve the data management challenges as a governmental task for road authorities to preserve all relevant information regarding the asset stock in a long-term perspective. According to the results of the before mentioned survey, in only one third of the cases monitoring data is, in addition to the report, stored at the road agency for later use or reuse for other purposes, see Figure 2a. This is mostly due to difficulties in negotiating how the data should be structured and stored, and how it can be technically shared between private companies and public authorities. The need for recommendations on data management is considerable, as more than half of the participants in the survey indicated, see Figure 2b.

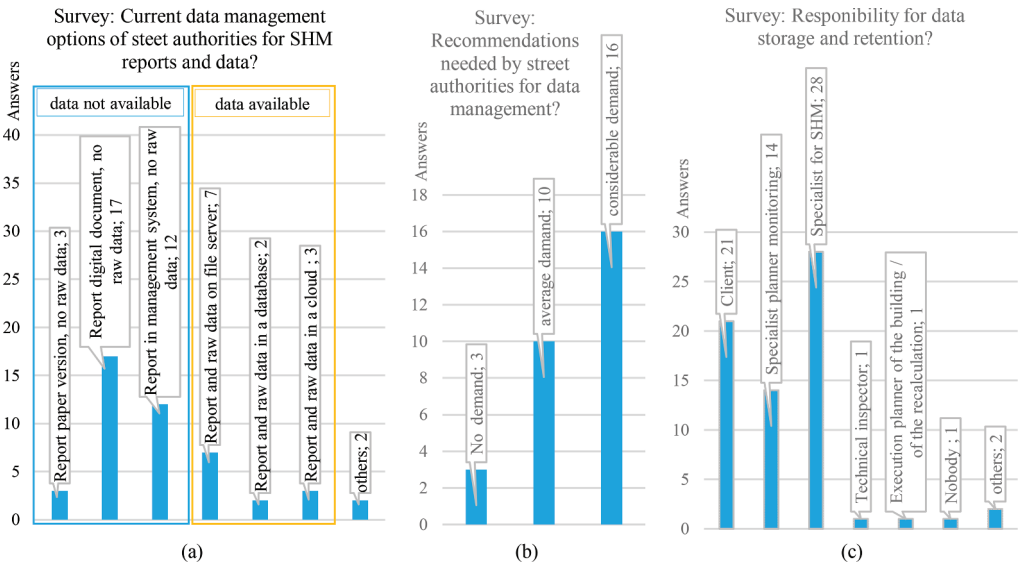


Figure 2. Survey result (a) currently used procedures for road authorities to store reports and data (multiple answers - 37 participants); (b) demand for recommendation in the field of data management (single answer - 29 participants); (c) responsibility for data storage and retention (multiple answers - 37 participants).

The need and responsibility to store the monitoring data exists for two stakeholders: for SSPSM/mounting planner and the owner/client, see Figure 2c. While the SSPSM need to handle the data that they acquire and analyze according to the contract, the road authorities need to be able to receive, archive and share the data for a specific infrastructure element. While for the administrative side, it is less important (unless the role of the structural assessment is fully covered by the road authority) to analyze the data in detail. The import interests and needs for road authorities has been collected during the expert workshop and taken from the survey evaluations. The requirements were captured in the form of *user stories*, that are short notes in a defined order:

'As a <role> I can <capability>, so that <receive benefit>'

This user stories are visualized as a user story map and will be made available as a collection to the road authorities to prioritize, their individual requirements when evaluating a data management software or development road map. One result of the discussion was that the value of SHM data, data governance and data sovereignty is a responsibility that needs to be addressed by road authorities, but currently the road authorities do not have structured processes to continuously evolve their capabilities to receive, archive and share SHM data including quality control, see (Herrmann, et al., 2017) and accounting. To fill this gap two business processes have been developed for the structured receipt of data from monitoring project, see Figure 3. The business process 1 starts with a given monitoring challenge. Depending on if the monitoring is part of a BIM tender of a new building (e.g. birth certificate), the tender of a monitoring concept or for a SHM installation the clients communicate their needs and technical capabilities for data management which are elaborated, extended and made compatible to the monitoring concept and current state of the art by the specialist planner and the SSPSM. This so-called employer's data requirement (EDR*)* is a document that specifies the data format, meta data, naming schemas, semantic linkages to models, data interfaces, limitations (API-calls, data amount), data delivery cycles, delay limits, pre-computed data evaluations, data aggregations, general purpose visualizations and quality/completeness checks, that SSPSM needs to deliver the data. The road authority acknowledges the filled EDR, when it satisfies their expectations and specifications. This EDR document will be stored along the data with revision tracking, so that each user of that data will find the relevant details about how the data can be retrieved and interpreted. As this is challenging, the EDR's template and the road authority's requirements should evolve with further monitoring projects.

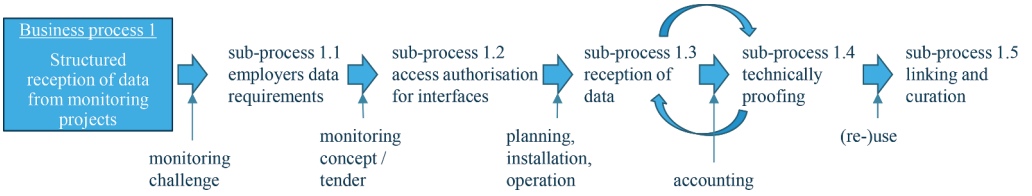


Figure 3. Business process 1 for road authorities to negotiate and realize the data delivery of SHM data acquired by the SSPSM.

After the EDR is finalized in the business process the road authority grants access to all required technical interfaces and the SSPSM delivers the data and meta data repeatedly, as agreed. The road authority checks the data delivery, using automated workflows and still needs to make the data source available in the used asset management systems, like 'SIB Bauwerke' or other catalogs, so that it will be findable and accessible. The business process 2 describes how the SHM data is used from a typically independent stakeholder that oversees the assessment of the structure, see Figure 4. If the SSPSM/specialist planner is also doing the assessment, then the responsibility to deliver reusable data with good meta data description and sufficient change/error management is even higher. Otherwise, the data may be unintelligible or even misinterpreted.

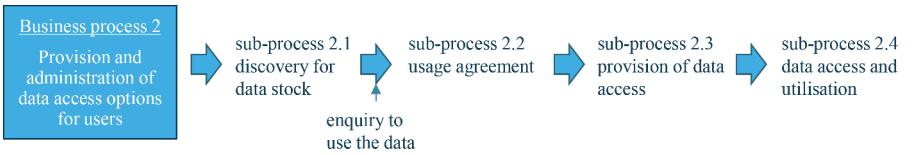


Figure 4. Business process 2 for road authorities to discover and share the available SHM data for structural assessment of structures under their responsibility.

The business process 2 involves the discovery of the available information about a realized monitoring activity on a structure and negotiates a usage agreement that gives both sides confidence of how the data and the access authorizations can be used, stored, and passed on. The road authority finally grants access, and the data can be used for any automated and manual data workflow.

The obligation to preserve the data long-term, that should typically be as independent from vendor-specific software, like database programs, helps to cleanly separate or export it so that it is available to a broad variety of dash-board solutions and digital-twin platforms. So, the data management might develop in the direction of a data broker in a healthy eco system of data producers and consumers for totally new business cases and maintenance routines.

4 SUMMARY

The maintenance management of Germany's road infrastructure is currently based on standardized inspections, where the structural condition is largely assessed visually and manually. The development of procedures and technical requirements for structural health monitoring is nowadays advanced and a widely used tool to reliably determine the structural condition of bridges and, if necessary, to predict future developments. Nevertheless, within the maintenance scheme of Germanys existing road bridges, monitoring is only used in exceptional cases. There are many reasons for this, but the most important is a lack of knowledge and experience in the practical application of monitoring. As part of a research project, the authors aim to develop a guideline for the application of monitoring measures on road bridges as an assistance instrument for the bridge administration bodies. This paper explains how an online survey as well as an expert interview workshop with participants from the road bridge authorities were used to extract the key issues that are still considered to be a challenge and for which a standardized procedure will be beneficial. These key issues include a lack of awareness about the structural use cases for which monitoring should be applied to provide information or improve the integrity of bridges as well as what the appropriate measurement technology will be, depending on the use case. Most importantly, a standardized monitoring process is missing or unknown as well as the parties necessarily involved in that process. In addition, there is a lack of knowledge about how the value of monitoring can be determined through economic feasibility studies and how the monitoring services can be tendered and awarded. A separate area of concern is data management. Here, the guideline suggests approaches and describes important boundary conditions to be considered.

The final guideline offers solutions to all these topics. In addition to a detailed guideline edition in the form of a report, the most important statements are condensed and published in a short and concise brochure. The whole process of guideline development was attended by consultation and discussion with the addressees from state and federal road authorities. This is understood as a necessary basis for the successful introduction and acceptance of the guideline.

The paper is based on parts of the research project carried out at the request of the Federal Ministry for Digital and Transport, represented by the Federal Highway Research Institute, under research project No. 15.0707/2022/LRB. The authors are solely responsible for the content.

REFERENCES

BMDV (ed.), 2019. BIM4Infra Handreichung und Leitfäden - Teil 6 - Streckbriefe der wichtigsten BIM-Anwendungsfälle [in German].

DBV (ed.), 2018. Merkblatt: Brückenmonitoring [in German].

DGZfP (ed.), 2022. Merkblatt B 09 - Dauerüberwachung von Ingenieurbauwerken [in German].

Empelmann, M. et al., 2023. *Konzepte für das Datenmanagement der Intelligenten Brücke.* Bergisch Gladbach: Fachverlag NW in der Carl Ed. Schünemann KG.

Herrmann, R., Rabe, J., Bolle, G. & Marx, S., 2017. Konzepte für Datenqualität und Datenablage bei Entwurf und Umsetzung von Monitoringsystemen [in German]. *Bauingenieur*, 92(12), pp. 537–545.

Hindersmann, I., 2021. Anwendung von Monitoring bei Brücken der Bundesfernstraßen und zukünftige Monitoringstrategien [in German]. *Fachkongress Digitale Transformation im Lebenszyklus der Verkehrsinfrastruktur: Tagungshandbuch 2021*.

Hindersmann, I., Müller, M. & Kaplan, F., 2023. Monitoring von Ingenieurbauwerken - aktuelle und zukünftige Anwendungsfälle [in German]. *2. Fachkongress Digitale Transformationder Verkehrsinfrasturktur - Tagungsband 2023*.

Kamariotis, A., Chatzi, E. & Straub, D., 2022. A framework for quantifying the value of vibration-based structural health monitoring. *Mechanical Systems and Signal Processing*, Volume 184.

Marzahn, G. et al., 2023. Bauwerksprüfung nach DIN 1076 [in German]. *Bautechnik*, 100(11), pp. 699–706.

Nieborowski, S. et al., 2023. Digitaler Zwilling Brücke im Betrieb [in German]. *Bautechnik*, 100(2), pp. 86–93.

Rigotti, M. et al., 2022. Design of IT platforms for monitoring data of transport infrastructure. *Project Report*, *EU Horizon 2020*, *IM-SAFE D4.3*.

Schubert, M. et al., 2020. Wirtschaftlichkeitsuntersuchungen von Monitoringmaßnahmen [in German]. *Berichte der BASt, Heft B 156*.

Straub, D. et al., 2017. Value of information: A roadmap to quantifying the benefit of structural health monitoring. *12th Intern. Conference on Structural Safety & Reliability (ICOSSAR 2017)*.


Taylor & Francis
Taylor & Francis Group
http://taylorandfrancis.com

SS12: Realising the extension of BIM for existing bridges

Organizers: N. Powers, V. Samec & M.A. Valenzuela Saavedra


Taylor & Francis
Taylor & Francis Group
http://taylorandfrancis.com

Bridge Maintenance, Safety, Management, Digitalization and Sustainability – Jensen, Frangopol & Schmidt (eds)
© 2024 The Author(s), ISBN 978-1-032-77040-6
Open Access: www.taylorfrancis.com, CC BY-NC-ND 4.0 license

Overview of the use of BIM for bridges across Australia and New Zealand

Nigel G. Powers
National Transport Research Organisation

ABSTRACT: Australia's freight task, and to a lesser extent in New Zealand, is growing at a rapid rate due to unprecedented population growth, coupled with increased demand from our trading partners in Asia and rapid changes in technology, e-commerce, and consumer behavior. A significant proportion of freight is transported using the road network and to remain competitive this network needs to facilitate fast, efficient, and effective access. This is a significant challenge with an ageing bridge network, regularly experiencing extreme climatic conditions and the freight industry constantly pushing to increase access and allowable loads.

Expectations on road infrastructure managers like Federal, State and Territory Governments, local government and private operators is very high and has become heightened even further with scrutiny via social and other forms of media. At the same time, there are significant pressures on government to provide greater level of service for other infrastructure they manage like schools, hospitals and law enforcement.

The above challenges create significant pressure on road infrastructure managers to minimize spend on the management of the network while attempting to meet the high expectations of the community. The use of Building Information Modelling (BIM) for bridges is seen as one of the tools that can assist road infrastructure managers in meeting the above challenges. To date its uptake has been limited with some authorities adopting BIM for major bridge structures and on recent large-scale projects but wider adoption is very limited.

The BIM survey outlined in this paper is part of the work being conducted by Task Group 5.6 – BIM in Structure Management for the International Association for Bridge and Structural Engineering (IABSE). This paper will explore the adoption of BIM across Australia and New Zealand and what is required for more significant adoption.

1 INTRODUCTION

1.1 *Australia and New Zealand challenges*

Australia's freight task, and to a lesser extent in New Zealand, is growing at a rapid rate due to unprecedented population growth, coupled with increased demand from our trading partners in Asia and rapid changes in technology, e-commerce, and consumer behavior. Overall, in Australia transport logistics was valued at over A$110 billion in 2010 (ACIL Allen Consulting, 2014) and has been steadily increasing since.

A significant proportion of freight is transported using the road network and to remain competitive this network needs to facilitate fast, efficient, and effective access. This is a significant challenge with an ageing bridge network, the regularly extreme climatic conditions and the freight industry constantly pushing to increase access and allowable loads. The majority of bridges we built and designed before 1950 to now outdated standards and for much lesser loads.

Expectations on road infrastructure managers like Federal, State and Territory Governments, local government and private operators is very high and has become heightened even

DOI: 10.1201/9781003483755-237

further with scrutiny via social and other forms of media. At the same time, there are significant pressures on government to provide a greater level of service for other infrastructure they manage like schools, hospitals, and law enforcement.

The above challenges create significant pressure on road infrastructure managers to minimize spend on the management of the network while attempting to meet the high expectations of the community. The use of Building Information Modelling (BIM) for bridges, also known as Bridge Information Modelling (BrIM) is seen as one of the tools that can assist road infrastructure managers in meeting the above challenges.

1.2 *IABSE task group 5.6 - BIM in structure management*

In November 2020, the International Association for Bridge and Structural Engineering (IABSE) formed Task Group 5.6 - BIM in Structure Management (Task Group 5.6). Task Group 5.6 aims to connect Bridge Management Systems (BMS) with existing BIM solutions, based on Open BIM standards.

The Mission Statement/Objectives of Task Group 5.6 is:

The Task Group aims to connect BMS (Bridge Management Systems) with existing BIM solutions, based on Open BIM standards. The complexity of maintenance/inspection requires organized, automated, open and transparent digital processes, which should consider both - structure and asset management data.

The BMS (Bridge Management System) aims to complete digital storage and exchange of data, cost as well as deterioration, optimization and analysis models and their interoperability with existing BIM solutions.

The vision includes 3D/4D/5D/6D software and hardware independent data exchange between different software technologies during life cycle and beyond, considering also monitoring, sensor equipment and damages on the structure along time axis. Open BIM technology for the interoperability from technical, semantic and organizational point of view is of main interest. (IABSE, 2023)

The Scope & Limitation of the group is:

As template for further structures only bridges will be focused.

Conceptually the connection of BIM model to BMS and vice versa should be focused. Therefore the existing documents, researches and current open BIM standard capability will be used.

Existing software solutions and BMS providers should be invited to present their possible consideration resp. realization of BMS connection in their established BIM workflows and BIM viewers.

The final goal is the IDM (Information Delivery Manual) – explaining how to connect BIM model with BMS and vice versa – in form of SED. (IABSE, 2023)

2 INPUT FROM THE INDUSTRY

2.1 *Bridge asset owners input*

To progress the research being undertaken by Task Group 5.6, input was required from bridge asset owners and operators across the world. It is important to understand the current situation worldwide, with the outcomes to be reported and inform further research and development. This will help to understand current operations, requirements and expectations. Ultimately it will help to develop a common standardized structure to exchange data between different systems, putting bridge asset owners in control to influence the process.

2.2 *Survey*

Task Group 5.6 developed a bridge asset owner survey in late 2022 into early 2023. To assist in achieve the goals of the project, the survey covered the following areas and asked the following questions:

- Introductory questions – covering how assets are managed?
  - How often do you have periodical inspections of your bridges?
  - Are these performed by your organization or is someone from outside hired to do this?

- How are data from inspection and maintenance and other information about the structure stored?
- How do you reference findings to the structure? Are you e.g., using a structured approach with unique IDs and standardized characterizations? Do you reference drawings or BrIM models?
- How is your budget for inspection and maintenance decided and how do you prioritize within this budget?
- Is your organization interested in BrIM and or BIM?

- General questions – covering how changes are identified, recorded, and managed?
  - How do you handle these changes today?
  - What is your system to prioritize repairs?
  - How do you arrive at the decision to restrict usage of a bridge?
  - Are all bridges/assets in your network stored in one common database, or is it fragmented to many systems?
  - Is all information split up in database format, or is your BMS appended with text files?
  - Do you have projects or cooperations with academia or software providers on improving your bridge information modeling, if so, what is your roadmap?
  - Access control could be important in some cases, e.g., to limit access to different types of information. Is this a feature that will be mandatory for you in the future?
  - How is your approach today for rating your current asset value and managing maintenance priorities?
  - How do you wish this process was?
  - Which factors need be considered or included in this process?
  - How do you ensure that the information in your asset management is correct?

- Visualization – covering asset data.
  - What type of visualization do you consider useful for you? This could be projection of damage onto the structure, tabulations of development of damage with time, or other information.
  - Could you expand on how you do this today, and identify features you wish to be available?
  - Which level of detail of damage description seems reasonable to you?
  - Based on your experience, could you elaborate on how important it is that that the dataset, model and visualization contain up-to-date information?
  - What would be an acceptable updating period?
  - What level of visualization detail do you think is minimum needed, and what level is optimum?
  - For which structural parts do you desire geometrical details of degradation (e.g., loss of effective concrete cover or loss of cross-section of rebars), and for which structural parts would a color code of degradation suffice (e.g., effectiveness of drainage, water circulation)?
  - What plans do you have to utilize this feature in your asset management system in the short and long term?
  - How do you store inventory data today?
  - Are foundation properties included in your models today (e.g., observations of settlement, scouring etc.)?

- Round-up Questions – covering asset systems.
  - What three key features will your perfect asset management system have, and how often will you use these features?
  - What nice-to have features do you wish were easily available from your dataset of current bridges?
  - What is your personal view of the hierarchy between BrIM and BMS? I.e., which one is the user front end and which the axillary data base in the background?

In February 2023, Task Group 5.6 circulated the survey to bridge asset owners across the world seeking their input into this important initiative.

3 SURVEY RESULTS – AUSTRALIA AND NEW ZEALAND

This paper will focus on the responses from bridge owners across Australia and New Zealand

3.1 *Survey participants*

The survey was sent to all government road and transportation authorities across Australia and New Zealand as they are responsible for a large proportion of road bridges across the two countries. The following organizations generously gave of their time to complete the survey:

- New Zealand Transport Authority (NZTA) – Waka Kotahi
- Main Roads Western Australia (MRWA)
- Department of Infrastructure and Transport (DIT), South Australia
- Department of State Growth (DSG), Tasmania
- Department of Infrastructure, Planning and Logistics (DIPL), Northern Territory

3.2 *Survey results*

The following sections outlines the key aspects of the responses to the survey from the survey participants in Australia and New Zealand.

3.2.1 *Bridge inspections, data, and BIM*

There was significant alignment between the respondents regarding bridges inspections and data. Regarding inspections, all have set frequencies for their bridge inspections although there is some variability in the timeframes as can be seen in Figure 1 below. The difference is timeframe is mostly driven by risk with older structures and those in poor condition having a shorter timeframe than newer structures, in good condition and good capacity. Inspections are undertaken by a mix of internal and external resources.

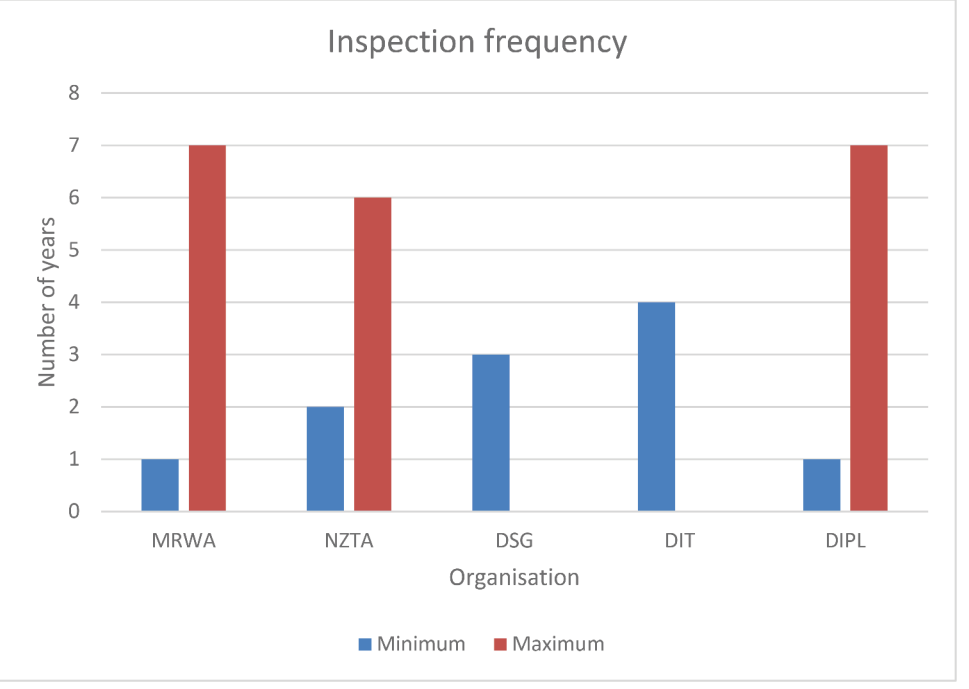


Figure 1. Bridge inspection frequency.

The data obtained for bridges and related structures is generally contained within a bridge or asset management system which has been specifically developed for each bridge owner. Overall, they all have individual asset identification for their structures electronically and/or physically on-site represented with an identification plate or similar marking. The data obtained from inspections is used to assist with the prioritization of works with all respondents acknowledging budgets are tight.

Overall, there is a very low uptake with BIM with all focused-on asset systems or BMS. There is some interest in adopting BIM in the future although the responses seem to indicate pessimism regarding its benefits.

3.2.2 *Bridge management*

Overall, there was also a significant amount of alignment on the management of bridges and data and systems supporting it. From a systems perspective, all are using a BMS to capture data on their bridges and related structures. In general, these systems have been developed specifically for the bridge owner. The data contained within the BMS is a mixture of formats depending on the dataset. Inventory information is held in basic, transferable format within the BMS but other aspects like reports and photos are saved in different formats.

The quality of data in the BMS is controlled in three main ways. Firstly, access is generally restricted to those within the organization and those external that have approval to use. The other two ways are related to the verification of the data contained in the BMS. Verification is often undertaken at the source of creation, i.e., the inspection report quality reviewed before being finalised. The other main approach was auditing within the system based on standards set by the bridge owner.

The use of data within the BMS was consistent within the responses received. The prioritization of funding and remedial works was often based on the most severe defects but also had an overlay of risk. The action of restricting bridge usage was in general based on the full assessment of all data to hand. The data required, as indicated by the respondents included:

- Damage extent,
- Cost of repair,
- Safety,
- Condition rating,
- Probability of failure,
- Level of Service,
- Legal,
- Risk,
- Environmental,
- Whole of Life Cost,
- Heavy vehicle usage, and
- Sustainability

The outcome of the assessment would require higher level approval due to the level of risk.

The valuation of structures was an area where there were some differences across the respondents with numerous different approaches. Some respondents had systems specifically for valuations, some utilize financial tools, others use overall bridge ratings and some it is a simple written assessment. Overall, there was agreement on the desire to have an automated way to conduct bridge valuations utilizing data within their system.

3.2.3 *Visualization*

Throughout this section of the survey there was strong alignment between the respondents in most areas. If they were to adopt BIM, the bridge owners wanted to have the following details:

- Damage overlay,
- Key Performance Indicators,
- Historical information on damage,

- Details on works programs including repairs undertaken,
- Material data for the structure,
- Geospatial information,
- Inspection data,
- Drawings,
- Photos, and
- Bridge Rating Index.

On the visualization of the data provided in the BIM most favored photos and inspection reports with some being open to schematic and simplified system data. The optimal solution though would be a combination of photo representation with as-built details. The respondents were all aligned with wanting details of degradation for all components, but all had minimal/incomplete data on foundations for their structures. Regarding the data kept in the BIM, most saw the updating of the data as critical with some of medium importance. The preference was for updating every 6-12 months but that depends on the level/risk for the structure.

At the time of the survey all respondents favored using a BMS over BIM with only some having interest or plans to further explore BIM. The features desired in their perfect BMS include:

- Quick/easy to find information,
- Easy upload of data,
- Automated,
- GIS referencing,
- Include all asset data include inspection records,
- Program management functionality,
- Risk and criticality,
- Load capacity,
- Status bar or dashboard for individual structures and the overall network,
- Tracking against Level of Service, and
- Backlog reporting.

4 CONCLUSION

Australia and New Zealand are facing significant challenges in the management of their road bridge infrastructure. The transportation of freight is critical for their economies, but their bridge stock is ageing and built to outdated standards. To continue to support the community and growth in their economy they need to seek ways to improve the way they manage their structures, and the utilization of BIM is one possible avenue.

The adoption of BIM is limited in Australia and New Zealand based on the responses to the survey. There is some interest, but all are focused on the management of their structures using a BMS. There appears to be a level of skepticism around the benefits of BIM. Some have used BIM for large bridge construction projects but not in the management of the lifecycle of an asset. Based on the responses this appears to be in part due to the lack of understanding of BIM and how it would complement their existing BMS. Also, based on the comments to the survey, there is concern that the level of investment in BIM would not be returned by the benefits of adopting it.

For BIM to be adopted across Australia and New Zealand a greater understanding of what BIM is and its benefits is required. An outline of the return on investment is required as it could take a significant investment of both time and resources to implement such as system. It would also require bridge owners to move away from familiar systems that mostly suit their current requirements.

ACKNOWLEDGEMENTS

I would like to acknowledge the following:

- IABSE Task Group 5.6 Chair Vanja Samec and the members of the Task Group for their contribution to the survey and collation of results.
- The bridge asset owners that generously gave their time to respond to the survey.
- Asanka de Silva, National Transport Research Organisation for his assistance in the collation and review of survey results for Australia and New Zealand.

REFERENCES

ACIL Allen Consulting. 2014. *The Economic Significance of the Australian Logistics Industry*. Australian Logistics Council.

IABSE. 2023. *Task Group 5.6*. Retrieved from IABSE: http://iabse.org/TG5.6.

Bridge Maintenance, Safety, Management, Digitalization and Sustainability – Jensen, Frangopol & Schmidt (eds)
© 2024 The Author(s), ISBN 978-1-032-77040-6
Open Access: www.taylorfrancis.com, CC BY-NC-ND 4.0 license

BIM-data of baseline digital twins for a new bridge maintenance system

C.S. Shim, G.T. Roh, D.H. Kang & J.W. Park
Chung-Ang University, Seoul, South Korea

ABSTRACT: With the growing deterioration of bridge structures in traffic networks, there is an urgent need for a reliable method to assess and predict bridge performance using diverse data sources. Building Information Modeling (BIM), currently being implemented in new construction projects, holds promise for providing crucial information to establish a maintenance baseline model by collecting and consolidating data from design to construction phases. However, the maintenance of existing bridges is hindered by a reliance on document-oriented information and the lack of effective integration of individual data within current bridge management systems (BMS) and information systems for inspection and repair records. To overcome these limitations, this paper aims to define key management factors and deliver a baseline digital twin model at the completion stage for maintaining existing girder-bridges. Additionally, inspection and maintenance history data generated during the maintenance stage are incorporated into the digital twin model. The paper presents the definition of BIM data for constructing a baseline digital twin specifically for common types of girder-bridges and demonstrates its functional implementation. A data-driven information delivery is presented for a typical prestressed concrete girder bridge. The effectiveness of the proposed approach is evaluated through actual examples of existing bridges.

1 INTRODUCTION

The increasing proportion of aging bridge structures emphasizes the urgent need for an appropriate maintenance plan and reliable method to assess and predict bridge performance using diverse data sources. Building Information Modeling (BIM), currently being implemented in new construction projects, holds promise for providing crucial information to establish a maintenance baseline model by collecting and consolidating data from design to construction phases. However, the maintenance of existing bridges is hindered by a reliance on document-oriented information and the lack of effective integration of individual data within current bridge management systems (BMS) and information systems for inspection and repair records. A system based on the concept of digital twins, which involves expanding this idea to introduce 3D models and related data into maintenance management systems, has been proposed (Jeon et al. 2023). In this process, a high-reliability, integrated data-driven information delivery system is required from design to operation [2]. To progress from the member-level data through the entire life cycle of a bridge using the data-driven system, a data management regime and optimization process are required. Data becomes the minimum unit of information required for business units and each stage, and utilizing this, digital models and updates in various aspects are carried out.

To overcome and satisfy these limitations and requirements, this paper aims to define key management factors and deliver a baseline digital twin model at the completion stage for maintaining existing girder-bridges from member unit to bridge system. Additionally, inspection and maintenance history data generated during the maintenance stage are incorporated

DOI: 10.1201/9781003483755-238

into the digital twin model. The paper presents the definition of BIM data for constructing a baseline digital twin specifically for common types of girder-bridges and demonstrates its functional implementation. A data-driven information delivery is presented for a typical pre-stressed concrete girder bridge. The effectiveness of the proposed approach is evaluated through actual examples of existing bridges.

2 DEFINITION OF DATA

The scope of BIM data extends from the member level that makes up the bridge to the system level. Depending on the life-cycle of the bridge, the data is segmented by a member, and accordingly, updates or exchanges of each piece of information take place. For flexible information exchange and optimization, it is essential to structure key information at each stage. And, to effectively utilize standardized data, pre-agreed data definitions between designers, fabricators, and assemblers must allow for seamless information exchange. The data for components is broadly categorized into geometry, material, performance, and external conditions (alignment, climatic conditions, fabrication, and construction-related schedules, etc.). Each piece of information is interlinked and dependent on data from the planning or design stages onward. Once such a system and procedures are established, the optimization of the data system occurs, ultimately enabling the utilization of accumulated data in the stages of sharing and maintenance. This leads to the establishment of a Digital Twin Model system for evaluation and prediction. Figure 1 illustrates the data flow of prestressed girders and the corresponding BIM model updated by this information.

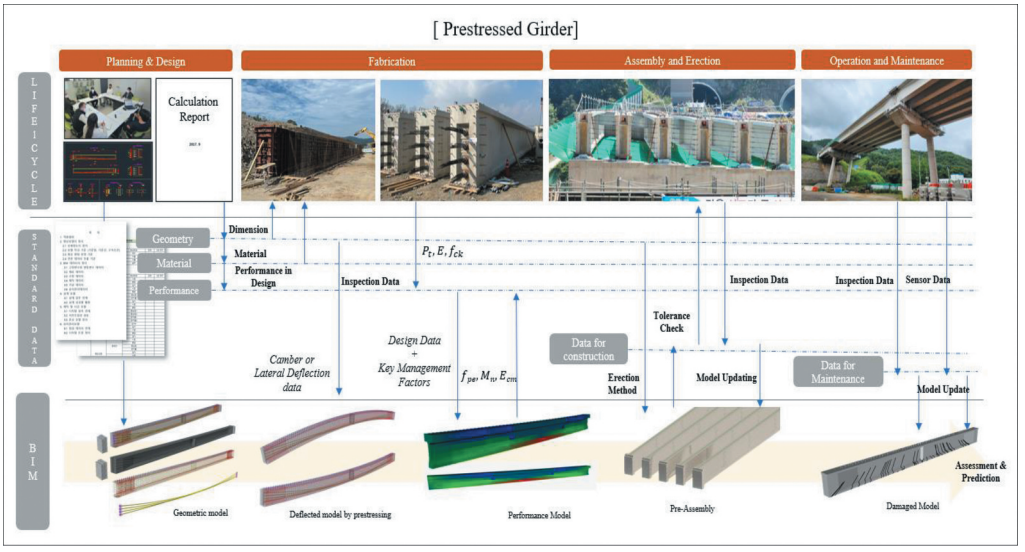


Figure 1. Data and model updating flow during the life-cycle of the prestressed girder.

The Digital Engineering Model, defined by applying data at each stage from the existing 3D geometric model, allows for a comprehensive examination of Design for Manufacture and Assembly (DfMA). This involves performance evaluation at the member level, consideration of information updates during fabrication and assembly stages, and application and evaluation in the design phase, all through the utilization of data and models. Additionally, it enables advanced checking of assembly for connection joints through pre-assembly simulation

of precast or prefabrication components, facilitating the early identification of assembly collisions. Once a system is established through data and data-based Digital Engineering Models (DEM) from the assembly stage to the as-built phase, the entire process's information and framework are managed as a baseline digital twin.

The baseline digital twin model is bifurcated into two branches for structural assessment during the operation and maintenance stages. Integrated information from these branches is utilized for evaluation and prediction. One branch comprises member force-related information for assessing the performance of components or bridges, while the other involves condition assessment by inputting or managing inspection data via the bridge maintenance management system.

To assess the strength and condition of structures, key management factors at the component level are necessary from the design stage. For instance, in the case of a girder bridge, structural components include girders and deck plates in the superstructure, and piers and abutments in the substructure. Updates for each component's key factors are based on information entered throughout the lifecycle. In the case of prestressed girders, during the design phase, factors such as geometric dimension section, concrete compressive strength, prestress material, and tension force are determined based on specifications for bending and shear strength. In the fabrication and as-built stages, actual values obtained from material tests, such as concrete compressive strength and elastic modulus related to the properties of materials, and the actual tension force specified in the tension report may differ from the design values, leading to inevitable variations in component strength.

Additionally, for prestressed concrete members, it is necessary to include data elements representing behaviors with time-dependent characteristics, such as relaxation, creep, and shrinkage, to accurately evaluate the performance of the structural member. However, determining precise values for these variables is challenging. Therefore, a stepwise management approach is adopted, using deflection values of members or strain data through sensors as indirect data. To achieve this, factor settings for component strength assessment are required, and these factors are continuously updated based on the input data. For prestressed girders, proposed key management factors include effective prestress stress (f_{ps}) and concrete elastic modulus (E_{cm}). The information input and updated throughout the lifecycle of the prestressed girder are presented in Table 1.

Ultimately, to assess the bridge system after the As-built stage, a system-level analytical model consisting of key factors of components is constructed. Based on data from field load tests conducted on the actual bridge, the lateral load distribution ratio is updated. Subsequently, a system is established to evaluate the member forces using standardized inputs in the common domain.

Table 1. Data definition for prestressed girder during its life-cycle

	Geometry Data	Material	Schedule(Date)	External Condition	Performance
Design	Dimension	F_{ck}, E_{cm}, f_{ps}, E_s	-	Bridge Alignment Humidity Temperature	M_{n_design} V_{n_design}
Fabrication	Deflection	F_{cm}, E_{cm}, $f_{first\ tension}$	Concrete casting(Date) 1st Prestressing(Date)	Humidity Temperature	$M_{n_fabrication}$ $V_{n_fabrication}$
Assembly	Deflection Inspection Data	F_{cm}, E_{cm}, $f_{second\ tension}$	Erection(Date) Deck(Date) 2st Prestressing(Date) Continuous(Date) Superimposed(Date)	Relative Location Humidity Temperature Support Condition	$M_{n_assembly}$ $V_{n_assembly}$

3 BRIDGE MANAGEMENT SYSTEM

When data, including design stage to construction stage information for each structural component of a bridge, is transferred to the Bridge Management System (BMS), maintenance procedures based on Building Information Modeling (BIM) are implemented in earnest. Periodically conducted public damage assessments and records of restoration are documented through various methods such as data, images, 2D inspection drawings, etc. This information is loaded or mapped onto the maintenance system, and it is visualized as shown in Figure 2. Damage information is typically mapped on a face-unit basis on the drawing of the structure and managed. However, the existing mapping approach, where image storage is designated as the management unit at the face-unit level, imposes challenges regarding storage space for the entity responsible for structure management. Damage information is managed as data before the mapping input stage, and since this data allows for individualized progress verification through shape modeling or numerical visualization methods, management through damage vectorization is possible rather than using the conventional mapping approach (Shim et al. 2019).

A sophisticated code system tailored for assessing bridge damages streamlines the automated compilation and quantification of defect data. Utilizing diverse image sources obtained from Unmanned Aerial Vehicles (UAVs) and Ground Penetrating Radar (GPR), in conjunction with damage maps, various image mapping techniques were employed with distinct approaches to visually represent the scrutinized data (Shim et al. 2019). The amassed inspection data and damage records for each bridge component can be systematically gathered, providing a robust foundation for informed decision-making. By harnessing federated data, digital twin models can be meticulously crafted for both individual bridge members and entire bridges (Jeon et al. 2024). These digital twin models, rooted in accumulated data, can effectively manage key performance indicators, enhancing the overall monitoring and assessment of bridge integrity.

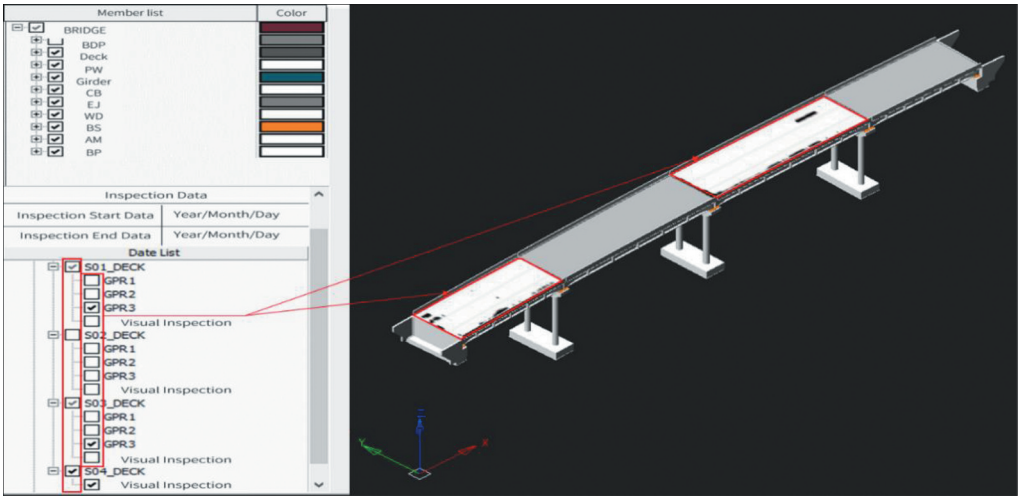


Figure 2. The bridge digital model with mapped damage information in BMS.

4 IMPREMENTATION TO A PRESTRESSED BRIDGE

4.1 *Prestressed concrete girder bridge*

The baseline digital twin concept is currently being applied to an expressway bridge in Korea. The bridge is comprised of prestressed concrete (PSC) girders with span lengths of 35m and 50m. In Figure 3, the bridge layout and the girders before erection on the shoe are illustrated. Steel lateral crossbeams and full-depth precast decks are assembled alongside the PSC girders.

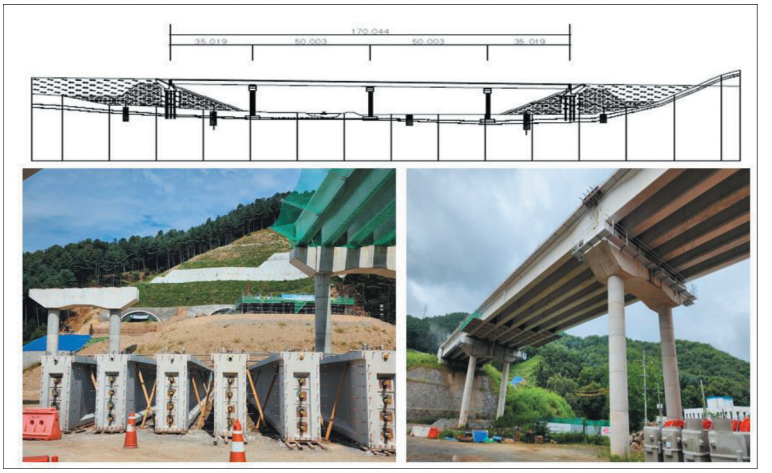


Figure 3. A prefabricated PSC bridge for implementation (In Korea).

In this project, we estimated the displacement of girders during the manufacturing phase through camber measurements. Utilizing the DEM, we predicted the deformations of girders based on camber measurement data over time and construction schedules, estimating concrete elasticity and initial prestress stress. These data can be collected by a common data environment (CDE) in a construction project. Figure 4 illustrates values related to the determination procedure of concrete elasticity and prestress stress after the first tensioning. The initial input concrete elasticity of 33,980 MPa and the initial prestress after short-term losses, such as elastic shrinkage and friction, were 1144 MPa in design phase, showing a significant difference from the values after actual tensioning. These results highlight the dependency of deformations on prestress and concrete properties as well as external influences, with key factors varying among girders within the same span. To construct a baseline digital twin model for the bridge, accurate assessments of material properties from production to hypothesis, and understanding the internal stresses, strengths, and stiffness of the actual components through updates, are essential.

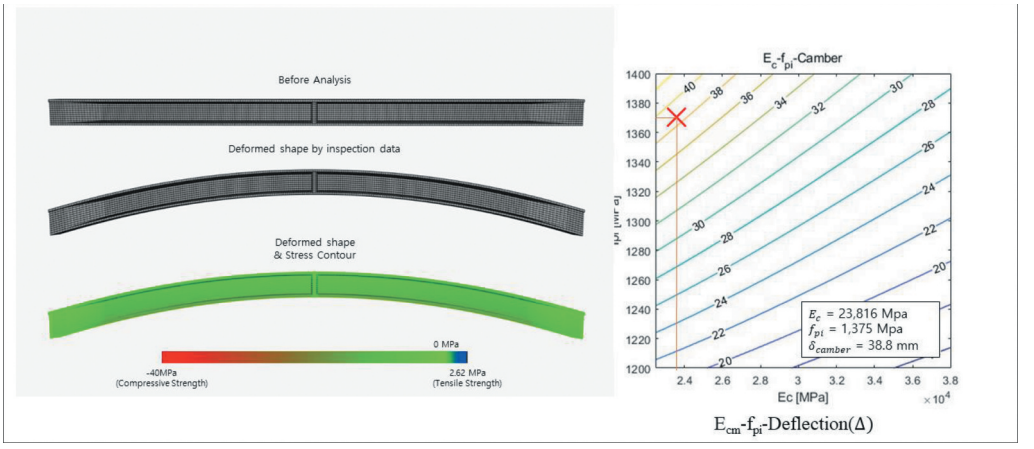


Figure 4. Key management factor of prestressed girder calculated from camber data.

5 CONCLUSION

As the number of aging bridges and the resulting cost of repairs continue to increase, the need for effective maintenance and performance evaluation becomes increasingly important. This

paper contributes to addressing these challenges by proposing a comprehensive definition of Building Information Modeling (BIM) data, establishing the foundation for generating baseline digital twins tailored to the maintenance requirements of common girder-bridges. The significance of a standardized data delivery system for bridges is underscored, particularly emphasizing the critical role of actual data during fabrication and assembly phases to ensure the reliability of baseline models and their as-built data at handover.

Three key points emerge as pivotal in advancing the efficacy of digitalized information delivery in bridge maintenance:

1) Recognizing the pivotal role of consistent data delivery between construction phases, this study emphasizes the necessity for a standardized approach. Notably, the inclusion of actual data during the fabrication and assembly phases is highlighted as crucial for establishing a dependable baseline model and ensuring accurate as-built data during handover.
2) The identification and selection of key indicators emerge as a critical aspect in evaluating the key performance of bridge members. Structural simulations for various scenarios are recommended as a means to comprehensively represent these indicators, providing insights into the diverse conditions and challenges that a bridge may encounter throughout its service life.
3) To facilitate effective data collection from construction projects, the establishment of a collaborative system, such as a Common Data Environment (CDE), is proposed. This collaborative framework can streamline data sharing and communication, fostering a cohesive approach to data collection from various stakeholders involved in the construction process.

In conclusion, the proposed framework not only establishes a robust basis for creating baseline digital twins for girder-bridges but also advocates for a standardized approach to data delivery, the selection of meaningful key indicators, and the implementation of collaborative systems for efficient data collection. These elements collectively contribute to an enhanced understanding of bridge performance and support informed decision-making in the realm of bridge maintenance.

ACKNOWLEDGEMENT

This research was conducted with the support of the "National R&D Project for Smart Construction Technology (RS-2020-KA156007)" funded by the Korea Agency for Infrastructure Technology Advancement under the Ministry of Land, Infrastructure and Transport, and managed by the Korea Expressway Corporation

REFERENCES

Chi-Ho Jeon, Duy-Cuong Nguyen, Gitae Roh & Chang-Su Shim. 2023. Development of BrIM-Based Bridge Maintenance System for Existing Bridges, *Buildings*, 13(9): 2332

Jeon, C.H., Shim, C.S., Lee, Y.H. & Schooling J. 2024, Prescriptive Maintenance of Prestressed Concrete Bridges Considering Digital Twin and Key Performance Indicator. *Engineering Structures*, will be published.

Shim, C. S., Dang, N. S., Lon, S., & Jeon, C. H. 2019. Development of a bridge maintenance system for prestressed concrete bridges using 3D digital twin model. *Structure and Infrastructure Engineering*, *15*(10), 1319–1332.

Bridge Maintenance, Safety, Management, Digitalization and Sustainability – Jensen, Frangopol & Schmidt (eds)
© 2024 The Author(s), ISBN 978-1-032-77040-6
Open Access: www.taylorfrancis.com, CC BY-NC-ND 4.0 license

Condition integration in BIM for existing bridges

M. Köhncke & S. Keßler
Chair of Engineering Materials and Building Preservation
Helmut-Schmidt-University/ University of the Federal Armed Forces Hamburg

ABSTRACT: Existing bridges are prone to different load action and exposure condition, which can alter their conditions and which could lead potentially to damages. Damages like cracks or spalling can affect the structures' durability and could reduce its service life. Consequently, Building Information Modelling (BIM) should continuously consider these changes in order to be able to assess the overall conditions of bridges or their components and to estimate their remaining service life at any point in time. Up to today, BIM is primarily a tool to supervise the design and construction phase and it requires further improvement to explore its potential for the operation phase of existing structures. A first step in this direction is the representation of damages in BIM, which ranges from linking photos or documents to fully integration of alphanumerical and geometric information. This contribution compiles and discusses the advantages and drawbacks of the existing approaches of damage integration in BIM and provides further guidance to use the knowledge on existing damages for the object-orientated damage analysis and the condition-based inspection planning.

1 INTRODUCTION

The administration of existing bridges is strongly depending on the information about the condition of the bridges. Currently, most information on existing bridges is still paper-based or in the form of scanned documents (Seitner et al. 2022). Even with Bridge Management Systems (BMS) only a part of the necessary bridge information is digitally available. This leads to a major issue for the progressing digitalization of administrations and authorities. While some information is partly machine-readable, it is often not machine-interpretable. Another advantage of digitalization is the accessibility of the information. Due to the long service life of bridges, exceeding 50 years, someone is not able to take care of one special bridge throughout its entire service life, from design to demolition. Changes in the responsible persons is necessary in bridge administration and these changes should not lead to loss of crucial bridge information. However, there is a risk of information loss over time, particular with paper-based documentation that underlies sometimes degradation due to poor storage conditions. Digital storage of the documentation seems to be less affected by these circumstances due to the smaller storage places needed for equivalent amount of information. Sometimes the documentation and further information on newer bridges are already stored in datacentres, which specialise in data storage and fulfil higher requirements on storage conditions. One approach connected with the digitalization is the method Building Information Modelling. The method BIM aims to overcome these issues by establishing one standard for the geometrical and alphanumerical representation of information of buildings in a centralized digital way. BIM is mostly used in the design and construction phase of buildings (Borrmann et al. 2021b). There are some approaches for the generation of BIM models for existing buildings, but these approaches are not widely used. These approaches often use optical methods like laser scanning or photogrammetry to set up a geometrical

DOI: 10.1201/9781003483755-239

model as a basis for a BIM model. This geometrical model will then be enriched with alpha-numerical information (Bednorz et al. 2020).

One challenge associated with this procedure is the representation of condition and other operation phase related information. For example, the geometrical model could show that some parts of a concrete beam are missing due to spalling, but the model itself lacks this awareness.

This contribution starts with a short overview of the use of BIM for bridges. Then some different approaches for damage representation are introduced followed by some use cases. Finally, a conclusion is drawn and a short outlook is given.

2 CURRENT USE OF BIM FOR BRIDGES

BIM aims to overcome the loss of information throughout the building lifecycle, which occurs during changes of the lifecycle phases and changes in stakeholders. These changes often lead to duplication of work because different software share no common interface or information gets distributed via PDF files and needs to be taken over manually to a different software (Borrmann et al. 2021b). BIM started in the design and construction phase in the building sector and slowly expanded to the infrastructure sector and other lifecycle phases. This expansion led to some gaps in use of BIM for bridges and especially in the operation phase. The transfer of BIM for existing buildings is still in progress and need development in different areas. This includes legal question who ownerships of the model after the design phase and organizational issues regarding how different stakeholder can work together without sharing the same software (Volk et al. 2014).

The standard data format for BIM is the Industry Foundation Classes (IFC), which determines the connection and storage of information (Borrmann et al. 2021a). The IFC-Bridge standard was one big step forward to the use of BIM in infrastructure, especially for bridges. However, the implementation of the standard in common BIM related software is still in progress. Nevertheless, there are already use cases for BIM for existing bridges. Besides the generation of as-built BIM models (Bednorz et al. 2020) there are approaches for the use of BIM models in bridge inspections (Hill et al. 2022) or for the support of Structural Health Monitoring (SHM) (Li et al. 2022). This contribution focuses on use cases of object-orientated damage analysis and the condition-based inspection planning. The execution of these use cases needs further information on the bridge's condition. Various approaches for representing conditions and damages will be presented in the following section.

3 APPROACHES FOR CONDITION AND DAMAGE REPRESENTATION

The needed information for the representation of conditions and damages highly depends on the use cases. In the context of BIM, this concept is named Level of Information Need (LOIN). It serves as an alternative draft to the Level of Development (LoD), which generalizes levels from the initial design stages to the as-built BIM model, which contains all the information on how the building was actually built. Apart from the general information necessary across use cases, like bridge number, span, construction type, construction year and current condition rating there are further information on the bridge depending on the construction type, which are useful for the administration of bridges. This information can be supplemented with information on the condition derived from inspections and tests.

According to the German standard for engineering structures in connection with roads, this information is usually stored in documents like the structure file and the inspection report (Bundesministerium für Verkehr, Bau und Stadtentwicklung 2004). Often, these documents are paper-based and partially digitalized for example in the database "SIB-Bauwerke". The storage of this information in BIM requires concepts for the representation of condition and damage information. Further requirements for the documentation of inspections of engineering structures are given in the German standard for maintenance of engineering structures

(Bundesministerium für Verkehr und digitale Infrastruktur 2017). This standard defines all necessary information, which need to be included in an inspection report. These are the main building part or construction part, which define the part the damage is assigned to. The damage description includes quantification of the damage and the assessment in the categories of durability, stability, and road safety on a scale from 1 to 4. Furthermore, the damage must be assigned to a suitable damage example and a statement is made whether the damage requires inspection in every visual inspection, even annually. Optional information may include the amount of the damage with dimensions, specific location relative to the building part, changes observed in the damage over time, and photos or sketches of the damage. Some of this information are inherent in the position of a damage in a digital representation for example, the main building part or the quantification of the damage in the geometrical parameters. Others need to be included separately in the representation via alpha-numerical attributes. For example, a beam gets the following attributes with the given values. The crack attributes are in alignment with the damage examples with the annex of German standard for maintenance of engineering structures (Bundesministerium für Verkehr und digitale Infrastruktur 2017).

Table 1. Example alpha-numerical attributes of a crack.

attribute	value
crack	yes
GUID	936DA01F-9ABD-4D9D-80C7-02AF85C822A7
crack_lenght [mm]	150
crack_width [mm]	5
crack_wet	yes
damage_example	025-08
frequent_inspection	yes
crack_location	3m from pillar 3, direction east
crack_type	transverse crack
assessment_stability	0
assessment_durability	3
assessment_road_safety	0

These attributes are machine-readable and compatible with different software. The disadvantage with this approach is the unclear description of the crack's position, which could lead to misjudgement of severity or traceability. The Globally Unique Identifier (GUID) is an attribute that allows the distinction between different building parts, which have the same attributes but are located in different locations. Every building part or BIM model element should have a GUID to give it a unique name for identification purposes.

Additional, these attributes can be extended with links to photos or sketches of the damages to give the person in charge of the structure a visual impression of the damage. This visual impression is easily implemented and offers the possibility to compare the damage over time. However, this approach lacks machine-readability of the information.

Another opportunity is the representation via geometrical or optical information. This approach depends on the method for the capturing of the optical or geometrical information. For example, a laser scan only contains points in a coordinate system based on distance measurements without further information regarding the association of a point with a specific building part. Currently there are research projects attempting to automate the segmentation of point clouds (Morgenstern und Raupach 2022). Especially for cracks, the missing measurement of depth is an issue. A different optical representation is the integration of photos from photogrammetry onto the surface of the building parts. This step goes beyond simply linking a photo, offering the opportunity to capture the condition of a whole structure at once. However, similar to linked photos, the information is visually interpretable for humans but not

machine-interpretable. First approaches on damage classification through deep learning are promisingly (Rodrigues et al. 2022). These approaches should not be seen as isolation, they can also be combined to achieve the desired result. Nevertheless, the damage representation enables further digitalization, illustrated through two use cases.

4 USE CASES FOR DAMAGE REPRESENTATION

One typical use case for damage representation is the conduction of further investigations of a damage known as object orientated damage analysis. The guideline for the object-orientated damage analysis in Germany outlines different necessary information during the conduction. For example, a textual description of damages should be supplemented with sketches. This underscores the need for a combination of alpha-numerical and geometrical information in the damage representation. Especially, the damage location is crucial for the assessment of a damage due to the variation of loads and resistance with position (McGuire et al. 2016). The current paper-based documentation of damage locations lacks the opportunity for quick further processing in different software or partial automation.

One result of an object-orientated damage analysis or the derived measurements could be the change of building information. Due to the current use of different software and databases in administration of existing bridges, repeated input of the same information is unavoidable throughout the entire process chain. A BIM based approach has the advantage that this change can be made in the same software environment. Therefore, the transmission or the repeated input in another software is not necessary. Even the integration of the results of an object-orientated damage analysis in BIM is an option. This allows for the centralization of not only the condition but also the assessment, streamlining the work of the responsible person.

Like the object-orientated damage analysis, the planning of condition-based inspections also requires detailed information on damage location and damage properties. The consideration of different damages with information on the different locations on the bridge enables a consolidated assessment. Therefore, up-to-date information on the main parameters of a bridge and environmental conditions is required. This information can be obtained by structural health monitoring (SHM) systems. Changes in the monitored parameters reaching a defined threshold can then trigger an alarm and the planning of a condition-based inspection. The exemplary integration of sensor data from an accelerometer in BIM via a GUID of the sensor is shown in Figure 1.

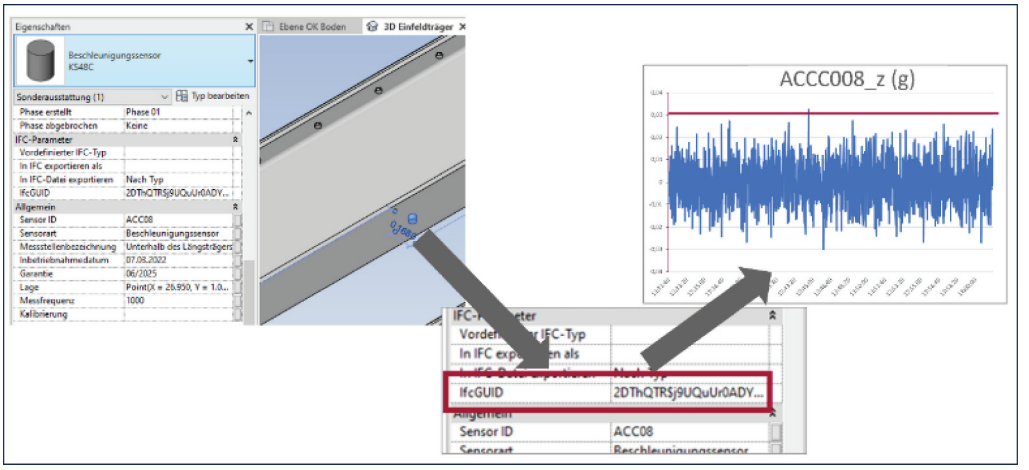


Figure 1. Integration of sensor data in BIM.

The planning of condition-based inspections could also benefit from BIM. For example, the central provision of condition information e.g. interpreted sensor data, connected with a representation of the damages in a BIM model, could simplify the selection of suitable non-destructive testing methods and necessary devices for inspection. The connection between SHM and BIM could facilitate the use of condition-based inspection. Unfortunately, the guidelines in Germany need to be adjusted to the new possibilities in inspection. Until this point, the advantages of condition-based inspection over time-based inspection cannot be fully realized.

5 DISCUSSION AND ANALYSIS

The increase in service life necessitates higher requirements in the availability and durability of the necessary structural information. The digital representation of condition information in BIM seems promising. The introduced approaches have different advantages and disadvantages concerning the practicability and the opportunity for further processing. Often, the practicability comes with a decrease in the possible automation. For example, the first mentioned approach, involving the sole integration of alpha-numerical attributes into building parts is easily done within the modelling software for BIM. On the upside, these attributes are machine readable, so this information can be transferred to other software with less effort and enabling further processing for tasks such as evaluating which category is rated worst for a particular damage. However, on the downside, these attributes are not machine interpretable which means that a software does not recognize the semantic information about the damage, only that a damaged building part differs from a non-damaged one. . Semantic information can be included in the geometric representation of a damage in IFC, but the geometric modelling of each damage is time-consuming. However, it offers the possibility that algorithms can use this information for sophisticated assessments of whole structures. Photos, like attributes in the building parts, can be read by machines but not interpreted correctly. It does not matter whether the photo is linked to a building part or assigned to its surface, further processing like labelling of damages and assigning photos to building parts is necessary until robust deep learning algorithms are included in the administration software and the labelling and assignment is automated. Until then, the required effort for digital representation should always be considered in the context of use cases and anticipated benefits.

6 CONCLUSION AND OUTLOOK

Depending on the use case, different approaches for the integration of condition and damage information are appropriate. For example, the integration of the condition rating of a structural component could easily be accomplished using an attribute. While the integration of damages like spalling requires a geometric representation for the estimation of the quantity for the repair measure. The condition and damage information integration in BIM could lead to progress in the digitalization of the administration of existing bridges, thereby, to a simplification and an increase in the administration efficiency. There are two key advantages in times of decreasing financial and personnel resources in the administration of infrastructure.

The current development in the generation of as-is-BIM models, together with the integration of SHM and the renewal of the guidelines and standards, could also enable the change to more condition-based inspection. The condition-based inspection approach could lead to a better allocation of resources for the maintenance and inspection of existing bridges than time-based inspections.

REFERENCES

Bednorz, J. Hindersmann, I. Jaeger, K. Marszalik, M. 2020. Methoden zur Generierung von As-Built-Modellen für Bestandsbrücken. In *Bautechnik* 97 (4): 286–294

Borrmann, A. Beetz, J. Koch, C. Liebich, T. Muhič, S. 2021a. Industry Foundation Classes – Ein herstellerunabhängiges Datenmodell für den gesamten Lebenszyklus eines Bauwerks. In: André Borrmann, Markus König, Christian Koch und Jakob Beetz (ed.), Building Information Modeling. Wiesbaden: Springer Fachmedien Wiesbaden (VDI-Buch): 95–146.

Borrmann, A. König, M. Koch, C. Beetz, J. 2021b. Die BIM-Methode im Überblick. In: André Borrmann, Markus König, Christian Koch und Jakob Beetz (ed.): Building Information Modeling. Wiesbaden: Springer Fachmedien Wiesbaden (VDI-Buch): 1–31.

Bundesministerium für Verkehr, Bau und Stadtentwicklung (ed.) 2004. Richtlinien für die Erhaltung von Ingenieurbauten. Leitfaden Objektbezogene Schadensanalyse. Berlin BMVBS.

Bundesministerium für Verkehr und digitale Infrastruktur (ed.) 2017. Richtlinien für die Erhaltung von Ingenieurbauten. Richtlinie zur einheitlichen Erfassung, Bewertung, Aufzeichnung und Auswertung von Ergebnissen der Bauwerksprüfungen nach DIN 1076. Berlin BMVI.

Hill, M. Bahlau, S. Butenhof, F. Degener, L. Klein, F. Kukushkin, A. et al. (ed.) 2022. Bauwerksprüfung mittels 3D-Bauwerksmodellen und erweiterter/virtueller Realität. Supporting bridge inspectors with interactive mixed reality visualisations of BIM process and geometry data. Bergisch Gladbach: Fachverlag NW in der Carl Ed. Schünemann KG

Li, X. Xiao, Y. Guo, H. Zhang, J. 2022. A BIM Based Approach for Structural Health Monitoring of Bridges. In: *KSCE J Civ Eng* 26 (1), 155–165

McGuire, B. M. Atadero, R. Clevenger, C. Ozbek, M. 2016. Using Building Information Modeling to track and assess the structural condition of bridges. Fort Collins: Mountain-Plains Region

Morgenstern, H. Raupach, M. 2022. Quantified point clouds and enriched BIM-Models for digitalised maintenance planning. In: *MATEC Web Conf*. 364, 5001.

Rodrigues, F. Cotella, V. Rodrigues, H. Rocha, E. Freitas, F. Matos, R. 2022. Application of Deep Learning Approach for the Classification of Buildings' Degradation State in a BIM Methodology. In: *Applied Sciences* 12 (15), 7403.

Seitner, M. Probst, R. Borrmann, A. Vilgertshofer, S. (ed.) 2022. Building Information Modeling (BIM) im Brückenbau. = Building Information Modeling (BIM) for bridges. Bergisch Gladbach: Fachverlag NW in der Carl Ed. Schünemann KG.

Volk, R. Stengel, J. Schultmann, F. 2014. Building Information Modeling (BIM) for existing buildings — Literature review and future needs. In: *Automation in Construction* 38: 109–127

Bridge Maintenance, Safety, Management, Digitalization and Sustainability – Jensen, Frangopol & Schmidt (eds)
© 2024 The Author(s), ISBN 978-1-032-77040-6
Open Access: www.taylorfrancis.com, CC BY-NC-ND 4.0 license

Cloud-based asset management for image-based inspections of infrastructures

G. Morgenthal & M. von Butler-Helmrich
Institute of Structural Engineering, Bauhaus-Universität Weimar, Weimar, Germany

ABSTRACT: The continuous safety and performance of infrastructures is of particular importance for a modern society. Demands for resource efficiency in the construction sector will require significantly longer service lives for structures in the future. New digital maintenance strategies can make this goal achievable. To realize the full potential of such digital maintenance strategies, asset management systems need to incorporate a heterogeneous and linked set of data and information such as condition data, digital models of the geometry and damage characteristics. At the same time, all available data and information must be easily accessible for decision makers to evaluate the current state of the structures and derive maintenance actions from it. This paper presents a cloud-based asset management platform that incorporates digital twin models obtained from automated image-based inspection and damage detection methods, enabling predictive maintenance based on permanent storage and tracking of highly accurate information about the location and extent of damage.

1 INTRODUCTION

In a modern society, the continuous availability and performance of infrastructure systems is of fundamental importance for quality of life, as they fulfill important supply functions and ensure the mobility of the population. Furthermore, demands for resource efficiency in the construction sector will require significantly longer service lives for structures in the future in the interests of conserving resources. At the same time, the time required for inspection and retrofitting measures should be minimized, as should the overall cost of maintaining the structures.

However, the current status quo for inspections are time-consuming and costly manual visual inspections that follow guidelines and regulations defined by each country or infrastructure owner. The results of these inspections, e.g. identified damage entities, are documented in a descriptive manner in bridge management systems, such that condition indices are derived and the planning of maintenance actions is enabled. While these regulations differ among others by the inspection intervals, the rating of individual damages, the method used for obtaining the overall condition index, and the components of the bridge management system (for an overview see for example ARCHES 2009, ASCAM 2012 and Chase et al. 2016), they all have in common a relatively high degree of subjectivity as shown by Bennetts et al. (2021). Further, a spatially accurate tracking of damage propagation over time is hardly achievable. Studies (Naraniecki & Marx 2019) on the robustness of condition indices show that the information value of these indices is limited and that the condition rating trends can vary considerably, even for similar structures.

A great potential for optimizing the inspection results derives from high-quality digital data on the structural condition, which enable a density of information for condition assessment that significantly exceeds the results of conventional structural inspections. Furthermore, Morgenthal et al. (2022) have shown that life cycle concepts based on multidimensional performance indices for a predictive maintenance can only be realistically implemented on the basis of digital data. The fundamental objective of digitized structural maintenance must therefore be a condition assessment that accounts for all relevant degradation processes of a structure by

DOI: 10.1201/9781003483755-240

(1) recording the current condition as accurately as possible, i.e. changes, especially damages, are reliably detected and characterized by location and damage extent,
(2) ensuring a close temporal monitoring of the damage development, and
(3) deriving quantitative evaluations on the condition of the structure or parts of the structure, aggregated from individual damages.

Digital methods, which can also be used in a complementary manner (see for example Simon et al. 2022), primarily include the already established technologies of continuous sensor-based monitoring as well as imaging methods. For the application of imaging techniques in structural condition assessment the authors have developed a scientific methodological framework (Morgenthal et al. 2019). The geometrically referenced linking of all data occurring in the process chain described there and the condition information extracted from it is based on the concept of a digital twin of the structure. The geometrical model of the structure is obtained by a high-resolution 3D reconstruction from the image data through photogrammetry, and with the INFRA//TWIN platform (INFRALYTICA 2023) a cloud-based software implementation with a high-performance web front end is available, which can be used for a related structure management.

This paper discusses the steps and requirements needed to generate digital twins of infrastructures that link highly accurate and detailed geo-referenced 3D building models with damage data that can be automatically generated using artificial neural networks or entered through manual inspections on the virtual model. Further, case studies are presented of projects where highly heterogeneous data sets of image-based inspections are integrated into the cloud-based asset management platform.

2 FROM IMAGES TO DIGITAL TWIN MODELS – BEST PRACTICE AND REQUIREMENTS

2.1 *Image data acquisition*

Various options are available for the acquisition of image data. Figure 1 shows examples of manual recording and the use of camera arrays and unmanned aerial systems (UAS or "drones") for (semi) automated data acquisition.



Figure 1. Examples of data acquisition techniques for generating image data (left: manual data acquisition, center: semi-automated data acquisition with customized camera array, right: automated data acquisition with UAS along pre-generated flight paths).

The use of image data for a structural condition assessment requires reliable detection of damage in the images, such that a minimum image quality (sufficiently low-noise, depth- and motion-focused as well as high-resolution) must be achieved. The limits of what can still be recognized in the image result from various factors, such as

- the physical relationships of the camera technology (object resolution or GSD)
- the acquisition conditions (wind, direct or indirect sun light, etc.),

- the relative camera orientation w.r.t. the surface of the structure, and
- the methods used for the image post-processing.

Furthermore, a systematic overlap of the images is required in addition to the minimum image quality to facilitate a photogrammetric 3D reconstruction to obtain a georeferenced 3D model of the structure (see Section 2.2). In this case an automated acquisition with pre-planned acquisition positions should be preferred to a manual acquisition. This can be done in different levels of detail according to the area-related required resolution as presented by Debus & Rodehorst 2021.

2.2 *Creation of linked digital models*

The transformation of the information contained in the acquired 2D image data into linked, digital 3D models, which can be used for the assessment of the structural condition of the structure, essentially requires three steps that run in parallel, each using intermediate results from the other processes: the photogrammetric reconstruction and georeferencing, the damage detection and classification in the images, and the linking of the data.

In order to create a common reference system and thus to be able to link all data later in a location-related manner, a 3D model is generated from the images by means of photogrammetric reconstruction. For structural inspection purposes, the structure-from-motion algorithm according to Schonberger & Frahm (2016) is usually applied. In this step, it is also important to georeference the reconstructed models. For this purpose, fixed points, which are clearly recognizable in the images, must be surveyed by tachymetry during the data acquisition. Besides ensuring the representation of the existing (as-built) geometry of the structure, the georeferencing provides a uniform coordinate system (e.g. national coordinate system or a local, project-related coordinate system) so that the following aspects become possible:

- several models of a structure at different levels of detail, depending on the focus of the investigation, can be combined into a common 3D model or replaced in certain areas,
- models of the same part of the structure captured during different data acquisition campaigns can be superimposed in a way that allows deformations or changes between the campaigns to be determined, and
- the reconstructed models of the 3D structure can be further set into relation to other digital models, such as simulation models.

To assess the condition of the structure, the extent and severity of existing damage must be quantified and classified accordingly. This requires sufficient image quality (see Section 2.1) to reliably detect anomalies in the image data. The damage can be either detected and classified using pre-trained artificial neural networks or entered through manual inspections on the virtual model. Through the relationship between 2D image data and 3D model from photogrammetric reconstruction, the extent of damage that spans multiple images can be determined by projecting it onto the 3D model. In addition, georeferencing allows the exact measurement of the damage geometry (e.g. crack width as presented by Benz & Rodehorst (2021)).

The data generated during an image-based inspection represents a very heterogeneous data set, both due to the file types that are used and due to the type of representation of the structure (e.g. geometry via a 3D point cloud, surface information in 2D image data, extracted damage information, location-related notes during data acquisition, etc.). In order to be able to make a holistic assessment about the condition of the structure, the data must be linked with each other so that (automatically) accumulated information can be derived. One possibility for geometrically highly accurate linking of heterogeneous data collected, even across multiple acquisition campaigns, is to use the multi-model approach and voxel-based methods, such as those proposed by Taraben et al. (2022a) and Taraben & Morgenthal (2022b). In this case, the synchronization of the informational coupling of the physical structure and the digital image according to Boje et al. (2020) is not ensured by continuous monitoring but at discrete points in time. In terms of the definition according to Errandonea et al. (2020), the application of the digital twin described thus falls between a condition-based and a predictive maintenance strategy. The following paragraphs mainly deal with the enhancement of the digital image.

2.3 *Condition evaluation and predictive maintenance*

The georeferenced and linked model created from the 2D image data (see Section 2.2) represents the necessary information for an assessment of the structural condition. In this context, the assessment can be carried out manually, assuming that an appropriate visualization is enabled and linked data can also be easily displayed, or (semi) automated, assuming that full linking of the data is available. The latter was shown, for example, for the determination of the condition index by Taraben et al. (2022a) by applying procedures currently used in practice.

Since the fully linked digital model can also contain other data in addition to the damage and structural data, key performance indicator-based methods (see for example Stipanović et al. 2017) can be applied to the condition assessment of the structure. Such methods allow for multi criterial predictive maintenance for example proposed by Bukhsh et al. (2020). Strategies for automatically generating condition metrics and performance indices as a basis for representing and interpreting the state of a structure will represent a viable research field for the foreseeable future.

3 CASE STUDIES OF CLOUD-BASED ASSET MANAGEMENT

3.1 *Example 1: Visual structural inspection in a digital twin*

The recorded and processed data from image-based methods is suitable for significantly reducing subjectivity in evaluation processes. On the one hand, a manual inspection can be carried out on the visualized 3D building surface and the linked 2D image data. On the other hand, anomalies on the surface can be measured digitally in both 3D and 2D space, as shown in Figure 2 (left).

Even if this ensures easy accessibility to all areas of the structure and excludes the effects of the weather, damage can be overlooked during the inspection process, especially in the case of very large surface areas. This is where the use of neural networks is suitable for automated damage detection. Using machine learning methods, detection is carried out by classifying relevant damage on the basis of prior training with annotated damage images. The relationship between the image and the 3D model means that damage detected in the image data can be projected onto the 3D model and geometrically referenced there and, if the image data is of sufficient quality, automatically measured. The result are georeferenced annotations, as shown in Figure 2 (right), containing information about damage characteristics such as type and extent. The automatically detected anomalies highlighted on the 3D model can then be evaluated in the same way as the conventional inspection process or linked with the other data in the digital twin of the structure to automatically determine the condition of the structure. Such methods can be a valuable support tool for damage detection and documentation.

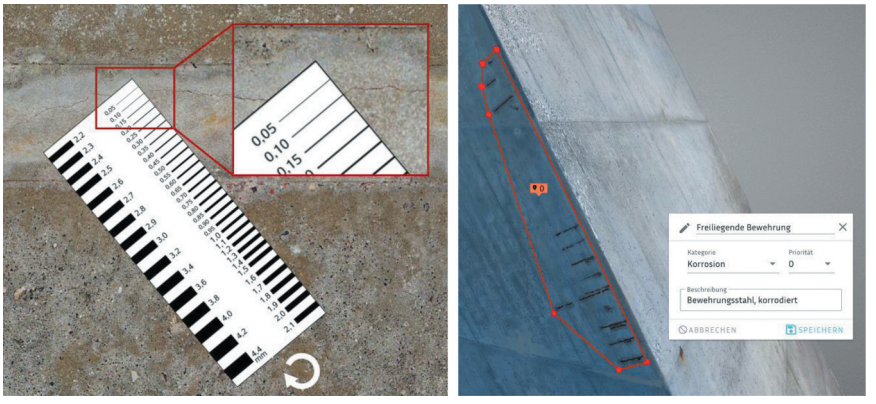


Figure 2. left: Manual measurement of crack width on the textured surface of a photogrammetrically reconstructed 3D model using a digitally superimposed crack width ruler; right: Display of an inspection note stored in the Digital Twin with categories of the evaluation (here: using the example of the INFRA// TWIN platform (INFRALYTICA 2023)).

The georeferenced location of the annotations also ensures that the conclusions and categorizations drawn for the assessment can be found directly on the 3D model of the structure and directly linked to any damage.

Although the surface of the photogrammetrically reconstructed model (corresponding to the underlying image data) achieves a very high resolution, it may be necessary in individual cases to include the original image data and the extent of damage recognizable there in the assessment. Thanks to the relationship between the 3D model and the 2D image data set from the photogrammetric reconstruction storage in the digital twin, the partial image data set associated with a 3D point can be found and displayed at any time, as shown as an example in Figure 3.

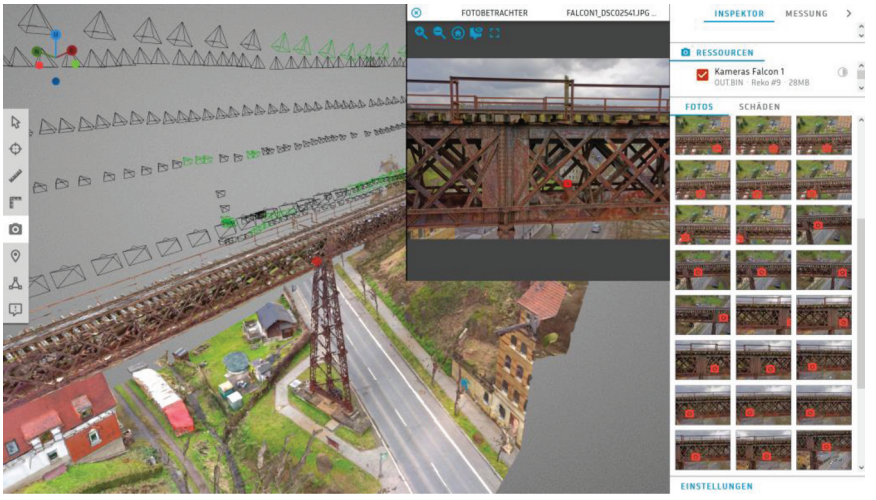


Figure 3. Display of a partial image dataset corresponding to the point selected on the 3D model incl. highlighting in green of the camera positions from which the selected point is visible and red camera symbol for highlighting the selected point in the images (here: using the example of the INFRA//TWIN platform (INFRALYTICA 2023)).

The precise georeferencing (usually within 10 mm) makes it possible to observe and compare the change between different images even without automated evaluation. Furthermore, georeferencing enables the extent of damage to be measured directly on the 3D structure model (see Figure 4). The link to the 2D image data allows the measured distances and areas to be recorded in the images with the real dimensions even if the representation is distorted.

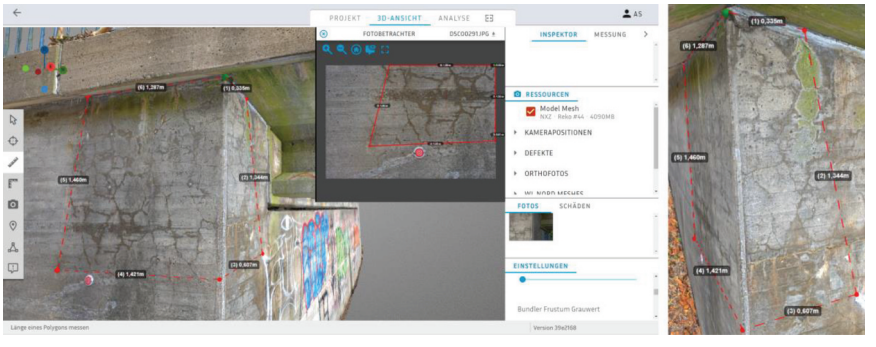


Figure 4. Measuring of damage dimensions (right: detailed view) on the georeferenced 3D building model (here: using the example of the INFRA//TWIN platform (INFRALYTICA 2023)).

3.2 *Example 2: Automated damage detection and progress monitoring*

Manual annotation of each individual damage in the image data is very time-consuming, especially with a large number of damage entities. The use of neural networks trained for the application area (including surface material and damage types) enables automated detection. The damage annotated in this way and stored in a database can then be referenced to the 3D model for further interpretation and linked in the digital twin, as shown in Figures 5 and 6.

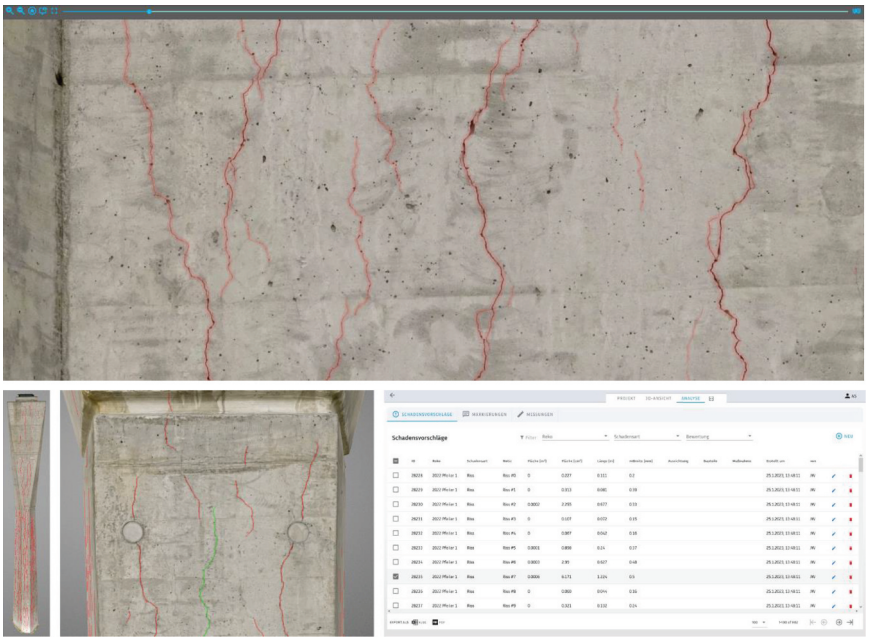


Figure 5. Visualization of cracks detected automatically with a neural network in a photo (top: image view with semi-transparent AI heatmap of crack detection) and projected onto the surface of the textured 3D model (bottom) incl. the link between damages selectable on the 3D model and their storage in a backend database (here: using the example of the INFRA//TWIN platform (INFRALYTICA 2023)).

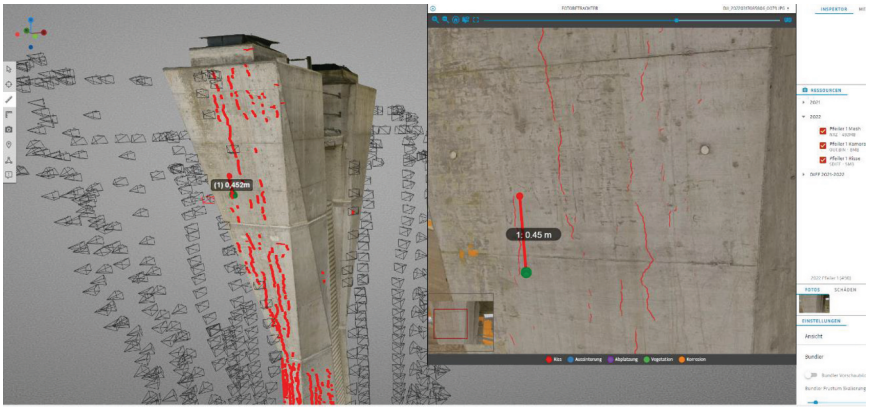


Figure 6. Visualization of cracks in the original image and the 3D-referenced crack pattern (here: using the example of the INFRA//TWIN platform (INFRALYTICA 2023)).

Meaningful applications of asset management platforms are also in the response of natural hazard mitigation and support of disaster response activities. Image data from e.g. flood events can be generated by drones fast and repeatedly and 3D models of affected areas can be provided through automatic data analysis and provision through cloud platforms in near real time (Schwarz et al. 2023). This allows crisis management and personnel on the ground to be provided with important information on structural deterioration, access restrictions and trends of flood propagation, see Figure 7.

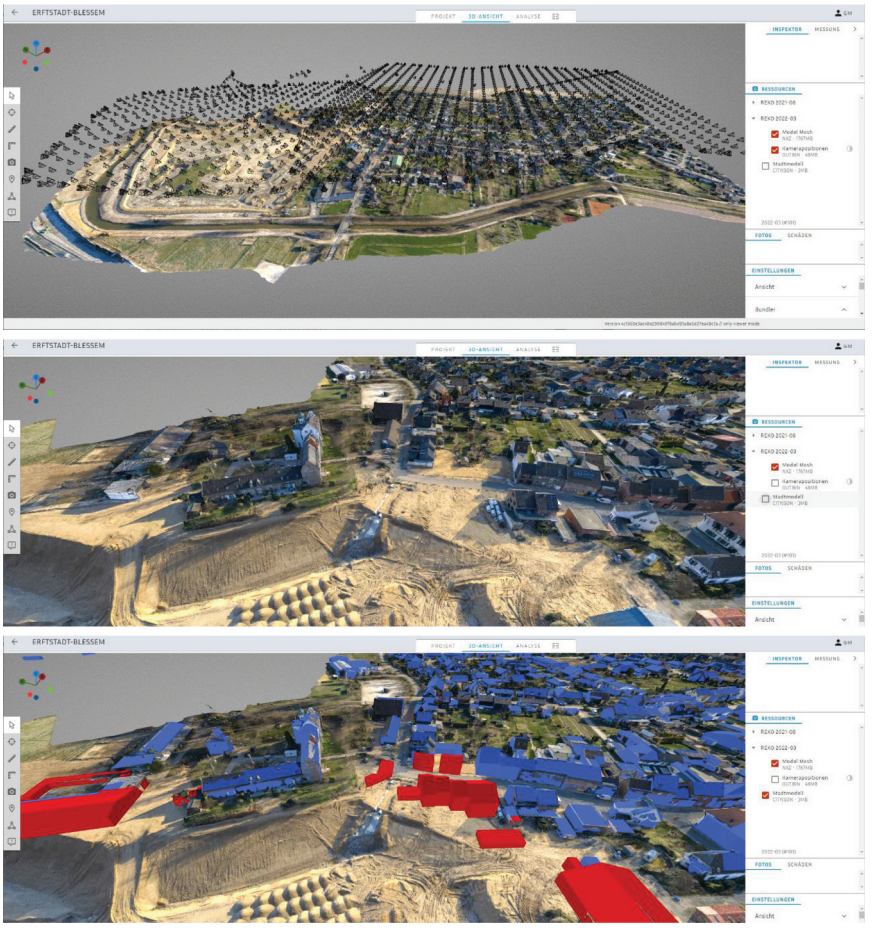


Figure 7. Visualization of flood affected areas based on drone imagery: drone positions (top), 3D model view (middle) and with damage interpretation models (degree of damage color coded, see Schwarz et al. 2023).

4 CONCLUSIONS AND DISCUSSIONS

The regular inspection of structures is essential to ensure the safety, serviceability and durability of infrastructures. The time, personnel and resource-intensive process of structural inspection can be supported by digital methods in the future, whereby the image-based structural inspection presented in this paper has particular potential.

Image-based digital structural inspection is suitable for achieving the three objectives of structural inspection effectively and efficiently thanks to the high-resolution image data and

its georeferenced linking in the digital twin. The paper presents possible application scenarios. When using the methods, however, it should always be noted that digital structural inspection cannot completely replace conventional structural inspection and must be subject to careful quality control in order to ensure that the generated image data contains sufficient information. In particular, digital structural inspection can provide valuable support in order to limit manual inspection to particularly critical areas and to reduce any subjective influences in the condition assessment with the help of automated evaluation algorithms. Further applications in disaster response are indicated.

REFERENCES

ARCHES. 2009. Assessment and Rehabilitation of Central European Highway Structures (ARCHES) - D09: Recommendations on the systematic decision making process associated with maintenance and reconstruction of bridges.

ASCAM. 2012. Asset Service Condition Assessment Methodology (ASCAM) - D03: Inventory Bridge Management practices.

Bennetts, J., Denton, S., Webb, G., Nepomuceno, D. & Vardanega, P. 2021. Looking to the future of bridge inspection and management in the UK. *Proceedings of the Tenth International Conference on Bridge Maintenance, Safety and Management (IABMAS 2020)*, pp. 3858–3866. CRC Press/Balkema, Taylor & Francis Group.

Benz, C., & Rodehorst, V. 2021. Model-based crack width estimation using rectangle transform. *17th International Conference on Machine Vision and Applications (MVA)*, pp. 1–5. IEEE.

Boje, C., Guerriero, A., Kubicki, S. & Rezgui, Y. 2020. Towards a semantic Construction Digital Twin: Directions for future research. *Automation in Construction* 114, pp. 103179

Bukhsh, Z. A., Stipanovic, I., & Doree, A. G. 2020. Multi-year maintenance planning framework using multi-attribute utility theory and genetic algorithms. *European transport research review* 12 (1), pp. 1–13.

Chase, S. B., Adu-Gyamfi, Y., Aktan, A. E. & Minaie, E. 2016. Synthesis of national and international methodologies used for bridge health indices.

Debus, P. & Rodehorst, V. 2021. Multi-scale flight path planning for UAS building inspection. *Proceedings of the 18th International Conference on Computing in Civil and Building Engineering (ICCCBE 2020)*, pp. 1069–1085. Springer.

Errandonea, I., Beltrán, S. & Arrizabalaga, S. 2020. Digital Twin for maintenance: A literature review. *Computers in Industry* 123, pp. 103316

Infralytica GmbH. 2023. INFRA//TWIN, available at https://www.infratwin.com/.

Morgenthal, G., Hallermann, N., Kersten, J., Taraben, J., Debus, P., Helmrich, M. & Rodehorst, V. 2019. Framework for automated UAS-based structural condition assessment of bridges. *Automation in Construction* 97, pp. 77–95.

Morgenthal, G., Rau, S., Hallermann, N., Schellenberg, K., Martín-Sanz, H., Schubert, M. & Kübler, O. 2022. Potenziale von Monitoringdaten in einem Lebenszyklusmanagement für Brücken. *BASt-Bericht B 190.* Bergisch Gladbach: Fachverlag NW in der Carl Ed. Schünemann KG.

Naraniecki, H. & Marx, S. 2019. Zustandsentwicklung und Prognose von Eisenbahnbrücken. *Beiträge zur 7. DAfStb-Jahrestagung mit 60. Forschungskolloquium*, pp. 103–118. Hannover: Institutionelles Repositorium der Leibniz Universität Hannover.

Schonberger, J. L. & Frahm, J.-M. 2016. Structure-from-motion revisited. *Proceedings of the IEEE conference on computer vision and pattern recognition*, pp. 4104–4113.

Schwarz, J., Maiwald, H., Abrahamczyk, L., Hallermann, N., Morgenthal, G. Methoden für digitale 3D-Lagebilder: Erfahrungen aus dem Hochwasser 2021. *Bautechnik* 100(2023), pp. 1–16

Simon, P., Helmrich, M., Herrmann, R., Schneider, R., Baessler, M., Lorelli, S. & Morgenthal G. 2022. Maintalbrücke Gemünden: Bauwerksmonitoring und -identifikation aus einem Guss. *Bautechnik* 99 (3), pp. 163–172.

Stipanović, I., Chatzi, E., Limongelli, M. P., Gavin, K., Bukhsh, Z. A., Palic, S. S., Xenidis, Y., Imam, B., Anzlin, A., Zanini, M., Klanker, G., Hoj, N. & Ademovic, N. 2017. WG2 Technical Report: Performance Goals for Roadway Bridges of COST ACTION TU 1406: Establishment of a Quality Control Plan. Boutik.

Taraben, J., Helmrich, M. & Morgenthal, G. 2022a. Datenmodelle für Digitale Zwillinge von Brücken und bildbasierte Zustandsaufnahmen. *Bautechnik* 99 (2), pp. 134–142.

Taraben, J. & Morgenthal, G. 2022b. Integration and comparison methods for multitemporal image-based 2D annotations in linked 3D building documentation. *Remote Sensing* 14 (9), p. 2286.

Bridge Maintenance, Safety, Management, Digitalization and Sustainability – Jensen, Frangopol & Schmidt (eds)
© 2024 The Author(s), ISBN 978-1-032-77040-6
Open Access: www.taylorfrancis.com, CC BY-NC-ND 4.0 license

Linking BrIM to BMS for bridges – validation of concepts

V. Samec
Independent Bridge and BIM Consultant, Austria

K. Aas-Jakobsen
Aas-Jakobsen AS, Norway

P. Hawryszków
Wroclaw University of Science and Technology, Poland

I. Heise
Technical University of Munich, Germany

M.A. Valenzuela
Pontificia Universidad Catolica de Valparaiso, Chile

C. Shim
Chung-Ang University, South Korea

ABSTRACT: Over the past two decades, Building Information Modeling (BIM) has emerged as a prominent facet of the digital transformation within the AEC sector. However, this transformational focus has predominantly centered on the design and construction of new bridges, overshadowing the critical realm of existing bridges constructed before the advent of BIM. The operational and maintenance phase of a bridge's lifecycle is the longest and most cost-intensive, heightened by the growing concerns of fatal accidents, climate change impacts, and the aging infrastructure of numerous bridges globally. This has sparked a global interest in shifting from a reactive to a preventive approach to bridge maintenance, entailing the seamless integration of digitalization into the operations and maintenance (O&M) lifecycle. The digital transformation of operation and maintenance processes carries the potential to significantly reduce costs and, most importantly, safety.

1 INTRODUCTION

The IABSE Task Group 5.6 has a dedicated mission: to bridge the gap between Bridge Management Systems (BMS) and existing BIM solutions. This initiative is grounded in Open BIM standards but accentuates the critical role of data models. The foundational concepts for this implementation were extensively deliberated upon at the IABSE Congress held in New Delhi, India (Aas-Jakobsen et al. 2023). The journey began with the identification and systematic categorization of use cases that facilitate the harmonious integration of Bridge Management Systems and BIM for existing bridges.

The pivotal stakeholders in this endeavor are the bridge owners and regulatory authorities, whose perspectives are paramount in shaping this market-oriented initiative. In our vision, the establishment of a universally accepted standardized framework for data exchange between disparate systems empowers bridge owners. This framework will grant them control over their bridge infrastructure's data, enabling informed and timely decision-making. The culmination of intensive interviews with bridge authorities and owners from around the world has led to the

DOI: 10.1201/9781003483755-241

creation of a comprehensive review document. This review will serve as the guiding compass for recommending the future integration between Bridge Management Systems and Open BIM.

2 VISION OF LINKING BIM TO BMS FOR BRIDGES

Many bridge owners hope that BrIM (Bridge Information Modeling) will be used throughout the structure's life cycle, from initial design to building, operation, and maintenance, and finally removal and recycling at the end of service – a one-stop shop for information. As part of a BMS, operation and maintenance data are currently collected in various forms and kept in multiple repositories. To maximize maintenance of individual structural assets and manage the asset as a portfolio of structures, BrIM and BMS should be linked so that information may be shared effortlessly, even for existing structures that do not yet have a BrIM model.

The complexity of maintenance/inspection requires organized, automated, open and transparent digital processes, which should consider both structural and asset management data.

It is assumed that the BMS aims to integrate digital storage, exchange of data, cost as well as deterioration, optimization and analysis models and their interoperability with existing BIM solutions (Hajdin & Samec 2022).

The vision of this work aims to form a foundation for 3D/4D/5D/6D software and hardware independent data exchange between different software technologies during life cycle and beyond, considering also monitoring, sensor equipment and damages on the structure along time axis. Open BIM technology for the interoperability from technical, semantic and organizational point of view is of main interest. Thus, the work is based on the following formulation:

BIM model should be the driver and front end and will provide a link to the BMS system. The BIM model should allow for bi-directional information flow with the BMS system (and other systems linked to the BIM) such that information is not duplicated. The aim of our TG is searching for all requests from BMS systems (in form of use cases) in order to report missing attributes within exiting Open BIM systems.

It is in the following assumed that in addition to structural information the BrIM model include or reference the design basis, which include location, bridge type, traffic definition, metocean data, information on hazard, geotechnical design data, geological design data, seismic input, etc. The focus of this work has been to the structural system.

In order to prioritize the direction of the work the following workflow was defined as shown in Figure 1:

- Identify and systematize use cases for linking BMS and BIM for bridges.
- Prioritize use cases based on market input.
- Propose structure for connecting BMS and BrIM.

The first step (Use Cases identification and systematization) was completed and reported in (Aas-Jakobsen et al. 2023). Relevant use cases for a BrIM model over its lifetime are identified, including their potential and eventual extension of IFC standard. Currently, IFC standard (widely recognized and used Open BIM standard) is used as the reference data scheme. For the future it is important to underline, that IFC is not the only possible exchange format.

This paper is describing the concept of BrIM and BMS linkage and its validation. For this purpose, stakeholders, bridge authorities worldwide have been answering a set of questions,



Figure 1. Workflow.

prepared by IABSE TG 5.6. Their point of view, requirements and practical needs will lead to the last step: development of missing parts within BrIM.

Our work is based on our hypothesis:

- The BrIM shall allow for bi-directional information flow;
- Information should not be duplicated in the connected systems.

3 USE CASES

In order to structure the work all tasks which BrIM, and BMS could be used for was sorted into use-cases. These were categorized into five groups: object data, data management, visualization, maintenance & repair information and user interface. All identified use case were described and the advantages with linking BrIM and BMS was identified, as well as necessary update of the IFC data scheme. The below discussion gives an overview of the main findings.

3.1 *Object data*

Object data is information needed for the object. The general bridge data should consist of existing documentation of the bridge from the construction site (including interventions after construction stage), geometrical model of the bridge as built (Isailovic & Hajdin 2022) or after retrofitting, geo location of the structure, hazard information, design basis, statical report, geological report, full set of drawings, reports from construction supervision (including deviations and vulnerable areas), bridge owner, designer, constructor, construction year, traffic class, traffic load, bridge class, generation of design codes, seismic zone, monitoring plan and instrumentation, time specification. Potentially all existing bridge data can be imported into the BIM tool.

Extended definition of structural and non-structural member specification shall be delivered on member topology, geometric extent and cross sections, materials, information of reinforcement, prestressing, surface treatments, environmental exposure, degree of strength utilization, geotechnical members like piles, anchors, appurtenances like bearings, expansion joints, etc., location of monitoring sensors and time dimension.

A mechanism is needed, which would identify the status of each element in the structure. The status should be able to reflect initial, unchanged, modified, replaced, added, and demolished entities. In addition, it should be able to reflect updated documentation in BMS system, including e.g. instrumentation. Storage should be organized such that historical data could be visualized and compared to similar structure and objects on other bridges.

Inspection and maintenance activity on bridge element should be stored in BrIM for planning and logging purposes. Damages must be stored in a way that it could be monitored and visualized and serve as input to a damage model. Modification, demolition, and construction of new elements need to be updated in BrIM and its geometric changes must be added such that visualization is possible. Thus, time stamp of changes is needed.

3.2 *Data management*

Data management is related to how the data and information in the model is used. The main purpose is to prepare the ground for fund optimization.

There are several BMS worldwide, all BMS have essentially a management process for all bridges, where one needs to identify the bridge, know its condition and act upon it when required. These three tasks are grouped into three main modules: i) Inventory; ii) Inspection; iii) Intervention. With evolution in technology and focus on the needs of bridge owners, these three main modules have been split into more specialized modules.

Since BMS in principles has to deal with a huge number of bridges, it is important to have a unique ID which can be used to link data relating to that particular bridge from other sources. BrIM model shall identify all the data fields that are essential for communication with BMS.

Currently existing structures are documented by 2D drawings. In the near future it is currently not realistic to automatically convert these drawings to full BrIM models. An alternative is to create simplified BrIM models that holds the information needed to communicate with BMS. Since BMS information contain information about how the structure develop with time, this parameter has to be added to the IFC scheme for seamless communication, as time and date stamp is critical in assessment of progression of deterioration within the bridge element. Deterioration modelling module is critical in BMS as it is based on the deterioration model created under this module that the management decision making during the Risk assessment and Priority and ranking tools are achieved. In addition to the 4^{th} dimension, we propose to add a 5^{th} dimension which describe the severity of distress in the element at that particular time zone.

3.3 *Visualization*

The visualization of information on a 3D numerical model of a bridge is crucial in the development of the link between BMS and BrIM. Indeed, an easy access to bridge information in its context, such as inventory data or bridge elements' conditions, can significantly improve maintenance workflows from inspection on site to prioritization of repair actions.

This use case aims to allow the visualization of generic data of the bridge: bridge type, geometric position of elements, material specifications, number of spans, dimensions, etc. These data can be presented under two forms: 3D view or table view. Besides, several milestones of the bridge life should be available: "as-built" model, "as-is" model, etc. (Tomczak et al. 2022).

3.4 *Maintenance and repair information*

Being fully aware of the complexity of various types of bridge damages (and their underlying deterioration mechanisms), the focus of our interest are not just its visible symptoms. In fact, rather than reinventing the common perception of damages in BMSs, the idea is to find the way to use BrIM for documenting damages which are identified in a traditional routine inspection process, based on a visual observation. Additionally, the focus might be extended to parameters for the damage evolution prediction.

In an object-oriented system, such as BrIM, each damage will be represented by an instance of certain class (i.e. type), described by certain set of attributes (i.e. properties). In principle damage classes are already implicitly defined in damage catalogs of various BMSs. The sets of properties describing damage types are included in catalogs too. Although similarly organized, damage descriptions differ between various BMSs. To make data communication between different BMSs easier, finding a consensus on damage description is necessary. This means that any damage type should be described by a set of properties which is a common denominator for majority of BMSs.

In BrIM terms, modeling of damage means enabling the new BrIM functionality of modifying the intact geometry of the damaged element by introducing damage location, affected area of an element, damage photos, relationship between the damage object and the affected element, etc.

For the bridge management, historical information is crucial both for documenting the historical development of damage, as well as for documenting element replacement, addition, and/or geometry adjustment. For this purpose, an extension of IFC schema is required.

Damage evolution prediction, performed by BMS, should be associated with particular BrIM element or the entire model. It can be done by externally referencing the damage evolution data and, perhaps, assigning a time attribute to it.

3.5 *User interface*

In the context of efficient maintenance of motorways and tunnels as-built drawings have been reworked to show the exact location of maintenance items and quantities for planning of maintenance rotations, tracking progress and tracing the history of interventions (e.g. refurbishment and partial replacement). The digital availability of detailed asset documentation simplifies the distribution and update of information (Sacks et al. 2018).

Exact and current asset information is even more vital for rescue teams. Also, for the online documentation of maintenance, immediate status update, quantity surveying and the billing workflows the use of portable tablet computers greatly improves the speed of processing and mobility of teams. The ultimate vision of utility managers is an augmented reality tool to look through solid material (pavement, concrete) onto hidden assets with their exact coordinates, network topology and status information.

Another advanced use of real-time interfaces with a digital twin is the use case of structural monitoring, either in temporary installation to measure the structural response for decision making, or in permanent big-data applications such as detecting changes in temperatures, humidity, forces, strains or vibration frequencies identify latent deterioration processes. The monitoring platform may just record data for later interpretation by postprocessing, or it may permit configurating new interfaces in the field, and even allow (by virtue of cloud computing) to run structural simulations and interpret the measurement data on the spot.

4 EXTENSION OF IFC FORMAT

Linking BrIM and BMS through extension of the IFC format opens up for seamless communication between the system. This will give the bridge owner the possibility to combine information stored during the design phase with data collected in the operation phase, thus, opening up for more informed and effective operations of individual structures, as well as easier comparison between structures.

The following key extension of IFC were identified:

- Introduction of time stamp to track change on elements and information.
- Introduction of unique IDs for elements.
- A mechanism which can store status of elements such as initial, unchanged, modified, replaced, added, and demolished entities. This could be done through a *IfcLifetime* entity type with attributes like *BirthDate* and *DeathDate*. By introducing IfcLifetime entity, the current as-is geometry of a bridge would be determined at any moment in time, as shown in Figure 2.
- Place holder for inspection and maintenance plans.
- Maintenance and repair functionality including deterioration prediction, costing and optimization.
- Connection to structural assessment software.
- Definition of damage properties and damage information modelling.
- A system that handles visualization of current status of the structure including accurate position of damage and vulnerable zones.

The proposed extension will work for both new structures with BrIM models and structures without BrIM models. For the latter, very simplified models can act as place holders for information and exchange with BMS, and then be expanded into the realistic models when needed.

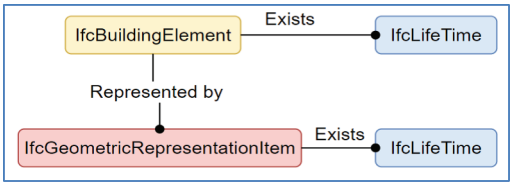


Figure 2. EXPRESS-G diagram illustrating the use of the proposed *IfcLifeTime* entity type.

5 BMS IN KOREA

In Korea, the BMS is meticulously tailored to cater to the distinct information needs of cable-supported bridges and conventional bridges. Specifically, for cable-supported bridges, the BMS incorporates sophisticated information systems such as a comprehensive health

monitoring system and a condition rating system equipped with detailed damage records. On the other hand, common bridges are overseen by an information system that meticulously tracks inspection and repair records for the entire bridge structure. The BMS dedicated to common bridges systematically accumulates invaluable inspection data, repair records, and essential information for the comprehensive assessment of bridge conditions and safety. This meticulous management extends to bridges owned by public agencies, ensuring a holistic approach to monitoring and maintaining the integrity of critical infrastructure.

Following the government's mandate for mandatory BIM adoption in public construction projects, the as-built BIM deliverables have assumed the role of foundational data for a BIM-based BMS (Nguyen et al. 2021). The IFC models submitted must undergo a conversion process to establish proper data links and optimize memory for seamless visualization. As maintenance tasks generate diverse data, encompassing images and Non-Destructive Evaluation (NDE) data, the primary objective is to efficiently transfer existing data to the new BMS, minimizing the need for manual input during this transition. Simultaneously, transitioning from the existing file-based maintenance system to a data-driven model, enabling Database-to-Database (DB-to-DB) transfers, presents a formidable challenge for bridge owners. This shift underscores the complexities inherent in modernizing maintenance systems while adhering to evolving technological standards (Won et al. 2021). In recent developments, public authorities have instituted a systematic approach for data accumulation throughout the project delivery, with the adoption of ISO 19650 as the standardized framework for handover data delivery (Shim et al. 2019). The architectural and data specifications of the as-built BIM must now factor in the specific requirements for new data and tasks that arise during the maintenance period as shown in Figure 3. Given the imperative of accurately assessing the key performance metrics of existing bridges facing deterioration, the new BMS is poised to offer a well-federated and dependable stream of data, ensuring comprehensive and reliable insights throughout the entire lifespan of the bridges. This strategic alignment ensures that the BMS is not only responsive to immediate project needs but also anticipates and addresses the evolving demands of bridge maintenance and performance assessment over time.

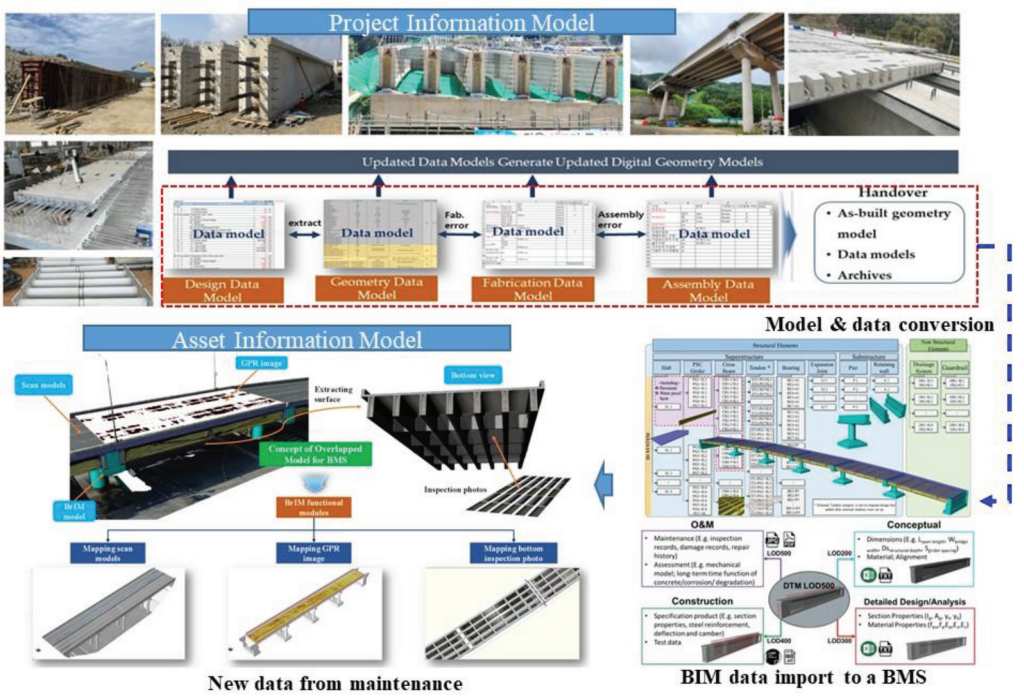


Figure 3. Information delivery from as-built BIM to BMS.

6 BMS IN SOUTH AMERICA

At the onset of 2015, the Technological Development Corporation established the BIM Forum in South America as a technical and permanent platform. This forum unites key professionals and institutions associated with Building Information Modeling (BIM) to channel technical concerns, knowledge, and information. Its purpose is to contribute knowledge and experiences from companies and professionals. The primary goal is to disseminate, develop, and foster best practices in all aspects of BIM, encompassing road infrastructure and bridges (Valenzuela et al. 2023).

The main countries involved in the BIM Forum include Argentina, Brazil, Colombia, Chile, Ecuador, Peru, among others, providing a foundation for various initiatives in each country. For instance, in Chile, the national strategic program "Construye 2025", under the "Plan BIM", aims to ensure that companies participating in future public tenders develop projects that are constructible and operable. These projects should contain integrated modeling and databases, demonstrating a comprehensive understanding of the BIM concept.

In alignment with this, the Roads Directorate, as part of its Bridges 2020-2030 program, has incorporated the BIM methodology within the lines of development and implementation (MOP 2022). The focus is specifically on the implementation of BIM in road infrastructure works, particularly in bridges, during certain project phases.

Academic support has played a crucial role in developing BIM, enhancing the technical capacity and skills of professionals. The primary application of BIM is evident in the design stage, especially for complex or unique bridges (cable-supported), under a master plan of road infrastructure, or specific requests during construction (e.g., Maipo bridge Pan-American route).

Highlighted projects include the "Trincheras Structural Project Concesión Américo Vespucio Oriente AVO1 (2018-2019)" in Chile, which was developed in BIM by the Concessionaire. Notable projects in Colombia include the "Intercambio vial San Juan con la Carrera, Medellin (2021)" and the "Troncal Alimentadora PLMB, Cali (2022)", both involving comprehensive BIM applications from site study and design coordination to visualization using VR + AR.

Costa Rica showcases studies involving the interaction between road infrastructure and bridges, such as the coordination of design on national road 1.

Currently, BIM implementation has extended to Operations and Maintenance (O&M), integrating methodologies for inspection and data review of pathology. Examples include Colombia's application to footbridges and initiatives in Chile by Municipalities, the Ministry, and EFE (Railway authorities) to digitalize O&M activities for existing structures (Seguel & Seguel 2021).

In conclusion, South America has developed several standards aligning with international requirements, as proposed by BIM Forum Argentina. These standards encompass fundamental concepts applied to design, construction, and operation, defining dimensions from 3D to 7D, implementation phases, and areas of application (architecture, infrastructures, including bridges), each at different stages of adoption in various countries and structures.

7 VALIDATION OF CONCEPTS

Various authorities, in total 22, in different countries have been interviewed over six months, using therefor developed questionnaire.

In general, bridge owners face the dual challenge of managing unique assets and determining the most effective inspection means. Various methods and systems are used for this purpose. The documentation of bridges with their conditions due to bridge inspections and the management of structures is generally done in a structured and digital manner. Either specially developed or commercially available systems are used for this purpose. It can be concluded that digital structure management with the recording of structure conditions has already arrived in principle in the institutions surveyed. Still, it must be assumed that different approaches to structuring, processing, and presenting the data exist.

The data that is or should be included in a bridge management system mainly relates to documenting conditions or condition developments. On the one hand, the relevance of

categorized and thus generalized condition descriptions in the form of condition grades, point- or scoring systems becomes apparent. These provide essential decision-making aids in higher-level management by making structures comparable. On the other hand, the survey of visualization requirements shows that component-related condition information and documentation, particularly damage and damage development, are also of considerable relevance. The respondents showed a clear preference for a representation that enables a linked representation of, e.g., damage details and affected components. While a photorealistic representation of buildings or parts of buildings is predominantly not considered necessary in this context, a significant proportion of respondents consider this valuable information in damage documentation. This underlines the heterogeneity of the data to be processed. There are different levels of consideration at which different types of condition descriptions become relevant. The required condition descriptions range from generalized categorization to highly detailed reports of individual damage incidents with additional documents such as photos or sketches. Neither BrIM nor BMS systems alone can fulfil all these requirements suitably. Instead, a flexible combination of the two approaches seems promising.

Another critical point is the provision of the collected bridge data. The challenge here lies in the different data users with varying legitimate interests. In addition to authorization levels that may become necessary due to administrative structures, a small proportion of the data is often publicly accessible. In Europe, for example, this requirement results from the INSPIRE (Infrastructure for Spatial Information in the European Community) directive of the European Commission. According to this directive, all 34 member states have been obliged since 2007 to make certain geodata sets (including transport networks and associated infrastructure facilities) available to the public. For many authorities, this makes the possibility of differentiating the provision of data according to different rights even more relevant. This is also reflected in the interviews conducted, in which most respondents stated that various levels of access control are also implemented in the existing systems.

The findings underscore the challenges in developing a system that combines a Bridge Management System (BMS) and Bridge Information Modeling (BrIM). The sector's complexity, varying needs, and preferences highlight the need for a nuanced and flexible approach to bridge asset management systems.

8 HIERARCHY OF BRIM AND BMS

BrIM is expected to significantly minimize errors, accelerate project delivery time, and cut implementation costs. However, research indicates that, despite the wealth of data generated using building management systems (BMS) of varied degrees of sophistication, the building operation and management stage is falling behind. Our survey includes the challenging question about hierarchy between BrIM and BMS, including GIS based system. It is consequently important to understand both frameworks, BrIM and BMS, as future linked data bases, improving the evaluation of bridge performance in use and provide feedback to the design stage, perhaps resolving design-related performance issues.

9 CONCLUSIONS

The current challenge for majority of existing bridges represents the fragmented data: data describing the structure and historical information on how the bridge has been managed is stored in many different formats and location, thus, it is fragmented. There is a lack of standardization of obtaining information about the state of the structure and its structural properties. For existing bridges currently data is stored in several formats. Several BMS systems exist worldwide, but not incorporated in Open BIM systems.

The BrIM model should allow for bi-directional information flow with the BMS system (and other systems linked to the BIM) such that information is not duplicated in the connected systems.

Short overview of BIM-BMS situation from Korea and South America was presented.

The aim of IABSE TG 5.6 is searching for all requests from BMS systems (in form of use cases) to report missing attributes within exiting Open BIM systems. Open BIM technology for the interoperability from technical, semantic, and organizational point of view is of main interest. We need to consider as-built BIM deliverables for new bridges. In our vision, the establishment of a universally accepted standardized framework for data exchange between disparate systems empowers bridge owners. The culmination of intensive interviews with bridge authorities and owners from around the world will serve as the guiding compass for recommending the future integration between Bridge Management Systems and Open BIM. Survey results from bridge owners and authorities worldwide will help us in prioritization of use cases and serve as further development input for software authorities. Further steps about will be reported in the next papers.

REFERENCES

Aas-Jakobsen, K., Hawryszków, P., Joshi, S., Berton, E., Isailovic D. & Hohberg M. 2023. Linking BrIM to BMS for bridges – concepts. *Proc. intern. IABSE Congress New Delhi*, *India*.

Hajdin, R. & Samec, V. 2022. BIM and BMS: Current status and Challenges. *Proc. intern. IABSE Symposium Prague, Czech Republic*.

Isailovic, D. & Hajdin, R. 2022. Geometry as a common ground for BMS and BIM. *Proc. intern. IABSE Symposium Prague*, *Czech Republic*.

MOP (Ministry of Public Work of Chile). 2022. In Ministerio de Obras Públicas de Chile (ed.), *Plan de puentes 2020-2030*. Santiago, Chile.

Nguyen, D.C., Nguyen, T.Q., Jin, R., Jeon, C.H. & Shim, C.S. 2021. BIM-based mixed reality application for bridge inspection and maintenance. *Construction Innovation* https://doi.org/10.1108/CI-04-2021-0069.

Sacks, R., Kedar, A. & Borrmann A. 2018. See Bridge as next generation bridge inspection – Overview, information delivery manual and model view definition. *J. Automation in Construction* 90: 134–145.

Seguel, J.L. & Seguel, C. 2021. USO BIM EN PUENTES CHILENOS Experiencia en la implementación en una oficina de puentes (in Spanish). *Proc. intern. 3rd Bridge Congress Valparaíso, Chile*.

Shim, C. S., Dang, N. S., Lon, S. & Jeon, C. H. 2019. Development of a bridge maintenance system for prestressed concrete bridges using 3D digital twin model. *Structure and Infrastructure Engineering* 15 (10): 1319–1332.

Tomczak, A., Van Berlo, L., Bolpagni, M., Krijnen, T. & Borrmann, A. 2022. A review of methods to specify information requirements in digital construction projects. *Proc. intern. IOP Conference Series Earth and Environmental Science* 10.1088/1755-1315/1101/9/09.

Valenzuela, M, Márquez, M., Roca, L. & Seguel, J.L. 2023. An Overview of the BIM implementation on Chilean Bridges. *Proc. intern. IABSE Congress New Delhi*, *India*.

Won, J. B., Park, J. W., Shim, C. S. & Park, M. W. 2021. Bridge-surface panoramic-image generation for automated bridge inspection using deep matching. *Structural Health Monitoring* 20(4): 1689–1703.

Bridge Maintenance, Safety, Management, Digitalization and Sustainability – Jensen, Frangopol & Schmidt (eds)
© 2024 The Author(s), ISBN 978-1-032-77040-6
Open Access: www.taylorfrancis.com, CC BY-NC-ND 4.0 license

Strategies for effective bridge information management with OpenBIM

C. Gragnaniello, G. Mariniello & D. Asprone
Department of Structures for Engineering and Architecture, University of Naples Federico II, Naples, Italy

ABSTRACT: This study focuses on the efficient management of infrastructure information using BIM (Building Information Modelling) models. With a specific emphasis on the assessment and maintenance of bridges, it examines the impact of using level of information need (LoIN) in BIM models and defines data schemas for guidelines related to bridge management. The paper highlights the definition of I-BIM models and interoperability. Applicability is demonstrated through an I-BIM digital model case study and the verification of information delivered.

1 INTRODUCTION

1.1 *Bridge information management*

The management of bridges is crucial to ensure their safety, efficiency, and durability over time. Infrastructure plays a key role in aiding the mobility of people and commodities, enabling development, and connecting countries [1]. However, with urban development and population growth, the volume of loads and vehicles crossing bridges has increased, causing high stress and deterioration on bridges. In addition, over time the materials used for bridge construction undergo a natural aging process.

Therefore, it becomes essential to adopt infrastructure management practices that aim to control the vulnerability of works and plan maintenance in a timely and efficient manner [2].

This involves several activities, such as periodically inspecting bridges to identify any signs of damage, assessing structural capacity to ensure that they can withstand the expected loads, and planning preventive maintenance actions [3,4].

In this context, the Bridge Management System (BMS) is a key tool for monitoring, assessing, and managing the condition of bridges. This provides a comprehensive view of the health of the infrastructure and identifies specific maintenance needs. BMS originated in the United States with the Pontis study initiated in 1975, evolving over time and providing a model for the development of similar systems around the world [5,6].

Over time, the concept of BMS has spread globally, adapting to the specific needs of different countries and regions. Nowadays, many countries have implemented or are implementing advanced bridge management systems that use increasingly sophisticated assessment and monitoring technologies and methodologies.

The evolution of BMS is an ongoing process, with an increasing emphasis on digitization, the use of advanced technologies such as Building Information Modeling (BIM), and the adoption of proactive approaches to infrastructure management [7,8,9].

Building Information Modeling (BIM) represents a digital methodology that is based on the creation and management of information models for buildings and infrastructure. Within BIM models are detailed and integrated information, including geometric, graphical, and documentary data describing the characteristics of constituent elements.

In the realm of existing bridges, BIM offers significant advantages. Studies, such as McGuire et al. [10], underscore BIM's capacity to optimize infrastructure management,

DOI: 10.1201/9781003483755-242

particularly for bridges. Furthermore, Hagedorn et al. [8] propose the use of BIM to manage transportation infrastructure assets, focusing on data description and updating, preparation of informational containers, integration with existing asset management systems, and the design of an informational portal.

I-BIM models streamline the assessment and maintenance of bridges by utilizing a single database, facilitating efficient and integrated management of bridge information. They enable the integration of damage data and inspection records within the same model, simplifying structural condition assessments without the need for data comparison across disparate sources, as shown by Nguyen et al. [9].

In addition, BIM models allow for the formulation of optimal maintenance based on on-site data. Shim et al. [11] propose a data schema for BIM models to establish a maintenance system for cable-stayed bridges, which effectively organizes data and demonstrates significant time-saving potential for maintenance work.

Ultimately, I-BIM models empower stakeholders to make informed decisions and execute efficient infrastructure management strategies for existing bridges.

1.2 *Scope of study*

The increasing adoption of BIM presents a significant challenge in ensuring the accuracy and certification of I-BIM models. This study addresses this challenge by concentrating on defining Levels of Information Need (LoIN) within bridge management processes, following EN 17412-1:2020 guidelines [12]. Specifically, it aims to answer the question of how to check I-BIM models to prevent errors during the delivery phase.

This study is divided into four sections: the second describes an approach that involves all the resources needed in a BIM management process, with a focus on bridge field. Moreover, in the third section is applied the methodology to a case study of a viaduct on a highway in Italy, to optimize the delivery of the project. Finally, the discussion and conclusions highlight the importance of clearly define the information requirements in a preliminary phase, to verify the consistency of I-BIM model delivered, with the support of CDE.

2 A BIM-BASED APPROACH TO IMPROVE BRIDGE MANAGEMENT PROCESS

The proposed approach considers the use of BIM as the main tool for information management of existing bridges. Emphasis is placed on the importance of defining the owner's information requirements in advance to ensure the creation of management models in line with specific requirements. This approach is based on the use of a Common Data Environment (CDE), an interoperable digital data sharing environment that facilitates collaboration among stakeholders by engaging them in an effective information flow. The CDE is structured into four distinctive folders: Work in Progress (WIP), Shared, Published, and Archive, according to ISO19650-1:2018 [13].

This approach optimizes the use of information requirements for data transmission, known as Exchange Information Requirements (EIRs). EIRs outline the requirements of the developer during the management of the bridge, including all activities necessary to preserve its structural integrity, which are outsourced to specialists in the field. EIRs include Levels of Information Need (LOINs), which are then translated into a machine-readable version: the Information Delivery Specification (IDS).

The main objective of this approach is to precisely define the location of all these elements within the CDE, and their use to optimize the information management of bridges, as shown in Figure 1. Initially, the various working groups collaborate within the WIP folder, where only they can access and work confidentially. However, for the models to comply with the requirements, it is essential that they have access to the EIRs at the beginning of the process. Next, the information moves to the Shared folder, which is also accessible to the owner, that allow the models to be shared and consolidated into a single federated model. These individual models or the federated model can be checked for consistency and conformity using IDSs. If

discrepancies are identified, the model is flagged and corrected by the corresponding working group before being moved to the Published folder.

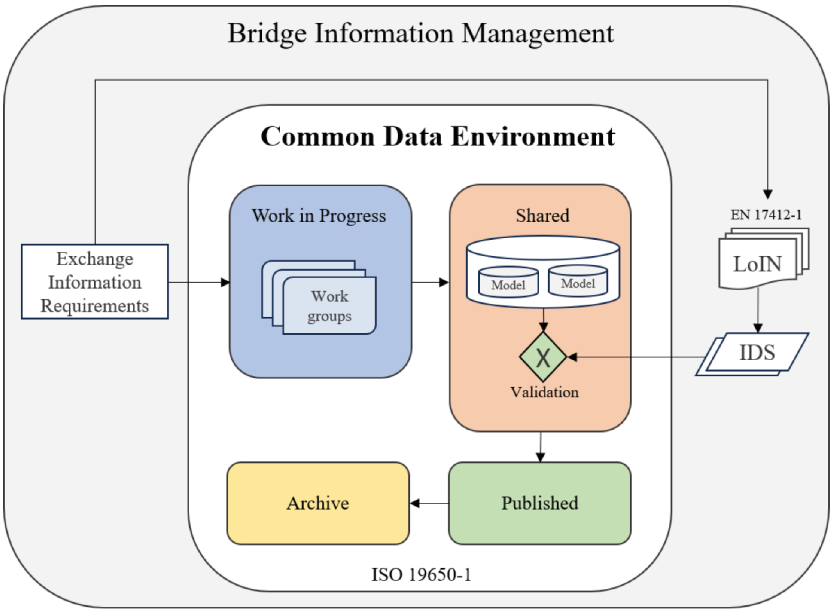


Figure 1. BIM-Based approach for bridge information management.

3 CASE STUDY: THE MORO VIADUCT

The "Moro" viaduct, constructed with prestressed reinforced concrete, consists of 25 spans, each spanning 45 meters. Its deck, approximately 19.10 meters wide, accommodates two lanes for traffic, separated by a central barrier. The piles supporting the viaduct comprise two box-shaped shafts, each measuring around 8.30x3.30 meters, connected by a pulvino beam on which six beams rest. These piles have columns founded on a single plinth resting on piles, with historical interventions focusing on beam swelling, support maintenance, and partial cortical restoration. Over the years, the viaduct has undergone several restorations, mainly concerning beam swelling, support maintenance, and cortical restoration of some parts of the beams.

The need for the Moro viaduct, translated by EIRs defined in the recruitment phase, was to have an I-BIM model with the geometric, documentary, and graphical information related to the bridge's actual state. In particular, the purpose of the model, to be delivered, was to be able to contain information related to the last inspections performed and the attention class in which the bridge fits, according to Italian regulations. For this purpose, it was defined a CDE, organized as described in Section 2, in a data sharing environment: usBIM.browser, by ACCAsoftware, to enable stakeholder collaboration in the infrastructure management process. In addition, the use of this data sharing environment allowed images of deterioration, documents, material tests and reports to be linked to the BIM model.

The I-BIM model (Figure 2) was created using the IFC4X3 standard, in accordance with the EIRs defined in the WIP folder. the IFC4x3 version, allows detailed representation of infrastructure elements, including bridges. With IFC 4x3 version, this bridge is coded as IfcBridge entities and fall under the IfcFacility category. Specifically, the model was developed by a block-based programming with tabular inputs and sections definition. The model represented the bridge as an IfcBridge entity and the constituent elements as IfcBridgeParts. The IfcBridgeParts were defined by the name of the part of the work they represent, with increasing numbering, while the spans were divided into IfcElements of beams, joints, supports, abutments, and foundations.

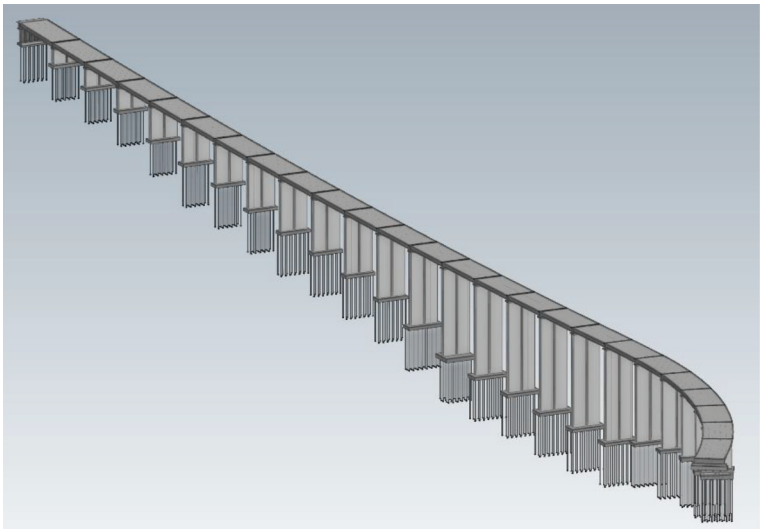


Figure 2. Case study I-BIM model.

Following the guidelines of EN 17412-1:2020 [12], the LoIN is defined by the purpose of the model delivery, namely the assessment of the bridge's condition. Additionally, the milestone is identified as the management phase where the owner acts. Furthermore, beams, columns, slabs, walls, piles, and footings are identified as the objects for which the LoIN is defined. Lastly, as alphanumeric information to manage the detected damage, a set of properties is defined as informational content: Pset_Condition.

Pset_Condition is composed by:

- AssessmentDate means the date on which the general condition of the asset/element is assessed.
- AssessmentCondition is the relative defectiveness value *DR*, calculated according to Italian "Guidelines for Risk Classification and Management the Safety Assessment and Monitoring of Existing Bridges" [3], represents the measurement of the condition state of the elements and is calculated in the following way:

$$DR = Gi \times k1 \times k2$$

In which *Gi* represents the weight of the defect; $k1$ represents the extension of the defect; $k2$ represents the intensity of the defect.

- AssessmentDescription is the qualitative description of the condition of the element considered for which it has been determined as the attention class value, approximately calculated according to the Italian Guidelines [3], attributed to the element depending on the value of the relative defectiveness index which characterizes it. If $DR < 5$, the attention class associated with the element is LOW; if $DR > 25$, the attention class associated with the element is HIGH; for all intermediate values between 5 and 25, the attention class associated with the element is MEDIUM.
- AssessmentType means the category of the last report concerning the assessment of the state of condition of the asset/element, or the type of assessment performed to evaluate the different items, in the case analyzed these are inspections.
- AssessmentMethod concerns the external reference to the assessment method or application used to perform the assessment.
- LatestAssessmentReport refers to the latest technical report on the condition, state of health of the asset/element.
- NextAssessmentDate is the date of the next condition inspection.

– AssessmentFrequency indicates the frequency with which the asset/element must be assessed, to have a clear estimate of their state of degradation.

After the insertion of all this information in the I-BIM model, the model was moved in Shared folder where the information produced must be verified. For this scope, applying the approach described in Section 2, it was generated and employed an IDS (Figure 3).

The IDS standard, developed by buildingSMART, with an XML language, translate LoIN into machine-readable language, ensuring coherence in BIM models [14]. As a distinguishing feature of the Open BIM approach, IDSs promote open data formats, fostering market development and interoperability. For the case study usBIM.IDSeditor was used to generate the IDS, which included all LoIN-specific information for the management phase.

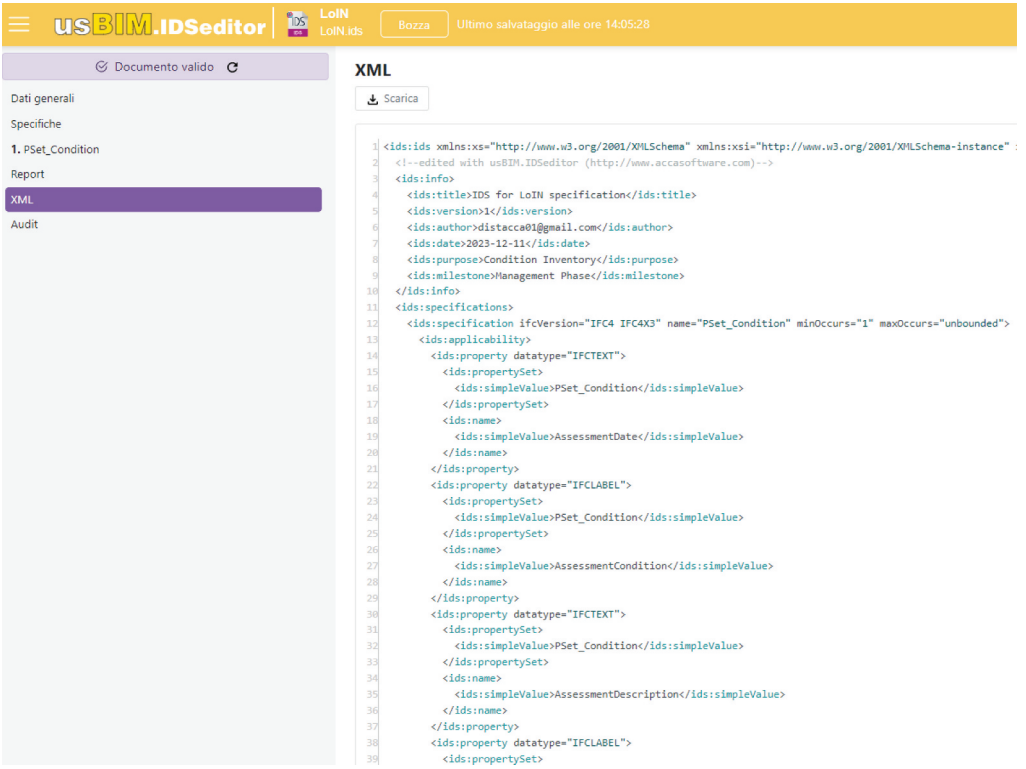


Figure 3. Example of IDS generation for the case study.

4 DISCUSSION

The use of the IDS made possible to verify the accuracy and adherence of the model against the pre-established information required, ensuring that the data and information provided were in accordance with expectations. This verification was carried out through usBIM.IDS, a tool directly applicable to our virtual environment containing the BIM model, which verifies the relevance of the information in real time. The tool usBIM.IDS notified the presence of all the information required. As shown in the following figure, if the information was missing, it would be notified and the IfcElement with the missing information would be highlighted with a different colour, in this case red. In addition, the error code for the failed verification is notified. In the present case, the code specifies that for that element, a specific requirement related to the insertion of the assessment data is not met. The model is therefore not verified, and a modification notification is

forwarded to the responsible team. After the modifications, the model is rechecked, and if it is verified through the IDS, it is shared in the published folder.

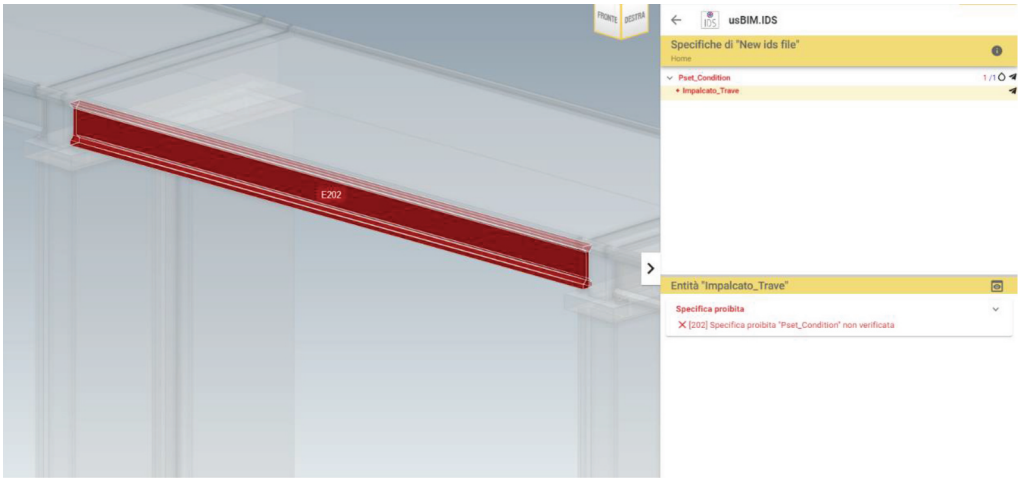


Figure 4. IDS verification for the case study.

The case study highlights the applicability of the proposed approach, which starts from the definition of specific needs related to I-BIM models and arrives at the possibility of verifying the information contained in the models themselves. The main result consists of an information checking strategy, to understand expeditiously what is missing in the model or what is contradictory to the specific needs. Therefore, it has been shown that through this procedure, it is possible to define whether in the I-BIM model of the case study information is present in the model or not, as shown in Figure 4, with the consequence of being able to reduce errors in the delivery phase.

5 CONCLUSIONS

The research has focused on exploitation of BIM approach to improve information management of existing bridges. The study particularly emphasizes the importance of specifying and verifying the information produced and exchanged, defining LoIN, and employing IDS, to check the data within BIM models. This approach is pivotal in all the process that involves model information sharing, fostering collaboration among stakeholders, and ensuring the consistency of data shared. The primary objective is a comprehensive understanding of all necessary information of bridge structures.

Specifically, the methodology is applied to a viaduct case study, in Italy, that shown the usefulness of a BIM-based approach to have a control on the I-BIM model shared, and suddenly identification of possible inconsistency in the delivery phase.

Finally, the application displays certain limitations, as the manual input required in the IDS generator. In addition, limited accessibility to tools such as usBIM.IDS limits their open use and potential for collaboration with infrastructure management stakeholders.

REFERENCES

[1] Frangopol, Dan M., and Min Liu. "Maintenance and management of civil infrastructure based on condition, safety, optimization, and life-cycle cost." Structures and Infrastructure Systems (2019): 96–108.

[2] Zonta, Daniele, Riccardo Zandonini, and Francesca Bortot. “A reliability-based bridge management concept.” Structures & Infrastructure Engineering 3.3: 215–235, 2007.
[3] Ministry of Infrastructure and Transport, Guidelines for the classification and management of risk, safety assessment, and monitoring of existing bridges, Superior Council of Public Works, 2020.
[4] AASHTO, Manual for Bridge Element Inspection, 2d Ed., 2019.
[5] Thompson, Paul D., et al. “The Pontis bridge management system.” Structural engineering international 8.4: 303–308, 1998.
[6] Woodward, R & Cullington, DW & Daly, AF & Vassie, PR & Haardt, P & Kashner, R & Astudillo, R & Velando, C & Godart, B & Cremona, C. Bridge management in Europe (BRIME)-deliverable D14-final report, 2001.
[7] Vignali, V, et al. “Building information Modelling (BIM) application for an existing road infrastructure.” Automation in Construction 128 (2021): 103752.
[8] Hagedorn, P., et al. “BIM-Enabled Infrastructure Asset Management Using Information Containers and Semantic Web.” Journal of Computing in Civil Engineering 37.1 (2023): 04022041.
[9] Nguyen, Duy-Cuong, et al. “BIM-based mixed-reality application for bridge inspection and maintenance.” Construction Innovation 22.3 (2022): 487–503.
[10] B. McGuire, R. Atadero, C. Clevenger, and M. Ozbek, “Bridge Information Modeling for Inspection and Evaluation,” Journal of Bridge Engineering, vol. 21, no. 4, Apr. 2016, doi: 10.1061/(asce)be.1943-5592.0000850.
[11] Shim, C. S., Kang, H., Dang, N. S., & Lee, D. (2017). Development of BIM-based bridge maintenance system for cable-stayed bridges. Smart Struct. Syst, 20(6), 697–708.
[12] EN 17412-1:2020, Building Information Modelling - Level of Information Need - Part 1: Concepts and principles.
[13] ISO 19650-1:2018, Organization and digitization of information about buildings and civil engineering works, including building information modelling (BIM). Information management using building information modelling. Part 1: Concepts and principles.
[14] Gragnaniello, C., Mariniello, G., Pastore, T., & Asprone, D. (2024). BIM-based design and setup of structural health monitoring systems. Automation in Construction, 158, 105245.


Taylor & Francis
Taylor & Francis Group
http://taylorandfrancis.com

SS13: Design, construction and evaluation of steel/FRP & concrete composite bridge structures

Organizers: H. Xin, X. Xu, R. Liu & J. He


Taylor & Francis
Taylor & Francis Group
http://taylorandfrancis.com

Bridge Maintenance, Safety, Management, Digitalization and Sustainability – Jensen, Frangopol & Schmidt (eds)
© 2024 The Author(s), ISBN 978-1-032-77040-6
Open Access: www.taylorfrancis.com, CC BY-NC-ND 4.0 license

Cyclic behavior of replaceable LYP steel coupling beam with corrugated web

J. He, S. Feng & Y. Ma
School of Civil Engineering, Changsha University of Science and Technology, Hunan, China

Q. Teng
Guangxi Transportation Science and Technology Group Co., Ltd, Guangxi, China

W. Lin
Department of Civil Engineering, School of Engineering, Aalto University, Espoo, Finland

ABSTRACT: A novel replaceable low yield point steel coupling beam with corrugated web and demountable connection is proposed for establishing a rapid recoverable system of bridge piers or shear walls. Six specimens using different material and shape of the webs, with different height-to-span ratio, were prepared and tested under cyclic loading as per AISC 341-16. Three kinds of failure modes were observed, such as local bucking at flanges, welding fracture at the flange-to-endplate connection, combined welding fracture at the flange-to-endplate connection and shear bucking at corrugated web. The utilization of a small height-to-span ratio and low yield point steel in the web can enhance the ductility and energy dissipation capacity of proposed steel coupling beam. All the findings from present investigation may provide reference for the application of proposed replaceable low yield point steel coupling beam with corrugated web for bridges and buldings.

1 INSTRUCTIONS

Earthquake resilient bridge pier has been developed recently, which consists of the main structures (piers) and the replaceable components (energy-dissipating coupling beams). Traditional reinforced concrete coupling beams can be replaced by steel coupling beams in bridge piers or shear wall systems, due to good hysteretic performance, stable mechanical properties, and "fuse" characteristic for the steel coupling beams (Shahrooz et al. 1993, Chen et al. 2007, EI-Bahey et al. 2012). The replaceable steel coupling beams were applied between the bridge towers in the New San Francisco-Oakland Bay Bridge, McDaniel et al. (2003) performed the cyclic tests on three specimens and verified the effective of the stiffened steel coupling beams in reducing the displacement, but the welding fracture took place at failure state. Fortney et al. (2007) & Nikoukalam et al. (2015) proposed demountable steel coupling beams with bolt connector using small cross-section to make sure shear-yielding in advance.

Corrugated steel web (CSW) has high shear strength and out-of-plane stiffness, which has been widely used in the steel girder bridges and shear walls (Wang et al. 2018, Qiu et al. 2022). Hajsadeghi et al. (2014) investigated the seismic performance of the coupling beams with CSWs by finite element simulations, considering the corrugation shape, thickness, and corrugated inclined angle of the CSWs, showing that the CSW coupling beams have excellent energy dissipation capacity. Aydın et al. (2016) conducted quasi-static tests on beam-to-column joints adopting steel coupling beams with CSWs, and concluded that the steel coupling beams with CSWs had the same seismic performance as the steel coupling beams with thicker steel plates. Zhang et al. (2017) proposed a recoverable assembled beam-column joints with CSWs, which was proved to have high bearing capacity and ductility, ensuring the main structure (beam and column) remained in elastic state

DOI: 10.1201/9781003483755-243

under severe earthquakes. Wang et al. (2021) proposed a type of coupling beam with longitudinal arrangement of corrugated steel plate (CSP), and carried out loading tests on CSPs with different geometries. The test results showed that the yield load and initial stiffness were mainly affected by the aspect ratio of the CSP. Considering the demountable performance of the steel coupling beams with CSWs, Quan et al. (2022) proposed a novel demountable corrugated shear panel damper (DCSPD) and investigated the effects of three key design parameters, including the corrugation direction, the thickness of CSW and flange.

In addition, experimental studies indicated that low yield point steel (LYP steel) with higher performance in terms of plastic deformation, ductility and energy dissipation than the common carbon steel, is preferred as the materials for earthquake-resistant components (Saeki et al. 1998). However, more stiffeners were required to avoid premature out-of-plane buckling when the flat webs of the coupling beams were made of LYP steel, and the failure mode of the coupling beams were mostly fracture of welding seam at web-to-stiffener (Zhuang et al. 2022).

Therefore, this paper proposed a novel replaceable LYP steel coupling beam with corrugated web (LCSW coupling beam), which can be designed as a shear coupling beam between two non-energy dissipating segments or as a flexure-shear coupling beam at the beam-to-column joint. The LCSW coupling beam consists of corrugated web with LYP steel, the top flange, the bottom flange, and the endplates. Six specimens with different height-to-span ratio, shape and material of the webs have been fabricated and tested under cyclic loading to investigate their seismic performance, such as the failure mode, stiffness degradation, residual deformation, and hysteretic energy dissipation.

2 EXPERIMENTAL INVESTIGATION

2.1 *Test specimens*

A total of six specimens were prepared and tested under the quasi-static cyclic loading. Figure 1 and Table 1 illustrate the structural details and main parameters of these specimens. The main different parameters considered in test specimens were the shape of the web (corrugated or I-shaped web), the material of the web (steel with yielding strength of 345MPa-Q345 or 160MPa-LYP160), and the height-to-span ratio [$H/(h_w+2t_f)$ =2.2 or 1.7]. The nomenclature of test specimens is shown in Table 1. For example, LCB22 shows the specimen with the height to span ratio of 2.2 using LYP160 steel corrugated web.

2.2 *Material properties*

The material properties of the flanges (Q345), the stiffener (Q235) and the webs (Q345 or LYP 160) were obtained from standard tensile coupon tests per BS EN ISO 6892-1 (BSI 2020). The properties obtained are modulus of elasticity (E_s), yield stress (f_y), ultimate tensile strength (f_p), and the ultimate elongation rate (δ). The results are given in Table 2 as average values of three coupon specimens.

2.3 *Test setup and measurements*

The test setup is shown in Figure 2a, a hydraulic actuator connected to the reaction frame, with load and displacement capacities of 500kN and 500mm, respectively, and with built-in load cell, was used to push and pull the test specimen through transmission beam bolted at the top endplate of specimen. The bottom endplate of test specimen was bolted to the ground beam.

Prior to the formal test, a preloading with 30kN was conducted to check the good contact between the support and loading equipment. After preloading, the lateral loading was applied to the test specimen by displacement-control method (see Figure 2b), as per AISC 341-16

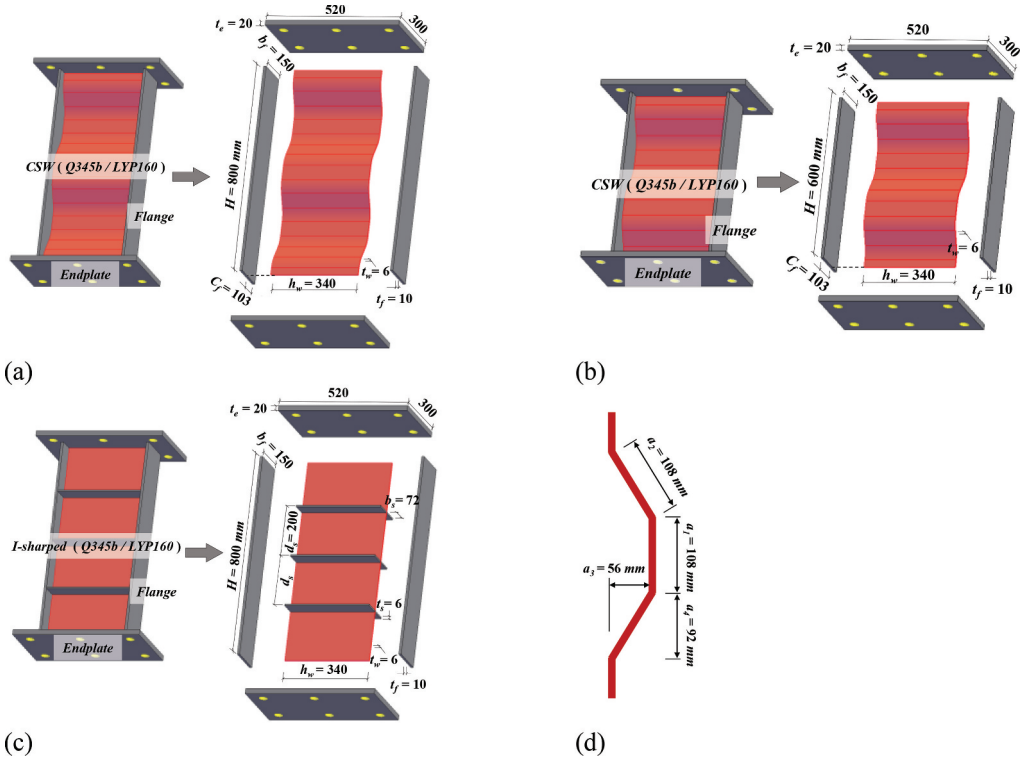


Figure 1. Components and dimensions of specimens: (a) Specimen QCB22 & LCB22; (b) Specimen QCB17 & LCB17; (c) Specimen QIB22 & LIB22; (d) Dimensions of LCSW.

Table 1. Parameters of test specimens.

No.	Specimens	Materials of web	Sharps of web	(h_w+2t_f)/H	h_w+2t_f/mm	H/mm
1	QCB22	Q345	CSW	2.2	360	800
2	QIB22	Q345	I-shaped	2.2	360	800
3	QCB17	Q345	CSW	1.7	360	600
4	LCB22	LYP160	CSW	2.2	360	800
5	LIB22	LYP160	I-shaped	2.2	360	800
6	LCB17	LYP160	CSW	1.7	360	600

Table 2. Material properties.

Steel	Elastic modulus E_s /GPa	Yield strength f_y /MPa	Peak strength f_p /MPa	f_p/f_y	Ultimate elongation rate δ/%
LYP160	195	198	379	1.91	33.34
Q235	202	339	488	1.44	20.17
Q345	196	385	538	1.4	18.21

(AISC 2016). The lateral displacement was defined as positive when the actuator was push to the west.

The arrangement of the strain gauges and the LVDTs are shown in Figure 3, note that the arrangement of the strain gauges for the specimens with flat web corresponds to that of the

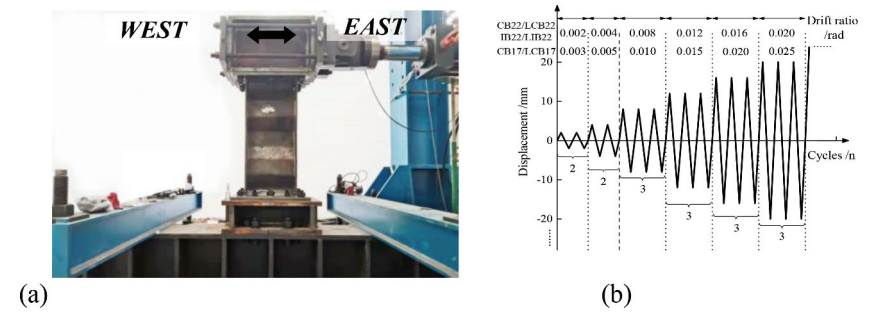


Figure 2. Test setup and loading protocol: (a) Sketch of test setup; (b) Loading protocol.

specimens with CSW. All the information obtained from the transducers, gauges, and load cells were automatically recorded by a data acquisition system at regular intervals during the test.

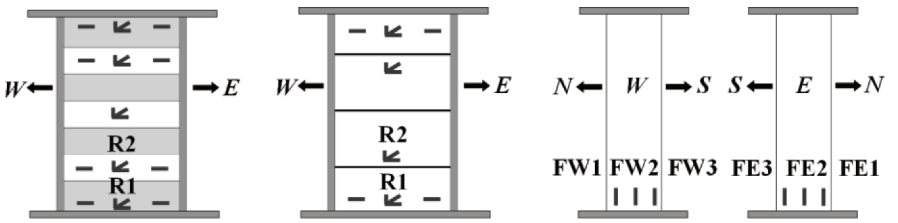


Figure 3. Measurement arrangement: (a) Layout of strain gauges and LVDTs.

3 TEST RESULTS AND DISCUSSIONS

3.1 *Failure process*

The failure process and phenomena were described under different lateral drift ratio. The lateral drift ratio was defined as the ratio of the lateral displacement to the height from the actuator to the bottom endplates. The failure process and modes for each specimen are shown in Table 3 and Figure 4, respectively.

Table 3. Failure process of test specimens.

	Damage features at drift ratio/rad						
Specimens	FB	WB or CSWB	WF	PWF	WT	Failure modes	Failure at drift ratio/rad
QCB22	0.030	0.057	NA	NA	NA	FB	0.057
QIB22	0.062	NA	0.020	0.065	NA	WF	0.065
QCB17	0.027	0.056	0.046	0.066	0.066	Combined WF & CSWB	0.066
LCB22	0.044	0.052	0.052	NA	NA	Combined WF & CSWB	0.052
LIB22	0.044	NA	0.056	NA	NA	WF	0.056
LCB17	0.052	0.056	0.070	NA	NA	Combined WF & CSWB	0.070

Note: FB- Flanges Buckling; WB or CSWB- Web Buckling; WF- Welding Fracture at flange-to-endplate; PWF- Penetrated Welding Fracture; WT- Web Tearing; NA- Not Applicable.

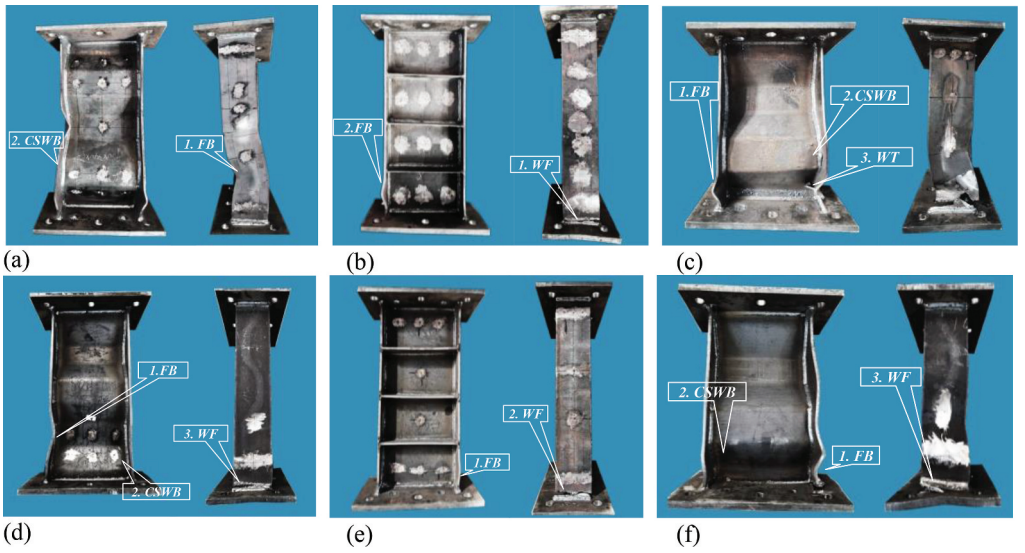


Figure 4. Damage features of specimens: (a) QCB22; (b) QIB22; (c) QCB17; (d) LCB22; (e) LIB22; (f) LCB17. (Note: 1, 2 and 3 represent the order of damage).

Three typical failure modes were observed, including local buckling of steel flanges, the welding fracture at flange-to-endplate connection, and the combination of welding fracture at flange-to-end plate connection and shear buckling of CSWs. In comparison to specimens with CSWs, specimens QIB22 and LIB22 with stiffened I-shape web did not present obvious local buckling of steel flanges due to three stiffeners attached on both sides of the web. Specimens QCB17, LCB22 and LCB17 all exhibited different degree of shear buckling at CSW near flange-to- bottom endplate connection. Moreover, the buckling degree at the CSW was more significant for the specimens with smaller height-to-span ratio (specimen QCB17, specimen LCB17). The buckling degree at the CSW was more significant for specimen using LYP160 steel (specimen LCB17) than that for the specimen using Q345 steel (specimen QCB17). So, both height-to-span ratio and LYP steel significantly influence the hysteretic deformation of the replaceable coupling beams. In addition, no obvious plastic deformation of high-strength bolts was found at the connection when all the specimens failed, thus the replaceable steel coupling beam could be easily demounted and assembled.

3.2 *Hysteretic curves and skeleton curves*

Figure 5 shows the hysteretic curves of test specimens, in terms of the relation between applied force and drift ratio. In the elastic-plastic stage, hysteretic curves show obvious nonlinearity due to yielding of steel webs or flanges, the slope of hysteretic curves decrease gradually with the increase of displacement amplitude, showing an obvious residual deformation due to plastic deformation of steel plates and relative slip at endplates caused by bolt connection. Besides, the energy dissipation capacity was enhanced gradually at the elastic-plastic stage. At the failure stage, the strength and stiffness decreased significantly due to cumulative damage of the test specimens, but the structures can still dissipate energy due to large displacements.

Figure 6 presents the comparison of the skeleton curves for specimens with different parameters. The strength hardening stage of the specimen with LYP160 steel is more obvious than that of the specimen with Q345 steel (see Figure 6a and Figure 6b). In terms of the lateral load in the positive direction, specimen LCB22 and specimen LCB17 reached the peak load (230.7kN, 282.6kN) at the drift ratio of 0.043 rad and 0.051 rad respectively, while the average peak load of QCB22 and QCB17 are smaller. Thus, the usage of LYP steel in the CSW increases the peak load. After the peak loading, the lateral force of test specimens with CSWs

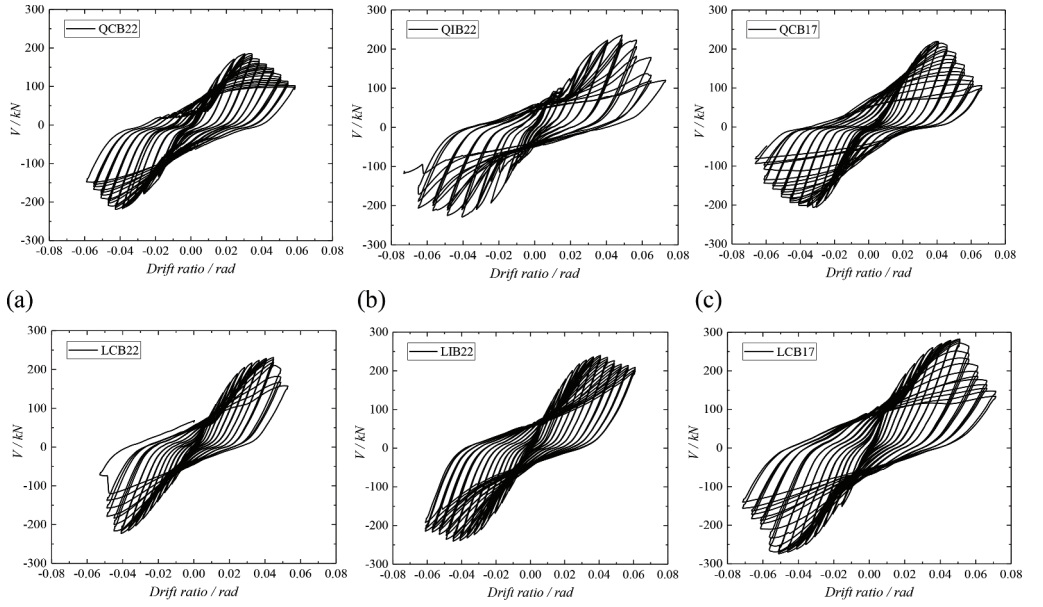


Figure 5. Hysteretic curves: (a) QCB22; (b) QIB22; (c) QCB17; (d) LCB22; (e) LIB22; (f) LCB17.

made of LYP160 steel decreased more obviously than that of test specimens with CSWs made of Q345 steel after the peak loading. Figure 6c shows the comparison of the skeleton curves for test specimens whose web were made of LYP160 steel, LCB17 has superior performance than other two specimens (LIB22 and LCB22) in terms of loading capacity and ductility.

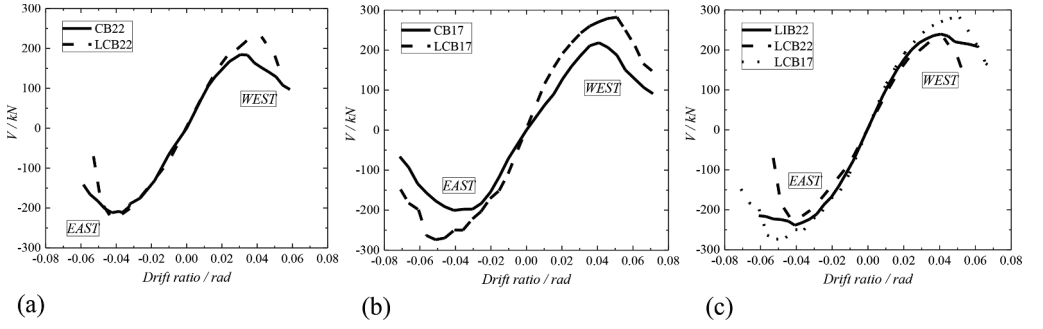


Figure 6. Skeleton curves: (a) LCB22/QCB22; (b) LCB17/QCB17; (c) Specimens with LYP160.

Overall, the utilization of LYP steel in the web improves the loading capacity of test specimens due to continuous strength hardening of LYP160 steel. However, the lateral deformation of the specimens with LYP160 steel CSWs is obvious, leading to local buckling of the flanges and reduction of lateral force. Thus, the flanges of steel coupling beam should be designed to prevent local buckling before ultimate lateral loading.

3.3 *Stiffness degradation*

The relation between stiffness degradation and the lateral drift ratio for all specimens are shown in Figure 7. The stiffness decreases as the lateral drift ratio increases, the stiffness of

specimen LCB17 is greater than that of the other specimens. The stiffness of the specimens with LYP160 steel webs is higher and the stiffness degradation is slower than those of the corresponding specimens with Q345 steel webs. Moreover, the stiffness degradation of the specimens with LYP160 steel webs behaved stably till peak loading, while the stiffness decreased rapidly during the failure stage owing to obvious shear buckling of CSWs with LYP160 steel and the excessive local buckling of steel flanges.

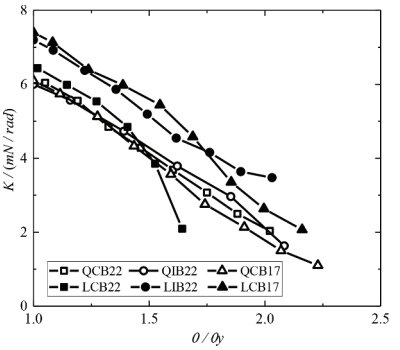


Figure 7. Stiffness degradation curves.

3.4 *Strain development*

Figure 8 shows the variation of the measured strain with the lateral drift ratio. The yield strain ε_{y1} and ε_{y2} are approximately 1000$\mu\varepsilon$ and 2000$\mu\varepsilon$ for LYP160 and Q345 steel steel respectively, which can be calculated according to the material properties of steel in Table 2 and are also presented in Figure 8.

The normal strains on the west flange were in compression while on the east flange were in tension when subjected to push loading. The strain values at the flanges were small before the rotation reached 0.020rad (see Figure 8a). As the lateral drift ratio increased, the west flange yielded first. The CSW did not yield when specimen QCB22 reached the yield point (0.029rad). When the lateral drift ratio reached to the ultimate point (0.039rad), the CSW entered the plastic stage until the specimen was damaged. The failure mode of QCB22 was flanges buckling. Thus, the energy dissipation capacity of the CSWs was not effectively utilized.

When the lateral drift ratio of specimen LCB22 reached the yield drift ratio θ_y (0.032rad in Figure 8b), only the strain at east flange (FE1) reached the yield strain. With the increase of the rotation, the strain at west flange (FW1) and east flange (FE1) increased significantly till the peak load. The strains at the flanges had just entered into plastic stage. Additionally, the shear strain at the CSW (R1) reached yield strain at the lateral rotation of 0.030rad, and the strain increased rapidly after the yield drift ratio θ_y, then reached the maximum around the peak load. The CSW with LYP160 steel deformed more obviously than the flange did after yield point thus became the main energy-dissipating component. Specimen LCB17 presented similar pattern of strain development as specimen LCB22 did (see Figure 8c).

Overall, the advantage of specimens with LYP steel in the web over the specimens with Q345 steel is that the web can enter into yield state earlier, increasing the energy dissipation capacity. During strength hardening stage, the stain at web (especially the web using LYP steel) increased significantly, and then the web became the main energy-dissipating component.

3.5 *Energy dissipation*

Figure 9a, b and c show energy dissipation coefficient (E) per cycle, the energy dissipation and cumulative energy dissipation of all test specimens, respectively. In the elastic stage (Δ/Δ_y<1), the dissipated energy of each specimen increases slowly. With the increase of displacement,

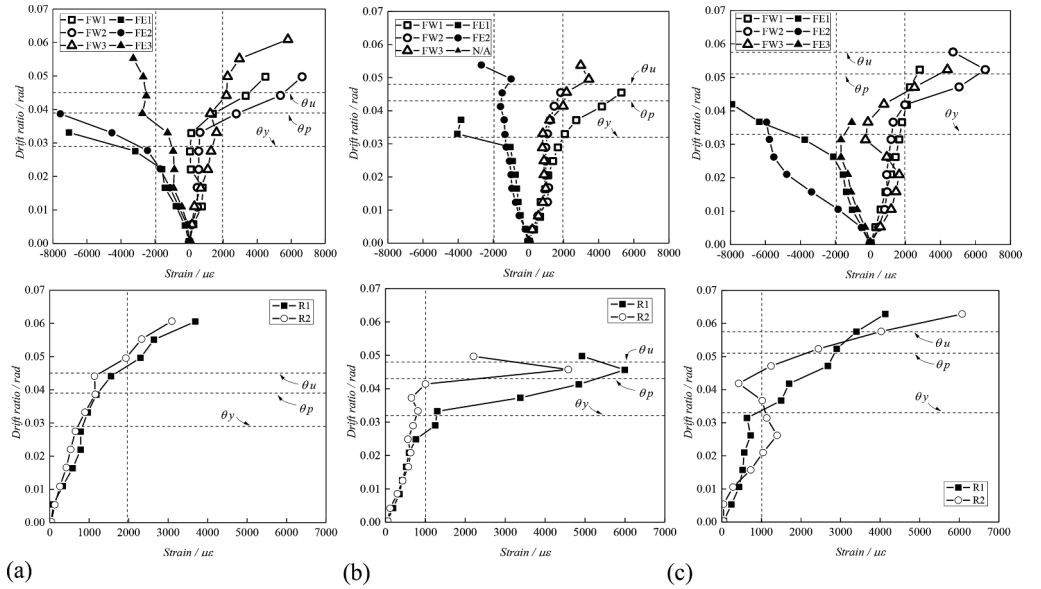


Figure 8. Measured strain development of specimens: (a) QCB22; (b) LCB22; (c) LCB17.

energy dissipation curves increased rapidly from yielding to failure of test specimens. For each loading level, the energy consumption of the second and third cycles was smaller than that of the first cycle (see Figure 9a and b). The energy dissipation coefficients (E) were in the range of 0.5 ~ 1.75 at failure stage showing good energy dissipation capacity for all test specimens.

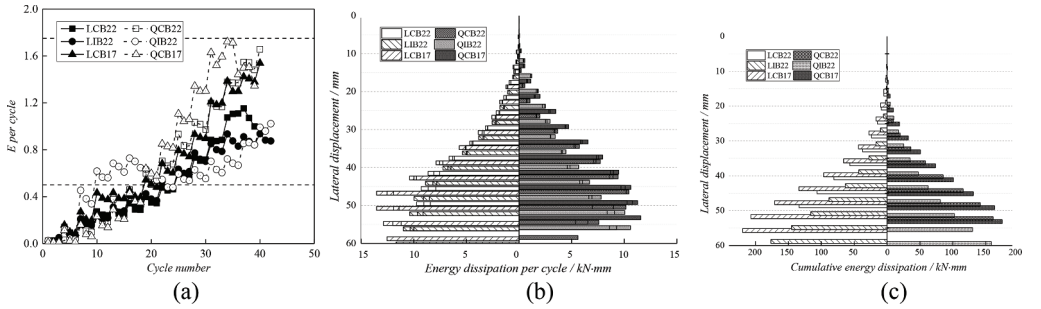


Figure 9. Comparison of energy dissipation capacity: (a) Energy dissipation coefficient per cycle; (b) Energy dissipation per lateral loading level; (c) Cumulative energy dissipation.

Specimens LCB17 and QCB17 with height-to-span ratio of 1.7 had the best energy dissipation among all the test specimens (see Figure 9b and c). Additionally, the utilization of LYP160 steel in the webs further improved the energy dissipation capacity, as the comparison between QIB22 and LIB22, between QCB17 and LCB17. The energy dissipation of specimen QCB22 was slightly higher than that of QIB22. Therefore, application of LYP160 steel and CSW in replaceable coupling beam improves its energy dissipation capacity.

4 CONCLUSIONS

(1) Three types of failure modes occurred for LCSW coupling beams under cyclic loading: local buckling of steel flanges, welding fracture at flange-to-endplate connection, and

combination of welding fracture at flange-to-endplate connection and shear buckling of CSWs. The replaceable steel coupling beam can be easily demounted and assembled since no obvious plastic deformation of high-strength bolts observed when the steel coupling beams failed.

(2) Height-to-span ratio and utilization of LYP steel significantly influence the cyclic behavior of the replaceable coupling beams. The utilization of LYP steel in the web improves the energy dissipation capacity, but enlarges the lateral deformation leading to local buckling of flanges.

(3) Application of LYP160 steel in the CSW coupling beams with smaller height-to-span ratio (1.7 in this paper; specimen LCB17) can enhance the hysteretic performance.

(4) The specimens with LYP160 steel in the web make their webs enter into yield state earlier, so the web becomes the main energy-dissipating component during strength hardening stage.

ACKNOWLEDGMENTS

The authors gratefully acknowledge the financial support provided by the National Natural Science Foundation of China (51978081, 52378127, 52211530037); the Natural Science Foundation of Hunan Province, China (2022JJ10049).

REFERENCES

AISC. 2016 Seismic provisions for structural steel buildings, in: ANSI/AISC 341-2016. AISC. Chicago.

Aydın, R. Yuksel, E. Yardımcı, N. & Gokce, T. 2016. Cyclic behavior of diagonally-stiffened beam-to-column connections of corrugated-web I sections. *Eng. Struct* 121: 120–135.

BS EN ISO 6892-1. 2020. Metallic materials - Tensile testing - Part 1: Method of test atroom temperature. European Committee for Standardisation. Brussels.

Chen, Z. Ge, H. & Usami, T. 2007. Study on seismic performance upgrading for steel bridge structures by introducing energy-dissipation members. *J. Struct. Eng* 53 (A): 540–549.

EI-Bahey, S. & Bruneau, M. 2012. Bridge Piers with structural fuses and bi-steel columns. II:analytical investigation. *J. Bridge. Eng* 17 (1): 36–46.

Fortney, P.J. Shahrooz, B.M. & Rassati, G.A. 2007. Large-scale testing of a replaceable "fuse" steel coupling beam. *J. Struct. Eng* 133 (12): 1801–1807.

Hajsadeghi, M. Zirakian, T. Keyhani, A. Naderi, R. & Shahmohammadi, A. 2014. Energy dissipation characteristics of steel coupling beams with corrugated webs. *J. Constr. Steel Res* 101: 124–132.

McDaniel, C.C. Uang, C. & Seible, F. 2003. Cyclic testing of built-up steel shear coupling beams for the new bay bridge. *J. Struct. Eng* 129 (6): 801–809.

Nikoukalam, M.T. & Dolatshahi, M.K. 2015. Development of structural shear fuse in moment resisting frames. *J. Construt. Steel Res* 114: 349–361.

Qiu, J. Zhao, Q. Yu, C. & Wang, Z. 2022. Lateral behavior of trapezoidally corrugated wall plates in steel plate shear walls, Part 2: Shear strength and post-peak behavior. *Thin-Walled Struct* 174: 109103.

Quan, C. Wang, W. Li, Y. & Lu, Z. 2022. Cyclic behaviour of demountable metallic corrugated shear panel dampers. *J. Build. Eng* 61: 105228.

Saeki, E. Sugisawa, M. Yamaguchi, T. & Wada, A. 1998. Mechanical properties of low yield point steels. *J. Mater Civil Eng* 10 (3): 143–152.

Shahrooz, B.M. Remmetter, M.E. & Qin, F. 1993. Seismic design and performance of composite coupled walls. *J. Struct. Eng* 119 (11): 3291–3309.

Wang, F. Yang, T.Y. Cui, Y. & Chen, T. 2021. Experimental and analytical study on the cyclic response of replaceable corrugated steel plate coupling beams. *Eng. Struct* 242: 112565.

Wang, S. He, J. Liu, Y. Xin, H. & Yao, H. 2018. Experimental study on cyclic behavior of composite beam with corrugated steel web considering different shear-span ratio. *Eng Struct* 180: 669–684.

Zhang, A.L. Li, S.H. Jiang, Z.Q. Fang, H. & Dou, C. 2017. Design theory of earthquakeresilient prefabricated sinusoidal corrugated web beam-column joint. *Eng. Struct* 150: 665–673.

Zhuang, L. Wang, J. Nie, X. & Wu, Z. 2022. Experimental study on the cyclic behaviour of shear coupling beams made of BLY160 steel. *Thin-Walled Struct* 174: 109072.

Bridge Maintenance, Safety, Management, Digitalization and Sustainability – Jensen, Frangopol & Schmidt (eds)
© 2024 The Author(s), ISBN 978-1-032-77040-6
Open Access: www.taylorfrancis.com, CC BY-NC-ND 4.0 license

Fatigue life extension for cracked OSDs using semi-rigid pavement layer

B. Wang
School of Aerospace Engineering and Applied Mechanics, Tongji University, Shanghai, China

R. Gong, D. Wang & A. Chen
Department of Bridge Engineering, Tongji University, Shanghai, China

ABSTRACT: The main problem of fatigue cracks on orthotropic steel deck (OSD) is the reduction of local stiffness that harms bridge serviceability, which may lead to pavement damages, lower driving comfort, and even corrosion on the top of the deck. Hence, measures to extend the fatigue life should be implemented to address these issues. This paper proposes to use a semi-rigid pavement made by methyl methacrylate (MMA) mortar on OSDs with existing fatigue cracks. The fatigue test is designed for a three-phase process: I) Pre-damage phase in which fatigue loading is applied on OSD specimens; II) Fatigue life extension phase in which fatigue loading is applied on the damaged OSD specimens with added semi-rigid pavement layers; III) Extra phase in which fatigue loading is increased to achieve the eventual failure of specimens. As a result, the specimens are always failed due to the penetrating crack at the rib-to-deck weld root. The crack is initiated in Phase I, then grows to penetrate through the deck plate first, and the semi-rigid pavement layer in the following phases. It can be addressed that the performance of the interface between MMA mortar and OSD is kept in a good shape, so that the semi-rigid pavement layer can not only help the prevention of crack growth, but also provide sufficient carrying capacity by forming a composite structure combined with the OSD.

1 INTRODUCTION

Orthotropic steel deck (OSD) is a popular structural type when building the mid-span and the large-span bridges. But the numerous welded joints on OSDs may lead to fatigue cracks under traffic loads in long-term services, as has been widely reported all over the world. Typical fatigue-prone welding details include rib-to-deck welds, rib-to-rib butt welds, rib-to-diaphragm welds and cut-outs.

To solve the fatigue issue on OSDs, studies have been carried out with respect to various welded joints. For the rib-to-rib butt welds, the rib-to-diaphragm welds, and the cut-outs, it is sound to reinforce the cracked detail by adding extra steel or FRP plates, which is quite effective in reducing the stress intensity factor (SIF) at the crack tip (Wang et al., 2016; Jiang et al., 2021). As for the rib-to-deck welded joint, however, the reinforcement tends to improve the stiffness of the OSD by adding structural layers, rather than to work on the cracked areas itself. It is mainly due to the difficulties in detecting and repairing the fatigue cracks on this detail, especially those grow to penetrate the deck plate.

Early studies based on cases of actual bridges have shown significant improvements in the fatigue performance of OSD by adding a concrete layer. For the reinforcement of the Caland Bridge in the Netherlands, it is concluded that by adhesively bonding a high-performance concrete layer on the OSD, the stress amplitudes at critical locations are reduced by about 60% to 92% (de Jong, 2007). Similar reinforcement is also proved feasible on OSDs, including the sandwich steel plate systems (de Freitas et al., 2017), the ultra-high-performance concrete (UHPC)

DOI: 10.1201/9781003483755-244

layer (Shao et al., 2019), and the steel-concrete composite system using waveform deck plates (Su et al., 2016).

It is worth noting that the aforementioned case study on Caland Bridge indicates that the strengthening layer can act solely to bear the loads even when the original OSD is completely damaged. It hence suggests that there is no need to adopt this kind of strong reinforcement until the penetrating cracks grow to have a length of about 100-150 mm (de Jong, 2007). In other words, for OSDs with limited-sized cracks, it is possible to fully consider their residual carrying capacity and carry out reinforcement using materials with moderate stiffness and ductility.

Therefore, for the fatigue life extension of OSDs, this paper proposes to use a semi-rigid pavement made by methyl methacrylate (MMA) mortar in a local zone on the OSD with existing cracks. It can be considered not only as the functional layer for the waterproof and driving comfort, but also as the structural layer that helps to reduce the crack growth rate. For the purpose, a fatigue test is designed by using different loading phases on OSD specimens with a semi-rigid pavement layer, as given in Section 2. In Section 3, the results are analyzed by comparion with those from specimens without the MMA layer, which manifests the effect of life extension of this approach. Accordingly, the conclusions are drawn in Section 4.

2 FATIGUE TEST DESIGN

2.1 *Specimens*

The specimen is designed for the rib-to-deck welded joint of OSD, which includes the deck plate and one U-rib. With respect to the common design in the current bridges using OSDs, the deck plate has a thickness of 12 mm or 14 mm, and the size is 800 mm × 400 mm. The U-rib is 280 mm in height, and the width is 300 mm at the top and 150 mm at the soffit. The specimens are all made of Q345D steel. According to the common way of OSD production, the test specimens were manufactured by CO2 gas metal arc welding, and the automatic welding is used on both sides of the U-rib synchronously, which helps to reduce the welding deformations and residual stresses. Also for investigating the effect of semi-rigid pavement, MMA is used as the extra layer by adhesively bonding on the specimen. It provides not only the function of waterproofing and bonding, but also considerable mechanical performances.

The boundary conditions on the specimens are simply supported on both sides. The rollers are set to contact with the specimen to provide the hinge, through which the forces are transmitted to the base of the test platform. During the experiment, the loads are applied on the top of the MMA layer or the deck plate (when there is no MMA layer). The loading area is 200 mm × 100 mm, with the position right above the rib-to-deck welded joint. The fatigue test specimen with the MMA layers is shown in Figure 1.

During the test, the strains near the weld root/toe on the deck and the rib are measured. For different longitudinal positions, strain gauges are installed on nine sections of the

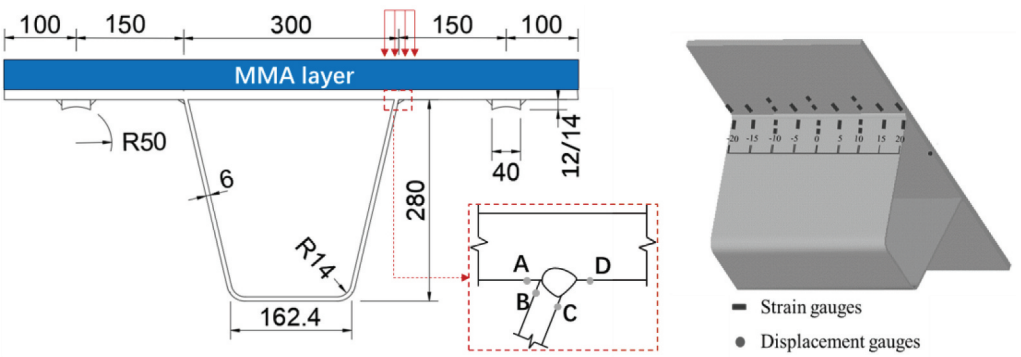


Figure 1. Design of the test specimens and the measuring points.

specimen, with an interval of 5 cm. Hereinafter, they are noted by the distance to the middle of the specimen, i.e. ±20 cm, ±15 cm, ±10 cm, etc. Each strain gauge is installed with a distance of about 5 mm to the root/toe, noted as measuring points A~D with respect to the position (see Figure 1). Additionally, for the C/D series with better accessibility, extra strain gauges are installed on three sections, with a distance of about 14 mm to provide the gradient.

2.2 *Verification test*

A verification test is first conducted to give a preliminary understanding of the effect of the MMA layer. The MMA layer on the OSD is 55 mm thick, and the load applied on the specimen is 30 kN. Figure 2 demonstrates the assembly of the test and the failure mode of the specimen in the end.

Accordingly, the fatigue life of this specimen is about 1.03×10^6 cycles, and the failure is caused by the crack initiated at the rib-to-deck weld root, which grows to penetrate the deck plate and the MMA layer above. Comparably, the previous fatigue test on specimens without having an MMA layer shows that the fatigue life is about 0.26×10^6 cycles (Wang et al., 2021). It means that a four-time fatigue life is given by adding the MMA layer.

Based on the strain data during the test, it can be stated that auxiliary stiffness provided by the pavement layer significantly reduces the stress amplitude at critical positions. Compared to unpaved specimens, the hot spot stress amplitude decreased from 251.98MPa to 164.89 MPa. According to the Basquin equation, the fatigue life can be estimated,

$$N(\Delta\sigma)^m = C \tag{1}$$

The reduction of hot spot stress by about 34.5% will result in a significantly larger fatigue life of OSD. By assuming that the exponent m equals three, the fatigue life is about 3.56 times the original one, which is quite close to the test results.

Based on the results, the fatigue life extension by adding an MMA layer is validated, and the design in the following tests can be given. The MMA layers are determined to have a thickness of 40 mm, for the sake of the test time and loading conditions.



Figure 2. Verification test on the OSD specimen with MMA layer.

2.3 *Load sequence*

Despite that the above verification test indicates a significant improvement in the fatigue life of OSD, further fatigue tests are required for the sake of the reinforcement for OSDs with existing cracks. Considering that the pavement is replaceable for actual bridges, the MMA layer can be added at a certain stage of the life cycle of OSDs. Hence, the load sequence in the test is designed to have three different phases.

1) Phase I: The fatigue load is applied on specimens without MMA layers. It produces pre-cracks on specimens, and the consumed fatigue life and the corresponding damages can be also estimated based on existing test results. Also for the recording of the crack status in this phase, a group of beach marking load cycles is applied in the end.
2) Phase II: The MMA layer is paved on the OSD specimen. The fatigue loads are then applied with beach marking loads in between, which are designed based on the previous study (Wang et al., 2019) to provide the crack growth progress during the test. The specimen may fail in this phase, and the fatigue test can be terminated.
3) Phase III: By the end of Phase II, the OSD should be severely damaged, while it is not always possible to address the fatigue cracks and to estimate the remaining test time. Only in this case, Phase III is applied, in which the load is increased by about 40% to show the failure mode of the specimen.

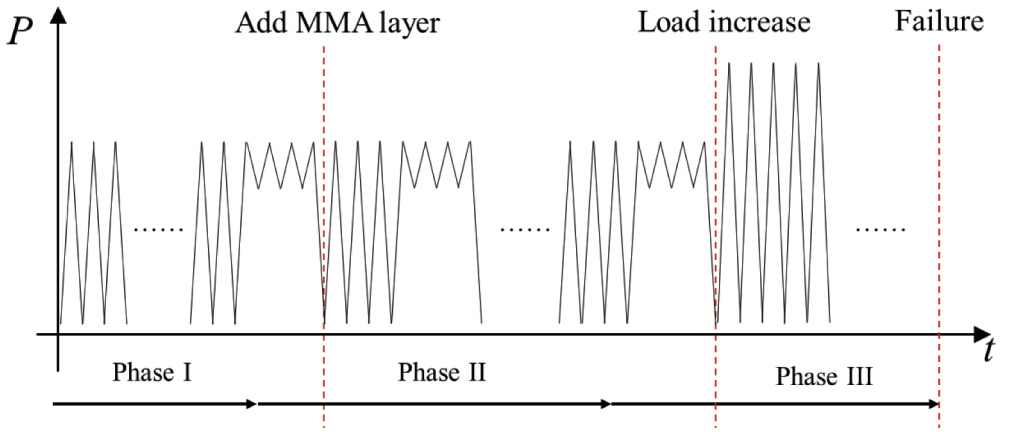


Figure 3. The three-phase load sequence of the fatigue test.

3 TEST RESULTS AND DISCUSSIONS

3.1 *Summary*

Based on the test design, a total of six specimens were tested, including three of them using 12-mm-thick decks, and the rest three using 14-mm-thick decks, which are noted as D12 and D14, respectively. The maximum fatigue loads are 25 kN and 35 kN, for the D12 and D14 groups, respectively, and the minimum loads are always set to 1 kN to keep the stability during the dynamic test. The loading frequency is 2Hz.

In order to manifest the effect from the MMA layer under different crack conditions, different cycle counts were used in Phase I, which are determined with respect to the variation of strains at critical locations. Because of the relatively large life in crack initiation and early-stage crack growth, the majority of the fatigue life of OSD is mainly consumed in this phase. The test conditions and the results are summarized in Table 1.

Table 1. Summary of the tests.

Specimen	P_{max} in Phase I&II (kN)	P_{max} in Phase III (kN)	Fatigue life (cycles)		
			Phase I	Phase II	Phase III
D12-1	25	35	350000	800000	347288
D12-2	25	\	500000	470607	\
D12-3	25	\	470000	730786	\
D14-1	35	50	328800	370000	112961
D14-2	35	\	401200	158557	\
D14-3	35	\	330000	333986	\

As a result, the specimens are always failed due to the penetrating crack at the rib-to-deck weld root. The crack is initiated in Phase I, and then grows to penetrate through the deck plate first, and the MMA layer in the following phases. In addition, it is worth noting that the interface between the MMA layer and the deck plate remains in good form even after the fracture by vertical cracks, as shown in Figure 4. Hence, it can be stated that the MMA layer can be easily implemented by adhesive bonding to OSDs, which shows the advantage in practical cases of bridges with existing fatigue cracks.



Figure 4. Failure of specimens due to penetrating cracks at the rib-to-deck weld root.

3.2 *Strain data analysis*

To better show the effect of the MMA layer, the strain data are analyzed. Since the specimens failed due to fatigue cracks at the rib-to-deck weld root, the data from the strain gauges for A series measuring points are specifically concerned. The data from A series measuring points on Specimen D12-2 and D14-1 are demonstrated in Figure 5, providing typical strain histories of the two-phase test and the three-phase one.

It is clear that, in Phase I, the strain at the crack site is decreasing, while those near the crack site are increasing, indicating the stress concentrations nearby. After adding the MMA layer, strain data from all gauges are reduced significantly. Consequently, the strain data can be kept in a relatively stable range in Phase II. Yet, the crack may continue to grow and affect the MMA layer, which demonstrates the brittle fracture behavior and thus leads to a rapid

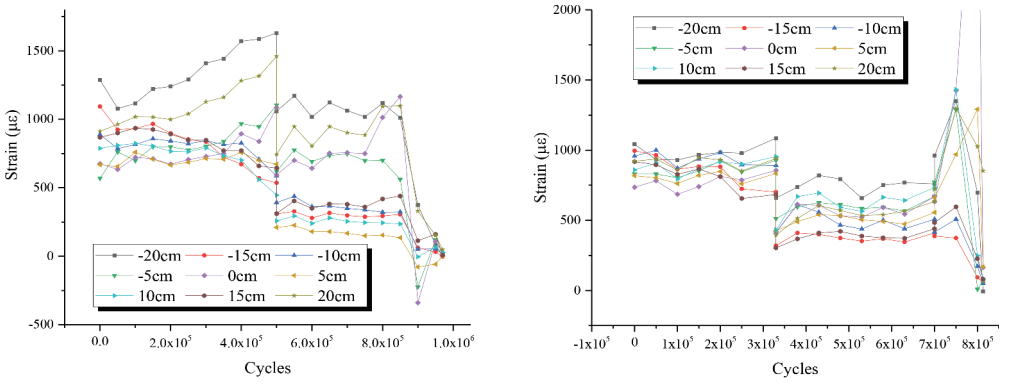


Figure 5. Typical strain histories of specimens: a) a two-phase test (Specimen D12-2) and b) a three-phase test (Specimen D14-1).

decrease for all strain data. Finally, the large deformations can be observed until they get out-of-limit, and the specimens are considered failed due to the fatigue cracks.

In a quantitative analysis on the strain data, it shows that the MMA layer can result in a strain reduction by about 40 to 55 percent. The effect can be even more prominent with the thinner MMA layer when compared with the verification test using a 55-mm-thick one. It can be attributed to the better usage of the mechanical performance of the MMA layer when the OSD is suffering severe fatigue damage. On the other hand, the 40-mm-thick MMA layer in the test can also provide better strength of the interface when connecting to the steel deck plate. As shown above, the well-behaved interface is observed after specimen failure. In contrast, the thicker layer may result in slower internal drying, affecting the curing effect, and leading to shrinkage and cracks during the curing process, thus reducing the adhesive strength with the steel deck plate.

3.3 *Estimation of OSD fatigue life extension*

The fatigue life extension by adding the MMA layer can be estimated based on the test results. Given that the fatigue crack is always initiated at the weld root near the section next to the longitudinal end, namely the one at ±15 cm, the strains from those measuring points are used to calculate the nominal stresses. The fatigue damage in each phase is then estimated using the S-N curve obtained by previous tests, which gives a fatigue strength of FAT 121.8 using the nominal stress method (Wang et al., 2021). Following the Miner's rule, the total damage can be provided by the summation of damage in each phase.

Table 2 presents the estimation of fatigue damage for all specimens in different phases. Obviously, the total damage of each specimen is larger than 1, though the results are quite scattered. It is not only induced by the randomness in fatigue issues of OSD, but also the paving process of the MMA layer that affects the material itself and the interface. Despite so, the worst cases, i.e. Specimen D12-2 and D14-2, have a total damage of about 1.9, meaning a 90% extension of fatigue life. Additionally, it is worth mentioning that the two specimens are loaded with a high cycle count in Phase I, causing severe damage before the MMA layer is paved.

Table 2. Estimation of fatigue damage.

		Fatigue damage D			
Specimen	Nominal stress (MPa)	Phase I	Phase II	Phase III	Total
D12-1	187.5	0.638	1.458	1.737	3.833
D12-2	190.3	0.954	0.898	\	1.852
D12-3	198.2	1.012	1.574	\	2.586
D14-1	198.6	0.712	0.802	0.714	2.228
D14-2	232.0	1.385	0.548	\	1.933
D14-3	253.0	1.478	1.496	\	2.974

4 CONCLUSIONS

This study presents a method to extend the fatigue life of OSDs with existing fatigue cracks by using the semi-rigid pavement layer made by the MMA mortar. Through the fatigue test, it can be stated that the MMA layer shows promising effects for this purpose. It not only helps prevent crack propagation, but also provides sufficient load-carrying capacity by forming a composite structure with OSDs. Based on a rough estimation of fatigue damage, a significant improvement in fatigue resistance can be provided, showing at least a 90% increase in fatigue life obtained for the test specimens. In addition, the interface between the MMA layer and the OSD is kept in good shape during the test, indicating that adhesive bonding can be also a practical way when connecting this type of reinforcement layer to the original OSD structures.

ACKNOWLEDGEMENTS

The authors are grateful for the financial support provided by the National Natural Science Foundation of China (No. 52238005, 51908423, 51978514), the Natural Science Foundation of Shanghai (No. 21ZR1467500), and the Open Fund of Zhejiang Provincial Key Laboratory of Road and Bridge Inspection and Maintenance (202204Z).

REFERENCES

de Freitas, T.S., Kolstein, H., & Bijlaard, F. (2017). Fatigue Assessment of Full-Scale Retrofitted Orthotropic Bridge Decks. *Journal of Bridge Engineering*, *22*(11).

de Jong, F. B. P. (2007). *Renovation techniques for fatigue cracked orthotropic steel bridge decks*. TU Delft, Delft University of Technology.

Jiang, X., Lv, Z., Qiang, X., & Zhang, J. (2021). Improvement of Stop-Hole Method on Fatigue-Cracked Steel Plates by Using High-Strength Bolts and CFRP Strips. *Advances in Civil Engineering*, *2021*, 6632212.

Shao, X., Luo, J., Cao, J., Fan, W., Wang, Y. (2019). Experimental Study of Steel-UHPC Lightweight Composite Bridge Deck Structure and Calculation of Crack Width (in Chinese). *Journal of Civil Engineering*, *52*(03), 61–75.

Su, Q., Tian, L., Zeng, M., Shao, C., Chen, L. (2016). Basic Performance Study of Orthotropic Folded Steel Plate-Concrete Composite Bridge Deck Panels (in Chinese). *Engineering Mechanics*, *33*(S1), 138–142.

Wang, C., Zhai, M., Houankpo, T.N.O., Tang, Y. (2016). Cold Maintenance Technology and Evaluation Method for Orthotropic Steel Bridge Deck Panels. *China Journal of Highway and Transport*, *29*(08), 50–58.

Wang, B., Nagy, W., De Backer, H., & Chen, A. (2019). Fatigue process of rib-to-deck welded joints of orthotropic steel decks. *Theoretical and Applied Fracture Mechanics*, *101*, 113–126.

Wang, D., Xiang, C., Ma, R., Chen, A., & Wang, B. (2021). Experimental study on the root-deck fatigue crack on orthotropic steel decks, *Materials and Design*, *203*, 109601

Bridge Maintenance, Safety, Management, Digitalization and Sustainability – Jensen, Frangopol & Schmidt (eds)
© 2024 The Author(s), ISBN 978-1-032-77040-6
Open Access: www.taylorfrancis.com, CC BY-NC-ND 4.0 license

Experimental and numerical study on static performance of steel cap beam

Shen Chong
Tongji University, ShangHai
Kyoto University, Kyoto

Su Qingtian
Tongji University, ShangHai

Li Jinguo
Tongji Architecture Design (Group) Co., Ltd., ShangHai

ABSTRACT: A new type of steel cap beam is proposed in this paper, combined with common steel plate composite girder bridges. Numerical simulation and scaled model test are used to study the static performance of hybrid structure which consists of steel cap beam and concrete column. In the test, the steel cantilever beam had the characteristic of bending and shear force under eccentric load and the root section was the most unfavorable. However, due to welding defects, the local buckling occurs at webs. By comparing the result of numerical and experimental study, in the state of ultimate bearing capacity, local buckling of webs is more likely to occur at the middle or the root section of steel cantilever beam, depends on whether there are welding defects at the transversal diaphragms. Specifically, the safety factor of steel cap beam in the test with welding defect is 2.8 while that of the finite element model without welding defect is 4.

1 INTRODUCTION

In recent years, traditional on-site pouring of concrete construction has been unable to meet the requirements for rapid and sustainable construction, and precast prestressed concrete bent caps have been preliminarily applied with the development of bridge assembly construction technology. However, problems such as the difficulty of transportation and hoisting caused by the excessive weight of precast bent caps, the large investment of component formwork and the inability to test the quality of grouting materials, make it difficult to be widely used [1-3].

Steel cap beam can effectively solve these problems and are mostly used in railway bridges instead of city bridges in China. Several scholars studied the structural form and mechanical properties of steel cap beam, [4] proposed a full prefabricated large-cantilevered high strength steel-UHPC composite bent cap and a theoretical calculation method for prediction of the ultimate flexural capacity on the basis of test result. [5-6] used the finite element method to study the parameters affecting the mechanical properties of steel cap beams and compared them with concrete cap beams. [7] studied the mechanical properties of the Hanshin Expressway by finite element and model test methods.

In this paper, scale model test and finite element method are used to study the static performance of the steel cap beam-concrete column hybrid structure, mainly focusing on the ultimate bearing capacity state of steel cap beam, conducting in-depth research on the failure modes of steel cap beam and causes, and summering reasonable safety factor of the structure.

DOI: 10.1201/9781003483755-245

2 TEST PREPARATION

2.1 *Design*

The specimen named as SLM is designed and manufactured with a 1: 4 scale ratio. As shown in Figure 1, the steel cap beam mainly consists of roof, webs, base plate and stiffener, and is welded by Q345 steel plates with different thicknesses, while the total length of the steel cap beam is 5.385 m, that of the cantilever beam is 1.893 m. The steel cantilever beam is subject to bending moments and shear force, whose shear force diagram is stepped because the shear force acts only above the diaphragms. Therefore, the section at 1.38 m from the end of the cantilever beam is set as the dividing section between thick plate and thin plate, while the thickness of the top plate, bottom plate and web of the outer cantilever beam end are 6mm, 6mm and 5mm, that of plates at other sections are 9mm, 9mm and 6mm respectively.

The size of concrete column in Figure 1 is 0.375m (transverse) × 0.55m (longitudinal)×2m, which uses vertical φ10 ribbed steel bars, φ4 transverse bars φ4 stirrups and C40 concrete. After bundling bars into cages, pouring into C40 concrete on site and curing for 2 weeks, the concrete column will be ready for installing steel cap beam and test.

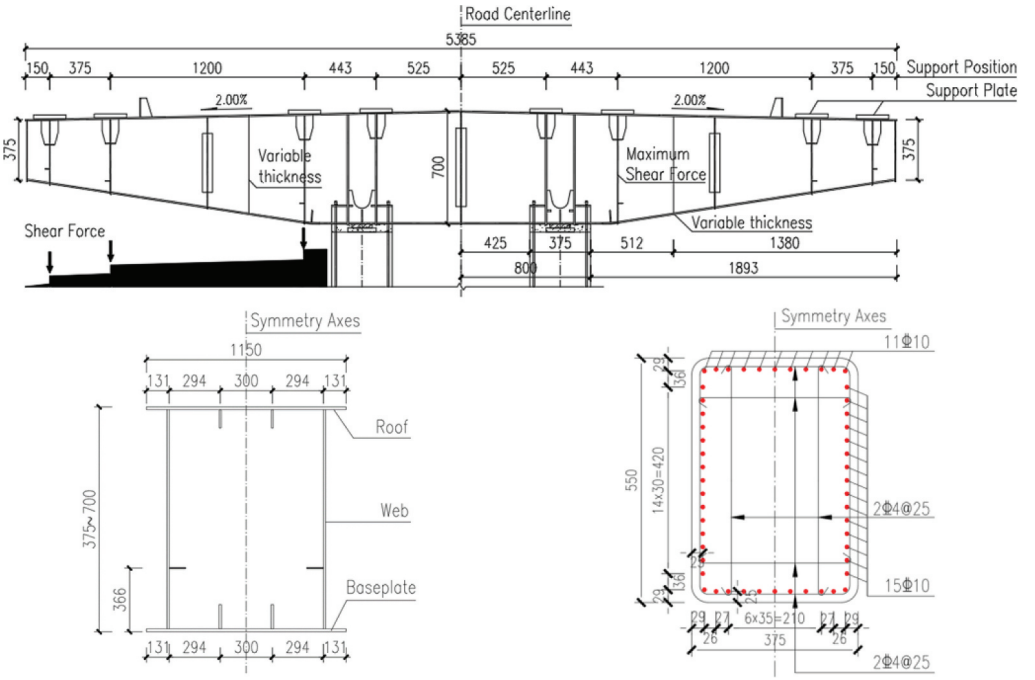


Figure 1. Design of steel cap beam and concrete column (Unit:mm).

As shown in Figure 2, a new type of reinforced flange anchorage connection structure is proposed for the joint section of steel cap beam and concrete column, which mainly consist of steel cap beam, flange, concrete column, rebars and UHPC. During the construction, steel cap beam is placed above the temporary support at the top of the column and nuts are tightened after rebars of concrete column passes through the reserved hole on plates of flange and steel cap beam, and finally pouring UHPC between the base plate of steel cap beam and the top section of concrete column.

2.2 *Loading system*

As shown in Figure 3, the loading system is a self-reaction device, including H-shaped steel beams and hydraulic jacks above the steel cap beam and steel base under the concrete columns, connected and tightened by prestressed steel tendons. The loading system passes

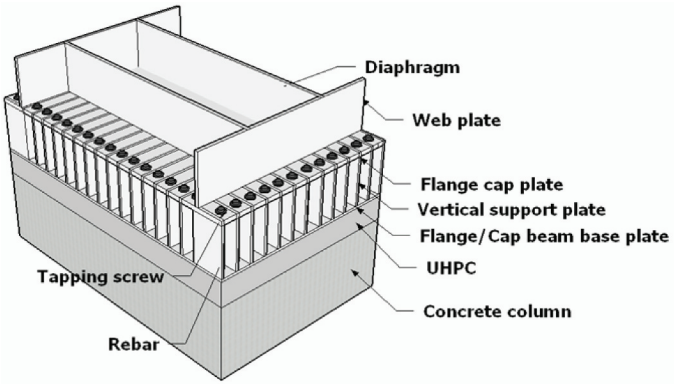


Figure 2. Reinforced flange anchorage connection.

vertical pressure on each support position of the steel cap beam through lifting jacks, and pre-loading is performed at the beginning of the experiment by applying 20kN each jack. The formal loading is divided into four loading stages: ① Four jacks provide 148.6kN respectively. ② The jacks at the end of cantilever beam provide 365.5kN of 17kN/level, and other jacks provide 209.6kN of 10kN/level. ③ Load in the same manner as ② until the steel plates yields; ④ Load until structural failure. (The average yield strength of steel is about 440MPa and the average ultimate tensile strain is about 600MPa).



Figure 3. Test on site.

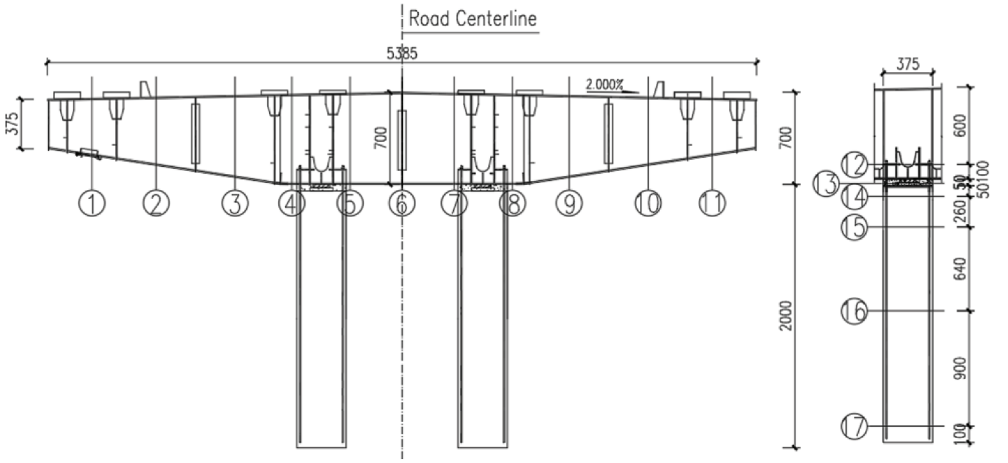
2.3 *Measuring arrangement*

Figure 4 shows the measuring arrangement of the test. The section 1~11 are set symmetrically on both side of the steel cap beam, while 3~5 unidirectional strain gauges are pasted on the roof and base plate to measure the transverse strain of the steel plate, 1~3 three-dimensional strain gauges are pasted on the web to measure the vertical shear strain.

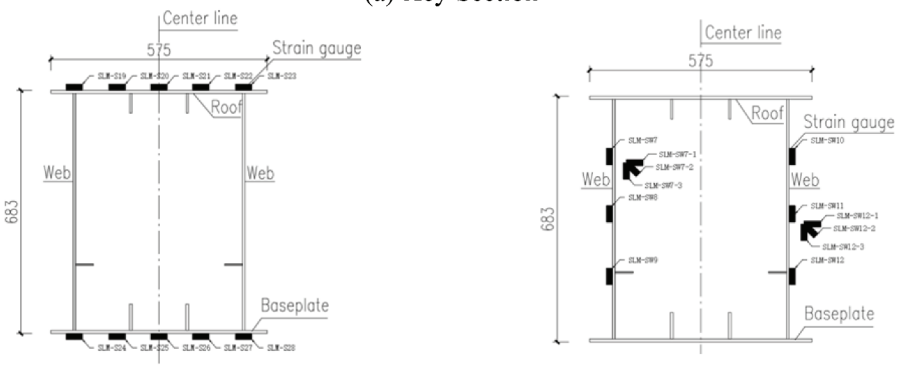
3 TEST RESULTS

3.1 *Failure model*

When the load at the end of cantilever beam on both sides was 1023kN and that of the root was 592kN, the failure occurred. Specifically, the steel cantilever beam deformed violently and



(a) Key Section



(b) Measuring Arrangement of Section4

Figure 4. Measuring arrangement.

produced a loud sound inside the box girder, and alone with the obvious deflection at the end of cantilever beam, three webs had local buckling failure at section 3 and section 9.

As shown in Figure 5, it was obvious that the local buckling of three webs occurred at the connection between the transverse rib and roof or the base plate, which deformed inward and developed about 45 °, possibly caused by the principal stress.

After the test, the steel cantilever beam was cut and the internal condition of the beam was observed. We found a welding defect that the transverse stiffeners and diaphragms were



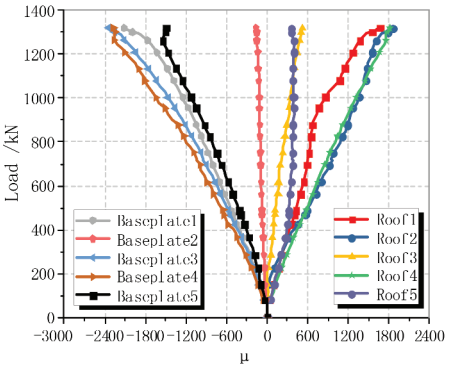
Figure 5. Failure model.

welded to the base plate respectively, but they were not welded together, which was different from the design. Considering that this diaphragm was close to the section for different plate thickness, local buckling may occur at this section instead of the root of cantilever beam due to the welding defects here, just as the test results.

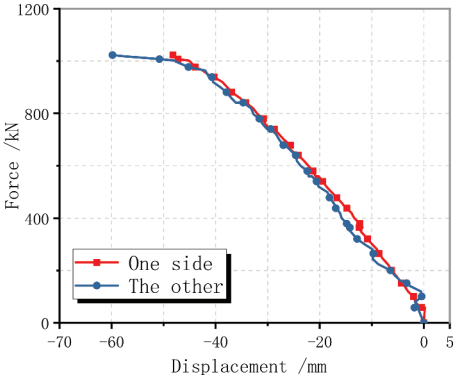
3.2 *Mechanical properties*

Figure 6 indicates the curve between the load and the strain or displacement of the key section of steel cap beam. Curve in Figure 6(a) is the load and the strain of the roof or base plate of section 4, where positive numbers represent tensile strain and negative numbers represent compressive strain. Specifically, five strain gauges are pasted on each plate and every curve shows obvious linear relationship between load and strain during the elastic phase of steel plate, and plateaus or mutations in the plastic phase. Curve in Figure 6(b) shows the linear relationship and the platform between the load and the vertical displacement of section 1. Figure 6(c) and Figure 6(d) respectively indicate the curve of the load and the maximum transverse strain of the base/roof plate form section 1 to section 5, from which we can conclude that section 4 is the most unfavorable.

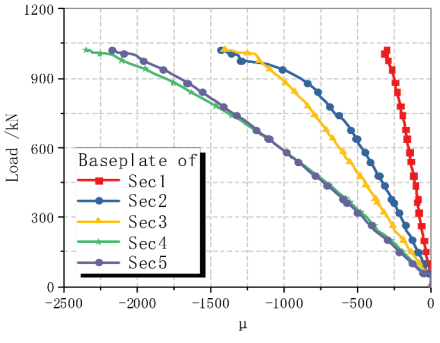
Moreover, it is obvious that the roof plate is tensile and the base plate is compressed, while webs are subjected to shear force. In section 3 that local buckling occurs, the tensile strain of the roof plate is 2594με and the compressive strain at the bottom is 1408με, also the shear strain of the web is 1318με. Although the strains at section 4 is higher than that of section 3, welding defects make section 3 more vulnerable.



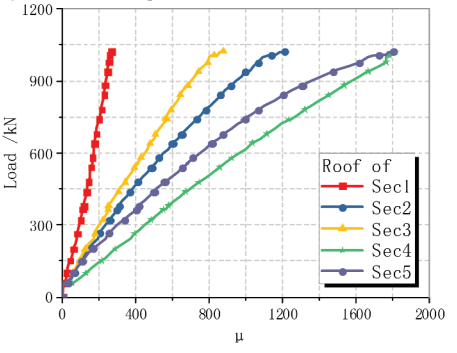
(a) Load - Strain curve at Section4



(b) Load - Displacement curve at Section1



(c) Load - Strain curve of Section1~5



(d) Load - Strain curve of Section1~5

Figure 6. Representative strain and displacement test results.

4 FINITE ELEMENT ANALYSIS

4.1 *Finite element model*

The ANSYS is used to calculate and analyze the static capacity of the hybrid structure pier. The shell181 element is used to simulate the steel cap beam and the solid65 element is used to simulate the concrete column and the UHPC post-pouring section, and the link8 element is used to simulate the reinforcement. Figure 7 shows the finite element model, and the bottom of the concrete column is constrained by all degrees of freedom, the load size and application position are consistent with the test above.

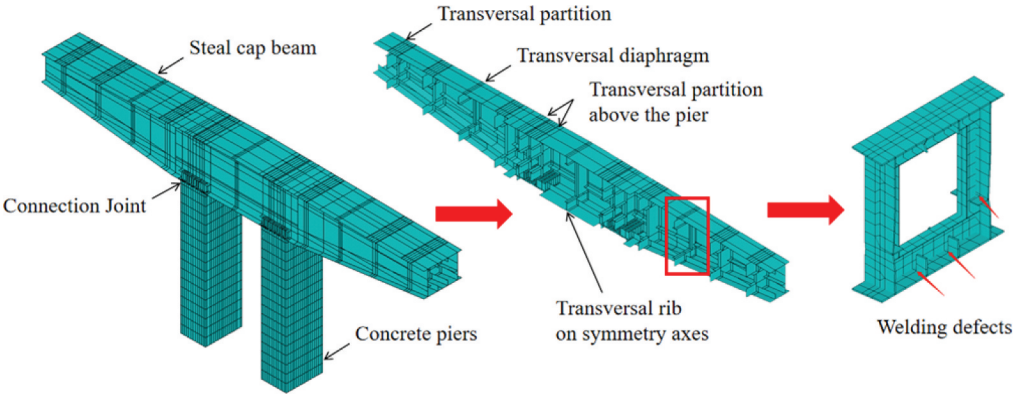


Figure 7. Finite element model.

4.2 *Results*

The calculation is divided into two situations. On the one hand, while considering the welding defects in Section 3.1, the stiffeners of base plate are disconnected from the diaphragm, both of which are only connected to the base plate respectively in the finite element model. In this case, it is found that the ultimate bearing capacity of the structure is about 1100kN, very close to 1023kN in the test, and local buckling occurs at the webs near the diaphragm when the structure fails, moreover, the transversal stress cloud is highly consistent with the test, as shown in Figure 8.

On the other hand, establish an FEM of the steel cap beam without welding defects by extending the stiffeners to connect with the diaphragm. Different from the results above, the load at the end of cantilever beam is 1488kN and that at the root section is 853kN, far higher than structure with welding defects. Obviously, in the ultimate bearing capacity state, the stress of the structure has not reached the maximum strength of the steel, so local buckling is more likely to occur at section 4 due to principle stress than at the middle of the steel cantilever beam.

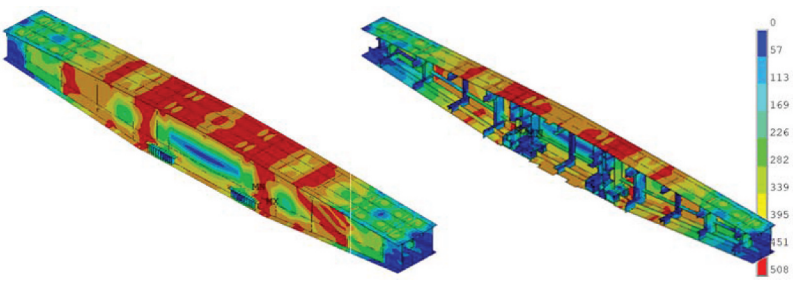


Figure 8. Mises stress diagram of FEM in ultimate Bearing capacity state (Unit:MPa).

4.3 *Safety factor*

Based on finite element analysis and model test results, to the steel cap beam with welding detects, the ratio of the load in ultimate bearing capacity state to serviceability state is about 2.8, however the safety factor of the steel cap beam without welding defect is 4 by finite element analysis. Therefore, the design of the structure is safe and can be optimized.

5 CONCLUSION

Based on the experimental and numerical study above, we can conclude that

(1) In the test, the steel cantilever beam had the characteristic of bending and shear force under eccentric load and the root section was the most unfavorable. However, due to welding defects, the local buckling occurs at webs, which deformed inward and developed about 45 °, possibly caused by the principal stress.
(2) By comparing the result of numerical and experimental study, in the state of ultimate bearing capacity, local buckling of webs is more likely to occur at the middle or the root section of steel cantilever beam, depends on whether there are welding defects at the transversal diaphragms.
(3) The safety factor of steel cap beam in the test with welding defect is 2.8 while that of the finite element model without welding defect is 4, and local buckling occurs at different places of webs.

REFERENCES

[1] Review on China's Bridge Engineering Research:2021[J].China Journal of Highway and Transport, 2021, 34(02):1–97.
[2] Yazdani, Nur, Ruiz, Francisco D. B. Comparative analysis of cast-in-place post-tensioned and steel-concrete composite bridge bent caps[J]. Journal of modern transportation, 2017, 25(03):194–204.
[3] National Academies of Science, Engineering, and Medicine. Prefabricated Bridge Elements and Systems to Limit Traffic Disruption During Construction.2004
[4] Shao, Xudong, Zeng, Huaqiao, Cao, Junhui. Flexural behavior of fully prefabricated large-cantilevered high strength steel-UHPC composite bent caps[J]. Journal of constructional steel research, 2023, 204.
[5] ZHOU Wenjun. Analysis on Application of Steel Capping Beam in Municipal Elevated Bridge[J] Urban Roads Bridges & Flood Control, 2021(06):313-317+31.
[6] Meng Lingqiang, LI Yunsheng, WANG Yuanqing. Finite Element Analysis of Bearing Performance of Viaduct Steel Cap[J]Journal of Shijiazhuang Tiedao University(Natural Science Edition), 2009,22 (01):38–42.
[7] The composite bridge foot of RC column and steel beam is suspected to move under the service load-[J]Construction Engineering Papers, 44-A3-1459.

Bridge Maintenance, Safety, Management, Digitalization and Sustainability – Jensen, Frangopol & Schmidt (eds)
© 2024 The Author(s), ISBN 978-1-032-77040-6
Open Access: www.taylorfrancis.com, CC BY-NC-ND 4.0 license

Real-time multi-objective topology optimization method via deep learning

Cheng Xiang
College of Civil Engineering, Fuzhou University, Fuzhou, China

Airong Chen, Dalei Wang & Rujin Ma
College of Civil Engineering, Tongji University, Shanghai, China

ABSTRACT: The goal of bridge design is to design and construct an elegant and safe bridge that meets all functional requirements at an acceptable cost. Topology optimization has emerged as a powerful tool for innovative bridge design. However, the inherent drawback of high computational cost in current topology optimization remains unresolved. Moreover, relevant research that mainly focuses on a single objective fails to meet the safety and usability requirements of the bridge. Therefore, in this paper, an iteration-free multi-objective topology optimization (MOTO) method based on deep learning is proposed in this paper, which can not only improve the computational efficiency of MOTO, but also meet the different structural demands. Firstly, a MOTO mathematical model based on constraint programming method was established, and the dataset with stiffness, strength and material consumption as optimization objectives was constructed. Secondly, based on the self-attention mechanism, a novel network is constructed, and trained. Finally, the performance of the proposed method was evaluated in terms of efficiency and accuracy. Results show that a significant reduction in computation cost of MOTO problem was achieved with little sacrifice on the performance of design solutions. The proposed method can provide new ideas for multi-objective design of bridges and promote the improvement of bridge design level.

1 GENERAL INSTRUCTIONS

Structural optimization seeks to pursue structures with higher efficiency (such as higher performance, lower costs, lightweight). Within the field of structural optimization, topology optimization (TO) is dedicated to identifying the optimal distribution of material within a given design domain under different constraints (loads, boundary conditions and volume fraction). Over the past few decades, TO has experienced rapid development, leading to the emergence of numerous numerical methods (Sigmund and Maute, 2013), such as SIMP, evolutionary approaches, level-set method and moving morphable components method (MMC). Despite their widespread adoption, traditional methods for solving TO are hindered by their computational expense, necessitating a large number of design variables and iterations during the optimization process. This computational inefficiency significantly hampers the practical application of TO, highlighting the urgent need for new methods to enhance its efficiency and practicality.

With the popularity of deep learning (DL), it has brought about significant advancements in various domains, and several DL methods have been developed in recent years to accelerate the topology TO process. Sosnovik and Oseledets (2019) give the first attempt to integrate DL by regarding TO as an image segmentation task. With the convolutional encoder-decoder architecture, the near-optimal structures can be obtained without any iteration. Yu *et al.* (2018) proposed an iteration-free method that utilizes a CNN to predict a low-resolution solution, which is subsequently fed into a GAN to enhance its resolution. Wang *et al.* (2021) and

DOI: 10.1201/9781003483755-246

Xiang *et al.* (2022) proposed a deep CNN with perceptible generalization ability for TO, enabled by a specially designed initial physical field input tensor, which can obtain 2D or 3D optimized structures in a split second even with previously unseen boundary conditions.

Some recently proposed advanced network architectures have also been introduced into TO task to improve the prediction accuracy. For instance, the attention mechanism, as the core of Transformer, is integrate into the TO task as a means to improve the predicting accuracy by *Zheng et al.* (2021). Seo and Min (2023)introduces the graph neural networks for accelerating topology optimization in irregular design domains, achieving near-optimal topologies by encoding complex non-Euclidean data into Euclidean form. Recent years also witnessed the adoption of physics-informed neural network (PINN) in TO with the aims at improving the accuracy of DL-based TO method. For instance, Zhang *et al.* (2021) gained the optimized structures by adopting the PINN that incorporating physical information of compliance into the loss function and replacing the element density update in TO with the neural network parameter update. Nevertheless, the PINN-based method required hundreds of FEA and frequent network parameter updates, making it even more time-consuming than conventional methods and failing to deal with the efficiency issue.

The aforementioned research has demonstrated the significant potential of integrating DL with TO. However, these studies mainly take the global response of compliance as the optimization objective, while in practical structural design processes, structural optimization involves a trade-off among different optimization objectives. For instance, it is often necessary to ensure structural stiffness while also achieving a reasonable stress distribution to avoid stress concentration (Xiang *et al.*, 2022). The existing research, which is primarily focused on specific optimization objectives, clearly falls short of meeting real-world requirements. Therefore, this paper presents an iteration-free method based on DL to address MOTO problem, with the aim of advancing the practical applications of TO technology. The remaining sections of the paper are organized as follows. In Section 2, a typical MOTO problem is introduced, and a mathematical model is formulated to achieve the MOTO. In Section 3, a dataset is generated for MOTO problem, and a novel UNet-based neural network is designed. Section 4 evaluates the performance of the neural network. Finally, Section 5 concludes the paper.

2 TYPICAL MULTI-OBJECT TOPOLOGY OPTIMIZATION PROBLEM

Currently, the compromise programming method is primarily used to address multi-objective optimization problems when the sub-objectives have different natures. Its fundamental idea is to normalize multiple sub-objective functions, allowing the objective function values to vary between 0 and 1, and then transforming the problem into a single-objective optimization problem by applying weights to each sub-objective. However, TO is commonly tackled using sensitivity-driven methods. The significant disparities in both the physical meanings and numerical values among different objectives may pronounced oscillations throughout the optimization process.

This research employed the constraint-based method that establish a primary optimization objective among multiple sub-objective functions. Subsequently, the other optimization objectives are treated as constraint conditions. In line with prevailing research, for the proposed MOTO problem, we employ compliance as the primary optimization objective, while treating stress and material consumption as constraints, as shown in Equation 1. This approach seeks to enhance optimization outcomes by prioritizing the minimization of compliance, while simultaneously addressing issues related to high stress scenarios and potential stress concentration phenomena. As a result, the optimized structure not only exhibits substantial stiffness but also satisfies the necessary strength requirements and considerations for economic performance. The mathematical model for minimizing compliance design under volume and stress constraints can be expressed as:

$$min\text{: } c(x) = \boldsymbol{U}^{\boldsymbol{T}}\boldsymbol{K}\boldsymbol{U} = \sum_{i=1}^{N} E_i(x_i)\boldsymbol{u}_{\boldsymbol{i}}^{\boldsymbol{T}}\boldsymbol{k}_{\boldsymbol{0}}\boldsymbol{u}_i$$

$$\text{s.t. : } \boldsymbol{K}\boldsymbol{U} = \boldsymbol{F}$$

$$V(x)/V_0 = V_f \tag{1}$$

$$\sigma_{vm}^{max} \leq \sigma_{vm}^{*}$$

$$0 < x_{min} \leq x_i \leq 1,\ i = 1, 2, \cdots N$$

Where c is the compliance, $\boldsymbol{K}$ is the global stiffness matrix, $\boldsymbol{U}$ is the global displacement vector, $\boldsymbol{F}$ is the global force vector, $\boldsymbol{k_0}$ is the element stiffness matrix for an element with fully distributed solid material, $\boldsymbol{u_i}$ is the element displacement vector, N is the number of elements in the discrete design domain, $V(x)$ and V_0 are respectively the material volume and the design domain volume, and V_f is the pre-defined volume fraction, σ_{vm}^{max} is the maximum von Mises stress value, σ_{vm}^{*} is the target stress constraint, x_i represents the relative density of the i-th element, x_{min} is a lower bound for the design variable, which is designed to avoid singularity. The element's Young's modulus $E_i(x_i)$ is determined by the element density x_i:

$$E_i(x_i) = x_i^q E_0 \tag{2}$$

Where, E_0 is the stiffness of the material, and q is a penalization factor in SIMP.

With regard to the local nature of stress (Le *et al.*, 2010), the popular p-norm global stress measure is adopted for approximating the maximum stress as follows,

$$\sigma_{vm}^{max} = \sigma_{PN} = \left(\sum\nolimits_{i=1}^{N} \sigma_{vm,i}^{p}\right)^{\frac{1}{p}} \tag{3}$$

Where $\sigma_{vm,i}$ denotes the von Mises stress of the i-th element, and p is the stress norm parameter, which is set as 6 for dataset generation following.

The level of stress constraint, denoted as σ_{vm}^{*}, will exert a significant influence on the topological structure of the design. Since in the proposed MOTO problem, σ_{vm}^{*} is introduced to optimize the stress distribution during the compliance optimization process, it is first required to know the stress level under the circumstances of minimizing compliance with volume constraints only, i.e., σ_0. The upper and lower limits of σ_{vm}^{*} are determined iterative: when the optimized structure under σ^* is equivalent to the optimized structure with the minimum flexibility under only V_f, it is considered that σ^* at this time has no effect on structural optimization, and this stress is the upper limit of the constraint stress σ_{vm}^{u} of the structure. When the stress constraint and V_f cannot be satisfied simultaneously, it is considered that σ^* at this time is the minimum stress value σ_{vm}^{l}. The stronger the constraint, the greater the impact on structural topology optimization, while the linear interpolation method cannot consider high stress areas much, so it is decided to use exponential interpolation method:

$$\sigma_{vm}^{*} = \frac{a}{b + S_f^k}\sigma_0 = \frac{\sigma_{vm}^{u}\sigma_{vm}^{l}}{\sigma_0\left(\sigma_{vm}^{l} + S_f^k\left(\sigma_{vm}^{u} - \sigma_{vm}^{l}\right)\right)}\sigma_0 \tag{4}$$

Where S_f is the stress fraction, defined by drawing upon the concept of volume fraction V_f: when $S_f = 0$, the stress constraint does not affect the topology results, and when $S_f = 1$, the stress exerts maximum influence on the results. k represents the exponent, which is set as 0.75.

3 THE PROPOSED NETWORK FRAMEWORK FOR MOTO

3.1 *Dataset generation and input tensor design*

Given that the MOTO problem is inherently nonlinear in nature, it is tackled using the MMA algorithm (Svanberg, 1987), which primarily capitalizes on the sensitivity of both objective and constraint functions in relation to design variables. Considering the intricacy of MOTO problems, this study aims to commence with the comparatively simple cantilever beam design domain and utilize the established MOTO mathematical model for data generation. A total of

20,000 samples were generated, with a distribution ratio of training set: validation set: test set = 8:1:1. During data generation, the load is applied to the free end of the cantilever within the load range illustrated in Figure 1, with a magnitude of 1.5N. To mitigate stress concentration, the load is evenly distributed across two adjacent nodes (i.e., 0.5N per node). The V_f and S_f are uniformly distributed. The construction of training samples follows specific guidelines:

1) Resolution: 40×80
2) Volume fraction V_f: 0.3-0.7 (Uniform distribution in increments of 0.1)
3) Stress fraction S_f: 0.0-1.0 (Uniform distribution in increments of 0.1)
4) Filtering method: density filtering with filtering radius of 1.5

In theory, the final topology form is a complex mapping of the initial conditions based on the optimization objective and constraints, this is also the theoretical basis for neural networks to solve TO problems. Since the initial conditions play an important role in determining the optimal topological forms of the structures, the way in which they are organized is closely related to the performance of the network. At present, there are usually two types of input modes of initial conditions, one is the mode of direct input, i.e., the load action position and the constraint position are directly input into the neural network (Yu et al., 2018). The other is the mode of indirect input, that is, the above-mentioned information is indirectly displayed through the initial physical fields (Wang et al., 2021, Yu et al., 2018). After trying different kinds of tensor types, the information-rich direct input tensor derived from the direct input mode, is found the optimal one for the MOTO problem. Specifically, the input tensor constitutes a 2-channel tensor (each channel of size 41×81), where the first channel encompasses information regarding boundary conditions and V_f, while the second channel represents load constraints and S_f information. Figure 1 provides an example of this input mode.

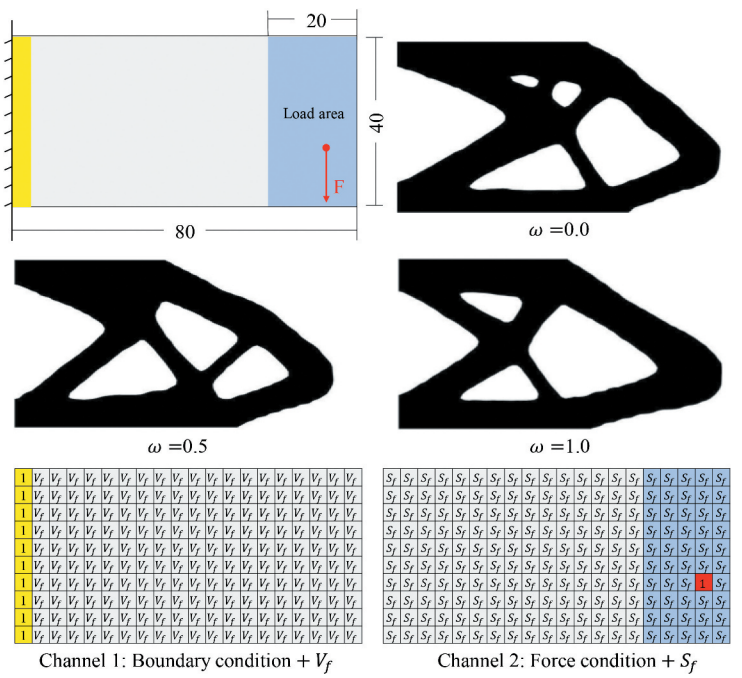


Figure 1. The optimized structures under different S_f and the information-enriched direct input tensor.

3.2 *The architecture of the neural network*

In current researches, a fundamental issue leading to structural disconnection arises from the lack of correlation between adjacent elements in disconnected positions. To address this

challenge, the self-attention mechanism, being the core unit of the transformer framework, demonstrates significant potential. By leveraging this mechanism, it becomes feasible to capture correlations among different input elements, thereby establishing stronger connections within the model and expanding the perceptual field range. Therefore, based on the self-attention mechanism, a novel extension of Unet called Shifted Windows Attention and Partial Convolution Unet (SWPUnet) is proposed, as illustrated in Figure 2.

SWPUnet retains the fundamental structure of Unet, encompassing three components: encoding, decoding, and skip connections. Compared to Unet, the key enhancement of SWPUnet, lies in the incorporation of shifted windows attention (SWA) (Liu *et al.*, 2021) within the skip connections. This enables the model to better capture the correlation between adjacent elements and enhance its attention to the regions with material distribution. The SWA module includes several SWA blocks, after tries many times, the optimal configuration of SWA, the structure of SWA block, as well as the participation of the self-attention mechanism in SWA blosk is presented in Figure 2.

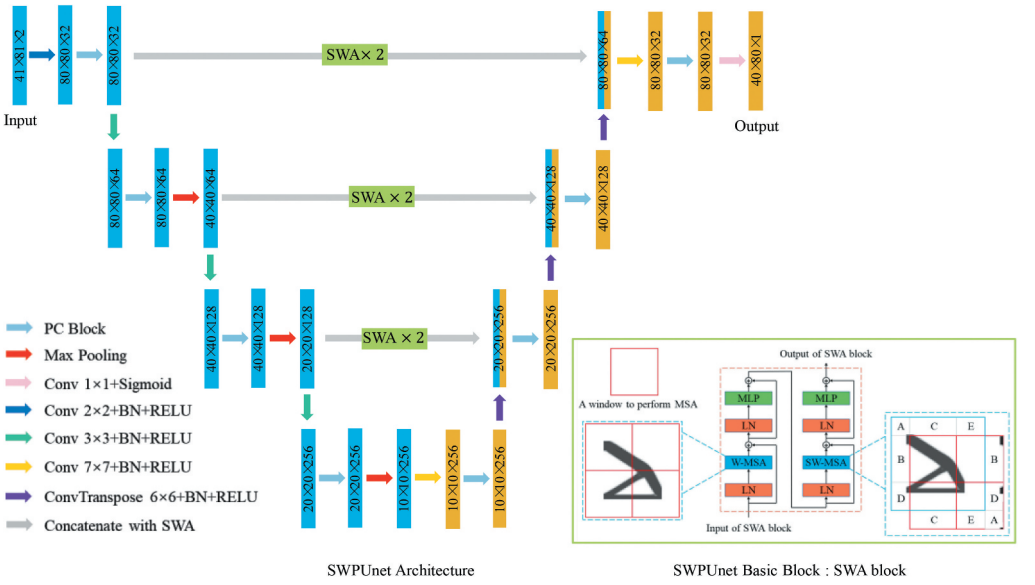


Figure 2. The architecture of SWPUnet.

3.3 *Training the network*

During the training process, the Adam algorithm (Kingma and Ba, 2014) was used to optimize the weights and biases of the networks to minimize the loss between the predicted structures and the simulated structures. The cross-entropy loss function is used in the training process. Besides, the L2 normalization is also widely used in designing loss functions to prevent overfitting. The mathematical formulation for the loss is expressed below:

$$Loss = -\frac{1}{N}\sum_{i=1}^{N}\left(y_i log h(x_i) + (1-y_i)\log(1-h(x_i))\right) + \frac{\lambda}{2}\sum_i \omega_i^2 \tag{5}$$

The first term is the cross-entropy loss, where y_i represents the ground truth of the i-th sample, $h(x_i)$ is the predicted structure from the neural network. The second part of the equation represents the L2 normalization, λ is the regularization weight, ω_i is the weight coefficient of the network, and N represents the total number of items being evaluated.

Figure 3 shows the history of loss on the training set and validation set during the training process. The validation loss reaches its minimum value of 0.18 at the 116th epoch, while the training loss still goes down and the overfitting appears. Therefore, the training process is stopped after 136 epochs.

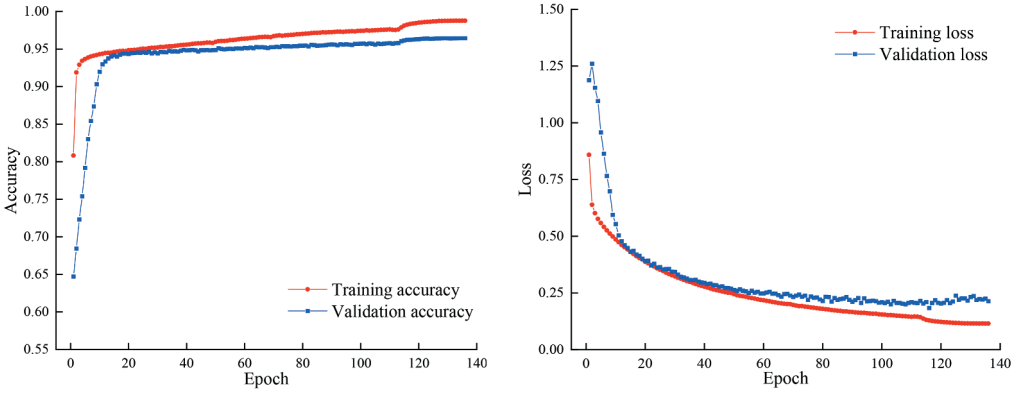
4 PERFORMANCE EVALUATION OF THE PROPOSED METHOD

The trained SWPUnet was used to predict the optimized structures with the samples in the test dataset. After that, the accuracy (i.e., the compliance, stress fraction, volume fraction, and pixel accuracy) as well as the efficiency of the proposed method was evaluated by comparing the obtained results with that of the conventional method.

In most cases, the proposed method and the conventional method can obtain almost the same final structures and von Mises stress distribution, as shown in Figure 4(a). The compliance error (E_c), p-norm stress error ($E_{\sigma_{PN}}$), volume fraction error (E_v), and pixel accuracy error (E_{pix}) of the predicted structures are -7.50%, -5.08%, 0.84%, and 5.18%, respectively. However, in terms of computational efficiency, compared with the traditional method that hundreds of iterations of finite element analysis and sensitivity analysis are required in the optimization process, the proposed iteration-free method can directly predict the optimized structure. The average computation time of the conventional method is 15.76 s, while the proposed method, once properly trained, can give a near-optimal result in 0.0076 s (9.4×10^{-4} s for data preprocessing and 4.42×10^{-3} s for model prediction), only 0.026% of traditional methods, with the efficiency improved by 99.97%. It should be noted that the considerable time of generating the dataset and training the neural network are not included. These results shows that the proposed method can effectively solve the MOTO problem without sacrificing structural performance. Details of the results are shown in Table 1.

Nevertheless, 5.9% samples in the test set appeared large error. Here, samples with E_c or $E_{\sigma_{PN}}$ greater than 20% are defined as large error samples, for it deviates from the optimization objective seriously. The reasons for significant errors can be mainly attributed to two factors. Firstly, there is a high sensitivity of stress to changes in the structural topology, which may result in significant stress concentrations in parts of the structure, even when the results obtained by two methods are similar to each other, as evidenced by the first case in Figure 4 (b). Another reason is the presence of disconnected structures in the results obtained by the DL method, as illustrated in the second case of Figure 4 (b). Similar observations have also been reported in related works (Yu et al., 2018, Wang et al., 2021), this can be attributed to the fact that the neural network training primarily focuses on the principle of pixel similarity. Therefore, in cases where the material distribution is inconsistent but the pixel similarity is close, the model will not penalize such instance.

Besides the unacceptable results, nearly half of the results are a pleasant surprise, that is, samples that performs better than traditional methods in the results, highlighting the significant advantages of the proposed approach. Here, it is defined that the predicted results of the proposed method outperform to the traditional method if the E_v of the result is within 1%, while the E_c and $E_{\sigma_{PN}}$ is smaller than -1%. Under these circumstances, the results of the DL method have smaller mean σ_{PN} than that of the conventional method, and better meet the optimization objective with little violation of constraint. Part of the samples of deep learning methods outperformed traditional methods in predicting results, as illustrated in Figure 4 (c).



a) Training and validation accuracy. b) Training and validation loss.

Figure 3. The accuracy and loss on training and validation set of the neural network during training.

Table 1. Comparison of the results between the proposed method and the conventional method.

	E_c	$E_{\sigma_{PN}}$	E_V	E_{pix}	OR	LER	Time saved
Average	-7.50%	-5.08%	0.84%	5.18%	49.75%	5.90%	99.97%

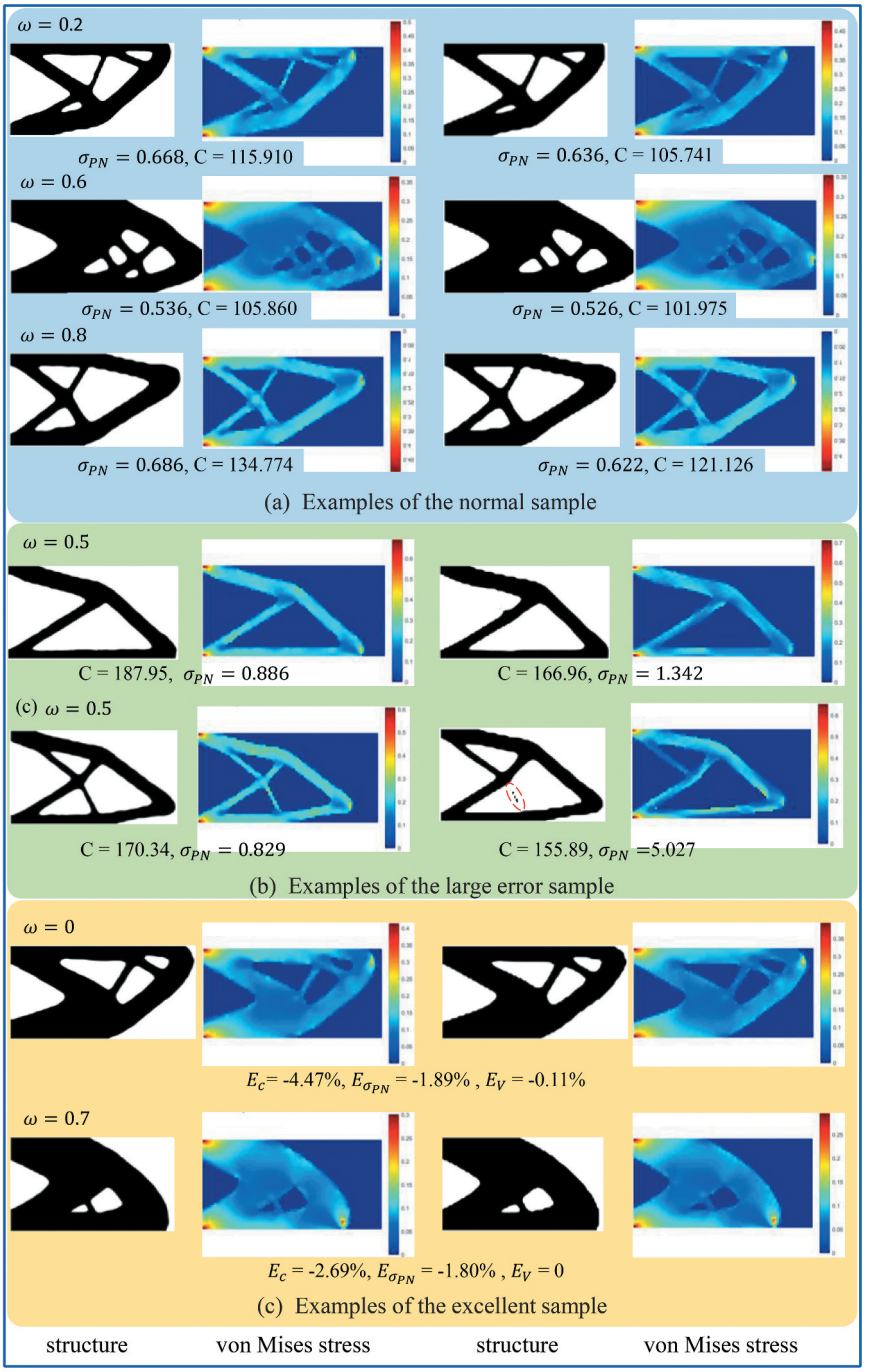


Figure 4. Comparison of traditional method and the proposed method.

5 CONCLUSION

In this paper, an iteration-free MOTO method based on deep learning is proposed in this paper, which significantly improve the calculation efficiency, and successfully extend the DL-based TO method to a multi-objective situation. In addition, nearly half of the predicted optimized structures performs better than tradition method, which shows the great potential and broad application prospects of the proposed method in the practice of innovative bridge design, particularly when considering diverse optimization objectives.

However, the method of using deep learning to deal with TO, especially the MOTO problem is still in its early stages. There are certain limitations both in this article and similar research. On the one hand, there appeared large errors for a few prediction results. The popular PINN may offer new insights for resolving this issue. On the other hand, current studies on the MOTO problem are confined to simple 2D cases, and expanding this approach to complex 3D bridge designs will be a crucial focus of our future work.

ACKNOWLEDGEMENT

The authors are grateful for the financial support provided by the National Natural Science Foundation of China (No. 52078365).

REFERENCES

Kingma, D. & Ba, J. 2014. Adam: A method for stochastic optimization, *International Conference on Learning Representations*. San Diego, CA, United states.

Le, C., Norato, J., Bruns, T., Ha, C. & Tortorelli, D. 2010. Stress-based topology optimization for continua. *Structural and Multidisciplinary Optimization* 41(4): 605–620.

Liu, Z., Lin, Y. T., Cao, Y., Hu, H., Wei, Y. X., Zhang, Z., Lin, S. & Guo, B. N. 2021. Swin Transformer: Hierarchical Vision Transformer using Shifted Windows. *2021 IEEE/CVF INTERNATIONAL CONFERENCE ON COMPUTER VISION (ICCV 2021)*.

Seo, M. & Min, S. J. 2023. Graph neural networks and implicit neural representation for near-optimal topology prediction over irregular design domains. *ENGINEERING APPLICATIONS OF ARTIFICIAL INTELLIGENCE* 123: 106284.

Sigmund, O. & Maute, K. 2013. Topology optimization approaches A comparative review. *Structural and Multidisciplinary Optimization* 48(6): 1031–1055.

Sosnovik, I. & Oseledets, I. 2019. Neural networks for topology optimization. *Russian Journal of Numerical Analysis and Mathematical Modelling* 34(4): 215–223.

Svanberg, K. 1987. The method of moving asymptotes—a new method for structural optimization. *International Journal for Numerical Methods in Engineering* 24(2): 359–373.

Wang, D., Xiang, C., Pan, Y., Chen, A., Zhou, X. & Zhang, Y. 2021. A deep convolutional neural network for topology optimization with perceptible generalization ability. *Engineering Optimization* 54(6): 973–988.

Xiang, C., Chen, A. & Wang, D. 2022. Real-time stress-based topology optimization via deep learning. *THIN-WALLED STRUCTURES* 181: 110055.

Xiang, C., Wang, D. L., Pan, Y., Chen, A. R., Zhou, X. Y. & Zhang, Y. Q. 2022. Accelerated topology optimization design of 3D structures based on deep learning. *Structural and Multidisciplinary Optimization*, Vol. 65 No. 3, pp.

Yu, Y., Hur, T. & Jung, J. 2018. Deep learning for determining a near-optimal topological design without any iteration. *Structural and Multidiplinary Optimization* 59: 787–799.

Zhang, Z. Y., Li, Y., Zhou, W. E., Chen, X. Q., Yao, W. & Zhao, Y. 2021. TONR: An exploration for a novel way combining neural network with topology optimization. *COMPUTER METHODS IN APPLIED MECHANICS AND ENGINEERING* 386: 114083.

Zheng, S., Fan, H. J., Zhang, Z. Y., Tian, Z. Q. & Jia, K. 2021. Accurate and real-time structural topology prediction driven by deep learning under moving morphable component-based framework. *Applied Mathematical Modelling* 97:522–535.

Bridge Maintenance, Safety, Management, Digitalization and Sustainability – Jensen, Frangopol & Schmidt (eds)
© 2024 The Author(s), ISBN 978-1-032-77040-6
Open Access: www.taylorfrancis.com, CC BY-NC-ND 4.0 license

A method for stochastic modelling of fatigue stresses in orthotropic bridge decks subjected to local and global traffic loading

A.G. Johansen
Entail AS, Oslo, Norway

F.-I.G. Giske
Multiconsult AS, Oslo, Norway

M. Storheim
Entail AS, Oslo, Norway

ABSTRACT: Fatigue loads and load effects are important aspects of the safety and resilience for many bridges. Long-span bridges are commonly designed with orthotropic steel deck bridge girders for weight optimization. Such bridge decks may be subjected to significant fatigue loading from heavy vehicle traffic, and in some cases the fatigue limit state will even be dimensioning for the stiffened deck plate. Typically, local wheel loads are assumed to dominate the fatigue stresses, and fatigue damage is calculated based on hot spot stress from local analyses. However, with increasing span length, global load effects from both traffic and environmental loads will increase in significance. This is particularly relevant for floating bridges, where the environmental loads may significantly contribute to the fatigue damage. Also, as more extreme suspension bridges and cable stayed bridges are sought, the combination of local and global effects will be important. With fatigue damage being highly nonlinear, fatigue analysis due to combined load effects is a challenging task, and a coupled approach is typically necessary to achieve sufficient accuracy. In this paper, a method to generate stochastic time series of hot spot stresses due to local and global load effects from traffic is proposed. The method is suitable for combination with other fatigue-driving load effects, achieving a reasonable total computational cost while maintaining accuracy.

1 INTRODUCTION

Orthotropic bridge decks may be subjected to significant fatigue loading from heavy vehicle traffic. As illustrated in Figure 1, the bridge deck will experience local load effects due to wheel pressure, as well as global load effects due to the global girder response. Typically, the local load effects are assumed to dominate. With increasing span length, the global load effects from both traffic and environmental loads are increasingly significant in the prediction of fatigue damage. This is particularly relevant for floating bridges, but also for other types such as suspension bridges and cable stayed bridges, with bridge technology being developed toward more extreme bridges. In this paper, a floating bridge is used as an example.

Orthotropic steel bridge decks are commonly used in long-span bridges and show good performance on long-span floating bridges as well. However, they have been prone to fatigue failure (Zhang et al. 2017). This type of bridge deck carries in-plane loads from global bridge deformations and out-of-plane loads from local loading such as traffic, and it is typically in areas where both these load types are present that cracks have been observed (Tsakopoulos & Fisher 2003). Matters are made more complicated by a difference in observed location of crack initiation in segmented model tests and full-scale structures (Chen & Lu 2013).

DOI: 10.1201/9781003483755-247

The stress amplitude and direction continuously change in a structural detail as a vehicle passes the bridge. Large efforts are made to improve the calculation methods, focusing on matters affecting the detailed response (Bohai et al. 2013, Zhiyuan et al. 2018, Ya et al. 2011) and the load pattern and combined loading mechanisms (Xu et al. 2012, Han et al. 2020, Zhang et al. 2013, Wu et al. 2012). Less work was found on the coupled local and global effect of loads such as traffic.

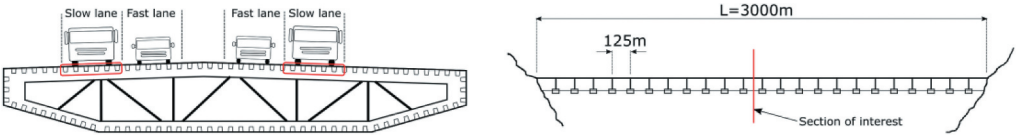


Figure 1. Orthotropic box girder for a four-lane bridge. Areas exposed to direct wheel loads and global loading are indicated in red boxes. A floating bridge is used as an example, considering a midspan section.

The motivation for the presented work is to provide a method that accounts for the combined local and global effect of fatigue loads from traffic in an accurate yet efficient manner. The outcome of the approach is synthetic time series of hot spot stresses which can be used to predict the fatigue damage from local and global traffic loads combined. Furthermore, the stress time series is suited for combination with a large set of environmental simulations of the bridge response, such that the total fatigue performance of the bridge from combined environmental and traffic loading can be assessed.

2 METHOD

The proposed method is motivated by structural details where both (i) out-of-plane stresses due to direct wheel loads and (ii) in-plane stresses due to global girder bending has significant contribution to fatigue. In the following these are denoted *local* and *global* load effects respectively. The proposed method has two main parts:

- Construction of vehicle influence lines, i.e. full stress histories at a fatigue hot spot for vehicles passing along the bridge, with both local and global load effects included.
- Application of a stochastic model for traffic simulation where a time realization of hot spot stress is established based on the individual vehicle influence lines.

2.1 *Global and local effects*

As illustrated in Figure 1, a 3 km span floating bridge is used as an example for the presented method. The bridge has four traffic lanes, two in each direction. The considered structural detail is a transverse welded splice in the deck plating at midspan between two pontoons. A location directly under the outer wheel path in lane 1 (slow lane) is considered, as shown in Figure 2. This detail is subjected to both global and local load effects and is of interest for floating bridges as both traffic and environmental loads may have significant contributions to fatigue. The stress of interest for the chosen detail is the normal stress in the bridge longitudinal direction, at the top of the deck plate. Three components contribute to this stress as illustrated in Figure 3, where bending of the bridge girder (global load effect), longitudinal stiffener (local load effect) and deck plating (local load effect) is shown.

The global contribution is accounted for by means of global influence lines. These can be obtained by stepping a unit axle load, e.g. a point load of 100 kN, along a global model of the bridge. The loads are applied for each traffic lane resulting in a set of sectional force influence lines $\boldsymbol{f}_{\text{infl}}(x, lane)$, where x is the load position along the bridge and *lane* is the lane number. In the general case, the stress influence lines due to global load effects can be calculated as

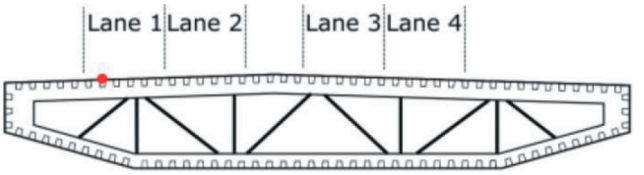


Figure 2. A transverse plate splice is considered with longitudinal stresses at the location shown in red.

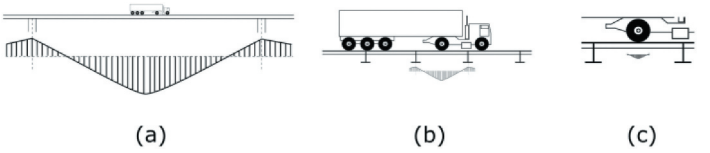


Figure 3. (a) Global girder bending. (b) Bending of longitudinal stiffener. (c) Bending of deck plating.

$$\boldsymbol{\sigma}_{\mathrm{G,infl}}(x, lane) = \boldsymbol{K} \times \boldsymbol{f}_{\mathrm{infl}}(x, lane). \tag{1}$$

Here, $\boldsymbol{K}$ is an n-by-6 matrix with stress transfer coefficients where n is the number of stress components in $\boldsymbol{\sigma}_{\mathrm{G,infl}}$, and $\boldsymbol{f}_{\mathrm{infl}}(x, lane)$ contains the sectional forces and moments:

$$\boldsymbol{f}_{\mathrm{infl}}(x, lane) = \begin{bmatrix} F_{x,\mathrm{infl}}(x, lane) \\ F_{y,\mathrm{infl}}(x, lane) \\ F_{z,\mathrm{infl}}(x, lane) \\ M_{x,\mathrm{infl}}(x, lane) \\ M_{y,\mathrm{infl}}(x, lane) \\ M_{z,\mathrm{infl}}(x, lane) \end{bmatrix}. \tag{2}$$

In the example considered here, the stress component of interest is the bridge girder normal stress $\sigma_{\mathrm{G,infl,n}}$. At the hot spot in question this component can be calculated by taking $\boldsymbol{K}$ as

$$\boldsymbol{K} = \begin{bmatrix} \frac{1}{A_x} & 0 & 0 & 0 & \frac{1}{W_y} & \frac{1}{W_z} \end{bmatrix}. \tag{3}$$

Here, A_x is the cross-section area at the considered section, W_y and W_z are section moduli for the stress point in question due to weak and strong axis bending respectively. The resulting global stress influence lines are shown on the left in Figure 4.

The local contributions are accounted for by means of a local FE model comprising a ~20 m section of the bridge girder with 4 m spacing between transverse frames. The model is a shell element model and is analyzed for unit axle loads, e.g. 100 kN, which are stepped along the length of the model. The loads are applied as pressure loads onto the deck plating according to the prescribed axle footprints in the traffic model. This results in a set of unit axle load influence lines $\boldsymbol{\sigma}_{\mathrm{L,infl}}(\tilde{x}, weave, axle)$ where $\boldsymbol{\sigma}_{\mathrm{L,infl}}$ is the vector of relevant stress components, $\tilde{x}$ is the axle position along the local model in the longitudinal direction, *weave* is the axle position in the transverse direction and *axle* is the axle type. In the example considered here, two stress components are relevant:

$$\boldsymbol{\sigma}_{\mathrm{L,infl}} = \begin{bmatrix} \sigma_{\mathrm{L,infl,m}} \\ \sigma_{\mathrm{L,infl,b}} \end{bmatrix} \tag{4}$$

These are the longitudinal membrane and bending stress components. These are mainly governed by stiffener bending (b) and plate bending (c) respectively, as illustrated in Figure 3. The normal stress at the weld toe location (top of deck plate) is obtained as $\sigma_{\mathrm{L,infl,n}} = \sigma_{\mathrm{L,infl,m}} + \sigma_{\mathrm{L,infl,b}}$.

The local stress influence lines are shown on the right in Figure 4 for axle type A. Weave 1-5 refer to transverse axle positions where the centre of one wheel footprint is located -200, -100, 0, 100, 200 mm from the hot spot, respectively. Here $\sigma_{\mathrm{L,infl,n}}$ is obtained by combination

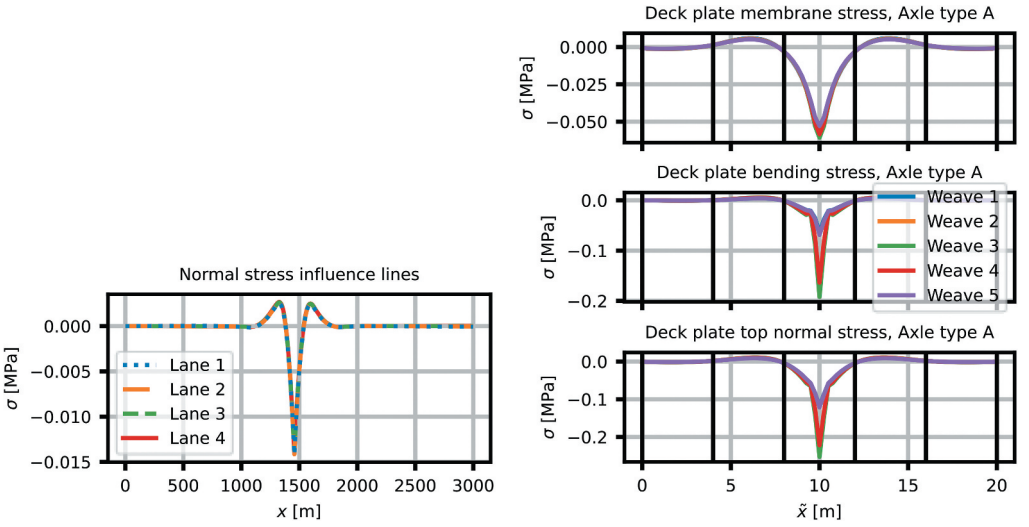


Figure 4. Global (left) and local (right) stress influence lines (stress per kN axle load) for the chosen fatigue detail. For the local stress (right), the deck plate top normal stress (bottom) is obtained by combination of membrane stress (top) and bending stress (middle).

of the membrane and bending components. Alternatively, depending on the FE software, the normal stress at the top of the deck plate can be read out directly.

2.2 *Vehicle stress histories*

The load specification is given by a fatigue load model for traffic. As an example, Fatigue Load Model 4 (FLM4) from the Eurocode (CEN, 2003) is considered. This model consists of five vehicle types, which are defined by the weight, position and wheel footprint of each axle. Vehicle type 3 from FLM4 is illustrated in Figure 5.

Based on the unit axle influence lines, vehicle influence lines are established for each vehicle in the traffic model. This is done by superposition of scaled and shifted influence lines for each axle associated with the vehicle. The axle influence lines are scaled according to weights and shifted according to axle position before they are summed to vehicle influence lines. The vehicle influence lines for local and global load effects are denoted by $\sigma_{\mathrm{L}}(\tilde{x}, \mathit{weave}, \mathit{veh})$ and $\sigma_{\mathrm{G}}(x, \mathit{lane}, \mathit{veh})$, respectively. $\tilde{x}$ and x now refer to the position of the first axle of the vehicle, and *veh* is the vehicle type. To account for vehicles driving in both directions, vehicle influence lines are established for both regular (front to rear) and reverse (rear to front) axle order. In Figure 6, the global and local vehicle influence lines are illustrated. In this example, we see that the local reverse vehicle influence lines correspond to the reverse of the regular ones. However, this would not be the case if the axle influence lines, cf. Figure 4 (right), did not have a symmetric shape. Globally, the axle order is less important, and the global vehicle influence lines are very similar.

Finally, by specifying the global location x_0 of the point $\tilde{x} = 0$ in the local model, the local and global stress components can be combined into a set of total vehicle influence lines for the complete hot spot stress $\sigma_{\mathrm{tot}}(x, \mathit{weave}, \mathit{lane}, \mathit{veh})$. For the lanes where vehicles are driving in the negative x-direction, the reverse local and global vehicle influence lines are combined. Otherwise, the regular ones are used.

Since the local and global load effects typically fluctuate on very different length scales, a non-uniform x-discretisation is preferred, with high density of data points only where local fluctuations are present. Another aspect is that the local load effects are only seen for vehicles in the lane directly above the detail in question, i.e. lane 1 for the considered example. This is illustrated in Figure 7 where the total vehicle influence lines for weave 3 of vehicle type 3 are shown

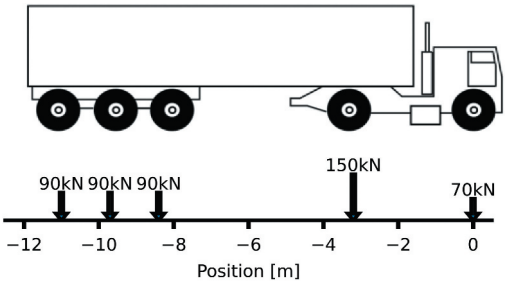


Figure 5. Axle weights and positions for vehicle type 3 of FLM4. Axle types are A, B, C, C, C front to rear.

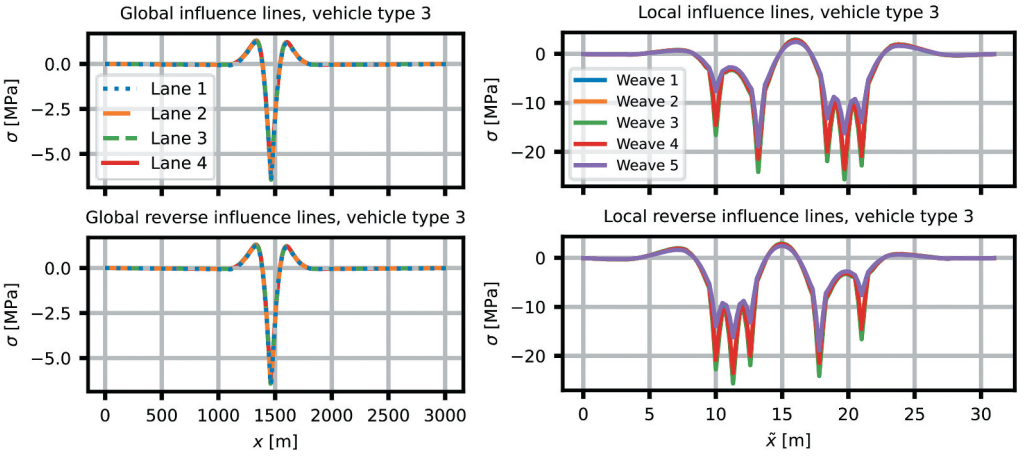


Figure 6. Global (left) and local (right) vehicle influence lines.

for all lanes. Lanes 1 and 2 have traffic moving in the negative x-direction, and it is seen that the local load effect in lane 1 is taken from the local reverse influence line in Figure 6.

2.3 *Stochastic load model*

Based on the individual vehicle influence lines, time realizations for the traffic load effects can be generated using a stochastic traffic model. The long-term distribution of vehicles is defined by the percentage of each vehicle type and the number of heavy vehicles per year in each lane. Considering the *long-distance* traffic type of FLM4, and an annual number of heavy vehicles per slow lane of $N_{\text{obs}} = 0.5 \cdot 10^6$ (traffic category 2), the long-term distribution is as given in Table 1.

From the long-term distribution, the number of vehicles of each type in each lane which statistically occur during the desired realization period, can be established. These vehicle numbers will in reality be random variables following the long-term distribution. However, by fixing the vehicle numbers for the given duration to their average values, we obtain realizations where the long-term distribution is preserved. In this way, a single short-term realization can be used to calculate yearly fatigue damage, without too large variation between realizations.

Once the number of vehicles for the desired realization period has been established, a simulation can be performed by applying the following steps:

1. Each vehicle is assigned a random weave position from a specified distribution. Typically weave 1-5 has a distribution of 7%, 18%, 50%, 18%, 7% (CEN, 2003).
2. For each lane the order of vehicles entering the bridge is picked at random.
3. For each lane the arrival times of vehicles entering the bridge are simulated using the Poisson process. This is described in Section 2.4 below.

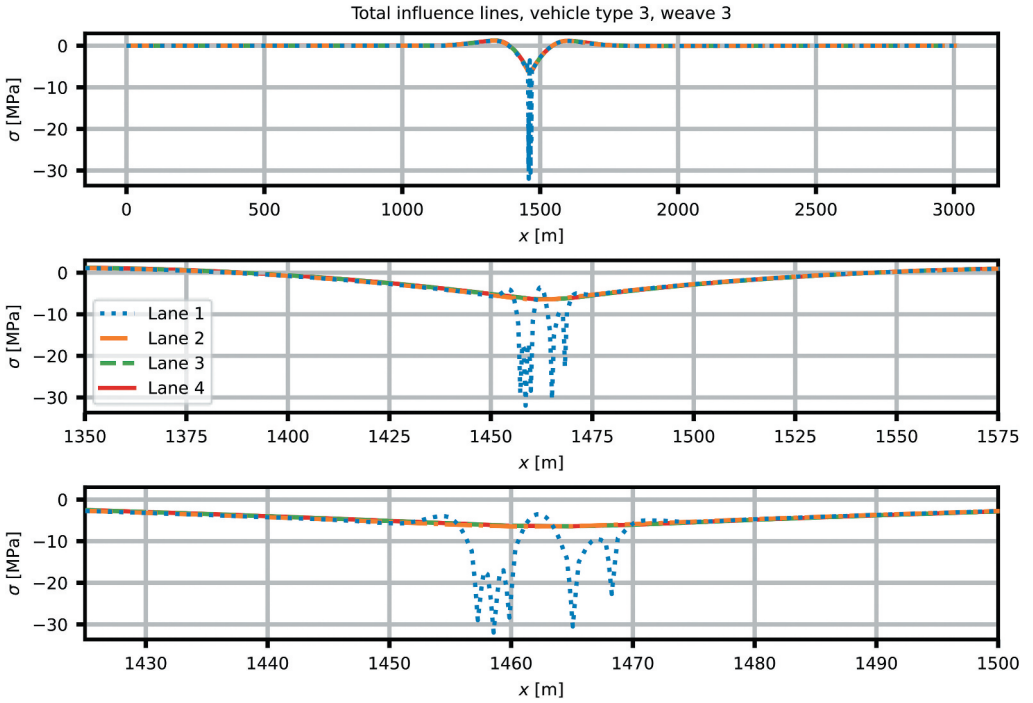


Figure 7. Total vehicle influence lines at considered hot spot for vehicle type 3 passing with weave 3. Local load effects are only included for the lane directly above the hot spot location (lane 1).

Table 1. Long-term distribution of vehicles.

Number of heavy vehicles					
Lane number	Lane 1	Lane 2	Lane 3	Lane 4	
Number per year	0.5e6	0.5e5	0.5e5	0.5e6	
Vehicle type distribution					
Vehicle type	Type 1	Type 2	Type 3	Type 4	Type 5
Percentage	20%	5%	50%	15%	10%

4. Vehicle influence lines are transformed to stress time series using a given vehicle speed. For the lanes where the traffic is moving in the negative x-direction, the influence lines are reversed.
5. A stress time series $\sigma(t)$ is generated by placing the vehicle time series at their respective arrival times and summing the contributions from each lane.

By simulating the arrival times explicitly, we can preserve the discretization of the influence lines with high resolution only when the local fluctuations occur.

2.4 *Simulation of arrival times*

Suppose N is the number of vehicles to be simulated within a specified duration T. First, we find the largest possible duration $T_{\max}$ such that any vehicle can arrive at $T_{\max}$ and still have its entire influence line pass within the duration T. The duration $T_{\max}$ is then split up as illustrated in Figure 8, where $t_2, \ldots, t_N$ are the $N-1$ interarrival times between the N vehicles and t_{sep} is the minimum allowed separation between the first axle of two vehicles. t_1 and t_{N+1} are buffer intervals that ensure random arrivals of the first and last vehicle in the time series.

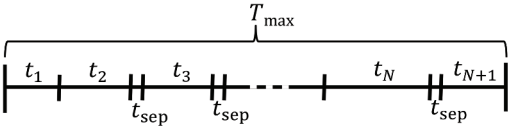


Figure 8. The duration $T_{\max}$ is split up by interarrival times and minimum allowed separations.

Phenomena described by an occurrence rate (i.e. number of events during a time interval) are commonly modelled using the Poisson process. For the Poisson process, the time between events is given by the exponential distribution with a rate parameter λ equal to the occurrence rate. Accounting for the minimum separations of t_{sep}, the intervals $t_1, \ldots, t_{N+1}$ represent $N+1$ events occurring during a time $T_{\max} - (N-1)t_{\text{sep}}$. Hence, we draw $N+1$ independent realizations $\tilde{t}_1, \ldots, \tilde{t}_{N+1}$ from an exponential distribution with a rate parameter

$$\lambda = \frac{N+1}{T_{\max} - (N-1)t_{\text{sep}}}. \tag{5}$$

The sum $\sum_{i=1}^{N+1} \tilde{t}_i$ will have an expected value of $T_{\max} - (N-1)t_{\text{sep}}$, but it will not exactly add up to this duration. To achieve intervals $t_1, \ldots, t_{N+1}$ that exactly add up to $T_{\max} - (N-1)t_{\text{sep}}$, a scaling is performed. Each interval is taken as $t_i = \tilde{t}_i / S$, where the scaling factor S is given by

$$S = \frac{1}{T_{\max} - (N-1)t_{\text{sep}} \sum_{i=1}^{N+1} \tilde{t}_i.} \tag{6}$$

It can be shown that S is gamma distributed with mean 1 and standard deviation $1/\sqrt{N+1}$. Thus, as long as N is reasonably large, the scaling factor S will be close to 1, and the exponential distribution of $\tilde{t}_i$ should be preserved for t_i in an approximate manner.

Having established the arrival time $t_{\text{arr},1} = t_1$ of the first vehicle and the interarrival times $t_2, \ldots, t_N$, the arrival time $t_{\text{arr},n}$ for vehicle number n is finally calculated as

$$t_{\text{arr},n} = t_1 + \sum_{i=2}^{n} \left(t_i + t_{\text{sep}} \right). \tag{7}$$

3 EXAMPLE RESULTS

A 10-hour simulation generated with the proposed method is shown in Figure 9, along with the contributions from each lane. Also, a more detailed view is shown for shorter time intervals around the time $t_{\min}$ when the lowest peak occurs. It is seen that in this case, the lowest peak is found when there is a simultaneous passing of two vehicles of type 3 in lane 1 and in lane 3. It can also be noted that the influence line from Figure 7 has been reversed, such that the effect of the front axle appears first in time. Based on the proposed methodology, time histories of hot spot stresses in relevant fatigue details can be established at a low computational cost. From there, cycle counting can be performed (e.g. by the rainflow method) to establish a stress range histogram where the "complete" effect of traffic is fully accounted for.

An interesting observation with the stochastic approach is an increase in stress when vehicles pass the considered cross-section simultaneously. This effect is illustrated in Figure 10, where the circles indicate events where the passings of vehicle type 3 in lane 1 have a simultaneous passing (less than 1.5s apart) of vehicle type 3 in lane 2 (red), lane 3 (green) or lane 4 (black). With type 3 being the heaviest and most common vehicle, it is seen that these passings capture the majority of the largest stress peaks, with simultaneous lane 4 (slow lane) passings being most common.

With the proposed method, several vehicles may contribute to the global response without a contribution to the local responses from direct wheel loads. Depending on bridge type and traffic model this effect may give a significant contribution to fatigue. A suspension bridge, for instance, will typically have global influence lines with a larger influence length, and the

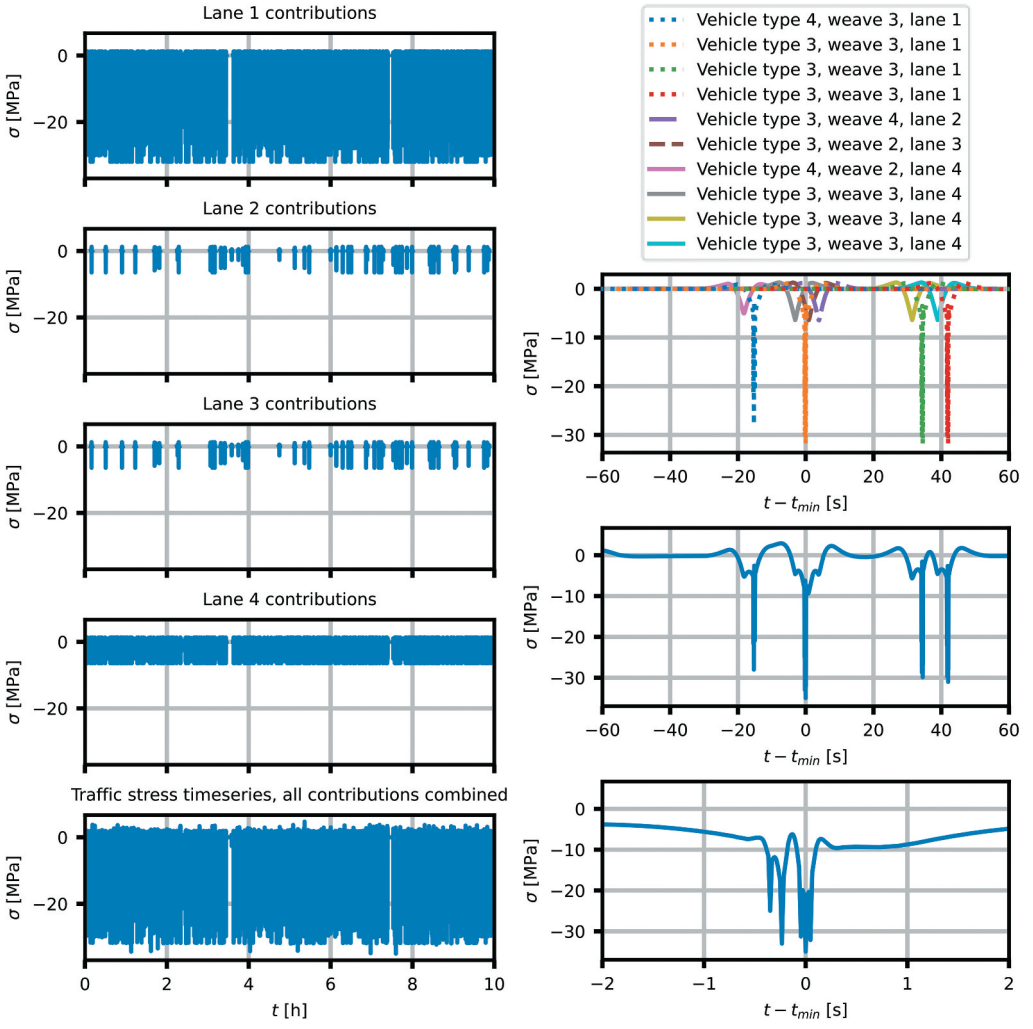


Figure 9. Left: A 10-hour simulation of hot spot stress showing contributions from each lane and finally the total combined stress. Right: Detailed view for shorter time intervals around the time $t_{\min} = 7.6$h when the lowest peak occurs. The upper plot shows the individual contributions from the different vehicles.

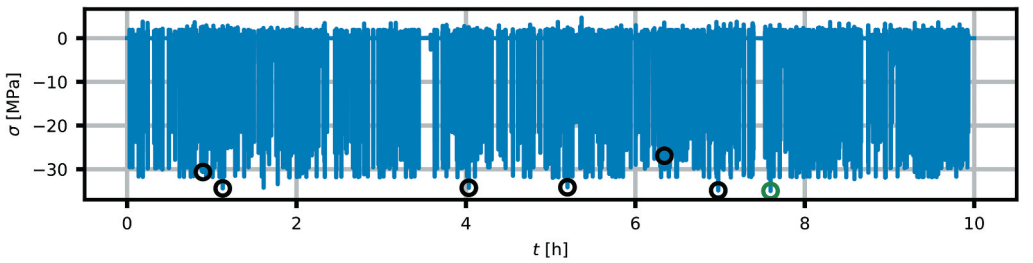


Figure 10. Circles indicate events where the passings of vehicle type 3 in lane 1 have a simultaneous passing (less than 1.5s apart) of vehicle type 3 in lane 2 (red), lane 3 (green) or lane 4 (black).

stress will vary more with the number of vehicles present on the bridge. In a deterministic

approach this effect would be tricky to account for. A more sophisticated model could also address daily variation such as rush traffic, varying vehicle speed etc.

4 CONCLUSION

The proposed method for stress time series generation can be used alone or in combination with environmental loading. This enables a thorough evaluation of the bridge fatigue performance, in which the combined effect of several dynamic processes can be captured at a computational cost that is feasible also in early design stages.

REFERENCES

Bohai, J., Rong, L., Ce, C., Hirofumi, M., & Xiongfei, C. (2013). Evaluation on root-deck fatigue of orthotropic steel bridge deck. *Journal of Constructional Steel Research*, *90*, 174–183.

CEN. (2003). *EN 1991-2 Eurocode 1: Actions on structures - Part 2: Traffic loads on bridges*.

Chen, S., & Lu, Y. (2013). Discussion of "Fatigue Evaluation of Rib-to-Deck Welded Joints of Orthotropic Steel Bridge Deck" by Samol Ya, Kentaro Yamada and Toshiyuki Ishikawa. *Journal of Bridge Engineering*, *18*(5), 450–451.

Han, Y., Li, K., Cai, C., Wang, L., & Xu, G. (2020). Fatigue Reliability Assessment of Long-Span Steel-Truss Suspension Bridges under the Combined Action of Random Traffic and Wind Loads. *Journal of Bridge Engineering*, *25*(3).

Tsakopoulos, P., & Fisher, J. (2003). Full-Scale Fatigue Tests of Steel Orthotropic Decks for the Williamsburg Bridge. *Journal of Bridge Engineering*, *8*(5), 323–333.

Wu, J., Chen, S., & van de Lindt, J. W. (2012). Fatigue Assessment of Slender Long-Span Bridges: Reliability Approach. *Journal of Bridge Engineering*, *17*(1), 47–57.

Xu, Y.-L., Chen, Z.-W., & Xia, Y. (2012). Fatigue assessment of multi-loading suspension bridges using continuum damage model. *International Journal of Fatigue*, *40*, 27–35.

Ya, S., Yamada, K., & Ishikawa, T. (2011). Fatigue Evaluation of Rib-to-Deck Welded Joints of Orthotropic Steel Bridge Deck. *Journal of Bridge Engineering*, *16*(4), 492–499.

Zhang, Q., Bu, Y., & Li, Q. (2017). Review on Fatigue Problems of Orthotropic Steel Bridge Deck. *China Journal of Highway and Transportation*, *03*, 14–39.

Zhang, W., Cai, C., & Pan, F. (2013). Fatigue Reliability Assessment for Long-Span Bridges under Combined Dynamic Loads from Winds and Vehicles. *Journal of Bridge Engineering*, *18*(8), 735–747.

Zhiyuan, Y., Bohai, J., Di, L., & Zhongqiu, F. (2018). Fatigue Strength and Root-Deck Crack Propagation for U-Rib to Deck Welded Joint in Steel Box Girder. *International Journal of Steel Structures*, *18*(5), 1589–1597.

SS15: Steel bridge rehabilitation

Organizer: M. Sakano


Taylor & Francis
Taylor & Francis Group
http://taylorandfrancis.com

Bridge Maintenance, Safety, Management, Digitalization and Sustainability – Jensen, Frangopol & Schmidt (eds)
© 2024 The Author(s), ISBN 978-1-032-77040-6
Open Access: www.taylorfrancis.com, CC BY-NC-ND 4.0 license

Application of microwave vibrometry in bridge monitoring & dynamic analysis

T. Bao & S. Bai
Inner Mongolia University of Technology, Huhhot, Inner Mongolia, China

ABSTRACT: Vibration measurement based on microwave sensing is a new non-contact vibration measurement technology developed on the basis of microwave radar micro motion sensing. Compared with the existing technology, its advantages include high sensitivity, multi scale, large detection range, strong environmental adaptability, low power consumption and miniaturization. In this paper, taking the Beijing-Baotou Railway Overpass as an example, the monitoring system based on microwave vibration measurement technology is used to extract the vibration monitoring data within six hours, and the data are analyzed in time and frequency domains. The signal characteristic indexes and the first two natural frequencies of the main bridge structure of the Beijing-Baotou Railway Overpass are calculated.

1 ENGINEERING BACKGROUND

In recent years, as large-span bridges have become more flexible and complex in both form and function, conventional means have struggled to grasp and predict their mechanical behavior under various operating environments and loading conditions. In the operation of bridges, ensuring structural safety and real-time structural health monitoring are major concerns not only for construction and design units but also for operation and management units. Therefore, it is necessary to adopt advanced monitoring means and automated monitoring technology to establish a bridge operation health monitoring management system with advanced technology, reasonable measures, practical and economical solutions, ease of management, openness, compatibility, and alignment with the needs of bridge management.

1.1 *Beijing-Baotou Railway Overpass*

The Beijing-Baotou Railway Overpass consists of left and right parts, with the left bridge spanning 2×75+3×(4×35)=570 meters and the right bridge spanning 2×35+2×75+2×35 +2×(4×35)=570 meters. The cross slope of the bridge deck ranges from 2% to 4% soil. The bridge starts at K123+138.5 and ends at K123+717.5, with a total length of 579 meters. The main bridge of the Beijing-Baotou Railway Overpass is a 2-span variable cross-section continuous steel structure (2×75 m), with a beam height ranging from 3.3 to 8.1 meters and a parabolic change ratio of 1.8 times. The approach bridge is a 35-meter cast-in-place continuous box girder with a height of 1.8 meters. The superstructure is made of C55 concrete, while C30 concrete is used for the approach bridge guardrail and C40 concrete for the main bridge guardrail. Anti-throwing nets are installed outside the bridge opening crossing the railway. The substructure of the main bridge consists of square column piers made of consolidated pier beams and C40 concrete. The substructure of the approach bridge consists of column piers, with the bent cap, pier shaft, tie beam, and retaining block made of C35 concrete, and the pile

DOI: 10.1201/9781003483755-248

foundation and cushion cap made of C30 concrete. The layout of the main bridge of the Beijing-Baotou Railway Overpass is shown in Figure 1.

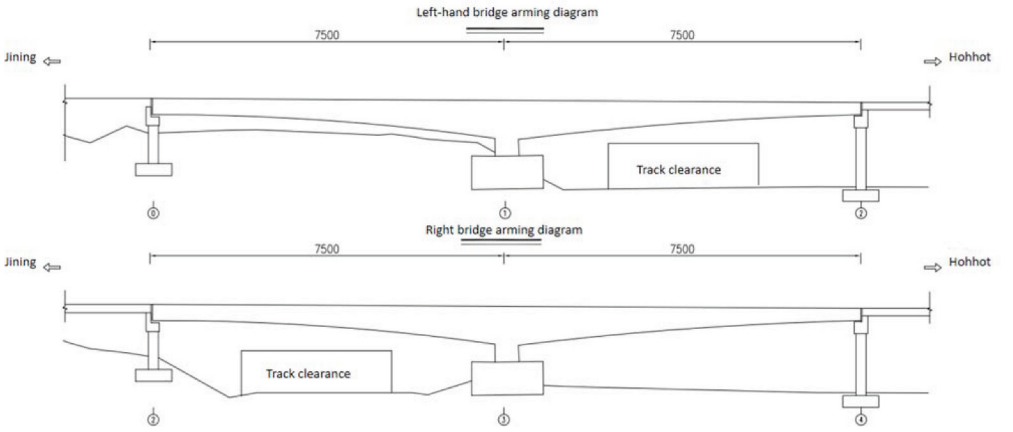


Figure 1. The layout of the main bridge of Beijing-Baotou Railway Overpass.

1.2 *Microwave vibrometry*

In monitoring the displacement influence line of bridge structures, arranging contact sensors is laborious and entails some risks. Optical fiber sensors, while accurate, have limited detection ranges in non-contact bridge vibration and deformation displacement monitoring. Large-scale distributed sensor measurement is required for the full-field synchronous test of large bridge structures, but sensor networking is complex, and the test efficiency is low, with high costs involved. The laser scanning method can expand the detection range to the meter level but can only achieve local bridge structure measurement, not meeting the requirements of full-field synchronous testing. The image method offers a large field of view but faces a contradiction between a large measurement range/field of view and high measurement accuracy. Achieving high-precision vibration and deformation measurement requires complex calibration and image stream data processing, demanding significant computation and vulnerable to environmental factors such as light. Given the challenges and limitations of existing technologies in vibration and deformation monitoring of large bridge structures, the sensor system based on microwave vibration testing provides a promising alternative for non-contact displacement measurement (Xiong et al., 2017, 2018, 2019, 2021; Ren et al., 2023). Vibration measurement based on microwave sensing is a new non-contact technology developed on the basis of microwave radar micro-motion sensing. Microwave radar transmits electromagnetic waves of a specific frequency and receives echo signals scattered by the target object. The movement of the target object generates nonlinear phase modulation, and the micro-motion information is derived by analyzing the modulation information of the baseband signal. Unlike widely used point sensors, microwave sensing can be considered a non-contact distributed sensing technology capable of extracting vibration displacement and deformation from numerous measuring points on the target structure within the observation range through a single device. It offers advantages such as high sensitivity, multi-scale capability, large detection range, strong environmental adaptability, low power consumption, and miniaturization. Currently, microwave vibrometry technology has been applied in vital sign monitoring (Ren et al., 2023), condition monitoring of aviation engine turbine blades, and holds promise in extracting displacement influence lines and health monitoring of large bridge structures (Xiong et al., 2020; Li et al., 2022).

This paper analyzes the vibration monitoring data of the main bridge of the Beijing-Baotou Railway Overpass within a six-hour period using microwave vibrometry technology and extracts its time-frequency and frequency-domain characteristic indicators to study the dynamic characteristics of the continuous rigid frame bridge under the influence of vehicles.

2 EQUIPMENT INSTALLATION

The commercial vibration and deformation microwave multi-point measurement instrument VDMM-L200, as shown in Figure 2-(a), has been successfully developed, with a measurement accuracy of ±2μm.

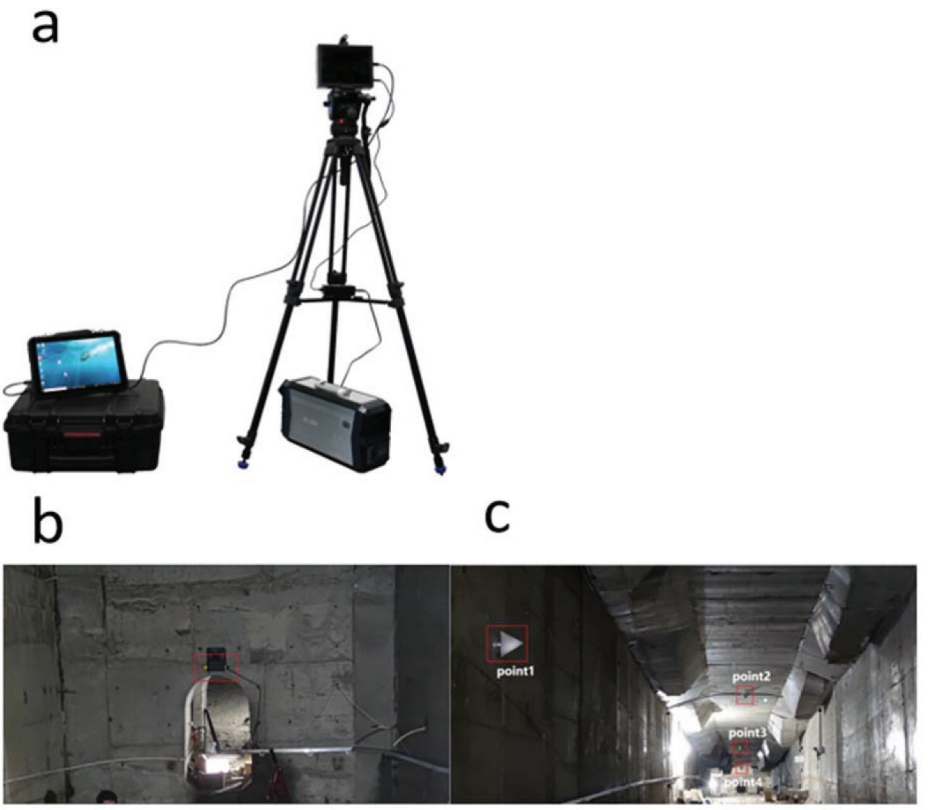


Figure 2. (a) Schematic diagram of microwave multi-point measurement instrument VDMM-L200;(b) Installation diagram of test instrument terminal;(c) Schematic diagram of target installation.

The testing distance is up to 200 meters, making it popular in the health monitoring field of large bridges and buildings. The microwave radar monitoring equipment is installed at the left pier, as indicated by the red box in Figure 2-(b). The target is installed in the box girder, as shown in Figure 2-(c), with the triangular reflector marked by the red box serving as the target. Measuring point 1 is located on the outer 1/2 side wall of the left side of the main bridge, while measuring points 2 and 3 are located on the top of the box girder. This paper utilizes the monitoring data from measuring points 1, 2, and 3, with a total monitoring time of 6 hours and a sampling frequencyf_s is set to 50Hz.

3 MONITORING DATA AND ANALYSIS

3.1 *Time domain analysis*

The deflection monitoring data for measurement points 1, 2, and 3 over a six-hour period are shown in Figure 3.

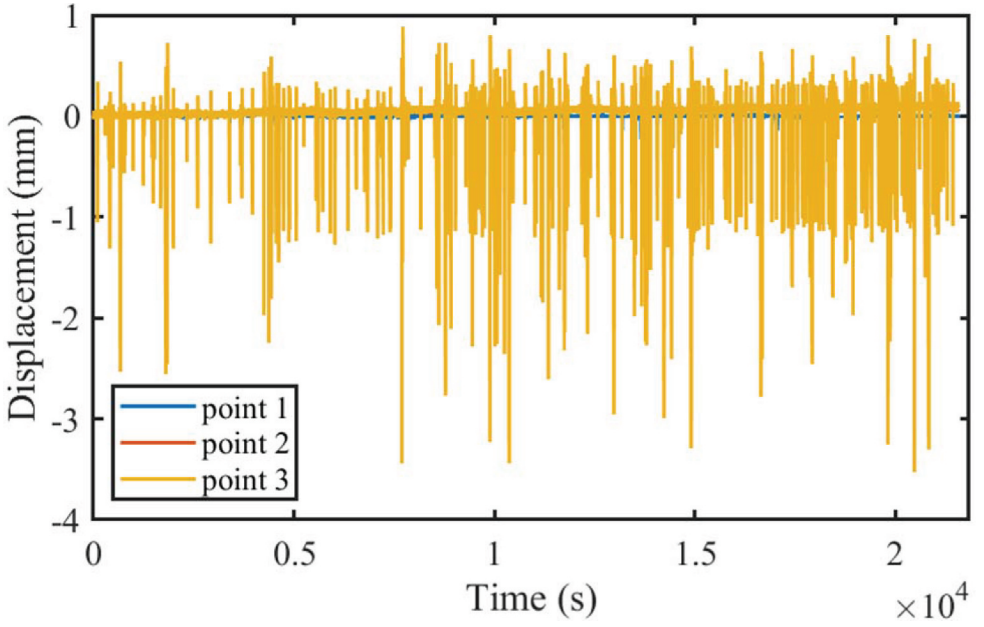


Figure 3. Waveform diagram of original monitoring data.

Applying Gaussian filtering to denoise the original signal, the window length is set to 15. The time history diagrams of measuring points 1, 2, and 3 after filtering are shown in Figure 4-(a)-(c).

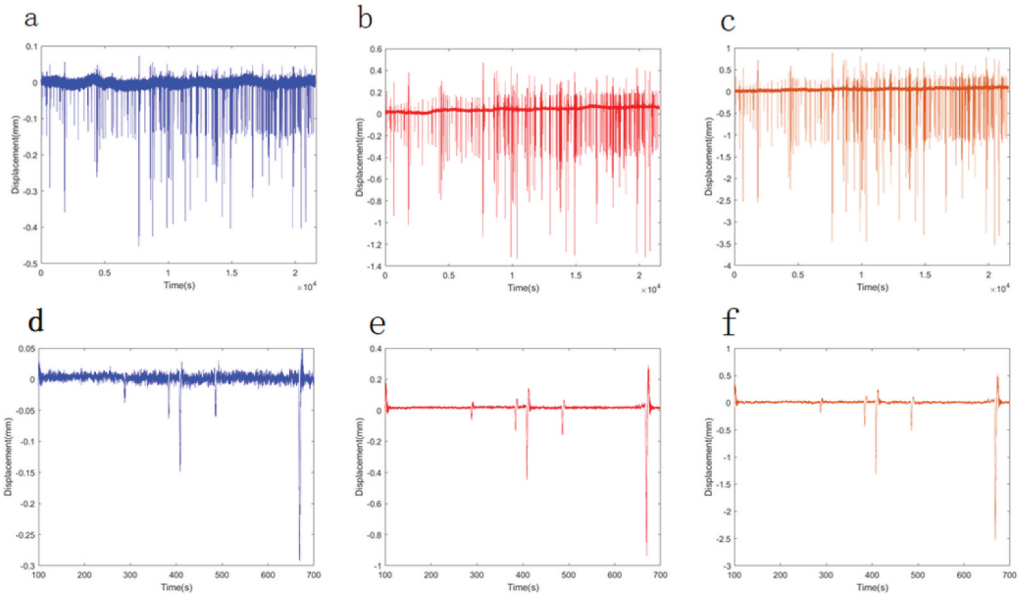


Figure 4. Waveform diagram of filtered monitoring data (complete) of point 1(a), point 2(b) and point 3(c);Waveform diagram of filtered monitoring data (partial) of point 1 (d), point 2(e) and point 3(f).

Taking the filtered monitoring signals of each measuring point within the range of 100s-700s as an example (Figure 4-(d)-(f)), it can be observed that each measuring point's waveform exhibits the following characteristics:

(1) The point will upturn when a vehicle passes but is not directly above the point.
(2) The vehicle causes bending and deformation at the measurement point when it directly passes over it.
(3) After a vehicle passes, the measuring point may buckle and exhibit free vibration.
(4) During vehicle passage, the deformation at the side wall where measuring point 1 is located is less pronounced compared to the deformation at the top of the box girder where measuring points 2 and 3 are situated. Within the 100s-700s range, the maximum deflections of measuring points 1, 2, and 3 are 0.2925mm, 0.9372mm, and 2.5314mm, respectively. The peak-to-peak values are 0.3424mm, 1.2282mm, and 3.0687mm, respectively. Across the entire time domain, the maximum deflections of measuring points 1, 2, and 3 are 0.4531mm, 1.3323mm, and 3.5243mm, respectively, with peak-to-peak values of 0.5252mm, 1.8025mm, and 4.4106mm, respectively. Time domain signal characteristics such as standard deviation (STD) and root mean square (RMS) can be extracted from monitoring data. The STD values for measuring points 1, 2, and 3 are 0.0249, 0.0680, and 0.1829, respectively, while the RMS values are 0.0253, 0.0772, and 0.1859, respectively.

3.2 *Spectrum analysis*

The time history curves of measuring points 1, 2, and 3 can be transformed through fast Fourier transform to revealing the spectrum distribution of the response, as depicted in Figure 5.

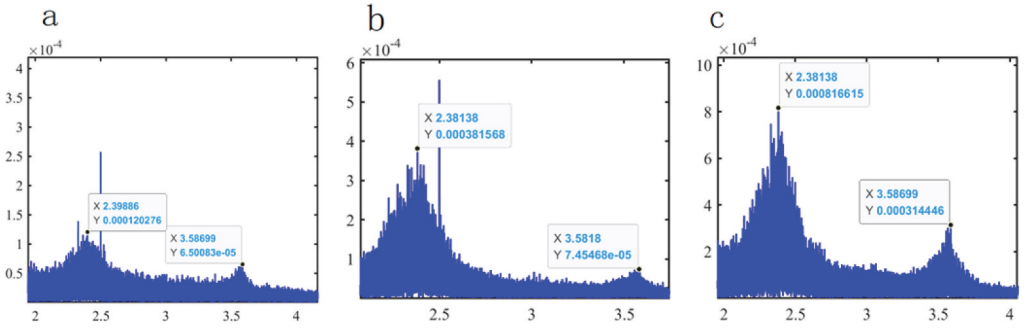


Figure 5. Spectrum diagram of measuring points 1(a), 2(b) and 3(c).

Through the spectrum diagram, the modes and corresponding amplitudes of the structure within the analysis frequency range can be determined. The frequency corresponding to the first peak on the spectrum curve represents the fundamental frequency of the structure. According to Figure 5-(a), the first-order natural frequency is 2.39886Hz, and the second-order natural frequency is 3.58699Hz. According to Figure 5-(b), the first-order natural frequency is 2.38138Hz, and the second-order natural frequency is 3.58180Hz. According to Figure 5-(c), the first-order natural frequency is 2.38138Hz, and the second-order natural frequency is 3.58699Hz. Based on the above data, the root mean square error of the first-order natural frequency is approximately 1.01%, and that of the second-order natural frequency is about 0.30%. It can be considered that the first-order and second-order natural frequencies obtained from the spectrum closely approximate the true values. The arithmetic mean value can be taken as the test result, yielding an arithmetic mean value of 2.38721Hz for the first-order natural frequency and 3.58526Hz for the second-order natural frequency.

4 CONCLUSION

This paper introduces the general situation of the Beijing-Baotou Railway Overpass project, utilizing microwave vibrometry technology to extract vibration signals at different positions

of the structure within a six-hour period, and studying the dynamic characteristics of continuous rigid frame bridges under random environmental excitation such as vehicle load and wind load. The following conclusions are drawn:

(1) During vehicle passage, the vibration signal of the measurement point exhibits the characteristics of upward-sinking-upward motion.
(2) Observing the maximum deflection and peak-to-peak value of each measurement point during the monitoring time, it was found that sidewall deformation was not significant, while top deformation of the box girder was relatively large. Two signal characteristics were calculated for the time-domain signals of each measurement point.
(3) Through spectrum analysis, the fundamental frequency of the bridge structure is 2.38721Hz, and the second-order natural frequency is 3.58526Hz.

ACKNOWLEDGEMENTS

This study was sponsored by the National Natural Science Foundation of China (Grant No. 12262027) and supported by the State Key Laboratory of Mechanical System and Vibration (Grant No. MSV202410).

REFERENCES

Li S.X., Xiong Y.Y., Wu G.Y., Ren Z.S., Meng G., Peng Z.K. Microwave Vibrometry: Noncontact Vibration and Deformation Measurement Using Radio Signals[J], IEEE Instrumentation & Measurement Magazine, 2022, 25(2), 16–26.

Li S.X., Xiong Y.Y., Xiangtian Shen, Peng Z.K. Multi-scale and full-field vibration measurement via millimetre-wave sensing[J], Mechanical Systems and Signal Processing, Volume 177, 2022, 109178.

Ren Z.S., Xiong Y.Y., Peng Z.K., Meng G., 3D microwave vibrometer: Contactless three-dimensional vibration measurements using microwave radars[J], Mechanical Systems and Signal Processing, Volume 183, 2023, 109622.

Xiong Y.Y., Chen S.Q., Dong X.J., Peng Z.K., Zhang W.M. Accurate Measurement in Doppler Radar Vital Sign Detection Based on Parameterized Demodulation[J], IEEE Transactions on Microwave Theory and Techniques, 2017, 65(11): 4483–4492.

Xiong Y.Y., Chen S.Q., Xing G.P., Peng Z.K., Zhang W.M. Static Clutter Elimination for Frequency-modulated Continuous-wave Radar Displacement Measurement Based on Phasor Offset Compensation[J], Electronics Letters, 2017, 53(22): 1491–1493.

Xiong Y.Y., Peng Z.K., Xing G.P., Zhang W.M., Meng G. Accurate and Robust Displacement Measurement for FMCW Radar Vibration Monitoring[J], IEEE Sensors Journal, 2018, 18(3): 1131–1139.

Xiong Y.Y., Chen S.Q., Xing G.P., Peng Z.K., Zhang W.M. High-Precision Frequency Estimation for FMCW Radar Applications Based on Parameterized De-alternating and Modified ICCD[J], Measurement Science and Technology, 2018, 29(7): 075010.

Xiong Y.Y., Peng Z.K., Jiang W., He Q.B., Zhang W.M., Meng G. An Effective Accuracy Evaluation Method for LFMCW Radar Displacement Monitoring with Phasor Statistical Analysis[J], IEEE Sensors Journal, 2019, 19(24): 12224–12234.

Xiong Y.Y., Peng Z.K., Gu C.Z., Li S.X., Wang D., Zhang W.M. Differential Enhancement Method for Robust and Accurate Heart Rate Monitoring via Microwave Vital Sign Sensing[J], IEEE Transactions on Instrumentation and Measurement, 2020, 69(9): 7108–7118.

Xiong Y.Y., Li S.X., Gu C.Z., Meng G., Peng Z.K. Millimeter-wave bat for mapping and quantifying micro-motions in full field of view[J], Research, 2021 (2021).

Bridge Maintenance, Safety, Management, Digitalization and Sustainability – Jensen, Frangopol & Schmidt (eds)
© 2024 The Author(s), ISBN 978-1-032-77040-6
Open Access: www.taylorfrancis.com, CC BY-NC-ND 4.0 license

Maintenance of large expansion joint in Honshu-Shikoku Bridges

M. Hongo, A. Moriyama, Y. Yano & Y. Yokoi
Honshu-Shikoku Bridge Expressway Company Limited, Kobe, Japan

ABSTRACT: Honshu-Shikoku Bridges have large and special expansion joints in order to deal with the deformation unique to long-span bridges, such as large longitudinal and in-plane displacement. There are several types of large expansion joints, and most of the link type expansion joints in Japan are used in the Honshu-Shikoku Bridges. The link type expansion joints installed in the Akashi-Kaikyo Bridge move up to ±1450mm. Although many minor damages were reported, maintenance of the link-type expansion joints is limited to small scale repairs or parts replacements. In order to continue to maintain more than 200 years, preparation for large-scale renewal work and replacement of these expansion joints expected in the future is necessary. This paper introduces the examples of damages and repair works of link-type expansion joints reported in the Honshu-Shikoku Bridges. Furthermore, the future maintenance strategies based on problems in maintenance over the past 30 years will be explained.

1 INTRODUCTION

Honshu-Shikoku Bridges Expressway Co., Ltd. (HSBE) operates and maintains three routes crossing the Seto-Inland Sea. Honshu-Shikoku Bridge consists of 17 long-span bridges including 10 suspension bridges, five cable-stayed bridges, one truss bridge and one arch bridge as shown in Figure 1. This group of long-span bridges in small area is very unique in the world. The Akashi-Kaikyo and Seto-Ohashi Bridges marked the 25th and 35th anniversary respectively in 2023. Honshu-Shikoku Bridges are important structures with no alternative route and must undertake a role as an emergency transportation route in case of a disaster.

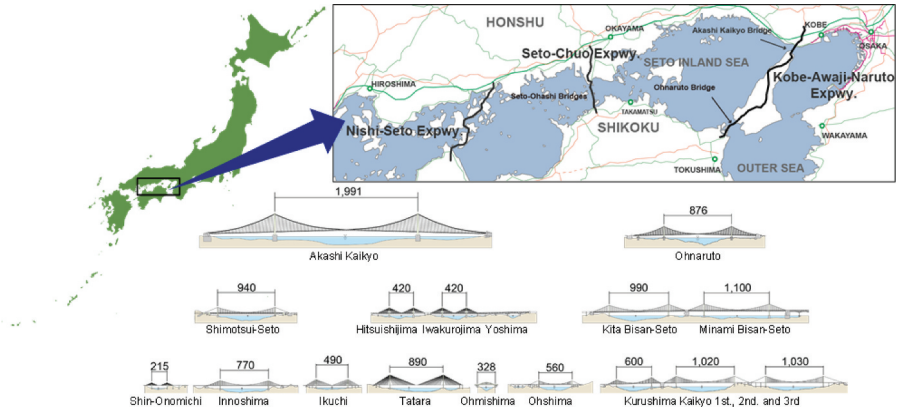


Figure 1. Location of Honshu-Shikoku Bridges.

DOI: 10.1201/9781003483755-249

The long-span bridges have large and special expansion joints in order to deal with the deformation unique to long-span bridges, such as large longitudinal and in-plane displacement. There are several types of large expansion joints. Four types of large expansion joint (finger type, rolling leaf type, link type and modular type) are mainly used for long-span bridges in Japan. Although each type has a unique structure, they have the same function in terms of dealing with the deformation. Especially, most of the link type expansion joints in Japan are used in Honshu-Shikoku Bridges including the Akashi-Kaikyo Bridge. Although many minor damages were reported, maintenance of the link-type expansion joints is limited to small scale repairs or parts replacements. In order to continue to maintain more than 200 years, preparation for large-scale renewal work and replacement of these expansion joints expected in the future is necessary.

In this paper, examples of damages and repair works of link-type expansion joints reported in the Honshu-Shikoku Bridges are explained. Furthermore, the future maintenance strategies based on problems in maintenance over the past 30 years will be explained.

2 LARGE EXPANSION JOINTS IN HONSHU-SHIKOKU BRIDGES

2.1 *Large expansion joints of long-span bridges*

Long-span bridges have large and special expansion joints in order to deal with the deformation unique to long-span bridges, such as large longitudinal and in-plane displacement. There are several types of large expansion joints as shown in Figure 2. Four types of large expansion joints (finger type, rolling leaf type, link type and modular type) are mainly used for long-span bridges in Japan. Although each type has a unique structure, they have the same function in terms of dealing with the deformation.

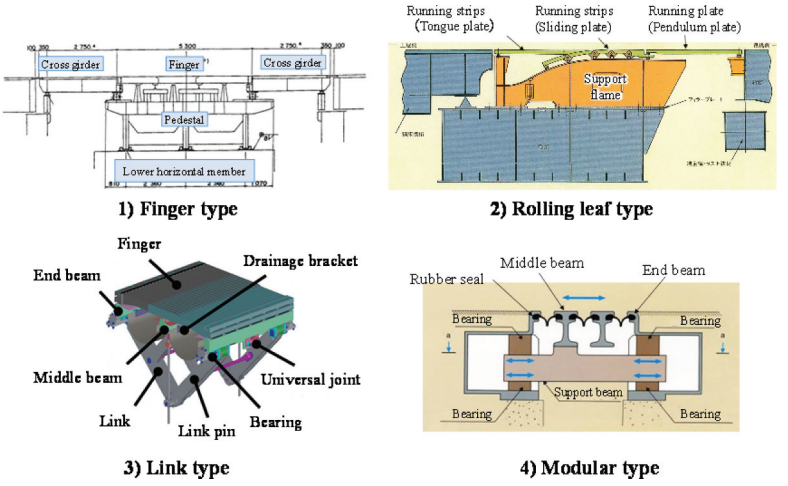


Figure 2. Large expansion joints for long-span bridges.

2.2 *Link type expansion joints*

In Japan, several types of large expansion joints are used as shown in Table 1 and especially most of the link type expansion joints are applied in the Honshu-Shikoku Bridges. In the Akashi-Kaikyo Bridge, designed movement range is up to +1,450mm and it indicates that the link type expansion joints are capable of dealing with large expansions and contractions (Figure 3).

Link type expansion joints are consist of link, link pin, bearing, middle beam, end beam, universal joint and finger (Figure 4). A link mechanism is applied as the load support mechanism, and the load is movably supported by the middle beam during expansion and contraction. Compared to other expansion joints, link mechanism is compact and suitable structural type for large expansion movement.

Link type expansion joints are capable of following displacement in all directions. For longitudinal displacement, the angle of the link mechanism changes. For transverse displacement, each unit follows by rotating in the horizontal in-plane around a universal joint. For vertical in-plane rotation, link and finger rotates around the connection of end beam. For horizontal in-plane rotation, each unit follows by displacement to expansion and contraction.

The unit width of the link type expansion joints is half the width of a lane, and each unit is removable, which has the advantage of superior workability in maintenance.

Table 1. Large expansion joints applied to bridges in Japan.

Expansion joint type	Honshu-Shikoku Bridges	Other Bridges in Japan
1) Finger type	Innoshima Bridge	Kanmon Bridge etc.
	Ohnaruto Bridge	
	Ikuchi Bridge	
2) Rolling leaf type	Shimotsui-Seto Bridge	Rainbow Bridge
	Kita Bisan-Seto Bridge	Hakucho Bridge
	Miani Bisan-Seto Bridge	Tempozan Bridge etc.
	Tatara Bridge	
	Kurushima-Kaikyo Bridges	
3) Link type	Akashi-Kaikyo Bridge	Kojimawan Bridge
	Hitsuishijima Bridge	
	Iwakurojima Bridge	
	Yoshima Bridge	
	Bannosu Viaduct	
	Ohshima Bridge	
4) Modular type	Ohmishima Bridge	Many bridges
	Yoshima Viaduct etc.	

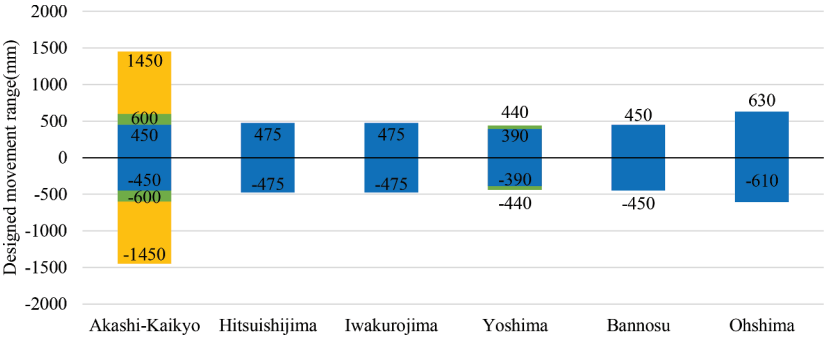


Figure 3. Designed movement range of link type expansion joints in the Honshu-Shikoku Bridges.

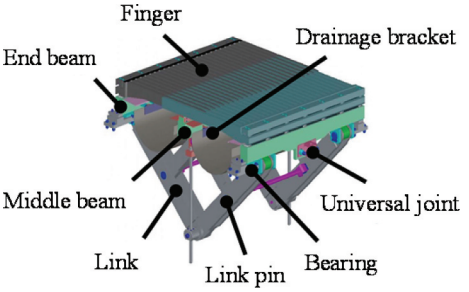


Figure 4. General view of link type expansion joints.

3 PROBLEMS OF LINK TYPE EXPANSION JOINTS

In this chapter, the major problems occurred in the past 30 years of maintenance of link type expansion joints. In the early stages of in-service, various types of damages have occurred due to the initial design of the expansion joint and structural improvements have been conducted each time. Failure and maintenance cases of link type expansion joints will be also explained.

3.1 *Noise problem during vehicle traffic*

Immediately after in-service, noise problem was reported during vehicle traffic. In order to determine the cause, investigation was conducted. The original structure had each independent finger pinned to the end beam. And it was found that the noise was caused by the gap between the pin and the pin hole, where the fingers bounce and hit as the wheel passes through. Figure 5 shows the mechanism of noise generation.

As countermeasures, two improvements were conducted as shown in Figure 6. First, the support structure of the fingers was changed. In detail, the pin that was causing noise was eliminated, and the anti-vibration rubber system was adopted to suppress the generation of noise and vibration. Second, the method of finger fabrication was revised. Originally, each steel plate separating finger was pinned and each finger could generate noise by moving individually. Therefore, casting integrated fingers were adopted instead of separating finger. By the two countermeasures mentioned above, noise problem caused by vehicle traffic was improved.

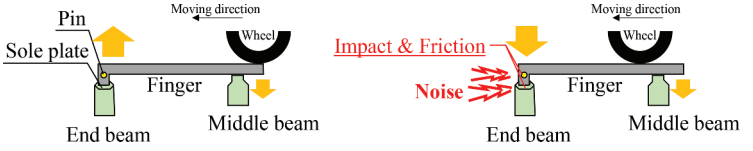


Figure 5. Mechanism of noise generation.

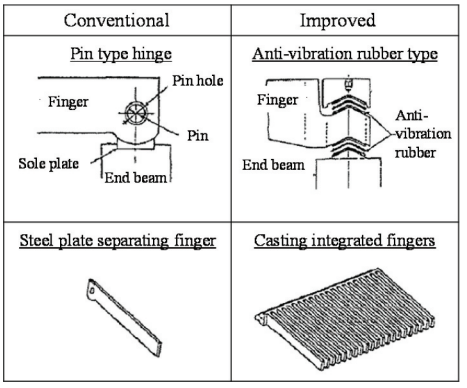


Figure 6. Improvement of support structure and finger.

3.2 *Breakage problem of finger*

Approximately five years after in-service, breakage problem of finger was reported. The vehicle passes through over the finger, a cause of the problem was investigated immediately. On the finger surface of link type expansion joints, a non-slip groove treatment is applied. As shown in Figure 7, previously non-slip groove treatment was conducted using flame cutting and the shape was rectangle. The corners of the groove profile were the cause of stress concentration, and fatigue cracks occurred due to the repeated wheel loading. In addition, residual

stress due to gas cutting during grooving was also considered. As countermeasures, flame cutting was replaced to machine cutting to deal with residual stress. And the shape of non-slip groove changed from rectangle to curved shape in order to reduce the stress concentration. After these improvements, there have been no reports of finger breakage.

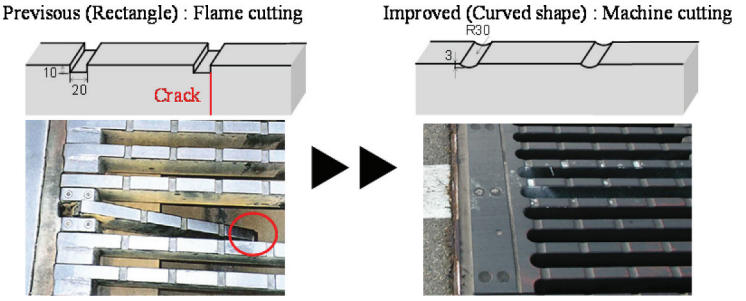


Figure 7. Improvement of finger shape of the surface.

3.3 *Failure and maintenance cases of link type expansion joints*

The damage caused by the initial design of the link-type expansion joint been described above, and a breakdown of link type expansion joint failures identified so far in the Honshu-Shikoku Bridges is shown in Figure 8. Damage resulting from poor construction or from the old structure described above is excluded. The majority of the cases are relatively minor failures such as deterioration of sealing due to aging, and cracking and peeling of the paint film. And failures related to the link mechanism has not been reported at this time.

Figure 9 shows the replacement of the universal joint. Corrosion of the universal joint leads to the restriction of transverse displacement. In order to prevent loss of rotational function of the universal joint, replacement is carried out at the appropriate timing. Loose bolts, etc. are repaired individually.

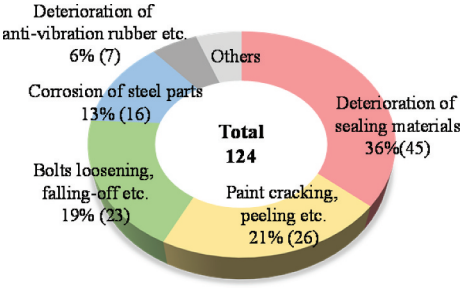


Figure 8. A breakdown of link type expansion joint failures identified in the Honshu-Shikoku Bridges.



Figure 9. Corrosion and replacement of the universal joint.

4 MAINTENANCE PLANS BASED ON PROBLEMS IN MAINTENANCE

The above chapters described problems that have been observed in link type expansion joints. In this chapter, strategies for maintenance management based on the problems that have occurred in maintenance are described.

4.1 *Reflection on maintenance related to deterioration of parts*

As mentioned above, the majority of the failure cases are relatively minor failures such as deterioration of some parts. Since components that have deteriorated over time need to be replaced on a periodic cycle, repairs and parts replacement are carried out based on the knowledge and experience that have been accumulated over the years. Table 2 and Figure 10 shows the estimated lifetime of rubber materials, sealing materials and painting based on the occurrence time of past deterioration. It shows that each component indicates the requirement for periodic replacement or repair of parts every 10 to 20 years.

These are all items that can be identified by close visual inspection, and are unidentified items that are structurally difficult to visually inspect, such as moving parts friction of the link mechanism. In order to understand the occurrence of deterioration and to consider the replacement period, a detailed investigation by overhaul will be conducted and the obtained results will be reflected to the maintenance plans.

Table 2. Estimated lifetime of parts (Link type expansion joint).

Parts name etc.	Estimated lifetime
Urethane rubber	10~20 years
Anti-vibration rubber	10 years
Dust rubber sealing for link	20 years
Seal ring for link	10 years
Painting layer	10~20 years



Figure 10. Deterioration of urethane rubber and anti-vibration rubber.

4.2 *Investigation of units standardization to ensure economic efficiency*

In order to accommodate the different design conditions of each bridge individually, the link type expansion joints applied in the Honshu-Shikoku Bridges have several designed movement ranges as shown in Figure 3 and each bridge has a variety of roadway widths.

Therefore, there is a wide variety of units when unit widths are included in addition to the designed movement range. Figure 11 shows the variation of unit width and designed movement range of link type expansion joint in Honshu-Shikoku Bridges. There are 28 types and a total of 214 units. There are also several units with very similar unit widths, indicating the possibility of standardization.

The size of the attached components of each type of unit varies slightly, which is one of the factors that increase production costs in maintenance. In preparation for periodic replacement

and repair of components and renewal of the expansion joint, investigations to standardize unit types and parts for the link type expansion joints in Honshu-Shikoku Bridges are currently underway. It is necessary to consider long-term maintenance and management from the design stage and standardization of parts is one of the efficient way when special structural members are applied.

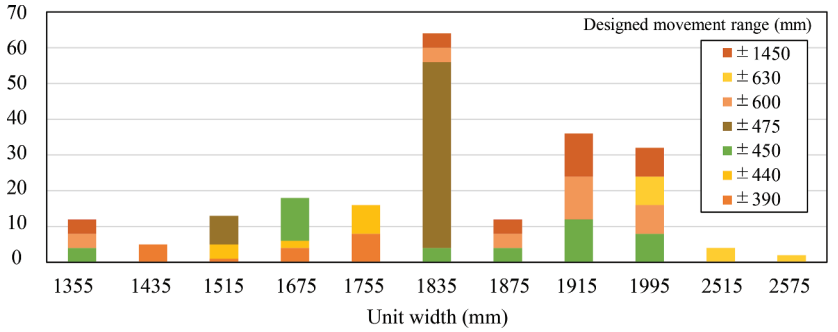


Figure 11. Variation of unit width and designed movement range (Link type expansion joint).

5 CONCLUSIONS

Link type expansion joints are applied to several long-span bridges in Honshu-Shikoku Bridges because of the compact structure and suitable structural type for large expansion movement. Although many minor damages were reported, maintenance of the link-type expansion joints is limited to small scale repairs or parts replacements. On the other hand, it is expected that large-scale repairs and renewal of the link type expansion joint will be more difficult due to its special characteristics, continuous maintenance, and technology inheritance. HSBE has started to discuss the standardization of the unit structure and the development of a maintenance policy for the long-term maintenance of the link type expansion joint.

Not only elastic devices, but also bridges with special structures require the establishment of a permanent maintenance system to prepare in advance for large-scale repairs and renewal associated with functional loss. It is necessary to consider long-term maintenance and management from the design stage when special structural members are applied.

HSBE will continue to undertake maintenance based on preventive maintenance in order to ensure that the long span bridge will be used over 200 years.

REFERENCES

Maruo S., Fujitani K. & Ishibashi K. 1995. Site Measurement on Link type Expansion Joint. *Honshi Technical Report* Vol.19 No.76: p27–35

Hayashi Y., Fujitani K. & Saeki N., 1996, Improvement on Link-type Expansion Joint, *Honshi Technical Report* Vol.20 No.79: p11–16

Bridge Maintenance, Safety, Management, Digitalization and Sustainability – Jensen, Frangopol & Schmidt (eds)
© 2024 The Author(s), ISBN 978-1-032-77040-6
Open Access: www.taylorfrancis.com, CC BY-NC-ND 4.0 license

Fatigue behavior of steel plates subjected to marine environment

A. Chang & Q.Q. Yu
Key Laboratory of Performance Evolution and Control for Engineering Structures of Ministry of Education, Tongji University, Shanghai, China
Department of Structural Engineering, Tongji University, Shanghai, China

ABSTRACT: Fatigue refers to a phenomenon in which stress of metallic structures at failure is significantly lower than the yield strength after long-term periodic loads. Corroded steel structures characterized by reduced nominal cross sections and complex surface morphology are prone to fatigue damage, and have attracted much attention in the community of civil engineering. This study presents a comprehensive study on the fatigue behavior of corroded steel plates. Specimens were first placed in a neutral salt spray environment and then loaded by fatigue. Effects of different placement angles on the morphology and fatigue behavior of the steel plates were investigated. A 3D laser scanner was adopted to obtain the corrosion morphology and later applied in the numerical simulation. A three-dimensional finite element model was proposed to calculate the stress concentration factor (SCF) and strain concentration factor (SNCF) of the specimen.

1 INTRODUCTION

Corrosion is one of major causes of structural durability problems. The annual disposal or replacement of materials due to steel corrosion consumes plenty of financial and material resources. In 2014, the cost of corrosion in China was at least 2127.8 billion RMB(~ 310 billion USD), accounting for 3.34% of GDP that year(Hou et al., 2017). Even if surfaces of the steel is protected by coating and other methods, occurrence of corrosion cannot be prevented after a certain period of time (Czarnecki and Nowak, 2008). The surface morphology of corroded steel can be divided into uniform corrosion and non-uniform corrosion. Uniform corrosion refers to reduction of steel cross-sectional areas, thereby reducing the nominal strength of steel and reducing the elongation capacity of steel (Garbatov et al., 2014). Non-uniform corrosion represented by pitting corrosion causes stress concentration on the steel surface and led to crack initiation and development at the bottom of the corrosion pit (Xu and Wang, 2015). Fatigue strength of carbon steel may degrade by as much as 50-90% when it suffers corrosion damage under its service environment (Kainuma et al., 2014).

Much work has been conducted on analysis of stress concentration on corroded steel surfaces. Kainuma et.al. evaluated the stress concentration factor (SCF) of the corrosion pits on steel plates placed in a natural environment by finite element analysis (FEA). It was found that maximum stress occurred at the maximum corroded depth on the corroded surface (Kainuma et al., 2014). Cerit et.al explored the relationship between the SCFs and corrosion pits with different aspect ratios. The SCF value increased linearly with increasing aspect ratio (Cerit et al., 2009). Zeng et.al. investigated the SCFs of stepwise corrosion pits. For different types of stepwise corrosion pits, the same corrosion pit parameter had completely different effects on the SCF (Zeng et al., 2022).

In the existing research, the stress concentration analysis of corroded surfaces was mainly based on numerical simulation, but no actual stress-strain measurement was carried out. In this paper, the finite element method was used to combine the morphology of the corroded

DOI: 10.1201/9781003483755-250

steel plate obtained by 3D laser scanning, and the numerical simulation analysis of the corroded steel plate was carried out. The strain field of corroded surface was gauged by DIC method during the fatigue test. Based on the numerical results of the surface strain distribution, the effect of the corroded surface on the SCF and SNCF was analyzed.

2 EXPERIMENT PROGRAMME

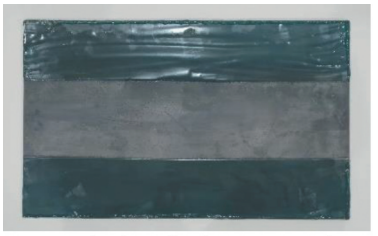
2.1 *Material and specimens*

The Q355b grade low-alloy steel was selected. The tested mechanical properties are given in Table 1. Three steel plates (500 mm×300 mm×6 mm) were exposed in the salt spray chamber, which were set in three angles to explore the effect of the salt spray angle, i.e., 0º, 45º, and 90º. Both ends of the plate were covered by using the epoxy resin to avoid corrosion of the clamping section (Figure 1a). The dog-bone specimens were cut from the rectangle plate by wire cutting. The dimension of steel dog-bone specimens were based on ISO 1099:2017 (ISO) (Figure 1b and Figure 1c). One specimen at each angle was cut for fatigue testing. They were set in spray chamber for 120 days, except for the 0º specimen, which was set for 240 days.

Table 1. Mechanical properties of Q355b steel.

f_y (MPa)	f_u (MPa)	δ (%)	E (10^5 MPa)
358.1	509.1	24.1	1.80

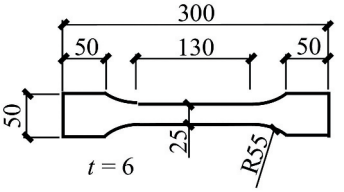
f_y - the yield strength, f_u - the ultimate strength, δ - the elongation ratio, E - the Young modulus.



(a) steel plate before corrosion



(b) dog-bone specimen for fatigue testing



(c) dimensions of the specimen for fatigue testing (unit in mm, not to scale)

Figure 1. Geometry and dimension of the test specimen.

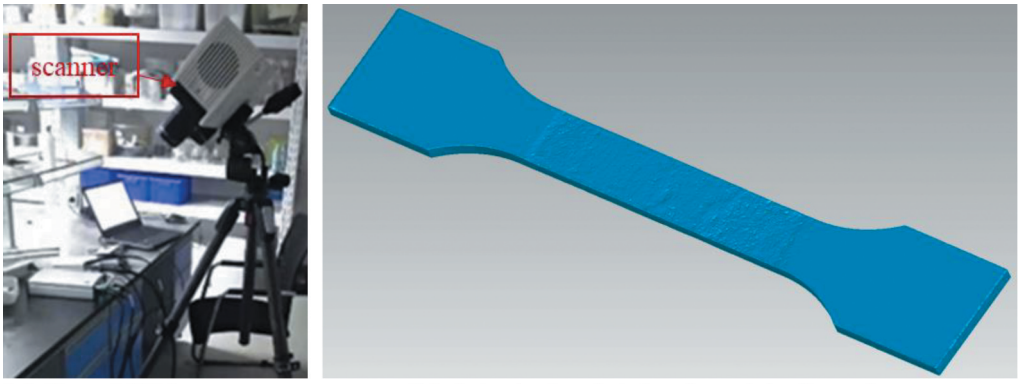
2.2 *Neutral salt spray accelerated corrosion test*

The salt spray tests were conducted according to ISO 9227:2006. The both sides of specimens were placed in a salt spray chamber fulfilled with salt fog generated by 5% weight NaCl and the temperature was 35 °C. Rust removal method was based on ISO 8407:2009(ISO). The

specimens after corrosion were first cleaned by a soft brush and then immersed into dilute hydrochloric acid solution for 20 minutes to scrub the tough rust. Next, they were rinsed with running water to remove the remains. Finally, they were dried with a dryer and weighed.

2.3 *Morphology scanning*

The specimens were scanned by Comet3D scanner with a minimum resolution of 20 μm to obtain the 3D surface morphology (Figure 2a). A typical point cloud model of specimen is illustrated in Figure 2b, which be used in finite element modeling.

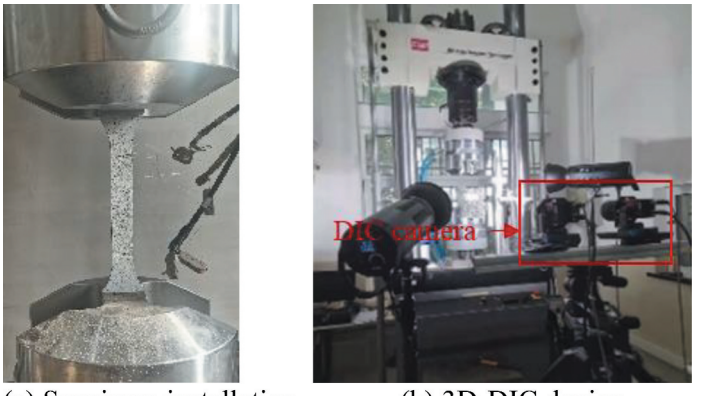


(a) Comet 3D laser scanner (b) A typical point cloud model of specimen

Figure 2. Morphology scanning.

2.4 *Test set-up*

The tests were performed on an MTS 322 servo hydraulic testing machine with a dynamic load capacity of 250 kN (Figure 3a). Cyclic tensile loads were applied to all the specimens with a frequency of 20 Hz and a stress ratio R (minimum load/maximum load) of 0.1 with the waveform being sinusoidal. The maximum in the spectrum was 250 MPa, which was about 50% ultimate strength of the material. The beach marking technique was adopted to record the crack propagation. Three-dimensional digital image correlation (3D-DIC) technology was used to measure the surface strain field (Figure 3b). Before the fatigue test was loaded, a monotonic tensile test was performed to allow DIC to measure the surface strain field of the specimen.



(a) Specimen installation (b) 3D-DIC device

Figure 3. Fatigue test set-up.

Table 3 presents a summary of the test program and results.

The mass loss ratio (η) is a common parameter to evaluate the corrosion degree in order to characterize the magnitude of mass loss in the corroded area. Because of the uncorroded area protected by epoxy resin, the value was corrected based on the ratio of the corrosion area to the total area, which was 2.5 in this study. The mass loss ratio η is calculated by Eq. (1).

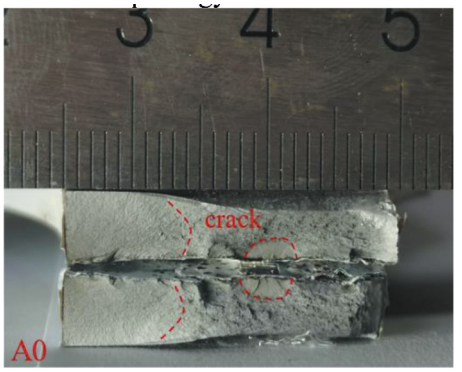
$$\eta = \frac{m_0 - m_1}{m_0} \times \alpha \tag{1}$$

where m_0 is initial mass of the specimen; m_1 is the mass of the specimen after corrosion, α is the ratio of the corrosion area to the total area.

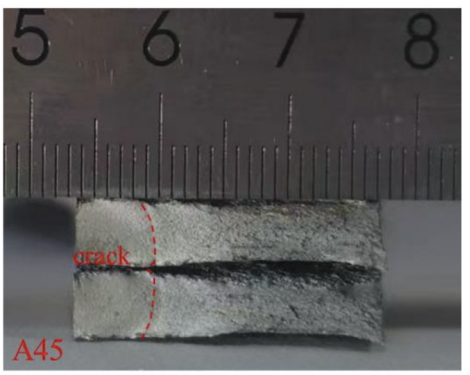
Table 2. Fatigue test results.

Specimens	Set angle	Corrosion time(days)	m_0 (g)	m_1 (g)	η	N
A0	0°	240	6647.0	6424.5	0.0825	582682
A45	45°	120	6671.0	6383.5	0.1075	417355
A90	90°	120	6664.5	6380.0	0.1050	229597

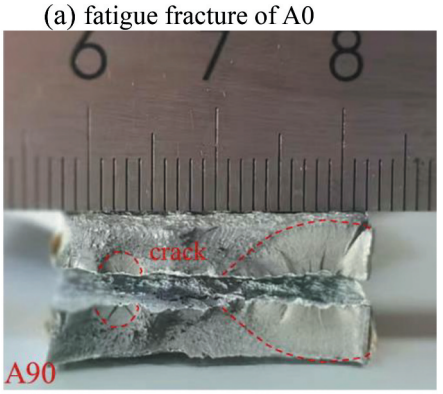
Cracks initiated at the corrosion pit on the surface of the specimen, and propagated simultaneously in both width and thickness directions. The crack front generally exhibited a semi-ellipse shape (Figure 4). At the late stage of crack development, the reduced cross-section



(a) fatigue fracture of A0



(b) fatigue fracture of A45



(c) fatigue fracture of A90

Figure 4. Fracture surface of specimens.

could not carry the maximum load applied in each cycle, and the specimen ruptured suddenly to produce the rough regions. In addition, multiple cracks were witnessed in Figures 4b and 4c due to the complex surface morphology.

With the strain field detected on the specimen surface before fatigue loading, stress concentration was observed, which was also in conformance with the location of fracture. The verification of fracture is described in 3.2.

With the increase of the η, the fatigue life of the samples dramatically decreased. It was also worth noting that, the specimens A45 and A90, with the approximate corrosion degree, were very different in fatigue life, which implied that corrosion morphology may have a greater effect on fatigue life.

3 FEM MODELING

3.1 *FEM model*

Three dimensional finite element models based on the configuration of tested steel plates were developed to simulate the experimental tests. The commercial software ABAQUS was employed. The steel plate were meshed using three-dimensional solid elements (C3D8R). The material properties refer to the material properties given in Table 1 for a elastoplastic constitutive model. one end of the model was fully fixed, the other was applied by a uniform tensile loading of 125 MPa, which was the maximum load in real fatigue test. A mesh size of 0.25 mm was selected for the corroded area (Cerit et al., 2009) and adaptive meshing was used to reduce the amount of elements (Figure 5b).

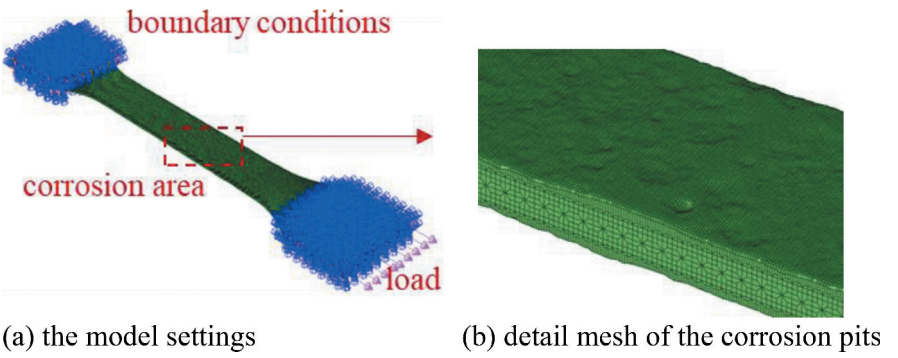


Figure 5. Typical FEM model of the corroded specimen.

3.2 *Strain field of numerical results*

The results of the three strain measurements or numerical method were shown in the Table 3. The finite element results and DIC results were shown in Figure 6.

Table 3. Strain comparison.

Gauges number	Position	DIC (με)	Strain gauges (με)	FEA (με)
0	Flat plate	1260	1095	1200
1	Corrosion pit	2071	1775	2746
2	Left side		1334	1454
3	Right side		1564	1667

The DIC measurement results were similar to the finite element strain distribution results. However, for corrosion pits, especially at the maximum strain, the measurement of the maximum strain may not be very accurate due to problems such as its resolution. The internal strain of the

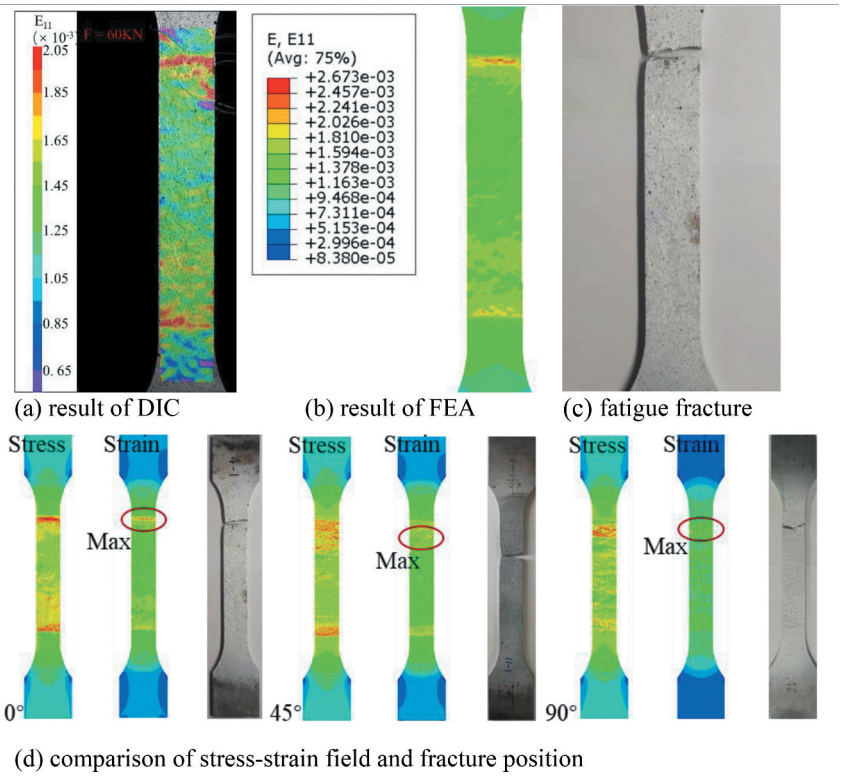


Figure 6. Strain field on the surface of the specimen.

corrosion pit often has a large abrupt change, and the DIC measurement had a high accuracy for the surrounding area of the corrosion pit. This inference can also be partially confirmed by the strain measurement near the corrosion pit in the strain gauge measurement, because it was actually more difficult to measure the strain at the bottom of the corrosion pit. At the same time, the reliability of the finite element calculation was verified by the strain gauges at each point, which had a error of about 10%. The SCF and SNCF on the surfaces of all the specimens were extracted according to Eqs. 2 and 3, respectively, and are performed in Figure 7.

$$K_\sigma = \frac{\sigma_{\max}}{\sigma_0} \tag{2}$$

where K_σ is SCF; $\sigma_{\max}$ is the maximum localized stress; σ_0 is the nominal stress of the specimen.

$$K_\varepsilon = \frac{\varepsilon_{\max}}{\varepsilon_0} \tag{3}$$

where K_ε is SCNF; $\varepsilon_{\max}$ is the maximum localized stress; ε_0 is the nominal stress of the specimen.

For different specimens, the variance of the SNCF was more obvious than that SCF (Figure), which may be caused by the higher maximum stress used in the fatigue test. At the same time, the SNCF seemed to have a higher explainability on the fatigue life of the specimen than the SCF. Due to the large stress, there are many areas on the surface of the specimen that enter the yield stage, but the areas with more significant strain concentration become the origin of the macroscopic cracks on the specimen. The SNCF of the specimen with the same corrosion rate was obviously different, which may be caused by the inconsistent surface morphology of the specimen under different placement angles.

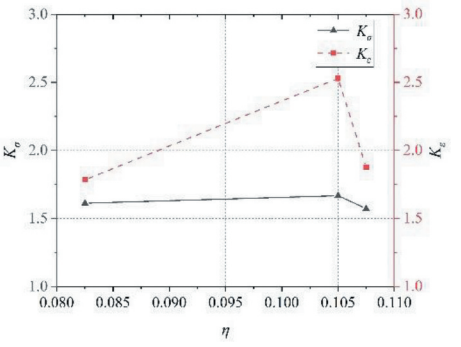


Figure 7. The SCF and SNCF of specimens.

4 CONCLUSIONS

In this study, steel plates were exposed to artificial salt fog spray and tested under fatigue. With the increase of the corrosion degree, the fatigue life significantly decreased. However, for the specimens with similar corrosion degree whereas different placement angle, the fatigue life differed much which may be due to the various specimen morphology. Finite element models were developed with the scanned surface characteristics and were validated in term of the surface stress distribution by using the experimental findings. The SCF and SNCF values of the samples were extracted and compared. It was found that the area where the strain is concentrated is more likely to be the basis for judging the origin of the crack.

ACKNOWLEDGMENTS

This study was financially supported by the proposal for Nation Natural Science Fund for Excellent Young Scientists Fund Program (Nos. 52222803).

REFERENCES

Cerit, M., Genel, K. & Eksi, S. 2009. Numerical investigation on stress concentration of corrosion pit. *Engineering Failure Analysis*, 16, 2467–2472.

Czarnecki, A. A. & Nowak, A. S. 2008. Time-Variant reliability profiles for steel girder bridges. *Structural Safety*, 30, 49–64.

Garbatov, Y., Guedes Soares, C., Parunov, J. & Kodvanj, J. 2014. Tensile strength assessment of corroded small scale specimens. *Corrosion Science*, 85, 296–303.

Hou, B., Li, X., Ma, X., Du, C., Zhang, D., Zheng, M., Xu, W., Lu, D. & Ma, F. 2017. The cost of corrosion in China. *npj Materials Degradation*, 1, 4.

ISO 8407: 2009. Corrosion of Metals And Alloys—Removal of Corrosion Products from Corrosion Test Specimens.

Kainuma, S., Jeong, Y.-S. & Ahn, J.-H. 2014. Investigation on the stress concentration effect at the corroded surface achieved by atmospheric exposure test. *Materials Science and Engineering: A*, 602, 89–97.

Xu, S.-H. & Wang, Y.-D. 2015. Estimating the effects of corrosion pits on the fatigue life of steel plate based on the 3D profile. *International Journal of Fatigue*, 72, 27–41.

Zeng, S., Ren, S., Gu, S., Gu, Y., Kong, C. & Zhou, Q. 2022. Effects of Size Parameters of Stepwise Corrosion Pit on Stress Concentration of Steel and Its Computation Model Establishment. *KSCE Journal of Civil Engineering*, 26, 2813–2825.

Bridge Maintenance, Safety, Management, Digitalization and Sustainability – Jensen, Frangopol & Schmidt (eds)
© 2024 The Author(s), ISBN 978-1-032-77040-6
Open Access: www.taylorfrancis.com, CC BY-NC-ND 4.0 license

Fatigue effect of welded gusset plate in steel-concrete composite bridge

S.L. Yan
CCCC First Highway Consultants Co.Ltd., Xi'an, China

S.Y. Jia
College of Aerospace and Civil Engineering, Harbin Engineering University, Harbin, China

S.W. Xu, J.N. Li & Y.Z. Wang
Yantai Research Institute, Harbin Engineering University, Yantai, China

ABSTRACT: Steel-concrete composite bridges are widely used because of their good structural properties but suffer from fatigue problems due to increasing vehicle loads and speeds. In order to investigate the fatigue response at welded gusset plates of steel-concrete composite bridges, finite element models of long-span steel-concrete composite bridges with three loading conditions and different gusset plate thickness are established, and the stress time history analysis is carried out. Finite element results show that the under the most unfavorable condition among the three conditions, the maximum stress occurs when the fatigue vehicle passes through the critical point. When the gusset plate thickness is 20 mm, the stress peaks for TC1, TC2 and TC3 conditions are 23.3 MPa, 27.4MPa and 14.8 MPa, respectively. Stress peak values decrease with an increase in thickness. Stress peaks for 12 mm, 16 mm and 20 mm thicknesses are 47.1 MPa, 37.3 MPa and 27.4 MPa, respectively.

1 INTRODUCTION

Steel-concrete composite bridge is a new type of bridge structure that connects concrete decks with steel beams through shear connectors, and it is widely applied in the construction of long-span bridges. Due to the increasing vehicle loads and speeds, the burden on bridge structures has escalated, leading to occurrences of bridge fracture and damage incidents. Therefore, it is important to carry out research on the fatigue performance of steel-concrete composite beams under vehicular loading (Hassanin et al., 2020).

In recent years, scholars from various countries performed research on the fatigue behavior of steel-concrete composite beams. Some scholars focused on the mechanical behavior of shear connectors. Shear connectors are commonly used in steel-concrete composite bridges to connect the concrete bridge deck and the top steel structure, providing a mechanism for shear transfer across the steel-concrete interface (Ovuoba & Prinz, 2016). Li et al. (2022) found that the presence of transverse shear significantly reduces the vertical shear strength and stiffness of bolted connections. Alsharari et al. (2022) also found that during the service life of a bridge, loading may cause bolt fractures near the end of the bridge, resulting in overall bridge failure.

Some scholars conducted research on the fatigue life asssesment of steel-concrete composite bridges. EI-Zohairy & Salim (2018) found that under the action of vehicular loads, the static strength of shear connectors in steel-concrete composite beams decreases with an increase in the number of loading cycles, resulting in a decrease in the load-carrying capacity of the beams. Matsuoka et al. (2019) discovered that European design standards set limits on the

DOI: 10.1201/9781003483755-251

acceleration of the bridge deck for high-speed railway bridges, but the influence of localized vibration of the bridge deck components is rarely considered when establishing the bridge vibration response model. Bhetuwal et al. (2021) conducted a detailed analysis on the fatigue life of a steel-concrete composite bridge under the influence of pavement conditions. The results showed that bridges with poor road conditions have a lower fatigue life compared to bridges with better road conditions. Many scholars have conducted in-depth research in the field of bridge fatigue. Some researchers have carried out fatigue tests on steel-concrete composite beam specimens to study the fatigue failure mechanisms and damage processes of composite beams under fatigue loading. Leitão et al. (2011) found that steel-concrete highway bridges experience dynamic actions of varying amplitudes due to vehicle traffic, leading to crack initiation and propagation in the structure. Martínez-Muñoz et al. (2020) investigated the degradation of stiffness in steel-concrete composite beams after being subjected to fatigue loading. The results indicated that the stiffness degradation is related to the macroscopic behavior of material fatigue damage and shear connection degradation.

Some scholars carried out research on the repair mrthods of steel-concrete composite bridges. Uy & Craine (2004) conducted a study on the strengthening of steel-concrete composite beams and found that the post-tensioning method improves the fatigue life of the components. Stylianidis & Petrou (2019) proposed a new analysis method to predict the moment-curvature relationship and overall flexural response of steel-concrete beams reinforced with FRP.

In summary, existing research on the fatigue response analysis of welded gusset plates in steel-concrete composite bridges is relatively insufficient. In this study, finite element analysis are carried out of models of a 400-meter span steel-concrete composite bridge, to identify the most unfavorable conditions for the fatigue details of welded gusset plates, considering the effect of gusset plate thickness. The finite element analysis results has guiding significance for fatigue design of welded gusset plates in steel-concrete composite bridges.

2 MODEL INTRODUCTION

2.1 *Model description*

A four-span (100 m + 100 m + 100 m + 100 m) continuous steel-concrete composite beam is selected for analysis. The main beam cross-section is a box-shaped composite section, consisting of a concrete bridge deck and a ribbed steel main beam, as shown in Figure 1. The concrete bridge deck has a width of 16.5 m and a thickness of 280 mm, designed for a one-way three-lane traffic layout. The steel beam has a height of 4.5 m, with a top plate thickness near the mid-support point of 65 mm and 50 mm elsewhere. The slopes of inner and outer webs are 1:3.1 and 1:2.9, respectively. The web thickness near the mid-support point is 28 mm, while elsewhere it is 24 mm. Four longitudinal stiffening ribs are arranged according to the compression area of the webs, of which the size is 280 mm × 26 mm. The bottom plate has a width of 6.6 m, with a thickness near the mid-support point of 24 mm and 20 mm elsewhere. Longitudinal stiffening ribs for the bottom plate are plate-type stiffeners measuring 260 mm × 24 mm, spaced at intervals of 650 mm.

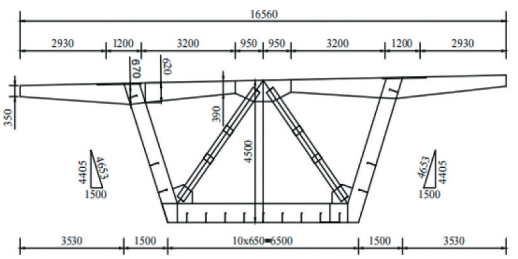


Figure 1. Cross-sectional diagram.

2.2 *Finite element model*

2.2.1 *Model establishment*

Figure 2 Illustrates the finite element model of the continuous steel-concrete composite beam bridge Employing solid elements for the bridge deck and shell elements for all steel members. The bridge deck was designed with three lanes corresponding to three different conditions (TC1, TC2 and TC3 from right to left). The connection between the bridge deck and the steel main beams was achieved using binding constraints.

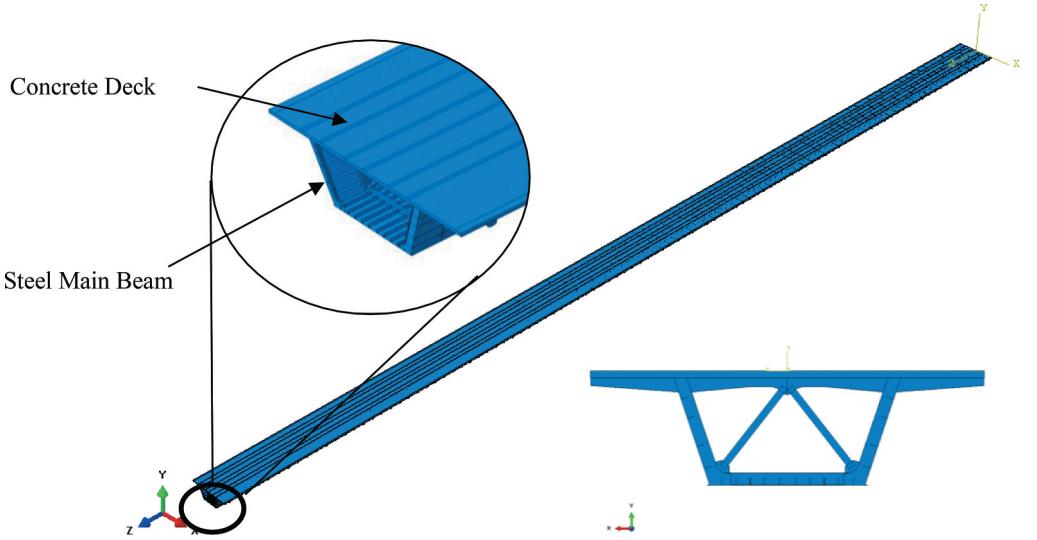


Figure 2. Finite element model.

The model was meshed using two different sizes. A Mesh of 0.2 m is applied to the entire bridge structure, while finer mesh of 0.04 m is applied specifically to the welded gusset plate at the critical region. Figure 3 shows the detailed mesh of the critical region.

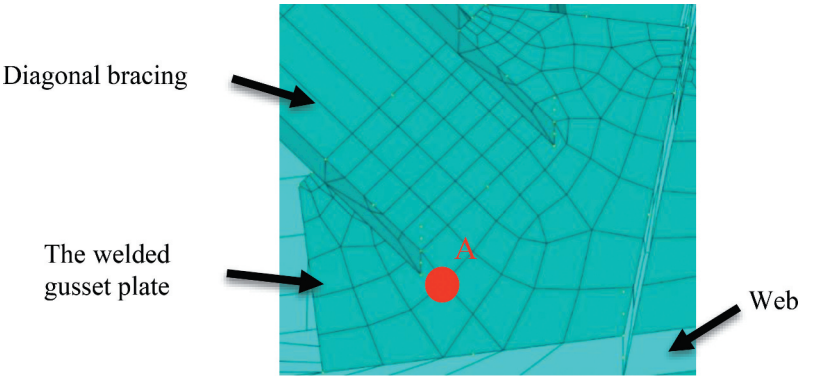


Figure 3. Mesh division at welded gusset plate.

2.2.2 *Material parameters*

The concrete bridge deck in the model is created using solid elements with C50 concrete material. The steel main beams are modeled using shell elements and constructed with Q345 steel material. The material parameters are shown in Table 1.

Table 1. Material parameters

Material	Density (kg/m³)	Young's Modulus (MPa)	Poisson's Ratio
C50	2500	3.25×10^4	0.2
Q345	7850	2.06×10^5	0.3

2.2.3 *Boundary conditions*

To ensure coordination of bridge displacement and deformation, the rotational constraints and translational constraints in the X and Z directions are released at the support point between the second and third spans of the bridge to simulate unidirectional (Y direction) movable bearings (BC-1). As for other support points, the rotational constraints and translational constraints in the X direction are released to simulate bi-directional (Z and Y directions) movable bearings (BC-2). Table 2 and Figure 4 show the layout of the bearings for the bridge.

Table 2. Boundary conditions.

Type*	U1	U2	U3	UR1	UR2	UR3
BC-1	Free	Fix	Free	Free	Free	Free
BC-2	Free	Fix	Fix	Free	Free	Free

*U1, U2, U3 are translations constraints in the X, Y, Z directions. UR1, UR2, UR3 are rotations about X, Y, Z directions.

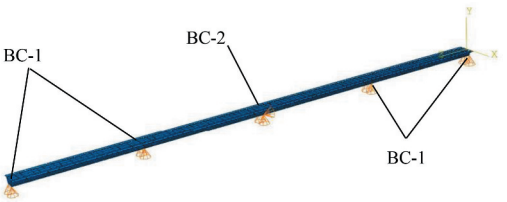


Figure 4. Bearing layout diagram.

2.3 *Load parameters*

Both permanent loads and variable loads are considered in the finite element analysis. Permanent loads can be divided into two stages. The first-stage permanent load is calculated based on the actual design drawings of the concrete and steel structures, considering their respective self-weights after adjusting for the corresponding component densities. The second-stage permanent load considers the bridge deck pavement, assumed to be 100 mm thick asphalt concrete, with a load intensity of 37.2 kN/m.

The fatigue vehicle model of Class II highways in General Specification for Design of Highway Bridges and Culverts (JTG D60) is adopted as variable loads. The fatigue load model for a single vehicle is illustrated in Figure 5. The standard values for the front axle load, middle axle load and rear axle load are 30 kN, 120 kN and 140 kN, respectively. These axle loads are distributed across two wheels, with a wheelbase of 1.8 m. The vehicle's moving speed is 10 m per second.

In order to achieve mobile loading in the software platform and obtain more accurate stress responses at fatigue details, concentrated loads are converted into equivalent distributed loads. Assuming the contact area of each front wheel with the ground is 0.2 m × 0.3 m and the contact area of each middle and rear wheel is 0.2 m × 0.6 m. The conversion results are shown in Table 3.

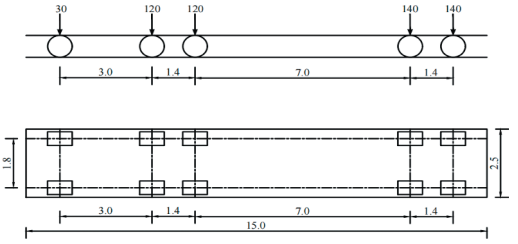


Figure 5. Single vehicle model for fatigue load.

Table 3. Equivalent distributed load parameters.

Axle Number	Axle Load(kN)	Wheel Load Area (m^2)	Equivalent Distributed Load(Pa)
1	30	0.06	250000
2	120	0.12	500000
3	120	0.12	500000
4	140	0.12	580000
5	140	0.12	580000

3 STRESS ANALYSIS

The gusset plate adjacent to the fourth span support (near the rightmost lane) was selected for stress analysis. For investigating stress responses at fatigue detail locations during the passage of vehicles, a stress focus point labeled as 'A' was placed at the typical fatigue crack initiation position of the gusset plate, as depicted in Figure 3.

3.1 *Stress-time history analysis*

Stress responses at the stress focus point are extracted as vehicles traverse the entire bridge under different conditions TC1, TC2 and TC3, corresponding to the three lanes (TC1 for the rightmost lane, TC2 for the middle lane, and TC3 for the leftmost lane). The stress-time history curves obtained for each lane are depicted in Figure 6.

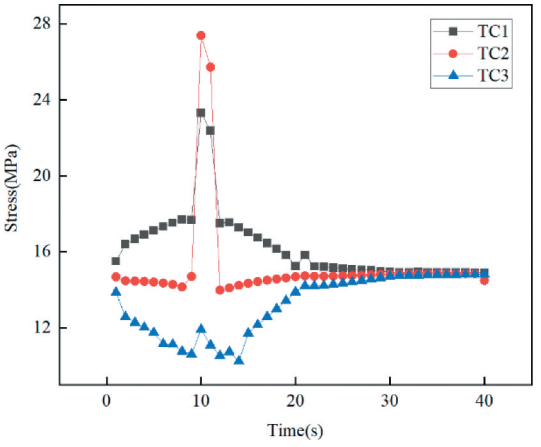
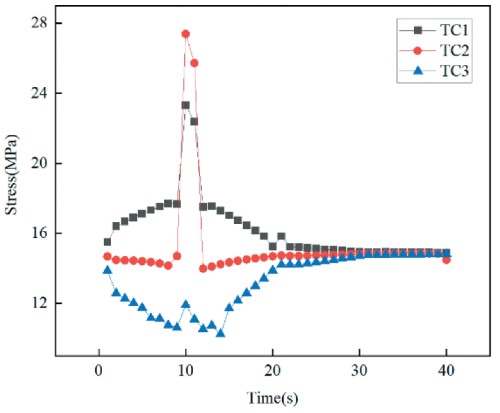
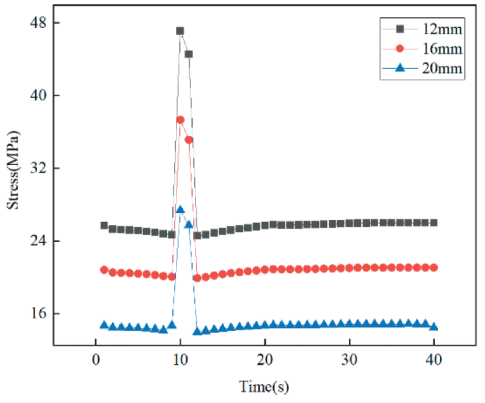


Figure 6. Stress-time history curves.

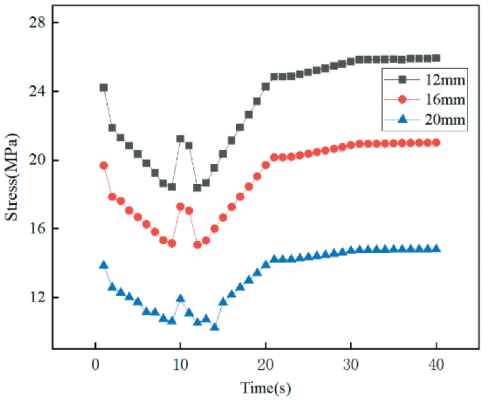
Based on the stress-time history curves, it is evident that when the fatigue vehicle travels in the middle lane (TC2 condition), the stress at the fatigue detail experiences higher levels.



(a) Stress-time history curves for different thicknesses under TC1 condition.



(b) Stress-time history curves for different thicknesses under TC2 condition.



(c) Stress-time history curves for different thicknesses under TC3 condition.

Figure 7. Stress-time history curves for different thicknesses under three conditions.

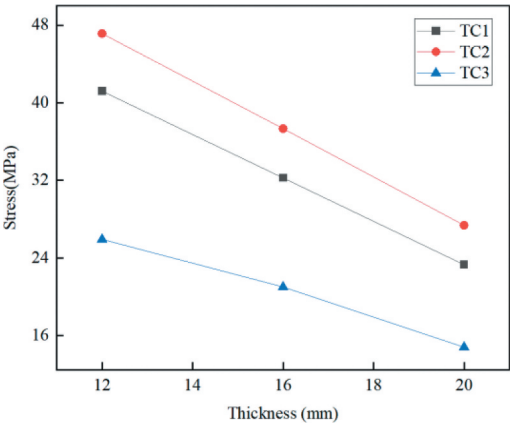


Figure 8. Stress peak curves for different thicknesses.

Conversely, when the fatigue vehicle operates on lanes further from the detail (TC1 and TC3 conditions), the stress at the fatigue detail remains lower. For TC1 and TC2 conditions, notable stress peaks are observed as the fatigue vehicle passes over the detail along the 'longitudinal direction. In TC3 condition, the maximum stress is witnessed as the fatigue vehicle departs from the bridge. The maximum stress peak at the fatigue detail for TC2 condition reaches 27.4 MPa, for TC1 condition it reaches 23.3 MPa, and for TC3 condition it reaches 11.9 MPa. Due to the influence of gravity, the stress levels tend to converge as the vehicle completes its passage.

In condition TC2, the stress peak at the focus point of the fatigue detail notably exceeds that under TC1 and TC3 conditions. When vehicle travels along the middle lane, it exerts the most substantial impact on the gusset plate, resulting in the highest stress.

3.2 *Analysis of the gusset plate thickness influence*

To consider the effect of varying gusset plate thickness on the stress response of fatigue details, finite element models with gusset plate thickness of 12 mm, 16 mm, and 20 mm are established. During the modeling process, while altering the gusset plate thickness in the same span bridge, other component dimensions remained constant. The stress-time history curves for different thicknesses under various conditions are depicted in Figure 7.

Figure 7 demonstrates stress peak values under various thicknesses and conditions. Under TC1 condition, the stress peaks at 41.2 MPa for 12mm thickness, 32.3 MPa for 16mm thickness, and 23.3 MPa for 20 mm thickness. For TC2 condition, the stress peaks at 47.1 MPa for 12 mm thickness, 37.3 MPa for 16 mm, and 27.4 MPa for 20mm. In TC3 condition, the stress peaks at 25.9 MPa for 12 mm, 21.0 MPa for 16mm, and 14.8 MPa for 20 mm thicknesses.

The stress peak curves for different thicknesses under various conditions are illustrated in Figure 8. Figure 8 illustrates that as the gusset plate thickness increases, the stress peak at the focal point decreases. The effect is uniform across different conditions, showing that thicker gusset plates result in lower stress at welding details. The stress peak values are maximum when the gusset plate thickness is 12 mm across all three conditions. Among these, the stress peak is highest under TC2 condition, reaching 47.1 MPa.

4 CONCLUSIONS

This paper established finite element models of a steel-concrete composite bridge and conducted finite element analysis to determine the unfavorable position and reveal the effect of gusset plate thickness on stress response. Based on the finite element analysis results, the following conclusions can be drawn:

(1) TC2 condition is the most unfavorable condition among the three conditions, under which the maximum stress occurs when the fatigue vehicle passes through the critical point.
(2) When the gusset plate thickness is 20 mm, the stress peaks for TC1, TC2 and TC3 conditions are 23.3 MPa, 27.4 MPa and14.8 MPa, respectively.
(3) Stress peak values decrease with an increase in thickness. Specifically, under TC2 condition, when the thickness is 12 mm, the maximum stress peak is 47.1 MPa. At 16 mm and 20 mm thicknesses, the stress peaks are 37.3 MPa and 27.4 MPa, respectively.

ACKNOWLEDGEMENT

The authors gratefully acknowledge the financial support provided by National Natural Science Foundation of China (Grant 52308160).

REFERENCES

Alsharari, F., Alaa, E.E., Mutnbak, M. & Salim, H. 2022. Effect of the progressive failure of shear connectors on the behavior of steel-reinforced concrete composite girders. *Buildings* 12: 596–804.

Bhetuwal, U., Shrestha, J.K. & Pradhananga, R. 2021. Fatigue life analysis of steel–concrete composite bridge considering road surface conditions. *Innovative Infrastructure Solutions* 7: 124–137.

EI-Zohairy, A. & Salim, H. 2018. Behavior of steel-concrete composite beams under fatigue loads 7. *Conference Proceedings of the Society for Experimental Mechanics Series* 7: 99–109.

Hassanin, A.I., Shabaan, H.F. & Elsheikh, A.I. 2020. The effects of shear stud distribution on the fatigue behavior of steel–concrete composite beams. *Arabian Journal for Science and Engineering* 45: 8403–8426.

Leitão, F.N., Silva, J.G.S., Vellasco, P.C.G.S., Andrade, S.A.L. & Lima, L.R.O. 2011. Composite (steel–concrete) highway bridge fatigue assessment. *Journal of Constructional Steel Research* 67: 14–24.

Li, J.H., Liu, Z.C., Deng, J. & Chen, F.Y. 2022. Bidirectional shear behavior of stud connectors in steel-concrete composite monorail track beams. *Structural Concrete* 24: 2951–2964.

Martínez-Muñoz, D., Martí, J.V. & Yepes, V. 2020. Steel-concrete composite bridges: design, life cycle assessment, maintenance, and decision-making. *Advances in Civil Engineering* 2020: 8823370.

Matsuoka, K., Collina, A., Somaschini, C. & Sogabe, M. 2019. Influence of local deck vibrations on the evaluation of the maximum acceleration of a steel-concrete composite bridge for a high-speed railway. *Engineering Structures* 200: 109736.

Ovuoba, B. & Prinz, G.S. 2016. Fatigue capacity of headed shear studs in composite bridge girders. *Journal of Bridge Engineering* 21(12): 04016094.

Stylianidis, P.M. & Petrou, M.F. 2019. Study of the flexural behaviour of FRP-strengthened steel-concrete composite beams. *Structures* 22: 124–138.

Uy, B. & Craine, S. 2004. Static flexural behaviour of externally post-tensioned steel-concrete composite beams. *Advances in Structural Engineering* 7(1): 1–20.

Bridge Maintenance, Safety, Management, Digitalization and Sustainability – Jensen, Frangopol & Schmidt (eds)
© 2024 The Author(s), ISBN 978-1-032-77040-6
Open Access: www.taylorfrancis.com, CC BY-NC-ND 4.0 license

Evaluation of fatigue environment in welded parts of orthotropic steel deck

K. Yoshida & H. Sekiya
Department of Urban and Civil Engineering, Tokyo City University, Tokyo, Japan

ABSTRACT: Orthotropic steel deck is made by welding together thin steel plates and have excellent workability. However, many fatigue damages have been reported due to local deformation caused by passing vehicles. To implement appropriate maintenance management against this fatigue damage, it is important to analyze the strain response near the welded parts in the orthotropic steel deck. In this study, field measurements were conducted on in-service orthotropic steel deck bridges using a load truck. Triaxial strain gauges were used to measure the strain response near the welded parts in the orthotropic steel deck. Based on the measurement data obtained while the load car was running, the strain response, the magnitude and direction of the principal strain at different fatigue crack-prone locations were compared and discussed.

1 INTRODUCTION

Orthotropic steel decks have been used in many urban expressways and long-span bridges because they are lightweight and can be constructed in a short time. Orthotropic steel decks are composed of a deck plate with a thickness of about 12 mm and thin steel materials such as transverse and longitudinal ribs, which are welded together. The direct loading from the wheel load of the car causes the orthotropic steel deck structure to behave in a complex manner, resulting in locally high stress at the intersection of the members, which is thought to lead to fatigue damage. In recent years, fatigue cracks have been reported in the welds between deck plate and U-ribs under heavy traffic and an increasing percentage of heavy vehicles. Although these cracks do not lead to immediate bridge failure when they occur, if left unchecked, they can propagate and lead to pavement damage, lack of road surface flatness, and other roadway deterioration. (Japan road association, 1997).

To implement appropriate maintenance management against such fatigue damage, it is important to analyze the strain response near the welded parts in the orthotropic steel deck. In this study, measurement tests using a load truck were conducted on an in-service bridge to analyze the strain response near the welds between the deck plate and the U-ribs.

2 TARGET BRIDGE AND MEASUREMENT OVERVIEW

2.1 *Target bridge*

The target bridge in this study is a three-span continuous orthotropic steel deck box girder bridge with a total length of 166.2 m and span lengths of 51.7 m, 62.0 m, and 51.7 m, respectively. It is 15.95 m wide and consists of a first traffic lane, a second traffic lane, a ramp for entering and exiting the parking area, and road shoulders. The main dimensions of the target bridge are asphalt pavement thickness of 80 mm, deck plate thickness of 12 mm, and U-ribs with a height of 240 mm, width of 320 mm, and plate thickness of 6 mm. Figure 1 shows a cross-sectional view of the box girder to be measured and the loading position of the tires.

DOI: 10.1201/9781003483755-252

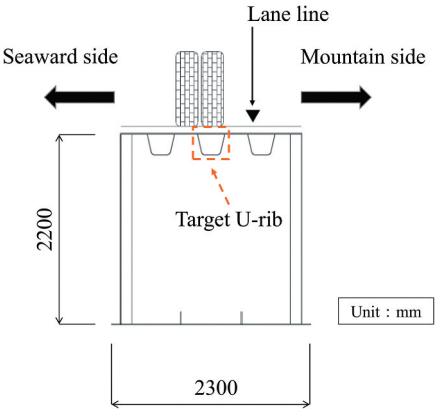


Figure 1. Cross-sectional view of the measurement location and tire position.

2.2 *Measurement method*

Measurements were taken at a section with a span length of 51.7 m, directly under the second traffic lane, in the general section of the box girder where there were no crossings of transverse ribs or other members. Figure 2 shows the geometry of the U-ribs and the position of the strain gauges attached to them. Triaxial strain gauges were used for measurement, and were attached to the deck plate and the U-rib at a distance of 10 mm from the weld end between the deck plate and the U-rib on both the seaward and the mountain sides (four positions). The sampling frequency of the strain gage is 500 Hz. Figure 3 shows the test vehicle used for the test. Ordinary trucks were used for the measurements. The test vehicle is four-axle vehicle with a total weight of 243.7kN. The front axle weight, the front rear axle weight, the rear front axle weight, and the rear rear axle weight are 46.9kN, 46.6kN, 74.6kN, and 75.6kN, respectively. Test vehicle traveling were also made six times. No lane closures were made during the measurement, which was conducted late at night when traffic volume was low. The load vehicle was driven at a speed of approximately 50 km/h.

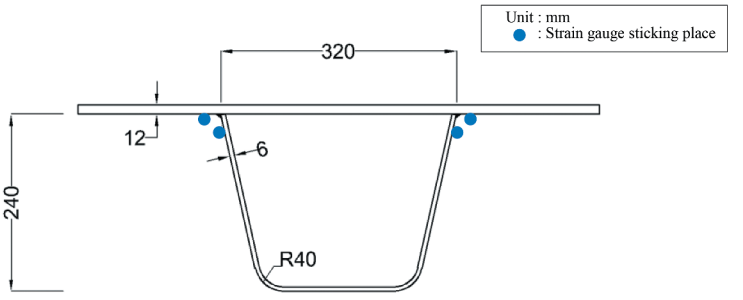


Figure 2. U-rib cross section and strain gauge sticking position.

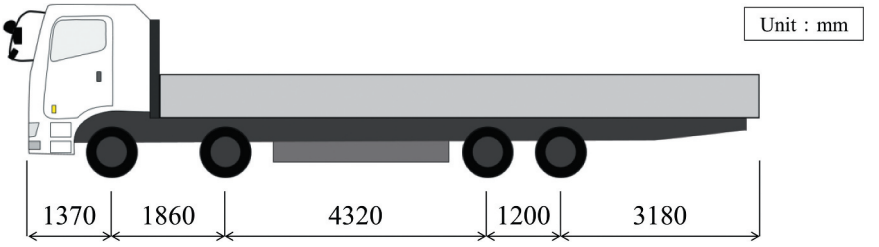


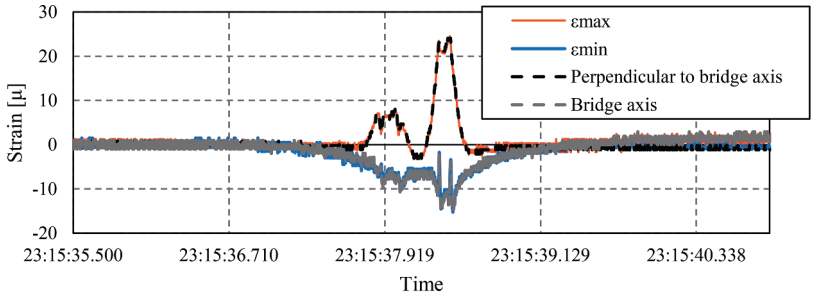
Figure 3. Test vehicle.

3 MEASUREMENT RESULTS

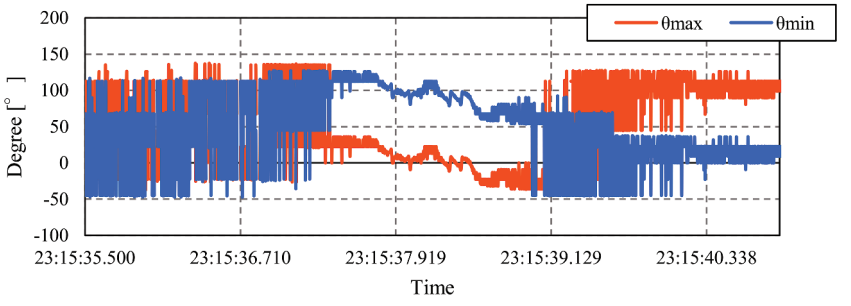
3.1 *Strain response of the deck plate on the seaward side*

Figure 4 shows the maximum and minimum principal strains calculated from the data obtained from the triaxial strain gauges attached to the deck plate on the seaward side, and the responses in the bridge axis direction and perpendicular to the bridge axis direction. The sharp responses in the minimum principal strain and in the direction of the bridge axis can be observed in four locations. This is thought to be due to the fact that the number of axles of the load car used in the test was four.

The peak values of the maximum and minimum principal strains at the time of vehicle passage were +24.5 μ for the maximum principal strain and -15.5 μ for the minimum principal strain, with the absolute value being greater for the maximum principal strain. It can be confirmed that the maximum and minimum principal strain responses are generally consistent with the responses in the direction perpendicular to the bridge axis and in the direction of the bridge axis, respectively. The maximum principal strain showed no response until the axles approached, and the response began to appear approximately 0.1 second before the first axle and changed to near 0 immediately after the axles passed, while the minimum principal strain began to gradually appear approximately 0.7 seconds before the axles passed and slowly changed to 0 after the axles passed. From this, it can be inferred that the influence line length is short in the direction perpendicular to the bridge axis and long in the direction of the bridge axis. With respect to the points where the strain response peaks at the passage of the load car, the maximum principal strain shows the largest response at the timing of the passage of the fourth axis, and the minimum principal strain also shows the smallest response at the time of the passage of the fourth axis. Figure 4(b) shows the respective angles of maximum and minimum principal strains on the seaward side of the deck plate shown in Figure 4(a). The angles



(a) Uniaxial strain response and principal strain response



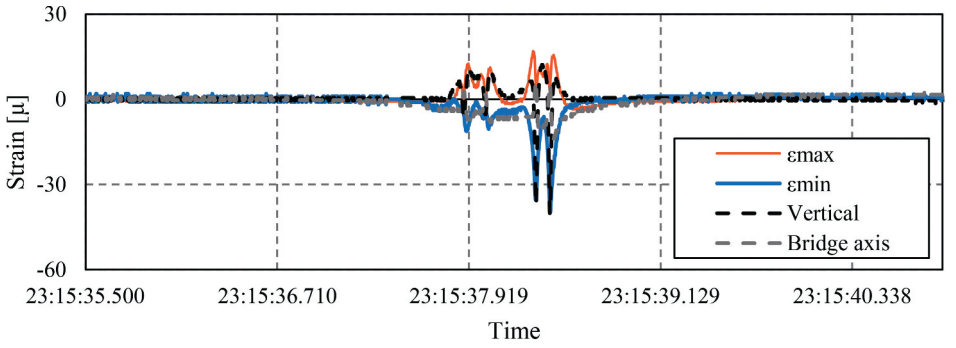
(b) Principal strain angle

Figurer 4. Measurement results of the deck plate on the seaward side.

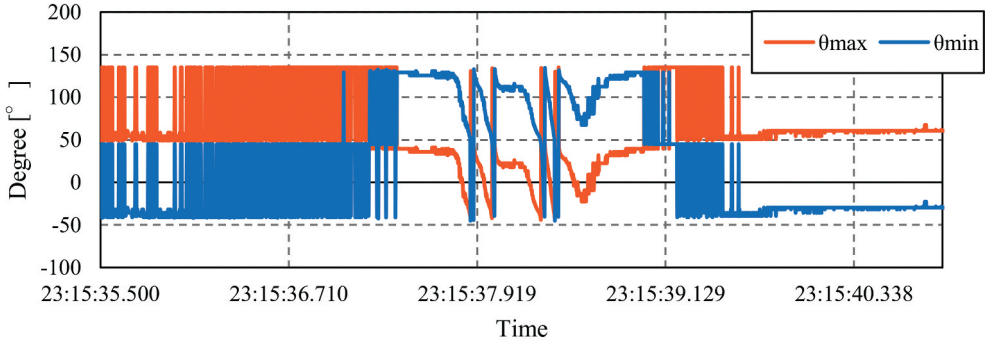
of principal strain at the deck plate are +0° and +180° in the direction perpendicular to the bridge axis and +90° and +270° in the direction along the bridge axis. Figurr 4(b) shows that the direction of the principal strain changes by about 50° before and after the passing of the load vehicle.

3.1.1 *Measurement results of U-rib on seaward side*

Figure 5 shows the maximum and minimum principal strains calculated from the data obtained from the triaxial strain gauges attached to the seaward side of the U-rib, as well as the vertical and axial responses of the bridge. Four sharp responses can be confirmed in Figure 5(a). It is thought that they are due to four axles of test truck. The maximum and minimum principal strain responses were generally consistent with the responses of the third and fourth axes in the vertical direction, but the results were inconsistent for other locations. The response in the bridge axial direction resulted in different strain values for both the maximum and minimum principal strains. The peak values of the maximum and minimum principal strains at the time of vehicle passage were +17.0 μ for the maximum principal strain and -40.0 μ for the minimum principal strain, with the absolute value being larger for the minimum principal strain. Figure 5(b) shows the respective angles of maximum and minimum principal strains of the seaward U-rib shown in Figure 5(a). The angles of principal strain at the U-ribs are +0° and +180° in the vertical direction and +90° and +270° in the bridge axis direction. Figure 5(b) shows that the angle of principal strain changes abruptly by a little less than +180° each time an axle passes through each axis.



(a) Uniaxial strain response and principal strain response

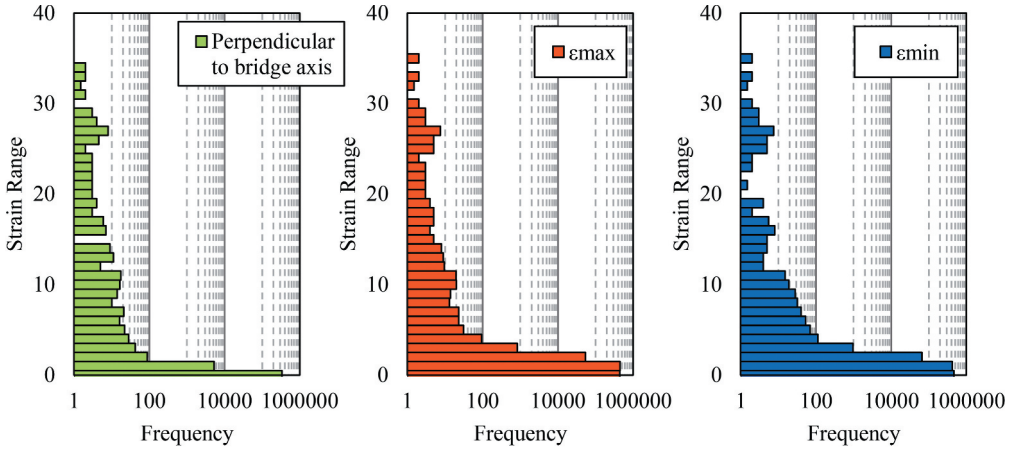


(b) Principal strain angle

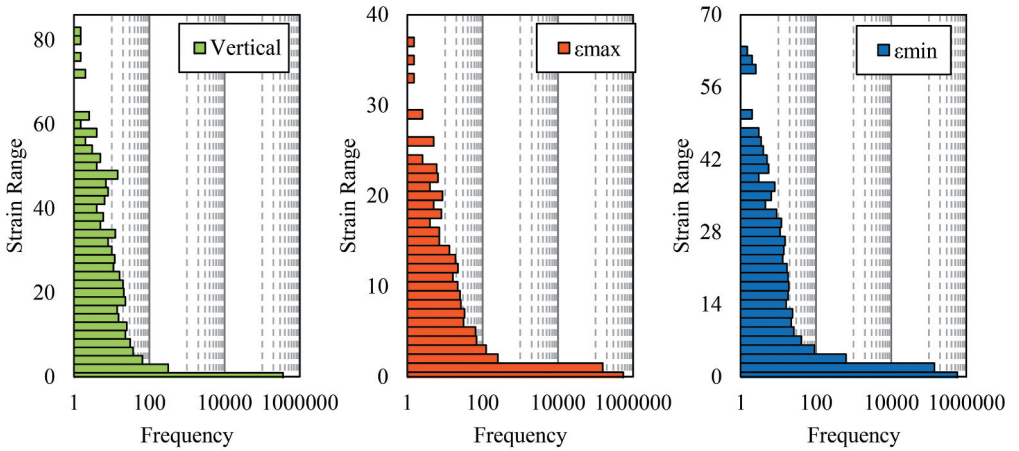
Figure 5. Measurement results of the U-ribs on the seaward side.

3.2 *Rain flow analysis*

Rainflow analysis was performed based on triaxial strain data from less than two hours of measurement testing. In this study, we utilized the Rainflow analysis to focus on the amplitude of strain response on the orthotropic steel deck. The analytical results for the deck plate on the seaward side in the direction perpendicular to the bridge axis, maximum principal strain and minimum principal strain are shown in Figure 6(a), and for the U-rib on the seaward side in the vertical direction, maximum principal strain and minimum principal strain are shown in Figure 6(b). From Figure 6(a), it can be confirmed that the maximum strain range in the direction perpendicular to the bridge axis and the maximum principal strain and minimum principal strain on the seaward side of the deck plate are generally the same. In the deck plate, the direction of the principal strain changes little, so it can be inferred that the results are identical to those obtained in the direction perpendicular to the bridge axis.



(a) Deck plate on the seaward side



(b) U-ribs on the seaward side

Figure 6. Rainflow analysis results.

Figure 6(b) shows that the maximum strain range for the seaward U-rib was 82 μ for the vertical direction, 35 μ for the maximum principal strain, and 63 μ for the minimum principal strain, with the vertical direction having the largest maximum strain range. Unlike the deck plate case described above, the U-ribs show an abrupt change in the angle of principal strain, which may account for the difference in the maximum strain range.

3.3 *Fatigue damage degree*

The fatigue damage degree was calculated using Equation (1) based on the results of the rainflow analysis calculated in 3.2.

$$D = \sum \left(\Delta\sigma_i{}^3 \times N_i\right) \tag{1}$$

D: fatigue damage degree, $\Delta\sigma_i$: strain range, N_i: frequency of $\Delta\sigma_i$. Based on the fatigue damage level, it is possible to evaluate the fatigue environment for active loading. Figure 7 shows the calculated fatigue damage values for the deck plate on the seaward side in the direction perpendicular to the bridge axis, maximum principal strain, and minimum principal strain, and for the U-rib on the seaward side in the vertical direction, maximum principal strain, and minimum principal strain. For the single axis in Figure 7, the results are shown in the direction perpendicular to the bridge axis for the deck plate and in the vertical direction for the U-ribs. Figure 7 shows that the highest fatigue damage degree of maximum principal strain response was obtained for the deck plate, and the highest vertical response was obtained for the U-ribs. Comparisons between the deck plate and U-rib sections showed that the fatigue damage levels differed significantly, with the U-rib vertical values approximately 3.6 times greater than the maximum principal strain of the deck plate.

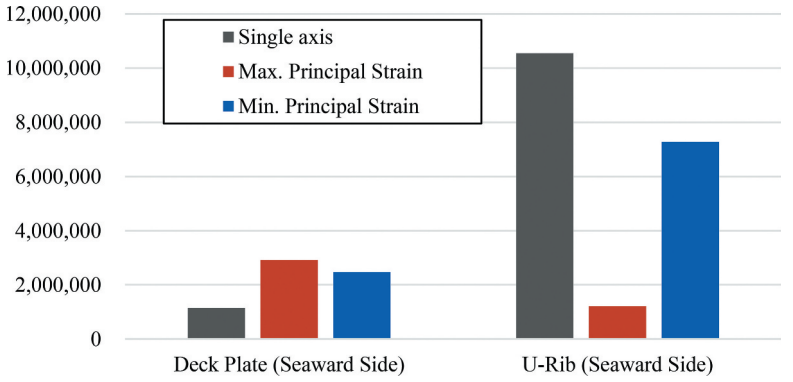


Figure 7. Fatigue damage degree calculation results.

4 CONCLUSIONS AND FUTURE STUDIES

Strain gauges attached to the orthotropic steel deck plate and U-ribs of the steel slab were analyzed for strain response during vehicle passage. The results are shown below.

1. The direction of the maximum principal strain in the deck plate was almost constant under test vehicle traveling.

2. The main strain direction of the U-ribs was not fixed in one direction and changed abruptly.
3. The strain ranges of the deck plates and the U-ribs were significantly different during vehicle passage, with the U-ribs having the largest strain range.
4. In the fatigue damage degree, the result based on the principal strain was not necessarily larger, and the fatigue damage degree of uniaxial was sometimes larger.

In the future, strain measurements will be conducted on slabs with Steel Fiber Reinforced Concrete (SFRC) pavement to verify the effect of strain reduction before and after SFRC pavement.

ACKNOWLEDGMENTS

The field measurements were supported by Metropolitan Expressway Co. Ltd.

REFERENCES

Japan road association (1997) Bridge Fatigue, pp.183.

Hayama, Mizuki. & Sekiya, Hidehiko. (2020) Visualization of Deformation of Trough Rib of Orthotropic Steel Deck Under Live Load Using MEMS IMUs and Contact Displacement Gauges, Journal of Bridge Engineering, Volume 25 Issue 10.

Tokida, Hideo., Yoshikawa, Tadashi. & Mori, Takeshi, (2020), Current Traffic Loads of Metropolitan Expressway Considering The Effect on Fatigue of Steel Bridges, Japanese Journal of JSCE, Vol.76, No.1, 139–151.

Bridge Maintenance, Safety, Management, Digitalization and Sustainability – Jensen, Frangopol & Schmidt (eds)
© 2024 The Author(s), ISBN 978-1-032-77040-6
Open Access: www.taylorfrancis.com, CC BY-NC-ND 4.0 license

A study of the effect of skew angle on natural frequencies of bridge girders

M. Satomi, R. Handa, Y. Sugimoto & H. Onishi
Iwate University, Morioka, Japan

ABSTRACT: Vibration test is one of the quantitative inspection methods, but it is expected that the plane geometry of bridges will affect the results of vibration test. In skewed bridges, there are several cases of bearings failing due to girder rotation during earthquakes, and the skew angle may affect the dynamic behavior of the bridge. The authors created bridge specimens to investigate the effect of skew angle on the vibration characteristics of bridges. The skew angle was varied from 60° to 90° in 10° increments to investigate how the natural frequency changes. In addition, the authors performed the FEM analysis to complement the experimental results. Experimental and analytical results show that the primary natural frequencies increase due to the skew angle. And factors such as bearing conditions were also affect the vibration characteristics.

1 INTRODUCTION

In Japan, many of the bridges in service today were built after the high economic growth period, and more than 50% of bridges will be in service for 50 years in 10 years' time. Many of these bridges are managed by local governments, which have small budgets for maintenance and management. In addition, there are some problems such as a shortage of civil engineers engaged in bridge inspections and a decrease in maintenance budgets in local governments (MLIT, 2023). To solve these problems, more simplified inspection and quantitative inspection methods for bridges is required. One of the simple and quantitative inspection methods for bridges is vibration tests. Vibration tests can determine the health of bridges by calculating vibration characteristics such as the natural frequencies of bridges, and many studies have been conducted on bridge damage detections (Chiba et al. 2022, Furukawa et al. 2005, Mimasu et al. 2018). However, further research is needed on the factors that affect natural frequencies. In addition, bridge monitoring systems using FE models and vibration measurements have been studied (Ntotsios et al. 2008, Whelan et al. 2009). Vibration measurements can be performed remotely in real time and are one of the simplified inspections. Therefore, we need to understand the vibration characteristics of each bridge type. We expected that the plane geometry of bridges effects on its vibration characteristics (Watanabe et al. 2014). It is well known that the reaction force becomes non-uniform and torsion occurs in a skewed bridge. Several cases of bearing damage due to girder rotation during earthquakes have been reported, and skew angle is expected to affect the dynamic behavior of bridges (Fujiwara, 2016). However, there are few examples of studies on the effect of skew angle or experiments with varying the skew angle of the specimen, and the degree of effect of skew angle has not been investigated sufficiently. Therefore, in this study, vibration experiments were conducted to investigate the effect of skew angle on vibration characteristics of bridge girders. In these experiments, the skew angle was varied from 60° to 90° in 10°. In addition, the 3D FE model was created based on the experiment specimens, and FEM analysis was performed to study how the natural frequencies change as the skew angle changes. The analysis was performed with an increased pattern of skew angles to examine the trend of change in natural frequencies as change in skew angle in more detail.

DOI: 10.1201/9781003483755-253



Figure 1. Overview of the specimen (Skew angle: 60°).

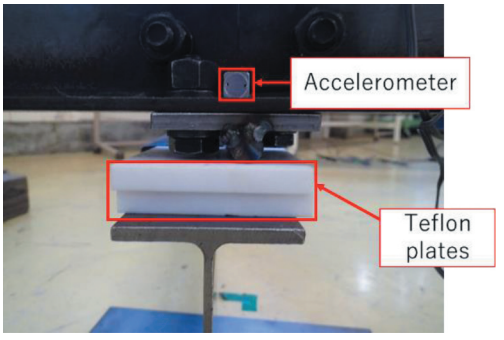


Figure 2. Reproduction of bearing conditions.

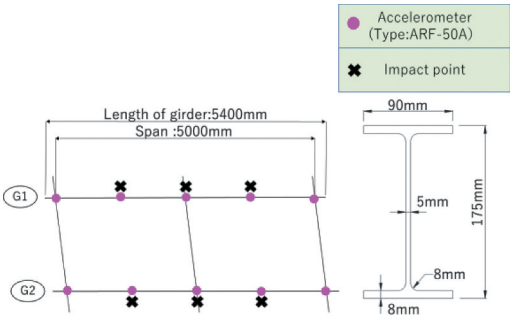


Figure 3. Measuring points of acceleration.

2 OUTLINE OF VIBRATION EXPERIMENT

2.1 *Test specimen*

In this paper, the test specimens were prepared assuming a small-scale bridge with two main girders. The overview of the specimen is shown in Figure 1 and the bearing section is shown in Figure 2. The specimens consisted of two main girders and three cross beams. The main girders were made of H steel of Japanese Industrial Standards (JIS standard) H175×90, with a girder length of 5400 mm and a span of 5000 mm. The cross beams were made of JIS standard Channel steel. The space of main girders was set to 750 mm, 1000 mm and 1250 mm, each with different sectional cross beams. Channel steel with cross sections of C125×65 for 750mm spacing, C150×75 for 1000 mm spacing and C200×80 for 1250 mm spacing was used. The

bearings were made of steel plates and round bar, and Teflon plates were placed between the bearings and the abutment to reproduce "pin-roller" as a bearing condition.

2.2 *Outline of experiment*

In this experiment, the vertical response acceleration was measured by applying vibration to the specimens of bridge girder to calculate the natural frequencies. Four patterns of skew angles of 90°, 80°, 70° and 60° were set as parameters. As another parameter, three patterns of girder spacing were set: 750 mm, 1000 mm and 1250 mm.

The locations of the accelerometers and impact points are shown in Figure 3. The specimens were subjected to vibration using a hammer. Since vibration form will vary depending on the impact positions, impact points were applied at 1/4, 1/2 and 3/4 of the span of each main girder. Response acceleration was measured at a total of 10 points on each main girder: at the bearing points on both sides of the main girder, at a quarter on the span, at the center of the span and at three quarter on the span. Accelerometers were installed on the upper surface of the lower flange of the main girder. Acceleration was measured at a sampling interval of 0.1 millisecond, for a total of 15 seconds (1 second before and 14 seconds immediately after the blow).

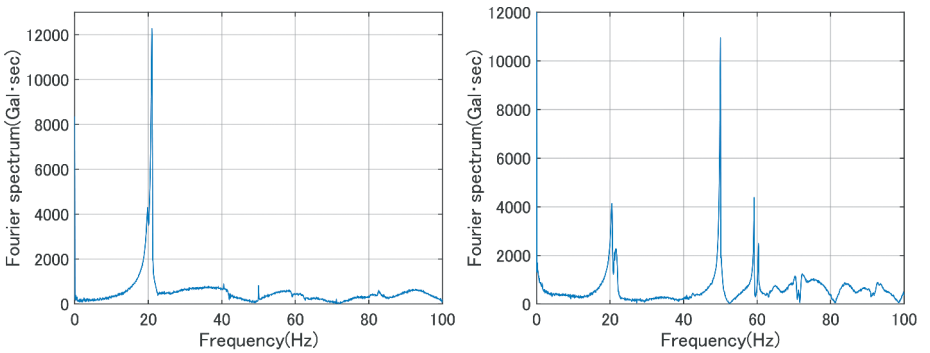


Figure 4. Example of amplitude spectrums.

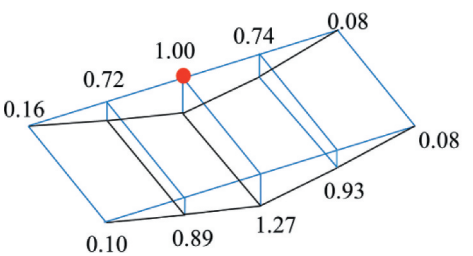


Figure 5. Mode of vibration (around 20 Hz).

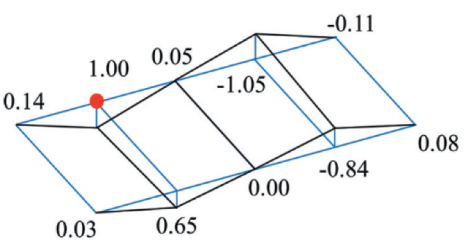


Figure 6. Mode of vibration (around 50 Hz).

3 EXPERIMENTAL RESULTS

3.1 *Comparison of amplitude spectrums*

mplitude spectrums processed the response acceleration data by Fast Fourier Transform (FFT) are shown in Figure 4. The amplitude spectrum when the impact point was the center of the span shows that two dominant frequencies appear around 20 Hz. In the experiment with different skew angles, it was also confirmed that the dominant frequency appeared around 20 Hz. These two dominant frequencies are considered to correspond to the bending and torsional natural frequencies.

The amplitude spectrum when the vibration applied at a quarter of the span shows that the dominant frequency appears around 20 Hz, similar to the result when the vibration applied at the center of the span. In addition, dominant frequencies also appeared around 50 Hz (Right of Figure 4). The similar results were obtained when the skew angle was varied, and when vibration applied at the three quarters of the span. These results show that the dominant frequencies vary depending on the point of the vibration.

3.2 *Vibration mode diagram*

Vibration mode diagrams were drawn to identify which vibration mode corresponds to the dominant frequencies obtained from the FFT.

The vibration mode diagram drawn using the dominant frequency around 20 Hz is shown Figure 5. The vibration mode diagram shows that the dominant frequencies near 20 Hz corresponds to the primary natural frequency. The two dominant frequencies correspond to bending and torsional natural frequencies.

The vibration mode diagram drawn using the dominant frequency around 50 Hz is shown Figure 6. The vibration mode diagram shows that the dominant frequencies at 50 Hz corresponds to the secondary natural frequency. Two natural frequencies, bending and torsional, were obtained as well as the primary natural frequencies.

3.3 *Natural frequencies*

The natural frequencies are summarized in Tables 1-3.

Table 1. Each natural frequency (Space of main girders:750 mm).

	Natural frequency (Hz)			
Skew angle	Bending primary	Torsional primary	Bending secondary	Torsional secondary
90°	20.14	21.13	49.90	-
80°	20.56	21.74	49.74	50.05
70°	20.68	21.44	49.94	49.98
60°	20.33	21.37	49.82	50.13

*Hyphen (-) means natural frequency could not be detected.

Table 2. Each natural frequency (Space of main girders:1000 mm).

	Natural frequency (Hz)			
Skew angle	Bending primary	Torsional primary	Bending secondary	Torsional secondary
90°	19.00	21.25	50.03	-
80°	19.91	21.21	49.74	50.05
70°	20.03	21.33	49.97	50.05
60°	19.61	20.37	49.82	49.74

Table 3. Each natural frequency (Space of main girders:1250 mm).

Skew angle	Natural frequency (Hz) Bending primary	Torsional primary	Bending secondary	Torsional secondary
90°	18.24	20.79	49.82	50.05
80°	18.88	20.98	49.82	49.74
70°	18.85	20.90	49.99	50.05
60°	18.77	21.21	49.94	50.17

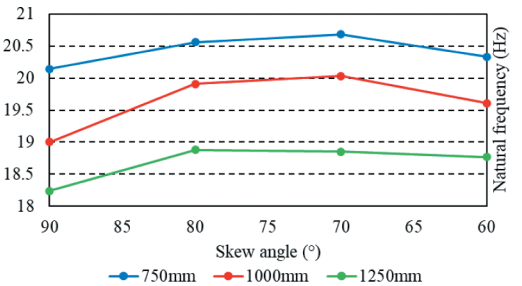


Figure 7. Bending primary natural frequency by space of main girders.

The natural frequencies vary by changing the skew angle on all patterns. For the bending primary natural frequencies, the other natural frequencies (the case of 80°, 70° and 60°) are larger than natural frequency at skew angle of 90°. Therefore, the bending primary natural frequency is larger in a skewed bridge than in a straight bridge. And while there is a slight variation between bending and torsion at the primary natural frequencies, there is minimal disparity at the secondary natural frequencies. The primary bending frequencies are consistently smaller than the primary torsion frequencies, but there is no consistent relationship at the secondary natural frequencies. For these results, the bending and torsional natural frequencies exist in a narrow range at the secondary natural frequencies and difficult to decompose.

Table 4. Comparison of experimental and theoretical values.

	Bending primary natural frequency (Hz)	Difference from theoretical value (%)
Theoretical value (pin-roller)	23.25	-
Measured value (750 mm)	20.14	-13.4
Measured value (1000 mm)	19.00	-18.3
Measured value (1250 mm)	18.24	-21.6

Table 5. Physical Properties Used In The Analysis.

Item	Physical property value
Poisson's ratio	0.3
Young's modulus (N/mm^2)	2.05×10^5
Density (ton/mm^3)	7.85×10^{-9}

The bending primary natural frequency for each girder spacing are shown in Figure 7. In terms of the difference in the girder spacing, the bending primary natural frequencies become smaller when the girder spacing is increased. The natural frequencies tend to decrease with

increasing girder spacing even when skew angle decreases. The bending primary natural frequencies tend to increase as skew angle decreases, but this is not the case for skew angle 60°.

3.4 *Comparison with theoretical values*

The natural frequencies obtained from this experiment are compared with the theoretical values to evaluate the accuracy of the experiment. Based on previous studies, it is considered that the fundamental bending natural frequencies of two-girder bridges with two main girders can be obtained from the analytical solution for simply supported beams, and equation (1) is used to calculate the bending primary natural frequencies of the specimens (Yoneda et al. 2006).

$$f_\eta = \frac{1}{2\pi}\left(\frac{\pi}{L}\right)^2 \sqrt{\frac{E_S I_{SZ}}{w/g}} = \frac{1}{2\pi}\left(\frac{\pi}{L}\right)^2 \sqrt{E_S I_{SZ}} \tag{1}$$

where f_η = fundamental bending natural frequency; L = maximum span; E_s = Young's modulus of steel; I_{sz} = moment of inertia about the centroid axis of the section converted to steel; m = mass per unit length.

The theoretical value of the bending primary natural frequency was calculated to be 23.35 Hz. Compared to the measured values of the bending primary natural frequencies for each girder spacing, a difference of 13.4% was observed even for the girder spacing of 750 mm, which has the smallest difference. One of the reasons for this difference from the theoretical value is that the restraint of the bearing was not sufficient. In this experiment, the bearings and the abutment were not fixed, and the bearings may lift when vibration applied to the specimen.

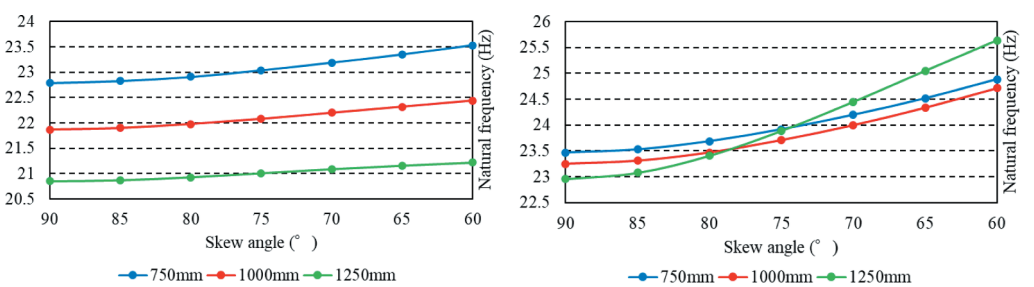
4 FEM ANALYSIS

4.1 *Outline of analysis*

FEM analyses were conducted to examine the effect of bearing conditions and skew angle in more detail. 3D FE models were created by shell elements based on the experimental specimen. The steel physical properties used in the analysis are shown in the Table 5. Two type of bearing conditions were considered: "pin-roller" and "pin-pin". We also attempted to reproduce the bearing conditions in the experiment by introducing spring elements in the bearing and the stiffness of the spring was varied. Skew angle was varied from 60° to 90° in 5° increments in the analysis to examine the effect of skew angle in detail.

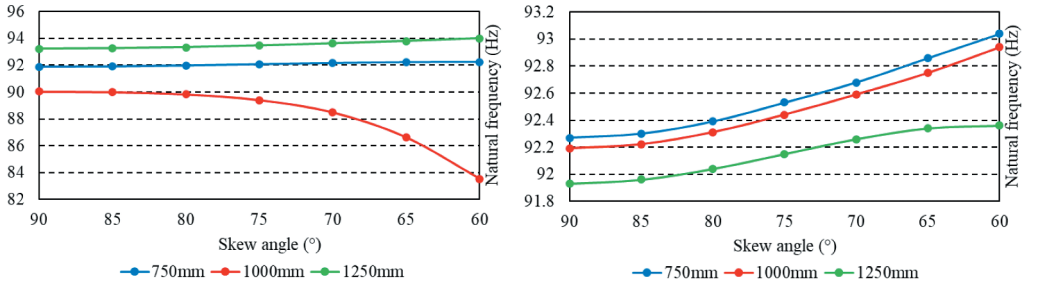
4.2 *Analysis results*

The results of the analysis are shown in the Figures 8-11. In term of the bending primary natural frequencies, when the bearing condition was "pin-roller", the natural frequencies vary with skew angle. In addition, the bending primary natural frequencies increased as the skew angle decreased. The torsional primary natural frequency also tends to increase with decreasing skew angle. A comparison of the bending primary natural frequency and torsional primary



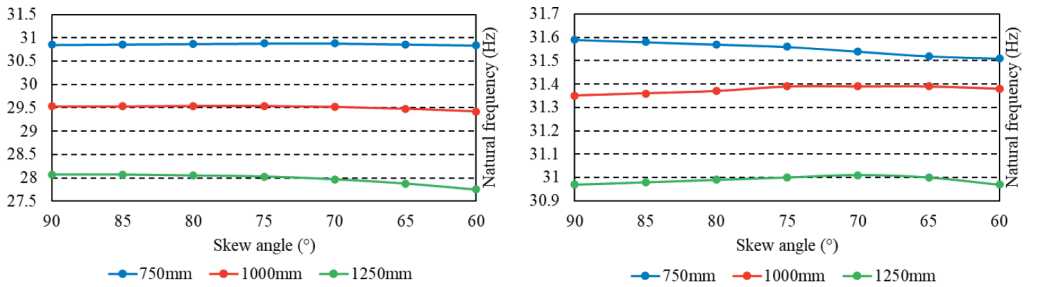
(a) Bending primary natural frequency. (b) Torsional primary natural frequency.

Figure 8. Primary natural frequencies by girder spacing (bearing condition: pin-roller).



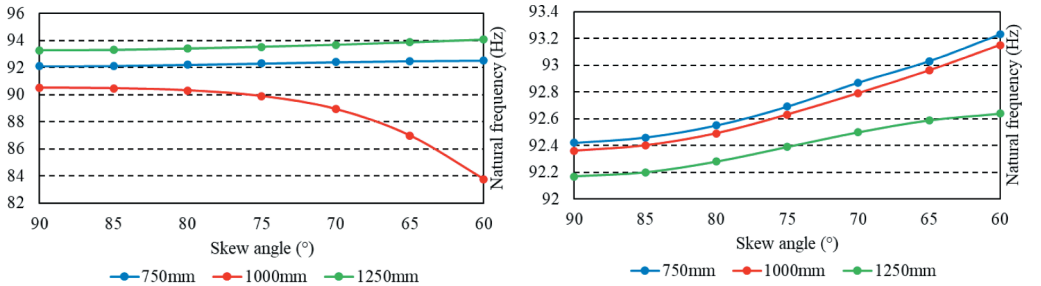
(a) Bending secondary natural frequency. (b) Torsional secondary natural frequency.

Figure 9. Secondary natural frequencies by girder spacing (bearing condition: pin-roller).



(a) Bending primary natural frequency. (b) Torsional primary natural frequency.

Figure 10. Primary natural frequencies by girder spacing (bearing condition: pin-pin).

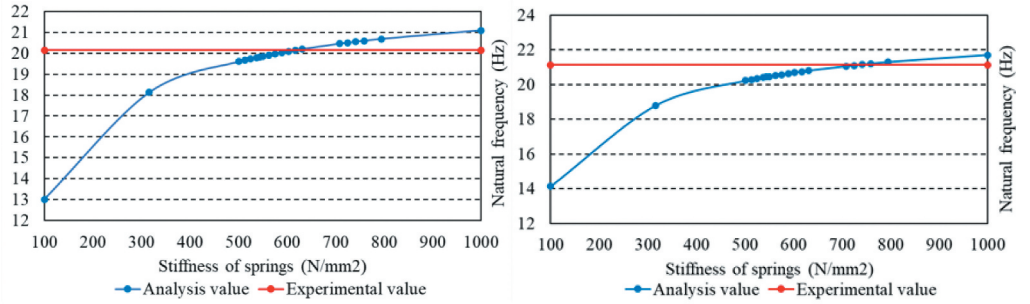


(a) Bending secondary natural frequency. (b) Torsional secondary natural frequency.

Figure 11. Secondary natural frequencies by girder spacing (bearing condition: pin-pin).

natural frequency shows that the torsional primary natural frequency is more affected by skew angle. This trend is also observed for the secondary natural frequencies. These results show that torsional natural frequency is more affected by skew angle than the bending natural frequency. This can be attributed to the torsional behavior observed in skewed bridge. When the bearing condition was "pin-pin", the primary natural frequencies show almost no change in natural frequencies with the change in the skew angle. In the secondary natural frequency, the degree of effect of skew angle doesn't change as the bearing conditions change. These results show that the degree of effect of skew angle changes as the bearing conditions change at the primary natural frequency.

Focusing on the difference in girder spacing, the bending primary natural frequency tends to decrease as the girder spacing increases, similar to the experimental results. One of the reasons for this trend is the use of cross beam of different sections for each girder spacing. It is possible that the difference in the weight of the bridge girders due to the different sections affects the change in the natural frequency.



(a) Bending primary natural frequency. (b) Torsional primary natural frequency.

Figure 12. An example of comparison of analytical and experimental values when spring stiffness is varied.

4.3 *Reproduction of bearing conditions*

In chapter 3, we considered that the difference between the theoretical and experimental values was caused by the poor reproducibility of the bearing conditions. In order to improve the reproducibility of the bearing conditions, we attempted to reproduce the bearing conditions in the experiment. Since it was expected that the vertical restraint was not sufficient during the experiment, we introduce spring elements in the vertical direction and analyzed.

Figure 12 Shows an example of comparison between analytical and experimental values when spring elements is introduced, and the spring stiffness is varied. The results of the analysis showed that the introduction of vertical spring elements resulted in analytical value that were close to the experimental values. By varying the stiffness of the spring elements, the analytical values were close to the experimental values at all natural frequencies. However, at each natural frequency, the spring stiffness at which the experimental and analytical values were close is different. For this result, it is considered that introducing the spring elements not only in vertical direction but also in other direction is necessary to fully reproduce the bearing conditions. The results of these analyses show that the accuracy of the experiments can be improved by ensuring sufficient vertical restraint.

5 CONCLUSION

In this study, vibration tests and analysis were conducted to investigate the effect of skew angle on the vibration characteristics of bridge girders. The following findings were obtained from the results.

1) In the vibration test, the natural frequencies differed depending on the impact point because the vibration form of the structure differs depending on the impact point.
2) The natural frequencies of bridge girders were affected by the skew angle. FEM analysis showed that the primary natural frequencies tend to increase with decreasing skew angle and torsional natural frequency is more sensitive to skew angle than bending natural frequency.
3) In primary natural frequencies, the degree of effect of the skew angle on the natural frequencies of the bridge girders varied depending on the bearing conditions. In the "pin-pin", there was little change in the natural frequencies due to changes in the skew angle. On the other hand, for the secondary natural frequencies, the degree of effect of skew angle doesn't change regardless of the bearing conditions.
4) The sectional shape of the cross beam and the girder spacing also affect the natural frequencies because these effects are attributed to the changes in mass of bridge girders.
5) In FEM, introducing spring elements in the bearing section reproduces the actual bearing condition. By introducing spring elements in various directions, it is possible to completely reproduce the actual bearing condition.

In the future, reproducibility of bearing conditions in experiments needs to be improved. In addition, it is necessary to investigate vibration characteristics not only of the bridge girders but also of the girders combined with the deck slab through experiments and FEM.

ACKNOWLEDGEMENT

This research was supported by NEXCO EAST Technical Research Grant. The authors would like to express their gratitude.

REFERENCES

Ministry of Land, Infrastructure, Transport and Tourism. 2023. Annual Report on Road Maintenance in Japan.

E. Ntotsios, C. Papadimitriou, P. Panetsos, G. Karaiskos, K. Perros, P. C. Perdikaris. 2009. Bridge health monitoring system based on vibration measurements. *Bulletin of Earthquake Engineering* 7:469–483

Y. Chiba, H. Onishi, S. Iwasaki, Y. Kimura and T. Sasaki. 2022. Examination of the deterioration determination method of the deck slab using the response acceleration obtained by the portable FWD test. *Journal of Structural Engineering* 68A:638-648.

A. Furukawa, H. Otsuka and F. Umebayashi. 2005. Experimental study on changes in vibration characteristics due to structural damage. *Proceedings of the JSCE Earthquake Engineering Symposium* 28. 19.

G. Watanabe, F. Tomohiro, S. Goto and H. Emoto. 2014. Health monitoring and identification of dynamic characteristic of skewed bridge based on the vibration test using a moving vehicle. *Journal of Structural Engineering* 60A:513-521.

H. Fujiwara. 2016. *Inspection, Evaluation and Maintenance Technology for Bearing Support System of Highway Bridges*. Subcommittee of Investigation for Bearing Support System of the Highway Bridge, Committee of Steel Structures, Japan Society of Civil Engineers.

T. Mimasu, Chul-Woo Kim, Y. Goi and G. Hayashi. 2018. Investigations on changes in modal properties caused by damages on a real steel plate girder bridge. *Journal of Japan Society of Civil Engineers (Applied Mechanics)* 74 No.2:513–522.

M. Yoneda and K. Edamoto. 2006. Practical evaluation method for fundamental natural frequencies of two-girder bridges based on beam theory. *Journal of Japan Society of Civil Engineers* 62A No.3:608–613.

M. J. Whelan, M. V. Gangone, K. D. Janoyan, R. Jha. 2009. Real-time wireless vibration monitoring for operational modal analysis of an integral abutment highway bridge. *Engineering Structures* 31 (10):2224–2235.

Bridge Maintenance, Safety, Management, Digitalization and Sustainability – Jensen, Frangopol & Schmidt (eds)
© 2024 The Author(s), ISBN 978-1-032-77040-6
Open Access: www.taylorfrancis.com, CC BY-NC-ND 4.0 license

The application of abrasive water-jet treatment on severely corroded weathering steel bridge

Y. Toyota
West Nippon Expressway Company Limited, Ibaraki, Osaka, Japan

S. Kainuma & S. Park
Kyushu University, Fukuoka, Japan

T. Ikeda
Ikeda Kogyo Company Limited, Hakodate, Hokkaido, Japan

T. Arakawa
Sugino Machine Company Limited, Namekawa, Toyama, Japan

ABSTRACT: In some environments where the amount of road salts or airborne sea salt particles are relatively high, weathering steels can be corroded remarkably. Under such conditions, weathering steel is unable to form its protective layer of rust, necessitating additional protective measures such as painting. Before repainting weathering steel, it is essential to completely remove not only the protective layer of rust but also any corrosion products. These corrosion products are physically very hard, necessitating chipping before abrasive blasting. However, a single blast treatment is often insufficient to completely remove the corrosion products, requiring multiple repetitions. Despite this, it can be challenging to fully remove chlorides remaining in deeply corroded areas. Such residual chlorides often cause localized corrosion under the coating. Abrasive water-jet treatment (AWT) has been developed as a new method for preparation of weathering steel surface. Abrasive waterjet is one of the cutting technology for cutting harder materials, which has been developed in the 1980s. AWT can remove rust layer containing corrosion easily with the ultra-high pressure water of Mach 2 and abrasive materials. Additionally, during AWT process, the water temperature rises, which effectively helps wash away residual substances containing chlorides. Due to these merits, AWT is superior to conventional surface treatment methods in terms of the removal of thick rust as well as the cleaning of surface residues. In this study, AWT was applied to an actual corroded bridge where it located in Japan, and it was verified the efficiency of removing corrosion products and chlorides. The results demonstrated that both the corrosion products and residual surface chlorides were completely removed in a very short period of time.

1 INTRODUCTION

In the low corrosive environments, weathering steels form protective rust layers on its surface, so that the progress of corrosion can be suppressed. However, in some environments where the amount of road salts or air borne sea salt particles are relatively high, weathering steel can be corroded remarkably as shown in the Figure 1.

In cases where the weathering steel is unable to form protective rust layer, it becomes necessary to promptly repaint the steel surface. Because it is usually difficult to improve the corrosive environment at the crosslinking point due to spraying road salts or air-borne sea salt particles.

Before repainting weathering steel, it is essential to completely remove not only the protective layer of rust but also any corrosion products. These corrosion products are physically very

DOI: 10.1201/9781003483755-254

hard, necessitating chipping before abrasive blasting. After that, blasting and water washing should be repeated several times to remove corrosion products and chloride until the amount of chloride that is remaining on its steel surface is less than the Japanese standard requirement of 50 mg/m^2.

However, the chloride remaining the bottom of the corrosion pit can't be removed completely. So, those chloride that is remained on the steel surface often causes local corrosions under the painting. To improve these problems, Abrasive water-jet treatment (AWT) has been developed as a breakthrough method for preparation of weathering steel surface. This paper reports the results of field application of the AWT method on a heavily corroded weathering steel bridge.



Figure 1. Severe corrosion of weathering steel bridge.

2 AWT METHOD

Figure 2 illustrates the effectiveness of the AWT method in removing corrosion products and chlorides from steel surfaces. This is achieved by using a water-jet stream at pressures above 200 MPa, containing hard abrasive particles. This method was developed utilizing the principles of the existing material cutting technique, Abrasive waterjet technology. Additionally, the adaptability of AWT for surface treatment under various operational conditions, such as nozzle types, pressure, and standoff distance, has been demonstrated through the author's prior research. The prior research shows that the maximum erosion depth varies depending on factors such as the type of nozzle, the size of the abrasive, and the standoff distance. Additionally, it is indicated that the AWT-treated specimens exhibit higher maximum erosion depth than the blasted specimens in case of the AWT process using 80 mesh garnet and divergent nozzle at a same standoff distance 100mm. However, the amount of thickness reduction is several tens of micrometers than the blasted specimens. By applying the AWT method to severely corroded steels, the high-pressure water fluid is penetrated into the cracks in the corrosion materials, the corrosion materials can be easily peeled off and removed. Besides, the fluid reaches the bottom of the tiny corrosion pit deeply so that almost all chlorides that are remained on the steel surface can be remove completely. AWT can remove rust layer containing corrosion easily with the ultra-high pressure water of Mach 2 and abrasive materials. Additionally, during AWT process, the water temperature rises, which effectively helps wash away residual substances containing chlorides. Due to these merits, AWT is superior to conventional surface treatment methods in terms of the removal of thick rust as well as the cleaning of surface residues. Therefore, the effect of corrosion materials and chlorides removal is drastically high so that AWT effectively removes hard rust layers and chlorides within a single treatment to achieve the desired coating surface conditions above Sa2 1/2 and surface salinity below the Japanese standard requirement of 50 mg/m^2. Therefore, the ATW method is expected to be one of the economic methods that can reduce to one process compared with traditional blasting, which requires multiple repetitive processes to remove corrosion products and chloride. Besides, consumption of abrasive materials is curtailed to a quarter of that required for abrasive blasting, which drastically reduces the abrasive waste and makes this methodology significantly more environmentally compatible.

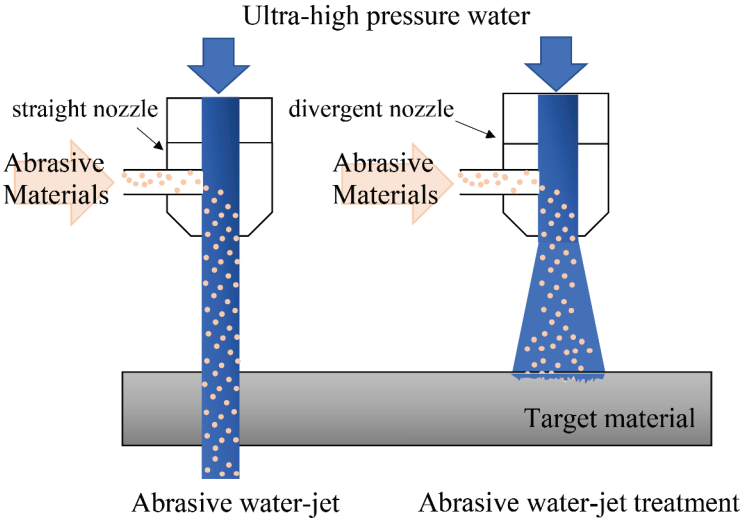


Figure 2. Overview of the AWT method.

3 FIELD TRIAL

3.1 *Outline*

In this study, the AWT method was applied to a severely corroded weathering steel bridge to assess its viability. This application demonstrated the AWT method's efficacy in eliminating corrosion products and chlorides from the structure. The bridge chosen for this test is a three-span continuous steel truss structure, built in 2001, and made of unpainted weathering steel. The bridge is located approximately 5km from the coastline and is affected by the sea breeze in Kagoshima - Japan, as shown in Figures 3 and 4.

The construction site is located more than 3km from the coastline (coastal coast of the Pacific Ocean) 2km, which can be applied to the non -painted weathering steel bridge, but the target bridge has been exposed air-borne sea salt particles amount of 0.09 to 0.97 MDD (dry gauze method: JIS Z 2382).

As a result, the effect of chlorides removal due to rainfall is hardly working because chlorides have always been supplied. Besides the bridge has been severely corroded owing to exposure to the moist environment (17°C, 75%RH). Therefore, severe corrosions have occurred in some parts of the bridge where are in wet situations in long times.



Figure 3. Bridge overview.

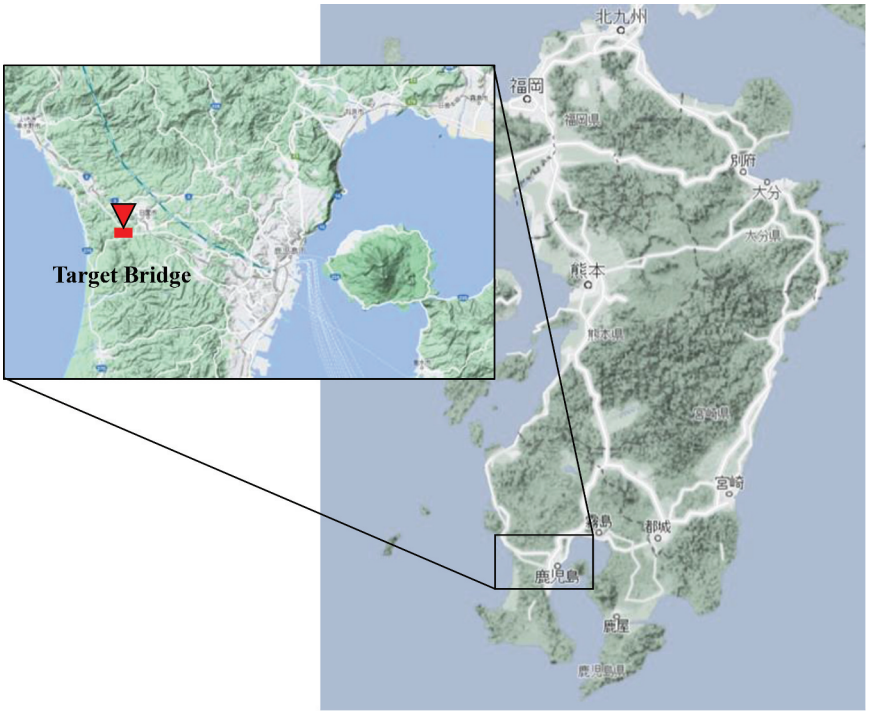


Figure 4. Bridge location.

3.2 *Trial method*

In this test, to verify the removal effects of corrosion products and chlorides in the severely corrosion areas using the AWT method, one of the diagonal member of truss bridge (19cm x 50cm) has been targeted.

The AWT method was applied to the target area until the severe corrosion could not be visually confirmed (about 120sec). As test condition, AWT was conducted with 80 mesh garnet, and standoff distance of 300mm. The detail test condition are shown in Table 1.

To confirm the corrosion removal efficiency of the AWT process, the method of measuring the amount of salt on the treated surface was conducted. Surface-soluble salts were measured using the Bresle patch test. The Bresle patch test was performed over a square patch of 1,250 mm^2 area in accordance with the ISO 8502-6 test method.

Table 1. AWT processing parameters.

Specimen	Nozzle type	Nozzle Diameter(mm)	Abrassive Materials	Stand-off Distance(mm)	Abrasive Supply	Pressure (MPa)	Water flow
AWT#80	AWT nozzle (Divergent)	5	Garnet #80	300	600	230	11.9

4 RESULTS OF FIELD TRIAL

Figure 5 shows the change in appearance of the treated surface after AWT process. Rust was observed before AWT, but immediately after AWT, the metallic color of the steel substrate can be observed on the entire surface. Consequently, it is apparent from visual examination

that the rust was removed entirely. Furthermore, the surface condition achieved the Sa2 1/2 level, which is optimal for quality before any coating or painting. Following the application of AWT, the quantity of salt residue on the treated surface was determined using the Bresle method, revealing values between 0 to 5mg/m^2. This is considerably below the standard threshold of 50mg/m^2. To further verify the chloride removal efficacy of the AWT method, the occurrence of flash rust was monitored over 96 hours after the treatment.

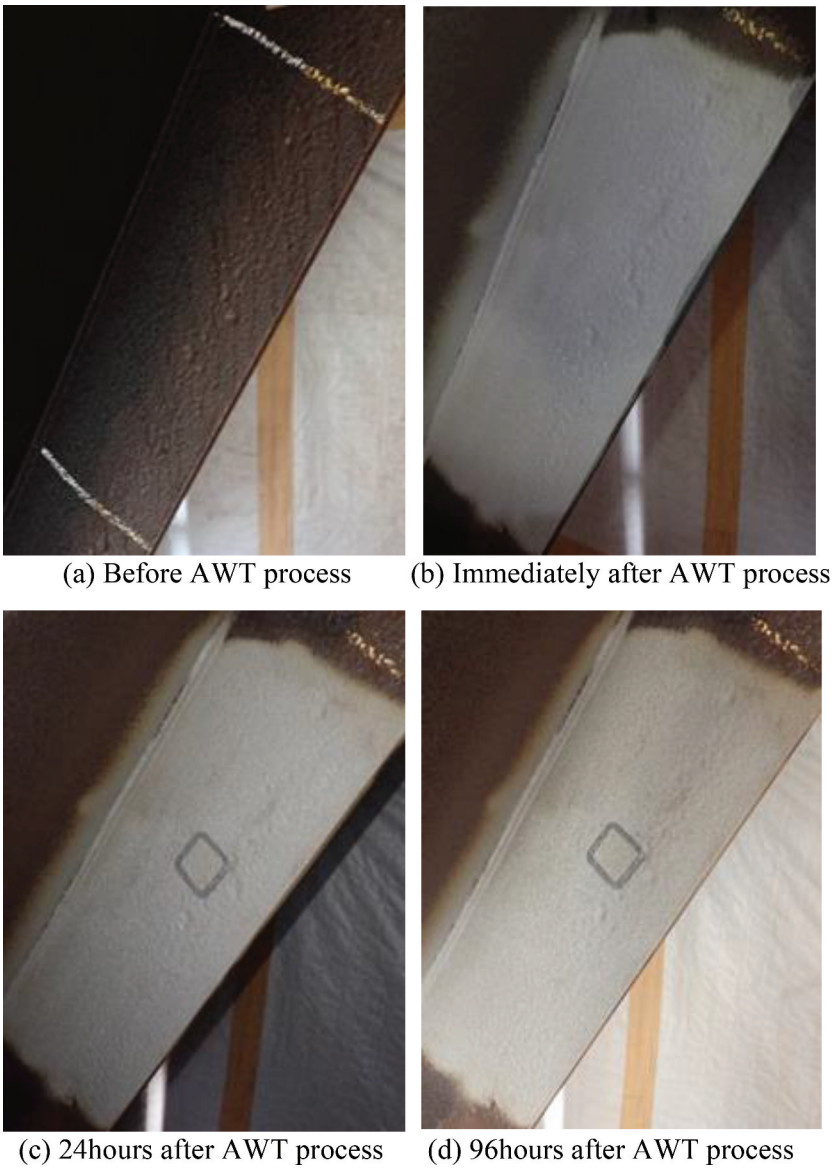


Figure 5. Surface condition after AWT process.

Figure 6 shows the pitting corrosion area that appeared on the steel substrate after the AWT process. Since corrosion products remain in deeply corroded areas, so that abrasive blasting is needed several times. On the other hand, in the case of the AWT method, it was confirmed that the pitting corrosion can be sufficiently removed in a single process.

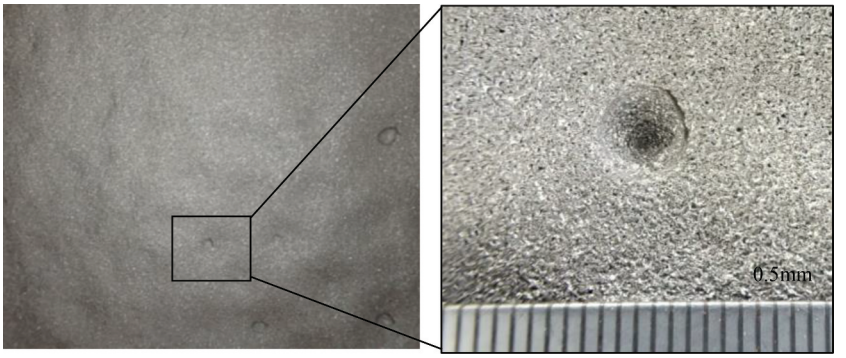


Figure 6. Surface condition after the AWT process.

5 CONCLUSIONS

The following are the main findings from tests of the AWT method's effectiveness in removing salt and rust from uncoated weathering steel bridges severely corroded by flying sea salt.

1) AWT method can achieve steel surface condition to Sa 2 1/2 level in a single process for severely corroded areas of weathering steel due to salt damage.
2) AWT method is effective in removing rust and chloride when applied to the severely corroded surface of weathering steel members.
3) The amount of chloride on the treated surface of heavily corroded weathering steel can be reduced to 0 to 5mg/m^2.

REFERENCES

Kainuma, S. 2023. Challenges and new techniques in surface preparation of existing steel structures, The 43rd corrosion and rust prevention technology presentation conference. Japan: Japan Association of Corrosion Control.

Park, S. Kainuma, S. Ikeda, T. Toyota, Y. & Morita, Y. 2023. Effect of surface characteristics of abrasive water-jet treatment on corrosion behavior of carbon steel. Japan: Zaiyo-to-Kankyo.

Japanese Road Association, 2014. Steel Road Bridge Corrosion Prevention Handbook. Japan: Japan Road Association.

Bridge Maintenance, Safety, Management, Digitalization and Sustainability – Jensen, Frangopol & Schmidt (eds)
© 2024 The Author(s), ISBN 978-1-032-77040-6
Open Access: www.taylorfrancis.com, CC BY-NC-ND 4.0 license

Analytical study on stress concentration zone of aseismic reinforced deck type arch bridge

M.O. Ouchi, T.S. Suzuki & H.S. Shirahata
Structural Safety Laboratory, Tamazutsumi, Setagaya-ku, Tokyo, Japan

ABSTRACT: Number of bridges used long periods in Japan has increased and some damages for their members caused to heavy transportation become apparent. Therefore, design methods of bridges have often revised for lifetime improvement. However, there are some cases that a bridge constructed before the change need a reinforcement to adapt the new criterion. In this study, take up a deck type steel arch bridge and reveal its fatigue performance, furthermore, the effect and influence for fatigue of aseismic reinforcement that method is Strengthening the Arch rib using Concrete jacket by finite element analysis. As a result, the post member that connects an arch rib and a stiffening girder tends to occur fatigue damages, especially the shortest post is weakest member of the arch bridge. And the reinforcement produces an effect that reduces a displacement of whole structure or stress.

1 INTRODUCTION

In Japan, the number of bridges often older than 50 years is increasing every year. During their long service life, damage to members caused by strong earthquakes and fatigue damage caused by heavy traffic are becoming more and more significant. Although design methods for road bridges have been revised in response to this experience, it is necessary to consider the introduction of reinforcement measures for bridges constructed prior to the changes.

In this study, we focused on arch bridges, especially deck type steel arch bridge, for which fatigue damage is rarely reported. Deck type steel arch bridge in this study were constructed 50 years ago and were reinforced with reinforced concrete wrapped around the arch ribs to increase their stiffness, which is almost unprecedented in the past. (Kakimoto, 1998) The arch ribs, which are the main members of the bridge, were thickened by this reinforcement, and although there is no structural change in the floor assembly, the bridge as a whole has undergone a significant change. In this study, a deck type steel arch bridge is picked up and its fatigue performance is evaluated, furthermore, the effect and influence for fatigue of aseismic reinforcement that method is Strengthening the Arch rib using Concrete jacket by finite element analysis.

2 TARGET DECK TYPE STEEL ARCH BRIDGE AND ANALYSIS MODEL

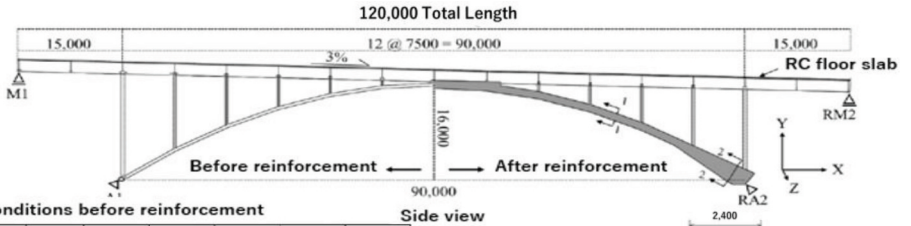
2.1 *Outline of the subject arch bridge*

The deck type steel arch bridge under study was put into service when the Tomei Expressway was opened to traffic in 1969 and is classified as a Class B Road bridge. The structural outline of the bridge is shown in Figure 1, and the cross-sectional dimensions of the reinforced concrete reinforcing are the same as those used in actual construction cases.

DOI: 10.1201/9781003483755-255

2.2 *Outline of analysis model*

ABAQUS CAE/6.13 (Dassault Systemes, 2013) was used in the general-purpose finite element analysis. Shell elements were used for the steel members, and solid elements were used for the RC slab and the concrete reinforced section after reinforcement. The material constants given to these elements are shown in Table 1. The unit weight of steel was increased by a factor of 1.2 to account for the weight of bolts and reinforcement materials, which were omitted in the modeling. In the analysis considering material nonlinearity, bilinear stress-strain curves were used for the steel, and the constitutive law in the specifications for highway bridges was used for the concrete. In the seismic analysis, dynamic analysis was performed considering material and geometric nonlinearity, and linear static analysis was performed for the analysis with vehicle loads to investigate the weakness in fatigue.



Restraint conditions before reinforcement

Position \ Directions		X	Y	Z	XR	YR	ZR
Arch base	AI	restraint	restraint	restraint	restraint	restraint	freedom
Bearing	MI	freedom	restraint	restraint	restraint	restraint	freedom

Restraint conditions after reinforcement

Position \ Directions		X	Y	Z	XR	YR	ZR
Arch base	RA2	restraint	restraint	restraint	restraint	restraint	restraint
Bearing	RM2	freedom	restraint	restraint	restraint	freedom	freedom

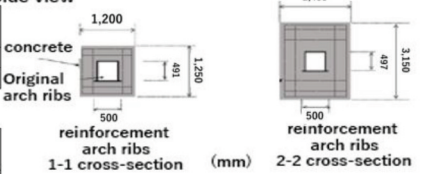


Figure 1. Overview of the structure of deck type steel arch bridges.

Table 1. Material constants considered in the analysis.

	Steels	Reinforced concrete
Unit weight (kN/m)	92.4	24.5
Modulus of elasticity (Gpa)	206	25
Poisson's ratio	0.3	0.2
Yield point (Mpa)	235	——
Design Base Strength (N/mm2)	——	24

3 ANALYSIS PROCEDURE AND RESULTS

3.1 *Analysis procedure*

The seismic waveforms used in the analysis were the waveforms of the 1968 Hyuga-nada earthquake for the L1 seismic motion and the 1995 Hyogo-ken Nanbu earthquake for the L2 seismic motion, both of which are for Class II ground. Seismic acceleration was input in the direction perpendicular to the bridge axis. In addition, only the dead load was considered for the loading condition.

3.2 *Evaluation method of the results*

Stress-strain (s-s) curves of the members were developed from the results, and the evaluation was based on the plasticization of the members. Since the effect of plasticization of main

members such as arch ribs on the entire bridge have not yet been clarified, plasticization of the main members is not considered as damage that is not easily repairable. In contrast, plasticization of secondary members such as lower transverse structures and tilted structures was allowed because they are relatively easy to repair.

The deck type steel arch bridges are classified as Class B bridges and must have a seismic performance2 against L2 earthquakes. Table 2 shows the definition of seismic performance in Japan. Based on this definition, we evaluated whether the bridge satisfies the required seismic performance against earthquakes based on the plasticization of the members.

3.3 *Analysis results*

3.3.1 *Results before reinforcement*

Figure 2 shows the S-S curves of the deck type steel arch bridge before reinforcement for the L2 earthquake, where the members of interest are the arch-rib joints and transverse supports, the arch-rib base, and the end-column base. None of the members did not plasticize during the L1 earthquake, and the results satisfied the requirements for seismic performance1.

In the L2 earthquake, all the arch ribs plasticized beyond the yield points indicated by the red dotted lines. The end columns, which are also primary members, did not plasticize. In addition, out-of-plane deformation occurred in the lower horizontal structure, which is a secondary member, and plasticization occurred. In the above results, it was judged that the subject arch bridge did not meet the required seismic performance2 due to the plasticization of the arch ribs, which were the main members.

3.3.2 *Results after reinforcement*

For the L2 earthquake, the reinforcement eliminated plasticization in the main members. However, plastic deformation was observed in a larger number of secondary members than before the reinforcement. However, as described in the previous section, this change is not problematic because the secondary members can be easily repaired.

The reinforcement was found to be effective in increasing the stiffness of the bridge as a whole, since plastic deformation of the main members no longer occurred, and in satisfying Seismic Performance 2, since the secondary members were able to absorb more seismic energy.

Table 2. Seismic performance specified in the specifications for highway bridges V in Japan.

Seismic Performance of bridges	Safety in seismic design	Seimic design serviceability	Seismic Design short term	Restorability long term
Performance of Bridges 1 Performance that does not soundness the integrity of the bridge due to earthquakes	Ensure safety against falling bridges	Ensure that the bridge functions as it did before theearthquake	Does not require restoration to restorefunctionality	Minor restoration is sufficient
Performance of Bridges 2 Performance that damages due to earthquakes are limited and that theearthquakes are limited and that thebridge can quickly recover its function	Ensure safety against falling bridges	Able to quickly recover its function as a bridge after an earthquake	Restoration to restore functionality can be handled by emergency restoration	Permanent restoration is relatively easy
Performance of Bridges 3 Performance that seismic damage is not fatal to the bridge	Ensure safety against falling bridges	——	——	——

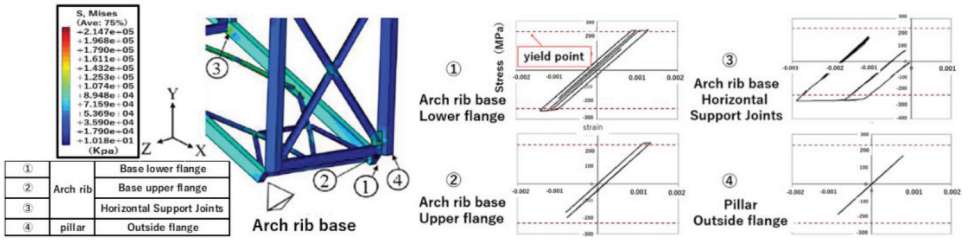


Figure 2. S-S curve for L2 seismic response of main member before reinforcement.

4 FATIGUE PERFORMANCE OF DECK TYPE STEEL ARCH BRIDGESWATASHIFECT OF REINFORCEMENT

4.1 *Analysis procedure*

Linear static analysis was conducted on the members which are expected to be subjected to fatigue damage by applying vehicle loads assuming heavy trucks, and the fatigue performance was evaluated from the stress and deformation behavior of the members. Three types of members were considered: ① vertical members, for which fatigue damage has already been reported; ② joints between stiffening girders and transverse girders; and ③ intersections between longitudinal girders and transverse girders, for which fatigue damage has frequently occurred, as shown in Figure 3. In order to clarify the differences in member length and location within the bridge, the area including the shortest vertical member adjacent to the arch crown was designated Part 1, and the area adjacent to it was designated Part 2.

In order to analyze these members with high accuracy, a method called zooming analysis (sub-modeling analysis) was used. The procedure of this analysis method is shown in Figure 3. The advantage of this method is that the same behavior can be reproduced, and accurate results can be obtained by performing the analysis on the overall model and then inputting the results of the overall model as boundary conditions to a sub model with a smaller element size that is cut from the model. In this study, static analysis was first performed on the entire arch bridge model with vehicle loads input, and then the sub models were used as the partial model and the detailed model in two stages. Three models of the focus member were created for each of Part 1 and Part 2, for a total of six models in the analysis. The same procedure was also used for the post-reinforcement model.

In the static analysis of the overall model, the load assuming a 3-axle 25-ton truck shown in Figure 4 was used in reference to the T-load specified in the specifications for highway bridges. However, due to the loading range, the load was equally distributed 20 tons to the four rear 2-axle wheels, or four loading surfaces (200 mm x 500 mm), where the load ratio is considered to be large.

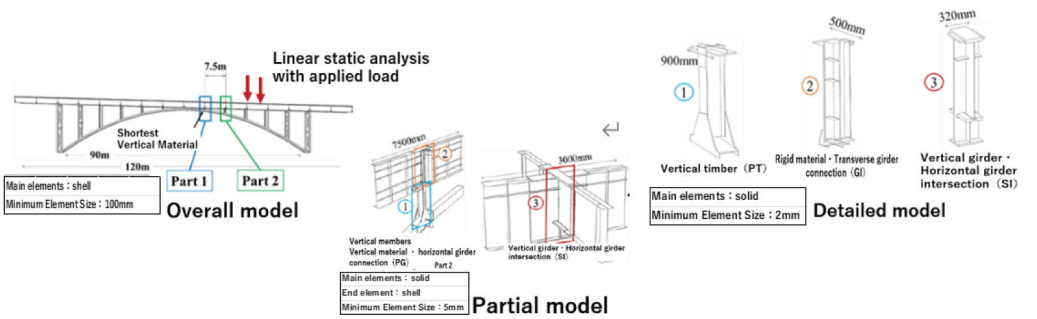


Figure 3. Zooming analysis procedure.

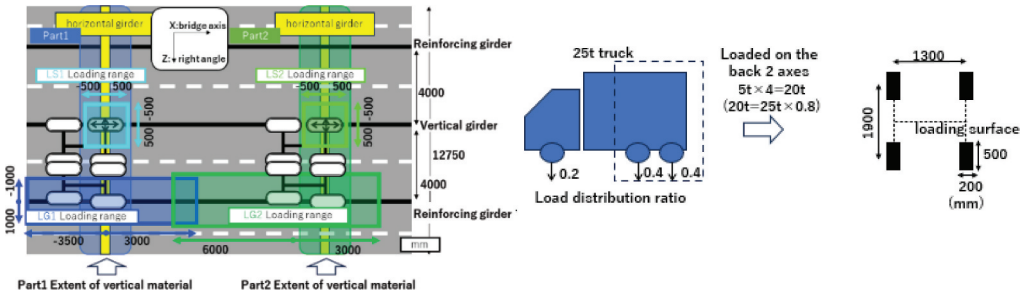


Figure 4. Load placement and travel range.

4.2 *Evaluation method of analysis results*

4.2.1 *Methods using stress influence surfaces*

The analysis was conducted by shifting the load, and the influence surface was created from the principal stresses obtained from the analysis. The load transfer was centered on the joints of the stiffening girders, longitudinal girders and transverse girders as shown in Figure 4, and the load at the joints of the transverse girders and longitudinal girders in the range including the Part1 vertical members is called LS1. Similarly, the load at the connection between the stiffening girder and the transverse girder in the area including the Part 1 vertical members is called LG1. The bridge axis direction is the X-axis, and the perpendicular direction of the bridge axis is the Z-axis, and the center of the joint is (0,0). The loads were shifted in the bridge axis direction and perpendicular direction by ±100 mm when focusing on the intersection of the vertical and transverse girders and by ±500 mm when focusing on vertical members and the joint between the stiffening girders and transverse girders. In the same way, the loads LS2 and LG2 were also shifted within the range including the Part2 vertical members.

4.2.2 *Method using hot spot stress*

When a fatigue crack initiates at a weld stop, the stress is maximum at the weld stop, but the stress at the stop is affected by the shape of the stop, so we used hot spot stress extrapolated from the base metal (hereinafter referred to as HSS), a method to evaluate the stress at the stop, which is affected by the shape of the stop. The HSS is calculated by extrapolating the stress from the reference point, which is located at a distance from the hot spot, using the weld stop as the hot spot. (Hobbacher, 2016)

The HSS was calculated from the analysis results of the load cases that showed the maximum and minimum values in the stress influence plane, and the difference was used as the stress range for fatigue verification by comparing it with the breakout limit of the constant amplitude stress of the welded joint. In the verification using HSS, the type of joints shall be either load-non-transmissive or load-transmissive cruciform welded joints, and the strength classes are E and F, respectively.

4.3 *Analysis results*

4.3.1 *Vertical members*

Figure 5 shows the deformation diagram of the Part 1 vertical material before reinforcement. The loading position is (X, Z) = (0,0) at LG1. The maximum principal stress diagram shows that secondary bending occurs in the vertical material. The out-of-plane deformation occurs at the vertical flange, and stress concentrations are observed at the bottom edge of the vertical member and at the welds between the vertical flange and the bottom flange of the stiffening girder. Since the stiffening girders and vertical members are welded, the HSS was calculated at this location. The results are shown in Figure 6. The stress range of the hotspots exceeding the

breakout limit indicates that fatigue cracks may occur at the welds of the vertical flanges. Since the Part 1 vertical members were completely wrapped around the concrete by the reinforcement, the HSS evaluation after the reinforcement is omitted because a comparison before and after the reinforcement is not possible.

The deformation of the vertical members in Part 2 was similar to that in Part 1, but the out-of-plane deformation of the vertical flange was different from that in Part 1. The stresses also tended to increase when the load moved to the arch crown side, i.e., to the adjacent Part 1 vertical member, and it was found that there was no difference depending on the member length. As shown in Figure 7, the displacement of the upper and lower edges of the reinforced Part 2 vertical members was smaller, and the secondary bending deformation was also slightly mitigated. However, there was no change in the out-of-plane deformation behavior of the vertical flange.

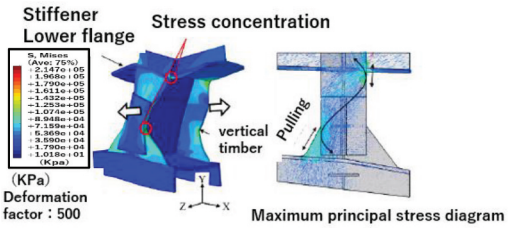
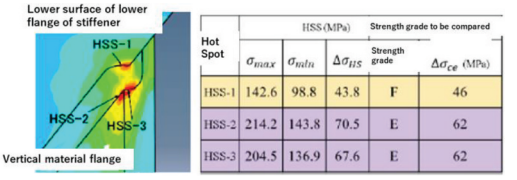


Figure 5. Deformation diagram of vertical material.



Hot Spot	HSS (MPa) σ_{max}	σ_{min}	$\Delta\sigma_{HS}$	Strength grade to be compared: Strength grade	$\Delta\sigma_{ce}$ (MPa)
HSS-1	142.6	98.8	43.8	F	46
HSS-2	214.2	143.8	70.5	E	62
HSS-3	204.5	136.9	67.6	E	62

Figure 6. HSS calculation results of the weld at the upper end of Part1 vertical material before reinforcement.

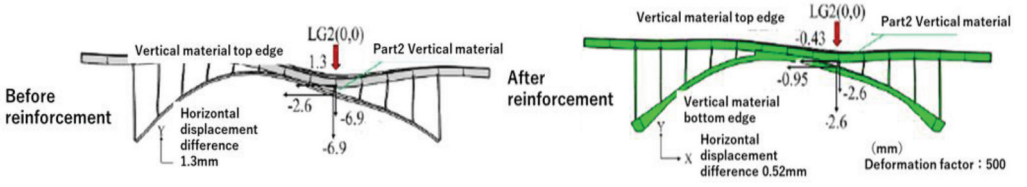


Figure 7. Effect of reinforcement on deformation of Part 2 vertical timbers.

4.3.2 *Connection between stiffening girder and transverse girder*

There was little difference in the deformation of this member shown in Figure 3②under load loading before and after reinforcement. Stress concentration was observed at the upper end of the connection plate weld between the vertical stiffener of the stiffening girder and the transverse girder web at the top of the member. No significant changes were observed in the above deformation behavior or stress development in this member regardless of the location of the member or whether it was reinforced or not, as shown in Part 1 and Part 2.

4.3.3 *Vertical girder/ transverse girder intersection*

In this member shown in Figure 3③, stresses were relatively high around the intersection of the longitudinal girder and the upper flange of the transverse girder and were particularly concentrated at the scallop of the connection plate of the longitudinal girder. The deformation behavior did not change depending on the location of the member or whether it was reinforced or not.

Figure 8 and Figure 9 show the results of the stress influence surface and HSS calculations, respectively, focusing on the scalloped welds at the top of the longitudinal girder connection plate, which is the location of the maximum stresses described above. The stress increased when the axle moved across the longitudinal girder from the influence surface in the minus direction perpendicular to the bridge axis, that is, when the axle moved across the longitudinal girder.

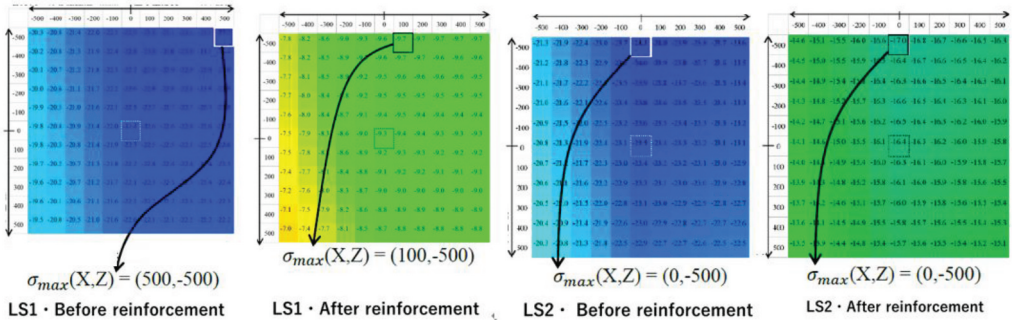
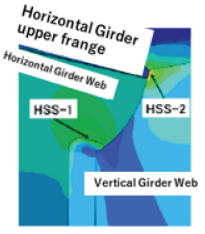


Figure 8. Stress affected surface of the weld at the top end of the longitudinal girder connection plate at the transverse girder web (LS).



Hot Spot	Before reinforcement						After reinforcement						Strength grade to be compared	
	Part 1			Part 2			Part 1			Part 2				
	σ_{max}	σ_{min}	$\Delta\sigma_{HS}$	σ_{max}	σ_{min}	$\Delta\sigma_{HS}$	σ_{max}	σ_{min}	$\Delta\sigma_{HS}$	σ_{max}	σ_{min}	$\Delta\sigma_{fi}$	Strength grade	(MPa)
HSS-1	-29.2	-38.7	9.5	-30.6	-41.3	10.7	-10.4	-16.6	6.2	-21.8	-30.6	8.8	E	62
HSS-2	-42.5	-48.6	6.1	-45.0	-48.9	3.9	-15.8	-20.6	4.8	-32.0	-34.8	4.8	F	46

Figure 9. HSS calculation results for welds at longitudinal and transverse girder intersections.

4.4 *Summary of results*

The hot-spot stress ranges focused on by each model are summarized and compared in Figure 10. As can be seen in the figure, the vertical member shown in Figure 3①, where secondary bending occurs, has the lowest fatigue durability among the vertical member, the connection between the stiffening girder and the transverse girder, and the intersection between the longitudinal girder and the transverse girder. Stress concentration occurs at the upper and lower ends of these members, and Part 1 vertical members adjacent to the arch crown, which have short member lengths, are particularly weak points in deck type steel arch bridges. Therefore, it was found that reinforcement measures are necessary mainly for the vertical members with short member lengths. On the other hand, the stress values and stress ranges of floor assemblies such as steel girders and steel slabs, where fatigue damage is frequently found, are lower than those of vertical members in the structure of deck type steel arch bridges.

In terms of stress effects, the stresses in the vertical members tended to be higher when the load shifted toward the arch crown and toward the outside of the bridge overhang. The outward movement of the load is considered to have increased the load-bearing ratio of the stiffening girders, and the vertical members directly below the stiffening girders were significantly affected. The addition of a vertical girder is considered to be an effective countermeasure. In addition, the stress in the floor assembly increases when the load shifts from just above the focus area to the center of the bridge. Therefore, it is considered that avoiding the position of the load or increasing the strength of the floor assembly is one of the ways to prevent fatigue. Comparison

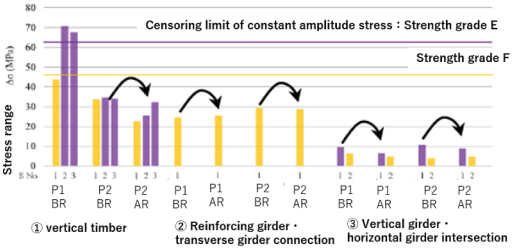


Figure 10. Comparison of stress ranges and truncation limits for each member.

of the results before and after reinforcement showed that the reinforcement reduced the stress in all members. This can be attributed to the decrease in overall bridge displacement due to the increased stiffness of the arch ribs. However, for the floor frames that were not structurally modified by the reinforcement, there were almost no differences in deformation behavior, stress state, or stress range between the pre- and post-reinforcement periods, and the reinforcement was not effective as an anti-fatigue measure. In addition, the fatigue durability of Part 2 vertical members, which could be compared by reinforcement, was confirmed, but secondary bending, which is the cause of damage, was still observed after reinforcement. Therefore, it is necessary to consider reinforcement measures to suppress the deformation.

5 CONCLUSION

In this study, finite element analysis was conducted to investigate whether seismic retrofitting of deck type steel arch bridge, which are considered to be inadequate for existing conditions, is also effective for fatigue retrofitting. The results are described below.

(1) For level 1 earthquake motion, plasticity did not occur even before reinforcement, and seismic performance 1 was satisfied. For level 2 earthquake motion, plasticity was observed, but the reinforcement eliminated the plasticity of the main members, thus satisfying Seismic Performance 2.
(2) From the viewpoint of fatigue, secondary stress concentration was observed at the upper and lower ends of the shortest vertical member connecting the arch rib and the stiffening girder before reinforcement, and fatigue damage was considered to occur. The stress value was about 100 MPa, but since this point was wrapped in reinforced concrete, it is considered that there was no stress concentration.
(3) The stress range at the top end of the second shortest vertical material was reduced from 35 MPa to about 25 MPa before and after reinforcement, respectively. The stress at the lower end was also reduced by 40 MPa. In addition, stresses at the joints between the stiffening girder and the transverse girder and between the longitudinal girder and the transverse girder were generally reduced by the reinforcement. The reason for this is that the stiffness of the arch ribs was increased, which suppressed the deformation of the bridge.
(4) However, the stress range increased by 1 MPa at the weld scallop at the intersection of the longitudinal and transverse girders. 5 MPa, which is sufficiently low compared to the fatigue design level of JSSC, is not considered to be a concern, but it should be noted that the stress range increased in some cases.

REFERENCES

Dassault Systemes: Abaqus/CAE User's Guide, 2013, http://130.149.89.49:2080/v6.13/books/usi/default.htm
Hobbacher, A.F.2016. *Recommendations for Fatigue Design of Welded Joints and Components (Edition)*.
Kamamoto, T.K. & Natsume, S.N. & Oshima, M.O. 1998. Strengthening the Arch Rib of Reversed Langer Steel Bridge using Concrete Jacket. The bridge and foundation engineering, Vol.32, No.11, pp.2–8.

Bridge Maintenance, Safety, Management, Digitalization and Sustainability – Jensen, Frangopol & Schmidt (eds)
© 2024 The Author(s), ISBN 978-1-032-77040-6
Open Access: www.taylorfrancis.com, CC BY-NC-ND 4.0 license

Rehabilitation methodology of a corroded steel-riveted highway bridge in an urban setting

I. Netzer & A. Kedar
Kedmor Engineers, Givataim, Israel

ABSTRACT: Current sustainability practices emphasize preserving existing bridges and extending their lifespan, as seen in the Namir Arches Bridge over the Yarkon River in Tel-Aviv. This 70-year-old Tied-Arch steel bridge faces challenges due to its corrosive coastal location and continuous use as a four-lane highway. The lack of maintenance and repetitive load-cycles over the years have led to deterioration. Ultrasonic field tests of the rivets revealed the bridge's condition, prompting the development of a rehabilitation plan involving the replacement of approximately 5,000 rivets. The replacement medium must have similar stiffness and capacity characteristics and avoid negative effects to the original plates. Options explored included: new rivets with a modern riveting machine, preloaded High-Strength Friction Grip (HSFG) bolts, and the chosen alternative of HSFG injection bolts. Beyond rivet replacement, the project addressed deteriorated abutments, and the replacement of expansion joints and safety barriers to ensure overall bridge functionality.

1 INTRODUCTION

1.1 *History of the Namir Arches Bridge*

The Namir Arches Bridge in Tel-Aviv, over the Yarkon river (Figures 1-2), was constructed in the mid 1950's to alleviate traffic congestion for northern to Tel-Aviv commuters. The bridge is a single 56 m span; the static scheme of the superstructure is a simply supported tied-arch bridge (Figures 3-4). The bridge was assembled on one riverbank and was moved to its final location utilizing the incremental launching method (Figure 5). The structural elemets are comprised of plates, angles and channels that are connected with rivets to create the structural members' sections and spliced connections (e.g., Figure 6). Two reinforced concrete abutments rest at either side of the river and are carrying the bridge and are loaded by four bearings: two roller bearings and two rocker bearings.



Figure 1. Namir Arches Bridge, Tel-Aviv, Israel (picture taken by author).

DOI: 10.1201/9781003483755-256



Figure 2. Namir Arches Bridge orientation, Tel-Aviv, Israel. (L) Google maps (R) gis Tel-Aviv.

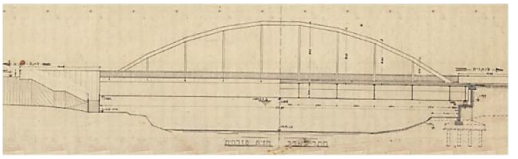


Figure 3. Elevation-section of the static scheme of the tied-arch bridge (Netivei Israel – National Transport Infrastructure Company).

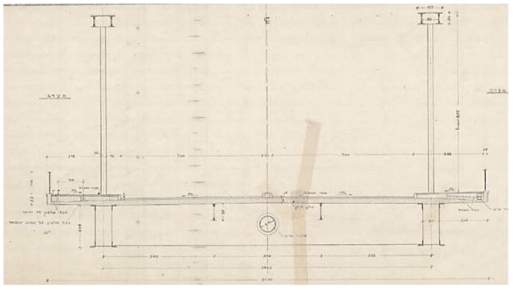


Figure 4. Bridge cross-section (Netivei Israel – National Transport Infrastructure Company).

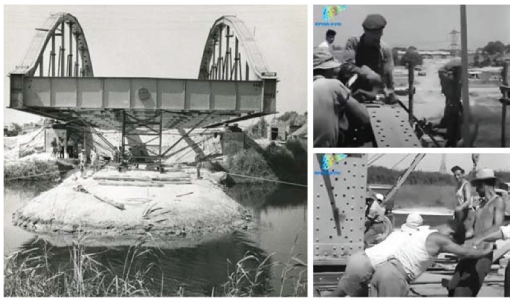


Figure 5. Photos of construction works: (L) cantilevering over the Yarkon River (TR) rivet installation (BR) launching was done mechanically by the on-site team (Israel State Archives).

1.2 *Current status of the bridge*

After approximately seventy years of continuous use, structural elements – both primary and secondary – exhibited significant structural damages (e.g., Figure 7). The current deteriorated state of the heavily corroded elements can be attributed to three predominant reasons:

a. Proximity to the Mediterranean Sea coastline: with a higher consistency of chlorides the effects of the corrosive environment are accelerated.

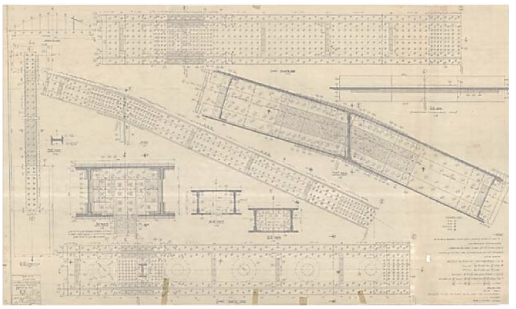


Figure 6. Example details of arch and hangar sections and splices (Netivei Israel – National Transport Infrastructure Company).

b. Fatigue cracking due to dynamic and repetitive load cycles: as this phenomenon was less known in the 1950's preemptive measures were not taken ahead and as a result damages were unsurprisingly seen in the higher stress regions.
c. Lack of maintenance over the years: in the past there were no structural retrofit works done to the bridge, rather just an architectural paint job for its now iconic blue color (Figure 1).

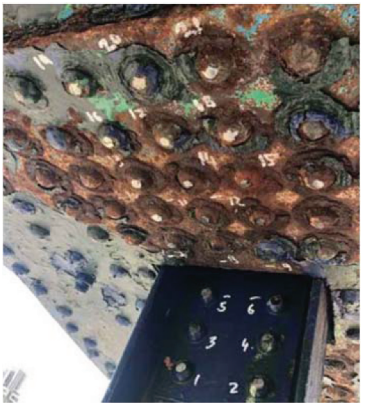


Figure 7. Corrosion in hangar-arch connection.

1.3 *Structural renovation – selection of design approach*

With the Namir Arches Bridge being in a poor state, the Tel-Aviv municipality has to address the issue. In terms of the detail level and the resulting design life extension period, there are several general approaches to be considered:

a. Rebuilding the bridge to meet current codes and standard practices, thus gaining a new and complete design life.
b. Retrofitting the existing bridge to meet current codes and standard practices, thus extensively prolonging its design life.
c. Rehabilitating the existing bridge to meet its original design criteria, based on codes and standard practices from the original design period. This will prolong the bridge's design life.

The Tel-Aviv municipality has selected to pursue the rehabilitation approach as it is expected to be the least costly, quickest to implement and leading to a more sustainable solution for the renovation of this urban construction site.

2 REHABILITATION DESIGN METHODOLOGY

2.1 *General background of the rehabilitation plan*

As mentioned above, the rehabilitation plan was devised with the objective of bringing the bridge back to a satisfactory operational state based on its original design and to increase its safety level in a sustainable fashion. Due to structural damages that were observed: the expansion joints, abutments and safety barriers were all designed to be replaced. Currently, whilst writing this text the Tel-Aviv municipality has begun work on the replacement of the expansion joints.

The most notable damage type, however, is that of the corroded rivets. In order to assess the degree of corrosion and its implications, a test program for a representative number of rivets was prepared. Kedmor Engineers were responsible for allocation of suspect rivets, based both on visual inspection and on expected vulnerable zones. EI-SHAR Metal Industries, an expert metallurgy lab, was responsible for the chosen test method and corresponding procedure; the ultrasonic field test was the selected method. Out of the 1,056 examined rivets approximately 15% were determined as unacceptable; around 10÷15% additional rivets were not able to be determined, deeming them as faulty as well; the remainder were found structurally acceptable. Prior to the field testing a calibration procedure was done. Ultrasonic tests were conducted on two different specimen types: a faultless rivet and a flawed rivet with a handmade visible damage cut in the shank of the rivet (Figure 8). Based on the test results an estimate placed ca. 5,000 rivets in need of replacement out of a total of ca. 20,000. It is of no surprise that most of the damaged rivets are in either high stress regions or near corrosion-inducive areas; even more so when the two cases coincide. Based on the findings a complete methodology for the replacement of faulty rivets is required.



Figure 8. Ultrasonic rivet test readings: (L) uncracked rivet; (R) cracked rivet.

Development of a rehabilitation plan for an existing bridge, specifically one with an outdated technology, requires meticulous planning and a strong understanding of the guiding principles of the structural behaviour, the mechanical properties and the material characteristics etc. From the outlook of the structural behaviour, it is crucial to understand that the bridge is comprised entirely of connected plates, angles and channels that are held by rivets. In addition, there are connection splices that are responsible for transferring from one set of a riveted cross-section to another. As the structure has already deformed and strained in the past, smooth operation is not to be expected and some difficulties are due: selection of any solution has to take that into account. Furthermore, the most important thing is to maintain joint action: when a rivet is replaced, it is imperative that it is replaced by a medium that has very similar stiffness, otherwise it will change the force distribution along the adjacent pieces. If the replacement medium is not stiff enough the older rivets will experience an increase in their respective applied loads that might cause a chain reaction. On the other hand, not every stiff alternative is a viable one. For example, although it has sufficient stiffness, utilizing welded a connection details replacement approach is not recommended due to the effect it has on the existing 70-year-old bridge structural steel plates. The welding causes the steel to become more brittle and reduce the fatigue strength.

Regardless of specifics, as only flawed rivets are to be replaced and the rest to remain in place, any approach will have to consider adequate compatibility between the existing and new elements as they must function together.

2.2 *Rehabilitation plan design alternatives*

Any design alternative should follow the aforementioned guiding principles. In the case of Namir Arches Bridge, there are a couple of key design criteria to consider: structurally, the replacement medium must exhibit rivet compatible behaviour with minimal to no slip. The fabrication process of rivets causes them to fill the plate-hole almost in its entirety giving very little room to experience movement (Ketchum 1919, Ghosh 2000). Operationally, the bridge is in the heart of the Tel-Aviv center and is an important traffic route. Therefore, the client's directive is that the bridge must remain operational throughout the rehabilitation works. Any design alternative must keep that in mind, and it is preferable that there will be as little closures as possible.

Several options were considered, primarily:

a. Installing new rivets with a new riveting machine: the benefit of using this structural solution is due to the inherent similarity of the systems. However, a clear disadvantage is the scarcity of professional equipment and personnel in the local market. Therefore, this option was not pursued.
b. Replacing the damaged rivets with High-Strength Friction Grip (HSFG) bolts: this is a common practice in the field of rehabilitation and/or retrofit projects of steel-riveted bridges (Åkesson 2010, Rickets 2017). In the case of Namir Arches Bridge very little, if any, preliminary treatment can be done on the plates; this is due to the client's condition that the bridge must remain operational. Resulting in expending significant efforts and resources to reach a lesser effectiveness due to low slip factor that is expected with varying degrees of corrosion throughout the bridge.
c. Replacing the damaged rivets with HSFG injection bolts: this design alternative suffers a negative grade due to the fact that it has not yet been utilized, neither by Tel-Aviv municipality nor in the Israeli market. Yet, it is still the most fitting design alternative from structural performance considerations as it poses a promising solution for the low slip factor of the HSFG bolts (ECCS 1994).

2.3 *Rivet replacement with HSFG injection bolts*

The injection bolt solution was developed in the Netherlands in the 1970's (Bouwman 1970) and was later established as a viable solution to replace rivets in existing structures (Kluwen 1981). The practice of replacing steel-riveted bridges (primarily railway bridges) with injection bolts can be seen in Northern and Western Europe.

Essentially, the system is similar to a typical bolted connection with a bolt thread and shank inserted in a designated hole joining several plates for a combined action. A drilled hole is administered in the bolt head and outer-to the shank diameter. An epoxy resin (or another

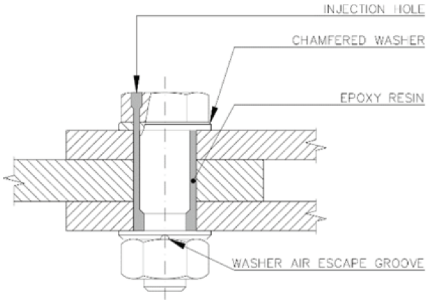


Figure 9. Injection bolt in a double lap joint (modified from ECCS 1994).

equivalent material) is inserted to fill the gap between the bolt shank and plates' walls (Figure 9). The force transfer mechanism is carried through bearing stresses rather than bolt shear in the shank/thread (e.g., Figure 10). The Injection bolts solution can also be applied for HSFG bolts. In that case, design for a dual action will include two different components. A shear component in the shear plane between the friction surfaces and a bearing stress component as detailed in Figure 10.

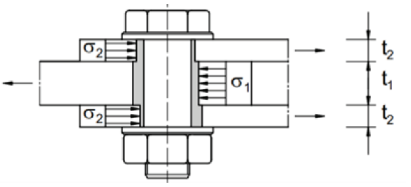


Figure 10. Stress distribution along bolt (EN 1993-1-8:2005).

The reason it is valid to assume joint action with these two components is due to the expected deformations regime. With the bolt hole filled and bearing compression surrounding and assuming sufficient stiffness, there is a de-facto non-slip behaviour leading to the HSFG participating in proportion. Nevertheless, in the Namir Arches Bridge project due to the unknown nature of the class of the friction surfaces and the expected slip factor, the bearing stresses of the injection bolts shall be designed as if there are no HSFG bolts at all. The latter shall be a secondary system assisting in increasing the redundancy of the rivet-substitutes. In addition, as the local market is inexperienced in design and execution of the injection bolts methodology, this 'belt + suspenders' approach was an advantage.

With the Namir Arches Bridge being in a corrosive environment close to the Mediterranean coast, durability considerations are crucial. The long-term durability of epoxy resin is negatively influenced by exposure to both wet and acidic environments (Uthaman et al. 2020), which can lead to degradation. It has been demonstrated that this phenomenon is mitigated by the preloading of injection bolts (Correia et al. 2016) and the application of a protective paint finish. This practice has performed well over the past 50 years (Grensigt and de Vries 2016). The epoxy resin specified in this project is RenGel SW404+HY2404, which is sufficient in the long-term for bearing stresses under 175 [MPa] (Kolstein et al. 2017).

2.4 *Meeting original design criteria*

With the Namir Arches Bridge being a rehabilitation project, the structural behaviour of the new elements needs to be assessed in comparison to the original design criteria. The first step is to adhere to the Allowable Stress Design (ASD) approach rather than the now common Limit State Design.

Upon review of the original calculation report, prepared by Eng. Shoshana Shacham (1955), and was luckily kept in pristine condition, it was clear that the allowable stress on each plate and rivet in the project was 140 [MPa]. Therefore, verification calculations of the bearing resistance of the resin were performed according to EN 1993-1-8:2005 cl. 3.6.2.

2.5 *Rivet replacement with HSFG injection bolts specification*

The procedure of rivet replacement with HSFG injection bolts shall be executed in several key phases. First, non-intrusive works; this entails preperation of the structural steel with sand blasting or other abrasive treatment. This is followed by carrying out the ultrasonic field tests for the bridge's rivets on-site and determining which rivets are disqualified and require replacement. Thereafter, establishing the workflow which methodically defines the order of which rivet is to be treated, in which element, within an element and with what time gap. For example, Figure 11 depicts the conceptual guideline replacement order of a few disqualified rivets in an element. This recommendation is aimed to increase the robustness whenever possible and to reduce unnecessary stresses in the plates.

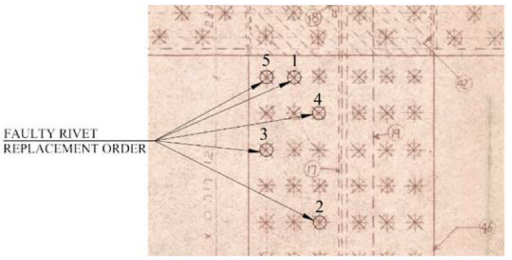


Figure 11. Rivet replacement order – conceptual guideline (modified from, Netivei Israel – National Transport Infrastructure Company).

Once a rivet has been disqualified a series of steps is to be carried in order to replace it with an HSFG injection bolt. Complete details are listed in the project specification; however, the main features can be summarized in making sure the drilled hole is clean from undesired outer agents and/or in a bad structural state. In addition, if necessary, a larger hole may be specified to accommodate the issue with a compatible larger bolt assembly. A partial list of the rivet replacement control table is shown below (Figure 12) for clarity. In essence, all bridge rivets were mapped according to the original design drawings to serve as a baseline for the replacement procedure (e.g., Figure 13 illustrates the interior plates and angles connections in the hangar-arch zone).

Finally, after finalizing with friction surfaces treatment for the open surfaces, the replacement HSFG bolts are preloaded in two phases with the resin injected between them. As the epoxy resin is a crucial component in the structural mechanism, details regarding the resin are included in the specification.

NO.	COMPONENT	RIVET DIAMETER [mm]	BOLT TYPE	BOLT LENGTH [mm]	DETAIL/ SECTION	ORIGINAL DRAWING	PRELOAD FORCE PHASE A 20% ULT. [t]	PRELOAD FORCE PHASE B 60% ULT. [t]
1	**Hangars**							
1.1	CONNECTION ZONE WITH MAIN TIE BEAMS	26	M24	105	Detail A		7.1	21.2
			M27	110	Detail A		9.2	27.5
1.2	TYPICAL SECTION	23	M22	75	Detail A		6.1	18.2
			M24	80	Detail A	65/1/א/ג	7.1	21.2
1.3	CONNECTION ZONE WITH ARCH - DIRECTLY TO HANGAR	26	M24	100	Detail A/Detail B	66/1/א/ג	7.1	21.2
			M27	100	Detail A/Detail B	67/1/א/ג	9.2	27.5
1.4	CONNECTION ZONE WITH ARCH - CONNECTIONS TO ANGLES AND PLATES	23	M22	105	Detail A	68/1/א/ג	6.1	18.2
			M24	110	Detail A		7.1	21.2
1.5	CONNECTION ZONE WITH ARCH - CONNECTIONS TO ANGLES AND PLATES	26	M24	110	Detail A		7.1	21.2
			M27	110	Detail A		9.2	27.5
2	**Arches**							
2.1	CONNECTION SPLICE OF ARCH PLATES - BETWEEN HANGAR NODES, TYPICAL SECTION	23	M22	80	Detail B		6.1	18.2
			M24	80	Detail B	65/1/א/ג	7.1	21.2
2.2	CONNECTION SPLICE OF ARCH PLATES - HANGAR ZONE	23	M22	105	Detail B	66/1/א/ג	6.1	18.2
			M24	110	Detail B	67/1/א/ג	7.1	21.2
2.3	INTERIOR ARCH STRENGTHENING DETAIL - INTERIOR ARCH ANGLES	20	M20	80	Detail B	68/1/א/ג	4.9	14.7
			M22	80	Detail B		6.1	18.2
2.4	ARCH END DETAIL - MAIN TIE BEAM CONNECTION ZONE	23	M22	95	Detail C		6.1	18.2
			M24	100	Detail C	63/1/א/ג	7.1	21.2
2.5	ARCH END DETAIL - MAIN TIE BEAM CONNECTION ZONE	26	M24	85	Detail C		7.1	21.2
			M27	90	Detail C		9.2	27.5

Figure 12. Rivet replacement by HSFG injection bolts control table (partial table, translated).

The methodology listed above is rather a guideline and not a recipe. While working on existing structures is never an easy task nor it is always as expected, in the case of the Namir Arches Bridge there are several issues that are worth mentioning.

First and foremost, the matter of access to small and closed spaces. This issue is true to both the required UT field tests of the rivets and more so to the replacement works, when required. Additionally, once the rehabilitation works of the structural steel rivets will commence unique and case-by-case specific details will be developed under the guiding principles of the methodical approach presented.

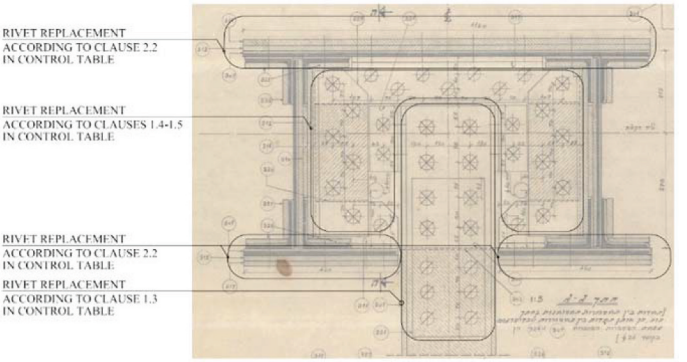


Figure 13. Detail B rivet replacement legend: hangar-arch connection (modified from, Netivei Israel – National Transport Infrastructure Company).

3 CONCLUSIONS

The rehabilitation project of the Namir Arches Bridge called for a tailor-made solution to prolong its design life and to ensure public safety throughout that period. Out of the aforementioned design alternatives, the HSFG injection bolts approach is the most suitable method with the remaining existing rivets kept in place.

This method results in a more robust product with an inherent greater redundancy at a relatively small premium.

REFERENCES

Åkesson, B. 2010. *Fatigue life of Riveted Steel Bridges*. London: CRC Press

Bouwman, L.P. 1970. Voorlopig overzicht van een onderzoek naar de invloed van het opvullen van epoxy-hars van de ruimte tussen boutsteel en gatwand bij verbindingen met diverse deklagen (Preliminary survey of the research on injection bolts). TU Delft, *Stevin rapport 6-70-7*

Correia, J.A.F.O., De Jesus, A.M., Pinto, J.C., Calçada, R.A., Pedrosa, B., Rebelo, C., Gervásio, H. & Da Silva, L. 2016, September. Fatigue behaviour of single and double shear connections with resin-injected preloaded bolts. In *IABSE Congress Stockholm*.

ECCS. 1994 *European recommendations for bolted connections with injection bolts*. Brussels: ECCS publication No. 79.Eurocode 3. EN 1993-1-8:2005. *Design of steel structures – Part 1-8: Design of joints*.

Ghosh, U.K. 2000. *Repair and Rehabilitation of Steel Bridges*. Rotterdam: Balkema

Gresnigt, A.M., & De Vries, P.A. (2016). Injection bolts update on Research and Applications. In *AIS-CECCS workshop* (Vol. 14).

Ketchum, M.S. 1924. *Structural engineers' handbook: data for the design and construction of steel bridges and buildings* (Vol. 2). McGraw-Hill Book Company, Incorporated.

Kolstein, H., Li, J., Koper, A., Gard, W., Nijgh, M., & Veljkovic, M. 2017. Behaviour of double shear connections with injection bolts. *Steel Construction*, *10*(4), 287–294.

Kluwen, H. 1981. Onderzoek naar het gedrag van injectiebouten indien deze worden toegepast ter vervanging van klinknagels in bestaande constructies (Research into the behaviour of injection bolts if they are applied to substitute rivets in existing structures). TU Delft, *Stevin rapport 6-81-9*

Rickets, N. 2017. *Railway Bridge Maintenance*. London: ICE Publishing

Uthaman, A., Xian, G., Thomas, S., Wang, Y., Zheng, Q. & Liu, X. 2020. Durability of an Epoxy Resin and Its Carbon Fiber- Reinforced Polymer Composite upon Immersion in Water, Acidic, and Alkaline Solutions. *Polymers*, *12*, 614.

Uthaman, A., Xian, G., Thomas, S., Wang, Y., Zheng, Q. & Liu, X. 2020. Durability of an Epoxy Resin and Its Carbon Fiber- Reinforced Polymer Composite upon Immersion in Water, Acidic, and Alkaline Solutions. *Polymers*, *12*, 614.

Bridge Maintenance, Safety, Management, Digitalization and Sustainability – Jensen, Frangopol & Schmidt (eds)
© 2024 The Author(s), ISBN 978-1-032-77040-6
Open Access: www.taylorfrancis.com, CC BY-NC-ND 4.0 license

Study on fatigue detection of weld toe in orthotropic steel deck

R. Harashima, C. Hashizume & H. Sekiya
Department of Urban and Civil Engineering, Tokyo City University, Tokyo, Japan

S. Morichika & M. Saeki
Department of Civil Engineering, Tokyo University of science, Chiba, Japan

ABSTRACT: Orthotropic steel deck bridges are employed in many urban expressways in Japan. Many fatigue cracks, which might be caused by overloading vehicles and long in-service periods, are found in the orthotropic steel deck. Since the cracks affect the safety of traveling vehicles, adequate maintenance should be conducted. The objective of this study was to develop a method of detecting a crack propagating in the deck plate through the change in strain response. In this research, fatigue tests were performed using small specimens that imitated a section of the deck plate and the trough rib of an orthotropic steel deck. The size of the deck plate was 1000 mm in length, 280 mm in width, and 12mm in thickness. The trough rib was 100 mm in length. As a result of the test, strain changes due to fatigue crack propagation on the weld toe at the upper side could be detected by measuring strain changes.

1 INTRODUCTION

Orthotropic steel deck bridges are employed in many urban expressways in Japan. This is because it can shorten the construction period and is lighter than concrete slabs. Many fatigue cracks, which might be caused by overloading vehicles and long in-service periods, are found in the orthotropic steel deck. Magnetic Particle Testing and Ultrasonic Testing have been used to detect fatigue cracks. However, it is necessary to consider a continuous monitoring system for earlier detection in the future. Therefore, this study investigates a fatigue crack monitoring system based on strain response analysis using strain gauges. Specifically, the detection of fatigue cracks is attempted from changes in the measurement results of the strain gauge installed at the weld, as shown in Figure 1.

2 SUMMARY OF THE TEST SPECIMENS

The test specimens were small specimens that imitated the U-ribs of the steel deck plate. The dimension of the specimen is shown in Figure 2. The dimension of the specimen follows the design guidebook of road bridges in Japan (Japan Road Association 2020). The deck plate thickness was set to 12 mm. The depth and length of the U-rib were set to 280 mm and 100 mm, based on previous research (Murakoshi et al. 2012) and the conditions of the testing machine. The material (Mori et al. 2006) was SM490YA. The amount of weld penetration was 75% or more. Since this experiment was conducted for root cracks, grinder treatment was performed at the weld toe, as shown in Figure 1.

3 FE ANALYSIS TO STUDY LOADING CONDITIONS

This chapter describes the Finite Elements Analysis (FEA) to validate the specimen model and determine loading conditions.

DOI: 10.1201/9781003483755-257

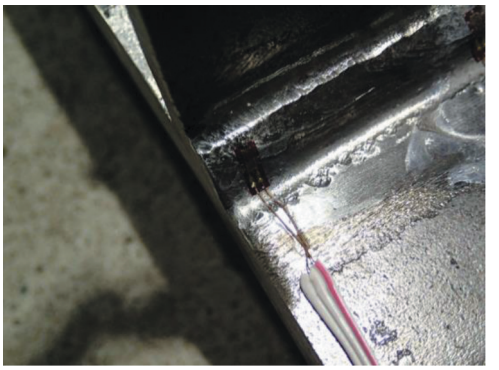


Figure 1. Strain gauge.

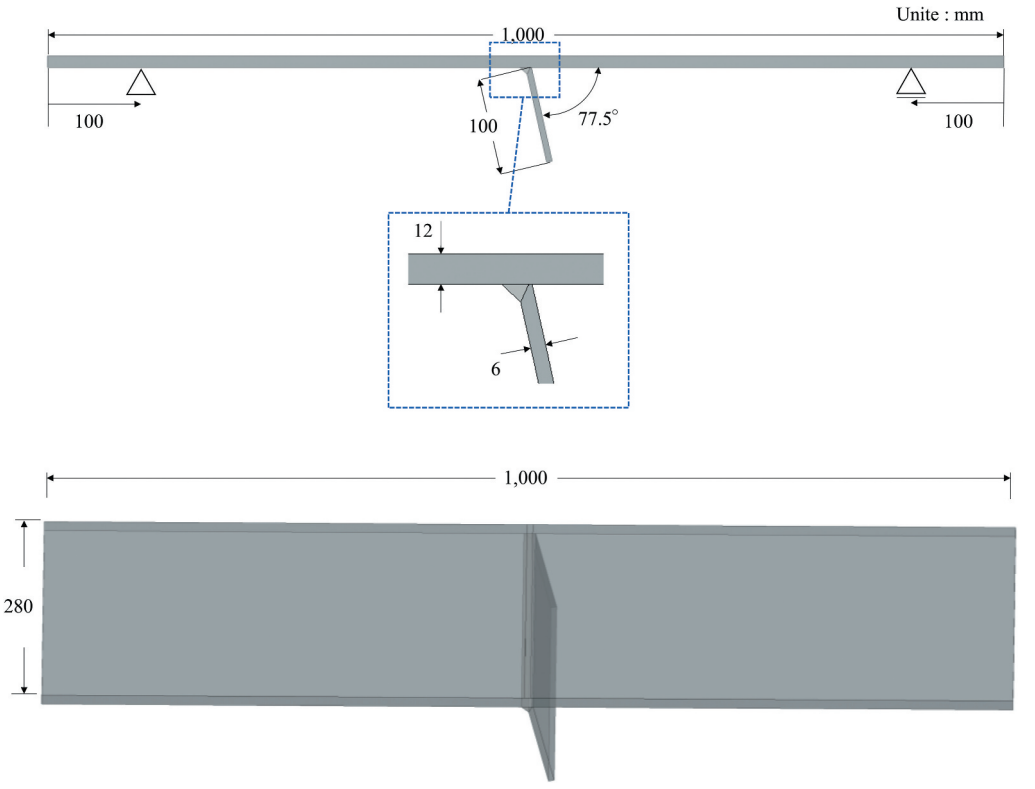


Figure 2. Dimension of the specimen.

3.1 *Investigation of loading position by FEA*

Loading positions were investigated by FEA. The software used for the FEM analysis was ABAQUS2022 Ver. 6.22. The specimen was modeled using solid element (C3D8R). The Young's modulus and Poisson's ratio of which are 205 GPa and 0.3, respectively. As stress concentration points, we focused on the weld toe at the upper side, the weld toe at the lower side, the weld roots at the upper side and left side of the weld between deck plate and trough rib, as shown in Figure 3. In the FEA, the effective notch method (Suganuma & Miki 2007) was used to evaluate the stress distribution in the weld root and toe. The radius of the effective notch was set to 0.5 mm. As shown in Figure 4, the loading position move at intervals of 50 mm. Assuming loading with a single tire, the loading area was 200 mm × 200 mm (square shape). The magnitude of

the load was set to 1 MPa. The Von Mises stress at the stress concentration points on the surface and in the center of the specimen are shown in Figure 5. The highest stress was observed at weld toe at the upper side in the center of the cross-sectional direction. Second and third highest stresses were the weld root at the upper side and the weld root at the left side, respectively. The maximum stress was found at the center of the specimen, just above the weld. FEA results showed that the cracks were most likely to initiate from the weld toe at the upper side. Grinder treatment was applied to the weld toe at the upper side to decrease the stress concentration, since the initial objective of the experiment was the detection of the fatigue crack from the weld root. Based on the FEA results, it was decided to place the load in the center of the specimen at an area of 200 mm × 200 mm. The loading patterns include crack introduction loading, beach mark introduction loading, and live load loading. The beach mark introduction loading was performed to investigate the relationship between strain response and crack propagation. The live load loading was performed to study the changes in the strain range under live loads. Crack introduction loading was applied with Sine waves of 10 kN maximum and 1 kN minimum at 100,000 to 150,000 cycles per cycle. The loading frequency was 2Hz to 4Hz. The beach mark introduction loading was given by Sine waves with a maximum of 10 kN and a minimum of 5.5 kN for 100,000 cycles per cycle. The live load was applied 50 cycles in each of the eight cases where the loads were set to achieve the assumed strain values.

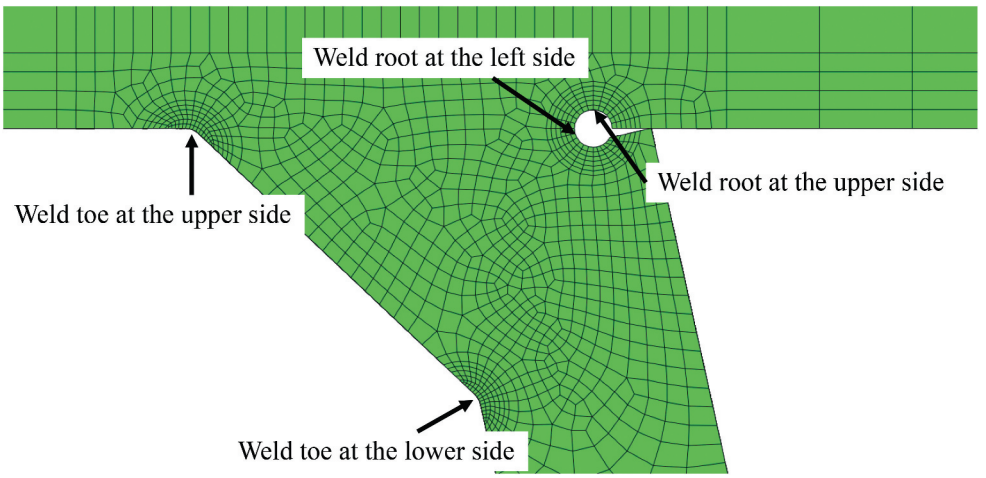


Figure 3. Stress concentration points.

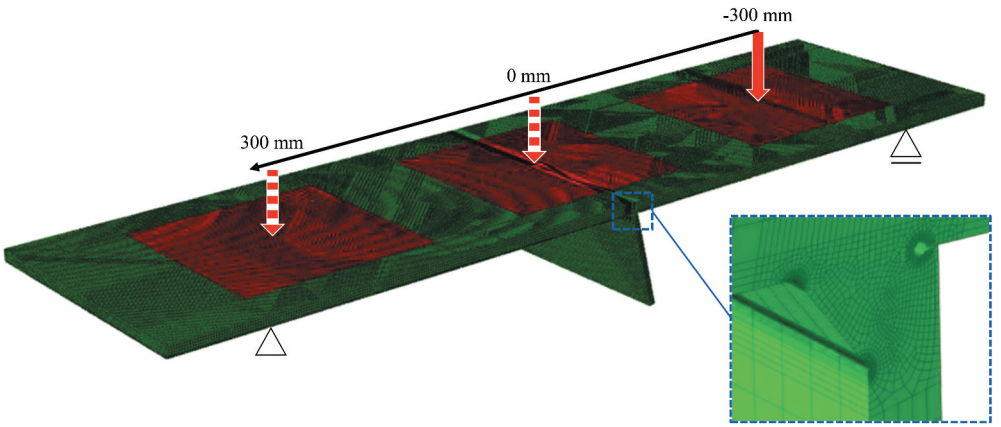


Figure 4. Consideration of loading position.

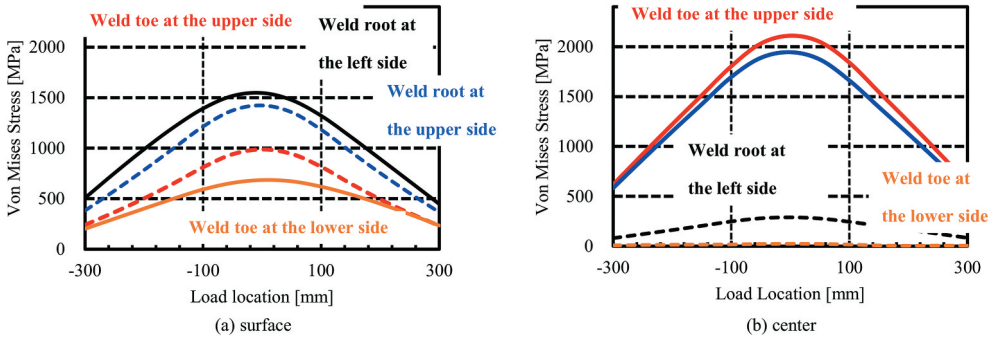


Figure 5. Comparison the stress concentration.

3.2 *Validation of FEA model*

FEM was used to examine the validity of the test specimens. The stress conditions between the U-rib model which includes the U-rib and the test specimen model which includes a part of U-rib were compared. The FEA model is shown in Figure 6. The load was applied to an area of 200 mm × 200 mm in the center of the specimen with the load of 1 MPa.

A contour plot of the Von Mises stress at the center of the specimen is shown in Figure 7. The stress distributions on the weld toe at the upper side are almost same. Furthermore, it can be confirmed that the stress is concentrated on weld root at the upper side. These results indicate that the trends of von Mises stress distribution for the U-rib model and the specimen model are similar.



Figure 6. FEA model.

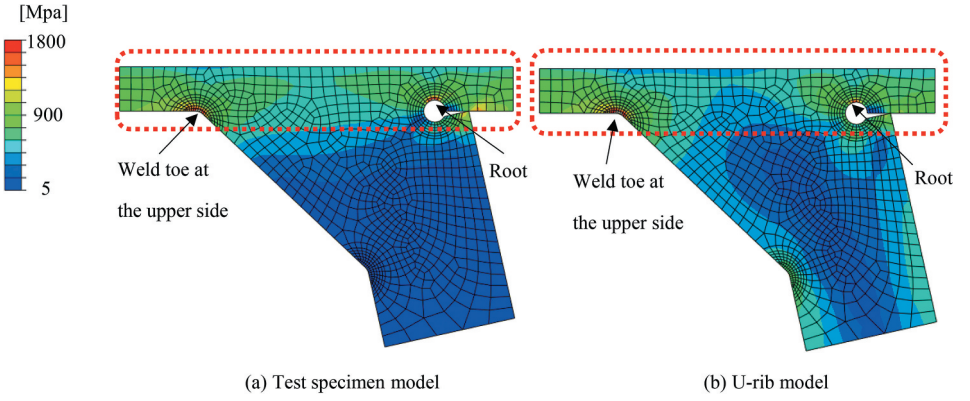


Figure 7. Comparison of stress distribution between test specimen and U-rib model.

4 SUMMARY OF MEASUREMENTS AND EXPERIMENTS

4.1 *Measurement locations*

Strain gauges were installed as sensors to measure the changes in strain response. Figure 8 shows the installation locations of the strain gauges and measurement number which is from

CH1 to CH17. CH1 to CH17 are strain gauges. CH1 to CH7 were installed for toe crack detection and CH8 to CH14 for root crack detection. CH17 was installed to confirm the strain response without the effect of the crack. Strain gauges were uniaxial and 3 mm length. The test set-up is shown in Figure 9. Fatigue tests are conducted by bending test.

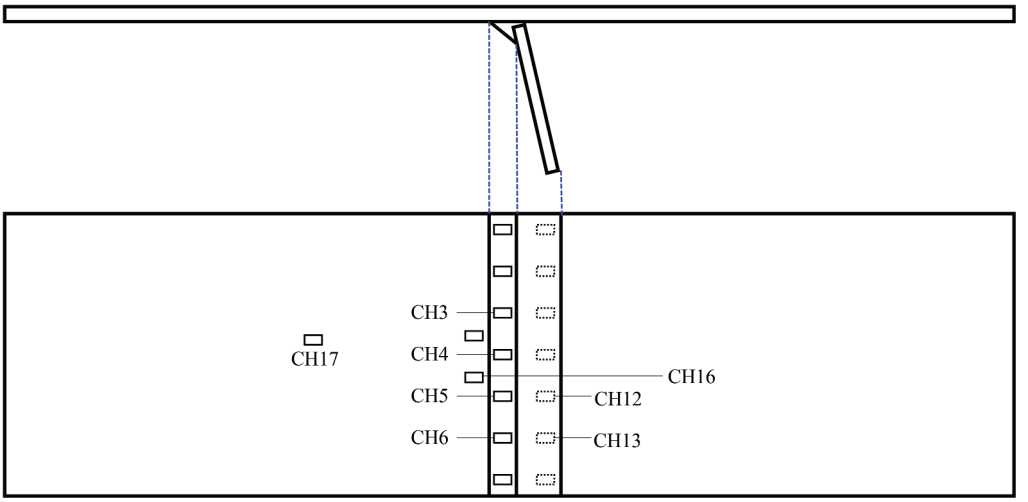


Figure 8. The installation locations and channels.

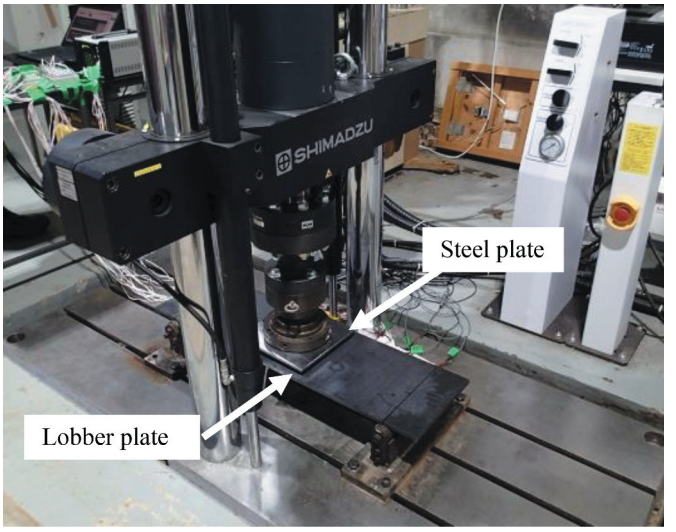


Figure 9. Fatigue test set-up.

5 RESULTS OF FATIGUE TEST

The crack initiated from the weld toe at the upper side which is between CH5 and CH6. The crack then propagated and penetrated by about 70%. Since the deflection was large, the fatigue test could not be continued. Therefore, it was cut using a thread saw. Figure 10 shows the test specimen after cutting.

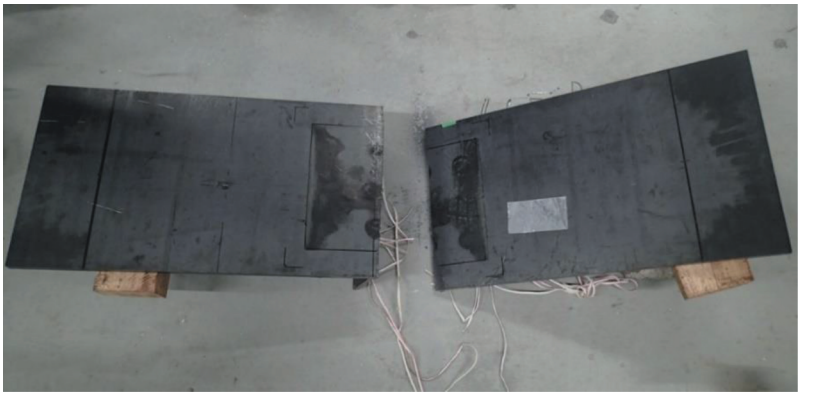


Figure 10. Test specimen after cutting.

5.1 *Beach mark*

Beach marks on the specimen fracture surface are shown in Figure 11. Beach marks were generated from 0.88 million cycles in each 0.1 million cycles. The crack initiation point was between CH5 and CH6 where is about 24 mm from CH5 and about 26 mm from CH6. The crack then developed on both sides. Fatigue cracks reached CH5 between 1.33 and 1.48 million cycles. Furthermore, the cracks reached CH6 about 1.39 million cycles. Cracks propagation in the direction of CH6 were found to have reached their ends between 1.58 million and 1.68 million cycles. Crack propagation began to accelerate from 1.18 million cycles, and 38.8 mm of crack propagation occurred between 1.58 million and 1.68 million cycles. Crack growth in the plate thickness direction was found to be slow, penetrating just above the crack initiation point at 1.68 million cycles.

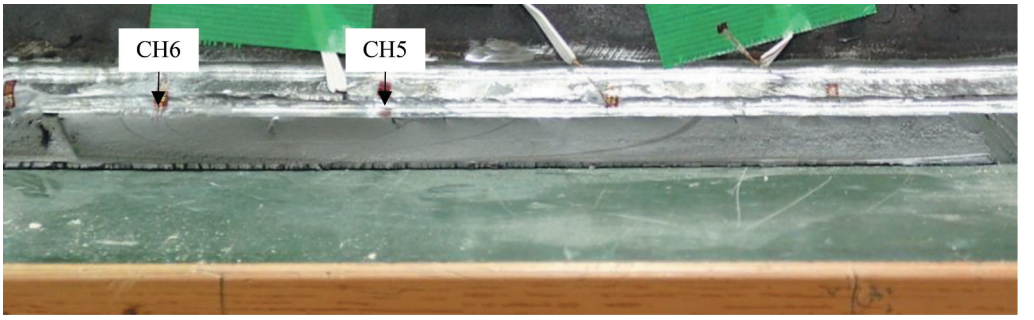


Figure 11. Beach mark.

5.2 *Strain measurement results*

The strain responses of CH3, CH4, CH5, CH6, CH12, CH13, CH16 and CH17 at 0.78 million cycles of crack introduction loading are shown in Figure 12. This amplitude is calculated for each loading cycles as the strain range, and is shown in Figure 13. In CH5, an increase in strain range was observed after 0.8 million cycles. The increase stopped at 1.32 million cycles, followed by a decrease. No change was observed in other CH. In all CHs, only CH5 showed the fastest change in strain response. The change in the strain range was calculated based on the strain range at 0.78 million cycles. The results are shown in Figure 14. The change in CH5 shows an increase of about 10% at 0.98 million cycles.

Beach mark shows that small cracks occur in about 0.88 million cycles. Considering the crack location and strain gauge strain variation, it is thought CH5 was able to detect a small

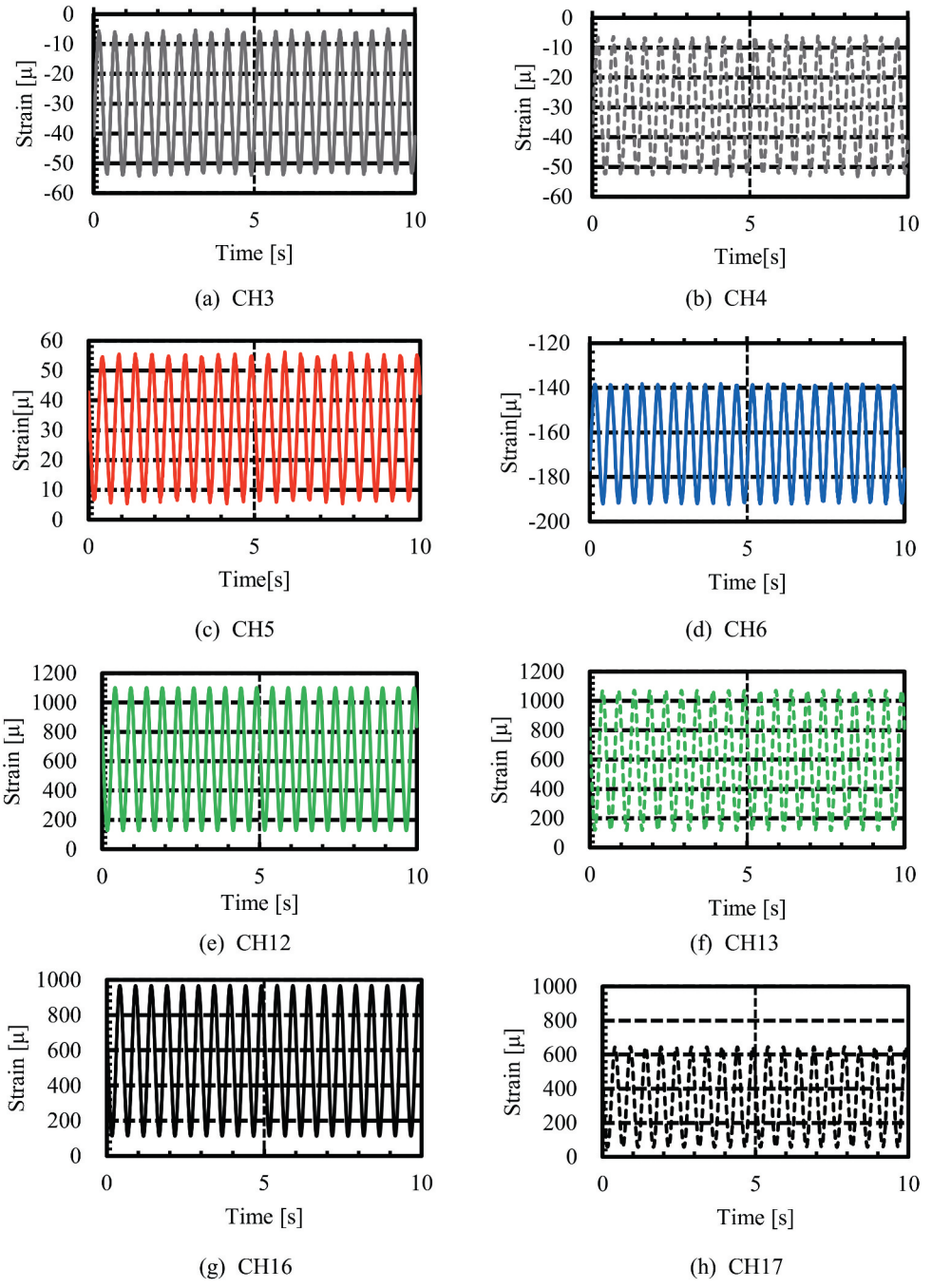


Figure 12. Strain response.

crack when the crack reached a distance of 15 mm from the sensor position. In CH6, strain range decreased by 10% when the crack propagated to 15 mm from the sensor. Furthermore, the strain range reached a maximum when the crack reached CH5. The strain range then decreased as the crack passed through CH5. When the crack propagated in the direction of CH6 and reached the edge of the specimen, the strain range of CH5 increased rapidly. These results indicate that strain gauges are able to capture the crack propagation.

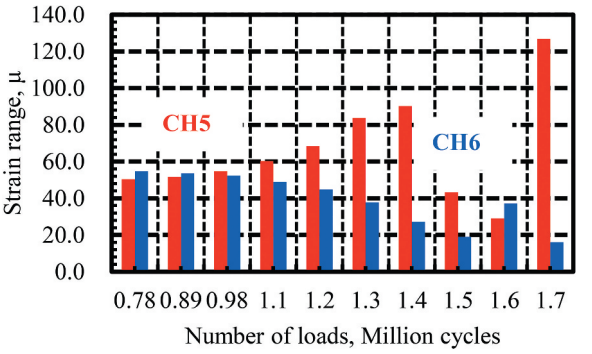


Figure 13. Strain range of loading cycles.

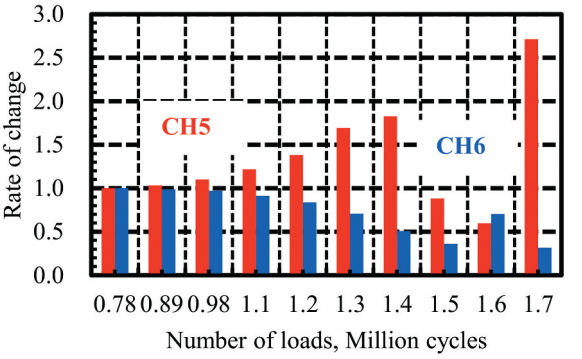


Figure 14. Rate of change in strain range.

6 SUMMARY

Strain changes due to fatigue crack propagation on the weld toe at the upper side could be detected by measuring strain changes. The strain changes due to fatigue crack could be detected by strain gauges which were installed 15 mm from crack position. When the crack reached the top of the sensor, the strain range reached a maximum and then showed a decreasing trend. In the future, we will conduct the experiment again to generate a deck-growth crack from the weld root. We will examine whether it is possible to detect deck-growth cracks by sensing strain gauges.

ACKNOWLEDGEMENT

This work was supported by JSPS KAKENHI Grant Number JP20K14814.

REFERENCES

Japan Road Association., 2020. *Steel Road Bridge Design Handbook*,Tokyo: MARUZEN Publishing, p146.

Mori, T., Shigihara, S., Nakamura, H., 2006. Fatigue tests in welded connections between deck plate and trough rib in steel plate deck inconsideration of weld penetration. *Journal of JSCE* A1.Vol.68, No.2.

Murakoshi, J., Takahashi, M., Koike, M., Kimura, T.,2012.Study on practical ultrasonic inspection method for fatigue cracks in steel orthotropic deckplates. *Journal of JSCE* A1.Vol.62, No.3.

Suganuma, H., Miki, C., 2007.Fague strength evaluation with effective notch stress of the weld between trough rib and deck plate on orthotropic steel deck. *Journal of JSCE* A1.Vol.63, No1.

Bridge Maintenance, Safety, Management, Digitalization and Sustainability – Jensen, Frangopol & Schmidt (eds)
© 2024 The Author(s), ISBN 978-1-032-77040-6
Open Access: www.taylorfrancis.com, CC BY-NC-ND 4.0 license

Fatigue crack detection in out-of-plane gussets using crack detection sensor

K. Sunada
Department of Urban and Civil Engineering, Tokyo City University, Tokyo, Japan

T. Kuroiwa & R. Kasakura
Tokyu Construction Co., Ltd. Institute of Technology, Kanagawa, Japan

H. Sekiya
Department of Urban and Civil Engineering, Tokyo City University, Tokyo, Japan

ABSTRACT: Due to the recent increase in traffic and vehicle weight, bridges are under severe service. As a result, many fatigue damages have been found during periodic inspections. Since it is expected that more fatigue damage will occur in the future, it is important to develop efficient and inexpensive maintenance methods. Therefore, in this study, experiments are conducted using small specimens that reproduce the out-of-plane gussets of steel bridges to verify the effectiveness of crack detection sensor. The specimens consist of a steel plate 90 mm wide, 700 mm long, and 12 mm thick, with a gusset plate 50 mm wide, 150 mm long, and 12 mm thick welded to it. Both materials were made of steel SM490 material and were not painted. The relationships between the response by the crack detection sensor and the conditions of fatigue crack are discussed.

1 INTRODUCTION

Bridges are in severe service due to the recent increase in traffic and vehicle weight. Therefore, many fatigue damages are found in steel bridges during periodic inspections. Fatigue damage occurs at locations where large strains occur repeatedly, such as at welded joints. When fatigue cracks are found by visual inspection, repair, and reinforcement should be considered according to the location of the cracks and their progress. Therefore, it is sometimes important to monitor the progress of fatigue cracks between the detection of fatigue cracks and repair or reinforcement.

Morichika et al. (2020) proposed fatigue crack detection using piezoelectric sensor. They conducted fatigue tests using I-digit fatigue specimens. The results showed that it is possible to detect the fatigue crack near the weld zone using a piezoelectric ceramic sensor as well as strain gauges.

In this study, we attempt to monitor the progress of fatigue cracks by utilizing a sensor used for crack detection in concrete. This crack detection sensor detects cracks by the breakage and emission of optical fibers caused by crack propagation. If this crack detection sensor can be applied to fatigue cracks in steel structures, it will be possible to easily determine fatigue crack growth during inspection. In this study, experiments using small specimens that reproduce the out-of-plane gusset of steel bridges are conducted to verify the effectiveness of the crack detection sensor.

The paper is organized as follows: Chapter 2 describes the experimental method. Chapter 3 describes the experimental results and discussion. Finally, Chapter 4 presents the conclusions.

2 EXPERIMENTAL METHODS

To verify the applicability of a crack detection sensor, which has the proven results in detecting concrete cracks, to fatigue crack detection, fatigue tests were conducted on a specimen

DOI: 10.1201/9781003483755-258

simulating an out-of-plane gusset. The objectives of this experiment were to verify the accuracy of fatigue crack detection, as well as to identify points for improvement.

Figure 1. shows the details of the crack detection sensor used in the experiments. The crack detection sensor is a sensor that detects cracks by the breakage and emission of light from an optical fiber as the crack propagates. The detection accuracy of the crack detection sensor is determined by the type of sensor and ranges from about 0.05 to 0.3 mm.

The crack detection sensor was attached in the same manner as the strain gauge was attached. The steel surface at the attachment point was smoothed with sandpaper, and the bonding point was cleaned with acetone. The sensor was then attached to the steel surface with adhesive.

The dimensions of the test specimen are shown in Figure 2. The dimensions of the specimen were 90 mm wide, 700 mm long, and 12 mm thick. A 12-mm-thick steel plate that imitated a gusset was welded to the center of the specimen as an all-around fillet weld with a weld leg length of 6 mm. All steels ware SM490YA, and no coated pavement was applied. The weld joint edges other than the focus point were machined by a grinder in advance to alleviate the stress concentration.

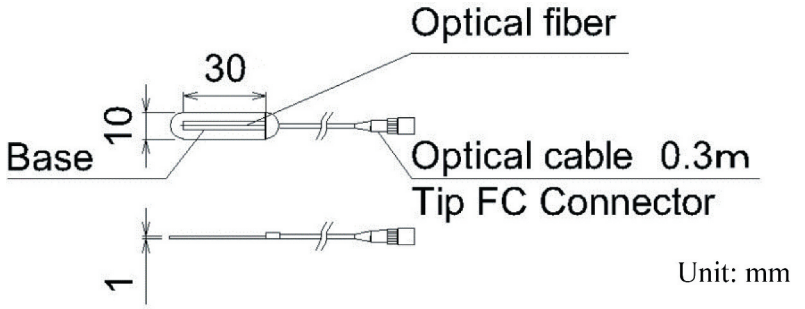


Figure 1. The details of the crack detection sensor.

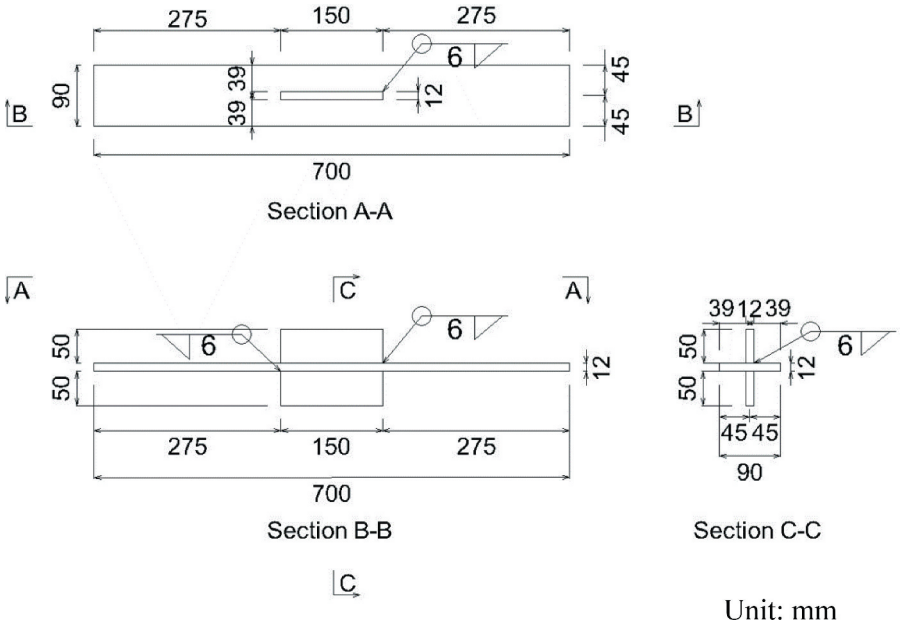


Figure 2. The dimensions of the test specimen.

The sensor locations are shown in Figure 3. In addition to the crack detection sensors, strain gauges were used to measure the nominal stress and to monitor the propagation of fatigue cracks. All strain gauges were 2 mm in diameter, and the sampling frequency was 100 Hz.

The fatigue machine with the specimen is shown in Figure 4. Two types of loading patterns, which include crack-introduced loading and beach-mark-introduced loading, were used as one cycle.

The loading pattern is shown in Figure 5. The crack initiation loading was intended for fatigue crack initiation and propagation, and the stress amplitude was set to approximately 120 MPa. The maximum and minimum loads were set to 135 kN and 5 kN, respectively, to achieve a load range of 130 kN, and 100,000 cycles of loading were considered as one set.The loading to introduce a beach mark to check the fatigue crack propagation was performed to introduce a beach mark.

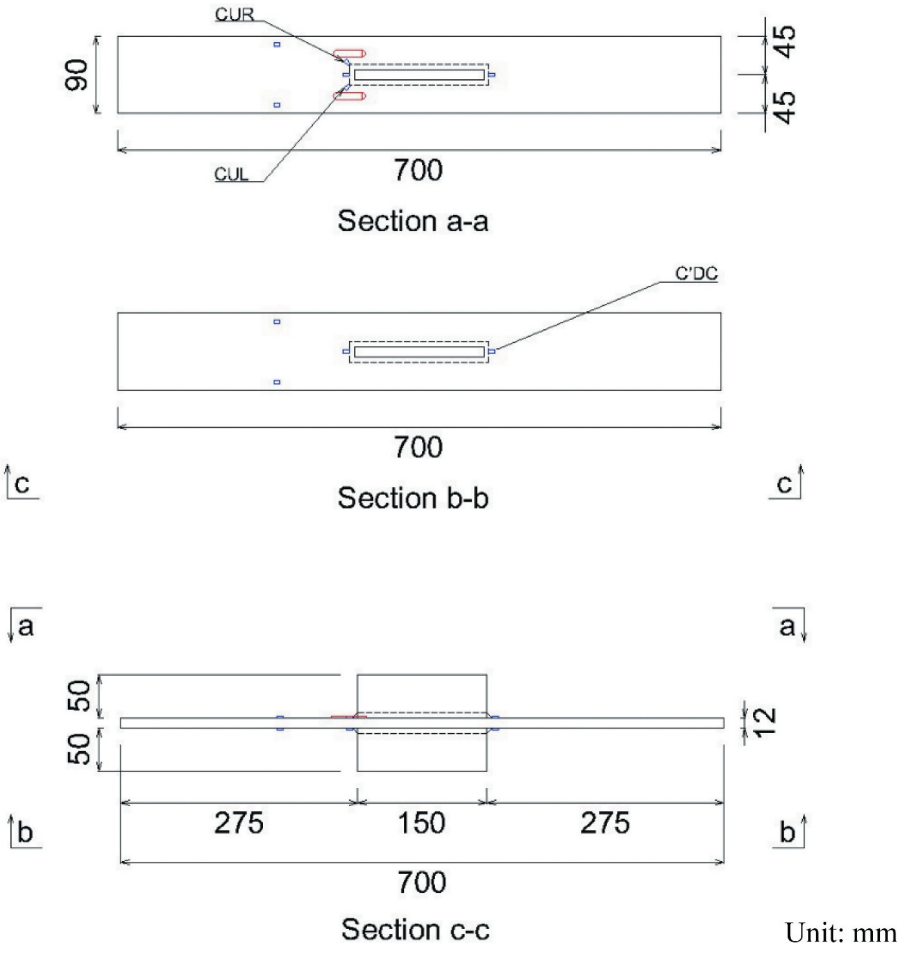


Figure 3. The sensor locations.

3 RESULTS AND DISCUSSION

The results of strain measurement using strain gauges, which were measured in conjunction with crack detection sensor, are shown in Figure 6.

In this experiment, fatigue cracks were assumed to occur at the points where strain gages CUR and CUL were attached. After 900,000 cycles of loading, the rate of change of C'DC had decreased, so grinder treatments were applied to remove it and prevent crack



Figure 4. Fatigue machine with the specimen.

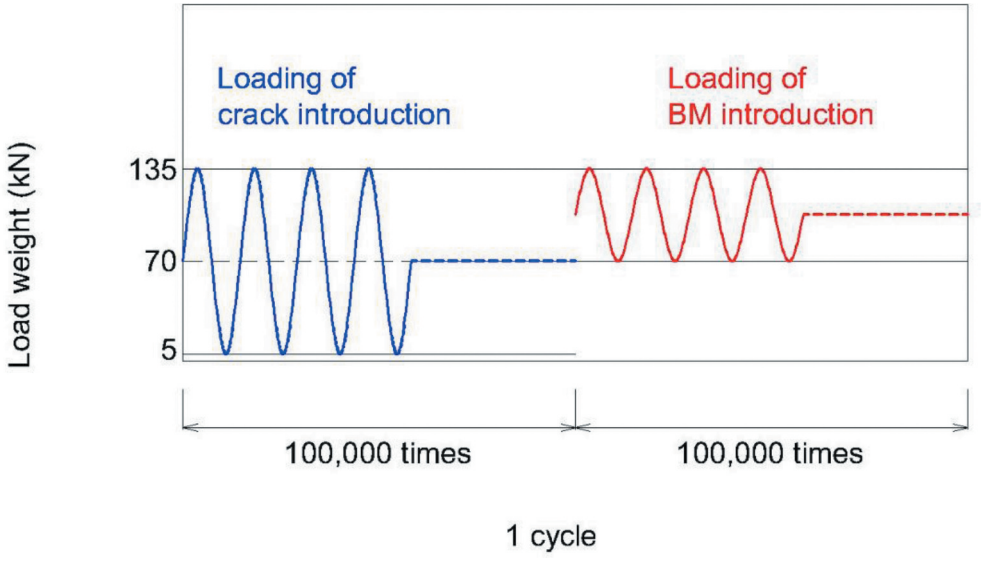


Figure 5. The loading pattern.

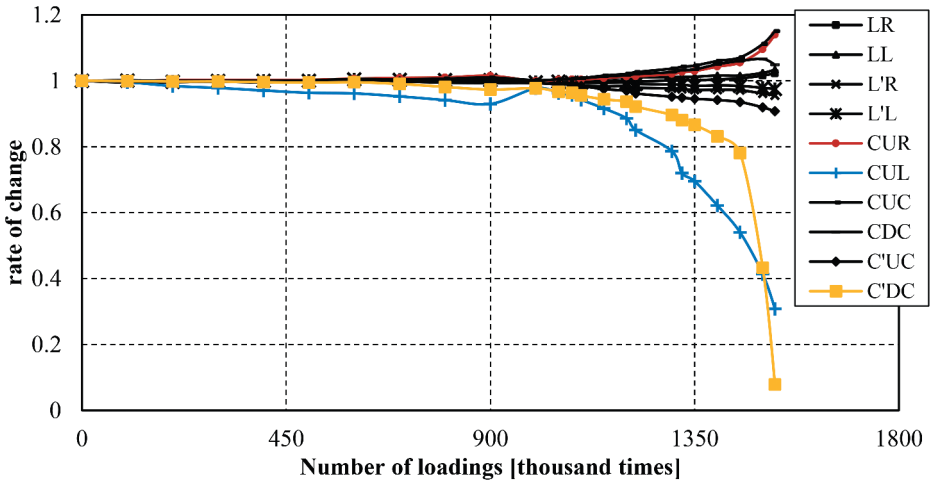


Figure 6. Strain measurement results using strain gauges.

propagation. Thereafter, since the rate of change of CUL was decreasing, it was expected that fatigue cracks would initiate at the planned locations, but at 1.5 million cycles, a sudden change in C'DC occurred. After confirming the position of C'DC, a fatigue crack with a length of about 40 mm was observed from the gusset plate side, so the target location was changed to the position of C'DC, and the crack detection sensor was replaced.

The conditions at the time of attaching the crack detection sensor and at the time of specimen rupture at the end of the test are shown in Figure 7. (a)-(b), respectively.

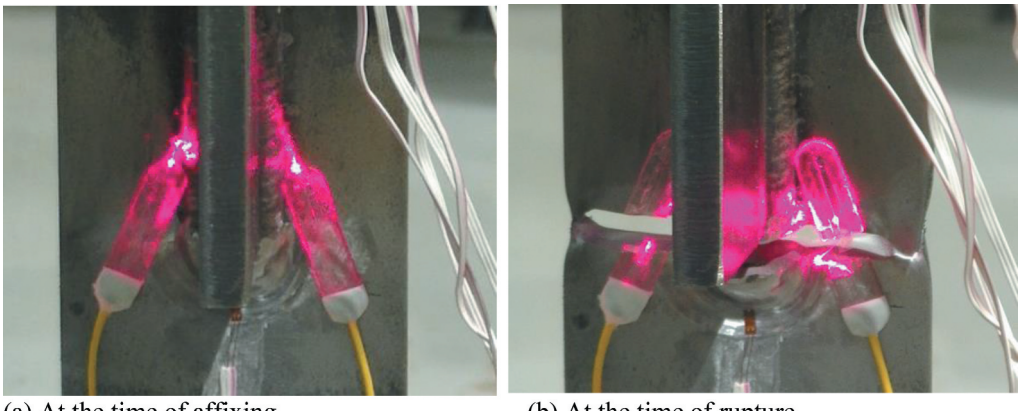
In Figure 7. (a), it is considered that the optical fiber was slightly broken due to the reattachment of the crack detection sensor, and the entire fiber emitted a slightly red light before the fatigue crack reached the sensor. If the optical fiber is not damaged and is correctly attached, only the upper end of the crack detection sensor emits light (Figure 8.).

As the crack propagated and the crack width increased, the light at the top of the sensor became slightly weaker, and the light emission at the crack was confirmed.

However, it is important to verify the response of the crack detection sensor at small crack widths.

Figure 7 (b) shows that when the specimen ruptured, the sensor also ruptured, and a strong light emission was observed at the ruptured point.

The fracture surface of the specimen is shown in Figure 9. Figure 9. shows that six beach marks were observed between 1 million and 1.5 million times of crack introduction loading.



(a) At the time of affixing (b) At the time of rupture

Figure 7. Changes in detection sensors.

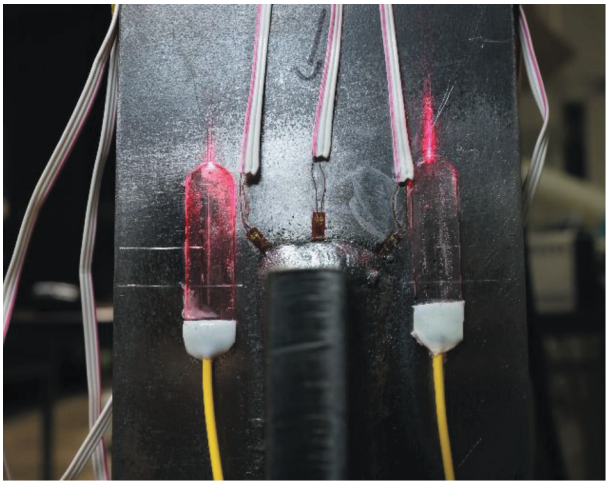


Figure 8. The correct state of the detection sensor when affixed.

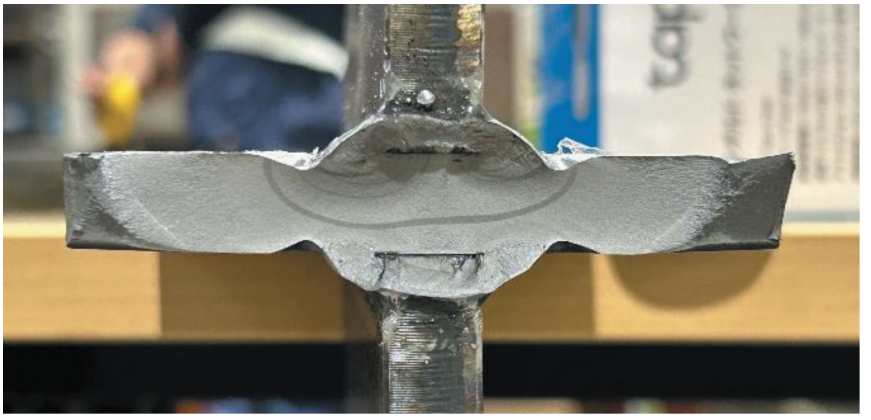


Figure 9. Fracture surface.

4 CONCLUSIONS

Although the crack detection sensor emitted light when the fatigue crack width was large or when the specimen was ruptured, the effectiveness of the sensor for small crack widths still needs to be verified.

In the future, we will continue to verify the effectiveness of the sensor using a crack detection sensor with high detection accuracy (detection accuracy: 0.05 mm).

ACKNOWLEDGEMENTS

Ms. Saito and Mr. Ohno supported the fatigue tests. We would like to express our gratitude to them.

REFERENCES

Morichika, S., Sekiya, H., Maruyama, O., Hirano, S. & Miki, C. 2020. Fatigue crack detection using a piezoelectric ceramic sensor. *Welding in the World* 64:141–149

Bridge Maintenance, Safety, Management, Digitalization and Sustainability – Jensen, Frangopol & Schmidt (eds)
© 2024 The Author(s), ISBN 978-1-032-77040-6
Open Access: www.taylorfrancis.com, CC BY-NC-ND 4.0 license

Fatigue crack monitoring by measuring strain without loading

T. Ishikawa & N. Matsumoto
Kansai University, Suita-shi, Osaka, Japan

K. Komon
Asco Co., Ltd., Tottori, Japan

ABSTRACT: The authors have previously proposed a method to evaluate fatigue crack initiation by monitoring changes in strain near the weld toe under unloading conditions. In this method, the alteration in strains resulting from the release of residual stress is utilized. However, if fatigue cracking has already initiated, the change in strain under the unloading condition at the weld toe is minimal. Therefore, the authors shifted their focus to the area around the fatigue crack tip. In this study, it was discovered that fatigue crack propagation can be detected through changes in strain under unloading conditions. Furthermore, considering the application to monitoring in real bridges, wireless strain measurement logger with LPWA was used to measure the strain at the crack tip under unloading conditions. It was found that the measurement results of the strain logger with LPWA show the same tendency to those of dynamic strainmeters.

1 INTRODUCTION

Fatigue damage is a typical cause of damage to steel road bridges, and many cracks have been found on steel bridges, particularly on urban motorways and on heavily trafficked routes. Smaller fatigue cracks are removed by grinding, however when the fatigue cracks have propagated 10 to 50 mm, emergency counter measures such as stop-hole methods (Miki et al. 1990; Okura and Ishikawa 2002; Chen 2016) are applied in Japan, until permanent repairs are conducted. Therefore, the technologies to monitor the fatigue crack growth at a low cost during their tentative repair to permanent repair is strongly required. Monitoring is also considered for cases where the slow fatigue crack growth or for fatigue cracks in secondary members.

Various methods have been proposed for fatigue crack monitoring, they are fatigue damage monitoring sensors (Komon et al. 2003) and crack gauges. However, they are not suitable for periodic checks of crack growth. Recently, the introduction of monitoring systems utilizing communication standards such as LPWA (Low Power Wide Area) enabling low-power and long-term measuring, which although limited in the amount of data to be transmitted, is advancing for cost-effective monitoring (Kobayashi and Ohara 2019, Sekiya et al. 2020).

The authors propose a method to evaluate the initiation and progression of fatigue cracks by periodically measuring strains near the welded end of a fillet-welded gusset joint without loading. Previous studies have focused on the welded end near the crack initiation point. Strains near the welded end exhibit significant changes during fatigue crack initiation and propagation, as this method measures the strain change resulting from the released residual stress. Furthermore, strain measurements without loading eliminate the need for applied loading, making it suitable for static measurements. Hence, the proposed method aligns with cost-effective monitoring, such as IoT monitoring using LTE-M or LPWA. However, proposed method is not suitable for evaluation of already well growth fatigue cracks, because the residual stress is mostly released for longer fatigue cracks.

DOI: 10.1201/9781003483755-259

This study focuses on the strain changes in the main plate section where fatigue cracks propagate, specifically in the vicinity of the fatigue crack tip. Strain measurements during unloading conditions in the vicinity of the fatigue crack tip are conducted in fatigue tests to clarify whether the evaluation of fatigue crack progression can be achieved through changes in strains during unloading conditions. Additionally, considering the application to monitoring in real bridges the strain changes were measured under unloading conditions by a developed strain data logger with LPWA and transmitted to the web server. The measurement results of the strain loggers with LPWA were found to show the same tendency as those of dynamic strainmeters.

2 FATIGUE TEST

2.1 *Test specimens*

In this study, bending fatigue tests were conducted using out-of-plane gusset-joint specimens. The strain at the tip of fatigue cracks developed in the test specimen was measured during without loading using dynamic strainmeters and wireless strain measurement devices. The fatigue tests employed the plate bending fatigue test machine as described in the references (Yamada et al., 2007). For all specimens, the fatigue tests were conducted with a stress ratio, R, as -1, resulting in the average strain corresponding to the without loading conditions.

The out-of-plane gusset welded-joint specimens used in this study consisted of a 12mm thick main plate and a 12mm thick, 100mm high gusset plate fillet welded together using semi-automatic CO_2 gas shielded arc welding. Fillet welds with equal leg lengths of 6mm were used. The mechanical properties and chemical compositions of the steel plate used in this study are listed in Table 1. In all specimens, JIS-SM490Y with a guaranteed yield stress of 365 MPa was used.

Table 1. Material properties and chemical compositions.

Steel	Thickness (mm)	Yield stress (MPa)	Tensile strength (MPa)	Elongation (%)	Chemical compositions (%)				
					C	Si	Mn	P	S
SM490Y	12	434	567	26	0.16	0.44	1.37	0.018	0.007

2.2 *Definition of crack length*

In this study, the crack length, shown in Figure 1, was defined as follows:

$N_{5\%}$: the stage where fatigue cracks originated from the end of the fillet weld, and the strain range of gauge AL decreased by 5%;

N_b: the stage where fatigue cracks originated from the end of the fillet weld and started progressing away from the weld towards the main plate.

N_{10}: the stage where fatigue cracks progressed 10mm away from the end of the fillet weld.

away from the end of the fillet weld.

Subsequently, N_{20} and N_{30} are defined the stage where fatigue cracks progressed 20mm and 30mm away from the end of the fillet weld. The crack initiated from the back surface of the main plate was defined as N_f. The fatigue test was finished when the crack length reached to N_{30}.

2.3 *Strain measurement positions*

Figure 2 shows the strain gauges positions attached to the main plate of the test specimens. Similar to the reference (Ishikawa et al., 2022), the stress range was determined by multiplying Young's modulus of the steel (E_s = 200 GPa) by the average value of the

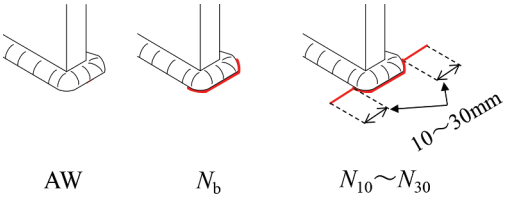


Figure 1. Definition of crack length.

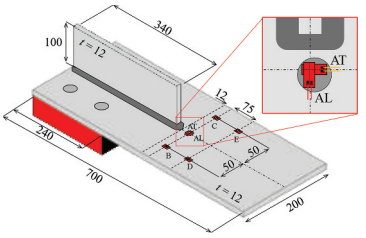


Figure 2. Out-of-plane gusset specimens.

strain range measured from strain gauges B and C during the initial loading. Figure 3 shows the strain gauge attachment positions at the crack tip. In specimen AW120, strain gauges with a gauge length of 5mm were attached radially at N_{10}, N_{20}, and N_{30} from the crack tip. In specimen AW90, strain gauges with a gauge length of 1mm were attached axially at ±5mm from the crack tip in the gusset axis direction and at N_{10}, N_{20}, and N_{30} in the crack propagation direction. Since the evaluation in this study focused on the progression of fatigue cracks, strain gauges were attached to AW120, and AW90 after N_b of fatigue crack progression.

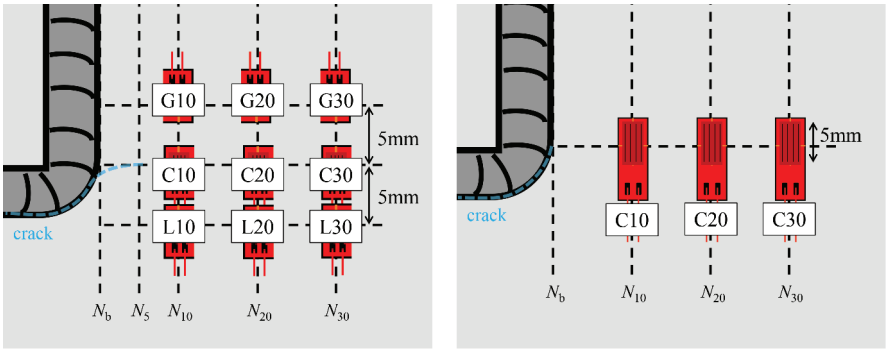


Figure 3. Strain gauges positions.

Table 2. Specimens and fatigue strength.

Specimens	Stress range (MPa)	Fatigue strength ($\times 10^4$)					
		$N_{5\%}$	N_b	N_{10}	N_{20}	N_f	N_{30}
AW120	122.1	10.2	21.4	34.8	45.6	45.6	54.9
AW90	90.8	35.5	63.9	96.9	119.3	131.8	142.1

3 STRAIN CHANGE UNDER UNLOADING CONDITIONS IN FATIGUE TEST

3.1 *Strain near the weld toe under unloading conditions*

Table 2 presents the fatigue test results for all specimens in this study and the fatigue strength for each crack length.

Figure 4 illustrates the relationship between the strain near the weld toe under unloading conditions since the start of the fatigue test and the number of cycles obtained from the fatigue test of AW120. This figure also includes the corresponding fatigue strengths. From Figure 5,

it can be observed that, due to the initiation and propagation of fatigue cracks, the strain under unloading conditions at gauge AL decreased as tensile residual stress was relieved. Gauges B and C show an increase in the strain under unloading conditions due to the redistribution of residual stress, while gauge AT exhibits an increase in compressive residual stress release. Gauges D and E, located away from the weld toe, show no significant changes. Therefore, even when fatigue cracks grow up to N_{30}, it is possible to evaluate the initiation and progression of fatigue cracks based on the changes in strain under unloading conditions near the weld toe, similar to the findings in the reference (Ishikawa et al. 2022).

Figure 5 represents the relationship between the strain change near the weld toe and the number of cycles from N_b in the fatigue test of AW120 under unloading conditions. It can be observed that the strain near the crack tip and near the weld toe changes with the growth of fatigue cracks. As can be seen from Figure 5, the change in strain under unloading conditions near the weld toe after the fatigue crack of N_b is smaller than the change of strain from the as-welded condition. Therefore, it is assumed that the change in strain under unloading conditions near the weld toe is not suitable for the monitoring of fatigue crack propagation, as the change in strain under unloading conditions becomes smaller for longer fatigue cracks.

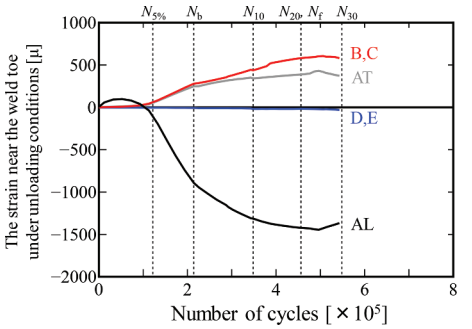


Figure 4. Strain change from as-welded condition.

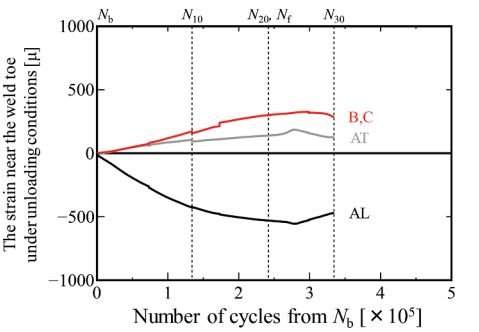


Figure 5. Strain change from N_b.

3.2 *Strain near the crack tip under unloading conditions*

Figure 6 presents the relationship between the strain change near the crack tip and the number of cycles from N_b in the fatigue test of AW120 under unloading conditions. It can be observed that the strain near the crack tip changes with the progression of fatigue cracks. From Figure 6, the strain near the crack tip under unloading conditions gradually increases with the progression of fatigue cracks. This is influenced by the redistribution of residual stress due to the progression of fatigue cracks and the transition of small-scale yielding at the crack tip with crack propagation. Additionally, it is noticeable that the strain increases sharply as the crack position approaches the strain gauges.

Figure 7 shows the results of magnetic particle inspection, MT, after the fatigue test of AW120. It can be seen from the figure that the crack tip aligns with the strain gauge. Since strain gauges were attached to match the center of gauges at N_{10}, N_{20}, and N_{30} with the crack tip in AW120, when the crack tip and strain gauge positions coincide, it indicates that the fatigue crack cut through the metal resistance of the strain gauge, making it unreadable just reaching each crack length. Therefore, it is considered that the evaluation of fatigue crack progression can be achieved not only by the values of strain under unloading conditions but also by the breakage of strain gauges.

Figure 8 illustrates the relationship between the strain near the crack tip under unloading conditions and the number of cycles from N_b, in the fatigue tests of AW90. From Figure 8, the strain near the crack tip under unloading conditions increases as the fatigue crack approaches the measurement position. This is considered to be due to the effect of small-scale yielding at the fatigue crack tip, similar to AW120. However, the strain under unloading

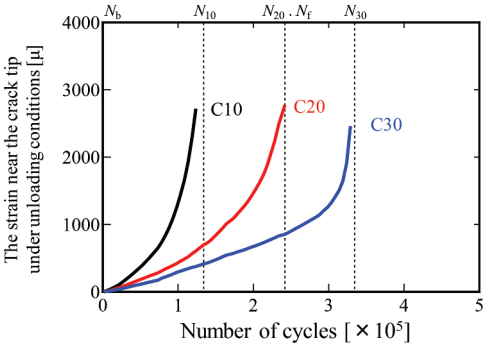


Figure 6. Strain change near the crack tip.

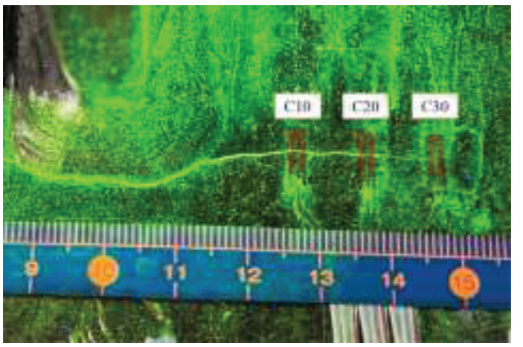
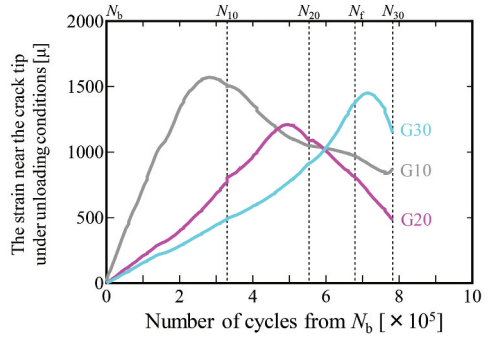


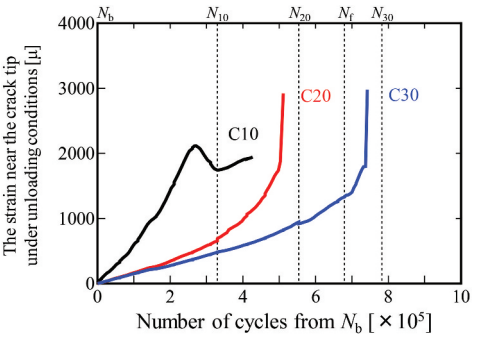
Figure 7. Fatigue crack on AW120.

conditions at C10 for AW90 decreases as the fatigue crack approaches, in contrast to other positions. Figure 8(d) shows the results of MT after the fatigue tests of AW90. From the fatigue crack in Figure 8(d), it is assumed that this is due to the distance between the fatigue crack and the strain gauge positions where the strain decreases under unloading conditions. Therefore, at position C10 for AW90, where the strain change due to the small-scale yielding at the crack tip was smaller when the crack approached, the trend differed compared with the strain change in Figure 6. Therefore, it is clarified that when the crack tip and strain gauge positions do not coincide, strain under unloading conditions increases once as the fatigue crack approaches, but then tends to decrease.

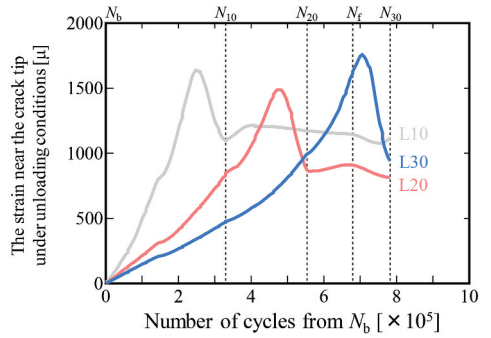
Therefore, when fatigue cracks have already propagated, measuring the strain under unloading conditions around the crack tip is more suitable than near the weld toe.



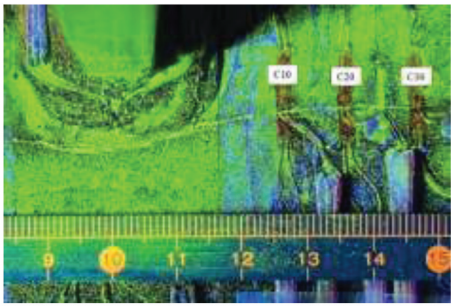
(a) Strain change in G10, G20 and G30



(b) Strain change in C10, C20 and C30



(c) Strain change in L10, L20 and L30



(d) Fatigue crack on AW90

Figure 8. Strain change under unloading conditions and fatigue crack on AW90.

Additionally, considering that the cut of strain gauges serves as a fuse for crack detection, it is advisable to use longer strain gauges with a length suitable for capturing the tip of the fatigue crack. On the other hand, even when the fatigue crack is away from the crack tip, it was shown that the strain under unloading conditions also changes significantly. Therefore, even when the fatigue crack is relatively small, and the progression direction is unpredictable, it is possible to monitor the progression of fatigue cracks.

4 FATIGUE CRACK PROPAGATION MONITORING VIA IOT

4.1 *Strain data logger with LPWA*

In the fatigue test of AW120, considering the application to monitoring in real bridges, the wireless strain measurement logger with LPWA was used to measure the strain at the crack tip under unloading conditions. The wireless strain measurement equipment consists of a single-board computer (Arduino Uno R3), LPWA communication device (Sigfox Shield for Arduino: UnaShield V2S), and a 2-channel strain amplifier shield AD8426 (Robotshop) for strain measurement, as shown in Figure 9. This small IoT device amplifies the voltage obtained from the strain gauge, converting it into integer data ranging from 0 to 1,023 for a voltage range of 0 to 5V (strain measurement range approximately ±2,000μ). This wireless strain measurement device allows strain measurements at approximately 1,000Hz. To connect the strain gauge (1mm gauge length, 2.4mm base width) used in regular fatigue tests, a bridge was formed using 120Ω metal film resistors (VISHAY) with an allowable error of ±0.1%. With this configuration, measurements were conducted every 2 hours for about 3 seconds each using a 2,500mA secondary battery, enabling a monitoring duration of six months. Furthermore, using the same configuration, displacement was measured with 2 channels, and monitoring was possible for 18 months.

In this study, data measured with the wireless strain measurement device were transferred through LPWA Sigfox, and fatigue crack progression monitoring was conducted on an online platform.

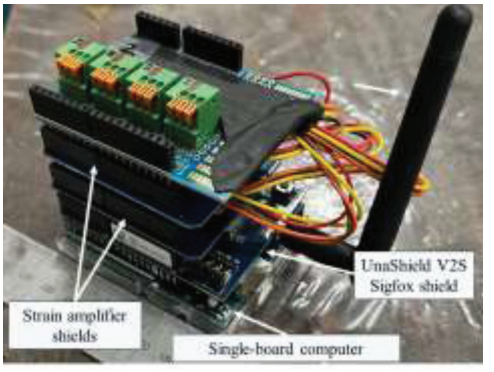


Figure 9. Strain data logger with LPWA.

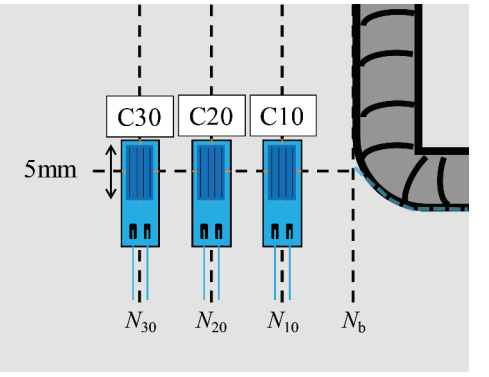


Figure 10. Strain gauges positions for IoT.

4.2 *Measurement positions*

To compare with the dynamic strain measurement in AW120, the strain gauges were attached right next to AL and next to the strain gauges B and C in Figure 2. For near the crack tip, the strain gauges of 5 mm gauge length were used as shown in Figure 10 for the wireless strain measurement with LPWA.

In this study, maximum and minimum strains were measured at the same intervals as the strains measured by dynamic strainmeters, for a period of approximately 3 seconds. The

average strain corresponding to the unloading conditions, which are average strains, was calculated and transmitted to the web server via LPWA.

4.3 *Results of fatigue crack growth monitoring via developed logger with LPWA*

Figure 11 shows the relationship between the change in strain under unloading conditions at strains AL, B and C and the number of cycles obtained from the fatigue test of AW120. The results obtained with the dynamic strainmeters (2,000Hz) from Figure 5 are also drawing. It can be observed from the figure that the strains under unloading conditions measured with the dynamic strainmeters and the wireless strain measurement logger are almost identical.

Figure 12 illustrates the relationship between the change in strain under unloading conditions at the crack tip and the number of cycles obtained from the fatigue tests of AW120. Similar to the measurements with the dynamic strainmeters in Figure 6, it can be seen that the strain under unloading conditions increases with the progression of fatigue cracks.

In AW120, the strain under unloading conditions increased by approximately 2,000 μ due to the fatigue crack growth. After that, the strain under unloading conditions remained constant at around 3000μ, this is because the fatigue crack propagation cut the strain gauge. In this manner, not only can fatigue crack growth be monitored from the change in strain under unloading conditions, but also alerts can be given by the cut of the strain gauge.

Therefore, as it was possible to monitor the fatigue crack growth using the strain data logger with LPWA, the developed wireless strain data logger could be used for the monitoring of fatigue crack growth on real bridges.

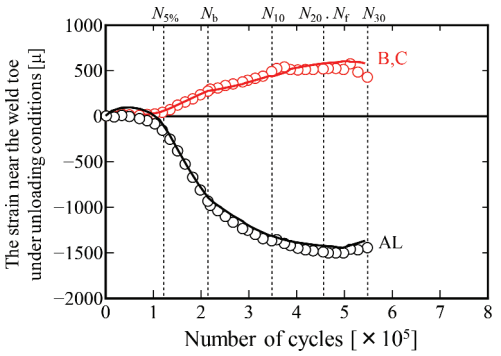


Figure 11. Strain change at AL, B and C.

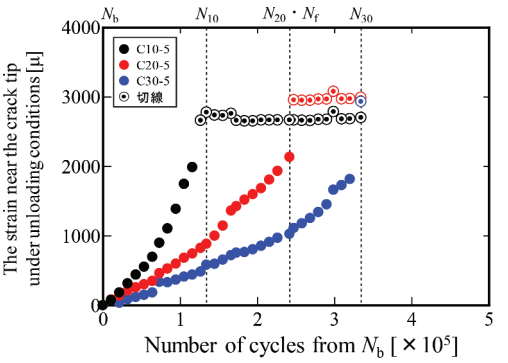


Figure 12. Strain change near the crack tip.

5 CONCLUSIONS

In this study, the authors focused on the strain changes near the crack tip under un-loading conditions for the crack propagation monitoring. Fatigue tests of out-of-plane gusset specimens were conducted to assess the propagation of fatigue cracks based on the changes in strain during unloading conditions. Additionally, the developed strain data logger with LPWA was used to measure the strain under unloading conditions. The main conclusions of this study are below:

1) Strain at the crack tip significantly increases during unloaded conditions due to the redistribution of residual stress and the small-scale yielding of fatigue cracks.
2) Longer strain gauges, capturing the tip of fatigue cracks more effectively, are recommended, as they can be used as an alert system when the fatigue crack propagation cuts the strain gauges.
3) Clear changes in strain during unloaded conditions were observed even in regions away from the crack tip, enabling the monitoring of crack growth in cases of relatively small cracks or unpredictable propagation directions.

4) Strain data loggers with LPWA were able to identify strain changes at the crack tip under unloading conditions and detect gauge cuts due to fatigue crack propagation. Thus, the feasibility of monitoring using IoT technology was demonstrated.

REFERENCES

Chen, N. Z., 2016, A stop-hole method for marine and offshore structures, *International Journal of Fatigue*, 88, pp. 49–57.

Ishikawa, T. and Matsumoto, N., 2022, Evaluation of strain change under unloading conditions by initiation and propagation of fatigue crack, *Journal of Structural Engineering A*, Vol. 68, pp. 554–563. (in Japanese)

Kobatashi, W., and Ohara, M., 2019, Real-time monitoring of flood inundation in urban area using LPWA, *Journal of Japan Society of Civil Engineers*, Ser. F3 (Civil Engineering Informatics), Vol. 75, No.1, pp. 36–47. (in Japanese)

Komon, K., Mori, T., Narumoto, A., Hirayama, S., and Abe, M., 2003, Development of fatigue damage monitoring sensor using crack propagation in thin stainless plate, *Journal of Structural Engineering*, No.738/I-64, pp. 245–255. (in Japanese)

Miki, C., Toyoda, Y., Mori, T., and Enokido, N., 1990, Fatigue of large-scale welded girders under simulated highway loadings, *Structural Engineering/Earthquake Engineering*, 7(2), pp. 283–291.

Okura, I., and Ishikawa, T., 2002, Stop-hole conditions to prevent re-initiation of fatigue cracks, *Steel and Composite Structures*, 2(6), pp. 475–488.

Sekiya, H., Kinomoto, T., Takaki, M., Maruyama, O. and Miki, C., 2020, Fundamental study on wire-less measurement in steel box girder bridge using LPWA, *Journal of Japan Society of Civil Engineers*, Ser. F3 (Civil Engineering Informatics), Vol. 76, No.1, pp. 53–62. (in Japanese)

Yamada, K., Ya, S., Baik, B., Torii, A., Ojio, T., and Yamada, S., 2007, Development of a new fatigue testing machine and some fatigue tests for plate bending, *IIW Document XIII-2161-07*, International Institute of Welding.

Bridge Maintenance, Safety, Management, Digitalization and Sustainability – Jensen, Frangopol & Schmidt (eds)
© 2024 The Author(s), ISBN 978-1-032-77040-6
Open Access: www.taylorfrancis.com, CC BY-NC-ND 4.0 license

Mechanical properties of steel tube with partially bonded CFRP

Y. Maeda, M. Mizutani & T. Ishikawa
Kansai University, Suita-shi, Osaka, Japan

ABSTRACT: CFRP bonded repair is the one of the repair methods for corroded steel structures. The workability of this method is better than the conventional steel patch repairs. Therefore, this method is sometimes applied for deteriorated sign posts and lighting columns. However, the debonding of CFRP from adhesive ends is one of the concerns about the CFRP bonded repair. To prevent the debonding of CFRP in the repair design, the shear stress or energy release rate in the adhesive layer is applied to the design verification in Japan. In this study, to evaluate the shear stress in adhesive layer, the shear-lag theory was applied to the steel tubes repaired by partially bonding CFRP subjected to bending moment. Additionally, the shear-lag theory of multiple bonded CFRP partially was also derived for the repair of the steel tubes under bending moment. Then, finite element analysis was performed to confirm the validity of the derived equations.

1 INTRODUCTION

Steel tube structures are used for signposts, steel tube trusses, and steel piers. The bases of sign posts and steel bridge piers embedded in road pavements such as concrete or asphalt are prone to crevice corrosion. In addition, the base of sign or light posts are often strengthened by ribs, therefore corrosion and fatigue cracks also occur at rib welding. Carbon fiber reinforced plastic (CFRP) bonded repair is one of the repair methods for steel tubes (Linden et al. 2014, Matsumura et al. 2017). This method is easy to handle and provides corrosion protection because CFRP has excellent material properties such as lightweight and corrosion resistant. CFRP bond repair have many applications for the repair corroded steel bridge members (Moy and Bloodworth. 2007).

CFRP-bonded repair of steel members has to check the prevention of the debonding of CFRP and to consider the force transmission delay by the adhesive layer. Shear stress, principal stress, or energy release rate in the adhesive layer are the parameters of check the prevention of debonding of CFRP in Japan(Japan Society of Civil Engineers (JSCE) 2018).

For the repair of deteriorated steel tubes by CFRP bonding, it has to check the prevention of debonding of CFRP. In addition, CFRP bonded repair requires a longer bond length than the repaired region because the CFRP at the adhesive ends does not transmit the sectional forces enough (JSCE, 2018).

Equations for calculating the shear stress and energy release rate in the adhesive layer and the required bond length when the CFRP bonded to the entire circumference of a steel tube have been proposed (Mizutani and Ishikawa. 2022). These equations were based on the shear-lag theory. The shear-lag theory assumes that the shear force in the adhesive layer transmitted the sectional forces between members, and mechanical properties can be evaluated by solving differential equations derived from the balance of forces in an infinitesimal element. However, it is not applicable for the cases which CFRP is partially bonded for steel tube structures, such as CFRP bonded repairs of the base of steel signposts with welded ribs. Partial CFRP bonding repair might be applied the partial corrosion in steel tube structures. Therefore, the authors consider that it is necessary to derive a theory that corresponds to partial CFRP bonding.

DOI: 10.1201/9781003483755-260

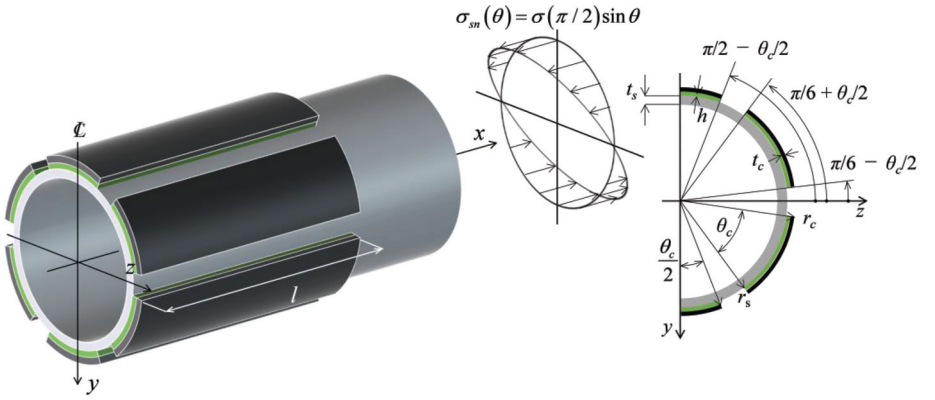


Figure 1. Dimension of partially CFRP bonded steel tube.

In this study, it is considered that the partially CFRP-bonded steel tube subjected to pure bending moments, as shown in Figure 1. The shared bending moments in the steel tube and CFRP, and the shear stress in the adhesive layer are derived by shear-lag theory. The derived shared bending moments and shear stress are validated using the finite element analysis. In addition, an equation for calculation of required bond length of partially CFRP bonded steel tube. Furthermore, the shear-lag theory for steel tubes with partially multiple CFRP bond repair is also derived.

2 SHEAR-LAG THEORY FOR PARTIALLY CFRP BONDED STEEL TUBE SUBJECTED TO PURE BENDING

2.1 *Dimension of model*

Figure 1 shows the steel tube with partial CFRP bond repair under pure bending. The CFRP is bonded symmetrically to the y and z axes in the range of θ_c in Figure 1. Therefore, the figure centers of the CFRP and steel tubes coincide. As shown in Figure 1, the outer radii of the steel tube and CFRP are r_s and r_c, respectively, the plate thicknesses of the steel tube and CFRP are t_s and t_c, and the thickness of the adhesive layer is h. The adhesive half-length of the CFRP is l.

2.2 *Differential equation and its solution*

The shear-lag theory for CFRP bonded steel tube has been proposed (Mizutani and Ishikawa. 2022). In this, the equations of shared bending moments of the steel tube and CFRP and the shear stress of the adhesive layer have been derived for the case of CFRP-bonded steel tubes subjected to pure bending. In the same way, the shared bending moment of the steel tube for the partially CFRP bond repair of steel tubes is derived by the following equation:

$$M_s = B_1 \cosh(c_b x) + B_2 \sinh(c_b x) + \xi_{0b} M \tag{1}$$

where,

$$c_b = \sqrt{\frac{G_e}{h}\left(r_s + \frac{h}{2}\right)^3 Z_b \frac{1}{E_s I_s} \cdot \frac{1}{1-\xi_{0b}}} \tag{2}$$

$$\xi_{0b} = E_s I_s / (E_s I_s + E_c I'_c) \tag{3}$$

E_s and E_c are Young's modulus of steel tube and CFRP, respectively, and I_s and I'_c are the sectional secondary moments of steel tube and CFRP, respectively.

In Equation (2), Z_b is the value of the definite integral with respect to the bonded range of CFRP. The number of partially CFRP bonded range is set to $2n$ by considering the symmetrical CFRP bonding. Z_b is given by the following equation:

$$Z_b = 4\int_{\theta} \sin^2\theta d\theta = n\theta_c \tag{4}$$

In the case of six part of CFRP bonding rage shown in Figure 1, Z_b is given by the following equation:

$$Z_b = 4\int_{\pi/6-\theta_c/2}^{\pi/6+\theta_c/2} \sin^2\theta d\theta + 4\int_{\pi/2-\theta_c/2}^{\pi/2} \sin^2\theta d\theta = 3\theta_c \tag{5}$$

The center of the bonded CFRP length is set to $x = 0$. The undetermined coefficient B_2 becomes zero because the bending moment M_s in the steel tube is symmetrical at $x = 0$. The undetermined coefficient B_1 is given by $B_1=(1\text{-}\xi_{0b})M/\cosh(c_b l)$ under the condition that the shared bending moment M_s in the steel tube at $x = l$ is equal to the applied bending moment M. Substituting the undetermined coefficients B_1 and B_2 into Equation (1), the shared bending moment M_s in the steel tube, is obtained. The shared bending moment M_c in CFRP is obtained from $M_c = M - M_s$. Therefore, the shared bending moment in the steel tube and CFRP and the shear stress in the adhesive layer are given by the following equations.

$$M_s = \left\{(1-\xi_{0b})\frac{\cosh(c_b x)}{\cosh(c_b l)} + \xi_{0b}\right\} M \tag{6}$$

$$M_c = (1-\xi_{0b})\left\{1 - \frac{\cosh(c_b x)}{\cosh(c_b l)}\right\} M \tag{7}$$

$$\tau(\theta) = \frac{c_b(1-\xi_{0b})}{(r_s + h/2)^2 Z_b}\frac{\sinh(c_b x)}{\cosh(c_b l)}\frac{I_s}{r_s}\sin\theta\sigma_{sn}(\pi/2) \tag{8}$$

where, $\sigma_{sn}(\pi/2)$ is the nominal stress ($\sigma_{sn}(\pi/2) = -M\, r_s/I_s$) acting on the steel tube end at $\theta = \pi/2$. The shear stress $\tau(\theta)$ in the adhesive layer is zero except the angle where the CFRP is bonded.

3 STRESS DISTRIBUTIONS OF PARTIALLY CFRP-BONDED STEEL TUBE

Finite element analysis was performed on the model subjected to pure bending moments using the analysis program Marc. The material properties applied to the analysis are listed in Table 1. The example of the analytical model is shown in Figure 2. The nominal stress acting on the steel tube end $\sigma_{sn}(\pi/2)$ is set as -100 N/mm^2.

The material property of CFRP in Table 1 takes into account the orthogonal anisotropy material of CFRP. CFRP is a composite material composed of carbon fiber and resin. It is known that when the volume of carbon fiber in CFRP is small, the shear deformation of the matrix resin cannot be ignored. A simple method has been proposed to account for the shear deformation of the matrix resin in CFRP into the height of the adhesive layer between the steel plate and CFRP for the shear-lag theory of CFRP bonded steel plates (Mizutani et al. 2019). This method is also used in this study. The shear-lag of CFRP can be accounted for by replacing the adhesive thickness h in Equation (2) with the converted adhesive layer thickness h' given by the following equation.

$$h' = h + \frac{t_c}{3}\frac{G_e}{G_{xy}} \tag{9}$$

Table 1. Dimension and material properties.

	Steel tube	CFRP
Thickness [mm]	$t_s = 4.5$	$t_c = 2$
Outer radios [mm]	$r_s = 108.15$	$r_c = 111.15$
Young's modulus [kN/mm^2]	$E_s = 200$	$E_c = 150$*
	Adhesive	
Thickness [mm]	$h = 1$	
Young's modulus [N/mm^2]	$E_e = 2500$	
Shear modulus [N/mm^2]	$G_e = 919$	
Range of bonding [°]	$\theta_c = 50$	

* In finite element analysis, the orthogonal anisotropy about the x-axis

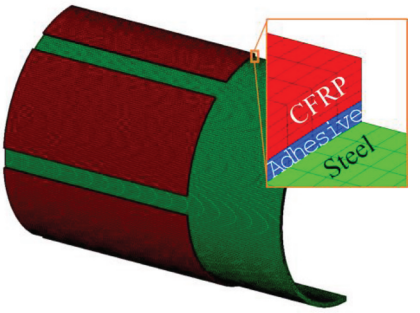


Figure 2. Example of FE model of partially CFRP-bonded steel tube.

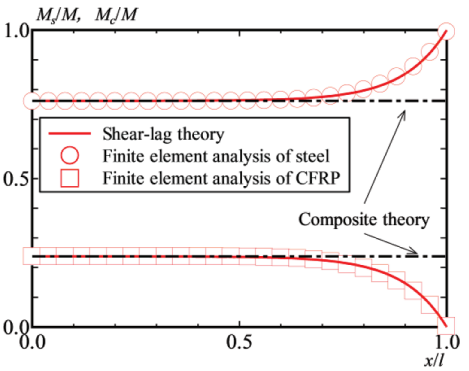


Figure 3. Shared bending moments of the steel tube and CFRP.

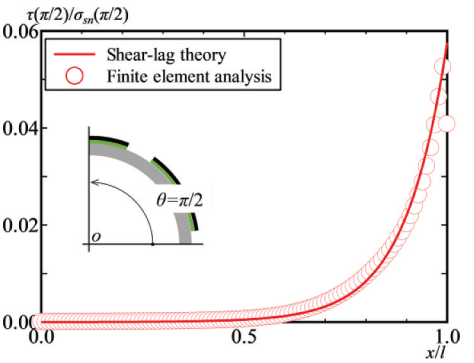


Figure 4. Shear stress in the adhesive layer.

where G_{xy} is the elastic shear modulus of CFRP in the x-axis direction.

Figure 3 shows the moment distribution of the analytical values and the theoretical values obtained from Equations (6) and (7). The vertical axis shows the shared bending moments M_s or M_c divided by the applied bending moment M. The horizontal axis is x divided by the half bond length l. The analytical values from the finite element analysis were converted from stresses in each section to bending moments. From Figure 3, it can be seen that the theoretical and analytical values have similar distributions. It can also be seen that the moments close to the composite theory as nearer to the center from the end of the adhesive.

The theoretical values of shear stress in adhesive layer obtained from Equation (8) and the analytical result are plotted in Figure 4. The vertical axis shows the shear stress $\tau(\pi/2)$ at $\theta = \pi/2$ divided by the applied stress $\sigma_{sn}(\pi/2)$ and the horizontal axis shows the distance x from the center of CFRP divided by the half bond length l. As can be seen from Figure 4, the theoretical and analytical values are good agreement.

4 REQUIRED BOND LENGTH AND CONVERGENCE VALUE OF SHEAR STRESS

4.1 *Required bond length*

As shown in Figure 3, the shared bending moments of the steel tube and CFRP close to the values of the composite theory as the x is close to zero. Until convergence to the composite theory, the sectional forces transmission between steel tube and CFRP is insufficient. Therefore,

it is necessary a longer CFRP bonding than the repair area of the steel tubes. The bond length outside the repaired area is called the required bond length (Mizutani and Ishikawa. 2022).

From Equation (6), if the bonded half-length l of the CFRP is sufficiently long, the moment in the steel tube converges to the value $\xi_{0b}M$ of the composite theory. For Equation (6) and $\xi_{0b}M$ to be equal, the bonded half-length l is infinite. Therefore, the rate of convergence of the steel tube stress to $\xi_{0b}M$, η_b is applied to determine the required bond length. The rate of convergence is defined by $\eta_b \geq M_s|_{x=0}/(\xi_{0b}M)$. The equation for the required bond length l_n in CFRP bonded steel tubes subjected to pure bending moment is given by the following equation;

$$l_n \frac{1}{c_b}\cosh^{-1}\left\{\frac{1}{\eta_b - 1}\cdot\left(\frac{1}{\xi_{0b}} - 1\right)\right\} = \frac{1}{c_b}\cosh^{-1}\left(\frac{1}{\eta_b - 1}\cdot\frac{E_c I'_c}{E_s I_s}\right) \tag{10}$$

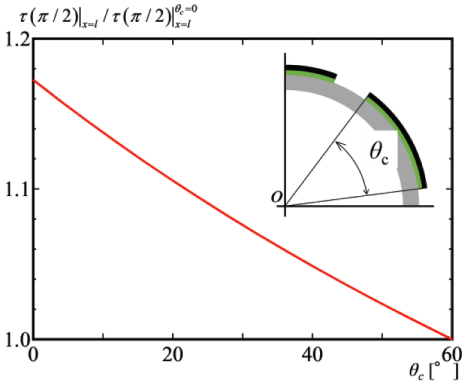


Figure 5. Shear stress in the adhesive layer.

4.2 *Convergence value of shear stress at CFRP end*

The energy release rate is one of the parameters used for design check of prevention of debonding of CFRP. The energy release rate is expressed as $G = (h\,\tau_e^2)/(2G_e)$ using the shear stress τ_e occurring at the CFRP end (JSCE. 2018). From Equation (8), if the bonded half-length l of CFRP is infinity, the shear stress $\tau(\pi/2)|_{x=l}$ at the CFRP end converges to the following equation;

$$\tau\left(\frac{\pi}{2}\right)\Big|_{x=l} = \frac{c_b(1-\xi_{0b})}{(r_s + h/2)^2 Z_b}\frac{I_s}{r_s}\sigma_{sn}(\pi/2) \tag{11}$$

Figure 5 shows the relationship between the range θ_c of bonding angles and the shear stress at the CFRP end. When $\theta_c = 60°$, the CFRP is bonded all around. As shown in Figure 5, the smaller the range of bonding angles, the higher the shear stress at the adhesive end. Therefore, the smaller the range of bonding angles is prone to debonding of CFRP. However, when θ_c=0°, there is no CFRP and no shear stress occurs.

The authors consider that the maximum value of shear stress shown in Figure 5 can be used to simplify the design check for the prevention of the debonding of CFRP. When the CFRP is bonded to the top of the steel tube, the shear stress is highest at $\theta = \pi/2$. The maximum shear stress at $\theta = \pi/2$ derived as θ_c in Equation (11) equals 0 is given by;

$$\tau\left(\frac{\pi}{2}\right)\Big|_{\theta_c=0} = \frac{M}{E_s I_s}\sqrt{\frac{G_e}{h}\cdot\frac{E_c I_c}{\pi(r_s + h/2)}} \tag{12}$$

Using Equation (12), the shear stress at the edge of the adhesive can be calculated simply, regardless of the adhesive angle. The shear stress value in Equation (12) can also be used to calculate the energy release rate.

5 EIGENVALUE ANALYSIS OF MULTI-LAYERED CFRP BONDED STEEL TUBE

5.1 *First-order simultaneous differential equations for strain*

Carbon fiber sheets and CFRP strand sheets are often used for CFRP bonded to steel tubes. These CFRP sheets are thin and are therefore bonded together in layers. Therefore, in this chapter, an eigenvalue analysis solution for steel tubes partially bonded with multiple layers of CFRP is conducted. The model is shown in Figure 6.

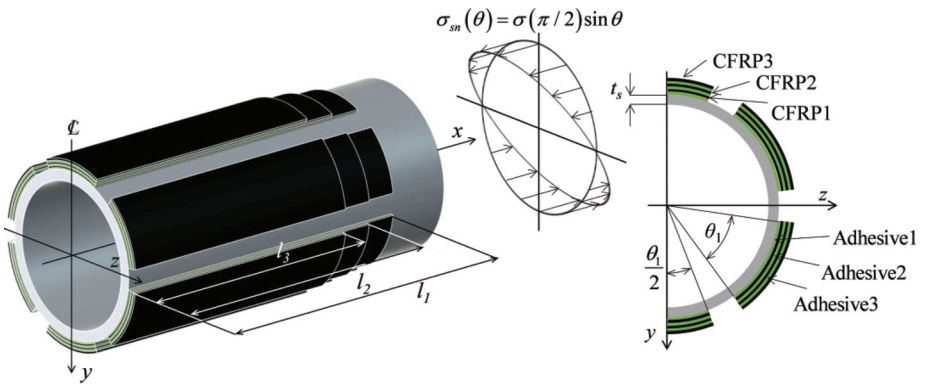


Figure 6. Dimension of multi-layered CFRP bonded steel tube.

Stress analysis methods based on eigenvalue analysis have already been proposed for steel tubes with multi-layer CFRP bonded repair around the circumference (Mizutani and Ishikawa. 2023). This method uses eigenvalue analysis to solve a first-order simultaneous differential equation based on shear-lag theory. This is because the calculation to solve the differential equation becomes more complicated as the number of CFRP layers increases.

In Chapter 2, the previous theory is extended to partially CFRP bonded steel tubes by considering the effect of the range of CFRP bonding angles (Z_b). The same extension was made for eigenvalue analysis in the case of multi-layer CFRP bonded steel tubes.

In eigenvalue analysis, the shared bending moments of the steel tube and CFRP and the shear stress of the adhesive layers are converted into strains and first-order simultaneous differential equations are developed. The simultaneous differential equations in matrix and vector form are given by;

$$d\varepsilon/dx = A_n\varepsilon \tag{13}$$

where $\boldsymbol{\varepsilon}$ is the strain vector. A_n is the coefficient matrix of the first-order simultaneous differential equations. The solution of Equation (13) is given by the following equation by solving the simultaneous homogeneous first-order differential equation expressed in matrix and vector form.

$$\varepsilon = Y_i\mathbf{C}_i = T_i e^{\Lambda_i x} T_i^{-1}\mathbf{C}_i \tag{14}$$

where T is a matrix consisting of the eigenvalue vectors of A_n. Λ is an eigenvalue of A_n and $\mathbf{C}$ is a vector of indeterminate coefficients. Vector $\mathbf{C}$ in Equation (14) is given by the boundary conditions and the continuity conditions of the strain in each axial segmental region of the members. Vector $\mathbf{C}$ is calculated from the following equation;

$$H\mathbf{C} = \mathbf{E} \tag{15}$$

where H is the coefficient matrix and $\mathbf{E}$ is the strain vector due to external forces and continuous conditions.

The vector **F**, which summarizes the shared bending moment in the steel tube and CFRP and the shear stress in the adhesive layer, is related to the strain vector **ε** by the following equation;

$$\mathbf{F} = G\sigma = GD\varepsilon \tag{16}$$

where

$$\mathbf{F} = \{\, M_s \quad M_{c1} \quad \tau_1(\pi/2) \quad \cdots \quad M_{ci} \quad \tau_i(\pi/2) \quad \cdots \quad M_{cn} \quad \tau_n(\pi/2) \,\} \tag{17}$$

$$\boldsymbol{\sigma} = \{\, \sigma_s \quad \sigma_{c1} \quad \tau_1 \quad \cdots \quad \sigma_{ci} \quad \tau_i \quad \cdots \quad \sigma_{cn} \quad \tau_n \,\}^T \tag{18}$$

$$\boldsymbol{\varepsilon} = \{\, \varepsilon_s \quad \varepsilon_{c1} \quad \gamma_1 \quad \cdots \quad \varepsilon_{ci} \quad \gamma_i \quad \cdots \quad \varepsilon_{cn} \quad \gamma_n \,\}^T \tag{19}$$

Table 2. Dimension and material properties.

	CFRP 1, 2, 3
Thickness [mm]	$t_c = 0.5$
Outer radios [mm]	$r_{c1} = 109.15$, $r_{c2} = 110.15$, $r_{c3} = 111.15$
Young's modulus [kN/mm^2]	$E_c = 250$*
Shear modulus of CFRP in axial direction [N/mm^2]	$G_{xy} = 919$ N/mm^2
	Adhesive 1, 2, 3
Thickness [mm]	$h = 0.5$
Young's modulus [N/mm^2]	$E_e = 2500$
Shear modulus [N/mm^2]	$G_e = 919$
Range of bonding [°]	50

* In finite element analysis, the orthogonal anisotropy about the x-axis

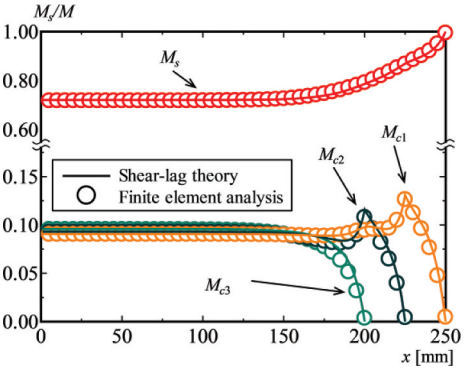


Figure 7. Shared bending moments of the steel tube and CFRP.

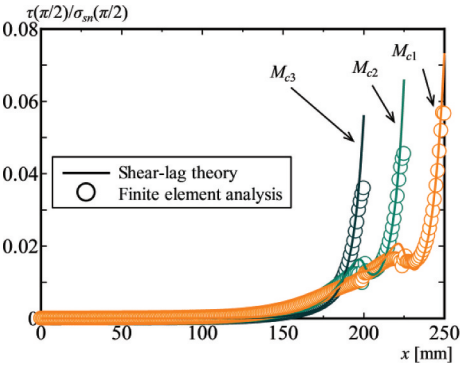


Figure 8. Shear stress in the adhesive layer.

$$G = diag\{\, I_s/r_s \quad I'_{c1}/r_{c1}\, 1 \cdots I'_{ci}/r_{ci} 1 \cdots I'_{cn}/r_{cn} 1 \,\} \tag{20}$$

$$D = diag\{\, E_s \quad E_{c1} \quad G_{e1} \quad \cdots \quad E_{ci} \quad G_{ei} \quad \cdots \quad E_{cn} \quad G_{en} \,\} \tag{21}$$

M_{ci} is the shared bending moment in CFRP i, and $\tau_i(\theta)$ is the shear stress in adhesive i. I'_{ci} and E_{ci} are the cross-sectional second moment and Young's modulus of CFRP i, respectively, and G_{ei} is the elastic shear modulus of adhesive i.

The matrix A_n in Equation (13) is a sparse matrix with mostly zero components. Therefore, the non-zero elements of A_n are shown in the following.

when $i = 1$

$$a_{1,3} = (r_s + h_1/2)Z_1 G_{e1}/(E_s A_s) \tag{22}$$

$$a_{2,3} = -(r_s + h_1/2)Z_1 G_{e1}/\left(E_{c1} A'_{c1}\right) \tag{23}$$

$$a_{3,1} = 1/h_1 \tag{24}$$

$$a_{3,2} = -1/h_1 \tag{25}$$

when $2 \le i \le n$

$$a_{2i-2,2i+1} = \left(r_{c(i-1)} + h_i/2\right)Z_i G_{ei}/\left(E_{c(i-1)} A'_{c(i-1)}\right) \tag{26}$$

$$a_{2i,2i+1} = \left(r_{c(i-1)} + h_i/2\right)Z_i G_{ei}/\left(E_{ci} A'_{ci}\right) \tag{27}$$

$$a_{2i+1,2i-2} = 1/h_1 \tag{28}$$

$$a_{2i+1,2i} = -1/h_1 \tag{29}$$

where r_{ci} is the outer radius of CFRP i and h_i is the thickness of adhesive i. Z_{bi} is the value of the definite integral with respect to the circumferential bond angle of CFRP i, as in the Equation (4). However, the bond width of CFRP $i + 1$ must not exceed the bond width of CFRP i ($Z_{bi} \ge Z_{b(i+1)}$).

5.2 *Shared bending moments and shear stress distribution in partially multi-layered CFRP bonded steel tubes*

Finite element analyses were performed to compare the results of Eigenvalue analysis. The material properties are shown in Table 2. The misalignment of CFRP ends were set to 25 mm each, so that the CFRP lengths are $l_1 = 250$, $l_2 = 225$, and $l_3 = 200$ mm. However, the material constants of steel tubes are the same as in Table 1.

Figure 7 shows the shared bending moment distribution in steel tubes and CFRP. The vertical axis shows the shared bending moments M_s or M_c divided by the applied bending moment M. From Figure 7, it is shown that the eigenvalue and finite element analyses have similar distributions. Figure 8 shows the shear stress distribution in each adhesive layer. The vertical axis shows the shear stress $\tau(\pi/2)$ at $\theta = \pi/2$ divided by the applied stress $\sigma_{sn}(\pi/2)$. Figure 8, it is shown that Eigenvalue analysis and finite element analysis have also similar distributions. Therefore, the shared bending moments in steel tubes and CFRP and the shear stresses in the adhesive layers can be calculated by Eigenvalue analysis of multi-layered CFRP bonded steel tube.

6 CONCLUSIONS

In this study, shear-lag theory was applied to steel tubes partially bonded with CFRP. Equations of the shared bending moments in steel tubes and CFRP and the shear stresses in the adhesive layer were derived. The validity of the equations given by shear-lag theory was confirmed by the finite element analysis. Additionally, convergence values of the required bond length and shear stresses were also derived. Furthermore, it was shown that the eigenvalue analysis results of the multi-layered CFRP bonded steel tube were also in good agreement with the finite element results.

REFERENCES

Japan Society of Civil Engineers, 2018. Guidelines for Repair and Strengthening of Structures Using Externally Bonded FRP. Tokyo: Maruzen Publishing Co., Ltd. (in Japanese)

Linden, J.N., Köpple, M., Elder, D. & Gibson, A.G. 2014. Fracture mechanics of crack propagation in composite repairs of steel pressure piping. *Journal of Reinforced Plastics & Composites 33*, No. 6: 526–532.

Matsumura, M., Chin, S., Nakao, R., Takemoto, K. & Sugiura, K. 2017. Static loading teste of steel column with corroded part strengthened by thermosetting preg CF sheets. *Proceedings of Japan Society of Civil Engineers A1 (Structure/Earthquake Engineering) 73*, No. 5: II_42-II_51. (in Japanese)

Miyairi, H., 2000. *Introduction to Adhesive Design for Mechanical Engineers*, Nikkan Kogyo Shimbun, Ltd (in Japanese)

Mizutani, M., Ishikawa, T. & Kitane, Y. 2019. Required length and energy release rate of CFRP bonded onto steel plate considering with effect of matrix resin. *Journal of Structural Engineering 65A*: 745–754. (in Japanese)

Mizutani & Ishikawa. 2022. Required length of CFRP and energy release rate for CFRP jointed steel tubes under pure bending conditions. *Bridge Safety*, *Maintenance, Management, Life-Cycle (Resilience and Sustainability)*, 1661–1669.

Mizutani, M. & Ishikawa, T. 2023. Step length based on convergence of energy release rate for multi-layered CFRP bounded steel tubes under pure bending. *Proceedings of Japan Society of Civil Engineer Vol.79*, No.1: 22–143. (in Japanese)

S. S. J. Moy. & A. G. Bloodworth. 2007. Strengthening a steel bridge with CFRP composites. *Proceedings of the Institution of Civil Engineers (Structures & Buildings 160)*, 81–93.

Bridge Maintenance, Safety, Management, Digitalization and Sustainability – Jensen, Frangopol & Schmidt (eds)
© 2024 The Author(s), ISBN 978-1-032-77040-6
Open Access: www.taylorfrancis.com, CC BY-NC-ND 4.0 license

Estimation of elastic buckling loads of defective steel plate repaired with CFRP

M. Mizutani, E. Yo & T. Ishikawa
Kansai University, Suita-shi, Osaka, Japan

Y. Hidekuma
NIPPON STEEL Chemical & Material Co., Ltd, Tokyo, Japan

M. Dogaki
Kansai University, Suita-shi, Osaka, Japan

ABSTRACT: Brittle debonding at adhesive ends may occur when carbon fiber reinforced plastic (CFRP) bonded steel members are subjected to high stress or large deformation, such as compressive buckling. Therefore, to prevent CFRP debonding, the use of a highly ductile putty material (elastic putty) between the steel member and the CFRP has been proposed. From the results of the test and analysis, when the elastic putty is inserted or the CFRP bond length is short, the buckling loads given by the eigenvalue analysis tend to be higher than that obtained by the tests or finite element results. This is because the eigenvalue analysis assumes a perfect composite condition of the steel plate and CFRP. Therefore, in this study, the estimation of the elastic buckling load of CFRP-bonded defective steel plates is proposed by using eigenvalue analysis to take into account the effect of transmission delay by adhesives and elastic putty.

1 GENERAL INSTRUCTIONS

In steel structures, the load-bearing capacity is reduced by loss of cross-section due to corrosion. In Japan, for rehabilitation of damaged steel structures, carbon fiber reinforced plastic (CFRP) has been bonded to damaged steel members since 2000. CFRP is a composite material consisting of carbon fiber and resin. It is lightweight, highly elastic, and corrosion-resistant. However, brittle debonding at adhesive ends may occur when CFRP-bonded steel members are subjected to high stress or large deformation, such as compressive buckling (Okuyama et al., 2011; Cao et al., 2023).

To prevent CFRP debonding, the use of a highly ductile putty material (elastic putty) between the steel member and the CFRP has been proposed (Okuyama et al., 2011; Kazem et al., 2016). The use of elastic putty reduces the stresses concentration in the adhesive and prevents debonding. In addition, by inserting elastic putty, the CFRP can follow large deformations caused by compressive buckling without debonding. However, the use of elastic putty increases the bonding CFRP length by the transmission delay of the sectional forces from the steel member to the CFRP, as well as the stress reduction effect on the steel member becomes smaller than that without the elastic putty.

Uniaxial compression tests and eigenvalue analyses were conducted to evaluate the buckling loads of CFRP-bonded steel plate with and without elastic putty (Ishikawa et al., 2022). From the results of the test and analysis, when the elastic putty is inserted or the CFRP bond length is short, the buckling loads given by the eigenvalue analysis tend to be higher than that

DOI: 10.1201/9781003483755-261

obtained by the tests or finite element results. This is because the eigenvalue analysis assumes a perfect composite condition of the steel plate and CFRP.

Therefore, in this study, the estimation of the elastic buckling load of CFRP-bonded defective steel plates is proposed by using eigenvalue analysis to take into account the effect of transmission delay by adhesives and elastic putty.

2 ESTIMATION OF ELASTIC BUCKLING LOADS

This chapter presents an estimation method of the elastic buckling load of CFRP-bonded defective steel plates. The elastic buckling loads are calculated based on Euler's buckling equation.

The elastic buckling loads can be calculated against the beams with different cross-sectional stiffnesses shown in Figure 1. Okuyama et al. (2011) presented an equation to calculate the elastic buckling load derived from Euler's buckling equation for beams with two different cross sections (beams 1 and 2), as shown in Figure 2(a). This assumes the case of CFRP bonded to intact steel plates. However, for the eigenvalue analysis of CFRP-bonded defective steel plate in Figure 2(b), three regions (beams 1 - 3) as 1/2 symmetry are required. Therefore, the authors derive Euler's buckling equations for the three regions. For the beam (beam i) in Figure 1, the differential equation for the displacement $w_i(x_i)$ is the following equation:

$$\frac{d^4 w_i(x_i)}{dx_i{}^4} - \alpha_i{}^2 \frac{d^2 w_i(x_i)}{dx_i{}^2} = 0 \tag{1}$$

here,

$$\alpha_i = \sqrt{P/(EI)_i} \tag{2}$$

x_i is the axial position from the left end of each beam i; $(EI)_i$ is the bending stiffness of beam i; P is the applied load.

The general solution of Equation (1) is:

$$w_i(x_i) = C_{1i} \sin \alpha_i x_i + C_{2i} \cos \alpha_i x_i + C_{3i} x_i + C_{4i} \tag{3}$$

where,

$$x_i = \begin{cases} x & (i = 1) \\ x - \sum_{j=1}^{i-1} l_j & (i \geq 2) \end{cases} \tag{4}$$

C_{ji} is the undetermined coefficient for beam i (j = 1 to 4).

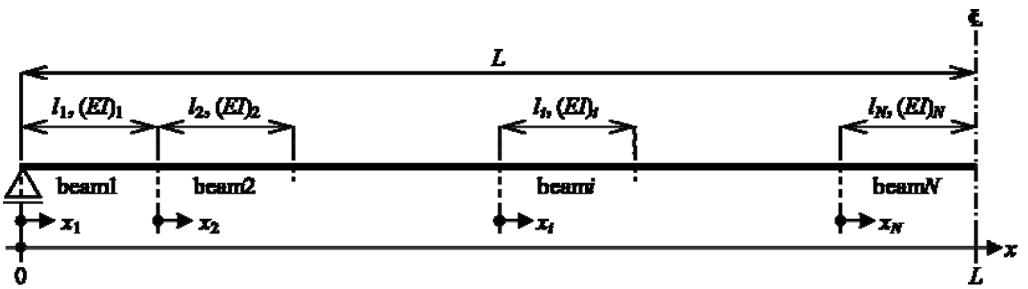
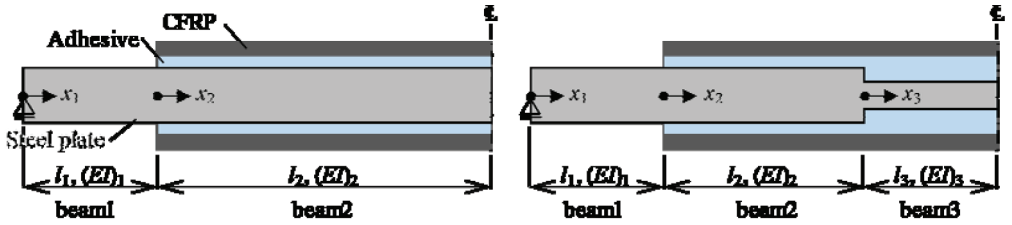


Figure 1. Simply supported beam with variable cross-sectional stiffness (1/2 symmetry).



(a) CFRP bonded intact steel plate (b) CFRP bonded defective steel plate

Figure 2. Beam with CFRP bonded to both sides of a steel plate (1/2 symmetry).

For beams 1 to 3 the total number of undetermined coefficients in Equation (3) is twelve. Each coefficient is given by the continuity and boundary conditions of the displacement $w_i(x_i)$, rotation angle $\theta_i(x_i) = dw_i(x_i)/dx_i$, bending moment $M_i(x_i) = -(EI)_i\, d^2w_i(x_i)/dx_i^2$ and shear force $Q_i(x_i) = -(EI)_i\, d^3w_i(x_i)/dx_i^3$ at each end of the beam i. Okuyama et al. (2011) and Mizutani et al. (2023) presented the equations for the undetermined coefficients in matrix and vector form as follows:

$$[B]\mathbf{C} = 0 \tag{5}$$

where, B is the coefficient matrix; $\mathbf{C}$ is the vector of undefined coefficients.

The condition for Equation (5) to have a non-trivial solution is:

$$\det[B] = 0 \tag{6}$$

For beams consisting of beams 1 to 3, such as CFRP bonded steel plates with sectional defect, the determinant of Equation (6) is the following equation:

$$\begin{aligned} &\alpha_1\alpha_2\cos(\alpha_1 x_1)\cos(\alpha_2 x_2)\cos(\alpha_3 x_3) - \alpha_1\alpha_3\cos(\alpha_1 x_1)\sin(\alpha_2 x_2)\sin(\alpha_3 x_3) \\ &-\alpha_2{}^2\sin(\alpha_1 x_1)\sin(\alpha_2 x_2)\cos(\alpha_3 x_3) - \alpha_2\alpha_3\sin(\alpha_1 x_1)\cos(\alpha_2 x_2)\sin(\alpha_3 x_3) = 0 \end{aligned} \tag{7}$$

The minimum applied load P (> 0) that satisfies Equation (7) is the elastic buckling load when the CFRP is bonded to the defective steel plate.

3 EVALUATION OF ELASTIC BUCKLING LOADS USING CONVERTED THICKNESS OF CFRP

Ishikawa et al. (2022) proposed a CFRP converted thickness for CFRP-bonded intact steel plate that focuses on the elongation of the steel plate with CFRP in Figure 2(a). This method was in good agreement with the results obtained by inserting elastic putty. However, this method is not applicable the CFRP bonded steel plate with sectional defects as shown in Figure 2(b). In this chapter, the converted thickness for Figure 2(a) is shown, followed by the converted thickness for Figure 2(b).

3.1 *Converted thickness of CFRP for CFRP bonded to intact steel plate*

A method for deriving the equivalent thickness of CFRP by focusing on the elongation of CFRP-bonded steel plates is presented. This method focuses on the axial displacement of the CFRP-bonded steel plate under compressive force. The axial displacement δ_s of the steel plate in the CFRP-bonded region is given by the following equation:

$$\delta_s = \int_0^{l_c} \varepsilon_s dx = \int_0^{l_c} \frac{N_s(x)}{E_s A_s} dx \tag{8}$$

where, ε_s is the axial strain of steel plate; l_c is the bonded half-length of CFRP; $N_s(x)$ is the axial force of steel plate; E_s is Young's modulus of steel plate; A_s is cross-sectional area of steel plate.

The axial force $N_s(x)$ of a steel plate is given by the following equation from the shear-lag theory (Ishikawa et al., 2013).

$$N_s(x) = \left\{ (1 - \xi_0) \frac{\cosh(cx)}{\cosh(cl_c)} + \xi_0 \right\} P \tag{9}$$

where,

$$c = \sqrt{\frac{b_c G_e}{h} \frac{2}{1 - \xi_0} \frac{1}{E_s A_s}} \tag{10}$$

$$\xi_0 = \frac{1}{1 + 2E_c A_c / E_s A_s} \tag{11}$$

$$G_e = \frac{E_e}{2(1 + \nu_e)} \tag{12}$$

b_c is the width of CFRP adhesion; h is the thickness of adhesive; G_e is the shear modulus of elasticity of adhesive; E_e is Young's modulus of adhesive; v_e is Poisson's ratio of adhesive; E_c is Young's modulus of CFRP; A_c is the cross-sectional area of CFRP.

Substituting Equation (9) into Equation (8) gives:

$$\delta_s = \frac{P l_c}{E_s A_s} \left\{ \frac{1 - \xi_0}{c l_c} \tanh(c l_c) + \xi_0 \right\} \tag{13}$$

On the other hand, the axial displacement of a steel plate based on the composite theory considering the converted cross-sectional area A_c' (= $b_c - t_c'$) with the thickness of CFRP as t_c', is given by the following equation:

$$\delta_s = \frac{P l_c}{E_s A_s} \cdot \frac{1}{1 + 2E_c A'_c / (E_s A_s)} \tag{14}$$

When the axial displacements of the steel plate in Equations (13) and (14) are equal, the equivalent thickness t_c' of CFRP is obtained by the following equation:

$$t'_c = \frac{E_s A_s}{2E_c b_c} \left\{ \frac{1}{(1 - \xi_0) \tanh(cl)/(cl) + \xi_0} - 1 \right\} \tag{15}$$

Since CFRP is bonded to a defective steel plate, as shown in Figure 2(b), in this study, the equivalent thickness t_c' of CFRP is calculated by substituting the bonding length l_n of CFRP on one side, excluding the defective section, into l in Equation (15). Using this converted thickness, when calculating the elastic buckling load from Equation (7), express its value as P_{VDcr}.

3.2 *Converted thickness of CFRP to CFRP bonded to defective steel plate*

As shown in the previous section, when CFRP is bonded to a defective steel plate subjected to compressive forces, the equivalent thickness of CFRP according to Ishikawa et al. (2022) is not

applicable. Therefore, the shear-lag theory (Ishikawa & Kitane, 2010) is used to derive the equivalent thickness of CFRP focusing on the axial displacement when CFRP is bonded to a defective section steel plate. The axial forces of the defective and reinforcing steel plates for a CFRP-bonded defective steel plate subjected to axial forces are given by the following equations, respectively:

$$N_s(x) = \{A_1 \cosh(c_d x) + \xi_d\} P \tag{16}$$

$$N_s(x) = [B_1 \cosh\{c(x - l_d)\} + B_2 \sinh\{c(x - l_d)\} + \xi_0] P \tag{17}$$

where,

$$c_d = \sqrt{\frac{b_c G_{ed}}{h_d} \frac{2}{1 - \xi_d} \frac{1}{E_s A_{sd}}} \tag{18}$$

$$\xi_d = \frac{1}{1 + 2E_c A_c / E_s A_{sd}} \tag{19}$$

$$A_1 = \frac{Z}{\cosh(c_d l_d)} \tag{20}$$

$$A_2 = 0 \tag{21}$$

$$B_1 = \xi_d - \xi_0 + Z \tag{22}$$

$$B_2 = \frac{c_d h_d}{ch} Z \tanh(c_d l_d) \tag{23}$$

$$Z = \frac{\frac{1-\xi_0}{\cosh(cl_n)} + \xi_0 - \xi_d}{1 + \frac{c_d h_d}{ch} \tanh(cl_n) \tanh(c_d l_d)} \tag{24}$$

$$l_n = l_c - l_d \tag{25}$$

h_d is the thickness of the adhesive at the sectional defect; G_{ed} is the shear modulus of elasticity of the adhesive at the sectional defect; A_{sd} is the sectional area of steel plate at defective section; l_n is the length of CFRP bonded area on one side of the reinforcement; l_d is the half length of the defective section.

Substituting Equations (16) and (17) into Equation (8), the axial displacements (δ_{sd} and δ_s) of the section deficient and reinforced sections, respectively, are given by:

$$\delta_{sd} = \frac{l_d}{E_s A_{sd}} \left\{ \frac{A_1 \sinh(c_d l_d)}{c_d l_d} + \xi_d \right\} P \tag{26}$$

$$\delta_s = \frac{l_n}{E_s A_s} \left[\frac{B_1 \sinh(cl_n) + B_2\{\cosh(cl_n) - 1\}}{cl_n} + \xi_0 \right] P \tag{27}$$

According to the composite theory of steel plate and CFRP, the axial displacements of the defective and reinforced sections are given by the following equations, respectively:

$$\delta_{sd} = \frac{Pl_d}{E_s A_{sd} + 2E_c A'_{cd}} = \frac{Pl_d}{E_s A_{sd} + 2E_c b_c t'_{cd}} \tag{28}$$

$$\delta_s = \frac{Pl_n}{E_s A_s + 2E_c A'_c} = \frac{Pl_n}{E_s A_s + 2E_c b_c t'_c} \tag{29}$$

When Equations (26) and (28) are equal, the converted thickness of CFRP in defective section, t_{cd}', is given by:

$$t'_{cd} = \frac{E_s A_{sd}}{2E_c b_c}\left\{\frac{1}{A_1 \sinh(c_d l_d)/(c_d l_d) + \xi_d} - 1\right\} \tag{30}$$

Furthermore, when Equations (27) and (29) are equal, the converted thickness of CFRP in reinforced section, t_c', is given by:

$$t'_c = \frac{E_s A_s}{2E_c b_c}\left[\frac{1}{\{B_1 \sinh(cl_n) + B_2(\cosh(cl_n) - 1)\}/(cl_n) + \xi_0} - 1\right] \tag{31}$$

Calculate the converted thickness t_{cd}' of the CFRP bonded to the sectional defective section by Equation (30) and the converted thickness t_c' of the CFRP bonded to the reinforced section by Equation (31), respectively. Using these converted thicknesses, when calculating the elastic buckling load from Equation (7), express its value as P_{VLcr}.

4 ELASTIC BUCKLING LOAD BASED ON EIGENVALUE ANALYSIS BY FINITE ELEMENT METHOD

In this chapter, the elastic buckling load is obtained from the eigenvalue analysis using the finite element method, and the validity of the elastic buckling load in Chapter 3 is confirmed. The eigenvalue analysis was performed using the finite element analysis program Marc.

Figure 3 Shows an example of the element division of the eigenvalue analysis model. The steel plate and adhesive (epoxy resin and elastic putty) were modeled with a 4-node plane stress element, and the CFRP was modeled with a 2-node linear beam element. The 1/2 symmetry model was used, the symmetry condition was given at the center of the member, and the

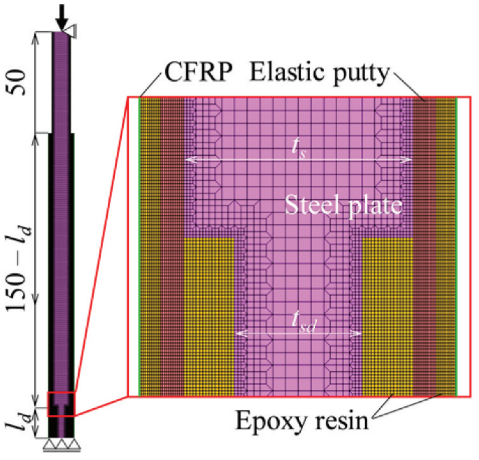


Figure 3. Model for eigenvalue analysis by finite element method.

Table 1. Dimensions and material properties of steel plates.

Width b_s [mm]	Thickness t_s [mm]	Half-length l_s [mm]	Young's modulus E_s [kN/mm^2]	Poisson's ratio ν_s
50	9	200	2.0×10^5	0.30

Table 2. Dimensions and material properties of Adhesives.

	Thickness h [mm]	Young's modulus E_e [N/mm^2]	Poisson's ratio v_e
Epoxy resin	0.6	2,500	0.34
Elastic putty	0.3	54.7	0.40

Table 3. Dimensions and material properties of CFRP.

Width b_c [mm]	Thickness t_c [mm]	Half-length $l_d + l_n$ [mm]	Young's modulus E_c [kN/mm^2]	Poisson's ratio v_c
50	0.286	150	2.0×10^5	0.30

top end was pin-supported at the center of the steel plate thickness. Compressive loads were applied at the top of the model, and eigenvalue analysis was performed using the BUCKLE function (Lanczos method, convergence error 0.0001).

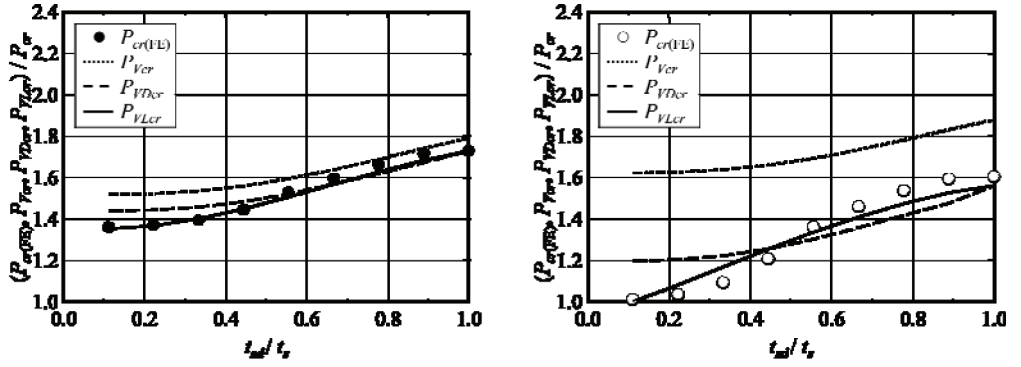
The material properties and dimensions of the steel plate, adhesive, and CFRP used in the analysis are shown in Tables 1 to 3. The section defect length of the steel plate was set to $2l_d$ =30 mm, and the remaining thickness of the plate, t_{sd}, was varied from 1 to 9 mm. The thickness of the CFRP was set to t_c = 0.286 mm.

Figure 4 shows the relationship between the elastic buckling load and the remaining thickness of the steel plate. The figure shows the effect of the remaining thickness of the steel plate on the elastic buckling load. The horizontal axis of the figure shows the remaining thickness of the steel plate t_{sd} divided by the thickness t_s of the intact section. The vertical axis is the buckling eigenvalue obtained by the finite element method or the elastic buckling load estimated in Chapter 3 divided by the buckling load P_{cr} (= 37.5 kN) of the intact steel plate only, as shown in the following equation:

$$P_{cr} = \frac{\pi^2 E_s I_s}{(2kl_s)^2} \tag{32}$$

where, I_s is the second moment of the weak axis of the steel plate ($b_s\ t_s^3/12$); l_s is the half-length of steel plate (l_s = 200 mm); k is the effective buckling coefficient (k = 1).

If the elastic putty is inserted in the calculations in Chapter 3, the adhesive thickness and shear modulus must take the epoxy resin and elastic putty into account. Therefore, the



(a) Without elastic putty (b) With elastic putty

Figure 4. Relationship between the elastic buckling load and the remaining thickness of the steel plate.

following equations were used to calculate the converted shear modulus of elasticity G_{Eq} and total thickness h_{Eq} of the adhesive when the elastic putty is inserted.

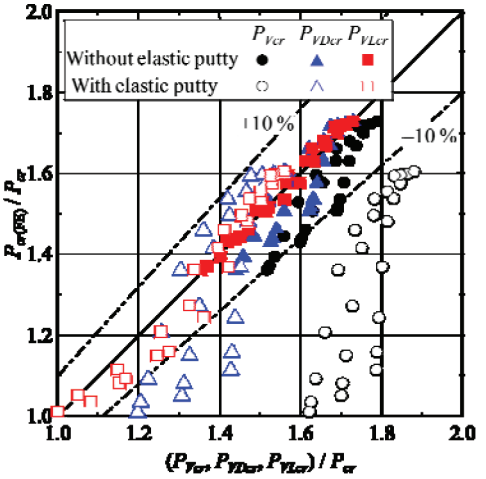


Figure 5. Relationship between eigenvalue analysis results and elastic buckling loads.

$$G_{Eq} = \frac{G_e(h_e + h_p)}{h_e + h_p G_e / G_p} \tag{33}$$

$$h_{Eq} = h_e + h_p \tag{34}$$

where, G_p is the shear modulus of elastic putty; h_p is the thickness of elastic putty. The defective section of the steel plate is assumed to be filled with epoxy resin, therefore, h_e includes the defective thickness of the steel plate.

The results of elastic buckling load estimation in Chapter 3 are compared with the results of eigenvalue analysis using the finite element method. In Figure 4, the results of the elastic buckling load P_{VDcr} using the CFRP equivalent thickness in Equation (15), the elastic buckling load P_{VLcr} for a defective steel plate in section using the equivalent thickness in Equations (30) and (31) are shown. Here, the elastic buckling load, P_{VLcr}, was calculated from Ishikawa et al. (2022) because CFRP adhesion to an intact steel plate occurs when t_{sd}/t_s = 1.0. The elastic buckling load P_{Vcr} from Okuyama et al. (2011), which assumes a composite beam of steel plate and CFRP, is also shown in Figure 4.

It is clear from Figure 4 that the elastic buckling load P_{Vcr} assuming a composite beam has a larger value than the eigenvalue analysis $P_{cr(\mathrm{FE})}$ of the finite element method, which does not agree when elastic putty is inserted. In addition, P_{VLcr} using Equations (30) and (31) is closer to the eigenvalue analysis $P_{cr(\mathrm{FE})}$ than P_{VDcr} using Equation (15). This is because P_{VLcr} takes into account the effect of force transmission at the section defect.

Figure 5 compares the results of the eigenvalue analysis with the elastic buckling load. For the calculation example in Figure 4, results for defect lengths of $2l_d$ = 10 and 20 mm are also included. The vertical axis in Figure 5 shows the eigenvalue analysis $P_{cr(\mathrm{FE})}$ obtained by the finite element method divided by the buckling load P_{cr} of the steel plate only, and the horizontal axis also shows the elastic buckling load P_{VDcr} or P_{VLcr} divided by the buckling load P_{cr}. Figure 5 shows that the buckling load P_{VLcr} using the converted thickness of CFRP in Equations (30) and (31) is within ±10 % of the buckling load $P_{cr(\mathrm{FE})}$ given by the finite element method in the calculation examples in this study. In addition, the buckling load P_{VDcr} using the converted thickness of CFRP in Equation (15) also has an error within ±10 % of the buckling load $P_{cr(\mathrm{FE})}$.

From Figures 4 and 5, the elastic buckling load P_{VLcr} can be estimated by using the converted thicknesses of CFRP in Equations (30) and (31) when elastic putty is inserted or when the cross-sectional deficiency is large. If no elastic putty is inserted or the cross-sectional defect is small, the elastic buckling load P_{VDcr} can be estimated by using the converted thickness in Equation (15).

5 CONCLUSION

This study presents an estimation of the elastic buckling load when CFRP is bonded to a defective steel plate. The proposed method was compared with the buckling eigenvalues obtained by the finite element method. The main results obtained in this study are as follows;

1) The axial force of a CFRP-bonded defective steel plate derived from shear-lag theory was used to show the converted thickness of CFRP focusing on the axial displacement.
2) Estimation equations for elastic buckling loads were derived for beams with three different cross-sections.
3) Estimation of the elastic buckling load using the proposed converted thickness is in good agreement with the results of the eigenvalue analysis using the finite element method.

REFERENCES

Cao, X., Chen, Y., Wang, H., Cheng, C., Zhou, X., Zhang, H., Kim, S.E. & Kong, Z. 2023. Experimental and numerical investigation of 800 MPa HSS welded T-section column strengthened with CFRP, *Thin-Walled Structures*, Vol. 184, 110510.

Ishikawa, T. & Kitane, Y. 2010. Required length and thickness of CFRP plate for bond repair of steel plate with a partial loss of cross-sectional area, *Journal of applied mechanics*, *JSCE*, Vol. 13, 911–920. (in Japanese)

Ishikawa, T., Miyashita, T. & Vigh, L.G. 2013. High-precision solution of steel plate strengthened with CFRP plates under uniaxial loading, *Journal of Japan Society of Civil Engineers, SerA1 (Structural Engineering & Earthquake Engineering (SE/EE))*. Vol. 69, 1, 89–100. (in Japanese)

Ishikawa, T., Gomi, K., Hidekuma, Y. & Dogaki, M. 2022. Estimation of elastic buckling load of CFRP bonded steel plates, *Steel Construction Engineering*, Vol. 29, 115, 115_53-115_64. (in Japanese)

Kazem, H., Guaderrama, L., Selim, H., Rizkalla, S. & Kobayashi, A. 2016. Strengthening of steel plates subjected to uniaxial compression using small-diameter CFRP strands, *Construction and Building Materials*, Vol. 111, 15, 223–236.

Mizutani, M., Yo, E. & Ishikawa, T. 2023. Estimation of elastic buckling load of steel plates with cross-sectional loss, *Journal of Structural Engineering*, *A*, Vol. 69A, 116–125. (in Japanese)

Okuyama, Y., Miyashita, T., Ogata, T., Fujino, K., Ohgaki, K., Hidekuma Y., Horimoto W. & Nagai, M. 2011. Uniaxial compression test of steel plate bonded FRP sheet for rational repair and reinforcement of web in steel girder bridge, *Journal of Structural Engineering*, *A*, Vol. 57A, 735–746. (in Japanese)

Bridge Maintenance, Safety, Management, Digitalization and Sustainability – Jensen, Frangopol & Schmidt (eds)
© 2024 The Author(s), ISBN 978-1-032-77040-6
Open Access: www.taylorfrancis.com, CC BY-NC-ND 4.0 license

Fatigue retrofit using TRS for trough rib-to-crossbeam connections in orthotropic steel decks

L.H. Ichinose
Japan Association for Non-Destructive Testing Industry, Osaka, Japan

A. Tanabe
Japan Civil Engineering Consultants Association, Osaka, Japan

Y. Teranishi
Hyougo Office of River and National Highway, Hyougo, Japan

M. Sakano
Hashimori Support Center, Osaka, Japan

ABSTRACT: Due to their lightness and cost effectiveness, orthotropic steel deck bridges are one of the most popular alternatives for bridges constructed in urban and metropolitan areas in Japan. However, fatigue is still a serious problem when considering durability in orthotropic decks. The present study focuses on the connection between trough ribs and crossbeams, particularly the welded joints around the slot at the bottom of trough ribs, where a great number of the fatigue cracks has been reported. A new fatigue retrofit method using TRS (Thread Rolling Screw), which secures the watertightness of trough ribs, was proposed for the connection between trough ribs and crossbeams in orthotropic steel decks and executed in a bridge in service. Dynamic loading tests and stress measurements under service load were performed in situ, before and after the execution of the retrofitting works to verify the effectiveness of the new retrofit method.

1 INTRODUCTION

Orthotropic steel decks, due to their lightness and short construction time are considered structurally advantageous for long-span bridges and also for bridges constructed in urban areas. However, orthotropic steel decks are also well known for their susceptibility to fatigue damages, what may compromise the structural durability in case no measures are taken. A large numbers of fatigue damages have been successively reported at the trough rib-to-crossbeam connections of orthotropic steel decks during routine inspections in Japan. In a previous paper (Ichinose et. al., 2021) friction-type one-side bolts were used to connect stiffening angles to trough ribs, but those bolts could not prevent water penetrating into trough ribs.

In the present paper, TRS (Thread Rolling Screw) were applied to connect stiffening angles to trough ribs to assure watertightness of the trough ribs as part of the "Research Project for Improvement of Fatigue Durability of Orthotropic Decks" (Sakano, 2018) to verify the effectiveness of a fatigue retrofit method proposed for trough rib-to-crossbeam connections in orthotropic steel decks. Stress measurements were carried out in a bridge in service, after the execution of the proposed retrofitting works and comparison were made with the results of stress measurement carried out previously before the execution of the retrofitting works (Ichinose et. al., 2018). Simultaneous to the field works, analytical studies and experiments in laboratory were also carried out as part of the referred Research Project and their findings were already partially reported. (Matsumoto et. al., 2018, Sakamoto et. al., 2018).

DOI: 10.1201/9781003483755-262

2 FIELD WORK

2.1 *Outline of the bridge*

The bridge selected for the field study was an orthotropic steel deck bridge completed in 1986 and retrofitted after the Hanshin-Awaji Great Earthquake. The 3-span continuous box-girder bridge, presented in Figure 1, is 214.790m long, with an average width of about 9.000m, which carried 2 traffic lanes. Stress measurements were carried out in the 62.790m lateral span and the location of the stress measurement was as presented in Figure 1. The figure also shows the bridge cross-section with the two traffic lanes.

The traffic volume on the bridge before the execution retrofitting works, according to the 2015 census, was about 36,640 vehicles (12 hours), of which 18.8% were heavy vehicles.

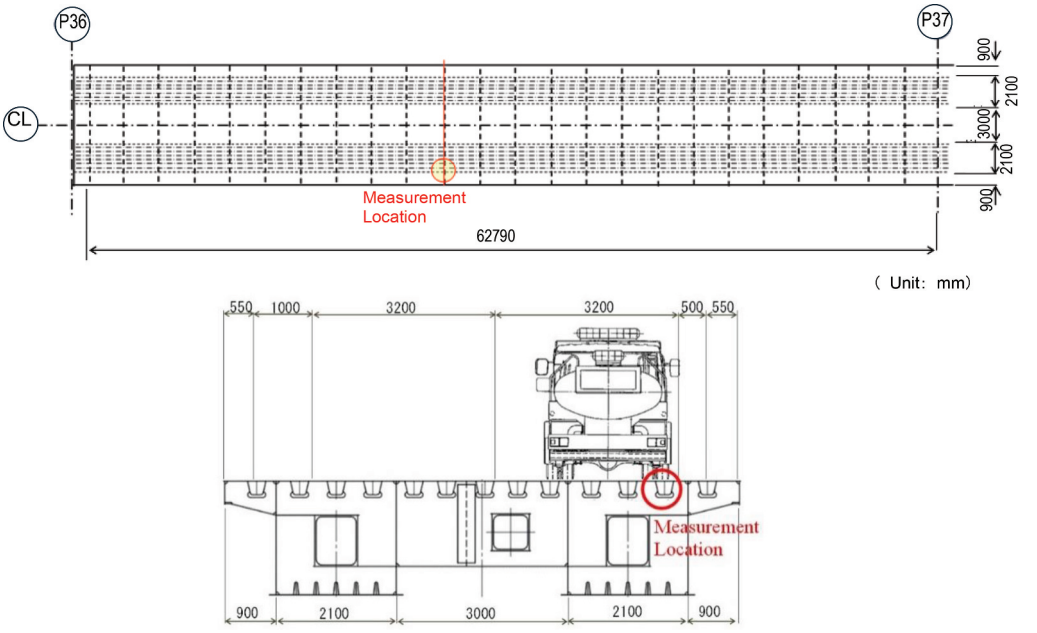


Figure 1. Measurement location (cross-section).

2.2 *Proposed retrofit method*

Fatigue retrofit method as shown in Figure 2 was proposed for trough rib-to-crossbeam connections in the orthotropic steel deck. As it is shown in the figure, two steel angle profiles were connected to both sides of the crossbeam web. One of the angle profile sides was connected to

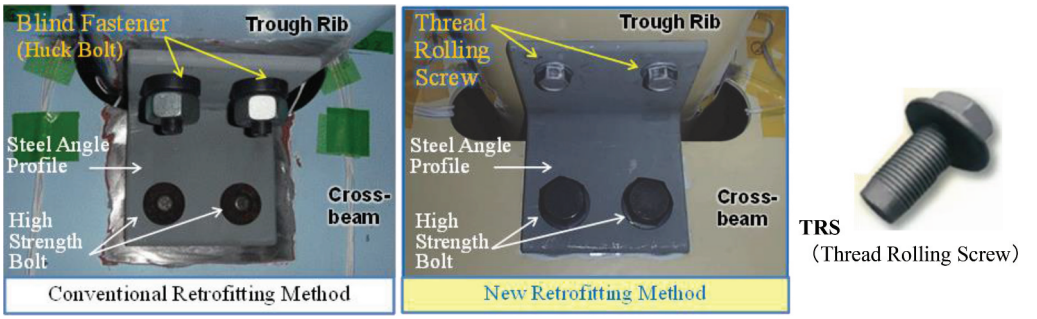


Figure 2. Retrofit methods of trough rib-to-crossbeam connections.

the bottom surface of the trough rib through TRS, instead of the friction-type blind fasteners (Huck bolts), which are conventionally used. The other side of the angle profile was connected to the crossbeam web through high tension bolts.

In previous studies the authors have found that the fatigue cracks on the welded joints around the slot at the bottom of trough ribs were caused by the relative horizontal movement of the bottom of the trough rib, and that connecting the bottom of trough rib to the cross-beam by a pair of angle profiles was effective to prevent such behavior of the trough rib. The new retrofit method was verified through fatigue tests and applied to actual structures (Ichinose et al. 2021, Tanabe et al. 2021).

The connecting angle profiles could have been installed using high-tension bolts, according to the conventional retrofit method. However, concerns on corrosion in the trough rib interior caused by air and water infiltration remained for the high-tension bolt connections, as well as for friction type one-sided bolts connections.

To prevent corrosion inside the trough ribs, TRS was proposed for trough rib side connection due to high air- and watertightness (Kagawa et al. 2018). The TRS is screwed into holes that are 0.5 mm narrower than its diameter, so that there is no space left between the TRS and base metal of the trough rib.

As the connecting mechanism of the conventional high-tension bolt is of friction type and the newly applied TRS connection is of bearing type, its influence on the effectiveness of the retrofit has to be verified. Therefore, field studies were carried out on angle profile retrofit applying TRS. The studies consisted of field measurements, including dynamic loading test and 72 hours continuous measurement of stresses under traffic load.

3 FIELD MEASUREMENTS

In order to clarify the stress conditions in the trough rib-to-crossbeam connections of the orthotropic steel deck before and after the execution of the retrofitting works and verify the effectiveness of the proposed retrofit method, dynamic loading test and 72 hours stress measurements under service load were carried out.

3.1 *Measurement points*

The measurement points and the respective strain gages are shown in Figure 3. Tri-axial gages were placed at a point 5mm from the cut-out welding toe on both sides of the crossbeam web and, at the trough rib, uni-axial gages were placed on each of the webs, 5mm from the weld toe. In addition, an uni-axial gage was placed at the bottom surface of the crossbeam lower flange in

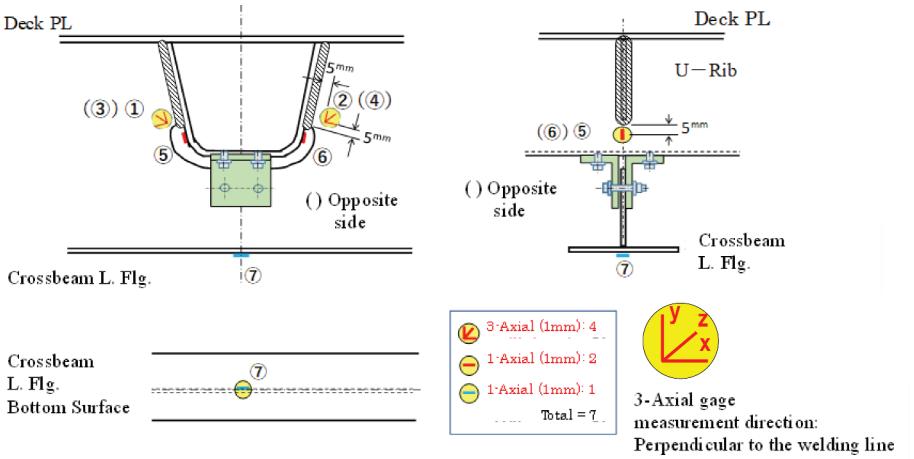


Figure 3. Measurement points and strain gage location.

order to confirm the overall behavior of the measurement area during dynamic load test and the 72 hours stress measurements. As shown in the figure, the measurements directions of the 3-axial gages were so that the direction x and y were, respectively perpendicular, and parallel to the welding line, and direction z was 45 degrees counter-clockwise towards the direction y.

3.2 *Dynamic loading test*

Dynamic loading test was carried out using the vehicle shown in Figure 4, a road sprinkler with a total weight of 137kN (front wheel = 42kN, rear wheel = 95kN). The vehicle drove on the bridge at a speed of about 60 km/h and positioned as shown in the cross-section in Figure 1.

The dynamic tests were carried out before and after the retrofitting works and stress measurements were performed at the same measurement points.

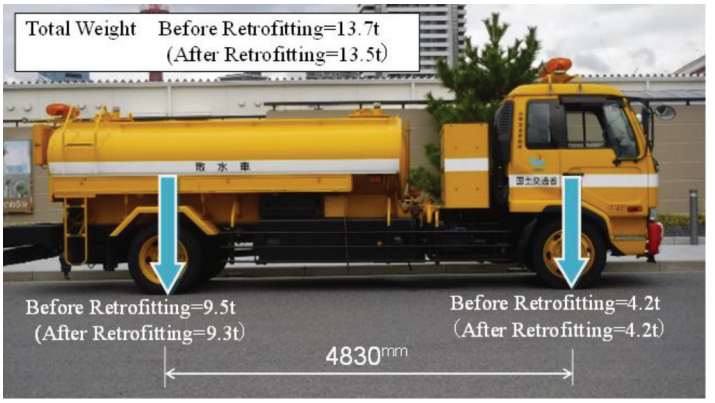


Figure 4. Testing vehicle.

3.3 *Stress measurements under traffic load*

After the dynamic loading test, 72 hours stress measurements under service load were carried out. The stress measurements were carried out according to the Guideline for stress frequency measurements (Provision) (Road Maintenance Technology Centre, 1996) and data of 3 consecutive weekdays (72hrs.) were collected. The analysis of the data was carried out applying both the peak-and-valley and the rain-flow methods.

4 RESULTS

4.1 *Dynamic loading test*

Although the dynamic loading test was carried out without traffic disruptions, each run of the test vehicle was carried out after assuring that no other vehicle was on the target span during the test to minimize the traffic influence. The test was carried out 3 times under the same loading conditions.

Figure 5 shows the maximum and minimum stresses measured at points ① to ⑦, when the test vehicle drove over the measurement location. The figure shows the measurements results for before and after the execution of retrofitting works. The maximum stress due to the test vehicle observed before the execution of the retrofitting works was about 13.5MPa (tension) at point ⑤, which decreased considerably to 6.1MPa after retrofitting. The minimum compression stress observed before retrofitting was -7.5MPa at point ③, which increased to -10.4MPa after retrofitting.

Tensile stress measured stress at point ① before retrofitting turned into compressive stress after retrofitting and compressive stress at point ④ turned into tensile stress after retrofitting, showing that the out-of-plane bending moment at the trough rib was constrained by the

addition of the angle profile at the bottom of the trough rib. This may be attributed to the fact that, the trough rib was slight asymmetric due to the transversal inclination of the road (deck) and also because the center of the retrofitting angle profiles did not coincide with that of the trough rib, causing the difference of behavior between point ① (and point ③), located at the left side of the trough rib and point ④ (and point ②), located at the its right side.

In addition, in the dynamic loading test, the maximum stress measured at the lower flange of the crossbeam, before retrofitting was 4.7MPa, whereas, after retrofitting, the measured stress was 4.6MPa, presenting almost no changes, from what it can be concluded that the crossbeam lower flange was not affected by the retrofitting works.

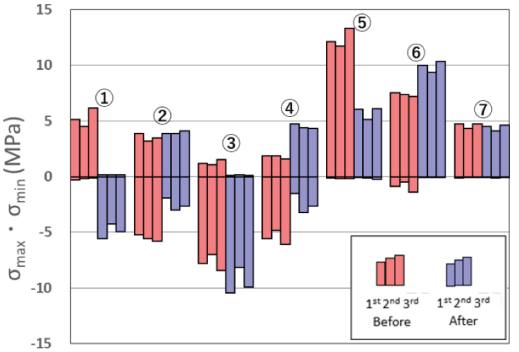


Figure 5. Dynamic loading test results (max. and min. stresses).

4.2 *Stress measurements under traffic load*

4.2.1 *Measured stress*

After the 3 days measurement, before and after retrofitting, the stresses were analyzed by the peak-valley method and their maximum and minimum values are shown in Figure 6. Before retrofitting, stresses at measurement points ① and ⑤ at the U-rib right side were predominately under tension, whereas and ② and ⑥, at the left side, were predominantly under compression. Stress at point ① was predominantly under tension and at point ③, on its opposite surface was predominantly under compression. However, after retrofitting, t point ② and ⑥ were predominantly under tensile stress and stresses points ① and ③ were predominantly compressive. The maximum stress measured before retrofitting, was 58 MPa, which was measured at point ⑤ at the left side of the U-shaped rib. This value decreased to about 48% (28 MPa) after retrofitting.

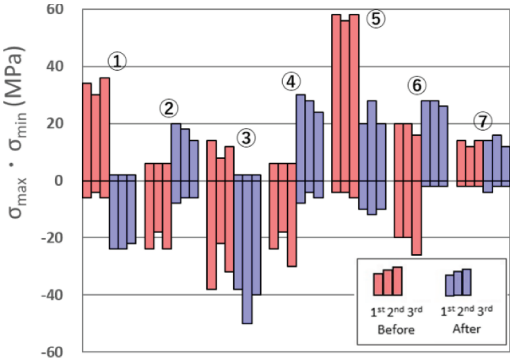


Figure 6. Max. and min. stresses according to the peak-valley method.

Figure 7 shows the variation of the stresses measured with time. The graphs show the stress variation for stresses measured when point ① presented the maximum value. As shown in the

graphs, stresses at points ① and ③, ② and ④, on the opposite surfaces of the crossbeam web, as well as ⑤ and ⑥, at opposite sides of the U-rib, presented opposite signs before retrofitting. After retrofitting, the stresses at these points presented the same signs as that of their respective pairs, showing that the crossbeam web out-of-plane flexure was restrained. In addition, the stresses decreased for all the measurement points.

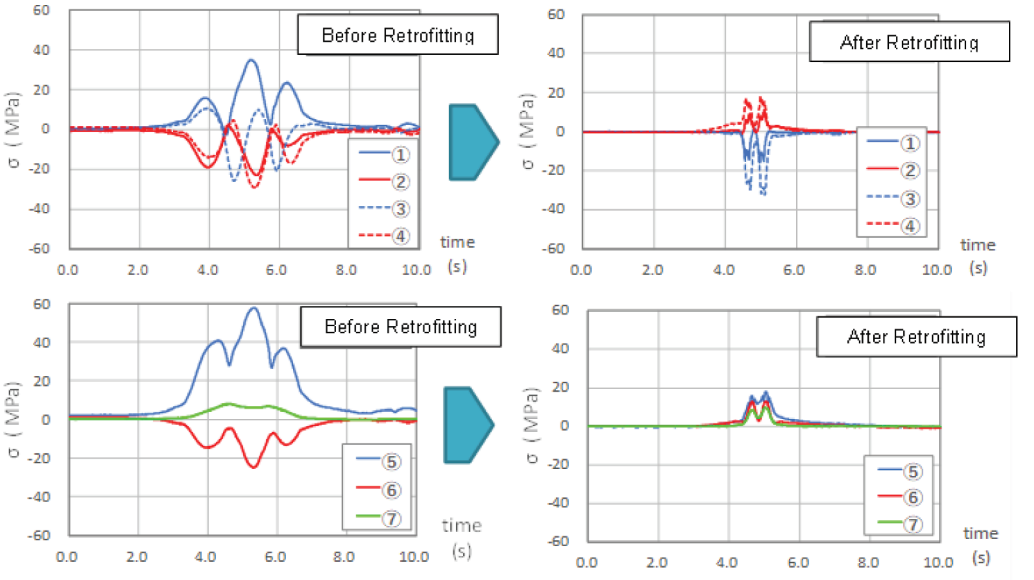


Figure 7. Example of stress variation (at maximum stress at point ①).

Figure 8 shows the histogram according to the peak-valley method for the measured stress at points ⑤ and ⑥. Stress at measurement point ⑤ before retrofitting varied from 20 MPa to 60 MPa and from -25MPa to 20MPa at point ⑥. After retrofitting, the stresses in the tensile range at point ⑤ decreased considerably, although there was a slight increase in the compression range. Tensile stress at point ⑥ presented a slight increase, whereas compressive stresses deceased to almost zero, after retrofitting. Both histograms configuration presenting similar shape after retrofitting.

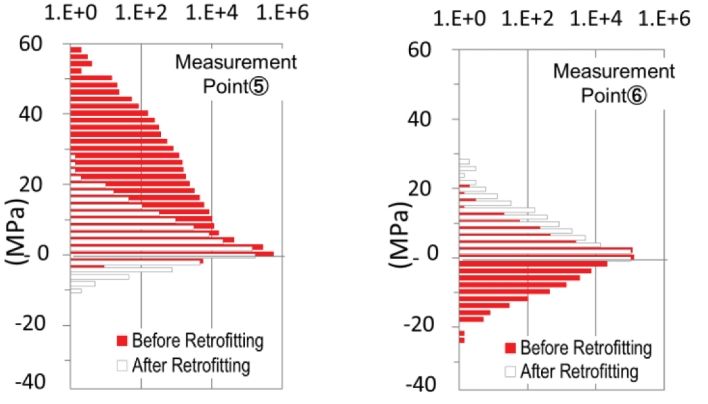


Figure 8. Measured stress histogram according to peak-valley method (measurement points ⑤ and ⑥).

It can also worth noting that, the maximum stress observed in the measurements under service traffic at the lower flange of the crossbeam before retrofitting was 14 MPa and, after

retrofitting, the maximum measured value for the same point was16MPa, whereas, the maximum stresses in the dynamic loading test was 4.7 MPa before retrofitting and 4.6 MPa after retrofitting, what represent a service traffic stress/dynamic load test ratio of about 3.0 times for before retrofitting and 3.5 times after retrofitting. This shows that during service load measurements a vehicle having an axle load equivalent to 29ton (before retrofitting) and 33ton (after retrofitting) have crossed the bridge during the period in which the measurements were being caried out.

4.2.2 *Stress range and fatigue life*

Table 1 presents the stress range and the fatigue life evaluated according to the Fatigue Design Recommendations for Steel Road Bridges (Japan Road Association. 2002). The maximum value for stress range was obtained at the measurement point ⑤ at the left side of the trough rib, where the measured stress exceeded 60MPa before retrofitting and the stress after retrofitting was reduced to 40% (below 40 MPa).

The shortest evaluated fatigue life was 55years (G class), at the measurement point ⑤, at the left side of the trough rib, which was extended to 30,000 years after retrofitting. For the other members, the stress life was over 10,000 years before retrofitting which improved to over 30,000 years, after retrofitting, proving that the structural durability has improved.

Table 1. Estimated fatigue life (before and after retrofitting).

	Member	Measurement Point	Class	2M-cycles Fatigue Strength (MPa)	Const. Ampl. Cut-off Limit (MPa)	Maximum Stress Range (MPa)	Equivalent Stress Range (MPa)	No. of Effective Cycles (cycles)	Fatigue Life (years)
Before Reinforcement	Cross-beam Web	①	F	65	46	40	-	-	∞
		②	F	65	46	30	-	-	∞
		③	F	65	46	50	49	2	20000
		④	F	65	46	36	-	-	∞
	U-Rib Side	⑤	G	50	32	64	39	608	55
		⑥	G	50	32	44	41	2	15000
	Cross-beam L. Flg.	⑦	D	100	84	16	-	-	∞
After Reinforcement	Cross-beam Web	①	F	65	46	26	-	-	∞
		②	F	65	46	28	-	-	∞
		③	F	65	46	52	51	1	34000
		④	F	65	46	38	-	-	∞
	U-Rib Side	⑤	G	50	32	40	38	1	37000
		⑥	G	50	32	30	-	-	∞
	Cross-beam L. Flg.	⑦	D	100	84	18	-	-	∞

5 CONCLUSIONS

From field measurements on the proposed fatigue retrofit method using TRS for the trough rib-to-crossbeam connection in an orthotropic steel deck bridge, the following can be concluded.

5.1 *On the measured stress*

Measurement of stresses before and after retrofitting showed that the horizontal movement of the trough rib in the bridge axial direction, as well as in the bridge transverse direction could be restrained. The maximum stress observed before retrofitting (point ⑤, 58MPa) was reduced to almost a half (28MPa) after retrofitting, confirming the effectiveness of the proposed retrofitting works.

In addition, measurements under service traffic showed that a vehicle having a maximum axle load equivalent to 33ton (after retrofitting) have crossed the bridge during the measurements.

5.2 *On the stress range and fatigue life*

The maximum value for stress range observed before retrofitting at point ⑤ (64MPa) was reduced by about 40% (40MPa) after retrofitting, which resulted in a considerable improvement of the expected fatigue life.

REFERENCES

Hanshin Expressway Corp. Ltd. 2012, Fatigue measures for steel bridges in the Hanshin Expressways, *3rd edition* (in Japanese)

Ichinose, L.H., Kunitoshi, S. and Sakano, M. 2021, Verification of effectiveness of fatigue retrofit for rib-to-crossbeam connections in orthotropic deck bridges, *Bridge Maintenance, Safety, Management, Life-Cycle Sustainability and Innovations (IABMAS 2020)*.

Japan Road Association. 2002, Fatigue design recommendations for steel road bridges (in Japanese)

Kagawa, Y., Kaneda, Y. and Endo, K. 2018, Study on air and water tightness of penetrated joint by thread rolling screw (diameter 16mm), *Proc. of 73rd JSCE, CS3-008*. (in Japanese)

Matsumoto, R., Tanabe, A., Kunitoshi, S., Sakano, M. 2018, Stress analysis of U-rib to crossbeam connections in orthotropic decks, *Proc. of 73rd JSCE, CS3-003*. (in Japanese) Road Management Technology Center 1996, Guidelines for stress frequency measurement (Provision) (in Japanese)

Sakamoto, C., Konishi, H., Ohmori, K., Ishikawa, T., Sakano, M. 2018, Verification ot effectiveness of fatigue measures in Rib-to-crossbeam connections in orthotropic decks, *Proc. of 73rd JSCE, CS3-004*, (in Japanese)

Sakano, M. 2018. Research Project on improvement of fatigue durability of orthotropic decks. *Proceedings of 73th JSCE*. CS3–001 (in Japanese)

Tanabe, A., Matsumoto, R., Kunitoshi, S. and Sakano, M. 2021, Analytical evaluation of fatigue retrofit for trough rib to transverse-rib welded joints in orthotropic steel decks, *Bridge Maintenance, Safety, Management, Life-Cycle Sustainability and Innovations (IABMAS 2020)*.

SS16: Redundancy in bridges: Design, fabrication and bridge maintenance

Organizer: A. Mosavi


Taylor & Francis
Taylor & Francis Group
http://taylorandfrancis.com

Bridge Maintenance, Safety, Management, Digitalization and Sustainability – Jensen, Frangopol & Schmidt (eds)
© 2024 The Author(s), ISBN 978-1-032-77040-6
Open Access: www.taylorfrancis.com, CC BY-NC-ND 4.0 license

Internal redundancy approach for built-up mechanically fastened steel tension members in the United States

Jason B. Lloyd
Nucor Corporation, Charlotte, NC, USA

ABSTRACT: Two USA-based AASHTO Guide Specifications were published in 2018, with 2022 interims. They offer the analytical framework needed to revisit the way we evaluate redundancy in steel bridges considering system-level and member-level redundancy for new or existing bridges. For the last four decades, the steel bridge industry in the United States has become accustomed to determining redundancy through engineering judgement married to a single approach, namely load path redundancy (referring to the number of primary girder lines). Publication of these new AASHTO Guide Specifications enables designers and owners to design outside the box that we put ourselves in 40 years ago. In addition, the Guide Specifications also include a methodology to establish an inspection interval for a special inspection of internally redundant members (IRMs) that is of sufficient depth to reliably detect a severed component. This is a major departure from the calendar-based approach to setting inspection intervals and is a big step toward developing an integrated fractur control plan. This paper discusses the development of the AASHTO Guide Specifications for internal redundancy, exploring the historical context and providing a working example of how the evaluation of an existing structure could demonstrate inherent redundancy previously not considered within the US bridge industry.

1 INTRODUCTION

Built-up member bridge construction practices using wrought iron can be traced to as early as the late 18th Century. From the 1840's onward, construction of long-span wrought-iron bridges in the UK continued the advancement of riveted connections and use of built-up member construction. The dawn of rolled steel mills in the late 19th Century and early 20th Century further advanced the use of built-up construction, making it the most widely used form of building and bridge construction. Hot-driven rivets were predominantly used to fasten multiple components, such as plates and angles, together until the 1950's to 1960's when high strength bolts and welding processes became preferred methods of construction. Today, thousands of bridges possessing built-up members continue to serve highway and railway industries and many are well over 100 years old! They remain a vital part of the US and international infrastructure systems, and in many cases have become historic and iconic structures.

While built-up construction may not be the most economical design option in current markets, some applications, such as built-up through-girders, built-up tie girders or built-up steel bents, could be smart choices when taking advantage of internal redundancy. An internally redundant member is defined as a primary steel bridge member in tension, or with a portion of it in tension, which has redundancy within the cross section, such that fracture of one element will not propagate through the entire member cross-section and is discoverable by the applicable inspection protocol.

This paper summarizes research that contributed to an American Association of State Highway Transportation Officials (AASHTO) guide specification that offers provisions for

DOI: 10.1201/9781003483755-263

the evaluation of built-up members for internal redundancy. It is called the AASHTO *Guide Specification for Internal Redundancy of Mechanically-Fastened Built-up Steel Members* (referred to hereafter as the IRM Guide Spec).

2 OVERVIEW OF THE IRM APPROACH

The new AASHTO IRM Guide Spec is another method engineers in the USA can use to extend the service life of many iconic, historic and economically valuable bridges. The IRM Guide Spec also provides a fresh perspective on how internal redundancy might be exploited in new designs to mitigate the risk of potential fracture events. It provides the industry with quantitative analysis for the purpose of showing redundancy and establishing rational inspection intervals for built-up members that are realistic about what can be reliably found during inspections and for what duration undiscovered damage could be safely tolerated. All of this, however, must be kept in context when discussing new steel bridges, designed and built to the standards of the AASHTO Fracture Control Plan (FCP), which has resulted in zero fractures in the past 45 years. That said, in the past 60 years no built-up member classified as a fracture critical member (FCM; now referred to in the USA as a nonredundant steel tension member, NSTM) is known to have triggered structural collapse due to the fracture of a single component. However, that is the assumption put on these member types. Three known cases of component failure in built-up NSTMs are the Hastings Tied Arch Bridge, USA, (two separate fractures), Milton-Madison Bridge, USA, (experimentally severed for research, simulating fracture to observe structural response), and the North Fork Mollola River Bridge, USA. In all three cases, the built-up NSTM did not result in partial or complete failure of the bridge and the bridges continued to safely carry service loads until repairs could be made. Keep in mind that risk is the product of likelihood and consequence. The IRM Guide Spec helps engineers evaluate the consequence of a component fracture, conservatively ignoring likelihood, linking damage tolerance to rational inspection requirements.

2.1 *The internally redundant member analysis methodology*

In the USA, the designation of a NSTM is left to the bridge designer (in the case of new design) or inspector/owner (in the case of existing bridges) to determine. Traditionally this has been decided through engineering judgement based on the number of girder lines, not a set of engineering calculations. This implies that the decision to define a member as NSTM has largely been made without regard to internal redundancy. The mechanical separation of components within an IRM produces an inherent fracture resistance at the component boundaries known as Cross-Boundary Fracture Resistance (CBFR). Full-scale experimental research showed that mechanically fastened built-up members possess CBFR independently of the toughness of the steel (Hebdon et al., 2017a; Lloyd et al., 2021). This is a beneficial outcome for owners because a majority of built-up members were fabricated long before the AASHTO Fracture Control Plan (FCP) of 1978 began requiring a minimum toughness level in base metal. The IRM Guide Spec equally applies to new designs and existing members, including all built-up flexural and axially loaded members, as well as members subjected to a combination of flexural and axial loading (e.g. tied arch tension ties). Simplified solutions allowing for hand calculations have been developed for a majority of the member types to date and more are currently being researched.

2.2 *Progression of IRM analysis*

The basic steps of analyzing a built-up member for internal redundancy using the IRM Guide Spec are:

1. Screening; criteria such as condition and remaining fatigue life
2. Strength limit checks in the assumed faulted condition
3. Fatigue life check in the assumed faulted condition
4. Special inspection interval

The provisions of the IRM Guide Spec first require that the member be screened for certain conditions, such as the presence of unmitigated damage and remaining fatigue life, to ensure a high likelihood of reliable, long-term performance. New and existing members must also meet specified proportioning limits provided in the Specification. Existing members that do not pass the screening criteria should be automatically excluded from further evaluation. The IRM Guide Spec is not intended to justify leaving a fractured component of a member in service once discovered, nor any other damage that may prohibit reliable service.

In step 2, the factored load is calculated using the reliability-based load combination called, "Redundancy II". Researchers used the same reliability-based procedures to develop Redundancy II that were used to establish the various load combinations of AASHTO LRFD Bridge Design Specifications (Connor et al., 2018). Factored loads are used to compute after-fracture stresses for strength and fatigue assuming that a single component within the member cross-section has failed. For flexural members, the outer cover plate generally is assumed to fail. This assumption is made for two primary reasons. First, the outer plate experiences the largest live load stress making it most likely to fatigue. Second, assumption of the outer plate failure has the greatest effect on section modulus, creating the most critical after-fracture capacity check. For axial members this process is iterated considering failure of a different component each time to find the controlling case, taking advantage of member cross-sectional symmetry. Gross and net section properties are checked for remaining strength in the assumed faulted condition. Laboratory testing and finite element parametric studies demonstrated that when a component is severed, localized stress amplifications occur in the adjacent component(s) as a result of load redistribution into and out of the adjacent component. Stress amplification factors are provided in the IRM Guide Spec to account for the local stress effects of shear lag and localized bending. For the strength limit state checks, the local amplification is not important, however, because local yielding, slip and load redistribution allow the section to fully develop the cross-section. Thus, amplification factors are set to unity. Factored demands are then compared to factored resistance, identical to a typical strength check made during design. If it is found that the member possesses sufficient strength in the faulted condition, the analysis may continue. If not, the member is removed from further analysis (for existing members) or for new designs the member cross-section is simply adjusted and re-evaluated.

Following strength limit checks, the third step in the analysis is fatigue life in the faulted condition. Unlike for strength checks, when considering the fatigue limit states for the faulted condition localized stress amplification of the live load stress ranges must be taken into account. The IRM Guide Spec provides simple equations and tables having illustrative cross-section types to help the user determine amplification factors to apply for each case. Fatigue detail categories for members in the faulted condition are provided, as well. These were established through full-scale experimental testing of members following failure of a single component (Hebdon et al., 2017b; Lloyd et al., 2021; Lloyd et al., 2023). If the member possesses positive fatigue life in the faulted condition, then it has satisfied the provisions of the IRM Guide Spec. Following a US Federal Highway Administration (FHWA) approved procedure, as per the National Bridge Inspection Standards (NBIS), the member can be reclassified as an IRM, thus being removed from an owner's NSTM inventory.

The final step is calculation of the special inspection interval. The special inspection replaces the arms-length NSTM inspection without changing requirements for routine inspection. The IRM Guide Specs include a methodology to establish the interval for special inspections intended to locate any tension component that has possibly fractured. This inspection of IRMs is referred to as a "Special Inspection" as defined in the US Code of Federal Regulations and must be sufficiently thorough enough to reliably detect a severed component. Conceptually, this is a significant departure from the somewhat arbitrary, calendar-based 2-year interval intended to find small fatigue cracks. The reality is small fatigue cracks are difficult for inspectors to find reliably and for that reason we can say with confidence that internal redundancy has been serving us well in our built-up members for well over a century.

As a note of interest to the reader, the US-based National Steel Bridge Alliance (NSBA) has developed Excel spreadsheet tools that perform the IRM analysis for multi-component axial members, multi-component flexural members, and two-component members. These free

IRM evaluation tools can be found on the NSBA Design Resources website (See www.aisc.org/nsba/design-resources).

3 IRM EVALUATION EXAMPLE

The following is an evaluation example of a few sections of an existing bridge. The intent is to demonstrate the application of the IRM analysis methodology. This method can be used for both evaluation of an existing bridge, as is demonstrated, or for the design of a new structure. Constructing bridges using built-up mechanically fastened tension elements will not always be the most cost-effective approach. However, due to the inspection requirements within the USA for members classified as NSTM, the overall service life costs can be drastically reduced by using this approach for certain member types, without compromising safety and performance. A few examples that make sense are the tie girders of tied arches, two-girder bridges such as through-girders, or steel straddle bents.

3.1 *Background for example bridge*

The bridge used in this evaluation example is a twin structure, each with two riveted built-up girders with parabolically haunched webs. A photo of the underside of the bridge is shown in Figure 1. The bridge is 732.4 m long with two end spans of 33.9 m and 14 symmetric interior spans of 44.47 m each. The yield strength of the steel was not explicitly stated in the design drawings. However, it did state that the unit stress of the structural steel was 124 MPa. This most likely means the yield strength was between 227.5 MPa and 248.2 MPa. However, because it was not stated the plans, the yield and tensile strengths were taken from AASHTO Manual for Bridge Evaluation Table 6A.6.2.1-1, where for a bridge built in 1958 the yield strength is listed as 227.5 MPa and tensile strength as 455 MPa.



Figure 1. Photo of the underside of the twin, two-girder bridges.

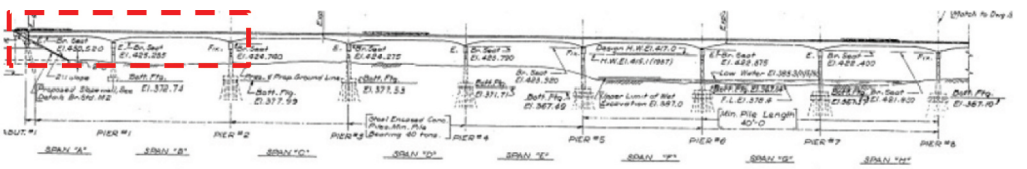


Figure 2. Original design drawings for the 1958 built-up riveted, two-girder bridge.

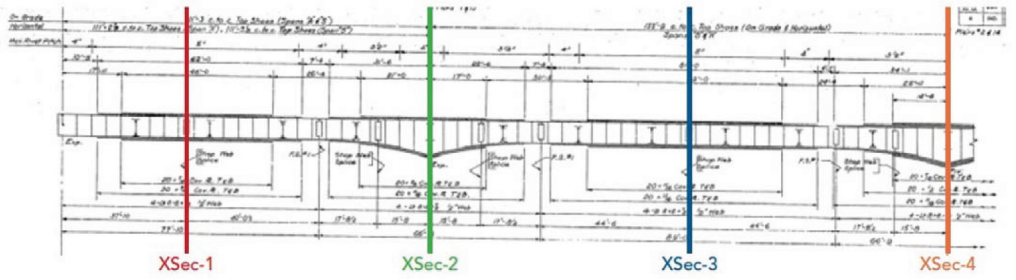


Figure 3. Blow-up elevation view of the built-up riveted girders (Span A and B), from Figure 2.

Figure 2 shows eight spans of the 16 symmetric spans of the bridge. The first two spans, shown encased within the red dashed line, are the two spans evaluated as part of this example (Span A & B). Note that the floorbeams are not included in the evaluation example. Due to the symmetry of the design, these girders make ideal candidates for quicker evaluation using "families" of identical members. This means that sections of the girders having the same dead and live load moments with the same cross-sectional properties, along with the same general condition, can be evaluated together. Any cross sections having different condition (e.g. section loss resulting in loss of capacity, unrepaired impact damage, etc.) or any having been repaired resulting in a different cross section (e.g. built-up plating to restore section), must be evaluated on an individual bases. This method proves advantageous for saving time when evaluating a bridge this long. Details for the member components will be provided throughout the example, as needed. Only members that carry a net tensile live load that exceeds any compressive dead load, in AASHTO's Strength Load Combination I, are required to be evaluated. Typically, for a flexural member this would include locations of maximum live load moment. Figure 3 provides the elevation view of the original design drawings where the field splices and haunched webs can be seen. For this example, four cross sections will be evaluated within the first two spans. Stress reversal zones are not evaluated here, although it would be recommended to do so in an actual bridge evaluation. The approximate four locations are shown with solid-colored lines at 0.4L of span A, center line of pier 1, 0.5L of span B, and center line of pier 2. These four locations represent the cross sections with the largest positive or negative live load moments in the first two spans.

3.2 *Summary of example bridge results*

The summary of results is provided in Table 1. These results were obtained by following the provisions of the IRM Guide Spec. It also contains the maximum special inspection interval for the cross section (or member) being evaluated. Guide Spec. Tables 3.1-1 and 3.1-2 provide guidance on determining the special inspection intervals. *XSec-1* was found to be a Case II member, having finite fatigue life in the unfaulted state and finite fatigue life in the faulted state. Thus, Table 3.1-2 from the IRM Guide Spec was used.

The total remaining fatigue life, N_f, was computed as 9.2 years. Being less than 20 years and greater than 5, the maximum permitted interval is calculated as $0.5N_f$, where the IRM Guide Spec allows for the result of $0.5N_f$ to be rounded up to the nearest next even-year interval. The user is referred to IRM Guide Spec article C3.1 for more information about rounding up to the next even-year interval.

Strength checks were made for the member cross-sections following the provisions of the IRM Guide Spec and recommended practices for flexural members, as described in Step 2 of Section 2.2 of the present paper. Two primary strength calculations are made, gross section yield on the faulted section (referring to the case where the outer-most cover plate is assumed to be failed), and net section fracture on the faulted section. Where "OK" is presented in Table 1, the cross-section was found to possess sufficient strength capacity in the faulted condition for both strength requirements.

Table 1. Summary of results for the example bridge IRM evaluation.

Cross Section	User Input Member ID	Faulted State Strength Check	IRM Special Inspection Interval Years
XSec-1	Span A, Positive Moment (0.4L)	OK	6
XSec-2	Negative Moment @ Pier 1	OK	8
XSec-3	Span B, Positive Moment (0.5L)	OK	6
XSec-4	Negative Moment @ Pier 2	OK	4

3.3 *Discussion of results and potential implementation*

Four cross sections were evaluated for the example bridge girder evaluation. Due to the symmetry of the spans, results can be extrapolated to cross sections of similar geometry and condition. It was found that all cross-sections met provisions of the IRM Guide Specifications resulting in Special Inspection intervals ranging from 4 to 8 years. Table 1 summarizes the results with the respective special inspection intervals. Keep in mind that these four cross sections represent the same continuous girder. They were selected as locations of highest live load, making them the likely most critical cross sections to evaluate. For continuous construction, stress reversal zones would also be recommended for evaluation. It would also be advisable to evaluate any location where cross-sectional properties change to ensure a critical demand-capacity ratio is not missed.

In this example, all cross sections passed the IRM evaluation requirements. Thus, the NSTM could be reclassified as an IRM. In the hypothetical case that a continuous girder has some cross sections that pass the IRM Guide Spec provisions and some that don't, it would fall upon the owner to decide how they wish to handle this. It could be that the continuous girder is divided into sections of positive and negative moment. Each section could be treated as a separate member with one or more cross sections evaluated for each member. Suggested cross sections to evaluate include those with maximum (or minimum for negative moment regions) live load moments, or those having abrupt section modulus changes, such as at the termination of a cover plate. (Only a single cross section was evaluated for each member in the example above to keep the example simple and brief.) Another possible solution, like the first, is to subdivide the girder some distance from the center line of the piers so that reversals zones are clearly included in a member, rather than falling on a dividing point. Consider that members need not be evaluated for internal redundancy at mechanically fastened splices (See IRM Guide Specifications 1.4), which will often be located at a stress reversal position on the continuous girder. A final strategy could be to implement a retrofit, such as strengthening, in areas that did not pass the IRM evaluation, making it so that the entire girder length does meet the IRM Guide Spec provisions and can be classified as IRM.

As is shown in this example, each cross section met the provisions of the IRM Guide Specifications. However, the analyses resulted in different special inspection intervals. This is a case where the owner would need to consider the options and decide if it makes sense to break out the sections of the girder and perform the special inspection for them on their different schedules or perhaps choose the section with the shortest inspection interval and perform the special inspection interval for the entire girder on that schedule such that the other special inspection interval requirements are exceeded. Suspending any unnecessary inspection of IRMs could save time, resources, and reduce lane closures and worker exposure to high-speed traffic helping to reduce risk. This aspect of implementation is not prescribed in the IRM Guide Specifications and therefore is incumbent upon the owner. There is ample flexibility built into the US Code of Federal Regulations for programming and conducting this type of inspection.

REFERENCES

AASHTO (2018a). *AASHTO Guide Specifications for Analysis and Identification of Fracture Critical Members and System Redundant Members*, (1st Edition), American Associations of State Highway and Transportation Officials, Washington, DC, USA.

AASHTO (2018b). *AASHTO Guide Specifications for Internal Redundancy of Mechanically-fastened Built-up Steel Members*, (1st Edition), American Associations of State Highway and Transportation Officials, Washington, DC, USA.

Connor, R. J., Bonachera Martin, F. J., Korkmaz, C., Varma, A. H., and Lai, Z. (2018) *NCHRP Report 883*:*Fracture-Critical System Analysis for Steel Bridges*. Transportation Research Board, National Research Council, Washington, D.C.

Hebdon, M. H., Bonachera Martin, F. J., Korkmaz, C., and Connor, R. J. (2017a). *Fracture Resilience of Steel Built-up Members Subjected to Flexure*. Journal of Bridge Engineering, American Society of Civil Engineers (ASCE). Doi: 10.1061/(ASCE)BE.1943-5592.0001059.

Hebdon, M. H., Bonachera Martin, F. J., Korkmaz, C., and Connor, R. J. (2017b). *Load Redistribution and Remaining Fatigue Life of Steel Built-up Members Subjected to Flexure Following a Component Failure*. Journal of Bridge Engineering, American Society of Civil Engineers (ASCE). Doi: 10.1061/(ASCE)BE.1943-5592.0001087.

Lloyd, J. B., Bonachera Martin, F. J., Korkmaz, C., and Connor, R. J. (2023). *Internal Redundancy of Mechanically Fastened Built-up Steel Axially Loaded Two-Channel Members*. Engineering Journal, American Institute of Steel Construction (AISC), Vol. 60, No. 4, pp. 197–223.

Lloyd, J. B., Bonachera Martin, F. J., Korkmaz, C., and Connor, R. J. (2021). *Internal Redundancy of Mechanically-Fastened Built-up Steel Axially Loaded Multicomponent Members*. Journal of Bridge Engineering, American Society of Civil Engineers, July, https://doi.org/10.1061/(ASCE)BE.1943-5592.0001743.

Bridge Maintenance, Safety, Management, Digitalization and Sustainability – Jensen, Frangopol & Schmidt (eds)
© 2024 The Author(s), ISBN 978-1-032-77040-6
Open Access: www.taylorfrancis.com, CC BY-NC-ND 4.0 license

Development of the current AASHTO integrated fracture-control plan for steel bridges

R.J. Connor
Jack and Kay Hockema, Professor in Civil Engineering, Lyles School of Civil Engineering, Purdue University, West Lafayette, IN, USA

ABSTRACT: There has been considerable research and interest in the topic of fracture-critical members (FCMs) during the past decade. As a result, the entire concept of what constitutes a nonredundant steel tension member has been completely revised and many long-standing ideas and opinions related to this classification of members have been shown to be overly conservative. After years of research, two new stand-alone AASHTO Guide Specifications that give codified direction on how to perform 3D system analysis to verify system redundancy, as well as AASHTO Guide Specifications to evaluate internal member-level redundancy of mechanically-fastened built-up members, have now been developed and adopted by AASHTO. This paper will summarize the background to the current views of FCMs and suggestions about how this new integrated approach to redundancy, in particular as related to the fatigue and fracture limits states is being implemented in the US.

1 INTRODUCTION

In the United States, there is a special classification of steel bridge structures. To be placed into this classification, a few criteria must be met, specifically, 1) that are deemed to have non-redundant members that are, 2) fabricated from steel, and 3) these members must be in tension. Members placed in this category are subjected to additional design, fabrication, and in-service inspection requirements in the name of increasing reliability. The concept originated in the mid-1970s following a relatively small number of major failures associated with tension members, or the portion of a member in tension. While the initiating cause may vary, the final mode of failure of the member was brittle fracture. As a response to these failures, the added requirements mentioned above were developed and implemented over a period of about 10 to 15 years for these members. Historically these members have been referred to as Fracture Critical Members (FCMs) in the United States codes and specifications. Today, such members are referred to as Nonredundant Steel Tension Members (NSTMs) and henceforth, will be referred to as such in this paper. For all practical purposes, NSTMs should be viewed equivalent to FCMs.

Despite the perception surrounding bridges classified as having NSTMs, there is actually very little evidence that would suggest such bridges have been more unreliable than other types of steel bridges. In fact, the previous term "Fracture Critical" has conjured up thoughts that such members are doomed to failure in the form of brittle fracture. However, such a view when compared to the actual in-service performance of such members could not be further truth. In fact, while it is true that catastrophic failure of a tension member has critical consequences, truss bridges, which are classified as having NSTMs, also have what the author refers to as BCMs, or "buckling critical members". However, non-redundant compression members in trusses exist without any additional concern regarding their criticality nor do they require any special fabrication or in-service inspection.

DOI: 10.1201/9781003483755-264

Nevertheless, as an industry, there is little concern that non-redundant compression members will suddenly fail in an unstable buckling mode. The reason is simple: the bridge engineering community as a whole believe the results of many years of experimental research and analysis. Thus, such members are not treated differently in design or during in-service inspection whether they are redundant or not. For some reason, the same is not true for tension members. While isolated failures of tension members have occurred, the US bridge engineering community, more specifically regulatory agencies, have *in the past* been very reluctant to accept the decades of research and advancements that have been made in the understanding of fracture mechanics, the availability of steels with superior toughness, advances in fabrication methods and non-destructive testing. Fortunately, the culmination of multiple more recent research projects coupled with decades of earlier research has resulted in a sea change in how redundancy is viewed in steel bridge structures. This paper will present a summary of how redundancy in steel bridge members subjected to tension is viewed in the US today, and in particular as related to steel bridge members in tension.

2 PERFORMANCE OF THE "MODERN" STEEL BRIDGE

As stated, NSTMs have traditionally been subjected to more stringent material, design, fabrication, and in-service inspection requirements. In the context of NSTMs, "modern" NSTMs will generally possess the following characteristics:

1. Meet more stringent CVN requirements;
2. Be fabricated to the AASHTO/AWS D1.5 Fracture Control Plan (FCP)) (AWS 2020);
3. Be designed using the nominal stress range approach for fatigue, generally using an infinite life approach;
4. Unlikely to possess details susceptible to distortion induced fatigue cracking which is responsible for most cracking observed in highway bridges.

In general, bridges built after about 1985 meet all of the above. It is also worth noting that nearly two decades ago, research related to constraint induced fracture (CIF) led to the develop of design criteria and retrofit strategies that have effectively eliminated the likelihood of this type of fracture (FHWA 2021). For example, in 2012 the first requirements were added to the AASHTO LRFD Bridge Design Specifications (AASHTO 2021) to prevent the use of details susceptible to this form of fracture. Fortunately, most if not all nonredundant girder bridges in the US which possess CIF susceptible details on NSTMs designed prior to this date have been retrofit in order to prevent this form of fracture. Recent work funding by the Federal Highway Administration (FHWA) has also led to improved design and retrofit guidance that will be incorporated into the 10th Edition of the AASHTO LRFD Bridge Design Specifications.

History has shown that steel bridges which meet all of above criteria are extremely unlikely to be susceptible to brittle fracture. In fact, the author has not been able to identify any NSTMs which have met the above criteria (a period of over 45 years) in which a brittle fracture has occurred. Thus, the improvements made in the design and fabrication of NSTMs have resulted in steel members that are highly reliable in terms of the fatigue and fracture limit state. Thus, brittle fracture is a very unlikely mode of failure in modern steel bridges.

3 DEVELOPMENT OF AN INTEGRATED FRACTURE CONTROL PLAN

Considering the above, about 10-15 years ago, the steel bridge industry and owners partnered to begin to undertake research that would allow a more systematic approach to addressing redundancy in both new and old steel bridges. More specifically, identify, conduct and then implement research that would address the risk associated with brittle fracture in nonredundant members more holistically. Ideally, the final outcomes would link the reliability of in-service inspection, the strength or performance of the member following a defined level of

damage, and the interval of the inspection. The approach is referred to herein as an Integrated Fracture Control Plan. In such an approach, the desired reliability is achieved and deficiencies in one area is made up through exploiting the strength of a more reliable component of the plan. For example, if in-service inspection can't reliably detect small cracks, the member design is changed to ensure that the critical crack size is much larger thereby ensuring the inspection can detect important damage. Interestingly, this approach is commonly utilized in other industries such as oil and gas and aerospace and is a proven and effective strategy.

Early on when laying out the research efforts needed, several areas were identified in which further study was needed. Four broad areas were considered.

1. Probability of detection associated with in-service inspection;
2. Internal member redundancy;
3. System redundancy;
4. Improved performance through exploiting the superior toughness of modern steels and modern fatigue design.

Items one through three will be discussed in this paper as they have been implemented, either directly or indirectly into the current bridge design practices in the US. The fourth item has not been directly implemented to date, though further work is ongoing. Hence, the fourth topic will not be discussed further in this paper.

4 PROBABILITY OF DETECTION

In the US, members identified as NSTMs are subjected to detailed arms-length in-service inspections. Historically, these inspections are required at intervals of 24 months or less. Such inspections are conducted with the objective of finding and documented small defects such as fatigue cracks *BEFORE* they lead to brittle fracture or some other serious outcome. However, while this is a valid strategy, when performing any type of inspection, one should consider the concept of probability of detection (POD) and hence ask the question; "Can the inspection reliably detect a defect before it becomes critical?".

Probability of detection studies are used to determine the probability of detecting a defect in a specified component under the inspection conditions and procedures provided or commonly used. In the case of highway bridges, this is almost always performed through a visual inspection. POD is typically expressed as a function of a quantifiable target parameter associated with the given flaw (e.g., length). While the target parameter is the single most influential factor in determining the probability of detection, it is also a function of many other physical and operational factors including the material, geometry, flaw type, NDT method, testing conditions and the inspector, their certification, education and experience (Georgiou 2006).

Probability of detection data can be analyzed as discrete data, where the response is binary, either a hit or a miss, or as continuous data, which is a signal response, tracking how close the noted size of the defect is to the actual size. Hit/miss data produces qualitative information indicating whether a flaw is present or absent.

Having such knowledge, the owner can make informed decisions to minimize risk as related to the effectiveness of the inspection program. For example, the following approaches could be explored to minimize risk if the POD data suggests that at identify the critical defect is unlikely.

- The consequence associated with member failure must be kept low via other means.
- The inspection strategy must be changed to result in increased POD, such as using another form of NDT in contrast to basic visual inspection.
- The owner simply accepts the risk of member failure and a high-risk level is deemed tolerable.

One may believe that inspecting more frequently would be a valid approach. However, such a strategy will generally only increase the likelihood of finding the failed component sooner. In fact, in the majority of cases where brittle fractures occurred, the public identified and

reported the damage, not a bridge inspector. More frequent but *unreliable* inspections will only be marginally effective in preventing member failure.

To investigate the likelihood of detecting a fatigue crack in a steel member, a large-scale POD study was performed at Purdue University [Snyder et al, 2015]. This study, which is believed to be the first statistically significant study of its kind focused on fatigue cracks in bridge members, revealed that the 50-50 crack length (i.e., that length with a 50% probability of an inspector hitting or missing) is on the order of one inch (25 mm) using visual inspection. Further, to achieve a POD of 90% requires cracks to be in the range of five inches (125 mm) in length. Other studies have shown similar results in terms of the overall low POD associated with visual inspection [Moore et al, 2001, Washer et al, 2014]. This is essential data to have when developing an integrated fracture control plan. Ideally, if the crack size that has a detection rate of 90% is known, one could infer that a member should at least be able to tolerate such a crack before catastrophic member failure would be expected. On the other hand, if there is a low probability of detection associated with the critical defect size, the strategy should not be to find small cracks since it is known such an approach is pointless (i.e., there is a low probability that such a crack would ever be found in the first place). As will be discussed, this data was very useful when combined with research items two and three listed above.

5 INTERNAL MEMBER REDUNDANCY

Mechanically-fastened built-up steel members have long been *perceived* to be highly resistant to complete and sudden catastrophic failure due to brittle fracture. While this type of redundancy was generally known to be present through anecdotal evidence, no guidance existed on how to establish if *adequate and reliable* internal redundancy is present in a given mechanically-fastened built-up steel member. Due to a lack of experimental evidence or existing standards, the Federal Highway Administration (FHWA) was not previously able to recognize this form of redundancy (Lwin, 2012).

To gain the needed data, Transportation Pooled Fund Project TPF-5(253) "Evaluation of Member Level Redundancy in Built-up Steel Members" was conceived and completed (Hebdon et al., 2017a & b,; Lloyd, 2018).

The resistance to complete member failure following brittle fracture in an individual component is referred to as cross-boundary fracture resistance (CBFR). Through full-scale experimental testing performed in the research, it was shown that brittle fracture in one component does not propagate into the adjacent component if certain conditions are met. The member is then checked to establish if there is sufficient strength in the faulted condition under prescribed load combinations. The experimental work was furthered through fatigue testing to establish how long a member in the faulted state could survive in this damaged condition (i.e., with one component completed failed). Using this information, conservative estimates could then be made to set an appropriate inspection interval and scope to ensure a second component will not fail prior to the next inspection. The research showed that members meeting specific proportion and condition requirements can be designated as Internally Redundant Members (IRMs) that do not need to be subjected to the traditional arms-length inspection associated with NSTMs. The research was recently incorporated into the AASHTO Guide Specifications for Internal Redundancy of Mechanically-fastened Built-up Steel Members which was approved by the AASHTO Subcommittee on Bridges and Structures in June of 2018 (AASHTO 2018a w/ 2022 interims). These specifications are applicable to both new and old steel bridge structures. Since complete member fracture is not a plausible failure mode, the member is reclassified as an IRM that is to be inspected in a way that will reliably detect broken components at intervals of up to ten years (*normal safety inspection intervals and scope of the deck, piers, etc. remain unchanged*).

It is also important to note that the primary objective of the in-service special inspections of IRMs is to detect fully severed components and not to find very small fatigue cracks emanating from any one of thousands of fastener holes. The POD study cited earlier showed that it is unrealistic to assume that small cracks can be identified with a high level of reliability using traditional visual inspection techniques. In contrast, the likelihood of detecting a severed

component in a built-up member, on the order of 10 inches long or more, is obviously much higher. In this way, the fracture control plan is "integrated" in that the inspection interval and capability of the inspector is linked to the tolerance of the member as a function of time since the fatigue life in the damage state is also known based on the large-scale testing.

6 SYSTEM REDUNDANCY

Another form of redundancy can be exploited through the use of advanced analytical tools. In such an approach, analysis is performed in which entire NSTMs are assumed to have failed and the structure analyzed to establish the consequence of the failure. To develop and codify the procedures to evaluate the redundancy of bridges with members traditionally designated as NSTMs through 3D system analysis, NCHRP Project 12-87a was conducted (Connor et al, 2018) in which the following questions were studied.

- What is an acceptable target reliability for a damaged structure?
- What level of live load should a faulted structure be capable of carrying?
- How should live load be positioned on the bridge?
- What criteria (service and strength) should be used to define failure?
- What is the exposure period during which the bridge should be assumed to be in the faulted state and how does this tie into future inspection needs?

The research resulted in the AASHTO Guide Specifications for Analysis and Identification of Fracture Critical Members and System Redundant Members, which was approved by the AASHTO Subcommittee on Bridges and Structures in June of 2018 (AASHTO 2018b w/ 2022 interims). This Guide Specification provides owners and engineers with a robust benchmarked analysis methodology that can be used to increase the effectiveness and efficiency of inspection in steel bridges with members traditionally classified as NSTMs. These specifications are also applicable to both new and old steel bridge structures. since it is shown the failure of the entire member would not lead to collapse, the member by definition is not an NSTM. As a result the member is classified as a SRM and need only be inspected at an interval and scope as any other redundant steel member.

Similar to IRMs, the overall FCP is integrated as inspection is not required to find small cracks, but rather complete broken members since analyses have shown that complete member failure can be tolerated under established load combinations. Thus, an integrated approach is used as the FCP.

7 SUMMARY AND CONCLUSIONS

This paper has presented a number of significant advancements that have been made which can be used to more rationally treat members traditionally classified as NSTMs and lower the perceived and actual risk associated with such members. Strategies have been developed and codified where internal redundancy and system redundancy can be used to show the consequence associated with a partial or complete member fracture, though highly unlikely is also low. Explicitly considering the fracture limit state in such a way allows for the development of an integrated fracture control plan in which the inspection interval, scope and capability of the inspector are linked to the tolerance of the member or structure as a function of time. Moving forward with an integrated fracture control plan allows a more rational treatment of these members that is based on engineering principles rather than perception and feeling. Because of these advancements, the National Bridge Inspection Standards (NBIS) in the US were updated in June of 2022 to allow these new approaches to be implemented by owners. This is major change in how redundancy in steel members subjected to tension is viewed as compared to the historical views of the past. The new approaches allow a clearer understanding of actual redundancy allowing owners to put limited inspection resources where they are most needed thereby increasing the reliability of their gaining inventory.

REFERENCES

AASHTO (2018a/2022). AASHTO Guide Specifications for Internal Redundancy of Mechanically-fastened Built-up Steel Members, (1st Edition), American Associations of State Highway and Transportation Officials, Washington, DC, USA.

AASHTO (2018b/2022). AASHTO Guide Specifications for Analysis and Identification of Fracture Critical Members and System Redundant Members, (1st Edition), American Associations of State Highway and Transportation Officials, Washington, DC, USA.

AASHTO. (2021). AASHTO LRFD Bridge Design Specifications. Transportation (9th Ed.), American Associations of State Highway and Transportation Officials, Washington DC, USA.

American Welding Society (AWS)., (2020). AWS D1.5:2020 Bridge Welding Code. Miami, FL.

Connor R. J., Bonachera Martin, F.J., Varma, A.H., Lai. Z., Korkmaz, C., "Fracture-Critical System Analysis for Steel Bridges", NCHRP Report 883, National Cooperative Highway Research Program (NCHRP), Washington, DC, 2018.

Hebdon, M. H., Bonachera Martin, F. J., Korkmaz, C., and Connor, R. J. (2017a). Fracture Resilience of Steel Built-up Members Subjected to Flexure. Journal of Bridge Engineering, American Society of Civil Engineers (ASCE). Doi: 10.1061/(ASCE)BE.1943-5592.0001059.

Hebdon, M. H., Bonachera Martin, F. J., Korkmaz, C., and Connor, R. J. (2017b). Load Redistribution and Remaining Fatigue Life of Steel Built-up Members Subjected to Flexure Following a Component

FHWA (2021) Evaluation of Steel Bridge Details for Susceptibility to Constraint-Induced Fracture, Final Project Report; Publication No. FHWA-HIF-21-046.

Lloyd, J.B., (2018). "Internal Redundancy of Mechanically-Fastened Steel Built-up Axially-Loaded Members". Diss. Purdue University, 2018. Web. Apr 2019.

Lwin, M., "Memorandum: Clarification of Requirements for Fracture Critical Members," Washington, DC, 2012.

Moore, M., Phares, B., Graybeal, B., Rolander, D., and Washer, G. (2001). Reliability of Visual Inspection for Highway Bridges (FHWA-RD-01-020). Federal Highway Administration, McLean, VA.

Snyder, L.R., Whitehead, J. Connor, R.J., Lloyd, J.B., "Probability of Detection Study for Visual Inspection of Steel Bridges Volume II - Full Project Final Report SPR 3820", Joint transportation Research Program, Indiana Department of Transportation, West Lafayette, IN, May 2015.

Washer, G.A, Connor, R.J., Looton, D.W., "Performance Testing of Inspectors Implementing NDT Technologies", Journal of the Transportation Research Record, No 2048, pp. 107–113, Washington, DC, 2014.

Bridge Maintenance, Safety, Management, Digitalization and Sustainability – Jensen, Frangopol & Schmidt (eds)
© 2024 The Author(s), ISBN 978-1-032-77040-6
Open Access: www.taylorfrancis.com, CC BY-NC-ND 4.0 license

Fabrication aspects of redundancy

R.D. Medlock
High Steel Structures, LLC, Lancaster, Pennsylvania, USA

ABSTRACT: There are special fabrication requirements for nonredundant steel bridges in the United States. As described in this paper, these include requirements for material, shop floor fabrication, and inspection.

1 INTRODUCTION

The Fracture Control Plan of 1978 introduced fabrication and inspection practices and special materials requirements for non-redundant members in bridges. These special practices and materials are now called, "Fracture Control", as in, "fracture control practices" and "fracture control material requirements".

Non-redundant members were then called, "fracture critical members", but recently new types and classifications of nonredundant members have been adopted (1):

Table 1. Steel bridge member redundancy classifications.

Redundancy Form / Member Designation	Description	Fracture Control Practice Required	Previous Description
Load Path Redundancy (2) / Load Path Redundant Member (LPRM)	A redundancy exists based on the number of primary load-carrying members such that fracture of the cross section at one location of a member will not cause a portion or all of the bridge to collapse.	No	Non-Fracture Critical
Nonredundant Steel Tension Member (3) (NSTM)	A primary steel member fully or partially in tension, and without load path redundancy, whose failure may cause a portion of or the entire bridge to collapse.	Yes	Fracture Critical
System Redundant Member (2)/System Redundant Member (SRM)	A redundancy that exists in a bridge system without load path redundancy, such that fracture of the cross section at one location of a primary member will not cause a portion of or all of the bridge to collapse.	Yes	New
Internally Redundant Member (2)/Internally Redundant Member (IRM)	A redundancy that exists within a primary member cross-section without load path redundancy, such that fracture of one component will not propagate through the entire member, is discoverable by the applicable inspection procerus, and will not cause a portion of or the entire bridge to collapse.	Yes	New

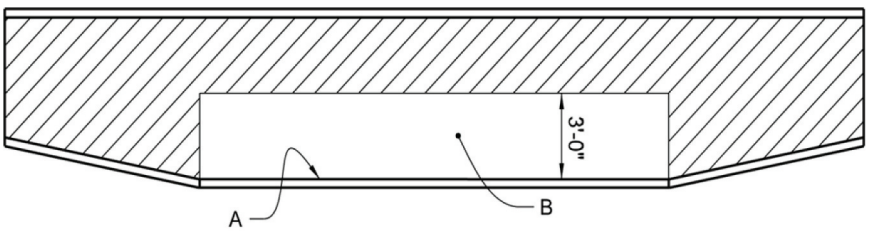
DOI: 10.1201/9781003483755-265

As shown in Table 1, two types of redundant members are new: SRMs and IRMs. Before, these members would simply have been considered non-redundant and therefore fracture critical. There are two key things to note about these members. First, neither carry the same special, stringent in-service inspection requirements that NSTMs carry (2). However, SRMs and IRMs do carry the same fabrication, inspection (shop inspection), and material requirements as NSTMs (4,5). This is because it is possible for SRMs or IRMs to lose their conditions that provide special redundancy and thus revert to NSTM status.

2 IDENTIFICATION OF NONREDUNDANT MEMBERS

Given that fabricators must procure special materials and perform special fabrication and inspection practices for nonredundant members, such members must be identified in contract documents. It is dynamic tensile loading that is of concern for non-redundant bridge members, and only components in tension may be appropriately designated as NSTM, SRM, or IRM. Thus, when engineers use non-redundant members, they must indicate which members are non-redundant, and they must indicate the areas of these components which will be in tension. Further, the AASHTO LRFD Bridge Design Specifications (6) require that engineers do so.

Engineers have used a variety of ways to identify non-redundant members. Such variety often leads to confusion or incomplete information. When fabricators are not clear about this or not sure that the plans correctly identify non-redundant members are their tension zones, they issue requests for information (RFIs). To guide engineers and help unify practices, the FHWA provides recommendations in their Bridge Welding Reference Manual (7).



FRACTURE CRITICAL DESIGNATION

Note: Shaded area indicates areas that are FC.

Source: FHWA

Figure 1. Excerpt from Bridge Welding Reference Manual (7) showing how to designate tension zone of non-redundant members (i.e., FC zones).

3 FRACTURE CONTROL MATERIALS

Steels for bridges are defined in ASTM A709, "Standard Specification for Structural Steel for Bridges". Materials for non-redundant members are indicated with an "F" appended to the grade, i.e., "50F" instead of "50T". The steel materials used for non-redundant members are the same as those used for redundant members except for toughness properties and some practice requirements. Each of the following are requirements for materials for non-redundant materials:

- CVN requirements are higher. See examples in Table 1 for select grades. Note that the values shown are for service temperature 2.
- CVN testing is more frequent – testing is done per plate as opposed to per heat. These are known as "P" and "H" frequencies, respectively.
- There are restrictions on the welded repairs mills are allowed to perform.

Table 2. Sample material requirement comparisons for non-redundant members.

Grade	Test Temperature	Minimum Charpy CVN Value	Minimum Average Charpy CVN Value
	degrees F	foot-pounds	foot-pounds
36T, up to 4"	40	NA	15
36F, up to 4"	40	20	25
50WT, up to 2"	40	NA	15
50WF, up to 2"	40	20	25
50WT, 2" to 4"	40	NA	20
50WF, 2" to 4"	40	24	30
HPS 70WT, up to 4"	-10	NA	25
HPS 70WF, up to 4"	-10	24	35

Fabricators purchase materials appropriate for the redundancy condition indicated on the design plans. If components or parts of components are specified fracture critical, NSTM, SRM, or IRM, then "F" designated materials are procured for the components or component parts. Mills provide these materials, and the material test reports (MTRs) produced by the mill indicate the materials as "F", and document that "H" frequency sampling was done for toughness testing.

There are times when fabricators desire to use a non "F" designated plate for a nonredundant application. In such cases, the fabricator will take a coupon from the plate and test it at the "F" temperature. In practice, plates always pass this testing.

4 SHOP DRAWINGS

Fabricators produce shop drawings to provide instructions to the shop about how to fabricate the bridge. The instructions in the shop drawings are complete, including what materials to use where and what components or parts of components are non-redundant. It is essential that instructions regarding non-redundancy are complete, correct, and clear. Otherwise, incorrect material may be used, or incorrect practices may be used on nonredundant components.

Fabricators document the requirements of the materials for each component in the bill of materials for that component. For example, if a flange or web is nonredundant, this associated material requirements will be designated in the bill of materials on the shop drawings which feature this component. Further, the shop drawings will indicate which portion of the components are non-redundant. As is the case with designs, fabricators indicate non-redundant zones on components with sketches.

Under the fracture critical program, fabricators indicate fracture critical components and zone as "FC". Under the new program, there are now three types of nonredundant members: NSTMs, SRMs, and IRMs. With each of these three member types requiring the same special non-redundant materials and practices, the bridge community has decided to designate nonredundant zones as "FC", for "fracture control" (1). To properly align the shop drawings with the specific member types in the design, fabricators will use a note on the shop drawing general notes sheet to mentions the type of redundancy (i.e., NSTM, SRM, or IRM) and also state that nonredundant components and zone will be designated as "FC". Thus, the shop coworkers and material purchasers will only need to recognize one special designation, "FC". This practice will help provide clarity and avoid errors.

5 FABRICATION

Under the Bridge Welding Code (8), there are several special fabrication requirements intended as extra precautions against fatigue or fracture during performance of the bridges. These may be categorized as hydrogen controls, welding practices, non-destructive examination, repairs, qualifications, and material processing requirements.

Special hydrogen control practices are described in Table 3. Already, the Bridge Welding Code (8) has stringent and effective welding hydrogen controls for bridge welding. The special requirements for nonredundant members take these a step further. In welding, the presence of too much hydrogen can cause discontinuities such as porosity or, more seriously, cracking. Hydrogen is always present, including in base metals, welding consumables, and in the air. It is impossible to eliminate it completely. As weld metal cools, free hydrogen accumulates in the grain boundaries of the nearly solidified base metal. In the presence of stress, such as shrinkage constraints, and depending on the hardness of the base metals being joined, cracks can form. Welding practices such as preheating and consumable controls minimize the amount of hydrogen present at the start of welding. Other controls such as post heat can drive off undesirable hydrogen even after solidification. For nonredundant members, these controls are increased for extra caution. Since hydrogen cracks sometimes do not form immediately upon solidification, nondestructive examination (NDE) of welds in nonredundant members is delayed as an extra precaution to ensure that any cracking that might occur has time to form.

Table 3. Hydrogen controls for welding of non-redundant members.

- Diffusible hydrogen requirements for electrodes
- Special drying and storage for shielded metal arc welding (SMAW) electrodes
- Submerged arc welding (SAW) storage and baking requirements
- Mixing of recovered SAW fluxes
- Drying & storage requirements flux-cored arc welding (FCAW) and GMAW electrodes
- Higher preheat requirements
- Postheat requirements for repairs
- Waiting time for NDT
- Preheat for repairs

Further to hydrogen controls, there are other welding practice restrictions to provide an extra bit of conservatism for welding on nonredundant members. These are described in Table 4. Electroslag and electrogas welding are precluded because research conducted by the federal highway administration (FHWA) (9) did not demonstrate that the ESW practice required by the Bridge Welding Code (8) would be suitable for nonredundant members. Regarding gas metal arc welding (GMAW) electrodes, the original authors of the Bridge Welding Code (8) were concerned that GMAW would not be suitable for welding nonredundant members. However, GMAW is indeed suitable for nonredundant members; metal cored GMAW has since be adopted for nonredundant members, and solid wire GMAW needs to be so adopted (it is indeed permitted for redundant members).

There are extra, more stringent requirements for welder qualification and requalification. For welding procedure qualification, there is no extra testing for nonredundant members, but tests do expire every five years, unlike procedure for redundant members, which no longer expire under the Bridge Welding Code (8). Regarding tack welding, in addition to higher minimum preheat (noted in Table 3), there are also minimum length requirements.

Table 4. Welding practices (other than special Hydrogen Controls).

- Electroslag (ESW) and electrogas (EGW) not allowed
- Gas-Metal Arc Welding (GMAW) only allowed with metal-core wire (not solid wire)
- Special packaging for consumables
- Charpy V-notch requirements for welding procedures
- Prequalification not allowed for E9018 electrodes
- Expiry of welding procedures qualification tests
- Tack welding only allowed inside joint
- Tack welding restrictions in Table 12.3
- Both radiography and side bends required for welder qualifications
- Annual welder requalification

In addition to the time delay mandate described in Table 3, there are other NDE requirements intended to provide an extra measure of caution described in Table 5. A particularly noted requirement is that for butt splices, both RT and UT are required, doubling the NDE over that conducted for butt splices on redundant tension shop splices. For ultrasonic testing (UT) there are more stringent requirements for recordable indications. "Recordable indications" are indications that do pass requirements; hence the Code is mandated the documentation of indications that are acceptable as a means of providing a possible starting point of investigation of an in-service weld that happens to prove problematic. "Prod" type magnetic particle (MT) probes are not allowed because if prod type probes are not used properly, arc-strikes can occur. Arc-strikes are not uncommon in fabrication, and when they occur, fabricators remove them, but this extra bit of caution is in place for non-redundant members as an extra bit of caution. For RT, wire-type image quality indicators (IQIs) are not allowed because hole-type IQI reveal angular distortion if any were to occur due to placement of the source.

Table 5. Nondestructive examination practices.

- Extra recordables for ultrasonic testing
- Only yoke magnetic particle testing (MT) allowed, i.e., not prod MT
- NDT Level II vs. I
- Wait time requirement before performing NDE
- Both radiographic testing (RT) & ultrasonic testing (UT) required on butt joints
- Only hole-type IQI (not wire type) allowed for RT

The need for repairs is inherent in steel bridge fabrication. If not done properly, repairs can introduce conditions that may lead to performance concerns. However, many repairs are routine, and good practice for executing them is well known and understood. Therefore, for most repairs, the Bridge Welding Code (8) defines requirements for most repairs and does not require discrete engineer approval for such repairs; these are known as "prequalified repairs". In the case of nonredundant members, the Bridge Welding Code (8) introduces extra caution in requiring engineer approval and written documentation for repairs that would otherwise be prequalified. For nonredundant members, repairs are divided into two categories: "critical" and "noncritical". For noncritical repairs, engineers may give preapproval, hence giving the engineer additional control over repairs that are otherwise routine. However, critical repairs may not be handled with preapproval. As shown in Table 6, there are also some extra repair practice requirements to introduce more conservatism. Also note that under general rules for welding nonredundant members, the welding procedures used to conduct welded repairs must be approved for use on nonredundant members.

Table 6. Repair practices.

- Grind out an extra 1/8" of base metal when removing welds
- MT of 12" beyond required in repair of fillet welds
- Written documentation required for all repairs, including those that do not require a nonconformance report
- Prequalified repair procedures are not allowed for critical repairs
- Preheat requirements for gouging for repairs
- Mandatory MT of repair excavation

There are five additional requirements for nonredundant members in Table 7, including two qualification requirements and three material requirements. Under Clause 1 of the Bridge Welding Code (8), steel bridge fabricators must be certified by the American Institute of Steel Construction (AISC) (10). For fabrication of nonredundant members, fabricators must satisfy additional AISC qualification requirements and carry an AISC fracture critical (FC) endorsement. To earn this endorsement, fabricators must demonstrate knowledge of special

requirements associated with nonredundant member fabrication. Fabricators must also have a person with three years' bridge fabrication experience on their quality control staff.

Finally, there are some special control requirements for nonredundant base metals. Base metal must be inspected for discontinuities. Some level of initial discontinuities is allowed, and these are defined by ASTM A6, "Standard Specification for General Requirements for Rolled Structural Steel Bars, Plates, Shapes, and Sheet Piling" (11). The requirements are the same for materials for nonredundant members; however, this extra inspection is required as a precaution to ensure unallowed discontinuities were not overlooked. The Code requires removal of a bit of material for universal edges and for sheared edges because these edges are not as uniform as thermally cut edges and might provide initial stress risers or might mask unacceptable discontinuities that would otherwise be noted. Generally base metal laminations are innocuous; however, the Bridge Welding Code (8) has extra conditioning requirements for laminations as an extra precaution against the possibility of a lamination at a butt splice resulting in a crack.

Table 7. Special qualifications and special material requirements.

- Requirement for AISC FC endorsement
- Requirement for lead inspector; must have three years' experience
- Preinspection of base metal surfaces
- Remove 3/16" from sheared or universal mill edges
- Special acceptability and repair for base metal laminations

6 SUMMARY

Since 1978, there have been special material, fabrication, and inspection requirements in place for nonredundant tension members. Previously, nonredundant members were known as "fracture critical" members; these are now known as either nonredundant steel tension members (NSTMs) or members with special redundancy, including both system redundant members (SRMs) and internally redundant members (IRMs). Regardless of these labels, these requirements have remained the same.

For materials, the differences amount to addition material characteristic testing and Charpy V-notch (CVN) requirements that are slightly more stringent. In practice, fabricators observe that material which satisfy tension requirements typically also will satisfy the special nonredundant requirements when testing is done. For fabrications and inspection, there are a wide range of additional requirements intended to introduce extra conservatism in practice. Many are minor additional requirements which do not have a significant impact on shop practices, while others are more significant. The most significant practices are those which impact the project schedule. These include requirements for engineer approval, which can introduce waiting for answers, and extra practices associated with NDE, including use of both radiography and ultrasonic testing for butt splices and the waiting period before testing.

REFERENCES

1. Connor, R., et. al., 2023, "Implementation of Redundancy Terms under 2022 NBIS", National Steel Bridge Alliance.
2. Title 23 Code of Federal Regulations (CFR) *Part 650.305 Subpart C*, *National Bridge Inspection Standards (NBIS)*.
3. Title 23 Code of Federal Regulations (CFR) *Part 650.305 Definitions*.
4. AASHTO, 2018, "Guide Specifications for Analysis and Identification of Fracture Critical Members and System Redundant Members".
5. AASHTO, 2018, "Guide Specifications for Internal Redundancy of Mechanically-Fastened Built-Up Steel Members".
6. AASHTO, 2020, "LRFD Bridge Design Specifications".

7. FHWA, 2019, “Bridge Welding Reference Manual”.
8. AASHTO/AWS, 2020, “D1.5 Bridge Welding Code”.
9. FHWA, 1987, “Improved Fracture Toughness and Fatigue Characteristics of Electroslag Welds”.
10. AISC, 2023, “AISC 207-23, Standard for Certification Programs”.
11. ASTM, 2021, “ASTM A6/A6M-21, Standard Specification for General Requirements for Rolled Structural Steel Bars, Plates, Shapes, and Sheet Piling”.

Bridge Maintenance, Safety, Management, Digitalization and Sustainability – Jensen, Frangopol & Schmidt (eds)
© 2024 The Author(s), ISBN 978-1-032-77040-6
Open Access: www.taylorfrancis.com, CC BY-NC-ND 4.0 license

UHPC beam end encasement for the design of maintenance-free steel bridges

B. Lassy, A. Hain & S. Motaref
University of Connecticut, Storrs, Connecticut, USA

ABSTRACT: Repair of corroded steel girder ends is a costly and time-consuming issue in the maintenance of highway bridges. Through a collaboration between the Connecticut Department of Transportation and the University of Connecticut, a repair method using Ultra-High Performance Concrete (UHPC) beam end encasement has been developed and successfully implemented on in-service bridges. This study broadens the use of this UHPC repair method by applying it to new bridge construction. The proposed design replaces traditional steel bearing stiffeners with durable UHPC bearing columns, protecting the beam ends from corrosion that occurs beneath leaking deck joints. This paper presents the design of a beam end and novel end diaphragm connection for a sample bridge. By eliminating the need for maintenance and repair of bridges with deck joints, this research has the potential to contribute to longer-lasting, high-performance bridges that benefit the nation's transportation infrastructure.

1 INTRODUCTION

The maintenance and inspection of bridges in the US is costly and time intensive but is essential for the safety of the nation's transportation infrastructure (ASCE, 2021). Damage or deterioration of individual elements of a bridge can contribute to the deterioration of additional elements (Ault & Dolph, 2018; Kayser & Nowak, 1989). Once corrosion begins, it is difficult and expensive to a) inspect; b) conduct the load rating to determine the remaining strength; c) repaint, clean, or otherwise maintain; and d) rehabilitate or replace the entire corroded element (Kere & Huang, 2019; Kogler, 2015). There has been significant research on beam end encasement using ultra-high-performance concrete (UHPC) to provide both a structural replacement for a typical steel bearing stiffener as well as providing a protective enclosure (Zaghi et al., 2017). This paper aims to expand this method to new construction for the design of maintenance free beam ends.

In a multiphase, decade-long project, researchers at the University of Connecticut (UConn) and engineers at the Connecticut Department of Transportation (CTDOT) teamed up to develop a rehabilitation method for corroded steel bridge girders (Hain & Zaghi, 2022; Zaghi et al., 2015, 2017). In this method, headed shear studs are welded (Figure 1b) to intact surfaces of corroded steel beam ends (Figure 1a), then the beam end is encased in UHPC (Figure 1c) to provide an alternate load path for bearing forces (Zmetra, 2015). Phase I of the research project, beginning in 2013, began with proof of concept experiments on half scale girders that showed the repair was successful in restoring the bearing capacity of the beam end beyond the undamaged capacity (Zaghi et al., 2015).

Phase II of the project built on the knowledge from Phase I and focused on validating design choices, specifically the strength of steel headed shear studs embedded in UHPC (Kruszewski, 2018)(Hain, Zaghi, Kamali, et al., 2019)(Kruszewski, Wille, et al., 2018). For studs embedded in UHPC, the failure mode was primarily controlled by stud shear failure (Kruszewski, Zaghi, et al., 2018). Limitations on spacing, cover, and thickness of the underlying web were developed

DOI: 10.1201/9781003483755-266

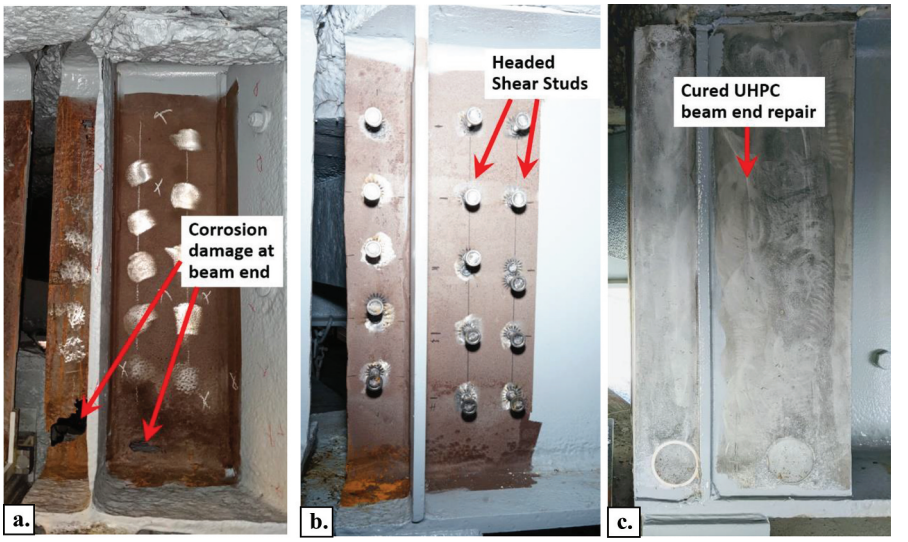


Figure 1. Beam end repair with uhpc encasement. a) corrosion damaged beam and bearing stiffener, b) headed shear studs are welded on to intact portions of the web, c) UHPC is poured over the corrosion and made integral with the beam end.

and validated with a series of push-off tests (Kruszewski & Zaghi, 2019)(Kruszewski & Zaghi, 2021). Phase II additionally included a full-scale girder test. The results showed that the repair restored the bearing capacity at the beam end and shifted the failure mode from web-crippling in the corroded region to web shear buckling in the first panel outside the extents of the UHPC repaired column (McMullen et al., 2018; McMullen & Zaghi, 2020).

Phase III focused on developing design guidelines for the repair to be used by practitioners and assisting CTDOT with the design and implementation of the repair on two highway bridges in Connecticut. The first bridge, repaired in 2019 in New Haven, CT, was a rolled steel girder bridge that carried highway traffic over rail lines (Hain, Zaghi, Fields, et al., 2019). While this presented a construction challenge, it showed the range of applicability for the repair. Due to the significant corrosion damage present, shear studs were laid out with consideration for the thickness of the underlying steel, leading to different layouts at different girders. The UHPC was poured overnight from the top of the deck through a core in the deck with PVC piping distributing it through the formwork (Hain & Zaghi, 2021). The second implementation in 2021 made use of partial height UHPC panels that extended from the bottom flange approximately one-third up the height of the web, allowing contractors to pour the UHPC into the top of the formwork without any distribution system (Lassy et al., 2023). The two beam end repairs the research team was involved with were fully instrumented and showed the successful force transfer through the studs into the bearing, findings which were back up through laboratory testing (Lassy et al., 2023). Due to the success of the multiphase research study, this repair was included in the Federal Highway Every Day Counts 6 Initiative (Haber & Ocel, 2020), and has begun gaining traction for projects around the country (CTDOT, 2020).

The main goal of this project is to extend the research from the beam end repair to new construction. The success of the beam end encasement method led to the concept of using a UHPC bearing column to replace a conventional steel bearing stiffener in new construction. This not only provides an alternative structural element for the bearing stiffener, but due to the proven durability and impenetrability of UHPC (Graybeal & Hartmann, 2003; Li et al., 2020), also acts as a maintenance-free protective coating to increase the service life of the bridge. The proposed design builds off the design guide produced for the beam end repair (CTDOT, 2020) with design options rooted in the AASHTO LRFD Bridge Design Specifications (AASHTO, 2020) and American Concrete Institute 318-19 Building Code Requirements

for Structural Concrete (ACI, 2019). The most significant challenge assessed for the UHPC bearing column detail is the connection between the UHPC and steel diaphragm. Several design options are documented in this paper to overcome this challenge.

2 DESIGN OF DIAPHRAGM CONNECTIONS

2.1 *Sample bridge*

A case study was conducted using the FHWA Design Example (Wilson et al., 2015) to generate a realistic example bridge. An important feature of the UHPC bearing column is the application on beam ends only. This feature has not been studied or designed for an intermediate bearing on a continuous span bridge, as there are significant structural differences. UHPC encasement aims to mitigate the leakage from deck joints, which can often be eliminated over a continuous bearing. However, the beam end encasement has been successfully implemented for the repair of the ends of continuous spans, where there is no negative moment. The end of a simple span beam has negligible moment to cause tension in the UHPC repair, while there is significant moment at the bearing of a continuous span. This should be avoided as such load effects have not been investigated and are not considered in the design guide.

Rather than performing a full bridge design for this project, the research team focused on the bearing column and diaphragm connections. The sample bridge selected for the study is a FHWA Example Steel Bridge, a continuous two span highway bridge designed to AASHTO LRFD specifications (AASHTO, 2020). The example bridge has five 1413 mm deep plate girders, a reinforced concrete integral deck, and standard steel bearing stiffeners and diaphragms. The diaphragm is a standard CTDOT k-frame diaphragm for steel girder bridges (Figure 2), which features a C channel and three angles welded to gusset plates attached to the diaphragm (CTDOT, 2003).

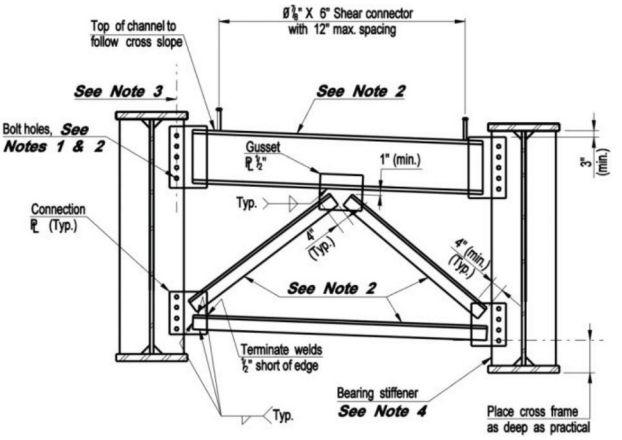


Figure 2. CTDOT standard K-frame diaphragm (CTDOT, 2003).

2.2 *Diaphragm design loads*

The FHWA example provides the loads on the bearing column (Wilson et al., 2015). However, it neglects the design for the diaphragm. To complete the design, the ASHTO LRFD specifications (AASHTO, 2020) were used to conduct a full design for both the bearing column and diaphragm connection. Horizontal loads are controlled by wind loading on the fascia girders, while vertical loading is controlled by the combination of dead and live loads from the bridge above. Seismic loading was not considered. The diaphragm is designed composite with the deck above, similar to the girders, with the top chord acting as a slab edge support. Based on AASHTO Article 9.7.1.4, "the edge beams may be designed as beams whose width may be taken as the effective width of

the deck specified in Article 4.6.2.1.4." For this design, the dead load was taken to be the weight of the haunch over the diaphragm only, with two calculations performed for live load. Based on AASHTO Article 4.6.2.1.4, the maximum live load moment is permitted to be found using AASHTO Table A4-1 and multiplying the moment per unit with by the corresponding full strip width of the edge beam. This was performed to find the total moment acting on the beam, and consequently, the reactions at the connections to the UHPC bearing columns. To check this method, the reactions were recalculated using principles from statics and a tandem wheel load over the diaphragm and found to be comparable to the values using Table A4-1. The controlling horizontal load was found to be 14.2 kN on the fascia girder from wind loading. The controlling vertical load was 206.4 kN at each connection point. For the design of the connection, both loads were considered.

2.3 *Bearing column design*

The bearing column was designed similar to a standard steel bearing stiffener, acting as a compression member at the beam end made up of the UHPC column and the steel web. Due to the high compressive strength of UHPC compared to conventional concrete, the UHPC column is only required to be approximately three times the width of an equivalent steel bearing stiffener. However, to attain the cover for the attachment studs and an appreciable level of protection for the beam end, the bearing column was increased in this design to 457 mm wide. Schematics of the beam end are shown below in Figure 3. Figure 3a and b show the detail of the stud spacing in CAD using a section and plan view, respectively. Figure 3c shows a final rendering with the cured UHPC. Currently, the CTDOT Bridge Design Manual Article 7.1.2.1c details a protective coating that extends (1.5×D) where D is the depth of the girder (CTDOT, 2003). Although the UHPC column does not extend a full 1.5D, the area of the bearing is the most critical structural component of the beam end, and this method can be combined with painting if necessary. The underlying stud pattern is centered over the centerline of the bearing, 229 mm from the edge of the beam. Due to the UHPC being placed prior to loading, the load path travels directly through the UHPC column between the flanges. The studs act primarily as an attachment mechanism, rather than the primary structural fuse in the beam end repair design. For this design, 16 studs were detailed on each side of the beam. The studs for each of the designs presented in this paper are 16 mm diameter by 76 mm length.

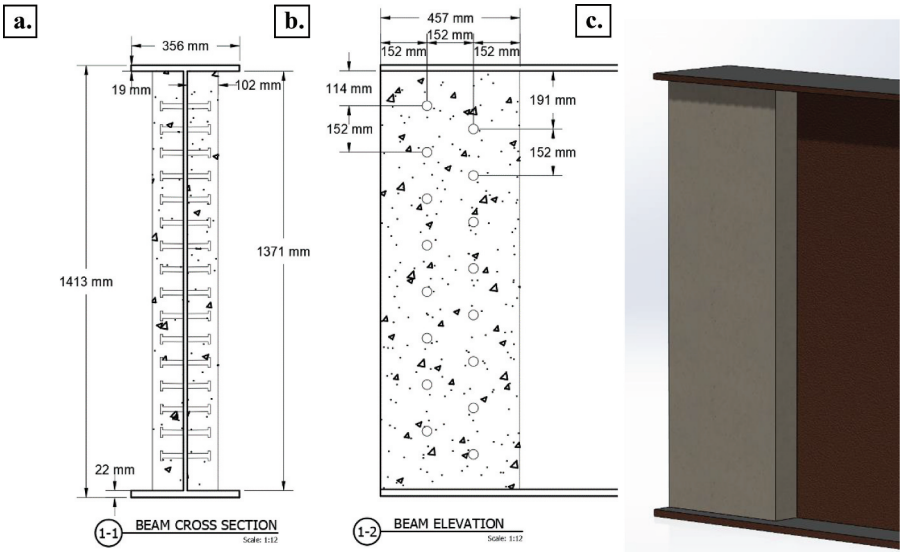


Figure 3. a) Cross sectional CAD schematic of UHPC bearing column, b) elevation view of UHPC bearing column, and c) 3D rendering of bearing column.

2.4 *WT-beam bolted connection option*

The first detail presented is a WT-beam connected to the front of the UHPC column with cast in place or post-installed anchors. This detail minimizes formwork complications when pouring the UHPC. For post-installed anchors, hammer drilling into UHPC permits the contractor to use standard anchor bolt installation methods with a high strength epoxy grout, and completely remove any interference with the formwork. Attaching the bolts to the formwork adds limited complexity to the formwork, but negates the need for any post installed anchors, which alleviates design concerns as the performance of bars embedded in UHPC is well studied (Choi et al., 2015; Kalthoff & Raupach, 2021). Using either anchor installation allows a WT beam to be bolted directly to the surface of the UHPC panel and the diaphragm welded to the WT-beam following a process well known to bridge contractors. It should be noted that in detailing this design, both anchors and shear studs must be arranged to comply with anchor spacing as defined in the ACI 318-19 Building Code Requirements for Structural Concrete (ACI, 2019) and shear stud requirements defined in the beam end repair guidelines (CTDOT, 2020).

A post-installed anchor bolt design using the Hilti PROFIS Engineering software (Hilti, 2023) was conducted to find a feasible anchor size and spacing for the required loading. Due to the short embedment depth permitted, the best working solution was two sets of eight anchor bolts for the top and bottom connections to the diaphragm. Figure 4a and b show the CAD layout of the WT-beams installed on the UHPC column, and Figure 4c shows a 3d rendering that includes the diaphragm connection. A significant challenge in the design is the limitation on concrete compressive strength for cast in place and post-installed anchors set by the ACI 318 committee and upheld in the ACI 318-19 Building Code and supported by research by Primevera. (ACI, 2019; Primavera et al., 1997). This research discovered that as the strength of the concrete increased past 55 MPa for post installed anchors and 69 MPa for cast in place anchors, the design equations became unconservative. However, the ACI Code notes that with tested verification, the limitation may be exceeded (ACI, 2019). While this is an area for further research, the research team continued with limited strength of the UHPC in the design of 55 MPa, as this will be conservative and allows designers to use standard concrete design software and ACI 318-19 formulas without conducting tests on each project.

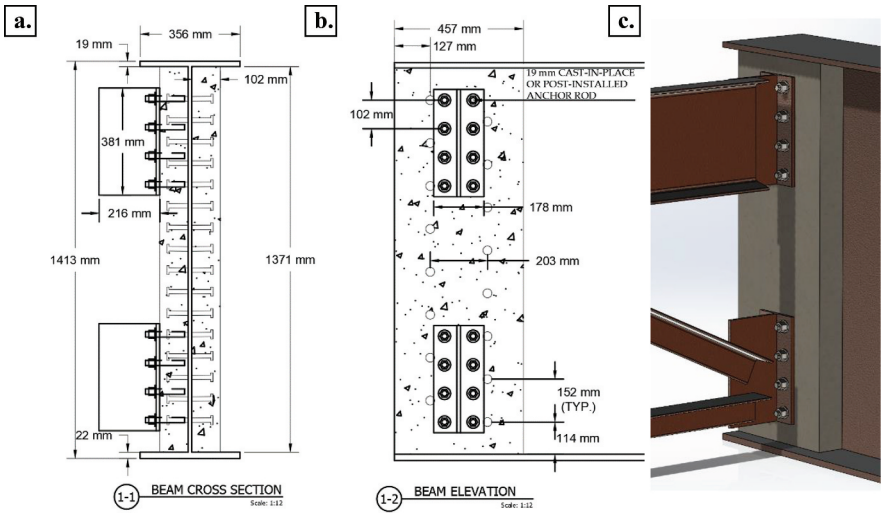


Figure 4. a) Cross sectional CAD schematic of WT-beam bolted option, b) elevation view of WT-beam bolted option, and c) 3D rendering of WT-beam bolted option.

2.5 *Embedded plate connection option*

The second set of connection options are embedded stiffener/gusset plates welded to the web with UHPC cast around them. Figure 5a and b show the CAD layout of the plate embedded in UHPC, and Figure 5c shows a 3d rendering including the diaphragm connection. These options provide a straightforward design and construction familiar to contractors with no additional design required for anchor bolts and no complications related to the design codes. One challenge is formwork construction around the gusset plates, requiring a tight fight for the formwork panel around the gusset plate. These designs require additional holes in the web and stiffener/ gusset plates to ensure one cohesive UHPC block. The sub-options include a bolted diaphragm connection and a welded connection. These options would be splitting the gusset plate into two separate gusset plates, once supporting the top channel and the second supporting the bottom chords of the diaphragm. The welded connections to the diaphragm chords could also be replaced with field-drilled bolted connections. As the UHPC acts as the main bearing column, and the stiffener/gusset plates do not span flanges, the design of the plates does not need to meet bearing requirements but does require design for diaphragm forces.

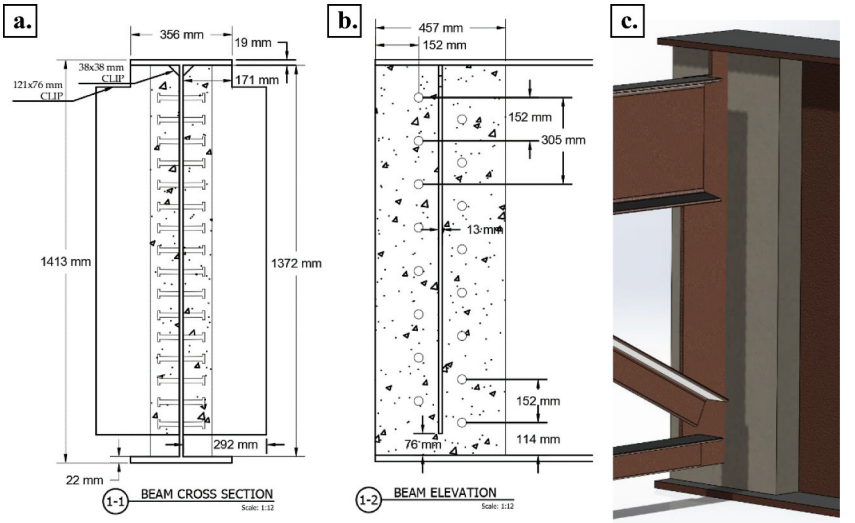


Figure 5. a) Cross sectional CAD schematic of embedded plate connection option, b) elevation view of embedded plate option, and c) 3D rendering of embedded plate option.

While this design primarily follows that of a gusset plate, several additional challenges are encountered. First, the UHPC bearing column is split into two sections with only small connection points. Additionally, each section of the UHPC column only has one row of studs and the minimal connection points may limit the studs on either side of the gusset/stiffener plates acting as a cohesive element. A second major complication is that the embedded plate cannot be easily replaced if it corrodes. Although the underlying web will remain intact, the diaphragm itself is still susceptible to corrosion and may require replacement. While the diaphragm cross members can be replaced, the embedded plate cannot be moved without removing the UHPC first.

3 FUTURE RESEARCH

The design of steel bridges with UHPC structural elements is a very new concept and has not been applied beyond rehabilitation. Significant research and development are required before bringing the proposed method to implementation. The current design and previous repair

have shown that it is viable to have a UHPC bearing column serve as a structural replacement for a steel bearing stiffener. In parallel, the research team is developing a life-cycle cost analysis comparing UHPC encasement, zinc metalizing, galvanizing, painting, and weathering steel. This analysis will provide valuable insight into the cost-effectiveness of UHPC as a protective method. Additionally, a forum with industry professionals was held and the data is being processed to evaluate the proposed diaphragm connection options in terms of cost effectiveness, design, and construction. Following analysis of this survey, the research team will take the best option and conduct a more in-depth design, including finite element analysis and performing full-scale tests on the diaphragm connection to the UHPC bearing column.

4 CONCLUSION

This work proposes a new design for a steel bridge bearing column by replacing the conventional steel bearing stiffener with a UHPC bearing column. While the majority of design for the beam can remain unchanged, the connection of a steel diaphragm to a UHPC bearing column presents a novel challenge to designers implementing this method. In this paper, two options are presented to overcome this challenge. The first option requires the embedment of steel anchor rods in UHPC, either cast in place or post-installed. The second option utilizes a modified steel stiffener and focuses on ease of design and construction. Both options are feasible but require significant further research before implementation can be considered. The designs presented in this paper provide multiple options for diaphragm connections to a UHPC bearing stiffener and identify several key areas where further research would benefit the existing literature on composite connections. The main learnings from this paper can be summarized below:

- UHPC beam end encasement is a promising method for eliminating corrosion under a deck joint in a steel bridge.
- A UHPC bearing stiffener can adequately sustain bearing loads at a beam end.
- Anchor bolts embedded in UHPC are a key area that further research is needed.
- Standard details for diaphragms can be integrated into a UHPC bearing column to minimize disruption to a steel bridge design process.

REFERENCES

AASHTO. 2020. *AASHTO LRFD Bridge Design Specifications*, *9th Edition*. American Association of State Highway and Transportation Officials.

ACI. 2019. *318-19 Building Code Requirements for Structural Concrete and Commentary*. American Concrete Institute. https://doi.org/10.14359/51716937

ASCE. 2021. *2021 Report Card for America's Infrastructure*. www.infrastructurereportcard.org

Ault, J. P., & Dolph, J. D. 2018. *Corrosion prevention for extending the service life of steel bridges*. National Academy of Sciences.

Choi, S., Joh, C., & Chun, S. C. 2015. Behavior and strengths of single cast-in anchors in Ultra-High-Performance Fiber-Reinforced Concrete (UHPFRC) subjected to a monotonic tension or shear. *KSCE Journal of Civil Engineering*, *19*(4), 964–973. https://doi.org/10.1007/s12205-013-0246-8

CTDOT. 2003. *BRIDGE DESIGN MANUAL 2003 Edition* (9/23). State of Connecticut Department of Transportation. httpss://portal.ct.gov/DOT

CTDOT. 2020. *Guidelines for the Utilization of Ultra-High Performance Concrete in the Rehabilitation of Steel Bridge Girder Ends*.

Graybeal, B. A., & Hartmann, J. L. 2003, January. Strength and Durability of Ultra-High Performance Concrete. *Concrete Bridge Conference*.

Graybeal, B., & Tanesi, J. 2007. Durability of an Ultrahigh-Performance Concrete. *Journal of Materials in Civil Engineering*, *19*(10), 848–854. https://doi.org/10.1061/(ASCE)0899-1561(2007)19:10(848)

Haber, Z., & Ocel, J. 2020. *EDC-6: UHPC for Bridge Preservation and Repair*. www.fhwa.dot.gov/everydaycounts

Hain, A., & Zaghi, A. E. 2021. Learnings from the Field Implementation of a Novel Ultra-High Performance Concrete Beam End Repair on a Corroded Steel Girder Bridge in Connecticut. In *Transportation*

Research Record (Vol. 2675, Issue 9, pp. 703–714). SAGE Publications Ltd. https://doi.org/10.1177/03611981211004128

Hain, A., & Zaghi, A. E. 2022. Field implementations of a novel UHPC beam end repair on steel girder bridges in Connecticut, USA. In *Bridge Safety, Maintenance, Management, Life-Cycle, Resilience and Sustainability* (pp. 2560–2567). CRC Press. https://doi.org/10.1201/9781003322641-320

Hain, A., Zaghi, A. E., Fields, T., Barakat, R., Cardinali, A., Culmo, M. P., & Lopata, T. 2019. Implementation of UHPC for the Repair of a Steel Bridge with Corrosion Damage in CT. *Second International Interactive Symposium on UHPC*, *06108*(860). https://doi.org/10.21838/uhpc.9684

Hain, A., Zaghi, A. E., Kamali, A., Zaffetti, R. P., Overturf, B., & Pereira, F. E. 2019. Applicability of 3-D Scanning Technology for Section Loss Assessment in Corroded Steel Beams. *Transportation Research Record*, *2673*(3), 271–280. https://doi.org/10.1177/0361198119832887

Hilti. 2023. *Hilti PROFIS Engineering* (3.088). Hilti Corporation. httpss://www.hilti.com/content/hilti/W1/US/en/business/business/engineering/profis-engineering.html

Kalthoff, M., & Raupach, M. 2021. Pull-out behaviour of threaded anchors in fibre reinforced ordinary concrete and UHPC for machine tool constructions. *Journal of Building Engineering*, *33*. https://doi.org/10.1016/j.jobe.2020.101842

Kayser, J. R., & Nowak, A. S. 1989. Capacity Loss Due to Corrosion in Steel-Girder Bridges. *Journal of Structural Engineering*, *115*(6), 1525–1537.

Kere, K. J., & Huang, Q. 2019. Life-Cycle Cost Comparison of Corrosion Management Strategies for Steel Bridges. *Journal of Bridge Engineering*, *24*(4). https://doi.org/10.1061/(asce)be.1943-5592.0001361

Kogler, R. 2015. *Steel Bridge Design Handbook: Corrosion Protection of Steel Bridges*.

Kruszewski, D. 2018. *Performance Evaluation of Shear Connectors Embedded in Ultra-High Performance Concrete as Part of a Bridge Repair Method*. httpss://opencommons.uconn.edu/dissertations/1963

Kruszewski, D., Wille, K., & Zaghi, A. E. 2018. Push-Out Behavior of Headed Shear Studs Welded on Thin Plates and Embedded in UHPC. *Engineering Structures*, *173*, 429–441. https://doi.org/10.1016/j.engstruct.2018.07.013

Kruszewski, D., & Zaghi, A. E. 2019. Design of Various Shear Connectors for Repair of Corroded Steel Girders with Ultra-High Performance Concrete. *Transportation Research Record*, *2673*(2), 521–530. https://doi.org/10.1177/0361198119826080

Kruszewski, D., & Zaghi, A. E. 2021. Load transfer between thin steel plates and ultra-high performance concrete through different types of shear connectors. *Engineering Structures*, *227*. https://doi.org/10.1016/j.engstruct.2020.111450

Kruszewski, D., Zaghi, A., & Wille, K. 2018. *Repair of Steel Beam/Girder Ends with Ultra High-Strength Concrete-Phase II Part 1*: *UHPC Push-out Experiments*.

Lassy, B., Hain, A., & Zaghi, A. E. 2023. Experimental Testing for Partial Height UHPC Beam End Encasement on Weathering Steel Bridges in Connecticut. *International Interactive Symposium on Ultra-High Performance Concrete*.

Lassy, B., Hain, A., Zaghi, A. E., Kanyo, Z. M., Chuong, B. K., & Cardinali, A. 2023. Rehabilitation of Corroded Steel Bridge Girder Ends using Partial-Height Ultra-High-Performance Concrete Encasement. *Transportation Research Record*. https://doi.org/10.1177/03611981231194629

Li, J., Wu, Z., Shi, C., Yuan, Q., & Zhang, Z. 2020. Durability of ultra-high performance concrete – A review. In *Construction and Building Materials* (Vol. 255). Elsevier Ltd. https://doi.org/10.1016/j.conbuildmat.2020.119296

McMullen, K. F., & Zaghi, A. E. 2020. Experimental Evaluation of Full-Scale Corroded Steel Plate Girders Repaired with UHPC. *Journal of Bridge Engineering*, *25*(4). https://doi.org/10.1061/(asce)be.1943-5592.0001535

McMullen, K., Zaghi, A. E., & Culmo, M. P. 2018. *Repair of corroded steel plate girders with ultra-high performance concrete* (N. Powers, D. M. Frangopol, R. Al-Mahaidi, & C. Caprani, Eds.; pp. 1350–1358). CRC Press. https://doi.org/10.1201/9781315189390

Primavera, E. J., Pinelli, J. P., & Kalajian, E. H. 1997. Tensile Behavior of Cast-in-Place and Undercut Anchors in High-Strength Concrete. *ACI Structural Journal*, *94*(5). https://doi.org/10.14359/507

Wilson, K. E., Bouscher, J. W., & Amrhein, W. A. 2015. *Load and Resistance Factor Design (LRFD) for Highway Bridge Superstructures - Design Examples*.

Zaghi, A. E., Kay Wille, Zmetra, K., & Mcmullen, K. 2015. *Repair of Steel Beam/Girder Ends with Ultra High Strength Concrete (Phase I)*. https://ntl.bts.gov

Zaghi, A. E., Wille, K., Zmetra, K., Mcmullen, K., Kruszewski, D., & Hain, A. 2017. *Repair of Steel Beam/Girder Ends with Ultra High-Strength Concrete-Phase II*.

Zmetra, K. M. 2015. *Repair of Corrosion Damaged Steel Bridge Girder Ends by Encasement in Ultra-High Strength Concrete* [Dissertation, University of Connecticut]. https://opencommons.uconn.edu/dissertations/769

Bridge Maintenance, Safety, Management, Digitalization and Sustainability – Jensen, Frangopol & Schmidt (eds)
© 2024 The Author(s), ISBN 978-1-032-77040-6
Open Access: www.taylorfrancis.com, CC BY-NC-ND 4.0 license

Identifying system redundant members in a steel arch bridge through advanced finite element analyses

A. Mosavi, H. Yuan, M. Tatarsky & M. Carter
Arup USA Inc.

ABSTRACT: The AASHTO LRFD Bridge Design Specifications define Non-Redundant Steel Tension Members (NSTM) as primary steel members subject to tension, whose failure could potentially lead to the collapse of a portion or the entire bridge. Bridges with NSTMs must adhere to special mandatory bi-annual hands-on inspections according to the National Bridge Inspection Standards (NBIS). These additional inspections, beyond routine checks, incur unnecessary costs for bridge owners.

Research indicates that bridges with traditionally designated NSTMs often retain significant strength reserves even after NSTM failure. AASHTO introduced a new guide specification in 2018 and outlined a detailed procedure for reclassifying NSTMs as System Redundant Members (SRMs). The procedure requires detailed nonlinear finite element analysis (FEA) to assess the available additional system redundancy.

This paper summarizes the FEA results for a newly designed steel arch bridge. AASHTO guideline procedure were directly followed to remove NSTM designation from the tension-tie members of this bridge.

1 INTRODUCTION

Non-load-path-redundant steel members were given a special designation of "Fracture Critical (FC)" following the collapse of the Silver Bridge in the US. This designation indicated that failure of these tension members could lead to collapse of the bridge. This term was first used in "AASHTO Guide Specification for Fracture Critical Non-Redundant Steel Bridge Members" in 1978 (AASHTO 1978). The most recent AASHTO LRFD Bridge Design Specifications (AASHTO 2017) define FCMs as "A steel primary member or portion thereof subject to tension whose failure would probably cause a portion of or the entire bridge to collapse". Special hands-on inspections have been mandatory for primary steel members designated as FCMs. These mandatory inspections impose additional costs for the owners. However, several studies have shown that bridges with traditionally designated FC Members (FCM) possess considerable strength reserves after the failure of these members. As the result, NBIS 2022 (FHWA 2022) has updated the terminology used for FCM to Non-Redundant Steel Tension Member (NSTM) to remove confusion around FCMs and failure criticality of these members. Also, a new AASHTO Guide Specification released in 2018 (AASHTO 2018) outlines a detailed procedure for reclassification of NSTMs as SRMs. The reclassified SRMs are not subjected to the same mandatory inspections as FCMs. As the result, bridge owners can save on their inspection costs and reallocate the saved budget to other priorities.

This paper summarizes the applied methodology and results of a study performed to reclassify NSTMs as SRMs in a new steel arch bridge. This bridge was a new design, and edge girders of the bridge were originally identified as NSTMs. A detailed nonlinear Finite Element Model (FEM) of the bridge was developed following the outlined procedure in the AASHTO Guide Specification. The critical bridge loading patterns are found, and detailed analyses are carried

DOI: 10.1201/9781003483755-267

out to assess the existing level of system redundancy in the bridge. The strength and serviceability requirements of the AASHTO Guide Specification are evaluated, and it is concluded that the edge girders in this bridge can be reclassified as SRMs. The outlined work established the methodology for adoption of the computationally intensive AASHTO procedure. The methodology will save a considerable amount of unnecessary inspection money for bridge owners during the bridge service life. In addition, it gives a better insight on the available redundancy within the structure and where the inspection effort should be better refocused.

2 METHODOLOGY FRAMEWORK

The AASHTO methodology starts with a screening process for the suitability of the candidate bridge. The full details of screening can be found in the AASHTO Guide Specification (AASHTO 2018). If the screening is satisfied, a detailed FEA is required to assess the available system redundancy for reclassification of the NSTMs within the candidate bridge.

The FEA methodology analyzes the structural responses of the candidate bridge at faulted states of the NSTM. FEA analyses shall be performed using a FE software capable of modelling the three-dimensional geometry, material and geometrical nonlinearity, kinematic constraints and a boundary conditions. Specific requirements set for the FEA software are outlined in the AASHTO Guide Specification (AASHTO 2018). This study has used LS-DYNA® which is a multi-purpose explicit and implicit finite element program capable of performing several types of nonlinear modeling.

Two failure locations at the middle and near the end of the tension tie member at its intersection with the arch are considered following the recommendations from the AASHTO Guide Specification (AASHTO 2018). The available system redundancy of the bridge is evaluated in these two failure scenarios assuming a full loss of steel beam cross-section.

Two redundancy load combinations are considered to investigate the performance of the bridge at its faulted state. The live loads are placed on the bridge deck maximize the demands in these load combinations for the remaining structure. The load combinations are:

1. Redundancy I: This load combination is designed to simulate the amplified dynamic effects during the free vibration immediately after the member failure. Only traffic lanes are considered for live loading of the bridge deck.
2. Redundancy II: This load combination assesses the performance of the faulted bridge under normal vehicular use after the failure event. Design lane loads are used to maximize the demands on the bridge.

The total factored load, *no*, for these redundancy load combinations are as following:

$$\gamma Q_n = (1 + DA_R)[\gamma_{DC} DC + \gamma_{DW} DW + \gamma_{LL}(LL + IM)] \tag{1}$$

Where DC is the dead load for structural and non-structural components, DW is the dead load of wearing surface and utilities, LL is the live load, DA_R is the dynamic load allowance, IM is the Impact factor. The load factors for these two load combinations are presented in Table 1.

Table 1. Load factors for the redundancy load combinations.

Load Combination	γ_{DC}	γ_{DW}	γ_{LL}	DA_R	IM
Redundancy I	1.05	1.05	0.85	0.4	0.0
Redundancy II	1.05	1.05	1.3	0	0.15

Both strength and serviceability requirements shall be met in these two redundancy load combinations in order to reclassify the NSTM to SRM. For the strength requirements, the following conditions shall be met in steel and concrete components:

– The average strain within the primary steel member shall remain smaller than five times the material yield strain. The average strain within the primary steel member shall also remain below 0.01. Also, the maximum strain anywhere within a primary steel member shall remain below 0.05.
– The compression strain within the concrete slab shall stay below 0.03.
– Also, both the foundation and substructure shall be able to support an additional 15 percent of the factored live load.

In addition, the following serviceability performance criteria shall be met to reclassify the NSTM to SRM:

– The maximum vertical deflection remains below L/50 for both the longitudinal primary member and floor beams, where L is the span length for the longitudinal primary member or distance between the remaining floor beams, respectively.

3 BRIDGE DESCRIPTION

This study is performed for a multiple tied-arch bridge, shown in Figure 1. The bridge has three arch spans. The two end spans are steel arch spans with hanger elements with an approximate span length of 260 ft. The middle span with the supporting steel arch below the deck is approximately 130 ft long. The total bridge length is over 650 ft. The bridge includes five traffic lanes, separated by a traffic median in the middle. Figure 2 shows the bridge deck typical cross-section with a total width of 101.5 ft.

The concrete column/abutments at the end spans and four foundation caps with drilled shafts in the middle support the steel arches at their ends. The arches are steel box girders. Tension tie members of the end spans are wide flange steel girders supported by the hanger

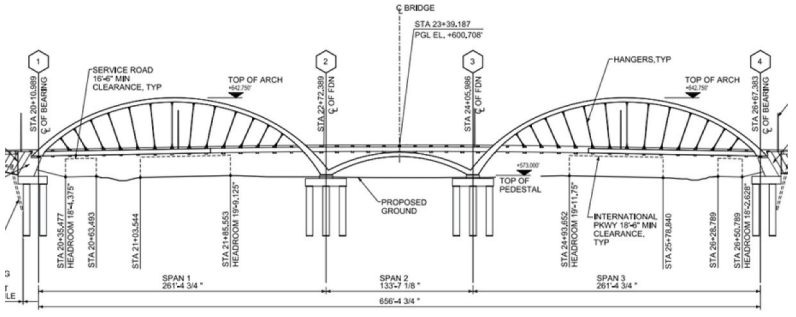


Figure 1. Steel arch bridge elevation view.

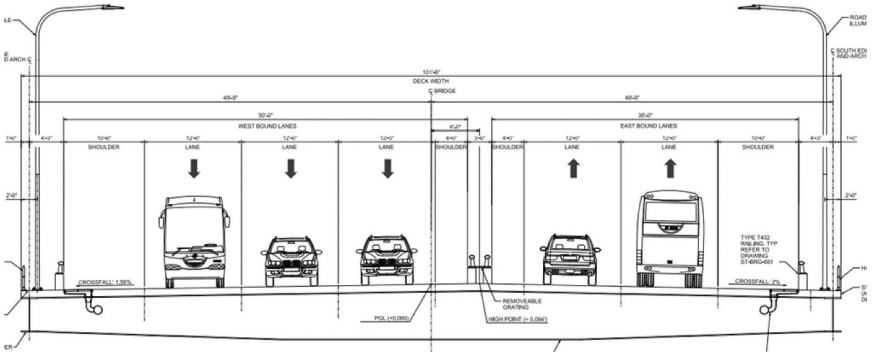


Figure 2. Bridge deck typical cross-section.

elements of the arch spans. The bridge deck is a 10.5" thick concrete slab compositely working with the floor beams and edge girders as shown in Figure 2. The floor beams running in transverse direction are placed at 15.5 ft spacings. The bridge is also designed with two sets of redundancy trusses as shown in Figure 3.

4 FINITE ELEMENT MODELING AND ANALYSES METHODOLOGY

AASHTO Guide Specification (AASHTO 2018) provides a guideline detailing the FEM requirements for the analyses. The outlined procedure intends to ensure the nonlinear behavior of the bridge at the fault state is properly captured by using the appropriate element type, size and properties for different material and component behavior. The FEM modeling in this study followed the provided guideline in great details. A 3-D detailed FEM of the bridge is developed is LS-DYNA as shown in Figure 3. A full description of the modeling approach for this study can be found in (Mosavi 2022).

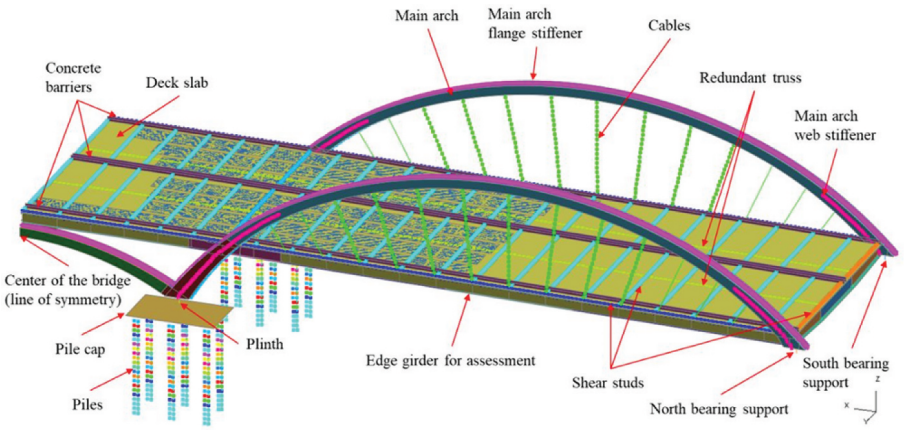


Figure 3. FE model of the candidate steel arch bridge.

Only half of the bridge is modelled with symmetrical boundary conditions at the line of symmetry to minimize the cost of analyses. This is shown still to be accurate as the location of the fault was within the end span and away from the line of symmetry.

All the primary steel members of the bridge are modelled using 4-noded linear Velichko-Lin -Tsay shell elements with reduced integration. These shell elements also have three integration points through thickness. All flanges and webs are modelled with a minimum of four shell as

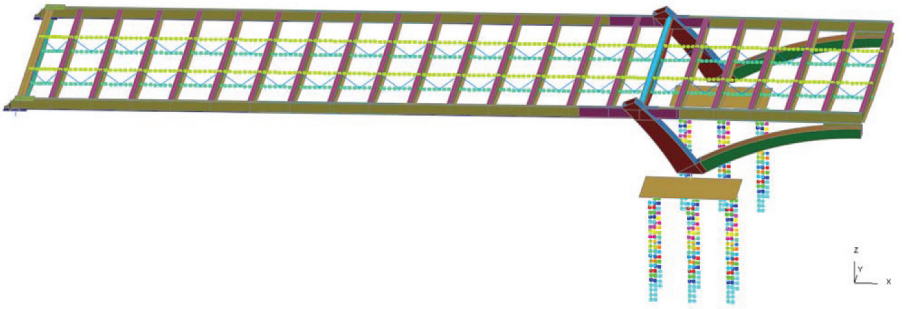


Figure 4. FE modeling of the redundancy trusses.

outlined per AASHTO Guide Specification (AASHTO 2018). The connections of the steel arch sections with the longitudinal tension tie edge girder and the transverse floor beam are modelled in full detail to ensure the true behavior of the connections. Also, both transverse and longitudinal stiffeners within the steel arch both girders are fully modelled to ensure analyzed strain values within the structure can be directly used without additional interpretations. Also, 2-noded nonlinear beam elements are used to model the secondary beam elements of the redundancy trusses as shown in Figure 4.

The foundation drilled shaft are modelled using linear beam elements. Also, linear spring elements are used in both transverse and longitudinal directions at every two feet along the length of the pile to model the force-displacement behavior of the soil around the piles. The pile cap was modeled using elastic linear shell elements. The pedestals on top of pile caps are modelled using linear beam elements, and nodes of the pedestal are connected to the nodes of the shell elements of the steel arch and pile cap using constraint equations. The abutment foundation at the end is not directly modelled since the abutment foundation is stiff and no major deformations are expected.

Nonlinear shell elements are used to simulate the concrete deck slab. This nonlinear composite shell element includes layers presenting cross-sectional properties of both top and bottom longitudinal and transverse reinforcements as shown in Figure 5. The thicknesses of these layers are calibrated to present the steel reinforcement cross-section correctly in both directions. The shell elements are modelled with representative nonlinear concrete and steel material curve as outlined per AASHTO Guide Specification (AASHTO 2018). The full details of the used nonlinear material curves can be found in (Mosavi 2022).

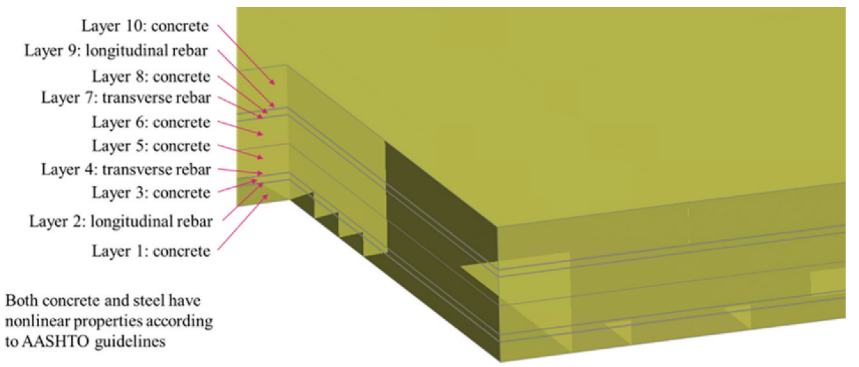


Figure 5. FE modeling of the concrete slab.

Shell studs are modelled using nonlinear beam elements. A set of nonlinear force-displacement curves are developed to model the full behavior of the shear studs in tensile and shear. These nonlinear curves are developed following the formulas outlined in AASHTO Guide Specification (AASHTO 2018). The full details of the developed tensile and shear properties of the shear studs can be found in (Mosavi 2022). The nonlinear beam elements of the shear studs are explicitly modeled with one node connecting to the top flange of the steel edge girders and floor beams and the other node connecting to the nodes of the shell elements of the concrete slab.

The hanger elements are modeled using tension-only cable elements. These elements did not possess any compression stiffness. Tensile failure force of the hanger elements is at 1044 kips and has an elastic modulus of 23000 kiss.

The material curves are used to simulate the nonlinear behavior of concrete slab with a 28-day compressive strength of 4000 psi. The steel nonlinear material curves are developed for ASTM A709 structural steel. Also, steel reinforcements are A706 Gr. 60.

Boundary conditions are simulated to represent the articulation plan presented in Figure 6. The boundary conditions at the median span foundations were modelled as discussed in the previous sections. The bridge had two expansion joints at its two ends. The boundary

conditions at the line of symmetry were modelled to simulate the symmetrical boundary conditions, and the bearings at the ends of the end span were modelled using beam elements to simulate the stiffness properties of the bearing.

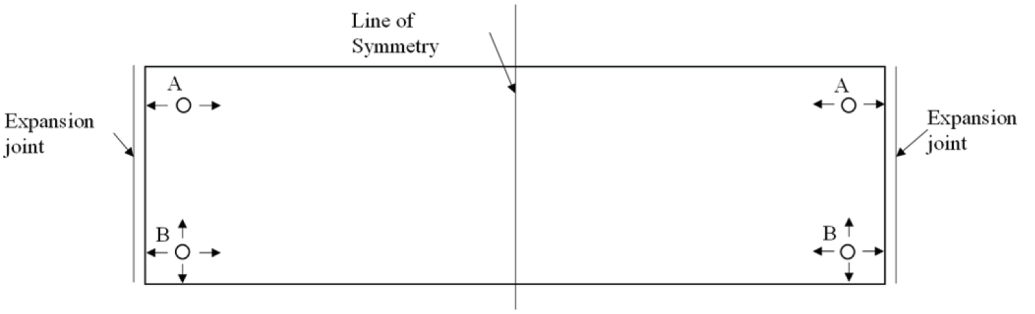


Figure 6. Articulation plan of the bridge.

Two damage scenarios are simulated. One is in the middle of the end span and the other one is at the end of edge girder close to its connection with the steel arch box girder. In both scenarios, the damages are assumed through the full height of the tension tie edge girder, and they are simulated by introducing two sets of nodes on either side of the simulated full height cracks.

Critical load patterns are identified to maximize the demand at the location of the simulated fault. Figure 7 shows the critical HL-93 vehicular live load pattern which maximizes the demand at the simulated fault location in the middle span for both redundancy I and II load combinations. Similarly, Figure 8 shows the critical HL-93 live load pattern for the fault location at the end of the end span for both of redundancy load combinations.

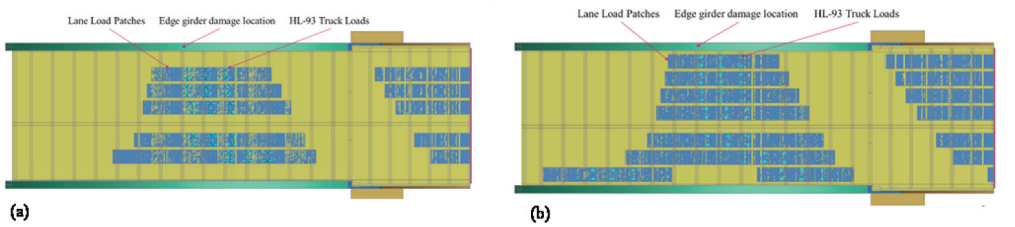


Figure 7. Vehicular live loads for (a) Redundancy I and (b) Redundancy II load combinations, Failure location in the middle span.

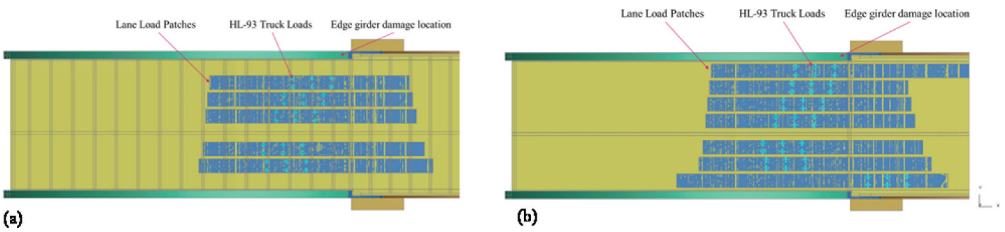


Figure 8. Vehicular live loads for (a) Redundancy I and (b) Redundancy II load combinations, Failure location in the end of the span.

5 DISCUSSION OF RESULTS

Strength performance requirements are checked by reviewing the strain values within the flange and web of the primary steel members. Figure 9 shows the von misses strains for both

redundancy I and II load combinations at the simulated fault scenario in the middle of the span, and Figure 10 shows the von misses strains in the primary steel members at the simulated fault state at the end of the end span. The average strain values within the primary steel members stayed below five time of the yield strain or 0.0086. The peak von misses strain is at 0.0014 for the midspan fault scenario and at 0.002 for the end span fault scenarios. These peak values are also comfortably lower than the maximum peak strain of 0.05. Additionally, the maximum compressive strains of the concrete are screened. The minimum principal strain within concrete slab remained comfortably below 0.0003. Only one single concrete shell element was found exceeding this strain limit, and this was considered a local numerical outlier. More details on the results of concrete strains and cracking can be found in (Mosavi 2022).

It is observed under both damage scenarios there were a few failing shear stud beams at the vicinity of the damage location. However, it did not result in a progressive failure and the area with the failed shear studs remained limited.

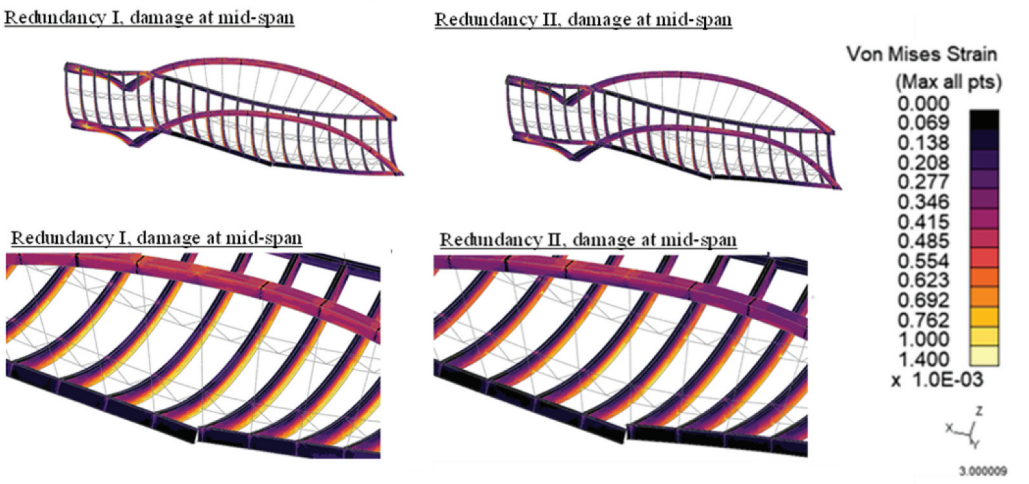


Figure 9. Von Misses strain plots of the primary steel members for the fault scenario in the middle of end span under redundancy I and II load combinations.

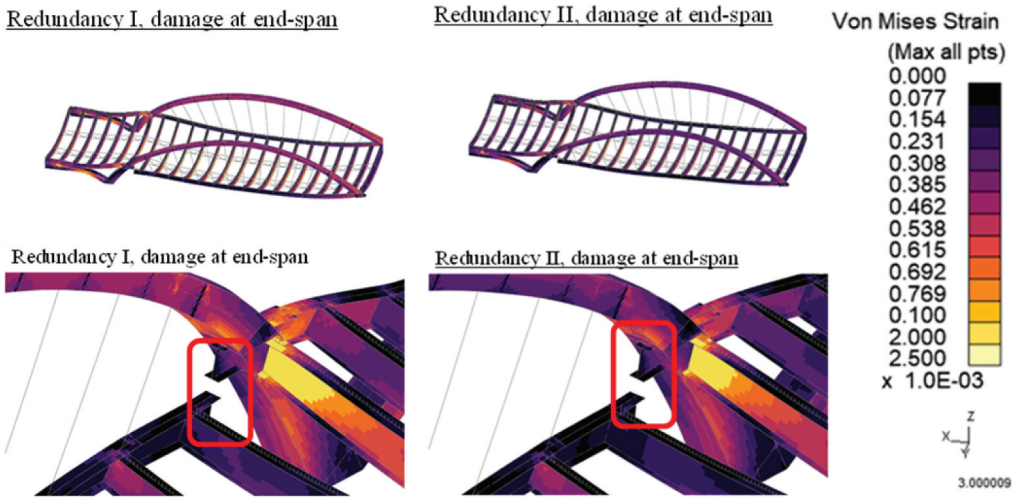


Figure 10. Von Misses strain plots of the primary steel members for the fault scenario at the end of end span under redundancy I and II load combinations.

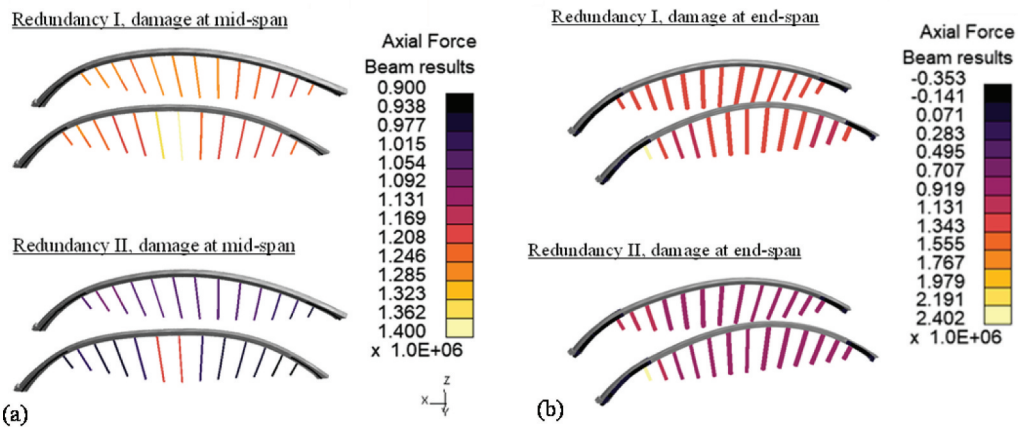


Figure 11. Hanger axial forces at both fault scenarios (a) middle of the span and (b) end of the end span under both redundancy I and II load combinations.

Overall, the deck loads previously carried by the edge girder redistributed either through the floor redundancy trusses to the other girders or to the steel arch box girders through the extra loads carried by the hanger elements. Figure 11 shows the distribution of the axial forces of the hanger elements under different redundancy load combinations at both fault scenarios. Also, all serviceability criteria were satisfied with deformations within the primary members remaining below L/50. More details on the results can be found in (Mosavi 2022).

6 CONCLUSIONS

This paper proposes reclassifying Non-Redundant Steel Tension Members (NSTMs) as System Redundant Members (SRMs) in a newly designed steel arch bridge, using a detailed procedure outlined in the AASHTO Guide Specification (AASHTO, 2017). The procedure involves detailed nonlinear FEA to assess the bridge's strength and serviceability performances under prescribed failure scenarios. The analysis of a new steel arch bridge, where edge girders were initially identified as NSTMs, revealed that strain levels in primary steel members and the concrete deck remained well below the prescribed AASHTO limits. Limited local cracking and shear stud failures were observed, confined to specific areas, with no progressive bridge failure. Maximum deflections also met serviceability requirements. Consequently, the study concludes that reclassifying edge girders as SRMs is safe, eliminating the need for bi-annual NSTMs inspections. This will potentially reduce the owner's operational maintenance cost of the newly designed bridge in a significant way.

REFERENCES

AASHTO. (1978). Guide Specifications for Fracture Critical Non-Redundant Steel Bridge Members, *American Association of State Highway and Transportation Officials*, *Washington, DC.*

AASHTO. AASHTO LRFD Bridge Design Specifications, Eighth Edition, LRFD–8. *American Association of State Highway and Transportation Officials*, *Washington, D.C.*, 2017.

FHWA, and DOT. National Bridge Inspection Standards—*23 CFR 650.C. Federal Register*, *Washington, D.C.*, 2022.

AASHTO. Guide Specifications for Analysis and Identification of Fracture Critical Members and System Redundant Members, First Edition. *American Association of State Highway and Transportation Officials*, *Washington, D.C.*, *2018*.

Mosavi, A,, Yuan, H., Tatarsky, M., Carter, M. Reclassifying Fracture Critical Members (Non-Redundant Steel Tension Members) to System Redundant Members in a Steel Arch Bridge, *Transportation Research Record: Journal of the Transportation Research Board*, *December* 2022.

SS17: Integrating digital twin with machine-learning techniques for structual damage identification

Organizers: J.F. Jiménez-Alonso, I. Duvnjak & I.M. Diaz


Taylor & Francis
Taylor & Francis Group
http://taylorandfrancis.com

Bridge Maintenance, Safety, Management, Digitalization and Sustainability – Jensen, Frangopol & Schmidt (eds)
© 2024 The Author(s), ISBN 978-1-032-77040-6
Open Access: www.taylorfrancis.com, CC BY-NC-ND 4.0 license

Bridge condition and performance monitoring: An engineering approach

P.S. McCarten
Transport and Main Roads (Retired), Hawkes Bay, New Zealand

ABSTRACT: Historically bridge inspection was focused on defect reporting to record the 'health' of network bridge stock. The introduction of asset management principles and practices resulted in a change to condition reporting of network bridge health. Concerns with the current method are the Bridge Index has low sensitivity to criticality, Bridge Inspectors are using 'bias' to report perceived condition, and, the Bridge Index while suitable for high level reporting could not be used in 'day to day' bridge management. Currently an experienced and trained Bridge Management Team is accepted for bridge intervention but being based on visual inspection reporting it has high subjectivity on the hidden features. This paper outlines an engineering approach to ensure the bridge health is identified and defined for reporting. The paper hence is focused on the hidden features and considers risk and criticality. The paper presents various case studies to show the need for monitoring.

1 INTRODUCTION

Through contractual requirements and ethical obligations Bridge Managers have a responsibility to ensure bridge user safety and bridge stock is consistently within the condition and performance requirements set by the bridge owner, typically a Road Controlling Authority (RCA). The bridge management contractual requirements may be specifically scheduled or they may be bound within general 'stewardship' responsibilities. Bridge management contracts will usually allow the Bridge Management Team flexibility on the work processes to be used. In this paper the Bridge Management Team (BMT) is assumed to consist of three nominated positions, being:

- Bridge Manager: Responsible for overall BMT performance and outputs, and, liaison with the RCA
- Bridge Inspector: Responsible for undertaking and gathering the inspection information needed for the contract. This may involve several inspection teams and specialist personnel as required
- Bridge Engineer: Responsible for reviewing the inspection information and assessing risk and implications. This may involve specialist personnel as required

The RCA sets out the general management requirements in respect to inventory and inspection data collection, intervention programming requirements, and, bridge condition reporting requirements to meet short and long term network objectives. It is recognized that advanced asset management is a process consisting of predictive modelling, risk management and optimized decision making to develop the required life cycle treatment options to meet the strategic targets. Bush et al. (2011) highlighted the importance of collecting complete, comprehensive and reliable data to define and report the linkage between bridge management and the wider strategic vision to achieve a sustainable and economic network.

McCarten (2012, 2014, 2016 and 2018) respectively set out the basic risk requirements and performance measures for the bridge stock recognizing that each bridge is a complex

DOI: 10.1201/9781003483755-268

engineered system. The previous McCarten (2012, 2014, 2016 and 2018) papers have considered the network with a probabilistic perspective but with a move to an engineering approach to managing bridge networks (Austroads 2021) there is a need to consider the specific issues affecting each bridge within the network.

This paper focuses on condition and performance monitoring following an engineering approach underpinned by high quality evidence and generally follows a proactive preventive maintenance approach. By necessity the identification process needs to identify, quantify and assess risk and criticality issues.

2 BACKGROUND AND MOTIVATION

While this paper is focused on Condition and Performance monitoring it is useful to understand historic approaches to bridge inspection reporting. A core part of a mature asset management system is learning and updating systems and practices to ensure future practice is meaningful and targeted to meet outcomes required in a cost effective and efficient manner. A prime motivation for this paper is recording failures and incidents that can improve practice.

Historically bridge inspection was considered a safety inspection focused on defect reporting by identifying issues to be included in a bridge maintenance program. The principal outcomes were to ensure the bridges were safe for continued use, and, report on issues identified as not meeting RCA accepted condition. Initially non-complying issues were defined by an experienced Bridge Engineer familiar with RCA requirements.

Bridge inspection programming was formalized in the early 1970's following the tragic failure of the Silver Bridge caused by eyebolt stress corrosion cracking in a connection detail with low redundancy. It was recognized that under historic inspection requirements bridge inspection reporting had a degree of subjectivity. In order to ensure complete bridge inspection reporting and set up a sound asset management approach many RCA have implemented Condition reporting using a segmented component methodology reporting the specified Condition States for the full extent of the complete range of components on each bridge. In order to remove the historic subjectivity RCA's have produced a suite of photographs showing all components for the range of Condition States to be reported (these vary but typically between 3 and 10 Condition States).

There has been much research on the Condition States approach to bridge inspection reporting, Sanford et al. (2000), Frangopol et al. (2001) and Catbas & Aktan (2002). McCarten (2004) provided a method for using bridge inspection information in 3P (Public Private Partnership) concessions and McCarten (2006) showed how a bridge stock index could be used to correlate bridge condition to financial investment. This latter paper showed that an investment of 0.3% of the total bridge replacement cost was required to maintain the condition steady. While this research shows the Condition States approach gives transparency, enhances asset management reporting and strategic visions for bridge networks there are concerns it has limited use for 'day to day' bridge management and is deviating from the 'safety inspection' objective. These concerns are related to Bridge Indices reporting an 'average' condition which is not reflective of defect criticality, and, Bridge Inspectors using 'bias' to report critical defects. These practices impact the integrity of the bridge management systems and processes.

It is widely accepted that visual inspections alone provide limited reliability in reporting bridge condition. Bridges are an engineered system, Aktan et al. (2013) and defects can be built into a structure. FHWA (2021) has recognized the risks of defects and requires BMT to report them. The defects may be original construction related which may develop under service or they may develop under service and continue to change. With changes in bridge inspection programming the significance of developing defects may not be recognized. Monitoring offers the opportunity to better define the nature of the defect and the defect risk/criticality.

For more than 20 years there has been significant progress in developing instrumentation, data collection at remote sites and data analysis methodologies to improve the quality and reliability of evidence for bridge management decision making. These technologies along with Non-Destructive Testing (NDT) and visual inspection provide a range of tools for cost effective targeted monitoring for 'day to day' bridge management.

NZTA (2013) reported a Road Efficiency Group Case Study: Bridge Management Frameworks – Managing Risk and Ensuring Value for Money that recognized "...the majority (of failures) are preventable if we can embed a structured approach to assessing and acting on vulnerabilities and learning from our experiences...". It is for these bridge management concepts and recognizing the importance of bridge safety the industry is moving toward an engineering approach for bridge management, Austroads (2021). It is these concepts that provide the motivation for this paper and the concepts are further expanded below.

3 CONDITION/PERFORMANCE DEFINITION

In this paper bridge Condition and Performance are considered with the following definitions:

- Condition: is the state of a Component with regard to its appearance, quality or working order. The Condition is reported by the states defined by the RCA. A Defect or Issue is a Condition that is adversely affecting a Component
- Performance: is the action or process of the Bridge performing a task or function. Performance reporting is focused on the Bridge ability to meet the required demands. A Defect/Issue is reporting an influence causing the Bridge to not meet the required demands

In an engineering approach to bridge management the BMT must recognize the reserve of strength accepted by the RCA through allowing lower load factors when rating a bridge compared to those used for bridge design. The BMT must understand the effects of construction defects on this strength reserve to know what is available for in-service deterioration effects and/or increasing load effects on the bridge network.

Irrespective of the way the Condition or Performance is reported under stewardship any Defect/Issue must be assessed by the BMT for risk and criticality on each Component or Bridge, whether that be strength or function. It is recognized that a visual inspection may not give the information needed and it is considered monitoring will be required to improve the quality and reliability of the information for bridge management decision making. Bush et al. (2011) sets out a risk and criticality approach to inspection and data collection.

Many RCA are setting strategic plans requiring an increase in bridge network robustness and resilience. The BMT must know the limitations of the existing bridge stock and even if all the bridge components are in excellent condition whether the Performance demands will be met.

4 BRIDGE CONDITION MONITORING

In general Bridge Condition Monitoring (BCM) is well defined and embedded into Bridge Management practice and there are many guides, Austroads (2018) and Austroads (2021), that set out the processes to follow and the planning required for monitoring. It also needs to be recognized that monitoring may identify the response of 'unknown defects' if the monitoring is well planned and the known defect effects fully identified, any residual defective response may be attributed to an 'unknown defect'. Due to cost of monitoring a risk and criticality, Bush et al. (2011), approach is suggested for monitoring selection. As reported in McCarten (2018) bridge failures and significant incidents are still occurring and the following practice changes are suggested:

a. Enforce the need to better understand the nature and risk of Defects/Issues reported, FHWA (2021). Include monitoring in bridge management investment funding, include monitoring in Bridge Inspection forms and consider it as 'day to day' bridge management
b. Align BMT condition risk reporting with bridge design standards. McCarten (2012) showed that any bridge with 3% AEP (Annual Exceedance Probability) likelihood of failure could be justified for replacement and hence should be monitored until replacement occurs. It is recognized that FHWA (1991) requires BMT to confirm bridge foundation failure is unlikely under the 0.2% AEP event due to the high number of waterway bridge failures
c. Avoid confusion with monitoring terminology/jargon (NDT, NDE, SHM and SM should be defined) to ensure common understanding of requirements and outcomes

d. The academic, consulting, BMT and RCA staff, the wider bridge management industry, must liaise and work together with any monitoring work recognizing the skill sets and value added by each party

While BCM tends to be considered for the structure and materials parts of a bridge the opportunities for monitoring other bridge risk components should not be discounted. The following case studies for BCM provide further guidance on this and follow a proactive preventive focus with monitoring:

- BCM Case 1: Foundations: A two span (20m overall length) one lane bridge failure occurred in a remote location with the central pier settling 180mm during a 10% AEP event. A review was undertaken to assess whether monitoring could have avoided traffic disruption and the need for a temporary bypass. The review determined a borehole positioned immediately adjacent the central pier may have given sufficient notice of the impending failure but the geotechnical analysis would have been required to clearly quantify skin friction effects. General 30mm/year degradation of the river bed had been recorded and was determined to be due to softening of the argillite basement material
- BCM Case 2: Substructure: A 30year old four span (100m overall length) two lane bridge carrying approximately 25,000 vehicles per day was planned for replacement with a one lane bridge. The main reasons for bridge replacement included existing half joint hammer head pier caps (considered by the RCA as a low redundancy component), poor condition as evidenced by cracking at the base of the pier cap upstand/rear of the half joint corbel, and, an analysis showing 'theoretical deficiency' in the pier cap load carrying capacity. Durability testing was undertaken confirming corrosion was not significant from both carbonation and chloride ion, the bridge located approximately 5km from the coast, This first stage investigation included bridge inspection identifying possible bearing movement issues. Subsequent investigation of the pier cap cracking showed this effect only extended approximately 0.5m to 1m from the pier cap ends, with the extent considered to be limited by the large 1.8m diameter central pier columns. The cracks were assessed to be associated with load sharing with the designed pier cap reinforcing – consisting of stiffer diagonal reinforcing and normal corbel flexural reinforcement. This second stage investigation confirmed the bearings had not 'locked' and were still accommodating the determined movements. The original design calculations and designer sketches showed there was more reinforcing in the pier cap than considered in the structural analysis. Hence it was determined that all structural matters were met, especially with the proposal to shift the traffic to the central part of the cap with the single lane configuration, and it was recommended the end cracks be epoxy injected to maximize cap durability and enhance shear transfer. The monitoring and investigation cost of approximately $0.5M showed bridge replacement (assessed at $12M construction cost only) could be deferred at least another 30years achieving a cost effective and sustainable outcome
- BCM Case 3: Superstructure beams: This 90year old 20 span (245m overall length) two lane bridge carrying approximately 15,000 vehicles per day is located in an aggressive coastal environment. The bridge can accommodate a 1.5% AEP flood event without overtopping and to date there have been at least two bridge submergences. At approximately 25 years old a bitumastic coating was applied to the beams to enhance service life. Unfortunately, the coating limited visual inspection of the beams. When the bridge approximated 55 years old significant signs of deterioration were being observed through some parts of the coating and a comprehensive concrete condition survey was undertaken. This survey highlighted several 'hidden details' including:

  a. Chloride ion corrosion dominated beam deterioration and pitting corrosion was significant
  b. The concrete while generally good had parts with low compaction, these were evidenced by more than normal number of voids. The voids were such that stirrup reinforcing bars could corrode away completely with no cracking or rust staining exhibited at the beam surface, even if the coating was not present

c. The main reinforcing consisting of 32mm diameter plain bars was assessed to have reduced bond due to the bar surface corrosion. The bar strength is very reliant on the end 180degree hooks. The slippage from the bond loss could be expected to impact beam response
d. The report noted the concrete condition survey sampled a range of different parts of the bridge to get an indication of the range of defects, but the survey should not be considered comprehensive in extent of each defect over the 20 span bridge

When the bridge approximated 60years old a major concrete repair was undertaken, approximate cost $1.0M. The repair was risk targeted focusing on the beams closest to the coast and parts of the inner beams with a coating applied to the beams and spans over the main river channel. The repair work included reinstatement of many 10mm diameter stirrups that had completely corroded through. Comprehensive records of the work completed were taken so future bridge managers would be aware of the parts of the structure repaired and hence be able to assess the extent of bridge not opened up and that could still have the deterioration/defects recorded in the concrete condition survey. Due to the potentially significant extent of 'hidden deterioration/defects' with pitting corrosion and main reinforcing bond loss being of particular concern, Structural Health Monitoring (SHM) using a known load test was promoted as a reliable and cost effective method for supplementing visual inspection monitoring. The BMT compiled a bridge management plan for the bridge and the RCA initiated investigations into replacement bridge and road realignment options

- BCM Case 4: Superstructure deck: This case study expands on that included in McCarten (2022) providing more background on the subject bridge and BCM work undertaken. The bridge now almost 65years old of 5 spans (217m overall length with 3 steel truss spans of 57.6m, 82.3m and 57.6m, and, two short steel beam land spans) and two lanes carrying approximately 6,000 vehicles per day. The steel truss superstructure was made continuous following the development of steel truss fatigue issues. The continuous superstructure was lively but within the RCA requirements. The low level of deck shear connectivity (20mm diameter shear studs at 1.8m centres) is considered to contribute to the superstructure liveliness. Overall bridge expansion/contraction movement occurs at the north end of the bridge with a large steel plate expansion joint. Significant traffic impact effects occur with the expansion joint. Major industrial development south of the bridge has generated significant numbers of fully laden trucks travelling southward over the bridge and due to the road geometry some of these trucks had been recorded crossing the bridge at approximately 130km/hr. The Weigh-In-Motion site set up in 2010 data analysis has confirmed overloading to approximately 20% over the legal axle limit occurs. As reported in McCarten (2022) the 1980 cracking in the 150mm thick deck was significant and a speed limit imposed. The early cracking pattern reflected construction practice but there was negligible drying shrinkage or plastic settlement cracking. Subsequent cracking reflected traffic operations and loading effects compounded by plain round deck reinforcing and the superstructure liveliness. The bridge is located 30km from the coast and carbonation had not reached cover depth so durability deterioration was minimal. When it was agreed to remove the speed restriction in the early 1990's a BCM program was initiated. As international bridge deck fatigue experience was limited a 'first principles' approach was adopted using an NDT Test load versus Displacement methodology at 5 yearly intervals, refer McCarten (1991). Throughout the monitoring period crack width and extent of cracking, using "crack windows", was undertaken. It was expected that should the crack widths exceed 0.5mm then there was a high probability of losing compressive membrane effects and the grid like cracking pattern reflecting the slab bottom reinforcing could develop quickly. McCarten (2022) reported cracking that resulted in water leakage through the deck, it was determined these discreet cracks were associated with deteriorated water proofing leakage and low temperature effects and did not appear to significantly affect the general deck cracking observed. Approximately 15 years following the installation of the new water proofing system the general deck cracking had reached the stage for deck rehabilitation, McCarten (2022). The deck was rehabilitated using low viscosity epoxy crack injection, to reinstate original deck integrity, and the deck strength enhanced using carbon fibre strips to provide robustness for reinforcing bond loss and deck liveliness.

5 BRIDGE PERFORMANCE MONITORING

In general Bridge Performance Monitoring (BPM) is immature and Bridge Management guides, Austroads (2021), recognize that methods for monitoring Performance measures are required. Austraods (2021) presents seven Bridge Performance measures being:

a. Heavy vehicle loading – ability of the bridge network to accommodate the heavy vehicle configurations defined by the RCA
b. Bridge geometry – curvature, lateral clearance and vertical clearance to safely accommodate heavy vehicle passage with or without other traffic as required by the RCA
c. Bridge structural safety – recognizing inherent structural deficiency, collision damage, vehicle fire on/under the bridge and sabotage
d. Bridge safety under natural hazard
e. Resilience under natural hazard
f. Bridge condition
g. Value for money

The Performance of a bridge is principally set by the 'original bridge design' standards, unless retrofitted since original construction. As design codes change with time, generally becoming more demanding in requirements, the older bridges become more and more 'non-conforming' but they are still providing a useful function. As urban development/growth progresses the transport demands on the bridge network will increase. The integration of Bridge Asset Management requirements with the Network (Bridge) Planning requirements utilizes a Network Optimization process to generate a Bridge Management Strategy (BMS) for each bridge on the network, McCarten (2020). A comparison of the BMS Performance demand with the Performance provided by that bridge will show the "Performance deficiency" of the bridge. It is considered this Performance deficiency could be quantified and measured, and, by setting a target "Performance deficiency" bridge upgrading or replacement requirements could be prioritized in a transparent manner.

Many RCA are recognizing the requirement for Network Optimization process and identifying strategic objectives that provide high financial returns and are assessing the funding demands for those strategic objectives to confirm viability. Those strategic objectives provide an optimized preventive approach to managing the Performance deficiency. Some case studies on BPM providing further guidance on this are given below:

- BPM Case 1: Heavy haulage routes: The RCA will liaise with key stakeholders to identify appropriate routes and performance requirements required for those routes. The bridges on each route will be assessed for monitoring, upgrading or replacement. Route viability will be assessed by economic analysis and BPM requirements determined accordingly with Performance deficiency being fully addressed
- BPM Case 2: Natural hazard prioritization: Many RCA recognized that with the significant improvement in earthquake design requirements, developed through the 1970's and 1980's, there was a need to implement seismic prioritization in the 1990's/2000's to identify seismic performance deficiency in the bridge stock. Much work has been undertaken with retrofits of bridges to ensure acceptable seismic performance in the network. More recently resilience is recognized as a Performance measure, Austroads (2021). It is considered further assessments may be required to ensure emergency routes have the required seismic Performance. It is also considered bridge waterway risks should be subject to a similar prioritization process. This is because with increasing rain and river flow monitoring the reliability of flood discharge assessments is improving and with bridge site monitoring there is improved understanding of the hydrologic processes. With, say, an additional 10 or 20 years of river monitoring the bridge risks may be quite different from that originally predicted with bridge design. It has been observed that bridge site flood discharge assessments typically increase with longer flow monitoring periods. Some RCA have recognized the significant number of bridge failures over waterways and set specific Performance requirements, FHWA (1991), to identify Performance deficiency for monitoring or programming bridge retrofit

- BPM Case 3: Bridge access: Many RCA recognize the need to be proactive in providing bridge/road users with specific advice for "safe access" during flood events, DTMR (2022). Austroads (2021) recognizes that for bridges susceptible to high scour risk then consideration should be given to bridge closures under significant flood events. These initiatives require improved waterway analysis to ensure realistic closure triggers are adopted, an understanding of network operations (alternative route management), development of bridge monitoring/warning systems, and, implementing improved methods for communicating with the travelling public. The implementation of bridge site monitoring improves the reliability of the closure triggers and CCTV offers 'real time' bridge site response for communication purposes, especially where the network has limited road access

6 DISCUSSION

This study has found that most bridge defects/issues/failures are foreseeable and preventable if a structured approach to assessing and acting on vulnerabilities, and, learning from industry experience is embedded into bridge management practice. RCA's need to be confident inspections fully cover the extent of each bridge and all defects are reported. While a defect may have been identified the nature and risks of the defect need to be understood to ensure reliable and comprehensive information is used in bridge management decision making. Monitoring, whether visual, NDT or SHM, offers the opportunity to develop an improved understanding of any defect. The challenge for the BMT is identifying the type and extent of monitoring required and this decision needs to be undertaken with the RCA to confirm funding requirements. In some defect cases special consultants/academia may be required to assist with this process. Bush et al (2011) provide a risk and criticality approach to data collection prioritization to assist with funding investment requirements. BMT skill sets and contractual obligations may impact activity allocation.

There is a need to have a consistent approach to risk reporting with that appropriately aligned with bridge design and allowing for remaining bridge service life. McCarten (2012) suggests that if bridge failure is predicted under a 3%AEP event then that could provide a trigger for formal bridge monitoring. The study shows that embedding monitoring into Inspection Forms and 'day to day' bridge management puts in place a structured approach to assessing vulnerabilities.

This study has found Performance Monitoring to be immature in part due to the difficulties translating strategic objectives to the Performance management of specific bridges. The case studies presented show that many RCA are undertaking work to improve network bridge performance in an optimized manner, but this is only targeting parts of the network. Natural hazard prioritization has been used to improve network robustness and it is suggested resilience and development of emergency corridors offer a way to upgrade other parts of the network. "Safe Accessibility" is being pursued by some RCA to show good stewardship and proactiveness to the travelling public. It is suggested monitoring is required to improve reliability with safe access triggers.

Condition and Performance monitoring are core to an engineering approach to bridge management and with the limitations of visual inspections recognized monitoring using NDT, SHM and other techniques suggested in the Case Studies must be embedded into 'day to day' bridge management.

7 CONCLUSIONS

From this review of the Condition and Performance monitoring requirements for a network of bridges with bridge management following an engineering approach it is concluded:

- BMT needs to improve bridge risk reporting, aligned with bridge design risks
- BMT needs to be responsible for better quantifying defects/issues, to improve reporting and reliability for forecasting intervention investment
- RCA needs to include monitoring on Inspection Forms and encourage BMT to embed monitoring into 'day to day' bridge management

- RCA needs to be more proactive in setting Performance measures for accessibility, ensuring safety of bridge users, and, improving bridge resilience/robustness particularly under natural hazards
- RCA needs to define the Condition and Performance measures, aligned with strategic planning, to be monitored and reported by the BMT

DISCLAIMER

The observations in this paper are those of the author and are presented to advance the topic in practice.

REFERENCES

Aktan, A.E., Moon, F. L. & Lowdermilk, D. S. 2013. Engineering and Management of Infrastructure Systems. Presented to the 6th International Conference on Structural Health Monitoring of Intelligent Infrastructure, Hong Kong.

Austroads, 2018. Guide to Bridge Technology: Part 7, Maintenance and Management of Existing Bridges. Austroads, Sydney, Australia.

Austroads, 2021. Engineering Guideline to Bridge Asset Management. Austroads, Sydney, Australia.

Bush, S., Omenzetter, P., Henning, T. & McCarten, P.S. 2011. A Risk and Criticality based approach to Bridge Performance data collection and monitoring. Structure and Infrastructure Engineering, Special Edition: Asset Management, Taylor & Francis, UK.

Catbas, F.N. & Atkan, A.E. 2002. Condition and Damage Assessment: Issues and some Promising Indices. Journal of Structural Engineering, ASCE, Vol. 128, No 8, August 2002, p 1026–1036.

Department of Transport and Main Roads, 2022. Road closure policy for wet weather and flooding. Engineering Policy, EP147, prepared by the Operations Section of the State of Queensland Department of Transport and Main Roads, Brisbane, Australia.

Federal Highway Authority, 1991. Evaluating Scour at Bridges. Technical Advisory Note prepared by the Hydraulics Section of the Office of Engineering, FHWA – T5140.23, October 1991, Washington D.C., USA.

Federal Highway Authority, 2021. Transportation Asset Management Plans: Case Study 4 – Managing Risks to Assets. Office of Infrastructure, FHWA-HIF-20-086, February 2021, Washington D.C., USA.

Frangopol, D.M., Kong J.S. & Gharaibeh E.S. 2001. Reliability–Based Life–Cycle Management of Highway Bridges. Journal of Computing in Civil Engineering, ASCE, Vol. 15, January 2001, p 27–34.

McCarten, P.S. 1991. Fatigue life of RC bridge decks. Paper IBC-91-42. Proceedings of International Bridge Conference (presented by ESWP), Pittsburg, USA.

McCarten, P. S. 2004. A systems method for defining Best Bridge Maintenance Management Practice. Proceedings of IABMAS'04 Conference, Kyoto, Japan.

McCarten, P. S. 2006. Bridge condition and health measures for needs analysis. Proceedings of IABMAS'06 Conference, Porto, Portugal.

McCarten, P. S. 2012. Bridge Risk Management: Back to basics. Proceedings of IABMAS'12 Conference, Stresa, Italy.

McCarten, P. S. 2014. Bridge performance measures: A fresh perspective. Proceedings of IABMAS'14 Conference, Shanghai, China.

McCarten, P. S. 2016. Bridge Performance Measures: Robustness- Redundancy. Proceedings of IABMAS'16 Conference, Iguazu Falls, Brazil.

McCarten, P. S. 2018. Bridge risk management: Credibility gaps. Proceedings of IABMAS'18 Conference, Melbourne, Australia.

McCarten, P. S. 2020. Bridge management: Data collection for bridge upgrades. Proceedings of IABMAS'20 Conference (On-line), Sapporo, Japan.

McCarten, P. S. 2022. Bridge deck fatigue: A case for proactive preventive bridge management. Proceedings of IABMAS'22 Conference, Barcelona, Spain.

New Zealand Transport Agency, 2013. Road Efficiency Group Case Study: Bridge Management Frameworks - Managing Risk and Ensuring Value for Money. Wellington, New Zealand.

Sanford, K.L., Herabat, P. & McNeil, S. 2000. Bridge Management and Inspection Data: Leveridging the Data and Identifying the Gaps. Transportation Research Circular 498, Transportation Research Board, Washington D.C., USA.

Bridge Maintenance, Safety, Management, Digitalization and Sustainability – Jensen, Frangopol & Schmidt (eds)
© 2024 The Author(s), ISBN 978-1-032-77040-6
Open Access: www.taylorfrancis.com, CC BY-NC-ND 4.0 license

Determination of precast concrete bridge slab connection stiffness by developing a digital twin

S. Ereiz, I. Duvnjak, J. Pajan, M. Bartolac, J. Košćak & D. Damjanović
Faculty of Civil Engineering, University of Zagreb, Zagreb, Croatia

ABSTRACT: The construction of bridges is usually a long-term task where the use of traditional concrete systems is challenging due to the installation of formwork, material falling from the scaffold and the disruption of traffic flow. Often, the use of such a system is limited due to the nature of the obstacle the bridge is spanning. As a solution to this problem, precast concrete slabs began to be produced and used in construction, which made construction easier but additionally caused problems for structural designers. One of the unknowns was how to interpret the connection between the slabs and how to describe the connection in the numerical model so that the global behavior of the structure matches the real behavior. This paper presents a determination of the precast concrete bridge connection stiffness by developing a digital twin. A pedestrian suspension bridge is selected as a case study. The digital twin of the precast slabs is developed by performing the numerical model and finite element model updating (FEMU). Based on the experimentally determined dynamic properties of the characteristic bridge slabs, the finite element model updating is performed. By updating the numerical model, the stiffness of the connection is determined.

1 INTRODUCTION

Among the various types of bridges, suspension bridges are increasingly used to span large spans and the richness of the architectural features and aesthetic aspects. However, their main cables and hangers may be subjected to corrosion and fatigue damage (Wickramasinghe & Wasanthi Ramyalatha, 2015). There is a need for a simple and reliable method to detect and locate this type of damage to subsequently make structural retrofitting and prevent further damage occurring (Zhang et al., 2019). SHM has emerged as an option that can meet this need (Heo & Jeon, 2016). Current SHM system are equipped with a variety of methods to detect damage of a local and global nature. The limitations of the local methods require non-destructive and global damage detection methods (Keshmiry et al., 2023). This has led to the continuous development of vibration-based damage detection (VBDD) methods in SHM systems (Chen, 2018). The basic principle of vibration based SHM is that damage changes the structural dynamic properties. Therefore, the change in structural dynamic properties can be used to detect damage. Due to the difficulty of detecting higher mode shapes in large structures such as suspension bridges, the applicability of existing damage estimates to this type of structure is limited (Comanducci et al., 2015). In addition, this type of structure oscillates in transversal, longitudinal, vertical, torsional, and combined mode shapes, making it difficult to identify the damage. According to the previous problem, a developing digital twin of the real structures and use it for the assessment of the structure is opened up (Hu et al., 2023). The advancement of the latest information technology and the widespread adoption of industrial information systems have spurred growing interest in the integration of cutting-edge technologies, including Digital Twins (DTs), into the civil engineering (Liu et al., 2020a). In this field, the finite element models are most commonly used for this purpose (Kaveh, 2014). To reflect the real structural behaviour, developed numerical mode is updated based on the experimentally determined

DOI: 10.1201/9781003483755-269

structural behaviour through the process of finite element model updating (FEMU) (Mottershead & Friswell, 2013). Utilizing DTs in engineering applications has the potential to greatly enhance the precision and intelligence of structural performance analysis. DT technology involves simulating the state and behavior of physical entities within a dynamic virtual model, offering high-fidelity representation (Liu et al., 2020b). Kessels et al. (Kessels et al., 2023) introduced different types of transient response features to update parameter values of nonlinear dynamic systems with increased computational efficiency and accuracy. In their work Ye et al. (S. Ye et al., 2020) they showed on the example of the freeway bridge in New Jersey that the operational monitoring of the bridge is sufficient for structural identification and that it enables the development of a 3D digital twin of the bridge that served in the formulation of meaningful interventions that can only be offered after model calibration. Jasiński et al. (Jasiński et al., 2023) presented the concept of DT development, its basic principles and features for its implementation in bridges where they highlighted the role of load testing in validating and updating the developed FEM model for further use in DTs. Jiménez Rios et al (Jiménez Rios et al., 2023) systematized information and knowledge on how information modelling of bridges, FEM and SHM can be combined and used to create DTs of bridges. Ghahari et al. (Ghahari et al., 2022) presented a Bayesian method technique for updating and developing a DT that includes the determination of various effects such as soil-structure interaction and the identification of measured structural responses. In their paper, Honghong et al. (Honghong et al., 2023) by reviewing, comparing and analysing 116 documents on Building Information Modelling (BIM) and DT concluded that the BIM framework can be significantly improved by DT to be implemented throughout the entire life cycle of a bridge. Ye et al. (C. Ye et al., 2022) made recommendations to encourage the adoption of bridge structure monitoring combined with the development of DTs in the form of numerical model development and their updating to realize industrial value. In this paper, the authors use DT to perform the FEMU of characteristic pedestrian suspension bridge slabs to solve problem of determination the stiffness of their connection. The following section provide some basics of the FEMU methodology used for the updating the DT of the characteristic slabs of the pedestrian suspension bridge. The section 3 provides the information about structure, initial numerical model of the characteristic slabs, experimental campaign, comparison between the predicted numerical model behaviour and the results of the experimental campaign while the last subsection describes the obtained results of the updating process. Section 4 discussed and evaluated the obtained results, since on the span slab the connection stiffness was determined through developing the DT and performing FEMU on span slab, while the obtained results are evaluated on the characteristic edge slab. The 5th section concluded the whole paper.

2 FINITE ELEMENT MODEL UPDATING - DIGITAL TWINS IN CIVIL ENGINEERING

For the practical engineering application, the updating process is usually performed considering the maximum likelihood method (MLM). According to this approach, the updating problem can be formulated as the combination of a bi objective optimization and a decision-making problem. The bi – objective optimization problem is defined in terms of the residuals between the experimentally obtained and numerically predicted structural dynamic properties. To optimize defined bi-objective function, nature inspired computational algorithms have been usually considered. According to the MLM the FEMU problem is transformed into an optimization problem. For this purpose, differences between the numerically predicted and experimentally obtained test results are defined in the form of the residuals. Using the structural dynamic properties natural frequencies residuals (r_t^f) are defined as relative differences, while the mode shape residuals (r_t^m) is most often defined in form of the modal assurance criterion and its derivates. General formulation of the FEMU problem under the multi objective approach can be defined as follow:

$$\min f(\theta) = (f_1(\theta)\, f_2(\theta)\,) = \; min\Big(\sum_{t=1}^{m_f} r_t^f(\theta)^2 \quad \sum_{t=1}^{m_m} r_t^m(\theta)^2 \Big) \tag{1}$$

where $f(\theta)$ represent the multi objective function, $f_1(\theta)$ and $f_2(\theta)$ is the first and second multi objective function residuals, m_f and m_m are the natural frequency and mode shape residual size; $r_t^f(\theta)$ and $r_t^m(\theta)$ are the residual vectors associated to the natural frequencies and normalized mode shapes. To guarantee that two types of residuals are well-balanced, they may be normalized as:

$$r_t^f(\theta) = \frac{f_{num,t}(\theta) - f_{exp,t}}{f_{exp,t}} \quad t = 1, 2, \cdots, m_f \tag{2}$$

$$r_t^m(\theta) = \sqrt{\left(\frac{\left(1 - \sqrt{MAC_t(\theta)}\right)^2}{MAC_t(\theta)}\right)} \quad t = 1, 2, \cdots, m_m \tag{3}$$

Optimizing defined objective function (Equation 1.), the optimal values of the parameters for which values the optimization is searching for are obtained. For the obtained values of parameters FE model the best represent the real structural behaviour and can serve for the other purpose such as structural maintenance, assessment, rehabilitation or defining the concept of the structural health monitoring.

3 FEMU OF PEDESTRIAN SUSPENSION BRIDGE

3.1 *Description of the structure*

Built in 1980, the suspension pedestrian bridge over the Drava River in Osijek is a testament to advanced engineering principles. With a span of 209,5 meters, the bridge has a statically prestressed catenary network, demonstrating precision in structural design to effectively connect opposite riverbanks. A parabolic suspension cable, securely anchored to blocks placed behind the bridge, spans 24-metre-high steel columns, highlighting the detailed engineering considerations. This integrates form and function, using precast concrete corridor panels suspended by inclined hangers on a parabolic suspension cable. The 5-meter-wide corridor itself contributes to the total width of the span, which is 6.12 meters. This architectural achievement exemplifies the merging of theoretical principles and practical application, establishing the suspension footbridge as a significant manifestation of scientific rigor and engineering excellence across the Drava River.

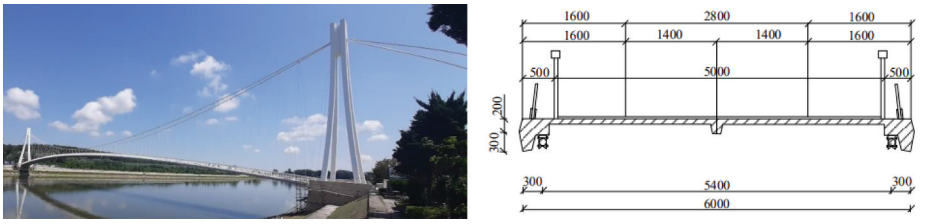


Figure 1. Pedestrian suspension bridge (a) view of the bridge (b) cross section of the bridge.

The span consists of prefabricated concrete slabs. There is a total of 50 of them, which can be divided into three types. The type 1 slabs are located at the beginning and end of the bridge (2 pieces). The type 3 slab is in the centre of the span (1 piece), while all other slabs are of type 2. These characteristic slabs have a dimension of 6 x 4 metres. The longitudinal and transverse ribs divide each slab into four parts. The lateral longitudinal ribs have a rectangular cross-section of 26 x 50 cm. The other ribs are 16 cm high, while their width varies: 12 x 18 cm for the longitudinal ribs in the centre, 12 x 15 cm for the outer transverse ribs and 16 x 22 cm for the central transverse ribs. The design value of the concrete cover thickness of the ribs is 2 cm, while the class of the concrete is MB 40. The slabs are 8 cm high, double-reinforced and have a design value for the concrete cover thickness of 1.5 cm. They are connected by a rigid, welded reinforcement in the lateral ribs. At one end, the slab is suspended from the hangers (ϕ21 mm),

while at its other end it is supported by a longitudinally movable mandrel (ϕ28 mm) that protrudes from the neighbouring slab. There are two tension cables under the slabs (Figure 1 (b)), which are anchored in the foundation of the pylon. The down main cable consists of (2 ϕ 61 mm) cables on each side of the bridge and forms a system of prestressing canaries that reduces the deformation of the deck and dampens vibrations. During the war the bridge (hangers) was damaged and two prefabricated slabs were broken through. The bridge was then rehabilitated to its original condition. In 2009, a new asphalt layer was installed, and the connection was repaired and rehabilitated. During the preparation of the concrete substructure for the installation of the asphalt, the concrete cover was removed in several lace by hydrodemolition of the concrete surface. In 2022, as part of the rehabilitation of the bridge, the connecting elements of the upper main cable were replaced, the asphalt layer was removed, beams of prefabricated slabs were reprofiled, the joints between prefabricated slabs were sealed, the corrosion protection of the steel elements was renewed, and the handrail was repaired. Based on the available drawings and documentation, the initial numerical model of the concrete slabs was developed to determine the connection stiffness between the concrete slabs.

3.2 *Initial numerical model*

Initial numerical modelling of the characteristic edge and span slab was performed using a commercial FE package ANSYS. FE model was developed using 3D linear BEAM 188, four node shell elements with six degree of freedom SHELL 181, uniaxial tension LINK 180 elements 1D longitudinal spring damper COMBIN14 elements with different degrees of freedom to define the connection between slabs and boundary conditions of edge slab. Material characteristics of steel was set as traditional (Bhadeshia & Honeycombe, 2017), while for the concrete it was set based on the information available in project documentation $E_{concrete}$ = 33 GPa, $c_{oncrete}$ =2548 kg/m^3, $\nu_{concrete}$=0,2. For cable elements E_{cable} = 160 GPa, ρ_{cable}=7850 kg/m^3, ν_{cable}=0,3. Properties of rigid elements was set as E_{rigid} = 210000 GPa, ρ_{cable}= 0,0001 kg/m^3, ν_{cable}=0,3. The stiffness of the connection elements between the slabs was set as k_{lon}=1x10^{10} N/m. On developed numerical model the modal analysis was performed to obtain the natural frequencies and mode shapes for considered mode t (Table 1.).

3.3 *Experimental investigation on characteristic edge and span slab*

To determine the boundary condition of the bridge, inspection of the bridge connection with the bank was performed and the dynamic parameters of the edge slab were determined. Since it was determined by visual inspection that the bridge is supported in the same way on both the left and the right bank (Figure 2. c) and d)), the measurement was performed only on one slab on the left bank. Determination of the structural dynamic parameters (natural frequencies and mode shapes) was proposed by Frequency Domain Decomposition (FDD) method.

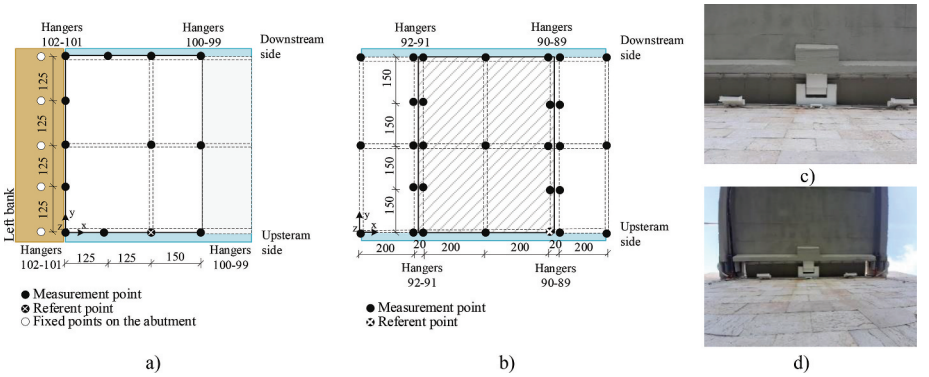


Figure 2. a) Arrangement of the measurement points (dimensions in cm) of the characteristic edge slab and b) characteristic slab in bridge span for which natural frequencies and mode shapes are determined c) boundary conditions on the left bank d) boundary condition on the right bank.

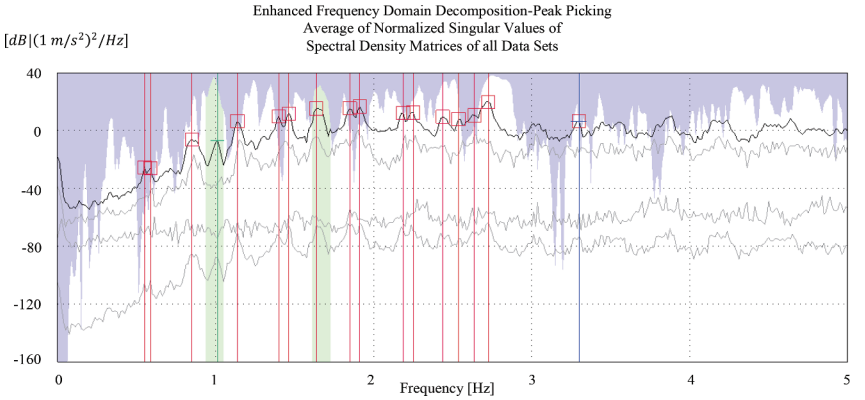


Figure 3. Characteristic record of Enhanced Frequency Domain Decomposition (EFDD) for the determination –average of the normalized singular values of spectral density matrices of all data sets for characteristic edge slab.

The slabs were vertically excited by pedestrian random walking for 2 minutes. Measurement of acceleration on the characteristic edge slab was performed in total 13 points (Figure 2. a)) while in the span slab it was performed in total 29 measuring points, for both in vertical direction. The natural frequencies were determined as the resonant peaks of the recorded singular values of the auto spectral densities (Figure 3.).

Based on determined natural frequencies values the mode shapes was also selected and assigned to the selected natural frequencies value. First mode characteristic for the edge, and second characteristic for the span slab are presented on the Figure 4.

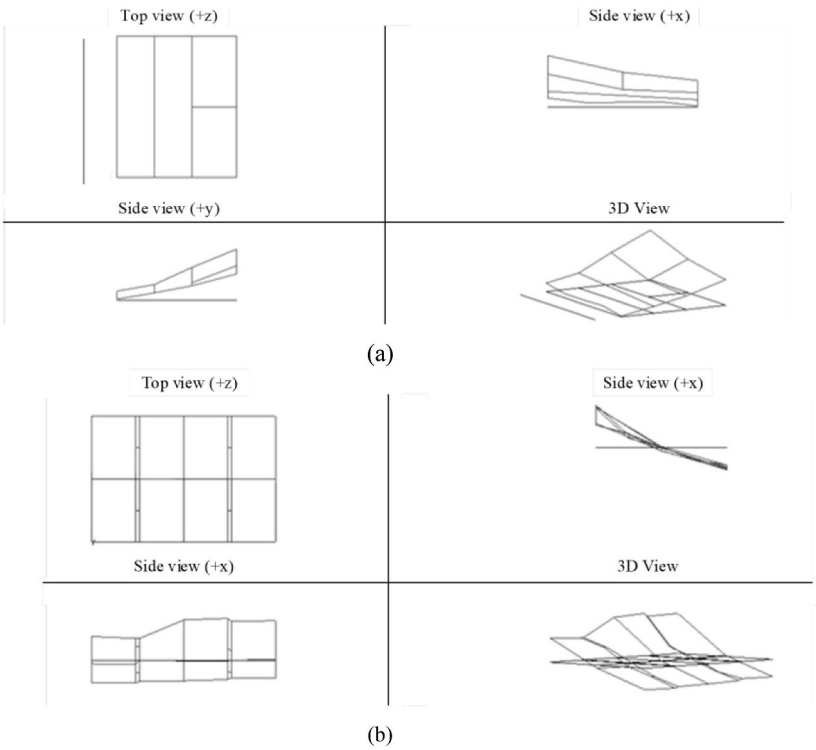


Figure 4. (a) First mode shape of edge slab (b) Second mode shape of span slab.

3.4 *Comparison between the experimental test results and initial model prediction*

The initial numerical model is tested based on comparative analysis (relative differences of the natural frequency and modal assurance criterion (MAC)) (Table 1.). The most relevant updating parameters were selected based on the sensitivity analysis (Sanayei et al., 2015). As a selection criterion, the ratio between the modal strain energy associated with physical parameters and the overall modal strain energy has been considered. The selected updating parameter include: the Young modulus of elasticity of concrete elements θ_1 [GPa]; (2) stiffness of the connection between the slabs elements - θ_2 [N/m]; (3) down main cable tension force - θ_3 [N]; (4) hangers tension force - θ_4 [N]; (5) Young modulus of elasticity of handrail elements – θ_5 [GPa]; (6) stiffness of the connection between the slabs and down main cables – θ_6 [N/m,]; (7) upper main cable tension force – θ_7 [N]. The vector of the initial values was set as follows: θ = [33 MPa $1x10^{10}$ N/m 1300 MPa 36,124 MPa 210 MPa 2.10 $x10^{11}$N/m^2 4760]. The constraints of the search domain are defined as: θ^l = [0,9 0,1 0,8 0,6 0,9 0,8 0,8] and θ^u = [1,1 2,0 1,2 1,1 1,1 1,2 1,2]

Table 1. The comparison of the numerically predicted and experimentally determined modal properties of the pedestrian suspension bridge edge and span slab.

	Edge				Span			
Mode t	f_t^{exp} [Hz]	f_t^{num} [Hz]	Δf_t [%]	MAC [/]	f_t^{exp} [Hz]	f_t^{num} [Hz]	Δf_t [%]	MAC [/]
1	0,587	0,568	3,2	0,967	0,587	0,567	3,4	0,934
2	0,850	0,863	-1,5	0,960	0,850	0,861	-1,3	0,972
3	1,013	1,172	-15,7	0,937	1,013	1,168	-15,3	0,794
4	1,462	1,145	21,7	0,870	1,400	1,146	18,1	0,712
5	1,850	1,795	3,0	0,802	1,650	1,695	-2,7	0,780
6	2,188	2,061	5,8	0,974	2,180	2,064	5,3	0,922
7	2,725	2,66	2,3	0,953	2,725	2,658	2,5	0,930
8	3,313	3,195	3,6	0,943	3,313	3,197	3,5	0,910

3.5 *Determination of the concrete slab connection stiffness*

The connection stiffness of the concrete slabs was determined using the approach described in the section 2 by determining the Pareto optimal front solution of the decision -making problem (determination of the knee point). For this purpose, the Harmony Search (HS) optimization algorithm has been considered (Manjarres et al., 2013) The updating process was performed by linking a FE analysis software, Ansys (*Ansys (2022)*), with mathematical software, Matlab (*Matlab (2022)*). The parameters of the HS algorithm were established as: population size PS=100; (ii) maximum number of iterations I_{max} =50; (iii) objective function tolerance $t_{of} = 1 \cdot 10^{-4}$; (iv) new population size $P_{s,\ new}$ = 40; (v) harmony memory pitch adjustment HMCR= 0.9 and (vi) pitch adjusting rate PAR=0.3. As a result of the FEMU the Pareto optimal front of considered residuals was determined. Based on the obtained set of optimal solutions, the best solution was select as knee point which correspond to the vector θ^*_{HS}= [0.9972, 0.8895, 1.0588, 1.0308, 1.0462, 0.8199, 1.0219]. The selected best optimal solution correspond to the numerical model properties: [32,908 $8{,}89 \cdot 10^9$ 1376,447 36,124 219,706 $1{,}721 \cdot 10^{11}$ 4864,130]. Based on the determined best optimal solution the stiffness connection between slabs was determined as k = $8{,}89 \cdot 10^9$ N/m.

4 DISCUSSION

Based on the connection stiffness value determined for the span slab, the edge slab was evaluated in a such way that the determined connection stiffness value was assigned to its one edge. The evaluation is performed based on the differences between the natural frequencies and the differences between the mode shapes expressed in the form of the MAC coefficient (Table 2).

Table 2. Correlation between experimental and updated natural frequencies and mode shapes on the edge and span slab.

	Edge				Span			
Mode t	f_t^{exp} [Hz]	f_t^{num} [Hz]	Δf_t [%]	MAC [/]	f_t^{exp} [Hz]	f_t^{num} [Hz]	Δf_t [%]	MAC [/]
1	0,587	0,596	-1,6	0,983	0,587	0,597	-1,6	0,999
2	0,850	0,841	1,0	0,976	0,850	0,843	0,9	0,967
3	1,013	1,027	-1,4	0,952	1,013	1,027	-1,3	0,940
4	1,462	1,500	-2,6	0,884	1,400	1,430	-2,2	0,903
5	1,850	1,839	0,6	0,815	1,650	1,659	-0,6	0,811
6	2,188	2,213	-1,2	0,990	2,180	2,203	-1,1	1,001
7	2,725	2,688	1,3	0,969	2,725	2,687	1,4	0,955
8	3,313	3,259	1,6	0,959	3,313	3,260	1,6	0,943

Based on the results presented in the Table 2 it can be concluded that the value of the stiffness of the panel connection determined on the basis of the dynamic parameters of the panel in the span corresponds to the stiffness of the connection between the edge panel and the rest of the bridge panels, which is visible not only from the difference in natural frequencies, but also from the value of the MAC factor.

5 CONCLUSION

To obtain a model of structure that corresponds as closely as possible to its actual behavior the digital twin models are developed. Developed models are combined with different known information from real structure to describe its behaviour as close as possible to correspond to actual behaviour. In this paper, for this purpose, the finite element model (digital twin) is combined with the finite element model updating process to determine the stiffness of connection between the slabs on the pedestrian suspension bridge. To update the developed numerical model the structural dynamic properties was determined on the one characteristic edge and one span slab. Based on the updating process of one span slab, the stiffness connection between slabs is determined and the obtained values are evaluated on the characteristic edge slab. Through described combination of digital twin and finite element model updating process it is possible to describe the structural behaviour to correspond to its actual and can be used for many other purposes such as structural maintenance, assessment, rehabilitation, conceptualization of the structural health monitoring concept, and many other. It is recommended for future research to perform the structural assessment based on the periodically performed measurement and updated the digital twin of structure.

REFERENCES

Ansys (2022). https://www.ansys.com/ (accessed Dec. 20, 2022). n.d.

Bhadeshia, H., & Honeycombe, R. 2017. *Steels: Microstructure and properties* (Fourth). Elsevier.

Chen, H.-P. 2018. *Structural health monitoring of large civil engineering structures* (1st editio). John Wiley and Sons Inc.

Comanducci, G., Ubertini, F., & Materazzi, A. L. 2015. Structural health monitoring of suspension bridges with features affected by changing wind speed. *Journal of Wind Engineering and Industrial Aerodynamics*, *141*, 12–26.

Ghahari, F., Malekghaini, N., Ebrahimian, H., & Taciroglu, E. 2022. Bridge Digital Twinning Using an Output-Only Bayesian Model Updating Method and Recorded Seismic Measurements. *Sensors*, 22(3), 1278.

Heo, G., & Jeon, J. 2016. An Experimental Study of Structural Identification of Bridges Using the Kinetic Energy Optimization Technique and the Direct Matrix Updating Method. *Shock and Vibration*, *2016*.

Honghong, S., Gang, Y., Haijiang, L., Tian, Z., & Annan, J. 2023. Digital twin enhanced BIM to shape full life cycle digital transformation for bridge engineering. *Automation in Construction*, 147, 104736.
Hu, K., Han, D., Qin, G., Zhou, Y., Chen, L., Ying, C., Guo, T., & Liu, Y. 2023. Semi-automated Generation of Geometric Digital Twin for Bridge Based on Terrestrial Laser Scanning Data. *Advances in Civil Engineering*, 2023, 1–13.
Jasiński, M., Łaziński, P., & Piotrowski, D. 2023. The Concept of Creating Digital Twins of Bridges Using Load Tests. *Sensors*, *23*(17), 7349.
Jiménez Rios, A., Plevris, V., & Nogal, M. 2023. Bridge management through digital twin-based anomaly detection systems: A systematic review. *Frontiers in Built Environment*, 9.
Kaveh, A. 2014. Computational structural analysis and finite element methods. In *Computational Structural Analysis and Finite Element Methods* (Vol. 9783319029).
Keshmiry, A., Hassani, S., Mousavi, M., & Dackermann, U. 2023. Effects of Environmental and Operational Conditions on Structural Health Monitoring and Non-Destructive Testing: A Systematic Review. *Buildings*, 13(4), 918.
Kessels, B. M., Fey, R. H. B., & van de Wouw, N. 2023. Real-time parameter updating for nonlinear digital twins using inverse mapping models and transient-based features. *Nonlinear Dynamics*, 111(11), 10255–10285.
Liu, Z., Shi, G., Zhang, A., & Huang, C. 2020a. Intelligent tensioning method for prestressed cables based on digital twins and artificial intelligence. *Sensors (Switzerland)*, 20(24), 1–20.
Liu, Z., Shi, G., Zhang, A., & Huang, C. 2020b. Intelligent Tensioning Method for Prestressed Cables Based on Digital Twins and Artificial Intelligence. *Sensors*, 20(24), 7006.
Manjarres, D., Landa-Torres, I., Gil-Lopez, S., Del Ser, J., Bilbao, M. N., Salcedo-Sanz, S., & Geem, Z. W. 2013. A survey on applications of the harmony search algorithm. In *Engineering Applications of Artificial Intelligence* (Vol. 26, Issue 8, pp. 1818–1831).
Matlab (2022). https://https://es.mathworks.com/products/matlab.html/ (accessed Dec. 20, 2022). n.d.
Mottershead, J., & Friswell, M. 2013. Finite Element Model Updating in Structural Dynamics. *Springer Science & Business Media*., 38.
Sanayei, M., Khaloo, A., Gul, M., & Necati Catbas, F. 2015. Automated finite element model updating of a scale bridge model using measured static and modal test data. *Engineering Structures*, 102(January 2021), 66–79.
Wickramasinghe, & Wasanthi Ramyalatha. 2015. *Damage Detection in Suspension Bridges Using Vibration characteristics* (Issue September).
Ye, C., Kuok, S.-C., Butler, L. J., & Middleton, C. R. 2022. Implementing bridge model updating for operation and maintenance purposes: examination based on UK practitioners' views. *Structure and Infrastructure Engineering*, 18(12), 1638–1657.
Ye, S., Lai, X., Bartoli, I., & Aktan, A. E. 2020. Technology for condition and performance evaluation of highway bridges. *Journal of Civil Structural Health Monitoring*, 10(4), 573–594.
Zhang, W., Li, T., Shi, L., Liu, Z., & Qian, K. 2019. An iterative calculation method for hanger tensions and the cable shape of a suspension bridge based on the catenary theory and finite element method. *Advances in Structural Engineering*, 22(7), 1566–1578.

Bridge Maintenance, Safety, Management, Digitalization and Sustainability – Jensen, Frangopol & Schmidt (eds)
© 2024 The Author(s), ISBN 978-1-032-77040-6
Open Access: www.taylorfrancis.com, CC BY-NC-ND 4.0 license

Damage detection of riveted truss bridge using ANN-aided AMS optimization method

B. Šplíchal & D. Lehký
Brno University of Technology, Brno, Czechia

K. Lamperová
Slovak Technology University, Bratislava, Slovakia

ABSTRACT: Aging transport infrastructure brings increased economic burden and uncertainties regarding the reliability, durability and safe use of structures. Early damage detection to locate incipient damage provides an opportunity for early structural maintenance and can guarantee structural reliability and continuing serviceability. This paper describes the use of the hybrid identification method, which combines a metaheuristic optimization technique aimed multilevel sampling with an artificial neural network-based surrogate model to approximate the inverse relationship between structural response and structural parameters. The method is applied to identify damage in existing riveted truss bridge. The effect of the damage rate and location on the identification speed and the accuracy of the solution is investigated and discussed.

1 INTRODUCTION

The increasing frequency of bridge and footbridge collapses highlights the critical importance of early detection of damage to ageing structures through structural health monitoring data. This plays a key role in maintaining the reliability of structures and ensuring the safety of people and property. Various monitoring and detection approaches have been proposed for practical early warning of structural damage (Gomez et. al. 2019, Avci et al. 2021). Among them, vibration-based methods, which use the vibration response of the monitored structure to evaluate its condition and identify damage, have gained wide popularity.

Damage means a change in the geometric or physical properties of the structure. A damaged structure exhibits a different mechanical response compared to an intact structure, with response parameters directly affected by changes in physical properties such as mass and, in particular, stiffness. Damage identification involves a mathematical process known as finite element (FE) model updating. This process modifies the original intact model to accurately match the damaged structure. Once a match is achieved, local adjustments to the model pinpoint the presence of damage.

Minimizing the residuals between the static and dynamic characteristics of the FE model and the characteristics of the damaged structure is an optimization problem that can be solved either directly or in conjunction with a sensitivity-based method (Jung & Kim 2013, Mordini et al. 2015, Zheng et al. 2015). In the methods presented in this paper, sensitivity analysis is used to normalize the effect of response parameters with different sensitivities on the extent and location of damage. This increases the convergence and refinement of the results. Another group of methods directly addresses the inverse relationship between the static and dynamic characteristics of the FE model and its response parameters. This relationship is often represented by a surrogate model such as an artificial neural network, Kriging, etc. (Lehký & Novák 2009, Yin et al. 2019).

In this paper, three methods are used to detect structural damage. The first method uses a metaheuristic optimization technique called aimed multilevel sampling (AMS) to efficiently

DOI: 10.1201/9781003483755-270

explore the design parameter space, achieving the best match between the deformed structure and its model. This method is enhanced by involving an artificial neural network (ANN) in finding the best realizations during the optimization process. In this paper, the method is referred to as ANN-aided AMS. The second method is a modification of the first method where, in order to reduce the computational complexity, ANN is used in only a limited number of iterations and in the remaining iterations the selection of the best sample is driven by the minimum value of the objective function. The last method treats model updating as an inverse problem and utilizes an ANN metamodel to approximate the inverse relationship between structural response and parameters. All methods are employed to identify damage in single-span riveted steel truss bridge. The study investigates the effect of damage rate and location on the identification speed and solution accuracy.

2 DAMAGE IDENTIFICATION

2.1 *FE model updating*

The method for identifying damage operates through a computational model of the structure. Consequently, the initial step in the identification process involves creating a precise Finite Element model and performing static and dynamic analyses of the considered structure. To meet the required accuracy for damage localization, the structural model is segmented into multiple regions, with stiffness parameters varied during the optimization process. A probability distribution is assigned to these stiffness parameters to establish an initial design space.

Following this, the stiffness parameters for each region are randomly generated in FReET reliability software (Novák et al. 2014) using the Latin Hypercube Sampling method (LHS), (Stein 1987). Subsequently, modal analysis is performed to ascertain eigenfrequencies and mode shapes. This generates random input data in the form of stiffness values for each region and output data consisting of static and dynamic response parameters for each simulation. These data are then utilized to identify the location and extent of damage within the structure. In this paper, the identification process is carried out using a metaheuristic optimization algorithm coupled with inverse analysis employing artificial neural networks.

2.2 *Aimed multilevel sampling optimization method*

The AMS optimization technique employed in this paper was chosen for its capacity to significantly reduce computational complexity (Lehký 2018). The fundamental concept involves breaking down the simulation process into multiple levels. At each level, advanced LHS sampling is conducted within a predefined design vector **d**. The sample with the most favorable properties, addressing the optimization problem definition, is subsequently chosen.

Following this, the design space for generating samples is narrowed down around this best sample $\mathbf{d}_{i,\text{best}}$. The next LHS simulation is executed *within* this reduced space. This process facilitates a more detailed exploration in the vicinity of the best-performing samples for the extreme value function. The reduction of the sample space is executed based on heuristic assumptions, constituting a pivotal aspect influencing the accuracy and performance of the AMS method.

There are two approaches to obtaining the best realization for the given design vector, $\mathbf{d}_{i,\text{best}}$. The basic approach is, that it can be derived as the optimal realization generated at the ith level for the structural vector **d**, corresponding to the minimum of the objective function $\phi(\mathbf{d})$, defined as:

$$\phi(\mathbf{d}) = \sum_{j=1}^{n} w_i \left[\frac{e_j - m_j(\mathbf{d})}{e_j} \right] \tag{1}$$

where, the term e_j represents the jth experimental static or dynamic property, serving as a structural response parameter to be aligned. Meanwhile, $m_j(\mathbf{d})$ represents the equivalent response parameter generated by the FE model. The parameters w_i are weight coefficients associated with the response parameters. Their role is to offset the influence of response parameters with lower sensitivity, which is crucial for accurately identifying the location and

extent of damage. These parameters ensure that even though some response parameters may have lower sensitivity, their contribution is considered in the identification process, preventing their neglect in the presence of more dominant response parameters.

An alternative approach is to view the problem as an inverse problem, where the inputs are the eigenfrequencies and mode shapes and the outputs are the stiffness values. However, for complex structures, this inverse relationship is impossible to find and the FE model must be replaced by a surrogate model, in our case the ANN. The neural network is trained using input–output pairs and then the best realization of the vector $\mathbf{d}_{i,\text{best}}$ is predicted. The basic idea of this method is to perform a large number of simulations using LHS on the initial design space, map the inverse space using a robust ANN, and then use it to predict the best realization. This method is hereinafter called "pure ANN".

The flagship of this paper is a method using ANN at each level of AMS. This method is called the ANN-aided AMS method. This method is the most complex of all the methods in this paper because it requires creating, training and simulating an ANN at each AMS level. Due to the time-consuming nature of the method, there is an alternative approach called here as the "hybrid method" that combines two approaches to estimate the best realization, namely using an ANN at every third level and using the minimum of the objective function at the other levels (Eq. 1).

3 REVITED TRUSS BRIDGE



Figure 1. Sideview of a riveted truss bridge in Trnovec nad Váhom (Slovakia).

The methods were applied to a steel railway bridge over the Váh River in Trnovec nad Váhom (Slovakia) (Figure 1). The steel bridge consists of 28 simply supported bridge objects, 14 on each of the two tracks. One of the tracks consists of truss bridges and the other is a combination of truss and box bridges. The total span of the bridge is 455.8 m. Objects are placed on concrete pillars (four on each pillar). This paper will focus on one of the truss bridges. The span of the selected bridge object is 31.3 m.

3.1 *Measurement of the dynamic response of the bridge*

A large part of the bridge passes through an inundation area, so access to individual objects was relatively easy. The dynamic response of individual bridge objects was measured using several measuring devices. The measurements were made during full operation without traffic restrictions. The displacements of the structure caused by passing trains were measured using the IBIS-S interferometric radar. From the time records of the displacements, it was also possible to determine the natural frequencies of the structure. In addition, appropriately spaced

accelerometers were used to accurately determine the eigenfrequencies and mode shapes. The measured data were used to verify the correctness of the FE model.

3.2 *FEM model*

A detailed FEM model of the bridge was created (Figure 2). Almost all structural elements (except for the lateral and transverse bracing) were created using shell elements. To better capture the response of the bridge when trains pass by, non-load-bearing parts, such as wooden sleepers and steel rails, were also modelled. The bridge was supported by a fixed bearing on one side and a sliding hinged bearing on the other side.

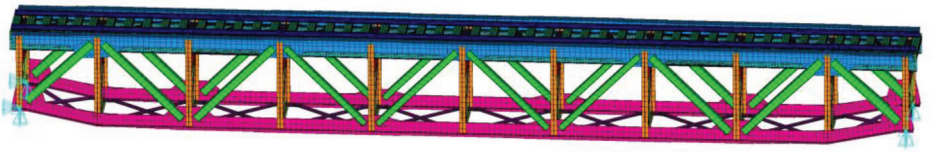


Figure 2. FEM model of the bridge.

The methods were applied to identify damage in three different cases – damage at one location, at three locations with the same and different levels of damage. The damage was modelled by reducing the Young's modulus of selected diagonal members. The original (undamaged) model was made of steel with a modulus of elasticity E = 210 GPa. A separate material model was created for each diagonal member, and the original modulus of elasticity E was multiplied by the coefficient k, which expressed how severe the damage to the member was. If the coefficient is equal to 1, the section was without damage (the coefficient less than 1 indicates damage). The coefficients k represent random variables for the FE model updating.

4 RESULTS

4.1 *Structure damaged in one location*

4.1.1 *Damage description*

The first analyzed case is the structure damaged in the fifth diagonal member, see Figure 3, where the damaged member is marked in red.

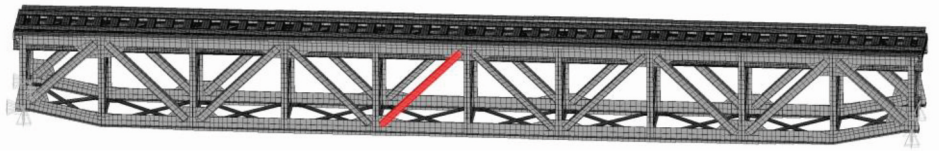


Figure 3. FEM model of the bridge with the damaged fifth diagonal member marked.

At the beginning of identification process, the initial design space was chosen in the range of 0.85-1.05 for all stiffnesses k. The total number of simulations was 1200, which for the AMS method was divided into 12 levels each of 100 simulations. The performance of each method is further compared in terms of error, which is calculated as:

$$Error = \sqrt{\sum_{i=1}^{n} \left(k_i^e - k_i^d\right)^2}, \tag{2}$$

where k_i^e is experimental stiffness of ith section, k_i^d is estimated stiffness of ith section, n is number of diagonals.

4.1.2 *ANN-aided AMS*

The first employed method is ANN-aided AMS method, where the best realization $\mathbf{d}_{i,\text{best}}$ at each AMS level is selected by an artificial neural network. The course of identification is shown in Figure 4, where on the left side is the evolution of the stiffness values during the optimization process and on the right side is the evolution of the error (Eq. 2).

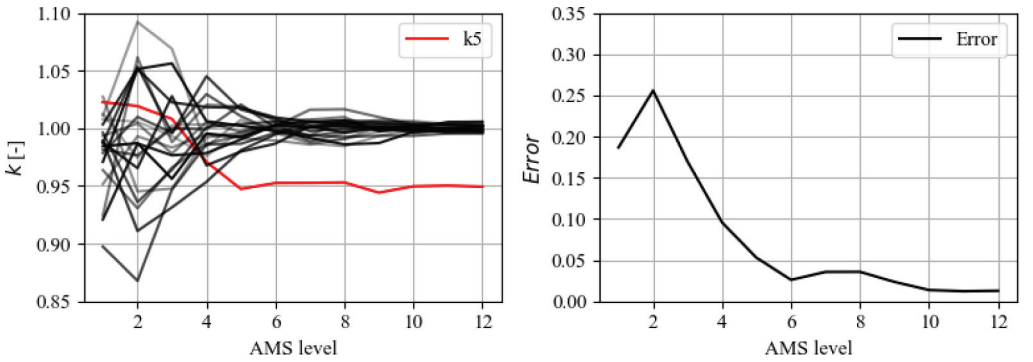


Figure 4. Case 1 optimization by the ANN-aided AMS: evolution of the stiffness values, with damaged segment k_5 in the red (left) and the evolution of the error (right).

4.1.3 *Hybrid method (ANN at every 3rd level)*

The second method is the hybrid method, which uses a combination of the objective function and artificial neural network. Compared to the first method, ANN is used only at every 3rd level, and the objective function is used at the other levels. The ANN helps to improve solution convergence while maintaining the speed of the classical AMS optimization method, see vertical changes in Figure 5.

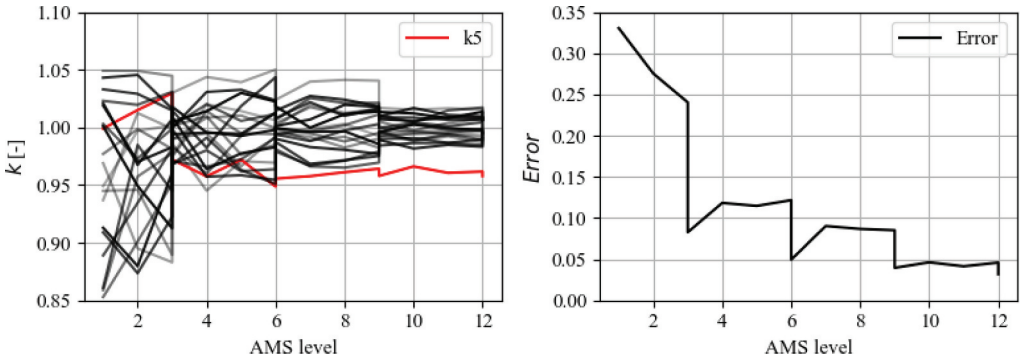


Figure 5. Case 1 optimization by the hybrid method: evolution of the stiffness values with damaged segment k_5 in the red (left), and the evolution of the error (right).

4.1.4 *Pure ANN*

The last method approaches optimization as an inverse analysis and uses ANN to replace the inverse relation. First, all 1200 simulations are calculated at once using the LHS method. The artificial neural network is then trained on all simulations and one prediction is provided. The method is not iterative and there is no sequential aiming. Figure 6 depicts the resulting stiffnesses of the diagonal members using a bar graph, with the damaged fifth member in red, and other undamaged members in shades of grey. The left side of the figure shows the best realization at the last AMS level (12th) provided by the ANN-aided AMS method, the middle is the

best realization at the last AMS level (12^{th}) calculated by the hybrid method, and the right-hand side is the damage prediction for the pure ANN. The results show that splitting the simulations into several levels using AMS brings better results than using ANN once for all available simulations.

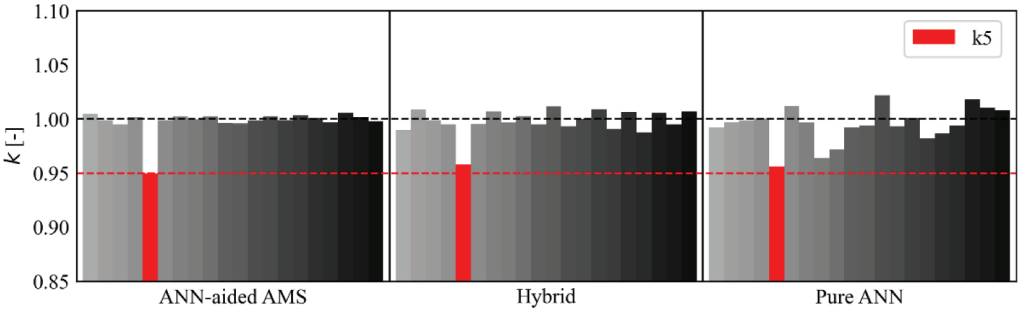


Figure 6. Comparison between ANN-aided AMS, Hybrid and Pure ANN methods.

A comparison of the errors for the first damage case for all methods is shown in Figure 7. The first column of the graph represents the ANN-aided AMS method, where the artificial neural network is used at each level, the error value is 0.0128. The second column represents the hybrid method, where ANN is used at every 3^{rd} level, the error value is 0.0319. The last column belongs to the pure ANN method, where only one ANN is used for all simulations, the error value is 0.0635.

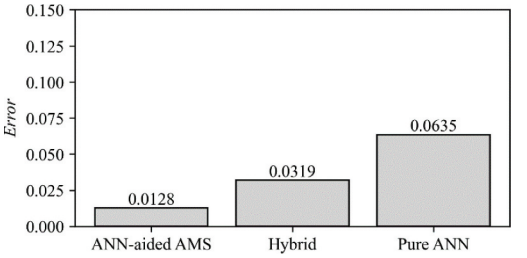


Figure 7. Comparison of the final optimization errors for the first damage case.

4.2 *Structure damaged in three locations with the same level of damage*

4.2.1 *Damage description*

The second case analyzed is the damage to the fifth, eighth and eighteenth diagonal members, as can be seen in Figure 8, where damaged members are marked in red. The damage magnitude is the same for all members and corresponds to a 5% reduction in stiffness.

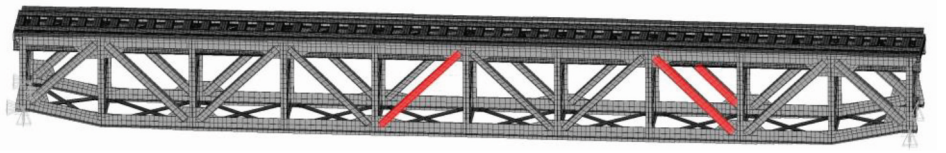


Figure 8. FEM model of the bridge with the damaged fifth, eighth and eighteenth diagonal member marked.

4.2.2 *ANN-aided AMS*

Given the best performance, only the ANN-aided AMS method was used, which uses an ANN to select the best realization at each AMS level. From the results depicted in Figure 9, it can be seen that all three damaged locations as well as the damage level were correctly identified.

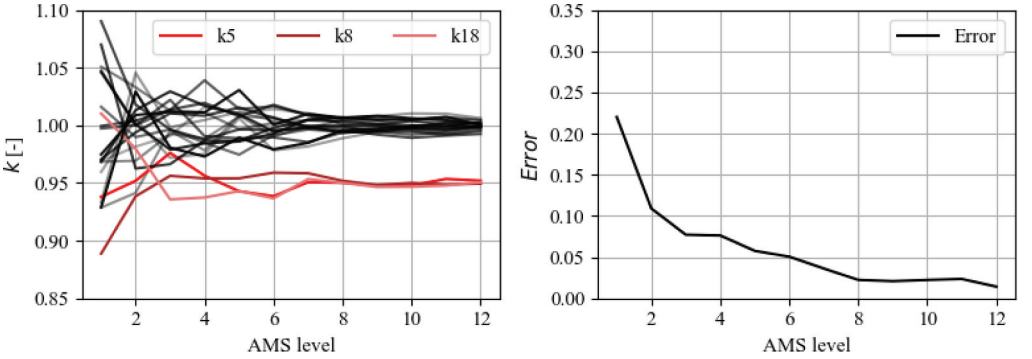


Figure 9. Case 2 optimization by the ANN-aided AMS: evolution of the stiffness values, with damaged segments in shades of red (left), and the evolution of the error (right).

4.3 *Structure damaged in three locations with different level of damage*

4.3.1 *Damage description*

The last case presented in this paper is a structure damaged in three different locations, each location having a different level of damage. The least damaged diagonal member is the eighth member (stiffness is reduced to 0.97), marked in light red, as shown in Figure 10. The most damaged member is the eighteenth member (stiffness is reduced to 0.93), the location is opposite to the eighth member, marked in dark red in the figure. In the fifth member, the stiffness is reduced still to 0.95, marked in red.

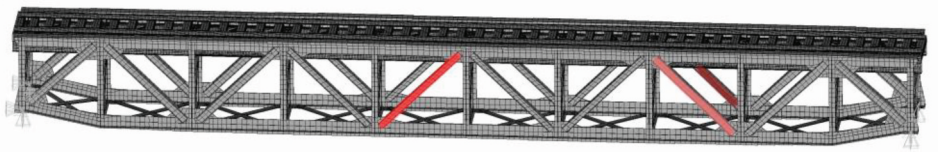


Figure 10. FEM model of the bridge with the damaged fifth, eighth and eighteenth diagonal member marked.

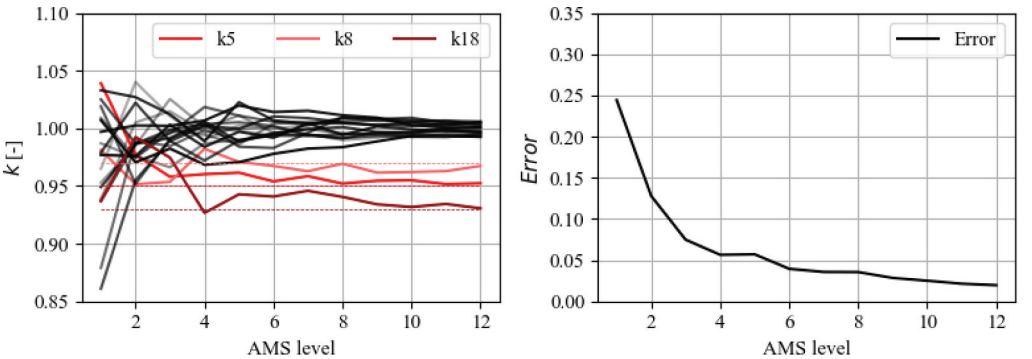


Figure 11. Case 3 optimization by the ANN-aided AMS: evolution of the stiffness values, with damaged segments in shades of red (left), and the evolution of the error (right).

4.3.2 *ANN-aided AMS*

As in the previous case, the ANN-aided AMS method was used. As can be seen in Figure 11, this method dealt with this problem really well. All damaged members were detected correctly, including an accurate estimation of the damage level.

5 CONCLUSION

The results of the analyzed damage cases show that the use of the AMS method in combination with an artificial neural network represents the most accurate approach to the task of damage identification. However, this method is the most time-consuming and computationally demanding of all the methods, since an ANN has to be created, trained, and simulated at each AMS level. An alternative is to use the classical AMS method, where the minimum of the objective function is used to select the best realization. This is a computationally relatively fast solution, but the disadvantages tend to be lower accuracy and slower convergence. A compromise between accuracy and time is the hybrid method, which combines the advantages of the classical AMS method and the use of ANNs at selected levels to improve convergence. When computational time is not an issue, the most efficient and accurate solution is the ANN-aided AMS method.

ACKNOWLEDGEMENT

The Czech authors thank for the financial support of the project No. 23-04712S awarded by the Czech Science Foundation, the project No. TM04000012, supported by the Technology Agency of the Czech Republic. The Slovak author thanks for the support of VEGA project No. 1/0230/22 provided by the Ministry of Education, Science, Research and Sport of the Slovak Republic.

REFERENCES

Avci, O., Abdeljaber, O., Kiranyaz, S., Hussein, M., Gabbouj, M., & Inman, D.J. (2021) A review of vibra-tion-based damage detection in civil structures: From traditional methods to Machine Learning and Deep Learning applications. Mech. Syst. Signal Process 147.https://doi.org/10.1016/j.ymssp.2020.107077

Gomes, G.F., Diaz Mendez, Y.A., da Silva Lopes Alexandrino, P., Simões da Cunha Jr., S., & Ancelotti Jr., A.C. (2019) A Review of Vibration Based Inverse Methods for Damage Detection and Identification in Mechanical Structures Using Optimization Algorithms and ANN. Archives of Computational Methods in Engineering 26, pp. 883–897. https://doi.org/10.1007/s11831-018-9273-4

Jung, D., & Kim, C. (2013) Finite element model updating on small-scale bridge model using the hybrid genetic algorithm. Structure and Infrastructure Engineering 9(5), pp. 481–495.https://doi.org/10.1080/15732479.2011.564635

Lehký, D., & Novák, D. (2009) Neural network based damage detection of dynamically loaded structures. Palmer-Brown; Draganova; Pimenidis; Mouratidis [eds.], Proceedings of the 11th Engineering Applications of Neural Networks (EANN 2009), London, UK, Communications in Computer and Information Science, vol 43. Springer: Berlin, Heidelberg, pp. 17–27. https://doi.org/10.1007/978-3-642-03969-0_2

Lehký, D., Slowik, O., & Novák, D. (2018). Reliability-based design: Artificial neural networks and double-loop reliability-based optimization approaches. Advances in Engineering Software, 117, 123–135. https://doi.org/10.1016/j.advengsoft.2017.06.013

Mordini, A., Savov, K., Wenzel, H. (2015) Damage detection on stay cables using an open source-based framework for finite element model updating. Structural Health Monitoring 7(2), pp. 91–102. https://doi.org/10.1177/1475921708089550

Novák, D., Vořechovský, M., & Teplý, B. (2014). FReET: Software for the statistical and reliability analysis of engineering problems and FreET-D: Degradation module. Advances in Engineering Software (Barking, London, England: 1992), 72, 179–192. https://doi.org/10.1016/j.advengsoft.2013.06.011

Stein, M. (1987). Large sample properties of simulations using Latin hypercube sampling. Technometrics: A Journal of Statistics for the Physical, Chemical, and Engineering Sciences, 29(2), 143–151. https://doi.org/10.2307/1269769

Yin, H., Ma, J.J., Dong, K., Peng, Z., Cui, P., & Yang, C. (2019) Model updating method based on Kriging model for structural dynamics. Shock and Vibration 2019. https://doi.org/10.1155/2019/8086024

Zheng, Z.D.; Lu, Z.R.; Chen, W.H.; Liu, J.K. (2015) Structural damage identification based on power spectral density sensitivity analysis of dynamic responses. Computers & Structures 146, pp. 176–184. https://doi.org/10.1016/j.compstruc.2014.10.011

Bridge Maintenance, Safety, Management, Digitalization and Sustainability – Jensen, Frangopol & Schmidt (eds)
© 2024 The Author(s), ISBN 978-1-032-77040-6
Open Access: www.taylorfrancis.com, CC BY-NC-ND 4.0 license

Evaluation of Low-cost Adaptable Reliable Accelerometer (LARA) technology

E. Delgado & V. Torralba
Tunnel and Bridge Technologies S.L

S. Komarizadehasl, G. Ramos & Jose Turmo
Department of Civil and Environment Engineering, Universitat Politècnica de Catalunya, BarcelonaTech

J.A. Lozano-Galant
Department of Civil Engineering, Universidad de Castilla-La Mancha

ABSTRACT: Structural health monitoring (SHM) applications are gaining increasing attention because they enable the early detection and characterization of damage during a prevention phase. Furthermore, SHM can also provide useful information associated with the condition and performance of a structure over time. SHM applications require a network of sensors to measure various structural parameters. However, the high cost of the required sensors is considered to be a limitation for their implementation in structures with limited monitoring budget. This paper presents an alternative low-cost solution to decrease the high cost of instrumentation. LARA (Low-Cost Adaptable Reliable Accelerometer) is a novel low-cost triaxial accelerometer based on Arduino and Raspberry Pi technologies. This system has a sampling frequency of 333 Hz and a noise density of 51μg/√Hz. This work presents an experimental campaign for the Operational Modal Analysis (OMA) of a footbridge using two types of sensors: a low-cost prototype LARA and a commercial one (HI-INC), in order to evaluate the reliability of the data acquired by LARA and to validate it as a low-cost accelerometer for SHM purposes.

1 INTRODUCTION

Since civil infrastructure and structures could be considered as the basis of contemporary civilization, it is crucial to prioritize the health of these systems (J. Lei et al., 2018). Evaluating structures along with their health-state assessment reduces repair and maintenance costs by detecting damage at the prevention stage and, eventually, for certifying infrastructure/structure safety (Peng et al., 2021b).

Structural health monitoring (SHM) applications provide statistics on the operating states of structures and their structural responses (Peng et al., 2021a) (X. Lei et al., 2022). To measure structural responses over time such as bending, deformation, rotation, temperature, humidity and accelerations, sensors are widely used in SHM systems (Komarizadehasl, Komary, et al., 2022). The information recorded by the sensors is used to estimate structural performance (Komarizadehasl, Lozano, et al., 2022). In fact, natural phenomena can be classified as static or quasi-static and dynamic (Atencio et al., 2022). On the one hand, some environmental parameters (such as temperature or humidity) change very slowly, so they can be considered to act in a quasi-static or static manner (Farré-Checa et al., 2022). On the other hand, some events (such as vibrations induced by traffic, environmental activities and waves from seismic events) are considered dynamic because their rate of change is significantly affected by time (Mobaraki et al., 2022).

DOI: 10.1201/9781003483755-271

According to the literature (see, e.g., (Komary et al., 2023)), the significant natural frequencies of most civil structures range from 0.2 to 100.0 Hz. It should also be noted that most of the environmental vibrations in civil structures are characterized by low amplitudes (Tran-Ngoc et al., 2018). The acceleration amplitude of these structures can be as low as 0.04 g. This characteristic shows the need to use accelerometers with low noise density and high sensitivity for SHM of bridges (Tran-Ngoc et al., 2018). Commercial MEMS accelerometers have a bandwidth of a few kHz. However, their design for higher frequencies has a lower noise density (Lee & Eun, 2022). It should be noted that the sensitivity of an accelerometer is indirectly proportional to the squared value of the resonance frequency. Therefore, the higher the sampling frequency of the accelerometer, the lower its sensitivity (Farrar et al., 2006). Because of this, many researchers have attempted to develop low-cost MEMS accelerometers with limited sampling frequency and vibration amplitude range for civil SHM (Shi et al., 2021).

The literature review shows a lack of works that include all the following points in a single approach for a low-cost accelerometer: (1) access to time information via the Internet for accurate sensor synchronization, (2) wireless control, (3) development of a synchronized data acquisition test, (4) measurement of ND and data resolution once the system is wired and, finally (5) performing experimental analysis of eigenfrequencies in real infrastructures.

Recently a Cost Hyper Efficient Arduino Product (CHEAP) was introduced by Komarizadehasl et al. (Komarizadehasl et al., 2021). Different laboratory tests were developed to validate CHEAP performance, and the results were compared with those of two commercial seismic accelerometers (PCB 393A03 and PCB 356B18).

The objective of this paper is to adapt CHEAP for solving all the detected problems and to develop a new reliable low-cost adaptive accelerometer (LARA). For this purpose, a laboratory test campaign was designed to validate the performance of LARA against its previous version. During the tests, frequencies between 0.1 Hz to 32 Hz and acceleration amplitudes in the range of [0.001- 9.806 m/s2] were tested. Further, another field test was developed on a short span footbridge in Barcelona. In this experiment, the eigenfrequencies measured by LARA were compared with those detected by a commercial dynamic sensor (HI-INC) (Komarizadehasl, Lozano, et al., 2022).

2 LOW-COST ADAPTABLE RELIABLE ACCELEROMETER (LARA) WITH POST-SYNCHRONIZATION CAPABILITY

Recently a Cost Hyper Efficient Arduino Product (CHEAP) was introduced by Komarizadehasl et al. (Komarizadehasl et al., 2021). LARA is an evolved version of CHEAP, it has a sampling frequency of 333 Hz, an acceleration range of ±2.0 g and an effective bandwidth of 165 Hz. LARA consists of two parts: (1) a sensing part: it contains the aligned accelerometers and the multiplexer, and (2) an acquisition part: composed of an Arduino and a Raspberry Pi (see Figure 1). LARA consists of five low-cost MEMS accelerometers aligned due to the fact that when averaging the results of a few accelerometers with unique inherent dynamic noises, the studied signal remains unchanged.

The advantages of LARA over CHEAP are the following: (1) higher bandwidth: it achieves a faster sampling rate (333 Hz) by efficiently rewriting all codes in the library, (2) independence: it does not need to be connected to a computer for data acquisition. LARA has a low-cost microprocessor that allows the acquired data to be saved on an SD card, a flash drive or portable hard disk, (3) triaxial data acquisition: having all LARA accelerometers aligned in the x, y, and z directions makes possible a triaxial data acquisition, and if it is necessary, it can operate as a uniaxial, biaxial accelerometer, (4) low Noise Density (ND), (5) time stamping and synchronization via the Internet: the Network Time Protocol (NTP) of LARA is activated, (6) experimental analysis: in this research, a short span was instrumented, and LARA eigenvalue analyses were compared with those of certified vibration detection devices, and (7) wireless accessibility: the user can access the stored data through the Internet. In this way, LARA can be controlled, updated via online commands and data can be recorded.

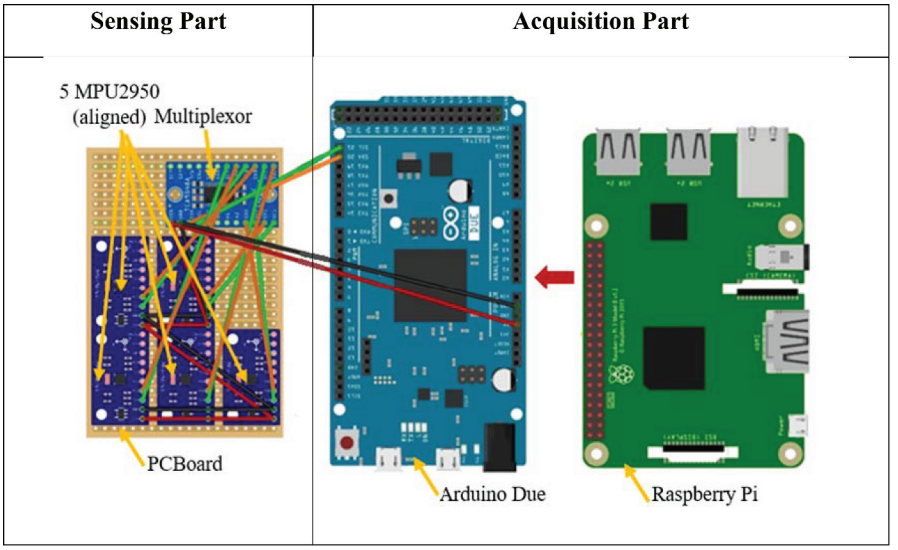


Figure 1. The sensing and acquisition part of LARA.

3 LABORATORY TESTS AND RESULTS

3.1 *Sensitivity, Noise Density (ND), and resolution evaluation*

This section compares the sensitivity, ND, and resolution results of a single accelerometer MPU9250 with CHEAP and LARA.

The sensitivity of accelerometers can be calculated as the ratio of the input (vibrations induced by the vibrating table) to the output (the information communicated by the accelerometer). This concept is measured differently for MEMS and analog sensors. While analog sensors report the sensitivity as V/g (voltage per gravitational acceleration), MEMS accelerometers report it as the Least Significant Bit per gravitational (LSB/g). The Analog to Digital Converter (ADC) formula for calculating the LSB is shown in equation (1) (Elhattab et al., 2019).

$$LSB = \frac{Input\ voltage}{2^{(number\ of\ bits)}} \tag{1}$$

Considering that MPU9250 accelerometers work with an input voltage of 2.5 volts and an ADC scale of 16 bits in equation (1), each LSB unit is equivalent to 0.03814 mV. Since datasheet of MPU9250 reports a sensitivity of 16 384 LSB/g for a range of ±2.0 g, the comparable sensitivity of MPU9250, CHEAP and LARA is calculated to be 625 mV/g.

A long-term test was performed to determine the ND and resolution of the devices. The ND values of the different accelerometers were calculated by applying equation (2) (Kwong, 2017).

$$ND = \sqrt{\frac{\sum_1^N (x_i - \mu)^2}{N * f}} \tag{2}$$

In Equation (2), the xi is the values read by the accelerometers in the time domain, μ is the average of all xi values, f is the sampling frequency of the accelerometer, and N is the number of used samples.

As a result, the calculated ND of MPU9250, CHEAP, and LARA for the z-directions were 390, 162, and 81 μg/√Hz, respectively. Additionally, the ND of LARA for both x and y directions was 51 μg/√Hz.

For a fair comparison between devices with different sampling frequencies, the same number of samples acquired was used in the test since the evaluation of the accelerometer resolution depends on the number of samples tested (*Data Acquisition Handbook*, n.d.). To illustrate the resolution of the accelerometers, the data was transformed from the time domain to the frequency domain by a Fast Fourier Transform (FFT).

Analyzing the frequency domain plots of the acquired LARA data for all axes, results show that the resolution of LARA for the x and y axes is 0.00005 m/s2. The resolution for the x and y directions is 44% better than for z-axis due to the absence of gravitational acceleration of the earth in those directions. As a result, the resolution of this accelerometer is evaluated to be 0.00005 m/s2.

After measuring the sensitivity, ND and resolution of LARA, it can be compared with other MEMS accelerometers. Several commercial applications of triaxial MEMS are presented in Table 1. The information shown in the table comes from data sheets provided by the manufacturers and from the measurements developed in this paper. The information is organized as follows: (1) number, (2) sensor's name, (3) sensitivity, (4) noise density, (5) acceleration range, (6) sampling frequency, (7) sensor cost (cost is based on data from 2021) (Komarizadehasl, Lozano, et al., 2022).

Table 1. Comparison of commercial triaxial MEMS accelerometers.

Nº	Name	Sensitivity (V/G)	Noise Density (μG/√ Hz)	Acceleration Range (G)	Sampling Frequency (Hz)	Cost (€)
1	IAC-Hires	2000	8	±2.0	800	1192
2	3713F112G	0.675	10	±2.0	500	2130
3	Unquake	0.400	25	±2.0	500	2500
4	Recovib Tiny	0.600	30	±2.0	500	1125
5	LARA	0.625	51	±2.0	333	140

Analyzing Table 1, indicates that LARA has a noise density very similar to commercial accelerometers and shows a wide range of prices of accelerometers solutions. Moreover, 3713F112G and IAC-Hires need extra data acquisition equipment for acquiring the vibrations which increases the cost. In the case of Unquake, Recovib Tiny, and LARA do not need any acquisition system for their data acquisition (Komarizadehasl, Lozano, et al., 2022).

3.2 *Frequency validation*

This section presents an experiment to validate the LARA frequency report. The vibration platform (INSTRON 8803) was programmed using Wave- Ma-trix2 Dynamic software. The jack can create several types of waveform with the frequency range from 0.1 to 100 Hz and its resonant frequency is 134 Hz. The direction of the vibration platform was in the z-direction.

To validate the accuracy of the accelerometers, 11 tests were performed with different frequency ranges (from 0.1 Hz to 32 Hz). To find the frequency report of the accelerometers, the raw data in the time domain of the accelerometers were transformed to the frequency domain using an FFT program written in MATLAB software.

The frequency error of the accelerometer was estimated by calculating the percentage error of the plot value compared to the reference value of the excitation device. Table 2 shows the comparison of the frequency errors of LARA, CHEAP and MPU9250 with the jack reference values.

Table 2 shows that a single MPU9250 reports the same frequency error as CHEAP from 2 Hz on. It also indicates that a single MPU9250 does not have enough resolution for

frequencies below 2 Hz. About CHEAP, it cannot display signals with a frequency lower than 0.4 Hz while LARA has a wider frequency range than MPU9250 and CHEAP and can detect signals down to 0.1 Hz with 0.5% error. In fact, LARA's frequency range is between 0.1 Hz and its bandwidth (165 Hz).

Table 2. Frequency validation of the accelerometers.

	PERCENTAGE OF ERROR PER SENSOR		
Frequency (Hz)	LARA	CHEAP	MPU9250
0.1	0.450 %		
0.2	0.295 %		
0.3	0.260 %		
0.4	0.050 %	0.470 %	
0.5	0.006 %	0.011 %	
2	0.005 %	0.025 %	0.025 %
4	0.000 %	0.000 %	0.000 %
8	0.003 %	0.003 %	0.003 %
10	0.004 %	0.004 %	0.004 %
16	0.001 %	0.001 %	0.001 %
32	0.003 %	0.003 %	0.003 %

4 REAL STRUCTURE TEST AND RESULTS

This section presents a field test performed on a short span footbridge to compare the measured eigenfrequencies of LARA with those of a high accuracy sensor (HI-INC). The footbridge under study is connected to an elevator box and, on the other side, is located on an abutment (see Figure 2). The commercial dynamic sensor (HI-INC) and LARA were mounted in the middle of the bridge span.

HI-INC is a dynamic inclinometer with a sampling frequency of 250 Hz, this sampling frequency is enough to acquire the main modal shapes of the footbridge. It should be noted that the reported noise density in its data sheet is 0.0004 deg/√Hz. This MEMS inclinometer was only used for comparing the eigenfrequency analysis of LARA.



Figure 2. A picture of the footbridge.

The process of installing the devices on the bridge consisted of manually connecting the sensors to the other monitoring components (power bank, 4G USB dongle, Arduino and Raspberry Pi). A Rasp- berry Pi was previously configured with a WiFi hotspot to enable the

communication of LARA over the Internet. In fact, after its on-site assembly, the Raspberry Pi was used to start the data acquisition process remotely via the Virtual Network Computing (VNC) software (Atencio et al., 2022).

Once the installation process was completed, LARA started working by following the next steps: first the acquired data were collected on the Raspberry Pi memory card and then the obtained data were transferred to a computer using VNC software.

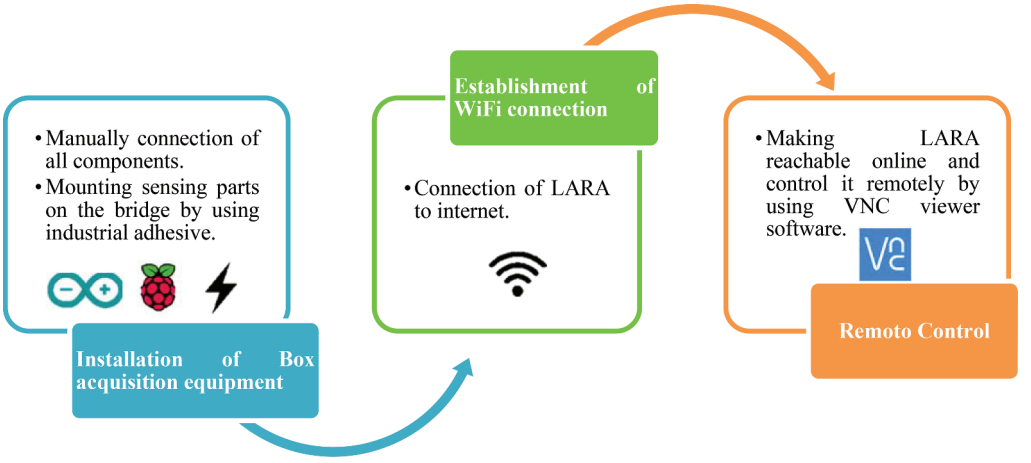


Figure 3. Mounting process of the sensors on the footbridge: LARA operation diagram.

The outputs of the eigenfrequency analysis of LARA are shown in Figure 4a–b for x and y axis, respectively.

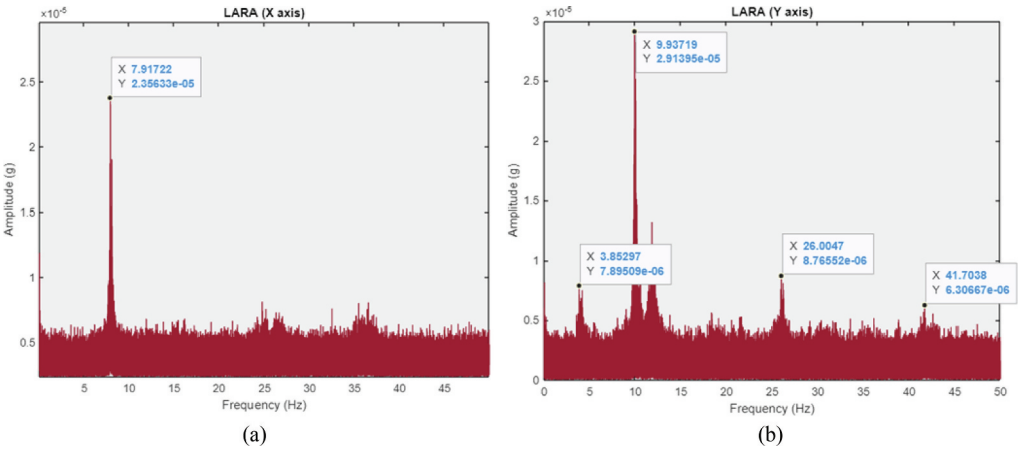


Figure 4. Eigenfrequency analysis of a footbridge using LARA for (a) longitudinal and (b) transversal directions of the footbridge.

As can be seen in the footbridge eigenfrequency diagrams, the structure does not show much excitation around its x-axis (longitudinal direction), while it shows a higher excitation around the other axis (y).

Table 3 presents the comparison of the results of the eigenfrequency analysis of LARA and the high accuracy dynamic inclinometer used (HI-INC).

Table 3. Comparison of the eigenfrequencies obtained between LARA and HI-INC.

	FREQUENCIES PER SENSOR		
Mode Shape	HI-INC	LARA	Difference (%)
1	3.90 Hz	3.85 Hz	1.28
2	7.91 Hz	7.91 Hz	0.20
3	9.94 Hz	9.93 Hz	0.88
4	26.25 Hz	26.01 Hz	0.91
5	42.81 Hz	41.70 Hz	0.27

Comparison of the measured eigenfrequencies of LARA with those of HI-INC shows a maximum error of 1.28%.

5 CONCLUSION

The development of low-cost sensors is essential for structural health monitoring (SHM) of structures with a low budget since these sensors can allow engineers to leave the equipment on the structure for monitoring. In previous work, a cost hyper-efficient Arduino product (CHEAP) was introduced, and its performance was validated in laboratory experiments. Improving both the hardware and software of CHEAP, a new Low Cost Triaxial Adaptive Reliable Adaptive Accelerometer (LARA) is introduced. The main advantages over its previous version are as follows:

(1) LARA achieved a faster sampling rate by rewriting the codes.
(2) LARA is independent of any connected computer for data sampling by using a Raspberry Pi connected to the Internet,
(3) LARA is a triaxial accelerometer.
(4) A reduced Noise Density.
(5) Having Internet time available is available for future data synchronization.
(6) LARA is a wireless accelerometer.

To evaluate the performance, resolution and ND of LARA, a set of laboratory experiments was performed. The results obtained show that LARA has lower ND ratio than MPU9250 and CHEAP for the same number of acquired data. In addition, comparison of MPU9250, CHEAP and LARA with shake table reports shows that LARA is more accurate in reporting frequency than MPU9250 and CHEAP in a laboratory experiment with the same time duration.

A field test has been performed over a 14m length footbridge located in Barcelona by using the LARA accelerometer. The frequencies obtained from the LARA eigenfrequency analysis have been validated by comparing its results with those obtained with a high-precision commercial sensor (HI-INC).

REFERENCES

Atencio, E., Komarizadehasl, S., Lozano-Galant, J. A., & Aguilera, M. (2022). Using RPA for Performance Monitoring of Dynamic SHM Applications. *Buildings 2022*, *12*(8), 1140. https://doi.org/10.3390/BUILDINGS12081140

Data Acquisition Handbook. (n.d.). Retrieved December 3, 2023, from https://www.mccdaq.com/support/Data-Acquisition-Handbook

Elhattab, A., Uddin, N., & OBrien, E. (2019). Extraction of Bridge Fundamental Frequencies Utilizing a Smartphone MEMS Accelerometer. *Sensors*, *19*(14), 3143. https://doi.org/10.3390/s19143143

Farrar, C. R., Park, G., Allen, D. W., & Todd, M. D. (2006). Sensor network paradigms for structural health monitoring. *Structural Control and Health Monitoring*, *13*(1), 210–225. https://doi.org/10.1002/STC.125

Farré-Checa, J., Komarizadehasl, S., Ma, H., Lozano-Galant, J. A., & Turmo, J. (2022). Direct simulation of the tensioning process of cable-stayed bridge cantilever construction. *Automation in Construction*, *137*, 104197. https://doi.org/10.1016/J.AUTCON.2022.104197

Komarizadehasl, S., Komary, M., Alahmad, A., Lozano-Galant, J. A., Ramos, G., & Turmo, J. (2022). A Novel Wireless Low-Cost Inclinometer Made from Combining the Measurements of Multiple MEMS Gyroscopes and Accelerometers. *Sensors 2022*, *22*(15), 5605. https://doi.org/10.3390/S22155605

Komarizadehasl, S., Lozano, F., Lozano-Galant, J. A., Ramos, G., & Turmo, J. (2022). Low-Cost Wireless Structural Health Monitoring of Bridges. *Sensors 2022*, *22*(15), 5725. https://doi.org/10.3390/S22155725

Komarizadehasl, S., Mobaraki, B., Ma, H., Lozano-Galant, J.-A., & Turmo, J. (2021). Development of a Low-Cost System for the Accurate Measurement of Structural Vibrations. *Sensors 2021*, *21*(18), 6191–6213. https://doi.org/10.3390/S21186191

Komary, M., Komarizadehasl, S., Tošić, N., Segura Pérez, I. S., Lozano-Galant, J. A., & Turmo, J. (2023). Low-Cost Technologies Used in Corrosion Monitoring. *Sensors 202*, *23*, 1309. https://doi.org/10.3390/S23031309

Kwong, K. (2017). *MEMS Accelerometer Specifications and Their Impact in Inertial Applications* (95th ed.). http://www.eecg.utoronto.ca/~johns/nobots/theses/pdf/2017_keiming_kwong_masc.pdf

Lei, J., Xu, D., & Turmo, J. (2018). Static structural system identification for beam-like structures using compatibility conditions. *Structural Control and Health Monitoring*, *25*(1), 1–15. https://doi.org/10.1002/STC.2062/ABSTRACT

Lei, X., Xia, Y., Komarizadehasl, S., & Sun, L. (2022). Condition level deteriorations modeling of RC beam bridges with U-Net convolutional neutral networks. *Structures*, *42*, 333–342. https://doi.org/10.1016/J.ISTRUC.2022.06.013

Mobaraki, B., Komarizadehasl, S., Javier, F., Pascual, C., Lozano-Galant, A., & Soriano, R. P. (2022). A Novel Data Acquisition System for Obtaining Thermal Parameters of Building Envelopes. *Buildings 2022*, *12*(5), 670. https://doi.org/10.3390/BUILDINGS12050670

Peng, T., Nogal, M., Casas, J. R., & Turmo, J. (2021a). Planning low-error SHM strategy by constrained observability method. *Automation in Construction*, *127*, 103707. https://doi.org/10.1016/j.autcon.2021.103707

Peng, T., Nogal, M., Casas, J. R., & Turmo, J. (2021b). Role of sensors in error propagation with the dynamic constrained observability method. *Sensors 2021*, *21*(9), 2918. https://doi.org/10.3390/s21092918

Shi, Y., Zhang, J., Jiao, J., Zhao, R., & Cao, H. (2021). Calibration Analysis of High-G MEMS Accelerometer Sensor Based on Wavelet and Wavelet Packet Denoising. *Sensors 2021*, *21*(4), 1231. https://doi.org/10.3390/S21041231

Tran-Ngoc, H., Khatir, S., Roeck, G., Bui-Tien, T., Nguyen-Ngoc, L., & Abdel Wahab, M. (2018). Model Updating for Nam O Bridge Using Particle Swarm Optimization Algorithm and Genetic Algorithm. *Sensors 2018*, *18*(12), 4131. https://doi.org/10.3390/S18124131

Bridge Maintenance, Safety, Management, Digitalization and Sustainability – Jensen, Frangopol & Schmidt (eds)
© 2024 The Author(s), ISBN 978-1-032-77040-6
Open Access: www.taylorfrancis.com, CC BY-NC-ND 4.0 license

Performance comparison between several SHM solutions: A viaduct of the Italian highway

M. Ciano, M. Malavisi & D. Buggiani
Movyon S.p.A., Engineering Division, Rome, Italy

L. Grottoli, D. Bolognini & F. Dacarro
European Centre for Training and Research in Earthquake Engineering (EUCENTRE), Pavia, Italy

ABSTRACT: The need of a continuous re-qualification of infrastructures, faced with an increasing demand for mobility, requires the definition of reliable methods, from technical and economical points of view, to evaluate the current conditions of an asset and predict its future state when affected by damages. Advanced SHM solutions could be usefully implemented to gather relevant information about the behavior of bridges and tunnels, through industrial technological systems that must be reliable, cost effective and have suitable performances to assess structural conditions. However, several monitoring solutions are available today, with very different characteristics, performance and costs, so it is difficult both to evaluate how these systems, often tested only in laboratory, perform under operating conditions and to find the right tradeoff between technical and economic needs. The case study of an Italian highway viaduct is presented in this work with the aim to compare different SHM solutions.

1 INTRODUCTION

1.1 *Context*

Economic growth requires adequate infrastructure to meet its full potential. Infrastructure managers need to adopt sustainable methodologies that address both technical and economic aspects, especially in response to the increasing demand for mobility. The primary objective is to assess the present condition of an infrastructure and predict future state and potential damage. In this regard, the deployment of advanced Structural Health Monitoring (SHM) solutions proves beneficial for obtaining pertinent information about the performance of bridges and tunnels. These solutions rely on advanced technological systems that must meet strategic criteria, such as reliability, accuracy, cost-effectiveness, and performance suitability for assessing structural conditions.

The continuous evolution of technology facilitates the widespread integration of Internet of Things (IoT) systems, aligning seamlessly with the requirements of an effective SHM solution. Rather than investing in costly new projects, governments and private-sector infrastructure players may address some infrastructure needs by getting more out of existing capacity through: i) boosting asset utilization: intelligent transportation systems can foster the use of an asset, typically at a fraction of the cost of adding the equivalent in physical capacity; ii) optimizing maintenance planning, for instance through a Total Cost of Ownership (TCO) approach (Ellram, 1993), which considers costs over the complete life of an asset and finds the optimal balance between long-term renewal and short-term maintenance.

Properly, a TCO approach can be implemented with an efficient SHM application by calibrating the cost-benefit balance (Keller & Poblete, 2011).

DOI: 10.1201/9781003483755-272

1.2 *Manufact*

To compare the performances of different SHM solutions, a Proof of Concept (PoC) has been implemented on a real viaduct. The PoC started in August 2023 with a focus on technological solution comparison rather than long term structural monitoring. The structure consists of two independent lanes; the static scheme can be summarized in 7 simply supported reinforced concrete 32m-long spans. The deck consists of 5 parallel equally spaced beams and 4 transverse beams (Figure 1).

The reasons why it was decided to monitor the previously described structure are various. First, the structure dates to 1968 and is representative of Italian construction, as 70% of the structures in the network were built between 1960 and 1980. Moreover, also the static scheme of the beams (simply supported elements) and the construction technique (precast reinforced concrete) are representative of the Italian stock. In addition, the typology of the beams deck, in terms of number of beams and span length, is very common in the network. The fact that the structure is easily accessible without any limitations for its operativity is very helpful.

The structure has also undergone a preliminary structural vulnerability assessment. In a future work, it will then be possible to correlate monitoring measurements with the output of the numerical analysis.



Figure 1. View of the viaduct.

1.3 *Requirements*

The choice on the instrumentations to involve in the case study was motivated by the need to consider, at the state of the art, the most common type of sensors used to monitor bridges, viaducts and infrastructures, following a series of requirements briefly analyzed below.

The system must be able both to be broken down into smaller, independent components, or modules, that can be easily replaced or modified without affecting the operativity of the entire system and to handle an increasing number of signals or workload.

Both dynamic and static acquisition protocols are often used in SHM solution to provide a complete and reliable assessment of the performance of a structural system. Dynamic acquisition protocols involve measurements of the structural response connected to environmental vibrations and strong motion events (e.g. earthquakes), the static ones address long-term monitoring of the manufact under ordinary loads and evaluate the changes in deflection and deformation. For these reasons, it is desirable that the system is suitable for various measurement techniques and signals (e.g. voltage, current, digital, etc.) and it is able to detect faults or failures on sensors, data acquisition and processing components minimizing downtime, false alarms, outliers or missed detections of important events.

A suitable choice is to adopt an acquisition sampling ≥1kHz/sec/channels in simultaneous fashion to post-processing data in terms of amplitude and frequency as well as phase correlation for advanced operational modal analysis; in parallel, a resolution ≥18bit and a signal to noise ratio (SNR) ≥120dB are fully in line with the state of the art of the most common acquisition system available on the market and is suitable for ensuring accuracy and adequate precision to the output.

The buffering and local storage capacity are very important features, which are helpful in case the system turns offline and to accommodate the amount of data collected during an assigned monitoring period. In any case, the optimization of the data storage is usually managed also by triggering strategies, which initiate data gathering in case of occurrence of specific events. A good rule is to provide different strategies (e.g. time-based, event-based, threshold-based) as long as the system is not overcomplicated.

2 DESCRIPTION OF THE STRUCTURAL MONITORING SYSTEM

The layout of the structural monitoring system was designed with the purpose of tracking the structural response in static and dynamic conditions over time and to be compliant with the output of the numerical model implemented.

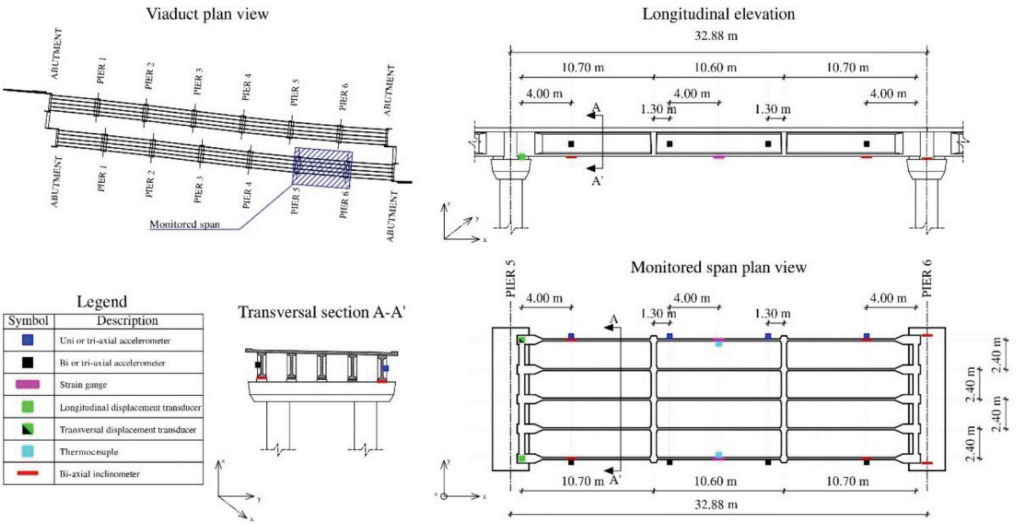


Figure 2. Sensor's installation layout.

The following types of sensors were included: accelerometers, inclinometers, displacement transducers, strain-gauges and thermocouples (Figure 2).

Integrated systems provided by four different suppliers were compared. The suppliers will hereafter be referred to as supplier A, B, C and D. Slightly different layouts were adopted for the installation of the sensors, whose specifications are listed in Table 1-Table 5.

Table 1. Accelerometers specifications.

	Supplier A	Supplier B	Supplier C	Supplier D
Quantity	12	8	12	8
Axis	1	3	1	1
Type	MEMS	MEMS	Piezoelectric	MEMS
Range	±2 g	±2 g	±5 g	±2 g
Sensitivity	4 V/g	-	1 V/g	4 V/g
Noise	7 μg/√Hz	25 μg/√Hz	2 μg/√Hz	7 μg/√Hz

Table 2. Inclinometers specifications.

	Supplier A	Supplier B	Supplier C	Supplier D
Quantity	6	6	6	4
Axis	2	2	2	2
Type	Analog	Analog	Analog	Analog
Range	±10°	±10°	±2°	±10°
Resolution	0.01°	0.01°	0.002°	0.01°
Accuracy	±0.15°	0.25°	-	±0.15°

Table 3. Strain gauges specifications.

	Supplier A	Supplier B	Supplier C	Supplier D
Quantity	2	2	2	2
Range	±300 με	±1500 με	-	±300 με

Table 4. Displacement transducers specifications.

	Supplier A	Supplier B	Supplier C	Supplier D
Quantity	2	2	2	2
Range	0-100 mm	0-50 mm	0-200 mm	0-150 mm
Non-linearity	0.15% F.S.	0.1% F.S.	0.05% F.S.	0.15% F.S.

Table 5. Thermocouples specifications.

	Supplier A	Supplier B	Supplier C	Supplier D
Quantity	2	2	2	2
Range	±100 °C	-40/+80 °C	-	±100 °C

The sampling rate for dynamic sensors was imposed at 200 Hz for all suppliers except Supplier B, which has adopted a sampling of 100 Hz. The sampling rate of static sensors was set to 10 Hz for suppliers A and D, 1 Hz for supplier C and 1 sample every 5 minutes for supplier B. The system architecture adopted for all the suppliers is depicted in Figure 3.

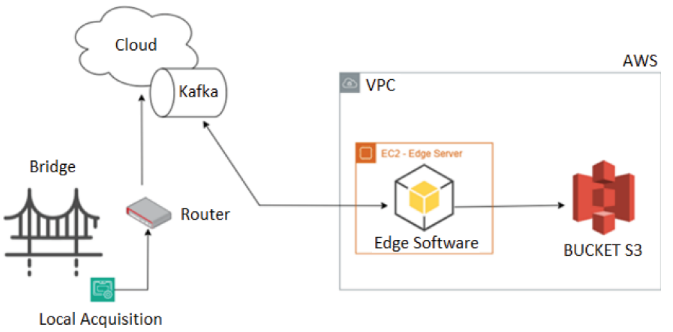


Figure 3. IoT system architecture.

The IoT system architecture idealization consists of:

- a local acquisition system for data sensors digitalization;
- a router for data transmission by mobile network;
- Kafka, message broker for robust management and to send the data flow;

- AWS, Virtual Private Cloud (VPC) composed by virtual machine (EC2-Edge Server) with an Edge Software ecosystem and Bucket S3 in order to manage data with object storage technology.

This IoT architecture is able to archive in cloud infrastructure data with a scalable potential.

3 STATIC MONITORING DATA ASSESSMENT AND COMPARISON

The static sensors of the monitoring installation include four inclinometers positioned on the external beams of the selected span, two sensors on each side (three suppliers installed two additional sensors on one of the piers), see Figure 2. Excluding a few tilt sensors, which exhibited electrical related malfunctions, the signals of the remaining inclinometers emphasize high amplitude peaks connected with traffic induced vibrations (Figure 4). This effect results more relevant on signals with a sampling rate of 10 Hz but it can be easily mitigated through a moving average to be adopted only in case the information on the dynamic content of the signal is not of interest.

Each supplier installed two strain gauges on the opposite sides of the external beams at the midspan. Strain gauges installation is a process which foresees a certain amount of expertise and that depends on a variety of factors including materials, geometry, surface conditions and more. Almost all the signals of the installed gauges are strongly affected by electrical noise. For this reason, the data related to the strain gauges are not shown.

Linear displacement transducers have been installed in both longitudinal and transversal direction, measuring the differential displacements between the external beams and a reference pier. These sensors appear to be slightly sensitive to electrical noise, see Figure 5.

Actually, the available data covered a period of four months (September to December 2023); if the displacements are observed on the longer period of time (Figure 6), it can be noted that the data coming from suppliers A, B and D are coherent between them, with differential displacement less than 3 mm. The static part of the systems also includes two thermocouples for each supplier installed on the external beams. The sensors were inserted into a drilled hole in the concrete to monitor its temperature drifts.

The available data of the thermocouples are shown in Figure 7 together with a longitudinal displacement transducer, as a comparison. In that figure it can be noticed the trend of the temperature, which decreases as a function of time, as expected. The three unexpected peaks arisen between the 90th and the 115th day correspond to real peaks of external temperature occurred exactly on December 1, 13 and 23, 2023, with values of about 20°C.

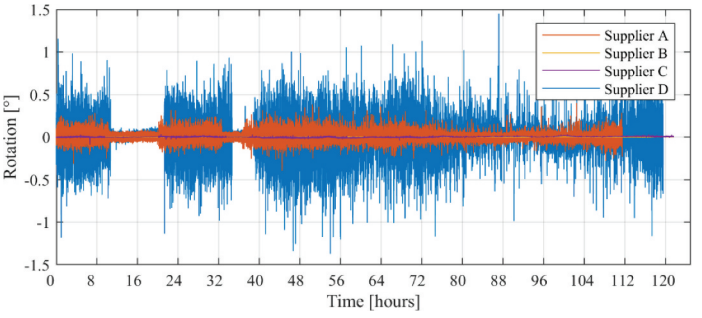


Figure 4. Signals of inclinometers.

The signal of the longitudinal displacement transducer seems to be coherent with te data coming from the thermocouples and since the nominal thermal coefficient of the displacement sensors is 5ppm/C° a variation of about 15°C between day 90 and 115 leads to a correlated expected drift in the displacement readings of 0.015mm due to environmental effects, consequently the remaining part of the displacement measured can be related to structural effects inducted by the temperature fluctuations.

More detailed analyzes and comparisons relating to long-term static monitoring will be performed when a greater amount of data will be available, at least 6 months (half of a seasonal cycle).

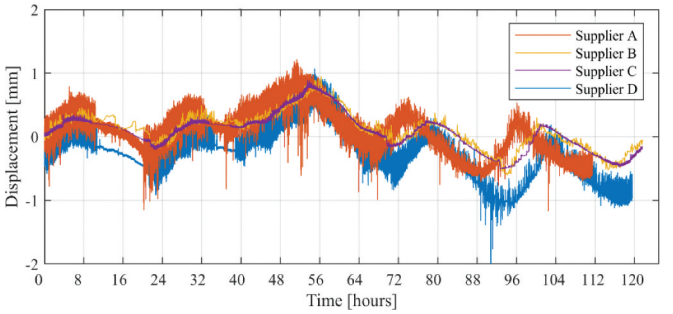


Figure 5. Signals of the longitudinal displacement transducers (limited time window, 120h).

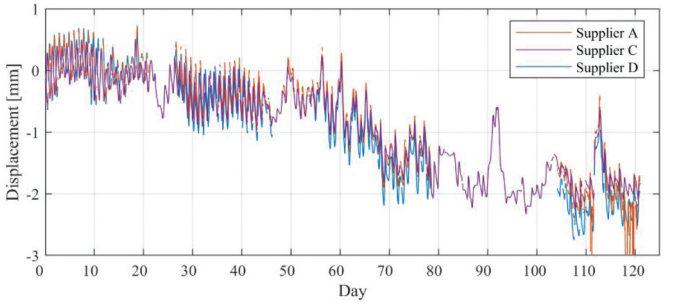


Figure 6. Signals of the longitudinal displacement transducers.

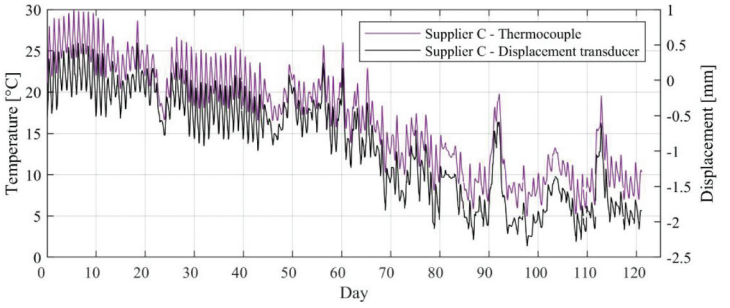


Figure 7. Signals comparison: thermocouple and longitudinal displacement transducer.

4 DYNAMIC MONITORING DATA ASSESSMENT AND COMPARISON

The dynamic acquisition in this context has been used to evaluate the main dynamic properties of the structure. All suppliers installed at least accelerometers to monitor accelerations in the vertical direction. Suppliers A and C added 4 more sensors, on one of the outer beams, to record accelerations in the transversal direction as well. Only Supplier B has exploited tri-axial sensors.

In this section the main results of operational modal analyses (OMAs), aimed to evaluate and compare modes and frequencies obtained from the different monitoring systems, are briefly summarized. In particular, the Operational Polymax Plus procedure has been used (Peeters B., 2012), (Siemens, 2023), since usually it has high computational efficiency and reliable stabilization diagrams even for highly damped systems and noisy signals.

A 0.1 Hz ÷ 100 Hz or 0.1 Hz ÷ 50 Hz bandpass filter has been imposed to all input signals. The different values of the upper band did not affect the results, since the stabilization diagram has been evaluated in the range 0 ÷ 30 Hz. The analysis has been developed along three

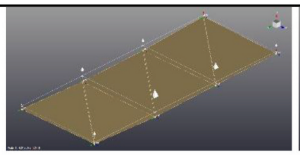
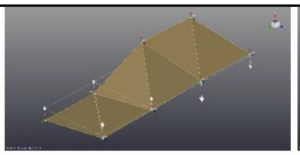
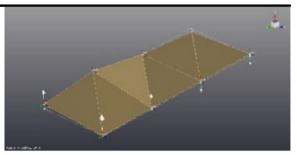
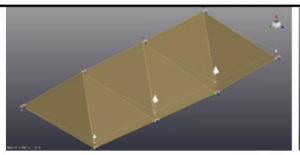
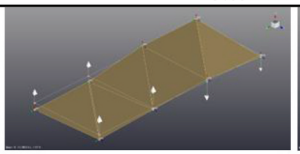
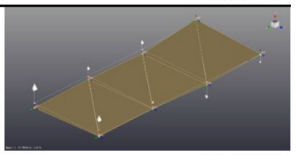
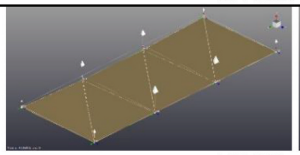
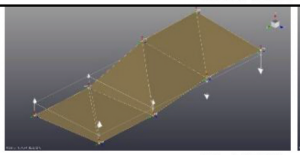
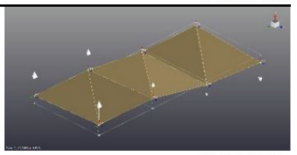
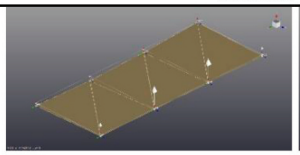
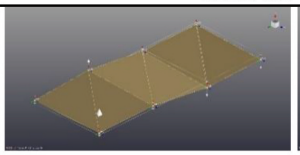
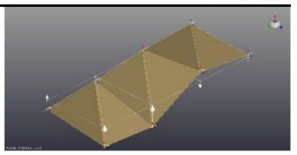
directions: vertical (Z), transversal (Y) and longitudinal (X). Only the configuration of accelerometric sensors of supplier B was suitable to analyze a 2D model of the bridge along all directions. Suppliers A and C refers to a 2D model along Z and a linear model in Y, with no data in X. Suppliers D considered only a 2D model in Z with no data along the other directions.

The most reliable results in Z direction have been provided by suppliers A, B and C (the last one identified the greater number of modes with a low scatter). Despite more scattered information, supplier D captured the values in common with the other systems. The common frequency values are 4.00-4.38 Hz, 13.30-13.80 Hz e 17.20-17.80 Hz (Table 6). The corresponding mode shapes, shown in Table 7, seem to be almost compatible between them. In Table 8 the frequencies for the transversal direction are shown.

Table 6. Frequency values along the vertical direction (the common frequencies are highlighted)..

	Supplier C	Supplier A	Supplier B	Supplier D
Mode 1	0.602 Hz	4.019 Hz	4.378 Hz	4.143 Hz
Mode 2	4.010 Hz	13.652 Hz	13.791 Hz	6.418 Hz
Mode 3	4.496 Hz	17.564 Hz	14.212 Hz	12.573 Hz
Mode 4	12.707 Hz	25.558 Hz	17.799 Hz	17.247 Hz
Mode 5	13.457 Hz	-	20.780 Hz	-
Mode 6	17.756 Hz	-	-	-

Table 7. Main mode shapes along the vertical direction.

Supplier	Mode 1	Mode 2	Mode 3
A	 4.019 Hz	 13.652 Hz	 17.564 Hz
B	 4.378 Hz	 13.791 Hz	 17.799 Hz
C	 4.010 Hz	 13.457 Hz	 17.756 Hz
D	 4.143 Hz	 12.573 Hz	 17.247 Hz

For what concerns the analysis in Y direction, an accelerometer of supplier A provided data with an amplitude significantly lower than the others. This issue clearly affected the results of supplier A.

The most reliable results were provided by supplier C, which was the only one able to capture the flexural mode shapes of the deck. From the monitoring systems of suppliers A and B incoherent mode shapes were obtained, in the sense that the deck expands and contracts as if it was not rigid in that direction or it is affected by movements at the ends (possible oscillations of the piers). Only supplier B provided results in the longitudinal (X) direction, which are characterized by a substantially high scatter. Four main frequency values have been obtained: 13.92 Hz, 15.87 Hz 22.49 Hz e 24.07 Hz. Nonetheless, only the first mode seems to be reliable.

Table 8. Frequency values along the transversal direction (the common frequencies are highlighted).

	Supplier C	Supplier A	Supplier B
Mode 1	4.119 Hz	7.082 Hz	7.190 Hz
Mode 2	12.762 Hz	12.893 Hz	12.981 Hz
Mode 3	17.692 Hz	17.688 Hz	17.701 Hz
Mode 4	20.579 Hz	20.640 Hz	24.076 Hz
Mode 5	22.348 Hz	21.409 Hz	26.353 Hz
Mode 6	-	22.458 Hz	-

5 CONCLUSIONS

In this paper a Proof of Concept based on four different monitoring systems installed on an Italian highway viaduct has been presented. The aim is to compare their functioning, the effectiveness of their results and essentially the technological solution. Each system consisted of several sensors to measure displacements, drifts, deformations, accelerations and temperature both in static and dynamic conditions.

During the period of the pilot test, the static part of the monitoring systems highlighted several issues inducted by electrical disturbances in terms of drift, spikes and broadband noise. Such phenomena could not be completely avoided. Disturbances from traffic, illumination system of a bridge or other electric sources is quite common and most of the time the monitoring system cannot be properly earthed to avoid such disturbances. These are the typical operational conditions on site. The software part of the system should include tools to identify such unwanted signals and attenuate the correlated negative effects. In most cases the characteristic of the signal was quite unique and could be detected by pattern recognition procedures. Electrical shocks are represented by extremely sharp rises, which means that the difference between two measurement points is orders of magnitude greater than normal signals.

The dynamic acquisition presented in some cases inaccuracies due to incomparable amplitudes of the accelerations of some sensor respect to the others. In any case it can be mentioned that system C provided reliable results in terms of frequencies and mode shapes.

Other results, particularly regarding the behaviour of the monitored structure, will be obtained only after a long-term observation period (i.e. at least one year).

REFERENCES

Ellram, L. (1993). Total Cost of Ownership: Elements and Implementation. *International Journal of Purchasing and Materials Management*, 1055-6001.

Keller, K., & Poblete, J. (2011). The Business Case for SHM. In S. Johnson, T. Gormley, S. Kessler, C. Mott, A. Patterson-Hine, K. Reichard, & P. Scandura, *In System Health Management* (p. 77–91).

Peeters B., E.-k.M. (2012). The new PolyMAX Plus method: confident modal parameter estimation even in very noisy cases. *In Proceedings of the ISMA: 2801-2813.*

Siemens. (2023). *Simcenter Testlab 2206*. https://community.sw.siemens.com/s/article/Simcenter-Testlab-2206-Download-and-Install-Instructions.

Bridge Maintenance, Safety, Management, Digitalization and Sustainability – Jensen, Frangopol & Schmidt (eds)
© 2024 The Author(s), ISBN 978-1-032-77040-6
Open Access: www.taylorfrancis.com, CC BY-NC-ND 4.0 license

Vibration-based NDT system for external tendons: Anomaly detection through machine learning classifiers

J. Naranjo-Pérez & J. Jiménez-Alonso
Universidad de Sevilla, Seville, Spain

I.M. Díaz, J.H. García-Palacios & C.M.C. Renedo
Universidad Politécnica de Madrid, Madrid, Spain

ABSTRACT: This paper proposes a new prototype for the non-destructive testing of external post-tensioning tendons. The system is based on the dynamic response of the tendon from which a series of structural performance indicators are identified, allowing to assess them and to make maintenance or replacement decisions in case anomalies are detected. The prototype developed is economical, easy to use, scalable (more sensors or performance indicators can be included) and portable, since all the necessary equipment is placed on a trolley. The system has been used for the evaluation of the external post-tensioning tendons of a 12-span railway bridge, with a total of 202 tendon segments analyzed. For each test, the system generates a report summarizing the calculated indicators and pointing out any anomalies detected. Considering the results of all the segments, an unsupervised clustering technique is applied to create groups with similar patterns where the results obtained are classified and the presence of outliers, i.e. tendon sections with anomalous behavior, is checked.

1 INTRODUCTION

In the design of new bridges and their rehabilitation, the use of external post-tensioning tendons is common due to their ease of installation and replacement if necessary. The presence of defects (corrosion of the strands or cracks in the grout) can accelerate the breakage of the tendon leading, in the worst case scenario, to the collapse of the structure (Anania et al. 2019). Therefore, due to the importance of these structural elements, numerous works have been carried out in recent years for the monitoring and evaluation of their structural integrity. In this context, two general applications can be mentioned: continuous monitoring of their structural health (Cigada et al. 2020) and non-destructive testing (NDT) for the estimation of tension force (Abdel & Glisic 2019, Chen at al. 2016). Within this second application, techniques based on dynamic response, acoustic or strain measurements can be commonly found in practice.

Regarding the methods based on dynamic response, this is related to their dynamic properties, which may be altered due to damage, structural anomalies or by the modification of their support conditions. Lee & Kang (2019) demonstrated that both the natural frequencies and the tension force of tendons decrease as the strands damage progresses. In the case of adherent tendons (bonded), the loss of steel section is not proportional to either the reduction in frequencies or the reduction in tension due to self-anchorage. However, between the frequencies, higher frequencies are more sensitive to damage and the ratio between them and the fundamental should be greater than the modal order due to the non-negligible moment of inertia provided by the grout. The main objective of this work is to propose an NDT system for external tendons which is able to measure and analyze the experimental vibrations, extract their modal parameters and monitor them, detecting changes or obtaining mechanical parameters of interest.

External post-tensioning tendons can be modeled as a cable with bending stiffness and their dynamic behavior will depend on: the boundary conditions (usually different from simply

DOI: 10.1201/9781003483755-273

supported due to the effect of bending at diaphragms and deviators), the tension force at that moment, the mass distribution along its length and the bending stiffness which is not negligible in general, especially in the case of short tendons subjected to significant tension forces. By knowing these parameters, the structural behavior of the tendon can be accurately evaluated. Since the conditions of the tendons are not visible due to the sheath and grout, NDT based on dynamic response can be a useful tool in the overall assessment of tendon mechanical behavior.

Several continuous tendon monitoring applications based on the dynamic response of tendons can be found in the literature that track natural frequencies and, indirectly, tendon tension force (considering the equation of a string without bending stiffness and only the fundamental frequency which provides significant errors in the tension force estimation) (Cigada et al. 2020). However, there are no prototypes of NDT equipment that complement more classical techniques such as ultrasonic and that carry out the dynamic analysis of the tendon and the calibration of its digital model in an automated way. This article presents an efficient (in terms of test time), scalable and portable NDT system for the evaluation of tendon anomalies that can be used for maintenance on successive occasions. The system, once the measurement has been performed, generates a report with several performance indicators (PIs) that allow evaluating the tendon segment and, finally, to compare them with more segments for a more exhaustive analysis of the complete tendon.

Changes in the tendon's tension force affect its structural behavior and is a parameter of interest for maintenance and structural evaluations. In fact, a significant drop in the tension force with an increase in the tension force of adjacent tendons is a clear indicator of an anomaly. The effect of bending stiffness makes the ratio between the frequencies and the fundamental clearly greater than the modal order. Reductions in this ratio indicate deterioration of the grout. In addition, higher modes are more sensitive to local effects (local strains, wire breakage or loss of stiffness) and their estimation has a direct impact on the number of measurement points, the configuration of the acquisition equipment and the post-processing digital filters.

The NDTT system (Non-destructive Tendon Tester) performs a real-time calibration of the tendon model (digital twin) minimizing the error between analytical and experimental natural frequencies and modal shapes. For the estimation of the experimental frequencies, the problem of the double peak, known as doublets (Sagüés et al. 2006), in the PSD (Power Spectral Density) is solved with a procedure based on weighting the peaks involved to obtain an average. On the other hand, an Operational Modal Analysis (OMA) is performed to obtain the vibration modes.

2 DESCRIPTION OF THE SYSTEM

The developed system for the non-destructive testing of the external tendons is herein described. The device consists of four elements (Figure 1): a trolley with shelves, the sensors and acquisition system, a laptop and a power supplier.

PCB seismic accelerometers are used to measure the dynamic response of the tendons. In particular, the model that is employed is B12 with nominal sensitivity of 10 V/g, resolution of $8 \cdot 10^{-6}$ g rms and frequency range from 0.15 to 1000 Hz. The accelerometers are placed in the tendon by using a magnet which is attached to ad-hoc braces screwed to the sheath equipped with metal plates. The other sensor is a piezoelectric force sensor integrated in an impact hammer. All the sensors are connected to the acquisition system (NI-cDAQ) through BNC connections. Figure 2 shows these devices.

The laptop runs an app programmed in MATLAB developed by the authors. This app launches the test and executes the whole process: a) measure of accelerations using LABVIEW, b) analysis of the signals to extract the behavior of the tendon, and c) generation of an immediate report of the test. By default, the app is configured with a sampling frequency of 1651 Hz, a test duration of 480 s (including ambient vibration test and free vibration test). However, this values can be modified in the setting tab of the app.

The electric generator has a power of 600 W and guarantees at least 8 hours of continuous work of the system.



Figure 1. Experimental setup of the system: trolley with the laptop and electrical generator, accelerometers and visualization of the impact in the laptop.



Figure 2. Sensors, acquisition system and electrical power supplier.

3 WORKING OF THE SYSTEM

3.1 *Measurements and analysis*

The dynamic response of the tendon is obtained by means of two experimental tests. The first one is an ambient vibration test where only environmental loads are applied. Subsequently, an OMA is performed to extract the natural frequencies and mode shapes of the tendon. Initially, the app is configured to extract up to the fourth vibration mode.

The second one is a free vibration test. To do this, the tendon is excited three times with the impact hammer and the free response is assessed to estimate the damping applying the logarithmic decay method. The mean value of the three dampings is given as result.

3.2 *Performance indicators*

Several PIs are defined to assess the structural condition of the tendon. These PIs are calculated from the two previous analyses. Currently, the system calculates ten PIs.

The first four PIs are the first four natural frequencies of the tendon. According to the vibrating string theory, natural frequencies should be proportional (or higher due to bending stiffness) to the modal order. If this is not fulfilled, it is indicated a loss in both the tension

force or the bending stiffness. The following four PIs are associated to the symmetry of the mode shape and is called Symmetry Aspect Ratio (SAR). To define the symmetry, the Modal Assurance Criterion (MAC) parameter of the two sides of the tendon is calculated. A value of 1 reveals a perfect symmetry whereas lower values indicates loss of symmetry possibly due to an irregular distributions of the mass along the length of the tendon. The ninth PI is the damping ratio calculated from the free response test. Changes in the damping ratio may be associated to grout cracking. Finally, the last PI is the tension force of the tendon. This PI is estimated from the updating of an analytical model of the tendon. This process is explained in next section. Table 1 shows the PIs computed by the NDTT.

Table 1. Description of the PIs calculated by the system.

Indicator	Definition	Description
P1	f_1	Fundamental natural frequency [Hz]
P2	f_2/f_1	Ratio between second and first natural frequency
P3	f_3/f_1	Ratio between third and first natural frequency
P4	f_4/f_1	Ratio between fourth and first natural frequency
P5	SAR_1	Symmetry aspect ratio of first mode
P6	SAR_2	Symmetry aspect ratio of second mode
P7	SAR_3	Symmetry aspect ratio of third mode
P8	SAR_4	Symmetry aspect ratio of fourth mode
P9	ζ_1	Damping ratio of first mode
P10	T	Tension force [N]

The ten PIs are the results of a particular segment of the tendon, i.e. each tendon will have between 3 to 9 test results. When all the segments of a tendon have been tested, a behavior matrix P_{ij} of the tendon is defined. The size of this matrix will be $10 \times N$, N being the number of segments. Subsequently, an anomaly matrix is computed. This is defined as:

$$d_{ij} = \frac{\hat{P}_{ij} - P_{ij}}{\hat{P}_{ij}} \tag{1}$$

where $\hat{P}_{ij}$ is a prescribed threshold of the i-PI and segment j. When the anomaly is positive, it is considered that the behavior is not as expected. Finally, a cumulative value of anomaly for each tendon is calculated as:

$$D = \frac{1}{N}\sum_j^N \left[\sum_{i\in M} r_i^1 d_{ij}\right]; \text{ with } \sum_{i\in M} r_i^1 = 1 \tag{2}$$

M being the vector containing the indexes of the PIs at the segment j such that $d_{ij} > 0$, and r_i^1 is the weight associated with indicator i. The weights are obtained from the initial values of the indicator weights as a function of the number of PIs greater than 0 (M vector length):

$$\sum_i^{10} r_i^0 = 1;\ \sum_{i\in M} r_i^0 = A \le 1;\ r_i^1 = \frac{1}{A} r_i^0 \tag{3}$$

where r_i^0 are the initial weights that are defined according to the relevance assigned to each PI. In the case that M contains all the PIs, the weights will be equal to the initial ones, otherwise they will be scaled using Equation (3).

3.3 *Theoretical approach for tension force estimation*

The tension force of the measured tendon segment is estimated by calibrating its analytical dynamic model using the results extracted from the OMA. To define the tendon model, it is considered simply supported at both ends. To consider possible irregularities in the supports

that move it away from the ideal support, the concept of equivalent length is used (Chen et al. 2018). Under this hypothesis, it is assumed that the modal shape can be represented by a tendon with an equivalent length (smaller or equal to the real one). The main advantage is that this model has analytical solution, which significantly reduces the simulation time, making possible its use for in-line application.

The equation for the transverse displacement of the tendon is:

$$EI\frac{\partial^4 v(x,t)}{\partial x^4} - T\frac{\partial^2 v(x,t)}{\partial x^2} + \rho_l \frac{\partial^2 v(x,t)}{\partial t^2} = 0 \tag{4}$$

where EI is the bending stiffness, $v(x,t)$ is the transverse (vertical) displacement, T is the tension force and ρ_l is the linear density. The natural frequencies and modal shapes are calculated as (Morse & Ingard 1986):

$$f_i = \frac{i}{2L_{eq}}\sqrt{\frac{T}{\rho_l} + \frac{\pi^2 EIi^2}{L_{eq}^2 \rho_l}};\ \phi_i(x) = sen\left(\frac{i\pi x}{L_{eq}}\right) \text{with } i = 1,\ 2,\ 3,\ 4 \tag{5}$$

Equal equivalent length is assumed here for all modes. The calibration is carried out by solving a minimization problem whose objective is to minimize the differences between analytical and experimental modal properties by iteratively modifying the tendon parameters. These parameters are: $\boldsymbol{T}$, $\boldsymbol{EI}$ and $\boldsymbol{L_{eq}}$.

This process is run using the genetic algorithm programmed in MATLAB (function ***ga***). The population size is set to 100 individuals and the number of iterations equal to 300. The algorithm is executed 20 times with the aim of computing a weighted mean value of the 20 tension forces. The weights are obtained as the inverse value of the objective function, i.e. the result that reaches a lower value of objective function has a higher influence.

4 EXAMPLE OF APPLICATION

The system has been applied in the monitoring of all the tendons of a continuous double-track railroad viaduct with single-cell box section. The total length is 558 m distributed over 12 spans. The bridge has a first-stage straight launching prestressing and a second-stage prestressing. The latter is external to the section and has a polygonal layout inside the box, anchoring at the diaphragms and breaking at the deviators at a quarter of the span. Each tendon, in general, covers three spans with three segments in each span, giving a total of 9 segments, except for the tendons of the end spans which cover only one or two spans. This bridge has been analyzed due to the notable deterioration that the external tendons have suffered over the years, leading to advanced corrosion processes that have even led to the collapse of one of the tendons. Therefore, the NDTT system developed is intended to shed light on the uncertainty that exists about the actual structural condition of the remaining tendons. Figure 3 shows the analyzed bridge and the external tendons inside the box. As can be seen, the deterioration led to the tendons being sling-joined together to prevent damage. In addition to replacing the collapsed tendon, maintenance work was carried out on the rest of the tendons, replacing some of them.

The application of the proposed system in the bridge was performed at night when no trains were running. Each test analyzes only one segment and is saved with its name so that the analysis of complete tendons and the whole post-tensioning system can be performed later. As mentioned above, several tendons of the bridge were replaced before the tests, having a different technology than the previous ones. Specifically, these were tendons with strands encapsulated in individual sheaths with grease inside and all of them in an outer sheath. In addition, the number of strands was different from previous tendons. Therefore, for the whole analysis the tendons were classified into: Class 1 (C1) the old tendons (bonded) and Class 2 (C2) the new tendons (unbounded). Thus, Class 1 tendons show the phenomenon of self-anchoring (adherent tendons) while Class 2 tendons show non-adherent behavior.



Figure 3. View of the bridge and external post-tensioning tendons.

The behavior matrix (P_{ij}) and the anomaly matrix (d_{ij}) of a particular 9-segment tendon are shown in Tables 2 and 3. Considering these values, the cumulative anomaly for this example was $D = 0.026$ (Equation 2). From the analysis of the results of all the tendons in the structure it was possible to detect that there were 3 tendons with clearly anomalous behavior. Figure 4a shows the histogram of the cumulative anomaly D for all the tendons, where, in particular, one of them had a significantly higher value with respect to the others. These three anomalous tendons correspond to old tendons, for which a thorough inspection was proposed. Figure 4b shows the tendon sections identified as anomalous and therefore candidates for replacement. Tendons 2.1, 1.2 and 4.4 show clearly anomalous behavior, in addition, 4.2 and 2.5 (identified with a diamond in the figure) would also be candidates for replacement.

Table 2. Example of behavior matrix of a particular segment of the bridge.

	N1	N2	N3	N4	N5	N6	N7	N8	N9
P1	14.19	6.80	14.16	13.78	6.51	13.49	14.06	6.81	14.35
P2	2.02	2.01	2.04	2.07	1.98	2.11	2.09	1.99	2.03
P3	3.07	3.03	3.14	3.20	2.92	3.25	3.20	3.01	3.11
P4	4.17	4.09	4.26	4.34	4.06	4.44	4.41	4.06	4.27
P5	1.00	1.00	0.96	1.00	1.00	0.99	1.00	0.99	0.99
P6	0.99	0.99	0.99	0.99	1.00	0.80	0.97	1.00	0.98
P7	0.99	0.98	0.94	1.00	0.95	1.00	1.00	0.99	0.98
P8	0.93	0.99	1.00	0.99	1.00	0.96	0.90	0.91	0.94
P9	0.15	0.24	0.08	0.13	0.07	0.09	0.12	0.10	0.13
P10	3957.87	3766.56	3956.61	3180.10	3474.74	3623.72	3969.84	3855.84	4211.76

Table 3. Example of anomaly matrix of a particular segment of the bridge.

	N1	N2	N3	N4	N5	N6	N7	N8	N9
P1	0.02	-0.01	0.02	0.05	0.04	0.07	0.03	-0.01	0.01
P2	-0.02	-0.01	-0.02	-0.04	0.01	-0.06	-0.05	0.00	-0.02
P3	-0.04	-0.03	-0.07	-0.08	0.01	-0.10	-0.09	-0.02	-0.05
P4	-0.03	-0.01	-0.05	-0.07	-0.01	-0.10	-0.09	-0.01	-0.05
P5	-0.05	-0.05	-0.01	-0.05	-0.05	-0.04	-0.05	-0.04	-0.04
P6	-0.10	-0.10	-0.10	-0.10	-0.11	0.11	-0.08	-0.11	-0.09
P7	-0.16	-0.15	-0.10	-0.17	-0.12	-0.17	-0.78	-0.16	-0.15
P8	-0.17	-0.23	-0.24	-0.23	-0.25	-0.20	-0.12	-0.14	-0.17
P9	-2.01	-3.80	-0.57	-1.69	-0.36	-0.75	-1.40	-0.96	-1.67
P10	-0.34	-0.28	-0.34	-0.08	-0.18	-0.23	-0.35	-0.31	-0.43

In addition to the calculation of cumulative damage indices, and given the large number of stretches analyzed, the use of an unsupervised machine learning technique has been proposed for the creation of groups (clusters) that have similar behaviors. With this technique, natural frequencies can be tracked and checked when one changes its behavior, i.e. it can be applied for

automated outlier detection. Furthermore, in the future, by applying transfer learning techniques, these classifiers can be used on similar bridges. In this study, the k-means technique has been used, which groups all the data into k groups characterized by their mean value. Due to the different types of segments (C1 and C2; inclined and horizontal; extreme spans and centered spans; etc.) there are a total of 8 groups. Therefore, the number of groups is $k = 8$. For the creation of the groups, an iterative process is performed and the results may vary between different calculations. To overcome this, 10 calculations (replicates) have been performed and the best of the 10 has been used based on the total sum of the distances between the points and the means. Figure 5 shows the graph with the groups obtained for the 4 natural frequencies. Each of the 8 colors represents a group and the repeated symbols indicate the frequency for which the analysis was performed (circles for the first frequency, squares for the second, pentagrams for the third and diamonds for the fourth). It should be noted that the groups with the same number for the 4 frequencies are not associated with each other, since the calculation has been made for each of the 4 frequencies independently. Clustering allows adding new values to previously created groups and verifying if it is in the right group. If not, it indicates that it does not have the expected behavior and proceeds to its detailed analysis. Using this clustering technique, outlier spans have been identified and it has been verified that these spans belonged to the tendons previously identified using the anomaly indicator.

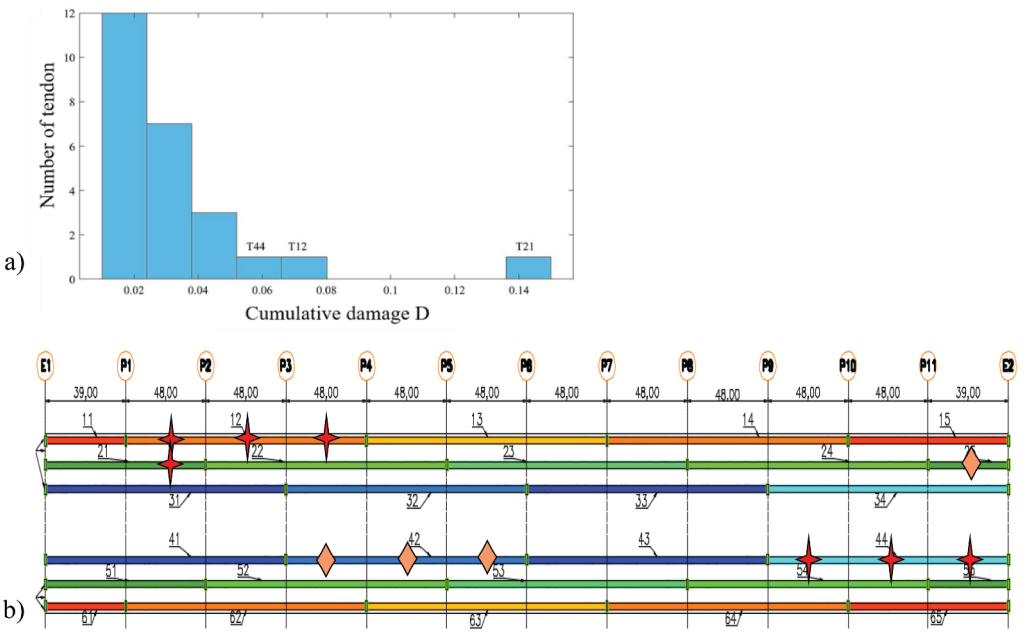


Figure 4. a) Histogram of the cumulative damage D and b) Segments with anomalous behavior.

5 CONCLUSIONS

In this paper, a new NDT system for external post-tensioning tendons has been presented and applied to a 12-span continuous bridge. The system calculates damage indicators on the one hand, and on the other hand, it performs an unsupervised clustering using machine learning techniques to identify tendon segment with abnormal behavior. By means of both procedures, some tendon sections with clearly anomalous behavior have been detected in the tested bridge. At the time of application of the system, new tendons had replaced the old ones and none of these were detected as anomalous. In conclusion, it was recommended to replace the anomalous ones or, if not, to strengthen the slinging and revise it periodically.

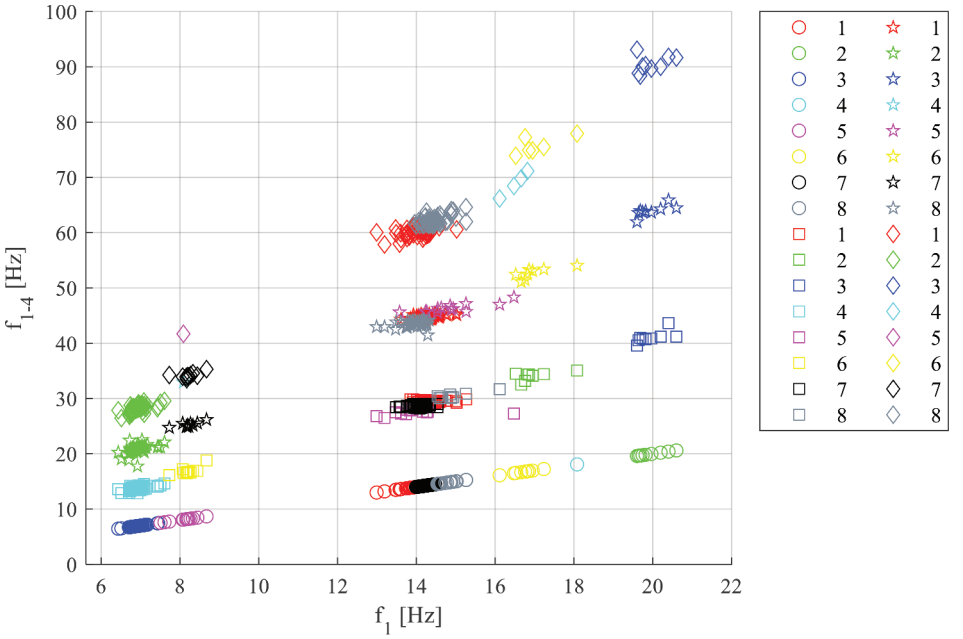


Figure 5. Clusters for the 4 natural frequencies. Each symbol represents a different frequency.

ACKNOWLEDGEMENTS

The authors acknowledge Grant PID2021-127627OB-I00 (Transport Infrastructures subjected to dynamic loading: assessment techniques for the sustainability, intelligent maintenance and comfort) funded by Ministerio de Ciencia e Innovación, Agencia Estatal de Investigación and 10.13039/501100011033 FEDER, European Union. Javier Naranjo-Pérez thanks Ministerio de Universidades for the Margarita Salas grant funded through the program 'European Union - NextGenerationEU'.

REFERENCES

Abdel, H. & Glisic, B. 2019. Monitoring of prestressing forces in prestressed concrete structures - An overview. *Structural Control and Health Monitoring* 26.

Anania L., Badalà, A. & D'Agata, G. 2018. Damage and collapse mode of existing post tensioned precast concrete bridge: the case of Petrulla viaduct. *Engineering Structures* 162: 226–244.

Chen, C.C., Wu, W.H., Leu, M.R. & Lai, G. 2016. Tension determination of stay cable or external tendon with complicated constraints using multiple vibration measurements. *Measurement* 86: 182–195.

Chen, C.C., Wu, W.H., Chen, S.Y. & Lai, G. 2018. A novel tension estimation approach for elastic cables by elimination of complex boundary condition effects employing mode shape functions. *Engineering Structures* 166: 152–166.

Cigada, A., Francescantonio, L., Malavisi, M. & Mancini, G. 2020. A damage detection strategy on bridge external tendons through long-time monitoring. In Pakzad S (ed), *Dynamics of Civil Structures, Volume 2. Proceedings of the 38th IMAC, A Conference and Exposition on Structural Dynamics*.

Lee, J.K. & Kang, J.W. 2019. Experimental evaluation of vibration response of external post-tensioned tendons with corrosion. *KSCE Journal of Civil Engineering* 23: 2561–72.

Morse, P.M. & Ingard, K.U. 1986. *Theoretical acoustics*. Princeton, USA: Princeton University Press.

Sagüés, A. A., Kranc, S.C. & Eason, T.G. 2006. Vibrational tension measurement of external tendons in segmental posttensioned bridges. *Journal of Bridge Engineering* 11(5): 582–589.

Bridge Maintenance, Safety, Management, Digitalization and Sustainability – Jensen, Frangopol & Schmidt (eds)
© 2024 The Author(s), ISBN 978-1-032-77040-6
Open Access: www.taylorfrancis.com, CC BY-NC-ND 4.0 license

Machine learning-based clustering and regression for assessing temperature-induced variations on external tendon's natural frequencies

L. Chillitupa-Palomino, C. Barrera-Vargas, J.H. García-Palacios & I.M. Díaz
E.T.S.I. Caminos, Canales y Puertos, Universidad Politécnica de Madrid, Madrid, Spain

J. Naranjo-Pérez
E.T.S.I, Universidad de Sevilla, Seville, Spain

ABSTRACT: Vibration-based techniques for external post-tensioning tendons have been used as non-destructive technique to assess their mechanical behavior. Thus, the continuous monitoring allows to assess their deterioration process through the continuous tracking of their natural frequencies, which may be used as damage indicators and for continuous force estimation. Hence, temperature dependencies on the frequency spectra of natural frequencies may mask potential damage among other problems such as double peaks or the existence of bracing systems. In this sense, this paper presents a mixed-cascade clustering for the frequency tracking together with the application of regression models (including linear regression and nonlinear autoregressive with exogeneous input neural network) to the classified data for identification of temperature dependencies. The proposed methodology has been applied to a case of study corresponding to several monitored tendons on a railway continuous concrete bridge.

1 INTRODUCTION

As civil engineering structures become mature, some structural aging effects may appear due to environmental conditions such as corrosion or operational factors like fatigue. Evaluating the structural condition becomes imperative; however, depending on the structural design, employing destructive testing may not be a viable option. Among the non-destructive testing (NDT) alternatives, vibration-based structural health monitoring (SHM) allows to extract features from the dynamic response that can be used as indicators of the structural condition of the structure. In particular, stiffness reduction or tension force losses implies abnormal reduction of the natural frequencies. However, the natural frequencies are also affected by environmental and operational factors that may mask anomalies (Gharehbaghi et al., 2022; Middleton, Fidler & Vardanega, 2016).

In the specific context of bridges featuring external post-tensioning tendons, vibration-based SHM stands out as an optimal alternative, given the discernible correlation between damage and natural frequencies (Lee & Kang, 2019; Zhang et al., 2022). As illustrated in Figure 1, there is a notable frequency variation corresponding to the progression of damage: frequencies decrease with increasing damage, and higher modes exhibit more pronounced variations, thereby rendering damage more visible. This frequency decrease is accompanied by a tension force loss due to the release or fracture of prestress wire and/or of bending stiffness due to grout damage.

Despite the evident correlation between frequency and damage, certain considerations must be taken into account before embracing frequency as a definitive performance indicator. Two crucial effects require attention when a frequency tracking system is going to be implemented:

DOI: 10.1201/9781003483755-274

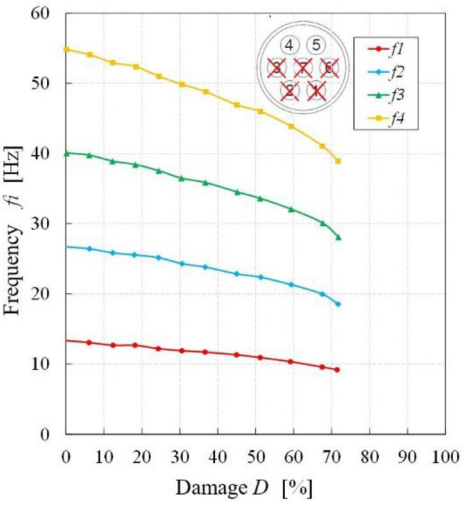


Figure 1. Damage – Frequency correlation adapted from (Lee & Kang, 2019).

I. Double peaks on Power Spectral Density (PSD).
   An important complication arises in experimental tests from the presence of peak doublets (Sagüés, Kranc & Eason, 2006). This may be due to the non-uniform strand arrangement inside the tendons and the different effective length due to different contact points at deviators.
II. Frequency variation attributable to temperature.
   In case of external posttensioning tendons, temperature variation affects importantly to the natural frequency estimation in such a way that NDT based on vibration measurement may not be as useful as expected.

To address the first effect, a cascade clustering process has been proposed. That is, two clustering processes are used to classify data before temperature dependency analysis. The first clustering process is utilized to identify daily and seasonal temperature cycles, as well as to detect coupling frequencies from adjacent tendon segments and outlier points. Subsequently, these outlier points are eliminated. The second clustering process serves to further filter out the outlier data, facilitating the creation of a robust and reliable regression model. This approach is specifically designed to mitigate the impact of the temperature variation on frequency and effectively address the challenges associated with the second effect.

When addressing the impact of temperature variation, the choice of regression methods becomes a pivotal consideration. Various techniques ranging from straightforward and explicit, exemplified by linear regression, to more complex and opaque approaches like neural networks, are available. The selection of an appropriate regression method depends on the specific characteristics of the dataset and the nuances of the relationship between temperature and the variable of interest. Simple and explicit methods, such as linear regression, offer interpretability and ease of implementation, making them suitable for scenarios where the underlying dynamics are relatively well-understood. On the other hand, black box methods like neural networks excel in capturing intricate patterns and non-linear relationships, providing a more flexible framework for modeling complex temperature effects. The decision to employ a particular regression method should align with the goals of the analysis, the nature of the data, and the desired balance between interpretability and predictive performance (Wang, Yang, Yi, Zhang & Han, 2022).

2 VIBRATION-BASED MONITORING OF EXTERNAL TENDONS

2.1 *Tendon description*

Tendons considered are of 2 types:

- Bonded:
  Bonded tendons, characterized by their sole protection through cement grout and a plastic tubing, often encounter corrosion issues, particularly in older instances. The corrosion problem is typically attributed to voids within the cement grout caused by inefficient filling techniques, creating spaces where water can accumulate around the steel strands. Notably, this category of tendons, particularly in aged conditions, does not exhibit a linear correlation between tendon damage and tension loss. This lack of linearity is attributed to the self-anchoring of the steel strands to the cement grout, posing challenges in accurately determining the extent of tendon damage. This fact makes frequencies less sensitive to damage than expected and makes the temperature-dependency removal crucial.
- Unbonded:
  Unbonded tendons distinguish themselves from bonded tendons through the inclusion of a second plastic enclosure filled with grease. This protective measure individually shields each cable, preventing water from reaching the steel strands. In contrast to bonded tendons, this type of tendon exhibits a much more linear correlation between tendon damage and tension loss since the tension loss is proportional to steel loss the absence of self-anchoring to the grease filling means that once a strand breaks, all tension along the strand is lost, contributing to the linear relationship observed in tension loss and tendon damage.

Figure 2 show an illustration of bonded and unbonded tendons.

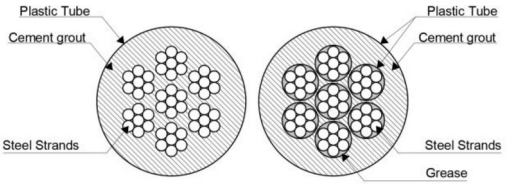


Figure 2. Bonded and unbonded tendons.

2.2 *Double peak on PSD*

As mentioned above, frequency doublets may appear due to:

- Non-homogeneous section
- Coupling frequencies from other segments
- Different contact points on boundaries
- Use of bracing systems

To show an example of this effect, the first frequency of a tendon with bracing is shown in Figure 3. As can be observed, the frequency estimates clearly jump into two different frequency groups, being one of them more persistent on time.

3 FREQUENCY TRACKING: CLUSTERING

3.1 *Mixed cascade clustering*

Due to the inherent characteristics of operational modal analysis, not every measurement yields a reliable value. This is attributed to the potential presence of coupling frequencies, and even when this issue is absent, measurements may be compromised due to insufficient excitation frequency, complicating the differentiation of the actual natural frequencies of the analysed tendon. To address these challenges, a clustering methodology has been proposed to filter

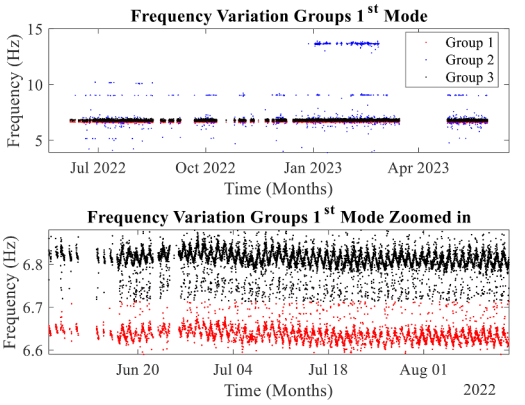


Figure 3. Clustering of coupling frequencies.

outlier data, detect trends, and separate coupling frequencies, facilitating the development of a robust regression model correlating temperature and frequency based on reliable data.

The method involves two clustering processes, with the first employing a Gaussian Mixture Model (GMM). GMM is a probabilistic model assuming data points originate from a mix of Gaussian distributions with unknown parameters (Bishop, 2006). This initial process identifies daily and seasonal temperature cycles, ideally resulting in two groups—one with outlier data and another with significant data. The latter is explored using a frequency vs temperature charts, often necessitating the removal of outlier data along this dimension. Two alternatives for this second classification are proposed hereof: the first involves using again GMM-based clustering process to separate outlier data from significant data, while the second employs Density-Based Spatial Clustering for Applications with Noise (DBSCAN). DBSCAN automatically creates clusters based on two parameters for each point: its border and the number of points inside that border (Ester, Kriegel, Sander & Xu, 1996). Although multiple clusters may be generated, the cluster numbered as -1 is crucial as it denotes outliers. Retaining the significant data obtained through either method results in a cleaner and reliable dataset, ready for applying regression methods. Figure 4 provides a flowchart of the proposed classification method which is illustrated by some plots.

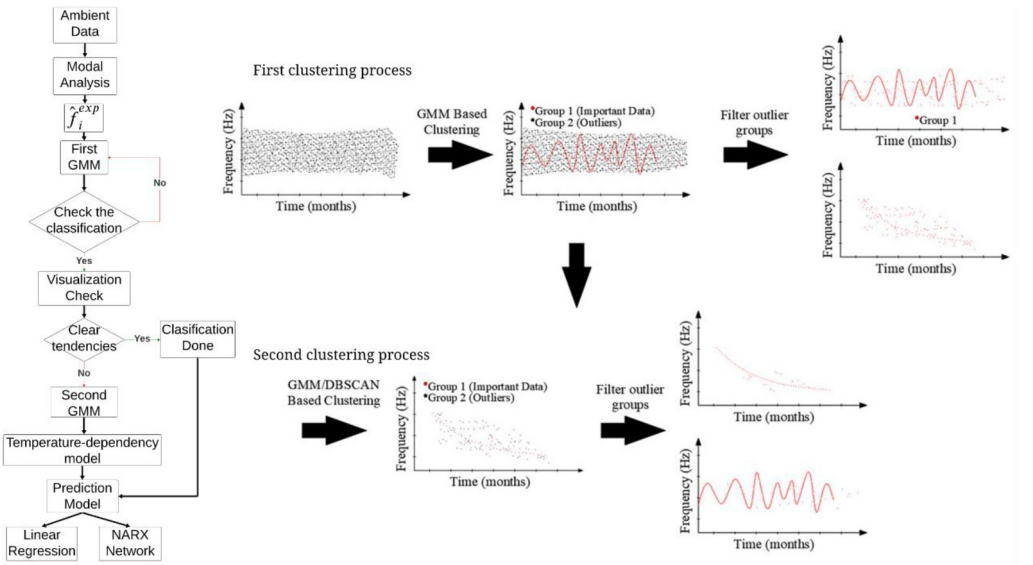


Figure 4. Cascade clustering process flowchart.

3.2 *Example of application*

The selected example involves one-year continuous monitoring initiative on a 12-span continuous concrete box-girder railway bridge featuring external post-tensioned tendons. The bridge initially incorporated six originally bonded tendons per span, which began exhibiting indications of stress-corrosion. For data acquisition, a monitoring system was deployed on the tenth span, comprising six accelerometers—one for each tendon—along with two accelerometers positioned on opposing borders, each located at a distance equivalent to one-tenth of the span from the center, and two displacement sensors (LVDTs) positioned at the midpoint of the horizontal section of the tendon. Additionally, an ambient temperature and humidity sensor was placed at the middle span inside the box-girder. Figure 5 illustrates the locations of these sensors and provides a visual representation of the tendon configuration at span 10.

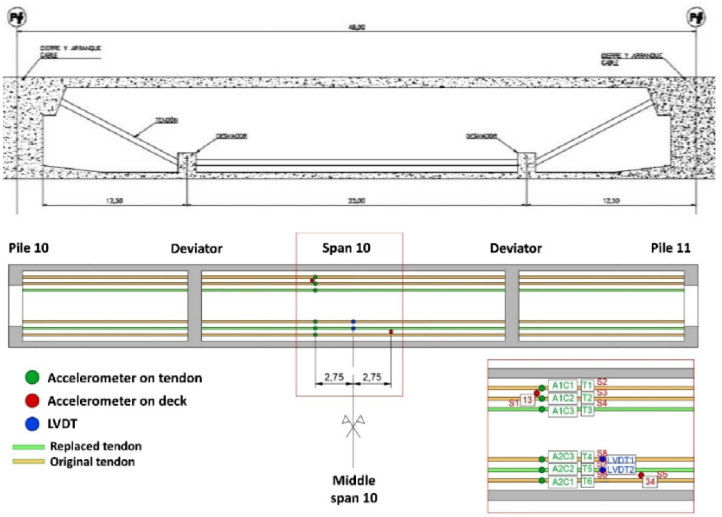
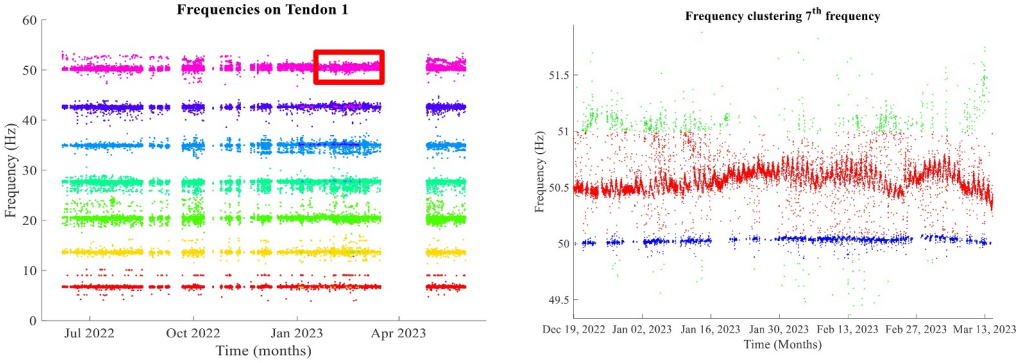


Figure 5. Sensor location.

The first 7 frequencies are obtained by peak picking on the PSD chart, this is done every 10 minutes over a one-yearperiod. These frequencies are illustrated in Figure 6. Initially, no discernible trend with temperature is evident in any of the seven frequencies. However, applying the cascade clustering process allows for the differentiation of day-night and seasonal cycles.



a) b)

Figure 6. a) First 7 natural frequencies of tendon 1. b) Zoom of resulting groups on the 7th frequency.

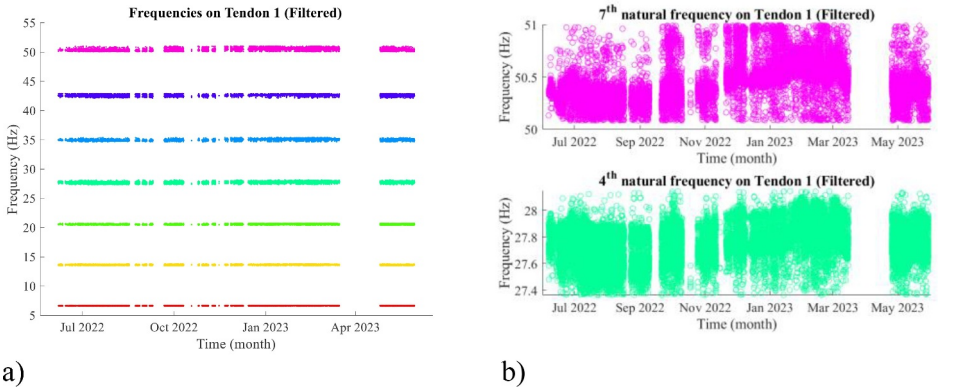


Figure 7. a) First 7 natural frequencies of tendon 1 after the first clustering process using GMM. b) Zoom of the 4th an 7th filtered natural frequencies.

Figure 7 illustrates the frequency distribution of tendon 1 after the first clustering process using GMM searching for ideally 2 groups but because of coupling frequencies could be more.

A second clustering process is executed to further eliminate outlier points. Figure 8 presents, as an exaple, the filtered dataset of modes 4 and 7 both using DBSCAN in this case, illustrating both the effectiveness of the method and the issues that need resolution.

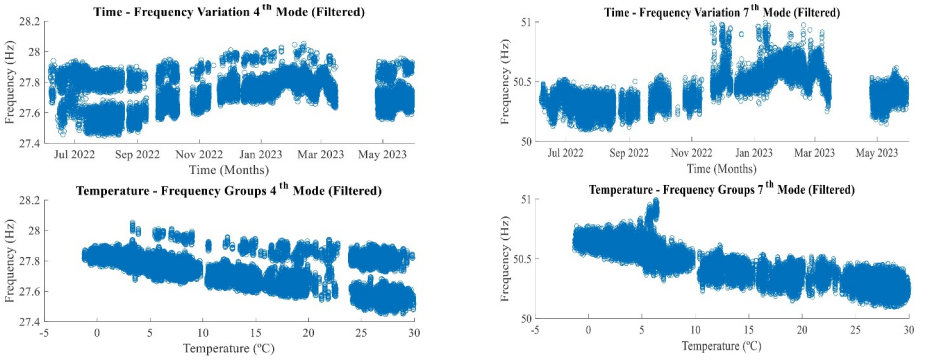
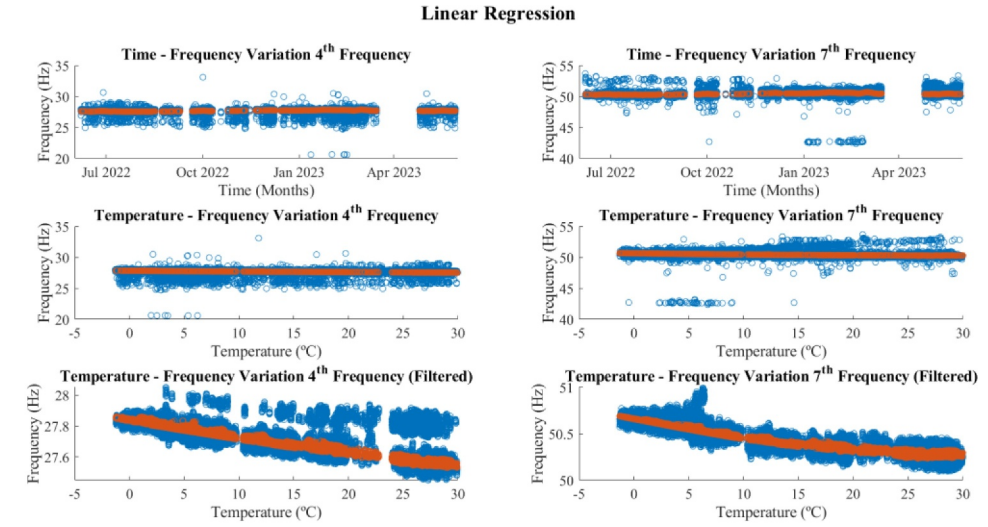


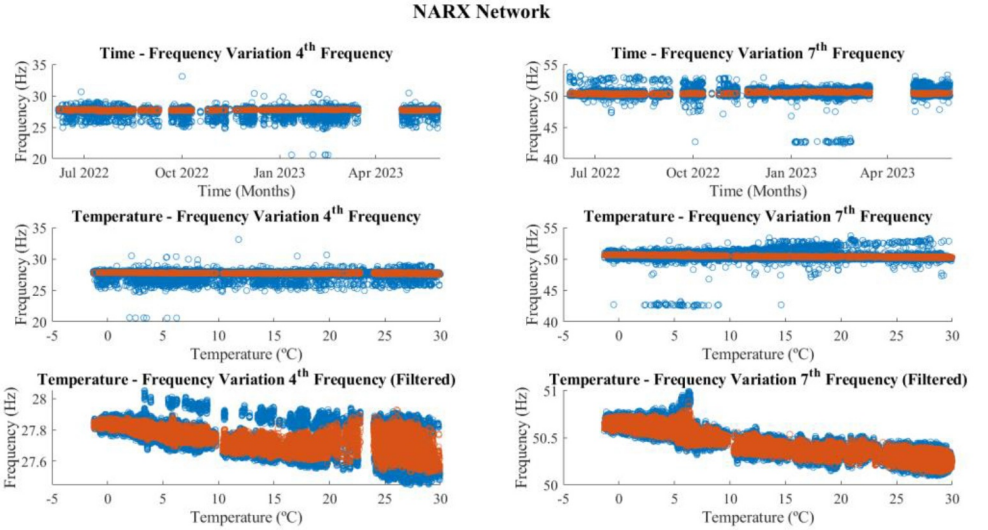
Figure 8. 4th and 7th filtered frequencies of the analysed tendon after the second clustering process using DBSCAN.

Following the acquisition of the classified dataset, two correlation methods were employed to establish a relationship between temperature and frequency. Among the numerous alternatives, linear regression and nonlinear autoregressive with exogeneous input neural network (NARX NN) were selected. The former was selected for its simplicity and fundamental nature in regression, while the latter, a specialized neural network for time-series analysis, was deemed ideal for this type of problem in which temperature changes take effect on frequencies after a period of time due to thermal inertia effect. Figure 9 illustrates the results obtained through the utilization of a linear regression and a NARX NN on the 4th and 7th natural frequencies.

It is evident that the NARX neural network can fit the majority of the data, but its consideration of coupling frequencies renders its predictions less reliable. Conversely, linear regression, although not as adept at describing the variation as the NARX NN, exhibits an advantage in its ability to disregard coupling frequencies that could not be filtered by the cascade clustering process.



a)



b)

Figure 9. Regression methods results a) Linear regression. b) NARX NN regression.

4 CONCLUSIONS

NDT of external tendons based on vibration data can be useful; however, some problems in the frequency estimates appear and make the use of natural frequencies as damage indicators awkward. Thus, methodology named as "cascade clustering process" comprising two successive clustering processes has been proposed. Two regression methods have been applied to the classified and compared: a basic method in the form of linear regression and a more complex approach using a NARX NN.

Linear regression demonstrates a notable capability to disregard coupled frequencies that may persist even after the cascade clustering process. This feature enhances its reliability in temperature effect elimination when coupled frequencies cannot be completely filtered.

Conversely, when there are no remaining coupling frequencies, the NARX neural network emerges as a superior alternative. Its capacity to effectively capture and describe the frequency variation surpasses that of linear regression.

As for future works, there is a keen interest in fully automating this process. Currently, the cascade clustering process involves numerous inputs that require manual configuration. Additionally, the differentiation between the analysed tendon's frequency and coupling frequencies, as well as the selection of GMM or DBSCAN for the second clustering process, relies on manual inputs that could benefit from automation. As depicted in Figure 8, coupling frequencies are not eliminated by the cascade clustering process in some modes. Consequently, there is a crucial necessity to enhance the clustering methods.

ACKNOWLEDGEMENTS

The authors acknowledge Grant PID2021-127627OB-I00 (Transport Infrastructures subjected to dynamic loading: assessment techniques for the sustainability, intelligent maintenance and comfort) funded by Ministerio de Ciencia e Innovación, Agencia Estatal de Investigación and 10.13039/501100011033 FEDER, European Union

REFERENCES

Bishop, C. 2006. *Pattern Recognition and Machine Learning* (1st ed.). New York: Springer New York.

Ester, M., Kriegel, H.-P., Sander, J., & Xu, X. 1996. A Density-Based Algorithm for Discovering Clusters in Large Spatial Databases with Noise. *Knowledge Discovery and Data Mining*. https://api.semanticscholar.org/CorpusID:355163.

Gharehbaghi, V. R., Noroozinejad Farsangi, E., Noori, M., Yang, T. Y., Li, S., Nguyen, A., et al. 2022. A Critical Review on Structural Health Monitoring: Definitions, Methods, and Perspectives. *Archives of Computational Methods in Engineering*, 29(4): 2209–2235.

Lee, J. K., & Kang, J. W. 2019. Experimental Evaluation of Vibration Response of External Post-Tensioned Tendons with Corrosion. *KSCE Journal of Civil Engineering*, doi:10.1007/s12205-019-0735-5.

Middleton, C., Fidler, P., & Vardanega, P. 2016. *Bridge Monitoring: A Practical Guide*.

Sagüés, A. A., Kranc, S. C., & Eason, T. G. 2006. Vibrational Tension Measurement of External Tendons in Segmental Posttensioned Bridges. *Journal of Bridge Engineering*, 11(5): 582–589.

Wang, Z., Yang, D. H., Yi, T. H., Zhang, G. H., & Han, J. G. 2022. Eliminating environmental and operational effects on structural modal frequency: A comprehensive review. *Structural Control and Health Monitoring*. John Wiley and Sons Ltd.

Zhang, Y., Feng, Z., Shi, S., Dong, Z., Zhao, L., Jing, L., et al. 2022. A quantitative identification method based on CWT and CNN for external and inner broken wires of steel wire ropes. *Heliyon*, 8(11).

Bridge Maintenance, Safety, Management, Digitalization and Sustainability – Jensen, Frangopol & Schmidt (eds)
© 2024 The Author(s), ISBN 978-1-032-77040-6
Open Access: www.taylorfrancis.com, CC BY-NC-ND 4.0 license

Integrating CWT and CNN for damage detection in high-speed railway bridges

J.F. Jiménez-Alonso & J. Naranjo-Pérez
Escuela Superior de Ingeniería, Universidad de Sevilla, Seville, Spain

C.M.C Renedo, J.H. García-Palacios & I.M Díaz
Escuela de Ingenieros de Caminos, Canales y Puertos, Universidad Politécnica de Madrid, Madrid, Spain

ABSTRACT: High-speed railway bridges, reinforced by external post-tensioning systems, are prone to suffer from fatigue problems under corrosion environments. In order to perform the structural assessment of these structures, during their overall life-cycle, structural health monitoring strategies are currently being implemented. Among the different strategies, vibration-based ones are normally employed in civil engineering applications due to its ability to global damage detection. According to these strategies, the measured dynamic response of the structure is compared between two states (the current and the original one) in order to assess the performance level. Nowadays, deep learning, a machine-learning computational tool, has been used to assist in this comparison task. An artificial neural network is usually trained for this purpose. For this training process, two extreme states are normally considered: (i) undamaged state; and (ii) damaged state. As it is not normally possible to obtain data of the damaged state of the structural system, an updated physics-based model is usually considered for this purpose. Therefore, the dynamic response of the damaged structure is simulated based on this updated model. In this manuscript, the performance of a classifier is assessed when it is implemented for the damage detection of a high-speed railway bridge. As an original (undamaged) state, an updated Bayesian finite-element-model of the structure is considered. Different level of uncertainty has been considered (variation range of the updating parameters) for this updated model. As damaged state, different levels of numerical damage have been generated. The dynamic response of the structure (vertical accelerations) has been compared for the damage detection. For the feature extraction, the continuous wavelet transform has been considered. As deep learning technique, a pre-trained convolutional neuronal network has been taken into account. Thus, the performance of the proposed classifier has been assessed, for this particular case-study, via the determination of both the confusion matrix and the accuracy ratio. Finally, the variation of the accuracy ratio in terms of the uncertainty of the updated model and the damage level has been studied in detail.

1 INTRODUCTION

Structural health monitoring (SHM) is currently the most powerful tool for civil infrastructure management (Ghiasi et al., 2019). One of the main objectives of the SHM is to establish an autonomous damage identification (DI) strategy (Anastasia et al., 2023). DI can be broken down into three different areas (Ghiasi et al., 2021): (i) damage detection (DD), (ii) damage diagnosis; and (iii) damage prognosis. Additionally, damage diagnosis can be sub-divided in three sub-areas to better characterize the damage (location, type and severity).

A SHM strategy involves the long-term monitoring of a structure, the extraction of the damage-sensitive features from the monitoring data, and the statistical analysis of these

DOI: 10.1201/9781003483755-275

features to determine the actual structural condition (Figueiredo et al., 2019). There are commonly two main methods to establish a SHM strategy: (i) physics-based methods; and (ii) data-based methods. The first methods are based on the resolution of an inverse problem, the finite element (FE) model updating problem, and they attempt to perform the DI process via the comparison of the main physical parameters of a FE model of the structure (Ereiz et al., 2022). The value of these physical parameters is obtained by a calibration process based on the measurements of the long-term monitoring. The data-based methods attempt to cope with the DI problem via the direct processing of the data recorded during the monitoring process. Currently, this data processing is performed considering the machine learning (ML) field. ML algorithms learn the structural behavior from the experimental data and perform the pattern recognition for DI.

Two types of ML methods can be applied to solve the DI problem: (i) unsupervised learning, when training data are only available from the undamaged structure; and (ii) supervised learning, when training data are available from the undamaged and damaged structure. This manuscript is focused on the use of supervised learning algorithms, and in particular, DL methods. These supervised DL methods are based on the use of artificial neural networks (ANN) for time series analysis and image classification. Thus, the DI problem can be reformulated as a classification problem.

Several strategies have been proposed to cope with the DI problem using ANN. Among the different proposals, the use of a particular type of ANN, the so-called convolutional neural networks (CNN), has been recently proposed by several researchers (Talaei et al., 2023). A CNN is a type of ANN specially designed to classify images. A great effort has been performed in different research fields to cope with this image classification problem. Thus, a high number of architectures of CNN have been proposed. In order to reduce both the data set and simulation time needed to train these complex DL algorithms, it is a common practice, to take advantage of these previous architectures and try to adapt them to different engineering problems. Therefore, a pre-trained CNN is usually modified to solve the DI problem (Chen et al., 2023).

A key-point, for the good performance of the classification method, is the so-called feature extraction phase. In this sense, the analysis of the statistical properties of the response of the structure considering the time and frequency domain is considered. In this sense, the dynamic response of the structure subjected to operational conditions has been commonly employed. As the dynamic response of the structure is a transient signal, the time-frequency content of the signal can be remarkable data for the feature extraction. The continuous wavelet transform (CWT) has been recently proposed for this purpose (Amanollah et al, 2023).

Several recent researches have proposed the use of a CWT-CNN method, based on pre-trained DL architectures, to solve the DD problem of civil engineering structures (Figueiredo et al, 2023). Despite the detailed analysis performed in this line, all these studies present a clear drawback, they have been developed assuming deterministic conditions (Figueiredo et al, 2011).

In order to shed some light to this problem, this manuscript focuses on the analysis of the performance of the abovementioned CWT-CNN method when it is implemented for the DD of high-speed railway bridges subjected to uncertainty conditions. This uncertainty is associated with the variation of the operational and environmental conditions. In order to quantify the uncertainty, a stochastic FE model updating technique is taken into account. Thus, the updated model has been used to simulate numerically both the undamaged and damaged behavior of the structure. In this manner, the importance of the use of stochastic FE model updating for the solution of the DD problem considering uncertainty conditions has been highlighted herein.

2 MACHINE LEARNING STRATEGIES FOR DAMAGE DETECTION

The formulation of the SHM problem, according to the ML method, can be described as a four-step problem. These four-steps are (Avci et al., 2021): (i) the operational evaluation; (ii) the data acquisition; (iii) the feature extraction; and (iv) the statistical modeling for feature

classification. Thus, the main objective of the method is to recognize and distinguish between the statistical patterns of two states of the structure: (i) the undamaged structure under operational and environmental influences; and (ii) the damaged structure under the same conditions. The process starts with the measurement of the behavior of the structure via a long-term monitoring system and finishes with the assessment of current state of the structure.

As the key-point of the process is the feature extraction, currently the use of DL algorithms has prevailed over other ML techniques. DL allows the autonomous extraction of the features of the data. For this reason, a DL algorithm has been considered in this study.

3 BAYESIAN FINITE ELEMENT MODEL UPDATING

In order to quantify the uncertainty associated with the variation of the main physical parameters of a structure associated with the variation of the operational and environmental conditions, the stochastic finite element (FE) model updating can be employed (Kamariotis et al., 2022). In this manner, the data obtained for a long-term monitoring of the structure can be used to characterize numerically the variation of the main physical parameters of the structure.

An initial FE model of the structure is commonly updated based on the experimental and numerical modal properties of the structure. Due to the stochastic character of the problem, as estimator, Bayesian inference, is considered. In this manner, the probabilistic distribution of the main physical parameters of the structure, θ, is estimated via the Monte Carlo sampling (Lye et al., 2021) of the Bayes' rule:

$$P(\theta/D) = \frac{P(D/\theta) \cdot P(\theta)}{P(D)} \tag{1}$$

where D represents the vector of the measurements (or observations); $P(\theta)$ represents the prior distribution; $P(D/\theta)$ represents the likelihood function of the parameters, $P(D)$ represents the evidence; and $P(\theta/D)$ represents the posterior distribution (the target distribution from which sampling is done).

Figure 1 shows the flowchart of the Bayesian FE model updating of a civil engineering structure. According to this flowchart, the linking between a FE analysis package (Ansys, 2023) and a mathematical package (Matlab, 2022) is considered.

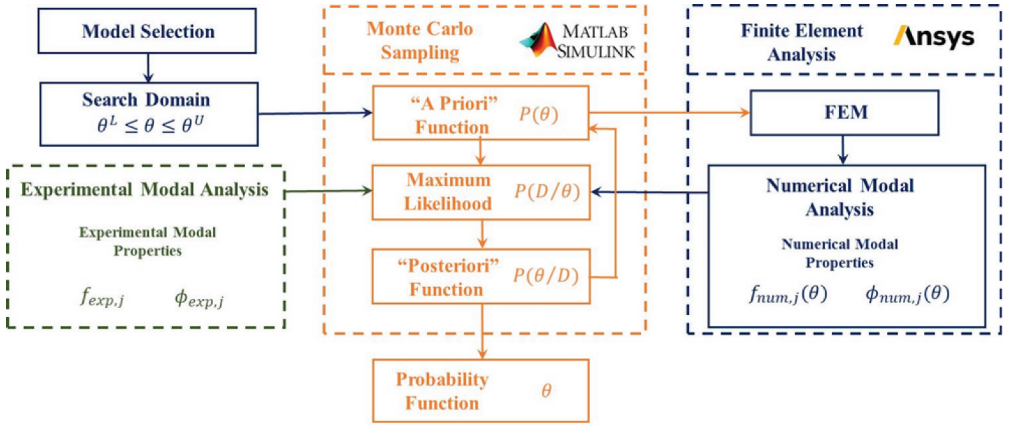


Figure 1. Flowchart for the Bayesian FE model updating of a civil engineering structure.

As a result of the Bayesian FE model updating process, a stochastic FE model of the structure is considered. According to this model, the main physical parameters that characterize

the behavior of the structure are defined as random variables. In this manner, this model can be used to simulate the abovementioned uncertainty conditions.

4 CONTINUOUS WAVELET TRANSFORM FOR FEATURE EXTRACTION

The dynamic response of bridges subjected to the crossing of a high-speed train is non-stationary in nature due to their frequency variation with time. Several researches have been performed to assess the deterioration state of these structures based on the data analysis of this response. Generally, the Fourier transform (FT) is used in these studies. FT breaks down a time series signal into its component frequencies. Therefore, FT is a mathematical decomposition of a signal in its discrete constituting components. Thus, FT allows transforming a signal from the time domain to the frequency domain.

For feature extraction, in signal processing, it is needed to transform the signal in time and frequency domains simultaneously. For this purpose, the FT is commonly used. However, this transform does not generate the actual time history of frequency variation when the frequency components are changing in the time domain. The FT of a time series signal, $x(t)$, is given below:

$$FT(w) = \int_{-\infty}^{\infty} x(t) \exp(-2\pi jft) dt \tag{2}$$

FT of a time series signal is the inner product between the given signal and the basis function, $\exp(-2\pi jft)$, in where t represents the time. FT is unable to detect any local variation in the time domain. Therefore, it is not ideal for non-stationary time signal analysis.

A partial solution to solve this problem, is the so-called the short-time Fourier transformation (STFT). In this transform a short-duration fixed window, $\mathbf{w}(\mathbf{t} - \tau)$, is used to extract all frequencies content in that time window. The STFT may be expressed as:

$$STFT(w, \tau) = \int_{-\infty}^{\infty} x(t)\mathbf{w}(\mathbf{t} - \tau) \exp(-2\pi jft) dt \tag{3}$$

However, the STFT presents a main problem, it has a fixed window (fixed frequency) which enables only short and fixed time–frequency resolution. In order to overcome this limitation, Wavelet transformation (WT) can be used.

WT is a computational tool that allows identifying local variations within a time series. This transform is a powerful technique to analyze random oscillation in a time series. As result of the WT a time-frequency spectrum is obtained. WT can be classified into two categories: (i) continuous Wavelet Transform (CWT); and (ii) discrete Wavelet Transform (DWT). The first category, CWT, is usually employed for feature extraction from time series. The idea of CWT was derived from short-time Fourier transform (STFT), where the time duration window is modified to extract all the frequencies within the window.

In this manner, the basic idea behind this transformation is the definition of the wavelet as a band-pass filter to the time series signal. This causes the translation and dilation of the mother wavelet. Therefore, this transform can expand a time series in the time and frequency domains at the same time. Therefore, CWT can examine and find a localized anomaly in time series analysis distributed at equal intervals. The CWT of a signal, $x(t)$, at scale, a, and time, b, can be defined as:

$$CWT(a, b) = \int_{-\infty}^{\infty} x(t) \frac{1}{\sqrt{a}} \psi^* \left(\frac{t - b}{a} \right) dt \tag{4}$$

where ψ is the mother wavelet; *is the complex conjugate; $CWT(a, b)$ are the CWT coefficients; a is the translation parameter; and b is the dilation parameter.

In this manner, small values of a cause the contraction of the mother wavelet producing high-frequency functions, while high values of a cause the stretching of the mother wavelet producing low-frequency.

In this study, the dynamic response of a high-speed railway is processed via a CWT. In this manner, the CWT coefficients are considered for the feature extraction. In particular, the scalogram, a frequency-time representation of these coefficients is considered for this purpose. Figure 2 shows the representation of the dynamic response of a high-speed railway bridge in the frequency-time domain.

5 PRE-TRAINED CONVOLUTION NEURAL NETWORKS FOR IMAGE CLASSIFICATION

As ML tool, a CNN has been considered in this study. A CNN is a special type of ANN which is specifically designed to classified images. One of the main advantages of using DL is that the algorithm extracts autonomously the features from the inputs (images).

As the design of this type of DL tool implies the determination of a high number of design parameters (associated with the parameters of the hidden layers of the ANN) a great data set together with a high simulation time is required to train the model. In order to overcome this limitation, the practical rule is to take advantage of a previously designed CNN and to adapt it to the new particular problem. This second approach, denominated as a pre-trained CNN, has been considered in this study. Among the different existing architecture, due to its good balance between complexity the accuracy of the results, the AlexNet CNN has been considered (Talaei et al, 2023).

In order to adapt this CNN to the DD problem, some layers of the CNN have been modified. In particular, the output layer has been modified to take into account the classification problem. Two classes have been considered for this purpose: (i) undamaged; and (ii) damaged state.

Finally, as data set of the pre-trained CNN a set of images must be generated. For this purpose, the CWT scalogram of the dynamic response of the bridges subjected to the crossing of a high-speed train has been considered. In this manner, the integration of the CWT and the pre-trained CNN allows designing an advanced classification model. Figure 2 shows a scheme of the CWT-CNN model.

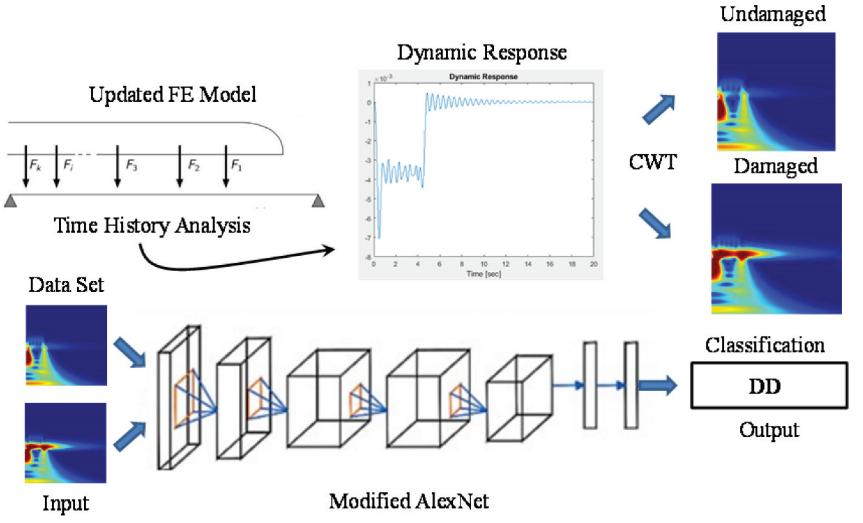


Figure 2. Flowchart of the CWT-CNN algorithm for DD.

6 VALIDATION EXAMPLE

As validation example, a single span high-speed railway bridge has been considered. The length of the span is about 58 m. The deck consists of a post-tensioned box-girder concrete structure. The depth of the deck is about 3.9 m. The following mechanical and material properties have been considered to model the structure: (i) cross-section area, 9.37 m^2; (ii) cross-section inertia, 19.59 m^4; (iii) concrete density, 2500 kg/m^3; (iv) concrete Young's modulus, 35000 MPa; (v) ballast mass, 13200 kg/m; and (vi) damping ratio, 2%.

A FE model of the structure is performed using a commercial FE package (Ansys, 2023). The dynamic response of the structure subjected to the crossing of a high-speed train is computed. The ICE2 train is considered for this purpose. As train velocity of 300 km/h has been taken into account. To compute the time history analysis a time increment of 0.01 sec and a total integration time of 20 secs have been considered. A full integration method has been considered. The damping matrix has been defined according to the Rayleigh method. The response of the structure is obtained considered undamaged and damaged conditions. The damage conditions have been simulated numerically reducing the stiffness of the structure. In order to take into account, the influence of the damage level in the performance of the classification method, a sensitivity analysis has been performed. Table 1 shows the damage level considered herein.

It is assumed that this FE model is updated, considering the Bayesian inference approach, based on the experiment modal properties identified from a long-term monitoring process. According to this, the FE model is re-defined according to a stochastic approach. Thus, three constitutive parameters have been updated as random normal variables (concrete density, concrete Young's modulus, ballast mass). As mean value of the normal distribution the aforementioned value has been considered. In order to taken into account, the influence of the variability of the operational and environmental conditions in the performance of the ML method, a sensitivity analysis has been performed. Table 1 shows the uncertainty level considered (range of variation of the random variables).

Subsequently, the dynamic response of the structure (times series), considering the two states (undamaged and damaged), has been transformed into an image using the CWT (scalogram). A data set, with 2000 images, has been considered to train (75% data set) and test (25 % data set) a pre-trained CNN (AlexNet) for each numerical simulation. In each simulation both a level of damage and uncertainty level have been taken into account. Ten epochs have been considered for the training process. The evolution of the accuracy of the pre-trained CNN in terms of the training together with the resulting confusion matrix are shown in Figure 3. The CWT-CNN model has been implemented in a mathematical package (Matlab, 2023).

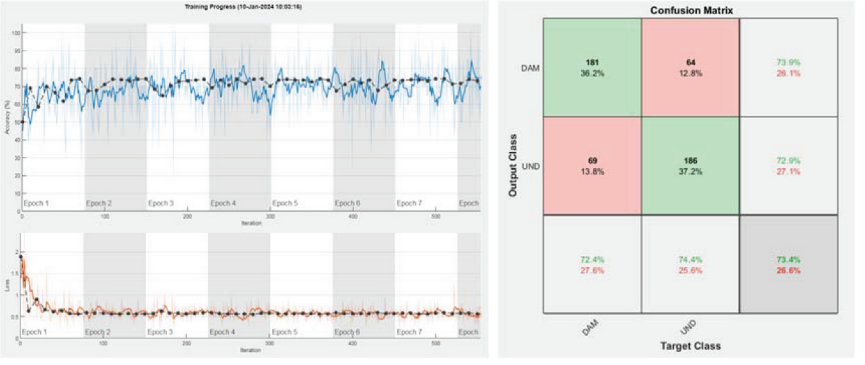


Figure 3. Training and testing process of the considered pre-trained AlexNet CNN.

As key-parameter to check the performance of the CWT-CNN method, the accuracy ratio is considered. The accuracy ratio is defined as the relation between the correct predictions of the model and the total predictions (based on the result of the confusion matrix). Finally, Table 1

shows the variation of the accuracy ratio of the neural network in terms of the uncertainty of the model and the damage level generated. As it is shown in Table 1, a clear reduction of the accuracy of the classification method is obtained when the uncertainty associated with the variability of the operational and environmental conditions masks a low damage level.

Table 1. Variation of the accuracy ratio of the pre-trained CWT-CNN in terms of the uncertainty of the model and the damage level generated.

	Damage level					
Uncertainty	0.05	0.10	0.15	0.20	0.25	0.30
0.05	0.984	1.000	1.000	1.000	1.000	1.000
0.10	0.884	0.988	1.000	1.000	1.000	1.000
0.15	0.790	0.938	0.990	1.000	1.000	1.000
0.20	0.734	0.892	0.968	0.992	1.000	1.000

7 CONCLUSIONS

In this manuscript, the performance of a CWT-CNN method is assessed when it is implemented for the DD of high-speed train bridges under uncertainty conditions. In particular, the influence of the uncertainty associated with the variability of the operational and environmental conditions is analyzed in detail. A stochastic method, a Bayesian inference technique has been considered for this purpose. Two possible states of the structure are considered (undamaged and damaged). The dynamic response of the structure subjected to the crossing of a high-speed train has been compared considering two scenarios undamaged and damaged structure. The damage state of the structure has been simulated numerically based on an updated Bayesian FE model of the bridge. The performance of a classification method, based on a ML algorithm, has been assessed herein. As method, the so-called CWT-CNN algorithm, has been considered. As input of the model, the CWT scalogram (image) of the dynamic response of the structure has been computed. As output, the damage state (undamaged or damaged) has been obtained. In order to reduce the training and complexity of the architecture of the DL algorithm, a pre-trained CNN has been taken into account, the AlexNet. As result of this study, a clear reduction of the performance of the proposal is achieved when the uncertainty conditions are high and the damage level is low. As consequence, further studies are needed to improve the performance of ML techniques when they are implemented to cope with the DI problem under uncertainty conditions.

ACKNOWLEDGEMENT

This publication has emanated from research conducted with the financial support of the research project "Transport Infrastructures subjected to dynamic loading: assessment techniques for the sustainability, intelligent maintenance and comfort" Grant number PID2021-127627OB-I00 funded by both Ministerio de Ciencia e Innovación, Agencia Estatal de Investigación and FEDER, European Union (10.13039/501100011033).

REFERENCES

Amanollah, H., Asghari, A., Mashayekhi, M. & Mehdi Zahrai S.M.. 2023. Damage detection of structures based on wavelet analysis using improved AlexNet. *Structures*, 56: 105019.

Anastasia S., García-Macías E., Ubertini F., Gattulli, V. & Ivorra S. 2023. Damage Identification of Railway Bridges through Temporal Autoregressive Modeling. *Sensors*, 23(21), 8830.

Avci, O., Abdeljaber, O., Kiranyaz, S., Hussein, M., Gabbouj, M. & Inman, D.J. 2021. A review of vibration-based damage detection in civil structures: From traditional methods to Machine Learning and Deep Learning applications. *Mechanical Systems and Signal Processing*, 147: 107077.

Chen, L., Chen, W., Wang, L., Zhai, C., Hu, X., Sun, L., Tian, Y., Huang, X. & Jiang, L.. 2023. Convolutional neural networks (CNNs)-based multi-category damage detection and recognition of high-speed rail (HSR) reinforced concrete (RC) bridges using test images. *Engineering Structures*. 276: 115306.

Ereiz, S., Duvnjak, I. & Jiménez-Alonso, J.F. 2022. Review of finite element model updating methods for structural applications. *Structures*. 41: 684–723.

Figueiredo, E., Moldovan, I., Santos, A., Campos, P. & Costa, J.C.W.A.. 2019. Finite element–based machine-learning approach to detect damage in bridges under operational and environmental variations. *Journal of Bridge Engineering*, 24(7): 04019061.

Figueiredo, E., Park, G., Farrar, C.R., Worden, K., & Figueiras, J.. 2011. Machine learning algorithms for damage detection under operational and environmental variability. *Structural Health Monitoring*, 10(6): 559–572.

Figueiredo, E., Yano, M.O., Da Silva S., Moldovan, I. & Bud, M.A. 2023. Transfer learning to enhance the damage detection performance in bridges when using numerical models. *Journal of Bridge Engineering*, 28(1): 04022134.

Ghiasi, R. & Ghasemi, M.R. 2018. An intelligent health monitoring method for processing data collected from the sensor network of structure. *Steel and Composite Structures*, 29(6): 703–716.

Ghiasi, R., Ghasemi, M.R. & Chan, T.H.T. 2021. Optimum feature selection for SHM of benchmark structures using efficient AI mechanism. *Smart Structures and Systems*, 27(4): 623.

Inc, T.M. ANSYS version 2023 R1 (2023R1). Canonsburg, Pennsylvania, United States: Ansys Inc., 2023.

Inc, T.M. MATLAB version: 9.13. 0 (R2022b). Natick, Massachusetts, United States: The MathWorks Inc.; 2022.

Kamariotis, A., Chatzi, E. & Straub, D. 2022. Value of information from vibration-based structural health monitoring extracted via Bayesian model updating. *Mechanical Systems and Signal Processing*, 166: 108465.

Lye A., Cicirello A. & Patelli E. 2021. Sampling methods for solving Bayesian model updating problems: A tutorial. *Mechanical Systems and Signal Processing*, 159: 107760.

Talaei, S., Zhu, X., Li, J., Yu, Y & Chan THT. 2023. Transfer learning based bridge damage detection: Leveraging time-frequency features, *Structures*, 57: 105052.

Bridge Maintenance, Safety, Management, Digitalization and Sustainability – Jensen, Frangopol & Schmidt (eds)
© 2024 The Author(s), ISBN 978-1-032-77040-6
Open Access: www.taylorfrancis.com, CC BY-NC-ND 4.0 license

Data-driven framework for damage detection in structural system

R. Ghiasi
Structural Dynamics and Assessment Laboratory, School of Civil Engineering, University College Dublin, Dublin, Ireland

J.F. Jiménez-Alonso
Escuela Superior de Ingeniería, Universidad de Sevilla, Camino de los Descubrimientos s/n Seville, Spain

A. Malekjafarian
Structural Dynamics and Assessment Laboratory, School of Civil Engineering, University College Dublin, Dublin, Ireland

ABSTRACT: This paper presents an automated methodology for data-driven damage detection (DD) based on feature extraction from the measured vibration responses of civil engineering structures subjected to ambient/operational conditions. To do so, after recording the dynamic response of the structure, feature extraction is performed in the time domain and then the best subset of measurement features that characterize the state of the structure is selected using Analysis of Variance (ANOVA) algorithm. Finally, DD is performed using a machine learning (ML) algorithm trained with selected features. To test the proposed framework, a dataset from a laboratory steel structure is used, and two supervised ML algorithms, K-nearest neighbor classification (KNN) and artificial neural network (ANN) were applied in order to classify damage states. The results showed that both classification techniques were able to successfully classify damage. In addition, the impact of using different feature extraction/selection methods on the accuracy of the proposed approach is studied in detail.

1 INTRODUCTION

Structural health monitoring (SHM) is one of the powerful tools for civil infrastructure management. The SHM process consists of permanent, continuous, periodic or periodically continuous acquisition of parameters by a sensor network, feature extraction and statistical modelling for feature classification to detect possible structural damages and to support the decision making (Ghiasi & Ghasemi, 2018; Avci et al., 2021). Damage is traditionally defined as changes in the material and/or geometric properties of the structures, including variations in the boundary conditions and system connectivity, which adversely affect the system's current or future performance. In contrast, normal condition refers to data acquired under different operational and environmental variability when the structure is known to be undamaged (Ghiasi et al., 2019; Ghasemi et al., 2018).

Significant efforts on SHM have been extensively undertaken (Avci et al., 2021). These studies could be mainly classified in two categories: a) physics-based approaches which are based on vibratory characteristics of structural systems including natural frequency, mode and curvature (Ghiasi et al., 2022), and b) data-driven approaches which extract sensitive features from sensor data to assess the structural conditions (Malekjafarian et al., 2022). In physics-based approaches, the captured sensor data are usually integrated in analytical models or simulations for calibration or interpretation to identify physical characteristics and assess the conditions of a structure. Although analytical models and simulation techniques are now well-established (Ereiz et al., 2022), rapid and accurate interpretation of large volumes of sensor data still lags

DOI: 10.1201/9781003483755-276

behind. Differently, by taking advantage of history sensor data, the data-driven models are robust to rapidly identify the key information from complex and heterogeneous sensor data, which may be no longer valid for the physics-based approaches (Ghiasi et al., 2019).

One of the important steps in data-driven approaches is extracting useful information from raw data which is called Feature Selection (FS) (Ghiasi et al., 2021). FS is generally used in machine learning (ML), especially when the learning task involves high-dimensional datasets. The primary purpose of feature selection is to choose a subset of available features, by eliminating features with little or no predictive information and also redundant features that are strongly correlated (Buckley et al., 2023). The availability of large amounts of data represents a challenge to classification analysis. For example, the use of many features may require the estimation of a considerable number of parameters during the classification process. Thus, the FS approaches is needed to tackle these problems.

The main focus of this research is facilitating the processing of datasets in SHM. Accordingly, the integrated system consisting of four blocks is proposed in this paper. After acquisition of acceleration response data of structure, statistical characteristics of structural response signals under ambient vibration are extracted, and feature vectors are obtained. Subsequently, the best feature subset is selected by the ANOVA analysis as FS algorithm based on importance score (Buckley et al., 2023). In the final step, selected features are employed to train a ML classification model based on the use of an ANN.

The proposed method's performance is evaluated on benchmark dataset of a steel laboratory structure (Jiménez Alonso et al., 2019). The structure has been excited by ambient vibration and the accelerations response of the structure in several characteristic points has been recorded.

Two comparative studies has been performed in order to evaluate the efficacy of the proposal: (i) the ANOVA approach has been compared to the Kruskal-Wallis (Bommert et al., 2020) criterion for FS; and (ii) the accuracy of the ANN classifier algorithm has been assessed in comparison to a conventional KNN classification model.

2 METHODOLOGY

The proposed data-driven approach for bridge health monitoring consists of four steps, which are shown in Figure 1, and the details of each of them are provided below.

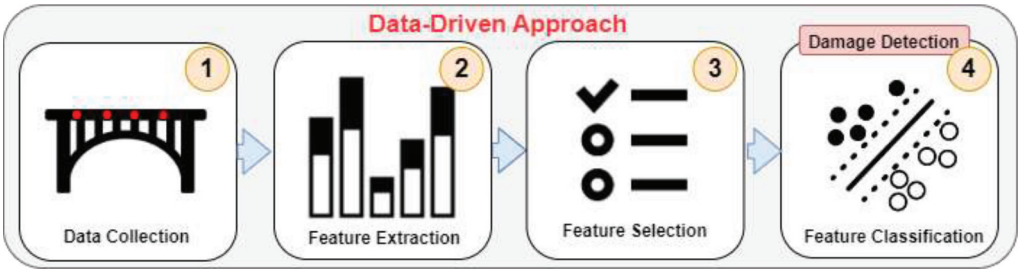


Figure 1. Proposed framework for direct monitoring of bridge.

In the first step, the acceleration response of the structure is recorded using accelerometer sensors on specific points of the structure. The response in the structure can be caused by different moving and static loads (Malekjafarian et al., 2022). In this paper ambient vibration is selected for structural excitation.

In the second step, the functions given in Table 1, are used to form the feature vectors from the data collected by sensors. These features are computed in time domain and provide a summary of the statistical characteristics of the signal over the feature extraction window. It should be mentioned that these features are selected based on the recommendations from previous works in this field (Buckley et al., 2023) and represent the energy, the time series distribution and the vibration amplitude of the signals in time-domain (Ghiasi & Malekjafarian, 2023).

In the third step, the best subset of extracted features will be selected using filter-based FS methods, which calculate the relevance of each feature with respect to the target classes. The features can then be sorted based on their individual relevance to the classes and a top percentage chosen for modelling. Filter methods are independent of classifiers and applied before any modelling is undertaken. A comparison of filter methods for high-dimensional data from different fields is provided in Ref. (Bommert et al., 2020). In this paper the 2 well-known filter-based approaches are used which are: ANOVA and Kruskal-Wallis (Bommert et al., 2020). In both algorithms, the Importance Scores (IS) is determined using F-statistic which compares the distribution variation between groups to the variation within the groups (Ghiasi et al., 2014).

Table 1. Time-domain features.

Feature	Function	Feature	Function
Root mean square	$rms = \sqrt{\frac{\sum_{n=1}^{N}(x(n))^2}{N}}$	Shape factor	$sf = \frac{rms}{\frac{1}{N}\sum_{n=1}^{N}\lvert x(n)\rvert}$
Variance	$var = \sigma^2 = \frac{\sum_{n=1}^{N}(x(n)-mean(x))^2}{(N-1)}$	Impulse factor	$cf = \frac{\max\lvert x(n)\rvert}{\left(\frac{1}{N}\sum_{n=1}^{N}\sqrt{\lvert x(n)\rvert}\right)^2}$
Skewness	$skewness = \frac{\sum_{n=1}^{N}(x(n)-mean(x))^3}{(N-1)\sigma^3}$	Crest factor	$crest = \frac{\max\lvert x(n)\rvert}{rms}$
Kurtosis	$kurtosis = \frac{\sum_{n=1}^{N}(x(n)-mean(x))^4}{(N-1)\sigma^4}$	Signal to noise and distortion ratio (SINAD)	Ratio of total signal power to total noise-plus-distortion power
Total harmonic distortion (THD)	Ratio of total harmonic component power to fundamental power	Signal-to-Noise Ratio (SNR)	Ratio of signal power to noise power

Finally, an ML classification model is used to classify various conditions of the laboratory steel structure. In this model, the input matrix includes the selected features of step 3, and the outputs are the corresponding damage conditions. In recent years, many ML approaches have been proposed or employed for various components of SHM in order to perform pattern classification, function approximation, and regression (Avci et al., 2021). In this paper, the performance of the ANN as a classification algorithm is compared with the kNN algorithm (with Euclidean distance and k = 5) (Gharehbaghi et al., 2023).

3 RESULTS: DAMAGE DETECTION OF A LABORATORY STEEL STRUCTURE

3.1 *Description of the benchmark structure and characterization of its modal properties*

As benchmark, a laboratory steel structure, that was designed and built in University of Almería (Universidad de Almería (UAL)) (Jiménez Alonso et al., 2019) is used to assess the performance of the data-driven based method. The structure consists of two parallel Warren trusses braced laterally by strut elements (Figure 2). The structure has a single span of 6 m in length. The depth of the structure is about 0.30 m. The two lateral Warren trusses are separated 0.60 m. All the elements of the structure are square tube profiles with dimensions 30x30x2 mm (Figure 3).

The stiffness of the upper chord at mid-span was reduced by severe damage (induced by a chainsaw). An ambient vibration test was performed experimentally to assess the dynamic behavior (modal properties) of the structure under the two considered states (healthy and damaged). The dynamic response (accelerations) of the nodes of the upper chords of the structure was recorded. Two points were considered as references. Each ambient vibration test was organized in 18 set-ups with a sampling frequency of 100 Hz and a duration of each step-up of 300 s. Three tri-axial force balanced accelerometers were used for the experimental ambient vibration tests. Figure 3 illustrates the gridline of the ambient vibration tests.



Figure 2. Laboratory footbridge at the Universidad de Almeria.

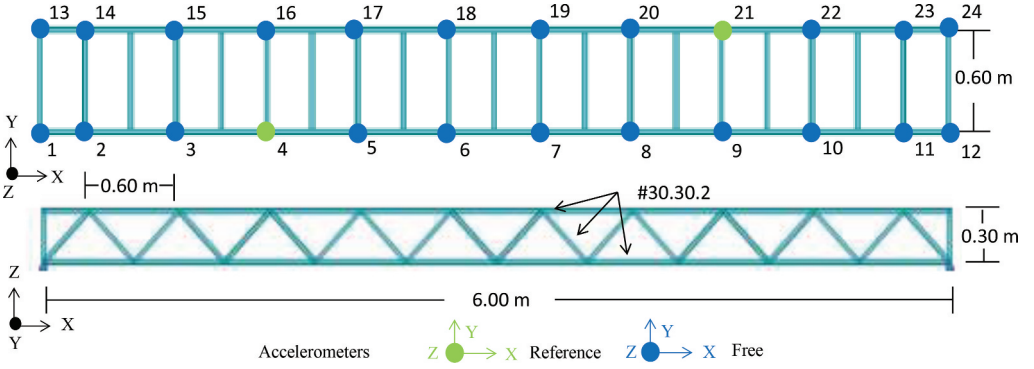


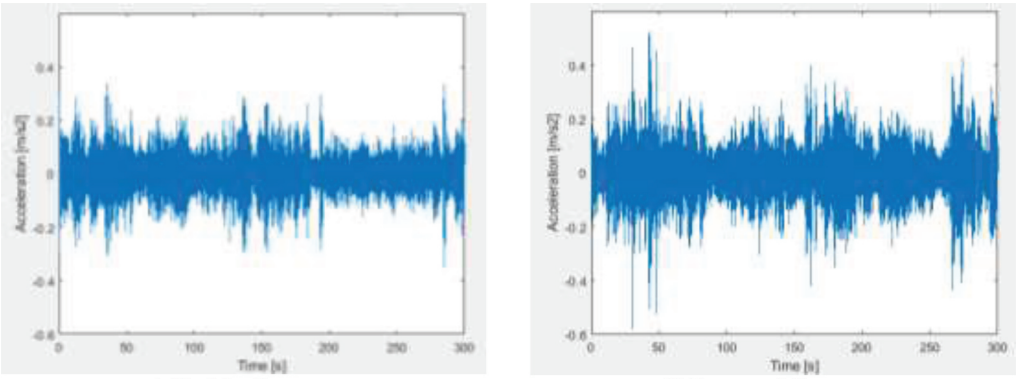
Figure 3. Gridline of the ambient vibration test.

The signal recorded during the ambient vibration tests was processed by an operational modal analysis algorithm (Magalhães et al., 2012). A frequency domain algorithm, the so-called Enhanced Frequency Domain Decomposition method, was considered for this purpose. The algorithm has been implemented in the mathematical software MATLAB (Inc, n.d.). Table 2 shows the variation of the experimental modal properties of the laboratory structure (natural frequencies and vibration modes) associated with the two scenarios (healthy and damaged). In Table 2, f_{exp}^{hea} is the experimental natural frequency of the healthy structure, f_{exp}^{dam} is the experimental natural frequency of the damaged structure, Δf_{exp} is the relative difference of the natural frequencies between the healthy and damaged structure and MAC_{exp} is the experimental MAC ratio (Magalhães et al., 2012).

Table 2. Comparison between the modal properties of the structure corresponding to the two considered states (healthy and damaged).

Mode	Description	f_{exp}^{hea} [Hz]	f_{exp}^{dam} [Hz]	Δf_{exp} [%]	MAC_{exp}[%]
1	1st Lateral	9.75	9.23	-5.33	0.97
2	2nd Lateral	14.50	11.48	-20.83	0.85
3	3rd Lateral	16..17	14.40	-10.95	0.91
4	1st Vertical	20.14	16.55	-17.83	0.95
5	2nd Vertical	23.74	23.44	-1.26	0.91
6	1st Torsion	25.14	21.38	-14.96	0.95

In order to illustrate the response of the structure under ambient conditions, the vertical acceleration of the structure recorded during the ambient vibration test is illustrated in Figure 4. The two considered states, healthy and damaged, are taken into account.



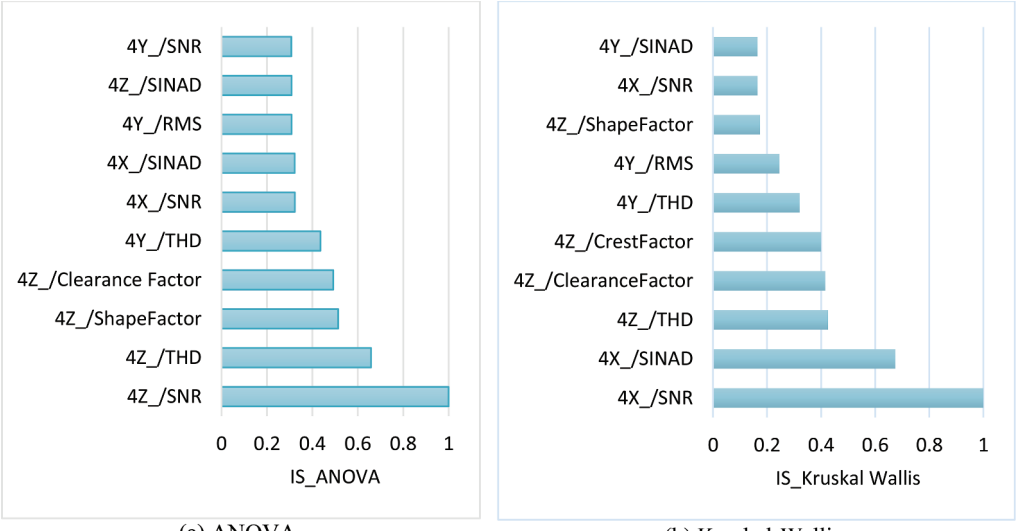
a) Healthy Structure b) Damaged Structure

Figure 4. Recorded signal at point 4 (accelerations in Z direction) considering the two states: (a) healthy structure and (b) damaged structure.

3.2 *Feature extraction and features selection*

After recording the dynamic response of the structure, the static characteristic shown in Table 1 is extracted from the signal in the time domain. In this study, only the response of sensor at point 4 is used. Therefore, considering that the accelerometer sensor stores the response in three directions, the total number of extracted features is equal to 30.

Then, in the third step of the proposed framework, using the FS algorithms, 10 damage-sensitive features are extracted from the entire set of features. The results of FS using ANOVA algorithm are shown in Figure 5 (a). In addition, the effect of using another algorithm for FS on the arrangement of selected features is shown in Figure 5 (b). Both algorithms use the IS to select damage-sensitive features. As shown in Figure 5, most of the selected



(a) ANOVA (b) Kruskal-Wallis

Figure 5. FS based on IS using two filter-based methods (in where "4Y_/FEATURE.", 4 is the position of considered sensor, Y is the considered measurement direction and FEATURE the considered function for FS).

features are related to the vertical direction (Z), which shows its importance and high sensitivity to damage in this benchmark structure.

3.3 *Feature classification*

After extracting the sensitive features in the third step, the last step is the proposed framework is DD using the ANN algorithm. The feature set selected by ANOVA is utilized as input for the algorithm, and the output represents the state of the structure. In addition, a 5-fold cross-validation procedure (Shen et al., 2023) was conducted to assess the average classification performance measures for the classification problem. The result of using ANN algorithm is shown in Figure 6(a). Also, a similar approach has been implemented using the kNN algorithm and its results are shown in Figure 6(b). By comparison of confusion matrixes, it can be seen that both algorithms have a high accuracy in detecting damage in this laboratory structure. Therefore, their true positive rate (TPR) is above 95% and the positive predictive value (PPV) is above 93%, which indicates the optimal accuracy of the proposed framework. Additionally, as it is illustrated by Figure 6, the performance of the ANN model is upper than the kNN model with a higher value of the abovementioned ratios. On the other hand, selecting the Kruskal-Wallis as the FS algorithm resulted in an overall accuracy of 92% with the ANN algorithm and 90% with the kNN algorithm. This indicates that the ANOVA algorithm has identified features with greater sensitivity to damage.

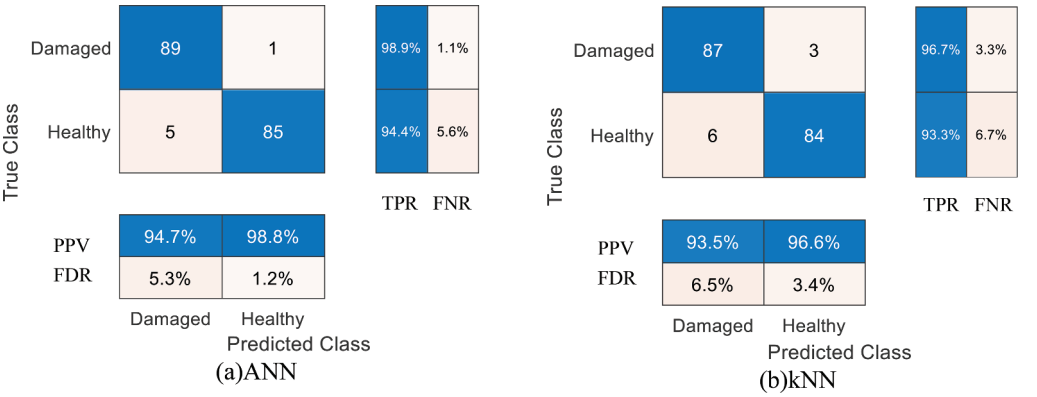


Figure 6. Confusion matrix for ML classifiers.

4 CONCLUSIONS

In this paper, a data-driven framework is presented for the feature selection in SHM problems. To evaluate the capabilities of the framework, the dynamic response of a laboratory steel structure subjected to ambient vibrations has been recorded for healthy and damaged conditions, and its time domain features have been used as input to ML classifiers. The results of this study show the sensitivity and effectiveness of the proposed method for detecting damage in bridges, and the classification accuracy of ANN and kNN is above 95%. A better performance of the ANN model is assessed when it is implemented for DD in this case study.

Moreover, the proposed framework can remove irrelevant and redundant information by choosing useful features as the input of the ML classifiers. These results highlight its potential to be used as a valuable tool for damage detection of civil engineering structures. Nevertheless, further studies are needed to characterize the performance of this proposal when it is implemented for DD in civil engineering structures subjected to environmental and operational conditions.

ACKNOWLEDGEMENT

This publication has emanated from research conducted with the financial support of two research projects: (i) Grant number 20/FFP-P/8706 funded by Science Foundation Ireland;

and (ii) “Transport Infrastructures subjected to dynamic loading: assessment techniques for the sustainability, intelligent maintenance and comfort” Grant number PID2021-127627OB-I00 funded by both Ministerio de Ciencia e Innovación, Agencia Estatal de Investigación and FEDER, European Union (10.13039/501100011033).

REFERENCES

Avci, O., Abdeljaber, O., Kiranyaz, S., Hussein, M., Gabbouj, M. & Inman, D.J. 2021. A review of vibration-based damage detection in civil structures: From traditional methods to Machine Learning and Deep Learning applications. *Mechanical Systems and Signal Processing*, 147: 107077. http://www.sciencedirect.com/science/article/pii/S0888327020304635.

Bommert, A., Sun, X., Bischl, B., Rahnenführer, J. & Lang, M. 2020. Benchmark for filter methods for feature selection in high-dimensional classification data. *Computational Statistics and Data Analysis*, 143: 106839. https://doi.org/10.1016/j.csda.2019.106839.

Buckley, T., Ghosh, B. & Pakrashi, V. 2023. A Feature Extraction & Selection Benchmark for Structural Health Monitoring. *Structural Health Monitoring*, 22(3): 2082–2127.

Ereiz, S., Duvnjak, I. & Jiménez-Alonso, J.F. 2022. Review of finite element model updating methods for structural applications. In *Structures*. Elsevier: 684–723.

Gharehbaghi, V.R., Kalbkhani, H., Noroozinejad Farsangi, E., Yang, T.Y. & Mirjalili, S. 2023. A data-driven approach for linear and nonlinear damage detection using variational mode decomposition and GARCH model. *Engineering with Computers*, 39(3): 2017–2034. https://doi.org/10.1007/s00366-021-01568-4.

Ghasemi, M.R., Ghiasi, R. & Varaee, H. 2018. Probability-Based Damage Detection of Structures Using Surrogate Model and Enhanced Ideal Gas Molecular Movement Algorithm. In A. Schumacher, T. Vietor, S. Fiebig, K.-U. Bletzinger, & K. Maute, eds. *Advances in Structural and Multidisciplinary Optimization: Proceedings of the 12th World Congress of Structural and Multidisciplinary Optimization (WCSMO12)*. Cham: Springer International Publishing: 1657–1674. https://doi.org/10.1007/978-3-319-67988-4_124.

Ghiasi, R. & Ghasemi, M.R. 2018. An intelligent health monitoring method for processing data collected from the sensor network of structure. *Steel and Composite Structures*, 29(6): 703–716.

Ghiasi, R., Ghasemi, M.R. & Chan, T.H.T. 2021. Optimum feature selection for SHM of benchmark structures using efficient AI mechanism. *Smart Structures and Systems*, 27(4): 623.

Ghiasi, R., Ghasemi, M.R., Noori, M. & Altabey, W. 2019. A non-parametric approach toward structural health monitoring for processing big data collected from the sensor network. In *Structural Health Monitoring 2019: Enabling Intelligent Life-Cycle Health Management for Industry Internet of Things (IIOT) - Proceedings of the 12th International Workshop on Structural Health Monitoring*.

Ghiasi, R. & Malekjafarian, A. 2023. Feature subset selection in structural health monitoring data using an advanced binary slime mould algorithm. *Journal of Structural Integrity and Maintenance*: 1–17.

Ghiasi, R., Noori, M., Kuok, S.-C., Silik, A., Wang, T., Pozo, F. & Altabey, W.A. 2022. Structural Assessment under Uncertain Parameters via the Interval Optimization Method Using the Slime Mold Algorithm. *Applied Sciences*, 12(4): 1876.

Ghiasi, R., Torkzadeh, P. & Noori, M. 2014. Structural damage detection using artificial neural networks and least square support vector machine with particle swarm harmony search algorithm. *International Journal of Sustainable Materials and Structural Systems*, 1(4): 303–320.

Inc, T.M. MATLAB version: 9.13. 0 (R2022b). Natick, Massachusetts, United States: The MathWorks Inc.; 2022.

Jiménez Alonso, J.F., López Martínez, J., Blanco Claraco, J.L., González Díaz, R. & Sáez Pérez, A. 2019. A topological entropy-based approach for damage detection of civil engineering structures. In *CMMoST 2019: 5th International Conference on Mechanical Models in Structural Engineering (2019), pp.* 35-42. Editorial Club Universitario.

Magalhães, F., Cunha, Á. & Caetano, E. 2012. Vibration based structural health monitoring of an arch bridge: From automated OMA to damage detection. *Mechanical Systems and signal processing*, 28: 212–228.

Malekjafarian, A., Corbally, R. & Gong, W. 2022. A review of mobile sensing of bridges using moving vehicles: Progress to date, challenges and future trends. In *Structures*. Elsevier: 1466–1489.

Shen, C., Zhang, P., Dollevoet, R., Zoeteman, A. & Li, Z. 2023. Evaluating railway track stiffness using axle box accelerations: A digital twin approach. *Mechanical Systems and Signal Processing*, 204 (August): 110730. https://doi.org/10.1016/j.ymssp.2023.110730.

Bridge Maintenance, Safety, Management, Digitalization and Sustainability – Jensen, Frangopol & Schmidt (eds)
© 2024 The Author(s), ISBN 978-1-032-77040-6
Open Access: www.taylorfrancis.com, CC BY-NC-ND 4.0 license

Measurement and structural behavior of suspended swaying pedestrian bridge

E.-S. Hwang
Department of Civil Engineering, Kyung Hee University, Yongin, Korea
HES Consultant Co., Seoul, Korea

S.-H. Shin
Cable Bridge Co., Seoul, Korea

T.R. Park
Ino-on Co., Seoul, Korea

D. Hwang
Institute of CEE, Seoul National University, Seoul, Korea(former)

ABSTRACT: Currently a number of suspended swaying pedestrian bridges are constructed and planned in Korea by mainly local governments. However, the structural behavior of these bridges is not completely known or analyzed and maintenance system has not been implemented yet compared to other road and railway bridges. In this study, various monitoring sensors and systems are applied on a typical swaying pedestrian bridge and longterm monitoring data are collected to investigate the behavior and performance of the bridge. To find the displacement and location movements, GNSS system has been installed on the two locations of the bridge: one at the center of the bridge and the other at anchorage of the bridge. Since the swaying bridge has the shape of suspended cable, the sag is very important static characteristics of the bridge and it can be effectively measured using GNSS system. Dynamic vertical and lateral displacement can also be monitored using this system. To collect the vibration and other environmental data such as wind and temperature, IoT (Internet of Things) system are proposed and installed on the same swaying bridge together with GNSS system. IoT system can measure the accelerations and inclinations as well as strains, temperature and wind speed and direction using its digital and analog inputs. IoT system also has a capability of transmitting data into any data storage via Wifi or LTE connection. Acceleration data may be used to calculate the dynamic characteristics such as natural frequencies and damping ratios. Together with the temperature and wind data, the variance of the sag, static and dynamic characteristics of the bridge may be investigated effectively. The results of this study can be used to develop the comprehensive design and evaluation criteria for swaying bridges.

1 INTRODUCTION

Currently a number of swaying pedestrian bridges are constructed and planned in Korea by mainly local governments, as shown in Figure 1. Also the length of the bridge increases competitively as the years go by. However, the structural behavior of these bridges is not completely known or analyzed and maintenance system has not been implemented yet compared to other road and railway bridges. In this study, various monitoring sensors and systems are applied on a typical swaying pedestrian bridge and long-term monitoring data are collected to investigate the behavior and performance of the bridge. To find the displacement and location

DOI: 10.1201/9781003483755-277

movements, GNSS (Global Navigational Satellite System) has been installed on the two locations of the bridge: one at the center of the bridge and the other at anchorage of the bridge. This system can monitor the settlement and movement at the anchorage ground as well as can increase the accuracy of the location data. Since the swaying bridge has the shape of suspended cable, the sag is very important static characteristics of the bridge and it can be effectively calculated using GNSS system. Dynamic vertical and lateral displacement can also be monitored using this system. To collect the vibration and other environmental data such as wind and temperature, IoT (Internet of Things) system are proposed and installed on the same swaying bridge together with GNSS system. IoT system can measure the accelerations and inclinations as well as strains, temperature and wind speed and direction using its digital and analog inputs. IoT system also has a capability of transmitting data wirelessly into any data storage via Wifi or LTE connection. Acceleration data may be used to calculate the dynamic characteristics such as natural frequencies and damping ratios. Together with the temperature and wind data, the variance of the sag, static and dynamic characteristics of the bridge may be investigated effectively. Based on the results of this study, long-term monitoring system is proposed and the comprehensive design and evaluation criteria for swaying bridges can be developed and verified.

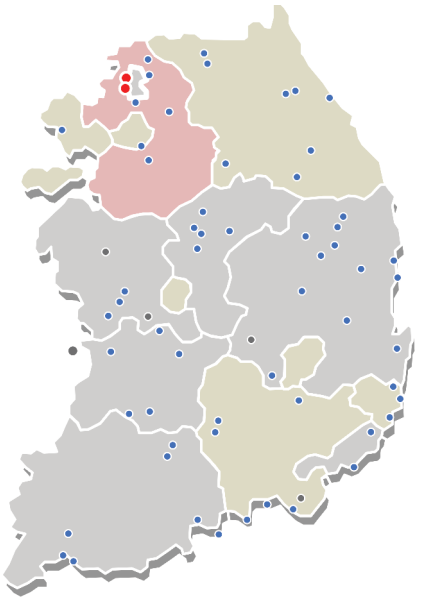


Figure 1. Locations of suspended swaying bridges in Korea.

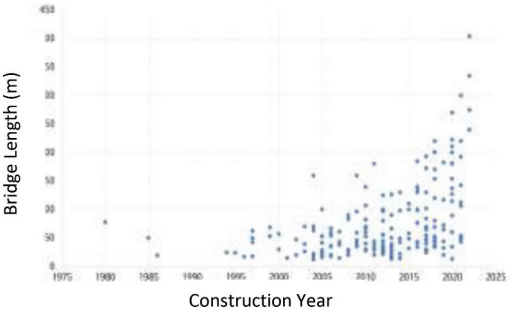
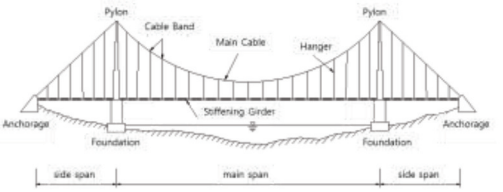


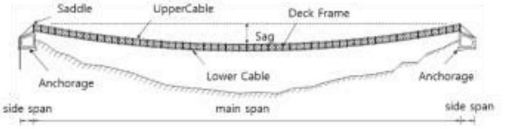
Figure 2. Increase of bridge length by construction year.

2 STRUCTURE OF SWAYING BRIDGES

There are generally two types of suspension swaying bridges; with or without pylons as shown in Figure 3. The swaying bridge with pylons has the similar shape with the conventional suspension bridges for roads or railways. To have swaying behavior, the deck frame or stiffening girder has segmental structure and no or minimum longitudinal stiffness. To design or evaluate swaying pedestrian bridges, several structural characteristics must be checked such as sag, static and dynamic displacement (vertical and lateral), deck accelerations, natural frequencies, damping, anchorage movement or inclination as well as wind and temperatures.



(a) Suspended swaying bridge with pylons



(b) Suspended swaying bridge without pylons

Figure 3. Types of suspended swaying bridges.

3 PROPOSED MONITORING SYSTEM FOR SWAYING BRIDGES

For general long span bridges such as cable-stayed or suspension bridges for roads and railways, comprehensive monitoring system has been installed as shown in Figure 4. It is equipped with many high-end and expensive sensors and data is monitored in real-time, displayed and stored. Also there is maintenance office near the bridge, some engineers and maintenance specialists. However, swaying pedestrian bridge usually have rather simple structural system and relatively small size in terms of bridge length and width. Consequently, construction cost and maintenance budget is low then it is impractical to have a large scale monitoring system. Furthermore, since the structural system is rather simple, there is a little space for installing sensors, electric cables. Therefore, low-cost, light, and wireless system is suitable for swaying pedestrian bridges.

To monitor the behavior of swaying bridges, several sensors should be used. Displacement data such as sag, static and dynamic displacement are measured by GNSS system. Sag is one of the most important characteristics of suspension-type structures and can be calculated as the distance between elevations of saddle and mid span of the cable. Settlement or movement of the anchorage also may be measured by GNSS. Accelerations and inclinations can be monitored by IoT sensor. It also has capability of transmitting data wirelessly by Wifi or LTE and connecting external sensors such as thermometer or wind gauge.

Figure 5 shows 1st version of the proposed monitoring system for swaying bridges. One GNSS includes two antennas (one in the midspan and one in the anchorage) and one receiver. Two IoT systems are installed on midspan and anchorage. Midspan IoT system is connected with wind sensor and thermometer measuring cable temperature. To verify the applicability of the long-term monitoring system, a test system with one GNSS and one IoT sensor was installed on a actual swaying bridge with main span length of 200 m as shown in Figure 6. It is also equipped with battery pack and solar charging panel for long-term monitoring. Data is transmitted via LTE to data server. Analysis of data measured by this monitoring system is explained in the next section.

After the successful application of the 1st version of monitoring system, it is upgraded to 2nd version to have more stable and reliable data collecting and easy installation. In the 1st version, GNSS data and IoT data are collected separately. But in the 2nd version, these are combined as one system so that the system becomes smaller and simpler and has more efficient data collection. The two combined systems are installed in midspan and anchorage, as shown in Figure 7.

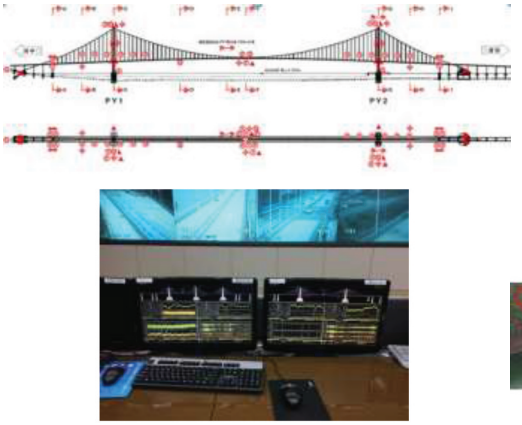


Figure 4. Typical monitoring system and real-time monitoring for general long-span bridge for roads and railways.

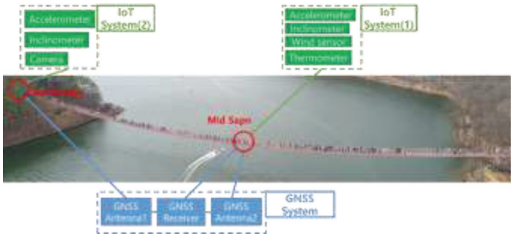


Figure 5. 1st version of proposed monitoring system for swaying pedestrian bridges.

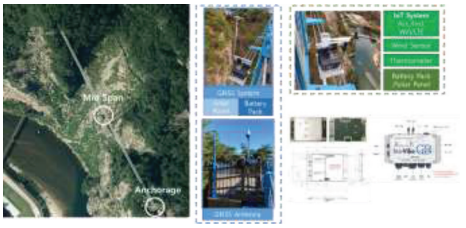


Figure 6. Installation of 1st version of proposed monitoring system on an actual swaying pedestrian bridge.

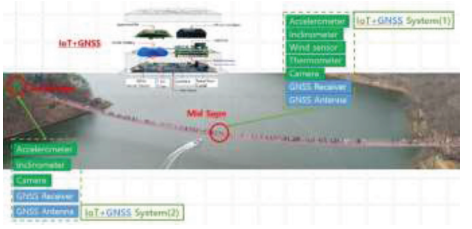


Figure 7. 2nd version of proposed monitoring system for swaying pedestrian bridges.

4 ANALYSIS OF MEASURED DATA

4.1 *Sag and vertical deflection*

The sag of the bridge can be calculated from altitudes of two antennas located at anchorage and midspan. Figure 8 shows the altitudes of two locations; anchorage (alt_val_x) and midspan (alt_val_y) during a day (from Dec. 29 9am to Dec. 30 9am, 2022). Even though the altitude of the anchorage is supposed to be constant, it shows some variations up to around 6.2 m due to the GNSS system error. However, since the same error also occurred on midspan altitude, sag can be accurately calculated from the relative altitudes of two points. Figure 9 shows the calculated sag of the same time period. It shows that sag varies as the temperature is increased or decreased. Figure 10 shows sag or vertical deflection during 1-minute time period. It shows the vertical dynamic deflection and some oscillations due to pedestrian walking.

To show the relationship between the sag and the temperature, 10-minutes' minimum, maximum and average value of the sag during a week (2022.12.29~2023.1.4) are calculated and shown in Figure 11 with the measured cable temperatures. It clearly shows that the sag and the temperature are in strong relationship. The sag in design document is 7.358 m based on the ambient temperature of 20 °C (Cable Bridge, 2017).

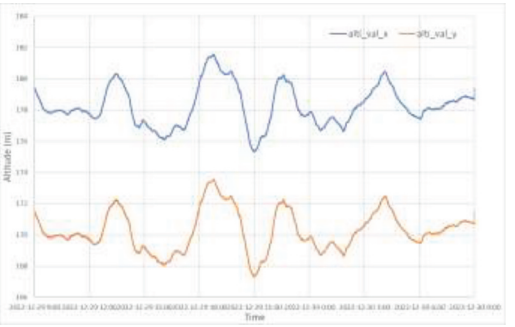


Figure 8. Altitudes of two GNSS antennas; anchorage (alt_val_x) and midspan (alt_val_y).

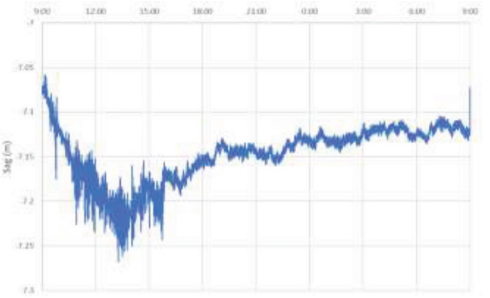


Figure 9. Measured sag during a day (2022.12.09~10).

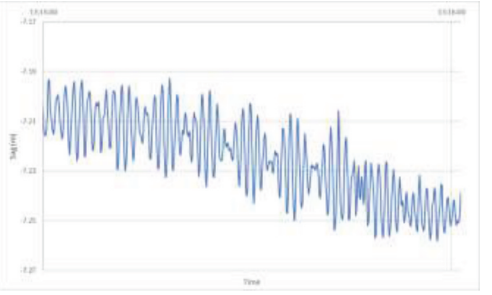


Figure 10. Measured dynamic deflection during 1 minute.

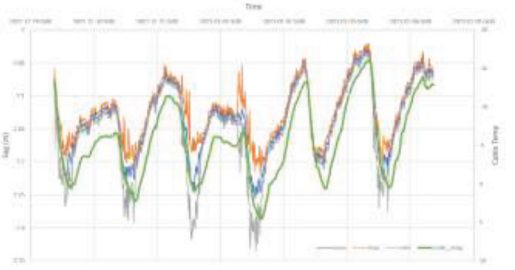


Figure 11. Measured sag and cable temperature during a week (2022.12.29~2023.1.4).

4.2 *Lateral displacement*

The lateral displacement is another characteristic of swaying bridges. To calculate the lateral displacement, the latitude and longitude from GNSS data is used. Figure 12 shows the variations of the latitude and longitude from two GNSS antennas. It shows larger lateral displacements during the opening hours of the bridge and less displacement during the night time without any pedestrian. The actual lateral displacement values should be calculated using geodetic considerations. There are a couple of methods to calculate the distance from latitude and longitude values. One is the relatively simpler method using the Haversine formula and the other is the method based on Vincenty formula. In this study, the Vincenty algorithm with inverse scheme is applied. Figure 13 shows the scatter plot during a day and maximum lateral displacement is about 92 mm and direction of lateral movement is perpendicular to the bridge axis.

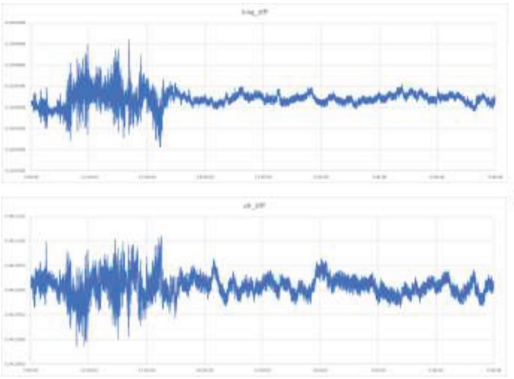


Figure 12. Variations of latitude and longitude of bridge midspan during a day (2022.12.09).

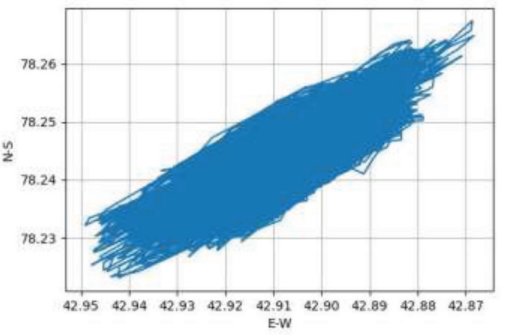


Figure 13. Lateral displacement of midspan GNSS antenna during a day (2022.12.09).

4.3 *Acceleration and natural frequencies*

Figure 14 shows accelerations in three directions during 10 minutes (2023.1.4 13:00:00~13:10:00). X-direction is longitudinal and accelerations are near zero. Y-direction is lateral and Z-direction is vertical. Vertical acceleration is larger than lateral acceleration. Figure 15 shows 10-minutes maximum and rms (root-mean-square) accelerations during a day (2023.1.6). The maximum vertical acceleration is about 0.4 m/s^2 and lateral acceleration is

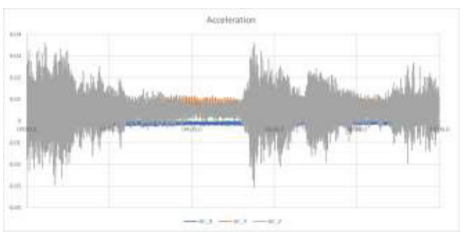


Figure 14. 10-minutes acceleration record in three directions (2023.1.4 13:00:00~13:10:00).

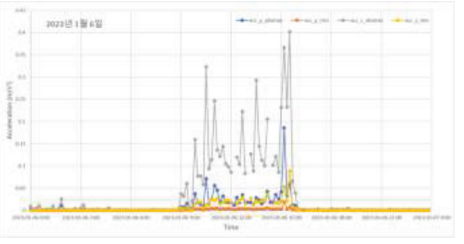


Figure 15. 10-minutes maximum and rms accelerations during a day (2023.1.6).

about 0.18 m/s^2, less than half of vertical acceleration. It also shows that the peak acceleration time is almost the same for vertical and lateral direction, which means that the torsional vibration may be dominant. In case of rms accelerations, the same trend is observed and maximum vertical and lateral rms accelerations are about 0.09 m/s^2 and 0.02 m/s^2, respectively.

Figure 16 shows 10-minutes vertical and lateral rms accelerations during a week (2022.12.29~2023.1.4). The tested swaying bridge is open to public usually from 9AM to 5PM during winter season and closed on every Monday. Since Jan. 2nd, 2023 is Monday, rms acceleration is nearly zero. Maximum rms vertical acceleration during this week is about 0.073 m/s^2 and maximum lateral acceleration is about 0.014 m/s^2.

Figure 17 and Figure 18 show 1-hour vertical acceleration records and corresponding PSD functions during opening hours (3pm~4pm) and closing hours (9pm~10pm), respectively. They show that the dominant natural frequencies are different. During the opening hours, dominant frequency is about 0.8 Hz, which is considered as one of the natural frequencies of the bridge. It also show a small peak at about 1 Hz, which is considered as the pedestrian walking frequency. However, during the closing hours, measured accelerations are about 0.01 m/s^2 and PSD function shows small peaks at 0.25 Hz, 0.54 Hz and 0.8 Hz, which are

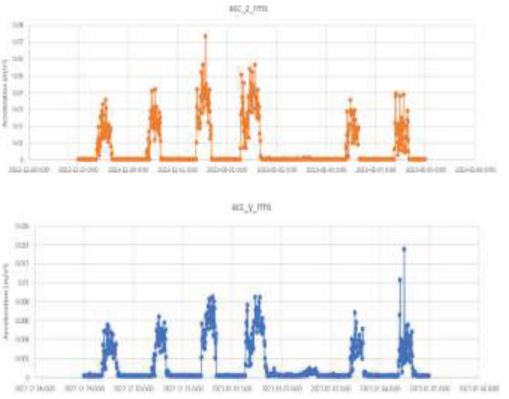
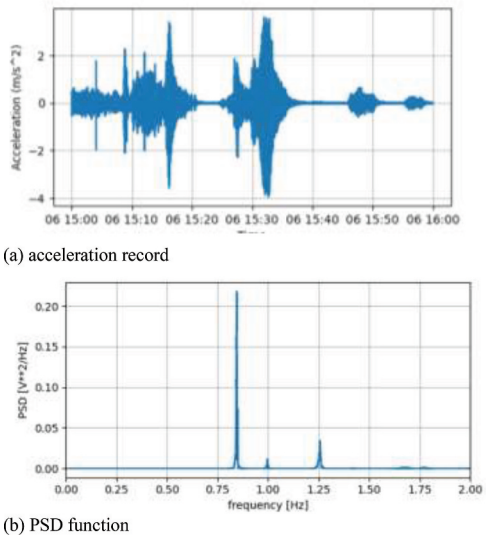


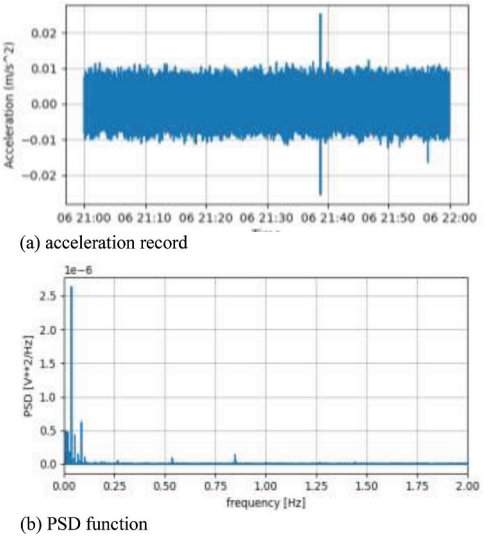
Figure 16. 10-minutes rms accelerations during a week (2022.12.29~2023.1.4).



(a) acceleration record

(b) PSD function

Figure 17. Acceleration records and corresponding PSD functions during opening hours.



(a) acceleration record

(b) PSD function

Figure 18. Acceleration records and corresponding PSD functions during closing hours (9pm ~ 10pm).

Table 1. Comparison of Natural Frequencies from Analysis and Tests.

		Natural frequencies (Hz)	
Mode No.	Mode shape	Analysis	Tests
1	1st lateral, sym.	0.255	0.239
2	1st vert., asym.	0.364	0.383
3	1st vert., sym.	0.491	0.503
4	1st lateral, asym.	0.541	0.525
5	2nd vert., sym.	0.601	0.682

natural frequencies of the bridge. In 2018, Korean Institute of Bridge and Structural Engineers test this pedestrian bridge and calculated natural frequencies by analysis and walking tests (KIBSE 2018). Results are shown in Table 1. It shows that the first natural frequency is

about 0.25 Hz (lateral symmetric mode). Since the IoT sensor is installed at midspan of the bridge, it can effectively show the first natural frequency in symmetrical vertical mode, which is about 0.5 Hz. More comprehensive analysis is required for analyzing vibration natural frequency and natural mode.

5 CONCLUSIONS

In this study, monitoring system using GNSS and IoT sensor for swaying pedestrian bridge is proposed and its applicability is analyzed using measurement data in real swaying bridge. Following conclusions can be made;

- Sag can be accurately measured by GNSS. It shows strong correlation with the temperature.
- Accelerations in three directions can be effectively monitored using IoT sensor.
- The proposed system can be effectively used as a long-term monitoring system.

More detailed analysis of long-term data is needed and results of this study are expected to be the basis for developing effective and economical monitoring system for swaying bridges as well as design and evaluation guidelines.

REFERENCES

Cable Bridge Co. (2017). Structural Calculation of Wonju Sogeumsan Swaying Bridge. Project Report.

Hwang, E.-S., Hwang, M. T. and Park, W. S. (2022). "Analysis of Vibration Characteristics of Swaying Bridges by Pedestrian Walking Tests." Proc. of Annual Convention of Korean Society of Steel Construction.

KIBSE (2018). Analysis on Structural Vibration of Wonju Sogeumsan Swaying Bridge. Final Report, Korean Institute of Bridge and Structural Engineers (in Korean).

Ministry of Land and Transportation (2021). Design Guidelines for Swaying Bridges. Korean Institute of Bridge and Structural Engineering (in Korean).

Ministry of Land and Transportation (2021). Manual of Safety Management for Swaying Bridges. Korean Institute of Bridge and Structural Engineering (in Korean).

Park, H. C., Hwang, E.-S., Kim, C. S. and Park, Y. J. (2022). "Research on Improvement of Safety Management for Swaying Bridges." Proc. of Annual Convention of Korean Society of Steel Construction


Taylor & Francis
Taylor & Francis Group
http://taylorandfrancis.com

SS18: Human-bridge managing interfaces through digital twinning

Organizers: R. Chacón, I. Stipanovic & J.R. Casas


Taylor & Francis
Taylor & Francis Group
http://taylorandfrancis.com

Bridge Maintenance, Safety, Management, Digitalization and Sustainability – Jensen, Frangopol & Schmidt (eds)
© 2024 The Author(s), ISBN 978-1-032-77040-6
Open Access: www.taylorfrancis.com, CC BY-NC-ND 4.0 license

A framework for an integrated & digitally-supported bridge management

S. Moghtadernejad, Z. Lounis & J. Zhang
National Research Council Canada, Ottawa, ON, Canada

ABSTRACT: Presently, there is an increasing need to exploit digitalization in the construction industry due to its potential benefits in improving productivity and reducing the costs and negative environmental impacts of construction activities. This puts bridge managers in a perfect position to leverage the recent technological advancements and data availability to move beyond their existing prescriptive approaches that are iterative, lack the consideration of climate change impacts and risks, and suffer from cost overruns. This study proposes a framework for managers to digitalize bridge management activities. The framework generates a modular system using BrIM, a bridge version of BIM and incorporates methodologies for bridge deterioration and failure risk modelling in the context of a changing climate. Moreover, it systematically accounts for changes in future demand and capacity of bridges as well as the associated uncertainties. This framework will enable intelligent maintenance decisions with minimal life cycle costs and impacts while ensuring acceptable service levels.

1 INTRODUCTION

Transportation infrastructure, including highway bridges, play a vital role in driving economic growth and improving societal well-being. Presently, Canada's infrastructure deficit is estimated to range from $50 billion to $570 billion (Infrastructure Canada 2018). For Canada's highway bridges, this translates to 40% of bridges needing maintenance and rehabilitation as they are in fair, poor and very poor conditions, according to the 2019 Canadian Infrastructure Report Card (CIRC-Blue Plan 2019). The situation becomes more serious when considering that by 2030, annual passenger traffic is expected to increase by 50% compared to 2015 estimates, and global freight volumes are projected to rise by 70%. This surge in demand necessitates an increase in investment in the expansion and maintenance of transportation infrastructures, including highway bridges. Moreover, future climate changes can also lead to higher climatic loads on highway bridges and accelerate the rate of deterioration, which may further increase the rehabilitation and replacement needs. In the absence of transformative change towards sustainable transportation, this could mean rising GHG emissions, increasing air and noise pollution, and reducing bridge safety and functionality. There are, therefore, major challenges in the bridge management sector to meet this additional demand, ensuring adequate levels of functionality, reliability, and safety, without putting extra pressure on the natural environment.

Overcoming the challenges of meeting an increasing demand, safety and functionality requirements, and climate adaptation, however, can exacerbate global warming by producing more carbon footprint if bridge management does not consider sustainability. This is because a significant portion of GHG emissions associated with the transportation sector is attributed to the construction, operation, and maintenance of transportation infrastructure assets. Hence, intelligently designed, well-built and well-maintained transportation infrastructure are

DOI: 10.1201/9781003483755-278

key to reducing transportation GHG emissions (Churchill et al., 2021). For the transition towards sustainability in bridge management to become a reality, it is necessary to have robust decision support models and tools that promote sustainable development in the construction, operation and maintenance, as well as in the decommissioning stages in addition to the planning and design stages.

2 CURRENT SITUATION

Despite recent advances in technology, highway bridges are still managed using prescriptive approaches that are unproductive, lack consideration of the high environmental footprint related to construction and rehabilitation activities and suffer from cost overruns and significant users' costs. The reason is that decision-makers often lack comprehensive and user-friendly tools and frameworks that can fully integrate sustainability criteria into the decision-making processes and can make appropriate trade-offs between environmental, economic and social dimensions over long periods (Hu et al., 2019; Lepech, 2006; Wang et al., 2018). Existing approaches and frameworks only partially integrate sustainability criteria in the decision-making process. For example, they concentrate only on one part of the life cycle of bridges and ignore the requirements during other stages, or they evaluate the life cycle impacts concerning one or a few criteria (Li et al., 2019). Many fail to allow objective comparison of solutions since they do not include appropriate guidance for evaluating the environmental impacts and the associated risks on the provided services. Additionally, existing frameworks neglect decision-makers' ability to make new plans in the future if new information presents itself and new needs emerge. Hence, they do not explicitly consider the long-term dynamic and iterative process that is used to plan the development and maintenance of bridges, thereby resulting in unproductive processes and tools that lead to less-than-optimal integration of new solutions.

The literature suggests that digitalization is necessary for bridge life cycle management as it centralizes data, enables real-time monitoring, optimizes resource allocation, enhances collaboration, facilitates performance evaluation, improves safety, and promotes productivity and life cycle sustainability (Dmitriev et al., 2020). However, the construction industry has traditionally been slow to adopt new technologies and practices. This hesitancy is primarily attributed to several factors, including the costs and complexities associated with adopting advanced tools, limited expertise in implementing new technologies, the absence of common guidelines for seamless collaboration among different stakeholders, and occasional resistance to change.

This emphasizes the need for the development of decision-support tools using a shared digital platform for an ecosystem of solutions to minimize the costs and negative environmental impacts of bridges including reduction of GHG emissions throughout their whole life cycles. The platform should include solutions for: (a) novel and sustainable materials, design, and construction techniques; (b) sustainable operation and maintenance, and decommissioning plans considering the long-term uncertainties and the associated risks; and (c) increased circularity in construction materials. To guarantee the adoption of the developed platform in practice without much resistance, it is necessary to ensure that it is easy to use and provides guidelines and training to the users.

Although a holistic platform should tackle the whole life cycle of bridges; however, it's crucial to compartmentalize modules for various stages of the bridge life cycle. This separation is necessary because tasks such as design, operations and maintenance (O&M), and decommissioning are typically managed separately by different professionals with allocated individual budgets. Moreover, existing bridges are already in the O&M phase which does not require the implementation of these innovative solutions in their initial design and construction.

As a first step towards filling the existing gaps, this paper will present a framework for O&M of bridge infrastructure that can be integrated with other modules of the bridge life cycle in a shared digital platform using the concept of Building Information Modelling (BIM) for bridges, BrIM. The framework will integrate necessary tools and models to systematically develop intelligent maintenance and operational plans by assessing the environmental impacts of different decisions, adapting to future demands and climate change and their uncertainties,

and minimizing life cycle costs while ensuring acceptable safety and high service levels. It supports data-driven decision-making and results in more sustainable, productive and efficient bridge management. Successful implementation of the framework in practice can also contribute to the reduction of the negative environmental impacts, specifically, GHG emissions associated with bridge operation and maintenance tasks through:

(a) developing optimized maintenance plans to extend the remaining service life of existing bridges, thus leading to savings in material and energy consumption as well as in reduction of owner's and users' costs;
(b) comparing different sustainable materials and advanced maintenance, repair and rehabilitation technologies with lower environmental footprints and selecting the optimal solutions for each project;
(c) promoting recycling/reuse of construction waste; and
(d) improving the productivity and facilitating collaboration and communication among various stakeholders involved in bridge management, to reduce the time and resources required for management activities and, ultimately, reduce the GHG emissions associated with these activities.

3 DIGITAL PLATFORM FOR BRIDGE MANAGEMENT

3.1 *Bridge maintenance management*

Bridge Management Systems (BMSs) have been extensively developed to streamline the maintenance and management of bridges through digital solutions. Several countries have devised their own BMSs, such as America's Preservation, Optimization, and Network Information System (PONTIS) (Golabi et al., 1993). These systems comprehensively capture and document bridge information throughout their entire life cycle. However, most BMSs are only used for information recording and storage and lack a dynamic integration within the decision-making process. This is mainly due to limited expertise in using these systems and the absence of common guidelines for seamless collaboration among decision-makers and stakeholders. This limitation results in inefficiencies in bridge maintenance workflows.

Researchers have explored numerous approaches for overcoming this limitation. There's a particular focus on incorporating BIM into bridge management, increasingly known as BrIM, as it provides a digital representation of detailed information regarding each bridge component. BrIM can be integrated with a spectrum of modern technologies, including big data analytics, augmented reality, the Internet of Things (IoT), wireless monitoring, and cloud-based real-time collaboration. This empowers bridge managers to devise efficient maintenance strategies, forecast potential restoration or replacement needs for bridge assets, and allocate resources efficiently. Consequently, this leads to minimized downtime, prolonged asset service life, decreased operational costs and improved communications and productivity. Figure 1 illustrates the potential benefits of managing bridges using BrIM.

To integrate BrIM technology with BMS, researchers have focused on establishing structural analysis models and evaluation systems. For instance, Lee et al. (2020) created BrIM models encompassing bridge components and their structural parameters information. Shim et al. (2019) introduced a novel generation of BMSs employing the concept of a digital twin BrIM model, thereby enhancing the decision-making process. Xu et al. (2019) constructed a comprehensive evaluation framework for bridge structural conditions, drawing from visual detection data. Orcesi et al. (2011) incorporated a data evaluation BrIM model pertaining to structural health monitoring into the cost analysis of bridge construction, optimizing bridge maintenance methodologies. Li et al. (2022) developed a long-span bridge health condition monitoring system that integrates bridge sensor data with an environmental BrIM model.

However, the main focus of the previous studies has been the integration of BrIM into bridge management and they lack considerations related to life cycle sustainability management or changes in future climate conditions and demand patterns.

3.2 *Data requirements of an effective digital platform for bridge management*

BrIM relies on creating digital 3D models and continuous communication and improvement of these models with information from the users. One can perceive this as a network of integrated data exchange where different collaborators supply a common environment with relevant data that will be required for specific cases. Hence, it is important to note that the creation of geometric models will not always be mandatory since the impact and value of pure information models are also significant. A graphical 3D model can greatly enhance user experience and the comprehensibility of outputs. However, the absence of such models, particularly for existing bridges, would not diminish the significant improvement in the quality of decisions and process productivity through the digitalization of the O&M decision-making process.

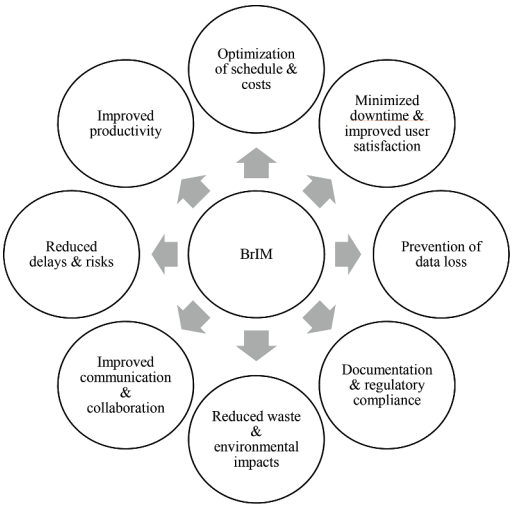


Figure 1. Potential benefits of managing bridges using BrIM.

Regardless of whether a 3D model is available or not, an effective digital platform for bridge management should encompass various features and functionalities to efficiently maintain bridges throughout their life cycle with minimal negative environmental impacts. Here are the key data requirements for such a platform:

- Structural design data or as-built models: This includes comprehensive information on the bridge's initial architectural and engineering designs. These details encompass blueprints, construction plans, material specifications, and structural configurations.
- Historical inspection and maintenance records: This includes detailed past inspection reports, maintenance schedules, and records of repairs or structural enhancements. These records provide a historical context regarding the bridge's maintenance history, identifying recurring issues, areas prone to damage, and the effectiveness of past maintenance strategies.
- Cost and resource data: This includes financial data related to maintenance, repairs, and replacement; which are associated with materials, labour, equipment, and any other resources utilized during these activities. Having such data is necessary for optimizing future budget allocations and assessing the cost-effectiveness of various maintenance strategies.
- Traffic data: This information helps in assessing the load, stress, and deterioration of bridges over time, considering that the deterioration rate and load carrying capacity are significantly influenced by the changes in traffic demand. The data includes information on traffic volume, vehicle classification, and traffic speed.
- Geographical Information Systems (GIS): Integrating geographical data such as maps, location-specific details, terrain information, and environmental factors that might impact

the bridge's condition. GIS data can provide insights into local weather patterns, nearby infrastructure, and geological aspects affecting the bridge's stability.

- Sensor or real-time data: This type of data is not mandatory but can significantly help with improving the bridge maintenance process. It includes data streams from various sensors installed on the bridge for real-time monitoring. These sensors capture critical structural health parameters like stress, strain, vibrations, temperature, and traffic load. Integrating this real-time data enables continuous monitoring of the bridge's condition and early detection of anomalies or potential hazards and the potential need for load posting of structurally deficient bridges.

3.3 *Models for effective bridge management*

Predictive analytics, life cycle sustainability analysis and optimization models are the core tools within effective bridge management. These tools leverage historical data, real-time monitoring, and advanced algorithms to predict potential bridge deterioration, assess risks, and estimate maintenance needs and select the most sustainable solution. Figure 2 provides an overview of the decision-making process and the models that should be embedded within the proposed digital platform.

Within the predictive analysis part, the bridge deterioration prediction models and failure risk estimations are incorporated. A comprehensive framework ought to take into account the impact of future changes in climate conditions and demand on the risks of failure, considering both gradual deterioration (such as accelerated deterioration due to climate change and alterations in traffic demand) and extreme events, such as heightened intensity and frequency of floods, scour, hurricanes, storms, and wildfire. This ensures that infrastructure managers are equipped with insights to proactively determine vulnerabilities and the maintenance needs of the bridge components. Using condition data and simulations during the predictive analysis stage, bridge managers can estimate the deterioration of bridge components over a defined time interval and assess the associated risks. This enables them to decide whether interventions will be necessary within that planning period or not.

If interventions are necessary, a list of potential solutions will be generated. These solutions will then be compared with regard to the Key Performance Indicators (KPIs) that define the life cycle sustainability of bridges. The life cycle sustainability model integrates the three pillars of sustainability, i.e., (a) environmental Life Cycle Assessment (LCA); (b) Life Cycle Costing (LCC); and (c) Social Life Cycle Assessment (S-LCA).

In LCA, the environmental impact of different intervention solutions is assessed across the entire life cycle of bridges (or bridge components). It quantifies various environmental aspects of interventions such as material and energy consumption, greenhouse gas emissions, recycling potential of materials, waste production, etc.

LCC evaluates the total direct and indirect costs of each solution throughout the life cycle of the bridge (or bridge component). It includes initial costs, impact on bridge durability and future intervention needs, users' costs and disposal costs.

S-LCA focuses on assessing the social and socio-economic aspects associated with different intervention solutions. It evaluates the social impacts throughout the life cycle, including factors like safety and user satisfaction. Presently, S-LCA has not reached the same level of maturity as the other two methods. This is due to the lack of clarity in the definition of S-LCA indicators, hence this area needs more research to reach broad application in practice. However, an initial step would be considering the effect of different intervention solutions on KPIs such as number of accidents and fatalities, traffic disruptions, and availability of the transportation network.

After a comparative analysis of various intervention solutions based on the defined KPIs, optimal intervention strategies for each bridge component will be identified. As a result, a compiled list of components requiring intervention during the upcoming planning period will be generated.

The next step would be the determination of optimal intervention programs that define optimal grouping and sequencing of interventions. The objective function is to maximize the net benefit; the benefit is defined as the reductions in failure risks and the net benefit is the benefit minus the overall costs of executing interventions.

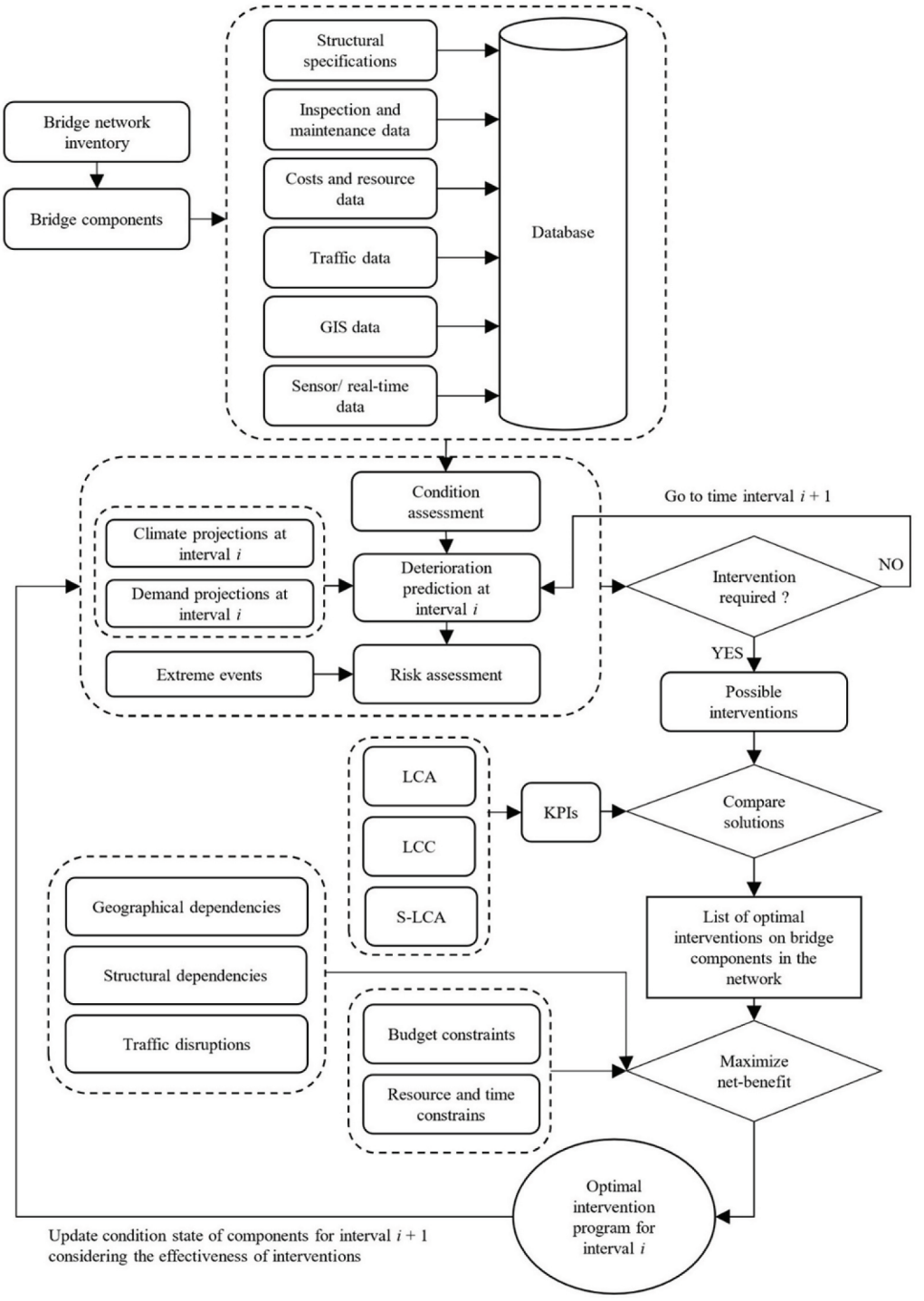


Figure 2. Framework for an integrated and digitally-supported bridge maintenance management.

It must be noted that optimizing the execution of network-level interventions within a defined planning period can be a very complex task. This objective demands a comprehensive approach that aligns various interconnected variables. When devising

intervention programs, it's essential to account for the synergies and interdependencies among structural components, the topological dependencies, and the impact of interventions on traffic flow. For instance, when undertaking interventions on different components of a bridge, consolidating these activities within the same planning period is more prudent than individual interventions across multiple planning periods.

The selection of the optimal execution timing for such interventions relies on the acceptable risk thresholds and evaluating the overall net benefit associated with executing interventions during each planning period.

Topological dependencies highlight the economic advantages gained from consolidating interventions on bridges situated in close proximity or within the same geographic area. By grouping interventions on interconnected or nearby assets, there's an opportunity to maximize economic benefits through efficient logistical operations, shared resources, and minimized disruptions to the surrounding environment. This approach allows for more efficient resource utilization and often results in cost savings, reduced downtime, and optimized workflows, ultimately contributing to enhanced overall project effectiveness. Minimizing traffic disruptions is a principal concern, as any intervention invariably affects transportation routes potentially leading to congestion, delays, and socioeconomic implications.

When developing the intervention programs, various constraints such as budget, time, or resource limitations, add another layer of complexity that cannot be overlooked in real-life practices and must be incorporated into the optimization model.

The output of this optimization would be an intervention program that illustrates the sequence, type and grouping of maintenance tasks in each planning period to maximize net benefit. Upon completion of the interventions, the digital platform will promptly update the condition state of the bridge components within the network. This update will reflect the efficacy of the executed interventions. These revised condition states will then be integrated into the analysis and predictive models for informing decisions during the subsequent planning period.

This platform is compatible with the long and dynamic nature of bridge maintenance management processes. This means that decisions will be initially made based on general and perhaps limited available data, years before their execution. As additional information becomes accessible, the planning process undergoes automatic updates, progressively becoming more comprehensive and refined. In the presence of 3D models or GIS mapping, interactive visualizations and reports should be generated to facilitate understanding of the data and the output intervention program.

4 NECESSARY CONSIDERATIONS

Achieving standardization across different phases is essential to leverage the benefits of digitalizing the bridge maintenance management process. When information is standardized, it can be efficiently preserved and used in a format that facilitates seamless integration and collaboration across various stages of a bridge life cycle, irrespective of the software being utilized. Consequently, the initial focus should be on exploring the requirements for developing information delivery specifications (IDS), BIM collaboration format (BCF), and a common data dictionary for bridge elements to be utilized by the O&M module of the integrated digital platform.

Data quality and accuracy are very crucial in digital asset management. If data integrity is endangered during storage or if updates are not consistently applied, the reliability of the digital bridge management systems can be undermined. This is because the accuracy of predictive maintenance models heavily relies on high-quality data. Moreover, particular attention should be directed towards addressing the uncertainty of the results, as forecast models (e.g., climatic data and loads and traffic demand projections) yield predictions that do not necessarily align with the real situation in the future.

Adherence to industry standards, codes, and regulations related to bridge management and safety is crucial. The platform should support compliance requirements and assist in regulatory reporting. Finally, robust security measures must be implemented to safeguard sensitive bridge data, ensure compliance with data privacy regulations and prevent cyber threats.

5 CONCLUSIONS

This paper proposed a framework for bridge managers to plan bridge maintenance activities using a shared digital platform. The framework generates a modular, interconnected system and incorporates methodologies for deterioration and failure risk modelling in a changing climate. This framework will develop intervention programs with minimal life cycle costs and impacts while ensuring acceptable safety and service levels. The platform is adaptable to changing future needs, increasing demands due to growth, climate change, extreme weather events, uncertainties, stakeholder demands, and new information. Using this platform, bridge managers can adjust their plans based on new information without going through unnecessary iterations. It also enables the tracking of the environmental and technical performance of various solutions for better future estimations.

While digitalizing the bridge management process, particularly in the context of maintenance management, presents several advantages, some limitations must be overcome for it to be efficiently implemented into existing workflows. One of the most prominent challenges is data integration and compatibility, as the existing systems often differ in formats and structures, necessitating intricate efforts to harmonize and synchronize diverse data sources. When implemented in practice, it is necessary to ensure that the platform is scalable to accommodate large bridge networks and capable of integrating with evolving technologies (e.g., automated structural health monitoring) and future upgrades.

REFERENCES

Churchill, S. A., Inekwe, J., Ivanovski, K., & Smyth, R. 2021. Transport infrastructure and CO2 emissions in the OECD over the long run. *Transportation Research Part D: Transport and Environment*, 95, 102857.

CIRC-Blue Plan. 2019. Canadian Infrastructure Report Card 2019. http://canadianinfrastructure.ca/en/index.html

Dmitriev A. & Plastunyak, I. 2020. Digital platforms for managing transport and logistics systems in the context of sustainable development de *E3S Web of Conferences*.

Golabi, K., Thompson, P.D., & Hyman. W.A. 1993. Pontis Version 2.0 Technical Manual: A Network Optimization System for Bridge Improvements and Maintenance. Report FHW A-SA-94-031. FHWA, U.S. Department of Transportation.

Hu, W., Shu, X., & Huang, B. 2019. Sustainability innovations in transportation infrastructure: An overview of the special volume on sustainable road paving. In *Journal of Cleaner Production* (Vol. 235). https://doi.org/10.1016/j.jclepro.2019.06.258

INFC 2018. Infrastructure Canada 2018. About Infrastructure Canada. https://www.infrastructure.gc.ca/about-apropos/index-eng.html#1 (accessed Nov. 7, 2018)

Lee, J. H., Park, J. J. & Yoon, H. 2020. Automatic bridge design parameter extraction for scan-to-BIM. *Appl. Sci*. **10**, 7346. https://doi.org/10.3390/app10207346.

Lepech, M. D. 2006. A paradigm for integrated structures and materials design for sustainable transportation infrastructure. *PhD diss.*

Li, H., Deng, Q., Zhang, J., Olubunmi Olanipekun, A., & Lyu, S. 2019. Environmental impact assessment of transportation infrastructure in the life cycle: Case study of a fast track transportation project in China. *Energies*, *12*(6), 1015.

Li, X., Xiao, Y., Guo, H. & Zhang, J. 2022. A BIM based approach for structural health monitoring of bridges. *KSCE J. Civ. Eng*. **26**, 155–165.

Orcesi, A. D. & Dan, M. F. 2011. Optimization of bridge maintenance strategies based on structural health monitoring information. *Struct. Saf*. **33**, 26–41.

Shim, C. S., Dang, N. S., Lon, S. & Jeon, C. H. 2019. Development of a bridge maintenance system for prestressed concrete bridges using 3D digital twin model. *Struct. Infrastructure. Eng*. **15**, 1319–1332. https://doi.org/10.1080/15732479.2019.1620789.

Wang, L., Xue, X., Zhao, Z., & Wang, Z. 2018. The impacts of transportation infrastructure on sustainable development: Emerging trends and challenges. *International Journal of Environmental Research and Public Health*, *15*(6), 1172.

Xu, X., Huang, Q., Ren, Y., Zhao, D. Y., Zhang, D. Y., & Sun, H. B. 2019. Condition evaluation of suspension bridges for maintenance, repair and rehabilitation: A comprehensive framework. *Structure and Infrastructure Engineering*. **15**, 555 567. https://doi.org/10.1080/15732479.2018.1562479.

Bridge Maintenance, Safety, Management, Digitalization and Sustainability – Jensen, Frangopol & Schmidt (eds)
© 2024 The Author(s), ISBN 978-1-032-77040-6
Open Access: www.taylorfrancis.com, CC BY-NC-ND 4.0 license

PONTI: An open WebGL-based tool in support to defect analysis and 3D visualisation of bridges

R. Fascia, F. Barbieri, F. Gaspari, F. Ioli & L. Pinto
Department of Civil and Environmental Engineering, Politecnico di Milano, Milan, Italy

ABSTRACT: The importance of monitoring bridges has extensively emerged in the last decade, considering recent bridge collapses in Italy. With over half of the country's bridges in service for more than 50 years, ensuring their serviceability is crucial. This requires inspections that document the condition of infrastructures. In this context, the development of customised, reproducible, and user-friendly web platforms plays a crucial role for exploring georeferenced 3D models of bridges acquired through laser scanning and drone photogrammetry. This paper focused on implementing Potree WebGL, a JavaScript library for the exploration of point cloud, native and custom functionalities to support bridge geometry reconstruction and defect documentation, as required by the Guidelines for Risk Classification and Management established by Italian Ministry of Infrastructure and Transport. Catering the needs of administrators, a standardised web platform called PONTI (Potree platfOrm for iNfrasTructure Inspection) has been developed to aid decision-making in road infrastructure maintenance and monitoring.

1 INTRODUCTION

In light of the bridge structural health deterioration observed in Italy in recent years (Malerba 2022), there has been a surge in studies addressing the most effective ways for managing information and data in support of infrastructure management and decision making on routine inspections and maintenance operations. Literature has widely documented the adoption of Geographic Information Systems (GIS) (Gaspari et al. 2023), Computer-Aided Design (CAD) software (Tanaka et al. 2019) and Building Information Modelling approaches (Tanaka et al. 2016, Ciccone et al. 2022) for the management of road networks, civil construction, and infrastructures (Einizinab et al. 2023). However, most of these solutions consists of proprietary software that requires licences or case-study-driven applications with limited possibility of customisation according to different scenarios (Zhang & Hu 2018). Moreover, the implementation of web-based platforms fostering also remote collaborations within experts is often limited by the difficulties in integrating different format of data (Caldera et al. 2021). In the last decade, the rapid evolution of functionalities supported by Web Graphic Libraries (WebGL) however suggests possible lightweight and low-cost solutions for sharing and visualising large amounts of 2D and 3D data on web browsers, allowing users to compare and analyse different file formats in a georeferenced environment (La Guardia & Koeva 2023). For example, Potree is an open-source WebGL framework (Schuetz 2016) designed to explore large point clouds together with meshes, vector data, 3D annotations and oriented images. Such a solutions allows to easily disseminate online products generated by techniques like laser scanning and photogrammetry – widely used for bridge and building surveys - that previously were difficult to share with users because they required the transfer of large amounts of data and the installation of dedicated applications (Gaspari et al. 2022).

This work presents the development and the functionalities of PONTI (Potree platfOrm for iNfrasTructure Inspection), an easy-to-implement and replicate template based on Potree JS for the definition of a web platform designed to facilitate the sharing of bridge inspection 3D

DOI: 10.1201/9781003483755-279

georeferenced products such as point clouds and oriented UAV images. The effectiveness of its adoption is tested for a case study in the framework of the Italian bridge inspection guidelines (MIT 2020, MIT 2022) by using the products in the platform to identify and evaluate extension and intensity of defects through a posteriori visual inspection of collected images.

2 METHODOLOGY

The methodology proposes the development of a 3D web platform that aligns with the requirements of the Italian Guidelines for bridge management. The workflow consists of three main parts: data preparation and processing, 3D platform design and implementation and defect detection and evaluation with the support of the platform (Figure 1).

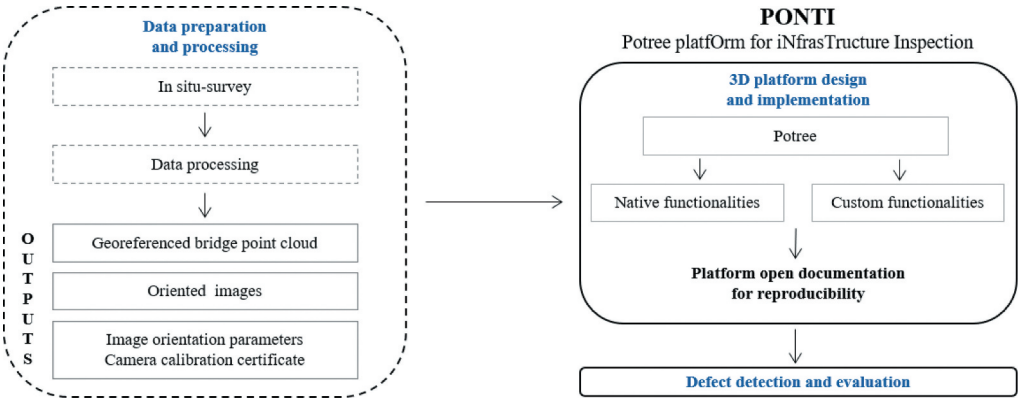


Figure 1. Workflow of the proposed methodology.

2.1 *Data preparation and processing*

Before defining the design of the platform, it is important to understand what type and format of products are required for it to function properly. The first requirement for the development of the web structure is the generation of a point cloud of the bridge, resulting for example from the processing of the data collected during the structure survey. This process involves the use of geomatics in-situ techniques such as traditional topography, photogrammetry and terrestrial laser scanning, followed by data processing in the laboratory to produce geo-referenced 3D products.

Once the point cloud of the bridge is obtained, it has to be classified according to the structural macro-components such as spans, piles, abutments and road surface. It is suggested to perform this step before the implementation of the platform, as it allows an immediate visualisation of the main parts of the structure. The classification of clouds can be done manually, for example using open-source software such as CloudCompare, or through advanced semantic segmentation methods (Xia et al. 2022). Another requirement for the platform to be efficient in sharing bridge point clouds is the presence of a terrestrial or UAV-photogrammetric survey and the insertion of oriented images into the visualisation of the 3D model. Such results are obtained through the reconstruction of the bridge 3D model, the orientation of the images and the georeferencing of the entire procedure in a global reference system. Once the photogrammetric processing is completed, the next step requires image files together with their exterior orientation parameters (i.e., the coordinates of the camera projection centres and the camera orientation angles in the world reference system at the time of each shot) and camera calibration certificate (i.e., the collection of the interior parameters of the cameras, including focal length, principal point coordinates and lens distortion parameters). These two pieces of information were derived from the photogrammetric processing aimed at reconstructing the 3D model.

2.2 *3D platform design and implementation*

The second step of the methodology initially consists in the design of the platform according to Potree WebGL native functionalities and custom needs for an effective user-friendly visual inspection of the digital 3D model of the structure. Potree offers flexible rendering of point clouds, the ability to perform measurements directly on the 3D model, and the ability to integrate oriented photos and georeferenced annotations without the need to install additional software packages. Its interface makes it easy to explore the 3D characteristics of the object, providing a better understanding of the model from both geometric and structural point of view. In addition, the ability to integrate and visualise oriented photographs of the object in a 3D context contributes to a higher level of detail and understanding, enriching the visual experience. Moreover, executing measurements on 2D objects like images and then automatically projecting them on the bridge point cloud avoids problem with the need of background in geomatics for managing a 3D object – the point cloud – that could require major efforts for non-familiar users.

To improve the visual inspection and facilitate the identification of defects in structures such as bridges, new functionalities have been implemented in the new PONTI platform. These include the visualisation of the point cloud with classified graphics, the management of chunk of images corresponding to the macro-components of the bridge to be inspected according to the Italian Guidelines, and the addition of geolocated annotations with media attachments as links.

In Potree's default configuration, the shared point cloud is generally displayed in RGB mode. The custom platform now offers a simplified classified view with its custom legend, which allows the 3D model of the bridge to be displayed in different colours according to the classification previously performed and also to be changed in visibility by hiding specific portions of it (Figure 2).

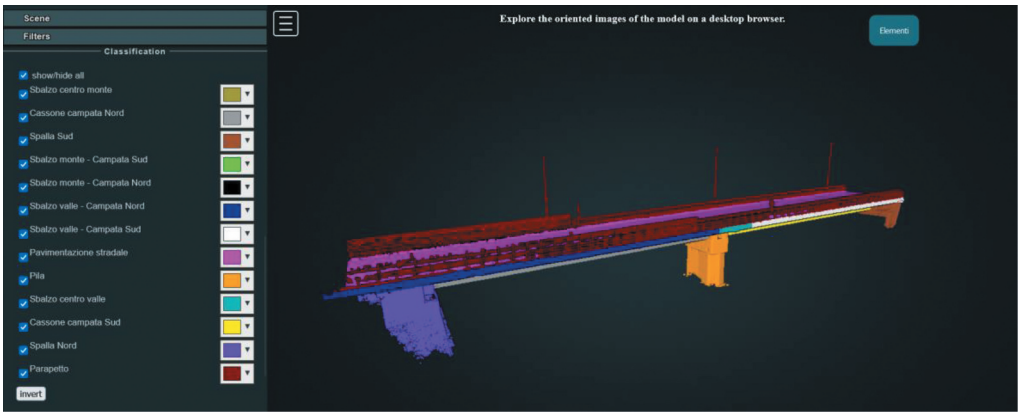


Figure 2. Classified view of the case study bridge in the PONTI template. The colours represent the structural macro-elements of the bridge: olive green - central cantilever; grey - north span caisson; brown - south abutment; green - south span mount cantilever; black - north span mount cantilever; blue - north span valley cantilever; white - south span valley cantilever; lilac - road surface; orange - pier; light blue - valley centre cantilever; yellow - south span caisson; violet - north abutment; red – parapet. It is possible to change the colours of each element according to user requirements.

The images can then be grouped into different folders/chunks according to the structural part of the bridge, together with the calibration certificates and images orientation parameters. In this way, the images are correctly geolocated and oriented in the 3D model viewer in relation to the structure according to the camera coordinates and the angle of view at the time of each shot. Indeed, in addition to reviewing the photos captured during the inspection and identify defects using the zoom and image measurement functions, it is also possible to get direct feedback on the location of the defect itself, as the photos are already organised

according to the structural elements of the bridge and spatially oriented on it in the 3D environment (Figure 3). The inclusion of a dedicated dropdown menu in the template provides users with the option to easily switch the view to a specific structural element of interest.



Figure 3. Oriented and geolocated image on the point cloud in the PONTI template. The image was taken during the drone survey and orientated using the calibration certificate and image orientation coordinates. Measurements can be made on the photographs. The photos are also divided into chunks/folders according to the structural element.

Geolocated annotations provide additional support in visualising and documenting defects found during visual inspection of bridges. Within the PONTI platform, each annotation is identified by a title and coordinates in the global reference system that defines the 3D scene. Each annotation is uniquely named, providing a direct link to the structural reference element (Figure 4).

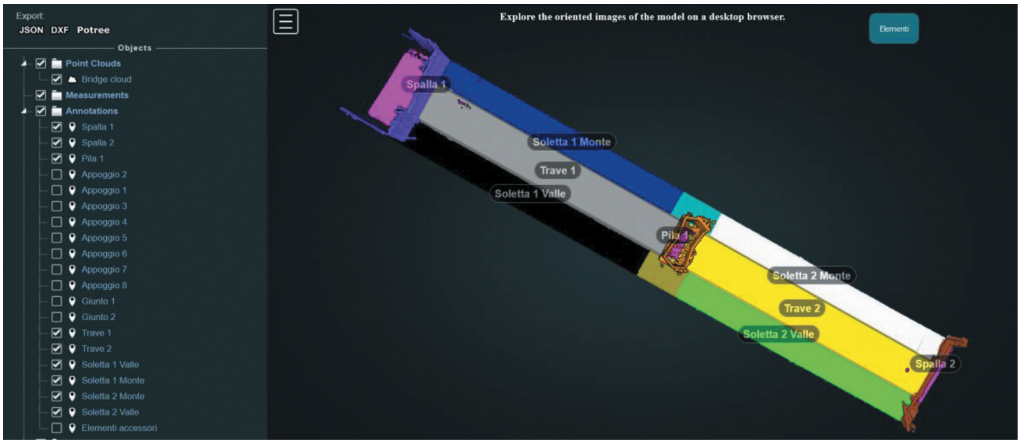


Figure 4. Visualisation of the classified point cloud in PONTI template with unique annotations associated with the bridge's structural macro-elements. It is possible to activate/deactivate the display of the tag. The image shows the following active: abutment 1, abutment 2, slab 1 mount, slab 2 mount, beam 1, beam 2, slab 1 valley, slab 2 valley.

2.2.1 *Platform open documentation for reproducibility*

Aiming at giving the possibility to researchers in the field to customise it, the template and the instructions for its adoption are freely accessible through a dedicated repository on GitHub, available at: https://github.com/labmgf-polimi/ponti.

The PONTI template indeed intends to guide users through the entire process of sharing bridge point clouds, providing instructions on how to get started, define the user interface (GUI), and integrate point clouds, oriented images, and annotations. The guide also explains how to customise the HTML and CSS to shape the appearance of the main page and sidebar, as well as specific details on how to integrate converted point clouds and oriented image files. It also provides detailed instructions on how to integrate oriented cameras, including details on how to load oriented images and camera parameters, and how to customise the dedicated script to correctly integrate them into the visualisation. The guide then explains how to add customised annotations to the point cloud, including steps for obtaining the coordinates of the desired points using Potree's measurement tool, editing the annotation file to correctly position and describe the annotations, and setting the camera view associated with each annotation.

2.3 *Defect detection and evaluation with the support of the platform*

In the final step of the workflow, the usability and effectiveness of the PONTI template is tested in support to the analysis of defects on structures. Currently, Level 1 of the Italian Guidelines requires a direct visual inspection and monitoring of the state of conservation of the structure through the compilation of reports documenting its condition. In order to facilitate the compilation of such document, defect sheets have also been created. These are reference documents that specify the description of the deterioration characteristics that should be identified during the inspection. The sheets are divided into five main groups according to element bridges material: steel, masonry, timber, reinforced/pre-stressed concrete and pre-stressed concrete. There are also additional sheets for abutments, footings, joints and accessories. Within each macro-group, there are several sheets that illustrate the various defects specific to the material considered with descriptions and images. In order to support objective observations on the structural defects, inspectors are also required to associate images to each defect detected and reported in each structural element sheet.

In this framework, PONTI is used to evaluate the effectiveness of its image data management in an a-posteriori visual inspection of survey pictures, with a particular focus on its ability to locate images on a 3D space, making measurement on them and connect them directly to the 3D reconstructed point cloud. Moreover, thanks to the classification of the bridge according to its macro-components and to the distinct annotations, it is easy to recognise the reference element on which the defect is manifested (Figure 5).

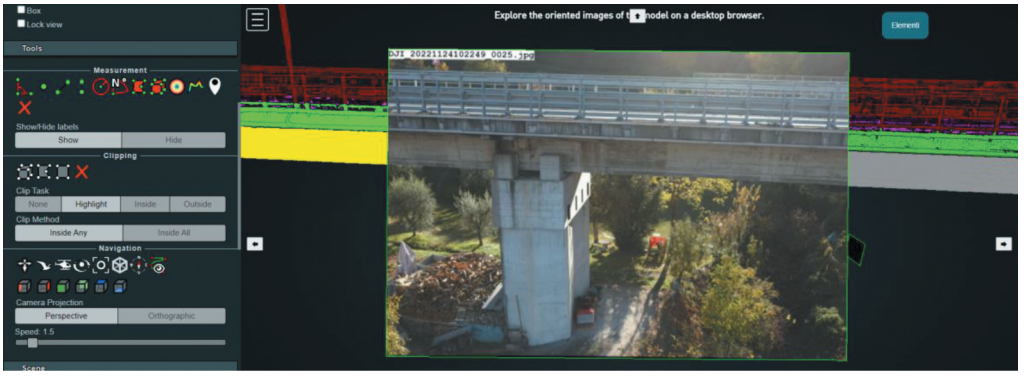


Figure 5. Oriented and geolocated image on the 3D model and displayed in the PONTI template. The image shows the presence of moisture spots on the structure. The image shows its nomenclature in the top left-hand corner.

3 CASE STUDY DATA COLLECTION

A bridge located in the municipality of Sulzano, in the province of Brescia, northern Italy, is analysed as a case study for the application of the described methodology. Its reinforced concrete structure consists of 2 spans (Figure 6).



Figure 6. Aerial view of the reinforced concrete bridge in Sulzano (Brescia) used as case study.

The process began with a preliminary visit to the sites to be surveyed in order to identify any obstacles or visual obstruction, such as vegetation or man-made objects. This was followed by the field survey phase. First, a topographic network was created for each structure in a local reference system using a total station (Leica Nova MS60) (Fagandini et al. 2017) to measure a series of targets placed on the structure and surrounding ground and used as Ground Control Points (GCPs), i.e., points with known coordinates both in the world reference system used to georeference and constrain the 3D model. Four of these targets were placed on the ground and measured with a GNSS antenna (Leica Viva GS14) for global georeferencing by roto-translation of the survey data processing products. The other targets were deploys directly on the structure and used as GCPs for the photogrammetric processing of nadiral (i.e., with the camera looking downwards) and oblique photographs taken during the UAV survey (DJI Matrice 300, RTK - DJI P1, DJI Mavic 2 Pro, DJI Phantom 4 RTK). Other images were taken manually with a handheld camera (Nikon D800). This integrated approach of aerial and ground photogrammetry was essential in areas close to vegetation, which could have compromised the efficiency of an UAV-photogrammetric approach. In parallel, point clouds were acquired by terrestrial laser scanning (Faro Focus M70). This combination of photogrammetry and laser scanning resulted in two point clouds, each derived from a different technique. The accuracy of the point clouds, assessed by error and residual analysis on targets not used as GCPs but used as check points (CPs, i.e., targets not used to georeferenced the 3D model, but to validate the model and ensure its accuracy), was compared to the required centimetre standards. To ensure accuracy, the results of the two techniques were checked during the post-processing phase on overlapping areas to identify any discrepancies. Once the accuracy requirements were met, the two separate point clouds were integrated and subsampled, incr. This process overcame the limitations of each technique, resulting in complete coverage of the structure. Following the data processing phase and before implementing the model in the PONTI template, the resulting point cloud was classified according to the structural macro-components of the bridge, such as piles, abutments, and spans. The images were processed and converted to .jpeg format to ensure lighter visualisation, with their orientation and associated camera parameters saved in separate text files. The PotreeConverter (Schuetz 2016) tool was used to convert the dense point cloud into a .json format compatible with Potree. The input data for the main functionalities and the basic structure of the 3D data exploration platform were created using a standard HTML structure, including the viewer and a sidebar with native tools for measurement and section extraction.

4 RESULTS AND DISCUSSION

The 3D point cloud represents the geometry of the bridge and provides a basis for understanding its structure, while the images and annotations allow immediate identification and anchor points for the visual analysis of the structural elements, together with their condition assessment and damage quantification. The classification of the point cloud according to structural macro-components facilitates the visual identification of the main parts of the structure. In fact, the introduction of this customisation makes it easier to recognise the different parts of the bridge like beams, abutments, piles and ancillary elements and contributes to a more effective overall understanding of the bridge. This rendering together with the dropdown menu for selecting the structural element to inspect also helps users to easily change the view in the scene according to the desired target element of the inspection as a simple shortcut that activate the corresponding oriented images chunk. By accessing each single image captured with UAV and compact cameras and loaded in the scene, users can conduct with simplicity an a posteriori visual inspection on the different reinforced concrete elements, comparing what they see in the picture with the references for defect quantification and evaluation provided by the Italian Guidelines. This approach revealed to be particularly effective in identifying qualitatively most of the standard defects such as passive and active moisture stains, detached concrete cover, cracks, exposure and/or corrosion of structural reinforcements as well as significant geometrical deformations.

However, some Guidelines-coded defects were difficult to identify as well as quantify due to visual obstructions, for example supports and portions of slabs. Such limitation is mainly connected anyway to the fact that most of the oriented images was captured by UAVs, not allowed to fly and stand less than a certain safe distance from the structure. A consequent problem hence regards the case of presence of thinner cracks that can be visually identified but whose severity and level on intensity can not be evaluated because their width is smaller than the geometrical resolution of the point cloud (around 1 cm). Regardless these limitations due to the surveying mode, the method was demonstrated valuable for evaluating the presence and the rough extension of the most severe defects, identifying their georeferenced position on a precise structural element, providing useful information for planning a subsequent more detailed in-situ investigation or for considering surveying technologies alternative to pure RGB cameras.

In addition, the inclusion of unique annotations has proved to be useful. This allowed the different structural parts of the bridge to be clearly identified with unique numbered labels such as ‘Beam 1’, ‘Beam 2’ and so on. Furthermore, the ability to integrate customised HTML content into the annotations facilitates the inclusion of multimedia attachments. For instance, for the case study, based on commissioners’ requests, in each structural element annotation it was included a direct link to a OneDrive space containing documents, files and additional images referring to the connected element. Indeed, PONTI’s open-source nature allows interested developers to implement the platform with new customisations even in contexts outside the Italian guidelines.

The custom features, together with the defect sheets, have proven to be effective tools for the rapid identification and association of bridge defects.

However, it is necessary to consider some aspects related to this method. The case study focuses on a reinforced concrete bridge, so the defect considerations are formulated using the Guidelines reference defect sheets specific to this material. As a result, the platform and defect detection considerations are different depending on the type of bridge examined, such as in the case of timber or masonry structures, which have different defect grades and defect maps to those of reinforced concrete structures. These considerations serve as a framework for improving and developing the PONTI template, testing also the integration of georeferenced data sourced from other type of instrumentations and surveying techniques.

5 CONCLUSION

The PONTI template presented in this work is an open-source resource for sharing and analysing bridge point clouds, providing a flexible and free approach to infrastructure

management, without the need for a licence. The practical application of the methodology on a bridge in Sulzano has demonstrated the efficiency of the platform in support of the a-posteriori visual inspection of a structure, making possible to identify the main defects standardised in the Italian Guidelines. The combination of georeferenced point clouds, images and annotations has indeed created an interactive environment that allows a comprehensive assessment of the geometrical state of the structure. It also has proven to be a flexible and accessible tool for different types of users, including administrators and non-expert users. The new implemented features, its open-source nature, the instructions for use and customisation and the intuitive interface make the platform user-friendly.

However, it is important to recognise some limitations, such as the possible presence of shaded areas in the 3D model and the challenge of visualising defects that are too small in the image, compromising the possibility of correctly quantifying. These aspects provide opportunities for further improvements by considering the integration in PONTI of compatible georeferenced data coming from other sources like for example thermal or multispectral cameras.

Future developments of the project aim to intensify the interaction between the platform and its users. Allowing users to download and upload annotations, adding comments and observations, could promote more collaborative work and a more comprehensive and up-to-date assessment of the bridge's conditions. A further step could be the introduction of coloured annotations that change according to the severity of the defect. For example, a colour could be associated with the weight G of the degradation in the defect sheets. This approach would allow an intuitive visualisation of defects. This functionality could also be associated to a database system that saves annotations made during an online session by the user and memorise them in the system when the viewing page of the platform is updated. This could be useful both in terms of a more collaborative approach between several users, and in terms of comparing the defects detected to provide a more accurate material pathology survey. In addition, the implementation of new functionalities is under study, such as the ability to compare the current state of the bridge with subsequent surveys over time, including different formats such as BIM representations, meshes, etc.

REFERENCES

Caldera, S., Mostafa, S., Desha, C., Mohamed, S. 2021. Exploring the Role of Digital Infrastructure Asset Management Tools for Resilient Linear Infrastructure Outcomes in Cities and Towns: A Systematic Literature Review. *Sustainability* 13(21):11965. https://doi.org/10.3390/su132111965

Ciccone, A., Suglia, P., Asprone, D., Salzano, A. & Nicolella, M. 2022. Defining a Digital Strategy in a BIM Environment to Manage Existing Reinforced Concrete Bridges in the Context of Italian Regulation. *Sustainability*, 14(18):11767. https://doi.org/10.3390/su141811767

Fagandini, R., Federici, B., Ferrando, I., Gagliolo, S., Pagliari, D., Passoni, D., Pinto, L., Rossi, L., Sguerso, D. 2017. Evaluation of the laser response of Leica Nova multistation MS60 for 3D modelling and structural monitoring. *In Computational Science and Its Applications–ICCSA 2017: 17th International Conference*, Trieste, Italy, Proceedings, Part IV 17 (pp. 93–104).

Einizinab, S., Khoshelham, K., Winter, S., Christopher, P., Fang, Y., Windholz, E., Radanovic, M., & Hu, S. 2023. Enabling technologies for remote and virtual inspection of building work. *Automation in Construction*, 156, 105096.

Gaspari, F., Ioli, F., Barbieri, F., Belcore, E., & Pinto, L. 2022. Integration of UAV-lidar and UAV-photogrammetry for infrastructure monitoring and bridge assessment. *The International Archives of the Photogrammetry, Remote Sensing and Spatial Information Sciences*, 43, 995–1002.

Gaspari, F., Barbieri, F., Demnati, I., Ioli, F., Pinto, L., & Toscani, V. 2023. Mobile mapping solutions for the update and management of traffic signs in a road cadastre free open-source GIS architecture, *The International Archives- of Photogrammetry, Remote Sensing and Spatial Information Sciences*, XLVIII-4/W7-2023, 61–66, https://doi.org/10.5194/isprs-archives-XLVIII-4-W7-2023-61-2023.

La Guardia, M., & Koeva, M. 2023. Towards Digital Twinning on the Web: Heterogeneous 3D Data Fusion Based on Open-Source Structure. *Remote Sensing*, 15(3), 721.

Malerba, P. G. 2022. About recent bridge failures. Bridge Safety, Maintenance, Management, Life-Cycle, Resilience and Sustainability, 56–80.

Ministry of Infrastructure and Transport - MIT, 2020. Linee guida per la classificazione e gestione del rischio, la valutazione della sicurezza ed il monitoraggio dei ponti esistenti.

Ministry of Infrastructure and Transport - MIT, 2022. Decreto ministeriale numero 204 del 1° luglio 2022. https://www.mit.gov.it/normativa/decreto-ministeriale-numero-204-del-1-luglio-2022.

Schuetz, M. 2016. Potree: Rendering Large Point Clouds in Web Browsers. *Master's thesis*, Technische Universitat Wien.

Tanaka, F., Hori, M., Onosato, M., Date, H., & Kanai, S. 2016. Bridge information model based on IFC standards and web content providing system for supporting an inspection process. In *16th International Conference on Computing in Civil and Building Engineering* (ICCCBE 2016) (pp. 1140–1147).

Tanaka, F., Tsuchida, M., & Onosato, M. 2019. Associating 2D sketch information with 3D CAD models for VR/AR viewing during bridge maintenance process. *International journal of automation technology*, 13(4), 482–489.

Xia, T., Yang, J. & Chen, L. 2022. *Automated semantic segmentation of bridge point cloud based on local descriptor and machine learning*. *Automation in Construction*, 133, 103992.

Zhang, J., & Hu, Q. W. 2018. A visualization progress management approach of bridge construction based on mixed panoramic and oblique photogrammetry. *In 2018 26th International Conference on Geoinformatics* (pp. 1–6). IEEE.

Bridge Maintenance, Safety, Management, Digitalization and Sustainability – Jensen, Frangopol & Schmidt (eds)
© 2024 The Author(s), ISBN 978-1-032-77040-6
Open Access: www.taylorfrancis.com, CC BY-NC-ND 4.0 license

Advancing bridge asset management in Indonesia: Integrating scan-to-BIM for digital twin approach

H.T. Saksena & R.P.P. Sastrawiria
Directorate General of Highways, Ministry Public Works and Housing of Indonesia

ABSTRACT: Bridge asset management is pivotal for ensuring safety within transportation networks. Indonesia, amid rapid infrastructure growth driven by post-pandemic economic surges in 2023, faces distinct challenges in advancing asset management. This study focuses extensively on Ministry of Public Works and Public Housing of Indonesia policies, specifically integrating Building Information Modeling (BIM) to enhance bridge asset management. It meticulously compares these policies with global standards, dissecting disparities between Indonesia's practices and international benchmarks. The research delves deeply into the Scan-to-BIM approach, spotlighting its role in creating Digital Twins for Long-Span Bridge projects across Indonesia, currently under extensive construction. It assesses BIM implementation evidence, gauging data quality, quantity, and utilization in comparison to global practices. This evaluation aims to align Indonesia's practices with global norms and evaluate their efficacy. The study explores the gap between BIM use in different countries and Indonesia, identifying contributing factors and suggesting strategies to bridge this divergence. Additionally, it addresses prevalent challenges in BIM policies, human resources, and tool implementation, proposing solutions drawn from existing literature. Discussions encompass diverse BIM workflows globally, outlining strengths and weaknesses while contextualizing their impact within Indonesia's context. Furthermore, it emphasizes the need for standardized deviation between point cloud and 3D models for precision in constructing Digital Twins through Scan-to-BIM methods in bridge projects.

Keywords: BIM(Building Information Modeling), Digital asset management, Digital Twin, Laser Scanning, Point Cloud

1 INTRODUCTION

1.1 *Background*

Bridge infrastructure serves a crucial role in transportation networks, facilitating safe and efficient movement for vehicles and pedestrians while connecting regions and communities. Their significance goes beyond structure, supporting economic activities and societal well-being by ensuring uninterrupted connectivity for goods, services, and people. Effective bridge asset management involves collecting and analyzing data on bridge condition, risk, and performance to inform decision-making and prioritize actions (Bennetts et al., 2020). (Wei et al., 2021) suggest using emerging technologies like BIM, GIS, and artificial intelligence to enhance information management, visualization, and collaboration in bridge asset management. This proactive management aims to preserve and improve bridge condition and performance.

Building Information Modeling (BIM) involves creating digital data that visually represents infrastructure objects across their lifecycle stages. According to various sources, including (Ali et al., 2022) (Musarat et al., 2023), and (Saraireh & Haron, 2020), BIM enhances

DOI: 10.1201/9781003483755-280

collaboration among stakeholders, improves project efficiency, quality, and integrates new technologies in construction. BIM is crucial in providing accurate data and meeting project expectations.

Scan-to-BIM, utilizing Laser Scanning, transforms real-world assets into precise 3D models, forming the basis for Digital Twin creation. This process, outlined by (Kang, 2023), supports decision-making, project optimization, and provides accurate information on cost, schedule, and sustainability. These Digital Twins, created through Scan-to-BIM, offer comprehensive visualization for maintenance planning, decision-making, and simulations without physical interaction with the asset.

Scan-to-BIM's integration with BIM and other cutting-edge technologies, as highlighted by (Olanrewaju et al., 2021), significantly enhances project delivery efficiency and quality. By providing accurate Digital Twins, Scan-to-BIM revolutionizes bridge asset management, aiding in decision-making for maintenance, performance optimization, and lifecycle management, ultimately ensuring the safety, economic continuity, and connectivity of transportation networks.

1.2 *Objectives*

Global government efforts significantly influence BIM adoption, with governments wielding substantial authority to drive operational changes within the construction (Borrmann et al., 2018). In Indonesia, the government's evolving policies for BIM implementation in bridge asset management face specific challenges detailed in this study, drawing from prior research to harmonize existing issues and optimize BIM utilization among stakeholders.

Implementation hurdles, including cost barriers, limited awareness and skills, legal complexities, and resistance to change, hinder BIM adoption (Olanrewaju et al., 2021). Indonesia encounters similar obstacles, where inadequate stakeholder understanding limits the optimal use of BIM-generated processes and outputs.

The global landscape of BIM integration policies varies widely, ranging from the UK's mandatory BIM Level 2 for government projects to diverse approaches in countries like the US, European nations (Norway, Finland, Denmark), Singapore, and South Korea (Charef et al., 2019). Indonesia, notably through the Ministry of Public Works, showcases a significant initiative in implementing BIM, notably demonstrated in transformative projects like the new capital city's development, leveraging BIM methodologies for sustainability and smart city planning.

Furthermore, the application of Scan-to-BIM in bridge asset management illustrates the innovative use of technology to elevate infrastructure maintenance and planning, generating highly accurate Digital Twins for bridges. This research delves into three key objectives: highlighting Indonesia's BIM implementation efforts, aligning these with global standards, and introducing Scan-to-BIM's potential in long-span bridge projects. Together, these objectives illuminate Indonesia's strides in embracing BIM technology, aligning policies with international standards, and leveraging innovative methodologies for effective infrastructure asset management.

2 POLICY ANALYSIS AND COMPARATIVE STUDY

2.1 *Indonesia's policies on BIM*

In Indonesia, the implementation of BIM is governed by various regulations, encompassing Government Regulation 2021, which pertains to the Implementing Regulations of Law 2002 focusing on Buildings. Additionally, PUPR Ministerial Instruction Number 2022 outlines strategies to prevent deviations in the PUPR Ministry's Goods/Services Procurement Process from 2022 to 2024. Further regulations such as PUPR Ministerial Regulation 2021 on Construction Implementation Guidelines and PUPR Ministerial Regulation 2018 regarding State Building Construction contribute to the framework governing BIM usage.

Specifically for the road and bridge sector, Road and Bridge Sector Guidelines 2023 provide comprehensive guidelines for the application of BIM within the realm of road and bridge construction. These guidelines intricately regulate the implementation of BIM, highlighting its role in various aspects, notably in bridge asset management across Indonesia. Furthermore, circular letters from relevant authorities, like Circular Letter 2023 from the Director General of Water Resources and Circular Letter 2022 from the Director General of Housing, offer detailed technical instructions and guidelines for leveraging BIM in infrastructure construction and housing projects respectively.

Examining Indonesia's scan-to-BIM guidelines, notable deviations from global standards arise. While Indonesia uses diverse laser scanning technologies for surveying, discrepancies lie in standardized tool specifications and data processing protocols. Unlike international practices ensuring uniformity and precision, Indonesia's guidelines lack explicit specifications for tools and data integration into 3D models, impacting consistency and accuracy. Despite Indonesia's detailed information collection through laser scanning, gaps in standardized tool specifications and data processing protocols persist. Aligning these aspects with global standards could significantly enhance the accuracy and effectiveness of scan-to-BIM processes in Indonesian road and bridge construction.

2.2 *Scan-To-BIM implementation on Indonesian bridges*

The completed Scan-to-BIM projects managed by Indonesia's Directorate General of Highways encompass a range of specialized bridges across diverse regions, such as the Musi IV Bridge in South Sumatera, Barelang Bridge in Batam Island, Sigandul and Serayu Bridges in Central Java, Kretek II Bridge in Yogyakarta, Sembayat Baru II Bridge in East Java, Alalak Bridge in South Borneo, Pulau Balang Bentang Panjang Bridge in East Borneo, and Bahtera Emas Bridge in South Sulawesi. These projects were executed with strict adherence to technical specifications and unique requirements during their construction phase. However, while the visualization of these bridges may seem impressive, the lack of robust quality assurance mechanisms post-processing raises concerns about the final data's quality. Despite precision engineering during construction, the absence of stringent post-processing quality checks may undermine the overall reliability and accuracy of the data obtained. Consequently, while these bridges stand as symbols of enhanced infrastructure and connectivity across Indonesia's diverse landscape, ensuring the reliability and accuracy of the final data becomes imperative for their true effectiveness and long-term utility.

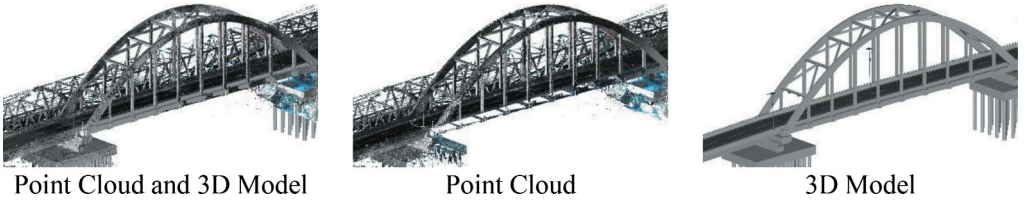


Figure 1. Sembayat Baru II Bridge digital asset from Scan-to-BIM approach.

3 ANALYSIS OF GAP AND FACTORS INFLUENCING BIM ADOPTION

3.1 *Bridging the gap: Comparative analysis*

The comparative analysis reveals Indonesia's progressive strides in BIM integration and Scan-to-BIM exploration but highlights significant disparities compared to global leaders like the UK, Norway, South Korea, and Singapore (Rocha & Mateus, 2021) While Indonesia's evolving policies show promise, they fall short compared to the UK's stringent BIM Level 2 mandates and Norway's comprehensive strategies, indicating a need for clearer directives and

standardized protocols. Moreover, Indonesia's moderate industry collaborations lag behind extensive partnerships seen in leading nations, demanding a faster pace of technological adoption to match Singapore and South Korea's advanced integration.

In Scan-to-BIM, Indonesia's exploration contrasts with established methodologies in the UK, Norway, and Singapore, signaling the need for adopting proven methodologies and advanced technology strategies (Saksena & Sastrawiria, 2023). Critical developmental areas emerge: explicit policy mandates, intensified industry collaborations, accelerated technological adoption, and focused adoption of established Scan-to-BIM methodologies from leading nations.

Table 1. Comparative analysis Indonesia's BIM framework and approach

Parameters	Policy Framework	Industry Collaboration	Technology Adoption	Standardization	Scan-to-BIM Approach
Indonesia	Ongoing integration efforts, emerging policies	Moderate collaborative initiatives	Emerging adoption, increasing awareness	Varied practices, limited standardization	Developing utilization, exploring potentials
Denmark	Extensive BIM initiatives	Industry-wide coordination	Advanced technology adoption	Uniform guidelines	Integrated in various projects
Finland	Emphasizes BIM	Active collaborations	Invests in technology	Standardized practices	Developing applications
Norway	Comprehensive BIM strategies	Unified industry practices	Innovative technology adoption	Established protocols	Proven application in projects
Singapore	BIM Excellence Program	Robust industry collaborations	Embraces digital innovation	Comprehensive standards	Implemented in major project
South Korea	Strong government support	Active industry partnerships	Cutting-edge tech integration	Unified standards	Advanced use in projects
UK	BIM Level 2 mandates	Extensive collaborations	Advanced technology integration	Unified protocols	Well-established methodologies
US	National BIM Standard	Collaborative approaches	Embraces BIM technologies	Standardized guidelines	Increasing use in projects

The table encapsulates diverse global approaches to Building Information Modeling (BIM) and Scan-to-BIM methodologies in infrastructure development. Denmark leads with extensive BIM initiatives, emphasizing coordination and technology adoption; Finland prioritizes BIM and collaboration while developing applications; Norway stands out for comprehensive strategies and proven application; Singapore excels with industry collaborations and real-world implementation; South Korea's government support drives cutting-edge tech integration; the UK mandates BIM Level 2 with advanced methodologies; the US steadily adopts BIM standards. Indonesia shows progress but faces challenges in standardization and collaboration, exploring Scan-to-BIM potentials and emerging policies, marking a developmental phase in BIM integration within infrastructure.

3.2 *Challenges in BIM implementation in Indonesia*

Embarking on Indonesia's journey towards seamless BIM integration exposes significant hurdles in policy, human resources, and tool implementation. Unlike the UK and Norway, Indonesia's evolving policies lack the granularity needed for standardized BIM adoption, posing challenges in uniform practices across projects. Digital twin creation, as highlighted by (Saksena & Sastrawiria, 2023), faces complexities due to diverse data, project dynamics, and multiple constraints, hindering recent BIM processes in Indonesia. Proficiency gaps in advanced BIM methodologies persist among professionals, limiting BIM's efficient use across project

phases, as noted in (Kineber et al., 2023), necessitating organizational and cultural readiness for embracing BIM in asset management. Furthermore, limited accessibility and familiarity with sophisticated BIM tools hinder their widespread adoption among professionals, restraining BIM's potential in transforming infrastructure development practices. Literature-based solutions suggest refining policies, upskilling the workforce, enhancing technological accessibility, and fostering collaborative efforts among stakeholders to advance BIM methodologies in Indonesian infrastructure projects.

Literature-based solutions suggest pivotal steps for enhancing BIM implementation in Indonesia. Clearer directives and stringent mandates within refined policies are crucial, fostering standardized BIM adoption across projects. Upskilling the workforce through comprehensive training programs can bridge proficiency gaps among professionals, while enhancing technological accessibility and affordability will ease BIM tool implementation. Collaborative efforts among stakeholders, facilitated by knowledge-sharing platforms, can create an ecosystem conducive to advancing BIM methodologies, driving Indonesia toward a more integrated BIM landscape in infrastructure projects.

4 COMPARATIVE WORKFLOWS AND IMPACTS

4.1 *Comparative analysis of BIM workflows*

The BIM delivery strategies across leading countries exhibit distinct advantages and disadvantages. For instance, the UK's stringent policy mandates foster standardized protocols and collaborative working, yet potential disadvantages might include initial implementation challenges and resource constraints. Conversely, while the US emphasizes national standards and industry collaboration, potential drawbacks could involve variations in state-level adoption and diverse stakeholder interests. Similarly, Norway's comprehensive BIM strategies showcase proven applications, but potential challenges may arise in scaling these strategies to match Indonesia's infrastructure diversity. Finland and Denmark's unified standards and innovative solutions present advantages in standardization and sustainability, yet challenges might surface in aligning these practices with Indonesia's developing infrastructure. South Korea's advanced technology integration and Singapore's comprehensive standards and digital innovation offer advantages in cutting-edge implementation; however, the potential challenge lies in adapting these high-tech approaches to Indonesia's varying technological landscape and resource availability. The impact within Indonesia's context hinges on leveraging these global practices to overcome challenges in policy refinement, skill development, technology accessibility, and fostering collaborative ecosystems suited to Indonesia's infrastructure complexities and developmental stages.

Leveraging these global BIM practices can offer valuable insights for Indonesia's infrastructure development. Indonesia can learn from stringent policy mandates like the UK's to foster collaboration, but should be mindful of initial challenges in implementation. Similarly, aligning strategies from Norway's comprehensive approaches with Indonesia's diverse infrastructure could pose challenges. Embracing collaborative models from the US while navigating state-level variations could provide a blueprint for Indonesia's industry cooperation. Further, lessons from high-tech integrations in South Korea and Singapore can inspire Indonesia's technological advancements but may require adaptation to suit local resource availability and infrastructure maturity. In essence, understanding these global practices' strengths and challenges empowers Indonesia to tailor BIM strategies to its developmental stages, focusing on refining policies, skill development, technology accessibility, and fostering collaborative ecosystems tailored to its infrastructure complexities and specific needs.

4.2 *Standardizing deviation point cloud vs 3D model in digital twin creation*

According to (Datta et al., 2023), common problems in BIM implementation include interoperability and standardization issues with software and data formats, leading to difficulties in data exchange across platforms and disciplines. Various BIM guidelines, like the US GSA BIM

guide and Finnish COBIM guidelines, show differences in defining tolerances and accuracy verification. While some, like the British PAS 1192 and Plowman Craven's BIM survey specification, suggest thresholds and verification methods, others lack explicit accuracy definitions. Existing standards from BuildingSMART International and ASTM International influence acceptable deviation ranges, aiding in tailored tolerance specifications. However, the absence of unified regulation points to the need for established maximum deviation standards between point clouds and 3D models in scan-to-BIM processes for bridges, crucial for data reliability, safety assessments, and predictive maintenance planning. Regulated deviations also enhance collaboration among stakeholders, streamline workflows, and ultimately optimize bridge asset management strategies. (Chen & Cho, 2018) highlight the importance of defined deviation standards and propose methods for measuring discrepancies between as-built conditions and BIM representations, contributing to data quality and integrity in bridge digital twins.

Moreover, regulated deviation standards foster interoperability and collaboration among stakeholders. With standardized tolerances, different entities involved in bridge projects can communicate effectively using common parameters, reducing misinterpretation and discrepancies. These standards also streamline the scan-to-BIM process, minimizing uncertainties and potential rework due to ambiguous accuracy requirements. This enhances efficiency in workflows, potentially reducing project costs and timeframes. Ultimately, regulated maximum deviations in scan-to-BIM creation for bridge assets optimize asset management by enabling better decision-making, predictive maintenance planning, and lifecycle management, thereby enhancing the overall effectiveness of bridge asset management strategies.

5 CONCLUSION

5.1 *Summary of findings*

The study delves into Indonesia's strides in BIM integration and Scan-to-BIM exploration, drawing comparisons with global leaders in the field. Indonesia shows progress in BIM implementation but lags behind nations like the UK, Norway, South Korea, and Singapore due to less stringent policies and differing methodologies in Scan-to-BIM approaches. This highlights the need for clearer frameworks and standardized protocols in Indonesia. Key influencers of this divergence include policy precision, industry collaborations, technological uptake, and standardization.

Recommendations advocate refining policies, bridging skill gaps, ensuring tech accessibility, fostering collaboration, and establishing standardized Scan-to-BIM protocols to address Indonesia's challenges in policy clarity, skill development, and technology accessibility.

In reviewing studies focused on BIM implementation and scan-to-BIM processes within bridge asset management, several critical insights have emerged. One key challenge identified across these studies lies in the lack of interoperability and standardization among various BIM software and data formats. This diversity poses significant difficulties in data exchange and integration across platforms and disciplines, leading to varying approaches to defining tolerances and accuracy verification within BIM guidelines.

Researchers advocate for the establishment of regulated maximum deviation standards between point clouds and 3D models in scan-to-BIM processes. This absence of a universal standard emphasizes the need to define tolerances, ensuring data quality and reliability for accurate digital representations of bridge assets. These regulated standards prove pivotal for safety assessments, informed decision-making, and predictive maintenance planning, aligning digital twins more closely with physical bridge structures.

Beyond ensuring data accuracy, regulated deviation standards foster better collaboration and interoperability among stakeholders. Common parameters help in effective communication, reducing misinterpretations and streamlining workflows. These standardized tolerances also promise increased efficiency, potentially cutting project costs and timeframes.

Ultimately, the application of regulated deviation standards within scan-to-BIM processes emerges as a linchpin for optimized asset management in bridge infrastructure. Their establishment facilitates improved decision-making, predictive maintenance planning, and overall

lifecycle management, thereby enhancing the effectiveness of bridge asset management strategies.

5.2 *Recommendations and future prospects*

The outlined roadmap for Indonesia's integration of BIM and Scan-to-BIM signifies both promise and challenges on the horizon. It highlights critical areas where significant progress is both necessary and achievable, demanding a holistic strategy to realign local practices with global benchmarks while addressing intrinsic developmental requirements.

Firstly, refining policy frameworks emerges as a cornerstone in Indonesia's journey. The need to revamp existing policies, mirroring the robust and stringent models observed in countries like the UK and Norway, becomes evident. This overhaul isn't solely about crafting stringent policies but ensuring their effective enforcement across the spectrum, fostering a consistent and regulated environment conducive to standardized BIM implementation in diverse infrastructure projects. This shift requires a harmonious blend of policy formulation and pragmatic enforcement mechanisms to ensure alignment with global benchmarks.

Secondly, the imperative for skill development among Indonesia's workforce looms large. Tailored training initiatives and certifications must be strategically introduced to bridge the prevailing skill gaps. These programs act as a catalyst, empowering professionals to proficiently wield sophisticated BIM methodologies and tools. The envisioned outcome is a workforce adept at harnessing these technologies effectively, thus fundamentally transforming their utility within Indonesia's infrastructure development landscape.

Thirdly, accessibility and affordability of cutting-edge BIM tools are pivotal. Promoting access to these tools and simplifying their user interfaces through strategic alliances or government-backed initiatives are essential catalysts for widespread adoption. This strategic move would democratize access to sophisticated BIM technologies, encouraging their utilization across diverse professional spectra within Indonesia's infrastructure development domain.

Furthermore, collaborative ecosystems are paramount. Encouraging the creation of platforms that facilitate knowledge exchange and interdisciplinary collaborations among stakeholders is crucial. These avenues are instrumental in fostering an environment conducive to embracing and propelling BIM methodologies forward. It's about forging synergistic alliances that transcend individual interests, emphasizing collective progress and innovation within Indonesia's infrastructure domain.

Finally, standardizing Scan-to-BIM methodologies is integral. Drawing lessons from successful global practices, particularly in laser scanning technologies and 3D model creation, will streamline and standardize protocols. This standardization ensures consistency, efficiency, and reliability in managing bridge assets within Indonesia's infrastructure landscape.

Overall, these recommendations collectively set the stage for Indonesia's ascendancy as a trailblazer in modern and efficient infrastructure development through BIM methodologies. They address intrinsic developmental requisites while aligning the nation with global standards, fostering a transformative trajectory in the realm of infrastructure development and management.

REFERENCES

Ali, K. N., Alhajlah, H. H., & Kassem, M. A. (2022). Collaboration and Risk in Building Information Modelling (BIM): A Systematic Literature Review. *Buildings*, 12(5). https://doi.org/10.3390/buildings12050571

Bennetts, J., Vardanega, P. J., Taylor, C. A., & Denton, S. R. (2020). Survey of the use of data in UK bridge asset management. *Proceedings of the Institution of Civil Engineers: Bridge Engineering*, 173(4). https://doi.org/10.1680/jbren.18.00050

Borrmann, A., König, M., Koch, C., & Beetz, J. (2018). Building information modeling: Why? What? How? In *Building Information Modeling*: *Technology Foundations and Industry Practice*. https://doi.org/10.1007/978-3-319-92862-3_1

Charef, R., Emmitt, S., Alaka, H., & Fouchal, F. (2019). Building Information Modelling adoption in the European Union: An overview. *Journal of Building Engineering*, 25. https://doi.org/10.1016/j.jobe.2019.100777

Chen, J., & Cho, Y. K. (2018). Point-to-point Comparison Method for Automated Scan-vs-BIM Deviation Detection. *Proceedings of the 2018 17th International Conference on Computing in Civil and Building Engineering*.

Datta, S. D., Sobuz, M. H. R., Mim, N. J., & Nath, A. D. (2023). Investigation on the effectiveness of using building information modeling (BIM) tools in project management: a case study. *Revista de La Construccion*, 22(2). https://doi.org/10.7764/RDLC.22.2.306

Kang, T. (2023). Scan to BIM Mapping Process Description for Building Representation in 3D GIS. *Applied Sciences (Switzerland)*, 13(17). https://doi.org/10.3390/app13179986

Kineber, A. F., Othman, I., Famakin, I. O., Oke, A. E., Hamed, M. M., & Olayemi, T. M. (2023). Challenges to the Implementation of Building Information Modeling (BIM) for Sustainable Construction Projects. *Applied Sciences (Switzerland)*, 13(6). https://doi.org/10.3390/app13063426

Musarat, M. A., Alaloul, W. S., Cher, L. S., Qureshi, A. H., Alawag, A. M., & Baarimah, A. O. (2023). Applications of Building Information Modelling in the Operation and Maintenance Phase of Construction Projects: A Framework for the Malaysian Construction Industry. *Sustainability (Switzerland)*, 15(6). https://doi.org/10.3390/su15065044

Olanrewaju, O. I., Kineber, A. F., Chileshe, N., & Edwards, D. J. (2021). Modelling the impact of building information modelling (Bim) implementation drivers and awareness on project lifecycle. *Sustainability (Switzerland)*, 13(16). https://doi.org/10.3390/su13168887

Rocha, G., & Mateus, L. (2021). A survey of scan-to-bim practices in the aec industry—a quantitative analysis. *ISPRS International Journal of Geo-Information*, 10(8). https://doi.org/10.3390/ijgi10080564

Saksena, H. T., & Sastrawiria, R. P. P. (2023). Implementation of Laser Scanning Technology for Digital Asset Management of Bridges in Indonesia: A Case Study of Pulau Balang Bridge in East Kalimantan. *Asia Australia Road Conference*. https://doi.org/https://doi.org/10.58674/phpji.v16i1.384

Saraireh, I. M. A. Q., & Haron, A. T. (2020). Understanding the Conceptual of Building Information Modeling: a Literature Review. *INTERNATIONAL JOURNAL OF CIVIL ENGINEERING AND TECHNOLOGY (IJCIET)*, 11(1). https://doi.org/10.34218/ijciet.11.1.2020.018

Wei, J., Chen, G., Huang, J., Xu, L., Yang, Y., Wang, J., & Sadick, A. M. (2021). BIM and GIS applications in bridge projects: A critical review. *Applied Sciences (Switzerland)*, 11(13). https://doi.org/10.3390/app11136207

Bridge Maintenance, Safety, Management, Digitalization and Sustainability – Jensen, Frangopol & Schmidt (eds)
© 2024 The Author(s), ISBN 978-1-032-77040-6
Open Access: www.taylorfrancis.com, CC BY-NC-ND 4.0 license

Material characterization for HBIM data structures on a masonry arch bridge

R. Chacón, C. Ramonell, H. Posada, L. Pelà, L. García-Ramonda, S. Gönen & A. Cabané
Universitat Politècnica de Catalunya, Barcelona, Spain

ABSTRACT: This paper presents a set of undertaken actions for characterizing masonry arch bridges using data structure suitable for proper embedment in Digital Twins and Heritage Building Information Modelling (HBM). Interfaces in bridge maintenance are relentlessly and increasingly sophisticated. For both new and existing bridges, these interfaces are tending towards their ability to deal with different sources of information. Comprehensive digital twins of heritage masonry arch bridges may include several sources of information gathered from the real asset. Measurements can be taken using many different techniques ranging from contact to contactless and from non-destructive to moderately destructive samples. In addition, these twins may base upon different numerical models aimed at predicting and anticipating the present and future behaviors of the asset, respectively. Masonry arch bridges are known for their complex material and structural characteristics. Digitizing these masonry properties is key for effective simulation and analysis, often involving homogenization of diverse material properties. The design of comprehensive information constructs able to store and federate multiple data layers within a single entity is still challenging. Layers must be connected using vast scoped solutions such as knowledge graphs, integrating measurements, simulations and other information sources. In this particular case study on a masonry arch bridge located in Catalonia, Spain, in-situ Non-Destructive Testing (NDT) data is conceptualized for proper infusion within HBIM schemas. This integration pursues a seamless information flow for analysis or predictive purposes.

1 INTRODUCTION

Masonry arch bridges can be found in numerous cities and landscapes across Europe and are renowned for their stunning and grand designs. Predominantly constructed from stone and/or brick, these bridges have exhibited excellent durability and structural integrity. They hold significant historical, scientific, and cultural values, with many being designated as world heritage sites. The resilient form of these bridges has been a key factor in their survival and continued functionality over centuries of service. However, most of these masonry structures are yet susceptible to varying degrees of irreversible damage due to natural disasters or the cumulative effects of environmental or serviceability exposure, with the materials being particularly vulnerable to such impacts. Consequently, it is crucial to forecast and anticipate potential collapses of those assets. Implementing strategic monitoring represents a crucial step in this endeavor.

Structural health monitoring (SHM) deployments includes the application of in-situ techniques for sensing and analyzing structural characteristics with the aim of diagnosing and detecting changes that could signify damage or degradation. The concept is decades old and it is nowadays benefiting from the use of more comprehensive information constructs within BIM (for organizational purposes), higher diagnosis capabilities with higher technological

DOI: 10.1201/9781003483755-281

readiness reached by characterization techniques (more varied and advanced ways of collecting data) and varied and sophisticated model-based or data-driven predictions for further prognosis. In the context of masonry bridges, one bottleneck is determined by the need of handling varied sources of collected data. The complexity and variety of characterization techniques and the non-standardized nature of their structural configurations pose challenges and thus, establishing threshold limits for anticipating collapse with data-informed warning indicators remains an intricate task.

For material characterization, an overall inspection of a masonry arch bridge traditionally encompasses different techniques. Non-destructive testing (NDT) and minor destructive testing (MDT) techniques, or a combination of both allow assessing the state of the components of the structure at a given episode (Cabané et al. 2023). Material characterization provides valuable insight related to the masonry components, i.e., mortars and units (fired clay or concrete bricks, cast or natural stones) and thus masonry as a homogenized continuum. In addition, static and dynamic proof load tests can shed light on the structural behavior at structural levels while geometrical surveys and visual identification of singularities contribute to the overall understanding of the behavior of the bridge.

BIM in civil engineering provides endless advantages for parametric modeling, 3D visualization, information management, and secondary development. It could also enhance efficiency and efficacy when handling information during construction phases. The operation and maintenance phase can also benefit from these information constructs. As a result, use of digital information of the asset encompasses design, construction and maintenance. In the particular case of heritage, HBIM stands for Heritage Building Information Modelling as an adaptation of the more widely known Building Information Modelling (BIM) technology, specifically tailored for historical and heritage buildings. HBIM focuses on digitally documenting, managing, and representing historic buildings and structures. Originally presented for characterizing geometric objects (Murphy et al. 2013), HBIM has permeated within many different types of heritage structures (López et al. 2018). In the specific field of masonry, BIM (and HBIM) schemas for masonry units and walls have been proposed in the literature (Gentry et al. 2016). In particular, these schemas are focused on new designs and designs using standard masonry units (MU). The field is active and advanced technologies, various types of software, and improved algorithms are under development to facilitate the automatic and rapid creation of structural HBIM models of heritage structures (Croce et al. 2022; Musella et al. 2021; Calvano et al. 2021).

SHM of masonry arch bridges can benefit from HBIM by leveraging frameworks in which information is retrievable and usable by different stakeholders (Wang et al. 2022). The synergy between SHM and HBIM provides vaster possibilities for encompassing information and better solutions for information integration, monitoring, and eventually, accurately anticipating the behavior of the asset. Recognizably, researchers have undertaken studies to develop Building Information Modeling (BIM) models for complex masonry arch bridges (Garozzo & Santagati, 2021). These efforts include parametric manual and AI-crafted modeling based on surveying and mapping data. The philosophy aims at integrating multi-source information such as history, geometry, material, detection, and repair data of heritage structures into BIM models. Researchers have proposed BIM parametric modelling for masonry vaults (Trovatelli et al. 2023). On an attempt of deploying comprehensive systems for anticipating the collapse of bridges, the Joncadella Viaduct, located in Catalonia, Spain is used systematically as an example of masonry bridge. The overall research project includes different types of measurements, simulations, surrogate models and analysis. All information legs are organized in the form of a multi-source information construct in the form of a digital twin. These actions belong to the Spanish National Research Project called PONT3 (www.pont3.es). In the particular case of actions deployed in this paper, the driving force of this research is underpinned by two primary research inquiries:

– What are the ontology structure for encapsulating the material characterization of masonry arch bridges?
– How can this domain of knowledge be leveraged for creating a Building Information Interoperable Model that emphasizes predicting potential collapses?

Advancing new ontologies or augmenting existing standards specifically for a thorough analysis of masonry bridges represents a significant stride that can contribute to assessing their health status. This endeavor necessitates a detailed examination of the available standards and ontologies. Developing a new data schema or an extension could additionally contribute to incorporating semantic layers into Heritage Building Information Modeling (HBIM) models. In this paper, advances on addressing this issue through a case study focusing on a specific masonry arch bridge located in Catalonia, Spain. This case study provides a practical application for initial examination of the theories and methodologies discussed, offering insights into their real-world implications and effectiveness in the context of the preservation and analysis of such historic structures.

2 THE CASE STUDY

2.1 *A brief history of the Joncadella Viaduct*

During the latter half of the 19th century, the expansion of railway networks in Europe spurred significant growth in the construction of stone and masonry arch bridges. While these bridges were generally built according to the 19th-century design standards for masonry arch structures, they also uniquely incorporated local construction techniques and materials. This blend of standardized design and local craftsmanship reflects the building practices of that era, serving as a historical testament to the architectural methods of the past. The Joncadella Viaduct is located in the Catalan region of "El Bages". It is part of the non-electrified "Manresa-Súria" railway line, primarily used for freight train traffic. Originally authorized as a mining railway to "Solvay & Cie" in 1918, the Joncadella Viaduct initially featured four masonry arches and a steel lattice girder deck with spans of varying lengths, all supported by masonry columns and abutments. Operational since 1924, it is currently operated by the *Ferrocarrils de la Generalitat de Catalunya* (FGC).. An exhaustive search of the documentation on the original structure has led researchers to several archives and museums of the area as well as documentation provided by historians. Reports date back to January 10th, 1919. The Manresa-Súria railway line, featuring a total of 6 viaducts, was undoubtedly built with the same technology, materials and construction processes. A historical photograph in Figure 1 illustrates the Manresa-Súria railway bridges under construction by "Construcciones y Ferrocarriles S.A." in 1920 and Figure 2 two photographs of the bridge with its initial design with a steel lattice girder deck during service.

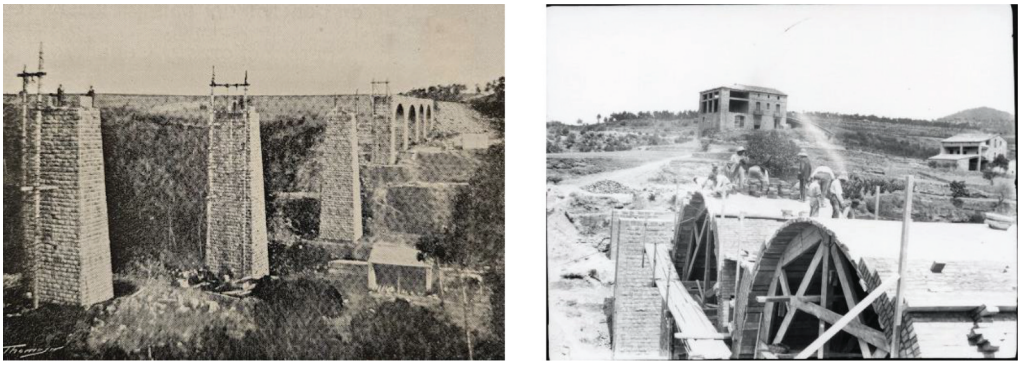


Figure 1. Left: The Joncadella Viaduct during early 20th century (Canet J. 1920). Right: The Cortes Viaduct (Fàbrega A. 2009). Both arch bridges under construction. Early 20th century.



Figure 2. The Joncadella Viaduct in November 1924 (Archive Comarcal del Bages, J.M. Rosal i d'Argullol collection, reference code ACBG30-154-N-1756 on the left and ACGB30-154-N-1764).

2.2 *The present of the Joncadella Viaduct*

Spanning roughly 169 meters in length and standing about 25 meters tall, the viaduct presently comprises thirteen spans. Initially, during the early 1920s construction phase, four of these spans were built as masonry arches. In a 1950 refurbishment project, the remaining nine spans were replaced with unreinforced concrete arches, taking the place of the original metallic truss that was heavily corroded and dismantled. The 1950s intervention and replacement works on the bridge were comprehensively documented, detailing the materials, structural elements, and construction process used. Figure 3 illustrate the concrete resulting arches that replaced the steel deck. Figure 4 provides both bird views and details of the viaduct in its present condition.



Figure 3. The Joncadella Viaduct during the second half of 20th century (Left: Roger (2008) Right: authors).

3 OBJECTIVES AND METHODOLOGY

The primary goal of this project is to proactively predict potential collapses across various bridge types. To achieve this, the methodology centers on creating an extensive information system that integrates diverse data sources, including measurements and numerical models. This system will not only assimilate various data inputs but also incorporate analytical and predictive tools. Central to this approach is the geometric model, which is grounded in



Figure 4. The Joncadella Viaduct bird view and detail of the masonry arch (Authors).

Heritage Building Information Modeling (HBIM) concepts. By combining HBIM with advanced data integration and analysis capabilities, the project aims to enhance bridge safety through early detection and prevention of structural failures. Figure 5 shows an overview of the encompassing techniques.

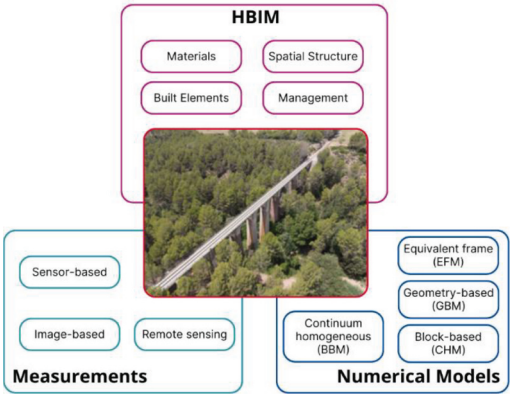


Figure 5. Different sources of information that must be encompassed together.

In this specific case study, it is crucial to highlight that the selected approach for numerical modeling relies on continuum models, which use homogenized material properties. This homogenization process combines both the properties of mortars and individual units to represent the masonry as a unified entity. To ensure accuracy and reliability, this methodology involves conducting specialized tests aimed at characterizing not just the mortars and individual units, but also the masonry as a whole. These specific characterization tests are integral to understanding the true nature and behavior of the materials in question. Additionally, the organization and management of the gathered information are heavily influenced by prior work in Heritage Building Information Modeling (HBIM). This approach in HBIM serves as a foundational framework for structuring and handling the diverse sets of data obtained from tests and analyses. By leveraging the principles and methods established in previous HBIM projects, the project can effectively organize and interpret the complex data. This structured approach not only enhances the accuracy of the numerical models but also ensures that the information is stored and managed in a way that is conducive to further analysis and application in the broader context of bridge maintenance and preservation.

4 NDT AND MATERIAL CHARACTERIZATION OF THE JONCADELLA VIADUCT

The Joncadella Viaduct is a protected cultural heritage, making it impossible to extract material or components that make up its structure for physical and mechanical characterization. For this reason, the characterization of its components requires the use of Minor Destructive Testing (MDT) and Non-Destructive Testing (NDT) Techniques. The MDT and NDT techniques used are increasingly recognized as valuable tools for characterizing and analyzing masonry. Concrete, stone, brick, and mortar, as individual components, can undergo assessment through penetration methods, pull-out tests, break-off tests, surface hardness tests, ultrasonic tests, and impact-echo tests. The research conducted on the Joncadella Viaduct focuses on utilizing the Pin Penetration Test (PPT), the Helix Screw Pull-out Test (HPT), the Torque Penetrometric Test (TPT), and the Rebound Hammer Test (RHT). The PPT involves measuring the depth of penetration of a steel pin to estimate compressive strength. Executed on concrete surfaces, stretcher brick faces, and mortar joints, a 3 mm diameter steel pin with a conical end is inserted into the Windsor Pin Instrument tool. The retraction nut is adjusted, ensuring the spring is in position, and the trigger is activated while maintaining firm contact between the device and the surface. A micrometer is then carefully inserted into the bottom of the hole to read the penetration. The HPT considers the pull-out load of a tie, inserted into a hole drilled into a brick or a mortar joint, as an indication of compressive strength. The mechanical tool and helices used are produced by Helifix Company UK. In the Joncadella Viaduct, the HPT is employed to test bricks and mortar joints. A 3 mm diameter pilot hole is made in the mortar, and a 4 mm one is made in the bricks, both with a depth of 35 mm. An helical tie with a diameter of 1/4 in. (6.3 mm) is embedded, and the Helifix mechanical tool is connected. Load is applied by turning a grip lever to progressively increase the load until failure. The TPT system measures the force required to twist the mortar using a notched tip inserted into the material with four protruding teeth. This test is conducted in mortar joints by inserting the notched tip into a 6 mm diameter pilot hole and subjecting the tip to torsion using a digital readout torque wrench until it reaches the maximum torque indicating material failure. The RHT measures the rebound of a spring-loaded mass impacting against the surface of a sample. The hammer test hits the concrete, stone, or brick at a defined energy, and its rebound is correlated with the material strength capacity. Figure 6 illustrates the MDT and NDT techniques described.



Figure 6. The MDT and NDT techniques. Left: PPT, centre: HPT, right: TPT.

5 NUMERICAL MODELLING STRATEGIES FOR MASONRY ARCHES

Masonry behavior is largely influenced by the mechanical properties of its blocks and mortar, and their interaction. For an accurate simulation of the mechanical behavior of an existing

masonry structure, it is essential to base the model on well-established mechanical properties, derived from experimental tests, and comprehensive geometrical and structural surveys (Lourenço 2002, Roca et al. 2010). The level of detail and accuracy needed for structural analysis dictates the choice of modeling strategies. These strategies differ in their approach to representing the notorious heterogeneity of masonry in numerical models. A recent classification provided by D'Altri et al. (2019) outlines the available strategies: a) continuum models; b) block-based models; c) macro-element models; and d) geometry-based models. Masonry also exhibits anisotropic characteristics, seen in its elastic properties, strength variations in different directions, and brittleness after peak stress. While regular brick masonry shows notable anisotropy, random stone masonry's lack of material regularity may result in less pronounced anisotropy in elasticity, strength, and brittleness. Defining the geometry of historic buildings, known for their intricate and irregular designs, is often complex and requires detailed surveys. Identifying the load-bearing elements within the building's geometry is a nuanced task dependent on the analyst's understanding of the structure. Furthermore, the applicability of this geometry in structural analysis poses its own challenges. While creating the structure's geometry in a CAD environment based on surveys is feasible, its integration into simplified structural analysis is more straightforward than in mesh-based analysis. The latter often encounters issues like mesh inaccuracies and compatibility problems, necessitating overly detailed meshes. Recent advances are directed towards utilizing 3D point clouds for automated mesh generation in historic buildings, aiming to overcome these difficulties. The refinement of these new methods is an active area of development, indicating the evolving nature of structural analysis in the context of historic buildings. Macro-modelling is one of the most popular and common numerical approaches due to its lesser computational demand when compared with other available strategies. Macro-modelling, which does not make any distinction between units and joints, may offer an adequate approach to characterize masonry structural response by considering the material as a fictitious homogeneous orthotropic continuum (Roca et al., 2010). Thus, an appropriate relationship between average masonry strain and stresses need to be established. To this end, the continuum parameters must be determined by means of experimental tests on specimens of sufficiently large size subjected to homogeneous states of stress. However, when it comes to existing masonry structures, such approach is not feasible. As an alternative, it is recommended the experimental assessment of the mechanical characteristic of the individual components of masonry by means of NDT or MDT (Pelà et al., 2016, 2018) and consider the obtained data as input parameters of a numerical homogenization technique. The homogenization procedure poses as a challenge due to the difficulties steaming from the accurate identification of mechanical properties and definition of reliable failure criteria for the homogenous equivalent material (Petracca et al., 2017). The proper definition and identification rely not only on the available empirical formulations provided by current standards, such as EC6 (European Standard, 2006), but also the heuristic-based criteria for the careful analysis of the experimental data, based on prior extensive experience.

6 MATERIAL DATA INTEGRATION

In the particular case of the case study, the integration of material data within a vaster information construct is presented in Figure 6. Site inspections include a series of material tests on several points of the masonry arches for both mortars and masonry units (MU). The data structure of the test program is prepared in a way it includes many samples together with crucial information about each sample. The measured value, an image, the exact location of the sample as well as open text are organized on reports for all tests. Information is sent to the geometrical model HBIM. Users of the HBIM can retrieve information of the testing program to infer structural properties of the masonry as an homogenized material. Numerical models can be based on processed information that can also be retrieved from the corresponding HBIM. A vaster information construct with decision-making capabilities such as

a comprehensive digital twin mustr be conceived in a way all information sources are seamlessly encompassed. Knowledge-graphs are used for integration purposes in this research (Ramonell et al. 2023).

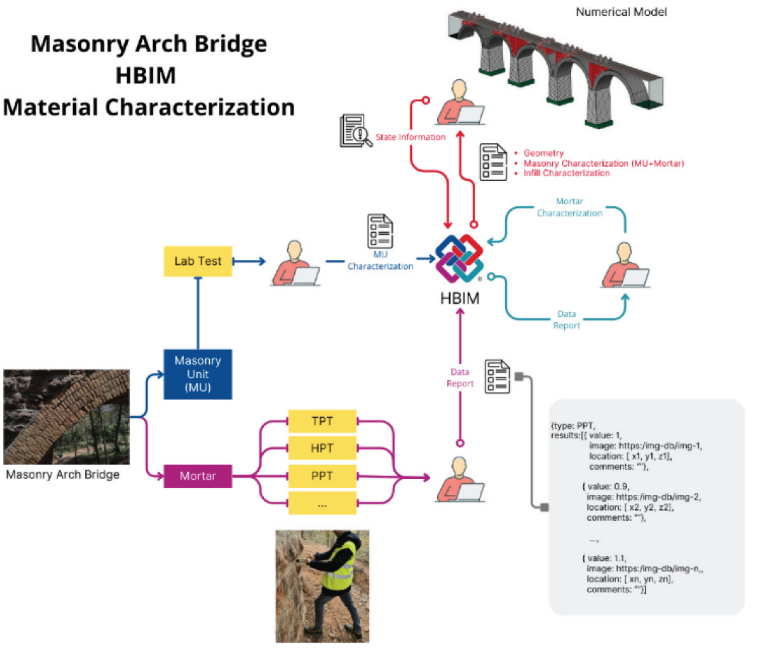


Figure 7. Schema for material characterization for the Joncadella Viaduct.

7 CONCLUSIONS AND FUTURE WORK

Anticipating collapse on masonry arch bridges implies encompassing information related to the physical condition of the bridge as well as related to accurate numerical predictions. A digital twin of a masonry arch bridges for decision-making processes can be used to organized all these data layers. This development necessitates meticulously designed material data structures. These structures should be crafted to seamlessly integrate information from in situ testing programs, ensuring a comprehensive representation of the bridge physical state. The key to successful digital twinning lies in the effective transmission of detailed, accurate data into Heritage Building Information Modeling (HBIM) constructs. This integration not only enhances the precision of the HBIM models but also ensures that every aspect of the bridge's material properties is accurately reflected and accessible for analysis, preservation, and maintenance planning.

ACKNOWLEDGEMENTS

The financial support from the Ministry of Science and Innovation (Spain), the State Agency of Research, and the European Regional Development Fund (ERDF) through the project PONT3 (PID2021-124236OB-C32). Authors also acknowledge the #KPI50 initiative of Ashvin, an H2020 project under agreement 958161 for the complementary support to the development of twinning techniques in new sites. The fifth author acknowledges the financial support of the European Union – NextGeneration EU through the postdoctoral grant Margarita Salas.

REFERENCES

Cabané, A. 2023. Doctoral Thesis. Mechanical characterisation of masonry in existing structures by means of laboratory and in-situ experimental techniques. Universitat Politècnica de Catalunya_BarcelonaTech.

Calvano, M., Martinelli, L., Calcerano, F., Gigliarelli, E. 2022. Parametric Processes for the Implementation of HBIM—Visual Programming Language for the Digitisation of the Index of Masonry Quality. *ISPRS International Journal of Geo-Information*. 11, 93.

Canet J. (1920). Barcelona Artística Industrial.

Croce, P., Landi, F., Puccini, B., Martino, M., Maneo, A. 2022. Parametric HBIM Procedure for the Structural Evaluation of Heritage Masonry Buildings. *Buildings*, 12, 194.

European Standard. (2006). Eurocode 6 - Part 3: Simplified calculation methods for unreinforced masonry structures.

Fàbrega, A. 2009. Grano Cum Salis. La Sal i la potassa a Súria. Ed. Ajuntament de Súria y Iberpotash, S.A. ISBN: 978-84-606-4808-6

Garozzo, R & Santagati, C. 2021. Digital Survey AI and Semantics for Railway Masonry Bridges Health Assessment. In th International Archives of the Photogrammetry, Remote Sensing and Spatial Information Sciences, Volume XLVI-M-1-2021. 28th CIPA Symposium "Great Learning & Digital Emotion", 28 August–1 September 2021, Beijing, China.

López F., Lerones P., Llamas J., Gómez-García-Bermejo J., Zalama E. 2018. A Review of Heritage Building Information Modeling (H-BIM). *Multimodal Technologies and Interaction* 2(2), 21.

Lourenço, P. 2002. Computations on historic masonry structures. *Progress in Structural Engineering and Materials*. 4(3):301–19.

Musella, C., Serra, M., Salzano, A., Menna, C., Asprone, D. 2021. H-BIM – Innovative and Digital Tools to Improve the Management of the Existing Buildings. *In. Proc. PROHITECH 2020 "4th International Conference on Protection of Historical Constructions". Athens, Greece. Volume: Protection of Historical Constructions*.

Pelà, L., Roca, P., & Aprile, A. (2018). Combined In-Situ and Laboratory Minor Destructive Testing of Historical Mortars. International Journal of Architectural Heritage, 12(3), 334–349. http://dx.doi.org/10.1080/15583058.2017.1323247

Pelà, L., Roca, P., & Benedetti, A. (2016). Mechanical Characterization of Historical Masonry by Core Drilling and Testing of Cylindrical Samples. International Journal of Architectural Heritage, 10(2–3), 360–374. http://dx.doi.org/10.1080/15583058.2015.1077906

Petracca, M., Pelà, L., Rossi, R., Oller, S., Camata, G., & Spacone, E. (2017). Multiscale computational first order homogenization of thick shells for the analysis of out-of-plane loaded masonry walls. Computer Methods in Applied Mechanics and Engineering, 315, 273–301. http://dx.doi.org/10.1016/j.cma.2016.10.046

Ramonell C., Chacón R., Posada, H. (2023). Knowledge graph-based data integration system for digital twins of built assets. Automation in Constrution. 156, 105109.

Roca, P., Cervera, M., Gariup, G., Pelà, L. 2010. Structural Analysis of Masonry Historical Constructions, Classical and Advanced Approaches. *Archives of Computational Methods in Engineering*. 17, 299–325.

Roger, G. 2008. *Els Ferrocarrils Catalans*. Molins de Rei. Futurgrafic.

Trovatelli, F., Falcao, A., Machete, R., Tanganelli, M., Bento, R. 2023. Parametric modelling in BIM for structural analysis of masonry vaults. *In: Gabriele, S., Manuello Bertetto, A., Marmo, F., Micheletti, A. (eds) Shell and Spatial Structures. IWSS 2023. Lecture Notes in Civil Engineering*, 437. Springer.

Wang, J., You, H., Qi, X., Yang, N. (2022). BIM-based structural health monitoring and early warning for heritage timber structures. *Automation in Construction* 144, 104618.

Bridge Maintenance, Safety, Management, Digitalization and Sustainability – Jensen, Frangopol & Schmidt (eds)
© 2024 The Author(s), ISBN 978-1-032-77040-6
Open Access: www.taylorfrancis.com, CC BY-NC-ND 4.0 license

Integration of BIM and MIVES to automate the sustainability assessment of viaducts

F. Lozano-Galant
Universitat Politècnica de Catalunya BarcelonaTech, Spain

J.C. Jurado
Universidad Politécnica Salesiana de Cuenca, Ecuador

A. de la Fuente
Universitat Politècnica de Catalunya BarcelonaTech, Spain

J.A. Lozano-Galant
University of Castilla-La Mancha, UCLM, Spain

J. Turmo
Universitat Politècnica de Catalunya BarcelonaTech, Spain

ABSTRACT: Among the multicriteria decision-making (MCDM) methods, the Integrated Value Model for Sustainability Assessment (MIVES) stands out for its ability to quantitatively assess sustainability of civil and construction engineering projects. The integration of this method with building information modeling (BIM) offers a holistic approach to construction project management, this allowing promoting better decision-making, collaboration, and ultimately, more successful and efficient construction projects. While literature explores the link between BIM and MIVES, efforts often lack consistent sustainability assessment automation. Current approaches mainly define MIVES indicators within the BIM model, without achieving a comprehensive evaluation automation. To address this issue, a novel methodology that combines MIVES and BIM is presented to automate the sustainability assessment. The proposed methodology automates the sustainability analysis of BIM digital twin in Revit using quantity tables and internal operators. In addition, a parametric programming tool in Dynamo is developed for direct MIVES and BIM coupling. The approach is validated using a real viaduct to assess sustainability and perform a sensitivity analysis in order to identify those indicators with the most influence on sustainability performance. Critically, this methodology is not limited to the sustainability assessment of bridges as it can be readily adapted to other types of infrastructure. Moreover, it is worth noting that the capabilities of this approach can be significantly augmented by incorporating data from sensors and diverse sources. This inclusion of sensor-derived or alternative data sources enhances the depth and accuracy of the insights drawn from the integrated MCDM-BIM framework.

1 INTRODUCTION

In the context of the ongoing fourth industrial revolution, often referred as Industry 4.0 (Pereiro et al. (2023)), Architecture, Engineering, and Construction (AEC) industry is undergoing a profound shift driven by digitalization. One prominent methodology at the forefront of this transformation is the pivotal role played by Building Information Modeling (BIM) (Fernandez-Mora et al. (2022)), which enables the generation of virtual replicas of the assets, such as civil infrastructures and buildings (Bellido-Montesinos et al. (2019)). The benefits of BIM

DOI: 10.1201/9781003483755-282

include improved collaboration among project stakeholders, enhanced visualization of project details, reduced errors and rework, efficient resource allocation, and better decision-making throughout a construction project's lifecycle (Caglayan & Ozorhon (2023)). It is essential to remark that BIM virtual replicas extend beyond the three-dimensional geometry of their elements, these are also enriched with multidisciplinary databases. Indeed, the integration of these databases empowers stakeholders to access and share precise and up-to-date information, resulting in improved project outcomes and more efficient decision making.

Decision making is also enhanced with Multi-Criteria Decision-Making (MCDM) methods, which facilitate the evaluation between alternatives characterized by multiple, usually conflicting, criteria. These methods are crucial in fields where decisions are complex and involve various factors and stakeholders. The main goal of MCDM is to identify the best option or to rank the options in order of preference, based on the given criteria. Examples of MCDM methods in the Architectural Engineering and Construction AEC field include: Building Research Establishment Environmental Assessment Method (BREEAM) (BREAM (2022)), Leadership in Energy and Environmental Design (LEED) (LEED (2022)), German Sustainable Building Council (DGNB in German) (DGNB (2018)), Civil Engineering Environmental Quality Assessment and Awards Scheme (CEEQUAL) (CEEQUAL (2019)), and (5) Integrated Value Model for Sustainability Assessment (MIVES) (Viñolas et al. (2009)).

Most of these methods are based on economic, environmental, and social criteria. Nevertheless, it is important to highlight that contrary to many MCDM methods, MIVES is not limited to building analysis, as it is a versatile methodology that can be readily adapted to any engineering discipline (Pons et al. (2016)).

MCDM methods offer several advantages when integrated with BIM, including (1) *Database enrichment*: The information contained within a BIM model, including geometric dimensions and compliance data to existing documentation and expert insights, is instrumental in determining the values for parameters used in MCDM methods. (2) *Information processing*: BIM streamlines the collection, categorization, alteration, updating, and analysis of project information. (3) *Information management*: BIM facilitates efficient exchange of information across the various disciplines engaged in a project.

The synergy of Multi-Criteria Decision-Making (MCDM) methods with Building Information Modeling (BIM) has been the subject of extensive research. A recent literature review (Tan et al. (2021)), analyzed 45 papers to demonstrate the collaborative benefits of MCDM and BIM. However, despite the versatility of MIVES and the advantages of the BIM methodology, the literature lacks studies that directly couple MIVES with BIM. To address this gap, this paper introduces a methodology for integrating MIVES with BIM models. This methodology is particularized to study the sustainability assessment of viaducts.

This conference paper is organized as follows: Section 2 examines the proposed methodology, initially detailing the steps involved in applying the MIVES method and subsequently describing its integration with BIM, including the employment of parametric algorithms to automate the information extraction for sustainability assessment. Section 3 presents a case study, the Las Arenas Viaduct in Spain, to demonstrate the step-by-step application of the proposed methodology to an actual structure. Section 4 presents the conclusions derived from this study.

2 SUSTAINABILITY ASSESSMENT METHODOLOGY

In this section, the theoretical background of the MIVES methodology is first described. Then, the application of MIVES for the study of the sustainability assessment of viaducts is presented. Finally, a parametric methodology to integrate MIVES with BIM software is detailed.

2.1 *MIVES*

MIVES is a sustainability-based approach that aims to facilitate decision-making among various options through a multi-criteria analysis. It is based on the use of the Analytic Hierarchy Process (AHP) to manage the hierarchical relationships among different parameters and to set priorities within the decision framework.

To enable the assessment of an alternative from an economic, environmental, and social perspective, MIVES provides a Sustainability Index (SI) ranging between 0 and 1. The calculation and use of this index for the decision-making process is based on the following steps (Pons et al. (2016)):

1. Definition of the problem and the decision needed.
2. The decision model diagram is structured in a decision tree that hierarchically arranges the characteristics of the parameters across three following levels: requirements, criteria, and indicators.
3. Defining the value functions to add homogeneity to the variables by their transformation to common, non-dimensional units named value functions (V). The value function corresponding to each ith indicator (V_i) quantifies the preference for a specific alternative, ranging from minimum (P_{min}=0) to maximum (P_{max}=1) levels of satisfaction. The methodology for calculating V_i involves the following steps: (i) determining whether the value function should ascend or descend, (ii) establishing the minimum (P_{min}) and maximum (P_{max}) thresholds, (iii) deciding on the form of the value functions, with common shapes being concave, convex, linear, or S-shaped, and (iv) formulating the V_i using the following equation:

$$V_i = K_i \left[1 - e^{-m_i \left(\frac{\left| P_{i,x} - P_{i,min} \right|}{n_i} \right)^{A_i}} \right] \tag{1}$$

where n_i is the value used, mi the value of the ordinate n_i, A_i the shape factor of the i^{th} indicator value function (A_i<1 concave, A_i =1 linear, and A_i >1 convex or S-shape), $P_{i,\,min}$ and $P_{i,\,max}$ are the minimum and the maximum value of the i^{th} indicator, respectively, $P_{i,z}$ is the score of alternative z that is under assessment, with respect to the i^{th} indicator under study, and K_i is a factor used to assure that the value of V_i will be within the bounded between 0 and 1. This factor is obtained as follows:

$$K_i = \left[1 - e^{-m_i \left(\frac{\left| P_{i,max} - P_{i,min} \right|}{n_i} \right)^{A_i}} \right]^{-1} \tag{2}$$

where the parameters n_i, m_i, and A_i are fixed according to the preferences of the decision maker.
4. Establishing the significance of each distinct factor involved in the evaluation process. This importance is assigned by relative weights in each requirement (α_i), criterion (β_i), and indicator (γ_i) of the requirements tree. The assignment of these weights can be determined both directly, or by an Analytic Hierarchy Process (AHP) based on a pairwise comparison of all elements with each other.
5. Defining the different alternatives for the proposed problem.
6. Evaluating the assessment of the different alternatives by studying their Sustainability Index (SI). This parameter can be calculated as follows:

$$SI = V\ (P_x) = \sum_{i=1}^{i=n} \alpha_i \cdot \beta_i \cdot \gamma_i \cdot V_i(P_{i,x}) \tag{3}$$

where $V(P_x)$ measures the degree of sustainability (value) of each of the defined alternatives with respect to a set of criteria $P_{i,x}$, and parameters α_i, β_i, and γ_i refer to the weights of the requirements, criteria, and indicators.
7. The SI of the different alternatives are compared to identify the most appropriate one (the one with the highest SI).

2.2 *Sustainability assessment of viaducts*

The MIVES method has been tailored for assessing the sustainability of viaducts. Accordingly, the decision tree (see Table 1) has been structured into three requirements (R) (Economic, R_1, Environmental, R_2, and Social, R_3), six Criteria (C) (Cost, $C_{1.1}$, Time, $C_{1.2}$, Emissions, $C_{2.1}$, Resources, $C_{2.2}$, Social indexes, $C_{3.1}$, and Safety, $C_{3.2}$), and eleven indicators (Total cost, $I_{1.1.1}$, Indirect cost, $I_{1.1.2}$, Maintenance cost, $I_{1.1.3}$, Dismantling cost, $I_{1.1.4}$, Execution time, $I_{1.2.1}$, CO_2 emissions, $I_{2.1.1}$, Raw material consumption, $I_{2.2.1}$, Energy consumption, $I_{2.2.2}$, Affected area, $I_{3.1.1}$, General disturbances, $I_{3.1.2}$, and Health and safety during construction, $I_{3.2.1}$,). Table 1 also includes the values of the weights (α, β, and γ).

Table 1. MIVES decision-making tree for the case study.

Requirement	α_i	Criteria	β_i	Indicator	γ_i
R_1 Economic	55%	$C_{1.1}$ Cost	70%	$I_{1.1.1}$ Total cost	60%
				$I_{1.1.2}$ Indirect cost	10%
				$I_{1.1.3}$ Maintenance cost	20%
				$I_{1.1.4}$ Dismantling cost	10%
		$C_{1.2}$ Time	30%	$I_{1.2.1}$ Execution time	100%
R_2 Environmental	25%	$C_{2.1}$ Emissions	60%	$I_{2.1.1}$ CO_2 emissions	100%
		$C_{2.2}$ Resources	40%	$I_{2.2.1}$ Raw material consumption	50%
				$I_{2.2.2}$ Energy consumption	50%
R_3 Social	20%	$C_{3.1}$ Social indexes	40%	$I_{3.1.1}$ Affected area	40%
				$I_{3.1.2}$ General disturbances	60%
		$C_{3.2}$ Safety	60%	$I_{3.2.1}$ Health and safety	100%

A detailed definition of each of the considered indicators is detailed in Lozano-Galant et al. (Lozano et al. (2023)).

2.3 *Parametric integration between MIVES and BIM*

The following steps were implemented to automate the connection between MIVES and BIM:

1. Analysis of the problem: The information of the viaduct under study is reviewed together with the definition of the problem.
2. Decision framework for MIVES: The different requirements, criteria, and indicators defined in the previous section are defined together with their respective weights (α, β, and γ), and their value functions following the decision-making tree in Table 1. The weights are determined based on the stakeholders' needs, taking into account economic, social, and environmental considerations.
3. BIM modelling: A virtual model of the viaduct is generated with the BIM methodology. The sustainability indicators must be included into the BIM model as project parameters. This process is carried out with the help of a parametric programming in Dynamo to export the information from excel as showed in Figure 1.
4. Definition of the value functions: Both the parameters and coefficients of the value functions of the considered parameters are defined in Excel. The data used to shape the value functions is obtained from the knowledge of each specific variable.
5. Calculation of the sustainability indexes (SI): Equation 3 is used to calculate the sustainability index.



Figure 1. Flow chart of the information.

2.4 *Introduction of sensor information*

Integrating sensor information into a BIM model represents a key step towards enhancing the comprehensiveness and real-time relevance of digital representations of structures. This integration facilitates a dynamic and data-rich environment where real-world data and digital models seamlessly converge. In addition, the introduction of sensor data into the BIM model provides a comprehensive historical record of a structure's performance.

For example, in the case of the LARA (Low-Cost Adaptable Reliable Accelerometer-Anglemeter) (Komarizadehasl (2022)), the sensor measurements can be stored on the Internet of Things IoT web server, and the link to this site can be straightforwardly associated with the attributes of the monitored elements within the BIM model. The traditional protocol for integrating the LARA monitoring data is based on the following steps (Figure 2): (1) Importing LARA data into the Things Speak platform, (2) Visualizing and plotting the results obtained from LARA into the IoT platform, and (3) Adding the IoT site link to the attributes of the monitored BIM element. As a result, the historical measurements can be visualized and incorporated into the BIM model.

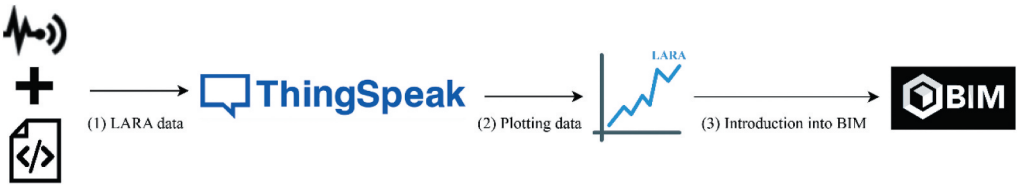


Figure 2. Flow of information to introduce LARA monitoring information in BIM.

In future works, information from actual sensors into the BIM model will be included into the MIVES analysis.

3 CASE OF STUDY

To validate the proposed methodology, the sustainability assessment was conducted on a case study, Las Arenas Viaduct. After describing the primary characteristics of the structure, the application of the proposed methodology is summarized, and the Sustainability Indexes for different scenarios are computed according to the method described in Section 2.1.

3.1 *Las Arenas Viaduct description*

Constructed in 2021, Las Arenas Viaduct stretches across the "Las Arenas" stream in Barcelona, Spain, and it is located on the C-58 road that liddinks Sabadell and Terrassa. The bridge extends over a total length of 128 meters and comprises four simply supported spans. Each span features a slab that rests on seven precast beams. A photography of the finished structure is presented in Figure 3.a.

The BIM model of the viaduct was constructed using Revit, based on the structural blueprints, achieving a Level of Detail (LOD) of 300. In this model, elements were organized into the following categories: (1) 'Columns' for the piles and piers, (2) 'Foundations' for the pile caps, (3) 'Walls' for the abutments, (4) 'Framing' for the deck beams, (5) 'Floor' for the deck slab, and (6) 'Structural Rebars' for the steel reinforcement embedded into the concrete elements. A capture of the model is presented in Figure 3.b.

A summary of the parameters and coefficients for the value function of the different indicators considered is presented the Table 2. This figure includes the shape of the value function (decreasing (D) or increasing (I) functions, these being linear (L_r), concave (C_e), convex (C_x) or S-shaped (S), the P_{max}, P_{min}, n_i, m_i, A_i, K_i, P_i, and V_i. For illustrative purposes the value functions of the indicators $I_{1.1.1}$ (Total cost) and $I_{2.1.1}$ (CO_2 emissions) are presented in Figure 4.

(a)



(b)

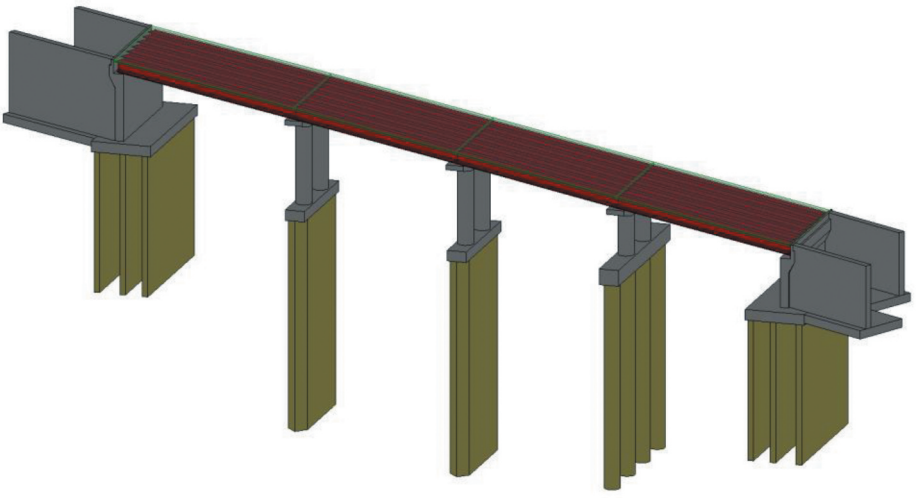


Figure 3. Las Arenas Viaduct: (a) Photography of the finished structure, and (b) BIM model.

Table 2. Parameters and coefficients for each indicator value function (Vi).

Indicator	Shape	P_{max}	P_{min}	n_i	m_i	A_i	K_i	P_i	V_i
$I_{1.1.1}$ Total cost	S-D	1036.18	414.47	625.00	10	1.90	1.00	828.94	0.707
$I_{1.1.2}$ Indirect cost	Cx-D	92.84	78.75	80.00	20	1.90	1.92	82.89	0.607
$I_{1.1.3}$ Maintenance cost	S-D	142.37	71.18	130.00	10	1.90	1.04	94.91	0.804
$I_{1.1.4}$ Dismantling cost	Cx-D	117.86	63.14	75.00	5	1.90	1.07	84.19	0.710
$I_{1.2.1}$ Execution time	S-D	98.00	52.00	160.00	20	2.00	1.24	65.00	0.709
$I_{2.1.1}$ CO_2 emissions	S-D	2682.91	1609.75	1500.00	3	1.45	1.19	2146.33	0.583
$I_{2.2.1}$ Raw material	S-D	12452.86	7471.72	12000.00	7	1.45	1.16	9962.29	0.596
$I_{2.2.2}$ Energy consumption	S-D	23914.29	14348.57	15000.00	4	1.45	1.14	19131.43	0.609
$I_{3.1.1}$ Affected area	Ce-D	6991.88	2913.29	5826.57	4	1.00	1.06	5826.57	0.568
$I_{3.1.2}$ General disturbances	Ce-I	0.00	10.00	3.00	1	1.00	1.04	3.40	0.703
$I_{3.2.1}$ Health and safety	Ce-D	1485.64	891.39	1000.00	3	1.00	1.20	1188.51	0.709

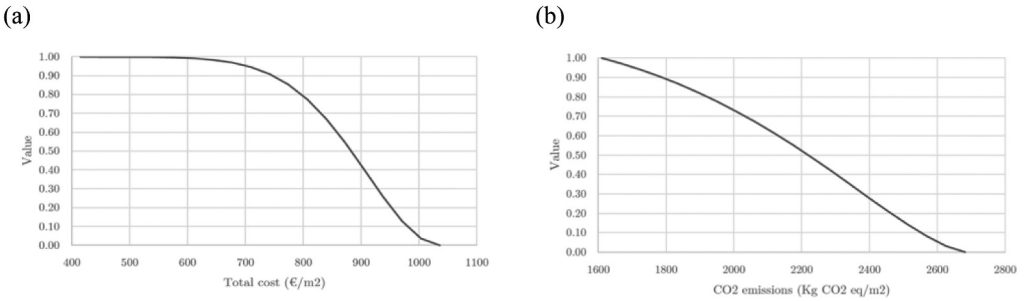


Figure 4. Value function of the indicators: (a) $I_{1.1.1}$: Total cost, and (b) $I_{2.1.1}$: CO_2 emissions.

3.2 *Results*

The sustainability index was examined across three scenarios, each characterized by distinct requirement weights (α). The initial scenario (SI_1) aligns with the reference case derived from the information outlined in Table 1. The second scenario (SI_2) reflects a sustainability balance scenario, where all requirement weights are uniformly set at $\alpha_1 = \alpha_2 = \alpha_3 = 33\%$. Lastly, the third scenario (SI_3) corresponds with a situation where the economic requirement's weight is highlighted, and environmental and social requirements are reduced in relation to the values established in SI_1 (specifically, $\alpha_1 = 75\%$, $\alpha_2 = 10\%$, and $\alpha_3 = 15\%$). It is important to note that both the criteria and indicator weights have remained constant across all three scenarios. Table 3 displays the resulting sustainability index values for each scenario, along with the respective weights assigned to each indicator. Additionally, the product of the different weights α_i, β_i, and γ_i is presented in the table.

Table 3. Sustainability indexes (SI) in the three analyzed scenarios.

Indicator	$[\alpha_1\beta_1\gamma_1]$	SI_1	$[\alpha_2\beta_2\gamma_2]$	SI_2	$[\alpha_3\beta_3\gamma_3]$	SI_3
$I_{1.1.1}$ Total cost	23.10%	0.163	14.00%	0.099	31.50%	0.223
$I_{1.1.2}$ Indirect cost	3.85%	0.023	2.33%	0.014	5.25%	0.032
$I_{1.1.3}$ Maintenance cost	7.70%	0.062	4.67%	0.038	10.50%	0.084
$I_{1.1.4}$ Dismantling cost	3.85%	0.027	2.33%	0.017	5.2%	0.037
$I_{1.2.1}$ Execution time	16.50%	0.116	10.00%	0.071	22.50%	0.159
$I_{2.1.1}$ CO_2 emissions	15.00%	0.087	20.00%	0.117	6.00%	0.035
$I_{2.2.1}$ Raw material	5.00%	0.030	6.67%	0.040	2.00%	0.012
$I_{2.2.2}$ Energy consumption	5.00%	0.030	6.67%	0.041	2.00%	0.012
$I_{3.1.1}$ Affected area	3.20%	0.019	5.33%	0.031	2.40%	0.014
$I_{3.1.2}$ General disturbances	4.80%	0.034	8.00%	0.056	3.60%	0.025
$I_{3.2.1}$ Health and safety	12.00%	0.085	20.00%	0.142	9.00%	0.064
	100.00%	0.678	100.00%	0.664	100.00%	0.698

The analysis of Table 3 shows that sustainability index of the reference scenario (SI_1) is 0.678. In this case, indicators such as total cost, execution time, CO_2 emissions, and health and safety during construction carry significant weight. This index displays slight fluctuations in the two alternative scenarios being considered. Remarkably, the scenario emphasizing the balanced requirements obtained a lower index with a value of SI_2=0.664. In contrast, the scenario focusing on the economic aspect demonstrates a slightly higher sustainability index (SI_3=0.698).

4 CONCLUSION

This paper proposes a new methodology for the evaluation of the sustainability assessment of viaducts. This approach is based on the integration of the MIVES method and the BIM

methodology using parametric programming tools. To illustrate the application of this method its step-by-step application to a real bridge (Las Arenas Viaduct) was studied for eleven economic, environmental, and social indicators.

The results obtained from the analyzed case study illustrate how the proposed methodology facilitates the automated analysis of diverse scenarios by considering both geometric and non-geometric information embedded in BIM databases. In the analyzed structure, a reference scenario was compared with two alternative scenarios- one emphasizing the sustainability balanced, and other simulating an economic crisis. The comparative analysis revealed that the sustainability index exhibited an increase when the significance of economic requirements was heightened, and conversely, it diminished when a balance among all requirements was maintained.

ACKNOWLEDGEMENTS

The authors are indebted to the projects PID2021-126405OB-C31, and PID2021-126405OB-C32 funded by MICIN/AEI/10.13039/501100011033/ and FEDER funds A way to make Europe. The financial support of the project F-00528 (PLEC2022-009441) with the title "Optimización topológica para una metodología de construcción de bajo impacto ambiental (Topological optimization for a low environmental impact construction methodology)" is also appreciated.

REFERENCES

Bellido-Montesinos, P. Lozano-Galant, F. Castilla, F. J. & Lozano-Galant, J. A. 2019. Experiences Learned from an International BIM Contest: Software Use and Information Workflow Analysis. *Journal of Building Engineering*, 21: 149–157.

BREAM. 2022. BREEAM International New Construction 2016 - Cover. https://files.bregroup.com/breeam/technicalmanuals/BREEAMInt2016SchemeDocument (accessed Sep. 07, 2022).

Caglayan, S. & Ozorhon, B. 2023. Determining Building Information Modeling Effectiveness. *Automation in Construction*, 151: 104861.

CEEQUAL, 2019. CEEQUAL Version 6 consultation information, *CEEQUAL Technical Manual – International Projects*.

DGNB. 2018. DGNB, New criteria set new construction building, *The DGNB Certification System*.

Fernández-Mora, V. Navarro, I.J. & Yepes, V. 2022. Integration of the Structural Project into the BIM Paradigm: A Literature Review. *Journal of Building Engineering*, 53: 104318.

Komarizadehasl S. Komary M. Alahmad A. Lozano-Galant J. A. Ramos G. & Turmo J. 2022. A Novel Wireless Low-Cost Inclinometer Made from Combining the Measurements of Multiple MEMS Gyroscopes and Accelerometers. *Sensors*: 5605.

LEED. 2022. LEED v4 for Building Design and Construction - current version | U.S. Green Building Council. https://www.usgbc.org/resources/leed-v4-building-design-and-construction-current-version (accessed Sep. 07, 2022).

Lozano F. Jurado J. C. Lozano-Galant J. A. de la Fuente A. & Turmo J. 2023. Integration of BIM and Value Model for Sustainability Assessment for application in bridge projects. *Automation in Construction*, 152: 1054935.

Pereiro, X. Cabaleiro, M. Conde, B. & Riveiro, B. 2023. BIM Methodology for Cost Analysis, Sustainability, and Management of Steel Structures with Reconfigurable Joints for Industrial Structures. *Journal of Building Engineering*, 77: 107443.

Pons O. de la Fuente A. & Aguado A. 2016. The use of MIVES as a sustainability assessment MCDM method for architecture and civil engineering applications. *Sustainability*, 8(5).

Tan T. Mills G. Papadonikolaki E. & Liu Z. 2021. Combining multi-criteria decision making (MCDM) methods with building information modelling (BIM): A review. *Automation in Construction*, 121: 103451.

Viñolas B. Cortés F. Marques A. Josa A. & Aguado A. 2009. MIVES: modelo integrado de valor para evaluaciones de sostenibilidad, *II Congrés Internacional de Mesura i Modelització de la Sostenibilitat*: 1–24.

SS20: Sensing technology and data processing algorithm towards bridge life-cycle maintenance and safety

Organizers: H. Qu, C. Guo & H. Zhang


Taylor & Francis
Taylor & Francis Group
http://taylorandfrancis.com

Bridge Maintenance, Safety, Management, Digitalization and Sustainability – Jensen, Frangopol & Schmidt (eds)
© 2024 The Author(s), ISBN 978-1-032-77040-6
Open Access: www.taylorfrancis.com, CC BY-NC-ND 4.0 license

A new multi-source data fusion method for seismic identification of bridge

An Chang & Hongya Qu
Department of Bridge Engineering, Tongji University, Shanghai, China

ABSTRACT: In this study, a novel parameter identification method based on data fusion algorithm is proposed. A set of sparse matrix equations on state variables is obtained by establishing the state space system of bridge structure parameters. Data passed into the equation is multi-source and heterogeneous, which includes time-history measurements of acceleration and velocity, and displacement estimation acquired from digital image correlation. Bayesian inference with multi-process modification is applied to solve the equation. With the capability of eliminating ill-conditioned equation, method is verified through shake table test. Applying the method to a series of raw test data, results show that estimation error of the identified seismic excitation time history is at a very low level, which represents good effectiveness. Material parameters calculated from the excitation recognition results of the tested specimen are also in good agreement with estimated results, indicating feasibility in practice.

1 INTRODUCTION

Bridge seismic monitoring data serves as a crucial foundation for assessing the post-earthquake functionality of bridges. In structural health monitoring (SHM), various sensors continuously measure and collect relevant physical quantities at predetermined measuring points on the structure, storing the data for subsequent collation and analysis. Commonly used sensors in SHM include displacement sensors, strain gauges, accelerometers, and so on. As sensing technology advances and detection demands increase, new devices and technologies such as speckle interference imaging, digital cameras, structured light projection have been applied in SHM. While these new technologies provide more available data and information for bridge SHM research, they also present new challenges.

The key challenge lies in effectively integrating multi-source heterogeneous sensor data with different data dimensions to achieve parameter identification, damage diagnosis, maintenance decision-making, and operational decision-making. This problem is known as multisource heterogeneous data fusion (MHDF). Currently, traditional time-frequency domain methods, machine learning techniques, probability theory and statistics, as well as heuristic algorithms are being applied as common MHDF algorithms (Hall 1998; Zhang 2021).

For the sensor information processing of building structure, the current research mainly focuses on the calculation of mechanical parameters under small disturbance, component damage monitoring, vehicle load identification and other directions, which mostly focuses on the analysis and fusion of SHM data under normal use state (Kralovec 2020; Wu 2020), while the research of MHDF for bridge seismic response detection data is still blank. The effect of earthquake on bridge structure usually presents strong randomness and nonlinearity, which may lead to sensor failure and data loss and error. When using image sensors, the extraction of global image displacement and other features of image signals is more complex than that of displacement meter and accelerometer due to its large amount of data and large data dimension (Chen, J.G. 2018).

DOI: 10.1201/9781003483755-283

The change of dynamic parameters of bridges in earthquakes has a significant effect on the evaluation of bridge seismic performance, but the traditional single-source and homogeneous sensor data often have certain limitations in the evaluation of the change process of bridge dynamic parameters in earthquakes, such as single identification parameter and low accuracy (Zhu 2020). For this problem, some scholars have conducted certain theoretical research. For example, Feng et al. (2015) first proposed a new method to simultaneously identify the vehicle axle load of bridge structural parameters and vehicle-bridge interaction system from a limited number of responses. In this study, the vehicle-bridge interaction of simply supported girder bridge and continuous girder bridge was mechanically modeled, and the dynamic control equation in the form of state space and matrix was established. Based on this study, Sun et al. (2015) proposed a new heterogeneous data fusion method for the node excitation identification problem of truss bridge. This method combined the new regularization method based on time domain Bayesian inference to solve the problem of ill-conditioned state equation.

However, the application of MHDF in bridge SHM in existing literature primarily focuses on conventional scenarios where the excitation is small and time-varying parameters of the structure are not considered. Earthquakes, being strongly nonlinear, random, and causing large displacements, can significantly affect the mechanical parameters of a structure or even lead to structural damage. Bridge SHM systems typically incorporate various heterogeneous sensors such as displacement sensors, acceleration sensors, image sensors, etc., resulting in a substantial amount of long-term data generation (Xiong 2002). Considering the growing demand for bridge disaster prevention and structural strength assessment purposes, it becomes imperative to develop MHDF algorithms that are suitable for seismic excitations and enable accurate identification of structural parameters by effectively utilizing sensor data during earthquake events.

This paper proposes a novel approach for identifying the time history of seismic excitations and structural parameters. The method employs the extended Kalman filtering (EKF) algorithm to update the matrix of structural parameters and external loads. Additionally, it utilizes the regression shrinkage method based on first-order and second-order norms to address singularity issues in the parameter matrix and correct baseline drift in dynamic parameters (e.g., velocity and displacement) caused by integration. Furthermore, a heuristic search algorithm is employed to calculate optimal mechanical parameters at each time step.

2 METHODOLOGY FORMULATION

2.1 *Basic ideas*

The proposed MHDF algorithm is shown in Figure 1. It aims to estimate the complete process of seismic excitation by utilizing time series data collected from heterogeneous sensors and to determine the changing pattern of structural parameters (e.g., elastic modulu3) under loading conditions. Initially, the sensor data are acquired, cleaned, and filtered, followed by extracting

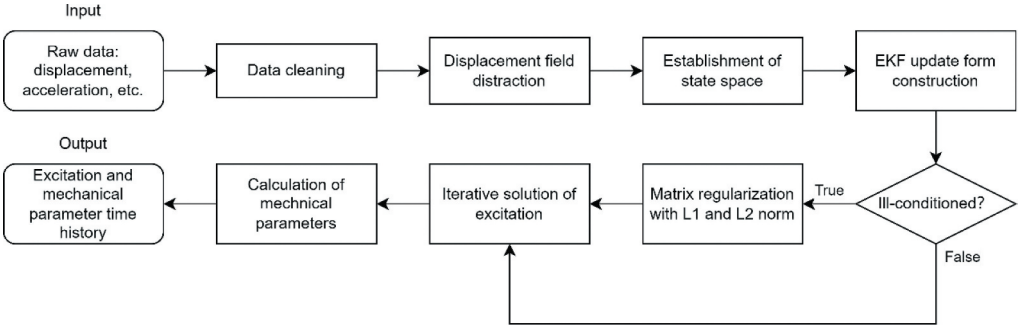


Figure 1. Flowchart of bridge parameter identification based on MHDF.

and modeling the displacement field of a specific section of the structure using digital image correlation (DIC) photography. By establishing a state space model and constructing an updated parameter matrix based on the EKF algorithm, the seismic excitation time history is iteratively solved. Subsequently, a search algorithm based on genetic algorithm is employed to update the model parameters, ultimately leading to acquirement of the relationship between structural parameters and loading condition.

2.2 *Data cleaning and extraction of displacement field*

Due to potential noise interference or sensor failure during data collection, it is necessary to perform basic cleaning and filtering on the original data. In this study, the noise is treated as a sparse vector representing differences throughout the entire process. By transforming the solution of the specific vector into a first-order norm minimization problem for estimating acceleration differences between time steps, hyperparameters can be approximated and adjusted to account for real acceleration drift errors. This approach is known as the first-order norm regression shrinkage method or LASSO method.

In the case of image sensors such as DIC, feature extraction is necessary to convert them into displacement fields within the shooting area. This is crucial for establishing the state equation and preventing potential singularity of parameter matrix in state equation. Figure 2 represents a frame selected from experimental DIC data of one pier from a simply supported beam bridge. The region can be modeled as the surface boundary of a columnar elastomer, and its mapping relationship with the node unit displacement of a multi-degree-of-freedom spring-damping model can be established through elastic theory.

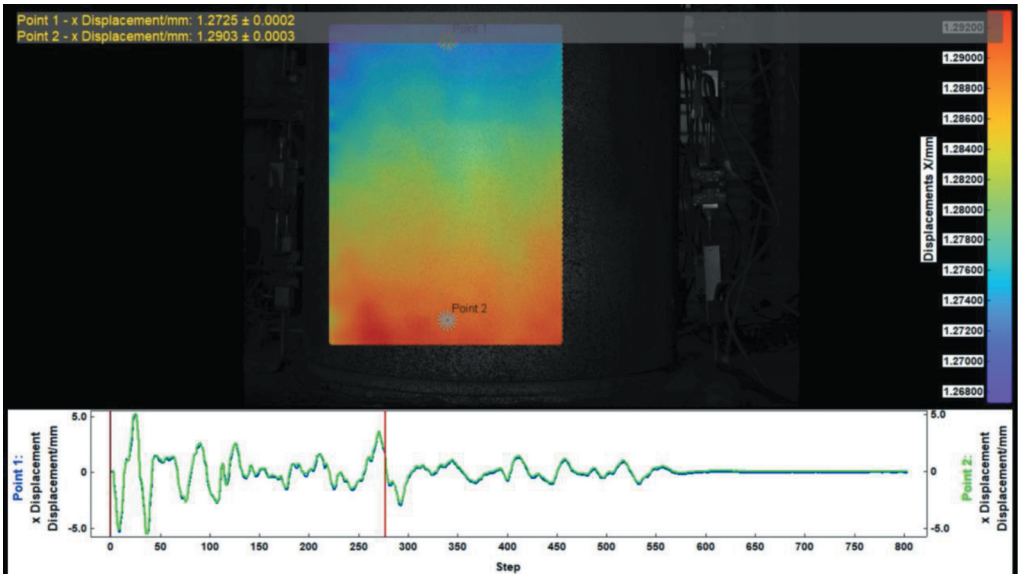


Figure 2. A frame selected from DIC displacement field data.

2.3 *State space construction and introduction of EKF*

The establishment of the state space in this study is based on the dynamic equations. The sensor data collected are primarily classified by dimensions such as displacement, acceleration, rotation angle, etc. Therefore, it is crucial to establish a correlation between the sensor data and structural parameters and external excitations. The studied structural parameters mainly include flexibility matrix, damping matrix, elastic modulus, etc., thus necessitating the

establishment of a mapping relationship between strain and displacement using geometric equations in elastic theory.

Subsequently, the dynamics differential equation is investigated. After processing each time step's state space with standardized matrices, seismic excitation can be solved using numerical methods such as Newmark-β. Given the inherent system nonlinearity in this study, EKF is employed for updating and predicting seismic excitation and parameter matrices. Since the mechanical parameters of the system itself may be time-varying, the use of EKF can better take into account the evolution of the system and avoid directly solving the coupling phenomenon of physical quantities that may exist (such as potential Duffing system), thereby improving the accuracy of recognition and the efficiency of denoising.

After establishing the state space, it becomes necessary to address the issue of ill-conditioning in the latent equation. The parameter matrix may become singular due to noise, potential collinearity, and other factors, rendering it unsolvable using ordinary least squares method. To overcome this challenge, regularization or regression shrinkage methods can be employed. Common regularization techniques include L1 regularization (LASSO regression) and L2 regularization (Ridge regression). In this study, we opt for utilizing the Elastic Net (EN) method which combines both L1 and L2 terms. EN offers sparsity through L1 regularization while effectively suppressing collinearity. By adjusting its hyperparameters, we can eliminate matrix singularity as well as enhancing computational efficiency. To clarify, the equation-solving problem is reformulated as a minimization problem involving a loss function comprising terms of first-order and second-order norms in every time step.

3 EXPERIMENTAL VERIFICATION

The effectiveness of the MHDF scheme was evaluated through shaking table test, as depicted in Figure 3. In this study, a scaled model of a simply supported girder bridge was subjected to shaking table experiments using amplitude modulation output of peak ground acceleration (PGA). Various parameters including the displacement and acceleration of the pier cap, displacement and acceleration of the bridge girder, and rotation of the girder were measured throughout the experiment. DIC monitoring was employed at the pier to obtain comprehensive displacement field data for fusion analysis.



Figure 3. The shaking table test of the double-column pier simply supported girder bridge.

The loading interval used in this study was set at 0.1 times the target PGA, gradually increasing with a step size of 0.1 times until reaching destructive deformation levels. The excitation source primarily relied on seismic records from the El Centro earthquake in the PEER seismic database. Additionally, white noise with an intensity level of 0.13g was applied between each load to ensure sufficient frequency domain coverage. The total loading time of the test was 52.55s, and the sensor monitoring step size was set to 0.0039s.

Through the aforementioned data fusion strategy, the drift vector of acceleration can be obtained as depicted in Figure 4. The state space is constructed by utilizing the modified acceleration and displacement information, and the update and prediction modes of EKF are iteratively solved to ultimately identify seismic excitation as the target recognition. Moreover, the identified seismic excitation's prediction results are evaluated using root mean square error, while residual autocorrelation testing is conducted. It is observed that the residual conforms to a random distribution with minimal error. The variation of pier elastic modulus obtained from material tests is compared with identified results, confirming accurate identification of elastic modulus under significant deformation and displacement conditions. An iterative process was conducted with an error threshold of 10^{-8}. It was verified that this method achieved convergence and yielded an average prediction error below 10%. Moreover, it demonstrates a relatively stable recognition outcome even under significant displacement conditions.

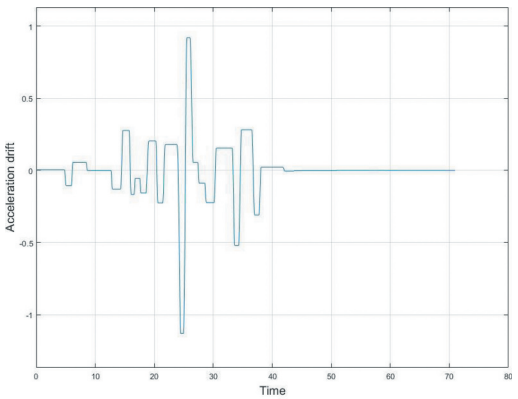


Figure 4. Identified acceleration drift vector.

4 CONCLUSIONS

In this paper, a new method is proposed for identifying bridge parameters and excitation time history in scenarios involving large displacement and strong nonlinear excitation. The method utilizes MHDF and primarily employs the extended Kalman filter to update and predict mechanical parameters and external excitation at each time step. To address potential ill-conditioned problems in the equations, L1 and L2 regularization techniques are employed. To validate the proposed method, numerical studies are conducted using ABAQUS to establish a finite element model, which is further verified through shaking table tests. The main findings of this study can be summarized as follows:

1. In the case of a single span simply supported beam model, displacement and acceleration parameters of the pier, cover beam, and main beam are considered. Despite strong earthquake scenarios, the proposed method effectively estimates the entire process of external load. When compared with actual test results, calculated results from our method exhibit smaller mean square error with residual errors conforming to random distribution patterns. This indicates that the data fusion approach is feasible in practical applications.

2. By standardizing procedures and employing first-order norm (L1) and second-order norm (L2) regularization techniques, we successfully eliminate ill-conditioned matrix problems while reducing computational complexity during EKF updating processes. Additionally, by establishing displacement-strain relationships through geometric equations, our proposed method enables obtaining time-varying processes of mechanical parameters for bridge structures.

REFERENCES

Chen, J.G., Adams, T.M., Sun, H., Bell, E.S. and Büyüköztürk, O., 2018. Camera-based vibration measurement of the world war I memorial bridge in Portsmouth, New Hampshire. *Journal of Structural Engineering*, *144*(11), p.04018207.

Chen, Y., Tan, C.A., Feng, M.Q. and Fukuda, Y., 2006, April. A video assisted approach for structural health monitoring of highway bridges under normal traffic. In *Smart Structures and Materials 2006: Sensors and Smart Structures Technologies for Civil, Mechanical, and Aerospace Systems* (Vol. 6174, pp. 592–609). SPIE.

Hall, D.L. & Llinas, J., 1997. An introduction to multisensor data fusion. *Proceedings of the IEEE*, *85*(1), pp.6–23.

He, Z., Wang, H. and Pan, P., 2023. A model-driven method based on multisource data for reproducing displacement time history. *Earthquake Engineering & Structural Dynamics*.

Kralovec, C. and Schagerl, M., 2020. Review of structural health monitoring methods regarding a multi-sensor approach for damage assessment of metal and composite structures. *Sensors*, *20*(3), p.826.

Sheng, Z.Q., Tang, C.P., Fan, H.T. and Zhang, C.B., 2011. Application of multi-sensor information fusion technology in machine-tool monitoring. *Applied Mechanics and Materials*, *88*, pp.714–717.

Smyth, A. and Wu, M., 2007. Multi-rate Kalman filtering for the data fusion of displacement and acceleration response measurements in dynamic system monitoring. *Mechanical Systems and Signal Processing*, *21*(2), pp.706–723.

Soman, R., Kyriakides, M., Onoufriou, T. and Ostachowicz, W., 2018. Numerical evaluation of multi-metric data fusion based structural health monitoring of long span bridge structures. *Structure and Infrastructure Engineering*, *14*(6), pp.673–684.

Sun, H. and Büyüköztürk, O., 2015. Identification of traffic-induced nodal excitations of truss bridges through heterogeneous data fusion. *Smart Materials and Structures*, *24*(7), p.075032.

Sung, W.T. and Chang, K.Y., 2013. Evidence-based multi-sensor information fusion for remote health care systems. *Sensors and Actuators A: Physical*, *204*, pp.1–19.

Wu, R.T. and Jahanshahi, M.R., 2020. Data fusion approaches for structural health monitoring and system identification: past, present, and future. *Structural Health Monitoring*, *19*(2), pp.552–586.

Xiong, N. and Svensson, P., 2002. Multi-sensor management for information fusion: issues and approaches. *Information fusion*, *3*(2), pp.163–186.

Zhang, P., Li, T., Wang, G., Luo, C., Chen, H., Zhang, J., Wang, D. and Yu, Z., 2021. Multi-source information fusion based on rough set theory: A review. *Information Fusion*, *68*, pp.85–117.

Zhu, H., Gao, K., Xia, Y., Gao, F., Weng, S., Sun, Y. and Hu, Q., 2020. Multi-rate data fusion for dynamic displacement measurement of beam-like supertall structures using acceleration and strain sensors. *Structural Health Monitoring*, *19*(2), pp.520–536.

Bridge Maintenance, Safety, Management, Digitalization and Sustainability – Jensen, Frangopol & Schmidt (eds)
© 2024 The Author(s), ISBN 978-1-032-77040-6
Open Access: www.taylorfrancis.com, CC BY-NC-ND 4.0 license

Defects detection of concrete bridge decks using UAV-based infrared thermography

H.B. Zhang & Z. Zhou
School of Civil Engineering and Architecture, Hainan University, Haikou, Hainan, China

G. Chen
Department of Civil, Architectural, and Environmental Engineering, Missouri University of Science and Technology, Rolla, Missouri, USA

ABSTRACT: Concrete bridges are vulnerable to both natural and man-made disasters, as well as aging and deterioration processes throughout their lifespan. Timely detection of defects in concrete structures is crucial for repair and decision-making purposes. However, traditional methods like visual inspection are time-consuming and expensive. Unmanned aerial vehicles (UAVs) equipped with infrared thermography (IRT) offer an efficient and cost-effective solution for detecting defects in concrete structures. This study presents passive and active IRT techniques for detecting common concrete defects, such as delamination and cracks. Principle and methods for quantifying these defects and evaluating the extent of damage are introduced. Experiments are conducted to validate the reliability of the algorithm. In conclusion, UAV-based IRT proves to be an effective method for detecting defects in concrete bridge structures.

1 INTRODUCTION

Bridges are the bottlenecks of infrastructure constitutes an essential component of the country's transportation network, which require sufficient maintenance to ensure their serviceability and safety. According to the report from American Road & Transportation Builders Association, more than one-third, or 220,000 of the nation's 618,000 bridges need structural repair, rehabilitation work or replacement (Black, 2022). Among all reinforced concrete bridge components, bridge decks have been the leading contributor to most deficient bridges in the United States (Maser et. al., 2012). Indeed, bridge decks have been identified as the most problematic, due to various forms of deterioration mechanisms.

Concrete delamination and cracking are the main reasons leading to bridge deck deteriation, which is attributed to many possible reasons, such as construction deficiencies, creep, temperature gradients, corrosion, and unforeseen over-load, etc. Once delamination and crack occurred, the path allows chloride ions, oxygen, and moisture more easily to penetrate adjacent concrete and rebar level, which will accelerate the process of rebar corrosion. The development of corrosion can cause delamination and concrete spalling, eventually reducing the load capacity of bridge deck and even threatening the safety of bridge when exposed to excessive external loads (Gucunski, 2010). Therefore, the localization and quantification of delamination and crack is critical importance to ensure the structural safety of concrete bridges and optimize maintenance and repair needs.

The evaluation of RC bridge decks is complex due to the heterogeneous nature of concrete. As a default bridge deck inspection methodology, visual inspection however has several limitations

DOI: 10.1201/9781003483755-284

including unavailable to inaccessible places, inability to detect hidden defects, and its operator sensitivity (Moore et. al., 2001). There are currently several Non-destructive Test (NDT) methods capable of reliable crack depth assessment for bridge decks based on acoustic, electric, electromagnetic, thermal, and other physical phenomena. Generally, such techniques utilize an approach to capture the characteristics of the medium from its response to an applied excitation (Gucunski, 2010 & ACI, 2013). However, it is difficult to access every concrete surface area located in the bottom of bridge deck with high altitude and other inaccessible places.

Infrared thermography (IRT) is a NDT technology that is often adopted for detecting characteristic thermal signatures related to RC bridge deck deterioration (Maser et. al., 2012 & Pozzer et. al., 2020). Such remote sensing technology provides data visualization in the form of real-time thermal images and does not require direct access to the surface under inspection. Currently, unmanned aerial vehicle (UAV) combined with IRT becomes more and more popular for bridge deck inspections, due to the advantages of no traffic block, fast, cost-effective, and reliable data collection. With the help of advanced artificial intelligent method, automatic bridge damage detection can be achieved more effectively and efficiently (Ding et. al., 2023). However, the delamination detection using UAV-based passive IRT method at the top of bridge deck in accordance with threshold defined by AASHTO has not been evaluated yet. In addition, the crack detection using UAV-based active IRT method in high resolution and fast way at the bottom of bridge deck has not been studied. Therefore, this study presents the case study of UAV-based passive and active IRT for delamination and crack detection, respectively, on the top and at the bottom of bridge decks.

2 PRINCIPLE

The principle of the passive and active IRT respectively for delamination and crack detection on the top and at the bottom of bridge deck is illustrated in the Figure 1. For passive IRT, solar is used for energy input. When a delamination layer initiated from the debonding between concrete and rebars, air occupies the space formed by the delamination. As a result, the thermal conductivity of the deteriorated region will be reduced. In the daylight, the delamination area will block the heat transfer from the top layer to bottom layer of concrete, and the heat will accumulate on the top of delamination area. This will result in a higher temperature difference between delamination and sound area. For active IRT, non-natural heat source should be adopted for crack detection at the bottom of the bridge deck. For example,

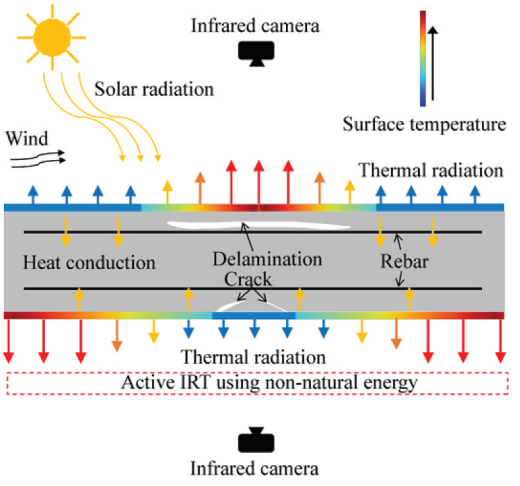


Figure 1. Schematic diagram of passive IRT and active IRT respectively on the top and at the bottom of bridge deck.

a thermal pulse is applied to a surface causing a non-stationary heat flow. The pulse heat conduction in the sound region is more efficient than cracking region, causing lower radiation heat and temperature at the bottom surface of the cracking region. These inhomogeneities in the near-surface region of the structural element, including delamination and crack, will result in measurable temperature differences in the local area of the surface.

3 PASSIVE IRT TEST

For passive IRT test, four specimens with artificial delamination were prepared. Each specimen was embedded with four large and eight delamination in different elevation. The dimension of the specimen is 114 cm in width, 183 cm in length, and 18 cm in height. The dimension and embedded depth of the delamination are presented in Table 1. The thermal properties of the materials used in this study is shown in Table 2.

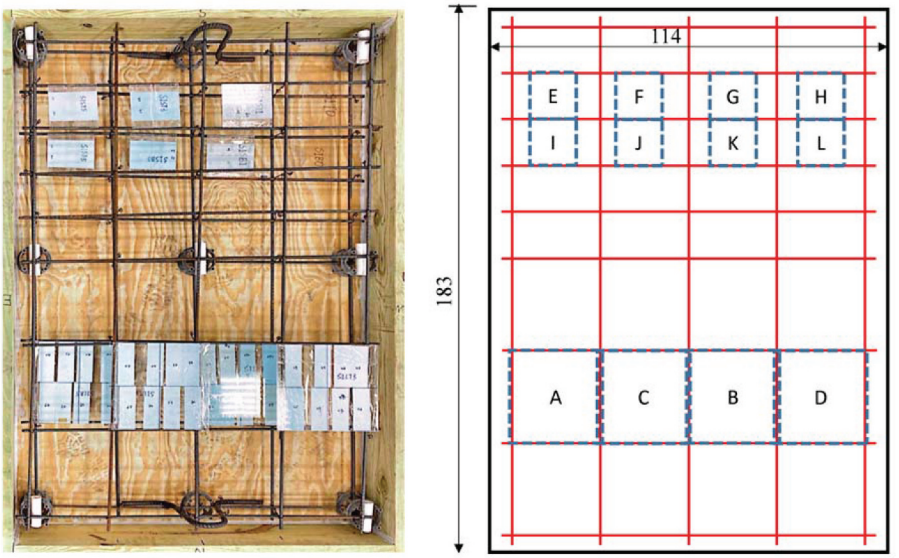


Figure 2. Specimen photo and schematic view for delamination detection of bridge deck. (Unit: cm).

Table 1. Dimension of delamination. (Unit: cm).

	A	B	C	D	E	F	G	H	I	J	K	L
length	30.5	30.5	30.5	30.5	15.2	15.2	15.2	15.2	15.2	15.2	15.2	15.2
Height	0.56	0.36	0.56	0.36	0.56	0.36	0.16	0.06	0.56	0.36	0.16	0.06
Depth	2.5	2.5	15.5	15.5	2.5	2.5	2.5	2.5	15.5	15.5	15.5	15.5

Table 2. Thermal properties of materials.

Material	k (W/m·K)	c (J/g·K)
Concrete	2.006	1.807
Steel rebar	45.000	3.500
Plastic board	0.213	1.274
Styrofoam board	0.024	0.025
Air	0.025	1.000

The four concrete bridge decks were placed side by side on a specially designed steel frame support to form a mock-up girder bridge, in order to mitigate the influence of the heat transfer from the ground. Ice block is used to provide an additional reference temperature to ensure the camera has been well calibrated in factory. An UAV (Model: DJI M600) equipped with a thermal camera was used to capture the thermal images at an altitude of 12 m above the bridge under sunlight. A weather station was set up on the Van to obtain weather information, such as wind speed, wind direction, ambient temperature, illumination intensity, etc. The tests were carried out at 14:00 as recommended by Washer et. al., 2010, when the temperature contrast between delamination and sound area is highest.

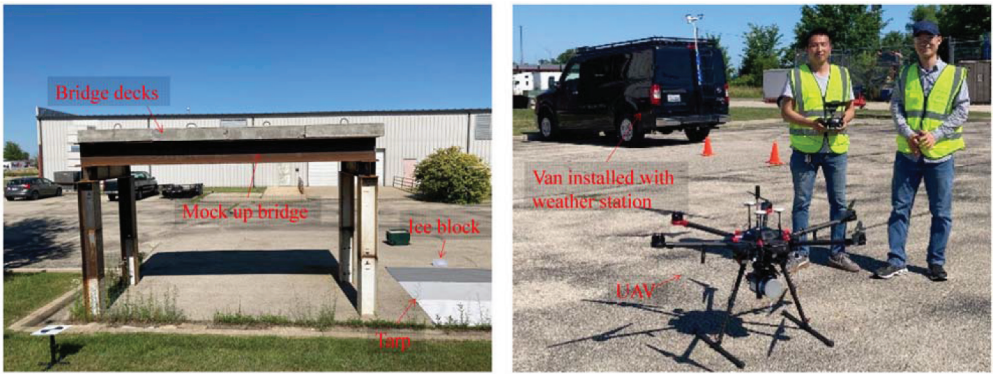


Figure 3. Test setup of passive IRT.

The thermal image of four bridge decks was transferred into binary image using gradient method, as shown in Figure 4. It can be found that all the shallow embedded large delamination and most of the shallow embedded small delamination can be detected through passive IRT method. However, some of the shallow embedded delamination with equivalent thickness of 0.06 cm cannot be distinguished due to the slight temperature difference. All the delamination with deep embedded of 15.5 cm cannot be detected. This test results satisfy the critical threshold levels in terms of size (15×15 cm) and embedded depth (2.5 cm) as defined by AASHTO.

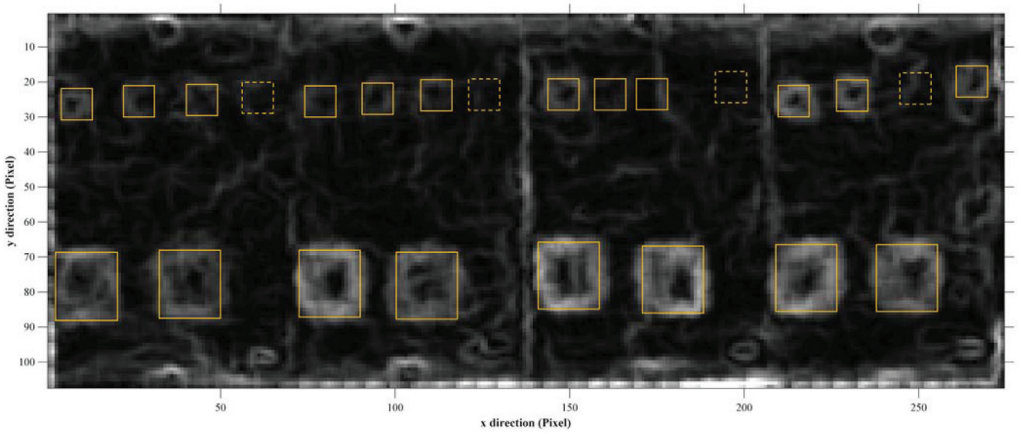


Figure 4. Delamination detection results for four concrete slabs.

4 ACTIVE IRT TEST

A concrete beam with artificial crack was prepared for active IRT test. Six cracks with the consistent width of 0.45 cm and depth of 1~6 cm at an interval of 1 cm were cut as shown in Figure 5. The ceiling drone that can fly against the bottom of bridge deck was designed and fabricated. The distance between the drone and the deck is only 18 cm, to get a best resolution of thermal and optical images. A laser generator is adopted as the non-natural heating source.

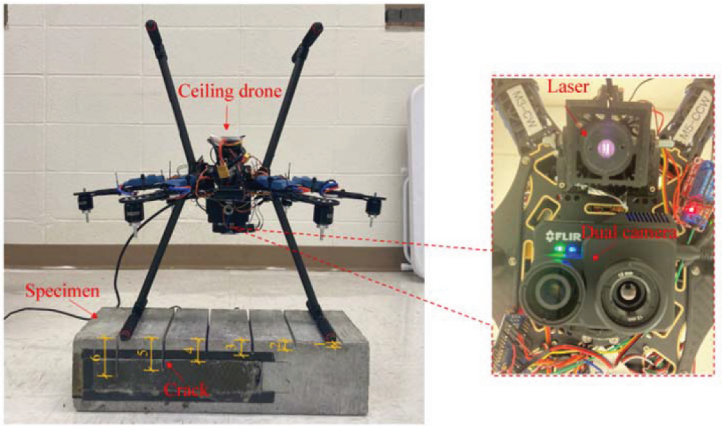


Figure 5. Test setup of active IRT. (Unit: cm).

The test results of thermal images of the crack detection with crack depth of 5 cm were presented in Figure 6. It can be found that the stable time of the thermal images at crack area is about 10 s. Similarly, other type of crack depth can be calculated as well, which was shown in Figure 7. It is shown that the relationship between stable time and crack depth is almost linear when the crack depth is larger than 1 cm. Therefore, utilizing the stable time of thermal image captured by active IRT, the crack depth at the bottom of concrete bridge deck can be obtained.

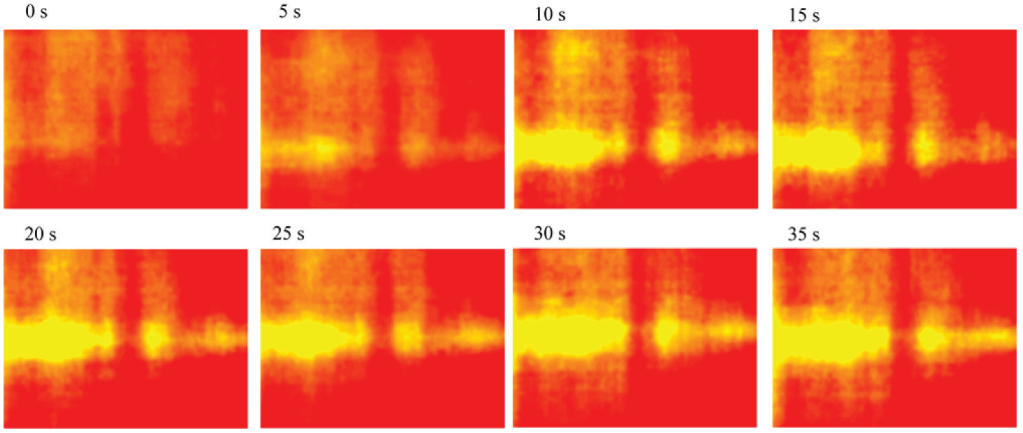


Figure 6. Test result for crack detection with crack depth of 5 cm using active IRT method.

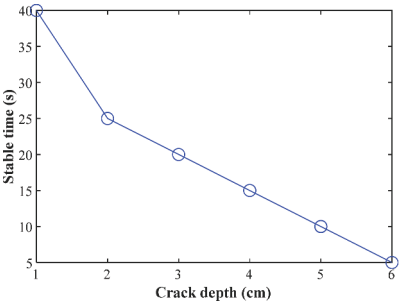


Figure 7. Relationship between crack depth and heating time.

5 CONCLUSION

This study presents case studies of UAV-based passive and active thermography for delamination and crack detection on the top and at the bottom of bridge deck, respectively. This method provides a fast and accurate way to quantify the deterioration of the bridge deck. The critical size and depth of the delamination as defined by AASHTO can be successfully detected. The relationship between stable time of thermal images and depth of the crack was established for ease of quantifying crack in practical application.

REFERENCES

ACI. 2013. Report on nondestructive test methods for evaluation of concrete in structures, 228.2R-13, American Concrete Institute Report.

Black, A.P. 2022 Bridge report. American Road and Transportation Builders Association, 2022. https://artbabridgereport.org/reports/2022-ARTBA-Bridge-Report.pdf (Access on 20/09/2023)

Ding, W. Yang, H. Yu, K. Shu, J. 2020. Crack detection and quantification for concrete structures using UAV and transformer. *Automation in Construction* 152: 104929.

Gucunski, N. and Nazarian, S. 2010. Material characterization and condition assessment of reinforced concrete bridge decks by complementary NDE technologies. Proceeding of Structures Congress (ASCE). Orlando, Florida, United States, DOI: http://dx.doi.org/10.1061/41130(369)40.

Maser, K. Martino,N. Doughty, J. Birken,R. 2012. Understanding and detecting bridge deck deterioration using ground penetrating radar. *Journal of Transportation Research Board* 2313(1): 116–123.

Moore, M. Phares, B. Graybeal, B. Rolander, D. Washer, G. Reliability of visual inspection for highway bridges, Final Rep. No. FHWA-RD-01-020, Federal Highway Administration (FHWA), Washington, DC, 2001. Chapter 1–4.

Pozzer, S. Pravia, Z.M.C. Rezazadeh Azar, E. Dalla Rosa, F. 2020. Statistical analysis of favorable conditions for thermographic inspection of concrete slabs. *Journal of Civil Structural Health Monitoring* 10(4): 609–626.

Washer, G. Fenwick, R. Bolleni, N. 2010. Effects of solar loading on infrared imaging of subsurface features in concrete. *Journal of Bridge Engineering* 15(4): 384–390.

Bridge Maintenance, Safety, Management, Digitalization and Sustainability – Jensen, Frangopol & Schmidt (eds)
© 2024 The Author(s), ISBN 978-1-032-77040-6
Open Access: www.taylorfrancis.com, CC BY-NC-ND 4.0 license

Senmos: A user-centered approach to structural health monitoring with applications on Lillebæltsbroen af 1935

Kasper Myrtue & Sandra D. Myrtue
KI Rådgivende Ingeniører, Denmark

Jakob Larsen & Pernille N.L. Sørensen
LIFA, Denmark

ABSTRACT: The increasing prevalence of Structural Health Monitoring (SHM) in recent years has led to a significant diversification of user profiles and a consequent demand for a more user-friendly approach in software and data exploration tools. Traditional SHM systems, tailored to large structures such as bridges and tunnels, often lack an intuitive interface and comprehensive data exploration facilities. In contrast, small-scale SHM systems frequently resort to a rudimentary file transfer protocol (FTP) server for data delivery. This research paper seeks to explore the prevailing usability issues associated with conventional SHM systems, focusing on two common use cases: alarm investigation and data correlation. Each use case is dissected to illuminate specific user experience components that often present challenges to users. Born out of the experience of developing Konmos[1], a structural health monitoring platform originally designed for the Great Belt Bridge in Denmark, Senmos represents an innovative departure from conventional SHM tools. Consciously designed with a user-centric approach, Senmos addresses usability concerns inherent in many traditional SHM platforms. The application of Senmos is then elaborated through a case study of its deployment on Lillebæltsbroen af 1935 in Denmark. By detailing how each user experience issue was resolved within the context of Lillebæltsbroen af 1935, we illustrate the effectiveness and adaptability of Senmos, providing evidence of its potential for broad scalability. The development of Senmos emphasizes the importance of considering the end-user experience in the design and implementation of SHM tools. As SHM practices continue to evolve, software solutions like Senmos that prioritize user experience, flexibility, and accessibility, will play an increasingly critical role in enabling efficient and effective monitoring for all types of structures.

1 INTRODUCTION

Structural Health Monitoring (SHM) has emerged as an indispensable tool for ensuring the longevity, safety, and optimal performance of infrastructure, especially structures such as bridges, tunnels, and skyscrapers. By employing a network of sensors, SHM systems constantly collect and analyze data to detect anomalies, assess damage, and predict the future health of structures. While the core objective of SHM is to provide real-time insights into the health of structures, the efficacy of this monitoring is closely tied to the tools and platforms that process, store, and present this data.

1. Kasper Myrtue & Nuno Martins (2021) SHM at the Great Belt Fixed Link in Denmark. SHMII 10 Conference.

DOI: 10.1201/9781003483755-285

Traditionally, the design of SHM platforms has been predominantly data-centric, focusing on the accurate collection and storage of sensor readings. Today, a broad spectrum of professionals, from field engineers to decision-makers, rely on SHM data. Yet, many of these individuals find themselves grappling with platforms that, while robust in data collection, often falter in user accessibility and intuitive data presentation.

Consider the conventional use of rudimentary file transfer protocols (FTP) for data delivery in smaller SHM systems. While FTPs are reliable, they are far from user-friendly, especially for those without technical backgrounds. Larger systems, tailored for monumental structures, often host vast troves of data but lack streamlined and intuitive interfaces for exploration. It's not uncommon for users to navigate through split systems or wrestle with hard-to-access data archives, leading to inefficiencies and potential oversights.

Senmos is a platform that seeks to reconcile the traditionally data-centered approach of SHM with the pressing need for user-centric design. Drawing inspiration from the principles of web platform usability, especially Nielsen's 10 heuristics[2], Senmos endeavors to transform how SHM data is accessed, visualized, and analyzed. But why is this shift towards user-centered design paramount for SHM's future? This article delves into the challenges of traditional SHM platforms, the paradigm shift introduced by Senmos, and the broader implications of aligning SHM tools with the evolving needs of its diverse user base.

In the development of Senmos, a user-centric design approach was selected from the beginning rather than the more traditional data-driven solutions. The 10 Usability Heuristics for User Interface Design by Jakob Nielsen were used for inspiration and to keep the right focus on the user's needs throughout the design of the user interface. While all 10 heuristics, or guidelines, are relevant, 3 in particular have had a huge impact on the user experience of the platform in comparison to traditional monitoring solutions:

1.1 *Visibility of system status*

Senmos very quickly lets the user know if sensors give errors or alarms, where the given sensors are located, and what caused the message. Furthermore, the overview dashboards quickly let the user get a live status of all sensors values in a logical and ordered format.

1.2 *Match between system and real world*

An important feature in Senmos, is the fact that rather than having to look through long lists of data and ID-numbers, the user can see live values and alarms depicted on images or drawings of their structure. This makes it easy and fast to pinpoint sensor type, location, and name and to see correlation between different sensors when looking at the data.

1.3 *Recognition rather than recall*

Throughout the platform the user is being presented with options rather than having to type in data themselves. This, for instance, is true for picking sensors through icons in menus, or clicking live values on dashboards to display data graphs. The sensors are easily sorted by type, location or status in several different ways, helping the user get to relevant data quickly without having to recall any ID's or names.

2. Molich, R., and Nielsen, J. (1990). Improving a human-computer dialogue, Communications of the ACM 33, 3 (March), 338-348.

2 COMMON USABILITY PROBLEMS IN TRADITIONAL STRUCTURAL HEALTH MONITORING

2.1 *Finding correlations in data*

The ability to discern correlations in structural health data is pivotal for understanding the dynamics of structures under various conditions, such as weather changes or load variations. Traditional SHM systems, however, often present a fragmented approach to data analysis, requiring civil engineers to manually plot and examine data files. This reliance on intuition and manual processes not only increases the likelihood of oversight but also restricts the depth of analysis, particularly when trying to distinguish between regular structural behavior and anomalies.

In contrast, Senmos revolutionizes this process by integrating data correlation tools directly within its platform. Unlike traditional or general-purpose cloud solutions, which may offer basic data plotting features without specialized focus, Senmos is tailored specifically for SHM. It provides an intuitive interface where users can effortlessly overlay various sensor data types to uncover hidden correlations. This feature is especially beneficial in cases like correlating strain gauge data with vehicular loads to assess road fatigue or analyzing weather impacts on structural behavior.

Senmos's correlation tools are designed for simplicity and effectiveness. Users can access a comprehensive data archive where any combination of sensors can be visualized together, making it straightforward to spot correlations, particularly with static sensors where movements occur over extended periods. For dynamic sensors, where detecting correlations can be more challenging due to rapid data fluctuations, Senmos offers a dedicated correlation plot feature. This tool allows plotting two sensors against each other, with the calculation of correlation coefficients, providing clear visual cues for positive or negative correlations.

Such advanced correlation capabilities in Senmos not only make it easier to discover meaningful connections between different data sets but also significantly reduce the time and effort required for data analysis. By lowering the barrier to data exploration, Senmos enables a broader range of users, from field engineers to decision-makers, to engage with SHM data more meaningfully. This approach contrasts sharply with older SHM methods or non-specialized cloud platforms, which often require more technical expertise and time-intensive procedures to achieve similar results.

2.2 *Investigating alarms*

In traditional SHM systems, when a sensor threshold is breached, the typical protocol is to dispatch an alarm email to the user, detailing the sensor's location and the value causing the alarm. However, this often leaves users at a crossroads, trying to determine the legitimacy of the alarm - is it a genuine structural issue requiring immediate attention, or merely a sensor malfunction?

Senmos seeks to revolutionize this process by enhancing user interaction and data accessibility. When an alarm is triggered, not only does the user receive the customary notification, but they're also presented with a clickable link. This link leads to a concise visualization of the past month's data for the sensor in question, displayed in an intuitive popup window.

This immediate access to relevant historical data facilitates rapid preliminary assessments. Sensor malfunctions often manifest as abrupt and large variations between data points, unrealistic for any real-world structural change. Such aberrations, caused potentially by a severed wire or a damaged sensor, can quickly be differentiated from genuine structural alarms.

Furthermore, noisy sensor outputs, which may send out alarms due to temporary spikes, can be discerned by analyzing the statistical mean of data over time. If this mean suggests that the actual structural movement is significantly less than the alarm value, it can be inferred that the alarm was possibly erroneous.

For those cases where a month's data isn't sufficiently illuminating, Senmos provides an expansive data archive. Here, users can juxtapose the data of the alarmed sensor with others, delve into tailored statistical views, or even isolate specific timespans for a more granular analysis.

The ability to swiftly and efficiently verify alarms not only instills confidence in the system but also empowers users to make informed decisions. When it comes to large infrastructure, where operational ramifications hinge on sensor outputs, such immediacy and clarity become paramount. Misinterpreting a sensor's alarm can lead to unnecessary interventions or, conversely, overlooking critical structural issues.

By simplifying and enhancing the alarm investigation process, Senmos ensures that users are no longer in the dark. Instead, they are equipped with the tools and insights necessary to discern genuine structural concerns from sensor anomalies, ensuring timely and appropriate responses.

3 CASE STUDY: LILLEBÆLTSBROEN AF 1935

Lillebæltsbroen af 1935 is owned and operated by Banedanmark, with sensor systems provided by the company LIFA for structural health monitoring. In 2023, the decision was made to implement Senmos as the data platform for monitoring this vital infrastructure. The primary objectives of deploying Senmos were to achieve real-time visualization of the bridge's condition, enable the extraction and analysis of historical data, and effectively manage sensor status and operation.



Figure 1. Lillebæltsbroen af 1935, senmos, overview dashboard.

3.1 *Sensor systems*

Lillebæltsbroen af 1935 features multiple sensor systems designed to monitor various aspects of the bridge's condition. These sensor systems are outlined in Table 1, with their respective functions described below:

1) Inclinometers on Pillars (8 units): Initially designed to monitor scour protection, these inclinometers served a critical role during a project aimed at safeguarding the bridge's pillars. Large rocks were strategically placed near the pillars to stabilize the soil around their foundations.

To ensure the pillars did not incline or tilt during the project, a monitoring system was devised. Initially, the system involved a steel wire threaded vertically through pillar 2 and 3, with a weight attached to its lower end. If any pillar exhibited angular movement, the steel wire would make contact with a small copper ring, completing an electrical circuit and triggering an alarm. However, this system had its limitations, including false alarms caused by birds nesting inside the pillars and a lack of detailed movement tracking.

To address these challenges and enhance monitoring precision, the steel wires and copper rings were replaced with inclinometers. These sensors provide real-time, precise measurements of the inclination of each pillar, allowing for continuous monitoring of pillar movement over time with high accuracy. This upgrade eliminated false alarms and enabled workers on the bridge to proactively track and respond to any subtle changes in pillar inclination.

2) and 3). Humidity and Air Temperature Sensors (16 units each): Positioned in the foundation of the pillars, these sensors track moisture and temperature levels to maintain sealed foundations and prevent moisture from continuously permeating the concrete by keeping the concrete and air on the inside fully humid.
3) Hydraulic System (1 unit): Monitored using a pressure sensor, this system tracks oil status and the condition of the enabling switch for the hydraulic buffer.
4) Total Stations (2 units): Located at land-adjacent pillars, total stations measure vertical displacements at the pillars.
5) Horizontal Displacement Sensors (11 units): These sensors monitor movement at expansion joints and rolling bearings.
6) Steel Temperature Sensors (4 units): Placed in one cross-section of the bridge, these sensors are used to correlate temperature changes with structural displacement to assess the impact of temperature variations.
7) Weather Station (1 unit): Positioned atop the bridge, this weather station includes an anemometer, rain gauge, air temperature, relative humidity, and air pressure sensors. It serves to analyze weather conditions and determine suitable conditions for bridge maintenance activities.

Table 1. List of sensors on Lillebæltsbroen af 1935.

Num.	Sensor type	Placement	Amount
1	Inclinometer	Inside pillars above sea level	8
2	Humidity	In pillar foundation below sea level	16
3	Air temperature	In pillar foundation below sea level	16
4	Hydraulics	In deck expansion joint	1
5	Total station	Externally on pillars	2
6	Displacement	In bridge deck	11
7	Steel temperature	Bridge deck	4
8	Weather station	Top of bridge	1

3.2 *Senmos on Lillebæltsbroen af 1935*

The implementation of Senmos on Lillebæltsbroen af 1935 aimed to achieve three key objectives in monitoring:

3.2.1 *Visualization of bridge conditions*

Each sensor system on the bridge is represented through a dedicated dashboard, simplifying real-time monitoring. As discussed in Section 3.1, these systems are configured to detect specific potential issues or to correlate data with other sensors. This arrangement allows for easy categorization by sensor type, facilitating straightforward value comparison and issue identification.

For instance, consider the inclinometers on pillars (see Figure 2). Live inclinometer data is displayed on a wire diagram of the bridge, offering a quick and clear overview of sensor

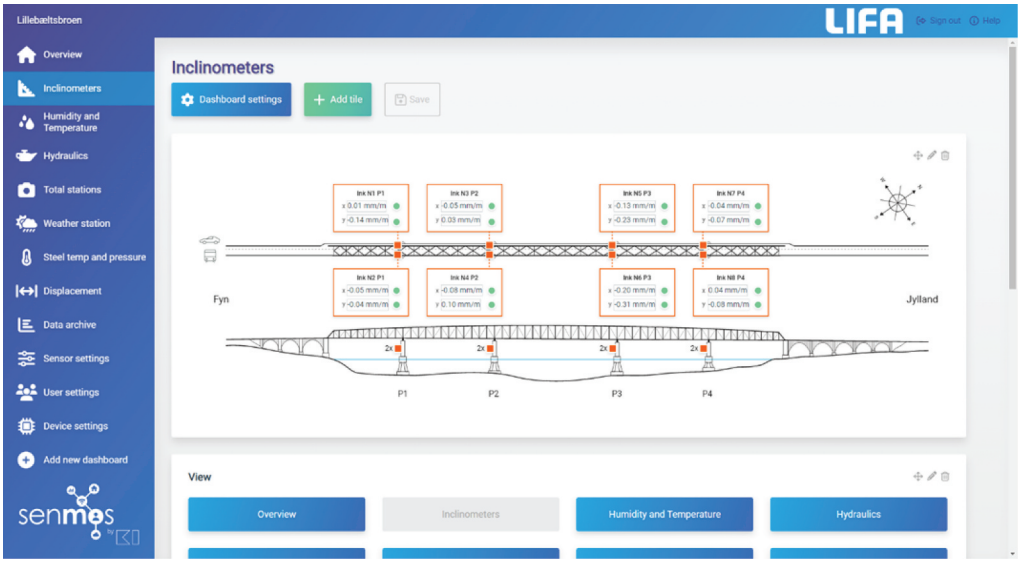


Figure 2. Inclinometers of pillars.

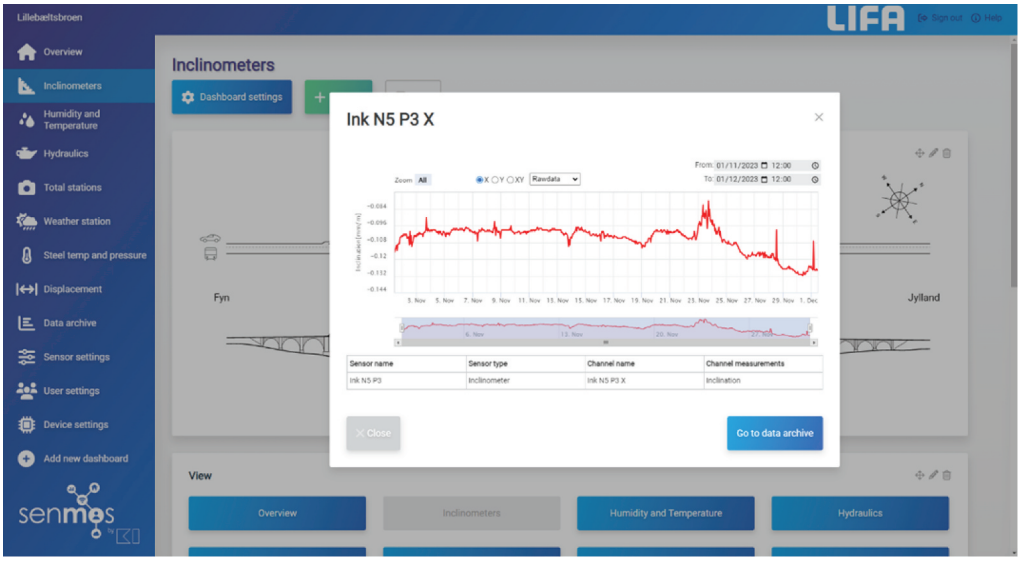


Figure 3. Pop-up with the last month of data from an inclinometer.

locations. Clicking on the live values in the white boxes (se Figure 2 the numbers inside the orange boxes) provides access to statistical information, with a pop-up window displaying the data from the past month (see Figure 3).

3.2.2 *Visualization of historical data*

Senmos offers access to a comprehensive data archive (see Figure 4) containing historical data from all sensors on the bridge. Users can plot various combinations of sensor data and, for instance, observe the correlation between steel temperature and pillar inclination, illustrating how temperature affects structural displacement (see Figure 4). All data is available for download and further analysis through the "generate data file" option in the menu to the right of the sensor graph.



Figure 4. Data archive displaying correlation between temperature and inclination of the pillar.

3.2.3 *Sensor status*

Structural health monitoring systems encompass a range of electrical components, including IoT devices, data loggers, and servers. Effective operation relies on service providers having up-to-date knowledge of the equipment. Senmos assists by displaying the date and time of the last received data from sensors, aiding in troubleshooting failure causes, and enabling email notifications if sensors cease sending data. These features collectively ensure ease of system maintenance and operational continuity.

4 CONCLUSION

In conclusion, Senmos represents a significant leap forward in the realm of Structural Health Monitoring (SHM) data platforms, driven by a steadfast commitment to user-centric design. As we've explored the challenges associated with conventional SHM systems and the paradigm shift introduced by Senmos, it becomes evident that this platform is not merely a technological advancement, but a fundamental transformation of how we approach structural health monitoring.

Senmos has successfully addressed some of the most pressing usability issues in traditional SHM platforms. Its adherence to Jakob Nielsen's usability heuristics has led to a platform that prioritizes user experience. The visibility of system status, the seamless matching of the platform with the real world, and the emphasis on recognition rather than recall have all contributed to Senmos's user-friendliness.

Moreover, the case study of Lillebæltsbroen af 1935 in Denmark exemplifies Senmos's real-world effectiveness. By providing intuitive dashboards for real-time monitoring, facilitating historical data visualization, and offering comprehensive sensor status management, Senmos has proven its adaptability and versatility in the monitoring of critical infrastructure.

The development and deployment of Senmos underscore the importance of considering the end-user experience in the design and implementation of SHM tools. In a world where the demand for efficient and effective monitoring of structures is ever-increasing, Senmos stands as a beacon of innovation and practicality. It not only enhances data accessibility and analysis but also empowers users to make informed decisions, ultimately contributing to the safety, longevity, and optimal performance of vital infrastructure.

As SHM practices continue to evolve, software solutions like Senmos that prioritize user experience, flexibility, and accessibility will play an increasingly critical role in ensuring the structural integrity of both large and small-scale structures.

ACKNOWLEDGEMENTS

Special thanks to Svend Erik Gaardmand and Banedanmark for allowing the use of the case "Lillebæltsbroen af 1935" for use in the article.

REFERENCES

Kasper Myrtue & Nuno Martins (2021) SHM at the Great Belt Fixed Link in Denmark. SHMII 10 Conference.

Molich, R., and Nielsen, J. (1990). Improving a human-computer dialogue, Communications of the ACM 33, 3 (March), 338–348.

Bridge Maintenance, Safety, Management, Digitalization and Sustainability – Jensen, Frangopol & Schmidt (eds)
© 2024 The Author(s), ISBN 978-1-032-77040-6
Open Access: www.taylorfrancis.com, CC BY-NC-ND 4.0 license

Investigation of the effect of surface condition variation on infrared imaging of concrete delamination

C. Cheng, D. Chen, H. Cai, S. Wang, R. Wang & X. Cheng
Chongqing Jiaotong University, Chongqing, China

ABSTRACT: Infrared thermography (IRT) has become an important non-destructive testing method for the layering of concrete bridge decks. One of the obstacles to making full use of infrared thermal imaging for detection in practice is the misjudgment of thermal images caused by the non-uniformity of bridge surface conditions (such as chromatic aberration) and the presence of foreign substances on the bridge deck surface. This "noise information" not only affects the data processing of infrared thermography detection but also changes the heat conduction process of the concrete deck under the solar heating cycle, which is a key factor in stimulating the thermal contrast of infrared thermography detection. In this paper, experimental studies are carried out to explore the effects of different surface conditions (bare concrete surface and painted surface of different colors) on the development of thermal contrast of concrete delamination in image inference. A simulated concrete platform with artificial delamination of the same buried depth was designed and constructed. The thermal image, heat flux and radiation intensity data of the solar natural loading environment are continuously recorded and analyzed, and the emissivity, absorption and reflectance of surface thermal radiation are revealed. The novelty of this study is that it captures two factors that influence the development of infrared thermography (IRT) sensing and delamination thermal contrast, which have rarely been reported in previous studies. On this basis, some suggestions are put forward to reduce noise and compensate for detection in thermal image processing.

1 INTRODUCTION

As an important transportation infrastructure connecting roads and highways, bridge plays a vital role in the operation of economic activities along roads and highways (Dabous et al., 2017). Bridges have a high-growing status in China's highway system, especially in the southwestern mountainous areas, and as of 2022, the number of bridges in China has reached 103,3200 (Transport, 2023). In addition, the bridge deck is an area where the wheels act directly, and the repeated heavy loads of vehicles will cause the bridge deck to crack (Koh et al., 1997), and rainwater will enter the cracks, which will then corrode the steel bars and gradually form delamination. Corrosion of steel bars is the most important factor that reduces the service life of reinforced concrete bridge decks, and it is also the culprit of the destruction of reinforced concrete bridge decks, which is in the form of cracking, delamination, and spalling (Oh et al., 2013, Tran et al., 2017). The degradation of the bridge deck not only affects the normal operation of traffic but in some cases can also threaten public safety (Oh et al., 2013, Raja et al., 2022). Therefore, the quality of the bridge deck directly affects the safety of the bridge and the comfort of driving. Regular inspection and long-term maintenance of the bridge deck is one of the most effective and indispensable means to ensure the normal operation of the bridge.

The current diagnostic methods based on infrared imaging for concrete deck delamination detection mainly focus on the criteria based on the surface temperature difference, that is, the

DOI: 10.1201/9781003483755-286

temperature difference (thermal contrast) between the defective area and the non-defective area. In 2013, Glenn Washer (Washer et al., 2013) discussed the effects of ambient temperature change rate and wind speed on the thermal contrast of soffit defects in the shadow of the bridge deck area. In 2015, Patricia Cotič (Cotič et al., 2015) also used thermal contrast evaluation techniques to study the applicability and limitations of cavities and delamination detection under concrete overburdens. A study in 2019 by Van Ha Mac (Mac et al., 2019) discussed the effects of different aspect ratios and different time windows of day on the thermal contrast of the specimen under passive excitation. In real bridges, there are differences in materials and different surface treatments (different colors of paint, different surface sanding methods, etc.) on the surface of the bridge deck, and the differences in these surface properties will affect infrared detection in terms of thermal contrast. In this paper, three artificial delamination with the same buried depth but with different surface properties (yellow paint, bare concrete, and white paint) were designed to explore the influence of the surface properties of the specimen under passive excitation on the thermal contrast.

2 EXPERIMENTAL WORK

2.1 *Specimen preparation*

As shown in Figure 1 (a), a concrete specimen CS20 with a size of 2100×900×100 mm^3 is designed as the testbed for deck simulation. Three polystyrene foams of the same size and shape with a thickness of 10 mm and a burial depth of 20 mm were embedded inside the specimen (as shown in Figure 1 b) to simulate the delamination inside the concrete bridge deck (see Table 1 for specific information). The polystyrene foam is selected to mimic the delamination with its thermal conductivity of k=0.027 w/m°C, which is similar to that of air k=0.024 w/m°C (Ta et al., 2023). For the concrete surface, 1.35m^2/kg of white paint and yellow paint were brushed on the top and bottom sides of the specimen surface to simulate the lane marking and the area of each color of paint is 900×800 mm^2. The middle part was bare concrete, which occupied an area of 900×500 mm^2 (as shown in Figure 1c). After the specimen is poured and cured, a heat flux sensor (XM269C, see details in Table 3) is attached to the center of each area surface correspondingly for data collection.

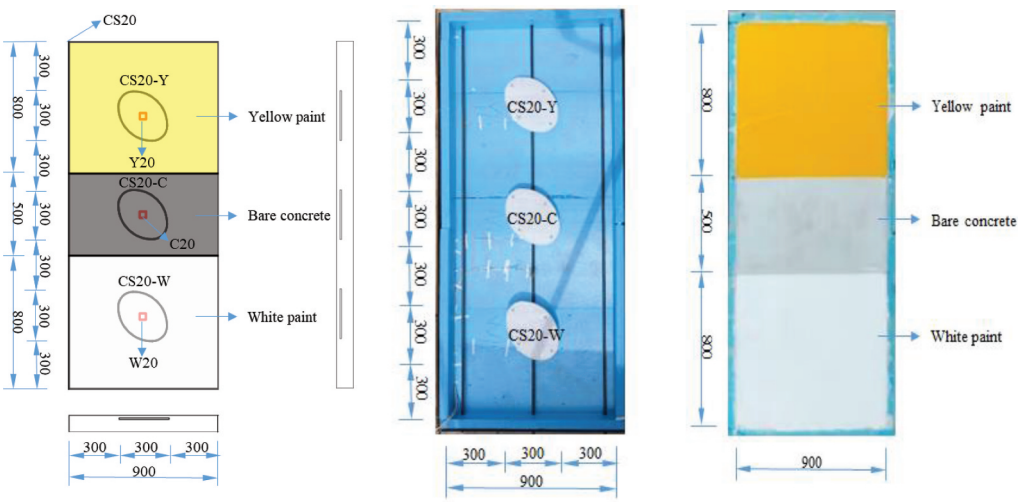


Figure 1. Specimen design and construction layout: (a) overall design and heat flux sensor layout; (b) artificial delamination arrangement; (b) Specimen after concrete pouring and surface painting.

Table 1. Detailed specification of the specimen CS20.

Delamination Annotation	The longest horizontal size (mm)	The longest vertical size (mm)	Area (mm^2)	Surface materials	Depth (mm)
CS20-Y	300	300	68508	Yellow paint	20
CS20-W	300	300	68508	White paint	20
CS20-C	300	300	68508	Bare concrete	20

2.2 *Experimental setup and equipment*

The experiment was carried out under the natural environmental conditions of the Science City Campus of Chongqing Jiaotong University in Chongqing, China as shown in Figure 2. To collect real-time meteorological data, a portable weather station (FT-BQX7) produced by Shandong Fengtu Internet of Things Technology Co., Ltd. was set up near the specimen to collect weather conditions, with a sampling frequency of every 15 minutes, and the measurement information included radiation intensity, atmospheric temperature, etc. (details are shown in Table 2). The heat flux sensor (XM269C) of Shanghai Anyi Scientific Instrument Co., Ltd., is used to measure the magnitude of the heat flux through the surface of the specimen (parameters are shown in Table 3), and the data is collected by the acquisition instrument DQ-100, which is collected every minute. In the natural environment, the MAG-F6 scientific thermal imaging camera of Shanghai Juge Technology Co., Ltd. was used to record a thermal image every minute (parameters shown in Table 4), with stability of ±0.3°C and an image resolution of 680×480 pixels (Ltd, 2022).



Figure 2. Layout of the experimental site.

Table 2. Parameters for the weather station (FT-BQX7).

Name	Wind velocity (m/s)	Wind (°)	Air temperature (°C)	Illumination (W LUX)
Measuring range	0~60	0~360	-40~60	0~20
Margin of error	±0.1	±2	±0.3	<±3%

Table 3. Parameters for the heat flux sensor (XM269C).

Name	Heat flow range (kW/m^2)	Sensitivity ($\mu V/(W/m^2)$)	Temperature (°C)	Accuracy
Measuring range	-150~150	1.5	-50~150	±3%

Table 4. Rarameters of IR thermal camera (MAG-F6).

Camera type	MGS-F6
Detector type	Uncooled microbolometer
Noise Equivalent Temperature Difference (NETD)	<0.05°C
Accuracy	±0.7°C or 0.7%
Resolution	640×480 pixels
Spectral range	8~14μm
Field of view	25°×19°

2.3 *Surface emissivity and absorptivity measurements*

Emissivity is a quantity that represents the energy of an object's radiant energy (Vollmer & Möllmann, 2017). The emissivity is one of the factors that have the greatest impact on the temperature measurement of the target captured by the infrared camera, so the emissivity of concrete and paint is particularly important. Based on previous studies (Vollmer & Möllmann, 2017, Institute, 2013), the emissivity of a dry normal concrete surface was set at 0.95 in this study. For yellow paint and white paint, the emissivity was calculated by the double reference body method (Li & Zhen, 2012), which was 0.96 and 0.965, respectively. Absorption rate represents the ability of an object to absorb energy. Because the absorption rate of solar radiation by concrete directly relates to the temperature accumulation and temperature effect in the concrete structure, the heat balance equation can be established on the surface of the specimen by using the principles of heat transfer and energy balance, and the absorption rate of various materials on the surface of the specimen can be calculated approximately based on experimentation (Wenyan & Yaoming, 2004). The absorption rates of yellow paint, white paint, and concrete surfaces were 0.593, 0.135, and 0.658, respectively.

3 RESULTS & DISCUSSION

3.1 *The detection variation under the solar loading cycle*

In this study, we analyzed the degree of detectability by analyzing the temperature difference between the delamination and non-delamination regions. Delamination is considered detectable when it can be visually distinguished from the infrared image (qualitative) or when its thermal contrast (ΔT) is no less than 0.5°C (according to the relevant American standard ASTM D4788-03). The thermal contrast is calculated from Eq. (1) (Tran et al., 2017, Ahlborn & Brooks, 2015):

$$\Delta T = T_{\mathrm{d}} - T_{\mathrm{nd}} \tag{1}$$

In the formula, T_d, T_{nd}, and ΔT represent the average surface temperature of the delamination zone, the average surface temperature of the non-delamination zone, and the difference between the average surface temperature of the delamination zone and the non-delamination zone, respectively. When ΔT>0, it means that $T_d > T_{nd}$, that is, the temperature of the delamination region is higher than that of the non-delamination region (the so-called "heat island" region); Conversely, the temperature in the delamination zone is lower than in the non-delamination zone (the so-called "cold island" zone).

As shown in Figure 3, the temperature calculation of the delamination region T_d is based on the average temperature in the red solid box, while the temperature calculation of the non-delamination region T_{nd} is based on the average temperature in the black solid box.

Figure 4 shows the ΔT curve of the specimen's 20 mm depth simulation stratification with three days of data acquired under natural conditions. They can be used to evaluate the ability of infrared imaging for detection as well as the best time window when the thermal contrast is sufficient for detection. Based on the figure, the period of detection can be divided into three

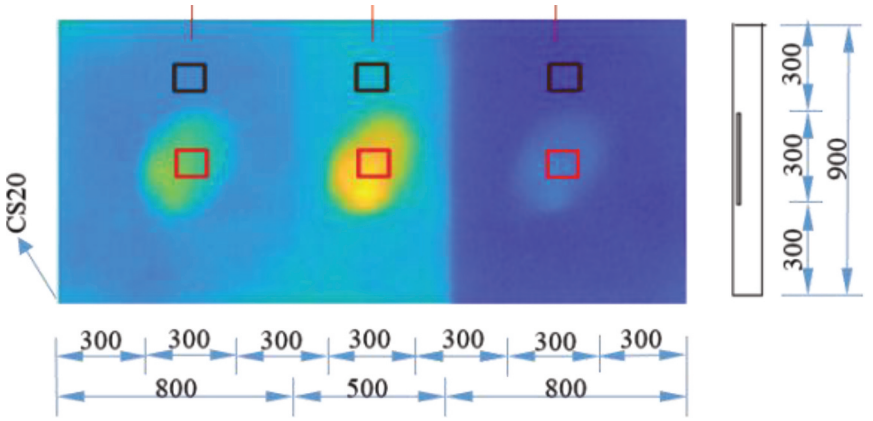


Figure 3. Temperature calculation of delamination and non-delamination areas.

phases. In phase I, the solar radiation is about to disappear and the only way to exchange heat is the convection heat exchange with the atmosphere and the radiation heat exchange of the environment. The temperature of the specimen is higher than the outside air temperature, and thus the specimen radiates heat to the outside. Due to the existence of the internal defect, the heat conduction rate in the delamination zone is different from the solid region, the ΔT is less than 0°C and the cold island area appears across all three regions. In addition, the defects with different surface conditions have developed different thermal contrasts meaning that the defects can be detected as cold regions with different temperature thresholds (maximum values of around 3.5, 3, and 20°C for concrete, yellow, and white surfaces). In phase II, the thermal contrasts in three surface regions become coincidental but still below 0°C meaning that the defects can be detected as cold regions with close temperature threshold (average contrast of -1.7 °C). In phase III, there is an inflection point at the intersection of II and III which may be majorly due to the start of solar radiation. After the solar loading, the thermal

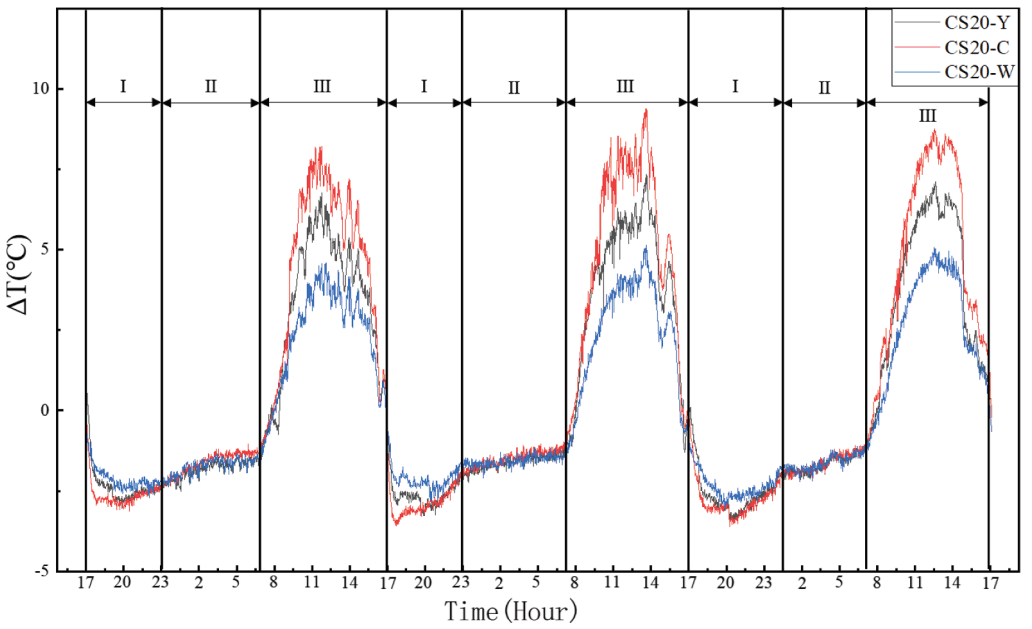


Figure 4. ΔT curves of heterogeneous materials on different surfaces under 20 mm deep delamination.

contrasts are developed dramatically and differently in three surface conditions. The maximum contrast can be reached at about 7, 5.7, and 4.5 °C for concrete, yellow, and white surfaces.

Figure 5 shows the heat flux curve attached to the center of the delamination regions. When the specimen emits heat to the environment, the sensor reads out positive values and vice versa. Between the time of 17:00 and 23:00 (phase I in Figure 4), the heat flux change is different for delamination under different surface conditions indicating the surface temperature may differ on each surface because of the consistent solar loading and air temperature during this period. During this period, the delamination area releases heat at different rates. Between the time of 23:00 and 7:00 (phase II in Figure 4), the heat flux for delamination under three surface conditions is almost the same around +25 w/m^2 indicating that the defect areas emit heat at the same rate. Between the time of 7:00 and 17:00 (phase III in Figure 4), the heat absorbed by the specimen increases dramatically, and the inside of the specimen gradually gains heat from the outside, making the value of heat flux less than 0. The delamination areas for all three regions share the same trend but with different magnitudes. The bare concrete, yellow, and white surface can reach a maximum rate of around -290, -260, and -120 w/m^2 which is correlated with the thermal contrast in Figure 4 respectively. It also found that during the day, at a certain point in time, the cloud obscures the sunshine which causes the curve to oscillate.

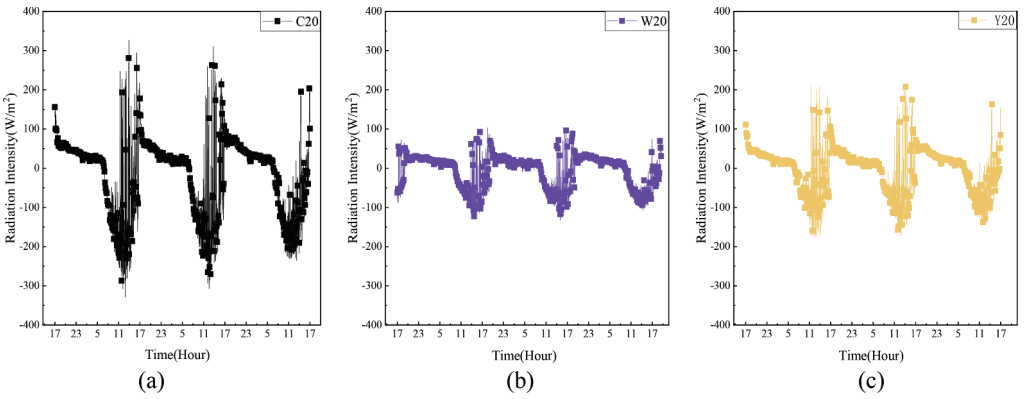


Figure 5. Surface heat flux curves of three surface conditions: (a) 20 mm depth delamination under bare concrete surface; (b) 20 mm depth delamination under white painting surface; (c) 20 mm depth delamination under yellow painting surface.

Figure 6 shows the solar radiant intensity plot during the experiment collected from the weather station. The solar loading starts around 6:30 and ends around 19:00. It can be used as an adjuvant analysis in addition to the ΔT curve and the heat flux curve. Between the time of 17:00 and 19:30, the intensity slowly decreases to zero showing the period of sunset. During this period, the thermal contrast is rapidly increasing for the delamination area in Figure 4 as well as heat flux in Figure 5. However, during the time between 16:30 and 17:30 the absolute value of thermal contrast is within ±0.5~1°C indicating the detectability of delamination remains low. Between the time of 19:30 and 6:00, the solar intensity is constantly zero showing the nighttime of the day. During this period, the thermal contrast and heat flux are relatively stable indicating the only influential factor of detection relates to the heat exchange between specimen and ambient. Between the time of 6:00 and 8:30, the intensity slowly increases showing the period of sunrise. During this period, the thermal contrast and heat flux increase rapidly. However, the absolute value of thermal contrast is within ±0.5~1°C indicating the detectability of delamination remains low. Between the time of 8:30 and 17:00, the radiant intensity rises first and then decreases rapidly, and the thermal contrast and heat flux curves follow the same trend.

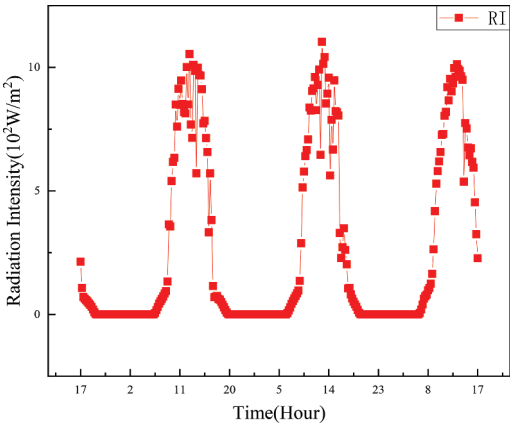


Figure 6. Solar radiation intensity.

3.2 *Effect of paint on the development of thermal contrast*

It found two time windows where the different surface conditions have a noticeable effect on the development of the thermal contrast. During the noon time when the solar radiation is relatively strong, the curve shows a hierarchical increase due to the different absorption rates of the surficial heterogeneous materials as shown in Figure 4. The ΔT of CS20-C is about 2°C larger than that of CS20-Y, and about 4°C larger than that of CS20-W. On the other hand, after about 2 hours of sunset, the ΔT of CS20-C is about 0.5°C larger than that of CS20-Y, and about 1°C larger than that of CS20-W. During the nighttime, there is no effect of solar radiation, and thus the curves coincide due to the same emissivity of the surface and similar heat exchange conditions. It also found that during phase II of Figure 4, the thermal contrast of delamination is constantly below zero (about -2 to -1.7 °C) indicating the potential time window for detection. Considering that the different surficial materials have different absorption rates but similar emissivity, the reason causing the difference in thermal contrast at daytime and sunset may be different. Further in-depth investigation is needed.

4 CONCLUSION

After three days under natural conditions, the delamination area can be detected under different surface conditions except for a period during sunrise and part of sunset whose developed thermal contrast is relatively low. In the daytime, the different surface conditions will have a major impact on the thermal contrast development of the delamination area due to the different absorption rates. The delamination under the bare concrete surface has a larger contrast than that under painted surfaces meaning higher detectability. In this period, the delamination can be detectable as hot regions in the thermal images. Right after the sunset, the different surface conditions also impact the thermal contrast development. The delamination area starts to become cold regions in the thermal images with different contrasts in terms of different surface conditions. During the nighttime, the surface condition has minimal impact on the thermal contrast, and the delamination area can be detected by using a similar threshold no matter what the surface conditions are. The above findings provide more insight and information for choosing the best time window and threshold for delamination detection when subjected to different surface conditions within the same bridge deck.

ACKNOWLEDGEMENT

This work is partially supported by the National Natural Science Foundation of China (No. 52108267), the General Program of Chongqing Natural Science Foundation (CSTB2022NSCQ-

MSX1379) and Special Funding for Chongqing Postdoctoral Research Projects (2021XMT007). The authors also would like to appreciate the help from Du Ke, Xianwang Zeng, Yi Wang, Liling Wang, Jie Xu, and Jianguo Liang who involve in the data collection and processing during the experimentation at the State Key Laboratory of Mountain Bridge and Tunnel Engineering

REFERENCES

Dabous, S. A., Yaghi, S., Alkass, S. & Moselhi, O. 2017. Concrete bridge deck condition assessment using IR Thermography and Ground Penetrating Radar technologies. *Automation in Construction*. 81 (340-354.

Transport, M. o. 2023. *Statistical Communiqué on the Development of the Transportation Industry in 2022* [Online]. Available: https://xxgk.mot.gov.cn/2020/jigou/zhghs/202306/t20230615_3847023.html [Accessed].

Koh, C., Ang, K. & Zhang, L. 1997. Effects of repeated loading on creep deflection of reinforced concrete beams. *Engineering structures*. 19(1), 2–18.

Oh, T., Kee, S.-H., Arndt, R. W., Popovics, J. S. & Zhu, J. 2013. Comparison of NDT methods for assessment of a concrete bridge deck. *Journal of Engineering Mechanics* 139(3), 305–314.

Tran, Q. H., Han, D., Kang, C., Haldar, A. & Huh, J. 2017. Effects of Ambient Temperature and Relative Humidity on Subsurface Defect Detection in Concrete Structures by Active Thermal Imaging. *Sensors*. 17(8).

Raja, B. N. K., Miramini, S., Duffield, C., Sofi, M. & Zhang, L. 2022. Infrared thermography detection of delamination in bottom of concrete bridge decks. *Structural Control Health Monitoring*. 29(3), e2886.

Washer, G., Fenwick, R., Nelson, S. & Rumbayan, R. 2013. Guidelines for Thermographic Inspection of Concrete Bridge Components in Shaded Conditions. *Transportation Research Record: Journal of the Transportation Research Board*. 2360(1), 13–20.

Cotič, P., Kolarič, D., Bosiljkov, V. B., Bosiljkov, V. & Jagličić, Z. 2015. Determination of the applicability and limits of void and delamination detection in concrete structures using infrared thermography. *NDT & E International*. 74(87-93.

Mac, V. H., Tran, Q. H., Huh, J., Doan, N. S., Kang, C. & Han, D. 2019. Detection of Delamination with Various Width-to-depth Ratios in Concrete Bridge Deck Using Passive IRT: Limits and Applicability. *Materials*. 12(23).

Ta, Q. T., Huh, J., Yim, H. J. & Tran, Q. H. 2023. Nondestructive detection of delamination in painted concrete structures through square pulse thermography. *Journal of Building Engineering*. 70(106360.

Ltd, S. J. T. C. 2022. *MAG-F6: Selection of Infrared Instruments for University Research* [Online]. Available: https://www.magnity.com.cn/product/id/74.html [Accessed].

Vollmer, M. & Möllmann, K. P. 2017. *Infrared Thermal Imaging (Fundamentals, Research and Applications) || IR Imaging of Buildings and Infrastructure*.

Institute, A. C. Report on Nondestructive Test Methods for Evaluation of Concrete in Structures. 2013. American Concrete Institute.

Li, Y. & Zhen, Y. 2012. *Infrared thermal imaging temperature measurement principle and technology*, Science Press.

Wenyan, L. & Yaoming, G. 2004. Experimental study on solar radiation absorption rate of concrete surface. *China Concrete and Cement Products*. 04), 8–11.

Ahlborn, T. M. & Brooks, C. N. 2015. Evaluation of bridge decks using non-destructive evaluation (NDE) at near highway speeds for effective asset management. Michigan Technological University.

Bridge Maintenance, Safety, Management, Digitalization and Sustainability – Jensen, Frangopol & Schmidt (eds)
© 2024 The Author(s), ISBN 978-1-032-77040-6
Open Access: www.taylorfrancis.com, CC BY-NC-ND 4.0 license

Structural health monitoring of the 1915Çanakkale Bridge in Turkey, the largest monitoring system for the longest suspension bridge in the world

S. Joye & M. De Witt
Sixense Monitoring, Nanterre, France

ABSTRACT: The 1915Çanakkale Bridge is outstanding and so is its Structural Health Monitoring. Designed and installed by Sixense upon the specification of the Client, the system will manage more than 1000 sensors. This monitoring architecture will allow to measure any external event happening on the Bridge such as strong wind, earthquakes, lightning, and heavy traffic. It will also record all the reaction behavior of the structure such as temperature, displacement, vibration, fatigue stresses. Amongst all the recorded data, dynamic records of such a slender structure is a key aspect. The acquisition system provided by Sixense will allow to record, compute, sample, and analyze a tremendous quantity of data related to the mechanical behavior of the structure. It will for instance allow rainflow counts of the stress cycles of the orthotropic slab in order to survey and prevent fatigue failure. But more than simply recording data for visualization and immediate maintenance, the system provided by Sixense will also allow predictive computations to model the future behavior of the infrastructure with regression analysis tools and will allow the owner of the bridge to anticipate the maintenance operations far in advance, out of critical service activity phases. This will increase the safety of the bridge, save money for the owner and allow this emblematic bridge to last for a very long time.

1 INTRODUCTION

The longest suspension bridge in the world is now open to traffic in Turkey with its 3563m length and a mid-span of 2023m. Located about 400km South West of Istanbul, the Bridge crosses the Çanakkale Strait (Dardanelles) to accelerate the traffic between Europe and Asia.

With more than 1000 sensors the SHM system implemented by Sixense allows to measure both environmental conditions and bridge mechanical response parameters. Besides the standard structural alert functionalities, the SHM system provides tools to anticipate the bridge performance in the long term.

2 THE BRIDGE

2.1 *Context an environment*

The Bridge is the fourth bridge linking Europe to Asia after the two well known Bosphorus bridges located in Istanbul and the 3rd Bosphorus Bridge Yavuz Sultan Selim located far North along the Black See. But this bridge in not over Bosphorus: located 500km South West it crosses the Çanakkale Strait just before the Agean Sea nearby the ancient city of Troy. Its purpose is to take into account the increase of traffic from Europe to Asia and to relieve some of the heavy traffic over the heavily congested Istanbul by derivating it south.

DOI: 10.1201/9781003483755-287

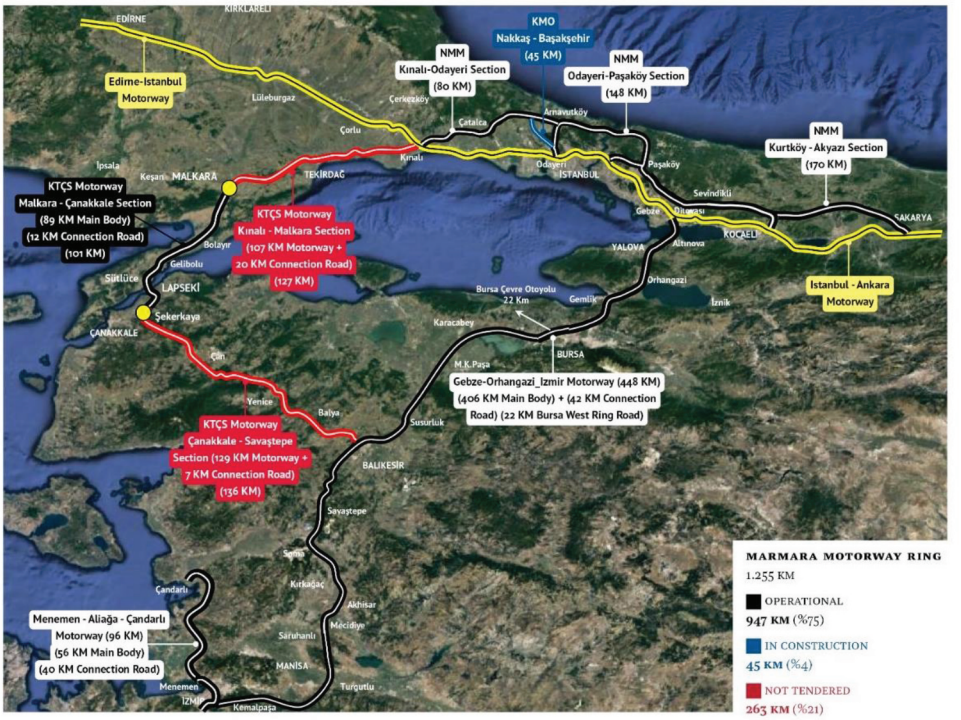


Figure 1. Routes between Europe and Asia.

2.2 *Bridge characteristics*

The Bridge has outstanding characteristics. Its mid span first with 2023m, it breaks the world record from the suspension bridge of Akashi Kaiko in Japan which has held the record since 1998 with 1991m mid span. The height of the tower is also a breakthrough. With a height of 318m it is higher than the Eiffel Tower in Paris.



Figure 2. 1915Çanakkale Bridge.

3 THE SHMS ARCHITECTURE

The SHMS architecture can be split between sensors and acquisition system. The sensors list may be split between environmental and traffic sensors and structural behaviour sensors.

3.1 *Environmental sensors*

The purpose of the environment and traffic sensors is to monitor the external loads that apply on the structures. This enable to alert on outstanding event that will raise alarm when predefined thresholds are overpassed. This can for instance allow to stop the traffic in case of wind or seismic events.

Monitoring of environmental loads can also enable to correlate the behaviour of the structure when submitted to specific environmental condition - for instance, wind against vibration - and verify the design calculation and hypothesis.

Table 1. Environmental sensors.

Sensor type	Quantity
Air temperature	3
Clearance - Laser distance sensor	2
Barometric Pressure	4
Humidity	4
Weather Station	6
Pyrometer	2
Seismic Station	2
Weight in Motion	2

3.2 *Structural sensors*

As environmental sensors, structural sensors enable to regulate the traffic in case of alarms raised by extreme vibrations for instance. But they are more particularly used to monitor the ageing of the structure or its long terms behaviour such as stress concentration, cumulative displacement, creep of the deck or even of corrosion of rebars inside the concrete deck.

Table 2. Structural sensors.

Sensor type	Quantity
Accelerometre	18
Asphalt Temperature	8
Steel Temperature	52
Cable temperature	4
Corrosion sensor	36
Displacement sensor	64
GPS	28
Inclinometer	74
Strain Gauge	508
Road Weather	4

3.3 *Integrated sensors*

The SHMS system is also designed to integrate data provided by external equipment such as dampers or buffers.

Table 3. Integrated sensors.

Sensor type	Quantity
Load Cell	16
Sensor in the Damper	4
Sensor in the Buffer	2

3.4 *Acquisition hardware units*

The acquisition hardware units are specifically design for the 1915Çanakkale Bridge. They enable the acquisition of either low frequency signal (ex. displacement) or high frequency signals (ex. accelerometers). They also enable the initial processing (summary statistics) and their transfer to data servers. Data acquisition units power supply is backed up by UPS (Uninterruptible Power Supply) to ensure they remain in service even in the unlikely event of a power failure.

4 THE SHM SOFTWARE

The Eversense SHM Software has been developed by Sixense for 15 years. However, the software has been specifically updated to include new functionalities requested by the specification of the Bridge.

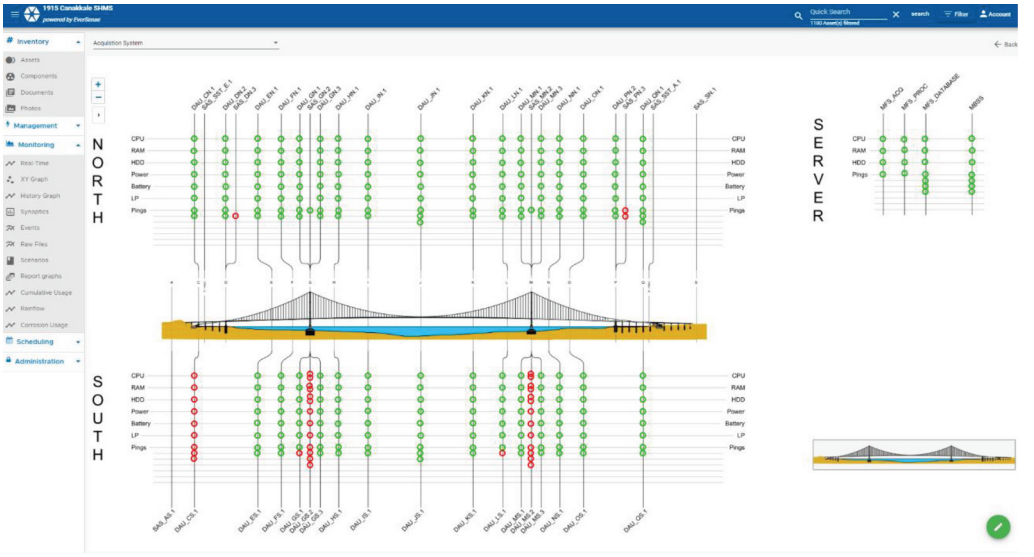


Figure 3. Eversense SHM software synoptic view.

It will enable to estimate the fatigue ageing of steel welds and component by a rainflow counting of the cumulated strains at specific locations. It will also enable predictive analysis of the behaviour of the Bridge by a comparison of bridge behaviour with environmental condition and application of specific predictive regression of the generated pattern. In this sense the software will act as a simplified but very useful full Digital Twin.

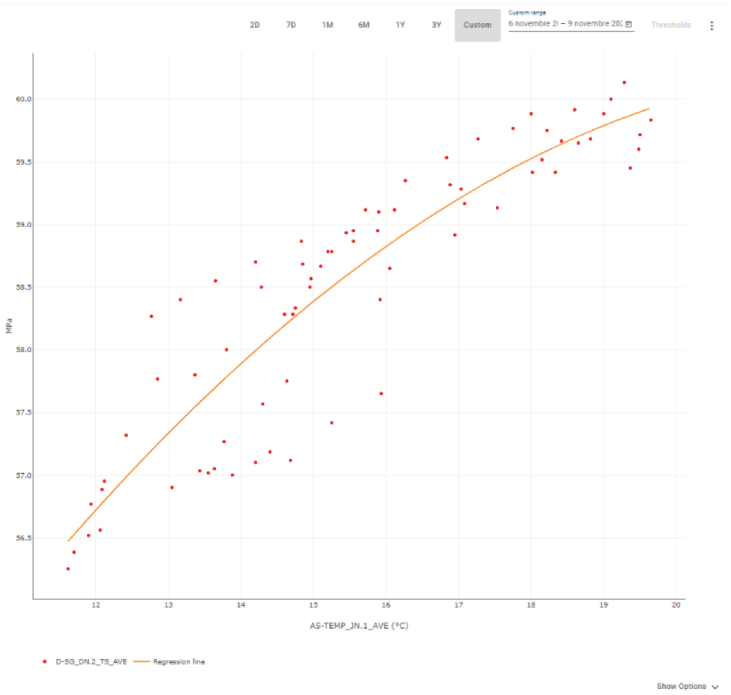


Figure 4. Stress measured by a differential strain gauge vs temperature and a trend curve obtained by regression plotted in Eversense software.

5 CONCLUSION

Worldwide increase of traffic is pushing civilisations to find new routes and new ways of reaching their destination always faster. Growing cities are desperately willing to deviate the traffic around to preserve their city centres form cars. Those goals are the sources for outstanding means or travelling when routes have no other choices that crossing sees.

The 1915Çanakkale Bridge is the result of such goals by outstandingly crossing the Çanakkale Strait over a main span of 2023m between towers becoming the new world record of the longest bridge main span.

Yet this Bridge is reaching such a great limit that is shall be backed by a significant and reliable structural health monitoring. Similarly, being designed and built to last more than 100 years this expectation cannot be reach without reliable information about the environment, the related structural response and an SHMS system allowing to correlate both in order to anticipate and advise about the maintenance of the structure. This is why Sixense SHM system has been chosen on this world record bridge.


Taylor & Francis
Taylor & Francis Group
http://taylorandfrancis.com

SS22: Advancements in intelligent monitoring and maintenance of bridge infrastructure

Organizers: S. Setunge, A. Alani, G. Heravi, R. Dissanayake, T. Bui-Tien, M. Mahmoodian & A. Sidiq


Taylor & Francis
Taylor & Francis Group
http://taylorandfrancis.com

Bridge Maintenance, Safety, Management, Digitalization and Sustainability – Jensen, Frangopol & Schmidt (eds)
© 2024 The Author(s), ISBN 978-1-032-77040-6
Open Access: www.taylorfrancis.com, CC BY-NC-ND 4.0 license

Real-time structural integrity assessment of bridge infrastructure

S.C. Jayasinghe
Department of Civil and Infrastructure Engineering, School of Engineering, RMIT University, Australia

T.M. Nanayakkara
Department of Manufacturing, Materials and Mechatronics Engineering, School of Engineering, RMIT University, Australia

A. Alavi
Department of Artificial Intelligence, School of Computing Technologies, RMIT University, Australia

M. Mahmoodian, A. Sidiq, Z. Sun, F. Shahrivar & S. Setunge
Department of Civil and Infrastructure Engineering, School of Engineering, RMIT University, Australia

ABSTRACT: Ageing infrastructure systems are easily prone to failure demanding frequent monitoring despite costs and risks. Digital twin offers an intelligent approach to overcome such limitations of traditional bridge monitoring. Current study focuses on implementing remotely connected real-time virtual models of bridges to visualize any induced stresses/strains of the actual bridge via the digital twin concept. It was first proposed to instrument a bridge with sensors and to follow an inverse approach to simulate the overall behavior using sensor measurements. A machine learning algorithm based finite element model has been suggested for this and three different algorithms were tested. All three machine learning algorithms accurately represented the behavior of the actual bridge in real-time. Overall, it was concluded that a combination of both physics-based and data-driven model development techniques is highly effective for real-time analyses and for the digital twining process. The proposed method can be extended to a large-scale bridge easily.

Keywords: Digital Twin, Machine Learning, Finite Element Method, Inverse Method, Structural Health Monitoring

1 INTRODUCTION

Civil infrastructure assets such as bridges, highways, and buildings are critical components of modern society. They provide essential services whilst supporting communities, industries, and economies as well. However, the aging infrastructure and the increasing frequency and severity of natural disasters have highlighted the need of having a systematic method of monitoring and maintenance of these assets (Mahmoodian, 2021). The traditional methods of inspection and maintenance are time-consuming, costly, and often reactive, leading to potential safety hazards and economic losses. According to cost estimates, Australia spends approximately $19 billion annually to maintain its road network (Austroads, 2016). Usually, bridges require between 0.4% and 2% of their construction cost for yearly maintenance activities (Mahmoodian et al., 2022). Consequently, for a bridge designed to last 100 years, its maintenance expenses could potentially reach twice the initial construction cost (Artus and Koch, 2020).

The emergence of digital twins offers a promising solution to address these challenges. Digital twins (DTs) are virtual replicas of physical assets that can be used for real-time monitoring,

DOI: 10.1201/9781003483755-288

analysis, and optimization (Callcut et al., 2021). The implementation procedure of digital twins initiates from the telemetry data collection from the operating asset and continue until the visualization of the real-time structural response via a digital model whilst accommodating a real-time connection in between. This allows to plan proper structural health monitoring (SHM) procedures based on the real-time behavior of bridges (Ye et al., 2019). Additionally, response-based acquisition units have become the prevailing choice, surpassing the popularity of image processing systems (Kaewunruen et al., 2021, Qiu et al., 2022). The digital replication can be accomplished either using a physics-based or data-driven methods (Mahmoodian et al., 2022) and also, a combination of them has demonstrated its ability to advance the functionality of a DT system (Ye et al., 2019). However, the majority of existing digital twins solely offer visualizations of the physical asset without depicting its structural integrity. Consequently, they are referred to as geometric digital twins and are primarily applicable during the structural design phase (Lu and Brilakis, 2019). Also, considering that the measured structural response serves as the input for the digital model, it is essential to adopt an inverse approach (Moi et al., 2020), which may often pose challenges due to its potential for ill-conditioning (Gupta, 2013, Wang et al., 2021). Recently, Artificial Intelligence (AI) techniques have been identified as potential algorithms for real-time FE modelling and for inverse structural analysis (Kononenko and Kononenko, 2018, Badarinath et al., 2021). Once trained, those algorithms will be able to do predictions for the given inputs immediately. However, they highly depend on the data availability.

In this light, the current study is proposing a novel methodology by aiming to demonstrate the feasibility of using digital twins and AI techniques for real-time structural analysis of bridges. It focuses on using Artificial Neural Networks (ANNs), Random Forest algorithms and Extreme Gradient (XG) boosting algorithms as surrogates for real-time inverse structural analysis via FEM. The sensor readings from IoT devices connected to the infrastructure will be fed into the trained model to perform real-time analysis and observe structural deformation.

The proposed methodology will enable the development of a system that can continuously monitor and analyze the structural health of civil infrastructure assets in real-time. This system can provide timely maintenance and intervention, reducing the risk of structural failure and ensuring the safety of the public and the environment. Also, this will contribute to the body of knowledge on AI-based surrogate models for structural analysis of civil infrastructure systems. It will demonstrate the potential of using digital twins and AI for real-time structural analysis and highlight the benefits of adopting these technologies for infrastructure monitoring and maintenance.

2 LITERATURE REVIEW

2.1 *Digital twins for bridges*

A digital twin of a bridge is anticipated to function as a dynamic digital representation, accurately reproducing and visually presenting every aspect of the bridge such as the geometry, materials, layout, inspections, and other pertinent details whilst facilitating a continuous data-flow with the actual bridge and providing stakeholders with the ability to respond promptly in emergency situations. (Ye et al., 2019). The commencement of the bridge digital twinning system involves gathering telemetry data. However, the crucial phase within this process is the implementation of the digital model. Researchers have utilized both physics-based and data-driven methods to construct virtual models (Shim et al., 2019, Ye et al., 2019, Lin et al., 2021, Febrianto et al., 2022). Each method comes with its own advantages and disadvantages that can have a substantial impact on the effectiveness of a digital twinning process. For instance, even though a physics-based method like FE modelling can detect damages, conducting real-time analysis is challenging due to its high computational cost. It is apparent that this kind of a method necessitates support from the other approach to boost its performance and produce results in real-time (Ye et al., 2019).

However, existing digital twins of bridges possess distinct limitations. The majority of existing digital twins showcase geometrical changes rather than considering the structural

performances (Lu and Brilakis, 2019). Also, they rarely incorporate real-time assessments of bridge structural integrity. Additionally, as sensors or image processing techniques document the performance of the real bridge, any faults in measurement instruments, environmental factors, or errors in storage devices may lead to the dispersion of measured data. Such dispersion has the potential to disrupt the entire digital twinning process (Ghahari et al., 2022). Hence, utilizing the technology to integrate actual environmental conditions with the generated models is crucial (Huang et al., 2015).

2.2 *Surrogates for real-time FE modelling*

Deemed as the widely used and powerful computational technique, FE analysis facilitates efficient structural analysis through advanced modeling and simulations (Marinkovic and Zehn, 2019). Also, FE modelling is the most popular physics-based technique for digital twins. However, in finite element (FE) modeling, a structure is divided into distinct elements (FE mesh) and these elements are analyzed individually rather than evaluating the entire structure as a whole (Logan, 2012). Consequently, it will produce highly accurate results albeit at a significant increase in computational costs. Thus, in response to these limitations, diverse surrogates have been introduced. Amongst, machine learning (ML) algorithms can be identified as one of the most promising approaches.

The application of machine learning algorithms has garnered significant attention, with numerous studies demonstrating its efficacy in real-time FE model analysis. Various machine learning algorithms have been employed to execute this specific task. Both FEM and ML algorithms individually hold significant predictive capabilities in various domains and their integration can be accomplished via three main distinct approaches: (i) Embedding ML algorithms directly into FEM architecture (Javadi et al., 2003, Tao et al., 2022), (ii) Developing empirical equations using generated data by FEM (Tohidi and Sharifi, 2016) and (iii) Conducting the entire FEM process to obtain desired outputs to given inputs after training via a dataset provided by FE analysis (Gudur and Dixit, 2008, Shahani et al., 2009). Amongst, the third approach is more suitable for an inverse approach of structural analysis as it allows to train an algorithm in between input and output values depending on the requirement (Kononenko and Kononenko, 2018).

Badarinath et al. (2021) assessed a one-dimensional beam, comparing three machine learning models: extreme gradient boosting trees, Random Forests, and Artificial Neural Networks (ANNs). Their findings highlighted ANNs as the most predictive method. Additionally, Vardhan and Sztipanovits (2022) also supported the effectiveness of deep learning by contrasting it with Random Forests and gradient boost regression models for sub-sea pressure vessel design via FEM. However, it is difficult to determine the best performing algorithm as all of these algorithms are highly relied on the dataset and the dataset will be completely different from one structure to another. Also, in terms of ANNs, the type of neural network also affects the performance of the trained model. Recent researches have focused on using Feedforward neural networks (Liu, 2019, Tran-Ngoc et al., 2021, Tao et al., 2023, Le-Duc et al., 2023), Recurrent neural networks (Ninić et al., 2017, Ghavamian and Simone, 2019), Convolutional neural Networks (Pizarro et al., 2021), Graph neural networks (Fu et al., 2023, Jiang and Chen, 2023), Radial basis functions (Lu et al., 2023) etc. Graph neural networks have attracted lots of interest for this specific application as it can indicate the FE mesh data in a graphical format and conduct the analysis in a more efficient way (Maurizi et al., 2022). It has been mentioned in most of the researchers a significant decrease in computational time when FEM replaced by ML algorithms. Also, the non-linearity in the structural behavior is not a problem for ML algorithms once trained by a proper dataset and these models are not highly sensitive for minor variations in the inputs.

3 METHODOLOGY: DEVELOPMENT OF THE DIGITAL TWIN

The methodology of this study has been proposed to develop the digital twin of a laboratory scaled bridge with the help of a machine learning approach for its real-time structural integrity

assessment. The methodology is twofold: Training the Artificial Neural Network, See Figure 1(a) and Real-time visualization of the structural response, See Figure 1(b).

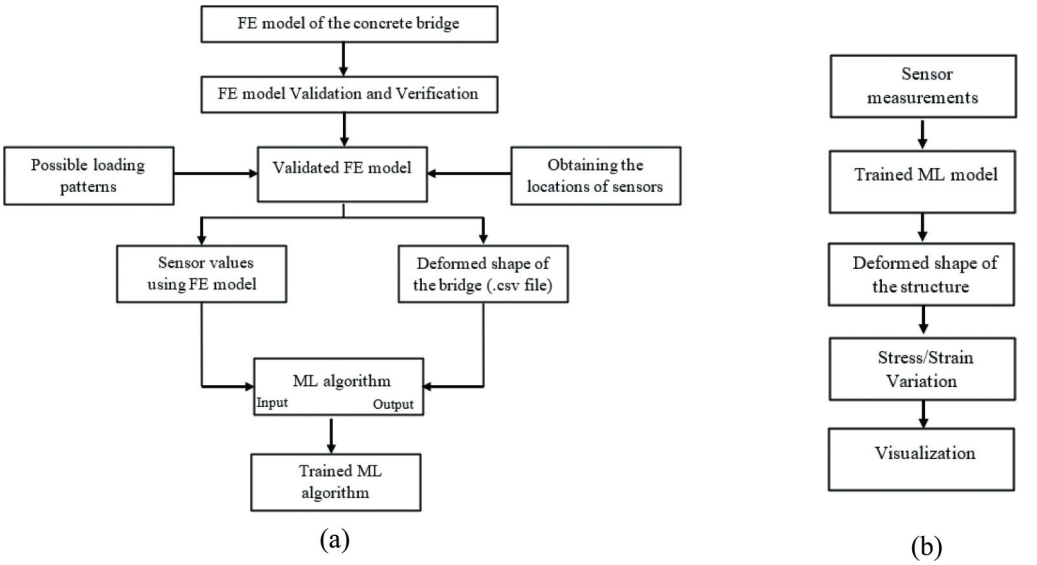


Figure 1. Methodology (a) Training of Neural Network (b) Real-time visualization.

3.1 *Experimental setup*

The selected bridge model, its geometry and sensor configurations are presented in Figure 2. SG refers to strain gauges. The model is a symmetrical roof truss with 13 circular cross-section members, each with a 6 mm diameter, made of stainless steel with a Young's modulus of 193 GPa. One end is a pin support, the other a roller support, and all joints are pin jointed. The truss, following manufacturer guidelines, can handle loads from -500N to 500N. Hence, all the possible loading patterns within that range were considered when generating the dataset and training the algorithm. The trained algorithm was used to feed randomly generated sensor data in real-time and allowed to visualize the stress variation in real-time.

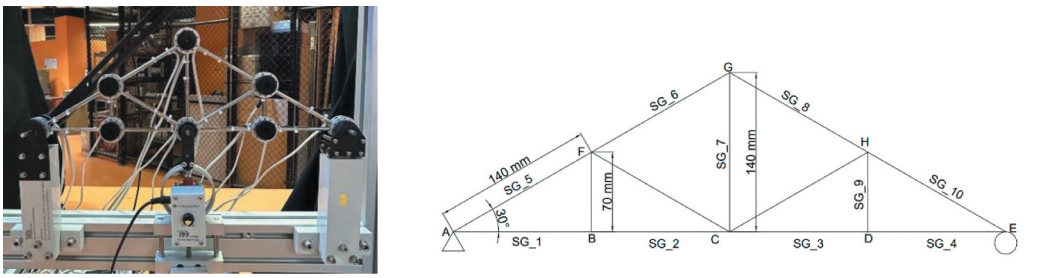


Figure 2. Structural setup and geometry of the laboratory model.

3.2 *Machine learning algorithms*

The FE model of the bridge was developed using python scripting and the analysis process was automated to generate a dataset as presented. Under the methodology three ML algorithms including the Random Forest (RF), Artificial neural networks (Multi-layer perceptron) and Extreme gradient (XG) boosting algorithms were followed to assess the predicting capacity of each of them towards the inverse structural modelling. Altogether 4000 records of strain values as the input and displacement of each node as the output were considered when

training the model. The data was split into 80% of training data, 20% of testing data and again 20% of testing data was considered for validation. Root mean square error (RMSE) value was used as the performance measure.

The RF algorithm stands out as a powerful ensemble technique that involves multiple independent decision trees with added randomness to obtain more accurate predictions (El Mrabet et al., 2022). Also, it has proved its effectiveness in different predicting tasks in the civil engineering domain (Huang et al., 2020, Liu et al., 2021). For the developed RF algorithm, 100 estimators were considered, and the cross-validation was also introduced to assess its performance.

Similarly, MLP based neural networks can be identified as the most popular neural network that includes a simple fully connected type of feedforward ANNs. It consists of three or more layers that includes an input layer, one or more hidden layers and an output layer. The nodes in each layer make relationships to conduct the prediction task effectively and MLPs show several successful attempts as a surrogate of FE modelling (Liu, 2019, Badarinath et al., 2021). For the developed MLP, min-max scaling was used to normalize the data to enhance the convergence of the training process. The feed forward neural network architecture was created using Keras, considering 4 layers with 2 hidden layers. A total of 10 inputs were fed to the model. Hidden layers consisted of 64 and 32 layers respectively and the size of the output layer was 13 as three nodes of the actual structure were constrained. The ReLU activation function and Adam optimizer were used whilst the RMSE was considered as the loss function. The model was trained for 100 epochs with the batch size of 32 with early stopping.

XG boost is also another powerful prediction algorithm that is based on the concept of gradient boosting and gained huge popularity due to its speed and performance. This also shows few successful attempts in predicting tasks in the civil engineering domain (de-Prado-Gil et al., 2022, Tuken et al., 2023). When developing the XG boost algorithm for the current study, initially the hyperparameters were tuned and the maximum depth of each individual tree was 15, min_child_weight was 9, learning rate was 0.1 and number of estimators were 100. Also, the tree-based models were obtained as the booster here. After training the ML algorithm, the best model was saved in order to use it when feeding the sensor data. The rest of the coding to visualize the stress variation was done using direct stiffness method and using the matplotlib library in python.

4 RESULTS AND DISCUSSION

4.1 *Machine learning models*

Three ML models including RF, ANN and XG boosting were trained using the developed dataset after conducting FE analysis of the truss structure for 4000 iterations. The data generation was automated. The obtained RMSE for both testing and validation are shown in Table 1.

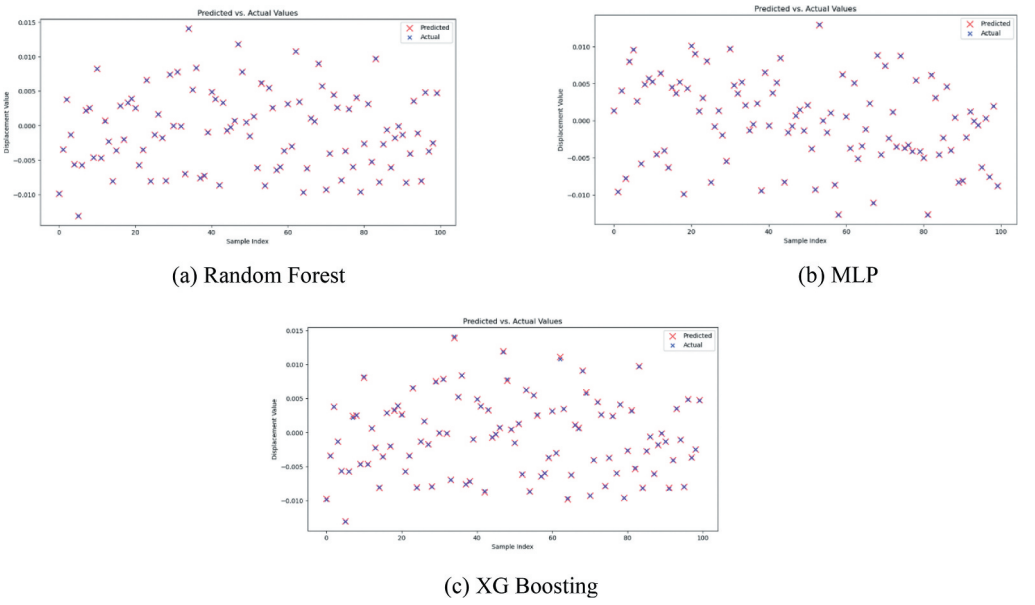
Table 1. RMSE of each tested algorithm.

Algorithm	Testing RMSE	Validation RMSE
Random Forest	0.000373	0.000341
MLP	0.000463	0.000473
XG Boosting	0.000470	0.000460

After training, 100 samples were randomly selected from the dataset to predict the output and a graph was created in between the actual output and predicted output for each model. Figure 3 depicts those graphs which compare the actual and predicted values. According to Table 1, the RMSE values were low for all three algorithms whilst the random forest algorithm shows the least RMSE values. Hence, the random forest showed the best performance regarding the inverse structural modelling whilst the feed forward architecture of ANNs and XG Boosting algorithm nearly similar RMSE values. Figure 3 also provides a similar observation.

4.2 *Real-time FE modelling*

The trained models were then fed with randomly generated sensor readings with a refresh rate of 1 second. All the three algorithms have the capability to generate the results in a time close to 20 milli seconds by proving its ability to conduct a real-time structural integrity assessment. As soon as the trained models provide an output, that output will be directly fed into a script that was written to visualize the stresses and deflected shape of a laboratory truss model. One output of that model is shown in Figure 4.



(a) Random Forest

(b) MLP

(c) XG Boosting

Figure 3. Comparison between predicted and actual outputs of each model.

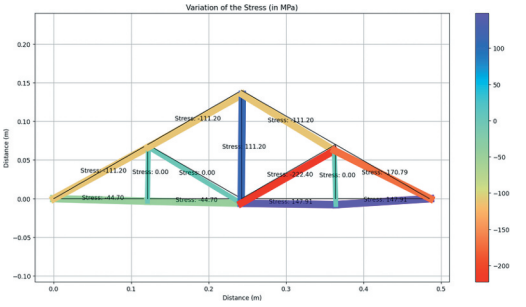


Figure 4. Real-time stress variation and deflected shape of the truss model.

The model indicates the elements with higher compression stresses in red color and higher tension stresses in blue color. Accordingly, it will provide the chance to decide which members carry out higher stresses and require a replacement.

5 CONCLUSION

This paper presents an implementation of a digital twin of a laboratory-scaled truss bridge. The bridge model was instrumented with ten strain gauges. Then, a dataset was

created including strain values and deformed coordinates of each node by conducting a finite element analysis for a series of loading patterns. Then, three machine learning algorithms including random forest, feedforward artificial neural network, and XG Boosting were developed and trained. The trained model was able to predict the real-time behavior of the bridge when actual strain gauge readings were fed into trained models. It was observed that all three models show relatively small error values when training whilst the random forest algorithm showed the best performance. All the three algorithms were able to predict the structural behavior of the bridge as soon as they receive a sensor reading and showed results immediately by proving their ability to conduct an inverse structural analysis in real-time. Also, it was noted that it is further possible to reduce the number of strain gauges of the truss model. However, to maintain the same accuracy, it is required to increase the size of the dataset. Overall, the proposed method was able to successfully visualize the stress variation of the bridge in real-time and it is clear that, this technique can be extended to a large-scale bridge.

REFERENCES

Artus, M. & Koch, C. 2020. State Of The Art In Damage Information Modeling For Rc Bridges – A Literature Review. *Advanced Engineering Informatics*, 46, 101171.

Austroads 2016. Reforming Remote And Regional Road Funding In Australia

Badarinath, P. V., Chierichetti, M. & Kakhki, F. D. 2021. A Machine Learning Approach As A Surrogate For A Finite Element Analysis: Status Of Research And Application To One Dimensional Systems. *Sensors (Basel, Switzerland)*, 21, 1–18.

Callcut, M., Cerceau Agliozzo, J.-P., Varga, L. & Mcmillan, L. 2021. Digital Twins In Civil Infrastructure Systems. *Sustainability (Basel, Switzerland)*, 13, 11549.

De-Prado-Gil, J., Palencia, C., Jagadesh, P. & Martínez-García, R. 2022. A Comparison Of Machine Learning Tools That Model The Splitting Tensile Strength Of Self-Compacting Recycled Aggregate Concrete. *Materials*, 15, 4164.

El Mrabet, Z., Sugunaraj, N., Ranganathan, P. & Abhyankar, S. 2022. Random Forest Regressor-Based Approach For Detecting Fault Location And Duration In Power Systems. *Sensors (Basel, Switzerland)*, 22, 458.

Febrianto, E., Butler, L., Girolami, M. & Cirak, F. 2022. Digital Twinning Of Self-Sensing Structures Using The Statistical Finite Element Method. *Data-Centric Engineering (Online)*, 3.

Fu, X., Zhou, F., Peddireddy, D., Kang, Z., Jun, M. B.-G. & Aggarwal, V. 2023. An Finite Element Analysis Surrogate Model With Boundary Oriented Graph Embedding Approach For Rapid Design. *Journal Of Computational Design And Engineering*, 10, 1026–1046.

Ghahari, F., Malekghaini, N., Ebrahimian, H. & Taciroglu, E. 2022. Bridge Digital Twinning Using An Output-Only Bayesian Model Updating Method And Recorded Seismic Measurements. *Sensors (Basel, Switzerland)*, 22, 1278.

Ghavamian, F. & Simone, A. 2019. Accelerating Multiscale Finite Element Simulations Of History-Dependent Materials Using A Recurrent Neural Network. *Computer Methods In Applied Mechanics And Engineering*, 357, 112594.

Gudur, P. P. & Dixit, U. S. 2008. A Neural Network-Assisted Finite Element Analysis Of Cold Flat Rolling. *Engineering Applications Of Artificial Intelligence*, 21, 43–52.

Gupta, D. K. 2013. *Inverse Methods For Load Identification Augmented By Optimal Sensor Placement And Model Order Reduction*. Proquest Dissertations Publishing.

Huang, J., Duan, T., Zhang, Y., Liu, J., Zhang, J. & Lei, Y. 2020. Predicting The Permeability Of Pervious Concrete Based On The Beetle Antennae Search Algorithm And Random Forest Model. *Advances In Civil Engineering*, 2020, 1–11.

Huang, J. M., Ong, S. K. & Nee, A. Y. C. 2015. Real-Time Finite Element Structural Analysis In Augmented Reality. *Advances In Engineering Software (1992)*, 87, 43–56.

Javadi, A. A., Tan, T. P. & Elkassas, A. S. I. Application of artificial neural network for constitutive modeling in finite element analysis. 2007 2003. 635–639.

Jiang, C. & Chen, N.-Z. 2023. Graph Neural Networks (Gnns) Based Accelerated Numerical Simulation. *Engineering Applications Of Artificial Intelligence*, 123, 106370.

Kaewunruen, S., Sresakoolchai, J., Ma, W. & Phil-Ebosie, O. 2021. Digital Twin Aided Vulnerability Assessment And Risk-Based Maintenance Planning Of Bridge Infrastructures Exposed To Extreme Conditions. *Sustainability (Basel, Switzerland)*, 13, 1–19.

Kononenko, O. & Kononenko, I. 2018. Machine Learning And Finite Element Method For Physical Systems Modeling.
Le-Duc, T., Nguyen-Xuan, H. & Lee, J. 2023. A Finite-Element-Informed Neural Network For Parametric Simulation In Structural Mechanics. *Finite Elements In Analysis And Design*, 217, 103904.
Lin, K., Xu, Y.-L., Lu, X., Guan, Z. & Li, J. 2021. Digital Twin-Based Collapse Fragility Assessment Of A Long-Span Cable-Stayed Bridge Under Strong Earthquakes. *Automation In Construction*, 123, 1.
Liu, G. R. 2019. Fea-Ai And Ai-Ai: Two-Way Deepnets For Real-Time Computations For Both Forward And Inverse Mechanics Problems. *International Journal Of Computational Methods*, 16, 1950045.
Liu, Y., Chen, H., Zhang, L. & Wang, X. 2021. Risk Prediction And Diagnosis Of Water Seepage In Operational Shield Tunnels Based On Random Forest. *Journal Of Civil Engineering And Management*, 27, 539–552.
Logan, D. L. 2012. *A First Course In The Finite Element Method*, Stamford, Ct, Cencage Learning.
Lu, J., Chen, Q. & Mohamed, H. 2023. Radial Basis Function Neural Network In Vibration Control Of Civil Engineering Structure. *Applied Mathematics And Nonlinear Sciences*, 8, 347–356.
Lu, R. & Brilakis, I. 2019. Digital Twinning Of Existing Reinforced Concrete Bridges From Labelled Point Clusters. *Automation In Construction*, 105, 102837.
Mahmoodian, M. 2021. Structural Reliability Assessment Of Corroded Offshore Pipelines. *Australian Journal Of Civil Engineering*, 19, 123–133.
Mahmoodian, M., Shahrivar, F., Setunge, S. & Mazaheri, S. 2022. Development Of Digital Twin For Intelligent Maintenance Of Civil Infrastructure. *Sustainability (Basel, Switzerland)*, 14, 8664.
Marinkovic, D. & Zehn, M. 2019. Survey Of Finite Element Method-Based Real-Time Simulations. *Applied Sciences*, 9, 2775.
Maurizi, M., Gao, C. & Berto, F. 2022. Predicting Stress, Strain And Deformation Fields In Materials And Structures With Graph Neural Networks. *Scientific Reports*, 12, 21834–21834.
Moi, T., Cibicik, A. & Rølvåg, T. 2020. Digital Twin Based Condition Monitoring Of A Knuckle Boom Crane: An Experimental Study. *Engineering Failure Analysis*, 112, 104517.
Ninić, J., Freitag, S. & Meschke, G. 2017. A Hybrid Finite Element And Surrogate Modelling Approach For Simulation And Monitoring Supported Tbm Steering. *Tunnelling And Underground Space Technology*, 63, 12–28.
Pizarro, P. N., Massone, L. M., Rojas, F. R. & Ruiz, R. O. 2021. Use Of Convolutional Networks In The Conceptual Structural Design Of Shear Wall Buildings Layout. *Engineering Structures*, 239, 112311.
Qiu, S., Wu, Z., Li, M., Yang, H. & Yue, F. 2022. Shape Monitoring And Damage Identification In Stiffened Plates Using Inverse Finite Element Method And Bayesian Learning. *Journal Of Vibration And Control*, 107754632210811.
Shahani, A. R., Setayeshi, S., Nodamaie, S. A., Asadi, M. A. & Rezaie, S. 2009. Prediction Of Influence Parameters On The Hot Rolling Process Using Finite Element Method And Neural Network. *Journal Of Materials Processing Technology*, 209, 1920–1935.
Shim, C., Kang, H. R. & Dang, S. 2019. *Digital Twin Models For Maintenance Of Cable-Supported Bridges*.
Tao, F., Liu, X., Du, H. & Yu, W. 2022. Finite Element Coupled Positive Definite Deep Neural Networks Mechanics System For Constitutive Modeling Of Composites. *Computer Methods In Applied Mechanics And Engineering*, 391, 114548.
Tao, W., Jiang, F., Li, L., Zhang, D., Guo, X. & Liao, W.-H. 2023. Dynamical Analysis And Vibration Estimation Of A Flexible Plate With Enhanced Active Constrained Layer Damping Treatment By Combinatorial Neural Networks Of Surrogates. *Aerospace Science And Technology*, 133, 108136.
Tohidi, S. & Sharifi, Y. 2016. Load-Carrying Capacity Of Locally Corroded Steel Plate Girder Ends Using Artificial Neural Network. *Thin-Walled Structures*, 100, 48–61.
Tran-Ngoc, H., Khatir, S., Ho-Khac, H., De Roeck, G., Bui-Tien, T. & Abdel Wahab, M. 2021. Efficient Artificial Neural Networks Based On A Hybrid Metaheuristic Optimization Algorithm For Damage Detection In Laminated Composite Structures. *Composite Structures*, 262, 113339.
Tuken, A., Abbas, Y. M. & Siddiqui, N. A. 2023. Efficient Prediction Of The Load-Carrying Capacity Of Ecc-Strengthened Rc Beams – An Extra-Gradient Boosting Machine Learning Method. *Structures (Oxford)*, 56, 105053.
Vardhan, H. & Sztipanovits, J. 2022. Deep Learning-Based Finite Element Analysis (Fea) Surrogate For Sub-Sea Pressure Vessel.
Wang, Y., Zhou, Z., Xu, H., Li, S. & Wu, Z. 2021. Inverse Load Identification In Stiffened Plate Structure Based On In Situ Strain Measurement. *Structural Durability & Health Monitoring*, 15, 85–101.
Ye, C., Butler, L., Calka, B., Iangurazov, M., Lu, Q., Gregory, A., Girolami, M. & Middleton, C. A Digital Twin Of Bridges For Structural Health Monitoring. 2019 2019. Destech Publications, Inc.

Bridge Maintenance, Safety, Management, Digitalization and Sustainability – Jensen, Frangopol & Schmidt (eds)
© 2024 The Author(s), ISBN 978-1-032-77040-6
Open Access: www.taylorfrancis.com, CC BY-NC-ND 4.0 license

Optimal sensor placement applications for bridge structural health monitoring using the effective independence method

Z. Sun, M.I. Manuel, M. Mahmoodian, A. Sidiq, R.W.K. Chan, S.C. Jayasinghe, F. Shahrivar & S. Setunge
Royal Melbourne Institute of Technology, Melbourne, VIC, Australia

ABSTRACT: Structural health monitoring (SHM) plays an increasingly significant role nowadays in ensuring the serviceability of large and complex bridge structures. Optimisation algorithms are employed to optimise the system settings, including the quality of the captured data and, hence, the SHM system's performance. This includes a selection of sensor types, numbers, and placement locations. Optimal sensor placement (OSP) aims to achieve cost-effective monitoring of bridges through minimal sensor adoptions. This study presents an application of the Effective Independence Method (EFI), one of the most adopted optimisation methods, to the case study bridge to derive an optimal solution. The generated sensor configurations are then evaluated in relation to their overall quality of sensor data collection, under predetermined project constraints, primarily the number of available sensor quantity and installation locations.

1 INTRODUCTION

In response to the rising demand for a more efficient, systematically consistent bridge integrity assurance approach, SHM was previously proposed in the field of civil infrastructure and mainly developed in bridge health monitoring (Aktan et al., 2001, Bui and De Roeck, 2012, Guidorzi et al., 2014, Bassoli et al., 2015, Saisi et al., 2018, Xin et al., 2022). The health monitoring of concrete bridges is commonly achieved through the employment of advanced sensors and intricate instrumentation for data acquisition to anticipate potential issues and detect structural damages. Being a source of instantaneous information on the structure, SHM allows bridge owners to access immediate structural assessments and timely responses when necessary. It allows for immediate maintenance responses with greater cost savings to be conducted before adverse changes in the structure. Ideally, to obtain information that is most representative of the dynamic characteristics of the bridge, the structure should be heavily populated with information-acquiring sensors to be able to extract as much data regarding the existing state of the structure. However, due to the costs and installation constraints for sensor technologies, the feasible number of sensors for installation on any single bridge for SHM is often limited (Li et al., 2012b, Pozo et al., 2021, Hassani and Dackermann, 2023). The typical installation of the wireless sensors was a result of the experience and knowledge of the installation team (Barthorpe and Worden, 2020). Nonetheless, as structures have grown in complexity, the problem of sensor placement has become a formalised one with the aim of achieving a balance between cost and the quality of information gathered by the sensors.

Sensor configuration, also known as sensor placement or deployment, constitutes the foundational process in establishing sensor networks for monitoring systems. OSP plays a critical role in elevating overall system performance, enabling optimal system utilisation, minimising downtime, and mitigating catastrophic failures. It is crucial to strategically position sensors to avoid incomplete information capture, such as inadequate modal data, which could compromise the precision of structural monitoring. Customising sensor configuration to suit the unique

DOI: 10.1201/9781003483755-289

requirements of each monitored system remains paramount. While engineering judgement often guides sensor placements, various computational methods have emerged to support OSP and streamline sensor deployments. The aim of OSP techniques is to achieve three key objectives: (i) minimise the number of sensors necessary, (ii) enhance system accuracy, and (iii) deliver a robust and optimal design. The overarching aim of OSP is to deliver precise data for potential issue and damage detection while simultaneously minimising sensor usage and ensuring comprehensive remote monitoring capabilities (Kralovec and Schagerl, 2020). Of the various research in OSP, the EFI is arguably the most adopted optimisation algorithms in the SHM of bridge structures (Friswell and Castro-Triguero, 2015, Demirlioglu et al., 2022, Hassani and Dackermann, 2023). The EFI method seeks the optimal set of degrees of freedom (DOFs) to place the sensors among all the candidate locations on the structure (Kammer, 1991). The user provides the candidate measurement locations. The optimal sensor configuration is determined based on the principle of linear independence of the mode shapes.

2 THEORETICAL BACKGROUND

The aim of EFI is to locate the most significant DOFs that accurately represent and communicate structural instability due to joint displacements. The determination of DOFs at joints is predicated on their potential for independent movements or rotations—essentially, the count of available directions in which these joints within a system can induce displacement. Consequently, these DOFs present favourable opportunities for the placement of sensors aimed at gathering data pertinent to structural damage detection. This is when the DOFs are deemed to provide the greatest amount of information about the structure. The linear independence of collected sensor data can be described as the minimisation of information redundancy and is an important quality indicator of EFI (Kim et al., 2018). Linear independence provides a concise set of unique displacements, which best represent the bridge's structural behavior. In structural dynamic applications, mode shapes refer to the characteristic patterns of vibration or deformation that a structure exhibits when subjected to dynamic loading. By iteratively deleting DOFs, which contributed the least linear independence from the mode shape matrix, EFI allows sensors at remaining candidate installation locations to collect the most significant structural responses. In other words, the errors between estimated mode shapes are minimised compared to the actual mode shapes (Kammer, 1991). This error is represented by the covariance matrix P and is displayed in E, q (1), where E is the expected value, q is the measure of modal displacement, andq' is the estimated modal displacement.

$$P = E\left[(q - q')(q - q')^T\right] = FIM^{-1} \tag{1}$$

The inverse of this covariance matrix P is the fisher information matrix (FIM), which is derived in E, q (5). FIM quantifies the amount of information that an observed set of data carries about the unknown parameters. In practice, Eghtesadi and McAuley (2016) identify the FIM as a summary of the potential impacts of model parameters on model predictions and have widely adopted it for the ranking of model parameters. Maximisation of FIM signifies greater information or precision about the parameters, indicating that slight changes in those parameters would significantly impact the likelihood of observing the given data. In other words, maximisation of FIM serves as a criterion for optimising sensor placement to ensure accurate parameter estimation or model identification. Hence, the determinant of the covariance matrix P can be minimised when the determinant of the FIM is maximised. The FIM is a product of the true mode shapes as shown in Φ_s and its transpose as shown in E, q (2).

$$FIM = \Phi_s^T \Phi_s \tag{2}$$

The EFI method begins with an initial placement of sensors determined by modal kinetic energy distribution at each candidate position towards the targeted mode shapes, as shown in E, q (3),

$$KE_{in} = \Phi_{in} \sum_j M_{ij} \Phi_{jn} \tag{3}$$

where for the n^{th} mode shape, KE_{in} is the kinetic energy for the i^{th} DOF, Φ_{in} and Φ_{jn} are the i^{th} and j^{th} coefficient of the mass matrix, and M_{ij} is the $i \times j$ term in the FE method mass matrix of the structure (Kammer, 1991). The mass matrix captures the distribution of mass within a structure or mechanical system and describes how this mass is related to the accelerations experienced by the system when subjected to external forces. It quantifies the inertia effects within the system, linking the accelerations of each DOF to the forces acting on those DOFs, considering the mass distribution and its influence on the dynamic behavior of the system. The contribution to kinetic energy at each location indicates the sensor's ability to retain structural dynamic information even where sensor noise is present (Heo et al., 1997). Thus, by initially ranking the candidate sensor location from the results of the kinetic energy distribution, the initial collection of sensor locations should yield greater resilience against sensor noise. The sensor output defined by is shown in E, q (4), where u_s is the sensor output and N is the Gaussian white noise vector with variance ${\Psi_0}^2$. The covariance matrix P can also be rewritten in the form of E, q (5) using the mode shape matrix and the white noise variance

$$u_s = \Phi_s q + N \tag{4}$$

$$P = [\Phi_S^T (\Psi_0^2)^{-1} \Phi_S]^{-1} = FIM^{-1} \tag{5}$$

In each iteration of the EFI, the independence distribution vector E_D is determined based on E, q (6), where Ψ_A and λ are the eigenvector and eigenvalue for the contribution of each DOF, respectively (Chai et al., 2022). The contribution of the i^{th} candidate sensor location to the FIM is determined by the i^{th} diagonal in E_D. The candidate sensor location with the least contribution to the EFI is removed. The process is continued until the target number of sensor locations is attained.

$$E_D = \Phi \Psi_A \lambda^{-1} (\Phi \Psi_A)^{-1} = \Phi [\Phi^T \Phi]^{-1} \Phi^T \tag{6}$$

The EFI method underwent validation through a trial conducted on a finite element (FE) model representing a space station (Kammer, 1991). Targeting the first 15 bending modes, the MATLAB implementation of the EFI process identified 70 sensor locations out of 187 candidates, achieving the desired mode shapes within 7 iterations. To ensure the validity of the EFI approach in this context, the FIM determinant was employed as a metric to assess the system's linear independence. Additionally, a comparative analysis was established, utilising sensor placement based solely on kinetic energy locations as a reference. Upon meticulous examination of the outcomes, it was observed that the EFI method yielded the largest determinant of the truncated FIM and demonstrated a condition number approaching 1, indicating a notably high level of linear independence. Moreover, the EFI approach exhibited superior computational efficiency compared to other sensor placement methods, primarily due to its ability to eliminate redundant sensors in each iteration, as highlighted by Kammer in 1991. Despite its initial design and verification within aerospace structures, this methodology has found widespread adoption in civil engineering applications, particularly in bridge infrastructure, owing to its demonstrated reliability (Li et al., 2012a, Sunca et al., 2021).

3 CASE STUDY IMPLEMENTATION

To provide a first glimpse into these questions, a numerical study has been carried out. For this purpose, Figure 1 shows a five-span SuperTee case study bridge situated over the water course located in Melbourne, Australia. A three-dimensional (3D) finite element model of the bridge was generated based on structural drawings and site observations using ANSYS. The employment of this modelling software is commonly accepted for FEM purposes (Lurie et al., 2018, Pachón et al., 2020, Hassani and Dackermann, 2023). The required modal information was extracted

from the numerical model to provide data for OSP analysis. The EFI method is adopted as the OSP algorithm and applied to determine 10 sensor locations with six target modes.



Figure 1. Five-span SuperTee bridge.

Figure 2 shows the typical cross-section details adopted for this study, which are verified according to available structural drawings.

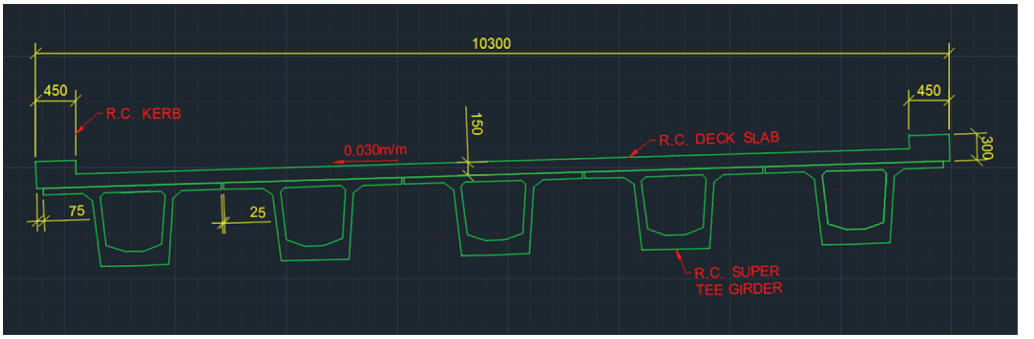


Figure 2. Typical bridge cross-section.

The bridge is accurately represented as a simply supported structure, with restraints positioned at the center edges of the super tee girders. The restraint configuration follows a pin-roller setup: specifically, the five nodes at the -x end are fixed in displacement across all three axes, while the five nodes at the +x end are constrained solely in displacement along the y- and z-axes. In its entirety, the adopted bridge model comprises 9,418 nodes and 5,258 elements. Each node encompasses three DOFs, enabling translation along the x-, y-, and z-axes, culminating in a total of 28,254 DOFs for the entire structure. The modal analysis is performed with the materials and geometry finalised, generating the first 4 mode shapes, shown in Figure 3. The displacements for each node in the x-, y- and z-directions are then compiled constructing the mode shape matrix φ, resulting in a 28,254x6 matrix. On the other hand, the 28,254x28,254 mass matrix M is determined by ANSYS based on the material and geometrical parameters given and could be only extracted through ANSYS scripting. The ANSYS model is also validated against the historical natural frequency measurements, the primary mode shape has been deemed to be mode 1, based on the participation factor solver embedded in ANSYS, the effective mass ratio is at 83% out of the total mass. This reflects the mass matrix is relevant to the field conditions.

The algorithm adopted in this study to implement the EFI on the bridge model follows E,q 2 and 6. The function of the initial EFI algorithm is outlined as follows: 1.import the mode shape matrix, 2.determine and record the initial independence distribution vector E_D using the complete mode shape matrix, 3. determine and record the initial determinant of the FIM using the complete mode shape matrix, and 4. perform the iterative process to delete candidate sensor locations. This iterative process includes: a. determine the lowest diagonal from the E_D, b. record, then delete the candidate sensor location with the lowest diagonal, and c. modify

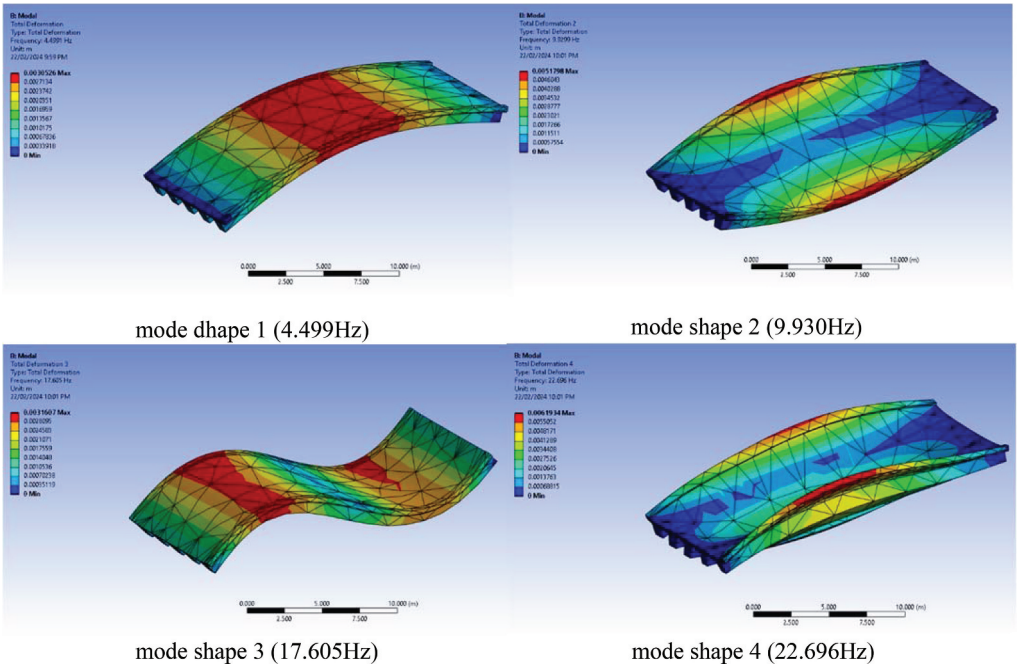


Figure 3. The first 4 mode shapes.

the mode shape matrix and calculate the new E_D and the new determinant of the FIM. The algorithm requires the mode shape matrix as input and returns the candidate sensor locations in order of deletion and the corresponding determinant of the FIM of the remaining sensor locations. Research on any existing EFI algorithm available for use prior to developing a novel MATLAB program. However, the search found that no EFI algorithm had been yet made available publicly and a new EFI algorithm was made specifically for this study. The algorithm executes its functions as intended and runs for about 4 hours for the 9,418 candidate sensor locations. Although there are 28,254 DOFs, in each iteration, the algorithm removes all the DOFs associated with the node to be deleted, reducing the number of iterations required.

4 RESULTS DISCUSSION

The developed EFI algorithm successfully truncating the list of candidate sensor locations until the desired 10 optimal locations are reached as shown in Figure 5, nine sensor locations are presented on the kerb and one at the bottom of the bridge girder.

Figure 4 displays a portion of the truncated list along with each DOF's corresponding contribution to the FIM determinant vector for the EFI. To simulate the feasibility of installation and operation on an actual bridge, only sensors located on the roadway of the bridge are selected for placement. Moreover, the faded circles indicate that the sensors are hidden from the view, located either under or on the side of the bridge deck. Additionally, the determinants of the FIM and the KE at each iteration for EFI arE Recorded And Then Plotted As Shown In Figure 6 and Figure 7 respectively. As shown in Figure 6, a comparison plot of FIM determinant derived from the case study EFI application is drawn against the original trend reported by Kammer (1991). As sensors are deleted, the FIM determinant trend follows the exponential decrease closely to the original study.

In addition, the graphical representation in Figure 7 exhibits the comparison between the kinetic energy (KE) derived from the EFI method alongside the original trend reported by

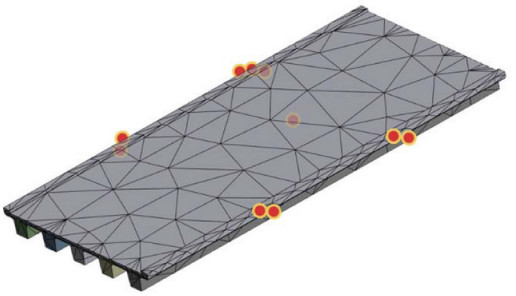


Figure 4. EFI identified sensor locations.

	A	B	C	D	E	F
1	Removed sensors	|FIM|				
9391	7574	1.51751E-11				
9392	1027	1.24856E-11				
9393	8541	1.03596E-11				
9394	8663	8.20842E-12				
9395	7601	6.39005E-12				
9396	815	4.75972E-12				
9397	1549	3.8455E-12				
9398	8542	3.10972E-12				
9399	1009	2.33558E-12				
9400	780	1.67693E-12				
9401	7712	1.22514E-12				
9402	7780	9.63016E-13				
9403	783	6.39872E-13				
9404	1006	3.93857E-13				
9405	8700	2.67123E-13				
9406	7723	1.942E-13				
9407	7577	1.26755E-13				
9408	7604	7.09861E-14				
9409	7758	3.5887E-14	Valid 10 sensors below			
9410	1019	2.3069E-14	OK			
9411	133	1.2194E-14	OK			
9412	7688	6.87845E-15	OK			
9413	7759	2.36841E-15	OK			
9414	7580	1.04657E-15	OK			
9415	8703	3.58021E-16	OK			
9416	7607	1.01428E-16	OK		Location	
9417	1030	8.32554E-19	OK		Roadway	
9418	7677	1.03327E-22	OK		Kerb	
9419	1016	1.87161E-69	OK		Girder	

Figure 5. EFI identified sensor ranking.

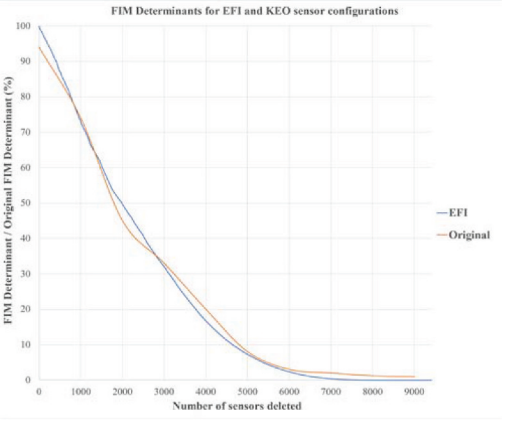


Figure 6. EFI FIM determinant retention.

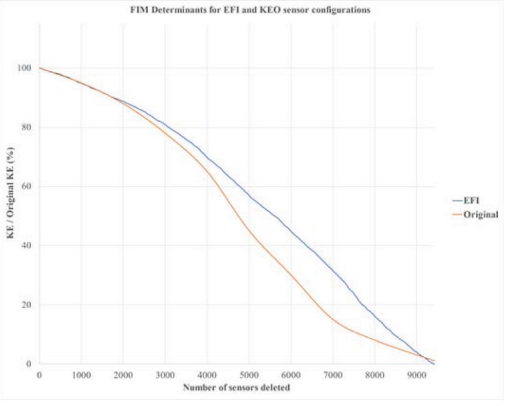


Figure 7. EFI KE retention.

(Heo et al., 1997). The original KE trend illustrates an almost linear correlation between the reduction in KE and the quantity of removed sensors. Despite a slight overall increase, the EFI case study application demonstrates a proportionate decrease in KE, mirroring the original linear trend while exhibiting a slight deviation over the entire plot. The EFI configuration shows a proportionate decrease in KE as a greater number of DOFs removed, suggesting its capability to retain sufficient KE along iterations. It is then practical to expect that adopting x% of considered sensor locations should retain at least x% of the total system kinetic energy. Likewise, to obtain the greatest KE in the system requires adopting as many sensors as possible. Yet, measuring KE could be argued as a better indicator of the accuracy of the adopted sensor configuration. Based on these findings, it can be argued that the implementation of the EFI method on the simplified reinforced concrete bridge model was successful as it follows the expectations listed in available studies.

5 CONCLUSIONS

In conclusion, the instrumentation of efficient and effective SHM systems on concrete bridges is crucial for ensuring the safety and longevity of these infrastructure assets. By adopting the EFI optimisation method, sensors can be strategically placed in key locations, ensuring the

accuracy of structural displacement measurements with a minimal number of sensors. This ensures bridge asset owners respond to sudden damages and potential failure in a timely manner though continuous bridge health monitoring. The development of a streamlined SHM system for concrete bridges, focusing on remote monitoring through optimal sensor placement and instrumentation methodologies, is of paramount importance. In this case-study, the adopted EFI method accurately predicted both the decreasing trend of FIM determinants and retained kinetic energy along with the iterative sensor deletion process, in close similarity to the previous studies. As the result, this system is expected to provide precise and reliable monitoring capabilities once sensors are correctly installed accordingly. In future, by leveraging advanced analytics and machine learning algorithms, the collected data could be analyzed to detect anomalies and deviations from expected behavior.

Overall, the development trial of an optimised SHM system with OSP for concrete bridges, supported by the successful implementation of the EFI method is a significant step towards ensuring the safety, longevity, and cost-effective maintenance of bridge infrastructure. By continuously monitoring the structural behavior of bridges, potential issues can be identified early on, leading to timely intervention. Ultimately, this will enhance the overall safety and performance of concrete bridges for the future.

ACKNOWLEDGMENT

The support and sponsorship of SmartCrete CRC under the project entitled '21.PP.0112 - Digital twin of reinforced concrete infrastructure for intelligent asset management' is acknowledged.

REFERENCES

Aktan, E., Chase, S., Inman, D. & Pines, D. Monitoring and managing the health of infrastructure systems. Proceedings of the 2001 SPIE conference on health monitoring of highway transportation infrastructure, 2001. Citeseer.

Barthorpe, R. J. & Worden, K. 2020. Emerging trends in optimal structural health monitoring system design: From sensor placement to system evaluation. *Journal of Sensor and Actuator Networks*, 9, 31.

Bassoli, E., Vincenzi, L., Bovo, M. & Mazzotti, C. Dynamic identification of an ancient masonry bell tower using a MEMS-based acquisition system. 2015 IEEE Workshop on Environmental, Energy, and Structural Monitoring Systems (EESMS) Proceedings, 2015. IEEE, 226–231.

Bui, T. & De Roeck, G. Design of a permanent structural health monitoring system on the Guadalquivir rail bridge based on baseline ambient vibration testing and optimal sensor placement. Proceedings of International Conference on Advances in Computational Mechanics, 2012. 967–981.

Chai, W., Yang, Y., Yu, H., Yang, F. & Yang, Z. 2022. Optimal sensor placement of bridge structure based on sensitivity-effective independence method. *IET circuits, devices & systems*, 16, 125–135.

Demirlioglu, K., Gonen, S. & Erduran, E. On the Selection of Mode Shapes Used in Optimal Sensor Placement. Sensors and Instrumentation, Aircraft/Aerospace and Dynamic Environments Testing, Volume 7: Proceedings of the 40th IMAC, A Conference and Exposition on Structural Dynamics 2022, 2022. Springer, 85–92.

Eghtesadi, Z. & Mcauley, K. B. 2016. Mean-squared-error-based method for parameter ranking and selection with noninvertible fisher information matrix. *AIChE Journal*, 62, 1112–1125.

Friswell, M. I. & Castro-Triguero, R. 2015. Clustering of sensor locations using the effective independence method. *AIAA journal*, 53, 1388–1391.

Guidorzi, R., Diversi, R., Vincenzi, L., Mazzotti, C. & Simioli, V. 2014. Structural monitoring of a tower by means of MEMS-based sensing and enhanced autoregressive models. *European Journal of Control*, 20, 4–13.

Hassani, S. & Dackermann, U. 2023. A Systematic Review of Optimization Algorithms for Structural Health Monitoring and Optimal Sensor Placement. *Sensors*, 23, 3293.

Heo, G., Wang, M. L. & Satpathi, D. 1997. Optimal transducer placement for health monitoring of long span bridge. *Soil dynamics and earthquake engineering (1984)*, 16, 495–502.

Kammer, D. C. 1991. Sensor placement for on-orbit modal identification and correlation of large space structures. *Journal of Guidance, Control, and Dynamics*, 14, 251–259.

Kim, T., Youn, B. D. & Oh, H. 2018. Development of a stochastic effective independence (SEFI) method for optimal sensor placement under uncertainty. *Mechanical Systems and Signal Processing*, 111, 615–627.

Kralovec, C. & Schagerl, M. 2020. Review of structural health monitoring methods regarding a multi-sensor approach for damage assessment of metal and composite structures. *Sensors*, 20, 826.

Li, B., Li, D., Zhao, X. & Ou, J. 2012a. Optimal sensor placement in health monitoring of suspension bridge. *Science China. Technological sciences*, 55, 2039–2047.

Li, I., Kumar, A., Beard, S. J. & Zhang, D. C. State-of-the-art pipeline structural health monitoring systems. SENSORS, 2012 IEEE, 2012b. IEEE, 1–4.

Lurie, S., Solyaev, Y., Rabinskiy, L., Polyakov, P. & Sevostianov, I. 2018. Mechanical behavior of porous Si 3 N 4 ceramics manufactured with 3D printing technology. *Journal of materials science*, 53, 4796–4805.

Pachón, P., Infantes, M., Cámara, M., Compán, V., García-Macías, E., Friswell, M. I. & Castro-Triguero, R. 2020. Evaluation of optimal sensor placement algorithms for the Structural Health Monitoring of architectural heritage. Application to the Monastery of San Jerónimo de Buenavista (Seville, Spain). *Engineering Structures*, 202, 109843.

Pozo, F., Tibaduiza, D. A. & Vidal, Y. 2021. Sensors for structural health monitoring and condition monitoring. MDPI.

Saisi, A., Gentile, C. & Ruccolo, A. 2018. Continuous monitoring of a challenging heritage tower in Monza, Italy. *Journal of Civil Structural Health Monitoring*, 8, 77–90.

Sunca, F., Okur, F. Y., Altunişik, A. C. & Kahya, V. 2021. Optimal sensor placement for laminated composite and steel cantilever beams by the effective independence method. *Structural Engineering International*, 31, 85–92.

Xin, J., Jiang, Y., Zhou, J., Peng, L., Liu, S. & Tang, Q. 2022. Bridge deformation prediction based on SHM data using improved VMD and conditional KDE. *Engineering Structures*, 261, 114285.

Bridge Maintenance, Safety, Management, Digitalization and Sustainability – Jensen, Frangopol & Schmidt (eds)
© 2024 The Author(s), ISBN 978-1-032-77040-6
Open Access: www.taylorfrancis.com, CC BY-NC-ND 4.0 license

Recent studies on the dynamic behaviour of various bridges in Spain

J.A. López-Aragón
Department of Continuum Mechanics and Theory of Structures, Universidad Politécnica de Madrid, Madrid, Spain
Ministry for Transport and Sustainable Mobility, Madrid, Spain

M.A. Astiz
Department of Continuum Mechanics and Theory of Structures, Universidad Politécnica de Madrid, Madrid, Spain
Carlos Fernández Casado, S.L., Madrid, Spain

ABSTRACT: This paper summarises the latest work carried out by the authors on the dynamic behaviour of various structures in Spain. After briefly reviewing the state-of-the-art on the subject, the description of the most relevant structures that are object of the study is included, a road and a railway bridge, as well as the installed monitoring and the dynamic analysis carried out. As most relevant results, the main conclusions for the road structure regarding the evolution over time of the dynamic parameters are presented, as well as the improvements in the calculation of the modal damping ratio. In this last case, the results obtained by applying different calculation methods are also shown, including an alternative methodology based on the reduction of the spectrum, whose main advantage is that it does not require the use of filters in multiple-degree-of-freedom systems, which contributes to reduce perturbations in the results.

1 INTRODUCTION

Technological evolution in recent years has made possible the extension of automatic structural health monitoring (SHM) systems for bridges, where dynamic parameters can be included as reference thresholds. However, given the singularities of bridges, the conclusions obtained in each case are not necessarily generalizable to similar cases. For this reason, academic studies carried out on real structures are of great interest, such as the two cases included in this communication: one road bridge, which is a long span metal arch, and another railway bridge, which is a continuous concrete girder.

Likewise, the studies carried out to date have shown the great dependence that exists in the case of the modal damping ratio on the calculation method. This paper summarises the new theoretical studies carried out in this regard, and proposes an alternative calculation method based on the reduction of the spectrum, thus minimizing the introduction of perturbations in the results. The results obtained in their application to one of the real structures are also included.

2 MAIN REFERENCES

Among the main references on the analysis of the dynamic behaviour of real structures, we can mention the studies carried out on the Europa Bridge (Austria), where the correlation between the first natural frequency and the ambient temperature was observed, as well as the

DOI: 10.1201/9781003483755-290

convenience to introduce corrections due to additional moving masses, which allowed the establishment of thresholds that could be used in an SHM system (Wenzel 2009); the work carried out by Magalhães, Cunha and Caetano in the monitoring of the Infante Don Enrique bridge in Porto (Portugal), which analysed the evolution over time of the dynamic parameters under the effect of environmental variables, such as temperature and recorded accelerations, which also made it possible to set thresholds for be used in an SHM system (Magalhães et al. 2008, 2009 and 2012); the analysis carried out by Gentile and Saisi on the evolution of the historic bridge of Paderno (Italy), where the relationship between the values of eigenfrequencies and changes in excitation (Gentile & Saisi 2010); the studies carried out by Soria, Díaz, García-Palacios and Ibán on a pedestrian walkway in Valladolid (Spain), which confirmed the great dependence of the modal parameters on temperature and that, once corrected, could be taken as a reference in a SHM system (Soria et al. 2016, Soria 2019); or the work carried out by Astiz on the dynamic behaviour of the cable stays of the Waterford Bridge (Ireland), in which it could be seen that the maximum accelerations in the cables were not due to traffic, but to the effect of wind (Astiz 2016).



Figure 1. Structures under study: E-1 (left) and E-2 (right) (Spanish Ministry for Transport and Sustainable Mobility, DGC and Adif).

Likewise, with regard to the possible identification of damage through variations in the dynamic behaviour of structures, the scale test carried out by Kölling, Reskin and Sargsyan can be mentioned, which demonstrated the appearance of new natural frequencies in the damaged structure, a reduction in the value of the main natural frequency and relevant modifications in the value of the modal damping factor (Kölling 2014); as well as the study carried out on the Regau Bridge (Austria), which showed a significant reduction in the frequency amplitude and a notable increase in the damping factor (Wenzel 2009).

Finally, in relation to the problem of the practical calculation of the modal damping ratio, the studies referenced by Wenzel on the Berlin Bridge in Halle (Germany) are of interest, where the disparity of results according to the calculation methods that were used (logarithmic decrement, adjustment to the theoretical curve and RDT) were revealed; as well as on the Regau Bridge (Austria), mentioned above, which also showed important differences both when the bandwidth method was used on the signal spectrum and depending on the type of filter.

3 STRUCTURES UNDER STUDY AND DYNAMIC ANALYSIS

3.1 *Description of the structures*

The objective of this study was the analysis of the experimental data recorded after the traffic opening of various structures, although this communication is exclusively focused on a road and a railway bridge, which are shown in Figure 1 (López Aragón & Astiz 2023).

The first of the structures is the road bridge known as "Arcos de Alconétar" (hereinafter, structure E-1). This viaduct is located on the A-66 highway, belonging to the State Highway Network in Spain, and allows it to cross the Tagus River.

This structure is composed of two twin structures 400 m in length, whose main spans are metal arches (spans of 220 m and 42.5 m rise) with an upper deck. Each of the arches is formed by two longitudinal pieces with a box section braced together. The deck, formed from a continuous section of composite steel–concrete structure, is simply supported on the metal pillars that rest on the arch and the reinforced concrete piers belonging to the access sections. The length of the spans, 26 m, is identical both in the access sections and in the main section. The steel used in the whole structure (arches, deck beams, and pillars on arches) is a weathering steel with improved resistance to atmospheric corrosion.

The second structure is the railway viaduct called "Arroyo del Valle" (hereinafter, structure E-2). This bridge is part of the Madrid – Segovia – Valladolid/Medina del Campo high-speed railway line, also in Spain.

The total length of the viaduct is 1755 m, divided into 2 extreme spans of 52.50 m and 25 intermediate spans of 66.00 m each. It is made up of a concrete box beam with a hollow box cross-section with a lower and upper slab and a variable depth between 3.30 m in the center of the span and 5.00 m in the pier support area. There are a total of 25 piers, with a hollow rectangular concrete box section. In addition, there is an ogival-type arch in the central area of the viaduct, formed by two semi-arches with a radius of curvature of 312.00 m and a hollow rectangular concrete box section so that the key of the arch materializes the fixed point of the structure, and both ends remain free.

3.2 *Monitoring*

In the case of structure E-1, the dynamic instrumentation was made up of 10 accelerometers (5 on each road), 2 anemometers and 2 vanes (on the left road). These accelerometers were located on each roadway as follows: three vertical accelerometers in the haunches of the arch (two in the south haunch and one in the north haunch) and two accelerometers in the key of the arch, one of them vertical and another transversal. The instrumentation was completed with a total of 37 thermometers and 2 laser distance meters to measure the movement of the expansion joints of the structure. The monitoring period in which there are dynamic records is between the months of March and September 2010.

In the case of structure E-2, the instrumentation that was implemented in the viaduct allowed the following variables to be controlled: pier movements, relative movements of pier/abutment– deck, accelerations due to centrifugal force and braking, vertical accelerations, wind speeds (gusts), train speeds, temperature and environmental conditions. For the study of dynamic behaviour, there were 15 accelerometers, 12 of which were vertical, 2 longitudinal and 1 transversal. The structure had this dynamic monitoring between the months of June 2008 and December 2009.

3.3 *Dynamic analysis*

Figure 2 shows an example of the type of dynamic analysis carried out in both structures. From the dynamic events recorded, the most representative ones during the monitoring period were selected (around 7% in both cases).

In each case, we started from the accelerograms of all the accelerometers (channels) corresponding to each event; sections of free vibrations were identified; analysis in the frequency domain was carried out, obtaining the eigenfrequencies; accelerograms corresponding to each natural frequency were filtered; and, finally, the modal damping factor associated with each natural frequency was obtained by applying different calculation methods. The whole obtained information was stored in a database.

Due to the typology of the E-2 structure, built mainly with concrete, accelerations were very reduced and the modal damping ratio was very high. This means that the entire structure was not excited by the passage of the moving load and gave rise to very short accelerograms, making it impossible to obtain precise values for both the natural frequencies and the modal damping ratios. Therefore, the rest of this communication will focus on the results obtained in the case of the E-1 structure.

4 EVOLUTION IN TIME OF THE DYNAMIC PARAMETERS

After the process indicated in the previous section, the study of the evolution of the dynamic parameters of the E-1 structure during the monitoring period was carried out (López-Aragón & Astiz 2014). In the case of the natural frequencies, a notable stability was observed, although certain variations occurred. In the case of the modal damping factor, although the results remained around certain values, greater variability was observed. In all cases, the possible relationship with other variables was studied: ambient temperature and arch

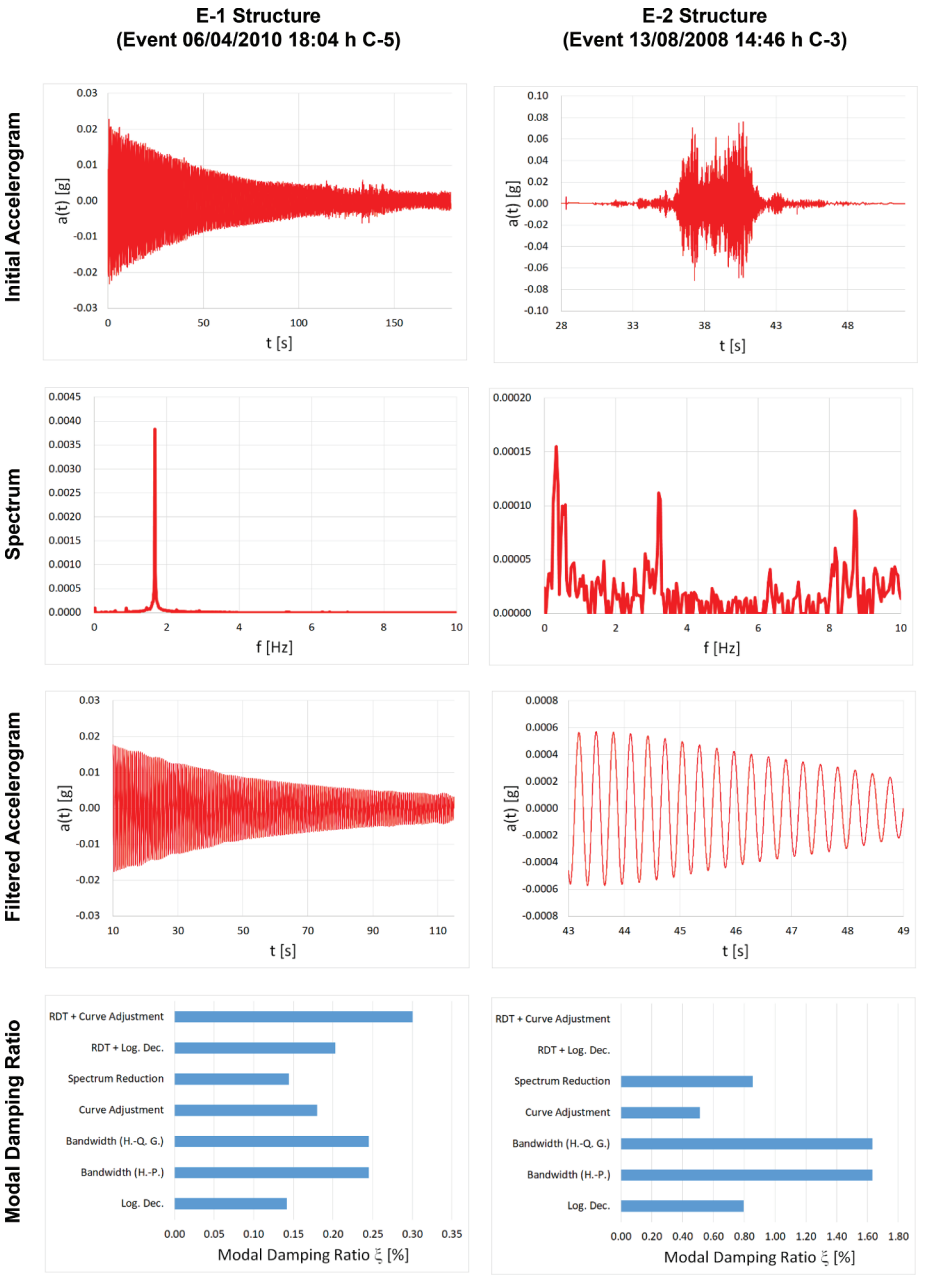


Figure 2. Example of the study of two accelerograms corresponding to structures E-1 and E-2.

temperature, average wind and maximum accelerations, both vertical and horizontal, since they represent the load to which the structure is subjected and, therefore, which resistant mechanisms are activated.

Table 1. E-1 Structure. Coefficients of determination for the mathematical models of the evolution of dynamic parameters.

	Coefficient of Determination (R^2)	
	Natural Frequency Model	Modal Damping Ratio Model
$f_{exp\ 1}$ = 0.396 Hz	0.66	0.30
$f_{exp\ 2}$ = 0.600 Hz	–	–
$f_{exp\ 3}$ = 0.878 Hz	0.58	0.04
$f_{exp\ 4}$ = 1.440 Hz	0.57	0.21
$f_{exp\ 5}$ = 1.674 Hz	0.24	0.30
$f_{exp\ 6}$ = 2.262 Hz	0.90	0.18
$f_{exp\ 7}$ = 3.018 Hz	–	–
$f_{exp\ 8}$ = 8.267 Hz	–	–

In the case of the natural frequencies, it was observed that there was an important relationship with the ambient temperature, which improved when the maximum accelerations were considered. However, practically no relationship with mean wind velocity was observed.

In the case of the modal damping ratio, the results –obtained using the logarithmic decrement method– showed a certain relationship with average wind velocity, which also improved when considering maximum accelerations. On the contrary, no relationship was observed with temperature, neither ambient nor arch.

For each natural frequency, when possible, a mathematical model was proposed that, taking into account these environmental variables, would allow correcting the values obtained for both the natural frequencies and the modal damping ratio. The results are summarised in Table 1. As it can be seen, the values of the coefficient of determination, R^2, are much higher in the case of the natural frequency models, even reaching 0.90. In them it was clearly seen that, when the temperature increases, a reduction in the value of the eigenfrequencies occurs. In the case of the modal damping ratio, the coefficients of determination are more reduced, and in some cases the behaviour is not clear, which may be due to the greater dispersion of the results.

In any case, the obtained results supported the possibility of incorporating dynamic parameters into a system for monitoring the structural health of this bridge, being able to set thresholds for them.

5 CALCULATION OF THE MODAL DAMPING RATIO

5.1 *General considerations*

As it was indicated in Section 2, several authors have warned about the variability of the damping factor ratios depending on the calculation method used. As an example, Table 2 shows the numerical results obtained for the accelerograms of the events shown in Figure 1. It can be seen that, in these specific examples, the damping values can even be doubled depending on the calculation method used. Therefore, it is important to know which calculation method for the modal damping factor is the one that is being used in SHM systems for bridges.

In addition, there are multiple variables that can influence the results, for example: in the logarithmic decrement method, the type of filter and the number of consecutive cycles that are considered; in the two formulations of the bandwidth method, it seems that the shape of the spectra has a lot of influence, especially if they show very sharp maxima; in the method of fitting to the theoretical curve, the discretization that is carried out to find the best fit; and in the random decrement technique (RDT), the duration set for the intervals and the threshold that is adopted. In conclusion, the used calculation methodology is a complex issue and has a great impact on the obtained results.

5.2 *Proposal for an alternative calculation method (Spectrum Reduction Method, SRM)*

To partially solve this problem, especially regarding to the disturbances introduced as a consequence of the application of the different filters, in the work carried out, it has been proposed an alternative method for the calculation of the modal damping ratio, based on the reduction of the signal spectrum (López-Aragón et al. 2024).

Table 2. E-1 and E-2 structures. Calculation of the modal damping ratio in two specific events applying various calculation methods.

	Modal Damping Ratio (%)	
Calculation Method	E-1 Structure (Event 06/04/2010 18:04 h C-5)	E-2 Structure (Event 13/08/2008 14:46 h C-3)
Logarithmic Decrement	0.142	0.795
Bandwidth (Half-Power)	0.245	1.631
Bandwidth (Half-Quadratic Gain)	0.245	1.630
Curve Adjustment	0.180	0.513
Spectrum Reduction	0.144	0.855
RDT + Log. Dec.	0.203	–
RDT + Curve Adjust.	0.300	–

As a summary, compared to the calculation of the modal damping ratio based on the study of the decrease in amplitude of the accelerogram in the time domain, this method is based on seeing how the Fourier transform of the original accelerogram decreases in the frequency domain, that is, its magnitude spectrum. To do this, the damping factor, ξ_k, for the desired natural frequency, f_k, is obtained from the following expression:

$$\xi_k = \frac{\ln\left(A_{k,q}/A_{k,q+n}\right)}{2\pi f_k \Delta t} \tag{1}$$

where $A_{k,q}$ y $A_{k,q+n}$ are the peak values of the spectrum for the k-th natural frequency in the initial spectrum section and in the last spectrum section, respectively; and Δt is the time distance between both spectrum sections.

The main advantage of this method is that it allows the study of multiple-degrees-of-freedom systems whose vibration modes are reasonably separated, which usually happens in bridges, without the need to apply filters to the initial signal to isolate each vibration mode.

As it can be seen in the reference where this method has been developed, the theoretical formulation does not restrict either the length of the spectrum sections or the number of separation cycles between them. However, the practical application suggests that, on the one hand, the sections must have sufficient length to adequately characterize the wave, that is, that the nature of the different excited natural frequencies is adequately manifested; and, on the other hand, the separation between the cycles must allow the damping of the structure to be appreciated in the free vibration regime. Likewise, to ensure that the vibration modes are reasonably separated, some prior knowledge of the structure is required.

Finally, it should be noted that, if damped free vibration does not predominate in the recorded accelerogram, this method would not be applicable, since the system would be excited by external forces and the formulation presented would not be applicable.

Both Figure 2 and Table 2 also include the values of the modal damping ratio obtained by applying the SRM methodology.

5.3 *Study on theoretical simulations*

To validate this method, the study was firstly carried out on several theoretical simulations, which modeled the behaviour of up to three superimposed waves, to which a random noise slightly higher than that expected from the measuring instruments was also added.

The average relative errors obtained through the study are shown in Table 3. It can be seen how the SRM method gave practically exact values (0.00%), followed by the logarithmic decrement (0.86%), the two formulations of the bandwidth (1.14% for half-power and 1.16% for half-quadratic), the two applications of the RDT method (2.15% combined with the logarithmic decrement and 3.06% combined with the curve adjustment) and, finally, the curve adjustment method (13.47%).

5.4 *Experimental analysis*

Likewise, the modal damping ratio of all the accelerograms corresponding to the dynamic events studied in the E-1 structure was recalculated by applying the same methods that were applied to the theoretical simulations.

Table 3. E-1 Structure. Average relative errors expected theoretically and recorded experimentally for the modal damping ratio.

Modal Damping Ratio Calculation Method	Averaged Relative Error (%)	
	Theoretical simulations	Registered Accelerograms
Logarithmic Decrement	0.86	–
Bandwidth (Half-Power)	1.14	428.38
Bandwidth (Half-Quadratic Gain)	1.16	336.71
Curve Adjustment	13.47	23.89
Spectrum Reduction	0.00	11.79
RDT + Log. Dec.	2.15	34.11
RDT + Curve Adjust.	3.06	81.52

In this case, those obtained using the logarithmic decrement method were adopted as reference values and the extent to which the results deviated by applying the rest of the methods was analysed. The results, which are shown in Table 3, show that the smallest differences were achieved with the SRM method proposed by the authors (11.79%), followed by the theoretical curve adjustment method (23.89%), RDT combined with logarithmic decrement (34.11%), RDT combined with curve adjustment (81.52%) and the two bandwidth formulations, the results of which were even several orders of magnitude higher (336.71% for half-quadratic gain and 428.38% for half-power).

It should be highlighted that the behaviour of the different calculation methods in the real accelerograms is quite different from when they were applied to the theoretical simulations, given that the variations are much higher, even of several orders of magnitude. This is especially relevant in the case of the two formulations based on the bandwidth method and, although more studies must be carried out in this regard, it seems to be related to the fact that the spectra are very sharply pointed in the case of this structure.

5.5 *Correlation between calculation methods*

In view of the clear dependence of the results on the calculation method adopted, another issue that was studied was the possibility of correlating the results obtained using two different calculation methods.

In that sense, it was noted that there was a great correlation between the results obtained through the SRM and the logarithmic decrement method (R^2=0.89) and, although smaller, also between the curve fitting method and the logarithmic decrement (R^2=0.65).

5.6 *Influence of the calculation methods in the damping predictive model*

Finally, another question that was studied is whether, as a consequence of the application of the other calculation methods, there was any significant change in the predictive model established for damping, the conclusions of which are summarized in Section 4. In this case,

although there could be some specific changes, both better and worse, in the study of the modal damping ratio corresponding to some of the eigenfrequencies, no significant changes were observed on average.

6 FUTURE STUDIES

As future studies, the following are proposed: the extension of the analysis of the behaviour of the dynamic parameters to the case of other real viaducts of different typologies; delve into the physical modelling of the correlations observed during the experimental analysis of the E-1 structure, especially between the eigenfrequencies and the temperature and the damping and the mean wind in the case of some of the eigenfrequencies; and, finally, carry out more studies on the variation of dynamic parameters as a consequence of the existence of damage to structures, both through the use of computational models, especially in the case of natural frequencies, and through use of scale tests, which would allow the study both in terms of the natural frequencies and the modal damping factor.

7 CONCLUSIONS

Throughout this paper some of the latest works carried out by the authors on the dynamic behaviour of various structures in Spain have been summarized, where the dynamic analysis of two real structures stands out, one road, which is a long span metal arch, and another railway, which is a continuous concrete girder.

From the point of view of the evolution over time of the dynamic parameters, it has been seen that, in the case of the road structure, it is possible to establish a model that considers several variables: temperature, the average wind and the maximum accelerations. In the case of the natural frequencies, very good correlations have been achieved taking into account the ambient temperature and the maximum accelerations, both vertical and transversal. In the case of the damping factor, although the correlations are smaller, a certain relationship with average wind velocity and maximum accelerations has also been observed.

Regarding the calculation of the modal damping ratio, the problems observed when applying the different calculation methods have been highlighted. As a consequence of this, an alternative calculation method proposed by the authors has been described, based on the reduction of the signal spectrum (Spectrum Reduction Method, SRM). The paper includes the most notable results of its application to both theoretical simulations and the experimental results recorded in the case of the road structure, which has given excellent results. Likewise, the possibility of correlating the results obtained between the logarithmic decrement and the SRM, as well as with the curve adjustment method, has been seen.

ACKNOWLEDGEMENTS

The authors wish to express their gratitude to the Spanish Ministry for Transport and Sustainable Mobility, particularly to the General Directorate of Roads (DGC) and the Administrator of Railway Infrastructures (ADIF), for facilitating access to the data of the monitored structures; to those responsible for Kinesia Data and IMC, for the necessary software for data processing; and to Ideam, for providing access to the computational model used during the construction of the E-1 structure.

REFERENCES

Astiz, M.A. 2016. Towards a standard policy for structural monitoring in cable-stayed bridges. In *Maintenance, Monitoring, Safety, Risk and Resilience of Bridges and Bridge Networks*. Boca Raton (FL, USA): CRC Press.

Gentile, C. & Saisi, A. 2010 Dynamic monitoring of the Paderno iron arch bridge (1889). In *Proceedings of the 6th International Conference on Arch Bridges (ARCH'10)*, *Fuzhou, China*, 2–4 October 2010.
Kölling, M., Resnik, B., Sargsyan, A. 2014. *Application of the Random Decrement Technique for Experimental Determination of Damping Parameters of Bearing Structures*. Berlin: BHS.
López-Aragón, J.A. & Astiz, M.A. 2014. An experimental analysis of the evolution of dynamic parameters of a long-span metal arch bridge. *Struct. Eng. Int*. 24 (1): 8–19.
López-Aragón, J.A. & Astiz, M.A. 2023. Some considerations about the incorporation of dynamic parameters in the structural health monitoring systems of bridges. *Appl. Sci*. 14: 33.
López-Aragón, J.A., Puchol, V. & Astiz, M.A. 2024, in press. Influence of the modal damping ratio calculation method in the analysis of dynamic events obtained in Structural Health Monitoring of bridges. *J. Civ. Struct. Health Monit*.
Magalhães, F., Cunha, A. & Caetano, E. 2008. Dynamic monitoring of a long span arch bridge. *Eng. Struct*. 30: 3034–3044.
Magalhães, F., Cunha, A. & Caetano, E. 2009. One-year dynamic monitoring of a bridge: Modal parameters tracking under the influence of environmental effects. In *Proceedings of the 4th International Conference on Structural Health Monitoring on Intelligent Infrastructure (SHMII-4)*, *Zurich (Switzerland)*, 22–24 July 2009.
Magalhães, F., Cunha, A. & Caetano, E. 2012. Vibration based structural health monitoring of an arch bridge: From automated OMA to damage detection. *Mech. Syst. Signal Process*. 28: 212–228.
Soria, J.M., Díaz, I.M., García-Palacios, J.H., Ibán, N. 2016. Vibration monitoring of a steel-plated stress-ribbon footbridge: Uncertainties in the modal estimation. *J. Bridge Eng*. 21: C5015002.
Soria, J.M. 2019. *Damage Identification and Condition Assessment of Civil Engineering Structures through Response Measurement*. Ph.D. Thesis, Madrid: Universidad Politécnica de Madrid.
Wenzel, H. 2009. *Health monitoring of bridges*. London: Wiley.

Bridge Maintenance, Safety, Management, Digitalization and Sustainability – Jensen, Frangopol & Schmidt (eds)
© 2024 The Author(s), ISBN 978-1-032-77040-6
Open Access: www.taylorfrancis.com, CC BY-NC-ND 4.0 license

Equivalent structural stress concentration factor for non-planar oblique butt joints

X. Wei & Q.L. Jia
The Department of Bridge Engineering, Southwest Jiaotong University, Chengdu, The PRC

ABSTRACT: Based on the finite element software ABAQUS, 135 non-planar oblique butt joint finite element models were established by considering different in-plane oblique angles and out-of-plane angles, aspect ratios, and stress ratios to investigate the equivalent structural stress concentration factor (ESSCF). The results show that the maximum ESSCF value only occurs at the obtuse angle point (hot point A1) of the weld toe on the concave side near the loading end and the obtuse angle point (hot point D1) on the convex side of the weld toe near the constraint end. As the out-of-plane angle increases, ESSCF at both points continues to grow at a nearly constant the in-plane oblique angle increases, the growth rate of ESSCF at hot point A1 gradually decreases, but the trend of ESSCF value change may increase or decrease; the change rate at hot point D1 remains almost constant, and the overall ESSCF decreases with an increase in in-plane inclination. As the stress ratio increases, ESSCF at hot point A1 continues to grow at a decreasing rate, while ESSCF at hot point D1 decreases at a decreasing rate. As the aspect ratio increases, ESSCF at hot point A1 continues to grow at an increasing rate, while ESSCF at hot point D1 decreases at an increasing rate. At the same time, the location of the maximum value tends to shift from hot point D1 to hot point A1 as the in-plane oblique angles, stress ratio, and aspect ratio increase but do not vary with changes in the out-of-plane angle. Finally, based on the ESSCF extraction results, formulas for calculating ESSCF at hot points A1 and D1 were obtained by LM-UGO fitting.

1 INSTRUCTIONS

With the innovative design of steel bridge structures, new and complex welded joints are being used in steel bridges, and their fatigue performance under long-term repeated loading deserves attention (Wei et al. 2017, 2018, Xiao et al. 2023). Non-planar oblique butt welded joints are commonly found in cable-girder anchorage structures of cable-stayed bridges, in which both oblique angle and out-of-plane angle exist between the two plates. The oblique angle can cause shear stresses at the weld toe, while the out-of-plane angles can cause bending stresses at the weld toe, both of which can affect the stress concentration at the weld toe, thereby affecting the fatigue life of the butt joint (Jie et al. 2017).

Including nominal stress method, hot spot stress method, notch stress method, and equivalent structural stress method, fatigue design and evaluation methods are recommended in the design standards, such as the International Institute of Welding (IIW 2000), the American Welding Society (AWS 2015), the American Petroleum Institute (API 2014), and the Eurocode 3 (CEN 2005). The equivalent structural stress method was proposed by Dong (2001) and used to predict the fatigue life of welded structures by constructing a master S-N curve based on structural stress. Unlike other stress methods, which rely on grid density for calculation (), the structural stress method is insensitive to the grid. It effectively converts the stress of complex three-dimensional regions of the structure into a two-dimensional crack problem (Kyuba et al. 2005). The equivalent structural stress is related to the structure's geometric

DOI: 10.1201/9781003483755-291

form, size, and weld toe position and is often obtained through finite element numerical simulation. The stress concentration degree of the structure can be quantified by the equivalent structural stress concentration factor (ESSCF).

Over the years, scholars have conducted much research on butt joints. Five types of specimens with different oblique butt-welding angles were used for the fatigue tests and subjected to fixed-directional loading to study the effect of oblique loading on the fatigue strength of butt-welded structures(Jen et al. 2008). Dong et al. (2019) evaluated the fatigue reliability of misaligned butt welded joints based on the structural hot spot stress method. Shen et al. (2019) derived the stress amplification factor considering the initial deformation effect of the thin plate based on the modified thick plate calculation formula. They compared the calculation results with traditional specifications. Su et al. (2020) studied the fatigue performance of the weathering steel Q345qNH butt welded joint without corrosion. The fatigue fracture mechanisms and the fatigue property evaluations of S355J2W steel butt-welded joints relieved welding residual stresses with and without welding reinforcement were systematically investigated by microstructure characterization and fatigue tests (Wang et al. 2023). At present, scholars have already done relatively complete research on butt joints, but there are still deficiencies in the study of non-planar oblique butt joints with both in-plane and out-of-plane angles.

This article establishes a finite element model of non-planar oblique butt joints using the ABAQUS software, analyzes the variation law of ESSCF at the weld toe with various parameters, and establishes a functional relationship for the ESSCF of non-planar oblique butt joints.

2 GEOMETRIC PARAMETERS

The geometric structure of a non-planar oblique butt joint is shown in Figure 1, where α is the oblique angle, γ is the out-of-plane angle, l is the distance from the obtuse-angle side weld toe to the edge of the test specimen, w is the plate width, and t is the plate thickness.

The oblique angle α and out-of-plane angle γ are the main research contents of this article. At the same time, the aspect ratio l/t and stress ratio σ/σ_0 are also the main factors affecting the ESSCF. This article takes the following values for each dimensionless parameter: α is taken as 30, 50, 70, γ is taken as 0, 4, 8, l/t is taken as 4, 6, 8, σ/σ_0 is taken as 0.5, 0.75, 1.0, 1.25, 1.5. The average stress σ_0 is taken as 100 MPa. A total of 135 models are established for parameterized research. In this study, the plate thickness t is 16 mm, and the plate width w is 50 mm.

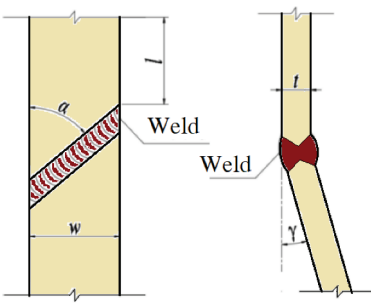


Figure 1. Non-planar oblique butt joint.

Many fatigue test results show that fatigue cracks in welded joints often start at the weld toe, and due to the relatively weak constraints at the structural boundary, cracks often originate at the intersection of the weld toe and the structural boundary. Therefore, this article focuses on solving and analyzing the eight hot spots at the weld toe, as shown in Figure 2. The

concave side of the loading end is the weld toe A, the convex side is the weld toe B, and the concave side of the constrained end is the weld toe C. The convex side is the weld toe D. Hot-point 1 is the location where the angle between the weld toe line and the plate edge is obtuse, and hot-point 2 is the location where the angle between the weld toe line and the plate edge is acute. Points A1 represent the hot spot at the obtuse angle of the weld toe A.

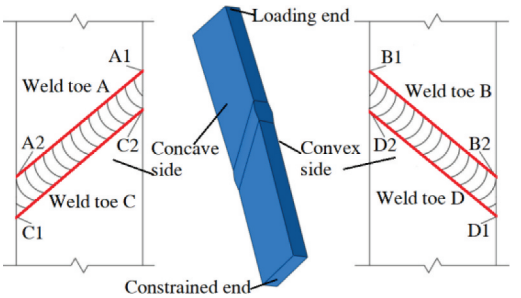


Figure 2. Hot-point in weld toe.

3 PARAMETRIC ANALYSIS OF ESSCF

3.1 *The definition of ESSCF*

According to the equivalent structural stress method, the stress in a welded joint can be decomposed into two parts, as shown in Figure 3. The first part of the stress is the structural stress that satisfies the equilibrium condition; the second part is called the notch stress.

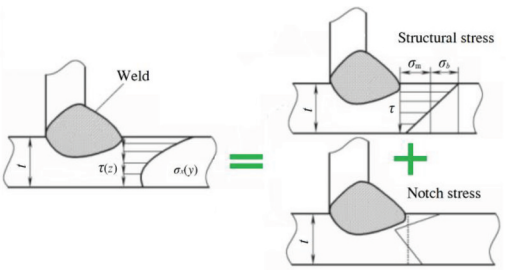


Figure 3. Structural stress and notch stress.

The structural stress, σ_s, is the sum of the membrane stress, σ_m, and the bending stress, σ_b. The membrane stress, σ_m, and bending stress, σ_b, within a section can be calculated using the following equations:

$$\sigma_m = \frac{1}{t}\int_{-t/2}^{t/2} \sigma_x(y)dy = \frac{f_y}{t} \tag{1}$$

$$\sigma_b = \frac{6}{t^2}\int_{-t/2}^{t/2} y\sigma_x(y)dy = \frac{6m_x}{t^2} \tag{2}$$

Where, t is the plate thickness; σ_x(y) is the distribution of structural stress along the plate thickness direction; f_y is the line force; m_x is the line moment.

After statistical analysis and fitting of a large number of experimental data, Dong defined the formula for equivalent structural stress range ΔS_s:

$$\Delta S_s = \frac{\Delta\sigma_s}{t^{(2-m)/2m} I(r)^{1/m}} \tag{3}$$

Where, m is the fatigue crack growth-related parameter obtained from experiments; $\Delta\sigma_s$ is the structural stress range; and I(r) is a dimensionless function of the load bending ratio r.

In this paper, the ESSCF is defined as the ratio of the equivalent structural stress S_s to the nominal stress σ_n.

$$ESCF = \frac{S_s}{\sigma_n} \tag{4}$$

Numerical analysis was conducted on non-planar oblique butt-welded joints, and the ESSCF for each hot spot at the weld toe were obtained according to Equation 4. The results showed that the maximum ESSCF occurred at points A1 or D1, which were located on the diagonal of the weld. As σ/σ_0, l/t, and α increased, the location of the maximum ESSCF shifted from point D1 to point A1. The location of the maximum ESSCF did not change with the change in γ. When γ=0, the ESSCF values at points A1 and D1 were the same.

3.2 *FE model of non-planar oblique butt joints*

Because the basis of structural stress is based on the equilibrium relationship, and the equilibrium relationship of force is insensitive to the number of nodes, the structural stress has the characteristic of grid insensitivity. The parameterized analysis model in this article adopts The C3D8R solid element in ABAQUS. In order to ensure the consistency of the number of structural stress samples extracted from each parametric model, the grid division is uniformly specified. The global element grid length is 5mm, the number of element divisions at the weld toe is 12, and the number of element divisions in the plate thickness direction is 4. The FE model of non-planar oblique butt joints is shown in Figure 4.

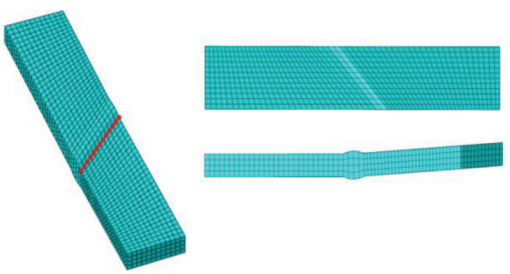


Figure 4. FE model of non-planar oblique butt joints.

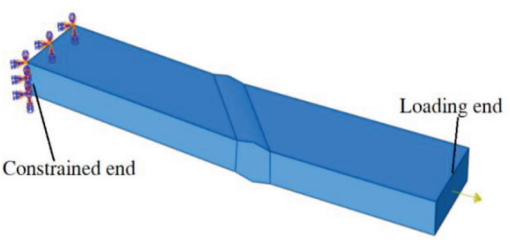


Figure 5. Loading and constrained condition.

One end of the model is the constrained end, and the other end is the loading end (Figure 5). The direction of the external load is consistent with the direction of the center line of the plate, acting on the center of the section. The degrees of freedom in all three directions of the constrained end are constrained.

3.3 *The influence of parameters on the ESSCF*

The variations in ESSCF at point A1 with different parameters are shown in Figure 6.

ESSCF at point A1 positively correlates with σ/σ_0, l/t, and γ. As σ/σ0 increases, the growth rate of ESSCF gradually decreases. With the increase of l/t, the growth rate of ESSCF gradually increases. As γ increases, ESSCF shows an approximately linear growth. As α increases, the growth rate of ESSCF gradually decreases. When α increases from 30 to 50, ESSCF increases accordingly; when α increases from 50 to 70, the change in ESSCF is relatively small and may slightly increase or decrease under different combinations of the other parameters.

The variations in ESSCF at point 4-1 with different parameters are shown in Figure 7.

It can be seen from Figure 7 that ESSCF at point D1 is positively correlated to γ. At the same time, the increase ratio of ESSCF increases with γ. ESSCF is negatively correlated to σ/σ_0 and l/t. With σ/σ_0 increasing, the rate of ESSCF decrease gradually slows down; with l/t increasing, the rate of ESSCF decreases gradually increases. As the increase of α, the rate of ESSCF change is almost constant, and ESSCF is approximately linearly changing. ESSCF decreases with the increase of α in different σ/σ_0 and l/t. When γ=0, ESSCF increases with the increase of α. When γ=4 or 8, ESSCF decreases with the increase of α.

4 CALCULATION FORMULAS OF ESSCF

4.1 *LM-UGO algorithm*

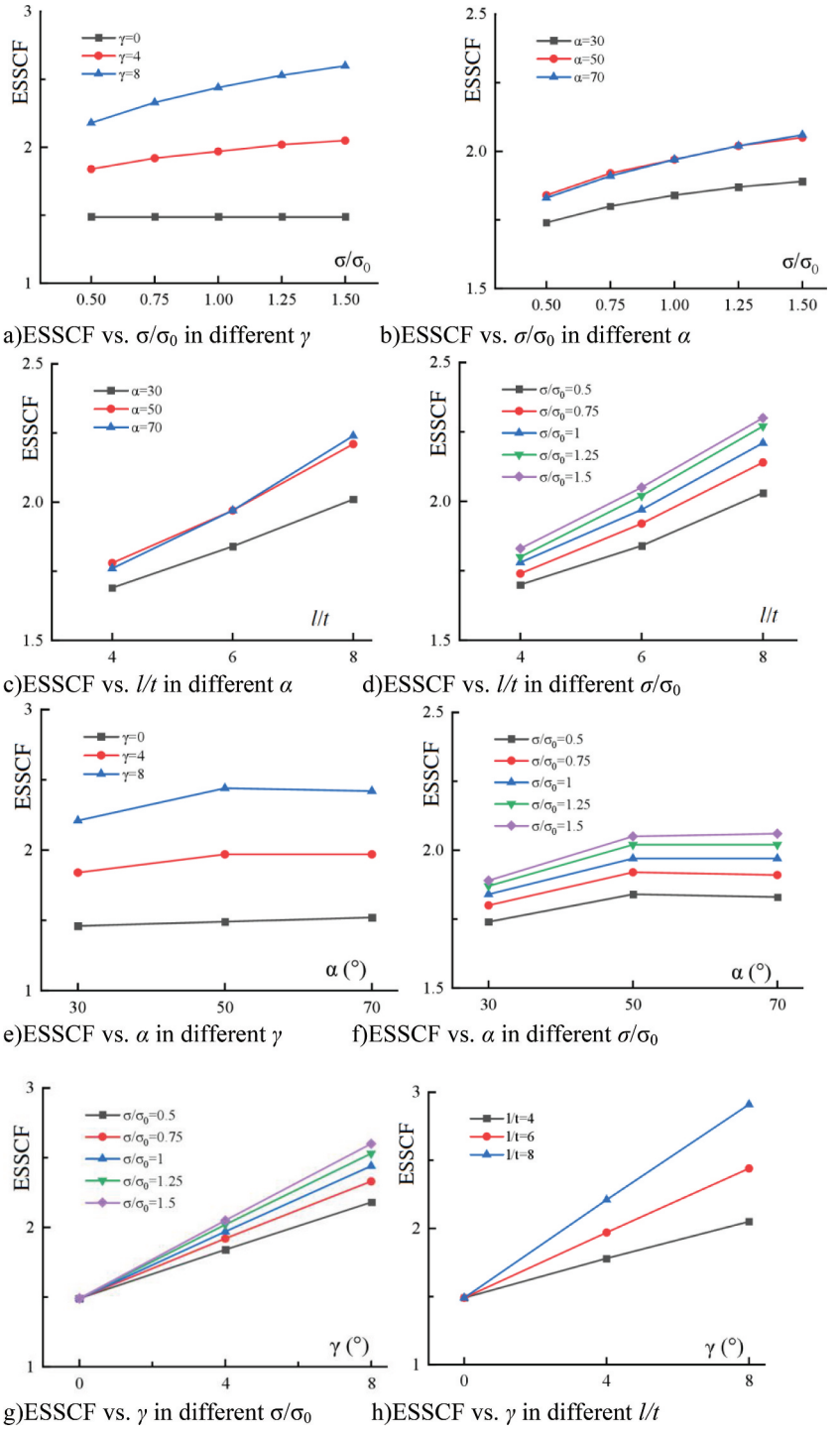
The most commonly used algorithms in nonlinear regression are the Marquardt method, Simplex algorithm, Simple surface climbing method, etc. However, regardless of the method, the user must provide appropriate initial parameter values. It is difficult to converge if the initial values are not set correctly. Providing appropriate initial parameter values in practical applications is pretty challenging, especially in cases with many parameters, and the difficulty increases sharply. However, the Levenberg-Marquardt algorithm and universal global optimization(LM-UGO) can solve this problem (Marquardt 1963). The most significant feature of this method is that it does not require users to provide initial values. With its robust optimization and error tolerance ability, in most cases, the correct results can be obtained starting with any random initial value, improving the solve rate and reducing the threshold for using it. Therefore, the LM-UGO algorithm was chosen to use in this article to calculate the function of ESSCF at points A1 and D1.

4.2 *Formula fitting at point A1*

In order to achieve high accuracy in fitting the formulas of non-planar oblique butt joints, this article uses polynomial functions for fitting. As described in section 3.2, ESSCF approximately linearly increases with the increase of γ. So γ was fitted linearly while fitting the other three parameters to the highest cubic term, considering all cross terms. Based on the fitting results, remove the coefficients with lower correlation. The final fitting formula is shown below, where the related coefficient R2=0.995.

$$ESSCF_{\mathrm{A1}} = 1.493 + \gamma\left(0.489\frac{l}{t}\frac{\sigma}{\sigma_0}\alpha - 0.541\frac{l}{t}\alpha^3 + 1.648\frac{l}{t}\alpha - 2.467\alpha\right) \tag{5}$$

The comparison between fit values and FEM values is shown in Figure 8a.



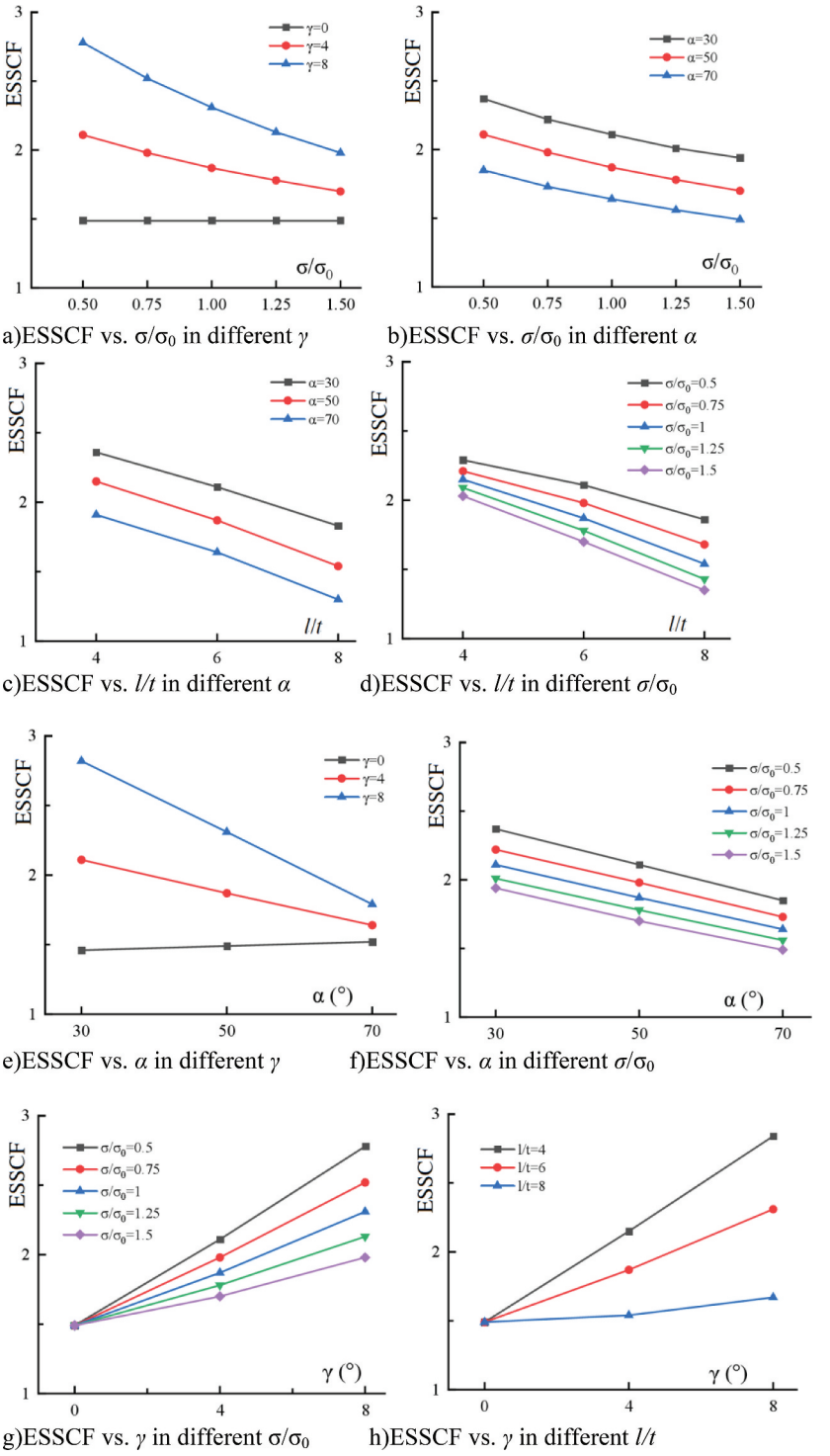
a)ESSCF vs. σ/σ_0 in different γ b)ESSCF vs. σ/σ_0 in different α

c)ESSCF vs. l/t in different α d)ESSCF vs. l/t in different σ/σ_0

e)ESSCF vs. α in different γ f)ESSCF vs. α in different σ/σ_0

g)ESSCF vs. γ in different σ/σ_0 h)ESSCF vs. γ in different l/t

Figure 6. ESSCF on point A1.



a)ESSCF vs. σ/σ0 in different *γ* b)ESSCF vs. *σ*/σ0 in different *α*

c)ESSCF vs. *l*/*t* in different *α* d)ESSCF vs. *l*/*t* in different *σ*/σ0

e)ESSCF vs. *α* in different *γ* f)ESSCF vs. *α* in different *σ*/σ0

g)ESSCF vs. *γ* in different σ/σ0 h)ESSCF vs. *γ* in different *l*/*t*

Figure 7. ESSCF on point D1.

4.3 *Formula fitting at point D1*

Unlike point A1, all parameters at point D1 exhibit non-linearity. Therefore, all parameters are fitted to the highest cubic term, while all cross terms are considered. Based on the fitting results, remove the coefficients with lower correlation. The final fitting formula is shown below, where the related coefficient R2=0.992.

$$\begin{aligned} ESSCF_{\mathrm{D1}} = {} & 1.490 - 1.275\gamma^3\left(\frac{l}{t}\right)^3\left(\frac{\sigma}{\sigma_0}\right)^2 + 0.249\gamma^2\left(\frac{l}{t}\right)^3\left(\frac{\sigma}{\sigma_0}\right)^2 + 0.279\gamma^2\left(\frac{l}{t}\right)^2\frac{\sigma}{\sigma_0} \\ & + 0.0915\gamma\left(\frac{l}{t}\right)^3 - 0.311\gamma\left(\frac{l}{t}\right)^2\frac{\sigma}{\sigma_0} - 1.665\gamma\left(\frac{l}{t}\right)^2 + 9.813\gamma\frac{l}{t} - 6.218\gamma\alpha^2 \end{aligned} \tag{6}$$

The comparison between fit values and FEM values is shown in Figure 8b.

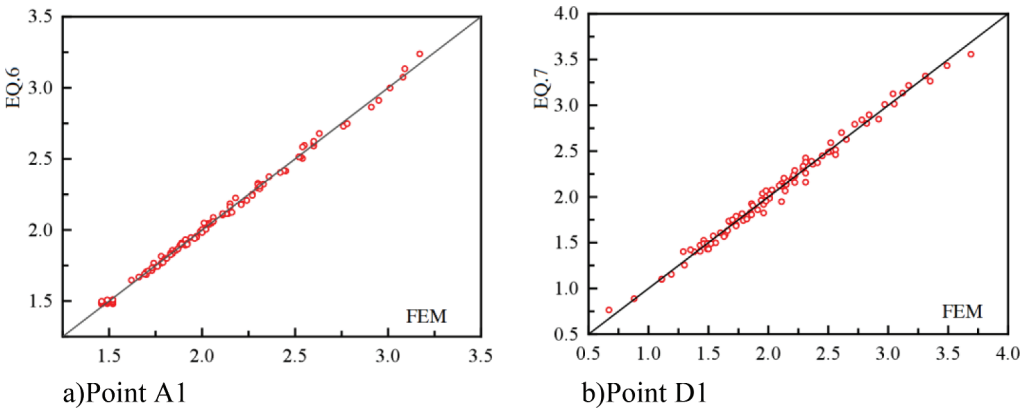


Figure 8. Comparison between fit values and FEM values.

5 CONCLUSION

(1) The maximum of ESSCF only appears at points A1 and D1, located at the obtuse side of the concave side of the load end and the obtuse side of the convex side of the constrained end. These two points are just at the diagonal positions of the structure relative to the weld seam.
(2) ESSCF is approximately linearly increasing with the increase of γ at points A1 and D1. The location of the maximum dose does not change with the change of γ.
(3) The increase rate of ESSCF decreases with the increase of α at point A1. At point D1, the change rate of ESSCF is almost unchanged. When γ=0, ESSCF increases with the increase of α. There is a trend that the location of the maximum of ESSCF shifts from point A1 to point D1 as α increases.
(4) ESSCF keeps on increasing with the increase of σ/σ_0 at point 1-1, and the increase rate gradually decreases. ESSCF keeps on decreasing with the increase of σ/σ_0 at point D1, and the change rate gradually decreases. The maximum ESSCF's location shifts from point D1 to point A1 as σ/σ_0 increases.
(5) at point A1, ESSCF increases with the increase of *l*/*t*, and the increase rate gradually increases; at point D1, ESSCF decreases with the increase of *l*/*t*, and the change rate gradually decreases. The maximum ESSCF's location shifts from point D1 to point A1 as *l*/*t* increases.
(6) Based on 135 non-planar oblique butt joint finite element models, ESSCF formulas at points A1 and D1 were fitted. The relative coefficient R^2 are 0.995 and 0.992. Two formulas reflect the relationship between ESSCF and various parameters at points A1 and D1 well.

REFERENCES

American Petroleum Institute (API). 2014. *API Recommended Practice 2A-WSD, Recommanded Practice for Planning, Designing, and Constructing Fixed Offshore Platforms-Working Stress Design*. Washington, USA.

American Welding Society (AWS). 2015. *AWS D1.1/D1.1M:2015, Structural Welding Code-Steel* Miami, USA.

CEN. EN 1993-1-9-2005, *Eurocode 3: Design of Steel Structures Part 1-9: Fatigue*. Brussels, CEN

Dong P. 2001. A structural stress definition and numerical implementation for fatigue analysis of welded joints.*International Journal of Fatigue*, 23:865–876

Kyuba, H., Dong, P. 2005. Equilibrium-equivalent structural stress approach to fatigue analysis of a rectangular hollow section joint.*International Journal of Fatigue*, 2005, 27(1):85–94.

Dong, Y., Teixeira, A.P., & Guedes Soares, C. 2019. Fatigue reliability analysis of butt welded joints with misalignments based on hotspot stress approach. *Marine Structures*, 65:215–228.

Eurocode 3: *Design of steel structures - Part 1-9: Fatigue*. European: 2010.

International Institute of Welding (IIW). 2000. *IIW Doc. XIII-1804-99, IIW Doc. XV-1035-99, Fatigue Design Procedure for Welded Hollow Section Joints*. Cambridge, UK: 2000.

Jen, Y.M., Chang, L.Y, Fang, C. F. 2008. Assessing the fatigue life of butt-welded joints under oblique loading by using local approaches. *International Journal of Fatigue*, 30(4):603–613

Jie, Z.Y., Li, Y.D., Wei, X. 2017. A study of fatigue crack growth from artificial corrosion pits at welded joints under complex stress fields. *Fatigue & Fracture of Engineering Materials and Structures*, (9):40.

Marquardt, D.W. 1963. An algorithm for least-squares estimation of nonlinear parameters. *Journal of the society for Industrial and Applied Mathematics*, 11(2): 431–441.

Shen, W., Qiu,Y., Li, C., et al. 2019. Fatigue strength evaluation of thin plate butt joints considering initial deformation[J]. *International Journal of Fatigue*,125:85–96.

Su, H., Wang, J., Du, J. 2020. Fatigue behavior of uncorroded butt welded joints made of bridge weathering steel. *Structures*, 24:377–385.

Wang, D.Q.Q., Yao, D. D., Wang, Q., et al. 2023. Evaluating the fatigue property of S355J2W steel butt-welded joint: Multiple notch effects. *International Journal of Fatigue*, 2023.

Wei, X., Wen, Z., Xiao, L., et al. Review of fatigue assessment approaches for tubular joints in CFST trusses. International Journal of Fatigue, 2018,113:43–53.

Wei, X., Xiao, L., Pei, S.L. 2017. Fatigue assessment and stress analysis of cope-hole details in welded joints of steel truss bridge. *International Journal of Fatigue*,100: 136–147

Xiao, L., Wei, X., Zhao, J.M. 2023. Hot spot stress concentration factor of CFST T/Y joints based on modified equivalent thickness. *Structures*, 51:910–925

Bridge Maintenance, Safety, Management, Digitalization and Sustainability – Jensen, Frangopol & Schmidt (eds)
© 2024 The Author(s), ISBN 978-1-032-77040-6
Open Access: www.taylorfrancis.com, CC BY-NC-ND 4.0 license

Electrochemical-chemical-mechanical phase field model for corrosion-induced cracking

Xurui Fang, Zichao Pan & Airong Chen
Department of Bridge Engineering, Tongji University, Shanghai, China

ABSTRACT: Evaluating the degradation process of concrete under corrosion-induced concrete fracture is significant in prolonging the service life of structures. This paper presents an electrochemical-chemical-mechanical phase field model to study the processes of non-uniform corrosion, reactive transport and precipitation of $Fe(OH)_2$, rust-induced cracking. The non-uniform corrosion is described based on the electrochemical theory and the precipitation reactions of Fe^{2+} and OH^- in the concrete pore are considered. The eigenstrain caused by rust is related to the volume fraction of corrosion products. The phase field regularized cohesive zone model is calibrated for concrete cracking. The phenomenon of rust movement through cracks can be observed by relating the diffusion coefficient of rust and the phase field variable. The proposed model is validated with the experimental data and shows good agreement with the experimental data.

1 INTRODUCTION

Rebar corrosion can cause concrete cracking, which reduces the structural load carrying capacity and jeopardizes structural safety. In the marine environment, chloride will invade into the concrete. When the chloride concentration on the rebar surface reaches the critical chloride concentration, the surface of the rebar will be depassivated and corrosion will begin to occur(Fang et al., 2023). The rebar corrosion will produce iron ions, these iron ions will not only produce precipitation in the vicinity of the rebar, but also enter the pores and cracks and then form corrosion products. If such behavior is ignored, it is possible to underestimate the corrosion degree of the rebar and thus overestimate the structure safety.

Over the past few years, extensive research has been conducted to investigate the transport of corrosion products. Tran et al. (2011) assumed that corrosion products entering the voids and cracks do not generate strain. Ožbolt et al. (2014) and Sola et al. (2019) described the transport of corrosion products by a convective diffusion equation. Fahy et al. (2017) related the transport of corrosion products to the pressure gradient generated by the confined volumetric expansion. Zhang and Angst (2021) investigated the transport and precipitation of corrosion products in cementitious materials. Korec et al. (2023) presented a mechanistic framework for corrosion-induced cracking in concrete that considers the reactive transport and precipitation of dissolved $^{Fe2+}$ and $^{Fe3+}$.

In this paper, we proposed an electrochemical-chemical-mechanical phase field model. The non-uniform corrosion is described based on the electrochemical theory and the precipitation reactions of Fe^{2+} and OH^- in the concrete pore are considered. The eigenstrain caused by rust is related to the volume fraction of corrosion products. The cracking of concrete is described by the phase field regularized cohesive zone model. The model was verified by an experiment. Finally, the crack pattern and volume fraction of corrosion products were studied.

DOI: 10.1201/9781003483755-292

2 NUMERICAL MODEL

2.1 *Transport and chemical reactions*

Seven agents are considered in saturated concrete: Cl^-, Na^+, OH^-, K^+, Fe^{2+}, $Fe_{(OH)_2}$, O_2. The transport of these agents can be described by Nernst-Planck equation:

$$\frac{\partial C_i}{\partial t} = \nabla \cdot D_i \nabla C_i + \nabla \left(\frac{z_i F}{RT} D_i C_i \nabla \Phi \right) + S_i \tag{1}$$

where D_i, C_i, z_i and S_i are diffusion coefficient, concentration, charge number and reaction rate of i-th ions, respectively; t is the time; F, R and T are Faraday constant, ideal gas constant and absolute temperature, respectively; Φ is the electrostatic potential.

The chloride binding effect is considered based on Langmuir isotherm, and the governing equation for chloride transport is(Liu et al., 2022):

$$(1 + \lambda_{Cl}) \frac{\partial C_{Cl}}{\partial t} = \nabla \cdot D_{Cl} \nabla C_{Cl} + \nabla \left(\frac{z_{Cl} F}{RT} D_{Cl} C_{Cl} \nabla \Phi \right) \tag{2}$$

where $\lambda_{Cl} = \frac{aC_{Cl}}{w(1+bC_{Cl})}$, w = 0.3; a=0.42 and b = 0.8 mol/L.

The electroneutrality condition is used in this study:

$$\sum_{i=1}^{N} z_i C_i = 0 \tag{3}$$

where N is the total number of ion species.

The diffusion coefficient of various agents is calculated according to the following equation (Zhang and Angst, 2021):

$$D_i = D_i^0 \frac{\delta \varphi}{\tau^2} \tag{4}$$

where D_i^0 is the diffusion coefficient in bulk water; δ, φ and τ are constrictivity, porosity and tortuosity, respectively. The diffusion coefficient varies with porosity.

In concrete, $Fe_{(OH)_2}$ is formed when the concentration product of OH^- ions and Fe^{2+} ions exceed the solubility product, and the reaction rate $S_{Fe(OH)_2}$ is expressed as:

$$S_{Fe(OH)_2} = k_r \cdot \left(C_{OH^-}^2 \cdot C_{Fe^{2+}} - k_{sp} \right) \tag{5}$$

where k_r is the deposition rate constant, k_{sp} is the solubility product.

2.2 *Electrochemical corrosion of rebar*

During rebar corrosion, electrochemical reactions of metal dissolution and oxygen consumption occur simultaneously on the rebar surface. The dissolution rate of Fe^{2+} ions increase with the increase in anodic current density i_{Fe}.

The anodic current density i_{Fe} and the cathodic current density i_{O2} are obtained based on Tafel equation:

$$i_{Fe} = i_{0,Fe} \times 10^{\frac{\Phi - \Phi_{Fe}}{\beta_{Fe}}} \tag{6}$$

$$i_{O_2} = \frac{C_{O_2}}{C_{O_2,s}} i_{0,O_2} \times 10^{\frac{\Phi - \Phi_{O_2}}{\beta_{O_2}}} \tag{7}$$

where $i_{0,Fe}$ and i_{0,O_2} are the exchange current densities of the anodic and cathodic reactions, respectively; Φ_{Fe} and Φ_{O_2} are the equilibrium potentials of the anodic and cathodic reactions, respectively; β_{Fe} and β_{O_2} are the anodic and cathodic Tafel slopes, respectively; $C_{O_2,s}$ is the oxygen concentration on the concrete surface.

2.3 *Precipitation eigenstrain*

The corrosion products will fill the volume left by the corroded rebar and the pores, and exert stress on the surrounding concrete matrix. Thus, the eigenstrain can be calculated as:

$$\varepsilon = \frac{1}{3}\left(\frac{\rho_{Fe} M_{Fe(OH)_2}}{(1-r_0)\rho_{Fe(OH)_2} M_{Fe}} - 1\right) \tag{8}$$

where ρ_{Fe} and $\rho_{Fe(OH)_2}$ are the density of Fe and $Fe_{(OH)_2}$, respectively; M_{Fe} and $M_{Fe(OH)_2}$ are the molar mass of Fe and $Fe_{(OH)_2}$, respectively; r_0 is the porosity of the corrosion product $Fe_{(OH)_2}$. In this study, we assumed that the a fraction of the pore volume will be filled before strain starts to develop(Sarkar et al., 2010), we introduce a coefficient f_0 to describe this case, and the eigenstrain is:

$$\varepsilon = \frac{1}{3}\left(\frac{\rho_{Fe} M_{Fe(OH)_2}}{(1-r_0)\rho_{Fe(OH)_2} M_{Fe}} - 1\right) \cdot \left(\varphi_p - f_0 \cdot \varphi_0\right) \tag{9}$$

where φ_p is the volume fraction of corrosion product; φ_0 is the initial porosity. It should be mentioned that the porosity will change due to precipitation and crack.

2.4 *Cracking of concrete*

The cracking of concrete is described by the phase field regularized cohesive zone model(Wu, 2017). In the phase field model, the discrete crack is regularized over a localization band Γ. The phase field variable $\phi(x, t)$ is introduced to represent the damage level. $\phi(x, t) = 0$ and $\phi(x, t) = 1$ denote intact and completely failed material states, respectively. It uses the gradient of the order parameter to automatically track the interface evolution, and the evolution of the order parameter follows the energy minimization principle. The damage and mechanical behaviors are governed by the following equations:

$$\begin{cases} \nabla \cdot \sigma + \boldsymbol{b} = 0 & \Omega \\ \sigma \cdot \boldsymbol{n} - \boldsymbol{f} = 0 & \partial\Omega_f \\ g'(\phi)\boldsymbol{H} + \frac{G_c}{c_0}\left(\frac{\alpha'(\phi)}{l_f} - 2l_0\nabla\cdot\nabla\phi\right) = 0 & \Gamma \\ \frac{2G_c}{c_0} l_f \nabla\phi \cdot \boldsymbol{n}_\Gamma = 0 & \partial\Gamma \end{cases} \tag{10}$$

where σ is the stress; $\boldsymbol{b}$ is body force acted on the body Ω; $\boldsymbol{f}$ is the traction on the boundary $\partial\Omega_f$; $\boldsymbol{n}$ and $\boldsymbol{n}_\Gamma$ are the outward unit normal vector of external boundary of Ω and Γ; G_c is the critical energy release rate; l_f is the phase field length scale; $c_0 = \pi$ is a scaling constant; $g(\phi)$ and $\alpha(\phi)$ are the degradation function and crack geometric function, respectively. The equations of $g(\phi)$ and $\alpha(\phi)$ are expressed as

$$g(\phi) = \frac{(1-\phi)^p}{(1-\phi)^p + Q(\phi)}, \quad Q(\phi) = a_1\phi + a_1a_2\phi^2 + a_1a_2a_3\phi^3 + \ldots \tag{11}$$

$$\alpha(\phi) = 2\phi - \phi^2 \tag{12}$$

where p=2, a_2= 1.3868, and a_3 = 0.9106. $\boldsymbol{H}$ is the history variable, reads:

$$\boldsymbol{H} = \max\left(\frac{f_t^2}{2E_0}, Y_t\right) \tag{13}$$

where f_t is the failure strength; E_0 is the Young's modulus; $Y_t = \frac{\langle\bar{\sigma}_1\rangle^2}{2E_0}$, $\bar{\sigma}_1$ is the major principal value.

3 RESULTS

In this section, the proposed model is validated by the experimental results xx. In their work, the corrosion initiation of the rebar was triggered in a cyclic drying-wetting environment. The specimens were then placed in an environmental chamber at 80% relative humidity and 33 °C to accelerate the corrosion propagation. A non-uniform rust distribution was obtained during the test.

In the simulation, the geometry and boundary condition of the mesoscale model is shown in Figure 1. The gray, red, orange, grayish green and blue represent matrix, ITZ, fine aggregate, rebar and ITZ between rebar and matrix, respectively. The size of the model is 100 × 100 mm. The rebar diameter is 10 mm. The top and edge cover thickness are 10 mm and 25 mm, respectively. The displacements in the vertical and horizontal directions on the left surface of the model are fixed. The surface chloride content is 1 wt% of cement. The other parameters in the numerical model are in Tables 1 ~ 3.

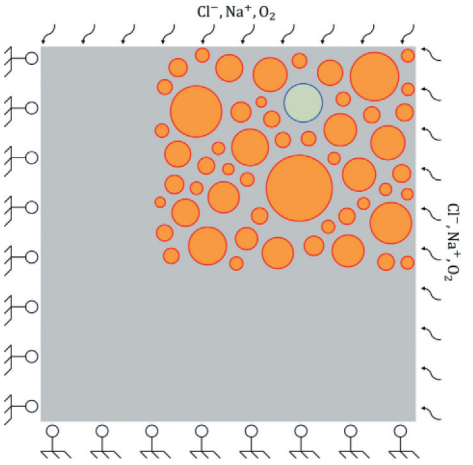


Figure 1. Geometry and boundary condition of the mesoscale model.

Table 1. Material parameters for different phases.

Phase	Young's modulus (MPa)	Poisson's ratio	Failure strength (MPa)	Fracture energy (N/m)
Aggregate	70000	0.2	-	-
Matrix	25000	0.2	6	60
ITZ	15000	0.2	3	30
Rebar	210000	0.3	-	-

Table 2. Electrochemical parameters in the simulation.

parameters	values
β_{Fe} (V/dec)	0.09
β_{O_2} (V/dec)	-0.14
Φ_{Fe} (V)	-0.78
Φ_{O_2} (V)	0.16
$i_{0,Fe}$ (A/m^2)	3×10^{-4}
i_{0,O_2} (A/m^2)	1×10^{-5}

Table 3. Diffusion coefficient and concentration in the simulation.

Variables	Cl^-	Na^+	OH^-	K^+	Fe^{2+}	O_2
Charge number	-1	+1	-1	+1	+2	-
Diffusion coefficient ($\times10^{-9}$m^2/s)	1	1.33	5.27	1.96	0.7	100
Initial concentration (mol/m^3)	0	0	60	-60	0	0.268
Boundary concentration (mol/m^3)	105	105	0	0	0	0.268

Figure 2 demonstrates the crack patterns in concrete. It can be seen that there is one crack progressing from the concrete surface to the rebar surface, and three other cracks progressing from the rebar surface into the concrete, one to the upper left, one to the upper right, and one to the lower right.

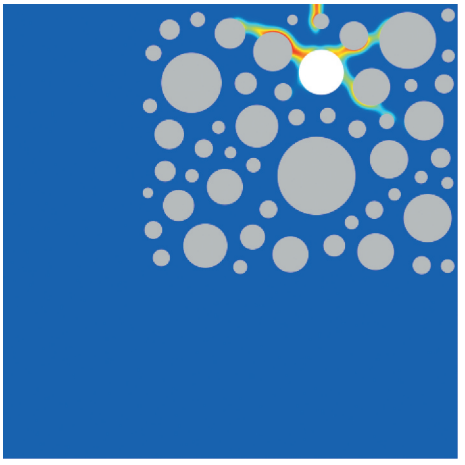


Figure 2. Crack patterns in concrete.

The comparisons of the experimental and numerical simulation results are illustrated in Figure 3. The black lines in the figure represent the numerical results, and the remaining three lines represent the experimental results. It can be seen that the trend of the simulated crack width with the corrosion degree is similar to that observed in the experimental results, indicating that the proposed model is efficient in addressing concrete cover cracking caused by rebar corrosion.

Figure 4 shows the damage level and concentration of $Fe_{(OH)_2}$ around the rebar. As can be seen from the figure, the concentration of $Fe_{(OH)_2}$ is smaller in the areas with more damage than in the areas with less damage. This is due to the fact that where the damage is large, the diffusion coefficient of Fe^{2+} is large and the Fe^{2+} ions are transported further away from the surface of the rebar and do not precipitate in the vicinity of the rebar surface.

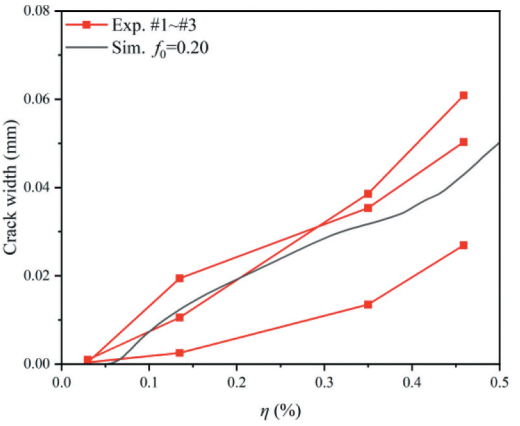


Figure 3. Comparisons of crack width between the experimental observations and numerical results.

Figure 5 shows the porosity in a radial direction from the rebar under different corrosion degree. It can be seen that because precipitation occurs first and faster near the rebar surface, the porosity near the rebar surface decreases. In the vicinity of 0.2 mm, the porosity decreases and then increases because the crack increases the porosity and the precipitation is not enough to

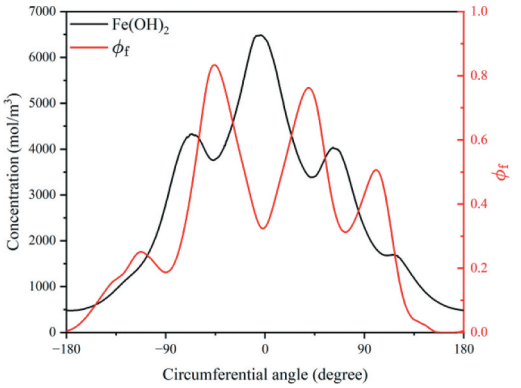


Figure 4. Damage level and concentration of $Fe_{(OH)_2}$ around the rebar.

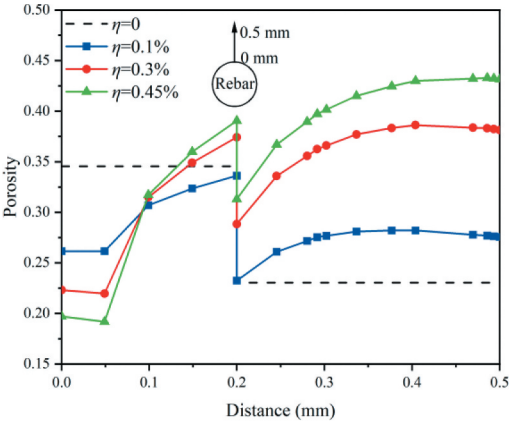


Figure 5. Porosity in a radial direction from the rebar.

offset the effect of the crack. In the matrix, there is less precipitation and the change in porosity is mainly affected by crack.

4 CONCLUSION

This paper presented a comprehensive electrochemical-chemical-mechanical phase field model to evaluate the degradation process of concrete subjected to rebar corrosion-induced fracture. The investigation encompassed non-uniform corrosion, reactive transport, $Fe(OH)_2$ precipitation, rust-induced cracking, and the movement of rust through cracks. The model considered precipitation reactions of Fe^{2+} and OH^- within the concrete pore space. The eigenstrain caused by rust is related to the volume fraction of corrosion products. The phase field regularized cohesive zone model is calibrated for concrete cracking. Validation against experimental data demonstrated the model's reliability, exhibiting a commendable agreement with the observed outcomes. The following conclusions can be drawn: (1) the concentration of $Fe_{(OH)_2}$ is smaller in the areas with more damage than in those with less damage; (2) damage leads to increased porosity, while precipitation decreases porosity, with the overall porosity variation pattern resulting from the interplay between these opposing factors.

REFERENCES

Fahy, C., Wheeler, S.J., Gallipoli, D., Grassl, P., 2017. Corrosion induced cracking modelled by a coupled transport-structural approach. Cem. Concr. Res. 94, 24–35. https://doi.org/10.1016/j.cemconres.2017.01.007

Fang, X., Pan, Z., Chen, A., Tian, H., Ma, R., 2023. Phase-field method for modeling non-uniform corrosion-induced cracking in concrete. Eng. Fract. Mech. 281, 109131. https://doi.org/10.1016/j.engfracmech.2023.109131

Korec, E., Jirásek, M., Wong, H.S., Martínez-Pañeda, E., 2023. A phase-field chemo-mechanical model for corrosion-induced cracking in reinforced concrete. Constr. Build. Mater. 393, 131964. https://doi.org/10.1016/j.conbuildmat.2023.131964

Liu, Q., Meng, Z., Hou, D., Zhou, Y., Cai, Y., Zhang, M., Tam, V.W.Y., 2022. Numerical modelling of electrochemical deposition techniques for healing concrete damaged by alkali silica reaction. Eng. Fract. Mech. 276, 108765. https://doi.org/10.1016/j.engfracmech.2022.108765

Ožbolt, J., Oršanić, F., Balabanić, G., 2014. Modeling pull-out resistance of corroded reinforcement in concrete: Coupled three-dimensional finite element model. Cem. Concr. Compos. 46, 41–55. https://doi.org/10.1016/j.cemconcomp.2013.10.014

Sarkar, S., Mahadevan, S., Meeussen, J.C.L., Van Der Sloot, H., Kosson, D.S., 2010. Numerical simulation of cementitious materials degradation under external sulfate attack. Cem. Concr. Compos. 32, 241–252. https://doi.org/10.1016/j.cemconcomp.2009.12.005

Sola, E., Ožbolt, J., Balabanić, G., Mir, Z.M., 2019. Experimental and numerical study of accelerated corrosion of steel reinforcement in concrete: Transport of corrosion products. Cem. Concr. Res. 120, 119–131. https://doi.org/10.1016/j.cemconres.2019.03.018

Tran, K.K., Nakamura, H., Kawamura, K., Kunieda, M., 2011. Analysis of crack propagation due to rebar corrosion using RBSM. Cem. Concr. Compos. 33, 906–917. https://doi.org/10.1016/j.cemconcomp.2011.06.001

Wu, J.-Y., 2017. A unified phase-field theory for the mechanics of damage and quasi-brittle failure. J. Mech. Phys. Solids 103, 72–99. https://doi.org/10.1016/j.jmps.2017.03.015

Zhang, Z.D., Angst, U., 2021. Modelling transport and precipitation of corrosion products in cementitious materials: A sensitivity analysis, in: Chen, A., Ruan, X., Frangopol, D.M. (Eds.), Life-Cycle Civil Engineering: Innovation, Theory and Practice. CRC Press, pp. 747–753. https://doi.org/10.1201/9780429343292-98

Bridge Maintenance, Safety, Management, Digitalization and Sustainability – Jensen, Frangopol & Schmidt (eds)
© 2024 The Author(s), ISBN 978-1-032-77040-6
Open Access: www.taylorfrancis.com, CC BY-NC-ND 4.0 license

Analysis of monitoring data on prestressed concrete bridges under construction

T. Ohno, H. Sekiya & I. Yoshida
Department of Urban and Civil Engineering, Tokyo City University, Tokyo, Japan

S. Morichika
Department of Civil Engineering, Tokyo University of Science, Chiba, Japan

A. Yasuda, M. Uno & N. Yoshiura
Bridge Management Division, Civil Engineering Headquarters, SHIMIZU CORPORATION, Tokyo, Japan

ABSTRACT: Balanced cantilever method is one of the bridge construction methods, has the advantage that construction can be carried out regardless of the environment under the girder. In this method, it is important to measure the deformation of the bridge at each event such as concrete placement, tensioning, temperature change, and solar radiation. Currently, these deformations are measured by level surveying. However, level surveying for each event is time-consuming and labor-intensive, making it a challenge to improve efficiency and reduce manpower. In this study, temperature, strain, inclination, and position data were measured on PC bridges under construction as a basic study of bridge deformation measurement, and the data were analyzed in detail.

1 INTRODUCTION

Structural Health Monitoring (SHM) has been extensively studied in structural engineering (Tran-Ngoc et al., 2019) (Tran-Ngoc et al., 2022). However, research on bridge monitoring during construction is currently limited. For example, in the construction of prestressed concrete (PC) bridges using the cantilever construction method, managing vertical displacement due to events such as concrete casting, tensioning, and solar radiation is crucial for quality control. Currently, this management is carried out using leveling survey. However, there is a need to save manpower and reduce costs due to reduced working hours and costs. Therefore, in a previous study (Morichika et al. 2022), sensors such as inclinometers and strain gauges to monitor the construction of bridges. There, three-dimensional deformation diagrams were created. This study evaluates the displacement of bridges due to temperature variations in air temperature and discusses the measurement accuracy required for alternative methods of leveling survey.

The paper is structured as follows. Chapter 2 describes the structure, construction conditions, and measurement conditions, Chapter 3 compares the measurement data during concrete casting, temperature changes, and tensioning operations, and Chapter 4 provides a conclusion and prospects.

2 TARGET BRIDGE

This chapter describes the target bridge in this study. The target bridge structure is a PC 3-span continuous ramen box girder bridge (corrugated web), with a bridge length of

DOI: 10.1201/9781003483755-293

121 m. The construction of the test bridge was carried out by constructing the pillars and casting the concrete symmetrically in one block from the pillars. There are three main phases of construction: concrete casting, tensioning of the bridge, and work vehicle movement. It is desirable to measure the deformation of bridges due to temperature changes at any time, but this is time-consuming and labor-intensive, so a labor-saving solution is urgently needed. In this study, the period when the concrete was cast, and the PC member was tensed in Block 8 (8BL) and Block 9 (9BL) was investigated. The distance from the pier to the tip at the time the measurements were taken was 52.5 m. External photographs and cross-sections of the subject bridge are shown in Figures 1 and 2.

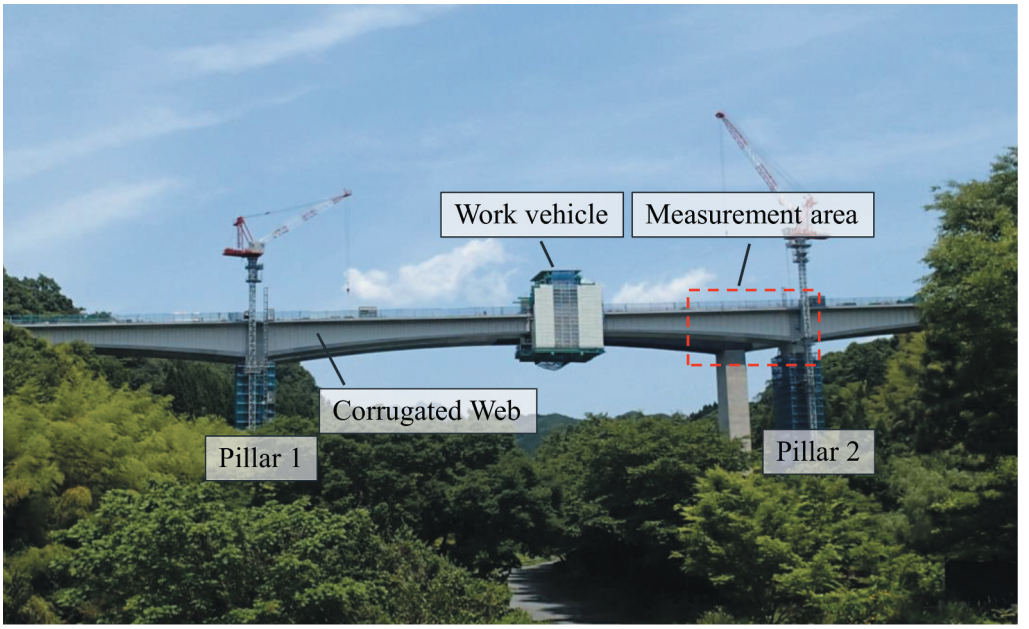


Figure 1. Appearance of the target bridge under construction.

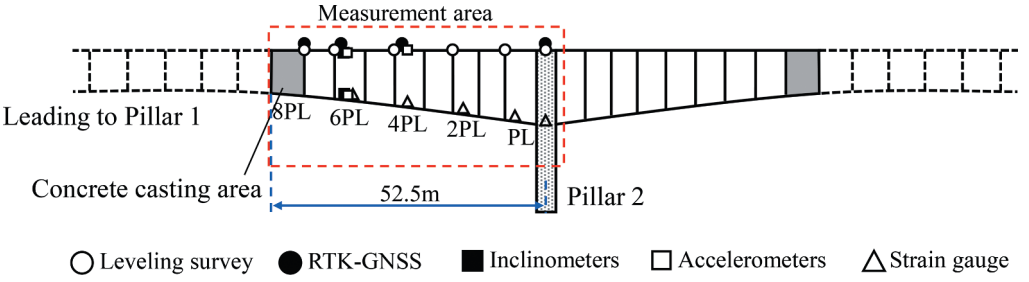


Figure 2. Details of the target bridge and measurement locations.

3 MEASUREMENT CONDITIONS

For the measurement of displacement, the Realtime Kinematic Global Navigation Satellite System (RTK-GNSS) was used in addition to the conventional method of leveling survey (Hussein et al. 2021) (Kubo et al. 2023). RTK-GNSS is a method that enables measurements on the order of centimeters by compensating for radio delays caused by the troposphere and

ionosphere. A wired inclinometer capable of measuring two axes and a three-axis Micro Electro Mechanical Systems (MEMS) accelerometer was used to measure the angle of inclination. The 3-axis MEMS accelerometers are easy to install because they can be installed with magnets (Sekiya et al. 2017) (Morichika et al. 2021). For strain measurements, a strain gauge with a gauge length of 67 mm, and a fiber-optic sensor were used. The survey positions and the locations of the various sensors are shown in Figure 2 and photographs of the installed sensors are shown in Figure 3.

Measurements were taken on both the upper and lower decks. For GNSS, the elevation angle must be open by about 15 degrees, so the GNSS is mounted on a pole and placed higher on the upper deck so that the measurement is not disturbed by worker traffic, etc. The strain gauge and fiber-optic sensors used for strain measurement were installed on both the upper and lower decks. Dummy gauges for temperature compensation were also installed for the strain gauges, as the analog signal output is particularly susceptible to temperature effects. In this study, however, only the data measured by strain gauges installed on the lower deck were treated.

4 MEASURED DATA RESULTS

4.1 *Relationship between vertical displacement and air temperature*

This chapter compares the measured data of the 8BL during concrete placement, temperature changes, and tensioning of the PC member. Figure 4 shows a plot of the vertical displacement results measured by level survey and GNSS for each event during the construction of 8BL and the outdoor temperature. However, the measurement positions are all at 8 BL at the tip and are based on 8:00 am, when the level survey was carried out at the beginning of the concrete placing day, and the differences from that point are shown.

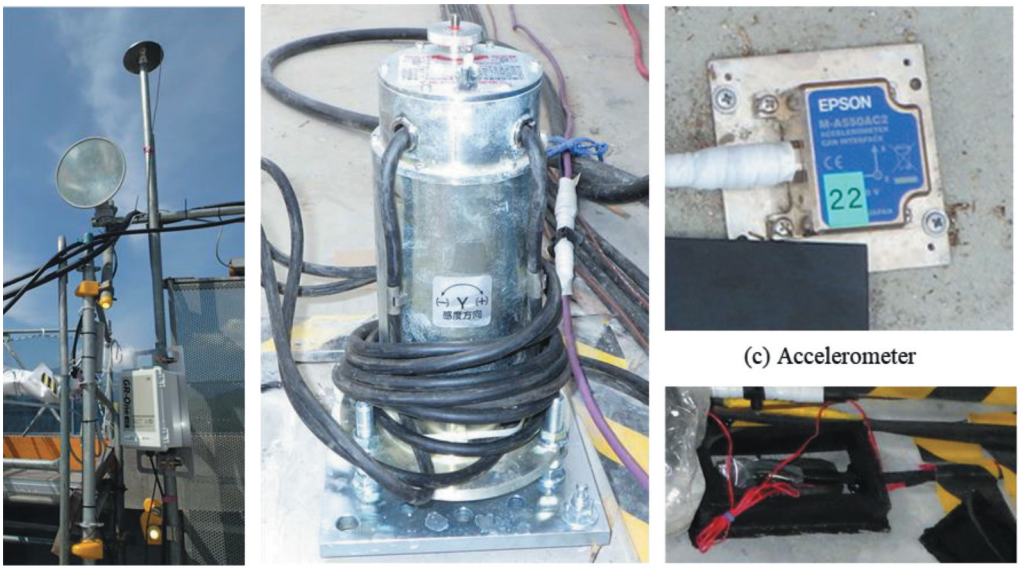


Figure 3. Measurement equipment used.

The black line in the diagram shows the vertical displacement measured by GNSS, the red dots show the vertical displacement measured by level surveying, a conventional method, and the blue line shows the air temperature around the target bridge as published by the JMA. Although the GNSS measurement data contained noise in centimeters, the behavior was

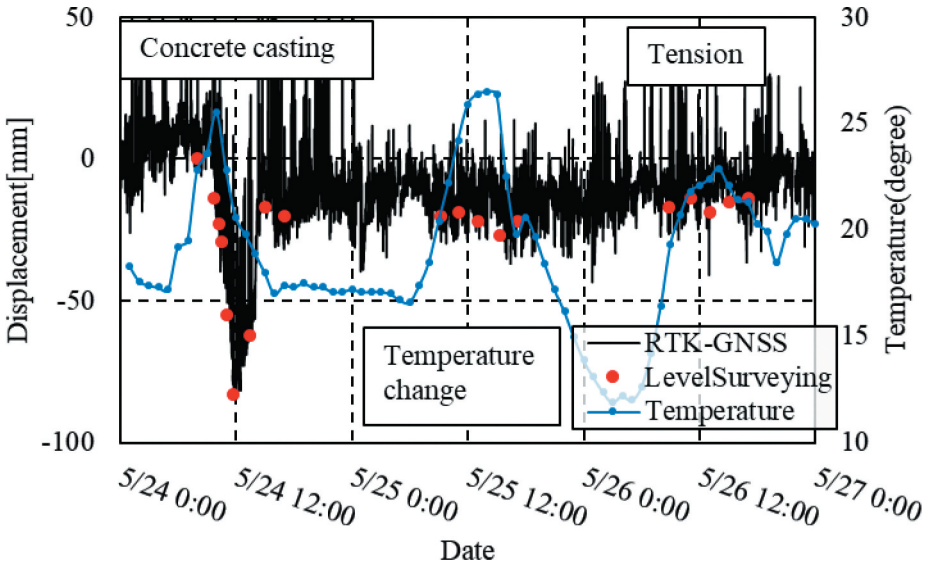


Figure 4. Relationship between vertical displacement and temperature during 8BL construction.

found to be consistent with the level survey results on the day of casting, when the vertical displacement was large throughout the day. However, for temperature changes with small vertical displacements and for days when tensioning operations were carried out, it was difficult to estimate the variables obtained by level surveying from the GNSS measurement data because the noise component was too large, and the results did not show sufficient measurement accuracy.

On the morning of 24 May, when the vertical displacement was greatest, 8 BLs of concrete were placed, with 12 m^3 of the lower deck completed at 10:30 and 20 m^3 of the upper deck placed at 11:45 for a total of 32 m^3 of concrete. The vertical displacement in this case is approximately 80 mm. In the afternoon of the same day, the pouring of the 8BL on the opposite side across P2 took place, with 12 m^3 of the lower deck being poured at 13:25 and 24 m^3 of the upper deck at 15:00, making a total of 68 m^3 of concrete poured since the morning. The vertical displacement returned by approximately 60 mm and the final vertical displacement of the bridge toe was approximately 20 mm. The following day, no major displacements occurred as there were no structural changes, but the temperature rose by approximately 10° C from early morning to midday, and this change caused displacements of up to 8 mm of vertical deflection downwards. The following day, the PC member was tensioned, but again no significant displacements occurred, with the maximum displacement being only 5 mm.

Displacements of more than 80 mm were observed at 8 BL at the tip during concrete placement, showing the potential of GNSS to replace conventional survey methods for such large displacements. However, the maximum displacement during temperature changes and when the PC member was under tension was approximately 8 mm, and the displacement response could not be captured by GNSS because the noise component was too large. Therefore, technology is required that can measure deformations on the order of mm. It was also found that the vertical displacement caused by a 10° C temperature change may be greater than the displacement caused by tensioning.

4.2 *Angle data*

The angle of inclination was measured using a wired inclinometer and a MEMS accelerometer. MEMS accelerometers output acceleration data in three axes, so conversion to an

inclination angle is necessary. The conceptual diagram and equation for calculating the inclination angle from the acceleration are shown in Figure 5 and Equation (1).

$$\theta = sin^{-1}\left(\frac{a_x}{g}\right) \tag{1}$$

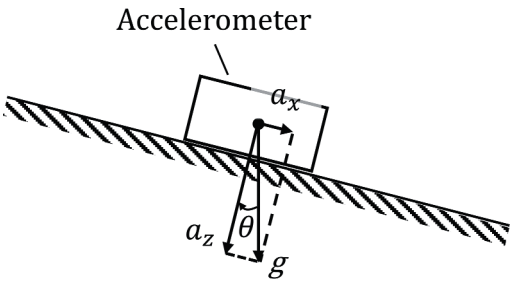


Figure 5. Relationship between measured acceleration and inclination angle.

The angles of inclination using the wired inclinometer and the acceleration data at the time of maximum displacement during concrete placement are shown in Figure 6. The angle of inclination is positive when the leading edge of the bridge is tilted vertically upwards when viewed from the column heads. As with the vertical displacements presented in the previous section, the differences are shown concerning 8.00 am, when the level survey was carried out at the beginning of the day of concrete placement.

The black line in Figure 6 shows the measured data from the inclinometer and the red line shows the angle of inclination calculated from the acceleration. A comparison of data from a wired inclinometer and an accelerometer installed at the same location shows that they have very equal inclination angles, indicating that the data from the accelerometer accurately measured the inclination angle.

A large inclination angle of -0.12° at the tip occurred at the time of casting, which was subsequently recovered to -0.04° by casting on the opposite side across P2. On the other hand, changes in inclination angle due to temperature changes and tensioning operations are small (about 0.02°) and therefore require highly accurate measurements.

4.3 *Strain data*

Strain measurements were carried out on the lower deck of the bridge. As in the previous sections, data on the strain during the construction of the 8BL are presented. However, the time is based on 8.00 a.m. on the day of casting and the difference is shown.

The measured data for strain showed that, compared to the inclination angle, the strain values were almost constant during concrete placement, irrespective of the installation location. The strain values at each location at 11:45 am, when the maximum displacement occurred, are shown in Figure 8 to confirm the response in more detail during the concrete placement. The strain gauge data for the lower deck showed values around -40 μ at all points, indicating that compressive forces were generated on the entire underside of the bridge and that the concrete placement deformed the bridge convexly upwards.

5 CONCLUSIONS

Various sensors were installed on bridges under construction and the measured data was analyzed in detail. The results show that a bridge of approximately 50 m in length deflects at its

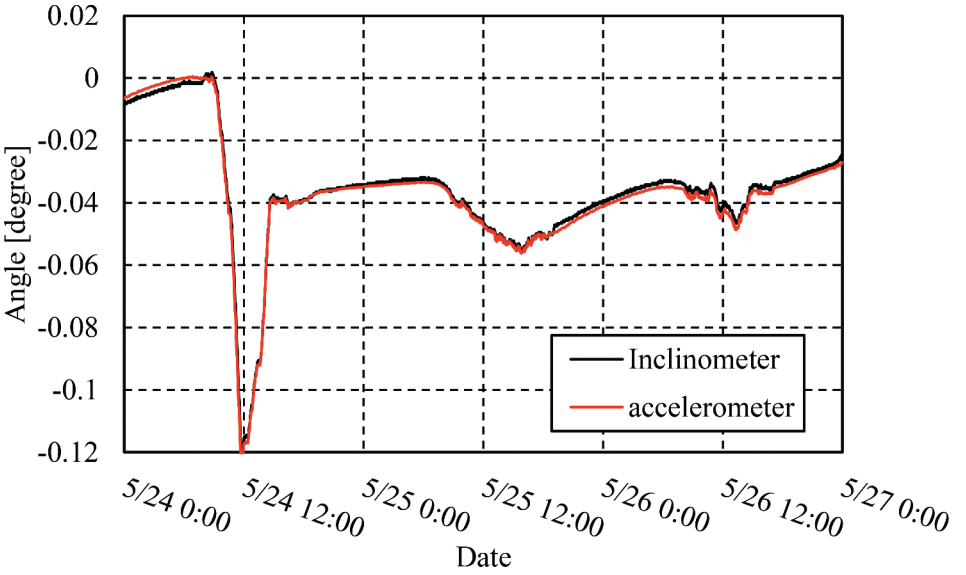


Figure 6. Inclination angle variation over time.

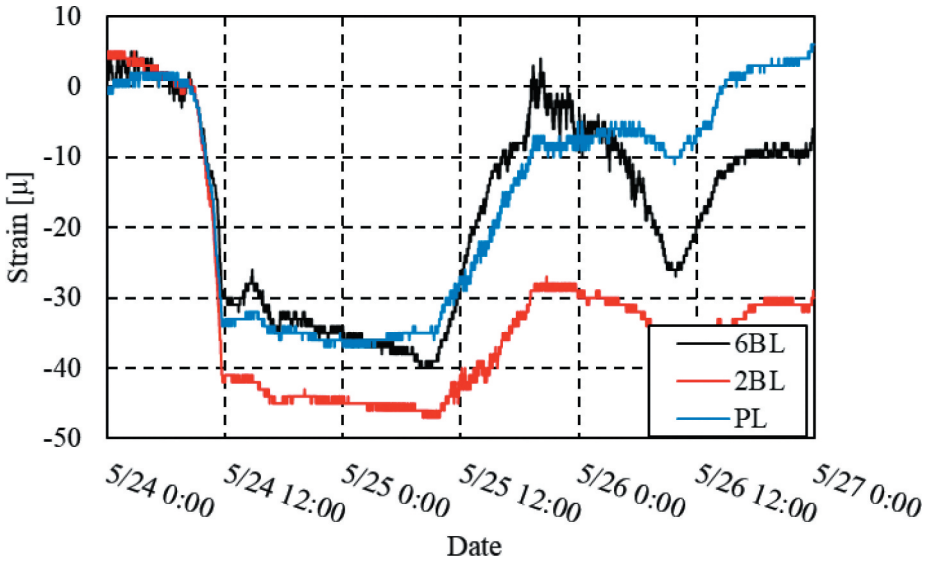


Figure 7. Time-series variation of strain.

leading edge by approximately 80 mm as a result of the concrete placement. For such large responses, the possibility of replacing conventional surveying with GNSS was demonstrated. The deformation of bridges due to temperature changes was found to be equal to or greater than that of PC member tensioning operations.

Prospects include the study and practical application of a method for estimating deformations on the order of millimeters in bridges under construction using measured strain, angle of inclination, and displacement data.

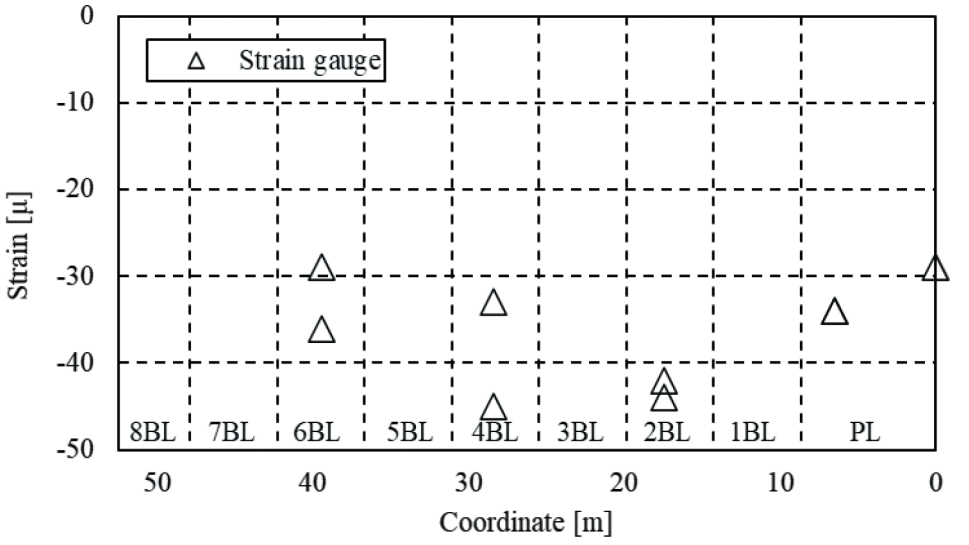


Figure 8. Strain on the bridge sub-base deck during pouring.

ACKNOWLEDGMENTS

This research was carried out as part of a joint research project with Shimizu Corporation. The authors would like to express their gratitude to all parties involved.

REFERENCES

Hussein, A.M., Panos, A.P., Craig, M.H., Gethin, W.R. & Lukasz, B. 2021. Monitoring the response of Severn Suspension Bridge in the United Kingdom using multi-GNSS measurements, *Structural Control Health Monitoring*, Volume 28, Issue 11: 1–29.

Kubo, N., Ozeki, T., Kobayashi, K., Narumi, T. & Yamaguchi, N. 2023. Improved Initial Integer Ambiguity Resolution When the Sky Visibility is Considerably Masked. *IEEE/ION Position, Location and Navigation Symposium (PLANS)*: 764–771.

Morichika, S., Sekiya, H., Zhu, Y., Hirano, S. & Maruyama, O. 2021. Estimation of Displacement Response in Steel Plate Girder Bridge Using a Single MEMS Accelerometer. *IEEE sensors journal*, Volume 21, No. 6: 8204–8208.

Morichika, S., Sekiya, H., Nakashima K., Yoshida I., Iwaki H. & Toshinami, T. 2022. Structural monitoring of PC bridges under construction based on measurable data. *Eleventh International Conference on Bridge Maintenance, Safety and Management (IABMAS 2022)*, https://doi.org/10.1201/9781003322641.

Sekiya, H., Kubota, K., Miki, C. 2017. Simplified Portable Bridge Weigh-in-Motion System Using Accelerometers. *ASCE, Journal of Bridge Engineering*, Volume 23, Issue 1: 1–15.

Tran-Ngoc, H., Khatir, S., De Roeck, G., Bui-Tien, T. & Abdel Wahab, M. 2019. Damage Assessment in Beam-Like Structures Using Cuckoo Search Algorithm and Experimentally Measured Data. *In: Wahab, M. (eds) Proceedings of the 13th International Conference on Damage Assessment of Structures. Lecture Notes in Mechanical Engineering. Springer, Singapore.* https://doi.org/10.1007/978-981-13-8331-1_27.

Tran-Ngoc, H., Khatir, S., Le-Xuan, T., De Roeck, G., Bui-Tien, T. & Abdel Wahab, M. 2022. Finite element model updating of a multispan bridge with a hybrid metaheuristic search algorithm using experimental data from wireless triaxial sensors. *Engineering with Computers*, Volume 38: 1865–1883.

Bridge Maintenance, Safety, Management, Digitalization and Sustainability – Jensen, Frangopol & Schmidt (eds)
© 2024 The Author(s), ISBN 978-1-032-77040-6
Open Access: www.taylorfrancis.com, CC BY-NC-ND 4.0 license

Piezo-Electric Dampers (PiDs) for energy harvesting purposes

J.F. Martins*, M. Francioli* & F. Petrini*
Sapienza University of Rome, Rome, Italy

ABSTRACT: Many modern bridges are able to sense their state in operational and emergency conditions through embedded sensors that constantly monitor structural damage conditions. However, the large amount of energy (supplied by the power grid or batteries) and wiring to operate the thousands of sensors required represents a concerning issue, entailing both a significant environmental impact (battery disposal) and disproportionate installation and maintenance costs (due to wiring and manual intervention). Energy Harvesting (EH) from induced vibrations has received emphasis allowing the development of efficient and reliable devices that convert into electrical energy the sensed perturbations occurred and piezoelectric materials have special attention given their natural capacity of converting mechanical into electrical energy. With the aim of Structural Health Monitoring (SHM), here is presented a device named PiD (piezoelectric damper) which, designed as an elastomeric bridge's bearing in which a piezoelectric fin is inserted, can harvest energy from induced vibrations.

1 INTRODUCTION

1.1 *Background*

Smart structures will facilitate the development of sustainable and resilient, modern/future European cities (Figure 1a) (Srinivasan et al 2001), (Rose 2011), sensing its own-status in operational and emergency conditions through embedded sensors (European Commission 2014) that constantly monitor the structural damage conditions (i.e., Structural Health Monitoring-SHM), often using wireless communication technology and allowing adaptive/rapid emergency response to different scenarios (e.g., accidental events) (Li 2016). However, a major challenge with current technology is the great amount of distributed energy (provided by the main sources or by batteries) and cables to operate the required thousands of sensors: this implies considerable environmental impact (batteries disposal) and disproportionate installation and maintenance costs (due to cabling, manual interventions). In this sense, Energy harvesting (EH) devices appear as a potential solution to sustain self-powered systems in alternative to batteries as well as to management operations; in accordance with an alternative to environmental impacting and cost-ineffective technologies, this work proposes a device named as Piezoelectric Dampers (PiDs), which represent an innovative type of device able to harvest energy from induced vibrations. They are battery and cable-free and they will embed piezoelectric materials and will be located in strategic joints providing power to wireless distributed sensors used for SHM. Piezoelectric (Pz) material receives a special look in engineering since it can convert the mechanical energy input into electrical energy. It can be said that PzEH technology is well-established at the micro- (Lu et al. 2011) and meso- (Tao et al. 2017) scale applications relevant to communication, space, and medical sectors where it is widely used for vibration or temperature gradient EH to power sensors and/or small actuators (Jung et al. 2011); however, no attempts were pursued to extend

*Corresponding authors: juliano.martins@uniroma1.it, mattia.francioli@uniroma1.it, francesco.petrini@uniroma1.it

DOI: 10.1201/9781003483755-294

PzEH usage in macro-scale civil engineering applications (such as in bridges), since specific properties of this material represented and still represent an obstacle for its diffusion in civil structural field. For example, Pz material has a limited stress resistance compared to structural material and it usually works well in a range of frequencies that doesn't belong to civil engineering field. Here are discussed the assumption made in order to avoid the aforementioned issues; however, there are still few literatures regarding this topic and the aim of the proposed study is to conceptualize a device that can be used for EH involving Pz material. Specifically, the idea is to design an innovative device that could replace a bridge's load bearing (Figure 2), guaranteeing both resistance and EH.

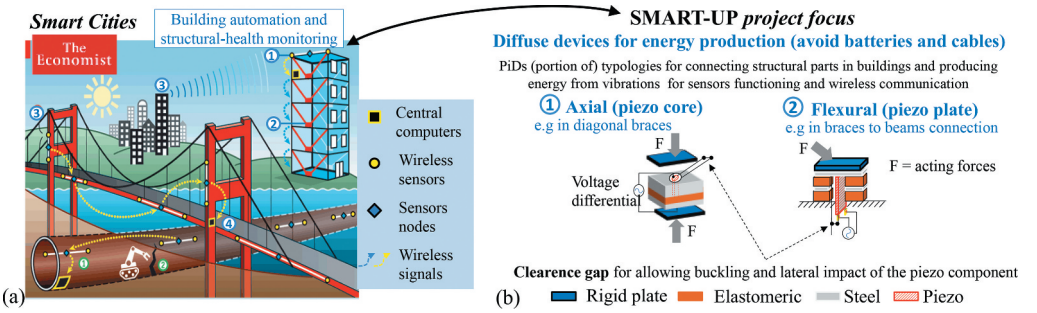


Figure 1. (a) smart structures operation in modern cities (The Economist Technology Quarterly); (b) position and schematic features of the PiDs.

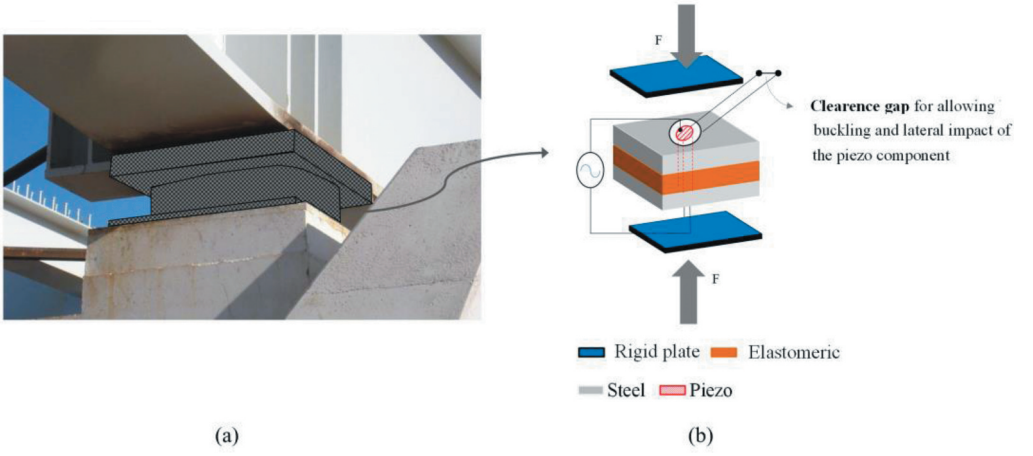


Figure 2. (a) Bridge's load bearing system; (b) concept of the proposed device (PiD).

2 METHODS

2.1 *Basic concepts regarding piezoelectricity and rubber bearings*

In accordance with the IEEE standard (ANSI 1988) the simplified piezoelectric constitutive equation is given by:

$$\begin{cases} S = sT + dE \\ D = dT + \varepsilon E \end{cases} \tag{1}$$

where S = strain; s = elastic compliance; T = stress; d = piezoelectric coefficient; E = electric field intensity; D = electrical displacement; and ε = permittivity.

Piezoelectric material operates in different modes depending on which direction the stress/strain occurs, as represented in Figure 3. Furthermore, there are two effects observed on those materials: direct and reverse. The direct effect is described as an electrical charge generated by mechanical stress, while the converse occurs when a strain is generated because of an applied electrical field. The piezoelectric material used on the d_{33} mode indicates that both voltage and stress occur in direction 3. When using d_{31} mode the piezoelectric will have the voltage acting in direction 3 (where the material is poled), and the mechanical stress/strain will occur in direction 1. In this last case, the use of thin bending elements is likely to occur, leading to a large strain in direction 1 developed due to bending. With that, d_{31} cases can be applied to a cantilever beam-type so larger strains can be produced with smaller input forces even if the electrical/mechanical coupling is lower than in the d_{33} modes. For the latter, more advanced structures configuration may be required as flex-tensional harvesters (Zhao et al. 2023).

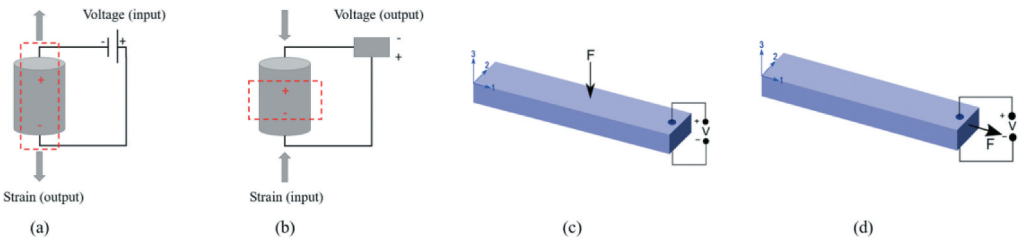


Figure 3. Effects of piezoelectric material direct (a) and converse (b) and operational modes piezo (c) d_{33} and (d) d_{31}.

One of the limitations that the PiD devices must surpass is the capability of supporting structural loads. Hence, to conceptualize the initial model it is taken in consideration the use of rubber bearings since it is a widely used equipment in civil engineering, and it is known for the capacity of working under high loads. Multilayer rubber bearings are devices that considerably decrease and/or dissipate the energy of a main structure to which it is attached, providing a damping mechanism. This type of device was used at first on structural elements of highways such as bridges or viaducts, then it started to be implemented on buildings to obtain seismic isolation. Conventionally, rubber bearings are laminated devices consisting of layers of different materials, as rubber (in order to provide period elongation and energy dissipation) and, usually, steel as reinforcing material which enhance the vertical bearing capacity. Moreover, the bearings are planned to sustain both the compressive load, given by the self-weight and live loads that act on the superstructures, and horizontal effects occurred by earthquakes or winds (Kelly et al. 2011), (Tubaldi et al. 2018). The use of such devices is mainly related to seismic isolations that works on minimizing or preventing structural damage in places such as buildings, bridges, and viaducts, providing a continuous operation by regulating the response of the structure (Ozkaya et al. 2011). Basically, rubber bearings can be subdivided into categories regarding the rubber material in low, natural, and high -damping rubber bearings (LDBR, NBR and HDRB, respectively); additional features may also be added to improve their performances, such as lead cores, reinforced fibers, and shape memory alloys (Ahmadipour et al. 2017). The efficiency of the bearings is related to their horizontal flexibility, vertical strength, and damping capacity: those functions are operated by rubber and steel layers. Since the PiDs concept lays on the idea of an element capable of supporting structural loads with a core denoted by a different material, few salient aspects are mentioned regarding the Lead Rubber Bearing (LRB, Figure 4), which is, among the others, the one with more similarities with the proposed device: LRB presents high damping capability due to the role of the lead core on shear displacements and in combination with the high damping rubber (Basshofi Habieb et al. 2019). It was introduced in New Zealand in the late 1970s, and presents elastomeric layers bonded to steel shim and fixing and

supporting plates at the top and bottom; the plus is that they are dotted with a lead core placed in the central part: the supporting steel plates confine the lead in the middle and restrain the whole isolator. LRBs bearings behave essentially as hysteretic damping devices since the lead goes inelastic; the lead core deforms plastically under shear deformation while energy dissipates through heat. It also provides an increase in vertical stiffness and energy absorption when compared to a low damping bearing (Ahmadipour et al. 2017). In this case, the stiffness of the structures may present a decrease because of the inelastic behavior of the lead, thus increasing structure's natural frequencies.

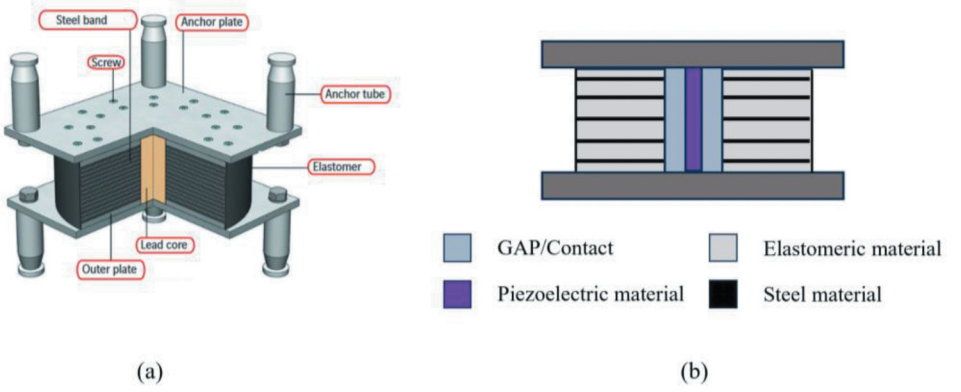


Figure 4. (a) Design of LRB (ISOSISM) and (b) section of the proposed device.

2.2 *Conceptual model for piezoelectric energy harvesters*

Despite the abilities of a piezoelectric material into convert energy, there are some limitations when such devices are implemented on civil structures, such as the load magnitude this material can support and its energy harvesting efficiency. Regarding the first aspect, it is possible to assume that the external part of PiD devices will be able to support the structural loads, while the internal core will be provided with piezoelectric energy harvesting. The choice of designing the PiD similarly as a rubber bearing guarantees every load's path, without compromising any possible structural function: they are thought as composite structural members comprising piezoelectric parts (in form of bars or fins), which resist loads either by axial or by flexural mode. A sufficient number of PiDs provided will constitute, as a whole, a self-powered parallel power system for sensors' energy needs, which is cable free (thanks to the wireless technology) and almost maintenance free (absence of batteries). However, PzEH from vibrations is proportional to the frequency of the dynamic loads and to the activated mass and here appears the other concern. In common (meso-, micro-scale) PzEH applications loading frequency is in the range of 0.1-10 kHz allowing for significant EH from small vibrating masses, while vibration frequencies in civil structures as bridges are orders of magnitude lower (within 1-25 Hz), reducing dramatically EH despite the larger masses involved. For this reason, the piezo components inside the PiDs will be designed to operate in two different kinds of nonlinear regimes: near-buckling conditions and impact dynamics. The first involves designing the piezo-bar inside the PiDs to buckle under the operating conditions, increasing both piezo strains and vibration frequencies with respect to the pre-buckling (linear) dynamic conditions (Friswell et al. 2012). The second regime allows impact of the vibrating piezo component, converting the low-frequency response to high frequency (Vijayan et al. 2015) and thus seeking a solution to maximize the energy production of piezoelectric harvesters when operating on civil structures: the maximum voltage and generated power from a vibrating mass are indeed mainly dependent on the frequency of vibration (the vibration mass is here the piezoelectric component). These two regimes (near-buckling and impact dynamics) will be enabled by the appropriate calibration of a "clearance gap" between the piezo fin and the other blocks being part of the PiDs, for allowing buckling and lateral impact of the piezo fin: those methods

receive the name frequency-up methods because they increase the frequency of vibration on the piezoelectric harvester and then their efficiency (Umeda et al. 1996), (Umeda et al. 1997).

In the proposed device configuration, as indicated in Figure 5, the impact phenomenon is likely to occur: the bar of piezoelectric material positioned in the core, as specified, is not in direct contact with the internal walls of the device but is detached from them by a certain gap (as represented by the back draw in the Figure 5b). When the PiD undergoes shortening due to the loads acting on the structure (PiDs are in fact designed to be positioned in the connection zones between structural elements), the bar can impact the aforementioned internal walls of the device, enabling the frequency-up conversion mechanism (the square dots in Figure 5b indicates the impact zone).

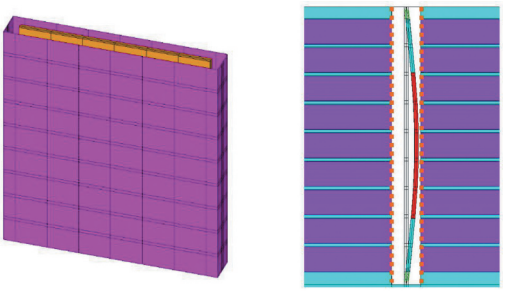


Figure 5. Contact (magenta) and target (orange) regions of the geometric model (a) and indication of the impact zones on a PiD device model (b).

3 APPLICATION

3.1 *Design of PiDs*

The materials used are steel, rubber and piezoelectric represented in blue, purple and red respectively (note that the steel shims in blue are also between purple – rubber – layers, Figure 6). The software used for the analysis is ANSYS® APDL: the element type chosen to represent the piezoelectric characteristics is the "SOLID5", which presents piezoelectric behavior, allowing the process of converting mechanical energy into electrical or vice-versa. The model used for further analyses is fully constrained at the bottom surface and horizontally constrained at top surface; vertical load is applied on the top plate and imperfections are taken into account by assuming a preferential buckling direction of the piezoelectric material component. Figures 6a and 6b presents the indication of the geometrical properties: W is the depth, L is the width (with W=L), Hi is the height of the internal core, t_{fix} is the thickness of the top and bottom plates, GAP is the gap between the piezo core and the lateral-internal walls that allows the buckling of the piezo-element (whose dimensions are named $PiezoW$ and $PiezoL$). Finally, t_r and t_s represent the height of the rubber and steel layers, respectively. The PiD dimensions (Table 1) are set by observing the maximum stress limit involved in the materials of the device: from literature (Usharani et al. 2017), (Anton et al. 2010) the maximum value for Pz material ranges around 45 MPa, which is the limit considered on this work, in order to secure the overall integrity. Besides the just mentioned values adopted for the geometric, Table 1 presents also the properties of the piezoelectric material: E is the young modulus, v Poisson constant, ε^T_{33} dielectric constant, d_{13} piezoelectric constant and ρ the material density. The clearance gap and the buckling of the piezo allow, as already stated, the PiDs to harvest significant energy even at the typical low-frequency range of vibration in civil structures; in order to catch in a correct way this phenomenon, the internal portion of the PiD is modeled using "contact" and "target" elements to have a simulation of an impact model during which the interaction among the surfaces is captured. One of the most challenging issues concerns the

simulation of the physical impact of the piezoelectric material core on the internal surfaces. In order to have a correct design, it is important to define i) which are the areas of impact and ii) what type of finite elements must be chosen to represent contact and sliding between 3-D target surfaces and a deformable surface. However, the region of contact is usually not known until the problem is run and, depending on loads, material, boundary conditions and other factors, surfaces can come into and go out of contact with each other in a largely unpredictable and abrupt manner. In the used model, element "CONTA174" is used to represent for deformable surfaces, while "TARGET170" is used for rigid bodies.

Table 1. The number of officially reported plague cases in the world.

$L = W$	$PiezoW$	$PiezoL$	GAP	Hi	t_s	t_r	t_{fix}	E	v	$\varepsilon^T{}_{33}$	d_{13}	r
800 mm	165mm	5mm	10mm	180mm	2.64mm	20mm	40mm	6.6E10Pa	0.2	1800	190e-12m/V	7800kg/m3

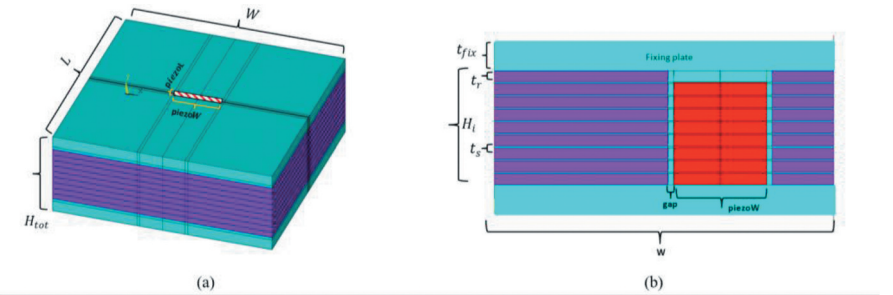


Figure 6. Geometry indication of the design parameters (a) and (b) section with indication of geometric parameters.

3.2 *Resistance's optimum value identification*

Given an eventual structural configuration in which PiDs can be inserted, it is possible to assume/reproduce a certain time-history for the relative displacement between the PiD nodes (Figure 7a) which will allow the evaluation of produced power. The time-history can be applied to the 3D PiD model/device as input on the top plate (the other one is assumed fully constrained for modeling purposes) and time-dependent analysis can be performed. Figure 7b represents a section of the device when the impact between the piezo core and the internal walls occurs, highlighting the clearance gap. The displacement of monitored core then is used in a subsequent analysis involving the piezoelectric energy harvester model: taking advantage of the possibility to combine structural and piezoelectric behavior in the same analysis, an electrical circuit element is added in order to obtain the power. The electric circuit is responsible for 'activating' the electrical part of the analysis which recognizes the piezoelectric behavior from mechanical to electrical energy or vice versa. Moreover, the addition of this element involves the appearance of a resistance (R) on the circuit, which influences the solution of the generated power. Since the solution obtained from the analysis is voltage (V) versus time, it is possible to obtain the root mean square (RMS) of the voltage by selecting two nodes on the different faces of the piezoelectric beam and then processing by the software tool. By Ohm's law, it can be presented that

$$P = V^2/R \tag{2}$$

where P is the power, V is voltage and R is the resistance applied on the circuit. Here the solution regards the Voltage (V) that is obtained by considering the RMS between the two nodes on opposite direction generated after performing the analysis, hence, by following the application of the Ohm's law, the parameter that may influence the obtained power is the Resistance

(R). In order to consider the optimum value for the resistance, different analyses were performed, varying the maximum displacement applied on the 3D PiD model and the frequency of vibration by introducing a generic sinusoidal signal. The results determined as optimum value a resistance of 2.5 KΩ (Figure 8). The presented methodology divided into levels appears to be a way of simplifying the performance of the PiD's device conception.

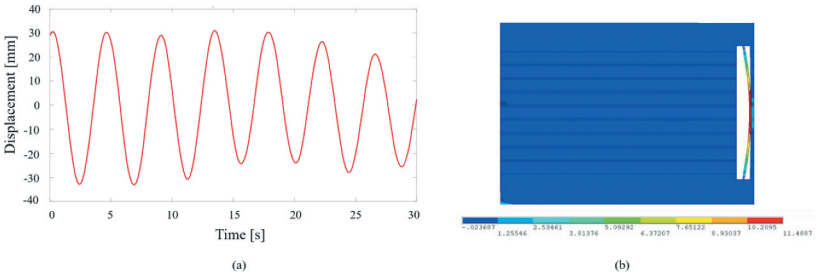


Figure 7. Time-History of the relative displacement (a) and section of PiD device with piezoelectric core impacting on lateral wall (mm).

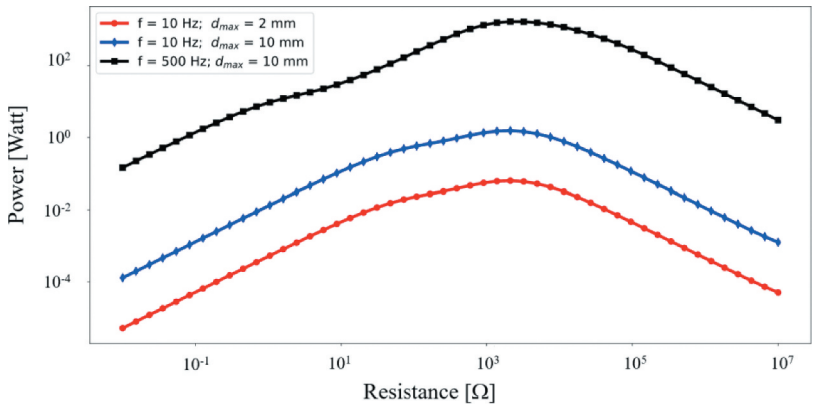


Figure 8. Optimum resistance observation in respect to different scenarios of frequency and maximum displacement.

4 CONCLUSION

A novel conception of a PiD device is here presented, showing the possibility of harvesting energy from vibration (as traffic induced vibration in case of bridges). This particular device is conceptualized as embedded in a structural member: the name, PiDs, stands for Piezoelectric Dampers. The importance for such devices results from the necessity of providing an infinitesimal amount of power to sensors and the novelty of this work is represented by the possibility of providing a solution to one of the main problems of sensors, power availability. PiDs are idealized to be energy harvesters by using piezoelectric materials, which produce electrical energy by converting the collected mechanical energy. In order to avoid some common problems that have made difficult the diffusion of piezo-material in civil engineering as the limited stress resistance (compared to structural material which doesn't allow to carry typical structural loads) and the different range of frequencies in which it usually works well (its behavior is at its best in a range that does not belong to civil engineering field), a design assumption was made: the PiD design started from a typical Lead Rubber Bearing device (LRB) in which the lead is replaced with a fin of piezoelectric material (in order to guarantee sufficient strength to resist structural loads) that does not occupy the whole core and that can buckle and impact on lateral walls,

increasing the vibration frequency and thus the harvested energy. However, it is necessary to be aware of the conditions of the materials if too much impact start happening; in this sense, the entity of the operational gap between the components and the size of the core are important aspects to consider among the design criteria. It is clear that further and in-depth research is still necessary on this topic, but the application has highlighted the feasibility of an innovative device that simultaneously guarantees structural support and energy harvesting from induced vibrations. Future developments, already partially under development, will concern both the implementation of experimental tests and finite element modeling that allows evaluating the behavior of PiDs in real situations (for example considering the loads induced by traffic passing on the deck of a bridge).

REFERENCES

ANSI & IEEE. 1988. IEEE Standard on Piezoelectricity Std 176-1987, New York: The Institute of Electrical and Electronics Engineers Inc

Ahmadipour, M. & Alam, M. S. 2017. Sensitivity analysis on mechanical characteristics of lead-core steel-reinforced elastomeric bearings under cyclic loading, *Eng Struct*, vol. 140: pp. 39–50.

Anton, S. R., Erturk, A., & Inman, D. J. 2010. Strength analysis of piezoceramic materials for structural considerations in energy harvesting for UAVs, *Proc. SPIE 7643, Active and Passive Smart Structures and Integrated Systems 2010*, 76430E.

Basshofi Habieb, A., Tavio, T., Milani, G., & Wijaya, U. 2019. 3D-Finite element modeling of lead rubber bearing using high damping material, *MATEC Web of Conferences*, vol. 276: p. 01013.

European Comission. 2014. The post-2015 Hyogo Framework for Action: Managing risks to achieve resilience. Brussels: UNGA.

Friswell, M. I., Ali, S. F., Bilgen, O., Adhikari, S., Lees, A. W., & Litak, G. 2012. Non-linear piezoelectric vibration energy harvesting from a vertical cantilever beam with tip mass, *J Intell Mater Syst Struct*, vol. 23, no. 13: pp. 1505–1521.

ISOSISM, SOSISM® Technical data sheet reference no.: FT En CV 513 (LRB), https://www.elemka.gr/media/5jlh522p/03_isosism_lrb.pdf.

Kelly, J. M. & Konstantinidis, D. A. 2011. Mechanics of Rubber Bearings for Seismic and Vibration Isolation. Chichester: John Wiley & Sons Ltd.

Jung, H.J., Kim, I.H. & Jang S.J. 2011. An energy harvesting system using the wind-induced vibration of a stay cable for powering a wireless sensor node, *Smart Mater Struct*, vol. 20, no. 7 075001.

Li, H.N., Ren, L., Jia, Z.G., Yi, T.H. & Li, D.S. 2016. State-of-the-art in structural health monitoring of large and complex civil infrastructures, *J Civ Struct Health Monit*, vol. 6, no. 1: pp. 3–16.

Lu, C., Raghunathan, V., & Roy, K. 2011. Efficient Design of Micro-Scale Energy Harvesting Systems, *IEEE J Emerg Sel Top Circuits Syst*, vol. 1, no. 3: pp. 254–266.

Ozkaya, C., Akyuz, U., Caner, A., Dicleli, M., & Pınarbası, S. 2011. Development of a new rubber seismic isolator: Ball Rubber Bearing (BRB), *Earthquake Engng Struct. Dyn*, vol. 40: pp. 1337–1352.

Srinivasan, A.V. & McFarland, D.M. 2001. Smart Structures: Analysis and Design. Cambridge: Cambridge University Press.

Tao, J. X., Viet, N. V., Carpinteri, A., & Wang, Q. 2017. Energy harvesting from wind by a piezoelectric harvester, *Eng Struc*t, vol. 133: pp. 74–80.

Tubaldi, E., Mitoulis, S. A., & Ahmadi, H. 2018. Comparison of different models for high damping rubber bearings in seismically isolated bridges, Soil Dynamics and Earthquake Engineering, vol. 104: pp. 329–345.

The Economist Technology Quarterly, Superstructures, http://www.economist.com/node/17647603, 2010.

Umeda, M., Nakamura, K., & Ueha, S. 1996. Analysis of the transformation of mechanical impact energy to electric energy using piezoelectric vibrator, *Japanese Journal of Applied Physics, Part 1: Regular Papers and Short Notes and Review Papers*, vol. 35, no. 5 B: pp. 3267–3273.

Umeda, M., Nakamura, K., & Ueha, S. 1997. Energy storage characteristics of a piezo-generator using impact induced vibration, *Japanese Journal of Applied Physics, Part 1: Regular Papers and Short Notes and Review Papers*, vol. 36, no. 5 SUPPL. B: pp. 3146–3151.

Usharani, R., Uma, G., Umapathy, M., & Choi, S.B., A new piezoelectric-patched cantilever beam with a step section for high performance of energy harvesting, *Sens Actuators A Phys*, vol. 265: pp. 47–61, 2017.

Vijayan, K., Friswell, M. I., Haddad Khodaparast, H., & Adhikari, S. 2015. Non-linear energy harvesting from coupled impacting beams, *Int J Mech Sci*, vol. 96–97: pp. 101–109.

Zhao, B., Qian, F., Hatfield, A., Zuo, L. & Xu, T.B. 2023. A Review of Piezoelectric Footwear Energy Harvesters: Principles, Methods, and Applications. *Sensors*, vol. 23, no. 13, 5841.

Bridge Maintenance, Safety, Management, Digitalization and Sustainability – Jensen, Frangopol & Schmidt (eds)
© 2024 The Author(s), ISBN 978-1-032-77040-6
Open Access: www.taylorfrancis.com, CC BY-NC-ND 4.0 license

Infrastructure structural health monitoring of bridge with polarimetric radar sensor

Lilong Zou
School of Computing and Engineering, University of West London, London, UK

Amir M. Alani
Faculty of Engineering, Computing and the Environment, University of Kingston, London, UK

ABSTRACT: The implementation of infrastructure structural health monitoring for bridges is crucial in thoroughly evaluating their condition and maintaining their structural robustness. Recently, novel technologies have been introduced for both static and dynamic evaluation, opening up exceptional opportunities in the fields of risk management and structural assessment. Notably, microwave radar sensors have been effectively utilized for the continuous surveillance of dynamic and static displacements in bridges via aerial deformation measurement techniques. However, a primary challenge for microwave interferometry arises from its inherent linear measurement nature, making it challenging to precisely locate damage and derive accurate displacement time-series for bridges. Furthermore, it is worth noting that vertical displacements typically hold more significance than horizontal displacements in the dynamic monitoring of bridges. Regrettably, microwave radar interferometry can yield only the line-of-sight (LOS) displacement of a monitored bridge. In this study, our primary objective is the remote surveillance of dynamic displacement responses in bridges using a polarimetric radar system. To achieve this, we employ various methodologies to surmount the inherent limitations of this technique. Further, we discuss the results obtained from our monitoring of a long-span metallic railway bridge and a reinforced concrete Shinkansen bridge. The ultimate goal of this research is to generate more comprehensive and precise data for bridge health monitoring through the use of a polarimetric sensor. As part of our approach, we conducted a polarimetric analysis to detect reflections from the deck of the bridges. Furthermore, details relating to the polarization orientation angle and the local incidence angle were processed under the acquisition geometry to compute the radar look angle. As a result, we were able to easily convert the bridge deformation fields in the vertical direction using the slant range distances. The maximum transient vertical deformation corresponding to the LOS deformation was also transformed while a train traversed the bridge

1 INTRODUCTION

As a key element in our infrastructure, bridges are pivotal for both economic growth and transportation efficiency. The maintenance and repair of aging bridge structures has become an increasingly critical issue worldwide. Traditional monitoring methods, such as on-site visual inspection, have significant limitations, often failing to detect non-visible problems. This has led to the rise of infrastructure health monitoring techniques, which are more effective in early problem identification and assessing the overall health of bridges. These techniques include vibration-based monitoring and innovative radar systems, such as Synthetic Aperture Radar (SAR) and Ground-Based Real Aperture Radar (GB-RAR), which have been advancing in recent years. Current research focuses on enhancing these technologies for more precise monitoring and assessment, including methods for dynamic deformation measurement and 3D imaging, to better manage and maintain bridge integrity (Zou et al., 2024).

DOI: 10.1201/9781003483755-295

In the last few decades, the field of infrastructure health monitoring, particularly for bridges, has seen significant advancements, becoming a critical tool in the maintenance and longevity of these essential structures. The evolution of this field owes much to the decreased costs associated with data collection, making comprehensive monitoring systems more feasible and widespread. The core objective of these systems is to detect potential issues at the earliest stage possible, thereby extending the lifespan of the infrastructure. Infrastructure health monitoring focuses not only on identifying damage but also on understanding the current state and load-bearing capacity of bridges (Tran-Ngoc et al., 2019). Damage, in this context, refers to any alterations in the material properties, boundary condition or overall integrity of the structure, caused by various factors including natural disasters, man-made events or gradual deterioration due to aging and environmental factors. The capability of these monitoring systems to provide an objective and continuous assessment of a bridge's condition is invaluable, especially in detecting issues before they escalate into major problems (Tran-Ngoc et al., 2021).

One of the most prominent methods in this field is vibration-based health monitoring. This approach is based on the principle that structural damage can be identified through dynamic testing, which evaluates the mechanical response of a structure to various stresses. Most vibration-based methods use fiber optic sensors and piezoelectric accelerometers, which are adept at capturing dynamic deformations over time. However, installing these systems can be challenging and potentially damaging, especially to historical bridges. In addition to vibration-based methods, microwave interferometric radar systems – particularly Synthetic Aperture Radar (SAR) and Ground-Based Real Aperture Radar (GB-RAR) – have become integral in bridge health monitoring. These systems use phase information from reflected microwave signals to detect displacements. Space-borne SAR offers wide-area monitoring, providing high-resolution data that can detect minute changes in a structure (Lazecky et al., 2016). On the other hand, GB-RAR is primarily used for the dynamic deformation monitoring of bridges, offering high accuracy and a non-invasive approach.

Despite their effectiveness, these radar systems have limitations, especially in providing comprehensive 2D or 3D images of a structure, which is crucial for a detailed assessment (Monserrat et al., 2014; Alani et al., 2014). Recent advancements have aimed to overcome these limitations. For instance, the introduction of polarimetric GB-RAR sensors has allowed a more detailed monitoring of bridge deformation. These sensors enhance the signal-to-noise ratio and can discern different structural properties of a bridge, allowing a more targeted and effective monitoring approach. Furthermore, recent research has explored methods by which to improve these radar systems. Techniques for obtaining 2D and 3D imaging have been proposed, enhancing the ability to monitor vertical and torsional movements. The use of multi-static GB-RAR systems and the integration of other technologies, such as terrestrial laser scanning, have furthered the capability to gather detailed structural information. In conclusion, the field of infrastructure health monitoring has evolved significantly, offering more precise and comprehensive methods for assessing the health of bridges. This evolution is crucial for ensuring the safety and longevity of these vital structures, and continued research and development in this area promise even more effective monitoring solutions in the future.

2 METHODOLOGY

2.1 *Microwave radar interferometry*

In the realm of microwave interferometric radar applications, a diversification of systems tailored to fulfill distinct objectives has occurred in recent years. These systems can be broadly categorized (based on the radar system's platform) into two principal classes: (1) space-borne Synthetic Aperture Radar (SAR) Systems and (2) ground-based Synthetic Aperture Radar Systems. Space-borne Interferometry SAR is adept at conducting efficient wide-area monitoring with a semi-continuous operation. It is proficient in detecting alterations in track geometry with commendable precision, measured in millimeters. These changes are ascertained through weekly measurement updates, complemented by superior spatial resolution. In instances

where infrastructural deformation predominantly occurs in the vertical and horizontal transversal directions, it is feasible to deduce the two-dimensional deformation vector utilizing multi-track radar data. However, it should be noted that the sensitivity of this deduction is contingent upon the track's directional orientation.

Deformation monitoring with InSAR requires phase observations from coherent scatterers, which can be double-different to phase differences between two locations and two epochs. From this, differential displacements can be derived by the multiplication of the phase differences with the radar wavelength (typically in the order of cms) and correcting for the two-way travel of the radar pulse. Coherent scatterers are primarily reflected from targets with stable phase values in time, such as buildings, bare rock and rails (Shao et al., 2018).

In satellite SAR interferometry, the differential interferometric phase is a combination of contributions from the systematic phase from the flat term $\Delta\phi_{flat}$, the topographic phase term $\Delta\phi_{topo}$, the deformation phase term $\Delta\phi_{def}$ and ionospheric $\Delta\phi_{ion}$, as well as the phase noise term $\Delta\phi_{noise}$. Hence, the interferometry phase in satellite SAR can be written as:

$$\Delta\phi = \Delta\phi_{flat} + \Delta\phi_{topo} + \Delta\phi_{def} + \Delta\phi_{ion} + \Delta\phi_{noise} + 2n\pi \tag{1}$$

where $2n\pi$ indicates the phase wrapping term. Following elimination of the non-deformation induced phase terms from the interferogram, the displacement phase in the radar line-of-sight (LOS) direction can be extracted. Radar measurements are only sensitive to the projection of the (3D) deformation phase $\Delta\phi$ onto the radar LOS. In practice, a local geodetic coordinate system is used for the projection containing the deformation components in the East, North and Up directions, respectively. With one satellite and single viewing geometry, estimation of the 3D deformation components based on the line-of-sight measurements is ill-posed, with three unknowns against one measurement. Therefore, it is impossible to determine 3D deformation from one satellite unless additional constraints can be introduced.

2.2 *Ground-based radar interferometry*

Ground and satellite-based radar interferometers follow the same basic principles. The only difference relates to viewing the geometry. As a kind of sensor, the ground interferometric radar can detect the displacement of the target in the target cone by using the phase information of the back-reflected microwave signal. If only a single-point scattering of monochromatic wave impact is considered, the phase difference of the backward reflected wave depends on the distance between the radar and the target. However, this phase information cannot be directly used for distance measurement because the phase must be affected by an ambiguity phase equal to half a wavelength. It is also affected by the nature of the air at the moment and the changes in the position of the sensor. Therefore, the interference phase $\Delta\varphi_{21}$ obtained at two moments can be expressed as (Zhang et al., 2018):

$$\Delta\phi_{21} = \Delta\phi_{def} + \Delta\phi_{atmo} + \Delta\phi_{geo} + \Delta\phi_{noise} + 2n\pi \tag{2}$$

where $\Delta\phi_{def}$ is the component related to the displacement; $\Delta\phi_{atmo}$ is the phase component due to the atmospheric effects during image acquisition; $\Delta\phi_{geo}$ contains the geometric phase component due to repositioning errors between the two acquisitions; and $\Delta\phi_{noise}$ is the phase noise component. Finally, the term $2n\pi$ relates to the phase wrapping corresponding to the ambiguity phase equal to half a wavelength. Interferometry phase accuracy depends not only on the ability of the electronic device to appreciate small phase rotation but also on the subsequent signal processing. In an ideal situation, using electromagnetic waves in the Ku band can achieve an accuracy of 0.1 mm, which is significantly higher than SAR interferometry observations.

In the case of the real aperture, the radar transmits a modulated signal that gives the sensor the capability to detect the displacement of targets that are more widely spaced than the resolution of the radar. In many applications, only-range resolution monitoring could be inadequate. In order to also provide angular resolution, it is necessary to rotate or move the microwave radar system. This makes it possible to obtain a 2D image in which the responses

of targets at the same distance from the radar can be discriminated in azimuth. In other words, moving the microwave radar system allows the obtaining of a 2D image of the displacement pattern and not simply a plot of its projection in the view direction. Although this is an important capability, it does result in the sensor becoming slower, heavier and bulkier; as such, it is an option not commonly implemented.

3 METHODOLOGY AND MONITORING RESULTS

3.1 *Monitoring of long-span metallic railway bridge*

The outstanding performance of the FastGBSAR-R (Zou et al., 2019) Interferometry radar sensor was implemented to investigate the dynamic behavior of the long-span metallic railway bridge. The sensor is a full polarimetric radar system featuring four horn antennas, two of which are used to transmit horizontal and vertical polarimetric electromagnetic waves while the remaining two are used to receive horizontal and vertical polarimetric reflective waves. The sensor was positioned on a tripod 10 m from the bridge, with the antennas pointed alongside the structure, as shown in Figure 1 (left). The measurements were taken during normal train traffic conditions. The aim of this study is to provide the dynamical monitoring of the bridge during a train crossing. The health condition of the bridge can be detected by judging the vertical deformation scale. The radar system can provide a radar profile within an extremely short sampling time. In this study, the pulse repetition frequency (PRF) was set to 500 Hz. The acquisition lasted approximately 300s. Under this monitoring condition, no movement occurred along the azimuth direction using a high PRF rate but the cost of this is a lack of azimuth resolution. All targets inside the antenna beam with the same slant range were recorded together, making it difficult to identify the corresponding target from the radar diagram. The Radar Cross Section (RCS) profiles of each polarimetric response of this bridge are presented in Figure 1 (right). Due to the scattering properties of the bridge and the acquisition geometry, the RCS decreases regularly as the distance increases. Identification of the bridge response commences at a 40 m range. The corresponding temporal profiles of the LOS deformation of each polarimetric component being passed by a train are shown in Figure 2 (left). It can be observed that, between 180s and 240s, deformation is measured in all the range profiles corresponding to the targets on the bridge.

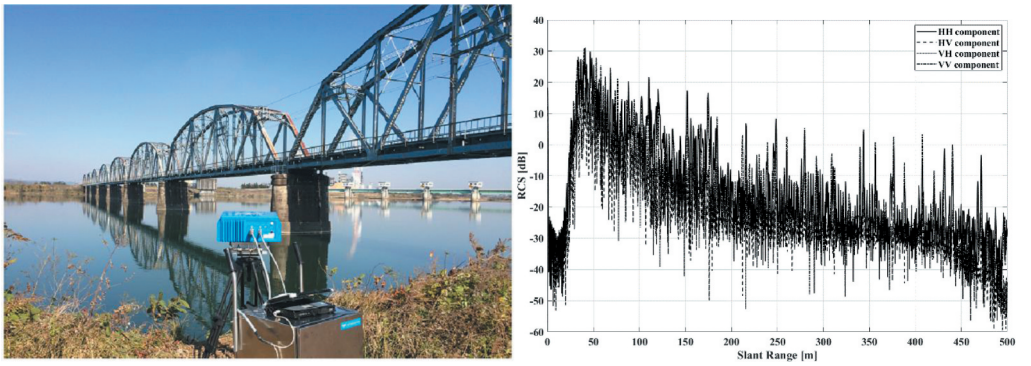


Figure 1. Polarimetric FastGBSAR-R system beside metallic railway bridge and RCS profile of HH, HV, VH and VV components.

Since radar has only a 1D range profile with distance resolution, the radar is able to distinguish objects on a distance basis only. In order to capture the overall bridge desk vertical vibration, an advanced methodology was proposed based on polarimetric analysis and acquisition geometry. The polarimetric responses hold all the information from the scatterers and all the polarimetric information can be written into a scattering matrix. Many current approaches that decompose the polarimetric scattering matrix are applied to more

meaningful, phenomenological parameter spaces. Based on these approaches, polarimetric information can be applied in our specialized case to target identification and classification. The proposed method can not only distinguish the resolution cell from the bridge desk, but also can provide vertical deformation information.

Due to the submeter-level spatial resolution of GB-RAR observations, a scatterer contains various noises. The total coherence can be modeled as:

$$\chi_{total} = \chi_{SNR} \cdot \chi_{vol} \cdot \chi_{add} \tag{3}$$

The loss of coherence caused by SNR decorrelation effects is represented by χ_{SNR}. The loss of coherence brought about by volume decorrelation effects is represented by χ_{vol}. The coherence loss resulting from extra residual sources, such as ambiguities and quantization mistakes, is represented by χ_{add}. The interaction between a radar wave and the target is characterized by total coherence, making the comparison of interferograms more straightforward. The precision of the determined signal phase difference $\Delta\phi$ error is correlated with the attained outcomes of the calculated deformations. It is possible to evaluate the signal phase difference based on the relationship between the total coherence value χ_{total} of the target and the GB-RAR observation using:

$$\Delta\phi^2 = \frac{1 - \chi_{total}^2}{2\chi_{total}^2} \tag{4}$$

Researchers have established that the SNR of scatterers plays a critical role in determining the accuracy of deformation monitoring in real-world measurements. In addition to considering the SNR value, the distance between scatterers within the scene must also be considered. Given that the obtained SNR values appear to be significantly overestimated, it is logical to establish a correlation between deformation and total coherence based on the preceding discussion, to enhance the real-world accuracy of deformation measurements under field conditions. In this paper, we implement an approach that combines the co-polarization deformation of scatterers according to coherence, to improve the estimation of the deformation time series. More specifically, the associated deformation of scatterers in the HH and VV channels is denoted as Def_{HH} and Def_{VV}, respectively. Employing the improved deformation method, their weighted average value was calculated (Chang et al., 2021):

$$Def_{LOS} = \frac{W_{VV} * Def_{VV} + W_{HH} * Def_{HH}}{W_{VV} + W_{HH}} \tag{5}$$

The designated weights for deformation in the HH and VV channels are represented by W_{HH} and W_{VV}, respectively. These weights can be influenced by the coherence of scatterers. In scenarios where coherence is elevated, scatterers are assigned significant weight. The precision of GB-RAR observational uncertainty and time series processing errors impacts considerably on the quality of the Def_{HH} and Def_{VV} deformation estimations.

H/Alpha analysis was then conducted, based on the full polarimetric responses of the RCS profiles. Entropy arises as a natural measure of the inherent reversibility of the scattering data and the alpha angle can be used to identify the underlying average scattering mechanisms. The H/Alpha plane can be subdivided into nine basic zones by considering different scattering behavior, to separate the data into basic scattering mechanisms. Each of these zones independently represents the pixel indexes corresponding to dominant scattering mechanisms identified by a backscattered signal (Lee et al., 2006). From the results of the H/Alpha analysis, we could see that most reflections emanated from a region with low entropy values. Regions in which entropy varies from 0 to 0.5 and alpha angle varies from 0° to 42.5° represent scattering from the Bragg Surface. Regions in which entropy varies from 0 to 0.5 and alpha angle varies from 42.5° to 47.5° represent the scattering from a target such as an isolated dipole (Lee et al., 2018). The reflections from these two regions mainly arose from the side surface of the metallic bridge. At this stage, the reflection from the side surface of the metallic bridge was selected from the RCS profiles, based on its polarimetric property.

We next focused on the reflections from these two regions and calculated the vertical deformation based on the acquisition geometry and radar polarimetry. The azimuth direction and ground range direction were determined by the radar H-pol and V-pol, respectively.

Polarization orientation angle (POA) is the angle of rotation about the radar line of sight (Lee et al., 2018). POA can be estimated from PolSAR data by the angle of the correlation between LL and RR circular polarizations (Lee et al., 2006), and can be expressed as:

$$\tan(-4\eta) = \frac{-4Re\left(\left\langle (S_{HH} - S_{VV})S_{HV}^{*}\right\rangle\right)}{-\left\langle |S_{HH} - S_{VV}|^{2}\right\rangle + 4\left\langle |S_{HV}|^{2}\right\rangle} \tag{6}$$

where ξ indicates POA. POA can also be obtained from the azimuth slope angle ω, ground range slope angle γ and radar look angle ϕ, based on the imaging geometry using the following equation (Moreira et al., 2013):

$$\tan(\xi) = \frac{tan\omega}{-tan\gamma cos\phi + sin\phi} \tag{7}$$

Since the sensor was positioned on a tripod 10 m distant from the bridge, the local incidence angle θ can be calculated by the following relationship:

$$\cos\theta = \frac{10}{R} \tag{8}$$

where R indicates the slant range distance from the radar sensor to the target, which can be obtained from the RCS profiles. The local incidence angle can also be derived in terms of the local slopes and radar look angle, and can be expressed as:

$$\cos\theta = \frac{tan\gamma sin\phi + cos\phi}{\sqrt{1 + tan^{2}\gamma + tan^{2}\omega}} \tag{9}$$

Hence, the radar look angle θ can be solved with the above equations. For deformation caused by passing trains, planar displacements contribute only minimally to the radar derived LOS deformation in most cases. Thus, it is recommended that planar deformation components are neglected when monitoring railway induced deformation on bridges regarded as having no planar deformations. With the known radar look angle ϕ, the bridge deformation fields in the vertical direction were easily converted with the slant range distances, as shown in Figure 2 (right).

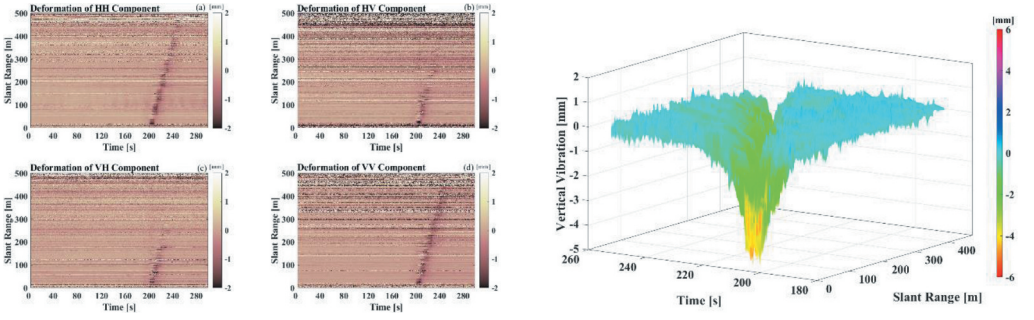


Figure 2. LOS deformation profiles and vertical deformation measured at metallic railway bridge while a train passes.

3.2 *Monitoring of reinforced concrete Shinkansen bridge*

The FastGBSAR-R Interferometry radar sensor was also implemented to investigate the dynamic behavior of the reinforced concrete Shinkansen bridge. The sensor was positioned on

a tripod under the edge of the bridge and the antennas were pointed along the structure, shown in Figure 3 (left). Measurements were carried out during the normal traffic conditions of the bridge. An aim of this study is to provide the dynamical monitoring of the bridge while being crossed by a Shinkansen train. The health condition of the bridge can be detected by judging the vertical deformation scale. In this study, the pulse repetition frequency (PRF) was set to 1000 Hz and acquisition lasted 300s. The Radar Cross Section (RCS) profiles of each polarimetric response of the bridge are presented in Figure 3 (right). The corresponding temporal profiles of the LOS deformation of HH and VV, while being passed over by a Shinkansen train, are set out in Figure 4 (left). It can be observed that, between 10s and 40s, displacement was measured in all the range profiles corresponding to targets on the bridge. The displacement is clear for targets located within 250 m of HH components but unclear for the VV component.

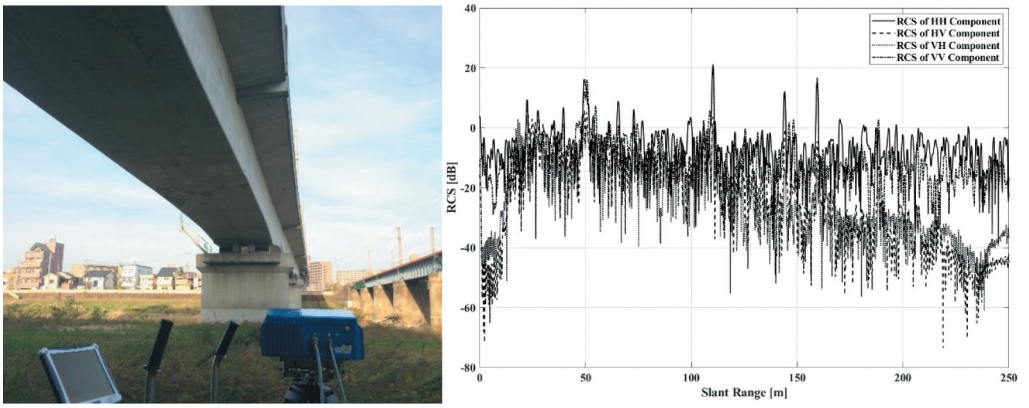


Figure 3. Polarimetric FastGBSAR-R system beside reinforced concrete bridge and RCS profile of HH, HV, VH and VV components.

Since the bridge deck surface is relatively smooth, the back reflected signals of each polarimetric component are very weak. The lower the signal to noise ratio (SNR), the lower the phase quality of the interferometry will be. It is not recommended that the interferometry phases of all reflections from the bridge deck are monitored, since just a small number of reflection points at the structure can retrieve an accurate displacement time series. From Figure 3 (right), three high RCS reflection points could be observed at approximately 50 m, 110 m and 160 m. H/Alpha analysis was carried out based on the polarimetric responses of the reflections. From the result of the H/Alpha analysis, we see that most of the coherent scatterers came from a region with low entropy and alpha values varying from 20° to 70°. This is

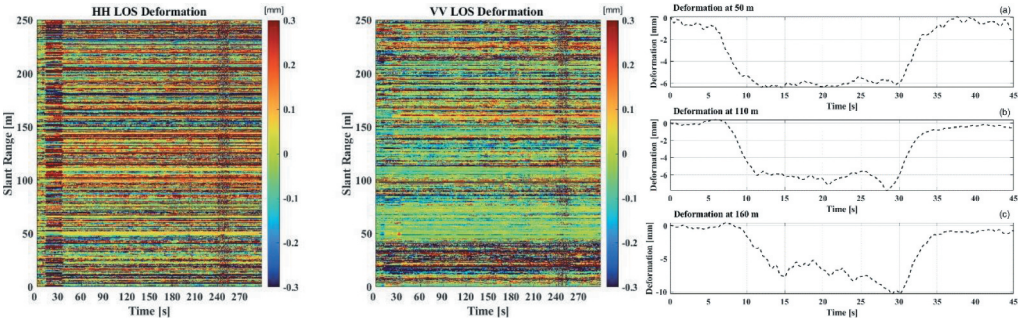


Figure 4. LOS deformation profiles and vertical deformation measured at reinforced concrete bridge while a Shinkansen train passes.

likely to mean that these reflections not only emanate from similar dihedral reflectors and dipole targets, but also similar Bragg surface targets.

It is clear that the reflections of the three points emanate from targets such as the dihedral reflector. Due to the acquisition geometry, we conclude that these reflections come from the horizontal desk with a vertical edge, which is similar to a dihedral corner reflector. The altitude difference between the sensor and the bridge desk is 2.5 m. Deformation of the three points in the vertical direction was easily converted with the slant range distances, as shown in Figure 4 (right). The maximum vertical deformation of the reinforced concrete Shinkansen bridge is around 10 mm. Each saw tooth of the deformation curve corresponds to a Shinkansen carriage.

4 CONCLUSION

Within the sphere of the structural health monitoring of infrastructure, Ground-based Real Aperture Radar (GB-RAR) interferometry has emerged as an innovative measurement technique. Its principal advantage is its capacity to generate comprehensive insights into the integrity of scrutinized structures. Nevertheless, technology is not without its limitations; specifically, the accurate localization of deformations within a structure represents a significant challenge, given that any point within a resolution cell can influence measurement. This paper introduces a suite of methodologies designed to counterbalance the inherent constraints associated with GB-RAR interferometry, particularly in the context of bridge monitoring applications. The investigation delves into the vertical deformation patterns of bridges, employing a polarimetric GB-RAR system augmented by sophisticated signal processing algorithms. Furthermore, the study explores the correlation between the modal parameters of a bridge and its structural properties. The signal processing strategies proposed herein are multifaceted, including the categorization of scattering characteristics via polarization analysis, the refinement of deformation forecasting by leveraging dual-polarization channels, and the estimation of radar look angles to compute vertical deformations. These methodologies collectively aim to enhance the precision of structural localization and vertical deformation measurements in bridge monitoring. Empirical findings presented in this research detail the dynamic behaviors of two distinct bridge types under varying load conditions, encompassing scenarios such as the transit of low-speed trains and the passage of high-velocity Shinkansen bullet trains. The outcomes underscore the efficacy of polarimetric GB-RAR, in concert with the advanced algorithms proposed, as a potent approach for the surveillance of bridge structures. This technique significantly enriches the quality and veracity of dynamic deformation monitoring, underscoring its utility in the domain of infrastructure health assessment.

REFERENCES

Alani, A.M., Aboutalebi, M. & Kilic, G., 2014. Use of non-contact sensors (IBIS-S) and finite element methods in the assessment of bridge deck structures. *Structural Concrete*, 15(2), 240–247.

Chang, L. & Stein, A., 2021. Exploring PAZ co-polarimetric SAR data for surface movement mapping and scattering characterization. *International Journal of Applied Earth Observation and Geoinformation*, 96, 102280.

Lazecky, M., Hlavacova, I., Bakon, M., Sousa, J.J., Perissin, D. & Patricio, G., 2016. Bridge displacements monitoring using space-borne X-band SAR interferometry. *IEEE Journal of Selected Topics in Applied Earth Observations and Remote Sensing*, 10(1), 205–210.

Lee, J.S., Ainsworth, T.L. & Wang, Y., 2018. Polarization orientation angle and polarimetric SAR scattering characteristics of steep terrain. *IEEE Transactions on Geoscience and Remote Sensing*, 56(12), 7272–7281.

Lee, J.S., KrogageR, E., Ainsworth, T.L. & Boerner, W.M., 2006. Polarimetric analysis of radar signature of a manmade structure. *IEEE Geoscience and Remote Sensing Letters*, 3(4), pp.555–559.

Monserrat, O., Crosetto, M. & Luzi, G., 2014. A review of ground-based SAR interferometry for deformation measurement. *ISPRS Journal of Photogrammetry and Remote Sensing*, 93, 40–48.

Moreira, A., Prats-Iraola, P., Younis, M., Krieger, G., Hajnsek, I. & Papathanassiou, K.P., 2013. A tutorial on synthetic aperture radar. *IEEE Geoscience and Remote Sensing Magazine*, 1(1), 6–43.

Shao, Z., Zhang, X., Li, Y. & Jiang, J., 2018. A comparative study on radar interferometry for vibrations monitoring on different types of bridges. *IEEE Access*, 6, 29677–29684.

Tran-Ngoc, H., Khatir, S., De Roeck, G., Bui-Tien, T., & Adbel Wahab, M., 2020. Damage assessment in beam-like structures using cuckoo search algorithm and experimentally measured data. In *Proceedings of the 13th International Conference on Damage Assessment of Structures: DAMAS 2019*, 9-10 July 2019, *Porto, Portugal* (pp. 380–385). Springer Singapore.

Tran-Ngoc, H., Khatir, S., LE-Xuan, T., De Roeck, G., Bui-Tien, T., & Adbel Wahab, M., 2021. Finite element model updating of a multispan bridge with a hybrid metaheuristic search algorithm using experimental data from wireless triaxial sensors. *Engineering with Computers*, 1–19.

Zhang, B., Ding, X., Werner, C., Tan, K., Zhang, B., Jiang, M., Zhao, J. & Xu, Y., 2018. Dynamic displacement monitoring of long-span bridges with a microwave radar interferometer. *ISPRS Journal of Photogrammetry and Remote Sensing*, 138, 252–264.

Zou, L. & Sato, M., 2019. An efficient and accurate GB-SAR imaging algorithm based on the fractional Fourier transform. *IEEE Transactions on Geoscience and Remote Sensing*, 57(11), 9081–9089.

Zou, L., Nico G., Amir A.M. & Sato, M., 2024. Strategy for vertical deformation of railway bridge monitoring using polarimetric ground-based real aperture radar system. *Structural Health Monitoring*, 1–12.

Bridge Maintenance, Safety, Management, Digitalization and Sustainability – Jensen, Frangopol & Schmidt (eds)
© 2024 The Author(s), ISBN 978-1-032-77040-6
Open Access: www.taylorfrancis.com, CC BY-NC-ND 4.0 license

Precise 3D simulations in bridge deck inspections of ground penetrating radar survey

Dingwu Dai, Yuhao Zheng & Hai Liu
Guangzhou University, Guangzhou, China

Lilong Zou
University of West London, London, UK

Amir M. Alani
University of Kingston, London, UK

ABSTRACT: Ground penetrating radar (GPR) is a non-destructive technology widely used for the structural mapping of bridge deck pavements. However, since traditional numerical simulation models have limitations in accuracy – inevitably resulting in dissatisfaction with current research – our study develops a refined three-dimensional GPR simulation model for enhanced imaging applications and fine structure inversion. The model comprises a mechanical construction, using a discrete element method (DEM) to accurately simulate coarse aggregate positioning. MATLAB is then employed for domain discretization and the integration of fine aggregate and asphalt binder. Subsequently, the study undertakes GPR numerical simulations using the finite-difference time-domain (FDTD) method with gprMax software. The results show a level of error between simulation results and empirical values below 2%, and a discrepancy between simulation results and measured data below 3%, demonstrating the high accuracy of the proposed method in simulating GPR responses in bridge deck pavements.

1 INTRODUCTION

Bridge structures play a vital role in economic development, cultural exchange and transportation within human society (Abouhamad et al., 2017). Affected by continuous repeated vehicle loading and other severe service conditions, such as high humidity in the natural environment and dramatic day/night temperature variations, bridge deck pavements typically suffer from distresses such as moisture damage, rutting, cracking and debonding (Alani et al., 2013). These issues are mainly caused by the mechanism of asphalt-aggregate debonding, which leads to a loss in pavement strength and stiffness and consequently shortens the service life of bridges (Zhang et al., 2020). Therefore, condition assessment and maintenance activities are essential for estimating the remaining service life of bridges that are structurally deficient or functionally obsolete. GPR stands out as one of the most effective Non-Destructive Evaluation (NDE) technologies for assessing bridge deck pavement deterioration due to its efficient data collection, rapid detection capabilities and high-resolution imaging. It has long been recognized as an exceptionally promising tool for capturing and quantifying the progression of deterioration in bridge decks, detecting debonding distribution and measuring the thickness of concrete cover, among other applications (Asadi et al., 2020).

GPR operates by transmitting high-frequency radio waves into the ground. As these waves encounter different subsurface materials, they are reflected back at varying intensities, depending on the material's electrical properties. The radar's receiving antenna captures these reflected signals while the remaining energy propagates further and gradually diminishes over

DOI: 10.1201/9781003483755-296

time (Varnavina et al., 2015). Therefore, the GPR application is based on electromagnetic wave propagation, indicating that numerical simulation using GPR can be realized by solving Maxwell equations, which mathematically express the relationship between fundamental electromagnetic (EM) field quantities and their dependence on their sources (Alani et al., 2014). GPR simulations enable the visualization of EM phenomena that are otherwise difficult to detect, significantly enhancing the accuracy of GPR interpretation. However, traditional modeling methods – which often simplify bridge pavement structures to homogeneous media – are becoming increasingly inadequate for contemporary complex research, such as the inversion study of the fine structure of bridge pavements. These simplified models can even lead to conflicting results between field test measurements and simulation outcomes. For example, research by Mezgeen et al. into the characteristics of GPR signals in response to varying crack widths in rigid pavements revealed a notable difference: cracks as narrow as 2mm (barely detectable in experimental measurements) were clearly observable in simulations (Zou et al., 2020). In reality, the material of bridge deck pavements, including asphalt concrete, is a multiphase, heterogeneous mixture composed of various substances. When high-frequency EM waves traverse through such a medium, a substantial amount of scattering wave occurs. This scattering leads to random features in the received signals, which is a primary reason for the significant discrepancies observed between the results of homogeneous model simulations and actual measurements. Therefore, it is essential for improving the accuracy of GPR numerical simulation to develop a multiphase random discrete medium model which more accurately reflects the actual conditions of bridge deck materials. However, methodologies for building numerical simulation models of composite media using GPR are scarce. Li et al. enhanced simulation accuracy by incorporating surface roughness, which increased heterogeneous scattering waves at interfaces (Zeng et al., 2023). However, irregular interfaces cannot accurately represent the random scattering waves occurring within the medium. Solla et al. combined image processing techniques (IPT) with the FDTD algorithm to achieve 2D GPR simulations of bridges (Solla et al., 2016). However, this method is heavily dependent on the quality of the input images and is not an automated process. Certainly, the integration of Computed Tomography (CT) technology with IPT can significantly enhance the efficiency of modeling, potentially achieving a one-to-one replication of the actual scenario in a three-dimensional model (Özkap et al., 2020). However, obtaining CT scan results for large-scale bridge deck pavements is impractical.

Considering the research discussed previously, this study introduces a Realistic Composite Medium Modelling (RCMM) approach tailored for actual composite mediums, with the aim of enhancing the precision of GPR numerical simulations on bridge deck pavements. The structure of this paper is as follows: a comprehensive description of the RCMM method is given in Section 2, followed by details of the validation process in Section 3. The final section offers a summary of our findings.

2 METHODOLOGY

In this paper, the bridge deck pavement is modelled as an asphalt concrete (AC) mixture. Aggregates, asphalt binder and air voids compose the three-phase heterogeneous media, excluding water, reinforcement mesh and other intricate structural elements typically found in bridge pavements. Given a specific designed air void content, the volume fractions of the other two phases are calculated as follows:

$$V_a = \frac{(1 - P_b) \times G_{mb}}{G_s} = \frac{(1 - P_b) \times (1 - V_{air}) \times G_{mm}}{G_s} \quad (1)$$

$$V_b = 1 - V_{air} - V_a \quad (2)$$

where V_{air} is the designed air void content; G_{mb} and G_s are the bulk density of asphalt mixture and aggregates, respectively; G_{mm} represents the maximum theoretical density of the asphalt mixture; and P_b signifies the asphalt content (Liang et al., 2022). The specific values of these

parameters can be derived from the design documents of AC mixtures. Compared with methods that depend on IPT, the RCMM method is independent of the need for high-definition images or the microstructure of real-world specimens, making it more adaptable for extensive modeling and precise parameter management. In this study, EDEM (a commercial DEM software) was employed as a promising tool to simulate both the location and orientation of coarse aggregate particles. To accurately simulate a realistic road model, we carried out two key simulations sequentially – settlement and compaction – based on the constitutive mechanical model of asphalt mixtures. Additionally, it is noteworthy that the irregularity of particles was achieved by importing various stone templates, each differing in angularity index and dimensional value. Considering the application of Yee's algorithm in the Finite-Difference Time-Domain (FDTD) method, the simulation domain was subsequently discretized into uniform cubic cells. The dimensions of these cells are designed to match the spatial resolution of the FDTD method, ensuring coherence between the simulation elements and the method's inherent structure. The three-phase pavement generation algorithm is summarized as follows:

1. Calculate V_s and V_b using Equation (1) and Equation (2).
2. Generate coarse aggregates with sizes larger than 2.36mm using EDEM, based on aggregate gradation data and Vs.
3. Discretize the simulation domain into a three-dimensional array using unit cubes and verify the aggregate gradation, noting that the dimensions of each cube should be smaller than 2mm to achieve the desired level of accuracy. After discretization, areas within the sample boundary that are not occupied by aggregates are designated as free space.
4. Complement the fine aggregates and asphalt binder by randomly substituting the free space elements within the sample boundary. This arrangement is accomplished by utilizing two distinct types of cube: aggregate-asphalt cubes and asphalt-void cubes. The former type represents elements where fine aggregates are mixed with asphalt binder at a specific ratio, whereas the latter represents elements combining asphalt binder and air voids in a certain proportion.

The dielectric properties of the materials were assigned following the completion of the FDTD model. In this study, all materials are considered non-lossy, implying that the imagery elements of their dielectric constants are not taken into account. In this work, the dielectric constants of free space and asphalt binder are set to 1 and 3, respectively (Leng et al., 2011). Subsequently, a two-phase Rayleigh model is employed to determine the dielectric constants for the aggregate-asphalt cube and the asphalt-void cube (Sihvola, 2000). Meanwhile, the ALL model is utilized to calculate the empirical values of the dielectric constant for asphalt concrete (AC) mixtures (Abufares et al., 2023).

3 LABORATORY TESTING AND NUMERICAL SIMULATION

In this section, we conducted laboratory experiments on GPR measurements for AC mixtures. The design parameters of the experimental specimens were utilized for two primary purposes: firstly, they were input into the ALL model to calculate the empirical values of the specimens' dielectric constants and, secondly, they served as input parameters for numerical modeling. To further underscore the accuracy of our proposed method, we also established a simulation model with identical parameters using the Random Sequential Adsorption (RSA) algorithm (Cao and Al-Qadi, 2021). Consequently, we compared the simulation outcomes from both methods with actual measurements and empirical values.

The thickness of the pavement layer of bridge deck pavements varies, as its design must incorporate factors such as the construction environment and vehicle density. In this research, thickness exceeding 10 cm significantly increases the experimental workload, while thickness below 5 cm causes the radar signals from the top and bottom surfaces to overlap, complicating the calculation of the dielectric constant using the two-way travel time (TWTT) algorithm. Consequently, three AC samples, each 10 cm thick, were designed and fabricated. Details of the designed parameters are summarized in Table 1 and the gradation curve is depicted in Figure 1.

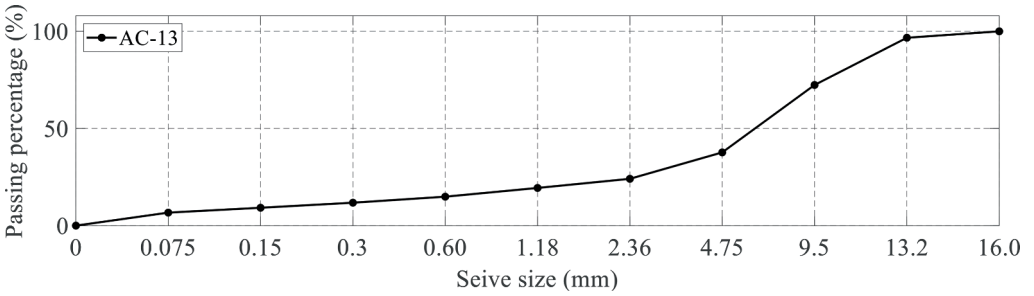


Figure 1. Aggregate gradation data of AC-13 mixture.

Table 1. Asphalt mixture information for specimens.

Characteristics	V_{air} (%)	G_{mm}(-)	G_s(-)	G_{mb}(-)	P_b(%)
AC-13*	6.00	2.69	2.93	2.53	5.00

*With a nominal maximum aggregate size of 13mm.

The laboratory GPR static tests were conducted using an IDS radar system, equipped with a palm antenna operating at a central frequency of 2 GHz. As depicted in Figure 2, a palm radar system was mounted at the center of each specimen for data collection. Due to the limited footprint of the antenna, individual data sets were obtained from each specimen. The time window for a single GPR A-scan was established at 20 ns, with a sampling rate of 2048 to ensure sufficient time-domain resolution for the TWTT method (0.0098 ns/sample). To prevent subsurface reflections from the floor decks (which are outside the scope of this study), a steel plate was placed beneath each specimen. Data collection involved eight measurements per specimen: four on the front side and four on the back side. Post-measurement processing included DC removal, bandpass filtering and time-window cutting for the received signals. Figure 3 illustrates a representative set of A-scan data, in which the reflection times of the upper and lower surfaces are extracted using the Hilbert transform. Figure 4 displays the experimental results for each plate, with average results being 8.34, 8.17 and 8.06, respectively.

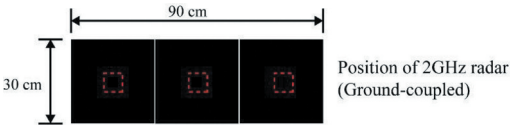


Figure 2. Laboratory experiment configuration.

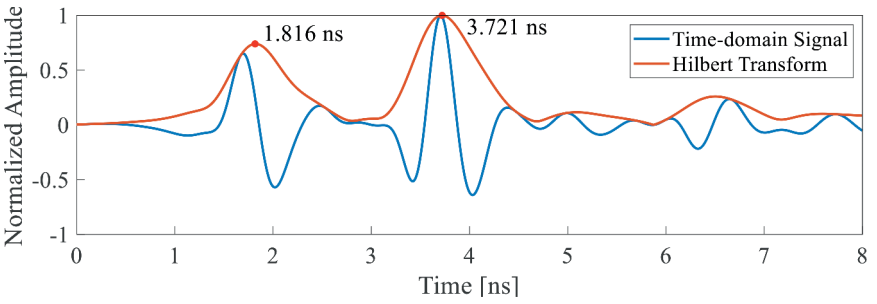


Figure 3. Example of measured A-scan data.

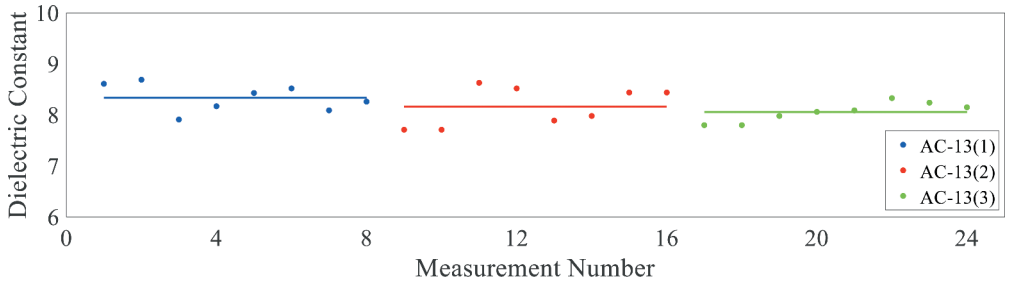


Figure 4. Dielectric constants for each AC mixture.

The numerical models were developed incorporating the same air voids, aggregate type, asphalt binder contents and aggregate gradations as depicted in Table 1 and Figure 1. Figure 5 presents a visualization of two simulated geometric models. It is noteworthy that, despite its theoretical capability, the RSA method encounters significant spatial configuration constraints in actual three-dimensional modeling. This limitation, characterized by increasing difficulty in avoiding overlaps between spheres as their number grows, makes effective spatial arrangement challenging within a limited area. Such constraints prevent the RSA method from effectively realizing a high-density, three-dimensional AC model. Therefore, we established the RSA-based AC model as a two-dimensional model with the dimensions 0.3m × 0.1m.

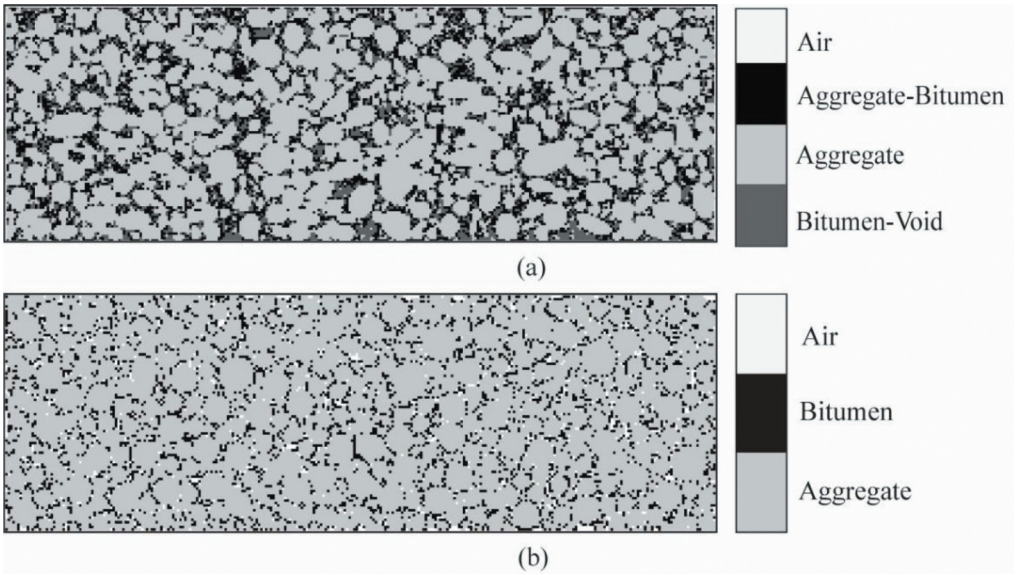


Figure 5. Visualization of (a) RCMM-based AC model and (b) RSA based AC model.

We continued to build the numerical simulation model based on FDTD using gprMax software. As depicted in Figure 6, the schematic of the FDTD model consists of two layers. The top layer was developed utilizing the generated heterogeneous models. The other was set as a Perfect Electric Conductor (PEC) due to its capability to strengthen the reflected waveform, which aids in the identification of TWTT. 'Tx' denotes the transmitting antenna and 'Rx' represents the receiving antenna. The Perfectly Matched Layer (PML) was employed to simulate EM wave propagation in an infinite space, effectively weakening EM waves at the boundary without generating any reflections. Additional model parameters are listed in Table 2.

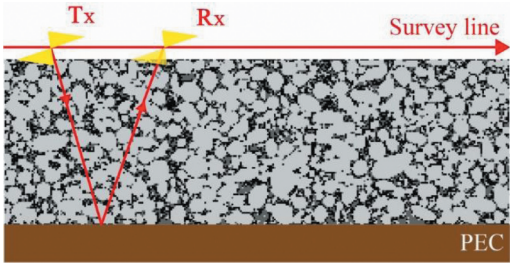


Figure 6. FDTD simulation model in gprMax.

Table 2. Asphalt mixture information for specimens.

Characteristics	Time window (ns)	Central frequency (GHz)	Function of excitation source (-)	Spatial resolution (m)	Antenna spacing (m)	Movement step (m)
Value	10	2	Ricker	0.001	0.06	0.01

The dielectric constant of the aggregates was found to be 10.5 (Parkhomenko, 1967). Subsequently, we calculated the dielectric constants for the aggregate-asphalt cubes and the asphalt-void cubes as 7.66 and 2.29, respectively. In the case of all materials, except for PEC, conductivity was set to 1e-5, indicating that the materials were assumed to be non-lossy.

After completing the simulations, Figure 7 showcases an example of the subtracted GPR A-scan signals, where the direct wave is removed. Consequently, Table 3 presents a comprehensive summary of various data types: average values from the simulations, empirical values derived from the ALL model, field experiment measurements, and discrepancies between both the simulated and empirical values as well as the simulated and measured

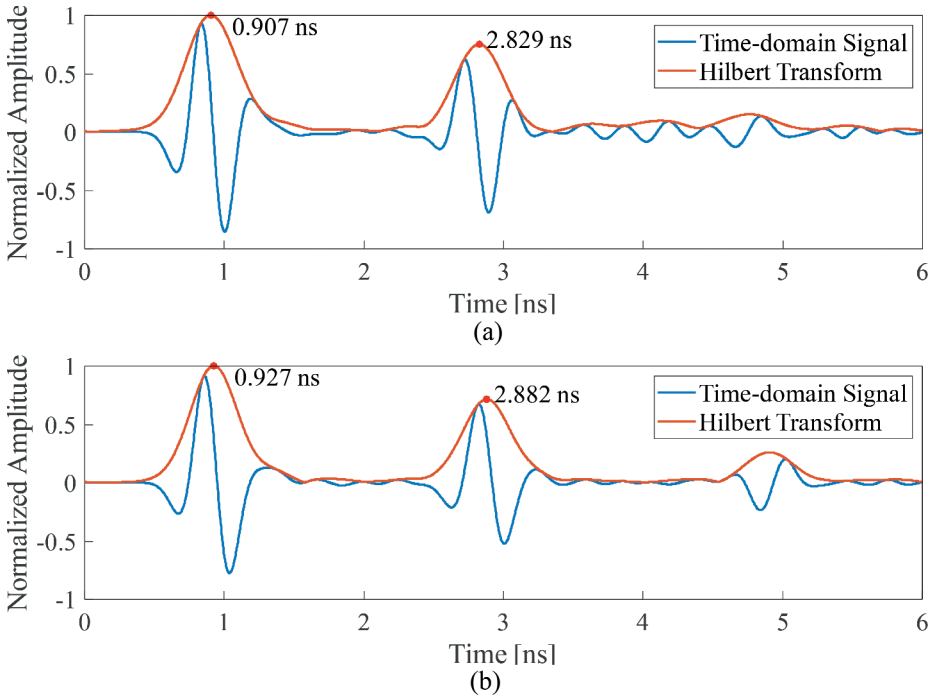


Figure 7. A-scan signals from (a) RCMM and (b) RSA Forward Simulations.

Table 3. Asphalt mixture information for specimens.

Characteristics	Values (-)	RCMM model result (-)	RSA model result (-)	Error with RCMM models (%)	Error with RSA-based (%)
AC-13(1)	8.34	8.30	8.60	0.5	3.1
AC-13(2)	8.17			1.6	5.3
AC-13(3)	8.06			3.0	6.7
AC-13(ALL)*	8.25			0.6	4.2

*Empirical value calculated by ALL model.

values. The data in Table 3 clearly indicates that, regardless of whether empirical values or measured results are considered, the refined model's simulation results significantly surpass those obtained from the RSA model.

4 CONCLUSION

In this study, we introduced the RCMM method – a novel approach in numerical modeling for simulations of bridge deck pavements using GPR. We began by constructing a three-dimensional structure with coarse aggregates as the skeleton, emphasizing the predominant volume fraction of aggregates relative to the other components. DEM was employed to position the coarse aggregates, incorporating irregular aggregate templates and an asphalt mechanical model for enhanced accuracy. Subsequently, we utilized MATLAB to discretize the simulation domain into Yee's grids. Innovatively, we introduced two types of grid element as aggregate-asphalt and asphalt-void elements during this phase to optimize the model's adaptability in the Yee grid. Finally, the model was encoded into a three-dimensional matrix and introduced into gprMax for GPR wave propagation. To validate our model's effectiveness, we conducted a comparative analysis against the RSA method, using identical parameters This comparison, backed by empirical data and actual measurements, revealed that our RCMM method significantly reduces simulation errors – less than 2% in comparison to empirical values and under 3% against measured data. These findings underscore the RCMM method's superior precision in simulating GPR responses for bridge pavement layers.

REFERENCES

Abouhamad, M., Dawood, T., Jabri, A., Alsharqawi, M. & Zayed, T. 2017. Corrosiveness mapping of bridge decks using image-based analysis of GPR data. *Automation in Construction*, 80, 104–117.

Abufares, L., Cao, Q. & Al-Qadi, I. L. 2023. Model development for moisture content and density prediction for non-dry asphalt concrete using GPR data. *International Journal of Pavement Engineering*, 24.

Alsharahi, G, Filali Bouami, M, Faize, A., Louzazni, M., Khamlichi, A. & Atounti, M. 2021. Contribution of analysis and detection the risks appearing in roads using GPR method: A case study in Morocco. *Ain Shams Engineering Journal*, 12, 1435–1450.

Alani, A.M., Aboutalebi, M. & King, M.J., 2013. Influence of fibre content on crack propagation rate in fibre-reinforced concrete beams. *International Journal of Civil, Environmental, Structural, Construction and Architectural Engineering*, 7(9), 1–7.

Alani, A.M., Aboutalebi, M. & Kilic, G., 2014. Integrated health assessment strategy using NDT for reinforced concrete bridges. *Ndt & E International*, 61, 80–94.

Cao, Q. & Al-Qadi, I. L. 2021. Development of a Numerical Model to Predict the Dielectric Properties of Heterogeneous Asphalt Concrete. *Sensors (Basel)*, 21.

Leng, Z., Al-Qadi, I. L. & Lahouar, S. 2011. Development and validation for in situ asphalt mixture density prediction models. *NDT & E International*, 44, 369–375.

Liang, X., Yu, X., Jin, Y. & Huang, J. 2022. Compactness prediction of asphalt concrete using Ground-Penetrating Radar: A comparative study. *Construction and Building Materials*, 361.

ÖZkap, K., PekŞEn, E., Kaplanvural, İ. & ÇAka, D. 2020. 3D scanner technology implementation to numerical modeling of GPR. *Journal of Applied Geophysics*, 179.

Parkhomenko, E. I. 1967. *Electrical Properties of Rocks*, Springer New York, NY.

Sihvola, A. 2000. Mixing rules with complex dielectric coefficients. *Subsurface Sensing Technologies and Applications* 1, 393–415.

Solla, M., Asorey-Cacheda, R., NúñEz-Nieto, X. & Conde-Carnero, B. 2016. Evaluation of historical bridges through recreation of GPR models with the FDTD algorithm. *Ndt & E International*, 77, 19–27.

Varnavina, A. V., Khamzin, A. K., Sneed, L. H., Torgashov, E. V., Anderson, N. L., Maerz, N. H. & Boyko, K. J. 2015. Concrete bridge deck assessment: Relationship between GPR data and concrete removal depth measurements collected after hydrodemolition. *Construction and Building Materials*, 99, 26–38.

Zeng, L., Zhang, X., Xie, X., Zhou, B., Xu, C. & Lambot, S. 2023. Measuring annular thickness of backfill grouting behind shield tunnel lining based on GPR monitoring and data mining. *Automation in Construction*, 150.

Zhang, J., Zhang, C., Lu, Y., Zheng, T., Dong, Z., Tian, Y. & Jia, Y. 2020. In-situ recognition of moisture damage in bridge deck asphalt pavement with time-frequency features of GPR signal. *Construction and Building Materials*, 244.

Zou, L., Yi, L. & Sato, M., 2020. On the use of lateral wave for the interlayer debonding detecting in an asphalt airport pavement using a multistatic GPR system. *IEEE Transactions on Geoscience and Remote Sensing*, 58(6), 4215–4224.

Bridge Maintenance, Safety, Management, Digitalization and Sustainability – Jensen, Frangopol & Schmidt (eds)
© 2024 The Author(s), ISBN 978-1-032-77040-6
Open Access: www.taylorfrancis.com, CC BY-NC-ND 4.0 license

New trends and possibilities of GPR in bridge inspection

M. Solla, A. Elseicy & A. Alonso-Díaz
CINTECX, Universidade de Vigo, Geotech research group, Spain

ABSTRACT: This contribution presents an overview of the GPR technique applied to bridge inspection, covering all the information that can be detected from both structural (layering, cover depth, etc.) and diagnosis (cracking, voids, corrosion, etc.) points of view. The use of Artificial Intelligence on GPR data will be also addressed, such as the use of Deep Learning methods to extract rebars or distresses like cracks or delamination. Moreover, data digitalization will be considered, with a special attention on GPR data formats to be integrated into GIS and BIM models, and other digital innovations like augmented reality and digital twins. Finally, a review of other non-destructive emerging methods commonly used with the GPR technique will be considered.

1 INTRODUCTION

Bridges are essential structures within the transportation infrastructure domain. They connect lands, and human communities in general, thus facilitating the movement of people and goods and representing a key factor in the economic, industrial, and social development. However, regular maintenance is required to ensure their safety and functionality. Bridges are exposed to several adverse aspects, such as aging, extreme weather conditions, changes in traffic loads, physical and chemical agents, and construction defects. Neglected maintenance can lead to deterioration, and in the worst case in collapse, and costly repairs.

The use of Non-Destructive Testing (NDT) evaluation is highly recommended for more complete inspections while preserving the integrity of these structures, particularly when they suffer from structural deterioration. There are various NDT methods that have been successfully applied for bridge monitoring. Among the different non-destructive methods, mechanical and electromagnetic technologies are especially important for structural imaging.

Conventionally, bridge inspection is based on visual inspection, instead of monitoring the real subsurface condition. Internal damage detection can prevent unpredictable and premature collapse of structures. Within the electromagnetic methods, the Ground-Penetrating Radar (GPR) is a geophysical and non-intrusive imaging technique widely used for routine subsurface inspections, due to its high-resolution and continuous imaging, in addition to its easy portability (compared to other techniques). GPR allows for data acquisition at high speed, continuously, using mobile acquisition units and in a non-contact mode. It enables to keep the bridge in-service during the GPR surveys, thus reducing costs and discomfort to users (Solla et al. 2021).

This work presents an overview of the applicability of the GPR method to bridge monitoring, including the information (findings) than can be detected, and the main limitations. Moreover, a case study is included showing the capabilities of the method for the documentation and evaluation of an ancient masonry arch bridge. A reflection on the use of emerging processing techniques based on artificial intelligence is also included. Another case study is also presented focusing on the use of deep learning (YOLOv8) for automatic rebar detection in concrete bridges. Finally, there is a brief discussion of complementary NDT methods that

DOI: 10.1201/9781003483755-297

have been commonly combined with GPR in the assessment of bridge structures, including the use of emerging techniques (such as Interferometric Synthetic Aperture Radar (InSAR) and drones or unmanned aerial vehicles (UAV) equipped with GPR). Further trends in the application are also commented.

2 GPR APPLIED TO BRIDGE INSPECTION

In bridge inspection, the GPR method has been successfully employed for a great variety of applications and different types of structures (masonry and concrete bridges).

Regarding masonry bridges (brick or stone), the GPR method has been demonstrated its capabilities in detecting:

- Thicknesses in ashlars (spandrel walls, ring arch, etc.) (Solla et al. 2014, Arêde et al. 2017).
- Filling distribution (probable material characterization) (Bergamo et al. 2015, Stavroulaki et al. 2016).
- Bridge foundations (Sánchez-Aparicio et al. 2019).
- Damages such as cracking, voids or cavities in stonework (Solla et al. 2011a).
- Moisture content (Kalogeropoulos & Brühwiler 2011).
- Evidence of restorations/reconstructions (Solla et al. 2016, Alani et al. 2017).
- Hidden structural elements such as arches or ancient geometries of the structure (Solla et al. 2010, Solla et al. 2011b).

With respect to concrete bridges, GPR has been successfully used in:

- Estimation of cover depth (Hugenschmidt & Mastrangelo 2006).
- Detecting and mapping reinforcing bars (Alani et al. 2013, Rathod et al. 2019).
- Moisture detection and water content estimation (Simi et al. 2012, Agred et al. 2018).
- Damage detection such as corrosion, cracking, delamination, etc. (Benedetto 2013, Abouhamad et al. 2017, Diamanti et al. 2017).
- Location of hidden elements and utilities (cable ducts, deck joints, etc.) (Sławski et al. 2016, Dinh et al. 2019).

It should be mentioned that the GPR method has been more widely used for the inspection of concrete bridge. Surveying masonry or concrete bridges differs in the GPR equipment and in data acquisition methods used. Ground-coupled antennas, usually single antennas mounted on a trolley or manually on a survey cart, are most generally used in masonry bridge surveying, while both ground-coupled and air-coupled antenna systems can be used in inspecting concrete bridges. For small survey areas and vertical surfaces (punctual areas), when more image resolution is required, ground-coupled antennas are most used. On the other hand, air-coupled antennas are generally mounted on a van or a vehicle (suspended) to conduct whole length of the bridge measurements, which allow operating at a higher speed (with lower resolution measurements) thus avoiding traffic disruption. Moreover, for large survey areas, and particularly to map utilities and reinforcement, the use of multi-channel systems is highly recommended. Array multi-channel systems are preferred because they cover wider width measurements (increasing the productivity and benefiting 3D visualization). Both air-coupled and array multi-channel systems are normally mounted on vehicles connected to a differential RTK GPS and an encoder-based distance measuring instrument (DMI) for real-time positioning.

The analysis and interpretation of GPR data in masonry bridges is often difficult due to the complexity of these structures and the heterogeneity of masonry and filling. Therefore, for these bridges, it is recommended to conduct more than one profile line to improve data quality and to prevent inappropriate data interpretation.

In the case of concrete bridges, the presentation of GPR data is usually carried out in the form of 3D maps, or time-slices, at different depths (amplitude/attenuation maps and deterioration/delamination maps). This way, it is possible to estimate the extent of deterioration. Nevertheless, some limitations can occur. In reinforced concrete bridges, the detection of

rebar is generally easy because the steel is a quasi-perfect reflector of the GPR waves, but deeper targets of interest can be masked. To overcome this limitation, collecting data in both polarizations is recommended. The reflections produced by metallic targets perpendicular to the data collection direction are weakly seen in data collected with dipoles parallel to the scanning direction, so that other potential targets below them can be more easily detected. In this regard, array multi-channel systems may use antennas arranged with different polarizations. Negatively, these systems have an excessive cost and decrease the survey speed (higher sampling rates are required). The later could result in higher survey costs and, more importantly, could interrupt the traffic flow.

Finally, for bridge structures in general, it is important to mention the technical difficulties experienced during data acquisition to access some parts of the structure (e.g., piers and spandrel walls). Further developments should therefore include the design of innovative devices for the automatic data collection such as drones or robots (Howlader et al. 2016, Gibb et al. 2018).

2.1 *Case study No. 1: Surveying the Arnuide Masonry Arch Bridge (Spain)*

The Arnuide Bridge is a medieval bridge located in the municipality of Vilar de Barrio, in the northwest region of Galicia, Spain. It has a gothic arch with a span of 11.65 m and presents a double slope profile, with a length of about 35 m and 3.50 m wide (Figure 1). In the construction of the bridge, granite ashlars were used as masonry with a regular morphology and without mortar in the joints (at least to the naked eye).



Figure 1. General view of the Arnuide Bridge.

The GPR survey was conducted using a ground-coupled pulsed system manufactured by Malå Geoscience, composed of a Proex control unit with a 500 MHz frequency antenna. The setting parameters used for data acquisition were trace-interval distance of 0.02 s and total time window of 75 ns composed of 512 samples per trace. To guarantee positioning, while measuring the profile lengths, marks were recorded during data acquisition at the joints between ashlars.

Figure 2 presents the GPR images collected along the pathway through the longitudinal direction of the bridge. Figure 2-a corresponds to the profile line close to the upstream side, while Figure 2-b corresponds to the profile line close to the downstream side. Both radargrams are shown from the upstream side, with the starting point (trace 0 in the x-axis) at the right margin upstream. The following characteristics and pathologies are interpreted:

(i) The reflections produced by the pavement/filling interface (orange line) and infill distribution in the form of layering (yellow lines).
(ii) Both the reflections produced by the filling/voussoirs interface (pink line) and voussoirs/air interface (red line), indicating the arch-ring thickness.
(iii) Different signal behavior at the right and left walls of the vault. In the right side (Zone 3), it is possible to observe the signal scattering produced by the existence of lateral

cracking through the extrados. Conversely, in the left side (Zone 2) signal attenuation occurs, which is most probably due to internal moisture.

(iv) Zone 1 highlights the presence of displacement (bulging) in ashlars. This area in the radargrams is likely associated with a more homogenous area, which could be related to a loss of filling by water infiltration. This agrees with the interpretation of signal attenuation due to moisture (iii). Moreover, observing the reflection produced by the voussoirs/air interface below this "empty" area, there is a jump in the beginning of the hyperbola showing lower travelled time distances.

(v) Zone 4, showing signal attenuation, corresponds to the area of the stonework having different masonry with presence of clay material.

(vi) The reflections produced by the air/water interface (blue lines), indicating the water level.

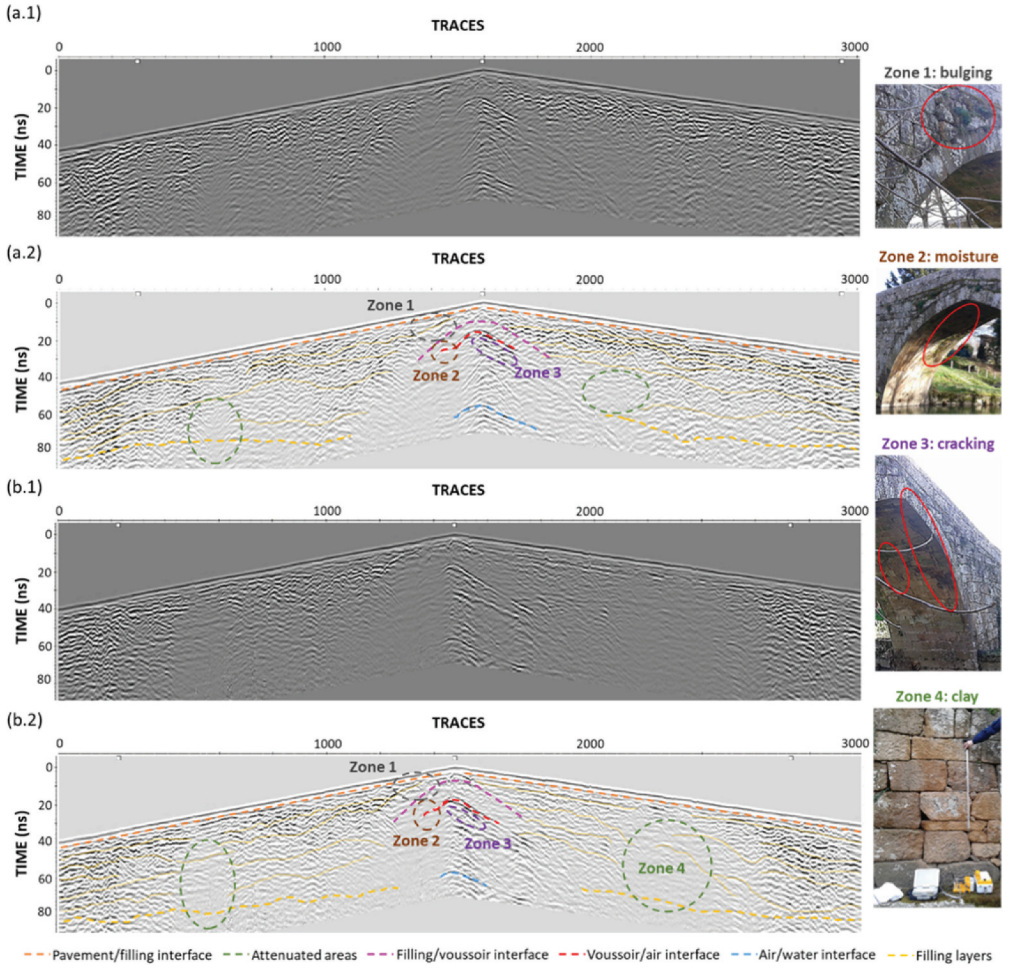


Figure 2. 500 MHz data obtained through the longitudinal direction of the bridge structure (1) and interpretation (2): a) profile line close to the upstream side and b) profile line close to the downstream side.

Figure 3 presents the radargram obtained in the transverse direction at the keystone, which allows to determine the pavement and keystone thicknesses. The pavement has a regular thickness of ~8 ns, whereas the arch-ring thickness at the keystone shows a variable depth, from lower thickness at the downstream (~5 ns) to higher thickness at the upstream side (~8 ns).

Using a pre-calibrated velocity of 0.12 m/ns for granite, the following thicknesses were computed: 0.5 m for pavement and 0.3 to 0.5 m for the granite ashlars at the keystone.

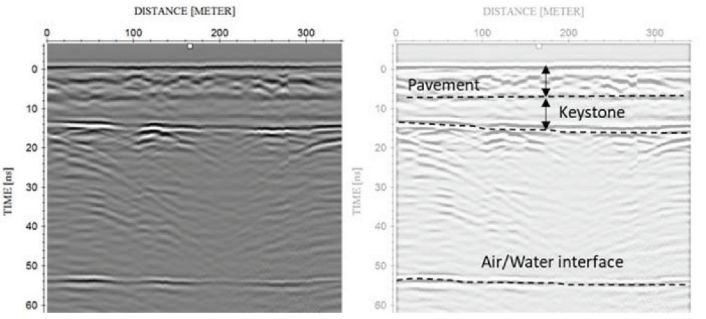


Figure 3. 500 MHz data obtained in the transverse direction at the keystone showing the interpretation of the pavement and keystone thicknesses.

3 INTELLIGENT DATA PROCESSING BASED ON DEEP LEARNING

GPR data collection can be fast and efficient when surveying concrete bridges, but a large amount of data are produced and extensive manual processing is required, which is time-consuming and labor-intensive. Moreover, the interpretation of the GPR data highly depends on the interpretational abilities of the operator to provide accurate information and reliable results, which is somewhat subjective. The introduction of Artificial Intelligence (AI) and cloud-based systems in condition monitoring, particularly in Structural Health Monitoring (SHM), has emerged as the top priorities for practicing engineers and researchers. AI is now an emerging technology to process GPR data and real-time analysis. Adapting state-of-the-art (SoA), AI technologies led to eliminating analysis subjectivity, saving processing time, and reducing the overall operation cost compared to traditional methods.

Recently, Deep Learning (DL) techniques and their application in signal processing and object detection became SoA thanks to their detection speed and accuracy compared to conventional image processing techniques. Several architectures can be applied to GPR data as 1D, 2D and 3D. DL applications help to eliminate analysis subjectivity by detecting hidden patterns between target features. Convolutional Neural Networks (CNN) is one of the DL architectures that has emerged to solve the complex data classification problem. CNN-based models can be used to detect the concrete cover depth (Wickramanayake et al. 2022). Moreover, object detection algorithms such as single-shot multibox detector (SSD) is used to detect corrosive environments (Zhang et al. 2022). The You Only Look Once (YOLO) method can also detect and localize steel bars and combine them with 1D CNN to estimate rebar diameters (Park et al. 2021). It should be highlighted that even though DL algorithms are widely used in computer vision tasks, they still need to be adequately explored with GPR data.

3.1 *Case study No. 2: Automatic rebar detection in concrete bridges using YOLOv8*

Manual rebar picking from GPR profiles of concrete bridge decks is a repetitive task that is time-intensive and labor-intensive. Analyzing the identified rebar reflections provides valuable data, enabling the extraction of peak amplitudes to generate bridge deck condition maps or estimate rebar dimensions. In this section, we present a case study leveraging the recent UltralyticsYOLOv8 object detection model to automate the localization and detection of rebar in concrete bridge decks.

A total of 1772 images were utilized for the experiment. The dataset was prepared by combining a subset the DECKGPRH1.0 dataset (Asadi et al. 2019) with profiles from a concrete bridge deck scanned using a 2.6 GHz antenna from SDNET2021 dataset (Eberichi et al.

2021), ensuring a diverse range of rebar scales within individual images. The influence of scale on the shape of rebar reflections is crucial for training a robust object detection model. According to the plotting scale, the rebar hyperbolic reflection can vary or overlap between adjacent rebars. To account for data variability, the training dataset incorporated multiple visualization scales, ranging from individual rebar reflections to longitudinal representations extending up to 3 meters. To standardize the input, all images were converted to grayscale and resized to uniform 256x256 pixel dimensions. Subsequently, the dataset was partitioned into train, validation, and test subsets, following a ratio of 7:2:1. A data augmentation technique was applied during training to increase the training data's size to enhance the model's robustness. The augmentation involved the random application of transformations, such as adjustments in image brightness, blur, noise, and exposure. Additionally, a random image mosaic was introduced to improve the detectability of rebar reflections. The size of the training data set was 6,205 after applying the augmentation.

The YOLOv8x model was trained from scratch for 210 epochs with a batch size of 16. The SGD optimizer was used with an initial learning rate of 0.02 and momentum of 0.9. The test dataset mAP50 was 0.992, while the mAP50-95 was 0.825. Figure 4 shows an example of prediction results on an unseen bridge deck.

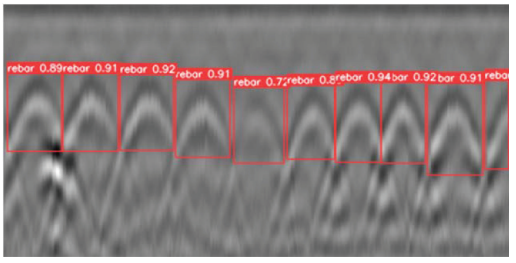


Figure 4. An example of the prediction results for a 2-meter profile.

4 COMPLEMENTARY NDT AND EMERGING TECHNOLOGY

The combination of GPR with complementary geophysical techniques is highly recommended. Each method provides different information owing to the physical properties of the construction materials, which allows for a more detailed investigation in the diagnosis of bridge stability. As discussed in Solla et al. (2021), the geophysical techniques that have been generally combined with GPR for the inspection of masonry bridges are sonic testing, ambient seismic noise, ultrasonic pulse echo and impact-echo, half-cell potential (HCP), hammer sounding resistivity, electromagnetic pulse induction (profoscope), infrared tomography and electrical resistivity.

The use of a multi-temporal InSAR (interferometric synthetic aperture radar) for bridge inspection has also been significantly increasing during the last few years. Studies undertaken on bridges have demonstrated the potential of the InSAR, together with GPR, to monitor subsidence at the transition zones of railway bridges (D'Amico et al. 2020). At network level, the InSAR allowed to detect differential settlements in transition zones and subsidence due to soil consolidation in high embankments; whereas, at project level, the GPR enabled to identify the possible causes of the displacements detected. Other authors (Alani et al. 2020) have combined GPR and InSAR technologies to investigate both the subsurface geometry and the structural displacements of masonry arch bridges certainly caused by water floods and the riverbed soil expansions. The work by Alonso-Díaz et al. (2023) has combined InSAR, GPR and FWD techniques for the assessment of road pavements, including the investigation of differential settlements in the transition zones of a concrete bridge.

The use of GPR mounted on drones or UAV (Unmanned Aerial Vehicle) has been also tested in experimental research, with some prototypes (García-Fernández et al. 2019,

Vergnano et al. 2022). This approach requires the design of novel portable antennas (Wu et al. 2019). Further progress could be focused on the development of antennas and UAV systems for surveying structural elements with poor accessibility (Esposito et al. 2023).

5 REMARKS AND FURTHER TRENDS

Transport infrastructure digitization is gaining popularity for monitoring and maintenance strategies, as reliable and effective information exchange is crucial to any industry. Misinterpretations or delays directly translate into increased cost and time requirements. Bridges are long-lasting investments that shall be functional for many decades and must deal with different domains and large amount of data that needs a collaborative environment to work together. This requires a framework for semantic integration of data sources that must deal with different types of data exchange standards. The arrival of Geographic Information Systems (GIS), Building Information Modelling (BIM) and Digital Twins (DT) to the transport infrastructure domain gives insights into latest developments in open standards for interoperability. The data from SHM inspection and monitoring can be used to create more confident information models, such as the GIS or BIM models (data), to support decision-making (Solla et al. 2020). There are different SHM studies using GPR data to create structural models for more detailed assessment of the bridge's structural load capacity and safety. The knowledge of the internal geometry and material characterization of the bridge allows engineers to perform more accurate numerical simulations (Alani et al. 2014, Bouzas et al. 2023). Nevertheless, GPR provides a subsurface representation which is rarely part of a geometric model. Thus, the representation of detailed geometries from standards still poses an open problem, as the SHM information to be added to the model may require of custom extensions of the standard or distributing semantic information points with custom SHM-related data.

ACKNOWLEDGMENTS

Work produced with the support of a 2022 Leonardo Grant for Researchers and Cultural Creators, BBVA Foundation. The BBVA Foundation takes no responsibility for the opinions, statements, and contents of this project, which are entirely the responsibility of its authors. This work also received financial support from the OVERSIGHT project (PID2022-138526OB-I00) funded by MCIN/AEI/10.13039/501100011033, UE. M. Solla acknowledges the grant RYC2019–026604–I funded by MCIN/AEI/10.13039/501100011033 and by "ESF Investing in your future". A. Elseicy acknowledges the Grant PREP2022-000030 for the training of predoctoral researchers funded by MCIN/AEI /10.13039/501100011033 and by FSE+. A. Alonso-Díaz acknowledges the funding received from the Xunta de Galicia through the ENDITí project (ED431F 2021/08).

REFERENCES

Abouhamad, M., Dawood, T., Jabri, A., Alsharqawi, M. & Zayed, T. 2017. Corrosiveness mapping of bridge decks using image-based analysis of GPR data. *Autom. Constr*. 80: 104–117.

Agred, K., Klysz, G. & Balayssac, J.P. 2018. Location of reinforcement and moisture assessment in reinforced concrete with a double receiver GPR antenna. *Constr. Build. Mater*. 188: 1119–1127.

Alani, A.M., Aboutalebi, M. & Kilic, G. 2013. Applications of ground penetrating radar (GPR) in bridge deck monitoring and assessment. *J. Appl. Geophys*. 97:45–54.

Alani, A.M., Aboutalebi, M. & Kilic, G. 2014. Integrated health assessment strategy using NDT for reinforced concrete bridges. *NDT&E Int*. 61: 80–94.

Alani, A.M., Tosti, F., Banks, K., Biancini-Ciampoli, L. & Benedetto, A. 2017. Non-destructive assessment of a historic masonry arch bridge using ground penetrating radar and 3D laser scanner. *Proc. IMEKO*, *Lecce, Italy*, 23-25 October 2017.

Alani, A.M., Tosti, F., Bianchini Ciampoli, L., Gagliardi, V. & Benedetto, A. 2020. An integrated investigative approach in health monitoring of masonry arch bridges using GPR and InSAR technologies. *ND&E Int*. 115: 102288.

Alonso-Díaz, A., Solla, M., Fontul, S., Marecos, V., Antunes, M.L. & Pais, J.C. 2023. A non-invasive and multi-scale approach to detect subsidence in pavements: InSAR, FWD and GPR. *Proc. of the 12th IWAGPR, Lisbon, Portugal*, 5- 7 July 2023.

Arêde, A., Costa, C., Gomes, A.T., Menezes, J.E., Silva, R., Morais, M. & Gonçalves, R. 2017. Experimental characterization of the mechanical behaviour of components and materials of stone masonry railway bridges. *Constr. Build. Mater*. 153: 663–681.

Asadi, P., Gindy, M. & Alvarez, M. 2019. A Machine Learning Based Approach for Automatic Rebar Detection and Quantification of Deterioration in Concrete Bridge Deck Ground Penetrating Radar B-scan Images. *KSCE J Civ Eng* 23: 2618–2627.

Benedetto, A. 2013. A three dimensional approach for tracking cracks in bridges using GPR. *J. Appl. Geophys*. 97: 37–44.

Bergamo, O., Campione, G., Donadello, S. & Russo, G. 2015. In-situ NDT testing procedure as an integral part of failure analysis of historical masonry arch bridges. *Eng. Fail. Anal*. 57: 31–55.

Bouzas, O., Conde, B., Matos, J.C., Solla, M. & Cabaleiro, M. 2023. Reliability-based structural assessment of historical masonry arch bridges: the case study of Cernadela bridge. *Case Stud. Constr. Mater*. 18:e02003.

D'Amico, F., Gagliardi, V., Bianchini Ciampoli, L. & Tosti, F. 2020. Integration of InSAR and GPR techniques for monitoring transition areas in railway bridges. *NDT&E Int*. 115:102291.

Diamanti, N., Annan, P. & Redman, J.D. 2017. Concrete bridge deck deterioration assessment using ground penetrating radar (GPR). *J. Environ. Eng. Geophys*. 22: 121–132.

Dinh, K., Gucunski, N. & Zayed, T. 2019. Automated visualization of concrete bridge deck condition from GPR data. *NDT&E Int*. 102: 120–128.

Eberichi Ichi & Sattar Dorafshan. 2021. "SDNET2021: Annotated NDE Dataset for Structural Defects". *Datasets*. 19. https://commons.und.edu/data/19.

Esposito, G., Salari, A., Catapano, I., Erricolo, D. & Soldovieri, F. 2023. UAV-based GPR prototype for structural monitoring of bridges: preliminary results and perspectives. *Proc. in Civil Engineering, EUROSTRUCT 6(5)*: 930-933.

Garcia-Fernandez, M., Alvarez-Lopez, Y. & Las Heras, F. 2019. Autonomous airborne 3D SAR imaging system for subsurface sensing: UWB-GPR on board a UAV for landmine and IED detection. *Remote Sens*. 11: 2357.

Gibb, S., La, H.M., Le, T., Nguyen, L., Schmid, R. & Pham, H. 2018. Nondestructive evaluation sensor fusion with autonomous robotic system for civil infrastructure inspection. *J. Field Robot*. 35: 988–1004.

Howlader, M.O.F., Sattar, T.P. & Dudley, S. 2016. Development of a Wall Climbing Robotic Ground Penetrating Radar System for Inspection of Vertical Concrete Structures. *Int. J. Mech. Mechatron. Eng*. 10: 1382–1388.

Hugenschmidt, J. & Mastrangelo, R. 2006. GPR inspection of concrete bridges. *Cem. Concr. Compos*. 28: 384–392.

Kalogeropoulos, A. & Brühwiler, E. 2011. High-resolution 3D condition survey of a masonry arch bridge using Ground Penetrating Radar. *Proc. of the First Middle East Conference on Smart Monitoring, Assessment and Rehabilitation of Civil Structures, Dubai, United Arab Emirates, 8-10* February 2011.

Park, S., Kim, J., Jeon, K., Kim, J. & Park, S. 2021. Improvement of GPR-Based Rebar Diameter Estimation Using YOLO-v3. *Remote Sens. 13*, 2011.

Rathod, H., Debeck, S., Gupta, R. & Chow, B. 2019. Applicability of GPR and a rebar detector to obtain rebar information of existing concrete structures. *Case Stud. Constr. Mater*. 11: e00240.

Sánchez-Aparicio, L.J., Bautista-De Castro, A., Conde, B., Carrasco, P. & Ramos, L.F. 2019. Nondestructive means and methods for structural diagnosis of masonry arch bridges. *Autom. Constr*. 104: 360–382.

Simi, A., Manacorda, G. & Benedetto, A. 2012. Bridge deck survey with high resolution Ground Penetrating Radar. *Proc. of the 14th International Conference on GPR, Shanghai, China*, 4-8 June 2012.

Sławski, Ł., Kosno, Ł. & S´wit, G. 2016. Evaluation of Precast Pre-post-tensioned Concrete Bridge Beams with the Use of GPR Method. *Procedia Engineering* 156:443–450.

Solla, M., Lorenzo, H., Novo, A. & Rial, F.I. 2010. Ground-penetrating Radar Assessment of the Medieval Arch Bridge of San Antón, Galicia, Spain. *Archaeol. Prospect*. 17: 223–232.

Solla, M., Lorenzo, H., Riveiro, B. & Rial, F.I. 2011a. Non-destructive methodologies in the assessment of the masonry arch bridge of Traba, Spain. *Eng. Fail. Anal*. 18: 828–835.

Solla, M., Lorenzo, H., Rial, F.I. & Novo, A. 2011b. GPR evaluation of the Roman masonry arch bridge of Lugo (Spain). *NDT&E Int*. 44: 8–12.
Solla, M., Riveiro, B., Lorenzo, H. & Armesto, J. 2014. Ancient Stone bridge surveying by ground-penetrating radar and numerical modeling methods. *J. Bridge Eng*. 19: 110–119.
Solla, M., Asorey-Cacheda, R., Núñez-Nieto, X. & Conde-Carnero, B. 2016. Evaluation of historical bridges through recreation of GPR models with the FDTD algorithm. *NDT&E Int*. 77: 19–27.
Solla, M., Gonçalves, L.M.S., Gonçalves, G., Francisco, C., Puente, I., Providência, P., Gaspar, F. & Rodrigues, H. 2020. A building information modelling approach to integrate geomatic data for the documentation and preservation of cultural heritage. *Remote Sens*. 12(24): 1–24.
Solla, M., Pérez-Gracia, V. & Fontul, S. 2021. A review of GPR application on transport infrastructures: troubleshooting and best practices. *Remote Sens*. 13: 672.
Stavroulaki, M.E., Riveiro, B., Drosopoulos, G.A., Solla, M., Koutsianitis, P. & Stavroulakis, G.E. 2016. Modelling and strength evaluation of masonry bridges using terrestrial photogrammetry and finite elements. *Adv. Eng. Softw*. 101: 136–148.
Vergnano, A., Franco, D., Godio, A. 2022. Drone-Borne Ground-Penetrating Radar for snow cover mapping. Remote Sens. 14(7): 1763.
Wickramanayake, S., Thiyagarajan, K. & Kodagoda, S. 2022. Deep Learning for Estimating Low-Range Concrete Sub-Surface Boundary Depths Using Ground Penetrating Radar Signals. *IEEE Sens. Lett*. 6 (3):6000704.
Wu, K., Rodriguez, G.A., Zajc, M., Jacquemin, E., Clément, M., De Coster, A. & Lambot, S. 2019. A new drone-borne GPR for soil moisture mapping. *Remote Sens. Environ*. 235: 111456.
Zhang, Y.-C., Yi, T.-H., Lin S., Li, H.-N. & Lv S. 2022. Automatic Corrosive Environment Detection of RC Bridge Decks from Ground-Penetrating Radar Data Based on Deep Learning. *J. Perform. Constr. Facil*.36(2).

Bridge Maintenance, Safety, Management, Digitalization and Sustainability – Jensen, Frangopol & Schmidt (eds)
© 2024 The Author(s), ISBN 978-1-032-77040-6
Open Access: www.taylorfrancis.com, CC BY-NC-ND 4.0 license

Øresund Bridge: Case study of a monitoring system for movement of bridge bearings

A. Paciacconi & T. Richli
Mageba SA, Bülach, Switzerland

ABSTRACT: Assessment of infrastructure conditions is currently a topic of great importance, but also a challenging one. Many significant pieces of infrastructure were built decades ago and have, since then been exposed to load cycles, weather, special events, and all other design scenarios. During this time period, a structure will experience structural degradation and reduction in remaining service life. In addition, over such a long time span, service conditions are likely to change and other phenomena can occur with unknown effects on the structures, which may not have been taken into consideration during original design. This spontaneously raises questions about the structure's condition and real time performance. Such questions are typically driven by a limited confidence in performance, directly stemming from limited information available. A monitoring system provides comprehensive information about the structures status and provides vital support for Engineers and Asset Managers involved in decision-making processes.

1 INTRODUCTION

This paper presents the case study of the Øresund Bridge, an outstanding stay cable bridge, carrying highway traffic and a rail system. Here, a system is installed to monitor bearings movements. The owner aimed to have accurate and clear data to clear the lack of information about bearings performances in the various scenarios of operation, for example seasonal changes of temperatures or passing trains. The system design and implementation has relied on special care and attention to the fine details, from ensuring long durability in harsh environment to undertaking accurate measurements in order to generate easy-to-use data. It consists of 28 sensors and 9 Data Acquisition Units (DAU) installed at the main bridge sections, for the whole bridge length from Sweden to Denmark. Excellent results have been achieved thanks to a pilot test performed prior to system development. Installation was first performed at only 2 bearings, simulating the real case. This enabled the engineers to gain more confidence and knowledge about the specific application, being able to fine tune the system design to better meet the end user needs and expectations. Data is being used to better understand bearing movements due to temperature, wind and passing trains. A catalogue of informative data will support in design of future refurbishment works, most of all bearing replacements upon end of service life.

2 ØRESUND BRIDGE

The Øresund Bridge is an outstanding piece of major infrastructure, the longest in Europe with both roadway and railway combined in a single structure, to provide connectivity across the Øresund strait between Denmark and Sweden. It runs approximately 8 kilometres (5.0 miles) from Sweden to the artificial island Peberholm in the middle of the strait, and from there onwards via the 4-kilometre Drogden Tunnel to complete the crossing to Denmark. Deck carries 4 lanes of highway traffic on the upper section and two railways tracks on the lower section. West and East approach viaducts consist of 23 and 28 spans respectively, each 140m in length. The cable-stayed span is 1090m in total, with the central section of 490m and clear height approx. 55 m above sea level to allow passage of vessel traffic beneath.

DOI: 10.1201/9781003483755-298



Figure 1. Øresund Bridge, aerial view of stayed cable span and artificial Peberholm island.

3 SYSTEM LAYOUT

The SHM system (Structural Health Monitoring system) is composed of 19 displacement sensors and 9 temperature sensors installed at the 9 bridge sections with expansion joints, from East Abutment to West Abutment. Sensors have been selected with specific features for this application, with high- performance under quasi-dynamic application, sufficient robustness to withstand a harsh marine environment, and very precise measurements of movements up to 0.1mm. In addition, sensor installation has been tailored to allow co-ordination below the weather protection skirt currently in place at the bearings which protects the sliding surface and sliding material. As a result, and to ensure longevity, sensors are not exposed to direct weathering.

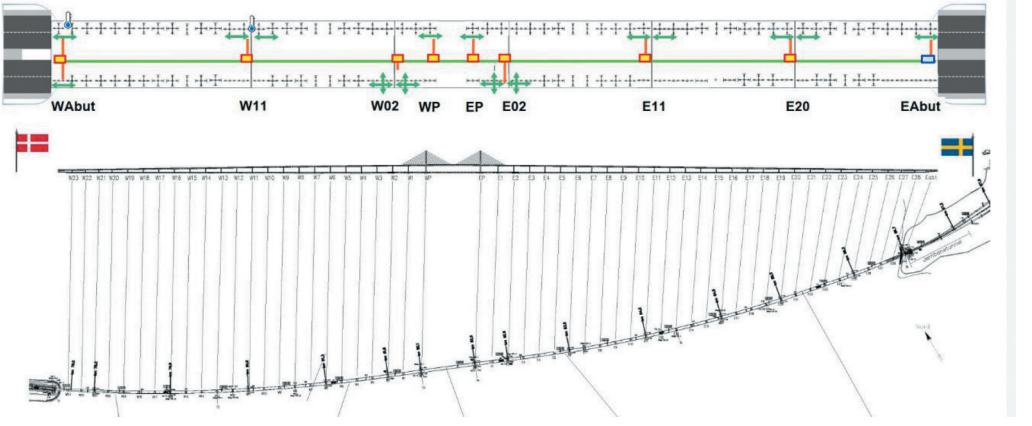


Figure 2. System layout: sensors and data acquisition units locations.

At each section being monitored, a Data Acquisition Unit (DAU) is also installed to collect the data from the sensors. DAUs are robust electronic cabinets used for industrial applications, highly resistant to corrosive agents and provided with internal heater and diagnostic sensors to prevent malfunctioning.

The DAUs feed the sensors, acquiring measurements and gathering data 24/7 at high frequency, but storage nor data processing is performed at the DAUs. Instead these are connected via the technical network to the Master Station located at the East Abutment.



Figure 3. Bearing being monitored and DAU.

The Master Station is the main unit equipped with an industrial computer where the monitoring software runs to, among other functions, gather data 24/7 displaying them in real time. Measurements undertaken by the sensors are calibrated to provide the bearings movements with respect to the middle position on the sliding plate. During commissioning, before hand over of the system to the bridge operator, such calibration has been double checked physically on site in order to confirm that the operator and the bridge owner can rely on accurate data.

Once stored at the Master Station, data is made available for the SCADA system, the supervisory and control system of the bridge owner for importing, further processing and reporting.

To ensure smooth operation, the bridge operator can remotely access the Master Station at any time, facilitating full control of the system to upgrade system configuration, measurement settings (sampling frequency, storage, etc.), perform troubleshooting in case of technical issues or control possible anomalies e.g. communication issues among the DAUs or internal temperatures not optimal for operation of such cabinets. The system is also equipped with self-diagnostic features to identify issues and in some cases restore the full functionalities. In any case, the operator is notified and informed.

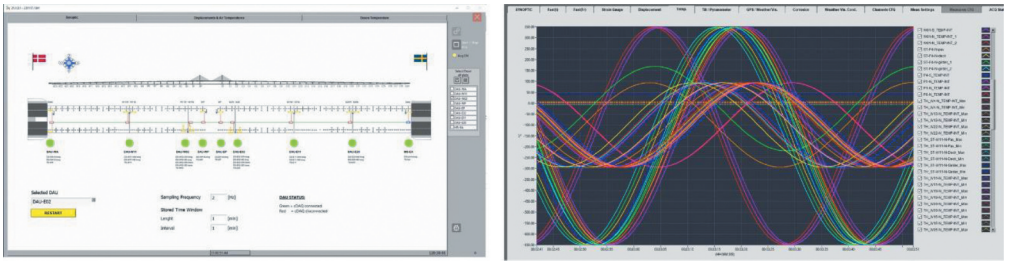


Figure 4. Interface of monitoring software, synoptic panel (left) and real time data visualization during simulation tests (right). For illustrative purpose only.

4 OPERATION, USAGE AND BENEFITS

The monitoring system has been carefully designed, paying special attention to detail, for example, precision in mechanical installation of sensors and software development to

provide data reliable, easy to use and suitable for direct interpretation. Therefore, the operator receives clear insight and information about the bearings directly from the system, without any further conversion steps, processing or analysis required. Other than saving time and efforts, this avoids possible misinterpretation of data.

One of the most important benefits is that, in general, the monitoring system allows continuous and automatic measurements, without the need for someone to go physically on site for an inspection. Visual inspections also have their importance but provide sparse information with isolated measurement and can only indicate the condition of the structure at that specific time in point, but do not give a detailed long-term overview of the behaviour.

The monitoring system operates 24/7, providing comprehensive information to understand behaviours, trends and performances over long time periods, for different weather conditions or traffic scenarios.

In addition, the quality and accuracy of information is far better with a proper monitoring system than with visual inspections referring to rapid movements, dynamic behaviour or the effects of live loads such as wind, road traffic and passing trains.

Current values and trends on the long term are obtained with sampling frequency of 2 Hz. The sampling frequency adopted has been chosen from the outcome of the pilot project, it results enough to capture the dynamic responses of interest but without generating an exaggerated amount of data. Thus, effects of wind and traffic on the bridge, which affect the bearing movements, are properly described.

First, data can be correlated to the temperature to cross check whether bearing movements meet expectations and understand possible deviations from expected values. Comparison of movements at different locations, either at corresponding locations in the northern & southern section or at different cross sections, enables a check on overall consistency of bearings movements.

Finally, trends show whether the bearings experience smooth or sudden movements, which can provide further insight as to the status of sliding material and possible friction transferred to the substructure.

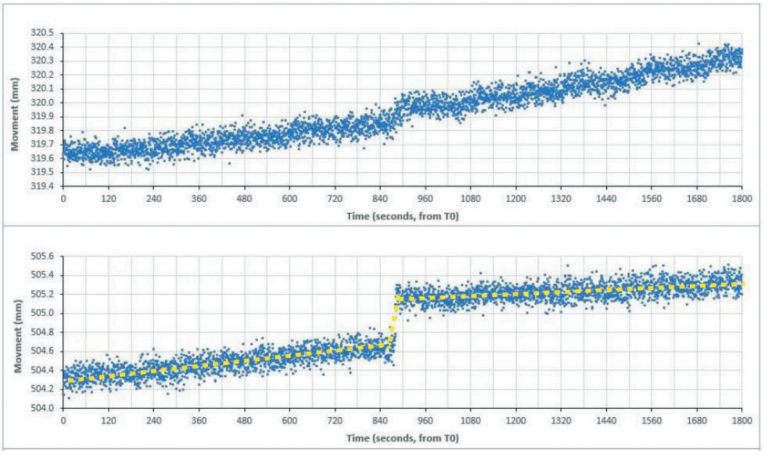


Figure 5. Example of data provided, movement vs time. For illustrative purpose only.

5 CONCLUSION

The SHM field is constantly developing thanks to active scientific research, and thanks to the development of new and upgrading technologies being developed to better support engineers and market needs. This project is a good example of how new technologies together with a well-thought detailed design of the monitoring system, often bespoke for the specific application, offer added value to the bridge maintenance, operation and assessment processes.

Bridge Maintenance, Safety, Management, Digitalization and Sustainability – Jensen, Frangopol & Schmidt (eds)
© 2024 The Author(s), ISBN 978-1-032-77040-6
Open Access: www.taylorfrancis.com, CC BY-NC-ND 4.0 license

Thermal response prediction of the MX3D bridge's operational dataset

T. Glashier & C. Buchanan
Department of Civil and Environmental Engineering, Imperial College London, London, UK

R. Kromanis
Department of Civil Engineering and Management, University of Twente, Enschede, The Netherlands

ABSTRACT: Environmental and operational variations (*eov*) remain a major obstacle for the successful transfer of structural health monitoring (*shm*) techniques from laboratory experiments, such as cracked beam experiments, to full-scale structures, such as long-span bridges. With evidence that timely interventions significantly increase the service-life and reduce the overall life-cycle cost of ageing infrastructure, carrying out *shm* in the presence of *eov*, such as temperature, is therefore of high priority within the bridge maintenance community. An iterative regression-based thermal response prediction (*irbtrp*) methodology is utilised within the temperature-based measurement interpretation (*tb-mi*) approach and is trained on the healthy condition of the bridge to predict its undamaged response to temperature fluctuations. The *tb-mi* approach and the irbtrp methodology are applied to the *mx3d* bridge in this study, demonstrating that their use enables earlier and more widespread damage detection amongst multiple sensor groups, compared to when no temperature effects are considered.

1 INTRODUCTION

Current infrastructure maintenance practices primarily involve routine visual inspection of structural surfaces (Aktan *et al.*, 1996), particularly for bridges where subjective assessments are often used to gauge the severity and extent of visible defects (Helmerich *et al.*, 2008), which results in data that tends to focus on individual structural components rather than offering a comprehensive view of the asset (Kong and Frangopol, 2003). In contrast, structural health monitoring (SHM) promotes condition-based maintenance, whereby interventions occur when specific real-time performance indicators surpass predefined thresholds (Brownjohn, 2007; Farrar and Worden, 2012). The field of SHM has garnered substantial momentum in recent decades, thanks to advancements in computing power, data handling capabilities, and storage, along with breakthroughs in deep learning research (Xu and Brownjohn, 2018; Ye, Tao and Yun, 2019; Zhao *et al.*, 2019; Azimi, Eslamlou and Pekcan, 2020), showcasing significant potential in supporting the maintenance of civil infrastructure.

SHM has proven its effectiveness in specific real-world infrastructure applications, such as conducting health assessments for bridges (De Roeck, 2003; Brownjohn *et al.*, 2015; Peiris, Sun and Harik, 2020; Turrisi, Zappa and Cigada, 2022) and damage detection using data-driven methodologies (Catbas, Gokce and Gul, 2012) as well as combinations with model-based techniques (Martín-Sanz *et al.*, 2020). Nonetheless, limitations remain that have affected its transition from controlled laboratory experiments to practical, real-world implementations (Brownjohn *et al.*, 2011; Masciotta *et al.*, 2016; Cawley, 2018). Figueiredo and Brownjohn (2022) have highlighted the primary challenges for SHM that include characterising the normal variations induced by environmental and operational variability (EOV) (Sohn,

DOI: 10.1201/9781003483755-299

2007) and shifting the focus towards real damage, away from cracked beam experiments. Overcoming these current limitations will help SHM research demonstrate successful infrastructure applications, and consequently positive return on investment (Figueiredo and Brownjohn, 2022).

This study focuses on minimising the influence that EOV has on the collected structural response of full-scale structures in operation. A temperature-based measurement interpretation (TB-MI) approach (Kromanis and Kripakaran, 2016; Glashier, Kromanis and Buchanan, 2023b) is adopted to analyse structural measurements following the removal of the thermal response. An iterative regression-based thermal response prediction (IRBTRP) methodology (Glashier, Kromanis and Buchanan, 2023a) learns and predicts the response of instrumented infrastructure to temperature variations and has been shown to be effective for a Laboratory Truss and the MX3D Bridge. In this study, the IRBTRP methodology is applied to the 2-year operational dataset of the MX3D Bridge (see Figure 1). This work evaluates the performance of the IRBTRP methodology to real-life structures and datasets.



Figure 1. The MX3D Bridge over the Oudezijds Achterburgwal canal in Amsterdam, the Netherlands, during the A) day and B) evening.

2 TEMPERATURE-BASED MEASUREMENT INTERPRETATION

The temperature-driven structural response is removed from the measured response prior to its interpretation within the TB-MI approach. This approach can be applied to infrastructure instrumented with sensors that measure its distributed temperature profile, using thermistors or thermocouples for example, and uses regression methodologies to characterise the thermal behaviour, such as an IRBTRP methodology that is outlined herein.

2.1 *Iterative regression based thermal response prediction methodology*

The structural response to static and dynamic loads has been shown to be masked by EOV, as well concealing damage-related features in the measured structural response. Damage detection techniques are hence less effective in the presence of EOV (Sohn, 2007; Figueiredo and Brownjohn, 2022). The IRBTRP methodology (Glashier, Kromanis and Buchanan, 2023a), described in Figure 2, was developed to accurately predict the normal response of a structure to temperature variations, to enable both a detailed understanding of its environmental response and a temperature-corrected and improved application of damage detection techniques. The healthy state of the structure is used as a reference period to understand its typical thermal response. This reference dataset is divided into training, validation, and testing periods. These segments are used for generating, selecting, and evaluating the regression model, respectively.

The initial stage of the methodology is data preparation (see Step 1 in Figure 2) to remove the influence of traffic loading and high-frequency noise in the input reference period signals. This is achieved, respectively, through a traffic load removal (TLR) algorithm (Glashier, Kromanis and Buchanan, 2023a), which uses load cell signals to detect the presence of traffic, and a moving average filter (MAF) to produce a dataset with only the distributed temperature and thermal response. The inputs to the model generation phase are therefore the distributed temperature and a single measured response signal (e.g., from a displacement gauge, inclinometer, or strain gauge).

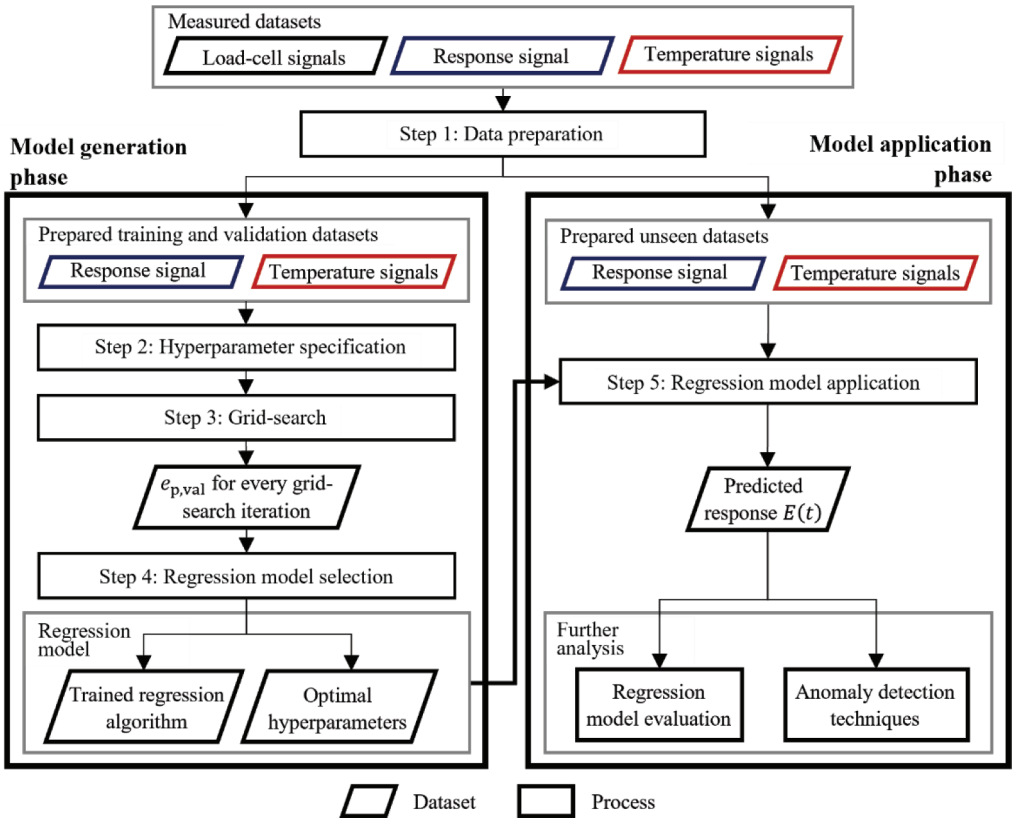


Figure 2. Flowchart of the IRBTRP methodology (Glashier, Kromanis and Buchanan, 2023a).

The IRBTRP methodology employs customisable parameters relating to measurement pre-processing, regression algorithms and post-processing, named hyperparameters, and regression algorithms to adapt and optimise itself to its application. A hyperparameter specification step identifies values that can simultaneously reduce computation time and minimize prediction errors. A grid-search is employed to optimise both hyperparameters and regression algorithms, with the regression model providing the lowest validation dataset error being selected. The models are then evaluated based on their performance on the unseen testing period, avoiding a biased assessment. Their prediction error is computed using the root mean squared error parameter e_p, defined as

$$e_p = \frac{\sqrt{\frac{1}{N}\sum_{i=1}^{N} E(t_i)^2}}{r_{\text{ref}}} \tag{1}$$

for N recorded data points, where $E(t_i)$ is the error signal (i.e., the difference between measured and subtracted signals) and r_{ref} is the signal's reference period range. The prediction error for the validation and testing subperiods are symbolised as $e_{\text{p,val}}$ and $e_{\text{p,test}}$.

3 THE MX3D BRIDGE

The MX3D Bridge is the world's first structure produced using metal additive manufacturing (AM), and is show in its Amsterdam location in Figure 1. The bridge's printed

components (i.e., the hollow handrails, substructure, and decorative end swirls) were separately printed by MX3D, and then hand welded along with the conventionally formed deck plate and two rectangular hollow section end beams. The bridge is fitted with a comprehensive sensor network that includes accelerometers (denoted by the notation A*XX*, where *XX* is the sensor number), displacement gauges (D*XX*), inclinometers (I*XX*), load cells (LC*XX*}), strain gauges (SG*XX*) and thermistors (T*XX*). The locations of the sensors used in this study are displayed in Figure 3. Additional information on the MX3D Bridge manufacturing process and dimensions can be found in (Glashier, Kromanis and Buchanan, 2023b).

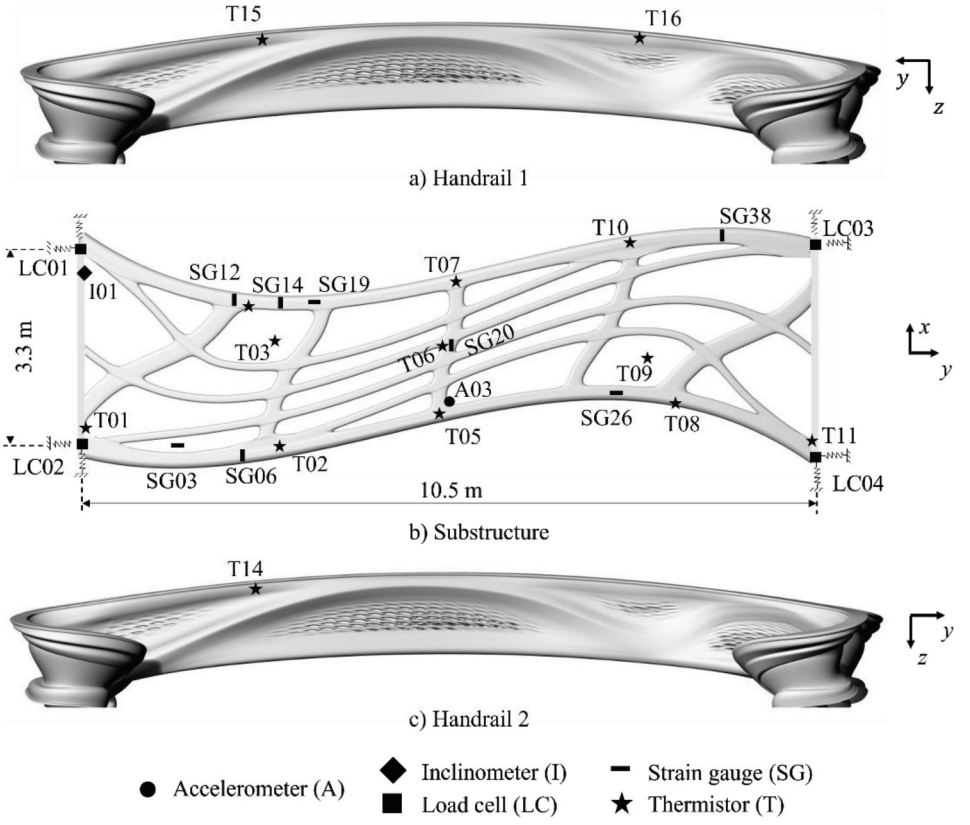


Figure 3. Locations of the MX3D Bridge sensors on the a) Handrail 1, b) Substructure, and c) Handrail 2 used in this study.

Following the bridge's installation in central Amsterdam in July 2021, a 2-year operational dataset was collected for research purposes into its long-term behaviour. Temperature and pedestrian loadings are the dominant sources of environmental and operational variations, respectively, for the MX3D Bridge. Typical measured operational responses from a load cell, strain gauge and a thermistor are provided in Figure 4 for a 48-hour period. The baseline of the LC03 load cell and SG10 strain measurements show a daily variation that correlates with thermistor T01's output. The change in the baseline of the load signal is caused by variations in the structure's self-weight distribution over its supports.

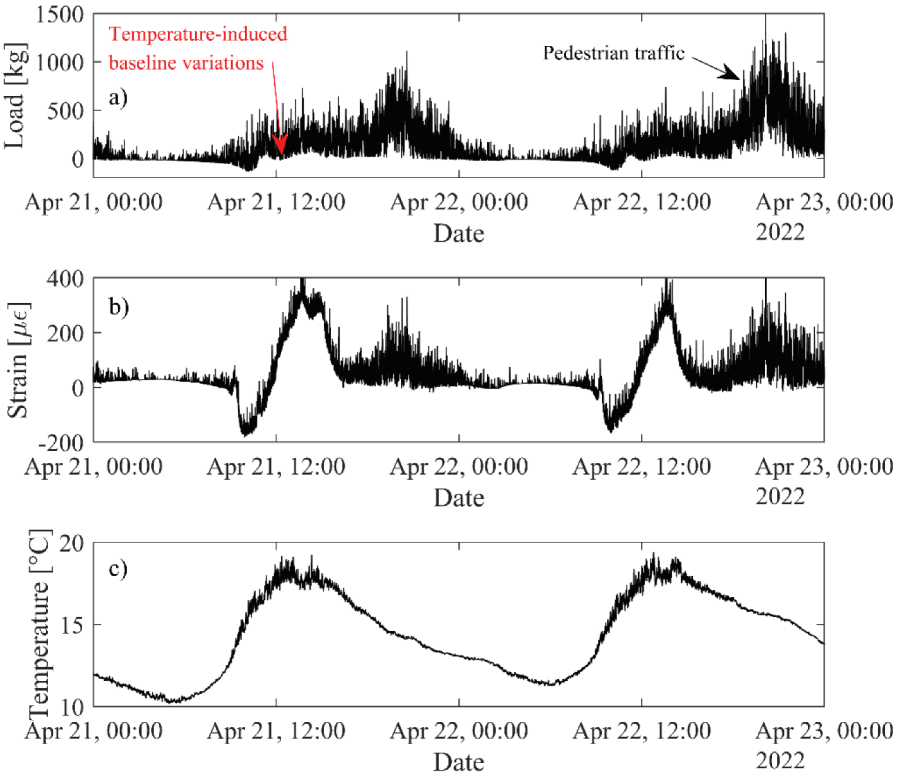


Figure 4. Typical measured response for a) LC03 load cell, b) SG10 strain gauge, and c) T01 thermistor over two days of the operational dataset.

4 APPLICATION TO THE MX3D BRIDGE

The TB-MI approach is applied to the MX3D Bridge operational dataset with the IRBTRP methodology being used to provide thermal response predictions. The first step of the methodology involves data preparation of the input signals that include the distributed thermistor and structural response signals. Traffic loading and measurement noise are removed through the application of the TLR algorithm (Glashier, Kromanis and Buchanan, 2023a) and a moving average filter, providing structural response signals free from operational variations. The specification of hyperparameters for the grid-search, and the consequent performance of the thermal response predictions are described in Sections 0 and 4.2, respectively.

4.1 *Hyperparameter specification*

The specification process determines the regions for each hyperparameter that can minimise both computation time and the prediction error. The selection process is carried out for all hyperparameters, but only illustrated using one pre-processing hyperparameter in this study. Figure 5 demonstrates the effect that the sampling rate of the training data has on accuracy and the computation time. Prediction errors are seen to rise with increasing sampling periods but are steady for < 10 minutes, whilst for sampling periods < 10 s, computing times grow rapidly. The values selected for computation within the grid-search are therefore 10 s, 1, and 10 minutes.

The outcome of the hyperparameter specification stage is summarised in Table 1, listing all the hyperparameter values along with the three regression algorithms investigated in this study: multiple linear regression (MLR) and robust regression (RR) as well as artificial neural

networks (ANN). The total number of hyperparameter combinations that are to be computed in the grid-search are 43,200 for MLR and RR, and 432,000 for ANN.

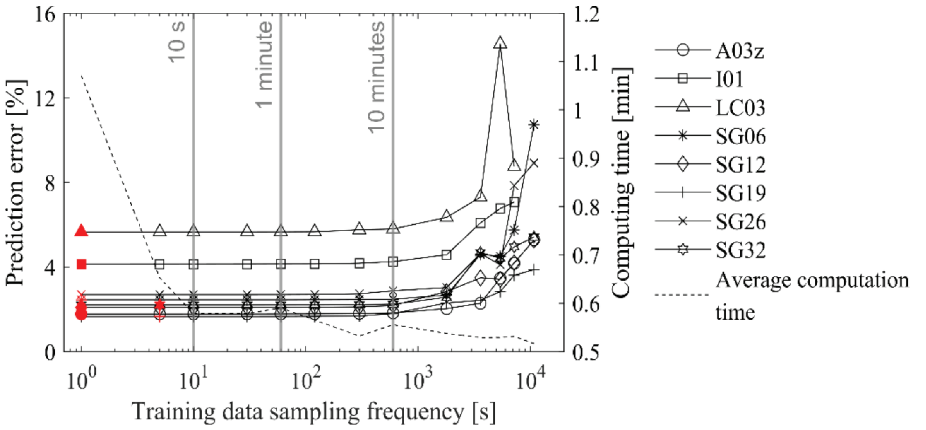


Figure 5. The effect of the training data sampling rate on prediction error and computing time (minima in red, and selected hyperparameters shown as solid grey lines).

Table 1. Summary of the IRBTRP methodology hyperparameters selected for modelling the MX3D Bridge.

Step	Hyperparameter	Grid-search value
Pre-processing	Inter-quartile range analysis (IQRA) window size	0 and 10 minutes
	Moving average filter (MAF) window size	0 and 2 minutes
	Training data sampling period	10 seconds, 1 and 10 minutes
	Number of principal components	5, 10, and 14
	Thermal inertia n°1 (TI_1)	0 to 11.5 hours in 30-minute steps for $TI_1 < TI_2$
	Thermal inertia n°2 (TI_2)	1 to 12 hours in 1-hour steps
Regression	N° ANN hidden layers (HL)	1 to 4
	N° ANN neurons per layer	1 5, 10 and 15 (HL = 1); 5, 10 and 15 (HL = 2); 10 and 15(HL = 3); and 15 (HL = 4)
	N° of networks in ANN ensemble	3
	N° cross-validation groups	20
Post-processing	IQRA window size	0 and 2 minutes
	MAF window size	0 and 2 minutes

4.2 *Thermal response predictions*

For the response signals measured on the MX3D Bridge by the sensors displayed in Figure 3, all hyperparameter and regression algorithms were computed in a grid search. The combination yielding the smallest validation error was selected as optimal and used to predict the structure's response for the testing period. The validation and testing prediction errors of the optimal regression models are reported in Table 2. The validation and testing errors of the optimal MX3D Bridge thermal response predictions. for a subset of the bridge's sensors. The measured and predicted signal of SG03 and SG20 strain gauges are displayed in Figure 6.

The overall thermal responses are accurately predicted for the training and the unseen testing sets, with average $e_{p,val}$ and $e_{p,test}$ of 2.0% and 2.1%. The predicted signals are compared to the measured signals (post data preparation), demonstrating a very good modelling of the structure's baseline response induced by temperature fluctuations (see Figure 6). Minimal increases between the validation and testing errors are observed, which confirms the accuracy of the regression models provided by the IRBTRP methodology. Previous work by the authors (Glashier, Kromanis and Buchanan, 2023a) had found significant increases in the testing errors however they were linked to non-negligible differences in the environmental conditions between the training and testing datasets.

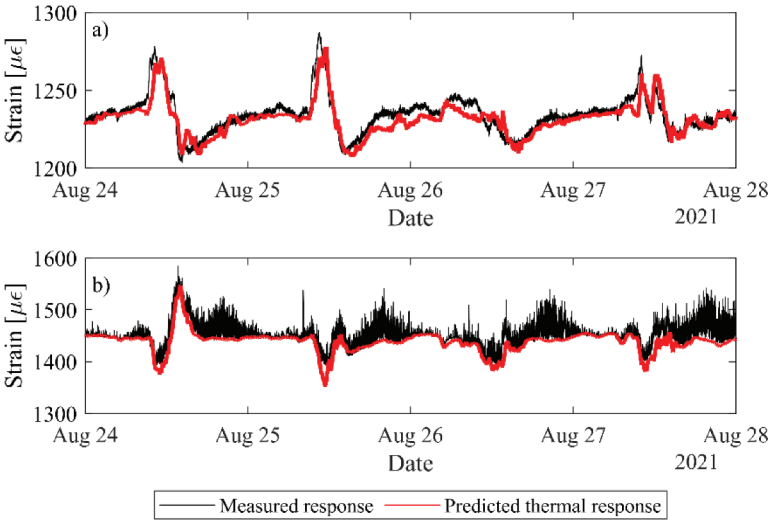


Figure 6. The measured response, and predicted thermal response of a) SG03 and b) SG20 strain gauges.

Table 2. The validation and testing errors of the optimal MX3D Bridge thermal response predictions.

	Optimal regression models			
Sensor	Regression algorithm	$e_{p,val}$	$e_{p,test}$	r_{ref}
A03z	MLR	3.0%	3.0%	0.029 m/s^2
I01	ANN	4.9%	4.9%	0.94 °
LC03	ANN	5.0%	4.4%	3.98 kN
SG03	ANN	1.6%	1.9%	225 $\mu \in$
SG06	ANN	0.9%	1.1%	490 $\mu \in$
SG12	ANN	0.6%	0.7%	370$\mu \in$
SG14	ANN	1.0%	2.3%	196 $\mu \in$
SG19	ANN	0.8%	0.8%	213$\mu \in$
SG20	ANN	0.6%	0.5%	551 $\mu \in$
SG26	ANN	1.3%	1.3%	124 $\mu \in$
SG38	ANN	1.8%	1.8%	3528 $\mu \in$
Average	–	2.0%	2.1%	–

As the bridge's structural response is driven by traffic as well as temperature (see Figure 4) and the regression models account for temperature variations, prediction errors cannot be evaluated for times of applied loading (e.g., pedestrians). For short-span structures, the response to applied loading makes up a larger part of the measured signal, whereas the response of long-span bridges is largely temperature-induced, encouraging the availability of

thermal response predictions at all times. For temperature-based measurement interpretation, it is recommended to minimise the variations in the operational conditions (e.g., minimally loaded or even unloaded).

Other than for A03*z,* artificial neural networks yielded the most accurate regression models for all sensors investigated in this work, indicating that simple regression techniques such as MLR and RR are not optimal for capturing the nonlinear relationship between a structure's distributed temperature and its response.

5 CONCLUSIONS

Temperature-based approaches for measurement interpretation of SHM datasets rely on accurate thermal response predictions to remove the effect of temperature variations from the measured structural response. So far, predictions for thermal response have been predominantly obtained for laboratory-set-ups, whilst the challenge remains to demonstrate that SHM techniques can be successfully applied to full-scale structures that are subject to environmental and operational variability (EOV).

Data preparation was applied to ready a 2-year operational dataset collected from the MX3D Bridge, including a step to detect the applied loading from pedestrians on the bridge, hence removing operational variations. The prepared dataset was then used in an iterative regression based thermal response prediction (IRBTRP) methodology to learn and predict the bridge's response to environmental changes in temperature. The structure's surface temperature measured by 14 thermistors suffices to provide accurate thermal response predictions of the MX3D Bridge for testing periods unseen during training, with average $e_{p,test}$ of 2.1%.

Further work will involve the application of anomaly detection techniques to the prediction error signals for the detection of structural change that may have occurred later on the bridge's structural dataset.

REFERENCES

Aktan, A. E. *et al.* (1996) 'Condition assessment for bridge management', *Journal of infrustructure systems*, 2(3), pp. 108–117. doi: 10.1061/(ASCE)1076-0342(1996)2:3(108).

Azimi, M., Eslamlou, A. D. and Pekcan, G. (2020) 'Data-driven structural health monitoring and damage detection through deep learning: State-ofthe- art review', *Sensors*, 20(10). doi: 10.3390/s20102778.

Brownjohn, J. M. W. (2007) 'Structural health monitoring of civil infrastructure', *Philosophical Transactions of the Royal Society A: Mathematical, Physical and Engineering Sciences*, 365(1851), pp. 589–622. doi: 10.1098/rsta.2006.1925.

Brownjohn, J. M. W. *et al.* (2011) 'Vibration-based monitoring of civil infrastructure: Challenges and successes', *Journal of Civil Structural Health Monitoring*, 1(3), pp. 79–95. doi: 10.1007/s13349-011-0009-5.

Brownjohn, J. M. W. *et al.* (2015) 'Operational deformations in long-span bridges', *Structure and Infrastructure Engineering*, 11(4), pp. 556–574. doi: 10.1080/15732479.2014.951857.

Catbas, F. N., Gokce, H. B. and Gul, M. (2012) 'Nonparametric analysis of structural health monitoring data for identification and localization of changes: Concept, lab, and real-life studies', *Structural Health Monitoring*, 11(5), pp. 613–626. doi: 10.1177/1475921712451955.

Cawley, P. (2018) 'Structural health monitoring: Closing the gap between research and industrial deployment', *Structural Health Monitoring*, 17(5), pp. 1225–1244. doi: 10.1177/1475921717750047.

Farrar, C. R. and Worden, K. (2012) *Structural Health Monitoring: A Machine Learning Perspective*. John Wiley \& Sons. doi: 10.1002/9781118443118.

Figueiredo, E. and Brownjohn, J. (2022) 'Three decades of statistical pattern recognition paradigm for SHM of bridges', *Structural Health Monitoring*, 21(6), pp. 3018–3054. doi: 10.1177/14759217221075241.

Glashier, T., Kromanis, R. and Buchanan, C. (2023a) 'An iterative regression-based thermal response prediction methodology for instrumented civil infrastructure', *Preprint submitted to Advanced Engineering Informatics*.

Glashier, T., Kromanis, R. and Buchanan, C. (2023b) 'Temperature-based measurement interpretation of the MX3D Bridge', *Preprint accepted by Engineering Structures*.

Helmerich, R. *et al.* (2008) 'Bridge inspection and condition assessment in europe', *Transportation Research Record*, 2044(1), pp. 31–38. doi: 10.3141/2044-04.

Kong, J. S. and Frangopol, D. M. (2003) 'Life-Cycle Reliability-Based Maintenance Cost Optimization of Deteriorating Structures with Emphasis on Bridges', *Journal of Structural Engineering*, 129(6), pp. 818–828. doi: 10.1061/(asce)0733-9445(2003)129:6(818).

Kromanis, R. and Kripakaran, P. (2016) 'SHM of bridges: characterising thermal response and detecting anomaly events using a temperature-based measurement interpretation approach', *Journal of Civil Structural Health Monitoring*, 6(2), pp. 237–254. doi: 10.1007/s13349-016-0161-z.

Martín-Sanz, H. *et al.* (2020) 'Monitoring of the UHPFRC strengthened Chillon viaduct under environmental and operational variability', *Structure and Infrastructure Engineering*, 16(1), pp. 138–168. doi: 10.1080/15732479.2019.1650079.

Masciotta, M. G. *et al.* (2016) 'A spectrum-driven damage identification technique: Application and validation through the numerical simulation of the Z24 Bridge', *Mechanical Systems and Signal Processing*, 70–71, pp. 578–600. doi: 10.1016/j.ymssp.2015.08.027.

Peiris, A., Sun, C. and Harik, I. (2020) 'Lessons learned from six different structural health monitoring systems on highway bridges', *Journal of Low Frequency Noise Vibration and Active Control*, 39(3), pp. 616–630. doi: 10.1177/1461348418815406.

De Roeck, G. (2003) 'The state-of-the-art of damage detection by vibration monitoring: The SIMCES experience', *Journal of Structural Control*, 10(2), pp. 127–134. doi: 10.1002/stc.20.

Sohn, H. (2007) 'Effects of environmental and operational variability on structural health monitoring', *Philosophical Transactions of the Royal Society A: Mathematical, Physical and Engineering Sciences*, 365(2007), pp. 539–560. doi: 10.1098/rsta.2006.1935.

Turrisi, S., Zappa, E. and Cigada, A. (2022) 'Combined Use of Cointegration Analysis and Robust Outlier Statistics to Improve Damage Detection in Real-World Structures', *Sensors*, 22(6). doi: 10.3390/s22062177.

Xu, Y. and Brownjohn, J. M. W. (2018) 'Review of machine-vision based methodologies for displacement measurement in civil structures', *Journal of Civil Structural Health Monitoring*, 8(1), pp. 91–110. doi: 10.1007/s13349-017-0261-4.

Ye, X. W., Tao, J. and Yun, C. B. (2019) 'A review on deep learning-based structural health monitoring of civil infrastructures', *Smart Structures and Systems*, 24, pp. 567–586. doi: 10.12989/sss.2019.24.5.567.

Zhao, R. *et al.* (2019) 'Deep learning and its applications to machine health monitoring', *Mechanical Systems and Signal Processing*, 115, pp. 213–237. doi: 10.1016/j.ymssp.2018.05.050.

Bridge Maintenance, Safety, Management, Digitalization and Sustainability – Jensen, Frangopol & Schmidt (eds)
© 2024 The Author(s), ISBN 978-1-032-77040-6
Open Access: www.taylorfrancis.com, CC BY-NC-ND 4.0 license

Identification of main cable shape of suspension bridge based on 3D point cloud

R. Pan, D. Dan & Y. Li
Tongji University, Shanghai, China

ABSTRACT: The main cable of the suspension bridge is the main and most important component of the structure. The main cable shape is mainly determined by the horizontal tension of the main cable, the suspension cable force, and its own load concentration. In the completed bridge state, the main cable shape can reflect the cable force of the suspension cable and also reflect its own internal force distribution. Therefore, the true shape of the main cable of the completed bridge is the key to study the stress state of the cable structure of the suspension bridge, which is of great significance to the long-term monitoring of the suspension bridge. In this paper, a method to identify the main cable shape of the suspension bridge based on a 3D point cloud is proposed, and the method is verified against the background of Honghe Bridge in Yunnan Province. The raw point cloud data of main cable was obtained through LiDAR. After noise reduction and registration of the raw data, the main cable point cloud is obtained through clustering algorithm. Then, using the circular tube axis algorithm, the measured central axis of the main cable is obtained. The construction phase of Suspension bridge is analyzed and the main cable model is obtained in the finite element software. Then, the finite element model is exported and registered with the measured point cloud to obtain the theoretical central axis. Finally, the theoretical central axis is compared with the measured central axis to obtain the main cable shape deviation result.

1 INTRODUCTION

The cable system of a suspension bridge is the key to bearing the full bridge load. For suspension bridges, precise construction quality control is particularly important. The identification and control of the main cable shape is a major project in suspension bridge construction monitoring. However, the identification of the main cable line of suspension bridges faces the following challenges: traditional methods for identifying the main cable line mainly rely on traditional measurement tools such as total stations and levels to measure some characteristic points of the main cable discretely. The results are not rigorous enough, and there are shortcomings such as low efficiency, large workload, and low data reliability. On the other hand, the geometric state of the suspension bridge structural system is more sensitive to temperature changes, and if the measurement time is too long, accurate main cable shape cannot be obtained. Therefore, an accurate and fast method for identifying the main cable shape of suspension bridges is needed.

3D laser scanning technology can accurately and efficiently measure the geometric information of objects (Tang, et al., 2010). The main principle of 3D laser scanning technology is to obtain the distance between the scanner and the measured point through a ranging system, and then obtain the horizontal and vertical angles from the scanner to the measured point through an angle measurement system to calculate the 3D coordinates of the measured point. After continuously scanning the measured object at a certain sample density, corresponding point cloud data can be obtained, thereby achieving a high-quality and comprehensive measurement of the object. This is something that conventional measuring instruments and methods cannot achieve.

DOI: 10.1201/9781003483755-300

Considering the shortcomings of traditional cable line recognition methods and the advantages of 3D laser scanning, this paper proposes a suspension bridge cable line recognition method based on 3D scanning. The point cloud data of the suspension bridge was obtained through LiDAR. The main cable point cloud was obtained through clustering algorithm. Obtain the measurement center axis of the main cable through the circular tube axis algorithm. Furthermore, the theoretical central axis is compared with the measured central axis to obtain the deviation results of the main cable line identification. The results indicate that the accuracy of the main cable line shape identified by this method is high, which has certain reference significance for practical engineering.

2 A METHOD FOR IDENTIFYING THE MAIN CABLE LINE SHAPE OF SUSPENSION BRIDGES USING 3D SCANNING TECHNOLOGY

The emergence of 3D scanning technology provides a new way to measure the continuous geometric shape of structures in space. This technology can comprehensively measure structures under complex environmental conditions and provide stronger support for the acquisition of position and appearance information of the tested object based on its large amount of data acquisition. At the same time, this technology greatly improves measurement efficiency and quality, and has good application prospects in structural detection. This section provides an introduction to the application methods of 3D scanning technology in identifying the main cable line shape of suspension bridges.

2.1 *3D scanning technology*

3D scanning technology transforms the traditional single point acquisition method into a new automatic and continuous way to obtain a large amount of point cloud data, which has the advantages of speed, high accuracy, and comprehensiveness, providing a new approach for measuring structures. Therefore, 3D scanning technology establishes a high-precision 3D point cloud model by obtaining actual spatial position information data such as points, lines, surfaces, volumes, and spaces of the target structure.

In the field of structural deformation monitoring, Stuart Gordon et al. (2001) used a 3D scanner to perform multi-site scanning of aged wooden bridge piers and analyze the coordinate differences between each station to complete deformation monitoring of the bridge piers in 2001. H S. Park et al. (2007) conducted deformation tests on simply supported steel beams using 3D scanning technology. Armasto J et al. (2010) applied 3D scanning technology to monitor the deformation of ancient stone arch bridges. Shi et al. (2014) attempted to apply 3D scanning technology to the monitoring of bridge pier shield excavation and proposed a 3D holographic modeling method based on triangular grid point cloud encapsulation. Matsumoto et al. (2018) proposed a spatial measurement method based on 3D ground laser scanning to capture the overall deformation of bridges. Through 3D scanning technology, the deformation of the pylon of the Twantay Bridge in Myanmar caused by anchor sliding was monitored. Yoon et al. (2018) proposed a method that minimizes the mismatch between shear grooves and shear connectors on bridge decks through 3D laser scanning and signal processing technology, and automatically identifies the optimal installation position of precast bridge decks on precast beams. Kwiatkowski et al. (2020) used FARO Focus 3D and Trimble TX8 scanners to scan and measure the main beams and cables of conveyor belt bridges, and the results showed that this method can be applied to deformation monitoring of bridge structures. Zhou et al. (2021) used 3D scanning technology to scan the main cables of suspension bridges and developed a method for inferring the force of suspension bridge suspension rods through the relationship between adjacent intersection points.

2.2 *Point cloud data preprocessing*

A point cloud is a collection of points with coordinates, vectors, and color information arranged in actual spatial positions, expressed in billions. The distance between points in

the point cloud obtained by a 3D scanner is very small, and various methods can be used to form patches and package them into a 3D model. When using a scanner to obtain point cloud data, the surrounding environment and the target structure itself may obstruct some components of the structure. This requires the use of multi-site scanning to collect multi-site clouds and obtain complete information of the target. Due to the need to move the scanner for multi-site scanning, the coordinate origin changes, resulting in the obtained point cloud data not being in the same coordinate system. This requires in-house personnel to register multi-site data. In addition, the point cloud data obtained by scanning generally includes some information about the surrounding environment. In order to present a better point cloud model and reduce the amount of data, data deletion and reduction are required. The point cloud model processed above still has a large number of noise points, which cannot meet the requirements of later analysis. Therefore, point cloud denoising is still needed (Tian F, et al., 2019).

The so-called "noise reduction" refers to the influence of on-site environmental factors such as human and machine vibration, which causes some noise points unrelated to the measured object to appear in the collected point cloud data. At this time, some filtering algorithms are used to filter out the point cloud data of occluded objects and some discrete points, retain the point cloud data of the target object, and use the "noise reduction" function to achieve structural noise reduction. Delete all point clouds unrelated to the curved tube structure (including all secondary components unrelated to the tube structure) in preparation for extracting the tube shape.

2.3 *Identification method for main cable line type*

The key to identifying the main cable line type is to extract the central axis of the main cable. This article proposes an algorithm for extracting the central axis of the main cable, and its main calculation process is as follows: the point cloud of the main cable is generally presented in spatial posture. To simplify the algorithm for extracting the central axis of the main cable and improve its computational efficiency, it can be segmented first, then the segmented main cable is projected onto a plane and linearly fitted. After segmentation, each microelement segment is fitted with a plane circle to obtain the plane coordinates of its center. Finally, the corresponding center space coordinates are found, and the spatial posture of each center is restored to complete the extraction of the axis. Set the collection of main cable point clouds as $P_{n\times 3} \in \{(x_i, y_i, z_i), i = 1, 2, 3, \cdots n\}$ and perform linear fitting on it, that is

$$\min \|\delta\|^2 = \sum [kx_i + b - y_i] \tag{1}$$

Calculate the slope of the linear fitting of the point cloud on the x-y plane according to formula (1), and then calculate the angle θ between the fitted line and the x-axis, where $\theta = \arctan k$. Rotate the point cloud clockwise around the z-axis with θ to obtain the point cloud in the x-z plane coordinate system. In computer graphics, the mathematical expression for this rotation process is to multiply $P_{n\times 3} \in \{(x_i, y_i, z_i), i = 1, 2, 3, \cdots n\}$ by equation A. The formula for A is as follows

$$A = \begin{bmatrix} \cos\theta & \sin\theta & 0 \\ -\sin\theta & \cos\theta & 0 \\ 0 & 0 & 1 \end{bmatrix} \tag{2}$$

Rotate and project each element segment onto the x-z plane using the above method, then fit the plane circle to obtain the center coordinates, and finally use the inverse matrix of formula (2) to restore the spatial orientation of the center. Finally, interpolate the centers of all microelement segments using a cubic spline curve to obtain the centerline of the main cable. All the above processes can be implemented by programming languages. The algorithm flow for identifying the main cable line type is shown in Figure 1.

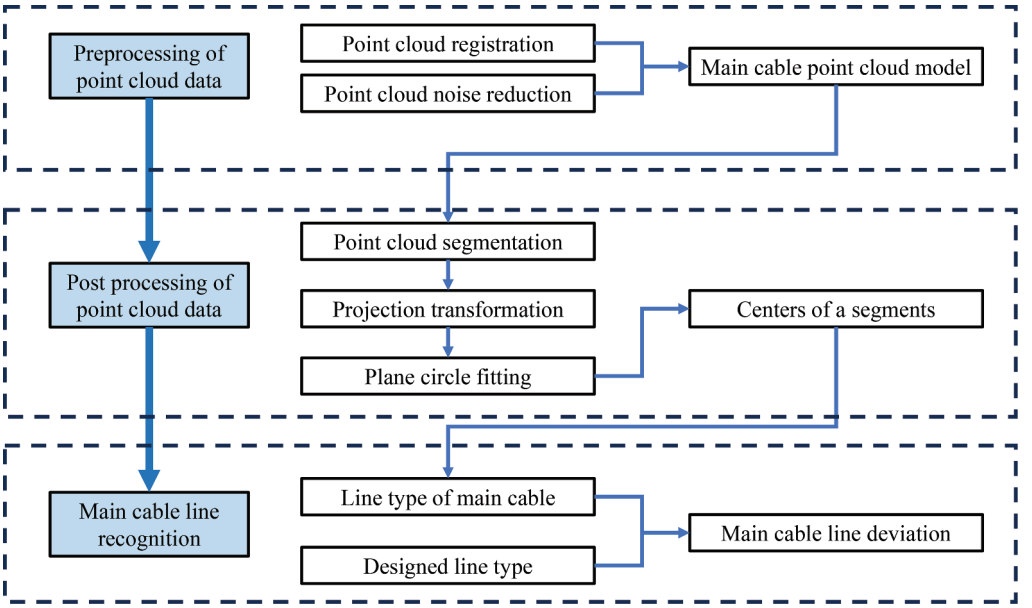


Figure 1. Algorithm flow for identifying the main cable line type.

3 CASE STUDY

3.1 *Case introduction*

This study uses the main cable point cloud data of the Honghe Bridge in Yunnan Province, China. The Honghe Bridge is a two-tower suspension bridge. The bridge is composed of cable towers, anchorages, suspension cables, suspension cables, and a deck system, with a total length of 1366 meters. The north approach bridge is 580 meters long, the south approach bridge is 80 meters long, and the main span is 700 meters long. The water surface is as high as 184 meters from the bridge deck, with the north main tower at a height of 181.29 meters and the south main tower at a height of 122.5 meters.



Figure 2. Honghe Bridge.

3.2 *Data acquisition*

This study used Livox Mid-70 LiDAR to collect point cloud data of the main cable of the bridge. Some parameters of the LiDAR are shown in the table below. LiDAR is shown in Figure 3.

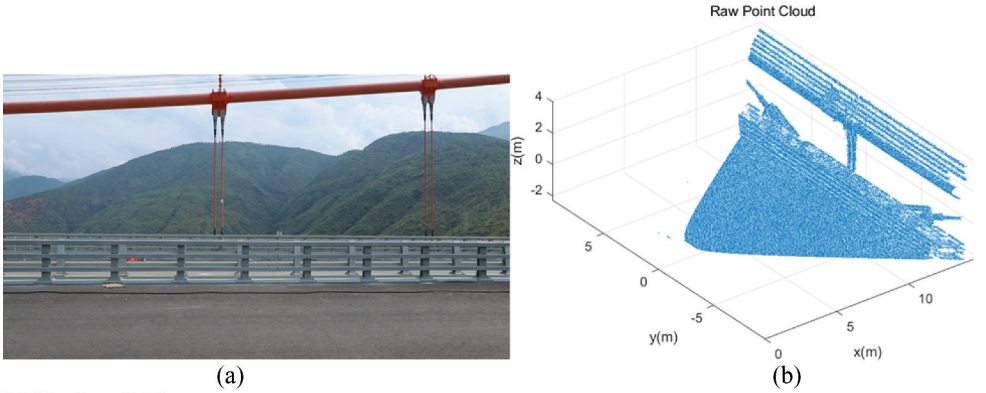
Table 1. LiDAR parameters.

Type	Livox Mid70
Size	97×64×62.7 mm
Weight	580g
Laser wavelength	905nm
Range	260m
FOV	70.4°
Distance measurement error	≤2cm
Angle measurement error	<0.1°



Figure 3. Livox Mid-70.

The testing field and the obtained main cable point cloud data are shown in the following figure.



(a) Testing field
(b) Raw point cloud data of main cable

Figure 4. Experimental data and source.

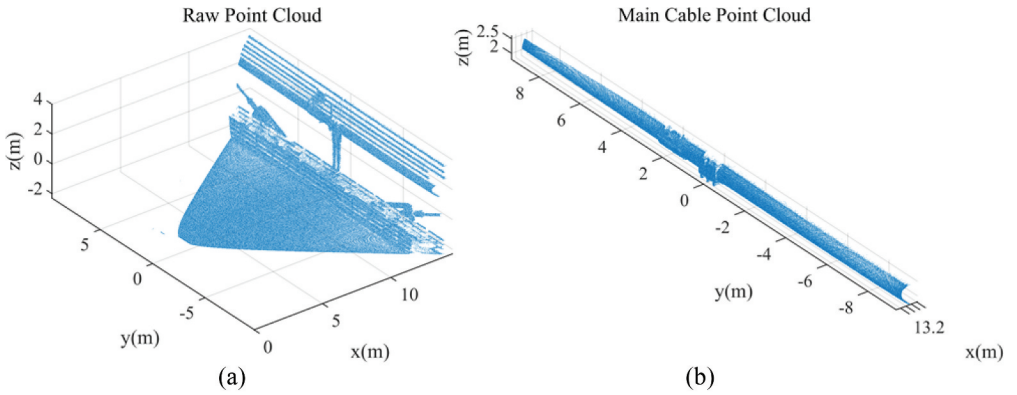
3.3 *Identification result*

Firstly, preprocess the original point cloud data to remove noise and unnecessary point cloud data, while preserving the point cloud data of the target object as much as possible. The results of data preprocessing are shown in the following figure.

Segment the preprocessed point cloud data, in order to balance computational efficiency and accuracy, the length of the microsegment is taken as 0.25m. One of the segmented main cable point cloud is shown in Figure 6(a).

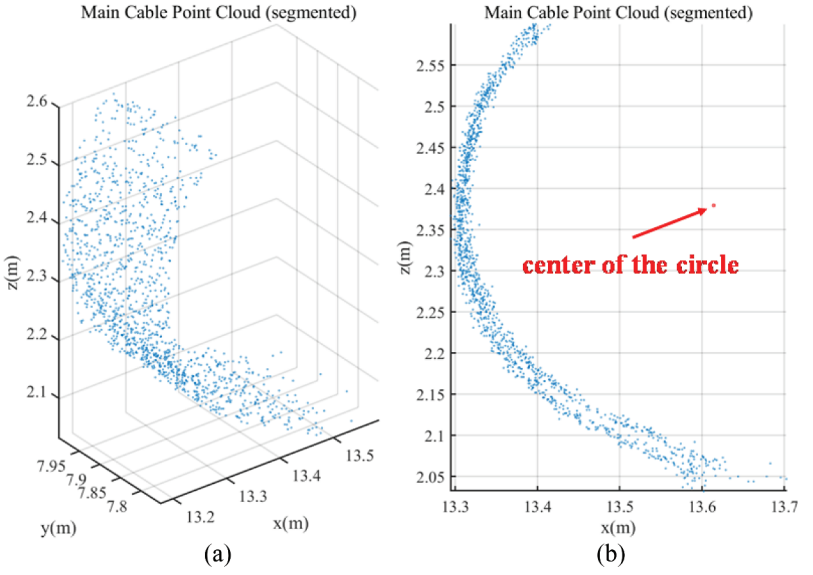
According to the method in section 2.3, rotate and project the point cloud of the segment, and find the center of the segment through the method of plane circle fitting. The result is shown in Figure 6(b).

After obtaining the centers of all segments, interpolate all control points through a cubic spline curve to obtain the centerline of the main cable. The results are shown in Figure 7.



(a) Raw cloud data
(b) Pre-processed point cloud data

Figure 5. Point cloud data of main cable.



(a) Segmented main cable point cloud
(b) Point cloud after projection transformation

Figure 6. Segmented main cable point cloud.

In Figure 7, the red curve represents the central axis of the main cable. From Figure 7, it can be seen that the central axis of the main cable identified by the above method is located at the center of the main cable point cloud. The accuracy of identification will be verified in the next section.

3.4 *Result verification*

In order to verify the accuracy of the main cable line identified by this method, the center axis identified is subtracted from the theoretical axis, and the vertical coordinate difference of each control point near the mid span is calculated to determine the recognition effect.

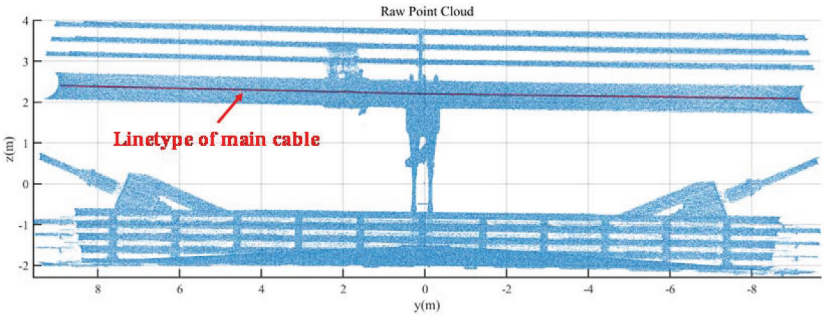


Figure 7. Line type of main cable.

Table 2. Result comparison.

Horizontal ordinate of control point (m)	Vertical coordinate of designed line type (m)	Vertical coordinate of identified line type (m)	D-value (m)
-8	2.093	2.096	-0.003
-6	2.120	2.123	-0.003
-4	2.144	2.147	-0.003
-2	2.169	2.172	-0.003
0	2.219	2.226	-0.007
2	2.234	2.259	-0.024
4	2.284	2.291	-0.006
6	2.328	2.333	-0.005
8	2.380	2.386	-0.006

From Table 2, it can be seen that the difference in vertical coordinates between the designed line type and the identified line type at the same control point is relatively small, indicating that the identified central axis of the main cable has high accuracy.

4 CONCLUSION

Research has shown that applying 3D scanning technology to the identification of the main cable line shape of suspension bridges is effective, and the following conclusions have been obtained.

(1) The three-dimensional LiDAR was used to quickly and comprehensively obtain rich data for the main cable of the suspension bridge. Combined with the influence of the micro segment point cloud projection circle, algorithm programming was used to automatically and efficiently extract the centerline shape of the structure. By comparing the reconstructed circular tube with the point cloud three-dimensional analysis given the centerline radius, the results show that the overall accuracy of the linear shape is high, the effect is stable, and it can meet the requirements of engineering measurement.
(2) The deviation between the detection method and the theoretical line shape of the suspension bridge was compared, and the results showed that the overall trend of the deviation between the two was basically consistent, and the deviation results of adjacent control points were close. The overall linear accuracy is high, which has certain significance for guiding the subsequent construction of the structure and ensuring on-site construction.

The proposal of this detection method has certain reference significance for the overall linear extraction of circular tube structures.

REFERENCES

Armesto J, Roca-Pardinas J, Lorenzo H, et al. (2010) Modelling masonry arches shape using terrestrial laser scanning data and nonparametric methods. *Engineering Structures* 32(2): 607–615.

Gordon S, Lichti D, Stewart M (2001) Application of a high-resolution, ground-based laser scanner for deformation measurements. *The 10th FIG International Symposium on Deformation Measurements*, 19–22 March 2001. Orange, California, USA.

Kwiatkowski J, Anigacz W and Beben D (2020) Comparison of Non-Destructive Techniques for Technological Bridge Deflection Testing. *Materials* 13(8).

Matsumoto K, Panting CAL, Kitratporn N, et al. (2018) Performance Assessment Using Structural Analysis and Spatial Measurement of a Damaged Suspension Bridge: Case Study of Twantay Bridge, Myanmar. *Journal of Bridge Engineering* 23(10).

Park HS, Lee HM, Adeli H, et al. (2007) A new approach for health monitoring of structures: Terrestrial laser scanning. *Computer-Aided Civil and Infrastructure Engineering* 22(1): 19–30.

Shi H, Bai M, Zhang Y, et al. (2014) Exploration in monitoring the shield excavation of adjacent bridge pier based on three-dimensional laser scanning technology. *International Journal of Earth Sciences and Engineering* 7(5):1985–1992.

Tang P, Huber D, Akinci B, et al. (2010) Automatic reconstruction of as-built building information models from laser-scanned point clouds: A review of related techniques. *Automation in Construction* 19(7): 829–843.

Tian F, Chen H, Yu M, et al. (2019) Super-voxel Based Point Cloud Segmentation Algorithm. *Proceedings of the conference on optoelectronic imaging and multimedia technology VI*, 21–23 October 2019. Hangzhou, Peoples R China.

Yoon S, Wang Q and Sohn H (2018) Optimal placement of precast bridge deck slabs with respect to precast girders using 3D laser scanning. *Automation in Construction* 86: 81–98.

Zhou Y, Xiang Z, Zhang X, et al. (2022) Mechanical state inversion method for structural performance evaluation of existing suspension bridges using 3D laser scanning. *Computer-Aided Civil and Infrastructure Engineering* 37(5): 650–665.

Bridge Maintenance, Safety, Management, Digitalization and Sustainability – Jensen, Frangopol & Schmidt (eds)
© 2024 The Author(s), ISBN 978-1-032-77040-6
Open Access: www.taylorfrancis.com, CC BY-NC-ND 4.0 license

A framework for bridge condition assessment using graph neural network

G. Marasco, S. Sadeghi Eshkevari, I. Dabbaghchian & S.N. Pakzad
Lehigh University, Bethlehem, PA, USA

D. Sen
Southern Illinois University, Carbondale, IL, USA

ABSTRACT: A heuristic approach based on visual inspections cannot provide an adequate and unbiased evaluation of bridges' structural state. Fatigue assessment methods, based on the structural dynamic response, turn out to be crucial to consider the current structural conditions. Conventionally, strain data under traffic loading are collected for fatigue assessment. Although direct measurements of strain signals allow effective structural health monitoring strategies, they would induce a considerable rise in costs and errors, specifically where an extensive sensor network is needed. To pursue higher reliability of the monitoring system, a machine learning approach to convert acceleration to strain signals is proposed from a life cycle assessment perspective. Graph neural networks (GNNs), a class of machine learning models recently emerging in the civil engineering field, are employed to achieve this task. The GNN enables the encoding of structural information to describe the relationship between its nodes, representing the structural joints, and creating a geometry-based architecture in this application. The approach has been validated on a numerical simulation and promising results have been obtained.

1 INTRODUCTION

Monitoring the health of structures such as bridges, subjected to dynamic loads and material aging, is essential for ensuring their structural integrity (Gulgec 2017). Bridge management systems (BMSs) are currently used for the management of bridge information and maintenance cost mitigation. They rely on periodical visual inspections presenting significant limitations due to constraints in both time and space.

Over the years, Structural Health Monitoring (SHM) strategies have been proposing to overcome such limitations, offering timely assessments of structural condition (Chiaia 2020a) saving time and costs as well as enhancing safety significantly. When assessing structural condition, methods related to damage condition and evaluation of remaining useful life are employed.

Damage detection techniques often revolve around either vibration-based (Magalhães 2011, Cronin 2021) or static-based approaches (Nguyen 2016). Vibration-based methods can reveal damage through shifts in modal parameters. However, factors like data volume, monitoring time, and environmental conditions (Chiaia 2020b) can impede accurately estimating these parameters, hindering early damage detection. Consequently, these methods are better suited for updating structural models rather than promptly detecting early deterioration. Static-based methods more readily achieve the second level of the hierarchical structure in damage identification, specifically targeting damage localization (Farrar 2012, Marasco 2022a). However, their application tends to incur greater expenses overall.

DOI: 10.1201/9781003483755-301

The evaluation of the remaining useful life is traditionally performed by collecting strain or stress data; they allow to evaluate the fatigue behavior of the structure by constructing rainflow diagrams (Fatemi 1998). Obtaining strain responses poses challenges due to limited access to critical areas, high associated costs, and labor-intensive nature of the process (Kim 2007, Childers 2001).

While recent studies have shown highly promising results in utilizing deep learning techniques to convert acceleration signals into strain signals, further investigations are required to determine the most suitable architecture for tackling this intricate task effectively. In (Gulgec 2019b), a long short-term memory (LSTM) architecture demonstrates effective performance in the task at hand. However, there remains a need for further exploration regarding LSTM computational cost and suitability, as indicated in (Gulgec 2020). Moreover, while LSTM excels in sequence prediction tasks, it may not be the optimal choice for simulating nonlinear models. Recent advancements in machine learning have illustrated notable performance improvements for time-series data compared to LSTM-centric approaches. Integrating different architectures, as demonstrated in (Le-Xuang 2024) where 1D Convolutional Neural Networks (1DCNN), LSTM, and Residual Networks (ResNet) are combined, can enhance overall performance. Additionally, cutting-edge algorithms such as Transformers and GNNs emerge as promising solutions worth considering.

This study aims at providing a deep learning framework for strain estimation by exploiting graph networks, one of the most recent emerging architecture in the civil engineering field. Graph-based data structuring, originating from fields like biology, recommender systems, traffic prediction, and computer vision, holds significant promise when applied to structural analysis. By representing a structure as a graph, the model captures spatial properties and element connections, thereby improving the model's understanding of structural responses. Currently, studies in the civil engineering field utilizing graph architecture are centered on two tasks: classifying damage and predicting static structural responses. Following are some of the main contributions. Dan et al. (Dang 2022) introduced a graph convolutional framework that directly utilizes vibration data for damage classification. Node features incorporate both node coordinates and the time-evolving patterns of recorded accelerations. Kim and Song developed a damage identification approach (Kim 2023) exploiting the structural response during an earthquake event. Whalen and Mueller (Whalen 2022) introduced a graph-oriented method tailored for trusses. Their approach encodes the structural geometry, supports, and applied loads within a graph framework to forecast displacement field resulting from static loads. Similarly, Song et al. proposed the utilization of graph neural networks in a self-supervised learning setup for elastic structural analysis (Song 2022).

Starting from the encouraging outcomes of a previous study (Marasco 2023), the present research aims at bridging the literature gap in addressing dynamic problems and the associated challenges with GNNs. It investigates the performance of a graph convolution neural network (GCN) architecture converting acceleration signal to strain signal at each structural node, evaluating what is the impact of physics information within this architecture. The method has been validated using synthetic data, showing promising results.

2 GRAPH NEURAL NETWORKS

GNNs are recent deep learning architectures that enhance the functionality of conventional neural networks such as CNNs (Gulgec 2019a), Recurrent Neural Networks (RNNs) (Eshkevari 2021, Eshkevari 2022), and Multi-Layer Perceptron (MLP) (Marasco 2022b) enabling them to process non-Euclidean input. In the conventional notation, a graph is typically represented as $G = (V, E)$, where V stands for the set of nodes (vertices) and E denotes the set of edges. Within structural contexts, nodes represent structural joints, while edges stand for the connecting structural elements that link these joints (Scarselli 2008)Two key matrices define a graph: the feature matrix and the adjacency matrix. The first one, $X \in R^{N \times D}$, contains the attributes of the nodes. The second one, $A \in R^{N \times N}$, contains information about the node connection. Here, N is the number of nodes and D is the attributes dimension. In this study,

sensor locations serve as nodes of an undirect graph, and vibration data along with physics information are their multidimensional attributes. Due to its nature, the present study addresses a regression problem at the node level. Among the various types of GNNs, this study specifically concentrates on GCNs. This architecture aggregates node information from neighboring nodes using convolutional techniques leveraging the graph's structure. GCNs have demonstrated success across diverse tasks and possess a strong ability to learn representations of graphs (Zhang 2019).

The key difference between CNNs and GCNs lies in how they merge vibration signals from multiple sensors. When CNN's kernel combines signals, it doesn't retain information about which sensor each time series corresponds to. Conversely, after the GCN operation, a revised set of node features is generated, combining signals exclusively from directly linked nodes. Therefore, it becomes possible to discern the data from each sensor following a GCN layer. In contrast to CNNs which combine considering their organization, GCNs leverage real mechanical interactions. They are designed to consider that adjacent data might not have direct mechanical interactions.

The GCN layer usually calculates, X^{l+1}, the node representation at layer $(l+1)$ based on, X^l, the representation at level l, by Equation 1:

$$X^{l+1} = \hat{D}^{-1/2}\hat{A}\hat{D}^{-1/2}X^l W + b \tag{1}$$

where, $\hat{A} = A + I$ represents the adjacency matrix with self-loops, $\hat{D}$ stands for its degree matrix, I is the identity matrix, and W denotes a weight matrix. Notably, this study does not apply the graph filter using the degree matrix to normalize the input adjacency matrix.

3 CASE STUDY AND GCN IMPLEMENTATION

In evaluating the graph architecture for the fatigue assessment task, a case study involving a two-span beam subjected to traveling loads, simulating vehicle weights on a bridge using Finite Element Software SAP2000, has been employed. The beam has two spans, each spanning 7.3 meters and divided into 8 equal-length elements. Figure 1a illustrates the geometry with sensor locations marked by blue rectangles for capturing the structural response in terms of accelerations and strains. To closely resemble a bridge dataset, adjustments were made to the natural frequencies, damping, and repetition of moving loads for the vibration dataset. Specifically, the first three mode frequencies are set at 1.9, 3, and 7.5 Hz.

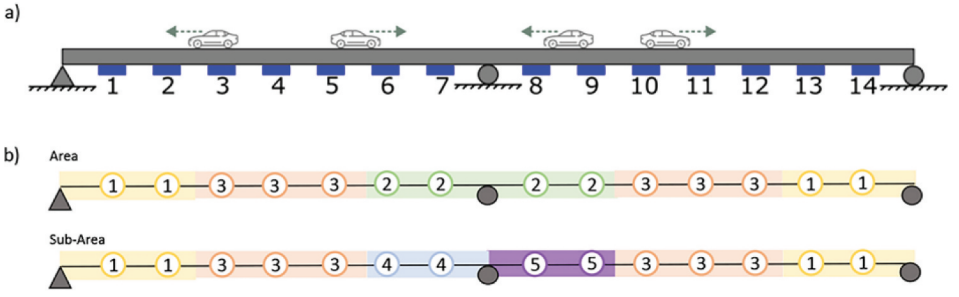


Figure 1. a) Two-span simulated beam b) Structural area and subarea.

Recordings of acceleration and strain time series were taken during a 4-minute period of vehicle movement, with data sampled at a frequency of 0.01 seconds. Subsequently, noise with an SNR of 15 was introduced. Normalization was performed by subtracting the average value and dividing by the standard deviation for each node individually. The signals were segmented into 4-second segments, each containing 400 samples with a step of 20 samples. Consequently, a dataset comprising 1181 signals, each containing 400 data points, was generated for each of the 14 nodes representing the graph's sensor locations.

The GCN architecture consists of several key components: GCN, normalization, dense, dropout, and dense layers. Initially, it employs convolutional and normalization layers to compress the input size from the attribute nodes' dimension (403 or more) down to 200. This reduction is aimed at capturing the most crucial features within the acceleration signal. Following this, the dimension remains fixed at 400 to make predictions for the strain signals. The dataset was split into training (70%), validation (20%), and testing (10%) subsets. Model training utilized the Adam optimizer with a learning rate set at 0.0001. However, the primary focus of this study was not on optimizing the model but rather on demonstrating the technique's applicability and highlighting the influence of physics-based information on performance. The network was implemented in Python, leveraging the Spektral library for coding, as detailed in (Grattarola 2021).

4 IMPACT OF PHYSICS INFORMATION

Evaluating the Graph Neural Network architecture's capacity to harness physics-based information involved investigating different approaches to incorporate this crucial data, acknowledging its fundamental importance in the process. To achieve this goal, both the feature and adjacency matrices have been used. The Time–Response Assurance Criterion (TRAC) has served as a metric to assess and compare the models' capability in accurately predicting the strain signals from the acceleration ones. Equation 2 shows its formulation, where X_t and $\overline{X_t}$ are the measured strain signal and the predicted strain signal, respectively.

$$TRAC = \frac{\left[X_t^T \bar{X}_t^T\right]^2}{\left[X_t^T X_t^T\right]\left[\bar{X}_t^T \bar{X}_t^T\right]} \tag{2}$$

Starting from an adjacency matrix composed of elements A_{ij} that are set to 1 if nodes i and j ae connected, including cases where i equals j, and are 0 otherwise, this study investigated how the results are influenced by the introduction of physics information into both the feature matrix and the adjacency matrix.

4.1 *Feature matrix*

As mentioned in Section *Graph Neural Networks*, the attributes of the nodes are represented by the feature matrix. In the first scenario S_1, apart from the raw signals, node coordinates and the normalized values of the first mode shape are also incorporated in the feature matrix by means of concatenation for each node. In the second scenario S_2, additional information specifying the structural area of each node is included. This was achieved by appending a vector that encodes this area information to each row of the feature matrix, essentially expanding the attribute vector of every node. This vector comprises ten repetitions of the index related to the structural area, concatenated with ten repetitions of the index linked to

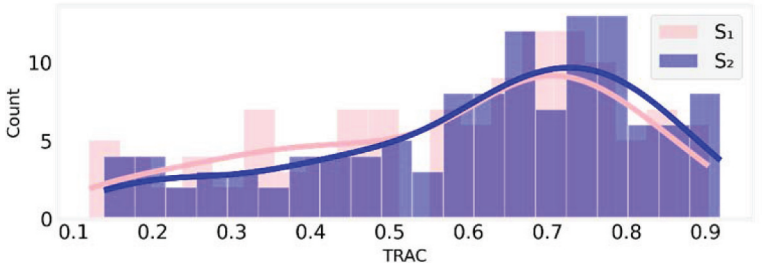


Figure 2. TRAC distribution for test dataset from case S_1 and S_2.

the sub-area. Figure 1b shows the splitting of the structure into distinct areas and subareas, each labeled with their respective associated indexes. Incorporating the structural area to which each node belongs provided a method to incorporate information regarding the influence of supports on the recorded signals.

Figure 2 illustrates the distributions of TRAC within the test datasets for scenarios S_1 and S_2. Table 1 summarizes the main statistical parameters (P) of such distributions. As can be observed, introducing additional physics-related information has yielded a positive effect on the overall performance. The mean, the mode, the minimum, and the maximum value of the TRAC distribution increase, as shown in the last column of Table 1.

Table 1. Statistical parameters for TRAC distributions for S_1 and S_2 scenarios.

Parameter (P)	S_1	S_2	$\Delta PS_2,S_1/PS_1$
Mean	0.58	0.62	6.9%
Mode	0.71	0.73	2.8%
Min	0.11	0.14	27.3%
Max	0.90	0.92	2.2%
Range	0.79	0.78	-1.3%
Skewness	-0.52	-0.71	36.5%
Kurtosis	-0.80	-0.41	49.5%

4.2 *Adjacency matrix*

Each structural system can be described using the eigenvalue decomposition approach by use of mode shapes and corresponding natural frequencies. Therefore, the structural properties can be represented by the mode shapes. The higher the difference in mode shape across nodes, the lower the spatial correlation (Kim 2023). The values of the elements, A_{ij}, within the modal-based weighted adjacency matrix, were calculated by:

$$A_{ij} = \sum_{i=1}^{n} T_i^2 e^{-\left|\bar{\phi}_{m,i} - \bar{\phi}_{m,j}\right|} \tag{3}$$

where T_i is the period of the m-th mode and $\bar{\phi}_{m,i}$ is the normalized mode shape of m-th mode at node i. The modes considered in this study are the first three. For research sake, such formulation has been used when node i and j are connected (S_3) and when node i and j are connected and equal (S_4). As shown in Table 2, S_4 has a narrower range then S_3 due to a greater minimum. Therefore, the use of this adjacency matrix allows to eliminate outliers.

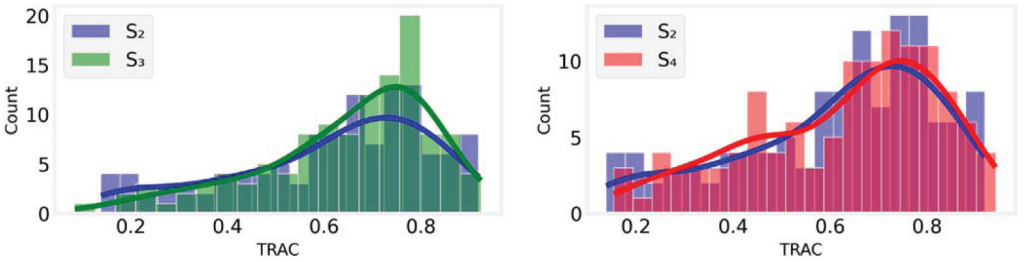


Figure 3. TRAC distribution for test dataset from case S_1 and S_2.

In S_3, an outlier is noticeable, yet the overall trend demonstrates improvement. In Figure 3, the green line portraying the S_3 distribution is situated below the blue line (representing S_2) on the left side and above it on the right side. The positive kurtosis value in S_3 indicates a distribution characterized by a distinct peak. S_4 shows an improvement in all the parameters

Table 2. Statistical parameters for TRAC distributions for S_3 and S_4 scenarios.

Parameter (P)	S_3	S_4	$\Delta PS_3,S_2/PS_2$	$\Delta PS_4,S_2/PS_2$
Mean	0.65	0.63	4.8%	1.6%
Mode	0.75	0.75	2.7%	2.7%
Min	0.08	0.15	-42.8%	7.1%
Max	0.92	0.94	0.0%	2.1%
Range	0.84	0.78	7.7%	0.0%
Skewness	-0.95	-0.61	33.8%	-14.0%
Kurtosis	0.34	-0.56	-183.0%	36.5%

with respect to S_2. The mean, mode, minimum, and maximum values of distribution S_4 are indeed greater of the ones of distribution S_2. The skewness shows a value slightly greater indicating a lower presence of outliers but the smaller value of kurtosis highlights a flatter shape of the distribution. In conclusion, both approaches showcase the positive influence of integrating physics-related structural mode information.

Alongside structural modes, another significant physical parameter affecting signal similarity between nodes is the distance separating them. As the distance increases, the weight assigned in the adjacency matrix decreases correspondingly. Figure 4 shows TRAC distributions associated with different values of n in Equation 4.

$$A_{ij} = \frac{\sum_{i=1}^{n} T_i^2 e^{-\left|\bar{\phi}_{m,i} - \bar{\phi}_{m,j}\right|}}{\left(d_{i,j}\right)^n} \tag{4}$$

The three curves corresponding to the three different values of n show a narrowing of the distribution with respect to S_2 and S_3 further deleting outliers. Equation 5 is proposed in the case in which the values on diagonal are not equal to zero.

$$A_{ij} = \sum_{i=1}^{n} T_i^2 e^{-\left|\bar{\phi}_{m,i} - \bar{\phi}_{m,j}\right|} \left(e^{-d_{i,j}}\right)^k \tag{5}$$

At varying of k, variations in the statistical parameters describing the distribution appear to show negligible impact.

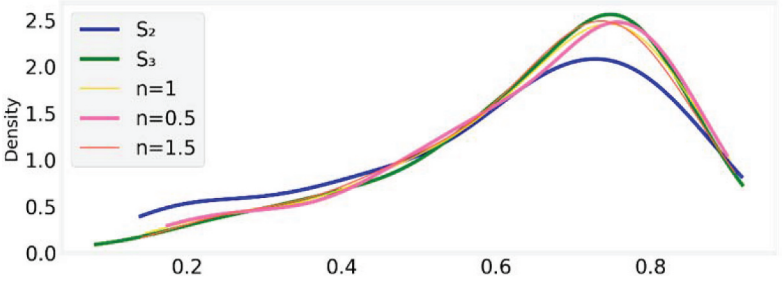


Figure 4. TRAC distribution for test dataset for different values of n.

5 CONCLUDING REMARKS

This study delved into utilizing graph convolutional neural networks to convert acceleration into strain signals for life-cycle assessment purposes. To validate the approach, a numerical case study was employed. The investigation aimed to discern the impact of integrating physics information within this framework. Despite the architecture's simplicity, with limited depth,

the accuracy of predictions was notably satisfactory and enhanced upon the inclusion of physics information. These promising outcomes serve as a foundation for future studies. Our forthcoming research endeavors involve developing more sophisticated methodologies and formulations to incorporate and leverage this invaluable information further.

REFERENCES

Chiaia, B., Ventura, G., Zannini Quirini. C. & Marasco, G. 2020a. Bridge active monitoring for maintenance and structural safety. *Proceedings of ARCH 2019: 9th International Conference on Arch Bridges*: 866–873.

Chiaia, B., Marasco, G., Ventura, G. & Zannini Quirini. C. 2020b. Customised active monitoring system for structural control and maintenance optimisation, *Journal of Civil Structural Health Monitoring*, 10 (2):267–282.

Childers, B. A., Froggatt, M. E., Allison, S. G., Moore Sr, T. C, Hare, D. A., Batten, C. F. & Jegley, D. C. 2001. Use of 3000 Bragg grating strain sensors distributed on four 8-m optical fibers during static load tests of a composite structure. Smart structures and materials 2001: *Industrial and commercial applications of smart structures technologies*, SPIE, vol. 4332: 133–142.

Cronin, L. M., Eshkevari, S. S, Sen, D. & Pakzad, S. N. 2021. Transfer learning for input estimation of vehicle systems. *IEEE International Conference on Acoustics, Speech and Signal Processing (ICASSP) 2021-2021*: 7953–7957.

Dang, V.-H., Vu, T.-C., Nguyen, B.-D., Nguyen, Q.-H. & Nguyen, T.-D. 2022. Structural damage detection framework based on graph convolutional network directly using vibration data. *Structures*. 38: 40–51.

Eshkevari, S. S., Tak ́a ̆c, M., Pakzad, S. N. & Jahani., M. 2021. DynNet: Physics-based neural architecture design for nonlinear structural response modeling and prediction. *Engineering Structures*. 229:111582.

Eshkevari, S. S., Cronin, L., Eshkevari, S. S. & Pakzad. S. N. 2022. Input estimation of nonlinear systems using probabilistic neural network. *Mechanical Systems and Signal Processing*. 166:108368

Farrar, C. R. & Worden, K. 2012. *Structural health monitoring: a machine learning perspective*. John Wiley & Sons.

Fatemi, A. & Yang L. 1998. Cumulative fatigue damage and life prediction theories: a survey of the state of the art for homogeneous materials. *International journal of fatigue*. 20(1):9–34.

Grattarola, D. & Alippi.C. 2021. Graph neural networks in tensorflow and keras with spectral. *IEEE Computational Intelligence Magazine*. 16(1): 99–106.

Gulgec, N. S., Shahidi, G. S., Matarazzo, T. J. & Pakzad. S. N. 2017. Current challenges with bigdata analytics in structural health monitoring. In Structural Health Monitoring & Damage Detection, Volume 7. *Proceedings of the 35th IMAC, A Conference and Exposition on Structural Dynamics 2017.:79–84.*

Gulgec, N. S., Tak ́a ̆c, M. & Pakzad, S.N. 2019a. Convolutional neural network approach for robust structural damage detection and localization. *Journal of computing in civil engineering*. 33(3):04019005.

Gulgec, N. S., Takáč, M., & Pakzad, S. N. 2019b. Innovative sensing by using deep learning framework. In Dynamics of Civil Structures, Volume 2: *Proceedings of the 36th IMAC, A Conference and Exposition on Structural Dynamics 2018*: 293–300.

Gulgec, N. S., Tak ́a ̆c,M. & Pakzad, S.N. 2020. Structural sensing with deep learning: Strain estimation from acceleration data for fatigue assessment. *Computer-Aided Civil and Infrastructure Engineering* 35 (12):1349–1364.

Kim, S., Pakzad, S., Culler, D., Demmel, J., Fenves, G., Glaser, S. & Turon, M. 2007. Health monitoring of civil infrastructures using wireless sensor networks. In *Proceedings of the 6th international conference on Information processing in sensor networks: 254–263.*

Kim, M. & Song, J. 2023. Near-real-time Identification of Seismic Damage by Graph Neural Network based on Structural Modes.

Le Xuang, T., Bui-Tien, T. & Tran-Ngoc, H. 2024. A novel approach model design for signal data using 1DCNN combing with LSTM and ResNet for damaged detection problem. *Structures* 59: 105784.

Magalhães, F. & Cunha, A. 2011. Explaining operational modal analysis with data from an arch bridge. *Mechanical Systems and Signal Process 25 (5)*: 1431–1450.

Marasco, G., Piana, G., Chiaia, B. & Ventura G. 2022a. Genetic Algorithm Supported by Influence Lines and a Neural Network for Bridge Health Monitoring. *Journal of Structural Engineering*. 148(9): 04022123.

Marasco, G., Oldani, F., Chiaia, B., Ventura, G., Dominici, F., Rossi, C., Iacobini, F. & Vecchi, A. 2022b. Machine learning approach to the safety assessment of a prestressed concrete railway bridge. *Structure and Infrastructure Engineering*: 1–15.

Marasco, G., Eshkevari, S.S. & Pakzad S.N. (2023). Graph Convolutional Neural Networks Based Strain Estimation. *Structural Health Monitoring 2023: Designing SHM for Sustainability, Maintainability, and Reliability - Proceedings of the 14th International Workshop on Structural Health Monitoring*: 1563–1570.

Nguyen, V.H., Schommer, S., Maas, S., & Zürbes, A. 2016. Static load testing with temperature compensation for structural health monitoring of bridges. *Engineering Structures. 127*: 700–718.

Scarselli, F., Gori, M, Tsoi, A. C., Hagenbuchner, M. & Monfardini, G. 2008. The graph neural network model. *IEEE transactions on neural networks*. 20(1):61–80.

Song, L.-H., Wang, C., Fan, J.-S. & Lu, H.M. 2022. Elastic structural analysis based on graph neural network without labeled data. *Computer-Aided Civil and Infrastructure Engineering*.

Whalen, E. & Mueller C. 2022. Toward reusable surrogate models: Graph-based transfer learning on trusses. *Journal of Mechanical Design*. 144(2).

Zhang, S., Tong, H., Xu, J. & Maciejewski R. 2019. Graph convolutional networks: a comprehensive review. *Computational Social Networks*. 6(1):1–23.

Bridge Maintenance, Safety, Management, Digitalization and Sustainability – Jensen, Frangopol & Schmidt (eds)
© 2024 The Author(s), ISBN 978-1-032-77040-6
Open Access: www.taylorfrancis.com, CC BY-NC-ND 4.0 license

An innovative approach for a sustainable monitoring of large infrastructures networks

M. Longo, S. Cirelli, D. La Mazza, I. Alovisi, P. Darò & G. Mancini
SACERTIS Ingegneria S.r.l., Roma, Italy

ABSTRACT: The progress made in the field of Structural Health Monitoring (SHM) has led monitoring systems to become an essential support tool for infrastructures management. The application of these systems on large infrastructures networks allows administrators to assess the remaining safety levels of managed bridges and, if necessary, helps in prioritizing and planning maintenance interventions. The need to implement a widespread monitoring system on a large scale clearly incurs costs that are often not compatible with the resources available. This problem gives rise to the need to optimize the use of monitoring systems. Sacertis Ingegneria, a leading company in the field of structural monitoring with over 150 continuously monitored structures, has responded to this need by offering various monitoring services, ranging in complexity. These services are evaluated and applied based on the characteristics and monitoring requirements of the structure under examination. This paper details distinct monitoring approaches proposed by Sacertis Ingegneria, differentiated by the adopted analysis method, which can be Model Driven, Data Driven, or a combination of both, and by the extension of the system (sensors layout) on the monitored elements (Local vs Global monitoring). Algorithms and Key Performance Indicators (KPIs) are so differentiated, as well as the scope of the analysis changes based on the chosen approach, ranging from an anomaly to a damage detection aim (Model Driven vs Data Driven approach). The choice of the approach depends on the structure itself, and the paper describes all the aspects to consider in this decision, including the health status of the structure, its strategic importance, its robustness, the consequences associated with potential closure or structural collapse, etc. Furthermore, the paper provides an illustrative example of the proposed monitoring approaches, comparing them and highlighting their advantages and limitations in a practical case study.

1 INTRODUCTION

Structural Health Monitoring (SHM) is a comprehensive solution designed to monitor various civil infrastructures, including bridges, tunnels, and monuments, assessing the impact of environmental factors, external actions, and damage processes on their structural response (Catbas 2009). The field of SHM has experienced significant advancements, establishing monitoring systems as indispensable tools for managing infrastructures effectively (Alovisi et al. 2022). Despite these developments, a crucial scientific gap persists - the optimization of structural monitoring to enable widespread implementation on a large scale without incurring prohibitively high costs. Overall, deterioration, material aging, widespread corrosion of steel reinforcing bars, corrosion of steel structures and components, increasing traffic volume and overloading, accidental damage combined with defects of design and construction, can cause a progressive loss of the infrastructures load carrying capacity (Fib Bulletin No. 109 2022). The application of these systems within extensive infrastructure networks plays a pivotal role in evaluating the ongoing safety levels of managed bridges. However, in order to have widespread monitoring systems on a large scale, it's necessary to invest costs that are often too high compared to the resources available, as highlighted in recent funded EU research projects

DOI: 10.1201/9781003483755-302

such as IM-SAFE (H2020 CSA IM-SAFE, 2020-2022), (Darò et al. 2022a), presenting Road Operators and Engineers with the challenging task of optimizing the use of monitoring systems across the network. In the following sections, a solution to this issue is proposed, also providing a practical application on a real case study.

2 METHODOLOGY

In response to this challenge, Sacertis Ingegneria, a leader company in structural monitoring, with over 150 structures (predominantly road bridges) under continuous monitoring, has developed a range of monitoring services with varying complexities (Darò et al. 2023). These services are meticulously assessed and applied, considering the monitoring requisites of the structure under scrutiny. The design of SHM systems, including the type and positioning of sensors, can be fine-tuned, ranging from a broad approach to a localized one. The diagnostic approach may vary not only between different structures but also within different spans of the same bridge. This variation is based on monitoring requirements or the state of conservation, blending more sophisticated Model-Driven (MD) analysis with Data-Driven (DD) approaches (Barthorpe 2011). Model-Driven diagnostic approaches are backed by detailed non-linear Finite Element Method (FEM) models updated based on the ongoing structural response, offering a profound understanding of the asset and supporting damage identification objectives. Conversely, Data-Driven approaches incorporate anomaly detection techniques to quickly pinpoint deviations from the standard behavior in structures, without providing correlations with safety levels. The instrumental equipment selected to reach the monitoring purpose are a series of sensors, like wired pre-assembled chains of MEMS accelerometers and inclinometers, temperature sensors and crackmeters, installed on the bridges key structural components to measure the identified Key Performance Indicators (Strauss et al. 2022a). An IoT smart gateway collects and pre-processes data in near-real time and sends them to the Cloud for further long-term analysis. These monitoring systems help optimizing the maintenance strategies, avoiding disasters, assessing risks according to the current safety methodologies and moving from a corrective to a preventive approach based on data analytics (Darò et al. 2022b), (Strauss et al. 2022b).

Ensuring the safety, performance, and long-term sustainability of assets relies significantly on the effective maintenance of infrastructure. This paper delves into the optimized approaches employed by Sacertis Ingegneria, integrating Model-Driven and Data-Driven solutions in practical applications across its network of continuously monitored bridges using MEMS sensors. It explores the extent of system deployment (sensor layout) on the monitored elements, differentiating between Local and Global monitoring strategies. Additionally, the paper discusses the selection of algorithms and KPIs tailor-fitted to the structural problem, offering a varied scope of analysis approaches, from anomaly detection to damage assessment (Data-Driven versus Model-Driven approach).

The selection of the most appropriate approach depends on various considerations, including the structural health, strategic significance, robustness, and potential consequences associated with shutdown or structural failure. This paper provides a comprehensive exploration of the factors influencing this decision-making process, highlighting the respective strengths and limitations of the diagnostic approaches through a practical case study analyzed using all the proposed approaches.

3 CASE STUDY

To highlight the potential of each specific approach, a structure has been identified as a case study (Cigada et al. 2021). It is a prestressed reinforced concrete slab bridge with two independent carriageways; each of them has a statically determined deck with a full-depth section with constant height in the longitudinal direction. For each of the two carriageways, the viaduct consists of n.9 spans, each with a total length of 35.0 meters, and a clear span between supports of 33.90 meters. This bridge, built in northern Italy in the early 1960s, is reflective of many Italian highway infrastructures in terms of its geometric and design features. It has been

chosen as a case study because it has several characteristics that make it suitable for the purpose: it is possible to identify one or more units (spans) that are repeated within the viaduct; the spans have the same features in terms of geometry, materials, reinforcements, loads, boundary conditions, etc..; further, in each carriageway, there is a span that, over the years, has experienced a performance loss due to the corrosion of prestressing reinforcements and has subsequently undergone structural strengthening interventions. In more detail, these two spans correspond to span number 4 in the south carriageway and span number 6 in the north carriageway. For the latter, the monitoring system was installed before the retrofitting intervention, and experimental data were collected in both the damaged and undamaged conditions (Cigada et al. 2021). A structural health monitoring system, consisting of 90 biaxial tiltmeters and 90 triaxial accelerometers, has been installed on the bottom surface of the decks. Specifically, each of the nine spans is equipped with a chain comprising 10 sensors (5 tiltmeters + 5 accelerometers). The sensors are interconnected using powerline communication technology. Two gateways, one per each carriageway, have been used to collect the data from the sensors and to send them to a cloud system.

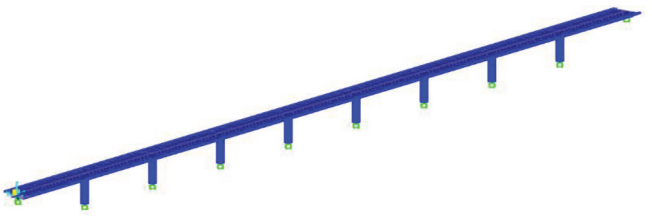


Figure 1. 3D view of the FEM model of a carriageway.

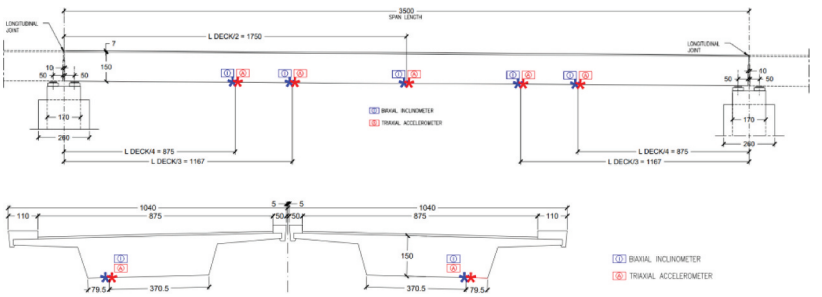


Figure 2. Longitudinal view of a span (top) and transversal cross section of both carriageways (bottom).

4 REAL APPLICATIONS OF DIFFERENT MONITORING APPROACHES

The case study presented in the previous section has been used as a mean to show with practical applications the possible implementation of the available approaches, such as Model Driven, Data Driven or a combination of both, with the aim to optimize the monitoring systems based on the diagnostics objective whilst highlighting the cost-benefits aspects of the selected monitoring strategy. In all approaches, the primary goal is to ensure the safety and durability of the infrastructure, based on the specific needs and the characteristics of the monitored structures with a decreasing Level of Approximations (LoA) of the analysis moving from a Model-Driven towards a Data-driven approach. In chapter 4.1 the attention is focused on the advantages of applying a Model-Driven damage detection diagnostics to the entire structure, with a detailed knowledge of the structural response based on the updated nonlinear FE model in face of a greater technical and economical effort. A mix of Model-Driven and Data-Driven analysis is also explored as a hypothetical solution, taking advantage of the bridge modularity. In chapter 4.2 the bridge is analyzed using the same dense sensing

monitoring system (same sensors number and positioning) however applying a Data-Driven approach only, assuming not to have the updated Digital Twin: in this second case the data analytics on similar spans supports an anomaly detection approach based on the comparisons of the clusters of homogeneous simply supported spans. Finally, in chapter 4.3 the analysis is restricted to a selection of sensors assuming a monitoring strategy that requires a minimal number of sensors installed on local positions, exploring the level of information available when choosing a Data-Driven approach with a light sensing scheme.

4.1 *Application 1: An optimized combination of model and data driven approach*

In the Model-Driven approach, the diagnostic service relies on a sophisticated numerical model using a Finite Element Model. This model is updated through calibrations, such as static and dynamic load tests, to accurately calibrate the initial condition of the monitored structure with the actual state. This allows for the establishment of a standard reference condition against which threshold levels can be assessed. These threshold levels are determined, based on predefined damage scenarios, on all the KPIs (static and dynamic) defined for the structure continuous monitoring. The instrumental equipment used in this approach consists of sensors of different type, well distributed along each key structural element, ensuring a comprehensive static and dynamic characterization and monitoring of the structure. This approach is particularly suitable for critical or strategic structures and requires a detailed numerical model that corresponds to the digital twin of the real structure. Referring to the highway viaduct outlined in paragraph 0, an illustration of the advantages of a Model-Driven approach can be observed by examining the monitoring data from span number 6 in the north carriageway. Figure 3 shows the results obtained from the static load test conducted on the span in 2019.

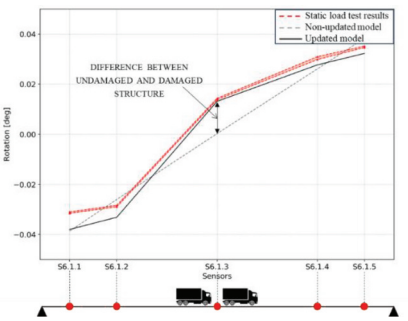


Figure 3. Static load test results on span number 6 of the north carriageway. Comparison between experimental data (red curves) and FEM results with both non-updated (grey curve) and updated (black curve) model.

The analysis of its deformation under a known load clearly indicates that the span exhibited significantly higher deformability than expected. The updating of the model, based on experimental data collected during tests, revealed the existence of damages that compromised the safety levels of the structure, necessitating a strengthening intervention (Cigada et al. 2021).

In some cases, the Model-Driven approach may also be used in conjunction with the Data-Driven approach, particularly when identifiable modularity exists in the structural static scheme. For instance, in the case of a multi-span bridge where spans share similarities in geometry, reinforcements, etc., a Model-Driven approach can be applied to the most critical span or to a typical span, and its threshold values, assessed on selected parameters, can then be transferred to all spans with similar characteristics.

In the context of the paper case study, an example of a monitoring system that combines Model-Driven (MD) and Data-Driven (DD) services can be illustrated. Let's assume two identical spans of the viaduct, theoretically indistinguishable, are monitored: one using the MD approach and the other using the DD approach. For example, consider spans number 6 on

both the north and south carriageways (i.e., spans with the same geometry, bearings condition, and location along the deck). In this example, span 6 of the south carriageway was modeled, and both static and dynamic load tests were conducted. Based on the results, an updated numerical model was obtained. Various damage scenarios were simulated on the updated FEM model, evaluating sensitive KPIs and establishing threshold levels corresponding to increasing degrees of damage (Warning and Alarm levels). These thresholds were then applied to the same KPIs calculated on the analogous DD span (span number 6 of the north carriageway).

In Figure 4 an application of this approach is illustrated: the selected KPI is the natural flexural frequency of the two spans. The south MD span (green curve) exhibits frequency values around 2.7Hz, with modeled warning and alarm thresholds represented by yellow and orange horizontal lines. The initial data collected in 2019 for this KPI on the south DD span (red curve) were below the warning level, suggesting the presence of potential damage. This would prompt a more in-depth analysis of this span, possibly upgrading the monitoring service to an MD one.

Notice, instead, how values collected after the retrofitting intervention on the span lie above both alarm and threshold levels, even though the frequencies consistently indicate its reduced stiffness compared to the MD span.

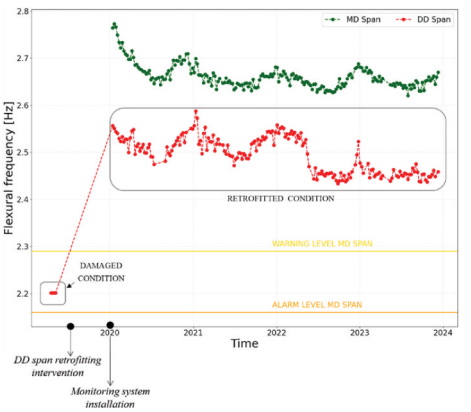


Figure 4. Example of combination of MD and DD services in the paper's case study. Evolution in time of the natural flexural frequencies of span number 6 on both the north (DD) and the south (MD) carriageways.

4.2 *Application 2: Data driven SHM*

A Data-Driven SHM solution is suitable for situations where comprehensive structural diagnostics may not be necessary or practical. It is often used for cases with lower criticality, non-strategic structures, or limited levels of degradation. The Data-Driven approach does not rely on the typical numerical structural modeling used in the Model-Driven approach; instead, it employs techniques for anomaly detection, such as machine learning, artificial intelligence, or statistical methods, to highlight any unfavorable trends in control parameters: the goal is to identify deviations from the standard behavior of the structure. Several Data-Driven techniques applied to the SHM field can be found in literature, such as those proposed by (H. Tran-Ngoc et al. 2019) or (Hung V. Dang et al. 2020 & Thang Le-Xuan et al. 2023).

The accuracy and robustness of the thresholds improve with the accumulation of a comprehensive history of recordings. Defining thresholds requires a history of data collected during the regular operation of the structure to capture seasonal variations and external influences. Any exceedance of thresholds requires on-site inspections to confirm the nature of the detected event. Thresholds defined with the Data-Driven approach can indicate an alert condition, signaling the need to monitor the evolution of the phenomenon without necessarily compromising the safety of the structure.

Typically, this solution involves an initial observation period (training period) covering the first months acquired by the structural health monitoring (SHM) system. This reference

period is crucial for establishing the standard behavior of all key performance indicators (KPIs) designated for monitoring. It is used to train data-based algorithms and consequently set thresholds capable of detecting anomalies. When opting for a Data-Driven solution, it is advisable to design a thorough sensor layout, encompassing various sensor types and locations. This facilitates an easy transition to a Model-Driven solution if anomalies in the structure intensify. A comprehensive sensor layout allows for a complete characterization of the monitoring object. Utilizing a well-designed network of accelerometers, operational modal analysis (OMA) algorithms can be applied to extract modal parameters such as frequency, damping, and mode shape. Vibrational analysis can also be conducted to study the vibrational behavior of each structural element, identifying both short and long-term anomalies through their vibrations under traffic. In static characterization, a similar depth of information can be achieved by correctly installing sensors like clinometers and crackmeters distributed on each span or near known defects (e.g., cracks).

Additional advantages of a Data-Driven solution emerge when modular elements are identifiable within the monitored structure. Comparative analyses can reveal anomalies when theoretically identical elements exhibit different responses. The paper proposed case study illustrates this point. The two carriageways are identical from a design standpoint, and repetitive modules can be identified between the 9 spans based on their bearings and geometry.

Continuous monitoring revealed an increase in vibrational levels in some spans in the longitudinal direction. Comparative analyses indicated that this increase in Y-axis (longitudinal) vibrations was concentrated in spans over the expansion joint. Initially attributed to the "normal" movement of spans due to thermal variations, this aspect became clearer a year later when a complete seasonal cycle was closed, highlighting variations in the vibrational indicator due to thermal factors. Figure 5 illustrates the behavior of the chosen KPI monitoring the vibrational levels of spans longitudinally over a year and a half of monitoring. Noticeable differences are observed between spans near and far from the expansion joint. While spans 4 and 5 exhibit significant oscillations in vibrations (increasing in winter and decreasing in summer), end spans (1 and 9) remain relatively stable over the reference period. In this instance, a comparative analysis facilitated the understanding that the rise in the vibrational indicator was not indicative of an anomaly but rather associated with the expansion joint. It underscored the importance of considering the joint as a critical element when studying the dynamic response of the viaduct. Moreover, this example highlighted and confirmed that a uniform treatment and a single training model for all spans may not be appropriate. A differentiation into at least three span categories is essential: the first category represents spans situated near the expansion joint, the second pertains to end spans, and the third encompasses central spans. In summary, a DD approach offers several advantages, such as the cost of the service, which is certainly lower than a Model-Driven approach, and the possibility, due to a complete instrumentation, of a comprehensive characterization of the viaduct from both a static and dynamic point of view. The drawback, however, lies in the lack of safety control, without the ability to detect structural damage, but this does not preclude the possibility of easily extending the service from DD to MD in case of anomalies.



Figure 5. Data driven approach application in the case study. Comparison of spans vibrational levels with respect to their distance from the structural joint.

4.3 *Application 3: Advantages and disadvantages of a light monitoring solution*

In case a light monitoring solution is opted for, the number and type of sensors installed on the structure is limited to key structural components and key positions to collect a set of data that aims to be representative of potential structural anomalies, acting as a 'sentinel' sensor that triggers further detailed analysis. In this case, no FE updated model nor diagnostics load test is available, therefore the attention is given primarily to the optimization of the cost implications in case of limited resources or in such cases where a structural preliminary analysis has confirmed that the state of conservation of the asset fully respects the reliability requirements with limited or absent signs of degradation. This approach implies that there is sufficient time to detect potential anomalies and time to intervene with either more detailed inspections/investigations, detailed analysis or proactive maintenance. The SHM objective changes from damage detection to anomaly detection. In the specific case under analysis, the hypothesis is to reduce the sensors to a minimum of n.1 MEMS triaxial accelerometer and biaxial clinometer at mid-span and concentrate on fewer Key Performance Indicators (Figure 6 (b)). As illustrated in Figure 6 (a), focusing on the natural frequencies as an example, clustering the response of similar spans allows to identify by comparison the damaged span as it stands out as a clear outlier from the standard values. This is a particularly representative case in which the first flexural mode is highly affected by the presence of the damage to the slab deck prestressing. However, as this approach allows to minimize the sensing technologies spreading the control over an increased number of assets, the absence of an updated FEM model impedes to directly correlate the damage entity/location and severity with the acquired data. In order to classify the identified anomaly, further inspections or analysis are required to inform the decision-making in terms of future corrective interventions. The clear advantage of optimizing the cost of information, favoring a diffused approach on a high number of assets with less sensors, is conversely accompanied by the drawback of losing redundancy in the measurements, limiting the analysis to local structural sections missing the global response (eg. impossibility to perform a full modal analysis) and decreasing the potentiality to identify anomalies or effects of damages due to the spatial distance between adjacent sensors. The thermal response correlate to the presence of the joints, as described in 4.2, would not be seen choosing a light sensing monitoring system.

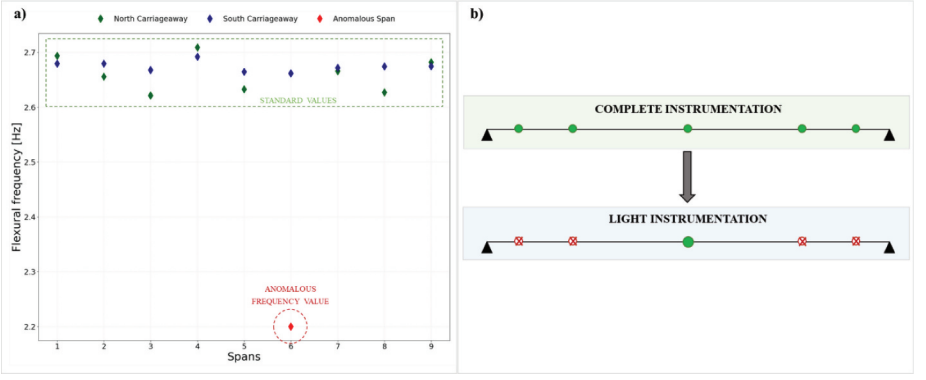


Figure 6. a) Comparison between spans flexural frequencies, when opting for a light monitoring solution. b) An example of sensors layout in a light monitoring approach.

5 CONCLUSIONS

As SHM solutions proved to be essential tools in infrastructure management, the deployment of these systems across extensive infrastructure networks enables administrators to evaluate the remaining safety levels of managed bridges and assists in prioritizing and planning maintenance interventions when necessary. However, implementing a widespread monitoring

system on a large scale often necessitates the optimization of monitoring system utilization. In response to this challenge, Sacertis Ingegneria has introduced various monitoring services of varying complexity. These services are assessed and applied based on the characteristics and monitoring requirements of the structure under examination. This paper delineates distinct monitoring approaches, distinguished by the adopted analysis method—whether Model Driven, Data Driven, or a combination of both—and by the extension of the system (sensor layout) on the monitored elements (Local vs Global monitoring). A case study of a modular prestressed reinforced concrete slab bridge with two independent carriageways has been analyzed, focusing on the differences and analogies between the n.18 spans. Algorithms and Key Performance Indicators (KPIs) are tailored accordingly, and the scope of the analysis varies based on the chosen approach, ranging from anomaly detection to damage identification goals (Model Driven vs Data Driven approach). The selection of the approach is contingent on the structure itself, and the paper thoroughly describes all considerations in this decision-making process, highlighting pros and cons of the monitoring and diagnostics options explored.

REFERENCES

Alovisi I et al (2022) New Sensor Nodes, Cloud, and Data Analytics: Case Studies on Large Scale SHM Systems. Structural Integrity 21:457–484.

Barthorpe R. J. (2011) On Model- and Data-based Approaches to Structural Health Monitoring. PhD thesis, University of Sheffield.

Catbas F.N., (2009) Structural health monitoring: applications and data analysis, Structural Health Monitoring of Civil Infrastructure Systems, Woodhead Publishing Series in Civil and Structural Engineering, Pages 1–39.

Cigada, A., Lucà, F., Malavisi, M., Mancini, G. (2021). Structural health monitoring of a damaged operating bridge: A supervised learning case study. In Pakzad, S. (ed.) Dynamic of Civil Structures, Volume 2. Conference Proceedings of the Society for the Experimental Mechanics Series, pp. 169–177. Springer, Cham. http://dx.doi.org/10.1007/978-3-030-47634-2_19.

Darò, P., Alovisi, I., Mancini, G., Negri, S., Bigaj-van Vliet, A., van Meerveld, H. (2022a) Lessons learned from proactive maintenance practices for concrete bridges, fib Congress Oslo, ISBN: 978-2-940643-15-8 - ISSN: 2617-4820.

Darò P., Longo M., Mancini G., Negri S., Bigaj-van Vliet A., Allaix D. L. (2022b), Data-informed safety assessment of concrete structures, fib Congress Oslo, ISBN: 978-2-940643-15-8 - ISSN: 2617-4820.

Darò, P., Alovisi, I., Mancini G., Longo M., La Mazza D., Cigada A., 'Dense sensing on roadway bridges network: new approach to data-informed assessment', 25 September 2023 http://dx.doi.org/10.1002/cepa.2024.

Fib Bulletin No. 109 (2022). Existing concrete structures life management, testing and structural health monitoring - State-of-the-art-report (151 pages, ISBN 978-2-88394-171-7, October 2023).

H2020 CSA IM-SAFE (2020-2022) Appraisal of methods for safety evaluation and risk management. https://im-safe-project.eu/, 2022.

H. Tran-Ngoca,b, S. Khatira, G. De Roeckc, T. Bui-Tienb, M. Abdel Wahab, (2019), An efficient artificial neural network for damage detection in bridges and beam-like structures by improving training parameters using cuckoo search algorithm. http://dx.doi.org/10.1016/j.engstruct.2019.

Hung V. Dang, Hung V. Dang, Hoa Tran-Ngoc, Tung V. Nguyen, T. Bui-Tien, Guido De Roeck, and Huan X. Nguyen, Senior Member, IEEE, (2020), Data-Driven Structural Health Monitoring Using Feature Fusion and Hybrid Deep Learning. http://dx.doi.org/10.1109/TASE.2020.

Strauss A., Bigaj-van Vliet A., Daró P., Sanchez, A., Granzner, M., Bergmeister, K. (2022a), Performance indicators for an objective assessment and through-life management of bridges and tunnels, fib Congress Oslo, ISBN: 978-2-940643-15-8 - ISSN: 2617-4820.

Strauss A., Bigaj-van Vliet A., Daró P., Van Meerveld H., (2022b), Condition-states and low limit maintenance thresholds of transport infrastructures in an European Context, fib Congress Oslo, ISBN: 978-2-940643-15-8 - ISSN: 2617-4820.

Thang Le-Xuan, Thanh Bui-Tien, Hoa Tran-Ngoc, (2023), A novel approach model design for signal data using 1DCNN combing with LSTM and ResNet for damaged detection problem. http://dx.doi.org/10.1016/j.istruc.2023.

Bridge Maintenance, Safety, Management, Digitalization and Sustainability – Jensen, Frangopol & Schmidt (eds)
© 2024 The Author(s), ISBN 978-1-032-77040-6
Open Access: www.taylorfrancis.com, CC BY-NC-ND 4.0 license

Field monitoring of bridge link slab performance under long-term and live load effects

A.M. Okeil
Department of Civil and Environmental Engineering, Louisiana State University, Baton Rouge, LA, USA

M. Canales
Universidad Tecnológica Centroamericana, Tegucigalpa, Honduras

ABSTRACT: Several details to eliminate bridge expansion joints have been proposed, and employed, in bridge construction. Expansion joints are known to require regular maintenance and are the cause of a host of problems including damage to girder ends and substructure components in the vicinity of the joints. The link slab detail is one of these alternatives that eliminates bridge expansion joints without introducing full bridge girder continuity. It has been gaining wide acceptance in North America and is becoming a standard construction detail. A bridge over the Ouachita River in Louisiana, US, employed the link slab detail to connect prestressed concrete bridge girder spans and was instrumented by six types of sensors, namely embedded sensors (sisterbars, strandmeters, and strain gages) and surface-mounted sensors (gapmeters and titlmeters). A total of 134 sensors were installed in three phases following construction sequence. The monitoring system recorded strains, girder end movements and rotations, and temperatures for the project, which employed different link slab details and segment lengths. The data was collected over a period of more than three years to study long-term effects as well as during a static live load test. Results show that cracking, which is mainly due to thermal effects, affects the performance of the link slab. The monitoring data also shows that jointless segments up to a length of 164.6 m (540 ft) performed well without excessive support movement.

1 INTRODUCTION

Precast prestressed concrete (PPC) girder bridges are considered one of the more efficient designs, which is reflected by the statistics in the National Bridge Inventory (NBI) (Federal Highway Administration 2016). They offer many advantages over traditional designs, such as ease of construction and durability. Prestressed concrete girders are usually precast offsite and transported for erection before pouring composite decks on site. As a result, full continuity between the girders has generally been sacrificed for the sake of ease of construction. As can be seen in Figure 1a, bridge deck joints traditionally have gaps of 1-3 inches under operating conditions (LA DOTD 2005). These gaps within the joints have the disadvantages of causing ride discomfort, debris accumulation, the need for maintenance to avoid leakage on the bridge substructure as a result of wear and tear caused by traveling vehicles and environmental exposure, which can cause corrosion of the substructure (Canales 2019). The direct costs associated with deck joints include construction, installation and maintenance. When deck drainage water is contaminated with chemicals such as deicing salts leaks through joints, it can damage the bridge superstructure and the pier caps below. This can lead to the damage of vital bridge parts, such as internal reinforcement, girder ends, caps and bearings. Accumulated debris in the joints may restrain deck expansion, causing increased pressures in bridge decks.

DOI: 10.1201/9781003483755-303

According to Lam (2011), expansion joints have not performed up to design expectations, in particular, during winter operations which has compromised the durability of many of these structures. Joints also make span unseating more likely for multiple-simple-span bridges in the event of earthquakes or floods and water surges during hurricanes (Okeil and Cai 2008). Therefore, there is need for reducing or eliminating expansion joints in bridge decks that are constructed as simple spans by developing continuity details that cover the gaps between adjacent spans. Several projects have looked into different continuity details (e.g. NCHRP Report 322 (Oesterle et al. 1989) and NCHRP Report 519 (Miller et al. 2004)). Several field investigations have also monitored the behavior of jointless bridge decks (Wing and Kowalsky 2005; Okeil et al. 2013). In Louisiana, the new John James Audubon Bridge was designed with a positive moment continuity detail (Hossain et al. 2014). It was observed that hairpin bars cause stress concentrations at girder ends that is likely to cause cracking in the bottom flanges (Okeil et al. 2013; Hossain and Okeil 2014). Conversely, the link slab detail, where continuity is only achieved in the deck slab (see Figure 1-b), does not establish full continuity as it allows girder ends to translate almost freely with respect to each other.

Analysis of this simple link slab detail has been the focus of many studies. Caner and Zia (1998) assumed that the contribution of the link slab is limited to additional flexural rigidity, which is small compared to the girder's. They also recommended debonding 5% of the span length for the link slab. Ignoring the restraining of girder rotations by the link slab will yield greater rotations than could actually be expected (Zhao et al. 2012). Therefore, Okeil and El-Safty (2005) proposed a simple design method for link slabs based on the three-moment equation method for analyzing continuous beams where the contribution of the deck was limited to its axial stiffness at the top of the girders. In another study, El-Safty and Okeil (2008) demonstrated that link-slabs may reduce the live-load stress range by 4.7% to 19.9% in comparison to simple span bridges. Au and Lam (2011) revised the flexural design approach to account for the compatibility between the deck and the girder displacements within the debonded length.

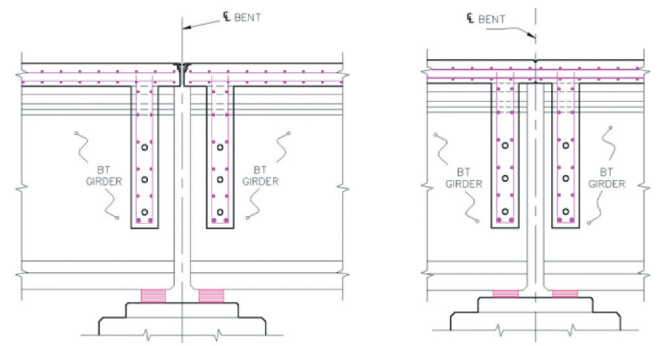


Figure 1. Typical details at bridge bents: (a) expansion joints, (b) link slab joints).

As can be seen, the link slab detail offers advantages over full continuity details such as ease of construction and elimination of stress concentrations. There is no consensus, however, on how this simple detail should be designed. This led to the initiation of another project to monitor the performance of a newly constructed bridge in Louisiana with the link slab details (Okeil and Canales 2020). In this study, details of a structural health monitoring system that was installed in the Ouachita River Bridge in Louisiana that is constructed with link slabs will be described. The bridge was selected to be a testbed for evaluating the performance of several link slab details. Data was collected over a period of more than three years to study long-term effects as well as during a static live load test. Results show that cracking, which is mainly due to thermal effects, affects the performance of the link slab.

2 MOTIVATION

Debris accumulation, deicing chemicals, improper selection of materials, or improper installation can cause the deterioration of expansion joints in bridges (Chang and Lee 2002), which in turn could lead to corrosion due to contaminated water leakage causing girder and pier deterioration. The cost of maintaining deteriorated expansion joints and the possible need for strengthening damaged substructure components has led to the call for reducing the amount of necessary expansion joints, or eliminating them altogether. The construction of fully continuous bridge decks can produce behavior similar to "blowups" in adjacent pavement through the compounding of the longitudinal pressures generated by thermal expansion (Burke 2004). Jointless bridge decks over simple span bridges reduces the need for expansion joints, and thus have a positive impact to bridge economics when properly implemented (Russell and Gerken 1994). Deck-only integration, or link slab, is the less intrusive alternative compared to full girder integration which may lead to girder end cracking (Hossain and Okeil 2014). This project was motivated by the lack of consensus on how link slabs should be designed. A field monitoring study was deemed important to understand the complex structural behavior of the simple link slabs detail.

3 METHODOLOGY

A structural health monitoring (SHM) approach was adopted to better understand the field behavior of link slabs. The Ouachita River Bridge was selected for this purpose and the long bridge, 3,275 ft (998.22 m) divided into 20 spans was constructed with different link slab details to study the best detail for future bridge construction projects. Sensors were embedded in the PPC girders as well as in the link slab. Additionally, sensors were also surface mounted to complete the SHM system.

3.1 *The Ouachita River Bridge*

The main bridge span over the river is a continuous steel girder segment with a total length of 980 ft (298.70 m). The rest of the bridge was divided into 17×135-ft (41.15 m) spans divided into a western approach (6 spans) and an eastern approach (9 spans). Figure 2-a and b shows the span length configurations for the western and eastern approaches. Figure 2-c shows the cross section of the bridge in these approaches, which consists of 7 standard AASHTO Bulb-T (BT-72) PPC girder spaced at 6′-8″ (1.69 m). The eastern approach consisted of one 4-span segment and 2 2-span continuous segments, while the eastern approach consisted of 4×2-span continuous segments in addition to one simple span.

3.2 *SHM system*

The SHM system was designed to capture the following: (1) force in the top and bottom link slab reinforcement, (2) differential displacements between adjacent girders at link slab locations, (3) displacement of the girder with respect to its supporting bent, (4) rotation of girder ends, (5) corresponding temperature for each of the recorded readings. Sensor placement was selected in order to obtain the necessary data at key locations within the structure and be able to effectively characterize link slab performance. Five types of sensors were employed in the designed monitoring system, namely embedded sensors (sisterbars, strandmeters, and straingages) and surface-mounted sensors (gapmeters and titlmeters). All of the selected gages are the vibrating wire gages, which is suitable for long-term monitoring as their readings do not drift with age (Bordes and DeBreuille 1985; Choquet et al. 1999). Table 1 lists the type and number of each of the employed sensors. A total of 134 sensors were installed in three phases. The sensors were installed at various locations as shown in Figure 3.

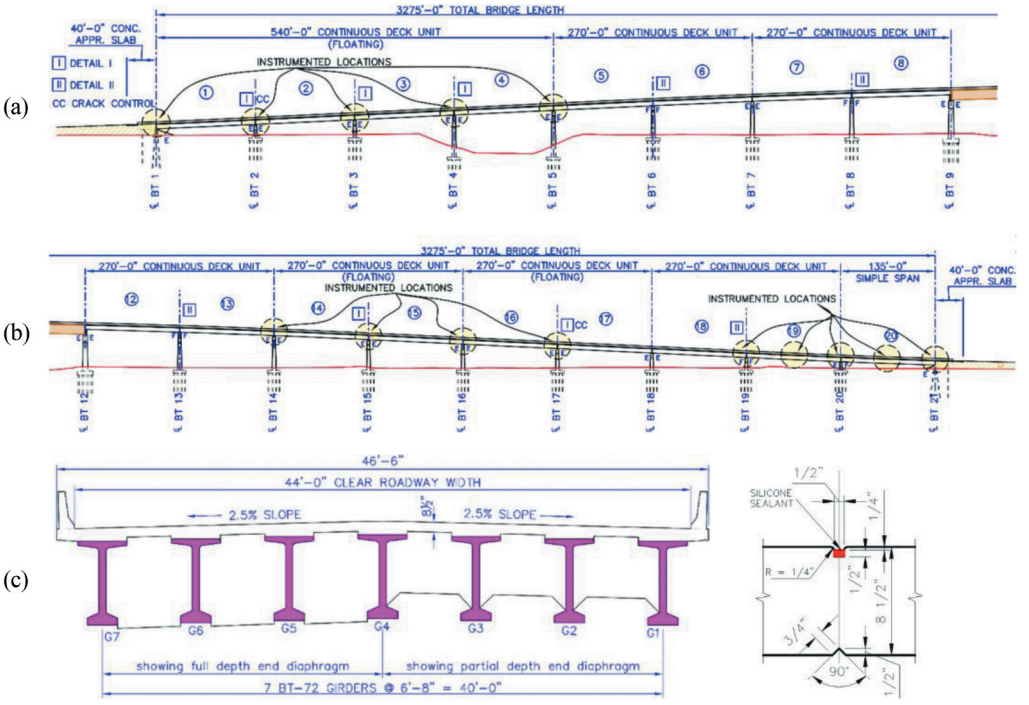


Figure 2. Ouachita River Bridge details: (a) western approach, (b) cross section, (c) eastern approach (1 ft= 0.3048 m; 1 in.=25.4 mm).

Table 1. Summary of sensors used in the Ouachita River Bridge.

Sensor Type	Measurement	Location	Number
Sisterbars	Strain in reinforcing steel	Embedded	18
Strandmeters	Strain in reinforcing steel	Embedded	36
Strain Gages	Strain in reinforcing steel	Embedded	2
Gapmeters	Displacement	Surface mounted	64
Tiltmeters	Rotation	Surface mounted	12
Weather Stations	Temperature and humidity	Surface mounted	2
Total:			134

Data from the SHM system was collected for a period of approximately 3 years and during one live load test where trucks were placed in 23 load cases were executed (11 positive moment and 12 negative moment). More details about the SHM system can be found elsewhere (Okeil and Canales 2020).

4 RESULTS

The SHM system provided a lot of data on many aspect of the behavior of continuous bridges with link slabs. In this section, a select few aspects of the behavior are presented.

4.1 *Girder end movement*

Figure 4 show plots of the relative girder end displacements based on from the gapmeters installed at the beginning and end of each segment. It should be noted that the plotted deformations are the cumulative deformation recorded at both ends of each segment.

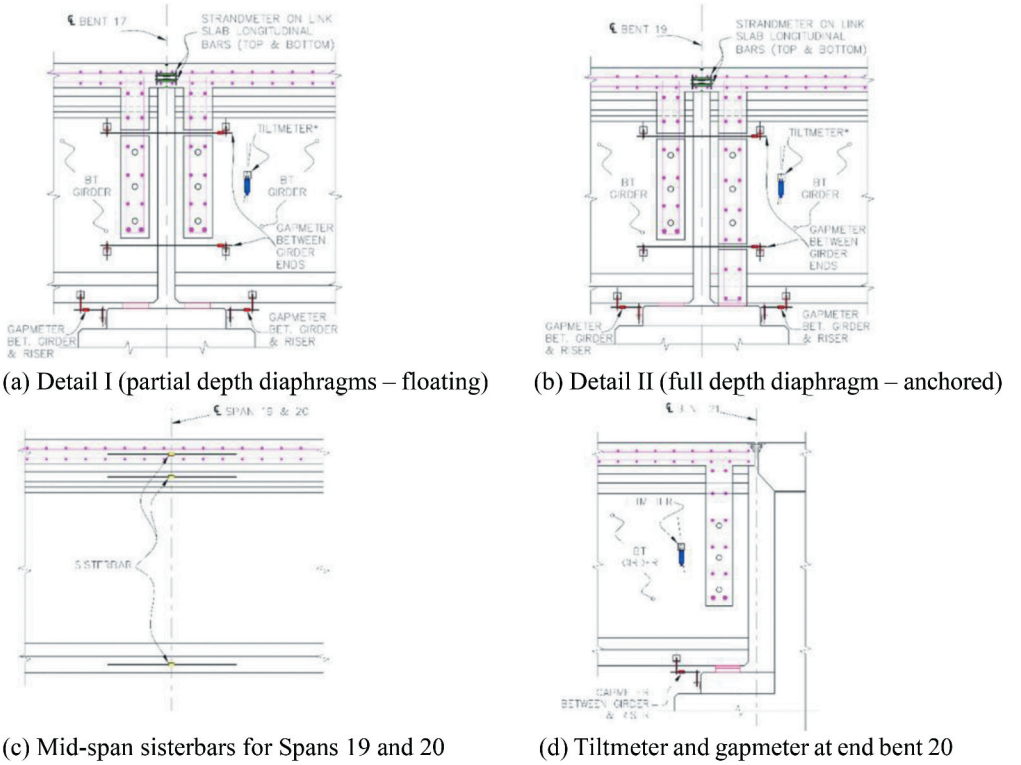


Figure 3. Placement of selected sensors at various locations.

$$\Delta = \Delta_{end} + \Delta_{beg} \tag{1}$$

The plotted results are for a period of about two years from March 2017 to February 2019. It can be seen that seasonal and daily temperature changes are directly correlated to the plotted relative girder end movements. This is expected as seasonal changes cause a uniform elongation, or shortening, of the entire bridge segment, while daily temperature changes are more affected by the temperature gradient, which causes girder camber leading to end rotations. In all cases, the girder end movements did not exceed 0.5 in (12.5 mm). The plots also show that floating segments experience smaller girder end movements (~ 0.2 in. [~5 mm]) compared to anchored segments. This implies that anchoring diaphragms, whether by design or due to unforeseen locking mechanisms, leads to more demands on the bearings.

4.2 *Relative angle between girder ends*

The relative angle between girder ends was extracted at locations where gapmeters were installed. Figure 5 shows the relative angle between girder end of Girder G7 at Bent 2 which is within the 4-span floating segment (see Figure 2-a). Like with girder end displacement, the observed relative angles are correlated with ambient temperature (not shown). It can be seen that the maximum relative angle between girder ends did not exceed 0.1°, which is small. However, given the large depth of the girders (81.5 in. (2.07 m)), this rotation imposes an extension on the link slab that causes tensile stresses that need to be addressed in design. Tensile force in the link slab of about 100 kip (445 kN) per girder were estimated at some locations (Canales 2019).

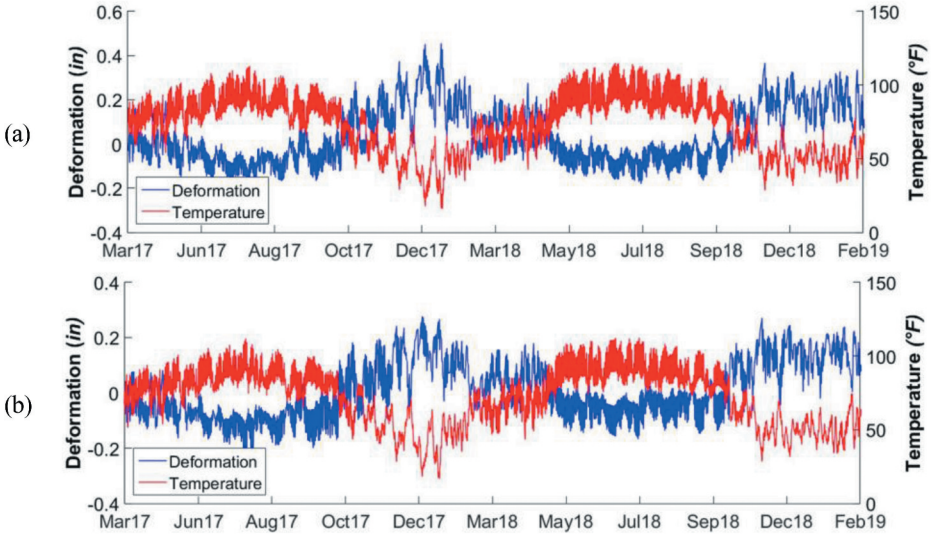


Figure 4. Girder G7 end displacement: (a) Span 2 (4-span floating segment), (b) Span 19 (2-span fixed segment).

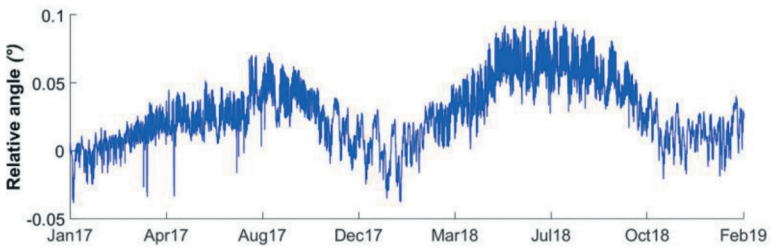


Figure 5. Relative angle between girder ends (Girder G7 at bent 2 (4-span floating segment)).

4.3 *Live load data*

As stated earlier, a load test was conducted to study the performance of link slabs under live loads. The trucks were position side by side for positive moment cases and in a truck train configuration (one on each span) for negative moment cases (see Figure 6). Figure 7 shows the link slab force in the link slab over Girder G7 at Bent 3. This plot shows that forces developed in the link slab for positive moment position P2 (side-by-side trucks over Span 2) and negative moment position N5 (truck train on Spans 2 and 3 over G7). In both cases, the link slab force is 20-40 kip (89 kN-178 kN) less than what was observed due to temperature changes. This implies that link slabs allow girder ends to rotate more freely under live loads and provide more release to restraint forces.

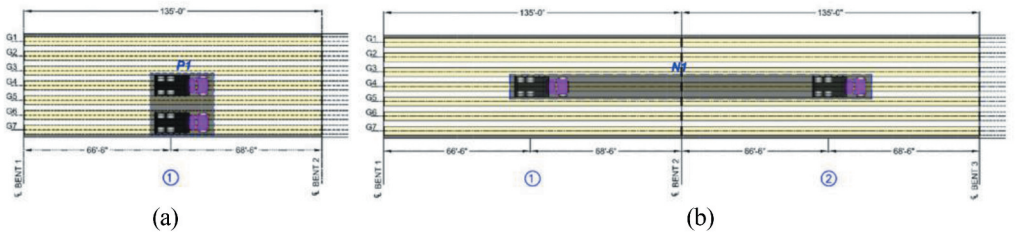


Figure 6. Positioning of trucks for load test: (a) positive moment case, (b) negative moment case.

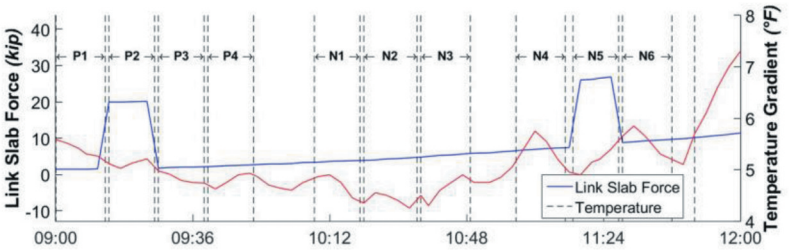
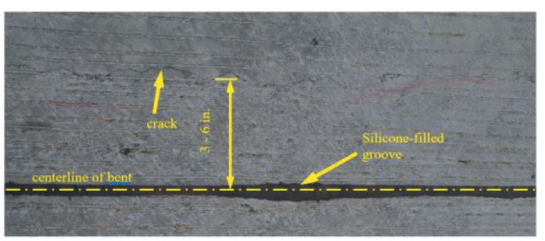


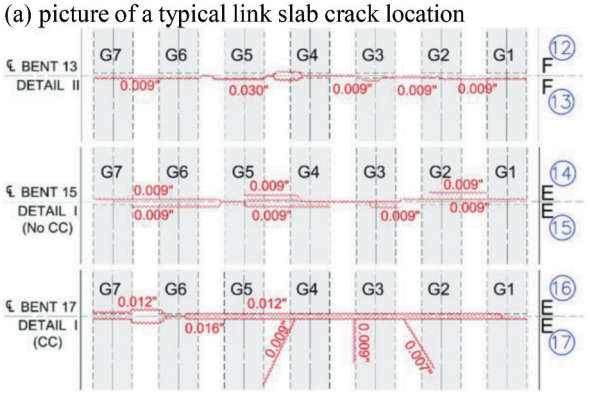
Figure 7. Live load forces in the link sab at Bent 3 for Girder G7 (4-span floating segment).

4.4 *Link slab transverse cracking*

Cast-in-place (CIP) reinforced concrete (RC) decks are known to crack in the transverse direction due to several reasons. Similarly, cracks were observed at all link slab locations even though certain crack mitigation strategies were employed at different bents such as saw-cut silicone filled groove to arrest cracks (see Figure 2-c). Cracks would disappear into the saw-cut groove intermittently but would reappear as transverse cracks running parallel to the groove approximately 3 to 6 in away from the groove. In other words, the crack control detail was not efficient in arresting the cracks. Figure 8 shows the crack pattern at Bent 13 (fixed bearings and anchored diaphragm) and Bent 15 (expansion bearings with partial diaphragm and no crack control) and 17 (expansion bearings with partial diaphragm with crack control detail). It can be seen that transverse cracks did not take place within the crack control groove as was intended. Cracks propagated away from the groove for most of the bridge width. Even though the observed crack width were not alarming, it is prudent to study ways for eliminating them such as by using Ultra-High Performance Concrete (UHPC) for link slab construction.



(a) picture of a typical link slab crack location



(b) link slab cracks at two bents with different configurations (1 in.=25.4 mm)

Figure 8. Transverse deck link slab cracking at bents 13, 15, and 17.

5 SUMMARY AND CONCLUSION

The Louisiana Department of Transportation and Development selected the Ouachita River Bridge to study the performance of link slab continuity detail, as well as quantify the influence of support conditions on its behavior. A SHM system consisting of various sensor types (sisterbars, strandmeters, straingages, gapmeters, tiltmeters and weather stations) with a total of 134 sensors was installed for long-term monitoring. A live load test was also conducted to test the instrumented spans under positive moment as well as negative moment. Data was collected over a period of more than 3 years, and sensor data was processed and corrected as per manufacturer instructions. Several analyses were performed to obtain different results including girder end displacement, relative angle between girder ends, and force in the link slab.

Continuous span segments up to 540 ft (164.6 m) in length performed well and did not show any signs of distress due to excessive expansions or contractions. Girder end rotations were affected by uniform temperature changes and temperature gradient changes. The small girder end rotations still caused notable link slab forces that need to be considered in design. It was found that the temperature gradient was found to generate larger link slab forces than live loads. With regards to link slab cracking, it was found that crack mitigation measure employed in the Ouachita River bridge did not perform as expected. Crack width formation is directly affected by temperature gradient variations throughout the day and seems to be unavoidable using reinforced concrete for the construction of link slabs. Therefore, it is recommended that the use of Ultra-High Performance Concrete (UHPC) for link slab construction be investigated.

REFERENCES

Au, A., and Lam, C. (2011). "Displacement Compatibility in Debonded Link Slab Design." *Bridge Office Rep.*, B. Office, ed., Ministry of Transportation, Ontario.

Bordes, J. L., and DeBreuille, P. J. "Some Facts about Long-Term Reliability of Vibrating Wire Instruments." *Proc., Reliability of Geotechnical Instrumentation*, National Research Council, 20–27.

Burke, M. P. (2004). "Reducing Bridge Damage Caused By Pavement Forces." *Concrete International*, 26(2), pp. 83.

Canales, M. (2019). "Performance Study of Link Slab Continuity in Prestressed Concrete Bridges." Ph.D. Dissertation, Department of Civil and Environmental Engineering, Louisiana State University, Baton Rouge, LA.

Caner, A., and Zia, P. (1998). "Behavior and Design of Link Slabs for Jointless Bridge Decks." *PCI Journal*, 43(3), pp. 68–80.

Chang, L.-M., and Lee, Y.-J. (2002). "Evaluation of Performance of Bridge Deck Expansion Joints." *Journal of Performance of Constructed Facilities*, 16(1), pp. 3.

Choquet, P., Juneau, F., DeBreuille, P. J., and Besette, J. "Reliability, Long-Term Stability and Gage Performance of Vibrating Wire Sensors with Reference to Case Histories." *Proc., 5th Symposium Field Measurements in Geomechanics*, 49–54.

El-Safty, A., and Okeil, A. M. (2008). "Extending the service life of bridges using continuous decks." *PCI Journal*, 53(6), pp. 96–111. WOS:000260895200006

Federal Highway Administration (2016). "National Bridge Inventory (NBI)." URL:<https://www.fhwa.dot.gov/bridge/nbi.cfm>, U.S. Department of Transportation. (Last Accessed: 02/14/2019).

Hossain, T., and Okeil, A. M. (2014). "Force transfer mechanism in positive moment continuity details for prestressed concrete girder bridges." *Computers and Concrete*, 14(2), pp. 109–125. doi:10.12989/cac.2014.14.2.109.

Hossain, T., Okeil, A. M., and Cai, C. S. (2014). "Field Test and Finite-Element Modeling of a Three-Span Continuous-Girder Bridge." *Journal of Performance of Constructed Facilities*, 28(1), pp. 136–148. doi:10.1061/(asce)cf.1943-5509.0000401.

LA Dotd (2005). *Bridge Design Manual*, Bridge Design Section, State of Louisiana, Department Of Transportation And Development, Baton Rouge, Louisiana.

Miller, R. A., Castrodale, R., Mirmiran, A., and Hastak, M. (2004). "Connection of Simple-Span Precast Concrete Girders for Continuity." NCHRP Report 519, T. R. Board, Washington, D.C., p. 191.

Oesterle, R. G., Glikin, J. D., and Larson, S. C. (1989). "Design of Precast Prestressed Bridge Girders Made Continuous." NCHRP Report No. 322, Transportation Research Board, Washington, D.C.

Okeil, A. M., and Cai, C. S. (2008). "Survey of Short-and Medium-Span Bridge Damage Induced by Hurricane Katrina." *Journal of Bridge Engineering*, 13(4), pp. 377–387. doi:doi:10.1061/(ASCE)1084-0702(2008)13:4(377).

Okeil, A. M., and Canales, M. (2020). "Evaluating Louisiana New Continuity Detail for Girder Bridges." 626, Louisiana Transportation Research Center, Baton Rouge, LA, p. 302.

Okeil, A. M., and El-Safty, A. K. (2005). "Partial Continuity in Bridge Girders with Jointless Decks." *Practice Periodical on Structural Design and Construction*, 10(4), pp. 229–238.

Okeil, A. M., Hossain, T., and Cai, C. S. (2013). "Field Monitoring Of Positive Moment Continuity Detail In A Skewed Prestressed Concrete Bulb-T Girder Bridge." *PCI Journal*, SPR 2013, pp. 80–90.

Russell, H. G., and Gerken, L. J. (1994). "Jointless Bridges -the Knowns and Unknowns." *Concrete International*, 16(4), pp. 44–48.

Wing, K. M., and Kowalsky, M. J. (2005). "Behavior, Analysis, and Design of an Instrumented Link Slab Bridge." *Journal of Bridge Engineering*, 10(3), pp. 331–344.

Zhao, J., Belutsky, I. Y., and Yatsura, V. G. (2012). "Study of Support Links Influence of Composite Bridges on Their Free Vibration Parameters." *Bulletin of PNU*, 27(4), pp. 79–86.

SS23: Structural health diagnosis under limited supervision for large bridges

Organizer: Y. Xu


Taylor & Francis
Taylor & Francis Group
http://taylorandfrancis.com

Bridge Maintenance, Safety, Management, Digitalization and Sustainability – Jensen, Frangopol & Schmidt (eds)
© 2024 The Author(s), ISBN 978-1-032-77040-6
Open Access: www.taylorfrancis.com, CC BY-NC-ND 4.0 license

Big model for bridge health diagnosis by cross-modal learning

Yang Xu*
Key Lab of Smart Prevention and Mitigation of Civil Engineering Disasters of the Ministry of Industry and Information Technology, Harbin, China
Key Lab of Structures Dynamics Behavior and Control of the Ministry of Education, Harbin, China
Harbin Institute of Technology, Harbin, China

ABSTRACT: Conventional deep-learning-based methods for bridge structural health diagnosis require complicated network structures and verbose from-scratch training with hyperparameter tuning. Because the pre-trained vision-language big model perceives fundamental knowledge of large-scale image and linguistic datasets, it should be of great potential to perform structural health diagnosis with full use of image and text datasets. This study performs a feasibility study towards establishing a big model for structural health diagnosis based on vision-language cross-modal learning. Specifically, an overall pipeline is proposed using a pre-trained vision-language big model of OFA (one for all, established by DAMO Academy in 2022). A series of Transformer modules based on the self-attention mechanism are stacked to unify pre-training tasks and downstream tasks in pure vision modality, pure language modality, and vision-language cross-modality learning. The results preliminarily demonstrate the feasibility and effectiveness of the vision-language cross-modal learning paradigm using OFA big model for structural health diagnosis.

1 INTRODUCTION

During the service period for decades, bridge structures are inevitably affected by various complex factors (including environmental erosion, material aging, fatigue load, and disaster events such as typhoons, earthquakes, and other emergencies), leading to the irreversible appearance and accumulation of structural damage. Various types of structural damage would occur, including concrete cracks, steel fatigue cracks, concrete spalling, and steel corrosion.

Timely identification of the location, morphology and geometrical characteristics of surface damage to ensure the resistance and service performance of structures is a crucial problem to be urgently solved in engineering practice. In recent years, with the development of artificial intelligence and collectible large-scale datasets, machine learning and deep learning have shown prominent potential in multiple application fields for structural health diagnosis (Xu et al., 2022a; Xu et al., 2022b). Bao and Li (2021) proposed a machine learning-based paradigm of structural health diagnosis using mathematical algorithms to process various monitoring data and predict the structural performance and state in high-dimensional feature space.

In deep learning-based methods, convolutional neural networks (CNNs) have been extensively utilized to extract the multi-level features of input images to map the damage annotations for various damage classification, localization, and change segmentation tasks (Xu et al., 2018; Xu et al., 2019; Qiao et al., 2021). In addition to image-based structural damage

*Corresponding author: xyce@hit.edu.cn

DOI: 10.1201/9781003483755-304

recognition, plenty of machine learning algorithms and deep learning models have been applied to crack propogation modeling(Xu et al., 2022c), fatigue reliability analysis (Chen et al., 2021), mechanical property prediction (Xu et al., 2023c), and multi-task modeling of structural component segmentation, damage segmentation, and condition assessment (Xu et al., 2023d).

Conventional deep-learning-based CNN models for bridge structural health diagnosis require complicated network structures and verbose from-scratch training with hyperparameter tuning. To reduce the dependency on data quantity and diversity, a model-agnostic meta-learning (MAML) with an attribute transferring method was proposed for structural damage identification based on the initial parameter optimization. Recently, meta-learning has been further developed in bridge damage recognition (Xu et al., 2021), and a task-significance-aware meta-learning paradigm has been established for structural damage segmentation (Xu et al., 2023b).

Besides CNNs, transformer is another type of widely-used deep learning model consisting of an encoder-decoder structure, in which the attention mechanism helps the model to remember longer sequential information (Vaswani et al., 2017). Initially, transformers were proposed to solve problems in natural language processing; later, vision transformers utilized superb contextual memorization and achieved outstanding performance in computer vision (Bi et al., 2021). Novel attention modules have been designed to merge into deep learning models and enhance the feature extraction of multi-type structural damage (Zhao et al., 2022; Xu et al., 2023a).

The success of pre-trained large-scale language models demonstrates that scaling-up models significantly improve task-agnostic few-shot performance and even surpass prior state-of-the-art fine-tuning approaches. By consistently increasing model parameters, researchers are trying to explore the performance-improving limitations of big models. In recent years, the conventional model design pattern of "different models for different tasks" is gradually transformed into the new trend, "one large-scale pre-trained model for various tasks". In this new pattern, researchers collect massive amounts of data, design advanced algorithms, and train big models for users with different demands. Among these big models, big multi-modal models can fuse different modal information and process them like human brains by training with large-scale multi-modal data. The goal of big multi-modal models is to align data from different modalities and acquire the ability to transfer their learned knowledge to various downstream tasks, ultimately approaching robust artificial general intelligence (AGI).

Large-scale pre-training models have led to revolutionary performance improvement in the natural language processing (NLP) community. The advent of BERT (Devlin et al., 2019) and GPT-4 (OpenAI, 2023) indicates the power of pre-training. After witnessing the great success of pre-training, many large-scale transformer-based vision models have also been proposed in recent years. The masked image modeling (MIM) method was proposed for pre-training methods to learn rich visual representations via masked part prediction conditioning on visible context. MIM also provides another direction for exploring the large-scale pre-training visual model.

Multi-modal pre-training big models are usually trained in an unsupervised way on a massive training dataset without annotations. Due to the enormous parameters and massive multi-modal data, the support of computing power is essential. Multi-modal data collection is significantly more challenging than unimodal data due to the scarcity of multi-modal data alignment. Most of the current multi-modal pre-trained large-scale models are vision-language models because of the easy access to image and text data pairs from the Internet.

The network modules for feature encoding of multiple input modalities are worthy of carefully tailoring, as different modalities may have unique characteristics, and thus, specific network structures are required. In general, current research on multi-modal models mainly focuses on video, image, speech, and language. Vision-language pre-training models, which take a large proportion in current research, extract image and text representation and learn to fuse image and text with pre-training tasks (Lu et al., 2019; Chen et al., 2020). These pre-trained models can easily accommodate several vision-language integration downstream tasks, mainly including comprehension tasks and generation tasks. For example, visual

grounding (VG), one of the most mainly investigated downstream tasks, aims to locate the most relevant object or region in an image based on a natural language query. The query can be a phrase, a sentence, or multi-round dialogue.

The remainder of this study is organized as follows. Section 2 describes the proposed overall framework for a big model of structural health diagnosis by cross-modal learning. Section 3 shows some validation results and discussion to verify the feasibility of the proposed method. Section 4 concludes the paper.

2 METHODOLOGY

In this study, we explore the viability of utilizing OFA (Wang et al., 2022), a unified big visual language model, for bridge structural health diagnosis. OFA is a task-agnostic and modality-agnostic framework that supports task comprehensiveness and unifies a diverse set of cross-modal and unimodal tasks, including image generation, visual grounding, and image caption, in a universal end-to-end sequence-to-sequence learning framework with no need for task-specific layers for downstream tasks. Pre-trained on only 20M image-text pairs, OFA have achieved great performance in a series of cross-modal tasks and uni-modal tasks.

The overall framework of the big model for structural health diagnosis based on vision-language cross-modal learning is shown in Figure 1. Firstly, single-modal pre-training tasks, including image infilling, masked image modeling, and masked language modeling, individually perform vision and language representation learning. Secondly, cross-modal pre-training tasks align visual and language features, including visual grounding, grounded captioning, image-text matching, image captioning, and visual question answering. Then, the pre-trained OFA model is fine-tuned on different downstream tasks with specified prompts following the prompt learning paradigm to transfer the well-learned knowledge based on frequently-used public deep learning datasets of Conceptual Caption 12M(CC12M), Conceptual Captions (CC3M), SBU, MSCOCO image captions (COCO) and Visual Genome Captions (VG Captions). Afterward, a fine-tuned OFA big model is utilized to generate text descriptions from structural images based on the universal tokenization of each image and the language description, which uses ResNet101 and BERT as the image encoder and text encoder, respectively.

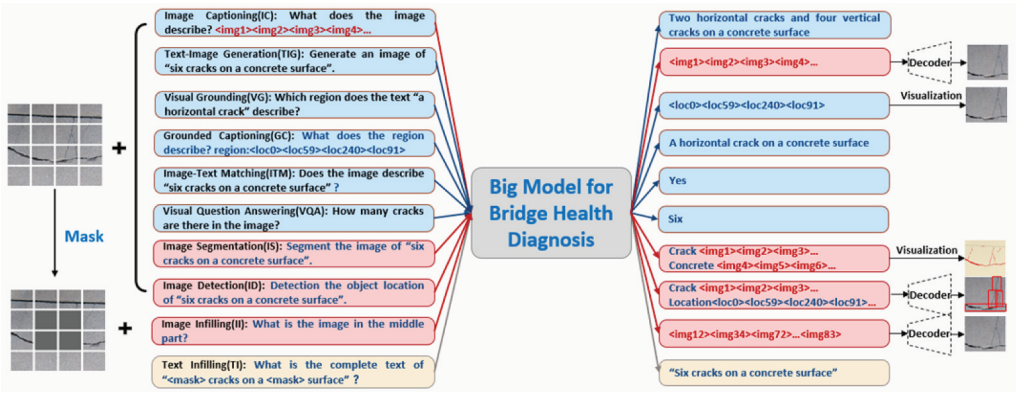


Figure 1. Overall framework of big model for structural health diagnosis by vision-language cross-modal learning.

The input data from different modalities undergo separate feature extraction and embedding representation processes. Subsequently, positional encoding is applied to the multi-modal data, enabling the corresponding token mapping to a unified representation space. This universal representation module establishes an integrated alignment framework for

multi-modal data, which is then fed into a pre-trained large-scale Transformer-based model for sequence modeling. Figure 2 shows the schematics of multi-modal feature representation and token alignment. Computational modules are designed with high-efficiency frozen-and-adaption strategy on visual-language pre-training tasks, as shown in Figure 3.

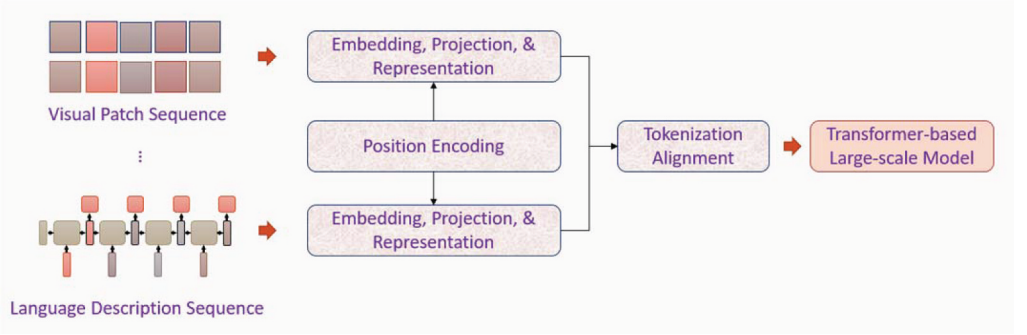


Figure 2. Schematics of multi-modal feature representation and token alignment.

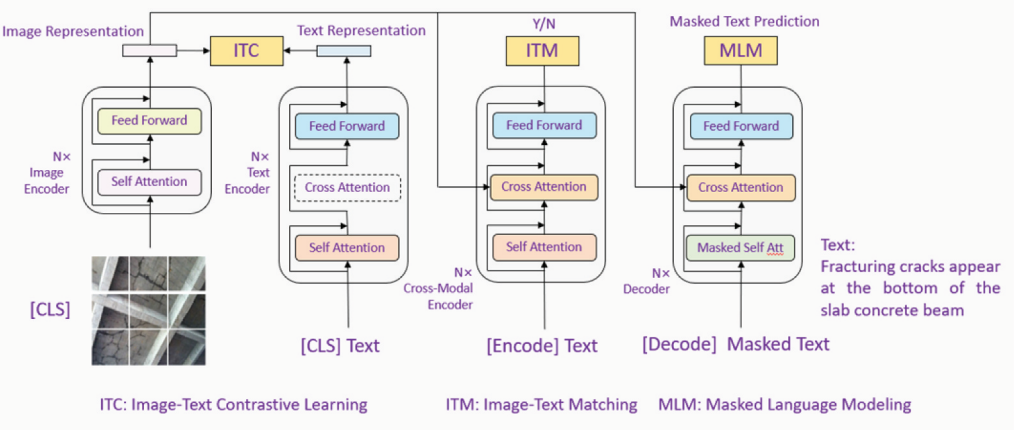


Figure 3. High-efficiency frozen-and-adaption strategy on visual-language pre-training tasks.

To identify the cross-modal features of multi-type structural components, material, and damage, the proposed big model utilizes different feature extraction modules to obtain the embedding feature vectors of damage images and texts, respectively. This setup enables that the model can possess the ability to merge the damage features in different modes through uni-modal feature extraction and cross-modal feature alignment. In addition, the model uses an additional decoding module to analyze the damage features extracted by the encoder to obtain the optimal text generation ability. Specifically, the calculation modules for uni-modal feature extraction of image and text are similar by stacking multiple self-attention layers. The visual-language cross-modal feature extraction module uses an additional cross-attention layer for feature fusion. The cross-attention layer accepts outputs of the image feature vector and text feature vector output from the image and text uni-modal encoder as inputs. The mask self-attention layer is added to the feature decoding module to keep the calculation of the training process consistent with the inference process of text generation for damage description. In the pre-training phase, three types of losses for image-text contrastive learning,

image-text matching, and mask language modeling are utilized to optimize the model on the collected bridge damage dataset of image-text pairs as

$$
\begin{aligned}
p_i^{i2t}(I) &= \frac{\mathrm{Exp}[\mathrm{Sim}(I, T_i)/\tau]}{\sum_T \mathrm{Exp}[\mathrm{Sim}(I, T)/\tau]} \\
p_j^{t2i}(T) &= \frac{\mathrm{Exp}\left[\mathrm{Sim}(T, I_j)/\tau\right]}{\sum_I \mathrm{Exp}[\mathrm{Sim}(T, I)/\tau]} \\
L^{ITC} &= \frac{1}{2}\sum_T \sum_I \left\{H\left[y^{i2t}(I), p^{i2t}(I)\right] + H\left[y^{t2i}(T), p^{t2i}(T)\right]\right)\}
\end{aligned}
\tag{1}
$$

where L^{ITC} denotes the image-text contrastive learning loss, I denotes image representation, T denotes text representation, Sim denotes cosine similarity, τ denotes annealing coefficient, H denotes the cross-entropy loss, y denotes the ground-truth one-hot vector.

$$
p^{itm}(I, T) = \mathrm{soft\,max}[\mathrm{MLP}(c)], L^{ITM} = H[y^{itm}, p^{itm}(I, T)] \tag{2}
$$

where L^{ITM} denotes the image-text matching loss, c denotes the image-text cross representation.

$$
L^{MLM} = H\left[y^{mask}, p^{mask}\left(I, \hat{T}\right)\right] \tag{3}
$$

where L^{MLM} denotes the mask language modeling loss, $\hat{T}$ denotes the masked text representation.

3 RESULTS AND DISCUSSION

Figure 4 shows some representative results of description generation for structural damage images. It can be found that the proposed method can successfully identify structural components (column, window, pavement, beam), materials (concrete, reinforced concrete, masonry, asphalt, protective layer), structural damage (crack, peal, corrosion, exposure, rusted, sink, broken, shear failure), location directions (bottom, surface, longitudinal, main reinforcement direction, middle, horizontal), and geometrical morphology (crisscross, X-shaped).



Figure 4. Validation results of description generation for structural damage images.

Figure 5 shows some representative results of attention map visualization for prompt-following logicality verification. It can be found that the generated phrase description could capture the semantic information and align image features of structural components, materials, structural damage, location directions, and geometrical morphology.

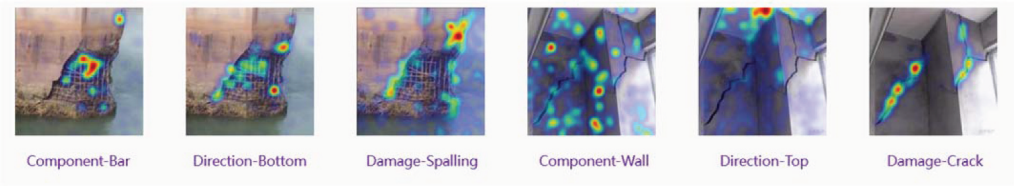


Figure 5. Attention map visualization for prompt-following logicality verification.

4 CONCLUSIONS

This study establishes a big model for structural health diagnosis based on vision-language cross-modal learning. The main conclusions are obtained as follows:

(1) An overall pipeline is proposed using a pre-trained vision-language big model of OFA with a series of Transformer modules. The image-self-attention, text-self-attention, image-text-cross -attention, and text-masked-attention mechanisms are stacked to unify pre-training tasks and downstream tasks in pure vision, pure language, and vision-language cross-modality learning.
(2) The proposed method can successfully identify structural components (column, window, pavement, beam), materials (concrete, reinforced concrete, masonry, asphalt, protective layer), structural damage (crack, peal, corrosion, exposure, rusted, sink, broken, shear failure), location directions (bottom, surface, longitudinal, main reinforcement direction, middle, horizontal), and geometrical morphology (crisscross, X-shaped).
(3) The results preliminarily demonstrate the feasibility and effectiveness of using a visionlanguage cross-modal learning framework based on the OFA big model for structural health diagnosis.

ACKNOWLEDGEMENT

Financial support for this study was provided by the National Key R&D Program of China [Grant No. 2021YFF0501003], National Natural Science Foundation of China [Grant Nos. 52192661, 51921006, and 52008138], China Postdoctoral Science Foundation [Grant Nos. BX20190102 and 2019M661286], Heilongjiang Provincial Natural Science Foundation [Grant No. LH2022E070], Heilongjiang Provincial Postdoctoral Science Foundation [Grant Nos. LBH-TZ2016 and LBH-Z19064], China University Innovation Fund - A New Generation of Information Technology Innovation Project [Grant No. 2022IT187], and Fundamental Research Funds for the Central Universities [Grant No. HIT.NSRIF202334].

REFERENCES

Bao, Y., & Li, H. (2021). Machine learning paradigm for structural health monitoring. Structural Health Monitoring, 20(4), 1353–1372.

Bi, J., Zhu, Z., & Meng, Q. (2021).Transformer in Computer Vision. 2021 IEEE International Conference on Computer Science, Electronic Information Engineering and Intelligent Control Technology (CEI), pp. 178–188, IEEE, 2021.

Chen, J., Chen, Z., Xu, Y., & Li, H. (2021). Efficient reliability analysis combining Kriging and subset simulation with two-stage convergence criterion. Reliability Engineering & System Safety, 214, 107737.

Chen, Y., Li, L., Yu, L., Kholy, Ahmed El, Ahmed, F., Gan, Z., Cheng, Y., & Liu, J. (2020). Uniter: Universal image-text representation learning. In ECCV, 2020.

Devlin, J., Chang, M., Lee, K., & Toutanova, K. (2019). BERT: Pre-training of Deep Bidirectional Transformers for Language Understanding. ArXiv, abs/1810.04805.

Lu, J., Batra, D., Parikh, D., & Lee, S. (2019). Vilbert: Pre-training task-agnostic visiolinguistic representations for vision-and-language tasks. In NeurIPS, 2019.

OpenAI. (2023). GPT-4 Technical Report. ArXiv, abs/2303.08774.
Qiao, W., Zhao, Y., Xu, Y., Lei Y., Wang Y., Yu, S., & Li, H. (2021). Deep learning-based pixel-level rock fragment recognition during tunnel excavation using instance segmentation model. Tunnelling and Underground Space Technology, 115, 104072.
Vaswani, A., Shazeer, N., Parmar, N., Uszkoreit, J., Jones, L., Gomez, A. N., Kaiser, Ł., & Polosukhin, I. (2017). Attention is All You Need. Advances in Neural Information Processing Systems, vol. 30, 2017.
Wang, P., Yang, A., Men, R., Lin, J., Bai, S., Li, Z., Ma, J., Zhou, C., Zhou, J., & Yang, H. (2022). Unifying Architectures, Tasks, and Modalities Through a Simple Sequence-to-Sequence Learning Framework. International Conference on Machine Learning.
Xu, Y., Bao, Y.Q., Zhang, Y.F., & Li, H. (2021). Attribute-based structural damage identification by few-shot meta learning with inter-class knowledge transfer. Structural Health Monitoring, 2021, 20(4): 1494–1517.
Xu, Y., Fan Y.L., & Li, H. (2023a). Lightweight semantic segmentation of complex structural damage recognition for actual bridges. Structural Health Monitoring, 14759217221147015.
Xu, Y., Fan Y.L., & Li, H. (2023b). Task-aware meta-learning paradigm for universal structural damage segmentation using limited images. Engineering Structures, 2023, 284, 115917.
Xu, Y., Li, S.L., Zhang, D.Y., Jin, Y., Zhang, F.J., Li, N., & Li, H. (2018). Identification framework for cracks on a steel structure surface by a restricted Boltzmann machines algorithm based on consumer-grade camera images. Structural Control & Health Monitoring, 2018, 25(2), e2075.
Xu, Y., Li, Y., Zheng, X., Zheng, X., & Zhang, Q. (2023c). Computer-vision and machine-learning-based seismic damage assessment of reinforced concrete structures. Buildings, 13, 1258.
Xu, Y., Qian, W., Li, N., & Li, H. (2022a). Typical advances of artificial intelligence in civil engineering. Advances in Structural Engineering. 2022, 25(16): 3405–3424.
Xu, Y., Qiao, W., Zhao, J., Zhang, Q., & Li, H. (2023d). Vision-based multi-level synthetical evaluation of seismic damage for RC structural components: a multi-task learning approach. Earthquake Engineering and Engineering Vibration.
Xu, Y., Tian, Y., & Li, H. (2022b). Unsupervised deep learning method for bridge condition assessment based on intra- and inter-class probabilistic correlations of quasi-static responses. Structural Health Monitoring-An International Journal, 22(1): 14759217221103016.
Xu, Y., Wei, S.Y., Bao, Y.Q., & Li, H. (2019). Automatic seismic damage identification of reinforced concrete columns from images by a region-based deep convolutional neural network. Structural Control and Health Monitoring, 2019, 26(3): e2313.
Xu, Y., Zhu, B., Zhang, Z., & Chen, J. (2022c). Hierarchical dynamic Bayesian network-based fatigue crack propagation modeling considering initial defects. Sensors. 2022, 22(18), 6777.
Zhao, J., Hu, F.Q., Qiao, W.D., Zhai, W.D., Xu, Y., Bao, Y.Q., & Li, H. (2022). A modified u-net for crack segmentation by self-attention-self-adaption neuron and random elastic deformation. Smart Structures and Systems, 2022, 29(1): 1–16.

Bridge Maintenance, Safety, Management, Digitalization and Sustainability – Jensen, Frangopol & Schmidt (eds)
© 2024 The Author(s), ISBN 978-1-032-77040-6
Open Access: www.taylorfrancis.com, CC BY-NC-ND 4.0 license

Large vision model-based crack segmentation under limited supervision

Yapeng Guo & Shunlong Li
School of Transportation Science and Engineering, Harbin Institute of Technology, Harbin, China

Yang Xu
School of Civil Engineering, Harbin Institute of Technology, Harbin, China

ABSTRACT: Crack segmentation is an important basis for automatic evaluation of the apparent state of bridge structures. The emergence of large vision models has revolutionized the basic process of object segmentation and demonstrated strong generalization ability. In this paper, a novel large vision model-based crack automatic segmentation method under limited supervision is proposed. By adding a crack segmentation head, the segmentation generalization ability of the large vision model is retained, and the automatic segmentation of cracks is realized. The effectiveness and accuracy of the proposed method are illustrated by comparing with the state-of-the-art crack segmentation methods on eight commonly used crack datasets.

1 INTRODUCTION

Crack identification is of great significance for obtaining and analyzing the appearance state of bridge structure, evaluating its service performance and making maintenance decisions (Adhikari et al., 2014, Koch et al., 2015, Yeum and Dyke, 2015, Cha et al., 2017). In view of the shortcomings of current manual inspection, such as strong subjectivity and low efficiency, researchers have begun to use computer vision to simulate the function of the human eye, and use mobile phones, drones and other devices equipped with cameras to collect crack images. A variety of crack automatic identification algorithms based on traditional digital image processing, machine learning and deep learning have been developed. Among them, the pixel-level crack segmentation method based on deep learning is more active and practical.

The current crack pixel-level segmentation methods take fully supervised learning as the main-stream. These methods involve training state-of-the-art object segmentation frameworks using crack image and pixel-level annotation data pairs. Innovative research in this field has focused on dataset construction, deep learning network optimization, loss function combination, and post-processing enhancement, leading to improved accuracy and algorithm efficiency in crack pixel-level segmentation (Li et al., 2019, Liu et al., 2019, Chen and Jahanshahi, 2020, Huyan et al., 2020, Kang et al., 2020, Zhang et al., 2021, Asadi Shamsabadi et al., 2022, Zhong et al., 2022, Guo et al., 2023, Xu et al., 2023, Zhang et al., 2023). However, the current crack segmentation models still have limited generalization ability due to constraints such as data size and segmentation framework efficiency, leaving ample room for improvement.

The advent of Segment Anything Model (SAM) has been likened to the GPT-3 moment in computer vision (Kirillov et al., 2023). SAM has been trained using over one billion masks on 11 million images and is designed as an interactive model that incorporates prompts during training. As a result, SAM can be applied to new image distributions and tasks through zero-shot learning, showcasing remarkable generalization ability. It can effectively segment unfamiliar scenes or objects. This large vision model has revolutionized the generalization ability of segmentation models in common object segmentation domains. Although SAM successfully captures some features of the crack image, two issues arise: (1) the segmentation

DOI: 10.1201/9781003483755-305

result lacks semantic information and does not conform to the requirements of the crack segmentation task, and (2) the accuracy needs improvement. Consequently, there is an urgent need to leverage the features learned by SAM and automate the crack segmentation task more effectively.

This paper focuses on the efficient application of large visual model in the task of automatic crack segmentation, aiming to provide a simple and accurate way to use the generalization ability of large visual model to improve the accuracy of crack segmentation under limited supervision. The remaining content of this article is arranged as follows. Section 2 introduces the architecture and objective function of the proposed method. Section 3 explains the dataset and implementation details. Section 4 shows the testing results. Section 5 summarizes the whole article.

2 METHODOLOGY

The proposed crack segmentation method based on fine-tuning SAM is mainly composed of crack image encoder and crack segmentation head, as shown in Figure 1. When training, all the parameters of the crack image encoder are frozen and not updated, only the parameters of the crack segmentation head are updated. The initial upsampling layer is to unify the crack image size to the input size of SAM. The crack image embedding refers to the high-dimensional features generated by the crack image after passing through the encoder.

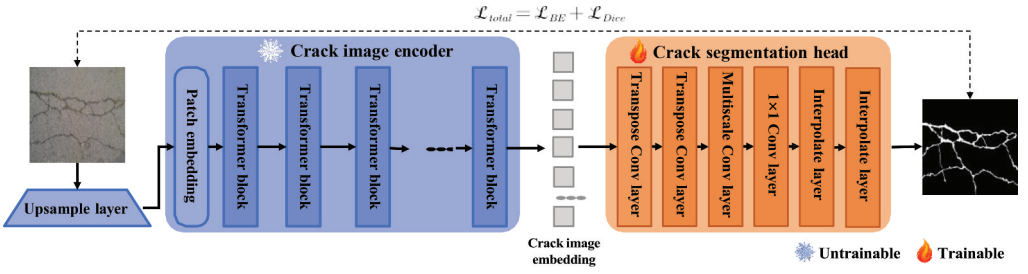


Figure 1. Framework of the proposed large vision model-based crack segmentation method.

2.1 *Crack image encoder*

The SAM architecture consists of three parts: image encoder, prompt encoder and mask decoder. Because the crack segmentation task does not require prompt input, this paper only uses the trained image encoder in SAM, because the encoder contains the general multi-level features of various objects.

The image encoder of SAM employs the pre-trained ViT-Base model. The original crack image is first upsampled to 1024 × 1024, and then the convolution with kernel size of 16 and stride of 16 is used to discretize the image into a vector of 64 × 64 × 768. The vector is flattened in order in length and width to 4096 × 768 with positional encoding, that is, 4096 tokens with a length of 768, so that the visual problem is transformed into a sequence to sequence problem. After the above patch embedding, the crack image will be sent to the transformer block. Each block consists of a normalization layer, a multi-head attention layer, another normalization layer, and a multi-layer perceptron (MLP).

2.2 *Crack segmentation head*

SAM uses prompts to assist object segmentation, that is, adding a prompt encoder and a mask decoder to process image embedding, prompt embedding, and output tokens after the

image encoder. Because the crack segmentation task referred to in this study is automatic and does not require prompt input, the second half of the SAM needs to be modified. This paper adds a crack segmentation head to achieve the required functions.

Specifically, the crack segmentation head consists of two transposed convolution layers, a multi-scale convolution layer, a 1 × 1 convolution layer and two interpolation layers (Zhang et al., 2022). The role of the transposed convolution layer is to perform 2 times upsampling on the encoded crack image embedding to restore spatial information. The multi-scale convolution layer is employed to obtain gain from feature fusion at different scales, that is, to learn information in different ranges around key pixels through back propagation gradient. The 1 × 1 convolutional layer is used to fuse the information of different channels and adjust the output dimension. The function of the interpolation layer is to further upsample to adjust the output dimension.

The objective function of the proposed method is the joint loss ($\mathcal{L}_{total}$) of binary entropy ($\mathcal{L}_{BE}$) and Dice ($\mathcal{L}_{dice}$), as shown in Equations (1)-(3). Where N represents the number of all pixels in an image, y_i and p_i are the ground truth label and prediction of the i^{th} pixel, and Y and $\hat{Y}$ are the ground truth and predicted crack masks, respectively.

$$\mathcal{L}_{total} = \mathcal{L}_{BE} + \mathcal{L}_{dice} \tag{1}$$

$$\mathcal{L}_{BE} = -\frac{1}{N}\sum_{i=1}^{N} y_i log(p_i) \tag{2}$$

$$\mathcal{L}_{dice} = 1 - \frac{2\left|\hat{Y} \cap Y\right| + 1}{\left|\hat{Y}\right| + |Y| + 1} \tag{3}$$

3 DATASETS AND IMPLEMENTATION DETAILS

This paper selected eight influential datasets to evaluate the proposed method, which were CFD (Shi et al., 2016), Crack500 (Yang et al., 2020), Cracktree200 (Zou et al., 2012), DeepCrack (Liu et al., 2019), EugenMiller (Yang et al., 2020), GAPs (Eisenbach et al., 2017), Rissbilder (Yang et al., 2020) and Volker (Yang et al., 2020) (Datasets 1-8). These datasets have large differences in the structural materials, structural parts, image quality, and image quantity, so they can effectively evaluate the generalization ability of crack segmentation models. All the training images (7754 in total) were divided into the training subset (90%) and validation subset (10%). All the testing images (the testing subset) were employed to evaluate segmentation methods in this paper.

The initial learning rate of fine-tuning the proposed crack segmentation model was set to 1e-5, the total number of training iterations was 24000, and the change of learning rate was multi-step, which became 0.1 times of the previous one at the 16000th and 20000th respectively. The fine-tuning process adopts the early stopping strategy, batch size was set to 2, r in LoRA was set to 4. The hardware platform employed for fine-tuning and testing the proposed method included: an Intel Xeon(R) E5-2620 v4 (CPU), an Nvidia RTX 3090 graphics processing unit (GPU) with 24GB memory and 128 GB of memory.

4 TESTING RESULTS UNDER KIMITED SUPERVISION

In this paper, the state-of-the art CNN-based crack segmentation model Deeplab v3p (Chen et al., 2018) and transformer-based crack segmentation model Segformer (Xie et al., 2021) are selected as the comparison methods. For fairness, these two methods used the weights trained on the large-scale segmentation dataset CityScapes (Cordts et al., 2016) as the basis for fine-tuning in this paper.

The trained weight parameters in SAM map the general features of object segmentation, so using the features in SAM and performing full-supervised fine-tuning has achieved significant accuracy improvement. The powerful generalization ability of SAM is also reflected in the few-shot task under limited supervision conditions, that is, using as few annotations as possible can also achieve acceptable segmentation results on new data distributions. In this section, the crack segmentation ability of the proposed method under limited supervision is explored by taking 1%-shot and one-shot cases as examples.

The 1%-shot case means that the data used to train the proposed method is randomly sampled from the training subset under the fully supervised condition at a ratio of 1%, and the 1%-shot training subset has a total of 77 images. The one-shot case means that an image is randomly selected from the training subset of each dataset as the one-shot training subset, that is, a total of 8 images. Table 1 illustrates the Dice scores of three methods on the test set under limited supervision.

Consistent with the theoretical analysis, when the size of training subset is sharply reduced, the segmentation accuracy of the proposed method on the eight datasets is reduced. Compared with the fully supervision, the average Dice scores of 1%-shot and one-shot decreased by 7.1 and 23.5, respectively. However, it is worth noting that compared with Deeplab v3p and Segformer, the accuracy of the proposed method has a Dice score improvement of 13.4, 9.5 and 3.8, 5.6 under two cases, respectively. More importantly, using only 1% of the training subset, the accuracy of the proposed method significantly exceeds that of Deeplab v3p trained under full supervision, which illustrates the strong generalization ability of the proposed method.

Table 1. Testing Dice scores (×100%) on eight datasets under limited-supervision.

		Dataset								
Data size	Method	1	2	3	4	5	6	7	8	Average
1%-shot	Deeplab v3p	31.4	54.0	21.9	69.4	33.6	13.5	30.6	60.1	42.9
	Segformer	47.2	60.0	17.3	65.6	44.8	23.0	47.0	64.2	52.5
	Proposed	54.2	65.8	21.1	70.5	48.1	32.9	48.3	66.8	**56.3**
one-shot	Deeplab v3p	41.7	29.9	16.4	55.3	34.8	16.5	24.5	50.5	30.4
	Segformer	47.0	22.4	22.2	51.4	48.7	34.8	36.1	58.9	34.3
	Proposed	44.8	34.1	16.5	59.3	54.2	34.7	39.3	58.0	**39.9**

5 CONCLUSIONS

This paper proposes a SAM-based crack segmentation framework, realizing the significant improvement on segmentation accuracy. The proposed method achieves significant accuracy improvement on eight widely used datasets under full supervision and limited supervision conditions, and the average Dice scores reach 56.3 (1%-shot) and 39.9 (one-shot), indicating the excellent fitting ability and generalization ability. The proposed crack segmentation method based on SAM provides a feasible way for the application of large vision model in the field of crack recognition. However, limited by the computational hardware resources of the authors, this study is carried out on the SAM with ViT-Base as the backbone. Future research will focus on light-weight work such as distillation of SAM model, making the application of large vision model under limited hardware conditions more feasible.

REFERENCES

Adhikari, R. S., Moselhi, O. & Bagchi, A. 2014. Image-based retrieval of concrete crack properties for bridge inspection. *Automation in Construction*, 39, 180–194.

Asadi Shamsabadi, E., Xu, C., Rao, A. S., Nguyen, T., Ngo, T. & Dias-Da-Costa, D. 2022. Vision transformer-based autonomous crack detection on asphalt and concrete surfaces. *Automation in Construction*, 140, 104316.

Cha, Y.-J., Choi, W. & BüyüközTürk, O. 2017. Deep Learning-Based Crack Damage Detection Using Convolutional Neural Networks. *Computer-Aided Civil and Infrastructure Engineering*, 32, 361–378.

Chen, F.-C. & Jahanshahi, M. R. 2020. ARF-Crack: rotation invariant deep fully convolutional network for pixel-level crack detection. *Machine Vision and Applications*, 31, 47.

Chen, L.-C., Zhu, Y., Papandreou, G., Schroff, F. & Adam, H. 2018. Encoder-Decoder with Atrous Separable Convolution for Semantic Image Segmentation. *arXiv e- prints*, arXiv:1802.02611.

Cordts, M., Omran, M., Ramos, S., Rehfeld, T., Enzweiler, M., Benenson, R., Franke, U., Roth, S. & Schiele, B. 2016. The Cityscapes Dataset for Semantic Urban Scene Understanding. *arXiv e-prints*, arXiv:1604.01685.

Eisenbach, M., Stricker, R., Seichter, D., Amende, K., Debes, K., Sesselmann, M., Ebersbach, D., Stoeckert, U. & Gross, H. M. How to get pavement distress detection ready for deep learning? A systematic approach. 2017 International Joint Conference on Neural Networks (IJCNN), 14-19 May 2017 2017. 2039–2047.

Guo, F., Qian, Y., Liu, J. & Yu, H. 2023. Pavement crack detection based on transformer network. *Automation in Construction*, 145, 104646.

Huyan, J., Li, W., Tighe, S., Xu, Z. & Zhai, J. 2020. CrackU-net: A novel deep convolutional neural network for pixelwise pavement crack detection. *Structural Control and Health Monitoring*, 27, e2551.

Kang, D., Benipal, S. S., Gopal, D. L. & Cha, Y.-J. 2020. Hybrid pixel-level concrete crack segmentation and quantification across complex backgrounds using deep learning. *Automation in Construction*, 118, 103291.

Kirillov, A., Mintun, E., Ravi, N., Mao, H., Rolland, C., Gustafson, L., Xiao, T., Whitehead, S., Berg, A. C., Lo, W.-Y., Dollár, P. & Girshick, R. 2023. Segment Anything. *arXiv e-prints*, arXiv:2304.02643.

Koch, C., Georgieva, K., Kasireddy, V., Akinci, B. & Fieguth, P. 2015. A review on computer vision based defect detection and condition assessment of concrete and asphalt civil infrastructure. *Advanced Engineering Informatics*, 29, 196–210.

Li, S., Zhao, X. & Zhou, G. 2019. Automatic pixel-level multiple damage detection of concrete structure using fully convolutional network. *Computer-Aided Civil and Infrastructure Engineering*, 34, 616–634.

Liu, Y., Yao, J., Lu, X., Xie, R. & Li, L. 2019. DeepCrack: A deep hierarchical feature learning architecture for crack segmentation. *Neurocomputing*, 338, 139–153.

Shi, Y., Cui, L., Qi, Z., Meng, F. & Chen, Z. 2016. Automatic Road Crack Detection Using Random Structured Forests. *IEEE Transactions on Intelligent Transportation Systems*, 17, 3434–3445.

Xie, E., Wang, W., Yu, Z., anandkumar, A., Alvarez, J. M. & Luo, P. 2021. Segformer: Simple and Efficient Design for Semantic Segmentation with Transformers. *arXiv e-prints*, arXiv:2105.15203.

Xu, Y., Fan, Y. & Li, H. 2023. Lightweight semantic segmentation of complex structural damage recognition for actual bridges. *Structural Health Monitoring*, 22, 3250–3269.

Yang, F., Zhang, L., Yu, S., Prokhorov, D., Mei, X. & Ling, H. 2020. Feature Pyramid and Hierarchical Boosting Network for Pavement Crack Detection. *IEEE Transactions on Intelligent Transportation Systems*, 21, 1525–1535.

Yeum, C. M. & Dyke, S. J. 2015. Vision-Based Automated Crack Detection for Bridge Inspection. *Computer-Aided Civil and Infrastructure Engineering*, 30, 759–770.

Zhang, H., Zhang, A. A., He, A., Dong, Z. & Liu, Y. 2023. Pixel-level detection of multiple pavement distresses and surface design features with ShuttleNetV2. *Structural Health Monitoring*, 14759217231183656.

Zhang, J., Chen, X., Qiu, Z., Yang, M., Hu, Y. & liu, J. Hard Exudate Segmentation Supplemented by Super-Resolution with Multi-scale Attention Fusion Module. 2022 IEEE International Conference on Bioinformatics and Biomedicine (BIBM), 6-8 Dec. 2022 2022. 1375–1380.

Zhang, K., Zhang, Y. & Cheng, H. D. 2021. CrackGAN: Pavement Crack Detection Using Partially Accurate Ground Truths Based on Generative Adversarial Learning. *IEEE Transactions on Intelligent Transportation Systems*, 22, 1306–1319.

Zhong, Q., Yanxin, L. & Qiang, Z. 2022. CrackT-net: a method of convolutional neural network and transformer for crack segmentation. *Journal of Electronic Imaging*, 31, 023040.

Zou, Q., Cao, Y., Li, Q., Mao, Q. & Wang, S. 2012. CrackTree: Automatic crack detection from pavement images. *Pattern Recognition Letters*, 33, 227–238.

Bridge Maintenance, Safety, Management, Digitalization and Sustainability – Jensen, Frangopol & Schmidt (eds)
© 2024 The Author(s), ISBN 978-1-032-77040-6
Open Access: www.taylorfrancis.com, CC BY-NC-ND 4.0 license

Vibration-based fatigue assessment and damage detection in bridge cables

B. Xu
Zhengzhou University, Zhengzhou, Henan, China
Technical University of Catalonia (UPC), Barcelona, Spain

J.R. Casas
Technical University of Catalonia (UPC), Barcelona, Spain

Z.R. Wu
Zhengzhou University, Zhengzhou, Henan, China

ABSTRACT: Cable monitoring and safety evaluation are crucial for cable-supported bridges in service. Due to its cost-effectiveness and convenience, vibration-based methods are widely used in cable monitoring. The fatigue assessment and damage detection of the cable using vibration monitoring data are developed in this paper. For the fatigue assessment of cables, a real-time monitoring and sensing scheme based on the amplitude and phase estimation method and the Miner's linear fatigue damage accumulation theory is proposed. It considers both the real stress amplitude spectrum as well as the changes in the mechanical properties of cables simultaneously. For cable damage detection, a method using the cable dynamic stiffness theory and time-varying frequency to detect damage in operational cables is proposed. In this method, empirical mode decomposition and moving average methods are used to remove the effects of traffic and temperature on cable frequency. K-means clustering method is used for identifying cable damage.

1 INTRODUCTION

Cables, as crucial load-bearing components of cable-stayed bridges, play a paramount role in determining the operational performance of the bridge. However, due to the coupling effect of harsh environment, complex live load, and insufficient maintenance, cables are prone to corrosion and fatigue damage, posing a serious threat to the safety of the bridge structure (Feng *et al.* 2022).

In cable fatigue analysis, simulation methods for obtaining cable load spectra usually involve statistical analysis of traffic loads over a period of time based on weigh in motion (WIM data), applying the obtained traffic load model to the bridge model (Jiang *et al.* 2020). The main problem addressed by this method is the accuracy of the vehicle load and finite element models. It is an ideal method to obtain fatigue load spectrum based on long-term actual cable data (Mao *et al.* 2019). However, the accuracy and durability of existing direct cable force measurement sensors cannot meet the requirements of fatigue stress.

In cable damage detection, early identification of the cable damage is essential for the assessment of the current condition, potential future life, maintenance and safety assessment of the cable (Li *et al.* 2019). In cable dynamic monitoring, although the collected data include responses to a combination of known and unknown loads, the obtained frequencies can characterize the

DOI: 10.1201/9781003483755-306

response of the structure to a constant static load by eliminating the effect of external dynamic actions. Therefore, cable damage can be identified by the processed frequency (Huang *et al.* 2018).

Cable dynamic monitoring is an essential part of the cable-stayed bridge health monitoring system. Applying cable dynamic parameters to the evaluation of cables is convenient and economical. Therefore, based on cable vibration monitoring data, this paper proposes a fatigue assessment method that considers the real fatigue load spectrum of the cable over entire lifespan and a cable damage identification method that considers the influence of external dynamic actions during operation.

2 BACKGROUND OF THE METHOD

Figure 1 establishes a simplified mechanical model of a taut cable without lateral forces, extensively used in cable-stayed bridges. This model assumes that the cable is continuous and nonextensible. It integrates essential cable parameters, including cable force H, cable length l_0, bending stiffness EI, sag d, and inclination angle θ. Such integration is crucial for accurately analyzing the dynamic characteristics of the cable. In the analysis, the cable is divided into two segments with chord length l_1 and l_2. To simplify the analysis, chord coordinate systems are established for each cable segment.

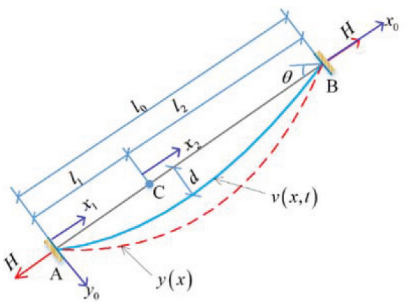


Figure 1. Cable mechanical model.

The cable illustrated in Figure 1 without considering internal damping and shear forces adheres to the motion differential equation presented in Eq.(1) under free vibration condition.

$$EI\frac{\partial^4 v(x_j,t)}{\partial {x_j}^4} - H\frac{\partial^2 v(x_j,t)}{\partial {x_j}^2} - h_j(t)\frac{d^2 y(x_0)}{d{x_0}^2} + m\frac{\partial^2 v(x_j,t)}{\partial t^2} = 0 \tag{1}$$

where, $v(x_j, t)$ is the dynamic configuration of the *jth* cable segment, $y(x_0)$ is the static configuration of the cable, which is approximated as a quadratic parabola, m is the mass per unit length, $h_j(t)$ is the vibration-induced additional cable force.

By employing the separation of variables and considering the boundary conditions of cable forces and displacements, the dynamic equilibrium equation Eq.(2) is derived (Dan *et al.* 2016).

$$\boldsymbol{Ka} = 0 \tag{2}$$

where, $\boldsymbol{K}$ is the cable dynamic stiffness matrix; $\boldsymbol{a}$ is the vector of boundary dynamic displacement amplitudes.

Based on Eq.(2), a cable frequency equation as indicated in Eq.(3) is derived (Xu *et al.* 2019). It is effective for accurately calculating cable frequencies when cable parameters are known.

$$det(\boldsymbol{K}) = 0 \tag{3}$$

3 FATIGUE ASSESSMENT OF THE CABLE

3.1 *Identification of fatigue load spectrum*

3.1.1 *Identification of time-varying cable force*

Since the variation amplitude of the time-varying cable force accounts for a small proportion of the total cable force, the sensing method must have sufficient accuracy. Therefore, this paper combines the BRAPES method and the exact formula fitting method, which can realize the accurate time-varying cable force sensing method with smaller cable force variation(Xu *et al.* 2022). In this way, the time-varying cable forces and frequencies can be identified based on the acceleration response of the cable.

3.1.2 *Cable bending stress sensing method*

The perception of bending stress is achieved by retrieving the joint load from the joint displacement and calculating the internal force of the section. According to the dynamic stiffness balance equation and Leung's theory, the equivalent joint external load and inertia force are obtained when the two ends of cables are consolidated. The bending moment and stress along time are as shown in Eq.(4) and Eq.(5) (Xu & Dan 2022).

$$M(t) = \sum_{j=1}^{j=n} \beta M(\omega_j) e^{i\left(\omega_j t + \phi_j\right)} \tag{4}$$

$$\sigma_C(t) = \frac{M(t)y}{I_z} \tag{5}$$

where, $M(\omega_j)$ represents the bending moment in the frequency domain, $\beta = k_B/(k_B + k_H)$ is the reduction coefficient, k_B is the bending stiffness of the cable section, k_H is the geometric stiffness provided by cable tension, y is the distance of the calculated point from the neutral axis of the cable section.

3.2 *Cable fatigue damage assessment method*

The calculation of fatigue damage adopts Miner's linear fatigue damage accumulation theory, and the expression is:

$$D = \sum D_i = \sum \frac{n_i}{N_i} (i = 1, 2..., k) \tag{6}$$

where, D_i is the damage experienced by n_i cycles under the action of the ith level stress level; n_i is the number of cycles of the ith level stress; N_i is the number of cycles to fatigue failure under constant ith level stress.

In the fatigue assessment, the S-N curve of the non-corroding and corroded steel strand under the average stress amplitude and the S-N curve of the cable considering the influence of the clamping effect and the anchoring effect are used (Birkenmaier 1980, Li *et al.* 2007).

$$\text{No corrosion}: \ lg(N) = 15.21 + 3.5\, lg\left(\frac{S_b - S_m}{S_b}\right) - 3.5\, lg(S_a) \tag{7}$$

$$\text{Corrosion}: lg(N) = 14.73 + 3.5\, lg\left(\frac{a(S_b - S_m)}{S_b}\right) - 3.5\, lg(S_a) \tag{8}$$

$$\text{Cable}: \ lg(N) = lg(C) - 3.5\ lg(1.6 S_{\text{ca}}) \tag{9}$$

where, S_b is the tensile strength of the material, S_m is the average stress, S_a is the corrected fatigue stress amplitude, a reflects the corrosion state of the section, S_{ca} is the fatigue stress

amplitude of the cable, N is the number of cycles, and C is the parameter of the S-N curve of the cable.

The schematic of the dynamic cable fatigue damage assessment method is shown in Figure 2.

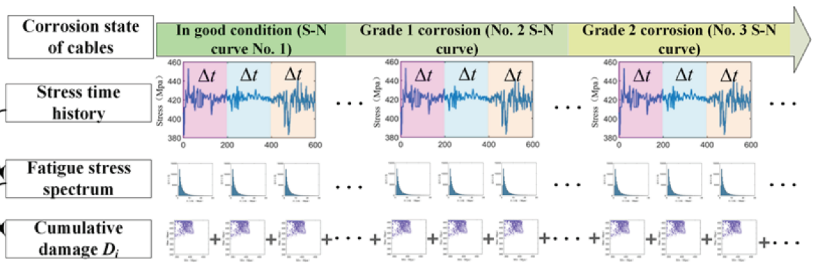


Figure 2. Schematic diagram of dynamic assessment of cable fatigue damage.

4 DAMAGE DETECTION

4.1 *Simulation of time-varying cable frequency considering traffic and temperature*

4.1.1 *Simulation of cable forces caused by traffic loads*

The traffic acts directly on the beam-deck and is transmitted to the cable through the anchoring points. The simulation of the static action of traffic loads on the cable is described by Eq. (10).

$$\Delta H_1(t) = \sum_{i=1}^{N} \alpha_i(t) W_i cos\theta \tag{10}$$

where, M_i is the weight of vehicle i; α_i is the load transfer coefficient, with a range of [0,1].

The simulation of the dynamic action of traffic loads on the cable is described by Eq. (11).

$$\Delta H_2(t) = M_{bi} a(t) cos\theta \tag{11}$$

where, M_{bi} is the mass of the beam segment supported by the cable, and $a(t)$ is the vibration acceleration of the beam at the location of the cable.

4.1.2 *Simulation of cable forces caused by temperature*

The cable tension caused by temperature can be calculated by Eq. (12)(Lepidi & Gattulli 2012).

$$\Delta H_3(t) = -EA\alpha_c \Delta T(t) \tag{12}$$

where, E is the elastic modulus of steel, A *is* cross-sectional area, α_c is the thermal expansion coefficient of steel; $\Delta T(t)$ is the temperature variation.

4.1.3 *Simulation of time-varying cable frequency*

Considering the influence of traffic loads and temperature on cable force, the time-varying force of an in-service cable can be expressed by Eq.(13).

$$H(t) = H_0 + \Delta H_1(t) + \Delta H_2(t) + \Delta H_3(t) \tag{13}$$

where, H_0 is the cable force under permanent load.

Once the time-varying cable force is determined, the corresponding time-varying cable frequency can be calculated using Eq.(3).

4.2 *Eliminating the influence of traffic loads and temperature on time-varying frequencies*

Moving average (MA) is used to eliminate the effect of traffic, while empirical mode decomposition (EMD) is used to eliminate the effect of temperature. Considering the order and number of applications of the two methods, the following two cases are analyzed: Method1 (MA-EMD-MA) and Method2 (EMD-MA) were compared in a previous study (Xu *et al.* 2023). To examine the effectiveness of these two methods, six types of trend data are selected from 24-hour time-varying force and frequency of the cable: (a) Upward trend; (b) Downward trend; (c) Convex curve; (d) Concave curve; (e) Outlier data; (f) Periodic curve. According to the results, comparing Method1 with Method2, it was found that the fluctuation of Method1 is less than Method2, and the results obtained by Method1 are all less than the cable frequency deviation when the cable moment of inertia damage reaches 5% for long cables with dense frequencies. This indicates that Method1 has better robustness. Therefore, this paper adopts Method1 for analysis.

4.3 *Qualitative identification of cable damage*

Although there is a significant shift in frequency when the cable has damage, the processed frequencies of different damage levels still overlap. Especially with longer cables, the frequencies are denser and the frequency changes caused by damage are smaller, making damage detection more challenging. The question of whether a cable has sustained damage can be regarded as a classification problem. This article uses the K-Means clustering method to achieve qualitative identification. The K-Means Clustering algorithm classifies data by minimizing the sum of squared distances between data points and the centroids within each cluster (Guo *et al.* 2022).

5 CASE STUDY

5.1 *Background of Yongjiang Bridge*

The A02 and A11 cables (Figure 3) of Yongjiang Bridge were used for verification. The bridge is a 105+97 m prestressed concrete single-tower cable-stayed bridge with 11 groups of 4 cables arranged in a harp shape with a spacing of 8 m. The cable parameters are shown in Table 1. The accelerometers are mounted on cables, and the vertical accelerometers are mounted in the middle span of the main beam. The bridge layout and sensor locations are shown in Figure 4.

Table 1. Cable parameters of Yongjiang Bridge.

Cable number	E/Pa	l_0/m	m/(kg m^{-1})	A/m^2	θ/ °	I/m^4	H_0/kN
A02	1.95E+11	102.436	40.846	8.825E-03	26.565	6.197E-06	2496
A11	1.95E+11	31.011	32.522	6.940E-03	26.565	3.832E-06	2060

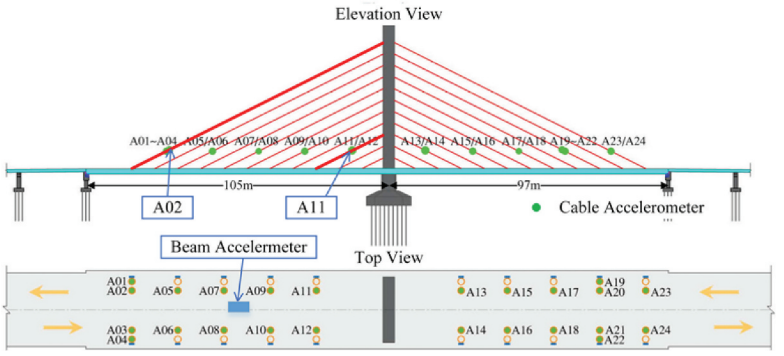


Figure 3. Cable sensor layout of Yongjiang Bridge.

5.2 *Fatigue assessment*

5.2.1 *Calculation of stress spectrum*

According to the aforementioned method, the time-varying cable force and the time-varying cross-section bending moment are calculated respectively. The 28-days of the acceleration data of the A02 and A11 cables were collected, and the time-varying cross-section bending moment was used to calculate the stress time history in the point at 0.1 l_0 along the cable length. Figure 4 is the stress time history of the A02 cable for 10 minutes.

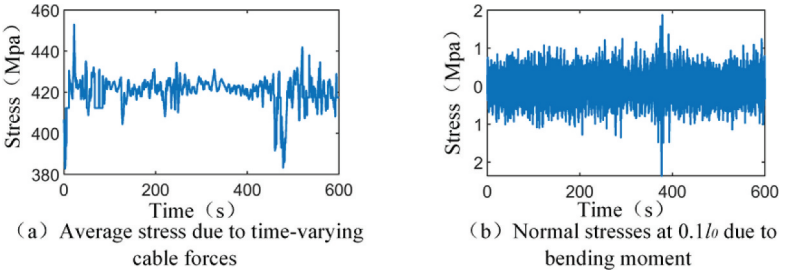


Figure 4. Stress history (10 minutes) of cable A02 due to axial force (a) and bending moment (b).

5.2.2 *Prediction of cable's fatigue*

Before estimating fatigue damage, the damage degree matrix is first calculated through the rainflow counting method. The accumulation of fatigue damage is the real fatigue damage of the cable. Figure 5 shows the fatigue damage matrix cloud diagram of the two cables.

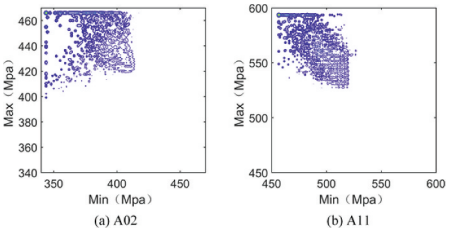


Figure 5. Nephogram of fatigue damage degree matrix of cables.

Table 2 gives the fatigue life estimated by different equations. Among them, Estimation 1 represents Eq. (7) or Eq. (8), and the stress amplitude adopts the average stress amplitude. Estimation 2 represents Eq. (9), and the stress amplitude adopts 1.6 times the average stress amplitude. When considering corrosion fatigue, the value of a is approximately 0.7.

Table 2. The fatigue life of cables (Unit: year).

	No consideration of corrosion		Consider corrosion	
Cable	Estimation 1	Estimation 2	Estimation 1	Estimation 2
A02	41368	7984	3905	754
A11	8324	1607	784	151

Table 2 shows that the fatigue life calculated by the stress amplitude of different formulas is quite different. Method 1 does not consider the interaction between the finished anchorage and the steel strand, and overestimates the fatigue life of the wire rope. The fatigue life calculated by method 2 is more reasonable. After considering the corrosion of the cable, the fatigue life of the

cable will be significantly reduced. For a bridge in operation, its cable is more susceptible to corrosion, and its service life will be significantly shortened under the combined effect of fatigue.

5.3 *Damage detection*

Since it is extremely difficult to get data from damaged real cables, the effectiveness of the method to remove the effect of external dynamic actions, as traffic and temperature, is verified by using real bridge cable data, but the damage detection can only be verified by numerical simulation.

5.3.1 *Eliminating the effects of traffic and temperature*

Based on the 24-hour acceleration data of the cable, the real time-varying frequency of cable A02 obtained through BRAPES is shown in Figure 6a. For the simulation of time-varying frequency, the method in reference (Ge *et al.* 2022) is used to simulate the traffic flow of Yongjiang Bridge, and $\Delta H_1(t)$, $\Delta H_2(t)$ and $\Delta H_3(t)$ of cable A02 are calculated by Eq.(10)-(12) also taking into account the temperature change along the day in the bridge location. The simulated time-varying frequency is shown in Figure 6b.

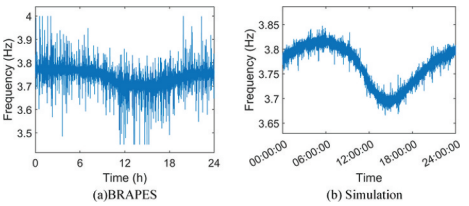


Figure 6. Time-Varying Frequency of Cable A02. a) From real acceleration data gathered with accelerometer in the cable. b) From simulation.

The time-varying frequency of the cable after removing the effects of traffic loads and temperature is shown in Figure 7.

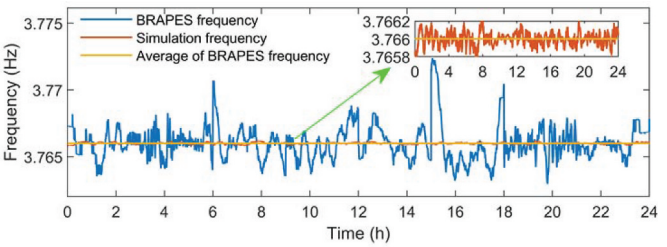


Figure 7. Time-varying frequencies processed by Method1.

From Figure 7, it can be seen that the post-processed simulated frequency has less variability, while the pots-processed measured frequency fluctuates more. However, by taking the average value of processed measured frequency as the representative value, it can be seen that the two coincide very well, with the maximum deviation less than 0.0002Hz. This indicates that the proposed simulation method is applicable for real cables.

5.3.2 *Simulation of cable damage*

The cable damage is simulated through the loss of the cable moment of inertia. For cable A11, five levels of damage: 0%, 5%, 10%, 15%, and 20% are considered. The corresponding calculated time-varying frequencies are shown in Figure 8.

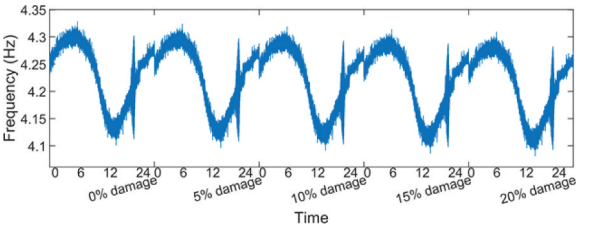


Figure 8. 24-hour of simulated time-varying frequencies of cable A11 for different levels of damage.

Method 1 (MA-EMD-MA) is used to remove the traffic load and temperature effects in the time-varying frequency, and the results are shown in Figure 9. As can be seen from Figure 9, it is feasible to evaluate whether cable damage has occurred based on changes in frequency.

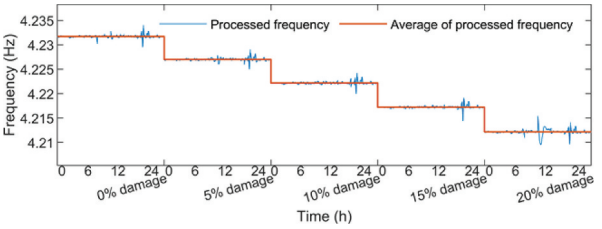


Figure 9. Processed time-varying frequency of cable A11 for different levels of damage.

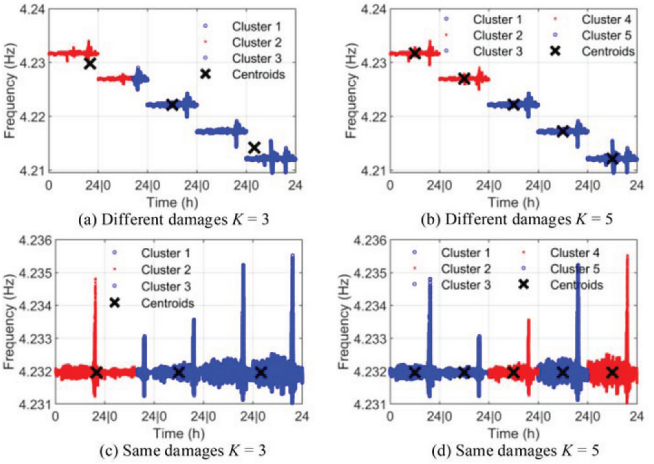


Figure 10. Results of time-varying frequency of cable A11 processed by K-means clustering.

5.3.3 *Qualitative identification of damage*

Figure 10 shows the application of the K-means clustering algorithm to cable A11 for the case of 5 levels of damage (a, b) and no damage (c, d) and different values of K. It can be seen that the accurate damage identification is only possible when K is equal to the number of damage levels, while when the data contains only one state, the centroids are the same, regardless of whether the K is correct or not. For real cables, the total damage levels of the cable are unknown, but they evolve gradually. Therefore, once the cable is damaged, the data will contain only two states. Therefore, the value of K=2 is recommended. If the clustering results are consistent, it is judged that no damage has occurred; if the clustering results are different, it is determined that the cable has sustained damage.

6 CONCLUSION

This article uses cable vibration as monitoring technique, and based on the vibration data, proposes two methods for cable fatigue assessment and damage detection. In the assessment of cable fatigue, a real-time stress perception method is first proposed, which includes time-varying cable tension and sectional bending stress. On this basis, a real-time monitoring and perception scheme for the fatigue state of service cables is established. In the cable damage detection, a qualitative assessment method for service cable damage based on time-varying frequencies is proposed. First, the MA-EMD-MA method is introduced to eliminate the operational and environmental variability from the cable frequency, and then K-means clustering method is used to qualitatively identify damage based on the offset of time-varying frequencies.

ACKNOWLEDGMENT

This study is funded by the National Natural Science Foundation of China (Grant No. 52108290); the China Postdoctoral Science Foundation (Grant No. 2022 M712906); the China State Scholarship Fund.

REFERENCES

Birkenmaier, M., 1980. Fatigue Resistant Tendons For Cable-Stayed Construction. *Iabse Proceedings*, 2, 65–78.

Dan, D.H., Xu, B. & Chen, Z.H., 2016. Universal Characteristic Frequency Equation For Cable Transverse Component System And Its Universal Numerical Solution. *Journal Of Engineering Mechanics*, 142 (4), 04015105.

Feng, J., Gao, K., Gao, W., Liao, Y. & Wu, G., 2022. Machine Learning-Based Bridge Cable Damage Detection Under Stochastic Effects Of Corrosion And Fire. *Engineering Structures*, 264, 114421.

Ge, L., Dan, D., Liu, Z. & Ruan, X., 2022. Intelligent Simulation Method Of Bridge Traffic Flow Load Combining Machine Vision And Weigh-In-Motion Monitoring. *Ieee Transactions On Intelligent Transportation Systems*, 1–16.

Guo, J., Wang, L., Fukuda, I. & Ikago, K., 2022. Data-Driven Modeling Of General Damping Systems By K-Means Clustering And Two-Stage Regression. *Mechanical Systems And Signal Processing*, 167, 108572.

Huang, J., Li, D., Li, H., Song, G. & Liang, Y., 2018. Damage Identification Of A Large Cable-Stayed Bridge With Novel Cointegrated Kalman Filter Method Under Changing Environments. *Structural Control And Health Monitoring*, 25 (5), E2152.

Jiang, C., Wu, C., Cai, C.S., Jiang, X. & Xiong, W., 2020. Corrosion Fatigue Analysis Of Stay Cables Under Combined Loads Of Random Traffic And Wind. *Engineering Structures*, 206, 110153.

Lepidi, M. & Gattulli, V., 2012. Static And Dynamic Response Of Elastic Suspended Cables With Thermal Effects. *International Journal Of Solids And Structures*, 49 (9), 1103–1116.

Li, X., Gao, C., Guo, Y., He, F. & Shao, Y., 2019. Cable Surface Damage Detection In Cable-Stayed Bridges Using Optical Techniques And Image Mosaicking. *Optics & Laser Technology*, 110, 36–43.

Mao, J.-X., Wang, H. & Li, J., 2019. Fatigue Reliability Assessment Of A Long-Span Cable-Stayed Bridge Based On One-Year Monitoring Strain Data. *Journal Of Bridge Engineering*, 24 (1), 05018015.

Xu, B., Dan, D., Zou, Y. & Lei, H., 2019. Research On Characteristic Function For Cable Inverse Analysis Based On Dynamic Stiffness Theory And Its Application. *Engineering Structures*, 194, 384–395.

Xu, B., Dan, D. & Yu, X., 2022. Real-Time Online Intelligent Perception Of Time-Varying Cable Force Based On Vibration Monitoring. *Engineering Structures*, 270, 114925.

Xu, B. & Dan, D., 2022. Whole-Field Online Real-Time Monitoring And Intelligent Perception Of Fatigue States Of Cables In Service. *China Journal Of Highway And Transport*, 35(6): 158–167.

Xu, B., Wu, Z. & Casas, J.R., 2023. Estimation Of Cable Damage Considering Traffic And Temperature Effect. *Barcelona: Technical University Of Catalonia (Upc)*.

Li, D., 2007. Damage Monitoring and health diagnosis for arch bridge suspender[D]. Harbin: Harbin Institute of Technology.

Bridge Maintenance, Safety, Management, Digitalization and Sustainability – Jensen, Frangopol & Schmidt (eds)
© 2024 The Author(s), ISBN 978-1-032-77040-6
Open Access: www.taylorfrancis.com, CC BY-NC-ND 4.0 license

Monitoring to secure the Ile-de-Ré viaduct France

S. Joye & M.De Witt
Sixense Monitoring, Nanterre, France

ABSTRACT: The Ile de Ré viaduct is a cantilever bridge made of 6 independent viaducts to link the Ré island to the city of La Rochelle in France. Built in 1988, it is 2926m long. Unfortunately, the viaduct experienced a failure of one of its external post tensioning tendon in 2018. The Department de la Charente-Maritime, owner of the bridge asked Sixense and Freyssinet to secure the structure for the replacement of the broken tendon. This securing operation consisted in 3 phases: ultrasonic inspection of the cable anchorage zone, installation of acoustic monitoring and finally, strapping of the group of cables together. The objective of the ultrasonic inspection was to qualify the current state of degradation of the anchorage. Indeed, the cause and location of cable failure was known to be within a short distance (within 2 m at the most) behind the anchorage. Failure was attributed to a corrosion phenomenon associated with a poor injection of cement grout inside the cable duct. Once the cable condition was qualified at the anchorage, the acoustic monitoring allowed to remotely detect any subsequent failure of wire inside the tendons. Any overpassing of the maximum allowed number of broken wires or any acceleration of failing wires would trigger an alert, and put the work in progress on hold. Finally, as an additional safety measure to secure the works within the bridge, the external post tensioning cables were strapped by group in order to prevent any whipping effect that would hurt the operator in case of cables failure. The quantity, strength, and location of straps has been carefully calculated with dynamic load cases. Thanks to this monitoring, the broken cable, 6 cables in poor state and more cable at risks were replaced between 2019 and 2023, allowing to secure the whole viaduct.

1 THE BRIDGE

The Ile de Ré viaduct is located on the Atlantic coast of France 500km south west from Paris. Built in 1988 it links the Ré Island to the main land. The 2962m of ocean water is crossed by a balanced cantilever bridge made of 6 independent viaducts.



Figure 1. View of the Ile de Ré viaduct.

DOI: 10.1201/9781003483755-307

2 AN EMERGENCY SITUATION

In september 2018, a broken cable from the post tensioning cable network was found broken down, laying on the floor. The tension released was sufficient to expulse the two anchorage heads out of their concrete blocks. The failure of the cable occurred within the massive anchorage concrete block at about 1m far from the anchorage head.

A preliminary inspection revealed that the anchorage head was lacking cement grout injection and this lack was compensated by polyurethane foam during the injection process.

The Charente Maritime Department, owner of the bridge, immediately organised a response to this unexpecting event with the help of specialised civil engineer experts. This response was structured in several stages:

- initial assessment of the stability of the bridge without the failed cables
- securing of the future operations by assessment of the condition of the other cable anchorages
- monitoring in time by installation of acoustic sensors the sound emitted by a broken wire makes it possible to detect any subsequent wire failure, following the principles of acoustic emission techniques),
- replacement of the broken cables
- identification of the 4 worst condition cables thank to the results of the ultrasonic inspection (Uscan technique) for later replacement,
- replacement of 2 additional critical cables.



Figure 2. Broken tendon inside the deck.

3 THE RESPONSE

3.1 *Securing*

3.1.1 *Ultrasonic reflectometry*

Ultrasonic reflectometry applied to prestressing cables (Uscan) has been developed by Gustave Eiffel University (UGE) and Sixense. It has been applied for 10 years on the stay cables of the Normandie Bridge. The principle of this non-destructive technique relies on the propagation of ultrasonic waves along the steel wires constituting the tendons and their reflection upon a broken wire.



Figure 3. Uscan measurement on strand extremity (anonymous project).

The ultrasonic sensor both acts as an emitter and receiver and the reflected signal are recorded for every single wire inspected for later analysis, and a possible defects identification. Typical defects involve generalised corrosion, fatigue cracks (for stay cables) and/or ultimately, wire breaks. The ultrasonic frequency is tuned according to the type of tendons: individually sheathed strands, strands poured in cement grout or individual parallel wires. The results are classified in 3 different levels: green, orange or red depending on the shape of the reflected signal.

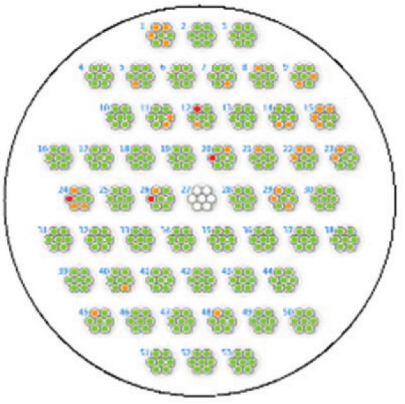


Figure 4. Uscan typical resulting pattern on anchorage head (anonymous project).

For the Ile de Ré viaduct, 85 anchorages were initially inspected during a campaign iniated just after the uncover of the broken tendon. A larger campaign was initiated in 2023 to assess the conditions of all anchorages in the bridge with the inspection of over 300 anchorages. In total this corresponds to over 50,000 wires, each individually inspected. The results of Uscan inspection allow the client to identify the cables with the worst condition that have to be replaced in priority.

After the removal of the first cables, visual inspections were carried on to confirm the reliability of the technique. With severe corrosion conditions, the wire break detection rates was found to drop significantly, but the technique was deemed to yield a sufficiently accurate assessment of the cable conditions to prioritize the replacement operations.



Figure 5. Uscan measurement in Ile de Ré viaduct.

3.1.2 *Acoustic monitoring*

After the condition of the cables was assessed by Uscan, an acoustic monitoring system was installed to detect any subsequent wire failure. The principle of the acoustic monitoring is to install acoustic sensors around and along external post-tensioning cable. Then any wire break occurring in a post tension cables is detected by the sensors and recorded by the associated data acquisition unit. Detection of the wire break generates an alert and the signal is analysed for confirmation of the wire break event. An Artificial Intelligence algorithm was trained to automatically filter false alarms generated by traffic noise or other external works.



Figure 6. Picture showing some acoustic sensors (in blue) located close to cable anchors in Ile de Ré viaduct.

The system was implemented during the operations in 2019 over a limited length of the bridge (where the broken tendon was uncovered). In 2023, the installation was completed to equip the entire bridge with an acoustic system. Over the past years, the system has detected about 30 wire break allowing the client to identify the cables at risk and in some cases led to cable replacements.



Figure 7. Data acquisition unit for acoustic monitoring.

4 THE FOLLOW UP

The acoustic monitoring system is still continuously monitoring the wire breaks that can occur during the service life of the structure. This system has been running since 2019 and is regularly detecting wire break. The Charente Maritime Department has commissioned a new work phase on the bridge in 2023, with an extended acoustic monitoring system, and additional works to ensure the structural stability of the bridge for the next decades. On specific periods with critical phases (cables dismantling), a dedicated specialist also helps identifying in quasi real-time potential acoustic events after the AI filter, to ensure the security of the working personnel.

5 EXPERIENCE

Sixense has performed many projects using Uscan ultrasonic reflectometry. The following table is giving the characteristic of our two major projects.

Table 1. Main work references for Sixense Uscan.

Project	Client	Type of anchorage	Number of Wire measured
Normandie	CCISE	Stay cable	109 000
Ile de Ré	CD 17	Prestressing	>50 000

Uscan technology has also be implemented on several infrastructures in France such as Bidouze Viaduc, Iroise bridge, Pont d'Isere, Chavanon viaduct or viaduct El Castro in Spain.

6 CONCLUSIONS

Uscan ultrasonic reflectometry is a patented method to assess the conditions of the structural cables in their anchorage zone. It applied for both stay cables or post tensioning cables giving a general assessment of the ageing at their anchorage area. It is particularly interesting to classify the state of the anchorages compare to others on order to prioritize the replacement of worst cables.

The Eversense Acoustics monitoring system allows to follow wire break during the lifetime of the bridge. It is a complex field requiring expertise in multiple domain such as sensors, analogical signal processing, advanced computer processing, acoustic skills and civil engineering

knowledge. Recent implementation of artificial intelligence program is securing the process by improving the filtering strategy and the outcome for the data analyst.

Uscan is giving a screen shot of the state of the cables whereas Acoustic monitoring allows to follow up the ageing through time. When combined together these technologies are complementary to assess the condition of structural cables and monitor their aging over time.


Taylor & Francis
Taylor & Francis Group
http://taylorandfrancis.com

SS25: Vulnerability assessment and retrofit of in-service bridges: Contributions and experiences

Organizers: M. Domaneschi, R. Cucuzza, G.A. Ferro, S. Mitoulis, M. Noori & V. Villa


Taylor & Francis
Taylor & Francis Group
http://taylorandfrancis.com

Bridge Maintenance, Safety, Management, Digitalization and Sustainability – Jensen, Frangopol & Schmidt (eds)
© 2024 The Author(s), ISBN 978-1-032-77040-6
Open Access: www.taylorfrancis.com, CC BY-NC-ND 4.0 license

Reliability of UT for the grouting inspection in PT bridges: A case study

I. Mazzatura
Department of Civil and Industrial Engineering, University of Pisa, Pisa, Italy
Department of Civil and Environmental Engineering, Universitat Politécnica de Catalunya, Barcelona, Spain

J.R. Casas
Department of Civil and Environmental Engineering, Universitat Politécnica de Catalunya, Barcelona, Spain

S. Caprili & W. Salvatore
Department of Civil and Industrial Engineering, University of Pisa, Pisa, Italy

ABSTRACT: The inspection of the condition of prestressing steel in post-tensioned structures is a challenging issue because of the potential presence of corrosion in the tendons not warned by any other visible degradation condition. The economic unfeasibility and technical difficulty of performing a large number of semi-destructive tests (endoscopies) require the identification and practical application feasibility of non-destructive testing techniques to optimize the inspection procedure and enhance its accuracy. Many real-world examples have evidenced that ineffective grouting, or even the lack of it, triggers the corrosion mechanism that, if not detected early, can lead to the brittle failure of the bridge. Therefore, failure of post-tensioned structures is normally associated with ineffective grouting. For this reason, it becomes of interest to localize and quantify grouting defects and voids in the tendons. Some non-destructive techniques are currently available; one of these being the Ultrasonic Tomography.

This paper presents the results of the combined application of Ultrasonic Tomography and endoscopies in the detection of un-grouted regions in a real bridge. The reliability of the Ultrasonic Tomography results is then obtained through the Probability of Detection (PoD) curves which are checked against the results given by the endoscopic testing campaign.

1 INTRODUCTION

Prestressed concrete bridges with bonded internal post-tensioning, in the following PT bridges, are difficult to investigate and assess. The high-strength steel cables are protected from dangerous conditions triggering corrosion by the grout, the metallic or plastic sheet of the ducts, and the concrete cover. Many protective layers are, therefore, provided, and for this reason, especially for the first constructions, there were no worries about their durability (Godart 2001). One of the serious and sudden events occurred in the UK in 1985 when a single-span PT bridge collapsed without any warning (Woodward 2001; Woodward and Williams 1988). The events led to the Department of Transport's (DoT) decision to ban the PT bridges with internal tendons until the design and construction standard could be reviewed, in September 1992. At the same time, DoT announced that all the PT Trunk bridges would be systematically inspected over a five years period. The moratorium was lifted for cast-in-place posttensioned concrete bridges in 1996 since the results of the Special Inspections revealed that the majority of structures have a good record of durability. Anyway, this fact focused the

DOI: 10.1201/9781003483755-308

attention on the methodologies to apply to inspect these structures, in particular in identifying not visible defects.

Regarding Italy, the triggering event was the collapse of the Polcevera viaduct, in August 2018. After that, many efforts were made to organize and standardize the inspection and assessment of bridges and viaducts of any typology. The publication of the Guidelines for Risk Classification and Management, Safety Assessment and Monitoring of Existing Bridges (MIT CSLP 2020) in 2020 stated a set of actions to be completed to inspect the structures depending on the level of knowledge to reach. In this context, PT bridges are presented as a "particular case", to be dealt with by executing the so-called Special Inspection. The main problem is that, even if some indications are given, there is a gap regarding the testing methodologies to apply and the definition of the number of samples. Some proposals have been made during the very last years to cover this lack (Mazzatura, Caprili, et al. 2023; Mazzatura, Salvatore, et al. 2023), and the research here presented is part of these wider topics.

The focus is on the possible non-destructive methodologies to apply in searching for defects in PT tendons. Since searching for corrosion is difficult, and since corrosion is often associated with the lack of grouting (i.e. voids within the ducts), a way to search for defects can be searching for voids. The underlying and main assumption is that the void sections are associated with the defective ones. Even if this assumption is conservative, detecting voids is easier through Non-Destructive Technologies (NDTs). Many NDTs are proposed in the state of the arts. In the present research, the choice is to apply the proposed method to a real bridge and investigate the reliability of the result provided by UT.

2 METHODOLOGY

A 14-span viaduct located on a Highway in the North of Italy was investigated. The followed methodology was the one explained in (Mazzatura, Caprili, et al. 2023). Even if the present paper will focus only on the individuation of ungrouted areas within the PT ducts, a few words will be spent in the following to explain the determination and the location of the samples to investigate. Starting from the consideration given by the Italian Guidelines (MIT CSLP 2020), and by the study of the available state of the art (in particular of (FHWA 2013; Highways England 2020)), a multiphase methodology is proposed. It works on subsequent levels of analysis, meaning that only for the most degraded structures is necessary to go through all the phases. The first two phases are mandatory for all the bridges: *phase 0* provides the knowledge of the structure and the determination of the number of samples to investigate, *phase 1* provides the overall assessment conditions through both non-destructive (ND) and semi-destructive (SD) technologies, *phase 2* consists in the deep analysis of the defectiveness individuated at the end of the previous one, and *phase 3* is optional and contains suggestions for the global analysis of the bridge. For the present structure, the first two phases are executed.

Once the number of samples was determined, the choice was to employ as NDT the Ultrasonic Tomography. On the basis of a laboratory testing campaign previously executed and presented both in (Mazzatura, Salvatore, et al. 2023), and in (Mazzatura et al. n.d.), the way of employing the instrumentation and some considerations useful for the critical elaboration of data had been determined. In particular, the main results are about the reliability of the NDT given in terms of Probability of Detection (PoD). The PoD model is an evaluation often carried out for Non-Destructive methodologies, widely employed in the context of aerospace and nuclear engineering, and standardized by ASTM (ASTM International 2015, 2018). Stated a certain confidence and for a given probability, by the PoD curve it is possible to determine the largest flaw that a system can miss.

The tests' campaign will be described, and the focus will be on the tests for the location of the grouting defects. Finally, a critical analysis of the results is given, considering the main outputs deriving from the PoD analysis.

3 EXPERIMENTAL CAMPAIGN

3.1 *Description of the structure*

The studied viaduct is located on a highway in the North of Italy. It has 14 spans of variable length for a total length of 600 m. Each span is either 45, 40, or 34 m; but the very large part (11) is 45 m. The deck has 4 posttensioned beams and 4 reinforced concrete cross members. The subject of the investigation campaign were the beams belonging to the large population, i.e. the ones of 45 m.

From the design documentation, it is known that each beam is posttensioned by 6 cables (Figure 1), each composed of 42 wires of 7 mm diameter. The longitudinal design layout of the cables is known as well (Figure 1), and also the design mechanical characteristics of both the concrete and the high-strength steel. The initial prestress is not known. The main information about the viaduct is summarized in Table 1.

Table 1. Main information.

Year	N_{spans}	L (m)	L_s (m)	N_{beams}/span	N_{cables} /beam	Cables' typology	f_t (MPa)	Initial prestress
1976	14	600	34-40-45	4	4-5-6	Parallel wires	1′600	Unknown

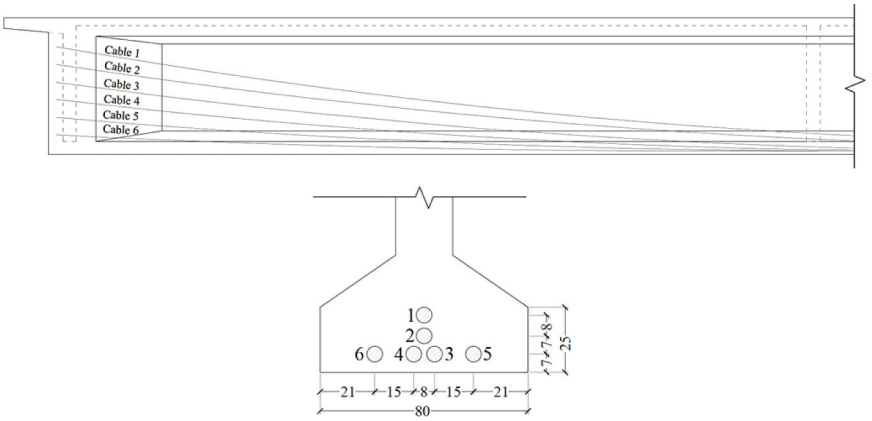


Figure 1. The upper figure shows the cables' trace, the lower one the middle-span cross-section.

3.2 *Number of samples and localization*

Many tests were performed on the structure. In the following, the focus will be only on the ones necessary to investigate the grouting defects within the ducts. First, a revision of the design documentation and the execution of a visual inspection is completed. This allows reaching a satisfying level of knowledge for the definition of the number of samples.

The basic assumption is that a sample corresponds to a cable and that a cable can be considered fully investigated if all the sites where voids are most likely to occur are tested. For more details, please refer to (Mazzatura, Caprili, et al. 2023).

In the present case, 14 samples resulted, therefore, 14 cables were chosen. A maximum of two tendons per beam are selected, to reasonably spread the testing campaign. Thus, 7 beams are chosen belonging to 3 different spans. The NDTs for the preliminary investigation aiming to define the layout of the cables (i.e. Ground Penetrating Radar), and the ones for the localization of voids (i.e. Ultrasonic Tomography), can be executed only in the areas shown in Figure 1, which corresponds to the ones in which the cables lies in the web of the beam and not in the lower part. The other locations (mainly the mid-span regions) were investigated through SDTs, i.e. endoscopies.



Figure 2. Inspected areas by GPR and UTs.

Endoscopies were also executed on the cables' trace in the web of the beam, both in areas warned by the Ultrasonic Tomography and in random areas.

3.3 *Preliminary investigation*

Before performing the investigations to locate grouting defects, it is necessary to collect some pieces of information about the structure. A revision of the design documentation was carried out, to identify potential conditions promoting damage, such as inadequate waterproofing and drainage system. The visual inspection is also fundamental to preliminary state the conservation status of the structure and to identify defects that can warn of possible deficiencies in the PT system. Particular attention must be given to cracks, whose presence could mean excessive losses in the precompression, and to defects showing the penetration of water/moisture inside the concrete section. Anyway, no worrying conditions were identified.

Once the overall condition of the structure is stated, and the number of samples to investigate is computed, it is possible to proceed with the preliminary in situ tests, mainly devoted to the location of the cables' layout. All the subsequent tests are concentrated on the cables, then it is important to exactly know their trace. In the present research, the Ground Penetrating Radar (GPR) was employed to locate the ducts.

GPR is a radar imaging technique using electromagnetic pulses transmitted to the element at very high frequencies. It was widely used (Terzioglu et al. 2018a) for achieving information about reinforcements' layout (Beben, Mordak, and Anigacz 2012; Kohl and Streicher 2006; Pasculli et al. 2018; dos Santos et al. 2014; Shaw et al. 2005; Soldovieri et al. 2006), the position of prestressing strands and metallic ducts (Clem, Schumacher, and Deshon 2015; Kohl and Streicher 2006; dos Santos et al. 2014; Terzioglu et al. 2018b), and the presence of voids in the concrete. From a practical perspective, the tests were executed by doing vertical scans (i.e. the 0, 1, … 10 sections in Figure 2) on the beam web each 100 cm. In each section, the location of each cable is identified. Finally, the single locations are joined to obtain the actual trace. As previously mentioned, the GPR test was executed in the areas of the beam where the cables lie in the web. These areas correspond to around the first 10 m from the beam heads. Indeed, it is not possible to execute the tests in other areas, such as the bulb of the beam, because the investigation surface is inclined. The trace of the cable represents the fundamental base for the execution of posterior tests.

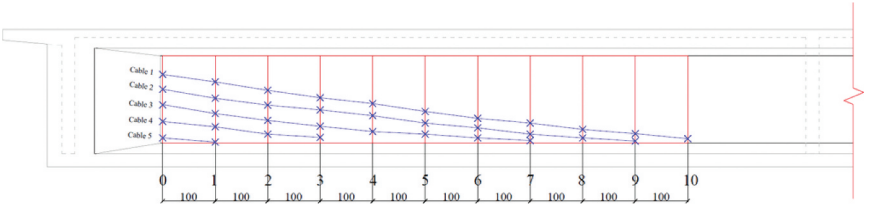


Figure 3. Operating modality for tracing cables.

3.4 *Investigations for the localization of voids*

The localization of voids was performed through Ultrasonic Tomography and endoscopies. Two cables per beam were inspected, and in detail cables 3 and 4. These are the cables that present largest areas on the web for feasible investigation. For instance, cable 1 and cable 2 are more visible in correspondence of the web, being the higher ones, but it is not possible to investigate them in the midspan region because they are located in the second order of PT reinforcements, having both a very large concrete cover, and the cables from 3 to 6 and the

ordinary reinforcements in the first order, making difficult the execution of any other kind of test (endoscopies and UTs), considering to execute them on the intrados of the beam (Figure 1 in the lower part shows the mid-span cross-section of the beam).

UTs were performed in all areas of the cables that could be tested, while endoscopies were performed in areas in which UTs gave no information (i.e. midspan region), in random areas (i.e. locations investigated but not warned by UT), and in critical areas (i.e. locations warned by UTs).

3.4.1 *Ultrasonic tomography*

UT was selected because of its quick and easy in-situ application. The in-situ conditions are often very adverse, mainly because of the height of the bridge, and therefore the uncomfortable work areas, and of the limited time available to complete the tests (it is often necessary to stop the traffic, or at least to limit it).

UT is reliable in estimating the thickness of elements/layers and in locating voids in PT ducts, especially when coupled with other testing methodologies (Martin et al. 2001; Muldoon et al. 2007). In the present campaign, the MIRA A10403d instrument, employing shear waves and dry point contact sensors was used. A stress pulse is generated through a mechanical impact of the sensors, even working as receivers. Part of the pulse propagates through the body, and part is reflected. Changes in the acoustic impedance are then captured. Through time-of-flight measurements, it is possible to locate discontinuities and therefore reinforcements, tendons, voids (cracks, honeycomb, delamination), or water defects (Muldoon et al. 2007). The testing apparatus gives images as results, elaborated through the SAFT algorithm (Schickert, Krause, and Mü Ller 2003; Stepinski and Lingvall 2010). Figure 4 shows the elaborated results of the UTs on one of the beams.

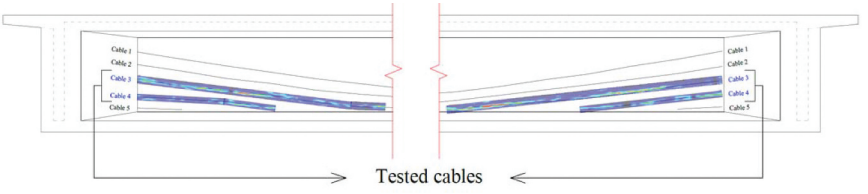


Figure 4. Results from UTs after postprocessing.

3.4.2 *Endoscopies*

To execute endoscopic investigations is necessary to locate the cable. In fact, a tiny spot (usually no more than 20 mm in diameter) is investigated. The endoscopies were executed firstly by performing a hole of a bigger diameter (20 mm), and then proceeding with a smaller one (10 mm); this methodology avoids smashing the metallic sheet of the duct on the tendon (Figure 5a.) and thus avoids performing a non-informative test.

Understanding the conservation status of the tendons through endoscopic investigations could be challenging, but it is a balanced compromise between an NDT and a full destructive investigation (i.e. the removal of the concrete cover, the metallic duct, and the grout).



a. *b.*

Figure 5. A. The mashed duct does not allow a correct evaluation; b. correct endoscopy with no evidence of grout.

4 RESULTS AND DISCUSSION

Starting from the results of a laboratory campaign for the definition of the Probability of Detection (PoD) curve for the UT investigating voids in PT metallic duct, the results of the in-situ testing campaign are elaborated. A critical discussion of the results is given with consideration about the overall observed state of conservation of the structure.

4.1 *Probability of detection*

The Probability of Detection is a methodology to evaluate the reliability of an NDT by furnishing as main information the largest flaw that the system can miss (given a certain probability and stated level of confidence). This piece of information is obtained by establishing a relationship between the probability of detecting a defect with its size, under representative application conditions. Since the main assumption is that the PoD depends only on the flaw size, it is very important to understand the other potential influencing parameters, that can be related to the geometry of the investigated body, environmental conditions, the testing set-up, and so on. Some details about the PoD construction are contained in (Mazzatura et al. n.d.); here the results of the PoD analysis are used to analyse the ones derived from the in-situ testing campaign.

The PoD useful for the present work is the one given in Figure 6, from (Mazzatura et al. n.d.). The displayed values are PoD(50%), i.e. the size of the void that the system can miss with a 50% probability and a 50% confidence level; PoD(90%), i.e. the size of the void that the system can miss with a 90% probability and a 50% confidence level; and PoD(90/95), i.e. the size of the void that the system can miss with a 90% probability and a 95% confidence level.

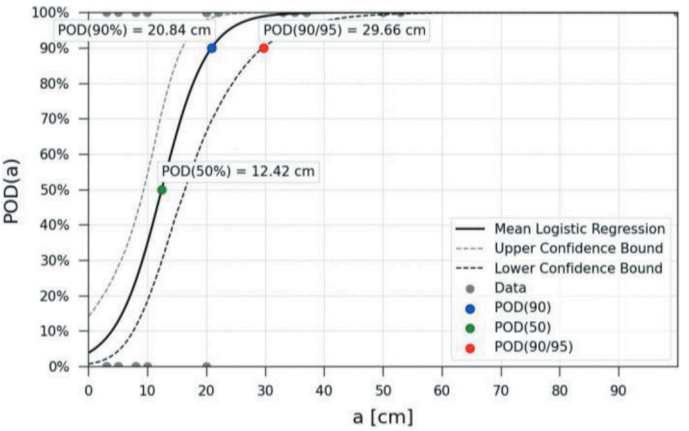


Figure 6. PoD curve for PT duct located at 15 cm from the investigation surface.

The last value, i.e. POD(90/95) is the interesting one, as the ASTM requires. The shown curve is obtained for defects located in cables lying 15 cm from the investigation surface and employing the same instrumentation calibration. This case represents the most similar one to the present testing campaign since the cables lie 11 cm from the concrete surface and all the tests were performed employing the same calibration.

4.2 *Critical analysis*

The results of the UTs and endoscopies were reported and compared as shown in Figure 7. Being the POD(90/95)= 25.66 cm (Figure 6), only the UTs showing a warn wider than 30 cm are considered as defective areas, i.e. voids inside ducts. In 4 out of 14 investigated cables, resulted in no defects at all.

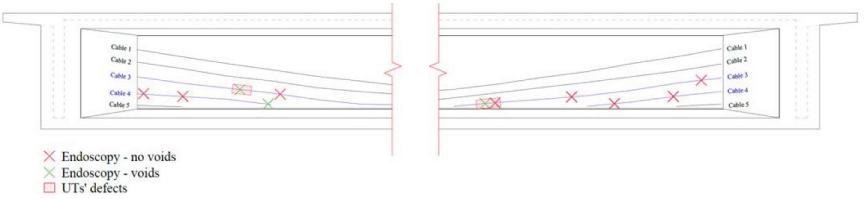


Figure 7. UTs defects and output of the endoscopic investigations.

In the other cables, some defects were signaled by the UTs. Table 2 gives a summary of the analysis. The last column represents the percentage of defective areas (L_{war}= warned length) on the total investigated length (L_{inv}= investigated length).

Table 2. Results of the UTs.

Span	Beam	Cable	UTs defective percentage ($L_{war}/L_{inv} \cdot 100$)
3	1	3	10%
3	1	4	30%
4	1	3	9%
6	1	3	8%
8	1	3	16%
8	1	4	43%
6	2	4	31%
8	2	4	6%
3	3	3	49%
3	3	4	55%

On a total of 56 endoscopies, 26 were executed in random areas of the cables and 30 in the areas warned by UTs. 63% of the tests in the warned areas reported the presence of voids; however, some of these voids are not located inside the duct but outside of it. The tests in random areas reported voids in 23% of the cases. No oxidized or corroded wires were found.

Table 3. Number of false positives and true positives.

	30 cm≤d<50 cm	50 cm≤ d <100 cm	100 cm≤ d <150 cm
Number of false positives	4	3	2
Number of true positives	4	7	7

By combining the output of the endoscopies and the UTs, it is possible to obtain the results summarized in Table 3. The assumptions are that if endoscopies are executed in correspondence of areas warned by UTs, and no evidence of voids is found, then false positives are identified; otherwise, if the endoscopies are not executed, or if the endoscopies are executed and voids evidence is found, then true positives are identified. It can be observed that the quote of false positives decreases with the length of the defects.

5 CONCLUSIONS

The present research deals with the inspection of PT bridges, with particular attention to the execution of tests for the location of voids. The focus is on Ultrasonic Tomography, employed on a 14-span bridge located in the North of Italy to investigate the status of grouting of 14 cables. The results of the investigations are elaborated in view of the reliability evaluation of the technique obtained thanks to a previous laboratory testing campaign. Some endoscopic investigations were conducted to check the reliability of the detection technique.

This case study shows that the PoD curves obtained in laboratory under controlled conditions and where only the flaw size is the variable, may have to be considered cautiously when applied to real bridges under uncertainties not encountered in the laboratory, related to the inspectors' ability to work in difficult environments, the variability due to in situ conditions, and others. The number of false positives encountered in real conditions, even for large voids has to be taken into account in further applications to real bridges.

However, by considering both the results of the NDT and of the SDT, mainly since no evidence of corrosion was found in any case, it is possible to affirm that the structure is in a good state of conservation, even if some voids within the ducts were found.

REFERENCES

ASTM International. 2015. *E3023-15 Standard Practice for Probability of Detection Analysis for â Versus a Data*.

ASTM International. 2018. *E2862-18 Standard Practice for Probability of Detection Analysis for Hit/Miss Data*.

Beben, Damian, Arkadiusz Mordak, and Wojciech Anigacz. 2012. "Identification of Viaduct Beam Parameters Using the Ground Penetrating Radar (GPR) Technique." *NDT and E International* 49:18–26. doi: 10.1016/j.ndteint.2012.03.001.

Clem, Daniel J., Thomas Schumacher, and Jordan P. Deshon. 2015. "A Consistent Approach for Processing and Interpretation of Data from Concrete Bridge Members Collected with a Hand-Held GPR Device." *Construction and Building Materials* 86:140–48. doi: 10.1016/j.conbuildmat.2015.03.105.

FHWA. 2013. "Guidelines for Sampling, Assessing, and Restoring Defective Grout in Prestressed Concrete Bridge Post-Tensioning Ducts."

Godart, B. 2001. "Status of Durability of Post-Tensioned Tendons in France." *Fib Bulletin No. 15 Durability of Post-Tensioning Tendons, Technical Report*, *Proceedings of a Workshop Held at Ghent University on 15–16 November 2001* 25–42.

Highways England. 2020. "CS 465 - Management of Post-Tensioned Concrete Bridges."

Kohl, Christoph, and Doreen Streicher. 2006. "Results of Reconstructed and Fused NDT-Data Measured in the Laboratory and on-Site at Bridges." *Cement and Concrete Composites* 28(4):402–13. doi: 10.1016/j.cemconcomp.2006.02.005.

Martin, J., K. J. Broughton, A. Giannopolous, A. Hardy, and M. C. Forde. 2001. "Ultrasonic Tomography of Grouted Duct Post-Tensioned Reinforced Concrete Bridge Beams." *NDT&E International* 34 (2):107–13. doi: https://doi.org/10.1016/S0963-8695(00)00035-9.

Mazzatura, Isabella, Silvia Caprili, Walter Salvatore, and Alessio Lupoi. 2023. "A Multi-Phase Survey Approach for Post-Tensioned Prestressed Concrete Bridge Decks." doi: 10.1201/9781003323020-487.

Mazzatura, Isabella, Joan R. Casas, Silvia Caprili, and Walter Salvatore. n.d. "Reliability of Ultrasonic Tomography in Detecting Grouting Defects in Post-Tensioned Structures by PoD Curves." *Engineering Structures, under Review*.

Mazzatura, Isabella, Walter Salvatore, Silvia Caprili, Simone Celati, Michele Mori, and Massimo Gammino. 2023. "Damage Detection, Localization, and Quantification for Steel Cables of Post-Tensioned Bridge Decks." *Structures* 57. doi: 10.1016/j.istruc.2023.105314.

MIT CSLP. 2020. *Linee Guida per La Classificazione e Gestione Del Rischio*, *La Valutazione Della Sicurezza Ed Il Monitoraggio Dei Ponti Esistenti*.

Muldoon, R., A. Chalker, M. C. Forde, M. Ohtsu, and F. Kunisue. 2007. "Identifying Voids in Plastic Ducts in Post-Tensioning Prestressed Concrete Members by Resonant Frequency of Impact-Echo, SIBIE and Tomography." *Construction and Building Materials* 21(3):527–37. doi: 10.1016/j.conbuildmat.2006.04.009.

Pasculli, Davide, Agnese Natali, Walter Salvatore, Francesco Morelli, and Davide Morandi. 2018. "Investigation of Reinforced Concrete Bridges by Using a Dual-Polarized High-Frequency GPR." *2018 17th International Conference on Ground Penetrating Radar, GPR 2018* 1–5. doi: 10.1109/ICGPR.2018.8441633.

dos Santos, Vinicius Rafael N., Waleed Al-Nuaimy, Jorge Luís Porsani, Nina S. Tomita Hirata, and Hamzah S. Alzubi. 2014. "Spectral Analysis of Ground Penetrating Radar Signals in Concrete, Metallic and Plastic Targets." *Journal of Applied Geophysics* 100:32–43. doi: 10.1016/j.jappgeo.2013.10.002.

Schickert, Martin, Martin Krause, and Wolfgang Mü Ller. 2003. "Ultrasonic Imaging of Concrete Elements Using Reconstruction by Synthetic Aperture Focusing Technique." *Journal of Materials in Civil Engineering* 15(3). doi: 10.1061/ASCE0899-1561200315:3235.

Shaw, M. R., S. G. Millard, T. C. K. Molyneaux, M. J. Taylor, and J. H. Bungey. 2005. "Location of Steel Reinforcement in Concrete Using Ground Penetrating Radar and Neural Networks." *NDT and E International* 38(3):203–12. doi: 10.1016/j.ndteint.2004.06.011.

Soldovieri, Francesco, Raffaele Persico, Erica Utsi, and Vincent Utsi. 2006. "The Application of Inverse Scattering Techniques with Ground Penetrating Radar to the Problem of Rebar Location in Concrete." *NDT and E International* 39(7):602–7. doi: 10.1016/j.ndteint.2005.12.005.

Stepinski, Tadeusz, and Fredrik Lingvall. 2010. "Synthetic Aperture Focusing Techniques for Ultrasonic Imaging of Solid Objects." Pp. 1–4 in *8th European Conference on Synthetic Aperture Radar*. Aachen.

Terzioglu, Tevfik, Madhu M. Karthik, Stefan Hurlebaus, Mary Beth D. Hueste, Stefan Maack, Jens Woestmann, Herbert Wiggenhauser, Martin Krause, Patrick K. Miller, and Larry D. Olson. 2018a. "Nondestructive Evaluation of Grout Defects in Internal Tendons of Post-Tensioned Girders." *NDT and E International* 99:23–35. doi: 10.1016/j.ndteint.2018.05.013.

Terzioglu, Tevfik, Madhu M. Karthik, Stefan Hurlebaus, Mary Beth D. Hueste, Stefan Maack, Jens Woestmann, Herbert Wiggenhauser, Martin Krause, Patrick K. Miller, and Larry D. Olson. 2018b. "Nondestructive Evaluation of Grout Defects in Internal Tendons of Post-Tensioned Girders." *NDT and E International* 99(October 2017):23–35. doi: 10.1016/j.ndteint.2018.05.013.

Woodward, R. 2001. "Durability of Post-Tensioned Tendons on Road Bridges in the UK." Pp. 1–10 in *fib Bulletin No. 15 Durability of Post-tensioning Tendons, Technical Report, Proceedings of a workshop held at Ghent University on 15–16 November 2001*, edited by L. Taerwe. Ghent.

Woodward, RJ, and FW Williams. 1988. "Collapse of Ynys-y-Gwas Bridge, West Glamorgan." *Proceedings of the Institution of Civil Engineers* 84(4):635–69. doi: https://doi.org/10.1680/iicep.1988.179.

Bridge Maintenance, Safety, Management, Digitalization and Sustainability – Jensen, Frangopol & Schmidt (eds)
© 2024 The Author(s), ISBN 978-1-032-77040-6
Open Access: www.taylorfrancis.com, CC BY-NC-ND 4.0 license

Resilience and sustainability assessment of a prestressed concrete viaduct

M. Domaneschi & R. Cucuzza
Department of Structural, Geotechnical and Building Engineering, Politecnico di Torino, Turin, Italy

R. Di Bari
Department Lifecycle Engineering, University of Stuttgart, Stuttgart, Germany

S. Argyroudis
Department of Civil and Environmental, Engineering, Brunel University London, UK

S. Mitoulis & N. Kopiika
Department of Civil Engineering, University of Birmingham, Birmingham, UK

ABSTRACT: The paper explores Greece's Polyfytos viaduct, the nation's second-longest bridge spanning 1,372 meters, renowned also for providing access to key power plants in South-East Europe. A resilience analysis of different retrofitting scenarios was conducted, including both transitability and structural capacity aspects, employing visual inspections, digital data collection, and advanced modeling techniques. The viaduct, conceptualized by Prof Riccardo Morandi and built in 1972-1975, displays typical degradation seen in pre-stressed and reinforced concrete bridges. Unlike previous research focused solely on retrofitting with LCA and LCC assessments, this study integrates resilience assessment, marking a pioneering holistic approach to viaducts refurbishment.

1 INTRODUCTION

1.1 *Summary*

Over the last five decades, the balanced cantilever method has become increasingly popular in constructing bridges with medium spans, typically ranging between 100 to 200 meters (Concrete Bridge Development Group, 2017). However, issues related to long-term material effects such as concrete creep, steel tendon corrosion, and others have been noted since the 1990s, resulting in excessive vertical deflections (Bažant and Chern 1984, Bažant and Kim 1991, Bažant and Panula 1980). These problems have led to instances of bridge deterioration, even partial collapse, primarily exacerbated by heightened traffic loads up to 5-6 times the original ones (Morgese et al. 2020) and potential construction complications (Lucko and De La Garza 2003). Despite multiple research efforts (Gu et al. 2011, Wang and Fu 2015, Domaneschi et al. 2020), a comprehensive mechanism to predict and calculate these faults remains elusive.

The lack of a standardized solution suggests to propose an alternative approach, moving away from traditional on-site inspections and extensive sampling. This paper suggests formerly a method for evaluating vulnerable assets with uncertain structural integrity, where destructive testing or extensive sample collection is not feasible. Drawing on digitalization and monitoring trends in the construction sector, the recommended approach relies on computer analysis and innovative tools like drone-based photogrammetry (Varbla et al. 2021). Emphasizing cost-effectiveness and environmental friendliness, this method aligns with the growing popularity of laser scanning technology (Lõhmus et al. 2018), capable of providing detailed results within limited time frames (Witcher 2017).

DOI: 10.1201/9781003483755-309

Furthermore, this study serves as a complement to prior research that focused on assessing various retrofit solutions for this bridge type, particularly concerning environmental sustainability and cost impacts. It aims to evaluate these solutions by quantifying their resilience considering both transitability and structural capacity issues in the resilience computation. Therefore, the result is to promote a holistic approach to the reinforcement and maintenance of existing viaducts, considering not only the classical technical aspects of structural engineering but also environmental impact, cost, and resilience in identifying the most suitable solution. The Polyfytos Bridge in Western Macedonia, Greece, has been chosen as the case study for this multi-step research effort.

1.2 *The Polyfytos Bridge*

The Polyfytos Bridge, constructed in 1975 within the Municipality of Western Macedonia, Kozani, Greece, stretches over the artificial Polyfytos lake, playing a crucial role in connecting local and national road networks. One section of the bridge, spanning 260 meters between piers 22, 23, and 24 (Figure 1), was built using the balanced cantilever method, contributing to the bridge's overall length of 1372 meters. Recent inspections, carried out by multiple inspectors, including one of the authors of this paper, revealed excessive deflections at the free ends of the cantilevers, a common issue in aging bridges constructed using this method (Markogiannaki et al. 2022). Initial evaluations highlighted corrosion and localized concrete damage, raising significant concerns about the bridge's structural soundness. Consequently, traffic restrictions, such as weight limitations for heavy vehicles and reduced speed limits, were imposed to minimize dynamic impacts.

Typically, extensive material sampling, destructive testing, and vibration/loading assessments are utilized to evaluate material conditions. However, due to concerns about critical points on the deck's capacity, the owners did not authorize these methods (Markogiannaki et al. 2022). Furthermore, because of the bridge's importance in the bustling national road network (part of the E65 Central Greece Highway), conducting tests that could disrupt traffic necessitates considerable challenges.



Figure 1. The Polyfytos bridge and the three piers under evaluation.

1.3 *Digital technologies toward bridge inspection*

A proposed method for digital damage assessment is introduced, employing sophisticated computational tools adaptable to diverse structural assets. While several monitoring systems utilizing sensor technology have been recommended in previous studies (Li et al. 2022, Zhou et al. 2021), none have achieved universal optimization due to varying levels of accuracy. The proposed innovative approach aims to minimize intrusion, time, cost, and environmental impact.

The suggested process starts with a report on the necessity for on-site inspections. High-tech surveying tools, such as drone-based photogrammetry, provide valuable data on deflections, rotations, and visible cracks without requiring physical access to the structure (Li et al. 2022). These measurements generate deflection curves for mathematical comparison with other datasets. Additionally, information sourced from design reports and literature complements this analysis, contributing to an advanced structural model.

Acknowledging existing knowledge gaps (Bažant and Jirásek 2018), the advanced model considers potential factors such as creep and shrinkage observed in similar structures.

Scenario-based analyses explore the impact of various parameters on the structure. By comparing the deflection curves from these scenarios with measured results, potential causes are identified, guiding further investigation without providing definitive conclusions.

While this approach may not offer conclusive findings, it provides engineers and asset stakeholders with reliable information, offering a digitally streamlined, cost-effective, time-efficient, and environmentally friendly solution with minimal structural intervention.

1.4 *Some remarks on corrosion issues*

The corrosion of tendons in prestressed concrete bridges poses a significant threat to their structural integrity, as seen in incidents such as the catastrophic failure of the Ynys-y-Gwas bridge in the UK in 1985 (Podolny 1992). Even early in a bridge's lifespan, events like the replacement of post-tensioned tendons in Florida's Mid-Bay bridge after eight years due to corrosion-related concerns emphasize the importance of this issue (Hartt and Venugopalan 2002).

This study primarily focuses on corrosion as the primary cause of the investigated bridge's deterioration, largely disregarding potential additional failure mechanisms such as scouring or spalling of the reinforced concrete. Exposure to moisture makes the exposed interface of a strand highly vulnerable to corrosion-induced damage. The concept of "localized corrosion" raises significant concerns as it could lead to substantial reductions in the strand's cross-section, resulting in severe decreases in its tension capacity. Variations may exist within a strut, with differences between corroded and uncorroded wires in the same section and corroded and uncorroded segments along its length (Bartolozzi et al. 2022, De Gaetano et al. 2020).

2 BRIDGE CONDITION

A more detailed description of the bridge, focusing on the segment examined in this research (piers #22, #23, #24 with cantilever and precast beams connected by half-joints), is presented in the study by Domaneschi et al. (2023), along with the utilization of prestressed concrete technique in construction. Additionally, specifics regarding geometry, constituent materials, conducted analyses, and degradation assessment are provided.

According to Domaneschi et al. (2023), an in-depth detailing of the current state of the bridge is presented utilizing a point cloud. This visualization offers insights into particular aspects of both the cantilever and the half-joint of the bridge.

The report also addresses the deflection of the most critical cantilever, noting a significant variance between the expected and measured elevations. The measured position reveals a considerable discrepancy, measuring 133mm and 207mm lower than the anticipated elevation.

These differences specifically highlight downward displacements at the tip or end of the most critical cantilever. Such considerable deviations from the expected positions may indicate potential structural concerns within this specific component of the bridge. Further investigation and analysis are crucial to determine the underlying causes and implement necessary measures to maintain the bridge's structural integrity and safety.

3 FRAMEWORK FOR THE ASSESSMENT

The comprehensive approach involves assessing the structure's condition, proposing various technical solutions, evaluating costs, analyzing environmental effects, and gauging resilience against diverse challenges. The ultimate selection of the retrofitting solution integrates these aspects, ensuring a balance between structural improvement, economic viability, sustainability, and long-term resilience. This framework aims to guide decision-making and implementation, aiming for a safer, more durable, and environmentally conscious infrastructure.

4 PRELIMINARY BRIDGE RETROFITTING MEASURE

The initial design for retrofitting the analyzed piers aims to improve the structural performance and safety of the bridge in accordance with standard regulations. As discussed earlier,

significant damage to the bridge is primarily attributed to inadequate maintenance, potential issues during construction, increased traffic, high loads during service, and exposure to harsh environmental conditions. The critical reduction in prestressing stress at the cantilever supports severely impacts the bridge's functionality. Thus, two viable retrofitting scenarios have been identified to restore its original functionality (Domaneschi et al. 2023).

- Scenario #1: Demolition and reconstruction involve demolishing the current continuous deck, comprising six tapered box girder cantilevers and three girder bridges, while retaining the existing piers. Reconstruction maintains the same structural configuration, materials, and behaviors due to the widespread use of the bridge's design.
- Scenario #2: Local interventions and replacement of the girder bridge sections incorporate installing external prestressing cables to restore proper compression stresses in the six cantilevers, enhancing the bridge's functionality. Additionally, it considers replacing three girder bridges with steel box girder sections to prevent cable corrosion. This solution results in improved slenderness and reduced load on the cantilevers.

For Scenario #1, the interventions include:

a) Disassembling the defective balanced cantilever segment of the deck and the reinforced concrete girder bridge using non-explosive agents that rely on chemical action instead of explosive charges.
b) Recreating the original structural design of the bridge by reconstructing the decks. Calculations for construction expenses cover both the concrete deck and steel reinforcement, encompassing the steel reinforcement within the deck and the necessary attachments to secure the new cantilever to the existing piers' head.
c) Installing elastomeric bearings at the cantilever's extremity.
d) Introducing expansion joints at the girder bridge deck level to prevent thermal constraints or damage to the traffic pavement.
e) Building the road surface, incorporating layers such as surfacing layers, an asphalt bond coat, protective layers, epoxy bonding, waterproofing, and a reinforced concrete deck.
f) Installing all requisite functional amenities, including road signs, safety barriers, and others

For Scenario #2, the interventions involve:

a) Removing only the Gerber bridge sections using a controlled approach.
b) Installing a steel box deck designed to minimize overall weight. This encompasses procedures related to creating the reinforced concrete slab utilizing the predalles system.
c) Employing hot-dip galvanization on all steel surfaces of the deck to apply a passivating treatment.
d) Substituting girder deck bearings with the FPS system to prevent any slippage between the deck and its supports.
e) Introducing expansion joints at the girder bridge deck level to avert thermal impacts or harm to the traffic pavement.
f) Constructing the road surface, which includes surfacing layers, an asphalt bond coat, protective layers, epoxy bonding, waterproofing, and a reinforced concrete deck.
g) Implementing all necessary functional amenities such as road signs, safety barriers, etc.
h) Introducing an external prestressing system by adding four cables along each cantilever to reinstate the original deflection. The design considerations involve utilizing cables of the same section as those depicted in the technical drawings and introducing compression stress to prevent any cracking.

5 EFFECTS OF THE RETROFITTING MEASURES

5.1 *Costs*

The financial assessments for each scenario were conducted utilizing the price catalogs provided by ANAS (2022) from Italy, with the exception of the evaluation for the cost of the

prestressing system, where the authors adopted the parametric cost outlined in Devitofranceschi (2018). Acknowledging potential variations in price lists across countries, the analysis primarily focused on comparing diverse retrofitting scenarios, noting that within the European community, discrepancies, while existent, are not considered significant.

For comparative purposes, a specific segment of the bridge was selected, encompassing all operations within an economic framework (one pier coupled with its associated cantilevers and one Gerber beam). The projected cost estimates for each scenario were derived from this slice, simplifying the extrapolation of the comprehensive intervention expenses. Table 1 provides a comprehensive overview of each intervention to facilitate the assessment of the total cost for individual scenarios. Ultimately, the final costs for each scenario clarify the higher financial impact associated with the first one (Domaneschi et al., 2023).

Table 1. Costs for each scenario.

Scenario #1 Phase	[k€]	Scenario #2 Phase	[k€]
(a)	80	(a)	25
(b)	2000	(b)	1100
(c)	11.2	(c)	9.5
(d)	13.5	(d)	11.2
(e)	106	(e)	13.5
(f)	133	(f)	76
		(g)	53
		(h)	35

5.2 *Environmental quality*

A Life Cycle Assessment (LCA) analysis, in parallel with the prior cost analysis, has been carried out for a comparative evaluation between the two scenarios and comprehend their collective environmental potential (Domaneschi et al., 2023). The selected functional unit for comparative assessment and benchmarking is the bridge's individual surface area (km² bridge). The analysis has predominantly centered on the Global Warming Potential impact category (GWP 100ys, CML 2001 calculated in ton CO_2 eq.), utilizing environmental data developed from GENERIS® software (Fraunhofer 2023). These data stem from available product-specific information (Environmental Product Declarations, EPD) and average datasets for common construction materials (Federal Ministry for Housing, Urban Development and Building 2023). For products lacking specific environmental information, like expansion joints and bridge support systems, average datasets have been employed for initial environmental assessments. For example, both bearing systems has been modelled as a double steel plate and an elastomeric intermediate element.

It is crucial to note that in the LCA, functional amenities such as facilities, electrical and drainage systems, as well as safety barriers, have been intentionally omitted from the analysis.

Table 2. Environmental impact for each scenario.

Scenario #1 Phase	[ton CO_2 eq]	Scenario #2 Phase	[ton CO_2 eq]
(a)	171	(a)	54
(b)	165	(b)	189
(c)	30	(c)	3.8
(d)	385	(d)	30
(e)	23	(e)	385
(f)	out of scope	(f)	26
		(g)	out of scope
		(h)	out of scope
Total	778	Total	690
Ton CO_2 eq./km²	0.6	Ton CO_2 eq./km²	0.5

These elements have been deemed beyond the scope, as the primary focus was exclusively on the restoration scenarios themselves.

Parallel to the cost analysis, GWP calculations are tabulated and consolidated within interventions in Table 2. The ultimate environmental impact for each scenario emphasizes a reasonable similarity between them (Domaneschi et al., 2023).

6 RESILIENCE ASSESSMENT

6.1 *Transit capability*

This section discusses the functionality curves of the system for both retrofitting scenarios under consideration. While interventions encompass the entire viaduct, the primary focus of this work is on analyzing the three main piers from #22 to #24, which feature the largest spans consisting of cantilevers connected by Gerber beams. Expert bridge engineering specialists, involved in designing, executing, reinforcing, and rehabilitating similar bridge structures have been consulted to establish reasonable and realistic parameters for plotting functionality curves for each intervention type.

The initial phases, such as selecting the intervention designer, assessing technical-economic feasibility, finalizing executive designs, and administration, are estimated to take 6-8 months before the bridge closes for interventions. Safety concerns identified in inspections starting in 2020 have led to traffic limitations and reduced load intensity. This includes traffic restrictions, lowering vehicle weight limits to 500 kN and speed limits to 40 km/h.

Both scenarios aim to utilize existing piers and related foundational structures. Additionally, both scenarios account for the bridge's closure due to its single-carriageway design, preventing reconstruction partitioning.

Figure 2 illustrates the functionality curves for the proposed solutions, starting at time 0 when either the whole deck or Gerber beams only are demolished, resulting in a complete bridge closure. In Scenario #1, demolition using explosives is estimated to take around 10 days, while for Scenario #2, controlled demolition of the Gerber beams will take approximately 20 days.

For the solution involving deck replacement or a portion of it, it is assumed that before demolition starts, the replacement structure is prepared nearby for swift replacement. Specifically, installing the new deck is estimated to take 3 months for Solution #1. Scenario #2, involving new Gerber beams and external prestressing cables for the cantilevers, is estimated to take 5 months.

Upon construction completion, the estimated timeline for testing, processing (technical-administrative approval), and full bridge reopening is set at 90 days. Post this period, it is assumed that the bridge's transit capability will be restored to 100%. Resilience values for the different scenarios considering a maximum closure period of 360 days are tabulated in Table 3.

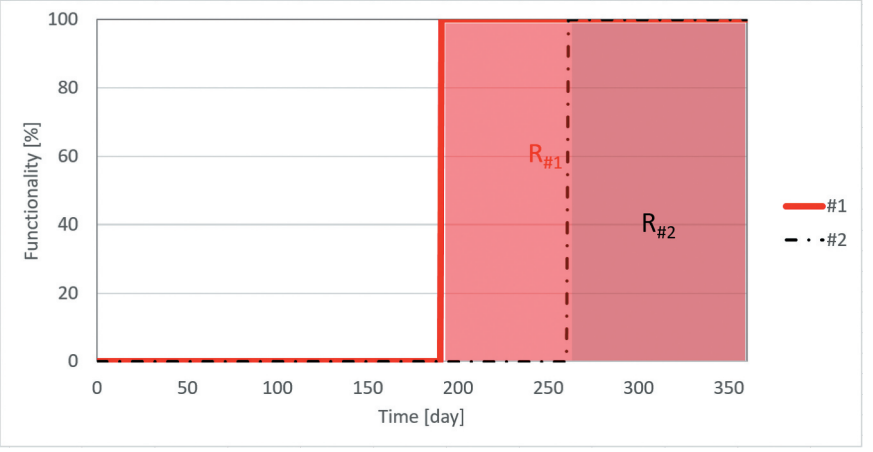


Figure 2. Functionality curves and resilience (transitability).

Table 3. Resilience values computed through transit capability.

Scenario	#1	#2
Resilience	0.47	0.28

6.2 *Capacity*

It is interesting to analyze the problem of assumed interventions by considering structural capacity and its restoration instead of transit capability. Consequently, for capacity analysis, purely administrative aspects are neglected. Obviously, it is necessary to introduce some assumptions, for example, it is assumed the linear pattern of the recovery curves, which in real conditions are associated with high uncertainty, including pauses, accelerations, and so on.

Shows the trends of the capacity curves for the various assumed scenarios, while Table 4 reports the resilience values computed concerning capacity.

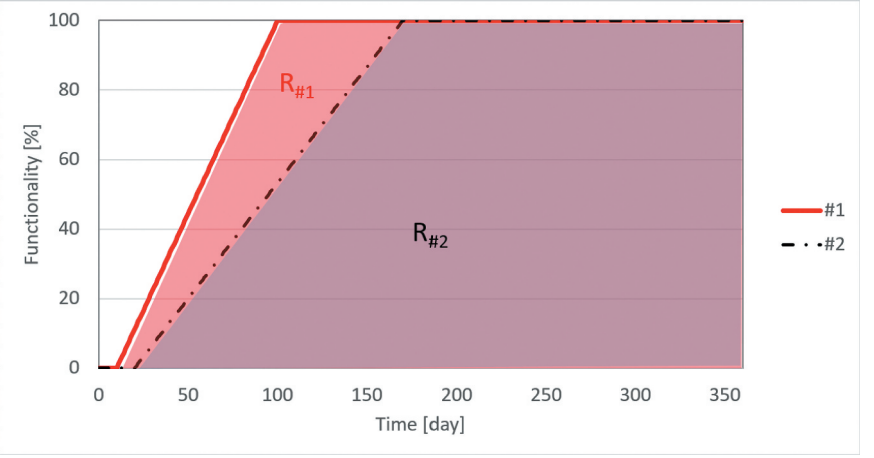


Figure 3. Functionality curves and resilience (capacity).

Table 4. Resilience values computed through capacity.

Scenario	#1	#2
Resilience	0.85	0.73

7 CONCLUSIVE REMARKS

This investigation assesses retrofit for the deteriorating Polyfytos Bridge using advanced surveying tools. A couple of different interventions are evaluated in terms of cost, sustainability, and resilience, aiming for a comprehensive (holistic) retrofit approach. Initial findings highlight cost disparities and interesting differences in resilience when transit capability is considered among interventions. On the other hand, the environmental impact, and the resilience values in terms of capacity results are reasonably equivalent.

Differences in resilience calculations, whether focused on transit capability instead of capacity, indicate how bureaucratic and administrative components might impact the process and, consequently, resilience by extending downtime. This underscores the significance of administrative efficiency in mitigating delays during retrofitting or maintenance processes for bridges. Streamlining bureaucratic procedures and administrative tasks can significantly minimize the downtime experienced during these critical infrastructure projects. Efficient

administrative processes contribute to shorter project timelines, reducing disruptions to the bridge's functionality and overall resilience of transport infrastructure.

ACKNOWLEDGEMENTS

The research has received funding from the (i) ERC Grant ID: 101007595 of the project ADDOPTML, MSCA RISE 2020; (ii) EU HORIZON-MSCA-2021-SE-01 Grant No: 101086413, ReCharged. Stergios Mitoulis and Sotirios Argyroudis received funding from the UK Research and Innovation (UKRI) under the Horizon Europe funding guarantee (agreements No. EP/Y003586/1, EP/X037665/1), for the project 'ReCharged - Climate-aware Resilience for Sustainable Critical and interdependent Infrastructure Systems enhanced by emerging Digital Technologies' (Grant No: 101086413). Dr. Andrea Benincasa - Nemesis Engineering (Turin, Italy) is gratefully acknowledged for his support in the assessment of the intervention phases for the resilience curves computation.

REFERENCES

ANAS S.p.A. 2022. Price list for New Construction and scheduled maintenance (in Italian). https://www.stradeanas.it/it/elenco-prezzi

Bartolozzi, M., Casas, J.R., Domaneschi, M. 2022. Bond deterioration effects on corroded RC bridge pier in seismic zone. *Structural Concrete* 23(1), 51–66.

Bažant, Z.P., Chern, J.C. 1984. Bayesian statistical prediction of concrete creep and shrinkage. *ACI Journal* 81(4), 319–330.

Bažant, Z.P., Panula, L. 1980. Creep Shrinkage Characterization for Prestressed Concrete Structures. *J. of the Prestressed Concrete Institute* 25, 86–122.

Bažant, Z.P., Kim, J.K. 1991. Improved prediction model for time-dependent deformations of concrete: Part 2 - basic creep. *Mater. Struct*. 24 (6).

Bažant, Z.P., Jirásek, M. 2018. Creep and Hygrothermal Effects in Concrete Structures. *Solid Mechanics and its Applications* 225. Springer, Dordrecht.

Concrete Bridge Development Group 2017. Development of prestressed concrete bridges. https://www.cbdg.org.uk/

Devitofranceschi, A. 2018. Repair of prestressed road viaducts: intervention techniques and cost-benefit analysis (in Italian). *Italian Concrete Days-AICAP*.

Domaneschi, M., De Gaetano, A., Casas, J.R., Cimellaro, G.P. 2020a. Deteriorated seismic capacity assessment of reinforced concrete bridge piers in corrosive environment. *Structural Concrete* 21, 1823–1838.

Domaneschi, M., Pellecchia, C., De Iuliis, E., Cimellaro, G.P., Morgese, M., Khalil, A.A., Ansari, F. 2020b. Collapse analysis of the Polcevera Viaduct by the Applied Element Method. *Engineering Structures* 214, 110659.

Domaneschi M., Mitoulis S.A., Cucuzza R., Villa V., Di Bari R., Siva G. 2023. RESTORATION OF A LANDMARK BALANCED CANTILEVER BRIDGE CONSIDERING DIFFERENT RESILIENCE AND SUSTAINABILITY STRATEGIES. *COMPDYN Proceedings*. EDS: Papadrakakis M., Fragiadakis M. PUBLISHER: National Technical University of Athens.

Federal Ministry for Housing 2023. Urban Development and Building. ÖKOBAUDAT. https://oekobaudat.de/

Fraunhofer 2023. IBP GENERIS®. www.generis-solution.eu

Guo, T., Sause, R., Frangopol, D., Li, A. 2011. Time-Dependent Reliability of PSC Box-Girder Bridge Considering Creep, Shrinkage, and Corrosion. *J. Bridge Eng*. 16(1), 29–43.

Hartt, W.H., Venugopalan, S. 2002. Corrosion evaluation of post-tensioned tendons on the Mid Bay Bridge in Destin, Florida. Florida Department of Transportation Research Center. Report 33890.

Li, S., Wang, W., Lu, B., Du, X., Dong, M., Zhang, T., Bai, Z. 2023. Long-term structural health monitoring for bridge based on back propagation neural network and long and short-term memory. *Structural Health Monitoring* 22(4), 2325–2345.

Lõhmus, H., Ellmann, A., Märdla, S., Idnurm, S. 2018. Terrestrial laser scanning for the monitoring of bridge load tests – two case studies. *Survey Review* 50:360, 270–284.

Lu, N., Beer, M., Noori, M., Liu, Y. 2017. Lifetime Deflections of Long-Span Bridges under Dynamic and Growing Traffic Loads. *J. Bridge Eng*. 22(11), 04017086.

Lucko, G., de la Garza, J.M. 2003. Constructability Considerations for Balanced Cantilever Construction. *Pract. Period. Struct. Des. Constr*. 8(1), 47–56.
Markogiannaki, O., Hang, X., Chen, F., Mitoulis, S., Parcharidis, I. 2022. Monitoring of a landmark bridge using SAR interferometry coupled with engineering data and forensics. *International Journal of Remote Sensing* 43, 95–119.
Morgese, M., Ansari, F., Domaneschi, M., Cimellaro, G.P. 2020. Post-collapse analysis of Morandi's Polcevera viaduct in Genoa Italy. *Journal of Civil Structural Health Monitoring* 10, 69–85.
Podolny, W. 1992. Corrosion of prestressing steels and its mitigation. *PCI journal* 37(5), 34–55.
Varbla, S., Artu, E., Raido, P. 2021. Centimetre-range deformations of built environment revealed by drone-based photogrammetry. *Automation in Construction* 128, 103787.
Wang, S., Fu, C.C. 2015. Simplification of Creep and Shrinkage Analysis of Segmental Bridges. *J. Bridge Eng*. 20(8), B6014001.
Witcher, T.R. 2017. From disaster to prevention: The silver bridge. *Civil Engineering Magazine Archive* 87(11), 44–47.
Zhou, J., Sun, Z., Wei, B., Zhang, L., Zeng, P. 2021. Deflection-based multilevel structural condition assessment of long-span prestressed concrete girder bridges using a connected pipe system. *Measurement* 169, 108352.

Bridge Maintenance, Safety, Management, Digitalization and Sustainability – Jensen, Frangopol & Schmidt (eds)
© 2024 The Author(s), ISBN 978-1-032-77040-6
Open Access: www.taylorfrancis.com, CC BY-NC-ND 4.0 license

Deterioration rate diagnosis to global climatic change: The case of Dnipro Dam in Ukraine

N.S. Kopiika & J. Ninic
University of Birmingham, Birmingham, UK

R. Cucuzza
Politecnico di Torino, Turin, Italy

S.A. Mitoulis
University of Birmingham, Birmingham, UK

ABSTRACT: Global climate change and increase of CO_2 emissions have dramatically influenced the deterioration processes in concrete structures worldwide. Thus, increased rate of carbonisation-induced corrosion for long-operated concrete structures has become one of the most critical durability issues in recent years. Although significant research has been conducted on the development of comprehensive approaches for evaluating the carbonisation effect on remaining resource, the application of existing models to particular case studies and bridging the gap between theory and practice is still underexplored, which is the main motivation for this study. Existing carbonisation-induced numerical models are investigated and applied to this case study. Results demonstrate the criticality of structural deterioration in conditions of global climatic change and this highlights the need to account for environmental changes in design and practice.

1 INTRODUCTION

In recent decades, an alarming change of climate was witnessed, the most important signs of which are relentless temperature increase and enhanced carbon dioxide emissions. According to Mauna Loa Observatory (MLO) measurements, the atmospheric CO_2 emissions increased by 100 ppm during last 60 years, which induced an increase in global air temperature by about 1° during last century (Bastidas-Arteaga et al, 2022; Talukdar et al, 2012). Recent patterns in climate change, including temperature and pollutant concentrations increment, changes in relative humidity and precipitation are widely recognized as one of the most pressing global challenges of our time. The consequences of these intertwined phenomena extend far beyond mere scientific curiosity; they encompass a complex web of ecological, economic, and societal ramifications. Within the scope of various influences, the phenomenon of global warming, characterized by an elevated CO_2 concentration, and the subsequent changes in temperature and relative humidity under specific circumstances, have the potential to expedite carbonation-induced corrosion. This, in turn, has the capacity to exert an impact on the longevity and operational capability of reinforced concrete (RC) structures (Saura-Gómez, et al, 2022; Coronelli, 2007; Anand et al, 2021; Lahdensivu et al, 2019). Given the predominant role of RC as construction type used in infrastructural assets and substantial direct and indirect expenses associated with their corrosion, even a minor acceleration of the corrosion process due to climate change can lead to substantial annual rises in maintenance and repair costs (Stewart et al, 2012). Considering that decreasing service life s in the context of a changing climate is among the most important research issues of interest, the development of approach to assess the level of deterioration of RC assets has reached its topicality during recent decades

DOI: 10.1201/9781003483755-310

(Ekolu, 2020; Inam et al, 2021). Most of existing studies in the literature provide the description of carbonization models, considering various influential factors. However, there is still insignificant amount of research, which would provide comprehensive illustration of application of such models on particular case studies- e.g. RC assets. Such demonstrative case study would provide valuable representation of the critical impact of structural deterioration in conditions of global climatic change and emphasize necessity to account environmental trends in design practice.

2 CLIMATE CHANGE AND CARBONATION-INDUCED CORROSION MODEL

Climate changes, reflected in various environmental factors (CO_2 concentration, temperature, humidity) have considerable impact on rate of deterioration especially in urban areas. In particular, corrosion damages in RC massive structures, operated during long time is a common problem for efficient exploitation of infrastructural systems. Initiation and propagation of corrosion damages, thus, could differ depending on structural type, loading schemes and aggressive environment, but in most cases include common stages: corrosion initiation, crack initiation and crack propagation. In this work damage due to carbonation induced corrosion will be considered, as one of the most common reasons of aged RC structures deterioration or even failure (Saura-Gómez, et al, 2022; Coronelli, 2007; Anand et al, 2021; Lahdensivu et al, 2019).

The point of carbonation -induced corrosion initiation (T_{init}) could be considered as the time when the carbonation depth reaches the surface of the rebar. Models for evaluation of carbonation depth, presented in the literature are based on Fick`s 1st low, and, according to Yoon et al. (2007) could be described by following Equation 1:

$$X_C = \sqrt{\frac{2D_{CO_2}}{\alpha} C_{CO_2} t} \tag{1}$$

where X_c = carbonation depth; C_{CO2} =atmospheric CO_2 concentration; D_{CO2} =CO_2 diffusion coefficient concentration. Further modification of this model was assumed by Stewart et al (2010) and Peng & Stewart (2014), by considering the time (t) dependent change in diffusion coefficient due to temperature ($f_T(t)$) and humidity ($f_{RH}(t)$) changes, as well as increased CO_2 levels in urban environment (k_{urb}), which could be expressed by Equations 2-3:

$$X_C(t) \approx \sqrt{\frac{2f_T(t)f_{RH}(t)D_{CO_2}(t)}{\alpha} k_{urb} \int_{to}^{t} C_{CO_2}(t)dt \left(\frac{1}{t-t_0}\right)^{n_m}} \tag{2}$$

$$D_{CO_2}(t) = D_1(t-t_0)^{-n_d} \tag{3}$$

where D_1 =diffusion coefficient after one year of operation of structure, which is assumed to increase in rate of age factor n_d; t_0 =time of beginning of exploitation; n_m = age factor for microclimatic conditions; k_{urb} =urban environment factor.

Increase of diffusion rate at high temperatures could be described according to Arrhenius Law:

$$f_T(t) = \exp\left(\frac{E}{R}\left(\frac{1}{293} - \frac{1}{273+T(t)}\right)\right) \tag{4}$$

In which the reference temperature of 20°C is considered; E= activation energy of the diffusion process; R =gas constant; $T(t)$=temperature change within the time (t) range.

According to Model Code for Service Life Design (fib, 2006), the impact of humidity changes ($RH(t)$) on the carbonation rate is taken into account by Equation 5:

$$f_{RH}(t) = \begin{cases} 0 & RH(t) \le 25\% \\ \left[\frac{1-(RH(t)/100)^{fe}}{1-(RH_{ref}/100)^{fe}}\right]^{g_e} & RH(t) > 25\% \end{cases} \tag{5}$$

where RH_{ref}= the reference humidity value (which in most cases is 65%); f_e and g_e=constant coefficients, equal to 5 and 2.5, respectively. Equation (5) reflects general trends of increase of diffusion rate up to RH=65%, while 100% humidity corresponds to f_{RH}=0. It is considered, the if RH is lower than the bottom level (25 %) carbonation would not begin due to small amount of water.

The degree of hydration (α) can be defined via Equation 6:

$$\alpha = 0.75 C_e C_{CaO} \alpha_H \frac{M_{CO_2}}{M_{CaO}} \tag{6}$$

where C_e=cement content; C_{CaO}=content of CaO in Portland cement; M_{CaO} and M_{CO2}= molar mass of CaO and CO_2, respectively; α_H= degree of hydration after more than 400 days, depending on water-cement ratio of concrete (w/c):

$$\alpha_H = 1 - e^{-3.38 w/c} \tag{7}$$

It could be assumed, that the stage of 1st crack initiation corresponds to time, when the 1st crack of 0.05 mm width is formed (T_{1st}), which is further followed by crack propagation and development, until the limit crack width is reached. (Stewart et al (2010))

Thus, further propagation of crack could be defined with the use of following model, which is obtained by reformulation of Stewart et al (2010):

$$\omega = \frac{i_{corr_20}(T - T_{init}) k_c ME(r_{crack}) r_{crack}}{0.0114 k_R} \tag{8}$$

where i_{corr_20}=corrosion current density at reference temperature (T_{ref}=20°C); ME(r_{crack})=error of the model, used for evaluation of crack propagation, which considers variabilities between model prediction and experimental data (assumed values of mean and COV are 1.04 and 0.09, respectively (Stewart et al (2010)). Also, ω=crack width; k_c=confinement factor, which is important for rebars, allocated at edges of RC structures, due to increased rate of crack growth at zones with insufficient concrete confinement. Other parameters in model are defined by Equations 9-11.

$$\psi_{cp} = \frac{Cov}{\varnothing f_t} \in [0.1 \ldots 1] \tag{9}$$

$$r_{crack} = 0.0008 e^{-1.7 \psi_{cp}} \tag{10}$$

$$k_r \approx 0.95 \left[\exp\left(-\frac{0.3 i_{corr(\exp)}}{i_{corr_20}} \right) - \frac{i_{corr(\exp)}}{2500 i_{corr_20}} + 0.3 \right] \tag{11}$$

where f_t=tensile strength of the concrete; $\varnothing$=diameter of the rebar; Cov=cover of concrete; r_{crack}=the rate of crack development, which is exponentially dependent on depends on the Cov, f_t, $\varnothing$. In order to consider accelerated corrosion rate ($i_{corr_20(exp)}$), required for enhancing crack development rate, loading rate correction factor k_r is introduced.

Equations listed above can be used for description of crack propagation within the time frame for RC structures, subjected to carbonation-induced corrosion. In particular the stage of corrosion damage (T_{sp}) corresponds to time when cracks in concrete cover reach the limit width (w_{lim} =1 mm). After the limit width of crack is reached, the corrosion of rebar is initiated, resulting in loss of steel bar cross-section, which, according to Stewart et al (2010) can be defined as:

$$\Delta\varnothing(t) = 2 \cdot 0.0116 \int_{T_{sp}}^{t} i_{corr}(t) dt \tag{12}$$

where temperature-dependent corrosion rate ($i_{corr}(t)$) is defined by equation, which is close correlation to Arrhenius equation:

$$i_{corr}(t) = i_{corr_20}[1 + K(T(t) - 20)] \tag{13}$$

Additionally, it is important to consider the effect of corrosion processes on material behavior. Cracking and spalling in the compressed concrete lead to more brittle behavior. Thus, enhanced transverse strains and longitudinal microcracking cause reduction of the compressive concrete, which is, according to model of Vecchio & Collins (1986) can be defined by (Coronelli & Gambarova (2004)):

$$f'_c = \frac{f_c}{1 + K\varepsilon_1/\varepsilon_{co}} \tag{14}$$

where ε_{co} =strain at the peak compressive stress f_c; ε_1 =average tensile strain:

$$\varepsilon_1 = \frac{n_{bars}\omega_{cr}}{b_o} \tag{15}$$

where b_0= initial width of the concrete cross-section; n_{bars}=number of bars in concrete cover; ω_{cr}=total crack width for a given corrosion level X_c:

$$\omega_{cr} = 2\pi(\upsilon_{rs} - 1)X_c \tag{16}$$

where ν_{rs}=ratio of volumetric expansion of the oxides.

The general scheme for the time margins of each stage of corrosion degradation, according to utilized carbonation model is given in Figure 1.

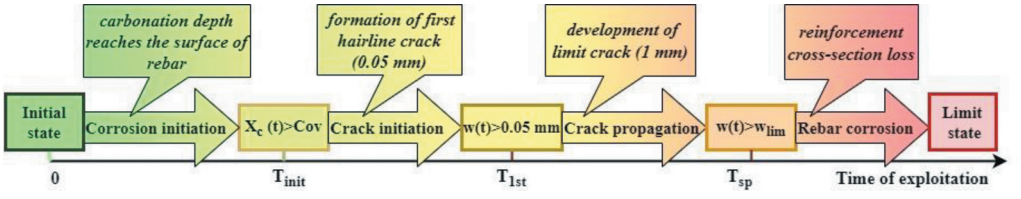


Figure 1. Main stages of degradation model.

3 CASE STUDY: RESULTS AND DISCUSSION

3.1 *Description of the case study -Dnipro HPP Dam-Bridge complex*

The Dnipro Hydroelectric Station (Dnipro HPPS) is the largest hydroelectric power station on the Dnipro River (Ukraine) and one of the most important network nodes, serving for both electric power provision for the most important industrial regions of country and enabling connection between two banks and communication within the country. As the part of transport infrastructure of Ukraine, the bridge of Dnipro HPP complex enables connection of the most important geopolitical centers and districts of the country, efficient operation of transport and logistic routes.

The Dnipro HPP consists of 49 supports that are connected from above by a monolithic reinforced concrete overpass. Its length is 760 meters, and its height is 60 meters (see Figure 2).

Dnipro HPPs complex is the oldest hydro-power station in the territory of Ukraine, which is the reason of increasing attention to its technical state and reliable operation regime. Its construction commenced in 1927, with the first hydro-unit being put into operation in 1932, while the design capacity of 560 MW was reached in 1939. Considering such long-term of operation of the

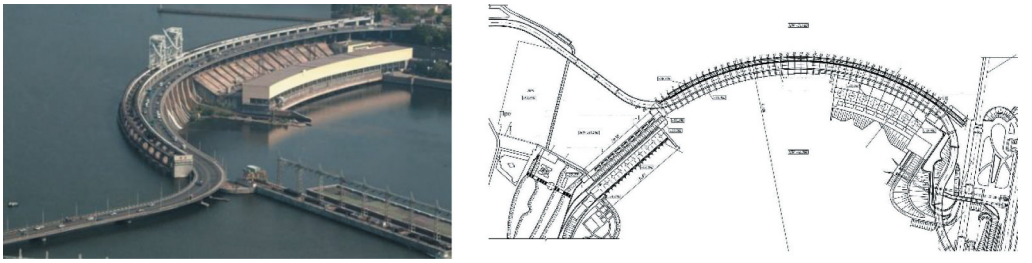


Figure 2. General view of the case study (Dnipro HPPS, Zaporizha, Ukraine).

structure in aggressive environment it is obvious, that its technical state and remaining resource requires specific attention: remote monitoring of deformations and structural state, on-site inspections of signs of deterioration, tracking damages growth. The HPP complex, in particular its bridge part is subjected to ageing, physical wear, intensive impact of humidity, etc. The strengthening measures, introduced during the last years enabled to slow down the process of destruction of structures. However, as was stated by Head of Ukrhydroenergo, based on trends of worsening of damages, the risk of destruction of the damn is increasingly reaching the emergency level (Press Service of Dnipro HPP in Politeks; Forpost). However, the ongoing military situation in Ukraine makes it impossible to conduct reconstruction works on this structure. Thus, the assessment of remaining capacity and corrosion-induced deterioration level is of prevalent importance.

3.2 *Climate changes in Ukraine and globally: Anthropological impacts*

Ukraine, as many other parts of the world has faced considerable climate changes during recent decades, which has become a growing concern, raising the public attention to necessity of adaptation measures and more precise assessment of structural deterioration parameters. In particular, a consistent increase in temperatures has been recorded, which is especially urgent for urban areas due to urban heat island effect (which is relevant for the case study in this research). Thus, according to the information of World Bank Group, temperature patterns for the examined period of time (period of exploitation of the case study, - 1932-2023) reveal the rise of annual mean average temperature by approximately 1.7 °C, while the August temperature anomalies show the increase by 2.54 °C per decade, according to NOAA National Centers for Environmental information (see Figure 3, a).

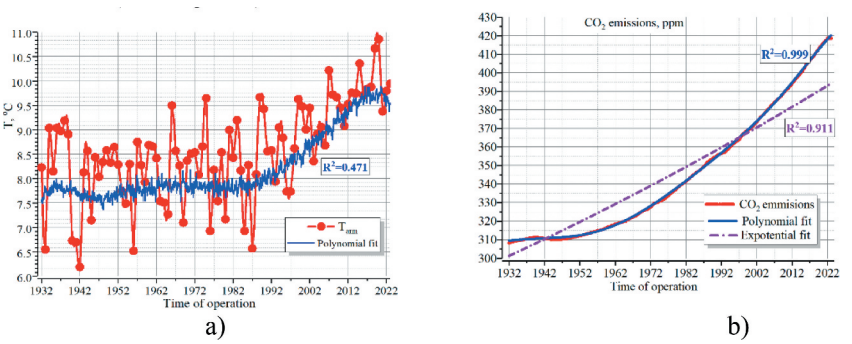


Figure 3. Patterns of climate changes in Ukraine for studied period of time (in the area of interest-Zaporizha, Ukraine): a) annual mean average temperature; b) The increase of CO_2 concentration.

The increase of CO_2 emissions and the rise in temperature are closely interlinked aspects of climate change, as increased levels of CO_2 in the atmosphere enhance the greenhouse effect, leading to a gradual rise in global temperatures. This issue has reached its topicality during recent years, as the concentration of CO_2 has ben steadily increasing after during last century

(see Figure 3, b) up to warning level, resulting in more frequent and severe heatwaves, changing precipitation patterns, and a rise in sea levels, among other effects.

3.3 *Assessment of deterioration due to carbonation induced corrosion*

Carbonation induced corrosion damage has critical impact on RC structures, subjected to long-term operation in aggressive environments, which is demonstrated with the use of case study. Deterioration model described above was used for assessment of level of corrosion damage to Dnipro HPP complex (Zaporizha, Ukraine). Values of initial parameters, used for the case study with reference sources are given in Table 1.

Table 1. Initial parameters for assessment of damage level of case study.

Parameter	Value	Units	Parameter	Value	Units	Reference
Structural parameters of the case study						
w/c	0.62	-	C_e	265	kg/m^3	Nilender (1937)
Cov	20	mm	Ø	25	mm	Nilender (1937)
f_t	2.46	MPa	f_c	21.57	MPa	Nilender (1937)
n_{bars}/b_o	5×10^{-2}	num/mm width	ε_{co}	1.6×10^{-3}	-	Nilender (1937)
$C_{CO2}(t)$	f(t)	ppm				SeaLevel.info
T(t)	f(t)	°C				climateknowledgeportal.worldbank.org
RH(t)	f(t)	%				power.larc.nasa.gov
Parameters of carbonation -induced corrosion model						
D_1	6×10^{-4}	cm^2/s	n_d	0.246	-	Peng & Stewart, 2016
n_m	0.12	-	k_{site}	1.140	-	Stewart et al, 2010
k_{urb}	1	-	$ME(r_{crack})$	1.04	-	Peng & Stewart, 2016
k_c	1.3	-	$i_{corr\text{-}20}$ ($i_{corr\text{-}exp}$)	2.586 (100)	$\mu A/cm^2$	Peng & Stewart, 2016
g_e	5	-	f_e	2.5	-	fib (2006)
E	40	kJ/mol	R	8.314	kJ/molK	
CaO		0.65				
M_{CO2}	44	g/mol	M_{CaO}	56	g/mol	
ν_{rs}	2	-	K	0.1	-	Coronelli & Gambarova (2004)
T_{ref}	20	°C	RH_{ref}	0.65	%	Peng & Stewart, 2016

Parameters and coefficients of empirical model of corrosion propagation were taken from the studied literature (see Section 2). In order to consider structural parameters of the particular case study, archive materials of experimental testing of the concrete samples from Dnipro HPP in 1930 were thoroughly studied.

Thus, with the use of equations and assumptions, described in previous section, the corrosion initiation and propagation in the particular case study was assessed and its effect on remaining capacity was evaluated.

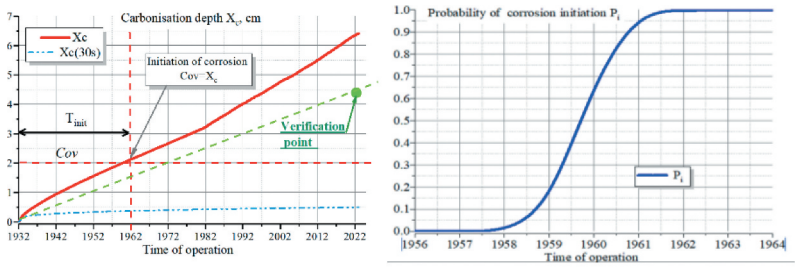
The cumulative probability of corrosion initiation (*Pi*) at time *t* is defined regarding the rapidity of carbonization depth propagation, defined by Equation (2):

$$P_i(t) = \Pr[Cov - X_c(t) < 0] \tag{17}$$

It is assumed, that the corrosion damage of reinforcement is initiated after the time when concrete cover severely cracks with limit width and its cumulative probability (P_s) at time *t* is:

$$P_s(t) = \Pr\left[t > T_{sp}\right] \tag{18}$$

It is important to emphasize, that the construction of this asset was performed with accordance to design regulations of early 1930s`, which do not meet the requirements of nowadays in terms of both sustainability, transport capability and resilience. In addition, design practices of that time did not consider climate changes and cumulative effect of carbonization induced corrosion. This becomes obvious from the values of concrete cover (20 mm), which does not ensure requirements of sufficient protection of rebar from corrosion (see Figure 4).

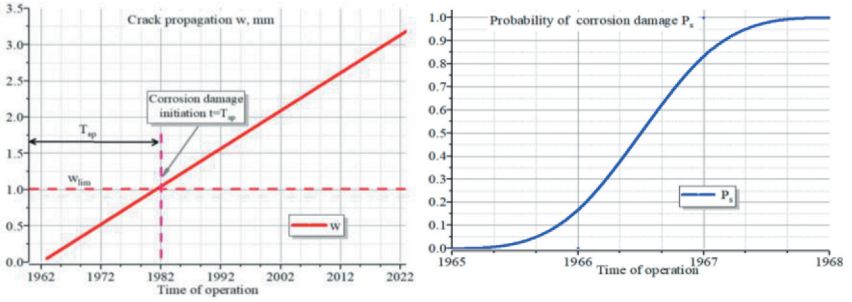


a) b)

Figure 4. Results of assessment of corrosion initiation stage for the case study: a) carbonization depth; b) probability of carbonization induced corrosion initiation.

Considering the results, illustrated in Figure 4, it can be assumed, that the corrosion initiation point was reached after 20 years of operation of structure (1932-1950), which was further followed by crack initiation stage, the indicator of which is formation of 0.05 mm hairline crack. Graph $X_c(30s`)$ on Figure 4 demonstrates the results of similar calculations (Equation 2), if climate effects are neglected, which reveals underestimation of deterioration impact on structural safety.

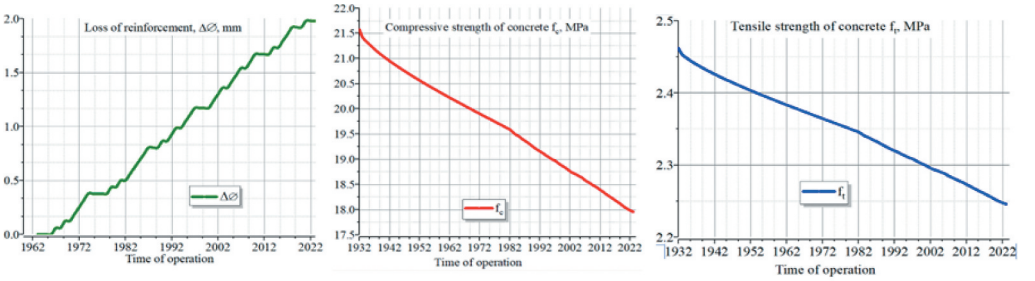
Application of crack propagation model to the Dam-Bridge structure has shown, that after the crack initiation (about 30 years of operation, -1932-1963), cracking width was increasing at enhanced rates and reached the limit value of 1 mm, evoking the beginning of corrosion damage to reinforcement (see Figure 5). Time-dependent corrosion loss or diameter of rebar according to Equation (12) follows the linear trend and for studied concrete structure could reach the value of about ΔØ=2 mm (see Figure 6,a). Finally, the approach for assessment of corrosion-induced strength decrease of concrete in long-term operated structures was applied to Dnipro HPP complex and results are demonstrated by Figure 6, b-c.



a) b)

Figure 5. Results of assessment of crack propagation and corresponding probability of corrosion damage for the case study: a) crack development; b) probability of initiation of corrosion damage.

Results, obtained with the use of proposed empirical model in general correspond to on-site observations, described in several technical reports (Onyshchenko, et al, (2021)). In particular,



a) b) c)

Figure 6. Time dependent degradation factors in corroded RC structure (case study): a)the rate of corrosion loss of the rebar diameter in the case study; b) decrease of concrete compressive strength; b) decrease of concrete tensile strength.

worsened condition of structural components was observed during visual and instrumental inspection by Galat, et al (2022), which manifested itself in increased number of cracks, areas of corrosion of concrete and reinforcement in comparison with previous inspections (2008, 2017 2021). Carbonation depth, assessed with the use of chemical reaction between phenolphthalein and the alkaline environment of concrete, reached the values up to 45 mm (Galat, et al (2022)), which is slightly lower than assumptions from empirical model (see verification point on Figure 4). Similarly, crack widths, measured during inspections were 1- 20 mm, thus the calculated values are within the range. However, although the assumptions of empirical model us this study overestimate the rate of corrosion propagation, it could still provide reliable qualitive supposition. Similar observations were reported in reports of governmental authorities, published in social media (Politeks; Forpost). Further adaptation and refinement of empirical model could be performed with the use of laboratory tests on concrete samples with particular concrete properties and particular conditions (Blikharskyy et al, 2021).

4 CONCLUSIONS

This paper employed a time-dependent analysis for interpreting the deterioration processes in RC structures due to carbonization-induced corrosion, which is becoming critical due to exacerbated environmental conditions as a result of climate change and increasing CO_2 in the atmosphere. Empirical models for the assessment of carbonisation-induced corrosion are introduced and applied to a real case study of an important asset of transport infrastructure in Ukraine. Results revealed the paramount role of climate changes and increased CO_2 emissions, witnessed recent decades, on rate of ageing and decrease of service life of RC structures, which is an important factor worldwide. To attain the desired service life for concrete structures it is essential to account for the environmental stressors in design practice, incorporating appropriate concrete cover with a margin of safety to mitigate the risk of carbonation-induced corrosion. Simultaneously, a more methodical approach, involving the analysis of concrete structures in real-world conditions across different environments, is necessary to address this matter effectively.

ACKNOWLEDGEMENTS

Authors would like to acknowledge of support received from the British Academy for this research (Award Reference: RaR\100770) and funding by the UK Research and Innovation (UKRI) under the UK government's Horizon Europe funding guarantee [grant agreement No: 10062091]. This is the funding guarantee for the European Union HORIZONMISS-2021-CLIMA-02 [grant agreement No: 101093939] RISKADAPT - Asset-level modelling of risks in the face of climate-induced extreme events and adaptation.

REFERENCES

Anand, N., Andrushia, D., Paul, D., & Arulraj, P. (2021). Condition assessment and analysis of a reinforced concrete building in India: a case study. Proceedings of the Institution of Civil Engineers-Forensic Engineering, 174(4), 89–104.

Atmospheric Carbon Dioxide (CO2) levels, 1800–present. Available at: https://www.sealevel.info/co2.html (open source, last assessed 30.10.2023)

Bastidas-Arteaga, E., Rianna, G., Gervasio, H., & Nogal, M. 2022. Multi-region lifetime assessment of reinforced concrete structures subjected to carbonation and climate change. *Structures*, 45, 886–899.

Blikharskyy, Y., Selejdak, J., Kopiika, N., & Vashkevych, R. (2021). Study of concrete under combined action of aggressive environment and long-term loading. Materials, 14(21), 6612.

Coronelli, D. (2007). Condition rating of RC structures: a case study. J Build Apprais 3 (1): 29–51.

Coronelli, D., & Gambarova, P. 2004. Structural assessment of corroded reinforced concrete beams: modeling guidelines. *Journal of structural engineering*, 130(8), 1214–1224.

Ekolu, S. O. 2020. Implications of global CO_2 emissions on natural carbonation and service lifespan of concrete infrastructures–reliability analysis. *Cement and Concrete Composites*, 114, 103744.

fib (Fe´de´ ration internationale du be´ ton) (2006) Model Code for Service Life Design. fib, Lausanne, Switzerland, Bulletin 34.

Forpost: The Dnipro HPP dam is collapsing due to the constant traffic of large-sized vehicles Available at: http://surl.li/nmskm (open source, last assessed 30.10.2023)

Galat, V. V., Slyusarenko, Y. S., Dombrovskyi, Y., Shuminskii, V., Mykolaiets, M., & Krylov, Y. (2022). Assessment of the technical condition of the structures of the spillway dam of the Dnipro HPP. Science and construction, 31(1), 13–23

Inam, I., Nasiry, M. K., Sediqmal, M., Wahdat, M. N., & Momand, I. 2021. A Study on the Carbonation Rate of Concrete Exposed in Different Climatic Conditions. *Australian Journal of Engineering and Innovative Technology*, 3(6), 128–136.

Lahdensivu, J., Lahdensivu, E., & Köliö, A. (2019). Case Study on the 20 Years Propagation of Carbonation in Existing Concrete Facades and Balconies. Nordic Concrete Research, 60(1), 1–12.

Nilender, Yu. A. 1937. Testing of Dnipro HPP. Moscow: Main editor of construction literature.

NOAA National Centers for Environmental information, Climate at a Glance: Global Time Series, published October 2023. Available at: https://www.ncei.noaa.gov/access/monitoring/climate-at-a-glance/global/time-series (open source, last assessed 30.10.2023)

Onyshchenko, A. M., Kovalchuk, V.V., Gibalenko, O. M., et al. 2021. Ensuring operating reliability of the bridge crossing of the Dnipro HPP drives. Bulletin of the NUVHP. Technical sciences, 4(96). 26–38

Peng, L., & Stewart, M. G. 2014. Spatial time-dependent reliability analysis of corrosion damage to RC structures with climate change. *Magazine of Concrete Research*, 66(22), 1154–1169.

Peng, L., & Stewart, M. G. 2016. Climate change and corrosion damage risks for reinforced concrete infrastructure in China. *Structure and Infrastructure Engineering*, 12(4), 499–516.

Politeka: Repairs will be delayed: a crack dating back to the USSR was discovered on the DniproHPP dam. Available at: http://surl.li/nmskg (open source, last assessed 28.10.2023)

Saura-Gómez, P., Rizo-Maestre, C., & Echarri-Iribarren, V. (2022). The Useful Life of Reinforced Concrete Structures with Reinforcement Corrosion Due to Carbonation in Non-Aggressive and Normal Exposures in the Spanish Mediterranean. Materials, 15(3), 745.

Stewart, M. G., Wang, X., & Nguyen, M. N. 2011. Climate change impact and risks of concrete infrastructure deterioration. *Engineering Structures*, 33(4), 1326–1337.

Stewart, M. G., Wang, X., & Nguyen, M. N. 2012. Climate change adaptation for corrosion control of concrete infrastructure. *Structural Safety*, 35, 29–39.

Talukdar, S., Banthia, N., & Grace, J. R. 2012. Carbonation in concrete infrastructure in the context of global climate change–Part 1: Experimental results and model development. *Cement and Concrete Composites*, 34(8), 924–930.

The POWER Project. NASA Prediction Of Worldwide Energy Resources. Available at: http://surl.li/nmsjw (open source, last assessed 30.10.2023)

Vecchio, F.& Collins, M. P. 1986. The modified compression field theory for reinforced concrete elements subjected to shear. *Proc. ACI*, 83(2), 219–231.

World Bank Group, Climate Change Knowledge Portal 2023. Available at: http://surl.li/nmsjc (open source, last assessed 28.10.2023)

Yoon, I. S., Çopuroğlu, O., & Park, K. B. 2007. Effect of global climatic change on carbonation progress of concrete. *Atmospheric environment*, 41(34), 7274–7285.

Bridge Maintenance, Safety, Management, Digitalization and Sustainability – Jensen, Frangopol & Schmidt (eds)
© 2024 The Author(s), ISBN 978-1-032-77040-6
Open Access: www.taylorfrancis.com, CC BY-NC-ND 4.0 license

Model-driven strategy for bridge measurement-system design

R. Galli & D. Briccola
University of Applied Sciences and Arts of Southern Switzerland (SUPSI), Mendrisio, Switzerland

ABSTRACT: Increasing traffic volumes on aging structures force bridge operators to periodically evaluate infrastructure performance and assess safety using code and model-driven analyses. Of course, the integration of prediction and monitoring techniques improves the management of critical infrastructures providing meaningful information, but it is not easy to interpret hundreds of data. Nowadays, disruptive IoT technical advances suggest that data-driven approaches must be preferred to model-based. This is potentially harmful as it is not true that the more data collected, the more information gained on elements' condition and structural safety. Moreover, since technical decisions are supported by finite-element analyses it appears useful to profit from a priori knowledge of the structural behavior to support sensor placement and enhancing data interpretation. That way, the natural bottleneck to the amount of data imposed by code verifications is automatically considered enabling time and resource savings for superior bridge management.

1 INTRODUCTION

A way to enhance societal and economic benefits while effectively reducing the construction industry's carbon footprint is by extending the service duration of existing bridges.

As a result, extensive structural analysis is essential to assess the actual load-carrying capacity of aging infrastructures. For instance, when dealing with main bridges in a road network, an uncertainty quantification framework is needed to estimate the evolution in time of structural performance. That poses significant challenges to the scientific and technical civil engineering community as it requires the collection of multiple information on actual material parameters and loads and an extensive knowledge of reliability assessment methods.

However, collecting more data does not necessarily correspond to gaining more information on structural performance. Despite the relevance of understanding cause-and-effect scenarios for decision-makers is evident, the technological development of sensors and disruptive Internet of Things (IoT) techniques, advocating for data-driven approaches, sometimes encourages a too simplistic overreliance on sensor-based data collection for early warning.

By contrast, structural health monitoring (SHM) can help collect data on actual traffic loads, detect unexpected structural performance, and identify structural deficiencies through sound engineering judgment. Especially when dealing with complex bridges, as reported by Malomo D. (2020), the pure detection of changes in the performance of specific elements in time, without being aided by robust structural analysis, is not enough to choose how to intervene. Hence, the integration of dynamic and static analysis is crucial to assess aging bridges (Bertola N. J. (2019)).

Following this approach, for a specific bridge typology, the study demonstrates that to get the best out of computational and monitoring techniques, a-priori structural assessment is unavoidable, and it lays the foundation for both effective monitoring system design and robust data interpretation. Symmetrically, data collected through monitoring are of value for updating structural model parameters using Bayesian techniques if and only if the number and location of sensors are accurately selected.

DOI: 10.1201/9781003483755-311

2 SIGNIFICANCE OF A MODEL-DRIVEN STRATEGY FOR SENSORS PLACEMENT

The thrust towards digital-twinned asset management, a relevant topic at the interface between science and policy, will increase, posing several challenges and opportunities to the civil engineering community. Nowadays, this trend is encouraged by the availability of ever-increasing amounts of data collected in real-time using different types of sensors and high-computing infrastructures. Nevertheless, this emerging approach will represent a game-changer paradigm for bridge management if, and only if, meaningful information emerges from processing data. In other words, monitoring data does not have a value of information by themselves but only after robust data interpretation through numerical models. As emphasized by Smith, I.F.C (2016), this approach goes beyond anomaly detection, typical of the early-warning approach, but stems from cause-and -effect research to inform decision-making processes according to structural identification purposes. In structural identification, other than data interpretation, numerical models can aid civil engineers in measurement-system design by defining sensor type, number, and location, overcoming currently qualitative rules-of-thumb approaches. Of course, the larger the number of sensors, the larger the possible sensor-placement configurations, but not necessarily the information gain. Therefore, the goal of each measurement-system design is to reach a balance between the less-invasive measurement system and the information gain. That enables civil engineers not to be overwhelmed by large amounts of not-valuable data and to design cost-effective data acquisition systems. Conversely, it is true that dealing with sparse data sets, as data collection points are few, poses relevant challenges. In short, two tasks are impactful: the sensor configurations selection based on sensor-placement methodology, and the identification of mechanical parameters according to the actual condition state of the bridge, based on structural identification methodology. Several sensor-placement methodologies exist (Papadimitriou, C. (2004), Argyris, C. (2017) and Papadopoulou, M. (2014)). As per the data-interpretation methodology, the Error Domain Model Falsification (EDMF) methodology helps identify plausible mechanical parameters for structural modeling by evaluating model-instance predictions against field measurements through an iterative approach at each sensor location. The mechanical parameters corresponding to those structural models grounded in engineering judgment, whose outcomes (model instances) are compatible with recorded data, within a threshold bound, feed a candidate-model subset (CMS), while the other structural models are dismissed. These bounds are calculated based on the modeling and measurement uncertainties and a target reliability of identification, according to a predefined confidence level that represents a tradeoff between accepting incorrect models and falsifying the correct one. The CMS is later used to assess structural performance evolution in time. The EDMF methodology has proved to be effective for structural identification purposes even in the case of biased structural models if enough data measurements are used. Unfortunately, this is not the case for bridges characterized by only a few sensors each due to costs and integration challenges. In case of biased (wrong) modeling and few data, the real set of mechanical parameters is at risk of falsification, as inferred from Goulet, J-A (2013). As a result, a greater effort in modeling is needed, especially when dealing with complex structures. For instance, for very old bridges characterized by an evident state of obsolescence, well-recognized standard degradation models, such as the one developed by Coronelli D. (2004) can be introduced in the structural model used for EMDF. This approach can potentially reduce model bias and therefore the model predictions -measurements discrepancies, accelerating the identification of the candidate-models set. In short, for structural identification purposes, a model-driven approach is a rewarding choice both for measurement-system design and data interpretation.

3 MODELING APPROACH

In the following two finite-element models were employed to uncover the distinctive structural behavior of a Maillart-type deck-stiffened bridge to provide a sound basis for the EMDF approach. Moreover, it is shown that the finite element models serve to obtain meaningful information for measurement system design, limiting the type and number of sensors.

As physics-based models represent an idealization of reality, modeling simplifications as omissions of secondary elements, changes in the load distribution, and avoidance of soil-structure interactions can affect static and dynamic predictions at several locations and to varying degrees, vinifying the EDMF approach for structural identification. For this reason, to reduce the model bias in EDMF, a sound analysis of the possible loading scenarios to provide meaningful model instances was carried out. Despite being comprehensive, the analysis was necessarily simplified for the sake of brevity as explained in the next section.

A detailed description of the reinforced concrete deck-stiffened bridge, finite element models, and loading scenarios follows. For the sake of brevity, the aleatory uncertainty on model parameters was not considered, and deterministic finite element analyses were carried out. Moreover, we hypothesize dealing with a new bridge, therefore a linear elastic analysis adopting for reinforced concrete E = 30GPa was carried out and geometrical nonlinearities were not accounted for.

3.1 *Bridge geometry and materials*

Inspired by an existing Maillart bridge crossing a river and built in reinforced concrete in the 50s in Tessin by Walter Krüsi, a detailed structural model was reconstructed to carry out both static and dynamic analysis. Figure 1 shows a view of the bridge taken as an example to derive the actual bridge geometry, there briefly described.

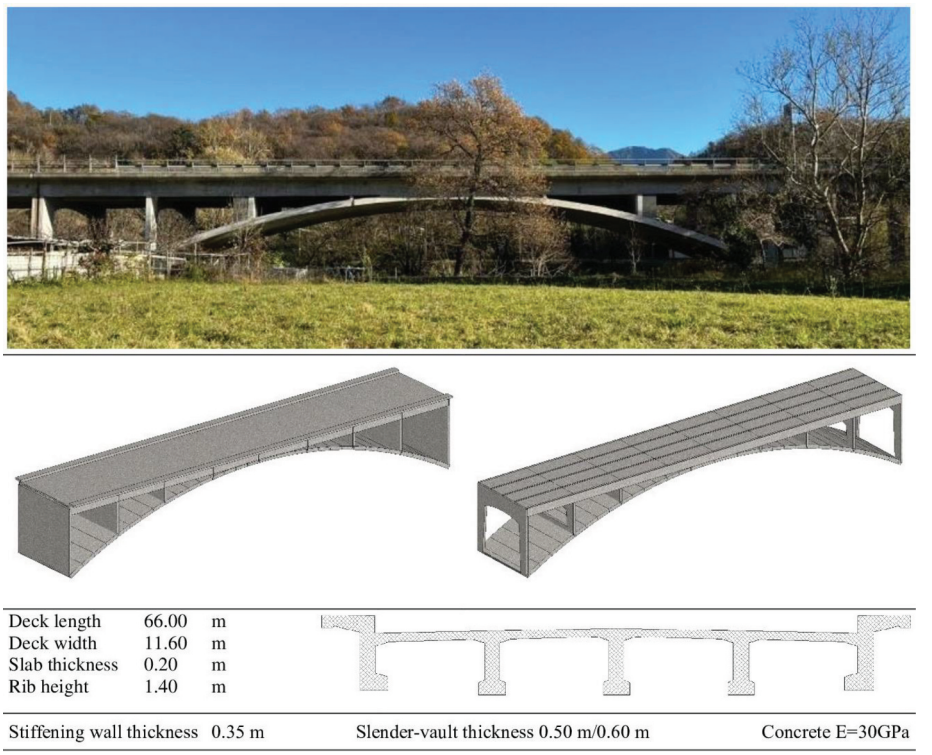


Figure 1. Viadotto Taverne-Torricelle, Lugano, 1951, finite element models and bridge characteristics.

3.2 *Finite element models*

1D- and 2D- finite elements were used to model the bridge and perform both static and dynamic analysis. Information gain, workload, and computational time are of course different. The number of elements and computational time, based on the computing PC performance in Table 1, are listed in Table 2. Despite a significant workload increase in modeling time, especially in applying traffic load according to influence line theory, and the intrinsic opportunity

with the 2D- model of getting information on torsional natural frequency and mode shapes, the two finite element models provide similar results as it will be shown in next section.

Table 1. Computing performance.

PC characteristics:	6 cores processor 2.30GHz with graphic board	16GB RAM

Table 2. Characteristics of finite element models.

1D - Finite element model	2D – Finite element model
147 beam elements	20,216 shell elements – 750 beam elements
5s for static and dynamic analysis	150s for static analysis – 350s for dynamic analysis

3.3 *Load case scenarios: Static analysis*

The self-weight, permanent loads (including pavement, safety barriers, additional equipment installations), and traffic loads were evaluated based on influence lines (1D- finite element model) and surfaces (2D- finite element model) according to design code specifications. In a highly collaborative structural system like this, the influence of kinematic fields such as localized settlements at springers and distortions like temperature and prestressing cannot be ignored. These factors can lead to significant internal force redistribution, potentially resulting in partial/global collapses. In case of localized settlements, both displacement direction and magnitude are meaningful to assess stresses in the deck. For this study, only horizontal component is of interest.

4 PROPOSED MEASUREMENT-SYSTEM BASED ON STRUCTURAL ANALYSIS

Accelerometers and strain gauges are valid monitoring sensors for structural identification purposes. Driven by cost-effectiveness and pursuing valuable structural health monitoring, the minimum number of such sensors can be established based on previous outcomes. To do that, the a priori knowledge of the dynamic response and the distribution of internal actions due to permanent, traffic, and imposed kinematic fields (temperature and localized settlements at springer) is meaningful.

Figure 2 shows the bending moment distribution along the deck as a function of increasing small (on the left) and large (on the right) horizontal displacement at the left/right springer.

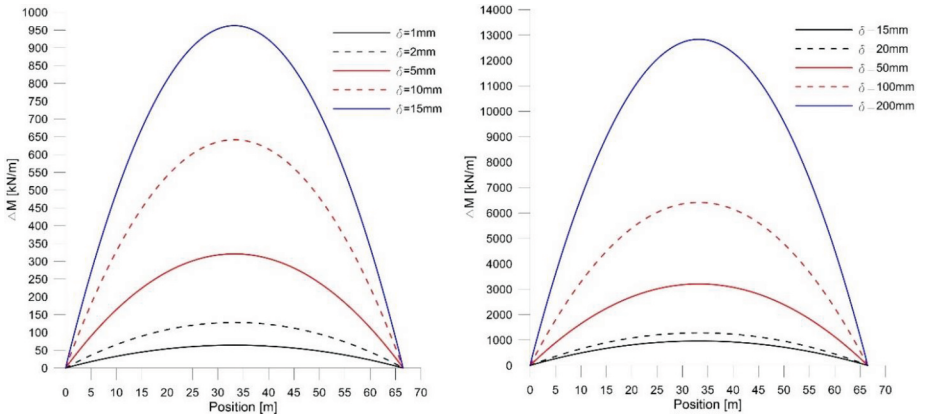


Figure 2. Additional bending moment along the deck due to a horizontal settlement occurring at one of the springers. Different magnitudes are considered.

A careful examination of the values obtained under a linear elastic analysis proves that there is not perfect direct proportionality between the settlement increase and the maximum bending moment at the midspan along the deck. That results from the high deck-arch collaboration typical of the Maillart-type deck-stiffened solution.

As the horizontal displacement's magnitude grows, the axial force in the vault diminishes, and there are noticeable variations in the bending moment along the deck. This illustrates the arch's stiffening effect on the deck: the lower the compression, the greater the bending moment along the deck.

Regarding the dynamic response, nine out of fifteen (the most important in terms of frequency for civil structures and participant mass, evaluated with modal analysis) are global modes, some of which are depicted with their nodes and antinodes in Figure 3. The two finite element models outlined in Section 3 differ in the natural frequencies and mode shapes they capture. Mode 11 signifies a global displacement along the longitudinal axis at a frequency of 15.42 Hz (1D-model) or 13.86 Hz (2D-model). Mode 4 represents a global displacement along the vertical axis, perpendicular to the deck, at a frequency of 3.42 Hz (1D-model) or 3.38 Hz (2D-model). Mode 1 is a rotation about the transversal axis at a frequency of 0.92 Hz (1D-model) or 0.83 Hz (2D-model). The 2D-finite element model's superiority lies in its ability to reveal torsional local and global mode shapes, which is crucial when dealing with highly collaborative structural systems.

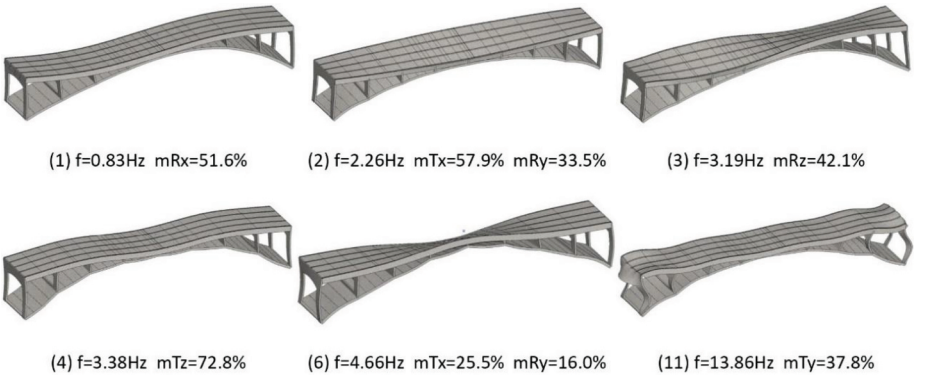


Figure 3. Eigenfrequencies and eigenmodes. Modes (1) Rotation about the transversal axis; (2) Translation along the transversal axis coupled with a rotation about the longitudinal axis; (3) Rotation about the vertical axis; (4) Translation along the vertical axis; (6) Translation along the transversal axis and rotation about the longitudinal axis; (11) Translation along the longitudinal axis.

The proposed model-driven strategy for bridge measurement system design follows:

(i) according to modal analysis, antinodes represent the most reasonable sections to place accelerometers as motion is maximum. The sensor number can be limited based on the accelerometer's capability of recording data in all directions after consideration of all mode shapes and corresponding antinodes.

(ii) after the installation of accelerometers, the comparison between model- and data-estimated natural frequencies can uncover possible cracking induced by corrosion, leading to stiffness changes. Severe material degradation has occurred if significant differences between model and data-driven natural frequencies exceed a threshold. Otherwise, linear elastic analysis is enough to determine the bridge's static structural response.

(iii) If that holds, adding to the measurement system strain gauges, suitable for strain measurements and internal action estimation, is crucial. That enables gaining more information on the structural response evolution over time. For the bridge under consideration, sections B, G, and I in Figure 4 are good points for strain gauge installation. Collected strain data can be analyzed using descriptive statistics to obtain meaningful information on data sets by evaluating measures of central tendency - like mean, median, and mode – and measures of variability like standard deviation variance, minimum and maximum,

kurtosis, and skewness, as well as quartiles. If the analysis of collected acceleration data reveals that no stiffness changes have occurred -see (ii) - then the mode of the strain data set can be considered because of permanent load, while variability relates to traffic loads (main variable action) or other loading actions.

(iv) Moreover, if no cracking occurred, it is worth adding tilt sensors at springers to detect settlements and interpret collected strain data evolution in time, considering the bending moment distribution shown in Figure 2.

(v) finally, temperature affects both internal force distribution in statically indeterminate structures and the performance of sensors like strain gauges. The use of thermocouples related to strain gauges and a priori knowledge of the temperature contribution to internal actions can be set as a benchmark against field measurements, eventually avoiding unnecessary model parameters updating. A bridge in operation experiences a significative non-linear temperature distribution that affects field measurements and depends on numerous parameters like bridge orientation, seasonal trends, solar radiation, pavement detailing, and cross-section shape (not only on its height).

Table 3. Location of nodes (e_0) and antinodes (e_{max}) for nine most important global modes.

Mode	1	2	3	4	5	6	7	8	11
Sec_e_{max}	E	I_{ext}*	E_{ext}	E	C	I_{ext}	I	G_{ext}	I
Sec_e_0	I	Axis	Axis	I	I	Axis	G	I	A

* The measurement is not in the axis for torsional modes.

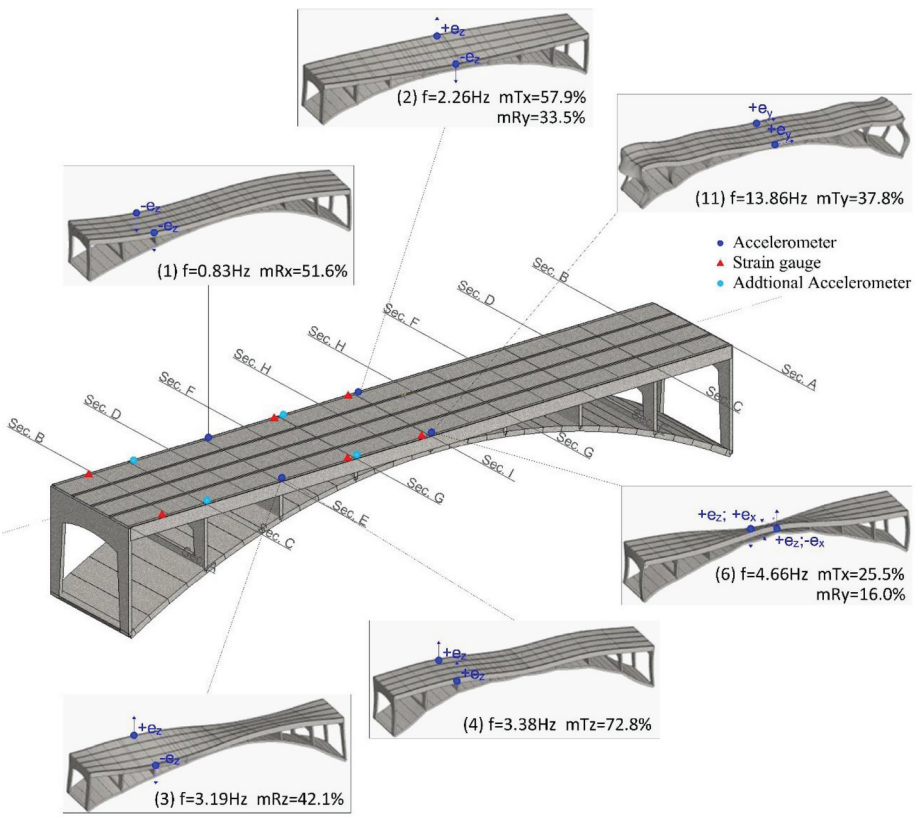


Figure 4. Sensor-placement plan based on static and dynamic analyses considerations.

In conclusion, the design of a measurement system is contingent on the type of monitoring activity, be it for damage detection or structural identification. Numerous sensors can be incorporated into a monitoring system. For example, strain gauges, which measure strain or deformation, and accelerometers, which evaluate the dynamic response of a bridge. Additionally, displacement sensors - such as laser, vibrating wire, or potentiometric technologies - and temperature sensors - like resistance or thermocouples - can be utilized. Lastly, load cells, which measure forces on a bridge (weight on the deck), and tilt sensors, which gauge the magnitude and direction of settlements, are other viable options.

Laying on that, the model-driven strategy proposed, and the model updating phase based on data is shown in Figure 5.



Figure 5. Steps of the proposed model-driven strategy for measurement-system design.

5 CONCLUSIONS

The benefits of bridge monitoring sensors include early detection of structural issues, cost savings on repairs, increased bridge lifespan, and improved safety for users. While challenges exist in terms of sensor installation, data management, and integration, future developments in wireless and MEMS (Micro-Electro-Mechanical Systems) sensor networks, IoT integration, and AI-based solutions hold promise for enhancing bridge monitoring systems. Advancements in the IoT enable the seamless connection between modeling and the digital realm through the

continuous exchange of recorded data and analysis outcomes. As highlighted by Bertola, N.J. (2020), robust data interpretation methodologies are imperative for asset managers to make informed decisions on intervention, while considering constraints on monitoring system invasiveness during bridge operation. Furthermore, considering the size of bridge stocks, and the available resources, the number and placement of sensors is usually limited. The goal is to minimize the number of installed sensors while retaining valuable information for structural identification. In the study, a model-centered approach to measurement-system design was proposed. A comprehensive examination of static and dynamic responses enables the determination of optimal sensor locations, the extent to which each accelerometer provides information on specific behaviors, and the assessment of mutual information gain among sensors. Moreover, a key objective was showing the need to integrate measurement-system design during the initial design phase. The methodology is flexible as it can be easily extended to other structures.

The key to success lies in tailoring the monitoring plan to the specific characteristics of each structure, thereby making a substantial contribution to ensuring the long-term safety of the infrastructure.

REFERENCES

Malomo, D. 2020. Numerical Study on the Collapse of the Morandi Bridge. J. Perform. Constr. Facil.

Bertola, N. J. 2019. A methodology for measurement-system design combining information from static and dynamic excitations for bridge load testing. *Journal of Sound and Vibration*

Smith, I.F.C. 2016. Studies of sensor data interpretation for asset management of the built environment. *Frontiers Built Environ*

Papadimitriou, C. 2004. Optimal sensor placement methodology for parametric identification of structural systems. *Journal of Sound and Vibration*

Argyris, C. 2017 Bayesian optimal sensor placement for modal identification of civil infrastructures. *Journal of Smart Cities*

Papadopoulou, M. 2014 Hierarchical sensor placement using joint entropy and the effect of modeling error. *Entropy*

Goulet, J-A. 2013 Structural identification with systematic errors and unknown uncertainty dependencies. *Computers & Structures*.

Coronelli, D. 2004. Structural Assessment of Corroded Reinforced Concrete Beams: Modeling Guidelines. *Journal of structural engineering*

Bertola, N. J. 2020. Strategy to Validate Sensor-Placement Methodologies in the Context of Spars Measurement in Complex Urban Systems. *in IEEE Sensors Journal*

Bridge Maintenance, Safety, Management, Digitalization and Sustainability – Jensen, Frangopol & Schmidt (eds)
© 2024 The Author(s), ISBN 978-1-032-77040-6
Open Access: www.taylorfrancis.com, CC BY-NC-ND 4.0 license

Quality assurance of intervention in reinforced concrete bridges

A.C.P. Martins, G.F.B. Milagres, J.M. Franco de Carvalho, C.A.F. Souza, F.G. Bellon, M.S. Andrade, D.S. Oliveira, K.M.L. César Jr & J.C.L. Ribeiro
Federal University of Viçosa, Viçosa, Brazil

ABSTRACT: Due to the nature of the loads and the environmental conditions to which bridges are exposed, these structures can be subject to rapid aging and deterioration. As a result, various pathological manifestations caused by chemical, physical, biological or mechanical agents may appear and develop. Thus, bridges require an effective monitoring and preventive maintenance program. Some types of materials, repairs and methodologies were discussed to evaluate the efficiency and control the quality of commonly used repair techniques, proposing an approach based on a database of inspected Brazilian bridges and their maintenance plans provided by the *Departamento Nacional de Infraestrutura e Transportes (DNIT)*. The most recurrent damage in reinforced concrete bridges were mapped and the most common repair interventions were identified. Finally, inspections were suggested to assist with quality control, acceptance and reliability of the repair, to ensure that the selected materials and techniques are suitable for each specific type of damage.

1 INTRODUCTION

Ensuring the integrity and safety of bridges requires continuous monitoring and timely execution of maintenance, repair, rehabilitation, or strengthening measures (Kasireddy & Akinci, 2015). Reinforced concrete structures suffer the loss of integrity over time due to degradation caused by chemical agents (alkali-aggregate reaction, corrosion, leaching, chloride and sulfate attacks, carbonation, efflorescence), physical (gradient of temperature, fatigue, overload, retraction, freeze-thaw cycles), biological (accumulation of organic matter, living organisms) or mechanical, and from this deterioration process arise pathological manifestations that affect the condition of the structures (DNIT, 2010; Helene, 2005; von Fay, 2015). Each of these agents can, individually or jointly, contribute in different ways to the emergence of damage in the structure. However, concrete deterioration is related to a single origin (Bolar et al., 2013).

The Bridge Management System (BMS) has the decision-making process as one of its most essential functions in bridge management, especially in prioritizing maintenance, repair, rehabilitation, and replacement (Contreras-Nieto et al., 2019; Lee & Kim, 2007). This process is vital to directing restricted budgets toward bridges that need maintenance and repair, requiring detailed information to select the most appropriate and cost-effective intervention strategies (Lee & Kim, 2007; Yehia et al., 2008). There is substantial pressure to extend the useful life of existing infrastructures, considering sustainability and their environmental impact. This circumstance forces the industry to offer more durable and efficient measures to preserve and repair concrete structures (Matthews, 2007).

Various repair and reinforcement materials and techniques have been implemented to rehabilitate these structures and fulfil the loads for which they were designed or even higher ones. However, it should be noted that several factors affect the selection and durability requirements of these interventions, such as the inappropriate selection of materials, lack of compatibility between the repair and the substrate, and the use of incorrect techniques for the intervention, creating the need to control the performance of the reinforcement, so that it is effective for the purpose for which it was carried out (Murthy et al., 2018; Su et al., 2021).

DOI: 10.1201/9781003483755-312

Techniques used to repair and reinforce concrete structures include sealing cracks by injection, stapling cracks, applying material to the surface to reconstruct or increase the cross-section, external prestressing, application of externally bonded reinforcement (EBR) or near-surface mounted (NSM), surface cleaning, application of corrosion inhibiting products, among others. Among the various techniques, several materials are used for different applications, depending on the need for the intervention. Existing materials include waterproofing, cement mortars, conventional concrete, polymer resins, polymer fibers, adhesives, and anti-corrosion protectors.

These materials and techniques aim to ensure that the structure has its mechanical strength restored or increased, as well as helping to protect the structure against aggressive agents, improving the chemical and physical resistance of the covering material of the structure, and can be applied as a preventive and corrective measure for the structural element (Sánchez et al., 2018).

As interventions on structures are carried out, greater inspection and maintenance requirements and criteria become essential since the interface between reinforcement or repair materials and the concrete substrate generally constitutes a zone of fragility for the reinforced structural element. Regarding the fatigue loading to which bridges are generally subjected, it is also necessary to monitor and assess the progressive damage that occurs in reinforced concrete structures that have been strengthened and repaired, and it is the duty of the person responsible predict the post-strengthening behaviour assessing the reliability of the techniques adopted (Brown et al., 2008; Manisekar, 2018; Song et al., 2022; Wang; Gupta, 2022).

This work surveys the main pathologies in a group of bridges inspected in Brazil by the *Departamento Nacional de Infraestrutura e Transportes (DNIT)*, which has work plans for maintenance interventions to map the occurrence of damage and make the association with maintenance and repair interventions in the structure. Based on these services, repair inspection methods before and after the intervention were listed to determine acceptability and guarantee the quality of the process.

2 RESEARCH METHODOLOGY

2.1 *Data collection and analysis*

For this study, 435 reinforced concrete bridges, inspected by the DNIT and with work plans for maintenance interventions, were selected and analyzed to map recurrent damage and associated maintenance services. These bridges constitute the *SGO - Sistema de Gerenciamento de Obras de Arte Especiais* and are managed by the DNIT. The bridges were classified according to structural typologies (Figure 1). The predominant structural system of the sample is a reinforced concrete beam (84.37%), followed by a reinforced concrete slab (11.03%).

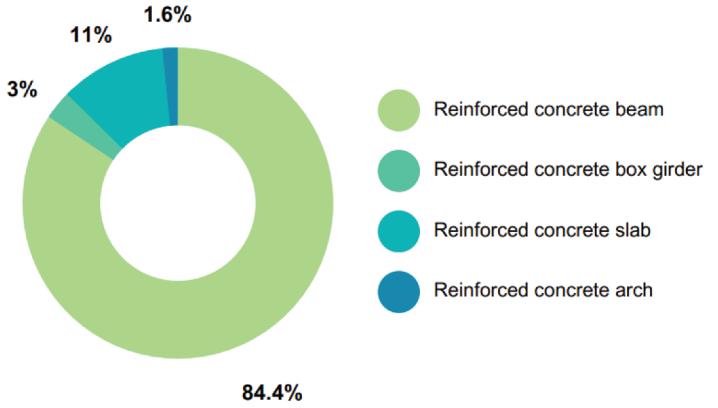


Figure. 1. Structural typologies of the bridges.

The sample universe of bridges was categorized for analysis based on two main criteria: the region of the country where the structure is located (Northeast, Southeast, North, South, Middle-West) (Table 1), and the longitudinal extent of the bridge, which was further classified into small spans, medium spans, or large spans (Table 2), the length of these structures varies from 4.30 to 693.65 meters and the width from 4.0 to 20.0 meters.

Table 1. Categorization of bridges by region.

Region	Sample universe	Percentage (%)
Northeast	168	38.62
Southeast	89	20.46
North	60	13.79
South	74	17.01
Middle-West	44	10.12

Table 2. Categorization of bridges by longitudinal extent.

Longitudinal extent	Sample universe	Percentage (%)
Small bridge: ≤ 30,0 m	219	50.,35
Medium bridge: 30,0 - 80,0 m	166	38.16
Large bridge: > 80,0 m	50	11.49

2.2 *Maintenance and repair interventions*

In this step, the methodology aimed to establish a correlation between the identified damages in the analyzed bridges and the corresponding repair services outlined in their respective work plans. For this purpose, each repair service underwent a detailed breakdown, with a clear description of its components, and an associated unit of measure was assigned to quantify the extent of repair required.

2.3 *Quality control of the intervention*

There are many non-destructive techniques used to evaluate and monitor structures, and they can also be applied to establish criteria for the acceptability and reliability of interventions, verifying the adherence of repair materials, delaminations, depth of cracks, among other properties. These methodologies include ultrasonic testing techniques such as impact echo, impact resonance, impulse response, along with acoustic emission and imaging techniques to determine the strength and assess the damage of concrete, among other methods (Gheorghiu; Rhazi; Labossiere, 2005; Hola; Schabowicz, 2010; Jaishankar et al., 2022).

The definition of quality control for interventions must involve the substrate of the structure repaired, acceptance of the quality of the products used, and the properties of the intervention (EN 1504). EN 1504 and ACI 228.2R provide guidelines for the checks to be carried out before, during and after a repair. In view of the stages that make up the repair activity, the type of test or observations that are appropriate for quality control of the intervention are established.

Concerning the condition of the substrate for applying the repair, both before and after the preparation stage, its properties must be checked, as shown in Table 3.

During the execution of the repair service, some checks are also necessary to ensure quality control of the repair and must be carried out, as shown in Table 4.

At the end of the services, to guarantee the correct execution, acceptability, and reliability of the services, inspections must be carried out by Table 5.

Based on the most recurrent damage to reinforced concrete bridges, the interventions carried out using non-destructive methods were associated with inspection, quality control, acceptability, and guaranteeing the reliability of the repairs carried out.

Table 3. Inspection methods for substrate condition.

Property	Inspection methods
Delamination	Hammer blow
Cleaning	Visual inspection
Surface roughness	Visual inspection, sand patch test or perfilometer
Surface resistance	Pulloff test; sclerometry
Cracks width and depth	Ultrasonic pulse velocity; Fissurometer
Crack activity	Glass plates; Extensometer
Vibration	Accelerometry
Moisture content	Visual inspection; resistivity test
Carbonation	Phenolphthalein; pH meter
Alkali-silica reativity	Cornell/SHRP rapid test
Freezing and thawing damage	Petrography
Steel area reduction	Ultrasonic pulse velocity
Presence of contaminants	Chemical analysis
Corrosion and cleaning of reinforcement	Visual inspection

Table 4. Inspection methods during intervention.

Property	Inspection methods
Temperature	Thermometer
Moisture	Higrometer
Precipitation	Visual inspection
Wind speed	Anemometer
Materials consistency	Consistency tests
Repair thickness	Visual inspection; cover meters

Table 5. Inspection methods to acceptability and reliability of interventions.

Property	Inspection methods
Location of delamination and voids	Impact-echo; Infrared thermography; Impulse response; Radiography; Ground penetrating radar
Coating finish	Visual inspection
Permeability	Karsten Tube Penetration Test
Injection of crack voids	Ultrasonic pulse velocity; Impact-echo
Bond strenght and quality	Pulloff test
Voids	Ultrasonic pulse velocity
Surface texture and color	Visual inspection
Rebar grip	Pullout test on steel bars

3 RESULTS AND DISCUSSION

3.1 *Damage mapping*

Table 3 presents the most recurrent types of damage identified in the group of bridges analyzed, together with the percentage occurrence of each. Through this table, it is possible to identify the main problems faced by the bridges analyzed, allowing maintenance and repair efforts to be directed towards the most recurrent types of damage and thus preserve the structural integrity and extend the useful life of these vital infrastructures.

1. Leaching and carbonation spotting: This type of damage refers to staining caused by the water infiltration into the concrete, followed by a chemical reaction with carbon dioxide from the air. These stains may indicate a deterioration process of the concrete, resulting in its loss of strength over time.

Table 6. List of the most recurrent damage types in analyzed bridges.

Damage	Unit	Occurrence (%)
Leaching and carbonation spotting	m²	90.57
Crack	m	85.52
Expansion joints damage	m	84.37
Disaggregated concrete	m²	69.66
Infiltration into the concrete	m²	66.21
Concrete displacement	m²	65.29
Uncoated reinforcement	m²	50.34

2. Crack: These are linear openings in the concrete, mainly caused by internal or external stresses that exceed the material's ability to resist. Cracks can compromise the bridge's structural integrity and facilitate the penetration of aggressive agents such as water and chlorides, leading to more significant damage.

3. Expansion joints damage: are designed to allow concrete to expand and contract in response to temperature changes. Damage to these joints can result in restriction of concrete movement, leading to cracking and failure of the structure.

4. Disaggregated concrete: This damage indicates significant degradation of the concrete around the reinforcement, leading to exposure and oxidation of the steel bars. The oxidation of the reinforcement can cause it to expand and break away from the surrounding concrete.

5. Infiltration into the concrete: the penetration of water, moisture, or other aggressive elements. Infiltration can accelerate the corrosion of reinforcement and contribute to the overall degradation of the concrete, making it less resistant.

6. Concrete displacement: This damage refers to situations where the concrete shifts or detaches, exposing the reinforcement. This can weaken the structure and increase susceptibility to other types of damage.

7. Uncoated reinforcement: This occurs when the steel bars of the reinforcement are not adequately coated with protective materials, making them more susceptible to corrosion. Corrosion of the reinforcement can lead to expansion and spalling of the concrete around it.

All these damages are common in reinforced concrete structures. It is not uncommon for bridges and other concrete structures to experience a combination of these types of damage over time. Factors such as environmental conditions, traffic loads, material properties, and design failures can contribute to the occurrence of these damages. These damages emphasize the importance of regular inspections, maintenance, and repair activities to ensure the safety, functionality, and longevity of reinforced concrete structures. By addressing these damages promptly, engineers and maintenance teams can extend bridges' lifespan and structural integrity.

3.2 *Damage and intervention association*

Each damage is associated with a set of maintenance and repair services. Certain simple damages correlate directly with maintenance and repair services (Table 4). However, in more intricate cases, the relationship between services depends on the specific element affected by the damage and the extent of reinforcement section loss, requiring a decision tree to represent this association (Figure 2).

Table 7. Common damages and services association.

Damage	Intervention type	Services
Leaching and carbonation spotting	Maintenance	Concrete surface cleaning with pressure water blasting
Expansion joints damage	Maintenance	Expansion joint cleaning
	Repair	Replacement of the expansion joint
Crack	Repair	Injection of structural adhesive based on low-viscosity epoxy resin

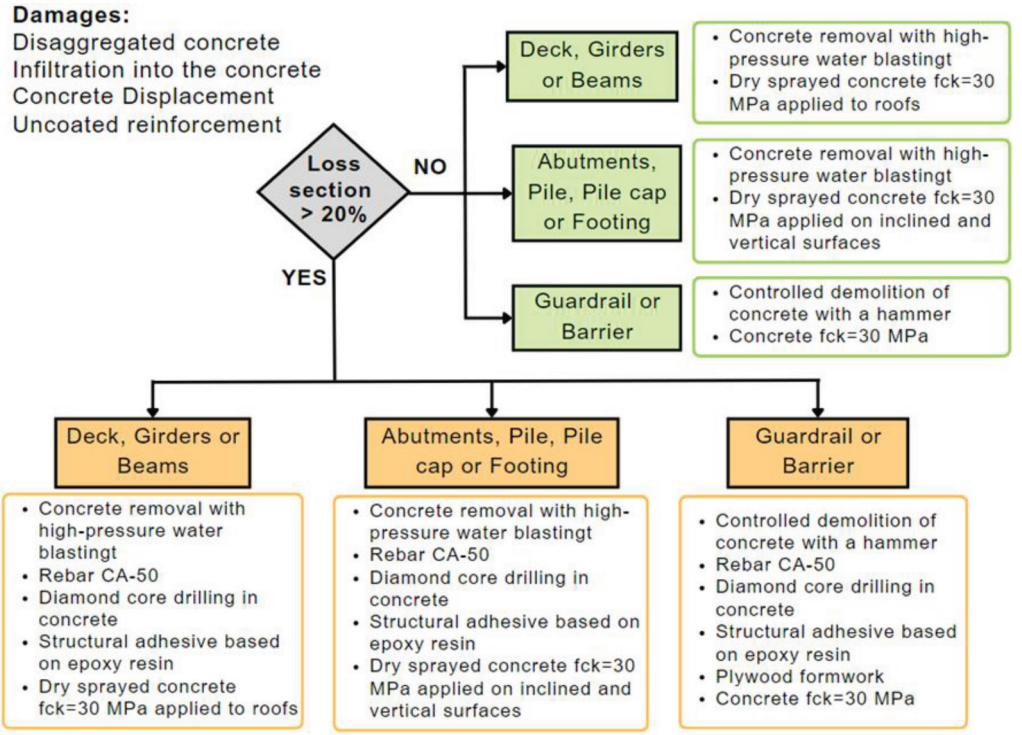


Figure 2. Decision tree for more complex repairs.

3.3 *Inspection methods*

For the services shown in Table 7 and Figure 2, Table 8 presents a proposal for some of the necessary inspections that involve the previous stages of the intervention, especially the substrate preparation, based on the recommendations of EN 1504 and ACI 228.2R. It should be noted that the inspection method depends on the service carried out and the type of surface damage.

Table 8. Necessary inspections in previous stages of the intervention.

Service	Damage	Inspection method
Concrete surface cleaning with pressure water blasting	Leaching spotting	Visual inspection and pulloff or sclerometry test for check the surface resistance
	Carbonation spotting	Visual inspection and Phenol-phthalein application
Expansion joint cleaning	Expansion joints damage	Visual inspection
Concrete removal with high-pressure water blasting or controlled demolition of concrete with a hammer	Disaggregated concrete	Visual inspection and pulloff test or sclerometry for check the surface resistance
	Infiltration into the concrete	Visual inspection and resistivity test
	Concrete displacement	Visual inspection and pulloff test or sclerometry for check the surface resistance
	Uncoated reinforcement	Visual inspection and pulloff test or sclerometry for check the surface resistance

Table 9 proposes some inspections during and after the intervention, based on the recommendations of EN 1504 and ACI 228.2R.

Table 9. Necessary inspections during and after the intervention.

Service	Inspection method
Replacement of the expansion joint	Visual inspection
Injection of structural adhesive based on low-viscosity epoxy resin	Glass plates or extensometer to identify crack activity and ultrasonic pulse velocity or impact-echo for check the crack injection
Concrete application	Consistency tests; visual inspections; Pulloff test and Ultrasonic pulse velocity
Steel bar anchoring with structural adhesive based on epoxy resin	Pullout test on steel bars

The proposed inspection methods and the results obtained during this stage are used to determine whether or not the intervention is acceptable, giving reliability to the repair or the need for a new execution.

4 CONCLUSIONS

Based on this study, it was possible to map the most recurrent damage in real reinforced concrete bridges and associate repair services with this damage more directly, making it possible to automate the decision-making process for intervention. The inspection methods proposed were related to the types of damage and services covered in the study, providing a range of possibilities. It is the responsibility of the engineer in charge of assessing the intervention services carried out to define which methods are best suited, ensuring that due attention is paid to the behavior of the structure and the repair after it has been carried out.

DECLARATION OF COMPETING INTEREST

The authors declare that they have no known competing financial interests or personal relationships that could have appeared to influence the work reported in this paper.

ACKNOWLEDGEMENT

This study was financed by the Departamento Nacional de Infraestrutura de Transportes (DNIT) - TED 703/2020. The authors thank the support of DNIT and Universidade Federal de Viçosa and also acknowledge the collaboration of the research groups SICon and TechBIM.

REFERENCES

ACI 228.2R-98.(1998). Nondestructive test methods for evaluation of concrete in structures. American Concrete Institute (ACI).

Bolar, A., Tesfamariam, S., & Sadiq, R. (2013). Condition assessment for bridges: a hierarchical evidential reasoning (HER) framework. *Structure and Infrastructure Engineering: Maintenance, Management, Life-Cycle Design and Performance*, 648–666. https://doi.org/http://dx.doi.org/10.1080/15732479.2011.602979

Brown, J. et al. (2008). Crack detection and fatigue related delamination in FRP composites applied to concrete. *Thermosense XXX*, 69390W.

Contreras-Nieto, C., Shan, Y., Lewis, P., & Hartell, J. A. (2019). Bridge maintenance prioritization using analytic hierarchy process and fusion tables. *Automation in Construction*, *101*, 99–110. https://doi.org/10.1016/j.autcon.2019.01.016

DNIT. (2010). Manual de recuperação de pontes e viadutos rodoviários. In *Departamento Nacional de Infraestrutura de Transportes*. Departamento Nacional de Infraestrutura de Transportes. http://ipr.dnit.gov.br/normas-e-manuais/manuais/documentos/744_manual_recuperacao_pontes_viadutos.pdf

EN 1504. (2006). Produtos e sistemas para protecção e reparação de estruturas de betão. Norma europeia (EN).

Gheorghiu, C.; Rhazi, J. E.; Labossiere, P. (2005). Impact resonance method for damage detection in RC beams strengthened with composites. *Nondestructive Evaluation and Health Monitoring of Aerospace Materials, Composites, and Civil Infrastructure IV*, 205.

Helene, P. (2005). *Manual de Reparo, Proteção e Reforço de Estruturas de Concreto*. Red Rehabilitar.

Hola, J.; Schabowicz, K. (2010) State-of-the-art non-destructive methods for diagnostic testing of building structures - anticipated development trends. *Archives of Civil and Mechanical Engineering*, 5–18.

Jaishankar, P. *et al.* (2022). Experimental investigation on Non-Destructive behaviour of repaired FRP concrete beams. *Materials Today: Proceedings*, 990–994. https://doi.org/10.1016/j.matpr.2022.05.078.

Kasireddy, V., & Akinci, B. (2015). Towards the Integration of Inspection Data with Bridge Information Models to Support Visual Condition Assessment. *Computing in Civil Engineering*, 644–651.

Lee, C. K., & Kim, S. K. (2007). GA-based algorithm for selecting optimal repair and rehabilitation methods for reinforced concrete (RC) bridge decks. *Automation in Construction*, *16*(2), 153–164. https://doi.org/10.1016/j.autcon.2006.03.001

Manisekar, R. (2018). Effect of External Post-tensioning in Retrofitting of RC Beams. *Journal of The Institution of Engineers (India): Series A*, 495–501. https://doi.org/10.1007/s40030-018-0312-9.

Matthews, S. (2007). CONREPNET: Performance-based approach to the remediation of reinforced concrete structures: Achieving durable repaired concrete structures. *Journal of Building Appraisal*, *3*(1), 6–20. https://doi.org/10.1057/palgrave.jba.2950063

Murthy, A. et al.(2018). Fatigue behaviour of damaged RC beams strengthened with ultra high performance fibre reinforced concrete. *International Journal of Fatigue*, 659–668. https://doi.org/10.1016/j.ijfatigue.2018.06.046.

Sánchez, M. et al.(2018). External treatments for the preventive repair of existing constructions: A review. *Construction and Building Materials*, 435–452.

Song, Xuemin et al. (2022). Cement-Based Repair Materials and the Interface with Concrete Substrates: Characterization, Evaluation and Improvement. *Polymers*, 7.

Su, N. et al.(2021). Assessment of effective patching material for concrete bridge deck -A review. *Construction and Building Materials*, 123520. https://doi.org/10.1016/j.conbuildmat.2021.123520.

Von Fay, K. F. (2015). *Guide to Concrete Repair* (Second, Issue August). U.S. Department of the Interior Bureau of Reclamation. https://doi.org/10.2307/j.ctt1x76d9j.11

Wang, B.; Gupta, R. (2022). Evaluating Flexural Performance of Repaired Reinforced Concrete Beams under Static and Repeated Loading Using Non-Destructive Methods. *Materials*, 6276.

Yehia, S., Abudayyeh, O., Fazal, I., & Randolph, D. (2008). A decision support system for concrete bridge deck maintenance. *Advances in Engineering Software*, *39*(3), 202–210. https://doi.org/10.1016/j.advengsoft.2007.02.002

Bridge Maintenance, Safety, Management, Digitalization and Sustainability – Jensen, Frangopol & Schmidt (eds)
© 2024 The Author(s), ISBN 978-1-032-77040-6
Open Access: www.taylorfrancis.com, CC BY-NC-ND 4.0 license

Fatigue analysis and maintenance strategies for details in long-span bridge girders

C. Deng, Y. Ren, X. Xu, Z. Fan & Q. Huang
School of Transportation, Southeast University, Nanjing, China

Y. Li
Guangdong Provincial Highway Construction Co.,Ltd., Guangzhou, China

ABSTRACT: Suspension bridges and cable-stayed bridges are dominant structures for super long-span bridges, where steel box girders, known as stiffened girders, are commonly used. Despite their advantages of light weight and easy construction, steel box girders are prone to suffer from severe fatigue damage. Excessive traffic volume and truck overloads are one of the external factors for the girders to have premature fatigue cracks. Critical details including U-ribs and truss diaphragms are reported to have the most fatigue cracks for their geometric features, seen at their welded joints. In this paper, fatigue performance of U-rib to deck joints, belonging to a suspension bridge, and truss-type longitudinal diaphragms, belonging to a cable-stayed bridge, is analyzed. Multi-scale finite element models (FEM) of the suspension and cable-stayed bridges are developed to calculate the fatigue life of the details under different load cases, based on cumulative fatigue damage law and S-N curves. The results are validated by field inspection records of the background bridges. Then, to prolong the life-cycle of the fatigue details, two maintenance actions are proposed and applied respectively. The thickness of the deck and U-rib of the suspension bridge is discussed and optimized through comparative study. On the other hand, the steel pipes of the diaphragms are replaced by bolted steel channels and the effects are proved to be satisfactory. These replacement strategies provide practical instructions for steel box girder maintenance and similar structures.

1 INTRODUCTION

Orthotropic steel girders (OSDs) are widely used in long-span cabled-stayed bridges and suspension bridges due to their light weight, high strength and construction convenience (Lu et al., 2019; Oh & Bae, 2013). Compared to bolted connections, welded connections are generally more commonly used for the complex internal structure in steel box girders. However, under alternating vehicle loads, fatigue cracks are prone to occur, which are difficult to discover at early stage but pose a huge threat to the safety of bridge structure as they grow. Inspection data revealed the presence of serious cracks in critical details, highlighting the urgent need of addressing fatigue issues. Multiple fatigue cracks were identified in different welded details of steel box girders. Notably, welded joints of U-rib to deck (Fu et al., 2018; Villoria et al., 2021; Yun et al., 2019) and rib-diaphragms (Guo et al., 2015) were reported to have serious cracks based on inspection data. Hence, U-rib to deck welded joints and longitudinal diaphragm welded joints are two critical fatigue details discussed in this study.

The fatigue behavior of these critical details has been fully investigated in many studies (Cui et al., 2020; Fu et al., 2018; Kainuma et al., 2017; Pengjun et al., 2019; Yang et al., 2016), in which S-N curve based linear cumulative fatigue damage theory and fracture mechanics are commonly used methods. Linear cumulative fatigue damage theory (Miner, 1945) is widely used in fatigue analysis due to its simple expression and convenience (Zhang et al., 2017). To obtain the fatigue effects under traffic loads, finite element (FE) numerical analysis and multi-

DOI: 10.1201/9781003483755-313

scale FE models are promising method as full-scale tests for large OSD is expensive and technically hazardous (Aygül et al., 2012; Cui et al., 2018; Yu et al., 2022; Zhang et al., 2015).

Fatigue cracking has become one of imperative issues of OSD (Zheng et al., 2019). However, few maintenance actions for OSD have been reported. Studies show that increasing the thickness of deck plate can significantly improve the fatigue life welded joints (Kainuma et al., 2017; Xiao et al., 2008). Ahmadivala et al. (2022) investigated the effect of applying a cement-based horizontal overlay by thickening the deck plate in the FE model. Some researchers proposed that a thickened U-rib edge can increase the fatigue strength of U-rib to deck joints (Heng et al., 2019, 2020; Luo et al., 2019; Zheng et al., 2019). Zhu et al. (2020a,b) suggested a thicker diaphragm and new cutout geometry under heavy traffic.

Previous studies focus on the thickness of deck plate or U-rib edge while some drawbacks remain unsolved. The traffic loads resembling real bridge traffic conditions are needed for acquiring accurate fatigue response. In terms of the maintenance measures, the effect of thickness of both the deck plate and U-rib is not further discussed. For another fatigue detail, i.e., the truss-type longitudinal diaphragm welded joint is seldom investigated, as well as its improvement measures. In this study, to evaluate the effectiveness of proposed measures and provide instructions for real bridge maintenance strategies, the FE models of two background bridges are developed. Then, the characteristics of real bridge traffic are analyzed and typical fatigue vehicle models are developed to apply on the FE models. The fatigue life of two welded details is calculated based on the linear cumulative fatigue damage analysis method. Finally, two replacement strategies are applied to two models respectively and subsequent fatigue life is estimated to make comparison with the former ones.

2 BRIDGE DESCRIPTION AND FE MODELS

Two critical details are analyzed in this study, i.e., the U-rib to deck welded joints of a suspension bridge and the truss-type longitudinal diaphragms of a cable-stayed bridge. Finite element models of the two bridges are developed. The modelling of the reinforced details is presented in 4.1 and 4.2.

2.1 *The suspension bridge*

One of the bridges chosen as a case study is a suspension bridge with a span of 1385m crossing the Yangtze River. The layout of the bridge is shown in Figure 1 and the detail of its U-rib of the deck is shown in Figure 2. The thickness of the girder deck plate and the U-rib adjacent to the deck is 12mm and 6mm respectively. According to the inspection records, the U-rib to deck welded joints of the OSD suffered from easily cracking. The number 12 U-rib, detected to have severe cracks,

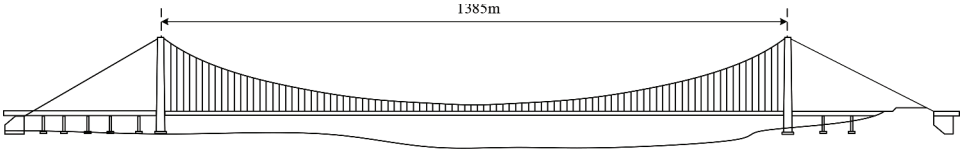


Figure 1. Layout of the suspension bridge.

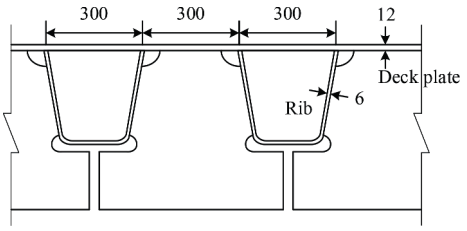


Figure 2. U-rib to deck welded joint (unit: mm).

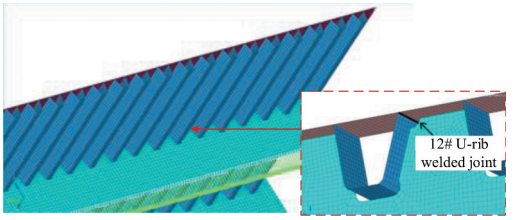


Figure 3. FE model A.

was chosen for the fatigue analysis. The main girder between two hangers was modeled by ANSYS software (model A), shown as in Figure 3, which has 48 U-ribs beneath the deck. For the concern of the computational efficiency, the bottom plate and its web members were simplified.

2.2 *The cable-stayed bridge*

Another background bridge is a cable-stayed bridge with a main span of 648m also crossing the Yangtze River. The main girder has two rows of longitudinal diaphragms. Two types of diaphragms were applied before reinforcement—solid types and truss types. In the truss-type diaphragms, top and bottom deck plates were welded by upper and lower chords, which are T-shape ribs, and they are connected by web members. It is noted that steel pipes were originally used as web members on this bridge, on which serious fatigue problems were detected. The inspection records indicated that some truss-type web members of the longitudinal truss diaphragms cracked at the welded joints and the cracks inclined to grow rapidly.

To obtain more accurate stress spectrum of the welded joint, a multiscale FE model (model B) of the cable-stayed bridge was established via ANSYS software, as shown is Figure 4. In the mid-span area, Shell elements were used to simulate the local model of the interested girder as well as one of its web members. Welded details of the web member were highly meshed to ensure the calculation accuracy.

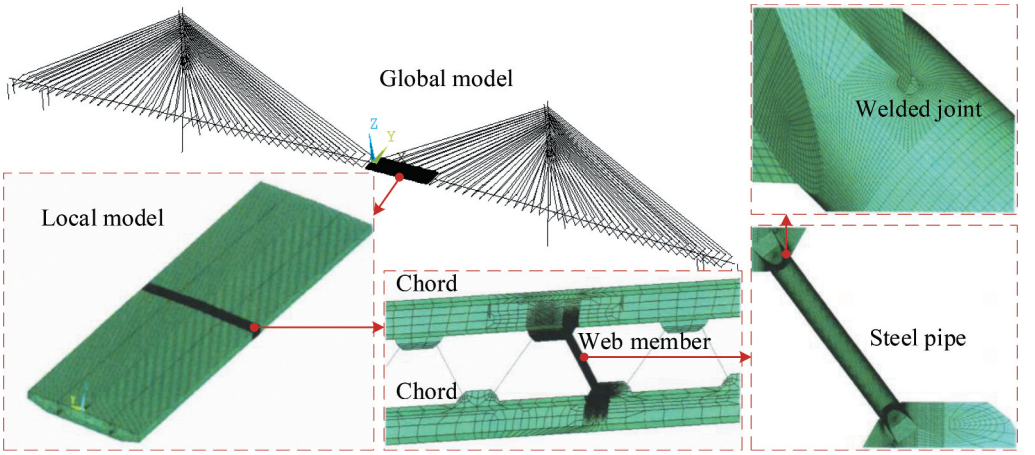


Figure 4. FE model B.

3 ACCUMULATIVE FATIGUE DAMAGE ANALYSIS OF CRITICAL DETAILS

3.1 *Fatigue damage analysis based on S-N curve*

Linier cumulative fatigue damage analysis, namely Stress-life method, is a widely used method to calculate the damage degree of steel components, which is based on S-N curve and the Miner's rule. The analysis of critical details includes three steps:

(1) Locate the most damaged details through field inspection or stress analysis.
(2) Obtain stress spectrum of the critical details under fatigue vehicle loads.
(3) Generate corresponding S-N curve and estimate fatigue life based on the Miner's rule.

S-N curve indicates the relation between stress and fatigue life, in which S represents stress range and N for number of cycles (Sun & Ye, 2022). The S-N curve used in the study is derived from the BS5400 (B.S.I. British standards BS 5400, 1980), which can be written as follows:

$$N \cdot \sigma^m = K_2 \tag{1}$$

where σ is the stress amplitude; m is the slope of the stress curve; N is the corresponding number of stress cycles; K_2 is the coefficient of fatigue strength.

The parameters of fatigue details discussed in Section 4 are shown in Table 1, based on BS 5400. Due to the variance of stress amplitude of steel girders, the S-N curves developed from constant amplitude fatigue tests are analyzed through the Miner's rule.

Table 1. The parameters of fatigue details.

Fatigue detail	Category	m	K_2
Rib to deck joints	C	3.5	4.23×10^{13}
Longitudinal diaphragms	D	3	1.52×10^{12}

According to the rule, fatigue damage brought by each variant stress cycle can be calculated as n_i/N_i and the cumulative damage is defined as the sum of damage derived from every cycle, which can be written as:

$$D = \sum_i \frac{n_i}{N_i} \tag{2}$$

where n_i is the cycle number of the stress amplitude calculated by rain flow method (Downing & Socie, 1982); N_i is the cycle number of the stress amplitude on the S-N curves; D is the cumulative damage.

It is assumed that fatigue failure happens when accumulative damage D reaches 1.0. However, low stress cycles in the stress spectrum also cause fatigue damage, which are modified by introducing proportional coefficient to consider their effect. Despite the deviation of the Miner's rule, it is applicable due to its simplicity.

3.2 *Fatigue vehicle loads*

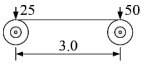
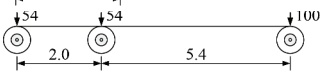
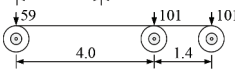
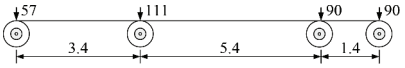
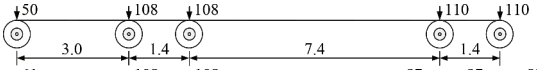
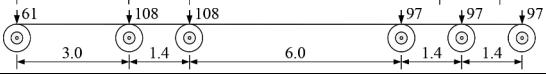
To reflect load responses of critical components under real traffic conditions, typical fatigue vehicle models are implemented from filed investigation to derive fatigue stresses. According to information from the Weigh-in-Motion (WIM) system from the background suspension bridge in 96 hours, 6 types of typical fatigue vehicle models are developed, as shown in Table 2, and their distribution on different lanes are shown in Table 3.

In order to estimate the traffic volume based fatigue life more accurately, a three-stage traffic growth model is introduced (Luo et al., 2021). The first stage is the short period after the bridge is put into service when the AADT grows linearly. In the second stage, traffic volume has an exponential growth curve until it reaches an upper limit. The traffic volume becomes stable at the upper limit in the third stage. The three-stage growth model can be written as follows:

$$y = \begin{cases} at + b_0 \\ e^{(b_1 + b_2 t)} \\ y_{\max} \end{cases} \tag{3}$$

where t is the time in years; a and b are the linear parameters of the first stage; b_1 and b_2 are the parameters of the second stage; $y_{\max}$ is the upper limit of traffic volume.

Table 2. The parameters of typical fatigue vehicles.

Vehicle type	Illustration*	Gross weight/kN	Proportion/%
1		75	39.63
2		208	13.12
3		261	15.28
4		348	4.46
5		486	3.87
6		568	23.63

* Length in meter and weight in kilogram.

Table 3. The lane distributions for different vehicles (%).

Vehicle type	1	2	3	4	5	6
Outside (slow) lane	12.60	65.44	14.55	67.95	68.77	63.18
Middle (driving) lane	37.41	31.10	52.91	30.67	29.86	34.83
Inside (fast) lane	37.41	31.10	52.91	30.67	29.86	34.83

4 FATIGUE ANALYSIS OF MAINTENANCE MEASURES

In this study, various maintenance strategies are simulated and analyzed through finite element simulation. In this section, the U-rib coupled with the deck of the suspension bridge (model A) and the longitudinal diaphragm of the cable stayed bridge (model B) are being replaced.

4.1 *Fatigue analysis of reinforced U-rib and deck*

Five reinforced models are developed considering different thickness combinations of U-rib and deck. Thickness of the details in FE models are shown in Table 4. Using the method in 3.1, the stress amplitudes and corresponding cycle numbers are calculated of the welded joints in each model. The cumulative fatigue damage of each detail under 6 million vehicles can be obtained by Equation 2, shown as in Table 4.

Table 4. The parameters and fatigue damage of fatigue details in different models.

Model	Deck/mm	U-rib/mm	Fatigue damage
Model A	12	6	2.06×10^{-1}
Model 1	12	8	1.99×10^{-1}
Model 2	12	10	2.11×10^{-1}
Model 3	14	8	3.31×10^{-2}
Model 4	16	8	7.83×10^{-3}
Model 5	18	8	1.22×10^{-3}

Compared to original model (model A), increasing the thickness of the U-rib has little influence on the damaged degree, which remains around 0.2, with the U-rib thicken from 6mm to 10mm. Based on that, when the thickness of the girder deck increases from 12mm to 18mm, D declines dramatically. It indicates that the thickness of deck dominates the fatigue life of critical details of U-rib to deck joints.

The traffic volume of the suspension bridge was 5400 thousand when it opened. Thus, the fatigue life of the joints of model A and model 5 without considering traffic growth can be deduced, which are 5.39 years and 925.93 years. According to field records, the welded joints of the bridge girder experienced fatigue cracks within the first 3 to 5 years, which aligns well with the estimated results. Based on the record of toll station on this bridge, the traffic volume stabilizes at $y_{\max}$ of around 2.6 million a year, as show in Figure 5. Therefore, the fatigue life of thickened deck in model 5 is 196.03 years and it can be expected that the critical detail generates no cracks during service time.

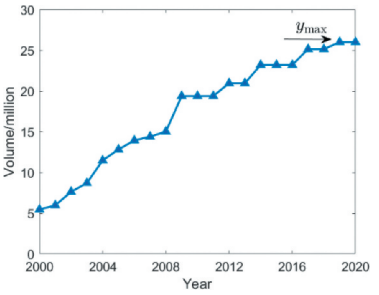


Figure 5. Traffic volume of the suspension bridge.

4.2 *Fatigue analysis of reinforced diaphragms*

The original steel pipes in the longitudinal diaphragms in the background cable-stayed bridge were replaced by two opposite steel channels with a height of 200mm, a few years after the inspection. The steel channels are connected back to back to the chords at gusset plates and stiffened by high-strength bolts, shown as in Figure 6. Using the high-strength bolts instead of welded joints can avoid stress concentration at the welded joints caused by geometric discontinuities. To quantify the effectiveness of the replacement method, one of the web members is simulated by steel channels, shown as in Figure 7. The detail category of the reinforced component belongs to C, according to BS 5400. Considering the similar geographic conditions between two bridges, the same fatigue vehicle loads in model A are applied to the reinforced model B. Using the method in 2.3, the D values of the fatigue detail before and after replacement are 0.422 and 0.0024, demonstrating the effectiveness of the replacement measure.

Since the opening of the bridge in 2005, the traffic volume in 2006, 2007, and 2008 was relatively low, with averages of 1.53, 2.01 and 2.30 million, respectively. After 2009, the annual traffic volume reached around 3.65 million. Based on the data, it could lead to the occurrence

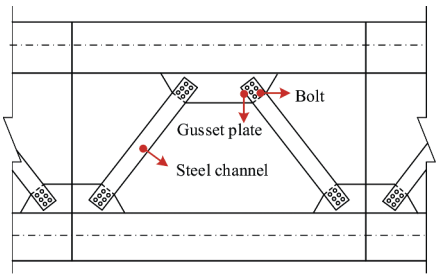


Figure 6. The layout of steel channels.

of fatigue cracks in the diaphragms within approximately 5.3 years. In fact, the bridge first observed the cracks at the welded joint of the diaphragms in 2008, approximately 3 years after its opening, which is in accordance with the simulation result. By Applying the same traffic growth as in model A, the fatigue life of reinforced diaphragm is expected to be 102.03 years, which is also promising for the safety of the OSD.

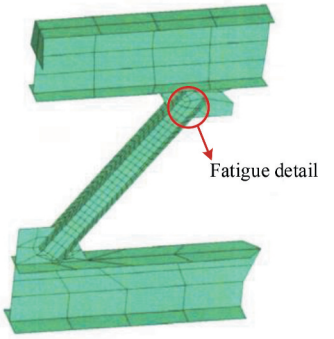


Figure 7. The local model of the steel channel.

5 CONCLUSION

This study presented a practical approach for fatigue analysis of OSD under vehicle loads. The proposed approach was applied to two types of fatigue details on the steel box girder, the web member to longitudinal diaphragm and the welded joints of U-rib to deck. In addition, improvement measures for two fatigue details were also investigated. Comparison of the fatigue life were made between the reinforced steel components and the original one to verify the effectiveness of the improvement measures. Based on the results, the following conclusion can be drawn:

(1) To simulate real traffic condition more accurately, vehicle characteristics such as vehicle type, lane distribution and traffic volume are analyzed.
(2) The fatigue analysis approach is applied to the welded joint of U-rib to deck and the joint of the truss-type longitudinal diaphragm. The fatigue damage of the critical details of U-rib to deck and the longitudinal diaphragm is 0.206 and 0.422 respectively. Both case studies obtain the fatigue life that are close to the real bridge components.
(3) Two maintenance strategies are presented for two details respectively. The thickness of U-rib and deck are modeled to increase to 8mm and 18mm, respectively. Results show that a thicker deck contributes more fatigue strength and the corresponding fatigue life is 195 years, considering traffic volume growth. On the other hand, the steel pipe of the diaphragm is replaced by the steel channels and the fatigue life after replacement is 102 years, using the proposed approach. Two strategies provide considerable improvement in fatigue life of two critical details, by 190 and 97 years, respectively.

REFERENCES

Ahmadivala, M., Berthellemy, J., Orcesi, A., Mattrand, C., Gayton, N., & Yalamas, T. 2022. A strategy for rib-to-deck crack propagation analysis and strengthening of orthotropic deck bridges. *Engineering Failure Analysis* 134: 106057.

Aygül, M., Al-Emrani, M., & Urushadze, S. 2012. Modelling and fatigue life assessment of orthotropic bridge deck details using FEM. *International Journal of Fatigue* 40: 129–142.

B.S.I. British standards BS 5400. 1980. Steel, Concrete and Composite Bridges. Part 10: Code of Practice for Fatigue. London: British Standards Institution.

Cui, C., Bu, Y., Bao, Y., Zhang, Q., & Ye, Z. 2018. Strain Energy-Based Fatigue Life Evaluation of Deck-to-Rib Welded Joints in OSD Considering Combined Effects of Stochastic Traffic Load and Welded Residual Stress. *Journal of Bridge Engineering* 23(2): 04017127.

Cui, C., Xu, Y.-L., Zhang, Q.-H., & Wang, F.-Y. 2020. Vehicle-induced fatigue damage prognosis of orthotropic steel decks of cable-stayed bridges. *Engineering Structures* 212: 110509.

Downing, S. D., & Socie, D. F. 1982. Simple rainflow counting algorithms. *International Journal of Fatigue* 4(1): 31–40.

Fu, Z., Ji, B., Zhang, C., & Li, D. 2018. Experimental study on the fatigue performance of roof and U-rib welds of orthotropic steel bridge decks. *KSCE Journal of Civil Engineering* 22(1): 270–278.

Guo, T., Liu, Z., Pan, S., & Pan, Z. 2015. Cracking of Longitudinal Diaphragms in Long-Span Cable-Stayed Bridges. *Journal of Bridge Engineering* 20(11): 04015011.

Heng, J., Zheng, K., Kaewunruen, S., & Baniotopoulos, C. 2019. Stochastic Traffic-Based Fatigue Life Assessment of Rib-to-Deck Welding Joints in Orthotropic Steel Decks with Thickened Edge U-Ribs. *Applied Sciences* 9(13): 2582.

Heng, J., Zheng, K., Kaewunruen, S., Zhu, J., & Baniotopoulos, C. 2020. Probabilistic fatigue assessment of rib-to-deck joints using thickened edge U-ribs. *Steel and Composite Structures* 35(6): 799–813.

Kainuma, S., Yang, M., Jeong, Y.-S., Inokuchi, S., Kawabata, A., & Uchida, D. 2017. Experimental investigation for structural parameter effects on fatigue behavior of rib-to-deck welded joints in orthotropic steel decks. *Engineering Failure Analysis* 79: 520–537.

Lu, N., Liu, Y., Deng, Y., & Deng, Y. 2019. Fatigue Reliability Evaluation of Orthotropic Steel Bridge Decks Based on Site-Specific Weigh-in-Motion Measurements. *International Journal of Steel Structures* 19(1): 181–192.

Luo, P., Zhang, Q., Bao, Y., & Bu, Y. 2019. Fatigue performance of welded joint between thickened-edge U-rib and deck in orthotropic steel deck. *Engineering Structures* 181: 699–710.

Luo, Y., Zheng, H., Zhang, H., & Liu, Y. 2021. Fatigue reliability evaluation of aging prestressed concrete bridge accounting for stochastic traffic loading and resistance degradation. *Advances in Structural Engineering* 24(13): 3021–3029.

Miner, M. A. 1945. Cumulative Damage in Fatigue. *Journal of Applied Mechanics* 12(3): A159–A164.

Oh, C.-K., & Bae, D. 2013. Fatigue test of an advanced orthotropic steel deck system using high performance steel for bridges. *International Journal of Steel Structures* 13(1): 93–101.

Pengjun, L., Zhang, Q., & Bao, Y. 2019. Predicting weld root notch stress intensity factors for rib-to-deck welded joint under deck loading modes. *International Journal of Fatigue* 128: 105212.

Sun, Z., & Ye, X.-W. 2022. Incorporating site-specific weigh-in-motion data into fatigue life assessment of expansion joints under dynamic vehicle load. *Engineering Structures* 255: 113941.

Villoria, B., Siriwardane, S. C., & Lemu, H. G. 2021. Review on fatigue life assessment methods for welded joints in orthotropic steel decks of long-span bridges. *IOP Conference Series: Materials Science and Engineering* 1201(1): 012036.

Xiao, Z.-G., Yamada, K., Ya, S., & Zhao, X.-L. 2008. Stress analyses and fatigue evaluation of rib-to-deck joints in steel orthotropic decks. *International Journal of Fatigue* 30(8): 1387–1397.

Yang, M., Ji, B., YuanZhou, Z., & Fu, Z. 2016. Fatigue behavior and strength evaluation of vertical stiffener welded joint in orthotropic steel decks. *Engineering Failure Analysis* 70: 222–236.

Yu, S., Li, D., & Ou, J. 2022. Digital twin-based structure health hybrid monitoring and fatigue evaluation of orthotropic steel deck in cable-stayed bridge. *Structural Control & Health Monitoring* 29(8): e2976.

Yun, H., Zhang, Q., Bao, Y., & Bu, Y. 2019. Fatigue assessment of longitudinal rib-to-crossbeam welded joints in orthotropic steel bridge decks. *Journal of Constructional Steel Research* 159: 53–66.

Zhang, Q., Bu, Y.-Z., & Li, Q. 2017. Review on Fatigue Problems of Orthotropic Steel Bridge Deck. *Zhongguo Gonglu Xuebao/China Journal of Highway and Transport* 30: 14–30 and 39.

Zhang, Q., Chuang, C., Bu, Y., Yiming, L., & Ye, H.-W. 2015. Fatigue tests and fatigue assessment approaches for rib-to-diaphragm in steel orthotropic decks. *Journal of Constructional Steel Research* 114: 110–118.

Zheng, K., Feng, X., Feng, X., Heng, J., Zhu, J., Zhu, J., Zhu, J., Zhu, J., & Zhang, Y. 2019. Fatigue Reliability Analysis of Rib-To-Deck Joints Using Test Data and In-Situ Measurements. *Applied Sciences* 9(22): 4820.

Zhu, Z., Xiang, Z., Li, J., & Carpinteri, A. 2020a. Fatigue damage investigation on diaphragm cutout detail on orthotropic bridge deck based on field measurement and FEM. *Thin-Walled Structures* 157: 107106.

Zhu, Z., Xiang, Z., Li, J., Huang, Y., & Ruan, S. 2020b. Fatigue behavior of orthotropic bridge decks with two types of cutout geometry based on field monitoring and FEM analysis. *Engineering Structures* 209: 109926.

Bridge Maintenance, Safety, Management, Digitalization and Sustainability – Jensen, Frangopol & Schmidt (eds)
© 2024 The Author(s), ISBN 978-1-032-77040-6
Open Access: www.taylorfrancis.com, CC BY-NC-ND 4.0 license

A comparison of Italian and UK guidelines on the vulnerability assessment of bridges

Alessandro Lipari & Paolo Clemente
ENEA Italian National Agency for New Technologies, Energy and Sustainable Economic Development

ABSTRACT: The vulnerability assessment of bridges has proven to be a challenging task: as of yet, there is no universal approach for carrying out the assessment; besides, in spite of recent technological advances, it still greatly relies on visual inspections, hence with a certain degree of subjectivity, and the assessment outcome may be affected by some factors that are not obvious, such as full accessibility of the bridge and presence of latent defects.

This paper compares the structural vulnerability assessment of existing highway bridges included in two national guidance documents, namely the well-established UK Design Manual for Roads and Bridges and the recent Italian Ministry of Infrastructure and Transport's Guidelines. Both documents present risk-based methods for assessing the structural vulnerability of bridges, while exhibiting fundamentally different approaches. For instance, the Italian assessment defines a vulnerability class, to be combined with hazard and exposure classes in order to determine a structural risk rating; then, the overall rating affects the actions that need to be taken, e.g. subsequent inspections, structural assessment or monitoring. On the other hand, the UK guidance uses a risk scoring system, which also includes some parameters not strictly related to vulnerability, in order to determine whether the interval between principal inspections may be increased from the minimum requirement of 6 years; some input data for such risk scoring are also used to determine whether a structural assessment is required. Finally, both vulnerability assessments are applied to two sample bridges, highlighting similarities and differences between the two guidelines.

The presented comparison may allow for a better understanding of the factors governing the assessment outcome, for potential improvement of guidelines, and ultimately for more effective intervention prioritisation.

1 INTRODUCTION

Bridges are critical parts of a transport network and ensuring their safety is paramount while they are ageing. However, this has proven to be challenging: the bridge stock may be close to or have exceeded its expected lifespan, traffic loads have increased over the years, climate change imposes unpredicted actions, maintenance operations may be costly and typically causing undesired traffic disruptions, available resources are often tight (Clemente, 2020, Buffarini et al., 2022).

Assessing their vulnerability is a crucial step before proceeding to any structural assessment or maintenance planning. Vulnerability is greatly related to bridge condition rating, although other factors should be considered, e.g. the structural scheme. Although monitoring systems have been used (Clemente et al., 2019, Bongiovanni et al., 2021), collection of data about bridge conditions is still greatly relying on visual inspections and, as such, the outcome has a certain degree of subjectivity. Moreover, condition rating is seldom standardised, even within the same country, potentially leading to inconsistent outcomes.

To tackle this, some countries have adopted national guidelines in an effort to reduce subjectivity and enhance uniformity in inspection and assessment tasks. Among these, the Italian

DOI: 10.1201/9781003483755-314

Ministry of Infrastructure and Transport has recently issued the "Guidelines on risk classification and management, safety assessment, and monitoring of existing bridges" (Ministero delle infrastrutture e dei trasporti, 2022), whereas in the United Kingdom the Design Manual for Roads and Bridges includes more established procedures for the inspection and assessment of existing highway bridges (Highways England, 2021, Highways England, 2020, National Highways, 2022). Both guidelines are risk-based and follow a comparable multi-level approach.

The Italian guidelines comprise of six levels (0–5): census (L0), inspection (L1), definition of a Class of Attention (L2); then, according to the outcome of L2, an existing bridge may be required to proceed to a preliminary assessment (L3), accurate assessment (L4), or a network resilience study (L5, applicable only to high importance bridges). The Italian guidelines endorse a multi-risk methodology, as they take into account four main risks: structural-foundational, seismic, landslide and hydraulic. For each risk, a vulnerability class is computed and then combined with hazard and exposure classes, resulting in a Class of Attention (CA). The combination of each risk CAs leads to an overall CA, upon which depend further actions, such as frequency of periodic inspections, additional inspections, structural assessment or monitoring.

The UK guidelines are based on a broader set of documents. The parts applicable to bridges can be broadly divided into inspection, structural review, and assessment. As such, these stages can be related to the Italian levels L1, L2, and L3-L4. Two separate risk-based procedures are established: one at the inspection stage for a potential extension of the interval between principal inspections of certain bridges, the other at the structural review stage for assessing the need for a structural assessment.

This paper focusses on the structural vulnerability assessment of existing highway bridges and compares the methodologies required to establish the inspection process, along with other parameters affecting the structural vulnerability. In this work, structural vulnerability is intended as the vulnerability of the structure against any actions, except for earthquake, landslide and hydraulic actions. An overview of the structural risk evaluation to establish the need for structural assessment is also given – this aspect has been discussed in greater detail in another work (Lipari et al., 2024). The procedures are then applied to two case studies, and similarities and differences are highlighted.

2 THE ITALIAN AND UK METHODOLOGIES

The Italian and UK methodologies to rate highway bridge conditions and to estimate the structural risk are outlined in the following. Obviously, the structural condition level is a crucial input in assessing the vulnerability of an existing bridge, although not the only one. Consideration of multiple factors is indeed a remarkable feature of both methodologies.

Methodologies developed for bridge condition indices can be broadly groped into four different approaches, or a combination of those (Chase et al. 2016):

- ratio-based methods: a Bridge Condition Index is assigned based on the ratio of the current condition to the condition of the structure after its construction;
- weighted averaging approaches: similar to the previous, but the condition ratings of all individual elements are weighted by their contribution to the structural integrity of the bridge;
- worst-conditioned approaches: the overall condition rating is that of the element in the worst condition;
- qualitative methods: conditions are not reported on a numerical scale.

2.1 *Methodology proposed in the Italian guidelines*

The methodology underlying the Italian guidelines is multi-level, multi-risk and qualitative. It has to be applied by all road managers for bridges and viaducts longer than 6 m.

Risk is consistently rated upon a combination of hazard, vulnerability and exposure, resulting in a CA, which can be Low (L), Medium-Low (ML), Medium (M), Medium-High (MH), or High (H). The vulnerability class bears the highest influence on the structural CA, as the hazard or exposure classes do not vary the overall CA as much (Santarsiero et al., 2021). The overall CA determines which further actions to take (Figure 1).

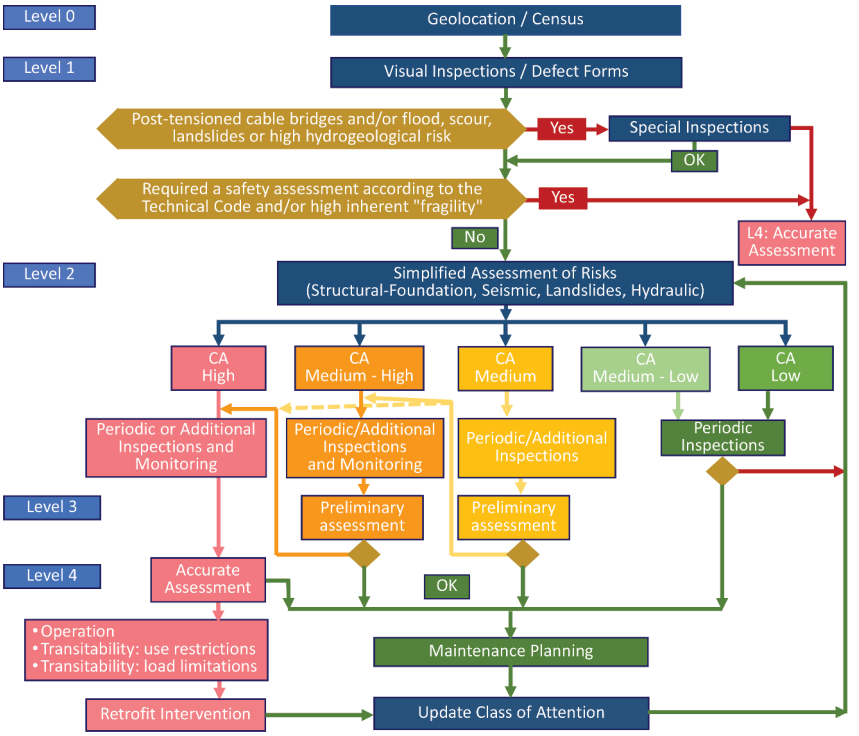


Figure 1. Multi-level approach according to Italian guidelines.

As can be seen, inspections can be classified into:

- *Periodic inspections*: to be carried out at minimum intervals, according to the CA resulting from an L2 evaluation and whether the structure had been previously subjected to periodic inspections or not; if so, intervals range from 6 months (CAs MH and H) to 2 years (CA L); otherwise, intervals are halved. Periodic inspections are visual, but it is recommended to carry out some basic non-destructive testing.
- *Additional inspections*: required to investigate the degradation process and the structural conditions whenever periodic inspections found significant damage, such for CAs M, MH or H. They must be carried out within 60 days from arising of their need, or at most every 2 years for CAs M, MH or H, and 5 years in other cases. Non-destructive tests must be performed, while load testing or dynamic testing may be performed.
- *Special inspections*: required for post-tensioned PSC bridges or landslide/scour/flooding-prone bridges; for post-tensioned PSC bridges, it is recommended to identify the tendon geometry from record information or non-destructive testing, and then to set out an investigation plan to ascertain the level of deterioration of the elements. In case of unsatisfactory results, an accurate assessment (L4) must follow.

The parameters required for determining the structural hazard, vulnerability and exposure classes are reported in Table 1.

Table 1. Input parameters for determining the structural risk.

Class	Parameter	Number of entry option
Hazard	Permitted load	5
	Average Daily Truck Traffic	3
Vulnerability	Level of deterioration	5
	Structural scheme	7
	Maximum span length	4
	Material	7
	Number of spans	2
	Speed of deterioration	3
	Design code	3
Exposure	Average Daily Traffic	3
	Average span length	3
	Alternative routes	2
	Obstacle crossed	3
	Transport of dangerous goods	2

The Level of Deterioration (LD) is based on an element-level damage survey, in which each defect type has its own listed severity (G = 1, 2, 3, 4, 5), and the inspector assigns its extent and intensity, each divided in 3 classes. From such detailed information, an LD can be computed for each element, then for each structural group (e.g., decks, piers, abutments, bearings, etc.), and ultimately for the whole structure. The LD of the whole structure is the worst LD among the structural groups, thus effectively endorsing a worst-conditioned approach, although some averaging is allowed when assigning the LD of a structural group, as long as there are no elements with levels MH or H.

An LD High (H) corresponds to severe defects (G = 4, 5) on critical elements, i.e., conditions for which the structural safety is at stake; a *critical element* is that highly subjected to degradation and whose damage could affect the global structural safety, such as half-joints or PSC tendons, or else an element in critical conditions. An LD Medium-High (MH) corresponds to severe defects (G = 4, 5) with high intensity on non-critical elements, but which could compromise the structural safety over time. An LD Medium (M) corresponds to defects G = 5 with low to moderate intensity on non-critical elements, or severe defects (G = 4, 5) with high intensity not potentially compromising the structural safety. An LD Medium-Low (ML) corresponds to defects G = 4 with low to moderate intensity on non-critical elements or numerous non-severe defects (G = 1, 2, 3), whereas an LD Low (L) has only a limited number of non-severe defects.

For full details, refer to Ministero delle infrastrutture e dei trasporti (2022) and ANSFISA (2022). Some relevant implications are reported here:

- when the LD is H, then the vulnerability class is H regardless of the other parameters; however, a vulnerability class H does not imply a level of deterioration H: in fact, a bridge with level of deterioration M or MH could have a vulnerability class H, depending on the other parameters reported in Table 1.
- when the vulnerability class is H, the structural CA is H regardless of the hazard and exposure classes; however, a structural CA H does not imply a vulnerability class H: in fact, a bridge with vulnerability class MH could have a structural CA H if either the hazard or the exposure class is H.

2.2 *Methodology proposed in the UK guidelines*

The UK methodology about inspections is set out in CS 450 (Highways England, 2021). Five types of maintenance inspections are applicable to structures with clear span greater than 0.9 m:

– *Safety inspections*: whose purpose is to identify significant deficiencies or signs of damage which represent or can lead to a danger to the public; they typically require frequent scheduling.
– *General inspections*: whose purpose is to provide information on the physical condition of all *visible* elements of the structure, consisting of a visual inspection of all parts that can be inspected without the need for additional access equipment; they shall be undertaken at intervals of 24 months.
– *Principal inspections*: whose purpose is to provide information on the physical condition of all *accessible* parts of a structure, consisting of a close examination within touching distance of the structure; they shall be undertaken at intervals of 72 months, or longer if appropriate, and are not required for spans below 1.8 m.
– *Special inspections*: whose purpose is to provide detailed information on a particular element, part, area or defect that is causing concern; they are considered in particular situations, e.g., cast iron structures, post-tensioned concrete bridges, structures with weight restrictions, damage following bridge strikes.
– *Inspections for assessment*: whose purpose is to provide the information required to undertake a structural assessment.

The interval between principal inspections may be increased to 8, 10 or 12 years, following a risk assessment comprising five categories, each with its own weighting W, as reported in Table 2. They include some parameters not related to structural vulnerability, such as those related to hydraulic risk and consequences of failure. The outcome is a total risk score T between 0 and 100, and the interval can be increased if $T \geq 65$.

Table 2. Input variables for determining the risk-based principal inspection intervals.

Category *(W)*	Parameter	Number of entry option	Risk score range
Structure type *(20%)*	Structural form	5	0-4
	Constituent material	10	0-4
	Age of the structure	4	0-2
	Headroom	3	0-1
	Span	3	0-2
Environment *(17%)*	Exposure to de-icing salts	3	0-3
	Scour	3	0-4
	Flooding	3	0-4
Inspection and assessment *(25%)*	Level of visual accessibility	6	0-5
	Likelihood of latent defects	4	0-3
	Assessment	4	0-4
Condition *(20%)*	Inspector's opinion (*)	3	2-3
	Condition performance indicator (average score) (*)	5	0-4
	Condition performance indicator (critical element score) (*)	5	0-6
	Signs of concrete deterioration (*)	3	0-3
Consequences *(18%)*	Applied loading	4	0-3
	Route supported	7	0-4
	Obstacle crossed	8	0-5
	Potential failure mode	3	0-2

(*) If conditions are not known or there are signs of concrete deterioration, interval remains at 6 years.

As can be seen, conditions are assessed using two criteria: the inspector's subjective condition rating (good, fair, or poor), and two *Condition Performance Indicators* (Condition PI). These are calculated using a severity/extent condition rating system on a scale 0-100: an *average* Condition PI score based on all elements, and a *critical* Condition PI score based on the

most critical element. PIs 40-65 are *poor*, 65-80 *fair*, 80-90 *good*, 90-100 *very good*. Note that, if the subjective condition rating is poor or a PI score is lower than 40 (which may be considered *very poor*), then this risk assessment is not permitted. Also, not all structures are in scope, e.g., complex structures are excluded.

Despite efforts in reducing subjectivity in the inspection process, including targeting the inspector's competency (Sandberg et al., 2022), several methods are used in practice for condition rating in the UK: one such method is reported in Atkins (2007), partly based on a previous method (Highways Agency, 2007), and outlined in the following.

Firstly, bridge elements are listed according to their importance, from Low to Very High importance. Examples of Very High importance elements are deck elements, half joints, piers; examples of High importance elements are abutments, bearings, joints, drainage, foundations.

Severity and extent of defects are assigned through 5 classes each, leading to an Element Condition Score, ECS, ranging from 1.0 (best) to 5.0 (worst). This is reduced by an Element Condition Factor ECF for Low to High importance elements, so as to determine the Element Condition Index ECI = ECS - ECF.

Moving from element-level to structure-level, two Structure Condition Scores are computed: the *average* SCS_{av} weighs the ECIs through an Element Importance Factor, ranging from 1.0 (Low importance) to 2.0 (Very High importance), whereas the critical SCS_{crit} is the maximum ECI among elements with Very High importance. Finally, as both SCSs range from 1 (best) to 5 (worst), they are rescaled into Condition PIs ranging from 0 (worst) to 100 (best).

Finally, every alternate Principal Inspection, a Structural Review is undertaken to determine the need for structural assessment, as set out in CS 451 (Highways England, 2020). The reviewer applies a Risk Appraisal, which is a numerical procedure based on the calculation of a risk score and a reliability score. Most input parameters are the same as in Table 2, albeit with different numerical values, while others differ, for instance change in condition or in loading since design or last assessment. A decision matrix then resolves the two scores to determine the need for assessment, recommending low to very high priorities.

3 APPLICATION TO CASE STUDIES

The procedures presented above are applied to two bridges belonging to Italian national roads and located in Southern Italy. The supported routes feature a single carriageway with two lanes and no restrictions in place.

3.1 *Case studies*

Bridge I is a three-span structure (maximum span 21.55 m), constructed presumably in the '80s and located in a rural area over natural ground. The structural scheme is made of a continuous RC beam-and-slab arrangement with diaphragms, supported over the piers (Figure 2a) and presumably over the abutments, which are neither visible nor accessible.

Defects are generally minor, with some areas of cracking in the external main beams (ECS = 3.3), likely due to corrosion of the embedded reinforcing bars (Figure 2b).



Figure 2. Bridge I: (a) main span view; (b) external beam with longitudinal cracking.

Bridge II is a large five-span structure (maximum span 89.8 m), constructed in the '70s and located in a rural area over a river at a great height. The first and the fifth spans are made of two deep RC beams with two end transverse beams. The structural scheme of the three main spans is made of steel-concrete composite girders supported over the piers, with half-joints (Figure 3a).

Defects are generally minor, except for some RC beams and piers which feature transverse and diagonal cracking (Figure 3b), likely due to shear (ECS = 4.3).



Figure 3. Bridge II: (a) bridge aerial view; (b) RC pier with diagonal cracking.

3.2 *Results and discussion*

According to the Italian guidelines, Bridge I has a ML level of deterioration; consideration of the other parameters in Table 1 increases the structural vulnerability class to M, mainly due to the effect of the speed of deterioration, whereas the hazard and exposure classes are respectively H and L. The resulting structural CA is M; therefore, besides periodic inspections every year, the structure has to undertake a preliminary assessment (L3), as well as an additional inspection if appropriate.

On the other hand, Bridge II has a MH level of deterioration; consideration of the other parameters in Table 1 results in a structural vulnerability class MH, whereas the hazard and exposure classes are respectively H and M. The resulting structural CA is MH; therefore, besides periodic inspections every 6 months, the structure has to undertake a preliminary assessment (L3), as well as an additional inspection, if appropriate.

When considering the UK guidelines, Bridge I has a good PI_{av} (82.0), while its PI_{crit} is poor (50.3). It would be possible to apply the procedure to extend the principal inspection interval, but since there are signs of concrete deterioration the interval remains at 6 years (Table 2). On the other hand, Bridge II has a fair PI_{av} (76.3), while its PI_{crit} is very poor (22.1), due to the shear cracks on a pier. As such, it is not allowed to increase the 6-year principal inspection interval.

When undertaking the UK structural review, both bridges are recommended to have a structural assessment with high priority. Bridge I is in better conditions, but the presence of critical elements, which cannot be adequately inspected during a principal inspection, leads to a more onerous score, and this is a parameter not included in the Italian rating.

Table 3 resumes the outcome of the inspection rating and assessment required. The PI_{crit} scores seem to be more onerous than the Italian LD, e.g., Bridge II is in the worst class in the UK, while in Italy is in the second worst. This is due to the fact that the most defective elements have not been considered critical elements, as defined in the Italian guidelines, whereas in the UK most structural elements are listed as of Very High importance, regardless of the significance of the observed defects on the structural integrity. On the other hand, the PI_{av} scores seem to align better with the Italian LD, in spite of the LD being based on the worst-conditioned element. This suggests that the UK condition rating is slightly more conservative than the Italian one. However, inspection intervals are considerably greater in the UK and, for the case studies presented, the recommendations for structural assessment are comparable.

Table 3. Outcome of inspection rating and assessment required according to Italian and UK guidelines.

	Italy			United Kingdom			
Bridge	LD	CA	Assessment	Opinion	PI_{av}	PI_{crit}	Assessment
I	ML	M	L3	Good	Good	Poor	High priority
II	MH	MH	L3	Fair	Fair	Very poor	High priority

Finally, it is worth noting that, for the Italian guidelines, priorisation within the class is not possible, as is the case for all qualitative methods, whereas for the UK guidelines it is possible to use the associated numerical values to establish a priority order.

4 CONCLUSIONS

In this paper, the Italian and UK risk-based methodologies for assessing the structural vulnerability of existing highway bridges are presented and applied to two case studies.

The vulnerability assessment is strictly related to the inspection process, although there are also other factors affecting the assessment. The Italian methodology is qualitative in nature and explicitly computes a vulnerability class, which is then combined to hazard and exposure classes to return Classes of Attention for specific risks, among which the structural risk. Conversely, the UK methodology is quantitative, but there is no explicit calculation of a vulnerability class.

Firstly, a stark difference is found in the time intervals between inspections: in Italy periodic inspections are at most every 2 years, with additional inspections as appropriate, whereas in the UK principal inspections are at least every 6 years, with general inspections every 2 years.

Secondly, the UK condition rating, in which average and critical condition performance indicators are scored on scales from 0 to 100, generally returns more conservative results than the Italian rating, which is assigned through five *levels of deterioration*, largely based on the worst-conditioned element. However, when examining the effects of the rating on the inspection process, the Italian guidelines seem more conservative: the UK scoring may be used to increase the interval between principal inspections through risk assessment, whereas the Italian level of deterioration is used to determine an overall Class of Attention, which may even reduce the interval of periodic inspections from the maximum of 2 years.

Thirdly, the two case studies show that results are comparable when evaluating the need of a structural assessment.

Finally, it must be noted that, in spite of both methodologies trying to reduce variation in the inspection process, subjectivity is still present, particularly when rating specific defects and estimating their importance on the structural behaviour.

ACKNOWLEDGEMENTS

This study was supported by Fabre (Research consortium for the evaluation and monitoring of bridges, viaducts and other structures, www.consorziofabre.it/en) within the activities of the Fabre-ANAS 2021-2024 research programme.

The authors are grateful to Niall McKay (AtkinsRéalis, UK) for his valuable comments.

REFERENCES

Ansfisa 2022. Istruzioni Operative per l'applicazione delle Linee Guida Per La Classificazione E Gestione Del Rischio, La Valutazione Della Sicurezza Ed Il Monitoraggio Dei Ponti Esistenti.

Atkins 2007. Guidance Document for Performance Measurement of Highway Structures Part B1: Condition Performance Indicator.

Bongiovanni, G., Celilli, A., Clemente, P., Giovinazzi, S. & Ormando, C. 2021. Seismic response of a r.c. viaduct during different earthquakes. In: Cunha, A. & Caetano, E., eds. 10th Int. Conf. on Structural Health Monitoring of Intelligent Infrastructure, 30 June - 2 July 2021 Porto.

Buffarini, G., Clemente, P., Giovinazzi, S., Ormando, C., Pollino, M. & Rosato, V. 2022. Preventing and Managing Risks Induced by Natural Hazards to Critical Infrastructures. Infrastructures, 7.
Clemente, P. 2020. Monitoring and evaluation of bridges: lessons from the Polcevera Viaduct collapse in Italy. Journal of Civil Structural Health Monitoring, 10, 177–182.
Clemente, P., Bongiovanni, G., Buffarini, G. & Saitta, F. 2019. Structural health status assessment of a cable-stayed bridge by means of experimental vibration analysis. Journal of Civil Structural Health Monitoring, 9, 655–669.
Highways Agency 2007. Inspection Manual for Highway Structures. London.
Highways England 2020. CS 451 Structural review and assessment of highway structures. Highway Structures & Bridges. Highways England.
Highways England 2021. CS 450 Inspection of highway structures. Highway Structures & Bridges. Highways England.
Lipari, A., Buffarini, G., Clemente, P., Mckay, N. & Ormando, C. in press. A comparison of Italian and UK methods for establishing the need for structural assessment of bridges. II Fabre Conference - Existing bridges, viaducts and tunnels: research, innovation and applications (FABRE24), 12-15 - February 2024 Genova, Italy.Ministero delle infrastrutture e dei trasporti 2022. Linee guida per la classificazione e gestione del rischio, la valutazione della sicurezza ed il monitoraggio dei ponti esistenti.
National Highways 2022. CS 454 Assessment of highway bridges and structures. Highway Structures & Bridges. Highways England.
Sandberg, J., Pires, C., Mckay, N., Laco, J. & Mitchell, R. 2022. Inspection and assessment. In: Parke, G. & Hewson, N. (eds.) ICE Manual of Bridge Engineering. Thirded. London: ICE Publishing.
Santarsiero, G., Masi, A., Picciano, V. & Digrisolo, A. 2021. The Italian Guidelines on Risk Classification and Management of Bridges: Applications and Remarks on Large Scale Risk Assessments. Infrastructures, 6.

Bridge Maintenance, Safety, Management, Digitalization and Sustainability – Jensen, Frangopol & Schmidt (eds)
© 2024 The Author(s), ISBN 978-1-032-77040-6
Open Access: www.taylorfrancis.com, CC BY-NC-ND 4.0 license

The knowledge process for the structural assessment of existing concrete bridges with post-tensioned cables: Application to a case study

A. Natali, S. Celati, D. Gaudioso & W. Salvatore
Department of Civil and Industrial Engineering, University of Pisa, Pisa, Italy

D. Coletta & M. Malavisi
MOVYON SPA | Gruppo Autostrade per l'Italia, Nuovo Centro Direzionale, Firenze, Italy

ABSTRACT: A structured project of knowledge is fundamental to comprehend the structural behavior of existing structures. The deeper and accurate is the level of analysis performed within, the lower is the approximation of evaluations and the higher the reliability of the outcomes. In the case of bridges with post-tensioned cables, this process gets trickier due to the hidden defects of the cables, indeed the level of approximation is also affected by the difficulty of not knowing *a-priori* their position and the impossibility of investigating all the cables. In this framework, this paper presents a methodology around the process of knowledge of these bridges, and its application to a case study. The aim of the method is reaching a deep level of knowledge for the proper characterization of the relevant variables, hence allowing to calibrate the values of the safety coefficients on the actual level reached, for a more accurate structural assessment.

1 INTRODUCTION

Nowadays, the road managers are dealing with the management of many infrastructures which for the most have reached the end of their design life with poor maintenance measures adopted in the time (Zhang, Liu, Liu, Lan, & Yang, 2022). Although some risk-based methodologies have been developed to provide instruments for expedite pointing out of critical evaluations (ANSFISA, 2022; Ministero delle Infrastrutture e dei Trasporti, 2020), a good amount of existing bridges (the damaged ones and/or with more vulnerable structural types, and/or the more exposed to traffic and those crossing urbanized areas or other infrastructures (Natali, Cosentino, Morelli, & Salvatore, 2023)) requires, or will soon require, an accurate assessment of the level of safety. For such purposes and to obtain reliable results, it is fundamental to properly define with limited uncertainties all the local and global parameters that characterize the capacity and the demand of the structure. Moreover, in the field of existing structures, it is also necessary to check the conservation status of the structure, pointing out defects and local/global vulnerabilities. Among the local level parameters, there are many to be statistically determined, so to be probabilistically treated (i.e. material strength and mechanical characteristics and hidden defects), and for which uncertainties (aleatory or epistemic) depend both on the accuracy of the measuring device and on the number of measures performed. Hence, besides choosing the more appropriate measuring devices and testing circumstances to maximise the related accuracy, to reach an appropriate and desired confidence level of the estimation it is necessary to properly evaluate the number of tests to be performed (the higher the number of the tests, the higher accuracy of the measures (Figure 1a) and the higher the confidence level, meaning reduction of uncertainties (Figure 1b)).

DOI: 10.1201/9781003483755-315

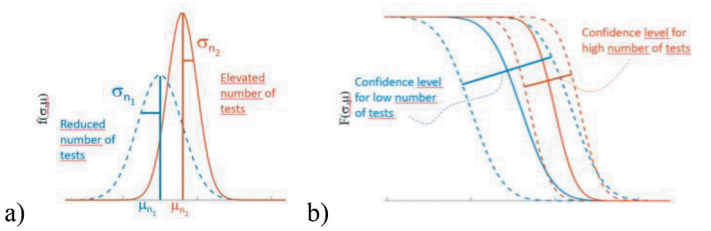


Figure 1. Examples of updating of a) Probability density function and b) Cumulative distribution function by increasing the number of tests (from n1 – reduced number of tests – to n2 – increased number of tests; with σ_i and μ_i, respectively, the standard deviation and medium value of the distributions).

The characterization of the local parameters gets harder when their population is not known in advance, as in the case of hidden defects of the pre-stressing system of Reinforced Concrete bridges with Post-Tensioned cables (RC-PT bridges). Indeed, in this case, the distribution and localization of defects is not known, so determining the amplitude of a significative sample is an iterative process. The method for the quantification and characterization of such defects is included in the procedure called "Special Inspection", which has been proposed and applied as showed within (Mazzatura, 2023; Mazzatura, Caprili, Salvatore, Casas, et al., 2023; Mazzatura, Caprili, Salvatore, Lupoi, & Ficociello, 2023). In this framework, this paper presents a methodology for designing the knowledge process aimed at the structural assessment of RC-PT existing bridges, with an application to a relevant Italian RC-PT viaduct. The aim of the method is reaching a deep level of knowledge for the proper characterization of all the relevant variables, including the hidden defects, hence allowing to calibrate the values of the safety coefficients on the actual level reached, for a more accurate structural assessment.

2 DESCRIPTION OF THE CASE STUDY AND DEFINITION OF THE PROCESS OF KNOWLEDGE

The 8-spans viaduct (Figure 2) is around 595 m long, and constituted of, starting from the left, three simply supported RC multi-beam decks and four *T-shaped* systems (the lateral ones are 70 m long, while the central ones are 116 m long). The peculiarity of the viaducts is the *T-shaped* systems, each one composed of one central pillar and two cantilever decks (Figure 3). The decks are composed of precast RC segments which are kept together and pre-stressed through post-tensioned Dywidag re-bars. The four *T-shaped* systems are, in the first construction stage, built one independent from the other one, then made continuous through shear connections. The constructive technique used for the realization of the decks of the *T-shaped* systems can be defined "intrinsically fragile", since the segments are kept together only by the pre-stressing system and the friction among the consecutive ones.

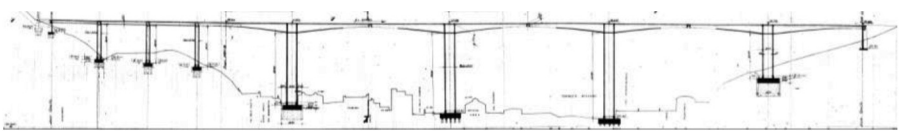


Figure 2. Longitudinal view of the viaduct.

The process of knowledge has been defined with the final aim of properly characterizing all the parameters that allow the definition of the demand and capacity of the structure, including the hidden defects that can be in the pre-stressing system, and organized as in the following: (i) Historical/critical analysis and of the original documentation; (ii) Investigation around the

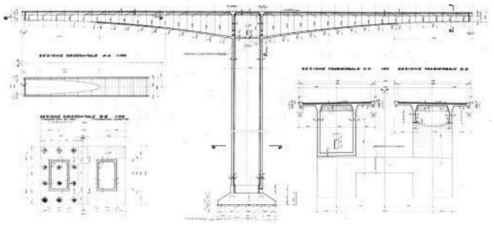


Figure 3. The *T-shaped* system.

global parameters that allow the definition of demand and capacity of the structure; (iii) Investigation around the local parameters for the definition of demand and capacity of the structure: characterization of materials, check of structural details, studies and *in-situ* surveys for the conservation status and damage of the Dywidag re-bars (the tests and *in-situ* actions have been planned accordingly to (Mazzatura, 2023; Mazzatura, Caprili, Salvatore, Lupoi, et al., 2023)). Furthermore, in parallel with the in-situ surveys, two numerical Finite Element (FE) models have been developed to understand, in the former, the stage constructions of the structure and its evolving stress state, and, in the latter, to simulate and calibrate the structural response of the structure to the external loads on the global investigations preformed, and then used for the evaluation of the demand. About point (i) of the methodology, there is plenty of original documentation available for this structure, together with a BIM model and all the results from a recent experimental campaign. This material has been used to characterize the current global and local geometry, the composition of the construction details and of the pre-stressing system, and, finally, the results from the experimental campaign have been adopted the for the *prior* materials mechanical characterization.

3 INVESTIGATIONS ON GLOBAL PARAMETERS

The investigations on global parameters comprehend global geometry, visual inspection for the conservation status, design of the in-situ surveys for the characterization of the natural frequencies of the system. Dealing with the global and constructive elements geometry, considering the plenty of material already at disposal from the original documentation, some spot measurements have been performed to check the correspondences, that have been positively verified. Regarding the conservation status of the structure, visual inspections have been performed and no local or global vulnerabilities have been identified - with reference to what it has been possible to inspect. The visual inspections have been completed with the so-called Special Inspections to investigate the conservation status of the pre-stressing system (§4.3). Finally, the dynamic behavior and natural frequencies of the system have been investigated through the Operational Modal Analysis (OMA). The OMA has been organized in different configurations that involve only the *T-shaped* systems. To better enhance the available instrumentation and time to perform such tests, the base configurations (Figure 4) involve two consecutive *T-shaped* systems, acquiring transversal (Y), vertical (Z) and longitudinal (X) directions in correspondence of the end zones of the decks, and Y and X directions in correspondence of the pillar. These acquisitions allow to catch the main modal shapes of the structure, including transversal vibration of the *T-shaped* systems, longitudinal movements of the viaducts, flexural and torsional movement of the decks. These base configurations are repeated for each couple of consecutive *T-shaped* system so that all configurations have at least one *T-shaped* system in common (in this way, the results can be merged and combined despite the non-simultaneity of the acquisitions). The tests were conducted during the night under conditions of complete disruption of vehicular passage, for a time acquisition of at least 45 minutes per each configuration (minimum time considering the expected first natural frequency).

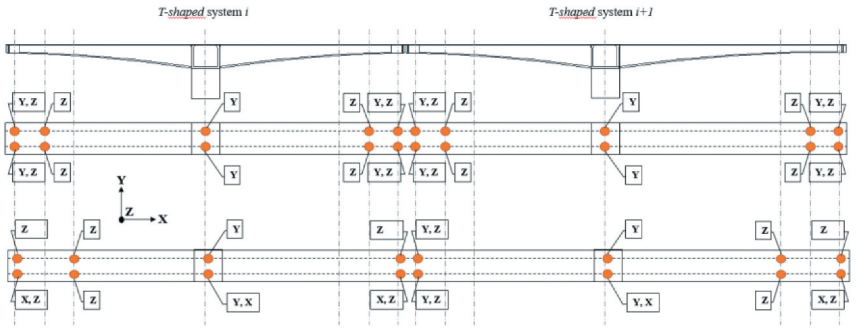


Figure 4. OMA tests: examples of the basic configurations for the acquisitions.

4 INVESTIGATIONS ON LOCAL PARAMETERS

The investigations on the local parameter include those for: checking the structural details, characterizing the materials properties, assessing the conservation status and damage of the pre-stressing system through *in-situ* surveys. Dealing with checking the structural details, *Georadar* has been used to have a view of the actual distribution of the reinforcement inside the segments of the decks, and then the correspondence with the original documentation has been positively verified. This matching allowed to consider the structural details fully characterized for the directly investigated zones and known with quite accuracy in the other zones.

4.1 *Concrete: Conservation status, prior material characterization and testing campaign*

The *prior* mechanical characterization of the concrete has been performed starting from the characteristic strength values according to the original documentation, and other assumptions and deductions according to literature and reference codes. Focusing into the *T-shaped* systems, concretes of pillars and decks' segments have to be analyzed separately. Table 1 gather the mechanical properties of the concretes: the characteristic cubic compressive strength R_{ck} has been deducted from the original documentation, which reported the parameter $\sigma_{r,28gg}$ as its corresponding value according to the standard of the time (R.D.L. 2229/1939 (*Norme per l'esecuzione delle opere in conglomerato cementizio semplice od armato. Regio Decreto Legge 16 novembre 1939.*, 1939)). $\sigma_{r,28gg}$ is equal to 400 kg/cm^2 for the pillars and 500 kg/cm^2 for the decks. The other parameters collected in the table are calculated consequently by adopting the related formulas from NTC2018 ("Norme tecniche per le costruzioni 2018- NTC 2018" 2018).

Table 1. Concrete: mechanical parameters according to the original documentation and derivations.

	Mechanical parameters						
Concrete	R_{ck}† [N/mm^2]	f_{ck}† [N/mm^2]	f_{cm}† [N/mm^2]	E† [N/mm^2]	ν†	G† [N/mm^2]	ϒ† [kN/m^3]
Pillars	40	33	41	33643	0.2	14018	25
Decks	50	42	550	35547	0.2	14811	25

† $R_{ck}/f_{ck}/f_{cm}$ = characteristic cubic/cylindrical/medium compressive strength; E = elastic modulus; ν = poisson modulus – not-cracked concrete; G = shear modulus – not-cracked concrete; ϒ = weight per unit volume.

The *prior* probabilistic modeling of the compressive strength of both the concretes has been done with the following assumptions: (i) a lognormal distribution is assumed; (ii) sample size *n'* is equal to 3 and degree of freedom *ν'* is equal to 10 (from JCSS Model Code JCSS probabilistic model code part 3: resistance models ("JCSS Probabilistic Model Code. Part 3:

Resistance Models," 2000)); (iii) the coefficient of variation CV' is assumed equal to 0.15, which is the typical value for concrete compressive strength ("JCSS Probabilistic Model Code. Part 3: Resistance Models," 2000); (iv) the characteristic strength value is the one deducted from the original documentation (40 and 50 N/mm^2 respectively for pillars and decks concrete). By this assumption, the *prior* probabilistic characterizations of pillars and decks concretes are defined by the following parameters: the characteristic values $\widehat{fc'}$ are respectively equal to 42.90 and 53.63 N/mm2, the medium values $\widehat{Rc'}$ are 51.69 and 64.62 N/mm2, and the standard deviations σ' are 5,343 and 6,681. The symbol 'is here adopted to distinguish *prior* knowledge from further updates.

In the framework of this study, the update of the *prior* distributions has been performed considering the experimental campaign recently executed, hence no other destructive or non-destructive tests have been performed. In the following, Table 2 collects the main information and deductions from the experimental campaign then used in this study to update the *prior* distributions.

Table 2. Relevant data from the experimental campaign for the characterization of decks and pillars' concretes.

Concrete	n†	μ† [N/mm^2]	σ†	f_{ck} † [N/mm^2]	E† [N/mm^2]	G† [N/mm^2]
Pillars	18	61,76	6,83	50,27	37987	15828
Decks	8	62,18	8,63	46,93	38064	15860

† n = sample size; μ = medium value of compressive resistance; σ = standard deviation; f_{ck} = characteristic value (5%); E = elastic modulus; G = shear modulus.

4.2 *PT cables: Special inspections for conservation status and tests for material characterization*

The Special Inspections for RC bridges with post-tensioned cables are required by the Italian Guidelines for existing bridges (Ministero delle Infrastrutture e dei Trasporti, 2020) to detect possible voids and defects in the pre-stressing system and quantify their severity. The general procedure for the design and execution of the Special Inspections (Mazzatura, Caprili, Salvatore, Lupoi, et al., 2023) is the following: (i) Phase 0a: Individuation of homogeneous populations within the pre-stressing elements, and relative zones to be investigated; (ii) Phase 0b: Special non-destructive surveys to assess the actual number and position of pre-stressed elements along the beam (through *Georadar* scans) and of possible voids (through *Tomography* scans); (iii) Phase 1a: Evaluation of the sample size and localization of the semi-destructive or locally destructive tests for each homogeneous population; (iv) Phase 1b: Execution of the semi-destructive or locally destructive tests. In this phase, concrete is removed till cable sheet, which is visually and through the *Endoscope* inspected to see its conservations status and detect possible damage. Then, a piece of sheet is cut away, together with grout, to assess the actual presence of voids and/or possible damage in the pre-stressing element (oxidation, corrosion, reduction of area). If defects are found in Phase 1b, it is necessary to progressively deepen the investigations.

Phases 0a to 1b have been applied in the framework of this study, with the additional evaluation of the mechanical properties of the Dywidag re-bars through hardness tests during Phase 1b. For each *T-shaped* system, and considering their symmetry, at least one zone has been individuated, corresponding to the changing of curvature of the Dywidag re-bars (Figure 5 – "Phase 0a"). After pointing out the exact location and geometry of the cables through *Georadar* acquisitions (no relevant differences with respect to the original drawings has been found), *Tomography* scans have been performed (Figure 5 – "Phase 0b") to localize possible defects. Figure 5 – "Phase 1a" shows in green the zones where Phase 1b actions have been executed: the green ones are those where defects could be present according to *Tomography* scans, while those in red are the other zones to be checked to conduct sample surveys. The Phase 1b activities highlighted that all the inspected spots are characterized by a good

conservation of the cables sheet, with no voids (grout fully present) and no oxidation of the Dywidag reinforcement. This suggests that there is a good probability that the pre-stressing system of the *T-shaped* structures is characterized by good conservation status, hence no further iterations of Special Inspections have been executed.

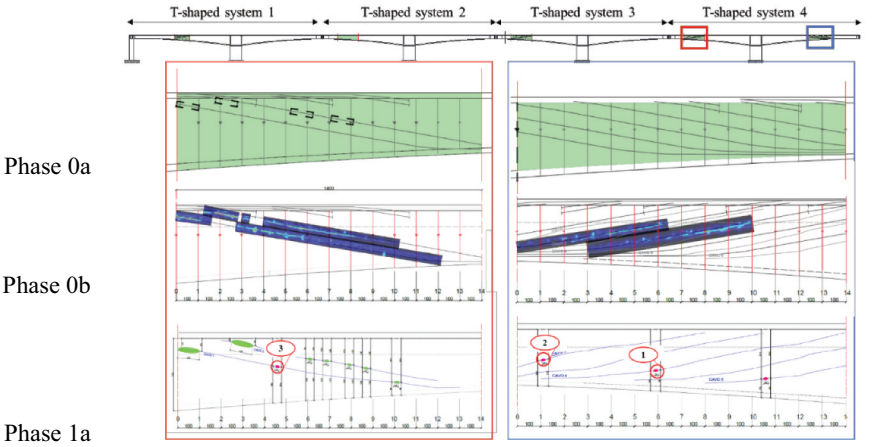


Figure 5. Special Inspections for the T-shaped systems: example of application to two inspected zones.

The hardness tests have been executed with a portable durometer in three zones (highlighted with red circles, Figure 5). A detailed procedure has been followed to obtain reliable results (Mazzatura, Caprili, Salvatore, Casas, et al., 2023). Table 3 gathers the results of the measurements and the correlations with the material strength according to ASTM E-140 (2019). The strength values derived from the tests are compatible with the one from the original documentation (where the ultimate tensile strength is at least equal to 10500 kg/cm^2). Despite only 3 tests could have been executed, the variability among them is quite low, and the low values of the coefficient of variation suggest the good executions of the measures, guaranteeing the reliability of the results.

Table 3. Measurements from the hardness tests.

Test spot	Medium Hardness [HV]	Ultimate tensile strength [N/mm^2]	CoV†	Sample size
1	294	919	1,6%	12
2	296	923	1,3%	12
3	299	936	4,7%	12

† CoV = Coefficient of variation.

The values deducted from the hardness tests have been used to update the *prior* characterization of Dywidag steel. The *prior* probabilistic modeling of tensile strength of Dywidag steel has been done with the following assumptions: (i) a lognormal distribution is assumed; (ii) sample size *n'* is equal to 50 and degree of freedom *v'* is equal to 10 (from JCSS Model Code JCSS probabilistic model code part 3: resistance models ("JCSS Probabilistic Model Code. Part 3: Resistance Models," 2000)); (iii) the coefficient of variation CV' is assumed equal to 0.025, which is the typical value for steel tensile strength ("JCSS Probabilistic Model Code. Part 3: Resistance Models," 2000); (iv) the characteristic strength value is the one deducted from the original documentation.

By this assumption, the *prior* probabilistic characterization of Dywidag pre-stressing system steel is defined by the following parameters: the characteristic value $\widehat{fy, p'}$ is equal to 884 N/mm^2 and the medium value $\widehat{fp, p'}$ is 1040 N/mm2.

5 POST-PROCESS OF THE RESULTS – GLOBAL PARAMETERS AND CALIBRATION OF THE FE GLOBAL MODEL

Two numerical FE models have been developed with the purposes of studying the evolution of the stress state and static scheme of the structure during construction, and of evaluating the demand in static condition. In the first model, all structural components were modelled using *beam* elements, with the aim of reproducing the construction phases from the assembly of the RC segments, the placement of pre-stressing system and post-tensioning application, to the variation of the static scheme following the insertion of shear connections. In this model, the cables have been modelled as elements working only in tension. In the second model, *shell* elements have been used to model of both deck and pillars to more accurately recreate the deformative behaviour of the structure, together with the structural response to external loads. In this model, the effects of pre-stressing system have been modelled by adopting the *equivalent loads* method and precautionary considering the relative short and long-term losses equal to 30%. In both models, global geometry has been deducted from the point cloud extracted from the BIM model at disposal, to represent the current geometrical configuration of the structure. The position of the pre-stressing system has been extracted from the original drawings, and updated, if necessary, thanks to the *Georadar* scans executed *in-situ* for the Special Inspection (§4.2). The constrains have been properly modelled through springs with difference stiffnesses for each degree of freedom in order to represent the actual behaviour. The second model has been appropriately calibrated based on the frequencies and modal forms obtained from the post-process of the accelerations acquired from the OMA executed *in-situ*. The data analysis and processing procedure allowed to point-out four main modes then adopted for the calibration of the FE mode (Figure 6): the modes 1 and 2 are flexional transversal modes in phase and in antiphase; the modes 4 and 6 are flexional vertical modes. The calibration procedure was conducted in a semi-automatic manner based on frequency matching, by verifying that the model's vibration modes were comparable with the experimental ones.

The parameters that have been updated in the calibration process are the elastic modulus of the decks and of the pillars, and the stiffness of the springs representing the shear connections between the consecutive *T-shaped* systems.



Mode 1. F= 0.47 Hz Mode 2. F= 0.71 Hz Mode 3. F= 1.36 Hz Mode 4. F= 1.56 Hz

Figure 6. Modal shapes of the FE model used for calibration process.

6 POST-PROCESS OF THE RESULTS – LOCAL PARAMETERS

The method to update the materials strength is defined according to ("JCSS Probabilistic Model Code. Part 3: Resistance Models," 2000) and considers, for the concrete, the knowledge acquired from the previously experimental campaign (Table 2) and, for the Dywidag re-bars, the values acquired from the hardness tests (Table 3). The so obtained *updated* probabilistic characterizations of pillars and decks concretes are defined by the following parameters: the characteristic values $\widehat{fc'}$ are respectively equal to 43.66 and 45,66 N/mm^2, the medium values $\widehat{Rc'}$ are 57,97 and 59,14 N/mm^2, and the standard deviations σ'' are 1,088 and 1,078. Regarding the Dywidag pre-stressing system, the characteristic values $\widehat{fy,pk''}$ is equal to 790,42 N/mm^2 and the medium value $\widehat{fp,p''}$ is 878,52 N/mm^2. With respect to the *prior* characterization, it can be noticed that most of the characteristic values have slightly reduced, but also the standard deviations, which highlights the increase of the accuracy of the evaluations.

7 EVALUATION OF SAFETY COEFFICIENTS ON THE ACTUAL LEVEL OF KNOWLEDGE

The partial safety coefficients have been calibrated following the entire process of knowledge and once the probability distributions of the material strength characteristics have been defined. According to JCSS formulations ("JCSS Probabilistic Model Code. Part 3: Resistance Models," 2000), the partial coefficients γ_M include both the model uncertainties γ_{mod} related to the type of mechanism to be checked and those related to the probability distribution of the material considered γ_{mat}, Equation (1).

$$\gamma_M = \gamma_{\mathrm{mod}} \cdot \gamma_{mat} \tag{1}$$

The model uncertainties follow a lognormal distribution with medium values μ and coefficient of variation CoV equal to, respectively, 1 and 0,1 for shear and torsion safety checks and 1,2 and 0,15 bending checks. The definition of the model uncertainties includes taking into consideration the aimed reliability index, that for the case study structure – consequence class 3 – is equal to 3,3, according to the fib Bulletin No.80 ("Partial factor methods for existing concrete structures. Fib Bulletin No. 80.," 2016). Following these considerations and by applying JCSS formulas, the resulting partial coefficient for modelling uncertainties are 1,11 for shear/torsion related safety checks ($\gamma_{mod,T}$) and 1,00 for bending related safety checks ($\gamma_{mod,F}$) Regarding the partial coefficients that considers material uncertainties γ_{mat}, JCSS formulations still have been adopted, which consider the *updated* mean values, standard deviations and final sample sizes following the whole and comprehensive process of knowledge performed on the study (§6). As an instance, γ_{mat} for pillars and decks concrete is 1,21, while for the Dyvidag steel is 1,10. Table 4 gathers the final partial safety coefficients to be adopted on concrete and steel materials composing decks and pillars of the *T-shaped* systems, when executing bending and shear/torsion safety checks, and compares these values to the ones according to NTC2018 ("Norme tecniche per le costruzioni 2018- NTC 2018," 2018). It can be noticed that there is a general reduction of the values thanks to the increase of knowledge reached.

Table 4. *Updated* partial safety coefficients for concrete and steel materials for bending and shear/torsion safety checks.

Material	Updated partial safety coefficients	Partial safety coefficients according to NTC2018 ("Norme tecniche per le costruzioni 2018- NTC 2018" 2018)	Variation
Pillars	$\gamma_{M,T}$† = 1,35	1,5	-10,0%
concrete	$\gamma_{M,F}$† = 1,21		-19,3%
Decks	$\gamma_{M,T}$† = 1,35	1,5	-10,0%
concrete	$\gamma_{M,F}$† = 1,21		-19,3%
Dywidag	$\gamma_{M,T}$† = 1,21	1,5	+5,22%
pre-stressing system steel	$\gamma_{M,F}$† = 1,10		-4,35%

† $\gamma_{M,T}$ = partial safety coefficient for shear/torsion safety checks; $\gamma_{M,F}$ = partial safety coefficient for bending safety checks.

8 CONCLUSIONS AND FUTURE WORKS

This paper proposes a methodology for the definition of the process of knowledge of existing pre-stressed reinforced concrete bridges with post-tensioned cables (RC-PT bridges). The aims of the proposed methodology is to properly characterize all the parameters that allow the definition of the demand and capacity of the existing RC-PT bridges, including a novel procedure for the detection and characterization of hidden defects ("Special Inspections" (Mazzatura, Caprili, Salvatore, Lupoi, et al., 2023)). Then, the safety coefficients for the semi-probabilistic static structural assessment are calibrated on the actual level of knowledge achieved. The

proposed method has been applied to a 8-spans RC-PT viaduct characterized by very peculiar decks are composed of precast RC segments which are kept together through post-tensioned Dywidag re-bars. The investigation campaign related to the local parameters, referring particularly to the mechanical characterisation of the materials, allowed to enlarge the sample size and thus its representativeness for the evaluation of the characteristic and average values of the resistances, bringing the decrease of the safety coefficients of the materials (Table 4). At the same time, the experimental investigations at global level allowed a proper calibration of the numerical mode, then more catching and representative of the actual structural behaviour and response of the whole system. The application of the proposed method highlights how a suitably designed and calibrated knowledge process may allow for a better characterisation of the relevant variables, thus reducing the relative uncertainties and possibly reducing the caution when assessing the level of safety.

REFERENCES

ANSFISA. 2022. Istruzioni Operative per l'applicazione delle Linee guida per la classificazione e gestione del rischio, la valutazione della sicurezza ed il monitoraggio dei ponti esistenti.

JCSS Probabilistic Model Code. Part 3: Resistance Models. 2000. .

Mazzatura, I. 2023. Damage detection, localization, and quantification for steel cables of post-tensioned bridge decks.

Mazzatura, I., Caprili, S., Salvatore, W., Casas, J. R., Gammino, M., et al. 2023. Inspection and assessment of PT structures: Results from application to an existing bridge.

Mazzatura, I., Caprili, S., Salvatore, W., Lupoi, A., & Ficociello, A. 2023. A multi-phase survey approach for post-tensioned prestressed concrete bridge decks.

Ministero delle Infrastrutture e dei Trasporti. 2020. Linee guida per la classificazione e gestione del rischio, la valutazione della sicurezza ed il monitoraggio dei ponti esistenti.

Natali, A., Cosentino, A., Morelli, F., & Salvatore, W. 2023. Multilevel Approach for Management of Existing Bridges: Critical Analysis and Application of the Italian Guidelines with the New Operating Instructions.

Norme per l'esecuzione delle opere in conglomerato cementizio semplice od armato. Regio Decreto Legge 16 novembre 1939. 1939.

Norme tecniche per le costruzioni 2018- NTC 2018. 2018. BibLus-net. https://biblus.acca.it/download/norme-tecniche-per-le-costruzioni-2018-ntc-2018-pdf/.

Partial factor methods for existing concrete structures. Fib Bulletin No. 80. 2016. .

Standard Hardness Conversion Tables for Metals Relationship Among Brinell Hardness, Vickers Hardness, Rockwell Hardness, Superficial Hardness, Knoop Hardness, Scleroscope Hardness, and Leeb Hardness. ASTM E140-12B. 2019.

Zhang, G., Liu, Y., Liu, J., Lan, S., & Yang, J. 2022. Causes and statistical characteristics of bridge failures: A review. Journal of Traffic and Transportation Engineering (English Edition), 9(3): 388–406.

Bridge Maintenance, Safety, Management, Digitalization and Sustainability – Jensen, Frangopol & Schmidt (eds)
© 2024 The Author(s), ISBN 978-1-032-77040-6
Open Access: www.taylorfrancis.com, CC BY-NC-ND 4.0 license

Sustainable repair of concrete structures in Denmark

Jens Mejer Frederiksen & Christian Møller Nielsen
COWI A/S, Lyngby, Denmark

ABSTRACT: Repair of concrete structures must be considered very carefully and preferably only be used if the cause of the damage has been clarified and will be remedied. Furthermore, the repair must be able to achieve a durability that is comparable to the remaining life of the surrounding structure. Correct repair and possibly supplementary protection of concrete structures is in many cases a more sustainable and cheaper solution than replacing the same structure.

By March 2024, the authorities responsible for the management and maintenance of infrastructures in Denmark publish new General Work Specifications for the repair and protection of concrete structures.

The paper summarizes how the common European standards for repair and protection of concrete structures (the EN 1504 series) have been and will be further implemented in Denmark. Examples from the specifications are shown. The approach is applicable for other countries as well. To apply the standards the presumed methodology must be used.

It is presupposed that personnel have the necessary skills and adequate equipment and resources to design, specify and execute the work in accordance with the relevant part of EN 1504 and the requirements of the project specification. The skill levels for each function in the value chain of a repair project has been defined in the standard DS 2425. A training programme has been defined as well and training lectures are being planned.

The paper gives short illustrative examples of typical obstacles that can be met by the inspector of concrete structure to be repaired, the person in charge of the elucidation of defining the cause of damage and hence the extend, the person in charge of the design, the person in charge of pricing the works, the person in charge of the supervision and the person in charge of the execution.

1 INTRODUCTION

Since the mid-1980s, the production of concrete in Denmark has been subject to specific regulations that ensure the expected service life of all significant concrete structures in the construction and civil engineering sector. The starting point for the technical service life is 50 years of durability without significant maintenance for building structures. For infrastructure, the requirements for the technical service life have since the mid-1980s been raised to 120 years. This has essentially been achieved by increasing the requirement for cover thickness by +10 mm combined with the obtained understanding of how to avoid premature concrete deterioration.

Since the regulations came into effect in around 1985, there has not been a single case of premature deterioration or lack of durability of conditional concrete structures in Denmark to date, which is naturally very satisfactory.

Unfortunately, the same cannot be said for concrete structures predating this period. Back then, the available knowledge on concrete degradation and risks associated with different constituents and compositions of concrete was not effectively applied. Therefore, there are still some older structures in both buildings and infrastructure that need to be repaired or have their service life extended.

The pathological signs of degradation and damage typically result from either 1) frost damage, 2) alkali-silica reactions, 3) carbonation, or 4) chloride ingress. The first two initially

DOI: 10.1201/9781003483755-316

only lead to damages to the concrete but can later affect the load-bearing capacity of the structure critically if they progress.

The latter two cause damages to the reinforcement, and these damages typically fall into two different problem types. 'Carbonation' results in a uniform and extensive corrosion of the steel in the concrete, leading to delamination of the cover layer with a risk of passers-by near the structure being hit by concrete fragments. 'Chloride ingress', on the other hand, leads to more hidden, localized pitting corrosion that can cause a critical reduction in the cross-section of the reinforcement and thus collapse of the structural component. This has happened a few times in Denmark – fortunately without any loss of life. Hence, there is a strong focus on preventing a recurrence.

Other reasons for repair like exposure to fire, physical damage and overloading are naturally also relevant, but these types of repairs do not correlate with the initial quality of concrete in the same manner.

Table 1. Overview of the special Danish requirements (cf. [3]) as they have been practiced with success since the mid-1980s – only small modifications have been introduced in the period. Numbers with * are valid for infrastructures with an expected service life of 120 years.

Exposure category	Passive, P	Moderate, M	Aggressive, A	Extra aggressive, E	
Exposure class according to EN 206	X0	XC2	XD1	XD2	
	XC1	XC3	XS1	XD3	
		XC4	XS2	XS3	
		XF1	XF2	XF4	
		XA1	XF3	XA3	
			XA2		
Examples	Indoor (dry) and subsoil	Facades and other outdoor without salt	Mild saline environments and submerged	Direct salt exposure and freezing plus swimming pools	
	Exposure category (group of classes)				
Property	P	M	A	E	Unit
$f_{ck,cyl} \geq$	12	30	35	40	MPa
eqv$(w/c) \leq$	-	0.55	0.45	0.40	(by mass)
Binder type (Cement, fly ash, silica fume)	Restrictions according to DS/EN 206 DK NA				-
Strength class for cement, minimum	32.5	42.5	MPa		
Cover $c_{\min} \geq$	10	20	30 (40*)	40 (50*)	mm
Crack width $w_k \leq$	-	0.4	0.3	0.2	mm
Pre-stressed $w_k \leq$	-	0.3	0.2	0.1	mm
Air content $\geq$	-	4.5 %	4.5 %	4.5 %	(fresh, by volume)

The special Danish durability requirements for concrete are based on the principles now known from EN 206 ([2]), Annex F, Table F.1. Table 1 above illustrates the slightly stricter requirements imposed on concrete in Denmark, [3] compared to the requirements in EN 206 ([2]). Furthermore, Danish regulations, [3] have stricter documentation requirements compared to EN 206([2]), with regards to providing evidence of the concrete mix design of each produced and delivered batch.

Despite concrete requirements that provide the expected technical service life, there is still a need for repairs on brand-new structures, perhaps even to a greater extent than previously. This is mainly due to errors during construction, where deficiencies in the concrete cover on the reinforcement and in the concrete itself are often observed.

Table 2. How to come from 'repair method' according to [5] to the suitable product type with the 'General Work Specification ID' (A to G), cf. [7].

Repair method according to EN 1504-9	Execution method	Product type	Remarks	GWS type ID
3.1	Hand placement	Mortar or concrete	Used for repairs that are small enough to be executed by hand placement of mortar or concrete. It is of highest priority that the product is easy workable.	A
3.2 4.4	Fluid casting	Concrete	Used for larger repairs that can be cast in form at thicknesses over 35 mm.	B
7.1 7.2		Mortar	Used for small repairs that can be cast in form at thicknesses below 40 mm.	C
3.2 4.4 7.1 7.2	Underwater form casting	Mortar or concrete	Casting in form underwater Concrete or mortar Special concrete or mortar that, in its fresh state, does not wash out and can displace water from the form, eliminating the need for drying. Otherwise, like ID B or C	D
3.3 4.4 7.1 7.2	Casting on large surfaces	Wet sprayed concrete	In the wet spray method, a pre-mixed mortar-concrete blend is conveyed through hoses by a screw pump and sprayed onto the desired surface by compressed air at the outlet.	E
		Dry sprayed concrete	In the dry spray method, a dry mortar or dry concrete mix is conveyed through hoses by compressed air, and water is added only at the outlet, just before the material hits the substrate	F
3.2 4.4 5.3 7.1	Casting with slope, profiling	Mortar or concrete	Used for overlaying a concrete structure, possibly for simultaneous creation/restoration of slope conditions on upward-facing surfaces. Otherwise, like ID B or C	G

These deficiencies often include 'insufficient cover thickness' and 'inadequate compaction'. Consequently, whereas repairs previously mainly were made due to ageing of structures, repairs are now made on brand-new structures before they are even handed over and put into use. This places significantly higher demands on the quality of the repairs and the lifespan of repairs.

2 IMPLEMENTATION OF EN 1504

Since before its implementation in 2009, the incorporation of the EN 1504 series (cf. [5] for an introduction) into Danish repair regulations has been prepared, and adjustments have been made continuously as experiences have been gathered afterwards. Despite this, there has been a relatively slow adaptation to the methodology that is intended to be used.

With the latest revision, cf. [7] and [8], an assessment of suitability and a declaration of suitability have been introduced, as CE marking alone does not guarantee that a product is suitable for the specific application.

For repair products for concrete, the contractor must now ensure that an assessment of suitability has been conducted for the chosen products. This assessment should include, among other things, the following:

- A written statement regarding the suitability of the offered product(s) for each of the proposed repair types.
- Each product should be suitable for the respective casting method(s).
- The type testing shall cover the declared casting method(s).
- Identification information regarding workability.
- Identification of the intended repair type or method according to [5].
- Compliance with any additional requirements specified in the repair regulations or project specifications, e.g. electrical conductivity in case of application of cathodic protection.

The suitability assessment and declaration serve to ensure that the selected repair products are appropriate for the intended repair type and that they meet the necessary performance criteria. This helps to ensure the quality and effectiveness of the repairs carried out.

In Table 2 and Table 3 a way to come from 'the repair method found according to EN 1504-9′ to a 'suitable repair product type' is suggested.

Table 3. Guidelines for selecting product type and execution method based on orientation of the casting joint according to [9].

GWS type ID	A	B	C	D	E	F	G
Product type and method of execution	Mortar or concrete for hand placement	Concrete for fluid casting	Mortar for fluid casting	Mortar or concrete for underwater casting	Wet sprayed concrete	Dry sprayed concrete	Mortar or concrete for overlaying and profiling
Method according to EN 1504-9, [5]	3.1	3.2 4.4 7.1 7.2	3.2 4.4 7.1 7.2	3.2 4.4 7.1 7.2	3.3 4.4 7.1 7.2	3.3 4.4 7.1 7.2	3.2 4.4 7.1
How should the repair be carried out:							
Bottom up (dry)	●	–	–	–	●	●	–
From up and downwards (dry)	●	●	●	–	(●)	(●)	●
On vertical surface (dry)	●	●	●	–	●	●	–
Under water (on vertical surface)	–	–	–	●	–	–	-

Legend: ● recommended, - not recommended, (●) possible but not recommended

3 COMPETENCES AND TRAINING PROGRAMME

EN 1504-9 (cf. [5]), Cl. 10, A.4.3.5 and Cl. A.10 are the places where the qualifications of people working with repair and protection of concrete structures are explicitly outspoken.

Cl. A.4.3.5 says:

"*... All assessments should be made by suitably qualified personnel with knowledge of investigation methods, structural design, maintenance, material technology and of the mechanisms which can contribute to the deterioration process of concrete structures...*"

Moreover Cl. A.10 states:

"*Personnel should be appointed who are familiar with protection and repair of concrete works and recognized as competent. This requirement requires to all persons involved in the repair process, including repair scheme designers, repair contractors and repair work inspectors. . .*"

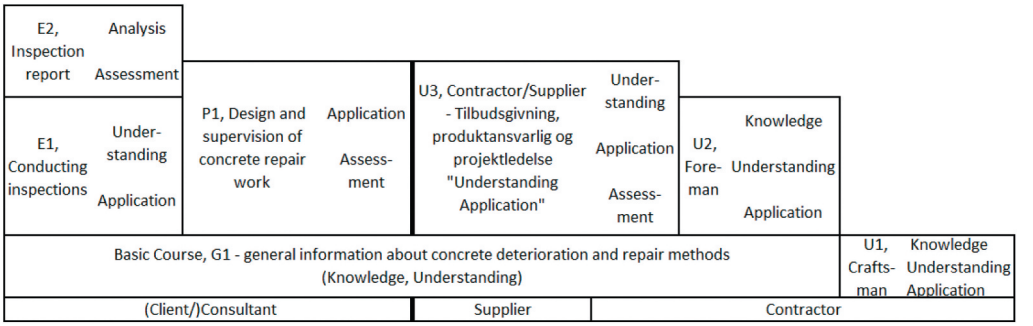


Figure 1. Schematic overview of the different courses being developed for training personnel to taking care of a repair project throughout the value chain and at all competence levels.

These general requirements and presumptions were adopted by the Danish concrete repair network named *Danrep* by unanimity. A task force was established and two years later the work crystalised in DS 2425, cf. [4].

In [4] Bloom's taxonomy [1] is used to define what skills levels are needed to carry out the individual functions in a repair project, cf. Figure 1 above. Further it defines how to verify obtained skill level at an exam. Several courses are being planned to provide the training. An overview of the courses and the corresponding skills levels is shown in Figure 1.

4 EXAMPLES

Below some examples are given – not to show the answers, but to illustrate the kind of cases that can be the reality in practice and what dilemmas they may encompass when it comes to the repair process. The examples shown are simple, but the dilemmas are generic.

A. **Insufficient compaction** of concrete structures that are to become watertight for many years is a severe execution fault. In Figure 2 an example of such a local defect is shown. Since there are requirements for watertightness a safe solution must be found. Additionally, the contractor has the duty as well as the right to reestablish the required quality. . .the following questions will typically arise:
   - What investigations are needed?
   - How can the Owner feel secure that the repair will be safe and durable?
   - How to make repairs with +50 years durability.
   - What measure will cause the minimal disruption to the progress on the construction site?

B. **Insufficient cleaning** of concrete surfaces prior to casting a new profiling layer may lead to lack a durability. The specification said: "*Before pouring new concrete against existing concrete, the surface must be cleaned by high-pressure washing or sandblasting so that it is free of organic material and layers that prevent good contact with the concrete.*"
   - The contractor regarded the surface shown in Figure 3 as being complying to the expectations. But does it?
   - The work was done as specified – a person did clean the surface with high pressure water. But is the outcome as specified?
   - The person responsible for the specification was sure it was a clear and concise text.



Figure 2. Poorly compacted concrete in a newly cast wall in a swimming pool.

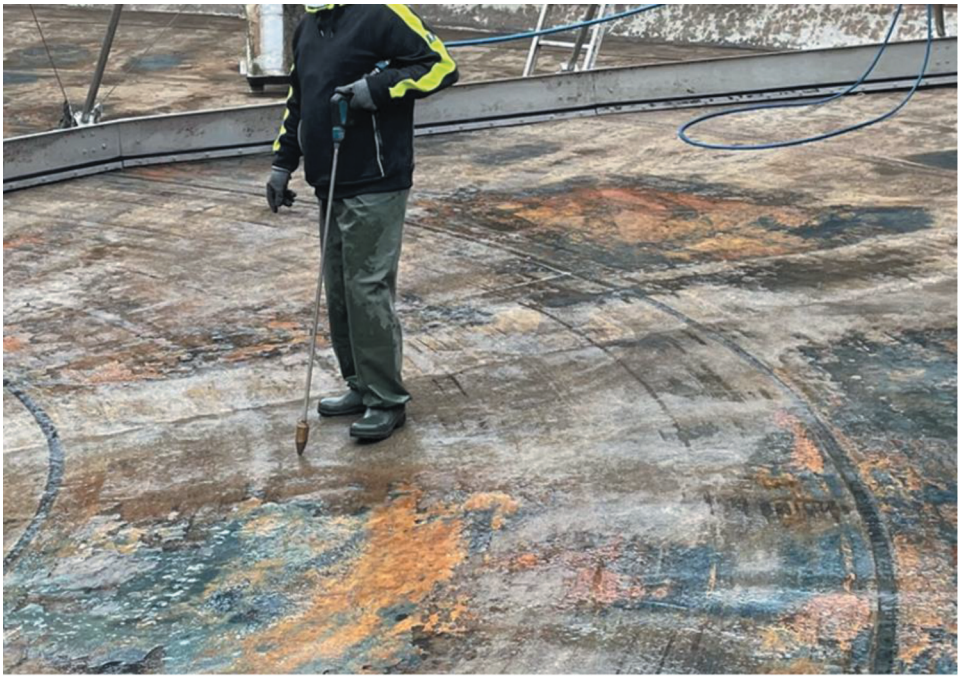


Figure 3. A surface after cleaning with high pressure water – but is the cleaning work finished and is the surface ready for application of a surface coating?.

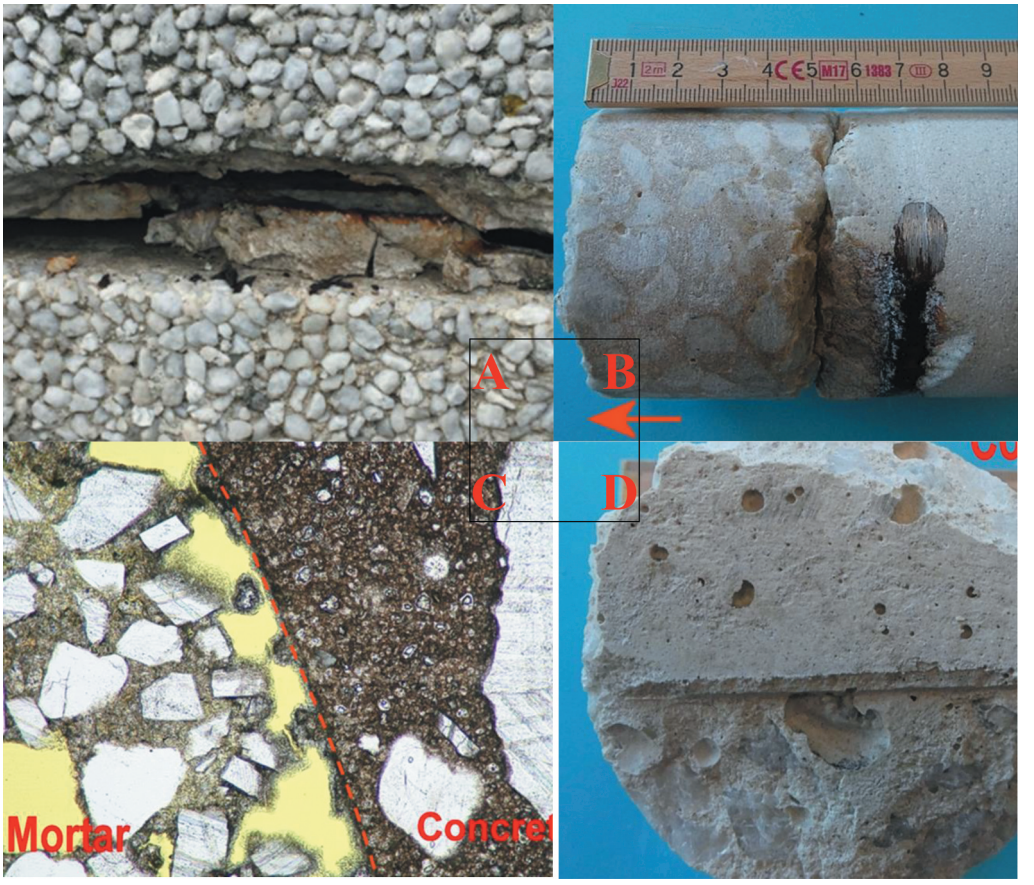


Figure 4. A) A local spot from a façade where a 0.2 kg piece of concrete spalled off. B) A sample taken in the damage (A) showing that the façade element is made up of concrete on the exposed side and mortar on the rear side. C) A close-up photo from microscopy of the sample (B)) showing a smooth casting joint between concrete to the right and a mortar to the left. D) shows that the rear side of the element has imprint of formwork i.e., formwork on the topside during casting.

- The person who did the pricing of the work may have thought that we can easily provide what is needed.

C. **The obvious cause of damage** can sometimes be misjudged and hence lead to misinterpretation and even misspecification of repairs. In Figure 4 is shown an example representing a façade of several thousands of square metres. The façade elements were casted with topside formwork on the rear side of the toe of the elements. This may have caused some irregularities during the casting manifested by trapped air pockets towards the formwork.

Hence, parts of the reinforcement may have been discovered to be exposed when demoulding. The issue of the trapped air pockets has called for a repair of the backside of the element's toe by applying a cement mortar.

This repair was made of low-quality mortar (compared to the concrete) and moreover proper preparation of the casting joint was not performed. Hence, this inadequate repair has enabled cracking (the poor casting joint), the consecutive corrosion and expansion of the reinforcement, and finally the concrete spalling.

The described casting irregularity may have easily been prevented by drilling air outlets or the like in the formwork. This measure was presumably applied, but not until it was discovered and thus after the production of some elements.

After a thorough inspection of the façade only a small number of initials faults like this was found. The key point of this example is that a thorough analysis to 'find the real cause of damage' must be made to specify the right repair – and that also the key to a successful repair according to [5].

The examples above touch on some of the issues that must be taken due care of in a repair project. I.e.:

- How to find and apply the correct measures to restore the properties of the structure without jeopardising the time schedule and the economy?
- How to define and communicate on what is sufficient to fulfil specifications of a qualitatively defined work?

5 SPECIFICATIONS

Besides following the route given in [5] via the exact cause of damage, the principles, the repair method and then choosing a suitable group of products (cf. e.g., Table 2 above) for the repair project, the new Danish General Work Specifications for repair and surface protection of concrete structures also direct a way to control the execution.

Stepwise requirements for the outcome of each work process of the repair work must be found acceptable to end up with a repair complying with the requirements for the repair work. For this the test methods given in EN 1504-10, [6] (meant for on-site use) can be applied. In Denmark these methods are supplemented by similar but more specific, simple test methods for use on site, cf. [11].

Finally, it shall be noted that with the new specifications [7] and [8] the authorities will aim at conducting repair works whenever needed and possible to obtain the most sustainable maintenance of the existing and new infrastructure as possible.

REFERENCES

[1] Bloom, Benjamin S., and David R. Krathwohl, *Taxonomy of Educational Objectives: The Classification of Educational Goals, by a Committee and University Examiners*. Handbook 1: Cognitive Domain. New York: Longman, 1956.

[2] EN 206:2013 *Concrete – Specification, performance, production, and conformity*.

[3] DS/EN 206 DK NA:2023 *Concrete – Materials. Rules for application of EN 206 in Denmark*. (in Danish)

[4] DS 2425:2021, *Skills levels for personnel responsible for the design, specification, and execution of protection and repair of concrete structures in Denmark according to DS/EN 1504-9*. (in Danish)

[5] DS/EN 1504-9:2009, *Products and systems for the protection and repair of concrete structures - Definitions, requirements, quality control, and conformity assessment - Part 9: General principles for the use of products and systems*.

[6] DS/EN 1504-10:2017, *Products and systems for protection and repair of concrete structures - Definitions, requirements, quality control, and assessment of conformity - Part 10: Application of products and systems and quality control of completed work*.

[7] General Work Specification and Special Work Specification Paradigm, Concrete Bridge – *Concrete Repairs* – GWS/SWS-P, Tender Specification, Infrastructures, March 2024. (in Danish)

[8] General Work Specification and Special Work Specification Paradigm, Concrete Bridge – *Surface Protection of Concrete Surfaces* – GWS/SWS-P, Tender Specification, Infrastructures, March 2024. (in Danish)

[9] Handbook – *Concrete Repairs* – Structures, Infrastructures, March 2024. (in Danish)

[10] Handbook – *Surface Protection of Concrete Surfaces* – Structures, Infrastructures, March 2024. (in Danish)

[11] Handbook – *Testing Methods – Repair and Surface Protection of Concrete* – Structures, Infrastructures, March 2024. (in Danish)

Bridge Maintenance, Safety, Management, Digitalization and Sustainability – Jensen, Frangopol & Schmidt (eds)
© 2024 The Author(s), ISBN 978-1-032-77040-6
Open Access: www.taylorfrancis.com, CC BY-NC-ND 4.0 license

Vulnerability assessment of timber piles by bending wave and dispersive wave testing methods

W. Zatar & H. Nghiem
Marshall University, 1 John Marshall Dr, Huntington, USA

ABSTRACT: Timber piles have been used to construct many aging bridges, locks, dams, levees, and other structures in the United States. Degradation of these piles may adversely affect their structural integrity and eventually cause catastrophic failure. This study utilizes state-of-the-art non-destructive testing (NDT) techniques to assist with vulnerability assessment of timber piles employed in aging bridges. Two timber piles were nondestructively tested in the laboratory, where one was undamaged and the other suffered damage at different locations. Test parameters include size and location of defects. Four NDT testing and evaluation methods were utilized for the timber piles. The NDT testing and evaluation methods are bending wave, dispersive wave, a combination of dispersive-bending wave, and parallel seismic. The Wavelet transform advanced signal processing method was used to post-process the NDT data. Peak identification method was used to detect the pile tip for both the bending wave and the dispersive wave/bending wave tests. The experimental results reveal that the dispersive wave/bending wave accurately detected the defects in the timber piles. The wavelet transform approach successfully detected the piles' shallow defect and the pile tip. The parallel seismic testing captured the pre-planned defects accurately in the timber piles.

1 INTRODUCTION

In the United States, numerous bridges span waterways to facilitate river navigation. Commonly employed as foundational elements for these bridges, wooden and steel piles support various civil and military infrastructures, safeguarding lives, the environment, and property against floods. Most pilings within the country's water resource infrastructure surpass 50 years old. Unfortunately, there is a lack of documented evidence regarding their structural health. This scarcity arises from the inherent challenges of inspecting pile foundations embedded in the soil and the considerable cost associated with assessing the condition of pilings in the United States water resource infrastructure. The undisclosed conditions of these pilings could give rise to significant risks throughout infrastructure inventories nationwide.

While foundation pilings are typically designed for long-term durability, their failure carries the potential for significant structural and catastrophic consequences. Defects along the piles can be a primary cause of such failures. Employing an efficient inspection or NDT technique becomes crucial for enhancing maintenance management, enabling engineers to predict the current conditions of the pilings accurately.

Non-destructive testing (NDT) methods can be categorized based on stress waves (also called acoustic or mechanical waves), electromagnetic waves, electrical/magnetic fields, and others (Xiao et al., 2019; Zatar et al., 2020). For deep foundations, the following NDT techniques are commonly used (Wightman et al., 2004; Olson, 1996):

- *Surface-based NDT methods*: Sonic echo/impulse response (SE/IR); Flexural (bending) wave (BW); Ultra-seismic (US); Spectral analysis of surface waves (SASW); Ground penetrating radar (GPR); Dynamic foundation response; Electrical resistivity imaging/induced polarization.
- *Subsurface-based (a.k.a. borehole-based) NDT methods*: Parallel seismic (PS); Borehole sonic; Borehole radar; Cross-hole sonic logging; Induction field; Borehole magnetic.

DOI: 10.1201/9781003483755-317

The impulse response/sonic echo (IR/SE) methods, as detailed by Olson (1996), Finno & Gassman (1998), and Finno (2010), have found widespread application in assessing the lengths, continuity, and integrity of both recently installed and operational deep foundations. These foundations include concrete or timber drilled shafts and driven piles. The methodology detects defects such as cracks, breaks, pile necking, lengths, bulbs (indicating diameter increases), and soil inclusions (Figure 1a). The IR/SE method uses surface reflection techniques to identify compressive wave reflections.

The bending wave (BW) method, as outlined by Olson (1996) and Finno (2010), diverges from the compressional waves employed in the IR/SE methods. Instead, the BW method utilizes flexural waves to ascertain deep foundations' unknown depth and integrity. Unlike the IR/SE methods, the BW method is specifically tailored for applications involving "rodlike" deep foundations, such as timber or concrete piles and drilled shafts that extend visibly above the ground or water surface (Figure 1b). An example of BW test results for a timber pile is shown in Figure 3.

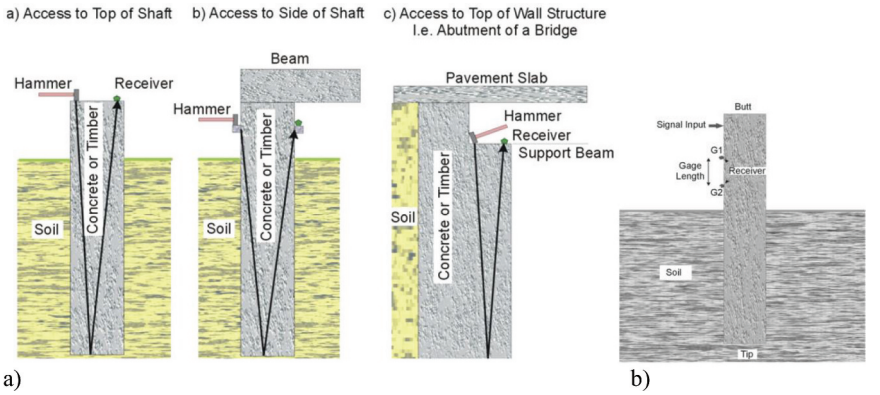


Figure 1. (a) IR/SE and (b) BW test methods.

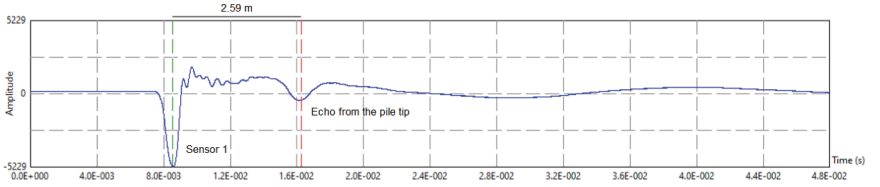


Figure 2. Examples of depth calculations using impulse response and sonic echo methods and BW test results for a timber pile.

The dispersive waves (DW) method can also be used to determine the cross-sectional integrity of a timber pile, as shown in Figure 3. The technique involves three significant steps:

1. Placing magnetic washers and accelerometers around a pile at "x" (x = circumference of the pile/4) apart around the circumference of the pile.
2. Striking on one washer and capturing the wave at the rest of the washers.
3. Calculating the velocity of the DW to travel from the impact washer to the other washers to gain information on the cross-sectional integrity of the pile.

Table 1 presents the comparison of test methods for timber piles.

The Parallel Seismic (PS) method, extensively studied by Niederleithinger (2012) and Liao et al. (2006), stands out as a prominent non-destructive testing (NDT) technique designed for borehole testing (Figure 4). This method has been widely researched and developed to determine the lengths of foundations with unknown dimensions. Notably, the PS method detects significant discontinuities within a foundation and provides valuable insights into the

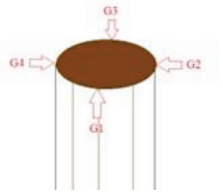


Figure 3. Cross-section integrity testing layout for a timber pile.

Table 1. Comparisons of NDT methods for timber piling.

Test Method	Investigation Type	Pile Exposure Required?
Mechanical Wave Velocity	Overall pile integrity	Yes, at least 4 ft
Cross-sectional using Dispersive Wave	Cross-sectional integrity on exposed pile only	Yes
Cross-sectional using Ultrasonic Wave	Cross-sectional integrity on exposed pile only	Yes

surrounding soil velocity profile. The procedure involves installing cased boreholes (water-filled if hydrophones are utilized) near the foundation under examination. The PS method proves particularly effective when testing long and slender piles (e.g., driven piles) is impractical using IR/SE techniques and when the top of foundations is inaccessible.

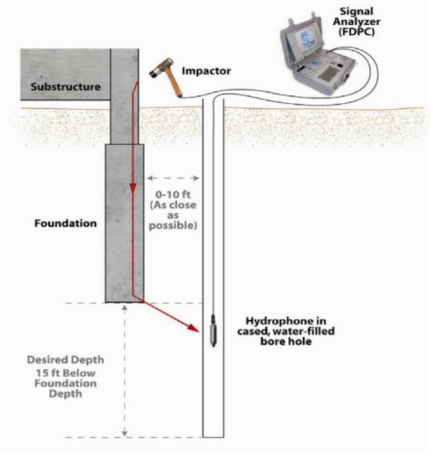


Figure 4. The Parallel Seismic (PS) method.

2 LARGE-SCALE TESTBED

A large-scale testbed has been designed to develop, test, and validate NDT methods for evaluating the conditions of wooden and steel piles. The testbed includes a three-dimensional steel-frame structure filled with sandy soils and pre-installed wood/steel pilings (Zatar et al., 2022a, 2022b). The steel frame was constructed with H-shaped columns, top/bottom beams, bracing systems, and perimeter steel walls (Figure 5). The overall dimensions of the frame are 2.74 × 2.74 × 3.05 m (width × length × height).

The experimental testing involves two pairs of timber piles and H-piles positioned strategically on the testbed. Each pair consists of one control pile devoid of artificial flaws and another intentionally featuring pre-planned defects. These four piles are situated at the corners of the testbed, as depicted in Figure 6. A 0.1-meter polyvinyl chloride (PVC) pipe, centrally positioned on the testbed, accommodates hydrophones for the parallel seismic (PS) non-

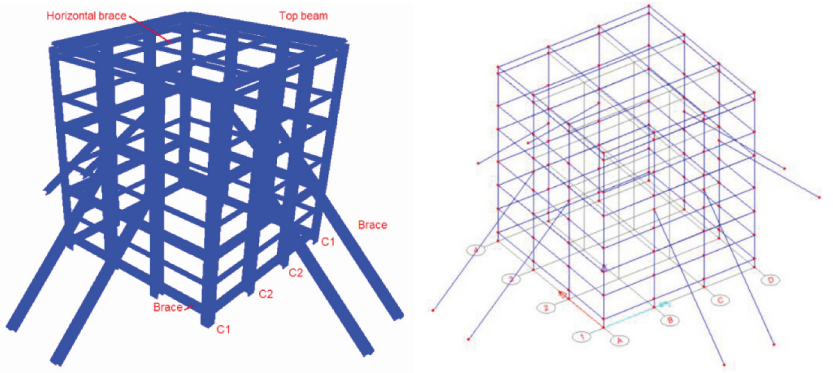


Figure 5. Overview and 3D model of the steel frame.

destructive testing (NDT) method (Figure 7). The elevation view of the testbed, incorporating the embedded piles, is presented in Figure 6. Key test parameters encompass:

1. Timber piles.
2. Various NDT methods were employed, including bending wave (BW), impulse response (IR), and parallel seismic (PS).
3. Sizes and locations of artificial defects on timber piles (Table 2).

Specifically, section losses in a rectangular shape representing the deterioration of the timber pile were deliberately introduced at 0.3 meters from the top (upper defects) and 0.3 meters from the bottom of the piles (lower defects). The piles were attached to the base plates connected to a strong floor (Figure 7). The bottom of the PVC pipe was sealed entirely to ensure it could hold the water needed to conduct the parallel seismic tests. The steel cage was filled with 30 tons of fine-grained construction sand (contained in more than 30 heavy-duty sandbags) to mimic the field environment of actual pile foundations. The testbed is ready to conduct laboratory testing of scaled wood piling to validate the condition assessment approach and water-filled plastic pipe and hydrophone, as shown in Figure 8.

Table 2. Test parameters.

Employed NDT methods	Type of defects	Size of defects	Location of defects
Bending Wave (BW) Parallel Seismic (PS) and Impulse Response (IR)	Section loss (rectangular shape)	0.25s × 0.5s	1' (12") from top of the pile

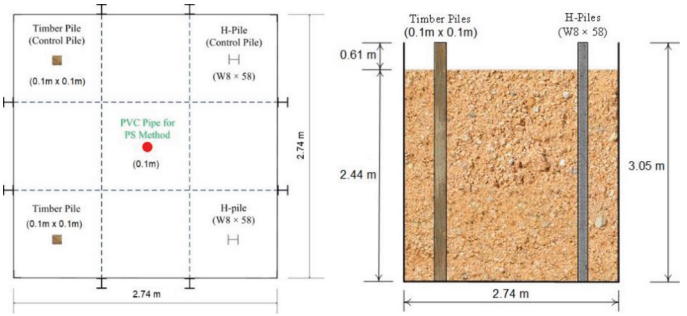


Figure 6. Plan (left) and elevation (right) views of the testbed showing the tested piles.



Figure 7. Piles and PVC pipe installed in the cage.



Figure 8. The testbed is ready to conduct laboratory testing of scaled wood piling for validation of the condition assessment approach (left) and water-filled plastic pipe and hydrophone (right).

3 TEST RESULTS

The sonic echo (SE) test method exhibits sensitivity to variations in pile impedance, which induces the formation of a reflected wave. A reduction in impedance, arising from factors like corrosion or decay, produces a reflected wave that, when combined with the incident wave, results in a downward peak (trough) in the signal. The process of interpreting a peak in the signal as a reflection indicative of a defect is called peak identification (PI). In a defect-free pile, only two peak reflections are typically observed in the measured signals, one from the impact impulse and the other from the reflection at the pile tip. The presence of intermediate peak reflections between the pile top and tip signals the existence of defects. However, the reflected wave from minor or deep defects may be weak and overshadowed by the incidence or reflected wave from the pile tip, posing challenges for the PI method in detecting such defects effectively. To address this limitation, wavelet transform (WT) comes into play. WT is widely employed for analyzing periodic, noisy, intermittent, and transient signals (Ni et al., 2017). Leveraging its sensitivity to phase information, the WT technique proves helpful in localizing pile damage, making it advantageous in scenarios where phase information is crucial for detection (Ni et al., 2017).

Three testing methods, including bending wave (BW), dispersive wave (DW), and mixed dispersive-bending wave (DW/BW), were conducted as schematically shown in Figure 9. Accelerometers and inhouse data acquisition were respectively used for sensing and recording the response of the tested piles subject to lateral and vertical impacts from different strikes produced by hard hammer (HH), baseball bat (BP), 1.8-kg sledgehammer (4-lb), bowling pin, and sphere. Different hammer types can generate distinctive frequencies of vibration. Some test results are presented in Figure 10 across Figure 13. The PI method can effectively be used to detect the pile tip in BW (Figure 9) and DW/BW (Figure 12) tests. The BW tests could only capture the upper defects (Figure 10). The combination of dispersive-bending waves (DW/BW) accurately determined upper and lower defects (Figure 12 and Figure 13). The WT method can detect the upper defect and the pile tip

(Figures 14, 15, and 16). The parallel seismic test was able to find both upper/more minor defects at the 12th strike (~0.91 m) and lower/more significant defects at the 36th strike (~ 2.74 m), as shown in Figure 17.



a) BW pile test b) DW pile test c) DW/BW pile test

Figure 9. Test setup.

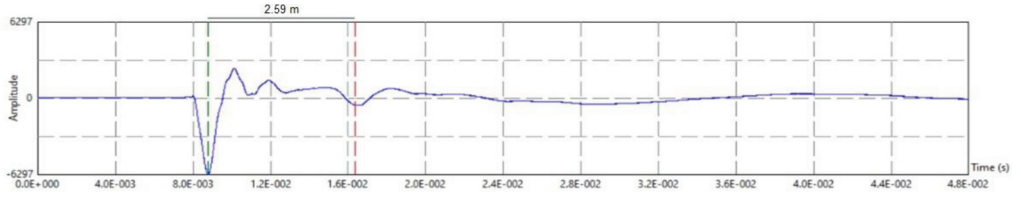


Figure 10. Pile tip location from BW test (PI method).

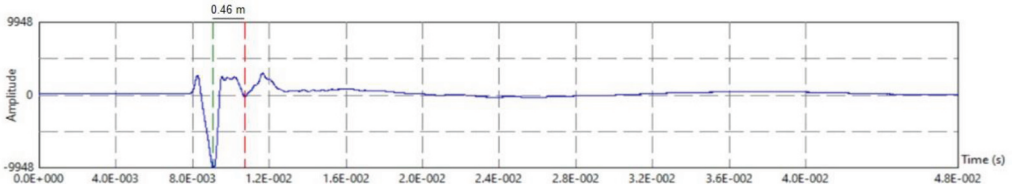


Figure 11. Upper defect location from BW test (PI method).

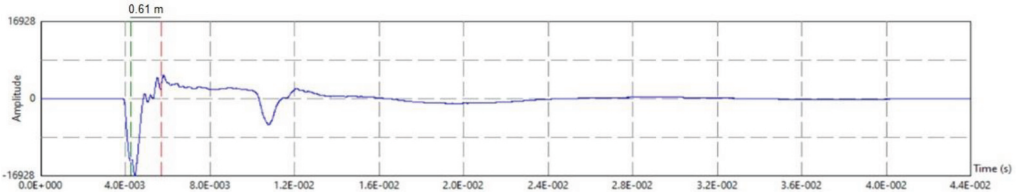


Figure 12. Upper defect location from DW/BW test (PI method).

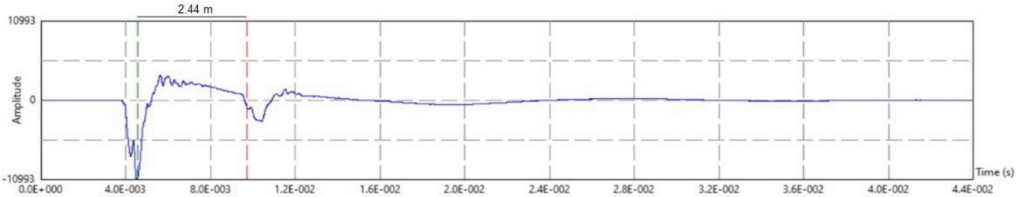


Figure 13. Lower defect location from DW/BW test (PI method).

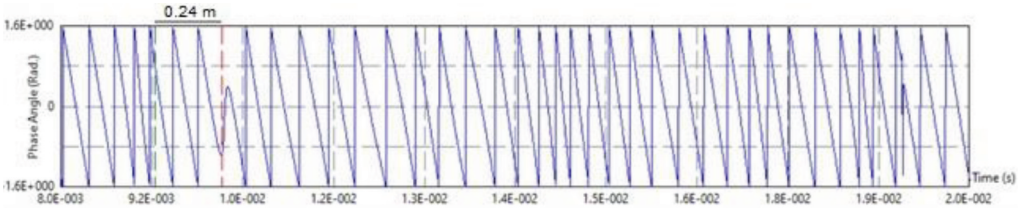


Figure 14. Upper defect location from BW test (WT method).

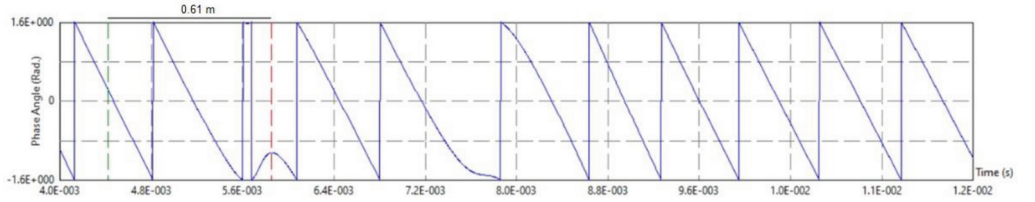


Figure 15. Upper defect location from DW/BW test for timber piles (WT method).

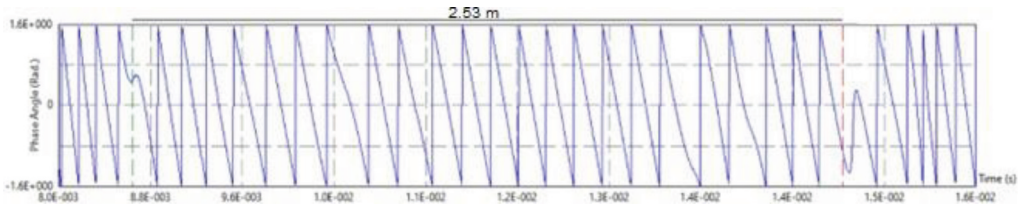


Figure 16. Pile tip location from BW timber piles test (WT method).

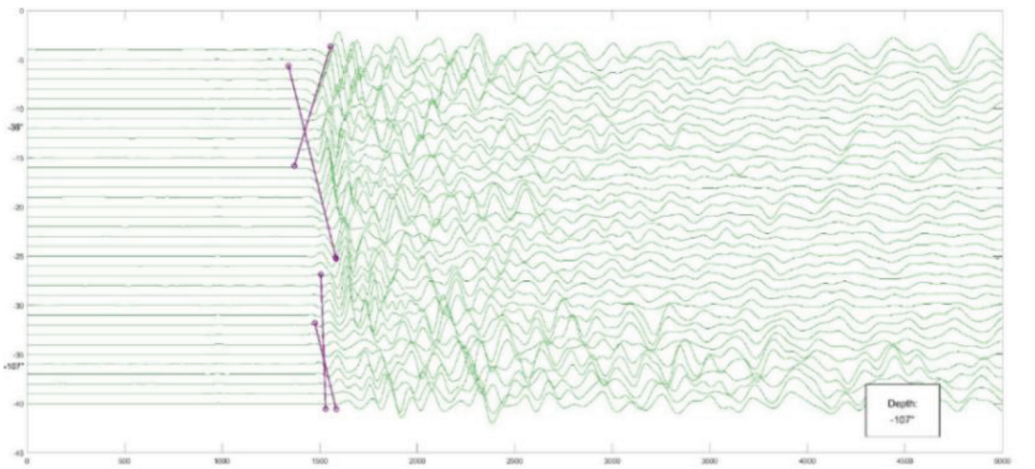


Figure 17. Parallel seismic test results.

4 CONCLUSIONS

Based on the obtained test results, the following conclusions were drawn:

- The peak-signal reflection method known as "peak identification (PI)" proved effective in detecting the pile tip in both bending wave (BW) and dispersive-bending wave (DW/BW)

tests. However, the BW test exhibited limitations in capturing lower defects. The combination of dispersive-bending wave (DW/BW) was identified as a successful approach in accurately determining pre-planned defects, encompassing the pile's upper and lower sections. Additionally, the wavelet transform (WT) method successfully detected shallow defects in the piles and accurately identified the pile tip.
- The parallel seismic (PS) test demonstrated accuracy and effectiveness in capturing upper and lower pre-planned defects in the timber pile.

ACKNOWLEDGMENTS

- This project was sponsored by the Engineer Research and Development Center (ERDC) and the U.S. Army Corps of Engineers (USACE). The financial support provided by the ERDC-USACE under contract No. W912HZ-19-SOI-0023 is gratefully acknowledged. The authors sincerely appreciate the tremendous and thorough mentorship ERDC experts Mr. Bradley Foust and Dr. Matthew Smith provided. Special thanks to Dr. Hai Nguyen and Dr. Haroon Malik for their invaluable contributions and outstanding leadership while conducting this study's experimental and analytical tasks. The authors also would like to thank the project team members from FDH Infrastructure Services for their assistance with this research project.

REFERENCES

Finno, R.J., and Gassman, S.L. 1998. Impulse response evaluation of drilled shafts. *Journal of Geotechnical and Geoenvironmental Engineering*, 124(10), 965–975.

Finno, R.J. 2010. 1-D wave propagation techniques in foundation engineering. In Art of Foundation Engineering Practice, 260–277.

Liao, S.T., Tong, J.H., Chen, C.H., and Wu, T.T. 2006. Numerical simulation and experimental study of parallel seismic test for piles. *International Journal of Solids and Structures*, 43(7-8), 2279–2298.

Ni, S.H., Yang, Y.Z., Tsai, P.H. and Chou, W.H. 2017. Evaluation of pile defects using complex continuous wavelet transform analysis. *NDT & E International*, 87, 50–59.

Niederleithinger, E. 2012. Improvement and extension of the parallel seismic method for foundation depthmeasurement. *Soils and Foundations*, 52(6), 1093–1101.

Olson, L.D. 1996. Nondestructive Testing of Unknown Subsurface Bridge Foundations: Results of NCHRP Project 21-5. Transportation Research Board, National Cooperative Highway Research Program (NCHRP), Research Results Digest No. 213.

Wightman, W., Jalinoos, F., Sirles, P., & Hanna, K. 2004. Application of geophysical methods to highway related problems. FHWA-IF-04-021.

Xiao, F., Chen, G., Zatar, W., and Hulsey, L. 2019. Signature Extraction from the Dynamic Responses of a Bridge Subjected to a Moving Vehicle using Complete Ensemble Empirical Mode Decomposition. *Journal of Low-Frequency Noise, Vibration, and Active Control*, SAGE.

Zatar, W., Nguyen, H., and Nghiem, H., 2020. Ultrasonic Pitch and Catch Technique for Non-Destructive Testing of Reinforced Concrete Slabs. *Journal of Infrastructure Preservation and Resilience*, 1(1), pp.1–13.

Zatar, W., Foust, B., Smith, M., Eick, B., Nghiem, H., Malik, H., Nguyen, H., Khan, R., Brearley, L., Pantha, T., and Cosgun, C. 2022a. Condition Assessment of Pile Foundations Embedded in Soil. 8th World on Structural Control and Monitoring (8WCSCM).

Zatar, W., Foust, B., Smith, M., Eick, B., Malik, H., Nghiem, H., Nguyen, H., Khan, R., Brearley, L., Pantha, T., and CosgunC.2022b. Develop Underwater Inspection Methods to Determine Condition of Pile Foundations Embedded in Soil, W912HZ–19–SOI–0027, 177 pages.


Taylor & Francis
Taylor & Francis Group
http://taylorandfrancis.com

SS26: Risk-informed decision making and asset management of highway bridge portfolios

Organizers: A. Du, X. Wang & A. Shafieezadeh


Taylor & Francis
Taylor & Francis Group
http://taylorandfrancis.com

Bridge Maintenance, Safety, Management, Digitalization and Sustainability – Jensen, Frangopol & Schmidt (eds)
© 2024 The Author(s), ISBN 978-1-032-77040-6
Open Access: www.taylorfrancis.com, CC BY-NC-ND 4.0 license

Maintenance plan optimization system based on remaining life prediction

A. Miyamoto
Prof. Emeritus, Dr. Eng., Yamaguchi University, Ube, Japan

ABSTRACT: In this paper, a maintenance plan optimization system (MPOS) which is a subsystem of the Japanese Bridge Management System(J-BMS) is described based on the results of remaining life prediction of the existing bridges. The proposed system that considered not only remaining life cycle cost (RLCC) but also rebuild cost stabilization is applied to existing bridge data on about 3,500 bridges that collected in J-BMS database (J-BMS DB) for practical use. Then, it is found that the system helps the efficiency of bridge engineers related to bridge management understand easily what are the major processes in the deteriorating bridges in the future, how to improve their performance, and what kind of repair/strengthening works is most convenient for the deteriorating bridges.

1 INTRODUCTION

The author has been developing a practical bridge management system (J-BMS) for bridge network in Yamaguchi Prefecture, Japan, which integrated with the concrete bridge rating expert system (BREX) that can be used to evaluate the serviceability (durability, load carrying capability) of existing concrete bridges (Miyamoto & Motoshita 2015). The J-BMS will be able to predict the deterioration process of existing bridge members, recommend a maintenance plan for repair and/or strengthening based on minimizing maintenance costs and maximizing quality, and estimate the maintenance costs in single bridge. In this system, the genetic algorithm (GA) technique was used to search for an approximation of the optimal maintenance plan. In this study, a comprehensive decision support system is developed for maintenance strategies with/without annual budget limitations based on life cycle cost analysis of an entire bridge inventory, which form part of a highway network. Especially, a maintenance plan optimization system (MPOS), a subsystem of the J-BMS, is described based on the results of remaining life prediction of the existing bridges. The proposed system that considered not only remaining life cycle cost (RLCC) but also rebuild cost stabilization is applied to existing bridge data on about 3,500 bridges that collected in J-BMS database (J-BMS DB) for practical use (Miyamoto, et al. 2009). Then, it is found that the system helps efficiency bridge engineers related to bridge management understand easily what are the major processes in the deteriorating bridges in the future, how to improve their performance, and what kind of repair/strengthening works is most convenient for the deteriorating bridges. In order to make the J-BMS developed by the authors a more practical tool, the MPOS that can be used for more than one bridge on the highway network has been developed. The system performs three tasks: (1) making it possible to draw up a maintenance plan that takes into consideration not only repair and strengthening based on structural soundness evaluation results but also reconstruction so that the peaks of future reconstruction costs can be saved; (2) provides a reconstruction cost stabilizing function to calculate a realistic service life of each bridge, and (3) drawing up a maintenance plan that satisfies the budgetary requirements for repair and strengthening for each year, taking into consideration budgetary constraints and construction requirements that can be specified by bridge administrators, and enabling the user to specify the year in which to perform repair or

DOI: 10.1201/9781003483755-318

strengthening for each bridge. Finally, the practicality of the proposed system has been verified by drawing up various maintenance plans by applying the system to the bridge data managed by Yamaguchi Prefectural Government.

2 OUTLINE OF J-BMS AND OPERATION FLOW

The J-BMS consists of the following three subsystems: (1) a bridge maintenance database system (J-BMS DB) for efficiently managing relevant data such as bridge specification data and inspection data, (2) a bridge deterioration diagnosis system (bridge rating expert system (BREX) and (3) a maintenance plan optimization system for drawing up an optimum maintenance plan (MPOS). Figure 1 shows the flow of operation of these subsystems (Miyamoto & Asano 2018). As shown in Figure 1, J-BMS is used as follows: (1) extract necessary data from the bridge specification database and the regular inspection database and download those data from J-BMS DB to BREX. Of the data thus downloaded, the inspection record data (xls. file) are used to enter, for example "main girder inspection" and "floor slab inspection" data, and the brx. file is used to enter, for example "bridge specifications" and "investigation/inspection" data. (2) Output BREX diagnosis data calculated from the input data as a CSV. file. The output data includes bridge name and BREX performance evaluation results such as "main girder-load carrying capability" and "floor slab-durability". Upload the CSV. file containing calculation data to J-BMS DB. Then the MPOS uses the uploaded data for making remaining life prediction and maintenance plan optimization.

3 DEVELOPMENT OF MAINTENANCE PLAN OPTIMIZATION SYSTEM (MPOS)

3.1 *System objectives*

The J-BMS that the authors have developed enables the user to specify an expected service life of each bridge so that a maintenance plan that satisfies the service life requirement for each bridge can be drawn up. In Yamaguchi Prefecture, however, about 57 percent of all bridges in the prefecture were built intensively in the 1950s to the 1970s (Morioka, et al. 2008). If, for example, maintenance plans for these bridges are to be drawn up by using an expected service life of 100 years, the resultant maintenance plans would call for the reconstruction of all those bridges in the 2050s to the 2070s. The proposed system, therefore, draws up a maintenance plan for each bridge in accordance with the maintenance planning flow shown in Figure 2, taking the reconstruction cost into consideration. The proposed flow consists largely of two steps: (1) drawing up a reconstruction plan for an existing bridge and (2) formulating a rational and effective maintenance plan, on the basis of that reconstruction plan, so that the repair/strengthening budget constraints and construction requirements for the year concerned can be met.

Each of the (numbered) items shown in Figure 2 is explained below:

(1) Service life maximization: A maintenance plan that maximizes the service life of an existing bridge is formulated in consideration of the conditions related to the bridge.
(2) Reconstruction cost stabilizing: The user specifies a reconstruction cycle according to the maintenance plan for maximizing the remaining service life of the existing bridge formulated as mentioned above so that annual reconstruction costs during that cycle are evenly distributed. This makes it possible to prevent reconstruction budget concentration and determine an expected remaining service life of the existing bridge. The next thing to do is to formulate a maintenance plan that satisfies this service life requirement.
(3) RLCC minimization: A maintenance plan that minimizes the repair/strengthening cost required during the expected remaining service life (remaining life cycle cost; RLCC). Under the maintenance plan thus formulated, however, repair and strengthening costs usually vary from year to year. The proposed system, therefore, performs either of the two tasks ((4) & (5)) described below.

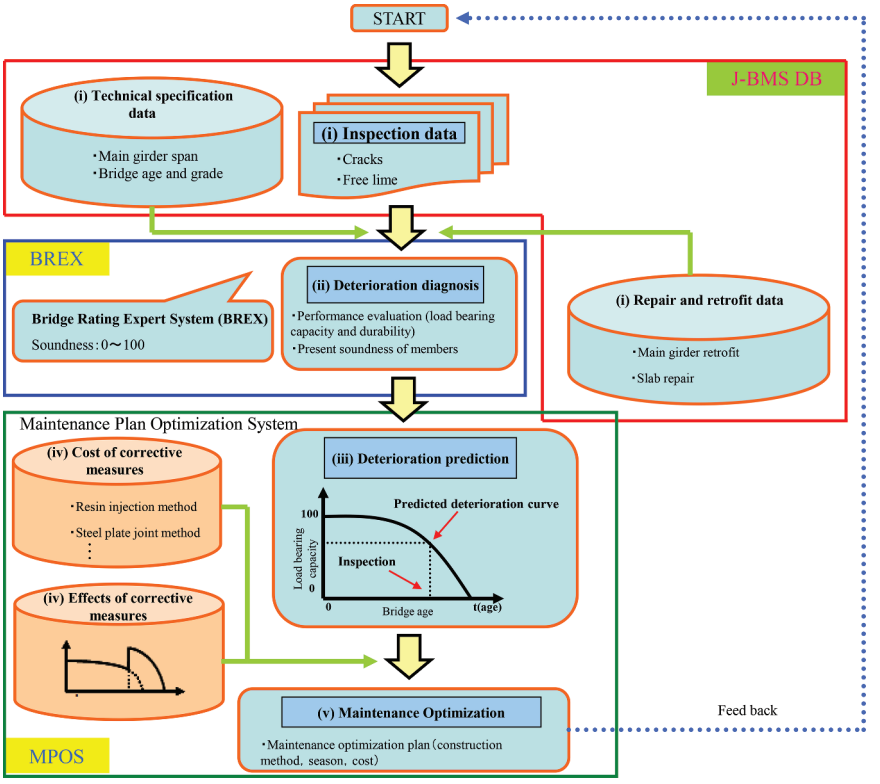


Figure 1. Whole configuration of J-BMS and operation flow in the system.

(4) Repair and strengthening cost stabilizing: The repair and strengthening costs are also distributed evenly.
(5) Planning within budget constraints: The upper limit of an annual budget is determined, and a plan is drawn up within budget. Thus, by shaving the peaks of repair and strengthening costs, the budget required for bridge management can be roughly estimated. Under increasingly tight budgetary constraints, however, the required amount of budget may not be available. The proposed system, therefore, performs the task described below.
(6) Allowing the user to specify a year in which to take action: By allowing the user to enter the upper limit of an annual budget, the system draws up a viable maintenance plan that meets the budgetary constraints.

3.2 *Bridge maintenance planning conditions*

This section describes the conditions that need to be specified for bridge maintenance planning.

3.2.1 *Bridge condition categories*

For the purposes of this study, the degree of deterioration of an existing bridge is expressed with an indicator called "soundness," which is rated on a five-point scale as shown in (Miyamoto & Motoshita 2015); Category V represents "the degree of material deterioration: low"; Category IV, "the degree of material deterioration: moderate"; Category III, "the degree of material deterioration: high"; Category II, "Influence on load-carrying capacity: minor"; and Category I, "influence on load-carrying capacity: major."

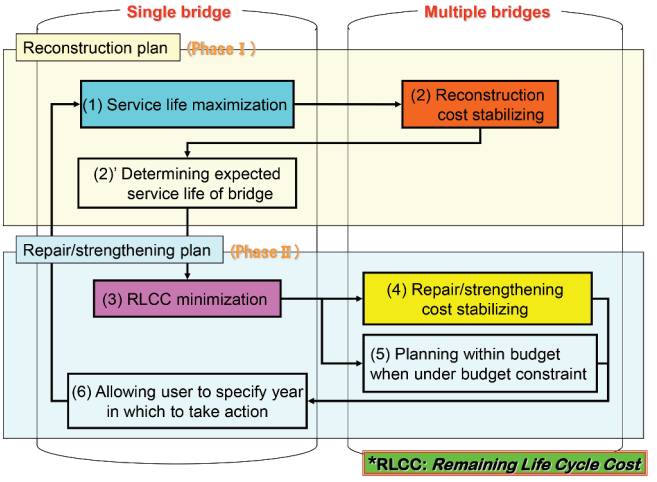


Figure 2. Maintenance plan optimization flow in MPOS.

3.2.2 *Deterioration curve*

Soundness, which is an indicator of the degree of deterioration of an existing bridge, was adopted as an indicator for maintenance planning. Soundness (vertical axis) h(t)n is measured on a 0 to 100, and its changes with time (deterioration curve) is expressed as,

$$h(t)_n = b_n - a_n(t - t_n)^c \tag{1}$$

where, t is the year; n, the number of times a remedial action was taken by year t; an is the slope of the deterioration curve at the time the nth remedial action has been taken; and b_n is the soundness of the existing bridge at the time the nth remedial action has been taken, which changes according to the effectiveness of the remedial action taken. The year of completion of the bridge is $t_{n=0}(=t_0)$, and c is the power exponent of the deterioration equation.

The deterioration curve expressed by Eq. (1) can be arbitrarily changed by adjusting the parameters a, b and c. The soundness in the year of completion of a bridge, b_0, and the power exponent c of the deterioration curve can be arbitrarily specified by the user. For the purposes of this study, b_0=100 and c=3 are used as the initial values.

The slope a_n of the deterioration curve can be calculated from the following equation by using the soundness $h(t)_n$ at the time of inspection:

$$a_n = \frac{(b_0 - h(t)_n)}{(t - t_n)^c} \tag{2}$$

where, the parameters a_n and b_n are updated every time repair or strengthening is carried out by using the following equations:

$$b_n = h(t_n)_n = h(t_n)_{n-1} + R \cdot \rho \tag{3}$$

$$R = \left(h(t_{n-1})_{n-1}\right) - \left(h(t_n)_{n-1}\right) \tag{4}$$

$$a_n = a_0 \cdot \eta^n \tag{5}$$

Figure 3 illustrates the effects of remedial actions on the deterioration curve. The symbols used in Eqs. (3), (4) and (5) the same as those used in Figure 3. In the equations, ρ is a parameter for reducing soundness recovery; a_0, the slope of the initial deterioration curve; and η, a parameter for increasing the rate of deterioration. In the determination of a deterioration curve, deciding on the method for determining the effects of remedial actions is a major challenge. In the proposed system, the slope of the deterioration curve, a_n, is

obtained by multiplying the slope of the initial deterioration curve, a_0, by η^n. If various data are accumulated in the coming years, the user can arbitrarily set the parameters η and ρ. The initial values of $\eta = 2$ and $\rho = 0.9$ have been adopted so that if maintenance actions have been taken in accordance with the upper limit of the number of maintenance actions shown in Table 1 (rightmost column), the maximum service life of an existing bridge becomes about 150 years.

3.2.3 *Repair/strengthening cost and the number of maintenance actions*
In the management of an actual existing bridge, repair/strengthening methods to be used may vary depending on the state of deterioration of the bridge. In this study, therefore, the repair/strengthening method, cost, area, and the upper limit of the number of maintenance actions are specified. The proposed system allows the user to specify the repair/strengthening cost, area, and the number of maintenance actions. As the initial values, the repair/strengthening costs and the upper limit of maintenance actions shown in Table 1 have been adopted. The costs (unit costs) in Categories I to III were determined based on the actual repair data. For the costs (unit costs) in Categories IV and V, data on actual repairs were not available because the damage to existing bridges is minor. If, however, existing bridges are to be maintained economically and efficiently, instead of repairing or strengthening them after their deterioration or damage has become apparent, it may be necessary to perform preventive repairs while deterioration or damage is still minor. This is why repair and strengthening methods have been specified for Categories IV and V, too. Table 1 needs to be modified to indicate more realistic maintenance actions or values according to various data such as data on examples of repair and strengthening.

3.3 *Details of maintenance plan optimization*

3.3.1 *Service life maximization*
The purpose of "(1) service life maximization" shown in Figure 2 is to draw up a plan that extends the service life of an existing bridge to the maximum extent possible. The objective function for this can be expressed as follows:

Objective function:

$$F_1 = Life \rightarrow \max \tag{6}$$

where, Life represents the remaining service life of an existing bridge (years), which can be calculated from the following equation:

$$Life = t_L - t_0 \tag{7}$$

where, t is time(years); t_0 is the year in which the bridge was built; and t_L is the end of the service life (years).

Constraints:

$$\sum_{t=t_0}^{t_L} x_{t,r} \leq n_{\max,r} \quad \begin{matrix} \text{incaseof no maintenance action at } t,\ r : x_{t,r} = 0 \\ \text{in case of maintenance action at } t,\ r : x_{t,r} = 1 \end{matrix} \tag{8}$$

where, x_t expresses whether or not a maintenance action is taken in year t; x_t,r expresses whether or not a maintenance action is taken in year t when in the category of state r; and $n_{max,r}$ is the upper limit of the number of maintenance actions taken in year t when in the category of state r. It is assumed, however, that in the year (t_L) in which an existing bridge reaches the end of its service life, the soundness $h(t_L)$=0. The soundness $h(t)$ is calculated from Eq. (1).

3.3.2 *Reconstruction cost stabilizing*
In this study, soundness and the categories of state have been related, and an upper limit is imposed on the number of maintenance actions allowed for each category of state. In order to

uniquely determine a maintenance planning result, therefore, existing bridges have been prioritized so that higher-priority bridges identified by the criterion shown below can be repaired or strengthened for a longer service life on a priority basis.

$$C_t \leq B_t \tag{9}$$

where, C_t is the reconstruction cost in year t; Bt is the reconstruction budget for year t; and t is years, where, $t \in [t_S, t_E]$, and t_S is the first year of the cost stabilizing period specified by the user, and t_E is the last year of that period. The reconstruction budget B_t is determined based on the total reconstruction cost during the cost stabilizing period.

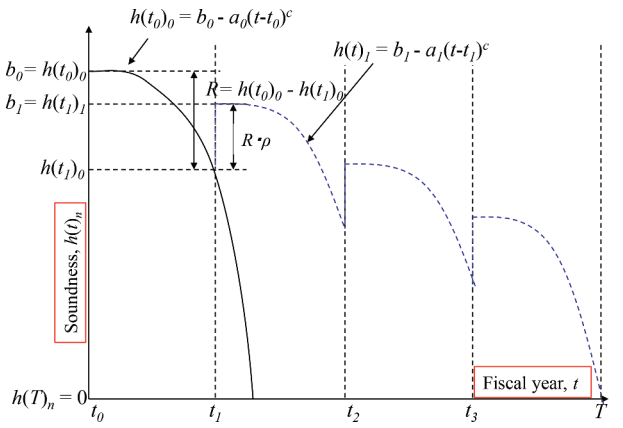


Figure 3. Effect of maintenance action on deterioration curve.

Table 1. Repair/strengthening costs & upper limits of the number of maintenance actions (assigned).

Category	State		Repair/strengthening method	Target area*	Unit cost (thousand yen/m²)	Upper limit of the number of maintenance actions
Ⅴ	Degree of material deterioration	Low	None	–	–	–
			Waterproofing	5%	16.0	1 time
Ⅳ		Moderate	None	–	–	–
			Repair(grouting)	10%	16.0	1 time
Ⅲ		High	None	–	–	–
			Repair (cross-sectional restoration)	20%	45.7	1 time
Ⅱ	Influence on load-carrying capacity	Minor	None (awaiting reconstruction)	–	–	–
			Strengthening (cross section + carbon fiber)	50%	130.5	1 time
Ⅰ		Major	Reconstruction	100%	1280.0	1 time

*: The ratio of repair or strengthening area by gross floor area(gross floor area =bridge length × wdth)(%)

3.3.3 *RLCC minimization*

The purpose of RLCC minimization is to formulate a plan that makes it possible to maintain the performance of an existing bridge until the end of its expected service period and minimizes the cost of doing so. The objective function, therefore, aims to minimize the repair and strengthening cost (RLCC) from the first year of the plan to the last year of the bridge's expected service life. The constraint is that the performance of the bridge needs to be maintained until the last year of its expected service life. These can be expressed as follows:

Objective function:

$$F_3 = \sum_{t=t_s}^{t_e} c_t \rightarrow \min \tag{10}$$

Constraint:

$$h(t) < level \tag{11}$$

where, t is the years ($t = t_S \sim t_e$; t_S is the first year of the plan, and t_e is the last year of the expected service life); $h(t)$, the soundness of an existing bridge in year t; and c_t, the repair and strengthening cost for an existing bridge in year t. The word "level" shown above represents "maintenance level." In order to prevent significant degradation of the performance of an existing bridge, the maintenance level is defined for the existing bridge, and the bridge is managed so that the soundness of the bridge does not become lower than the predetermined maintenance level. For this purpose, it is assumed that the maintenance level in Eq. (11) corresponds to the soundness $h(t)$=0, and the existing bridge is managed so that the soundness h(t) does not become smaller than zero. For the repair and strengthening cost c_t, the values shown in Table 1 are used.

3.3.4 *Planning within budget constraints*

If an annual budget for repair and strengthening needed to maintain the performance of existing bridges is set at a low level, adequate repair or strengthening cannot be performed. As a result, the bridges cannot be maintained until the last year of their expected service life, and it becomes necessary to reconstruct some of those bridges. If, however, an objective function is defined simply so as to enable as many existing bridges as possible to fulfill their service life, the following problems arise:

(1) Priority may be given to less-costly small-scale bridge repair or strengthening rather than more expensive large-scale bridge repair or strengthening.
(2) A system that indicates different reconstruction cycles every time it draws up a plan under the same constraints is not reliable enough for practical use.

To solve these problems, it was decided to provisionally prioritize existing bridges and draw up a plan that satisfies the following criterion and selects bridges to be repaired or strengthened according to that priority.

$$C_t \leq B_t \tag{12}$$

where, C_t is the repair and strengthening cost in year t; B_t is the repair and strengthening cost for year t.

The upper limit B_t of the repair and strengthening budget for year t in the constraint expression can be calculated from the following equation:

$$B_t = B_{t_S} \cdot (1+\gamma)^{t-t_S} + \alpha \tag{13}$$

$$B_{t_s} = \frac{\sum_{t=t_S}^{t_E} C_t}{\sum_{t=t_S}^{t_E} (1+\gamma)^{t-t_S}} \tag{14}$$

where,
γ is the rate of increase in annual budget; α is an additional cost to be added to annual budget.

3.3.5 *Allowing the user to specify a year in which to take action*

In cases where an existing bridge is repaired or strengthened, this function enables the user to specify a year in which to carry out repair or strengthening work, taking into consideration various factors related to construction work such as traffic restriction. In this study, the specification by the user of a year in which to take a maintenance action is used as a constraint, and a plan that takes "allowing the user to specify a year in which to take action" into

consideration is drawn up in accordance with the flow of the planning process shown in Figure 2. This is expressed by the equation shown below. In the equation, x_t, which indicates whether or not a maintenance action is taken in year t takes the value of "1" when a maintenance action is taken in year t and takes the value of "0" when no maintenance action is taken in year t. Thus, the user is free to select "0" or "1."

$$x_t = \begin{cases} 0 & : \text{in case of no maintenance action at year } t \\ 1 & : \text{in case of maintenance action at year } t \end{cases} \tag{15}$$

4 IMPLEMENTATION INTO J-BMS AND PRACTICAL APPLICATION

The proposed system, MPOS as mentioned above is installed into J-BMS as a subsystem. In this chapter, the system is applied to an actual bridge network in Ube City area, Yamaguchi Pref., Japan (total 169 concrete bridges) to evaluate its effectiveness (Yamaguchi Pref. Gov. 2003). And the example of specific maintenance plan from the MPOS is shown with corresponding computer displays for easy to understand.

Figure 4 shows a screen display of deterioration curve/specification input data for maintenance actions which is displayed when starting of this system. As shown in Figure 4, the screen which the deterioration estimation and specification of maintenance actions for main girder, as an example is composed form 3 different forms of purpose like shown below, namely a main window and 2 windows in order to display bridge data: ①**Flow**: The form that allows the user to access optionally into each function, and the process which is executed on the system is clarifies (function display). It is composed from the button of "Initial setting", "Data assignment", "Service life maximization", "Reconstruction cost stabilizing", RLCC minimization", P/S cost stabilizing", "Planning within budget" and "User set of specify year for action". By clicking on flow button, it is able to perform the correspondence step, ②**Data reference window**: The form to call up the screen which displayed bridge data. It is composed from the button of "Single" and "Group", and ③**Setting screen**: The different specification screen for each step of flow is displayed, and the input of data and condition is done by the user.

When the read in of the data file is complete, by clicking on the "Next" button near the right top of the screen, "single bridge data confirmation screen" and "bridge group data confirmation screen" as shown in Figure 5 are displayed, and the main window calls up "service life maximization specification screen" which is shown in Figure 6.

In the bridge group data confirmation screen (Figure 5), the information for all bridges which have been read in data is able to be confirmed. The details of bridge group data confirmation screen are described below: **(i) Reconstruction bridge number:** In this part, the graph is drawn with horizontal axis as fiscal year and vertical axis as maintenance action cost or number of bridges that need the maintenance action. In the example of Figure 5, the number of reconstruction bridges for each year is displayed, and 7 bridges is the biggest amount for the number of reconstruction bridge in a year, **(ii) Progress of soundness:** In this part, the graph is drawn with horizontal axis as fiscal year and vertical axis as bridge proportion. It shows the progress and distribution of soundness which has been classified in 5 condition categories (CategoryI~V) as shown in section 3.2.1. The soundness progress of main girder is shown in the example of Figure 5. It is able to selecting the target member (main girder or floor slab) from the check box in the lower part, **(iii) Maintenance action details:** The maintenance action for all bridges which read in data has been done is displayed in table format. The items of table are composed by the "(Maintenance) action year", "Bridge name", "Member", "Measure method" and "Costs". In the example of Figure 5, there is a part of before service life maximization which only "Reconstruction" is done. Then, in order to do "Reconstruction" for the whole bridge, it is different with the maintenance which is done on the member, so that in item of "Member" there is nothing being input. And by clicking on "Detail display" button on the right below the screen, the detail screen is displayed in different window, and **(iv) Total costs:** The total cost of reconstruction and maintenance which are done in the period of plan is displayed here. And by clicking on "Display of general information" button, it is able to confirm the detail information by opening the different window.

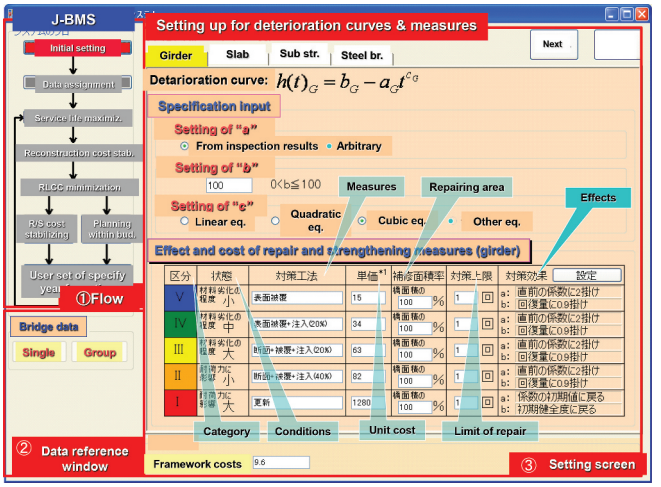


Figure 4. Deterioration curve/specification input screen of maintenance actions (for main girder).

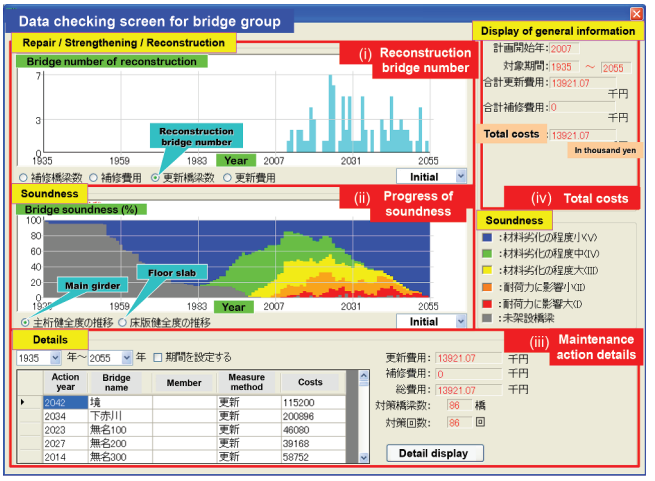


Figure 5. Screen display for bridge group data confirmation.

As the next step, service life maximization is then done due to the maximization setting of bridge service life. Based on the number of "Service life maximization setting" screen which is shown in Figure 6, the explanation is mentioned below: **(i) Calculation method for optimization:** The calculation technique which is used when performs the service life maximization is selecting here. Presently, for the calculation technique, only "Calculation time priority (Ramification model)" which is shown in service life maximization in step 1 is able to execute. In future, the development of "Precision priority (all search)" and "Standard (PSO)" is performing and the mounting is under planning, **(ii) Setting of effects:** The setting of maintenance action effects which is used in the calculation of service life maximization is done here. The setting of maintenance action effect is composed by "Measures", "Unit cost", "Repairing area", "Limit of repair" and "Effects". The annual value of this system is input by maintenance action setting which is shown in the setting of maintenance action effect. User is allowing to specify optionally in "Measures". It is able to specify "Effects" from pull down menu. Presently similar with the existing system, the value of slope "slope coefficient η =2", only the recovery "soundness recovery ρ = 0.9" is able to be selected (see section 3.2.2), **(iii) Action button:** By clicking on "Service life maximiz." button, the service life maximization calculation

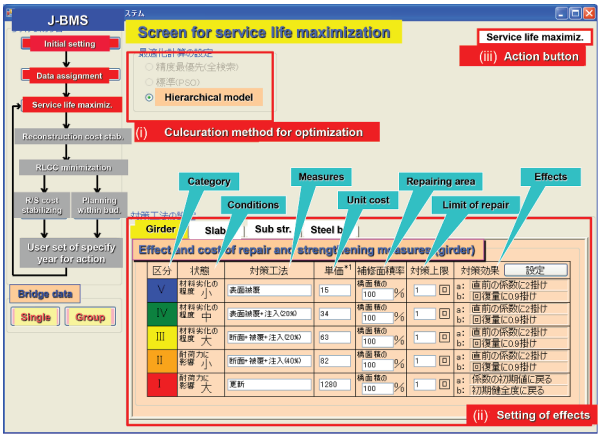


Figure 6. Screen display for service life maximization specification.

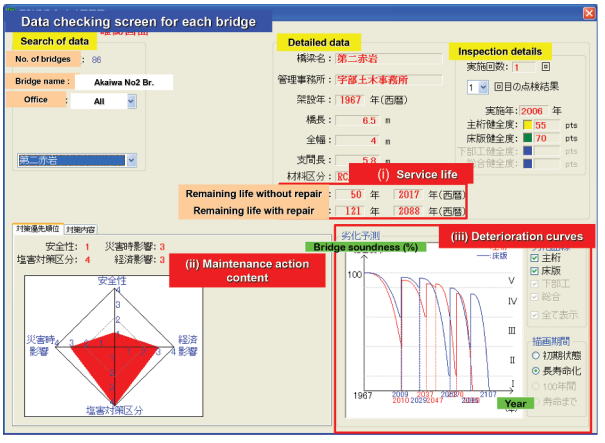


Figure 7. Single bridge data confirmation screen after performed the service life maximization.

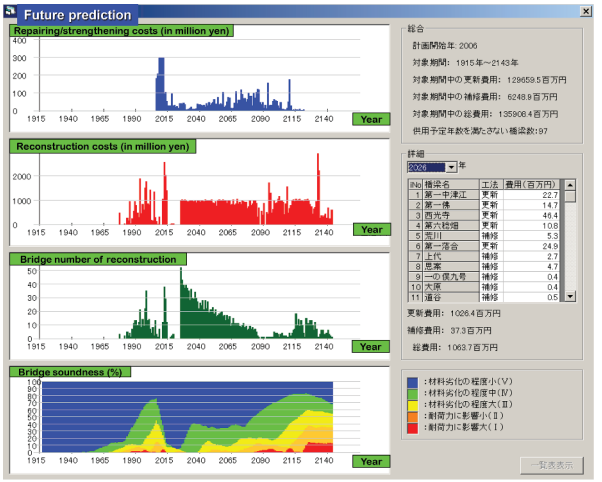


Figure 8. Future prediction screen after performed the RLCC minimization (bridge group).

is performs based on the contents which is input in "(i) Calculation method for optimization" and "(ii) Setting of effects". After the action is taken, the single bridge data confirmation screen is automatically showed.

The single bridge data confirmation screen after performed the service life maximization is shown in Figure 7, each of the number is described below: **(i) Service life:** The service life maximization is not performed, only initial service life is displays, and by performing the service life maximization, the bridge service life (the limit of bridge service life) after the service life maximization is displayed in Figure 7. In the example of Figure 7, the initial service life which is calculated from the normal inspection result is 50 years, reconstruction is need in 2017. However, by performing the service life maximization, the bridge service life could be extended until 121 years, which meant that reconstruction is need in 2088, **(ii) Maintenance action content:** The maintenance action that is taken for the selected bridge is displayed here. The maintenance action perform year is the year when the soundness is recovered in **"(iii) Deterioration curves"**. The maintenance action for main girder and slab are taken separately.

Figure 8 shows the result of a proposed optimal maintenance plan from the MPOS as the final step. From this figure, we found that it becomes easy understand what are the major processes in the deteriorating bridges in the future, how to improve their performance, and what kind of repair/strengthening works is most convenient for the deteriorating bridges.

5 CONCLUSIONS

The main conclusions of this study are as follows:

1) An integrated bridge management system for Yamaguchi Prefectural Government has been developed based on a basic policy for systematic bridge management, practical database system, etc with IT-based advanced monitoring system.
2) The system was applied to an actual bridge network in Ube City area, Japan to evaluate its effectiveness. As the results, it will be able to make the priority of repair/strengthening works of existing bridges based on the various information from the database system, then the system helps bridge administrators to establish the rational maintenance strategies.

REFERENCES

Miyamoto, A. and Motoshita, M. 2015. Development and practical application of a bridge management system(J-BMS) in Japan, *Civil Engineering Infrastructures Journal*, 48(1), 189–216.

Miyamoto, A. and Asano, H. 2018. Application of J-BMS to performance evaluation and remaining life prediction of an existing RC bridge, *Civil Engineering Infrastructures Journal*, 51(2), 321–337.

Miyamoto, A., Ito, D. and Ichiki, A. 2009. Development of a bridge management database system: J-BMS DB'09", *Infrastructure Management Series 11*, The Research Center for Environmental Safety, Yamaguchi Univ., 1–44.

Morioka, H., Ishida, J. and Miyamoto, A. 2008. Maintenance strategy for civil infrastructures in Yamaguchi Pref., *Proc. of 4th Choshu-London Memorial Symp. in Lifetime Eng. of Civil Infrastructure*, 4, 1–38.

Public Works and Construction Dept. of Yamaguchi Pref. Gov. & Yamaguchi Univ. 2003. *Inspection manual for J-BMS and it's utilization, 2003 Aug. version.*

Bridge Maintenance, Safety, Management, Digitalization and Sustainability – Jensen, Frangopol & Schmidt (eds)
© 2024 The Author(s), ISBN 978-1-032-77040-6
Open Access: www.taylorfrancis.com, CC BY-NC-ND 4.0 license

Risk-informed approach to determining optimal bridge inspection frequency for periodic replacement policies

Arnold X.-X. Yuan & Wang Chen
Department of Civil Engineering, Toronto Metropolitan University, Toronto, Ontario, Canada

ABSTRACT: Bridges are a critical part of a highway transportation system. As bridges deteriorate, inspection becomes an essential task of a transportation agency's Bridge Management System to ensure that the structures are safe and that infrastructure renewal funds are effectively and efficiently allocated and invested. However, the current Ontario Structural Inspection Manual provides a rigid specification regarding the bridge inspection frequency: typically, two years. While this is deemed a conservative approach, it is imperative to review and enhance the current inspection strategy considering bridge type, age, and other factors that would affect the likelihood and consequences of accelerated bridge deterioration and, in the worst case, bridge failures. For this purpose, a research project was recently initiated, aiming to develop a risk-informed value of information framework to determine an optimal lifecycle inspection profile of a bridge. The paper presents a simplified version of the analysis framework. It contains a gamma process-based bridge performance deterioration model, Bayesian model updating, and value of information analysis considering both aleatory and epistemic uncertainties for age-based preventive replacement programs. Some interesting preliminary results of individual bridges are presented.

1 INTRODUCTION

Bridges are subject to various environmental and loading stresses. As a result, their structural reliability declines, slowly but steadily, with time. However, due to the large variations and uncertainties underlying the various degradation mechanisms, the deterioration rates fluctuate among bridges and along their ages. Therefore, bridge inspection plays a vital role in capturing these uncertainties and assisting maintenance and rehabilitation decisions involved in bridge asset management.

Currently, most transportation agencies employ a periodic bridge inspection strategy. Enacted through Ontario Regulation (O. Reg. 104/97) under the Public Transportation and Highway Improvement Act (PTHIA), Ontario adopted a bridge inspection frequency of 2 years in 1997, although the inspection frequency for major culverts (≥3m span) was later relaxed to 4 years if they were in good condition as outlined in the OSIM (MTO, 2018). Similarly, the Federal Highway Administration (FHWA) recommends a routine bridge inspection program at regular intervals not to exceed 24 months (FHWA, 2012). Frequent inspections will affect MRR decisions in cases where the results of two consecutive tests may be unlikely to change within the safety critical threshold, due to deterioration affected by measurement errors (Yang and Xie, 2021), as well as the safety and delay risk that inspection activities pose to inspectors and the public. Given this, a risk-informed inspection interval that takes into account the risk of missing inspection and the value of inspection can improve resource utilization efficiency and operational

DOI: 10.1201/9781003483755-319

effectiveness. Therefore, it is important to review the current inspection program and if possible, propose a new set of inspection policies for bridges based on their disparate risk profiles.

Early bridge inspection planning research aimed to maximize the overall reliability of the bridge network for a given inspection budget (Kim and Frangopol, 2011). The reliability-based approach holds that MMR is required when a structure reaches a critical threshold. The generic inspection planning process is to model the optimal inspection planning problem based on the defined reliability function, hoping to get the optimal inspection plans with the objective of minimizing the LCC and appropriate reliability constraints, or an optimal hazard threshold under maximizing life expectancy. Early research on reliability-based bridge inspection planning dates back to the 1970s in the airplane industry. In civil structural engineering, Sorensen (1993) described how inspection information could be used for bridge I&M decision-making. Much work followed subsequently, including, e.g., Barone and Frangopol (2013), Orcesi and Frangopol (2011), Kwon and Frangopol (2011), Barone and Frangopol (2013) and Xu and Azhari (2022). However, most of the reliability-based inspection studies focused on conceptual development trying to answer the question of how inspection planning should have interacted with maintenance optimization. The methodology taken there is largely probabilistic without much empirical support.

Recent data-driven deterioration modelling provides new opportunities for inspection planning using a value of information (VOI) framework (Howard, 1967, Straub and Faber, 2004, Pozzi and Kiureghian, 2013, Papakonstantinou and Shinozuka, 2014). VOI is defined as the difference between the lifecycle costs of a maintenance program with and without inspection. Current VOI research in the field of bridge asset management focuses on exploring the influencing factors affecting VOI for implementing rational inspection. Quirk et al. (2018) may be the first to analyze the VOI of inspection in a bridge management system by using Bayesian updating and analyzing the VOI of different parameters (prior probability, the likelihood of inspector-assigned condition ratings, and the economic) and scenarios (no information, perfect information, imperfect information). However, the time dependence associated with detection techniques will also have a significant impact on the decision outcome. To further analyze the utility of inspection information for decision-makers, Liu and Frangopol (2019) proposed a new framework for decision-making using inspection data, comparing two techniques with different probability of detection (POD) on VOI. Results show that the NDT with a low POD can achieve a higher VOI in the early years of service. Yang and Frangopol (2022) pointed out that POMDP is a promising method due to its excellent performance in complex I&M decision scenarios.

Despite all these, there are several major drawbacks of the existent VOI studies related to inspection planning. First, many studies did not consider the temporal variation of bridge deterioration. When the temporal variation is explicitly modelled, the VOI analysis does not consider the epistemic or sampling uncertainty related to the stochastic deterioration models. The purpose of the paper is to develop a holistic VOI analysis framework for determining the optimal inspection interval for bridges. In this framework, the bridge performance is measured by the Bridge Condition Index (BCI), which is widely used in Ontario and several other provinces across Canada. The BCI deterioration is modelled as a nonstationary gamma process, of which the shape parameter is further parameterized as a set of functions of multiple bridge attributes. Based on this nonstationary gamma process deterioration model, the VOI analysis can readily take into account reductions in both temporal uncertainty and epistemic uncertainty. This feature represents the unique and novel feature of the proposed VOI analysis framework.

The rest of the paper is organized as follows. Section 2 presents the deterioration model that was calibrated with Ontario's Open Bridge Performance Database. Section 3 presents the preliminary results of the VOI analysis. Section 4 concludes the paper with a few outstanding issues to be addressed in the future.

2 THE BRIDGE DETERIORATION MODEL

2.1 *Fundamentals of non-stationary gamma process*

The gamma process is well considered one of the most realistic and yet most flexible stochastic process models for modelling the monotonic and gradual deterioration occurring in long-life civil infrastructure systems. The gamma process has independent nonnegative increments that follow a gamma distribution with the following probability density function:

$$f(x) = \frac{\beta^{\alpha} x^{\alpha-1}}{\Gamma(\alpha)} e^{-\beta x}, \tag{1}$$

for $x > 0$. The shaper parameter α and the scale parameter β both must be positive. Such a gamma process is stationary when its mean path is a linear function of time. Sample paths of a gamma process are monotonically increasing, making it a good candidate for modelling physical deterioration phenomena in various infrastructure systems. To characterize the non-linearity exhibited in many real deterioration phenomena, the shape function can be extended into a time-dependent function. A common form is the so-called Weibull function as

$$\alpha(t) = \theta_2 \left(1 - e^{-\left(\frac{t}{\theta_3}\right)^{\theta_4}} \right) \tag{2}$$

As a result, a nonstationary gamma process is constructed, and its increment, defined as $\Delta X(t) = X(t + \Delta t) - X(t)$, is known as a gamma distribution, with the shape parameter given as $\Delta\alpha(t) = \alpha(t + \Delta t) - \Delta\alpha(t)$. More discussions of gamma process can be found in Noortwijk (2009).

The Bridge Condition Index (BCI) which is widely employed in Canada measures bridge condition with a range from 100 to 0. A newly built bridge has a BCI of 100, and its condition is expected to decline gradually with time. Therefore, the decline in BCI of a specific bridge relative to the perfect condition (BCI = 100) can be modelled by a nonstationary gamma process.

Since different bridges may have different designs, loading conditions, and climate, geotechnical and hydraulic conditions, the modelling can be further extended in three ways. One is through the fixed-effects modelling approach by expressing the model parameters as the following:

$$\theta_i(z_j) = \exp\left[a_{i0} + a_{i1} z_{j1} + \cdots a_{iA} z_{jA}\right] \tag{3}$$

where $i = 1, \ldots, 4$ denotes the labelling of the scale and parameters with $\theta_1 = \beta$ for the scale parameter; $j = 1, \ldots, B$ denotes the bridge (B is the total number of bridges in an inventory); $\mathbf{z_j} = (z_{j1}, \ldots, z_{jA})$ represents the bridge attributes (A is the total number of attributes); and a_{ik} represents the model parameter for θ_i and attribute z_k ($k = 0,\ 1, \ldots,\ A$). The parameterized model can be estimated using the maximum likelihood method. The other modelling approach is through the use of the random effects by considering $(\theta_1, \ldots,\ \theta_4)$ as a dependent random vector. In this approach, each bridge is thought to have its own set of model parameters, whose values are a random realization of the random vector. More details of the modelling approach can be found in Yuan and Pandey (2009).

2.2 *Sources of data*

The data source used in this study is the bridge conditions in Ontario dataset obtained from the Open Government Portal, and the maintenance history as well as traffic volume data provided by the Ministry of Transportation Ontario (MTO). This dataset contains an inventory

of 5054 bridges, with BCI records spanning from 2000 to 2020. The database also contains important attributes. However, other essential information such as the construction year and the last MRR activity was obtained from MTO directly. The attributes considered in the study included material, structure, highway function, number of spans and length of spans, geographical region, and the last maintenance records. Figure 1 presents the geographic distribution of structures in this dataset. Note that the bridge and culvert are both included in open data, but only the bridge will be focused on.

2.3 *Deterioration modelling results*

After data cleansing, data from 380 bridges were considered for the natural deterioration modelling from the first life cycle. The bridge attributes were available but not considered in this paper. As the first step, each bridge was fitted individually with the nonstationary gamma process model. A few mean paths of the individually fitted gamma process models and their BCI observations are plotted in the left panel of Figure 1. From the plots, it is clear that the deterioration pattern varies significantly from one bridge to another. The scatterplots of the model parameters of the 380 bridges are shown in the right panel. It further confirmed the great variability of the deterioration patterns. It is interesting to see that θ_1 and θ_2 are highly negatively correlated, and so are θ_3 and θ_4. The variances of $\log \theta_i$ are 1.83, 2.22, 12.8 and 1.08, respectively.

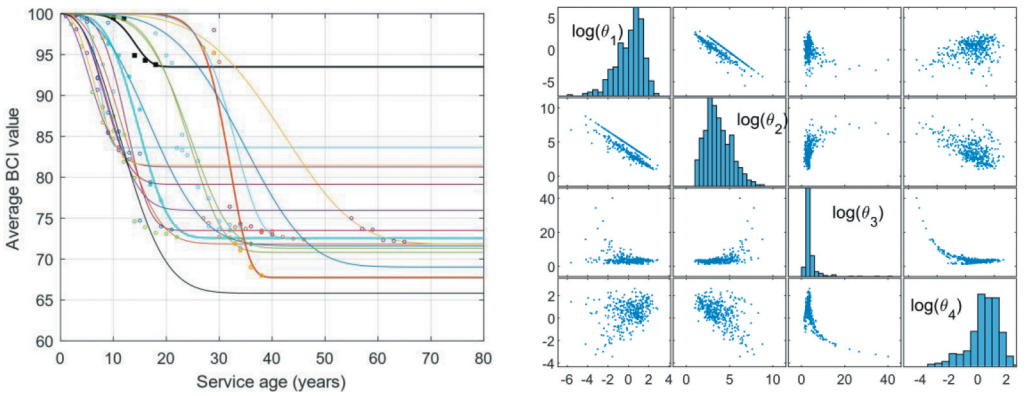


Figure 1. Sample individually fitted mean curves and the scatterplots of the model parameters.

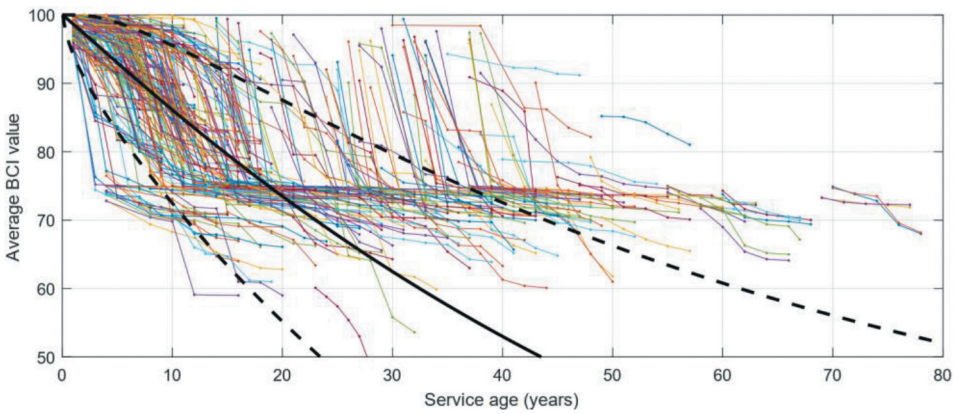


Figure 2. The pooled gamma process model and the observed individual sample paths.

The BCI data of the 380 bridges are then pooled and fitted to one common gamma process with the same model structure. The mean path and the 95% lower and upper bounds as well

as the observed individual sample paths are shown in Figure 2. The lower and upper bounds do not cover 95% of the sample paths, as they are supposed to do. This suggests that the bridge deteriorations exhibit significant heterogeneity that must be more carefully modelled.

Since the focus of the study is not on the deterioration modelling, further deterioration modelling results are not reported. From the value-of-inspection perspective, it is now clear that inspection can collect and accumulate BCI deterioration data that would help not only develop a more accurate deterioration model for the whole bridge inventory, but also develop a bridge-specific model, which then would help refine bridge-specific maintenance and rehabilitation plans. It is this point that the paper would like to illustrate in the following VOI analysis.

3 VALUE OF INSPECTION ANALYSIS

3.1 *The framework*

The basic notion of the value of information was established by Howard (1967). When it is applied for inspection planning, the VOI is calculated using the following simple formula:

$$\mathrm{VOI} = \mathrm{LCC}_0 - \mathrm{LCC}_1 \tag{4}$$

where LCC_0 and LCC_1 represent the lifecycle cost of the referencing bridge management program and that of an enhanced program, respectively. Several key questions need to be answered:

1) What is the referencing management program? This can be an age-based preventive replacement program. Alternatively, it may be a predictive condition-based maintenance program. Different referencing programs take different assumptions, which will definitely affect the VOI calculation.
2) What is the overall structure of the inspection program? For example, is it a periodic program with a fixed interval, or a non-periodic one?
3) What is the enhanced bridge management program? Is it a predictive condition-based program or an adaptive maintenance program?

In this study, the referencing program is an age-based, periodic preventive replacement program. The bridge lifetime is considered as a random variable of which the distribution is derived from the nonstationary gamma process model with randomized parameters as shown in Figure 1. The randomized parameters are assumed because, for a new bridge, it is unclear which set of parameters will fit the bridge. A bootstrap simulation is used to generate the random lifetime. The bridge life is defined as the time when the BCI drops for the first time below 50. The renewal theory is applied to obtain the optimal preventive replacement age for such a bridge. For that purpose, it is assumed that the preventive replacement cost is one unit, and the failure or corrective replacement cost is five units as the baseline, although a cost of ten units will also be used as a sensitivity analysis.

The inspection program is considered periodic. Different inspection intervals are considered: one year, two years, and four years. As new data are collected, the bridge-specific deterioration model is updated via Bayesian updating. With the new deterioration model, a forward-looking inspection plan is updated until the end of the planning horizon. The planning horizon is taken as 100 years. For brevity, this paper does not consider a preventive maintenance strategy; but rather, only preventive replacement is considered. In addition, the paper does not consider an aperiodic inspection program either, even though it may be more cost-effective. This is left for the future to investigate.

A unique feature of the proposed VOI analysis framework is the consideration of both temporal uncertainty and epistemic uncertainty. The temporal uncertainty was accounted for by the independent increments underlying the gamma process model, whereas the epistemic parameter uncertainty was characterized by Bayesian analysis. Yuan et al. (2021) presented an example of such analysis for a one-step inspection and maintenance program. However, the

problem we presented here was an extension for sequential decision-making involved in bridge management. Another extension is the use of a nonstationary gamma process. This requires additional computation that calls for advanced simulation techniques such as Markov chain Monte Carlo simulation.

3.2 *Models and parameters*

In the following VOI analysis, the optimal inspection interval is evaluated for an imaginary new bridge, which may be a random replica of the inventory of the 380 bridges. Without inspection, the lifetime of the imaginary bridge is a random variable of which the probability distribution can be derived from the gamma process model with a random set of parameters. For consistency, the four-parameter gamma process model is confined with $\theta_1\theta_2 = 100$. The bridge is said to reach its service life (and hence need replacement) whenever its BCI reaches 50 or below. Only the age-based replacement policy is considered. The inspection cost is taken as one unit, or \$1, whereas the preventive and corrective replacement costs are \$100 and \$500, respectively.

Since the gamma process model involves multiple parameters that are dependent on one another, a full-course Bayesian updating will be very computationally intense. To address the computational issue, a simplified, discretized scheme is employed. Specifically, since the new bridge is considered as a random replica of the inventory, the prior belief probability is taken as 1/380. As new data are accumulated, the belief probability is updated out of the 380 disparate cases. It is expected that the posterior probability will converge to the correct bridge identity. In other words, the Bayesian updating becomes a bridge identification problem.

3.3 *Results*

The baseline information before inspection is undertaken is a lifetime distribution that is derived from the gamma process model with parameters randomly drawn from the samples shown in Figure 1. The survival function of the lifetime distribution is shown in the left panel of Figure 3. The probability distribution exhibits a long tail, a common feature of mixed models. Based on this lifetime distribution, the cost rate curve of an age-based replacement program is shown in the right panel, which demonstrates that the optimal replacement age is 24.3 years with a minimized cost rate of \$5.88 per year.

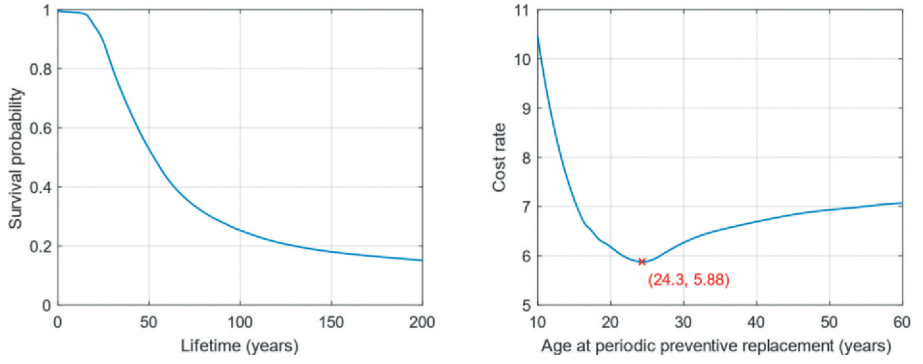


Figure 3. The survival function (left) and the cost rate function of an age-based replacement program (right).

As deterioration data accumulate from inspection, the optimal replacement age and the probability of the identified model keep updating. As a demonstration, Figure 4 shows the evolution of the two quantities over time at four different inspection intervals. With a given inspection interval, the posterior probability of the identified model increases along with time. As the inspection interval increases, less data accumulates and as a result, the rate of increase

in the posterior probability decreases. Both results are expected. Such a clear pattern is not shown in the posterior optimal replacement age, however. This is because the posterior optimal replacement age is a result of both an updated deterioration model and an accurate observation of the current BCI state. The former is an effect due to a reduction in epistemic uncertainty, whereas the latter is an effect due to a reduction in temporal uncertainty.

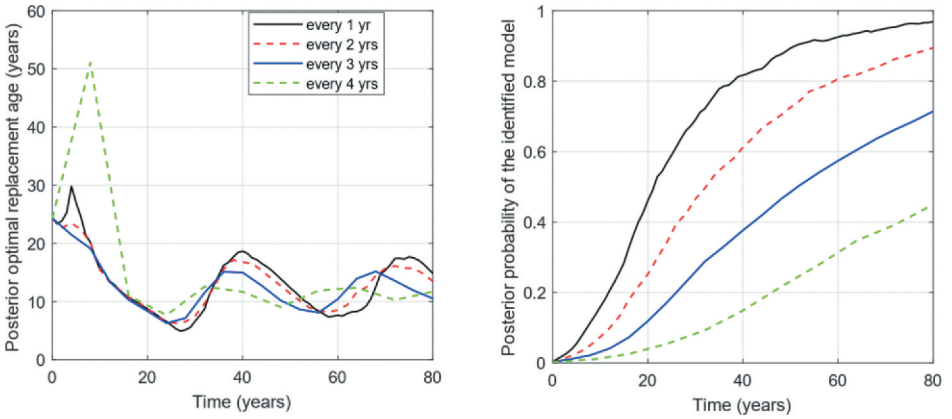


Figure 4. Evolution of the predicted remaining life (left) and the posterior probability of identified deterioration model (right) for bridge B100.

The average cost rates within the 80 years of planning horizon at different inspection intervals ranging from 1 to 8 years are computed using simulation. A few random samples are shown in Figure 5 for demonstration. The broken line represents the average cost rate for an age-based periodic replacement program without inspection. The optimal inspection interval with the minimal average cost rate is highlighted with a red arrow. The same bridge (B100) used in Figure 4 is also shown in Figure 5(d). For this bridge, an inspection interval of 4 years is optimal. Since different bridges have different deterioration patterns, the optimal inspection interval also varies. For the nine sample bridges, the minimal average cost rate with inspection is always lower than the cost rate without inspection, although the difference is almost negligible for bridges B150 and B200.

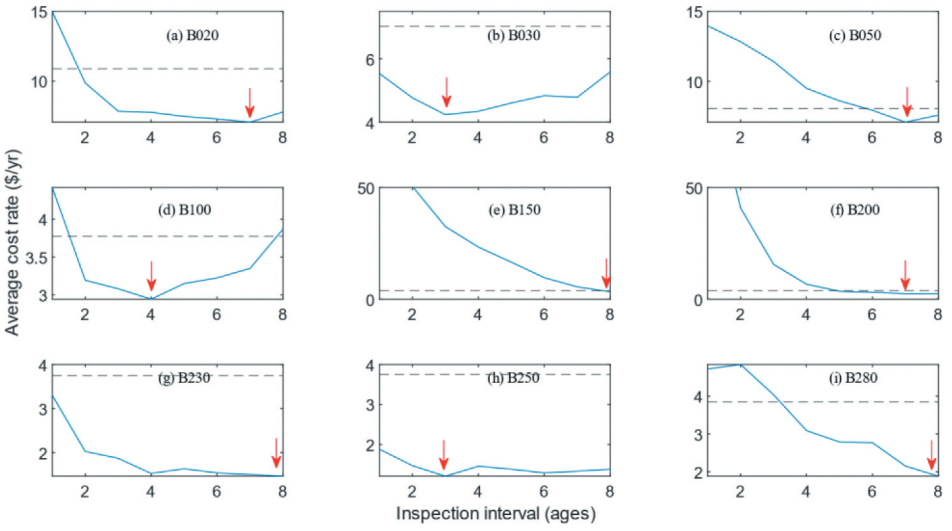


Figure 5. Sample results of the average cost rates at different inspection intervals.

The whole inventory of the 380 bridges is analyzed and the results are shown in Figure 6. Surprisingly, about 40% of the bridges have an optimal inspection interval of 8 years or even more. Only 8 out of the 380 bridges use the current inspection period – 2 years – as the optimal interval. This result is quite surprising and deserves further investigation. Another interesting observation of the analysis is made in the right panel of Figure 6: There are 31 points lying under the line of equality, suggesting a negative value of inspection. Further examination found that 14 of the 31 bridges have an optimal inspection interval of less than 8 years. This suggests that these bridges are better off doing no inspection. Note that the inspection cost is assumed to be 1% of the preventive replacement cost ($1 vs. $100). If the inspection cost increases, the number of bridges that are better off doing no inspection will also increase.

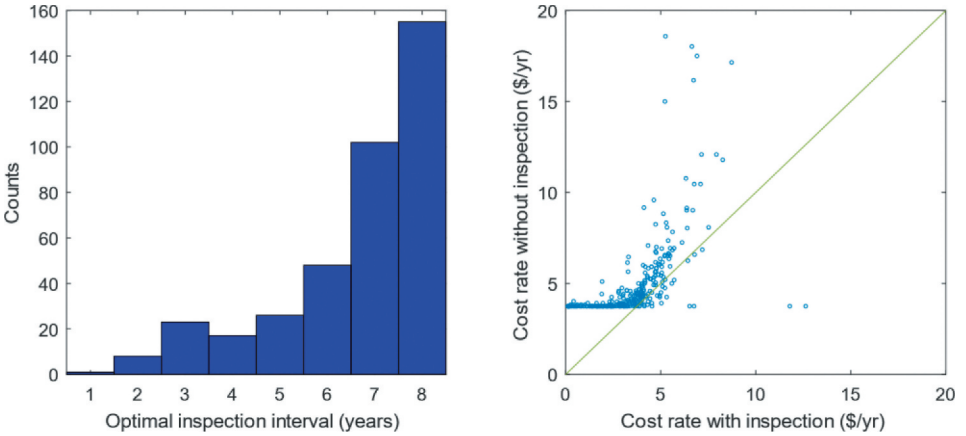


Figure 6. Histogram of the optimal inspection interval (left) and comparison between the cost rates with and without inspection (right).

It is worth highlighting that the optimal inspection intervals presented above are based on only a preventive replacement policy. Although the inspection results are utilized to update the replacement policy (in terms of the optimal replacement age), condition-based maintenance and rehabilitation policies may increase the value of inspection. This is left for future investigations.

4 CONCLUSIONS

Employing the notion of the value of information, this paper presents a novel approach to determining the optimal bridge inspection interval. The approach is unique in that it considers both the value of inspection in reducing temporal uncertainty and the value of inspection in reducing parameter uncertainty. The results showed that when only periodic replacement policies were practiced, the inspection intervals could be extended for a majority of the bridges in the inventory with some even better off doing no inspection. The inspection intervals are expected to be shortened when condition-based maintenance and rehabilitation policies are adopted together with an inspection program. This is left for further investigations in the future.

REFERENCES

Barone, G. & Frangopol, D. M. 2013. Hazard-Based Optimum Lifetime Inspection and Repair Planning for Deteriorating Structures. *Journal of Structural Engineering*, 139.

FHWA 2012. *Moving ahead for progress in the 21st century act (MAP-21), a summary of highway provisions*, Washington, DC: Federal Highway Administration.

Howard, R. A. 1967. Value of Information Lotteries. *Ieee Transactions on Systems Science and Cybernetics*, Ssc 3, 54-&.

Kim, S. & Frangopol, D. M. 2011. Inspection and monitoring planning for RC structures based on minimization of expected damage detection delay. *Probabilistic Engineering Mechanics*, 26, 308–320.
Kwon, K. & Frangopol, D. M. 2011. Bridge fatigue assessment and management using reliability-based crack growth and probability of detection models. *Probabilistic Engineering Mechanics*, 26, 471–480.
Liu, Y. & Frangopol, D. M. 2019. Utility and Information Analysis for Optimum Inspection of Fatigue-Sensitive Structures. *Journal of Structural Engineering*, 145.
MTO 2018. *Ontario Structure Inspection Manual (OSIM)*, Ontario, Canada, Ministry of Transportation of Ontario.
Noortwijk, J. M. V. 2009. A survey of the application of gamma processes in maintenance. *Reliability Engineering & System Safety*, 94, 2–21.
Orcesi, A. D. & Frangopol, D. M. 2011. Use of Lifetime Functions in the Optimization of Nondestructive Inspection Strategies for Bridges. *Journal of Structural Engineering*, 137, 531–539.
Papakonstantinou, K. G. & Shinozuka, M. 2014. Planning structural inspection and maintenance policies via dynamic programming and Markov processes. Part II: POMDP implementation. *Reliability Engineering & System Safety*, 130, 214–224.
Pozzi, M. & Kiureghian, A. D. 2013. Computation of Lifetime Value of Information for Monitoring Systems. *Structural Health Monitoring 2011: Condition-Based Maintenance and Intelligent Structures, Vol 2*, 1799–1806.
Quirk, L., Matos, J., Murphy, J. & Pakrashi, V. 2018. Visual inspection and bridge management. *Structure and Infrastructure Engineering*, 14, 320–332.
Sorensen, J. D. 1993. Reliability-based inspection planning for structural systems. *In*: Thoftchristensen, P. & Ishikawa, H. (eds.) *Reliability and Optimization of Structural Systems, V.*
Straub, D. & Faber, M. H. 2004. System effects in generic risk-based inspection planning. *Journal of Offshore Mechanics and Arctic Engineering-Transactions of the ASME*, 126, 265–271.
Xu, G. W. & Azhari, F. 2022. Data-driven optimization of repair schemes and inspection intervals for highway bridges. *Reliability Engineering & System Safety*, 228.
Yang, D. Y. & Frangopol, D. M. 2022. Risk-based inspection planning of deteriorating structures. *Structure and Infrastructure Engineering*, 18, 109–128.
Yang, Y. N. & Xie, H. M. 2021. Determination of Optimal MR&R Strategy and Inspection Intervals to Support Infrastructure Maintenance Decision Making. *Sustainability*, 13.
Yuan, X.-X., Higo, E. & Pandey, M. D. 2021. Estimation of the value of an inspection and maintenance program: A Bayesian gamma process model. *Reliability Engineering & System Safety*, 216, 107912.
Yuan, X. X. & Pandey, M. D. 2009. A nonlinear mixed-effects model for degradation data obtained from in-service inspections. *Reliability Engineering and System Safety*, 94, 509–519.

Bridge Maintenance, Safety, Management, Digitalization and Sustainability – Jensen, Frangopol & Schmidt (eds)
© 2024 The Author(s), ISBN 978-1-032-77040-6
Open Access: www.taylorfrancis.com, CC BY-NC-ND 4.0 license

Fragility assessment of water-crossing bridge structures exposed to flood hazards

J.M. Patel & J.E. Padgett
Department of Civil and Environmental Engineering, Rice University, Houston, TX, USA

ABSTRACT: Given the scarcity of available studies related to flood-fragility assessment of bridges and the expected increase in frequency of future flooding events, this study is focused on deriving parameterized fragility models relevant to a class of bridges that capture both primary and secondary effects of flood events. Different parameter combinations of a multi-span simply supported concrete girder bridge class are considered, leveraging finite-element analyses to assess the performance of different bridge components subjected to flooding scenarios. Following statistical sampling and analyses across a comprehensive range of bridge parameters and loading and site conditions, probabilistic flood-fragility functions are derived using statistical regression models for the different failure modes considered. The results highlight the important role of combined primary and secondary effects in exacerbating bridge damage potential during floods. The developed fragility models can be combined with scenario-based or probabilistic flood models to support regional risk and resilience modeling for transportation infrastructure.

1 INTRODUCTION

Transportation infrastructure is repeatedly exposed to natural hazards which cause significant damage to components such as bridges and roadways and lead to cascading consequences for response and recovery efforts in affected communities (Argyroudis et al., 2019; Boakye et al., 2022). Severe storm and rainfall events can produce heavy flood-flow discharge which cause significant hydraulic forces to act on various components of water-crossing bridges and give rise to secondary effects from flooding such as scouring of bridge foundations. More than 50% of historical bridge collapses in the United States are attributed to flooding or secondary flood-related effects (Wardhana & Hadipriono, 2003; Xiong et al., 2023). Although the risks associated with water-crossing bridge structures subjected to flooding are widely recognized, the literature is scarce regarding probabilistic models of bridge damage potential considering the range of sources of uncertainties and parameters affecting bridge performance when subjected to flooding.

Previous studies have developed flood fragility curves for water-crossing bridge structures considering the effects of water pressure loading, scour formation, and debris accumulation (Anisha et al., 2022; Argyroudis & Mitoulis, 2021; Kim et al., 2017). However, these fragility analyses were either performed for a specific case study bridge structure, or the fragility curves were conditioned on a single intensity parameter which may not capture the full complexity of the loading scenario or the variations on structural parameters that may be of interest in a regional analysis. Ahamed et al. (2021) examined the effects of considering flow hydraulics and geotechnical uncertainties in the flood fragility assessment and found the significance of both, implying the fragilities developed without considering comprehensive intensity parameters may not be able to represent the appropriate flooding scenario. To assist comprehensive flood-risk and resilience assessment, flood fragility models should consider: (a) both primary (hydraulic loads) and secondary effects (scour formation and debris damming) stemming from a flooding event, (b) uncertainties associated with hydraulic, geotechnical, and bridge parameters, and (c) potential for generating fragilities for a given bridge parameters and variable flooding scenario. Recently, the notion of

DOI: 10.1201/9781003483755-320

parameterized fragility modeling has been advanced (i.e., models that estimate the conditional failure probability of a structure given not only a scalar hazard intensity measure, as common in traditional conditional reliability models, but instead a vector of predictors related to the hazard or structural parameters). While such models have been developed for different types of bridges considering different hazard scenarios beyond flooding (e.g., Jeon et al., 2019; Saeidpour et al., 2018), the existing literature on developing flood fragility functions for water-crossing bridge structures is scarce. Recently, there have been a few studies performed to develop flood fragility models (Anisha et al., 2023; Khandel & Soliman, 2021; Mendoza Cabanzo et al., 2022). However, these studies did not consider comprehensively the primary and the secondary effects of floods, or the analysis was restricted to specific bridge component only.

To address these gaps in the literature, the primary objective of this study is to develop parameterized flood fragility models associated with different failure modes of water-crossing bridge structures which can be used for bridge damage state probability prediction. The multi-span simply supported concrete girder bridge is selected as a representative case study bridge, as this bridge class is found to be particularly vulnerable during flood events (Padgett et al., 2008; Xiong et al., 2023). Flood hazards including hydrodynamic flood loads, buoyancy effects, scour formation, and wooden debris accumulation are considered in this study. Uncertainties related to the bridge, flood, and geotechnical parameters are considered in the analysis. The probabilistic fragility models are developed using logistic regression, given its closed form functional representation. The study proposes different fragility models for different failure modes that can be used to assess the safety of water-crossing bridges subjected to flood events.

2 FLOOD HAZARD QUANTIFICATION

2.1 *Water pressure effects*

Columns of water-crossing bridges generally have continuous exposure to water pressure forces due to riverine flow. Depending on the severity of a flood event, the bridge superstructure may also become exposed to flood flow. The horizontal force (F_h) due to the water pressure of the fluid flow can be calculated by:

$$F_h = 0.5 C_D \rho v^2 A \tag{1}$$

where C_D is the drag coefficient, ρ is the mass density of the fluid, v is the velocity of the flow, and A is the submerged cross-sectional area of the bridge pier (and portion of a bridge deck, if submerged) normal to the direction of the streamflow.

In addition to horizontal loads, uplift buoyancy forces act on the bridge superstructure when flow depth exceeds the height of the bridge substructure. This may lead to bridge deck unseating, resulting in bridge failure (Padgett et al., 2008; Xiong et al., 2023). The uplifting buoyancy force (F_b) can be calculated using Archimedes principle:

$$F_b = \rho g V \tag{2}$$

where V is the volume of the submerged superstructure; and g is the gravitational acceleration constant. This failure mode is commonly observed in the United States when the flow depth exceeds the deck level of simply supported bridges, particularly in older bridges which tend to lack any vertical connection between the bridge deck and bearings (Balomenos et al., 2020; Xiong et al., 2023). Assuming that resistance to vertical uplift forces on a bridge deck comes only from self-weight, the limit state functions g_1 and g_2 for this failure mode can be defined as:

$$g_1 = W - F_b \tag{3a}$$

$$g_2 = \mu W_{sub} - F_h \tag{3b}$$

where W is the self-weight of the bridge superstructure; W_{sub} is the submerged weight of the bridge superstructure; and μ is the friction coefficient at the connection between the bridge superstructure and the substructure. If adequate or alternative bearings and connections are provided between the superstructure and substructure, these limit state functions can be altered to accommodate the appropriate resistances. Failure is assumed if either Equation 3(a) or (b) yields a negative value.

2.2 *Scour formation*

When the shear stress caused by flood flow exceeds the critical shear stress of soil particles in the channel bed, these soil particles are transported along with the flow of water which results in the formation of a cavity in the channel bed. This phenomenon, when occurring along a water-crossing bridge foundation, is referred to as bridge scour formation. When scour is formed at a bridge location, the bridge foundation is additionally exposed to lateral hydrodynamic loads (as represented in Equation 1). Also, the unsupported length of the impacted column increases which may cause structural instability of the bridge. For bridges with deep foundations, the lateral and frictional resistance of the foundation system can also decrease due to the loss of the soil layer above. Hence, considering the effects of scour formation while assessing bridge safety is crucial.

2.3 *Wooden debris accumulation*

Trees falling into the river because of their proximity to the riverbank and high winds or soil erosion is a common phenomenon observed in flood events (Hughes et al., 2023; Panici & De Almeida, 2020). Large volumes of accumulated wooden debris may result in debris-damming on the upstream side of the bridge pier or its superstructure, increasing the horizontal demand on the bridge. This causes additional overturning moments at the base. The loads exerted by the debris accumulation can be calculated using Equation 1 with C_D estimated for debris and by considering A as the projected area of debris accumulation (AASHTO, 2021; Elliot et al., 2012; Hughes et al., 2023). Present study assumes wedge-like shape of the debris accumulation and its critical dimensions (maximum size of the accumulated debris for the given flow condition) are calculated from the regression equations proposed by Panici & De Almeida, (2018).

3 FLOOD FRAGILITY ANALYSIS OF WATER-CROSSING BRIDGE STRUCTURE

The previous section enumerated various primary and secondary effects of riverine flood flow. The demands imposed on bridge components due to flood flow can result from both laterally and vertically applied forces. As such, two bridge failure modes are considered in this study: (a) deck unseating, and (b) excessive pier movement. These two failure modes broadly cover the bridge failure patterns observed during past flood events (Padgett et al., 2008; Xiong et al., 2023). This section presents the modeling of flood loads for bridge analysis and the development of fragility functions for different failure modes of the bridge. Given the vulnerability of multi-span simply supported (MSSS) concrete girder bridges against flood hazards, this study considers different configurations of this bridge class to develop the fragility models for the identified failure modes.

3.1 *Finite element modeling of the bridge*

OpenSees (McKenna et al., 2000) is adopted to perform the bridge response and flood load analyses of different bridge configurations, as it has been widely used for analyzing parameterized bridges models subjected to various hazards (Nielson, 2005; Pregnolato et al., 2022). Figure 1 shows the representative sketch of the two-dimensional (2D) bridge model. This

model was derived from a previously validated three-dimensional (3D) bridge model that has been used for seismic excitation as well as for hydraulic wave analysis (Balomenos et al., 2020; Nielson, 2005). The representative 2D model consists of a cross-sectional bridge deck and girders, representative bearings, bridge columns, and a foundation system. The deck-girder along the 2D cross-section is modeled using *elasticBeamColumn* elements connecting each girder-end node. For simply supported spans, the masses are lumped at the girder-end nodes and are assigned based on the specified span length and girder properties (girder weight, cross-sectional area, deck weight) for each analysis. The girders rest on a series of elastomeric bearing pads with steel dowels, modeled using a combination of bilinear *Steel01* material and *Hysteretic* material in *OpenSees*. The columns of the bridge are modeled using displacement-based beam-column elements (*dispBeamColumn*) with fiber-defined cross-section to model confined core concrete (*Concrete04*), steel reinforcement (*Steel02*), and unconfined cover concrete (*Concrete04*). The pile foundation considered in this study is of "drilled-shaft" type which is also modeled using displacement-based beam-column elements (*dispBeamColumn*). The soil resistance is modeled using appropriate *P-y* springs in the horizontal direction, *T-z* springs along the vertical axis, and *Q-z* springs at the tip of each pile, following the modeling strategy of Kameshwar & Padgett (2018). Depending upon the specified soil erosion level, these soil springs are removed from the eroded soil region to account for the scour in the analysis. For simplicity, this study uses uniform scour around each pier. A nonlinear static analysis considering maximum flow conditions of the flood event time-history is performed in this study using *algorithm Newton* as the solution algorithm which is based on the Newton-Raphson method.

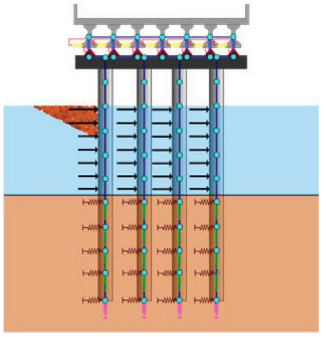


Figure 1. Schematic diagram of case study concrete-girder bridge.

3.2 *Experimental design and bridge parameters*

In order to cover a wide range of bridge, flood and geotechnical parameter combinations, the Latin Hypercube Sampling design was implemented to ensure that the parameter space covers the entire range of the parameter bounds. Table 1 shows the different parameters and their bounds considered in this study. These bounds are collected based on the existing water-crossing bridge inventory from the Houston-Galveston near-coast region. The uncertainty bounds for different drag coefficients are considered based on the results from past studies (Almasri & Moqbel, 2017; Nasim et al., 2019).

This study develops separate fragility functions for the two failure modes considered: (a) excessive pier movement, and (b) deck unseating. The soil type is broadly classified into two categories: cohesive soil and cohesionless soil; and their respective range of soil parameters are propagated into the analysis cases. Two different sets of 20,000 experimental samples are generated for cohesive and cohesionless soil. For each generated sample, the *OpenSees* bridge model is run and the results are extracted to develop parameterized fragility functions. Further, since the flood flow height is required to reach beyond the substructure level for imposing demands on the superstructure, additional 20,000 samples are generated specifically to

Table 1. Ranges of different parameters used to generate Latin Hypercube design samples.

Parameter	L †	U ‡	Parameter	L	U
Column diameter, D_{col} (m)	0.4	1.50	Scour depth, d_{scour} (m)	0	$0.9h_{pile}$
Deck slab thickness, t_{deck} (m)	0.1	0.25	Drag coefficient for pier, $C_{D,\ pier}$	0.7	1.2
No. of girders, n_{gd}	3	9	Drag coefficient for deck, $C_{D,\ deck}$	1.2	2.0
No. of piers per bent, b_n	2	8	Drag coefficient for pier in presence of wooden debris, $C_{D,\ debris}$	1.0	2.5
Deck width, w_{deck} (m)	5.0	24.0	Flood water density, ρ_w (kg/m^3)	900	1100
Span length, l_{span} (m)	6.1	39.6	Flow depth, y (m)	1.0	h_{bridge}
Column height, h_{col} (m)	1.5	17.3	Flow velocity, v (m/s)	1.5	15
Depth of bent, h_{bent} (m)	0.6	1.5	Debris log length, L (m)	0.5	18
Length of drilled pile, h_{pile} (m)	1.5	22.4	Angle of internal friction for soil particles, Φ (degree)	22.8	40
Unit weight of soil, γ (kN/m^3)	12.7	22.5	Cohesion between soil particles, C (kPa)	10	192
Girder type: AASHTO I, II, IV, Type C					

*$h_{bridge} = h_{col} + h_{bent} + h_{girder} + t_{deck}$; †L: lower bound; ‡U: upper bound

examine the deck unseating failure of the bridge considering flood flow depth to vary from the bottom of the girder to the top of the deck level, using the limit states defined in Equation 3.

3.3 *Fragility modeling*

To represent the response of the bridge component of interest, appropriate engineering demand parameters (*EDP*s) are selected for each failure mode. Similar to previous literature for seismic hazard, curvature ductility is chosen as the *EDP* to capture the pier movement (Nielson, 2005). The lognormally distributed capacity limit state of the column is adopted from Nielson (2005). *EDP* for the deck unseating failure mode is selected as its displacement in the horizontal or vertical direction, in accordance with their defined limit states in Equation 3.

EDPs from each analytical simulation are compared with the capacity estimates for each failure mode for the respective component, and the outcome is recorded as a binary variable with 1 representing the case in which demand exceeds the capacity (failure) and 0 represents the case in which demand does not exceed the capacity (no failure). In this study, parameterized fragility functions are developed using logistic regression, which is selected due to its easily transferable closed-form expression. The general form of the logistic-regression model can be expressed as:

$$P[\text{failure}|\mathbf{X}] = \frac{1}{1 + \exp[-l(\mathbf{X})]} \tag{4}$$

where $\mathbf{X}$ is the vector representing polynomial terms of model parameters along with its coefficients. Out of the different parameters used for the analysis, a subset of parameters can be chosen that provides the expected performance of the model. This study utilizes 10-fold cross-validation on the training samples for more robust estimates of the model parameters and to avoid overfitting of the model. The logistic regression model is trained using 70% of the data from the total dataset and tested on the remaining 30% of the data. The parameters considered for each model and the model coefficients are presented in the following sub-sections.

3.4 *Excessive pier movement*

The lateral resistance of the bridge is predominantly characterized by the soil type of the foundation. Since the majority of resistance to pier movement comes from the soil, separate fragility models are developed for bridge foundations in cohesive soil and cohesionless soil. The model estimated coefficients of the polynomial functions $l(\mathbf{X})$ along with their goodness-of-fit estimates evaluated on the test dataset are:

Cohesionless soil (Accuracy: 0.88, Precision: 0.88, F1-score: 0.88):

$$l(\mathbf{X}) = -3.38 - 5.47D - 0.21h_{\text{pile}} + 0.57d_{\text{scour}} + 0.39y + 0.69v + 0.0041V_{\text{debris}} + 1.35I_{\text{debris}} \tag{5}$$

Cohesive soil (Accuracy: 0.84, Precision: 0.85, F1-score: 0.84):

$$l(\mathbf{X}) = -3.67 - 3.61D - 0.13h_{\text{pile}} + 0.41d_{\text{scour}} + 0.32y + 0.52v + 0.0035V_{\text{debris}} + 1.08I_{\text{debris}} \tag{6}$$

The effect of debris accumulation is included by considering the debris volume parameter V_{debris} in the model. For training purposes, the set of the results from experimental design samples without considering debris loads (V_{debris} = 0) are merged with the same set of sample results considering the debris accumulation loads so that the single model is able to predict excessive pier movement failure probability for the two different scenarios. One additional binary categorical feature is introduced (I_{debris}) while training the model which should be taken as 0 when debris effects are neglected and 1 when debris accumulation is considered.

3.5 *Deck unseating analysis*

The estimated coefficients of polynomial function $l(\mathbf{X})$ to develop fragility model for the deck unseating failure mode are:

$$l(\mathbf{X}) = -14.25 + 7.75Z_{\text{c}} + 0.88v + 0.12l_{\text{span}} - 0.05w_{\text{deck}} \tag{7}$$

While selecting these parameters, the accessibility factor was considered so that it could be used for real-time bridge condition assessment. Parameter Z_c represents the height of flood water above the base of the superstructure. The velocity of the flow can be found from the preinstalled current meter readings. The goodness-of-fit estimates of the model on the test dataset are as follows: Accuracy: 0.89, Precision: 0.89, F1-score: 0.89.

4 DISCUSSION

To illustrate parameter sensitivity, a representative MSSS concrete girder water-crossing bridge is selected as a case study. The case study structure is a three-span bridge with a span length of approximately 20 m, a deck width of 12 m, and concrete girders of the AASHTO-IV class. The substructure consists of 4 equal-height circular columns 6.1 m in length and 0.51 m in diameter. The foundation of the bridge is of a drilled shaft type (pier extends and goes through the soil) with a length of 7.6 m and the soil type is cohesionless soil. Assuming no effects of scour formation or debris accumulation, fragility curves of this bridge are generated conditioned on the depth of flow parameter, for excessive pier movement (flow velocity of 7 m/s) and deck unseating (flow velocity of 4 m/s) failure modes (Figure 2). Considering this as a reference case, different parameters in the model are varied to assess the sensitivity of each parameter.

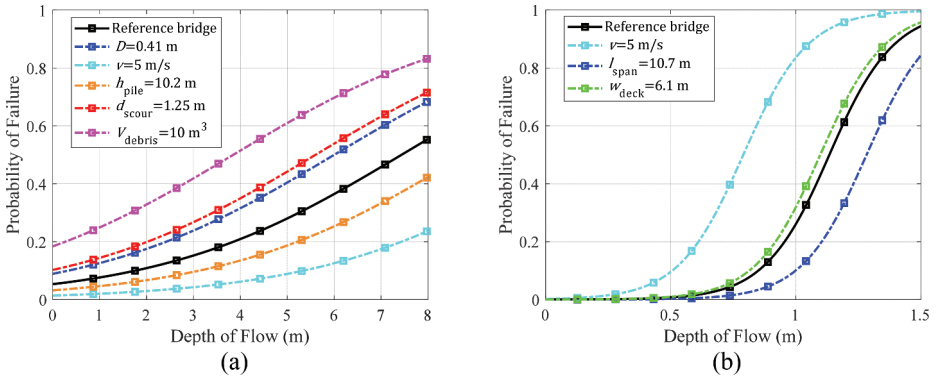


Figure 2. Parameter sensitivity of the proposed flood fragility models developed for (a) excessive pier movement, and (b) deck unseating failure mode.

When the bridge pier diameter is decreased from 0.51 to 0.41 m, significant variation is observed in the flood fragility curve as shown in Figure 2(a). Since the lateral bending capacity of the pier is directly proportional to the moment of inertia of its cross-section, minor change in the pier diameter significantly affects the lateral resisting capacity of the pier, resulting in higher movement of a pier with a smaller diameter when subjected to horizontal forces. Figure 2(a) also represents the fragility curves developed by considering different pile lengths. In the case of lateral loading, the resistance is provided from the soil pressure in the lateral direction. Hence, increasing the pile length provides higher lateral resistance, resulting in lower bridge fragility. It can also be observed that the fragilities change significantly when the flow velocity is changed or the effect of debris accumulation is considered, as evident from Figure 2(a). The formation of the scour at the bottom of the pier crucially affects the structure's lateral and vertical resistance capacity, which can be observed in Figure 2(a) where an increment in the scour depth significantly increases the fragility of the pier damage.

As shown in Figure 2(b), increasing the flow velocity from 4 to 5 m/s dramatically increases the fragility for deck unseating failure mode. On the other hand, decreasing the span length leads to reduction in the fragility. The lateral forces acting on the simply supported superstructure increases with its length for the given flow depth, whereas, the frictional resistance is only provided from its supports. Thus, when bridge decks with higher span length are exposed to the lateral and uplift forces from the floodwater, it attracts higher demands that results in more fragile cases compared to the bridges with shorter spans. Finally, reduction in the deck width leads to lesser self-weight of the superstructure for the given span length, resulting in increasing fragility.

5 CONCLUSION AND FUTURE SCOPE

This study develops parameterized flood fragility functions for a multi-span simply supported (MSSS) concrete girder bridge class to evaluate its failure probability when subjected to a flooding event. Along with the primary stressors caused by the flood flow in terms of the horizontal water-pressure and uplift forces, the study also considers the secondary effects stemming from the flood hazard in the form of scour at the bridge foundation and wooden debris accumulation at the location of bridge columns. Given the type of loading a bridge experiences during flooding conditions, the bridge failure modes are broadly classified into two categories: deck unseating and excessive pier movement. The proposed parameterized flood fragility functions for each failure mode are developed herein using logistic regression. Considering the uncertainties associated with bridge parameters, foundation parameters, and flood-hazard parameters in the statistical sampling, finite-element simulations of the analytical bridge model are performed to generate training dataset for fitting the logistic regression model. The developed fragility functions indicated a high level of accuracy on the test dataset. These models provide useful insights into the contribution of different

parameters on the likelihood of bridge failure when subjected to different flooding scenarios. Application of the proposed models is demonstrated using a representative case study bridge and model parameter sensitivity analysis is performed. Results suggest that the coupled effects from high-velocity flow and the formation of scour at the pier bottom significantly reduce the lateral resistance of the foundation system and increase the failure threat for water-crossing bridge structures. Bridges with slender piers are more likely to experience damage, whereas, narrow bridges (because of lesser superstructure weight) are prone to unseat from their support during extreme flooding events. The proposed fragility models can also help identify bridges vulnerable to flood hazard, and accordingly, suggest prospective interventions based on the insights gained from a parameter study. Moreover, the proposed fragility models can be easily implemented for regional flood-risk and resilience studies given its closed-from formulation. Real-time bridge safety can also be assessed by coupling the proposed fragility models with a situational awareness framework for safer vehicular routing during a flood event. Additionally, while the flood fragility models proposed in this study are developed for a specific bridge class, the presented methodology can be adopted for the development of fragility models for other types of bridge classes. Future work related to this topic may additionally explore the effects of abutment scour or non-uniform scour formation which may result in uneven bridge settlement.

ACKNOWLEDGEMENT

The authors would like to acknowledge the Rice University Civil and Environmental Engineering Department for the support. The authors would also like to acknowledge the support of this research by the National Science Foundation (NSF) PIRE grant under award number 1545837. Any opinions, findings, and conclusions, or recommendations expressed in this paper are those of the authors and do not necessarily reflect the views of the sponsors.

REFERENCES

AASHTO. (2021). *American association of state highway and transportation officials*.

Ahamed, T., Duan, J. G., & Jo, H. (2021). Flood-fragility analysis of instream bridges – consideration of flow hydraulics, geotechnical uncertainties, and variable scour depth. *Structure and Infrastructure Engineering*, *17*(11), 1494–1507. https://doi.org/10.1080/15732479.2020.1815226

Almasri, A., & Moqbel, S. (2017). Numerical Evaluation of AASHTO Drag Force Coefficients of Water Flow Around Bridge Piers. *Journal of Engineering Materials and Technology*, *139*(2), 021001. https://doi.org/10.1115/1.4035253

Anisha, A., Jacob, A., Davis, R., & Mangalathu, S. (2022). Fragility functions for highway RC bridge under various flood scenarios. *Engineering Structures*, *260*, 114244. https://doi.org/10.1016/j.engstruct.2022.114244

Anisha, A., Sahu, D. K., Sarkar, P., Mangalathu, S., & Davis, R. (2023). High dimensional model representation for flood fragility analysis of highway bridge. *Engineering Structures*, *281*, 115817. https://doi.org/10.1016/j.engstruct.2023.115817

Argyroudis, S. A., & Mitoulis, S. A. (2021). Vulnerability of bridges to individual and multiple hazards-floods and earthquakes. *Reliability Engineering & System Safety*, *210*, 107564. https://doi.org/10.1016/j.ress.2021.107564

Argyroudis, S. A., Mitoulis, S. A., Winter, M. G., & Kaynia, A. M. (2019). Fragility of transport assets exposed to multiple hazards: State-of-the-art review toward infrastructural resilience. *Reliability Engineering & System Safety*, *191*, 106567. https://doi.org/10.1016/j.ress.2019.106567

Balomenos, G. P., Kameshwar, S., & Padgett, J. E. (2020). Parameterized fragility models for multi-bridge classes subjected to hurricane loads. *Engineering Structures*, *208*, 110213. https://doi.org/10.1016/j.engstruct.2020.110213

Boakye, J., Guidotti, R., Gardoni, P., & Murphy, C. (2022). The role of transportation infrastructure on the impact of natural hazards on communities. *Reliability Engineering & System Safety*, *219*, 108184. https://doi.org/10.1016/j.ress.2021.108184

Elliot, R. C., Froehlich, D. C., & MacArthur, R. C. (2012). Calculating the Potential Effects of Large Woody Debris Accumulations on Backwater, Scour, and Hydrodynamic Loads. *World Environmental and Water Resources Congress 2012*, 1213–1222. https://doi.org/10.1061/9780784412312.123

Hughes, W., Santos, L., Lu, Q., Malla, R., Ravishanker, N., & Zhang, W. (2023). Probabilistic risk assessment framework for predicting large woody debris accumulations and scour near bridges. *Structure and Infrastructure Engineering*, 1–18. https://doi.org/10.1080/15732479.2023.2177875

Jeon, J.-S., Mangalathu, S., Song, J., & Desroches, R. (2019). Parameterized Seismic Fragility Curves for Curved Multi-frame Concrete Box-Girder Bridges Using Bayesian Parameter Estimation. *Journal of Earthquake Engineering*, *23*(6), 954–979. https://doi.org/10.1080/13632469.2017.1342291

Kameshwar, S., & Padgett, J. E. (2018). Parameterized Fragility Assessment of Bridges Subjected to Pier Scour and Vehicular Loads. *Journal of Bridge Engineering*, *23*(7), 04018044. https://doi.org/10.1061/(ASCE)BE.1943-5592.0001240

Khandel, O., & Soliman, M. (2021). Integrated Framework for Assessment of Time-Variant Flood Fragility of Bridges Using Deep Learning Neural Networks. *Journal of Infrastructure Systems*, *27*(1), 04020045. https://doi.org/10.1061/(ASCE)IS.1943-555X.0000587

Kim, H., Sim, S.-H., Lee, J., Lee, Y.-J., & Kim, J.-M. (2017). Flood fragility analysis for bridges with multiple failure modes. *Advances in Mechanical Engineering*, *9*(3), 168781401769641. https://doi.org/10.1177/1687814017696415

McKenna, F., Fenves, G. L., & Scott, M. H. (2000). *Open system forearthquake engineering simulation* [Computer software].

Mendoza Cabanzo, C., Santamaría, M., Sousa, H. S., & Matos, J. C. (2022). In-Plane Fragility and Parametric Analyses of Masonry Arch Bridges Exposed to Flood Hazard Using Surrogate Modeling Techniques. *Applied Sciences*, *12*(4), 1886. https://doi.org/10.3390/app12041886

Nasim, M., Setunge, S., Zhou, S., & Mohseni, H. (2019). An investigation of water-flow pressure distribution on bridge piers under flood loading. *Structure and Infrastructure Engineering*, *15*(2), 219–229. https://doi.org/10.1080/15732479.2018.1545792

Nielson, B. G. (2005). *Analytical fragility curves for highway bridges in moderate seismic zones*. Georgia Institute of Technology.

Padgett, J., DesRoches, R., Nielson, B., Yashinsky, M., Kwon, O.-S., Burdette, N., & Tavera, E. (2008). Bridge Damage and Repair Costs from Hurricane Katrina. *Journal of Bridge Engineering*, *13*(1), 6–14. https://doi.org/10.1061/(ASCE)1084-0702(2008)13:1(6)

Panici, D., & De Almeida, G. A. M. (2018). Formation, Growth, and Failure of Debris Jams at Bridge Piers. *Water Resources Research*, *54*(9), 6226–6241. https://doi.org/10.1029/2017WR022177

Panici, D., & De Almeida, G. A. M. (2020). Influence of Pier Geometry and Debris Characteristics on Wood Debris Accumulations at Bridge Piers. *Journal of Hydraulic Engineering*, *146*(6), 04020041. https://doi.org/10.1061/(ASCE)HY.1943-7900.0001757

Pregnolato, M., Winter, A. O., Mascarenas, D., Sen, A. D., Bates, P., & Motley, M. R. (2022). Assessing flooding impact to riverine bridges: An integrated analysis. *Natural Hazards and Earth System Sciences*, *22*(5), 1559–1576. https://doi.org/10.5194/nhess-22-1559-2022

Saeidpour, A., Chorzepa, M. G., Christian, J., & Durham, S. (2018). Parameterized Fragility Assessment of Bridges Subjected to Hurricane Events Using Metamodels and Multiple Environmental Parameters. *Journal of Infrastructure Systems*, *24*(4), 04018031. https://doi.org/10.1061/(ASCE)IS.1943-555X.0000442

Wardhana, K., & Hadipriono, F. C. (2003). Analysis of Recent Bridge Failures in the United States. *Journal of Performance of Constructed Facilities*, *17*(3), 144–150. https://doi.org/10.1061/(ASCE)0887-3828(2003)17:3(144)

Xiong, W., Cai, C. S., Zhang, R., Shi, H., & Xu, C. (2023). Review of Hydraulic Bridge Failures: Historical Statistic Analysis, Failure Modes, and Prediction Methods. *Journal of Bridge Engineering*, *28*(4), 03123001. https://doi.org/10.1061/JBENF2.BEENG-5763

Bridge Maintenance, Safety, Management, Digitalization and Sustainability – Jensen, Frangopol & Schmidt (eds)
© 2024 The Author(s), ISBN 978-1-032-77040-6
Open Access: www.taylorfrancis.com, CC BY-NC-ND 4.0 license

Combining condition deterioration and seismic risks for bridge asset management

A. Ghavidel
Graduate Research Assistant, The University of Texas at San Antonio

A. Du
Assistant Professor, The University of Texas at San Antonio

S. Kameshwar
Assistant Professor, Louisiana State University

ABSTRACT: Traditionally, bridge asset management has been primarily focusing on chronic aging-related deterioration, overlooking the impact of earthquake hazards. Despite extensive research on bridge deterioration and seismic risks, there's a gap in combining both factors in life-cycle cost analysis (LCCA). This study introduces a framework integrating bridge condition deterioration and seismic risks in LCCA, thereby enhancing decision-making of highway bridges. Markovian deterioration process and probabilistic seismic damage analysis are integrated for time-dependent condition rating and seismic damage estimation. The proposed framework can quantify life cycle costs for different maintenance and retrofit strategies. In addition, the framework accommodates different risk perceptions with proposed weighting factors. A sensitivity analysis on a case-study bridge explores the influence of factors and local seismicity on LCCA, making this framework a valuable tool for risk-informed, long-term bridge asset management.

1 INTRODUCTION

Bridge asset management is crucial to ensuring the functionality and operation of regional transportation networks. Traditionally, bridge asset management mainly deals with chronic deterioration resulting from natural aging processes (Assaad & El-adaway, 2020; de Dieu et al., 2020; Sabellano et al., n.d.). Yunovich et al. (2003) demonstrated this by conducting cost analysis throughout the lifespan of reinforced concrete bridge decks, using a corrosion-related deterioration. Kong & Frangopol (2003) introduced a framework to evaluate the life-cycle analysis of structures as they deteriorate. They specifically pointed out challenges arising from uncertainties in changing loads over time, resistance factors, and maintenance interventions.

On the other hand, many studies have focused on bridge damages caused by earthquakes and the overall costs throughout the life cycle (Omidian et al., n.d.; Torti et al., 2022). Kumar et al. (2009) used a probabilistic approach to calculate the life-cycle cost of reinforced concrete bridges that are prone to corrosion in earthquake-prone areas. Padgett et al. (2010) proposed a method to assess the best retrofits for bridges. This approach is based on considering seismic life-cycle costs and conducting a cost–benefit analysis. This method combines probabilistic seismic hazard models, the vulnerability of bridges in their original and retrofitted states for different levels of damage, and the related costs of both damage and retrofitting.

Despite considerable research efforts in quantifying the probabilistic deterioration and evaluating seismic fragility and risks in highway bridges, there is a noticeable gap in the literature regarding the integration of these two crucial stressors into a cohesive LCCA framework. This study aims to address this gap by introducing a new framework that incorporates both the deterioration of bridge conditions and seismic risks into the LCCA of highway bridges. This approach provides

DOI: 10.1201/9781003483755-321

a more comprehensive understanding of the relative contributions of these external threats. By considering the effects of aging-induced deterioration and the potential for sudden and catastrophic seismic damages simultaneously, this framework becomes a valuable tool for making informed decisions in long-term bridge asset management. Moreover, in traditional LCCA, decisions are typically based on predetermined rules and schedules. The proposed LCCA framework can further enable dynamic and adaptive AI-based (e.g., reinforcement learning) decision-making processes by offering episodic random simulations over a planning horizon.

In the following sections, we will offer a comprehensive explanation of the methodology and application of this LCCA framework. We will use a case-study highway bridge to demonstrate its practicality. Moreover, a sensitivity analysis will be carried out to examine the influence of changing weighting factors and local seismicity on the LCCA results. This analysis aims to highlight how different perceptions of risk can impact decision-making in bridge asset management.

2 INTEGRATED CONDITION DETERIORATION AND SEISMIC DAMAGE MODELING

2.1 *Markovian bridge condition deterioration*

The bridge component condition deterioration is modeled via Markov processes. Markov state transition probability matrices under chronical aging deterioration (i.e., do-nothing) are obtained for three bridge components (deck, super structure, and substructure) based on the national bridge inventory (NBI) data (FHWA, 2022):

$$P_{DECK} = \begin{bmatrix} 1.00 & 0.00 & 0.00 & 0.00 & 0.00 & 0.00 & 0.00 & 0.00 & 0.00 \\ 0.00 & 1.00 & 0.00 & 0.00 & 0.00 & 0.00 & 0.00 & 0.00 & 0.00 \\ 0.00 & 0.00 & 1.00 & 0.00 & 0.00 & 0.00 & 0.00 & 0.00 & 0.00 \\ 0.00 & 0.00 & 0.0114 & 0.9886 & 0.00 & 0.00 & 0.00 & 0.00 & 0.00 \\ 0.00 & 0.00 & 0.00 & 0.0174 & 0.9826 & 0.00 & 0.00 & 0.00 & 0.00 \\ 0.00 & 0.00 & 0.00 & 0.00 & 0.0227 & 0.9773 & 0.00 & 0.00 & 0.00 \\ 0.00 & 0.00 & 0.00 & 0.00 & 0.00 & 0.0268 & 0.9732 & 0.00 & 0.00 \\ 0.00 & 0.00 & 0.00 & 0.00 & 0.00 & 0.00 & 0.0714 & 0.9286 & 0.00 \\ 0.00 & 0.00 & 0.00 & 0.00 & 0.00 & 0.00 & 0.0452 & 0.1011 & 0.8537 \end{bmatrix} \quad (1)$$

$$P_{Super} = \begin{bmatrix} 1.00 & 0.00 & 0.00 & 0.00 & 0.00 & 0.00 & 0.00 & 0.00 & 0.00 \\ 0.0282 & 0.9718 & 0.00 & 0.00 & 0.00 & 0.00 & 0.00 & 0.00 & 0.00 \\ 0.00 & 0.0107 & 0.9893 & 0.00 & 0.00 & 0.00 & 0.00 & 0.00 & 0.00 \\ 0.00 & 0.00 & 0.0147 & 0.9853 & 0.00 & 0.00 & 0.00 & 0.00 & 0.00 \\ 0.00 & 0.00 & 0.00 & 0.0194 & 0.9806 & 0.00 & 0.00 & 0.00 & 0.00 \\ 0.00 & 0.00 & 0.00 & 0.00 & 0.0246 & 0.9754 & 0.00 & 0.00 & 0.00 \\ 0.00 & 0.00 & 0.00 & 0.00 & 0.00 & 0.0276 & 0.9724 & 0.00 & 0.00 \\ 0.00 & 0.00 & 0.00 & 0.00 & 0.00 & 0.00 & 0.0532 & 0.9468 & 0.00 \\ 0.00 & 0.00 & 0.00 & 0.00 & 0.00 & 0.00 & 0.0282 & 0.0995 & 0.8723 \end{bmatrix} \quad (2)$$

$$P_{Sub} = \begin{bmatrix} 1.00 & 0.00 & 0.00 & 0.00 & 0.00 & 0.00 & 0.00 & 0.00 & 0.00 \\ 0.00 & 1.00 & 0.00 & 0.00 & 0.00 & 0.00 & 0.00 & 0.00 & 0.00 \\ 0.00 & 0.0142 & 0.9858 & 0.00 & 0.00 & 0.00 & 0.00 & 0.00 & 0.00 \\ 0.00 & 0.00 & 0.0208 & 0.9792 & 0.00 & 0.00 & 0.00 & 0.00 & 0.00 \\ 0.00 & 0.00 & 0.00 & 0.0302 & 0.9698 & 0.00 & 0.00 & 0.00 & 0.00 \\ 0.00 & 0.00 & 0.00 & 0.00 & 0.0282 & 0.9718 & 0.00 & 0.00 & 0.00 \\ 0.00 & 0.00 & 0.00 & 0.00 & 0.00 & 0.0207 & 0.9793 & 0.00 & 0.00 \\ 0.00 & 0.00 & 0.00 & 0.00 & 0.00 & 0.00 & 0.0654 & 0.9346 & 0.00 \\ 0.00 & 0.00 & 0.00 & 0.00 & 0.00 & 0.00 & 0.0349 & 0.0925 & 0.8726 \end{bmatrix} \quad (3)$$

The effect of maintenance actions should also be incorporated into the modeling framework, as these intervention actions may improve and restore the bridge component conditions. Since this research adopts a component-based approach, three generic component-level maintenance actions are considered including: 1-minor maintenance, 2-major maintenance, and 3-replacement. The resulting Markov transition matrices are shown in Eq. 4-6. It is assumed that the three generic bridge components share the same transition probability matrices for under maintenance actions.

$$P_{minor} = \begin{bmatrix} 1 & 0 & 0 & 0 & 0 & 0 & 0 & 0 & 0 \\ 0 & 1 & 0 & 0 & 0 & 0 & 0 & 0 & 0 \\ 0 & 0 & 1 & 0 & 0 & 0 & 0 & 0 & 0 \\ 0 & 0 & 0 & 1 & 0 & 0 & 0 & 0 & 0 \\ 0 & 0 & 0 & 0 & 0.9 & 0.1 & 0 & 0 & 0 \\ 0 & 0 & 0 & 0 & 0 & 0.8 & 0.2 & 0 & 0 \\ 0 & 0 & 0 & 0 & 0 & 0 & 0.7 & 0.3 & 0 \\ 0 & 0 & 0 & 0 & 0 & 0 & 0 & 0.6 & 0.4 \\ 0 & 0 & 0 & 0 & 0 & 0 & 0 & 0 & 1 \end{bmatrix} \tag{4}$$

$$P_{major} = \begin{bmatrix} 1 & 0 & 0 & 0 & 0 & 0 & 0 & 0 & 0 \\ 0 & 1 & 0 & 0 & 0 & 0 & 0 & 0 & 0 \\ 0 & 0 & 0.3 & 0.4 & 0.3 & 0 & 0 & 0 & 0 \\ 0 & 0 & 0 & 0.1 & 0.3 & 0.6 & 0 & 0 & 0 \\ 0 & 0 & 0 & 0 & 0.1 & 0.2 & 0.7 & 0 & 0 \\ 0 & 0 & 0 & 0 & 0 & 0.05 & 0.1 & 0.85 & 0 \\ 0 & 0 & 0 & 0 & 0 & 0 & 0.05 & 0.05 & 0.9 \\ 0 & 0 & 0 & 0 & 0 & 0 & 0 & 0.02 & 0.98 \\ 0 & 0 & 0 & 0 & 0 & 0 & 0 & 0 & 1 \end{bmatrix} \tag{5}$$

$$P_{replacement} = \begin{bmatrix} 0 & 0 & 0 & 0 & 0 & 0 & 0 & 0 & 1 \\ 0 & 0 & 0 & 0 & 0 & 0 & 0 & 0 & 1 \\ 0 & 0 & 0 & 0 & 0 & 0 & 0 & 0 & 1 \\ 0 & 0 & 0 & 0 & 0 & 0 & 0 & 0 & 1 \\ 0 & 0 & 0 & 0 & 0 & 0 & 0 & 0 & 1 \\ 0 & 0 & 0 & 0 & 0 & 0 & 0 & 0 & 1 \\ 0 & 0 & 0 & 0 & 0 & 0 & 0 & 0 & 1 \\ 0 & 0 & 0 & 0 & 0 & 0 & 0 & 0 & 1 \\ 0 & 0 & 0 & 0 & 0 & 0 & 0 & 0 & 1 \end{bmatrix} \tag{6}$$

2.2 *Seismic damage and risk modeling*

In this section, system-level bridge seismic fragility models will be used to provide probabilistic seismic damage estimates. The general functional form of the system-level seismic fragility model is shown in Eq. 7, which follows a lognormal distribution:

$$P(DS|PGA) = \Phi\left(\frac{ln\ (PGA) - ln\left(med_{sys}\right)}{\xi_{sys}}\right) \tag{7}$$

where med_{sys} is the mean value of the system fragility, and ξ_{sys} is the dispersion, or logarithmic standard deviation, of the system fragility. $\Phi(.)$ is the standard normal cumulative distribution function. Peak ground acceleration (PGA) is used as the intensity measure. The as-built state fragility models for the four damage states (slight, moderate, extensive and complete) and modification factors that reflects the effect of retrofit on the bridge system fragility of Multi-Span Simply Supported (MSSS) concrete bridge are adopted from Padgett et al. (2010). Then the annual rate of exceeding a certain damage state can be calculated as follows:

$$\lambda_{annual}(DS) = \int_{IM} P(DS|IM) \left| \frac{d\lambda(IM)}{dIM} \right| dIM \tag{8}$$

where λ(IM) denotes the annual rate of exceeding a certain IM, which is available from site-specific seismic hazard curve (e.g., from the USGS Unified Hazard Tool). Under the homogenous Poisson earthquake occurrence assumption, the annual probability of exceeding certain damage state can be finally calculated as follows:

$$P_{annual}(DS) = 1 - e^{-\lambda_{annual}(DS)} \tag{9}$$

It is assumed that all seismic damages will be repaired right after the earthquake impact. For slight and moderate damage state, it is assumed that the repair actions won't have any effect on the bridge condition ratings, but for extensive and complete damages, it is assumed that the repairs will restore the bridge conditions to the best condition.

3 COST QUANTIFICATION

3.1 *Annual direct cost*

The annual direct costs related to the intervention actions carried out in each year are quantified. The direct costs of the intervention actions are represented as percentages of the total construction cost for the bridge components or the entire bridge. Three maintenance actions and various seismic retrofit actions are considered, and their associated costs are obtained from the references (Du & Ghavidel, 2022; FHWA, 2021; Heath et al., 2004; Huang et al., 2014; Padgett et al., 2010). Seismic repair and cost estimates for various damage states are adapted from Padgett et al. (2010).

3.2 *Annual indirect cost*

In addition to the direct costs associated with intervention actions in bridge asset management, it is crucial to consider the indirect costs, which encompass the socioeconomic consequences arising from the disruption to the traffic-carrying capacity of bridges. These indirect costs comprise three components: (1) vehicle operation costs; (2) time costs incurred by passengers and trucks; and (3) safety costs, calculated based on empirical equations in the literature (Du & Ghavidel, 2022; Mackie & Stojadinović, 2005).

3.3 *Total life-cycle cost*

The above direct and indirect costs are then aggregated into the total annual cost. For the cost aggregation, weighting factors are introduced for the indirect costs as they are typically much higher than the direct costs. Moreover, different weighting factors are considered for the indirect costs induced by bridge condition deterioration/maintenance actions and by seismic repairs to reflect different risk perceptions.

$$C_{total} = (C_{D0} + C_{D1} + C_{D2}) + w_1 C_{I1} + w_2 C_{I2} \tag{10}$$

where C_{D0}, C_{D1}, and C_{D2} respectively denote the direct cost due to seismic retrofit, maintenance, and seismic repair. C_{I1} and C_{I2} denote the indirect costs due to bridge condition deterioration/maintenance and due to seismic damages/repair. w_1 and w_2 denote the indirect cost weighting factors for condition deterioration/maintenance and due to seismic damages/repair, respectively.

The estimates for both direct and indirect costs are computed for a specific year and should ultimately be aggregated to determine the life-cycle cumulative costs. This enables a straightforward comparison of various intervention actions, while explicitly incorporating different sources of uncertainties. The time-cumulative cost C_T over a T-year period is calculated as follows:

$$C_T = \sum_{t=1}^{T} \gamma^t C(t) \tag{11}$$

where $C(t)$ denotes the annual cost estimate at year t, $\gamma \in (0,1)$ is a discount factor to account for the effect of inflation and delayed reward, where in this study a discount factor of 0.96 is considered (USDOT, 2018).

4 CASE STUDY AND EVALUATION

4.1 *Case study setup*

In this section, a comprehensive analysis of a case-study bridge (as shown in Table 1), selected from the NBI database (FHWA, 2022), is conducted. The objective is to evaluate the effectiveness of the developed framework for bridge life cycle cost analysis considering a 75-year life cycle, considering 10,000 random life-cycle episodes to incorporate the different sources of uncertainties. This assessment is performed by considering the bridge located in two distinct cities (San Francisco and Memphis) with different seismic hazard.

Table 1. Case study bridge specifications.

Bridge parameter	Deck area (m^2)	Detour length (km)	Average Daily Traffic (Vehicle/day)	Truck ratio (r_{truck})
Value	809.25	19	14740	0.02

To assess the impact of various maintenance strategies on the life-cycle cost of the bridge, several prescribed maintenance scenarios are considered as follows, each offering unique insights into the interplay of maintenance actions and life cycle dynamics.

- Scenario #1: Do nothing
- Scenario #2: Minor maintenance every 10 years
- Scenario #3: Major maintenance every 25 years
- Scenario #4: Replacement of all components at the 35^{th} year
- Scenario #5: A condition-based policy:

  If components in good condition: Do nothing
  If components in fair condition: Minor maintenance
  If components in poor condition: Replacement

Furthermore, several practical assumptions have been incorporated into the framework, including:

- The replacement of the substructure will lead to reconstruction of the entire bridge.
- The replacement of the girder is assumed to lead to the replacement of the deck.
- Initial component conditions are randomly sampled from the categories of good and fair conditions (CR = 9 - 5). This stochastic approach reflects the bridge condition rating uncertainty.

Additionally, several seismic retrofit strategies, namely steel jacketing (SJ), seat extender (SE), shear key (SK), and their combinations are introduced in conjunction with maintenance scenarios.

4.2 *Cost-benefit analysis of different seismic retrofit strategies*

This section presents a detailed cost-benefit analysis to evaluate the effectiveness of various seismic retrofit strategies. This sensitivity analysis is focusing exclusively on seismic hazard-related costs to assess the effectiveness of retrofit strategies in mitigating earthquake-induced expenses. To this aim, the bridge condition ratings are assumed to be at the best conditions all the time to isolate the contributions solely from seismic hazard and retrofitting. Table 2 summarizes the results, providing a comprehensive overview of cost-benefit ratios (i.e., the reduced indirect cost compared to the no retrofit scenario respect to the increased direct cost compared to the no retrofit scenario) for diverse retrofit strategies.

Table 2. Cost benefit ratio of different seismic retrofit strategies.

Retrofit Strategies		No Retrofit	SJ	SE	SK	SE+SK	SJ+SE	SJ+SE+SK
Memphis	CI*	683484	508194	588998	666805	595245	485322	517671
	CD†	8670	173989	48789	50143	90562	215457	257606
	CBR‡	N/A	1.06	2.36	0.40	1.08	0.96	0.67
San Francisco	CI*	2297066	1828645	2207142	2399218	2196767	1763731	1716294
	CD†	29723	191646	68371	72564	109678	232368	273312
	CBR‡	N/A	2.89	2.33	-2.38	1.25	2.63	2.38

* CI: Indirect cost
† CD: Direct cost
‡ Cost benefit ratio (CBR) = $(CI_{No\ Retrofit} - CI_{Retrofit})/(CD_{Retrofit} - CD_{No\ Retrofit})$

As indicated in Table 2, the cost-benefit ratios vary across different retrofitting scenarios and geographical locations with different local seismicity. Between the two cities, it is observed that it is more cost-effective to implement seismic retrofit for the San Francisco case, which may experience more frequent earthquake events compared to Memphis.

4.3 *Life cycle cost analysis of different maintenance strategies*

In this section, a life cycle cost analysis is carried out. Figure 1 shows the direct, indirect, and total costs (direct cost + 0.05 × indirect cost) of different maintenance strategies for San Francisco, with each curve corresponding to a specific maintenance strategy outlined in Section 4.1. Analyzing the figure reveals higher direct costs for "Replacement at 35th year" scenario and condition-based policy, while "Do nothing" scenario and "Minor maintenance every 10 years" scenario lead to lowest cumulative direct costs. Based on Figure 1 (B), condition-based policy demonstrates the lowest cumulative indirect costs, suggesting a balanced approach. Figure 1 (C) presents the total cost across various strategies for bridge, with a similar trend to the indirect cost curves. The above results can effectively reveal how the cumulative direct and indirect costs vary for different maintenance strategies.

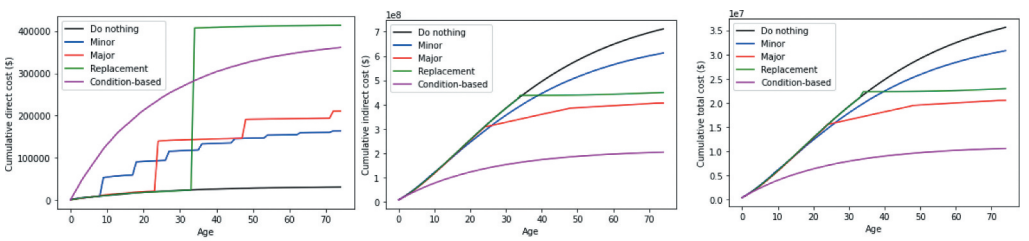


Figure 1. Cost curves for case study bridge: (A) Direct cost, (B) Indirect cost, and (C) Total cost.

For demonstration purposes, Figure 2 shows the influence of weighting factors on earthquake-induced indirect costs for the condition-based policy incorporated with a multi-retrofit scenario (SJ+SE+SK). The analysis of three weight configurations consistently shows that: as earthquake hazard weights (w_2) increases, indirect costs also rise proportionally, with a more significant impact in San Francisco. According to Figure 2, increasing earthquake-induced indirect costs from 5% to 100% results in a 30% increase for San Francisco and a 10% increase for Memphis in terms of cumulative indirect costs. This visualization can assist decision-makers, by highlighting the significance of weight selection in seismic risk assessments.

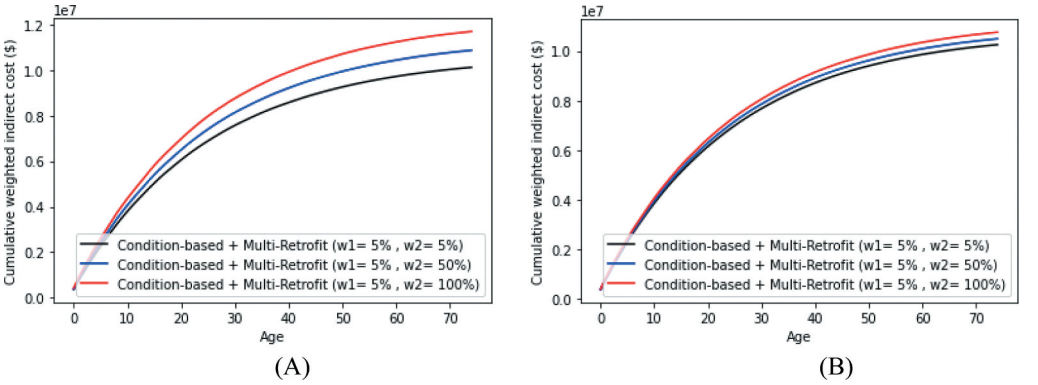


Figure 2. Different weighted indirect cost for case study bridge: A) San Francisco, B) Memphis.

5 CONCLUSION

This study introduces a simulation framework that enables episodic random simulations over a planning horizon for life-cycle cost analysis (LCCA) of highway bridges. This framework for the first time integrates the effects of bridge condition deterioration and seismic risks, by leveraging Markovian deterioration modeling and probabilistic seismic risk analysis. This framework can flexibly consider different maintenance and seismic retrofit strategies, and compare their efficacy in terms of life-cycle costs. Furthermore, by introducing different weighting factors, this approach enables the aggregation of indirect costs from different sources, facilitating cost assessment aligned with the stakeholders' risk attitude.

Ultimately, this research aims to empower decision-makers, engineers, and stakeholders involved in bridge asset management with a powerful tool that fosters more informed, risk-aware, and long-term-focused strategies for safeguarding bridge infrastructure in seismic-prone regions. The integration of bridge condition deterioration and seismic risks in the LCCA framework presented herein marks a significant step toward enhancing the resilience and longevity of our transportation networks. This framework can be further integrated with artificial intelligence to offer AI-informed sequential decision support for more proactive long-term bridge asset management.

ACKNOWLEDGEMENTS

This study is funded by the Federal Highway Administration (FHWA) under Contract No. 693JJ321C000027.

REFERENCES

Assaad, R., & El-adaway, I. H. (2020). Bridge infrastructure asset management system: Comparative computational machine learning approach for evaluating and predicting deck deterioration conditions. *Journal of Infrastructure Systems*, *26*(3), 04020032.

de Dieu, G. J., Chingui, J. A., & Botir, E. (2020). A Review of Bridge Management System: Deterioration Models. *Asian Journal of Engineering and Technology (ISSN: 2321–2462)*, *8*(2).

Du, A., & Ghavidel, A. (2022). Parameterized deep reinforcement learning-enabled maintenance decision-support and life-cycle risk assessment for highway bridge portfolios. *Structural Safety*, *97*, 102221.

FHWA. (2021). *Bridge replacement unit costs* [dataset]. https://www.fhwa.dot.gov/bridge/nbi/sd2021.cfm

FHWA. (2022). *National Bridge Inventory Data* [dataset]. https://www.fhwa.dot.gov/bridge/nbi/ascii.cfm

Heath, A. C., Pestana, J. M., Harvey, J. T., & Bejerano, M. O. (2004). *California Department of Transportation*.

Huang, Y., Parmelee, S., & Pang, W. (2014). Optimal retrofit scheme for highway network under seismic hazards. *International Journal of Transportation Science and Technology*, *3*(2), 109–128.

Kong, J. S., & Frangopol, D. M. (2003). Life-cycle reliability-based maintenance cost optimization of deteriorating structures with emphasis on bridges. *Journal of Structural Engineering*, *129*(6), 818–828.

Kumar, R., Gardoni, P., & Sanchez-Silva, M. (2009). Effect of cumulative seismic damage and corrosion on the life-cycle cost of reinforced concrete bridges. *Earthquake Engineering & Structural Dynamics*, *38* (7), 887–905.

Mackie, K. R., & Stojadinović, B. (2005). *Fragility basis for California highway overpass bridge seismic decision making*. Pacific Earthquake Engineering Research Center, College of Engineering . . ..

Omidian, P., Khaji, N., & Aghakouchak, A. A. (n.d.). *Developing a Resilience-Based Optimization Framework for Life-Cycle Costing Infrastructure Management*.

Padgett, J. E., Dennemann, K., & Ghosh, J. (2010). Risk-based seismic life-cycle cost–benefit (LCC-B) analysis for bridge retrofit assessment. *Structural Safety*, *32*(3), 165–173.

Sabellano, R., Bandpey, Z., & Shokouhian, M. (n.d.). Evaluating and Predicting Deterioration of Bridges Using Machine Learning Applications. *Structures Congress 2023*, 150–163.

Torti, M., Venanzi, I., Laflamme, S., & Ubertini, F. (2022). Life-cycle management cost analysis of transportation bridges equipped with seismic structural health monitoring systems. *Structural Health Monitoring*, *21*(1), 100–117.

USDOT. (2018). *Benefit-cost analysis guidance for discretionary grant programs*. USDOT Washington, DC.

Yunovich, M., Thompson, N. G., & Virmani, Y. P. (2003). Life cycle cost analysis for reinforced concrete bridge decks. *NACE CORROSION*, NACE–03309.

Bridge Maintenance, Safety, Management, Digitalization and Sustainability – Jensen, Frangopol & Schmidt (eds)
© 2024 The Author(s), ISBN 978-1-032-77040-6
Open Access: www.taylorfrancis.com, CC BY-NC-ND 4.0 license

A short-term hyperlocal meteorological forecast tool for mitigating bridge risks

Christos T. Georgakis
Department of Civil and Architectural Engineering, Aarhus University, Aarhus, Denmark
Mathesi Aps, Denmark

Nikos Lagaros, Pantelis Tsakalis & Ilias Chamatidis
Department of Structural Engineering, National Technical University of Athens, Athens, Greece
Mathesi Aps, Denmark

Cristoforo Demartino
Department of Architecture, Roma Tre University, Rome, Italy
Mathesi Aps, Denmark

ABSTRACT: A short-term hyperlocal meteorological forecast is an important tool for mitigating bridge risks as it empowers bridge operators and maintenance teams with timely and accurate weather predictions. Accurate predictions enable proactive responses to adverse conditions. Bridges are particularly vulnerable to extreme weather events, which can compromise their structural integrity and pose significant hazards. For instance, heavy rain can lead to flooding and erosion around bridge foundations, high winds can impose dynamic loads that strain the bridge's superstructure, freezing temperatures can cause ice accumulation and expansion within concrete or steel components, and fog can severely limit visibility for drivers, increasing the likelihood of accidents. This study presents a short-term hyperlocal meteorological forecast framework designed to assist in the real-time decision-making processes on the bridge. The proposed framework leverages cutting-edge machine learning algorithms, integrating a blend of local and global sensor systems to continuously collect real-time data. The data also forms a comprehensive dataset for the training process. The capacity of the framework to provide real-time weather insights for one geographic location is evaluated. In this context, this study critically examines one potential application of the proposed framework in predicting wind gusts, scrutinizing its versatility and efficacy in addressing diverse weather-related challenges faced by bridge management. Furthermore, the potential of the framework to enhance the resilience of transportation networks by minimizing disruptions and structural damage caused by adverse weather events is discussed and quantified.

1 INTRODUCTION

Bridges, as critical components of transportation infrastructure, are highly susceptible to adverse weather conditions (Markolf *et al.*, 2019). The integrity and safety of these structures can be significantly compromised by extreme weather events, necessitating proactive and effective management strategies. The importance of hyperlocal meteorological forecasts in mitigating bridge risks is becoming increasingly evident.

Recent studies highlight the growing role of machine learning and artificial intelligence in improving real-time decision-making for high-impact weather events, which are known to disrupt infrastructure (McGovern *et al.*, 2017). Machine learning algorithms have shown significant potential in enhancing weather data modeling, a computationally intensive task, by learning from data and producing relevant predictions (Trieu *et al.*, 2021).

The advancement in the application of machine learning for predicting extreme weather conditions has been remarkable. Lee and Chen (2021) developed a hybrid machine learning method that effectively predicts long-range precipitation under extreme weather conditions,

DOI: 10.1201/9781003483755-322

demonstrating the capability of machine learning to handle statistical variations caused by such conditions. Lucente *et al.* (2019) employed machine learning to predict high impact climate events like El Niño, highlighting the significance of machine learning in climatology. Mdegela *et al.* (2023) applied machine learning to classify extreme rainfall events, a key factor in predicting rainfall-induced floods. Lastly, Fang *et al.* (2021) surveyed the use of deep learning in predicting extreme weather, underscoring the role of advanced neural networks in meteorology.

This paper focuses on a short-term hyperlocal meteorological forecast framework, leveraging advanced machine learning algorithms. Following this introduction, the outline of this paper is as follows: Section 2 delves into the foundational concepts, methodologies, and theoretical underpinnings of the study, providing a detailed overview of the technological and algorithmic infrastructure utilized. In Section 3, the focus shifts to the specific tool developed for meteorological forecasting, discussing its design, functionality, and operational mechanisms, particularly its efficacy in short-term and localized weather predictions. Section 4 illustrates the practical implementation of this tool through various case studies or real-world scenarios, highlighting its effectiveness and practical utility. Section 5 expands on the versatility of the tool by exploring a wider range of possible scenarios and fields where the tool could be significantly beneficial. The paper concludes with Section 6, which synthesizes the key findings and insights from the research, discusses its limitations, and suggests directions for future research, emphasizing the broader impact and potential of the study in meteorological forecasting and related areas.

2 FRAMEWORK

The proposed framework for a short-term hyperlocal meteorological forecast tool for mitigating bridge risks is depicted in Figure 1. The proposed framework has versatile applicability across a range of scenarios; however, the forthcoming sections will specifically illustrate its application in the context of preventing truck overturning incidents caused by extreme lateral wind gusts. It signifies a step for risk mitigation for bridge operations, particularly in areas prone to severe weather events that could endanger vehicles crossing the structure.

The local weather station plays a pivotal role in the architecture, as it supplies real-time, site-specific atmospheric data, such as wind speed, wind direction, wind gusts, temperature, humidity, etc. which are critical for predicting the likelihood of high wind gusts that could compromise vehicular stability on bridges. This data is analyzed alongside information from one or more global weather stations that provides a broader context of weather patterns and predictions, thereby enhancing the system's ability to forecast local weather conditions (e.g., thunderstorms, etc.) imminent in the area of the the weather station.

Central to the operational efficacy of this system is the ML forecast algorithm. The predictive model within this system offers flexible operational modes: it can be executed locally, given that the computational demands are not substantial for edge computing. This local execution allows for rapid response times and reduces the need for constant cloud connectivity, which can be crucial in time-sensitive situations. Alternatively, the model can operate in cloud mode, harnessing greater computational power and resources. By potentially omitting data from the global weather stations, the framework can be streamlined to run entirely locally. This configuration, while less computationally intensive, still provides the capacity for accurate short-term forecasts, sufficient for initiating the early warning systems necessary to mitigate the risks of high wind events on bridge infrastructure.

The integration of hyperlocal real-time data with historical weather patterns to inform ML algorithms represents a significant advancement in location-specific weather forecasting. This methodology is corroborated by studies indicating that ML can substantially enhance the precision of weather-related risk assessments (Hall *et al.*, 2019; McGovern *et al.*, 2017). The framework's ability to rapidly process and analyze complex datasets exemplifies the tangible benefits of integrating AI with traditional meteorological techniques, enabling a more proactive approach to infrastructure safety management.

In the following, this paper seeks to present the technical design and operational testing results of the ML-based forecast tool, providing a detailed examination of its effectiveness in reducing the risk of truck overturning incidents on bridges. Through this exploration, the paper contributes

valuable insights to the domains of meteorology, civil engineering, and traffic safety, offering a replicable model for similar applications in other high-risk infrastructure scenarios.

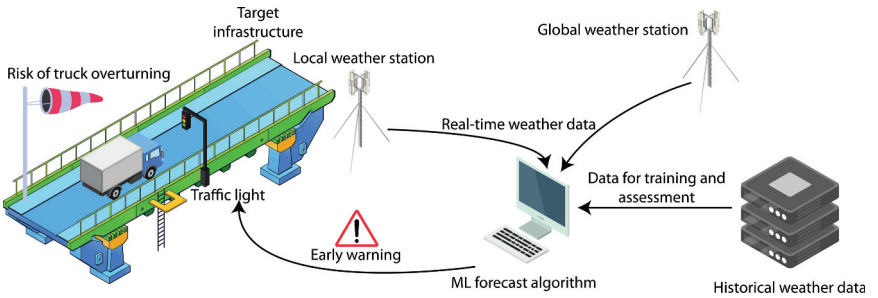


Figure 1. Proposed framework: example of application of the case of truck overturning under extreme lateral wind gusts.

3 SHORT-TERM HYPERLOCAL METEOROLOGICAL FORECAST TOOL

The short-term hyperlocal meteorological forecast tool is designed as a practical solution for accurate weather forecasting, particularly useful for bridge safety and transportation infrastructure.

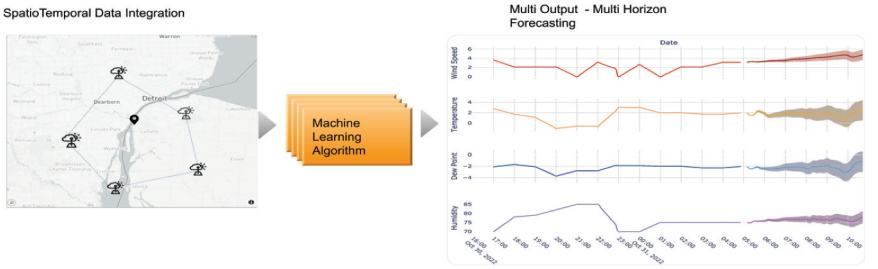


Figure 2. Short-term hyperlocal meteorological forecast tool: example of inputs and outputs.

The tool utilizes deep neural networks for its forecasting capabilities, chosen for their efficiency in processing complex weather data (see Figure 2). The core machine learning algorithm leverages Long-Short-Term-Memory (LSTM) and Convolutional (CNN) layers and has the following characteristics:

- **Multivariate and Multi-Output Forecasting**: The tool can handle multiple weather variables simultaneously and produce forecasts for several weather parameters. This feature allows for a comprehensive understanding of potential weather conditions.
- **Spatiotemporal Data Integration**: The framework combines data from local and global weather stations to train the machine learning algorithm. This ensures that the forecasts consider both local weather nuances and broader meteorological trends.
- **Customizable Inputs**: The tool's architecture permits customization through parametrized inputs, allowing it to be tailored to specific environmental conditions and user needs.
- **Scalability**: Designed to handle increasing amounts of data, the tool is scalable, ensuring its continued effectiveness as forecasting needs evolve.

The tool takes an input of past short sequences and forecasts a multi-horizon forecast of the desired time steps.

4 APPLICATION

High winds and wind gusts pose a significant hazard on highways and bridges, notably increasing the risk of vehicle accidents and particularly the overturning of high-profile vehicles

like trucks, buses, and trailers. This risk is heightened on highways where the combination of higher speeds and wind-induced forces can result in dangerous vehicular movements. Accurate short-term forecasting of wind gusts enables timely alerting of drivers and transportation authorities, who can then implement crucial safety measures, including speed restrictions, rerouting, and temporary road closures.

4.1 *Database*

The area chosen for this analysis is Cheyenne, Wyoming, USA, which is characterized by its high average wind speeds. Cheyenne's geographic and climatic conditions contribute to frequent and intense wind events, making it an ideal location for examining the impacts of wind on road safety. The significance of this choice is underscored by previous research and data indicating a notable correlation between the area's high wind speeds and the occurrence of wind-related vehicle accidents (Neupane *et al.*, 2022). By focusing on this area, the analysis aims to understand better the dynamics between high wind conditions and road safety.

The dataset is historical weather data from the stations nearest to the analysis point. The data starts from 2005-03-14 up to 2023-11-01 and comprised from 5 min interval of weather measurements. The data is split into three sets: training, validation and test set. The local station is ASOS station CHY and global station is chosen as the LAR station.

4.2 *Results*

The datasets are further split in sequences of 180 min interval (36 timesteps), the model is set to forecast 90 min interval (18 timesteps). The results and the performance of the proposed framework will be evaluated both in relation to forecasting the exact values but also in terms of distinguishing exceedance of thresholds relevant to the application. The model is forecasting the wind gust magnitude (Figure 3) and the vertical and horizontal components of the wind.

The forecast performances are assessed by using the following metrics: Mean Absolute Error (MAE) and Root Mean Squared Error (RMSE). Table 1 illustrates the regression model's capability in forecasting wind-related parameters, with a particular focus on wind gusts and wind direction. Notably, the model demonstrates higher accuracy in predicting specific components of wind gusts (U and V) compared to general gust measurements, as indicated by lower MAE and RMSE values.

The model is evaluated in relation to the detection of values above a particular threshold. Specifically, for the assessment of truck overturning risks, the critical threshold is set at 20 m/sec (Baker et al., 2022). Figure 4 presents a confusion matrix, offering a detailed visual representation of the model's performance in this context. In this analysis, there are 331 instances where

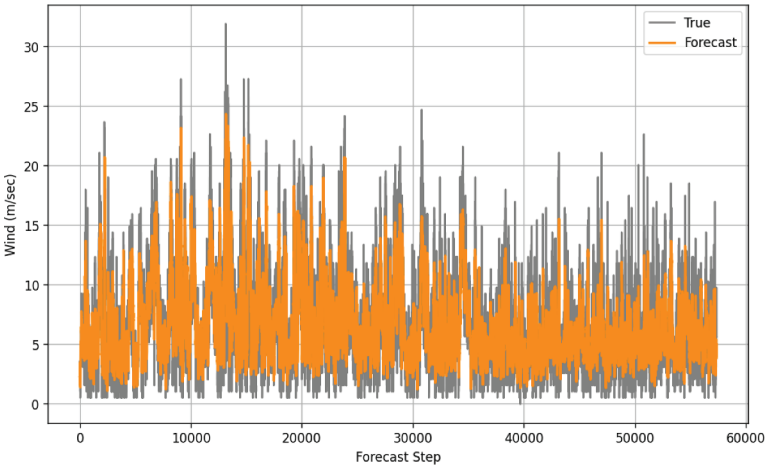


Figure 3. The complete test set true and forecasted wind gust values; each step is a 5-min interval step.

Table 1. Regression forecast performances.

	MAE	RMSE	Units
Wind Gust	1.61	2.21	m/sec
Wind Gust-U	1.24	1.72	m/sec
Wind Gust-V	1.36	1.94	m/sec
Wind Direction	23.81	-	degrees

TARGET / OUTPUT	Below 20m/s	Above 20m/s	SUM
Below 20m/s	56834 99.07%	201 0.35%	57035 99.65% 0.35%
Above 20m/s	159 0.28%	172 0.30%	331 51.96% 48.04%
SUM	56993 99.72% 0.28%	373 46.11% 53.89%	57006 / 57366 99.37% 0.63%

Figure 4. Confusion matrix for each 5 min observation of test set converted to binary above or below the 20m/sec threshold.

the wind gust surpasses the established threshold. The model demonstrates a high level of precision in identifying these occurrences, achieving an impressive accuracy rate of 99.3%. Additionally, its performance is further underscored by a robust Receiver Operating Characteristic (ROC) Area Under the Curve (AUC) score of 0.97, indicating excellent predictive capability.

Referring to Table 2, the model incorrectly forecasts 201-time steps where wind gusts exceed 20 m/sec. Upon closer analysis of these false positives, it is observed that 70% of these instances feature wind gusts above 15 m/sec. Despite being below the critical threshold, such wind speeds can still represent a significant risk for various types of vehicles.

Table 2. Statistics of false positives.

Samples	201	-
Mean Wind Gust (m/sec)	16.3	m/sec
Standard Dev (m/sec)	3.18	m/sec
30% percentile (m/sec)	15.43	m/sec

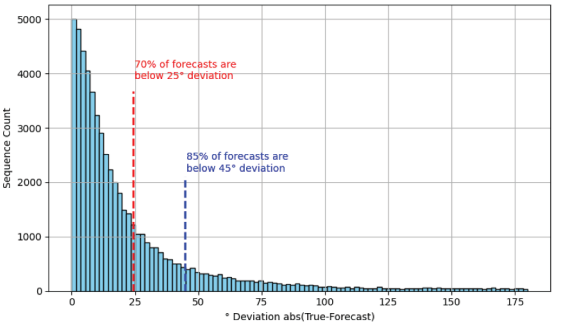


Figure 5. Distribution of absolute angle difference between true and forecasted wind vectors for each step.

The error in wind direction forecasting is quantified by the absolute difference between the true wind vector's angle and that predicted by the forecast model. As illustrated in Figure 5, the histogram of forecast deviation shows that 70% of forecasts have an error within 25°, and 85% fall within a 45° deviation. This distribution indicates a generally reliable directional forecast, with a significant majority of predictions deviating less than half a right angle from the actual wind direction.

5 VARIOUS POTENTIAL APPLICATIONS

The proposed short-term hyperlocal meteorological forecast tool can be used as an approach to bridge safety and operational efficiency. Its capacity to anticipate and react to various weather-related risks is pivotal in mitigating potential hazards (Figure 6).

Here, we explore five key applications of this innovative tool:

- **Icing Prevention:** Bridges are particularly susceptible to icing, which poses a significant risk to vehicular stability and safety. The forecast tool can predict temperature fluctuations and humidity levels that lead to ice formation, enabling preemptive deployment of deicing measures. By doing so, it ensures the maintenance of safe passage during cold spells and winter storms, thereby reducing the incidence of accidents related to slippery surfaces (Wu and Peng, 2011).
- **Truck Overturning Alerts:** High winds can lead to the overturning of high-profile vehicles like trucks, especially on exposed bridges. The tool's capability to provide real-time wind speed and direction forecasts allows for the issuance of timely alerts. These alerts can inform traffic management systems and drivers, prompting necessary precautions such as vehicular speed restrictions or temporary traffic halts, thus averting potential overturning incidents (Lim, Kim, and Kim, 2020).
- **Flood Prediction and Management:** Flash floods represent a formidable threat to bridge integrity and road user safety. The forecast tool's integration of high-resolution rainfall estimates offers a proactive flood management approach. This approach not only fortifies flood preparedness but also facilitates the execution of emergency plans such as road closures and traffic redirection, thereby safeguarding both infrastructure and commuters (Naulin, Payrastre, and Gaume, 2013).



Figure 6. Key applications of the short-term hyperlocal meteorological forecast tool.

- **Visibility and Fog Detection:** Reduced visibility from fog is a frequent challenge in bridge environments. The forecast tool's ability to predict low-visibility events enables the activation of safety protocols, such as fog lighting and signage, and the implementation of speed reduction measures. This not only prevents accidents due to poor visibility but also enhances the overall safety of the driving experience during adverse weather conditions (Chun-Hua, 2008).
- **Structural Health Monitoring:** Extreme weather events exert considerable stress on bridge structures, which can lead to wear and eventual failure. The forecast tool's detailed weather predictions allow for timely structural assessments and maintenance scheduling. Such predictive maintenance ensures the longevity of the bridge and uninterrupted service, reducing the likelihood of catastrophic structural failures (Lin, Peng, and Wu, 2010).

The Short-Term Hyperlocal Meteorological Forecast Tool is pivotal not only for immediate safety measures but also for the long-term maintenance of bridge structures. In addition to its various applications, an essential function is its capacity to predict environmental conditions leading to structural corrosion and degradation:

- **Corrosion and Degradation Prediction:** The tool's precise weather data assists in forecasting conditions like high humidity and salinity, particularly detrimental to bridges. This ability to anticipate corrosive weather conditions allows for preemptive maintenance actions, such as applying corrosion-resistant treatments or scheduling detailed inspections. This proactive approach in combating corrosion and degradation is vital for the longevity and safety of bridge structures, helping to avert costly repairs and ensuring structural integrity over time (Wu and Peng, 2011).

6 CONCLUSIONS

In conclusion, the proposed framework of the short-term hyperlocal meteorological forecast tool, as outlined in this study, demonstrates a significant potential in enhancing bridge safety and operational efficiency. Its versatile applicability across various scenarios, particularly in preventing truck overturning incidents caused by extreme lateral wind gusts, highlights its utility in addressing specific and critical weather-related challenges.

The tool's advanced predictive capabilities, powered by machine learning algorithms, allow for accurate forecasting of high-risk weather conditions, such as strong lateral winds that pose a significant risk to high-profile vehicles on bridges. By providing timely alerts and actionable insights, the framework enables proactive measures to be taken, thereby mitigating the risk of accidents and enhancing the overall safety of bridge infrastructure.

Moreover, the framework's adaptability to different scenarios underscores its potential as a valuable asset not only for specific weather events but also for broader applications in infrastructure management and safety. The detailed exploration of its application in truck overturning prevention serves as a compelling example of how hyperlocal weather forecasting can be effectively utilized in practical, high-stakes environments.

The short-term hyperlocal meteorological forecast tool showcases diverse applications, crucial for both immediate safety and long-term bridge maintenance. Its key strengths lie in accurately predicting and addressing various risks including icing, truck overturning due to high winds, flash floods, fog-induced visibility issues, and structural damage caused by environmental factors.

Additionally, the tool's capabilities extend to long-term structural health monitoring. By predicting weather conditions that could lead to corrosion, it aids in preventive maintenance, thereby reducing the risk of long-term structural damage and extending the lifespan of bridge infrastructure. Overall, this study presents a robust and innovative approach to leveraging meteorological data for enhancing infrastructure safety. The short-term hyperlocal meteorological forecast tool stands as a testament to the advancements in technology and data analytics, offering a promising solution for mitigating bridge risks in various challenging scenarios.

ACKNOWLEDGEMENTS

Nikos D. Lagaros acknowledges the support of the Hellenic Foundation for Research and Innovation (H.F.R.I.) under the "2nd Call for H.F.R.I. Research Projects to support Faculty Members and Researchers", AMOSS project: "Additively Manufactured Optimized 3D Printed Steel Structures", (Project Number: 02779)

REFERENCES

Markolf, S. A., Hoehne, C., Fraser, A., Chester, M. V., & Underwood, B. S. (2019). Transportation resilience to climate change and extreme weather events–Beyond risk and robustness. *Transport policy*, *74*, 174–186.

McGovern, A., Elmore, K., Gagne, D., Haupt, S. E., Karstens, C., Lagerquist, R., Smith, T. M., and Williams, J. K. (2017). Using Artificial Intelligence to Improve Real-Time Decision-Making for High-Impact Weather. Bulletin of the American Meteorological Society, 98, 2073–2090.

Trieu, N.-T., Pottier, B., Rodin, V., and Huynh, H. X. (2021). Interpretable Machine Learning for Meteorological Data. *2021 The 5th International Conference on Machine Learning and Soft Computing*.

Sravanthi, N., Venkat, M. L., Harshini, S., and Ashesh, K. (2020). An Ensemble Approach to Predict Weather Forecast using Machine Learning. *2020 International Conference on Smart Electronics and Communication (ICOSEC)*.

Lee, M.-H., and Chen, Y. J. (2021). Precipitation Modeling for Extreme Weather Based on Sparse Hybrid Machine Learning and Markov Chain Random Field in a Multi-Scale Subspace. *Water*, 13(9), 1241.

Lucente, D., Duffner, S., Herbert, C., Rolland, J., and Bouchet, F. (2019). Machine Learning of committor functions for predicting high impact climate events. *arXiv: Atmospheric and Oceanic Physics*.

Rizvee, M. A., Rahman, M. A., Al-Hasan, M., Tareque, S. M., and Hasan, M. Z. (2020). Weather Forecasting for the North-Western region of Bangladesh: A Machine Learning Approach. *2020 11th International Conference on Computing, Communication and Networking Technologies (ICCCNT)*.

Ferrari, S., Lazzaroni, M., Piuri, V., Salman, A., Cristaldi, L., Rossi, M., and Poli, T. (2012). Illuminance prediction through Extreme Learning Machines. *2012 IEEE Workshop on Environmental Energy and Structural Monitoring Systems (EESMS)*.

Lazarevska, E. (2018). Wind Speed Prediction based on Incremental Extreme Learning Machine. *Proceedings of The 9th EUROSIM Congress on Modelling and Simulation, EUROSIM 2016, The 57th SIMS Conference on Simulation and Modelling SIMS 2016*.

Mdegela, L., Municio, E., De Bock, Y., Luhanga, E., Leo, J., and Mannens, E. (2023). Extreme Rainfall Event Classification Using Machine Learning for Kikuletwa River Floods. *Water*.

ang, W., Xue, Q., Shen, L., and Sheng, V. (2021). Survey on the Application of Deep Learning in Extreme Weather Prediction. *Atmosphere*.

McGovern, A., Elmore, K. L., Gagne II, D. J., Haupt, S. E., Karstens, C. D., Lagerquist, R., Smith, T., and Williams, J. K. (2017). Using artificial intelligence to improve real-time decision-making for high-impact weather. In Bulletin of the American Meteorological Society, 2073–2090.

Liu, Y., Horsburgh, J. S., DeVecchio, D. E., Jackson, E., Cao, Y., and Wei, X. (2015). Using machine learning to predict water temperature in lakes and reservoirs. In *Journal of the American Water Resources Association*, 1023–1032.

Wu, H., and Peng, D. (2011). Research of the Forecast and Early Warning System for Bridges. *Advanced Materials Research*, 243-249, 1978–1983.

Lim, J., Kim, S., and Kim, H.-K. (2020). Short-Term Forecasting of the Occurrence Time of Strong Wind Speed during a Typhoon based on LSTM for Sea-Crossing Bridge Operation. In *IABSE Conference, Seoul 2020: Risk Intelligence of Infrastructures*.

Naulin, J., Payrastre, O., and Gaume, E. (2013). Spatially distributed flood forecasting in flash flood prone areas: Application to road network supervision in Southern France. *Journal of Hydrology*, 486, 88–99.

Chun-hua, L. (2008). Analysis of Urban Traffic Safety in the Bad Weather. Taiyuan Science and Technology.

Lin, W.-Z., Peng, D., and Wu, H. (2010). Research on the Early-Warning System with the Static Method for Bridge Safety. In 2010 International Conference on Internet Technology and Applications.

Baker CJ and Soper D (2022). Calculation of the overturning wind speed of large road vehicles at exposed sites. Proceedings of the Institution of Civil Engineers – Transport.

Adarsha Neupane, Noriaki Ohara, and Kathy Ahlenius. Blowover Risk Assessment for Tractor-Trailer Trucks in High Winds Using a Blowover and Statistical Model. Transportation Research Record: Journal of the Transportation Research Board.


Taylor & Francis
Taylor & Francis Group
http://taylorandfrancis.com

SS27: Life-cycle performance safety, reliability, and risk of bridges and infrastructure systems under climate change

Organizers: F. Biondini, Z. Lounis & M. Ghosn


Taylor & Francis
Taylor & Francis Group
http://taylorandfrancis.com

Bridge Maintenance, Safety, Management, Digitalization and Sustainability – Jensen, Frangopol & Schmidt (eds)
© 2024 The Author(s), ISBN 978-1-032-77040-6
Open Access: www.taylorfrancis.com, CC BY-NC-ND 4.0 license

Remaining fatigue service life of the Hillsborough River Bridge in PEI, Canada

C. MacAulay, G. MacDonald, A. MacDonald & R. Keefe
Harbourside Engineering Consultants, Stratford, Prince Edward Island, Canada

D. Evans
Prince Edward Island Transportation and Infrastructure, Charlottetown, Prince Edward Island, Canada

ABSTRACT: The Hillsborough Bridge is Prince Edward Island Department of Transportation and Infrastructures (DTI's) signature structure, which connects the capital city of Charlottetown with the bordering community of Stratford and southern portion of Kings County. It is the busiest section of highway in the province with a peak average annual daily traffic (AADT) of about 40,000 vehicles per day (vpd). Any service interruption at this location would necessitate a 57 km detour, causing significant user costs and delays. Originally a ferry crossing, it was replaced by a railway bridge in the early 1900, supported on 11 masonry piers with a turnstile (or swing) span to allow navigation of the Hillsborough River. This was replaced in 1962 with a truss structure, which carried two-lanes of automobile traffic. The deck truss still exists today.

Several modifications to the truss structure have since been completed including: widening of the structure to four lanes by used of a variable depth trapezoidal box structure, as well as strengthening some transverse members and truss joints to aide in the installation of municipal services and an Active Transportation Corridor.

Harbourside Engineering Consultants Ltd. (HEC), with the support of DTI, are conducting a Remaining Fatigue Life analysis of the deck-truss structure (the scope does not include the box girders). Due to the unique nature of the structural system in place, the analysis requires detailed modelling of the elements and connections, including the newer trapezoidal box details and connection to the deck truss.

This paper details the approach, including the use of a model calibrated using structural response data from controlled loadings, in determining the remaining fatigue life for the truss portion of the Hillsborough River Bridge per CSA S6:19 (Canadian Highway Bridge Design Code).

1 INTRODUCTION

The Hillsborough River Bridge in Charlottetown, PEI, Canada is an aging piece of infrastructure that is critical to the local traffic network. Originally constructed in 1959, the bridge superstructure is a 3-span (78 m – 91 m – 78 m) steel box truss and in 1996 was widened on each side by variable depth steel box girders. The following is a report on the fatigue life analysis for the truss members of the Hillsborough River Bridge, located between Charlottetown and Stratford, PEI, Canada.

In 2021, an arm's length inspection of the structure, performed by Harbourside, identified several fatigue prone details on the truss and a subsequent investigation, using non-destructive testing, revealed the presence of cracks at some of these details. These cracks were drilled as part of repairs to attempt to arrest their growth (Harbourside, 2023).

The analysis was conducted to determine the theoretical residual fatigue life is for each detail. Concerns identified in the analysis could potentially be addressed prior to or during the upcoming coating project.

DOI: 10.1201/9781003483755-323

To provide additional context for the report, a brief history of known major upgrades and evaluations of the structure is provided as follows:

- Originally constructed in 1959, the bridge superstructure is a 3-span (78 m – 91 m – 78 m) steel box truss and in 1996 was widened on each side by variable depth steel box girders. During the widening project, the box truss underwent a significant reinforcing program which stiffened many of the members of the truss due to the anticipated increase in load effects (CBCL, 2018), including the addition of post-tensioning bars for some bottom chord members.
- In 2015, Bridge Diagnostics Inc. (BDI) was hired by Prince Edward Island Transportation and Infrastructure (PEITI) to complete load tests and field verified modelling on the structure to better quantify the structure's behaviour. BDI worked alongside Stantec during this process. CBCL also had a role as they had performed an analysis on the structure in 2014. CBCL used the results of BDI's testing to update their own model and provided dead load effects and member capacities to BDI (BDI, 2016).
- In 2017, additional member strengthening was completed in anticipation of future works.
- In 2019, two sewage pipes were added to the structure supported by W-sections spanning between lower floorbeams. IFT drawings for the pipes (Stantec, 2019) do not reflect the as-built condition, but the as-built condition was used in this analysis.
- In 2021, an active transportation (AT) trail was installed on the west side of the structure, which had the effect of narrowing the traffic lanes and shifting them to the east.
- In 2021, Harbourside, with the assistance of a Tacten Rope Access Team, completed a detailed arm's length inspection on the truss members and connections to develop tender documents for repairs and recoating.
- In 2022, Harbourside with the assistance of a Tacten Rope Access Team, completed NDT testing on select welded details, as well as repairs on three locations that were found to have cracks.

2 ASSUMPTIONS

A list of all major assumptions made during the analysis is provided below:

- A loss of sectional area due to corrosion of 5% was assumed to be present on all members. Due to severe corrosion noted on elements within group BC1.1, the loss of area due to corrosion was assumed to be 20% for these elements. This is consistent with CBCL's assumptions (BDI, 2016). No allowance was made for future corrosion.
- Evaluation of the structure was completed as per Section 14 of CSA Group (2019). The traffic lanes marked on the structure were assumed to be the design lanes.
- The passage of a CL-625 design vehicle causes one stress cycle for each member as per Table 10.5 in the Canadian Highway Bridge Design Code.
- The fatigue analysis considered the full life of the structure since construction in 1959. The poor (Detail Category E and E1) fatigue details were added in 1996. Prior to 1996, the truss members would have been Detail Category D (due to riveted connections). Analysis demonstrated the Category E and E1 details for the stress range and number of cycles post 1996 governs over the Category D detail for the full life of the structure. Fatigue damage from the Category D and E details have not been summed together as the defect(s) introduced by the welding of the cover plates is remote from the original rivets when considering the cross sections of the elements.
- The Dywidag post-tensioning (PT) rods were post tensioned to 20 kN as per CBCL (2018). The primary members of the bottom chords are back-to-back C-channels and the ends of the post tensioning rods connect to the bottom chord by bearing on horizontal shear plates welded onto the back side of each channel. The post tensioning rods are also supported vertically at regular intervals via saddles (vertical plates with holes for the rod, welded to transverse angles which are in turn welded to top flanges of the bottom chord channels).
- The concrete deck was assumed to be uncracked over the piers. BDI (2016), indicated that at the load levels they tested the deck appeared to be acting in an uncracked manner over the pier and their test loads were similar to the weight of the fatigue truck.

– The concrete deck was assumed to be fully composite with top chord as per the results of BDI (2016).
– The concrete deck stiffness was based on a compressive strength of 55 MPa as per the results of BDI (2016).
– The total weight of the paint and bolts/rivets was assumed to be 4% of the truss self weight.
– The density of sewage within the pipes was assumed to be 1200 kg/m^3.
– All tack welds noted in the 2021 inspection are assumed to be removed.

3 MODEL GENERATION

Harbourside received CAD files for BDI's model geometry and a text file containing information from BDI's model, such as member section properties and material properties. The CAD files were converted to a S-Frame 3D finite element model and the section and material properties from the text file were imported into the model. Harbourside performed geometry checks throughout the model to verify it was representative. Harbourside also checked the section properties for a random selection of 10% of the members to verify BDI's values.

To confirm that Harbourside's model agreed with BDI's model, Harbourside prepared four test load cases and requested BDI perform the same four test load cases. By comparing the results of the two models, Harbourside determined:

– The original model considered the truss members with fixed end member releases, not pins.
– The original model did not model the real support conditions. Instead, the original model only considered vertical supports, with a couple of transverse and longitudinal supports added for model stability. In addition, each of the box girder bearings were modelled as a pair of closely spaced rigid vertical supports.
– The original model did not include any post tensioning force in the PT rods.
– The original model had the PT hangers shear connected to the PT rods (i.e., the rods/chords could transfer axial load between each other at each hanger).
– The results from the original model were produced using a linear static analysis.
– In the original model the TC5 and TC6 top chords had the incorrect section properties. The section properties of TC5 and TC6 had been reversed. These are the top chord members above and adjacent to the piers.
– The box girder-to-truss members at the abutments and piers were not considered in the original model (only the top beams between the box and the truss at the piers).
– Harbourside's S-Frame model matched the stiffness of the original model to within ±6%. In other words, a comparison of the vertical deflection values at various locations throughout the bridge were within ±6% between the two models.
– Total vertical reactions to a pier/abutment were within 0.4%.

After reviewing the results of the BDI to Harbourside model comparison (in particular, the stiffness and reactions) Harbourside determined that the two models were behaving similarly and therefore Harbourside's model could be considered calibrated to BDI's model. There were, however, some concerns in BDI's model that needed to be addressed. It is worth noting that it is possible some of the issues may have been generated during the model translation process, or BDI accounted for them in some other way that was not indicated in their report or subsequent communications. To address these concerns, prior to performing the analysis, the following adjustments were made to the Harbourside model:

– The support conditions were adjusted to better reflect the true conditions. The pair of closely spaced rigid supports under each box girder were replaced with a single vertical support per bearing, and the longitudinal and lateral supports were modelled with stiff springs and placed at the locations indicated in the drawings.
– The PT rods were post tensioned to 20 kN.
– The intermediate PT rod hangers were deleted from the model. They were acting as shear connectors and axial load from the PT rods was being transferred into the bottom chord at

each hanger location. In reality, aside from a small amount of friction, the rods are free to slide inside the hangers and can only transfer axial force into the bottom chord at the ends of each rod.
- Harbourside used a non-linear static analysis to generate results. The non-linear analysis allows for the PT rods to be modelled as tension only members. In BDI's model, it is possible for the rods to take compression which results in a decrease in the bottom chord compressive force.
- Harbourside corrected the TC5 and TC6 section properties. These members are in the bays directly above and adjacent to the piers (U9 to U15 and U23-U29) and they have a significant local effect on the stiffness of the truss frames when considering the truss members to have fixed end connections (as BDI did). Using the correct section properties reduces moments in the bottom chord members by approximately 25%. The effects are not as significant in the truss model using pinned connected members.
- Harbourside added the box girder-to-truss members at the abutments and piers that were missing.
- Harbourside adjusted the area of the longitudinal deck stringers to be near zero as it was noted that they were taking axial load due to global bending action. It is unclear if this was happening in the original model but upon review of the drawings and photos from site, it is clear the stringer connections would not be capable of transmitting significant axial forces. Loads were added to the dead load case to compensate for the loss of stringer area.

4 ANALYSIS

Every member was assigned a fatigue category following guidance in CSA Group (2019). The details on Dwg. No 25 of the Hillsborough Bridge Improvement drawings (CBCL, 2018) and S02 of the Truss Strengthening Drawings (CBCL, 2017) show the fatigue prone details. The fatigue categories assigned range from Class D to Class E1. There were no details prone to distortion induced fatigue noted on the truss. Photo 1 and Photo 2 show typical as-built post tensioning details on the truss bottom chord.



Photo 1. Example of post tensioning end connection, category E fatigue detail (Harbourside, 2023).

PEITI provided historical AADT values for 1990-2021, as well as the estimated precent trucks and growth rate. From this information Harbourside was able to determine the annual daily truck traffic (ADTT) and the total number of truck cycles from 1996-2021 at (23.76 million), as well as make predictions for the additional number of cycles for each year after 2021 using an annual growth rate of 1.38% (calculated from the data provided). From 1959 to 1996, traffic was assumed to grow at a rate of 1.38% and consisted of 5% trucks.

To complete the detailed analysis, Harbourside first determined the stress in each truss member due to the dead load of the structure. Although fatigue calculations are only based on



Photo 2. Example of post tensioning hanger connection, category E1 fatigue detail (Harbourside, 2023).

the range of stress caused by the passage of a single CL-625, load-induced fatigue was disregarded when the compressive stress was at least twice the maximum tensile live load stress in locations where the stresses resulting from the permanent loads are compressive as per CSA Group (2019).

Based on the phasing sequence (see Figure 1) provided in the Hillsborough Bridge Improvement drawings (CBCL, 2018) there is a condition where the boxes have been installed and the deck above them is composite while the concrete deck over the truss is still wet (non-composite) and separated from the box girder deck by a gap. During this stage the load effects in the truss members from the self-weight of the steel and concrete, and the load effects from the post-tensioning would have been locked in. The load effects from the asphalt, barriers, and sidewalks on the composite section were superimposed to get the total dead load effects prior to the addition of the AT Trail. The change in dead load due to the addition of the AT Trail was also captured and added. The maximum tensile live load stress caused by the passage of a CL-625 was then compared to the combined dead load effects for each member, to determine if load-induced fatigue could be disregarded.

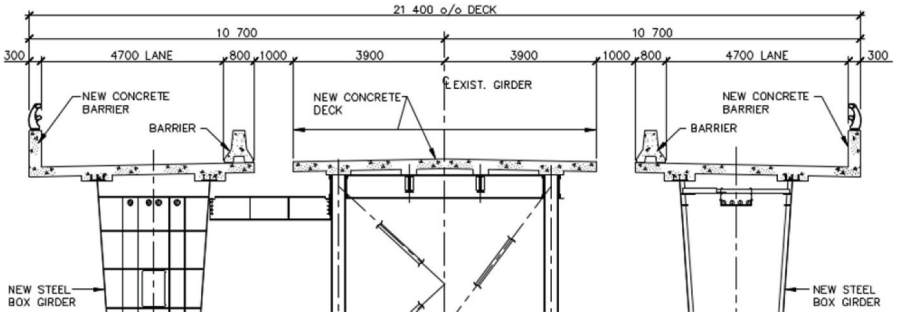


Figure 1. Phase 3 of Bridge Expansion (CBCL, 2018).

From CSA Group (2019), for load induced fatigue, except as otherwise specified, bridge components shall satisfy Equation 1, below:

$$0.52 C_L f_{sr} < F_{sr} \tag{1}$$

where C_L = 1.0 when the weight of the design vehicle ≤ 625 kN; f_{sr} = calculated stress range due to the passage of a single CL-625; and F_{sr} = fatigue stress range resistance of a member or detail.

Furthermore, to determine the fatigue stress range resistance CSA Group (2019), indicates:

$$F_{sr} = \left(\frac{\gamma}{N_c}\right)^{\frac{1}{3}} \tag{2}$$

$$\text{If } F_{sr} = \left(\frac{\gamma}{N_c}\right)^{\frac{1}{3}} < F_{srt},\ F_{sr} = \left(\frac{\gamma'}{N_c}\right)^{\frac{1}{5}} \frac{F_{srt}}{2} \tag{3}$$

where γ = fatigue life constants pertaining to the fatigue detail category; N_c = specified number of design cycles; and F_{srt} = constant amplitude threshold stress range.

The stress range in each truss member caused by the passage of a single CL-625 truck was calculated for each of the travel lanes, with the bridge in the pre-AT trail condition. The stress range for each member was compared to the stress curve for the member's respective fatigue category, and the maximum number of cycles before failure was determined. There are three zones on the fatigue detail stress curve, as shown in Equations 2 and 3, and when the stress range is low enough that it does not exceed half of the constant amplitude threshold stress range the number of cycles is deemed to be infinite for that member i.e. infinite fatigue life. Based on the stress ranges calculated, many of the truss members were determined to fall into this zone; and therefore, have an infinite fatigue life. Equation 1 and Equation 3 can be combined and rearranged as shown below in Equations 4 to 6, to describe the process above.

$$\text{If } 0.52 f_{sr} < \frac{F_{srt}}{2}, N_c = \infty \tag{4}$$

$$\text{Else if } 0.52 f_{sr} < F_{srt}, N_c = \left(\frac{\gamma'}{F_{sr}{}^5}\right) \tag{5}$$

$$\text{Else } N_c = \left(\frac{\gamma}{F_{sr}{}^3}\right) \tag{6}$$

The maximum number of cycles was compared to the number of truck cycles prior to 2021 (pre-AT Trail) and the percent usage was determined. The results from the passage of a single CL-625 truck under the new lane configuration (post-2021 and the addition of the AT Trail) were analysed. For every member, following the same process as described above, working with the fatigue curves and the calculated stress range, the maximum number of truck cycles before failure was determined. Then, following Equation 7, the already used fatigue life was subtracted (i.e., if a member had used 10% of its fatigue life prior to 2021, the post 2021 maximum number of cycles was reduced by 10% as well).

$$\left(1 - \frac{N_{pre\ 2021}}{N_{c,\ pre\ 2021}}\right) \times N_{c,\ post\ 2021} = N_{remaining} \tag{7}$$

where $N_{pre\ 2021}$ = number of design cycles seen by the bridge between 1996-2021; $N_{c,pre\ 2021}$ = maximum specified number of design cycles (from Equations 4 to 6) for stress range pre-2021; $N_{c,post\ 2021}$ = maximum specified number of design cycles (from Equations 4 to 6) for stress range post 2021; and $N_{remaining}$ = remaining number of design cycles. As noted in the assumptions, fatigue damage from the Category D and E stresses have not been summed together as the defect-(s) introduced by the welding of the cover plates is remote from the original rivets when considering the cross sections of the elements.

The ADTT values calculated from the PEITI data were then projected forward using the provided growth rate to determine how long each member can safely remain in service. For

simplicity, if the remaining fatigue life was determined to be more than 50 years (from 2023) the forward projections stopped, and the member's lifespan was labelled as "50+".

5 RESULTS

The members were grouped into three categories (based on percent fatigue life used from 1996) and a graphical representation of this is shown in Figure 2. Only half of the truss members are shown because the results are symmetrical about the centreline of the truss (U19-L19). Elements in green have used 0% of their fatigue life, elements in yellow have used between 0% to 10% of their fatigue life and elements in red have used between 10% to 31% of their fatigue life.

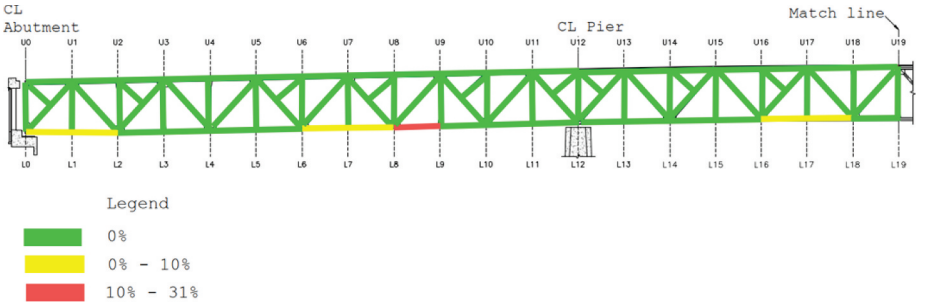


Figure 2. Percentage of fatigue life used.

L8-L9 and L29-L30 on both the North and South trusses were determined to have used 31% of their fatigue life (as of 2021) and have the least remaining fatigue life at 33 years (from 2023). The governing detail on all the yellow and red members is the post tensioning hanger as it is a category E1 Fatigue Detail. If this detail is removed, then all the members except L16-L17 and L22-L23 move to category E (because of the cover plates). L16-L17 and L22-L23 move to category D, as they don't have cover plates but are riveted. The resulting effect is that all members would have 50+ years of remaining fatigue life.

During the 2022 inspection of the welds completed by Harbourside, cracks were noted in three locations (Harbourside, 2022):

- East truss, on L10-U11 near U11 (see Photo 5)
- East truss, on L10-U11 near L10
- East, truss, on U27-L28 near L27



Photo 3. Example of cracked weld (Harbourside, 2023).

While all the cracks are located on members with poor fatigue details (category E cover plates), none of the cracks were located on members noted above that are suspected of having a reduced fatigue life. As discussed in Fisher, Kulak & Smith (1998), there are several reasons why cracks may occur in steel members including, large number of cycles, a large stress range, out-of-plane distortion, corrosion, inappropriate fabrication procedures, poor welding procedures, and large defects. The results of this analysis suggest the cracks were not caused by a large number of cycles or large stress range. Large defects, out-of-plane distortion and significant corrosion were also not observed. This leads Harbourside to believe that the cracks seen on the structure are likely the result of poor welding procedures or inappropriate fabrication procedures.

6 CONCLUSION

Harbourside has completed a theoretical remaining fatigue life analysis for the truss portion of the Hillsborough River Bridge. The analysis was performed after several poor (category E and E1) fatigue details were noted on the truss and subsequent non-destructive testing revealed the presence of cracks in some locations. Due to the complex, indeterminate nature of the structure a detailed model was required. This model used was calibrated using structural response data from controlled loadings. The results of the analysis indicate that theoretically, the structure has approximately 33 years of remaining service life based on the governing elements and with small repairs the remaining service life could be extended to greater than 50 years.

The results of the analysis do not point to load induced fatigue damage alone being the direct cause of cracks observed in some members and further investigation is required to understand the cause of these cracks and the risk associated with them.

7 RECOMMENDATIONS

Harbourside recommends that that metallurgical testing be performed on the L10-U11 and U27-L28 members as well as select other members to be determined. Specifically, Harbourside is recommending Charpy impact tests, yield strength tests, and chemical analyses of both the cover plates and original truss steel. The chemical analysis will provide insight into the weldability of the steel, while the Charpy impact test will help determine how brittle the steel is. As noted in Fisher, Kulak & Smith (1998), brittle fracture is an undesirable situation and low fracture toughness bridge steels can result in brittle fracture under normal service loads when cracks develop. Understanding the fracture toughness of the steel will help Harbourside understand the likelihood of a brittle fracture. The yield strength tests will be useful in other phases of the project and can be completed for minimal additional cost. This information will help narrow down the possible causes for the observed cracks.

Harbourside recommends that the PT rod hangers on all members are removed and replaced with a bolted detail (details for this were provided in Harbourside's Coating and Repairs Package previously submitted to PEITI). During the removal process care needs to be taken to ensure that main chord members aren't damaged and that the welds are ground smooth in the direction of the applied stress. By completing these repairs, the remaining fatigue life of the truss can be considered to be greater than 50 years (post 2023).

Assuming the above noted repairs are completed, a regular monitoring plan for all members (beyond the standard biennial inspections) is not recommended at this time; however, the locations that were noted to be cracked should be re-examined prior to recoating and on a regular basis thereafter, to assess whether the drilled holes have been effective in arresting the crack growth. Particular attention should also be given to the severity of member corrosion during each biennial inspection. Corrosion of the truss members can have a negative impact on the fatigue life of the structure because corrosion reduces the member cross sectional area, increasing stresses. Severe corrosion can also induce discontinuities which cause stress concentrations.

During the 2021 inspection of the structure by Harbourside and Tacten, tack welds were noted on the gusset plates (Harbourside 2023). Harbourside has not considered these tack welds in the fatigue analysis, and experience has shown that these types of tack welds can induce cracks in members and gussets. It is Harbourside's understanding that these tack welds will be removed during the planned recoating project. This is an extremely important assumption in this assessment.

REFERENCES

CSA Group. 2019. Canadian Highway Bridge Design Code S6:19. Toronto: Canadian Standards Association.

CBCL. 2018. Hillsborough River Bridge Improvement Contract 94846, Record Drawings. Charlottetown: CBCL Ltd.

BDI. 2016. Field Testing and Modeling Report: Hillsborough River Bridge – Charlottetown, PEI. Boulder: Bridge Diagnostics, Inc.

Fisher, J.W., Kulak. G.L., Smith I.F.C. 1998. A Fatigue Primer for Structural Engineers. Chicago: National Steel Bridge Alliance.

Harbourside. 2023. Detailed Review and Inspection/Maintenance Plan Development for Steel Fatigue Prone Details on the Hillsborough Bridge. Charlottetown: Harbourside Engineering Consultants.

BIBLIOGRAPHY

CBCL. 1996. Hillsborough River Bridge Improvement Contract 94846. Charlottetown: CBCL Ltd.

CBCL. 2017a. Hillsborough Bridge Truss Strengthening, Project 142613.03. Charlottetown: CBCL Ltd.

CBCL. 2017b. Hillsborough Bridge Strus and Pier Diaphragm Modifications, Project 142613.04. Charlottetown: CBCL Ltd.

CBCL. 2020. Hillsborough Bridge Active Transportation Corridor. Charlottetown: CBCL Ltd.

CSA Group. 2019. Commentary on CSA S6:19, Canadian Highway Bridge Design Code. Toronto: Canadian Standards Association.

Fisher, J.W. 1989. Executive Summary: Fatigue Cracking in Steel Bridge Structures. ATLSS Report No. 89-03. Bethlehem: Lehigh University.

Harbourside. 2023. Hillsborough Bridge Coatings and Repairs Project (DRAFT). Charlottetown: Harbourside Engineering Consultants.

McCulloch & Co., 1959. The Hillsborough Bridge Superstructure Charlottetown, PEI.

Stantec. 2019. Wastewater Delivery System to CPCP Package – E Hillsborough Bridge Forcemain. Charlottetown: Stantec Consulting Ltd.

Bridge Maintenance, Safety, Management, Digitalization and Sustainability – Jensen, Frangopol & Schmidt (eds)
© 2024 The Author(s), ISBN 978-1-032-77040-6
Open Access: www.taylorfrancis.com, CC BY-NC-ND 4.0 license

Climate change challenges: A study on bridge accessories and structural performance

D. Greco, A. Moscatelli & D. Briccola
University of Applied Sciences and Arts of Southern Switzerland (SUPSI), Mendrisio, Switzerland

ABSTRACT: Structural bearings and bridge expansion joints are accessories requiring an accurate design, inspection, and maintenance, as their malfunctioning can cause a bridge to depart from its expected behavior and their replacement is a costly activity due to passenger and freight traffic interruption. Because of their exposure to water, deicing agents, and silt, they experience a high level of wearing that limits their serviceability far beneath the warranty period ensured by manufacturers. Climate change exacerbates this trend: storms and hail increase the volume of bridge deck water runoff and cause clogging of expansion joints due to the accumulation of grit and gravel and severe damage to bearings, leading to restrained movements. That causes the onset of distress in structural elements and triggers further damage. A study on the impact of restrained movements at increased temperatures according to Tessin climate change scenarios in 2085 for RCP8.5 has been carried out.

1 INTRODUCTION

The impact of climate change on the frequency and magnitude of natural hazard-related events is evident worldwide (ITF, 2016). By contrast, the potentially highly damaging impact on the built environment, specifically on viaducts and bridges, needs further effort from the scientific and professional community to develop effective adaptation strategies. More in detail, the consequences of increased temperatures and precipitation, especially when considering worst-case emission scenarios, directly affect (i) the design of new bridges in terms of detailing reinforcement for cracking control and design of bearing devices and expansion joints and (ii) the maintenance of existing infrastructures to uncover the relationship between climatic indicators and degradation processes. The paper tackles the impact of climate change on bridge design through a simplified approach, leaving the rigorous uncertainty treatment to further studies on the topic. First, a review of the most common damages on bridge accessories are presented; then, the study focuses on evaluating the impact of temperature variations on bridge superstructure actions in presence of bridge accessories malfunctioning. In Tessin, about 42% of bridges are multi-span box girder bridges in reinforced and prestressed concrete: for this reason, the numerical application focuses on a three-span prestressed concrete box girder bridge.

2 CLIMATE CHANGE RELATED IMPACTS ON BRIDGES

Currently, 52% of expansion joints and 22% of bearing devices in Tessin undergo a pronounced degradation, opening questions on their actual service duration compared with that declared by manufacturers and the bridge one. As stated in Lima et al., 2010 damage to these elements results in average maintenance costs of 20% of the total maintenance cost and their replacement leads to subsequent traffic disruptions and indirect economic losses. Therefore, their condition assessment to timely detect defects that could affect their behavior and compromising their functionality is a crucial activity in bridge management. In fact, as shown

DOI: 10.1201/9781003483755-324

in Figure 1, malfunctioning of expansion joints, and bearing devices can jeopardize the condition of both the super- and sub-structure leading to cracking phenomena on the deck, efflorescence and spalling at half-joint sections, and pouring along the piers together with a diffused degradation of material properties.

For instance, the main cantonal road-network in Tessin comprises 138 bridges with bearing devices and expansions joints 52% on average of which have already undergone multiple localized repair work during their lifespan. Here, bearing devices and expansion joints attain level 3 on a five-levels scale for condition assessment spanning from good to bad conditions, as shown in Figure 2 and Figure 3. Expansion joints are always more damaged than bearing devices because of their direct exposure to deicing salts, abrasion due to traffic loads and thermal degradation.

Their clogging due to the accumulation of sand can lead to premature cracking of the pavement and increased corrosion risk for the deck (Palu et al., 2019). Additionally, there appears to be a correlation between the condition assessment of bearings and expansion joints: for almost all sampled bridges, a level 3 condition assessment of bearing devices corresponds to a level 3-4 condition assessment of expansion joints. Moreover, since degradation phenomena considerably affect the structural capacity, particular attention must be given to head sections in case of prestressed systems where very corrosion-sensitive anchor heads are usually placed. A further difference exists between bridges located in the northern or southern regions of Tessin. Despite the reduced traffic, bridges in the north are more damaged than those in the south: this evidence can be easily understood if one considers the prolonged use of deicing salts in cold regions rather than in hotter ones. Conversely, in the south damage to expansion joints concentrates close to the Italian border, where are daily detected high traffic volume.

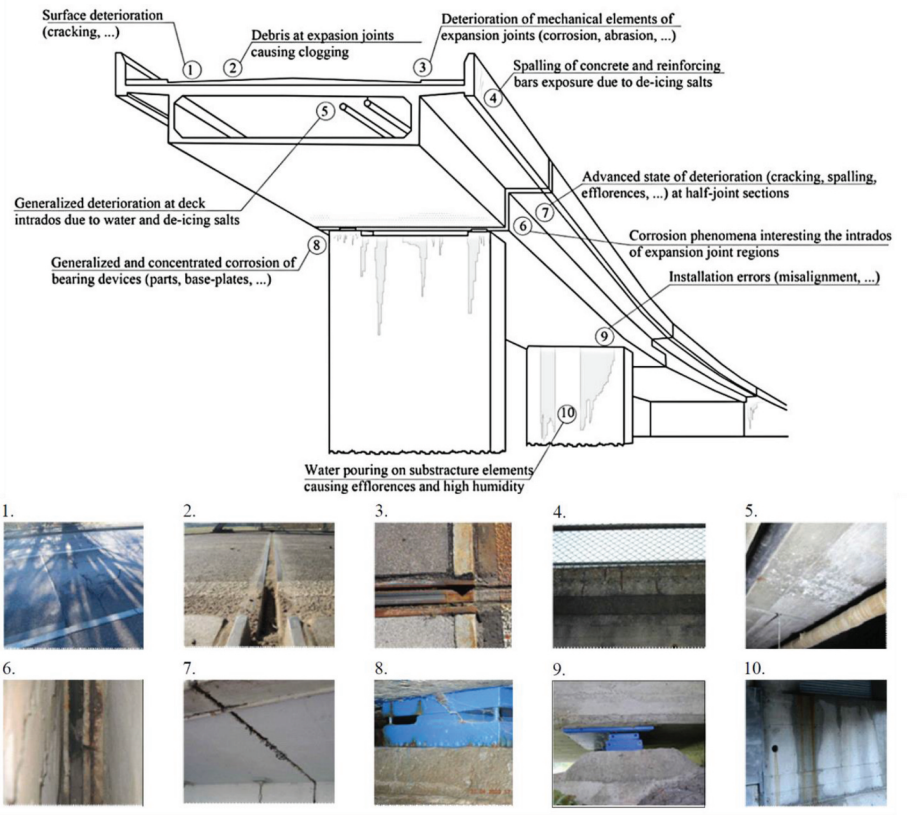


Figure 1. Damages detected on reinforced and prestressed bridges: localization and common appearance.



Figure 2. Common damages on structural bearings (circle) and expansion joints (square) classified according to the corresponding chromatic scale: level 1- good (dark green); 2 - acceptable (light green); 3 - damaged (yellow); level 4: poor (orange); 5: bad (red).

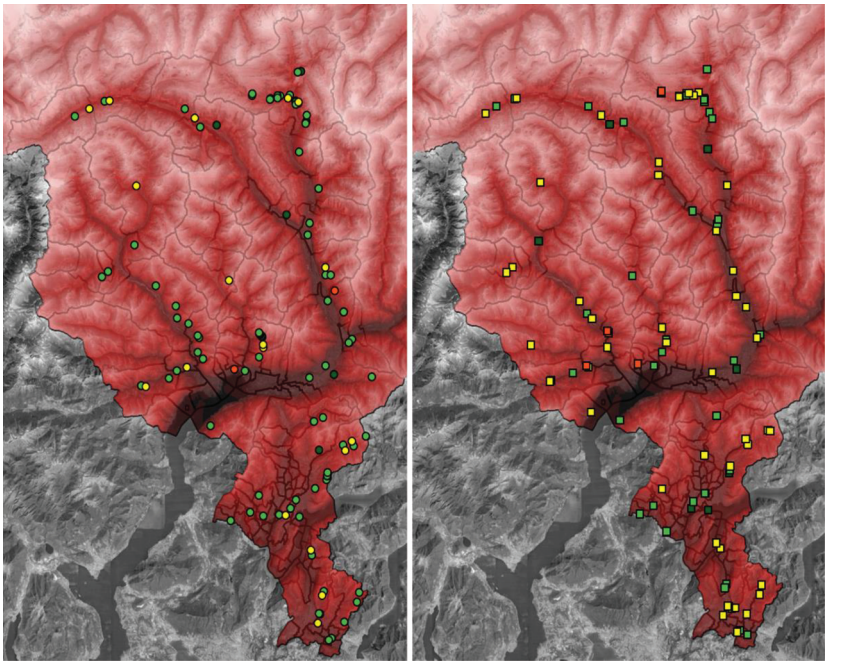


Figure 3. Condition assessment of bearings (left) and expansion joints (right) overlapped with yearly average temperature map RCP 8.5 in 2085. According to the following chromatic scale level 1- (dark green); 2 - acceptable (light green); 3 damaged (yellow); 4: poor (orange); 5 bad (red).

In short, the issues related to bridge accessories are manifold (Ramberger et al., 2003), with many being prompted and exacerbated by climate change, a global phenomenon whose impacts are local, due to either different object's exposure to hazard or specific climate-structure interaction. The impact of climate change on bridges and viaducts can be summarized as in Figure 4. In general, increasing temperatures amplify the magnitude of axial forces (in hyperstatic systems) and bending moments. The increased intensity of rainfall results in significant water runoff volume and subsequent pouring and augmented risk of corrosion. This risk is further intensified by deicing salts, a byproduct of the number of frost days, especially in northern areas of Tessin. Additionally, extended dry summers, leading to the accumulation of dust, sand, and silt on the road platform, in combination with extreme autumn and winter rainfalls, make material to accumulate at expansion joints and bearing devices impeding their proper operation, giving rise to undesirable stresses in the superstructure as reported in Kromanis et al., 2016. The phenomena described above can be aggravated by the presence of pre-existing kinematic and degradation co-factors. All this results in rapidly deteriorating structural problems and in the worst case to failure. If nowadays the impact of climate change on existing structures is a well-recognized field of studies, the same cannot be said as it concerns new structures. Only recently

the quantification of the effects of climate change on load magnitude has been started to be scrutinized as demonstrated in Croce et al., 2018 and Ghosn et al., 2022.

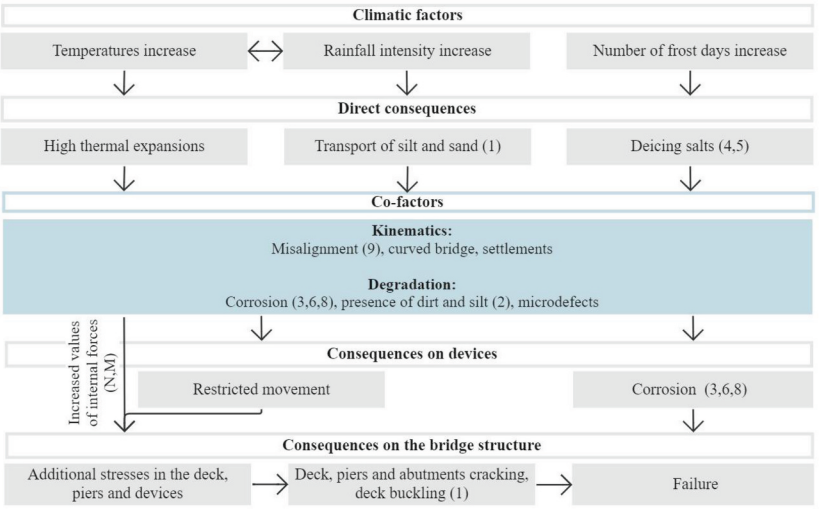


Figure 4. Impact of climate change on existing bridges. Numbers refer to code introduced in Figure 1.

3 CLIMATE CHANGE RELATED DISPLACEMENT DEMAND AND INTERNAL ACTIONS: A CASE STUDY

Structural analysis focused on quantifying the impact of temperature variations due to climate change on bridge bearings movements and superstructure internal actions (mainly axial force and bending moment see Figure 4) considering the RCP8.5 emission scenario in 2085. Simultaneously, prevented movements due to malfunctioning or damages of support devices and expansion joints, exacerbated by clogging due to stormwaters, were considered. Despite the high degree of level of epistemic uncertainty characterizing climate change and related impact on materials and structures would require a sophisticated uncertainty quantification framework, a deterministic approach has been preferred to quantify, in short, the effect of neglecting actual forecast temperature values in designing new bridges.

3.1 *Bridge description and model assumptions*

A three-span box girder bridge ideally located in the north region of Tessin was studied. The geometry and material characteristics are illustrated in Figure 5. As for the prestressing action, five parabolic tendons are placed on each side of the deck: three of them extend over the central and lateral spans, two only over the central span. Figure 6 (right) shows the original bridge bearing layout and those corresponding to restrained movements; expansion joints are placed at the bridge abutments. The structure was modelled by means of beam-type finite elements and actual loads were calculated for comparison according to current design codes. A linear-elastic analysis was carried out to assess the bridge longitudinal behavior.

3.2 *Analysis*

As indicated in several studies (Jaccoud et al., 1982 and Tayşi et al., 2015, Li et al., 2004) the temperature on a box girder section is influenced by many factors among which the material thermal coefficient, the deck height, as well as the pavement characteristics, just to cite few. The thermal loads (see Figure 6(left)) prescribed by the Swiss technical standard SIA 261:2003

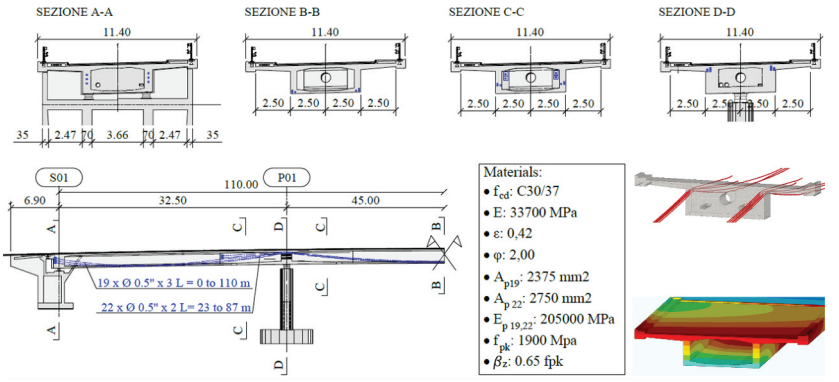


Figure 5. Bridge geometry, material characteristics and FE model views.

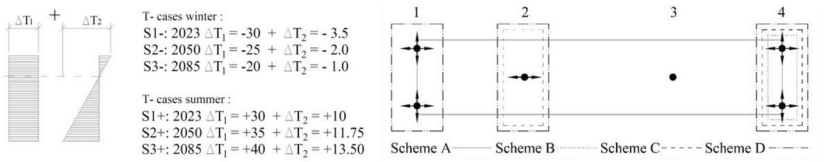


Figure 6. Temperature gradients related to climate scenarios (left) and progressively clogging bridge bearing layout indicated graphically with dotted and dash-dotted lines indication (right). No allowed displacement at: bearing 3 (Scheme A); bearing 3,4 (Scheme B), bearing 2,3,4 (Scheme C), bearing 1,2,3,4 (Scheme D).

provide practitioner engineers with appropriate esteems about temperature variations DT1 (uniform temperature distribution), DT2 (linear distribution relative to the centroid) and DT3 (non-linear distribution) with respect to the average temperature. For reinforced and prestressed concrete structures, DT1 assumes a value of ±20°C to be increased by 50% for joint and bearings movements requirements calculation. Moreover, considering a 2m-depth deck DT2 must be considered equal to 10°C for warm top surface (in summer) and equal to -3.5°C for cold bottom surface (in winter). The representativeness of these values may be jeopardized by climate change particularly under 2085 RCP 8.5 scenario. To roughly estimate the increase in DT1 and DT2 components, annual and seasonal average temperatures, as well as maximum and minimum daily temperatures, made available by the Swiss National Centre for Climate Services NCCS, were analyzed. All temperature loading scenarios used in the analyses are calculated from available data (2085 RCP8.5 scenario). In particular three scenarios were considered: the current reference scenario S1, the 2050 scenario S2 and the 2085 scenario S3. For each of them, the temperatures DT1 and DT2 were determined for both winter (-) and summer (+). For the sake of brevity, these calculations are not shown explicitly; the values taken into account are shown in Figure 6 (left).

In the analysis, various bridge bearing layouts were examined, taking into account their progressive clogging caused by material (sand, silt, dust) debris; these are illustrated in Figure 6 (right).

4 RESULTS DISCUSSION

The results of the analysis carried out to quantify the impact of climate change on superstructure internal actions and bridge accessories movement requirements follow.

Figure 7b illustrates the axial force increase resulting from impeded displacement at supports and expansion joints according to scheme A, B, C, and D (see Figure 6). These

eigenstresses manifest as compression for $DT_1 > 0$ (summer) and tension for $DT_1 < 0$ (winter), respectively diminishing or increasing the prestressing action, shown in Figure 7a. It is important to note that the condition of fully restrained movements at bearings may occur gradually. Therefore, the corresponding axial force values represent an upper limit with a low probability of occurrence. Nevertheless, even with a considerable reduction in axial stress values, corresponding to partial restrained movements at supports, the consequences on structural behavior are not negligible.

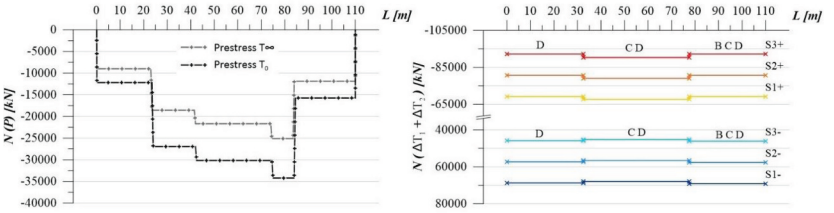


Figure 7. Axial force diagrams due to prestressing (on the left) and restrained bridge accessories movements caused by malfunctioning (on the right). Negative values represent compression, while positive tension.

The displacement requirement at the left of fix support (scheme A, B, Figure6) due to actual temperature gradients (S1, 2023) is equal to 22.5 mm of extension if DT > 0, or 10 mm of shortening if DT < 0 (Figure 8b). Compared to these values, for the S3 scenario (2085), there is a 37% increase in summer extension and a 50% reduction in winter shortening. Similar comments hold for schemes C, D under different climate-change scenarios.

These additional displacements may pose relevant challenges to well-preserved expansion joints and bearing devices during their service duration. Additionally, these values must be combined with shortening values due to prestressing after discounting losses due to shrinkage and creep shown in Figure 8a. These values (shortening) limit the displacement requirement at bearings in summer (S+ scenarios), but represent an unfavorable contribution in winter (S- scenarios), when, combining both effects (temperature gradients and actual prestressing) could lead to a total shortening displacement of 32 mm.

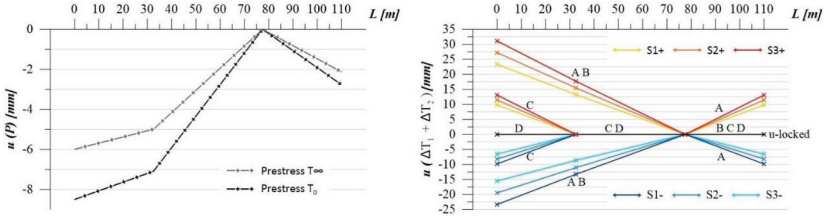


Figure 8. Horizontal displacement due to prestressing, shrinkage, and creep (on the left) and climate change related temperature-gradient scenarios (on the right). Negative values represent shortening, while positive extension.

The additional bending forces due to ΔT2 component (Figure 9b) result in a greater magnitude of positive bending moments along the spans and lower magnitude of negative bending moments at the supports for T>0 (summer) and, conversely, in a lower bending moment along the span and a grater at the support for T<0 (Figure 9a). With respect to scenario S1, these values undergo a 50% magnitude increase for S3+ scenario (extrados 5.81° - intrados 7.60°C) and a 70% reduction for S3- scenario (extrados -0.43°C and intrados 0.57°C).

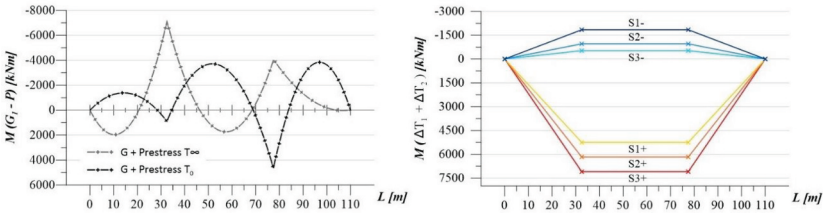


Figure 9. Bending moment diagrams due to permanent loads and prestressing (on the left) and climate change related temperature-gradient scenarios (on the right). Negative values represent stretched top fibers, while positive stretched bottom fibers.

Figure 10 shows the bending moment distribution under service condition compared with the value of the bending moment at first cracking for scenarios S - (winter) under partially restrained movements at bearings. An axial force N = 22500 kN, corresponding to roughly half of the extreme values in case of fully restrained movements due to accessories malfunctioning, was accounted for in the analysis. The tensile force reduces the prestressing action lowering the resistance to first cracking. As a result, the portion of the deck across the supports cracks: this can seriously compromise the bridge service duration favoring chlorides penetration into concrete cover (see deicing salts) and threatening the effectiveness of hogging prestressed tendons in case of defects in ducts and surrounding grout.

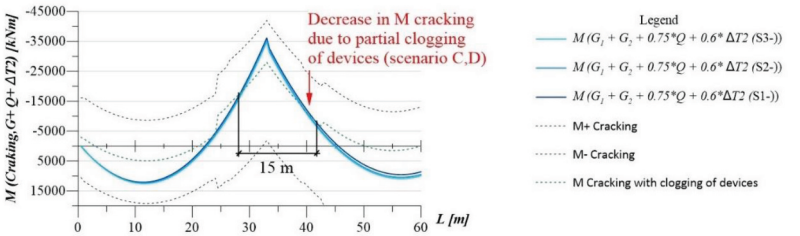


Figure 10. Cracking moment at support according to scheme C and D under service condition and winter temperature-gradient scenarios.

5 CONCLUDING REMARKS

In conclusion, the study allows to reflect on the challenges brought about by climate change on new structures by discussing the results of a deterministic analysis on a prestressed concrete three-span box girder bridge ideally located in the north of Tessin for the 2085 RCP 8.5 scenario.

Despite the epistemic uncertainty character of the phenomenon would require a proper uncertainty quantification framework (the current forecast values are being revised at a national level), the simplification adopted, motivated by reasons of synthesis, enables the identification of possible climate change impact on common structural scheme in case of small to medium-span bridges.

The analysis carried out highlights that increasing temperatures amplify the magnitude of bending moments and axial forces (in case of restrained movements).

The initial analysis on bridge accessories condition encourages further considerations on the interplay between climate stressors and material degradation. Bearings and expansion joints, due to their exposure to multiple factors (water, dirt, wear, and tear), are vulnerable to degradation, harshened by climate change fast kinetics.

In fact, the transport of silt and sand from the road platform to the joints caused by heavy autumn rains coupled with the severe corrosion caused by deicing salts are scenarios with an increasing probability of occurrence especially in the northern region of Tessin. Prevented bearing movements combined with temperature increase can lead to extended and severe

cracked zones along bridges and viaducts. The effects are amplified in case of structures with a high degree of flexural indeterminacy.

Finally, the study highlights the need for the technical community and policy makers to address the issues of climate change to properly:

- design, inspect and maintain expansion joints and bearings, exploiting the potential of structural monitoring on existing viaducts.
- organize a measurement campaign on a territorial scale involving different types of structures (steel, concrete, etc.) to establish a relationship between environmental and structural temperature gradients.
- adopt a rigorous uncertainty quantification framework to deal both with aleatory and epistemic uncertainty (Monte-Carlo and Bayesian methods, etc.) and correctly assess the structural reliability.
- reflect on the opportunity to update design code prescription to evaluate environmental actions and assess the impact of climate change by using deterministic analysis or, alternatively, encourage the adoption of a reliability framework for risk management of climate change and related impacts.

REFERENCES

ITF. Adapting Transport to Climate Change and Extreme Weather: Implications for Infrastructure Owners and Network Managers. OECD Publishing, 2016.

Lima, Joao Marques, and Jorge de Brito. "Management system for expansion joints of road bridges." Structure and infrastructure engineering 6.6 (2010): 703–714.

Palu, Susan, and Hussam Mahmoud. "Impact of climate change on the integrity of the superstructure of deteriorated US bridges." Plos one 14.10 (2019): e0223307.

Ramberger, Günter, and Jörgen Robra. "Structural bearings and expansion joints for bridges." Structural engineering international 13.4 (2003): 268–270.

Kromanis, Rolands, Prakash Kripakaran, and Bill Harvey. "Long-term structural health monitoring of the Cleddau bridge: Evaluation of quasi-static temperature effects on bearing movements." *Structure and Infrastructure Engineering* 12.10 (2016): 1342–1355.

Croce, Formichi, Landi, Mercogliano, Bucchignani, Dosio, Dinova, "The snow load in Europe and the climate change: Climate Risk Management" (2018).

Ghosn, M., and B. R. Ellingwood. "Risk-based design and safety assessment of structures in a changing climate." Bridge Safety, Maintenance, Management, Life-Cycle, Resilience and Sustainability. CRC Press, 2022. 1377–1384.

Jaccoud, Jean-Paul. "gradients de temperature dans les ponts-resumes des connaissances actuelles et indications pour le dimensionnement." *ingenieurs et architectes Suisse* 82.23 (1982).

Tayşi, Nildem, and Sallal Abid. "Temperature distributions and variations in concrete box-girder bridges: experimental and finite element parametric studies." *Advances in Structural Engineering* 18.4 (2015).

Li, Dongning, Marc A. Maes, and Walter H. Dilger. "Thermal design criteria for deep prestressed concrete girders based on data from Confederation Bridge." *Canadian Journal of Civil Engineering* 31.5 (2004).

Bridge Maintenance, Safety, Management, Digitalization and Sustainability – Jensen, Frangopol & Schmidt (eds)
© 2024 The Author(s), ISBN 978-1-032-77040-6
Open Access: www.taylorfrancis.com, CC BY-NC-ND 4.0 license

Fatigue life assessment of steel wires with multiple corrosion pits based on peridynamics

Y. Yang, Q.W. Zhang, J.F. Liu, Y.F. Ji & Y.C. Ni
Tongji University, Shanghai, China

ABSTRACT: Pitting corrosion, which results in crack initiation of steel wires, is a critical degradation form shortening the cable's fatigue life. The simulation of crack growth has been a challenging issue in the community of classical continuum mechanics as the assumption of displacement continuity is no longer valid at the crack. In this study, we attempt to employ the Peridynamic (PD) theory to evaluate the fatigue life of steel wires with multiple corrosion pits. The PD theory allows for the spontaneous initiation, propagation, and interaction of cracks, making it particularly suitable for analyzing multiple crack problems. Firstly, a numerical meshfree model of steel wires is established. Utilizing a novel crack tip detection algorithm proposed in this study, the propagation, interaction and merging process of multiple corrosion pits are investigated based on the PD fatigue model. The numerical model is validated and calibrated through comparison with the linear elastic fracture mechanics for the case of a single corrosion pit. Furthermore, fatigue simulations for steel wires with multiple corrosion pits are conducted to obtain the relationship between the remaining area rate and fatigue cycles. The effect of relative circumferential position of pits on the cross-section is investigated. Additionally, a comparative analysis is carried out between the fatigue life of steel wires containing two pits and that of a single pit with an equivalent damaged area. The results indicate that the residual fatigue life of steel wires with multiple pits will be affected by the circumferential position of pits. Converting two pits into a single pit based on an equivalent damaged area will lead to an overestimation of the fatigue life. The pd theory provides a promising new approach for assessing the fatigue life of steel wires with multiple corrosion pits.

1 INTRODUCTION

Due to long-term exposure to natural environments and sustained high-stress states, bridge cables are vulnerable to sheath breakage, resulting in corrosion and mechanical deterioration of steel wires. Pitting corrosion, which is the dominant factor decreasing the fatigue life of corroded steel wires, has been extensively investigated. Despite the intricate and random nature of the pitting morphology, both experimental and numerical results validate that crack initiation takes place at the bottom of the pit(Zheng et al., 2020). The semi-elliptical model is widely utilized and probability distribution models for the depth and radius of the pits are established(Guo et al., 2022, Li et al., 2021). For the residual fatigue life of steel wires with single corrosion pit, Jie et al., 2020, Ma et al., 2019 utilized the Theory of Critical Distances (TCD) (Taylor, 2008) method to predict fatigue life. Cui et al., 2020, Wang et al., 2020 established a damage evolution model for corroded steel wires based on Continuum Damage Mechanics (CDM). Wang et al., 2022, Zheng et al., 2019 calibrated the crack growth rate and predicted fatigue life using the Paris law based on Linear Elastic Fracture Mechanics (LEFM).

While the occurrence of multiple pits is commonly observed, the fatigue life of steel wires with multiple pits remains highly uncertain. Probabilistic methods are predominantly employed to predict the fatigue life of steel wires with multiple pits. The mass loss rate was

DOI: 10.1201/9781003483755-325

introduced to modify the S-N curve considering corrosion(Jiang et al., 2018, Zheng et al., 2017).Ye et al., 2021 introduced the initial crack size to correct the S-N curve. Lan et al., 2018 proposed a three-parameter Weibull model considering the influence of corrosion and stress amplitude, and estimated the model parameters based on experimental data(Ma et al., 2022). Probabilistic methods demand a significant amount of fatigue test, which is both time-consuming and costly. An urgent need for numerical simulation methods exists, while Classical Continuum Mechanics (CCM) based methods encounter significant obstacles as the assumption of displacement continuity is no longer applicable at the crack, posing challenges in dealing with multiple cracks. Among CCM based methods, TCD methods(Chen et al., 2021), LFEM methods(Ye et al., 2020) have been utilized to address multiple cracks, but with limited applicability.

Peridynamic theory, a novel nonlocal theory(Silling et al., 2007), enables the spontaneous initiation, propagation, and final rupture of cracks(Ha et al., 2011, Silling et al., 2010, Yaghoobi et al., 2017), making it particularly suitable for handling multiple cracks. The PD fatigue model was initially proposed by (Silling et al., 2014) and validated by (Zhang et al., 2016). Recently, the PD fatigue model have been employed to address various problems(Bang et al., 2021, Hong et al., 2021, Ma et al., 2020), demonstrating its applicability and accuracy in fatigue-related issues.

In this study, we attempt to employ the PD theory to investigate the residual fatigue life of steel wires with multiple corrosion pits. A novel crack detection algorithm was proposed to track the crack tip during the fatigue simulation process. Subsequently, numerical results obtained from PD simulations of steel wires with a single corrosion pit were compared with results from LFEM. Finally, the residual fatigue life of steel wires with multiple corrosion pits was investigated. Parameter analysis on the relative position and initial damage area was conducted.

2 PERIDYNAMICS THEORY

2.1 *Bond-Based Peridynamics(BBPD)*

In the framework of PD theory, a material body is discretized into a set of discrete material points, as shown in Figure1. Each point **x** only interacts with points within a specified distance δ, called horizon. The interaction between two points is called a bond. Points falling inside horizon are called neighbors of point **x**, and all neighbors consist the family of **x**, denoted by H_x. The PD equation of motion is defined by Eq.(1):

$$\rho\ddot{\mathbf{u}}(\mathbf{x},t)=\int_{H_x}\mathbf{f}(\mathbf{u}(\mathbf{x}',t)-\mathbf{u}(\mathbf{x},t),\mathbf{x}'-\mathbf{x})dV\mathbf{x}'+\mathbf{b}(\mathbf{x},t) \tag{1}$$

where ρ denotes material density, $\ddot{\mathbf{u}}(\mathbf{x},t)$ is the acceleration of point **x** at time t, **b**(**x**,t) is the body force of point **x**, **f**(**u**(**x'**, t) – **u**(**x**, t), **x'**–**x**) is the pairwise bond force function that point **x'** exerts on point **x**. In BBPD, the bond force function is defined by Eq.(2):

$$\mathbf{f}(\mathbf{u}(\mathbf{x}',t)-\mathbf{u}(\mathbf{x},t),\mathbf{x}'-\mathbf{x})=\mathbf{f}(\boldsymbol{\eta},\boldsymbol{\xi})=\mathbf{cs}\mu\frac{\boldsymbol{\xi}+\boldsymbol{\eta}}{|\boldsymbol{\xi}+\boldsymbol{\eta}|} \tag{2}$$

where c denotes the microelastic modulus, which characterizes the stiffness of a bond. For 3D problems, $c = 12E/\pi\delta^4$. $\boldsymbol{\xi}=\mathbf{x}'-\mathbf{x}$ denotes the relative position vector of **x** and **x'** before deformation, $\boldsymbol{\eta}=\mathbf{u}'-\mathbf{u}$ denotes the relative displacement vector of **x** and **x'**, $_s$ denotes the bond stretch which is $(|\boldsymbol{\xi}+\boldsymbol{\eta}|-|\boldsymbol{\xi}|)/|\boldsymbol{\xi}|$. μ is a scalar function to introduce fracture into PD theory. Once the bond stretch exceeds the critical stretch s_c, μ is equal to 0. Otherwise μ is equal to 1. The critical stretch s_c is related to the critical energy release rate G_c and the material fracture toughness K_c. Once the bond is broken, it is irreversible. And the damage of material point **x** can be defined by Eq.(3) as the ratio of broken bonds to total number of bonds connected to point **x**.

$$\varphi(\mathbf{x}) = 1 - \frac{\int_{x' \in H_x} \mu(\mathbf{x}, \boldsymbol{\xi}) dV_{x'}}{\int_{x' \in H_x} dV_{x'}} \tag{3}$$

One critical limitation of traditional PD theory is that the horizon δ must be constant, which results in a significant increase in computational costs as the computational domain expands. To address this issue, the dual-horizon peridynamics(Ren et al., 2017), which allows for non-uniform discretization with varying horizons, is utilized in this study.

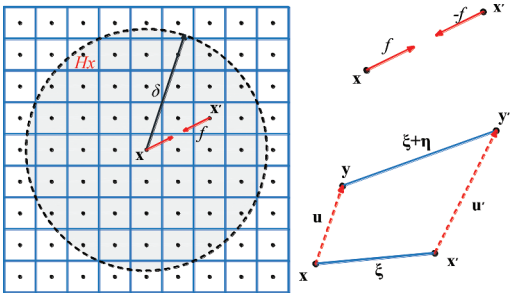


Figure 1. The horizon, family, pairwise bond force function of BBPD.

2.2 *Peridynamic model for fatigue cracking*

In peridynamic fatigue model, a new parameter λ called bond remaining life is introduced to describe the failure process of a bond under fatigue load. λ is initially 1, and gradually decreases to 0 during the fatigue loading process. Once $\lambda \leq 0$, the bond is irreversibly broken, resulting in fatigue damage in corresponding material point. Drawing from the Paris law, the relationship between λ and fatigue cycles N is defined by Eq.(4):

$$\frac{d\lambda}{dN}(N) = -A\varepsilon^m \tag{4}$$

where A and m are material constants, ε the cyclic bond strain under fatigue load which equals to $|(1-R)s_{\max}|$, where $s_{\max}$ is the stretch of the bond under the maximum load and R denotes the stress ratio.

In crack nucleation phase, A_1 and m_1 can be calibrated with the $\varepsilon - N$ curve. In crack growth phase, the crack propagation speed can be derived from Eq.(4) and denoted as:

$$\frac{da}{dN}(N) = \beta A_2 \varepsilon_{core}^{m_2} \tag{5}$$

where ε_{core} is the cyclic strain range of the core bond, which is the bond with the maximum strain range near the crack tip. β is a shape influence factor representing the geometric influence on the strain distribution. A_2 and m_2 can be calibrated with the Paris law(Eq.(6)):

$$\frac{da}{dN}(N) = c\Delta K^M \tag{6}$$

By comparing Eq.(5) with Eq.(6), m_2 is set to be equal to M as the stress intensify factor is proportional to strain. While there is no explicit expression for β, A_2 cannot be directly obtained. To determine A_2, a calibration process must be performed. Firstly, a fatigue calculation process needs to be conducted with an arbitrary value A_a to obtain the crack growth rate $(da/dN)_a$. Because the crack growth rate (da/dN) depends linearly on A_2, A_2 can be calibrated by Eq.(7):

$$A_2 = A_a \frac{da/dN}{(da/dN)_a} \tag{7}$$

where *da*/*dN* can be obtained from the Paris law or experiment data.

3 NUMERICAL SIMULATIONS

3.1 *Model discretization, boundary conditions and static solution*

A numerical model for steel wires with a length of 50mm and a diameter of 7mm is firstly established, as shown in Figure 2. The crack region is set at the middle of the wire, and a mesh density $\Delta x_1 = 0.2\ mm$ is applied, while the remaining region is meshed with a lower mesh density $\Delta x_2 = 0.5\ mm$. In PD theory, virtual boundary region and load region must be specially assigned. The displacement in all directions is fixed for the material points in the boundary region. An external load will be applied on material points in the load region. Horizons δ_1 and δ_2 are set to be $3.015\Delta x_1$ and $3.015\Delta x_2$ respectively, and the boundary region and the load region are set to be $3\Delta x_1$ and Δx_2 respectively in length(Bobaru et al., 2016). A surface without thickness is defined as a pre-existing crack. Bonds through the crack surface are initially set to be broken to introduce the initial crack.

The adaptive dynamic relaxation method(Kilic et al., 2010) is used to accelerate the static solution. The construction of the family list is facilitated through the utilization of the k-dimensional tree algorithm, while parallel computing is applied to compute the peridynamic force.

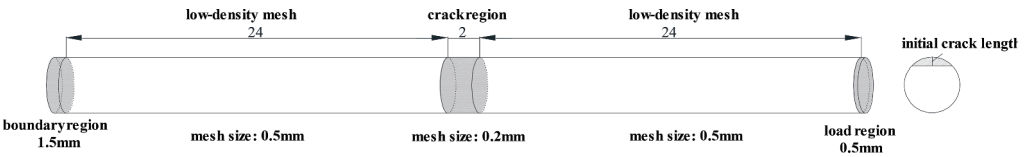


Figure 2. Model discretization of steel wires (unit: mm).

3.2 *A novel crack tip detection algorithm for PD fatigue analysis*

As a pre-crack exists, the crack nucleation phase is ignored and material points within horizon of the crack tip will directly switch to the crack growth phase. Therefore, it is essential to detect the crack tip at every step during the fatigue simulation process, while few crack tip detection algorithms are available in literature. Zhang et al., 2016 converted the PD damage map to black and white images to detect the crack tip. Ma et al., 2023 identified all particles with a local damage coefficient greater than 0.39 as the crack tip. Zhu et al., 2021 utilized the status of bonds which connect a material point with its neighbouring material points only to locate the crack tip. However, these crack tip detection algorithms are only suitable for 2D problems. In 3D problems, the crack tip forms a curve instead of a point, making it more challenging to detect the crack tip.

Therefore, a novel crack tip detection algorithm is proposed in this study. Once the damage index φ_i is calculated for all material points, the normalized damage index $\varphi_{i,\ n} = \varphi_i/\varphi_{max}$ is introduced. $\varphi_{\max}$ is the max damage index of points near crack tip, which is approximately 0.393 for 2D problems and 0.385 for 3D problems(Freimanis et al., 2018). Then points with $\varphi_{i,\ n}$ between 0.48 and 0.52 is identified as the crack tip. Note that due to the limited mesh size, there are typically insufficient points to constitute a continuous curve. Consequently, additional points are generated through an interpolation algorithm. An inverse distance interpolation algorithm is applied in this study.

The remaining life of bonds within horizon of the crack tip is calculated by Eq.(4), and the minimum cycle ΔN needed to break a bond is obtained. Once a bond is broken, a new static

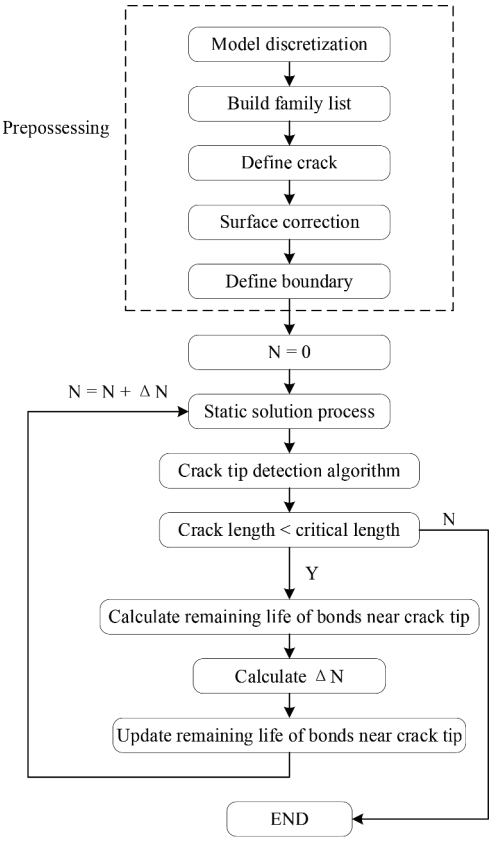


Figure 3. Flowchart of fatigue analysis.

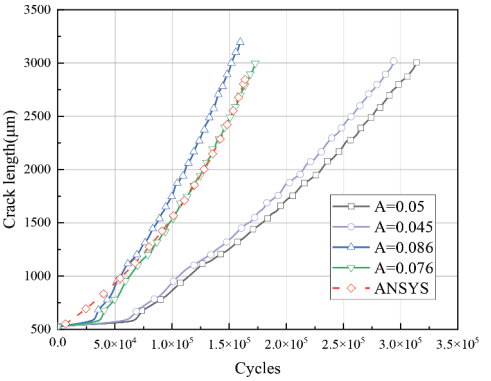


Figure 4. Calibration process of A_2.

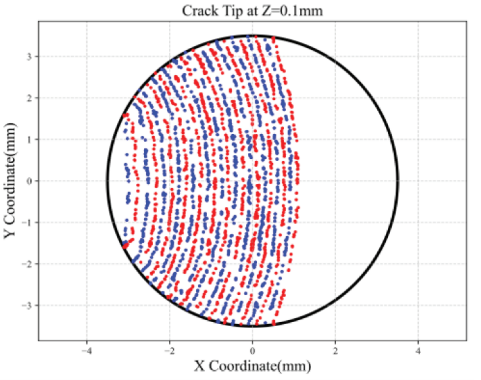


Figure 5. Crack growth path.

solution needs to be run to update the cyclic strain of each bond, which is computationally inefficient. Time mapping(Silling et al., 2014), critical damage factors(Zhang et al., 2016) and the number of cyclic broken bonds are introduced to improve computational efficiency. The broken bonds ratio r, defined as the proportion of broken bonds to the total number of bonds near the crack tip, is proposed in this study. ΔN can be determined as the minimum number of cycles needed to break a certain percentage of bonds. r is set to be 2% combining computational efficiency and accuracy. The fatigue analysis procedure is illustrated in Figure 3.

4 NUMERICAL RESULTS

4.1 *Model calibration and validation*

A fatigue load, with a stress amplitude σ_a = 150MPa and a stress ratio R = 0.1, is applied to the numerical model shown in Figure 2. The PD fatigue parameters A_2 and m_2 are determined according to section 2.2. The values of c and m are set to 3.98e-9 and 1.26 respectively when R = 0.1 (Wang et al., 2022), therefore m, is set to be equal to 1.26. A_2 is calibrated as 0.076 through a series of trial calculations, as shown in Figure 4. The ANSYS Workbench with SMART crack growth is employed here to provide a standard solution of LEFM. The obtained crack growth path is illustrated in Figure 5, which is consistent with theoretical and experimental results.

To further validate the PD fatigue model, the fatigue life of steel wires with a single corrosion pit is analyzed. Various initial crack lengths, specifically 0.3 mm, 0.5 mm, and 0.7 mm,

are applied to investigate the influence of the initial crack length. The relationship between crack length and the number of cycles (a-N curves) obtained from ANSYS, FRANC3D and PD are compared, as shown in Figure 6. The fatigue life decreases with an increase in the initial crack length, and the simulation results from the PD fatigue model exhibit consistent with the FEM results.

4.2 *Fatigue life of steel wires with multiple corrosion pits*

A distinctive advantage of PD theory is its ability to solve problems related to multiple crack propagation and interaction without additional defined criteria. In this section, the fatigue life of steel wires with multiple corrosion pits is investigated. Circumferential double pits on the cross-section are taken into consideration, and the relative angle θ of the two cracks is used to indicate their relative position as shown in Figure 7(a). Firstly, the crack propagation behavior of two cracks with $\theta = \pi/3$ and an initial crack length of 0.3mm is analyzed. The two cracks initially propagate independently, subsequently interact, and ultimately merge into a single crack, as illustrated in Figure 7(a).

Parameter analysis on θ is then conducted. As multiple cracks exist, the remaining area rate is selected to indicate the crack growth speed, which is also the direct result of nondestructive test in field testing(Ni et al., 2021). Figure 7(b) and (c) illustrate the relationship between the remaining area rate and fatigue cycles for different θ. As shown in Figure 7 (b), the rate of remaining area reduction is insensitive to θ when the fatigue cycles is relatively low, while certain diversity appears for different θ when the fatigue cycles increase. The most unfavorable situation occurs when $\theta = \pi/2$, while $\theta = \pi$ leads to the lowest remaining area reduction rate, with the relative difference about 12% when the remaining area rate comes to 50%. This phenomenon can be explained by the stress intensity factor in LFEM as shown in Figure 8. The stress intensity factor along the crack tip when $\theta = \pi/2$ is generally higher than that when $\theta = \pi$, resulting in an accelerated rate of crack growth. The same conclusion can be drawn from Figure 7 (c) where the initial crack length is 0.3mm. Note that the fatigue cracking develops at the slowest pace when $\theta = \pi/6$. This is more likely due to that the two cracks merges into a single crack at an earlier stage, therefore the remaining area reduction rate is more convergent to that of a single crack.

Furthermore, the fatigue life of steel wires with two pits is compared to that of a single pit with an equivalent damaged area as shown in Figure 9. Two cracks each with a size of 0.5mm are considered equivalent in damaged area to a single crack with a size of 0.8mm. Relative to the most conservative result of two-crack situation, the fatigue life of steel wires with a single crack exceeds that of two-crack situation. The same conclusion can be drawn when the initial crack length is set at 0.3mm as shown in Figure 9. These results indicates that the presence of two cracks produces a higher risk compared to a single crack with the same damaged area, and, in application, simply converting multiple cracks into a single crack will overestimate the fatigue life of steel wires.

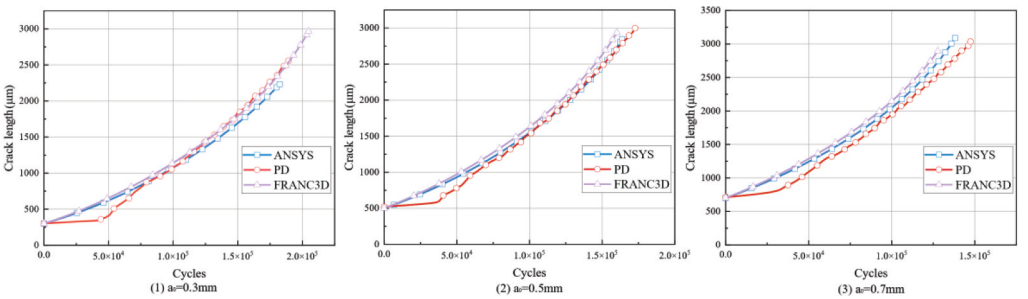
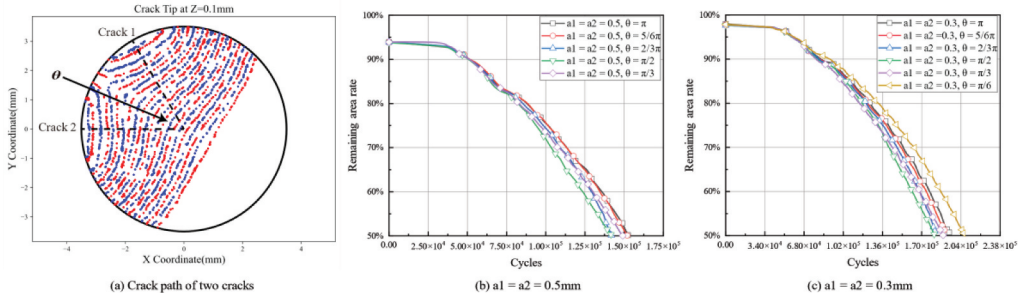


Figure 6. The relationship between crack length and the number of cycles with various initial crack length.



(a) Crack path of two cracks (b) a1 = a2 = 0.5mm (c) a1 = a2 = 0.3mm

Figure 7. The relationship between the remaining area and fatigue cycles under different θ.

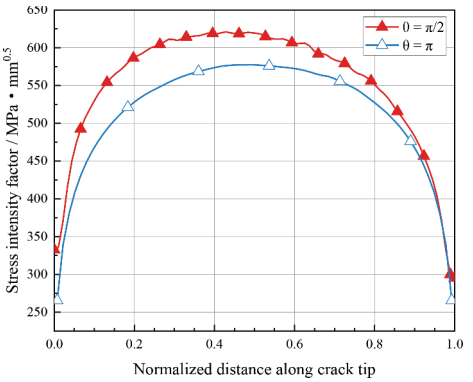


Figure 8. Stress intensity factor along the crack tip obtained using LFEM.

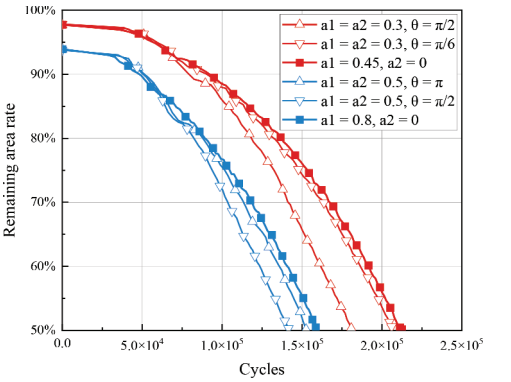


Figure 9. Comparison of the fatigue life of steel wires with two pits to that of a single pit with an equivalent damaged area.

5 CONCLUSIONS

In this study, the PD fatigue model was employed to conduct a fatigue analysis on steel wires with multiple corrosion pits. A novel crack tip detection algorithm was proposed to track the crack tip during the fatigue simulation process. The PD fatigue model was validated and calibrated through a comparative analysis with the numerical results obtained from LFEM. The effect of relative circumferential position of pits was investigated, and the fatigue life of steel wires containing two pits and that of a single pit with an equivalent damaged area was compared. The following conclusions can be drawn based on numerical results:

(1) The PD fatigue model is capable of capturing the propagation, interaction and merging process of multiple cracks on steel wires. The proposed crack tip detection algorithm can accurately track the crack tip.
(2) The relative circumferential position of two cracks has certain effect on the residual fatigue life, especially for the greater fatigue cycles. It is more unfavorable when $\theta = \pi/2$, while the two cracks merge into a single crack at an earlier stage, hence leads to a longer fatigue life.
(3) The existence of multiple cracks poses a greater risk than that of a single crack, when the damaged area is the same. Simply converting multiple cracks into a single crack would result in an overestimation of the fatigue life of steel wires.

The conclusions in this study are primarily drawn from numerical results, and corresponding experiments will be conducted to further validate these conclusions. The approach of translating the damage area into the size and quantity of the pits requires further investigation, which enables engineers to directly utilize the outcomes of non-destructive testing for assessing the residual fatigue life of corroded steel wires.

REFERENCES

Bang, D. J., Ince, A., Oterkus, E. & Oterkus, S. 2021. Crack growth modeling and simulation of a peridynamic fatigue model based on numerical and analytical solution approaches. *Theoretical and Applied Fracture Mechanics*, 114.

Bobaru, F., Foster, J. T., Geubelle, P. H. & Silling, S. A. 2016. *Handbook of peridynamic modeling*, CRC press.

Chen, C., Jie, Z. & Wang, K. 2021. Fatigue life evaluation of high-strength steel wires with multiple corrosion pits based on the TCD. *Journal of Constructional Steel Research*, 186.

Cui, C., Chen, A. & Ma, R. 2020. An improved continuum damage mechanics model for evaluating corrosion-fatigue life of high-strength steel wires in the real service environment. *International Journal of Fatigue*, 135.

Freimanis, A. & Kaewunruen, S. 2018. Peridynamic Analysis of Rail Squats. *Applied Sciences-Basel*, 8.

Guo, Z., Chen, H. & Yao, G. 2022. Bayesian prediction of the stress concentration effect on high-strength wires with corrosion pits. *Engineering Failure Analysis*, 131.

Ha, Y. D. & Bobaru, F. 2011. Characteristics of dynamic brittle fracture captured with peridynamics. *Engineering Fracture Mechanics*, 78, 1156–1168.

Hong, K., Oterkus, S. & Oterkus, E. 2021. Peridynamic analysis of fatigue crack growth in fillet welded joints. *Ocean Engineering*, 235.

Jiang, C., Wu, C. & Jiang, X. 2018. Experimental study on fatigue performance of corroded high-strength steel wires used in bridges. *Construction and Building Materials*, 187, 681–690.

Jie, Z. & Susmel, L. 2020. High-strength steel wires containing corrosion pits: stress analysis and critical distance based fatigue life estimation. *Fatigue & Fracture of Engineering Materials & Structures*, 43, 1611–1629.

Kilic, B. & Madenci, E. 2010. An adaptive dynamic relaxation method for quasi-static simulations using the peridynamic theory. *Theoretical and Applied Fracture Mechanics*, 53, 194–204.

Lan, C., Bai, N., Yang, H., Liu, C., Li, H. & Spencer, B. F., Jr. 2018. Weibull modeling of the fatigue life for steel rebar considering corrosion effects. *International Journal of Fatigue*, 111, 134–143.

Li, R., Miao, C., Feng, Z. & Wei, T. 2021. Experimental study on the fatigue behavior of corroded steel wire. *Journal of Constructional Steel Research*, 176.

Ma, J., Bai, N., Zhou, Y., Lan, C., Li, H. & Spencer, B. F. 2022. Generalized hierarchical Bayesian inference for fatigue life prediction based on multi-parameter Weibull models. *International Journal of Fatigue*, 162.

Ma, X., Wang, Y., Wang, X., Yin, W., Liu, L. & Xu, J. 2023. Investigation on fatigue crack propagation behaviour of U71Mn and U75V rails using peridynamics. *Engineering Fracture Mechanics*, 281.

Ma, X., Xu, J., Liu, L., Wang, P., Feng, Q. & Xu, J. 2020. A 2D peridynamic model for fatigue crack initiation of railheads. *International Journal of Fatigue*, 135.

Ma, Y., Wang, G., Guo, Z., Wang, L., Jiang, T. & Zhang, J. 2019. Critical region method-based fatigue life prediction of notched steel wires of long-span bridges. *Construction and Building Materials*, 225, 601–610.

Ni, Y., Zhang, Q. & Xin, R. 2021. Magnetic flux detection and identification of bridge cable metal area loss damage. *Measurement*, 167.

Ren, H., Zhuang, X. & Rabczuk, T. 2017. Dual-horizon peridynamics: A stable solution to varying horizons. *Computer Methods in Applied Mechanics and Engineering*, 318, 762–782.

Silling, S. A. & Askari, A. 2014. Peridynamic model for fatigue cracking. Sandia National Lab.(SNL-NM), Albuquerque, NM (United States).

Silling, S. A., Epton, M., Weckner, O., Xu, J. & Askari, E. 2007. Peridynamic states and constitutive modeling. *Journal of Elasticity*, 88, 151–184.

Silling, S. A. & Lehoucq, R. B. 2010. Peridynamic Theory of Solid Mechanics. *In*: Aref, H. & Vandergiessen, E. (eds.) *Advances in Applied Mechanics, Vol 44*.

Taylor, D. 2008. The theory of critical distances. *Engineering Fracture Mechanics*, 75, 1696–1705.

Wang, G., Ma, Y., Guo, Z., Bian, H., Wang, L. & Zhang, J. 2022. Fatigue life assessment of high-strength steel wires: Beach marks test and numerical investigation. *Construction and Building Materials*, 323.

Wang, Y., Zheng, Y. Q., Zhang, W. H. & Lu, Q. R. 2020. Analysis on damage evolution and corrosion fatigue performance of high-strength steel wire for bridge cable: Experiments and numerical simulation. *Theoretical and Applied Fracture Mechanics*, 107.

Yaghoobi, A. & Chorzepa, M. G. 2017. Fracture analysis of fiber reinforced concrete structures in the micropolar peridynamic' analysis framework. *Engineering Fracture Mechanics*, 169, 238–250.

Ye, H., Duan, Z., Tang, S., Yang, Z. & Xu, X. 2020. Fatigue crack growth and interaction of bridge wire with multiple surface cracks. *Engineering Failure Analysis*, 116.

Ye, H., Yang, Z., Duan, Z., Liu, J. & Huang, R. 2021. S-N Fatigue Curve Determination for Corroded High-Strength Bridge Wires. *Journal of Engineering Mechanics*, 147.
Zhang, G., Le, Q., Loghin, A., Subramaniyan, A. & Bobaru, F. 2016. Validation of a peridynamic model for fatigue cracking. *Engineering Fracture Mechanics*, 162, 76–94.
Zheng, X., Xie, X. & Li, X. 2017. Experimental Study and Residual Performance Evaluation of Corroded High-Tensile Steel Wires. *Journal of Bridge Engineering*, 22.
Zheng, X. L., Xie, X., Li, X. Z. & Tang, Z. Z. 2019. Fatigue crack propagation characteristics of high-tensile steel wires for bridge cables. *Fatigue & Fracture of Engineering Materials & Structures*, 42, 256–266.
Zheng, Y. & Wang, Y. 2020. Damage evolution simulation and life prediction of high-strength steel wire under the coupling of corrosion and fatigue. *Corrosion Science*, 164.
Zhu, N., Kochan, C., Oterkus, E. & Oterkus, S. 2021. Fatigue analysis of polycrystalline materials using Peridynamic Theory with a novel crack tip detection algorithm. *Ocean Engineering*, 222.

Bridge Maintenance, Safety, Management, Digitalization and Sustainability – Jensen, Frangopol & Schmidt (eds)
© 2024 The Author(s), ISBN 978-1-032-77040-6
Open Access: www.taylorfrancis.com, CC BY-NC-ND 4.0 license

Fatigue life estimation for long span suspension bridges due to buffeting

Z.Z. Banday & A. Fenerci
Norwegian University of Science and Technology, Ålesund, Norway

T.M. Lystad & O.A. Øiseth
Norwegian University of Science and Technology, Trondheim, Norway

ABSTRACT: Buffeting-induced vibration of long-span cable-supported bridges is critical for the serviceability and fatigue performance of these structures. Such problems are more prevalent in long-span bridges located in complex terrain and subjected to gusty wind. One of the long-term adverse effects includes the cyclic loading induced by the buffeting which may cause fatigue of the material. As a case study for this work, fatigue life due to buffeting-induced vibrations has been estimated for the longest-span suspension bridge in Norway, the Hardanger Bridge. This bridge is situated in the Norwegian fjords, characterized by consistent and strong winds. The terrain-induced variability in the turbulence field is considered by modelling the field as a joint probabilistic model of turbulence parameters. Utilizing a Finite Element model of the bridge, the modal parameters of the bridge are extracted. Subsequently, the classical multi-modal buffeting analysis is performed to obtain the stress spectra of the hot-spots along the bridge girder. Considering uncertain mean wind velocity and turbulence parameters, fatigue damage is calculated using a Bayesian updating approach, where new simulation points were sequentially added to the training data set. Consequently, the fatigue life of the bridge girder is obtained by numerical integration.

1 INTRODUCTION

Fatigue failure is a critical threat, holding the potential for catastrophic consequences for the structural integrity of bridges. Over the course of decades, bridges bear the brunt of fatigue damage induced by vehicular traffic and wind loads, sometimes manifesting in bridge collapses or costly repairs (Gu, 1999). In the field of contemporary bridge design, the increasing prevalence of longer main spans intensifies the need to address fatigue-related challenges during the structural planning phase as well as the operational phase.

In this work, we study the cyclic loading induced by buffeting forces, impacting the slender girder of the Hardanger Bridge. Nestled in the Norwegian fjords, regions characterized by complex terrain topography and strong wind patterns, this bridge has proven invaluable for understanding the interplay between wind induced forces, and structural resilience. Notably, the Hardanger Bridge has an unusually slender design, as the bridge deck is a mere 18.3 meters wide, with a narrow separation of 14.5 meters between cable planes. A detailed cross section of the bridge girder is shown in (Figure 1). We study the stochastic nature of wind-induced forces, focusing on the buffeting of the bridge girder. Subsequently, we study the cyclic forces induced by buffeting and the accompanying fatigue damage. It must be noted that the Hardanger bridge has been monitored for many years using accelerometers and anemometers (Fenerci, 2021), the anemometry data were used to devise a probabilistic turbulence model that describes the long-term wind characteristics at the site.

DOI: 10.1201/9781003483755-326

We introduce and use a Gaussian process regression (GPR) surrogate model, based on nonparametric regression. Considering the unpredictability of wind forces, we set up surrogate models for the Fatigue Damage Accumulation (FDA) for three points along the girder. These models are sequentially updated, and the result is a computationally cheap and accurate estimate of the fatigue damage.

This study is presented below in the following two sections. Section 2 explains the mathematical tools needed to perform the analysis, namely the buffeting analysis, the probabilistic wind field, and the surrogate modelling using GPR. Section 3 is devoted to the results from the analysis, followed by some discussions and the conclusion.

2 PROCEDURE FOR FATIGUE ANALYSIS

This section will provide the foundation necessary for carrying out the fatigue analysis. We briefly discuss the probabilistic wind spectra and the buffeting theory, introducing the environmental factors. Later, a detailed introduction to Gaussian process regression, kernel functions, surrogate modelling and its sequential updating is presented.

2.1 *Stress spectra from the buffeting response of the bridge*

As opposed to the flutter of the bridges, buffeting of bridges is a stable and random response to the turbulence of the oncoming wind flow. Buffeting seldom leads to catastrophic failures but over large time scales, buffeting can result in fatigue damage accumulation. To begin with, the buffeting response of Hardanger Bridge was calculated in the frequency domain using the classical multimode theory (Scanlan, 1978).

For this purpose, a wind model based on the Kaimal-type spectra, and Davenport's coherence formula for the cross-spectra was used. These are defined as:

$$\begin{aligned} \frac{S_{u,w}f}{\sigma_{u,w}^2} &= \frac{A_{u,w}f_z}{(1+1.5A_{u,w}f_z)^{5/3}}, \quad f_z = \frac{fz}{U} \\ C_{u,w} &= \exp -\left(K_{u,w}\frac{f\Delta x}{U}\right) \end{aligned} \tag{1}$$

where f is the frequency, U is the mean wind velocity, z is the height above the ground, and $A_{u,w}$ are spectral parameters. $\sigma_{u,w}$ are the standard deviations of the turbulence of the wind in the along-wind (u) and vertical (w) directions, while $K_{u,w}$ are the decay coefficients. Δx is the separation along the distance of the bridge. Furthermore, utilizing a Finite Element model of the bridge (Petersen, 2019), we extract the still-air displacement mode and force mode shapes of the bridge deck. The aerodynamic features of the deck, namely the steady-state force coefficients and aerodynamic derivatives, are obtained through forced vibration tests (Siedziako, 2017).

The spectral density matrix G_{FF} of the three components of the sectional forces (SF_1, SM_1, SM_2) at any point along the span of the bridge is obtained by using the cross spectral density matrix of the buffeting load $\tilde{G}_{QQ}$, the frequency response matrix $\tilde{H}(\omega)$, and the section force mode shapes Φ_F, as:

$$G_{FF}(\omega, x) = \Phi_F(x)[\tilde{H}(\omega)\tilde{G}_{QQ}(\omega)\tilde{H}(\omega)^T]{\Phi_F}^T \tag{2}$$

Further, by using a transfer function T, we proceed to calculate the stress spectrum $G_{\sigma\sigma}(\omega, x)$. by using the Euler beam theory:

$$G_{\sigma\sigma}(\omega, x, \kappa) = T(\kappa)\, G_{FF}(\omega, x)\, T^T(\kappa), \quad T(\kappa) = \begin{bmatrix} \frac{1}{A} & \frac{z(\kappa)}{I_y} & \frac{y(\kappa)}{I_z} \end{bmatrix} \tag{3}$$

with κ depending on the position of the point along the cross-section of the bridge girder chosen for the analysis. In this work, three points are chosen for the analysis as shown in

(Figure 1). Each point is assigned its coordinates $(y(\kappa),\ z(\kappa))$, with the shear center of the girder cross-section as the origin. The moments of inertia along the strong and the weak axes are denoted by I_z and I_y, respectively.

2.2 *Probabilistic wind field for the site*

The calculation of the rate of the fatigue damage accumulation, requires a joint probability distribution function of all wind parameters. Wind speeds at the girder of the Hardanger Bridge have been monitored for several years by researchers. Using this this long-term full-scale wind data, a probabilistic model of the wind field was proposed by (Fenerci, 2018). The model fits a Weibull distribution for the mean wind speed, while the remaining six parameters are seen to follow a log normal distribution. In this work, the influence of the turbulence field in the along-wind direction is investigated. The parameters are listed in the table below:

Table 1. The wind and the joint probability distribution parameters at the bridge site for easterly winds.

Wind field parameter	Distribution type	Distribution parameters
U	Weibull	$\lambda = 5.1941, \mathrm{K} = 1.7946$
$\sigma_u \vert U$	lognormal	$\tilde{\mu} = 0.122 + 0.039U,\ \ \tilde{\sigma} = 0.28$

2.3 *Stress time-history simulation and rainflow counting.*

To proceed, we take the stress spectra, $G_{\sigma\sigma}(\omega, x, \kappa)$obtained from the buffeting analysis. We can simulate the time history of the stresses and perform rainflow counting. The SN-curves proposed by NS-EN 1999-1-3 are used. To tackle the scatter of the damage calculated for each set of set of the wind field parameters, 60 Monte Carlo simulations of 600 secs each are realized. The scatter of the damage obtained from the 60 simulations is similar. To this end, the damage used to train the surrogate model is taken as the average of these 60 simulations. Equipped with this understanding, we can commence the establishment of a surrogate model for a comprehensive long-term analysis.

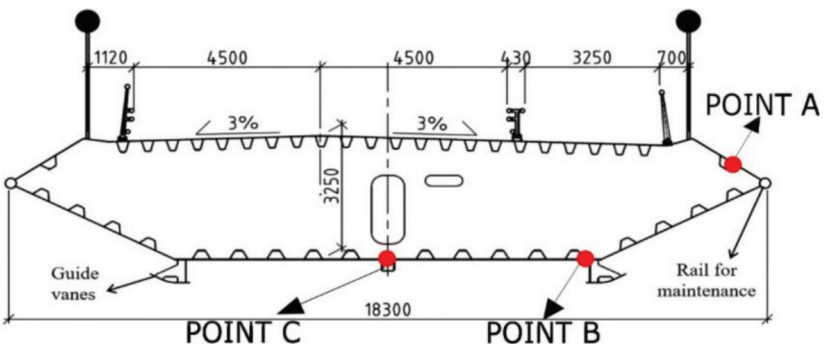


Figure 1. Cross section of the Hardanger bridge along with the three points checked for fatigue damage.

2.4 *Gaussian process regression*

Conversely, complexity of computing the rate of fatigue damage accumulation increases if we consider more wind field parameters to be uncertain. If n is the number of uncertain factors considered, then the computational complexity ~ $O(c^n)$, where c is a constant. To this end, we make use of surrogate modelling and Gaussian process regression to make the operation computationally cheaper.

At its core, Gaussian process regression is a non-parametric regression that uses a prior distribution over functions and uses Bayesian inference to update the distribution based on the observed data (Williams 1995). The result is a posterior distribution that reflects the likely functions fitting the data. Combining this property with the fact that GPR provides uncertainty measurements on the predictions and is valid for multiple dimensions, makes it suitable for our problem.

Mathematically, a Gaussian process is defined by its mean and the covariance function. Assume we have a data stored in $X = [x_1, x_2, \ldots, x_n]$. We proceed by defining the mean and the covariance functions as $m(x) = E[f(x)]$ and $k(x, x') = E[(f(x) - m(x))(f(x') - m(x'))]$, respectively. So, for a Gaussian process with non-zero mean, it is denoted as:

$$f(x) \sim N(m(x)),\ k(x, x) \tag{4}$$

Usually, the observed data is assumed to have some noise, leading to $y \sim \mathcal{N}(m(x)),\ k(x, x) + \sigma_n^2 I$ noise. Now, if we want to make predictions over new points $X^* = [x_1^*, x_2^*, \ldots, x_m^*]$, with $f^* = [f(x_1^*), f(x_2^*), \ldots, f(x_m^*)]$. The conditional distribution over the unknown points remains Gaussian even after the model is updated with more data points. Consequently, we can write:

$$\begin{bmatrix} f \\ f^* \end{bmatrix} \sim ND\left(\begin{bmatrix} M_X \\ M_{X*} \end{bmatrix}, \begin{bmatrix} K(X, X) + {\sigma_n}^2 I & K(X, X^*) \\ K(X^*, X) & K(X^*, X^*) \end{bmatrix} \right) \tag{5}$$

Where M_X and M_{X_*} represent the mean values of the training set and the test set respectively. The term ND denotes a multivariate Gaussian distribution. The values for the new points are predicted using the conditional likelihood and the covariance matrix. These covariance functions are dependent on the Euclidean distance $D(X, X^*)$ between X and X^*. For this work, the squared exponential kernel was used and is defined as:

$$K_{\{RBF\}}(D) = \sigma_{\{f\}}^2 \exp\left(-\frac{1}{2l^2} D^2 \right) \tag{6}$$

Where σ_f and l are the hyperparameters, termed as the scaling factor and the length scale, respectively. A higher value of the length scale and lower value for the scaling factor results in a smoother and more global fit for the data. However, tuning these hyperparameters is essential for making useful predictions.

2.4.1 *Surrogate modelling and updating process:*
A surrogate model is set up for calculating the rate of fatigue damage accumulation (FDA). The model is initiated by calculating the FDA (Lutes, 1984) for a single set of environmental factors. The vector σ_s contains the standard deviations of the surrogate model, while the vector D_{pred} stores the predicted values of the FDA. To this end, we can define a learning function P_{next}, that chooses the next set of environmental factors to be used for updating the model (Lystad, 2023).

$$P_{next} = argmax\left\{ \sigma^{(1-n)} [D_{pred}\, f(\psi_1, \psi_2, \ldots \psi_m]^n \right\} \tag{7}$$

where ψ_i is the i^{th} environmental factor used. $f(\psi_1, \psi_2, \ldots \psi_m)$ is the joint probability distribution function of the m wind parameters. The factor n is used as a weighting factor to prioritize those sets of wind parameters which contribute the most towards the FDA. A value close to zero will result in a quasi linear spacing of the training data points over the entire range of the environmental parameters, which is suboptimal. To avoid this issue, we give precedence to those combinations of the environmental factors that contribute the most to the FDA, setting a value of $n = 0.15$.

The learning function helps our model to quickly converge. Once the convergence is achieved, the damage accumulated for the length of stress signal chosen is calculated as (Gramstad, 2020):

$$FDA = \int_{\psi_1} \int_{\psi_2} \dots \int_{\psi_m} D_{pred}(\psi_1, \psi_2, \dots, \psi_m) f(\psi_1, \psi_2, \dots, \psi_m) d\psi_1 d\psi_2 \dots d\psi_m \tag{8}$$

In the context of the surrogate model, two distinct stopping criteria were selected to determine its convergence. The maximum number of points in the training data or the number of iterations to calculate the learning function, and the relative change in the FDA due to the addition of a new training data set. The limits are chosen based on the number of uncertain environmental factors leveraged for the surrogate model. We now proceed to perform the analysis in the next section and report the results.

3 RESULTS

Initially, the surrogate model is set-up and involves the mean wind velocity, denoted as U, as the singular uncertain parameter. Subsequently, the complexity and precision of the model is enhanced through the incorporation of the standard deviation of along-wind turbulence, denoted as σ_u, as uncertain. It is noteworthy that in the context of these surrogate models, when an environmental factor is not treated as uncertain, the analysis opts for their most probable value derived from the Joint Probability Density Function (PDF).

3.1 *Single uncertain parameter*

Prior to delving into the presentation of results, it is important to provide contextual information about the working of the algorithm. In the context of the squared exponential kernel, the initial configuration involved setting the standard deviation of observation noise and the length scale to unity, while the scale factor was initialized to 5. It is noteworthy that these hyperparameters undergo updates as the model is progressively trained with additional data points. In pursuit of convergence, two termination criteria were also established. The first one regards the maximum number of iterations, which was set to 30 for the case of single environmental factor, namely U. The second one regards the relative change in the FDA over each iteration. For this study, convergence was said to have been achieved when the addition of a new point in the training data set resulted in the relative change of less than 0.1% in the FDA.

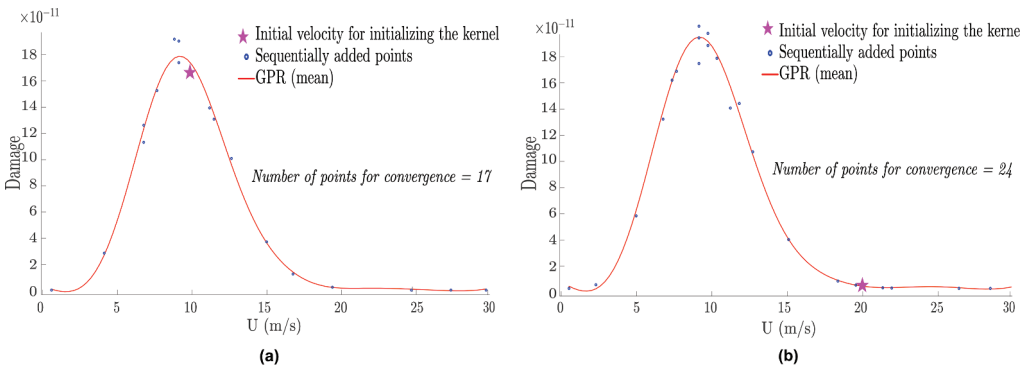


Figure 2. Two surrogate models for FDA at point A for uncertain mean wind velocity, showing two different velocities to initialize the kernel.

The algorithm performs in an optimal way with the value of $n = 0.15$ (Figure 2) shows two surrogate models for the fatigue damage at point A. It is evident from these plots that the mean wind velocities in the range from 5 *m/s* to 15 *m/s* contribute the most to the accumulated damage. This can be attributed to their high probabilities of occurrence. Consequently, to compute the integral in Equation (8), the model needs to have a better fit close to this peak. This implies the necessity of having a greater number of data points within this interval near the peak. Unfortunately, the location of this peak is not a prior knowledge. Nevertheless, (Figure 2a) was initialized with a velocity close to the with $U = 10$ *m/s*, while Figure (2b) was initialized with $U = 20$ *m/s*, and the convergence was achieved in less than 30 iterations for both the cases. The learning function can quickly locate the peak of the damage curve, irrespective of the value of the mean wind velocity used to initialize the kernel.

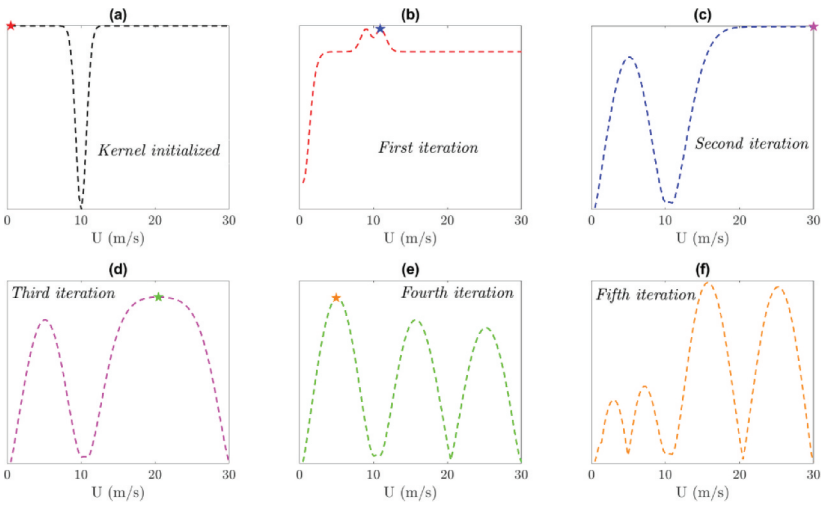


Figure 3. The learning function for the first five iterations, with the marker on each plot denoting the maximum value of the function. The kernel was initialized with a velocity of 10 m/s. The values of the leaning function have been normalized for enhanced clarity.

The learning function is computed at each test velocity as a weighted average of the predicted damage and the standard deviation of the prediction, as shown in Equation (7). This implies that velocities with minimal impact on damage will be given lower priority compared to those near the peak. Consequently, the learning function tends to concentrate most data points in the vicinity of the peak, with fewer points distributed elsewhere, as illustrated in (Figure 2). This process of sequential updating becomes more apparent when we refer to the plots in (Figure 3). The normalized values of the learning function for the first five iterations are plotted. The kernel is initiated with $U = 10$ *m/s*. The training function is plotted in (Figure 3a) and shows a constant value except in the vicinity of this sole training point. The pentagram marks in the plots show the maximum value of the learning function, with the corresponding velocity being chosen as the next point for training. We observe lower values of the learning function corresponding to velocities within the training data, attributed to a decreased standard deviation of the Gaussian Process Regression in the vicinity of the training data points.

Table 2. The fractional fatigue damage accumulated by the three points.

Points	A	B	C
Cumulative damage (100-year period)	0.0066	0.0052	0.003

The FDA calculated at each iteration changes since the mean of the GPR evolves. The addition of the first few points results in a substantial change to the value of the FDA. This is tracked quantitatively using the relative change of the FDA, plotted in Figure (4). We notice that after twelve iterations, the surrogate model is already pretty accurate and converges fully after twenty iterations. Table (2) presents the predicted values of the fraction of the fatigue damage that will be accumulated at the three points in the girder over a 100-year period. The computed values are beneath the expected values, providing evidence of the exceptional aerodynamic characteristics of the cross-section.

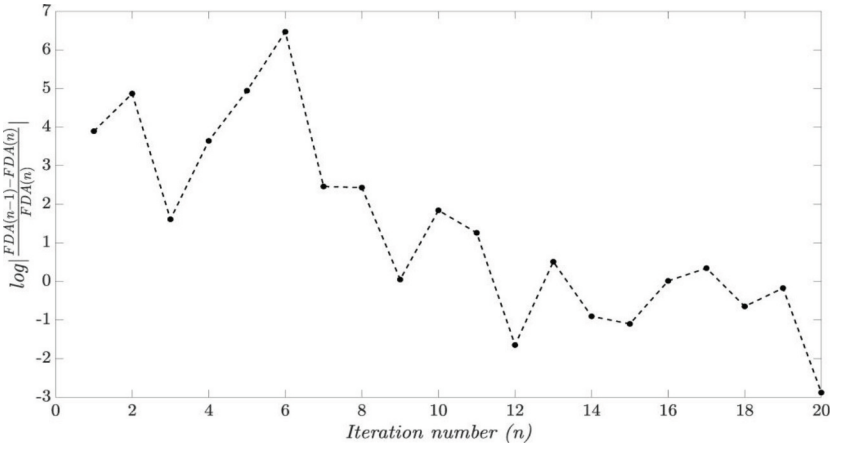


Figure 4. Plot showing the convergence achieved after 20 iterations. The relative change in the FDA has been plotted for each iteration.

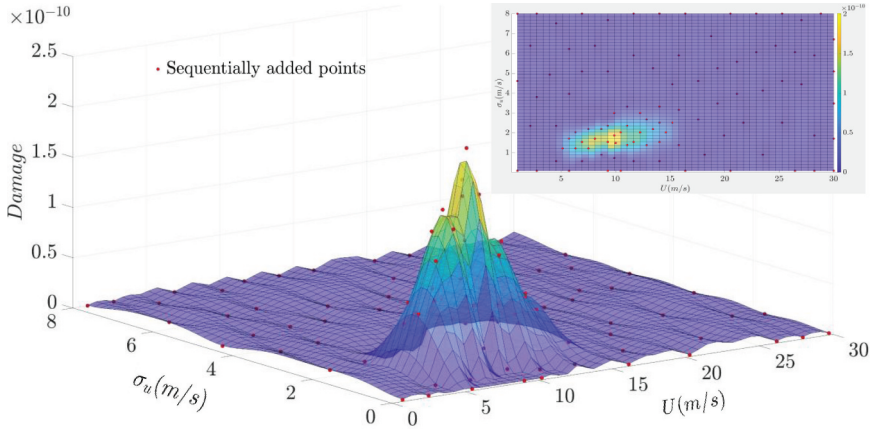


Figure 5. A surrogate model for FDA using two uncertain wind parameters. The insert plot depicts a higher density of points chosen by the algorithm near the peak of the surface.

3.2 *Two uncertain parameters*

In this section, we perform the fatigue analysis considering two uncertain environmental factors. The parameter chosen is the standard deviation of the turbulence intensity in the horizontal direction and orthogonal to the bridge, denoted by σ_u. This choice was motivated by the fact that σ_u has a greater impact on the buffeting response of a bridge, hence the fatigue.

As the number of uncertain parameters increases there is a significant uptick in the number of iterations the algorithm needs to perform to reach convergence. This is where sequential updating has the potential to cut the computational effort.

A 100-point surrogate model is depicted in Figure. (5). The kernel was initialized with $U = 15\ m/s, \sigma_u = 4\ m/s$. The convergence was not achieved after 99 iterations. However, the value of the relative change in FDA was close to the termination criterion and stood at $0.46\% > 0.1\%$. The insert plot in Figure. (5) depicts the points chosen by the learning function, making it evident that the peak is more densely represented. For this case of two uncertain wind parameters, using the algorithm without a learning function is computationally expensive, and the peak of the surface is not well represented. This issue exacerbates when more uncertain parameters are used.

3.3 *Conclusions*

The sequential updating algorithm presented in this work, emerges as a robust and efficient methodology for buffeting-induced fatigue analysis in the presence of uncertain environmental factors. Our study demonstrates the efficacy of a sequential updating algorithm for fatigue analysis in a long-span suspension bridge, in scenarios with uncertain wind-field parameters. The use of a learning function streamlines the selection of training points for the surrogate model of fatigue damage, reducing computational effort, a crucial advantage when dealing with more uncertain parameters. The initial analysis, focusing on a single uncertain parameter, showed rapid convergence, with the surrogate model achieving accuracy after a few iterations.

Expanding to two uncertain parameters, the algorithm's capability to handle increased complexity was demonstrated. Despite increased computational demands, the sequential updating algorithm remains viable for optimizing training point selection, enhancing convergence efficiency. This approach shows promise in applications where accurate fatigue damage prediction is crucial for structural integrity assessments.

REFERENCES

Gu, M., Xu, Y. L., Chen, L. Z., & Xiang, H. F. (1999). Fatigue life estimation of steel girder of Yangpu cable-stayed bridge due to buffeting. Journal of Wind Engineering and Industrial Aerodynamics, 80(3), 383–400.

Fenerci, A., Andreas Kvåle, K., Wiig Petersen, Ø., Rønnquist, A., & Øiseth, O. (2021). Data set from long-term wind and acceleration monitoring of the hardanger bridge. Journal of Structural Engineering, 147(5), 04721003.

Scanlan, R. H. (1978). The action of flexible bridges under wind, II: Buffeting theory. Journal of Sound and vibration, 60(2), 201–211.

Petersen, Ø. W., & Øiseth, O. (2019). Finite element model updating of a long span suspension bridge. In Proceedings of the international conference on earthquake engineering and structural dynamics (pp. 335–344). Springer International Publishing.

Siedziako, B., & Øiseth, O. (2017). On the importance of cross-sectional details in the wind tunnel testing of bridge deck section models. Procedia engineering, 199, 3145–3151.

Fenerci, A., & Øiseth, O. (2018). Site-specific data-driven probabilistic wind field modeling for the wind-induced response prediction of cable-supported bridges. Journal of Wind Engineering and Industrial Aerodynamics, 181, 161–179.

Williams, C., & Rasmussen, C. (1995). Gaussian processes for regression. Advances in neural information processing systems, 8.

Lutes, L. D., Corazao, M., Hu, S. L. J., & Zimmerman, J. (1984). Stochastic fatigue damage accumulation. Journal of Structural Engineering, 110(11), 2585–2601.

Lystad, T. M., Fenerci, A., & Øiseth, O. (2023). Full long-term extreme buffeting response calculations using sequential Gaussian process surrogate modeling. Engineering Structures, 292, 116495.

Gramstad, O., Agrell, C., Bitner-Gregersen, E., Guo, B., Ruth, E., & Vanem, E. (2020). Sequential sampling method using Gaussian process regression for estimating extreme structural response. Marine Structures, 72, 102780.

Bridge Maintenance, Safety, Management, Digitalization and Sustainability – Jensen, Frangopol & Schmidt (eds)
© 2024 The Author(s), ISBN 978-1-032-77040-6
Open Access: www.taylorfrancis.com, CC BY-NC-ND 4.0 license

Cellular automata damage models incorporating climate change effects for life-cycle assessment of concrete bridges

G.V. Nava, A. D'Iorio & F. Biondini
Politecnico di Milano, Milan, Italy

ABSTRACT: The accuracy of life-cycle assessment of concrete structures exposed to corrosion due to ingress of chlorides and other aggressive agents can depend significantly on the diffusion models adopted. In addition, daily weather fluctuations and long-term changes in climatic conditions can exacerbate the effects of chloride attack, accelerating the onset of corrosion and increasing the rate of damage. This paper presents a novel approach to chloride diffusion simulation and corrosion modeling under climate change using cellular automata. The proposed model is based on the extension of a general formulation established in previous works for life-cycle assessment of concrete structures under corrosion by adapting cellular automata to account for the evolution over time of the environmental parameters that influence the initiation and propagation of corrosion, i.e. temperature and relative humidity, in a changing climate. The methodology is applied to life-cycle structural assessment of a bridge pier under corrosion considering different climate change scenarios. The results allow to quantify the impact of climate change on chloride diffusion, corrosion damage, and structural performance over time.

1 INTRODUCTION

Structures and infrastructure systems suffer over time from the detrimental effects of aging, fatigue, and deterioration processes due to attack by aggressive agents and other damage mechanisms that impair their original structural performance (Ellingwood 2005). These damaging effects may lead to unsatisfactory structural safety and performance, including structural and functional obsolescence. Life-cycle-oriented design, assessment, maintenance and management criteria, methods and procedures are hence necessary to guarantee adequate levels of structural safety and reliability over the entire lifespan of structures (Biondini & Frangopol 2016).

Among various structural degradation phenomena, chloride-induced corrosion in reinforced concrete (RC) structures is particularly damaging, especially for RC bridges whose structural members are frequently exposed to chloride attack. In this context, diffusion and damage models that can accurately reproduce chloride ingress, corrosion initiation and damage propagation are essential for life-cycle structural assessment. Fick's diffusion model is often applied in a simplified one-dimensional form to describe chloride ingress (fib 2006). However, depending on the exposure and shape of structural members, the diffusion process can be better described by two- or three-dimensional concentration gradients (Biondini et al. 2004, Titi & Biondini 2016).

In addition, climate change associated with continued greenhouse gas emissions will lead to increased global warming, which, in turn, leads to exacerbate multiple and concomitant hazards (IPCC 2023), such as the occurrence of extreme events of increased magnitude and frequency and the acceleration of aging and structural deterioration processes. Rising temperature and changes in relative humidity can affect the diffusivity of concrete and the rate of corrosion damage, leading over time to impair the life-cycle structural performance and the residual structural lifetime (Stewart et al. 2011, Nava et al. 2023).

DOI: 10.1201/9781003483755-327

This paper presents a novel approach to chloride diffusion simulation and corrosion modeling under climate change using cellular automata. The proposed approach is based on a general formulation established in previous works for probabilistic life-cycle assessment of concrete structures under corrosion (Biondini et al. 2004, 2006). The main novelty is the extension of cellular automata and evolutionary computation techniques to account for climate change effects by incorporating the variability over time of the environmental parameters that influence the initiation and propagation of corrosion, i.e. temperature and relative humidity. The methodology is applied to life-cycle structural assessment of a RC bridge pier under corrosion considering different climate change scenarios. The effects of uncertainties in the mechanical and environmental damage stressors are also investigated in probabilistic terms. The results allow to quantify the climate change impact and highlight the importance of the proper modelling of degradation processes and environmental conditions over the entire structural lifetime.

2 CLIMATE CHANGE AND FUTURE EMISSION SCENARIOS

Climate change models are based on greenhouse gas emissions which depend on how the future may evolve with respect to a range of different socio-economic variables. Future climate is simulated under different scenarios such as the shared socioeconomic pathways (SSP) combined with the representative concentration pathways (RCP), i.e. SSP-RCP scenarios (IPCC 2023).

SSPs are a set of scenarios developed to describe plausible alternative trends in the evolution of society and ecosystem over a century timescale without considering climate change or climate policies and consist in a narrative storyline describing societal future, and a quantitative description of socio-economic drivers such as population, gross domestic product and urbanization. SSP1 and SSP5 represent scenarios for human development emphasizing education, health, and economic growth. However, SSP5 leans towards an energy-intensive, fossil-based economy, while SSP1 shifts towards sustainability. In contrast, SSP3 and SSP4 envision pessimistic trends with minimal investment in education or health, rapid population growth, and rising inequalities. SSP3 prioritizes regional security, while SSP4 emphasizes large inequalities within and across countries, leading to societies highly vulnerable to climate change. Finally, SSP2 envisions a central pathway where trends continue historically without significant deviations (O'Neill et al. 2016). On the other end, RCPs specify the radiating forces at the end of the century based on different emission trajectories (van Vuuren et al. 2011). A set of five scenarios has been considered in the VI IPCC assessment report (IPCC 2023): SSP1-1.9 and SSP1-2.6 representing a low emission scenario pathway leading to warming below 1.5°C and 2.0°C respectively in 2100; SSP2-4.5 represents a medium emission scenario; SSP3-7.0 and SSP5-8.5 represent a high and a very high emission scenarios, respectively. In the comparative investigation presented in this paper, scenarios SSP2-4.5 and SSP5-8.5 are considered.

3 DIFFUSION AND CORROSION MODELING UNDER CLIMATE CHANGE

3.1 *Cellular automata simulation of diffusion*

The mathematical description of the diffusion process of chemical components within solid media typically involves equations relating the mass diffusion rate to the concentration gradient responsible for the net mass transfer (Glicksman 2000). The simplest model to describe this process is the Fick's second law leading to a linear relationship between the mass flow and the concentration gradient as described by the following differential equation:

$$\nabla[D(\mathbf{x},t)\nabla C(\mathbf{x},t)] = \frac{\partial C(\mathbf{x},t)}{\partial t} \tag{1}$$

where $D=D(\mathbf{x},t)$ and $C=C(\mathbf{x},t)$ are the diffusion coefficient and mass concentration, respectively of the component at point $\mathbf{x}=\mathbf{x}(x, y, z)$ and time t, and $\nabla(\cdot) = \mathbf{grad}\,(\cdot)$.

The closed-form solution of Fick's diffusion equation can be obtained only for simple problems. Cellular automata are used in this study for numerically solving the diffusion equation

(Biondini et al 2004). This technique relies both on temporal (i.e. time step subdivision) and spatial discretization (i.e. regular uniform grid of cells with state variables associated to each cell). In case of diffusion, the state of a cellular automaton at time t is fully defined by the concentration $C_i = C_i(t)$ at each cell i. Evolution occurs at discrete time steps according to parallel state transitions determined by local rules. At time t_{k+1}, the variables C_i^{k+1} are synchronously updated based on the concentration values ${C_{i,n}}^k$ in the neighborhood n of cell i at the preceding time instant t_k, where the neighborhood typically includes the cell itself and adjacent cells within a specified radius r. The diffusion process described by the Fick's model in d-dimensions ($d = 1,\ 2,\ 3$) can be reproduced by adopting $r = 1$ and the following local evolutionary rule (Biondini 2011):

$$C_i^{k+1} = \Phi_0 C_i^k + \sum\nolimits_{j=1}^{d} \left(\Phi_j^- C_{i-1,j}^k + \Phi_j^+ C_{i+1,j}^k \right) \tag{2}$$

where $C_i^k = C(\mathbf{x}_i,\ t_k)$ is the concentration at cell i and time instant k, Φ_0, Φ_j^-, and Φ_j^+ $(j = 1, \ldots, d)$ are evolutionary coefficients. According to mass conservation law, the evolutionary coefficients must fulfil the following normality rule:

$$\Phi_0 + \sum\nolimits_{j=1}^{d} \left(\Phi_j^- + \Phi_j^+ \right) = 1 \tag{3}$$

For isotropic medium, the symmetry condition $\Phi_j^- = \Phi_j^+ = \Phi_1 (j = 1, \ldots, d)$ should be imposed to avoid directionality effects, i.e. $\Phi_0 = (1 - 2d\Phi_1)$. In this way, the evolutionary rule can be rewritten as follows:

$$C_i^{k+1} = \Phi_0 C_i^k + \frac{1 - \Phi_0}{2d} \sum\nolimits_{j=1}^{d} \left(C_{i-1,j}^k + C_{i+1,j}^k \right) \tag{4}$$

Based on the diffusivity D, a proper discretization in space Δx and time Δt has to be chosen:

$$D = \frac{1 - \Phi_0}{2d} \frac{\Delta x^2}{\Delta t} = \Phi_1 \frac{\Delta x^2}{\Delta t} \tag{5}$$

Standard value of central evolutionary coefficient for constant diffusivity is Φ_0=1/2.

3.2 *Cellular automata with time-variant diffusivity*

Concrete diffusion results to be affected by material aging and changes in environmental conditions. Experimental studies have shown an increase in the concrete diffusivity along with the increase in temperature and relative humidity. To account for aging and nonstationary climate conditions, the diffusion coefficient can be expressed as follows (Chirdeep et al 2023):

$$D(t) = k_e\ k_c\ k_t\ D_{ref}\ f_T(t) f_{RH}(t) f_a(t) \tag{6}$$

where D_{ref} is the reference diffusion coefficient for T=20 °C and RH=75%, k_e, k_c, and k_t are environment, curing, and test method factors, respectively, and $f_T(t)$, $f_{RH}(t)$, and $f_a(t)$ are functions which account for temperature and relative humidity variation and aging process, respectively.

The functions $f_T(t)$ and $f_{RH}(t)$ are computed as follows (Martín-Pérez et al. 2001):

$$f_T(t) = e^{\frac{E}{R}\left(\frac{1}{293.15} - \frac{1}{273.15 + T(t)}\right)} \tag{7}$$

$$f_{RH}(t) = e^{\left[1 + \frac{(1 - RH(t))^4}{(1 - 0.75)^4}\right]^{-1}} \tag{8}$$

where E is the activation energy of the chloride's diffusion process (40 kJ/mol), R is the gas constant (8.314×10^{-3} kJ/mol), T is the temperature in Celsius degrees, and RH is the relative humidity. The aging function can be evaluated as a function of the aging factor a, as follows:

$$f_a(t) = \left(\frac{0.0767}{t}\right)^a \tag{9}$$

The variability in time of diffusivity can be incorporated in the cellular automata formulation by updating over time (a) the time step Δt, (b) the evolutionary coefficients Φ_0 and Φ_1, or (c) both the time step Δt and coefficients Φ_0 and Φ_1. Updating the time step only may be not practical for implementation purposes and it is also not feasible for inhomogeneous conditions, such as when diffusivity is modified locally by cracking (Biondini et al. 2004). In fact, chloride ingress may change significantly with the increase of crack width (Bazant et al. 1987, Kwon et al. 2009). Updating evolutionary coefficients only is a more convenient approach that also allows for local variations in diffusivity over time. However, when such variations become important, as it may occur under climate change effects, evolutionary coefficients may deviate significantly from initial values. In this case, simultaneous updating of the time step and evolutionary coefficients is useful to maintain the evolutionary coefficients within appropriate values.

3.3 *Corrosion damage modeling*

For a steel bar located at point $\mathbf{x}_b$, corrosion initiates at time t_{cr} when chloride concentration attains a critical threshold C_{cr}, or $t_{cr} = \min\{t \mid C(\mathbf{x}_b, t) \geq C_{cr}\}$. Corrosion propagation, expressed in terms of corrosion penetration rate p_s (mm), is described based on Faraday's law as follows:

$$\frac{\partial p_s}{dt} = 0.0116\ R_f\ i_{corr} \tag{10}$$

where i_{corr} is the corrosion electric current density ($\mu A/cm^2$), and R_f is the pitting factor, i.e. the ratio between the maximum depth measured at pit and the average penetration calculated indirectly from the weight loss of the steel bar (Stewart & Al-Harthy 2008).

Corrosion propagation is affected by the variation of environmental parameters, such as temperature and relative humidity, as well as chloride concentration and formation of corrosion products. To account for these effects, the corrosion rate is expressed as follows (Nava et al 2023):

$$i_{corr}(t) = i_{corr,ref}\varphi_{RP}(t)\varphi_T(t)\varphi_{RH}(t)\varphi_C(t) \tag{11}$$

where $i_{corr,ref}$ is the reference corrosion rate for T=20 °C and RH=75%, and the functions $\varphi_{RP}(t)$, $\varphi_T(t)$, $\varphi_{RH}(t)$, and $\varphi_C(t)$ account for the formation of rust products and variation of temperature, relative humidity, and chloride concentration, respectively. The following functions are adopted (Liu & Weyers 1998, Vu & Stewart 2000, Stewart et al. 2011, Guo et al. 2015):

$$\varphi_{RP}(t) = 0.85t_p^{-0.29} \tag{12}$$

$$\varphi_T(t) = [1 + K_T(T(t) - 20)] \tag{13}$$

$$\varphi_{RH}(t) = e^{-6000(RH(t)-0.75)^6} \tag{14}$$

$$\varphi_C(t) = \frac{C(t) + C_{cr}}{2\ C_{cr}} \tag{15}$$

where t_p is the time since corrosion initiate, and K_T=0.025 or K_T=0.073 for temperature $T \leq 20°C$ and $T > 20°C$, respectively.

Corrosion damage is modeled based on corrosion penetration in terms of a damage index δ_s representing the percentage of loss of cross-sectional area of the steel bar. The reduction of steel bar ductility and the damaging longitudinal splitting cracks in the concrete surrounding the corroded bars due to the formation of oxidation products are taken into account as reported in Biondini and Vergani (2015), i.e. based on a reduction of both steel ultimate strain capacity ε_{su} and concrete compression strength f_c, eventually leading to spalling of concrete cover.

4 APPLICATION

4.1 *Case study: RC bridge pier*

The two-column RC bridge pier shown in Figure 1a is considered. Each column bent has a two-cellular cross-section with the geometry and reinforcement layout shown in Figure 1b. The concrete cover is 4 cm. Figure 1b shows also the fiber structural model developed in OpenSees (Mazzoni et al. 2006). Material constitutive laws are based on a parabola-rectangle model for concrete (concrete 01) and elastic-plastic model with strain hardening for steel (steel 01).

The life-cycle structural performance of the bridge pier is investigated at cross-sectional level under axial force N=7.1 MN by assuming the bridge pier exposed to chloride attack over the inner and outer surfaces with uniform concentration C_s. Diffusion and damage modeling are based on cellular automata with grid cell size Δx = 1 cm and time step Δt = 0.09 years (Figure 1c). Random variables, probability distributions, descriptors, and bounds are listed in Table 1.

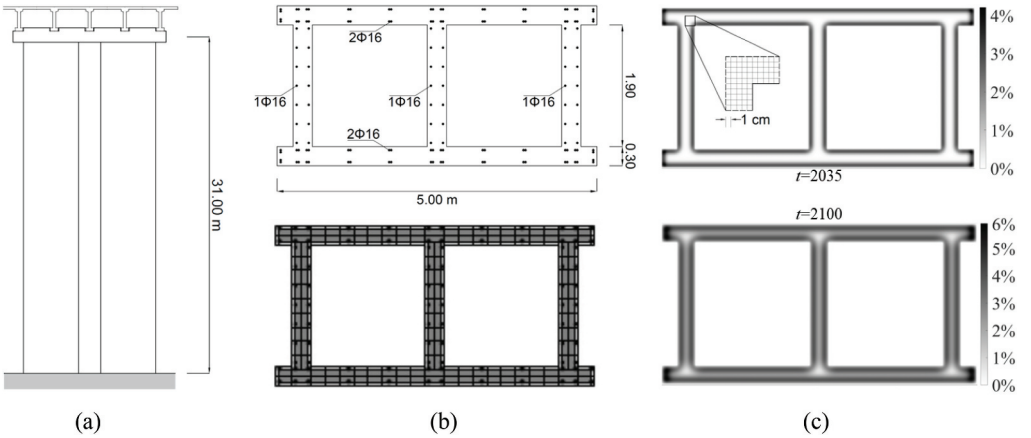


Figure 1. (a) RC bridge pier; (b) Geometry, reinforcement layout, and structural model of the cross-section; (c) Detail of the grid of cellular automata and contour maps of the concentration ratio $\Delta C=(C_{SPP5\text{-}8.5}-C_{HIST})/C_s$ quantifying the difference of chloride concentration predicted with climate change, i.e. $C_{SPP5\text{-}8.5}$, and without climate change, i.e. C_{HIST}, normalized to surface concentration C_s, at years 2035 (top) and 2100 (bottom).

Table 1. Random variables, probabilistic distributions, descriptors, and bounds (Stewart & Al-Harthy 2008, Titi & Biondini 2016, Nasr et al 2022).

Random Variable	Distribution Type	Mean	C.o.V.	Bounds
Surface chloride concentration C_s [%wt./c]	Truncated Normal	3.0	0.30	$C_s \geq 0$
Critical chloride concentrations C_{cr} [%wt./c]	Beta	0.60	0.25	$0.2 \leq C_{cr} \leq 2$
Environmental factor k_e [-]	Gamma	0.676	0.169	$k_e \geq 0$
Curing factor k_c [-]	Beta	0.8	0.125	$0.4 \leq k_c \leq 1.0$
Test method factor k_t [-]	Truncated Normal	0.832	0.0288	$k_t \geq 0$
Reference diffusivity D_{ref} [10^{-12} m^2/s]	Truncated Normal	15.8	0.20	$D_{ref} \geq 0$
Aging coefficient a [-]	Beta	0.362	0.677	$0 \leq a \leq 0.98$
Reference current density $i_{corr,ref}$ [μA/cm^2]	Lognormal	2.586	0.67	$i_{corr} \geq 0$
Pitting factor R_f [-]	Gumbel	6.2	0.18	$R_f \geq 0$
Concrete compression strength f_c [MPa]	Lognormal	36.3	0.18	$f_c \geq 0$
Steel yielding strength f_y [MPa]	Lognormal	497.3	0.1	$f_y \geq 0$

Climate projections are based on the EC-Earth3-Veg-LR climate model (Döscher et al. 2022). Figure 2 shows the projection of mean annual temperature (Figure 2a) and relative humidity

(Figure 2b) with resolution of 250 km in Lombardy Region, Italy, including historical data from 1970 to 2014 (light gray line) and two climate scenarios from 2015 to 2100: medium emission scenario SSP2-4.5 (dark gray line) and very high emission scenario SSP5-8.5 (black line).

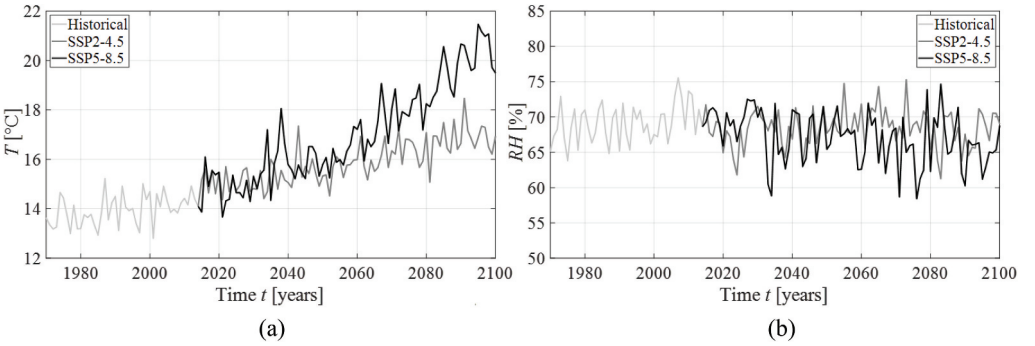


Figure 2. Historical and future climate projections: (a) Mean annual temperature; (b) Relative humidity.

4.2 *Life-cycle structural assessment under climate change*

The influence of climate change is investigated with reference to chloride diffusion, steel bar corrosion, and cross-sectional bending capacity. A deterministic life-cycle analysis is firstly carried out by assuming the mean values listed in Table 1 as nominal values. The contour maps shown in Figure 1c provide the concentration ratio $\Delta C=(C_{\text{SPP5-8.5}}-C_{\text{HIST}})/C_s$ to quantify the difference between chloride concentration predicted for the climate change scenario SPP5-8.5, i.e. $C_{\text{SPP5-8.5}}$, and based on historical climate, i.e. C_{HIST}, with respect to surface concentration C_s, at years 2035 (top) and 2100 (bottom). A difference of about 5% on the outer layers of the box cells holds over the entire lifetime, leading to reduce the corrosion initiation time and increase the corrosion rate of the reinforcing steel bars. This is shown in Figure 3a by means of the evolution over time of the damage index δ_s of the steel bars #1 and #2 located at midspan and end of the bottom flange, respectively, for historical vs SSP5-8.5 climate scenarios. The impact of corrosion damage is reflected at cross-sectional level on the evolution over time of the bending moment vs curvature capacity curves, as shown in Figure 3b, with markers indicating cracking, yielding and ultimate conditions. It is worth noting that climate change effects involve a reduction of both bending strength and curvature ductility with respect to the prediction based on historical climate. Figures 3c and 3d allow to quantify this reduction over the investigated timeframe for the capacity ratio of both ultimate bending moment M_u (Figure 3c) and curvature ductility $\mu=\chi_u/\chi_y$ (Figure 3d), where χ_y and χ_u are the values of bending curvature at yielding and ultimate, respectively. These diagrams provide an effective quantitative measure of the impact of a changing climate also in terms of time lag between the two investigated scenarios, historical vs SSP5-8.5, associated with the attainment of target values of ultimate bending moment and curvature ductility capacity ratios, i.e. $M_u(t)/M_u(t_0)$ and $\mu(t)/\mu(t_0)$.

The probabilistic life-cycle analysis is performed by Monte Carlo simulation (Table 1). The impact of climate change compared to the prediction based on historical climate is confirmed also in probabilistic terms, as shown by the histograms of the probability density functions reported in Figure 4 for corrosion initiation time t_{cr} of bar #1 (Figure 4a) and bar #2 (Figure 4b) for scenario SSP5-8.5, and ultimate bending moment M_u at year 2100 for scenario SSP2-4.5 (Figure 4c) and scenario SSP5-8.5 (Figure 4d). It is worth noting that for several realizations the severity of the corrosion scenario leads over the investigated lifetime to an almost complete corrosion of the steel reinforcement ($\delta_s \rightarrow 1$). The number of realizations associated with this critical condition increases when the effects of climate change are considered (Figures 4c and 4d).

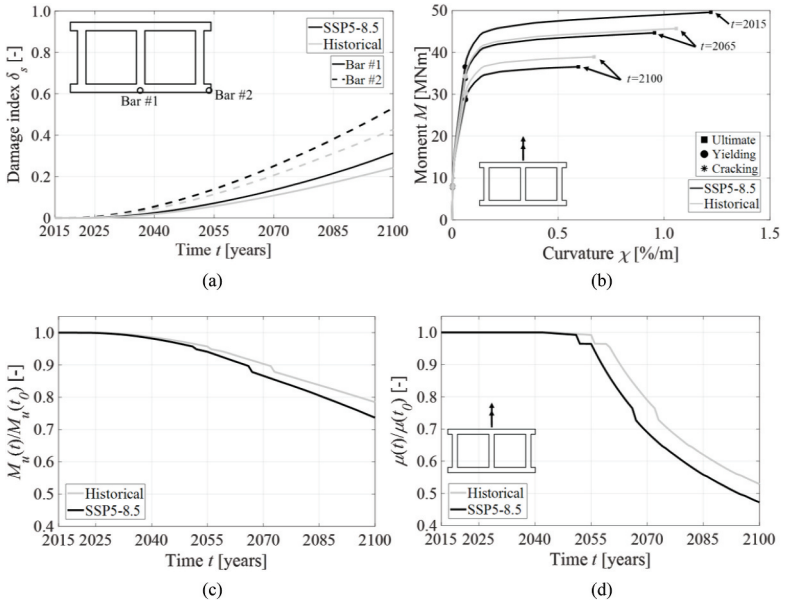


Figure 3. Deterministic life-cycle structural analysis (nominal structure) under historical vs SSP5-8.5 climate scenarios: (a) Evolution of damage index δ_s of bars #1 and #2, and (b) bending moment M vs curvature χ capacity curves at different time instants; Time-variant capacity ratio of (c) ultimate bending moment, $M_u(t)/M_u(t_0)$, and (d) bending curvature ductility, $\mu(t)/\mu(t_0)$.

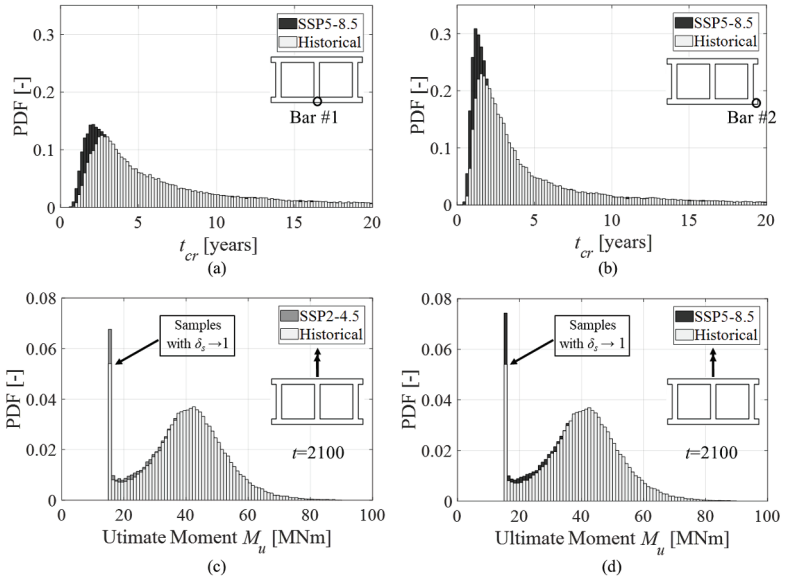


Figure 4. Probabilistic life-cycle analysis considering historical, SSP2-4.5, and SSP5-8.5 climate scenarios: histograms of the probability density functions of corrosion initiation time t_{cr} of (a) bar #1 and (b) bar #2 under historical vs SSP5-8.5, and ultimate bending moment M_u at year 2100 under historical vs (c) SSP2-4.5 and (d) SSP5-8.5.

5 CONCLUSIONS

An approach to chloride diffusion simulation and damage corrosion modeling under climate change using cellular automata has been presented. The proposed cellular automata model, which is an extension of a general formulation proposed in previous works, incorporates the evolution in time of the environmental parameters which affects corrosion initiation and propagation, i.e. temperature and relative humidity. The results obtained by applying the proposed model to life-cycle assessment of a RC bridge pier under different climate scenarios allow to quantify the impact of climate change on chloride diffusion, corrosion damage, and structural performance over time. These results confirm the importance of incorporating the effects of climate change in diffusion and damage models for life-cycle design, assessment, maintenance and management of RC bridges exposed to corrosion. Further research is ongoing along the lines established in Biondini et al. (2004) to extend the proposed approach to account for concrete cracking and other local damaging effects that may interact with the diffusion process and related corrosion damage.

ACKNOWLEDGEMENTS

This study has been carried out within the activities of the ReLUIS-DPC 2022-2024 research program, funded by the Presidenza del Consiglio dei Ministri - Dipartimento della Protezione Civile (DPC).

REFERENCES

Bazant, Z. P., Sener, S. & Kim, J. K., 1987. Effect of cracking on drying permeability and diffusivity of concrete. *ACI Materials Journal*, 84(5), 351–357.

Biondini, F., 2011. *Cellular automata simulation of damage processes in concrete structures*. Chapter 10 in: *Soft Computing Methods for Civil and Structural Engineering*, Y. Tsompanakis & B.H.V. Topping (Eds.), Saxe-Coburg Publications, Stirlingshire, Scotland, 229–264.

Biondini, F., Bontempi, F., Frangopol, D. M. & Malerba, P. G., 2004. Cellular automata approach to durability analysis of concrete structures in aggressive environments. *Journal of Structural Engineering*, 130(11): 1724–1737.

Biondini, F., Bontempi, F., Frangopol, D. M. & Malerba, P. G., 2006. Probabilistic service life assessment and maintenance planning of concrete structures. *Journal of Structural Engineering*, 132(5), 810–825.

Biondini, F. & Frangopol, D. M., 2016. Life-cycle performance of deteriorating structural systems under uncertainty: Review. *Journal of Structural Engineering*, 142(9): F4016001.

Biondini, F. & Vergani, M., 2015. Deteriorating beam finite element for nonlinear analysis of concrete structures under corrosion. *Structure and Infrastructure Engineering*, 11(4): 519–532.

Chirdeep, N. R., Shekhar, S. & Bahurudeen, A., 2023. Climate change impact on seismic vulnerability of aging highway bridges. *ASCE-ASME Journal of Risk and Uncertainty in Engineering Systems, Part A: Civil Engineering*, *9*(4), 04023041.

Döscher, R., Acosta, M., Alessandri, A., et al. 2022. The EC-Earth3 Earth system model for the Coupled Model Intercomparison Project 6. *Geoscientific Model Development*. 15(7), 2973–3020.

Ellingwood, B. R., 2005. Risk-informed condition assessment of civil infrastructure: state of practice and research issues. *Structure and Infrastructure Engineering*, 1(1), 7–18.

fib, 2006. *Model Code for service life design*. Bulletin 34. Fédération internationale du béton/International Federation for Structural Concrete, Lausanne, Switzerland.

Glicksman, M.E. (2000). *Diffusion in solids*. New York, NY: Wiley.

Guo, Y., Trejo, D., & Yim, S., 2015. New model for estimating the time-variant seismic performance of corroding RC bridge columns. *Journal of Structural Engineering*, 141(6): 04014158.

IPCC, 2023. *Summary for Policymakers. Climate Change 2023: Synthesis Report.* Contribution of Working Groups I, II and III to the Sixth Assessment Report of the Intergovernmental Panel on Climate Change.

Kwon, S. J., Na, U. J., Park, S. S. & Jung, S. H., 2009. Service life prediction of concrete wharves with early-aged crack: Probabilistic approach for chloride diffusion. *Structural Safety*, 31(1), 75–83.

Liu, T., & Weyers, R. W., 1998. Modeling the dynamic corrosion process in chloride contamined concrete structures. *Cement and Concrete Research*, 28(3): 365–379.

Martın-Pérez, B., Pantazopoulou, S. J. & Thomas, M. D. A., 2001. Numerical solution of mass transport equations in concrete structures. *Computers & Structures*, 79(13), 1251–1264.

Mazzoni, S., McKenna, F., Fenves, G. L., et al., 2006. *Open system for earthquake engineering simulation user manual*. Pacific Earthquake Engineering Research Center: University of California, Berkeley.

Nasr, A., Honfi, D. & Larsson Ivanov, O., 2022. Probabilistic analysis of climate change impact on chloride-induced deterioration of reinforced concrete considering Nordic climate. *Journal of Infrastructure Preservation and Resilience*, 3(8), 1–16.

Nava, G.V., Capacci, L., Biondini, F. & Casti, L., 2023. Life-cycle structural reliability of RC bridge piers under corrosion in a changing climate. *Eighth International Symposium on Life-Cycle Civil Engineering* (IALCCE 2023), Milan, Italy, July 2-6, 2023. In: Biondini, F., Frangopol, D.M., (Eds.), 2023. *Life-Cycle of Structures and Infrastructure Systems*. CRC Press, London, UK (Open Access): 1625–1633.

O'Neill, B. C., Tebaldi, C., van Vuuren, D. P., et al. 2016. The Scenario Model Intercomparison Project (ScenarioMIP) for CMIP6, *Geoscientific Model Development*, 9, 3461–3482.

Stewart, M. G. & Al-Harthy, A., 2008. Pitting corrosion and structural reliability of corroding RC structures: Experimental data and probabilistic analysis. *Reliability Engineering and System Safety*, 93(3): 373–382.

Stewart, M. G., Wang, X. & Nguyen, M. N., 2011. Climate change impact and risks of concrete infrastructure deterioration. *Engineering Structures*, 33(4): 1326–1337.

Titi, A. & Biondini, F., 2016. On the accuracy of diffusion models for life-cycle assessment of concrete structures. *Structure and Infrastructure Engineering*, 12(9): 1202–1215.

van Vuuren, D. P., Edmonds, J., Kainuma, M. et al., 2011. The representative concentration pathways: An overview. *Climatic Change*, 109: 5–31.

Vu, K. A. T., & Stewart, M. G., 2000. Structural reliability of concrete bridges including improved chloride-induced corrosion models. *Structural Safety*, 22(4): 313–333.


Taylor & Francis
Taylor & Francis Group
http://taylorandfrancis.com

SS28: Probability-based life-cycle design analysis of bridge engineering

Organizers: L. Wang, J. Peng, J. He, W. Lin & X. Zhou


Taylor & Francis
Taylor & Francis Group
http://taylorandfrancis.com

Bridge Maintenance, Safety, Management, Digitalization and Sustainability – Jensen, Frangopol & Schmidt (eds)
© 2024 The Author(s), ISBN 978-1-032-77040-6
Open Access: www.taylorfrancis.com, CC BY-NC-ND 4.0 license

Robustness evaluation of a twin I-girder bridge

P. Acharya*, R. Hao* & W. Lin*
Department of Civil Engineering, School of Engineering, Aalto University, Espoo, Finland

ABSTRACT: With the increasing popularity of twin I-girder bridges, lack of robustness of this bridge type has always been a major concern. Though the AASHTO (2012) specification considers all twin I-girder bridges as non-redundant and fracture critical structures, the robustness of these structures can be improved through design criteria updates and the addition of auxiliary members. This study aims to evaluate the robustness of simply supported twin I-girder bridges. Experimental testing was conducted on two scaled bridge specimens (intact and damaged) under asymmetric loading conditions, and the structural responses were analyzed. Obtained test data were used to validate the developed finite element model and non-linear analyses were performed for further investigation. In this study, the robustness of twin I-girder bridge is studied with different vertical positions of crossbeam, considering different damage locations. The results obtained indicate an enhanced system robustness when the crossbeams are positioned at the lower end of the girder.

1 INTRODUCTION

According to the Euro-code definition, robustness refers to the capacity of a structure to endure events such as fire, explosions, impact, or human error consequences, without suffering damage that is significantly greater than the original cause (EN 1991-1-7). To achieve structural robustness and minimize the risk of disproportionate collapse, various alternative measures should be incorporated into the structural design. These measures encompass the following: 1) ensuring structural integrity and solidarity, 2) implementing a second line of defense, 3) incorporating multiple load paths or redundancy, 4) employing progressive failure or zipper stopper techniques, and 5) harnessing the advantages of strain hardening (Partov et al., 2017).

Twin I-girder bridges is increasing its popularity among the steel-concrete composite bridges among European and other countries due to its easy constructability and other benefits including low weight to span ratio (Lin et al., 2020). These twin I-girder bridges are considered as a non-redundant structure, according to AASHTO (2012) due to lack of load distribution capacity under local failure. Under the member failure condition, these bridges are more susceptible towards collapse of whole structure. Therefore, these structures are considered as a non-robust structure. However, several investigations (Lin et al., 2013; Park et al., 2012) have indicated that various composition of structural members and boundary conditions such as bracing systems, girder continuity and deck system can provide alternate load transfer paths for redistribution, thus escalating structural redundancy and robustness of the system. In their study, Lam et al. (2014) investigated the redundancy level of models for twin I-girder bridges. Their research revealed that multi-span continuous twin I-girder bridges possess adequate redundancy levels and can be classified as redundant structures. Furthermore, the inclusion of lateral X-type bottom bracing was found to increase the redundancy level. The researcher (Lin et al., 2013) also noted that the efficiency of the bridge was improved by incorporating I-shaped cross beams, which offer an alternative load path. In overall, the

*Corresponding authors: pramod.acharya@aalto.fi, rui.hao@aalto.fi, weiwei.lin@aalto.fi

DOI: 10.1201/9781003483755-328

redundancy level and robustness of bridge is a result of combined action of various structural parts of the structural system.

This paper studies the post fracture performance of twin I-girder bridge under damage caused by fatigue and corrosion process. It also extends to the parametric study on twin I-girder bridge due to the effect caused with different crossbeam location across the vertical height of main girder.

2 EXPERIMENTAL PROGRAM

Two twin I girder bridge prototypes, one in an intact form and another with an artificially induced fatigue crack were subjected to the laboratory testing to examine the mechanics and structural performance behavior under asymmetrical loading condition as shown in Figure 1(a). Specimens were designed based on Japanese bridge design specifications. Test specimens were steel concrete composite structures with steel reinforced concrete of 4.4m × 1.2m × 0.12m dimension with double layered steel reinforcement of ϕ10mm and steel I-shaped girders of height 300mm and 150mm flange width spaced 800mm from each other. Each I-shaped girders were connected with reinforced concrete slabs with shear stud connectors designed under compliance with JSCE specification (JSCE, 2009). I-shaped crossbeams connecting two main girders placed every 800mm spacing to provides stability against lateral forces. In addition, vertical stiffeners were placed every 400mm spacing to prevent local buckling. Figure 1 provides design details of the bridge specimens along with details on sensor types and position. One of the bridge specimens was subjected to damage in the form of an artificial crack induced through torch cut of 4.5mm created in lower flange and web of main girder as shown in Figure 1(b). The location of such damage was chosen at mid-span, next to the welded area of vertical stiffener. The intact specimen, hereafter known as Specimen 1, was utilized to investigate the performance of the bridge under normal conditions. On the other hand, Specimen 2, which had a fatigue failure in one of its girders, was employed to gain insights into the behavior of the bridge after experiencing a fracture.

2.1 *Material properties*

The concrete slab was constructed using concrete with mean cylindrical compressive strength of 29.3 MPa. This strength value was determined through a compressive strength test conducted on three cylindrical concrete specimens. For reinforcement, SD345 steel bars with a nominal diameter of D10 were employed. The steel components, including the steel girder, crossbeam, and vertical stiffeners, were made from SM490 structural steel with varying thicknesses. The main girder consisted of a 6 mm thick web plate and a 12 mm thick flange, each possessing distinct yield and ultimate strength values. To connect the steel girder with the concrete slab, stud connectors of SS400 were utilized. Details on material properties of concrete, reinforcement bars, and structural steels of various thickness can be seen in Table 1.

Table 1. Material properties.

Materials	Type	Youngs Modulus (GPa)	Yield Strength (MPa)	Yield Strain (μ)	Ultimate Strength (MPa)
Concrete	C35	29.5	-	-	-
Steel Plate (6mm)	SM490	200	450	2250	577
Steel Plate (8mm)	SM490	200	427	2135	556
Steel Plate (12mm)	SM490	200	389	1945	548
Rebar (D10)	SD345	200	406	2030	544
Stud Connector	SS400	200	235	-	400

2.2 *Instrumentation and loading test procedure*

To measure vertical deflection at strategic points, Linear Variable Differential Transformers (LVDTs) were employed, while various strain gauges were attached to measure strains in girder web and flange, concrete surface, reinforcement bars, and studs. Additionally, LVDTs in stud connectors were utilized to measure two distinct types of strains, namely shear and bending strains.

The bridge specimen being tested was supported by two roller supports. Displacement controlled asymmetrical load was applied just above the main girders (Girder 1) until functionality failure of the bridge specimens. To distribute the concentrated load over the flange width, loading plates measuring 200 mm × 150 mm × 30 mm were employed.

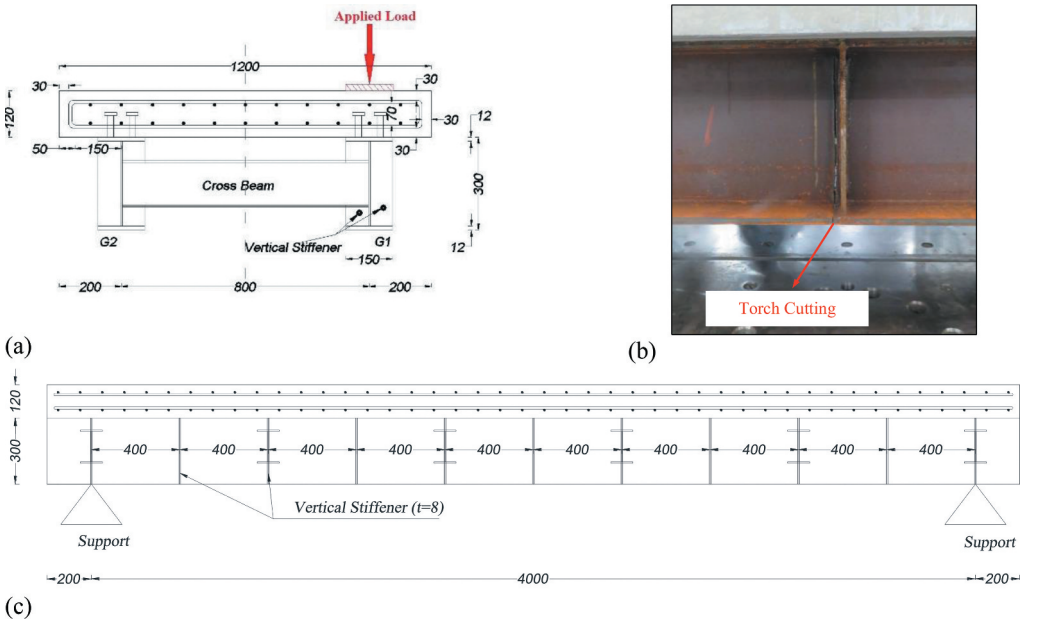


Figure 1. Geometric description of bridge specimen: (a) Transverse section of bridge; (b) Torch cut damage on steel girder; (c) Longitudinal section of bridge.

3 NUMERICAL MODELLING AND VALIDATION

The 3-dimensional finite element model was utilized to conduct numerical modelling and simulation, which was achieved using commercial software ABAQUS. A static non-linear analysis was carried out to simulate the material and geometrical non-linearities. The numerical model of the bridge specimen, featuring various elements and a fatigue crack model, is depicted in Figure 2. For damaged bridge model, fatigue crack is introduced through a geometric cut of 4.5 mm wide created in lower flange and web of main girder.

Three distinct element types were utilized in constructing the numerical model. The concrete model was represented by the solid element C3D8R, while the steel reinforcement and stud connectors were modeled using the beam element B31. The structural steel was represented by the shell element S4R. The reinforcement bars and stud connectors were embedded within the solid concrete element, and a hard contact interaction was established between the concrete surface and the upper flange of the steel girders, with a friction coefficient of 0.5. The simply supported boundary condition was modeled with a pin support at one end and a roller support at the other end. Finally, a displacement-controlled load increment method was enforced for load application at the top of the concrete slab, with a maximum downward displacement of 40mm allowed.

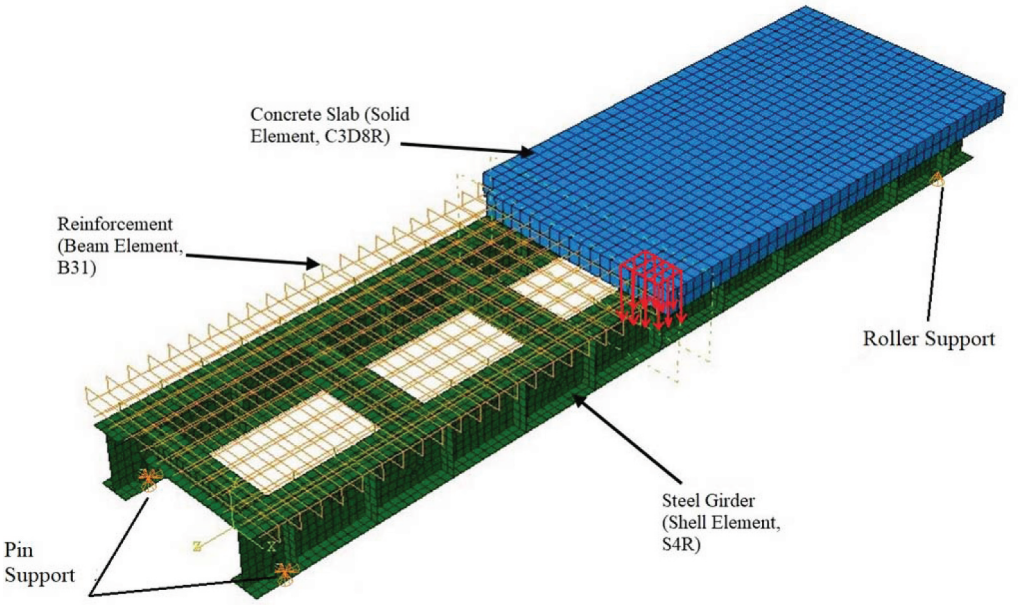


Figure 2. Finite element model with boundary conditions and the corresponding element type for different parts.

3.1 *Material properties modelling*

The concrete properties were modeled in accordance with the JSCE specification for concrete structures, following the stress-strain curve depicted in Figure 3. This allowed for the simulation of both compressive and tensile behavior of the concrete. The model also included the plasticity of the concrete in a damaged state. The compressive behavior of the concrete was determined based on equations (1) and (2), where σ_c, ϵ_c, f_{cd}, f_{ck}, and ϵ_{cu} represent the compressive stress, compressive strain, design compressive strength, characteristic compressive strength, and ultimate compressive strain of the concrete, respectively. On the other hand, equations (3) and (4) define the tensile behavior of the concrete, where σ_t, ϵ_t, f_{tk}, and ϵ_{tk} represent the tensile stress, tensile strain, characteristic tensile strength, and compressive strain corresponding to the characteristic tensile stress of the concrete, respectively.

$$\sigma_c = \begin{cases} k_1 f_{cd} \cdot \frac{\in_c}{0.002} \cdot \left(2 - \frac{\in_c}{0.002}\right); \ \in_c \ \leq 0.002 \\ k_1 f_{cd} \ ; \ \in_c \geq 0.002; \ k_1 = 1 - 0.003\, f_{ck} \end{cases} \tag{1}$$

$$\in_{cu} = \frac{155 - f_{ck}}{30000}; \ 0.0025 \leq \ \in_{cu} \ \leq 0.0035 \tag{2}$$

$$f_{tk} = 0.23\, {f_{ck}}^{2/3} \tag{3}$$

$$\sigma_t = f_{tk} \left(\frac{\in_{tk}}{\in_t}\right)^{0.4} \tag{4}$$

The material properties of reinforcement steel and stud connecters were designed based on the relationship depicted by Figure 4(a) as per JSCE specification. Figure 4(b) represents the stress-strain relationship for structural steel plates adopted from JSCE specification for steel and composite structures. The stress value (σ) for $\epsilon \geq \epsilon_{st}$ is defined by Eq. (5) and (6) for

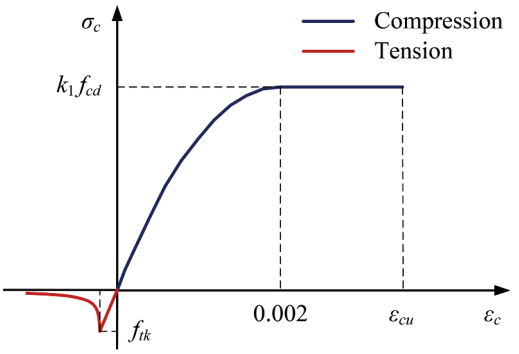


Figure 3. Stress-strain relationship of concrete.

structural steel plates. Table 1 provides a summary of information regarding the elastic modulus, yield stress, yield strain, and ultimate stress capacity of steel reinforcement and structural steel plates with varying types and thicknesses.

$$E = \frac{d\sigma}{d\in} = E_{st}.e^{-\xi\left(\frac{\in}{\in_y}-\frac{\in_{st}}{\in_y}\right)} \tag{5}$$

$$\frac{\sigma}{\sigma_y} = \frac{1}{\xi}\frac{E_{st}}{E}.\left[1 - e^{-\xi\left(\frac{\in}{\in_y}-\frac{\in_{st}}{\in_y}\right)}\right] \tag{6}$$

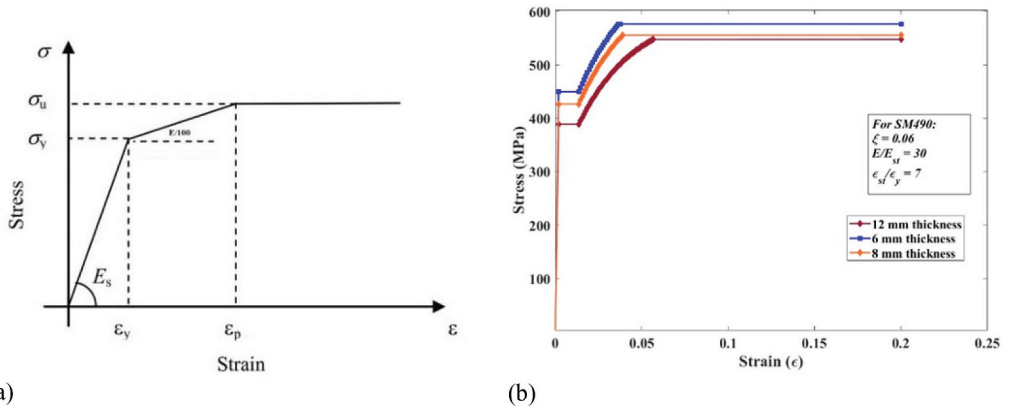


Figure 4. Stress-strain relationship of: (a) steel reinforcement and stud connectors;(b) structural steel plates.

3.2 *Numerical model validation*

The numerical model built in ABAQUS were validated through comparison of analysis results with experimental results. Figure 5 represents the load-displacement curve for both intact and damaged specimen for the load application point at midspan position. Result indicated a close agreement between the results with structural response obtained from numerical analysis with that of experimental results. This provides a validation for the numerical models developed for both intact and damaged specimen.

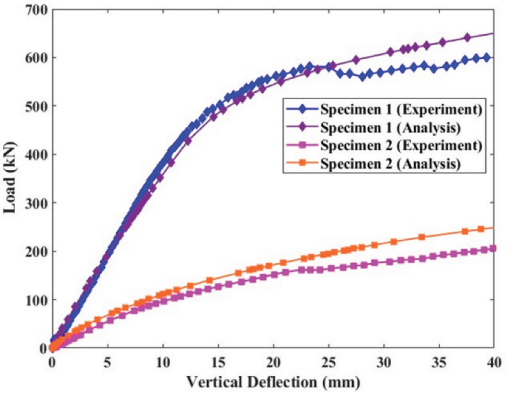


Figure 5. Load-deflection response of bridge specimens with load at mid-span position.

4 PARAMETRIC STUDY

4.1 *Effect of crossbeam position on the robustness of I-girder bridge*

With the shift in position of crossbeam across the vertical depth of main girder changes the transverse geometry of the bridge structure as a system, which in turn changes the performance response of the structure against the applied load. This behavioral change is due to change in mechanics for load transfer. This paper examines the impact of vertical shifts in the crossbeam position along the girder height on the overall performance of a bridge structure. The study analyzes three different positions for the girder - top, middle, and bottom - without making any geometrical changes to the crossbeam. The investigation results are presented in Figure 7 through the load vs. deflection curve and are analyzed for three different damage scenarios where the fatigue crack position and loading position are at the mid-span, quarter-span, and near the end support, as illustrated in Figure 6.

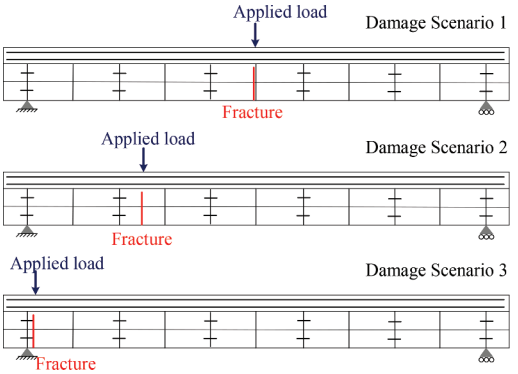
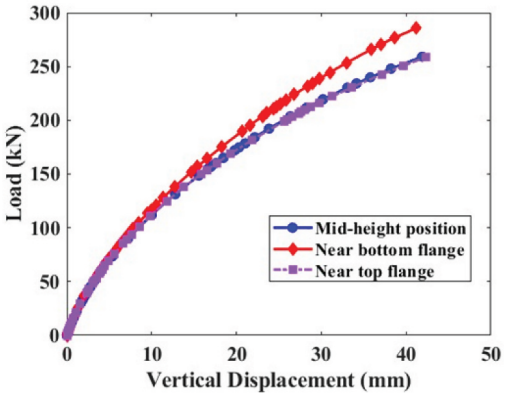
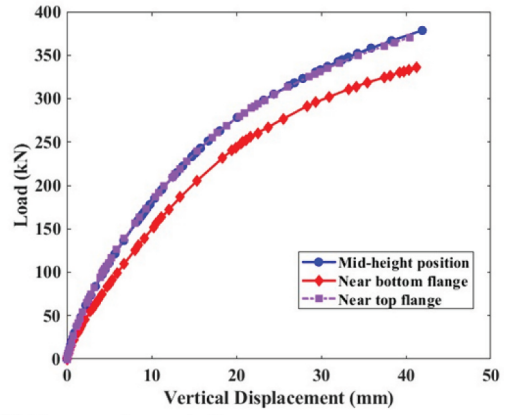


Figure 6. Damage scenarios with different damage location and load application point.

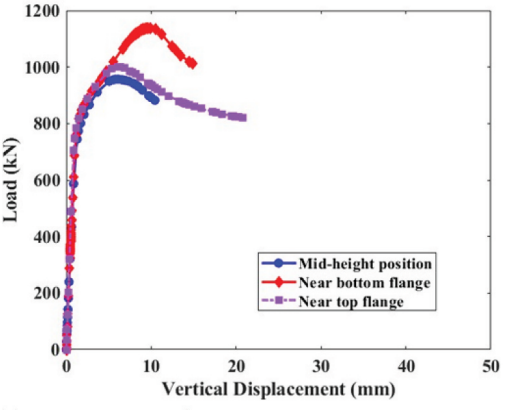
The findings revealed that the positioning of the crossbeam at the top and mid-height of the girder had minimal impact on all three damage scenarios. However, the performance varied when the crossbeam was placed at the bottom position. By incorporating the crossbeam at the bottom position, the structural capacity improved for Damage Scenario 1 and Damage Scenario 3 but decreased for Damage Scenario 2. The proximity of the crossbeam to the lower flange of a twin I-girder bridge can influence the torsional rigidity of the structure



(a) Damage Scenario 1



(b) Damage Scenario 2



(c) Damage Scenario 3

Figure 7. Load-deflection response curve for various damage scenarios with crossbeam location at three different positions along the vertical depth of girder: (a) Damage Scenario 1; (b) Damage Scenario 2; (c) Damage Scenario 3.

(see Figure 7). Under torque application, the twin I-girder bridge's primary beams undergo warping deformation, resulting in deformation in opposite longitudinal directions. By positioning the crossbeam at a lower level on the girder, the bridge's bending and torsional capacity are enhanced. This is achieved by enlarging the closed transverse section, resulting in improved performance for Damage Scenario 1 and Damage Scenario 3. However, the result is opposite for damage scenario 2, where the overall performance of the bridge specimen decreases when crossbeam is located near the lower flange.

5 CONCLUSION

The objective of this study was to analyze the performance of composite I-girder bridges after experiencing fatigue cracks. Both experimental and numerical investigations were carried out on a simply supported composite twin I-girder bridge, considering both intact and damaged systems. The FEM model was built and further verified by experimental results, and then parametric nonlinear analyses were conducted to assess the influence of factors such as crossbeam cross-section, crossbeam position, and damage location on the safety of the bridge models in the post-fracture condition. The findings of this research can be summarized as follows:

Vertical position of the crossbeam along the girder height, has an influence on the overall performance against capacity degradation. The findings revealed that positioning the crossbeam near the bottom flange resulted in better performance for damage scenarios occurring at mid-span and near the support end. However, the performance degraded when damage occurred at the quarter-span position. Similarly, placing the crossbeam near the upper flange had the same effect as positioning it at mid-height.

REFERENCES

AASHTO, 2012. AASHTO LRFD bridge design Specification.

EN 1991-1-7: Eurocode 1: Actions on structures - Part 1-7: General actions - Accidental actions. (2006).

Japan Society of Civil Engineers (JSCE), 2009. Standard Specifications for Steel and Composite Structures.

Lam, H., Lin, W., Yoda, T., 2014. Effects of bracing systems on redundancy of three-span composite twin i-girder bridge. Journal of Structural Engineering 60.

Lin, W., Ph, D., Asce, M., Lam, H., Ph, D., Yoda, T., Ph, D., Asce, M., 2020. Experimental study on steel – concrete composite twin i-girder bridges 25, 1–10.

Lin, W., Yoda, T., Taniguchi, N., Hansaka, M., 2013. Performance of strengthened hybrid structures renovated from old railway steel bridges. Journal of Constructional Steel Research 85, 130–139.

Park, Y., Joe, W., Park, J., Hwang, M., Choi, B.H., 2012. An experimental study on after-fracture redundancy of continuous span two-girder bridges. International Journal of Steel Structures 12, 1–13.

Partov, D., Petkov, M., Matuski, V., Zhelev, D., 2017. 14.04: Temporary steel structures: for strengthening of a large excavation for new metro in sofia. ce/papers 1, 3871–3880.

Bridge Maintenance, Safety, Management, Digitalization and Sustainability – Jensen, Frangopol & Schmidt (eds)
© 2024 The Author(s), ISBN 978-1-032-77040-6
Open Access: www.taylorfrancis.com, CC BY-NC-ND 4.0 license

Fatigue reliability analysis for welding details under traffic flow

Qiaona Zheng, Zichao Pan, Xurui Fang & Rujin Ma
Department of Bridge Engineering, Tongji University, Shanghai, China

Benjin Wang
School of Aerospace Engineering and Applied Mechanics, Tongji University, Shanghai, China

ABSTRACT: Fatigue cracking is the prevalent disease observed in welding details of orthotropic steel decks, especially in deck-rib welded joints. This paper presents a framework for evaluating the fatigue reliability of deck-rib welded joints under the simulated traffic flow based on the S-N curve and linear damage theory. First, we build a combined shell-solid finite element model of the typical area on the panel of a steel arch bridge to obtain the stress influence surface function of the key joint. Then, the traffic flow model is established according to the probability distribution of vehicle parameters. The stress time history curve of the welded joint is further studied. Based on the above analysis, the time-varying fatigue reliability curves of welding details under different traffic flows are investigated. The proposed framework can provide further insight into the management and maintenance of orthotropic steel decks for bridges under construction and existing bridges.

1 INTRODUCTION

The orthotropic steel deck (OSD) has been widely used in modern bridge construction due to its advantages, such as high strength-to-weight ratio, rapid construction, and durability (Deng et al., 2018; Yang et al., 2020). However, the welding detail, especially the deck-rib weld joint, as a critical detail in the OSD structure, is susceptible to fatigue damage under traffic flow loading. Once the accumulation of fatigue damage exceeds the fatigue resistance, the structure will have brittle failure and even lead to the collapse of the bridge (Fisher and Barsom, 2016; Ya et al., 2011). This process involves the random influence of many factors. Therefore, the fatigue reliability assessment of welding details is of paramount importance to ensure the structural integrity and fatigue safety of steel bridges.

In the study of fatigue performance, the initial step involves acquiring the fatigue stress spectrum of critical nodes. This can be accomplished through numerical simulation based on finite element analysis (Sim and Uang, 2012) or through assessment methods based on real bridge inspections (Liu et al., 2010). While the latter method offers greater precision, the former is more universally applicable. Subsequently, fatigue life or reliability is forecasted and assessed using an appropriate fatigue damage model, primarily derived from experimental data. Zhang et al. (2013) investigated the fatigue reliability of steel bridge panels of a large-span cable-stayed bridge under coupled vehicle and wind loads by finite element analysis. Guo et al. (2012) compared vehicle inspection data with evaluation data based on finite element analysis, and demonstrated the consistency of the results of the two analyses. In addition, a large number of scholars (Fang et al., 2020; Ma and Zhang, 2020) have discussed the effects of different conditions such as welding process and foundation scour on the fatigue damage of welded joints in steel bridge decks. Such studies focus more on deterministic analysis.

This paper aims to present a comprehensive analysis of fatigue reliability for welding details under traffic flow loading, with a specific focus on the deck-rib weld joint of the OSD. On the

DOI: 10.1201/9781003483755-329

basis of simulated traffic flow, the fatigue stress history of a steel bridge panel weld detail is analyzed by finite element, and the time-varying fatigue reliability of the structure under the influence of traffic flow parameters is further investigated.

2 FATIGUE DAMAGE AND RELIABILITY MODEL

Fatigue damage in welded structures is a complex phenomenon influenced by various factors such as material properties, stress concentration, and loading conditions. In this context, the fatigue damage function needs to be established first. Moreover, fatigue reliability estimation methods play a crucial role in quantifying the probability of fatigue failure, considering uncertainties in material properties and loading conditions.

2.1 *Fatigue damage function*

There are two commonly used models for the fatigue damage evolution process, one is the fatigue cumulative damage model based on the stress range number (S-N) curve, and the other is the linear elastic fracture mechanics model (LEFM) based on the Pairs crack extension theory. It is generally accepted that the LEFM method is more applicable to structures with initial cracks or defects, whereas the S-N curve method, which uses an abstract fatigue damage model, is widely applicable (Chen et al., 2011).

Definitions of S-N curves are given in different national and regional codes (AASHTO, 1990; European Committee for Standardization, 2005). The OSD with open stiffening ribs, especially the deck-rib details, is characterized by low stress and high number of cycles under vehicle loading. For this type of welding details, the International Institute of Welding (IIW) recommends the use of hot spot stresses in combination with S-N curves to assess fatigue strength (Hobbacher, 2016). The hot spot stresses are obtained by linear derivation of the reference point stresses, as shown in Figure 1. It can be calculated as

$$\sigma_{hs} = 1.67 \cdot \ \sigma_{0.4t} - 0.67 \cdot \ \sigma_{1.0t} \tag{1}$$

where t is the thickness of the base material; $\sigma_{0.4t}$ and $\sigma_{1.0t}$ are the reference point stresses; σ_{hs} is the hot spot stresses. In addition, for variable amplitude loading, the welding detail fatigue S-N curve is expressed as

$$\Delta\sigma_R^3 N_R = K_C = \Delta\sigma_C^3 \times 2 \times 10^6 (\Delta\sigma_R \ \geq \Delta\sigma_D) \tag{2a}$$

$$\Delta\sigma_R^5 N_R = K_D = \Delta\sigma_D^5 \times 1 \times 10^7 (\Delta\sigma_R \ \leq \Delta\sigma_D) \tag{2b}$$

where $\Delta\sigma_R$ is the stress range; N_R is the number of cycles; $\Delta\sigma_C$ is the fatigue detail category, while $\Delta\sigma_D$ is constant amplitude fatigue limit (CAFL); the fatigue strength coefficient is defined as K_C if $\Delta\sigma_R$ is larger than $\Delta\sigma_D$, and K_D if not. In this study, considering the effects of welding improvement process and other factors, combined with the recommendations of IIW, FAT90 is selected as the calculation curve. The parameters are listed in Table 1.

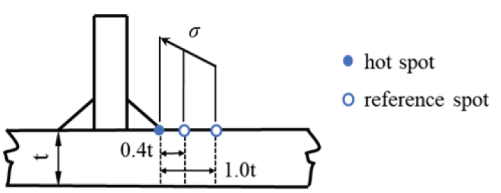


Figure 1. Definition of structural hot spot stress.

Table 1. The parameters of recommended S-N curve.

$\Delta\sigma_C$ (MPa)	$\Delta\sigma_D$ (MPa)	K_C	K_D
90	52.7	1.458×10^{12}	4.046×10^{15}

According to Equation(2a,b) and the Palmgren-Miner rule(Miner, 1945), the fatigue damage under vehicle loading can be obtained as

$$\mathrm{D} = \sum\nolimits_{S_i \geq \Delta\sigma_D} \frac{n_j S_i^3}{K_C} + \sum\nolimits_{S_j \leq \Delta\sigma_D} \frac{n_j S_j^5}{K_D} \tag{3}$$

where n is the number of corresponding stress range S. The stresses under vehicle loading can be converted to equivalent constant amplitude stresses by the equivalence principle, and the equivalent stress range S_{eq} and corresponding number of cycles N is

$$S_{eq} = \left(\frac{\sum_{S_i \geq \Delta\sigma_D} \frac{n_i S_i^3}{K_C} + \sum_{S_j \leq \Delta\sigma_D} \frac{n_j S_j^5}{K_D}}{N/K_D} \right)^{1/5} \tag{4}$$

$$N = \sum\nolimits_{S_i \geq \Delta\sigma_D} n_i + \sum\nolimits_{S_j \leq \Delta\sigma_D} n_j \tag{5}$$

The determination of equivalent stresses lays the foundation for subsequent fatigue performance analysis.

2.2 *Fatigue reliability estimation methods*

Based on the fatigue cumulative damage model, the fatigue limit state equation can be established as (Liu et al., 2016)

$$F(X) = \Delta - D = \Delta - \frac{N S_{eq}^5}{K_D} \tag{6}$$

where Δ is the Fatigue limit of a structure. When $F(X) < 0$, it is considered that fatigue damage has occurred in the structure, then the reliability index can be calculated by the following equation

$$\beta = \varphi^{-1}\left(1 - p_f\right) = \varphi^{-1}\left(1 - p(F(X) < 0)\right) \tag{7}$$

In Equation (7), the uncertainty in Δ and K_D can be quantified by a lognormal distribution. The statistical parameters are shown in Table 2. Then the Monte Carlo method can be used to obtain the time-varying reliability of the target structure under the influence of traffic flow.

Table 2. Statistic information of parameters.

Random Variable	Distribution Type	Mean Value	COV	Source
Δ	Lognormal	1	0.3	(Liu et al., 2016)
K_D	Lognormal	4.046×10^{15}	0.45	(Hobbacher, 2016)

3 FINITE EIEMENT ANALYSIS OF WELDING DETAILS

The numerical simulation in this study consists of two parts. The first part is the analysis of the stress response of welding details under single vehicle loading, which is shown in this section. The second part is the simulation of the traffic flow, which will be shown in the Section 4.

3.1 *Finite element model*

The fatigue problems of the bridge deck under vehicle loads are primarily influenced by the system comprising the bridge deck, transverse beams, and longitudinal ribs. Additionally, due to the short stress influence line of the orthotropic steel bridge deck, the stress calculation results of the local segment model align closely with those of the main beam's overall model. Consequently, this section opts to utilize the local steel bridge deck to establish a full-scale finite element model.

The bridge is a center-bearing steel truss arch bridge featuring orthotropic steel bridge panels consisting of welded open ribs. The numerical model includes four diaphragms and eleven stiffening ribs, with a total length of 9 m and a total width of 4.4 m, as depicted in Figure 2, covering the stress influence range when wheels pass by. The material for the model is Steel Q345, and a UHPC layer is also designed on the bridge deck. The mechanical properties of these two materials are given in Table 3.

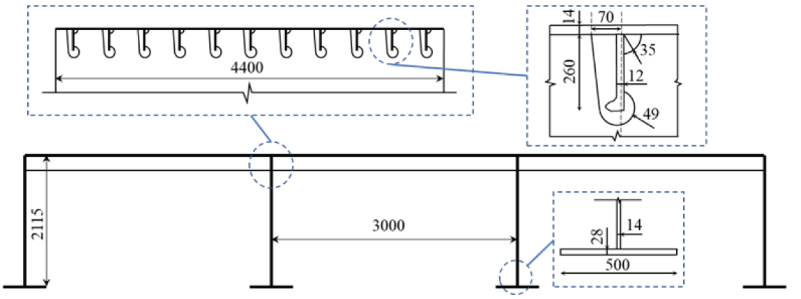


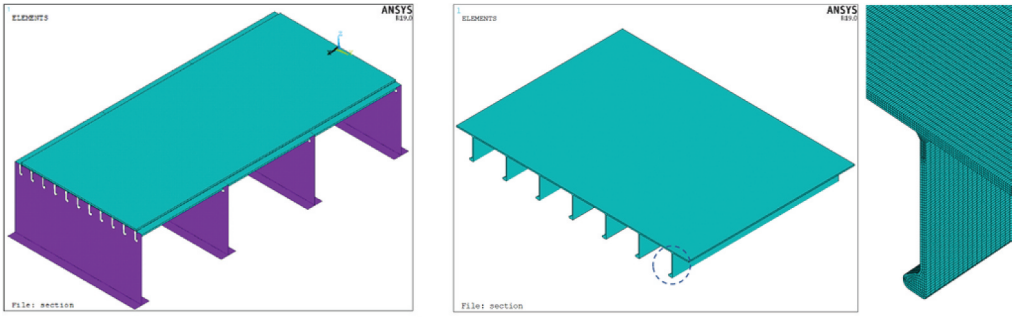
Figure 2. Model component section (unit: millimeters).

Table 3. Mechanical properties of Q345 and UHPC.

Materials	Density(kg/m^3)	Elasticity modulus(N/m2)	Poisson's ratio
Q345	7850	2.1×10^{11}	0.3
UHPC	2700	4.5×10^{10}	0.2

The finite element model is established using SHELL181 cell in ANSYS and the UHPC layer is modeled using SOLID185 cell, and the contact between the two is set to be permanently bound, which is simulated by CONTA174 cell, as shown in Figure 3(a). The lower edge of the modeled transverse bulkhead is fixed and the bridge deck slab displacement is constrained. To study the hot spot stress of the deck-rib welded joint, it is necessary to refine the model of the central position of the rib. A local three-dimensional model is created using SOLID185 elements, with dimensions of 2.0m × 2.8m, and incorporating 7 ribs (Figure 3(b)). The solid model is connected to the shell model using CONTA175 elements to ensure deformation coordination. A fine mesh is required due to the large stress variation near the welding details, and a relatively coarse mesh is used for the rest of the locations to improve computational efficiency.

In the fatigue assessment of bridges, vehicle loads are generally considered in three forms: vehicle load spectra, standard fatigue vehicles, and a heavy vehicle from the standard live load for static strength design(Zhou et al., 2010). Each country's bridge design code provides different models for fatigue vehicle loads. Considering the engineering background of this study, the model adopts the recommended fatigue load calculation model III from the Chinese code for the assessment. Figure 4 illustrates the axle load and contact conditions of this load model. The pavement layer of the bridge has a certain impact on fatigue stress. The thickness of the pavement layer on the bridge is 0.04 m. Assuming that the load spreads at a 45° angle when transmitted downwards, the actual load area acting on the UHPC layer is 0.68m × 0.28m. The coupling effect between adjacent wheels in the fatigue load model is minimal.



(a) (b)

Figure 3. The finite element model: (a) the whole model; and (b) mesh of the solid model.

Therefore, when analyzing local stress, it is sufficient to apply loading using a single wheel to obtain the stress influence function for subsequent fatigue damage analysis.

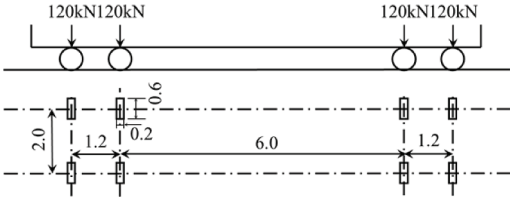
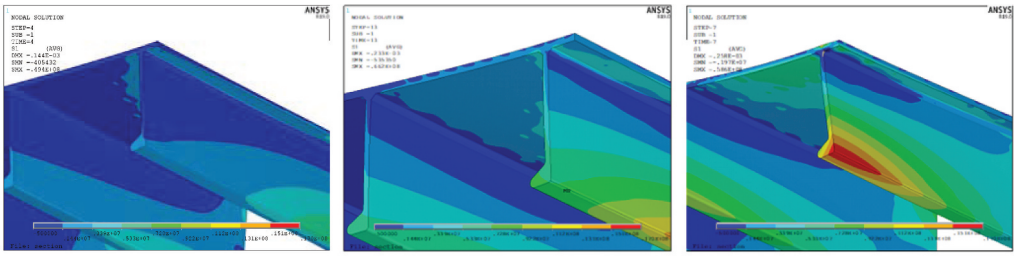


Figure 4. The recommended fatigue load calculation model (unit: meters).

3.2 *Stress response analysis*

The numerical model is loaded and analyzed to obtain the structural response. The results show that the variation of the hot spot stress on both sides of the stiffener section is basically symmetrical in the transverse direction, with differences within 1%. Therefore, the following text only explains the hot spot stress situation on one side of the weld. Figure 5 shows the distribution of the first principal stress near the weld. Stress concentration is prone to occur at the weld position.



(a) (b) (c)

Figure 5. The first principal stress distribution in the simulation (unit: pascals), when the relative position of load center is: (a) 1m; (b) 0.5m; and (c) 0.

Subsequently, the stresses at the reference point under various working conditions are extracted for calculating the hot spot stresses. This allows for the plotting of the stress influence surface under the action of a single wheel, as shown in Figure 6, where the coordinates represent the position of the wheel load center on the bridge deck.

The stress analysis results indicate that as the distance between the wheel load center and the weld decreases, the impact on the weld becomes more significant, leading to a sudden

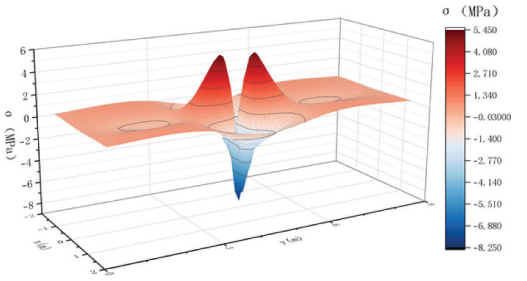


Figure 6. Hot spot stress influence surface.

change in the weld stress. The maximum hot spot stress value is approximately 5.45 MPa, while the minimum value is approximately -8.25 MPa. This finding describes the static response of the structure under the influence of a single wheel. To capture the structural stress history under the standard fatigue vehicle load model (Figure 4), it is essential to account for the dynamic amplification factor, set at 1.3 in this study. The results are depicted in Figure 7, where the horizontal axis denotes the relative position of the center of the first row in the model to the hot spot of the target spot, and the vertical axis represents the hot spot stress.

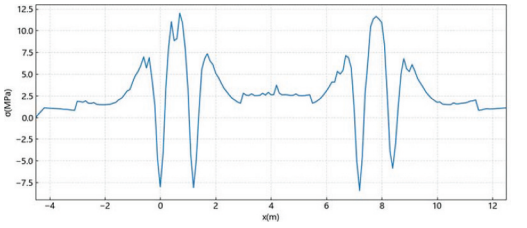


Figure 7. Stress history under the standard fatigue vehicle load model.

4 FATIGUE RELIABILITY EVALUATION

In this section, a comprehensive assessment of the structural reliability is made incorporating the traffic flow model and fatigue damage accumulation.

4.1 *Traffic flow model*

A traffic flow model is essential for capturing the varying load conditions experienced by the bridge structure over its service life. The load model involves various factors such as vehicle type, speed, and spacing. Due to limited operational data, this study references the probability distribution characteristics of vehicle parameters for similar-grade highway bridges in China when establishing the traffic flow load model. After fitting the probability distribution functions, the Monte Carlo method is employed for sampling, and single lane traffic is simulated.

Firstly, contributions of small and medium-sized vehicles to bridge fatigue damage are minimal, with large vehicles being the primary source of damage (Dou et al., 2016; Liu et al., 2017). Therefore, the traffic flow model primarily focuses on standard fatigue vehicles, corresponding to a stress amplification factor of 1.3. Subsequently, based on a highway design speed of 60 km/h, the assumed vehicle operating speed is 15 m/s. Following the recommendations of Eurocode 3, the lateral distribution of the wheels is fitted to a standard normal distribution. The uncertainty of the spacing is stronger and is related to the operational state. Therefore, the daily operation of the bridge is divided into two phases: dense operation (14 hours) and sparse operation (12 hours). In the former, the spacing is based on the safe driving distance at the bridge's design speed, using a Weibull distribution with a shape parameter of 6.5 and a scale parameter of 8; in the latter, the spacing is appropriately increased.

Taking into account the vehicle speed, spacing, and operational state, the equivalent traffic flow can be estimated based on multiple sampling results. Under dense operation, approximately 22 vehicles pass every 10 minutes, while under sparse operation, around 16 vehicles pass every 20 minutes. Therefore, the daily equivalent traffic flow for this single-lane traffic flow model is 2328 vehicles, with an annual equivalent traffic flow of approximately 850,000 vehicles.

4.2 *Results of the fatigue reliability analysis*

Based on the stress influence surface of the weld joint and the traffic flow model, stress time history is computed. Subsequently, the rainflow counting algorithm (Socie, 1992) is employed to analyze the stress time history. Under dense operation, S_{eq} at the hot spot is 20.02 MPa, while under sparse operation, it is 19.63 MPa. Further analysis of the damage situation in conjunction with the S-N curve yields an expected fatigue life of the structure of 699 years.

With the results and statistical information listed in Table 2, the fatigue reliabilities of the deck-rib details can be calculated. Meanwhile, this study quantifies the process of traffic flow growth and stabilization using a simplified three-stage traffic growth model. Three models are defined: Model I does not consider traffic growth; Model II assumes a 1% annual traffic growth rate for the first five years of operation (Stage 1), followed by an accelerated growth rate of 3% for the next 15 years (Stage 2), and then traffic saturation in Stage 3 with no further growth; Model III assumes annual growth rates of 2% and 5% for the first two stages. The resulting time-varying fatigue reliability indices are shown in Figure 8.

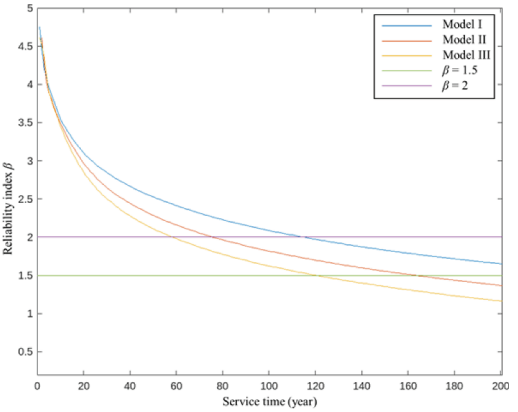


Figure 8. Time-varying fatigue reliability indices.

When the reliability index is 1.5 and 2.0, the structural failure probabilities are 6.68% and 2.28% respectively. The calculation results indicate that the structural reliability index is initially high but decreases over time. Within the 100-year design service life of the bridge, the reliability index remains greater than 1.5. However, contrasting the results of different models, it is evident that traffic growth significantly accelerates the decline in reliability. Under the influence of Model I, the reliability index decreases to 2 after approximately 115 years, while for Model II and Model III, this occurs at 76 years and 59 years respectively. Therefore, it is necessary to monitor changes in bridge traffic flow within the service life, conduct regular inspections, and take timely measures to prevent fatigue failure.

5 CONCLUSIONS

This study investigates the fatigue reliability of deck-rib welded joints in the OSD under simulated traffic flow, utilizing the S-N curve and linear damage theory. The results indicate that

the welding details exhibit quality fatigue performance and maintain satisfactory reliability within the bridge's design service life. However, the study also highlights the significant impact of traffic flow development during the bridge's operational period on the fatigue reliability of the weld, emphasizing the need for monitoring and regular inspections based on actual traffic conditions. Overall, the findings are expected to contribute to the development of robust design guidelines and maintenance strategies for enhancing the fatigue performance and safety of OSDs and steel bridge structures.

ACKNOWLEDGEMENTS

The authors wish to express their gratitude to the National Natural Science Foundation of China under the Grant (No. 52238005).

REFERENCES

AASHTO, 1990. Guide Specifications for Fatigue Evaluation of Existing Steel Bridges, 1990. AASHTO, Washington. DC.

Chen, N.Z., Wang, G., Guedes Soares, C., 2011. Palmgren–Miner's rule and fracture mechanics-based inspection planning. Engineering Fracture Mechanics 78, 3166–3182.

Cui, C., Bu, Y., Bao, Y., Zhang, Q., Ye, Z., 2018. Strain energy-based fatigue life evaluation of deck-to-rib welded joints in OSD considering combined effects of stochastic traffic load and welded residual stress. Journal of Bridge Engineering 23, 04017127.

Deng, Y., Li, A., Feng, D., 2018. Fatigue Reliability Assessment for Orthotropic Steel Decks Based on Long-Term Strain Monitoring. Sensors 18, 181.

Dou, Y., Zhang, J., Hu, C., 2016. The improvement of the design standard of overloaded highway. International Journal of Security and Its Applications 10, 151–162.

European Committee for Standardization, 2005. EN 1993-1-9 Eurocode 3. Design of steel structures—part 1-9: fatigue. European Committee for Standardization (CEN) Brussels, Belgium.

Fang, Z., Ding, Y., Wei, X., Li, A., Geng, F., 2020. Fatigue failure and optimization of double-sided weld in orthotropic steel bridge decks. Engineering Failure Analysis 116, 104750.

Fisher, J.W., Barsom, J.M., 2016. Evaluation of Cracking in the Rib-to-Deck Welds of the Bronx–Whitestone Bridge. Journal of Bridge Engineering 21, 04015065.

Guo, T., Frangopol, D.M., Chen, Y., 2012. Fatigue reliability assessment of steel bridge details integrating weigh-in-motion data and probabilistic finite element analysis. Computers & Structures 112–113, 245–257.

Hobbacher, A., 2016. Recommendations for fatigue design of welded joints and components. Springer.

Liu, M., Frangopol, D.M., Kwon, K., 2010. Fatigue reliability assessment of retrofitted steel bridges integrating monitored data. Structural Safety 32, 77–89.

Liu, Y., Li, D., Zhang, Z., Zhang, H., Jiang, N., 2017. Fatigue Load Model Using the Weigh-in-Motion System for Highway Bridges in China. Journal of Bridge Engineering 22, 04017011.

Liu, Y., Xiao, X., Lu, N., Deng, Y., 2016. Fatigue Reliability Assessment of Orthotropic Bridge Decks under Stochastic Truck Loading. Shock and Vibration 2016, e4712593.

Ma, X., Zhang, W., 2020. Fatigue Life of Weldment Details of Existing Orthotropic Steel Bridge Considering the Scour Effects. Journal of Bridge Engineering 25, 04020078.

Miner, M.A., 1945. Cumulative damage in fatigue.

Sim, H.B., Uang, C.M., 2012. Stress Analyses and Parametric Study on Full-Scale Fatigue Tests of Rib-to-Deck Welded Joints in Steel Orthotropic Decks. Journal of Bridge Engineering 17, 765–773.

Socie, D., 1992. Rainflow cycle counting: A historical perspective. The Rainflow Method in Fatigue 3–10.

Ya, S., Yamada, K., Ishikawa, T., 2011. Fatigue Evaluation of Rib-to-Deck Welded Joints of Orthotropic Steel Bridge Deck. Journal of Bridge Engineering 16, 492–499.

Yang, H., Wang, P., Qian, H., 2020. Fatigue behavior of typical details of orthotropic steel bridges in multiaxial stress states using traction structural stress. International Journal of Fatigue 141, 105862.

Zhang, W., Cai, C.S., Pan, F., 2013. Fatigue Reliability Assessment for Long-Span Bridges under Combined Dynamic Loads from Winds and Vehicles. Journal of Bridge Engineering 18, 735–747.

Zhou, Y., Bao, W., Zhai, H., Liu, Y., 2010. Study of standard fatigue design load for steel highway bridges. China Civil Engineering Journal 43, 79–85.

Bridge Maintenance, Safety, Management, Digitalization and Sustainability – Jensen, Frangopol & Schmidt (eds)
© 2024 The Author(s), ISBN 978-1-032-77040-6
Open Access: www.taylorfrancis.com, CC BY-NC-ND 4.0 license

Static and fatigue tests for hybrid welded-bolted demountable shear connectors

J. He, Z. Wang & L. Wang
School of Civil Engineering, Changsha University of Science and Technology, Hunan, China

G. Vasdravellis
Institute for Infrastructure and Environment, Heriot-Watt University, UK

H. Xin
School of Human Settlements and Civil Engineering, Xi'an Jiaotong University, China

ABSTRACT: A welded-bolted hybrid demountable shear connector was proposed for use in steel-concrete composite buildings and bridges. According to Eurocode 4, four standard push-out static tests and four high-cycle fatigue tests were carried out to assess the structural performance of the hybrid connector, respectively. The experimental results show that the initial stiffness, shear resistance, and slip capacity of the proposed connector are higher than those of traditional welded studs. The hybrid connector can be regarded as a ductile connector with a slip capacity higher than 6 mm. Moreover, the primary fatigue failure mode observed was stud fracture at the base. The presence of grout inside the tube significantly increased the WDSC's fatigue life by 5.4 times. The study also analyzed stiffness degradation and relative slip evolution during fatigue cycles. All the findings from present investigation may provide reference for the application of proposed demountable shear connector in sustainable steel-concrete structures.

1 INSTRUCTIONS

The infrastructure construction sector plays an important role to reduce carbon dioxide (CO_2) emissions, waste, and natural resources consumption, thus to achieve the Net-Zero carbon emissions targets (Arsova et al. 2021). Therfore, recent research efforts have been devoted to develop demountable structural systems which can be easily disassembled and reassembled with minimal damage or waste. Also, demountable structural system taking advantage of reusing the structural components, which can maintain their embodied energy content, eliminate the environmental impact of disposal, and save the energy required to produce a new one (Brambilla et al. 2019).

Steel-concrete composite construction is a popular construction method for bridges, buildings, and other infrastructures, due to the advantages of high strength and stiffness, and accelerated construction (He et al 2014). Demountable shear connectors (DSCs) are beneficial to the deconstruction, retrofitting or replacing of damaged slabs and improve the construction efficiency. Therefore, different kinds of DSCs were developed and investigated: Dallam (1968) firstly investigated high strength friction-grip bolts as shear connectors in the 60s by test. Liu et al. (2015) found that high strength friction-grip bolts embedded in geopolymer precast concrete slabs showed high strength and slip capacity. Dai et al. (2015) tested and indicated that the bolted Threaded Nelson shear studs have comparable strength, higher slip capacity, but lower initial stiffness, comparing with welded studs. Feidaki et al. (2019) proposed ductile demountable steel hollow section connectors with high initial stiffness and slip capacity, as well adjustable strength. In order to improve low stiffness at the initial loading stage for demountable bolt connectors,

DOI: 10.1201/9781003483755-330

making full use of good performance of headed studs, and considering the needs of structural disassembly, the authors proposed a welded demountable shear connector (WDSC), consists of a grout-filled steel tube and a partially threaded stud, connecting steel beams to concrete slabs in composite structures. The details including the configuration, construction and deconstruction of WDSC can be referred to Suwaed et al. (2022), as shown in Figure 1.

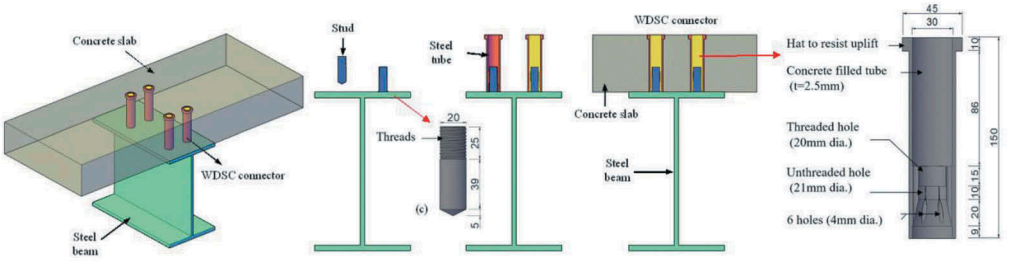


Figure 1. Steel-concrete composite girder with WDSCs.

The static and fatigue behavior of shear connectors is critical in the design of steel-concrete composite structures, particularly in bridges subjected to traffic loads. In present study, a series of standard push-out tests, on the basis of Eurocode 4, were performed to evaluate the static and fatigue performance of the WDSC under monotonic and fatigue loading. The load-slip curves, failure modes, strength and stiffness of WDSC were obtained during static and fatigue loading. Moreover, S-N diagrams were determined through fatigue loading tests, to facilitate their practical application.

2 EXPERIMENTAL INVESTIGATION

2.1 *Test specimens*

Eight standard push-out test specimens were designed and fabricated according to Eurocode 4 (2005). Each specimen is composed of an HEB260 steel section (256 mm in width, 260 mm in height, 10 mm in web thickness and 18 mm in flange thickness), two concrete slabs (650 × 600 ×150 mm), and four WDSCs at each slab, as shown in Figure 2. Two layers of deformed rebars with diameter of 10 mm were placed in each slab to prevent concrete slab cracking.

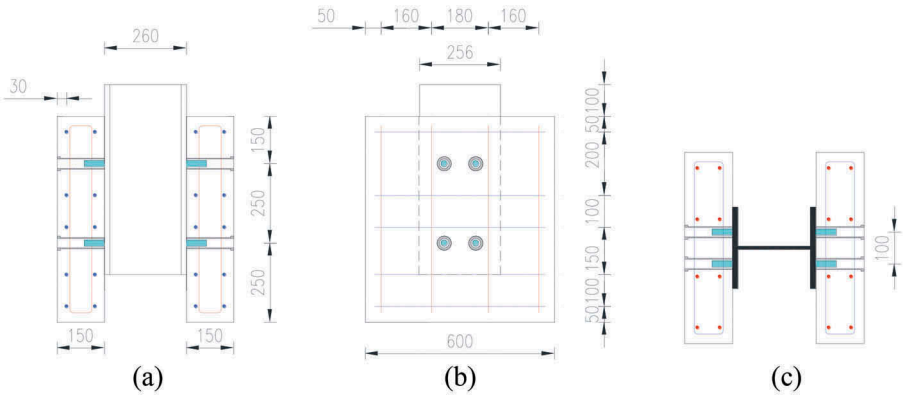


Figure 2. Test specimens (unit: mm): (a) elevation view; (b) side view; (c) plan view.

Eight specimens were prepared and tested, four of them (Group 1) are subjected to static loading, the others (Group 2) are subjected to fatigue loading. Each group has three specimens arranged WDSC filled with flowable grout in steel tube and one without filled grout. In Group 1, the effects of the compressive strength of concrete slab (40 to 54 MPa), loading method (Monotonic-M and Cyclic-C loading) were considered, while in Group 2, constant amplitude fatigue loading is applied for each specimen, but different loading range (Lower limit- Upper limit) was considered, as shown in Table 1.

Then, another four specimens were prepared and subjected to fatigue loading, in which three specimens arranged WDSC filled with flowable grout in steel tube and one without filled grout. Constant amplitude fatigue loading was applied for each specimen, but different loading range (Lower limit- Upper limit) was considered, as shown in Table 1. The upper limit of the loading range were chosen as 700, 600, 500 kN, which account 7/16, 3/8, 5/16 of theoretical ultimate load, considering that the WDSC can be in the elastic and elastic-plastic stages, respective. The stress ratio was chosen as 0.1 for all the specimens.

Table 1. Push-out test specimens.

Specimen group	Specimen name	Grout strength (N/mm^2)	Concrete slab strength (N/mm^2)	Loading procedure		
				Type	Loading method	Loading range
Group 1	S1	47.5	40.7	Static	M	0-F_F
	S2	47.5	48.0		C+M	(5%-40%) $F_{u,e}$ + 0- F_F
	S3	No grout	49.2		C+M	
	S4	47.5	53.7		C+M	
Group 2	F1	48	60.1	Fatigue	C	60-600kN
	F2	No grout	60.1		C	60-600kN
	F3	48	60.1		C	50-500kN
	F4	48	60.1		C	70-700kN

2.2 *Material properties*

Concrete tests were conducted on the in-situ concrete and grout mix of each specimen. The concrete cubes (100×100×100 mm) were casted on the same day as the corresponding specimen using the same concrete mix to perform compressive tests. Table 1 summarizes the average compressive concrete and grout strength of three cubes at test day.

The material properties of the stud and tube were obtained from standard tensile coupon tests (ASTM. 2011). The properties including the modulus of elasticity, the yield stress or 0.2% proof stress, the ultimate stress and the tensile strain corresponding to the ultimate stress for the stud are 193GPa, 454MPa, 658MPa and 0.049, for the tube are 205GPa, 333MPa, 645MPa and 0.185, respectively.

2.3 *Test setup, loading procedure and measurements*

A servo hydraulic testing machine, with load and displacement capacity of 2000 kN and 1200 mm respectively, was used to push the steel section against concrete slab, as shown in Figure 3.

The loading procedure includes two types: static and fatigue loading. As for the static loading, one specimen is subjected to monotonic loading, the other three is subjected to the combined cyclic and monotonic loading in accordance with Eurocode 4, which divided into two steps: Step 1, load was gradually increased up to 40% of the estimated ultimate shear force $F_{u,e}$ and then reduced to 5% of $F_{u,e}$, and this loading cycle was repeated for 25 times; Step 2, monotonic static load was applied using displacement control method with a speed of

0.005 mm/s, and the loading was stopped until the failure of test specimen or the loading capacity of test specimens dropped to 80% of the peak load. As for the fatigue loading, constant amplitude cyclic loading is applied, but different loading range (Lower limit- Upper limit) was considered for each specimen, as shown in Table 1. The fatigue loading was conducted by load control using a continuous sinusoidal waveform with a loading frequency of 0.5 Hz.

Four linear variable differential transformers (LVDTs) were arranged to monitor relative slip between the steel section and the concrete slab, while two LVDTs horizontally placed near the bottom layer of WDSC to measure lateral separation between the slab and the steel section.

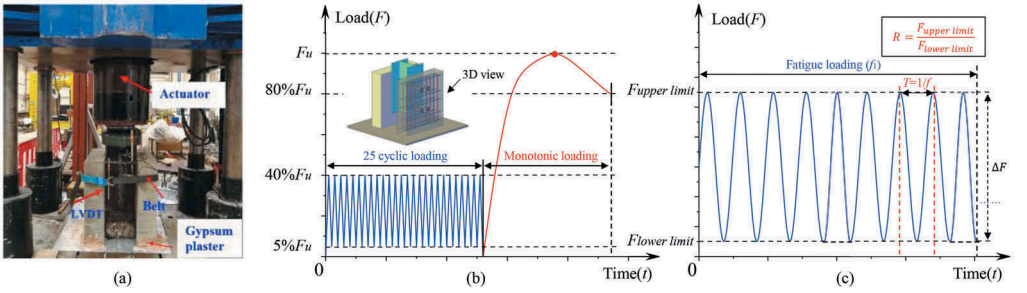


Figure 3. a) Test setup; b) static test loading protocol; (c) fatigue test loading protocol.

3 STATIC TEST RESULTS AND DISCUSSIONS

3.1 *Failure mode*

The typical failure mode of static test specimens was stud shank shear failure, where above the welded collar. Local concrete crushing in front of the tubes was also observed under ultimate load, the damage degree depends on the slab's concrete strength, as shown in Figures 4.



Figure. 4. Failure mode of specimens.

3.2 *Load versus displacement response*

Figure 5a shows the load versus slip responses of all specimens from static loading tests. The load-slip curves can be divided into three phases. The first phase is characterized by linear elastic deformations in the concrete slab and the shear connector, which starts from zero slip to 0.3 - 0.5 mm of slip. In the second phase, the load increases nonlinearly with the slip until the ultimate

load, since the tube and stud bending and bearing against the grout and concrete. In the third phase, the slip develops rapidly, and the load capacity reduces suddenly due to shearing failure of the stud. From Figure 5a, the in-filled grout (47.5MPa) for S2 improved the ultimate strength by 12% and the shear stiffness by 3.4 times in comparison to S3. When the concrete strength of the slab increased from 40.7 MPa to 53.7 MPa for S1 and S4, the shear strength and stiffness increased by 8% and 5%, respectively. Thus, increasing concrete strength of the slab slightly improve the shear strength and stiffness when the specimens failed due to stud's shear off.

Figure 5b shows the load versus separation responses of static test specimens. The separation at ultimate load is 0.57, 0.49, 0.51 and 0.87 mm for S1-4, respectively, which only accounts for 6~13% of the corresponding slip. Thus, the separation between concrete slab and steel flange satisfies the requirement recommended by Eurocode 4 that the slab uplift (i.e., slab separation) should be no more than 50% of the corresponding slip displacement at a shear load equal to 80% of the shear resistance. This proves the effectiveness of the hat at the top of the tube to prevent separation of the slab from the steel section.

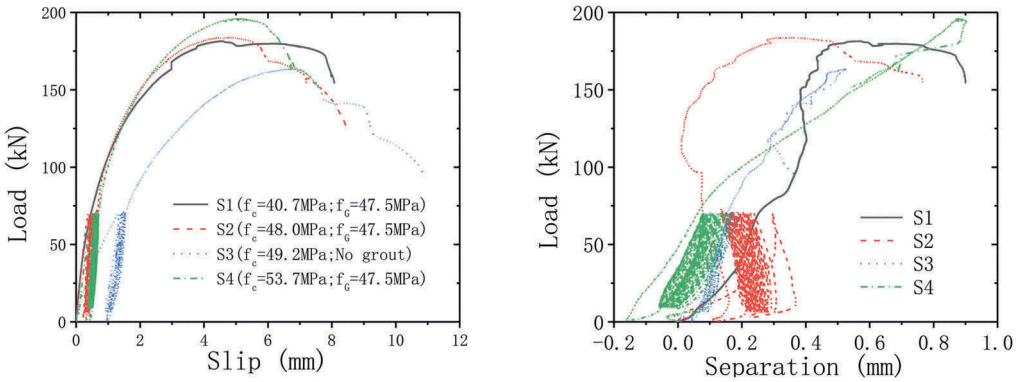


Figure 5. (a) Load versus slip responses for specimens; (b) Load versus separation responses for specimens.

4 FATIGUE TEST RESULTS AND DISCUSSIONS

4.1 *Fatigue failure mode*

The failure process of four fatigue push out specimens was basically the same. The relative slip and separation between steel section and concrete slab gradually increased with the increasing of fatigue cycles. When the fracture of the welded studs occurred at one slab, whose slip and separation is larger than the other one, the concrete slab was separated from the steel section, as shown in Figure 6a.

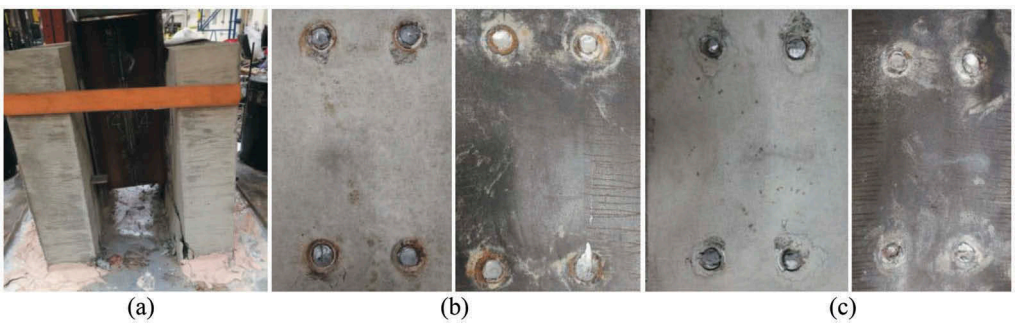


Figure 6. Failure mode of (a) front view; (b) F1 with grout (c) F2 without grout.

Figure 6c-6f describes the fatigue failure characteristic of the WDSC, including the fracture of the welded stud and cracking or crush of the grout and concrete. Smaller cavities were observed vertically below the WDSC subjected to fatigue loading (the area of cavity about quarter of stud section) than that subjected to static loading (the area of cavity about half of stud section) as presented in Xu et al. (2018). The welded stud was greatly deformed for WDSC (F2) without grout filled in the tube. The fracture surface of the failed stud was substantially flush with the surface of the steel plate, dominated by pure shear failure. Ratchet marks caused by multiple crack initiation were found in fatigue failures. The cracks initiated at the weld collar and gradually propagated under continued cyclic loading. Crack progression marks (Beach marks, semi-circular shaped marks) were also observed as shown in Figure 7c. Final fracture zone (Figure 7b) depends on the load magnitude, the severe loading condition result in a large fracture zone.

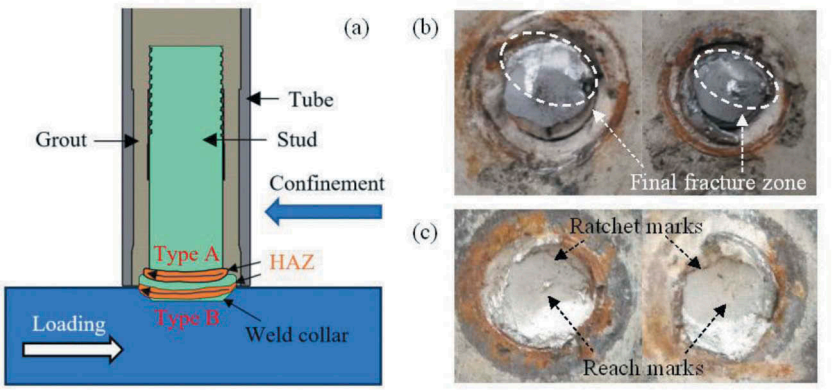


Figure 7. (a) Typical failure mechanism and fatigue fracture zone (b) concrete side; (c) steel side.

4.2 *Fatigue life and S-N curves*

Table 2 lists the loading cycles until failure corresponding to different stress ranges. The fatigue lives of specimens F1 to F4 were 10909, 2016, 41092 and 5326 cycles, respectively. The fatigue life increases significantly as the reducing of stress level. Under the same fatigue stress range, the fatigue life of the specimen F1 is 5.4 times that of the specimen F2. It can be concluded that the fatigue life of the WDSC with grout filled in the tube is much more than that of the WDSC without grout, although their shear strength only changes about 12% in static push out test. The grout improved the shear stiffness of the WDSC, which reduce the relative slip, thus decrease the cumulative damage, resulting in extend fatigue life.

Table 2. Loading cycles until failure corresponding to different stress ranges.

Specimen	Min. Load F_{min} (kN)	Max Load F_{max} (kN)	Min. stress τ_{min} (MPa)	Max. stress τ_{max} (MPa)	Stress range $\Delta\tau$ (MPa)	R	Cycles until failure ($N_{f,test}$)
F1	7.5	75	24	240	216	0.1	10909
F2	7.5	75	24	240	216	0.1	2016
F3	6.25	62.5	20	200	180	0.1	41092
F4	8.75	87.5	28	280	252	0.1	5326

The S-N curve generally depicts the relationship between the fatigue life and stress range. There are three distinct models: "EC model", "BS model" and "Peak Load model" (Johnson 2000). Although the "EC model" does not consider the static shear strength of the stud, it is used in Eurocode 4 (2005) and Specifications for design and construction of highway steel-concrete composite bridge (Ministry of Transport of the People's Republic of China. 2015), as following.

$$\log N + m\log\Delta\tau = C \tag{1}$$

where N is the number of fatigue cycles, m is the slope of the S-N curve, $\Delta\tau$ is the stress range, and C is a constant.

The test data of the WDSC subjected to fatigue loading is plotted in a log–log coordinate system as show in Figure 8. Linear regression analysis of log $\Delta\tau$ on logN was conducted, and the mean regression curve with a 50% survival probability (Hobbacher. 2016) for the WDSC with grout is expressed as Eq. (2):

$$\log N + 7.631\log\Delta\tau = 21.922 \tag{2}$$

A survival probability no less than 95% is recommended for fatigue design. So, the regression curve with a 95% survival probability was also performed, the S-N curves with a 95% survival probability for fatigue design for WDSC with grout is expressed as Eq. (3):

$$\log N + 7.631\log\Delta\tau = 21.618 \tag{3}$$

Eqs. (2, 3) are also plotted in Figure 8. When $N = 2 \times 10^6$, Eq(2) gives the mean shear stress range $\Delta\tau cm = 112$ MPa for WDSC with grout, the characteristic shear stress range $\Delta\tau ck = 100$ MPa for WDSC with grout, respectively.

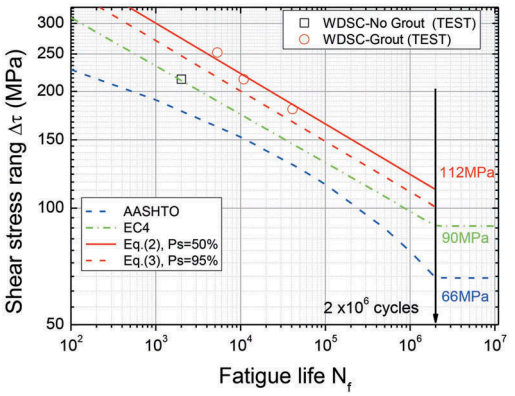


Figure 8. S-N curves for WDSCs.

The test results of fatigue lives for the WDSC were also compared with that for shear studs recommended by specifications—AASHTO (2014) and Eurocode4 (2005). The related S-N curve and the test results with the regression line are shown in Figure 8. It can be seen that both Eurocode 4 (2005) and AASHTO (2014) evaluations have large safety redundancies, especially AASHTO (2014). The slop of fitted S-N curve for WDSC with grout is 7.678, which is smaller than 8 recommend by Eurocode 4. The stress range at 2 million cycles ($\Delta\tau$) for the WDSC was also compared to the specifications. The fatigue strength was taken as 112 MPa for WDSC with grout, estimated from the S-N curves with a 50% survival probability, is larger than fatigue strength for stud connectors which was taken as 90 MPa, recommended by Eurocode 4, also higher than 66 MPa recommended by AASHTO.

5 CONCLUSIONS

- All the specimens including WDSC with or without in-filled grout show ductile shear failure at the base of stud shank and surrounded concrete crush, all specimens achieved a slip capacity higher than that required by Eurocode 4, i.e., higher than 6 mm.
- Slightly smaller shear strength but greater slip capacity is achieved when the tube is not grout-filled. In addition, there is no tolerance or initial slip issue, and the initial stiffness is comparable to that of traditional welded studs.
- Under high-cycle fatigue loading, the WDSC exhibited a consistent shear failure mode at the base of the short stud, no cracking but only minor concrete crushing in the concrete slab was observed. The degree of concrete crushing under fatigue loading was lower than that under static loading.
- The grout significantly improved fatigue life of WDSC, a 5.4-fold increase compared to the WDSC without grout, due to the enhanced stiffness caused by the infill grout.

ACKNOWLEDGMENTS

The authors gratefully acknowledge the financial support provided by the National Natural Science Foundation of China (51978081, 52378127, 52211530037); the Natural Science Foundation of Hunan Province, China (2022JJ10049).

REFERENCES

AASHTO. AASHTO LRFD bridge design specifications, Washington, DC. 2014.

Arsova S, Corpakis D, Genovese A, and Ketikidis, P. H. The EU green deal: Spreading or concentrating prosperity? Resources Conservation and Recycling, 2021, 171(1):105637.

ASTM. Standard test methods for tension testing of metallic materials. ASTM E8/E8M. West Conshohocken, PA: ASTM, 2011.

Brambilla, G., M. Lavagna, G. Vasdravellis, and C. A. Castiglioni. 2019. Environmental benefits arising from demountable steel-concrete composite floor systems in buildings. Res. Conserv. Recycl. 2019, 141: 133–142.

Dai, X., Lam, D. and Saveri, E. Effect of Concrete Strength and Stud Collar Size to Shear Capacity of Demountable Shear Connectors, J. Struct. Eng. 2015, 141(11): 04015025.

Dallam, L. N. Pushout tests with high strength bolt shear connectors. Rep. 68-7, Dept. of Civil Engineering, Univ. of MissouriColumbia, Columbia, MO. 1968.

EN 1994-2, Eurocode 4: Design of Composite Steel and Concrete Structures - Part 2: General Rules and Rules for Bridges, European Committee for Standardization, Brussels. 2005.

Feidaki, E., Vasdravellis, G., He, J., and Wang, S. Steel-Yielding Demountable Shear Connector for Composite Floors with Precast Hollow-Core Slab Units. J. Struct. Eng., 2019, 145(8): 04019076.

He, J., Liu, Y., Pei, B. Experimental study of the steel-concrete connection in hybrid cable-stayed bridges. J Perform Constr Facil, 2014, 28(3), 559–70.

Hobbacher, A. Recommendations for the fatigue design of welded joints and components, Springer, 2016.

Johnson, R.P. Resistance of stud shear connectors to fatigue, J. Constr. Steel Res. 2000, 56 (2): 101–116.

Liu, X., Bradford, M., Lee, M. Behavior of high-strength friction-grip bolted shear connectors in sustainable composite beams. J. Struct. Eng. ASCE, 2015, 141: 04014149.

Ministry of Transport of the People's Republic of China, Specifications for design and construction of highway steel-concrete composite bridge JTG/T D64-01-2015. Beijing, China Communications Press, 2015.

Suwaed, A. S. H., He, J., Vasdravellis, G. Experimental and Numerical Evaluation of a Welded Demountable Shear Connector through Horizontal Pushout Tests. J. Struct. Eng., 2022, 148(2): 04021274.

Xu, Chen., Sugiura, Kunitomo., and Su, Qingtian. Fatigue Behavior of the Group Stud Shear Connectors in Steel-Concrete Composite Bridges. J. Bridge Eng., 2018, 23(8): 04018055.

Bridge Maintenance, Safety, Management, Digitalization and Sustainability – Jensen, Frangopol & Schmidt (eds)
© 2024 The Author(s), ISBN 978-1-032-77040-6
Open Access: www.taylorfrancis.com, CC BY-NC-ND 4.0 license

Optimization of maintenance program for bridge cable in service lifetime

Shijie Liao*, Jianxin Peng, Lei Wang & Jianren Zhang
School of Civil Engineering, Changsha University of Science and Technology, Changsha, Hunan, China

ABSTRACT: The complex service environment and increasing traffic volume make the maintenance of service bridges more and more important, and how to improve the service life of bridge members and reduce bridge operation and maintenance costs by optimizing maintenance strategies is a hot issue today. In this paper, a state transfer matrix is constructed based on NBI bridge inspection data, and an optimization model for state maintenance of bridge cables is proposed by using semi-Markov process theory. Taking a large-span cable-stayed bridge as a case study, where the objective is to maintain the normal service level of the ties for 200 years, the most economical maintenance programs for the cables is proposed based on the whole-life-cycle maintenance cost. This case study can provide an effective reference for bridge maintenance departments.

Keywords: Semi-Markov process, Bridge Cable, Maintenance Strategy

1 INTRODUCTION

The frequency and load of bridges are growing daily due to the ongoing expansion in urban traffic. Over 7.5% of American bridges are currently deficient, and the government is under a lot of pressure due to large maintenance costs. The United States has an infrastructure financing gap of up to 2.59 trillion US dollars, according to figures [1]. The frequent repair or replacement of bridges increases the consumption of energy and materials and also causes damage to the environment. The cable, which is the fundamental part of a cable-stayed bridge, assists the construction of the bridge in carrying weight, distributing the load on the bridge tower, transferring force, etc. Its working performance is directly related to the normal use state of the cable-stayed bridge. Under the requirements of ensuring the safe service state of the cable, the frequency and cost of maintenance and repair are minimized, which is of great significance for the operation and maintenance safety of the bridge structure and social and economic stability.

The cable service process is often subject to wind loads, vehicle loads, and external corrosive environmental erosion, making it prone to corrosion and fatigue damage. Some studies have shown that the probability of the occurrence of these two types of damage accounted for the impact of the cable operating life factors, respectively, at 52% and 35% [2]. Numerous scholars have carried out research on the corrosion and fatigue damage of cable slanting. Nakamura et al. [3] conducted fatigue tests on corroded galvanized steel wires with different corrosion levels, and the results show that the increase in corrosion rate leads to a reduction in the fatigue strength of steel wires. According to Wu et al. [4], on the bridge of the old cable performance indicators for experimental research, test results show that the yield strength, tensile strength, and elongation of the steel wire are not significantly weakened, but the number of fatigue tests is only 308,000 times, far below the standard of 2 million times. Lan et al. [5] established a multi-parameter Weibull model of cable fatigue life, derived a maximum

*Corresponding author: csliaoshijie@163.com

DOI: 10.1201/9781003483755-331

likelihood algorithm for model parameter estimation, and proposed an EM algorithm for model parameter estimation considering truncated data according to conditional probability.

The above studies discussed the correlation between corrosion and fatigue damage of bridge cable ropes and clarified the deterioration mechanism of cable ropes' performance. Some scholars further carried out the research on cable rope repair and replacement strategies in the life cycle, considering structural deterioration and cycle cost. M. ASCE [6] and others studied the cable-stayed cable repair and replacement strategy of a cable-stayed bridge in service and arrived at the most economical solution based on the whole life cycle cost assessment. Wang Libin et al. [7] proposed the cable life function and the series-parallel model of the cable system and combined the life function with the whole life cycle cost to put forward the cable optimization maintenance strategy.

The existing studies focus on the replacement strategy of bridge cable, while there are few studies on the comprehensive consideration of maintenance strategies, such as maintenance cycles, maintenance methods, This paper constructs the state transition matrix and establishes the state degradation model of the stay cable based on the semi-Markov process. At the same time, taking a cable-stayed bridge as an example, based on the whole life design concept, the maintenance strategy of the combination of cable-stayed maintenance and replacement is proposed, which can provide a useful reference for the bridge maintenance department.

2 SEMI-MARKOV PROCESS

Given two events, A and B, and the probability of the occurrence of event A is greater than 0, then:

$$P(B|A) = \frac{P(AB)}{P(A)} \tag{1}$$

In the semi-Markov process, the residence time of each state is T_i, assuming that the random variable T_i follows a certain probability distribution. Let $f_i(t)$, $F_i(t)$ and $S_i(t)$ be the probability density function, probability distribution function, and survival probability distribution function of the residence time of state i respectively. If the structure is in state 1 at time t, the conditional probability of it moving to state 2 at the next time is calculated as follows:

$$P[X(t+dt) = 2|X(t) = 1] = \frac{f_1(t)dt}{S_1(t)} \tag{2}$$

The time for state i to transfer to state j is $T_{i\text{-}j}$, so that $f_{i\text{-}j}$ (t), $F_{i\text{-}j}$ (t), and $S_{i\text{-}j}$ (t) are the probability density function, probability distribution function, and survival probability distribution function of $T_{i\text{-}j}$, respectively. If the structure is in state i at time t, the conditional probability of it moving to state i+1 at the next moment is calculated as follows:

$$P[X(t+dt) = i+1|X(t) = i] = \frac{f_{1-i}(t)dt}{S_{1-i}(t) - S_{1-(i-1)}(t)} \tag{3}$$

3 STATE DEGRADATION MODELLING OF SLOPING CABLES

The service status of the cable is divided into four categories based on NBI's test results: status 1 means excellent; status 2 means good; status 3 means medium; status 4 means qualified. The service level below status 4 means unqualified, the function of the cable has failed.

The life of the corroded cable generally obeys the Weibull distribution. For the general case of the Weibull distribution, you need to solve the β_i and λ_i two parameters. You can choose any two times of NBI data. By solving the algebraic equations to obtain the target parameters, the calculation process is as follows in Equations 4 and 5. The parameters of the first four states are calculated as shown in Table 1.

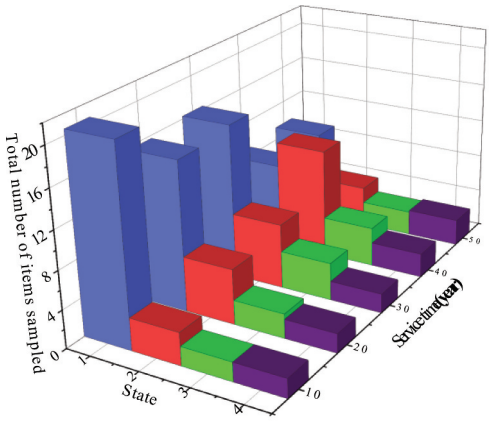


Figure 1. Cable state distribution.

$$\begin{cases} S_i(u) = \exp\left[-(\lambda_i u)^{\beta_i}\right] \\ S_i(v) = \exp\left[-(\lambda_i v)^{\beta_i}\right] \end{cases} \Rightarrow \begin{cases} \ln[S_i(u)] = -(\lambda_i u)^{\beta_i} \\ \ln[S_i(v)] = -(\lambda_i v)^{\beta_i} \end{cases} \Rightarrow \ln\left(\frac{\ln[Si(u)]}{\ln[Si(v)]}\right) = \beta_i \ln\left(\frac{u}{v}\right) \tag{4}$$

$$\beta_i = \frac{\ln(\ln[S_i(u)]) - \ln(\ln[S_i(v)])}{\ln(u) - \ln(v)} \lambda_i = \frac{1}{u}(-\ln[S_i(u)])^{1/\beta_i} \tag{5}$$

Table 1. Value of Weibull distribution parameter.

State i	u	$S_i(u)(\%)$	v	$S_i(v)(\%)$	β_i	λ_i
1	10	46.91	20	16.75	1.23	0.08
2	20	52.20	30	19.64	2.26	0.04
3	30	55.73	40	24.28	6.43	0.03
4	40	93.57	50	6.42	16.67	0.02

The state transfer probability $P^{i,i+1}$ between two different moments, e.g., $P^{2,3}$, is calculated according to equation (3) as follows:

$$P^{2,3} = \begin{bmatrix} 0.9416 & 0.0584 & 0 & 0 & 0 \\ 0 & 1 & 0 & 0 & 0 \\ 0 & 0 & 1 & 0 & 0 \\ 0 & 0 & 0 & 1 & 0 \\ 0 & 0 & 0 & 0 & 1 \end{bmatrix} \tag{6}$$

When the cable is put into use, each part of the cable is in state 1, and no transfer occurs between states. It can be assumed that the initial state vector is $A(0)$. After serving for a period of time, the updated state transition matrix $A(t)$ can be obtained by the following formula:

$$A(t) = A(0) \prod_{k=0}^{t-1} p^{k,k+1} \tag{7}$$

The maintenance effect of the cable is generally determined by the state of the cable before maintenance and the maintenance means used. Define the repair matrix *rep* as shown in equation 8, where $r_{i,1}$ is the probability that state i returns to state 1 after repair.

$$rep = \begin{bmatrix} 1 & 0 & 0 & 0 & 0 \\ r_{2,1} & 1-r_{2,1} & 0 & 0 & 0 \\ r_{3,1} & 0 & 1-r_{3,1} & 0 & 0 \\ r_{4,1} & 0 & 0 & 1-r_{4,1} & 0 \\ r_{5,1} & 0 & 0 & 0 & 1-r_{5,1} \end{bmatrix} \tag{8}$$

When maintenance is performed at year t, the state transition matrix after maintenance is updated as follows:

$$A(t)^{new} = A(t)rep \tag{9}$$

4 CASE ANALYSIS

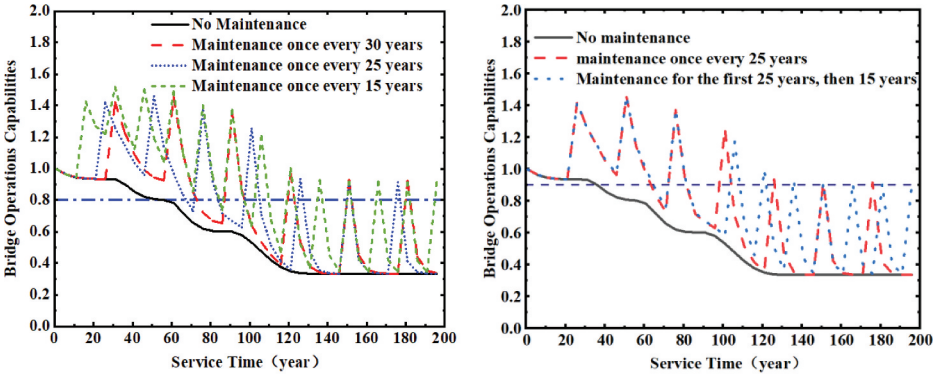
This paper takes a large-span cable-stayed bridge as a case study, whose cable-stayed cables are parallel steel wire cables, and the steel wire used for the cables is a 7mm zinc-aluminium alloy high-strength, low relaxation steel wire with a tensile strength of 2100 MPa. Combined with the construction background of the bridge, the target service life of the bridge is formulated as 200 years. According to the study of scholars Fu et al. [8], the longest-stay cable has the greatest impact on the strain of the main beam; that is, the outermost cable has the most important function among all cable members. Therefore, the mid-span cable numbered NM40 is selected as the object of the study, and the stress-free length between the anchor points of the cable is 610m, with a total weight of the cable body of 65.6t.

Select maintenance intervals of 15 years, 25 years, and 30 years. In this case, it is assumed that after one repair, all the cable bodies of states 1 and 2 can be restored to state 1, while 90% of state 3 can be returned to state 1, 80% of state 4 can be returned to state 1, and only 50% of the cable bodies that have reached the limit of normal use can be returned to state 1 after repair. If the cable is replaced, the states and their state transition matrix will be restored to the initial stage. Establish the service level matrix Re, Re^T=[1 0.8 0.6 0.4 0.2] as shown in section 3. Considering the degradation of cable status, the service level under different service times is calculated as follows:

$$Q = sum(A(t)[Re]/5) \tag{10}$$

According to the bridge access requirements in the NBI, the normal service level of the cable is set to be maintained above 0.9. Combining equations 8 and 9, the service level of cable can be calculated for different maintenance strategies, and the results are shown in Figure 2(a). Without maintenance, the cables fails at 36 years; at a maintenance interval of 30 years, the cables fails at 70 years; at a maintenance interval of 25 years, the cables fails at 60 years; and at a maintenance interval of 15 years, the cables fails at 70 years. Between 100 and 200 years, the service level under all three maintenance strategies is lower than 1. In order to improve the service level of the cables in the last 100 years, the number of maintenance visits in the last 100 years is taken to be encrypted, and the result is shown in Figure 2(b), which shows that the maintenance effect is not satisfactory.

The above results show that a repair-only strategy cannot ensure that the cable will maintain its normal service level throughout its 200-year service life. In order to keep the bridge structure in service during its design life, a combination of repair and replacement strategies is required, including the replacement of the cable when the service level after repair no longer returns to 0.9. According to Figure 2a, cables that do not undergo maintenance will be replaced in the 35th year of service; for maintenance intervals of 25 years, replacement is in the 60th year of service; for maintenance intervals of 30 years and for maintenance intervals of 15 years, the failure of the cable occurred around 70 years; therefore, it should be replaced in the 70th year of service.



(a) (b)

Figure 2. Service level of cable under different maintenance strategies.

5 MAINTENANCE COST ANALYSIS

In this paper, the present value formula of a one-time payment is used to discount, and the expected cost of each repair or replacement is calculated as follows:

$$E\left[C_{main}^{t}\right] = A(t) * C_{main} * (1+\gamma)^{-t} \tag{11}$$

Where γ is the interest rate, the latest interest rate of 3.65% was chosen for the calculation; C_{main} is the maintenance cost of the diagonal cable.

The maintenance cost of the stay cable in this paper is estimated according to the national industry standard JTG/T5612-2020[9]. As shown in Table 2 below, the calculation shows that the maintenance cost of the NM40 cable is about 260,000 yuan, and the replacement cost is about 1.55 million yuan.

Table 2. Maintenance cost unit price quota.

Maintenance Mode	Unit Price		Maintenance Mode	Unit Price		
Cable Repair	Project Base Price	430yuan/m	Parallel Wire Cable Replacement	Project Base Price	Demolition 3588.9yuan/t	Installation 20000.7yuan/t

According to the maintenance strategy, the statistics of the maintenance items of the cable are shown in Table 3, and the maintenance cost under each maintenance strategy is shown in Figure 3,

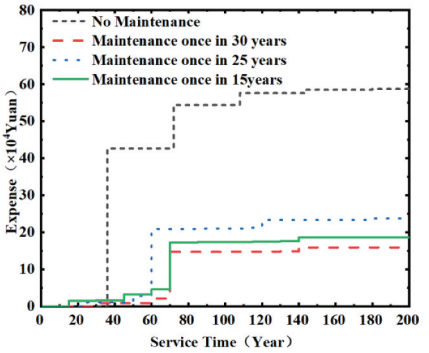


Figure 3. Maintenance costs expectations.

which shows that the maintenance cost expectation is the lowest at a maintenance interval of 30 years, which is only 159,200 yuan. And the cost of maintenance every 15 years is lower compared to the strategy with a maintenance interval of 15 years and a maintenance interval of 25 years, mainly due to the fact that there are fewer cable replacements during the service life of the bridge.

Table 3. 200 years of Nerazo maintenance project statistics.

Maintenance Strategy	No Maintenance	Maintenance once in 30 years	Maintenance once in 25 years	Maintenance once in 15 years
Maintenance (Times)	0	5	6	11
Cable Changes (Times)	5	2	3	2

6 CONCLUSION

This paper establishes a state maintenance optimization model based on a semi-Markov process, selects the inspection data of NBI to calculate the state transfer matrix of the diagonal cable, and combines it with the maintenance optimization model to derive the service level of the cable under different maintenance strategies in 200 years.

Taking a cable-stayed bridge as an example, the maintenance cost of the bridge during its life cycle is calculated. The results show that the service life of a cable-stayed cable-stay is about 60 to 80 years using only maintenance, and furthermore, encrypted maintenance during the latter 100 years is not satisfactory. Considering the full life-cycle maintenance cost of the zip wire within 200 years, the lowest maintenance costs of 159,200 yuan were achieved by using maintenance at 30-year intervals and replacement at 70-year intervals.

ACKNOWLEDGMENTS

This study was supported by the National Key R&D Program of China (Grant No. 2021YFB2600900), the National Natural Science Foundation of China (Grant No. 52078056 and 52208166), Changsha University of Science and Technology postgraduate research innovation project (Grant No.CSLGCX23154).

REFERENCES

[1] ASCE. Report card for Americas infrastructure. Reston: The American Society of Civil Engineers. New York, ASCE, 2021.
[2] Shu L, Xu HS, Zeng YJ, Yan DH. Of the various factors affecting the service life of stay-cables operation analysis. Sino-Foreign Highway, 2017 (01): 84–88.
[3] Nakamura S, Suzumura K .Experimental Study on Fatigue Strength of Corroded Bridge Wires.,Journal of Bridge Engineering 2013, 18(3):200–209.
[4] Wu ZX, Sheng HJ, Zheng M, Wang W, Chen J. Test inspection and residual life assessment of old cables of cable-stayed bridges. Sino-Foreign Highway, 2015, 35(01):103–108.
[5] Lan CM, Ren DL, Xu Y, Li N, Liu ZQ. Fatigue performance evaluation of parallel steel wire cable inclined cable I: steel wire fatigue life model. Journal of Civil Engineering, 2017, 50(06):62–70.
[6] Armin B. M, Christopher A.L. Evaluation, Rehabilitation Planning, and Stay-Cable Replacement Design for the Hale Boggs Bridge in Luling, Louisiana. Journal of Bridge Engineering, 2010(4): 364–372.
[7] Wang LB, Li AQ, Ma XL, Ding S. Research on the maintenance and replacement strategy of diagonal cable system based on life function. Journal of Civil Engineering, 2012, 45(06):162–170.
[8] Fu ZQ, Ji B, Yang M, Sun HB, Maeno H. Cable Replacement Method for Cable-Stayed Bridges Based on Sensitivity Analysis. Journal of Performance of Constructed Facilities, 2015, 29(3): 04014085.
[9] Ministry of Transport of the People's Republic of China. Highway bridge maintenance project budget quota: JTG/T 5612-2020. 2020.

Bridge Maintenance, Safety, Management, Digitalization and Sustainability – Jensen, Frangopol & Schmidt (eds)
© 2024 The Author(s), ISBN 978-1-032-77040-6
Open Access: www.taylorfrancis.com, CC BY-NC-ND 4.0 license

Probabilistic inspection planning for the life cycle management of railway bridges

I. Ames, T.N. Bittencourt & M.M. Futai
University of São Paulo (USP), São Paulo, São Paulo, Brazil

A.T. Beck
University of São Paulo (USP), São Carlos, São Paulo, Brazil

H. Carvalho
Federal University of Minas Gerais (UFMG), Belo Horizonte, Minas Gerais, Brazil

ABSTRACT: The durability and reliable operation of bridges play a critical role in society's development and economic growth. Nevertheless, the existing structures' deterioration over time, increasing structural demands, and exposure to extreme events may raise safety concerns and consequently limit the bridges' lifetime. The service life extension and durability of these structures rely on successful maintenance, repair, and rehabilitation activities supported by the rational use of inspection and monitoring information. In general, as the repair decision follows inspection results, a timely and accurate inspection plan can avoid unnecessary early repair and prevent repair being administered only when the degradation is at an advanced stage, resulting in a structurally deficient operating bridge with a high failure risk and complex and costly rehabilitation strategies. At all stages involved in the decision-making process, the presence of uncertainties associated with the onset and spread of damage, the occurrence of extreme events, the accuracy of inspections, and the effect of maintenance actions must be recognized, so that the structure's long-term performance is rationally quantified during the life cycle. Additionally, because of the limitations of visual inspections, non-destructive testing can be employed to enhance the level of inspection reliability and contribute to a better prognosis of structural performance, thereby supporting the decision process. By developing appropriate inspection and repair policies through an optimization framework, safety and cost requirements can be achieved during a structure's life cycle. In this sense, this work aims to demonstrate the application of an optimum inspection planning framework for a deteriorating reinforced concrete railway bridge affected by reinforcement corrosion based on a probabilistic analysis.

1 INTRODUCTION

The service life extension and durability of deteriorating bridges rely on successful maintenance, repair, and rehabilitation activities supported by the rational use of inspection and monitoring information. Such interventions have a crucial impact on the structure's life cycle by mitigating the deleterious effects of deterioration that lead to decommissioning and failure of systems. Concomitantly, they impose an inevitable increase in their life-cycle costs, once the maintenance and use phases frequently figure as the primary sources of environmental and economic impacts during the service life (Navarro et al. 2019, Yang & Frangopol 2019).

In general, as the decision to repair a deteriorating bridge follows inspection results, an optimized inspection plan can avoid unnecessary early repair and prevent the repair from occurring only when the degradation is at an advanced stage, resulting in a structurally deficient operating bridge with a high failure risk and complex and costly rehabilitation strategies (Abdallah et al. 2022). At the same time, owing to the conflicting cost and performance requirements, the utilization of optimization algorithms subsides the finding of appropriate

DOI: 10.1201/9781003483755-332

management techniques throughout the structure's life cycle (Barone & Frangopol 2014; Orcesi et al. 2018). To this end, at all stages involved in the decision-making process, the presence of uncertainties associated with performance prediction models, the onset and spread of damage, the occurrence of extreme events and their effects on the structure, the effect of inspection and maintenance actions, and others, must be recognized (Biondini & Frangopol 2016; Frangopol et al. 2017; Frangopol & Soliman 2016).

In the context of probabilistic decision-making, Barone et al. (2014) formulated a life cycle inspection and condition-based repair optimization framework considering the entire system of deteriorating components, minimizing both the failure rate and the expected costs of inspection and maintenance. A methodology for probabilistic assessment and optimal life cycle management of bridges was proposed by Kim et al. (2013) to obtain the time and types of inspection and condition-based repair events, satisfying the maximization of the expected service life and the minimization of the expected life cycle cost. The inspection and repair schedules, as well as the criteria for performing repair, were obtained by Zou et al. (2019b), considering the minimization of life-cycle costs (inspection, repair, and failure) and, alternatively, the minimization of the probability of failure over the life cycle of a fatigue-prone detail. The optimal schedule for condition-based maintenance with perfect and imperfect inspection information, as well as detection-based maintenance, was investigated. Kim & Frangopol (2018a) proposed a probabilistic inspection planning for fatigue-prone structures based on multi-objective optimization with weighted objectives, where a single solution was obtained to optimize six different objectives. A framework with two multi-objective optimization processes, before and after damage detection, was proposed by Kim et al. (2019), where the information collected in the scheduled inspections was used to update the probabilistic model of fatigue crack propagation and optimize the repair schedule, minimizing the maintenance delay and total maintenance cost. Barone & Frangopol (2013) considered uncertainties in both the detection and the propensity of the repair to be performed. The use of the instantaneous failure rate function was analyzed, and an iterative process to determine the number and instants of inspection and repair was suggested. Gong & Frangopol (2020) aimed to provide a decision-making framework considering managers' risk perceptions. A multi-objective optimization was performed to obtain the optimized inspection interval and load rating threshold for maintenance, in terms of expected repair and failure costs. The utility theory and the cumulative prospect theory were used to evaluate the preference between the solutions obtained. Gomes & Beck (2014) developed an investigation to establish the optimal moment of the first inspection, the interval between subsequent inspections, and the appropriate criterion for performing repair, to minimize the costs involved in inspection, repair, and failure for a renewable system.

This work focuses on the application of a risk-based optimum inspection planning framework for a deteriorating reinforced concrete railway bridge affected by carbonation-induced reinforcement corrosion.

2 RISK-BASED LIFE-CYCLE OPTIMIZATION

The process of bridge inspection and repair planning involves predicting structure deterioration and loading occurrence, interpreting the ability of the inspections to detect the developing damage and the repair outcomes, and formulating a comprehensive optimization problem that can reflect realistic expectations for efficient life-cycle management while considering the uncertainties involved in the life-cycle events (Frangopol 2011).

2.1 *Service life prediction under uncertainty*

In concrete structures, deterioration can occur through efflorescence or leaching, sulfate, carbon dioxide and chloride attack, corrosion, and alkali-aggregate reaction, as well as physical damage mechanisms, like ice/defrost cycles, thermal expansion, abrasion, erosion, shrinkage, and fatigue (Ellingwood 2005). However, depending on the characteristic of the structure utilization, the stochastic nature of the loading events indicates that the failure event may not be governed only by the strength loss due to damage progress and, thus, a combination of both loading and deterioration leads to structural failure in a first-crossing failure problem.

2.1.1 *Corrosion in reinforced concrete structures*

The life cycle of structures subject to corrosion consists, in general, of the period of corrosion initiation, where aggressive agents are transported inside the concrete to the surface of the reinforcements, and the propagation period, where the depassivation of steel allows the beginning of corrosion until the structure reaches the end of its service life. When present in a sufficient amount, aggressive elements such as chlorides and carbon dioxide can destroy the passive layer that initially protects the steel bars against the deterioration process. The duration of the initiation phase depends mainly on the transport rate of the aggressive elements, environmental conditions, and design parameters (Guo et al. 2015). In the case of concrete structures, the degenerative effects of reinforcement corrosion manifest as superficial stains caused by corrosion products, the cracking and spalling of concrete cover, reduction of reinforcement cross-section area, and bond loss (Ribeiro et al. 2020). Based on Faraday's law, the diametrical reduction of a steel bar under corrosion Δd in an instant t_n can be estimated by Equation 1 (Val et al. 1998):

$$\Delta d(t_n) = 0.0232 \int_{t_{oc}}^{t_n} i_{corr}(t)dt \tag{1}$$

where t_{oc} is the corrosion onset time (in years), the corrosion current density $i_{corr}(t)$ is expressed in μA/cm², and d in mm.

2.2 *Probability of damage detection*

The application of non-destructive testing plays an important role in obtaining a better prognosis of structural performance when compared to visual inspections, subsiding the decision process with more reliable information (Soliman et al. 2013). Acoustic emission, ground penetrating radar, electrical resistivity, half-cell potential, impact-echo testing, infrared thermography, and pachometer are examples of non-destructive tests that can be applied to concrete structures (Lee et al. 2014). The advancement of non-destructive testing methods and inspection techniques indicates that comprehensive planning of inspections should consider the type of method to be utilized (Abdallah et al. 2022).

The probability of damage detection, also referred to as the "detectability function", is the conditional probability of detecting damage given the defect size or damage degree, δ, and can be utilized to describe different inspection techniques in terms of their quality (Kim et al. 2011, Soliman et al. 2013, Yang & Frangopol 2018). This relationship can be statistically represented by shifted exponential, logistic curve, and standard normal cumulative distribution functions (Kim & Frangopol 2011). The higher the inspection quality, the lower the mean value of damage detectable by the inspection method, $\delta_{d,i}$. Although more accurate lifetime predictions may result from better inspection quality, the cost of technology and required expertise increases as more refined methods are employed. In this way, the choice of the appropriate moment to perform the inspection balances the level of damage, the inspection cost and quality, and, consequently, the cost of failure. The event for damage detection can be expressed as Equation 2.

$$D = \left[\delta_{d,i} - \delta \leq 0\right] \tag{2}$$

2.3 *Modeling of repair events*

Conventional repair methods for already damaged concrete bridges include the utilization of patches, overlays, sealers and coatings, crack injection, cathodic protection, and chloride extraction (Tabatabai et al. 2004). To represent the effect of protective and recovery measures, simplified assumptions have been utilized in optimization frameworks, including the replacement of components – and resulting reestablishment of initial capacity or initial lifetime, also regarded as "as good as new" repair (Barone et al. 2014, Benítez et al. 2020, Bismut & Straub 2021, de Angelis et al. 2017, Gong & Frangopol 2020, Kim et al. 2019, 2013, 2011, Kim & Frangopol 2018a, 2018b, 2016, Sun et al. 2018, Tolentino & Ruiz 2014, Yang & Frangopol 2018, Zhang et al. 2020, 2019, Zou et al. 2021a, 2021b, 2020, 2019); the suppression of deterioration rate for a period of time, that may be deterministic (Barone et al. 2014, Gong & Frangopol 2020, Vereecken et al.

2020), or random (Kim et al. 2013, Kim & Frangopol 2016); partial recovery of initial structural properties – that is usually modelled as an uncertain variable (Benítez et al. 2020, Zhang et al. 2019, Zou et al. 2021a); and reduction of the deterioration rate (Abdallah et al. 2021).

Usually, the repair events are classified according to the criterion for their application. In a detection-based repair strategy, the repair is performed once the damage is detected, and the event for detection is the same as for repair. A condition-based repair, in turn, occurs if the measured defect exceeds a repair criterion, which is typically defined as a damage level for repair $\delta_{r,i}$. In this case, when the damage is encountered during an inspection, the flaw is measured in an in-depth inspection, and the repair decision is made upon the measurement results. The event for repair differs from the event for inspection and can be expressed as:

$$R = \left[\delta_{r,i} - \delta \leq 0\right] \tag{3}$$

2.4 *Expected life cycle cost*

The total expected life cycle cost can be calculated according to the event tree depicted in Figure 1, where an inspection event at $t_{insp,i}$ can result in the events of damage detection and in-depth inspection resulting in the need for repair type 1 (D&R1), damage detection and in-depth inspection resulting in the need for repair type 2 (D&R2), damage detection and in-depth inspection resulting in no repair (D&$\overline{\text{R}}$), and no detection ($\overline{\text{D}}$). Each one of the intervention events can lead to a survival (S) or failure (F) event in the time gap before the subsequent inspection event.

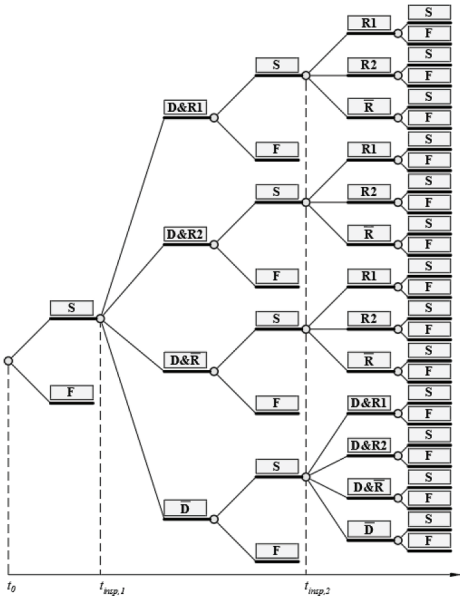


Figure 1. – Event tree for two inspection events and two repair options.

2.5 *Optimization problem formulation*

Based on the information obtained through life-cycle analyses, the optimization problem can be formulated to determine the optimal inspection times $\boldsymbol{t_{insp}}$ and repair thresholds δ_r for the available repair options to minimize the expected total costs consisting of inspection costs C_{insp}, repair costs C_r, and failure costs C_f:

$$\begin{gathered} Find: \boldsymbol{t_{insp}} = \left\{t_{insp,1}, \ldots, t_{insp,n}\right\}, \boldsymbol{\delta_r} = \left\{\delta_{r1},\ \delta_{r2}\right\} \\ That\ minimizes:\ E[C_{tot}] \\ Subject\ to: t_{insp,i} - t_{insp,i-1} \geq 2 \end{gathered} \tag{4}$$

3 CASE STUDY

To demonstrate the application of the optimization of life-cycle interventions, a Brazilian reinforced concrete railway bridge is studied. The structure has three simply supported spans of 18.67m and a broad-gauge ballasted track where the primary rolling stock consists of trains transporting iron ore. To characterize the loading events, wheel-load measurements conducted during instrumentation campaigns were utilized to compute the annual maximum bending moment through a moving-load dynamic analysis.

The degradation of the structure is simulated by the progress of general corrosion and carbonation depassivation of steel as the onset mechanism. To this end, the model proposed by Papadakis & Tsimas (2002) is applied to simulate the carbon dioxide ingress, and the model proposed by Ghods et al. (2008) is used to simulate the corrosion current density with values of concrete resistivity calculated according to Zhang et al. (2021). The damage is represented as a reduction of the main girder steel cross-sectional area, that is utilized as an input to calculate the resistant flexural capacity of the reinforced concrete cross-section yearly. The fraction of the steel cross-sectional area lost due to the corrosion progress is considered as the representation of the damage degree. Furthermore, the effect of concrete cover cracking due to corrosion products is investigated by applying the thick-walled cylinder model (Bažant 1979, Chernin & Val 2011).

To investigate the effect of inspection quality, the degree of damage detectable by the inspection method (δ_d) is varied, assuming values from 1×10^{-4} to 1×10^{-2}, represented by a normal distribution with a coefficient of variation of 0.1. Two repair methods are considered available for decision-making: the utilization of patch repair as a minor repair method; and the reestablishment of the initial resistant capacity as a major repair method applied in cases of more severe damage observation. The effect of patch repair is represented by the stagnation of damage progress for a random period, described by a uniform random variable U(4 years, 10 years) (Tabatabai et al. 2004). The effect of the bending moment occasioned by the passing train is, however, kept unchanged, to address both the failures governed by the degradation of the strength barrier and loading.

The costs of in-depth inspection, patch repair, major repair, and cracking of concrete cover are assumed as 2/3, 2, 10, and 1×10^3, respectively. In contrast, the cost of failure is varied assuming values from 1×10^5 to 5×10^5. The cost of non-destructive testing for damage detection can be associated with its quality by the expression (Mori & Ellingwood 1994):

$$C_{insp,i} = \left(1 - \delta_{d,i}\right)^b \tag{5}$$

where b is assumed as 190. The optimization problem is solved by utilizing the Genetic Algorithm from the Matlab Global Optimization Toolbox.

4 RESULTS

The utilization of the mentioned deterioration models resulted in a mean value of the depassivation time of 62.51 years with a standard deviation of 22.79 years. The mean time of concrete cracking due to corrosion products was 75.29 years with a standard deviation of 48.69 years.

The solution to the optimization problem is presented in Table 1. As seen in Figures 2a and 2b, the optimal repair criteria values for both repair types tend to decrease with higher inspection quality and cost of failure. This is because detecting damage earlier (Figure 3a) allows repairs to be made at lower damage levels, thereby reducing the associated expected life-cycle costs, since to higher failure costs, the relative repair costs decrease compared to the potential expected failure cost reduction. This is further supported by scheduling higher quality inspections earlier in the service life as observed in Figure 2d. However, observing Figure 2c, for higher values of δ_d and failure costs, the number of inspections increases, as the relative costs of inspections decrease compared to failure costs.

Figure 3a Illustrates the expected damage detection delay for the optimized solutions. The schedule with $C_f = 5 \times 10^5$ and $\delta_d = 1 \times 10^{-4}$ exhibited the shortest delay in detecting the developing damage, (20.28 years). However, the highest probability of detecting damage before

Table 1. – Optimization results.

δ_d	Equivalent anode area [mm²]	C_f	n_{insp}	t_{insp}	δ_r	$E[C_{tot}]$
1×10^{-4}	1.81		1	31	1e-4, 3e-4	381.59
5×10^{-4}	9.06		1	46	6e-4, 7e-4	381.30
1×10^{-3}	18.12	1×10^5	1	46	1.1e-3, 1.4e-3	381.21
5×10^{-3}	90.58		1	63	4.9e-3, 5e-3	381.02
1×10^{-2}	181.16		1	72	9e-3, 9.1e-3	381.23
1×10^{-4}	1.81		1	53	5e-4, 1.5e-3	524.71
5×10^{-4}	9.06		1	46	6e-4, 7e-3	524.70
1×10^{-3}	18.12	2×10^5	1	53	1.4e-3, 1.5e-3	524.69
5×10^{-3}	90.58		1	65	4.6e-3, 4.7e-3	525.00
1×10^{-2}	181.16		1	72	9.2e-3, 9.3e-3	525.92
1×10^{-4}	1.81		2	24, 45	1e-4, 6e-4	667.45
5×10^{-4}	9.06		2	28, 52	3e-4, 4e-4	667.46
1×10^{-3}	18.12	3×10^5	2	29, 49	4e-4, 5e-4	667.29
5×10^{-3}	90.58		2	54, 78	1.4e-3, 1.5e-3	668.34
1×10^{-2}	181.16		6	37, 53, 68, 70, 83, 87	2.5e-3 2.6e-3	670.03
1×10^{-4}	1.81		2	24,45	1e-4, 6e-4	810.25
5×10^{-4}	9.06		2	28, 52	3e-4, 4e-4	810.21
1×10^{-3}	18.12	4×10^5	1	63	1e-3, 1.3e-3	811.33
5×10^{-3}	90.58		4	45, 61, 68, 78	1e-4, 1.9e-3	811.98
1×10^{-2}	181.16		6	42, 54, 64, 67, 69, 82	6e-4, 8.8e-3	814.84
1×10^{-4}	1.81		2	29, 53	1e-4, 2e-4	952.77
5×10^{-4}	9.06		2	28, 52	3e-4, 4e-4	952.96
1×10^{-3}	18.12	5×10^5	3	23, 29, 49	4e-4, 5e-4	953.81
5×10^{-3}	90.58		3	44, 51, 71	9e-4, 1e-3	955.62
1×10^{-2}	181.16		8	50, 52, 54, 58, 65, 67, 69, 76	7e-4, 1.1e-3	959.39

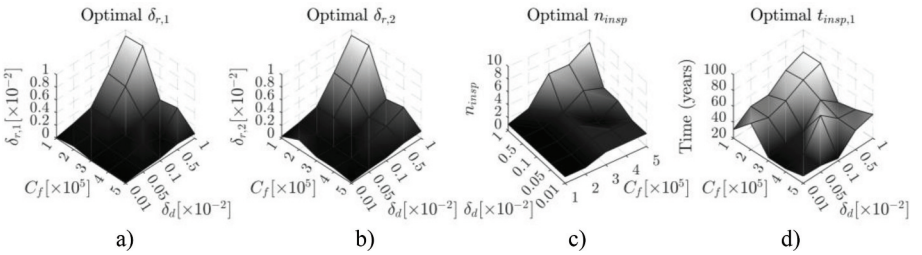


Figure 2. – a) Optimal δ_{r1}; b) Optimal $\delta_{r,2}$; c) Optimal n_{insp}; d) Optimal $t_{insp,1}$.

failure (Figure 3b) was observed for $\delta_d = 1 \times 10^{-3}$ and $C_f = 4 \times 10^5$, with a probability of 0.41, corresponding to the highest probability of repair (0.12) as well (Figure 3c). Moreover, the expected reduction in the life cycle costs increases with the utilization of more refined inspection methods and assigning higher values to the cost of failure (Figure 3d).

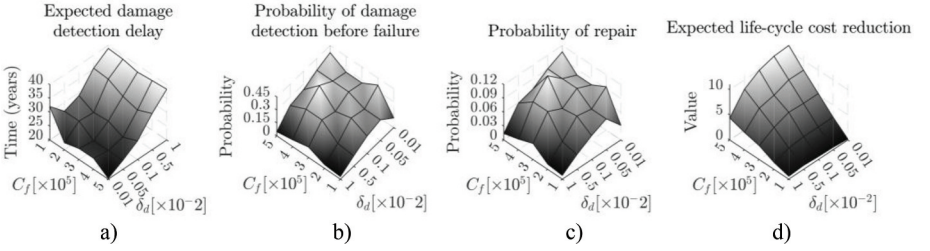


Figure 3. – a) Expected damage detection delay; b) Probability of damage detection before failure; c) Probability of repair; d) Expected life-cycle cost reduction.

5 CONCLUSIONS

This paper presented an application of probabilistic inspection planning for a reinforced concrete railway bridge subjected to carbonation-induced corrosion. The uncertainties in the deterioration process, loading occurrence, inspection detectability, and repair effectiveness are considered to determine the optimized inspection times and repair criteria. The results showed that improving the probability of damage detection before failure and the probability of repair does not necessarily lead to the maximum expected life cycle cost reduction, as the optimization procedure identifies the best arrangement on the choice of inspection times and damage levels for performing repair for a given inspection quality and cost of failure. In this way, it is possible to reduce the expected total costs by employing the resources of inspection and repair rationally during the life cycle, even for relatively late deterioration initiation and low deterioration rates, thus subsiding the process of decision-making with a risk-based point of view.

REFERENCES

Abdallah, A.M., Atadero, R.A. & Ozbek, M.E. 2021. A Comprehensive Uncertainty-Based Framework for Inspection Planning of Highway Bridges. *Infrastructures* 6: 1–33.

Abdallah, A.M., Atadero, R.A. & Ozbek, M.E. 2022. A State-of-the-Art Review of Bridge Inspection Planning: Current Situation and Future Needs. *Journal of Bridge Engineering* 27.

Barone, G. & Frangopol, D.M. 2013. Hazard-Based Optimum Lifetime Inspection and Repair Planning for Deteriorating Structures. *Journal Of Structural Engineering* 139.

Barone, G. & Frangopol, D.M. 2014. Life-cycle maintenance of deteriorating structures by multi-objective optimization involving reliability, risk, availability, hazard and cost. *Structural Safety* 48: 40–50.

Barone, G., Frangopol, D.M. & Soliman, M. 2014. Optimization of life-cycle maintenance of deteriorating bridges with respect to expected annual system failure rate and expected cumulative cost. *Journal of Structural Engineering* 140.

Bažant, Z.P. 1979. Physical Model for Steel Corrosion in Concrete Sea Structures - Theory. *Journal of the Structural Division* 105: 1137–1153.

Benítez, P., Rocha, E., Varum, H. & Rodrigues, F. 2020. A dynamic multi-criteria decision-making model for the maintenance planning of reinforced concrete structures. *Journal of Building Engineering* 27 (100971).

Biondini, F. & Frangopol, D.M. 2016. Life-Cycle Performance of Deteriorating Structural Systems under Uncertainty: Review. *Journal of Structural Engineering* 142: 1–17.

Bismut, E. & Straub, D. 2021. Optimal adaptive inspection and maintenance planning for deteriorating structural systems. *Reliab Eng Syst Saf* 215.

Chernin, L., & Val, D. V. 2011. Prediction of corrosion-induced cover cracking in reinforced concrete structures. *Constr Build Mater* 25: 1854–1869.

de Angelis, M., Patelli, E. & Beer, M. 2017. Forced Monte Carlo Simulation Strategy for the Design of Maintenance Plans with Multiple Inspections. ASCE-ASME *Journal of Risk And Uncertainty In Engineering Systems Part A - Civil Engineering* 3.

Ellingwood, B.R. 2005. Risk-informed condition assessment of civil infrastructure: state of practice and research issues. *Structure and Infrastructure Engineering* 1: 7–18.

Frangopol, D.M. 2011. Life-Cycle performance, management, and optimisation of structural systems under uncertainty: Accomplishments and challenges. *Structure and Infrastructure Engineering* 7: 389–413.

Frangopol, D.M., Dong, Y. & Sabatino, S. 2017. Bridge life-cycle performance and cost: analysis, prediction, optimisation and decision-making. *Structure and Infrastructure Engineering* 13: 1239–1257.

Frangopol, D.M. & Soliman, M. 2016. Life-cycle of structural systems: recent achievements and future directions. *Structure and Infrastructure Engineering* 12: 1–20.

Ghods, P., Isgor, O.B. & Pour-Ghaz, M. 2008. Experimental verification and application of a practical corrosion model for uniformly depassivated steel in concrete. *Mater Struct* 41: 1211–1223.

Gomes, W.J.S. & Beck, A.T. 2014. Optimal inspection planning and repair under random crack propagation. *Eng Struct* 69: 285–296.

Gong, C. & Frangopol, D.M. 2020. Condition-Based Multiobjective Maintenance Decision Making for Highway Bridges Considering Risk Perceptions. *Journal of Structural Engineering* 146.

Guo, Y., Trejo, D. & Yim, S. 2015. New Model for Estimating the Time-Variant Seismic Performance of Corroding RC Bridge Columns. *Journal Of Structural Engineering* 141.

Kim, S. & Frangopol, D.M. 2011. Cost-based optimum scheduling of inspection and monitoring for fatigue-sensitive structures under uncertainty. *Journal of Structural Engineering* 137: 1319–1331.

Kim, S. & Frangopol, D.M. 2016. Efficient multi-objective optimisation of probabilistic service life management. *Structure and Infrastructure Engineering* 13: 147–159.
Kim, S. & Frangopol, D.M. 2018a. Decision making for probabilistic fatigue inspection planning based on multi-objective optimization. *Int J Fatigue* 111: 356–368.
Kim, S. & Frangopol, D.M. 2018b. Multi-objective probabilistic optimum monitoring planning considering fatigue damage detection, maintenance, reliability, service life and cost. *Structural and Multidisciplinary Optimization* 57: 39–54.
Kim, S., Frangopol, D.M. & Soliman, M. 2013. Generalized probabilistic framework for optimum inspection and maintenance planning. *Journal of Structural Engineering* 139: 435–447.
Kim, S., Frangopol, D.M. & Zhu, B. 2011. Probabilistic Optimum Inspection/Repair Planning to Extend Lifetime of Deteriorating Structures. *Journal of Performance of Constructed Facilities* 25: 534–544.
Kim, S., Ge, B. & Frangopol, D.M. 2019. Effective optimum maintenance planning with updating based on inspection information for fatigue-sensitive structures. *Probabilistic Engineering Mechanics* 58: 1–12.
Lee, S., Kalos, N. & Shin, D.H. 2014. Non-Destructive Testing Methods in the U.S. for Bridge Inspection and Maintenance. *Journal of Civil Engineering* 18, 1322–1331.
Navarro, I.J., Martí, J. V & Yepes, V. 2019. Reliability-based maintenance optimization of corrosion preventive designs under a life cycle perspective. *Environmental Impact Assessment Review* 74: 23–34.
Orcesi, A., Cremona, C. & Ta, B. 2018. Optimization of design and life-cycle management for steel–concrete composite bridges. *Structural Engineering International* 28: 185–195.
Papadakis, V.G. & Tsimas, S. 2002. Supplementary cementing materials in concrete: Part I. Efficiency and design. *Cem Concr Res* 32: 1525–1532.
Ribeiro, D.V. et al. 2020. *Corrosão e Degradação em Estruturas de Concreto*: Teoria, controle e técnicas de análise e intervenção, 2nd ed. GEN, Rio de Janeiro.
Soliman, M., Frangopol, D.M. & Kim, S. 2013. Probabilistic optimum inspection planning of steel bridges with multiple fatigue sensitive details. *Eng Struct* 49: 996–1006.
Sun, P., Cui, F., Qin, H. & Hou, X. 2018. Study on Regular Inspection Frequency of Bridge Based on Seismic Vulnerability Analysis. *Shock and Vibration* 2018 .
Tabatabai, H., Ghorbanpoor, A. & Turnquist-Nass, A. 2004. *Rehabilitation Techniques for Concrete Bridges*. Wisconsin.
Tolentino, D. & Ruiz, S.E. 2014. Influence of structural deterioration over time on the optimal time interval for inspection and maintenance of structures. *Eng Struct* 61: 22–30.
Val, D. V, Stewart & M.G., Melchers, R.E. 1998. Effect of reinforcement corrosion on reliability of highway bridges. *Eng Struct* 20: 1010–1019.
Vereecken, E., Botte, W., Lombaert, G. & Caspeele, R. 2020. Bayesian decision analysis for the optimization of inspection and repair of spatially degrading concrete structures. *Eng Struct* 220: 111028.
Yang, D.Y. & Frangopol, D.M. 2018. Probabilistic optimization framework for inspection/repair planning of fatigue-critical details using dynamic Bayesian networks. *Comput Struct* 198: 40–50.
Mori, Y., Ellingwood, B. 1994. Maintaining Reliability of Concrete Structures. II: Optimum Inspection/Repair. *Journal of Structural Engineering* 120: 846–862.
Yang, D.Y. & Frangopol, D.M. 2019. Life-cycle management of deteriorating civil infrastructure considering resilience to lifetime hazards: A general approach based on renewal-reward processes. *Reliab Eng Syst Saf* 183: 192–212.
Zhang, Q., Lun, P.-Y. & Li, X. 2021. A simplified approach for prediction of concrete resistivity: experimental study and mathematic model. *Mater Struct* 54 (155).
Zhang, W.-H., Qin, J., Lu, D.-G., Thöns, S. & Faber, M.H. 2020. VoI-informed decision-making for SHM system arrangement. *Struct Health Monit*.
Zhang, X.-S., Chen, J.-Q. & Wei, J.-H. 2019. Condition-based scheduled maintenance optimization of structures based on reliability requirements under continuous degradation and random shocks. *Journal of Zhejiang University: Science A* 20: 272–289.
Zou, G., González, A., Banisoleiman, K. & Faber, M.H. 2019. An integrated probabilistic approach for optimum maintenance of fatigue-critical structural components. *Marine Structures* 68.
Zou, G., Faber, M.H., González, A. & Banisoleiman, K. 2021a. A simplified method for holistic value of information computation for informed structural integrity management under uncertainty. *Marine Structures* 76.
Zou, G., Faber, M.H.,González,A.& Banisoleiman, K. 2021b. Fatigue inspection and maintenance optimization: A comparison of information value, life cycle cost and reliability based approaches. *Ocean Engineering* 220.
Zou, G., Faber, M.H., González, A. & Banisoleiman, K. 2020. A holistic approach to risk-based decision on inspection and design of fatigue-sensitive structures. *Eng Struct* 221(110949).

SS29: Risk-based assessment and prioritization of bridge stocks

Organizers: N. Scattarreggia & R. Monteiro


Taylor & Francis
Taylor & Francis Group
http://taylorandfrancis.com

Bridge Maintenance, Safety, Management, Digitalization and Sustainability – Jensen, Frangopol & Schmidt (eds)
© 2024 The Author(s), ISBN 978-1-032-77040-6
Open Access: www.taylorfrancis.com, CC BY-NC-ND 4.0 license

Management of earth retaining structures based on condition and criticality

J.L. Amado, M.A. Pratas, B. Monteiro, A. Costa & M. Pinheiro
Infraestruturas de Portugal, S.A., Almada, Portugal

ABSTRACT: This article presents a risk-based framework for managing earth retaining structures (ERS) in the Portuguese National Road and Railway Network, managed by Infraestruturas de Portugal, S.A. With a substantial inventory of over 20,000 ERS in mainland Portugal, the company has developed a specialized management system aligned with industry best practices in asset management.

1 INTRODUCTION

In the pursuit of enhancing operational efficiency and optimizing resource utilization, the application of asset management principles and techniques has been tailored for earth retaining structures, commonly known as retaining walls. The conceptual framework of the management system revolves around a model founded on systematic processes of data collection, analysis, and decision-making.

The data collection phase commences with Inventory campaigns, encompassing the compilation of jurisdictional and technical information. This includes geometric and locational details concerning road or railway infrastructure. The amassed data serves as the foundation for computing a criticality index, a metric that assesses the significance of each asset in aligning with organizational objectives and desired goals.

Central to the structural analysis process are Principal Inspections, utilizing predefined observations as indicators to evaluate component condition and derive an overall rating for each Earth Retaining Structure. This rating is integrated with factors such as seismic risk, precipitation, and load considerations, resulting in a semi-quantitative condition index. By integrating the qualitative condition rating with these factors, the Condition Index furnishes a comprehensive evaluation of the health and safety of each earth retaining structure.

The Condition Index functions as a measure of the probability of failure, while the Criticality Index offers insights into the consequences of failure. Through an integrated approach using a risk matrix, resource allocation can be optimized, facilitating inspection scheduling and intervention prioritization based on risk assessment outcomes. This article delves into the indicators utilized in condition and criticality analysis, elucidating the processes supporting risk-informed decision-making.

2 STRATEGIC MODEL

2.1 *A collaboration process*

The management of earth retaining structures (ERS), hereafter referred to as ERS, is conceptualized as a collaborative process involving specific participants, interlinked activities, both internal and external to the process, and standard outputs, as articulated by Amado et al. (2019). Drawing on best practices outlined in ISO/IEC (2013) and ISO 9000:2015, which defines a process as a set of interrelated activities, the strategic model emphasizes understanding the desired outcome when implementing a management system.

DOI: 10.1201/9781003483755-333

The prioritization of maintenance and investment needs, along with defining inspection frequencies, constitutes the overarching goals of the system. Differentiating these needs is contingent on varying levels of risk, determined through a matrix combining the structure's condition with its criticality. The condition rating reflects the structure's response to designed conditions, obtained through principal inspections, structural health monitoring, and information about the operating environment. Simultaneously, the criticality index hinges on the structure's impact on organizational objectives, integrating physical characteristics and functional location. Inventory and principal inspection activities serve as the cornerstone of the system, complemented by routine inspections for preventive maintenance needs and monitoring when necessary. The strategic model, illustrated in Figure 1, provides a clear representation of activities and their interdependencies without representing exceptions or actors for immediate perceptibility.

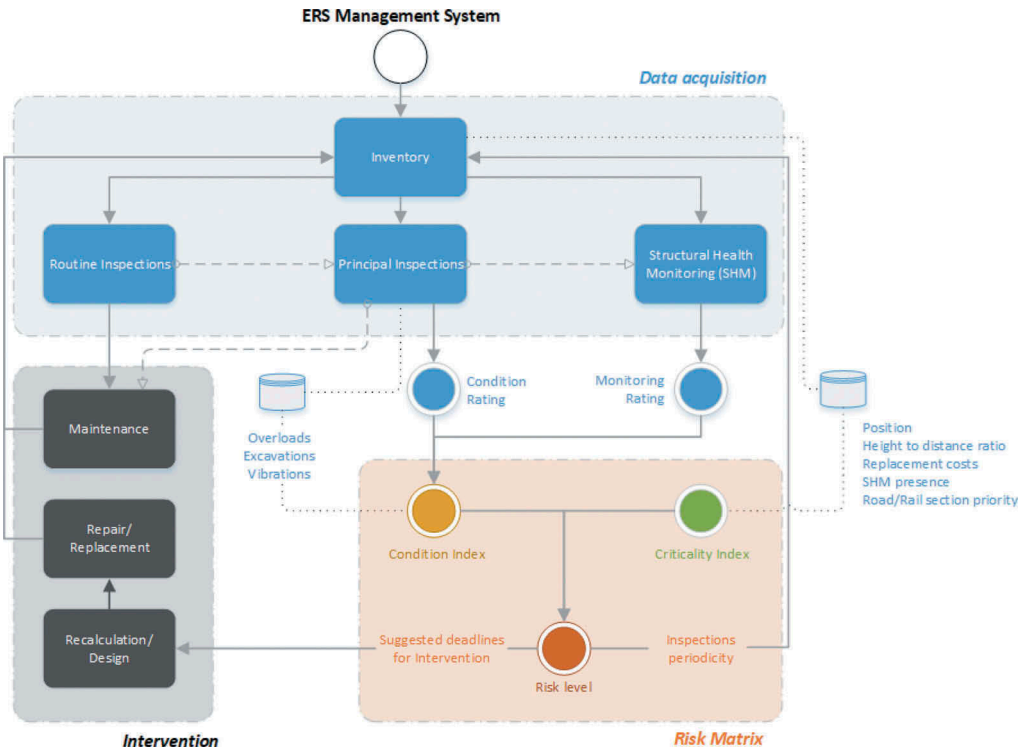


Figure 1. Infraestruturas de Portugal's strategic model for the management of earth retaining structures.

2.2 *Risk informed decision-making*

The risk-based decision model employed by Infraestruturas de Portugal for retaining structures is rooted in the Risk Level, calculated based on a Condition Index and a Criticality Index. These indices encompass intrinsic and external factors, combined through weighted averages, as depicted in Figure 2.

The methodology employed by Infraestruturas de Portugal for calculating the risk level of earth-retaining structures is more comprehensively illustrated in the model presented in Figure 3. This model identifies the factors included in the calculations of each index, along with the relevant parameters considered for each factor, where applicable.

As depicted in Figure 3, the parameters (level 4) used in the calculation of the factors (level 3) are analyzed on a discrete scale from 1 to 5, based on established intervals. Their combination is

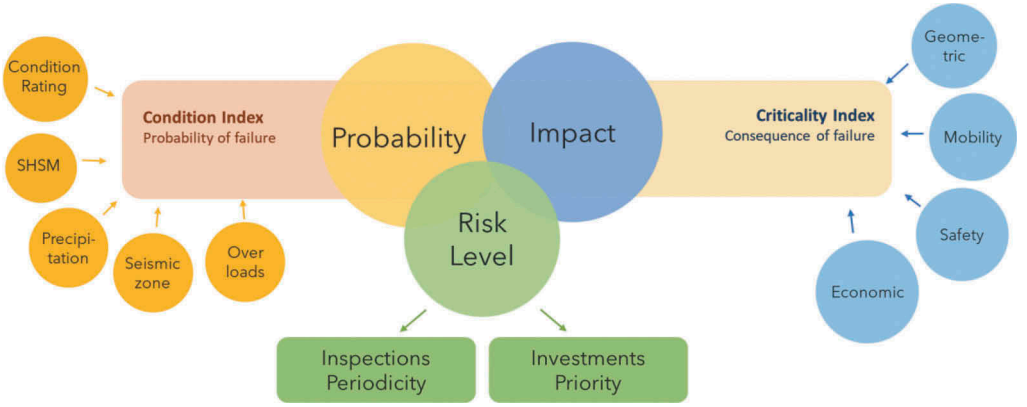


Figure 2. Infraestruturas de Portugal's risk-based decision model.

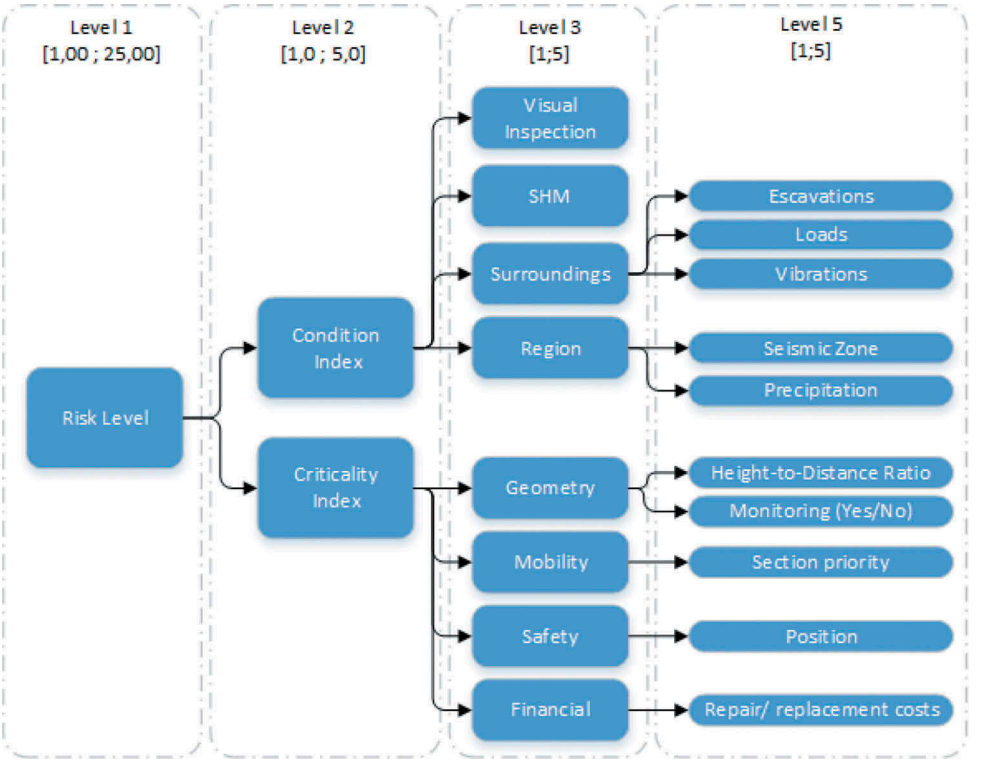


Figure 3. Infraestruturas de Portugal' earth-retaining structures methodology for risk level calculation.

performed through a weighted average. Similarly, the factors (level 3) are also assessed on a discrete scale from 1 to 5, and their combination through a weighted average results in an index (level 2) on a continuous scale from 1 to 5. Finally, the simple multiplication of the two indices (level 2) yields a Risk Level (level 1), falling within a discrete scale from 1 to 25.

As stated, the parameters and factors, analyzed on discrete scales, are combined through weighted averages to generate two indices, Condition and Criticality index.

The Condition Index intends to be a qualitative measure of the observable physical state of the structure under operational conditions and design loads. It serves as an indicator of reliability and acts as a proxy for the probability of failure. This index integrates a qualitative condition

rating derived from visual inspections with factors including monitoring results, environmental conditions, and surroundings, offering a comprehensive assessment of the overall health and safety of the structures. Conversely, the Criticality Index assesses the significance of an asset in accomplishing organizational objectives and fulfilling desired goals, considering its impact on the organization, stakeholders, and the overall system. As depicted in the Figure 3, criticality is determined by geometric factors, positioning in relation to the transportation corridor (for protection or support), segment priority, and estimated costs related with its typology and size.

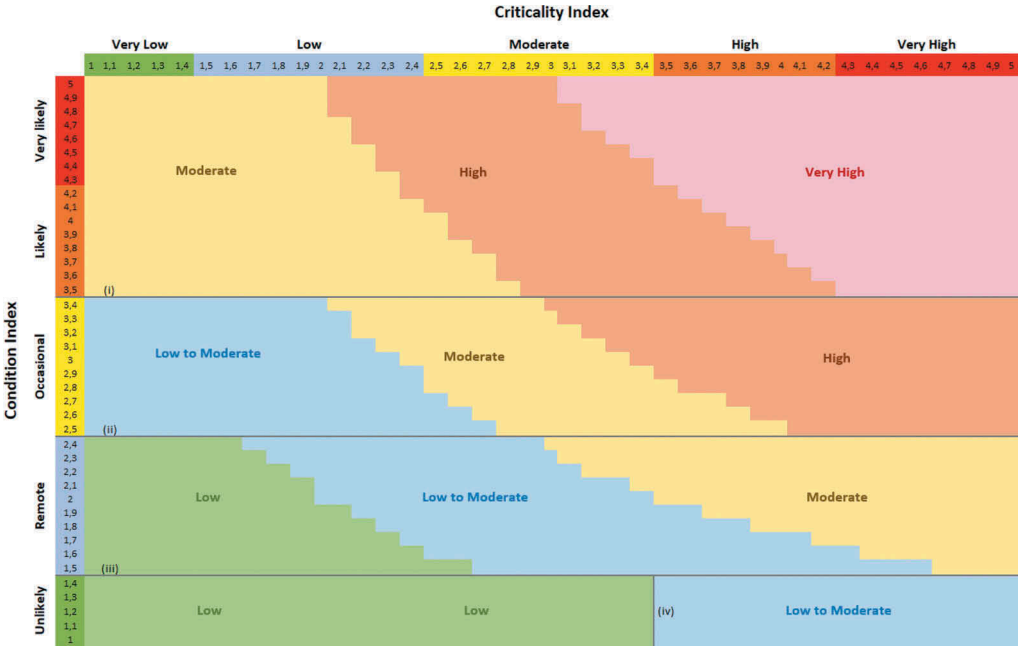


Figure 4. Infraestruturas de Portugal' risk matrix for the management of ERS.

Table 1. Risk levels for earth retaining structures and subsequent actions

Risk Level		Inspection Intervals	Intervention time frame
< 4	Low	Routine inspections up to 2 yrs Principal inspections upon request	No actions beyond annual routine maintenance.
< 7	Low to Moderate	Routine inspections up to 2 to 4 yrs Principal inspections up to 6 years	Actions to be planed under maintenance contracts.
< 10	Moderate	Routine inspections up to 2 to 4 yrs Principal inspections up to 4 yrs	Medium-term intervention needed.
< 15	High	Routine inspections up to 2 yrs Principal inspections up to 2 yrs	Medium-term intervention needed. Risk mitigation measures in the short-term.
≥ 15	Very High	Principal inspections up to 1 yr	Short-term intervention needed. Risk mitigation measures including immediate circulation restrictions.

Building upon the preceding risk matrix, five risk levels were established, each corresponding to specific subsequent actions concerning inspection frequencies and intervention timeframes, as illustrated in Table 1.

3 PERFORMANCE INDICATORS

3.1 *Inspection protocol*

As delineated in Section 2, the Condition Index incorporates data derived from visual observations, particularly those conducted during Principal Inspections. To institute a comprehensive framework for these diagnostic procedures, a protocol for inspections was formulated. This protocol centers on three pivotal components: Wall, Drainage, and Influence Area, encompassing all pertinent elements of the ERS. Throughout the inspection, specialized technicians undertake visual assessments

Table 2. Condition rating assigned in principal inspections.

Condition Rating (CR)	Description
1	No damage
2	Low severity damage
3	Medium severity damage, in a limited to medium extent
4	Medium severity damage, in a medium to high extent
5	Severe damage

Table 3. Elements and observations/indicators for condition assessment of the wall component.

Elements	Observations/ Indicators	Detail
Surface Finishing Materials	Disintegration	
	Blisters or swelling	
	Detachment or peeling	
	Hairline cracking	
Wall body	Failure	
	Deformations	Bulging; Flexure; Settlement; Disarray of wall elements; Abnormal joint opening
	Displacements	Horizontal displacement; Rotation to the extrados; Rotation to the intrados
	Cracks	Horizontal; Vertical; Diagonal
	Loss of material from the backfill	
	Surface degradation	
	Damage to joint mortar	Cracking; Degradation and loss of cohesion; Vegetation growth
	Corrosion/section loss in metal elements	
	Stains, runoff, or efflorescence	
Foundation	Foundation exposure	
	Soil deformation	Bulging; Subsidence
Parapet installed on the wall	Abnormal inclination	
	Deformation	
	Malfunctions	
Safety Barrier installed on the wall	Abnormal inclination	
	Deformation	
	Malfunctions	
Other elements or equipment installed on the wall	Abnormal inclination	
	Deformation	
	Malfunctions	

and allocate ratings within the 1 to 5 range to indicators linked with identified defects. These ratings aim to articulate the severity and scope of the damages, in accordance with the general description delineated in Table 2. Additionally, for each observation, a distinct description has been formulated and is accessible to inspectors in a dedicated manual (Infraestruturas de Portugal, unpubl.). This manual furnishes comprehensive guidance and directives on how to evaluate and assign ratings to each indicator, thereby ensuring uniformity and precision in the inspection process.

The performance indicators for the elements within the Wall component, along with the corresponding assessment details are summarized in Table 3.

For the elements within the Drainage and Influence Area components, Table 4 and Table 5 respectively present the performance indicators and assessment details.

Table 4. Elements and observations/indicators for condition assessment of the drainage component.

Elements	Observations/ Indicators	Detail
Drainage Inlets and Outlets	Blocked	
	Damaged	
Rear Gutters	Blocked	
	Damaged	
Frontal Gutters	Blocked	
	Damaged	
Side Gutters	Blocked	
	Damaged	

Table 5. Elements and observations/indicators for condition assessment of the influence area component.

Elements	Observations/ Indicators	Detail
Backslope or embankment on the rear side	Deformations	Bulging; Subsidence; Abnormal inclination of trees
	Displacements	Falls; Slides; Erosion
	Cracks	Horizontal; Vertical; Diagonal
	Vegetation	
	Presence of water in the backfill	
Buildings or constructions on the rear side	Settlement	
	Cracks	
	Evidence of failure	
Pavement or sidewalk on the rear side	Settlements	
	Bulges	
	Cracks	Transverse/oblique; Longitudinal
Frontal slope or embankment	Deformations	Bulging; Subsidence; Abnormal inclination of trees
	Displacements	Falls; Slides; Erosion
	Cracks	Horizontal; Vertical; Diagonal
	Vegetation	
Buildings or constructions on the frontal slope or embankment	Settlement	
	Cracks	
	Evidence of failure	
Pavement or sidewalk on the frontal slope or embankment	Settlements	
	Bulges	
	Cracks	Transverse/oblique; Longitudinal

After assigning ratings to each observed indicator, a rating is computed for each of the three components of the structure (wall, drainage, and influence area), along with an overall

rating for the entire structure. This comprehensive rating serves as the primary determinant in the calculation of the Condition Index, as discussed in section 2.2. For detailed insights into the inspection protocol, encompassing the algorithm employed for computing the condition rating for each component and the wall as a whole, readers are referred to Amado (2023a).

In summary, this calculation takes into consideration the varying degrees of relevance associated with the made observations, with some deemed critical, following the methodology proposed by Butler (2016) and Rasdorf (2016). This approach prevents the masking of severe situations through the adoption of a simple average. If any component receives a rating exceeding 4, the overall rating assumes that value. In other instances, the rating is calculated using a straightforward average. An additional rule pertains to the Wall component, stipulating that the overall rating cannot be lower than the rating assigned to this component.

Building upon the findings of the COST ACTION TU1406 project (Hajdin 2018, Pakrashi 2019), the inspection protocol of Infraestruturas de Portugal also documents the causes of defects and underlying damage processes. This documentation provides valuable insights for evaluating the structure's condition. Noteworthy causes, including capacity issues, material deterioration, execution problems, natural phenomena, and maintenance deficiencies, are recorded to enhance the assessment process and pave the way for future development of degradation models, thereby facilitating long-term planning.

4 DISCUSSION

This article has presented a simple and comprehensive risk-based framework for managing retaining walls, encompassing a strategic model, criticality and condition assessments, and risk analysis to support decision-making. A set of performance indicators was also proposed based on a general discretization of the structures in components and elements. The integration of these entities forms a robust and feasible management approach, ensuring the resilience and reliability of earth retaining structures. This framework's applicability extends beyond ERS, offering potential benefits for managing diverse asset types. Notably, bridges emerge as a pivotal domain wherein the framework can be adeptly employed, showcasing its potential benefits for strategic asset management. According to Amado (2023c) the company is currently testing the efficacy of this framework in overseeing overhead sign gantries, thereby establishing a precedent for its successful implementation across various asset classes.

REFERENCES

Amado, J., Freire, L., Santos, F. A. 2019. Framework for the Management of a Large Stock of Earth Retaining Structures. *Towards a Resilient Built Environment Risk and Asset Management*: 780–787. Zurich: International Association for Bridge and Structural Engineering (IABSE).

Amado, J., Pratas, M. A., Monteiro, B., Costa, A., Pinheiro, M. M. 2021. Expedit Condition Assessment of Earth Retaining Structures managed by Infraestruturas de Portugal, S.A. (in Portuguese). *Proceedings of the 17º Congresso Nacional de Geotecnia*. Lisboa: Sociedade Portuguesa de Geotecnia (SPG) & Laboratório Nacional de Engenharia Civil (LNEC).

Amado, J.L., Pratas, M.A., Monteiro, B., Costa, A. and Pinheiro, M. 2023a, Indicators for the Management of Earth-Retaining Structures. *Ce/papers* 6: 1344–1350.

Amado, J., Pratas, M. A., Monteiro, B., Costa, A., Pinheiro, M. M. 2023b. Tools for performance management of earth retaining structures: Implementation in Infraestruturas de Portugal S.A. *Transportation Research Procedia* 72: 2078–2085.

Amado, J. L., Martins, A. C., Rodrigues, N., Minas, N. 2023c. Modelo Estratégico do Sistema de Gestão de Pórticos de Sinalização da Infraestruturas de Portugal, S.A. (in Portuguese). *RAE - Revista De Ativos De Engenharia* 1(1): 31–42.

Butler, C. J., Gabr, M. A., Rasdorf, W., Findley, D. J., Chang, J. C., & Hammit, B. E. 2016. Retaining wall field condition inspection, rating analysis, and condition assessment. *Journal of Performance of Constructed Facilities* 30(3): 04015039.

Hajdin, R., Kušar, M., Mašović, S., Linneberg, P., Amado, J., and Tanasić, N. 2018. WG3 Technical Report. Establishment of a Quality Control Plan. Guimarães: Eurostruct Association.

International Organization for Standardization (ISO). 2015. ISO 9000:2015 - Quality management systems - Fundamentals and vocabulary. Geneva: ISO.
International Organization for Standardization (ISO). 2014. ISO 55000:2014 Asset management — Overview, principles and terminology. Geneva: ISO.
Infraestruturas de Portugal (Unpublished a). GR.IT.GEO.010 Manual for Principal Inspections of Earth Retaining Structures (in Portuguese), Almada.
Infraestruturas de Portugal (Unpublished b). IP.MN.031 Earth Retaining Structures Management System (in Portuguese), Almada.
Institute of Asset Management. 2015. Asset Management - an anatomy. Bristol: IAM.
ISO/IEC. 2013. ISO/IEC 19510:2013(en) - Information technology - Object Management Group Business Process Model and Notation. Geneva: ISO/IEC.
Pakrashi, V., Wenzel, H., Matos, J., Casas, J., Strauss, A., Stipanovic, I., Hajdin, R., Kedar, A., Guðmundsson, G., Limongelli, M.-P., Xenidis, Y., Skaric Palic, S. 2019. Drafting Of Guideline/ Recommendations Of Cost Action TU1406. *WG5 Technical Report*. Guimarães: Eurostruct Association.
Rasdorf, W., Butler, C. J., Findley, D. J., Gabr, M. A., & Bert, S. A. 2016. Framework for Defining Asset Features to Monitor and Assess Earth-Retaining Structures. *Transportation Research Record* 2579(1): 8–16.

Bridge Maintenance, Safety, Management, Digitalization and Sustainability – Jensen, Frangopol & Schmidt (eds)
© 2024 The Author(s), ISBN 978-1-032-77040-6
Open Access: www.taylorfrancis.com, CC BY-NC-ND 4.0 license

Automatic calibration of structural BIM models applied to bridges

F. Lozano-Galant
Universitat Politècnica de Catalunya BarcelonaTech, Spain

E. Atencio
Universidad Pontificia de Valparáiso, Chile

N. Tošić
Universitat Politècnica de Catalunya BarcelonaTech, Spain

J. González-Arteaga
University of Castilla-La Mancha, UCLM, Spain

Y. Xia
Tongji University, Shanghai, China

J.A. Lozano-Galant
University of Castilla-La Mancha, UCLM, Spain

ABSTRACT: Building Information Modeling (BIM) enables the creation of digital twins that simulate physical assets like buildings and infrastructure. Achieving an accurate representation of the true structural behavior necessitates calibrating the properties of these virtual models using real on-site measurements. The calibration process holds particular significance for the federated structural model, as on-site damages can potentially compromise crucial mechanical attributes, jeopardizing the asset's safety and integrity. Although Structural System Identification (SSI) methods can derive actual parameters from on-site measurements, integrating these calibrated properties into BIM models poses challenges. Typically, the calibration process involves manual operations, such as modifying predefined structural databases and updating properties for damaged elements. This manual approach introduces complexities and potential inaccuracies. This paper proposes a novel approach using Robot Process Automation (RPA) to automate the calibration of BIM structural models. The proposed RPA tool automates the generation of new sections in the structural database and the assignment of updated mechanical properties to damaged elements. By leveraging RPA, the integration of SSI results into BIM models can be significantly enhanced, improving interoperability between architectural and structural federated models. Furthermore, this automation supports informed decision-making in structural assessment and maintenance. To validate the proposed tool, a case study is presented involving the calibration of mechanical properties in a real steel bridge. Autodesk software, including Revit and Robot Structural Analysis, is utilized in this case study. The findings demonstrate the effectiveness and potential benefits of the proposed RPA tool in streamlining the calibration process and ensuring the accuracy of BIM structural models.

1 INTRODUCTION

In the context of the ongoing fourth industrial revolution, often referred as Industry 4.0, Architecture, Engineering, and Construction (AEC) industry is undergoing a profound shift driven by digitalization. One prominent methodology at the forefront of this transformation is the pivotal role played by Building Information Modeling (BIM). BIM methodology is based on a federated approach that integrates multiple discipline-specific models into a single, cohesive virtual and holistic representation of a construction project. This integration fosters

DOI: 10.1201/9781003483755-334

improved communication, reduces errors, and improves decision-making throughout the construction project's lifecycle. However, as highlighted by Bellido et al. (2019), challenges related to interoperability among disciplines frequently emerge.

To properly reproduce the actual structural response of a structure, BIM models need to be calibrated. This calibration involves aligning the models with the real mechanical properties of the structural elements including the effects of structural pathologies, such as steel corrosion and concrete cracking. The calibration of the structural parameters, such as axial or flexural stiffnesses, is traditionally carried out by Structural System Identification (SSI) techniques from the static or dynamic structural response measured on site. An overview of some of the most common SSI methods, as well as future trends in the field are presented in Lei et al (2018) and Wu and Jahanshahi (2020). Currently, most SSI methods remain disconnected from the BIM methodology, operating independently with their own structural models. The few studies presented in the literature about this topic focus primarily on calibrating the mechanical and material properties of a structural model exported from the BIM model. This is the case of Bouzas et al. (2022), focused on the calibration of corrosion degradation in a steel bridge. In this work, the BIM model of the bridge is first exported to a dedicated structural software, specifically Ansys. Subsequently, an optimization algorithm was used to update the steel plate thicknesses to minimize the discrepancy between the predicted dynamic response and the actual observed behavior on site. A literature review of other works focused on the geometric parameter updating of BIM models was presented in Osadcha et al. (2023).

Robotic Process Automation (RPA) refers to an advanced technology that employs business rules and activity structures to automate tasks traditionally performed by humans, replicating the same user interface interactions as a human operator. The advantages of RPA include a user-friendly interface, faster and more streamlined programming, and direct execution in productive environments. Asatiani and Penttinen (2016) provide a comprehensive examination of RPA's application in various industries, such as banking, healthcare, and manufacturing. Noteworthy examples of RPA in the construction field include the work of Atencio et al. (2022), who proposed automating the management of low-cost sensors for dynamic structure monitoring using RPA tools, and Jiang and Ling (2022), who suggested employing RPA to automate the operation of building equipment in BIM models. In this context, this paper proposes the application of RPA to automate the calibration of the mechanical properties of BIM models.

This conference paper is organized as follows: Section 2 illustrate the identified problems associated with calibrating structural parameters in BIM models. In Section 3, the utilization of RPAs is presented for the automatic calibration of structural damages in BIM models. Section 4 presents the application of the proposed methodology in a case study. Finally, the main conclusions are drawn in Section 5.

2 INTEROPERABILITY PROBLEMS BETWEEN REVIT AND ROBOT

Connecting structural elements across different software platforms may result in the loss of either geometry or structural attributes. To illustrate these challenges, this section examines interoperability problems in two specific information flows: from Revit to Robot and from Robot to Revit. Additionally, this section shows the challenges of the manual calibration of structural parameters.

2.1 *From Revit to Robot*

In the BIM modeling software Revit, structural elements like beams or columns are organized into families. The analytical model attributes of these families are interconnected with predefined structural databases, such as "EuroPro.xml" for steel profiles. Consequently, when a structural element is added to the BIM model, its structural attributes, such as area and inertia, are automatically retrieved from the corresponding database. The EuroPro database is structured as follows: (1) Definition of the name, section, and shape parameters for various steel shape families, (2) Mathematical equations determining the steel profile boundary based on the defined geometry, and (3) Values of the dimensions and mechanical properties for different steel profiles. Figure 1 illustrates the definition of the IPE 220 profile in the "EuroPro.xml" database.

```
        <row ID="21892" NAME="IPE" DIM1="220" DIM2="0" DIM3="0" SHAPE_TYPE="20" MASS="26.1958" SURF="0.847598" H="0.22"
B="0.11" EA="0.0059" ES="0.0092" RA="0.012" RS="0" GAP="0" SX="0.00333705" SY="0.00201485" SZ="0.00130764"
IX="0.0000000886" IY="0.0000277184" IZ="0.00000204886" IOMEGA="0.0000000226723" VY="0.055" VPY="0.055" VZ="0.11"
VPZ="0.11" MSY="0.000285426" MSZ="0.0000581119" TORS="0.000007776" SHEAR_Qy="0.001352" SHEAR_Qz="0.001147" GAMMA="0"
SYMBOL="" A_1="0" A_2="0" HAS_MATS="false" MATERIALS="" POINTS="" IS_THIN="false" B_2="0" ES_2="0" P1_L="0" P1_T="0" P2
_L="0" P2_T="0" P3_L="0" P3_T="0" P4_L="0" P4_T="0" NAME1="IPE 220" NAME_REVIT="IPE220" IYn="0.0000277184"
IYb="0.0000277184"/>
```

Figure 1. Fragment of the definition of the IPE220 in the "EuroPro.xml" database.

Not all mechanical parameters specified in the databases are readily visible in the corresponding Type Properties in Revit. This discrepancy is particularly evident in the case of flexural inertias (I). This lack of accessibility of the structural parameters prevents its direct customization within Revit.

2.2 *From Robot to Revit*

The mechanical properties of predefined structural elements can be manually adjusted in Robot and incorporated into structural analyses. Nevertheless, the structural attributes of the customized profiles in Robot are not accurately imported into Revit. This interoperability problem arises because the updated mechanical value is not included into the steel profile database (Euro-pro.xml) employed by Revit. Consequently, the customized parameter cannot be properly imported as a BIM object.

2.3 *Manual calibration*

To ensure the interoperability of customized structural sections, it becomes essential to modify the structural databases. However, manually updating the profiles database presents various challenges and limitations. Firstly, the process is time-consuming and labor-intensive, demanding considerable effort to manually adjust and update the model's parameters and attributes. Secondly, manual calibration is susceptible to human error, relying on individual judgment and interpretation, which can introduce inaccuracies and inconsistencies into the model. Additionally, manual calibration lacks a systematic and standardized approach, making it difficult to replicate the calibration process in other projects. Finally, as the model evolves over time, manual calibration becomes cumbersome to maintain and update, potentially resulting in outdated or inaccurate information.

To automate the solution of these three problems, Robotic Process Automation (RPA) protocols are developed in the subsequent section.

3 AUTOMATIC CALIBRATION WITH ROBOTIC PROCESS AUTOMATION

The process for calibrating the BIM models consists of the following steps:

- Step 1: Generation of the analytical model. The BIM model of the structure is initially created in Revit. In this model, the structural elements are assumed to be undamaged, and their properties are extracted from a predefined database. For example, in the case of normalized steel profiles the "EuroPro.xml" database case be used. Subsequently, the analytical model of the structural elements is generated in Revit.
- Step 2: Exporting the analytical model. The analytical model is exported from Revit to Robot Structural Analysis using the integration with Revit Structure dialogue box.
- Step 3: Introduction of the damages in Robot. The effects of the different damages in the mechanical properties and their assignation to the structural elements are defined into a Microsoft Excel sheet. This information is then used to create new damaged sections and assign them to the corresponding elements, thus updating the structural model. This updated model can be used to investigate the effects of damages on structural reliability.
- Step 4: Calibrated structure in Revit. The updated Robot model is imported back into Revit using the integration with the Revit Structure dialogue box.

After manually specifying the necessary information, Steps 3 and 4 can be automated to calibrate the identified structural damages into the analytical model using Robot. This automated procedure is based on the creation of new sections for each damaged element in the structural database, uploading the damaged sections, updating the sections of the damaged elements in Robot, and subsequently updating the model in Revit. This process is automated through an RPA, that is based on the following two protocols: (1) Automatic updating of the structural databases to facilitate the transfer of analytical models between Revit and Robot, and (2) Automatic updating of structural damages in the BIM digital twins. The steps of this RPA are summarized in Figure 2 and elaborated as follows:

- RPA 1: (1) Reading damage information. The RPA opens the Excel sheet input data, reads, and stores the information of the damages, including their name, the values of their mechanical properties, and their allocation to the structural element's identificatory (ID). Then the Excel sheet is closed, and (2) Updating the database with the damaged sections. The RPA opens the .xml database of mechanical properties and creates a new section for each of the damaged properties detailed in the Excel sheet. Then the database is saved and closed.
- RPA 2: (3) Loading the damaged sections in Robot. The RPA opens Robot and loads the damaged sections introduced into the structural database, and (4) Updating the cross-sections of the damaged elements. In this step, the damaged elements are assigned the damaged sections according to the definition of the Excel sheet.

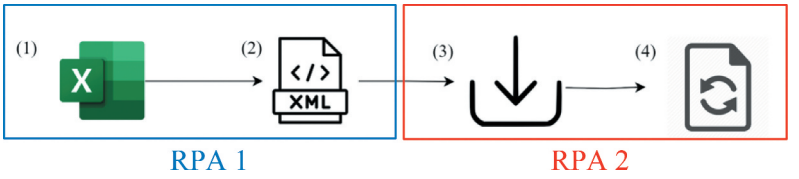


Figure 2. Septs followed by the developed RPAs.

In the following section, the proposed methodology is applied in a case study.

4 CASE STUDY

This section applies the proposed methodology for automating the calibration of structural damages in BIM models to a case study. Firstly, the geometry and the BIM model of the structure are described. Next, the pathologies identified during the on-site inspection of the structure are reviewed. Finally, the application of the RPA protocols to automate the calibration of the structural parameters in the BIM mode is presented.

4.1 *Geometry and BIM model*

The analyzed structure is the Pajareles footbridge, a suspension bridge located in Albacete, Spain, and built in 1935. This bridge includes two steel pylons and a span of 85 meters. The steel deck, measuring 2.35 meters in width, is connected to the main suspension cables through vertical hangers. A picture of this structure is presented in Figure 3. Since no drawings of the structural elements were available, a point cloud was generated on-site using a drone for aerial flights. The resulting point cloud was subsequently processed and cleaned using Autodesk Soft-ware Recap.

The point cloud data was used to create the BIM model presented in Figure 4. The structure depicted in this figure is composed of normalized steel profiles, each family indicated by a different color. The geometry and mechanical properties of the sections in the structure (FL4x30, FL5x60, HEB160, IPN100, CAE30x3, CAE50x5, CAE120x15, ROND10, ROND30, UPN80, UPN140, and UPN 160) were obtained from the "EuroPro.xml" database.



Figure 3. Picture of the Pajareles footbridge.

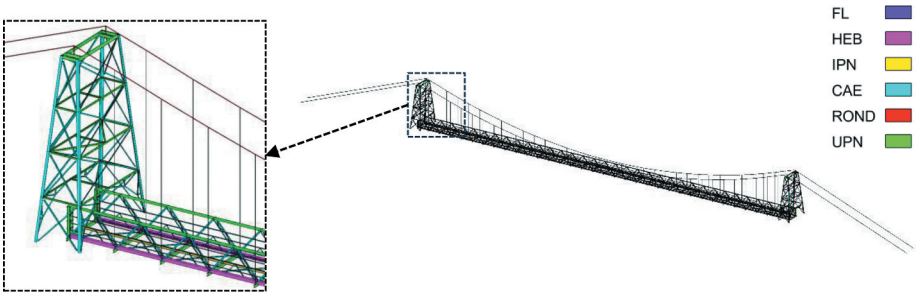


Figure 4. BIM model of the Pajareles footbridge.

The analytical model of the structure was then created in Revit. The obtained model is presented in Figure 5 and it includes 747 analytic bar elements.

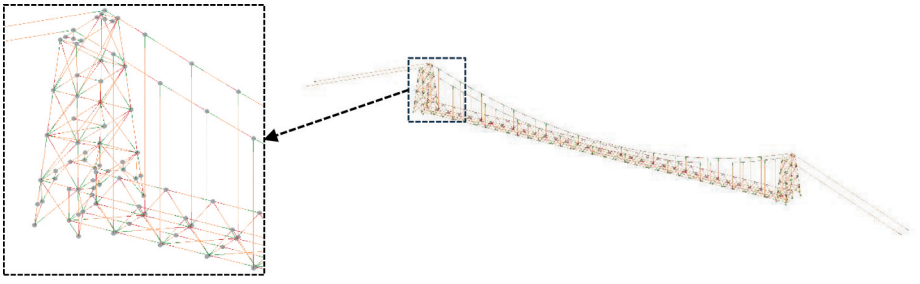


Figure 5. Analytical model of the Pajareles footbridge.

4.2 *Inspection on site*

To assess the condition of the structural elements, an on-site inspection of the Pajareles footbridge was conducted in 2022. This inspection revealed that the majority of steel elements exhibited significant corrosion in most structural elements. In order to study the application of the proposed calibration methodology, a scenario involving damage to all structural members was examined. In this situation, corrosion-related pathologies were presumed to result in significant decreases in mechanical properties, especially concerning areas and inertias, in contrast to the standardized values of the corresponding steel profiles. To simulate the corrosion-induced strength reduction, a random percentage ranging from 0% to 15% was employed as an average value for the entire bar. This percentage was based on previous tests reported in the literature (e.g., Ducuan et al. (2020)).

The perceptual corrosion damages are graphically represented in Figure 6. This illustration incorporates a color-coded filter to categorize the perceptual corrosion damages into three ranges: lower than 5%, between 5% to 10%, and between 10% to 15%.

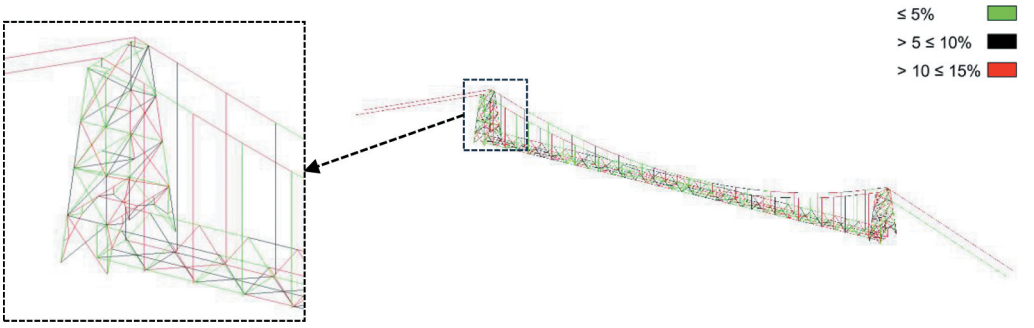


Figure 6. Assumed corrosion damages in the elements of the BIM model.

4.3 *Automatic calibration of the BIM model*

The procedures delineated in Section 3 for automating the calibration of mechanical properties due to corrosion effects were specifically customized for the given case study in the RPA software UiPath.

Following the establishment of the BIM model and the incorporation of damaged information (Step 1), RPA 1 was developed to automate the updating of structural databases, streamlining the transfer of analytical models between the BIM models (Step 2). The input data for this process is sourced from the Excel sheet outlined in Figure 7, and the resulting output encompasses the updated profile database, specifically the Euro-pro.xml database. The actions followed by RPA 1 in can be summarized as follows:

(i) The Euro-pro.xml database is uploaded in .txt format.
(ii) The length of the .txt file is retrieved and stored in a new variable.
(iii) The list of corrosion damages is imported from the Excel sheet.
(iv) The .txt file is copied into a string variable.
(v) The .txt file undergoes a comprehensive editing process, involving an analysis and update of the steel profile family information based on the damaged elements defined in Activity iii.
(vi) The modified .txt file is exported to .xml format to enable compatibility with Revit an Robot software.

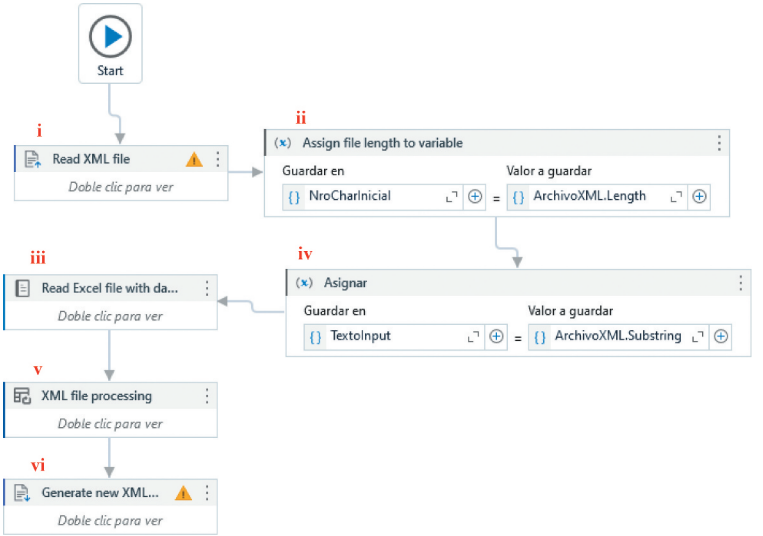


Figure 7. RPA 1 in UiPath highlighting the followed steps.

RPA 2 was customized to facilitate the automated updating of structural damages within the BIM model of the case study. The input data for this process included both the updated profile database and the analytical model in Robot, while the resulting output corresponds to the analytical model updated with the specified corrosion damages. As illustrated in Figure 8, RPA 2 is organized into two distinct modules—one operating within Revit and the other within Robot. The detailed activities carried out by each of these modules are summarized as follows:

(i) Access the BIM model through its Revit .rvt file.
(ii) Export the analytical model of the case study from Revit to Robot using the integration with the Revit Structure dialogue box.
(iii) Import the updated database containing the damaged sections into Robot.
(iv) Extract the list of families for the damaged sections.
(v) Load each damaged family into Robot.
(vi) Import the list of damages from the Excel sheet.
(vii) Attribute the updated properties to the damaged elements. This process involves modifying the section type of the damaged elements from their original designation to the corresponding damaged one in the table of properties of the beam elements within Robot. This task can be automated by pasting the section name specified in the Excel sheet into the section type column for the respective beam elements.

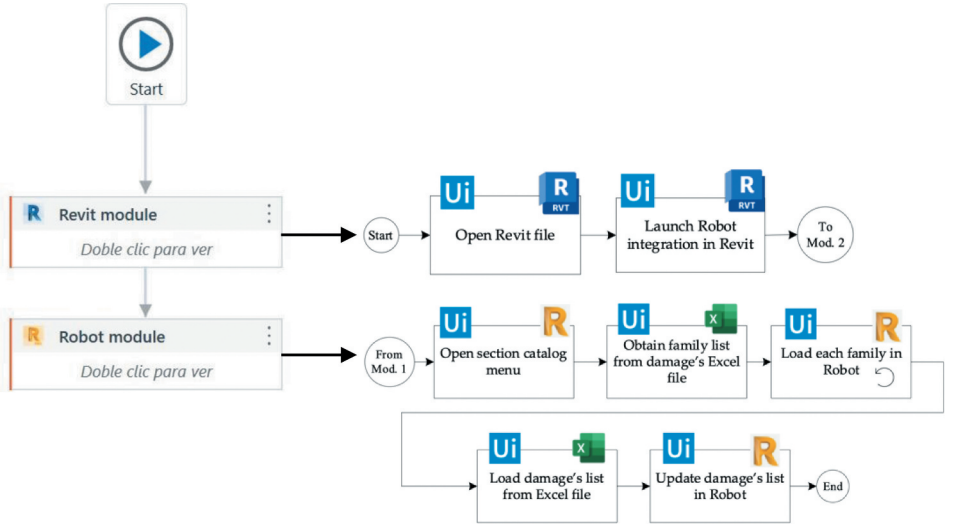


Figure 8. RPA 2 in UiPath highlighting the followed steps.

The calibrated analytical model was transferred from Robot to Revit employing the integration with the Revit Structure dialogue box. The resulting model is presented in Figure 9. It is worth to remark that both the nomenclature and attributes of the elements corresponds with the updated mechanical sections. To exemplify this characteristic, the properties of five damaged sections (UPN_1 160, UPN_2 160, HEB_160, HEB_4 160, and IPN_5 100) are highlighted in the figure.

5 CONCLUSION

This paper proposes a novel tool for automating the calibration of building information modelling (BIM) structural models. This methodology is based on an innovative use of robot process automation (RPA) tools that automates, from a user-friendly and intuitive approach, both the

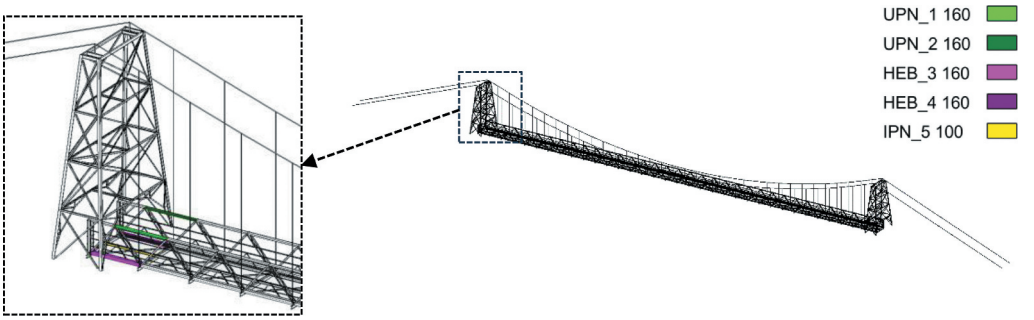


Figure 9. RPA 2 in UiPath highlighting the followed steps.

generation of new sections in the structural database, and the assignment of the updated mechanical properties to damaged elements. State of the art BIM, including Revit and Robot Structural Analysis, and RPA, UiPath, software is used in this study to ensure robust and reliable results. This work contributes to bridging the gap in the automation of BIM models. The effectiveness of the proposed tool is validated in the calibration of the effects of corrosion pathologies in the structural model of a suspension bridge.

ACKNOWLEDGEMENTS

The authors are indebted to the projects PID2021-126405OB-C31, and PID2021-126405OB-C32 funded by MICIN/AEI/10.13039/501100011033/ and FEDER funds A way to make Europe. The financial support of the project F-00528 (PLEC2022-009441) with the title "Optimización topológica para una metodología de construcción de bajo impacto ambiental (Topological optimization for a low environmental impact construction methodology)" is also appreciated.

REFERENCES

Bellido-Montesinos, P. Lozano-Galant, F. Castilla, F. J. & Lozano-Galant, J. A. 2019. Experiences Learned from an International BIM Contest: Software Use and Information Workflow Analysis. *Journal of Building Engineering*, 21: 149–157.

Lei, J. Nogal, M. Lozano-Galant, J.A. Xu, D. & Turmo, J. 2018 Constrained observability method in static structural system identification, *Struct Control Health Monit*, 25(1), doi: 10.1002/STC.2040.

Wu R.T. &. Jahanshahi M.R. 2020. Data fusion approaches for structural health monitoring and system identification: Past, present, and future, *Struct Health Monit*, 19(2): 552–586.

Bouzas, O. Cabaleiro, M. Conde, B. Cruz, Y, & Riveiro B. 2022. Structural health control of historical steel structures using HBIM, *Autom Constr*, 140: 104308, doi: 10.1016/J.AUTCON.2022.104308.

Osadcha, I. Jurelionis, A. & Fokaides, P. 2023 Geometric parameter updating in digital twin of built assets: A systematic literature review, *Journal of Building Engineering*, 73: 106704, doi: 10.1016/J.JOBE.2023.106704.

Asatiani, A. & Penttinen, E. 2016 Turning robotic process automation into commercial success-Case OpusCapita, 2043, doi: 10.1057/jittc.2016.5.

Atencio, E. Komarizadehasl,S. Lozano-Galant, J.A. Aguilera, M. 2022 Using RPA for Performance Monitoring of Dynamic SHM Applications, *Buildings*, *12(140)*: 1140, doi: 10.3390/BUILDINGS12081140.

Jiang H. & Ling, R. 2022 Using RPA+BIM for High Efficient Operation of Smart Building's Equipment Room, doi: 10.20944/PREPRINTS202210.0045.V1.

Dacuan, C. N. Abellana, V. & Canseco, H.A. 2020 Mechanical Properties of Corroded-Damaged Reinforced Concrete Pile-supporting Wharves, Civil Engineering Journal, 6 (1): 2375–2396, doi: 10.28991/CEJ-2020-03091624.

Bridge Maintenance, Safety, Management, Digitalization and Sustainability – Jensen, Frangopol & Schmidt (eds)
© 2024 The Author(s), ISBN 978-1-032-77040-6
Open Access: www.taylorfrancis.com, CC BY-NC-ND 4.0 license

Sustainable-centered approach for bridge management: A game-changer paradigm

D. Duzzi & D. Briccola
University of Applied Sciences and Arts of Southern Switzerland (SUPSI), Mendrisio, Switzerland

ABSTRACT: Bridge owners and operators are responsible for delivering users reliable infrastructures within the road network to develop a prosperous economy and a well-functioning society. As bridges are essential components of the transport road network, especially in alpine countries like Switzerland, switching from bridge- to network-based prioritization rankings to ensure a predefined level of sustainable development considering available resources is paramount. That implies the definition of simplified indexes based on specific indicators to establish a bridge's importance at the network level. The traffic volume, the distance of each artifact from cantonal first aid facilities, the bridge condition assessment, a simplified vulnerability-to-degradation measure, and exposure to natural hazards play a role. The proposed approach, developed for Tessin, could be extended to countries with few principal axes and numerous valleys, like Switzerland. The strategy appears as a potential game-changer paradigm for management of stocks of viaducts and bridges considering multi-hazard risks.

1 INTRODUCTION

In an era characterized by rapid evolutions and continuous changes, the built environment increasingly manifests its vulnerability during extreme weather events. Direct and indirect social, environmental, and economic damages are significant and can jeopardize the well-being of entire nations. Therefore, it is evident that climate change seriously threatens the built environment, and there is an emerging need to develop strategies to implement adaptation actions that reduce damage. Asset managers should guarantee sustainability under all circumstances, not only when natural hazards or extreme weather events occur. That is more desired, the greater the value of the assets considered, like with critical infrastructures, among which road and rail transport infrastructure are prominent.

Especially in Alpine and pre-Alpine countries like Switzerland, the recognition of the socio-economic value of bridges within the transport infrastructure is a driving force for asset managers to identify actions to ensure network continuity in time (availability), space (maintainability), and performance commensurate with changing environmental and operating conditions. Operators must guarantee users a reliable system of bridges characterized by operational efficiency, structural safety, and durability. Nowadays, climate change jeopardizes durability: degradation processes tend to accelerate, become more severe, and increase in time and space. In this framework, damages take the role of additional risks for existing bridges and viaducts.

Not least, increasingly around the world and in Europe, the aging of transportation infrastructure (such as bridges), which are the foundations of modern society freeways, is receiving more and more interest in the wake of the "Morandi bridge" and "Caprigliola bridge" collapse. In fact, many artifacts were built in the period after World War II up to the 1960s, years in which many European nations laid the foundations of modern highway systems, for example, in Italy the 760 km of the "Autostrada del Sole" highway system linking Milan to

DOI: 10.1201/9781003483755-335

Rome and Naples was built, in which 853 bridges and viaducts and 38 tunnels were constructed to complete the work. Nowadays, many European artifacts are reaching their nominal design life, especially there is a need to allocate resources for their assessment, repair and upgrading (see e.g. (Calvi, G.M., 2019) and (Scattarreggia, N., 2022)).

To worsen the already complex framework, the interdependence, deferred in time, between the changes that occur at the global level and those at the local level plays a crucial role. Additionally, adaptation strategies to changes, due to the socio-economic and geo-political structure that has come into being, can only be elaborated and implemented at local level and territorial scale because of the economic resources available and the importance of the individual heritage objects within the reference infrastructure networks. Thus, there is a need to develop management strategies capable of implementing the long-sought paradigm shift related to prioritizing systemic interventions based on simple parameters.

Moreover, to deal with the inherent uncertainty of bridge management due to the continuous and sudden change of boundary conditions (environmental factors, traffic, state of preservation), while respecting operational and economic constraints, it is necessary to move toward management processes establishing thresholds of accepted risk without compromising the well-being of communities. For a unified multi-parameter management, it is essential to make a paradigm shift: consider anomalies and defects affecting condition assessment like risks. That is conceptually feasible due to the randomness in space and time that characterizes climate change.

In such a way, related damages, like durability limitation and the potential impairment of safety and structural efficiency, can be treated together with damages induced by natural hazards. Moreover, based on a priori structural reliability assessments, the technical community can establish an acceptability threshold. Indeed, the growing push for sustainability calls for further reflections on the need to consider it, not only as a discriminating parameter between different maintenance options, but as a cue to devise a sustainable bridge and viaduct management strategy on a territorial scale.

For Tessin, some indicators and indexes are proposed. They measure the importance of each artifact within the infrastructure network in terms of sustainable development, at least concerning the two dimensions society and economy, without neglecting the importance of the structural aspect. The importance metric translates automatically into a scale of attention that allows prioritizing in-depth verification and/or intervention activities since the socio-economic impact of any maintenance work is clearly proportional to the importance of the artifact at the network level. After a description of the social, economic, environmental, and structural aspects considered and the indicators selected, the structure of the indexes of economic, social, and structural vulnerability importance is presented. Finally, a sort of sustainability footprint of the entire road network is shown for bridges and viaducts of the main and secondary roads in Canton Ticino.

The section further development outline the main adaptation measures that should be implemented to extend the methodology beyond the target territory (see e.g. (Mitoulis, S.A., 2021); (Stipanovic, I., 2020) and, (Gaowei, X., 2022)).

2 FROM DATA TO INDEXES: SPATIAL AND CLUSTERING CONSIDERATIONS

With the aim of quantifying the systemic importance of each artifact through a cumulative measure, three indexes were introduced namely the Social Significance Index, the Economic Significance Index, and the Structural Vulnerability Index. Defining an Environmental Significance Index would have required either to introduce a metric related to (i) Life Cycle Assessment, or (ii) to natural hazards. In the first case, that would have meant encompassing the requirement of simplicity at the basis of the developed strategy; in the second case, the inherent uncertainty on the occurrence of natural hazards is emphasized by climate change therefore its representativeness appears too weak. As a result, the Environmental dimension of sustainability was not accounted for in this study.

2.1 *Indicators*

Each index is in turn composed by indicators related to the three dimensions of sustainability and the technical dimension related to structural safety and vulnerability.

The indicators used for indexes formulation are given in Table 1.

The indicators are extrapolated from a set of data collected at the territorial level, timely updated by the Cantonal Statistical Office, and aggregated through specific weights to form significance indexes.

Table 1. List of indicators for each dimension of interest.

Dimension	Social	Economic	Environmental	Structural
Indicator	(I) Number of inhabitants (II) Distance of each bridge from the first aid facility	(I) Number of registered cars (II) Average Daily Traffic	(I) Location and level of risk associated with each natural hazard	(I) Structural scheme (II) Bridge length (III) Bridge condition assessment

2.2 *Data elaboration*

Data collected were subjected to geographical and statistical elaboration.

Clustering criteria based on regional considerations helps in determining the importance of a bridge in terms of socio-economic value through the quantification of indicator SI_1, SI_2 and EI.

For instance, the number of inhabitants that lives close to a bridge and use it to commute every day to work can be considered a measure of the economic importance of an artifact. Likewise, the number of inhabitants that lives close to a bridge also represent a measure of the social importance of the artifact that, during leisure time, represent the access to specific recreational sites or, in case of emergence, to reach first aid centers.

Statistical elaboration (descriptive statistics) of indicators and/or other collected data enables the definition of specific weightings, as explained for each significance index.

2.3 *Indexes*

As anticipated, three indexes were defined to measure the importance of a bridge, and therefore the impact of its temporary closure, within the cantonal road network.

Each index can maximum attain the unitary value and indicators are weighted by means of parameters ranging from 0.25 to 1.00.

2.3.1 *The social significance index*

Table 2. The social dimension of sustainability.

Dimension	Indicator	Description	Index
Social	SI_1	Minimum distance (as the crow flies) of each bridge from the nearest First Aid-equipped hospital.	$SSI_k = \gamma^{I,k}{}_{SI} \cdot \frac{SI_1}{max(SI_1)} + \gamma^{II,k}{}_{SI} \cdot \frac{SI_2}{max(SI_2)}$ **
Social	SI_2	Number of inhabitants belonging to the social contributory area of each artifact.	

**Where γ are the weightings, values assigned to the index based on the percentiles obtained through descriptive statistics, $\gamma_{SI}^{I,k}$ is based on the number of inhabitants per bridges.

2.3.2 *The economic significance index*

Table 3. The economic dimension of sustainability.

Dimension	Indicator	Description	Index
Economic	EI	Average Daily Traffic (ADT) value subdivided based on the automated traffic control station-artifact distance rational. For artifacts along international routes, the ADT value is equal to that of the reference station.	$ESI_k = \gamma_{EI}^{I,k} \cdot \gamma_{EI}^{II,k} \frac{EI^k}{max(EI)} \cdot \gamma_{EI}^{III,k}$ *

*Where γ are the weightings values assigned to the index based on the percentiles obtained through the descriptive statistics, $\gamma_{EI}^{I,k}$ is based on the registered cars numbers in the whole region, $\gamma_{EI}^{II,k}$ is based on the ADT and, $\gamma_{EI}^{III,k}$ is the value given to the type of configuration of the asset (series and parallels).

2.3.3 *The structural vulnerability index*

Finally, the large number of artifacts in the area and reasons for operational sustainability led to the definition of a simplified vulnerability index as a function of artifact type and length. The probability of damage occurrence was implicitly assumed proportional to the length of each artifact. In this way, a masonry bridge is less vulnerable than a viaduct responding to the structural scheme of an arch-frame artifact, and for the same structural scheme, an artifact bypassing a larger obstacle is more vulnerable (see e.g. (Sonnenberg, A., 2018) and (Thompson, P.D., 2018)).

Table 4. The structural dimension.

Dimension	Indicator	Description	Index
Structural	VI	Value of the structural vulnerability of an artifact in relation to its static type.	$SVI_k = \gamma_{VI}^k \cdot \frac{VI^k}{max(VI)}$ ***

***Where γ_{VI}^k is a weighting value based on the different static scheme per bridges.

3 BRIDGE SYSTEMIC SIGNIFICANCE AND CRITICALITY

For each bridge, after the definition of the social and economic significance index, its systemic importance at the territorial scale can be defined. This requires normalizing each index against the maximum value attained along each involved dimension.

As a result, each artifact attains a precise position in a two-dimensional plane identified by the Social Significance Index (x-axis) and Economic Significance Index (y-axis). There each bridge can be represented by a point with a specific shape and color to take into account different structural typologies and artifact condition assessment, as explained in Figure 1.

If a bridge is identified by a point lying along the bisector, it means that within the cantonal road network is equally important respect to social and economic metrics. More in detail, by measuring the distance of each point from the axes 'origin, a measure of the bridge significance in the road network can be obtained.

Of course, the greater the importance of a bridge – the point-origin distance –, the greater the impact of its, albeit temporary, unavailability could produce in the road network.

Conversely, in terms of sustainable development, the maximum benefit could be obtained if and only if asset managers move along the bisector first.

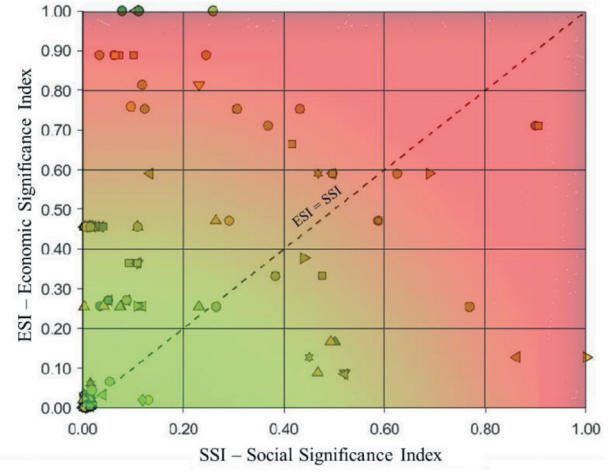
The bridge significance can change over time as the number of inhabitants, the traffic volume, etc. do, therefore points can roam in the SSI-ESI plane.

The plane is ideally subdivided in region that contains bridges with limited to great social and/or economic importance following a green-to-red blended chromatic scale.

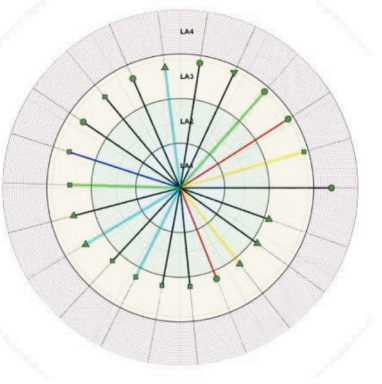
Additionally, the bridge significance and its structural vulnerability index define the so-called bridge level of attention. This level of attention can be visualized in a 3D space, the so-called sustech (sustainability-technical) management space SSI-ESI-SVI, bounded by the axes of Social Significance Index, Economic Significance Index and Structural Vulnerability Index. Asset managers and decision makers can refer to this aggregate measure to define inspection priorities and diagnostic campaigns.

Given that all indexes can attain at maximum a unitary value within the network, in case of unlimited resources, asset managers will have to deal with bridges represented by points close to unpoint (1,1,1) in the space SSI-ESI-SVI as in Figure 3.

It will then be sufficient to calculate the complementary part to unit of the point(bridge)-origin distance in the SSI-ESI-SVI space to obtain for each bridge a so-called systemic level of criticality. For each bridge condition assessment class, asset managers can plot the level of criticality on a radial basis. The higher the level of criticality, the greater the attention bridge managers have to place on that specific bridge.



a)

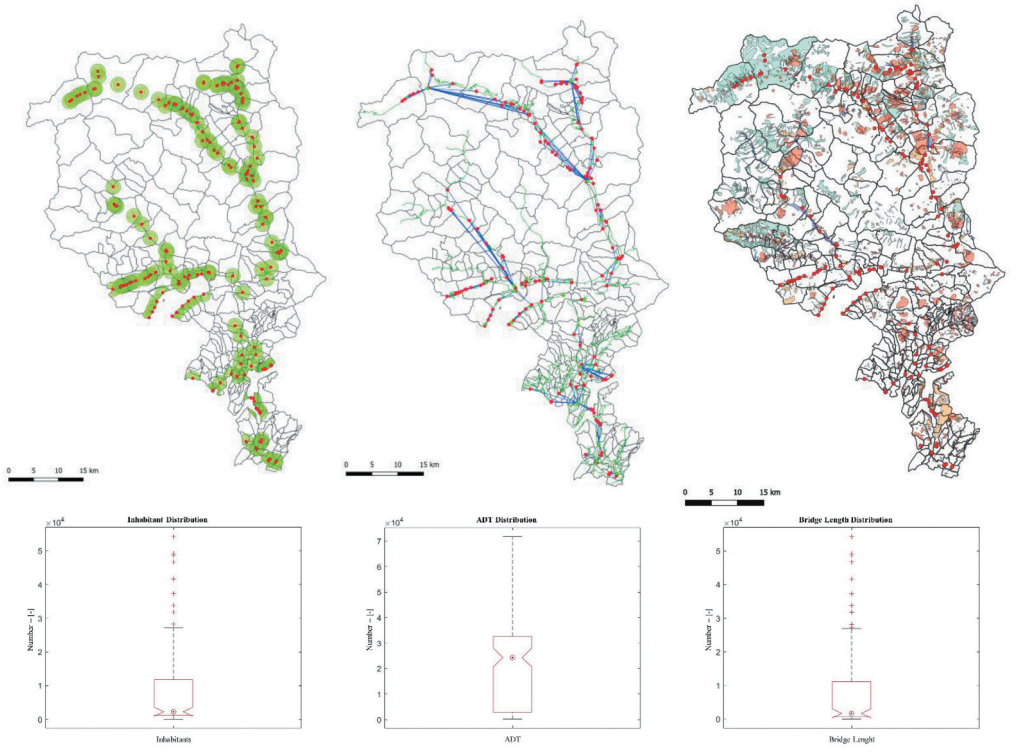


b)

ID Type	Type Name	Preservation state 1	2	3	4	5	Symbol
1111	Simple Beam Bridge						
1112	Multi Beam Bridge						
1121	Frame Bridge						
1123	Arch Bridge						
1124	Tied Arch Bridge						
1125	Framed Arch Bridge						
1193	Slab Bridge						
2311***	Mixed Bridge						

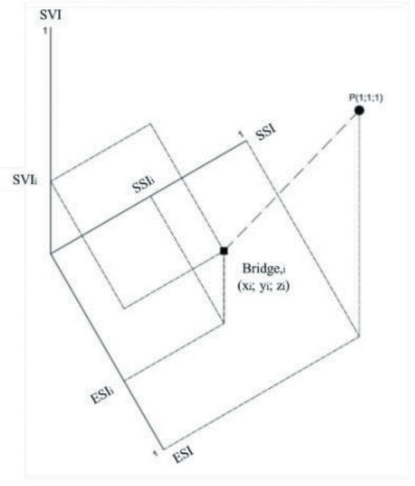
c)

Figure 1. a) Bridge socio-economic importance and related impact; b) Level of criticality of bridges for each condition assessment and related natural hazard level of risks (red-high degree, blue-medium degree, yellow-low degree, green-remaining degree, cyan-indicative danger); c) Overview of the multiplicity of structural types and states of preservation applicable to the artifacts analyzed.



a) b) c)

Figure 2. a) Map of inhabitants about a bridge and associated with descriptive statistics; b) Map of bridge average daily traffic distributions and associated with descriptive statistics; c) Map of natural hazards associated with descriptive statistics of bridge lengths.



a)

ID type	Type name	Symbol	IV
1111	Simple Beam Bridge		0.40
1112	Multi Beam Bridge		0.16
1121	Frame Bridge		0.20
1123	Arch Bridge		0.05
1124	Tied Arch Bridge		0.24
1125	Framed Arch Bridge		0.50
1193	Slab Bridge		0.10
2311	Mixed Bridge		0.40

b)

Figure 3. a) The *sustech* (sustainability-technical) management space ESI-SSI-BVI and a representation of a bridge level of attention b) Indicator of vulnerability based on different types of structural scheme.

4 DISCUSSIONS

The systemic significance and level of criticality measures were conceived with the clear intent of considering technical and contextual aspects in a concise manner.

To validate the representativeness of the measures introduced and their soundness, a sensitivity analysis with respect to each of the indicators and weighting introduced is required.

This extensive analysis is object of a different contribution on the subject (Briccola, D., 2024) and it is not included here just for the sake of brevity.

Due to the high level of heterogeneity in bridge condition assessment, this parameter was intentionally excluded from the definition of systemic measures. However, pursuing a pure clustering approach, for each bridge condition assessment class, asset managers can plot the level of criticality on a radial basis. The higher the level of criticality, the longer the segment in the radial plot and the greater the attention bridge managers have to place on that specific bridge. The information associated with the environmental dimension (natural hazards) and structural typology appear in the radial priority diagrams by means of a chromatic and geometric code, see Figure 1b (see e.g. (Duzzi, D., 2023), (Itoh, Y., 1997) and (Y. Yang, D., 2020)).

Doing that, no information is lost, and asset managers can choose to pay attention to specific aspects from time-to-time, pursuing strategic choices (see e.g. (Frangopol, D.M., 2001)).

Moreover, considering resource constraints and policy, asset managers can fix thresholds to aggregate bridges based on their level of criticality. Once again, these thresholds are dynamic as they can change depending on resource availability subject to political strategies.

5 CONCLUSIONS

The proposed strategy for managing operations on cantonal bridges and viaducts at a territorial scale is based on a comprehensive understanding of the context and the complex variables involved, including bridge number and typology, as well as spatial and operational considerations.

The ultimate objective is to ensure that the infrastructure assets remain resilient and sustainable in the face of continuous change. The strategy considers four basic elements: economy, society, environment, and technical components, to achieve a sustainable development informed by technical aspects.

The article presents indicators and indexes to measure the significance of each artifact within the cantonal transportation network. Although these indicators are specific to the Swiss context – especially Tessin –, they can be easily extended to territories with similar orographic characteristics with valleys and few major commutation axes. The proposed strategy is agile, as it is based on timely data collection and updates, enabling managers to replan decisions to capitalize on emerging opportunities. This potential can be effectively captured by aligning it with pre-existing policies and strategies as well as available resources.

Furthermore, the proposed strategy aligns well with a predictive maintenance approach, rather than a corrective one. By projecting economic, social, environmental, and structural data for a predetermined reference time interval, a picture of the evolving importance of each artifact within the network can be obtained. Based on these results, effective choices can be made to ensure the development of resilient and sustainable infrastructures.

REFERENCES

Calvi, G. M., Moratti, M., O'Reilly, G. J., Scattarreggia, N., Monteiro, R., Malomo, D., Calvi, P. M., Pinho, R. (2019). "Once upon a Time in Italy: The Tale of the Morandi Bridge", Structural Engineering International, 29(2), 198–217, https://doi.org/10.1080/10168664.2018.1558033

Scattarreggia, N., Salomone, R., Moratti, M., Malomo, D., Pinho, R., Calvi, G. M. (2022). "Collapse analysis of the multi-span reinforced concrete arch bridge of Caprigliola, Italy", Engineering Structures, 251:113375, https://doi.org/10.1016/j.engstruct.2021.113375

Mitoulis, S. A., Domaneschi, M., Cimellaro, G. P., Casas, J. R. (2021). "Bridge and transport network resilience – a perspective". Bridge Engineering, 175(3), https://doi.org/10.1680/jbren.21.00055

Stipanovic, I., Connolly, L., Skaric Palic, S., Duranovic, M., Donnelly, R., Bernardini, I., Bakker, J. (2020). "Reliability Based Life Cycle Management of Bridge Subjected to Fatigue Damage", Frontiers In Built Environment, 6, https://doi.org/10.3389/fbuil.2020.00100

Gaowei, X., Fengdi, G. (2022). "Sustainability-oriented maintenance management of highway bridge networks based on Q-learning", Sustainable Cities and Society, 81, https://doi.org/10.1016/j.scs.2022.103855

Sonnenberg, A. (2018). "The development of a modern bridge asset management system", Maintenance, Safety, Risk, Management and Life-Cycle Performance of Bridges, IABMAS 2018: 239–245, https://doi.org/10.1201/9781315189390

Thompson, P. D. (2018). "Risk assessment for bridge management system", Maintenance, Safety, Risk, Management and Life-Cycle Performance of Bridges, IABMAS 2018: 246–253, https://doi.org/10.1201/9781315189390

Briccola, D. & Duzzi, D. (2024). "Sustainable Management of Existing Bridges: Development of a Territorial Strategy", Journal of Management in Engineering, [Manuscript submitted for publication]

Duzzi, D. (2023). "Strategy for the Sustainable Management of Bridges: Territorial Considerations on Integrating Environmental and Socio-Economic Impacts into Decision-Making Processes", Master Thesis, SUPSI.

Itoh, Y., Hammad, A., Liu, C., Shintoku, Y. (1997). "Network-Level Bridge Life-Cycle Management System", Journal of Infrastructure Systems, 3(1), https://doi.org/10.1061/(ASCE)1076-0342(1997)3:1(31)

Y. Yang, D., M. Frangopol, D. (2020). "Life-cycle management of deteriorating bridge networks with network-level risk bounds and system reliability analysis", Structural Safety, 83, https://doi.org/10.1016/j.strusafe.2019.101911

Frangopol, D. M., Kong, J. S., Gharaibeh, E. (2001). "Reliability-Based Life-Cycle Management of Highway Bridges", Journal of Computing in Civil Engineering, 15(1), https://doi.org/10.1061/(ASCE)0887-3801(2001)15:1(27)

Bridge Maintenance, Safety, Management, Digitalization and Sustainability – Jensen, Frangopol & Schmidt (eds)
© 2024 The Author(s), ISBN 978-1-032-77040-6
Open Access: www.taylorfrancis.com, CC BY-NC-ND 4.0 license

Expediting the bridge management practice: A structural reliability-based method

F. Brighenti, M.F. Bado, F. Poli, F. Romeo & D. Zonta
Department of Civil, Environmental and Mechanical Engineering, University of Trento, Trento (TN), Italy

J.D. Rotilio & A. Ferman
Società Autostrade Alto Adriatico S.P.A., Trieste (TS), Italy

ABSTRACT: A significant percentage of assets within the Italian national bridge stock have exceeded their nominal design service life, leading to an escalating number of structural failures over time. While it is impractical to replace all existing infrastructure, the focus has shifted to maintenance and upkeep, commonly achieved through the implementation of well-planned and prioritized maintenance interventions. To effectively manage their bridge stock, infrastructure managers thus require a prioritization tool capable of rapidly assessing the urgent need for maintenance of a particular unit. The present study introduces a novel and expeditious structural reliability model. Specifically, this model provides a comprehensive framework for evaluating risk factors related to overload and degradation, seismic response, hydraulic and landslides conditions, and a detailed formalization of the most widespread ones i.e., overload and degradation. The latter was developed to be applied to the bridges of the Italian highway operator Autostrade Alto Adriatico to enhance their stock management processes. The simplified reliability model presented in this article represents a departure from the complex and time-consuming methodologies currently employed, as it efficiently provides an informative value of Structural Reliability in a proper and expeditious manner. This expeditious approach allows infrastructure managers to promptly discern bridges in critical condition, enabling the swift detection of rapidly deteriorating structures and ensuring timely interventions to enhance user safety.

1 INTRODUCTION

The global landscape of infrastructure is undergoing a critical phase, as a substantial number of bridges have either surpassed or are on the verge of surpassing their intended design life and consequently exhibit potentially severe defects. This predicament is alarmingly widespread, with 42% of American bridges aged 50 years or more, of which 7.5% are structurally deficient, as reported by the American Society of Civil Engineers (ASCE) in 2021 (ASCE 2021). The repercussions of this aging infrastructure are dire, with approximately 178 million trips occurring daily on structurally deficient bridges, posing a significant risk to public safety. In the 2011-2021 decade, 60 bridge failures occurred worldwide (Bado & Casas 2021). This grim reality has manifested in numerous structural failures, including the tragic collapse of the Morandi Bridge in Genoa, Italy, in 2018, resulting in the loss of 43 lives (Calvi et al. 2019).

Addressing this crisis presents a formidable challenge, primarily due to budgetary constraints and the environmental and logistical complexities associated with widespread demolition and reconstruction efforts which, as observed by Regier & Hoult (2014), makes it not feasible to replace all the structures that have surpassed their intended service lives. Consequently, the most viable strategy involves meticulous assessment and strategic maintenance of the bridges still deemed serviceable (Faber 2002). Hence, the importance of determining their

DOI: 10.1201/9781003483755-336

deterioration level, serviceability performance and public safety through a series of inspections, monitoring and maintenance protocols (Bado et al. 2022).

Effective maintenance protocols are not merely about preserving the structural integrity of bridges; they are about maximizing the utilization of economic resources while safeguarding the lives of those who use these critical infrastructural assets (Chase et al. 2016, Denysiuk et al. 2016). Achieving this delicate balance requires up-to-date knowledge concerning durability, defect evolution, and structural reliability (Deng et al. 2014). This knowledge must be continuously updated through regular inspections and the extraction of key data on the asset conservation state. Timely intervention in deteriorating structures can yield significant benefits with minimal financial outlay. Critically, given the constraints of infrastructure managers' budgets, it is imperative to prioritize maintenance interventions based on a rigorous assessment of structural reliability (Frangopol 2019).

Most of the modern-day approaches to the management of bridge stocks are based on the evaluation of the bridge Condition States (Zonta et al. 2007). This one implicitly assumes that the reliability of the bridge is somehow related to the Condition State. Yet, as highlighted by Das (1996), these evaluations often overlook the direct influence of structural defects on bridge reliability and load-carrying capacity. Despite the expectation that bridges in poor structural health would exhibit lower reliability indexes, a direct correlation between the two variables is not straightforward. For instance, an old bridge can be unsafe, even if impeccably preserved, due to inadequate load-carrying capacity resulting from changes in traffic patterns. Conversely, a deteriorated bridge might still possess sufficient capacity.

In the current landscape, there are sophisticated methodologies available for the comprehensive evaluation of bridge structural reliability. However, many of these methods are time-consuming and intricate, making them less than ideal for swiftly assessing bridges in urgent need of maintenance. Infrastructure managers require rapid assessments to prioritize interventions effectively. To expedite this evaluation process and subsequently prioritize bridge maintenance interventions, this article proposes a simplified structural reliability model. This model thus enables infrastructure managers to swiftly identify bridges undergoing rapid deterioration, ensuring timely intervention and enhancing user safety.

2 STRUCTURAL RELIABILITY: ITS THEORETICAL BACKGROUND IN BRIEF

Structural Reliability, a fundamental aspect of bridge engineering, is a concept rooted in the probabilistic quantification of a bridge's safety coefficient, delineating its capacity to meet specific structural requirements (Luo et al. 2009). Central to this assessment is the Probabilistic Reliability Theory, providing indispensable methodologies for evaluating Structural Reliability and, consequently, the Probability of Failure. A plethora of practical numerical techniques has been developed, including the Monte Carlo simulation (Tonelli et al. 2023), Importance Sampling, Response Surface Approximation (Rajashekhar & Ellingwood 1993), and Moment Methods such as the First-Order reliability method (Hasofer & Lind 1974) and the Second-Order reliability methods (Hohenbichler & Rackwitz 1988, Luo et al. 2009).

It is important to note that although the First-Order method is considered one of the most efficient computational approaches for Probabilistic Structural Reliability (Luo et al. 2009), the Second-Order method is widely employed for reliability calculations and code calibration purposes as well (Melchers & Beck 2018). Typically, a structure's reliability is quantified using a Reliability Index, determined based on probabilistic data, technical models, and additional bridge-related information (Möller & Beer 2004). This Reliability Index serves as a crucial parameter used by infrastructure managers to prioritize maintenance interventions for their inventory (Zonta et al. 2007). Crucially, the Reliability Index inversely correlates with the Probability of Failure P_F, exemplifying that higher β values translate to lower collapse probabilities (Der Kiureghian & Liu 1986).

In structural reliability analysis, dealing with the computational complexities, often involves resorting to a method known as First-Order Second-Moment (Ayyub & Haldar 1984). Essentially, Second-Moment reliability methods, encompassing both First-Order and Second-Order

Methods, simplify the complexities by expressing all uncertainties related to a structure's reliability in terms of expected values (first moments) and covariances (second moments) of the input parameters (Cornell 1969, Ditlevsen 1981). This means estimating the approximate mean and variances of Z (μ_Z and ${\sigma_Z}^2$, respectively) using information derived from the means ($\mu_{x,i}$) and variances (${\sigma_{x,i}}^2$) of the fundamental random variables X_i (Ayyub & Haldar 1984). These Second-Moment methods find extensive application in reliability calculations and are instrumental in code calibration purposes as well (Melchers & Beck 2018).

Certainly, the Limit State Function is commonly conceptualized as the disparity between a system's resistance (R) and the corresponding load effect S (Denysiuk et.al. 2016), thus Z is defined by Equation (1).

$$Z = R - S \tag{1}$$

Given this perspective and assuming the uncorrelation hypothesis of R and S, a Reliability Index β can be defined using the First-Order Second-Moment Method, as outlined in Equation (2):

$$\beta = \frac{\mu_Z}{\sigma_Z} = \frac{\mu_R - \mu_S}{\sqrt{{\sigma_R}^2 + {\sigma_S}^2}} \tag{2}$$

Where the symbols μ_R, μ_S are the mean value of R and S respectively and ${\sigma_R}^2$ and ${\sigma_S}^2$ are the variance of R and S, respectively.

When assuming both R and S follow a lognormal distribution, Equation (2) can be reformulated as Equation (3) in terms of Expected Value $E[\cdot]$ akin to the formulation by Rosenblueth and Esteva (Ditlevsen & Madsen 2007).

$$\beta = \frac{E[\ln R] - E[\ln S]}{\sqrt{Var[\log R] + Var[\log S]}} \cong \frac{\ln E[R] - \ln E[S]}{\sqrt{V_R^2 + V_S^2}} = \frac{\ln \mu_R - \ln \mu_S}{\sqrt{V_R^2 + V_S^2}} = \frac{\ln \mu_R - \ln \mu_S}{V_z} \tag{3}$$

In this context, $V_R = \sigma_R/\mu_R$ signifies the Coefficient of Variation for R, $V_S = \sigma_S/\mu_S$ indicates the Coefficient of Variation for S and $V_z = \sqrt{(V_R^2 + V_S^2)}$ represents the Limit State Coefficient of Variation. Notably, the latter, encapsulates the overall uncertainty of a specific model based on Equation (1) including uncertainties in its parametrical distribution, variance, and load effects calculation methodologies, among others.

3 A NOVEL APPROACH TO THE ASSESSMENT OF STRUCTURAL RELIABILITY OF BRIDGES

In the framework of contemporary engineering practices, the assessment of structural reliability has become increasingly intricate, necessitating advanced methodologies (Luo et al. 2009). However, to streamline the evaluation process and expedite the prioritization of bridge maintenance interventions, there arises a compelling need for a swift and simplified structural reliability model. Addressing this need, this article introduces an innovative approach, streamlining the complexities inherent in the reliability assessment of bridges.

Navigating the complexities of Structural Reliability, this article delves into the intricacies of the Limit State Function, emphasizing the integral role of Reliability Index (β) in this context (Ayyub & Haldar 1984). This index, representing the difference between the resistance (R) and the load effect (S) of a structure, is pivotal in gauging reliability. The formulation of β, often derived using the First-Order Second-Moment Method, encapsulates the mean values and variances of R and S, shedding light on the reliability landscape (Ayyub & Haldar 1984). Despite the inherent challenges, this method offers a pragmatic approach, especially when dealing with lognormal distributions of R and S, enabling a nuanced evaluation of reliability

(Cornell 1969). Armed with these foundational concepts, this article introduces a simplified model for bridge structural reliability assessment, bridging the theoretical underpinnings with practical applications.

To achieve this, our novel model incorporates several simplifications and assumptions:

1. Reference Condition: A designated reference state denoted by the subscript "0."
2. Log-Normal Distributions: Resistance R and Load Effect S follow log-normal distributions: $R \sim L(\mu_R, V_R)$ and $S \sim L(\mu_S, V_S)$ respectively.
3. Resistance Coefficient of Variation: V_R of an undamaged bridge aligns with the reference code's Resistance Coefficient of Variation $V_{R,0}$, making $V_R \equiv V_{R,0}$.
4. Constant Load Effect: S remains constant according to the reference code. In fact, by selecting the most recent available code as the reference, it is implied that the traffic load on all present-day bridges irrespective of their original design code or current state of damage conforms to the specifications outlined in the reference codes., i.e., $S \equiv S_0$ (consequently $L(\mu_S, V_S) = L\left(\mu_{S,0}, V_{S,0}\right)$.
5. Uncorrelated Risk Factors: Risk factors influencing bridge reliability are considered uncorrelated.

When a bridge transitions from its reference state 0 to a generic state ≠0 due to its service life, its structural reliability varies. In this context, the reliability index of the bridge in the generic state is denoted as β, while the index for the same bridge in its just-built state, designed as per the reference code 0, is noted as β_0. Leveraging these assumptions and Assumptions 1-5 along with Equation (3), the relation between these two reliability indices can be calculated Equation (4).

$$\begin{aligned}\beta &= \frac{\ln\left(\frac{\mu_R}{\mu_{s,0}}\right)}{V_z} = \frac{\ln\left(\frac{\mu_R}{\mu_{s,0}}\frac{\mu_{R,0}}{\mu_{R,0}}\right)}{V_z} = \left\{\frac{\ln\left(\frac{\mu_{R,0}}{\mu_{s,0}}\right)}{V_z} + \frac{\ln\left(\frac{\mu_R}{\mu_{R,0}}\right)}{V_z}\right\} \cdot \frac{v_{z,0}}{v_{z,0}} \\ &= \left\{\frac{\ln\left(\frac{\mu_{R,0}}{\mu_{s,0}}\right)}{v_{z,0}} + \frac{\ln\left(\frac{\mu_R}{\mu_{R,0}}\right)}{v_{z,0}}\right\} \cdot \frac{v_{z,0}}{v_z} = \left\{\beta_0 + \frac{\ln\left(\frac{\mu_R}{\mu_{R,0}}\right)}{v_{z,0}}\right\} \cdot \frac{v_{z,0}}{v_z}\end{aligned} \tag{4}$$

The reliability index β can be computed for different risk factors based on the analysis objectives.The risk model proposed in the present article calculates a Reliability Index and the Probability of Failure P_F for the main risk factors associated with civil engineering structures: risk for Overload and Degradation (D), Seismic risk (S), Hydraulic risk (H) and Landslides risk (L). Furthermore, under the Assumption 6, the risk factors can be combined in order to extract a unique value of Total Probability of Failure P_F as in Equation (5).

$$P_F = P_{F,D} + P_{F,S} + P_{F,H} + P_{F,L} = \phi(-\beta_D) + \phi(-\beta_S) + \phi(-\beta_H) + \phi(-\beta_L) \tag{5}$$

In the present article the authors proceed to showing only the calculation-modus-operandi of $P_{F,D}$, commonly the most impactful and widespread risk. The Overload and Degradation Risk encompasses two core components: Overload risk linked to different codes than the reference one, leading to varying Traffic Loads, and Degradation risk, representing capacity reduction due to structural defects. The Overload and Degradation Risk sees the above two risks combined into one, in light of the fact that they both have a direct influence on the Carrying Capacity of a bridge.

Before delving in the extrapolation of $P_{F,D}$, it should be kept in mind that, whenever dealing with any of the above introduced risks, additional uncertainties beyond mathematical modeling $V_{z,0}$ come into play, denoted as ΔV_z. These uncertainties arise from variations in the bridge's state from its reference condition, persistently increasing over time.

Indeed, whenever mathematical modelling uncertainties are the only ones being discussed – as in the previous section – the overall uncertainty V_z coincides with $V_{z,0}$ i.e., $V_z = V_{z,0}$ (which fundamentally is $V_z = \sqrt{V_{z,0}^2}$). Whereas when other uncertainties are present, then the overall

uncertainty V_z can be expressed as $V_z = \sqrt{\left(V_{z,0}^2 + \Delta V_z^2\right)}$. The parameter ΔV_z represents the variation of uncertainty arising whenever a divergence of the state of the bridge from its reference condition. Considering that a variation of the state occurs from the first moment that the bridge is built (environmental factors, constant use, etc.), this one is always positive.

In light of the fact that both degradation and overload are inherently correlate as both impact the Carrying Capacity of a bridge, they are unified into a single Uncertainty Variation ΔV_z and Reliability Index β_D.

4 MATHEMATICAL FORMULATION FOR ASSESSING THE OVERLOAD AND DEGRADATION RELIABILITY OF BRIDGES

The authors will now guide you through the steps to derive the mathematical formulation of β_D. Starting with the undamaged state of a bridge and Equation (4), we'll now express the $\ln \mu_R$ and $\ln \mu_{R,0}$ terms. To achieve this, we employ the fractile or lower/upper percentile of order 5% related to the log-normal probability distribution of the Resistance evaluated against its median value $R_{50\%}$ utilizing Equation (6) (Melchers & Beck 2018).

$$\ln R_k = \ln R_{50\%} - 1.645 * V_R \tag{6}$$

Here, the characteristic value of the Resistance R_k is equal to $R_{d,U} * \gamma_R$, where $R_{d,U}$ denotes the Design Resistance of a bridge in its undamaged condition, and γ_R signifies the Resistance Safety Coefficient. Based on Assumption 3, Equation (6) and the system in Equation (7), we can deduce the mean value of Resistance $\ln \mu_R$, as follows:

$$\begin{cases} \ln R_{50\%} = \ln R_{d,U} + ln\gamma_R + 1.645 * V_R \\ ln\mu_R = lnR_{50\%} + \frac{V_R^2}{2} \end{cases} \rightarrow \ln \mu_R = \ln R_{d,U} + \ln \gamma_R + 1.645 * V_R + \frac{V_R^2}{2} \tag{7}$$

Note that, the same equation can be formulated for the reference condition 0 (in terms of $R_{d,0}$, $\gamma_{R,0}$ and $V_{R,0}$). On the grounds of Equations (4) and (7) and Assumption 6, the difference between the two Reliability Indexes can be evaluated as per Equation (8).

$$\beta_D = \left\{ \beta_{D,0} + \frac{\ln\left(\frac{R_{d,D}}{R_{d,0}}\right)}{V_{z,0}} \right\} \cdot \frac{v_{z,0}}{v_z} = \left\{ \beta_{D,0} + \frac{\ln\left(\frac{R_{d,D}}{R_{d,0}} \cdot \frac{R_{d,U}}{R_{d,U}}\right)}{V_{z,0}} \right\} \cdot \frac{v_{z,0}}{v_z} = \left\{ \beta_{D,0} + \frac{\ln\left(\frac{R_{d,D}}{R_{d,U}} \cdot \frac{R_{d,U}}{R_{d,0}}\right)}{V_{z,0}} \right\} \cdot \frac{v_{z,0}}{v_z} \tag{8}$$

Let's consider the known effects of (1) Permanent Load G, (2) Traffic Load calculated according to the reference code $Q_{d,0}$, and (3) Traffic Load calculated using a specific outdated code $Q_{d,U}$. Based on these factors, the following extrapolations can be made:

- $R_{d,\mathrm{D}} = G + Q_{d,\mathrm{D}}$ representing the Resistance of a bridge in its damaged condition;
- $R_{d,0} = G + Q_{d,0}$ representing the Design Resistance calculated according to the reference code;
- $R_{d,U} = G + Q_{d,U}$ indicating the Design Resistance calculated based on an outdated code and, significantly, in its undamaged state. It's essential to note that this value aligns with the Resistance of the bridge in its newly constructed state, reflecting the construction standards of the past years;
- $I = Q_{d,U}/Q_{d,0}$ denoting the Performance Index. Generally, if we consider the more recent code as the reference, then $I < 1$. This is because modern-day reference traffic loads tend to be more conservative than their outdated counterparts.

Given these considerations, the authors now delve into the $R_{d,U}/R_{d,0}$ ratio presented in Equation (8). This ratio signifies the potential Resistance deficiency of a bridge solely due to

its design with an outdated code compared to the reference one. Referred to as the Capacity Index C, it can be elaborated as per Equation (9).

$$\frac{R_{d,U}}{R_{d,0}} = \frac{1 + \frac{Q_{d,U}}{G} * \frac{Q_{d,0}}{Q_{d,0}}}{1 + \frac{Q_{d,0}}{G}} = \frac{1 + \frac{Q_{d,U}}{Q_{d,0}} * \frac{Q_{d,0}}{G}}{1 + \frac{Q_{d,0}}{G}} = \frac{1 + I * \frac{Q_{d,0}}{G}}{1 + \frac{Q_{d,0}}{G}} = C \tag{9}$$

Now, let's shift our focus to the damaged state of a bridge. In this scenario, Equation (8) not only includes the $R_{d,U}/R_{d,0}$ ratio (representing the undamaged condition) but involves also a new ratio, $R_{d,\mathrm{D}}/R_{d,0}$ (D for damaged condition). This definition therefore encapsulates both the impact of overload and damage on the Carrying Capacity of the bridge. This ratio can be expressed as $R_{d,D}/R_{d,0} * R_{d,U}/R_{d,U} = R_{d,D}/R_{d,U} * R_{d,U}/R_{d,0}$.

Whilst the $R_{d,U}/R_{d,0}$ ratio has already been defined as the Capacity Index C, the $R_{d,D}/R_{d,U}$ ratio represents the Resistance deficiency of a bridge solely due to the presence of damage. This ratio is now referred to as the Damage Index $D \in (0, 1)$. It's important to note that this index can be calculated in various ways, such as through meticulous static calculations or simulations, predefined reduction values linked to different damage levels, visual inspections, instrumental damage diagnosis, and so on.

Considering these factors, Equation (8) can be reformulated as Equation (10). Equation (10) incorporates both D and C, reflecting the bridge's state transition.

$$\beta_D = \beta_{D,0} + \frac{\ln\left(\frac{R_{d,D}}{R_{d,0}}\right)}{V_{z,0}} = \beta_{D,0} + \frac{\ln\left(\frac{R_{d,D}}{R_{d,U}} * \frac{R_{d,U}}{R_{d,0}}\right)}{V_{z,0}} = \beta_{D,0} + \frac{\ln(D * C)}{V_{z,0}} \tag{10}$$

As previously mentioned, the variation of the state of the bridge versus its initial/reference condition 0 (integrated through D and C), inevitably brings along an increase in uncertainty. This needs to be accounted for in terms of reliability. In particular, the output of Equation (10) needs to be decreased of an amount equivalent to the increase in uncertainty i.e., the ratio $V_{z,0}/V_z \in (0, 1)$, as in Equation (11).

$$\beta_D = \left\{\beta_{D,0} + \frac{\ln(D * C)}{V_{z,0}}\right\} \frac{V_{z,0}}{V_z} \tag{11}$$

Finally, incorporating the Overload and Degradation Reliability Index β_D, Equation (12) calculates the Probability of Failure $P_{F,D}$ using the standard normal cumulative distribution function:

$$P_{F,D} = \phi(-\beta_D) = \phi\left(-\left\{\beta_{D,0} + \frac{\ln(D * C)}{V_{z,0}}\right\} \frac{V_{z,0}}{V_z}\right) \tag{12}$$

Note that, being the Reliability Index calculated for both the bending limit state M and the shear one V, the overall Overload and Degradation Reliability Index β_D is assumed as their minimum: $\beta_D = \min(\beta_{D,M},\ \beta_{D,V})$.

Nonetheless, being the reference period of the model 50 years, the degradation over this time should be taken into account as well. The approach can be integrated with a sophisticated degradation model rooted in Markov Chains (Ayyub & Haldar 1984), offering a nuanced depiction of the evolution of the parameters associated with structural defects. In this framework, the pivotal element of the Markov Chain is encapsulated in Transition Matrixes T, delineating the likelihood of maintaining the current state on the diagonal elements and the probabilities of transitioning to subsequent states on the elements external to the diagonal, facilitating a robust foundation for projecting the system's behavior.

The evolution of the defect can therefore be dynamically captured by iteratively modifying the Transition Matrix T through matrix multiplication, leading to the derivation of state

probability vectors which, in turn, crystallizes the likelihood of specific states of degradation after a defined temporal interval (Ayyub & Haldar 1984). Crucially, the methodology accommodates scenarios where the defect is both present and absent during the initial inspection, forming a nuanced narrative of the defect's evolutionary trajectory over time.

Key structural parameters, namely the weighted average value of Damage Index D_i, the coefficient of variation $V_{z,i}$ in consideration of such weighted average value of Damage Index, and Reliability Index for a return period of 1 year $\beta_{D,01}$, can then be extracted from the state probabilities, offering a dynamic portrayal of the structural system's health at any given i-th year. The temporal descent of D_i underscores the structural deterioration over time, while the ascent of $V_{z,i}$ is emblematic of evolving uncertainties in the model projection and defect degradation. Reliability Index $\beta_{D,01}$ is discerned for the undamaged reference state with a 1-year return period through meticulous consideration of Poisson processes (Ayyub & Haldar 1984), laying the groundwork for computing the Probability of Failure $P_{F,D,i}$ at various time horizons, encompassing all conceivable status of defect during the initial inspection. This meticulous procedure culminates in the creation of a robust matrix of projected collapse probabilities, enriching the understanding of the structural system's resilience.

This innovative approach not only simplifies the complex task of structural reliability assessment but also provides a comprehensive framework for evaluating multiple risk factors, paving the way for efficient and informed bridge maintenance strategies.

5 CONCLUSIONS

The global scenario of aging bridges poses an intricate challenge, with many of these structures exhibiting potentially severe defects as they approach or surpass their nominal design life. The impracticality of replacing all these structures underscores the necessity for an alternative approach: preserving the assets still functional through judicious, scheduled maintenance interventions. Achieving this preservation imperative hinges on a nuanced understanding of bridge performance, specifically in terms of structural reliability.

Modern strategies for managing bridge stocks predominantly rely on the evaluation of bridge Condition States, a method that erroneously assumes a direct relationship between these states and structural reliability. This oversimplification obscures the actual impact of structural defects on bridge reliability and load-carrying capacity. For instance, an aging bridge, even if meticulously preserved, can be perilous if its original load-carrying capacity no longer aligns with contemporary traffic demands. Conversely, a deteriorating bridge might possess adequate capacity, complicating the evaluation further.

In response to this complexity, a myriad of intricate methodologies have emerged for comprehensive bridge structural reliability assessments. However, not all of these methodologies are conducive to swift application. Addressing this gap, our article presents a groundbreaking solution: a simplified structural reliability model. This innovative model integrates crucial risk factors such as Overload, Degradation, Seismic, Hydraulic, and Landslides, focusing primarily on Overload and Degradation—the two most widespread risk factors. Crucially, our model incorporates an element of uncertainty inherent in the assumed model and the presence of Overload and Degradation, providing an extensive understanding of structural reliability.

The simplified reliability model represents a departure from the nowadays complex and time-consuming methodologies, as it is able to provide an informative value of Structural Reliability in a proper and expeditious manner. On the grounds of such swift reliability assessment, this model empowers infrastructure managers to swiftly identify bridges undergoing rapid deterioration. This timely identification ensures interventions occur promptly, significantly enhancing user safety and safeguarding critical infrastructure assets.

ACKNOWLEDGEMENT

The studies presented here were carried out as part of the activities envisaged by a research agreement between the University of Trento and Autostrade per l'Italia SpA, and supported by Fondazione CARITRO Cassa di Risparmio di Trento e Rovereto (grant number 2021.0224), MIUR PON RI 2014-2020 Program (Project MITIGO, ARS01_00964), the Agreement between the High Council of Public Works (CSLLPP) and the ReLUIS Consortium implementing Ministerial Decree 578/2020 and Ministerial Decree 240/2022, and the Agreement between the Italian Department of Civil Protection (DPC) and the ReLUIS Consortium. The contents of this paper represent the authors' ideas and do not necessarily correspond to the official opinion and policies of CSLLPP and DPC.

CONFLICTS OF INTEREST

The authors confirm that there are no conflicts of interest.

REFERENCES

ASCE. 2021. ASCE Report Card for America's Infrastructure 2021 - A comprehensive assessment of America's infrastructure Executive summary. In *ASCE*.

Ayyub, B. M., & Haldar, A. 1984. Practical Structural Reliability Techniques. *Journal of Structural Engineering*, *110*(8), 1707–1724.

Bado, M. F., & Casas, J. R. 2021. A review of recent Distributed Optical Fiber Sensors applications for Civil Engineering Structural Health Monitoring. *Sensors*, *21*(5), 111–123.

Bado, M. F., Tonelli, D., Poli, F., Zonta, D., & Casas, J. R. 2022. Digital Twin for Civil Engineering Systems: An Exploratory Review for Distributed Sensing Updating. *Sensors*, *22*(9), 3168.

Calvi, G. M., Moratti, M., O'Reilly, G. J., Scattarreggia, N., Monteiro, R., Malomo, D., Calvi, P. M., & Pinho, R. 2019. Once upon a time in Italy: The tale of the Morandi Bridge. *Structural Engineering International*, *29*(2), 198–217.

Chase, S. B., Adu-Gyamfi, Y., Aktan, A. E., & Minaie, E. 2016. Synthesis of National and International Methodologies Used for Bridge Health Indices. In *Federal Highway Administration* (Issue FHWA-HRT-15-081).

Cornell, C. A. 1969. A probability-based structural code. *Journal Proceedings*, *66*(12), 974–985.

Das, P. C. 1996. Bridge management methodologies. *Recent Advances in Bridge Engineering. Proceedings of the US-Europe Workshop on Bridge Engineering. Technical University of Catalonia, Spain and Iowa State University*.

Deng, X., Hu, Y., & Deng, Y. 2014. Bridge condition assessment using D numbers. *The Scientific World Journal*, *2014*.

Denysiuk, R., Fernandes, J., Matos, J. C., Neves, L. C., & Berardinelli, U. 2016. A Computational Framework for Infrastructure Asset Maintenance Scheduling. *Structural Engineering International*, *26* (2), 94–102.

Der Kiureghian, A., & Liu, P.-L. 1986. Structural reliability under incomplete probability information. *Journal of Engineering Mechanics*, *112*(1), 85–104.

Ditlevsen, O. 1981. Principle of normal tail approximation. *Journal of the Engineering Mechanics Division*, *107*(6), 1191–1208.

Ditlevsen, O., & Madsen, H. O. 2007. *Structural Reliability Methods* (Issue September). Department of Mechanical Engineering, Technical University of Denmark.

Faber, M. H. 2002. Risk-Based Inspection: The Framework. *Structural Engineering International*, *12*(3), 186–195.

Frangopol, D. M. 2019. Life-cycle performance, management, and optimisation of structural systems under uncertainty: accomplishments and challenges. In *Structures and Infrastructure Systems* (pp. 5–29). Routledge.

Hasofer, A. M., & Lind, N. C. 1974. Exact and invariant second-moment code format. *Journal of the Engineering Mechanics Division*, *100*(1), 111–121.

Hohenbichler, M., & Rackwitz, R. 1988. Improvement of second-order reliability estimates by importance sampling. *Journal of Engineering Mechanics*, *114*(12), 2195–2199.

Luo, Y., Kang, Z., & Li, A. 2009. Structural reliability assessment based on probability and convex set mixed model. *Computers and Structures*, *87*(21–22), 1408–1415. https://doi.org/10.1016/j.compstruc.2009.06.001

Melchers, R. E., & Beck, A. T. 2018. *Structural reliability analysis and prediction*. John wiley & sons.

Möller, B., & Beer, M. 2004. *Fuzzy randomness: uncertainty in civil engineering and computational mechanics*. Springer Science & Business Media.

Rajashekhar, M. R., & Ellingwood, B. R. 1993. A new look at the response surface approach for reliability analysis. *Structural Safety*, *12*(3), 205–220.

Regier, R., & Hoult, N. A. 2014. Distributed Strain Behavior of a Reinforced Concrete Bridge: Case Study. *Journal of Bridge Engineering*, *19*(12), 1–9. https://doi.org/10.1061/(ASCE)BE.1943-5592.0000637

Tonelli, D., Beltempo, A., Cappello, C., Bursi, O. S., & Zonta, D. 2023. *Reliability analysis of complex structures based on Bayesian inference*. https://doi.org/10.1177/14759217231152798

Zonta, D., Zandonini, R., & Bortot, F. 2007. A reliability-based bridge management concept. *Structure and Infrastructure Engineering*, *3*(3), 215–235. https://doi.org/10.1080/15732470500315740.

Bridge Maintenance, Safety, Management, Digitalization and Sustainability – Jensen, Frangopol & Schmidt (eds)
© 2024 The Author(s), ISBN 978-1-032-77040-6
Open Access: www.taylorfrancis.com, CC BY-NC-ND 4.0 license

Development of a bridge rating tool for optimised multi-hazard life-cycle-based maintenance

M. Calò, N. Scattarreggia, G. Mucedero & R. Monteiro
IUSS – School for Advanced Studies, Pavia, Italy
RESISK s.r.l., Pavia, Italy

ABSTRACT: Providing and maintaining a resilient and sustainable transport infrastructure is a main priority nowadays for a solid economic development. While infrastructure plays an important role in the economies of most countries, it also represents a considerable cost. The financial consequences of neglecting maintenance are often only seen in terms of reduced asset life and premature asset replacement expenses. However, more importantly, neglecting maintenance implies increased costs of operating facilities and waste of financial resources when failure/out-of-service occurs. In Italy, recently observed bridge collapses have put pressure on management authorities to set up procedures for prioritisation of asset maintenance, that led to the introduction in 2020 of specific guidelines on risk classification and management, safety assessment and monitoring of existing bridges. However, because of the qualitative description of the risk foreseen by such guidelines, management entities are not able to produce fine-grained prioritisation rankings of bridges within a network. This paper presents the development of a bridge rating application, using C# language, integrating the results of guideline-based rankings with those obtained through available or newly proposed risk-based quantitative methods. The goal is to provide operational support to the relevant bridge management stakeholders, with more refined prioritisation rankings that become particularly helpful when dealing with large bridge stocks.

1 INTRODUCTION

Bridges play a crucial role in infrastructure systems, and their interruption or failure can result in not only loss of life but also significant economic and traffic disruptions. In Italy and many other countries, the backbone of the existing road infrastructure was constructed after World War II, meaning that numerous bridges are now over 50 years old. Recent failures like the collapse of the Morandi bridge in Genoa (Calvi *et al.* 2019) and the multi-span arch bridge between Albiano Magra and Caprigliola (Scattarreggia *et al.* 2022) have raised concerns, prompting the need for assessment and, if necessary, intervention. However, in a resource-constrained world, it is essential to adopt a rational approach to determine which bridges require further analysis.

Detailed safety assessments of bridges can be performed using current code-based methods, potentially revealing the need for structural retrofitting or replacement, but their application is highly demanding for large-scale assessment. This situation has emphasized the need to find rapid techniques to assist in evaluating large portfolios of bridges. Consequently, there have been recent efforts to develop practical risk assessment methods, such as those proposed by (Bertola and Brühwiler 2023; Meoni *et al.* 2023; Zizi *et al.* 2023; Abarca *et al.* 2023), following similar studies conducted in past decades (e.g., Castorani *et al.* 2011). Despite substantial progress in bridge evaluation, particularly in assessing damage and deterioration in many countries, Italy has only recently introduced guidelines (Ministry of Infrastructure and Transportation 2020) for a unified and effective approach to manage existing bridges. However, these guidelines may conflict with the procedures of the main bridge management entities (e.g., ANAS, RFI), which are now required to adopt the national guidelines.

DOI: 10.1201/9781003483755-337

The Italian guidelines use a multi-level, multi-hazard approach for assessing the risk of existing bridges, considering various hazards such as structural, seismic, landslide, and flooding. They take on the challenge of addressing the issues concerning existing bridges by employing a comprehensive approach that involves multiple levels of assessment. Indeed, this method begins with regional-scale risk evaluations, which rely on a qualitative assessment of bridges. It then proceeds to establish rules for conducting more detailed assessment procedures. Importantly, this approach takes into account various types of hazards arising from structural vulnerabilities and the surrounding environment. This leads to the assignment of an overall class of attention (CoA) and results in a qualitative assessment and categorization into five main classes. As a result, the primary drawback of these guidelines is their qualitative nature, making it challenging to rank bridges falling within the same CoA, unlike quantitative methods.

This paper presents the development of a bridge rating application, using C# language, used to store bridge data collected over time, which is employed to evaluate the CoA according to the current Italian guidelines. The web application provides the capability to arrange and verify data, conduct queries, process information, and present the results visually. The post-processing enabled by the tool permit to analyse the outputs from different viewpoints, thus better plan maintenance interventions. Additionally, the tool is integrated with a recently proposed risk-based quantitative indicator proposed by Hamidpour *et al.* 2023 to operationally support relevant bridge management stakeholders, with more refined prioritisation rankings that become particularly helpful when dealing with large bridge stocks to facilitate the decision-making process. This permits to overcome the limitations of the Italian Guidelines, which, relying on five classes of attention, need to be integrated with additional parameters. For instance, the introduction of a defect index related to gravity/traffic loads (the most relevant hazard as per the Italian Guidelines) enables the planning of maintenance interventions to groups of bridges with the same issues, rather than addressing each bridge individually according to their relative importance. An approach based on clusters of bridges sharing similar types of defects, albeit with varying degrees of extent and severity, helps minimizing both economic and social costs.

A case-study stock of thirty real bridges located in northern Italy is analysed using the developed web tool application. Although the primary objective is to provide a description of the platform that permits to organise recorded data and monitor deadlines, it is also used here to derive the multi-hazard risk classification, in a digital format, according to the recently issued Italian Guidelines. Furthermore, the developed tool permits to carry out priority sub-rankings through vulnerability indicators, taking advantage of the required input data (thus readily available) for the Italian Guidelines application.

2 ADOPTED RATING METHODS

2.1 *Italian Guidelines*

The 2020 MIT Guidelines propose a multi-level and multi-component approach that classifies bridges in risk categories through the processing of qualitative metrics, specific to each of the considered hazards: a) structural/foundational; b) seismic; and c) flood/landslide. The framework foreseen by the Italian Guidelines for the derivation of the Class of Attention (CoA) is briefly summarized in the following steps:

- Data Collection: Gather comprehensive data about the bridge, including its design, construction materials, historical records, and past inspection reports;
- Visual Inspection: Perform visual inspections of the bridge to identify any visible defects or damage. This includes assessing the condition of various components, such as piers, girders, abutments, joints, and superstructure. Report of the extent and severity of damage, corrosion levels, and any signs of distress;
- Data Assessment: Evaluate the collected data and analyse it in accordance with predefined criteria and thresholds set by the Italian Guidelines;
- Classification: Based on the assessment results, classify the bridge into one of several predefined classes of attention, namely High (H), Medium-High (M-H), Medium (M), Medium-Low (M-L), and Low (L), indicating the level of attention that must be given to a bridge for a

specific hazard. Finally, using logical models, the final CoA is derived from the CoA for each hazard.

Particularly, the procedure that leads to the identification of the CoA is divided in the three well-known main components of risk: a) hazard; b) exposure; and c) vulnerability, each of which being assigned one of the five possible attention levels. This is done by processing qualitative characteristics of each bridge and road to which it belongs using a specific set of tabular values and according to logic trees. These guidelines have been recently analysed and evaluated by Santarsiero *et al.* (2021), where a thorough summary of the entire classification methodology is presented.

2.2 *Index for quantifying the Vulnerability under Gravity loads (V-G)*

The vulnerability index for Gravity loads (V-G) is herein introduced for a refinement of the prioritization carried out using the Italian Guidelines. It is derived from the risk-based assessment method proposed by Hamidpour *et al.* 2023, which employs a quantitative priority ranking (PR) model that, in a simplified manner, through a weighted average, combines vulnerability (V), exposure (E), and hazard (H) indicators. Consequently, quantitative risk-based scores are derived for each bridge and can be used to identify prioritization schemes. While interested readers are referred to the work by (Hamidpour *et al.* 2023), a brief overview is given for what concerns the main assumptions behind the definition of the vulnerability component of interest for the present study.

The vulnerability (V) is calculated according to Equation (1), which is composed of two primary subcomponents: one representing the "as-built" vulnerability based on the structural characteristics (V_{Str}),and the other representing the vulnerability associated to damages and defects reported in the bridge elements (V_{Def}). The consideration of defects either due to construction errors (see e.g., Pinho *et al.* 2023) or deterioration over time due to ageing (see e.g., Scattarreggia *et al.* 2021) is of high relevance to the quantification of the residual capacity and structural performance of existing bridges. V_{Str} is essentially determined based on the parameters foreseen by the Italian guidelines described in §2.1 (e.g., year of construction, static scheme, number of spans, etc.), while V_{Def} is assessed using the procedure adopted in the Unit Kingdom (UK) for the definition of a Bridge Condition Index (BCI) with some modifications. Particularly, the UK method categorizes bridge defects into two conditions for each bridge: the average defect condition (herein identified as *Avg. Def.*) and the critical defect condition (herein identified as *Crit. Def.*). The assessment based on *Avg. Def.* defines the overall condition of the bridge based on all its damaged and undamaged elements, whereas the one that uses *Crit. Def.* associates the extremely poor condition of a specific element that holds significant importance in the overall structural integrity of the bridge. The latter is the one foreseen in a qualitative manner by the Italian Guidelines. As a result, V_{Def} can be either defined considering *Avg. Def.* or *Crit. Def.* to take into account the condition of the bridge. It is worth mentioning that V_{Def} is defined as the reverse of the BCI and is normalized to the range (0,1).

$$V = \sqrt{\frac{V_{Str}^2 + V_{Def}^2}{2}} \tag{1}$$

This study is focused on the quantification of the damage/defects for planning future interventions and the subsequent overall vulnerability. The BCI is determined by considering the severity and extent of damages observed in the bridge components during visual inspections, as well as the importance of elements. To be able to adopt the UK BCI method using the available information provided by the application of the Italian Guidelines, the equivalences given in Table 1 are adopted with the Italian Guidelines for what concern the score of the damage extent and severity.

Furthermore, the Italian guidelines assign a weight (G) to each type of damage, ranging from 1 to 5, which represents the severity of damage, considering the bridge construction material. This aspect is not covered by the UK-BCI method. For instance, in reinforced concrete elements, reinforcement corrosion (G=5) and broken brackets (G=4) are regarded as more severe damage types than active moisture stains (G=3), detachment of the concrete cover (G=2), or spider web cracks (G=1). Accordingly, Hamidpour *et al.* 2023 proposed to

Table 1. Equivalence adopted for damage extent and severity between Italian Guidelines and UK – BCI method.

ITA-Guidelines (k_1)	UK-BCI	ITA-Guidelines (k_2)	UK-BCI
0.2	C	0.2	2
0.5	D	0.5	3
1.0	E	1.0	4

incorporate this parameter into the UK-BCI damage assessment process by multiplying the damage weight ratio (G/5) by the damage severity score, k_2. This adjustment helps to account for the varying importance of different damage types based on their relative significance. Finally, the UK-BCI method foresees importance factors for elements under gravity loads, which are herein adopted as reported in by Hamidpour *et al*. 2023.

3 BRIDGE RATING WEB TOOL

The main purpose of the web-service application in C# language and developed with Microsoft Visual Studio is to provide an easier interface for an operational support to stakeholders having access to a more refined prioritization ranking. In addition, the tool is capable of collecting and computing future interventions within the portfolio of bridges based on the inspections conducted and the observed level of degradation. This aspect is related to life-cycle–based maintenance of bridges, which is beyond the scope of this study hence is not discussed in this paper.

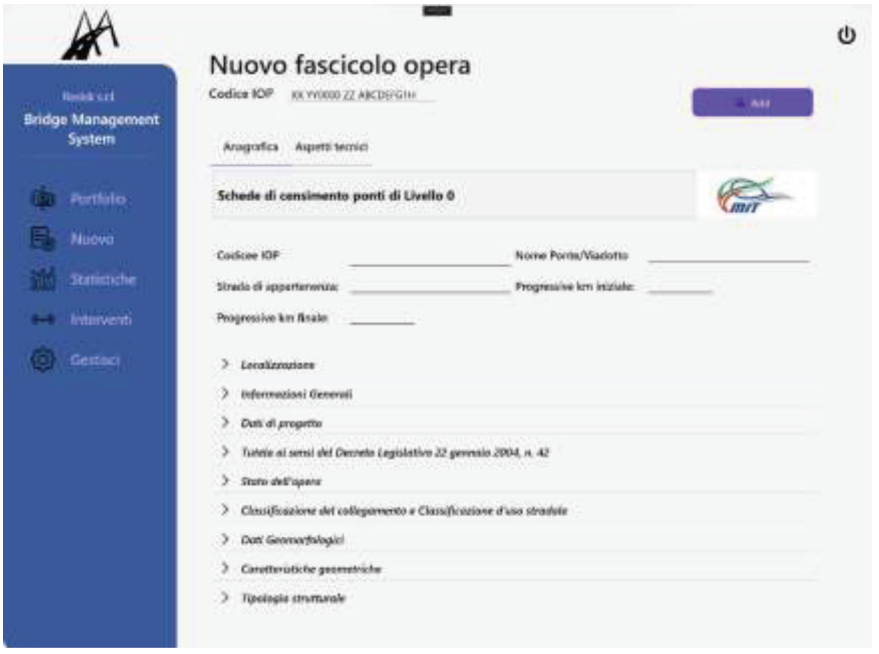


Figure 1. Main interface web-tool interface. Sample of information required for level 0 and 1 of the Italian Guidelines.

The main input data primarily focused on the first three levels of the Italian Guidelines is illustrated in Figure 1, including level 0 (gathers available data for individual bridges from design documents and results of periodic inspections), and level 1 (site inspection outcomes to verify the current state of degradation and the possibility of having structural and non-structural components affected by serious defects).

For what concerns Level 2, for each bridge, the information collected through Levels 0 and 1 will be used to consider risks taking into account hazard, vulnerability and exposure of the related structural vulnerabilities and the surrounding environment, as: (i) structure-foundations, (ii) earthquakes, (iii) flood related, and (iv) landslide related. When the information is combined, a total class of attention (CoA) of the bridge under examination is assigned (Figure 2). Based on such assignment, bridge owners can take appropriate measures spanning from normal periodic inspection to more detailed safety assessment.

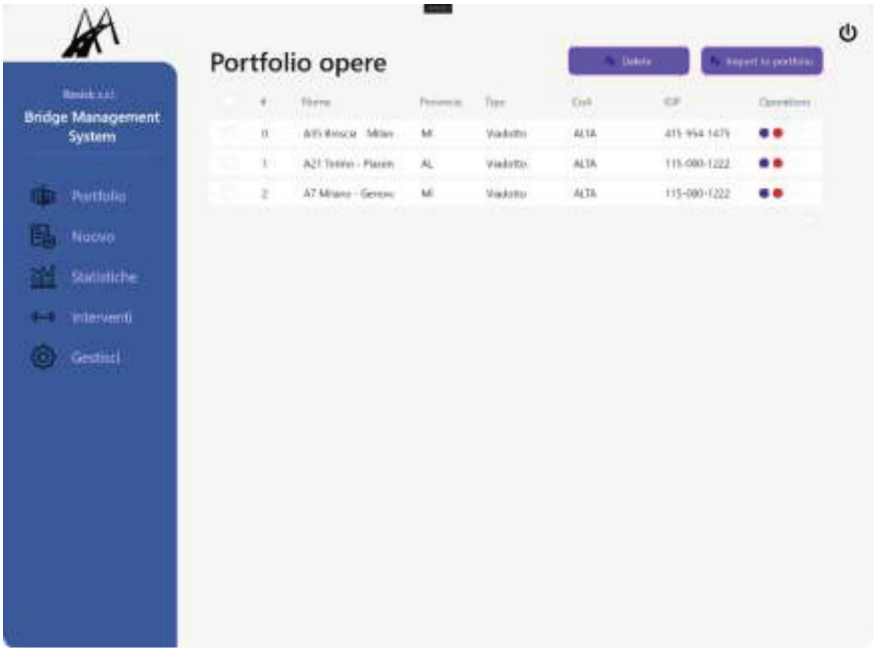


Figure 2. Example of portfolio after the user have completed the input data: the Class of Attention (CoA) is automatically determined for each bridge.

Based on the qualitative approach of the Italian guidelines, several bridge structures may have the same CoA, which makes it difficult to establish a rational decision-making process for determining the priority of bridges for further assessment or intervention. For this reason, the vulnerability indicator introduced above has been considered of interest and implemented in the tool to increase the resolution of priority among bridges belonging to the same CoA, while posing high priority to the health condition under gravity loads as recommended by the current Italian Guidelines.

4 CASE-STUDY BRIDGE STOCK

The risk assessment of thirty highway viaducts and overpasses situated in the northern Italy, described in Hamidpour *et al.* 2023, is used here to illustrate the tool. Figure 3 provides an overview of the key characteristics of these bridges obtained from the analysis of the data collected using the web platform. The data pertaining to the structural and geometric attributes of the bridges, as well as details about defects and damages, was gathered through visual inspections. In addition to this information, data regarding the geotechnical properties and potential hazards at the bridge sites was also collected. Expert teams conducted these assessments in accordance with the aforementioned Italian guidelines.

The collected bridges were predominantly constructed between the 1960s and 1990s, feature a straightforward design with a supported deck system comprising steel girders and a concrete

slab. Many of the bridges have multiple spans with either constant or varying lengths, with the largest span usually of 25 m, with two of them reaching up to 50 m. The total length of the bridges varied from approximately 15 to 125 m. The bridges are positioned alongside major roadways that typically carry an average daily traffic volume exceeding 25,000 vehicles.

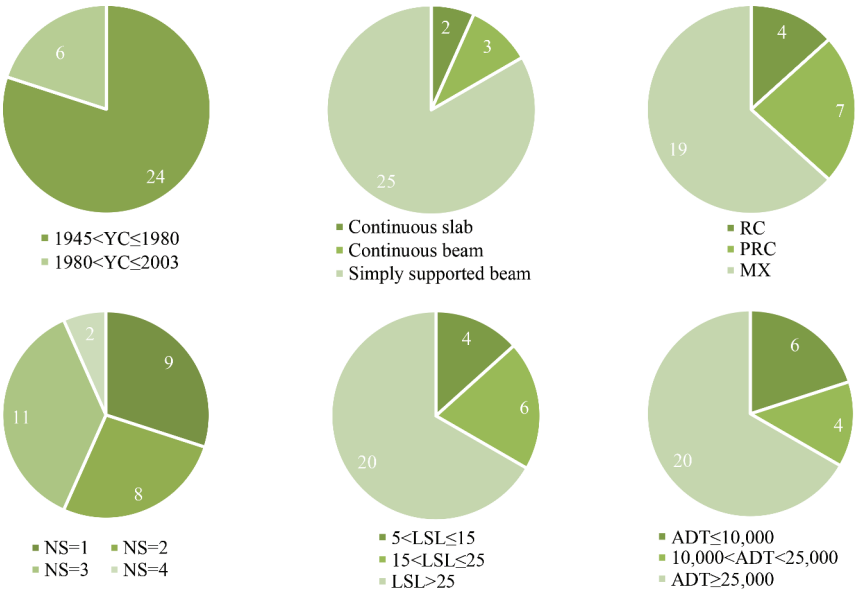


Figure 3. Main features of the analysed case-study bridge stock.

5 PRIORITIZATION RESULTS

5.1 *Application of Italian Guidelines*

The case-study stock was analysed by means of the developed tool and the obtained results, in terms of initial data post-processing, are illustrated in Figure 4. In what follows, the state of conservation of the bridges is analysed distinguishing the typical damages for element groups, as well as the severity. Following the analysis of defects, the total CoA and its disaggregation per hazard is presented. Finally, the derivation of the Vulnerability index for Gravity loads (V-G), described in §2.2, is used to produce sub-priority rankings among bridges that belong to the same CoA.

State of conservation

Figure 4 statistically represents the collected data concerning defects and damages observed in the case-study bridges. The chart displays the frequency of the most severe damages for different bridge components, along with their corresponding weights (G) based on the Italian Guidelines specifications. Among the observed damages, corroded bars were mostly found in piers, reinforced concrete girders, abutments, and slabs. According to the ITA-Guidelines, steel bar corrosion is classified as the most severe type of damage in reinforced concrete elements, with a rating of G=5. On the other hand, steel girders were more frequently affected by corrosion (G=4) and oxidation (G=2), while bearings primarily suffered from oxidation. With the statistical analysis of this data, automatically produced by the tool, bridge operators can have an idea of how the analysed bridges are in terms of state of conservation. The data will also serve as one of the inputs for the derivation of the Classes of Attention for each hazard.

Class of Attention (CoA)

Figure 5 shows the Classes of Attention (CoA): Low, Medium-Low, Medium, Medium–High, and High, obtained from the application of the Italian Guidelines to the analysed bridge stock. As presented in Figure 5-a) the majority of bridges belong to the High CoA. Particularly, the disaggregation of results in terms of hazard shown in Figure 5-b) indicate

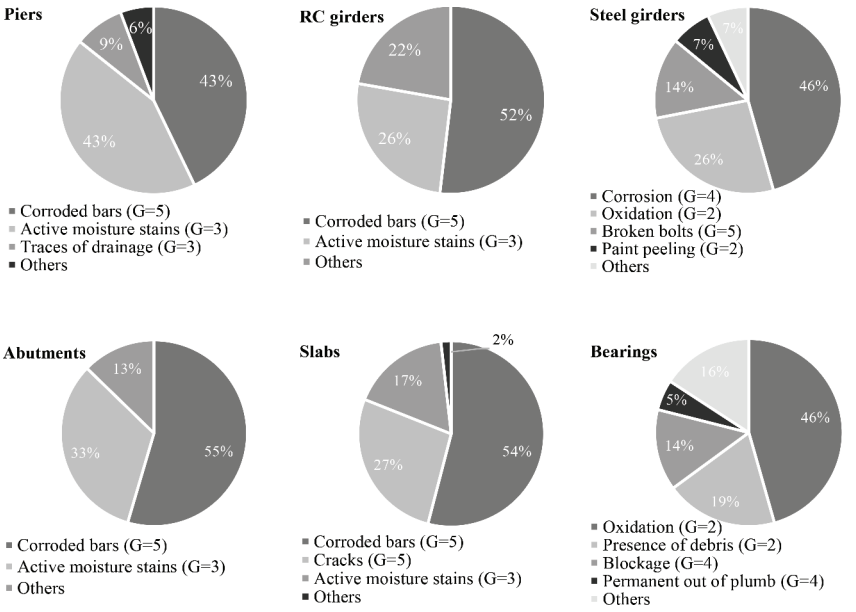


Figure 4. Defects scheduled for main bridge components.

that most of the bridges in the high total CoA are due to the high structural/foundational CoA. Notwithstanding, decision-makers experience difficulties to identify high priority cases due to the grouping of large number of bridges in a single CoA. The problem is likely even more serious when increasing the number of bridges within a stock. The vulnerability indicator previously described is therefore introduced in the following section to derive priority sub-ranking in each CoA to assist decision-makers in planning further actions.

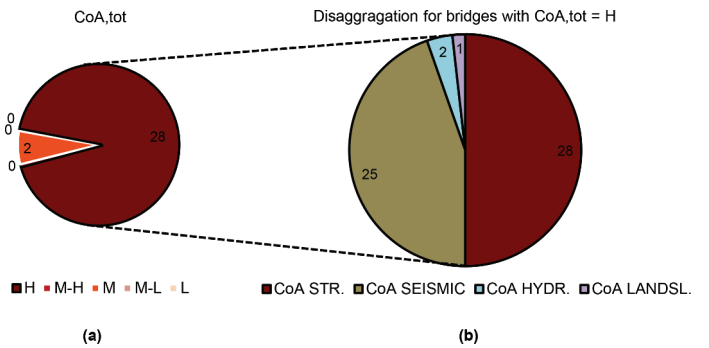


Figure 5. (a) Total Class of Attention ($CoA_{,tot}$) and (b) CoA for each hazard for bridges with HIGH $CoA_{,tot}$.

5.2 *Prioritization refinement using the Vulnerability index for Gravity loads (V-G)*

In a similar fashion to the scheme followed for the application of the Italian Guidelines, the V-G index is defined for each bridge and a priority ranking based on this indicator is derived. Considering the prioritization schemes given by the Italian Guidelines that group bridges in five classes, this indicator is used to obtain sub-ranking for bridges belonging to each CoA. According to Hamidpour *et al.* 2023, the V-G index has been calculated for each bridge by using the two conditions of deterioration for the definition of vulnerability associated to defects, both average and critical. Figure 4 presents the analysis and further post-processing results, which highlight that many bridges among those analysed present similar indicators aside of the defect condition used for the definition of the vulnerability implying a uniform

condition of conservation/deterioration of the bridge. On the other hand, cases where the vulnerability due to the critical defects is much higher than the one associated to the average condition imply that localised defects are responsible for a potentially higher vulnerability. Finally, the ranking of bridges belonging to the High CoA has been produced ordering structures from the most to the less critical according to the vulnerability that accounts for the critical defects condition. Consequently, a comparison between the V-$G_{,crit}$ and V-$G_{,avg}$ clearly shows that, depending on the indicators used to produce the ranking, the priority order may change. Still, considering that the proposed method is applied to bridges that belong to a pre-identified CoA according to the Italian Guidelines, the results do not invalidate the overall conclusion foreseen by the legally binding guidelines.

6 CONCLUSIONS

The developed bridge rating web application utilizing C# language marks a significant step towards enhancing bridge management processes. It can collect data and guide future interventions of the portfolio of bridges based on conducted inspections and the given level of degradation for their optimal management over time. The feature related to the large-scale risk assessment of bridge portfolios by means of simplified methods is given particular attention. To this end, the developed tool combines guideline-based rankings, namely the Italian Guidelines, with a vulnerability indicator incorporating deterioration considerations through a risk-based quantitative method available in current literature. The integration of diverse metrics offers a more comprehensive evaluation of bridge conditions and assists in the refinement of risk assessment of bridges belonging to the same Class of Attention (CoA), ultimately empowering stakeholders involved in bridge management. By analysing the stored data, the tool automatically assesses the CoA and the corresponding vulnerability indicator under gravity loads of each bridge within the considered stock. As result, the inclusion of the vulnerability indictor permits to increase the resolution of priority among bridges belonging to the same CoA highlighting their relative priority, while posing high attention to the vulnerability under gravity loads as recommended by the current Italian Guidelines. Finally, a case-study of thirty real bridges has been analysed to show the potential of the developed tool with its implemented methods of providing operational support to the relevant bridge management stakeholders, with more refined prioritisation rankings that become particularly helpful when dealing with large bridge stocks.

REFERENCES

Abarca A, Monteiro R, O'Reilly GJ (2023) Seismic risk prioritisation schemes for reinforced concrete bridge portfolios. 1–21.

Bertola NJ, Brühwiler E (2023) Risk-based methodology to assess bridge condition based on visual inspection. Structure and Infrastructure Engineering 19:575–588.

Calvi GM, Moratti M, O'Reilly GJ, et al (2019) Once upon a Time in Italy: The Tale of the Morandi Bridge. Structural Engineering International 29:198–217.

Castorani A, Rosario Santo A DI, Fratino U, et al (2011) Methodological approach to evaluate multihazard risk on bridges and viaducts. Italian journal of engineering geology and environment 2011:19–32.

Hamidpour S, Scattarreggia N, Nascimbene R, Monteiro R (2023) A risk-based quantitative approach for priority assessment of ageing bridges accounting for deterioration.

Meoni A, García-Macías E, Venanzi I, Ubertini F (2023) A procedure for bridge visual inspections prioritisation in the context of preliminary risk assessment with limited information. Structure and Infrastructure Engineering.

Ministry of Infrastructure and Transportation (2020) Linee guida per la classificazione e gestione del rischio, la valutazione della sicurezza ed il monitoraggio dei ponti esistenti. Italy.

Pinho R, Scattarreggia N, Orgnoni A, et al (2023) Forensic estimation of the residual capacity and imposed demand on a ruptured concrete bridge stay at the time of collapse. Structures.

Scattarreggia N, Salomone R, Moratti M, et al (2022) Collapse analysis of the multi-span reinforced concrete arch bridge of Caprigliola, Italy. Eng Struct 251:113375.

Zizi M, Bencivenga P, De Matteis G (2023) Handling policies for Italian existing bridges with a territorial approach: the case study of Caserta, Italy. Structures 48:1306–1321.

Bridge Maintenance, Safety, Management, Digitalization and Sustainability – Jensen, Frangopol & Schmidt (eds)
© 2024 The Author(s), ISBN 978-1-032-77040-6
Open Access: www.taylorfrancis.com, CC BY-NC-ND 4.0 license

Enhancing bridge monitoring through supervised anomaly classification

I. Bayane, J. Leander & R. Karoumi
Structural Engineering and Bridges, KTH-Royal Institute of Technology, Stockholm, Sweden

ABSTRACT: Bridge monitoring is a useful tool for alerting to changes in behavior and supporting informed bridge management decisions. However, the triggering of alerts is often based on predefined thresholds, which results in incomplete anomaly detection, leading to excessive false positives or negatives. This highlights the need for an efficient anomaly detection approach adapted to bridges. This paper presents a supervised classification framework for detecting and classifying anomalies in bridge monitoring data. The framework involves labelling data from existing datasets and training a classification algorithm to detect similar anomalies in new measurements. The focus is on strain measurements labelled using a predefined time series taxonomy, as illustrated by a case study of a bascule railway bridge. The framework demonstrates high accuracy in detecting and classifying anomalies, making it easy to identify their causes. It triggers alerts only when necessary and provides a reliable method for detecting changes in behavior.

1 INTRODUCTION

Recent technological advances have given rise to data-driven methods for bridge management exploiting the latest innovations in sensors, data processing, high-speed internet, and cloud computing, which makes bridge monitoring increasingly complementing traditional inspection methods. Within this context, new techniques are being developed to process monitoring data and finding patterns that deviate from expected behavior, to help identify potential damage and assess bridge behavior.

The detection of patterns in data that are inconsistent with expected behavior is called anomaly detection, and the inconsistent patterns are called anomalies. Anomaly detection in time series has received considerable attention in various fields including computer science, the stock market domain and medical applications (Mejri et al.). However, in civil engineering, research on anomaly detection and classification in monitoring data remains limited. Current research focuses mainly on the use of numerical modelling (Ghiasi et al.) and laboratory experiments (Li et al.) for this purpose, with limited validation at full scale. Uncertainties in numerical simulations and questions about the transferability of laboratory results to real-world scenarios pose challenges in applying knowledge to full-scale case studies. Bridging this gap requires the exploration of field data, which is challenging in the absence of labelled datasets.

To address this challenge, the study suggests the use of anomaly taxonomy and monitoring data to generate labeled datasets for training and testing. The established anomaly taxonomy for time series, originally designed for evaluating anomaly detection algorithms, provides a broad classification of anomalies across various domains (Choi et al.; Golmohammadi and Zaiane; Lai et al.; Yu et al.). This taxonomy, discussed by Choi et al. (2021), categorizes anomalies into three main types: point, contextual, and collective outliers. An updated taxonomy by Lai et al. (2021) further distinguishes between point outliers (comprising global and contextual outliers), and pattern outliers (including trend, shapelet, and seasonal outliers).

DOI: 10.1201/9781003483755-338

Based on this defined taxonomy, this paper proposes a framework for supervised classification of anomalies in bridge monitoring data, providing guidance for the creation of synthetic datasets for training and testing. This study focuses on strain measurements due to their local and direct sensitivity to damage. Emphasis is placed on monitoring data during loading events, which include train passages and bridge openings.

2 METHODOLOGY

The supervised classification framework is presented in the following sections. Monitoring data used in this study is described, with the extracted features used for anomaly detection and classification. Anomaly types are introduced, derived from observations over years of measuring strain variations in bridges, and informed by a taxonomy that evaluates metrics for outliers in time series. Subsequently, the process of constructing and labeling datasets with the identified anomaly types is then presented. The datasets are separated into testing and training subsets. Classification is then performed using a supervised learning model based on a decision tree classifier. The methodology is shown in Figure 1.

2.1 *Monitoring data*

The presented methodology involves capturing local behavior of bridge structural elements at critical points using strain gauges. Monitoring is performed continuously over long periods with a high frequency to capture the effect of different loading events. The case study focuses on a steel bascule-railway bridge constructed with riveted truss members from 1914 to 1916. Strain variations are continuously measured at critical truss members with a high frequency of 200 Hz, over a 15-month period from December 2021 to March 2023.

2.2 *Data preprocessing*

To facilitate anomaly detection and classification, monitoring data is divided into subsets corresponding to distinct loading events. After extracting features for both anomaly detection and classification and before and after injecting synthetic anomalies, a normalization is performed according to equation 1.

$$x = \frac{X - \min(X)}{\max(X) - \min(X)} \tag{1}$$

where $X(X_1,\ X_2, \ldots, X_n) \in R^n$ is the measured-strain vector during a loading event, and x is the normalized measurement vector.

2.3 *Feature extraction*

The features used for anomaly detection are Minimum, Maximum, Mean, Covariance, Kurtois, RMS, PRMS, RSS, and peak-to-peak. These features are defined in equations 2–8.

$$\text{Mean } (\mu)\ \ \mu = \frac{1}{n}\sum_{i=1}^{n} X_i \tag{2}$$

$$\text{Covariance } (cov)\ \ cov = \frac{1}{n-1}\sum_{i=1}^{n} (X_i - \mu)^2 \tag{3}$$

$$\text{Kurtois } (K)\ \ K = \frac{\frac{1}{n}\sum_{1}^{n} (X_i - \mu)^4}{\left(\frac{1}{n}\sum_{1}^{n} (X_i - \mu)^2\right)^2} \tag{4}$$

$$Root - Mean\ Square\ (RMS)\ \ RMS = \sqrt{\frac{1}{n}\sum_{i=1}^{n} X_i^2} \tag{5}$$

$$\text{Peak to RMS}\ (PRMS)\ \ PRMS = \frac{\max|X|}{\sqrt{\frac{1}{n}\sum_{i=1}^{n} |X_i|^2}} \tag{6}$$

$$\text{Root} - \text{Sum of Squares}\ (RSS)\ \ RSS = \sqrt{\sum_{i=1}^{n} |X_i|^2} \tag{7}$$

$$\text{Peak to Peak (P2P)}\ \ \text{P2P} = \max\ (X)\ - \min\ (X) \tag{8}$$

For the supervised classification process, more features are extracted from strain measurements, and ranked to identify the relevant features for classification. The extracted features include the statistical features defined in Equations 2–8, along with various factors like clearance factor, crest factor, and shape factor. The set of features also includes parameters like those used for acoustic emission(Bayane and Brühwiler, 2020), such as the time of the highest amplitude point, the number of threshold crossings from the first to the highest point, and the count of signal crossings above a threshold. The threshold here is defined as half of the peak-to-peak amplitude. Additional features include properties related to the power spectrum, such as its maximum, as well as the time and frequency of its occurrence.

To select the most relevant features for classification, they are ranked using the minimum-redundancy maximum-relevance algorithm. The algorithm minimizes feature set redundancy while maximizing its relevance to the response variable. The redundancy and relevance are quantified through the mutual information of variables, involving pairwise mutual information among features and the mutual information of a feature with respect to the response(Darbellay and Vajda; Ding and Peng). The top six features are then selected from the initially defined features for the classification process.

2.4 *Anomaly detection*

Anomalies are detected using the isolation forest algorithm that clusters instances in a dataset by building an ensemble of random decision trees. It measures an instance's anomaly score based on the number of splits needed to isolate it. The algorithm is based on the idea that anomalies are easier to isolate and require fewer splits than normal instances. It provides scores between 0 and 1, with higher scores indicating more pronounced anomalies.

2.5 *Anomaly types*

Observed anomalies in strain measurements are occasional, gradual, or permanent shifts, that are in the form of points or patterns. They are due to diverse factors such as electrical or mechanical disturbances (power supply fluctuations, electromagnetic fields, wheel impact), variations in applied load (a loading interruption or changes in loading characteristics), or strain release associated with damage. Five outlier types are defined from these observations as illustrated in Figure 2:

2.5.1 *Global outliers*

Points in the signal that exhibit significant deviation from the rest. These are typically spikes frequently caused by electrical disturbances. They are defined as point shifts exceeding the maximum or falling below the minimum strain levels recorded during loading events.

2.5.2 *Contextual outliers*

Points in the signal that deviate from their contextual surroundings within a specified range of neighboring time points. These deviations are attributed to minor shifts in strain measurements typically caused by inherent electrical noise that persists after sensor calibration, and

mechanical noise due for example to wheels. They are defined as small point shifts within the normal range of variation between the minimum and maximum strain values.

2.5.3 *Trend outliers*
A pronounced shift in strain measurements resulting from a sudden release of strain, often associated with the occurrence of damage. They are defined as a continuous-constant shift of strain during the loading event.

2.5.4 *Shapelet outliers*
Random fluctuations in strain gauge output resulting from electrical or mechanical disturbances, including power supply fluctuations and electromagnetic fields or random variations in strain measurements caused by loading irregularities. They are defined as a change in the shape of the signal.

2.5.5 *Drift outliers*
Gradual shifts in strain gauge output over time, attributed to aging, temperature variations, or humidity, or a slow increase in damage. They are defined as a linear drift of strain over time.

2.6 *Injecting synthetic anomalies*

Synthetic anomalies are introduced into strain variations recorded during loading events, with the associated context determined from observed strain variations during similar events. The assumption is made that each loading event contains one type of anomaly. This assumption is applied to simplify dataset labelling and facilitate anomaly classification, although it's recognized that certain events may involve multiple types of anomalies.

2.6.1 *Global outliers*
This anomaly type is generated by randomly selecting a time step r from the interval $[1, n]$ and replacing x_r with a value that either exceeds the maximum value or falls below the minimum value. This process is shown in Equations 9–10, where λ presents a random number within the range $[0, 1]$.

$$x_r = x_r + \lambda \max(x) \tag{9}$$

$$x_r = x_r - \lambda \min(x) \tag{10}$$

2.6.2 *Contextual outliers*
This anomaly is generated by randomly selecting a time step r from the interval $[1, n]$ and replacing x_r with a value between the maximum and the minimum values. This process is shown in Equation 11–12, where λ presents a random number within the range $[0, 1]$.

$$x_r = \lambda(\max(x) - x_r) \tag{11}$$

$$x_r = \lambda(\min(x) + x_r) \tag{12}$$

2.6.3 *Trend outlier*
This anomaly type is synthesized by changing the trend of the measurement vector leading to a permanent shift. The anomaly is injected within the signal's 10% to 90% range, ensuring a substantial change without affecting the entire signal. This process is shown in Equation 13, where m presents a random integer between $0.1n$ and $0.9n$, and λ presents a non-zero random number within the range $[-1, 1]$.

$$\forall i \in [m, n] \; x_i = x_i + \lambda \tag{13}$$

2.6.4 *Shapelet outlier*

This anomaly type is generated by changing the shape of the signal for a subset of points. To avoid changing the entire signal, this anomaly is injected within the signal's 10% to 90% range, ensuring a change without affecting the entire signal. The initiation point and length of the modified subset are determined by two random variables. The procedure is detailed in Equation 14, where m_1 and m_2 present random integers within the range of $0.1n$ to $0.9n$, with $m_2 > 1.1m_1$. Additionally, f denotes a function, that is adapted based on the context to change the shape of the signal, and it is for the case study, a random constant, or a sinusoidal function based on the nature of the loading event.

$$\begin{gathered} \forall i \in [m_1, m_2]\ x_i = f(\ x_i)[\lambda,\ x_i] \\ \text{such us } f(x_{m_1}) = \ x_{m_1} \\ \text{and } f(\ x_{m_2}) = \ x_{m_2} \end{gathered} \tag{14}$$

2.6.5 *Drift outliers*

This type of anomaly is generated by adding a linear trend to the measurement vector, as it is shown in Equation 15, where λ presents a random number within the range $]0, 1]$.

$$\forall i \in [1, n]\ x_i = \ x_i + \lambda i \tag{15}$$

2.7 *Dataset labelling*

To label monitoring data, synthetic anomalies are introduced into anomaly-free data. The anomaly-free data is identified from measurement vectors by selecting the vectors with the lowest scores obtained from the isolation forest algorithm. The resulting vectors are normalized according to Equation 1. Anomalies are introduced into the normalized vectors with an assigned label, and the vectors are again normalized and subjected to feature extraction.

2.8 *Anomaly classification*

Classification is performed using the binary classification decision tree, which is a supervised machine learning model that operates based on a tree structure for binary classification. The nodes of the tree present decision points based on input features, leading to recursive splits until a final classification is reached at the leaves. Trained on labeled datasets, it learns decision patterns and relationships for categorizing instances into two classes.

The study uses a supervised classification model trained on selected top six features and class labels from synthetic datasets. The training and test sets are split 80%/20%. Model performance is evaluated using a confusion matrix to determine classification accuracy. Classification is performed using the 'fitc-tree' function in MATLAB R2023. The prediction results were obtained using the 'predict' function with default configurations for optional arguments in both the classifier and predictor.

3 CASE STUDY

In this section, the methodology is applied to strain data obtained from a bascule-railway bridge, focusing on various critical components. For detailed information and datasets, refer to Leander et al.(2023). Three loading events are identified: train passage, bridge opening, and bridge closing. The analysis focuses on strain variations from two critical components during train passages and bridge openings, as strain variations during bridge closing are similar to those observed during bridge opening.

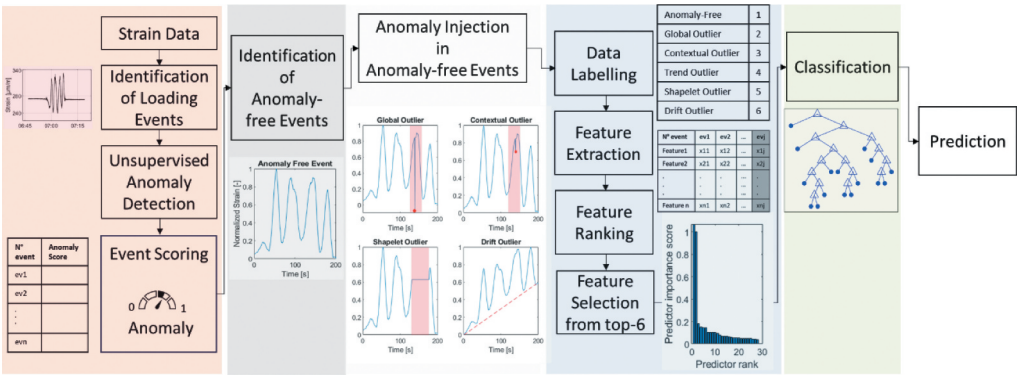


Figure 1. Proposed methodology.

The dataset is separated into loading events labeled "opening" or "train passage." Anomaly scores, ranging from 0 to 1, are assigned using the isolation forest algorithm. The 300 events with the lowest scores, corresponding to one month of continuous monitoring, are selected as anomaly-free events. Synthetic anomalies are introduced into these events, each labeled to indicate the specific anomaly type added (Figure 2).

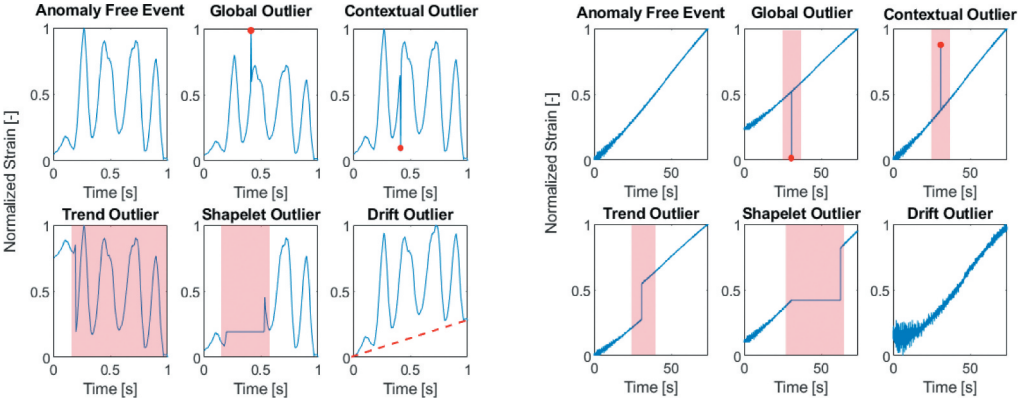


Figure 2. Normalized strain variations during train passage (left), and bridge opening (right) with anomaly-free event compared to the same event containing injected anomalies.

The supervised classification model is trained on 80% of the synthesized datasets (240 events for each class) and validated with the remaining 20% (60 events for each class). A binary classification decision tree is then used to classify unlabeled monitoring data. Figure 3 illustrates the confusion matrix, with known and predicted classes for train passages and bridge opening loading events.

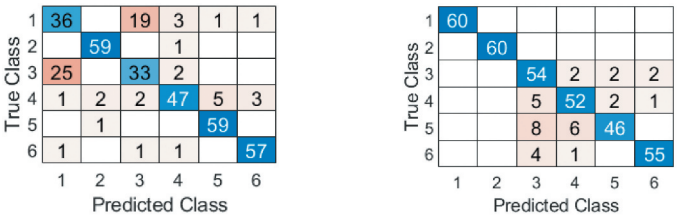


Figure 3. Confusion Matrix for the known and predicted classes, for train passage events (left) and bridge opening events (right).

The supervised classification model demonstrates robust performance during bridge opening achieving a 90% test accuracy. It correctly classifies anomaly-free events and global outliers, identifying 91% of drift outliers, 90% of contextual outliers, 86% of trend outliers, and 76% of shapelet outliers.

For train passage events, the model exhibits an 80% test accuracy. It accurately identifies 98% of global and shapelet outliers, 95% of drift outliers, and 78% of trend outliers. However, challenges arise in accurately classifying contextual outliers, often misclassifying them as anomaly-free events, which is similar with anomaly-free events being misclassified as shapelet outliers.

The observed decrease in model performance for contextual outliers and anomaly-free events during train passages is attributed to electrical and mechanical vibration associated with the train and wheels, contributing to the normal occurrence of contextual outliers. In contrast, bridge-opening events, where such vibration is absent, result in higher precision (90%) in contextual outlier classification.

The trained supervised classification model is used to predict and classify anomalies in new measurements collected over 15 months of continuous monitoring, comprising 5048 train passages including different train types, and 2642 bridge openings. Among train-passage events, 76% are identified as anomaly-free, 20% as contextual anomalies, and 4% as anomalies related to various train types, categorized as shapelet, trend, or drift outliers.

For bridge-opening events, 97% are classified as anomaly-free, while 3% exhibit anomalies, manifesting as signal shifts, loading irregularities (e.g., breaks or sudden stops during bridge opening), and strain releases associated with damage, as illustrated in Figure 4.

It is possible to achieve a high-precision classification within 300 events for training and testing, which corresponds to one month of continuous monitoring. Precision can be further enhanced by increasing the number of events considered for training.

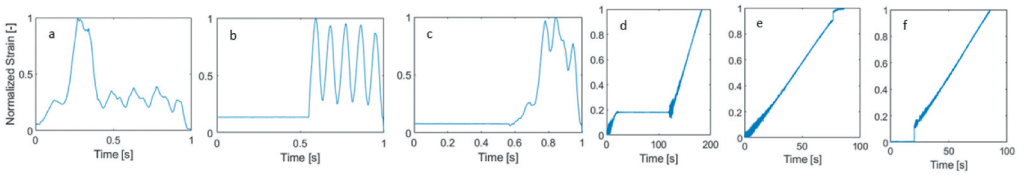


Figure 4. Examples of detected and classified anomalies: a-c) Unrecognized-train configurations during train passage; d) a stop during bridge opening, e) strain release linked to damage during bridge opening; f) signal loss during bridge opening.

4 CONCLUSIONS

In this paper, a context-specific framework is introduced for the supervised classification of anomalies in strain monitoring data. The supervised model exhibits strong performance, demonstrating its reliability in real-world scenarios, by achieving 80% accuracy for train passages and 90% accuracy for bridge opening events over 15 months of monitoring. Three important conclusions are drawn:

- The integration of time series anomaly taxonomy with empirical observations provides a framework for supervised anomaly detection and classification in bridge monitoring.
- The generation of synthetic datasets from monitoring data demonstrates the potential to achieve high-precision classification within one month of monitoring, which offers a practical approach for rapid implementation.
- The application of the framework to real strain data from a bascule bridge validates its efficiency to provide bridge owners with an automated method for detecting anomalies related to damage, irregular loading, and sensor failures.

Future work will explore multivariate monitoring data, combine data from different strain gauges and introduce additional classes of combined anomalies.

REFERENCES

Bayane, Imane, and Eugen Brühwiler. "Structural Condition Assessment of Reinforced-Concrete Bridges Based on Acoustic Emission and Strain Measurements." *Journal of Civil Structural Health Monitoring*, vol. 10, no. 5, Nov. 2020, pp. 1037–55. *Springer Link*, https://doi.org/10.1007/s13349-020-00433-0.

Choi, Kukjin, et al. "Deep Learning for Anomaly Detection in Time-Series Data: Review, Analysis, and Guidelines." *IEEE Access*, vol. 9, 2021, pp. 120043–65. *DOI.org (Crossref)*, https://doi.org/10.1109/ACCESS.2021.3107975.

Darbellay, G. A., and I. Vajda. "Estimation of the Information by an Adaptive Partitioning of the Observation Space." *IEEE Transactions on Information Theory*, vol. 45, no. 4, May 1999, pp. 1315–21. *IEEE Xplore*, https://doi.org/10.1109/18.761290.

Ding, Chris, and Hanchuan Peng. "Minimum Redundancy Feature Selection from Microarray Gene Expression Data." *Journal of Bioinformatics and Computational Biology*, vol. 3, no. 2, Apr. 2005, pp. 185–205. *PubMed*, https://doi.org/10.1142/s0219720005001004.

Ghiasi, Alireza, et al. "Damage Detection of In-Service Steel Railway Bridges Using a Fine k-Nearest Neighbor Machine Learning Classifier." *Structures*, vol. 45, Nov. 2022, pp. 1920–35. *ScienceDirect*, https://doi.org/10.1016/j.istruc.2022.10.019.

Golmohammadi, Koosha, and Osmar R. Zaiane. "Time Series Contextual Anomaly Detection for Detecting Market Manipulation in Stock Market." *2015 IEEE International Conference on Data Science and Advanced Analytics (DSAA)*, IEEE, 2015, pp. 1–10. *DOI.org (Crossref)*, https://doi.org/10.1109/DSAA.2015.7344856.

Lai, Kwei-Herng, et al. "Revisiting Time Series Outlier Detection: Definitions and Benchmarks." *Proceedings of the Neural Information Processing Systems Track on Datasets and Benchmarks*, vol. 1, Dec. 2021. *datasets-benchmarks-proceedings.neurips.cc*, https://datasets-benchmarks-proceedings.neurips.cc/paper/2021/hash/ec5decca5ed3d6b8079e2e7e7bacc9f2-Abstract-round1.html.

Leander, John, et al. "Dataset for Damage Detection Retrieved from a Monitored Bridge Pre and Post Verified Damage." *Data in Brief*, vol. 51, Dec. 2023, p. 109729. *ScienceDirect*, https://doi.org/10.1016/j.dib.2023.109729.

Li, Zhenkun, et al. "Real-Time Drive-by Bridge Damage Detection Using Deep Auto-Encoder." *Structures*, vol. 47, Jan. 2023, pp. 1167–81. *ScienceDirect*, https://doi.org/10.1016/j.istruc.2022.11.094.

Mejri, Nesryne, et al. *Unsupervised Anomaly Detection in Time-Series: An Extensive Evaluation and Analysis of State-of-the-Art Methods*. arXiv:2212.03637, arXiv, 3 Jan. 2023. *arXiv.org*, https://doi.org/10.48550/arXiv.2212.03637.

Yu, Yufeng, et al. "Time Series Outlier Detection Based on Sliding Window Prediction." *Mathematical Problems in Engineering*, vol. 2014, Oct. 2014, p. e879736. www.hindawi.com, https://doi.org/10.1155/2014/879736.

Bridge Maintenance, Safety, Management, Digitalization and Sustainability – Jensen, Frangopol & Schmidt (eds)
© 2024 The Author(s), ISBN 978-1-032-77040-6
Open Access: www.taylorfrancis.com, CC BY-NC-ND 4.0 license

Reshaping bridge inspection with AI, 3D tools and BIM: Outcomes from an R&D initiative

T. Mendonça, V. Brito & S. Costa
Betar Consultores Lda, Lisbon, Portugal

J. Matos & S. Fernandes
ISISE, University of Minho, Guimarães, Portugal

ABSTRACT: This paper offers an in-depth review of a European-funded R&D project involving Minho University, the Center for Graphical Computation, and Betar, a Portuguese company specializing in asset management and bridge inspection. The project's goal was to digitally transform Betar's existing BMS system by integrating BIM standards, AI, and 3D technologies. Key developments included a computer vision AI for defect detection in bridges, a BIM-to-3D model conversion tool, a mobile app for efficient inspection using 3D models, a user-friendly tool for generating 3D models in the absence of BIM models, and frameworks for degradation prediction and maintenance optimization. The paper details the project's objectives, developed tools, and main outcomes, providing a practical assessment of these tools, their operational details, and real-world applicability based on pilot tests. It also discusses the challenges faced, key learnings, and future research directions to enhance civil engineering and infrastructure maintenance.

1 INTRODUCTION

1.1 *Context*

Transport infrastructures, such as highways, railways, airports, and ports, play a crucial role in economic development, supporting personal well-being and economic growth. These assets are vital for national and international development, both socially and economically. They contribute indirectly to economic development through various channels, highlighting their importance in wealth generation (International Transport Forum, 2013).

In the late 20th and early 21st centuries, developed countries invested heavily in transport infrastructure. In Portugal, after joining the European Union in 1986, the transport sector, especially highways, saw significant improvements to meet socioeconomic development needs (Diário da República nr. 188/2003, 2003). Traditional infrastructure design focused on minimizing initial investment costs, often leading to high maintenance costs.

The introduction of Life-Cycle Cost analysis marked a shift towards balancing investment and maintenance costs (Hammervold et al., 2013). Despite financial constraints, strategic infrastructure investments have been crucial in Portugal's transport sector. The 2008 financial crisis, however, led to reduced public investments in transport infrastructures.

Currently, the ageing of transport infrastructures in Portugal poses maintenance challenges. The Auditors Court identified urgent maintenance needs, particularly in railways, which are generally older than highways (Simões et al., 2020). Despite these issues, Portugal ranks high in global infrastructure quality but faces problems in railway infrastructure, with a significant portion of railway tracks and bridges below adequate quality levels (Simões et al., 2020).

The decrease in public investments is a common problem worldwide, affecting the quality of transport infrastructure (World Economic Forum, 2019). Modern structures have shorter

DOI: 10.1201/9781003483755-339

lifespans due to economic and time constraints in construction. The Morandi Bridge collapse is a recent example highlighting the consequences of inadequate maintenance (Calvi et al., 2018).

The World Economic Forum recommends re-igniting public and private investment in infrastructure, education, and innovation to boost national economic growth (World Economic Forum, 2019). Environmental sustainability has become a key consideration in infrastructure projects, affecting the feasibility and public support for new constructions.

Implementing a national asset management system for transport infrastructures is essential (Simões et al., 2020). Such a system supports decision-making and helps policymakers collect high-quality data for investment prioritization, crucial under tight budget constraints. The OECD notes the need for a cross-country analytical framework to assess the impact of transport infrastructure on economic development, highlighting challenges in data management across different systems (International Transport Forum, 2013).

A renovation of asset management of such kind should most probably come with the help of digitalization tools and industry 4.0 advances. In fact, bridge inspection is traditionally a labor-intensive task, sometimes involving safety risks to inspectors and demanding great investment in expert training to reduce subjectivity and error. Introducing artificial intelligence (AI) in inspection activities, namely machine learning and computer vision is a clear path forward, by enabling automated, accurate and efficient defect detection. Computer vision has been a very hot topic in a wide variety of applications and industries, and progress moves rapidly with the advancements in algorithmic sophistication and increased computation capabilities in easily accessible hardware. There are several deep learning models available to train, and much of the algorithm efficiency results from the quality of the training dataset.

Any reference to digitalization in the construction sector immediately leads to the topic of Building Information Modelling (BIM). BIM is one of the major topics in the construction industry and is believed to be the most adequate option to support the digital transition in this sector (Santos et al., 2022). Gathering and sharing information about structures has always been a challenge in civil engineering, and there is a transformative potential in BIM that brings a holistic approach to design, construction, and maintenance, encompassing not only the geometric aspects but also the functional characteristics of the bridge, creating a shared knowledge resource. The integration of BIM in BMS systems is still in the early stages, but as BIM use gains traction in design and construction phases, it will inevitably be used in the operation phase where BMS systems are a pivotal tool.

1.2 *Existing bridge management systems*

GOA.BI is a technologically driven project designed to address challenges in the management of highway and railway infrastructures. It aims to establish a smart interface to assist various stakeholders, including owners, transport agencies, and inspectors, in managing the lifecycle of transport infrastructures. These infrastructures involve a diverse array of assets starting with bridges, viaducts, and tunnels, and contemplating other structural assets present in road and rail infrastructure. The project's foundation is an integrated Asset Management System, primarily based on the concept of a Bridge Management System (BMS), which provides a versatile framework adaptable to various infrastructure assets.

The importance of BMS in infrastructure conservation has been recognized by many owners, given the structural complexity and significant investment needed over different lifecycle stages of bridges (Costa et al., 2019). BMS software should support maintenance management by developing maintenance timelines and strategies that balance cost efficiency with performance, considering the societal, economic, and environmental impacts.

Globally, numerous BMS have been developed, including BRIDGIT, Pontis, FinnRABMS, and others (Mirzaei et al., 2014). The evolution of BMS began in the 1960s, driven by the need to address the increasing deterioration of bridges. The United States pioneered this approach following the Silver Bridge collapse, leading to the creation of the National Bridge Inspection Standard (NBIS) in 1968. Initially, bridge management relied on replacement theory and basic mathematical models, which later evolved to incorporate data from

inspections into more sophisticated maintenance planning. By the 1990s, American BMS like BRIDGIT and Pontis were using detailed condition states derived from inspections to guide maintenance decisions (Neves et al., 2003; Santamaria et al., 2019).

In Portugal, the bridge management system GOA® - Gestão de Obras de Arte, developed by Betar, Lda., became a significant tool in the national market. Launched in 1997, GOA filled a market gap and was first implemented by Lisbon's City Council and subsequently by Refer, the Portuguese Railways Company. The 2001 Hintze Ribeiro Bridge collapse, a major tragedy in Portugal, underscored the importance of effective bridge management systems and led to the wider adoption of GOA (Carmo, 2021). Over two decades, GOA has evolved with continuous improvements and has even expanded internationally.

GOA encompasses a comprehensive inventory process for asset characterization, including administrative and technical data, component identification, and material details. The system is structured to continuously receive updated information, primarily from various types of inspections: routine, principal, underwater, and surveys. Routine inspections focus on service quality and traffic safety, recommending preventive maintenance tasks. Principal inspections, conducted every four to six years, are more detailed, assessing structural damages and assigning condition states to components. Also available are modules for planning activities and for maintenance management, allowing for the complete tracking of a defect lifecycle within the structure. Other supporting modules, like extensive reporting features and BI and online map integration constitute a complete tool for managing bridges and similar assets.

2 GOA.BI PROJECT

After twenty years of evolution and wide adoption, GOA has helped bridge owners to guarantee security and better management of over 20.000 bridges. GOA allows for the collection of data and making it available for use under a tested and successful system, which has in recent years been successfully implemented in Mozambique, with various other opportunities arising in countries in Europe and other Portuguese speaking nations.

However, several major challenges are growing in importance, which constituted the reason for this project. There is a growing demand for actionable information by managers that can help the decision-making process, for prioritizing strategies and forecasting while reducing costs. The maturity and effectiveness of asset management systems for bridges has also propelled owners to look to other relevant assets, following an increasing awareness of economical, security, environmental and reputational risks both from owners and broad society. The leading idea behind this project is that the digital transformation of the system can address many of the rising challenges.

Data is organized and readily available, but it is still difficult to extract meaningful information that can help management activities. Also, processes in the field, like inspection, are still largely manual and form based. Asset characterization data is still difficult and expensive to obtain and maintain in ways that bring added value to the user. It involves extended visits to the site, is susceptible to errors and very frequently requires post-processing of the information to extract data required by the manager (for example, estimating the area of a pier for painting may require intermediate processing of height and cross-section data).

Bridge Information Modelling (BrIM) technology facilitates the visualization, characterization and retrieving of geometrical data, used throughout the different activities of asset management. BrIM technology will also facilitate the extension of the system to other structural assets. Traditional static records must be completely changed (changing data models and user interface) when a new asset is characterized. With BrIM models, new assets can be introduced to the system without major disruption to the software.

Inspection is one of the main activities of the system and still requires time-consuming visits by the inspection teams. Inspectors must record all relevant data associated with the bridge or structure in a descriptive fashion, and mobile tools still include major hindrances to effective and fast inspection. Simplified mobile BrIM technology can facilitate work for the teams in the field, simplifying location and characterization of defects. BrIM technology also shows the

potential to enable autonomous drone inspection, easily correlating information between drone sensors and the model.

The extraction of relevant information from the data, namely concerning defect location, defect characterization, the evolution of the defect through time and defect tracking between different inspection records has always been difficult to perform due to analogue methods and traditional data models that struggle to effectively model geometric data. These shortcomings have also hindered reliable implementations of prediction models and other forecasting tools. The use of BrIM technology during the recording of inspection data solves many of the underlying problems and helps implement more reliable tools for forecasting and decision making.

2.1 *Objectives and proposed solutions*

The project's consortium defined as the main objective the development of a new bridge management system designated GOA.BI. This new system should exist and be accessible both in the format of a desktop web-based platform and in the format of an intelligent interface platform. The former is intended for the central management team; thus, it is a full version of the system, including all its modules. The latter is to be used by in-situ inspectors, which will access it employing mobile devices. Hence, this needs to be a lighter version only including a smaller number of features and a reduced number of modules.

Besides the objectives directly related to the development of a new bridge management system, main tools developed included:

- The training and use of a computer vision AI tool for detecting defects in bridges, working alongside the inspector for accurate identification of defects;
- The development of a BIM-to-3D-model conversion mechanism that facilitates seamless BIM model integration with the BMS system;
- A mobile application, supported by the 3D model, for fast and accurate inspection;
- The development of a user-friendly 3D model generation tool specifically designed to address scenarios where BIM models are absent;
- The deployment of degradation prediction models and a maintenance optimization framework;

2.2 *Implementation*

The success of the project depends on good coordination between all intervening co-promoters. In that sense, the activities for each objective were designed to extract the best of each promoter and better pursue the objectives of the project.

A total of eight activities were foreseen, ranging from industrial research to experimental development. The major tools developed are described in the following sections.

2.2.1 *BrIM module*

In the development of the BrIM module for the project, a comprehensive approach was adopted, emphasizing data-driven design methodologies. The module's framework was structured around a detailed data diagram, which meticulously outlined the requirements for information exchange and storage.

A pivotal feature of the module is the integration of Building Information Modelling (BIM) Authoring. This allowed for the application of various modelling protocols, enhancing the module's versatility and effectiveness in creating digital representations of bridge infrastructures. Additionally, the module adopted an object-oriented approach to alignment modelling, which significantly increased the accuracy and adaptability of the digital models.

Technologically, the module leveraged tools such as IfcOpenShell-python, combined with commercial algorithmic tools for 3D digital modelling. This synergy facilitated the effective extraction and processing of Industry Foundation Classes (IFC) model data, focusing on key parameters like element IDs, dimensions, and specific locations. The processing phase utilized four distinct algorithm sets, each dedicated to handling different aspects of the data: input,

location, dimension, and geometry. These algorithms were crucial in developing a parametric bridge model that could dynamically adapt to varying data inputs. The BrIM Module consists of two essential tools: the one described previously, that constitutes an assisted tools for BIM model import to that BMS, and a second tool, that offers simple model construction features. Because existing bridges and structures seldom have an existing BIM model (more so in the case of a maintenance specific model) it was necessary that the new platform enabled the creating of maintenance appropriate 3D models. Overall, the two tools are complementary are guarantee that a 3D model can always be used within the app to use during inspection and for post-inspection activities.

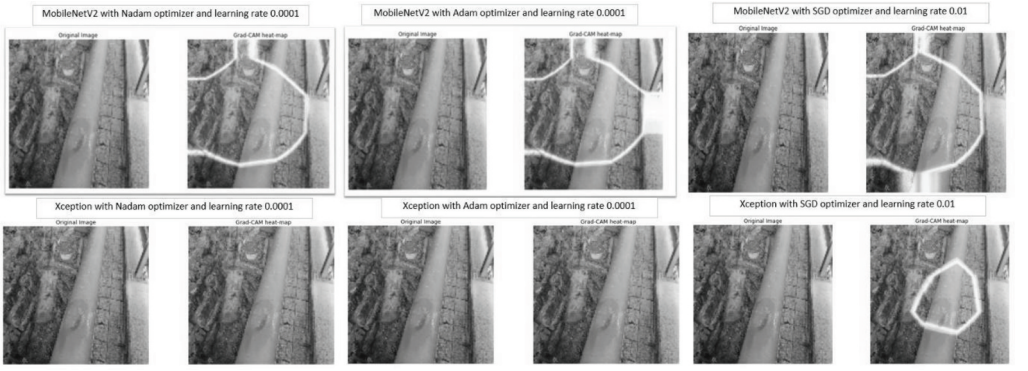


Figure 1. Model performance comparison.

2.2.2 *Defect detection using AI*

This module was designed to allow for the automatic detection of anomalies in bridge structures using advanced deep learning vision algorithms. The initial phase of the development involved constructing a comprehensive image database.

This database was crucial for training the deep learning algorithms and was initially populated with a diverse range of images sourced from Betar. It encompassed six different types of defects commonly found in bridge structures. The meticulous process of manual image processing undertaken was a critical step in ensuring the accuracy and quality of the data. The images were carefully processed, annotated, and categorized to facilitate effective machine learning.

Following this, the dataset was strategically segmented into three parts: training, testing, and validation sets. This segmentation was vital for the proper training of the algorithms and for evaluating their effectiveness and accuracy in real-world scenarios. Additionally, data augmentation techniques were employed to enhance the diversity and robustness of the dataset. These techniques involved modifying the existing images in ways that are likely to occur in real-life scenarios, thereby preparing the algorithms for a wide range of possible defect presentations.

The core of the module was the Intelligent Sensor for Optical Inspection. This component utilized TensorFlow, a powerful open-source software library for machine learning, alongside various Convolutional Neural Network (CNN) architectures. These architectures were specifically chosen and optimized for their ability to classify and identify anomalies in the images effectively.

The testing phase of the module was comprehensive and rigorous. It focused on scrutinizing the performance metrics and classification accuracy of the algorithms, particularly on previously unseen samples. This phase was crucial in determining the practical applicability and reliability of the module in real-world conditions. A notable innovation in the testing phase was the incorporation of Grad-CAM, a sophisticated visual explanation technique. Grad-CAM provided clear visual explanations for the decisions made by the CNN models, highlighting the specific areas in the images that influenced the algorithms' conclusions. This

transparency was instrumental in refining the models and in building trust in their decision-making processes.

The tool was implemented within the GOA.BI platform as a confirmation feature to the inspector's work. Images are uploaded and classified in the field by the inspector. On the server side, the algorithm runs and compares the classification from the inspector to its own result. If they are the same, no action is performed (with the guarantee that the defect identified in the image was double-checked!); if there is a difference, the inspector is prompted, asking about the divergence. The final decision remains in the hand of the inspector and its ultimate decision is used as feedback to the algorithm, guaranteeing increasing accuracy.

In summary, the development of this module was a major milestone in the integration of Vision AI tools and machine learning technologies into a BMS commercial product. It exemplifies the potential of these technologies to revolutionize infrastructure monitoring and maintenance, enhancing safety, efficiency, and reliability. The meticulous development process, from the creation of a comprehensive image database to the rigorous testing and validation of the algorithms, underscores the commitment to quality and precision in applying AI to real-world engineering challenges.

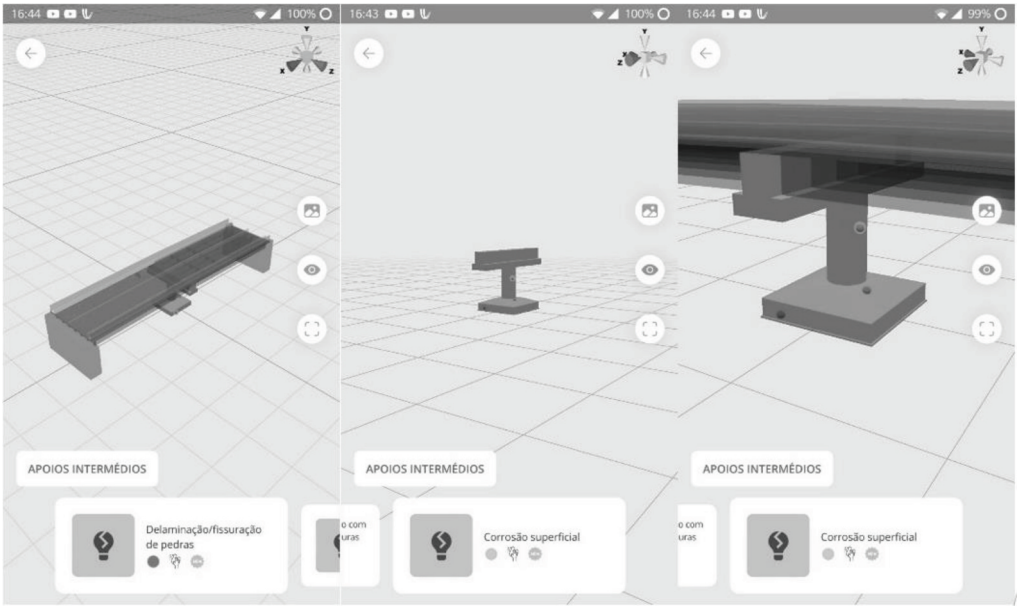


Figure 2. Mobile app views of the 3D model.

2.2.3 *Mobile 3D platform*

The mobile application interface was meticulously tailored for on-field work, focused on creating a user-centric, efficient, and responsive tool for infrastructure management.

The mobile app includes a variety of functionalities: multi-language, inspection campaign details and selection, tracking and management of planned inspections, inspection creation, bridge rating, defects lists and a rich visual user interface. Additionally, the inclusion of auxiliary table data ensures that users have access to all necessary information at their fingertips. The development process also emphasized the integration of 3D models into the mobile platform. This integration not only enhances the visual and interactive experience of the users but is transformative in the quality of the information that is recorded.

By recording precise geometric information of defect location, the app allows for the effective creation of a maintenance *digital twin*, with an enormous field of possible use cases with beneficial impact. Starting in inspection results that are easier to share and interpret, maintenance planning and activities that are less prone to error and a new dimension of data that

allows for a new generation of prediction and optimization algorithms, enriched by defect location data and geometric and physical data from the structure.

The development underscores a commitment to enhancing the efficiency, accuracy, and accessibility of bridge infrastructure management through technological innovation, while maintaining a grounded and practical perspective on its application in the field.

2.2.4 *Mixed reality module*

Unity was used as the development engine to design the prototypes for the mobile, holographic and desktop/web applications. The holographic application was developed for HoloLens, specifically HoloLens 2, and mainly uses the user's hands and fingers as the interface for interacting with and manipulating the holograms.

The 3D models that are created and used throughout the platform are consumed by the mobile and holographic applications. Through the mobile application, the user can visualise the model and record defects detected during the inspection, and with the holographic application it can see and manipulate the complete 3D model of the bridge.

The holographic application was developed in Unity using the MRKT (Mixed Reality Toolkit) augmented reality framework and includes the following features: i) choice of language; ii) Bridge visualisation on a 3D map; iii) Visualisation of bridge information; iv) Viewing photographs; v) Viewing the list of inspections; vi) Viewing and interacting with the 3D model of the bridge superimposed with inspection results.



Figure 3. Mobile app use during pilot testing.

2.3 *Testing and pilot*

In the development of the project a comprehensive testing and validation phase was undertaken. This phase was crucial in refining the application, ensuring its effectiveness and suitability for the intended end-users.

A pivotal aspect of the development process involved integrating the application into real-world field inspections. This practical application provided invaluable insights into the application's performance under actual operating conditions. Inspections of various bridges were conducted, allowing for a thorough evaluation of the application's functionality in diverse scenarios.

The focus was significantly placed on assessing the user experience. It involved gauging the application's usability, understanding how intuitive the interface was for the users, and determining the ease with which users could navigate and utilize the various features. Performance metrics were also meticulously recorded, providing quantitative data on the application's speed, responsiveness, and reliability.

User feedback was a critical component of the testing phase. Feedback from the end-users, who interacted with the application during the bridge inspections, was gathered systematically. This feedback encompassed aspects of user satisfaction, including the application's practicality, efficiency, and overall usability. It served as a direct indicator of the application's alignment with the real needs and preferences of its users.

Another key area of focus was the system's agility – its ability to perform efficiently under various conditions. Observations were made on how the application handled large data sets, its performance in different network conditions, and its adaptability to various user inputs and scenarios. Based on the feedback and performance metrics, several areas for improvement were identified, leading to iterative enhancements of the application.

The development was finalised with the execution of a pilot session executed on two integral days of field work (inspections to bridges), with the app being used by two different inspectors from Betar's team. All phases of the development of the work were gauged, from bridge and model creation to field work. Results from the feedback collected allowed for the validation of the interface, confirming the benefits in speed and accuracy of the data collection when compared with typical workflows.

3 CHALLENGES AND INSIGHTS

In the development of a bridge management system incorporating BIM technology numerous challenges and insights have emerged. The project navigated the fluid landscape of BIM standards, notably IFC, confronting the hurdles posed by their novelty and instability. This situation impeded seamless integration, demanding adaptability and innovative problem-solving to align with the evolving digital framework.

Concurrently, the implementation of AI for defect detection required a substantial investment in image collection and preparation. This foundational stage, while resource-intensive, was crucial for ensuring the model's accuracy and effectiveness. It highlighted the necessity of a robust groundwork for AI applications, especially in domains where precision is paramount.

Field manipulation of 3D models presented a unique set of challenges. The complexity of interacting with intricate models in a real-world context revealed a gap between digital sophistication and practical utility, underscoring the need for user-friendly interfaces and real-world applicability in technological solutions.

The ambition of real-time image processing via AI faced technical constraints, particularly the necessity for high computational power and optimized algorithms. This aspect of the project underscored the importance of computational advancements and algorithmic efficiency in real-time data processing applications.

Balancing the complexity and thoroughness of data collection with the need for operational efficiency in fieldwork was a recurring theme. Developing methods that streamline data capture without compromising data quality emerged as a critical factor in enhancing field operations' efficiency.

In addition to these challenges, the project navigated issues related to data security and privacy, especially pertinent given the sensitivity of infrastructure data. The integration of various technologies also highlighted the need for interoperability between different systems and platforms, requiring a harmonized approach to ensure seamless functionality.

From these challenges, several key insights were gained. The fluidity of BIM standards, though challenging, offered a platform for continuous improvement and adaptation in asset management systems.

The project's experiences emphasized the importance of user-centric design, particularly in field applications. Solutions that prioritize intuitive interfaces and align with real-world fieldwork conditions can effectively bridge the gap between technological innovation and practical usability. Furthermore, the development of strategic data collection methods that balance depth with speed can significantly improve operational efficiency. The project's experiences also highlighted the importance of continuous learning and adaptation in the face of technological advancements and changing industry standards.

In summary, the project offered a rich learning experience, providing key insights into the integration of advanced technologies in infrastructure management. The lessons learned extend beyond the scope of this project, offering valuable guidance for future endeavours in digital asset management and infrastructure inspection.

REFERENCES

Berardinelli, U., Neves, L.C., Matos, J.C., Guimarães, H., 2015. An advanced highway asset management system, in: 4th International Symposium on Life-Cycle Civil Engineering, IALCCE 2014. CRC Press.

Calvi, G.M., Moratti, M., O'Reilly, G.J., Scattarreggia, N., Monteiro, R., Malomo, D., Calvi, P.M., Pinho, R., 2018. https://doi.org/10.1080/10168664.2018.1558033 29, 198–217.

Carmo, J., 2021. The Hintze Ribeiro bridge collapse and the lessons learned, in: River Basin Management - Sustainability Issues and Planning Strategies. IntechOpen, p. 19.

Denysiuk, R., Fernandes, J., Matos, J.C., Neves, L.C., Berardinelli, U., 2016. Struct. Eng. Int. 26, 94–102.

Hammervold, J., Reenaas, M., Brattebø, H., 2013. J. Bridg. Eng. 18, 153–161.

International Transport Forum, 2013. Understanding the Value of Transport Infrastructure - Guidelines for macro-level measurement of spending and assets. France.

Isailović, D., Petronijević, M., Hajdin, R., 2019. The future of BIM and Bridge Management Systems, in: IABSE Symposium, Guimaraes 2019: Towards a Resilient Built Environment Risk and Asset Management.

Kunert, U., Link, H., 2013. DIW Econ. Bull. 3, 12–17.

Mirzaei, Z., Adey, B., Klatter, L., Thompson, P., 2014. Over-view of existing Bridge Management Systems. Report by the IABMAS Bridge Management Committee.

Neves, L., Frangopol, D.M., Hogg, V., 2003. Condition-Reliability-Cost Interaction in Bridge Maintenance, in: Ninth International Conference on Applications of Statistics and Probability in Civil Engineering, ICASP9.

Omar, T., Nehdi, M.L., 2018. Infrastructures 2018, Vol. 3, Page 36 3, 36.

Santamaria Ariza, M., Zambon, I., S. Sousa, H., Campos eMatos, J.A., Strauss, A., 2020. Struct. Concr. suco.201900434.

Santamaria, M., Fernandes, J., Matos, J., 2019. Overview on performance predictive models – Application to bridge management systems, in: IABSE Symposium, Guimaraes 2019: Towards a Resilient Built Environment Risk and Asset Management.

Simões, L., Silva, M., Patrocínio, T., Castro, Â., Marçal, C., 2020. Operacionalidade de Infraestruturas e Transportes. Lisboa, Portugal.

Soilán, M., Sánchez-Rodríguez, A., Del Río-Barral, P., Perez-Collazo, C., Arias, P., Riveiro, B., 2019. Infrastructures 2019, Vol. 4, Page 58 4, 58.

World Economic Forum, 2019. The Global Competitiveness Report 2019.

Costa, S., Brito, V., Mendonça, T., 2019. Transport Infrastructures and Asset Management in Portugal: Past, Present and Future, in: IABSE Symposium 2019 Guimarães Towards a Resilient Built Environment - Risk and Asset Management. pp. 1750–1757.

Diário da República n.o 188/2003, S.I.-A. de 2003-08-16, 2003. Decreto-Lei n.o 182/2003.

Santos, C., Coelho, M., Matos, J., Costa, S., Brito, V., 2022. BMS and BIM: the Portuguese scenario, in IABSE Symposium 2022 Prague Challenges for Existing and Oncoming Structures.

Bridge Maintenance, Safety, Management, Digitalization and Sustainability – Jensen, Frangopol & Schmidt (eds)
© 2024 The Author(s), ISBN 978-1-032-77040-6
Open Access: www.taylorfrancis.com, CC BY-NC-ND 4.0 license

A quantitative methodology for risk-based priority ranking of deteriorated bridges: Application to a bridge stock

S. Hamidpour, N. Scattarreggia, R. Nascimbene & R. Monteiro
University School for Advanced Studies (IUSS) of Pavia, Italy

ABSTRACT: Bridges play a crucial role in a nation's infrastructure, facilitating connectivity in road networks. Recent global incidents of bridge failures have heightened concerns about the existing bridge structures, prompting the development of more effective bridge management techniques. Italy, among other countries, has addressed this concern by introducing national guidelines for the risk assessment and management of bridge portfolios. While these guidelines offer a detailed multi-level and multi-hazard approach, their qualitative nature limits enhance precision of risk classification for a specific bridge stock. This study addresses this limitation by presenting a quantitative approach to evaluate bridge risk conditions. The method provides quantifiable expressions for vulnerability, exposure, and hazard, considering both the general robustness of the bridge structure and the presence of defects and damages. Leveraging the Italian guidelines' specifications, the priority ranking approach employs a refined scoring system to convert qualitative bridge characteristics into quantitative parameters. The study focuses on prioritizing 130 bridges in northern Italy through both the priority ranking method and the ITA-Guidelines. It thoroughly assesses the ITA-Guidelines' classes of attention for various risk parameters and compares the outcomes with the priority ranking method.

1 INTRODUCTION

Ageing bridge structures have become a significant global concern in recent decades, driven by the increased occurrence of bridge failures worldwide (e.g., the muti-span arch bridge failure in 2020 in Italy,Scattarreggia et al., 2022). These structures are subjected to various forms of deterioration and degradation, which can compromise their structural integrity. Ensuring the safety and reliability of these critical infrastructure elements is essential to prevent unforeseen failures that could lead to severe consequences, including harm to human life, disruption of transportation networks, and economic losses. Implementing prioritization methodologies for assessing the overall condition and risk of bridges is crucial to help managing bodies decide over further assessment, maintenance, rehabilitation or demolition of the bridges to prevent or minimize further socio-economic consequences.

This subject has gained significant interest in recent years with numerous studies exploring various aspects. Meoni et al. (2023) proposed a priority ranking method for bridges that considers both risk assessment and visual inspection costs, aiming to develop a visual inspection plan. Zizi et al. (2023) introduced an empirical risk assessment method based on seismic hazard to establish a priority ranking for bridges, for planning detailed on-site visual inspections. Bertola & Brühwiler (2023) formulated a risk-based approach to assess the condition of bridges by linking the degradation state of the bridge with the consequences of element failure, utilizing visual inspection data. Ivanković et al. (2021) developed an approach for the prioritization of bridges for repair purposes, utilizing data from damage inspections. Kim et al. (2018) developed a method for prioritizing maintenance, considering diverse risk factors optimized through an examination of conventional methods and insights from engineering

DOI: 10.1201/9781003483755-340

consultants. The Federal Highway Administration of the United States (FHWA, 2022) issued instructions for the condition assessment of highway bridges to ensure their safety. As outlined in FHWA (2016) numerous other bridge health indices are currently utilized worldwide, along with recent optimal prioritization methodologies proposed by researchers, such as Abarca et al. (2023) or D'Apuzzo et al. (2022).

Italy has around 120,000 bridges, mainly built between the 1950s and 1970s (Pinto & Franchin, 2010; Santarsiero et al., 2021). Many of these bridges may lack sufficient durability due to outdated construction standards, which precede the introduction of modern design regulations (e.g., NTC 2018); may encounter challenges with current traffic demands; and may alter in their residual capacity due to unknown defects, e.g., the ones correlated to construction errors (e.g., Pinho et al., 2023). Inadequate maintenance coupled with ageing was evident in recent failures like the Annone overpass (di Prisco et al., 2018) and the Morandi bridge (Calvi et al., 2019). To address this, the Italian Higher Council of Public Works introduced the Italian guidelines, to regulate the risk assessment and management of existing bridges (ITA-Guidelines, 2020). These guidelines classify bridges into five Classes of Attention (CoA): High (H), Medium-High (MH), Medium (M), Medium-Low (ML), and Low (L). While each class indicates the level of attention required for a bridge, due to their qualitative definition of risk, these guidelines hinder prioritization within the same CoA.

This study presents a quantitative approach to prioritize bridge importance, addressing the limitations of qualitative methods, such as the ITA-Guidelines (Hamidpour et al., 2024). The approach utilizes closed-form expressions for definition of vulnerability, exposure, and hazard parameters aligning with the ITA-Guidelines and recent methodologies (Zizi et al., 2023). Vulnerability combines structural features as outlined in the ITA-Guidelines and defects using the approach foreseen for the United Kingdom Bridge Condition Index (UK-BCI, 2007). This innovative quantitative integration using two distinct guidelines elevates the comprehensiveness of vulnerability assessment. Exposure assesses the bridge and network-level impacts of a bridge failure. Hazard considers commercial vehicle traffic and expected Peak Ground Acceleration (PGA) of an event with 475-year return period. The priority ranking is determined as a weighted combination of these three parameters showing the relative priority of a bridge within a stock. The study involves the application of the priority ranking method and the ITA-Guidelines to assess 130 bridges located in northern Italy. A thorough evaluation of the ITA-Guidelines' classes of attention for different risk parameters is carried out, and a comparative analysis is conducted between the results obtained from the adopted priority ranking and the ITA-Guidelines.

2 RISK-BASED PRIORITY ASSESSMENT METHOD

The risk-based assessment methodology used in this study is described in Hamidpour et al. (2024), to which interested readers are referred for additional details. It incorporates three primary parameters: vulnerability (V), exposure (E), and hazard (H), each quantified knowing the general and physical characteristics of the bridge and the road to which it belongs through equations outlined in this section. The priority ranking (PR) is then determined as the weighted combination of these three parameters, as per Equation 1. The formulations have been crafted in parallel with the fundamental principles outlined in the ITA-Guidelines as the main reference for the mentioned quantitative methodology. Furthermore, the UK-BCI approach has been used to evaluate the vulnerability of bridges by considering the extent and severity of the existing damages and defects in a quantitative manner.

$$PR = 0.4(V + E) + 0.2H \tag{1}$$

2.1 *Vulnerability*

In vulnerability definition, two primary factors are considered representing vulnerability attributed to structural characteristics ($V_{Str.}$), and vulnerability arising from the condition of damages and defects in the bridge elements ($V_{Def.}$). The two components are combined using the Root Mean Square (RMS) method to obtain the overall vulnerability of bridge as in

Equation 2. While the $V_{Str.}$ is defined using the ITA-Guidelines specifications, the $V_{Def.}$ is determined based on the previously mentioned UK method for bridge condition index (BCI) using the formulations presented in Equation 3 and 4, respectively.

$$V = \sqrt{({V_{Str.}}^2 + {V_{Def.}}^2)/2} \tag{2}$$

Structural vulnerability, denoted as $V_{Str.}$, considers five characteristic parameters: V_{YC}, V_{SS}, V_{LS}, V_{NS}, and V_{DM}, which respectively represent the influence of the year of construction, structural static scheme, largest span length, number of spans, and deck material. The determination of structural vulnerability involves converting the bridge specifications to numerical values, as specified in Table 1. The weights assigned to parameters in Equation 3 and the values in Table 1 are primarily aligned with the ITA-Guidelines, with some modifications based on recent research findings (e.g., Zizi et al., 2023), along with expert judgment.

$$V_{Str.} = 0.25(V_{YC} + V_{SS}) + 0.2V_{LS} + 0.15(V_{NS} + V_{DM}) \tag{3}$$

Table 1. Structural vulnerability parameters ($V_{Str.}$).

Year of construction	V_{YC}	Static scheme	V_{SS}	Largest span length (m)	V_{LS}
YC≤1945	1.00	Simply supported beams/slab (SSB/S)	1.00	LS<5	0.10
1945<YC≤1980	0.75			5≤LS<15	0.30
1980<YC≤2003	0.50	Continuous beams/slab (CB/S)	0.90	15≤LS<25	0.70
2003<YC≤2018	0.25			LS≥25	1.00
YC>2018	0	Arches (A)	0.80		
Number of spans	V_{NS}	Deck material	V_{DM}		
NS=1	0.10	Steel and reinforced concrete (MX)	0.80		
NS=2-4	0.30	Prestressed concrete (PRC)	0.90		
NS=5-7	0.60	Reinforced concrete (RC)	0.95		
NS=8-10	0.90	Masonry (M)	1.00		
NS>10	1.00				

Regarding the other component of bridge vulnerability associated with defects, denoted as $V_{Def.}$, it is assessed using the UK method based on data obtained from visual inspections of the bridge elements damages (Equation 4). This method generates an index (BCI_{UK}) considering the extent and severity of defects observed at the element level and indicates two states of conservation: "Avg-Def." and "Crit-Def.". The "Avg-Def." state provides a comprehensive evaluation of the bridge condition, illustrating the extent of deterioration across all damaged and undamaged bridge elements. In contrast, the "Crit-Def." state signifies the criticality of the structure due to the exceptionally poor condition of a critical element, deemed essential to the overall integrity of the bridge. Further details about the evaluation of the bridge condition indicator can be found in Hamidpour et al. (2024).

$$V_{Def.} = 1 - (BCI_{UK}/100) \tag{4}$$

2.2 *Exposure*

The exposure parameter for a bridge (E) is calculated using Equation 5, where E_{AT}, E_{DL}, E_{MS}, E_{EB}, and E_{RC} represent the average daily traffic on the entire roadway, detour length in the event of bridge closure, mean span length, entity bypassed by the bridge, and road category, respectively, reflecting in the scores given in Table 2.

$$E = 0.3E_{AT} + 0.2(E_{DL} + E_{MS} + E_{EB}) + 0.1E_{RC} \tag{5}$$

Table 2. Exposure parameters (E).

Average daily traffic (vehicle/day)	E_{AT}	Detour length (km)	E_{DL}	Mean span length (m)	E_{MS}
AT≤10k	0.80	DL≤1	0	MS<5	0.10
		1<DL≤10	0.25	5≤MS<15	0.30
10k<AT<25k	0.90	10<DL≤20	0.50	15≤MS<25	0.70
AT≥25k	1.00	20<DL≤40	0.75	MS≥25	1.00
		DL>40	1.00		
Entity bypassed	E_{EB}	Road category	E_{RC}		
"High" social/public effects (railways, main roads, constructed areas)	1.00	Highway or railway (HRW)	1.00		
		Main suburban road (MSR)	0.90		
"Medium" social/public effects (secondary roads, waterways and water bodies)	0.70	Secondary suburban road (SSR)	0.80		
		Urban road (UR)	0.70		
"Low" social/public effects (Natural grounds and areas)	0.20	Local road (LR)	0.60		

2.3 *Hazard*

This study incorporates two potential sources of hazard, specifically traffic load and seismic action. As indicated in Table 3, the determination of the hazard component considers the frequency of commercial vehicles per lane (H_T) and the ratio between the Peak Ground Acceleration (PGA) expected to be exceeded every 475 years at the bridge's location and the highest anticipated PGA in the Italian territory (H_S), as per the seismic hazard maps (i.e., 0.35g).

Table 3. Hazard parameters (H).

Commercial vehicle/day	H_T	PGA ratio	H_S
CT≤300	0.50	Event with 475-year return period/	
300<CT<700	0.75	Highest expected event in Italy	PGA(g)/0.35
CT≥700	1.00		

3 SELECTED CASE-STUDY BRIDGE INVENTORY

The studied inventory encompasses 130 viaducts and overpasses in Lombardy region, northern Italy. Figure 1 provides an overview of the primary characteristics of the bridges and their statistical distribution. The data including geometrical, geotechnical, and structural features, along with potential on-site hazards and structural element damages was made available by the managing operator through visual inspections following the protocol prescribed by the ITA-Guidelines. The predominant design of most bridges includes a simply supported deck system with steel girders and concrete slabs, and they were mainly constructed between years 1960 and 2010. A significant number of bridges have multiple spans (mostly 3 spans) with varying or uniform lengths; typically, the largest span length varies from 6 m to 70 m, with one bridge spanning up to 125 m. These bridges are situated mostly on local roads or highways with an average daily traffic between 10,000 and 32,000 vehicles throughout the entire road, and the daily commercial traffic from 300 to 12,000 vehicles per lane. As the majority of the bridges primarily span over highways, their surrounding area may encompass high social or economic consequences in the event of failure.

4 RISK ASSESSEMENT OF THE CASE-STUDY BRIDGES

4.1 *ITA-Guidelines*

The ITA-Guidelines prescribe a multi-level multi-hazard procedure to evaluate the risk associated with existing bridges. The process initiates with an extensive data collection through visual

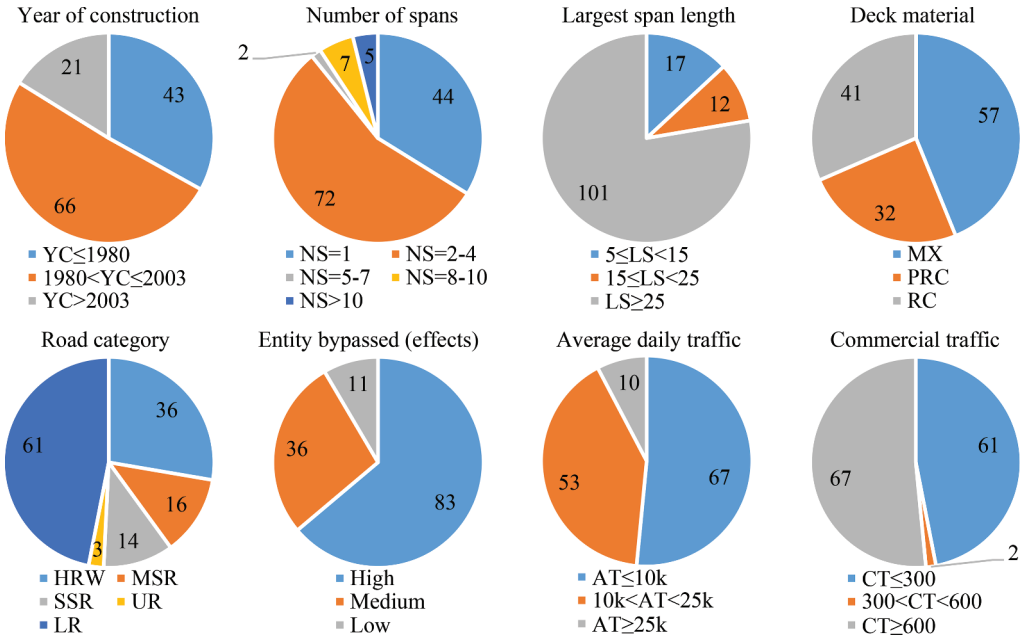


Figure 1. Summary of primary characteristics of bridges and their statistical distribution.

inspections, covering various aspects such as geometrical, structural, and geotechnical characteristics, as well as potential on-site hazards and structural element damages and defects. This data is then used to categorize bridges into different classes of attention based on hierarchical logic models for risk components, which are vulnerability, exposure and hazard. This preliminary classification indicates the required level of attention for each bridge under a specific hazard. By combining the classes of attention associated with all relevant hazards through a hierarchical model, an overall CoA is obtained for bridges. According to ITA-Guidelines, in defining the possible combinations, greater weight is given to the structure-foundation (traffic) CoA as it is linked to the operability of bridges. This means that if it is high, the overall CoA is high, irrespective of the CoAs related to seismic, hydraulic, and landslide hazards.

Figure 2 illustrates the outcomes of such evaluations for the case study inventory introduced in Section 3, displaying the CoA for various risk parameters. The CoA has been assessed separately in two risk categories including structure-foundation and seismic as outlined in the ITA-Guidelines. Since the structure-foundation risk considers commercial traffic as the potential hazard, it is denoted as traffic CoA in this study. The results indicate relatively higher seismic CoA for bridges considering defects, attributed to the presence of high-importance defects including oxidation and corrosion in seismic-critical components of the bridges, such as support devices and piers. On the other hand, vulnerability shows almost similar results for traffic and seismic CoAs, as both incorporate very similar input physical and geometric parameters during the evaluation procedure. Moreover, exposure remains identical for traffic and seismic CoAs, as the studied bridges do not feature strategic nature considering seismic emergency conditions, resulting in the same seismic CoA as traffic. Since the Lombardy region is not an area with a high seismicity, seismic hazard CoA for all bridges results as medium, while due to the intense daily traffic of roadways, the traffic hazard CoA is classified as medium-high and high. The analysis of results revealed that a greater number of bridges are assigned a high CoA in traffic risk category compared to the seismic counterpart (95 and 77 bridges, respectively). The overall CoA, resulting from the combination of traffic and seismic CoAs, yields to 95 bridges identified as requiring a high level of attention. This implies that most of the studied bridges demand further detailed assessments in accordance with current technical standards for construction.

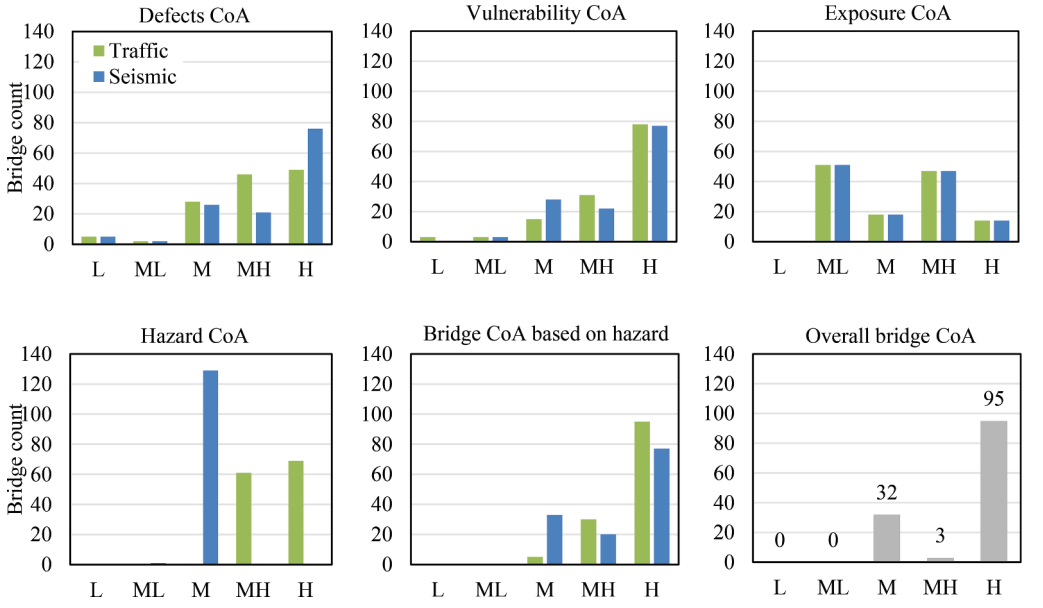


Figure 2. Statistical distribution of bridges based on the ITA-Guidelines CoA considering defects, vulnerability, exposure, hazard, bridges CoA based on hazard, and overall bridge CoA.

4.2 *Quantitative priority ranking*

The priority rankings of the studied bridges, calculated using Equation 1 and considering different approaches to determine the vulnerability parameter as defined in Equations 2 to 4, are depicted in Figure 3. The results indicate that when defects are accounted for, mainly when using the indicator based on the critical one (i.e., Crit-Def.), the total number of bridges with higher priority ranks for both traffic and seismic hazards increases. For instance, Figure 3 shows that none of the bridges fell within the range 0.6-0.8 or higher, and within the range 0.8-1.0 when neglecting the presence of defects (i.e., the case "Str. & wo-Def.") under seismic and traffic hazards, respectively. On the other hand, when defects are accounted for, either in average or critical states, some bridges move to ranges that imply higher priority. In other words, including the contribution of defects to vulnerability confirmed a more severe risk condition for the bridges. Finally, an overall look indicates most bridges are ranked in the ranges of 0.6-0.8 and 0.4-0.6 under traffic and seismic hazards, respectively.

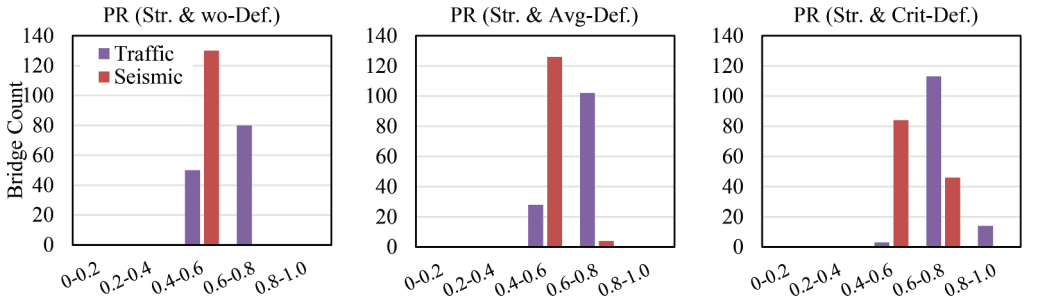


Figure 3. Statistical distribution of bridges based on the priority ranking (PR) for seismic and traffic hazards, under various vulnerability definitions: Str. & wo-Def., Str. & Avg-Def., and Str. & Crit-Def.

4.3 *Comparison of the results*

Since the ITA-Guidelines incorporates defects in the risk classification of bridges, in this section the priority ranking method results are discussed when defects are considered in determination of the vulnerability. To provide consistency between the results of the two methods, the priority ranking subranges of the presented method, defined in intervals of 0.0-0.2, 0.2-0.4, 0.4-0.6, 0.6-0.8, and 0.8-1.0 were viewed as the Low (L), Medium-Low (ML), Medium (M), Medium-High (MH), and High (H) classes of attention of the ITA-Guidelines, respectively. According to Figure 4, for the traffic hazard, the results of the priority ranking method with the vulnerability case of "Str. & Avg-Def." show that many of the bridges are classified within the 0.6-0.8 subrange (equivalent to the medium-high CoA), while most bridges were classified as high CoA according to the ITA-Guidelines. For the seismic hazard, with similar vulnerability, most bridges were classified in the 0.4-0.6 subrange (equivalent to the medium CoA), whereas using the ITA-Guidelines, most bridges are classified in the medium-high and high CoAs. Even when considering the critical defects, resulting in a higher vulnerability and consequently higher priority rankings than the case of the average defects, the ITA-Guidelines approach tends to classify the bridges at higher levels than the proposed method by Hamidpour et al. (2024). The method's ability to generate individual bridge scores provides a notable advantage in determining relative priorities within extensive inventories, especially when multiple bridges share the same CoA.

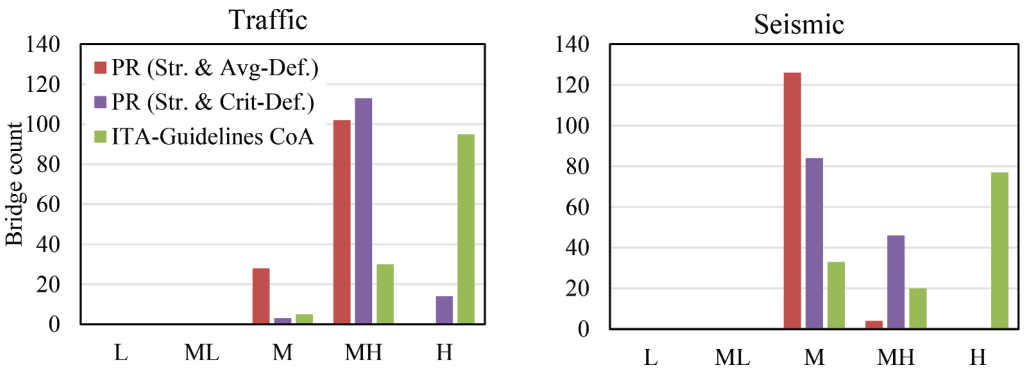


Figure 4. Comparison of the statistical distribution of bridges using the priority ranking (PR) method or the ITA-Guidelines' CoA for traffic and seismic hazards.

5 CONCLUSIONS

This study addresses the risk associated with existing ageing bridge structures, showing an application of a recently proposed risk priority method to a bridge inventory that encompasses 130 bridges in the Lombardy region, in northern Italy. While acknowledging the comprehensive multi-level, multi-hazard approach of the Italian guidelines issued in 2020 for risk assessment and management of existing bridges, this study highlights their limitation in creating a refined risk classification for bridge stocks due to their qualitative description of risk. Such a limitation is overcome by providing quantitative rankings, interpreting the qualitative characteristic of bridges and roads into numerical values, as proposed by the adopted approach (Hamidpour et al., 2024). Both methods were applied to the case-study bridge stock, conducting a thorough evaluation of the Italian guidelines classes of attention (CoA) for various risk parameters and a comparison between the results of the two methods. The primary findings confirm that considering bridge defects and damages amplifies vulnerability, resulting in a higher risk priority ranking. Furthermore, the research highlights variations in a bridge's priority ranking within the stock based on the specific hazard source, with an overall tendency for traffic-related risk to rank higher than the seismic counterpart. The study concludes that the selected

quantitative method offers more refined priority ranks for the 130 bridges, helping their relative priority ranking when they feature the same CoA according to the Italian guidelines. This provides an advantage for bridge operators managing large inventories, allowing for a more refined determination of relative priorities of bridges.

REFERENCES

Abarca, A., Monteiro, R., & O'Reilly, G. J. 2023. Seismic risk prioritisation schemes for reinforced concrete bridge portfolios. *Structure and Infrastructure Engineering*, 1–21.

Bertola, N. J., & Brühwiler, E. 2023. Risk-based methodology to assess bridge condition based on visual inspection. *Structure and Infrastructure Engineering*, *19*(4), 575–588.

Calvi, G. M., Moratti, M., O'Reilly, G. J., Scattarreggia, N., Monteiro, R., Malomo, D., Calvi, P. M., & Pinho, R. 2019. Once upon a Time in Italy: The Tale of the Morandi Bridge. *Structural Engineering International*, *29*(2), 198–217.

D'Apuzzo, M., Evangelisti, A., Rasulo, A., & Nicolosi, V. 2022. Simplified approach to integrate seismic retrofitting prioritization with social cost evaluation: A case study in central Italy. *Journal of Traffic and Transportation Engineering (English Edition)*, *9*(3), 447–460.

di Prisco, M., Colombo, M., Martinelli, P., & Coronelli, D. 2018. The technical causes of the collapse of Annone overpass on SS.36. *Proceedings of Italian Concrete Days*.

Guidance document for performance measurement of highway structures part B1: Condition performance indicator. 2007. *Association of Directors of Environment*, *Economy Planning and Transport*, Lincoln, United Kingdom.

Guidelines for risk classification and management, safety assessment and monitoring of existing bridges (In Italian). 2020. *Ministry of Infrastructure and Transport*, Rome, Italy.

Hamidpour, S., Scattarreggia, N., Nascimbene, R., & Monteiro, R. 2024. A risk-based quantitative approach for priority assessment of ageing bridges accounting for deterioration. *Submitted*.

Ivanković, A. M., Skokandić, D., Marić, M. K., & Srbić, M. 2021. Performance-based ranking of existing road bridges. *Applied Sciences (Switzerland)*, *11*(10).

Kim, D., Lee, Y., & Lee, M. 2018. Development of Risk-Based Bridge Maintenance Prioritization Methodology. *KSCE Journal of Civil Engineering*, *22*(10), 3718–3725.

Meoni, A., García-Macías, E., Venanzi, I., & Ubertini, F. 2023. A procedure for bridge visual inspections prioritisation in the context of preliminary risk assessment with limited information. *Structure and Infrastructure Engineering*, 1–27.

Pinho, R., Scattarreggia, N., Orgnoni, A., Lenzo, S., Grecchi, G., Moratti, M., & Calvi, G. M. 2023. Forensic estimation of the residual capacity and imposed demand on a ruptured concrete bridge stay at the time of collapse. *Structures*, *55*, 1595–1606.

Pinto, P. E., & Franchin, P. 2010. Issues in the upgrade of Italian highway structures. *Journal of Earthquake Engineering*, *14*(8), 1221–1252.

Santarsiero, G., Masi, A., Picciano, V., & Digrisolo, A. 2021. The Italian guidelines on risk classification and management of bridges: Applications and remarks on large scale risk assessments. *Infrastructures*, *6*(8).

Scattarreggia, N., Salomone, R., Moratti, M., Malomo, D., Pinho, R., & Calvi, G. M. 2022. Collapse analysis of the multi-span reinforced concrete arch bridge of Caprigliola, Italy. *Engineering Structures*, *251*.

Specifications for the national bridge inventory, Publication No. FHWA-HIF-22-017. 2022. *Office of Bridges and Structures*, *U.S. Department of Transportation*.

Synthesis of national and international methodologies used for bridge health indices. 2016. *U.S. Department of Transportation, Federal Highway Administration*.

Update of the «Technical standards for construction», NTC 2018, (In Italian). 2018. *Ministry of Infrastructure and Transport*, Rome, Italy.

Zizi, M., Bencivenga, P., & De Matteis, G. 2023. Handling policies for Italian existing bridges with a territorial approach: the case study of Caserta, Italy. *Structures*, *48*, 1306–1321.

Bridge Maintenance, Safety, Management, Digitalization and Sustainability – Jensen, Frangopol & Schmidt (eds)
© 2024 The Author(s), ISBN 978-1-032-77040-6
Open Access: www.taylorfrancis.com, CC BY-NC-ND 4.0 license

An index-based method for risk assessment of existing bridges subjected to multiple hazard

L.A. Grieco
University of Naples Federico II, Naples, Italy

N. Scattarreggia & R. Monterio
University School for Advanced Studies IUSS, Pavia, Italy

F. Parisi
University of Naples Federico II, Naples, Italy

ABSTRACT: Recent bridge collapses have highlighted the urgent need for rapid risk analysis methods to support infrastructure managers in the selection and prioritization of disaster risk mitigation measures. As far as existing road bridges are concerned, their construction was mainly carried out between the 1960s and 1980s, implying that many of those structures have exceeded or are reaching their typical 50-year nominal lifespan. Previous studies have shown that bridges often fail due to a range of natural and human-induced hazards, including floods, vehicle impact, and overloading. Such hazards together with earthquakes should be duly considered into disaster risk assessment of existing bridges. Therefore, the identification of critical structures within a large bridge portfolio should rely upon comprehensive multi-hazard risk assessment approaches. This study presents an index-based methodology for disaster risk assessment of existing bridge portfolios, accounting for a variety of natural and human-made hazards and their potential impact on the roadway network. The proposed risk-based methodology considers various factors that influence structural vulnerability and potential consequences of bridge failure, depending on the specific nature of each hazard. Additionally, the structural condition of the bridges is taken into account when computing single-hazard risk indicators for traffic, seismic, fire, and vehicle impact. These indicators are then integrated into a multi-hazard risk measure using multiple formulations. The final part of the study shows the application of the methodology to a set of road bridges located in northern Italy. The analysis results are compared with those provided by methods available in the literature, discussing the benefits of the proposed methodology.

Keywords: Multi-hazard risk assessment, existing bridges, risk indicators, risk-based ranking, comparative analysis

1 INTRODUCTION

The importance of bridges in road infrastructure cannot be underestimated. Bridges are not merely structural components of a road infrastructure, but an integral part of the socio-economic development and overall well-being of a nation. The significance of bridges in road infrastructure lies in their ability to connect people, promote economic growth, enhance safety, and contribute to the efficient movement of goods and people. Therefore, investing resources on design, construction, and maintenance of bridges is a wise and essential step in ensuring the prosperity of a region or a country as a whole. All around the word, especially in Italy, the backbone of existing road infrastructure dates back to the Second World War, which implies that many of the existing bridges are 50 years old or more. Their natural ageing in combination with the recently observed collapses, e.g., the Morandi bridge in Genoa (Calvi et al. 2019), the multi-span arch bridge

DOI: 10.1201/9781003483755-341

between the municipalities of Albiano Magra and Caprigliola (Scattarreggia et al. 2022), have prompted the need for assessment and, if necessary, intervention. However, in a world where resources are limited, it is needed a rational prioritization approach to support decision-makers allowing the identification of critical structures when dealing with large bridge portfolios. Available approaches for bridge prioritization typically involve the use of indices associated with information on the structural elements (e.g. Bianchi et al. 2022).

A risk-based approach for prioritizing bridges is a systematic method that considers factors such as structural integrity, safety, maintenance needs, and potential consequences of failure for the definition of a priority ranking. Several statistical studies have shown that bridges often suffer failure due to either natural or human-related events (see e.g. Deng et al. 2016). Optimal prioritization approaches should therefore be multi-hazard in addition to having features for an easy application on a large scale. As result, it is important to use quantitative approaches to create a ranking of bridges based on their criticality (Moon et al. 2009), contrary to those based on a qualitative description of risk. Indeed, qualitative approaches do not permit to obtain refined rankings, thus rendering difficult their employment for the management of existing bridges, as the recently issued Italian guidelines foresee (MIT 2020).

In this study, single-hazard risk-based quantitative methods associated with road traffic and seismic ground shaking (Hamidpour et al. 2023b), fire (Kodur et al. 2013), and vehicle impact (Kim et al. 2020) have been selected from those available in the literature. Initially, a brief overview of each of the adopted methods is given. Subsequently, individual risk-based indicators used to derive multi-hazard risk indicators (I_{MH}) according to different well-established combination approaches are described. A group of thirty real bridges located in northern Italy was selected as case-study with the aim of applying the proposed quantitative multi-risk approach for bridge risk prioritization. Single-hazard indicators have been defined for all bridges, and then combined according to the selected approaches for the definition of multi-risk indicators. Obtained results were compared with each other, and the impact on the priority ranking of each multi-hazard combination commented. Finally, a comparison between the proposed quantitative method and the qualitative Italian guidelines is carried out.

2 SINGLE-HAZARD METHODS FOR QUANTITATIVE RISK ASSESSMENT

2.1 *Road traffic and seismic risk*

The weighted multi-factor average model proposed by Hamidpour et al. (2023b) is used for road traffic and seismic hazards to evaluate the priority index of existing bridges. It accounts for hazard (H), vulnerability (V) and exposure (E) components, that are combined according to specific weights as in Eq. (1):

$$PR = 0.2H + 0.4V + 0.4E \tag{1}$$

Multi-parameter formulations are employed to determine each risk component (i.e. H, V, and E), based on the general characteristics of bridges, road category, and their hazards when providing numerical values. In particular, this approach foresees that the overall vulnerability is determined according to Eq. (2), thus, in addition to the structural characteristics, the level of deterioration/defects is also explicitly accounted for.

$$V = \sqrt{\frac{V_s + V_D}{2}} \tag{2}$$

The structural vulnerability (V_s) considers five characteristic parameters including the year of construction, static scheme, largest span length, number of spans and deck material. On the other hand, the vulnerability due to defects (V_D) represents the bridge condition, which accounts for the deterioration effects resulting from the structures ageing and lack of maintenance. This term is defined based on the United Kingdom Bridge Condition Index (UK-BCI) approach (2007). The exposure component of the bridge is estimated using parameters that

account for average daily traffic, detour length, mean span length, entity bypassed and road category. Each of these parameters would represent the expected losses for the bridge itself and the network to which it belongs. Finally, the hazard is evaluated differently depending on whether it is due to traffic load or seismic loading, considering the frequency of commercial vehicles per lane (H_{CT}) and the expected Peak Ground Acceleration (PGA) at the bridge site (H_E), respectively. Further details can be found in Hamidpour et al. (2023b).

2.2 *Fire risk*

The simplified methodology proposed by Kodur and Noser (2013) is employed to identify the most critical bridges regarding the effect of fire, through the determination of an Importance Factor (IF). The method takes into account hazard, vulnerability, and exposure. Specifically, five classes are identified, each of which is composed of parameters that in turn include sub-parameters:

- Class I (ψ_g): Geometrical features, material properties, and design characteristics. The sub-parameters are the number of lanes, age, current standard rating in terms of functionality, and the additional presence of service features.
- Class II (ψ_h): Hazard (fire) likelihood. The sub-parameters are the response time in terms of necessary time before actions, architectural/historical importance, threat perception according to historical fires close to the bridge, and probable fire scenario in terms of consequences.
- Class III (ψ_t): Traffic demand. The sub-parameters are the average daily traffic and location of nearby facilities.
- Class IV (ψ_e): Economic impact. The sub-parameters are the presence of alternative routes, time and cost expected for repair.
- Class V (ψ_f): Expected fire losses. The sub-parameters are life and property losses, and environmental damage.

Each sub-parameter is assigned a weighting factor ($\varphi_{i,x}$) between 1 (best) and 5 (worst). The importance factor (IF) can be estimated indirectly by an overall class coefficient (λ) calculation:

$$\lambda = \sum \Delta_x \psi_x \tag{3}$$

$$\psi_x = \sum \frac{\varphi_x(max)}{\varphi_{total}} \tag{4}$$

The maximum factor ($\varphi_{x(max)}$) corresponds to the highest weight that the sub-parameters can assume for each parameter. Once the λ value has been calculated, the method proposes to assign an arbitrary IF (from 0.2 to 1.5) to qualitatively describe the risk grade from "low" to "critical".

2.3 *Vehicle impact risk*

The risk associated to vehicles impact on bridge piers is evaluated using the method by Kim et al. (2020), who proposes a priority index based on the vulnerability and hazard components. The parameters that need to be taken into account for the hazard evaluation include the type of lower road, the existence of bridge columns within 9 m of the road verge, the distance from industrial sites, and truck accessibility to the road. On the other hand, the vulnerability is characterized taking into account the service years, the current safety level, the number of columns, the minimum diameter of the column(s), the slenderness ratio, and the design load.

The method foresees an initial screening through the so-called "preliminary risk analysis" (PRA) to determine if a bridge is exposed to such kind of hazard. This initial step is conducted by checking for the presence of the following parameters: the existence of a bridge column, the type of bridge column, and the existence of a lower road near a bridge column. As result, bridges without columns, as well as wall-section piers, are not analysed and thus categorized

into the "No Risk" (NR) group, because of the unlikely probability of failure under vehicle impact. Bridges that pass the preliminary risk analysis, are further analysed according to the proposed "simplified risk analysis" (SRA). It is foreseen that both hazard and vulnerability are defined as the sum of weighting factors (from 1 (best) to 3 (worst)) assigned to each parameter, according to the definition of sub-parameters. The standard deviation method (SDI Method) is used to evaluate the scale that defines the attribution of the weighting factor, with reference solely to the quantitative parameters (e.g., number of columns, slenderness ratio, and distances).

Finally, according to SRA, the risk index (I) for each bridge is calculated through the additive combination of hazard (I_H) and vulnerability (I_V) indices according to Eq. (6):

$$I = (I_H + I_V)/2 \tag{6}$$

The two components of the risk index (I_H and I_V) are evaluated individually by normalizing the sum of the weighting factors assigned to each sub-parameter, to the sum of the maximum value that the weighting factor assumes for each of the sub-parameters considered.

3 MULTI-HAZARD RISK ASSESSMENT

3.1 *Qualitative assessment according to the Italian guidelines*

The Italian guidelines method for risk assessment of existing bridges is based on a multi-level and multi-hazard approach that considers the presence of various hazards, i.e. structural/foundational, seismic, landslide, and flood. The guidelines are articulated on six levels (from 0 to 5) of assessments, with increasing complexity and accuracy. Level 2 analysis relates to the Class of Attention (CoA) definition based on the data acquired in Levels 0 and 1 (see MIT 2020) regarding, e.g., location, road use, year of construction, geometrical characteristics, and defects (based on visual inspections), as well as potential risks associated with landslide and flood. The CoA is determined by considering the hazard, vulnerability, and exposure components, with the results being High (H), Medium-High (M-H), Medium (M), Medium-Low (M-L), and Low (L). Logic trees, based on relevant parameters (see MIT 2020), are employed to calculate CoAs associated to a single hazard as well as for their combination. Thus, the derived CoA represents a qualitative description of the risk. Among all analysed hazards, the structural/foundational-related CoA assumes the highest importance and governs over all the others. The method foresees further actions according to the obtained CoA, as, for instance, immediate accurate evaluations for High CoA and preliminary assessments for Medium-High and Medium CoA. The CoA also addresses the decisions on future interventions to be carried out (e.g., monitoring and safety assessment).

3.2 *Proposed quantitative multi-hazard assessment*

The individual risk indicators (I_{Hj}) briefly described above are combined to obtain a total multi-hazard risk indicator (I_{MH}), similarly to what carried out by Scattarreggia et al. (2023). To this end, two combinations are considered: i) a quadratic combination of individual risk indicators, normalized with respect to the number of considered hazards (N_H) (see Eq.7), and ii) a summation of individual risk indicators, but considering the possibility of using weighting factors (C_{Hi}) that can be applied to each risk, e.g., according to the level of knowledge of input required (see Eq.8).

$$I_{MH_i} = \sqrt{\frac{\sum_j {I_{Hj}}^2}{N_H}} \tag{7}$$

$$I_{MH_i} = \frac{\sum_j C_{Hj} I_{Hj}}{\sum_j C_{Hj}} \tag{8}$$

4 APPLICATION TO A BRIDGE STOCK

4.1 *Case-study description*

The multi-hazard methodology has been applied to a group of thirty real bridges, located in primary roads of the Lombardy region in northern Italy (Hamidpour et al. (2023a)). These bridges are viaducts and overpasses, that were mainly built during the second half of the last century (from 1962 to 1967). Most of them (63%) present a deck composed by mixed-steel reinforced concrete and a simply supported beam static scheme (83% of the portfolio). The bridges are located on highways with an average traffic flow of more than 25.000 vehicles per day, indicating a significant amount of daily traffic. The majority of the bridges under study is single or few-span (2 or 3) structures, and most feature decks that are simply supported and have a longest span length of over 25 m. Simple supports are used at the extremities of parallel beams in single or multi-span bridge decks in simply supported beam systems. When they are continuous, they pass continuously over the central piers to span between the abutments. A cast-in-place slab covers every span in continuous slab bridges. Finally, the RC piers on every bridge are either multi-column or single-wall. The statistical distribution of these bridges in terms of year construction (Figure 1 (a)), static scheme (Figure 1(b)), deck material (Figure 1(c)), average commercial daily traffic (Figure 1(d)), largest span length (Figure 1(e)) and number of spans (Figure 1(d)) are shown below.

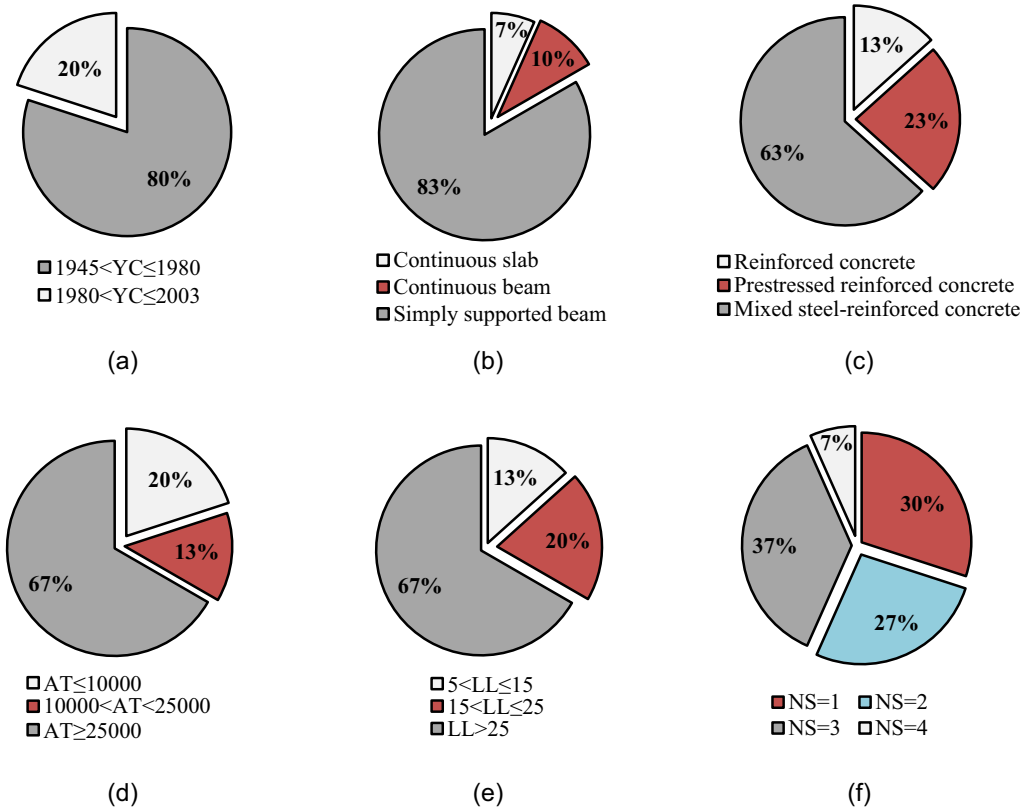


Figure 1. (a) Year of construction, (b) static scheme, (c) deck material, (d) average daily traffic, (e) largest span length and number of spans (f) for the analysed bridges.

4.2 *Quantitative multi-hazard risk assessment*

Although the Italian guidelines propose a multi-level multi-hazard method, their qualitative nature precludes from ranking bridges within the same CoA, as quantitative approaches do. However, instead of the Italian guidelines relying on four hazard classes, namely gravity loads, landslides, floods, and earthquakes, the method provided herein explores the possibility to account for two additional key anthropic hazards, namely vehicle impact (against piers) and fire. Therefore, the quantitative methods introduced in Section 2, are herein applied to evaluate the single-hazard risk indicators that are subsequently used for the assessment of the multi-hazard indicators. Accordingly, the individual risk indicators, i.e., structural/road traffic (I_G), seismic (I_S), fire (I_F), and impact (I_I), were computed, and results are shown in Figure 2. It is herein noted that for the evaluation of index I_I, the exposure component was integrated following the approach of Kodur et al. (2013), in such a way that all the quantitative methods examined, even if simplified manner, account for the three typical components of risk, namely hazard, vulnerability and exposure.

For the evaluation of the seismic indicator two levels of earthquake intensity have been considered: Lower Level (LL) and Upper Level (UL) which correspond to a 10% probability of exceedance in 50 years (which corresponds to a return period of 475 years) and a 5% probability of exceedance in 50 years (with a return period of 975 years), respectively (hence the use of the $I_{S,LL}$ and $I_{S,UL}$ notations in Figure 2). Similarly, for the evaluation of the road traffic hazard indicator two states of damage/defects are considered (according to UK-BCI method): average (Avg.) and critical (Crit.) defects. Particularly, the state named "average" is an overall picture of the bridge condition through a weighted indicator, obtained considering the state of conservation of all elements and considering their importance for the bridge safety. On the other hand, the state identified as "critical" associates the bridge condition to the wors condition among the critical elements for the bridge safety.

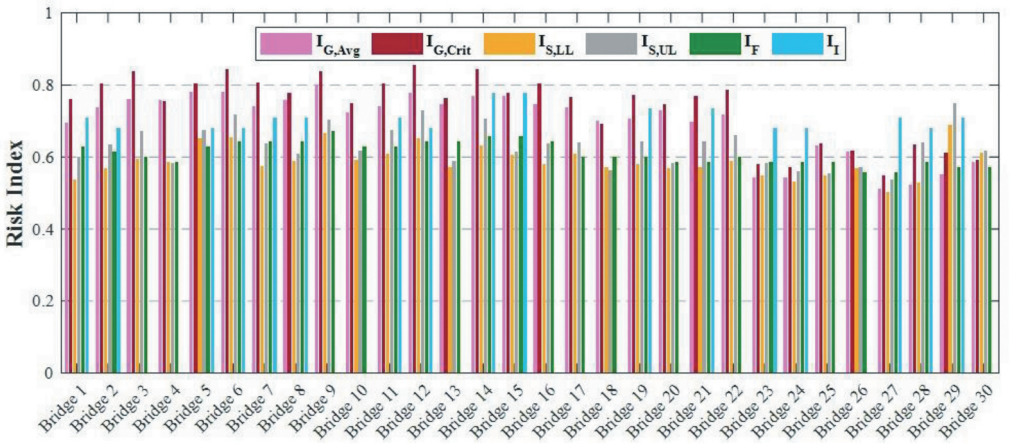


Figure 2. Single-hazard risk indices for the bridges examined.

Once the single-hazard indicators have been evaluated, they can be employed for the multi-hazard assessment. Indeed, assuming $I_{G,Avg}$ as road traffic indicator and considering both the lower $I_{S,LL}$ and the higher $I_{S,UL}$ levels of seismic action, in combination with I_F and I_I, two multi-hazard risk indicators I_{MH1} and I_{MH2} can be calculated using Eq. 7, respectively. Similarly, Eq. 7 can be used to compute another indicator I_{MH3} by combining $I_{G,Crit}$, $I_{S,UL}$, I_F and I_I. Based on the former, Eq. 8 is used to carry out an additional combination using various weighting factors for the different hazards (I_{MH4}). For example, given the comparatively low probability of occurrence (when computable) of fire

and impact hazards, C_F and C_I were set to 0.25. The highest weight was attributed to the road traffic risk indicator C_G=1, due to its larger likelihood in comparison to the other hazards (a logic also followed by the Italian guidelines). C_S=0.5 was used as the seismic-related weight. As a result, Figure 3 shows the total multi-hazard risk indicators (I_{MH}) obtained for the four combinations considered. Results obviously show that thanks to the quantitative nature of indicators a refined ranking can be obtained as opposite to the qualitative grouping of Italian Guidelines. The comparison between I_{MH3} and I_{MH4} highlights the importance of the UK-BCI approach employed for the assessment of the structural condition. On the other hand, the comparison between I_{MH1} and I_{MH3} indicates that the intensity level of the seismic action would not have played a relevant role in the definition of the total risk, reflecting the low hazard of the region where the bridges are located. Finally, I_{MH3} points out bridges that are more vulnerable to structural and seismic actions, given that both fire and impact were weighted minorly.

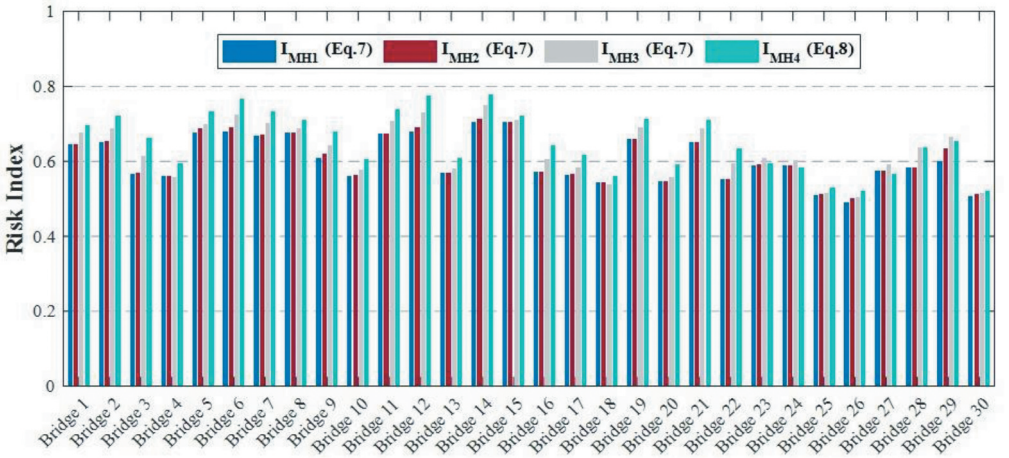


Figure 3. Multi-hazard risk indices proposed for existing bridges examined.

4.3 *Comparison between proposed quantitative approach and Italian guidelines*

According to the Italian guideline's procedure, the analysed bridges fall in the "High" and "Medium" CoA (26 and 4, respectively), considering seismic and road traffic as the only hazards (fire and vehicle impact are not considered by these guidelines). Due to the large number of bridges falling in the same CoA, a managing entity would not be able to prioritize interventions on the selected bridge stock, as opposed to the ranking obtained in Section 4.3 using the proposed multi-hazard quantitative method. Assuming a correspondence between High (H) to Low (L) risk condition ranges of the Italian guidelines with the proposed multi-hazard indicator via the equivalent scale given in Table 1, the proposed method allows grouping bridges as illustrated in Figure 4. Particularly, the comparison is conducted as follows: (i) using Eq. 7 and Eq. 8 considering the single-hazard indicator $I_{G,Crit}$ due to road traffic (i.e. gravity loads) and the seismic indicator $I_{S,UL}$; (ii) using only the single-hazard indicator $I_{G,Crit}$, that has been preferred with respect to $I_{G,Avg}$ considering it match better with the CoA as observedby Hamidpour et al. (2023a).

The comparison in Figure 4 leads to similar observations to Hamidpour et al. (2023a), indeed $I_{G,Crit}$ produces the closest results to the Italian CoA. On the other hand, when both the traffic and seismic indicators are combined according to Eq. 7 and Eq. 8, i.e., I_{MH7*} and I_{MH8*}, respectively, the differences slightly increase.

Table 1. Equivalence adopted between Italian guidelines CoA and multi-hazard indicators (I_{MH}).

ITA CoA	High	Medium-High	Medium	Medium-Low	Low
Proposed I_{MH}	0.60-1.00	0.35-0.60	0.20-0.35	0.10-0.20	0.00-1.00

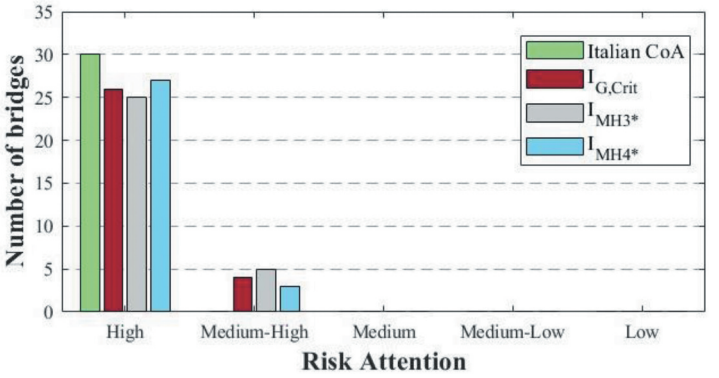


Figure 4. Comparison between Italian CoA and multi-hazard risk indicators range proposed.

5 CONCLUSIONS

This work proposed a preliminary multi-hazard risk analysis method for large bridge portfolios by calculating quantitative indicators (I_{MHi}), combining individual risk estimates (I_{Hi}) using existing literature methods. The road traffic, seismic, fire, and vehicle impact risks are considered for the computation of the total multi-hazard risk indicators (I_{MHi}). The goal was to propose a quantitative multi-hazard assessment approach, as opposed to the qualitative approach of the Italian guidelines, according to which ranking bridges belonging to the same class of attention is not an easy task. It has been shown that the prioritization process is influenced by the type of combination used for multi-hazard risk aggregation. The use of a multi-hazard approach based on the unbundled assessment of individual hazards helps to develop targeted intervention techniques, while increasing the level of knowledge for each bridge (i.e. targeted inspections) allows to obtain a more accurate multi-risk classification. To this end, for prioritization purposes, the efforts in increasing the resolution of the Italian guidelines could be their integration with more quantitative parameters, which may also permit the inclusion of extreme hazards (such as the herein-included fire and vehicle impact). Notwithstanding the promising results that were obtained with this preliminary study, future developments should aim to propose a more comprehensive multi-hazard quantitative method, also improving the multi-risk aggregation procedures, e.g., by using statistically calibrated weighting factors (C_{Hj}) and investigating the importance of uncertainties associated to the input data needed for the calculation of each single-hazard indicator on a final multi-hazard indicator.

REFERENCES

ATKINS (2007). *Guidance Document for Performance Measurement of Highway Structures Part B1: Condition Performance Indicator*, Lincoln, United Kingdom.

Bianchi, S., Biondini, F. (2022). Bridge Condition Assessment Using Supervised Decision Trees, *EUROSTRUCT*, 200: 1108–1116.

Calvi, G.M., Moratti, M., O'Reilly, G.J., Scattarreggia, N., Monteiro, R., Malomo, D., et al. (2019). Once upon a Time in Italy: The Tale of the Morandi Bridge, *Structural Engineering International*, 29 (2): 198–217.

Deng, L., Wang, W., Yu, Y. (2016). State-of-the-Art Review on the Causes and Mechanisms of Bridge Collapse. *Constr. Facil.*, 30(2): 04015005.

Hamidpour, S., Scattarreggia, N., Nascimbene, R., Monteiro, R. (2023a). *Evaluation of prioritization schemes for bridge stock assessment*, NZSEE 2023 Annual Conference.

Hamidpour, S., Scattarreggia, N., Nascimbene, R., Monteiro, R. (2023b). A risk-based quantitative approach for priority assessment of ageing bridges accounting for deterioration, submitted for publication.

Ministry of Infrastructure and Transportation (2020). *Linee guida per la classificazione e gestione del rischio, la valutazione della sicurezza ed il monitoraggio dei ponti esistenti*, *Parere CSLLPP n. 88|2019*, Rome, Italy.

Moon, F.L., Laning, J., Lowdermilk, D.S., Chase, S., Hooks, J., Aktan, A.E. (2009). *A pragmatic risk-based approach to prioritizing bridges*, Proceedings of SPIE.

Naser, M.Z., and Kodur, V.K.R. (2013). Importance factor for design of bridges against fire hazard, *Engineering Structures*, 54:207–220.

Kim, K., and Lee, J. (2020). Fragility of Bridge Columns under Vehicle Impact Using Risk Analysis, *Advances in Civil Engineering*, 7193910.

Scattarreggia, N., Salomone, R., Moratti, M., Malomo, D., Pinho, R., Calvi, G.M. (2022). Collapse analysis of the multi-span reinforced concrete arch bridge of Caprigliola, Italy, *Engineering Structures*: 251.

Scattarreggia, N., Grieco, L.A., Monteiro, R., Parisi, F. (2023). A preliminary methodology for multi-hazard risk assessment of large bridge portfolios using quantitative indicators. *Proceedings of 14th International Conference on Applications of Statistics and Probability in Civil Engineering, ICASP14*, Dublin, Ireland.

Bridge Maintenance, Safety, Management, Digitalization and Sustainability – Jensen, Frangopol & Schmidt (eds)
© 2024 The Author(s), ISBN 978-1-032-77040-6
Open Access: www.taylorfrancis.com, CC BY-NC-ND 4.0 license

The Italian guidelines for risk and safety evaluation of existing bridges: A case study

P.P. Rossi & N. Spinella
Department of Civil Engineering and Architecture, University of Catania, Catania, Italy

A. Recupero
Department of Engineering, University of Messina, Messina, Italy

ABSTRACT: After some catastrophic collapses of bridges, detailed guidelines on risk classification and management, safety assessment and monitoring of existing bridges have been issued in Italy in 2020. This paper presents one of the first experimental applications of these guidelines to a large stock of bridges of two highways located in the Sicilian region (southern of Italy). The first three levels of analysis recommended by the Italian Bridges Guidelines have been applied, and they comprise census, visual inspection and calculation of the so-called class of attention of bridges. The results of these analyses made it possible to collect an experimental database of 358 in-service road bridges, which has been stored and catalogued by means of a customized web application. The web application allows to organize and check data, make queries, processing and visualizing the results. The experimental results are described in detail and analyzed, underlining both abilities and limitations of the examined levels of analysis of the Italian Bridges Guidelines. Moreover, a group defect index is introduced to classify groups of bridges for which the same types of defects with different level of extension and intensity have been detected. It is a prioritization method which allows to plan the same type of maintenance intervention on a group of bridges, more than on a single bridge, reducing economic and social costs.

1 INTRODUCTION

Bridges are critical components of transportation infrastructure, because they provide essential connections for users and services. They may deteriorate quickly, due to the lack of maintenance and/or the increase of traffic load. Therefore, the probability of collapse, as well as the associated economic and social costs, grows rapidly. Almost the Italian territory is prone to several natural hazards, like earthquakes, landslides, and floods. Furthermore, the infrastructure heritage of Italy is one of the oldest in Europe. In the past, only a few Italian regions and handlers have made investments on the management and risk assessment of bridges by means of partnerships with academic research groups or experts in order to obtain support for activities of safety verification of bridge structures or develop their own guidelines (Zonta & al., 2007, Limongelli & al., 2022a, Limongelli & al., 2022b). The Polcevera bridge collapse in 2018 (Calvi & al., 2018) has raised the management and maintenance of bridge to an issue of utmost interest in the country.

In 2020 the Italian Ministry of Sustainable Infrastructure and Mobility (MIT) issued the Italian Bridges Guidelines (IBG) for the classification and the risk management, safety evaluation and monitoring of existing bridges (MIT, 2020). The main scope of the IBG is to ensure a standard and uniform method for the assessment of the level of risk of existing bridges and, then, to plan the monitoring and maintenance activities. The IBG propose a multi-level approach (levels from 0 to 5) with growing degrees of detail. The approach considers different

DOI: 10.1201/9781003483755-342

risks associated with structure-foundation, earthquakes, landslides and floods. The first level of analysis of IBG aims to obtain an inventory of the examined bridges; the second aims to achieve an evaluation of the degradation conditions of bridges by means of visual inspections. The third level allows to determine, for each type of risk, the Class of Attention (CoA) of each bridge. The CoA provides an indicator for the handler to establish the subsequent actions on bridges (i.e. assessment or planning of monitoring systems).

The recent literature about the IBG is mainly focused on the first levels of analysis (from L0 to L2). For instance, Scalbi & al. (2002) presented an application of IBG to a set of sixteen Prestressed Concrete (PC) bridges located in the Lombardia and Calabria regions. As result of the use of the IBG, the authors highlighted the relevance of the maintenance plans in the through-life management of the structure. Zizi & al. (2023) applied the first three levels of analysis of the IBG to a set of sixty road bridges of the Province of Caserta (located in the south of Italy). Based on their results, the authors proposed a preliminary risk model suitable to define an inspection priority ranking.

This article presents the results of the first three levels of analysis of the IBG on more than 350 road bridges of two highway sections in Sicily, a region located in the south of Italy. This campaign was commissioned in the recent past by the handler, the Consortium of Sicilian Highways (CAS), and is one of the first experimental campaigns performed in Italy on a large stock of bridges based on the IBG (MIT, 2020, 2022). The analysis of the results is intended to highlight pros and cons of the IBG. Moreover, a global defect index is introduced as a tool for prioritization of interventions on bridges. It allows handlers to outline a plan of similar interventions on large groups of bridges. Carrying out the interventions suggested by the proposed approach, the number of bridges that need a detailed and expensive analysis (higher than L3 in the IBG) can be reduced.

The authors note that the analyses presented in this paper refer to the entire stock of bridges, without any reference to the single bridge. The use of the results of census and visual inspection is authorized by the data owner (CAS). Based on the results of the visual inspections, the CAS has carried out proper restoration works on their bridges to ensure adequate safety levels.

2 THE ITALIAN BRIDGES GUIDELINES

The IBG implement a multilevel approach. It encompasses six levels of analyses (from L0 to L5) which require different activities as summarized below:

- L0. Inventory of the main characteristics of the bridge and collection of the available documentation;
- L1. Visual inspection of the structure in order to recognize defects and structural and geometric characteristics of the bridge, as well as geo-morphological and hydraulic characteristics of the area;
- L2. Estimation of the CoAs based on hazard, vulnerability and exposure parameters determined at levels L0 and L1. The level of CoAs [structure-foundation (CoA-SF), seismic (CoA-S), landslide (CoA-L) and flood (CoA-F)] may be high, medium-high, medium, medium-low or low. Once the level of the CoAs has been determined, actions are planned. In particular, specific inspection campaigns are mandatory for bridges with medium or medium-high CoAs whereas accurate structural assessments (L4) are required for bridges with high CoAs;
- L3. Preliminary assessment of the structure in order to recognize the need for a detailed analysis of L4. The numerical calculations required at level L3 aim to estimate the minimum safety level required by the codes at the time of construction of the bridge compared with the safety level required by the current code NTC18 (MIT, 2018).
- L4. Accurate assessment of the bridge according to NTC18 and IBG.
- L5. It is currently not described in the IBG.

This study focuses on the first three levels of the IBG (L0, L1 and L2) which are related to the classification of risks and management of interventions. The visual inspections carried out on the two sections of the Sicilian highways were intended to evaluate the structure-

foundation and seismic risks only. As a consequence, the CoAs related to the other risks (CoA-L and CoA-F) are not evaluated and discussed in this paper.

case study

2.1 *Description of the stock of data*

As a demonstrative case, the procedures of the IBG have been applied to a stock of bridges of two sections of the Sicilian highways managed by CAS. These bridges belong to the highway named A18, which connects the towns of Messina and Catania (east side of the Sicily Island) and A20, which connects the towns of Messina and Buonfornello (north side of the Sicily Island). Highways A18 and A20 are more than 50 years old because they were built in the early 1970s. The east side of Sicily has been involved by relevant seismic events (i.e. the Messina strait earthquake in 1908). Nevertheless, the bridges that were built before the '70s were designed without significant seismic provisions.

2.2 *Collection and management of the database*

The inventory and visual inspection activities have produced results in the form of photos and spreadsheet files. At first, these data have been checked by means of an automatized protocol in order to find eventually gross errors due to the inspection activity. For example, the most common errors concerned: the coordinates of the bridge location and the structural type of the bridge deck [sometimes PC bridges were catalogued as Reinforced Concrete (RC) one]. The lack of a predetermined list of allowed responses and the absence of a clear guide to some of the questions included in the forms have caused these kinds of mistakes. In addition, values of intensity and extension factors equal to 0.2, 0.5 or 1 were provided by the inspectors also when the forms allow only a specific value (i.e. 1).

The revised data have been collected in a large database. To create, read, update, delete and quickly select and analyze portions of the database, a customized web application has been built (Costantino & al., 2023).

2.3 *Web application*

The web application includes several components. Each component runs specific tasks, i.e. inventory of bridges, compilation of inspection forms and computation of CoA. All data are stored server-side on a MySQL relational database. An application Program Interfaces (APIs) system allows the exchanges of data between client and server. In addition, data can be imported or exported in MS Excel and/or JSON format.

2.4 *Main characteristics of considered bridges*

The bridges are in number of 142 and 216 on highways A18 and A20, respectively, and have been grouped as a function of the deck material, i.e. RC, PC or Steel-Concrete (SC). As

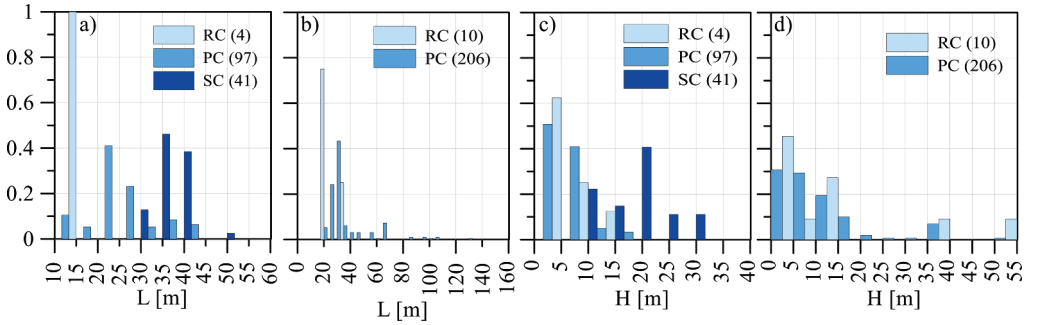


Figure 1. Relative frequency of the length of girders (L) and the maximum height of piers (H) for (a, c) highway A18 and (b, d) highway A20, respectively.

regards the PC bridge decks, pre-stressed strands were mostly utilized on highway A18, while post-stressed strands were used on highway A20.

Figure 1 shows the relative frequency of the values of girder length and maximum pier height grouped for the highway sections (A18 and A20) and for the type of the deck material considered (RC, PC or SC). The girder length of the bridges on highway A18 is mostly in the range between 20 and 30 m. Instead, the girder length of the bridges on highway A20 is mostly in the range between 35 and 40 m, but, in some cases, it exceeds 100 m. The maximum pier height is strictly related to the morphology of the landforms which characterize the territory. The maximum pier height is about 30 m for some bridges of the highway A18 and is over 50 m for some bridges of the highway A20.

3 RISK ANALYSIS

The CoA of a bridge is a function of hazard, vulnerability, and exposure for each risk considered in this work: structure-foundation and seismic, respectively. Risks are analyzed according to primary and secondary parameters described in the IBG.

In particular, the hazard relative to the structure-foundation risk depends on the maximum permissible mass of vehicles and on the frequency of transits of commercial vehicles. Therefore, the handler has provided the data regarding the transit of all vehicles along the considered sections of the highways and, then, an analysis of traffic has been performed. The average of the transits per day was always high for the A18 highway, while on the highway A20 the average of the transits per day was medium from toll-gates 1 to 14 and low from toll-gates 14 to 28. Similarly, the exposure depends on the average daily traffic and average span length, alternative routes and bypassed entity.

The hazard associated with the seismic risk depends on the local characteristics of the ground, both in terms of Peak Ground Acceleration (PGA) and subsoil stratigraphy. The former has been provided by the inspectors based on the national seismic hazard map, the latter has been assumed as the worst condition in accordance with the standard code. The exposure to seismic actions is simply estimated as equal to the one estimated for the structure-foundation risk or it is corrected if the bridge has a strategic function in case of emergency.

The vulnerability of both types of risk considered, structure-foundation and seismic, is mainly estimated as a function of the level of defectiveness as explained in the next section.

3.1 *The level of defectiveness*

The level of defectiveness is determined from the results of the visual inspections and based on the criteria indicated in the IBG. For each type of element, the IBG provide a list of pre-established defects with a different grade of importance (G) from 1 to 5. Each defect is identified by the inspector by means of a level of extension (k_1) and intensity (k_2) factors and, where applicable, indicating if the detected defect can affect or not the statics of the bridge. Moreover, the IBG indicate a list of Critical Elements (CEs), like half-joints, prestressing tendons and extensive crack pattern, which are particularly prone to degradation phenomena and, then, they can significantly affect the structural behavior of the bridge. According to the authors the list of CEs reported in the IBG is not exhaustive. Owing to this, it has been integrated considering also movements undermining bridge foundations (ril_fond_1), diagonal (ca-cap_10) and crushing cracks (ca-cap_13), bending of rebars (ca-cap_17), breakage of the prestressing bars or anchorages failure (cap_12) and oxidation of prestressing wires (cap_8).

Selecting the results of the inspection activities, which were catalogued by means of the web application, it has been possible to know how many times (N) a defect has been detected on the considered group of bridges at a certain level (0.2, 0.5 or 1.0) of k_1 or k_2. The number of times a defect has been detected is $N_{ki,l}$, where $i = 1, 2$ and $l = 0.2, 0.5$ or 1.0. For instance, Figure 2 shows $N_{k1,l}$ and $N_{k2,l}$, which are referred to the defects detected on the primary and secondary beams of the PC decks of highway A18. The defects detected on the PC beams mainly involve the external surface of the PC beams and are: water traces due to inefficient rainwater drainage systems (dif-gen_1), passive (ca-cap_1) and active (ca-cap_2) humidity

spots, erosion of the external layer of concrete (ca-cap_3), spalling of the concrete cover (ca-cap_5) and presence of oxidized and corroded rebars (ca-cap_6) (Figure 3).

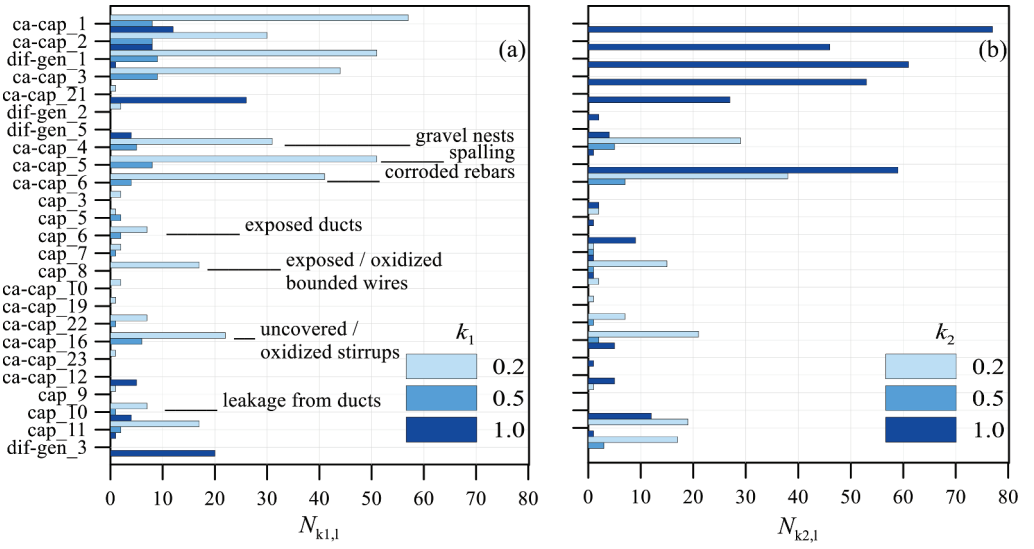


Figure 2. Number of defects detected on "PC primary and secondary beams" of bridges on highway A18 at different (a) extension and (b) intensity grades.



Figure 3. Photos of some defects detected on PC beams.

4 CLASSES OF ATTENTION

The CoAs have been calculated for each bridge of the highways A18 and A20 using hazard, vulnerability and exposure. The possible combinations of values of these components of risk are indicated in the IBG, which report five different tables for each level of hazard (high, medium-high, medium, medium-low and low), and allow the estimate of the CoA following a procedure described by means of flow charts.

Figure 4 summarizes the results of the calculations in terms of structure-foundation (CoA-SF) and seismic CoAs (CoA-S). The bar charts show that the CoA-S is generally higher than the CoA-SF for the bridges of both highways considered. It can be explained because the hazard related to CoA-SF depends on the traffic loads frequency and is higher on highway A18 than on highway A20. By contrast, the seismic hazard is influenced by the seismicity level of the zone of the bridge in terms of both PGA and soil class. The exposure to CoA-S is higher than the one to CoA-SF due to the strategic function of the bridges in case of earthquakes.

The application of the IBG to the stock of bridges considered returns that 56 and 114 of the 358 bridges have been classified as in high CoA-SF and CoA-S, respectively. Therefore, a more detailed and more onerous investigations would be required.

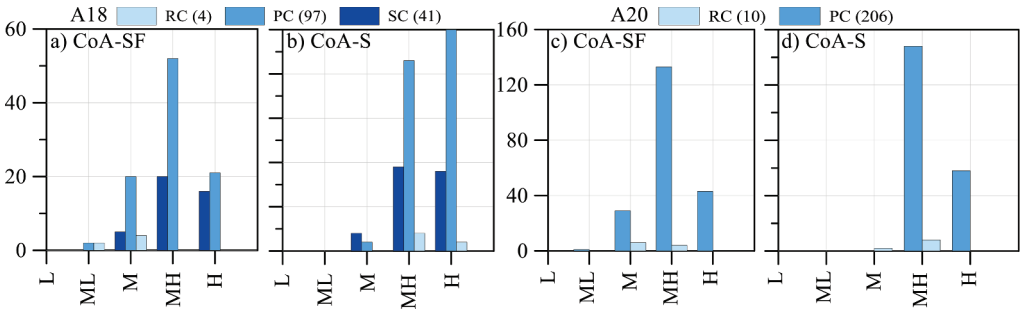


Figure 4. Structure-foundation (SF) and seismic (S) classes of attention of bridges: (a, b) highway A18 and (c, d) highway A20.

Furthermore, bridges with problems due to their structural type and /or material (i.e. bridges with post-tensioned strands) should be preliminary subjected to special inspections and, as a consequence of that, the level 4 of analysis could be necessary to some other bridges with consequent costs often not compatible with the budget of the handler.

5 A SIMPLE INDEX TO PLAN INTERVENTIONS

The prioritization index proposed in this section is based on the principle that management companies, in order to reduce economic and social costs, are generally inclined to carry out the same type of maintenance intervention on a group of bridges, more than on a single bridge. Therefore, the data concerning the defects detected by visual inspection have been analyzed to identify the defects that are mostly influential on the level of defectiveness of the group of bridges. The elaboration of data leads to obtain a Group Defect Index (GDI) inclusive of extension, intensity and importance grades of defects.

First, two indexes (K_1 and K_2) are first calculated for each defect detected on the considered group of bridges to incorporate the weight of the extension or intensity grade factor (k_1 and k_2) of the examined defect. The two indexes are calculated by means of the following relation:

$$K_i = \frac{\sum_l l \cdot N_{ki,l}}{N_b} \tag{1}$$

where i indicates extension ($i = 1$) or intensity ($i = 2$) factors, $N_{ki,l}$ is the number of times a defect with assigned values of the extension or intensity factor ($l = 0.2$, 0.5 or 1.0) has been detected in the group of bridges and N_b is the number of bridges where the specific defect could be detected.

To take into account also of the grade of importance of the defect, the GDI of a defect is defined as:

$$GDI = (G/G_{max})\sqrt{K_1 K_2} \tag{2}$$

$G_{max} = 5$ being the maximum grade of importance of defects. The GDI returns a value between 0 and 1. The higher the GDI value, the greater the influence of the defect in the level of defectiveness of the group of bridges examined. The GDI does not depend on the number of bridges considered because K_1 and K_2 are normalized with respect to N_b, and then it can be used to prioritize interventions.

For instance, in Figure 5 the defects of the PC and RC beams of the bridges on highway A18 have been considered and the GDI has been calculated. The defects with the highest GDI

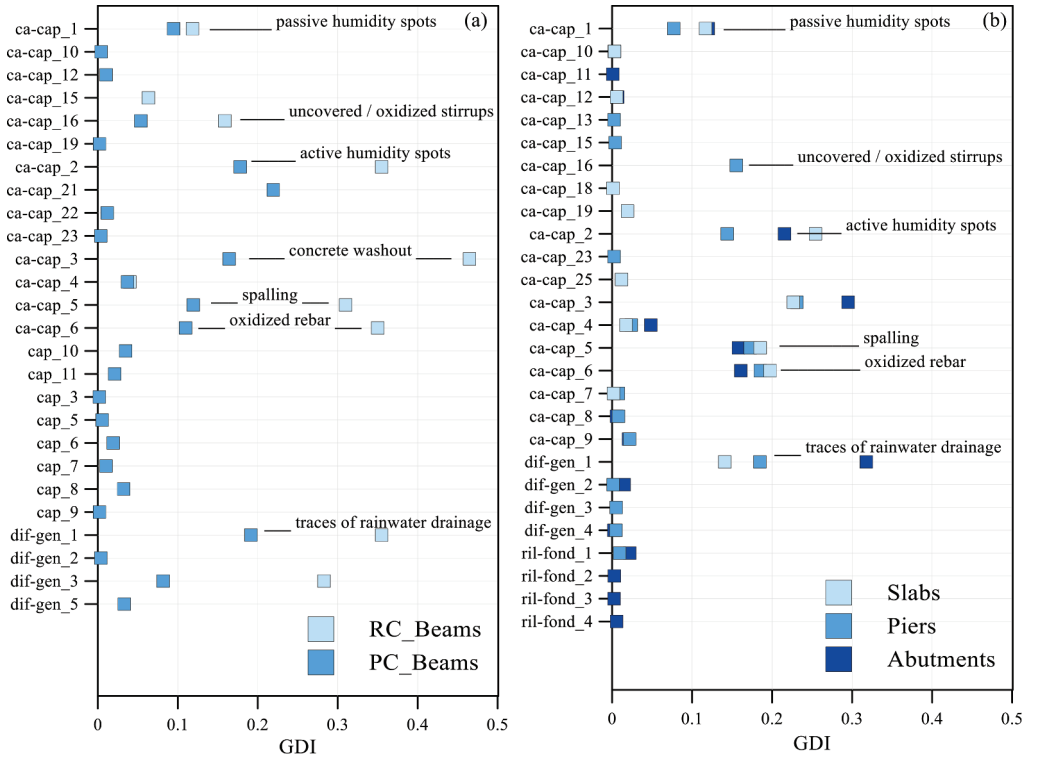


Figure 5. Group defect index for bridges of highway A18: (a) PC and RC beams, (b) slabs, piers and abutments.

values involve the concrete surface of the beams, as previously observed. In detail, the highest values of GDI are related to water traces due to inefficient rainwater drainage systems (dif-gen_1), passive (ca-cap_1) and active (ca-cap_2) humidity spots, erosion of the external layer of concrete (ca-cap_3), spalling of the concrete cover (ca-cap_5) and oxidized and corroded steel bars (ca-cap_6). The defects on slabs, piers and abutments of bridges on highway A18 (Fig. 6b), characterized by the highest values of GDI (≈ 0.35), are practically the same as those of PC and RC beams. In particular, the GDI values of the weightiest defects on slabs, piers and abutments range from 0.10 for traces of rainwater drainage (dif_gen_1) of concrete slabs to about 0.35 for concrete washout (ca-cap_3) of abutments. Defects characterized by deterioration due to erosion of the external layer of concrete (ca-cap_3) of slabs and piers and oxidized steel bars (ca_cap_6) of concrete piers have values of GDI between 0.15 and 0.20. These results highlight an overall high priority of interventions needed to mitigate the effects of inefficient rainwater drainage systems, on RC beams as well as on slabs, piers and abutments.

6 CONCLUSIONS

The paper presents the experimental results obtained applying the methodology proposed by the Italian guidelines on existing bridges. The procedures have been applied to a bridge stock of 358 bridges located along two highways of Sicily Island (south of Italy). The data acquired by visual inspection activities have been stored in a web application to expedite the analysis.

The results of the visual inspections have led to the main conclusion that the most common defects detected on the considered bridges involve cracking and spalling of the concrete cover of the reinforced and prestressed concrete members and are basically due to the lack of maintenance of the structures during past decades.

Moreover, the application of the Italian guidelines to the stock of bridges considered, has allowed outlining the following main observations and proposals:

- The role of the critical elements is significant on the results of the visual inspections because it leads to high levels of defectiveness and, then, to high levels of the Class of Attention. Therefore, to more accurately estimate the effects of a critical element on the level of defectiveness of the bridge, the authors suggests that the effects should be related to the effective level of degradation of the critical element as a function of extension and intensity grades of the defect.
- The structure-foundation and seismic classes of attention are high in 22% and 36% of the inspected bridges. Therefore, a detailed structural and seismic assessment activity on a large number of bridges is mandatory.
- A Group Defect Index has been suggested and it allows owners to cluster groups of bridges through aggregation of data referring to the detected defects in a single numerical index. The proposed index can be useful to plan interventions on groups of bridges and optimize the economic and social costs.

ACKNOWLEDGEMENTS

The authors thank the Consortium for the Sicilian Highways (CAS) that has authorized the use of the data of census and visual inspection of the examined bridges. The research study has been supported by the University of Catania within the research project "DU.SO.CA.P. – Durabilità e SOstenibilità delle strutture in Cemento Armato e Precompresso" 2020/2022 PIA.CE.RI". Moreover, the studies presented here have been carried out as part of the activities envisaged by the Agreement between the High Council of Public Works (CSLLPP) and the ReLUIS Consortium implementing Ministerial Decree 578/2020 and Ministerial Decree 240/2022. The contents of this paper represent the authors' ideas and do not necessarily correspond to the official opinion and policies of CSLLPP.

REFERENCES

Calvi G.M., Moratti M., O'Reilly G.J., Scattarreggia N., Monteiro R., Malomo D., Calvi P.M. & Pinho R. 2018. *Once upon a Time in Italy: The Tale of the Morandi Bridge*. Structural Engineering International 29:198–217.

Costantino G., Messina D., Recupero A., Rossi P.P. & Spinella N. 2023. *A web platform for management and analysis of existing bridges*. *Procedia Structural Integrity* 44:1220–7.

Italian Ministry of Infrastructures and Transportations. D.M. 17 December 2020. Linee Guida per la classificazione e gestione del rischio, la valutazione della sicurezza ed il monitoraggio dei ponti esistenti.

Italian Ministry of Infrastructures and Transportations. D. M. 01 July 2022. Linee Guida per la classificazione e gestione del rischio, la valutazione della sicurezza ed il monitoraggio dei ponti esistenti.

Italian Ministry of Public Works. D.M. 17 January 2018. Nuove Norme tecniche per le costruzioni. *Gazzetta Ufficiale*, vol. 42.

Limongelli M.P., Gentile C., Biondini F., Di Prisco M., Ballio F. & Belloli M. 2022. The Monitoring Guidelines of the Lombardia Region in Italy. *Engineering Proceedings* 17:1–16.

Limongelli M.P., Gentile C., Biondini F., Di Prisco M., Ballio F., Zonno G., Borlenghi P., Bianchi S., Capacci L., Anghileri M., Zani G., Scalbi A., Flores Ferreira K., D'Angelo M., Cazzulani G., Benedetti L., Somaschini C., Bernardini L., Belloli M., Resta F., Vigo P. & Colombo A. 2022. Bridge structural monitoring: the Lombardia regional guidelines. *Structural Engineering International*.

Scalbi A., Zani G., Di Prisco M. & Mannella P. 2022. The role of maintenance plans on serviceability and life extension of existing bridges. *Structural Concrete* 24(1):127–142.

Zizi M., Bencivenga P. & De Matteis G. 2023. Handling policies for Italian existing bridges with a territorial approach: the case study of Caserta, Italy. *Structures* 48:1306–21.

Zonta D., Zandonini R. & Bortot F. 2023. A reliability-based bridge management concept. *Structure and Infrastructure Engineering* 3:215–35.


Taylor & Francis
Taylor & Francis Group
http://taylorandfrancis.com

SS30: Virtual inspection

Organizers: P. Linneberg & S. Gjerding


Taylor & Francis
Taylor & Francis Group
http://taylorandfrancis.com

Bridge Maintenance, Safety, Management, Digitalization and Sustainability – Jensen, Frangopol & Schmidt (eds)
© 2024 The Author(s), ISBN 978-1-032-77040-6
Open Access: www.taylorfrancis.com, CC BY-NC-ND 4.0 license

Immersive visualization for enhanced operations and management of bridges

B. Aryal
Bentley Systems, Pittsburgh, USA

P. Linneberg
COWI A/S, Kongens Lyngby, Denmark

ABSTRACT: In recent years, technology has made it possible for us to have a better view and understanding of existing conditions. One such aspect is the use of Unmanned Aircraft Systems (UAS) and Photogrammetry to create photorealistic reality models, which have yielded significant benefits by allowing inspectors, bridge maintenance personnel, and engineers to have a clearer view of what is happening on critical infrastructure and to also perform many of the tasks virtually that would have previously required expensive travel, access equipment, and manual labor. Not to mention the impact on the normal operations of a transportation infrastructure asset (reduced availability and safety). In this paper, we will provide a demonstration of these capabilities and how Transportation Owners and Engineering Firms are starting to apply them on projects to see tangible benefits in terms of costs, time, environmental impact, and safety.

1 INTRODUCTION

In recent years, technology has made it possible for us to have a better view and understanding of existing conditions of our transportation infrastructure. One such technology is the use of Unmanned Aircraft Systems (UAS) and Photogrammetry to create photorealistic reality models, which have yielded significant benefits by allowing inspectors, bridge maintenance personnel, and owners/operators to have a clearer view of what is happening (as-is condition) on critical infrastructure and to also perform many of the tasks virtually that would have previously required expensive travel, expensive access equipment, and extensive manual labor. Not to mention the impact on the normal operations of a transportation infrastructure asset (reduced availability and safety for the users).

There is a significant opportunity to harness additional benefits using virtual and augmented reality (VR and AR). By allowing multiple users to access structures and to view them at a real-world 1:1 scale, we can start to collaborate on bridge projects without everyone being physically on-site. The opportunity to conduct virtual inspections incl. performance prediction and the ability to conduct better Quality Assurance/Quality Control means that we can derive much higher quality, consistent, and objective data that can lead to transparent and better decisions and outcomes. This becomes ever more important as the inventory of bridges and structures that are close to and beyond their design service life continues to grow. It is not sustainable to replace all these structures, and all owners and operators need to develop an optimal strategy to inspect and maintain them.

Introducing a digital twin for bidirectional communication is not new to infrastructure engineering. For decades real time sensor-based updating of Finite Element Models for offshore jacket structures have been performed which again formed the basis for risk-based inspection planning. The digital twin can be local (e.g., cracking of certain area) or global (e.g., deformation of an entire structure). The qualification and assurance of digital twins based on Finite Element Models is described in ref. (DNV, 2020). Somewhat similar to

DOI: 10.1201/9781003483755-343

offshore jackets, bridges are also large infrastructure objects that are often difficult to access and often require complex analyses. Digital twins of bridges have also been used for some time, e.g., for analysis of various hazard scenarios (e.g., strike of lightning on stay cables) so the owner/operator can prepare in advance and thereby increase network resiliency.

Integration of digital technologies and tools in current bridge management workflow needs to be intuitive, reliable, flexible and support transparent decision-making. This holds for new bridges with BIM models, birth certificates (digital as-constructed information) etc. but also for existing bridges with all the challenges that comes with these structures.

Technologies, such as UAS, Photogrammetry, VR/AR, Machine Learning as an application of Artificial Intelligence (AI-ML), and Internet of Things (IoT) can allow us to do more with less and still ensure safe operations of these critical infrastructure. In this paper, we will discuss and demonstrate capabilities and how infrastructure owners and operators and their consultants are starting to apply them on projects to see tangible benefits in terms of costs, time, environmental impact, and safety. Easy access to as-is information may also pave the way for innovative and sustainable structures, materials and inspection and maintenance approaches with yet unproven track record.

Establishment of a photorealistic model is described (chapter 2), followed by a summary of the benefits from an immersive inspection workflow and having a photorealistic model in general (chapter 3). Introducing a second and third layer of new technologies on top of the photorealistic model - virtual and augmented reality (chapter 4) and artificial intelligence and machine learning (chapter 5) is also discussed.

2 ESTABLISHMENT OF PHOTOREALISTIC REALITY MODELS

In Denmark and elsewhere it is common to use a traditional hierarchy of inspections, comprising routine, principal, and special inspections as primary source of information on bridge condition and performance. In particular, principal inspections, often performed within a 5-year interval, should be performed within an arms-length reach of all surfaces according to national codes and guidelines. This principle implies difficult access on major bridges (often coast to coast) by use of rope access and/or underbridge inspection gantries. Performing such inspections comes with a risk to the bridge users (due to traffic restrictions) as well as the inspection personnel working at heights and/or near water. Furthermore, this inspection type is labor-intensive and costly – especially when dealing with major bridges.

In recent years, several bridge owners and their consultants have with success implemented a UAV-based immersive inspection workflow on some of their major bridges. The immersive inspection workflow often starts with a drone flight where RGB and for concrete bridges often also thermal images are obtained. The aircraft could be a DJI M300 RTK or similar. RGB and thermal images might be captured simultaneously with a DJI Zenmuse H20T camera (20 MP zoom camera, 12 MP wide camera and 640x512 px radiometric thermal camera) or similar. The temperature difference between night and day should be minimum 5 degrees for optimum use of the thermal images for detection of concrete delamination, honeycombing etc. The latter defects are otherwise only obtainable using hammer tapping and/or by use of NDT equipment at the concrete surface. It is generally recommended to use the same device for RGB and thermal image capturing respectively during the entire operation.

Real time kinematic positioning (RTK) is used for geo reference of the pictures, which is a 3D representation of the image location in real time. For other bridge structures, a surveyor establishes separate fix points on the structure for geo reference. It must be acknowledged that GPS signal is limited below bridge girders and when flying in their interior. The drones operate in a predefined flightpath at approx. 15 m from the bridge structure. The flight path is determined from weather conditions, drone capability (tight spaces), light conditions, quality of sensors (cameras), restrictions due to traffic, fix points for image reference, etc., which requires domain knowledge within reality capture. Careful planning is key. It is expected that flightpaths can be semi-automated in the future. Automated flight paths can also be of use, when performing a second future reality model.

The imagery is captured with an overlap of approximately 70-80%, which creates a highly detailed 3D mesh. The mesh is then overlayed with the RGB and possibly thermal photos. In special vulnerable zones such as concrete half-joints and splash zone of concrete piers, imagery is captured with an overlap of 80 % for more detailed 3D mesh. It requires domain knowledge within bridge condition management (vulnerable zones, damage mechanisms, resolution needed for defect finding, etc.) to establish a detailed 3D model suitable for immersive inspection. Usually, all pictures are stored as part of the reality capture model and the reality model can be used for easy navigation to the best picture displaying the area of interest.

Using the reality capture model an immersive inspection can be performed at the office. This allows for collaboration between the inspector and various experts if needed be.

Furthermore, immersive inspection allows for the inspector to be well rested and to be able to go back-and forth between locations of interest. Defects and repairs can be annotated on the reality capture model for easy communication between consultant, owner and contractor and all captured data are stored for easy reuse – maybe in connection with defect prognosis at or after the next principal inspection. The use of a reality capture model increases objectivity, transparency and flexibility, i.e., they allow for better decisions.

Furthermore, one or several trained artificial intelligence (AI) models for defect detection are being used. They assist the inspector during virtual inspection especially at vulnerable zones (could be a concrete crack-overlay that highlights flow of forces at half-joints or beneath bearings). Based on the finding from immersive inspections the owner can launch targeted special inspections if certain defects need a more thorough investigation using non-destructive or destructive testing.

Along with the reality mesh, it is quite valuable to be able to add data from other sources that have historically been kept in either a paper format or digital format but on a different/siloed platform. One such example is building information modeling (BIM) data that could be added to the model to give more information from the original design. For an older bridge, this data might not exist. But consultants and owner/operators are more and more seeing the value of putting information into the model that shows all of the historical data made throughout the lifecycle of the bridge. Also, a BIM model could be helpful when inspection data lead to rehabilitation or replacement plans.

3 BENEFITS OF IMMERSIVE INSPECTIONS AND PHOTOREALISTIC MODELS IN GENERAL

Application of immersive inspection comes with a range of benefits. The most important benefits are listed below in random order:

- Reality capture models allow for efficient information sharing, cooperation, and communication between consultant, owner, and contractors.
- Reality capture models provide a good reference point for daily operation of major bridges, e.g., during planning of maintenance works at meetings between various stakeholders (contractors, consultant, and owner).
- Reality capture models can contain and present: 'birth certificates' (as-constructed information), condition assessments as a snapshot in time (incl. warranty inspection i.e., condition at year zero), information of performed and planned repair works and monitoring data. It is seen that a reality capture model represents a snapshot in time information and needs updating when important activities take place (inspection and repair works).
- Combining reality capture models established at different times allows for better prognosis and transparent decision-making. This benefit is not capitalized from day one.
- Immersive inspections decrease the need for labor-intensive inspections and costly access equipment.
- Immersive inspections increase the safety for inspection personnel (less time exposed to traffic, working at heights and near water) as well as asset users (risk of accidents due to traffic restrictions).

- Decrease of inspection costs, maybe not during the first inspection due to establishment of the reality model, but during the following inspections (entire bridge or element-clusters at major bridges).
- UAV's can carry different equipment and in the same flight, e.g., RGB photo for photorealistic models and thermal photo for identification of concrete delamination, honeycombing etc. – and with the current development pace it is expected that more equipment will come.
- No need for manual description of defect location. This may reduce manual labor, increase precision when a special inspection is launched, increased possibility of prognosis and add transparency in decision-making.
- Inspection can be performed by well rested personnel with the possibility of going back and forth between locations (did we miss a repeatable defect?).
- Decrease of environmental impact (detour, congestion, trucks on site for inspection gantries and for traffic restrictions with lights).

There are also some challenges and barriers for people using this digital technology:

- Reality capture and structural experience is required, i.e., domain knowledge is required. Experience with reality capture modelling comprises flight paths for reality capture models of high quality, drone types and carry-on equipment, lighting needed and max wind speed. This is an area of fast development where flightpaths assistance/automation is becoming available. Structural experience comprises reality model resolution needed for defect detection (again dependent on deterioration process and material) and understanding of vulnerable areas that are of special interest (either prone to deterioration or limiting the capacity of the structure in question). Artificial Intelligence assisted defect detection experience comprise knowledge on the accuracy of models, needed training etc.
- Speed and model quality can be obstacles because immersive inspections are always compared to visual inspection. If areas are difficult to reach (often the case for major bridges) speed will not "be a problem". Furthermore, reality capture models usually store all photos, i.e., quality should not be a problem if the reality capture model is established with 70-80% overlay which is generally recommended.
- Introduction of new technologies and tools in organizations comes with a cost and requires new skills. However, a cost-benefit analysis should pave the way for implementation, at least for bridges with difficult access.
- Storing of information should be 'balanced'. It must be decided what data/information should be stored directly in the reality capture model for efficient presentation and decision making and what data should be stored or kept in the bridge management system (BMS), database or a structural health monitoring system (SHMS). A link between the reality capture model and BMS and possibly other systems is key. Similar questions arise regarding new structures and their BIM model.

4 VIRTUAL AND AUGMENTED REALITY

A reality model lets bridge experts see the model from anywhere and easily move around to see different angles of a large bridge structure that would otherwise be hard to reach and comprehend. Once the model is made, there is usually little extra work needed to view it on mobile devices like phones, tablets, or even augmented reality (AR) and virtual reality (VR) headsets. While looking at reality meshes on a desktop is well known, the AR/VR tools offer a chance to improve the workflows, get more information and enhance collaboration among stakeholders.

Virtual Reality (VR):

Virtual reality offers a way to simulate the experience of a physical visit to a bridge site while allowing the user to easily navigate views of the entire structure. Inspecting bridge components such as the top of a bridge pier would be hard to reach, and present issues related to required equipment, traffic management, safety risks and travel time to and from the site.

Furthermore, viewing the model in VR allows the user to view at a 1:1 scale and then quickly switch to a zoomed in overhead view of the overall structure.

The VR environment provides a realistic viewing experience with enhanced features, and the added advantage of being able to co-experience it with other project stakeholders who may be geographically distant. It is plausible to envision multiple engineers evaluating the seriousness of a bridge inspection problem, while looking at the flaw in actual size from different offices.

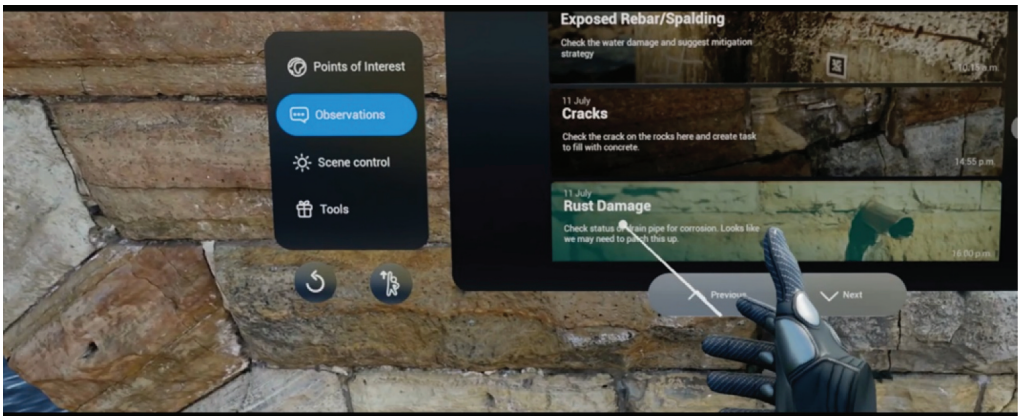


Figure 1. Using a VR app to remotely annotate observations.

Another potential for this technology is in the realm of public involvement, which is a key element in bridge operation and management. Through traditional data and deliverables, it can be difficult to convey how traffic will be impacted by inspection and maintenance projects to public motorists who depend on that infrastructure. Through a combination of a design and reality model data along with VR technology, we can offer more effective visualizations, which makes it significantly easier to convey impacts for a public that is not used to seeing 2D plans, cross-sections, or engineering details.

Augmented Reality (AR):

While virtual reality can bring the bridge to the office, augmented reality can now bring digital data into the field. Recently, AR hardware has been developed that is integrated into personal protective equipment, like hardhats so that personnel in the field can safely use the equipment and combine the insights and usability of the reality mesh with the inherent value of being able to physically view the bridge components.

We can envision many use cases for AR, but these 3 are the most apparent:

Viewing hidden design components – Often the as-built drawings that are provided at the completion of a project can be lacking in information, unreliable or in a format that is difficult to valuably use to make maintenance decisions. Being able to visualize hidden features like rebar or buried utilities against the backdrop of the physical structure empowers professionals to have a more complete picture and make more informed decisions. This is accomplished by integrating an accurately georeferenced model into the AR view. It should be noted that for many older structures, this information may not be readily available, and more work and data acquisition may be required to identify hidden components and convert the data to a digital format. However, AR presents this potential advantage for future design and construction projects. Integrating AR and building data-rich models into current workflows will pay dividends well into the future.

Comparing inspection or design notes while onsite – An accurate high-resolution reality model presents the opportunity to create annotations and inspection items in the office that can be subsequently viewed onsite as georeferenced locations on the model. Integrating these notations into the AR viewable model allows inspectors to leverage the benefits of the reality

model while in the field. The notes created in the office can be verified and amended in the field with the backdrop of the physical structure.

Visualizing potential rehabilitation/replacement components – Similar to integrating existing hidden BIM design components into a reality view, the ability to physically walk the bridge and view proposed design items at a 1:1 scale can provide a more complete picture and help identify clashes or potential construction challenges. Unlike the hidden design components, the ability to integrate new BIM components into an existing model does not present the same technical or logistical challenges and is a feature that can be easily added throughout the maintenance lifecycle of a bridge.

The potential for AR to revolutionize the way we see our infrastructure is certainly there, but there are also technical challenges that must be addressed. While AR technology continues to mature, VR technology is already mature enough to deliver significant benefits to everyone involved in infrastructure projects ref. (Bentley, 2021).

As an early proof of concept of Augmented and Virtual Reality, Microsoft HoloLens 2 (HL2) has been used along with Microsoft Azure Remote Rendering (ARR) technology to stream reality data to the headset device. The streaming service requires a strong and stable network connection with a minimum requirement of 40 Mbps download and 5 Mbps upload. The HL2 comes with a version of Windows, which has a familiar user interface for most users. The headset requires an initial configuration to calibrate the device for each user and can also use their retina for login purposes. For the HL2, an application (App) was developed and deployed, which can integrate with single-sign-on (SSO) systems to access 3D models that reside in cloud services. A proof-of-concept project between COWI and Bentley was conducted where a HL2 App was used to stream reality data from a cloud service.

The process for this immersive visualization required the user to first generate a QR code from a web application, which then allowed the use of the HL2 device to read and then launch the application to access that specific model. The App allows the user to view the model in table (small) scale as well as full (1:1) scale. The hologram of the reality capture model can be moved, rotated, and extended with the use of gestures and finger movements. The 1:1 scale allows the user to fly around in the model giving access to areas that would be difficult or impossible to do on-site. Within the App it is also possible to inspect the structure and annotate maintenance items and observations. A pin is placed for each of these annotations and details can be added either by writing on the hologram keyboard or by dictating the text. These annotations can then be synchronized to a web application for further collaboration with other users.



Figure 2. Using HoloLens 2 at site (upper right picture is the AR-image as seen by the inspector).

5 ARTIFICIAL INTELLIGENCE AND MACHINE LEARNING

Bridge inspections can be a tedious yet risky task. An inspector must correctly spot, measure, and categorize damage processes and defects such as deck cracking as part of a thorough bridge inspection. The data they collect is useful for bridge inspection reports and for maintenance and design purposes. Inspectors have to visit the site and examine every part of the bridge to assess condition/performance and report it properly in the system.

Artificial Intelligence can help make the workflow better by providing assistance to the inspectors. Some examples have appeared with machine vision technology that lets inspectors get a more consistent and objective understanding of issues, such as cracking, spalling, or corrosion.

For instance, to solve the problem of finding cracking on bridge decks, we can use thousands and thousands of images. These images can come from regular inspection photos, from a dataset that is open to the public, or from drone images, to train a detector that can find cracking on bridge elements. The AI-ML detector can go through all the 2D images to detect and then mark the cracks in the photos. A post-processing cleaning step can find and remove known false positives. The reality capture model should be based on pictures of similar resolution as used for training of the AI-ML models. This allows for the best defect detection.



Figure 3. Sample of a cracked concrete surface (left) and crack-overlay (right).

Each 2D image with the crack information can then be sent to software to create a 3D mesh, which can then project the identified cracks on the surface of the deck. This 3D view lets the user quickly assess the overall state of the bridge without having to zoom in on the reconstructed model. Even before getting the actual analysis and numbers, this lets the user evaluate the condition qualitatively with little effort.

These auto-detected cracks can also be turned into 3D-lines, which can then let us interact with them as individual cracks that can be edited, deleted, or extract information about their geometry. Some examples of the type of analysis that can be done include individually selecting each crack and instantly getting the length, selecting all of the cracks to get the total crack length and even more importantly crack width in the chosen area – both options relevant for pavement repair but not very interesting for concrete bridges.

While cracking on concrete bridges is a good use case, other types of defects can also be found using this workflow. For example, spalling is a very common (and troublesome) issue on large concrete structures. Spalling is a big issue for infrastructure owners because 1) it may weaken the structure integrity, 2) even when it does not, it greatly increases the chances for more spalling to happen and other elements to degrade (like rebars in reinforced concrete, which then corrode when exposed to humidity) and 3) concrete may hit underpass traffic.

Because spalls affect areas rather than lines like a crack would do, new types of detectors are needed to find them. There are some challenges, such as the AI model not being able to find the exact boundaries of spalling areas and the tendency to produce a lot of false positives.

As the goal of such automated inspection is to assist engineers in their task, a few of these false positives can be accepted, however, a high number of mistakes is problematic, because it would require a lot of time from the engineer to exclude them and would lead to a general distrust of the AI system. Using several new AI techniques, detectors for spalling are now able to not only put a rectangular bounding box around the area of concern, but can also highlight the affected areas accurately, so that you can get a much better measurement of overall spalling.

Besides using machine vision for supporting inspections, AI-ML has the potential power to help our industry move at a faster pace from reactive to preventative or even cognitive maintenance. For example, with the emergence of Internet of Things (IoT) sensors that can collect a large amount of data about a bridge's performance over time, we can not only use this information to alert us when the readings are out of range, but we can use the time-series data to predict performance. This type of analysis could be supporting us to move from the traditional scheduled-based inspection and maintenance to risk-based inspection and maintenance.

6 CONCLUSION

Digital technologies have a lot of potential to improve the way we do bridge inspections and maintenance. They can help us collect more consistent data and analyze it faster and more effectively, which can benefit bridge owners, inspectors, and the public who use them. Some of the early users of tools and technologies like UAS, AI-ML, and IoT have already seen benefits, such as: less field time, more reliable data for analysis, better bridge repair suggestions, better communication and cooperation, lower costs, and less environmental impact by using less equipment. Technology is advancing quickly, and this is only the start. In the immediate future it is foreseen that we will have more trained defect detection models for various materials, image resolution, lighting conditions etc. and efficient integration of data from various sources (crow sourcing from connected cars, satellite data, sensors/IoT on the structure, etc.). But technology is not enough to change the way we manage our bridges. We also need to train people to use these technologies and we need to update our processes so that we can use UAS more confidently and regularly in our operations and trust the power of AI-ML to help our bridge engineers make the best choices on how to maintain our growing number of structures that are aging beyond their expected design life.

REFERENCES

Bentley 2021. A Perfect Storm: Bridge Inspections Re-imagined with Drones, AI/ML, Photogrammetry, and Mixed Reality (Presented by Bentley Systems) | NVIDIA On-Demand, *GTC Digital April 2021*.

DNV. 2020. DNV-GL Recommended Practice – Qualification and assurance of digital twins, *DNVGL-RP-A204*, *Edition October 2020*.

Jensen, J. S. 2023. Digital transition in asset management of bridges – Advantages and challenges; *Proc. IALCCE 2023*, *Milan*, *2-6 June 2023*. London: CRC Press.

Linneberg, P. 2022. Unmanned Areial Vehicle (UAV) supported bridge inspections; *Proc. IABMAS 2022*, *Barcelona*, *11-15 July 2022*. London: CRC Press.

Bridge Maintenance, Safety, Management, Digitalization and Sustainability – Jensen, Frangopol & Schmidt (eds)
© 2024 The Author(s), ISBN 978-1-032-77040-6
Open Access: www.taylorfrancis.com, CC BY-NC-ND 4.0 license

Digital transition in asset management – Virtual inspections of bridges

N.L. Barnes
COWI A/S, Kongens Lyngby, Denmark

E.D. Hartwich
The Danish Road Directorate, Fløng, Denmark

ABSTRACT: In Denmark, bridge managers are obligated to conduct principal inspections every sixth year. Today, most inspections of bridge structures are outsourced to consultancy companies performing visual inspections on-site, facing challenges such as traffic restrictions, subjectivity and consistency in documentation, and difficult access- and working conditions. However, the ongoing digital transformation of O&M of bridges offers viable solutions through the integration of technical equipment including drones, sensors, software, etc. in the inspection process, leading to significant environmental, economic, and technical benefits. By employing high-quality RGB photogrammetry and thermal imagery captured by drones etc., a Reality Capture Model, a visual Digital Twin of the structure, is generated. The COWI Virtual inspection software facilitates principal inspections with AI-aided defect detection enabling multiple specialists to annotate damages or defects directly on the RCM and revisit the bridge structure when necessary. Additionally, the thermal imagery, when combined with RGB photos, enables the detection of delaminations, honeycombing, and water ingress in concrete structures. In 2023, a virtual principal inspection of the pylons on the Faroe Bridges and the Queen Alexandrines Bridge is conducted. This paper presents key findings from pilot projects to complete virtual inspections and highlights the benefits and challenges associated with the transition to virtual inspection methodologies and future AI-driven- and performance-based asset management.

1 INTRODUCTION

The digital maturity of the construction sector was reported as very low back in 2016 (McKinsey 2016). Compared to other industries there seems to be great potential in terms of both technical and economic benefits of the digital trasition in the construction sector. In the recent years there have been a great focus on the Operation and Maintenance (O&M) of bridges originating from e.g., bridge collapses, increasing environmental focus, and the attention to service life and Life Cycle Cost of structures and materials accelerating the digital transition.

In Denmark, the asset manager is obligated to conduct visual inspections every sixth year to maintain the level of safety, foresee critical defects, and avoid costly repairs. Most of the inspections are outsourced to consultancy companies performing traditional inspections. The traditional inspections are carried out with rope-access or from a lift or platform challenged by e.g., traffic restrictions, high initial costs, subjectivity, and consistency in documentation (Moore et al., 2001), and access - and working conditions.

The use of Unmanned Aerial Vehicles (UAVs) has accelerated in the construction sector in within both inspections and supervisions of structures. The high-quality sensors, Real Time Kinematics (RTK), and improved software have made it possible to establish detailed 3D-meshes and Reality Capture Models suitable for virtual inspections. RGB Photogrammetry and AI-aided defect detection is used to detect visual defects e.g., cracks, corrosion, etc.

DOI: 10.1201/9781003483755-344

and thermal imagery is used to detect e.g., delamination, loose repairs, honeycombing, and water ingress. UAV-based photogrammetry has proven safe, cost-, and technically efficient on multiple bridge projects with the use of both RGB and thermal imagery (Lindberg et. al, 2022 and Sandager Jensen 2023).

The digital transition within asset management and O&M is rapidly improving, and this paper provides key findings from pilot projects to complete virtual principal inspections performed today and the prospects within performance-based asset management and predictive maintenance.

2 ASSET MANAGEMENT OF BRIDGES

The inspections are performed according to general procedures and manuals for principal inspections. The observations from the principal inspections are noted on tablet or paper and documented in a report including selected photos (primarily the founded defects). In addition, the observations are translated into a condition rate for each structural element (intermediate piers, abutment, pavement, bearings, etc.), according to the codified procedures. The inspector also provides a timing and cost estimates of needed repair or replacement works, and the asset manager plans for future repair work based on this principal inspection report.

The visual inspection is cost-effective when performed by qualified personnel. However, the documentation rely on subjectivity as only selected defects are reported. The inspector should also be able to separate visual defects from critical defects and acknowledge when to upgrade the principal visual inspection to a special inspection and perform non-destructive tests or service life assessment, load capacity assessment, proof-loading, etc.

An essential aspect of asset management is determining the 'optimal point in time' for repair or replacement of structural elements based on the inspection data and condition rating considering the Key Performance Indicators (KPIs) reliability, availability, safety, economy, and environment relevant for bridge management when considering service life of bridges (COST TU1406, 2018 and Linneberg, 2020). Structural Health Monitoring Systems (SHMS), bearing capacity (Finite Element modelling), and defect modelling is key input to the decision making regarding long term maintenance strategies. It requires Artificial Intelligence to objectify and find the strategies and the optimal point in time for repair and replacement of structural elements.

The traditional inspections are reported by the inspector into existing Bridge Management Systems (BMS), which cannot accommodate the integration of different data sources. Such improvement of the current portfolio BMS incl. full integration of a risk-based management system considering multiple maintenance strategies (and KPIs) is technically challenging and costly. Therefore, the digital transition is only improved gradually.

2.1 *The Danish Road Directorate*

The Danish Road Directorate is the asset manager of the Danish state roads and adjacent civil structures including bridges. They have shown increasing interest in UAVs and a more cost-effective alternative to traditional inspections the recent years. As bridge maintenance costs continue to rise, this has become a priority. Consequently, several pilot projects exploring the possibilities of UAVs, Digital Twins, and virtual inspections were initiated in 2019. One such project involved the collaboration between the Danish Road Directorate and COWI A/S in 2020. The main focus was to establish a Reality Capture Model of the Faroe Bridges (presented later in this paper). This model was intended for general operational purposes and to facilitate the principal inspection of concrete emergency walkways.

The pilot project marked the beginning of an ongoing collaboration between the Danish Road Directorate and COWI A/S. As case studies in this paper, the recent principal virtual inspections of the Faroe Bridges and the Queen Alexandrines bridge are examined. Notably, both bridges cross water, presenting significant potential for cost-effective inspections when utilizing UAVs.

One of the challenges facing the Danish Road Directorate is the large number of relatively small and easily accessible structures for which the state is responsible. When considering the establishment of Reality Capture Models for these smaller structures, careful assessment of the costs versus the value they can create is essential. In addition to their applications in the operational phase, RCMs can also yield valuable information for future road and bridge projects during the planning and construction phases, thus enhancing the overall data foundation for the Danish Road Directorate.

3 CASE STUDIES

Two case studies from Denmark have been selected to illustrate the utilization of UAVs, Reality Capture Models, and the general workflow when working with virtual inspections: The Faroe Bridges and The Queen Alexandrines Bridge. Both bridges have been part of pilot projects prior to complete inspections which is described in further details in the following presentations of the two bridges.

3.1 *The Faroe Bridges*

The Faroe Bridges connect Falster and Zealand via the Faroe Island in Denmark. These bridges opened to traffic in 1985 and is carrying four lanes of highway traffic. The connection consists of a cable-stayed bridge in the south, connecting Falster to Faroe. It has a length of 1,726 m, a main span of 290 m, and a clearance from the sea of 26 m. In the north, there is a concrete beam bridge (orthotropic steel box girder) connecting Faroe to Zealand, with a total length of 1,596 m and a clearance from the sea of 26 m (The Danish Road Directorate, 2023).

The Danish Road Directorate owns and operates the bridge, while COWI A/S has provided consultancy services related to its operation and maintenance. The cable-stayed bridge is shown in Figure 1. In 2020, the Danish Road Directorate commissioned COWI A/S to establish a Reality Capture Model of both bridges, used for general operations and principal inspection of concrete emergency walkways (spanning over 6.5 km) and bridge piers (34 in total).

In total four UAV flights were conducted for the pilot project: The first flight established reference points. The second flight established RGB photogrammetry for the entire model. The third flight obtained close-up photos of emergency walkways, and the fourth captured close-up photos, including thermal imagery of all bridge piers.

The inspection was carried out in an early edition of COWI Virtual Inspection. Following a virtual visual inspection with RGB-imagery and thermal images, an inspection of six bridge piers using rope access were carried out. The inspectors found the same significant defects (delaminated areas of similar size) as the virtual inspection alongside minor defects as cracking and poor in-situ grouting of voids from the removal of scaffolding. Furthermore, the virtual inspection discovered a few defects in the splash zones that were not accessible during the rope access inspection. In 2023, a principal inspection of the two pylons of the cable stayed bridge is conducted.

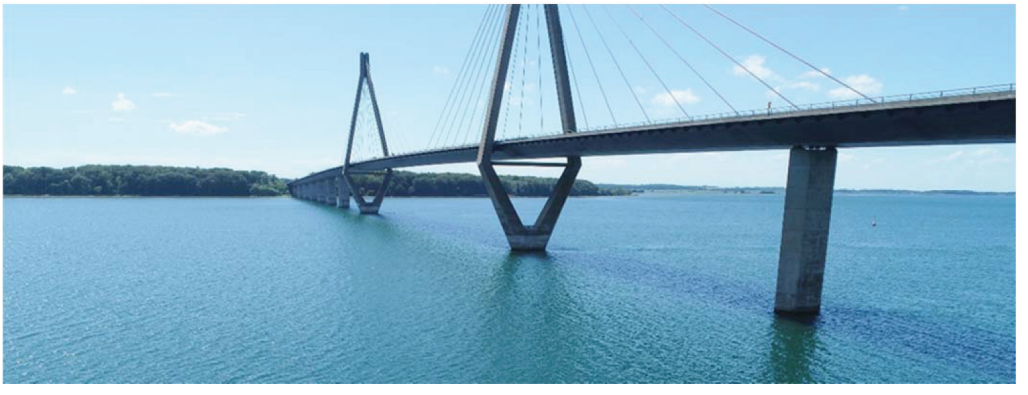


Figure 1. The Faroe Bridges (Cable Stayed Bridge in South).

3.2 *The Queen Alexandrines Bridge*

The Queen Alexandrines Bridge, also known as the Moen Bridge, connects Zealand with Moen in Denmark. The bridge opened to traffic in 1943 and is carrying two lanes of traffic and two pedestrian walkways. It has a total length of 745,5 m, with a main span of 127,5 m and a clearance from the sea of 26 m (The Danish Road Directorate, 2023). The construction is an open arch bridge with five approach spans cast in reinforced concrete on each side of the main arch span constructed in steel.

The Danish Road Directorate is responsible for owning and operating the bridge, with consultancy services provided by COWI A/S for its operation and maintenance. The Queen Alexandrines Bridge is shown in Figure 2. In 2022, the Danish Road Directorate commissioned COWI A/S to establish an RCM of one approach span. The model was integrated into COWI Virtual Inspection as part of a pilot project for visual inspections.

The Reality Capture Model of the bridge was based on both RGB – and thermal imagery captured simultaneously with the use of a drone, without any traffic restrictions. The principal inspection was carried out using annotations in the model to illustrate visible damages e.g., cracks, spalling, organic growth, graffiti, etc. The annotations are directly linked to the specific area of the model and are easy to revisit to e.g., consult or verify with a specialist. In 2023, a Reality Capture Model of the bridge is established as part of a principal inspection of the entire bridge.



Figure 2. The Queen Alexandrines Bridge.

4 DATA COLLECTION

In 2023, the Reality Capture Models of the two bridges are established using similar methods. The models are created by processing RGB-images captured with a drone trough photogrammetry. The captured pixels ranges from 1.2 to 7.8 mm. In addition to the visual surface, thermal images are also simultaneously captured. The drones follow a predefined flight path, approximately 15 m from the bridge structures. The flight path is dependent on weather conditions, drone capability (e.g., tight spaces which require a drone capable of bumping into the structure), light conditions, quality of sensors (cameras), restrictions due to traffic, fix points for image reference, etc., which requires domain knowledge within reality capture. When operating in Denmark, the drones are not allowed to pass or fly above traffic lanes without permission.

To ensure accurate geo-reference, real-time kinematic positioning (RTK) is utilized for the Faroe Bridges, providing a 3D representation of the image locations in real time. For the

Queen Alexandrines Bridges, a surveyor establishes separate fixed points on the structure for geo-referencing purposes.

Typically, the imagery is captured with an overlap of approximately 70%, resulting in a highly detailed 3D mesh. In vulnerable zones (e.g., splash zone), imagery is captured with an overlap of around 80% to produce an even more detailed 3D mesh. This mesh is then overlayed with the RGB photos. The creation of a detailed 3D model suitable for visual (virtual) inspection requires domain knowledge within bridge condition management, considering factors such as vulnerable zones, damage mechanisms, and the necessary resolution for defect detection.

5 VIRTUAL INSPECTIONS

5.1 *Workflow of virtual inspections*

The RGB-images are processed in commercial Bentley software to establish the Reality Capture Model. The models with adjacent RGB- and thermal images are then imported into the COWI Virtual Inspection tool. It is a web-based platform where the virtual inspections are carried out. The platform allows the users to manually annotate defects, use AI for defect detection, attach files or URLs to the model or defect, and generate a principal inspection report of annotated defects. The workflow of the two case studies is elaborated in the following.

5.1.1 *The Faroe Bridges*

The pylons of the Faroe Bridges are established as two separate RCM-models and imported with adjacent RGB- and thermal images into COWI Virtual Inspection. The COWI Virtual Inspection platform is shown with the northern pylon in Figure 3. The screen of the platform is split into three showing the model, annotations, and the images. A double click on the model will give the user the 30 best images in the picture panel.

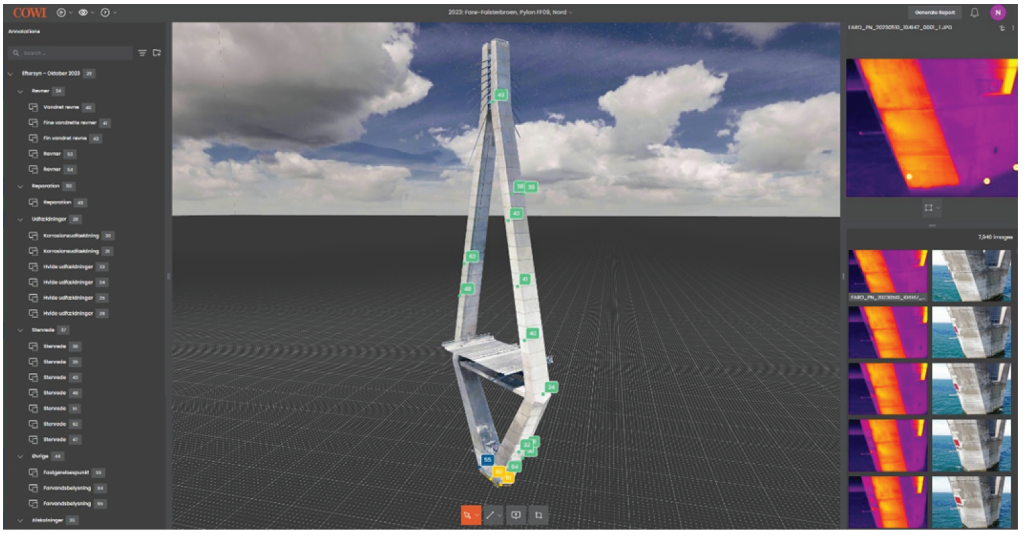


Figure 3. Pylon of the Faro Bridges in COWI Virtual Inspection.

A principal inspection is carried out using manual annotations to illustrate visible defects e.g., cracks, spalling, corrosion, coating defects, etc. The defects are registered with severity level 1-5 (green to red), a short description, recommended action, and custom tags (location). The defect annotations are linked to the specific area of the 3D-model and are easy to revisit e.g., consult

or verify with a specialist. Thermal imagery identifies areas that have a temperature difference down to 0.1-0.2 degrees Celsius compared to the surrounding structure.

The thermal imagery is primarily used to screen the concrete surface above the highway for possible delaminations to ensure safety for the drivers passing the bridge. In the splash zone thermal imagery is also used to detect spalling and loose repairs in the splash zone where cathodic protection is established. A principal inspection report is generated in COWI Virtual Inspection with all the annotated defects and two adjacent images: Overview and close-up image of the annotated defect.

The virtual principal inspection is combined with a manual inspection of the interior concrete surfaces of the pylon. A pilot project was carried out using the same method with image processing based on RTK, but it was not optimal with the plain concrete surface and no GPS in the pylons. Instead, the manual inspection is supported with drone videos and imagery from inaccessible areas inside the pylon. Both inspections are collected in a general inspection report with overall summary of defects and recommendations.

5.1.2 *The Queen Alexandrines Bridge*

The Queen Alexandrines Bridge is established as two separate RCM-models: Span 1-6 and 7-12 and imported with adjacent RGB- and thermal images into COWI Virtual Inspection. The COWI Virtual Inspection platform is shown with model of span 7-12 in Figure 4.

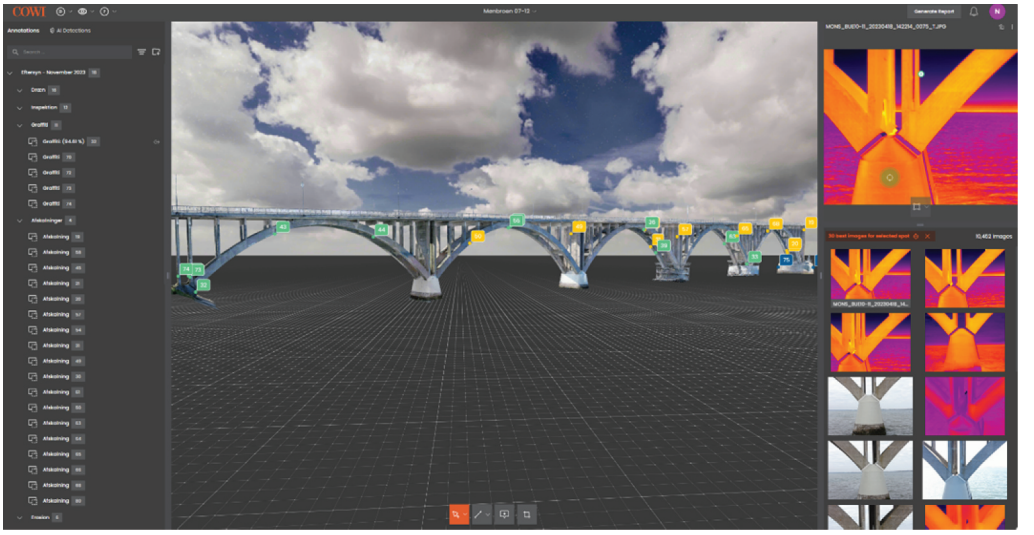


Figure 4. Span 7-12 of the Queen Alexandrines Bridge in COWI Virtual Inspection.

The approach of the virtual inspection is similar to the one carried out for the pylons of the Faroe Bridges. However, AI defect detection is implemented in the beginning to screen the bridge structure for cracks, graffiti, and corrosion. The defect detections are rated true og false to train the general AI-model, and the AI detection is moved to the annotations for the principal inspection if it is within the scope of the inspection. An example of an AI-detected crack is shown in Figure 5.

The AI-models are in general trained with the mindset, that false positives are accepted (they are sorted out during the manual visual inspection), but a false negative of a given size or in vulnerable regions (e.g., shear cracks in bridge half joints) is not accepted. In addition, it is important to use AI models that are trained for similar damage types and image resolution.

The thermal images are primarily used to screen the concrete surfaces on the main arches for possible delamination and loose concrete repairs. A principal inspection report is generated in COWI Virtual Inspection with all the annotated defects.

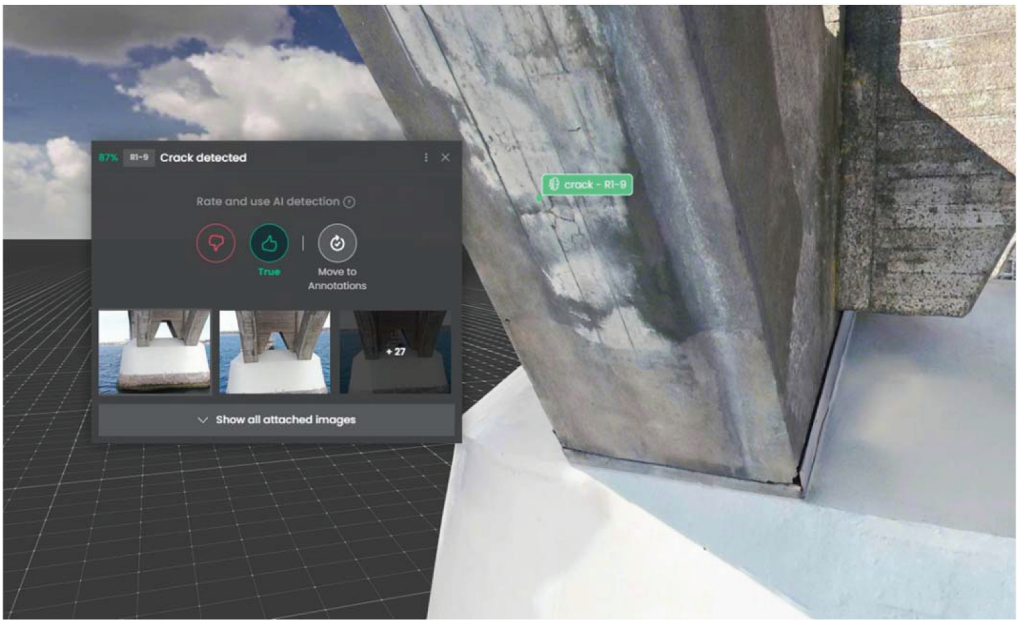


Figure 5. Example of an AI-detected crack in soffit of concrete arch of the Queen Alexandrines Bridge.

The virtual inspection is combined with a manual inspection of the interior and structural elements above road level as pavement, dams, railings, and main span including embankments. The main span consists of a steel arch with hangars and trusses. That type of structure is problematic when establishing an RCM-model with image processing and the drone images are instead used to supplement the manual inspection of the main span. Both inspections are collected in a general inspection report with overall summary of defects and recommendations.

5.2 *Advantages and challenges*

The COWI Virtual Inspection platform allows multiple specialists to take part in the visual inspection leading to transparency in decision-making and less subjectivity. The bridge is inspected with well-rested personnel, and it is possible to revisit structural elements to look for repetition patterns in defects or consult a specialist.

At the Queen Alexandrines Bridge it is not profitable to do a principal inspection of the entire bridge every fifth or sixth year. The bridge is constructed with arches and columns, which are difficult to inspect from a lift, platform, or rope-access. The RCM-model gives a great visual model of the entire structure. If necessary, it is easy to point out structural elements or areas where a special inspection should be caried out. The Danish Road Directorate can access the model and hereby get full documentation of the bridge inspection, not only selected defects. Beside the models, the images, annotations, and the 3D-model is handed over in open-source formats to the DRD, which makes it possible for them to access the data from other platforms.

The Reality Capture Model may also be used to e.g., annotate daily operation jobs for operation personnel, plan future repair works, etc. The model creates a solid foundation for collaboration with all stakeholders incl. owners, contractors, and consultants without being present at the bridge site and without possible traffic restrictions.

Though many advantages have been pointed out, some challenges remain: The data collecting process still requires highly trained personnel to establish a detailed photo-realistic 3D model and depends on the quality of sensors (cameras etc.), traffic laws, and restrictions when flying with UAVs, flight plans, lighting conditions, weather, and temperature (when using thermal imagery).

The implementation of the Reality Capture Model in 'codified' procedures and manuals, and in current BMS software remains one of the greater challenges. The digital transition requires more performance-based assessment and not only codified procedures and traditional reporting. The Danish Road Directorate is openminded and has agreed to do separate inspection reports to upload in their Bridge Management System.

6 FUTURE PERSPECTIVES

When working with O&M of older bridges as the two bridges presented in the case study, the drawings, images, structural verification reports, etc. from construction are rarely well-documented. The establishment of an RCM-model gives full documentation of the older bridge as a first step in O&M. The same applies for a newly constructed bridge. It can both work as supervision in collaboration with the contractor or as a 'Birth Certificate' of the bridge. The bridge owner has a great focus on the BIM-models to be handed over as part of the As-built information. It might be the time to demand a Reality Capture Model, which gives full documentation of the structure with defects from the beginning and works as a solid foundation for future O&M activities.

Companies specialized in BIM have acknowledged the great potential for digitalization within Operation and Maintenance (O&M). It is competencies like this that will take the RCM-models to the next step with integration of both BIM-models and FE-models and improve the quality of the O&M ensuring repairs and replacement of structural elements at the 'optimal point in time'.

7 CONCLUSIONS

It requires domain knowledge within bridge condition management and reality capture to establish a detailed 3D model suitable for visual (virtual) inspection. With improved sensors, software, and UAVs, the data collection -and integration process still becomes less time consuming and more cost beneficial. Virtual inspections performed on Reality Capture Models delivers less subjectivity and full 3D documentation in an improved workflow with full transparency. In addition, UAV-based inspections increase bridge availability, and increase safety for bridge users and workers.

The workflow of Virtual Inspections is continuously improved as seen in the two case studies from pilot projects to principal inspections with both RGB and thermal imagery to detect visual and certain non-visual defects. However, it is important to acknowledge the limitations and move on to a special inspection when needed.

The integration of the Reality Capture Model within the principal inspection regime improves workflow, ensure full documentation, and supports finding the 'optimal point in time' to repair and replace structural elements considering multiple Key Performance Indicators for bridge owners and operators.

REFERENCES

COST TU1406, 2018, Hajdin, R., Kusar, M., Masovic, S., Linneberg, P., Amado, J., Tanasic, N., WG3 Technical report, Establishment of a Quality Control Plan, ISBN: 978-86-7518-200-9.

Linneberg, P., 2020, From condition to performance assessment of bridges – The challenge, *IABMAS 2020*.

Linneberg, P., Jensen, F. M., Hartwich, E. D., Holt, P., 2022, Unmanned Aerial Vehicle (UAV) supported bridge inspections, *IABMAS 2022*.

McKinsey Global Institute, 2016, Digital Europe: Pushing the frontier, capturing the benefits, www.mckinsey.com/mgi.

Moore, M, et al., 2001, Reliability of Visual Inspection for Highway Bridges, *FHWA-RD-01-020*.

Sandager Jensen, Jens, Digital transition in asset management of bridges – Advantages and challenges, *IALCCE 2023*.

The Danish Road Directorate, 2023, Dronning Alexandrines Bro og Farøbroerne, *Oversigt over broer og tunneler (vejdirektoratet.dk)*.

Bridge Maintenance, Safety, Management, Digitalization and Sustainability – Jensen, Frangopol & Schmidt (eds)
© 2024 The Author(s), ISBN 978-1-032-77040-6
Open Access: www.taylorfrancis.com, CC BY-NC-ND 4.0 license

Norwegian coastal bridges

T. Kvamstad
COWI AS, Trondheim, Norway

H.A. Moe
COWI AS, Oslo, Norway

I.A. Lervik
Møre and Romsdal County Molde, Norway

ABSTRACT: Due to Norway's topography with fjords and islands the demand for bridges is high. The age of these bridges, specifically those constructed between 1960 and 1990, coupled with harsh climate and exposure to seaborn chloride, indicates an anticipated increase in the need for maintenance in the near future. This paper give insight in challenges the asset managers of Møre and Romsdal county is facing. This is illustrated by the case studies of Remøy bridge from 1967 and Runde bridge from 1982. The result of a special inspection by COWI demonstrates how different maintenance strategies is needed based a detailed investigation of the deterioration state. The Remøy bridge will rely on a strategy of Controlled Detoriation to maintain an acceptable Safety level. For the Runde Bridge the rehabilitation strategy is to extend service life by investment in new and modern cathodic protection systems. To be able to inspect and perform maintenance to the bridges in a sustainable way, new technologies must be taken into use and further developed. In this paper drone inspections with thermal images, NDT inspection of post-tensioned strands and rehabilitation with cathodic protection will be discussed.

1 INTRODUCTION

Norway has the second-longest coastline in the world, measuring 100,915 km when including all the islands. With its topography characterized by fjords extending up to 205 km into the country and approximately 300 islands with permanent residents, there is a high demand for bridges.

In general, Norway's regional policy since World War 2 has aimed to reduce centralization and promote development across the country. A crucial aspect has been ensuring access to healthcare, schools, and transportation networks for all citizens. As part of this effort, the construction of bridges to replace ferries has been prioritized, even in areas with relatively few permanent residents. The coast is home to important export industries within the maritime industry, seafood industry, and power-intensive industries. These industries rely on bridges that are open and with high load-carrying capacity.

Coastal areas of Norway are home to over 7,000 public road bridges, where the majority are reinforced concrete bridge (Bruaas, T.). The first reinforced concrete bridges were built in the 1920s, and the number of bridges constructed annually increased rapidly and peaked in the 1970s. According to the BRUTUS database, which catalogs Norwegian public bridges, approximately 60% of the bridges have either already reached, or will soon reach an age, where extensive maintenance is required. The main challenge faced by bridges in coastal areas is corrosion of the reinforcement due to the presence of chlorides. Seawater and air born chlorides can result in pitting corrosion, which deteriorate the health state and safety of the structures. The required concrete cover thickness for bridges has varied over the years since the first regulations were

DOI: 10.1201/9781003483755-345

established in 1926. From 1973 to 1988, it reached its lowest at 25 mm - 30 mm (Bathen, L 2021). Considering that this period coincided with the peak in the construction of new bridges, we anticipate a rapid increase in corrosion-related damage in the coming years.

Post-tensioned bridge technology gained popularity in Norway, particularly for longer span bridges along the coast. The industry faced challenges, particularly with grouting. However, significant improvements in grouting quality were achieved following the release of the first version of the Norwegian Concrete Association (NCA) publication number 14 in 1986. Several bridges with insufficient grouting from before 1982 have been identified. With the recent release and implementation of the NPRA Report number 718 "Post-tension concrete bridges - Inspection manual" in 2021, more bridges with corrosion on post-tensioned reinforcements are expected to be discovered.

The high costs involved and the challenge of keeping bridges open with only limited closure times due to lack of alternative routes require the application of new technologies. Several major older bridges are single lane and may be the only access point to a community and industry. Closure for more than a few hours has high user inconvenience cost and, in some cases, not acceptable.

The Norwegian bridge owners are obligated to seek sustainable solutions when managing their bridge portfolio. To keep the existing bridge for as many years as possible will in most cases be the correct solution. The decision of whether a bridge should be strengthened, maintained or go through controlled deterioration has to be based on LCA and LCC with input of sufficient data.

2 MØRE AND ROMSDAL COUNTY MUNICIPALITY

In the Norwegian Public Road association, a bridge is a traffic carrying element spanning more than 2,5 m. In Møre and Romsdal county road network, there are a total of 1021 structures that are managed according to the national bridge management regulations. This includes 872 road bridges, 50 pedestrian and bicycle bridges, 56 ferry docks, 34 avalanche protection structures, and nine loose material tunnels/tunnel portals that bear traffic loads.

The bridge management regulations require regular inspections, to ensure control over the condition of these structures. Currently, three percent of the road bridges in the county road network have severe damages/deficiencies that pose a threat to the bridge's bearing capacity or the safety of the users, as shown in Figure 2. There is a significant maintenance need for road bridges. The main reasons are the age of the bridges, how they were constructed, and the environment they are exposed to. A national goal of a 100-year lifespan for bridges was established around 1990. This goal resulted in much stricter requirements regarding concrete composition, concrete cover, and considerations for the environment in which the structure is placed. These stringent requirements do not apply to structures built between approximately 1960 and 1990. The regulations at that time were based on a lifespan of 50-60 years. Figure 2 shows that 60 percent of the county road bridges in Møre and Romsdal were constructed during that period.

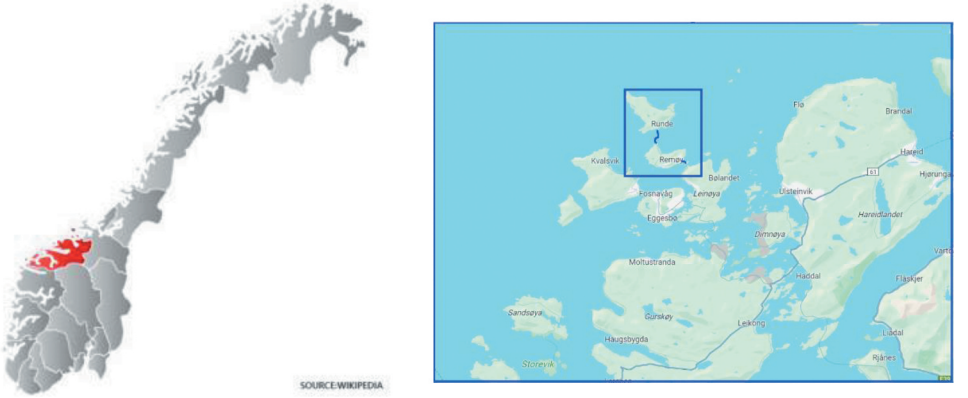


Figure 1. Left: Map of Norway and Møre and Romsdal County Municipality showed in red. Right: Location of Remøy Bridge and Runde Bridge outlined in blue (Map: Wikipedia).

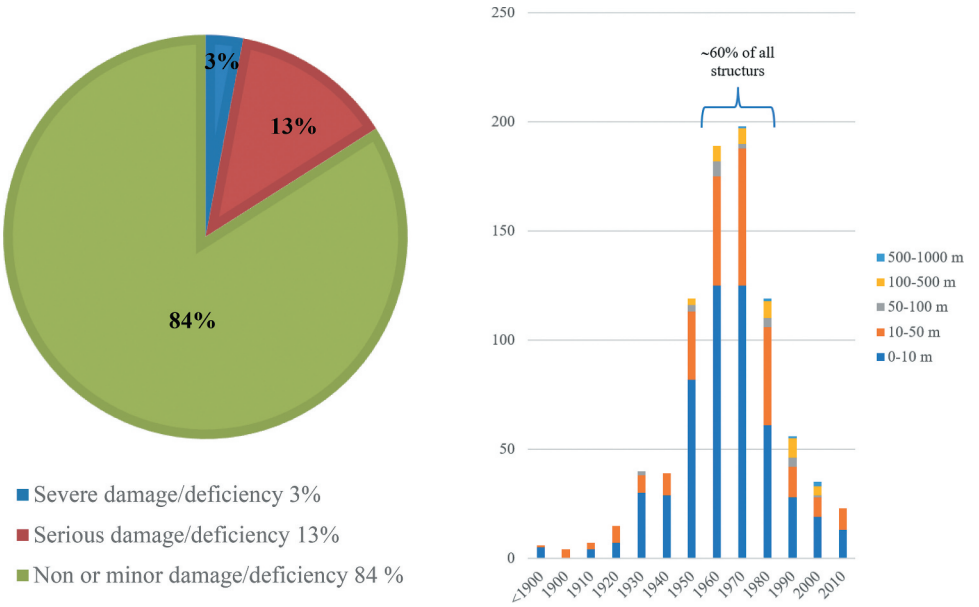


Figure 2. Road Bridges in Møre and Romsdal County. Left: Condition. Right: Year of construction.

Møre and Romsdal county situated on the coast of Norway is characterized by its challenging geography, islands, fjords and mountain areas, combined with scattered settlements. Despite of this, Møre and Romsdal is one of the country's largest export counties. According to the National Exportation Report from 2022, the export per employee of the county was 700 000 NOK. This is almost four times the export intensity of Innlandet County and more than double the export intensity of Oslo. The high export intensity is driven by significant exports from the maritime industry, seafood industry, and power-intensive manufacturing in the region (Menon Economics, 2023). Hence, it is of vital importance to have an operational road network with high bearing capacity.

Knowing that over half of the total bridge length pr. meter built between 1960-1990 is located over the sea, this indicates a significant need for major maintenance or replacement of bridges in the coming years. The leading repair method for large reinforced concrete bridges in coastal areas is cathodic protection (CP) systems. As CP rehabilitation is an expensive investment, it is crucial to apply the correct repair strategy and method. Amount of damaged concrete to be replaced is often a key cost driver. This leads to time consuming inspections and field work, including visual inspections and surface testing with hammer sounding.

3 CASE STUDY

Møre and Romsdal County's challenges and need for investments in bridge operation and maintenance is illustrated by the case studies of the Remøy and Runde, located at the coastline in the south-western part of the region. The bridges carry a single lane of traffic and a narrow pedestrian walkway, and is the only access to the islands Remøy and Runde, see Figure 1. The Remøy bridge opened to traffic in 1967, with a 2023 annual average day traffic (AADT) of 1000. The Runde bridge opened to traffic in 1982 where it replaced the previous ferry connection to Remøy, with a 2023 AADT of 300 (Vegkart.no).

Both bridges are situated in harsh climates, exposed to deterioration from chloride driven corrosion. In 2023 Møre and Romsdal FK commissioned COWI AS to perform a special inspection of both bridges. The purpose of the inspections was to recommend a short term and long-term maintenance strategy. An overview of the inspection program is listed in *Table 1*.

Table 1. Special inspection program conducted for the Remøy and Runde Bridge, June 2023.

	Remøy	Runde
Under Bridge Lift Access *(night closure of traffic)*	x	x
Rope Access *(night closure of traffic)*		x
Drone inspection with Reality Capture Model and Thermal images	x	x
Visual inspection and Sound hammering	x	x
Chloride samples (RCT-method)	x	x
Concrete core testing	x	x
NDT (Non-Destructive Testing) of PT-reinforcement	x	x
Inspection and data collection of Cathodic protection system	x	x
EKP measurement to assess ongoing corrosion		x
Local inspection of ongoing corrosion on reinforcement	x	x

3.1 *The Remøy Bridge (1967)*

The Remøy bridge is a 340-meter-long slender beam bridge opened to traffic in 1967. The bridge consists of 20 spans, a T-shaped beam cross section with varying height. The 40 m main span and adjacent side spans are prestressed with Dywidag bar system. The need for a ship navigation clearance of 17-meter results in high slender columns, as well as steep slopes.

As a combination of the harsh climate conditions and the design rules at the time of constructions with limited concrete cover, the Remøy bridge today is at a state of rapid increasing deterioration. The slender design has few reserves with regards to bearing capacity.

The inspection by COWI concluded that Remøy bridge has extensive concrete damages mainly due to chloride driven corrosion and that the damages developed from last inspection. Photos from drone inspection was important when comparing to previous inspections and assessing the rate of deterioration. Also, the cathodic protection system does not function as intended anymore. Although a load capacity check shows sufficient bearing capacity on short term, the location and shape of cracks on the main beam indicate that they may have occurred due to high loading.



Figure 3. The Remøy bridge. (Photo: COWI AS).

The recommended strategy for Remøy bridge is controlled deterioration and the county need to invest in a new bridge within 5-15 years. The reason for this is both the high chloride content and rapid development of damages, but also the lacking robustness that is required to perform maintenance at the same time as it is traffic on the bridge.

On a side note, the bridge has a slightly longer twin bridge, the Nerlandsøy bridge, build at the same year where damages have yielded the need for a replacement, and a new bridge is under construction and opens to traffic in 2025. The total cost for the new Nerlandsøy bridge is estimated to 850 MNOK. The need for a high-bridge due to the Norwegian Coastal Authority sailing lead requirements is a key cost driver.

3.2 *The Runde Bridge (1982)*

The Runde Bridge from 1982 is a post-tensioned concrete box girder bridge, where the main span of 118 m is constructed as an extradosed cantilever girder. The bridge lands on a 1,2 km long mole, and the sea currents around the mole and pillars leads to heavy currents. The asset manager has informed that the snow plough runs over the bridge to remove seaweed after heavy storms.

The Runde Bridge is located in extremely harsh climate, facing the open Nordic Sea to the west. The severe chloride impact has led to increasing deterioration from concrete damages and corrosion. At the end of the 1990's the bridge was in need for a corrosion protection system, and early 2000 a Cathodic protection system was installed at bottom slab of the girder, as well as on most pillars.

The inspection conducted by COWI AS showed increasing deterioration, and a non-functioning CP-system that needs to be replaced on both pillars and underside of bridge-deck. Due to the robust design of the box girder, no damages with consequence for the short-term bearing capacity was identified. To reach this conclusion it was vital to investigate the state of non-visual parts as cast-in post-tensioned tendons. This inspection of PT-tendons was conducted as non-destructive testing (NDT) based on ultrasonic pulse combined with local inspection.

The single-lane traffic as well as heavy wind led to difficult and expensive inspection, and hence will lead to an even more difficult and expensive repair. Result show that, depending on strategy chosen, the Møre and Romsdal county will face an investment of between 30 MNOK and 80 MNOK to extent the service life.

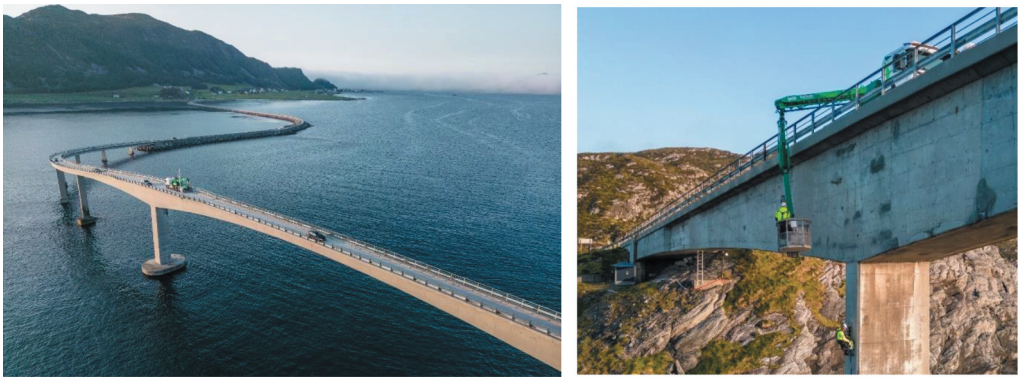


Figure 4. The Runde Bridge (Photo: COWI AS).

4 CHALLENGES AND OPPORTUNITIES

4.1 *Controlled deterioration*

When selecting a repair and rehabilitation strategy for a deteriorating structure – including a controlled deterioration strategy - the estimate of the remaining lifetime is often based on experience. To avoid serious bridge failures a conservative estimate must be used when predicting the remaining lifetime. Additionally, the effect on the extension of lifetime because of various repair and rehabilitation option is associated with some uncertainty due to the lack of an efficient tool to proper evaluate the effect. This uncertainty with respect to the remaining lifetime – and the effect of repair and rehabilitation options – means that there is a lack of information when determining the optimal bridge rehabilitation strategy, which may often lead to a non-optimal spending of budgets.

When a bridge such as the Remøy bridge undergoes a controlled deterioration strategy it is vital to have the required and updated information on the current deterioration of the bridge and an estimate on the development of deterioration – concrete, reinforcement, and

post-tensioning system. A controlled deterioration strategy is maintained by maintaining the load bearing capacity, so an updated load bearing capacity model and a trustworthy model of the current and future deterioration is vital. Only when having this, is it possible to evaluate the needs for actions from the current day and until a replacement bridge is in place. as well as consequences for on delaying the replacement on:

- Safety and robustness associated with the condition and load-bearing capacity
- Increased cost to inspection routines
- Increased costs associated with load-reducing measures
- Increased cost to acquiring knowledge to maintain safety (data collection, calculations)
- Socio-economic consequences (traffic regulations, closure time for inspections and maintenance work)

The actions required in this period may range from doing nothing, perform new inspections to update and validate the deterioration model, local strengthening projects, local repair projects to slow deterioration, reduction of allowable loads on the bridge and so forth.

4.2 *Virtual inspections*

As a pilot project initiated by Møre and Romsdal County, a Reality Capture Model was included in the inspection program for Remøy and Runde bridge. The Reality Capture 3D models and inspection software were delivered by the drone inspection specialist company Axess Digital AS. COWI AS contributed to the flight plan before data collection and conducted the virtual inspection reporting in the Axess Bridge software.

A Reality Capture Model offers a visual overview of the bridge and full documentation for future operation and maintenance activities. A Reality Capture Model is established from RGB images captured primarily with Unmanned Aerial Vehicles (UAVs) as drones etc.

In addition to the visual surface, thermal images are simultaneously captured. The drones follow a predefined flight path, approximately 15 m from the bridge structures. The flight path is dependent on weather conditions, drone capability (e.g., tight spaces which require a drone capable of bumping into the structure), light conditions, quality of sensors (cameras), and fix points for image reference. The imagery is captured with an overlap of approximately 70%, resulting in a highly detailed 3D mesh, which is then overlayed with images to create a visual digital twin. The models with adjacent RGB- and thermal images are then imported into commercial software for inspections. The platform allows the users to manually annotate defects and generate a report of annotations. An example is shown for Runde bridge in Figure 5.



Figure 5. Rundebru in axess inspection app with annotated defects and adjacent images.

The thermal imagery is used as a supplement to the RGB photos and can identify areas with temperature changes at the surface of the concrete e.g., delamination, certain cracks and joints, concrete repair, and water ingress which may not be visible on RGB photos.

Using UAVs leads to reduced traffic disturbance and a short time on site which overall reduce the initial cost e.g., truck mounted under bridge inspection units, rope access, lifts, etc. for visual inspections. The virtual inspection is a good starting point for special inspections, offering a visual overview of the entire bridge before collecting concrete cores or dust samples for further material analysis, manual inspection with hammer test using rope-access, etc. of a limited part of the bridge. It provides full documentation with less subjectivity compared to manual inspections on site.

4.3 *Cathodic protection rehabilitation*

The use of impressed current cathodic protection as part of rehabilitation strategies for the bridges in the coastal areas started in the late 1980′ties and early 1990′ies. At the Runde bridge an extensive cathodic protection system was installed in 2001/2002. Protection was applied to 6 of the 8 pillars and the entire bottom of the concrete box girder. For the pillars a carbon fibre-based anode mesh embedded in 3-5 mm cement mortar was installed on all external surfaces, whereas discrete drilled-in anodes (3 mm diameter TI-MMO rods) embedded in a graphite paste were installed in the bottom plate from the inside of the box girder. A modular rectifier and monitoring system was installed inside the box girder. Compared with traditional TI-MMO mesh embedded in sprayed concrete both anode types allowed for at faster and more effective installation as the mesh on the pillars was only covered with a thin (3-5 mm) mortar and all discrete anodes were installed from inside the box girder eliminating traffic nuisance and the need for scaffolding. In terms of the anode types used the installation was considered a pilot project as the performance was not well known.

After installation, operation and maintenance inspections were carried out at regular intervals to evaluate the performance of the system, and particularly the adopted anode systems. Over the first decade, it was observed that the current output from the carbon fibre mesh decrease significantly over the years, and it was reported that samples of the anode mesh collected from the structure showed signs of deterioration. Also, it was from observations suggested that the low current output was also a result of failing anode mesh connections. Also, the performance of the discrete drilled in anodes was observed to decrease over time. This was observed to be a result of drying out of the graphite paste causing both a high electrical resistivity and shrinkage reducing the contact to the concrete surrounding the anodes. From the inspection performed in 2023 it was concluded that the system no longer provided any protection that could be considered when evaluating the remaining service life of the bridge.

Approximately, at the time of installation of the system at Runde bridge, a cathodic protection system was also installed at the Remøy bridge nearby. Here cathodic protection was applied to all pillars and the bottom side of the bridge deck. Due to the slender design of the bridge an anode conductive paint was chosen as anode system in order not to increase the weight of the bridge. The conductive paint system was one of the first generations where silver wires were used as primary anodes/current distributors. A good performance of the anode system was observed over the first approximately 10 years. However, since then the performance in terms of the current output has decreased gradually due to mainly spalling of and cracks in the conductive paint as well as rupture of the primary anodes (silver wires). Similar to Runde bridge it was in 2023 concluded that the system no longer provided any protection that could be considered when evaluating the remaining service life of the bridge.

Despite the need for testing novel anode systems as well as other components for cathodic protection systems the experiences from Runde and Remøy bridge clearly demonstrate that proven technologies and materials should be used when applying cathodic protection to the many bridges at the Norwegian west coast. Not only are the bridges and thus cathodic protection systems exposed to the extremely harsh climate at the west coast meaning that the materials used should highly durable. But also, the costs of maintenance, repair and eventually replacement are high due to the often remote locations and harsh climate making construction work difficult.

Development within cathodic protection systems has during the recent years been focused on rectifier and monitoring systems with a trend going in the direction of automated cloud based systems. This allows for a better performance monitoring of the systems and optimised maintenance and repair.

When designing and planning future cathodic protection systems for these bridges it should be ensured that all embedded and difficult to access/replace components such as anode systems, reference- and monitoring electrodes, cables and wires have the longest service life possible. For traditional TI-MMO based anode systems this is often +50 years. Other components such as reference electrodes, wires and cable have a somewhat lower service life, typically not longer than 25 years. As a result of this the installations should be designed and installed allowing for easy replacement of all components expected to be replaced during the design service life of the cathodic protection system. To optimise performance monitoring and maintenance automated rectifier and monitoring systems with remote access or cloud solutions combined with data management should be considered for future installations. For these systems the service life is most often not defined by the service life of the electronics itself, but rather limitations in use, repair, and maintenance due to outdating. Thus, the risk of testing novel systems is limited compared with e.g. anode systems.

5 CONCLUSIONS

The bridge owner must rely on detailed knowledge about degradation rates and available repair methods to maintain their bridge portfolio in a sustainable manner. The challenges and need for future investment in bridge maintenance and inspections are illustrated by asset manager Møre and Romsdal County and the case studies of Remøy bridge and Runde bridge. These illustrate how chosen repair strategy requires advanced bridge inspection methods, including visual inspection with challenging access, data collection from material testing, as well as NDT-inspections of post-tensioned cables.

The case studies also serve as examples of different maintenance strategies based on the deterioration state, age and access. The Remøy bridge will rely on a strategy of Controlled Detoriation to maintain an acceptable Safety level. For the Runde Bridge the rehabilitation strategy is to extend service life by investment in new and modern cathodic protection systems. Both bridges show how the County face major investments, especially when related to annual average day traffic of the road network.

With the increasing volume of aging bridges, there is an urgent need to develop new technologies and methods for inspection of bridges. Drone-inspection enables efficient access to structures, with high resolution images and thermal camera/infrared technology to identify delamination and corrosion. These technologies are still evolving, and further research in these areas will be necessary.

REFERENCES

Bruaas T., 2019, Long term Performance of cathodic protection (CP) of marine bridge, inspection of Sortland bridge 27 year after CP installation, Mater Thesis NTNU.

Menon Economics, 2023, MENON-Publikasjon nr. 79/2023 Eksportmeldingen 2022 – Et årlig dypdykk i. Norges eksport, menon-eksportmeldingen-2023-med-fylkesvedlegg.pdf (nho.no)The Norwegian Road Association, 2022, FOU Program Better Bridge Maintenance 2017-2021, End-Report 21_09_22 SVV rapport 865 bruvedlikehold.pdf (unit.no)

Karlsson A., Boström E., Jilderda P., 2021, Post-tensioned concrete bridges, Inspection Manual, FoU program Better Bridge Maintenance 2017-2021. The Norwegian Road Association, Report no. 718, 2022

Bathen, L (2021): STAR Post-tensioning practice in Norway 1960-2021, bidrag til fiB WG 1.15 «Bulletin; Management of post-tensioned concrete bridges». Statens vegvesen notat MIME 20/31348-8.

Bathen, L (2021): STAR Post-tensioning practice in Norway 1960-2021, bidrag til fiB WG 1.15 «Bulletin; Management of post-tensioned concrete bridges». Statens vegvesen notat MIME 20/31348-8.

Bridge Maintenance, Safety, Management, Digitalization and Sustainability – Jensen, Frangopol & Schmidt (eds)
© 2024 The Author(s), ISBN 978-1-032-77040-6
Open Access: www.taylorfrancis.com, CC BY-NC-ND 4.0 license

Virtual supervision of the new Storstrøm Bridge: Status and potential with CVI

T. Norsk
COWI A/S, Kongens Lyngby, Denmark

ABSTRACT: The New Storstrøm Bridge, currently under construction, is comprised of 44 prefabricated girders manufactured onshore, which are then shipped and assembled with the pierheads offshore. Usually, all bridge constructions have a Principal inspection every six years, which also applies to this bridge. Unlike other construction projects the strategy for the New Storstrøm Bridge is to inspect and repair any minor initial defects on the elements before they are mounted offshore. For this strategy the COWI Virtual Inspection (CVI) routine is used. The CVI software facilitates Principal inspections using Reality Capture Models (RCM) and makes it possible to revisit the bridge structure without having to visit the structure on site.

This project, utilizing CVI benefits, supports the digitization of Principal Inspection procedures and the product (RCM model). In the long run, it can merge with the digital twin of the structure, serving as a baseline for future operational and maintenance procedures.

1 INTRODUCTION

The New Storstrøm bridge is a bridge under construction comprised of 44 prefabricated girders manufacture onshore, which are shipped and assembled with the pierheads offshore. On Figure 1 a visualization of the new Storstrøm Bridge is shown. The new Storstrøm Bridge will replace the old Storstrøm Bridge from 1937, which has served its design lifetime and has an outdated design. The New Storstrøm Bridge is part of the new rail line from Copenhagen to Germany, where the Femern Belt Tunnel between Denmark and Germany is currently under construction.

The bridge is approximately 4 km long with a span of approximately 70 m between pier heads and with an average clearance to sea at 26 m. It will be a two-lane bridge for vehicles together with a two-lane railway crossing that starts at Masnedø and connects with Orehoved on Falster, see Figure 1. This paper introduces the progress of the New Storstrøm bridge with CVI and the future possibilities introducing a digitalization tool.



Figure 1. Illustration of the new Storstrøms Bridge and alignment for the new and old version (from wwww.vd.dk).

DOI: 10.1201/9781003483755-346

The bridge is under construction and almost half of the girders have been cast and mounted offshore pr. December 2023, see Figure 2.



Figure 2. New Storstrøm bridge with indication of progress of project (from wwww.vd.dk).

The plan is that the project is complete by 2026 to be a part of the new route from Germany to Scandinavia through the finalization of the Fehrman project.

For creating the best possible departure of the bridge inspections are performed and repair strategies are formed on a very early stage a short time after casting and hardening of the girder elements. Instead of doing manual inspection it is planned to use the project as a Pilot project for a more digital approach, introducing COWI virtual inspection CVI.

2 COWI VIRTUAL INSPECTION

Usually, inspection of major bridges is performed from a permanent inspection platform, by boat or using rope access. This provides several challenges regarding traffic access and working conditions, dependency on weather, high initial cost (lifts etc.) and difficult conditions for onsite documentation. Furthermore, manual inspection is very time consuming when dealing with major structures and with any uncertainty of the inspection, the inspection worker would be required to go on site again, resulting in lost time and higher expenses.

Using drones to take high-quality RGB photogrammetry supplemented with thermal imagery of the structure a Reality Capture Model (RCM) can be generated for the purpose of inspecting the structure from a computer instead of on site.

The RGB-images are processed in commercial Bentley software to establish the RCM model.

The captured pixels ranged from 1.2 to 7.8 mm. The drones follow a predefined flight path, approximately 15 m away from the bridge girder structure. The flight path is dependent on weather conditions, drone capability (e.g., tight spaces), light conditions, quality of sensors (cameras), fix points for image reference, etc., which requires domain knowledge within reality capture.

By generating a high-quality RCM, the construction only needs to be visited once with drones and afterwards the RCM can be utilized via computer and inspected by multiple people if needed.

CVI is the software platform, where the RCM models can be review and notes can be tagged to individual locations in the model.

CVI brings significant flexibility to the project for both inspection workers and the quality assurance process, allowing the digital model to be examined in the office.

CVI is a part of the ongoing digital transformation for Operation and Maintenance (O&M) that the industry is undergoing at the moment.

2.1 *Benefits from using CVI on the Storstrøm Bridge*

To heighten the quality of the Storstrøm bridge it was decided that CVI would be used in the early stages of the construction of the bridge. See the following list for the overall benefits of using CVI for the Storstrøm bridge:

- Due to the size of the project, it is optimal to be able to inspect the construction from a computer (allowing several specialists to analyse the bridge without visiting site)
- Each individual girder is split into its own RCM model, which allows for a detailed analysis for each girder separately.When the bridge is completed, all these individual models will be collected into at single model of the whole bridge.
- A benefit with CVI on the Storstrøm bridge compared to other major bridges is that it is under construction, so the drone flying has no challenges regarding traffic or pedestrians.
- Possibility to visit the bridge as many times as needed without having to visit site.
- Easy access for visual inspections on areas that might be difficult or impossible to visit on site.
- Overview of photographic data of each element on the bridge stored and easy accessibility for this data through a RCM model.

2.2 *Disadvantage from using CVI on the Storstrøm Bridge*

The disadvantages with using CVI on the bridge is listed below:

- Slightly more expensive to initialise the process of doing the virtual inspection as well as being labour intensive (highly trained personnel is needed to capture photos and generating RCM models)
- There is a certain time window to do the virtual inspection, otherwise the bridge girder elements are shipped offshore. This would result in additional cost to perform the virtual capture and if needed the actual repairs to possible defects identified on the elements. However, due to the speed of the girder construction onshore and the girders being shipped onshore, it has been necessary to do the drone inspection offshore as well. Using current technology, the drone inspection has been able to be done from onshore and has therefore not resulted in additional inspection costs.

3 CVI ON THE NEW STORSTRØM BRIDGE

It was decided that the New Storstrøm bridge is part of a pilot project for usage of CVI on major bridges in Denmark. The first RCM model of the Storstrøm bridge was conducted in early 2023. An external company was hired in to perform drone inspections on the bridge, preferably while the girder elements are still located on land after casting. Here both RGB image and thermal capture is performed from the drones, which is later handed over to COWI to be used in CVI as RCM models.

From the RCM models it is fast and easy to inspect each girder. Additionally, the model allows for quality check of the reported defects from other experienced inspection engineers. It is observed that after casting of the prefabricated girders some minor errors such as honeycombing, cracks (with or without deposit) or delamination is present.

The identified defects are subsequently mapped within CVI, enabling the generation of a report and later an appropriate repair strategy can be created.

Since it is a pilot project, the inclusion of extra inspections after casting, along with the subsequent repair strategy and the actual repair of elements, is still being integrated into the inherent workflow of the Storstrøm Bridge construction. However, as of now, it has not become a seamless part of the natural workflow.

Incorporating the routine into the workflow during the initial phase is expected to result in cost and time savings over the lifespan of the structure. Addressing repairs in the early stages can help prevent more extensive repairs that might become necessary later, ultimately averting structural failure.

3.1 *Example from CVI – Bridge girder G13S*

Girder G13S is used as an example from the Storstrøm Bridge project. From Figure 3 a snapshot is seen from the software including listing of the different noted defects in the structure. A colour table is used for different condition rating, from 1 (least severe defects) to 5 (more severe defects):

- Green for least defect severity of 1
- Yellow for severity of 2
- Orange for defect severity of 3
- Light red for defect severity of 4
- Red for worst defect severity of 5
- Blue for unknown severity or to highlight a query to the supervision team.

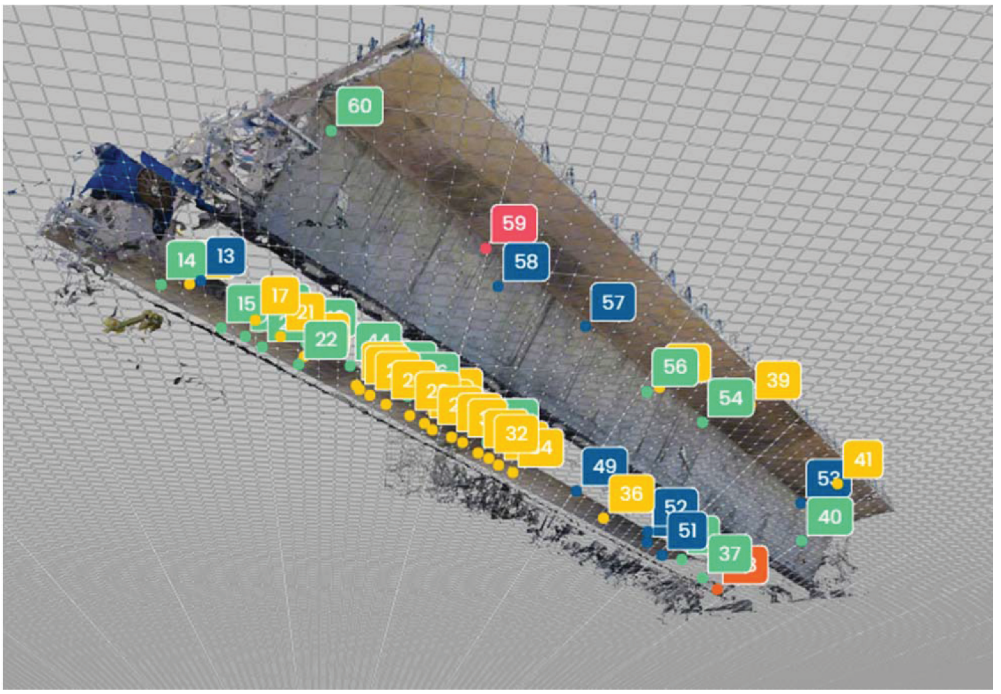


Figure 3. Snapshot of girder G13S from CVI representing recorded defects.

In this example some minor defects are found and placed in CVI with varying severity. Many of the defects are of similar nature, one example is that cracks are forming on the wings of the structure with a cross-sectional direction. From Figure 4 an example can be seen of

a cross-sectional crack on the wing of the girder G13S, which is flagged in CVI with a defects severity of 2.

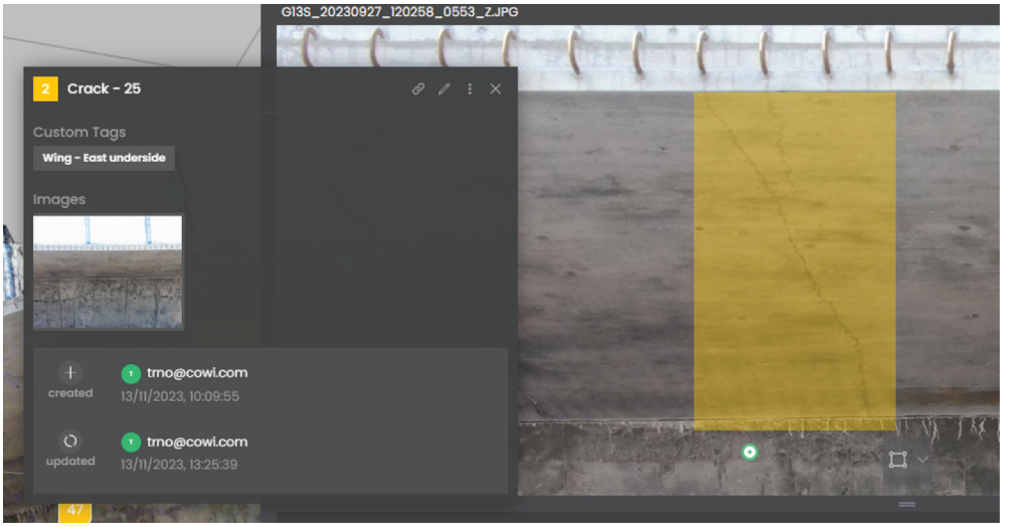


Figure 4. Snapshot of crack from G13S on the Eastern wing underside.

The whole RCM model, seen on Figure 3, consist of lots of individual high-quality photos merged together to a 3D model, which is packed into a manageable model. The registration of defects is done on photos and not in the overall RCM model. A photo used for a registration is seen on Figure 4. The RCM model for this girder consist of approximately 2000 high-quality photos (RBG and thermographic).

All registered "defects" are not defects in the common understanding. In this approach "defects" refer to minor initial defects that needs to be repaired before handover of the bridge to the bridge owner – and – it refers to "defects" which are discolouring, cracks planned during construction, minor casting defects that do not require repair og remediation. However, for future drone based inspections, this is vital knowledge. This means that all "defects" have been treated during construction and they do not need to be reevaluated during future inspections.

3.2 *Reparation strategy*

After conducting a virtual inspection on a single girder, a report can be created and exported using CVI to showcase defects in a preferred format, such as arranging them from most severe defects to least severe defect or organizing them based on their specific locations. This report can work as a presentation of the virtual inspection that has been perform and a repair strategy can be discussed with the contractor. The RCM model itself can also serve as a tool to identify and discuss individual defects during a live meeting with the contractor.

3.3 *Corporation with the contractor*

The utilization of RCM models facilitates smoother collaboration between the contractor and consultant. The digital model serves as an excellent navigation tool, eliminating the need to locate defects on-site. Moreover, the ability to navigate through a model within minutes contrasts with the hours required on foot, addressing accessibility concerns. It is easier to pinpoint exactly where the defect is from the RCM models and prepare the repair strategy with the contractor.

3.4 *Status on the use of CVI on the Storstrøm Bridge*

As of November 2023 a total 20 girders have been virtually captured and uploaded to the CVI software. Several of these have been through the first round of checking.

4 FUTURE USE OF CVI

There are several opportunities to further develop CVI, as listed below:

1. Developing the automatization part of the program using AI image recognition to limit the need of personnel to quality assure the results. This is not in the pipeline for this project, but is under development – and expected to be used later on and before handover of the bridge
2. Combining the RCM model part of CVI with the digital twin of the structural model together with structure defects registrations to have a more developed BIM model for future requirements from clients.

4.1 *Possibility with automated AI image recognition of defects*

CVI represents a significant advancement in more intelligent methods of digitizing work performed during inspections, traditionally conducted by field personnel. Taking the next step towards smarter inspection methods involves incorporating AI for the detection of structural defects seen through CVI. Currently, the process of defect recognition through AI is still in progress, but there is potential to achieve fully automated inspection through the integration of CVI and automated AI defect recognition, which might be possible in the next couple of years. This would have to be quality assured by comparing a traditional inspection through CVI with an AI inspection.

In the grander scheme, the integration of CVI and AI reflects a strategic move towards a future where infrastructure inspections are seamlessly fused with state-of-the-art technologies, paving the way for safer, more efficient, and technologically advanced projects in the realm of structural assessment and maintenance and mitigating human mistakes.

4.2 *Using the RCM model for advanced BIM models*

Introducing the reality capture model into a digital twin would allow for the next generation of BIM models and could benefit the operation and maintenance process of a construction lifetime. Even the development of a structures defect could be captured automatically comparing RCM models from different moments in time and a repair strategy could be developed and executed on the right time. This would be beneficial for economy optimization, structural safety and green transition (optimising when to repair).

5 OPERATIONAL BIM

In modern day a lot of focus is on operational BIM and digital twins. With CVI a huge step is taken towards the first point of operational BIM, but with a bit more development the two can be combined, such that the images and notes in CVI could be combined with a real BIM model.

It is not exactly known where the future of BIM is heading and what format will be the main format, but it is certain that more information will be required in models. For operational BIM there is not captured any information on operation and maintenance in complex BIM models. This could be a future aspect of the CVI tool to incorporate defect and note tagged RCM model into digital twins of the real structure.

6 CONCLUSION

Incorporating CVI into the building process of the Storstrøm bridge seems like an advantageous way to create lots of data for the bridge on the concretes initial condition. It also serves as a way of quickly identifying problematic areas to be repaired, such that the bridge can have a departure without initial concrete defects. Collaboration with the contractor using CVI as a tool to present and discuss defects works smoothly.

The integration of the Reality Capture Model within the principal inspection regime improves workflow, ensure full documentation, and supports finding the 'optimal point in time' to repair and replace structural elements considering multiple Key Performance Indicators for bridge owners and operators.


Taylor & Francis
Taylor & Francis Group
http://taylorandfrancis.com

SS31: O&M of major bridges

Organizers: R. Percy & J.L. Jensen


Taylor & Francis
Taylor & Francis Group
http://taylorandfrancis.com

Bridge Maintenance, Safety, Management, Digitalization and Sustainability – Jensen, Frangopol & Schmidt (eds)
© 2024 The Author(s), ISBN 978-1-032-77040-6
Open Access: www.taylorfrancis.com, CC BY-NC-ND 4.0 license

Sustainability monitoring of cable systems

J. Laigaard Jensen, J.F. Melén & I.F. Alcover
COWI A/S, Kongens Lyngby, Denmark

ABSTRACT: Corrosion is a major threat to the sustainability of cable bridge systems. Corrosion is probably the largest threat to exceedances of bridge owner's maintenance budgets just as corrosion is a persistent threat to the sustainability of the cable-borne bridges. Many years of experiences with different generations of cable systems shows that water ingress is a problem both with respect to main cables, suspenders and cable stay lower anchorages. As the cable system as such is a primary non redundant part of the structural system, such durability issues may be costly to mitigate and may reduce the sustainability of the bridge as a whole. In order to handle proactively such threats, the paper presents cases and discusses the pros and cons of different monitoring approaches. Monitoring in this context may be inspection, testing or continuous automatic monitoring. Based on hand-on experiences, the paper reviews different monitoring approaches.

1 INTRODUCTION

1.1 *The corrosion challenge of cable borne bridges*

The world assets of medium-sized and large bridges comprise a large population of cable borne bridges which provide important infrastructure links. Hence, to keep the infrastructure fully functional, the integrity of these bridges must be maintained. The cable systems of the bridges are non-redundant and are thus a critical structural system to maintain. As the bridges are generally large and expensive assets, their integrity is also an important element of the sustainability of the infrastructure both with respect to environment and socio-economic costs.

Although cable vibrations are often considered as a major problem of cable systems, experiences show that, from an operation and maintenance point of view, the threat of corrosion is a problem of at least the same magnitude if the economic consequences are considered, Laigaard et al. (2012). Corrosion is triggered by the combination of water and oxygen accelerating further if impacted by chlorides from e.g. road de-icing salts. As gravity generally controls water ingress, water ingress and corrosion are generally a problem related to lower anchorages of cables.

Records of experiences show that corrosion of cable systems on many occasions have caused the need for replacement or large rehabilitation works on the entire cable systems, e.g. Andersen (1999), Bloomstine & Zinck (2016), Laigaard et al (2016). With the focus on cable stays and suspension bridge suspenders, this paper will highlight some important cases and describe the causes, the monitoring, and the handling of cable corrosion problems. The challenges of water ingress and corrosion in cables are described generally in e.g. Laigaard et al. (2017).

2 SCENARIO WITH LACK OF SUSTAINBILITY

2.1 *Sustainability of cable-borne bridges*

Cable borne bridges have been used for major crossings for far more than hundred years. Figure 1 shows an approximate overview of the age distribution of existing cable borne

DOI: 10.1201/9781003483755-347

bridges. The two plots show that about 60% of all cable borne bridges are more than 20 years old and about 40% of the bridges were inaugurated from 1960 to 2000. Hence, in the future there will no doubt be a significant need for monitoring and maintaining the corrosion exposed cable systems. As an illustration, it may be recalled that the use of steel ropes goes back to about 1830 and the first bridge to use galvanized wires was Brooklyn Bridge opened in 1883 However, the use of black steel has continued well into the 20th century and corrosion protection may not yet have reached a stage of perfection.

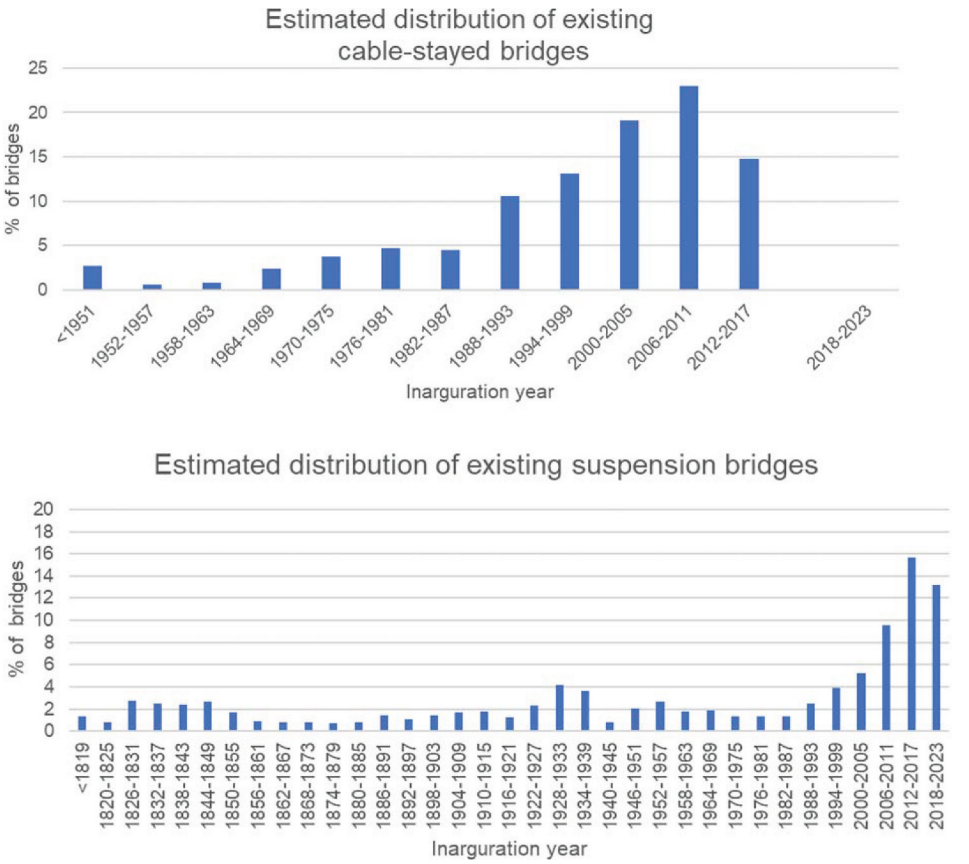


Figure 1. Age distribution of suspension bridges and cable stay bridges based on data from https://structurae.net/en/structures/bridges (November 2023).

The service life of the cable systems of such bridges may be subjected to discussion. However, for a modern bridge hardly any manufacturer or designer warrants a cable service life of more than 100-120 years, which often will be the formally stated service life of the bridge.

Based on experiences from the last two decades, a cautious estimate of cable service life could be suggested to be around 60 years even when new bridges are being designed. The cautiousness in giving service life estimates is somewhat illustrated by the fact that modern bridges are designed with replaceable cables to allow for replacement before the end of the service life of the bridges themselves. Hence, the suggested 60 years' service life for a cable system is somehow not up to date with the novel sustainability agenda. Based on the above-mentioned age distribution, it may therefore be concluded that today's owners and consultants are looking into a major challenge regarding extending an ambition of a 60 years' service life to a much longer service life. Here it should be noted that due to the nature of corrosion, the handling of this challenge is an urgent problem. This is illustrated in Figure 2, which

shows that, in some cases, corrosion of a cable stay may develop quire rapidly over only 6 years. Hence, it is evident that there is need for detecting and monitoring corrosion in cable system in due time before complete replacement is required.

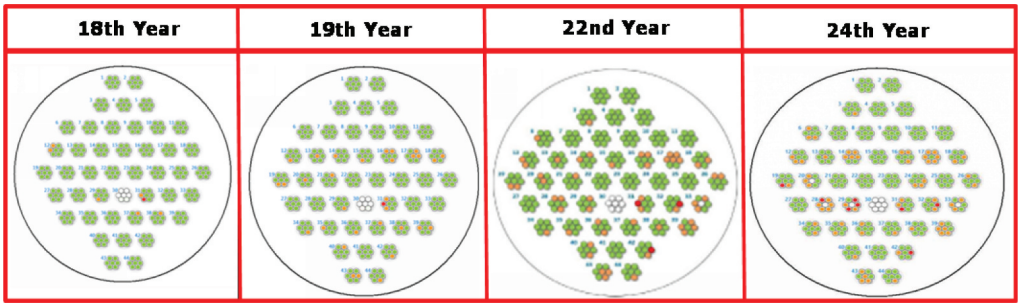


Figure 2. Example: development of corrosion in parallel strand cable anchorage based on ultrasound testing. green: uncorroded; orange: corrode; red: broken (Laigaard. et al. 2022).

The scenario outlined stresses the need for monitoring strategies of the cable condition allowing for:

- A systematic and persistent approach on monitoring the condition of cable stays and suspenders to maintain and prolong their service life as much as possible.
- Sufficient early detection of irreversible corrosion degradation to allow for replacement of cables one by one without costly and time-consuming temporary strengthening arrangements. Such arrangements will be needed when many cables have reached a severe corrosion degradation at the same time.

2.2 *Monitoring of corrosion condition*

Corrosion monitoring of the condition of cables will be the main topic in the following sections which will consider the following categories of monitoring:

- Visual inspection (manual or by endoscopy, photogrammetry, infrared techniques)
- Non-Destructive-Testing (ultra-sound, magnetic flux techniques, chemical analysis of water samples)
- Destructive Testing (inspection, metallurgy assessment and tensile testing)
- Permanent automatic continuous monitoring (vibration, acoustic emission)

The challenges of monitoring the corrosion condition will depend on the cable system, which for modern bridges may comprise the following cable systems, Gimsing & Georgakis (2013):

- Spiral strands – predominant used in sixties and seventies.
- Fully locked coil – predominant used in fifties, sixties, and seventies.
- Grouted parallel wires – predominant used in sixties, seventies, and eighties.
- Parallel seven wire strands - predominant used from mid-nineties.

2.3 *Examples of corrosion cases*

There are numerous reports on cases with cable corrosion for the four types of cables described above and there are good reasons to assume that several existing bridges are being operated and maintained without awareness of an on-going risk of water ingress and corrosion. This is understandable as it is difficult to inspect and document corrosion problems in cable systems before the problems have become serious and detectable by visual inspection. Unfortunately, this often means that problems often have grown into a size making them costly to mitigate. In some very unfortunate, but few cases, the difficult detection may even result in having severe bridge failures.

Table 1 shows several selected examples of cases which have led to significant costs with need for cable replacements, traffic restrictions/closure and unwarned cable failures. Many of these older generation bridges have had a significant shorter service life than the above suggested 60 years' service life of modern bridges. Figure 3 shows examples of cable failures after only 16-19 years of service life.

Table 1. Overview of bridges with records of corrosion problems in cable systems. S: Suspension Bridge; CS: Cable stay bridge.*) Approximate year of awareness of corrosion issue.

Bridge	Bridge type	Year	Cable type	Year of corrosion detected	Mitigation
A.L. McDonnald Bridge	S	1955	Spiral strands	**2015-2017**	Replacement
Strömsund Bridge (S)	CS	1956	Locked coil	2014	Replacement
Maracaiobo Bridge (Ven)	S	1962	Locked coil	1974-78	100% Replacement
Kravik Fjord Bridge (N)	S	1963	Locked coil	1982-2016*)	Inspection and maintenance program
Älvsborg Bridge (S)	S	1967	Locked coil	2007*)	Replacement
Morandi Bridge (I)	CS	1967	Tendons inconcrete.	2016*)	No mitigation – failed.
Pierre La Porte Bridge (CAN)	S	1970	Spiral ropes	2015	Inspection and replacement program
Erskine Bridge (UK)	CS	1971	Spiral strands	2018*)	Planning of dehumidification.
Kohlbrand Bridge (D)	CS	1974	Locked coil	1976	100% Replacement
Zarate-Brazo Bridge (Arg)	S	1977	Parallel wires	1996	50% Replacement
Tjörn Bridge (S)	CS	1982	Locked coil	2010-2013	25%v Replacement
Luling Bridge (USA)	CS	1983	Parallel wires	1983-1985	PE repair
Pont de Normandie (F)	CS	1995	Parallel Strands	2011	Program for testing, monitoring and replacement.
Uddevalla Bridge (S)	CS	2000	Parallel strands	2000-2011*)	Monitoring

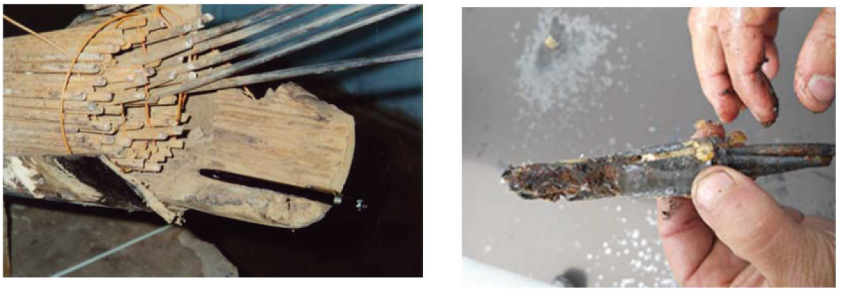


Figure 3. Examples of cable failures: left: 19-year-old parallel wires in grout of suspender. right: 16-year-old modern parallel strand.

3 VISUAL INSPECTION

3.1 *Visual inspection*

Visual inspection will rarely be able to detect corrosion in cables due to very limited access for inspecting the most exposed part of the cable wire (Figure 4). Most visual positive detections of

corrosion will not occur before irreversible corrosion damages have taken place. Only in cases where lower anchorage systems are quite open and easily accessible, it will be possible to detect corrosion. However, in some cases with parallel strand systems, it may be an option with a jack to extract a cable strand to inspect the anchored position for signs of corrosion. Hence, the primary objective of visual inspection is mainly pro-active maintenance of sealings, drainage and other elements in the multi-level protection systems of cable systems. Figure 5 illustrates examples of such inspection objectives. For the free lengths of cable systems, visual inspection may be efficient in detecting defects in paint, cable tubes and embedment in cement/grout. For such cases, visual inspection may be assisted by use of infra-red cameras equipped on drones or robots.

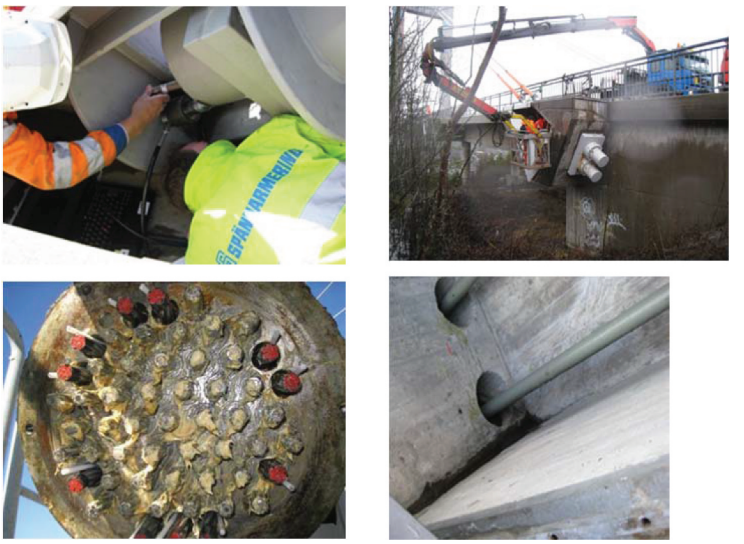


Figure 4. Access condition will rarely allow direct visual contact to the anchorage point in the lower anchorage which is most exposed to corrosion. left: parallel strand anchorage. right: locked coil anchorage.



Figure 5. Visual inspection of drainage, sealings and barriers against water ingress may considered as primary objective of visual inspection. left: parallel strand anchorage. right: locked coil anchorage.

4 TESTING

4.1 *Non-destructive testing*

Non-destructive test methods relevant for cable stays and suspenders for detecting corrosion may be summarized to comprise:

- Testing of coatings and grout by a Schmidth hammer or similar may provide insight in signatures of cavities of defects in the coatings and grout.
- Magnetic flux induction may be relevant in the cases where there may be a corrosion risk along the free length of the cable. This will be the case where parallel wires are embedded in a grout or cement solid. Having said this, the severe corrosion risk could often still end up being on odd locations not suitable for using magnetic flux method.
- Ultrasound may be applied as a very efficient tool for assessment of corrosion and wire ruptures of parallel wire strands. Figure 6 shows an example of the use of ultrasonic testing for a cable stay bridge. The reliability of ultrasound may be as high as 80% for detection of strands with broken wires, (Laigaard et al. (2022).



Figure 6. Ultra-sound testing applied on parallel strand system at lower anchorage.

4.2 *Destructive testing*

Destructive testing of cables may be carried out to obtain an in-depth understanding of the actual corrosion and possibly provide a basis for calibrating NDT methods. This may involve on-site testing as well as dismantling of cable elements with subsequent testing in laboratory. One often activity will be to do tensile testing of corroded cable segments to assess their capacity. Figure 7 shows an example with subtraction of cable strands from a bridge with subsequent tensile testing and calibration with ultrasonic testing carried out on bridge. This case

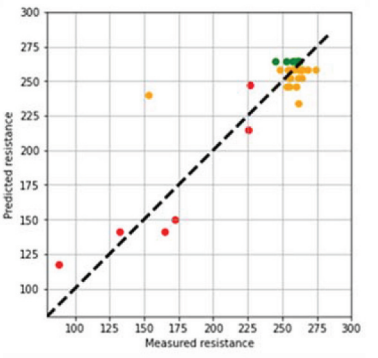


Figure 7. Results of tensile testing of segments of parallel strands with subsequent calibration with the ultrasound testing carried out on bridge Laigaard et al. (2022).

resulted in an increased reliability of the ultrasonic testing carried out and estimation of tensile resistances of strands/stays based on the results of periodic ultrasonic tests.

5 MONITORING

Monitoring methods may comprise a range of options with somewhat different objectives:

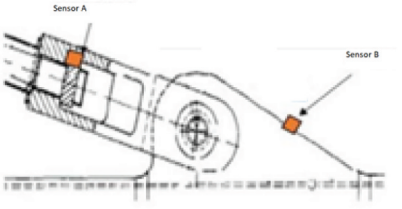
- Use of corrosion cable strand dummies in anchorages to provide early warning of corrosion. Periodic inspection of such dummies may reveal early signs of corrosion. This may provide early warnings of corrosion in a cable system. The only limitation is that the cable anchorage system design needs to have space allowing the use of dummies subjected to the same exposure as the installed cables Laigaard et al. (2017).
- Measurement of moisture due to water ingress or condensation. Some cable systems, which may be difficult to visually inspect, may still allow the detection of moisture by use of sensors having spacings and cavities as part of their lower anchorage design. This may allow continuous monitoring of moisture and thus assessment of the corrosion risk and the effect of different mitigations Parodi et al. (2024)
- Periodic chemical assessment of water tapped from the anchorage can provide indication of on-going corrosion and thus raise the need for further assessment. However, this may also only provide a somewhat late indication of corrosion as a significant amount of corrosion indicators have to be present in the tapped water.
- Vibration testing may be used to observe changes in natural frequencies. However, this will almost always only provide a very late detectable indication of corrosion.
- Acoustic emission by sensor measuring the dynamic impact response induced by the failure of individual wires. If signal noise from normal loading in the cable system can be removed by signal processing, the method can provide information about the occurrence of individual wire ruptures by measuring the sound wave propagation due to energy release caused by wire rupture. However, the method is only of interest as an alarm system for bridges, which already have a severe corrosion problem in the cable system.



a) Use of cable dummies



c) Tapping of water for chemical analysis.



b) Acoustic monitoring of cable anchorage for detection of wire ruptures.

Figure 8. a) Use of cable dummy for monitoring of corrosion, b) acoustic monitoring as mean for detecting wire or strand failure, c) water tapping for chemical testing for traces of corrosion from cable wires.

6 CONCLUSION

The existing population of cable borne bridges shows that there is a significant challenge regarding corrosion monitoring of the cable systems. The cable system of many of the existing bridges can be expected to have a service life which will be significantly shorter than the bridges themselves. This both will cause a burden regarding sustainability, costs of operation and maintenance and may also cause reduction of the infrastructure capacity over significant periods of time.

For this challenge, there should be a focus on developing corrosion monitoring of cables further. Firstly, for making pro-active maintenance to extend the service life beyond the current state-of-the-art ambition, which this paper has suggested to be of the order of 60 years. Secondly, further development of corrosion monitoring will also be of great significance in postponing the time of replacement by prudent mitigation actions. Any extension of service life will support the need for a more sustainable bridge infrastructure.

For meeting these challenges, the paper points to a need for further development of corrosion monitoring for the cable systems using the concepts of: Inspection, Testing and Monitoring as shown in Figure 9. The corrosion monitoring of cable systems is far from a simple task. No method alone is sufficient to monitor the condition of a cable system. However, the paper shows that different tools together may form the basis for developing corrosion monitoring of cable systems further with the aim of providing pro-active maintenance in due time and extend service lives further and obtaining control when weaknesses have caused severe corrosion problems.

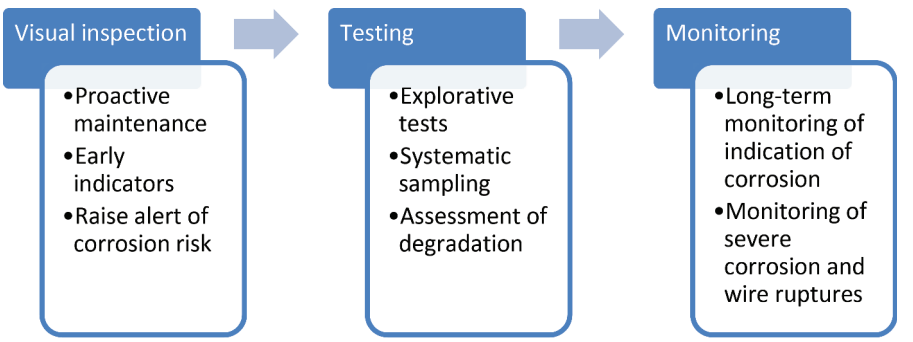


Figure 9. Framework for a systematic development of corrosion monitoring of cable systems.

REFERENCES

Andersen, E. 1999. Emergency Rehabilitation of the Zárate-Brazo Largo Bridges, Argentina. Proceedings of IABSE Conference. Malmö.

Bloomstine, M.L., Zinc, M. 2016. Strömsund Cable-Stayed Bridge – Cable Corrosion and Replacement, Proceedings of ISCBOC. Halifax.

Gimsing, N.J. and Georgakis, C.T. 2013. Cable Supported Bridges, Concept and Design, 3rd ed. Wiley.

Laigaard, J, Sørensen & O, Bitsch, N. 2012. Maintenance of bridge cable systems. Proceedings of IABMAS. Italy: Balkema.

Laigaard, J., Skoglund, M., Darholm, T., Maglica. 2016. A. Replacement of Corroded Cable Stays on Tjörn Bridge. Proceedings of IABSE Conference, Stockholm:.

Laigaard, J., Farreras-Alcover, I., Joye, S. & Laguerre, L. 2022, Data mining corrosion and failure in cable stays, Proceedings of IABMAS Barcelona: Balkema.

Laigaard, J., Lambertsen, J., Zinck, M. & Stefansson, E., 2017. Challenges with Water Ingress in Bridge Cable Systems. Journal of Steel Construction vol. 10 (2017) no. 3. Berlin: Ernst & Sohn Verlag.

Parodi, A., Laigaard, J., Steffanson, E. & Melen, J.M. 2024: Moisture monitoring in cable anchorages before and after dehumidification. Proceedings of IABMAS. Copenhagen: Balkema.

Bridge Maintenance, Safety, Management, Digitalization and Sustainability – Jensen, Frangopol & Schmidt (eds)
© 2024 The Author(s), ISBN 978-1-032-77040-6
Open Access: www.taylorfrancis.com, CC BY-NC-ND 4.0 license

Tjörn bridge O&M challenges and mitigation

J. Laigaard Jensen, A. Larsen, A.H. Langager, S. Ussing & J.F. Melén
COWI A/S, Kongens Lyngby, Denmark

A. Maglica
Trafikverket, Jönköping, Sweden

ABSTRACT: This paper presents a summary of the service life of The Tjörn Bridge. The focus is highlighting deviations of the expected maintenance, replacements, and upgrades from the expected service life of the bridge. The objective is to identify the bridge components and operational conditions, which often may be deviating from the expected planned service life in connection with the design of a bridge. The Tjörn Bridge being a 366 m span cable stay bridge from 1981 has reached an age where maintenance tasks have started to increase. Some tasks, such as general degradation of paint, pavement, joints etc., have been in line with expectations, whereas other have been unexpected and thus called for mitigation. The Tjörn Bridge was constructed over a record short duration of 18 months as it replaced the old bridge which collapsed due to a ship collision.

1 INTRODUCTION

1.1 *The service life of Tjörn Bridge*

This paper describes the service life of the Tjörn bridge and significant events and decisions in the service life from 1981 until today (2023) to investigate how the actual life of the bridge may deviate from what was planned and expected when the bridge was decided and carried out.

The Tjörn Bridge, shown in Figure 1, is located 50 km North of Göteborg in Sweden in a temperate climate, Kahmann (1982). Figure 1 shows that the bridge is 645 m long with a main span of 366 m. Cable stays are painted locked coil cables of 46 m to 160 m lengths with diameters ranging from 77 mm to 108 mm arranged in pairs. The bridge forms the major fixed connection between the island of Tjörn and the mainland via the two islands Almön and Källön. The bridge was opened in 1981 after only 18 months of construction, as it replaced an arch bridge, which collapsed on 18th January 1980 due to a ship collision with the loss of 8 lives. On January 31, 1980, a new bridge was decided. Tender was carried out and on June 19, 1980, a contractor was chosen, and the bridge was opened for traffic November 9, 1981, where design, procurement and construction had been finalized. The winning tender had the 3rd lowest price but with the fastest execution time, which was decisive for the selection.

1.2 *Bridge design, construction and operation*

The Tjörn Bridge, being 42-year-old, gaps over at least two generations of owners, contractors and consultants and it is therefore very relevant to ask how the bridge's service life turned out compared to the original intentions and expectations regarding operation and maintenance of the bridge.

Looking into the service life of bridge components and the operation and maintenance carried out, it may provide some insights into how the actual service life turned out. It may reveal if the bridge, after decades of operations, have met expectation when they were planned, tendered, and the bridge commissioned. Of course, this could be considered as a somewhat

DOI: 10.1201/9781003483755-348

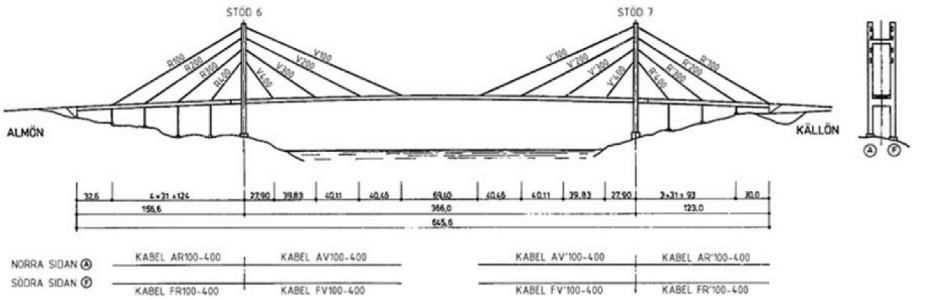


Figure 1. Overview of the Tjörn Bridge.

academic question, as the involved professionals rarely will be the same persons after several decades have passed. However, it may still be interesting to pursue the answers to the question, as there could perhaps be room for improvements in the way we plan, design, construct, commission, operate and maintain bridges.

When bridges are designed, the service life and level of required maintenance are directly or implicitly considered with expectation on:

- The service life and level of required maintenance considered both for individual bridge components and for the bridge. In modern terms this is accomplished through service life design but has in the past been carried out through use of proven concepts and materials although there have been periods where new concepts and materials have been introduced with unintended consequences. As simple and well-known examples the use of new concrete mix recipes (e.g. alkali chisel), new cable stay system and post tensioning system (corrosion due to water ingress), reinforced concrete exposed to deicing salts (insufficient concrete cover), could be mentioned.
- Construction quality which per experience often is challenged in tenders exposed to e.g. tough price competition and accelerated project time schedules or unclear tender requirements. Once a weakness is introduced in the phase of design and construction, it is a well-known experience that this weakness will trend to follow the bridge over long period of time with a potential significant impact on inspection, maintenance, service life and overall, its sustainability. In addition, it may in some cases happen that bridges suffer from lacking maintenance attention due to lack of organization, funding or simply just manpower.

Considering the owners, their consultants, and contractors in many ways control the life of the bridge throughout its service life, there are good reasons to look back and see if we can learn something or if there has been circumstances out of our control when the bridge has ended up in another way than anticipated when the bridge was decided. However, before looking at what may have deviated from expectation, it may be necessary to start with what was likely to be expected from the service life of a bridge like Tjörn Bridge.

2 THE EXPECTED SERVICE LIFE OF TJÖRN BRIDGE

There is no knowledge of anybody who can describe the expectations to the service life of the Tjörn Bridge when it was designed and constructed, Brodin (1984, Kahmann & Koger (1982). Instead, we have referred to more than forty years old written descriptions and design calculations. It was designed during an era before the concept of service life design, life cycle cost and sustainability were on the agenda and basically, we can only look back and evaluate what we think would be the expected service life of the design and the applied materials.

Based on today's standards, the bridge would have been required to have a service life of at least 120 years in accordance with SS-EN 1992-1-1. Prior to the development of Eurocode there was a more informal expectation that bridges should last at least 100 years. Table 1

shows what we with today's insight would expect to be the service life of the different main components of a new bridge. The irreplaceable elements would be expected to have a service life of minimum 100 years. From the descriptions of the bridge design and construction, the state-of-the-art durability precautions were part of the design, and it was designed to last a considerable number of years. However, no explicit durability design was carried out with a holistic view both with respect to interaction among bridge components and the life cycle from design, construction to operation.

It may be noted that the definition of service life does not consider the development of inadequate functionality due to changes operational needs compared to the intentions in the applied design. Examples could for instance be a change of configuration of road lanes, a need for larger bearing capacity, noise screens etc.

Table 1. Expected service life of bridge main components.

Selected main components	Overall service life	Maintenance
Concrete piers and pylon	120	Not replaceable
Concrete girder	120	Not replaceable
Orthotropic deck	120	Not replaceable
Cable system	60	Replaceable
Bearings	50	Replaceable
Expansion Joints	30	Replaceable
Edge beam	80	Replaceable
Pavement	25	Replaceable
Deck membrane	60	Replaceable
Barriers	40	Replaceable
Railings	40	Replaceable
Lift	20	Replaceable
Gantry	20	Replaceable

3 THE ACTUAL SERVICE LIFE OF TJÖRN BRIDGE

Overall, it may be anticipated that all bridges have components which last unexpectedly short but nevertheless it is interesting to study the reasons for why the service life became shorter, which in our case is demonstrated for the Tjörn Bridge. Subsequently this may be brought further by benchmarking of group of bridges. Hence, the achieved service life of main bridge components to now, can be compared with expected service and the reasons for unforeseen short service lives can be scrutinized to identify the roles of design deficits, lack of construction quality or maintenance carried out or changes in the operation of the bridge.

Table 2 shows actual service life experiences until 2023 based on listing of recorded maintenance carried out on the bridge from 1982. The table shows the achieved service life for bridge main components with identification of components with unexpectedly short service life. By color identification the maintenance of components is marked with the group of bridge components it belongs to.

The table indicates that the following types of components may at some point of the more than 40 years' service life have experienced an unexpected shorter service life:

- Parts of the concrete
- Components of cable system
- Orthotropic deck welds
- Structural Monitoring System installed due to need for wind assessment for planning of a reconfiguration of deck cross section (new barriers and jump prevention parapets).

In the following, reasons explaining the achieved service life of these four bridge components will be investigated.

Table 2. Overview of maintenance history from 1982 to 2023. Maintenance data from Swedish Transport Administration (Trafikverket). Comment on service life: "Expected" and "Unexpected" compared to design expectations.

Color legend:

Concrete:
Steel:
Cable:
Electrical:
Drainage:
Pavement:
Articulation:
Ground:

Year	Main bridge components maintenance	Achieved Life	Comment on service life
1995	Edge beam, concrete repair	13	Unexpected
1995	Edge beam railing concrete repair	13	Unexpected
1998	Pavement replacement	16	Unexpected
2001	Edge beam railing concrete repair	19	Expected
2001	Cross bream injection	19	Unexpected
2003	Drainage channel cleaning	21	Expected
2003	Cable damper replacement	21	Expected
2003	Cable repaint	21	Expected
2005	Cable anchorage, change	23	Unexpected
2005	Electrical switchboard upgrade	23	Expected
2005	Inspection hatch upgrade	23	Expected
2005	Ventilation adjustment	23	Expected
2006	Water sealing	24	Expected
2006	Cross bream concrete repair	24	Expected
2006	Cross beam sealing	24	Expected
2006	Piers concrete repairs	24	Expected
2006	Piers concrete sealing	24	Expected
2006	Bearing plinth concrete repair	24	Expected
2010	Expansion joint replacement	28	Expected
2010	Railing repaint/replacement	28	Expected
2010	Pavement maintenance/replacement	28	Expected
2010	Steel edge beam repaint	28	Expected
2010	Concrete edge beam sealing	28	Expected
2010	Bearing Plinth concrete repair	28	Expected
2010	Bearing Plinth sealing	28	Expected
2010	Erosion protection abutment	28	Expected
2011	Inspection gantry overhaul	29	Expected
2011	Cable anchorages cleaning	29	Unexpected
2013	Cable anchorage watertightness&access	31	Unexpected
2015	Cable, concrete repair	33	Expected
2016	Cable replacement	34	Unexpected
2019	Cable replacement	37	Unexpected
2019	Inspection update, ladders	37	Expected
2020	Cable replacement	38	Unexpected
2020	Rope anchorages pylon top	38	Expected
2020	Electrical update/lightning protection	38	Expected
2020	Inspection update hatches	38	Expected
2020	Water tightness cover	38	Expected
2020	Hatch/door correction	38	Expected
2021	Tie down cable paint	39	Expected
2021	Structural monitoring system	New	Unexpected
2022	Inspection gantry overhaul	40	Expected
2023	Cable replacement	41	Unexpected
2023	Welding repairs deck	41	Unexpected

4 CASES OF EXPERIENCED SHORT SERVICE LIFES

4.1 *Repair of concrete edge beam*

Although the repair of concrete appears somewhat early with a service life of 14 years, it may not have been a complete surprise that the edge beams of the bridge was the most vulnerable component needing repair due to the use of de-icing salts. The applied concrete mix and a concrete cover may very likely have been state-of-the-art at the time in 1981. However, it appears reasonable to assume that the eighties (the time where the bridge was designed and constructed) had significant less focus on durability than in the following decades, where considerably more attention was given to concrete recipes and choice of concrete cover, Johansson & Johansson (2007). Hence it is considered that the current state-of-the-art with improvements in design over time have resulted in considerably more durable edge beams than obtained in 1981.

4.2 *Replacement cables stays after 35 years.*

Table 3 shows that cable stays of the bridge have been replaced in a program running since 2015. As indicated in Figure 2, the reason was that through inspections it was found that the lower anchorages of the cables in the approach spans over a longer period appeared to have been exposed to water due to lack of sealing against water as well as blocked drainages. The corrosion led in 2013 to the rupture of some wires in two of the lock coiled cables with wires, which were protected by hot dipped galvanized wires and a paint coat on the cable. The short service life of 34 years compared to an expected service life of at least 50 years may be attributed to:

- Lack of designed access to the lower anchorage is likely to have made it difficult to carry out inspection and maintenance.
- Lack of drainage caused by construction tolerances not providing sufficient room for drainage in some anchorages.

The corrosion of the cables was mitigated by improved access to lower anchorages, 1:1 replacement of cables but with extruded HDPE sheeting instead of paint and with improved water drainage. In addition, safety of the bridge during the replacement program was ensured by a safety assessment of the bridge with corroded cables. In total these mitigation works can be considered one of the largest costs in maintenance carried out so far. The details of replacement of the cables are described in Table 3 (Jensen et al. 2016). The cables of the approach spans were given highest priority as they were the most critical ones regarding the bridge global integrity.

Table 3. Overview of cable replacements on Tjörn Bridge.

Year	Number of cables	Position
2015	2	Eastern approach span
2019	14	Eastern approach span
2021	16	Western approach span
2024	8	Main span
To be planned	24	Main span

4.3 *Repairs of orthotropic steel deck structure*

Some fatigue cracks were identified after 38 years of services, which is quite early considering that the overall service life of the deck would be expected to be at least 100 years. In 2018 the results of a load capacity assessment showed insufficient fatigue capacity of the orthotropic steel deck (12 mm deck plate with 24 6 mm throughs spanning 4 m). This initiated the execution of an inspection program, which in total until 2023 have led to the identification of four cracks:

- Two cracks in welds in mouse holes between cross girder and through no. 14 and 15 at diaphragm no. 27. These cracks are small and kept under observation.



Figure 2. Condition of lower cable anchorage in 2013.

- One potential Crack at a stiffener against the deck plate at diaphragm no, 32 - 33. The crack could probably be attributed to inadequate welding and has been repaired.
- One crack in the bottom of the through no. 9 between diaphragm no. 90 and 91. The crack may have its origin from the construction and had been repaired.

The causes for the cracks have been evaluated to be due to quality issues from construction with several locations with the poor welding quality not meeting nowadays standards. These observations combined with the results of the fatigue evaluation of the bridge means that there are some concerns for occurrence of fatigue cracks in the future. At the same time, it may be noticed that traffic has increased from approximate 12200 (1980) to 19210 Average Daily Traffic (ADT) (2019), which also will contribute in detrimental way. Hence these concerns have been addressed through a continued inspection and repair program. For now, the extent of the mitigation program is moderate but over time there will be a risk of further development of cracks.

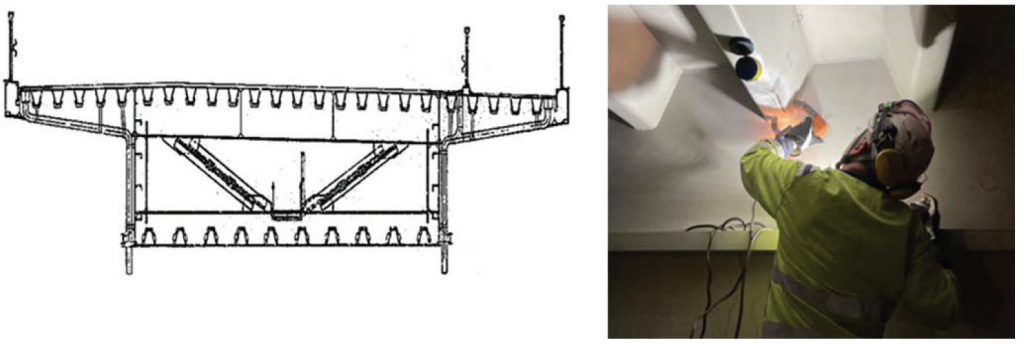


Figure 3. Left: Deck cross section. Right: Repair of crack at through-diaphragm interface.

4.4 *Wind assessment by structural monitoring system (SHMS), numerical calculations and wind tunnel testing*

In 2020, it was decided to carry out a wind investigation with the objective of assessing the wind response of the bridge deck ahead of an upgrade of the bridge. This service life activity may not be considered as a maintenance activity as such but rather an operation assessment and upgrade of the bridge. The assessment comprised the installation of a structural monitoring system as well as a detailed study of wind performance of the deck through a finite element calculation, aerodynamic simulations and wind tunnel testing. There were two reasons for the assessment carried out:

- Investigation of the overall aerodynamic properties of the deck as a basis for planning a future reconfiguration of the bridge railings (barriers, suicide prevention fences) including road lane division. For the original and a future configuration of the bridge deck, assessment of aerodynamic performance of the bridge was carried out by simulation of the aerodynamic

stability by COWI in-house software DWMFLOW and finite element modal analysis with subsequent verification through wind tunnel testing. The investigation was supplemented by results from SHMS, among other damping estimates. The latter confirmed the observed vortex shedding with 169 mm amplitudes and 3.6% log. Dec damping at winds of 13 m/s. The investigation was supplemented by results from SHM, among other damping estimates. The results of the assessment have shown a reconfiguration of deck cross section is indeed feasible and may even improve the aerodynamic performance of the bridge.

- In addition, the assessment has served as a clarification of the concern of occurrence deck vibrations raised by traffic and maintenance personnel. The deck vibrations are identified as vortex-induced oscillations which occur at certain wind conditions with wind roughly perpendicular to the bridge with 10-minute average wind speeds of 12.5 m/s and 14.5 m/s with frequency of occurrence of 0 to 7 days per year. These observations match well the predicted wind speed for vortex induced oscillations in the bridges first order vertical bending mode from wind tunnel test. Results from installed structural monitoring system verified the frequency and magnitude of these deck vibrations (Figure 4) and is used to continuously evaluate the need for any mitigation. The SHMS has now a permanent purpose in observing the wind response of the bridge to support the safe operation of the bridge. Currently the SHMS is a stand-alone system but in the longer perspective, the owner pursues a strategy on having such systems on several major large cable borne bridges in Sweden to support the operation of the bridges.

The need for this wind assessment with installation of SHMS was of course never foreseen when the bridge was planned and designed. Overall, the wind assessment may be said to have been triggered by the fact that:

- Traffic has increased from approximate 12200 (1980) to 19210 ADT (2019) which may have led to less tolerances for perceived insecurity through e.g. occurrences of large deck vibrations.
- In society, there has been a development of a non-acceptance towards the occurrence of suicides with jumps from bridges over time.
- Pylons have through capacity assessment turned out to be sensitive the loss of a cable stay combined with development of heavy traffic has led to higher requirements to traffic barriers.

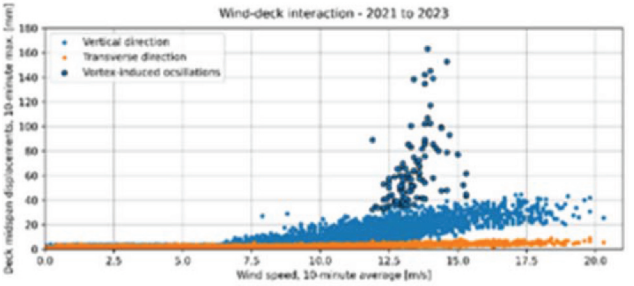


Figure 4. Wind induced vertical deck displacement at midspan (2021-2023). Arrow marks vortex shedding incidences.

5 DISCUSSION & CONCLUSION

With Tjörn Bridge as an example, the paper has compared the actual service life from the bridge inauguration in 1981 with what was expected when the bridge was planned, designed and constructed. The bridge was as an replacement established over only 18 months, and overall it may be concluded that the bridge has performed very much in line with the service life expectations except for a few durability challenges due to weaknesses in the design and construction quality and some changes in the operational conditions of the bridge.

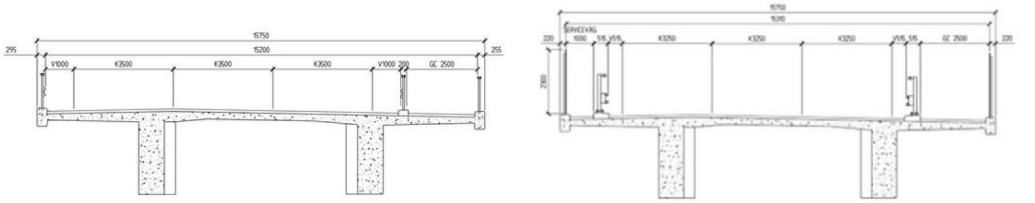


Figure 5. Left: Existing deck cross section. Right: Investigated future deck cross section.

5.1 *Durability challenges*

The bridge has overall performed quite well except for the problems with corrosion of cable stays. The durability challenges have overall been quite conventional with the somewhat early needed repairs of the concrete edge beams probably as the most unexpected. Nevertheless, the corrosion of the cable stays has been a significant cost in the service life of the bridge. The reason for this may be attributed to weaknesses in the design concept, which also has been experienced on other bridges with similar cable systems e.g. Saul & Humpf (2007). This design weakness has combined with deficits in construction quality led to failure in obtaining the intended drainage in the lower cable anchorages and thus resulted in the severe corrosion problem. The problem has been mitigated by a replacement program for all cable stays.

5.2 *Operational challenges*

Changes in operations have also challenged the operation and maintenance of the bridge in two ways:

- Increased traffic loads compared to design assumptions, have due to some deviations in quality of deck welding resulted in some fatigue cracks in the orthotropic steel deck. These challenges are now handled by an inspection program and follow-up repairs.
- More dense traffic has also had operational consequences on the bridge deck. Firstly, a larger focus from society on the need for parapets preventing people from jumping from the bridge triggered the need for an aerodynamic assessment (incl. installation of a SMS) of a deck reconfiguration with a jump prevention parapet. Secondly, pylons vulnerable to loss a cable stay combined with heavier traffic has pointed to a need for upgrade of the road barriers together with a reconfiguration of the deck cross section. Thirdly, it may be noticed that over there the years has been a development on attention on driving conditions being influenced by wind, which also has been addressed by the installation of a structural monitoring system.

5.3 *How to handle the unexpected service life*

The above isolated deviation from the expected service life may not easily be handled. However, it underlines the need for focusing on establishing a sound basis for the design and construction of a bridge, where focus should not only be on complying with standards but also on robustness and risks in the operation and maintenance phase of the service life of the bridge.

REFERENCES

Brodin, S. 1984. Tjörnbron. Stockholm: Vägverket, Västra Aros. ISBN 91-7810-123-9.

Jensen, J.L., Skoglund, M. & Maglica, A. 2016. Safe replacement of Cable Stays on Tjörn. Bridge. IABSE Conference 2016.

Kahmann, R. & Koger, E. 1982. Die Neue Tjörnbrücke – Konstruktion, Statik und Montage der Stahlkonstruktion. Springer-Verlag. Bauingenieur (1982), pp 379–388.

Saul.S. & Humpf, K. 2007. Inspection, Maintenance and Replacement of Stay Cables Munich.: Munich Bridge Assessment Conference, MBAC 2007.

Johansson, T. & Johansson, D. 2007. Lund: Betongtäckskiktets inverkan på sprickinducerad corrosion. University of Lund.

Bridge Maintenance, Safety, Management, Digitalization and Sustainability – Jensen, Frangopol & Schmidt (eds)
© 2024 The Author(s), ISBN 978-1-032-77040-6
Open Access: www.taylorfrancis.com, CC BY-NC-ND 4.0 license

Moisture monitoring in cable anchorages before and after dehumidification

A. Parodi, J.Laigaard Jensen, E. Stefansson, H. Sønderby & J.F. Melén
COWI A/S, Kongens Lyngby, Denmark

A. Maglica
Trafikverket, Jönköping, Sweden

ABSTRACT: Water presence in lower cable anchorages has been a long-term challenge on the Uddevalla Bridge in Sweden, as on several other cable-stayed bridges. To find an ultimate solution to the possible corrosion development, a moisture monitoring system has been installed in two selected anchorages. Over 1½ year, the system has provided the base of data required for tracking the formation of condensation, the mechanisms of water ingress and the efficiency of the drainage ways. All the above has also been assessed in relation to different interventions carried out on the anchorages. The monitoring system is currently used to evaluate the effectiveness of a prototype dehumidification system, designed to ensure an internal relative humidity below 40%, which will eliminate the risk of corrosion development. A potential way forward is to develop the moisture monitoring system into a digital twin, enabling to extrapolate the moisture assessment to all anchorages of the bridge.

1 INTRODUCTION

Lower cable anchorages of cable-stayed bridges are often subject to the challenge of water ingress during the service life, which implies a significant risk of corrosion for the cable strands. For Uddevalla Bridge (Sweden – see Figure 1), water ingress has been a long-term challenge and although several preventive measures have been adopted, the problem remains and the concern regarding corrosion has not been resolved (Laigaard et al, 2017).

Since the discovery of water in the lower cable anchorages already in 2000 – year of inauguration – the bridge owner Trafikverket (Swedish Transport Administration) has followed the conditions of the cables closely. After more than 20 years of operation, it was decided to investigate in detail the issue and its causes, with the aim of finding an ultimate solution. In order to carry out a continuous investigation throughout different seasons and environmental conditions, it was therefore decided to design and install a moisture monitoring system.

COWI has procured and installed the monitoring equipment (May 2022) and performed the subsequent data processing and interpretation. The system has been installed on two anchorages – specifically identified as 101V and 115V – selected as representative of all other anchorages (see Figure 1).

The recorded data have been processed and analyzed to monitor the parameters directly related with moisture throughout the different seasons, with special focus on mapping the causes behind the presence of water. This includes an effort in differentiating the moisture generated by air condensation from the moisture associated with rain ingress, as well as checking the watertightness of the anchorage casings, tracking the water flows, and validating the efficiency of the drainage ways.

DOI: 10.1201/9781003483755-349



Figure 1. Photos of the Uddevalla Bridge, one of the monitored anchorages (101V) and one of the Leaf Wetness Sensors on the cable wires.

The information gathered by data analysis has been used to design and calibrate a prototype dehumidification system, installed on the two monitored anchorages at the end of May 2023. After the installation, the data obtained from the monitoring system acquired the additional objective of evaluating the dehumidification system effectiveness, before possibly extending its installation to all stay anchorages of the bridge.

The following sections present in detail the hardware and setup of the monitoring system, the approaches for data analysis and interpretation, the main results, and the conclusions – along with the potential way-forward.

2 MONITORING SETUP

The monitoring system has been procured, installed on site, and programmed for data acquisition and communication by COWI. The layout of the system is described in the following. Table 1 and Figure 2 should be referred to, for details regarding hardware and sensor positions.

The monitoring system features air temperature sensors, relative humidity (RH) sensors, surface temperature sensors and Leaf Wetness Sensors (LWS).

The air temperature and RH sensors have been installed on the inside of the protection pipe of the anchorages, with the aim of identifying the air conditions in the anchorages and to provide the basis for calculating the dew point in the condensation assessment (see section 4).

The surface temperature sensors have been installed on the wire surface, on the protection pipe surface (both internal and external) and on the DAU cabinet (hidden from solar radiation, for correlation with the surface temperature measured on the anchorage), with the aim of providing a full overview of the surface temperatures and, consequently, of the formation of condensation.

LWS are normally used in agriculture for monitoring wetness conditions in greenhouses and are designed to mimic the thermodynamic and radiative properties of real plant leaves. In that context, the LWS data are normally meant to be interpreted binarily – i.e., as "dry" or "wet" – as in the standard agricultural application there is no need for quantitative wetness data proportional to the amount of water on the sensor. For this reason, deploying LWS to monitor moisture and water flow in stay anchorages was initially considered experimental, without any ambition of capturing anything more precise than a simple binary indication on presence/absence of water. Nevertheless, as shown in the following sections, it has been proved that LWS data can be highly more informative than expected, and that data trends can be used to differentiate the wetness due to condensation from the wetness due to water flow – see section 5.

The LWS have been installed at strategic positions (on the wires, on the surface of the protection pipe and in the base pipe) to track the water flow paths. Special solutions have been

adopted to make sure that the water flowing on a surface instrumented with a LWS would not "skip" the sensor's surface – e.g., by applying silicon to guide the water flow onto the sensor surface, as shown in Figure 1. At each anchorage, one of the LWS (LWS4) has been installed outside on the DAU cabinet, which is exposed to rain, to serve as a rain sensor.

Table 1. Details of the monitoring hardware.

Item	Supplier	Model	Quantity
Air temperature and humidity sensor	Campbell Scientific	HYGROVUE5	1
Surface temperature sensor	Campbell Scientific	CS241 PT1000	4
Leaf Wetness Sensor	Campbell Scientific	LWS DECAGON	4
Data Acquisition Unit	Campbell Scientific	CR1000X	1

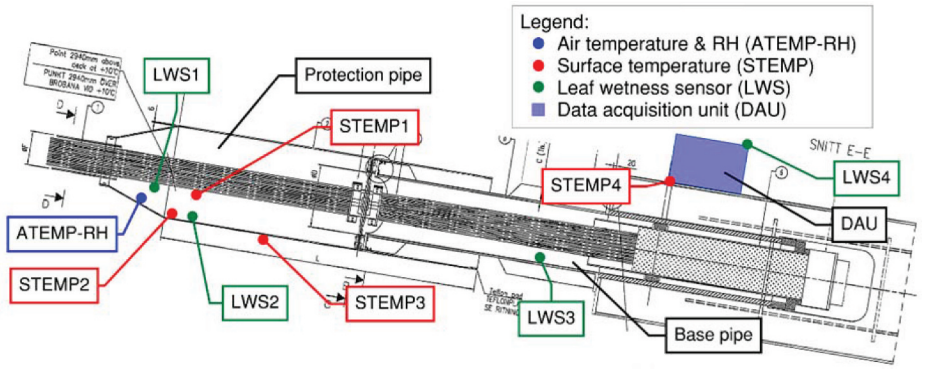


Figure 2. Layout of the monitoring system, identical in the two monitored anchorages 101V and 115V.

3 DATA PROCESSING AND VALIDATION

The data obtained from all sensors have been analyzed to understand, to the extent possible, the behavior of humidity and temperature conditions in the monitored anchorages, while keeping into account the execution of interventions and the geometrical differences between the two anchorages.

As an example, extracts of air temperature, air relative humidity (RH) and surface temperature data are shown in Figure 3 to Figure 5.

Figure 3 shows a noticeable difference both in air temperature and RH during the warmest hours of the day, especially in summer, between the two anchorages. It has been interpreted that this phenomenon is related to the different size and inclination of the two anchorages. Specifically, the air inside of anchorage 101V – smaller and more inclined – is more efficiently heated and dried than in anchorage 115V, especially under more intense solar radiation during summer days.

The analysis of the surface temperature sensors has provided information on how the different surfaces (of wires, protection pipe and base pipe) are subject to temperature variations with a timing consistent with their position. As an example, Figure 4 shows how the outer surface of the protection pipe in anchorage 101V is heated earlier and more efficiently during the first sunny hours of the day, while the internal surface, as well as the wires, are heated with a delay of several hours. In general, the temperature of all anchorage and wire surfaces show – at different times of the day – higher peaks compared to the data from surface temperature sensors on the DAU cabinet hidden from sun radiation. This highlights that the sun radiation has a significant impact also on the distribution of the surface temperatures, in addition to the effect on air temperature and RH as mentioned above.

The measured data have also been used to test the effects of different interventions on the anchorages. As an example, Figure 5 shows an extract of the wetness data from LWS2 (installed on the internal surface of the protection pipe). On December 21st, 2022, the gaiter sealing at the top of the protection pipe (see example in Figure 8) was removed from anchorage 101V. Given that LWS2 would normally provide values around 170 mV when dry, it appears evident that the removal of the gaiter sealing has caused an increase in the recorded wetness peaks during all the following rainy periods.

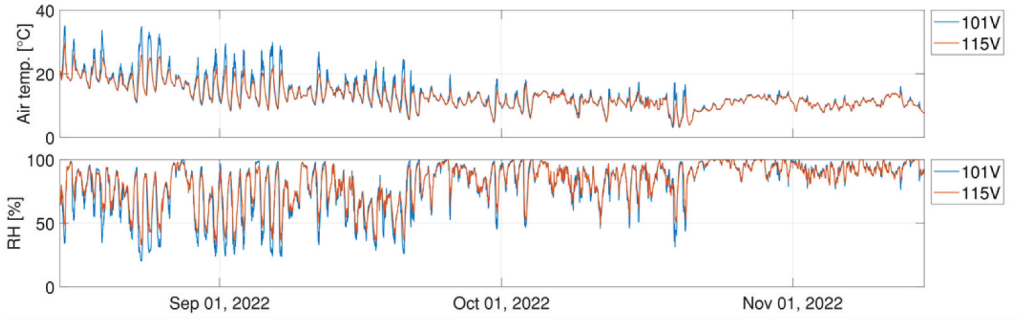


Figure 3. Time series of air temperature and RH in both anchorages.

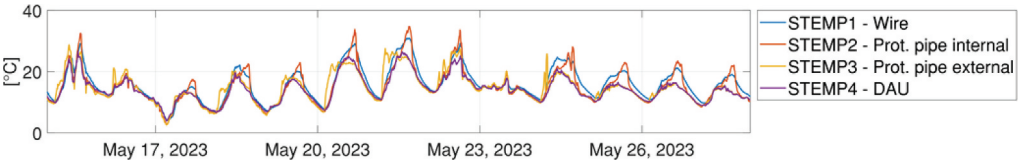


Figure 4. Time series of surface temperature data in 101V.

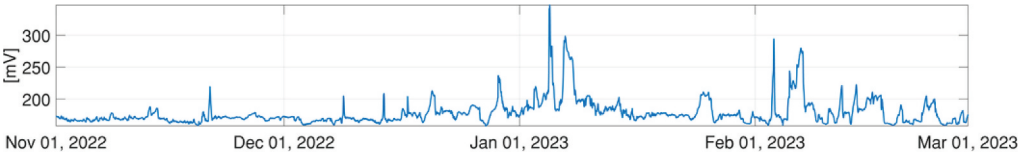


Figure 5. Time series of wetness measured by LWS2 (on protection pipe internal surface) in 101V.

4 CONDENSATION ASSESSMENT

Air temperature, RH and surface temperature data have been used as basis to track the situations in which the conditions triggering the formation of condensation would be met on the different surfaces of the anchorages.

More in detail, the air temperature and RH data have been used to calculate the dew point of the air enclosed in the anchorages. The dew point is defined as the temperature below which air must be cooled to become saturated with water vapor (RH≥100%), assuming constant air pressure and water content. Hence, if a surface has a temperature below the dew point, the air will condensate when it gets in contact with this surface. The measured surface temperature data have therefore been used to assess when condensation can form on the instrumented surfaces.

An example of the outcome of this assessment is shown in Figure 6, where the difference between surface temperature and dew point is plotted. Values below zero identify situations where the conditions for condensation are met. The data are extracted from a period in which an

airtight bellow sealing had been installed between protection pipe and base pipe of 115V (January 2023 – see example in Figure 8), but before the installation of the dehumidification system (May 2023). This means that the air conditions inside 115V were sealed and isolated from outdoor conditions, which caused a significant increase of RH in the anchorage and, consequently, a more intense formation of condensation compared to 101V – as evident from Figure 6.

The results of the condensation assessment obtained throughout time have been summarized by calculating the percentage of time per month with formation of condensation on the internal surfaces of the anchorages. The outcome is shown in Figure 7. As expected, the formation of condensation becomes more intense during the winter months, due to higher RH and lower temperatures. These summary results have also been useful in identifying the effects of the interventions carried out on the anchorages, e.g., the above-mentioned installation of a bellow sealing on 115V before the installation of the dehumidification system, which implied a big gap in the formation of condensation between the two anchorages starting from January 2023.

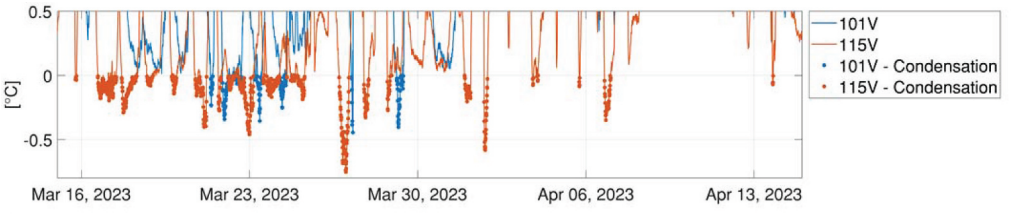


Figure 6. Time series of difference between surface temperature and dew point, based on measurements by STEMP2. Negative values correspond to formation of condensation.

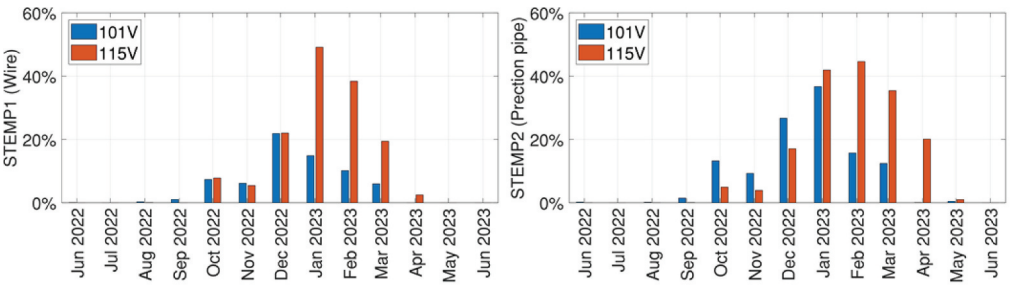


Figure 7. Monthly summary of percentage of time with condensation on wire and protection pipe surfaces.



Figure 8. Sealing gaiter and bellow in anchorage 101V.

5 WATER INGRESS ASSESSMENT

The data recorded with the LWS have been used as basis to assess the magnitude of the water ingress issue during rain. As anticipated in section 2, although LWS were initially expected to provide purely binary information (i.e., sensor "dry"/"wet"), LWS data have proven to be significantly more informative if the focus is on the wetness trends in time (see Figure 9). Firstly, it has been possible to identify the formation of condensation as a slow and gradual increase of wetness that can be developing through several hours. On the other hand, the start of water flow has been associated with sudden "jumps" in the wetness readings. It shall be noted that, given the nature of the wetness measurements, it is only possible to identify when the water flow starts – i.e., when a jump in the data is produced – but not the duration of the water flow. This is because the wetness produced by a water flow after its initiation is affected by the continuity of the rain, it can be easily confused with the wetness produced by condensation, and the drying time can be heavily affected by the air humidity.

As part of the water ingress assessment, all data recorded during the monitoring period have been analyzed to seek sudden jumps in the wetness data due to the start of water flow on the different surfaces instrumented with LWS. The results have been summarized in a similar fashion to what was done for the condensation assessment (see section 4), by calculating the percentage of time during which water flow is initiated during rainy days. The results are shown in Figure 10. For clarity, as the data are available with a frequency of 10 minutes, the above-mentioned percentage has been calculated as the ratio between the number of 10-minute intervals with a jump in wetness and the number of 10-min intervals in which the readings from LWS4 (installed outside of the anchorage and serving as a rain sensor) are above a certain threshold, i.e. when the sensor is wet due to rain.

LWS2 (installed on the surface of the protection pipe) is the sensor recording the highest rate of water flow. Given the position of LWS2 at the top of the protection pipe of both anchorages, this water flow is considered directly produced by rain ingress from the top of the protection pipe. Anchorage 115V appears to be the most sensitive anchorage to rain ingress.

LWS3 (in the base pipe) records a higher water flow rate than LWS1 (on the wires), which has come as a surprise when interpreting the data. As a matter of fact, the water flow recorded by LWS3 would be expected to be equal to or less than the water flow recorded at LWS1, since the main – and possibly only – path enabling rain leakage into the protection pipe to reach the base pipe should be through the wire surface. An explanation for why this expectation has not been met may be that the water flow recorded by LWS3 is not caused by the rain ingress at the top of the protection pipe, but by the condensation formed on all anchorage surfaces and then flowing down into the base pipe. This mechanism is more evident in 101V than in 115V, which is due to the different size of the two anchorages. Specifically, the drops of condensation formed on the protection pipe or wires of 101V need to flow for a shorter distance before dripping into the base pipe. To conclude, it is considered that only a minor portion – if not negligible – of the water flow recorded in the base pipe is directly produced by rain ingress at the top of the protection pipe.

The effects on rain ingress associated with different interventions on the anchorages have also been assessed. For example, it has already been described in section 3 how the removal of the sealing gaiter at the top of the protection pipe of 101V in the end of December 2022 has caused an increase in the water flow rate in the following months – which can also be noticed in Figure 10.

A significant increase in water flow rate is also noticed from January 2023 in 115V. This is most likely related to the installation of the bellow sealing between base pipe and protection

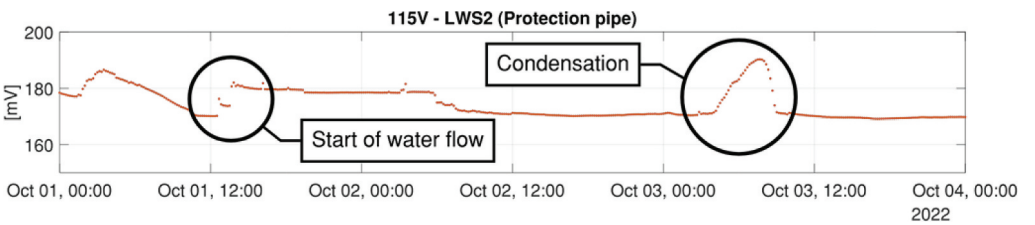


Figure 9. Example of wetness readings associated with start of water flow and with condensation.

pipe at the end of December 2022, which has triggered a very intense formation of condensation – as described in section 4. It is highly plausible that such an intense formation of condensation eventually produces a notable water flow.

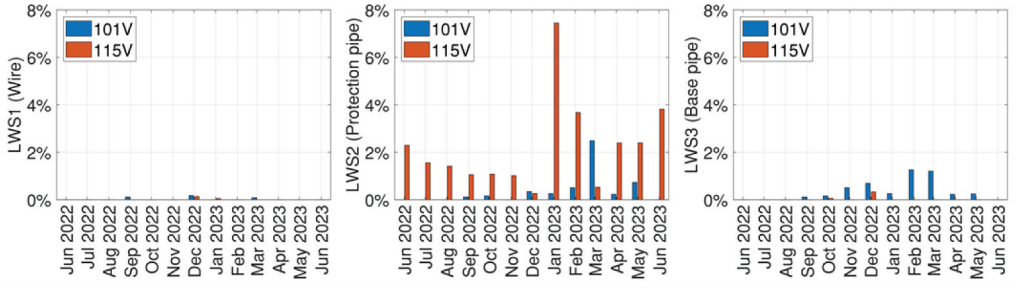


Figure 10. Summary of percentage of time in which water flow is initiated during each month.

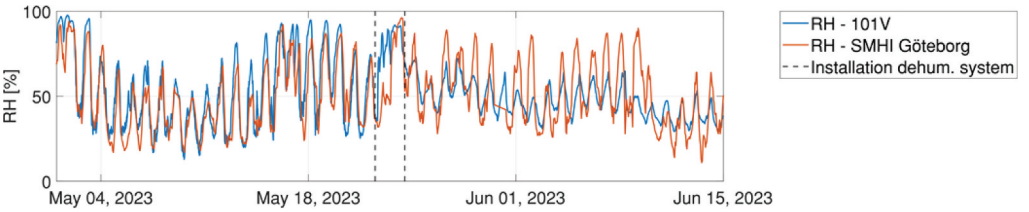


Figure 11. RH data from 101V and from the SMHI weather station at Gothenburg.

6 EVALUATION OF PROTOTYPE DEHUMIDIFICATION SYSTEM PERFORMANCE

In order to mitigate the issue of the water presence in the lower cable anchorages, Trafikverket has decided to install and test a prototype dehumidification system in each of the two monitored anchorages. The monitoring system has therefore acquired the additional objective of validating the efficiency of the dehumidification system before it is possibly extended to dehumidify all anchorages of the Uddevalla bridge.

This process is currently ongoing, and the dehumidification system is being calibrated to achieve the desired air conditions inside of the anchorages, namely a relative humidity below 40%, which is expected to eliminate the formation of condensation and to facilitate the drying process of the water potentially leaking into the anchorage during rain.

In general, the efficiency of the dehumidification system is tracked by simply comparing the RH measured inside of the anchorages and the RH measured by the nearest SMHI (Swedish Meteorological and Hydrological Institute) weather station in Gothenburg. As an example, the plot in Figure 11 shows an extract of the RH readings from anchorage 101V, where the impact of the dehumidification system is already evident right after its installation.

The evaluation of the dehumidification system's performance is currently ongoing, and the system is being calibrated to achieve the desired effect. To this aim, optimal settings for dry air production will be identified after the system has been operational for a certain period in airtight anchorages, protected from weather conditions.

7 CONCLUSION AND FUTURE DEVELOPMENT

This paper has presented the main outcomes of the moisture monitoring system installed on two selected lower cable anchorages of the Uddevalla bridge.

The monitoring system, procured and installed by COWI (including programming of data logging and communication), continues showing an excellent performance in providing data of high quality. The initially moderate expectations regarding the experimental deployment of Leaf Wetness Sensors (LWS) have been exceeded, as a base of highly informative data have been collected, allowing to map the paths of water flows and the efficiency of the drainage ways.

Specific assessments have been carried out to investigate the magnitude of the main issues behind the presence of water in the anchorages, namely condensation and rain ingress. Both assessments have resulted in monthly summaries estimating the percentage of time affected by the two issues.

Based on both raw and processed data, the effect of different interventions on the anchorages has been successfully evaluated, identifying changes in air conditions and water flow intensity inside the anchorages.

Finally, the performance of a prototype dehumidification system is now being monitored since its installation at the end of May 2023 on both monitored anchorages. The efficiency of the dehumidification system can be tracked by comparing the outdoor relative humidity with the one measured inside the anchorages, while its operation is being calibrated to achieve the desired objective of an internal relative humidity below 40%.

Among the future developments of the monitoring project, the possibilities for extrapolating the data from the monitored anchorages to all the other anchorages are being investigated. After more than a year of continuous monitoring, air temperature, humidity and surface temperature data are available for all seasons, which constitutes a quite complete basis of data under diverse weather conditions.

As described in section 3, the trend of air temperature, humidity and surface temperature are strongly correlated with the geometry – i.e., size and inclination – of the anchorages. It is therefore considered that air temperature, humidity, surface temperature, and, as a consequence, the condensation rate, can be extrapolated from the monitored anchorages to all other anchorages, by considering their geometry.

A less straightforward operation may be the extrapolation of the water ingress results, as they directly depend on the watertightness (i.e., leaks and imperfections) of each anchorage. A possible way-forward to obtain a basis for the extrapolation could be to perform inspections on all anchorages and rate their watertightness.

All the above initiatives for future development converge into the general idea of establishing a digital twin that would enable estimating the consequences of environmental conditions, mitigation, and other changes with respect to the extent of the water presence issue. This digital twin approach may provide an efficient way of assessing the exposure to corrosion risk for all anchorages, based on their geometry.

REFERENCES

Bloomstine, M.L. & Melén, J.F. 2017. Main Cable Dehumidification – Flow Testing and Other Innovations, *Proceedings of the 9th New York Bridge Conference*, August 21-22, 2017, New York City, USA

Laigaard, J. & Lambertsen, J., Zinck, M., Stefansson, E. 2017. Challenges with Water Ingress in Bridge Cable Systems, *EUROSTEEL 2017*, September 13–15, 2017, Copenhagen, Denmark

Melén, J.F. & Bloomstine, M.L. 2018. Optimal Maintenance of Suspension Bridge Cable Systems, *IABSE Conference 2018 – Engineering the Past, to Meet the Needs of the Future*, June 25-27, 2018, Copenhagen, Denmark

Bridge Maintenance, Safety, Management, Digitalization and Sustainability – Jensen, Frangopol & Schmidt (eds)
© 2024 The Author(s), ISBN 978-1-032-77040-6
Open Access: www.taylorfrancis.com, CC BY-NC-ND 4.0 license

Analysing ultrasonic testing data to optimise stay cable maintenance

A. Boyez & R. Percy
COWI UK Limited, London, UK

J. Laigaard Jensen & I. Farreras Alcover
COWI A/S, Lyngby, Denmark

ABSTRACT: Corrosion caused by water ingress is a significant risk for parallel-strand cable systems lower anchorages. When this risk is realised on a bridge, implementing a robust maintenance strategy is needed to ensure safety and minimise operational impacts. This makes ultrasonic reflectometry a valuable tool for bridge owners since it can estimate the condition of individual wires from the anchorage.

Sixense's UScan® has been applied to the stay cables of Pont de Normandie since 2012, and since COWI started advising the bridge operator CCIT-SE in 2019, complementary testing and analysis has allowed to assess the reliability of ultrasonic testing and to maximise the value of ultrasonic testing data.

The paper builds on this experience to discuss how ultrasonic testing can be used to inform stay cable maintenance and replacement and proposes further steps to better enable proactive maintenance that minimises costs and operational impacts while extending the life of stay cables.

1 INTRODUCTION

Stay cables on major long span bridges are critical components within primary load paths, historically with limited or no redundancy. While more modern bridges are usually designed to permit one or two stay cables to be temporarily absent, earlier bridges may either have no redundancy or cater only for a single stay to be removed, typically under reduced traffic loads. The majority of stay systems use spiral strand or parallel strand systems: the later has become more widely used and is the one considered in this paper.

Corrosion of the wires making up stay cable strands may lead individual wires and strands to fail, threatening the integrity of stay cables. Considering their limited redundancy, water ingress prevention is a design priority, but corrosion remains a possibility, so that effective methods for corrosion detection become critical. Indeed, without data on the extent of corrosion, bridge owners and operators cannot accurately assess the bridge's reliability or efficiently plan stay replacements.

In this context, stay lower anchorages are problematic as they combine susceptibility to water ingress with limited access. Most of the length of strands within the anchorage is not visible beyond the anchorage plate, leaving Non-Destructive Testing (NDT) as the only option to determine the extent of corrosion before wire and strand failures become apparent.

This paper explores the use of periodic ultrasonic testing data to inform safe operation and maintenance of cable-stayed bridges subject to stay lower anchorage corrosion. Context on the issue is provided and the testing method presented before practical applications of data analysis and visualisation from COWI's work on Pont de Normandie are presented. Finally, short-term and long-term optimisation of stay condition testing and management is discussed.

DOI: 10.1201/9781003483755-350

1.1 *Corrosion in parallel strand stay cable lower anchorages*

The top right of Figure 1 shows the cross-section of a typical parallel strand stay cable: multiple strands are arranged in parallel to approximate a circular cross-section, and generally protected by an outer high-density polyethylene (HDPE) sheath. Modern steel strands are typically formed of 7 high-strength steel wires, which, for corrosion protection, are individually galvanised. The complete strand is then covered with wax and an extrusion of high-density polyethylene (HDPE) - refer to the bottom left of Figure 1.

At the anchorages, strands are separated and individually anchored using steel wedges, which requires removing the HDPE extrusion (refer to top left of Figure 1). This leaves the strands and constituent wires more vulnerable to corrosion (refer to centre left of Figure 1). Anchorages are often injected with wax, but this further mitigation does not always prevent water ingress.

This weakness to water ingress is particularly relevant at the lower anchorage since gravity will help water find a way past imperfect and aging seals into the anchorage, and this is indeed where many corrosion issues have been documented in stay cables (Jensen 2017).

1.2 *Inspection, testing and monitoring of stay cable lower anchorages*

The challenge with corrosion in parallel strand stay cable lower anchorages is the difficulty to view or reach the location where corrosion is most likely to occur, that is within the length of strand not protected by HDPE, as this area is either within or beyond the anchorage plate. Some options for inspection, testing and monitoring are discussed below:

1. Stay cable checks: when a strand breaks, it may pierce or distort the stay's outer sheath and become visible. While checking for this is easy to implement, it provides only partial information after a breakage.
2. Anchorage visual inspection: signs of corrosion, missing wires or missing strands may be identified from the anchored end. This requires access, preparation (removal of the anchor cap and wax), and potentially restoration (reinjection of wax), and is more likely to provide information when the corrosion process is advanced.
3. Endoscopy: in theory, a fiberscope thin enough to be inserted between the strand and its anchorage hole should allow to check for signs of corrosion along the exposed strand length. In practice, residual wax makes it impractical. Requirements for this method are the same as for visual inspection.
4. Acoustic emissions monitoring: in theory, this continuous monitoring identifies wire breaks when they occur, building an incremental picture of the stay degradation. In practice, any downtime could lead to wire breaks being missed, and false negatives and false positives are a possibility that must be accounted for in assessing the output. Acoustic emissions monitoring requires 2 sensors per stay to determine/confirm the location of breakage, an acquisition network and specialist signal interpretation, but once installed access should not be needed other than for maintenance. This cannot provide information on pre-existing stay condition.
5. Ultrasonic reflectometry: this test, further described below, provides a snapshot of the absolute corrosion level of each wire. It requires access, preparation (removal of the anchor cap and wax, machining of the wires) and restoration (reinjection of wax).

Destructive testing of loaded strands is to be avoided considering their structural function. On the other hand, failed or replaced strands can be extensively tested, which yields valuable information on the accuracy of testing and monitoring techniques and on strand properties. This will not however directly inform the condition of the remaining strands.

1.3 *Challenges of stay replacement*

Stay replacement involves several challenges, including traffic restrictions, which may be necessary for public and worker safety and structural capacity; and the removal of elements such as protective covers and sheaths, stay damping devices, and ancillaries such as monitoring sensors, cabling and lighting.

These challenges, together with works set-up costs, make stay replacement a complex and costly operation, especially when a low number of stays is replaced. Forward planning and

maximising stay life are therefore essential to reduce maintenance costs and environmental impact.

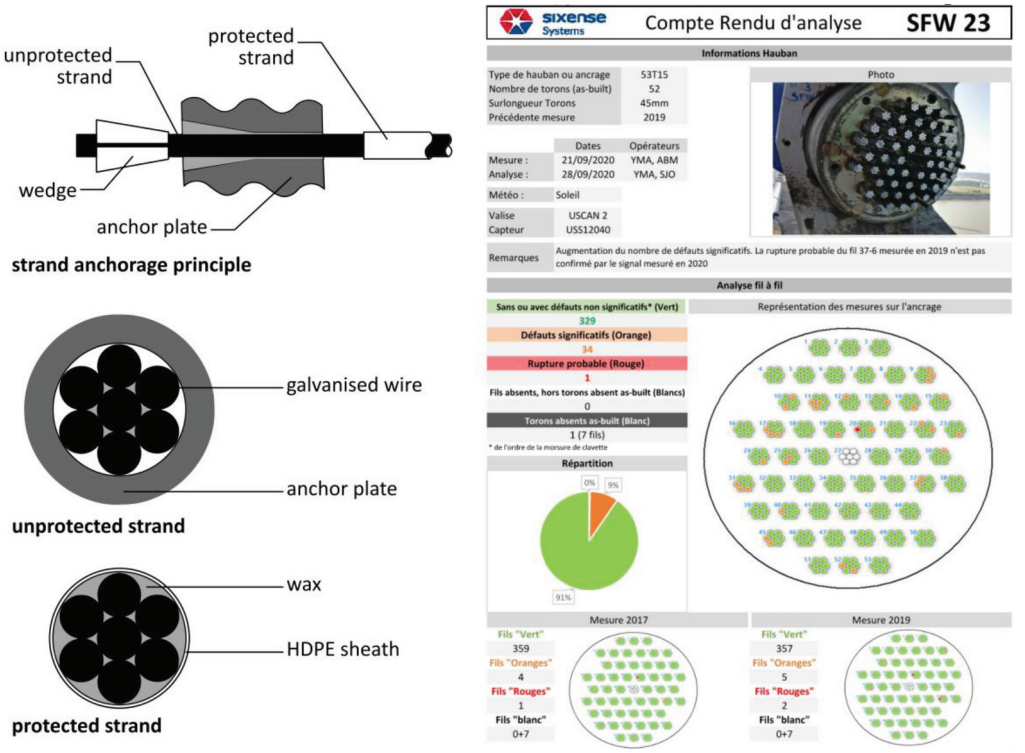


Figure 1. Left – strand anchorage section and cross-sections of the unprotected and protected sections of the strand. Right – results of UScan® testing of a Pont de Normandie stay before its replacement in 2020.

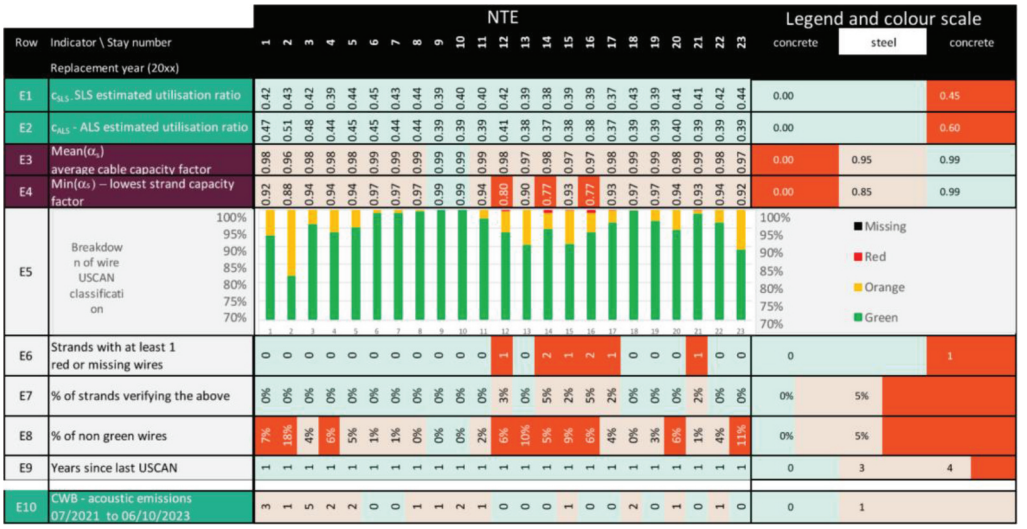


Figure 2. Extract from COWI's Pont de Normandie summary table bringing together all available stay information, including UScan® and stay condition indicators derived from it.

Table 1. Colour classification used by Sixense to report UScan® results from Pont de Normandie stays.

Wire colour classification	Signal reflection	Meaning
Green	None/poor	A defect such as corrosion is unlikely.
Orange	Significant	A defect such as corrosion along the wire is likely.
Red	High	A failure along the wire is likely.
White	N/A	Wire physically absent but was present at construction.
Black	N/A	Wire absent from construction, by design.

2 ULTRASONIC REFLECTOMETRY TESTING OF PARALLEL-STRAND CABLES

Ultrasonic reflectometry is a non-destructive test that can be applied to detect flaws in steel wires and steel strands. An ultrasound is emitted at an anchored end, and the recorded response signal is analysed to identify flaws such as surface corrosion or ruptures.

The ultrasonic guided wave reflectometry applied to stay cables further discussed below, UScan®, has been developed and patented by Gustave Eiffel University (UGE) and Sixense (Laguerre et. al 2011, 2020).

2.1 *Requirements and output*

For parallel-strand cables, UScan® can be applied to individual wires. The wave is generated and detected by an ultrasonic transducer held in contact with the wire end, which requires preparation so that the wire section is clean, flat, and orthogonal to the strand axis. Signal can be detected for ranges between a few decimetres and a few metres, which covers the length of wire most susceptible to corrosion in an anchorage. The signal is then analysed to classify individual wires into categories (see Table 1 for the wire colour classification used by Sixense).

The right side of Figure 1 illustrates how Sixense typically reports UScan® test results for parallel-strand cables – it provides useful contextual information on top of the classification of each wire, such as the date of measurement and processing, results from previous investigations, and a picture of the anchorage at the time of inspection.

2.2 *Consistency and reliability*

UScan® is subject to uncertainties and errors from multiple sources including, in no particular order, ultrasonic equipment calibration, wire surface preparation, signal contamination, stay/strand/wire mislabelling, signal interpretation process, erroneous data entry. Since its inception, the UScan® methodology has been refined to eliminate or mitigate some of the above (e.g., measuring each wire twice), however cross-checking throughout the process remains essential to maximise data quality.

Stay replacements provide an excellent opportunity to establish the reliability of ultrasonic testing: the classification into corrosion categories from a detailed visual inspection of removed wires can then be compared with wire classifications from a recent UScan® test. It should be kept in mind however that the results of such an exercise only apply to an instance of UScan® and cannot be fully generalised to other instances if the test methodology changes.

3 ANALYSIS OF USCAN TESTING DATA FROM PONT DE NORMANDIE

3.1 *History of ultrasonic testing on Pont de Normandie*

The discovery of 2 broken strands in one of the bridge's stay cables in 2010 led to investigations that established the cause as corrosion in the lower anchorage. In parallel, the lower anchorages of other stays were visually inspected, revealing some corrosion but no visible ruptures. The limited information to be gained from visual inspection triggered a research and development for better testing methods which culminated in the selection of ultrasonic reflectometry.

In 2012/13, UScan® was applied on Pont de Normandie to test the bridge's 184 stay cables. Since 2017, a rolling program to test all stays over 4 years has been ongoing.

The observation of strands breaking out of their stay aerodynamic sheath in 2018 and 2019, in combination with UScan® results, prompted the replacement of a further 3 stays in 2020. This was used as an opportunity for testing of the replaced stays, including tensile resistance tests and cross-checking of UScan® wire classification (see Table 2).

Other related activities have included the evaluation of the stays' design loads, and a trial acoustic emission monitoring system with 2 acoustic sensors per stay has been running since July 2021.

COWI became involved as a consultant to the bridge owner in 2019 and has since been working with UScan® data and other sources to provide meaningful information. The bridge is operated by CCIT Seine Estuaire (CCITSE), concessionaire for the French state.

3.2 *UScan® data quality and reliability assessment*

Although the responsibility for UScan® data quality lies with Sixense, several data quality checks can be conducted by other analysts. Such checks include verifying the consistency of information provided on individual stay reports. While these may be basic, they can identify mistakes that would impact the analysis, and are easy to automate – it makes sense to perform them as reports are generated. Incorporating similar consistency checks with other sources of information (e.g., composition of stays from construction records) is also beneficial.

The next level of checking involves the comparison of successive measurements on the same stay. Since the true wire condition can only degrade over time, the expectation is that individual wires can only evolve in the following order, although colours might be skipped: green, orange, red and white. In Laigaard (2022), such a method is presented. It relies on encoding the colour classification of wires constitutive of a strand into a scalar that increases with corrosion. If this number decreases between two successive measurements of a strand, at least one of the results must be erroneous. Although the error might come from multiple sources, aggregating the results of this method for stays tested at the same time can reveal trends that are likely to be due to differences in UScan® measurement or processing. Conversely, a reduction in the prevalence of non-physical evolutions of UScan® wire classifications over multiple campaigns would point to the reliability of UScan® increasing over time.

The best way to assess the reliability of UScan® data is to compare it with visual inspection results from replaced cables. Such a comparison exercise was undertaken during the replacement of 3no. Pont de Normandie stays in 2020, the results of which show a good correlation between UScan® and visual inspection (see Table 2 and Laigaard (2022)).

These results are recast in Table 3 on the basis that UScan® is a test to detect wire breaks, showing that UScan® in 2020 could reliably classify a wire into dichotomous "un-broken" or "broken" categories (being correct 97% and 71% of the time respectively). A similar analysis focused on UScan® as a test to detect corrosion reveals that it correctly places a wire in the "intact" category 87% of the time, and in the "corroded" category 50% of the time. This lesser performance is explained by the allusiveness of early corrosion and can be mitigated by data processing strategies. Overall, the above results are impressive and show UScan® is altogether a reliable method to assess wire condition.

The quantification of UScan® reliability informs the interpretation of the data and can even be explicitly taken into account using Bayesian probabilistic modelling to infer the actual

Table 2. Breakdown of UScan® wire category counts based on laboratory visual inspection categories for 971 wires from the 2020 replacement of 3no. Pont de Normandie stays.

Visual inspection levels*	Green	Orange	Red
Levels 1, 2 & 3	720	69	3
Levels 4, 5 & 6	102	21	7
Level 7	5	20	24

* Levels are grouped to match the UScan® colour categories.

condition. It should be noted however that this quantification corresponds to UScan® performed at a certain point in time and that changes to the methodology are expected to have an impact on its reliability.

Table 3. Alternative breakdown of the results shown in Table 2.

Visual inspection levels*	Green+Orange*	Red+White*
Levels 1-6	912 [97%]	10 [29%]
Level 7	25 [3%]	24 [71%]

* Category groups correspond to un-broken or broken.

3.3 *Meaningful indicators and data visualisations*

UScan® data is discrete categorical data with high granularity (every wire in a stay is attributed a category), which can make interpreting and summarising it difficult. Some of the strategies used by COWI's to achieve this are discussed below.

The first strategy is aggregation, an example of which is the use of normalised stacked bar plots reflecting the total count of wires in each colour category within a stay (see Figure 2). This plot allows to see the proportion of wires likely to be corroded or broken within a stay but also to compare it across stays, which helps clearly identified which appear to be in the worst condition. Another example of aggregation is the definition of colour categories for strands based on that of its constitutive wires. Such a strand categorisation makes sense for two reasons: first because remedial action cannot be taken on individual wires, and second because corrosion in a wire means the whole strand is likely to be exposed to water and corrode eventually.

The second strategy is encoding, i.e. transforming categorical data into numerical data, which makes ranking and aggregating easier. An example of encoding is the strand Damage Indicator (DI) defined in Laigaard (2022), which captures the colour categories of 7 wires making up a strand into a scalar that increases with the signs of corrosion. Another example is the definition of a strand capacity factor that estimates the proportion of tensile resistance maintained by a strand using the UScan® classification of its constitutive wires. This relies on a linear regression model fitting tensile testing data to UScan® results for a sample of strands from the 3 stays replaced in 2020, see Laigaard (2022).

The third strategy is the focus on meaningful indicators and synoptic data visualisations, exemplified by Figure 2. Along the rows, it shows estimated utilisation ratios, capacity factors, underlying UScan® results, condition indicators, contextual information and Acoustic Emission results. Along the columns, it shows stay cables according to their location. Discrete conditional colour formatting helps to highlight hotspots. While it summarises and juxtaposes a lot of information, it is designed to remain readable, so that it can serve as a tool for contextualisation, comparison and prioritisation. Figure 2 shows only one fan for readability, but the full version shows the 8 stay fans of Pont de Normandie in an A3 sheet of paper, condensing a large amount of information digestible manner.

3.4 *Degradation rates and predictive models*

While Figure 2, reading like a snapshot of the condition of the stay cables, is a useful tool for management, it has limitations. The first is that it shows the latest available UScan results, which on Pont de Normandie can be up to 4 years old and are necessarily asynchronous. This must be kept in mind when interpreting it, which is why the age of the underlying UScan is indicated. The second is that it doesn't offer forecasting information, which would benefit long-term planning. Options to address this latter issue include the characterisation of degradation rates and the definition of predictive models, both informed by historical data. Pros and cons of potential empirical and Bayesian approaches to both options are discussed below.

An empirical approach could be to plot the historical evolution of a numerical condition indicator for a stay, and to extrapolate the future evolution on this basis. This method can be

refined by using statistics (e.g., averaging the rate for all stays), by grouping individuals (e.g., making the rate conditional on the current condition) or by exploiting the granularity of the data (e.g., looking at strand degradation rates rather than stay degradation rates), and the physics of degradation can help inform the refinement used (one could for instance expect that different stays will see different degradation rates due to differences in exposure to water). While implementation can range from simple to complex depending on the level of refinement, the empirical approach is limited by two considerations: first, UScan® is susceptible to censoring (the exact time of a change in wire condition between two measurements is uncertain), and second, UScan®, although generally reliable, can and does misclassify wire conditions, as seen in Table 2 and Table 3. While an empirical approach can be informative if the associated uncertainty is kept in mind, quantifying this uncertainty is difficult.

A Bayesian modelling approach can elegantly deal with the limitations of empirical approaches and inherently quantifies uncertainty within the model structure. It is possible to bake into such a model that UScan® measurements are discrete observations of condition and that the true wire condition can only degrade with time. Both misclassification probabilities as inferred from laboratory testing data and variability within stays and strands can be incorporated. A trained model can flexibly estimate the true condition, which can be used to derive relevant condition indicators, and provides the associated uncertainty, making it an ideal tool for long-term planning. Multiple candidate model structure can be considered, ideally informed by corrosion process modelling.

4 STAY CABLE MAINTENANCE OPTIMISATION USING ULTRASONIC TESTING

4.1 *Extent and frequency of ultrasonic testing*

As discussed in the previous section, ultrasonic testing of stay cables' lower anchorages enables a range of analyses that can inform stay cable maintenance. While the minimum amount of data necessary will depend on the analysis, the reliability and value of these analyses can only increase with more ultrasonic testing data and other relevant information from inspection, testing, design and assessment, the acquisition of which comes at a cost for the bridge operator.

The ultrasonic testing regime must balance operational and financial costs of ultrasonic testing with the need for informative analysis outcomes. The following elements should be considered:

1. Testing costs: whether direct or indirect, many factors can influence them. Testing more stays per ultrasonic testing campaign is likely to reduce costs but operational constraints can limit the extent of the campaigns (weather, concurrent maintenance works). Costs can be expected to reduce over time as experience is gained, but only to an extent, unless specific process improvements are developed and implemented.
2. Condition knowledge: if the extent of corrosion is unknown, testing all stays to establish a benchmark should be a priority. Conversely, if the condition is understood, the frequency of testing should be proportional to the known corrosion level.
3. Stay criticality: the frequency of testing should be proportional to the criticality with respect to safety and structural integrity, to be informed by specific assessments.
4. Confidence in testing and data analysis: as confidence in ultrasonic data and derived results such as degradation rates or projection increases, the frequency of testing could be reduced.

On Pont de Normandie, the outcome of these considerations is a rolling program where a quarter of the stays (46 stays) are tested each year (so that no result is ever older than 4 years), complemented by more frequent testing of stays exhibiting the worst condition. This serves the dual purpose of keeping results up to date and of accumulating more data to enable more advanced analysis, while ensuring the condition of the most degraded stays is monitored closely.

4.2 *Ultrasonic testing informed maintenance decision making*

Conceptually, ultrasonic testing informs two aspects of stay cable lower anchorage corrosion: detailed results for individual stays allow to determine the local severity of corrosion, while an

overview of results for many stays informs the global extent of the issue. Up-to-date knowledge of the extent and local severity of corrosion, combined with understanding of bridge-specific circumstances, allows stakeholders to answer the following questions:

1. Should traffic restrictions, mitigation measures, contingency plans be prepared/implemented?
2. Should further testing be conducted, what should it target and what should its extent be?
3. Should complementary monitoring (e.g. acoustic emission monitoring) be considered?
4. Should selected strands or stays be replaced, and how soon?
5. Should corrosion prevention measures (such as dehumidification) be considered?

Figure 2 is an example of how to design ultrasonic testing data visualisation to facilitate the identification of the local severity and global extent of the stay lower anchorage corrosion issue, making it a useful tool to inform maintenance decision making. Its usefulness is further enhanced by the integration of further information such as stay utilisation levels, corroded strand resistance and acoustic emission monitoring. It is part of a report that is updated every time new UScan® results become available.

4.3 *Optimising replacement planning*

Bridge operators are typically working under tight budget constraints, so that they might be limited in their ability to replace stays within a given period. This, combined with sustainability considerations, makes optimising replacement planning a high priority.

A major obstacle to optimal planning is imperfect and incomplete information at the time decisions are made. A reasonable reactive replacement strategy, such as replacing the worst stay based on current information whenever new information becomes available, might prove far from optimal if the replaced stays were adjacent and would have had enough capacity to be replaced in a single, delayed operation, at a significantly lower cost. In this example, a better understanding of the relationship between the condition of a stay and the associated urgency of its replacement could lead to a better replacement strategy and an extended stay cable life.

For the issue considered here, investigations complementary to ultrasonic testing, although associated with a cost, enable further value to be obtained from ultrasonic testing: specific assessments of stay loading and redundancy can inform the criticality of individual stays, laboratory testing of replaced stays can quantify the reliability of ultrasonic testing and link condition with capacity, and complementary monitoring such as acoustic emissions monitoring have the potential to increase the robustness of the condition assessment.

For Pont de Normandie, COWI prepared a stay management plan that covered the above points. This document, periodically updated to take into account new information, provides a high-level summary and recommendations on the stay corrosion issue to enable proactive maintenance.

Replacement planning could be further optimised by the ability to estimate current and future condition based on available data. Such predictions might be valuable even if they are not particularly refined provided they can highlight a range of realistic scenarios that can be specifically assessed in terms of criticality (e.g. 3 adjacent stays might need to be replaced at once, or 8 stays might need replacing in 3 years).

COWI is working on a proof-of-concept Bayesian model that incorporates UScan® historic data, mis-classification rates, and the physics of degradation to provide estimates of current and future actual condition, and quantify their uncertainty. Such a model would evaluate the probability of a given replacement scenario occurring within a defined timeframe. If successful, this would be an excellent tool to optimise replacement planning.

5 CONCLUSION

The difficulty of assessing strand condition within stay lower anchorages, combined with the limited redundancy of stay cables, makes corrosion a significant challenge for cable-stayed bridge. For parallel strand stay cables, ultrasonic reflectometry testing can be a solution to

this problem. A testing strategy cognisant of the bridge's specificities and incorporating information from complementary analysis, assessment, monitoring can enable proactive maintenance that extends the life of stay cables and minimises operational and financial costs.

The management of Pont de Normandie's stay lower anchorage corrosion using UScan® testing illustrates the benefits of this approach: the bridge owner now has a reliable means of assessing stay condition as well as synoptic data visualisations to help inform decisions, and can look forward to condition predictions that quantify uncertainty to better inform long-term planning.

ACKNOWLEDGEMENTS

The authors would like to acknowledge Chambre de Commerce et d'Industrie Seine Estuaire (CCITSE) for their support and for giving permission to publish this paper, as well as Sixense for their assistance in reviewing this paper.

REFERENCES

Jensen, J.L., Lambertsen, J., Zinck, M. & Stefansson, E. 2017. Challenges of water ingress into bridge cable systems. Steel Construction 10(3): 200–206

Laguerre, L., Durand O. & Colin, R., 2020. Method for detecting a defect in a metal wire of a set of metal wires, in particular for an anchoring area of a civil engineering structure. U.S. Patent No 10,816,511, 27 oct. 2020.

Laguerre, L. & Treyssede, F., 2011. Non destructive evaluation of seven-wire strands using ultrasonic guided waves. European journal of environmental and civil engineering, 15(4), 487–500.

Laigaard, J., Farreras Alcover, I., Joye, S. & Laguerre, L. 2022. Data mining corrosion and failure in cable stays. In Casas, J.R., Frangopol, D.M., & Turmo, J. (eds.), *Bridge Safety, Maintenance, Management, Life-Cycle, Resilience and Sustainability; Proc. of the 11th intern. conf. on Bridge Maintenance, Safety and Management (IABMAS 2022)*, *Barcelona, Spain*, 11-15 July 2022. London: CRC Press.

Bridge Maintenance, Safety, Management, Digitalization and Sustainability – Jensen, Frangopol & Schmidt (eds)
© 2024 The Author(s), ISBN 978-1-032-77040-6
Open Access: www.taylorfrancis.com, CC BY-NC-ND 4.0 license

The maintenance project of the special anti-seismic devices of the longest Italian bridge

A. Greco
Speri Spa, Rome, Italy

A. Lupoi
Sapienza University of Rome, Rome, Italy

ABSTRACT: The *elastoplastic damper* devices are frequently used to control the seismic response of structures and, in particular, of continuous bridges. Unlike other anti-seismic devices, the elastoplastic dampers are seismic restraints with *hysteretic elastoplastic* response capable of controlling the horizontal force level and of dissipating energy due to the earthquake. Sometimes such devices are coupled to *temporary* constraint devices, which are hydraulic type (shock-transmitters) generally. In case of seismic action, the hydraulic device is able to transmit the forces to the elastoplastic damper, while in case of service load, it does not offer resistance and allows the movements. Due to their performance characteristics, the elastoplastic dampers coupled to shock-transmitters have been used to control the seismic response of the longest Italian bridge, located on A12 highway in Tuscany Region. The paper shows the details of the maintenance project of the devices of the bridge, with a focus on the causes of any and all damage which have been detected during the surveillance.

1 INTRODUCTION

The article deals with the assessments and the choices regarding the improved maintenance project of the bearing and anti-seismic devices of the longest Italian bridge, which is located on the A12 highway, in Tuscany Region.

The abovementioned maintenance project of anti-seismic devices was part of a wider intervention strategy, which has been developed on the basis of certain damage found through the monitoring activity on the bridge's devices. This monitoring activity was made necessary due to (i) the significant length of the bridge (9 km), and (ii) the wide number of the anti-seismic devices (1047 units), and (iii) the peculiarity of such devices, consisting of elastoplastic dampers and oleo-dynamic components coupled to each other.

Moreover, the monitoring activity of anti-seismic devices was useful to constantly check the state of the anti-seismic devices and to arrange a proper intervention plan which will be adopted over the years in relation to the levels of the monitored damage. The limits of these levels have been identified in advance and throughout numerical analysis. The main benefit of this approach has allowed us the optimization of the costs related to the project.

For the sake of completeness, we have also carried out a safety static and seismic assessment of the bridge before starting the maintenance project of the devices, which has confirmed their compliance with Italian technical standards required by D.M. 17/01/2018. The outcome of this assessment was crucial as we have opted for a maintenance project of the anti-seismic devices rather than replacing them completely.

The article also describes the depth-analysis on the reveled damage which affecting the anti-seismic devices, and which has been carried out with the aim at better understanding the causes of such damage. This analysis has allowed us to consider within the project, the proper measures to have to be adopted for improving the functionality and the durability of all such devices.

DOI: 10.1201/9781003483755-351

In conclusion, we would like to point out that the maintenance of the devices, rather than their replacing, was opted on the basis of three factors: i) the positive outcome of the safety assessment; ii) the increasing of residual service life of the devices up to 50 years obtaining in this way the same service life of a new devices; iii) the lower costs of the maintenance interventions compared to a full replacement.

2 THE BRIDGE

2.1 *Description of the bridge*

The bridge was built in 1993 and it is located on A12 Italian highway. The length of the bridge is 9619 m, and it is considered the longest Italian's bridge (Figure 1).

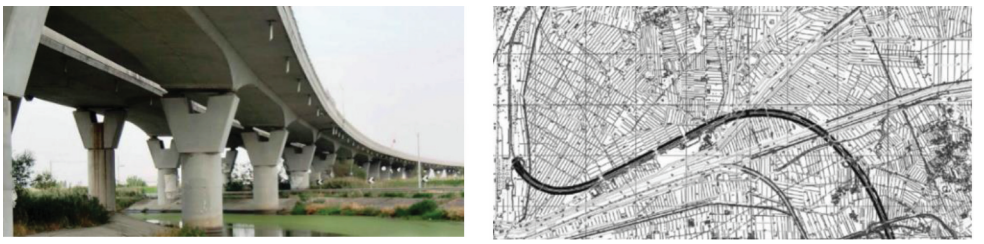


Figure 1. View of the bridge (left); cadastral plan of the bridge (right).

The bridge consists of no.27 continuous deck with separate carriageways; no.230 piers and no.2 abutments. The single deck consists of no.10 spans: the eight internal spans are 45 m long, while the two external ones are 33 m long. The single deck, of 12,25 m width (11,25 m for driveways), is built with the *incremental launching method.* Each single span is characterized by parabolic profile (from 2,3 m to 1,1 m) with *precast* concrete plate section. The pre-stressing system of the decks consists of 21ϕ7 with a ultimate tensile strength f_{ptk} and yield tensile strength $f_{p(0.1)k}$ equal to 1800 MPa and 1600 Mpa, respectively. The piers and foundations are in ordinary reinforced concrete, with a cubic resistance of R_{ck} 45 MPa and 55 MPa, respectively. Pier stems are characterized by a circular or rectangular section and a variable height ranging from 4,1 m to 13,6 m. Foundations piles are 65-70 m long with a ϕ1200 diameter do due the poor characteristics of the soil.

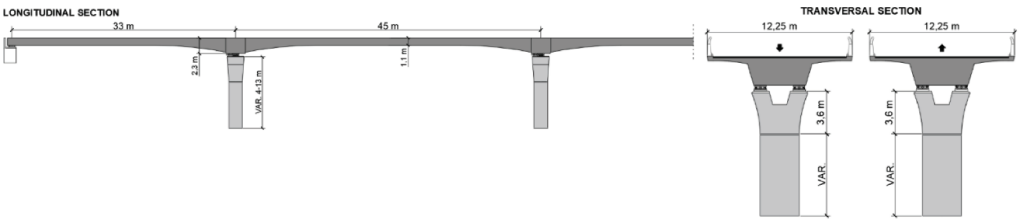


Figure 2. Longitudinal (up) and transversal (down) sections of the bridge.

2.2 *Bridge bearings and anti-seismic devices*

The deck is connected to the piers by special devices which have a dual function: the vertical load transfer and the seismic protection. The total number of the devices, considering the two carriageways, is equal to 1047, no. 2 for each pier of the bridge. The constraint scheme of each continuous deck is characterized by two fixed type devices located in the central pier, two free sliding type devices installed on the two external piers and two longitudinal sliding type devices on the remaining eight pears (Figure 3) which are coupled to hydraulic devices (shock-transmitters).

The latter devices ensure the longitudinal movement in case of service load (thermal action, creep, shrinkage, post-stress relaxation), while the transversal movement are bounded.

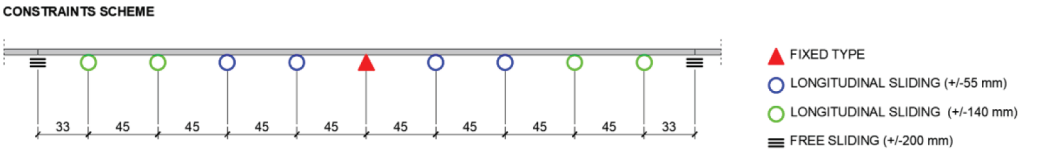


Figure 3. Constraints scheme.

Fixed and longitudinal device are able to transmit the horizontal forces through elastoplastic element characterized by *tapered* shape (also called *tapered pin*). These elements are developed to dissipate a rate of seismic energy by yielding and guarantying many stable hysteresis loops [1], [2]. The yielding force and ductility of such *tapered pin* are defined precisely.

The details of the longitudinal special device of the bridge, coupled to oligodynamic device, are shown in Figure 4.

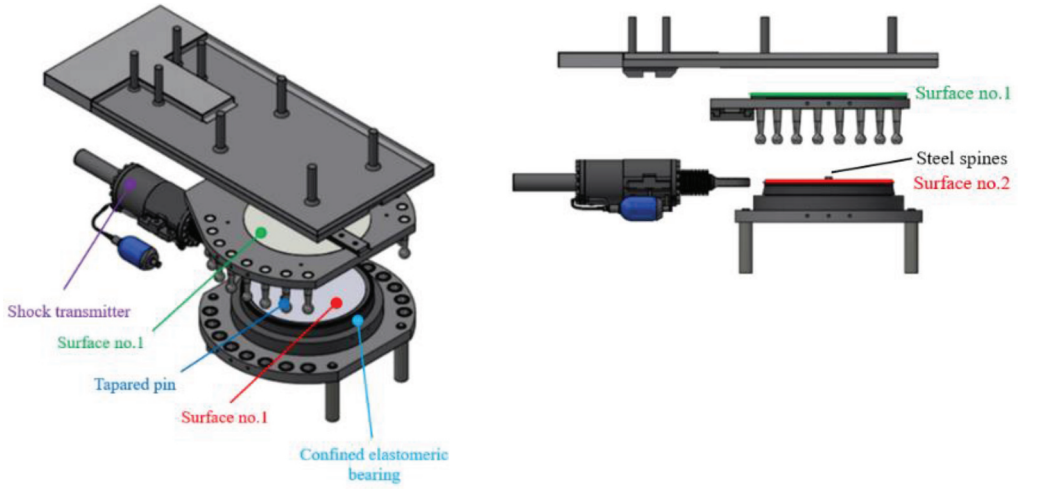


Figure 4. Tridimensional view (left), details (right).

The main components of the special device are the following:

1. Confined elastomeric bearing which is able to transmit vertical load.
2. Dissipative components which consist of no.16 *taperd pin* (built with stainless steel AISI 304) which dissipate seismic energy by yielding and hysteresis loops.
3. Hydraulic device (shock transmitter) connected both to the deck and to dissipative components. In case of seismic action, the hydraulic device has the ability to transmit the forces to the elastoplastic damper, while in case of service load, it does not offer resistance but allows the movements.
4. No.2 sliding surfaces made of PTFE which are characterized by low friction (the surface no.1 is highlighted in green in Figure 4, while the surface no.2 is highlighted in red color);
5. No.2 steel spines characterized by circular diameter and by made of S355 which are able to transmit service breaking action only.

The device allows a different performance which depends on the type of action. In particular, the sliding occurs at the surface no.1 or no.2 in case of service load or seismic action,

respectively. In case of seismic action, the steel spines break, and the hydraulic device transmits the force to the dissipative components which start their hysteresis loops by deformation.

The braking action transmission is ensured by steel breakage spines which allow to spread the forces in all devices of the continuous deck.

In terms of construction, the hydraulic device (shock-transmitter) consists of a piston sliding in a cylinder, filled with silicone or any other kind of oil. The piston is equipped with seal in order to separate the cylinder in two parts [3].

The hydraulic circuit is characterized by two valves with two calibrate orifices (one on the pressure side and the other one on the vacuum side) through which the fluid flows. In case of service loas, the orifices are opening, while for seismic action, the orifice on the pressure side closes and ensures the transmission of the forces.

The circuit is also connected to an external nitrogen accumulator which pressure is dependent of the outside temperature. The nitrogen accumulator is able to compensate the volume of oil in the cylinder, which is variable, due to its compressibility.

The shock-transmitters of the bridge, ones of the first type on the market, is rigidly connected to the deck of the bridge, while its piston is connected to steel sliding plate of the bearing by cylindrical hinges. These kinds of connections only allow the rotation in the horizontal plan as opposed to the ones currently in use which also allow the rotation in all planes (spherical hinges).

The dissipative components, as stated earlier, consist of no.16 *taperd pin* developed to dissipate a rate of seismic energy by yielding and guarantying many stable hysteresis loops. The total yielding force is equal to 640 kN (40 kN for each pin) which corresponds to a displacement equal to 8 mm. The maximum displacement to failure is equal to 70 mm (Figure 5).

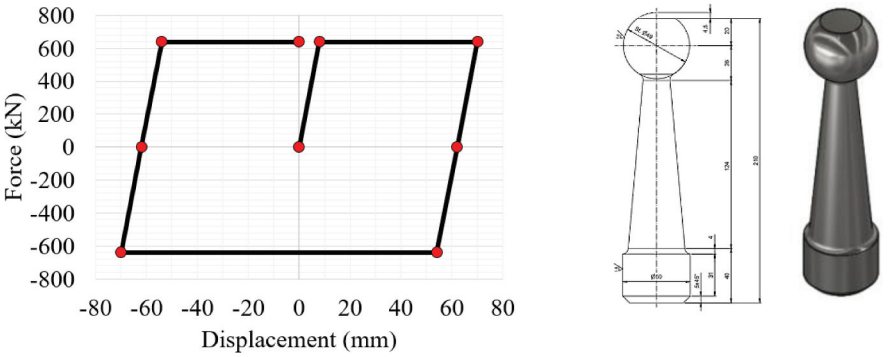


Figure 5. Diagram Force/Displacement of no.16 *elastoplastic taperd pin* (left); detail of the single taperd pin (right).

The performance parameters of all devices are shown in the Table 1 below.

Table 1. Performance parameters of the devices of the bridge.

	Vertical Load	Long. load	Transv. load	Long. displacement	Transv. displacement
Tipo	kN	kN	kN	mm	mm
Fix	12000	640	640	-	-
Longitudinal sliding	12000	640	0	+/-140 (+/-55)*	-
Free sliding	4000	-	-	+/-200	+/-200

* The excursion capacity is equal to +/- 140 mm or +/-50 mm for the longitudinal sliding device located at external or internal side respectively (Figure 3).

3 DAMAGE ASSESMENT AND CAUSES ANALYSIS

3.1 *Damage assesment*

During the bridge monitoring activity were detected multiple types of damage on the bridge's devices in the latest years. Such damage mainly interested the hydraulic devices and the elasto-plastic components, while the elastomeric confined bearings are very preserved.

Below we have listed the main damage captured by on-site inspection followed by photographic details (Figure 6):

a) Elastoplastic tapered pin deformed or broken.
b) Oil leakage from the shock-transmitters.
c) Circuit of the hydraulic device lockout.
d) Deterioration of the sliding PTFE surfaces and loss of planarity.
e) Oxidation of the metallic components.



Figure 6. Mainly damage of the devices.

3.2 *Causes analysis*

Firstly, an assessment of the damage has been carried out with the aim at better understanding the causes of such damage. This assessment was helpful to evaluate and then to adopt the most appropriate measures for restoring and improving the functionality and the durability of the bridge's anti-seismic devices.

The outcome of the assessment has revealed that the main cause of the damage to the device consists of lockout of the hydraulic circuit of the shock-transmitters which leds the deformation or the breaking of the tapered pin for service load.

In particular, have been identified two different behaviors:

i. Malfunctioning of the hydraulic circuit.
ii. Reaching the displacement limit stop of the device.

With regard to letter (i), the main cause of the malfunctioning of the circuit could be the orifices obstruction of the calibrate valves and in particular, the sliding of the piston in the cylinder wears out the seal and such wearing causes the releases of elastomeric particles which obstruct the orifices of the valves (without protection filter) by blocking the device (Figure 7).

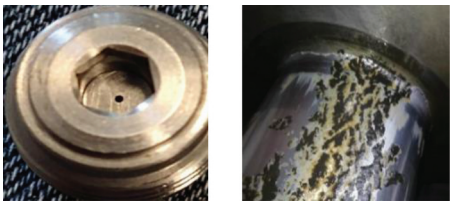


Figure 7. Calibrated orifices of the valves (left); particles of the seal in floating in the oil (right).

The valves are the most important elements of the system as well as the activation velocity of the device, which should be the same in both push directions of the piston (i.e. pressure and vacuum direction). Therefore, the tolerance of orifices' diameters shall be deemed crucial as such tolerance should be the same for both orifices of the valves and, if possible, for the all devices of

the bridge as well. The different activation velocity of the oleodinamic device might lead a delay time in their response by causing damage to themselves and to the bridge.

With regard to letter (ii), it is possible that certain oleodinamic devices might have reached the displacement limit, due to the thermal and rheological effect [4], and then consequently the blocking of the devices should have occurred. In fact, the numerical analysis of the bridge, which will be presented clearly in the next chapter no.4, will show that the maximum displacement of one device could be equal to 62,8 mm (12,8 mm due to thermic action, 50 mm due to rheological effect) and, therefore, greater than its own capacity which is 55 mm (Figure 8).

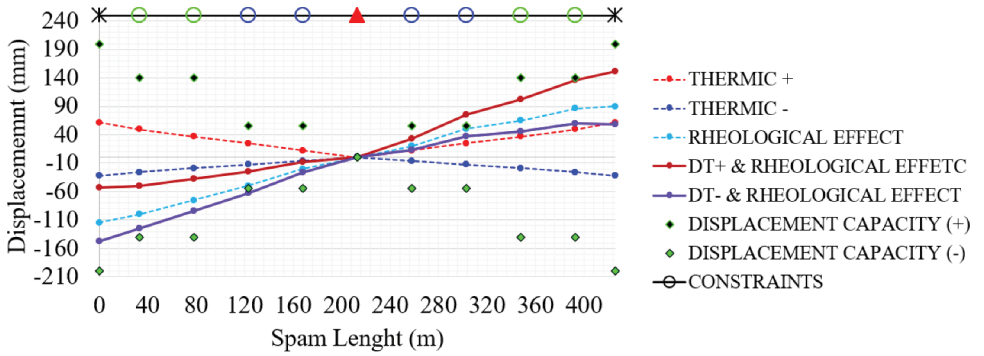


Figure 8. Thermal and rheological displacement of the device of the single continuous deck.

Additionally, it was possible to identify contributing factors by the assessment which factors may have been decisive for the damage detected on the bridge's devices:

iii. Type of the connection of the piston of the shock-transmitters to the bearing steel plate. In particular, the connection of the devices consists of cylindrical hinges only allows the rotation in the horizontal plan and not the one in the vertical plane, as clarified in chapter 2. This aspect could have arisen a parasitic bending moment and – consequently – an high pressure on the seals of the piston and their deterioration (Figure 9). The modern devices, in fact, are characterized by spherical hinges instead of cylindrical hinges in order to avoid these latter negative effects.

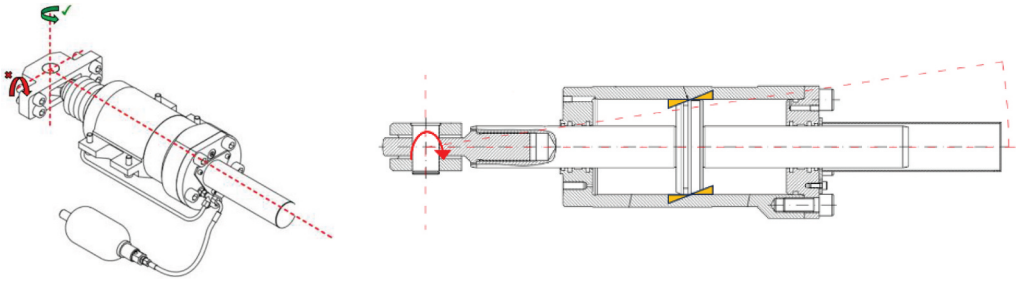


Figure 9. Cylindrical hinges of the device (left); negative effect of the blocked rotation on the seals of the piston (right).

iv. Deterioration and consequently loss of flatness of the PTFE surface of the bearing which could have increased the friction resistance and caused the deformation of the tapered pin for service loads.
v. General deterioration of all components due to the exposure to atmospheric agents.

4 NUMERICAL ANALYSIS

As preliminary phase of the maintenance project of the devices, a safety static and seismic assessment was carried out and it has confirmed their compliance with Italian technical standards required by D.M. 17/01/2018. The outcome of such seismic assessment was crucial to evaluate and then to opt for a maintenance project of the anti- seismic devices rather than for their complete replacement.

The response of the bridge (and its special devices) has been captured by FE model, managed with the support of the SAP2000 code (Figure 10). The model represents the single typological deck of the bridge which consists of no.10 spans and no.11 piers (total length equal to 426 m).

Decks and piers are modelled with frame elements [5], while the shock-transmitters interposed between deck and each pier are modelled with elastoplastic links. Such links are characterized by law governing performance of tapered pin (Figure 5). In addition, the model considers the construction phases by a specific *staged construction*, including the different response of the special anti-seismic devices for service or seismic loads.

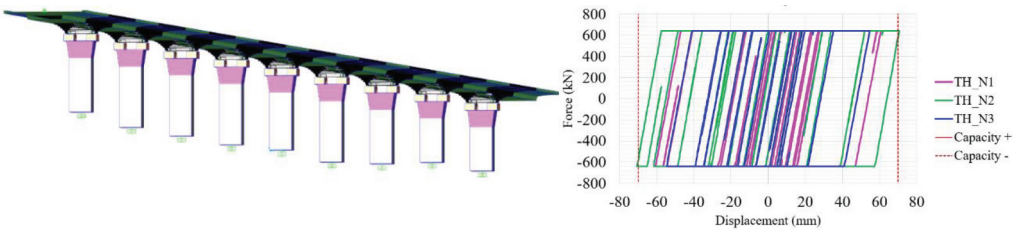


Figure 10. FE model of the typological deck of the bridge (left); hysteresis loop of the elastoplastic devices (right).

The dynamic response of the structure is estimated by carrying out dynamic non-linear analyses with direct integration [6]. Seismic input is applied by displacements time history with a duration equal to 20 s in the three directions of the seismic action and characterized by 8000 steps of 0,0025 s. The thermic and rheological action are considered by equivalent thermic load applied to the deck, while the traffic loads have been modeling by moving load. Figure 10 shows the typically hysteresis loop of the elastoplastic device obtained for the seismic action. The graph outlines that the maximum displacement of the elastoplastic devices is within the range of their capacity excursion. This positive response, as already pointed out in the preamble of this chapter 4, has allowed us to opt for a maintenance project of the anti-seismic devices by avoiding their radical substitution.

5 THE MAINTENANCE PROJECT OF THE DEVICES

The main goal of the maintenance project, which is the object of this paper, was the restoring and the improvement of the functionality of the special anti-seismic devices of the bridge and the adoption of the proper measures to increase their durability. On the basis of the monitoring activity of anti-seismic devices it has been arranged an intervention plan which will be adopted over the years in relation to the levels of the monitored damage with the aim at optimizing the maintenance costs.

The maintenance project has identified two main cases of intervention:

a) In case of tapered pin deformed or broken (or poor general state of preservation): the project provides for the full replacement of special devices, including all their relevant components (elastomeric confined bearing; elastoplastic components and hydraulic device).

b) In case of tapered pin not damaged (and good general state of conservation): the project only provides for the maintenance of the hydraulic devices (shock-transmitters).

Regarding the case (a) the main action that needs to be considered is the raising of the bridge which is, however, an operation much expensive. Due do this latter aspect, the initial choice to rebuild the *tapered pin* was excluded. Therefore, the intervention involves the full replacement of the devices with other ones which are characterized by the same performance but built according to the requirements of the current standards. In particular, it is required that the new devices have (i) the "CE" marking, and (ii) the connection with spherical joint, and (iii) the orifices of the valves with protection filter which shall be characterized by appropriate tolerances of their diameters. The new devices which have been installed on one pier of the bridge recently are shown in Figure 11.



Figure 11. New devices installed on one pier of the bridge.

Regarding the case (b), it was defined an accurate procedure in order to restore the oleodinamic devices. The procedure provides for the restoring of all components of such devices, in particular the replacement of the oil and the insertion of a filter in the calibrated valves' orifices, together with the complete replacement of such valves, to capture the potential particles which may be in suspension in the oil. In addition, the procedure requires an accurate preselection and coupling of the valves by specific algorithm with the aim at ensuring the tolerance of the diameter of the orifices within the range provided by current standards (<5%). This approach permits to have the same activation velocity in both push directions of the piston (i.e. pressure and vacuum direction) and for all devices of the bridge.

We should also point out that the checking tests on no.20 calibrated valves' orifices (with a diameter of 0,4 mm as per project), which were performed during the disassembly of certain devices of the bridge, have shown that the value of the current tolerance of their diameters is equal to +/-0,1 mm. This means that the tolerance is approximately equal to 56% versus 5% required of current standards.

Subsequently, the cylinder shall be painted according EN ISO 12944 (C5M) and the devices' stems shall be double chromed. All devices will be tested according EN 15129 before their reinstallation on the bridge. Regarding the assembly phases, particular care must be taken to the excursion adjustment of the device, considering the thermic displacement at that time. Rheological displacements, instead, are now stabilized to 30 years from the construction of the bridge and, therefore, they can be overlocked.

6 CONCLUSION

The article has showed the assessment of the damage and the details of the maintenance project related of the special anti-seismic devices of the longest Italian bridge, which consist of elastoplastic dampers coupled with shock-transmitter. The preliminary assessment of the damage detected on the devices has permitted to identify the main causes of such damage and to consider, within the project, the proper measures to have to be adopted for improving the functionality and the durability of all such devices.

On the basis of the project that was carried out and which was detailed in this work, we might point out the following main aspects:

1. The adequate tolerance of the diameter of the valves' orifices is relevant to ensure the greatest performance of the hydraulic devices. A low value of such tolerance in fact permits to

have the same activation velocity in both push directions of the piston (i.e. pressure and vacuum direction) and for all devices of the bridge. This aspect allows to avoid potential at hydraulic devices and at the whole structure, as well.
2. The presence of the filter protection of the valves' orifices of the hydraulic devices is decisive to avoid their obstruction, the blocking of such devices and any further damage both to the devices and to the bridge.
3. It is crucial the connection of the hydraulic devices to their support by spherical joint in order to avoid parasitic bending moment and – consequently – high pressure on the seals of the piston and their deterioration.
4. It is decisive a correct estimate of the thermic and rheological effects on the continuous bridges and their devices, to choose the compatible excursion capacity of such devices and to avoid permanent damage both to them and to the bridge. Regarding this matter, it is important to consider the correct adjustment of the device during the assembly phase.
5. The continuous monitoring of the bridges' behaviour and their devices is the best approach to plan the intervention strategy over the time and to optimize the maintenance costs.

REFERENCES

[1] T. Kobori, Y. Miura & E. Fukuzawa, T. Yamada, T. Arita, Y. Takenaka & N. Miyagawa, N. Tanaka & T. Fukumoto. *"Development and application of hysteresis steel dampers"*. Earthquake Engineering, Tenth World Conference, 1992 Alkema, Rotterdam. ISBN 90 5410 060 5.

[2] Panos Tsopelas, Michael C. Constantinou. *"Study of Elastoplastic Bridge Seismic Isolation System"*. Journal of Structural EngineeringVolume 123, Issue 4.

[3] Sleemah, A.A.; Constantinou, M.C., *"Investigation of Seismic Response of Structures of Buildings with Linear and Nonlinear Fluid Viscous Dampers"*. Tech Rep. NCEER-97-0004, National Centre for Earthquake Engineering. Research, State Univ. of New York (SUNY) at Buffalo, NY, (1997).

[4] Mola, F., *"Gli Effetti della Viscosità nei ponti a travata Continua. Evoluzione degli Schemi Strutturali"*, 1999. Politecnico di Milano.

[5] Zienkiewicz O.C., Taylor R.L., "The finite element method". McGraw Hill, Vol. I., 1989, Vol. II, (1991).

[6] E. L. Wilson, I. Farhoomand, K. J. Bathe. *"Nonlinear dynamic analysis of complex structures"*. (1972). The Journal of the international association for earthquake engineering.

Bridge Maintenance, Safety, Management, Digitalization and Sustainability – Jensen, Frangopol & Schmidt (eds)
© 2024 The Author(s), ISBN 978-1-032-77040-6
Open Access: www.taylorfrancis.com, CC BY-NC-ND 4.0 license

Experiences with repair of fatigue cracks in an orthotropic steel deck, New Little Belt Bridge, Denmark

P.L. Sørensen & N. Bitsch
COWI A/S, Kongens Lyngby, Denmark

J. Præst
The Danish Road Directorate, Copenhagen, Denmark

ABSTRACT: Since 2017 a numbers of fatigue cracks, at approximately 160 locations, has been observed in the orthotropic steel deck of the New Little Belt Suspension Bridge in Denmark. The bridge was in 2017, 47 years old, and this was the first time to observe fatigue cracks in the steel deck of the bridge girder. For a bridge owner this can be a crucial observation, as it is well known that repair of fatigue cracks in orthotropic steel decks can be difficult to repair in a proper way and the repairs are normally costly. More to that it is difficult to foresee how this will develop, as the kilometres of welds and number of fatigue prone details are enormous. Despite the difficulties and uncertainties, the bridge owner needs to consider the related crack repair costs in budgeting of the O&M costs in the remaining lifetime of the bridge.

1 INTRODUCTION

The Little Belt Suspension Bridge carries the E20 motorway over the crossing between the island of Funen and the mainland of Jutland, connecting east and west Denmark. The bridge was opened in 1970 and it carries three lanes of traffic in each direction. The average daily



Figure 1. Overview of New Little Belt Suspension Bridge.

DOI: 10.1201/9781003483755-352

traffic numbers have seen a steady increase since the opening, from around 15,000 vehicles to around 100,000 vehicles at present which is close to maximum capacity.

The suspension bridge has a main span of 600 m and two side spans of 240 m for a total length of l,080 m, see Figure 1. The approach spans have a total length of 620 m, giving a total length of l,700 m for the entire connection.

The superstructure is a closed steel box girder with a width of 33.3 m and a height of 3.0 m. The inside of the steel box girder is protected from corrosion by means of dehumidification. As this bridge was the first in the world to have this system installed, it was decided to also apply a paint system as backup. This paint system has a base layer that contains lead and a tar asbestos based top coat. After 50 years there is no sign at all of corrosion, even not at the non protected surfaces.

The width of the carriageway and paved area is 26.6 m. The pylons are ll8 m tall and made of reinforced concrete.

The suspension bridge has altogether six (6) expansion joints, as the bridge girder is divided in three (3) independent sections, two (2) side span sections and one (1) main span section.

During a general visual inspection in 2017, indications of fatigue cracks in the orthotropic steel deck were observed for the first time. A special inspection was performed and the indications of cracks were confirmed by NDT. Eddy current testing (ET) and ultrasonic testing (UT) methods were used.

2 DECK STRUCTURE

At the time of design of New Littlebelt Suspension Bridge in the mid 1960′es there was only very limited experience with wearing surface on orthotropic steel decks (OSD) in Denmark. Danish codes and regulations for bridges were based on the allowable stress method and no fatigue analysis was required to be performed.

However, some experiences from Great Britain and West Germany with OSD's were available and both the Client and the designers were, already at that time, very aware that fatigue was an issue that should be taken into consideration, and so several work groups were formed with the task of finding an optimum pavement to be used on the OSD and to find the best welding methods. Several tests were also completed to verify the composite effect between pavement and OSD and assist in the selection of details and welding procedures during the bridge design. For instance, it was decided to select an automatic submerged arc welding procedure for the vital trough deck weld, as this method would yield fewer welding defects compared to a manual welding process and it possesses better fatigue performance. Test results reported in [2] confirm this.

The final design was an orthotropic steel deck structure with closed troughs that act as the upper flange in the closed steel box girder. The troughs have a height of 250 mm, thickness of 6 mm, width at the deck of 300 mm and spacing of 600 mm, see Figure 2. Troughs are welded with a part penetration butt weld with up to 2 mm root gap. The plated bulkheads have

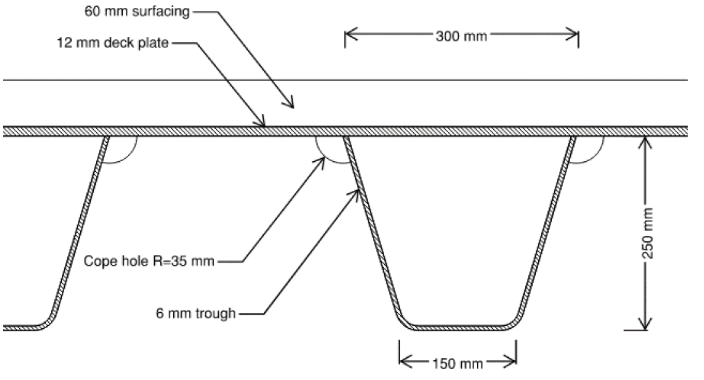


Figure 2. Trough layout.

a spacing of typically 3.0 m, but the spacing can vary down to 1.0 m at site connections. There are no cope holes in the transverse bulkheads at the bottom of the troughs, but there are R=35 mm cope holes at the trough to deck weld, ref. (COWI 1970).

On top of the 12 mm steel deck is a wearing surface with a total thickness of 60 mm. The original surfacing on the OSD was composed of the following layers:

- Adhesive primer
- 4 mm waterproofing
- 25 mm bearing course, Mastic Asphalt 0/8 mm
- 30 mm wearing course, Mastic Asphalt 0/12 mm with 8/12 mm embedded chippings.

The original surfacing had a very good durability and was first partly replaced in 1999/2000 were 5 mm of the bearing course and the entire wearing course was replaced with a 35 mm Stone Mastic Asphalt (SMA) layer. The SMA layer was then replaced again in 2013/2014. Full replacement of the pavement is planned to be executed in 2026 – 2027.

3 ANALYSES

Longitudinal cracks in the pavement close to the central node were observed in 2016, ref. (Ferreras et al. 2017). To evaluate the effect of a damaged pavement on the fatigue life of the OSD, two (2) different analytical methods were undertaken of a section of the OSD.

The first method consisted of a finite element analysis. An accumulated fatigue damage of D=0.7 after 100 years of usage was estimated with composite effect included for the trough deck weld near a bulkhead. The accumulated fatigue damage without composite effect was calculated to D=5.0 which simulate a fully cracked pavement.

The second method consisted of data analysis from a monitoring campaign that included nos. fifteen (15) strain gauges and pavement temperature sensors. This method had the advantage of being based on actual traffic loads and included the temperature influence on the composite effect. The fatigue damage was estimated to D=0.35 after 100 years of usage.

Assuming some composite effect from the pavement, no fatigue cracks should be expected in the bridge service life in areas that is not influenced by the impact from the expansion joints. However, if there is no composite effect due to deterioration of the pavement, fatigue cracks must be expected in the trough deck welds throughout the bridge during the service life.

4 OBSERVED CRACKS IN 2017

During a general visual routine inspection in the summer of 2017, indications of fatigue cracks in the orthotropic steel deck were first observed. The superstructure contains many kilometers of welds, and the visual inspections primary focus was on welds close to the expansion joints under the slow lane with spot checks further away from the expansion joints. These locations were selected based on the following criteria's:

- Structural details that will cause high stress concentrations.
- High local stresses and a high number of wheel passages from heavy vehicles.
- Additional impact factor from heavy vehicles passage of expansion joints.
- Experience from fatigue damage in similar structures.

The paint system with its orange base layer and black top coat provided a good background where crack indications stood out quite clearly, see Figure 3. There were however some concerns that small fatigue cracks could develop, hidden by the asbestos based top coat and thus not observed in a visual inspection. This concern was addressed by performing NDT inspections later in 2017.

All crack indications were in the through to deck plate welds in through nos. 14 and 17 which correspond to the typical wheel positions of heavy vehicles in the slow lane, see Figure 4.

All crack indications were also located close to the bulkheads after the expansion joints in the driving directions.

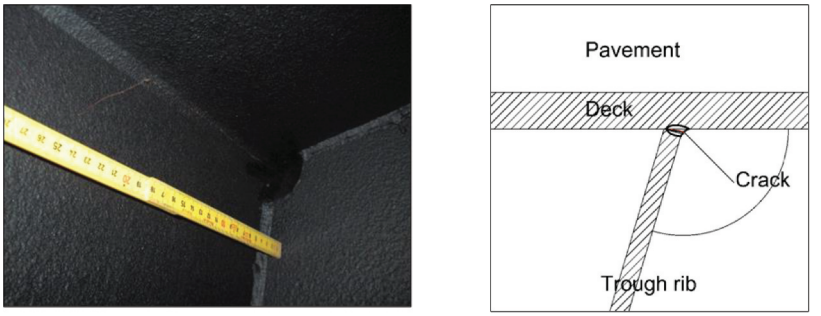


Figure 3. Fatigue crack indication in trough to deck weld.

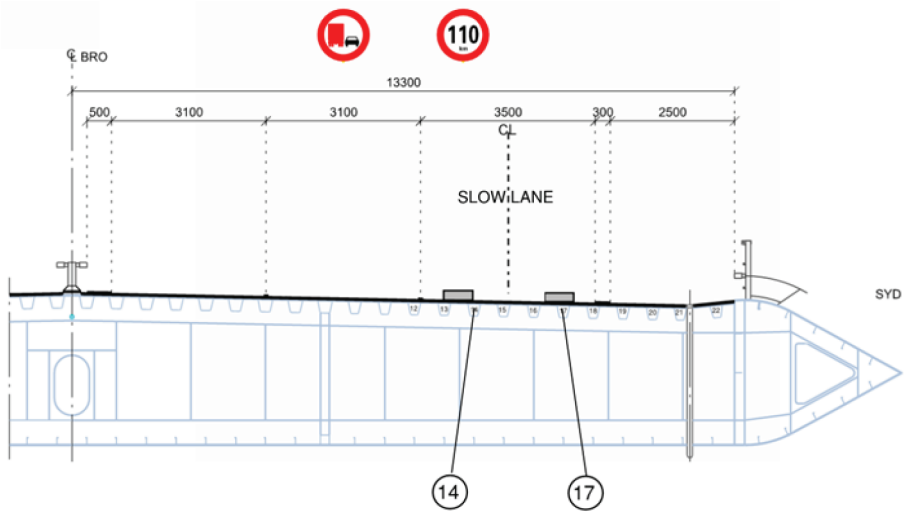


Figure 4. Cross section with typical wheel locations of heavy vehicles.

Following the general visual routine inspection, a program for the execution of a special inspection, with particular focus on the fatigue cracks, was prepared. Meetings with NDT experts from FORCE Technology were held and it was decided to use ultrasonic testing (UT) and eddy current testing (ET) in the special inspection.

A special inspection with assistance from FORCE Technology was performed later in 2017 with NDT methods. The crack indications were confirmed and areas without crack indications nearby were also tested with negative results. It was thus confirmed to a certain extent, that no hidden cracks, that could not be observed by visual inspection, were present.

A total of ten (10) cracks were found with a total length of approx. 2.5m. The cracks initiates at the weld root near the bulkhead cope hole and propagate through the weld bead to the face. They are often termed through bead cracks. They extend away from the bulkhead for approx. 150 – 200mm and then turn down into the parent metal in the trough rib, until they reach a position in the trough rib where the crack driving stress is sufficiently small. There were not any indications of cracks initiating at the root and extending up into the deck plate.

Seven (7) cracks were limited to the trough deck weld and would typically extend 50 - 100mm on each side of the transverse bulkhead. Three (3) had developed to a length of typically 150 – 200mm on each side of the transverse bulkhead and had then continued down in a skew angle into the parent metal in the trough rib as shown in Figure 3 left above. All the three (3) long cracks were in the same area after an expansion joint and on the left side of trough no. 14.

5 STUDY OF REPAIR METHODS

A study of repair methods was performed in the spring of 2018 based on COWIs experience from similar bridge structures with fatigue damage and published articles on the subject. A total of eleven (11) options was identified, that could be used either alone or in combination:

1. Do nothing.
2. Move traffic lanes approx. 0.6m.
3. Drill stress relieving holes at crack tip of cracks that have continued down into trough rib.
4. Strengthening of troughs by bolting a steel plate over one weld.
5. Strengthening of troughs by bolting a steel plate over two welds.
6. Strengthening of troughs by filling the troughs with a filling material, such as polyurethane.
7. Weld repairs from inside of the box girder.
8. Weld repairs both from inside and outside of the box girder.
9. Weld repairs from inside combined with bolted splice plates on the deck.
10. Bolted splice plates on the deck plate combined with bolted splice plates on the trough ribs.
11. Replace asphalt surfacing with high strength concrete overlay with steel fibers.

The options were compared and ranked, based on several parameters such as documented effect, impact on total bridge dead load, ease of execution, impact on traffic on bridge and economy.

Based on the limited number of cracks detected and COWIs successful experience with crack repair by welding, it was decided to go ahead with option 7) "Weld repairs from inside of the box girder". This method does not change the stiffnesses of the deck structure or introduce additional weight and can be performed without the need to close traffic above repairs, which was of very high importance to the bridge owner, the Danish Road Directorate.

The unit price of weld repair was initially estimated to 9,000 USD per nos. and it was expected, that the unit price could be reduced if the number of repairs was increased. A large part of the cost of option 7) is due to removal of the toxic paint system. Therefore option 4) was also seriously considered as the paint system does not need to be removed except very locally and this option is generally considered cost effective. However, it was not selected due to lack of documented long-term fatigue performance.

6 MOCKUP

As preparation for the weld repairs, it was decided to manufacture two (2) mockups of troughs, deck plate and surfacing, see Figure 5 - left, where a preproduction test, including weld preparation and welding, could be tested under near realistic conditions. Welds shall be performed without backing and particularly the weld repairs in the trough rib is considered difficult to execute. It was decided to use a multi run Tungsten Inert Gas (TIG) welding procedure specification because high quality welds by experience can be achieved with TIG welding, due to the excellent weld bead control.

The welds on the mockup was tested by both radiographic testing (RT), ultrasonic testing (UT), magnetic particle testing (MT) and macro examination. All with good results. Furthermore, surfacing temperature was measured to max. 250°C directly above the trough deck plate weld repairs. The adhesive primer is damaged at temperatures around 180°C and was therefore damaged over a width of approx. 3cm above and along the weld repairs. Thus local damage and possible local repair of the surfacing must be expected with this repair method.

A method statement for the weld repairs was prepared based on the experiences obtained from the preproduction test. The main tasks were:

- Preparation
  - Removal of paint.
  - Coordinate temporary traffic markings. It was necessary to close the emergency lane locally to bring personnel and equipment into the box girder.
  - Coordinate with NDT inspector.

- Removal of crack and weld preparation
  - Removal of crack and weld preparation with grinder and rotating file.
  - Check with VT/MT that crack tip is removed.
- Welding
  - Perform horizontal weld in position “horizontal overhead” (PD) from bulkhead and out on both sides.
  - Perform weld in trough rib in position “vertical down” (PG) on both sides. Both vertical up (PF) and vertical down (PG) had been tested on mockup with PG giving the best results.)
- NDT
  - Check weld with VT/RVT/MT/RT.

It was decided to drill two (2) Ø16mm holes in the trough rib on the opposite side of the weld repair, so remote visual testing (RVT) of the weld repair could be carried out with an endoscope, see Figure 5 - right.



Figure 5. Mockup – left. Two (2) Ø16 holes for RVT – right.

7 WELD REPAIR CAMPAIGN

Weld repairs were carried out late in 2018 based on the method statement and the WPS and with full traffic in the roadway lane above. All repairs were welded by the same expert TIG welder. The results were generally good and a typical weld repair is shown in Figure 6 - left.

A crack indication was found by RT in one (1) of the trough weld repairs, see Figure 6 – right, and this was then cut away and repaired again with satisfactory result. The remaining nine (9) weld repairs were satisfactory in the first repair.

The weld repairs were in total quite time consuming because the cracks were scattered over four (4) locations and thus personnel and equipment had to be moved four (4) times. With



Figure 6. Weld repair of trough deck plate weld left, crack indication in trough weld repair right.

taking down and setting up traffic markings, movement to a new location could take almost a full day. Also the NDT inspector was not present full time and one day hold time before NDT could be performed had to be respected. With all in place the welding in itself did not take long for the expert TIG welder.

The unit cost for a weld repair ended up to approx. 6,500 EUR per nos. with a rough split of 25% for removal of paint and 75% for NDT, weld repair and traffic markings.

Some of the lessons learned were:

- Great care should be exercised with the weld preparation and the root gap should not be too large.
- High quality pictures of the root side of weld repairs, could be obtained with a flashlight and the camera from a mobile when put in front of the two Ø16 holes. Much higher quality than by endoscope, see Figure 7.
- Only expert TIG welders should be used, and welder should preferably practice on a mockup before actual production welding.
- Allowing traffic above the weld repairs increased the weld duration slightly, but from an overall perspective, this had little impact on the total duration.
- Cracks shall preferably be repaired before they turn down into the parent metal of the trough side.

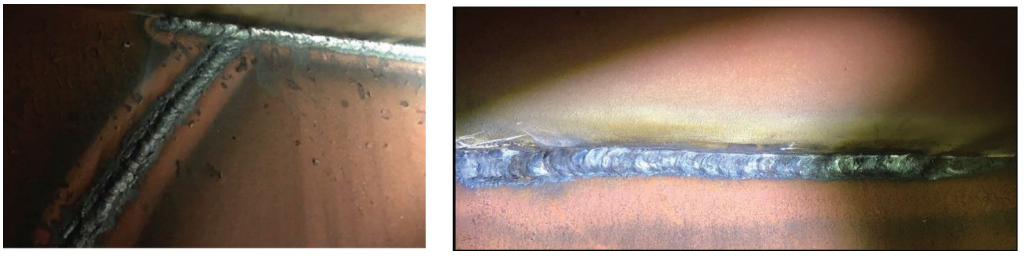


Figure 7. Root side of weld repair, first repair left and last repair right.

8 FOLLOW UP ON WELD REPAIRS AFTER 2018

Since 2018 visual inspections has been carried out every year and afterwards all observed fatigue cracks have been repaired. The repair works has been tendered out and agreements made with a contractor for a 3-year repair period.

It has in the tendering process been found beneficial to specify five (5) types of repairs, characterized by the length and the location of the fatigue crack. The unit cost in 2023 for a weld repair is in average approx. 3,000 EUR per nos. with a rough split of 20% for removal of paint and 80% for NDT, weld repair and traffic markings. Compared to 2018 prices a reduction of 54%. The costliest fatigue crack repair is 3,800 EUR.

70% of the fatigue cracks are observed at an early stage (Type 1), where the fatigue crack is limited to the deck to trough weld. The next 27% fatigue crack observations (Type 2) are observed when the fatigue crack is extended from the deck to trough weld, down (10 – 100 mm) in the trough side.

A visual inspection supplemented with NDT methods was performed approx. one (1) year after the weld repairs. No crack indications were found in any of the weld repairs.

However, three (3) new trough deck plate bead through cracks were observed and confirmed by MT. These newly discovered cracks were located before the expansion joints in trough nos. 14 and 17. The areas before the expansion joints have not been in similar focus, as the areas after the expansion joints, in earlier visual inspections and it is therefore not known how long they have been there.

The continuous discovery of new cracks highlight the necessity for conducting visual inspection on a regular basis in areas under the slow lanes. The dynamic effect on the front axles of

a lorry passing the expansion joint will also have a dynamic impact back on the rear axles that have not yet reached the expansion joint that need to be considered.

The remaining fatigue life of the trough deck weld under the fast lanes is likely several decades and need only be spot checked every five years.

9 CONCLUSION

The steel box girder of New Little Belt Bridge contains close to 100km of trough to deck plate welds and it was fabricated during a time where the knowledge of fatigue assessment of steel bridge deck details was much less developed than today. Also, modern welds are generally of higher quality than the welds on the New Little Belt bridge. The deck plate and trough thickness are smaller than current Eurocode recommendation and ultimately, and from that point of view, it is only a matter of time before fatigue cracks will start to appear. However, it depends very much on the original weld execution quality, pavement condition and traffic loads if cracks will start to develop on a large scale within the bridge service life. General fatigue issues thus could represent an enormous potential cost for the bridge owner.

At present, after fifty-three (53) years of operation, at total of one hundred and fifty-seven (157) fatigue cracks have been detected in the trough to deck weld close to the bulkheads, see heatmap in Figure 8. Most cracks have been located close to the expansion joints and beneath trough nos. 14 and 17 which correspond to typical wheel positions of heavy vehicles in the slow lane, see Figure 4.

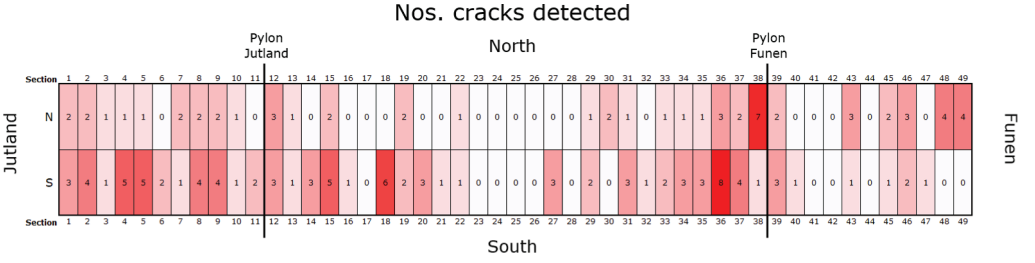


Figure 8. Heatmap of cracks per December 2023.

All the discovered fatigue cracks from the period 2018 – 2023 have successfully been repaired by welding based on a method statement that was prepared after preproduction tests on a mockup.

The expansion joints cause an additional impact that roughly can be estimated to a 30% increase of wheel loads for pavements of good quality. As the fatigue life is a function of stresses to the power of five (5), it is very vital that the pavement and expansion joints are continuously kept in good condition.

Because heavy vehicles are restricted to driving in the slow lanes and lighter vehicles does not cause fatigue damage, it is anticipated that the remaining fatigue life of the trough deck weld under the fast lanes is likely several decades.

REFERENCES

COWI 1970. *Motorway Bridge across Lillebælt, Design and Construction of the Bridge*. Copenhagen.

de Jong, F.B.P. 2006. *Renovation techniques for fatigue cracked orthotropic steel bridge decks*. PhD Thesis Technische Universiteit Delft.

EN 1993-2 2007. *Eurocode 3 – Design of steel structures – Part 2: Steel Bridges*.

Farreras-Alcover et al. 2017. Fatigue life prediction of New Little Belt steel deck under a cracked pavement section. EUROSTEEL 2017.

Hirayama et al. 2014. *Report on Repair of Fatigue Cracks of the Orthotropic Steel Decks in the United Kingdom*. Steel Construction Today & Tomorrow.

Kolstein, M.H. 2007. *Fatigue classification of welded joints in orthotropic steel bridge decks*. PhD Thesis. Technische Universiteit Delft.

Bridge Maintenance, Safety, Management, Digitalization and Sustainability – Jensen, Frangopol & Schmidt (eds)
© 2024 The Author(s), ISBN 978-1-032-77040-6
Open Access: www.taylorfrancis.com, CC BY-NC-ND 4.0 license

The organization, O&M operations and inspections of the 1915Çanakkale Bridge

F. Aytekin
Çanakkale Motorway and Bridge Construction Investment and Operation Inc., Turkey

A.M. Kızılkaya
Intertoll Turkey Operation and Maintenance Inc., Turkey

ABSTRACT: The 1915Çanakkale Bridge provides the crossing of the Dardanelles between Gelibolu-Lapseki as part of the 101-kilometer long Malkara-Çanakkale Motorway. The 1915Çanakkele Bridge is the longest suspension bridge in the world with a main span of 2023 meters, symbolizing the 100th anniversary of the Republic of Turkey, and featuring the world's tallest towers at a peak height of 334 meters with the addition of Seyit Onbaşı artillery shell figures to the 318-meter steel tower height. The1915Çanakkale Bridge is a world record bridge that was built in a record time of just four years providing an alternative route to the busy city of İstanbul. The long main span combined with extreme wind loads and possible earthquakes, put engineering capabilities to the test. The O&M sub-contractor organization, inspections, and monitoring systems offer an intriguing case study. Operational since March 18,2022 the 1915Çanakkale Bridge and Malkara-Çanakkale Motorway Project critical for enhancing regional connectivity.

1 INTRODUCTION

The Malkara-Çanakkale Motorway and 1915Çanakkale Bridge Project represent a monumental engineering accomplishment that has significantly enhanced Turkey's transportation infrastructure. This visionary project was conceived as an essential component of the 101-kilometer Malkara-Çanakkale Motorway, which has now been brought to fruition with the construction of the 1915Çanakkale Bridge. The bridge spans Çanakkale Strait (Dardanelles) between Gelibolu and Lapseki connecting Europe and Asia. Not only it is a testament to exceptional engineering prowess, but it also holds deep symbolic significance as it commemorates the 100th anniversary of the Republic of Turkey.



Figure 1. 1915Çanakkale Bridge.

DOI: 10.1201/9781003483755-353

1.1 *Strategic importance*

The countries within the region have constructed railways and integrated motorways across Anatolia, Caucasia, and Asia to support the development of the Silk Road. This historical trade route originates in the Far East and extends all the way to Europe, along the "Middle Corridor" To facilitate this, they have taken important steps to develop a multi-directional transportation network on the Asia-Europe-Middle East axis and implemented projects to develop transportation.

As a result, mega projects are being built in an integrated manner. The 1915Çanakkale Bridge is of great importance in this regard. It not only connects mega-projects such as Yavuz Sultan Selim Bridge, Northern Marmara Motorway, Osmangazi Bridge, North Aegen Port, and Gebze-Orhangazi-İzmir Motorway but also increases the benefits and importance of this corridor.

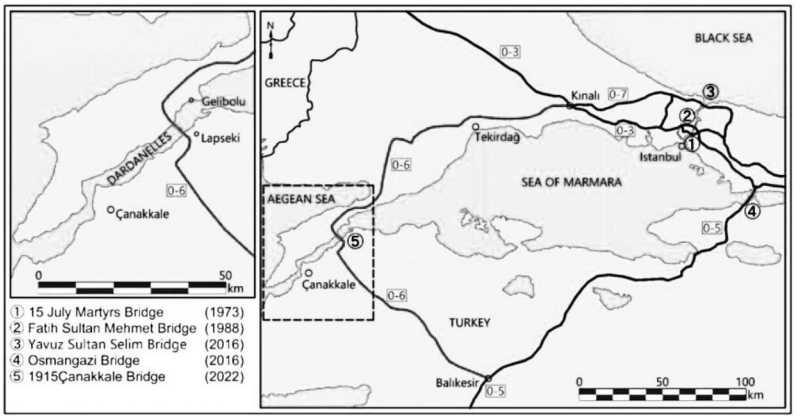


Figure 2. Transportation network between mega-projects (Til 2023).

1.2 *Design basics*

The Bridge faces several challenges including aerodynamics, ship traffic, seismic activity and adverse soil conditions. To address the windy conditions, a wind-resistant twin-box steel girder design is being implemented. The tower foundations are designed to withstand intense ship traffic and seismic hazards. The construction timeline requires fast-track construction methods, influencing the overall design approach.



Figure 3. Twin-box steel girder deck.

The deck arrangement was finalized following wind tunnel testing aimed at enhancing traffic comfort through the implementation of wind barriers. Prefabricated parallel wire strands

were used for main cables and high-grade steel was used for the tower to reduce the quantities and consequently construction time and seismic mass.

1.3 *Organization, information*

The General Directorate of Highways commissioned the 1915Çanakkale Bridge and Motorway Project to a Turkish-Korean joint-venture in 2017 within the framework of the public-private partnership model. Limak and Yapı Merkezi from Turkey and Daelim and SK E&C from Korea make up this joint-venture named DLSY JV which established a joint-venture company specific to the project, under the name of Çanakkale Motorway Bridge Construction Investment Management Inc.

Project Length: 101 Km. (88 km Motorway + 13 km Link Road)

Duration: 16 Years 2 Month 12 Day (Construction + Operate) (5 Years 6 Month Construction+10 Years 8 Month 12 Operation Day)

Appointed Company: Çanakkale Otoyol Yatırım ve İşletme A.Ş. Contractor: Daelim – Limak – SK – Yapı Merkezi

Operator Company: Intertoll Turkey Operation and Maintenance Inc

2 ORGANIZATION AND PARTNERSHIP MODEL

2.1 *Organization structure*

The Kınalı-Tekirdağ-Çanakkale-Savaştepe Motorway Project Malkara-Çanakkale section, including the 1915Çanakkale Bridge, has been commissioned by the General Directorate of Highways to a Turkish-Korean joint-venture under the name of Çanakkale Motorway Bridge Construction Investment Management Inc. The joint-venture has been awarded a Build-Operate-Transfer contract for the project.

Intertoll Turkey Operation and Maintenance Inc. is the O&M sub-contractor related to the operation and maintenance project Malkara-Çanakkale section, including the 1915Çanakkale Bridge is part of Intertoll Europe, an independent infrastructure developer, operator & maintenance provider, and toll operator with its head office in Budapest, Hungary.

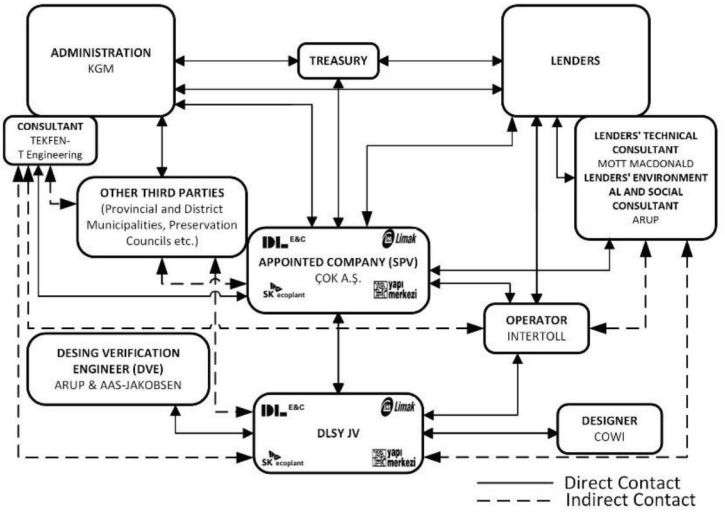


Figure 4. Organization scheme.

2.1.1 *Public-private partnership model*

Public-private partnership (PPP) generally refers to the implementation of investments and services through a contractual agreement, involving the sharing of costs, risks, and returns between the public and private sectors. Originally conceived as a means to secure financing for national infrastructure projects, PPP has evolved into a model emphasizing the effective managerial capabilities of

the private sector. In this framework, the public sector is strategically positioned to focus on areas such as investment coordination, overarching planning, supervision, and policy formulation (T.C. Kalkınma Bakanlığı 2012).

3 INSPECTIONS AND MAINTENANCE

3.1 *Inspection and maintenance protocols*

Inspection and maintenance activities are arranged according to the relevant specification of the General Directorate of Highways, I&M manual by the bridge designer and suppliers O&M manuals. Inspection and maintenance activities are classified into five types "routine inspections/maintenance", "principal inspections", "special inspections" "major maintenance", and "surveying". These types of help organize the activities involved in keeping equipment and infrastructure safe and working well.

Routine I&M tasks are typically carried out with a frequency of weeks, months or annually. The nature of the work is visual inspection and ad-hoc maintenance by walking or driving on the bridge. Routine I&M performed by the permanent I&M personnel.

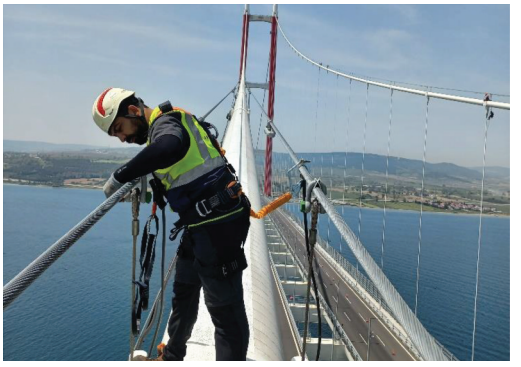


Figure 5. Main cable routine inspection.

Table 1. Suspension Bridge and Approach Viaducts routine inspection plan.

Routine inspection of substructure	Routine inspection frequency
Tower foundation elements above the sea level	Annually
Tower (Outside)	Annually
Tower (Inside)	Annually
Anchor Blocks (Outside)	Annually
Anchor Blocks (Inside)	Annually
Concrete Piers	Annually
Routine inspection of superstructure	Routine inspection frequency
Steel Deck Exterior	Annually
Steel Deck (Inside)	Annually
Main Cable System	Annually
Hanger Rope System	Annually
Bearings	Semi-Annually
Expansion Joints	Monthly/ 3 Monthly/Semi-Annually
Surfacing, Pavement, Maintenance Walkway	2 times a month
Concrete Deck Exterior	Annually
Concrete Deck (Inside)	Annually
Routine inspection of substructure	Routine inspection frequency
Barriers, Parapets, Wind Barriers and Ancillaries	2 times a month
Access Facilities	The relevant access structure during the inspection
Hydraulic Buffers and End Stops (Structural Parts)	Annually
Drainage System	Semi-Annually



Figure 6. Concrete surface visual inspection by using drone.

Principal inspections comprise a closer visual inspection with the objective of assessing the current condition of the structure, reviewing the development of defects, and assessing and planning the need for maintenance. Principal inspections are carried out at fixed intervals, which are typically defined as intervals of 5 or 10 years in the designer manual.



Figure 7. Principal inspection of bearings.

Special inspections normally involve the use of specialist personnel and equipment to conduct and evaluate measurements and testing. They are typically initiated based on the conclusions of principal inspections or routine I&M, where the results indicate the need for special inspections to clarify the condition of the structure and the need for repair. After extreme events with potentially large structural consequences for example fire, earthquake, ship impact high winds and vehicular collisions.

3.2 *Maintenance strategies*

In addition to adhering to the recommendations outlined by the supplier's O&M manuals a maintenance plan has been developed with the primary objective of preserving and maximizing the structural integrity and service life of the suspension bridge. The maintenance program comprises both routine and ad-hoc interventions for addressing any identified damages during inspections to ensure the bridge's stability throughout its lifespan.

Table 2. Suspension Bridge and Approach Viaducts routine maintenance plan.

Routine maintenance of the bridge elements	Maintenance Frequency
Litter collection (Anchorage Blocks (Outside), Revetment, Abutments)	Semi-Annually
Litter collection (Anchorage Blocks (Inside), Piers (Inside))	Annually
Litter collection (Suspension Bridge Decks (Inside))	Annually
Litter collection (Approach Viaducts Decks (Inside))	Annually
Litter collection maintenance walkway	Annually
Cleaning of expansion joints	2 times a month
Cleaning of bearings	Annually
Cleaning of drainage system	Semi-Annually
Cleaning of road elements	Maintenance Frequency
Cleaning of traffic signs	When needed
Cleaning of guardrail and wind barriers	When needed



Figure 8. Cleaning of expansion joints.

3.2.1 *Winter maintenance*

During the winter, meteorological data are monitored which have been taken from the General Directorate of Meteorology and outsourced services for winter maintenance, and preventive maintenance work is initiated for the suspension bridge when the asphalt temperature taken by patrol on site drops below 2°C. Urea solution is used to prevent the negative effect of NaCl on the steel surface of the suspension bridge. If snowfall is normal and urea solution can melt the snow, snow ploughing is not performed. Under extreme conditions, if the solution used is not sufficient to melt the snow on the bridge, snow ploughing is also carried out in all 3 lanes. In cases where the width of the shoulder is not sufficient to accumulate snow due to heavy snow conditions, winter maintenance is carried out with snow ploughing in 2 lanes only, as there is no shoulder on the bridge section. It is planned to use magnesium chloride and corrosion inhibitor solution at temperatures too low for urea solution to function.

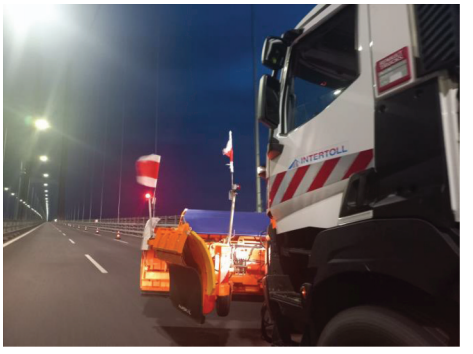


Figure 9. Preventive winter maintenance.

4 CONCLUSION

In conclusion, the paper provides a comprehensive overview of the organization, operations, and inspections of the 1915Çanakkale Bridge, a monumental engineering achievement that significantly enhances Turkey's transportation infrastructure. The 1915Çanakkale Bridge emerges as an unparalleled engineering marvel, proudly claiming the title of the world's longest suspension bridge with its extraordinary 2023-meter main span. Positioned as a pivotal component within the extensive 101-kilometer Malkara-Çanakale Motorway, this iconic structure transcends its physical dimensions, embodying Turkey's rich history and commemorating a century of the Republic.

The strategic significance of the 1915Çanakkale Bridge is evident in its role connecting major projects such as the Yavuz Sultan Selim Bridge, Northern Marmara Motorway, Osmangazi Bridge, North Aegean Port, and Gebe-İzmir Motorway, contributing to the development of modern Silk Road. The organization and partnership model, implemented as a public-private partnership, reflects effective collaboration between Turkish and Korean entities.

The section on inspections and maintenance outlines a comprehensive approach to ensuring the longevity and safety of the 1915Çanakkale Bridge. The protocols for inspections and maintenance strategies showcase a meticulous and proactive maintenance plan.

In summary, the 1915Çanakkale Bridge stands not only world record in terms of its impressive dimensions but also as a testament to the successful project management, innovative engineering, and effective public-private collaboration. The operational and maintenance practices detailed in this paper reflect a commitment to ongoing safety, functionality, and regional connectivity facilitated by this extraordinary infrastructure project.

REFERENCES

Til, M.A. 2023. *Risk-Based Strategies for Bridge Maintenance Chapter 5 1915Çanakkale Bridge: deck construction technology developments*. Darlington, UK

T.C. Kalkınma Bakanlığı 2012. *Dünyada ve Türkiyede Kamu-Özel İşbirliği Uygulamalarına İlişkin Gelişmeler, Turkey*

Bridge Maintenance, Safety, Management, Digitalization and Sustainability – Jensen, Frangopol & Schmidt (eds)
© 2024 The Author(s), ISBN 978-1-032-77040-6
Open Access: www.taylorfrancis.com, CC BY-NC-ND 4.0 license

Traffic wind hazards on the Storebælt East Bridge and mitigation

A. Larsen, L.F. Pedersen & N. Bitsch
COWI consulting engineers, Kgs. Lyngby, Denmark

F.R. Gottfredsen
Sund & Bælt, København V, Denmark

ABSTRACT: The present paper gives an account of theoretical and experimental work carried out for identifying and improving the wind traffic climate for vehicles crossing the Storebælt bridge. The theoretical work involved development of the balance model for wind overturning and a survey of stability parameters for various classes of road vehicles. The experimental work involved wind tunnel tests for determination of aerodynamic coefficients to be applied in the theoretical balance model yielding revised wind restrictions for vehicles travelling the bridge.

1 INTRODUCTION

The wind climate experienced by the traffic crossing cable supported bridges is influenced by structural components such as pylons, anchor blocks, crash barriers and other equipment rising above the roadway. These elements create local zones of increased wind speed or shelter relative to the approach wind speed well upwind of the bridge. Abrupt changes in the wind speed requires responsive counter steering by the driver to maintain the driving path. Also, excessive momentary wind loads may cause overturning of light high sided vehicles. A statistical survey of wind related vehicle accidents encountered on the Storebælt East Bridge revealed that 33 out of 56 accidents recorded in the period 1998 - 2019 happened in the vicinity of the pylons and the anchor blocks involving overturning of light and high sided box trailers town by private cars, commercial vans or lorries, Figure 1.

The fact that most of the wind related accidents involved overturning of light high sided vehicles initiated a theoretical and experimental investigation into the wind hazards and wind screens and traffic restrictions for mitigation.

2 SIMPLE THEORETICAL BALANCE MODEL FOR WIND OVERTURNING

A vehicle travelling at a constant speed V in a wind field having a local speed U and a direction β with the travel path will be met by a relative wind speed V_r at inflow angle α, Baker (1991), Figure 2, left:

$$V_r = \sqrt{(V + U cos\beta)^2 + (U sin\beta)^2}$$
$$sin\alpha = \frac{U sin\beta}{\sqrt{(V + U cos\beta)^2 + (U sin\beta)^2}} \quad (1)$$

The forces acting on the vehicle is the restoring moment of gravity $M_g = ½Bmg$ about the lee wheel contact point and an overturning moment due to the wind $M_w = 1/2\rho V_r^2 LHz_a C_M$ where C_M is the aerodynamic overturning moment coefficient. C_M is a function of the inflow

DOI: 10.1201/9781003483755-354



Figure 1. Wind overturning accident near the pylon involving a small empty box trailer towed by a car.

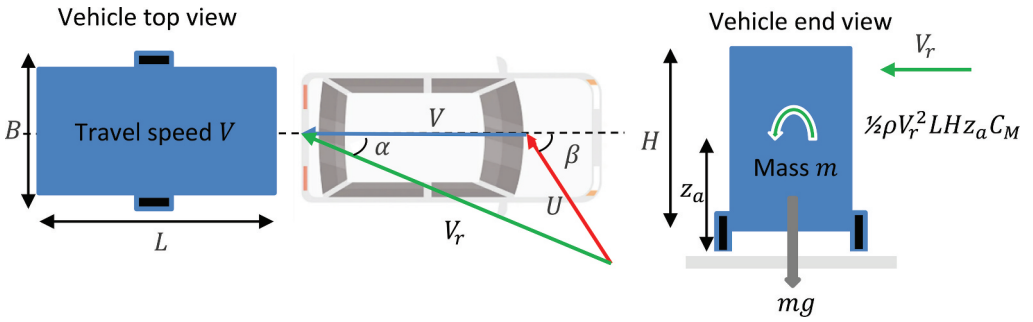


Figure 2. Characteristic dimensions, wind speeds and forces acting on a travelling vehicle.

angle α and is often well approximated by sinus function $C_M(\alpha) = C_{M90} sin\alpha$ for box shaped high sided vehicles (Baker, 1991) with C_{M90} being the nominal value for cross winds. C_{M90} is to be determined from wind tunnel tests for the vehicle types in question.

The relative wind speed at which the vehicle is expected to overturn is obtained by equating the overturning moment of the side wind force and the restoring moment due to gravity:

$$1/2Bmg = z_a 1/2\rho {V_r}^2 LHC_M \Rightarrow {V_r}^2 = \frac{S}{C_{M90}\, sin\,\alpha} \tag{2}$$

where $S = Bmg/\rho LHz_a$ is the stability parameter combining the width of the wheelbase B, the length and the height of the vehicle L, H, the height of the aerodynamic center z_a above the roadway mass, the mass m, the air density ρ and the gravity acceleration g as illustrated in Figure 2.

Inserting (1) into (2) allows the overturning condition to be expressed as function of the vehicle speed V, the wind speed U and wind direction β:

$$U^4\left(1 + \left(\frac{V}{U}\right)^2 + 2\left(\frac{V}{U}\right)cos\beta\right) = \frac{S^2}{C_{M90}^2}\frac{1}{sin\beta^2} \tag{3}$$

which must be solved numerically for the general case. In the case of cross winds, $\beta = 90$ deg. (3) reduces to the analytical expression:

$$V_{OT} = \frac{1}{U}\sqrt{\frac{S^2}{C_{M90}^2} - U^4} \tag{4}$$

where V_{OT} (m/s) is the travel speed at which the vehicle is expected to overturn when subjected to a local wind speed U (m/s). Numerical solutions to (3) reveals that it displays a shallow minimum for $\beta \approx 70$ deg. as is also reported in Baker (1991). Using (4) instead of (3) overestimates the travel speed by approximately 4% at $\beta \approx 70$ deg. A fair approximation for practical applications.

Application of (4) for investigation of the traffic crossing the Storebælt East Bridge requires that the stability parameter S and the overturning moment coefficient C_{M90} are determined.

3 STABILITY PARAMETER

The stability parameter S combines the vehicle size and inertia properties of the overturning as discussed above. The stability parameter for different types of vehicles crossing the Storebælt bridge was determined from vehicle manufacturers and providers databases.

The many and diverse vehicles crossing the bridge were divided into commercial and private categories.

The commercial vehicle category included high sided truck trailers empty or full, vans, mini-buses, city busses and tourist buses.

The private vehicle category included small and large high sided box trailers, caravans, auto campers, large, midsize, and small passenger cars and sports utility vehicles (SUV).

The survey revealed a certain variation in the numerical value of S depending on model and make. Based on the variability of the stability parameter within each vehicle group it was decided to define a characteristic value S_c as the mean S_m minus one standard deviation S_σ to be applied for stability calculations. The characteristic stability parameter for commercial vehicles such as vans, mini busses and city/tourist busses falls in the range $1500 < S_c < 2500$ whereas the characteristic stability parameter for private vehicles like passenger cars and SUVs falls in the range $2500 < S_c < 5600$.

The lowest and thus most critical stability parameters are found for large and small commercial or private box type trailers, Table 1. The small and popular box trailer which can be rented at most service stations, home improvement retailers and large furniture stores in Denmark displays the lowest characteristic value $S_c = 480$ making it the most vulnerable vehicle with respect to wind induced overturning.

Table 1. Stability parameters for typical high sided commercial and private vehicles.

Vehicle type	Truck trailer – empty	Large box trailer - empty	Caravan	Small box trailer - empty
				
Stability parameter				
Mean S_m	1490	1000	1100	700
Standard deviation S_σ	140	300	100	220
Characteristic $S_c = S_m - S_\sigma$	1350	700	1000	480

4 OVERTURNING MOMENT COEFFICIENT

The overturning moment coefficient for wind constitutes the aerodynamic parameter necessary of evaluation of vehicle overturning travel speeds to be determined from wind tunnel testing. It is noted that C_{M90} appearing in (4) refers to the local wind speed U meeting the vehicle at a given section of the travel path. The local wind speed experienced on a bridge is dependent on the shelter

or speed up effects caused by bridge components located upwind of the vehicle. To obtain the best possible estimates of the overturning moment coefficients from the wind it was decided to measure the overturning moments M_w acting directly on a generic box trailer model located at different locations on models of representative parts of the Storebælt East Bridge and to refer the overturning moment coefficient, now termed C_M, to the speed U_0 of the undisturbed wind approaching the bridge model: $C_M = M_w/1/2\rho U_0^2 LHz_a$. The consequence of this choice is that C_M now becomes a function of the shape of the vehicle as well as its position on the bridge.

4.1 *Wind tunnel tests*

The wind tunnel tests were carried out at FORCE Technology, Kgs. Lyngby, Denmark. The models of the Storebælt East Bridge included λ_l = 1:30 scale deck/pylon and deck/ anchor block assemblies and was tested with and without local wind screens arranged as vertical picket fences having an open area ratio of 50%, Figure 3. All tests were run in turbulent flow of 10% intensity characteristic for the Great Belt site. The approach wind speed U_0 was measured by a pitot tube situated at deck level and well upwind of the bridge models.

The vehicle model was chosen to represent a generic box trailer having full scale dimensions L = 2.3 m, H = 2.8 m, B = 1.3 m and z_a = 1.6 m. The vehicle model was mounted on a heigh frequency force balance having a first resonance frequency of 25 Hz. The vehicle/force balance assembly was inserted in pits in the slow lane of the bridge deck model at preset distances from the pylon or anchor block such that the top of the model mount was flush with the roadway leaving a 0.2 m gap to the trailer bottom plate, Figure 3, bottom.

All measurements reported were made for cross winds (β= 90 deg.) at a model scale approach wind speed of U_{0ms}= 8 m/s taking 60 sec. time histories of the overturning moment M_w.

Data processing involved low pass filtering of the recorded timeseries at 17 Hz to avoid contamination of the measured signals by the force balance resonance. Assuming a full scale wind speed of U_{0fs} = 25 m/s the time scale of the tests is obtained as $\lambda_t = \lambda_l U_{0fs}/U_{0ms} \approx$ 1:10 indicating that the 60 sec. sampling period is a good representation of standard meteorological averaging period of 10 min. and capable of resolving gusts down to approximately 1 sec. full scale.

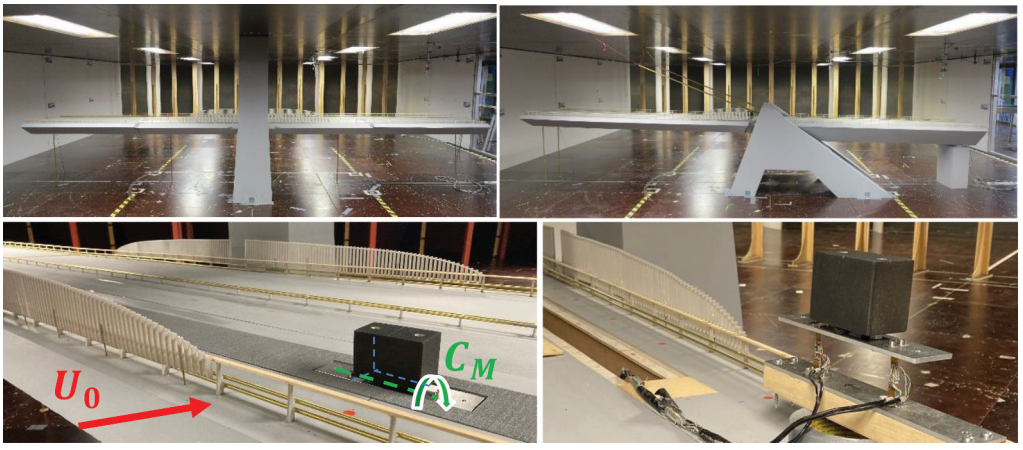


Figure 3. 1:30 scale wind tunnel models of the Storebælt bridge. Photo: FORCE Technology.
Top: Pylon/deck (left) assembly and anchor block/deck assembly (right) featuring local wind screens.
Bottom: Model box trailer located in the slow (windward) lane. High frequency balance/model assembly.

4.2 *Wind action at the pylons without wind screens*

Figure 4. top right, displays an excerpt of the C_M time series measured at a position 7 m from the center line of the 9 m wide pylon, i.e., at a position approximately one vehicle length before entering the shelter zone. The times series is converted to full scale time by applying the

time scale λ_t. It is noted that the mean value of the overturning moment coefficient is approximately 1 (horizontal line) whereas the peak reaches 2.7 and the minimum 0.17 within the 10 sec. time window displayed. Video recordings of overturning box trailers indicates that the overturning is a fast process of 1 – 3 sec. duration thus governed by the peak value of C_M.

The Fourier transformation of the time series (below, right) displays a wide band signal slightly decreasing with increasing frequency and a prominent narrow band peak at the non-dimensional frequency $fD/U_0 = St = 0.12$ where $D = 9$ m is the cross-section dimension of the pylon leg. The broad band signal is interpreted to be due to random turbulence. The narrow band peak at $St = 0.12$ is identified as the Strouhal Number for von Kármán vortex shedding from a square section prismatic structure as proposed in EN1991-1-4. The large variation of C_M due to the vortex shedding action in the vicinity of the pylon is believed to be a significant ingredient in the frequent overturning accidents close to the pylons. Following (4) a factor 3 increase of C_M yields a 70% reduction of the approach wind speed at which a vehicle overturns.

The spectral composition of C_M suggests that the peak value can be obtained as the sum of the mean value C_{Mm}, the standard deviation of the contribution from the vortex shedding $C_{M\sigma vtx}$ and the standard deviation of wide band turbulence $C_{M\sigma wb}$:

$$C_{Mp} = C_{Mm} + \sqrt{2}C_{M\sigma vtx} + 3.5C_{M\sigma wb} \tag{5}$$

Application of (5) to the spectrum in Figure 4 yields $C_{Mp} = 2.34$ while the absolute maximum value of the time series is $C_{Mmax} = 2.4$ thus supporting the spectral summation.

It is interesting to note that the relatively high speed of the vehicle compared to the relative slow time variation of C_M (a period of about 3 seconds) means that some vehicles may experience a quiet situation when passing into or out of the near wake of the pylon whereas other vehicles may enter or exit the pylon wake when the overturning moment is at its peak. A vehicle travelling at 80 km/h will travel 22 m in one second. From the time trace of C_M it is observed that a vehicle entering the pylon wake at time about 412.5 will experience a moment overturning coefficient $C_M < 0.5$. Contrary, a vehicle entering the wake at time 414.5 will experience an overturning coefficient $C_M > 2.0$.

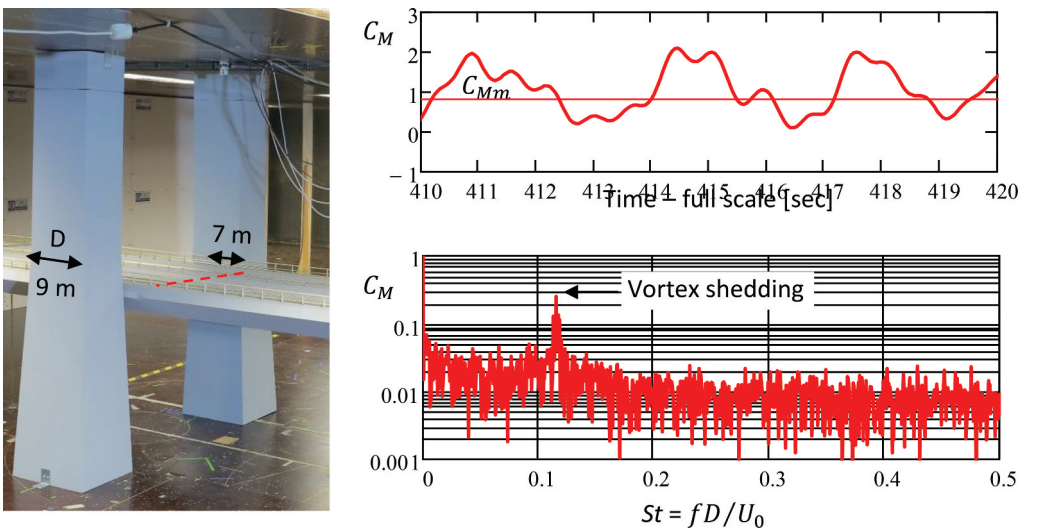


Figure 4. Full scale time trace and frequency spectrum obtained at a position 7 m from the center line of the pylon. As built situation without local wind screens.

4.3 *Overturning moment coefficients at the pylons and effect and extent of the wind screens*

The discovery of the effect of wind band turbulence and narrow band vortex shedding close to the pylon suggested that shielding of the vehicles by wind screens may reduce the mean wind

loading and break up the coherent vortex patterns in wind flow. To this end the model wind screens were fitted to the pylon/deck and anchor block/deck models, Figure 3.

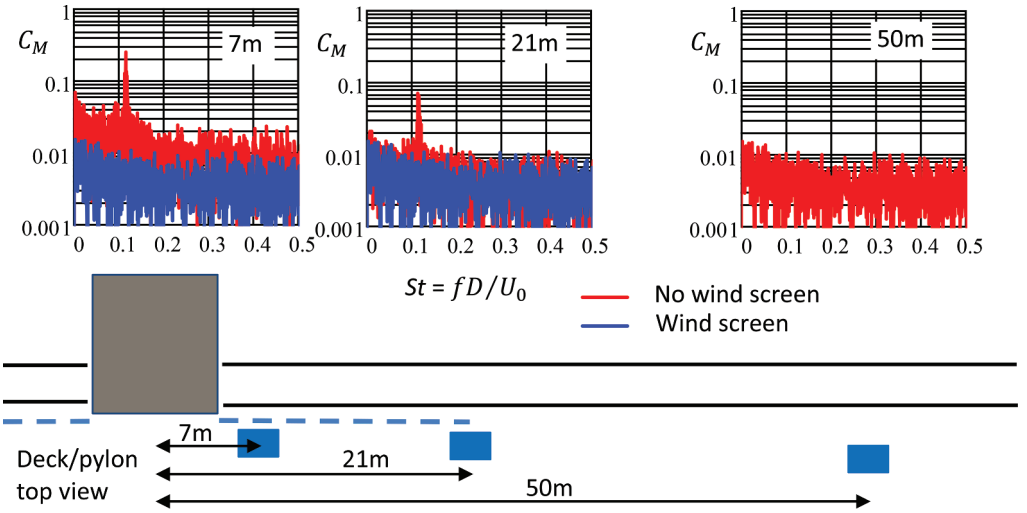


Figure 5. Moment coefficient spectra at positions 7m, 21m and 50m from the pylon center line.

Figure 5 shows spectra of overturning moment coefficient measured at 3 positions of the model vehicle 7 m, 21 m and 50 m from the center line of the pylon. The spectral distribution for the as built situation without wind screens shows that the magnitude of the vortex peak as well as the wide band contribution decreases when moving away from the pylon. At the position 50 m from the pylon the vortex peak has completely disappeared. At a position 21 m the vortex peak has decreased by a factor of 5 relative to the 7 m position and the wide band contribution is roughly at the same level as at the position 50 m from the pylon center line. This finding suggested that a wind screen extending approximately 21 m each side of the pylons would control the vortex shedding loading on passing vehicles.

Overturning moment coefficients measured at 7 m and 21 m before and after fitting of 3.5 m tall, 20 m long wind screens having an open area ratio of 50% show that the wind screens are very efficient in decreasing the peak C_{Mp}, the mean C_{Mm} and the dynamic components $C_{Mdyn} = \sqrt{2}C_{M\sigma vtx} + 3.5C_{M\sigma wb}$ of the overturning moment coefficient, Figure 6.

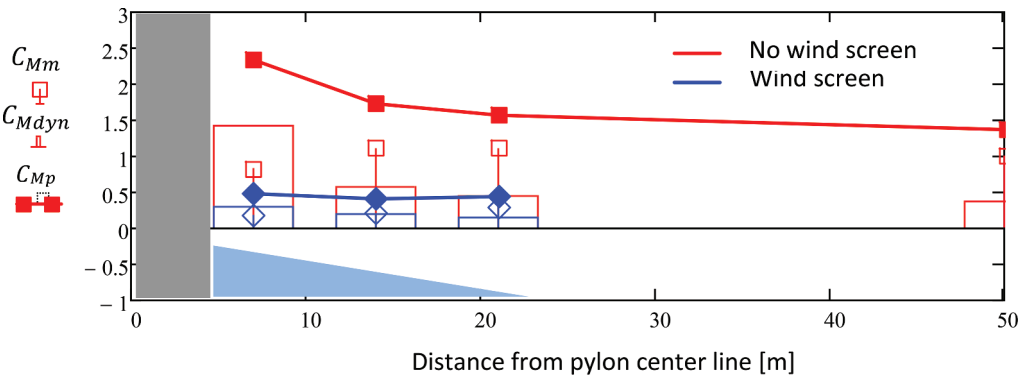


Figure 6. Mean (⊔), dynamic (⊓) and peak (▬) overturning moment coefficients as function of distance from the pylon center line following (5).

4.4 *Overturning moment coefficients at the anchor blocks*

The two anchor block structures of the Storebælt East Bridge, Figure 3, form triangular structures rising approximately 6 m above the roadway at each side of the bridge girder forming the transition from the 4.4 m deep suspension bridge girder to the 7.5 m deep girders of the approach bridges. The similarity between the shelter zones at the pylons and the anchor blocks suggests that it is desirable to fit identical wind screens from the anchor block extending into the suspension bridge side spans. The operation and maintenance of moveable traffic barriers situated at the point of transition from the anchor blocks to the approach bridges would be rendered difficult by the presence of the wind screens. Thus, it was desirable to omit the wind screens at this location.

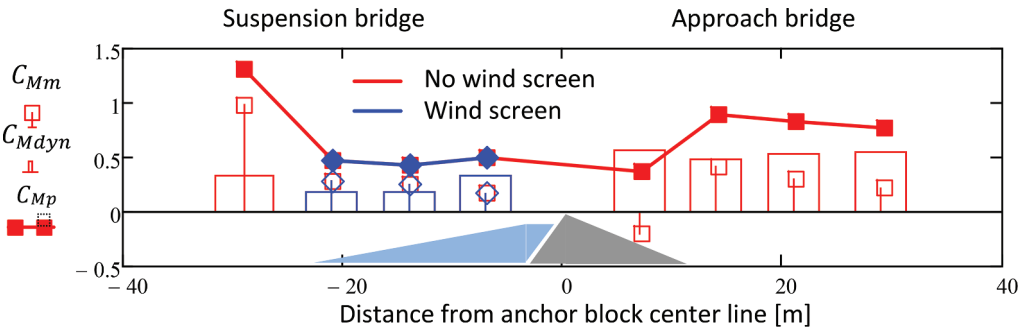


Figure 7. Mean ( ), dynamic ( ) and peak ( ) overturning moment coefficients as function of distance from the pylon center line following (5).

From Figure 7 it is noted that the wind screens at the suspension bridge side of the anchor block reduces the overturning moment coefficients as efficiently as is the case in proximity of the pylons. At -29 m onto the suspension bridge side span and past the wind screens, C_{Mp} = 1.31 which for practical purposes is identical to C_{Mp} = 1.37 measured at the 50 m position in the deck/pylon model, Figure 6. At 29 m onto the approach bridge it is noted that C_{Mp} = 0.77, about 60% of the peak overturning moment coefficient measured at the identical position on the suspension bridge. It is speculated that this effect is due to the larger section depth of the approach bridge which diverts parts of the of the wind flow otherwise impinging on the trailer model.

5 OVERTURNING WIND SPEEDS

The theoretical travel speed speeds V_{OT} (km/h) as function of the approach flow wind speed U_0 (m/s) are calculated from (4) using the characteristic stability parameter S_C = 480 (Table 1) and peak moment coefficients C_{Mp} obtained from the wind tunnel tests, Figure 8.

Small box trailers are allowed to travel at a maximum speed of 80 km/h on highways and thus also on the Storebælt bridge. Thus, it is a appropriate travel speed for evaluating the corresponding approach wind speeds at which the vehicle is expected to overturn.

From Figure 8 (left) it is noted that the small box trailer is at risk for overturning at an approach wind speed of 9 m/s at a position 7 m from the center line of the pylon if wind screens are not fitted, C_{Mp} = 2.34 (red curve). In presence of the wind screes the estimated overturning wind speed becomes 28 m/s at this position proving the efficiency of the wind screens (blue curve). At some distance from the pylon center line (50 m, C_{Mp} = 1.37) the approach wind speed for overturning becomes 14 m/s at a travel speed of 80 km/h (magenta curve) which must be considered as a theoretical limiting wind speed for the small box trailer travelling on the bridge.

On approaching the anchor blocks from the approach bridges, Figure 8 (right) the minimum approach wind speed for overturning is 18 m/s, C_{Mp} = 0.89 (magenta curve). When passing the shelter of the anchor blocks and the wind screens the approach wind speed for overturning

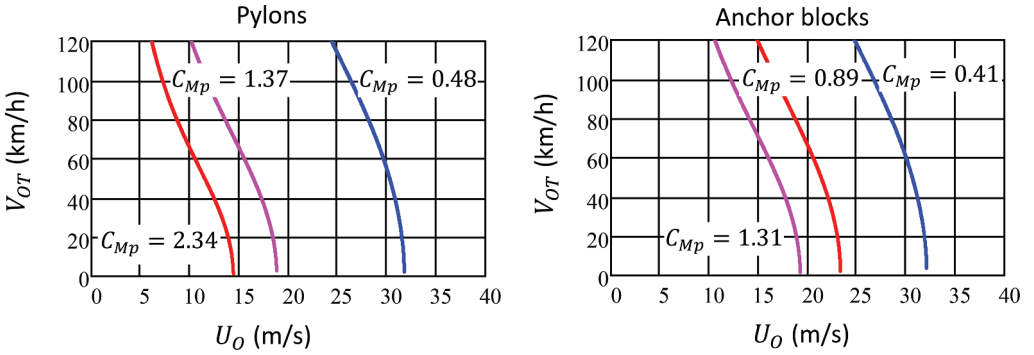


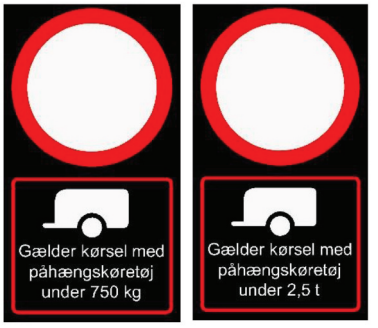
Figure 8. Calculated travel speeds for overturning V_{OT} as function of the approach wind speed U_0 on the suspension bridge (left) and approach bridges (right).

increases to 28 m/s, C_{Mp} = 0.41 (blue curve). On exit of the wind screens on the suspension bridge the approach wind speed for overturning becomes 14 m/s, C_{Mp} = 1.31 (magenta curve) at the travel speed of 80 km/h. This evaluation demonstrates that the approach bridges provide better sheltering of the traffic than the suspension bridge does. Also, the evaluation supports the decision not to install wind screens at the approach side of the anchor blocks.

6 TRAFFIC RESTRICTIONS AND SIGNS

Calculation of vehicle travelling speeds for overturning were carried out for various classes of vehicles leading to implementation of a set of revised wind related restriction for crossing the Storebælt bridge. The new restrictions are summarized in Table 2 along with the new sign boards developed for enforcing the restrictions in high wind situations. The approach wind speed referred to in Table 2 is the wind speed component normal to the bridge alignment.

Table 2. New traffic restrictions based on wind tunnel tests.

Approach wind speed	Restrictions	New Sign boards	
< 10 m/s	No restrictions	Small box trailer	Large box trailer
10 – 15 m/s	Small box trailers not allowed - (weight below 750 kg) Other vehicles: Speed limit 110 km/h		
15 – 20 m/s	Small, large box trailers and Caravans not allowed - (weight below 2.500 kg) Other vehicles: Speed limit 90 km/h		
20 – 25 m/s	Small, large box trailers and Caravans not allowed - (weight below 2.500 kg) Other vehicles: Speed limit 70 km/h		
25 m/s	Bridge closed		

REFERENCES

Baker, C. J. 1991. Ground vehicles in high cross winds, part I: Steady aerodynamic forces. *Journal of Fluids and Structures*, Vol 5, 69–90.

Smith, R. W., Barker, C. P. 1998. Design of wind screens, experience and applications on major bridges. *Bridge Aerodynamics*, Larsen & Esdahl (eds). Balkema Rotterdam.

EN-1991-1-4: Eurocode 1: Action on structures – Part 1-4: General actions – Wind actions. 2ed, 2007.

Bridge Maintenance, Safety, Management, Digitalization and Sustainability – Jensen, Frangopol & Schmidt (eds)
© 2024 The Author(s), ISBN 978-1-032-77040-6
Open Access: www.taylorfrancis.com, CC BY-NC-ND 4.0 license

Fatigue crack propagation simulation of Haibach hole for orthotropic steel bridge deck

Z. Kang
Xi 'an Rail Transit Group Company Limited, Xi 'an, China

J. Kang
China Railway Major Bridge Reconnaissance & Design Institute Co., Ltd, Wuhan, China

L.W. Xu, P.Y. Li & C.S. Wang
Department of Bridge Engineering, School of Highways, Chang'an University, Xi'an, China

ABSTRACT: To study the fatigue crack propagation mechanism at Haibach hole for orthotropic steel deck, the multi-scale whole-bridge digital twin model was established based on a highway-railway dual-purpose bridge case study. The digital fatigue test of the Haibach hole was carried out based on fracture mechanic theory and the eXtended Finite Element Method (XFEM). The welding process numerical simulation near Haibach hole was performed. The result shows there is the high residual tensile stress at the cutout edge. The cracks at diaphragm cutout edge and weld toe at U-rib propagation were simulated coupled with the effect of multi-stress field. The result shows that the crack could not be in the plane but will deflect a certain angle during the propagation process. The cumulative strain energy release rate result reveals that the fatigue cracks at Haibach hole edge are I mode crack and I mode crack at U-rib weld toe.

1 INTRODUCTION

Orthotropic steel deck is widely used in bridge construction because of its excellent mechanical properties, convenient construction and environmental protection (Wang *et al.*, 2015). However, due to its complex structural form, the orthotropic steel bridge deck inevitably introduces welding defects and welding residual stress in the manufacturing process, and there is wheel loads directly acting on the steel bridge deck during operation. These factors make the fatigue cracking problem of orthotropic steel bridge deck very serious (Wang & Feng, 2009).

Relevant researchers mostly use the method of physical fatigue test to study fatigue property of orthotropic steel deck (Wang *et al.*, 2017, Fisher & Barsom, 2016). Physical fatigue test, especially full-scale fatigue test, can directly observe the fatigue crack propagation behavior and obtain the corresponding fatigue strength.But the physical fatigue test cycle is large and the cost is high. The digital fatigue test provides a new way for the fatigue research of steel bridge. A refined numerical model of fatigue details of orthotropic steel bridge deck is established, and the information of different stages of physical real bridge is mapped to the numerical model to construct a digital twin model of fatigue crack propagation.

Traditional finite element method is widely used in the current digital fatigue test of orthotropic steel bridge deck. Liu et al. (Liu *et al.*, 2016) established finite element models from the component and segment scales respectively, predicted the fatigue crack propagation path, evaluated the number of cyclic loadings, and proved the reliability of the fracture mechanics parameter analysis of the three-dimensional solid model. Wang et al. (Wang *et al.*, 2019) established a three-dimensional fracture mechanics model of riveted steel bridge before and after reinforcement, and considered the effect of corrosion fatigue. The results show that this method can well evaluate the residual fatigue life of riveted steel bridge under the coupling

DOI: 10.1201/9781003483755-355

effect of corrosion and fatigue. Zong et al. (Zong *et al.*, 2015) used FRANC3D to simulate and analyze the fatigue crack propagation of CT specimens based on the theory of linear elastic fracture mechanics, and obtained the residual life of fatigue cracks more accurately.

When the traditional finite element method is used to simulate the crack propagation, it is necessary to divide the grid repeatedly after the crack propagation. Repeated meshing reduce the computational efficiency. Belytsehko et al.and Moës proposed the extended finite element method (XFEM) (Belytschko & Black, 1999, Moës *et al.*, 1999), based on the partition of unity finite element method (Melenk and Babuska, 1996). This method can well solve the disadvantages of the traditional finite element method. Based on XFEM, Chen et al. (Xiang *et al.*, 2022) studied the fatigue life calculation under the condition of double crack propagation, and analyzed the influence of the angle between the crack and the roof, the initial crack size and the aspect ratio of the crack on the fatigue crack propagation behavior. Wang et al. (Wang *et al.*, 2017) established a segment model of orthotropic steel bridge deck, considering the influence of welding residual stress, and realized the fatigue crack propagation of main details based on numerical fracture mechanics and XFEM.

In the existing research, the segment model is used to carry out the digital fatigue test and the simulation of welding residual stress is mostly small-scale simulation, which is different from the actual welding situation in the factory. Therefore, it is necessary to put forward reasonable boundary conditions of welding residual stress simulation corresponding to the actual situation. Moreover, there is less research on the Haibach cutout fatigue property. With the development of traffic, more and more railway bridges use Haibach cutout as the form of digging cutout in the diaphragm of orthotropic steel bridge deck, and the force is complex. Therefore, the propagation mechanism of typical fatigue cracks at the top deck-U rib-diaphragm Haibach cutout detail under multi-field coupling needs to be clarified. In this paper, an orthotropic steel bridge deck in a highway-railway bridge is taken as the case study, and the digital twin model of this whole bridge is established. The welding process is simulated, and the actual welding boundary conditions are adopted. Considering the multi-field and the fatigue crack propagation behavior is researched. The propagation mechanism of typical fatigue cracks at the Haibach cutout of the top deck-U rib-diaphragm under multi-field coupling is revealed.

2 CASE STUDY AND NUMERICAL MODEL

2.1 *Case study*

A continuous steel truss bridge is taken as the case study. This is a highway-railway dual-purpose bridge. The height is 12m and the width is 30.5m of the steel truss girder. The main body of the steel beam is made of Q370q steel. As shown in Figure 1, the thickness of the roof of the deck is 16mm; the longitudinal stiffener adopts a closed trapezoidal section. The thickness of the longitudinal rib web is 8mm, the thickness of the top deck is 10mm, the top width is 300mm, the bottom width is 180mm, the height is 280mm, the diaphragm cutout radius is 20 mm and the spacing is 600mm. The cut-out form of the diaphragm is Haibach cutout. The full penetration fillet welds

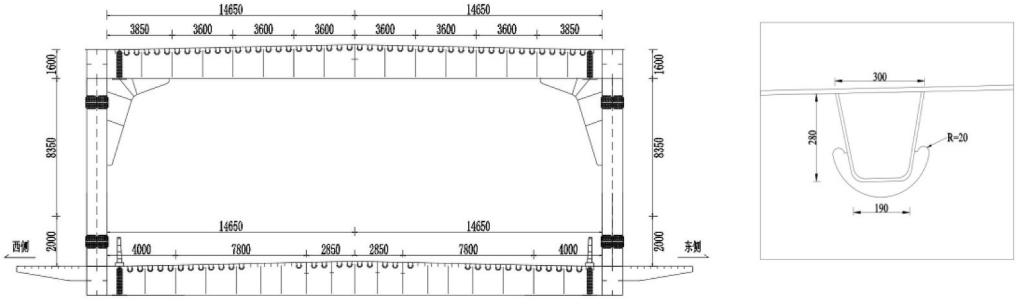


Figure 1. Structural dimensions of steel bridge deck.

are used for the connection welds between the orthotropic steel top deck and the U-rib, and the connection welds between the diaphragm plate and the U-rib.

2.2 *Digital twin model*

Taking into account the calculation cost and calculation accuracy, the cross-scale sub-model modeling method was used to establish a full-bridge digital twin model. At the full bridge scale, the main truss, stiffening string, upper deck system and lower deck system are simulated by beam element. Five internode lengths were selected to establish a 68m long segment steel truss girder substructure, which was simulated by shell element. The key parts containing fatigue cracks are simulated by solid elements. In the cross-scale model, the main girder segment model and the welded sub-model adopt the shell-solid coupling constraint, and the beam element model and the main girder segment model adopt the coupling constraint. According to the bridge span arrangement and the bearing arrangement, the continuous beam boundary constraint is applied in the numerical model. The cross-scale full-bridge model is shown in Figure 2.

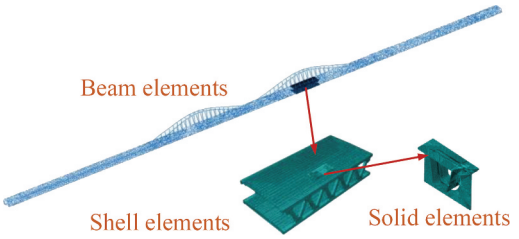


Figure 2. The cross-scale full-bridge model.

3 SIMULATION AND ANALYSIS OF WELDING PROCESS

The influence of residual stress at the weld on the fatigue performance cannot be ignored. The researchs of relevant scholars show that there is a large residual stress at the connection weld (Wang *et al.*, 2013). In this paper, a numerical model of fatigue details at the weld of U-rib and diaphragm is established for thermal-mechanical coupling analysis. This lays a foundation for the simulation of crack propagation under multi-field stress coupling.

3.1 *Welding simulation model*

The welding simulation solid sub-model shown in Figure 3 is selected in the connection area of U-rib and diaphragm. The width of the sub-model is 600mm, the longitudinal length is 200mm, the height is 400mm, the thickness of U rib is 8mm and the thickness of diaphragm

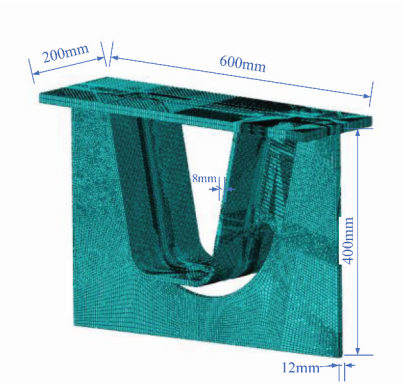


Figure 3. Welding analysis model.

plate is 12mm. The mesh size is refined to 1mm at the connection details of the U-rib and the diaphragm to ensure the calculation accuracy of the residual stress field and the matching degree between the mesh size and the initial crack size during the subsequent fatigue performance analysis. At the same time, taking into account the computational efficiency, the grid size gradually changes smoothly from 1mm to 8mm from the focus area to the outside. The eight-node hexahedral heat transfer element is used to calculate the temperature field, and the eight-node linear hexahedral element is used to calculate the residual stress field.

3.2 *Welding simulation method*

In the simulation of the whole welding process, the 'birth and death element method' is used to simulate the filling process of multi-pass welds, and the welding residual stress analysis of U rib-diaphragm connection weld is carried out by sequential coupling method. In the thermal analysis, the stress on the 'dead element' and its constraint on the adjacent elements are also close to zero. During the welding process of the diaphragm and U-rib connection weld, the weld element set is continuously activated with the movement of the welding heat source. In the process of thermal analysis, only thermal boundary is needed. However, when analyzing the welding stress field, it is necessary to apply mechanical boundary conditions in the welding model to ensure that the structure does not appear rigid body displacement and does not constrain the free deformation of the weld. The boundary conditions of the welding residual stress model are shown in Figure 4. Welding heat input and welding heat source model are the main influencing factors of welding temperature field. This paper assumes that the thermal efficiency η is 0.75 and adopts the double ellipsoid heat source model (Goldak *et al.*, 1984).

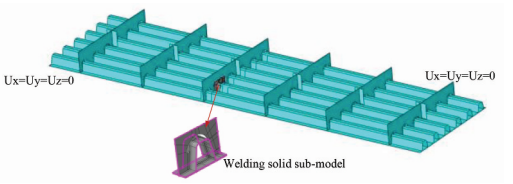


Figure 4. Boundary conditions of welding residual stress model.

3.3 *Welding residual stress analysis*

Taking the welding temperature field as the external load, the stress boundary conditions of the whole welding process are set up to carry out the thermal analysis of the whole welding process. The welding residual stress around the weld has reached or approached the yield value of the steel, indicating that the welding residual stress has a great influence on the stress distribution of the fatigue details of the Haibach cutout.

In order to analyze the distribution characteristics of welding residual stress, three paths are selected for analysis, which reflect the transverse direction of the weld toe and the diaphragm cutout edge. The distribution of welding residual stress is shown in Figure 5. The transverse residual stress at the weld toe is the largest near the weld toe, and gradually decreases away from the weld toe. The distribution trend is similar to the vertical residual stress distribution. Under the action of vehicle load, the detail has a combination of tensile-tensile stress cycle and welding residual stress, resulting in fatigue failure of the detail. It can be seen that there is a large welding residual tensile stress along the edge of the Haibach cutout, and it shows a trend of increasing first and then decreasing, and the stress at the later welding is significantly greater than the stress at the earlier welding, indicating that the welding residual stress at the earlier welding will be reduced during the later welding process. The welding residual stress reaches the maximum at about 50mm from the weld toe at the edge of the Haibach cutout, and the maximum can reach 350MPa.

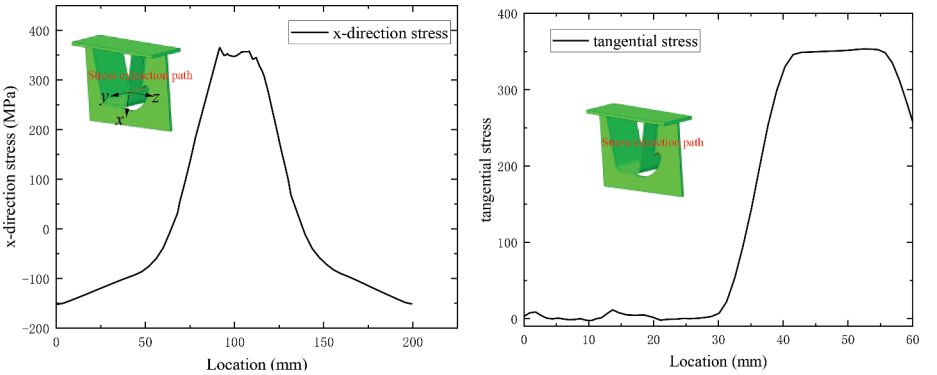


Figure 5. Welding residual stress distribution.

4 FATIGUE CRACK PROPAGATION SIMULATION

4.1 *Extended finite element method*

Based on the partition of unity finite element method, Belytsehko and Moës proposed a new calculation method in 1999. The finite element method (XFEM) allows the crack to be independent of the grid, and there is no need to re-divide the grid during the crack propagation. XFEM introduces the enrichment function into the displacement function of the traditional finite element method, and reflects the discontinuity of the crack by strengthening the degree of freedom of the element nodes around the crack. The enrichment function includes the crack tip asymptotic function and the jump function, and the two-dimensional plane grid with cracks.

4.2 *Fracture mechanic theory*

Under the action of fatigue load, the rate of change of crack length a and cycle number N is called the fatigue crack growth rate, and the da/dN-ΔK curve describes the fatigue growth performance of the material. The da/dN-ΔK curve in double logarithmic coordinates can be obtained by constant amplitude fatigue test on the central crack tensile specimen or compact tensile specimen with sharp notch and prefabricated crack. As shown in Figure 6, the curve can be divided into three regions (Paris & Erdogan, 1963):Zone I is the low rate region of fatigue crack growth. When ΔK is less than the lower limit value ΔK_{th}, the fatigue crack will not expand, and ΔK_{th} is the stress intensity factor threshold of fatigue crack growth. Zone II is the medium rate zone of fatigue crack propagation, in which the fatigue crack propagates stably. There is a good linear relationship between lg (da/dN) and lg (ΔK), and the linear relationship is the famous Paris formula. Zone III is a high-rate zone for fatigue crack propagation. In this zone, crack propagation will expand rapidly, and then the structure will fracture. Usually, the contribution of this zone to life is not considered.

In order to directly apply the strain energy release rate calculated by VCCT method and improve the calculation speed of fatigue crack propagation simulation, the composite crack propagation power criterion is adopted, and its expression is (Xu & Yuan, 2009):

$$\frac{G_I}{G_{IC}} + 1.9\frac{G_{II}}{G_{IIC}} + 2.1\frac{G_{III}}{G_{IIIC}} = 1.0 \tag{1}$$

Among them, G_I, G_{II}, and G_{III} are type I, type II, and type III strain energy release rates; G_{IC}, G_{IIC} and G_{IIIC} are type I, type II and type III critical strain energy release rates, respectively.

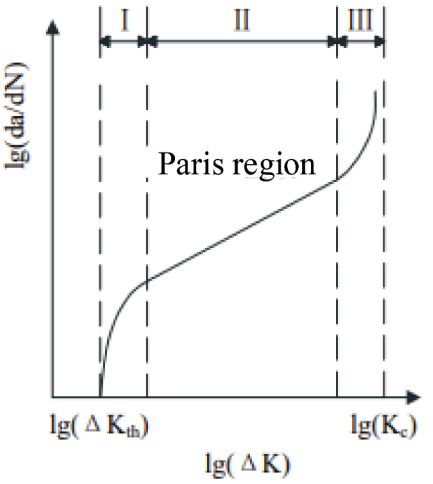


Figure 6. D*a*/d*N*-Δ*K* dependence.

4.3 *Fatigue crack growth analysis*

4.3.1 *Fatigue crack propagation at the weld toe of the U-rib side of the U-rib and diaphragm connection weld*

The initial crack at the weld toe of the U-rib side is a semi-elliptical crack, and its fatigue crack ruler is a_0/c_0= 0.5mm/1mm. The initial crack plane is along the thickness direction of the U-rib, the short half axis of the crack is in the thickness direction of the U-rib, and the long half axis is at the weld toe of the U-rib side. With the increase of loading times, the crack propagates longitudinally along the U-rib, and the angle between the crack and the U-rib weld is formed due to the influence of welding residual stress, as shown in Figure 7. When the number of cycles reaches 2.65 million, the crack penetrates the U-rib web plate, and the crack remains semi-elliptical shape. After that, the crack shape gradually expands from plane to both ends to space arc shape. The strain energy release rate at the crack tip is extracted and the strain energy release rate curve is drawn, as shown in Figure 8. It can be seen that the value of G_{I} is greater than G_{II} and G_{III}, and G_{II} and G_{III} are less than 10 % of G_{I}, and their effects are negligible. This shows that the cracks are mainly type I cracks, and the effects of type II and type III cracks can be ignored. It can be concluded that the fatigue crack at the weld toe of the U rib side of the U rib-diaphragm connection weld is a type I crack.

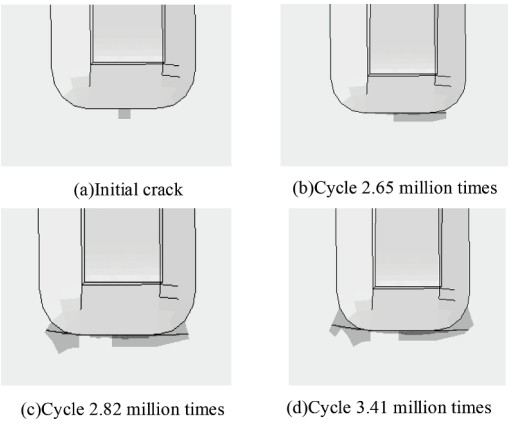


Figure 7. Fatigue crack propagation at weld toe of U rib side.

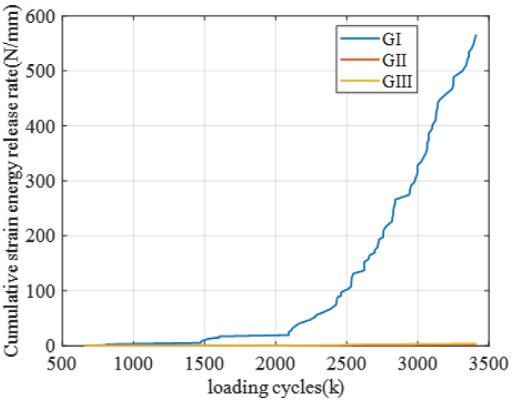


Figure 8. Cumulative strain energy release rate of fatigue crack propagation at weld toe of U-rib side.

4.3.2 *Fatigue crack propagation at the edge of Haibach cutout*

The initial crack at the edge of the diaphragm is 1/4 elliptical crack, and the initial crack size is a_0/c_0=0.5mm/1mm.The initial crack plane is along the thickness direction of the diaphragm, the short half axis of the crack is in the thickness direction of the diaphragm, and the long half axis is in the normal direction of the edge of the diaphragm. The fatigue crack propagation at the edge of the diaphragm hole is shown in Figure 9. When the cumulative cycle of fatigue wheel load reaches 2 million times, the crack propagation direction remains in the normal direction of Haibach cutout edge. When the number of cycles reaches 6.73 million, the crack propagation direction is not in the initial direction and begins to deflect. After that, the crack propagation direction gradually deflects to the diaphragm. The cumulative strain energy release rates G_{I}, G_{II}, and G_{III} at the side weld toe of the diaphragm during crack propagation are shown in Figure 10. It can be seen that the cumulative strain energy release rate changes slowly at the initial stage of crack propagation, and gradually increases with the increase of cycle times. It shows that in the initial stage of crack propagation, the tensile-tensile stress of the initial crack is small and the crack propagation rate is slow. After that, due to the multi-field coupling effect, the tensile-tensile stress at the crack gradually increases, and the crack growth rate begins to increase. The value of G_{I} is greater than that of G_{II} and G_{III}, and the values of G_{II} and G_{III} are less than 10 % of G_{I}, and their effects can be ignored. This shows that the cracks are mainly type I cracks, and the effects of type II and type III cracks can be ignored. It can be concluded that the fatigue crack at the Heibach notch is a type I crack.

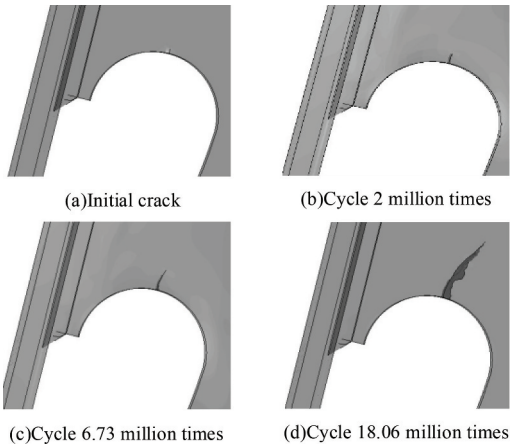


Figure 9. Fatigue crack propagation at Haibach cutout.

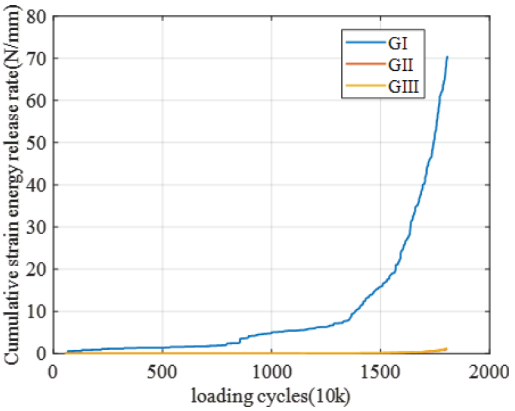


Figure 10. Cumulative strain energy release rate of fatigue crack propagation at Haibach cutout.

5 CONCLUSION

1) In this paper, a multi-scale full-bridge digital twin model was established. The global model is simulated by beam element and truss element, the sub-model and steel deck is simulated by shell element, and the sub-model of top deck-U rib-diaphragm is simulated by solid element. The fatigue problem of steel deck can be studied under multi-field coupling.
2) There is a large welding residual stress in and around the weld, which is close to the yield strength of the steel. There is a large residual tensile stress at the top deck-U rib-diaphragm excavation detail group. It can be concluded that the welding residual stress has a non-negligible effect on the fatigue performance of the steel bridge deck.
3) Coupling with the multi-field stress, based on the XFEM, the digital twin simulation of the typical cracks at fatigue-prone details of Haibach cutout was carried out. The results revealed that the fatigue crack at the weld toe of the U-rib side of the U-rib and diaphragm connection weld is a type I crack and the fatigue crack at the Haibach notch is type I crack.

ACKNOWLEDGEMENT

The authors gratefully acknowledge the financial support provided by the Innovation Capability Support Program of Shaanxi (2019TD-022), Scientific Research and Development Project of China Railway Major Bridge Reconnaissance & Design Institute CO., Ltd and Chang'an University Central University Basic Scientific Research Fund Green Highway Key Special Support Plan (300102219309).

REFERENCES

Belytschko, T. & Black, T. (1999), Elastic crack growth in finite elements with minimal remeshing, *International journal for numerical methods in engineering*, 45(5), 601–620.

Fisher, J. W. & Barsom, J. M. (2016), Evaluation of cracking in the rib-to-deck welds of the Bronx–Whitestone Bridge, *Journal of Bridge Engineering*, 21(3), 04015065.

Goldak, J. & Chakravarti, A., et al. (1984), A new finite element model for welding heat sources, *Metallurgical Transactions B*, 15(2), 299–305.

Liu, Y. M. & Zhang, Q. H., et al. (2016), Numerical simulation method for 3D fatigue crack propagation of orthotropic steel bridge deck, *China Journal of Highway and Transport*, 29(7), 89–95.

Melenk, J. & Babuska, I. (1996), The partition of unity finite element method: Basic theory and applications, *Computer Methods in Applied Mechanics and Engineering*, 139(1-4), 289–314.

MoËs, N. & Dolbow, J., et al. (1999), A finite element method for crack growth without remeshing, *International journal for numerical methods in engineering*, 46(1), 131–150.
Paris, P. C. & Erdogan, F. (1963), A critical analysis of crack propagation laws, *Journal of Basic Engineering*, 85(4), 528–533.
Wang, C. S. & Duan, L., et al. (2017), Steel bridge long-term performance research technology framework and research progress, *Advances in Structural Engineering*, 20(1), 51–68.
Wang, C. S. & Feng, Y. C. (2009), Review of fatigue research for orthotropic steel bridge decks, *Steel Construction*, 24(09), 10-13+32.
Wang, C. S. & Fu, B. N., et al. (2013), Fatigue Test on Full-scale Orthotropic Steel Bridge Deck, *China Journal of Highway and Transport*, 26(02), 69–76.
Wang, C. S. & Wang, Y. Z., et al. (2019), Fatigue Performance Evaluation and Cold Reinforcement for Old Steel Bridges, *Structural engineering international: journal of the International Association for Bridge and Structural Engineering (IABSE)*, 29(4), 563–569.
Wang, C. S. & Zhai, M. S., et al. (2015), Life-cycle cost based maintenance and rehabilitation strategies for cable supported bridges, *International Journal of Advanced Steel Construction*, 11(3), 395–410.
Wang, C. S. & Zhai, M. S., et al. (2017), Numerical fracture mechanical simulation of fatigue crack coupled propagation mechanism for steel bridge deck, *China Journal of Highway and Transport*, 30 (03), 82–95.
Xiang, C. & Wang, D., et al. (2022), Numerical simulation of root-deck crack propagation of orthotropic steel bridge deck, *Structure and Infrastructure Engineering*, 18(7), 1076–1090.
Xu, Y. & Yuan, H. (2009), Computational analysis of mixed-mode fatigue crack growth in quasi-brittle materials using extended finite element methods, *Engineering Fracture Mechanics*, 76(2), 165–181.
Zong, L. & Shi, G., et al. (2015), Experimental investigation and numerical simulation on fatigue crack behavior of bridge steel WNQ570 base metal and butt weld, *Construction and Building Materials*, 77419–429.

Bridge Maintenance, Safety, Management, Digitalization and Sustainability – Jensen, Frangopol & Schmidt (eds)
© 2024 The Author(s), ISBN 978-1-032-77040-6
Open Access: www.taylorfrancis.com, CC BY-NC-ND 4.0 license

Digital fatigue test of steel truss girders in long-span suspension bridge with double-deck

Q.L. Wu
Department of Bridge Engineering, College of Highways, Chang'an University, Xi'an, China

T.K. Zhang
Guangdong Bay Area Traffic Construction Investment Co., Ltd, Guangzhou, China

J. Xu
CCCC Highway Consultants Co.,Ltd, Beijing, China

S. Liu
Guangdong Bay Area Traffic Construction Investment Co., Ltd, Guangzhou, China

C.S. Wang
Department of Bridge Engineering, College of Highways, Chang'an University, Xi'an, China

ABSTRACT: The steel truss girders with double-deck are widely used in long-span suspension bridges due to its superior mechanical properties and traffic capacity. However, the fatigue mechanism of such bridges under multi-lane loads is uncertain. In order to clarify this issue, full size digital fatigue test considering detail welding residual stress (WRS) is carried out. Based on the theory of Extended Finite Element Method (XFEM) and the Linear Elastic Fracture Mechanics (LEFM), the fatigue crack propagation law of the details is researched. The results show that the WRS of the fatigue-prone detail is close to the yield strength of the steel. Thus, the influence of WRS should be considered in the fatigue assessment. Then, the cracking of fatigue details is caused by out-of-plane distortion under the multi-field coupling effects. Moreover, the fatigue cracks are Mode I-II-III combined cracks dominated by Mode I through analysis of fracture parameters.

1 INTRODUCTION

The double-deck steel truss girder is widely used in long-span bridges due to its high spanning capacity, large traffic volume and superior structural performance. For the double-deck truss girder, the joints intersect many members such as chords, web members and crossbeams, resulting in a more complex force transmission path. With the improvement of welding technology, full-welded integral joints are gradually used in steel truss girders instead of splicing joints. It has a high degree of factory manufacturing and superior overall mechanical performance. However, there are many fatigue-prone structural details in the welded integral joints, and initial defects such as large welding residual stress (WRS) and deformation are also introduced during the welding process. The vehicle loads are transmited to the truss by crossbeams. The bending moment generated at the end of the crossbeams will drive the joints and chords to twist. Therefore, out-of-plane distortion will occur in the connecting area between the crossbeams and the joints. Distortion-induced fatigue cracks initiate and propagate under the cyclic vehicle loads, severely threaten service safety and life of truss girder bridges.

DOI: 10.1201/9781003483755-356

Current research methods on fatigue performance in the field of steel bridges mainly include two aspects: (1) Carry out physical fatigue tests to evaluate the fatigue strength of sturcture details (Wei et al. 2017, Wang et al. 2022); (2) Conduct fatigue assessment based on in-situ monitoring of real bridges (Wang et al. 2013). However, the cost of physical fatigue testing is high, and it is difficult to fully ensure that the stress state of the physical model is consistent with that of the actual structure. During in-situ monitoring of real bridges, fatigue cracks are always shielded and scattered. It is difficult to monitor fatigue cracks at joints accurately in real-time. With the continuous development of computing science, the numerical fracture mechanics method that combines fracture mechanics with Extended Finite Element Method (XFEM) has gradually been applied to fatigue analysis of bridges (Wang et al. 2017). By establishing a multi-scale full-bridge numerical model, WRS and initial defects are introduced in the fatigue detail, fatigue cracks propagate under the action of vehicle cycle loads, and the fatigue cracking mechanism of structural details is studied (Wang et al. 2022).

In this paper, a multi-scale numerical fatigue model of a long-span suspension bridge with double-deck is established, and the sequential coupling method is used to simulate the WRS of the crossbeam-joint structural detail sub-model. Based on linear elastic fracture mechanics (LEFM) and XFEM, crack propagation analysis is carried out under the multi-field coupling effect of dead load, live load and WRS field to explore the cracking mechanism and propagation behavior.

2 MULTI-SCALE DIGITAL FATIGUE TEST MODEL

The suspension bridge of 2180 m main span with double-deck steel truss girder is selected as the research object. Both upper and lower decks adopt a multi-crossbeam system, which is arranged in eight-lane layout each deck with a total width of 43.6 m. The standard section length of the steel truss girder is 16 m, the height of the upper and lower chords is both 1.7 m, and the width of the chord is both 1 m.

By the analysis of the moving load of the whole bridge and the identification of fatigue sensitive details, the joints in the about L/5 region are determined as the most unfavorable fatigue control joints for evaluation. The layout of the whole bridge is shown in Figure 1.

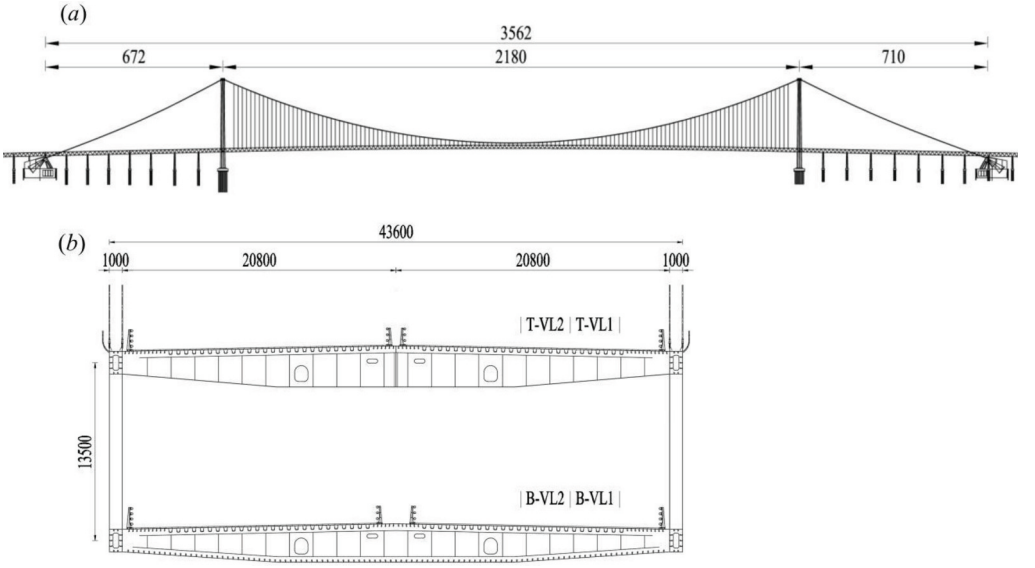


Figure 1. The layout of the whole bridge: (*a*) bridge elevation (Unit: m); (*b*) cross section of stiffing girder (Unit: mm).

In order to fully reflect the stress state of the joints in whole bridge and ensure calculation efficiency and accuracy, multi-scale finite element model of suspension bridge is established, containing SOLID element sub-model considering the detailed geometric configuration. Solid sub-model is embedded into the SHELL element model of five standard segments by means of "Shell-Solid Coupling". The whole bridge model including main cables, hangers, towers and truss girder is simulated by BEAM/TRUSS elements. It is constrained with segment SHELL element model by "Coupling" means to realize force transmission and displacement constraints. Initial crack is semi-ellipsoidal, whose length is 2 mm and depth is 0.5 mm.

The solid mesh size at the crack insertion position is accurate to 1mm. In order to improve the computational efficiency, mesh transition technique is used to increase the mesh size from 1 mm to 8 mm. The multi-scale calculation model is shown in Figure 2.

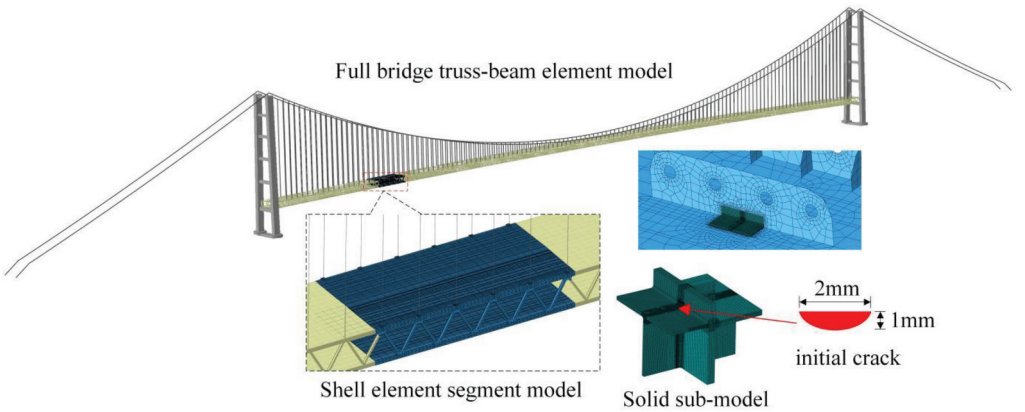


Figure 2. Multi-scale FEM of the suspension bridge.

3 WRS SIMULATION

3.1 *Welding simulation method*

The WRS field of the solid sub-model in welding process is calculated by sequential coupling method. The truss adopts Q355 steel, and the deck system adopts Q420 steel. The thermal-physical and thermodynamic performance parameters of Q355 and Q420 steel are defined respectively (Sun et al.2016). The welding wire and the corresponding base metal use the same material property. Due to large thickness of plates, welds are simulated by multi-layer and multi-pass welding means. A rational cooling interval is set between two adjacent layer welds to ensure an appropriate interlayer temperature. The passivated elements are gradually activated to simulate the travel process of the welding.

Firstly, welding temperature field is calculated. The solid sub-model element attribute is set by eight-node hexahedron DC3D8. In the welding process, the double ellipsoid heat source model is selected as the heat input model to convert electric energy into heat energy, which is expressed (Goldak et al. 1984) as:

$$q_r(x,y,z) = \frac{6\sqrt{3}f_r Q}{\pi^{3/2}abc_r}\exp\left\{-3\left[\frac{x^2}{a^2}+\frac{y^2}{b^2}+\frac{(z-z_0-vt)^2}{{c_r}^2}\right]\right\}\ (Z \geq 0) \tag{1}$$

$$q_f(x,y,z) = \frac{6\sqrt{3}f_f Q}{\pi^{3/2}abc_f}\exp\left\{-3\left[\frac{x^2}{a^2}+\frac{y^2}{b^2}+\frac{(z-z_0-vt)^2}{{c_f}^2}\right]\right\}\ (Z<0) \tag{2}$$

where f_f and f_r are constants of the heat deposited in the front and rear quadrants; Q is the heat input per-unit time; v is the welding speed; t is the welding time; z_0 is the position of the heat source in the z-direction at the beginning. The heat source model geometric parameters a, c_f and c_r are independent and they can have different value.

Based on results of the temperature field, the WRS field is calculated. Temperature field is applied to the solid sub-model as a predefined load. On the basis of the original solid sub-model mesh division method, element type is modified to an eight-node hexahedron C3D8R, and activation order of weld elements is guaranteed to be consistent with the thermal model. Symmetrical mechanical boundary constraints are used on the edges of the solid sub-model.

3.2 *WRS analysis resluts*

In the process of welding thermal analysis, it is necessary to adjust the input of current, voltage and the heat source model size to ensure that welds can be fully penetrated. The melting point of steel and welding wire is 1450℃.

Figure 3 shows temperature field distribution of the welding process. The color of the area where the temperature exceeds 1450℃ is eliminated. It can be seen that the molten pool above 1450℃ can penetrate the cross section of the welds, which further indicates that the parameter setting of the heat source model is reasonable.

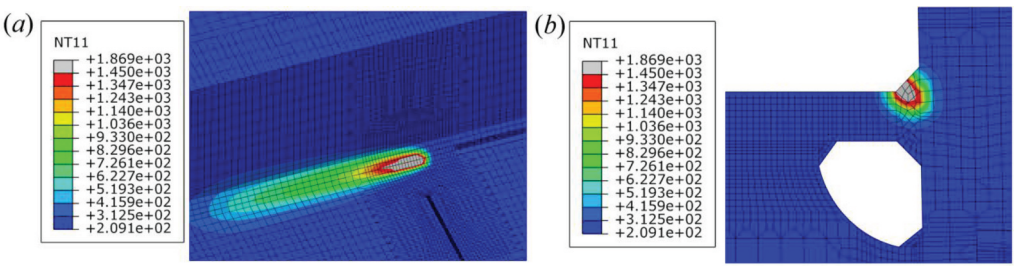


Figure 3. Temperature field distribution(Unit: ℃): (*a*) Molten pool plane; (*b*) Molten pool section.

Based on results of the temperature field, the WRS field is calculated. WRS distribution results of different paths are extracted, as shown in Figure 4. It can be seen that WRS is tensile stress closed to the yield strength. As the welding goes on, WRS of the previously weld decreases, indicating that the subsequent welding process will affect the WRS distribution in the previous welding area.

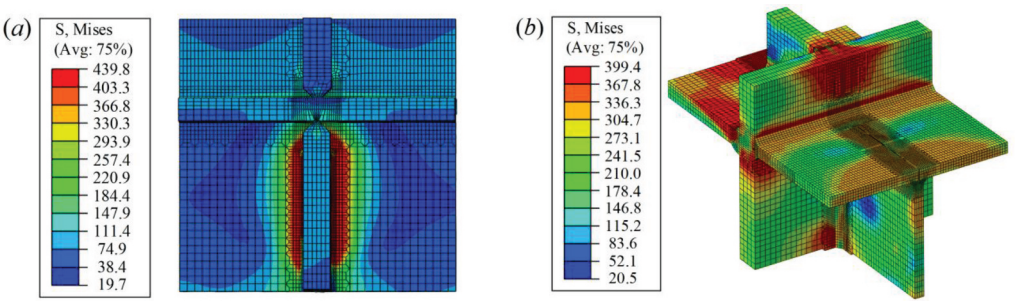


Figure 4. WRS field distribution (Unit: MPa): (*a*) welding process; (*b*) welding completion.

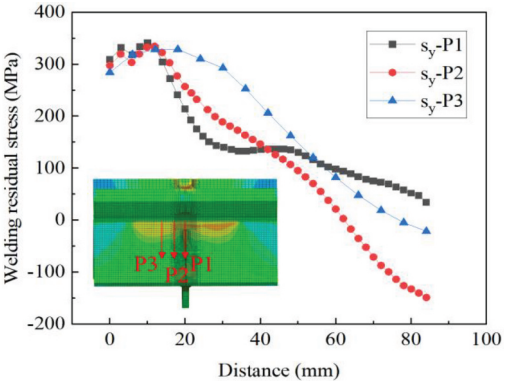


Figure 5. WRS distribution along different path.

The WRS in the vertical weld toe direction under different paths at the extracted details is shown in Figure 5. It can be seen that the farther away from the weld toe, the WRS gradually decreases. The WRS of P2 begins to transform into compressive stress at 58 mm from the weld toe, whose gradient is the largest of three paths.

4 DETAIL STRESS RESPONSE ANALYSIS

4.1 *Fatigue vehicle load*

In order to analyze the stress response of the fatigue details of the joints under the action of live load, the fatigue load model II (FLM II) from the *Chinese Specifications for Design of Highway Steel Bridge* (JTG D64-2015) is selected as the fatigue load. FLM II is consisted of double vehicles with 40 m center distance. Single vehicle is six-axis truck which weighs 425kN. Each wheel load area is 0.20 m×0.60 m. Regardless of the stiffness contribution of the 75mm thick asphalt pavement layer to the structure, it is treated as a secondary load on the bridge deck. Single wheel load area is diffused to the steel bridge deck through the asphalt pavement layer at an angle of 45°, so the calculated area of a single wheel load is 0.35 m×0.75 m.

4.2 *Analysis of stress response results*

The joints of the double-deck truss girder intersect with multiple members such as hingers, chords, crossbeams and web members. Due to three-dimensional spatial lane distribution feature, the FLM II on different lanes will have different effects on the details of joints. It is necessary to comprehensively consider the stress response of the details caused by different loading cases. Different combinations of double-deck lane loads are designed to determine the most unfavorable loading cases, as shown in Table 1. Based WRS field and the dead load stress field, the stress response of the details under different loading modes is calculated, as shown in Figure 6. When the rear axle of the FLM II is just acting on the crossbeam connected to concerned joint, stress at the details reaches the peak. The stress amplitude of details under Case 3 is the largest, reaching 46.3 MPa. Effect of bottom lane loading cases on top joint details can be ignored from fatigue damage perspective.

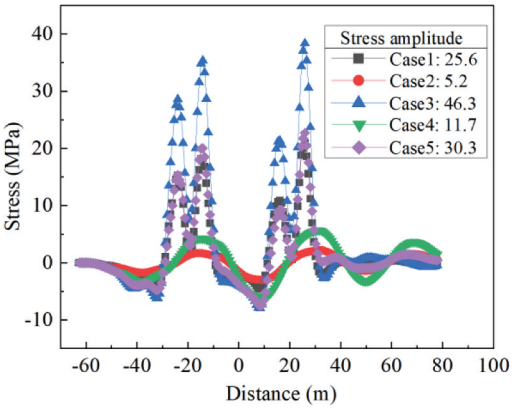


Figure 6. Stress distance-history of fatigue detail.

Table 1. Designed load scenery of FLM 2.

Load cases	FLM 2 loading lane
Case 1	T-VL1
Case 2	B-VL1
Case 3	T-VL1+T-VL2
Case 4	B-VL1+B-VL2
Case 5	T-VL1 +B-VL1

5 DIGITAL FATIGUE ANALYSIS

5.1 *Methodology*

Cracks cannot directly pass through the element when using traditional finite element method. And the mesh needs to be re-divided at every step of propagation to make crack surfaces and the element edge match each other, resluting extremely low calculating efficiency. XFEM introduces the enrichment function in the displacement approximation function to reflect the geometric discontinuity problem in crack propagation. The displacement function equation in the XFEM is expressed (Belytschko et al. 1999, Moes et al. 1999) as:

$$u(x) = \sum_{I \in \mathrm{P}} N_{\mathrm{I}}(x) \left[u_{\mathrm{I}} + \underbrace{H(x) a_{\mathrm{I}}}_{\mathrm{I} \in K_{\Gamma}} + \underbrace{\sum_{\alpha=1}^{4} F_{\alpha}(x) b_{\mathrm{I}}^{\alpha}}_{\mathrm{I} \in K_{\Lambda}} \right] \tag{3}$$

Where a_{I} is additional degrees of freedom (DOF) of the penetrating element; b_{I}^{α} is additional DOF of crack tip element; K_{Γ} is penetrating element nodes set; K_{Γ} is crack tip element nodes set.

5.2 *Crack propagation path simulation*

FLM II wheel load position of the most unfavorable loading case is selected for cyclic loading. Calculation results of crack propagation path with and without considering WRS field are extracted seperately, as shown in Figure 7. It can be seen that crack deflects along the length and depth direction under cyclic loading without considering WRS field. After considering WRS field, the crack propagation path and morphology basically do not change, indicating that the WRS field has no effect on the crack propagation morphology.

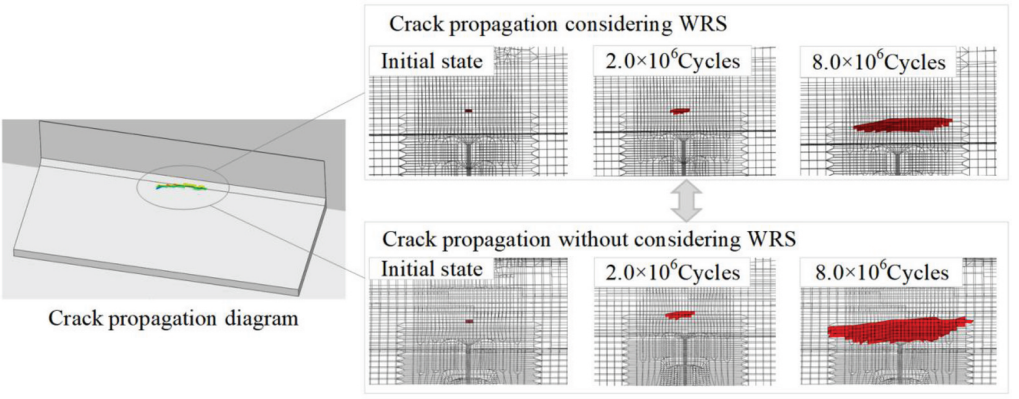


Figure 7. Crack propagation path comparison with and without considering WRS.

Further analysis shows that without considering the WRS, the crack extends 54 mm along length direction and 10 mm along depth direction under 8 million loading cycles. When considering the WRS field, the crack extends 76 mm along the length direction and 14 mm along the depth direction, basically penetrating the plate thickness. Crack growth rate considering WRS field is about 1.4 times than that without considering WRS field.

5.3 *Analysis of cumulative strain energy release rate*

The strain energy release rate (SERR) during crack propagation is calculated based on the virtual crack closure technique. Cracks will propagate when meeting $G_{th}<\Delta G<G_{pl}$. By calculating the SERR during crack propagation, mechanism and law of crack propagation are further analysed. The cumulative SERR under crack propagation with and without considering WRS field is extracted respectively as shown in Figure 8. It can be seen that in the process of crack propagation, ΣG_I is much larger than ΣG_{II} and ΣG_{III}, and the three forms of cumulative SERR with or without WRS are basically the same. In the process of crack propagation, the proportion of ΣG_I in the total SERR increases rapidly. However, ΣG_{II} and ΣG_{III} increase slowly, where (ΣG_{III} /ΣG_I) is about 2.0 times and 1.5 times of (ΣG_{II}/ΣG_I), corresponding to the crack propagation with and without considering WRS, respectively. It shows that the proportion of ΣG_{III} increases considering the WRS. The fatigue cracks are Mode I-II-III combined cracks dominated by Mode I, consistent with the crack growth paths.

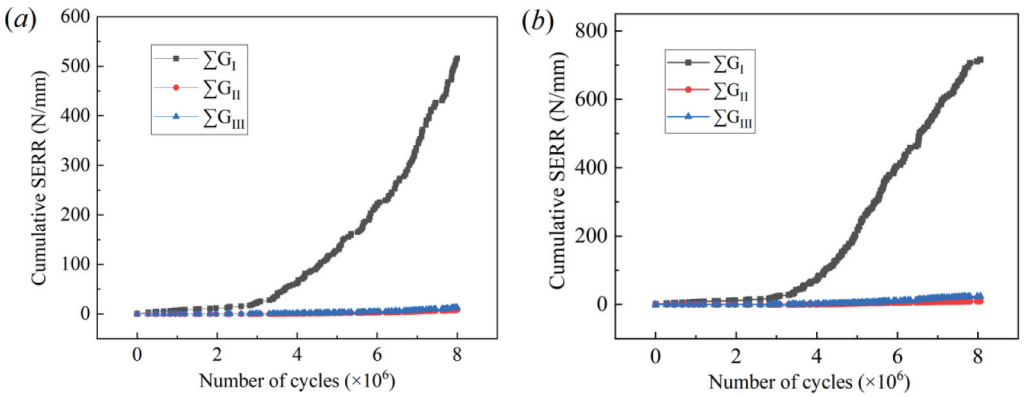


Figure 8. Cumulative SERR during the crack growth simulation: (a) without considering WRS; (b) considering WRS.

6 CONCLUSION

The digital fatigue analysis of integral joints in double-deck steel truss girder of long-span suspension bridge based on LEFM and XFEM methods is studied and applied in this paper. By establishing a multi-scale numerical model of the whole bridge, the dead-live load stress field and the WRS field are introduced to simulate the fatigue crack propagation, and crack propagation law is further revealed. The specific conclusions are as follows:

(1) According to the calculation results of WRS in multi-layer and multi-pass welding, the WRS of the detail reaches 320 MPa, which is about 90.1% of the yield strength. The post-welded weld can reduce the WRS of the previous weld.
(2) It is calculated that the most unfavorable vehicle loading position of the joint fatigue details is that the vehicle heavy axis acts directly above the crossbeam connected to the concerned joint, while the effect of the bottom-layer vehicle on the top-layer joint details can be ignored.
(3) Based on the calculation results of cumulative SERR, $\sum G_{\mathrm{I}}$ is much larger than $\sum G_{\mathrm{II}}$ and $\sum G_{\mathrm{III}}$, and the proportion of $\sum G_{\mathrm{III}}$ increases while WRS is considered. The fatigue cracks are Mode I-II-III combined cracks dominated by Mode I, consistent with the crack growth paths.
(4) Crack growth rate considering WRS field is about 1.4 times than that without considering WRS field, indicating that the influence of WRS cannot be ignored in the fatigue analysis of welding details.

ACKNOWLEDGEMENT

The authors gratefully acknowledge the financial support provided by the Program of the Innovation Capability Support Program of Shaanxi (2019TD- 022), Research on Anti-fatigue Fracture Performance and System High Resilience Design Method of Long-span Suspension Bridge with Wide Double-deck Steel Truss Girder and Chang'an University Central University Basic Scientific Research Fund Green Highway Key Special Suzpport Plan (300102219309).

REFERENCES

Wei, X. et al. 2017. Fatigue assessment and stress analysis of cope-hole details in welded joints of steel truss bridge. *International Journal of Fatigue* 100: 136–47.
Wang, C. S. et al. 2022. Distortion-induced fatigue behavior of vertical stiffener web gaps in steel girder bridges. *Thin-walled Structures* 180: 10892
Wang, C. S. et al. 2013. Fatigue evaluation of a strengthened steel truss bridge. *Structural Engineering International* 23(4): 443–9.
Wang, C. S. et al. 2017. Numerical fracture mechanicalsimulation of fatigue crackcoupled propagation mechanism for steel bridge deck. *China Journal of Highway and Transport* 30(3): 82–95.
Wang, C. S. et al. 2022. Digital fatigue test of detail group at deck-U rib-diaphragmaccess hole of steel bridge deck in cable-stayed bridge. *Journal of Traffic and Transportation Engineering* 22(06): 67–83.
Sun, J. M. et al. 2016. Numerical simulation of residual welding stress in multi-pass T-joint of thick Q390 high strength steel plate using instantaneous heat source. *Transactions of the China Welding Institution* 37(7): 31–34,38.
Goldak, J. et al. 1984. A new finite element model for welding heat sources. *Metallurgical Transactions B* 15: 299–305.
Belytsehko, T. et al. 1999. Elastic crack growth in finite elements with minimalremeshing. *International Journal for Numerical Methods in Engineering* 45(5): 601–620.
Moës, N. et al. 1999. A finite element method for crack growth without remeshing. *International Journal for Numerical Methods in Engineering* 46(1): 131–150.
Ministry of Transport of the People's Republic of China. 2015. Specifications forDesign of Highway Steel Bridge. JTG D64-2015, Beijing.

SS32: Data-driven asset management

Organizers: I.F. Alcover, M. Saberi & J. Winkler


Taylor & Francis
Taylor & Francis Group
http://taylorandfrancis.com

Bridge Maintenance, Safety, Management, Digitalization and Sustainability – Jensen, Frangopol & Schmidt (eds)
© 2024 The Author(s), ISBN 978-1-032-77040-6
Open Access: www.taylorfrancis.com, CC BY-NC-ND 4.0 license

Change detection using Bayesian multivariate linear regression

R.J. Hollamby & I.F. Alcover
COWI

ABSTRACT: For civil engineering infrastructure, the objectives of monitoring are often to quantify current performance behavior and seek to detect changes in behavior or status that could be attributed to component damage or degradation. For structures, responses such as displacements and stress changes are often strongly influenced by the effects of wind loading, traffic and temperature, the latter presenting via correlated daily and seasonal variations between structural components, often of differing materials. Displacements due to temperature change can be significant, and loading imparted by traffic is often only indirectly measured. In contrast, comparatively small deformations of the structure can be expected due to component degradation or localized failure. Without a principled approach to data analysis there is a risk that such subtle changes will be go unnoticed due to the complex daily, seasonal, and random volatility of the variable actions.

Through monitoring two long span bridges in Normandy, France, COWI have developed analysis methods that use measured data from several different sensor types to deliver insights with regards to the defined monitoring objectives. Bayesian multivariate linear regression has been found to be a versatile and scalable model class for predicting structural responses, owing to its compatibility with the linear system theory by which structures are typically analyzed. In this class of model, action-related measurement channels (e.g., temperatures, wind speeds) are typically used as regressors, with response measurements being the dependent variables. Response predictions obtained from deployed models serve to contextualize new measured data and identify anomalous responses. Sophisticated model variants, in which some of the parameters are time-varying, can serve to expose any long-term trends or changes that may be evident, yet otherwise masked, within the measured data. This approach constitutes an efficient automated methodology for processing large data quantities that scales well. Inferred model parameters deliver information that is relevant for digital twinning and asset management purposes. The practical application of this methodology is illustrated via a few case studies analyzing real data.

1 INTRODUCTION AND MOTIVATION

The following generic objectives are commonly encountered when working with structural monitoring data from civil engineering infrastructure:

1. Is the structure behaving as predicted? *Design verification/behavior characterization*
2. Is the behavior of the structure changing over time (months, years)? *Long term trend/degradation monitoring*
3. Can we identify rare events/unusual occurrences? *Anomaly detection*

The above are important for proactive asset management, to keep infrastructure functional and safe and give advance warning of any degradation or impending failures that could occur, so that component replacements and/or other interventions can be made.

DOI: 10.1201/9781003483755-357

The responses of civil engineering infrastructure, such as displacements and stress changes, are usually strongly influenced by the combined effects of wind loading, vehicular traffic and temperature, the latter typically presenting via complex variations and temporal lags between structural components. For long span bridges, displacements due to temperature can be very significant; often movement ranges more than 1m are witnessed as structural temperatures increase from Winter to Summer. In contrast, comparatively small deformations of the structure can be expected because of component degradation or localized failure. Without a principled approach to data analysis, the daily, seasonal, and random volatility of these variable actions can easily mask the temporal variations that are of interest, per the generic objectives listed above.

2 BAYESIAN MULTIPLE LINEAR REGRESSION

2.1 *Formulation for use with metric data*

Multiple linear regression is one of the oldest and simplest regression analysis techniques within the field of Machine Learning. But despite its simplicity it represents a convenient mathematical model that has wide applicability in the analysis of structural monitoring data, owing to its compatibility with the linear (or linearised) theory by which most civil engineering structures behave and/or have been designed.

A more versatile variation of the traditional deterministic multiple linear regression model is a Bayesian multiple linear regression model, which can be written in its most elementary form as:

$$\mathrm{Y}_t = [\beta]X_t + \alpha + \varepsilon$$

where X_t is a vector of n regressor variables at time t, Y_t is the vector of m dependent, or response, variables at time t, $[\beta]$ is the gradient matrix of shape $[m,n]$, α is the bias/intercept vector and ε is the process noise vector. In this most elementary form, $\varepsilon \sim Normal(0, [\Sigma_\varepsilon])$, where $[\Sigma_\varepsilon]$ is a diagonal covariance matrix formed from standard deviations vector σ_ε.

The advantage of this model structure is that each of the parameters are physically meaningful. For example, the gradient coefficients that form $[\beta]$ express the proportional influence that each of the regressor variables has on the dependent variables. In a bridge engineering context, these will typically be the influence of wind, traffic and temperature on responses such as displacement, rotation or stress. Once inferred such gradients are readily compared vs Finite Element (FE) model predictions e.g., of displacement due to temperature and/or wind separately, i.e., facilitate FE model calibration.

2.2 *Extensions to the basic formulation*

The metric formulation above can be extended in several ways, also summarized in Table 1:

- α can be allowed to vary with time t, be this via a step-change at unknown time $t=t_1$, a ramp trend or other pre-defined or inferred temporal variation, or simply by adopting a different α parameter for different time intervals, e.g., monthly
- σ_ε can be allowed to vary with time also. Where this is being included to account for unmeasured inputs, such as vehicular traffic, it would be natural to adopt a different σ_ε parameter on weekdays and during trafficked hours.
- Alternative noise models for ε could also be adopted. For example, rather than using a Normal distribution, a Students T-distribution could be used, such that the model structure may then be termed *Robust* Bayesian Multiple Linear Regression, [1], since parameter estimation is less sensitive to outliers in the measured data.

Besides tracking real changes in the bias of responses, use of time-varying bias can help accommodate, identify or be tolerant of small offsets that can occur due to routine monitoring

system maintenance activities, e.g., disconnection and remounting of sensors. Having used the data to infer offsets attributed to such activities, suitable corrections to the measured data can be made, to correct for these effects.

Terms in $[\beta]$ would not normally be varied with time since this would imply a change in system responsiveness to loading actions. Notwithstanding this, there is no technical reason why $[\beta](t)$ couldn't be adopted, except doing so would give increased potential for over-fitting and poor model generalization, especially when other model parameters are also allowed to be time varying. Having estimated parameters via Bayesian inference, a useful back-substitution is to determine the posterior distribution in the reference response vector, Y_{ref}:

$$Y_{ref}(t) = [\beta](t)X_{ref} + \alpha(t)$$

where the regressor vector X_{ref} is defined to have suitable reference values. For example, zero entries when considering variable actions such as wind or temperature difference, or 15°C (of other suitable annual average value for the site) when considering absolute structural component temperatures. Suppose Y were a vector of position coordinates. Evaluating Y_{ref} in this way naturally defines the "reference positions at a uniform temperature of 15°C in zero wind", i.e., the reference positions compensating for the effects of wind and temperature. In many applications this is itself is a useful metric to have inferred from the measured data. Furthermore, considering the variation of $Y_{ref}(t)$ provides a natural answer to facilitate the review of the existence of long-term trends. Since $[\beta]$ is usually treated as time-invariant, $Y_{ref}(t)$ is just a re-positioning (ideally centralizing) of the $\alpha(t)$ offset within the space represented by the variables comprising X. Thus, changes in $Y_{ref}(t)$ are inferred exogenous changes attributable to variables not included in X.

A further use of this model is to evaluate the posterior predictive distribution in the response vector $\hat{Y}(t)$. This is useful for contextualizing new data and for the detection of anomalies. These could be short-term outliers, attributable to incidents such as traffic jams, or more persistent deviations of the measurements from model predictions.

Table 1. Extensions to the basic linear regression formulation and their practical applications.

Parameter		Practical applications
Posterior predictive responses	$\hat{Y}$(t)	Data contextualization; predict responses given measured actions, X(t)
		Anomaly detection; significant differences between predicted responses $\hat{Y}$(t) and measured responses Y(t) (residuals)
		Model evaluation: identify situations in which current model does not perform well, to seek to improve model
Time-varying bias or reference response	α(t)	Long-term trend detection
	or	Inference of offsets due to reinstallation of sensors
	Y_{ref}(t)	Assessment of abrupt changes following events taking place at known time t
Time-varying gradients	$[\beta]$(t)	Assessment of long-term changes in responsiveness to loading actions
Time-varying noise	σ_s(t)	Account for time-varying influence of traffic, if not measured directly and included in X

It should be noted that whilst in general it is common for the variables comprising X to be metric variables, such as wind speed and temperature, the framework of the linear model can be easily generalized to include dichotomous or categorical regressor variables, as may often be encountered when working with measured data from infrastructure. Similarly, through appropriate selection of inverse link function, the dependent variables can also be of non-metric type. Refer application examples below and [2] for further details of generalized linear models.

Similarly, it should be noted that a generalized linear model is applicable in any situation where a model structure is linear *in the parameters*. For example, power law relationships between X and Y, as are encountered when considering wind responses for example, can be inferred according to a linear model by transforming both X and Y using logarithms.

Whilst often X may comprise measured physical data, e.g., wind speed measurements from anemometers, stress changes from strain gauges or temperature measurements from thermocouples, this is not essential. For example, suppose the natural frequencies of the structure have been identified via one of the methods of Operational Modal Analysis. For flexible structures these data will routinely be found to vary with temperature and other loading (wind/traffic), hence it is natural to wish to seek to subtract-off these effects via determining the 'reference' natural frequencies (e.g., at 15°C and when subject to no wind or traffic), to examine if these are changing meaningfully with time (months, years).

Regarding adjudging for *significant* changes, the Bayesian approach provides an expressive means of assessment. For example, suppose we define a model with a step-change bias $\alpha(t)$ as follows:

$$\alpha(t) = \alpha_1 for\, t < t^*$$

$$\alpha(t) = \alpha_2 for\, t t^*$$

whereby the switch time t^* may in some applications be defined as a constant, or otherwise via a suitable prior (e.g., Uniform distribution, bounded by start/end times of monitoring period). By evaluating the posterior distribution in $\Delta\alpha = \alpha_2 - \alpha_1$ we can conduct Bayesian hypothesis testing to assess the significance of the change. Similarly, if t^* is not defined via a constant we can review for a grouped posterior on the switch time at which the unknown change in bias $\Delta\alpha$ occurred.

In summary, a Bayesian Multiple Linear Regression model, especially when extended as described above, proves a good choice when working with structural monitoring data, owing to its inherent compatibility with the linear theory of structures and the way in which its parameters can be used to deliver on monitoring objectives.

2.3 *Software implementation*

Modern probabilistic programming packages such as Stan, JAX and PyMC can be used to naturally define this model, including any of the variants listed above. PyMC, [3], has been used by the author since this Python-based package interfaces well with associated data analysis and provides an especially clean syntax and other supporting functionalities that promote debugging and clear communication of the intent of the model. Having defined parameter prior distributions (either informative or weak, according to any univariate or multivariate probability distribution) together with the model structure as described above, inference of the model's free parameters is conducted via Markov Chain Monte Carlo (MCMC) sampling, by using advanced gradient-based inference engines such as No U-Turn Sampling (NUTS) as implemented by PyMC. This provides samples from the joint posterior distribution in the parameters.

Regarding the obtention of joint posterior parameter samples, this proves especially useful when the variables comprising X are strongly correlated, as is often found to be the case with structural temperature measurements, e.g., from steel and concrete bridge components. In such cases the joint posterior distribution in the influence parameter terms in $[\beta]$ will exhibit strong correlation, which makes these harder to interpret in isolation, but this doesn't undermine the usefulness of the model otherwise. Notwithstanding this, useful projections to evaluate temperature differences and average temperatures are nonetheless useful for restoring the physical interpretability of such parameters.

3 APPLICATION EXAMPLES

For over 4 years COWI have been responsible for the analysis and interpretation of monitoring data recorded from two major cable-supported bridges in Normandie, France: Pont de

Normandie and Pont de Tancarville, see Figure 1. These structures are instrumented with hundreds of sensors that measure environmental conditions (such as structural temperatures, wind speed & direction) and bridge responses (such as position, displacement, inclination, tension force, and strain). Monitoring objectives are diverse but cover each of the main classes of problem listed in the Introduction.

In the sub-sections below some examples of how Bayesian multivariate linear regression has been applied to assist the interpretation of data and the management of these structures.



Figure 1. Pont De Normandie (left, center) and Pont de Tancarville (right).

3.1 *Pont de Normandie: Geometry and stay load review following stay cable replacement*

Following concerns regarding their condition three stay cables on Pont de Normandie were replaced, between June 2020 and December 2020. Stay replacement involved de-tensioning existing stays and then successive tensioning operations to install new stay cables. Such operations would result in a redistribution of load within the remaining stay cable system as well as temporary vertical (Z) displacements of the deck. Data from the monitoring system was used to verify that the works had not permanently altered the distribution of loads within the stay system or the vertical position of the deck.

Four of the remaining stay cables have been instrumented since the original construction of the bridge using load cells. These devices record the absolute tension force sustained by the strand to which they are affixed. For a given instrumented stay, 3 or 4 strands are instrumented. In addition, the bridge is instrumented with GPS receivers, from which XYZ displacements in a bridge-aligned coordinate system are calculated relative to datum positions. Structural temperatures of typical deck and pylon cross-sections are measured. Two anemometers positioned close to midspan measure wind speed and direction.

From linear regression analysis using data prior to the stay replacement works it was established that the 10-minute-mean strand tension for a given stay could be predicted reasonably accurately given the 10-minute-mean structural temperatures and 10-minute mean wind statistics. Various candidate models were considered, with model performance and generalization (overfitting) assessed using distinct training and test datasets, each comprising data from a minimum of 3 months. The most parsimonious model uses the effective steel deck temperature (itself a weighted average from 7no deck temperature sensors) and the transverse component of mean wind speed -squared as regressors. To largely eliminate the influence of traffic, which is not itself monitored directly, only data recorded at 03:00am (when traffic is invariably light) was included in the analysis.

To use such data before, during and after the works an extension of the linear regression model structure was required. The bias vector $\alpha(t)$ was allowed to vary at pre-defined monthly intervals; this was sufficiently granular given the works programme and furthermore some fine-tuning of the assignment of the monthly bias parameters to data was made, given known key dates. During stay replacement gradient parameters [β] would not be expected to vary and

hence are modelled as time-invariant. Similarly, σ_s, which represents the goodness-of-fit of the model in this context, was also modelled as time-invariant. Each of the parameters are arrays i.e., allowed to be distinct for each of the instrumented stay cables.

Posterior distributions in all model parameters were inferred using MCMC and NUTS as implemented by PyMC. Reference responses Y_{ref} were defined at X_{ref}=[15,0] i.e. 15°C uniform deck steel temperature and zero transverse wind speed. In this application $Y_{ref}(t)$ is of greatest interest, a key conclusion being to determine whether the Y_{ref} after completion of the works differs significantly from Y_{ref} prior to the works (recall that Y includes both stay load and deck displacement response channels).

Figure 2 presents time series plots of the measured data from regressor X and dependent Y variables. Posterior predictive stay loads $\hat{Y}(t)$ determined according to the model structure and X(t) data are overlaid via median curves and prediction bands, which represent equal-tailed 90% credible intervals. Monthly-varying reference loads $Y_{ref}(t)$ parameters are shown via right-hand vertical axes, these evaluated based on $X_{ref} = [15, 0]$, i.e., 15°C deck temperature and zero transverse wind speed.

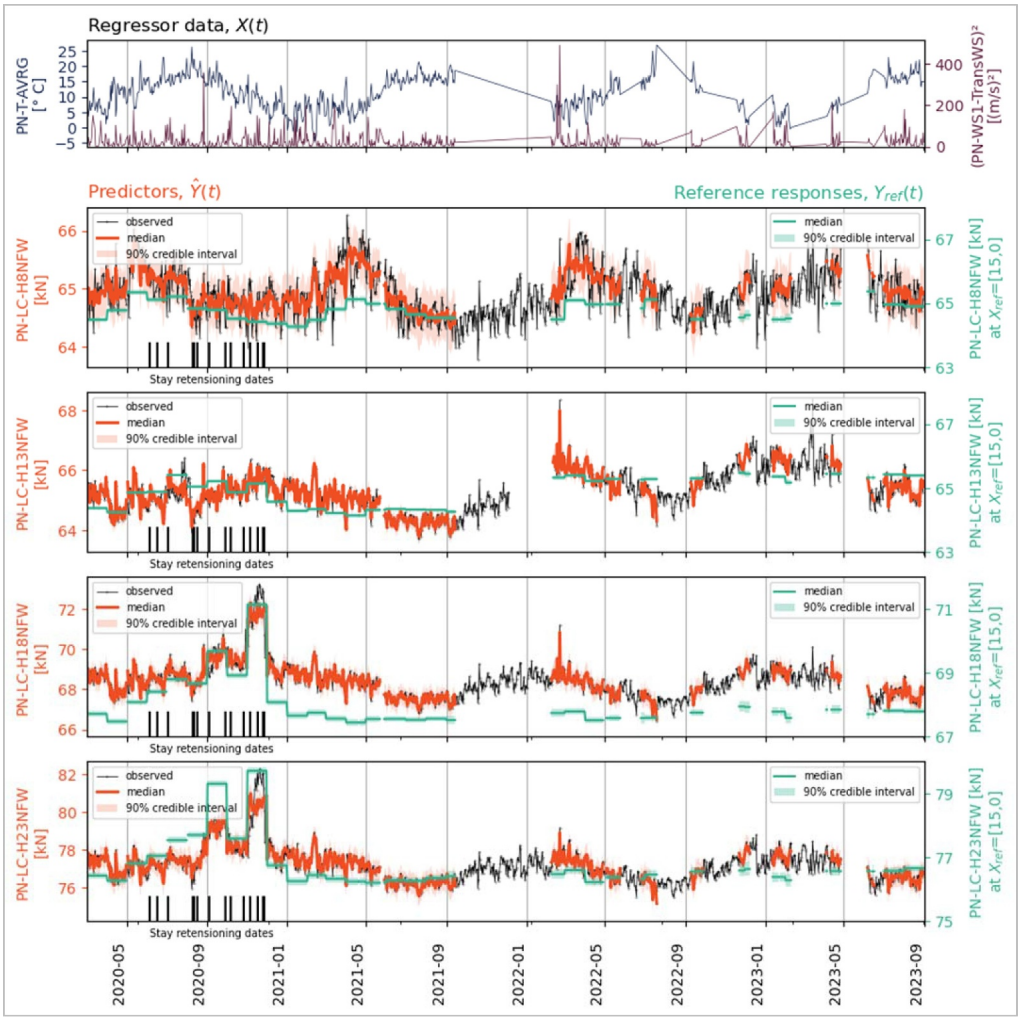


Figure 2. Time series of measured and predicted 10-minute mean stay load data, given measured temperature and wind speed data (refer top subplot). Time series of reference stay loads are plotted via right-hand vertical axes. Key dates in the stay replacement works programme are overlaid for context.

Some responses were hardly influenced by the stay replacement works (e.g., H8NFW strand forces; this stay cable is remote from those replaced) but others were temporarily disturbed yet return to their pre-works values following completion of the stay replacement works. This provided quantitative evidence to reassure the owner-operator of the bridge that the works had not permanently altered the geometry of internal strand forces of the bridge.

3.2 *Pont de Normandie: Correlation of stay wire break events vs environmental conditions*

Each of the 184 stay cables of Pont de Normandie have been monitored using acoustic emission (AE) monitoring, as part of a set of proactive stay management plan, which also includes periodic use of ultrasonic non-destructive testing, laboratory tests and visual inspections, in response to concerns about corrosion at their lower anchorages. Since 2021 AE monitoring has been delivered by Mistras, who classify filtered AE waveforms to identify events compatible with wire breaks. Such events are denoted "Confirmed Wire Breaks" (CWB) with discrete data giving their time of occurrence and stay anchorage.

It should be emphasized that the count of CWB events per year is small. COWI have been engaged to review the data and assess its implications for structural condition. This includes a review of correlations with measured environmental data, e.g., measured temperatures and wind speeds. Other AE monitoring systems have suffered from false-positive events at times of strong rainfall, hence reviewing for dependence on rain conditions was also important.

To explore the correlations in the data a generalized linear regression model was formulated as follows:

- *X* data include discrete wind speed categories, in 5m/s bins, and a Boolean raining/not raining channel, this being classified from the measured rainfall rate data.
- *Y* data are the integer counts of CWB events per hour, aggregated across all stays. *A vector Y could have been used by adopting different aggregations, e.g., distinct for each stay or sum of counts within a stay fan, but this was not done.*
- Metric CWB rate parameters [λ] take the place of the gradients [β] in metric formulation. [λ] is a tensor with multiple dimensions; two in this application, to define joint wind speed and raining/not raining categories respectively. *This would be extended to additional dimensions if different aggregation levels were used.*

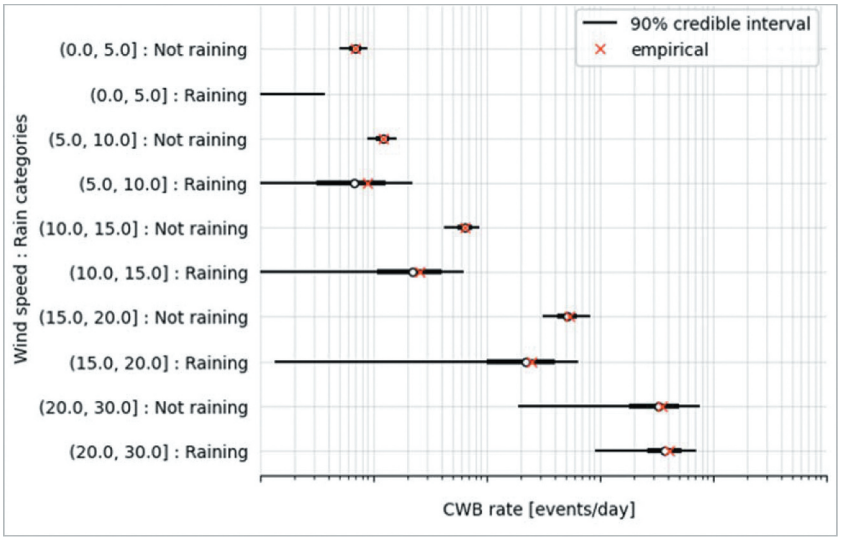


Figure 3. Posterior Distributions On Conditional Cwb Rate Parameters For Joint Wind Speed [M/S] And Rain Categories. Please Note The Horizontal Scale Has Been Obscured For Reasons Of Confidentiality.

- Poisson distribution is used as inverse link function. I.e., the observed CWB count data is regarded as a realization of a Poisson process with parameters [λ], with appropriate [λ] selected according to enumerated wind & rain categories of each data point in X, i.e., each hour of data.
- Weak priors were assumed for the model parameters, i.e. [λ], to let posterior distributions be inferred freely given the data only.

This provides a principled means of analysis that makes use of diverse data and respects their distinct types. Different quantities of data in the various joint categories are reflected in the posterior distributions in [λ] inferred; greater uncertainty is found for under-represented joint categories. The posterior distributions can be compared (refer Figure 3) and directly deliver insights; in this case it was shown that CWB events occur at significantly increased rate as wind speed increases. Furthermore, the presence of rain was shown to not have a significant modifying effect, the posterior rate parameters for a given wind speed category overlap.

3.3 *Pont de Tancarville: Post-fire assessment*

A further application of linear regression came following a major fire on the road deck of Pont de Tancarville in 02/09/2022. A truck lost control, crashed and caught fire, coming to rest adjacent to one of the suspension hangers. Given the intense heat from the fire there was concern that the hanger could have been irreversibly damaged by this event.

Immediately following the fire, the bridge was closed to all traffic, this being diverted considerably via Pont de Normandie. COWI provided advice to the owner-operator (CCITSE) on procedures for conducting a robust post-fire assessment of the crossing prior to its reopening. One aspect of this was to review the monitoring system data, which recorded both the vibrations resulting from the truck's impact and the bridge deformations before, during and after the event.

One aspect of that data review was to apply linear regression analysis to check for any abrupt change in response e.g., vertical displacement following the fire, using techniques like those described in Section 3.2. No significant step-changes in reference positions of the deck or pylon were noted, which provided reassurance when considered in conjunction with findings from close visual inspections.

4 CONCLUSIONS

As demonstrated through application examples, despite its simplicity Bayesian multivariate linear regression has been shown to be a versatile model class that is well suited to the analysis of structural monitoring data. The physical interpretability of its parameters lends itself to FE model calibration, due to its compatibility with the linear theory of structural behavior. Comparison of predicted and measured responses allows for automated detection of anomalies. Use of time-varying parameters can allow subtle long-term change in response to be exposed, which may otherwise be masked by daily and seasonal variations in response attributable to changes in environmental loading. Generalized linear model structures can be used to deliver similar benefits using diverse data types (metric and nominal).

ACKNOWLEDGEMENTS

The authors would like to acknowledge the following: Chambre de Commerce et d'Industrie Seine Estuaire, CCITSE, (Client) for their support of this project and for giving permission to publish this paper; the PyMC team, for their development and support.

REFERENCES

[1] T. Wiecki, "GLM: Robust Linear Regression," [Online]. Available: https://www.pymc.io/projects/docs/en/v3.11.4/pymc-examples/examples/generalized_linear_models/GLM-robust.html.
[2] J. Kruschke, Doing Bayesian Data Analysis: A Tutorial with R, JAGS, and Stan, Academic Press, 2014.
[3] "PyMC: a probabilistic programming library for Python," [Online]. Available: https://www.pymc.io/.

Bridge Maintenance, Safety, Management, Digitalization and Sustainability – Jensen, Frangopol & Schmidt (eds)
© 2024 The Author(s), ISBN 978-1-032-77040-6
Open Access: www.taylorfrancis.com, CC BY-NC-ND 4.0 license

Scoring system for technical evaluation of technologies for remote monitoring of bridges

Mogens Saberi
COWI, Lyngby, Denmark

Kevin McPherson
TRL, Crowthorne House, Nine Mile Ride, Wokingham, Berkshire, UK

Fengqiao Zhang
TU Delft, Delft, The Netherlands

Anna Arvidsson
VTI, Linköping, Sweden

Simon Fjendbo
DTI, Taastrup, Denmark

Carl Van Geem
BRRC, Brussels, Belgium

Maja Kreslin & Andrej Anžlin
ZAG, Slovenian National Building and Civil Engineering Institute, Ljubljana, Slovenia

ABSTRACT: Transportation infrastructure demands reliable, cost-effective, environmentally friendly, and safe solutions. It is, therefore, crucial to leverage both the knowledge gained from current practices and the potential offered by emerging technologies. This paper uses the scoring system approached in the INFRACOMS project to offer a framework for asset managers and technology providers to identify areas of improvement and make informed decisions regarding selecting and implementing remote condition monitoring solutions. We focus on two technologies for bridges, like bridge weigh-in-motion and digital inspection and centre around four areas: data analysis, visualisation and integration and potential for practical decision-making. Technologies are evaluated based on their intended use, acknowledging that some may have multiple applications due to novel sensor installations or data interpretation/visualisation methods. Consequently, a technology may undergo multiple appraisals within this system. We showcase the benefits of the scoring system, alignment with specific use cases, and potential for broad applicability.

1 INTRODUCTION

The application of consistent, reliable information is a key component of highway asset management. The information and the tools to help interpret and apply data have continuously evolved. However, National Road Authorities (NRAs) are not yet fully exploiting their potential in the highway environment. By bringing these components of sensing and measurement together, NRAs could better understand highway assets and improve reactive and proactive asset management decisions.

This paper describes a scoring system to appraise new technologies mapped for bridges and pavements in the INFRACOMS project (www.infracoms.project.cedr.eu/). INFRACOMS is

DOI: 10.1201/9781003483755-358

a CEDR Transnational Road Research Programme Call 2021 project (July 2022 – June 2024). It aims to equip NRAs with the capability to leverage the technological evolution in data/ monitoring.

The first action in the project consisted of identifying the information needs, gaps, and priorities of different NRAs in terms of their data collection and monitoring approach and a list of current and emerging measurement technologies. This is reported in Deliverable D1.1 Current Practice, Future Need and Gap Analysis (Arvidsson et al. 2023a).

Commonly used appraisal methodologies that can be used to evaluate the effectiveness, suitability, and potential impact of new technologies for an organisation include Technology Readiness Levels (TRLs), Cost Benefit Analysis (CBA), Life Cycle Cost Analysis (LCCA), Risk Assessment, and Multi-Criteria Decision Analysis (MCDA). Elements of these commonly used methodologies are included in the INFRACOMS Appraisal Methodology.

The INFRACOMS Appraisal Methodology is designed around technology use cases, that is, a particular application of a technology by an NRA. Some technologies may have more than one technology use case within an NRA. In general, each technology use case should be subject to a separate appraisal, as their costs and benefits, risks and limitations will be different. The appraisal methodology was designed and fine-tuned by applying it to several examples of emerging technologies. INFRACOMS will ultimately deliver a Technology Database and a Technology Appraisal Toolkit to CEDR. The database will comprise appraisals and will be the subject of a future publication.

In this paper, a sequence of appraisal methodology developed within the INFRACOMS project is presented and applied to two different technologies. They were mapped as promotional case studies. First, Section 2 presents a concept of the appraisal methodology, following its technical scoring system in Section 3. Section 4 is intended to apply the scoring system for two technologies: Bridge Weigh-In-Motion (BWIM) and COWI Digital inspection platform (CVI). For each technology, a brief description is given, followed by comments on the scoring results and emphasis on future areas of improvement. In the last chapter, the main conclusions from the paper are drawn.

2 APPROACH OF THE INFRACOMS PROJECT

The proposed INFRACOMS Appraisal Methodology is presented in Figure 1. The processes shown in orange boxes represent the core components of an INFRACOMS appraisal. The blue boxes are filtering and prioritisation processes, representing the ways in which the methodology can be tailored to individual NRAs.

An INFRACOMS appraisal has three (3) core processes with increasing levels of detail and complexity: a Pre-Evaluation, an Evaluation, and a Case Study. These core processes apply at the level of the technology use case. Although the appraisal focuses on a specific technology use case, the Pre-Evaluation and Evaluation stages are still considered generic and useful to any NRA considering applying that technology in a similar use case. Case Studies are normally conducted with an individual NRA and are more focused.

The pre-evaluation process is a high-level analysis of the anticipated benefits, limitations and costs and an assessment of the readiness level of the technology for a particular use case from the supplier's perspective. It also scores the technology for the particular use case against the key imperatives of the NRA. Pre-evaluation should be accomplished quite quickly (in perhaps 2 – 3 hours). It would require general knowledge of technologies and their applications and an understanding of the potential applications of the NRA.

The evaluation process is a more detailed breakdown of the technology's benefits, limitations, and cost factors within the proposed use case, including a more in-depth technical evaluation and an assessment of the steps required to implement it in an NRA. It provides an assessment of the readiness level of the technology from the NRA's perspective. Evaluation would take longer (perhaps 2 – 3 days of inputs). It would require input from a specialist or expert in the field and discussion with the technology supplier to gain a full understanding of the technology and its potential application for an NRA. Detail information on this can be found in Arvidsson et al. (2023b).

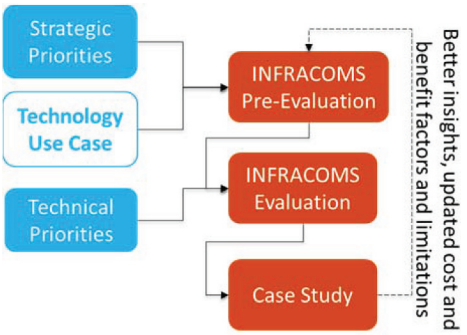


Figure 1. The concept of the INFRACOMS appraisal methodology.

Both the pre-evaluation and evaluation processes also consider the strategic and technical priorities of the NRA. The NRA must establish Strategic Priorities concerning the key imperatives that the NRA wishes to address using emerging technology. Four key imperatives were established in the first action of the project (Arvidsson et al. 2023a): safety, environment, socio-economic, and availability. The NRA must establish Technical Priorities to define its technical priorities concerning the capabilities for using and integrating technology. Four key components that were identified for use in a technical evaluation are (Arvidsson et al. 2023b):

- The need for associated data analysis
- Ease of data visualisation
- Potential for improvement in decision-making
- Ease of data integration.

The ranking between these priorities may differ for different NRAs. A technology may be less relevant for an NRA when it does not address any of the priorities.

3 INFRACOMS SCORING SYSTEM

The current paper focuses only on the technical evaluation of a technology found in the INFRACOMS appraisal methodology. The appraisal components in the technical evaluation include the following items as specified above: The need for associated data analysis, ease of data visualisation, potential for improvement in decision-making, and ease of data integration. Appraisal regarding cost and implementation in an NRA's organisation is for example, not considered in this paper.

The INFRACOMS technical appraisal includes a simple scoring mechanism to allow for the comparison of technologies. The above four components are scored from 1 (lowest) to 5 (highest), indicating the level of technological maturity and potential for improvement. Before scoring, the technology must be described in a specific format to inform the evaluator adequately. An example of the scoring mechanism for the appraisal of data visualisation can be seen below in Figure 2. There are 4 items that should be scored for data visualisation, namely:

- Does the technology come with a visualisation platform?
- Can visualisation data be extracted?
- Current state and prognosis?
- Compliance with client visualisation requirements for decision support?

The concept is that the evaluator will choose a box from each column that they believe best aligns with the current technology from their perspective. The final score is the average of all four items.

A radar diagram where each 'spoke' represents the technical score for a component provides a concise interpretation of the strengths and weaknesses of the technology in each of the

technical evaluation areas. Two practical examples of the scoring system are provided in the next chapter.

DATA VISUALIZATION				
DESCRIPTION OF ANALYSIS:				
FINAL SCORING	DOES THE TECHNOLOGY COME WITH A VISUALISATION PLATFORM?	CAN VISUALIZATION DATA BE EXTRACTED?	CURRENT STATE AND PROGNOSIS	COMPLIANCE WITH CLIENT VISUALIZATION REQUIREMENTS FOR DECISION SUPPORT
5 – Visualization provides complete information for decision support / gap closure	Yes, Technology comes with clear and useful visualisation platform. The platform requires some basic training.	Yes, The visualized data can easily be extracted and used for further analysis	The visualization provides information of current state and prognosis can be easily visualised within the platform	The visualization provided gives sufficient and clear information for decision support and open for future developments
4 – Visualization provides complete information for decision support, but some traning are required to interpretate visualization	Yes, Technology comes with clear and useful visualisation platform but the visualization requires detailed technical training to interpret results	Yes, The visualized data can easily be extracted and used for further analysis	The visualization provides information of current state. Prognosis and trends needs to be done manually but this does not require expert staff.	The visualization provided gives sufficient and clear information for decision support
3 –A visualization will provide information for decision support but work is required to develop this	No, But proper visualization/interpretation can be made using simple plotting tools which can generate 2D/3D plots. No specialized staff needs to develop the visualisation platform	Yes, Data can be extracted and used for further analysis but some work are needed to extract the data	The visualization provides information of current state. Prognosis and trends needs to be done manual but this work do not require expert staff.	If the data are visualized it provides sufficient and clear information for decision support
2 – Visualization provides information for decision support, but expert staff are required to interpret visualization	Yes, Technology comes with clear and useful visualisation platform but the visualization requires expert to interpret results	Yes, The visualized data can be extracted and used for further analysis but work from expert staff are needed to extract the data	The visualization provides information of current state. Prognosis and trends needs to be done manual by expert staff.	The visualisation provides information for decision support.
1 – Visualisation only provides partial information for decision support and expert staff are needed to interpret	No,In order to make proper visualisation complex programming are required (e.g. 3D-'as-is'-model based on photogrammetry, possibly paired with AI for automated identification of defects). Expert staff needs to develop the visualisation platform	Yes, The visualized data can be extracted and used for further analysis but work from expert staff are needed to extract the data	The visualization provides information of current state. Prognosis and trends needs to be done manual by expert staff.	The visualisation only provides partial information for decision support; there is a need for additional information

Figure 2. Scoring sheet for data visualisation.

4 APPLICATION OF SCORING SYSTEM

4.1 *Bridge Weigh-in-Motion system*

Bridge Weigh-In-Motion (BWIM) enables measuring the axle and gross weights of vehicles passing over a bridge in the free flow traffic (Moses, 1979, Žnidarič et al. 2017). This technology is based on the dynamic response of the bridge due to moving vehicles in terms of strains, measured with different sensors strategically placed under the bridge. The acquired data is then processed using specialised algorithms to estimate the vehicle data, i.e. gross vehicle weights, axle weight, axle spacing, velocity, etc. Data and information obtained by the BWIM system can be used for two different areas:

- Heavy traffic management.
- Bridge safety assessment.

One significant application of BWIM systems lies in managing heavy traffic. These systems identify overweight vehicles, ensuring the protection of road infrastructure. Moreover, by eliminating the need for vehicles to stop at weigh stations, BWIM facilitates smoother traffic flow. Additionally, it contributes valuable statistical data for traffic policymaking (Figure 3, left).

BWIM systems are also crucial for bridge assessment services, particularly in performing Soft Load Testing (SLT). SLT offers a cost-effective and efficient alternative to traditional load tests by utilising free-flowing traffic data without road closures. This method provides essential parameters for bridge assessment, including strains, influence lines (Figure 3, right), load distribution factors, and dynamic amplification factors.

The effectiveness of BWIM in both heavy traffic management and bridge safety assessment was evaluated using the INFRACOMS scoring system, providing insights into its efficiency and practicality in real-world applications.

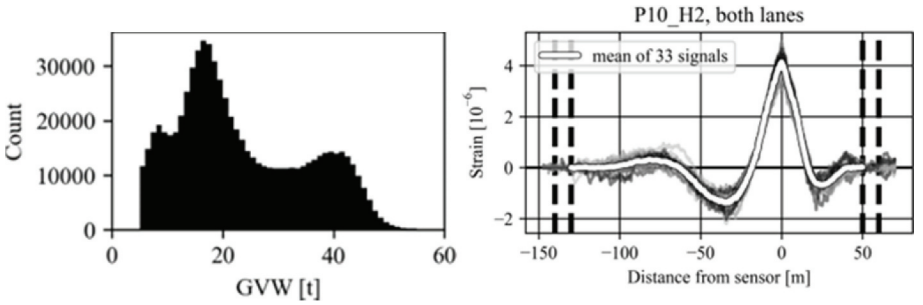


Figure 3. Gross vehicle weight (GVW) and strain data obtained by BWIM for Heavy traffic management (left) and for Bridge Safety assessment (right) (Hekič et al., 2022).

4.1.1 *Scoring results*

As mentioned, BWIM technology offers several layers of data and can be used for both pavements and bridges. The technology scoring was performed similarly, addressing pavement management and bridge management issues. Our findings show that BWIM scores, if we evaluate average ranking values of 2.5 for bridge safety assessment and 4.2 for heavy traffic management (Figure 4). Remember that a score of 5 is reserved for technologies that have achieved full development with little to no room for further advancement.

Although modest, the average score of 2.5 assigned to BWIM in bridge safety assessment has much potential to increase its score. The data for heavy traffic management scores particularly high in Data Visualization and Data Integration, indicating that it is well-suited for comprehensive analysis and seamless synthesis with other data sets. Conversely, the bridge safety assessment data shows lower performance, especially in Data Analysis and Data Integration, suggesting that while it is sufficient for practical decision-making, there is substantial room for improvement in its analytical and integrative capabilities. This suggests that while BWIM has significant capabilities, it demands additional involvement and advanced expertise from bridge engineers to enhance its relevance and improve its standing on the scoring scale.

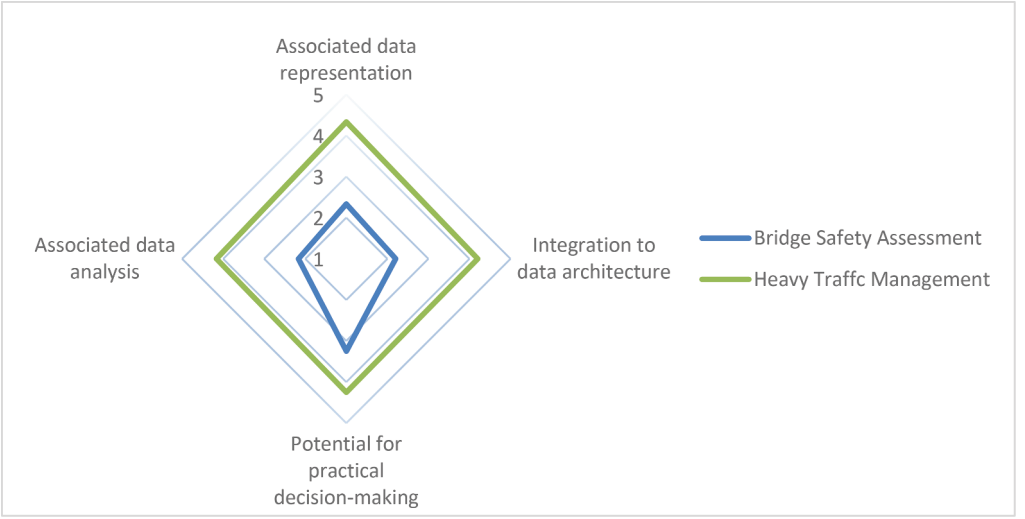


Figure 4. Scoring results for the B-WIM technology are shown on a radar diagram for two different applications.

4.1.2 *Future potential*

The future of BWIM technology is at a promising juncture, with vast potential for enhancing the operational efficiency of road networks. It is an indispensable tool in dual areas, such as Heavy traffic management and Bridge safety assessment. As described in Section 4.1.2, the B-WIM technology already automates key technical aspects like data analysis, visualisation, integration, and practical decision-making. However, for bridge safety assessment services, a gap remains in achieving the desired level of automation for its full practical deployment.

Looking ahead, the modular architecture of the BWIM system harbours the capacity for substantial upgrades, potentially transforming it into a comprehensive Structural Health Monitoring (SHM) system. Its ability to connect a diverse array of sensors and draw a direct correlation between vehicle impact and the consequent structural response — deformations, accelerations, or displacements — sets it apart from other SHM systems. Integrating bridge assessment expertise can unleash the full spectrum of BWIM capabilities, making it an even more powerful instrument in the infrastructure monitoring and maintenance domain. The future enhancements are not just incremental but could mark a paradigm shift in how bridge health is monitored, with BWIM technology offering this advanced step.

4.2 *Digital inspection platform*

The lifetime of structures such as bridges depends on how good we are at maintaining them. If we can postpone decommissioning, we can save massive amounts of time and natural as well as financial resources. An important step in extending the lifetime of structures is to perform reliable and accurate inspections. Traditional inspections are challenged by traffic restrictions, high initial costs (rope access, platform, lift, etc.), subjectivity, and consistency in documentation and working conditions. Establishing a Reality Capture Model or Virtual Twin is important in optimising inspections and moving towards a digital transition within bridge asset management. The model is created from photogrammetrically processed images efficiently collected using camera-mounted unmanned aerial vehicles (UAV).

Within the INFRACOMS project, a case study of digital inspection was taken into account, where COWI's Virtual Inspection platform (CVI) was used. It uses of UAV and artificial intelligence to create a given structure's virtual twin and detect deterioration. The data reveals the structural condition, enabling you to plan for and handle issues while they are still minor and easy as well as inexpensive to correct. By gathering all data in one platform, you can access the full overview from any location and perform your virtual inspections from the office.

First, drones capture high-quality images of the entire structure's surface, which are used to create a photorealistic 3D model. Using a combination of normal colour photography and thermographic images enables you to see "hidden" defects not always visible to the naked eye,

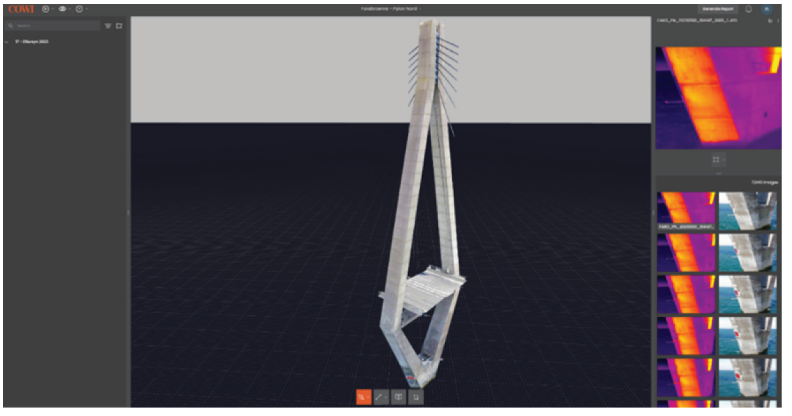


Figure 5. The COWI Virtual Inspection platform illustrates the bridge pylon, where a thermographic camera is used to detect hidden defects.

like delaminated concrete or water seepage. Next, the data is processed, and artificial intelligence is used to detect the defects. Bridge inspection experts then qualify the defects that require repair or further follow-up. All information is gathered in a web-based platform, where data can be shared or revisited at any time.

Inspections using drones on large bridges can significantly reduce the need for lifts, boats, climbing, and rappelling equipment and thereby optimising the inspection process both in terms of safety cost and reliability

Drones with thermography camera provide greater possibility to collect data from the entire structure than hammer tapping, which often only collect data from selected random samples (Figure 5). Direct coupling between photos and geographical position facilitates tracking the development of defects at later stages. Unlike in traditional surveys, where defects are often grouped and only one or few typical pictures are taken for each group, in the COWI Virtual Inspection Platform, pictures are taken for every individual defect.

4.2.1 *Scoring results*

The CVI platform is scored using the INFRACOMS scoring system in the Figure 6. The INFRACOMS scoring is done on a case where the CVI platform was used on a large bridge in Europe.

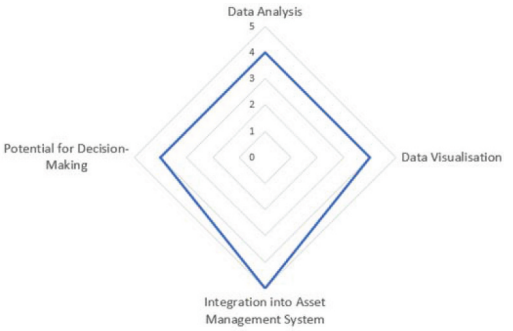


Figure 6. Scoring results for the COWI virtual inspection platform on a radar diagram.

Data visualisations - A 3D Reality Capture Model is created automatically by CVI containing annotated defects and it also includes all RGB – and thermal images. By clicking on any part of the generated 3D model, the 30 best images for the selected spot are shown in a picture panel. In addition, a conventional PDF report is generated in CVI. The report includes a written summary and an auto-generated description of findings based on annotations with additional photos of the defects

Data analysis - Crack detection is performed automatically using a well-trained AI algorithm. An expert, however needs to review and confirm be identified cracks.

Integration into asset management system - In the current case, the data from CVI was not integrated into an existing asset management system. All collected data, including analysis results and expert assessments, where centralised in a web-based platform, facilitating seamless collaboration and data sharing among stakeholders

Potential for decision making - Structural experts need to evaluate the severity and repair urgency of detected defects, enabling informed prioritisation for efficient maintenance planning to ensure that repairs are made at the optimal point in time. Future RCM models can be compared to previous models to identify new defects and defect development to ensure that repairs are made at the optimal point in time. The CVI will improve the quality assurance (QA) process since you have a complete view of the structure and not only pictures taken at locations which are selected by the engineer who is performing the inspection.

4.2.2 *Future potential*

Trials are currently being conducted using smartphones to broaden the use of CVI to smaller structures. While smartphone cameras possess adequate resolution, challenges persist in achieving a finely detailed resolution crucial for precise positioning. This high level of detail is essential for generating a functional 3D model while merging the captured images.

5 CONCLUSIONS

This paper has presented a scoring system for the technical evaluation of technologies which can be used in remote bridge monitoring applications. This scoring system is part of the technology appraisal concept developed within the framework of the INFRACOMS project. It focuses on four key areas: data analysis, data visualisation, decision-making potential, and data integration. These criteria are crucial for assessing the viability and effectiveness of technologies. Two technologies were mapped as appropriate for showcasing the scoring system, i.e. bridge weigh-in-motion systems and digital inspection platforms.

Our findings reveal that each technology has distinct strengths and limitations, as evidenced by the case studies. For instance, bridge weigh-in-motion systems demonstrate high utility in heavy traffic data management but indicate a need for improvement in bridge safety assessment applications since, at this point, it requires the full engagement of the bridge safety assessment experts. This understanding is critical for bridge owners and asset managers to make informed decisions that align with their strategic and technical priorities. Digital Inspection Platform already provides benefits for the landscape bridges at this stage. On the other hand, to scale its application for the whole bridge stock, there should be development in the area of smartphone usage and simplification with respect to the importance of the structure in the whole transport network.

Looking ahead, this scoring system lays the groundwork for more advanced studies and the integration of emerging technologies in the field of bridge or asset management. It holds the potential to guide future research, fostering innovations that further enhance the efficiency, safety, and sustainability of infrastructure management.

ACKNOWLEDGEMENTS

We acknowledge financial support from the Slovenian Research Agency through the research programme No. P2-0273 and Slovenian Motorway Agency (DARS) to provide data for the case study analysis.

REFERENCES

Arvidsson, A. et al. Current Practice, Future Need and Gap Analysis. 2023a, Report D1.1 of the INFRACOMS project: https://www.infracoms.project.cedr.eu/reports-deliverables [Accessed on 6/12/2023]

Arvidsson, A. et al. Appraisal Methodology. 2023b Report D2.1 of the INFRACOMS project: https://www.infracoms.project.cedr.eu/reports-deliverables [Accessed on 6/12/2023]

Hekič, D., Anžlin, A., Kreslin, M., Kalin, J., Žnidarič, A. 2022. Using B-WIM system-generated performance indicators to support model updating of a multi-span viaduct. In Casas, Joan Ramon (ed.), Frangopol, Dan M. (ed.), Turmo, Jose (ed.), *bridge safety, maintenance, management, life-cycle, resilience and sustainability: proceedings of the Eleventh International Conference on Bridge Maintenance, Safety and Management (IABMAS 2022)*, Barcelona, Spain.

Moses, F. 1979. Weigh-In-Motion system using instrumented bridges. ASCE Transportation Engineer*ing Journal* 105(3):233–249.

Žnidarič, A., Kalin, J., Kreslin, M. 2017. Improved accuracy and robustness of bridge weigh-in-motion systems. *Structure and Infrastructure Engineering* 14(4):412–424.

Bridge Maintenance, Safety, Management, Digitalization and Sustainability – Jensen, Frangopol & Schmidt (eds)
© 2024 The Author(s), ISBN 978-1-032-77040-6
Open Access: www.taylorfrancis.com, CC BY-NC-ND 4.0 license

Regional impacts of natural disasters on road bridges in the Philippines

M.J. Adarne & M. Henry
Shibaura Institute of Technology, Tokyo, Japan

ABSTRACT: Bridges serve as a vital infrastructure that links the Philippines' island and mountainous regions and promotes trade, quality of life, and movement of people. However, these bridges are susceptible to natural disasters such as typhoons, earthquakes, and floods, representing significant hazards and resulting in temporary or permanent disruptions to the economy and people's lives. Therefore, this research aims to assess the impact of natural hazards on road bridges in the Philippines at the regional level by analyzing two years of government-collected data for 2020 and 2021. It will investigate the physical damage that these natural hazards bring to bridges, as well as the financial losses incurred by bridge infrastructures due to these natural calamities and compare the results across regions. Understanding the effects of natural disasters and how they vary between regions will help agencies responsible for bridge management in developing a strategy to mitigate those effects and prepare for the economic implications.

1 INTRODUCTION

The Philippines has placed a significant emphasis on infrastructure development in recent years, acknowledging its critically important purpose as the foundation of the economy, a driver of social activities, and a facilitator of increasing levels of interconnection among various regions, islands, cities, and provinces. Infrastructure investment increased from 3% of GDP on average between 2011 and 2016 to over 5% in 2018, with the goal of reaching over 6% (MGS Insurance, 2022). To facilitate the movement of people, goods, and services throughout the archipelago, roads and bridges connect metropolitan centers, remote provinces, and rural communities in the sixteen regions of the Philippines. The transportation of products and tourists across regions sustains economic growth by supporting industries, agriculture, and tourism. In addition, these infrastructure projects will ensure that rural populations not only benefit from better connections to essential services such as healthcare and education but also facilitate access to these benefits for rural people (DPWH Atlas, 2022). In all sixteen regions, roads and bridges stimulate socioeconomic development by promoting integration and seamless connectivity.

Bridges serve an essential role in connecting islands and regions while also playing an important part in natural calamities and disaster preparedness. One of their critical tasks is to maintain a connection with areas impacted by disasters, making them a vital lifeline during these times of need. By providing connectivity, bridges facilitate rapid emergency response activities and contribute to saving lives and minimizing the impact of disasters on affected communities (Utilities One, n.d.). Therefore, bridges are needed to support rapid emergency response activities, especially when access to crucial services, rescue operations, and critical operations is hampered due to the isolation of certain islands, cities, and areas. However, it should be noted that these crucial infrastructures are not immune to the adverse impacts of natural disasters. This vulnerability is underscored by the country's notable position as the 8th

DOI: 10.1201/9781003483755-359

highest on the global risk index and its designation as the 9th most disaster-exposed country, according to the World Risk Report (World Risk Report, 2021). In 2021, the country's total cost of damages caused by natural disasters exceeded 60 billion pesos or 1.1 billion USD (Statista, 2021). The speed at which a nation recovers from a disaster is influenced by its level of development (Taghizadeh-Hesary et.al, 2019). Developing countries, like Philippines, are generally more susceptible to and more severely affected by natural disasters of all varieties than developed countries. As a result, the average citizen's welfare is further compromised (Cavallo et.al, 2009).

The present study aims to identify regions susceptible to various types of bridge damage resulting from natural disasters through data collection. Data was obtained from the Bureau of Maintenance (BOM) of the Department of Public Works and Highways (DPWH) regarding natural disasters that have damaged bridge infrastructures in the Philippines, together with the estimated cost of damages for the years 2020 and 2021. Data cleaning was done, and different types of bridge damage caused by natural disasters were identified, together with an estimate cost of damage. The results offer significant contributions to future readiness efforts by facilitating the development of mitigation strategies that allocate and prioritize resources strategically, with a particular emphasis on bridge structures that are susceptible to damage in areas susceptible to disasters.

2 RESEARCH METHODOLOGY

2.1 *Research data*

This study used data from BOM, DPWH obtained from 16 Regional Offices (R.O) and reported by their corresponding District Engineering Offices (DEO). The condition of the bridge structure prior to the occurrence of natural disasters is not determined. However, the damages that occurred to bridge structures prior to natural disasters are collected and reported. The geographic location of each region within the Philippines is illustrated in Figure 1. Following natural disasters, the maintenance division of DEO conducts an inspection, records the physical damages subjectively, and estimates the cost of such damages. These damages typically consist of road slips, potholes, landslides, scouring, base failure, bridge and road protection damage, and other infrastructure-related issues.

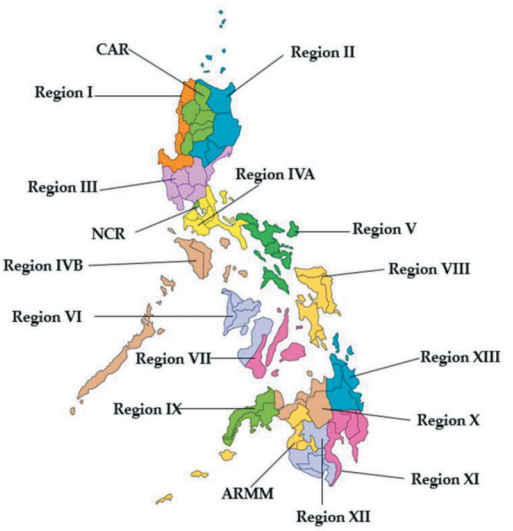


Figure 1. Map of the Philippines with regions (Nnadari et.al 2021).

2.2 *Description of damages*

In 2020 and 2021, 82 different types of bridge structure damages were identified as the result caused by natural disasters. The damages were categorized into three distinct groups: the superstructure damages group contained 37 different types of damage, the substructure damages group contained 17 different types of damage, and the bridge protection damages group contained 28 different types of damage. This categorization facilitated the identification of the specific components of the bridge structures that were most susceptible to damage in the event of such natural disasters.

2.2.1 *Superstructure*

The upper portion of the bridge comprises structural elements above the bearings that support the deck, and these damages can potentially compromise the bridge's stability (Fontanez, 2021). Since this section is always exposed when infrastructure is damaged by natural disasters, this section of the bridge is more susceptible to damage.

2.2.2 *Substructures*

Damages that affect the structural components below the bearings, including piers, abutments, and foundations, are referred to as substructure damages (Fontanez, 2021). This particular section of the bridge is frequently subjected to flooding and scouring caused by excessive rainfall. In addition, the materials typically used in this area consist of masonry and concrete, which are susceptible to deterioration under various natural conditions.

2.2.3 *Bridge protection*

To ensure the bridge's longevity and avoid damage, structures that protect them from natural disasters are important. To prevent structural damage from natural disasters, it may be necessary to install riprap slope structures, stone masonry, and scour preventative measures, all of which are expected to receive damage initially (Harasti et.al, 2021). Bridge protection is undertaken with the goal of helping preserve bridges.

3 RESULT AND DISCUSSION

3.1 *Road infrastructure damage events in 2020 and 2021*

The frequency of infrastructure damage for the years 2020 and 2021 is presented in Table 1. The data shows that natural disasters caused a greater number of infrastructure damages in 2020 as compared to 2021. It can be seen that there were 2,778 instances when infrastructures were damaged by natural disasters, with road infrastructure accounting for 1,670 (60%) of the total number of damage events, bridge infrastructure for 245 (9%), and other infrastructures, including flood control, school buildings, etc., comprising 863 (31%).

Table 1. Total number of infrastructure damages for the years 2020 and 2021.

Types of Infrastructures	2020	2021	Total	Percentage
Total data	1,473	1,305	2,778	100%
Road	832	838	1,670	60%
Bridge	147	98	245	9%
Other Infrastructure	494	369	863	31%

After cleaning the two-year data, 245 damage events of bridge structures were identified. Two damage events were determined to have missing data, making up 1% of the total number of damage events in the data. The absence of these two data points in the analysis can be attributed to the lack of specific information regarding the type and extent of the damage. While there were reported incidents of damage in the area, the exact details were not recorded. As a result, these

missing data points were not included in the analysis due to the absence of recorded information regarding the type and scope of the damage. Following that, considering the significance of traffic conditions during repairs, bridge structure defects were classified into three different groups: superstructure, substructure, and bridge protection, as previously explained. Additionally, it was discovered that while there have been recorded instances of bridge damage in Regions IX and XII, there are no reported incidents for the years 2020 and 2021.

As shown in Table 2, bridge structures were affected by four types of natural disasters over this period of two years. The frequency distribution of damage events indicates that typhoons caused the greatest number of road bridge damage in 2020 and 2021, accounting for 86% of the total, whereas tropical cyclones accounted for 11%.

Table 2. Number of occurrences of natural disasters that caused damage to bridge structures, N=245.

Natural Disasters	2020	2021	Total	Percentage
Tropical Storm	0	27	27	11.0%
Typhoon	141	70	211	86.1%
Continuous Rain	0	1	1	0.4%
Earthquake	6	0	6	2.4%

Although the overall data indicates that the bridge structures constituted a lower percentage of damage events, it is important to take a wider range of factors into consideration before concluding that they are less vulnerable. The particular information like the intensity of the impact of disasters, the kinds of damage, and the local conditions are all important factors in determining the vulnerability of the infrastructure.

3.2 *Regional distribution of bridge structure damage events*

Figure 2 illustrates that, in comparison to all other regions, Region V, Region VII, and Region II experienced the highest number of damage events in bridge structures as a result of natural disasters. Region V, also referred to as the Bicol Region, experienced 117 bridge-damaging events (48% of the total number of damage events in 2020 and 2021), and it's also been reported that the Bicol Region is characterized as having a significant number of potentially damaging wind speeds (Thinkhazard.org., 2020). In addition, its frequent cyclones and

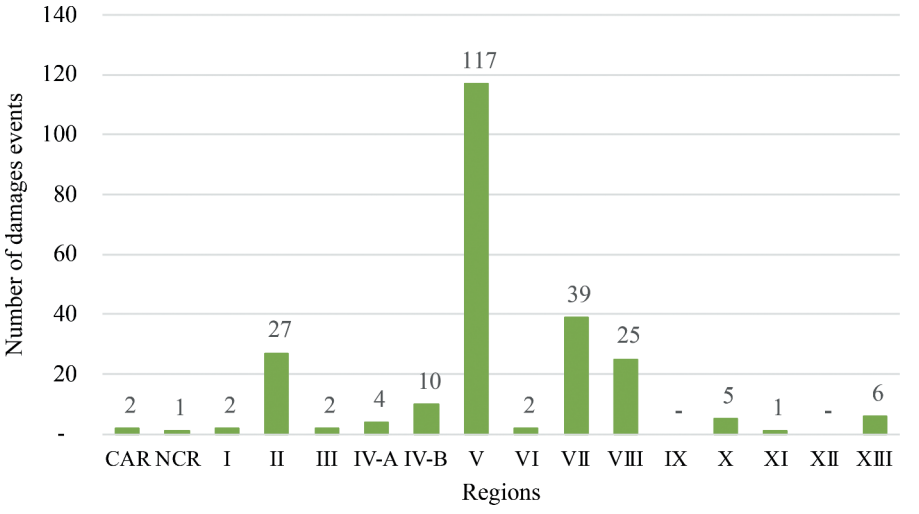


Figure 2. Number of bridge structure damage events due to natural disaster by region.

floods contribute to its location as one of the most disaster-prone areas due to its geophysical locations (preventionweb.net., 2022).

The Central Visayas region, specifically Region VII, experienced the second-highest number of damage events, with 39 events (16%) recorded in 2020 and 2021. This high incidence of bridge damage can potentially be attributed to the unique geographical composition of the area, which includes several outlying islands, one main island, and one smaller island. Additionally, the interior of the region's provinces is characterized by expansive highlands, while the coast features narrow strips of arable land. A significant portion of the province's land area, accounting for 62% of the total, is hilly and mountainous. Consequently, the susceptibility of bridges in this region to damage events may be heightened due to these geographical factors (Arkipelago, 2020).

Region II, generally known as Cagayan Valley, experienced 27 damaging events (11%) in bridge structures due to its geographical location along the Pacific Ocean, making it prone to frequent typhoons. The region's diverse topography, including plains, mountains, and a major river system (Cagayan River), contributes to heightened flooding risks and landslides, particularly during the typhoon season. Heavy rainfall is caused by the tropical environment and being in the path of typhoons, increasing these hazards. The region's economic reliance on agriculture increases the effects of natural disasters, making adequate risk mitigation and disaster preparedness measures critical (Cuntapay A.B., 2015).

3.3 *Physical damage to bridge structures due to natural disasters*

Since the physical or actual damage was divided into three groups, the percentage of damage for each group was calculated by dividing the number of actual damage occurrences within that group by the total number of damage events recorded during the specified period. As per data in Figure 3, the largest number of damage to bridge structures in 2020 and 2021 in the Philippines was found for superstructures, which was observed in 45.7% of the damage events. This indicates that superstructures were most susceptible to damage during this time frame. Bridge protection incurred the second-highest percentage of damage at 44.4%, while substructure damages incurred the least at 21.8% of the total damage event.

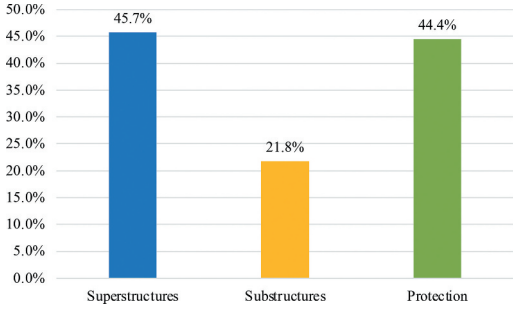


Figure 3. Percentage of damage events for which each type of damage was observed.

After a thorough analysis of the regional implications of bridge damages, it is evident that Region V greatly impacted the structural integrity of bridges. During the combined period of 2020 and 2021, Region V accounted for 18.1% of superstructure damage, 8.2% of substructure damage, and 17.7% of bridge protection damage, as depicted in Figure 4. These percentages were derived by calculating the actual group of damages experienced by Region V, divided by the total of 243 recorded damage events within the specified time frame. Additionally, Region V is the one that is most impacted by all three categories of disasters. This illustrates how much the bridge structures in this area were impacted by natural calamities. Region VIII, which accounted for 8.6% of superstructure damage, follows closely to Region V in terms of superstructure damage. However, Region VIII's substructure and bridge protection damages were comparatively smaller, making only 1.2% of the overall damages. It's interesting to take into account that, at 8.2%, Region VIII came in second for contributing to damages to bridge protection. These results

demonstrate how susceptible bridges in Region V are to natural calamities and the necessity of preventive measures and specific attention to increase their resilience. It also highlights how important it is to take certain geographic areas into account when developing mitigation strategies for reducing and dealing with natural disaster-related bridge damage.

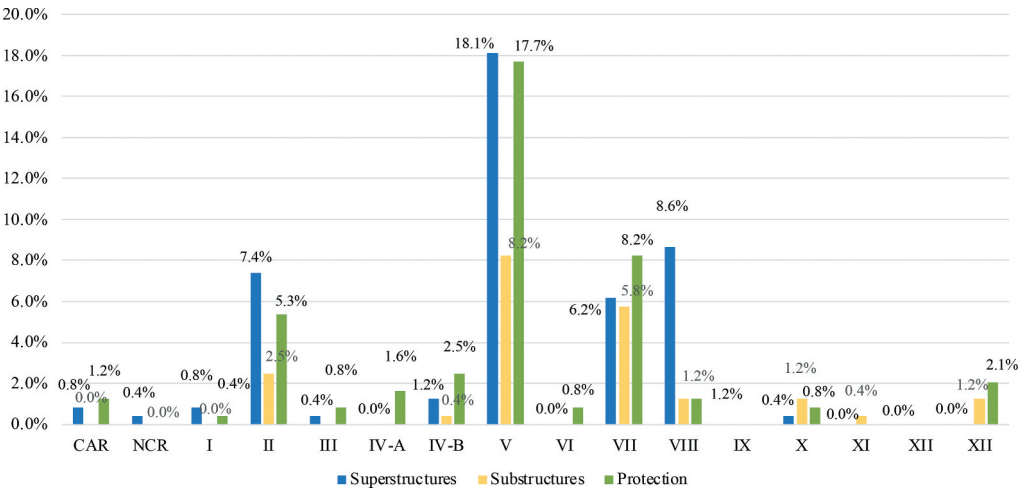


Figure 4. Percentage of damage events in each region for which each type of damage was observed.

3.4 *Estimated cost of damages to bridge structures*

Figure 5 shows the total estimated cost of damages to bridges caused by natural disasters in each region for the years 2020 and 2021. It can be observed that Region V suffered the highest estimated cost of damages, amounting to Php 1,254.1M, followed by Region II with Php 252.8M and Region VII with Php 160.0 M. Evidently, Region V has the highest estimated cost of damages as well, given that it suffered the highest percentage of damages, as shown in Figure 3. After reviewing Figure 3, it becomes apparent that Region VII incurred a greater proportion of cost damages in comparison to Region II. However, an examination of the financial implications of these impacts, as illustrated in Figure 5, shows an interesting finding. Despite Region VII experiencing a greater number of natural disasters and sustaining a larger number of damages in Figure 2, it was actually Region II that incurred a higher estimated cost of damages than Region VII.

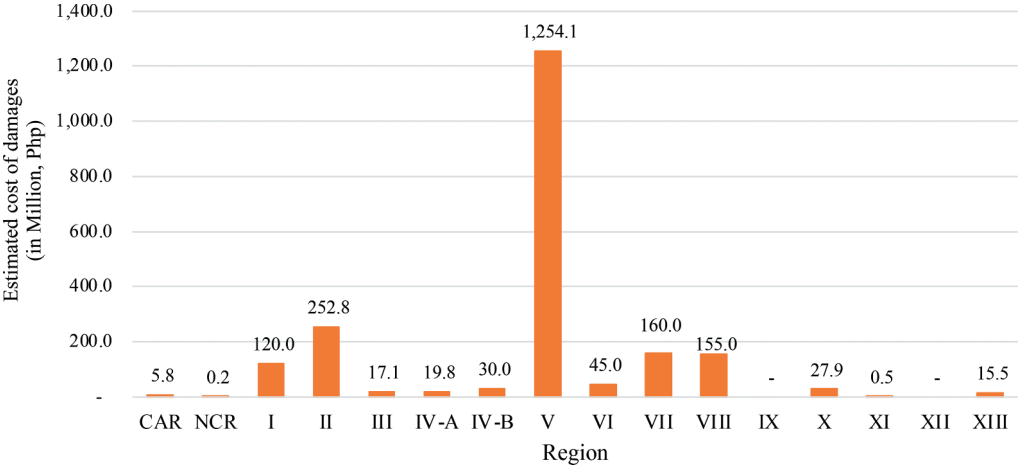


Figure 5. Percentage of the estimated cost of damage per region in the year 2020 and 2021.

One possible explanation for this discrepancy is that the severity and scale of the disasters in Region II were more significant. Even though Region VII had a greater frequency of events, factors such as the severity of typhoons, the vulnerability of infrastructure, and the specific types of natural disasters can all contribute to variations in the economic impact on different regions. All these factors must be considered when evaluating the economic impacts of natural disasters on different regions. Merely estimating the amount or percentage of the damages sustained might not offer a comprehensive understanding of the actual cost incurred. Gaining insight into the socioeconomic factors that extend beyond mere frequency may help in a more accurate assessment and mitigation of the financial impact of natural disasters in particular regions. By considering the severity and specific characteristics of natural hazards in each region, policymakers and stakeholders can develop more targeted strategies to mitigate the economic impact of future disasters and allocate resources effectively for post-disaster recovery and reconstruction efforts.

4 CONCLUSION

Based on a study investigating the impact of natural disasters on the infrastructure of the Philippines in 2020 and 2021, it was found that bridges experienced less damage than road structures. In addition, bridges also had a lower occurrence of structural damages when compared to road structures. These findings highlight the relatively better resilience of bridges in the face of natural disasters as compared to road structures. Moreover, the comparative susceptibility of bridge structures to road structures depends on various conditions, relying solely on the percentage of damage events may not accurately represent the structures' overall vulnerability.

In terms of damage distribution among regions, Region V has seen much more extreme damage events, with the greatest impact on bridge structures, resulting in a significant number of damages. As a result, this region suffered the most damage to bridge structures and the highest estimated cost of damages compared to any other region.

Another key observation is that Region II experienced more severe financial implications despite having a lower number of damages to bridge structures compared to Region VII. This suggests that the severity of the damage in Region II was greater. It is essential to note that the number of damages does not always correlate with the financial losses, as factors like damage type, severity, and location can significantly influence the financial implications.

Furthermore, when assessing the impact of natural disasters on different regions, it is important to consider the economic growth and overall state of each region's economy. Road authorities must evaluate multiple factors, including geographic location, magnitude of the natural disasters, current economic conditions, and infrastructure status in the affected regions. Taking a comprehensive approach will help in developing evidence-based strategies and efficiently allocating resources for future loss mitigation and post-disaster recovery.

Examining the economic factors provides a broader understanding of the financial implications of the damages. The growth and stability of a region's economy can influence the ability to fund repairs and recovery efforts effectively. Regions with stronger economies may be better equipped to allocate resources towards infrastructure repairs, while regions with weaker economies may face more significant challenges in addressing the damages. Hence, policymakers and stakeholders should analyze these underlying factors rather than solely relying on the number of damages. By taking a holistic approach, they can develop evidence-based strategies and allocate resources efficiently. This comprehensive perspective will help mitigate future losses and facilitate a more effective post-disaster recovery.

The research promotes awareness and knowledge of transportation infrastructure damages and the cost implications of road infrastructure damages caused by natural disasters. This paper will provide useful information to experts, relevant government agencies, construction industries, and the general public in order to decide on appropriate countermeasures or mitigation strategies for the transportation infrastructure and to better prepare the budget for the future maintenance of road infrastructures, allowing for a quick and timely response during and after natural disasters. Additional data from previous years will also need to be incorporated into the research to investigate the overall pattern of road infrastructure damage caused

by natural disasters. Furthermore, it is strongly advised to conduct additional regional studies and consider the condition of each road infrastructure as well as the magnitude of natural disasters to acquire a greater understanding of road infrastructures and create possible solutions on how to reduce the vulnerability of road infrastructure.

5 RECOMMENDATION

Investing in high-resolution camera-equipped drones can significantly benefit the Regional and District Engineering Office of DPWH in the Philippines for assessing bridges after natural disasters. Drones offer a cost-effective and efficient solution, providing a comprehensive aerial view and real-time data capture of bridge conditions in affected areas. Equipped with LiDAR sensors, these drones allow for detailed 3D scanning of bridge structures, facilitating accurate evaluation of damages. By swiftly deploying drones, the DPWH can make timely decisions regarding repair and rehabilitation efforts, optimizing resource allocation within budget constraints. This technology enables faster response efforts, facilitates prioritization of maintenance activities, and ultimately aids in the speedy recovery and functionality of bridges in the aftermath of natural disasters, enhancing disaster preparedness and resilience efforts.

ACKNOWLEDGMENT

The authors would like to thank the Japan International Cooperation Agency (JICA) for their support through the Road Asset Management Platform (RAMP), the Shibaura Institute of Technology (SIT) for providing the environment for the research, The Department of Public Works and Highways (DPWH), Philippines for sharing the data and information needed and the Unified Project Management Office (UPMO), DPWH for their warm support.

REFERENCES

Aleksandrova, M., 2021. World Risk Report 2021.

Cavallo, E.A. and Noy, I., 2009. The economics of natural disasters: a survey.

Harasti, A., Gilja, G., Potočki, K. and Lacko, M., 2021. Scour at bridge piers protected by the riprap sloping structure: A review. *Water*, *13*(24), p.3606.

Nnadiri, G.U. et al. (2021) Comparison of driving forces to increasing traffic flow and transport emissions in Philippine regions: A spatial decomposition study, MDPI.

Taghizadeh-Hesary, F., Yoshino, N., Mortha, A. and Sarker, T., 2019. Quality infrastructure and natural disaster resiliency (No. 991). ADBI Working Paper Series.

Utilities One. (n.d.), The Role of Road and Bridge Construction in Disaster Preparedness. <tiesone.com/the-role-of-road-and-bridge-construction-in-disaster-preparedness,>.

Arkipelago, 2020, Kapuluang ng Pilipinas webiste. (2020). Retrieved from Arkipelagohttps://kapuluanng pilipinas.wordpress.com/.

Cuntapay A.B., 2015, Regional Profile, Denr.gov.ph, https://r2.denr.gov.ph/index.php/about-us/regional-profile.

DPWH ATLAS 2022, Dpwh.gov.ph., https://www.dpwh.gov.ph/dpwh/DPWH_ATLAS/index.htm.

Fontanez, D.R., 2021 The Different Components of a Bridge, U.S. Bridge, https://usbridge.com/the-different-components-of-a-bridge/.

Mgs-Ronel (2022), MGS Insurance, Philippine Infrastructure and Bridges, MGS Insurance< https://mgsinsurance.ph/blogs/philippine-infrastructure-and-bridges/ Accessed 23 Nov. 2023.

Preventionweb.net, 2022, Mainstreaming disaster risk reduction into agriculture: a case study from Bicol Region, Philippines, https://www.preventionweb.net/publication/mainstreaming-disaster-risk-reduction-agriculture-case-study-bicol-region-philippines.

Statista, 2021, Philippines: Cost of damage during calamities 2021, https://www.statista.com/statistics/1264085/philippines-value-of-damaged-infrastructures-during-calamities/.

Thinkhazard.org, 2020, Think Hazard - Region V (Bicol region) – Cyclone, <https://thinkhazard.org/en/report/2361-philippines-region-v-bicol-region/CY>.

Bridge Maintenance, Safety, Management, Digitalization and Sustainability – Jensen, Frangopol & Schmidt (eds)
© 2024 The Author(s), ISBN 978-1-032-77040-6
Open Access: www.taylorfrancis.com, CC BY-NC-ND 4.0 license

Improved structural assessment of Newport Bridge using smartphone-based technologies

J. Winkler
Digital Engineering Solutions – DES & AtkinsRéalis, Warsaw, Poland

N. McKay
AtkinsRéalis, Stockton, UK

C. Hendy
AtkinsRéalis, Epsom, UK

ABSTRACT: The ongoing operation & maintenance costs regarding physical infrastructure are extremely high and asset owners continue to experience budgetary constraints. One of the biggest challenges is a lack of practical tools and low-cost solutions for structural health monitoring. However, developments in smartphone technologies have opened new opportunities for optimizing bridge inspection including rapid data collection on asset health. Bridge inspectors can use smartphones during visual inspections vastly improving accessibility and efficiency. The Tees Newport Bridge is a vertical-lift road bridge in England. Bridge inspection revealed that the bearing and bearing support steelwork had failed leading to joint displacement and impact on road users crossing the bridge. AtkinsRealis was called to carry out the assessment and evaluate bridge safety. This paper shows how smartphone-based applications were used for scanning, creating 3D photogrammetric models and monitoring of bridge deformations to understand structural response to the bearing failure. To the authors knowledge this is one of the world's first examples where regular smartphones were used for generating the 3D model of a complex bridge and also for capturing and analyzing structural displacements with mm-accuracy. Low-cost, smartphone-based tools are potentially game-changing with respect to structural health monitoring and asset condition reporting, enabling engineers and clients to manage their assets as efficiently and safely as possible.

1 INTRODUCTION

1.1 *Description of structure*

Tees Newport Bridge is located between the A66 and the A19 and carries the A1032 two lane dual carriageway and associated footpaths over the River Tees with Stockton-on-Tees to the west and Middlesbrough to the east. The structure comprises 11 spans and was constructed circa 1934. Lifting span is simply supported, 80m long between the centres of the bearings and approximately 20m wide. It comprises a pair of primary Pratt trusses with curved top chords, connected by bracing frames. The span is connected to lifting girders which are suspended by 80 steel cables (or "ropes"), in 8 groups of 10, which pass over sheaves at the top of the towers and connect into counterweights on the other sides. There are four groups of cables and two counterweights at each corner of the lifting span. The roadway is carried by a steel frame deck comprising secondary transverse girders spanning between the primary trusses, with longitudinal tertiary girders between each transverse girder. Quaternary transverse girders span between the tertiary longitudinal girders to provide support to the mass concrete, non-composite deck (Figure 1).

DOI: 10.1201/9781003483755-360



Figure 1. The Tees Newport Bridge.

1.2 *Context and client issues*

During the mid 20th Century the bridge was in constant use and would be lifted twice daily. However, this gradually declined, and upon the construction of the Tees Barrage approximately 1.5 miles upstream, the need for lifting the deck ceased. The last known lift occurred on 18th November 1990. The route over the bridge nevertheless continued to see large volumes of traffic. North shore industry along the bank of the Tees saw much commuter traffic and this continued throughout the latter part of the century, even following the construction of the A19 Tees Viaduct that crosses the river just south-west of Tees Newport Bridge. Daily traffic volumes continue to be high with Annual Average Daily flows of circa 20,000 vehicles.

In 2023, bridge inspection revealed that the bearing and bearing support steelwork had failed leading to joint displacement and impact on road users crossing the bridge. In addition, the condition of other key elements including the remaining bearings, buffer mechanisms and lifting cables became a concern as the support conditions changed following the bearing failure (Figure 2). Reports of "locking off" the bridge deck following its last lift in 1990 indicated that load in the cables may have been removed or reduced. Subsequent inspection of the tower steelwork indicated that this wasn't in fact accurate. Angles connected to the tower legs above the main deck prevented the deck from lifting excessively. However, with only upward movement restricted and a gap of around 40mm between deck and angle lock off, the deck was still carried by the vertical cable runs passing over large sheaves at the head of each tower and connecting to the counterweight system. The counterweight system was indeed finely balanced with approximately 90% of the total permanent load from the deck passing into the cables. The remaining 10% supported on the rocker bearings and transferring approximately 20 tonnes of load into each supporting pier.

Failure of the north-west bearing and support steelwork led to downward displacement of the deck and this was seen along the comb joint across the width of the bridge at this end. With the deck so finely balanced and significant load taken by the cables, any forward mitigation would need more comprehensive understanding of associated movement under live load. As an immediate measure traffic was directed away from the north side of the bridge through lane closure and towards the central section of the bridge. The finely balanced support conditions and complex structural arrangement presented a logistical headache when considering potential mitigation methods.

2 SPECIAL INSPECTION

The initial bridge inspection was followed up with special inspection (SI) of the bearing and this was carried out by AtkinsRealis in April 2023. The inspection identified the full extent of



Figure 2. Inspection images of the cables and the bearing assembly post-failure.

the problem in terms of collapsed stool and fracture throughout most of the stool width. In addition, there was a clear gap at the head of the bearing indicating that the deck was supported entirely on the cables at this corner. The inspection also considered the condition of the fixed end bearing assemblies at the east end of the bridge and the corresponding condition of the south-west bearing at the free end. Whilst the condition at the fixed end indicated corrosion of key elements these remained relatively intact and serviceable. The bearing assembly at the south-west corner however indicated similar deterioration mechanisms as that at the north-west corner although not as severe. Nevertheless, it was clear that stabilizing the deck under load as an initial measure would require work to both corners at the west end of the bridge.

To support the SI a 3D photogrammetric scan was undertaken using LIDAR enabled iOS device. Inspectors carried out the scan from below the bridge obtaining access to the pier head. Scanning included pier head, bearing and original buffer assembly. Access to the south of the assembly was restricted by the deck steelwork however sufficient data was obtained from the remaining 3 sides of the assembly. The scan has enabled holistic condition appraisal of the assembly as well as basic measurement of key dimensions including collapsed bearing stool height, gap between bearing and deck soffit, deck steelwork dimensions, etc. The 3D scan has proved invaluable in supporting the contractor in designing and locating temporary jacks as well as providing valuable data for the replacement bearing design.

3 MOBILE DIGITAL IMAGE CORRELATION (DIC) SURVEY

Understanding of the deck movement under load was critically important and this was true to understand structural response post bearing failure but also structural response to temporary jacking. As such, monitoring was required. In advance of jack installation and more comprehensive physical monitoring, deployment of mobile Digital Image Correlation (DIC) was carried out. AtkinsRealis started to use DIC technology in structural health monitoring in 2014 (Winkler et al. 2014) and continue to expand the use of this technology in recent years

(Winkler et al. 2022). AtkinsRealis carried out a basic movement monitoring for all four corners of the bridge in May 2023.

3.1 *Methodology and equipment*

The method uses a smartphone mounted on a tripod, at a static position. The phones camera picks up two points, a static point used as a datum and an active point which moves under dynamic load. The ISO certified software developed by Digital Engineering Solutions (DES) records a video of the load moving over the bridge and calculates the relative displacement between the static and active points and presents the information on a graph of displacement against time (Figure 3).



Figure 3. Mobile Digital Image Correlation (DIC) survey.

The survey (data collection and video analysis) was carried out successfully using a regular smartphone by an engineer with no prior monitoring experience proving scalability and easiness of use of the smartphone based DES technology. Survey was susceptible to shadow at a pixel level, however it can be considered a useful in determining the extent of movement above and below the bridge, under normal traffic.

4 RESULTS

4.1 *North-West corner*

Figure 4 shows movement of the north-west corner buffer while Figure 5. shows peak movement of the expansion joint (approx. 10mm) at the nearside lane position.

The results support the theory of the movement being predominantly at the north-west and south-east corners. At the north-west corner, it was noted that the range of movement under heavy traffic was not sufficient to close the approximately 60mm gap above the northwest bearing, suggesting the deck is predominantly free and supported on the buffer, acting as a spring support, in combination with the cables.

4.2 *Full scale monitoring*

Deployment of full scale structural health monitoring was conducted before the jacking operations at the north-west corner of the bridge. Preliminary findings from the mobile DIC survey indicated the extent of movement expected at each corner both upward and downward in response to traffic load. It is clear when comparing the full monitoring output to the DIC output that the magnitude of movement under load is consistent.



Figure 4. North-West corner buffer movement.



Figure 5. North-West corner expansion joint movement.

5 CONCLUSIONS (KEY BENEFITS & SUCCESS FACTORS

Bridge inspection of the Tees Newport Bridge revealed that the bearing and bearing support steelwork had failed leading to joint displacement and impact on road users crossing the bridge.

AtkinsRealis was called to carry out the assessment and evaluate bridge safety. It has been demonstrated that smartphone-based applications can be successfully used for scanning (15 min to capture images), creating 3D photogrammetric models and monitoring of bridge deformations to understand structural response to the bearing failure. Ease of deployment of mobile DIC and early value of movement information in supporting the decision to keep the bridge open to traffic should be emphasized. To the authors knowledge it was one of the world's first examples where regular smartphones were used for generating the 3D model of a complex bridge and also for capturing and analyzing structural displacements with mm-accuracy. Low-cost, smartphone-based tools are potentially game-changing with respect to

structural health monitoring and asset condition reporting, enabling engineers and clients to manage their assets as efficiently and safely as possible.

REFERENCES

Winkler J., Fischer G., & Georgakis C.T., Measurement of local deformations in steel monostrands using digital image correlation. 2014; *Journal of Bridge Engineering* (ASCE), 19(10).

Winkler, J., Bormlund, F., Havelykke, M. D., 2022, Improved structural health monitoring of Great Belt Bridge hangers and deck using digital image correlation. *Proceedings of the Eleventh International Conference on Bridge Maintenance, Safety and Management (IABMAS 2022)*, *Barcelona, Spain*, *July 11-15*. 2022; 9781003322641

Bridge Maintenance, Safety, Management, Digitalization and Sustainability – Jensen, Frangopol & Schmidt (eds)
© 2024 The Author(s), ISBN 978-1-032-77040-6
Open Access: www.taylorfrancis.com, CC BY-NC-ND 4.0 license

Artificial intelligence to identify defects on bridges inspected by drone

S. Flawinne
Public Service of Wallonia, Liège, Belgium

ABSTRACT: Drones and artificial intelligence are fast-growing technologies that offer considerable potential for the inspection of large, high-rise structures, such as viaducts. Drones can lead to safer and more economical inspections. Several years ago, Belgium's Service Public de Wallonie (SPW) began carrying out full drone inspections of its major structures. This survey includes photos, 3D model, orthomosaics of defects and database of defects.

The advantages of drone inspection are numerous. It allows precise visualization of hard-to-reach areas, as well as global analysis directly from orthomosaics. It also enables full digital documentation of the defects via the database.

However, the number of defects identified on large-scale structures can be extremely large. Manual detection of all these defects is time-consuming. So the SPW is now working with an artificial intelligence solution that can automatically identify defects in the structure on photos and positioning defect contours on 3D CAD models of the bridge.

1 INTRODUCTION

Drones are an emerging technology that holds significant potential for inspecting tall and large structures such as bridges and viaducts. Compared to traditional visual inspections, the use of drones can be safer and more cost-effective, avoiding indirect costs associated with road closures and the rental of inspection lifts. However, detection of all the defects identified on large-scale structures can be extremely time-consuming. Artificial intelligence is a solution that can help solve this operation much faster and more efficiently.

2 INSPECTION OF LARGE BRIDGES BY DRONE

To assess the feasibility and limitations of using drones for inspecting large structures, the Public Service of Wallonia has initiated test projects on four viaducts.

For each viaduct, a drone inspection was conducted, including:

- Capturing photos of each defect
- Creating a 3D model through photogrammetry
- Generating orthophotos with defects outlined and sorted by layers, all at a millimeter-scale photo resolution
- Compiling a database documenting all defects by type and location

The requested ground sample distance (GSD) for both photos and orthophotos is a minimum of 1mm. This means that each side of a pixel in a photo or orthophoto will have a maximum length of 1mm. The GSD will be calculated using the Equation 1 below: $R = Tp{*}H/p \leq 1\ (mm)$

Where:

- R is the ground sample distance (GSD)
- Tp is the size of the photosite in mm (pixel size on the sensor of the camera used)

DOI: 10.1201/9781003483755-361

- H is the maximum distance in mm between the camera during measurement and the structure being photographed
- p is the focal length used in mm

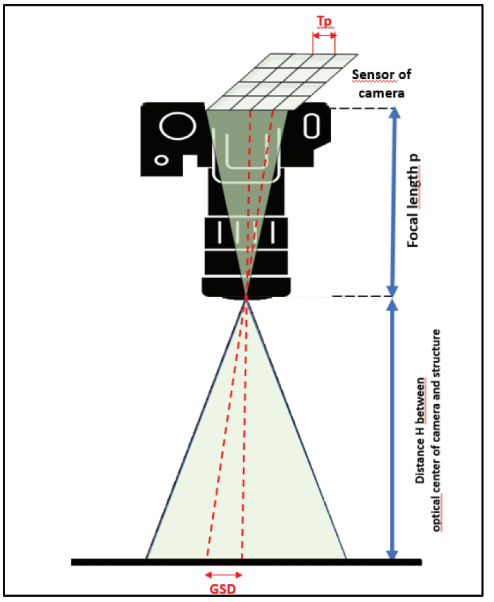


Figure 1. Calculation of ground sample distance (GSD).

The four inspected viaducts are the Onoz, Remouchamps, Sécheval, and Horion viaducts. These viaducts are of high significance in the Walloon Region and have substantial dimensions, spanning over numerous traveled roadways. Their sizes range from 300m to 1 km in length. Table 1 provides a description for each viaduct, including the deck size and the type of structure.

Table 1. Deck size and type of structure of each viaduct.

Bridge name	Deck size	Type of structure
	m^2	
Onoz	23638	Concrete girder bridge
Remouchamps	33770	Steel girder bridge
Sécheval	19630	Steel girder bridge
Horion	8430	Steel girder bridge

The Figure 2 illustrates each of the four viaducts.

Several different drones were used for photo capture, but, in general, the characteristics of the drones used were fairly consistent, namely:

- Weight ranging between 10 - 15 kg
- Flight autonomy between 40 and 60 minutes
- Excellent resistance to wind and turbulence
- Obstacle avoidance sensor system
- Three-axis stabilized camera gimbal capable of pivoting vertically from +90 to -90°

The last point is crucial because it's necessary to have a camera that can be oriented upwards to capture the underside of the deck, which is often the most important and complex part for inspecting large viaducts. However, most commercial drones do not offer such a solution.



Figure 2. Illustration of each viaduct.

The cameras mounted on these gimbals were often models with a full-frame 36x24mm sensor and a resolution ranging from 24 to 45 megapixels. The focal length often varied around 50mm.

Based on the camera's characteristics, it is possible, through Equation1, to calculate the necessary distance between the structure and the camera to achieve a minimum resolution of 1mm. This calculated distance showed that the camera had to be positioned between 5 and 8 meters from the photographed surface.

To construct 3D models of the structure as well as orthomosaics, a photogrammetric process is required. Photogrammetry involves creating accurate 3D models of objects and environments using photos taken from different angles. Once scaled, distance measurements on the 3D model or its 2D projection (orthomosaic) can be made. Figure 3 schematically illustrates the transition from photographs (represented by the blue rectangles) to a comprehensive 3D photogrammetric model.

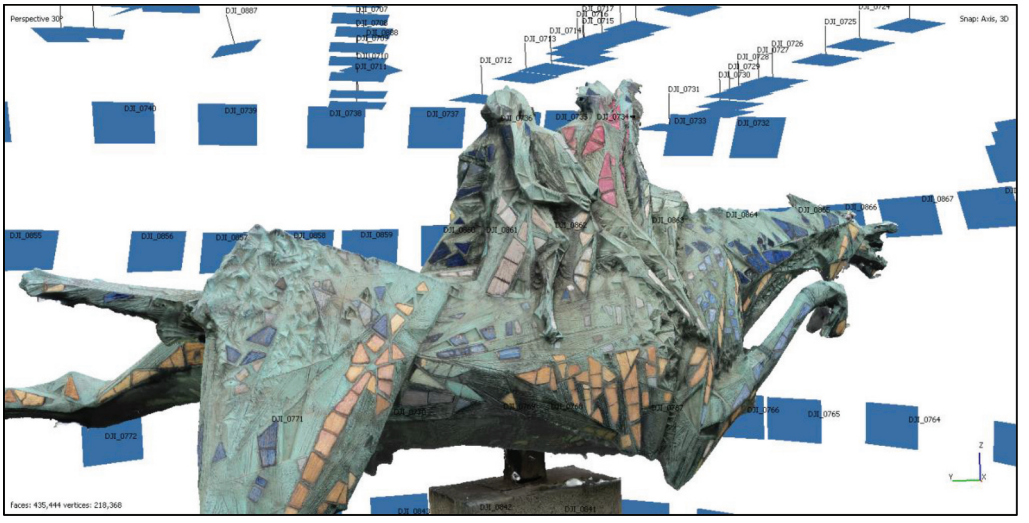


Figure 3. Transition from photos to 3D model.

An absolutely necessary condition for creating a 3D model through the photogrammetric process is to have an overlap (common area) between two successive photos. This overlap must be a minimum of 60% on the same strip (usually 80%) and a minimum of 20% between strips. Therefore, each taken photo will only have 20 to 40% of the area not yet captured compared to the previous photo in the same strip.

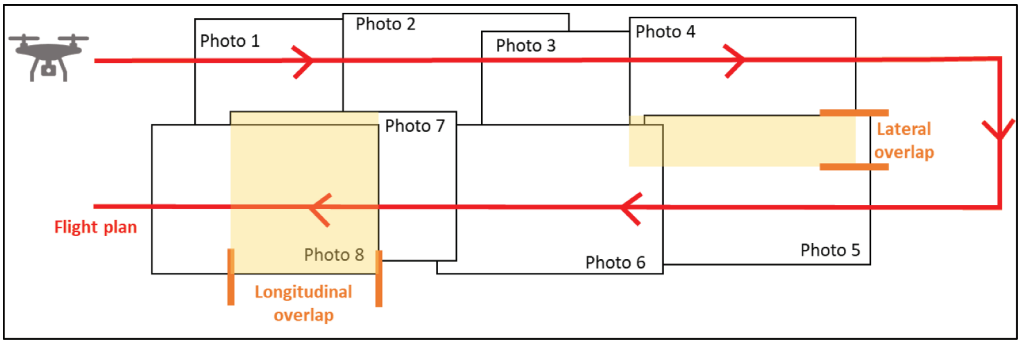


Figure 4. Overlapping of photos.

The photogrammetric process, therefore, entails a significant increase in the number of photos required to create a 3D model and orthomosaics compared to the number of photos needed to simply capture the entire structure. Table 2 indicates the number of photos taken for each bridge and the number of defects identified in these photos.

Table 2. Number of photos taken by drone and number of defects identified.

Bridge name	Number of photos	Number of defects
Onoz	30141	5418
Remouchamps	19271	2712
Sécheval	4355	2702
Horion	9585	3927

From these photos, a photogrammetric 3D model is created. This model is projected in a reference direction to generate orthophotos of various elements of the structure. The orthophotos are then analyzed to identify each defect. These defects are then listed in a database, along with their location, size, and type of defect. Figure 5 illustrates the different steps of analysis.

Layers are drawn on the orthophotos at the defect locations to visualize them directly. Each color represents a type of defect. Figure 6 shows, for example, the orthophotos with colored layers for each of the piers and undersides of the spans of the deck of the Onoz viaduct.

The advantages of such drone inspections have proven to be manifold. Such an inspection on large structures allows for precise visualization of hard-to-reach areas and a comprehensive analysis of large sections of the structure directly through orthophotos. Moreover, it can be conducted more quickly and with fewer risks for inspectors. It also enables accurate digital documentation of detected defects through the database.

While conducting a drone inspection of a large viaduct proves highly advantageous for helping asset managers synthesize and assess the bridge's condition, several important aspects can be considered drawbacks:

- Current regulations prohibit the overflight of traveled roadways by drones of such weight. Therefore, it is necessary to close and divert traffic beneath the structure during flight operations.

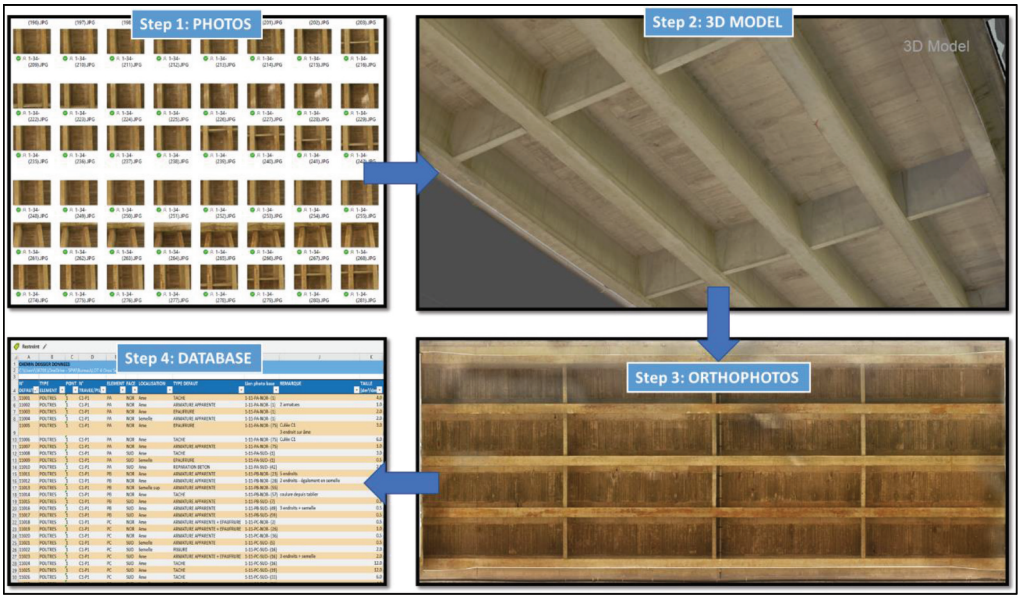


Figure 5. Different steps of analysis. Onoz viaduct.



Figure 6. Orthophotos of Onoz viaduct with layers on the defects.

- The number of defects observable in photos taken at close range on a large structure is extremely high. The time required for analyzing this amount of data and creating layers and a database is consequently very high.
- Inspections of each structure are mandated every three years. It is not feasible to conduct a complete drone inspection with such regularity. Therefore, conventional inspections are performed between two drone inspections. But, the time required to link the defects from such an inspection to those from the mass of defects captured by drone is significant.

3 ARTIFICIAL INTELLIGENCE FOR VIADUCTS INSPECTION BY DRONE

If the technology doesn't provide leverage on regulations, it's not the case for the last two issues raised. Indeed, working with an artificial intelligence solution can solve those problems by automatically:

- identifying defects in the structure on photos. The AI categorizes these defects, estimates their size and annotates the contours of the defects on the photos
- positioning defect contours on 3D CAD models of the bridge
- finding a defect already identified during a previous inspection, and estimating the change in defect size from two successive inspections

In the first phase, SPW worked with an artificial intelligence, developed by the company Dynamic Infrastructure, capable of automatically recognizing each type of defect on a structure, regardless of the category, such as:

- Cracks
- Moisture stains
- Rust stains
- Visible corroded reinforcements
- Gravel nests
- Spalls

On each photo analyzed by the AI, defects were outlined and tagged according to their type. Figure 7 displays the tags of defects automatically identified by the AI on several photos (the colors do not indicate the type of defect but rather their severity).



Figure 7. Tags of defects automatically identified by AI.

To assist the structure manager in analyzing the bridge, the defect detection cursor was adjusted with a strong tolerance. This means that the AI is configured to, in case of uncertainty, tag a defect even if it is not one. This scenario is, however, quite rare since the correct detection rate of the AI used is 99%. However, this approach ensures that all existing defects are effectively identified (which may not have been the case with a defect detection cursor set to low tolerance).

As the goal is not to rely entirely on AI, a human eye must review the tagged photos to validate the AI results. However, it is much simpler and faster to identify tagged defects that are not defects than the reverse. Currently, an experienced operator can, in this way, check hundreds of photos in one or two hours.

The operator takes advantage of this phase to assign a chosen severity level to defects they deem appropriate. Consequently, defects are not only classified by type but also by severity.

Still in the first phase, the AI solution used can automatically link and identify the same defect from one photo to another. It calculates the relative evolution (in percentage) of the defect's size or intensity from one photo to another, even if the photo is taken from a different angle. This allows for automatic detection of whether defects have changed in size from one inspection to another. Figure 8 illustrates an example of defect evolution identified by the AI.



Figure 8. Example of defect evolution identified by the AI.

While the solution proposed by AI at the end of the first phase already brings many benefits, there are still some limitations that ideally should be addressed to significantly improve the impact of AI. Indeed, at this stage, it is not possible to:

- Measure the absolute size of a defect
- Automatically position the defect in 3D on the structure for a general overview

These capabilities were possible with drone inspections but required significant manual work to synthesize the data. The idea, therefore, was to enhance the process offered by AI by recreating the process of a drone inspection but in an automated way. In a second phase, the AI has been reworked by Dynamic Infrastructure to automate this process.

The concept is to use this new process on a series of major structures. The steps are as follows:

1. Drone photo capture of the structure with overlap
2. Identification of defects in the photos by AI
3. Creation of a low-quality photogrammetric 3D model. This model is used to calculate the size of defects and position them on a CAD 3D model.
4. Projection of the outlines of identified defects onto the 3D model. The CAD model is lighter than the photogrammetric model and therefore easier to navigate. Clicking on the outlines reveals the characteristics of the defect.

Figure 9 illustrates the ongoing development process for the Onoz viaduct.

This new process overcomes the limitations imposed by AI in the first phase (no calculation of absolute defect size, no positioning on a 3D model). Furthermore, once this process is completed, it is entirely possible for future inspections to capture simple photos of defects from any location and without overlap. The AI will then be able to link the defects photographed during this new inspection to the defects already identified and positioned on the 3D model previously. It can also automatically verify if the defect has increased in size. It is simply necessary that the initial photo capture of the bridge processed by the AI is done in a way that

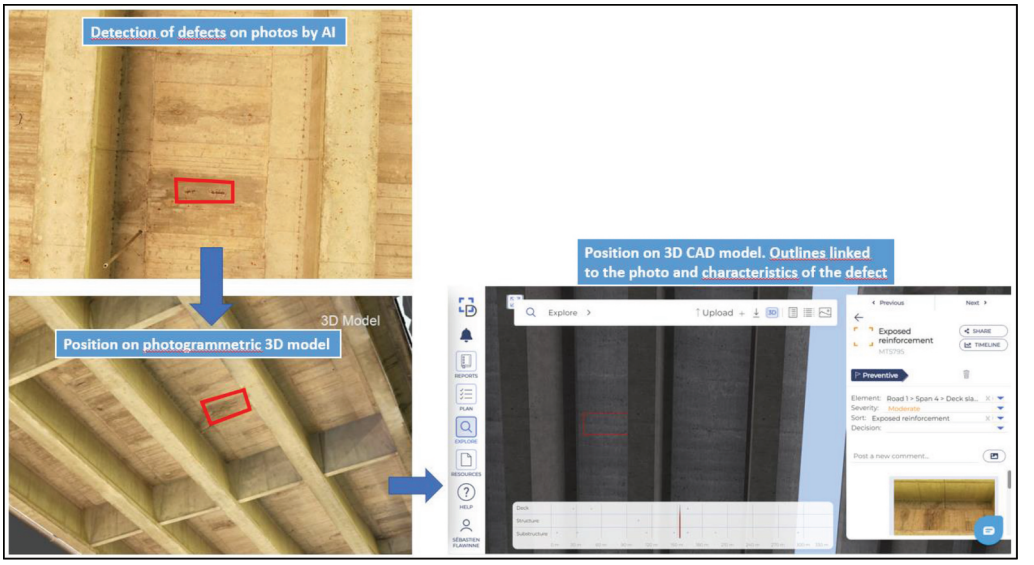


Figure 9. Process of automatic inspection of major structures by AI. Onoz viaduct.

allows for the creation of a photogrammetric 3D model, meaning taking a significant number of photos to ensure the necessary overlap (this photo capture can be done using drones or other methods).

That's why SPW reserve this process for major structures that involve a significant analysis time and that will be greatly facilitated by this method.

4 CONCLUSIONS

As a manager of infrastructure assets, the inspection of major structures by drones offers numerous advantages. Four viaducts have been inspected using this tool, and the results have been conclusive. The quality of photos at close range, the ability to quickly visualize all defects on orthophotos, and the creation of a database for a detailed analysis greatly facilitate the decision-making support for the asset manager.

The limitations of such inspections are more on the side of drone operators, who must undertake significant work to capture and, most importantly, sort and format all the data. To overcome these difficulties, the implementation of a tool using artificial intelligence to automatically perform the identification and categorization of defects greatly eases the operators' work. A human eye is still necessary to verify the results. However, by combining drone inspections with powerful AI, the inspection and analysis of major structures are significantly simplified and comprehensive.

Bridge Maintenance, Safety, Management, Digitalization and Sustainability – Jensen, Frangopol & Schmidt (eds)
© 2024 The Author(s), ISBN 978-1-032-77040-6
Open Access: www.taylorfrancis.com, CC BY-NC-ND 4.0 license

Improved structural health monitoring of the Lincent Bridge using innovative camera-based system

L. Rivituso & S. Flawinne
Service Public de Wallonie, Direction de l'Expertise des Ouvrages, Belgium

J. Winkler
Digital Engineering Solutions – DES, Poland | AtkinsRéalis, UK

ABSTRACT: The Service Public of Wallonia (SPW) oversees 6,000 bridges in Belgium, relying on specialized departments for their operation and maintenance.

Structural Health Monitoring (SHM) is crucial for managing aging infrastructure. To achieve that goal SPW began to use a camera-based monitoring system. The system is compatible with all commonly available cameras (including smartphones) and enables precise monitoring of structural displacements with no traffic disruption.

This paper shows the outcome of 2-year long structural health monitoring campaign. The camera-based system was used on the Lincent Bridge, where settlement caused concrete beams to become trapped. The monitoring system initially employed conventional sensors, resulting in inconclusive results. In 2021, SPW introduced solar-charged cameras, revealing that the expansion of beams was pushing one of the abutments.

The DES system, showing over 90% correlation with temperature sensors, provided unique insights unattainable through conventional methods. These findings were instrumental in assessing the situation and initiating necessary renovations.

1 INTRODUCING THE ISSUE

The structure in question is a highway bridge located on the E40 (connecting Liège to Brussels) near Lincent. It consists of two similar bridges, each with slightly different widths, corresponding to traffic flow in opposite directions. These bridges span over a local road.

With a total length of 25 m, the structure comprises a deck section with longitudinal beams covering 15 m, followed by a frame bridge section for the remaining 10 m.

During the structure inspection, SPW observed that certain longitudinal beams were compressed between the frame and the abutment. This observation indicates the presence of unforeseen movements within the structure. It's essential to highlight that this compression primarily stems from settlement issues, with temperature effects exacerbating the situation. It is also crucial to emphasize that the compression is concentrated in specific areas at the end of the beams.

Topographic surveys were conducted to assess whether any parts of the structure had potentially shifted from the original construction plans. It was observed that the frame bridge had tilted from its original position, resulting in the pushing and compression of the longitudinal beams between the abutment and the frame.

Before undertaking the costly rehabilitation measures proposed by a consulting firm to restore the structure to its original state, SPW wanted to ensure that the situation was still evolving.

An initial instrumentation campaign using traditional sensors (inclinometers, displacement sensors, etc.) was conducted. However, the results from this campaign proved to be complex and challenging to analyze, preventing SPW from determining the overall behavior of the structure.

DOI: 10.1201/9781003483755-362



Figure 1. The Lincent Bridge.

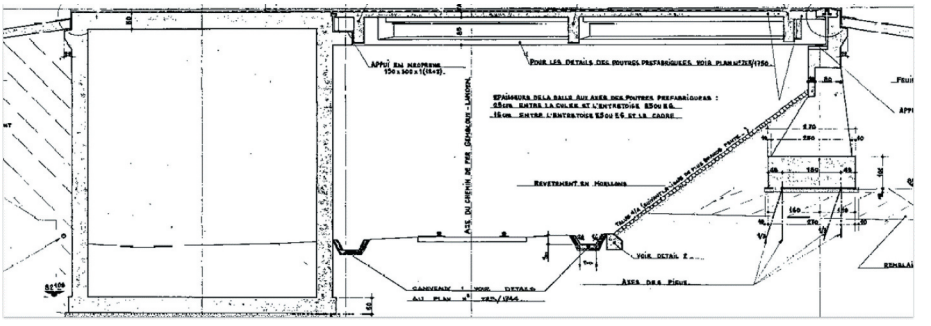


Figure 2. Cross section of the Lincent Bridge.



Figure 3. Crushing concrete as a result of a contact between the beam and the abutment/frame section.

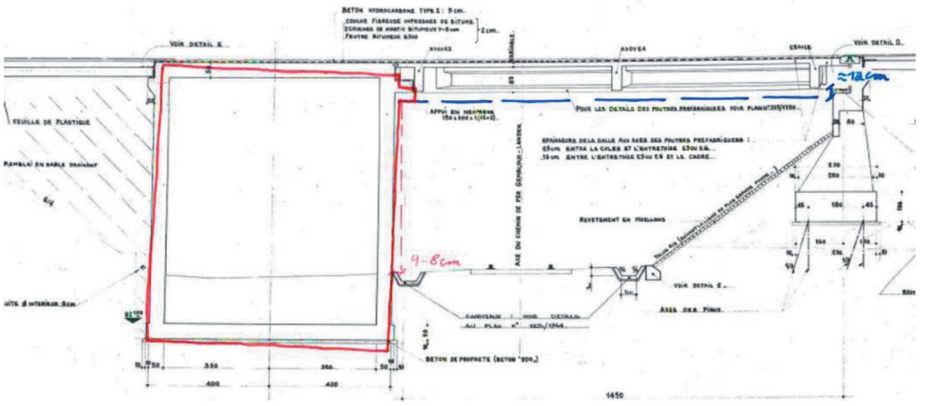


Figure 4. Displacement of the frame and beams.

2 ISSUES ENCOUNTERED WITH TRADITIONAL INSTRUMENTATION

In 2020, the traditional instrumentation campaign commenced, incorporating linear displacement sensors, inclinometers, temperature probes, and strain gauges installed on-site, with data transmitted via telemetry.

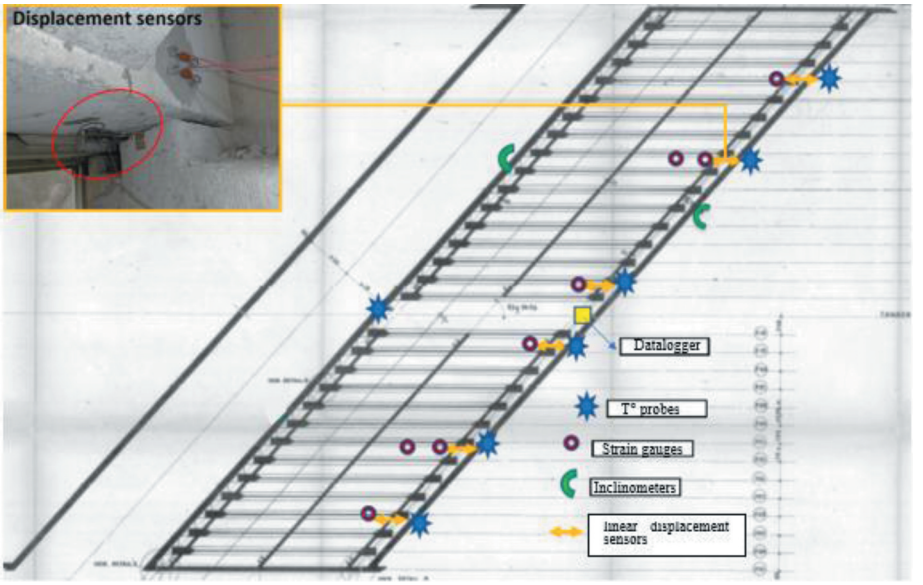


Figure 5. Distribution of traditional instrumentation.

Inclinometers placed on the frame revealed that the frame had ceased to tilt, exhibiting only slight cyclic movements around 0.03°, attributed to temperature variations. The challenge arose in determining how the abutment behaved concerning the beam movement, adding complexity to the study.

The displacement sensors at the beam-abutment junction provided movements perfectly correlated with temperature suggesting that the beam wasn't constrained in its movements according to the coefficients of expansion. Surprisingly, the coefficient of expansion derived from these values was twice the expected value, which is unexpected given the contact between the beams and the abutment.

It is noteworthy that these results were obtained based on a single temperature probe within the structure (at a depth of 15cm). In this instance, temperature gradients were not calculated, as this study did not aim to undertake such complexity.

The abutment is also equipped with inclinometers, and their results proved equally intriguing. Data analysis uncovered a partial correlation with temperature, with maximum displacements reaching 0.15°, equivalent to a 16 mm displacement at the top. This movement significantly exceeded that of the frame. These findings present a contradictory scenario, as while the beams are theoretically free to expand, the inclinometers suggest a pushing motion against the abutment.

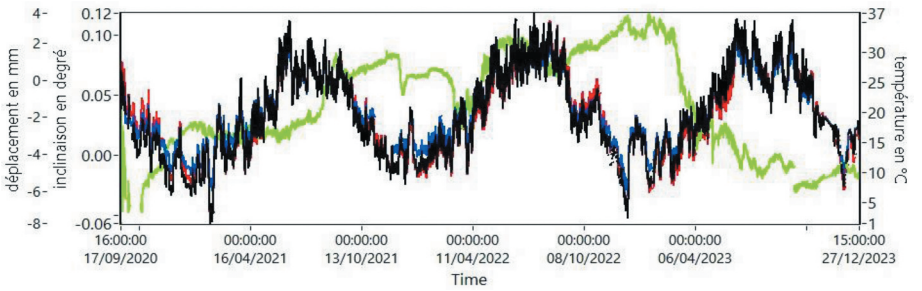


Figure 6. Temperature curve (red); beams displacement (black and blue); Abutment's rotation (green).

The issue stems from using linear displacement sensors, focusing on relative displacement studies (between the abutment and the beam, for example). The overall complex movement of the structure led to sensor results unsuitable for in-depth analysis. The possibility of the beam undergoing rotational movement upon contact with the abutment makes interpreting results from linear sensors particularly challenging.

Given this complexity, a comprehensive study of the overall movement of different elements was necessary for a profound understanding. Consequently, SPW adopted an innovative approach, exploring the use of Digital Image Correlation (DIC).

While this method has proven effective in laboratory settings (Winkler et al. 2014, Winkler et al. 2015) its application in the field remains underutilized but holds promise as an alternative solution (Winkler & Hendy 2017).

3 IMPLEMENTATION OF DIC INSTRUMENTATION

The DIC method is ideal for tracking the evolution of displacements over time. To implement this instrumentation, two surveillance cameras, powered by solar panels, were installed on the back wall of a railway bridge located 30 meters from the structure under investigation.



Figure 7. Camera-based system powered by solar panels.

These two cameras provided an overall view of the Lincent Bridge (frame, beams and abutment). Two cameras were necessary to capture all elements due to their restricted field of view (FOV). Nonetheless, the study could have been conducted with a single camera filming the entire scene but with a lower precision. SPW used cameras to observe the 2D displacements (in the image plane) of various points on the structure. These points facilitate the study of the following elements:

- The frame itself
- The longitudinal beams
- The abutment
- A point outside the structure considered fixed

On-site, these different points were marked with circular targets with a diameter of 5 cm.

This instrumentation remained in place from November 2021 until September 2023. During this period, images taken at regular intervals (every hour) by the cameras were directly transmitted to FTP owned by SPW. Consequently, DES Vision Software was used to conduct the displacement study.



Figure 8. Positions of cameras and their FOV.

4 STUDY IN THE DES SOFTWARE

The displacement study was conducted in two parts. The first part aimed to determine whether the frame section of the structure continued to tilt. The second part focused on understanding how the abutment behaved in relation to the movement of the longitudinal beams.

On-site, the traditional sensors installed during the initial instrumentation attempt were still in place. These sensors were utilized to validate certain results.

4.1 *Study of the frame movement*

The investigation into the frame's movement constituted the initial step in the analysis process conducted in the DES Vision Software. This study determined that there were no changes in the inclination of the frame. The results aligned with those obtained from the inclinometers.

Analyzing the frame's movement was the easier part of the study. The subsequent focus was on determining whether the DIC study conducted in DES Vision Software could provide insights into the abutment's movement.

4.2 *Study of the abutment movement*

To conduct this study, SPW chose to examine the displacement of three distinct points in the image, located respectively on the abutment (orange dot), one of the longitudinal beams (red dot), and the pier (purple dot) on which the beams rest. The displacement of these points was

studied relative to a point considered fixed within the image (the bridge's stone parapet represented by a blue dot). The study is conducted in a "relative" manner, but it effectively examines the overall movement of a single element.



Figure 9. Selected points for conducting the study.

The study of the abutment displacement provided values with a very good correlation with temperature (around 90%) and an expansion coefficient approaching expected values.

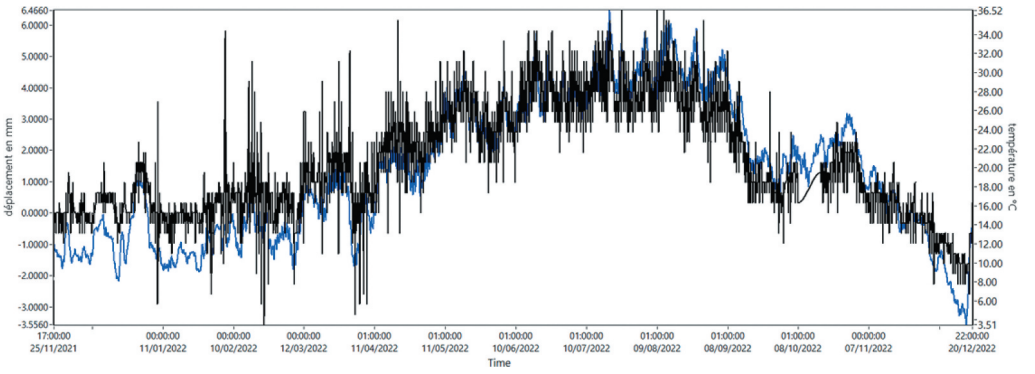


Figure 10. Abutment's displacement curve from DES (black) and temperature curve (blue).

SPW then focused the attention on studying the displacement of beams and the abutment. The results provided by Digital Image Correlation (DIC) reveal a perfect correlation between the movement of the beams/pier and the motion of the abutment.

Indeed, the beams and pier exhibit similar motion patterns in response to temperature variations. This motion is attributed to the contraction/expansion of the beams during different temperature cycles.

Consequently, these beams exert force against the abutment, a phenomenon not explicable by traditional sensors. This underscores the importance of augmenting conventional instrumentation with DIC for a comprehensive understanding of the structural dynamics.

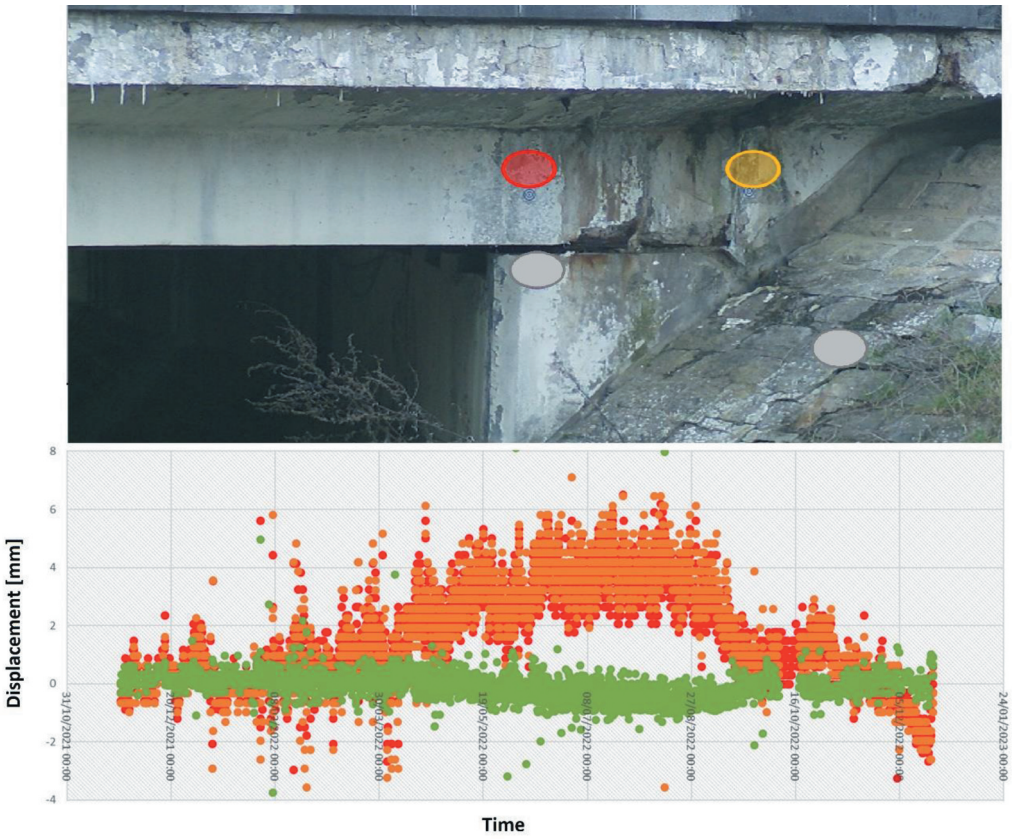


Figure 11. Displacement of the beam (red), displacement of the abutment (orange) and difference between them (green).

5 CONCLUSION

In conclusion, the study using Digital Image Correlation (DIC) proved to be an effective method for assessing the complex displacements of the Lincent Bridge. The installed cameras provided data for analyzing the movements of the frame, longitudinal beams, and abutment. This approach offered a complementary perspective to traditional sensors, providing precise information on absolute displacements.

By integrating the DIC method into the instrumentation toolkit, SPW overcame the limitations of traditional sensors and gained a more comprehensive understanding of the bridge's behavior. This innovative approach proved valuable for making informed decisions regarding the management and rehabilitation of the structure.

REFERENCES

Winkler J., Georgakis C.T., Fischer G., Wood S., & Ghannoum W. Structural response of a multi-strand stay cable to cyclic bending load. *Journal of Structural Engineering International*. 2015; 25(2): 141–150, DOI:10.2749/101686614X14043795570138.

Winkler J., Fischer G., & Georgakis C.T., Measurement of local deformations in steel monostrands using digital image correlation. 2014; *Journal of Bridge Engineering* (ASCE), 19(10).

Winkler, J., Hendy, C., 2017, Improved Structural Health Monitoring of London's Docklands Light Railway Bridges Using Digital Image Correlation. *Structural Engineering International*. 2017; 27(3): 435–440.


Taylor & Francis
Taylor & Francis Group
http://taylorandfrancis.com

SS33: Sustainability in bridge design, operation and maintenance

Organizers: M.H. Faber & P. Linneberg


Taylor & Francis
Taylor & Francis Group
http://taylorandfrancis.com

Bridge Maintenance, Safety, Management, Digitalization and Sustainability – Jensen, Frangopol & Schmidt (eds)
© 2024 The Author(s), ISBN 978-1-032-77040-6
Open Access: www.taylorfrancis.com, CC BY-NC-ND 4.0 license

Life-cycle assessment of RC trough bridges in Sweden and Colombia: A comparative Study

S.L. Leiva-Maldonado
Universidad de la Salle, Bogota D.C., Colombia

J. Gonzalez-Libreros, C. Wang & G. Sas
Luleå University of Technology, Luleå, Sweden

P. Simonsson
Ramboll, Sweden

D. Sas
iTid Tarinfo AB, Sweden

ABSTRACT: This paper discusses the life-cycle assessment (LCA) of concrete trough bridges, which make up about 20% of Sweden's railway bridge inventory. The LCA focuses on environmental impact and considers European Union emission regulations. It uses a 7.20m x 3.10m railway bridge in Rättelöv, Sweden, as a case study, along with a similar structure in Colombia. The study includes embodied carbon calculations, covering materials production, construction, use, and disposal. Approximately 70% of emissions occur during materials production and bridge use, with a focus on STA construction processes. While alternative life-cycle profiles weren't extensively explored, changes in working actions' schedules were considered. Additionally, a life cycle cost analysis (LCCA) was conducted, highlighting emissions from materials production, construction, and reconstruction as significant contributors. Recommendations and discussions for the Colombian case were proposed due to limited regional emission data.

1 INTRODUCTION

The focus of infrastructure project analysis can vary depending on the primary objectives of the decision-maker. The choice of analysis method, such as determining service life, assessing environmental impact, conducting life-cycle cost analysis (LCCA), optimizing schedules, or enhancing networks, depends on the specific goals of analysis. In the context of bridges, historically, costs have been the primary driving factors behind both past and current processes. For example, Leiva-Maldonado et al., (2023) and Leiva-Maldonado & Bowman, (2023) present current developments for superstructure selection based on LCCA. Regarding service-life extensions or maintenance scheduling, different approaches considered various aspects of bridge construction methods and technologies (Bouhaya et al., 2009; Du & Koroumi, 2013; Zhang et al., 2011). However, life-cycle assessments (LCA), is a method to determine public policies based on environmental load and impact are scanty and far apart in time. O P Gibbons & J J Orr, (2020) indicate that the carbon reduction potential decreases as the project stages develops. The higher reduction potential can be achieved in the planning and design stages, close to 100% and 80% respectively. Therefore, this research serves as a valuable tool for decision-makers during the planning process and may be advantageous for the involved agencies. Specifically for Swedish bridges, Hammervold et al., (2013) presented a comparative environmental

DOI: 10.1201/9781003483755-363

LCA case study, where different bridge material types were considered (structural steel, structural concrete, and wood). This research is one of the earliest and most important made about LCA specifically for bridges located in the Scandinavian peninsula, stating that is possible to decide upon environmentally effective design alternatives, a target of emissions and environmental impact, which is more than relevant in current practices.

Based on experience and research, some broad principles for conducting LCA (Collings, 2006): First, the initial environmental impact is proportional to its initial cost, and second, the long-term environmental burden will be approximately proportional to the amount of maintenance required. Thus, bridge structures with less working actions during its service-life would also be structures with less environmental burden in the future. In other words, even though the LCA could be made, if data is not available to calculate the environmental impact, the LCCA could be used as an indirect method to select the design option with the less environmental impact. Therefore, and specifically talking about LCCA, to determine the true cost of a bridge structure, the cost to build, inspect and maintain the bridge over the entire lifespan of the bridge, is needed. This involves not only the estimation of initial costs, but also future costs, so called "long term costs". This is a better measure of the real cost of a bridge, rather than the initial, or first cost.

There are few data or prior published studies regarding the life-cycle cost of entire bridge structures in Sweden and those are focused mainly on road bridges. However, there are approximately 4000 railway bridges in Sweden managed by the Swedish Transport Administration (Trafikverket), of which a common construction type is the reinforced concrete trough bridge (RCTB -close to 20%-), which is a structure that consists of a slab carried by two longitudinal main beams which transfer loads towards the supports (Gustafsson, 2021). A substantial number of the RCTB structures are approaching the end of their service lives which consequently implies that the replacement of some of these bridges can be expected in the near future (Åkergren, 2021). A comprehensive analysis focused on the LCC and the LCA as a complementary tool of structural behavior analyses, is of the most relevance to preserve and optimize agency budgets and environmental impact.

Some researchers have approached this problem in the past, for example, Du & Koroumi, (2013) made the LCCA comparison of two different railway superstructure options including the environmental performance, concluding that the slab reinforced concrete (RC) option has a better environmental performance over all due to the implementation of easier maintenance working actions. On the other hand, other studies focused the attention on the environmental footprint of specific working actions, such as deck replacements as described by Zhang et al., (2011). It can be seen in the literature that the existing research treated the environmental impact issue for different materials and working actions. However, no evidence of a comprehensive approach to perform an analysis for a specific bridge type but also to apply such techniques into the analysis of railway bridges such as RCTB have been found.

Therefore, a study to evaluate LCA and LCCA in railway bridges, specifically in the ones considered the most common (RCTB) would be useful for efficient, cost-effective, and environmentally responsible future planning. In this document, a first approach to this problem is presented, determining both the LCCA and LCA of a RCTB structure. Additionally, a comparative analysis is presented for a similar structure (reinforced concrete -RC- bridge) located in Colombia. Hence, different challenges and aspects of LCCA and LCA applied to Colombian structures are discussed, making a "roadmap" for future developments and research in the region.

2 METHODOLOGY

The present preliminary study is divided into two main analyses, one focused on the LCA and the second on the LCCA. However, both analyses were done for the RCTB, the case of the RC bridge was performed only for the input data available. The primary obstacle to implementing both methods arises from the insufficient regional information. Therefore, a discussion about the minimum requirements needed is presented in each section.

2.1 *Environmental life-cycle assessment*

There are different methodologies to compute LCA as stated by Hammervold et al., (2013). For example, and specifically for Nordic bridges, software's called *BridgeLCA* and *BridgeLCC* were developed to calculate LCA and LCCA respectively (*ETSI Project III - Task Group 5*, 2013), using *SimaPro* and the *Ecoinvent* database. Nonetheless, in this research the approximation proposed by The Institution of Structural Engineers is used (O P Gibbons & J J Orr, 2020). The guide supports the sustainability objective to achieve net-zero carbon emissions by 2050. As stated in the appendix of the guide, the process proposed involves more databases than the ones used in *BridgeLCA*, including Ecoinvent, EPD Norge among others. The method uses different factors in production, service, and end-of-life phases. The environmental impact of this guidance refers to its carbon dioxide equivalent emissions ($kgCO_2e$), also known as global warming potential (GWP). The best practice is to consider whole life embodied carbon emissions (Stages A – D in the guide, see Figure 1). Consequently, minimization of embodied carbon emissions is achieved contemplating future emissions, including end of life scenarios, reusability, and recyclability. The general approximation is described in Equation (1). In the case of minimum or unavailable data for stages B-D, the minimum analysis must be made considering only stage A because those emissions will be released before 2050. Additionally, uncertainties are higher for stages B – D. Also, most embodied carbon emissions are associated with stage A, which means that most of the reductions can be achieved in this time frame. Therefore, careful consideration of Environmental Product Declarations (EPD) of construction products is needed.

$$\begin{aligned} kgCO_2e = {} & ECF_{A1-A3} + \sum_{j=1}^{n} ECF_{A4,j} + \sum_{i=1}^{n} ECF_{A5W,i} + EC_{A5a} + ECF_{B1-B3} \\ & + \sum_{k=1}^{n} ECF_{B4,k} + ECF_{B5} + EC_{C12} + \sum_{k=1}^{n} ECF_{C34,l} + \sum_{k=p}^{n} ECF_{D,p} \end{aligned} \tag{1}$$

Where:

$kgCO_2e$ =	Life-Cycle total embodied carbon
ECF_{A1-A3} =	Embodied carbon factor for stages A1 to A3 (product phase)
$ECF_{A4,j}$=	Embodied carbon factor for stage A4 for the *j*th material
$ECF_{A5W,i}$=	Construction waste embodied carbon factor for the *i*th material
EC_{A5a} =	Embodied carbon from construction site activities
ECF_{B1-B3} =	Embodied carbon factor for stages B1 to B3
$ECF_{B4,k}$=	Replacements emissions for the *k*th material
ECF_{B5} =	Refurbishment emissions factor
EC_{C12} =	Demolition and deconstruction emission factor
$ECF_{C34,l}$=	Waste processing and disposal embodied carbon factor for the *l*th material
$ECF_{D,p}$=	Reuse emission factor (stage D)

2.2 *Life-Cycle Cost analysis (LCC)*

To determine the life-cycle cost, detailed information, and data on the bridge initial costs and long-term bridge inspection, repair, and maintenance costs are needed. Consequently, and with the aim of presenting and comparing different options (not only for bridge construction but also for bridge maintenance) the costs of a single life-cycle event will be projected back to obtain the net present value (NPV). The comparison of such NPV's will be used for selecting the most cost-effective Life Cycle Cost Profile (LCCP) for trough bridges. LCCP's was also considered to determine the environmental impact of all the options considered. It is important to remark that structural behavior of the superstructure type is needed prior to the LCCA, this information is vital to understand the possible deterioration and the feasible maintenance/preventive/rehabilitation schedule for different deterioration degree. However, since structural behavior is out of the scope of this research, information of such will be assumed based on previous research (Åkergren, 2021;

Gustafsson, 2021; Thun et al., 2006). Additionally, LCCA implementation in the Swedish infrastructure (road bridges) is presented in multiple research (Du & Koroumi, 2013; Safi et al., 2012, 2013, 2015). The general model is presented in Equation (2) (Leiva-Maldonado & Bowman, 2023), where the discount rate (i) and the service life (SL) of each option, and the time of execution of each working action (t) are considered in design costs (CD), construction costs (CC), inspection costs (IC), maintenance costs (MC), rehabilitation costs (RC) salvage costs (SV), and user costs (UC).

$$\mathrm{BLCCA}_{(i,SL)} = \mathrm{CD}_{(i,t)} + \mathrm{CC}_{(i,t)} + \mathrm{IC}_{(i,t)} + \mathrm{MC}_{(i,t)} + \mathrm{RC}_{(i,t)} + \mathrm{UC}_{(i,t)} + \mathrm{SV}_{(i,t)} \quad (2)$$

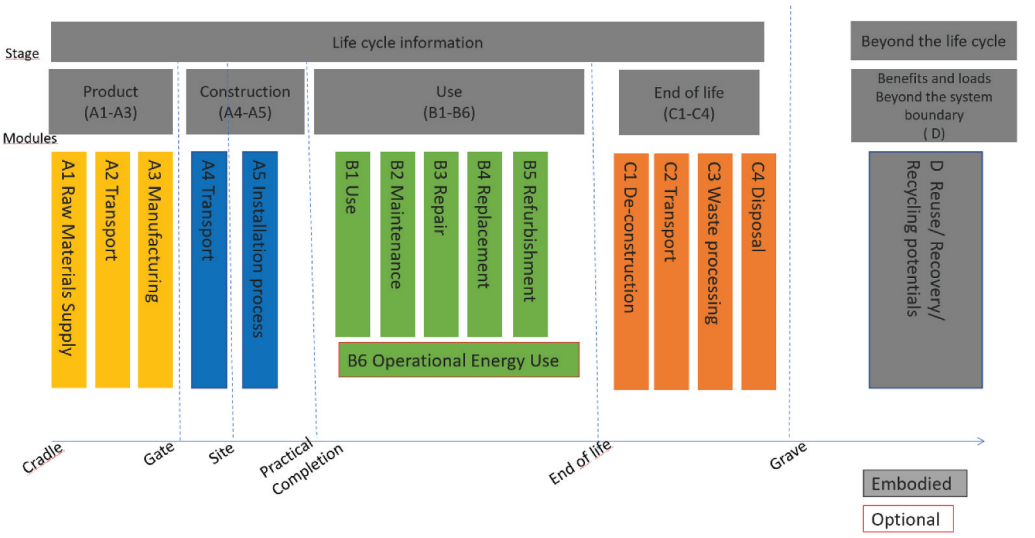


Figure 1. BS EN 1578 Life-cycle stages (O P Gibbons & J J Orr, 2020).

3 CASE OF STUDY

Trough bridges are built as a slab suspended between two longitudinal main edge-beams that carry the loads towards the support. The structure typically forms a "U-shape" which allows to be filled with ballast to distribute loads from the sleepers, rails, and traffic. The traffic load is transferred to the ballast using sleepers on which the rail is fastened. According to Trafikverket, the most common sleeper type in Sweden is the concrete sleeper which is used in almost 71% of the tracks. Figure 2 shows an example of a RC trough bridge located in Rättelöv in Sweden.

The structure used is the Lautajokki bridge, an RC trough bridge with a longitudinal span length of 7.20m and width of 3.10m (reinforcement and geometrical details are presented in the appendix of the research made by Gustafsson, (2021)). Bill of materials showed that 9.36m^3 (22.470kg) of concrete, 1.860kg of reinforcement steel, 462kg of wooden formwork, 864kg of UIC60 steel rails, 310kg of normal concrete sleepers (0.20x0.20x2.65m^3 every 0.60m) and 24.028kg of crushed stone ballast was needed for the construction of the superstructure.

A separate discussion is needed for the Colombian considerations. Due to the lack of railway development, few structures can be catalogued as railway bridges, and those are mainly structural steel superstructures (Márquez, 2017). However, similar bridge types can be seen in slab road bridges. Therefore, to make impactful research for the region, road bridges must be the focus of the investigation. However, as stated by the *International Trade Administration* \(International Trade Administration, 2023), Colombia launched a railway master plan to develop cargo and passenger railway lines. Thus, estimation of LCA and LCC in through bridges could be useful to support this master plan.



Figure 2. RC trough bridge located in Rättelöv, Sweden (Åkergren, 2021).

4 LCCA

For the LCCA analysis, costs related to the different service-life activities are needed. Different sources were used to determine costs, not only for construction but also for future working actions. However, it is important to remark that for more precise computations, historical cost records can be used, with them, probability density functions (PDF's) could be fitted. Those PDF's will be used for a stochastic model (Monte Carlo Simulation) that considers the inherent probability of cost estimation. Nonetheless, for this preliminary research historical records are not available. Therefore, cost estimation was modeled as a PERT distribution with a minimum and maximum value of 0.75 and 1.25 times the reference values presented in Table 1 respectively. Additionally, a similar model was used for the discount rate, which expected value was assumed as 3.5% (*BridgeLCC*).

Table 1. Construction cost (CC) and future working actions costs estimation.

Bill of Materials (CC)

Item	Unit	Quantity	Price per Unit (SEK) 2012	Price per Unit (SEK) 2023	Total Price SEK	Source
Concrete	m^3	9.36	4000.00	6399.24	59896.87	BridgeLCC
Reinforcement Bars	kg	1860	55.00	87.99	163660.52	BridgeLCC
Formwork	m^3	28.52	1300.00	2079.75	59314.54	BridgeLCC
Rails	m	14.4	-	1694.65	24402.99	1
Expansion Joints	m	6.2	30000.00	47994.29	297564.58	BridgeLCC
Ballast	kg	24028	-	0.56	13359.81	1
Concrete Sleepers	m^3	1.378	4000.00	6399.24	8818.15	BridgeLCC
				Total Initial Cost	**627017 SEK**	
				Initial Bridge Cost/m2	**28092 SEK**	

1. https://compassinternational.net/railroad-engineering-construction-cost-benchmarks/

Future Working Actions

Item	Time Interval	Reference Quantity %	of	unit	Price per Unit (SEK) 2012	Source
Regular Inspection	1 Years	100	Total Bridge Area	m^2	12	Dafi, (2013)
General Inspection	3 Years	100	Total Bridge Area	m^2	40	Dafi, (2013)
Mayor Inspection	6 Years	100	Total Bridge Area	m^2	70	Dafi, (2013)
Cleaning Salts	1 Years	100	Total Bridge Area	m^2	6	Dafi, (2013)
Cleaning Vegetation	1 Years	10	Total Bridge Area	m^2	7	Dafi, (2013)
Maintenance Railings	2 Years	10	Railing Length	m	250	Dafi, (2013)
Expansion Joint Ref	25 Years	100	Exp Joint Length	m	3000	BridgeLCC
Expansion Joint Rep	50 Years	100	Exp Joint Length	m	30000	BridgeLCC
Railing Ref	25 Years	10	Railing Length	m	1695 [2]	Compas Int[1]
Railing Rep	50 Years	100	Railing Length	m	1695 [2]	Compas Int[1]
Ballast Rep	25 Years	100.00	Ballast volume	ton	556 [2]	Compas Int[1]

1. https://compassinternational.net/railroad-engineering-construction-cost-benchmarks/
2. Cost year reference 2022

For the future working actions, Trafikverket experience and recommendation given by Safi, (2013) were considered and are presented in Table 1. As a result, the LCCP presented in Figure 3 was used. However, as described by Sinha et al., (2009), the action year of each activity depends on the bridge condition of that year and the budget availably. The action year can vary from 2 to 5 years depending on bridge condition. Therefore, for this analysis, for repair, replacement and rehabilitation activities, a Poisson distribution was modeled with a minimum and maximum value of "action year $\pm$ 5years" respectively. For the MC simulation, a licensed program developed by *Palisade*^{TM} called *@RISK*® was used. The number of iterations (10000) employed corresponds to the stabilization of the mean and variance of the output variables. A pseudo random number generator (Mersenne Twister) and a Latin Hypercube sampler were utilized. Results of the simulation and the sensitivity analysis are presented in Figure 4. This study only considers superstructure analysis, substructure depends on local

conditions and specific site variables. In addition, user costs are also omitted due to the same conditions.

The main limitation encounter for the Colombian analysis is the lack of reliable scientific information or comprised official costs databases. The Colombian national road institute (INVIAS) has spare available data that needs to be gathered, cleaned up, and organized, to make the LCCA computation. Additionally, maintenance and inspection schedules are not normalized, and depend on the local authorities and constrained budget allocations. On the other hand, bridge service life needs a separate discussion. According to the local Colombian bridge standard design code (CCP14), the service-life for bridge structures is 75 years, however, no scientific research was found that analyze condition ratings or bridge inspections to predict future conditions. Conversely, Sweden base information regarding service-life can be obtained from different researchers (Racutanu, 1999; Safi, 2013), which indicates a service-life of 100 years. Nonetheless, a comprehensive study about deterioration rates including current practices is also needed.

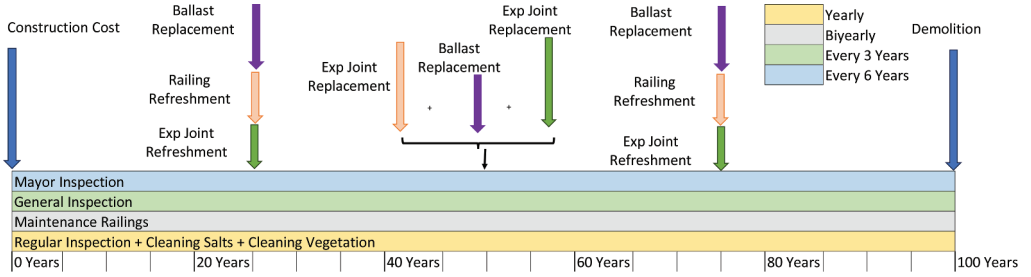


Figure 3. LCCP - Reinforced concrete trough bridges.

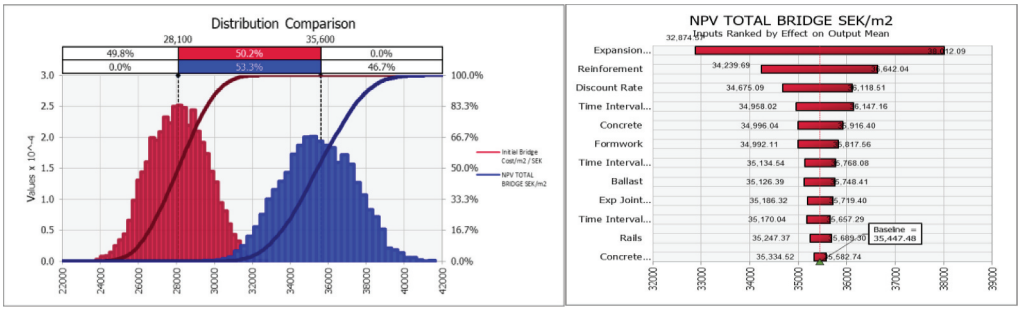


Figure 4. Simulation results and sensitivity analysis for total bridge cost per area.

5 ENVIROMENTAL LCA

As described before, considering data from specific EPD's is key to accurately computing the environmental emissions. Declarations vary depending on geographical location. For this analysis, EPD Norge and EPD Latin America databases were considered. Sweeden EPD's according to O P Gibbons & J J Orr, (2020) are dictated by the International EPD database, meaning that the closest accurate data is the one mentioned in the basics of this sections. Bridge quantities presented in Table 1 and maintenance schedule presented in Figure 3 were used for the computation of emissions. Nevertheless, EPD's depends severely on the productions processes of the companies making the declaration. Therefore, variability is inherently elevated. Hence, to make standardized LCA, minimum CO_2 emissions for each stage must be established by regional authorities. Where minimum CO2 emissions data are not available, recommendations from O P Gibbons & J J Orr, (2020) were used.

Specifically, for the presented analysis, the following variables were considered for each major stage. Emission for stage A1 to A3 were obtained from the EPD's described before. Transportation computed in stage A4 are based on local measurements, for the Sweden option, basic emission were taken from Uppenberg & Åhman, (1998), additionally, for the Colombian analysis, research made by Agudelo et al., (2021) was considered. Particularly, for the Colombian case, and as mentioned before, railway development is limited, therefore, only dump truck material transportation was used. Moreover, for locally produced materials 50km transportation was assumed, for national products 300km, for non-transoceanic international material 1.500km and finally, for transoceanic importation 10.000km, as suggested by O P Gibbons & J J Orr, (2020). Conversely, for demolition (C2) only 50km local transportation was assumed. Stages C3-C4 namely waste processing disposal emissions were taken from each material EPD. In cases like reinforcing bars and ballast from the Swedish option, and all materials except reinforcing bars and formwork in the Colombian case, no emissions were reported in the EPD's, therefore, a minimum of 0.013kgCO_2 per unit was contemplated. Reuse and recovery (D) emissions were also reported as the EPD's for each material. Finally, stage B only considered subsection B4 since use and maintenance (B1-B4) emissions are considered marginal (inspections and cleaning as presented in Figure 3). Stage B5 is only considered when planned changes in use are defined at the conception of the project. Operational carbon emissions (B6-B7) could be impactful for buildings, however, for infrastructure projects as bridges, those emissions can be neglected. Results of the LCA are presented in and Figure 5.

Stage	Sweden		Colombia	
	$kgCO_2e$	rel %	$kgCO_2e$	rel %
ECF_{A1-A3}	7005.69	52%	10576.10	49%
$ECF_{A4.i}$	238.05	2%	1161.00	5%
$ECF_{A5W.i}$	298.12	2%	365.61	2%
EC_{A5a}	333.59	2%	333.59	2%
ECF_{B1-B3}	0	0%	0.00	0%
$ECF_{B4.k}$	4719.74	35%	8461.84	39%
ECF_{B5}	0	0%	0.00	0%
EC_{C12}	344.34	3%	513.39	2%
$ECF_{C34.l}$	411.58	3%	247.89	1%
$ECF_{D.D}$	-618.03	-5%	-76.90	0%
Total $kgCO_2e$	12733.07		21582.53	

Stage	$kgCO_2e$		rel %	
	Sweden	Colombia	Sweden	Colombia
Stage A	7875.45	12436.31	58.99%	57.42%
Stage B	4719.74	8461.84	35.35%	39.07%
Stage C	755.92	761.27	5.66%	3.51%
Stage D	-618.03	-76.90	-4.63%	-0.36%
Total $kgCO_2e$	12733.07		0.95	

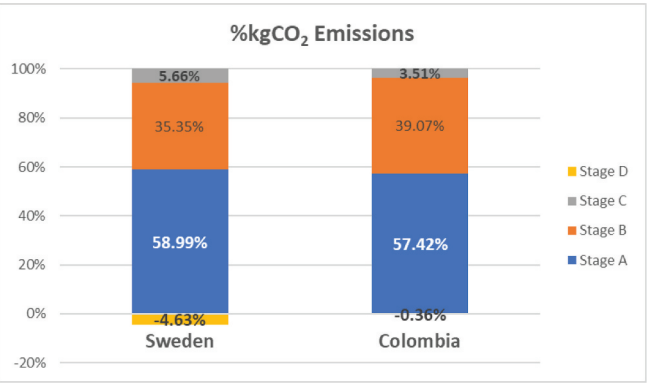


Figure 5. LCA CO_2 total emissions.

6 CONCLUSION

A first approximation to LCCA and LCA for Swedish railway reinforced concrete trough bridges was presented. Also, a parallel analysis for the same structure was performed for the Colombian case. Monte Carlo simulations were executed for the LCCA, using PERT and Poisson PDF's only for the original case. The lack of railway development in Colombia as well as the minimum or inexistent behavior or cost information made the LCCA unfeasible. However, the Colombian major railway master plan makes this preliminary study of total interest for the region. A LCCP was proposed for RCTB, including inspection, maintenance and replacement working actions. Sensitivity analysis showed that the most impactful variables of the analysis are dictated by material costs and the discount rate. On the other hand, LCA was performed for both options. Specific EPD's and transport emissions for each region were used. Results showed that higher emissions are expected for the Colombian structure. Results are driven by the greater emissions presented in material production and internal transportation. Again, the lack of railway Colombian development make internal transportation by dump trucks mandatory, which significantly impact the emissions outcome. Finally, as

presented in the LCA, most of the emissions are reported during production, and replacement phases (Stage A – 58% – and B –35%–), meaning in those activities it is expected to have more potential of emission reductions.

REFERENCES

Agudelo, J. R., Agudelo-Santamaria, A. F., Moreno-Sanchez, R., & Lopez-Garcia, A. F. (2021). *Factores de Emisión de los Combustibles Colombianos (FECOC+) Fase 2.1: Determinación de los factores de emisión de vehículos pesados de carga (camiones y tractocamiones) a la altitud del área metropolitana de Bucaramanga*. https://www1.upme.gov.co/DemandayEficiencia/Documents/Informe_final_FECOC_fase_21.pdf

Åkergren, D. (2021). *RC Trough Bridges : A Parametric Study using FEM and an Analysis of their Current State*. Luleå University of Technology.

Bouhaya, L., Le Roy, R., & Feraille-Fersnet, A. (2009). Simplified environmental study on innovative bridge structure. *Environmental Science &Technology*, *43*(6), 2066–2071. https://doi.org/10.1021/es801351g

Collings, D. (2006). An environmental comparison of bridge forms. *Proceedings of the Institution of Civil Engineers - Bridge Engineering*, *156*(4), 163–168. https://doi.org/10.1680/bren.2006.159.4.163

Du, G., & Koroumi, R. (2013). Life cycle assessment of a railway bridge: comparison of two superstructure designs. *Structure and Infrastructure Engineering: Maintenance, Management, Life-Cycle Design and Performance*, *9*(11), 1149–1160. https://doi.org/10.1080/15732479.2012.670250

ETSI Project III - Task Group 5. (2013). http://etsi.aalto.fi/Etsi3/TG5.html

Gustafsson, J. (2021). *Influence of load distribution on trough bridges*. Luleå University of Technology.

Hammervold, J., Reenaas, M., & Brattebo, H. (2013). Environmental Life Cycle Assessment of Bridges. *Journal of Bridge Engineering*, *18*(2). https://doi.org/https://doi.org/10.1061/(ASCE)BE.1943-5592.0000328

International Trade Administration. (2023). *Colombia - Country Commercial Guide*. https://www.trade.gov/country-commercial-guides/colombia-infrastructure

Leiva-Maldonado, S. L., & Bowman, M. D. (2023). Superstructure bridge selection based on Life-Cycle cost analysis for short and medium span bridges. *Engineering Structures*, *285*(April), 116031. https://doi.org/10.1016/j.engstruct.2023.116031

Leiva-Maldonado, S. L., Bowman, M. D., & Gomez, D. (2023). Life-cycle cost profiles selection for different superstructure bridge types. *Structures*, *54*(July 2022), 1–13. https://dx.doi.org/10.1016/j.istruc.2023.04.105

Márquez, L. (2017). The Colombian railways: 4 recurring subjects in the literature. *Estudios Gerenciales*, *33*(143), 187–194. https://doi.org/10.1016/j.estger.2017.04.003

O P Gibbons, & J J Orr. (2020). How to calculate embodied carbon. In *The Institution of Structural Engineers*.

Racutanu, G. (1999). The Real Service Life of Road Bridges in Sweden - A Case Study. *Durability of Building Materials and Components 8*, 56–70. https://www.irbnet.de/daten/iconda/CIB2042.pdf

Safi, M. (2013). *Life-cycle costing: Applications and Implementation in Bridge Investment and Management* [Royal Insitute of Technology (KTH)]. www.ircwash.org/projects/life-cycle-costing-tools?tab=posts

Safi, M., Sundquist, H., & Karoumi, R. (2015). Cost-Efficient Procurement of Bridge Infrastructures by Incorporating Life-Cycle Cost Analysis with Bridge Management Systems. *Journal of Bridge Engineering*, *20*(6). https://doi.org/10.1061/(asce)be.1943-5592.0000673

Safi, M., Sundquist, H., Karoumi, R., & Racutanu, G. (2012). Integration of Life-Cycle Cost Analysis with Bridge Management Systems: Case Study of Swedish Bridge and Tunnel Management System. *Transportation Research Record*, *2292*(1), 125–133. https://doi.org/10.3141/2292-15

Safi, M., Sundquist, H., Karoumi, R., & Racutanu, G. (2013). Development of the Swedish bridge management system by upgrading and expanding the use of LCC. *Structure and Infrastructure Engineering*, *9*(12), 1240–1250. https://doi.org/10.1080/15732479.2012.682588

Sinha, K. C., Labi, S. A., McCullouch, B. G., Bhargava, A., & Bai, Q. (2009). *Updating and Enhancing the Indiana Bridge Management System (IBMS)* (Issue December). https://doi.org/10.5703/1288284314306.This

Thun, H., Ohlson, U., & Eklfgren, L. (2006). Concrete Strength in Old Swedish Concrete Bridges. *Nordic Concrete Research*, *December*, 1–14. https://pure.ltu.se/portal/files/3422699/Article.pdf

Uppenberg, S., & Åhman, M. (1998). *Climatic Impact of Future Swedish Transports*.

Zhang, C., Amaduddin, M., & Canning, L. (2011). Carbon dioxide evaluation in a typical bridge deck replacement project. *Proceedings of the Institution of Civil Engineers - Energy*, *164*(4), 183–194. https://doi.org/10.1680/ener.2011.164.4.183

Bridge Maintenance, Safety, Management, Digitalization and Sustainability – Jensen, Frangopol & Schmidt (eds)
© 2024 The Author(s), ISBN 978-1-032-77040-6
Open Access: www.taylorfrancis.com, CC BY-NC-ND 4.0 license

Reducing the climate impact (GWP) from bridges in a Danish highway project

J. Olesen & P.G. Pedersen
COWI A/S, Kongens Lyngby, Denmark

C.V. Scholten
Vejdirektoratet, Hedehusene, Denmark

ABSTRACT: This article focuses on the analysis of the carbon emissions of different concrete road bridges together with possibilities of reducing their carbon footprint. Reducing carbon emissions is of increasing importance to owners, consultants and contractors alike, the whole industry is in transition to reduce their impact. Infrastructure projects have a significant carbon footprint due to the large quantities of consumed materials.

A key focus for the project owner, The Danish Road Directorate, is to reduce the carbon emissions from the construction of Kalundborg Motorway Stage 3. For the road bridges in the project, a life cycle analysis is made comparing the carbon emissions of different types of concrete bridges. The potential savings in carbon emissions from choosing the concrete bridge type is significant and the results of the analysis are highlighted and elaborated in this article.

1 INTRODUCTION

Sustainability, especially lowering of the carbon footprint (CO_2e), is a focal point in the design, tendering, and construction of the Kalundborg Motorway Stage 3, Regstrup-Kalundborg. In this the project, several analyses have been conducted on the influence of different bridge types on the carbon footprint. This includes road bridges, pedestrian bridges, and wildlife crossings. These analyses were carried out during the outline and project proposal phases and will continue during the detailed design phase.



Figure 1. Left: Location of project in Denmark (red box). Right: Alignment plan, the Kalundborg Motorway Stage 3, from Regstrup to Kalundborg (red line).

DOI: 10.1201/9781003483755-364

Bridges have a significant carbon footprint due to their size and thereby use of construction materials. This article includes examples and results from specific analyses conducted on the project "Kalundborgmotorvejens Phase 3, Regstrup-Kalundborg".

The Kalundborg Motorway Stage 3, from Regstrup to Kalundborg, is part of the Danish Infrastructure plan 2035, "Danmark Fremad"/"Denmark Forward", (Ministry of Transportation, 2021). The project consists of 20 km of road widening and 10 km of new road. The project includes 26 major structures, including 2 new pedestrian bridges, 11 new road bridges, 6 new wildlife crossings, and 7 existing structures, as well as 17 smaller structures (small wildlife crossings/pipes).

The Danish Road Directorate (Vejdirektoratet) are the owner of the project, and COWI are the consultant. The project is expected to be tendered in 2024-2025 and completed by 2028.

It is one of the first projects where the Danish Road Directorate focuses on minimizing the carbon footprint of structures such as bridges as well as other civil structures. Minimizing the carbon footprint is an unavoidable area of focus, especially considering the Danish goal of a 70% CO_2 reduction by 2030 compared to 1990. This target is from The Danish Climate Act (Ministry of Climate, Energy and Utilities, 2019). Carbon reduction is an area of focus for clients, consultants, manufacturers, and contractors alike. There are significant developments in the construction industry in this area, and therefore the article also provides details on the status of the industry's progress and direction.

2 THE ANALYSIS ON THE PROJECT

With a larger number of bridges (20+), there is significant potential to reduce the carbon footprint. Analysis is conducted in the concept design and project proposal phase of the project. It focuses on a predetermined location within the project. This location is representative to a larger portion of the bridges in the project. The road bridges in the analysis are assumed to be constructed with concrete. The analysis solely focuses on the carbon footprint of the structures but should be seen as part of the overall effort to minimize the project's carbon footprint.

At the specific location 7 different possible types of bridge layouts are identified, including both overpasses and underpasses (OP/UP). In addition, the bridge types also differ in terms of the number of spans, with either 1, 2, or 4 spans. The designs also vary depending on the type of the abutment, with either vertical walls/abutments close to the edge of the under passing road or sloping embankments (verges) under the bridge end. These types are referred to as closed/open bridge-ends which is what is seen from a user perspective passing the bridge. In Figure 2 below, the 7 different bridge types investigated are illustrated.

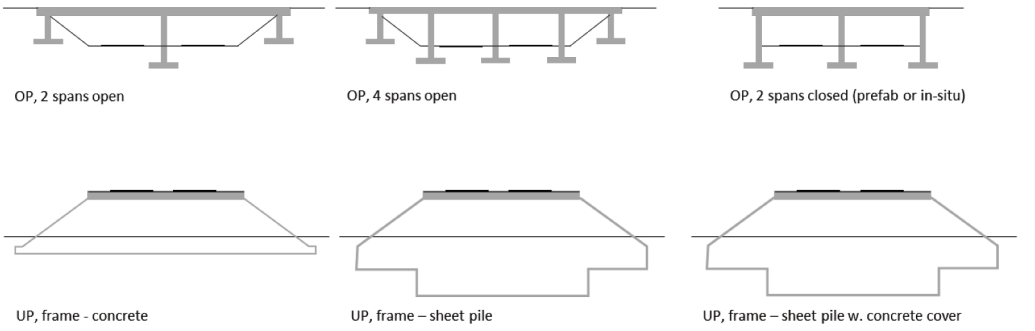


Figure 2. The 7 bridge types in the analysis (the "OP, 2 spans closed" is investigated with both prefab concrete beams and in-situ cast concrete deck).

The analysis is conducted using the Danish Road Directorate and Banedanmark's joint life cycle assessment tool, InfraLCA. Life cycle assessments are evaluations of the overall climate and environmental impacts of one or more material/ product throughout their entire life cycle.

In this analysis, the focus is solely on the carbon footprint (GWP). The GWP is calculated in CO_2-equivalents, which is the impact from greenhouse gasses calculated as an equivalent amount of CO_2. When conducting such analyses with organizations like the Danish Road Directorate or Banedanmark, the tool InfraLCA is commonly used.

The aim was to use the predefined data in the program, including; emission factors, transport distance, and service life, to keep the analysis as generic as possible. However, some inputs must be adjusted to provide a reasonable basis for the analysis that aligns with the project's assumptions. The program and other details of the analysis are not further discussed here.

The version of InfraLCA used (version 2.11) includes the following life cycle phases: A1-A3, A4, (A5) & B4 (cf. EN 15804). Phases A1-A3 represent raw material extraction, transportation, and production of the material/product. Phase A4 represents transportation, for example, from the factory to the construction site. Phase A5 represents the construction phase, this is not included in the analysis due to insufficient incorporation in the utilized version of InfraLCA. Phase B4 represents replacement at the end of the lifespan. It is noted that the newest version of InfraLCA additionally includes phase C (demolition and disposal) and phase D (reuse). The analysis conducted generally includes the following categories: concrete, concrete elements, reinforcement, prestressing reinforcement, sheet piles, soil anchors, pavements, insulation, and earthworks.

In the project, various options for carbon reductions are considered in the project's different phases, these are reflected in the CO_2-evaluation. The process is shown in Figure 3 below (the figure reflects the project's progress according to the Danish Road Directorate's project phases, phase 1-6).

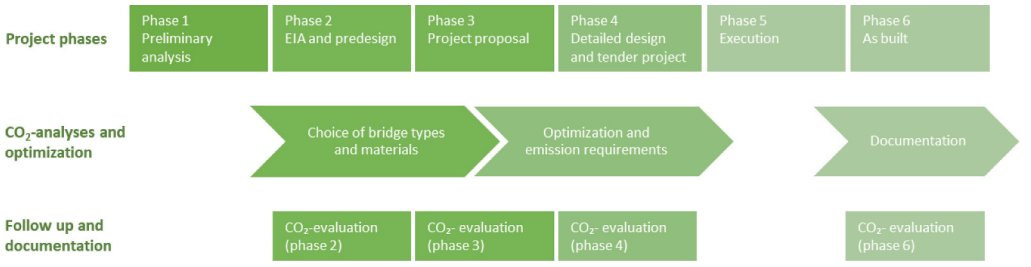


Figure 3. Process for carbon reduction throughout the design lifecycle - consultant CO_2-evaluation for each larger structure in the project.

The Danish Road Regulation, "Design Basis for Bridges" (Danish Road Regulation, 2023) Section 3.2, has been updated to outline the requirements for implementation of carbon reducing measures during the design phase. These requirements reflect the strategy of the Danish Road Directorate to reduce carbon emissions from structures they build and own.

The choice of bridge type and materials is the first step in reducing the carbon footprint of these structures. The next step is to optimize the selected bridge type during the detailed design phase, typically by reducing the quantity of materials. Emission requirements (in tenders) and other execution guidelines are then incorporated into the tender material and used in throughout the execution.

3 RESULTS

In Table 1, the results of the analysis of the 7 bridge types are shown, the results are divided into life cycle phases and include a summation of all life cycle phases. An indexing in relation to the 2-spans bridge (lowest footprint) has also been conducted to facilitate comparison.

As seen in Table 1 (A1-A3, A1-A3/Index), there are relatively large differences in the total carbon footprint of the different bridge types based solely on the footprint from the production of materials. Particularly, the underpasses (UP) have a high carbon footprint. This is mainly due

Table 1. Results from the analysis in InfraLCA of the 7 bridge types. Total [t CO_2e].

Bridge type	A1-A3	A4	B4	Sum (A1-A4+B4)	Index* (Sum, A1-A4+B4)	Index* (A1-A3)
	[t CO_2e]				[-]	
OP (overpasses), open						
2 spans	234	351	36	620	1.0	1.0
4 spans (short)	273	354	36	663	1.1	1.2
4 spans	291	355	39	685	1.1	1.2
OP, closed						
2 spans (prefab)	350	356	23	729	1.2	1.5
2 spans (in-situ)	367	359	23	749	1.2	1.6
UP (underpasses)						
Frame (concrete)	403	325	20	748	1.2	1.7
Frame (sheet pile)	427	333	20	780	1.3	1.8
Frame (sheet pile + conc.)	503	335	20	859	1.4	2.2

*Relative to the result of "2 spans open"

to the assumed location and the narrow crossing road (approx. 10m), which applies to several bridges in the project. The UP and closed type OPs will require larger walled substructures, which have a negative impact on the carbon footprint. However, the results for the different types can be influenced by the width of the bridge. For a wider highway bridge, the carbon footprint of the substructure will be relatively smaller compared to the superstructure for these bridge types.

Furthermore, the results for materials transport (A4) are noteworthy. The primary contribution to this phase is the transportation of soil, especially for the bridge approach embankments. When constructing on flat terrain, significant amounts of soil are involved. It should be noted that the chosen location in this project is a particular case, and the amount of soil at this location is considerably larger than the average amount for the project as a result of special bridge approaching embankments. The footprint of soil transportation at this location is just below 300 t CO_2e, while on most other locations of the same size in the project, it is around 100 t CO_2e due to significantly smaller approach embankments structures.

Maintenance/partial replacement (B4) of a bridge account for a smaller portion of the footprint since concrete bridges require minimal maintenance. The primary differences in these results come from the replacement of pavements where there are differences in road and bridge deck areas for the different bridge types.

To make comparisons and establish requirements, there is a need for some benchmark values. In the Table 2 below, the CO_2e footprints are presented per square meter of bridge deck area. Both for the total bridge deck area and per square meter of "crossing area". "Crossing area" defined as the area overlapped by underpassing and overpassing road. The latter benchmark value has the advantage of being based on a constant (crossing area) which is independent of the bridge type for a specific location.

As seen in Table 2, the clear differences observed in the total carbon footprint are also reflected when calculated per area. The variation is significant for the results per square meter of bridge deck, while it eliminates the variances between bridge types and is (relatively) smaller for the result per square meter of crossing area. However, it is evident that the choice in bridge type for this specific location has a significant influence on the overall footprint. It is expected that the carbon footprint per bridge deck area/crossing area will become an important way to measure the carbon footprint of bridges.

It should be noted that the carbon emission factors for primary materials such as concrete, reinforcement, prestressing reinforcement, sheet piles, etc., have a crucial impact on the results and, therefore, the comparison of bridge types. Therefore, careful selection of emission factors is important.

From this analysis, the results indicate that the 2 spans open bridge has the lowest carbon footprint among the investigated bridge types.

Table 2. Results calculated pr. m² bridge deck/crossing area.

Bridge type	A1-A3 [t CO_2e]	Bridge deck area, [m²]	(A1-A3) [kg CO_2e/m²] (deck area)	Crossing area [m²]	(A1-A3) [kg CO_2e/m²] (crossing area)
OP (overpasses), open					
2 spans	234	506	462	254	921
4 spans (short)	273	506	540	254	1075
4 spans	291	548	531	254	1146
OP, closed					
2 spans (prefab)	350	326	1074	254	1378
2 spans (in-situ)	367	326	1126	254	1445
UP (underpasses)					
Frame (concrete)	403	286	1409	254	1587
Frame (sheet pile)	427	286	1493	254	1681
Frame (sheet pile + conc.)	503	286	1759	254	1980

3.1 *Analyses of other structures in the project*

Similar analysis was conducted on other types of structures within the project with the aim of minimizing the overall carbon footprint of the project's structures. This included an analysis of the wildlife bridge, for several large wildlife passages, in addition to a footbridge where several materials and bridge types are analysed and investigated.



Figure 4. Rendering of a possible wildlife crossing on the project.

3.2 *Other bridge related carbon emissions*

During construction, many activities lead to carbon emissions. These can include test drilling, cooling/heating at concrete casting, lowering of groundwater, operation and maintenance in addition to traffic-related factors.It is generally more challenging to quantify these emissions, and many of them are not yet included in the analysis conducted by commonly used tools such as InfraLCA.

Further analysis has been undertaken to identify and quantify carbon emissions for aspects related to bridge design and construction that are not accounted for in InfraLCA calculations. These was focused on detours and traffic congestions during bridge construction works.

The results indicate that detours and traffic congestions can have a significant impact on the total carbon emissions, and in some cases the carbon emissions associated with detours and traffic congestion may exceed the carbon footprint of the bridge itself.

These considerations highlight the complexity of calculating the total carbon footprint of a structure and emphasize the importance of conducting an overall assessment as early as possible in the project, considering all relevant factors.

4 OPTIMIZATION POTENTIALS AND WORK FOR FUTURE PHASES

In the next phase of the project (detailed design), further carbon reducing measures will be implemented. This includes investigating the following:

- Cut outs/voids in structural parts
- Ribbed structural parts
- Varying thicknesses
- Differentiation of concrete types/strengths
- Optimizing surfacing/materials on slopes beneath bridge
- Stressing reinforcement vs. height of structure
- Optimization of the layout of the substructure

In the tender documents, requirements for minimizing the carbon footprint will be imposed on the contractor's execution. These requirements can include:

- Soil management
- Emission requirements for materials/products
- Construction site management requirements
- Construction machines fuel type
- Maximum transport distances
- Reuse of interim structures
- Minimization of waste and spills
- Recycling and reuse

These optimization opportunities and quantification aim to minimize the overall CO_2 footprint of the project and promote sustainable construction practices.

4.1 *Challenge requirements, norms, and standard practices*

There are high demands placed on materials, design, and execution when constructing structures with long lifespans (120 years). If the goal of 70 % reduction in carbon emissions is to be achieved, there is a need to adjust more parameters than investigated here. This includes, but is not limited to, the choice and composition of materials, which should be considered, researched, and tested to determine the necessary requirements to ensure these lifespans, not only in terms of material selection but also during designing and execution.

However, it is crucial to ensure that the durability of the structure is not compromised in the attempt of lowering the carbon emissions, as it may otherwise result in higher carbon emissions due to subsequent repairs than what is gained from optimization. Additionally, there will be a greater need for the maintenance of existing structures and allowing for increased reuse in various contexts.

5 THE POTENTIAL REDUCTION AND PERSPECTIVES

The described analysis and presented results should be seen as a study in projects phases 1-3 (see Figure 3), where aspects such as materials, type of structures, and initial optimization are analysed. Additionally, there is room for further optimization in the detailed design phase and the possibility to establish carbon requirements in the tender material for compliance during

construction, as reflected in Figure 3. When setting requirements or comparing products, environmental product declarations (EPD) are essential. EPDs are declarations that contains information on several environmental impacts from a specific product or material, and this is how the global warming potential, measured as carbon emission, is documented. The trend is that EPDs are becoming increasingly demanded as documentation for the materials and products used in larger quantities within infrastructure projects.

If the bridge type with the lowest footprint (2 spans open) is considered, there is expected potential for further reductions in carbon footprint in the next phases, as described below. Currently, it is estimated that there is a possibility of reducing carbon emissions in phases A1-A3 by around 10 % by minimizing material consumption, especially concrete and reinforcement.

Maximum emission requirements for the most common materials are expected to further reduce the carbon footprint by approximately 15-20 % in phases A1-A3. Refer to Table 3 below.

It should be noted that transportation (A4), especially earthworks and transportation of soil, is expected to shift towards electric or hydrogen-powered vehicles, leading to a movement towards zero emissions.

Looking towards 2030, it is anticipated that concrete for construction purposes will have a carbon footprint of around 200 kg CO_2e/m³, while reinforcement will be around 375 kg CO_2e/t due to advancements in material technology (projection estimates from Vejdirektoratet). This would reduce the total reduction for phases A1-A3 by 45 % compared to the "basic-case" 2022 estimates for the "2 spans open" bridge.

Table 3. An approximate assessment of the carbon footprint for the 2 spans open bridge type over time.

Year	1990 (baseline)	2022 (basic case)	2022 (optimistic)	2030 (expected)
Estimates of emissions factors (concrete/reinforcement)	-	392 kg CO_2/m³ 1060 kg CO_2/t	353 kg CO_2/m³ 600 kg CO_2/t	200 kg CO_2/m³ 375 kg CO_2/t
A1-A3 [t CO_2e]	360*	234	175**	130***
A1-A3 [kg CO_2e/m^2 bridge deck]	711*	462	346**	257***
CO_2-reduction compared to 1990 baseline	0%*	35%	51%**	64%***

*Estimate based on industry experience (Teknologisk Institut, 2020).
**Based on possible emission values.
***Estimates based on expected approximate emission values.

In Table 3, during the period from 1990 to 2030, there is an estimated CO_2e reduction of nearly 65%, suggesting that the climate goal of a 70% CO_2 reduction by 2030 is not unrealistic but requires continued development and effort.

It can be added that there is a natural limitation in reducing carbon emissions in concrete in the short term, as about half of the carbon emissions come from the chemical process when cement clinker is heated. To further reduce the footprint of concrete, Carbon Capture Storage (CCS) can be a possibility. CCS is to capture and storage the CO_2. There are also opportunities in changing/new concrete compositions. For reinforcement/steel, there are already technologies (SSAB) that, in the long run, will be able to produce steel using hydrogen and green electricity with a CO_2e emission close to 0.

6 CONCLUSION & GOING FORWARD

Civil structures in infrastructure projects have a significant carbon emission. It is clear, that analysing the necessary type of bridge structure for a specific location can have a significant positive impact in lowering the total environmental impact. In this specific location the

differences were up to a factor 2. However, this will vary depending on the specific location and size of crossing. Therefore, it is important to choose the right type of crossing where possible in respect of other project constraints.

It is also clear, that the large amounts of earth moved has a significant impact on the overall carbon emission. Detailed plans for earthworks are important in reducing the overall carbon emissions.

Looking at the goals for the carbon emissions in Denmark (Ministry of Climate, Energy and Utilities, 2019), there is still way to go when focusing on bridges.

When the process of deciding if something should be built, what should be build and how it should look, the process of optimising the defined structure starts (build nothing, build less, build clever, build efficiently). To reach our goals, it is very important to have a continued focus in this phase as well, as we have an opportunity to reduce the carbon emission further.

A lot of initiatives and development is ongoing in the industry, and if large infrastructure projects shall be a reality in the future, it is important to maintain this ongoing development.

REFERENCES

Danish Road Regulation 2023, *Design Basis for Bridges*, guideline for bridges, Projekteringsgrundlag for broer (vejregler.dk)

Ministry of Climate, Energy and Utilities 2019, *The Danish Climate Act*, https://kefm.dk/aktuelt/nyheder/2019/dec/klimalov

Ministry of Transportation 2021, *Danmark Fremad*, Danish infrastructure plan 2035, https://www.trm.dk/politiske-aftaler/2021/aftale-om-infrastrukturplan-2035-aftale

SSAB, "HYBRIT technology", fossil free steel production, https://www.ssab.com/en/fossil-free-steel/insights/hybrit-a-new-revolutionary-steelmaking-technologyTeknologisk Institut, 2020, *CO2 beregninger på broer*

The Danish Road Directorate, "InfraLCA", LCA-tool developed by the Danish Road Directorate, (https://www.vejdirektoratet.dk/infralca)

The Danish Road Directorate, "InfraLCA", LCA-tool developed by the Danish Road Directorate, (https://www.vejdirektoratet.dk/infralca)

Bridge Maintenance, Safety, Management, Digitalization and Sustainability – Jensen, Frangopol & Schmidt (eds)
© 2024 The Author(s), ISBN 978-1-032-77040-6
Open Access: www.taylorfrancis.com, CC BY-NC-ND 4.0 license

Static behavior of steel-concrete bridge under pier girder consolidation

Wei Xie & Qingtian Su
Tongji University, ShangHai

ABSTRACT: There are some advantages of steel-concrete composite bridge in the case of pier girder consolidation, such as greater overall stiffness, less maintenance work. However, the combination zone of composite girder and concrete pier which needs to transfer bending moment, shear force and axial force is under complicated stress state. Combined with Sutai expressway project in Tongxiang, this paper conducts research on its static behaviour. Firstly, stress distribution law of the structure during construction and service stage is studied by establishing an overall three-dimensional solid model, and the influence of some structural system parameters on its static behaviour is analysed. Then, a local model which minutely simulates the combination zone of composite girder and concrete pier is established to reveal the failure mechanism by nonlinear finite element analysis, and effects on stiffness, ultimate capacity and failure mode are investigated by varying shear span ratio, embedded depth of steel plates and reinforcement ratio. The conclusions obtained in this paper can provide references for the same type of bridges.

1 INTRODUCTION

During the service period of bridge bearings, numerous problems may arise, including deflection, disengagement and deterioration[1-2]. The typical life expectancy of bridge bearings ranges from 15 to 20 years. However, improper construction or maintenance methods can significantly shorten this lifespan. Consequently, it becomes necessary to repeatedly close the traffic and replace bearings within the designated bridge lifespan, thereby increasing the later maintenance expenses. Furthermore, bridge overturning accidents resulting from overload phenomena occur frequently in China, yet the current study on tensile bearing remains relatively limited. In soft soil foundation areas, the constraint effects of shallow soil on pile foundations are not significant, therefore, pier-girder consolidation structures can be considered to solve the above problems.

In recent years, the steel-concrete composite girders have been widely applied in the simply supported bridges since the merits of concrete compressive strength and steel tensile strength can be efficiently utilized. Additionally, compared with concrete girders, steel-concrete composite girders exhibit less noticeable shrinkage and creep effects, making them a more suitable choice for the superstructure.

The combination zone of composite girder and pier is a typical stress disturbance zone, characterized by complex stress distribution and force transmission mechanisms. In recent years, many scholars have carried research on the mechanical behaviour of this joint. [3-4] have proposed an innovative beam-to-pier joint, and respectively studied the joint response under monotonic and cyclic loading. [5-6] have proposed a deck-to-pier connection structure suitable for earthquake-prone areas based on the German specifications, and studied the differences between the two structural systems of pier-beam consolidation and non-pier-beam consolidation through experiments. [7] has studied the seismic performance of the joint between steel-concrete composite girder and concrete pier under cyclic loading through

DOI: 10.1201/9781003483755-365

a double cantilever model test. [8] has dis-cussed the seismic characteristics and failure mode of beam-to-pier joint through shaking table test and finite element analysis.

2 ENGINEERING OVERVIEW

The simply-supported system to rigid-frame system is adopted for the Tongfu viaduct bridge, which is implemented by post pouring concrete cross beam. This paper takes it as engineering background, the span layout of which is 3×30m. Figure 1 shows the cross section at pier. The height of pier is about 10~20m.

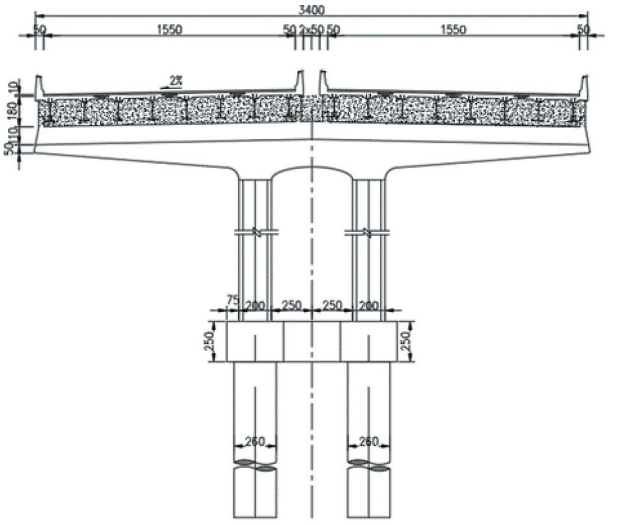


Figure 1. Cross section at pier (unit: mm).

The beam-to-pier joint is as Figure 2 shows. The connection between steel and concrete is achieved by adopting perforated plates and welding studs. The concrete slab in the hogging moment zone tends to crack, so two methods are employed to address this issue. The first method involves adjusting construction sequences. Initially, the steel girder and concrete slab are prefabricated and assembled in the factory, then erected in place. Subsequently, the concrete cross beam is poured to connect main girder and pier. The second method is to pour an ultra-high performance concrete (UHPC) layer, with a thickness of 100mm, within a range of 6m at the top of pier.

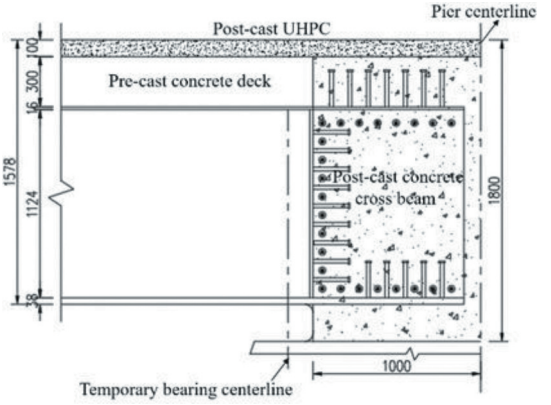


Figure 2. Beam-to-pier joint (unit: mm).

3 NUMERICAL SIMULATION

This paper establishes an overall three-dimensional solid model to study the overall mechanical behaviour of steel-concrete composite bridge in the case of pier girder consolidation during construction and service stages, and studies the influence of some structural system parameters. Due to the fact that the combination zone of composite girder and concrete pier is under complicated stress state, it is essential to establish a detailed local model to investigate its stiffness, ultimate capacity and failure mode by nonlinear finite element analysis.

3.1 *Overall mechanical behaviour*

3.1.1 *Finite element model*

This paper establishes an overall three-dimensional solid model by the general finite element software ANSYS for stress analysis, as Figure 3 presents. In this model, steel plates are simulated by SHELL93 element, while concrete components are simulated by SOLID95 element. The actual construction process of the bridge is considered in the calculation. The steel girder and concrete slab are prefabricated and combined in the factory, and then erected in place. Subsequently, the concrete cross beam is poured to connect main girders and piers. The EKILL and EALIVE commands are used to simulate the construction process. The boundary conditions of the model during service stage are as follows, displacements in Y and Z direction are restricted on both sides of steel bottom plates, and nodes at the bottom of piers are restricted in all directions. The dead load, vehicle load and the effect of temperature, foundation displacement and concrete shrinkage and creep are considered in the finite element calculation. The most unfavorable condition is found through combination of load effects.

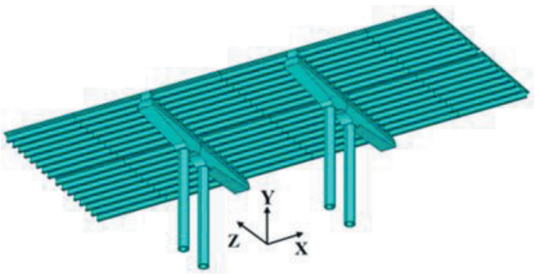


Figure 3. Three-dimensional solid model.

3.1.2 *Numerical results*

Through combination of load effects, the following three cases are determined. Case 1: the hogging moment zone is under the most unfavorable state; Case 2: the midspan area of the side span is under the most unfavorable state; Case 3: the midspan area of the middle span is under the most unfavorable state.

Figure 4 presents the longitudinal normal stress distribution of the structure under Case 1. It can be seen from Figure 4(a) that the maximum tensile stress values 13.0MPa and occurs at the upper edge of the junction section of main girder and concrete cross beam. It demonstrates that pouring UHPC at the surface of hogging moment zone is essential. Figure 4(b) shows that the closer to the outer lane, the greater the compressive stress of the concrete cross beam is. This is mainly due to the fact that eccentric loading is considered when arranging the vehicle load. The maximum compressive stress reaches 32.4MPa, which is caused by stress concentration. Figure 4-(c) shows that tensile stress of top plate in the middle of the side span is 98.1 MPa, and the compressive stress of bottom plate is 70.2 MPa.

Maximum longitudinal normal stresses of different components are listed in Table 1. It should be noted that the maximum stresses of steel plates given in the table are obtained in the

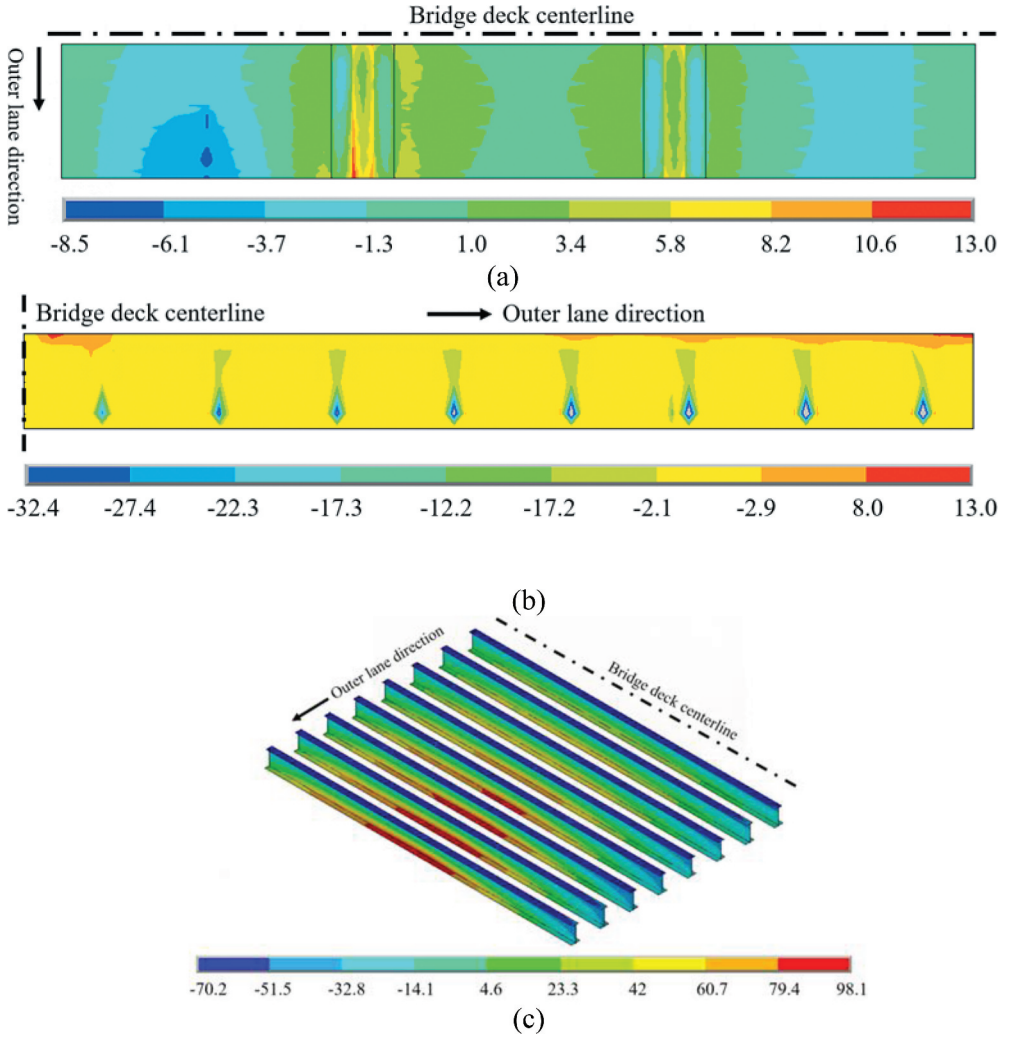


Figure 4. Longitudinal normal stress distribution of (a) concrete slab; (b) concrete cross beam and (c) steel plates of side span under Case 1.

midspan region. The stress of concrete slab reaches 13.0MPa, while that of steel structure is far less than the material limit. It can be concluded that the stress state of concrete slab in the hogging moment zone plays a crucial role in the design of steel-concrete composite bridge in the case of pier girder consolidation.

Table 1. Maximum longitudinal normal stresses of different components (unit:MPa).

		Side span		Middle span	
	Concrete slab	Top Plate	Bottom Plate	Top Plate	Bottom Plate
Case 1	13.0	-70.2	98.1	-64.6	17.9
Case 2	10.3	-54	113.5	-48.0	26.0
Case 3	9.9	-51.3	53.9	-50.2	80.7

Note: Positive number represents tensile stress, negative number represents compressive stress.

3.1.3 *Parameter study*

Effects on the static behaviour of the structure are investigated by varying span, pier height and the longitudinal length of concrete cross beam in this paper. The parameter study only con-siders the effects of dead load and vehicle load.

Figure 5 illustrates the longitudinal tensile stress distribution of the upper edge of concrete slab under different span, pier height and longitudinal length of concrete cross beam. When the span changes from 20m to 40m, the maximum longitudinal tensile stress of the upper edge of concrete slab increases from 5.5MPa to 16.8MPa. In addition, it can be seen from Figure 5-(a) that length of tensile area of concrete slab is about 0.4L. When the pier height changes from 10m to 50m, the maximum longitudinal tensile stress of the upper edge of concrete slab near the side span decreases from 10.7MPa to 10.1MPa, that near the middle span increases from 8.0MPa to 8.2MPa. It can be concluded that pier height slightly affects stress distribution of the upper edge of concrete slab. With the increasing of the longitudinal length of concrete cross beam, the longitudinal tensile stress of the upper edge of concrete slab within the concrete cross beam area decreases, while that outside the concrete cross beam area increases. When length of concrete cross beam changes from 0.6m to 2.0m, the maximum longitudinal tensile stress of the upper edge of concrete slab changes from 12.3MPa to 10.3MPa.

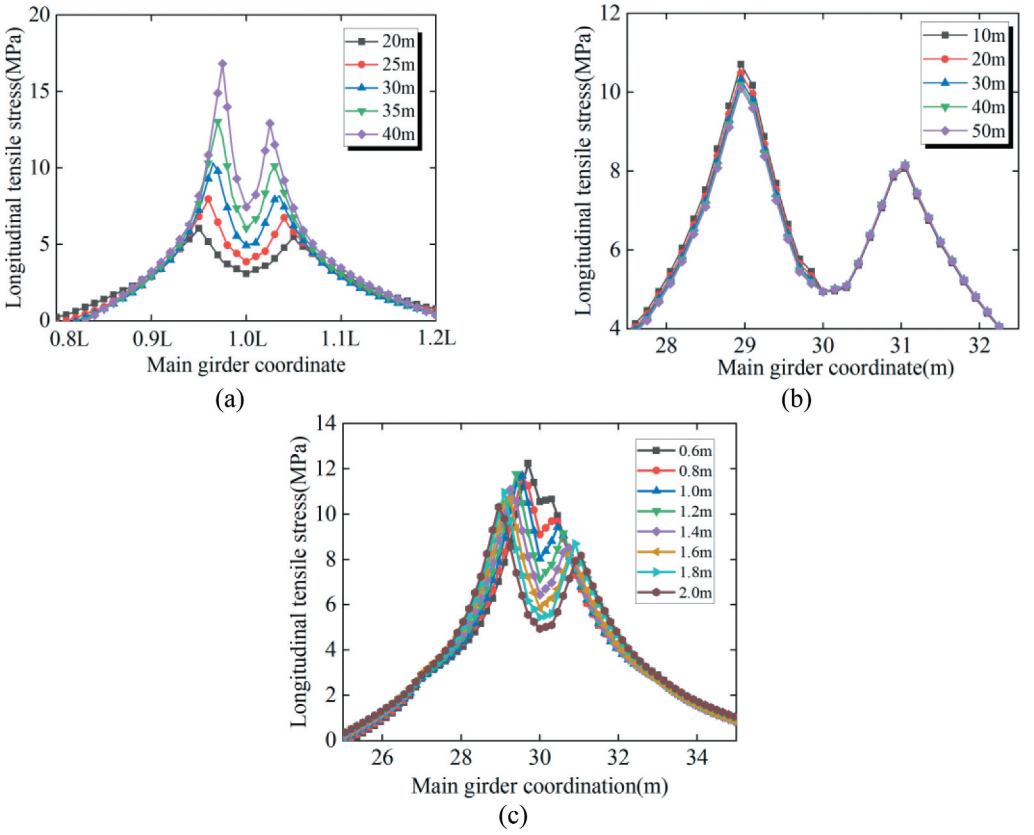


Figure 5. Longitudinal tensile stress distribution of the upper edge of concrete slab under different (a) span; (b)pier height and (c) longitudinal length of concrete cross beam.

3.2 *Local mechanical behaviour*

3.2.1 *Finite element model*

This paper establishes a local model which minutely simulates the combination zone of composite girder and concrete pier, as Figure 6 shows. The longitudinal length of the local model

is taken as length of the hogging moment region. In this model, steel plates are simulated by shell element, and loaded plates, the UHPC layer, concrete slab and cross beam are simulated by solid element. Rebars simulated by truss element are embedded in the concrete. Concrete and steel plates are tied together. The boundary conditions of the model are as follows, nodes at the bottom of concrete cross beam are restricted in all directions. Displacement-controlled loading is applied on both sides. Dynamic explicit analysis, which can increase the calculation speed, is used to numerically solve the iterative equation.

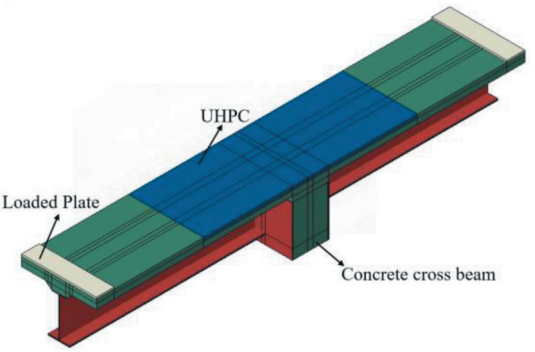


Figure 6. Local model.

The concrete damaged plasticity (CDP) model is employed to simulate the mechanical behavior of the concrete. For C50, the stress-strain relationship of C50 is referred to the current specifications of China, and for UHPC, the stress-strain relationship in tension is referred to Gao[9], and that in compression is referred to Wang[10], as Figure 7 shows. The classic bilinear model is adopted for reinforcement bars and steel plates.

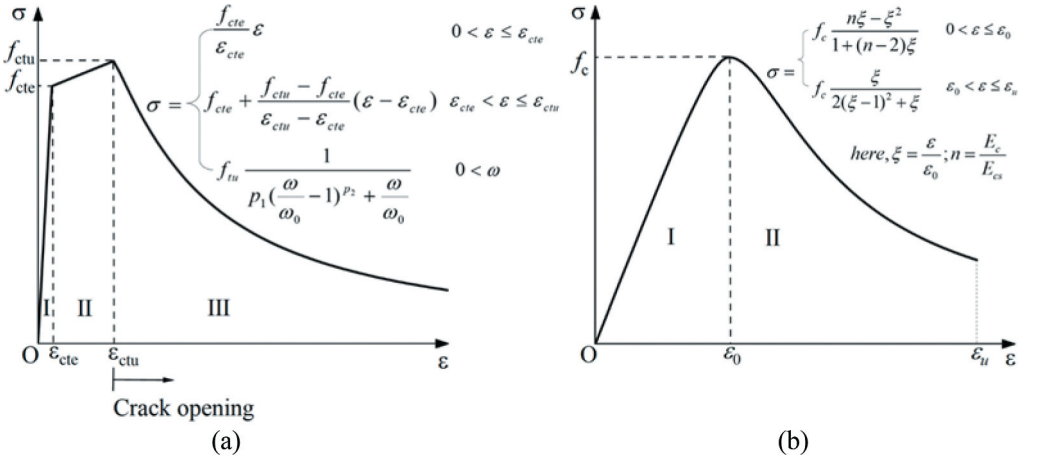


Figure 7. Constitutive models of UHPC: (a) tension; (b) compression.

3.2.2 *Numerical results*

Figure 8 demonstrates the load-displacement relationship of the structure. It is found that with the increasing of load, the cracking of normal concrete layer is earlier than that of UHPC layer on the surface. When the load reaches 466kN, the maximum tensile stress of C50 concrete reaches 2.64MPa, and the beginning of C50 concrete damage marks the end of the linear elastic stage. The UHPC layer begins to crack under a load of 600kN. The failure mode of the structure is the yielding of longitudinal rebars. The ultimate bearing capacity corresponding to the peak point is about 1468kN, and the corresponding vertical displacement is 37.0mm.

The longitudinal stress of rebars at the peak point reaches 400MPa, but steel bottom plates have not yielded, and the Mises stress values 332MPa. Figure 9 shows the concrete tensile damage at the peak point. It can be seen that severe damage happens to normal concrete compared with UHPC. The concrete cross beam also suffered tensile damage, which may be due to the fact that steel plates are embedded in the concrete and the relative displacement is not allowed.

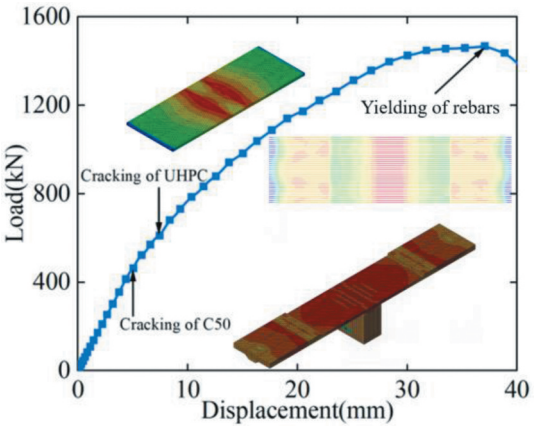


Figure 8. Load-displacement relationship.

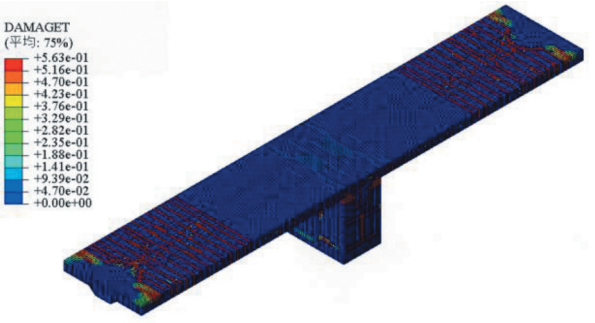


Figure 9. Concrete tensile damage at the peak point.

3.2.3 *Parameter study*

Effects on the static behaviour of the structure are investigated by varying shear span ratio, embedded depth of steel plates and reinforcement ratio in this paper. Table 2 lists the detailed parameters of the local model.

Table 2. Detailed parameters of local model.

Parameters	values
Shear span ratio	**3.8**, 3.2, 2.2, 1.6, 1.0.
Embedded depth	0.15m, 0.25m, **0.35m**, 0.45m, 0.5m.
Reinforcement ratio	0.88%, 1.04%, 1.2%, 1.36%, **1.68%**.

Note: Bold number indicates the parameters of the standard model.

The change of shear span ratio is achieved by varying the cantilever length on both sides. The shear span ratio mainly affects failure mode of the structure. When the shear span ratio is

less than 1.6, shear failure occurs in the structure, which is manifested by yielding of web, as Figure 10 shows.

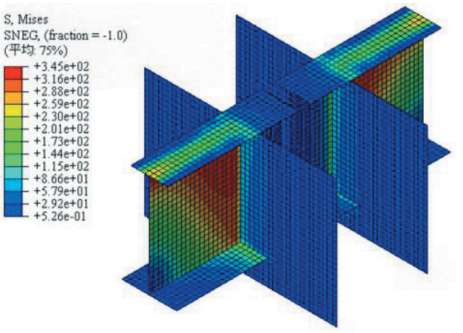


Figure 10. Failure mode.

Figure 11 shows the load-displacement relationship of structure under different embedded length of steel plates and reinforcement ratio. When the embedded depth of steel plates changes from 0.15m to 0.50m, the ultimate bearing capacity increases from 1333kN to 1639kN. When the load is less than 983kN, the load-displacement relationship of the structure under different embedded depth is almost identical, which is mainly due to the fact that the concrete cross beam begins to damage in a wide range when the load is greater than 983kN. With the increasing of reinforcement ratio, the stiffness and ultimate bearing capacity of the structure both increase. When the reinforcement ratio changes from 0.88% to 1.68%, the ultimate bearing capacity increases from 1282kN to 1490kN.

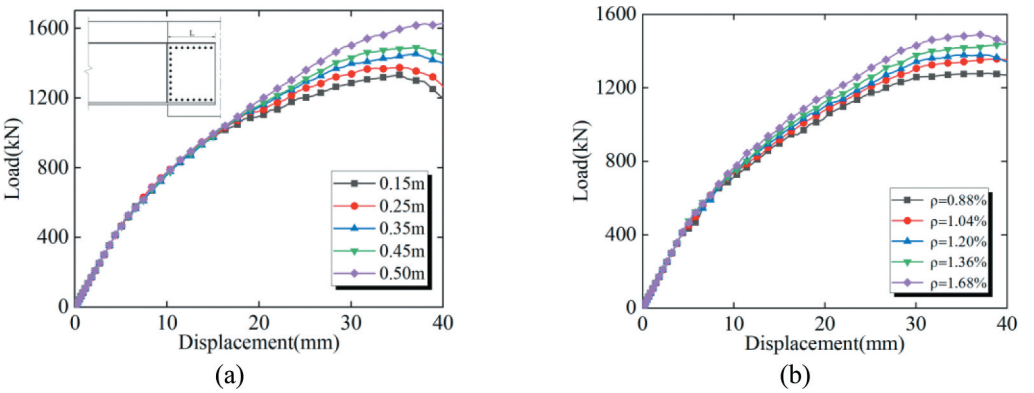


Figure 11. Load-displacement relationship under different (a) embedded length of steel plates and (b) reinforcement ratio.

4 CONLUSIONS

Based on the above investigations, the main conclusions are

(1) Stress state of concrete slab in the hogging moment zone plays a crucial role in the design of steel-concrete composite bridge in the case of pier girder consolidation.
(2) With the increasing of span, the longitudinal tensile stress of the upper edge of concrete slab increases.With the increasing of pier height, the maximum longitudinal tensile stress of the upper edge of concrete slab near the side span decreases, while that near the middle span increases. With the increasing of the longitudinal length of concrete cross beam, the longitudinal tensile stress of the upper edge of concrete slab within the concrete cross beam area decreases, while that outside the concrete cross beam area increases.

(3) With the increasing of load, the cracking of normal concrete layer is earlier than that of UHPC layer on the surface.
(4) Shear span ratio mainly affects the failure mode of the structure. When the shear span ratio is less than 1.6, shear failure occurs in the structure, which is manifested by yielding of web, and when the shear ratio is more than 1.6, bending failure occurs in the structure, which is manifested by yielding of longitudinal rebars.
(5) With the increasing of embedded depth of steel plates and reinforcement ratio, the ultimate bearing capacity of the structure both increase.

REFERENCES

[1] Wu Yifeng, Xu Hong, Li Aiqun, Zhang Yan. Review on Operating Disease and Effects of Bridge Plate Rubber Bearing[J]. Earthquake Resistant Engineering and Retrofitting, 2021, 43(05):104-113 +95.
[2] Dong Zhenhua, He Cunzhe, Cheng Shoushan, Li Pengfei. Shear Performance of Common Plate Rubber Bearing with Friction Slipping[J]. China Journal of Highway and Transport, 2020, 33(02):83–93.
[3] Zordan T, Briseghella B. Nonlinear Experimental Response of Non-conventional Composite Steel and Concrete Connection[J]. Frontiers of Architecture and Civil Engineering, 2009, 3(1):42–49.
[4] Briseghella B, Zordan T. An Innovative Steel-concrete Joint for Integral Abutment Bridges[J]. Journal of Traffic and Transportation Engineering, 2015, 2(4):209–222.
[5] Abbiati G, Cazzador E, Alessandri S. Experimental Characterization and Component-based Modelling of Deck-to-pier Connections for Composite Bridges[J]. Journal of Constructional Steel Research, 2018, Volume 150, Pages 31–50.
[6] Paolacci F, Giannini R, Alessandri S. On the Cyclic Behaviour of New Pier-to-deck Connections for Short-medium Span Composite I-girder Bridges[J]. Journal of Traffic and Transportation Engineering, 2018, 5(6): 439–453.
[7] Taghinezhadbilondy R, Yakel A, Azizinamini A. Deck-pier Connection Detail for the Simple for Dead Load and Continuous for Live Load Bridge System in Seismic Regions[J]. Engineering Structures, 2018, Vol.173: 76–88.
[8] Lin Yuanzheng, Kaiming Bi, Zong Zhouhong. Seismic Performance of Steel-concrete Composite Rigid-frame Bridge: Shake Table Test and Numerical Simulation[J]. Journal of Bridge Engineering, 2020, 25(7).
[9] Gao Xiaolong, Wang Junyan, Guo Junyuan, Liu Chao. Axial Tensile Mechanical Properties and Constitutive Relation Model of Ultra-high Performance Concrete under Cyclic Loading[J]. Acta Materiae Compositae Sinica, 2021, 38(11):3925–3938.
[10] Wang Zhe, Nie Xin, Fan Jiansheng, Lu XinYing, Ding Ran. Experimental and Numerical Investigation of the Interfacial Properties of Non-steam-cured UHPC-steel Composite Beams[J]. Construction and Building Materials, 2019, Vol.195: 323–339.

Bridge Maintenance, Safety, Management, Digitalization and Sustainability – Jensen, Frangopol & Schmidt (eds)
© 2024 The Author(s), ISBN 978-1-032-77040-6
Open Access: www.taylorfrancis.com, CC BY-NC-ND 4.0 license

On CO_2 efficiency and trade-offs between safety and sustainability in concrete bridge management

M. Liu
School of Civil Engineering, Harbin Institute of Technology, China
Department of the Built Environment, Aalborg University, Denmark

J. Olesen & P. Linneberg
COWI A/S, Denmark

D.G. Lu
School of Civil Engineering, Harbin Institute of Technology, China

M.H. Faber
School of Civil Engineering, Harbin Institute of Technology, China
Department of the Built Environment, Aalborg University, Denmark

ABSTRACT: Roadway transportation systems contribute significantly to global Green House Gas (GHG) emissions. Although there has been significant progress in identifying how to reduce embedded GHG in construction, we do not know how efficient our decisions are in creating sustainable welfare. To achieve this knowledge, it is necessary to investigate how structures contribute to economic growth, life safety, resilience and sustainability, relative to their associated embedded GHG emissions. In the present paper a framework is provided on how the GHG efficiency of different strategies for roadway bridge design and integrity management may be modelled and quantified. The application of the framework is illustrated on an example considering typical design decisions for ordinary concrete highway bridges and it is shown that optimal decision in this respect have the potential to reduce embedded GHG emissions by a factor of two.

1 INTRODUCTION

The urgency to mitigate climate change has made the reduction of carbon emissions a global imperative, particularly in the short to mid-term. Civil structures and building structures play a big role in global greenhouse gas emissions. The global embodied GHG emissions from construction amounts to nearly 20% of global emissions caused by human activities (Faber, 2020). At the same time, infrastructure is expanding rapidly across the globe, driven by economic growth and increasing urbanization. This expansion brings significant environmental challenges. As critical elements of infrastructure, the construction, maintenance, and operation of civil structures, hereunder concrete bridges are significant contributors to global greenhouse gas emissions, particularly CO_2 emissions. This necessitates a focused effort to understand and mitigate the carbon footprint associated with the lifecycle of concrete bridges– as one example. To enable the construction industry to engage effectively in redesigning best practices, it is necessary to shift the focus of leading principles. These principles should be grounded in achieving the desired functionality of the built environment with maximum efficiency, especially in terms of minimizing environmental impacts like CO_2e emissions (all greenhouse gas emissions converted to the equivalent effect of CO2 on climate change), rather than relative to costs alone. To redesign best practices in this regard, however, necessitates that we are able to:

DOI: 10.1201/9781003483755-366

– Assess the efficiency of structural designs and strategies for structural integrity management in providing the desired functionality relative to associated effects on impacts to the environment, reliability/safety and economy.
– Understand the trade-offs between life safety, economy and reductions in impacts to the environment (at global and local scale) under different strategies for the development of societal infrastructure with respect to quality and quantity.

Presently, knowledge on these two points is very sparse; in fact no previous study of such nature has been identified by the authors.

The present paper focuses on the modeling of the relationship between bridge construction and integrity management decisions and their impact on associated life-cycle costs and embedded CO_2e emissions. Bridge structures made by reinforced concrete are addressed in the present paper but the general approach presented may be easily adapted to structures made of other materials. To investigate how different strategies for design affect the life-cycle cost and embedded CO_2e emissions, different design scenarios are explored by altering the cross section, material type, target reliability, and cover depth. Our analysis aims to support decisions for design of concrete bridges, contribute to decision making at political, regulatory, and operational levels on how to ensure and optimize sustainable and affordably safe development of infrastructure.

2 DECISION SUPPORT FRAMEWORK FOR BRIDGE MANAGEMENT

2.1 *Brief introduction of the decision support framework*

This framework is established based on previous research (Nishijima & Faber, 2009) in which optimal strategies for the development of infrastructure systems was addressed from the context of socio-economic optimization. In the present paper, focus is on the modeling of the relationships between the decisions related to the quality and quantity of the bridges and the consequences in terms of life-cycle cost and embedded CO_2e emissions during the life-cycle of the structures. In this framework, the quality of the structures is considered as the reliability/safety and durability of the structures and the quantity of the structures are considered as the material consumption such as the consumption of concrete and steel. There are trade-offs between the decisions on the quality and quantity of the structures considering the life-cycle cost and embedded CO_2e emissions as consequences. Decisions which may improve the reliability/safety level of the structures could lead to higher material consumption. Opting for higher reliability/safety in structural design reduces the probability of failures, thereby decreasing the expected embedded CO2e emissions from replacements or repairs caused by failures, but the higher material consumption may also at the same time be associated with a higher emissions.

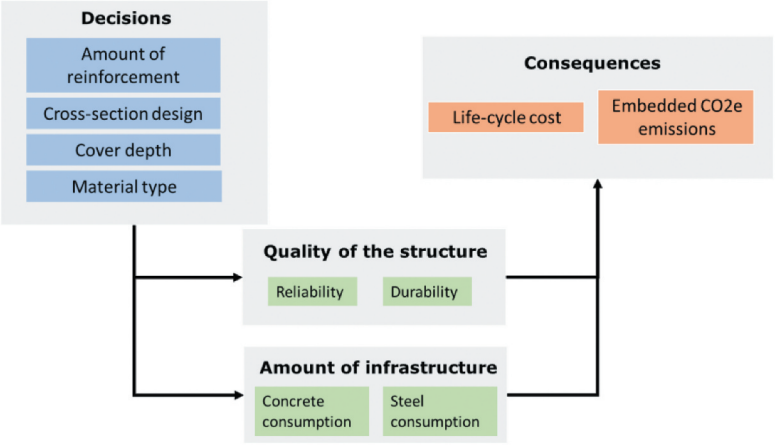


Figure 1. Principal relationships between decisions on the quality and quantity of bridges and consequences with respect to embedded CO_2e emissions and life-cycle cost.

2.2 *Modeling of failure events*

2.2.1 *Failures due to extreme operational loads*

The approach utilized for calibrating design codes, as demonstrated by Faber & Sorensen (2003), is adapted to model the failures due to extreme operational loads. In this way, instead of modeling structures in detail, only the failure modes relating to different types of materials and load cases are considered.

For purposes of simplicity, and without loss of practical relevance, it is assumed in the design process of the bridge girder cross section that the pre-stress reinforcement is designed to carry all the dead load. As a consequence the event of failure of the cross section is modelled as the event that the tensile force from the live loads in the mild reinforcement is larger than the yield capacity, which is expressed as:

$$g(z) = z \times F_{\mathrm{y}} - F_{\mathrm{load,l}} \tag{1}$$

where $F_y = f_y \times A_{\mathrm{s}}$ represents the tensile capacity of mild reinforcement, f_y is the yield strength of the mild reinforcement and A_{s} is the area of the longitudinal reinforcement; $F_{\mathrm{load,\ l}}$ is the tensile force from the live loads; z is the design parameter (e.g., cross-section parameter) which is adjusted such that the annual probability of failure is equal to a given target value $P_{\mathrm{f}}^{\mathrm{T}}$.

It is acknowledged that pre-stressing cables possess additional capacity which, under realistic conditions, would contribute to the ultimate capacity of the structure in response to live loads. However, in the present paper, we adopt this simplification to facilitate straightforward, preliminary estimates of the environmental impact, specifically in terms of CO2 emissions, associated with varying levels of safety. More detailed model of the limit state should be introduced in the future work.

The probabilistic model for the parameters entering Equation (1) are given in Table 1.

Table 1. Uncertainty model for the considered failure mode.

Basic variable	Distribution	Mean	CoV
Tensile capacity (F_y)	Log-normal	1	0.07
Tensile force from the live loads ($F_{\mathrm{load,l}}$)	Gumbel	1	0.3

2.2.2 *Modeling of degradation*

Research into the probabilistic modeling of deterioration processes has received considerable attention. The report by Duracrete (1999) provides a comprehensive review of the current understanding as it pertains to reinforced concrete (RC) structures compromised by chloride-induced reinforcement corrosion. Different limit state functions describe different condition states, which are related to the serviceability and the safety of the structure.

In the present paper, a simplified model is utilized to describe the ingress of chlorides into concrete (Malioka,2009), which is expressed as:

$$C(z,t) = C_s\left[1 - erf\left(\frac{z}{2\sqrt{tD}}\right)\right] \tag{2}$$

where $C(z, t)$ represents the chloride concentration at a distance z from the concrete surface at time t, C_s represents the the surface chloride concentration, D represents the chloride diffusion coefficient and $erf(\cdot)$ is the error function.

Corrosion will essentially begin when the chloride level at the depth of the reinforcement will exceed a critical threshold level, C_{CR}. Assuming both the surface chloride concentration and the diffusion coefficient as constant, the time till corrosion initiation, T_{CI}, at the first layer of reinforcement may be determined as follows:

$$T_{CI} = \frac{d^2}{4D}\left(erf^{-1}\left(1 - \frac{C_{CR}}{C_S}\right)\right)^{-2} \tag{3}$$

where d is the cover depth, which replace z in Equation (2), $erf(\cdot)$ is the inverse of the error function and can be expressed for computational purposes as:

$$erf^{-1}(\cdot) = \frac{\Phi^{-1}(\cdot)}{\sqrt{2}} \tag{4}$$

The limit state function for visible corrosion at time t can be expressed as:

$$g_{CV}(t, \mathbf{X}) = T_{CI}(\mathbf{X}) + T_V - t \tag{5}$$

where $\boldsymbol{X}$ is a vector that includes all the stochastic variables in the limit state function, T_V represents the time from corrosion initiation to visible corrosion. As suggested by Johnsen et.al. (Johnsen et.al., 2003), T_V is estimated as 10 years.

The deterioration of concrete structures is a random phenomenon that shows significant spatial variability. In the present paper, the model proposed by Straub et.al. (Straub et.al., 2009) is utilized. To model the spatial variability in concrete structures, areas with similar characteristics are grouped into zones. It is assumed that there is no interdependency between different zones. Then the zones are further discretized into elements. To assess the size of these elements, as well as their dependency structure, a study of the correlation length or radius of the parameters governing the degradation process must be carried out. In Straub (2009), the correlation length is identified as 80 cm.

Table 2. Uncertainty model for the degradation model.

Basic variable	Unit	Distribution	Mean	Std. dev.
d	mm	Log-normal	45/50/55	8/9/10
D	mm²/ year	Log-normal	μ_D	24
C_s	Weight-% of concrete	Log-normal	μ_{C_s}	0.04
C_{CR}	Weight-% of concrete	Normal	0.1	0.03
μ_D	mm²/ year	Normal	30	3
μ_{C_s}	Weight-% of concrete	Normal	0.24	0.02

2.3 *Life-cycle analysis*

Life-cycle assessment (LCA) is extensively utilized to evaluate the energy and environmental impacts throughout the lifespan of products and services. This is particularly relevant in the context of civil structures, which encompasses various stages such as material production, construction, maintenance, operation, and end-of-life (ISO 14040, 2006). These stages correspond to the A1 to C4 categorization in Life Cycle Assessment, see Figure 2.

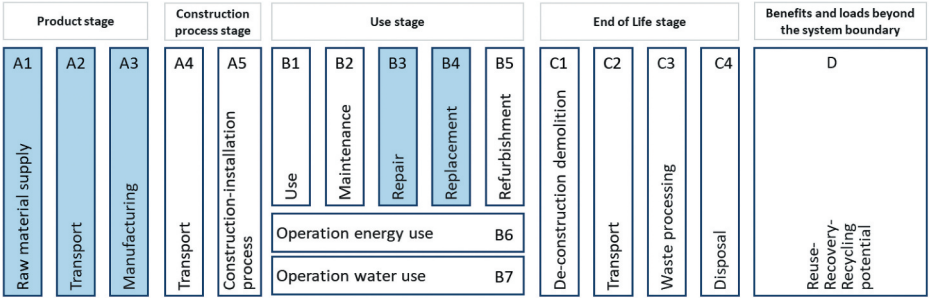


Figure 2. Life-cycle stages (ISO 14040, 2006).

2.4 *Life-cycle cost and embedded CO_2e emissions*

Considering different decisions related to the design and integrity management of the bridges, the life-cycle cost $E[C_T]$ can be expressed as:

$$E[C_{\mathrm{T}}\ (\mathbf{a})] = E[C_{\mathrm{C}}\ (\mathbf{a})] + E\left[C_{\mathrm{Repair}(\mathbf{a})}\right] + E\left[C_{\mathrm{Replacement}}\ (\mathbf{a})\right] \tag{6}$$

where **a** is the vector that represents the decision variables, $E[C_{\mathrm{C}}\ (\mathbf{a})]$ is the initial cost depending on the design decisions which lead to different material consumption and construction cost; $E\left[C_{\mathrm{Repair}(\mathbf{a})}\right]$ represents the repair cost, which depends on the decisions related to the degradation process of the structures such as cover depth and inspection and repair plan; $E\left[C_{\mathrm{Replacement}}\ (\mathbf{a})\right]$ represents the replacement cost which depends on the reliability of the structures.

The life-cycle embedded CO_2e emissions can be expressed as:

$$E[E_{\mathrm{T}}\ (\mathbf{a})] = E[E_{\mathrm{C}}\ (\mathbf{a})] + E\left[E_{\mathrm{Repair}(\mathbf{a})}\right] + E\left[E_{\mathrm{Replacement}}\ (\mathbf{a})\right] \tag{7}$$

where $E[E_{\mathrm{C}}\ (\mathbf{a})]$ is the embedded CO_2e emissions at the production phase (A1-A3), which also depends on the design decisions which lead to different material consumption; $E\left[E_{\mathrm{Repair}(\mathbf{a})}\right]$ represents embedded CO_2e emissions from the repairs (B3) (assuming embedded CO2e from inspection being minimal and somewhat similar for all scenarios) and $E\left[C_{\mathrm{Replacement}}\ (\mathbf{a})\right]$ (B4) represents the emissions from replacement. The considered stages in the life-cycle analysis are highlighted in Figure 2. It should be noted that the emissions calculated here are all expected values, which are the results after taking into account the uncertainty of the system. They are not directly calculated emissions in a given scenario.

3 ILLUSTRATIVE EXAMPLE

3.1 *Introduction of the example bridge*

The example bridge is a two-span continuous bridge, see Figure 3, and the detailed superstructure cross-section for the basic case is shown in Figure 4.

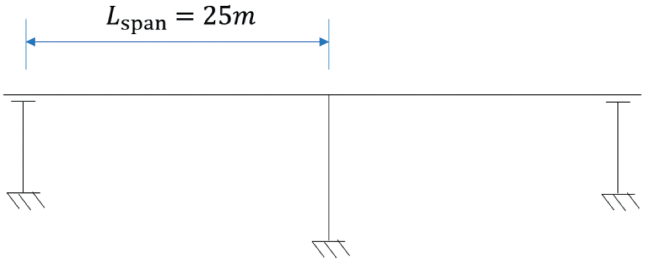


Figure 3. Two-span continuous bridge.

In the following, only the superstructure of the bridge is being considered.

3.2 *Design scenarios*

In the example, various design scenarios are explored by altering the cross section, material type, target reliability, and cover depth. Consequently, 18 distinct design scenarios are examined. Scenario 1 is the basic case shown in Figure 4. More scenarios could be investigated, but some of the most obvious are investigated here. These scenarios are indeed possible and reasonable, but some of them ar not allowed due to existing codes and guidelines. Even though these scenarios are not all currently implemented in practice, their inherent potential emphasize the needs for changing these regulations.

The first group of scenarios encompasses those with a reliability/safety level equivalent to the basic case, characterized by a failure probability, $P_f^T = 10^{-6}$. These scenarios are introduced as follows:

– Using a new type of cement, "FUTURECEM", which is a more sustainable cement based on the LC3 technology, can possibly reduce the CO_2e emissions significantly while

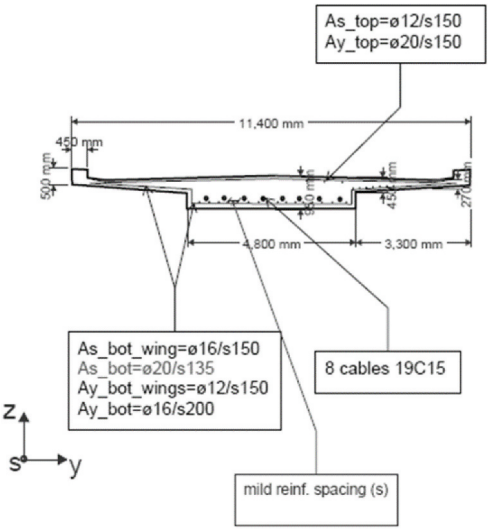


Figure 4. Cross-section for the basic case.

maintaining high performance, and is currently being implemented in various construction projects (Scenario 8).

- Using LC3 (Limestone Calcined Clay Cement), which is an environmentally friendly concrete technology that combines calcined clay and limestone to reduce clinker content, thereby lowering CO_2e emissions while possibly maintaining or enhancing the performance of traditional Portland cement (Scenario 9).
- Cut outs in the cross section, a technique involving intentional voids or openings in structural elements, effectively reduces concrete consumption. To maintain the bending capacity, this scenario necessitates an approximate 10% increase in the consumption of mild reinforcement (Scenario 10).
- Using lower strength concrete, C30. To preserve the bending capacity in this scenario, it's necessary to increase the consumption of mild reinforcement by about 5% (Scenario 11).
- Using recycled concrete. By repurposing concrete from the demolished structures, the aggregate and clinker in the concrete can be substituted by the recycled This approach reduces the consumption of raw materials and lowers CO_2e emissions (Scenario 12).
- Reduce the cross-section height with 10cm. To maintain the capacity, this scenario necessitates an approximate 30% increase in the consumption of mild reinforcement (Scenario 13).
- Reduce the cross-section height with 20cm. To maintain the capacity, this scenario requires an approximate 75% increase in the consumption of mild reinforcement (Scenario 14).
- Reduce the cross-section height with 20cm and using high-strength mild reinforcement (700 Mpa). To maintain the capacity, this scenario requires an approximate 40% increase in the consumption of mild reinforcement (Scenario 15).

Then different reliability levels are considered, which are calibrated according to Equation (1). Scenarios related to lower reliability/safety level ($P_f^T = 10^{-5}$) are considered as follows:

- Reducing mild reinforcement based on the basic case (Scenario 2).
- Using low strength concrete (Scenario 3).
- Reduce the cross-section height with 10cm (Scenario 4).
- Reduce the cross-section height with 20cm (Scenario 5).
- Reduce the cross-section height with 20cm + 700 MPa reinf. (Scenario 6).
- LC3 concrete + Reduce the height of the cross section with 20cm + 700 MPa reinf. (Scenario 16).

Scenarios related to higher reliability/safety level ($P_f^T = 10^{-7}$) are considered as follows:

– Increasing mild reinforcement based on the basic case (Scenario 7).

Finally, to investigate the effect of cover depth, on basis the basic case (cover depth is 45mm), two other scenarios are considered by reducing or increasing the cover depth by 5 mm.

3.3 *Results*

Figure 5 shows the expected value of life-cycle total emissions. The emission factors utilized in the example come from InfraLCA, a tool developed by the Danish Road Authority (2021). The emission factors for the FUTURECEM and LC3 are assumed according to the research in Antoni et al. (2012) and the report from Aalborg Portland (2020).

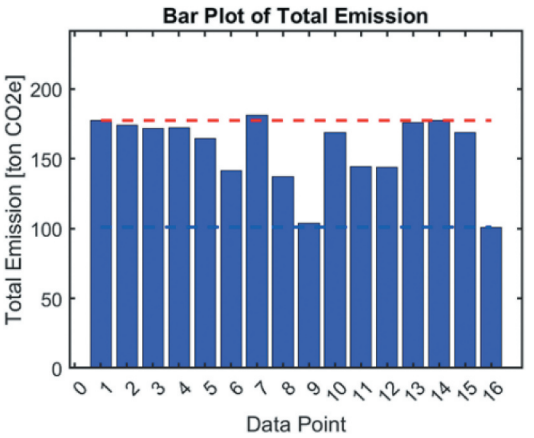


Figure 5. Expected value of life-cycle total emissions (A1-A3 + B4).

It is observed that all scenarios with lower reliability/safety levels have been observed to reduce embedded CO2e emissions when compared to the basic scenario, conversely, the scenario with higher reliability/safety level is associated with an increase in embedded CO_2e emissions compared to the basic scenario. Keeping the basic-case reliability/safety level, it is still possible to reduce emissions by utilizing low emission materials such as LC3 and FUTURECEM or utilizing high strength steel. Scenario 16 can reduce emissions by more than 40%. Additionally, there is a minimal difference in the total cost across the various scenarios.

By calculating the expected value of life-cycle total costs, it is found that there is a minimal difference in the total cost across the various scenarios - within a margin of 5%. The purpose of the calculation here is to estimate the cost difference due to changes in material type, material consumption, and reliability level. Since many materials are not yet available on the market, the results here are based on assumptions.

Table 3 shows the results about expected value of total embedded CO_2e emissions for different cover depths. It is observed that increasing the cover depth by 5mm can reduce the annual embedded CO_2e emissions (yearly emissions) by 20% compared with the basic case. It is important to understand that this does not imply a reduction of total emissions at the initial point.

Table 3. Expected value of CO_2e emission with different cover depth.

Cover depth	Emission (production (A1-A3)) [t CO_2e]	Expected value of emission from major repair (B3) [t CO_2e]	Expected value of total CO_2e emissions (A1-A3 + B3)	Life [yr]	Annual carbon emission [t CO_2e/yr]
40 mm	175.21	2.67	177.88	100	1.78
45 mm	177.36	3.88	181.24	135	1.35
50 mm	179.91	5.96	185.87	175	1.06

4 CONCLUSION

The efficiency of roadway bridge design and strategies for structural integrity management in providing the desired functionality relative to associated effects on impacts to the environment, safety and economy are assessed. This study demonstrates that there are multiple strategies to effectively reduce embedded CO_2e emissions in civil structures. The utilization of lower strength concrete (scenario 6 and 11), incorporation of high strength steel (scenario 5 and 15), and the use of low emission materials (scenario 8, 9, 12, and 16) have all shown promising results. Notably, these strategies have the potential to decrease emissions by more than 40%. Additionally, increasing the concrete cover thickness (the concrete outside the reinforcement), while also initially increasing the embedded CO_2e emissions during the production phase, has the long-term benefit of reducing the frequency of major repairs and extending the lifespan of structures, thereby reducing annual embedded CO_2e emissions. The findings of the present study emphasize the vital necessity for industries to expedite the qualification of new materials for various uses and exposures. It's imperative that this information is shared swiftly and incorporated into new policies, codes, standards, and guidelines.

REFERENCES

Aalborg Portland. (2020). FUTURECEM – ny cementtype med reduceret CO2-udledning.

Antoni, M., Rossen, J., Martirena, F., & Scrivener, K. (2012). Cement substitution by a combination of metakaolin and limestone. *Cement and concrete research*, 42(12), 1579–1589.

DuraCrete. (1999). Probabilistic Performance based Durability Design of Concrete Structures. BRITE EU-RAM Project no. 1347.

Faber, M. H., & Sørensen, J. D. (2003). Reliability-based code calibration: the JCSS approach. In *Applications of Statistics and Probability in Civil Engineering: Proceedings of the 9th international conference on applications of statistics and probability in civil engineering* (pp. 927–935). Millpress.

Faber, M. H. (2020). GLOBE–Global Consensus on Sustainability in the Built Environment—Report. *Structural Engineering International*, *30*(4), 600–601.

ISO 14040:2006 - Environmental management.

Johnsen, T. H., Geiker, M. R., & Faber, M. H. (2003). Quantifying condition indicators for concrete structures. *Concrete international*, *25*(12), 47–54.

Malioka, V. (2009). *Condition indicators for the assessment of local and spatial deterioration of concrete structures* (Vol. 321). vdf Hochschulverlag AG an der ETH Zürich.

Nishijima, K., & Faber, M. H. (2009). Societal performance of infrastructure subject to natural hazards. *Australian journal of structural engineering*, *9*(1), 9–16.

Straub, D., Malioka, V., & Faber, M. H. (2009). A framework for the asset integrity management of large deteriorating concrete structures. *Structure and Infrastructure Engineering*, *5*(3), 199–213.

UNOPS 2021, Infrastructure for climate action, 2021.

Vejdirektoratet. (2021). InfraLCA.

Bridge Maintenance, Safety, Management, Digitalization and Sustainability – Jensen, Frangopol & Schmidt (eds)
© 2024 The Author(s), ISBN 978-1-032-77040-6
Open Access: www.taylorfrancis.com, CC BY-NC-ND 4.0 license

Fatigue design of continuous thermite-welded rail

Y.C. Park & J.Y. Lee
Department of Civil Engineering, Inha University, Incheon, Republic of Korea

ABSTRACT: Since continuous rails are made by welding a certain length of rail, there is a pos- sibility that fatigue cracks may occur due to train passage. Since thermally welded long rails are constructed in the field, there is a higher probability of welding defects compared to other welding methods. Therefore, the fatigue life of continuous rails can be determined by the fatigue life of thermite-welded connection. In this study, the fatigue life of thermite-welded continuous rails presented in existing studies was verified. The fatigue strength of thermite-welded continuous rails was evaluated based on linear elastic fracture mechanics by analyzing the existing experi- mental results. The fatigue life and crack shape at failure were used to obtain the initial crack size for crack growth analysis. The stress intensity factor range threshold utilized to obtain the fatigue limit is determined by the stress ratio. Changes in residual stress due to seasonal temperature changes cause changes in the stress ratio acting on the rail, and therefore changes in the fatigue limit occur depending on the season. Considering these features, a fatigue design method for ther- mite-welded continuous rail is proposed.

1 INTRODUCTION

Fatigue cracks in rails can be caused by welds or by friction between the rail and the wheel. Welds are particularly susceptible to fatigue cracking due to inherent nature of welding, with large re- sidual stresses and micro-discontinuity at the interface of the weld and the rail. Welding methods for rails include flashbutt welding, gas tack welding, thermite welding, and submerged arc weld- ing. Among them, thermite welding is a method of joining rails by installing molds on the rails in the field, which has the advantage of simple welding equipment, no need for power equipment, and short welding time, but it has the disadvantage of quality deviations depending on the skill of the operator, low strength of the welded part as a casting, and a lot of padding in the web and lower part of the rail. In particular, it can be considered the most vulnerable to fatigue cracking because the fatigue strength is lower than other welding methods due to the strength of the casting and the presence of the filler metal.

Several studies have experimentally characterized the fatigue performance of thermite-welded connection. The fatigue strength of thermite welds has been studied experimentally by Ishida (1990) and Park (2016). The experiment conducted by Ishida (1990) was a full-scale rail fatigue test for thermite-welded connection with the purpose of studying the relationship between rail surface irregularities and rail bending fatigue life. The test method was a four-point bending fatigue test, and the results of the test are shown in Figure 1. The test conducted by Park (2016) was a full-scale rail fatigue test for thermite-welded connection for the purpose of studying the rela- tionship between rail surface irregularities and rail bending fatigue life. The test method is a three- point bending fatigue test, and the results of the test are shown in Figure 2.

As shown in Figures 1 and 2, S-N curves for various probability of fracture were presented based on the linear-log scales of the stress range and number of cycles to failure. As per linear elastic fracture mechanics, crack growth rate is linear to the stress intensity factor when both are illustrated in log-log scale. Thus, S-N curves for welded connections recommended in many fa- tigue design guidelines are in the form of log-log scale, so that both Ishida (1990) and Park (2016) are violating the basic rule of linear elastic fracture mechanics.

DOI: 10.1201/9781003483755-367

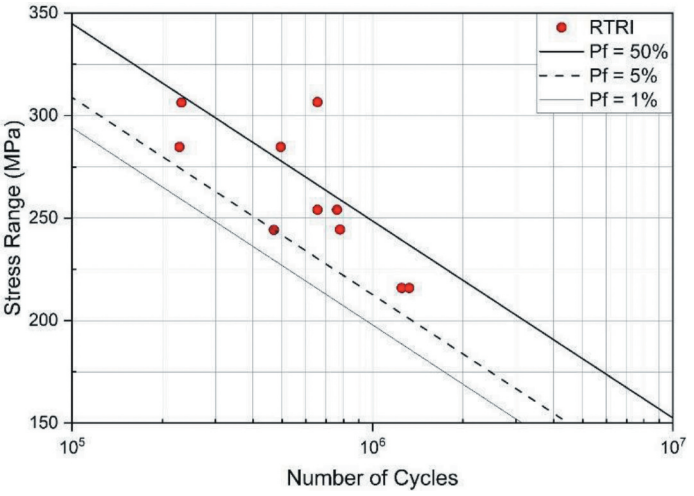


Figure 1. Fatigue test results conducted by Ishida (1990).

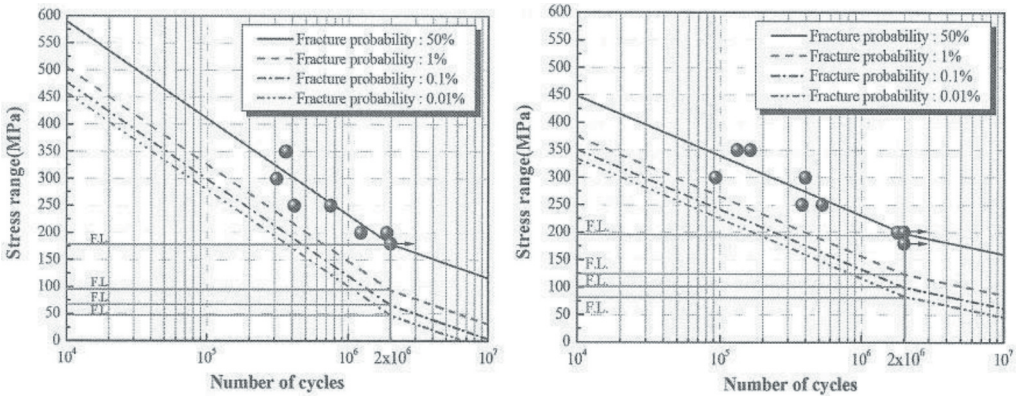


Figure 2. Fatigue test results conducted by Park (2016): (a) 50 kg/m rail; and (b) 60 kg/m rail.

The maintenance guidelines for continuous rail in Korea are divided into rail replacement cy- cles based on rail wear by rail type and cumulative tonnage. The criteria for rail replacement consists of the degree of wear, cumulative tonnage and visual inspection. The rail replacement criteria items that are currently applied are reviewed from a linear elastic fracture mechanics per- spective for a more reasonable rail life assessment.

A method of determining the fatigue life of the thermite-welded rail was developed by simulating different crack growth under repeated loading based on linear elastic fracture mechanics. Fatigue crack growth simulation was performed based on the fracture surface data from previous fatigue tests (Park 2016), and the expected initial crack size was estimated. Based on the fatigue test data, S-N curves for 5 and 50% of the probability of failure on log-log scale.

2 S-N CURVE OF THERMITE-WELDED RAIL

Fatigue test data for thermite-welded rail was collected from various documents and are shown in Figure 3 (Ishida 1990, Park 2016, Sung 2021, Yang 1998). Fatigue life of 51 specimens with the stress ranges from 100 to 450 MPa. No significant difference was observed from the new and used rails and 50 kg and 60 kg rails.

S-N curves for the probability of failure *Pf* of 50% and 5% were estimated, and those were:

$$P_f \ of \ 50\% : \log N = 15.25 - 3.92 \log S_r \quad (1)$$

$$P_f \ of \ 5\% : \log N = 14.88 - 3.92 \log S_r \quad (2)$$

where, N = fatigue life; and Sr = stress range.

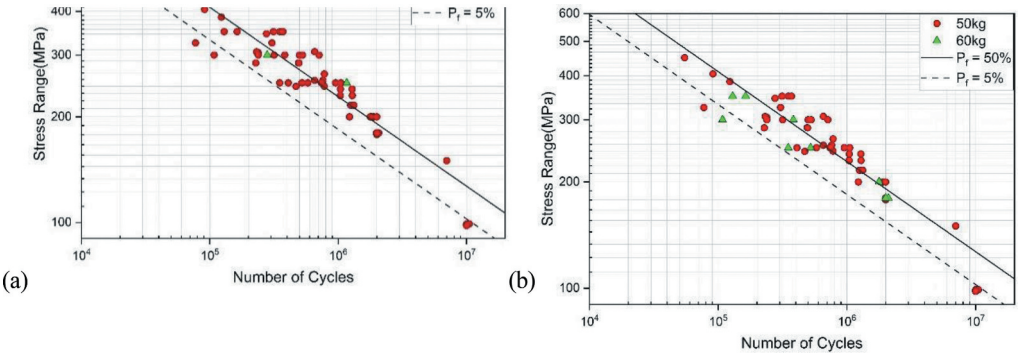


Figure 3. Fatigue test data of thermite-welded rail and S-N curve: (a) comparing used and new rail; (b) comparing 50kg and 60 kg rail.

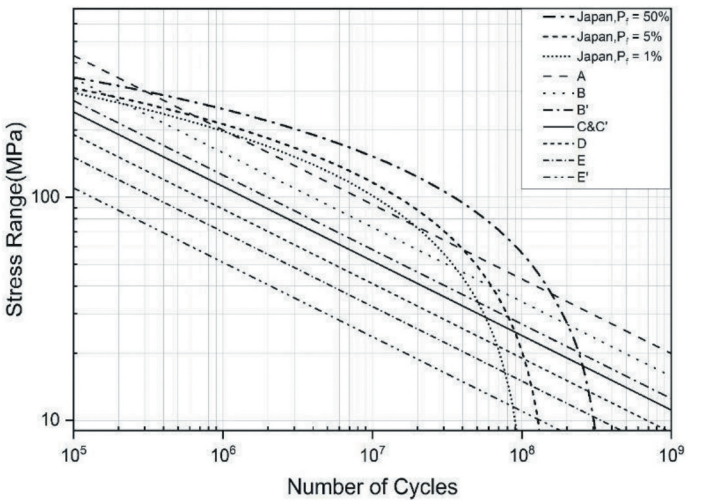


Figure 4. Comparison of S-N curves from AASHTO (2020) and Ishida (1990).

Figure 4 shows the S-N curve by probability of failure from Ishida (1990) and the S-N curve from AASHTO (2020) on a log-log scale. As shown in this figure, for stress ranges where exper- imental or regression data are available, fatigue life is likely to be severely under-estimated for sections in the lower stress range. The plotting of fatigue life against stress range on a linear scale follows a trend from the early days of fatigue research in the 19th century, and even then it was known that the relationship between stress range and fatigue life was not linear, but exponential, so it is a clear error to plot the S-N curve on a linear-log scale as in previous studies. It is consistent with the theory of linear elastic fracture mechanics that the S-N curve of steel has a linear rela- tionship in the stress range higher than the fatigue limit on the logarithmic scale. Since the fatigue tests in the previous studies were conducted at a stress range of 200 MPa or higher than the actual stress range, the fatigue life at stress ranges beyond the data used in the regression analysis is not reliable, but it is judged to be linear in

this range according to the results of fatigue tests of other structural steel joints and the theory of linear elastic fracture mechanics.

Under normal conditions, the stress range developed by the traffic of train is less than 100 MPa. However, all fatigue tests were conducted at the stress range greater than 100 MPa. To construct robust fatigue design curve including the fatigue limit, fatigue test data which includes the stress range at lower stress range level is required. Unfortunately, fatigue test data is not available for lower stress range levels, analytical approach based on linear elastic fracture mechanics (LEFM) was performed to estimate fatigue limit of the thermite-welded rail.

3 ESTIMATE FATIGUE LIFE AND FATIGUE LIMITS FOR THERMITE WELDS BASED ON LEFM

3.1 *Key factors affecting fatigue performance*

It has been known that the fatigue crack growth rate depends on the stress intensity factor range. When the stress intensity factor range is greater than the threshold ΔKth and less than the fracture toughness KIc, fatigue crack growth rate linearly increases as increasing stress intensity factor range in log-log scale (Figure 5). This relationship is called the Paris Law (Paris & Erdogan 1963). The following equation expresses the relationship:

$$\frac{da}{dN} = C \times (\Delta K)^m \text{ or } \log\left(\frac{da}{dN}\right) = \log C + m \times \Delta K \tag{3}$$

where a = crack size; N = number of stress cycles; C and m = material constants; and ΔK = stress intensity factor range.

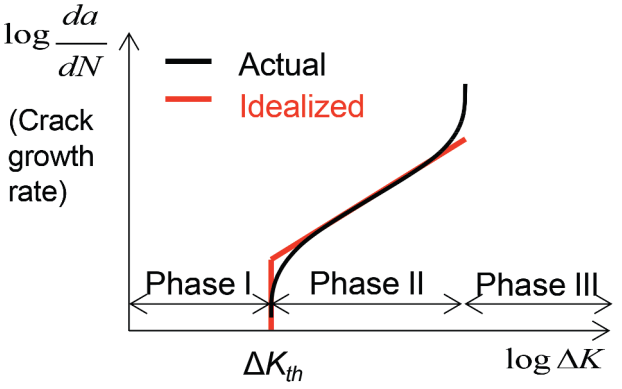


Figure 5. Relationship between crack growth rate and stress intensity factor range.

According to the Paris Law equation, the main factors affecting fatigue life are crack size, material constants and fracture toughness KIc. To determine these factors, test results conducted by Yang (1998) were considered. The material constants C and m and the fracture toughness KIc of the rail are tubulated in Table 1. The factors were measured from the upper and lower parts of rail. The values of the material constants were averaged, and lower value of the fracture toughness KIc was considered to be conservative. It should be noted that the averaged value of m = 3.7, which is the slope of the crack growth rate with respect to the stress intensity factor range, is close to the slope of the S-N curve shown in Figure 3 and Equations 1 and 2.

3.2 *Estimating initial crack size*

Initial crack size in the thermite weld was estimated from the test results conducted by Park (2016). As shown in Figure 6, width and depth of the fatigue crack were 54.0 and 17.6 mm,

Table 1. Material constants C and m and fracture toughness KIc of rail (Yang 1998).

Factors	Upper part	Lower part	Average
C	4.21×10^{-14}	7.10×10^{-17}	7.13×10^{-15}
m	3.2	4.2	3.7
KIc (MPa√mm)	1429	1398	–

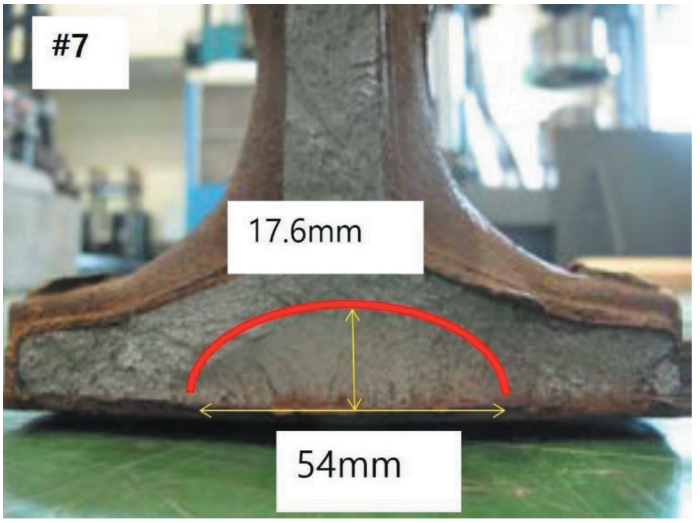


Figure 6. Fracture surface and fatigue crack of thermite-welded connection (Park 2016).

respectively. Applied stress range was 200 MPa with minimum stress of 30 MPa at the bottom fiber of the specimen, the fatigue life was 1.9 million cycles. Stress intensity factor was calculated at the deepest point of the crack and was 1423 MPa√mm. The fracture toughness KIc of 1398 MPa√mm was validated. Newman-Raju solution for elliptical edge crack was applied to calculate the stress intensity factor (Newman & Raju 1984).

Initial crack was assumed to be elliptical edge crack and the size was estimated by conducting crack growth simulation from the final crack to the initial crack using Equation 3. Estimated initial crack depth and width were 0.51 mm and 22.5 mm, respectively. The specimen shown in Figure 6 demonstrated the fatigue life close to the probability of failure of 50%. Thus, initial crack size which could provide probability of failure of 5% presented in Figure 3 was estimated to obtain conservative fatigue limit.

Range of the crack depth was assumed to be 0.7~1.3 mm, and aspect ratio of the initial crack (depth to width ratio) was assumed to be 1/200~1/50. The crack depth and the aspect ratio were divided into 30 levels, and crack growth simulation was conducted using Equation 3. To consider the effect of the stress range, stress ranges of 100, 200 and 300 MPa were considered.

Estimated initial crack sizes for various stress ranges are tabulated in Table 2.

Table 2. Estimated initial crack size for various stress ranges.

Stress range (MPa)	Crack depth (mm)	Crack width (mm)
100	1.21	62
200	1.10	59.3
300	0.98	51.5

3.3 *Estimating fatigue limit*

As shown in Figure 3a, fatigue life of used rails is not different compared to the new rails indicating fatigue cracking has not occurred on the rail in service. Since the train load on the rails is not highly variable, it can be assumed that these rails will not develop fatigue cracks no matter how long they are used. Therefore, knowing the fatigue limit, the stress range below which fatigue cracking will not occur in thermite-welded rail, can have a significant impact on the maintenance of rails in service.

The stress range at which crack growth may not occur when applying the initial crack size to estimate the fatigue limit was identified based on LEFM. According to Barsom & Rolfe (1999), stress intensity factor range threshold ΔKth, which can determine the fatigue limit, is determined by the following equation:

$$\begin{aligned} \Delta K_{th} = {} & 7(1 - 0.85R)MPa\sqrt{mm} && \text{for } R0.1 \\ = {} & 6MPa\sqrt{mm} && \text{for } R<0.1 \end{aligned} \tag{4}$$

where, R = stress ratio. The stress ratio is determined by the maximum and minimum values of the stress range. To determine the maximum and minimum stress, the actual stress acting on the rail should be determined, but it is very difficult to measure actual stress. As an alternative, fatigue limit for varying stress ratio was estimated. The fatigue limit was determined using following equation:

$$Sr = \frac{\Delta K_{th}}{Y(a)\sqrt{\pi \mathrm{a}}} \tag{5}$$

where, $Y(a)$ = correction factor. The fatigue limit obtained by varying the stress ratio from 0.1 to 0.6 for the stress range of 100 MPa are shown in Table 3.

Table 3. Fatigue limit at the stress range of 100 MPa.

Stress ratio	0.1	0.2	0.3	0.4	0.5	0.6
Fatigue limit (MPa)	163	148	133	118	103	87

4 CONCLUSION

To estimate the fatigue life and fatigue limit of thermite-welded rail, this study analyzed the re- sults of previous fatigue test results and estimated the initial crack size. Fatigue limit based on the linear elastic fracture mechanics was estimated considering the initial crack size and fatigue test results. The main conclusions of this study are follows:

(1) S-N curve for the fatigue design or the maintenance of the thermite-welded rail was proposed based on previous fatigue test results. S-N curve of thermite-welded continuous rail for the 5% probability of failure was $\log N = 14.88 - 3.92\log Sr$.
(2) The crack width and depth of the initial crack in the thermite weld, obtained by considering the size of the fatigue crack identified in the fracture surface of a fatigue tested specimen and the fatigue life for a 5% probability of failure, are approximately 0.98~1.21 mm and 51.5~62.0 mm, respectively.
(3) The fatigue limit was estimated by considering various stress ratios, and the fatigue limit was estimated to be approximately 90 MPa for the most conservative case, a stress ratio of 0.6.

The results of this study are based on previous experimental results and a number of assump- tions. In order to better characterize the fatigue properties of thermite-welded connection for ef- fective maintenance, it is necessary to further confirm the following points:

- magnitude of residual stresses around the weld after thermite welding
- range of stresses caused by vehicle traffic on the rails at various locations
- stress changes due to changes in the environment around the rails, such as tempera- ture changes, deflection of the bridge, rail lifting, etc.
- fatigue life when the range of stresses experienced by the rail is formed around the fatigue limit.

ACKNOWLEDGEMENT

This work was supported by Korea Research Institute for defense Technology planning and ad- vancement (KRIT) grant funded by the Korea government(Defense Acquisition Program Admin- istration).(No. 22-102-C001-001)

REFERENCES

AASHTO. 2020. *LRFD bridge design specifications, 9th ed.* Washington DC: American Association of State Highway and Transportation Officials.

Barsom, J.M. & Rolfe, S.T. 1999. *Fracture and fatigue control in structures: Application of fracture mechanics*. West Conshohocken: ASTM.

Ishida, M. 1990. *Relationship between rail surface irregularity and bending fatigue of welded part in long rails*. Tokyo: Railway Technical Research Institute (in Japaness).

Newman, J.C. & Raju, I.S. 1984. *Stress intensity factor equation for cracks in three-dimensional finite bodies subject to tension and bending loads*. Washington DC: National Aeronautics and Space Administration.

Paris, P. & Erdogan, F. 1963. A critical analysis of crack propagation laws. *Transactions of the ASME* December: 528–534.

Park, Y.G. 2016. *Establishment of general rail replacement and maintenance guidelines*. Anyang: Korea Agency for Infrastructure Technology (in Korean).

Sung, D.Y. 2021. *Research for estimating railroad facility maintenance standards such as rail life*. Daejeon: Korea National Railroad Administration (in Korean).

Yang, S.C. 1998. *Investigation on characteristics of welded connections in rail*. Uiwang: Korea Railway Research Institute (in Korean).

SS37: Nordic Operation and maintenance strategies for bridges: Pioneering a sustainable future

Organizers: T. Bangsgaard, D. Honfi & B.T. Svendsen


Taylor & Francis
Taylor & Francis Group
http://taylorandfrancis.com

Bridge Maintenance, Safety, Management, Digitalization and Sustainability – Jensen, Frangopol & Schmidt (eds)
© 2024 The Author(s), ISBN 978-1-032-77040-6
Open Access: www.taylorfrancis.com, CC BY-NC-ND 4.0 license

Risk-based evaluation of fire protection on cable-supported bridges

N.P. Høj
HOJ Consulting, Brunnen, Switzerland

M. Bjelkerud
RED Consulting, Oslo, Norway

H. Matre
Norwegian Public Roads Administration, Oslo, Norway

ABSTRACT: The procedure and practical application of a risk-based evaluation of the fire exposure, fire impact and fire protection of cable supported bridges is presented.

The goal is to adapt fire protection to the actual risk of the individual structure. Whereas it may be sufficient to follow guidelines and common practice for more modest structures, larger cable supported bridges may benefit from a specific study based on the actual structure and exposure.

1 INTRODUCTION

The main steps in a risk-based evaluation include: hazard identification, estimation of probabilities and consequences, aggregation of the risk picture and evaluation of acceptability and risk reducing measures.

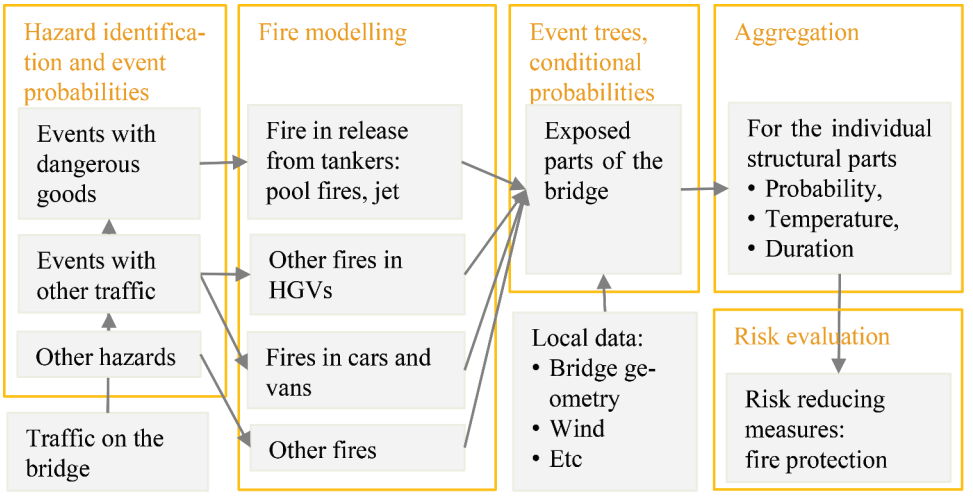


Figure 1. Structure of the risk-based evaluation of fire protection.

DOI: 10.1201/9781003483755-368

2 HAZARD IDENTIFICATION

The first step identifies the main scenarios: fires in dangerous goods transports, in other trucks or vehicles, and fires from other sources. The estimation of the probabilities is dependent on the traffic volume, the traffic composition, and an estimate of the local basic events probabilities. Local conditions which indicate increased or reduced incident probabilities need to be taken into account. The timely development of traffic and incident rate will have to be considered, and either a reference year can be decided or the development over time can be integrated.

Whereas the statistical basis for accidents on road and fires in tunnels is well represented in literature and in public statistics, the event probabilities for various types of fires on bridges need to be based on assumptions and estimates. The data for events with dangerous goods are available for open roads and for tunnels. With the focus on the most severe fires in dangerous goods, these data can be applied for bridges as well. A more comprehensive and generally accepted basis may be established and shared internationally by authorities and scientists.

The main initial events distinguish fires in road vehicles as results of accidents and "spontaneous" fires, igniting without prior accidental events.

Furthermore, the fires are distinguished with respect to fires in light vehicles (cars and vans), heavy goods vehicles (HGV) and transports of hazardous (flammable) goods.

The fires in dangerous goods are modelled as pool fires (flammable liquids spill on the road and ignited) and jet fires (flammable liquids or gasses released from pressure tanks and ignited). Other fires in general flammable solids may be modelled separately for the various substances, alternatively a model can be adapted and made representative for the various solid substances.

Other hazards may include fires in buildings or other infrastructure near the bridge or, for bridge over waterways, fires in vessels under the bridge. Also fires in the technical equipment in the bridge, lightning, and sabotage (and similar) have been identified as hazards. The effect of these types of hazards are not discussed further in this paper.

The probability of these initiating events will need to be established.

Further detailing in the hazards include the circumstances of the fire, i.e., the location of the fire, the wind and other meteorological conditions during the fire, the size of the leak, etc. These circumstances are modelled in terms of event trees and based on initial event probabilities and conditional probabilities for the circumstances, the probability of each scenario of the event tree is determined.

3 FIRE MODELLING

3.1 *Pool fires*

In the present paper the fire modelling is focused on pool fires and jet fires. As the first step in the model for pool fires, the release is modelled. Some of the relevant parameters are: the type of liquid (for example: petrol or diesel fuel), volume and geometry of the tank, diameter/size of the hole in the tank, location (height) of the hole.

$$\dot{m} = A_d \cdot C_d \cdot \rho \cdot \sqrt{2 \cdot g \cdot h_V} \tag{1}$$

where
C_d = release coefficient (= 0.6)
A_d = hole area (m^2)
g = 9.81 m/s^2
h_V = the height of the liquid in the tank
ρ = mass density of the fuel (kg/m^3)
Petrol: ρ = 700–800 kg/m^3
Diesel fuel and similar: ρ = 830–950 kg/m^3

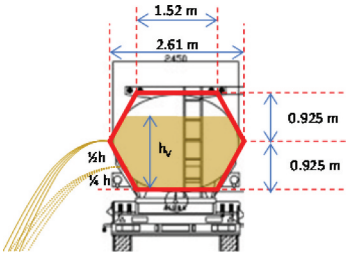


Figure 2. Example of release from a tanker.

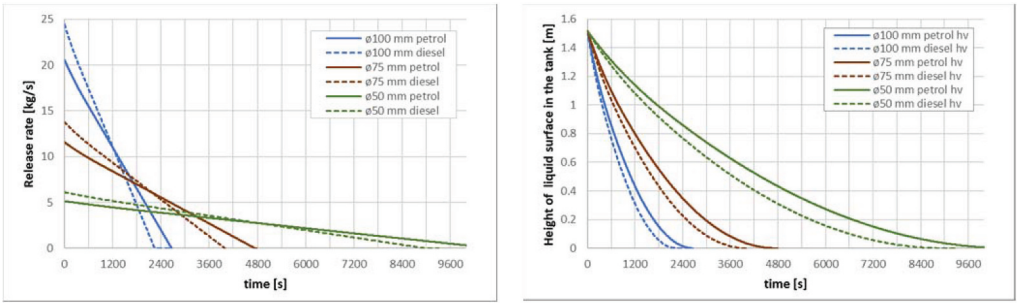


Figure 3. Release rate and height of liquid surface as function of time for a 40 m^3 tank (shown in Figure 2).

Based on the results presented above the average release rate and the duration of the release can be determined for various hole diameters (ø50 mm, ø75 mm and ø100 mm), locations of the hole (¼ h, ½h) and petrol and diesel fuel. The results vary from long durations with low release rate (say, ø50mm, ½h, petrol: duration 2000 s, avg. release 5 kg/s) and vice versa (say, ø100mm,½h, petrol: duration 500 s, avg. release 18 kg/s).

The area of the pool resulting from the release is dependent on the combustion rate and the drainage. The arrangement of the drainage system and the geometry of the bridge deck on the determines the effective mass from through the drain grate.

$$A_1 \approx \frac{l_{w1}}{\sin(\arctan(c/g))} \cdot 2.4 \cdot V^{0.46} \tag{2}$$

where V = the release rate in l/s
c = the cross slope
g = the gradient
l_{w1} = the distance from the release to the kerb
$A_2 \approx \frac{d}{2} \cdot \frac{(V - V_{comb})^{0.5}}{c}$, where
d = the distance between the drain grates

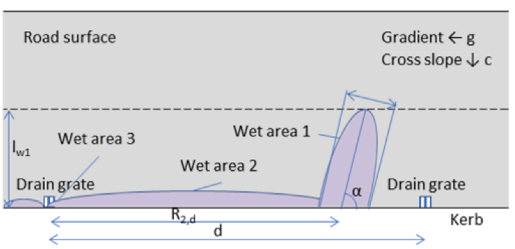


Figure 4. Formation of pools on the bridge deck with drain grate and kerb.

V_{comb} = the combusted volume of fuel for A_1+A_2

With a similar formula (subtracted the drained volume) a third pool will form if the first drain grate has insufficient capacity for V–V_{comb}.

The heat release from the fire is calculated (simplified) as:

$$\dot{Q} = \dot{m}'' \cdot A \cdot \Delta H_c \approx A \cdot 2.64 MW/m^2 \tag{3}$$

where

$\dot{m}''$ = the combustion rate (for petrol 0.055 kg/(m^{2}s))

ΔH_c = the combustion heat (for petrol 48 MJ/kg)

The generalised flame length is based on circular pools. Based on the areas determined from the principles in Figure 4 an equivalent pool diameter, D_{pool}, is determined as function of release rate, distance to the drain grate and the geometry of bridge deck and drainage system. In the actual case equivalent diameters in the range 7 – 16 m^2 were estimated.

Various estimations have been proposed for estimating the flame length as function of the pool diameter. The empiric relation proposed by Heskestad, 1995 expresses the length as function of the heat release and diameter:

$$L_{flame} = 0.235 \cdot \dot{Q}^{2/5} - 1.02 \cdot D_{pool}$$

Without wind the flame is considered to be vertical and cylindrical. The wind velocity, u_w, will influence the direction and reach of the flame.

$$cos\theta = 0.7 \cdot [u^*]^{(-0.49)}, \text{if } 0.7 \cdot [u^*]^{-0.49} \leq 1 \tag{4}$$

$$cos\theta = 1, \text{ if } 0.7 \cdot [u^*]^{-0.49} > 1 \tag{5}$$

Where

$$u^* = u_w / u_c$$

$$u_c = g \cdot m'' \cdot D_{pool} / \rho_{air}$$

u_w = the wind velocity (m/s).

$$\frac{D'}{D_{pool}} = 1.5 \cdot Fr^{0.069}; \text{ where } Fr = \frac{{u_w}^2}{g \cdot D_{pool}} \tag{6}$$

Hereby:

$$x = sin\theta \cdot L_{flame} + D' + 1/2 \cdot D_{pool} \tag{7}$$

$$H = cos\theta \cdot \left(L_{flame} - \left(D' - D_{pool}\right)\right) \tag{8}$$

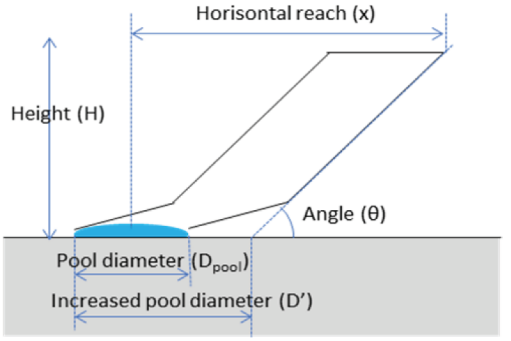


Figure 5. Determination of horizontal and vertical reach of flames.

With these calculations the vertical and horizontal reach of the flames and the fire durations have been determined as function of location on the bridge deck, hole size and location, liquid type and volume, drainage, and wind speed. The exposure of the various structural components of the bridge is investigated in event trees.

3.2 *Jet fires*

Jet fires occur when flammable liquids or gasses are released from pressure tanks and ignited. The pressure in the tank (and hereby the release rate) depends on the surface of the fluid in the tank in relation to the hole. When the surface of the liquid has come under the hole, the release required evaporation, and the pressure and release is reduced (RWS, 2005).

$$L_f = 18.5 \cdot m^{0,41} \ [m] \tag{9}$$

$$D_f = 0.1 \cdot L_f \ [m] \tag{10}$$

$$m_{liq} = \varphi \cdot m_{Bernoulli} = \varphi \cdot A_d \cdot \ C_d \cdot \sqrt{2 \cdot dP \cdot \rho}$$

$$m_{gas} = \ A_d \cdot \ C_d \cdot \psi \cdot \sqrt{(2 \cdot p^2 \cdot M_W)/(R \cdot T)}$$

where
dP is the pressure difference tank– atmosphere
ρ is the mass density of the gas
A_d is the hole area
C_d is the release factor = 0.62
φ is empirically 0.75
ψ is empirically 0.48

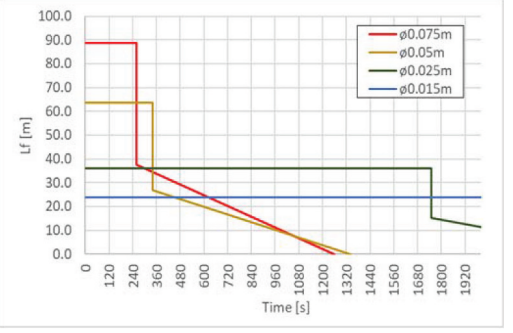


Figure 6. Example of determination of flame length from a jet fire in propane (40 m^3 tank, hole at ½h).

The flame from a jet fire is a concentrated beam, the direction of the release is determined by the location of the hole, the wind may bend the direction and the length of the flames are assumed to grow with 33% in tailwind and reduce 15% in headwind.

With these calculations the reach of the jet flames and the fire durations have been determined as function of location on the bridge deck, hole size and location, liquid type and volume, drainage, and wind speed. The exposure of the various structural components of the bridge is investigated in event trees.

4 EVENT TREES

The event trees are detailed with the exposure of structural components, depending on the randomised fire location, the flame size, direction and temperature, the bridge geometry, and the local meteorological conditions. The structural components of a suspension bridge are considered: the main cable, one or more hangers, the pylon and the bridge deck.

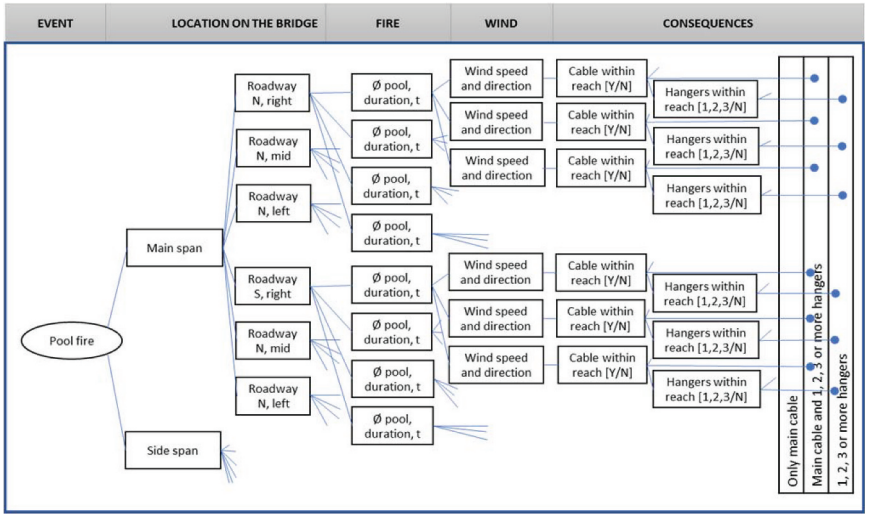


Figure 7. Part of (a simplified) event tree for exposure of main cable and hangers to flames from a pool fire.

Event trees are methodologically quite simple, however, with many variables, event tree grow rather large and difficult to oversee. In Figure 7 a simplified part of the event tree for pool fires is illustrated. In the event tree the location of the fire between the Northern roadway and the Sothern roadway are distinguished because the bridge in the present example is not symmetrical. Side span and main span is distinguished because hangers are only placed on the main span. For jet fires similar event trees are established. Furthermore, event trees for the exposure of the pylon (and the girder) are established from the same basic principles.

As part of the event tree evaluation all the conditional probabilities will have to be established, for example the probability of various locations on the fire, probability of various fire events, probability of wind speed and – direction (wind rose) etc.

In addition to this the main consideration is to which degree the various structural elements are exposed to the flames. This exercise requires the geometrical calculation of the reach of the fires from the specific location and the distance to cable, hangers, pylons etc.

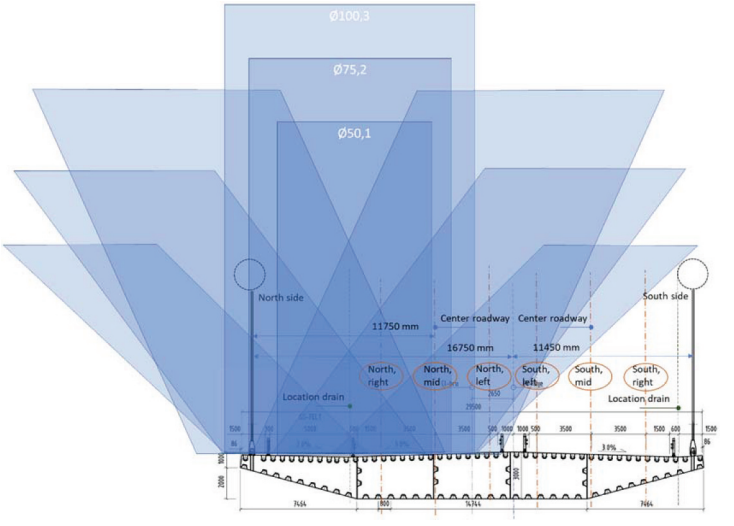


Figure 8. Principal illustration of the flames from severe pool fires at one location and with wind speeds of -4 m/s, 0 and 4 m/s transversal on the bridge deck.

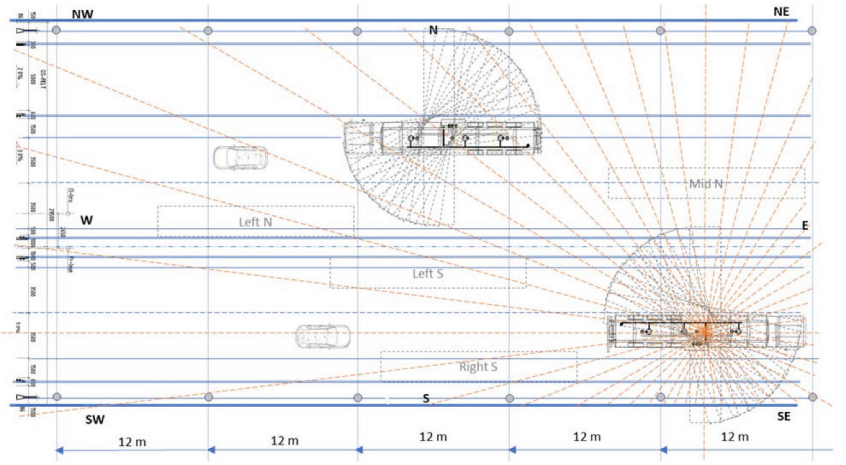


Figure 9. Principal illustration of the flames from jet fires at one location and the horizontal distances to hangers.

5 AGGREGATION

For each of the structural components (cables, hangers, girder, pylons), the exposure is determined as probability, duration, and temperature.

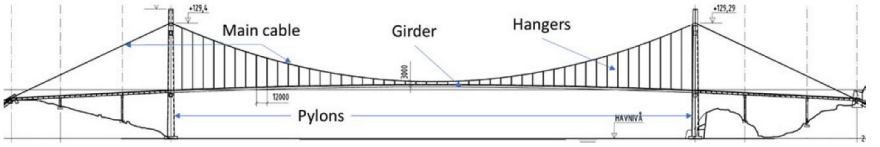


Figure 10. Main components of the suspension bridge.

5.1 *Main cables, hangers and pylons exposed to pool fires*

Based on a large number of scenarios combining hole size, location of the bridge cross section, wind speed, wind direction etc. and the associated conditional probabilities, it can be determined that approximately 30% of all pool fires on the bridge have a flame length and direction which will engulf the main cable. With the event probability of a pool fire, the annual exposure probability of any of the two cables is estimated to 3 E-06 in the present case. The asymmetric design makes one side slightly more exposed than the other. This exposure probability is determined for the reference year, and it will be dependent on the timely development of the traffic and the event rates.

The hole size determining the release is correlated with the duration of the fire. Hence, a relation between exposure probability and duration can be established as shown in Figure 11.

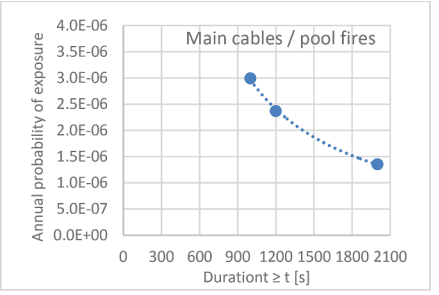


Figure 11. Annual probability of exposure and duration of pool fires engulfing the main cable.

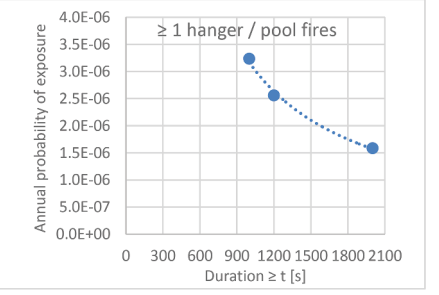


Figure 12. Annual probability of exposure and duration of pool fires engulfing at least one hanger.

In similar aggregations of scenarios as for the main cable, it can be determined that approximately 40% of all pool fires on the bridge have a flame length and direction which will engulf the at least one hanger. The design of the bridge without hangers in the side span has of course a major influence on this figure. With the event probability of a pool fire, the annual exposure probability of any of the two cables is estimated to 3.3 E-06 in the present case.

The hole size determining the release is correlated with the duration of the fire. Hence, a relation between exposure probability and duration can be established as shown in Figure 12.

The exposures shown in Figure 11 and Figure 12 are very similar, however, the criticality of the exposure differs significantly. On one side the exposure of a hanger to a high flame temperature will relatively quickly heat up the entire hanger and change the strength and stiffness of the hanger, whereas the main cable may only be heated on the surface and remain a significant part of its strength and stiffness after a fire. The exposure of the main cable may lead to repair but not to replacement, whereas the hanger more likely will have to be replaced after the exposure.

On the other side the bridge is designed so that one or more hangers can be replaced. A failure of a hanger is hereby not a failure which endangers the structural stability of the bridge. In the present case, the bridge design has taken into account that up to three hangers are lost without impairing the integrity of the bridge.

For this reason, it is important to calculate the probabilities of ≥2, ≥3, ≥4, etc cables exposed to the pool fire. In the present case it was determined that the probability decreased with approximately a factor 10, when one more hanger was considered. The annual probability of more than 3 hangers exposed to a pool fire is therefore approximately 100 times less than shown in Figure 12.

Similar calculations can be made for the exposure of the pylons to pool fires, but as the probability of a fire located on the bridge within reach of the flames from a pool fire, is about a factor 10 lower for the pylon as it is for the main cable.

5.2 *Main cables and hangers exposed to jet fires*

In spite of the much longer reach of flames from jet fires, the probability of reaching the main cable is significantly lower than for the pool fires because the width of the flames is narrow, and the direction is most likely horizontal. Horizontal jet flames will in most part of the bridge not reach the main cable. On the other hand, the hangers are more exposed on a larger part of the bridge.

With aggregations of event probability and conditional probabilities, the relation between annual exposure and duration can be established as shown in Figure 13 and Figure 14.

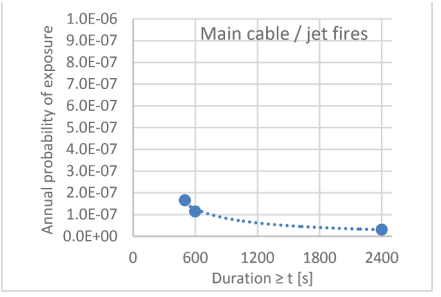


Figure 13. Annual probability of exposure and duration of jet fires engulfing the main cable.

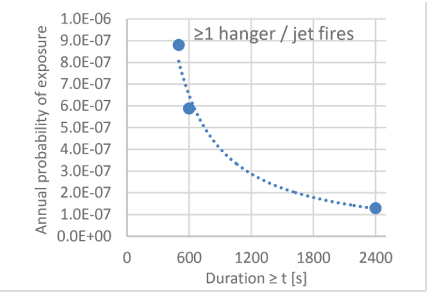


Figure 14. Annual probability of exposure and duration of jet fires engulfing at least one hanger.

The probabilities of ≥2, ≥3, ≥4, etc cables being exposed to the jet fire decreases with approximately a factor 2 when one more hanger is considered. The longer reach of the flames results in a relatively higher share of cases where several hangers are affected. On the other hand, the annual probabilities are very low.

The lower part of the pylon may also be exposed to flames from jet fires, and even the bridge deck may in some circumstances be exposed to jet flames. The probabilities for these exposures are in the order of magnitude as for the main cable.

5.3 *Other vehicle fires*

Other vehicles fires may be modelled in a similar way. Fires in cars and light vans are much more likely, but the exposure of the structural components will be limited. Fires in HGVs may potentially result in severe fires. As part of the studies of the present bridge these fires were preliminarily equivalated with adapted small pool fires. Based on these studies it was found that the main cable at midspan and near the anchor blocks can be reached by 6 m high flames, which may occur with an annual probability of over 1 E-04. The probability of fires in HGVs reaching more than two hangers is much lower.

5.4 *Discussion*

Most fires have little impact on the structural behaviour and the main consequence will be repair and reinstatement. In some cases, the structural integrity may be compromised. The probability of these events is very low, but, on the other hand, the consequences can be extraordinarily high.

The vulnerability of the bridge is dependent on the degree of redundancy and robustness in the structural system. The reserves in the components' capacities and the material fire behaviour are important as well.

6 RISK EVALUATION AND FIRE PROTECTION

The last step in the analysis is the risk-based evaluation of the effect measures and the costs of these in order to arrive at a cost optimal decision.

According to the national bridge guideline, accidental loads with annual probabilities over 1E-04 cannot be disregarded. In the present example, fire loads for HGV fires should be further considered and/or designed for. The design may evaluate whether the heating from the flame temperature of e.g. the main cable is exceeding a level, where fire protection is necessary for the exposed areas, or whether the integrity is not affected, and reasonable repairs can be performed after a severe fire.

For the pool fires and jet fires the possible consequences of the heating may be more severe, but the annual probabilities found in the study were all under 1E-04. It should be noted that the guideline does not state that accidental loads with annual probabilities under 1E-04 must be disregarded. In some cases, the consequence of failure can be so severe in terms of material loss (possible bridge collapse), loss of lives, traffic disturbance etc., that also events with small probabilities are worth to consider in a risk-based approach. In these considerations, the expected consequences (i.e., the expectation value in terms of probability times consequences) is transformed into monetary values and compared with the expected costs of various risk reducing measures. If the benefit of reducing the consequences exceeds the costs, then the risk reducing measure should be implemented. The lower the probabilities of the events are, the more difficult it will be to identify relevant cost-efficient measures.

Based on the results of the studies, it was identified that expensive safety measures may most likely not be cost efficient. The study was performed before the final design, and the possible safety measures were merely identified and discussed roughly based on the likely efficiency. Cost efficient safety measures may involve fire protection of the most exposed parts (fire insulation, fire paint or similar) or shielding against the flames.

7 CONCLUSION

A method for risk-based evaluation of fire and fire design of large cable-supported bridges. The method includes, modelling of the bridge, the specific geometry of the bridge, the traffic on the bridge, the local event rates. Furthermore, it includes hazard identification and modelling of the events in terms of event trees with associated conditional probabilities. The aggregation of the results leads to establishment of probabilities and duration of fires. The exposure is determined as the time, when the structural components are impacted by the flame temperature. Finally, these results are used to determine whether the design can be adapted and/or further cost-efficient safety measures need to be implemented.

For the actual case, the required safety measures could be limited to selected, most exposed areas, for which safety measures with relative low costs could be applied.

REFERENCES

NPRA, 2021: Brann- og eksplosjonspåvirkning på Sotra Bru, Norwegian Public Roads Administration, NPRA 2021, Exempted public availability Off.l. §23.1. §24.3.1

Heskestad, G., 1995: Fire Plumes. In SFPE Handbook of Fire Protection Engineering; National Fire Protection Association: Quincy, MA, USA, 1995; Section 2, Chapter 2–2 C

RWS, 2005: Methods for the calculation of physical effects Due to releases of hazardous materials (liquids and gases) «Yellow Book», Publicatiereeks Gevaarlijke Stoffen 2, Ministerie van Verkeer en Waterstaat, 3rd edition, 2nd revised print 2005.

Bridge Maintenance, Safety, Management, Digitalization and Sustainability – Jensen, Frangopol & Schmidt (eds)
© 2024 The Author(s), ISBN 978-1-032-77040-6
Open Access: www.taylorfrancis.com, CC BY-NC-ND 4.0 license

Maintenance strategies by the Swedish Transport Administration

F. Olsson
Swedish Transport Administration, Gothenburg, Sweden

ABSTRACT: The Swedish Transport Administration, Trafikverket, manages approximately 17,000 road bridges and 4,000 railway bridges. The Bridge and Tunnel Management System (BMS) provides support throughout the process from construction to assessment and prioritization of measures. The BMS is also used by a majority of Swedish municipalities. Beside the BMS there are guidelines that support the Bridge officers through the different stages such as inspection, planning, prioritization and finally performance of maintenance measures.

1 ASSET MANAGEMENT

This article will describe how the Swedish Transport Administration works with maintenance of structures during the whole life-cycle.

The Bridge Management System (BMS) that the Swedish Transport Administration uses supports management of not only bridges, it also gives support for managing other important structures such as retaining walls, troughs, ferry quays, tunnels and rock walls. Most of the Swedish counties and other big infrastructure owners also use this BMS.

Within the Swedish Transport Administration there is a formalized handover of new structures such as bridges from the building project to the asset steward. Correct as-built information in right time gives good opportunities for a cost-effective asset management.

The first main-inspection of a bridge is made short before it is open for traffic. After that all bridges are inspected close at hand at least every six years. If needed the interval of inspection is shorter. For some critical components and types of bridges there can be extra inspections in between the main inspections.

The inspections are carried out according to a special methodology and the bridge inspector assesses both the physical and functional state of the bridge.

All bridges that are in need of any condition-based maintenance measures within the next 6 years must have an individual strategy. For bridges that are in need of complete reconstruction the corresponding time is 12 years. Specified major bridges such as suspension bridges and cable stay bridges must have an individual strategy that covers at least next 20 years.

For road bridges the predetermined maintenance such as keeping the bridges free from dirt and vegetation is procured in integrated bridge maintenance contracts, contract time 3-5 years and 600-1,000 bridges/ contract. The contracts also include a contractor organization that can perform corrective maintenance.

2 INFORMATION OF THE ASSETS

2.1 *Type of assets stored in the Swedish Bridge Management System (BMS)*

The bridge and tunnel management system supports users in the management of bridges, tunnels and other structures. Bridge owners, consultants, planners etc. receive support and information about structures through the system.

The BMS contains a searchable database containing the structures that are registered. In the database, users can register new data and update information. One of the great benefits of

DOI: 10.1201/9781003483755-369

managing structures in the BMS is the ability to carry through effective measures for each individual structure. The BMS provides control over the condition of bridges, tunnels and other structures and information on what needs to be done to maintain or improve their standard.

The Swedish Transport Administration, municipalities in Sweden, Stockholm Public Transport, the Port of Gothenburg and others use the BMS for the management of their structures, and it is the Swedish Transport Administration that manages the system. The system is industry-wide and is used by many different actors such as consultants, contractors and administrators.

Outside the Swedish Transport Administration there are more than 20,000 structures, owned by the municipalities and some other major infrastructure owners in the BMS. Most of those structures are bridges.

Table 1. Structures owned by Swedish Transport Administration. Registered in the BMS.

	Number of structures	
Structure	Road	Railway
Bridges	16,860	4,535
Tunnels	319	520
Rock slopes	27,995	5,294
Culverts (≤ 2.0m)	-*	20,608
Retaining walls	460	103
Troughs	62	51
Ferry quays	123	-
Noise barriers	-*	624
Other structures	224	78
Total	46,043	31,813

*For the road-system noise barriers and culverts with largest span ≤ 2.0 m are not managed in the BMS.

During the 60s and early 70s there were many big infrastructure projects and many major bridges were built during this period, eg the bridge from mainland Sweden to Oland, the Alvsborgs bridge in Gothenburg and the bridges on the Essinge route in Stockholm. This means that a large part of the Swedish bridge area now has reached the age of 50-60 years and these bridges need fundings for bridge maintenance.

During the 90s there were also many new bridges built, It can be explained by recession were the state wanted to stimulate the construction industry by building new highways.

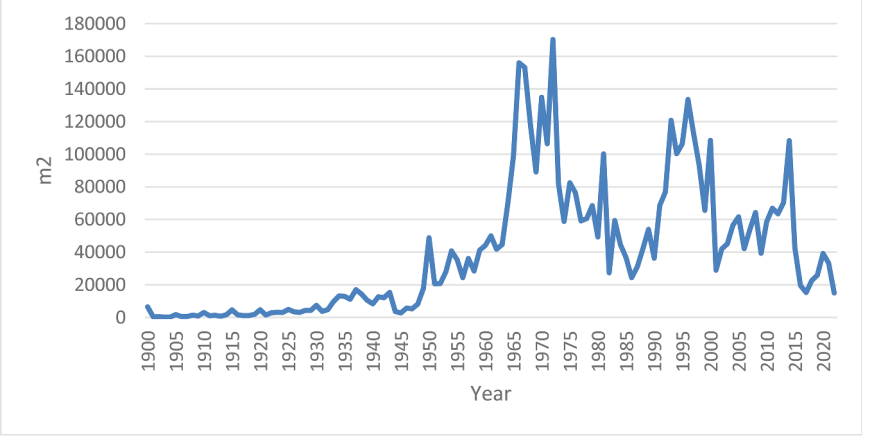


Figure 1. Bridge surface built each year, and still in traffic. (Bridges in the road-system).

2.2 *New and updated information about the assets*

Within the Swedish Transport Administration there is a formalized handover of new asset-information from building projects to asset-managers at the maintenance and operational departments. A plan for handover is established before any contracting-works have started. There are designated persons who have the role as handover-coordinators representing the building department and receiving-coordinator representing the maintenance and operational departments. These two roles support the building projects to deliver correct information in correct time in each of the management-systems that the Swedish Transport Administration uses.

When the contract-works are finished, approved and all information is handed over there is a formal receiving. This also means that the maintenance department takes the responsibility for conducting warranty inspections and having contact with the contractor if there are any problems that occur during the time of warranty.

3 INFORMATION ABOUT CONDITION

3.1 *Inspection*

The first inspection of a new bridge, tunnel or other structure is made before it's taken in traffic, second inspection before end of warranty (5 years). After that all bridges are inspected at least every six years, shorter intervals may be considered if the condition of the bridge is poor. Bridge inspections is a service contracted by the Swedish Transport Administration to external consultants with specialized expertise in the field. The inspections are conducted according to a specific methodology, and both the physical and functional condition of the bridge are assessed. The methodology is described in the BMS. The inspections are registered directly in the BMS as structured data. There for there are rarely any inspections-reports being written. The Swedish Transport Administration (2021), TRVINFRA-00213 Standard for inspection of bridges and other structures.

The functional condition is evaluated based on several parameters: the functional properties of the structural part, the functional requirements set during the design, the current and previously measured values, and the expected future deterioration of the damaged structural part.

The identified deficiencies are classified based on whether they affect the bridge's load-bearing capacity, traffic safety, durability, or other factors. The condition is described using the condition classes 0, 1, 2, or 3:

3: Deficient function at the time of inspection 2: Deficient function within 3 years 1: Deficient function within 10 years 0: Deficient function beyond 10 years

Bridges with damages in condition class 3 regarding traffic safety or load-bearing structural elements should be investigated within three months. Inspections form the basis for planning maintenance measures such as painting, replacement of parapets, railings, and waterproofing, as well as reinvestment.

3.2 *Special inspections*

Special inspections and damage investigations are carried out when required to follow up or study in detail individual structural parts/elements or damages.

For specific bridges/ bridge-elements the guidelines require that special inspection must be carried out in between the main-inspections.

For prestressed concrete bridges built before 1980, the main inspections shall be supplemented by special inspections of prestressed structural parts. This special inspection shall be carried out every three years.

For road bridges with modular expansion joints older than 20 years the main inspections shall be supplemented by special inspections of the joints. This special inspection shall be carried out every three years for road bridges with a traffic of > 10 000 vehicles per day.

4 PLANNING AND PRIORITIZATION

4.1 *Planning*

In the BMS there is a specific module that supports the bridge manager in planning of measures on structures. The planning is registered in the BMS. Planning aims to describe the overall action needs for a structure to ensure expected functionality at the lowest life cycle cost. In object planning, various action strategies are analyzed to find the strategy that provides lowest societal cost to maintain existing or restore the original functional standard. Based on external needs, object planning may also involve improving the functional standard. Object planning and the selected action strategy form the basis for short-term planning and the specification of requirements for the design and procurement of measures.

Within planning and prioritization there are guidelines and regulations published by the Swedish Transport Administration. Swedish Transport Administration (2021), TRVINFRA-00214 Standard for object-planning of bridges and other structures.

A main strategy (S1) is to be established for a structure with need for measures within each planning period. The S1 strategy should include all actions during the remaining lifetime of the structure, up to a maximum of 60 years, and conclude with a reconstruction (reinvestment) if such measure is expected within a 60-years period. The first action in S1 should have a validity period during which the S1 is intended to be carried out. No conflict with applicable delivery standard is allowed for the S1.

A structure with S1 strategy should also have an associated S2 strategy. S2 should describe the consequences if actions according to the S1 are not carried out within the validity period and is used to calculate the profitability of the S1. S2 may come into effect no earlier than the year after the expiration of the validity of the S1. S2 should further more have a validity period of 1 year. The profitability factor for the measure is calculated as follows: Profitability factor = (S2 total - S1 total)/S1 production

Table 2. Planning period is decided as below.

Category	Planning period
Structures with need of a condition based maintenance measure	6 years
Structures with a need of reconstruction (reinvestment)	12 years
Structures with planned improvement or risk reduction	12 years
Structures within category Major bridges*	20 years

*Suspension bridges, cable stay bridges and a handful of other major bridges.

4.2 *Prioritization*

When each structure with need of measures within the planning period has a main strategy (S1) and an associated S2, there has to be a comparison between different bridges and measures. When the overall need for funds is greater than the allocated funds, this has to be done. The BMS planning-module supports this by calculating which measures that are most cost-effective in

Table 3. Prioritization of measures on structures in the road system.

Priority	
1	Inspections and predetermined maintenance
2	Corrective maintenance on bridges with deficient functional condition
3	Maintenance measures on major bridges, moveable bridges and tunnels
4	Condition based maintenance on other bridges and structures. To support this allocation, the BMS planning-module is used. Since the socio-economic costs of different strategies are evaluated, high traffic roads are valuated higher than low traffic roads
5	Rock-slopes

a life-cycle cost perspective, the higher profitability-factor the better. All planned structures are presented in a list with measures and which year, within the validity period, they should be carried out. This list works as input for new projects in the maintenance plan. There also has to be taken into account other costs such as inspection and predetermined maintenance as well as other known local conditions and dependencies that exist.

5 MAINTENANCE MEASURES

Finally, after the prioritization there is a list of objects that shall be carried out the next four years within the budget that is given. By the end of each year there is a formal handover from the planning departments the executing departments. The executing departments are of course involved during the planning.

Bigger repairs are often contracted individually and smaller repairs can be contracted in groups (2-5 objects) so that the contract value at least reaches 5 MSEK. Bridge repairs are mostly procured as execution contracts.

The pre-scheduled maintenance is procured as Integrated bridge maintenance, which is a turn-key contract. There are 23 Integrated bridge maintenance contracts and they are geographically spread over the country. The predetermined maintenance consists of clearing of vegetation and cleaning (removal of de-icing salt, dirt etc). These contracts also include immediate corrective maintenance such as traffic damages and other unforeseen incidents, for instance due to extreme weather. They can also include same common repairs such as repair or replacement of edge beams and parapets, expansion joints or water proofing layers.

Almost 30% of the total budget for road-bridges goes to reinvestments, from small culverts and steel-pipe bridges to larger bridges.

6 MAINTENANCE MEASURES

Finally, after the prioritization there is a list of objects that shall be carried out the next four years within the budget that is given. By the end of each year there is a formal handover from the planning departments the executing departments. The executing departments are of course involved during the planning.

Bigger repairs are often contracted individually and smaller repairs can be contracted in groups (2-5 objects) so that the contract value at least reaches 5 MSEK. Bridge repairs are mostly procured as execution contracts.

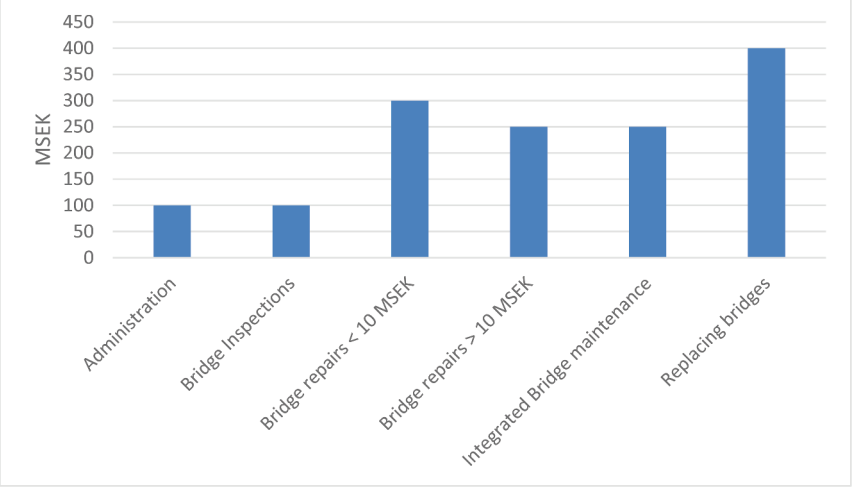


Figure 2. Costs of bridge maintenance in the road system, approximately 1,400 MSEK/ year.

The pre-scheduled maintenance is procured as Integrated bridge maintenance, which is a turn-key contract. There are 23 Integrated bridge maintenance contracts and they are geographically spread over the country. The predetermined maintenance consists of clearing of vegetation and cleaning (removal of de-icing salt, dirt etc). These contracts also include immediate corrective maintenance such as traffic damages and other unforeseen incidents, for instance due to extreme weather. They can also include same common repairs such as repair or replacement of edge beams and parapets, expansion joints or water proofing layers.

Almost 30% of the total budget for road-bridges goes to reinvestments, from small culverts and steel-pipe bridges to larger bridges.

7 CONCLUSIONS

A successful management of structures requires a successful management of working procedures. For a big organization such as the Swedish Transport Administration there must be guidelines that support the bridge officers so that decisions of maintenance measures are based on the condition and lowest life cycle costing. The Bridge Management System, BMS, is one tool that helps us to accomplish an effective asset management.

The procedures from inspections, to planning and prioritization must be easy to follow and well known in the organization. Keep it simple.

It's finally important that planned measures are carried out cost-effectively, that our tender specifications are transparent with a balanced risk distribution. The Swedish Transport Administration aims to be the supplier's first choice. We believe that is cost-effective for the Swedish Transport Administration and profitable for the suppliers.

REFERENCES

The Swedish Transport Administration (2021), TRVINFRA-00213 Standard for inspection of bridges and other structures

The Swedish Transport Administration (2021), TRVINFRA-00214 Standard for object-planning of bridges and other structures

Bridge Maintenance, Safety, Management, Digitalization and Sustainability – Jensen, Frangopol & Schmidt (eds)
© 2024 The Author(s), ISBN 978-1-032-77040-6
Open Access: www.taylorfrancis.com, CC BY-NC-ND 4.0 license

Evaluation of post-tensioned bridges by state-of-the-art techniques

G. Rapaport
Ramboll Finland Oy, Kuopio, Finland

ABSTRACT: Based on the author's long experience, implementing suitable state-of-the-art non-destructive testing techniques in condition evaluation of post-tensioned bridges' invisible prestressing system is an essential approach for ensuring post-tensioned bridges' safe usage, long time durability and appropriate level of asset management. It also assists in determining the remaining service life of those bridges. There are thousands of aging post-tensioned bridges getting close the end of their service life. Due to reasons like environmental stresses, construction and maintenance faults the safe usage of bridges may be uncertain or even dangerous. In extreme cases this may lead even to sudden collapses of bridges.

Applying NDT techniques in post-tensioned bridges enables evaluation of the prestressing system grout injection, which is critical for the system durability and functionality. The introduced NDT techniques, ultrasound tomography and Impact-Echo, used together with slightly invasive investigations assist in this important evaluation.

1 INTRODUCTION

There is great amount of aging post-tensioned bridges, in many cases on critical transportation routes, built mostly in the 1960s-1970s. The condition of the bridges' prestressing system is usually unknown. Hidden faults and damages due to various reasons may threaten the safe usage of bridges. In some cases, the results might be catastrophic, causing a bridge collapse, as witnessed in 2018 when the Morandi Bridge in Genoa Italy suddenly collapsed.

Many post-tensioned bridges have reached renovation time or are getting close to the end of their designed service life. Their condition should be assessed and their safe usage should be verified. A serious challenge is that "traditional" inspection techniques do not provide any indications on the internal prestressing system even though it has a crucial role in the bridge load carrying capacity. It should be noted that at least part of the older post-tensioned bridges were planned as "fully prestressed structures" with only a small amount of regular reinforcement. Therefore a fault in the prestressing system is serious and possibly dangerous.

With correct implementation of suitable NDT techniques (ultrasound tomography and impact-echo) it is possible to evaluate tendon duct grout injection of post-tensioned structures. The injection grout (cementitious based) has a crucial role in protecting the prestressing steel against corrosion, which may cause dangerous damage mechanisms. The injection grout has also important structural role as will be explained. When considering these aspects it is obvious that successful grout injection is critical significance in ensuring the bridge safe and correct functionality.

NDT techniques also assist in pinpointing logical locations for applying invasive measures, i.e. opening of tendon ducts. The main purpose of the invasive measures is to confirm the NDT evaluation and to evaluate the condition of the prestressing system components.

Obviously, NDT techniques may also be applied to grout injection evaluation during construction of new post-tensioned bridges as a quality assurance measure. This ensures from the

DOI: 10.1201/9781003483755-370

beginning of the bridge service life its correct functionality and reveals possible problematic durability issues concerning the bridge prestressing.

The introduced NDT methods, used together with slightly invasive investigations, have already been successfully applied by the author in over 150 inspections of post-tensioned bridges in the past 15 years.

2 DURABILITY PROBLEMS OF POST-TENSIONED BRIDGES

A crucial factor affecting mostly the long-term durability of post-tensioned bridge prestressing steel is the success of the grout injection into the tendon ducts. The injected grout has two main roles:

- Providing permanent protection to the prestressing steel (high strength steel) against corrosion and preventing ingress of water, chlorides, air and humidity into the duct. Corrosion may cause at some point fractures of the prestressing steel due to Hydrogen Embrittlement and Stress Corrosion Cracking.
- Intermediating the prestressing forces from the prestressing steel to the concrete structure. Deficient intermediation of the prestressing forces to the concrete structure might result in reduced load carrying capacity of the bridge.

To provide sufficient protection to the prestressing steel the grout should be of adequate quality and thickness. This also demands correlation between the diameter of the duct and the amount of prestressing steel installed inside it. Obviously, proper injection work procedure and use of adequate injection grout mass is critical for the success of the injection.

The most acute durability problems are usually found at the prestressing system anchoring zones (moist and chloride stresses from leaking expansion joints and casting defects) and in the ducts' extreme low (water accumulation risk) and high points (leaking joints or waterproofing).

The risk caused by corrosion of prestressing steel, especially if chlorides are present (→ causing pitting corrosion), is severe because the steel is usually concentrated only in few tendons which provide most of the load carrying capacity of the bridge. If few tendons fail it can trigger a catastrophic sequence.

3 "TRADITIONAL" INSPECTION TECHNIQUES CONCERNING POST-TENSIONED BRIDGES

Traditional inspection techniques which are regularly applied in reinforced bridge inspections do not provide sufficient information concerning the condition of the internal prestressing system, which is the key factor of post-tensioned concrete bridges. Corrosion detection techniques such as the half-cell potential measurement and the electrical resistivity measurement are suitable for evaluating the corrosion process of regular reinforcement, not of prestressing steel (physical contact with the steel is also needed).

Opening ducts for ocular estimation of the prestressing system is risky and difficult as the exact location and depth of the duct is uncertain. Use of suitable Ground Penetrating Radar can assist to some extent in locating the actual positions of ducts, but it cannot reveal the success of ducts grout injection. Applying suitable NDT techniques is proven to be beneficial in these cases, as will be discussed here.

4 NDT TECHNIQUES SUITABLE FOR GROUT INJECTION EVALUATION OF DUCTS

This section shortly introduces the NDT techniques applied by the author in tendon ducts injection evaluation of post-tensioned bridges. More elaborate introductions can be found in different professional publications. Due to various reasons only injection evaluation of corrugated steel ducts which are close to surface can be reliably performed with NDT techniques.

4.1 *Ultrasound tomography*

Ultrasound tomography is suitable for concrete structures integrity evaluation usually when the concrete structure surface is reachable. Ultrasound tomography enables fast, accurate and sufficiently deep scanning from one surface of the concrete structure (Germann Instruments 2014). Experienced user of the system can perform quick onsite interpretation of the testing results. It is important to mention that tomography testing results' interpretation is based on relative comparison of the obtained testing results (there are no absolute thresholds). This is why the experience and understanding of the technique by the user are crucial when performing evaluations with this technique.

Ultrasound tomography is probably the most suitable NDT technique for grout injection evaluation of post-tensioned bridge tendon ducts. It is also useful in detecting and evaluating casting defects and in general a concrete structure's integrity.

The tomographer creates 3D representation of internal reflecting interfaces that may be present inside a concrete object. It is based on the ultrasonic Echo method using transmitting and receiving transducers in a "Pitch-Catch" configuration. It uses an antenna composed of an array of dry point contact transducers, which transmit into the concrete low frequency shear waves. The transducers are spring loaded to conform to an irregular surface. The effective scanning depth is about up to 0,5 m in heavily reinforced structures.

The testing results are presented in tomograms in 3D and different cross-sections by visualization software (Synthetic Aperture Focusing Technique algorithm based).

Detection of a defect with ultrasound tomography: if a defect inside a concrete object exists in the form of a sufficiently large concrete-air interface, a portion of the transmitted stress wave will be reflected by it and the reflected wave will arrive at the receiver sooner than reflections from the back wall. The SAFT software determines the location of a defect by analyzing the arrival times of the reflected pulses. When evaluating prestressing systems, continuous and intensive S-waves reflections along and at the depth of a duct might indicate voided duct.

4.2 *The Impact – Echo system (IE)*

The Impact-Echo technique is also suitable for concrete structure's integrity evaluation, usually when the concrete structure surface is reachable. Impact-Echo enables rather fast and deep yet pointwise evaluation. Experienced user of the system can perform quick interpretation of the testing results onsite, but a deep understanding of this technique is needed. The Impact-Echo technique is suitable for performing grout injection evaluation of tendon ducts (usually applied together with the ultrasound tomographer technique for increased reliability), for evaluating hidden defects inside the concrete, fracturs, delaminations etc.

The Impact-Echo testing method is also introduced in ASTM C1383-15 "Standard Test Method for Measuring the P-Wave Speed and the Thickness of Concrete Plates Using the Impact-Echo Method".

The impact-echo method is based on monitoring the periodic arrival of reflected stress waves (P- waves) and enable to obtain information on the depth of reflecting interfaces (e.g. void/defect). By that the integrity of a concrete object could be evaluated. The Impact-Echo components include mechanical spherical impactor source (different sizes of impactors are available), a high fidelity displacement transducer for measuring the surface displacement and a laptop with the Impact-Echo software needed for data acquisition, analysis and storage.

The technique principle: the impactor generates a short-duration pressure wave, which travels into the concrete and is reflected from the backside of a solid test object or from an internal anomaly. The P-wave is reflected sever-al times and the arrival of the reflected P-wave is detected by the displacement transducer on the test object surface. The impactor contact time is a function of the impactor diameter and is influencing the frequency do-main. The time domain waveform is converted to a frequency response (amplitude spectrum) using a FFT algorithm (a mathematical method to convert and presented data as function of frequency).

When evaluating prestressing systems, we look for dominant signal peaks at the depth and location of the tested tendon. If found at least at several spots along the duct → suspicious

indication. Similarly to grout injection evaluation by tomography system, also here appropriate understanding and experience in performing these types of tasks is required.

5 TENDON DUCT EVALUATION BY SLIGHTLY INVASIVE METHODS

It's always recommended to complement NDT by slightly invasive measures, when possible. Evaluation of a tendon duct with slightly invasive methods means opening a tendon duct and evaluating the different components of the prestressing system (see Figure 1 Left and Middle): the duct, the injection grout and the prestressing steel (strands). It is also possible to drill just slightly into a duct a small hole and to evaluate the duct injection by use of an endoscope (see Figure 1 Right), but in this case corrosion estimation of the prestressing steel is not possible.

NDT pinpoints logical locations of tendon duct opening. The opening should be done very carefully so it is a time-consuming process. Usually only 1-2 ducts will be opened per inspected bridge (at least in the first phase).

The main objectives of opening a tendon duct:

- Verifying NDT results.
- Verifying the exact duct location, its dimensions, material and condition.
- Evaluating the injection grout: quality, thickness, voids, chloride ion content evaluation (also of water if found inside the duct).
- Verifying the type of the prestressing system, dimensions of strands.
- Corrosion estimation of the prestressing steel (Räsänen & Salparanta 2003). In Finland, determining the corrosion classes: 0 (not corroded). . .4 (severely corroded).



Figure 1. Diamond drilling during opening of a tendon duct, opening of a tendon duct and exposing the injection grout (Left and Middle). Right: drilling by a small diameter drill-bit (d6 mm) few millimeters into a duct. Dry injection grout is visible.

6 EXAMPLE TEST CASES

This section presents some test cases demonstrating the NDT techniques and invasive measures in bridge inspection tasks the author was involved in.

6.1 *Test case 1*

About 150 m long prestressed concrete continuous box-girder bridge (Finland) built in 1968, see Figure 2 Left. The prestressing system type is KA Sigma Oval which is known to be sensitive to hydrogen embrittlement thus additional stresses such as faulty grout injection and corrosion of the prestressing steel are a real concern. The expansion joints of the bridge leak and de-icing salts are used here during wintertime.

Grout injection was evaluated at several locations of the bridge along 1,5 m of the theoretical locations of ducts. Applied NDT techniques were ultrasound tomography and Impact-Echo. Some of the NDT results for one of the anchorage zones (figure 2 Right) are shown in the Figure 3.

In the presented investigated zone ultrasound tomography revealed continuous and intense reflections along two scanned ducts and at their depth (ducts A and B). Nevertheless, "ringing" observed is the B scans at depth of about 175 mm from the concrete surface could indicate that the ducts are not completely empty of injection grout. Duct C is classified as non-suspicious according to tomography. The Impact-Echo test results at this investigation zone correlated well with the tomography results providing suspicious indications along ducts A and B (dominant signal peaks were detected along the duct and at the depth of the duct) and non-suspicious indications along duct C. According to the NDT results the duct A that was classified as "suspicious" was opened at a selected test point.

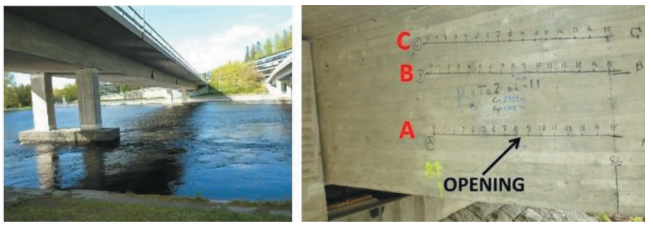


Figure 2. A side view of test case 1 bridge and the location of the presented investigation zone.

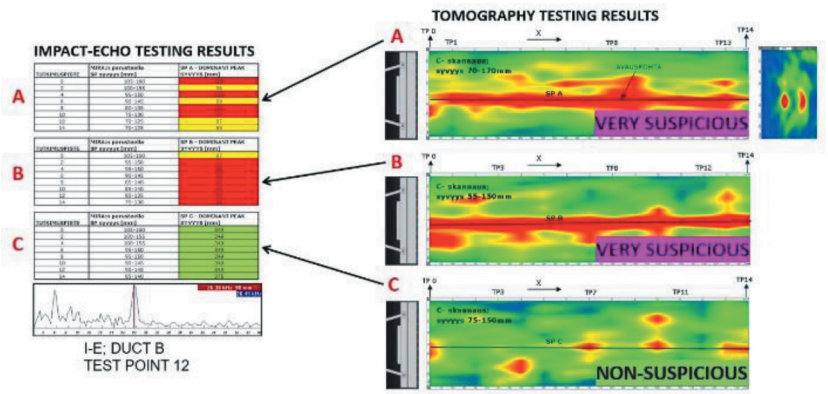


Figure 3. Ultrasound tomograms (C scans and B scan at a point along duct A) along investigated ducts A, B and C (See Figure 2) and Impact-Echo test point results summarized in a table (red-yellow colours are suspicious) and a dominant peak example at one test point.

Findings according to the opening of the duct (see Figure 4):

- The duct is partially injected (5 mm void). The injection grout is foamy and of low quality. The chloride content of the injection grout was <0,01 Cl^- % concrete weight → no penetration of chlorides from near leaking expansion joint has occurred.
- The prestressing steel corrosion class is estimated to be between 1 to 2 (light to mild). No pitting corrosion was observed.

6.2 *Test case 2*

About 102 m long prestressed concrete continuous box-girder bridge (Finland) built in 1971, see Figure 5 Left. The prestressing system is CCL 12 Ø 0,5" strands in each tendon duct. The expansion joints had been leaking intensively till the recent repair of the bridge. De-icing salts are frequently used during wintertime at the location of the bridge.



Figure 4. Voided duct. Light to mild corrosion of prestressing steel.



Figure 5. Side view of test case 2 bridge and the investigation zone related to the ultrasound tomography results presented in Figure 6.

Tendon ducts' grout injection was evaluated at various locations of the bridge along 1-2 m of the theoretical locations of the ducts, see Figure 5 Right. Applied NDT techniques were ultrasound tomography and Impact-Echo (partially). Some of the NDT results of one of the girders' anchorage zones are shown in Figure 6.

In the presented investigation zone the ultrasound tomography reveals continuous and clearly intense reflections along the scanned duct and at its depth. No "ringing" reflections were visible → very "suspicious" to be completely empty of injection grout.

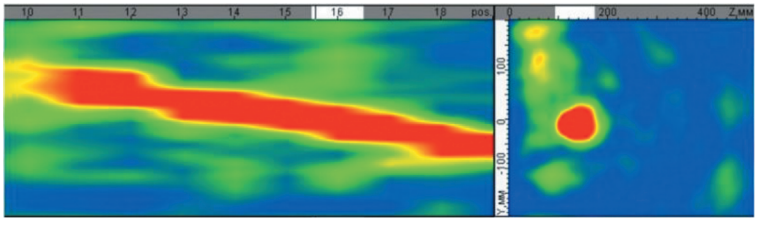


Figure 6. Side view of test case 2 bridge and ultrasound tomograms (C and B scan) along a duct and at the depth of the duct.

Opening of the tendon duct (Figure 7) revealed it is completely empty of injection grout and the prestressing steel is severely corroded (estimated Corrosion Class "3A"). Such a severe corrosion degree of the strands might significantly increase the risk of hydrogen embrittlement and/or SCC of the strands and therefore should be considered as a significant risk to the bridge durability.



Figure 7. Severely corroded prestressing steel in the opened empty duct.

7 CONCLUSIONS

Evaluation of tendon duct grout injection by applying suitable state-of-the-art NDT techniques and by performing slightly invasive measures at locations pinpointed by NDT results is proven to be beneficial in detecting substantial durability problems. These problems may pose risks to the prestressing system and affect the bridge functionality and sometimes its safe usage.

In some cases, acute faults were detected which required fast measures such as strengthening, setting traffic load limitations and even removal of bridges from service. Possibly some disasters were and will be avoided thanks to efficient evaluation of the prestressing system of bridges.

Applying these NDT techniques also during construction work of new bridges can ensure the post-tensioned system adequate quality from day zero and assist in preventing long term durability problems.

REFERENCES

ASTM C1383-15 (2022) "Standard Test Method for Measuring the P-Wave Speed and the Thickness of Concrete Plates Using the Impact-Echo Method"

Räsänen, O & Salparanta, L (2003) Evaluation of Degree of Rusting of Concrete Reinforcement. Helsinki 2003. Finnish Road Administration. Finnra Reports 48/2003.

GERMANN INSTRUMENTS, NDT Systems, Bringing NDT Theory and Practice, Catalog NDT 2014 (www.germann.org)

Bridge Maintenance, Safety, Management, Digitalization and Sustainability – Jensen, Frangopol & Schmidt (eds)
© 2024 The Author(s), ISBN 978-1-032-77040-6
Open Access: www.taylorfrancis.com, CC BY-NC-ND 4.0 license

Development and implementation of digital inspection notebook for bridges

M. Tai
Setsunan University, Osaka, Japan

H. Shirahata & T. Kawai
Tokyo City University, Tokyo, Japan

T. Aoki & H. Hara
East Japan Civil Aviation Bureau, Ministry of Land, Infrastructure, Transport and Tourism, Tokyo, Japan

S. Takagi
Shutoko Technology Center, Tokyo, Japan

ABSTRACT: In this study, we have developed a digital inspection notebook in the bridge inspection process to prevent the oversight of damages and deterioration and ensure reliable inspections. Then, we evaluated and identified the challenges associated with the implementation of the digital inspection notebook in actual bridge inspections. By utilizing the digital inspection notebook, it became possible to display similar bridge damage cases and to record the inspection results on a 3D model of the bridge. This received positive feedback as it facilitated a better understanding of structural details and easier identification of areas susceptible to damages or changes. However, it was concluded that improvements are needed to enhance the usability in the field due to the complexity of equipment operation and increased input tasks on-site, as well as the difficulty of capturing images in narrow areas using the tablet device's camera. Based on the issues, we have improved the system in terms of the tool operation and showing of areas prone to damages or changes.

1 INTRODUCTION

Bridge Maintenance requires an establishment of a maintenance cycle consisting of inspection, diagnosis, measure and record which needs to be carried out continuously. That is, inspection within this maintenance cycle is a crucial first step in identifying any damage in the components, leading to subsequent diagnosis and measure. Therefore, inspectors responsible for conducting these inspections must possess sufficient knowledge and skills related to inspections and are required to appropriately report the condition of the bridge, which serves as the basis for the soundness through close visual inspection and similar methods.

On the other hand, bridge inspections may lead to "overlooking damage and deterioration" and "misjudgment of inspection results". The "overlooking damage and deterioration" occurs when the inspection is conducted, but crucial areas are missed, or when damage is overlooked due to a lack of knowledge regarding what constitutes damage. The "misjudgment of inspection results" is believed to arise from insufficient learning about similar damage cases and so on. Annual report of road maintenance in Japan (Ministry of Land, Infrastructure, Transport and Tourism. 2022) has reported significant variation in the proportion of damages classified as severity levels III (early measure stage) and IV (emergency measure stage) among different local authorities in bridge inspections. While the influence of regional characteristics is possible, there

DOI: 10.1201/9781003483755-371

is variability even in neighboring prefectures where the environment is considered to be similar. This suggests that "the overlooking damage and deterioration" and "misjudgment of inspection results" can be attributed to the knowledge and skills deficiency of the inspectors. To prevent such overlooking and misjudgment, it is necessary to understand areas prone to damages by referring to past inspection records of the target bridges and inspection results of similar bridges, and conduct inspections with the assumption of potential damages. However, many inspection records are primarily stored in paper format, and there is not a fully developed system that can be effectively utilized in the field. Therefore, there is a demand for the establishment of a system that allows on-site access to similar damage cases and past inspection records, enabling an understanding of critical inspection points for each bridge.

As mentioned above, the Ministry of Land, Infrastructure, Transport, and Tourism in Japan is actively promoting DX (Digital Transformation) in the field of infrastructure by harnessing data and digital technology. Various initiatives aimed at streamlining and improving the efficiency of maintenance and management using digital technologies, such as 3D data, are being undertaken by various public and private institutions. Kubota et al. (2021) developed a system for small-scale bridges without on-site signage of bridge names. This system utilizes RFID and QR codes to display the bridge name and a brief overview on tablet devices, with the goal of improving inspection efficiency, eliminating inspection errors and omissions, and enhancing the reliability of inspection results. Asai et al. (2018) investigated the construction of an inspection support tool that allows inspectors to annotate notes on images captured at the site using tablet devices, which are then displayed in an augmented reality (AR) space. Emoto et al. (2019) involves the development of a system that provides access to essential information for inspections, such as bridge specifications and inspection history, using augmented reality (AR) when scanning a bridge card with a smartphone camera. This system aims to enhance the efficiency of inspection tasks. Ibayashi et al. (2022) is working on the development of a bridge overview inspection system for small-scale bridges. This system enables inspectors to capture images of discovered damage using the built-in camera of a tablet device and automatically generate inspection reports.

As described above, in recent years, there have been efforts to develop systems that enable the acquisition of information related to bridge specifications and maintenance records as inspection support tools using digital data. However, there has been limited development of support tools focused on preventing the overlooking of damage, its diagnosis, and record. Therefore, the authors have developed a digital field notebook that prevents overlooking damage and deterioration in bridges and expects efficient and reliable inspections (Tai et al. 2023). In the present study, the developed digital field notebook was subjected to practical implementation and verification on real bridges. This process allowed the identification of the issues encountered and provided an opportunity to reflect on further development.

2 OVERVIEW OF DEVELOPED DIGITAL INSPECTION FIELD NOTEBOOK

In this chapter, an overview of the digital inspection field notebook developed by the authors are provided. The development of the digital inspection field notebook was carried out using the Unity game development software, which is a versatile tool used not only in game development but also in various other fields. Additionally, the chosen device for the digital inspection field notebook needed to have the following features:

- Portable for use in inspection sites
- Capable of capturing photos of inspection points
- Able to record inspection results
- Allows access to past inspection records and damage cases
- Capable of touchscreen operations (swiping, tapping, etc.)

In this study, a device that satisfies these requirements was selected, which is the Windows Surface Go3 with a weight of 544g, a 10.5-inch display, and an 8MP autofocus camera on the rear. The configuration of the digital field notebook system is shown in Figure 1.

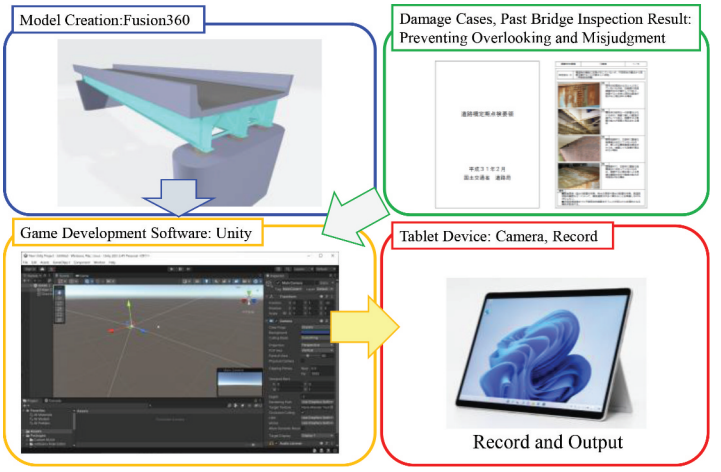


Figure 1. Configuration of digital field notebook system.

(1) 3D Bridge Model and Verification Function of Inspection Perspective
A 3D model of target bridge is created in VR space using the general-purpose 3D CAD software Fusion 360 by Autodesk. By creating 3D models for all bridge components, it becomes possible to conduct pre-inspection learning, confirming inspection points and inspection perspectives before the actual inspection. This allows for the visualization of inspection tasks and planning. Figure 2 depicts the general view of the bridge targeted for implementation verification and the created 3D model of the bridge.

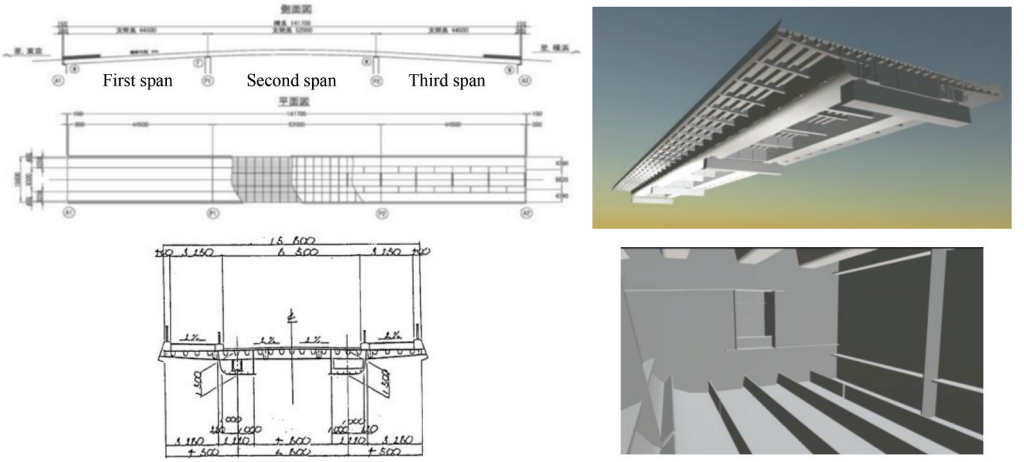


Figure 2. 3D model creation (a) Drawing of target bridge, (b) 3D model of target bridge.

(2) Confirmation of Similar Bridge Damage Cases and Prevention of Misjudgment
In bridge inspections, bridges with similar designs and construction environments often exhibit similar types of damage. Therefore, understanding damage cases from similar bridges and verifying the assessment of damage severity can help prevent misjudgments. While such verifications are commonly conducted as part of pre-inspection preparations, enabling on-site verifications, in addition to the preparatory phase, can contribute to preventing “overlooking damage and deterioration” and “misjudgment of inspection results”. This approach is believed to facilitate high-quality inspections.

Therefore, the digital inspection field notebook includes a feature that allows for the verification of damage cases and their assessment results from similar bridges. As illustrated in Figure 3, this feature compiles information on damage conditions and assessment cases as specified in the "Periodic Bridge Inspection Guidelines (Ministry of Land, Infrastructure, Transport and Tourism, 2019)". The included categories are corrosion, fatigue, fracture, deck plate, and others (such as bearing components or missing bolts). It also provides information on the target bridge's specifications and inspection considerations. Importantly, these pieces of information are customizable, allowing users to tailor them to the specific characteristics of the bridge under inspection.

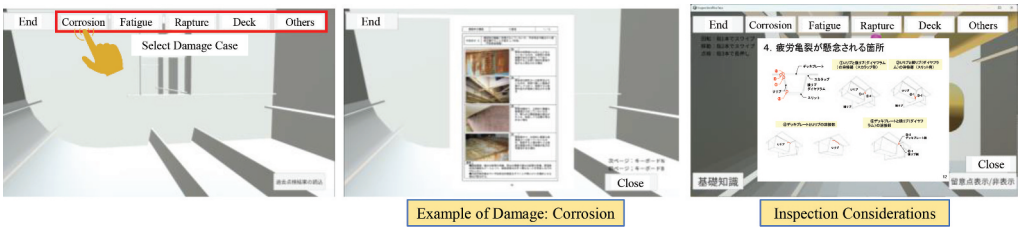


Figure 3. Confirmation feature for damage cases and inspection considerations.

(3) Verification of Past Inspection Records

When conducting inspections, it is of utmost importance to review past inspection records to identify areas where damage has occurred. Comparing the locations of damage or anomaly and assessing their progression and extent from previous inspection records is essential to prevent oversight and to make accurate assessments of the severity of damage. Therefore, to facilitate on-site verification of the occurrence, progression, and expansion of damage or deterioration, as shown in the example in Figure 4, the digital inspection field notebook has a feature that reads past inspection record data and displays markers in the form of spherical icons on the bridge's 3D model, indicating the locations where inspections were conducted. These spherical markers are displayed in different colors each time past inspection record data is loaded, allowing users to trace back through previous records to confirm damage or structural change data. As a result, during inspections at the site, inspectors can reference the occurrence of damage or deterioration from past inspection records, compare them with the actual damage, and prevent oversights or omissions during the inspection. This capability also allows for considerations regarding the progression of damage or deterioration when making assessments.

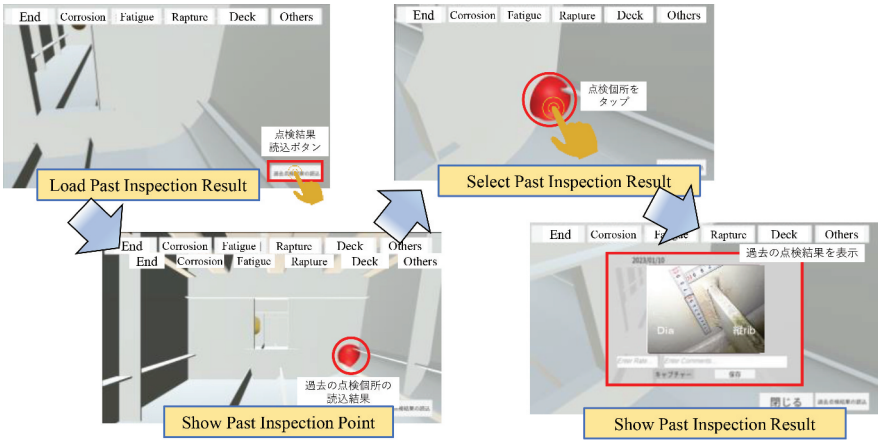


Figure 4. Feature for reviewing past inspection results on 3D bridge model.

(4) Record of Inspection Results

The ability to record inspection results is an essential feature in any field notebook, as accurate record enables proper diagnosis. In the digital field notebook, there is a function to capture photos using the rear camera of the Windows Surface Go3 device during inspections and record the inspection results. Specifically, as shown in Figure 5, users can tap on inspection points on the bridge's 3D model and choose to capture a photo. This action activates the device's rear camera, allowing for the photographing of the inspection point. After taking the photo, users can input information such as the component name, the damage severity classification, and commentsregarding the damage. This information is then saved as an inspection record. Once the inspection record is saved, similar to the inspection record verification feature described earlier, spherical markers appear on the bridge's 3D model. Users can tap on these markers to review the recorded content. As the markers are visually placed at the inspection points, it becomes easy to determine which locations have been inspected. This feature is valuable in preventing overlooking inspections.

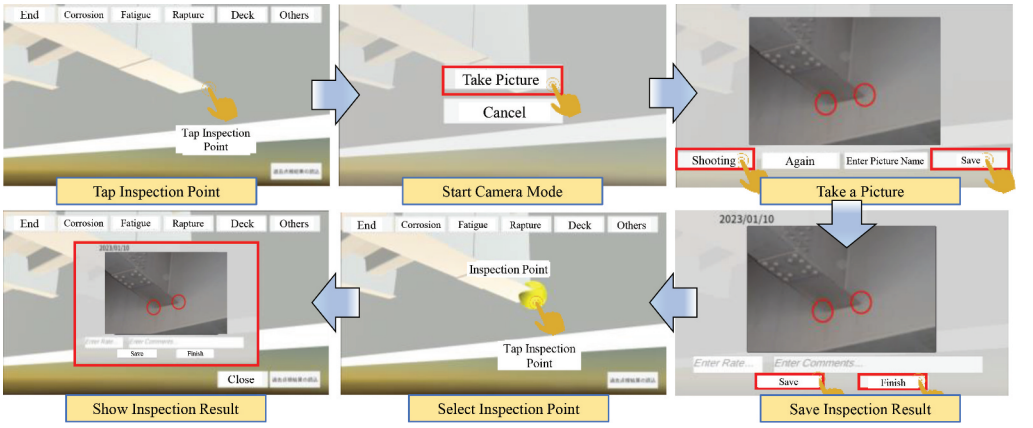


Figure 5. Record of inspection results.

3 IMPLEMENTATION OF DIGITAL INSPECTION FIELD NOTEBOOK

3.1 *Implementation testing method*

To validate the effectiveness of the digital field notebook mentioned above, an implementation test was conducted on the bridge illustrated in Figure 2. The testing method involved comparing the number of damage detections before and after implementing the digital field notebook. Specifically, the test involved two groups: one consisting of junior inspectors (with less than 3 years of inspection experience) and the other with mid-level inspectors (with over 10 years of inspection experience). For the test, the bridge's first and third spans were selected. Skilled inspectors with over 20 years of experience conducted visual inspections for these spans. Subsequently, the junior inspector group performed visual inspections on the third span before implementing the digital field notebook and the first span after implementing it. The mid-level inspector group inspected the first span before implementing the digital field notebook and the third span after implementation. The test aimed to compare the number of damage detections between skilled inspectors and junior or mid-level inspectors. The effects of implementation were evaluated through a questionnaire, and the results are presented in Table 1. The status of the implementation verification is illustrated in Figure 6.

Table 1. Questionnaire items and results.

For Pre-training			
Q1	Time required for pre-training	Average of 1.3 hours	
Q2	Understanding of structural features	Comprehensible	3
		Incomprehensible	0
Q3	Explanation of structural features	Comprehensible	3
		Incomprehensible	0
Q4	Understanding of potential fatigue crack initiation points	Comprehensible	3
		Incomprehensible	0
Q5	Explanation of potential fatigue crack initiation points	Comprehensible	3
		Incomprehensible	0
Q6	Understanding of potential corrosion occurrence region	Comprehensible	3
		Incomprehensible	0
Q7	Explanation of potential corrosion occurrence region	Comprehensible	3
		Incomprehensible	0
Q8	Usefulness of pre-training		
	Basic information (bridge specifications)	Necessary	4
		Unnecessary	0
	Structrural features	Necessary	4
		Unnecessary	0
	Potential fatigue crack initiation points	Necessary	4
		Unnecessary	0
	Potential corrosion occurrence region	Necessary	4
		Unnecessary	0
	Structure of reinforcing members	Necessary	4
		Unnecessary	0
Q9	Usability	Easy to operate	1
		Difficult to operate	3

For Inspection			
Q1	Record method of inspection	Easy to operate	0
		Difficult to operate	4
Q2	Did you check the consideratoins during the inspection?	Checked	1
		Unckecked	3
Q3	Is the tablet device cumbersome during the inspection?	Comprehensible	3
		Incomprehensible	1
Q4	Size of tablet device	Just as well	4
		Small	0
		Large	0
Q5	Inspection efficiency	Efficient	0
		No change	1
		Inefficient	3
Q6	Prevention of overlooking damage and deterioration	Decrease	3
		No change	1
		Increase	0
Q7	Usability	Easy to operate	0
		Difficult to operate	4
Q8	Items to be added or modified	Free description	



Figure 6. Situation of implementation.

3.2 *Results of implementation*

A summary of the inspection results from skilled inspectors and junior/mid-level inspectors before and after the implementation of the digital field notebook is presented in Table 2. In the first span, the detection rate of fine paint cracks, which are precursors to the development of fatigue cracks, improved from 38% for mid-level inspectors before implementation to 50% for junior inspectors after implementation. On the other hand, there were no detections of paint deterioration by junior inspectors after implementation, and neither group of junior/mid-level inspectors detected rust. In the third span, both mid-level and junior inspectors missed the paint cracks and rust discovered by skilled inspectors. In the case of paint deterioration, junior

inspectors before implementation had an 88% detection rate, which was superior to the 50% detection rate of mid-level inspectors after implementation. Since the targeted bridge in this test had a low occurrence of damage or deterioration within the box girder, the effects of implementing the digital field notebook were not clearly evident. To understand this factor, an analysis was conducted based on post-implementation questionnaires.

Table 3 shows the result of free description in questionnaire. Based on the results, it is likely that the application of the digital field notebook enhances pre-learning by providing a better understanding of structural details and making it easier to grasp locations prone to damage or deterioration compared to traditional drawings. However, the complexity of the field notebook's operation and the increased data input at the site may lead to a decrease in inspection efficiency and concentration, potentially not resulting in a clear improvement in inspection accuracy following implementation. Therefore, in the future, efforts should focus on improving usability, streamlining data input processes, and exploring equipment combinations to enhance inspection efficiency and concentration in the field. This will be crucial for the development of a more user-friendly system that effectively supports inspection activities.

Table 2. Comparison of inspection results before and after implementation.

First Span				Third Span			
	Type of damage	Number	Ratio		Type of damage	Number	Ratio
Skilled Inspector	Paint crack	16		Skilled Inspector	Paint crack	2	
	Paint degradation	3			Paint degradation	16	
	Rust	3			Rust	2	
	Total	22			Total	20	
Mid-level Inspector (Before Implementation)	Paint crack	6	38%	Mid-level Inspector (After Implementation)	Paint crack	0	0%
	Paint degradation	2	67%		Paint degradation	8	50%
	Rust	0	0%		Rust	0	0%
	Total	8	36%		Total	8	40%
Junior Inspector (After Implementation)	Paint crack	8	50%	Junior Inspector (Before Implementation)	Paint crack	0	0%
	Paint degradation	0	0%		Paint degradation	14	88%
	Rust	0	0%		Rust	0	0%
	Total	8	36%		Total	14	70%

Red: Mid-level inspector Black: Junior Inspector :Before Implementation :After Implementation

Table 3. Results of free description in questionnaire.

・**About Operation**
Radius of rotaion is too large.
Operation by finger is difficult.
Key plan is needed to identify current place.
・**About Data Input**
It's easier to operate when damage type can be selected from a dropdown.
Modification or re-editing function is needed.
・**About Photography**
Camera in the tablet device is not suitable to apply photography for narrow space.
It is difficult to come into focus by the tablet device.

・**About Usage effect**
It would be more efficient as it shows areas that should be inspected.
The tablet offers clear display screens, but it was not suitable for taking photos in particularly confined or challenging angles.
It could be a matter of getting used to it, but the operating the screen takes up so much attention that it can lead to a decrease in the focus on visual inspection of damages.
The visuals are easy to understand, and even after creation, others can intuitively understand the location of damages.
The 3D model is easier to understand the structure compared to drawings.
If it were possible to extract unfolded views and mark drawings from the 3D field book, it would lead to more efficient internal operations.

3.3 *Improvement of digital field notebook*

Based on the above results, the developed digital field notebook was improved. To reduce the overlooking the damage, The system added a feature to prevent overlooking of potential damage in critical locations by changing the color on the bridge's 3D model. For instance, in

the steel deck, there is concern about fatigue crack initiation from the welded joints of vertical ribs directly under the wheel load. Additionally, at field joints, being a site for on-site painting, there is a higher possibility of paint film degradation and corrosion compared to other areas. Therefore, as shown in Figure 7, the system visually highlighted such critical locations with potential damage or deterioration, allowing for easy visual recognition during pre-inspection and inspection.

Furthermore, the input method has been changed to screen buttons, adding a sketch feature on the 3D model, using dropdown menus for selecting damage levels, and incorporating a handwriting note feature (Figure 8). These improvements have enhanced usability. Implementation verification and continuous improvement are planned for the future.

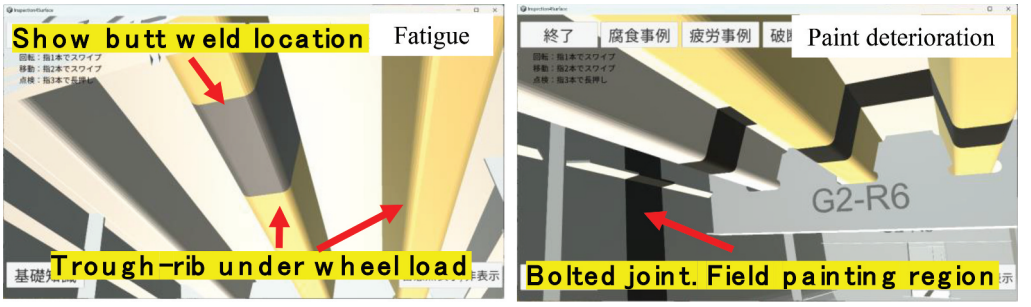


Figure 7. Examples of visually highlights such critical locations with potential damage.

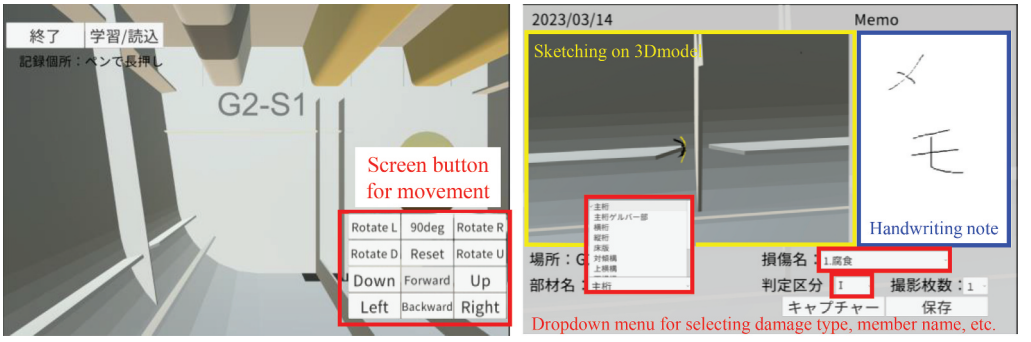


Figure 8. Example of improvement for the input method.

4 SUMMARY

In this study, the authors developed a digital inspection field notebook aimed at preventing the “overlooking of damage and deterioration” and “misjudgment of inspection results” in bridge inspections and ensuring efficient and reliable inspection processes. This system was implemented in actual bridge inspections, and an evaluation of its effectiveness and identification of issues were conducted.

By using the digital inspection field notebook, inspectors are able to display areas on the 3D model of the bridge in the tablet’s VR environment, based on damage instances from similar bridges where damage and deterioration are likely to occur. This feature enhances the understanding of structural details and locations prone to damage or changes compared to traditional drawings. However, there are challenges to be addressed, such as the complexity of equipment operation and the difficulty of capturing images in confined areas using the tablet’s camera.

To address these challenges, several improvements have been proposed, including changing the input method from tapping and swiping to button-based controls, implementing touchscreen pens for handwritten input, and streamlining data input through dropdown menus. These improvements is expected to reduce the workload in field inspections, ensuring that inspectors can concentrate on their work and preventing the overlooking of damage or deterioration. By directly inputting damage or change locations on the 3D model and enhancing the accuracy of inspection records, the system contributes to the advanced maintenance and management of infrastructure. The authors plan to work on further improvements to build a system that enhances inspection reliability and efficiency while reducing the workload on inspectors.

ACKNOWLEDGEMENT

This work was performed with financial supports from JSPS KAKENHI Grant Number 21K04565 and Tokyo City University Prioritized Studies.

REFERENCES

Asai, M., Hirose, M. and Yasumuro, Y. 2018. AR display of hand-written memo for information sharing in bridge inspection, *Journal of Japan Society of Civil Engineers, Ser. F3 (Civil Engineering Informatics)*, Vol.74, Issue 2, pp.II_118-II_124.

Emoto, H., Ono, T., Nakamura, H. and Kawamura, K. 2019. Development of bridge inspection system regarding with accessing inspection data using augmented reality, *Journal of Japan Society of Civil Engineers, Ser. F3 (Civil Engineering Informatics)*, Vol.75, Issue 2, pp.II_25-II_33.

Ibayashi, K. and Maruyama, A. 2022. Development and demonstration experiment of a bridge brief inspection system using tablet computers for local governments, *Infrastructure Maintenance Practices*, Vol.1, Issue 1, pp.8–17.

Kubota, S., Ishii, Y., Maruyama, A. and Yasumuro, Y. 2021. Information display system for small bridges using RFID and QR codes, *Journal of Japan Society of Civil Engineers, Ser. F3 (Civil Engineering Informatics)*, Vol.77, Issue 2, pp.II_9-II_15.

Ministry of Land, Infrastructure, Transport and Tourism HP. 2019. Periodic bridge inspection guideline.

Ministry of Land, Infrastructure, Transport and Tourism HP. 2022. Annual report of road maintenance <https://www.mlit.go.jp/road/sisaku/yobohozen/pdf/r03/r03_09maint.pdf>

Tai, M., Shirahata, H. and Kawai, T. 2023. Development of digital twin inspection field notebook for periodic bridge inspection, *Infrastructure Maintenance Practices*, Vol.2, Issue 1, pp.136–142.

Bridge Maintenance, Safety, Management, Digitalization and Sustainability – Jensen, Frangopol & Schmidt (eds)
© 2024 The Author(s), ISBN 978-1-032-77040-6
Open Access: www.taylorfrancis.com, CC BY-NC-ND 4.0 license

Towards a service life extension of the Øresund Fixed Link

I. Björnsson & S. Thöns
Division of Structural Engineering, Faculty of Engineering, Lund University, Lund, Sweden

S. Celati
Department of Civil and Industrial Engineering, School of Engineering, University of Pisa, Italy

B. Hergart
Øresundsbron Konsortiet, Malmö, Sweden

ABSTRACT: The Øresund Fixed Link is a 15,9 km road and railway connection between the southerly Swedish city of Malmö and its neighbor across the Øresund strait, Copenhagen, in Denmark. The link, which opened in 2000, consists of an elevated bridge, including a high stay cable bridge, an artificial island, as well as a submerged tunnel. The operators of the link, Øresundsbron Consortium, have recently, as part of a comprehensive sustainability strategy, initiated a project for extending the service life of the link. The project, which is being carried out by researchers at Lund University, aims to develop decision support for service life extension of the bridge and tunnel structures to 200 years. The tasks include the identification, modelling, and analysis of service life relevant scenarios (as a basis for service life quantification) as well as decision scenario modelling and analyses considering possible future repair actions. A brief overview of the project is provided along with a general framework for service life quantification. Preliminary results for an example, concerning active corrosion initiation of the immersed tunnel roof, are also provided. This work highlights the potential benefits of industry-academic collaboration towards improved infrastructure operation and maintenance and, by extension, sustainability.

1 INTRODUCTION

1.1 *Background*

The proper operation and management of transport infrastructure assets is critical to ensure a well-functioning transportation network. Approaches to this have evolved and developed substantially over time. The focus early on was on repairing only when damage was observed (corrective maintenance) followed by developments towards preventative and then condition-based (or predictive) maintenance (Moubray 1997). More recently, emphasis has been on integrating risk or decision analysis-based methodologies to improve and optimize the management and operation of bridges and other infrastructure assets (e.g., Faber 2008, Björnsson et al. 2019, Thöns 2018). Recent research efforts have focused on the development and implementation of more advanced computational models for deterioration, identifying and calculating structural-performance indicators, evaluating life-cycle costs, and optimizing inspection, maintenance, and repair strategies (Sánchez-Silva et al. 2016, Zhang et al. 2021, Abdallah et al. 2022). However, the operational phase of built infrastructures such as bridges or tunnels is seldom, if ever, considered during design. Thus, ensuring continued operation, satisfactory performance, and structural safety over time can be a daunting and costly task for the bridge owner and manager.

The operation and management of medium to small scale infrastructure assets is commonly the responsibility of national or regional authorities, e.g., the Swedish Transport Administration

DOI: 10.1201/9781003483755-372

in Sweden or the Danish Road Directorate in Denmark. In these cases, the number of assets (bridges or tunnels) being maintained may be in the tens of thousands leading to a limited number of resources available for each individual structure. On the other hand, for larger scale infrastructures, such as the Millau Viaduct in France or the Øresund Fixed Link between Sweden and Denmark, ownership and management is the purview of a dedicated agency or company. In these cases, efforts are directed towards operating and maintaining a single large-scale infrastructure. In practice, it is commonly these types of structures that will, e.g., be equipped with expensive monitoring systems or employ state-of-the-art inspection technologies (such as drones) to support maintenance decisions. This is quite reasonable as the failure of these types of structures would result in very significant consequences; the collapse of the Polcevera Viaduct in Genoa in 2018 is a stark example of this (Calvi et al. 2019).

1.2 *Øresund Fixed Link (Øresundsbron)*

The Øresund Fixed Link, referred to locally simply as Øresundsbron, is a 15,9 km long road and railway connection between Southern Sweden and Denmark, see Figure 1. The link, which was opened to traffic in 2000, consists of a 7,8 km long elevated bridge, a ca 4 km artificial island, as well as a 4 km immersed tunnel. The bridge structures can further be subdivided into two approach bridges as well as a high stay-cable bridge to allow for transit of larger seagoing vessels. The bridge superstructure is a double-deck configuration with a lower steel truss supporting railway traffic positioned below a concrete slab for road traffic (Gimsing 2000a). The submerged (or Drogden) tunnel consists of 20 concrete tunnel segments on gravel bed foundation with immersion joints (Gimsing 2000b).



Figure 1. View of the Øresund Fixed Link (view from the artificial island Pepparholmen towards Malmö).

The link is owned and operated by the Øresundsbron Consortium, a company owned equally by the Swedish and the Danish state. The operators have a vision for the link to become the most sustainable infrastructure in the world. This vision is illustrated by four

targets: 100 extra year service life, 100% open for traffic, 100% free from severe accidents, and 100% free from CO_2. The strategies and main activities for approaching these visionary targets include a remarkable cut in energy consumption (by more than 55%) and installation of solar energy plants (now providing 45% of the needed electricity). The most sustainable action, however, is to prolong the service life of the link from the original design criteria which was 100 years. To support this action, an ongoing collaborative research project was recently initiated together with researchers at the Division of Structural Engineering, Lund University, Sweden. This paper briefly describes this project and describes methods for service life quantification. An example is also provided concerning reinforcement corrosion in the roof of the submerged tunnel.

2 SERVICE LIFE EXTENSION

2.1 *Background*

Extending the service life of infrastructures is an effective measure to improve sustainability by delaying or avoiding the need for expensive and resource-intensive replacements. The current design of these structures is often based on a design life of 100 years. The actual service life, which requires considering the operation phase, is limited by both technical and economic factors (Thöns et al. 2024). For the former, time-dependent considerations of structural safety and serviceability are central. Varying structural deterioration mechanisms, such as fatigue or corrosion, degrade structural integrity while the intensity and severity of certain hazards may also increase over time. Active measures to treat these risks are embedded in the management and maintenance of these structures, e.g., through preventive measures, periodic inspections, repairs, strengthening, etc. However, it is sometimes difficult, impractical, or impossible to avoid or repair certain structural damages, placing a technical limit on service life. Economic factors similarly place limits on service life if the required measures become too costly. In extreme cases, replacing the structure entirely may be the optimal solution. Another issue, commonly observed in practice, is obsolescence - when the structure is no longer deemed useful, e.g., owing to changes in the local transportation network (Mattsson 2008). However, this issue is difficult to consider a-priori and will not be discussed further in this paper.

2.2 *Collaborative project description*

In 2022, a collaboration was initiated between Øresundsbron Consortium and the Division of Structural Engineering, Lund University in Sweden. A pre-study was carried out to prepare a modelling basis for the service life management and service life extension to 200 years (Thöns & Björnsson 2023a, 2023b). The focus in the pre-study was on the structural components and systems of the link including the approach bridges, the high bridge, and the immersed tunnel. As of fall 2023, a continuation of the project is underway with the following objectives:

1. Modelling and analysis of service life relevant scenarios for different structural groups and deterioration mechanisms.
2. Service life quantification with repair strategies and additional information.
3. Quantification of service life extension costs and utilities.
4. Identification of efficient service life extending integrity management strategies.

The project is founded on methods of applied engineering and decision analysis research for the service life quantification and service life management as illustrated in Figure 2. The first step is to identify and model service life relevant scenarios for different structures and substructures considering relevant failure and deterioration mechanisms. Thereafter, the service life can be quantified provided time-dependent probabilistic models can be developed. At this stage it is also important to consider discrepancies or deviations from design assumptions as well as the current condition and loading on the structure (based, e.g., on previous inspections and repairs).

The remaining service life can then be determined based on compliance with corresponding target reliabilities as specified according to, e.g., JCSS (2001-2015) and ISO 2394 (2015).

Actions (such as, e.g., repair and strengthening) may be taken to extend the service life of the link and observations (i.e., information) can be used to update and predict the structural condition for the support of implementing these actions. These service-life extending strategies lead to economic and environmental benefits but may be costly and include potential structural risks. Furthermore, these strategies can be explicitly modeled and analyzed using a (pre-posterior) decision analysis framework. Finally, the analysis of the resulting decision scenarios allows for the identification of optimal service life extension and management strategies by maximizing the expected utility composed of potential benefits, consequences, and costs.

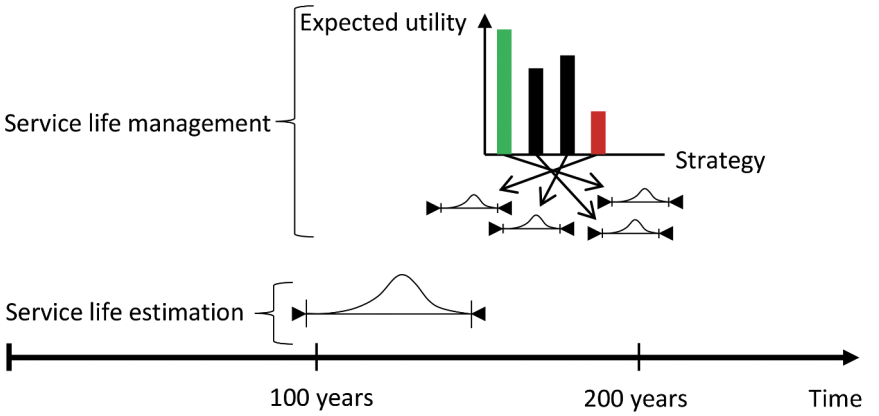


Figure 2. Visualization of the service life extension, service life management and decision-support model.

3 SERVICE LIFE QUANTIFICATION

3.1 *Introduction*

Determining the service life of an infrastructure is not a straightforward task and multiple approaches may be adopted. Herein, three will be briefly mentioned: (1) estimation by failure databases (of similar structures), (2) estimation by expert opinions, and (3) probabilistic modeling. For the first, published incident or failure databases can be utilized as a basis for estimating an average failure rate for a sample population with associated rates for different causes; see, e.g., Cook (2014). However, such estimates should be regarded with care as failure data is rarely complete, may contain incomplete or poor descriptions, etc. (Stewart & Melchers 1997). Furthermore, an average failure rate may be misleading as structures in general (and especially large-scale infrastructures) are unique; both with regards to their configuration and the circumstances to which they are enduring (e.g., loading history).

The second approach concerns estimations by synthesizing opinions from a group of experts. Established methods include expert elicitation (see, e.g., Ayyub 2001, Ioannou et al. 2022) and the Delphi method (see, e.g., Beiderbeck et al. 2021). Such approaches are useful in cases where uncertainties are high. However, as with using failure databases, the acquired results from expert opinions, which may be highly subjective, should be regarded with care. On the other hand, both the previously mentioned approaches may be useful in accounting for phenomena which are more difficult to model numerically (e.g., failures resulting from gross human errors).

Finally, an explicit probabilistic modelling of service life limiting scenarios can be carried out. Critical service life ending scenarios are identified, characterized by a structural condition that fails to meet safety standards and is unmodifiable. In other words, a condition that is

both unsafe and irreparable. Such a condition can be caused by technical or by economic limitations; see Thöns et al. (2024) for further details. The technical service life quantification relies on a probabilistic model including (1) a structural deterioration mechanism describing the time-dependent condition of the system, and (2) a criterion for when failure is reached. To illustrate this, the phenomenon of active reinforcement corrosion is presented in the next section.

3.2 *Reinforcement corrosion*

Active corrosion of reinforcement in concrete structures is a highly relevant deterioration phenomenon. Once active corrosion is initiated, the loss of load carrying capacity will occur as the steel area becomes reduced. Over time, this can lead to failure of a structural component or system. In this paper, we consider the initiation stage for active corrosion (without assessing the time-dependent structural reliability of a corroded RC structure). Thus, service life quantification based on these probabilistic models would require further assessing the impacts of this process to structural performance. On the other hand, they can provide a good starting point for prioritizing different service life ending scenarios, e.g., if the results indicate a relatively high or low probability of active corrosion for a critical structural member.

3.2.1 *Active corrosion initiation*

In a marine environment, corrosion can become active if both the concentration of chlorides at the rebars' level overcomes the critical threshold and the pH of the concrete surrounding the rebars is lower than ca. 9 (Melchers and Li 2009). This statement holds for sound concrete (no cracks developed).

Chlorides' concentration rises due to diffusion of chloride ions from the concrete surface, while a pH reduction is herein considered due to the carbonation process of concrete. Because carbonation is inhibited for submerged structures, the corrosion of submerged elements is, in this (preliminary) phase, neglected. Both processes are considered to develop independently, therefore the time to active corrosion (T_{ac}), or time needed for chlorides to reach the reinforcement (T_{ich}) and carbonation to advance (T_{ica}), can be estimated from:

$$T_{ac} = \max\left\{T_{i_{ch}}; T_{i_{ca}}\right\} \tag{1}$$

The subsequent sections describe the models adopted for each of these processes.

3.2.1.1 Chloride diffusion

The concentration of chloride ions at time t and depth x inside the concrete can be modelled using Fick's second law as follows:

$$C(x,t) = C_0 + \left(C_{s,\Delta x} - C_0\right)\left[1 - \mathrm{erf}\left(\frac{x - \Delta x}{2\sqrt{D_{app,c}(t)\cdot t}}\right)\right] \tag{2}$$

where C_0 is the concrete initial chloride content [wt.-%/c], $C_{s,\Delta x}$ is the chloride content at depth Δx [wt.-%/c], Δx is the depth of the convection zone [mm], $D_{app,c}(t)$ is the time-dependent chloride diffusion coefficient [mm^2/year], and $erf(\cdot)$ is the error function. The value of the apparent chloride diffusion coefficient $D_{app,c}$ can be evaluated from:

$$D_{app,c}(t) = k_e D_{RCM,0} k_t B(t) \tag{3}$$

where $D_{RCM,0}$ is the chloride diffusion coefficient [mm^2/year], k_t is the environmental transfer parameter equal to 1, and $B(t)$ is the ageing function. The environmental variable, k_e, can be determined according to:

$$k_e = \exp\left(b_e\left(\frac{1}{T_{ref}} - \frac{1}{T_{real}}\right)\right) \tag{4}$$

where b_e is the regression parameter [K], T_{ref} is the reference temperature equal to 293 K (20°C), and T_{real} is the temperature of the element or of the environment [K]. The ageing function is estimated from:

$$B(t) = \left(\frac{t_0}{t}\right)^a \tag{5}$$

where t_0 is the reference time (equal to 0.0767 years) and a is the ageing coefficient [-].

If the initial chloride content of concrete is considered equal to zero, the time needed for the chloride concentration to overcome the critical threshold at the steel (reinforcement) surface can be evaluated as follows:

$$T_{i_{ch}} = X_{ch} \cdot \left[\frac{1}{4k_e k_t D_{RCM,0} t_0^a}\left(\frac{c - \Delta x}{\text{erf}^{-1}\left(1 - \frac{C_{cr}}{C_{s,\Delta x}}\right)}\right)^2\right]^{\frac{1}{1-a}} \tag{6}$$

Eq. (6) is derived rearranging Eqs. (2-5) and replacing C_0 with the critical chloride threshold C_{cr} [wt.-%/c], and x with the concrete cover c [mm]. X_{ch} is an added variable that accounts for the model uncertainties.

3.2.1.2 Carbonation

The time to carbonation initiation is herein determined using an empirical model, see Eq. (7) (Silva et al. 2014).

$$T_{i_{ca}} = \begin{cases} \frac{c^2}{k_d^2} \text{ for } RH \leq 70\% \\ \frac{c^2}{k_w^2} \text{ for } RH > 70\% \end{cases} \tag{7}$$

In addition to the concrete cover c [mm], the following parameters are defined:

$$k_d = S_1 \cdot [CO_2] - S_2 \cdot EC - S_3 \cdot f_c + S_4 \tag{8}$$

$$k_w = S_5 \cdot [CO_2] - S_6 \cdot C_l - S_7 \cdot f_c + S_8 \tag{9}$$

Table 1. Carbonation model parameters.

Parameter	Distrib.	Mean	St. Dev.
S1	N	0.556	0.024
S2	N	-3.602	0.482
S3	N	-0.148	0.033
S4	N	18.734	1.785
S5	N	3.355	0.088
S6	N	-0.019	0.003
S7	N	-0.042	0.013
S8	N	10.830	0.571

N: Normal (Gaussian distribution)

In Eqs. (8) & (9) [CO_2] is CO_2 content [%], *EC* is the exposure class (equal to 1 for *XC1*, 2 for *XC3*, and *3* for XC4), C_l is the clinker content [kg/m3], and f_c is the concrete compressive strength [MPa]. The eight regression parameters (S_i) are modelled as hyperparameters according to Table 1.

Table 2. Description of the input variables for probabilistic analysis of corrosion in immersed tunnel roof.

Variable	Distr.	Mean	St. Dev.	Min	max	Ref.
X_{ch}	LN	1	0.05	-	-	[1]
c [mm] *	N	50	6.01	0	-	[2]
μ_{Cs} [wt.-%/c]	U	1	0.29	0.5	1.5	[2]
$C_{s,\Delta x}$ [wt.-%/c]	LN	μ_{Cs}	0.75μCs	-	-	[2]
C_{cr} [wt.-%/c]	B	0.6	0.15	0.2	2	[2]
Δx [mm]	D	0	-	-	-	[2]
RH [%]	B	72	10	0	100	[3]
[CO2] [%] **	U	0.065	0.0087	0.05	0.08	
T_{real} [K]	N	281	5	-	-	[2]
T_{ref} [K]	D	293	-	-	-	[2]
b_e	N	4800	700	-	-	[2]
a	B	0.3	0.12	0	1	[2]
$D_{RCM,0}$ [mm^2/year]	N	280.67	56.13	-	-	[2]
$C_{em,C}$ (cement content) [kg/m3] *	U	325	11.55	305	345	
f_c [MPa] ***,*	LN	56.50	11.33	-	-	
C_l [%Cem,C] ****	U	0.925	0.014	0,90	0,95	

N: Normal; D: Deterministic; B: Beta; LN: Log-normal; U: Uniform.
[1] Straub et al. (2009), [2] fib (2015), [3] Derks (2004)
*Ranges provided in construction requirements and Gimsing (2000b). **Inferred from Dong et al. (2017). ***f_{ck} = 40 MPa with CoV = 0.20. ****Typical range for clinker content of Portland cement.

4 EXAMPLE - REINFORCEMENT CORROSION IN IMMERSED TUNNEL ROOF

This example concerns active corrosion of reinforcement in the immersed tunnel roof of the Øresundsbron. A reduction in capacity of the roof section due to corrosion would be very severe as watertightness of the immersed tunnel element would be compromised. The results are preliminary and are related to the initiation of active corrosion, without considering the structural integrity of the tunnel roof as potential corrosion progresses.

For the inner surface of the tunnel roof (XD1), a type A concrete (Gimsing 2000b) is employed. The nominal cover is 50 mm with a tolerance of ±10 mm, the water-to-cement ratio is 0.45, and the characteristic compressive strength (f_{ck}) is 40 MPa. Input variables and distributions are summarized in Table 2.

The survival function, defined as the complement of the cumulative distribution function (1-CDF), for the T_{ac} variable is shown in Figure 3 for the studied example. The 90% survival probability is highlighted for illustrative purposes. In this example, utilizing higher survival probabilities (e.g., based on target reliabilities for ultimate limit state) is not suitable as the initiation of active corrosion would not lead to failure. Finally, a sensitivity analysis reveals that the concrete quality (strength), cover, and chloride content have the highest impact on the results; see Figure 4.

5 DISCUSSIONS AND CONCLUSIONS

Extending the service life of infrastructures is an effective measure to improve sustainability. Recently, the Øresundsbron Consortium have adopted this strategy for the Øresund Fixed

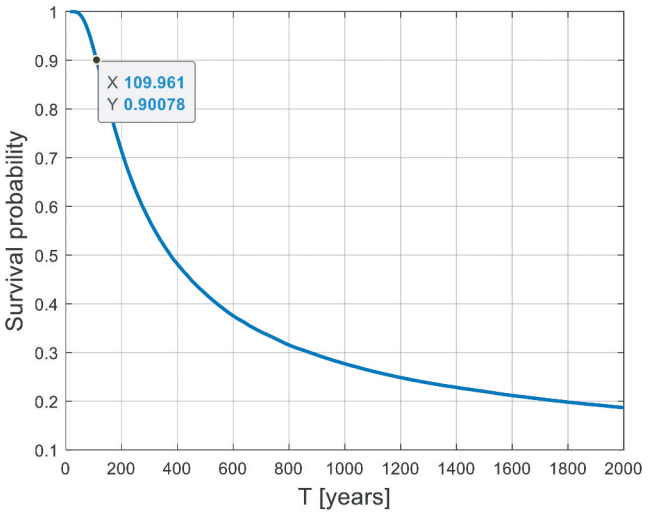


Figure 3. Survival function of the variable T_{ac} (time to active corrosion) for the inner ceiling of immersed tunnel (50mm cover).

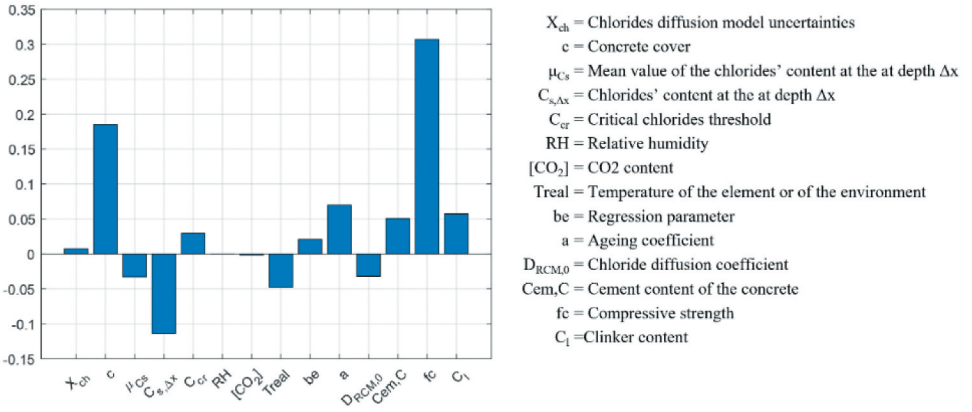


Figure 4. Spearman correlation coefficient of the input variables for time to active corrosion of the inner ceiling of the immersed tunnel (50mm cover).

Link located between south Sweden and Denmark. Specifically, the aim is to increase the service life from 100 years to 200 years. To support this, an industry-academic collaboration was established to implement current state-of-the-art research in the operation and management of the link. The ongoing research project aims to provide decision support for service life management and extension of the link. A first step in this direction concerns the development and implementation of probabilistic models for service life quantification. The provided example focuses on one deterioration mechanism (reinforcement corrosion) at a critical location in the link (the immersed tunnel roof). The preliminary results provide a basis for service life quantification which can then be extended to determine optimal maintenance actions and information acquirement strategies, providing direct decision support for the infrastructure operator. Investigations are ongoing concerning other deterioration mechanisms and critical sections/details, including steel fatigue of critical details of the bridge superstructure and at cable anchors.

REFERENCES

Abdallah, A.R. Atadero & Ozbek, M. (2022). A State-of-the-Art Review of Bridge Inspection Planning: Current Situation and Future Needs. *Journal of Bridge Engineering*, **27**(2), 03121001.

Ayyub, B.M. (2001). *A practical guide on conducting expert-opinion elicitation of probabilities and consequences for corps facilities*. Institute for Water Resources, Alexandria, VA, USA.

Beiderbeck, D., Frevel, N., von der Gracht, et al. (2021). Preparing, conducting, and analyzing Delphi surveys: Cross-disciplinary practices, new directions, and advancements. *MethodsX*, 8, 101401.

Björnsson, I., Ivanov, O.L., Honfi, D. & Leander, J. (2019). Decision support framework for bridge condition assessments. *Structural Safety*, **81**, 101874.

Calvi, G., Moratti, M., O'Reilly, G., et al. (2019). Once upon a time in Italy: The tale of the Morandi Bridge. *Structural Engineering International*, **29**(2), 198–217.

Cook, W. (2014). *Bridge failure rates, consequences, and predictive trends*. PhD Thesis: Utah State University.

Derks, H. (2004). *DARTS, Durable and Reliable Tunnel Structures – Benchmarking of the 2nd Benelux tunnel (immersed tunnel)*.

Dong, J., Tao, Y., Xiao, Y. & Tu, T. (2017). Numerical simulation of pollutant dispersion in urban roadway tunnels, *J. Comput. Multiph. Flows*, **9**(1), 26–31.

Fib (2015). *Benchmarking of deemed-to-satisfy provisions in standards: durability of reinforced concrete structures exposed to chlorides, state-of-the-art report*. Fédération internationale du béton, Bulletin no. 76. Lausanne, Switzerland.

Ioannou I, Cadena JE, Aspinall W et al. (2022). Prioritization of hazards for risk and resilience management through elicitation of expert judgement. *Nat Hazards*, 112, 2773–2795.

ISO 2394 (2015). *General Principles on Reliability for Structures ISO 2394*.

JCSS (2001-2015). *Probabilistic Model Code, JCSS Joint Committee on Structural Safety*.

Mattsson, H.Å. (2008). *Integrated Bridge Maintenance: Evaluation of a pilot project and future perspectives*. Doctoral dissertation, KTH School of Architecture and Built Environment, Stockholm.

Melchers, R.E. & Li, C.Q. (2009). Reinforcement corrosion initiation and activation times in concrete structures exposed to severe marine environments. *Cement and Concrete Research*, **39**(11), 1068–76.

Moubray, J. (1997). *Reliability-Centered Maintenance*, 2nd Edition. Industrial Press, New York.

Gimsing, N. J. (2000a). *The Øresund Technical Publications: THE BRIDGE*. Øresundsbro konsortiet.

Gimsing, N. J. (2000b). *The Øresund Technical Publications: THE TUNNEL*. Øresundsbro konsortiet.

Sánchez-Silva, M., Frangopol, D.M., Padgett, J. & Soliman, M. (2016). Maintenance and operation of infrastructure systems: Review. *Journal of Structural Engineering*, **142**(9): F4016004.

Silva, A., Neves, R. & De Brito, J. (2014). Statistical modelling of carbonation in reinforced concrete. *Cement and Concrete Composites*, **50**, 73–81.

Stewart, M.G. & Melchers, R.E. (1997). *Probabilistic Risk Assessment of Engineering Systems*. Chapman & Hall

Straub, D., Malioka, V. & Faber, M.H. (2009). A framework for the asset integrity management of large deteriorating concrete structures, *Struct. Infrastruct. Eng*., **5**(3), 199–213.

Thöns, S. (2018). On the Value of Monitoring Information for the Structural Integrity and Risk Management. *Computer-Aided Civil and Infrastructure Engineering*, **33**(1), 79–94.

Thöns, S. & Björnsson, I. (2023a). *Pre-study: Öresund-Bridge Service Life Extension (EXTEND)*. Project report.

Thöns, S. & Björnsson, I. (2023b). *Workshop documentation: Öresund-Tunnel Service Life Extension (EXTEND)*. Workshop report.

Thöns, S., Björnsson, I. & Celati, S. (2024). On service life quantification and service life management. *II Fabre Conference – Existing bridges, viaducts, and tunnels: research, innovation, and application.*

Zhang, W.H., Lu, D.G., Qin, J., Thöns, S. & Faber, M.H. (2021). Value of information analysis in civil and infrastructure engineering: a review. *J. of Infrastructure Preservation and Resilience*, **2**(1), 16.


Taylor & Francis
Taylor & Francis Group
http://taylorandfrancis.com

SS39: Digital enabled asset management of major bridges

Organizers: T. Friis & I. Gualtero


Taylor & Francis
Taylor & Francis Group
http://taylorandfrancis.com

Bridge Maintenance, Safety, Management, Digitalization and Sustainability – Jensen, Frangopol & Schmidt (eds)
© 2024 The Author(s), ISBN 978-1-032-77040-6
Open Access: www.taylorfrancis.com, CC BY-NC-ND 4.0 license

Extending great belt bridge bearing service life using mobile computer vision

J. Winkler
Digital Engineering Solutions – DES & AtkinsRéalis, Warsaw, Poland

M.D. Havelykke & F. Bormlund
Sund & Baelt A/S, Copenhagen, Denmark

ABSTRACT: Our industry is facing a global problem with aging infrastructure. We need asset health data to extend service life of structures and thereby decarbonize our sector. Current structural monitoring tools are too expensive and not scalable enough. However, mobile computer vision technology has a potential to revolutionize structural monitoring by providing easy to use and affordable tools like regular smartphones. Great Belt East Bridge forms a part of the critical Scandinavian infrastructure. Inside the bridge anchor block there are several structural elements like bearings that ensure safe operation of the bridge. The bridge owner (Sund & Bælt) was concerned about the proper functioning of the bearings. This paper shows how Sund & Baelt technicians with no prior monitoring experience used a regular smartphone to capture and analyse bridge asset health data with sub-mm accuracy. The DES mobile app allowed for rapid data collection and analysis of the bearing behavior. The visual data obtained from the app triggered maintenance actions that ensured proper functioning of the bearings. Today, the mobile app for asset condition survey is used in connection with Sund & Bælt's operation and maintenance of the bridge. According to the bridge owner the mobile app has a potential to revolutionize bridge structural health monitoring worldwide.

1 INTRODUCTION

1.1 *Context and client goals*

The total value of the world's infrastructure is estimated at $50 trillion and ageing rapidly. Despite $70 billion spent on bridge maintenance alone there is a growing number of catastrophes in both developed and developing countries. The existing tools for monitoring and infrastructure management are usually too expensive and too complicated and therefore, most repairs are reactive and costly. The infrastructure will continue to develop and the constant reduction in maintenance budgets is posing serious challenges but at the same time creating an opportunity and a demand to introduce digital technologies. Sund & Bælt is Scandinavia's largest private infrastructure asset owner and has total responsibility for the operation and the maintenance of the Great Belt Bridge, Öresund Bridge (linking Denmark and Sweden) and Fehmarn Tunnel (world's longest immersed tunnel) Figure 1.

The Danish, state-owned holding company's strategy is to digitalize operations of the large infrastructure assets in collaboration with external technology partners like Digital Engineering Solutions - DES. The client have been using the DES mobile system and AtkinsRealis expertise to enhance their monitoring and measuring capabilities on the bridge. The data about structural performance (including damage detection) acquired by Structural Health Monitoring systems (Farrar & Worden, 2007) are used to develop maintenance strategies to

DOI: 10.1201/9781003483755-373



Figure 1. Sund & Bælt is Scandinavia's largest private infrastructure asset owner.

reduce operations costs and to improve reliability (Winkler & Hendy 2016, 2017). Sund & Bælt 2025 sustainable goals include:

- Reduction of operational costs: 2% per year
- Keeping constant cost level after 2024/2025 despite aging asset
- Maintaining quality and accessibility

1.2 *Structure description*

The Great Belt East Bridge has a central span of 1624 m with 535 m side spans and pylons reaching up to 254 m. The bridge carry a four lane motorway plus emergency lanes. 31 m wide welded steel box girder is continuous between the anchor blocks over the whole suspension bridge length (Figure 2).



Figure 2. Great Belt East Bridge.

The total length of the Great Belt Fixed Link is 18km long consisting of a road suspension bridge, a railway tunnel and a box-girder bridge for both road and rail traffic.

2 PROBLEM

2.1 *Bearing PTFE plate deterioration*

Inside the anchor block there are several structural elements like bearings that need to be monitored to ensure safe operation of the bridge. During one of the inspections it was noticed that the PTFE plate was getting worn out excessively indicating bearing malfunction (Figure 3).



Figure 3. Bearing and deteriorated PTFE plate.

The client was trying to identify the cause of the bearing problem. The first assumption was related with the mechanical issue (the friction between the PTFE plate and the bearing was potentially impacted as the plate was positioned on uneven stainless-steel plate). During a follow up inspection it turned out that the steel plate below stainless steel was deformed, causing local deformation. The second assumption was related with the bridge suspension span moving more than intended (due to f.x. increased traffic) and thereby inducing bigger movement on bearings.

The client decided to use the mobile app to capture additional monitoring data. It should be noted that there was a displacement sensor already installed on the bearing providing data on longitudinal movements. However, the client considered potential bearing rotation as a primary concern and wanted to gather visual data on the movement mechanism to better understand the overall behaviour.

3 SOLUTION

3.1 *DIC mobile app*

Mobile phones have never been just "phones." From camera to games, mobiles have always offered more than the standard calling experience. Now, the abilities of mobile phones have taken a new turn. Nowadays, smartphones come with superior-quality cameras. When integrated with computer vision and Digital Image Correlation (DIC) algorithms, these cameras can be used to provide professional services.

Computer vision give mobile devices the ability to see and process visual information like objects or images. Computer vision is becoming increasingly popular globally and is being applied in a wide range of industries. However, the application of mobile computer vision in structural health monitoring was virtually non-existent.

Sund & Baelt being one of the world's most innovative/digitally focused infrastructure asset owners was looking for smart solutions and recently adopted a technology that combines easiness of use, digitisation and flexibility in data collection & analysis. The technology was developed by DES - a pioneer in connecting AI with mobile computer vision for optimal structural monitoring (Figure 4).



Figure 4. Mobile DIC app developed by DES.

The method uses a regular smartphone mounted on a tripod, at a static position. Two setups for mobile monitoring were arranged: Setup 1 was used for capturing data on rotations while Setup 2 was used to simultaneously collect data on bearing movement (Figure 5). The mobile app system was collecting data for 2 days continually and the distance between a smartphone and the bearing was kept constant throughout the monitoring period. Light was provided by the client and the calibration procedure was done by implementing a known dimension into the software.

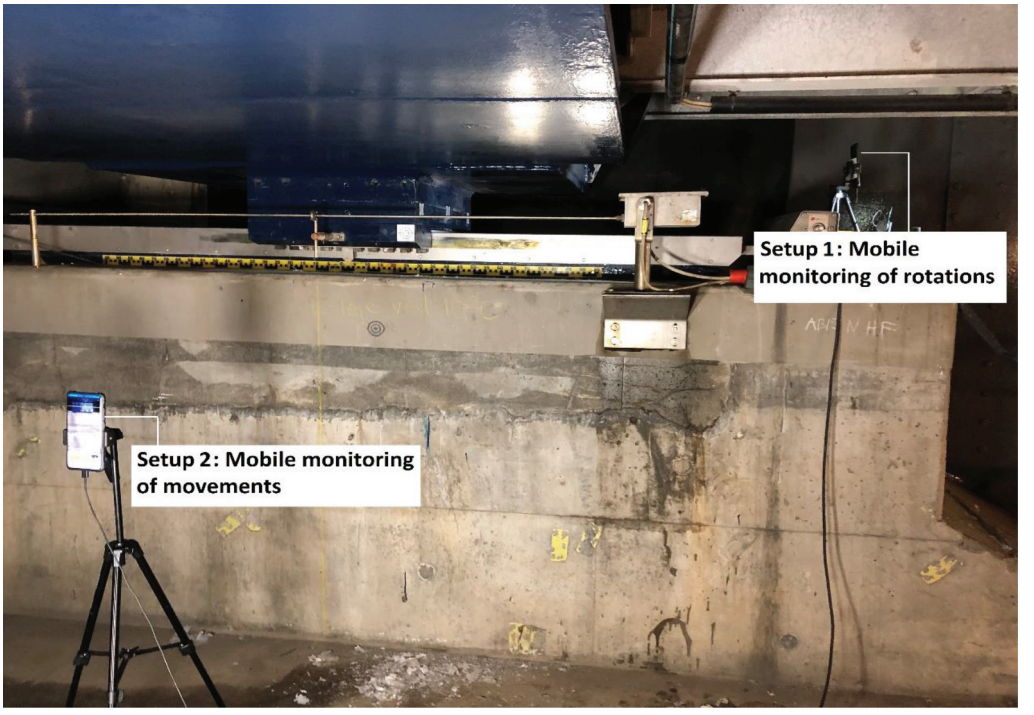


Figure 5. Mobile DIC setups for bearing monitoring.

Visual data acquired from the mobile setups were used to investigate bearing rotational movements (Setup 1). The results showed that there was no rotation of the steel part sitting on top of the bearing (Rotation 1 – see Figure 6) . However, the images collected over time clearly showed a rotation of the bearing plate (Rotation 2 – see Figure 6) and the subsequent rapid deterioration of the PTFE material. These results supported the assumption of an uneven steel plate affecting the behavior of the bearing.

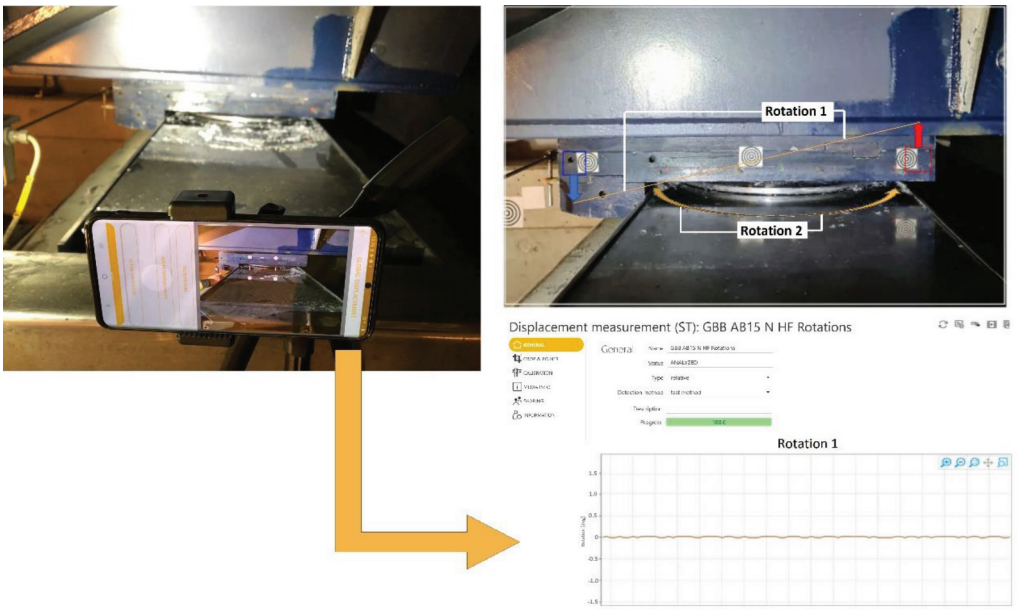


Figure 6. Setup 1: Mobile monitoring of bearing rotations.

To better understand the holistic bearing behaviour the mobile app was also employed to simultaneously collect data on movement (Figure 7). The results showed that the movement of the bearing exceeded the anticipated amount.

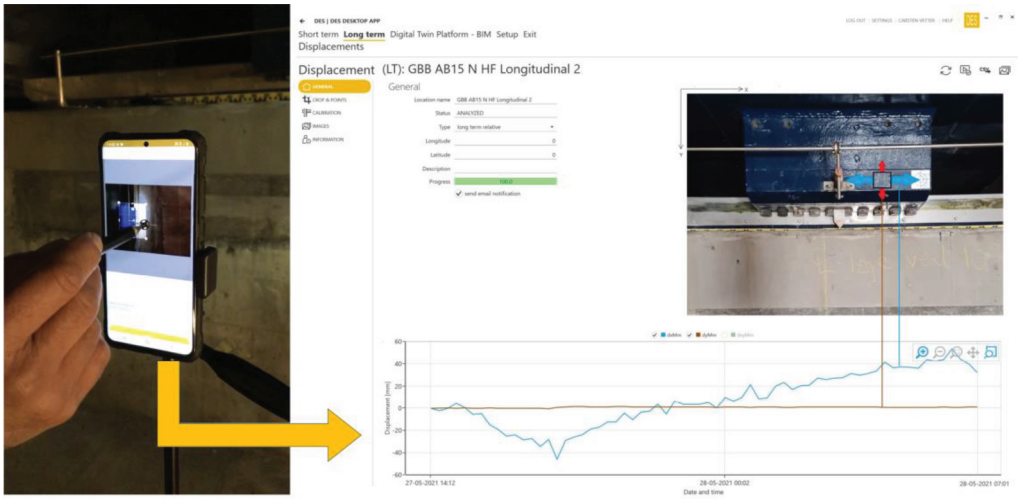


Figure 7. Setup 2: Mobile monitoring of bearing movement.

No specialist equipment or training was required to take and analyse the measurements. The mobile app uses AI and computer vision to analyse vidoes or images and the results are returned in as little as few minutes. The user sets the parameters for the capture and the algorithms incorporated into the app do the rest.

The mobile app measurements are highly accurate and have been validated multiple times against traditional equipment. A calibration certificate has been issued by an accredited laboratory according to the standards for European ISO 9513 and American ASTM E83-16.

4 MAINTENANCE ACTION

The client took two maintenance actions following the mobile app monitoring investigation. First was related with replacement of the stainless-steel plate to ensure proper bearing behaviour (no rotational movements) and replacement of the PTFE plate (Figure 8).



Figure 8. Maintenance action to replace the damaged elements of the bearing (PTFE plate).

Second maintenance action involved correction of the hydraulic pressure of the buffers to reduce bearing movement to allowable limits. The mobile app allows repetitive measurement for comparison purposes which showed that the bearing movement after the maintenance action and correction was as intended (23 mm at the highest point rather than 75 mm - see Figure 9).

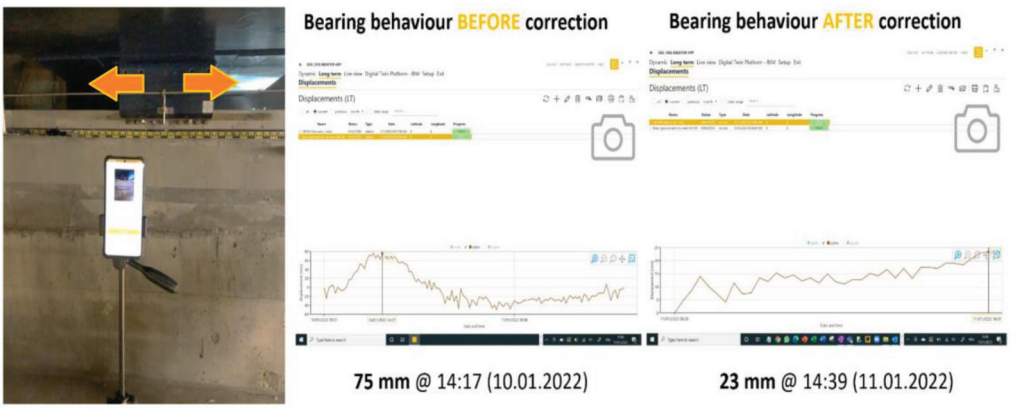


Figure 9. Movement of the bearing before and after hydraulic pressure correction.

5 CONCLUSIONS

Sund & Baelt is now able to take measurements anywhere along the bridge girder (more than 1.6 km long) using the DES mobile app. Previously, collecting additional monitoring data on expansion joints, bearings, decks or girders was too expensive. Traditionally, highly qualified experts along with specialized equipment are required for this level of monitoring. It also took a long time for the data to be analyzed and results produced. Now with the easy-to-use app functionality with its visual inspection and sub-millimeter measurement capability, accurate results can be acquired in a matter of minutes and available at the point of measurement if necessary.

The mobile app measurement triggered maintenance actions that ensured safe operation of the bearings and extended service life of critical structural elements.

Sund Baelt considers the mobile app SHM system as ground-breaking and disruptive technology that enables fundamental changes in the way bridge monitoring and asset management is carried out.

REFERENCES

Farrar, C.R., Worden, K. 2007. An introduction to structural health monitoring. *Philosophical Transactions of the Royal Society A: Mathematical, Physical and Engineering Sciences*, 365(1851), pp.303–315.

Winkler, J., Hendy, C. 2016. Improved Structural Health Monitoring of Bridges using Digital Image Correlation. *8th International Conference on Bridge Maintenance, Safety and Management (IABMAS 2016)*, DOI https://doi.org/10.1201/9781315207681

Winkler, J. Hendy, C., 2017, Improved Structural Health Monitoring of London's Docklands Light Railway Bridges Using Digital Image Correlation, Str*uctural Engineering International* 27(3): 435–440, DOI:10.2749/101686617X14881937384648.

Bridge Maintenance, Safety, Management, Digitalization and Sustainability – Jensen, Frangopol & Schmidt (eds)
© 2024 The Author(s), ISBN 978-1-032-77040-6
Open Access: www.taylorfrancis.com, CC BY-NC-ND 4.0 license

30 years' experience of optimizing the use of corrosion sensors

P.H. Møller
Ramboll, Hannemanns Allé 53, Copenhagen S, Denmark

S. Gjerding
Sund & Bælt Holding, Vester Søgade, Copenhagen, Denmark

ABSTRACT: For 25 years corrosion sensors at the concrete structures of the Great Belt Link in Denmark have been tested by various standard methods, but the results did not allow for a satisfactory evaluation of the corrosion in the splash zone, partly because of cathodic protection from anodes in the water installed at the Great Belt Link. The use of alternative/traditional inspection methods is difficult in the splash zone and therefore it was investigated if corrosion evaluation in this very important zone could be improved by optimizing the use of the corrosion sensors. The sensor setup was changed from separate sensor parts to all sensor parts being connected to the reinforcement which allowed detailed evaluation of the complex conditions in the splash zone governed by macro-cell corrosion and protection/prevention from the water anodes. Introduction of continuous monitoring allowed to document the influence from weather conditions on the corrosion conditions in the splash zone.

1 CORROSION SENSORS IN CONCRETE STRUCTURES, LITERATURE REVIEW

Around 1990 the main concept for corrosion sensors was introduced. The concept consists of sensor anodes arranged in a ladder system and the corrosion status of each sensor anode is mainly evaluated by measuring short-time (5 sec.) macro-cell current. The system layout, the measurement methods and 10 years' experience of the system is presented in (Raupach et al. 2000). The main purpose of this system is to determine the time of reinforcement corrosion initiation, but the measuring methods do not allow for evaluation of the corrosion rate after initiation.

To allow for taking account of the propagation phase methods for measuring corrosion rate after initiation were introduced. A review of relevant methods is presented in (Figueira 2017). Usually the Linear Polarisation Resistance (LPR) method is used, and a presentation and evaluation of the LPR methods is found in (Nygaard et al. 2012). Design of a sensor system and the results from continuous LPR measurements from 3 years field exposure is found in (Sørensen et al. 2013). The results from (Sørensen et al. 2013) showed an intermediate phase between the change of corrosion status from passive to active. During the intermediate phase status changes several times between active and passive. After the intermediate phase status stabilizes as active.

To measure corrosion rate at surfaces subjected to partial cathodic protection the sensor setup and the measuring methods must be adjusted. An example of such adjustments and the results from 10 years field testing is presented in (Møller et al. 2018).

Earlier corrosion systems were monitored by "snapshot" measurements, i.e., measurements with typical intervals between 1 and 5 years, but the long-term results (Sørensen et al. 2013) and (Møller et al. 2018) have shown that the results are significantly influenced by seasonal changes and fluctuations of corrosion status during the intermediate state between permanent active and permanent passive status. By a more "continuous" monitoring, e.g., measurement intervals between 1 hour and 1 week, interpretation of the results could be significantly more precise and reliable.

DOI: 10.1201/9781003483755-374

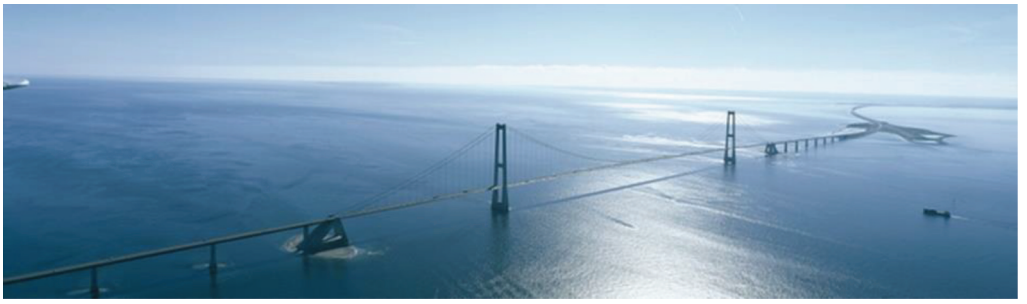


Figure 1. Great Belt Link, High bridge (front) and Low bridge (back).

2 CORROSION SENSORS AT THE GREAT BELT LINK

The Great Belt Link, see Figure 1, is 17 km long and consists of 7 km High bridge (road), 7 km Low bridge (road and rail) and an 8 km rail tunnel. At the 2 bridges a total of 222 corrosion sensors are installed and 224 sensors are installed in the tunnel. This paper only describes the sensors in the High bridge where sensors are installed at levels between -1.2 m and +14 m. In the splash zone sensors are installed at levels 0, +1.2 and +2.5 m. Sensors in casting joints are installed in level +4 m and + 12 m.

The sensor layout and the initial test methods for the Great Belt Link sensors are according to (Raupach et al. 2002). Measurements were planned to be performed as "snapshot" measurement campaigns at all sensors every 1-5 years. The purpose of the sensors was to determine the time for reinforcement corrosion initiation.

3 GOVERNING CORROSION CONDITIONS AT THE GREAT BELT LINK

To improve the corrosion evaluation by sensors the governing factors of corrosion development at the piers were inspected by traditional inspection methods. The main results were:

- The structures below water are corrosion protected by galvanic anodes to prevent corrosion in cracks formed during fabrication of the caissons. Surface based measurements showed that parts below level 0 m are fully protected by the water anodes and the parts just above level 0 m are partly protected. However above +2.5 m protection is low.
- Chloride measurements indicate that corrosion initiation is highly dependent of the distance to the water level, i.e., 100 years at water level but > 500 years 5 m above water level, see Figure 2.
- Above +4 m concrete AC resistance is so high, that risk of macro-cell corrosion is low. In the splash zone AC resistance is much lower and risk of macro-cell corrosion is thereby significantly increased.

The Great Belt Link is designed for a service life of 100 years but the possibility for an extension to 200 years is highly prioritized.

4 EARLIER RESULTS FROM CORROSION SENSORS AT THE GREAT BELT LINK

After conducting a few initial measurement campaigns, the results revealed that the electrochemical potential of the intended cathode (platinized titanium) was significantly reduced due to the high concrete moisture level in the lower splash zone and underwater zone. Consequently, the role of the intended cathode could shift to that of an anode in the context of the 5 sec. macro-cell current measurement method. As a result, it was concluded that the

interpretation of the original sensor measurements was unreliable for sensors located underwater and in the lower part of the splash zone.

Since chloride measurements clearly indicate that the highest corrosion risk occurs within the lower splash zone, the interpretation challenges in this area substantially diminish the value of the suggested sensor concept. Consequently, the 5 sec. macro-cell current measurements were replaced with LPR measurements, and a new measurement campaign was carried out. However, performing LPR measurements in the lower splash zone posed difficulties, leading to reduced reliability. Furthermore, LPR measurements do not account for the possible corrosion protection provided by the water anodes. The presence of such protection in the lower splash zone could significantly reduce corrosion, rendering a sensor system incapable of considering cathodic protection from water anodes less valuable.

Additionally, the relatively frequent manual measurements incurred non-negligible costs. Therefore, it was necessary to consider whether reducing the focus on sensor measurements in favor of traditional corrosion monitoring methods would be more practical.

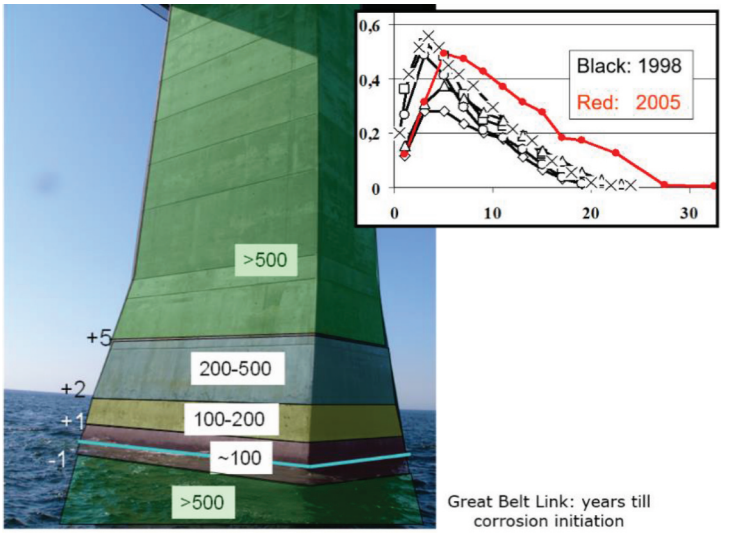


Figure 2. Time till reinforcement corrosion initiation (years) based on chloride ingress simulation.

5 OPTIMIZING THE RELEVANT SENSOR MEASURMENT METHODS

5.1 *General*

The traditional inspection showed that corrosion problems might arise within a 200-year service life in the zone between 0 meters and +4 meters. Outside this zone, the corrosion risk is very low. Therefore, corrosion measurements should be optimized for the zone between 0 and +4 meters. Experience has shown that repairing corrosion damage in concrete is very expensive. Consequently, it is highly important to prevent the development of corrosion damage that would necessitate concrete repairs. Cathodic protection is expected to be the most relevant prevention method, and the cost of cathodic protection depends significantly on where the anodes are being installed:

– Underwater installation costs are low, and maintenance costs are very low.
– Above approx. level +2 m installation costs and maintenance costs are moderate.
– Between 0 and +2 m installation cost are very high, and maintenance costs are also high.

The most relevant strategy for corrosion prevention in the zone between 0 and +4 m is to maximize protection from water anodes and only install anodes above +2 m when/if the prevention provided by water anodes is insufficient. To implement this strategy, sensor measurements should be able to address the following questions:

– When will corrosion be initiated in the zone between 0 and +4 m?
– What is the upper limit of corrosion protection from the water anodes?
– What is the upper limit of corrosion prevention from the water anodes?
– When must anodes above level +2 m be installed?

Within the zone between 0 and +4 m the traditional inspections indicate the following:

– Uniform corrosion can be relevant throughout the entire zone above water.
– Macro-cell corrosion can be relevant for æbetween 0 to +4 m but not likely above +4 m.
– Cathodic protection from water anodes is relevant for the zone up to +4 m but it is unlikely to be effective above this zone.

5.2 *Measurement of uniform corrosion rate*

At the Great Belt Link, the uniform corrosion rate is measured using the LPR method. This method is generally well accepted, and the requirements for testing equipment are relatively low. According to Nygaard et al. (2012), LPR is primarily measured through methods that induce a controlled current or methods that induce a controlled change in the steel potential. During earlier tests at the Great Belt Link, both types of LPR methods were tested to optimize their use in the splash zone. The main observations specific to the splash zone were as follows:

– Potential fluctuations are significant, during moderate to high winds (refer to Figure 4). However, even under relatively calm conditions, variations remain noticeable. To minimize the dependency on weather conditions, LPR measurements should be robust in the face of potential fluctuations.
– Polarization measured without compensation for Ir-drop can be up to 10 times higher than polarization measured with Ir-compensation. Therefore, precise compensation for Ir-drop is essential for accurate LPR results.

To achieve the highest robustness against fluctuating potentials, the simplest LPR method (galvanostatic) was selected. Signal strength was enhanced by allowing a high polarization voltage (20 mV) and a relatively long polarization time (60 seconds). Polarization and depolarization were recorded by an external logger with a scan rate of 3 Hz, enabling measurement of Ir-drop both when power was switched on and when it was switched off (see Figure 3). This approach aimed to test the reliability of the measurement.

The adjusted LPR equipment was tested. Originally the equipment was intended to be tested during both calm and wind weather conditions. Unfortunately, no tests were performed during any calm periods. As such the results of all tests are taken during windy weather conditions.

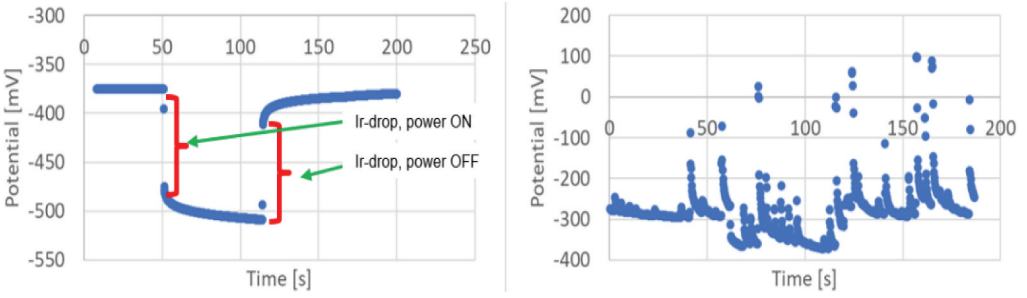


Figure 3. LPR-measurement level +1.2 m. Left: determination of Ir-drop. Right: sensor showing high noise.

The main results indicate that reliable LPR-measurements can be performed for levels above +1.2 m in most weather conditions, but for the critical sensors in levels 0 m and +1.2 m, measurements can only be performed in relatively calm weather.

5.3 *Testing measurement of cathodic protection methods*

According to the code for cathodic protection of concrete structures: ISO 12696:2022, Cathodic protection of steel in concrete (ISO 12696) the criteria for full cathodic protection are:

- The steel potential must be more negative than -884 mV (MnO_2/NaOH (0.5 mol/l))
- Depolarisation over a 24-hour period must be higher than 100 mV.

In addition, the protection can be evaluated from the design guidelines of ISO 12696:

- Cathodic prevention: current density should fall between 0.02 and 0.2 μA/cm^2.
- Cathodic protection: current density should fall between 0.2 and 2 μA/cm^2.

To establish cathodic protection each sensor anode is connected to the reinforcement by a separate cable.

The steel potential criterion can be tested directly by disconnecting the connection cable and measure the sensor anode potential with the reference electrode of the sensor. However, the calibration of these electrodes cannot be checked directly and therefore this measurement should be verified. Verification can be performed by handheld measurements (drop-cell) in the water.

To test the depolarisation criterion the connection cable is disconnected, and the anode depolarisation is measured over a 24-hour period.

The current density criterion is tested by measuring current flow through the connection cable.

5.4 *Macro-cell measurement*

Under real conditions, corrosion will start at a small area of the outer reinforcement and the other parts of the reinforcement will act as a cathode, possibly causing macro-cell corrosion. To simulate real corrosion initiation, the sensor anode should therefore be connected to the reinforcement. Through this connection both the influence from macro-cell corrosion and possible cathodic protection can be measured.

Each sensor anode is connected to the reinforcement through a separate cable, and by measuring the current flow in each cable the macro-cell corrosion can be measured. If current flow is negative, i.e., the anode is more negative than the reinforcement, the macro-cell corrosion rate can be calculated by Faradays Law showing that a current density of 1 μA/cm^2 corresponds to a corrosion rate of 11.6 μm/year. However, to determine the total corrosion rate, the local corrosion at the anode must also be considered. The local corrosion rate can be estimated from LPR measurements, but the sensor anode must be disconnected from the reinforcement and allowed to depolarize before LPR measurements are taken.

5.5 *Testing of cathodic protection and macro-cell measurement*

The most important outer anodes were connected to the reinforcement by separate cables. For one month, the current flow through these cables was monitored. Afterwards the anodes were disconnected and LPR and depolarisation was measured. Through this arrangement either the cathodic protection or the macro-cell corrosion is measured. If current flow is positive, cathodic protection current density is measured, and if current flow is negative, macro-cell corrosion is measured. Results are shown in Table 1.

Table 2. Main results from LPR-and macro-cell current testing.

Level/ orientation	Potential vs.		LPR, un-connected	Macro-cell corr.	CP current	1 h depo-larization.
	ERE10	Reinfor.				
	mV	mV	µm/year	µm/year	µA/cm^2	mV
+4 m/S	-350	-150	5	2 - 3		-84
+2.5 m/S	-180	-125	5	2 - 5		-55
+2.5 m/W	-100	+85	1-2	0 - 1	+0.05	+50
+1.2 m/S	-250	-200	40	30 - 60		-120
+1.2 m/W	-50	+340	5-18		-0.5-+5	+40
0 m/S	-738*	+90	80		-0.1-+0.2	+2
0 m/W	-940*	+75	40		-0.1-+0.1	+2
-1.2 m/S	<-940*	+360	33		0-+0.1	+2
-1.2 m/W	-996*	+66	Approx. 60		0-+0.02	+3

*Potentials measured after test period

6 DISCUSSION

6.1 *Upper level of protective effect from anodes in water*

The sensor anodes at level +1.2 m W and +2.5 W were most likely in a passive state before the cathodic protection from the water anodes was established (green in Table 1) because anode potential is 100-200 mV higher than reinforcement potential. After connection, macro-cell corrosion was low <1-2 µm/year and 1 hour depolarisation was 40-50 mV, see Figure 4. Ramboll has compared depolarisation after 1 hour and 24 hours on other structures and it showed the following: At level +1 m 24- hour depolarisation was 3 times higher than 1-hour depolarisation. At level +3 m the 24-hour depolarisation was approx. 2 times higher than 1-hour depolarisation. It is therefore likely that the measured protection of the passive anodes fulfils the ISO 12696 100 mV criterion for full cathodic protection.

However, for the anodes showing signs of corrosion initiation (red in Table 1), before connection to the water anodes, the depolarisation is negative. This indicates macro-cell corrosion and no cathodic protection. This means that the reinforcement will not be protected, but instead connection to the reinforcement will seriously increase corrosion.

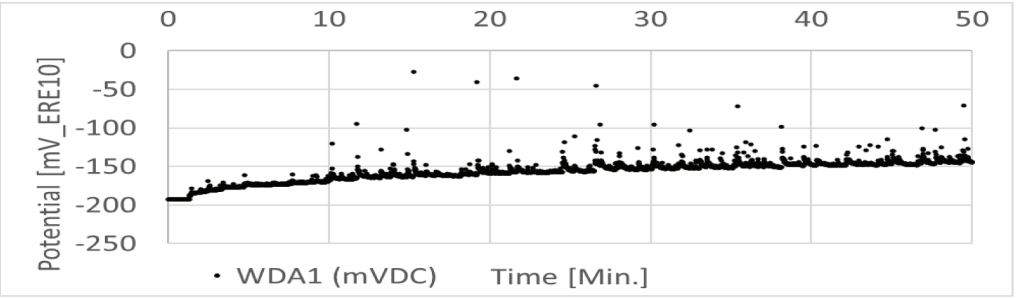


Figure 4. Level +2.5m W. 50 minutes depolarization. Depolarization is not finalized.

The measurements thereby indicate that the protection from the anodes in water can have a significant preventive effect up to level +2.5 m but cannot stop ongoing corrosion at level ≥+1.2m.

6.2 *Protection in and close to water*

The potentials of the 2 anodes at level -1.2 m and anode *0 m/W* at level 0 m fulfil requirements for full cathodic protection and according to ISO 12696 their corrosion rate is therefore negligible. However, the potential of the anode *0 m/S* at level 0 m does not fulfil the criterion, but the magnitude, development, and the depolarisation of the macro-cell current of this anode is very similar to the macro-cell current of the other 3 anodes, see Figure 5. For all 4 anodes current is high initially but is highly reduced after 1-2 days and reduces further to 0.01-0.04 μA/m^2. This very low current changes the natural corrosion potential of the anodes by 66 and 360 mV, which indicate that the cathode reaction (oxygen reaction) is highly restricted by poor oxygen access. The poor oxygen access is also responsible for the very low depolarisation rate of 2-3 mV/hour.

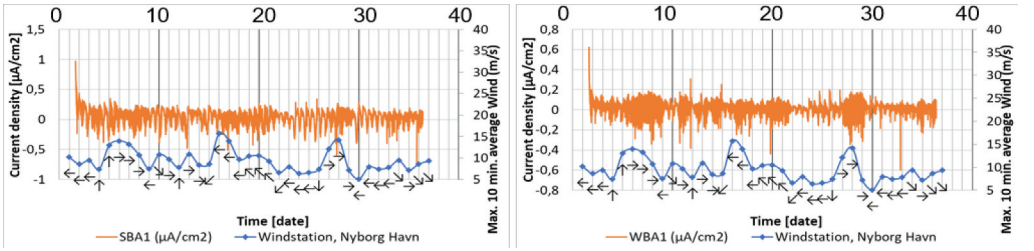


Figure 5. Macro-cell current. Left, level 0 S. Right Level 0 W. Same current size and development.

All 4 anodes in and close to water exhibits the same overall polarisation and depolarisation development and therefore all these anodes will most likely have the same negligible corrosion rate.

6.3 *Influence from macro-cell corrosion*

For actively corroding anodes at level +2.5 and +4 m (red in Table 1) a moderate uniform corrosion and a moderate macro-cell corrosion rate is measured after these anodes are connected to the water anodes. At the actively corroding anode at level +1.2 m, much higher corrosion rates of both uniform and macro-cell corrosion is measured.

The uncertainty of the measured LPR corrosion rate is expected to be quite high at +1.2 m and upwards, but for level 0 and below the uncertainty is expected to be extreme. For level 0 and below corrosion rates are most likely lower than 2 μm/year, but rates >50 μm/year are measured.

The macro-cell corrosion can be measured accurately. However, for the connected sensor anodes, the rate might be realistic for reinforcement corrosion, because anode/cathode ratio for the sensor anodes is lower than for the reinforcement. The measured influence from macro-cell corrosion is therefore expected to be overestimated. However, even if accounting for this incorrect anode/cathode ratio, the macro-cell corrosion at level +1.2m is expected to be very high.

6.4 *Intermitted protection and long-term protection development from water anodes*

In Figure 6 it is clearly seen that the protective effect from the water anodes is highly increased during high winds. The measurements indicate that high winds increase the upper limit of significant protection of actively corroding anodes from less than +1.2 m in calm weather to more than +2.5 m in high winds. To determine the accumulated benefit from the water anodes

it is therefore important to understand the effect of intermitted protection. ISO 12696 mentions this but it is not quantified. The depolarisation measurements indicate that intermitted protection can have a high effect for preventive protection, but the results are insufficient to draw solid conclusions.

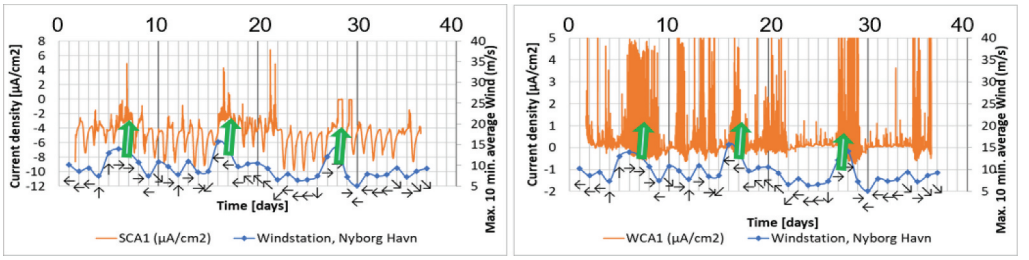


Figure 6. Relation between high wind (green arrows) and protective current from the water anodes. Left +1.2m S, actively corroding anode (macro-cell current reduced by wind). Right +1.2m W, passive anode (cathodic protection current increased by wind).

Regarding the long-term effects of establishing cathodic protection, the electric field caused by the protective current will generally slow chloride migration towards the reinforcement, and thereby increase time until the critical chloride concentration is developed at the steel surface and thereby delay corrosion initiation. Furthermore, cathodic protection reduces the aggressivity of the concrete at the steel surface by forming protective hydroxides and by removing aggressive chloride ions. Corrosion is expected to initiate when a given level of the $[Cl^-]/[OH^-]$ ratio is exceeded. The production of OH^- and the reduction of Cl^- by the cathodic protection thereby increases the critical chloride concentration. Corrosion initiation is thereby delayed because chloride migration is reduced, and a higher concentration must be established before corrosion starts. It is well known that the protective effect of cathodic protection will improve over time and the effect of the water anodes measured after just one month protection will most likely be increased significantly over the years.

7 SUGGESTED MEASUREMENT PROCEDURE FOR SENSORS IN THE SPLASH ZONE

Based on these results, the following measurement procedure is suggested:

- Base situation: all anodes are connected to the reinforcement and macro-cell current is monitored.
- At regular intervals each anode is disconnected, and 1 h depolarisation measured.
- After depolarisation LPR is measured whereafter anodes are reconnected to reinforcement

Due to very fluctuating conditions in the splash zone frequent logging is necessary for satisfactory monitoring of the conditions. For sensors >+4 m or <0 m frequent logging is not needed. To explore the possibilities of protecting the splash zone without anodes in the problematic zone 0 to +2 m it might be necessary to perform test installation of anodes just above +2 m and to test the effect of maximizing the protection from the water anodes, e.g., by more anodes.

8 CONCLUSION

The use of corrosion sensors for concrete bridges was analysed and concluded that the original test methods were unable to give a full picture of the corrosion in the splash zone. This is problematic since this zone mostly is governing for the condition of the bridges. Analysis

showed that the corrosion conditions in the splash zone are very complex and the usual evaluation from simple chloride ingress measurement are insufficient. Furthermore, it was found that installation of sacrificial water anodes could provide good corrosion prevention. The use of corrosion sensors was therefore optimized for the use in connection with water anodes.

The measurements indicated that macro-cell corrosion between outer- and inner reinforcement can accelerate corrosion highly. Measurements indicated that water anodes could prevent corrosion up to level +2.5 m, but that they might not stop ongoing corrosion even at level +1.2 m. This indicates the value of timely installation of water anodes. However, measurements showed that the corrosion conditions in the splash zone fluctuates highly, mainly from the sea waves, and to obtain a realistic picture of the corrosion conditions, continuous monitoring is necessary. Furthermore, the measurements indicate that corrosion might be highly reduced by poor oxygen access in the zone just above the water line.

For the concrete structures of the Great Belt Link, it is concluded that the main corrosion problem for obtaining 200-year service life is to prevent corrosion development without installing anodes in the zone 0-+2 m. The optimized use of the sensors can provide valuable information for designing this corrosion prevention. However, the full effect of these preventive measure is expected to improve over a long time and the monitoring period must therefore be long. Furthermore, the effect of the preventive measures fluctuates highly by the weather conditions and therefore detailed continuous monitoring is necessary. However, even with such detailed monitoring evaluation is difficult because the usual design models are insufficient for the fluctuating conditions in the splash zone. However, the monitoring can improve these models.

REFERENCES

Raupach, M. & Schiessl, P. 2000. Monitoring Corrosion Risk in Concrete Structures-Review of 10 Years Experience and New Developments, Fifth CANMET/ACI international Conference on Durability of concrete.

Figueira, R. B. 2017. Electrochemical Sensors for Monitoring the Corrosion Conditions of Reinforced Concrete Structures: A Review. Applied sciences.

Nygaard, P. V. & Geiger, M. R. 2012. Measuring the corrosion rate of steel in concrete – effect of measurement technique, polarisation time and current. Materials and Corrosion.

Henrik Erndahl Sørensen & Ulf, Jönsson 2013. Monitoring of Reinforcement Corrosion in Field Exposed Concrete Blocks. IABSE symposium.

Peter H. Møller & Hans-Aage Munk Cordua 2018. Monitoring of the performance of concrete repair. IABSE conference Copenhagen.ISO 12696:2022, Cathodic protection of steel in concrete.

ISO 12696:2022, Cathodic protection of steel in concrete.

Bridge Maintenance, Safety, Management, Digitalization and Sustainability – Jensen, Frangopol & Schmidt (eds)
© 2024 The Author(s), ISBN 978-1-032-77040-6
Open Access: www.taylorfrancis.com, CC BY-NC-ND 4.0 license

Digital technologies for bridge damage detection: Drones and AI for remote inspections

D. Buggiani, M. Malavisi & A. Baldacci
Movyon s.p.a, Roma, Italy

ABSTRACT: Transportation infrastructure have a considerable impact on the economic, social and political growth of nowadays society. In particular, highway bridges, due to their inherent vulnerability, are affected by aging and degradation processes over time, which lead to a loss of the expected performances. Periodic inspection is therefore essential to ensure their safety and serviceability. In common practice, defects assessment is performed through visual inspections carried out by engineers that come close to the bridges to perform the inspection. However, these activities are laborious, require huge cost and time and have significant safety implications. Moreover, there might be a wide disparity in the quality of visual inspections depending on the experience, knowledge, and competence of inspectors. To cope with these issues, the use of drones, can allow performing visual inspections, maximizing damage identification quality and minimizing costs as well as user safety. This work illustrates an innovative and powerful methodology to perform completely remote visual inspections using drones. In particular, a tool to perform remote inspections using the digital twin of a bridge is presented, combining state-of-the art 3D reconstruction methods with AI technologies for defects detection and high-resolution 3D rendering. The tool empowers inspectors with a Web application which improves and speeds up the process of defects detection, verification and tracking through time. We demonstrate significant improvements upon precision and recall of defects detection with respect to on-site inspections even in the most challenging cases. Significant experience from different Italian bridges is shown, confirming the opportunities and challenges of performing remote inspections applying the developed methodology.

1 INTRODUCTION

In 2020, the Guidelines for risk classification and management, safety assessment and monitoring of bridges have been issued in Italy as regulatory instrument for existing structures (MIT, 2022; Junwon Seoa, 2018). According to these guidelines and related operating instructions, every bridge must be subjected to visual inspections performed at regular intervals ranging from a minimum of 3 months to a maximum of 2 years, depending on the risk level of the bridge. Traditional inspections require experienced engineers to physically go on site and visually analyze all components of a bridge, in order to identify any defects or deterioration phenomenon and report it to the infrastructure manager. However, this entails strong impacts in terms of costs and time as well as social consequences on the highway operation caused by lane or roadway closures. Moreover, these activities involve considerable risks for safety of workers as well as an inaccurate, non-measurable and non-repeatable detection of defects, especially in hard to reach locations or parts of complex bridges, with inadequate lighting and conditions.

In recent years, many studies (M. Mandirola, 2022), (F. Giacobbe, 2018), (In-Ho Kim, 2022), (Jin Fan, 2019) have focused on the possibility of using Unmanned Aircraft System (UAS, according to the definitions proposed in the current European Union Regulations EU 2019/945 (EU, 2019)) commonly known as drones, equipped with different cameras and

DOI: 10.1201/9781003483755-375

sensor technologies, as an efficient and cost-effective support, or in some cases an alternative, for visual inspection activities, being able to reduce the impacts on traffic, costs, times and operators' safety in many inspection scenarios. Furthermore, drones have some advantages over conventional inspection practices regarding the inspection's quality, allowing quantifiable, measurable and repeatable defects identification over time (Junwon Seoa, 2018).

However, if, on the one hand, the use of drones appears to be a promising alternative for carrying out remote inspections on bridges in a safer and more efficient way, on the other hand the amount of data collected by the drone needs to be appropriately managed and made available to the inspector for carrying out the inspection as he would do on site. Indeed, UAS collect a massive amount of data during a flight, that require to be stored, postprocessed, analyzed and elaborated to be effectively used by structural engineers. (FHWA, 2021) underlined how appropriately manage data collected by drones can be one of the most challenging aspects of using this inspection methodology.

This paper describes a comprehensive practice-oriented approach and related platform, named ARGO 3D, for drones-based inspection. ARGO 3D is part of the larger ARGO asset management platform, developed by Movyon and Autostrade per l'Italia companies, for assisting highway and bridge managers in their choice of optimum improvements to the bridge network that are consistent with the national regulations, long-term objectives, and budgetary constraints.

The starting point for ARGO 3D platform is the standardization and control of all phases of bridges inspection process and data and, at the same time, the development of all the tools needed to use data collected during flights. Indeed, many research study were conducted regarding drone inspections, but there are still limitation in the standardization of the process, in the easy and effective use of data and in the availability of technologies able of covering the end-to-end remote inspection process. The developed platform solved these challenge problems by automating and integrating the entire bridge inspection procedure in a single easy to use inspection tool, perfectly aligned with Italian regulations.

The main contribution of the work is, thus, to propose drones-based inspection methodology and describe the innovative technological platform ARGO 3D, emphasizing how it is able to optimize the entire process, starting from inspection mission planning to data acquisition, processing and delivery, providing inspectors with all the tools needed to use data collected during flights and carry out bridge inspection in a much simpler and faster way than on the field.

2 BRIDGE INSPECTION USING DRONES: METHODOLOGY

This paper illustrates a methodology aimed at covering the whole end-to-end remote inspection process. The methodology has been fully implemented in the ARGO 3D platform. The term "inspection process" underlines the fact that there are several aspects that must be taken into account during bridge inspections, some related to field operations, other connected to some technical pre-process (e.g. digital twin creation or AI algorithms) and, finally, some related to the interaction with the platform users with the role "Inspector".

Before describing the proposed approach, some important pre-requirements that need to be considered before and during the data collection and necessary to obtain a suitably reconstructed 3D model are illustrated:

- a correct GSD (ground sampling distance), not too big if the focus is to be able to see same narrow defects (f.i. cracks), not too small otherwise the amount of data cannot be managed.
- a certain overlapping among pictures during the image collection, that allow to correctly reconstruct the 3D model with the less possible human interaction.
- a correct GPS positioning of the images.
- some GCP (ground control points) to be able to determine the correct roto-translation, scale and georeferenced 3D model.
- as much surface of the infrastructure as possible must be covered with pictures, since every not covered part cannot be reconstructed and, hence, cannot be represented in the digital twin.

Once the flights technical requirements have been defined, the proposed methodology includes, for each bridge to be inspected:

i. **Data collection** through a drone flight around the bridge, according to the standards preliminarily define. Collected data must be appropriately managed, with a process that ensures that all the information has the correct quality and completeness, and that the whole data chain is signed and not repudiable.
ii. **3D reconstruction of the bridge**, i.e. the digital twin, to be used to carry out remote inspection. A digital twin is a 3D virtual model of a bridge, obtained using photogrammetric techniques or LiDAR, that can be used to view structures from different perspectives and angles, as being on the structure itself.
iii. **Damage identification through AI algorithms**, where deep learning-based data analytics and modelling are applied for processing and analyzing drones images, pre-identifying damages on the structure.
iv. **Inspection planning and assignment** on ARGO 3D platform, so that the inspector in charge, the inspection date and all the information related to the inspection are univocally traced inside the platform.
v. **Remote inspection execution** by the inspector and in particular: (a) the inspector accesses ARGO 3D platform and is able to view the digital model of the bridge and the simplified 3D model side by side, with the defects identified by the AI algorithms and those from previous inspections already highlighted on the 3D model; (b) the inspector selects the bridge component to be inspected on the 3D simplified model; (c) using "drawing" tools, the inspector can trace a defect (or select one identified by AI algorithms) and select its type from a drop-down menu, in accordance with the list of defects provided by the Italian guidelines; (d) the identified defect is automatically associated with the selected component; (e) the system automatically sends an image of the defect to the central system to be stored; (f) when all defects have been identified, the inspector can close the inspection and all defects are stored in the platform.
vi. **Automatic inspection report production**: once the inspection is completed, the system produces a report that assesses the state of the infrastructure, in a format compliant with the current Italian Guidelines, digitally signed by the inspector.

3 ARGO 3D - BASED INSPECTIONS

3.1 *Asset registry and standard visual inspections*

Standard bridge visual inspections can be performed using ARGO platform, the extended technological platform for managing and monitoring infrastructure life cycle.

The platform contains the digital inventory of all the bridges of Autostrade per l'Italia network, which are decomposed in smaller components (beams, piers, abutments,..) and stored in an asset management system, following a four levels hierarchy that allows to have a unique and fully replicable way to store all the bridge information (Figure 1). Using the bridge registry data, ARGO can automatically build simplified 3D models, following the BIM format, used to have a visual representation of the bridge to, on the one hand, verify the correctness of all the geometric data stored in the platform and, on the other hand, "guide" the inspector during the inspection on site.

ARGO visual inspection tool allows to carry out on-site inspection activities with the support of a platform that:

- allows to plan the inspections, assign and execute them in a traceable manner.
- provides inspectors with a mobile app, that help the human to be sure to fulfill all the checks that are recommended by Italian guidelines and by the company in charge of the infrastructure. The mobile app, in fact, through the visualization of the simplified 3D model of the bridge, helps users to be sure to inspect all the components and report any defects found on the structure.

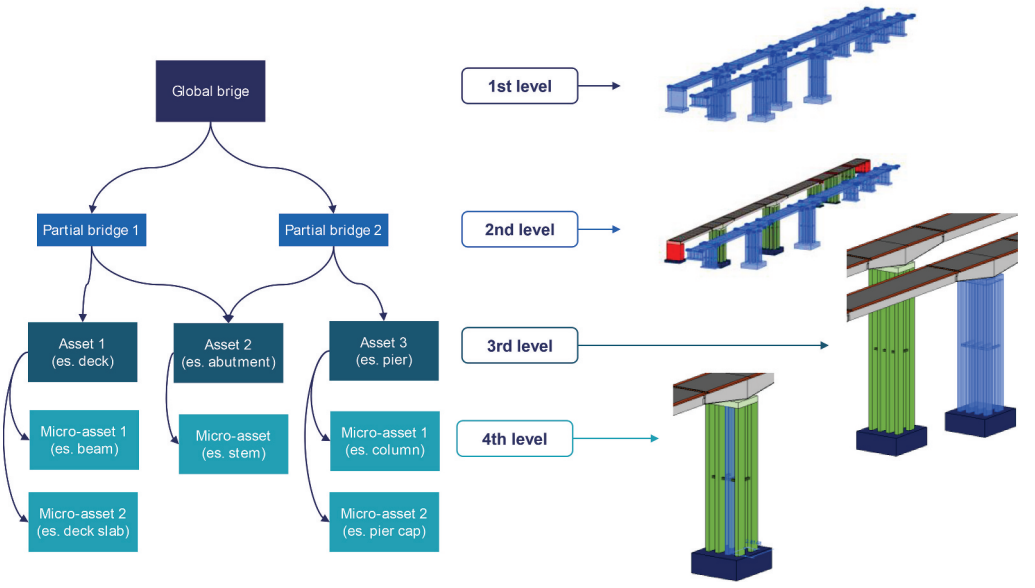


Figure 1. ARGO four-level hierarchy for the simplified 3D models.

- allows comparing over time the state of a defect, having easily available the information of the previous state of the same defect found during previous inspections.
- forces the user to upload images of all detected defects, in order to have a visual traceability of the state of the structure over time.

3.2 *Remote inspections tool*

Together with the tool supporting ordinary inspections, a part of the ARGO platform, called ARGO 3D, is specifically dedicated to remote inspections. More in detail, the platform allows to carry out inspections completely remotely, making available to the inspector all the tools that allow carrying out the activity exactly as if he were in the field but being comfortably in his office.

Indeed, the user, if a remote inspection has been assigned to him and after login in the platform, will see all the workorders whose he is in charge of, and, if the task is related to an inspection that can be performed remotely, he will access the web application "ARGO 3D".

As described before, there are some pre-requirements that must be covered in order to perform a remote inspection:

- All the pictures of the bridge must have been already collected during a drone flight.
- The digital twin of the bridge must already be reconstructed from the images (and eventually from laserscanner).
- AI inference must have been already executed over all the images that has been used for the 3D reconstruction.

Given that the requirements are fulfilled, when the user access "ARGO 3D", the tool allows to view the digital twin of the bridge, giving the inspector the possibility to rotate it, translate it and increase/decrease the zoom to literally "navigate" it; this first basic functionality actually enables the user to do the same thing he usually does during a visual inspection: look at the bridge.

The digital twin of the bridge can be viewed from any PC equipped with an Internet browser, without the need for dedicated workstations with special hardware features (e.g. very powerful GPUs). This is possible because ARGO 3D is a web application that exploits the principle of multiresolution, in order to progressively download the details of the infrastructure

required for the inspection, as you zoom in or out. In particular, every time the user zooms in to see a more detailed view of a component of the bridge, a set of more detailed textures and geometry features are download and shown into the web application. On the contrary, if the 3D model is viewed in a mono-resolution way, the web application should download the whole set of data (both for geometry and texture), that must match a strict tradeoff between something that is "detailed enough" to perform an inspection and something that can be downloaded and viewed in a browser without a too high memory consumption. This tradeoff, as can be easily imagined, can lead to a unfeasible configuration if the bridge is too big.

In addition to the mere visualization of the structure, since the purpose of this tool is to carry out visual inspections, it is possible to exploit the potential of the 3D model to identify defects on the bridge and draw the area of the detected defect directly on the surface of the solid. Once the presence of a defect has been detected, in fact, it is possible to locate it precisely using a drawing tool that allows to draw a polygon on the 3D geometry, identifying the area where the defect is located. This area can be measured with an accuracy equal to that of the 3D reconstruction.



Figure 2. Digital twin of a bridge.

Moreover, ARGO 3D contains the list of all the defects foreseen by the Italian Guidelines; this means that, once a defect has been identified and a polygon has been traced, the inspector can select the type of identified detect from a drop down list and perform a defect-type association, which is automatically stored in a specific database for subsequent analysis.

As is done for traditional inspections using ARGO mobile tablet application, each defect must be associated with a component of the infrastructure. To do this, the inspector can use

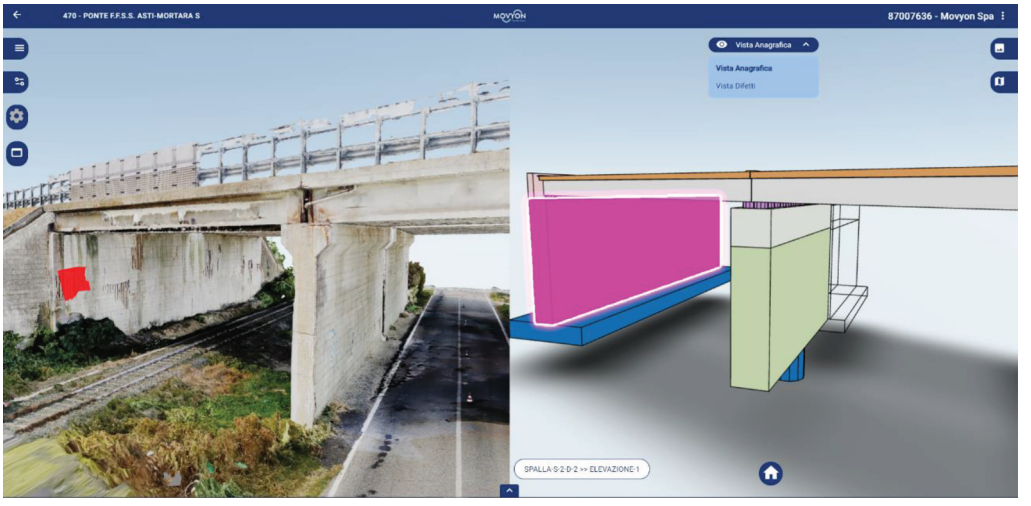


Figure 3. Digital twin of bridge and simplified 3D model, used for remote inspections.

the simplified 3D model of the bridge (the one automatically built from the digital inventory), which can be displayed in a side-by-side window, or, if available, use the digital twin previously segmented into components. In particular, in the last cited case, the application allows to use all the power of the simplified 3D model (strictly related to the digital inventory), in a seamless way, since its information are embedded in the digital twin.

3.3 *Automatic damage identification using AI*

Once the bridge surface images along a predetermined trajectory are collected, artificial intelligence algorithms can be used to automatically identify damages on the structure. Indeed, inside the ARGO 3D platform, the reconstruction of the digital twin is flanked by another fundamental process, which can be enabled before the inspector's intervention, i.e. the automatic detection of defects through the use of Artificial Intelligence (AI) techniques.

The use of modern deep convolutional networks for the semantic segmentation of images or the so-called 'object detection' (i.e. the identification of elements of interest by means of "bounding boxes") makes it possible to suggest, when the remote inspection application is opened, a series of defects that must then be confirmed or rejected by the human operator.

The automatic defect identification software, developed and integrated into ARGO 3D, is now able to recognize five classes of defects on concrete: cracks, exposed reinforcement, crawl spaces, efflorescence and moisture stains (work is underway to increase this number).Approximately 15,000 images (approximately 30% were synthetically generated) were used to train and then test the artificial intelligence algorithms, which are currently able to identify defects with very high precision.



Figure 4. Output of AI algorithms on the 3D model (left) and original image (right).

The usage of these algorithms, before the inspector activity begins, is intended to help him in his decision-making by showing not a 'blank' digital twin, but a digital twin with some suggestions, thus mimicking what is already being done in the medical field, where the use of AI as decision support for doctors in the interpretation of X-rays, CT scans, etc. is yielding excellent results (Scott J. Adams, 2021). This means that, when the inspector accesses the platform, what he sees is not the simple digital twin of the structure, reconstructed starting from the images collected by the drone, but a reconstruction of the bridge on which the main defects have already been pre-identified using AI, which he can confirm or modify. This represents a great time saving for the inspector and significantly reduces the human risk of "forgetting" some defect.

In addition, in order to speed up and optimize the process, the synergy between the collected pictures and the digital twin has been exploited, providing a dual and simultaneous AI-identified defects visualization on photos and bridge reconstruction model (Figure 4). In particular, making use of the knowledge about the position of the cameras and the projection of the images on the digital twin, defects suggested by the AI will be visible both on the photos and directly on the digital twin, providing a precise location of the defect in three dimensions and allowing inspector to perform geometric measurements. In this way, it will be immediate for the inspector to visualize what has been detected by the AI, correct it or add information.

This ability to precisely locate defects in three dimensions allows also the observation and analysis of defects history and the comparison among different surveys carried out over months or years, resulting in a powerful tool for predictive/forecasting analyses, to be used for optimizing maintenance and intervention planning.

3.4 *Towards merging ordinary and remote inspections*

In the transition from traditional on-site inspections to remote ones, carried out using ARGO 3D application, or in a possible alternation between the two types of inspections on a same bridge, it is essential to be able to use the information and data coming from both sources in a completely integrated way.

To achieve this goal, an algorithm has been implemented within ARGO 3D platform that, by leveraging on the tablet's GPS data and images characteristics, manages to 'record' the tablet's shooting position in relation to the digital twin model. The use of computer vision and AI algorithms then makes it possible to search for the same defect within the tablet photo and on the digital twin model, effectively linking the photos taken by the tablet with the digital twin.

The advantages of this approach are twofold: on the one hand, all the information saved during traditional inspections are recovered, and on the other hand, the defects reprojected on the 3D model are correctly labelled (because they are derived from human validation on the tablet). In this way, it is possible to reuse as much as possible all the information collected during classic inspections to strengthen and enrich what is shown in the 3D model.

3.5 *Data management*

As mentioned in the previous paragraphs, one of the main challenges associated with remote inspections is the organized management of a large amount of unstructured data collected during drones-based surveys, such as images, 3D models and point clouds.

In order to be able to manage this type and amount of data, ARGO 3D makes available to the user a graphical interface, that stands in front a back-office module, through which it is possible to upload data associated with an infrastructure, and, for those who have the appropriate role, to verify and validate this data.

The back-office module also includes a number of automatic checks that make certain validations of the uploaded data, e.g. checks on image quality, presence of location information (GPS) and checks that all raw files have been uploaded correctly.

Once the deliverables have been fully validated, the Digital Twin becomes usable in ARGO3D.

Another need that is covered by the back-office module is to be able to give the inspector completing a remote inspection reasonable certainty that the model he is operating on is actually reconstructed from images from a certain date.

To give this type of guarantee to the inspector, the module allows the person uploading the images and data, relating to a certain survey made on a certain date, to sign these data, thus making the entire chain from data collection to remote inspection traceable and non-repudiable.

3.6 *Conclusions*

This paper describes ARGO 3D platform, part of the larger ARGO platform, developed by Movyon and Autostrade per l'Italia, which aims to enable remote inspections of bridges.

The platform synthesizes the experience of digitization via mobile apps of the entire inspection process together with the new technologies of 3D models and digital twin, giving birth to a remote inspection tool that contains tools that enable: (a) data management and traceability (back office module), (b) the execution of inspections without the need for ad hoc workstations (web application with multi-resolution principles), (c) many capabilities to help the user in his decision making role (AI algorithms) and (d) the possibility to reuse all the information already available (recording tablet position with the 3D model).

Remote inspections performed with ARGO 3D are fully consistent with Italian Guidelines and, once finalized, are related to a detailed report signed by the inspector, and to a set of structured information (images, polygons that define defects and related metadata, etc) stored in the ARGO asset management platform.

Of course, many open points are still to be covered and investigated, and only a large-scale adoption of this tool, and consequently, of this approach, can confirm its effectiveness.

REFERENCES

Eu, C. D. (2019). *2019/945 of 12 March 2019 on unmanned aircraft systems and on third-country operators of unmanned aircraft systems*.

F. Giacobbe, E.B. (2018). Inspection of Components with the Support of the Drones. *International Research Journal of Engineering and Technology*.

Fhwa. (2021). *Collection of Data with Unmanned Aerial Systems (UAS) for Bridge Inspection and Construction Inspection*.

In-Ho Kim, S. Y.-J. (2022). A Comparative Study of Bridge Inspection and Condition Assessment between Manpower and a UAS. *MDPI*.

Jin Fan, M. S. (2019). Applications of Drones in Infrastructures: Challenges and Opportunities. *International Conference on Aerial Robotics and Drone.*

Junwon Seoa, L. D. (2018). Drone-enabled bridge inspection methodology and application. *Automation in Construction*.

M. Mandirola, C.C. (2022). Use of UAS for damage inspection and assessment of bridge infrastructures. *International Journal of Disaster Risk Reduction*.

Mit, M. o. (2022). *Linee Guida per la Classificazione e Gestione del Rischio, la Valutazione della Sicurezza ed il Monitoraggio dei Ponti esistenti.*

Scott J. Adams, R. D. (2021). Artificial Intelligence Solutions for Analysis of X-ray Images. *Canadian Association of Radiologists Journal*

Bridge Maintenance, Safety, Management, Digitalization and Sustainability – Jensen, Frangopol & Schmidt (eds)
© 2024 The Author(s), ISBN 978-1-032-77040-6
Open Access: www.taylorfrancis.com, CC BY-NC-ND 4.0 license

Service life strategies on hanger cables of the Great Belt Bridge

P. Holmstrøm, D. Lang, T. Friis & M.N. Svendsen
Rambøll Danmark A/S, Denmark

M.D. Havelykke
Sund&Bælt Holding A/S, Denmark

ABSTRACT: This paper will present the scenarios considered for replacement of hanger cables, including considerations from an operational perspective. In summary, the investments are made up front in terms of preparatory activities for future hanger replacements in case this is urgently required, as well as digital health monitoring and inspections enabling data-driven decisions on activities. For the case that a cable is lost (e.g., from a fire), urgent replacement would be desired. Preparatory activities include an engineered manual for handling forces and displacements of hanger replacements, detailing of bespoke equipment and sourcing of replacement hangers.

Global analyses to obtain hanger forces, girder deflections etc. are required in advance of hanger replacements, and thus these are made up front considering scenarios of partial or full hanger replacements with associated special traffic configurations.

A digital health monitoring system is used together with site inspections to give a longer warning for other replacement scenarios and enable data-driven decisions on mitigating actions to prolong the service life. After 25 years of service, the strategies for replacement have been re-assessed, taking into account the experience gained of the hangers in operation at this specific bridge through inspection, digital health monitoring and incidents on the bridge.

1 SERVICE LIFE IN GENERAL OF THE HANGER CABLES

1.1 *The Great Belt Bridge*

The Great Belt Bridge (Storebæltsbroen), inaugurated in 1998, is one of the largest suspension bridges in the world, with a main span of 1624m and hangers up to 177m in length. The suspension bridge is part of the 18km Storebælt Crossing which consist of the suspension bridge including approach viaducts, a twin box girder bridge and a twin bored railway tunnel. The structure is owned and operated by A/S Storebælt which is a subsidiary of Sund&Bælt Holding owned by the State of Denmark. A photo of the Great Belt Suspension Bridge is shown in Figure 1.

The hanger cables comprise of fully locked coil cables with HDPE sheathing and anchored in the ends by poured spelter cone type sockets. There are 176 hangers on the bridge in different lengths connecting the bridge deck girder to the main cables, and each hanger consists of two separate locked coil cable strands. In total 352 fully locked coil strands varying from 2m to 177m. The cable strands are installed in three different sizes (diameter/MBL) and with four different types of end socket configurations.

As it is assumed that replacement of hanger cables will be required at some point throughout the service life of the suspension bridge, the global structural integrity of the bridge is designed and prepared for replacement of the hangers, including sudden rupture of a single hanger from an accidental case. Any such replacement work will lead to traffic restrictions on the bridge, depending on the space required for the work site and structural safety of the bridge.

The top socket of the hanger strands is fixed to a cable clamp of the main cable, and the lower socket is placed inside the bridge girder and is accessible only from the interior of the girder. A further general description of the cable system can be found in Gimsing et al. (1998).

DOI: 10.1201/9781003483755-376

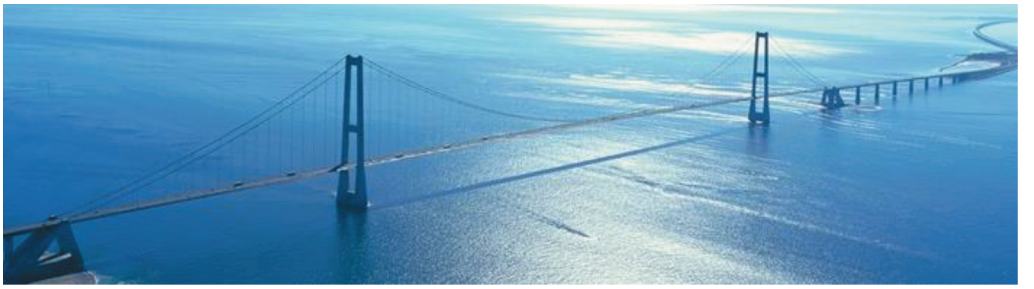


Figure 1. Photo of the suspension bridge of the Great Belt Crossing – also referred to as the East Bridge.

1.2 *Replacement scenarios*

Replacement of hangers would be required in case of fracture of the strand or damage to such an extent that the safety of the strand is compromised. For the Great Belt Bridge, the strategy for replacement depends on the root cause for replacement. Three different scenarios have been identified that would require replacement of one or more of the hangers depending on the type of damage on the cable. These three scenarios are listed in Table 1 and are described in more detail in the following. Some scenarios are likely to be more predictable than others.

Table 1. Replacement scenarios.

Root cause	Predictability	Expected no. of hangers to be replaced
I. Deterioration	Planned	All or most in same campaign
II. Fatigue	Semi-urgent	Selected 4 to 32
III. Accident	Urgent	One

I. *Deterioration of materials and corrosion*
Having a robust and well-proven design, the recurring inspections and investigations is expected to provide sufficient warning to secure the possibility of a well-planned replacement of the hangers. This general breakdown of material properties is considered to cover all hangers on the bridge equally, as the deterioration is assumed to be similar on all hangers, when a proper level of maintenance is kept. Thus, it is likely that all of the hangers are to be replaced in this scenario.

II. *Fatigue damage*
Fatigue damage of the strands is very difficult to detect until wire fractures occur, and given the expected location of wire fractures, these might even be difficult to detect using currently available none-destructive testing methods. Thus, this scenario might lead to urgent replacement of hangers in case of fatigue fracture. In order to mitigate this risk and predict the time for replacement, indirect monitoring of the fatigue damaged are installed as described in section 2. Replacement due to fatigue damage is likely to cover several hangers but not all – e.g. the ones longer than a certain length that are prone to heavy oscillations.

III. *Accidents on the bridge*
Accident scenarios are unpredictable by nature, and would cover fire incidents, explosions, collision from road, sea or air or other unpredictable types. It is assumed that these scenarios will lead to urgent replacement of a single hanger as these are expected to be local incidents.

This paper will not go into detail about deterioration of materials and corrosion as this is likely to be several years ahead still. The replacement work for this scenario will be a large campaign of replacing many hangers, that is assumed to be handled in due time in a well-planned schedule. The paper, thus, focuses on semi-urgent and urgent hanger replacement caused by fatigue and accidents, respectively.

2 RISK OF SEMI-URGENT REPLACEMENT AND SHMS

2.1 *The hanger monitoring*

Selected hangers undergo continuous monitoring using accelerometers to observe the oscillations of the cables, which have been identified to exhibit substantial oscillations intermittently Gjelstrup (2011). This monitoring initiative has been ongoing for approximately two decades. The current monitoring configuration involves accelerometer measurements in two horizontal directions on seven hangers situated around the western pylon. Specifically, all four hangers in position 2 from the pylon, along with hangers in positions 1, 3, and 4 to the southeast of the pylon, are subject to monitoring. These accelerometers are positioned 4.5 meters above the bridge deck and operate with a sampling frequency of 25Hz, which is feasible for cables on a bridge of this size, given the nature of vibrations relevant for analysis. A photo of a double stranded hanger with accelerometers installed above the damper is seen in Figure 2.

During 2023 and the beginning of 2024, the sensors within the hanger monitoring system are replaced, and additional sensors are introduced. As a general modification, the measurement height on the hangers is now adjusted to 10 meters above the bridge deck. In total, 10 hangers are monitored, and on one hanger, the setup is expanded to include 2 dual-axis accelerometers, 2 tri-axial accelerometers, and 5 dual-axis inclinometers. For more on the SHMS see Lollesgaard and Brøndum (2018) and Myrtue et al. (2021).

2.2 *Prediction of semi-urgent replacement (fatigue assessment)*

As previously outlined, a selected set of hangers is under constant surveillance, and the measurements are scrutinized with a focus on various aspects contributing to operational and maintenance considerations:

- *Surveillance and analysis of oscillation levels:*
  Utilized for planning, design, and evaluation of potential mitigation actions.
- *Estimation of fatigue lifetime:*
  Enables timely planning for potential replacement and assessment of the need for actions extending the lifetime.
- *Continuous monitoring of load distribution:*
  Provides insight into changes that could indicate damages, facilitating immediate detection and cost-effective measures. Enables surveillance of change in load distribution during replacement of hangers.
- *Surveillance of estimated hanger damping:*
  Continuous evaluation of performance of external dampers. Dampers with poor performance can be replaced to ensure longevity of the hangers.

The oscillations in the cables induce bending stresses and fretting wear at the ends, potentially leading to cable fatigue. Therefore, one of the primary motivations for hanger

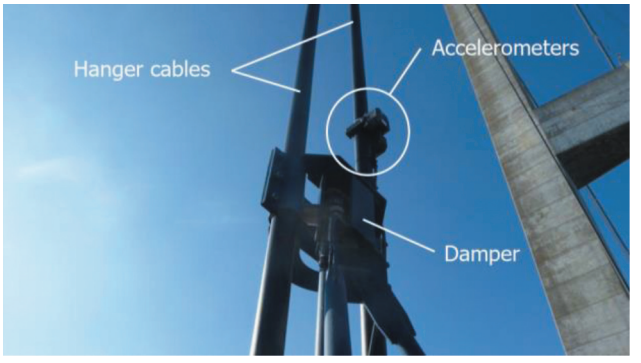


Figure 2. Photo of the double stranded hanger with accelerometers installed above the damper.

monitoring is to estimate fatigue damage resulting from these oscillations. The fatigue damage estimation involves several steps:

I. Virtual sensing to estimate stresses at critical positions.
II. Rainflow counting based on ASTM E1049-85 to determine stress ranges and count on an hourly basis.
III. Conversion of stress ranges and count into hourly damage values using an appropriate S-N curve and the Palmgren-Minor rule.
IV. Estimate of the fatigue lifetime based on the calculated fatigue damage.

Current estimates of the fatigue lifetime indicate a disappointingly low level. However, these calculations are considered conservative with an overestimation of stresses. In response, two actions have been initiated:

- Enhance of the measurement setup in spring 2023 to cover more hangers and increase sensor density on one hanger for a better understanding of vibration characteristics and thereby a reduction in conservatism in the fatigue damage estimation.
- Designing additional dampers for hangers in positions 3 and 4 from the pylons, complementing existing dampers installed in 2007 on the two longest hangers on each side of the pylons.

A pilot project has also been conducted to assess the feasibility of estimating the hanger tension forces from the acceleration measurements and thereby the load distribution between the hangers. The idea is to monitor the load distribution during replacement of hanger or immediate detection of potential damages large enough to cause elongation of a cable, which will cause a minor redistribution of the hanger forces. Potentially this can be detected immediately by the existing measurement setup and appropriate measures can be carried out in a timely and cost-effective manner.

The estimation of the hanger forces has been conducted by a continues estimation of the lower natural frequencies and mode shapes using automated operational modal analysis Friis et al. (2021), which have then been transformed into hanger forces by a model. In Figure 3, the tension force corrected for environmental and operational variations (EOV) (wind, temperature and traffic) is shown for one hanger for 2021 with moving average values and horizontal lines marking relative changes in tension force at 1%, 2%, and 3%. It is seen that the moving average of 7 days stay within the borders of a relative change of just 1% which indicate that there's potential to automatically detect damages that cause the load distribution to change 1% or more.

The hanger monitoring has already proven valuable for operational and maintenance purposes. It has illuminated vibration levels, identified potential future issues, and prompted timely and cost-effective actions to ensure current and future operational safety. Proactive

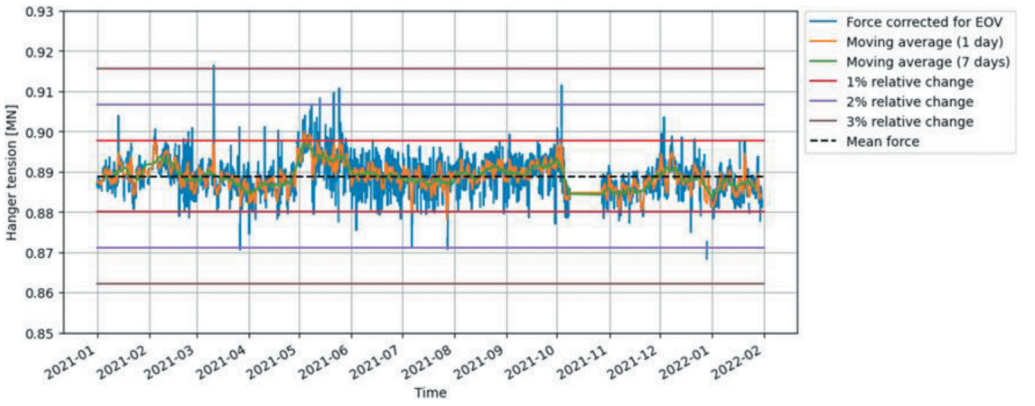


Figure 3. Tension force corrected for environmental and operational variations (EOV) for one hanger for 2021 with moving average values of 1 and 7 days and horizontal lines marking relative changes in tension force at 1%, 2%, and 3%.



Figure 4. Fire accident in 2020: (left) Truck on fire, (right) Undamaged hanger.

measures taken in the early stages of bridge life may contribute to extending its intended lifetime beyond the original design expectations. The reader is referred to Friis et al. (2023) for more on structural health monitoring of the Great Belt Suspension Bridge and the benefits for operation and maintenance.

3 RISK OF URGENT REPLACEMENT

In 2015, the general risk assessment of the bridge was revised using knowledge from the fire incidents on the bridge and other suspension bridges in Denmark. It was concluded that fire incidents are not as unlikely as assumed previously, and a general increased focus of fire incidents on major brides was included. Consequently, it was decided to install fire protection of the main cable during 2018/2019. Fire protection was not installed on the hanger cables, as the bridge is prepared for replacement of these.

In 2020, a near miss fire incident occurred at the hangers, when a truck fully loaded with bottles of cocktail liqueur caught fire. The truck was located close to one of the longer hanger cables, but luckily with a favourable wind direction. Hence no damage to the nearby hanger cables was observed. Photos from the incident can be seen in Figure 4.

After this near miss incident, it was decided to prepare an engineered technical manual for urgent replacement of hanger cables in order to be fully prepared for a similar case. One of the main challenges of urgent replacement is the lead time for sourcing a new hanger cable as these are bespoke at each location. Several concepts were investigated including having temporary hangers on stock, that can be adjusted in length and installed quickly until the permanent replacement hanger is available. But the result is to have a drum on stock of hanger replacement cable but with sockets installed at one end only and separate sockets ready for installation. If an accident occurs, the cable will have to be cut to correct length, the socket installed using resin socketing and installed permanently on the bridge. By this concept, bridge closure and traffic restrictions are kept to a minimum.

4 ENGINEERED MANUAL FOR URGENT REPLACEMENT OF A HANGER CABLE

In general, operation and maintenance of the Great Belt Bridge are handled using pre-defined technical instructions for the work that can be foreseen. These technical instructions cover various annual inspection works as well as replacement and repair of selected and critical members of the bridge. Several of these technical instructions were prepared when the bridge was built, and some are added or modified at later stages. After it has been acknowledged that urgent

replacement of the hangers might be required, as earlier mentioned, Sund&Bælt decided to prepare the technical instruction for replacement of hanger cables. This is made through a series of engineered manuals. To account for the many variations, a series of 5 manuals has been produced, each covering a range of the hangers such that the series account for all hangers.

The manuals can be viewed as a step-by-step guide to replace the hangers. The manuals describe which pieces of equipment is used at what times, what the expected loads and deformations are as well as how working areas are to be established on the bridge. All of this has been developed with a focus on minimal disruptions to the bridge users, as the bridge is critical infrastructure. The manuals therefore also include traffic limitations required for the different stages of the hanger replacement. The manuals are created with a reversibility principle, meaning that all steps in each procedure are fully reversible such that the replacement work can be terminated at any step, and the bridge reversed to its previous condition. This is an important safety principle in case unforeseen actions occur during the work.

4.1 *Global FE-model*

Replacement of any given hanger cable will impose a changed load distribution locally in the girder and in the nearby hangers, both for self-weight as well as for special load scenarios relevant for the temporary replacement situation. The quantification of force changes and deformations due to the various hanger replacement scenarios was performed using Ramboll's in-house FE-model of the bridge, developed in SOFiSTiK. The global FE-model is shown in Figure 5.

The model comprises a detailed, fully geometrical non-linear construction stage simulation, considering large displacements and geometric stiffness effects. The staged simulation produces an accurate calculation of main cable forces with large sag effects, as well as accurate hanger forces. This includes a special hanger force redistribution which was implemented as part of optimizations in the detailed design, essentially by transferring load from the (otherwise highly loaded) hangers next to the towers, to their adjacent hangers. The load transfer was achieved by making the hangers at positions 2 from the towers somewhat longer than the target geometry would otherwise prescribe, as well as making the hangers at positions 1 (adjacent to the towers) and positions 3 somewhat shorter. Similar adjustments were also made at the anchor blocks and all of these are represented in the model.

Influence-line analyses were an important part of the assessments. A control load, P = 100kN, moving longitudinally with steps = 10m along the bridge span was defined. The influence-line (i.l.) for the three different transverse positions shown in Figure 6a have been derived considering the situation of intact bridge: next to the south hangers, y = -13.5m (1), midway between the south hangers and the deck centreline, y = -6.75m (2), and next to the north

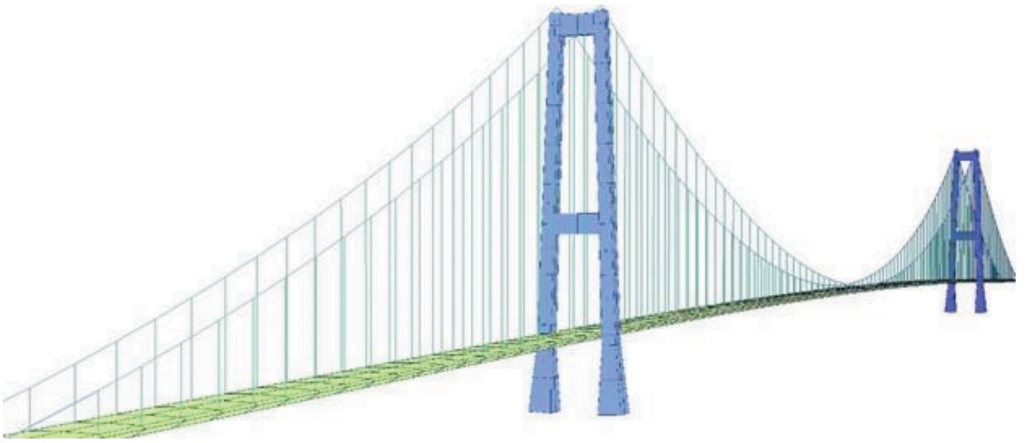


Figure 5. Ramboll's in-house FE-model of the Great Belt Suspension Bridge.

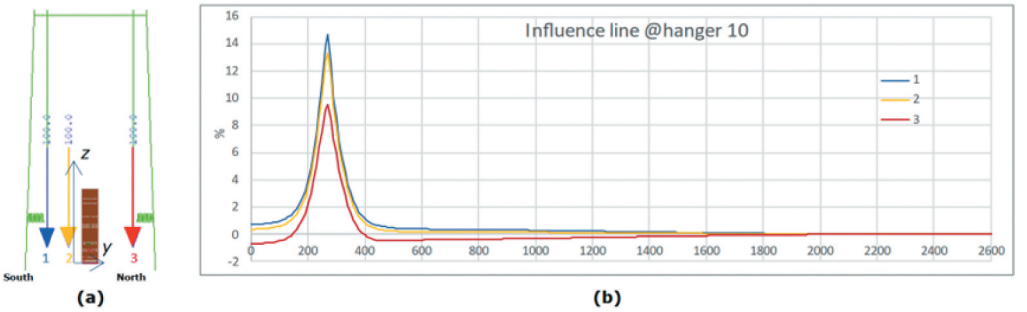


Figure 6. (a) Control loads in transverse direction. (b) Influence line of axial force in hanger no. 10.

hangers, y = 13.5m (3). The transverse distance between the hangers is 27m. It was concluded that the i.l.s are strongly affected by the transverse position of the loads, i.e. torsional effects are present. For example, Figure 6b shows the i.l. of the axial force in hanger no. 10, counting from the eastern anchor block.

A load located longitudinally between 0m to 180m is unfavourable for the force in hanger 10 if applied at position 1 or 2 counting from the pylons, whereas it is favourable in position 3. Position 1 and 2 produce similar i.l.s and position 2 was used for further analyses. Therefore, the traffic loads running on the north side of the deck will be defined on the i.l. for position 3, and the traffic loads running on the south side on the i.l. from position 2. For example, analysing hanger 10 south, it would take 15% of a load located at that hanger position and only 9% of a load located at the north side of the deck, as shown in Figure 6.

4.2 *Detailed design of equipment and replacement cables*

Replacing a hanger cable will be a challenging task which require meticulous planning and preparation. Even though the global structural integrity of the bridge is designed for replacement originally, the local structural effects and practical access issues must be considered too. In order to be prepared for an urgent replacement scenario, Sund&Bælt decided to invest in bespoke equipment designed to replace any hanger. Some of the main variations to consider in this design are:

- 3 different hanger diameters sizes (diameter/MBL)
- 4 different types of bottom sockets – 3 different principles to unload the hanger
- 4 different type of top sockets – 2 different principles of top anchorage
- Cable clamps varying in size and slope
- Hanger lengths in range of 2m to 177m
- Weight of hanger strands in range of 0.5 tonnes to 11 tonnes
- Hanger forces varying from 0.8MN to 2.9MN
- Varying deflection and movement when unloading

When one hanger is unloading it will shorten, the neighbouring hangers will elongate and the main cable will straighten. The sum of these 3 main contributions is the total extension which needs to be handled when unloading a hanger cable. The global FE-model of the bridge is used to quantify the extension and force to be handled at each location in order to design different types of unloading equipment.

As the hanger cables already are prepared for unloading from the girder interior, this concept is kept for the replacement scenarios. However, it was found that the total extension to be considered at some locations is larger than the free-space inside the girder, and consequently the unloading of the hangers has to be carried out by several jack strokes instead of one. The setups for unloading the hangers in both one and two strokes respectively are shown in Figure 7.

The equipment used for unloading the cable is also used for loading the replaced cable. The same applies for lowering/lifting the new cable. The bespoke equipment is procured and stored such that it is ready for use in case an urgent replacement is needed.

For the replacement work, the hangers are divided into categories of *short hangers* (<60m), which are readily accessible using a mobile crane, and *long hangers* (>60m) which are not accessible with a mobile crane or requires a mobile crane too large to fit on the bridge.

After the unloading of the hangers, the pin connecting the hangers to the main cable needs to be removed such the cables can be lowered onto the bridge deck and removed. For the short hangers a mobile crane can be used, while for the longer hangers a setup using strand jacks and a 'table' mounted on the cable clamps are used, refer Figure 7. The table, which is designed for the purpose, needs to accommodate the varying size and slopes of the cable clamps. Both short and long hangers are demounted using the same approach, where the hangers are lifted to unload the pin, and the pin is then removed and the hangers are lowered. The same approach is used for installation of the new cables, but in reverse.

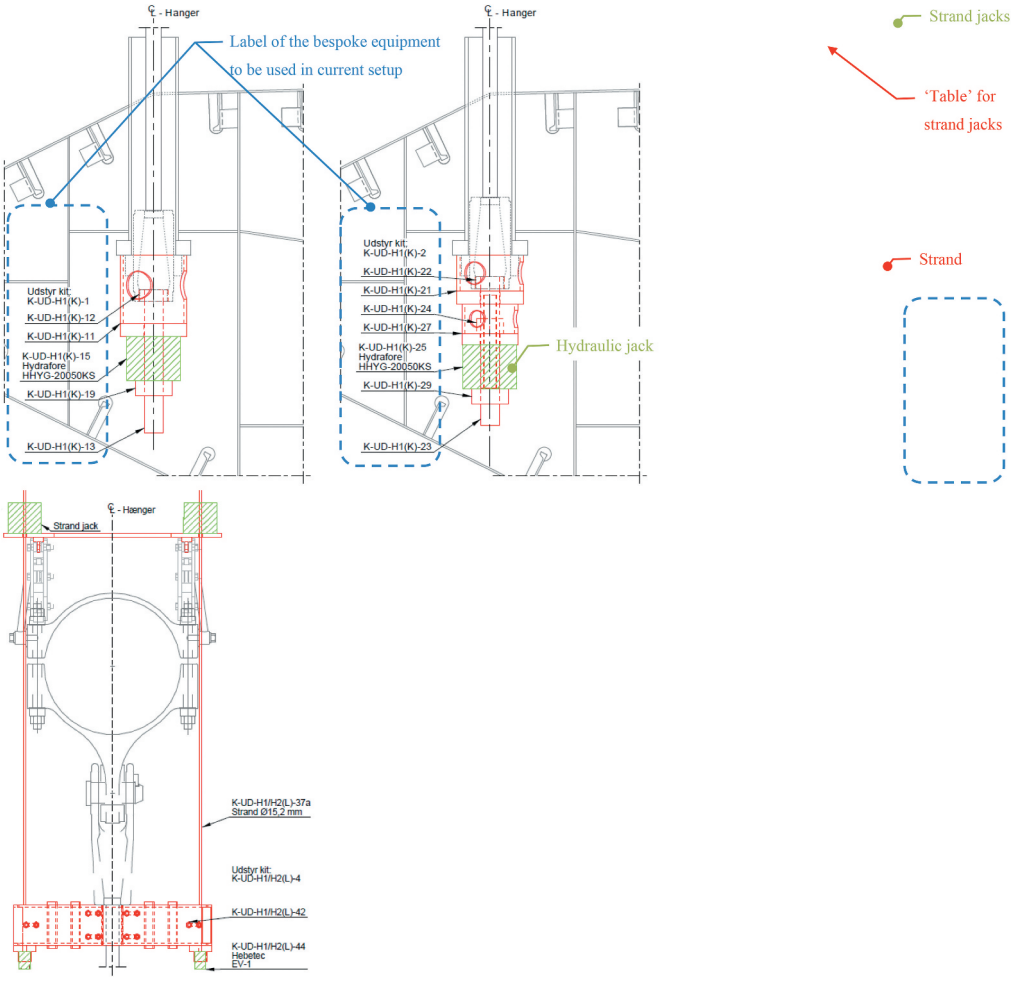


Figure 7. Typical setup for unloading hanger strands. (left) setup for short extension and (middle) setup for long extension. (right) Strand jacking from main cable.

5 CONCLUSIONS

SHMS on hanger cables can be used to get a better understanding of cable vibrations and these results may be used for estimation of remaining fatigue life. However, as it is an indirect method of determining the fatigue damage, uncertainties still remain. But it allows a downgrade of the predictability of fatigue fracture scenarios from urgent to semi-urgent when considering the service life strategy.

When preparing for replacement of hangers, knowledge of the magnitude of forces and displacements that shall be handled on site is crucial. The global FE-model is an important tool to obtain this.

Following accidental cases on the bridge, urgent replacement of hanger cables might be required, but these may typically have a long manufacturing lead time. To mitigate the time with traffic restrictions on the bridge, preparatory activities are being carried out in due time. These includes preparations of engineered manuals for the replacement work and sourcing of bespoke equipment and replacement hangers to keep on stock in case of an accident. One of the main issues is lead time required for a replacement hanger.

REFERENCES

Friis, T., Tarpø, M., Katsanos, E., & Brincker, R. 2021. *Best linear approximation of nonlinear and non-stationary systems using Operational Modal Analysis*. Mechanical Systems and Signal Processing, 152 (4), 107395. doi:10.1016/j.ymssp.2020.107395

Friis, T., Nielsen, S. T., Lollesgaard, M., Bangsgaard, T. B. & Havelykke, M. D. 2023. *Structural Health Monitoring of the Great Belt Suspension Bridge and the Benefits for Operation and Maintenance*. The International Bridge Conference (IBC). Washington DC.

Gimsing, N.J., et al. 1998. *East Bridge*. Copenhagen: Storebæltsforbindelsen

Gjelstrup, H. 2011. *Understanding and Simulating wind-induced vibrations of iced vertical cables*. Kgs. Lyngby: Technical University of Denmark (PhD thesis).

Lollesgaard, M., & Brøndum, R. 2018. *Great Belt Bridge – Structural monitoring*. IABSE Conference – Engineering the Past, to Meet the Needs of the Future. Copenhagen. doi:10.2749/copenhagen.2018.401

Myrtue, K., Martins, N., Lollesgaard, M., Bangsgaard, T. B., Havelykke, M. D., Bormlund, F., & Ingolfsson, E. 2021. *SHM at the Great Belt Fixed Link in Denmark*. 10th International Conference on Structural Health Monitoring of Intelligent Infrastructure (SMHII 10). Porto.

Bridge Maintenance, Safety, Management, Digitalization and Sustainability – Jensen, Frangopol & Schmidt (eds)
© 2024 The Author(s), ISBN 978-1-032-77040-6
Open Access: www.taylorfrancis.com, CC BY-NC-ND 4.0 license

Data-driven maintenance of Bogibeel Bridge - large scale structural health monitoring

H. Gjelstrup, T. Bangsgaard & F. Houseini
Rambøll Denmark A/S, Copenhagen S, Denmark

ABSTRACT: The Bogibeel Bridge in India, spanning the Brahmaputra River, is a 4.94 km rail-cum-road bridge pivotal for Northeast India's infrastructure. Its design incorporates 41 spans with steel truss girders and a concrete slab. This paper focuses on the bridge's advanced Structural Health Monitoring (SHM) system, which employs around 920 sensors for continuous monitoring of key structural aspects like strain, temperature, vibration, and displacement. A critical feature of this SHM system is its integration with the bridge's asset management, allowing automated reporting and alarms based on data analysis for proactive maintenance. This innovative approach combines sensor-based data, cloud computing, and automated analytics to move maintenance from reactive to predictive, enhancing operational efficiency, safety, and cost-effectiveness. By early detection of structural issues, it ensures timely intervention, minimizing downtime. The adopted approach to the SHMS on the bridge, significantly improves safety, efficiency, and cost-effectiveness, demonstrating a pioneering model for smart infrastructure management.

1 BACKGROUND

The Bogibeel Bridge, India's longest rail-cum-road bridge, is not only a critical infrastructural asset spanning the Brahmaputra River in Assam but also a modern marvel of engineering for its blend of functionality and resilience. Completed in December 2018, this 4.94-kilometer bridge enhances Northeast India's transportation network and plays a vital role in national defense logistics due to its strategic location near the Assam-Arunachal Pradesh border.

The construction of the Bogibeel Bridge addresses strategic, economic, and social needs in Northeast India. It significantly improves connectivity within the region, reducing the distance between Dibrugarh and Guwahati by 55 km and linking key sections of the North-East Frontier Railway. This enhancement in connectivity boosts trade and economic activities while easing travel and congestion. Furthermore, the bridge's proximity to the Indo-China boundary in Arunachal Pradesh underscores its strategic military importance. The introduction of a state-of-the-art SHM system aligns with these strategic needs, ensuring the bridge's health and longevity through advanced monitoring and maintenance.

This paper examines the Bogibeel Bridge's innovative maintenance approach, focusing on its Structural Health Monitoring (SHM) system. This advanced system marks a paradigm shift in infrastructure maintenance, transitioning from reactive to proactive strategies by leveraging sensor technology and data analytics.

Traditionally, bridge maintenance relies on periodic inspections and manual assessments. Inspectors physically examine the structure for visible signs of wear, corrosion, or damage. This approach is often reactive, with repairs conducted in response to identified issues. While effective for detecting surface-level problems, it can miss internal or subtle structural weaknesses. Furthermore, manual inspections are labor-intensive and can lead to prolonged traffic disruptions. In contrast, the Structural Health Monitoring (SHM) system being employed on the Bogibeel Bridge offers continuous, real-time monitoring, allowing for proactive maintenance and early issue detection, thus enhancing safety and operational efficiency.

DOI: 10.1201/9781003483755-377

The paper aims to highlight the integration with asset management, and enhancements in safety and efficiency brought by the SHM system. The implementation of this system exemplifies a dynamic, responsive approach to infrastructure maintenance, setting a precedent for future large-scale projects.

2 BOGIBEEL BRIDGE STRUCTURAL DESIGN

The Bogibeel Bridge is a composite welded steel truss bridge with reinforced concrete, designed to carry a double line broad gauge railway on the lower deck and a three-lane road on the upper deck. The bridge comprises 41 spans, each measuring about 125 meters (End span, 33.4 meters).

The bridge's unique construction involved the creation of three distinct types of spans, in addition to the end spans. This design approach was necessitated by the bridge's deployment onto its pillars, which were the initial structures erected. The construction process involved welding multiple spans together and then pushing them onto the pillars. This method necessitated varying steel thicknesses, leading to the requirement of the three span types (labeled A, B, and C) along with the end spans. After positioning the spans accurately, the welds were removed, resulting in the bridge consisting of 41 individual spans. The picture in Figure 1 shows the Bogibeel bridge under the deployment of some of the spans.

The structural design of the Bogibeel Bridge, characterized by its repetitive span structure, uniquely facilitates the application of the Structural Health Monitoring (SHM) system. The uniformity in design across the 41 spans, each featuring steel truss girders and a concrete slab, allows for strategic deployment of the SHM system on select spans. This approach not only exemplifies efficient resource utilization but also ensures comprehensive monitoring. By selectively equipping spans with sensors, the SHM system can extrapolate data to assess the overall structural integrity, optimizing maintenance and ensuring the bridge's longevity.



Figure 1. Bogibeel Bridge under the deployment of span to the piers.

3 STRUCTURAL HEALTH MONITORING SYSTEM FOR BOGIBEEL BRIDGE

As the SHMS system is currently being implemented, the system overview, shown in Figure 2, is outlining the data flow and analysis process. The design is geared to leverage the bridge's repetitive span structure, enabling efficient sensor placement and data extrapolation for structural assessment.

The SHMS collects and conditions monitoring data from critical elements of the Bogibeel Bridge, providing temporary storage, data processing, system control, operation, and data management within the Structural Health Monitoring Control Room. At the time of writing this paper, the sensor installation is about to commence, which results in the absence of data from the system for this publication.

The system ensures the aggregation of critical data pertinent to the bridge's performance and enables future evaluations of the Bogibeel Bridge's structural health. The SHMS works in conjunction with visual inspections to facilitate targeted maintenance, enhance safety, identify

critical structural components, assess wear on moveable parts, and estimate the bridge's remaining lifespan. The architecture of the SHM system is depicted in Figure 2."

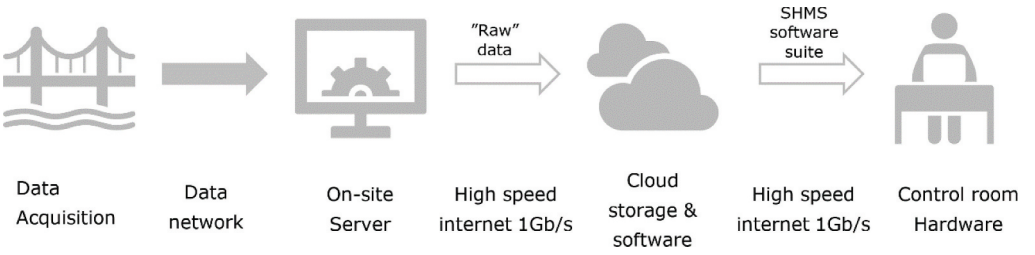


Figure 2. System overview.

The Structural Health Monitoring (SHM) system of the Bogibeel Bridge employs a comprehensive array of sensors, amounting to approximately 920 instruments, to ensure continuous and precise monitoring of the bridge's structural integrity. These sensors are strategically positioned across the bridge, mainly on four different spans, identified as Span A, B, C, and the south end span. They monitor a range of environmental parameters, operational and environmental loads, and the bridge's structural response. Figure 3 illustrates the different spans of the Bogibeel Bridge, including the sensor locations on all spans and piers.

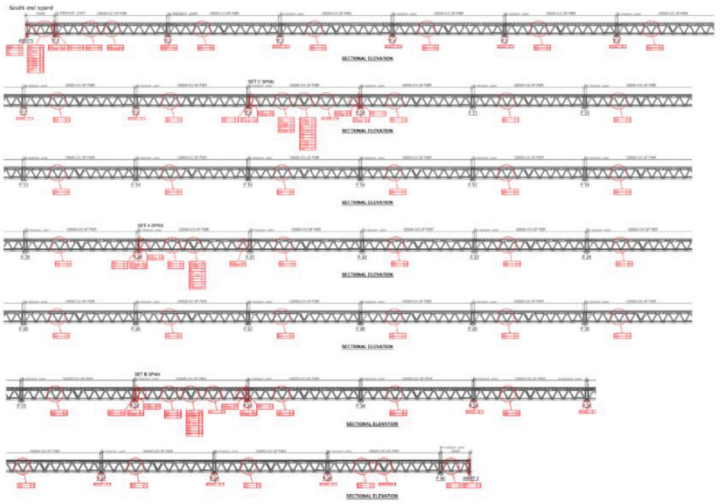


Figure 3. Overview of the different spans comprising the Bogibeel Bridge and the indication of sensor locations.

The SHM system for the Bogibeel Bridge includes a variety of sensors for monitoring environmental conditions, operational and environmental loads, and structural responses. Environmental sensors, such as Triaxial Ultrasonic Anemometers and Temperature & RH sensors, gather data on conditions impacting the bridge. Sensors like Dynamic Weigh in Motion sensors and Scour Monitoring Sensors track the loads affecting the bridge and its piers. To gauge the bridge's structural response, instruments like Load Cells and Accelerometers among others, measure aspects such as strain, load, acceleration, and corrosion.

These sensors are mainly positioned on four key spans, but all spans are equipped with accelerometers and GPS sensors to allow data extrapolation via numerical modeling, thus boosting the SHM system's effectiveness. Tables 1 through 3 detail the types and quantities of sensors installed on the bridge for various monitoring purposes.

Additionally, the SHM system incorporates a database with warning and alarm values to facilitate updates corresponding to changes in the bridge's condition. This database ensures a straightforward method for modifying important values when the bridge's structural characteristics change.

Table 1. The number of sensor and their type (Environmental Parameters).

Sensor/Instrument	Measurements	Qty.
Triaxial Ultrasonic Anemometer	Wind speed & direction in all directions	8
Visibility & Fog detector	Visibility	3
Pyranometer	Solar radiation	3
Barometer	Air pressure	3
Rainfall gauge	Rainfall rate & total rainfall	3
Temperature & RH sensor	Ambient Temp. & Relative humidity in air	12
Asphalt Temperature	Temperature	18
Concrete Deck Temperature	Temperature	18
Steel Deck Temperature	Temperature	45
Video Surveillance	Video surveillance	6

Table 2. The number of sensor and their type (Loads- Operational and environmental loads).

Sensor/Instrument	Measurements	Qty.
Dynamic Weigh in Motion sensor	Load of road traffic & speed	3
Sonic motion sensor	Train traffic detection	4
Scour monitoring sensors	Scour at piers	12

Table 3. The number of sensor and their type (Response Measuring sensors).

Sensor/Instrument	Measurements	Qty.
Load cell	Vertical Load on bearing	16
Static strain gauge	Strain in concrete	202
Dynamic strain gauge	Strain in structural steel	300
Accelerometer	Acceleration/ frequency of the girders	86
Displacement Transducer	Displacement of girder	28
GPS rover & reference stations	Deflection of girder	84
Tiltmeter & Inclinometer	Tilt of pier & rotation of girder	27
Corrosion sensor	Corrosion of concrete Rebar	40

4 DATA PRESENTATION AND ANALYSIS

All data from the SHM system is provided to the cloud-based SHMS software suite as "raw" data in SI units, with data preprocessing done on the data acquisition units (DAUs). Upon receiving data from the DAUs, the SHMS software suite can perform post-processing on both "online data" and "historical data." This process offers users options for displaying data in various formats, detailed below.

The terms 'online' and 'historical' data denote the real-time or stored data in the SHMS software, respectively, with 'online' data indicating immediate, live data and 'historical' data referring to records maintained on the cloud server.

Figure 4 illustrates the sensor locations on the Bogibeel Bridge and the alarm status for different sensor types. The left side of the figure shows an overview, while the right side zooms in on the response sensors. Users can access the latter by clicking on the corresponding row.

Similarly, detailed data for individual sensors can be accessed by selecting the sensor type. Figure 5 displays the SHMS software interface when the Load Cell option is selected, showing both the bridge location and a detailed view for better data origin understanding.

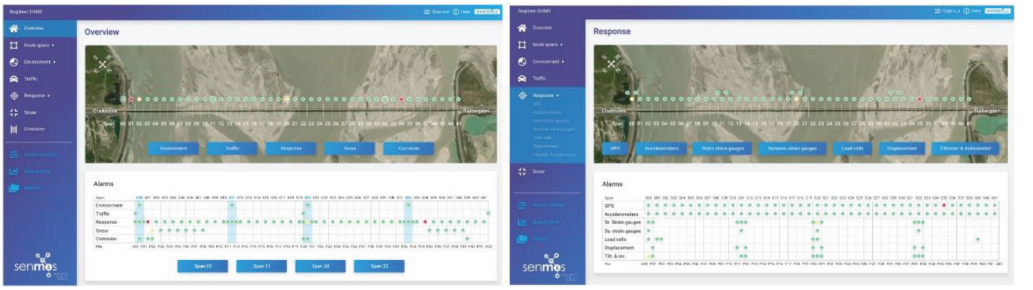


Figure 4. Overview of the sensor location and their alarm status in the SHMS software (Left) and a zoom in on the Response alarm status overview (Right).

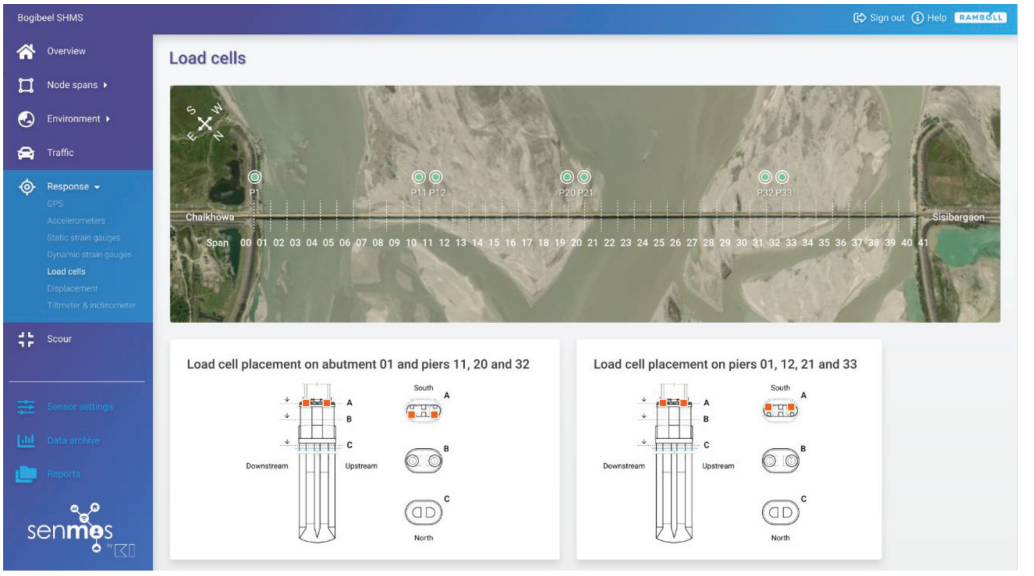


Figure 5. Detailed location information for the Load cells on the Bogibeel Bridge.

4.1 *Data presentation*

As previously mentioned, data is categorized into online and historical types. Table 4 provides an overview of the presentation options for these data types.

Each plot mentioned in Table 4 includes options for displaying limit characteristics. This feature allows for the visualization of both warning and alarm levels alongside measured data, offering an insight into the bridge elements' proximity to their utilization limits.

Figure 6 shows some examples of the mention plots. Here a correlation plot is seen to the left and rainflow and accumulated damage is seen to the Right. Example of the different limits are also shown in the plot.

4.2 *Analysis*

Post-processing scripts, as part of data analysis, are essential for creating desired data presentations. These scripts can be applied to both online and historical data. Table 5 outlines the available post-processing scripts for different data types.

Virtual channels can also be created as part of the analysis, which in the realm of data analysis for structural health monitoring plays a pivotal role in synthesizing complex insights from raw sensor data. These channels are not direct sensor outputs but are constructed through mathematical algorithms that manipulate and combine data from one or more physical sensor

Table 4. Data presentation.

Online data	Historical data
Images with displayed sensor values and alarm indicators.	Timeseries, with limit characteristics.
Tables with sensor values and alarm indicators.	Rainflow histograms, with detail class characteristics
Timeseries plots with online data.	Polar, with envelope characteristics.
– Online data scripts available with this graph is described in section 5.2 Post-processing scripts.	
Tables with latest sensor threshold	Histograms, with limit characteristics.
Tables with latest sensor errors (connection, configuration, and threshold errors)	Correlation, with envelope box characteristics
Online timeseries graphs with incoming values	Autocorrelation, with characteristics.
Historical graphs with a predefined specified period	Fatigue accumulation, with limit characteristics
Weather display for the region.	Accumulation over a set period, with limit characteristics
	Frequency plot, with limit characteristics.

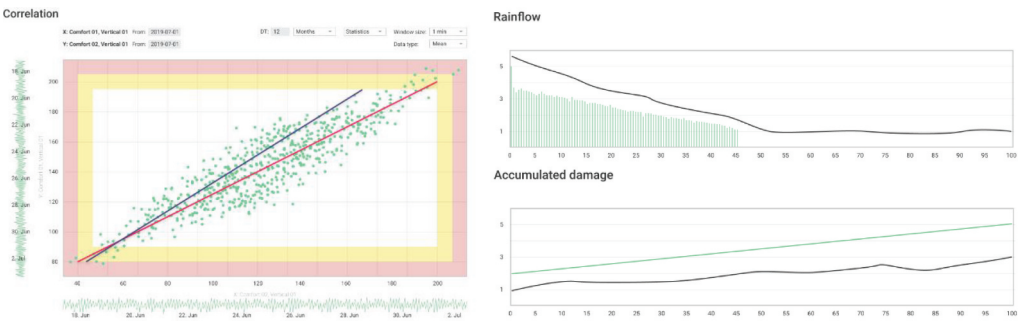


Figure 6. Example plots showing a correlation plot with warning and alarm limits (Left) and plots of rainflow count (Top right) and its related accumulated damage (Bottom right).

Table 5. Post-processing scripts.

Online data	Historical data
Low-pass filter	Statistics (mean, max, min, std, accumulated change)
High-pass filter	Rainflow-counting and fatigue utilization
Band-pass filter	FFT/Spectral Densities
Moving average (ranging from sampling frequency to 1 hour) with associated statistical values	Cross-correlation and auto-correlation analysis
Simultaneous plotting of up to 256 channels	Combination of channels (virtual channels)
Gain and offset applied to sensor channels	Gain and offset applied to sensor channels

channels. By applying basic mathematical operations such as addition, subtraction, multiplication, a new channel is created—this composite channel encapsulates a specific aspect of the bridge's performance that cannot be captured by a single sensor. All post-processing scripts shown in Table 5 are thought to be usable on the virtual channels, just as if they were physical channels. For instance, if physical channels measure variables like strain and temperature independently, a virtual channel could represent the adjusted strain value that accounts for temperature effects, giving a more accurate indication of structural stress. This process of creating virtual channels enhances the interpretability of the data, allowing engineers to construct tailored indicators that are closely aligned with the bridge's unique monitoring needs. The

creation and analysis of such channels are crucial for the detection of subtle patterns or trends that signify potential issues, thereby enabling preemptive maintenance actions.

Using the post-processing scripts and virtual channels, warning and alarm systems can be configured to alert bridge owners to significant changes in the recorded data. Here the alarms are passed on to the management program SMART, which will be touch on in section 5 of this paper. For example, Figure 7 demonstrates a frequency check using defined intervals from the bridge's limit characteristics.



Figure 7. Frequency range check on example data for the Bogibeel Bridge.

5 MAINTENANCE STRATEGY

The new and innovating approach to the maintenance strategy is based on using the Specialized bridge asset management program SMART together with a link to the SHMS software where alarms and reports are automatically uploaded to SMART and placed under the correct hierarchical member in SMART. Figure 7 shows a schematical setup for this process and which data flows from the SHMS to SMART.

The Alarms and reports send from the SHMS software will create item/job in SMART which will then be a part of the maintenance planning for the bridge. The automation of placing reports and alarm in the SMART bridge management program will optimize the workflow by providing asset managers access to the information. Having the information under the right structural members and placed in the job interface in SMART is providing an easy way to prioritize the work needed on the bridge, that being "normal" maintenance, checking alarms/sensors or anomalies reported in the automated reports from the SHMS.

The implementation of the SHMS with the aim of integrating its data into the SMART software is a strategic move that enhances the usability of the information gathered by the SHMS. By integrating SHMS data as native data within the SMART system, it ensures seamless workflow and utilizes the established capabilities of the SMART system for efficient task management. This integration allows for an optimized use of SHMS data, making it more accessible and actionable for users, thus enhancing overall maintenance efficiency and decision-making for the bridge.

The optimization will help lower the cost of maintaining the bridge over its lifetime. Comisu et al. (2017) explore the structural health monitoring systems of bridges, indicating the potential of permanent monitoring systems to reduce the operating costs of inspections and maintenance by 25%, and to reduce the overall life costs of bridges by 10% by applying lifetime prediction models.

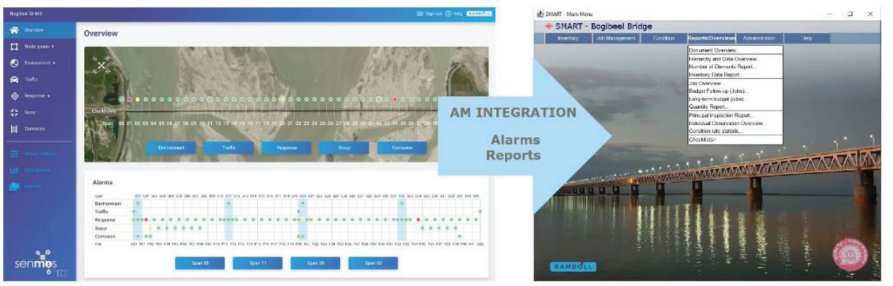


Figure 8. SHMS cloud software and its integration with the assets management software SMART.

6 FUTURE PERSPECTIVES AND INNOVATIONS

Structural Health Monitoring (SHM) systems in bridge maintenance is pivoting towards predictive methodologies where Deng et al. (2023) review the current developments in structural health monitoring within the last five years. Apart from this review of exiting sensor and data handling/analysis technologies and enhanced sensors, AI-driven analytics will facilitate early detection of structural issues, leading to timely interventions. This shift is expected to improve bridge safety and longevity while optimizing maintenance. Emerging technologies, including IoT, drones, robotics, and AI, are set to revolutionize SHM systems. Advances in sensor technology, particularly with nanotechnology, will improve SHM system precision and durability, steering bridge maintenance towards more effective and future-focused practices.

On the note of nanotechnology then this technology is starting to influence structural health monitoring in bridges, by providing advanced tools and materials for enhanced maintenance and safety. Han et al. (2023) discuss the use of nanosensors, which are emerging as promising tools for assessing the structural integrity of bridges whereas Zheng et al. (2019) talks about nanocomposites for structural health monitoring.

7 CONCLUSION

This paper has detailed the ongoing implementation of a Structural Health Monitoring System (SHMS) on the Bogibeel Bridge, marking a pivotal shift in bridge maintenance and safety methodologies. The SHMS, with its extensive network of approximately 920 sensors, is poised to transition bridge maintenance from traditional reactive methods to a more proactive, data-driven approach. Once operational, this system is expected to significantly enhance the safety and efficiency of the bridge, setting a precedent for future infrastructure projects.

The anticipated outcomes of this SHMS implementation include improved early detection of structural issues and a more efficient maintenance response. This proactive strategy is projected to extend the bridge's service life, ensure safety, and optimize maintenance costs. However, it's crucial to recognize the current challenges, such as the complexities involved in data validation and interpretation in the initial phases of the system's operation.

Future research opportunities plentiful in the realm of SHMS. The integration of emerging technologies like artificial intelligence and the Internet of Things could potentially enhance the predictive accuracy of SHMS. Furthermore, expanding the system to encompass environmental impact assessments might provide a more comprehensive approach to infrastructure maintenance.

In sum, the ongoing installation of the SHMS on the Bogibeel Bridge represents a significant stride towards adopting modern engineering solutions for improving the durability and reliability of crucial infrastructure. As the field of structural health monitoring advances, it is expected to revolutionize maintenance strategies for large-scale structures globally, potentially marking a new era of infrastructure management.

REFERENCES

Han, D., Hosamo, H., Ying, C., & Nie, R. 2023. "A Comprehensive Review and Analysis of Nanosensors for Structural Health Monitoring in Bridge Maintenance: Innovations, Challenges, and Future Perspectives." Applied Sciences, 13(20), 11149.

Deng, Z., Huang, M., Wan, N., & Zhang, J. 2023. "The Current Development of Structural Health Monitoring for Bridges: A Review." Buildings, 13(6), 1360.

Comişu, C.-C., Taranu, N., Boacă, G., & Scutaru, M.-C. 2017. "Structural Health Monitoring System of Bridges." Procedia Engineering, 199, 2054–2059.

Zheng, Q., Han, B., & Ou, J. 2019. "NanoComposites for Structural Health Monitoring." In Nanotechnology in Eco-efficient Construction (Second Edition): Materials, Processes and Applications, 227-259. Woodhead Publishing Series in Civil and Structural Engineering.

Bridge Maintenance, Safety, Management, Digitalization and Sustainability – Jensen, Frangopol & Schmidt (eds)
© 2024 The Author(s), ISBN 978-1-032-77040-6
Open Access: www.taylorfrancis.com, CC BY-NC-ND 4.0 license

Digital health monitoring of the Great Belt Suspension Bridge

T. Friis, S.S. Christensen, S.T. Nielsen, M. Lollesgaard & T.B. Bangsgaard
Rambøll Danmark A/S, Denmark

M.D. Havelykke
Sund & Bælt Holding A/S, Denmark

ABSTRACT: This contribution demonstrates how operation and maintenance of one of the largest suspension bridges worldwide have significantly benefitted from a structural health monitoring (SHM) setup with +400 sensors developed in a unique collaboration between consultants at Ramboll, contractors and the owners from Sund & Bælt. The Great Belt Fixed Link in Denmark opened in 1998 and consists of an 18 km road and railway link composed of a tunnel, a continuous multi-span beam-type bridge, and a suspension road bridge with a main span of 1624m, the current 6th longest worldwide. The aim of the tailormade SHM setup is to provide knowledge of structural performance, deterioration and remaining lifetime to the asset managers that can accordingly plan maintenance and actions for mitigation of undesirable structural performance to ensure economical and sustainable asset management and safe operation. The paper provides an overview of the SHM system followed by case studies showing SHM outputs and how these are used in the operation and maintenance. Specifically, it is presented how the SHM provides insight into the vibration phenomena and fatigue lifetime of the hangers, insight into fatigue lifetime of the main girder including influences of operational and environmental parameters, and insight into wear and lifetime of the bearings. It is revealed how this valuable information are used in decision making of the operation and maintenance of the suspension bridge. Lastly, further improvements of the monitoring system and subsequent analyses are discussed with respect to the further value it brings for the asset managers.

1 INTRODUCTION

The Great Belt Fixed Link in Denmark opened in 1998 and connects the islands of Zealand and Funen. It consists of an 18 km road and railway link composed of a tunnel, a continuous multi-span beam-type bridge (the West Bridge), and a suspension road bridge (the East Bridge) with a main span of 1624m, the current 6th longest worldwide (3rd longest outside of China). The Great Belt Suspension Bridge is a landmark engineering marvel. The Great Belt Suspension Bridge is not only a symbol of Denmark's technological advancements, but also a vital link for the country's infrastructure.

The combination of aging infrastructure, advances in technology and concerns of safety and sustainability have all contributed to the growing popularity of Structural Health Monitoring (SHM) in the past decades. The advances in technology have made it easier and more cost-effective to implement SHM systems and the increasing emphasis on safety and sustainability has also contributed to the popularity by creating the need for more knowledge of the structural condition to ensure the correct level of safety and by addressing the importance of longevity to fulfil sustainability goals (Straarup et al. 2022). Thus, an SHM system is an essential tool in management, maintenance and operation of large infrastructure, where these systems are designed to provide real-time information about the structural condition and

DOI: 10.1201/9781003483755-378

behavior of a bridge, allowing asset managers to detect and address potential problems before they become comprehensive.

The SHM system on the Great Belt Bridge is designed to continuously monitor the condition and behavior of the bridge and its mechanical equipment, e.g., tuned mass dampers and hydraulic buffers, and detect any changes that could indicate potential structural or mechanical problems and supply information for both the present and future maintenance decision-making process. The system consists of a network of sensors and monitoring equipment that is distributed throughout the bridge, see Figure 1. The SHM system on the Great Belt Bridge is considered to be one of the most advanced in the world, and it has played a key role in ensuring the safety and longevity of this important infrastructure in a cost-effective manner (Lollesgaard & Brøndum 2018, Myrtue et al. 2021).

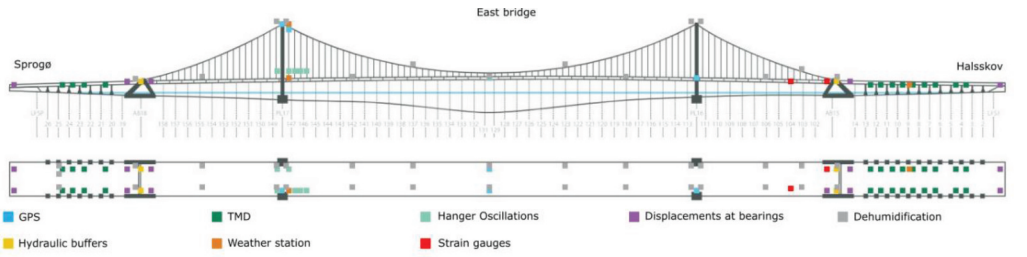


Figure 1. Sensor positions on the Great Belt Suspension Bridge.

In this paper, the current SHM system of the Great Belt Bridge is shortly described followed by a description of the analysis outcome of the measurements and the related benefits for operation and maintenance for a selection of the measurement systems. The focus is on the monitoring of the hangers, bearings and main girder. Towards the end the paper, a discussion of further improvements of the SHM system and the related benefits is provided along with a discussion of the present transformation towards digital enabled asset management.

2 STRUCTURAL HEALTH MONITORING SYSTEM

The entire SHM system is named Konmos, which stands for Structural Monitoring, Great Belt (**kon**struktions**mo**nitering, **S**torebælt in Danish). The system includes approximately 650 sensors distributed on the West Bridge and East Bridge with associated data storage and data access (user interface) on Azure Cloud. The structural monitoring of the suspension bridge consists partly of measurement systems that were installed during the construction of the bridge, and partly of systems that have been installed as the need arose. The Konmos system itself was established in 2015 with its own user interface and data storage for sensors on the West Bridge. Existing sensor systems on the East Bridge were connected to Konmos in 2018-2019.

The user interface is an intuitive tool that makes it easy for anyone who needs information from construction monitoring to quickly access an overview of measurement data from a wide range of different sensors. The user interface provides flexible options for presenting measurement data, making it easy to get an overview and create figures for reports and email correspondence. For further description of the SHM system see (Lollesgaard & Brøndum 2018, Myrtue et al. 2021).

2.1 *Bearing monitoring*

The bearing displacements are monitored on both the West Bridge and the East Bridge and have been in place since the construction of the link. The bearing measurements on the suspension bridge measure horizontal displacements in the direction of the bridge at 12 bearings.

The sensors are placed on each side at the ends of the suspended span and on each side at the ends of the two approach spans, see Figure 1. Specifically, the displacement sensors measure all relative movements with submillimeter resolution between the bridge deck and the support with a sampling frequency of 10 hz, and a photo of a bearing with the measuring equipment can be seen in Figure 2.

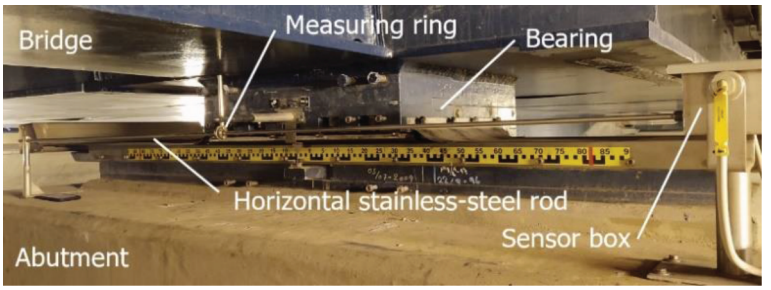


Figure 2. Photo of abearing with the sensor for monitoring bearing displacements on the East bridge.

2.2 *Strain monitoring of the main girder*

The system is established in the late part of 2019 and consists of a temperature sensor and 29 strain gauge sensors, which respectively measure temperature in the steel deck and strains in the steel in relation to fatigue of welds on troughs in the upper side of the bridge deck in sections 101 and 104, see Figure 3. Here it can be seen that the sensors in section 101 are located approx. 10 m from the anchor block under the westbound lanes. The sensors in section 104, on the other hand, are located approx. 120-160 m from the anchor block under the eastbound lanes.

Strains are measured in section 101 close to the expansion joints, as it is assessed as one of the more severely affected locations in terms of fatigue, since the expansion joint is expected to give rise to an additional impact from the passing vehicles compared to the other sections of the bridge. The impact results from the lack of evenness at the transition between the expansion joint and the adjacent road surface. Section 104 is thought to be more representative of the rest of the bridge deck in the suspension section. The focus is also on measuring strains under

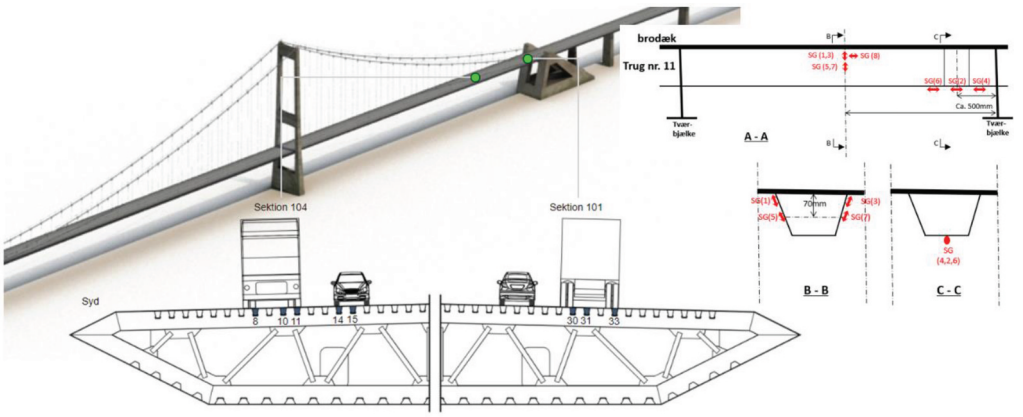


Figure 3. Figures from the Konmos user interface showing the locations of the strain gauges. Section A-A is a longitudinal section in the girder.

slow-moving lane, as the response from traffic is, as expected, greatest here. Moreover, the measurement setup is measuring continuously with as sampling frequency of 600 Hz to capture the fluctuation of stress in the steel caused by relatively fast-moving local traffic load.

2.3 *Hanger monitoring*

Selected hangers are permanently monitored with accelerometers to continuously monitor the vibrations of the cables that have been found to oscillate with large amplitudes from time to time (Gjelstrup 2011). The present monitoring setup consists of accelerometer measurements in 2 horizontal directions on 7 hangers around the western pylon. All 4 hangers in position 2 from the pylon, as well as hangers in positions 1, 3, and 4 Southeast of the pylon, are monitored. The accelerometers are mounted 4.5 m above the bridge deck and sample with a frequency of 25 Hz.

Sensors in the hanger monitoring system have been replaced during the 2023 and additional sensors are added. The new setup cover 10 hangers and on one hanger, the setup is expanded to include 2 dual-axis accelerometers, 2 triaxial accelerometers, and 5 dual-axis inclinometers.

3 ANALYSIS OF MEASUREMENTS AND BENEFITS FOR OPERATION AND MAINTAINANCE

In the present section, the analysis outcome of the measurements and the related benefits for operation and maintenance are presented for a selection of the measurement systems. The focus is on the monitoring of the hangers, bearings and main girder.

3.1 *Bearing monitoring*

The continuous monitoring of the longitudinal displacements at the bearings are analyzed in several different ways from more simple verification of maximum displacements not exceeding the physical limits to more advanced estimation of bearing lifetime. The outcome of the analyses has the following benefits for operation and maintenance:

- Surveillance of larger, slow temperature related displacement with alarm system for detection of critical displacement in respect to physical limits of the bearings, expansion joints and supports incl. assessment of the presence of warping effects. Potential problems are detected before they become adverse and preventive measures can be planned well in advance.
- Estimates of bearing lifetime can potentially be used to ensure timely planning of maintenance and full utilization of bearings before replacement.
- Analysis of governing parameters of the bearing displacement was used to optimize pressure settings of hydraulic buffers which damp longitudinal displacements of the bridge deck. This led to decrease in longitudinal displacements of the suspended bridge deck. The optimization approx. doubled the expected lifetime of the bearings under the main span.

Studies of the measured displacements have shown that the wear of the bearings is caused by accumulation of smaller and faster displacements over time caused by traffic and wind load rather than larger and slower displacements caused by temperature changes. This is in line with the general knowledge of the employed bearings, where the lifetime is given by the accumulated displacement over time but also from the velocity of the displacements. On that basis, estimates of lifetime are obtained based on measured displacements and estimated velocities to get an equivalent accumulated displacement that is comparable to the capacity stated by the manufacturer.

A study of the accumulation of equivalent displacement showed a necessity to reduce the smaller and faster displacements of the main girder. The settings of the hydraulic buffers in the ends of the main span of the suspension bridge were then optimized to reduce the

longitudinal displacements even further, which has been shown to significantly reduce wear and approximately double the expected lifetime of the bearings. The study also revealed the importance of the bearings being able to withstand small and fast displacements, which was important information for the consideration of bearing types and material during bearing replacement. The chosen material can better absorb the small and fast displacements that these bearings have been found to be affected by, which in turn lead to even less maintenance in the future.

Figure 4 shows equivalent accumulated displacement over time from one of the bearings in the main span from June 2021 before optimization of the damping (blue) and June 2022 and after the optimization (orange). A significant difference in the accumulation is seen between these two periods, which leads to the significantly increased lifetime. Moreover, the lines are shown to have sudden changes in inclination, which is found to be a result of the difference in the amount of heavy traffic passing during the weekdays and during the weekend.

3.2 *Strain monitoring of the main girder*

It is known from older bridges with orthotropic steel girders that issues with fatigue cracks of welded connections occur within the lifetime of the bridge. On that basis, it is quite important for operation and maintenance to know when it is expected that the fatigue cracks can occur and where. Thus, the current setup is used to continually estimate the fatigue lifetime of selected welded connections, which is essential input for the planning of current and future actions with respect to inspection and maintenance of several kilometers of welds, and for a potential planning of mitigating actions that will prevent comprehensive problems in the future.

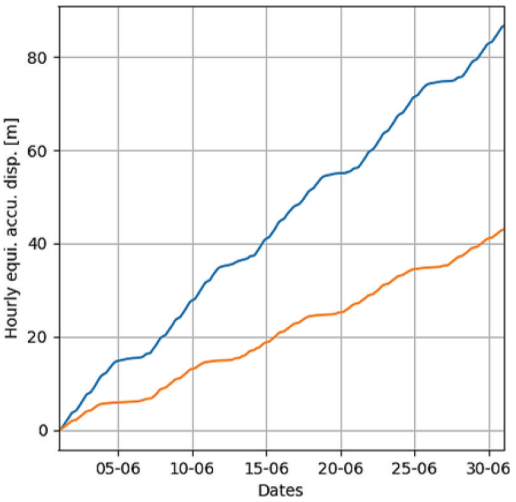


Figure 4. Equivalent accumulated displacement from June 2021 in blue (before optimization of the damping) and June 2022 in orange (after optimization of the damping). The measurements are from a bearing supporting the main span (AB18 NW).

The fatigue lifetimes of selected welded connections are currently estimated based on more than 3 years of continuous measurements of strain. The measured strains are transferred into stresses, and from the time series of stress, rainflow counting is conducted based on ASTM E1049-85 to get stress ranges and counts. The stress ranges and counts are turned into values of damage using the S-N curves of the standard DS/EN 1993-1-9 2007 and the Palmgren-Minor rule. For the final estimate of fatigue lifetime, the estimated damages are scaled based on traffic counts of heavy traffic and a prognosis of traffic development over the Great Belt Bridge in the future.

The estimated remaining fatigue lifetime of the selected welded connections is ranging from approximately 50 years (characteristically) in the heaviest loaded location under the slow-moving lane to a theoretical infinity of least loaded location under the fast-moving lane. This knowledge is essential input for the planning and prioritizing of current and future actions with respect to inspection and maintenance. Additionally, this knowledge and a continues monitoring is also essential input for potential planning of mitigating actions in the future that will prevent comprehensive problems that might arise as the bridge ages beyond the lifetime of the heaviest loaded welds, and thereby extending its lifespan and minimizing the costs over time.

The strain gauge monitoring has also provided increased insight into the relation between the asphalt and the lifespan of the bridge deck, where temperature and the condition in terms of thickness and unevenness of the pavement have shown to have a significant impact. The temperature decreases the stiffness of the asphalt causing larger stress changes in critical locations. In Figure 5, a plot is seen of the damage on a weld between trough and top plate for one year computed from the measurements on an hourly basis over hourly mean road temperature and hourly traffic count of trucks and busses. From these results it is clear that the hours with higher amount of fatigue damage only occur at higher road temperatures and with many heavy traffic passages.

The knowledge of how much the road temperature affects the lifespan of the weld in the main girder is beneficial input to the operation and maintenance since it shows the importance of choosing and maintaining an asphalt pavement with the right properties (thickness and stiffness) to prevent fatigue cracks and not just for the sake of the comfort of the passing traffic. Even for design of new bridges, it shows the importance of these considerations of the asphalt pavement to ensure the longevity of the welds of the girder and prevent expensive maintenance work when the bridge becomes older. Additionally, the asphalt pavement in slow-moving lane with passage of trucks has been renewed during 2022 to ensure the longevity of the Great Belt Suspension bridge and the comfort of the passing traffic. Preliminary studies of the strain gauge measurements have shown that the renewal of the asphalt might have a significant positive effect on the lifetime of the welds in the top part of the main girder.

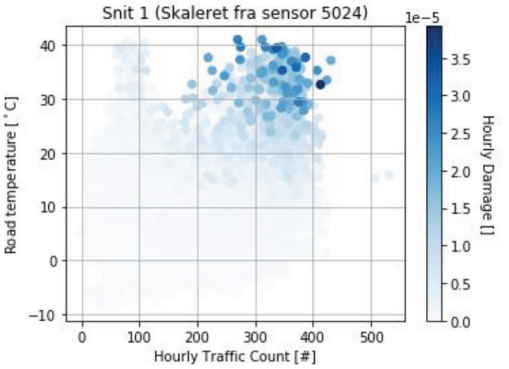


Figure 5. Hourly damage over hourly mean road temperature and hourly traffic count of trucks and busses for a weld between trough and top plate. The measurement period is from February 2021 to February 2022.

3.3 *Hanger monitoring*

As previously described, selected hangers are permanently monitored, and the measurements are analyzed with focus on the following benefits/input for operation and maintenance:

- Surveillance and knowledge of oscillation levels and phenomena which is also employed for planning, design, and evaluation of potential mitigation actions.

- Estimation of fatigue lifetime for timely planning of potential replacement and assessment of the need for mitigation actions that can extend the lifetime.
- Surveillance of estimated hanger forces as continuous monitoring of the load distribution, where changes in the load distribution potentially can indicate damages. Thus, potential damages can be detected immediately, and appropriate measures can be carried out in timely and cost-effective manner. This is elaborated in the current section.
- Surveillance of estimated hanger damping to continuously evaluate performance of external dampers. Dampers with poor performance can be replaced to ensure longevity of the hangers.

The continuous monitoring of the oscillations for more than 3 years has given insight into the oscillation levels and frequency of the occurrence of the higher vibration levels. Maximum vibration levels are found with amplitudes in the range of 1.5-2.0 m at the center of the hangers.

The oscillations of the cables cause bending stresses and fretting wear at the ends where the curvature is largest, which potentially can result in fatigue of the cables. Thus, one of the main reasons for monitoring the hangers is to estimate the fatigue damage from these oscillations.

The estimation of the fatigue damage and lifetime is carried out in several steps. At first, the subject of virtual sensing is employed to estimate virtual measurements of displacements and stresses at the critical positions. Secondly from the time series of stress, rainflow counting is conducted based on ASTM E1049-85 to get stress ranges and counts. Then stress ranges and counts are turned into values of fatigue damage using an appropriate S-N curve and the Palmgren-Minor rule.

At this point in time, the estimates of fatigue lifetime have been found to be towards a disappointing low level. The current calculations, however, have also been assessed to be quite conservative with an overestimation of the stresses. On that basis, two actions have been set in motion: i) The measurement setup has been expanded during 2023 to cover more hangers but also to have more sensors on one hanger. The latter is planned to give a better insight into the structural characteristics of the hangers and reduce the aforementioned conservatism. ii) Additional dampers have been designed for some of the hangers and are currently being produced. Vibration dampers were already installed in 2007 on the two longest hangers on each side of the pylons (i.e., 8 damped hangers at each of the two pylons). The additional dampers are planned to cover hangers in position 3 and 4 from the pylons.

In one case, the external damper (local viscous) of a hanger was found completely defect during maintenance, which led to a continuous estimation of modal damping from the measured accelerations using Operational Modal Analysis in order to monitor the performance of the external dampers. For the specific hanger, it even led to an evaluation of the damper concept by estimating the modal damping before and after replacement of the damper cylinder, see Figure 6. It was found that the dampers in one position did not supply a sufficient level of damping due to the damper not having a large enough movement range and not providing the optimal force level. New dampers are planned for the one position to ensure longevity of the hangers.

The monitoring of the hangers has already given much value for operation and maintenance. Vibration levels are known, and potential future problems are illuminated and analyzed, and actions have been set in motion in a timely and cost-effective manner to ensure safe operation now and in the future. By already carrying out preventive action in the early ages of the bridge, the lifetime is potentially expanded past the intended lifetime during design.

4 DISCUSSION AND DIGITAL ENABLED ASSET MANAGEMENT

A good yield with significant operation and maintenance cost benefits is already achieved from monitoring, as described for a selection of the measurement systems in the previous section. Nonetheless, there is still a greater yield to be gained if the monitoring hardware, the subsequent analyses and its implementation in the operation and maintenance procedures are

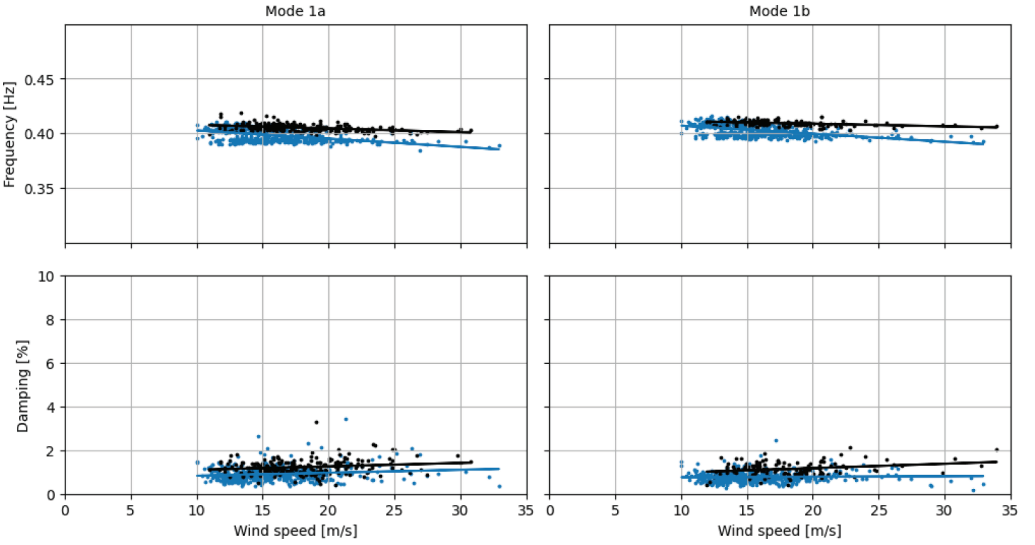


Figure 6. Lowest natural frequency and damping as a function of the 10-minute mean wind speed for a hanger in position 1 from a pylon. Blue represent data from before the defect damper cylinders on the hanger were replaced, and black represent data from after the damper cylinders were replaced. Mode 1a and 1b are the two closely-spaced fundamental modes of the hanger.

expanded and developed further, so that the maintenance moves further towards being condition-based or predictive, as it can help to provide or increase the following benefits even further:

- Lower maintenance costs - optimization of inspection intervals and reduction of manual inspection, timely planning and full utilization of elements before replacement.
- Extend lifespan - some elements have a predetermined design life, which may prove to be longer under actual conditions. Factors that reduce lifespan can be identified and rectified, so that construction parts last longer.
- Increase safety - when actual conditions are known and monitored, uncertainties are reduced and reliability increases. In other words, the deterioration of structural components over time can be detected or even predicted to avoid possible accidents and collapses.
- Increased sustainability - the monitoring provides more knowledge about the condition of the structure, whereby climate-damaging maintenance, renovations, and partial replacements are prevented with countermeasures in due time or not carried out until necessary.
- Minimize downtime - when the condition of the structural components can be predicted, maintenance and repairs can be planned well in advance and arranged so that traffic is disturbed as little as possible.
- Improve the customer/user experience - structural-related conditions that may worsen the customer/user experience can be reduced and rectified.
- Knowledge sharing and collaboration with universities and other bridge owners - increased yield through research and knowledge sharing.

Digital enabled asset management is the process of using digital technologies to optimize the management of physical assets throughout their lifecycle, from design and procurement through to operation, maintenance, and decommissioning. This approach involves the use of digital tools such as sensors, data analytics, algorithms and machine learning to collect and analyze data on asset performance, condition and usage, and to use this information to make more informed decisions about how to manage and maintain assets. By leveraging digital technologies, asset managers can gain real-time insights into asset health, anticipate and prevent failures, and optimize maintenance schedules, leading to reduced downtime, increased asset

longevity, and lower overall costs. Digital-enabled asset management also enables better collaboration between stakeholders in the asset management ecosystem, such as owners, operators, maintenance teams, and suppliers, by providing a shared digital platform for data collection, analysis, and decision-making. Overall, digital enabled asset management offers significant benefits for organizations across a wide range of industries, helping them to improve asset performance, reduce costs, and increase overall efficiency and effectiveness (Straarup et al. 2022).

The maintenance and operation of the Great Belt bridge has taken the first steps towards an implementation of digital enabled asset management as is evident from the present paper. The transformation is, however, not straightforward and will naturally face challenges and difficulties, and take time. Changing set ways of conducting operation and maintenance is not done overnight and will most probably be conducted in both small and large steps. In order to have predictive maintenance and optimized inspection, the knowledge obtained from the monitoring has to be transferred into practical ways of inspection and maintenance. The latter is a challenge often underestimated, which will inevitably demand willingness to change to be successful.

REFERENCES

Bangsgaard, T. B., Gjelstrup, H., Scullion, A., & Faulkner, P. (2018). Structural Health Monitoring System for The Queensferry Crossing. IABSE Conference – Engineering the Past, to Meet the Needs of the Future. Copenhagen. doi:10.2749/copenhagen.2018.431

Gjelstrup, H. (2011). Understanding and Simulating wind-induced vibrations of iced vertical cables. Kgs. Lyngby: Technical University of Denmark (PhD thesis).

Lollesgaard, M., & Brøndum, R. (2018). Great Belt Bridge – Structural monitoring. IABSE Conference – Engineering the Past, to Meet the Needs of the Future. Copenhagen. doi:10.2749/copenhagen.2018.401

Myrtue, K., Martins, N., Lollesgaard, M., Bangsgaard, T. B., Havelykke, M. D., Bormlund, F., & Ingolfsson, E. (2021). SHM at the Great Belt Fixed Link in Denmark. 10th International Conference on Structural Health Monitoring of Intelligent Infrastructure (SMHII 10). Porto.

Straarup, L., Abdalla, G., Visser, M., & Bangsgaard, T. B. (2022). A Digital Twin for the Fehmarnbelt Tunnel – preparing for Digital Enabled Asset Management. ITA-AITES World Tunnel Congress, WTC2022 and 47th General Assembly. Copenhagen.

Bridge Maintenance, Safety, Management, Digitalization and Sustainability – Jensen, Frangopol & Schmidt (eds)
© 2024 The Author(s), ISBN 978-1-032-77040-6
Open Access: www.taylorfrancis.com, CC BY-NC-ND 4.0 license

Data-driven preventive maintenance and service life extension of the Sunshine Skyway Bridge – Tampa FL, USA

I.A. Gualtero, P.E., A.H. Alvi, P.E. & S.D. Womble, P.E.
T.Y. Lin International, Tampa FL, USA

J.J. Jacobsen, P.E.
Florida Department of Transportation District Structures Maintenance Engineer, Tampa FL, USA

V.S. Collie, P.E.
Florida Department of Transportation Skyway Bridge Project Manager, Tampa FL, USA

ABSTRACT: The Sunshine Skyway Bridge, inaugurated in 1987, was born out of necessity following a tragic vessel collision that destroyed the southbound main span, killing 35 people. Conceived by the accomplished French engineer, Jean M. Mueller, this iconic bridge boasts a 366 m cable-stayed main span, complemented by a 1,219 m main unit featuring 11 spans employing a combination of cable-stayed box girder and balanced cantilever post-tensioned concrete box girder components for the back spans. Acknowledging the significant milestone of the bridge reaching its 37th year,, the Florida Department of Transportation is actively engaged in intensive efforts to extend the service life of the bridge. This paper delineates the innovative *Data-Driven Preventive Maintenance and Service Life Extension* approach currently being applied to the Sunshine Skyway Bridge. Spearheaded by TYLin, the approach integrates structural monitoring employing nearly 100 sensors, encompassing conventional structural health monitoring (SHM) sensors combined with custom-built sensors designed to cater specifically to the distinctive monitoring requirements of this structure. Concurrently, a finite element model is under development to precisely represent the as-built structure. This model will be fine-tuned with sensor data, culminating in the creation of a comprehensive digital twin of the bridge, which is poised to enhance comprehension of the bridge's behavior and furnish crucial data for gauging the remaining service life of critical components such as stay cables and stay cable dampers. In tandem with monitoring and modeling, the data procured from sensors undergoes advanced post-processing techniques using "Big Data" analytics. Currently, this data is used to train a *machine learning model*, enabling real-time prediction of structural parameters. This capability will facilitate the instantaneous identification of any parameter deviating from the normal range, thereby enhancing the bridge's overall safety and performance.

1 INTRODUCTION

The Bob Graham Sunshine Skyway Bridge, a renowned and vital structure recognized as the State of Florida's "flagship bridge" stands as an symbol of resilience and innovation. Completed in 1987, its inception followed the tragic failure of the original Skyway Bridge's South Bound Main Span due to a vessel impact, resulting in a catastrophic event that claimed 35 lives. This poignant history underscores the critical importance of the current bridge as a vital link, spanning 6.66 km across Tampa Bay and connecting the communities of Pinellas and Manatee Counties. The bridge boasts a cable-stayed main span and high-level approach spans constructed

DOI: 10.1201/9781003483755-379

with precast segmental concrete superstructure and substructure. Additionally, the trestle spans feature AASHTO concrete beams and a conventional concrete pile/bent design. A distinctive feature of the bridge is the inclusion of forty-two total continuous stay cables, with twenty-one gracefully running through each of the two towers along the center line, providing indispensable support to the entire structure. In light of the Sunshine Skyway Bridge's extremely aggressive environmental conditions, corrosion has emerged as the primary challenge. This persistent threat manifested in significant issues with the post-tensioning (PT) system during the early 2000s, necessitating substantial cost to rectify the deficiencies. In light of the bridge reaching its 37th year, the Florida Department of Transportation (FDOT) remains steadfast in their ambitious endeavor to to extend the bridge's operational lifespan to an impressive 100 years.

Recognizing this ambitious objective, FDOT has astutely acknowledged that traditional, reactive maintenance approaches are insufficient for such a challenging task, and in collaboration with engineering consultant T.Y. Lin International (TYLin), has adopted innovative methodologies and cutting-edge practices, with a particular focus on Data-Driven Preventive Maintenance. The utilization of data-driven preventive maintenance not only enhances the bridge's current structural health but also positions it to successfully navigate the challenges of the future. As the bridge continues to gradually age, these initiatives underscore a commitment to safety, longevity, and the seamless functionality of this iconic structure for generations to come.



Figure 1. The Sunshine Skyway Bridge.

2 STRUCTURAL MONITORING

The structural monitoring system in this bridge encompasses a diverse array of structural sensors, incorporating accelerometers, displacement sensors, strain gauges, GPS units, weather stations, acoustic sensors, water sensors, and thermocouples. This comprehensive suite comprises nearly 100 sensors, with an ongoing commitment to expanding this network by installing additional sensors annually, see Figure 2. These augmentations are thoughtfully tailored to meet the evolving monitoring requirements of the bridge, ensuring a dynamic and responsive approach to safeguarding its structural integrity.

2.1 *Accelerometers*

The accelerometers are tactically placed at three general locations, the top of the tower, the stay cables, and the interior of the superstructure.

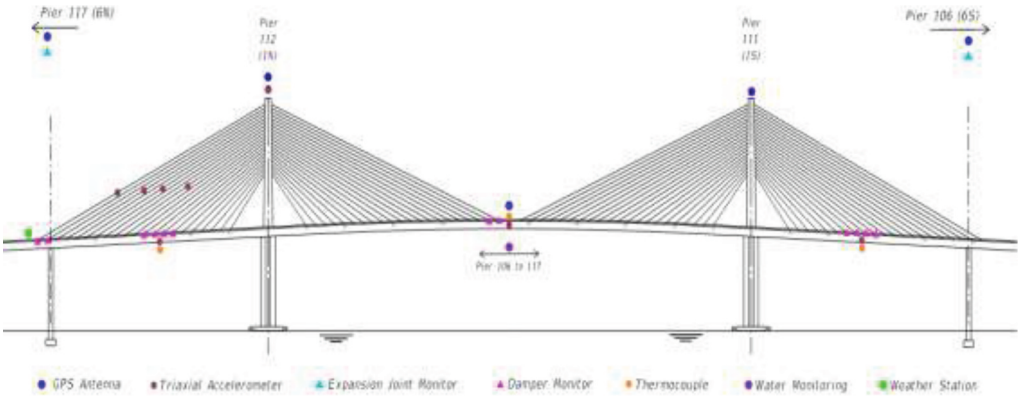


Figure 2. Location of structural monitoring sensors.

2.2 *Stay cable and tower accelerometers*

Presently four stay cables are instrumented with triaxial MEMS accelerometers. These accelerometers are installed on the top side of the cable and located about 15.2 m above deck level. They have a 100Hz sampling rate and a 16-bit resolution at +/- 2g scale. The cable accelerometers are wired to a data logger housed in a cabinet located in the median of the bridge.

Consistency in monitoring technology is maintained using the same triaxial MEMS accelerometers as were installed on the stay cables and at the summit of the north tower in 2016.

2.3 *Deck accelerometers*

Deck accelerometers have been tactically placed at critical points including the center of the main span and the center of the two back spans. Installed between 2021 and 2023, the specifications are: Triaxial MEMS accelerometers with 16-bit resolution, and a 50Hz sampling rate. These accelerometer units are portable, and real-time communication is obtained through an embedded 5G cellular modem. The raw accelerometer data is compressed using an algorithm that allows compression rates of 30x.

Additionally, these accelerometer units are equipped with a triaxial gyroscope, enabling the measurement of angular velocities along three axes. This gyroscopic data is particularly crucial for monitoring torsional vibration modes.

2.4 *Expansion joint monitoring*

The expansion joint monitoring sensor provides real-time measurements of joint movement with a high resolution of 0.1mm. The system, equipped with redundant sensors, can capture absolute values, not just differentials from reboot time. It features acoustic monitoring for continuous noise level surveillance in the joints. Another highly innovative aspect of these sensors is the incorporation of on-demand video, enabling visual confirmation of alarms and time-lapse capabilities for the joint system as shown in Figure 3. The system operates on a cellular basis through an embedded 5G cellular modem.

Furthermore, the system integrates thermocouples to monitor internal temperature, advantageously placed at the top slab, web, and bottom slab of the box girder. These temperature sensors are positioned at the midspan of both the main span and the back spans.

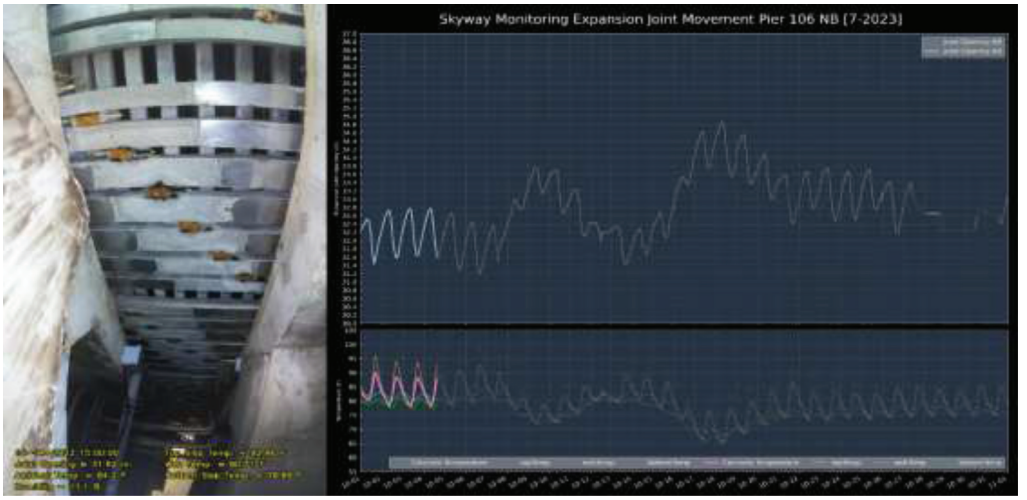


Figure 3. Example of joint timelapse video and movement and temperature plots.

The joints, situated at the ends of the 1,219-m main span unit, are 61-cm, 20-ton, modular joints replacements for the original joints, which were replaced via emergency contract in 2004 due to premature damage. The current joints have been in service for 19 years.

2.5 *Cable damper monitoring*

The stay cable dampers consist of two damper sets at each end of each cable, each set consisting of three damper shocks situated within the interior of the superstructure. These dampers are connected to the stay cables through two struts, linking to the cables approximately 1.5 m from the top of the median slab.

At present, monitoring systems are integrated into 12 stay cables, specifically targeting the cable dampers. They operate in real-time, capturing the movement of the dampers with an impressive 0.1 mm resolution. The sensors operate at a sampling rate of 5 Hz and offer a maximum amplitude range of 5 cm, providing detailed insights into the dynamic behavior of the cable dampers.

2.6 *Water presence monitoring*

Water presence near PT tendons has persistently posed challenges in this bridge, prompting the incorporation of a water monitoring system. To address the expansive coverage needed, wireless IoT water presence sensors were deployed. These sensors operate on a plug-and-play basis, facilitating placement at any location with power access, instantly initiating the reporting of water presence conditions to a gateway unit. Designed with measures to prevent electrical currents from accelerating corrosion on bridge components, the 20 installed sensors are purposefully placed in areas prone to water intrusion. The system's flexibility allows for seamless integration of additional wireless sensors as needed.

2.7 *Future sensors*

2.7.1 *Midspan deflection*

We are currently developing a real-time deflection monitoring system for the bridge's main span, designed to meet specific criteria: suitability for long spans, high resolution (up to 0.1mm), high accuracy (+/- 2 mm), real-time readings at a 2 Hz sample frequency, and no

long-term drift in deflection readings. Notably, this system does not require a clear view of the sky, allowing it to be entirely housed within the bridge. Additionally, its accuracy remains unaffected by structural vibrations, severe weather conditions, or space weather phenomena like solar storms.

This system empowers us to track changes in the main span deflection resulting from daily temperature variations and live loads. The high resolution and sampling frequency enable monitoring of low-frequency oscillations as well. By focusing on mid-span deflection with these specifications, we can promptly identify unexpected structural changes, offering valuable insights into potential issues with stay cables or live load overloads.

2.7.2 *Stay anchor strain gauges*

As part of a pilot program, we will monitor strains and stresses at the stay cable anchor block spacers. While these sensors won't provide stay cable tensions directly, they offer a precise method to track changes in stay cable tensions since installation. This monitoring system represents the optimal approach for promptly detecting any sudden changes in stay cable tension, particularly in response to strand or cable failures.

3 DATA EVALUATION

3.1 *Data collection and presentation*

Data from various sensors is transferred through either a fiber optic network or a 5G cellular network, reaching a Microsoft Azure cloud server. Next, decimated data is presented on a web interface. Simultaneously, raw data files are automatically uploaded to TYLin servers for additional post-processing. All systems are equipped with programmed sensor alarm trigger levels, ensuring that SMS text messages are promptly sent when alarms are triggered.

3.2 *Postprocessing*

The gathered data undergoes evaluation, and a comprehensive report is furnished to the FDOT on a monthly basis or following significant events, such as severe weather occurrences.

The raw data acquired from accelerometers is presented as acceleration time history, denoting changes in the acceleration of the member over time. While this data alone may not yield extensive insights into structural behavior, additional processing unlocks valuable structural parameters.

Initiating the data processing, the first step involves normalizing raw acceleration magnitudes. This normalization is imperative due to variations in acceleration axes over time, induced by minor shifts in accelerometer orientation caused by the thermal movement of the structure. To achieve normalization, the mean of a 500-point moving average is subtracted from each data point, resulting in an acceleration time history centered over the 0g axis.

The normalized acceleration data is further transformed into a frequency domain plot using the Fast Fourier Transform algorithm applied to a 10-second time slice. The frequency domain plots illustrate all frequencies present in the data slice, facilitating the identification of the most predominant frequency. These dominant frequencies are tabulated for each slice, and the collective frequency distributions for a given time are depicted in a histogram for each member and evaluated time period.

Crucial to structural assessment is determining the extent of cable, tower, or deck movement during wind-induced oscillations. However, this calculation is complex, and the derived value is considered an estimate. The peak to peak displacement (amplitude x 2) is computed by applying sinusoidal motion equations, establishing a relationship between frequency, acceleration, and amplitude using Equation 1 below.

$$D = \frac{G * A}{2 * \pi^2 * F^2} \tag{1}$$

where: D= Displacement (m), A= Max acceleration (g), F= Oscillation frequency (Hz), G= 9.8066 m/s^2

To apply the equations accurately and obtain precise estimates, it is crucial to isolate low-frequency oscillations and eliminate high-frequency vibrations from the data. This is achieved through the application of a low-pass filter, effectively removing frequencies higher than 2 Hz from the signal. Subsequently, the displacement equation is applied to the filtered signal. The low-pass filter is implemented by excluding frequencies above 2 Hz from the frequency domain, followed by signal reconstruction through the inverse FFT algorithm in the time domain.

The scale of postprocessed raw data in this evaluation is substantial, with each channel generating approximately 17 million data points daily. Given the immense size of the datasets, conventional data processing applications proved inadequate for handling this volume, necessitating the utilization of "Big Data" procedures implemented in the versatile computer programming language, Python.

In light of the complexity of the post-processing algorithms and to enhance confidence in the results, a decision was made to validate these scripts using computer-generated signals with predetermined parameters. The signals (acceleration vs. time) underwent processing using the same scripts employed for raw data, and the output was meticulously compared with known signal parameters. This iterative verification process continued until the analysis output was consistently aligned with the known parameters.

As shown in Figure 4, the output data is presented comprehensively in a summary plot, showcasing acceleration, frequency, amplitude, wind speeds, and directions (arrows). Following this summary plot, additional plots depict histograms of frequency distribution and 10-second snapshots illustrating the 10 maximum amplitudes and accelerations. These snapshots serve as visual verification of the data presented in the summary plots, enhancing the interpretability and reliability of the results.

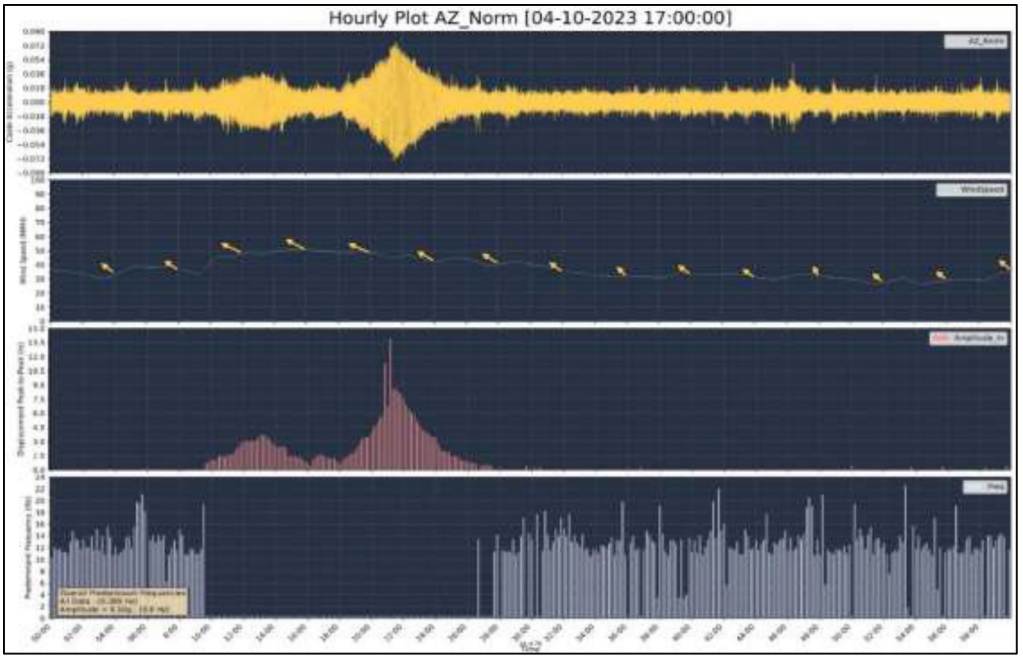


Figure 4. Example of deck accelerometer post-process data during a high oscillation event.

4 DATA-DRIVEN PREVENTIVE MAINTENANCE

Bridges are vital components of transportation networks, necessitating robust maintenance strategies to ensure their longevity and structural integrity. Traditional maintenance approaches often rely on reactive responses to issues, leading to increased costs and potential disruptions. The emergence of data-driven preventive maintenance presents a revolutionary approach, where the power of data analytics is harnessed to predict, prevent, and address maintenance needs proactively. Data-driven preventive maintenance revolves around the continuous collection, analysis, and interpretation of various data sources related to bridge health. This includes structural data, environmental conditions, traffic patterns, and historical performance records.

The objective of data-driven preventive maintenance is to proactively identify potential issues before they escalate, enabling timely interventions that mitigate risks and extend the service life of the bridge. To achieve this objective, a series of impactful measures have been implemented, including:

4.1 *Stay cable service life evaluation (fretting analysis)*

The Skyway Bridge employs a unique saddle system for attaching cable-stays to the towerhead. In this system, the strand bundle constituting each cable is guided through a steel cable saddle, rather than being terminated with an anchorage in the towerhead. The saddle configuration of the strand bundle introduces radial forces resulting from the curvature of the cable bundle as it passes through the tower resulting in fretting stress.

The assessment of stay cable service life, specifically focusing on fretting analysis, involves utilizing collected cable acceleration data to measure oscillation cycles. A complex analysis to determine fretting stress on the cables was conducted in 2019 but there wasn't sufficient data to conclude the study. This measured data provides a more accurate input for cable fretting evaluation, surpassing the previous estimation derived from wind studies. Additionally, the data gathered from damper monitoring and cable accelerometers contributes to obtaining an improved estimate for the cable damping ratio, a pivotal input in the fretting analysis. The integration of these data sources enhances the precision and reliability of the evaluation process, leading to more informed insights into the service life of stay cables.

4.2 *Cable damper service life and replacement evaluations*

Cable damper monitoring provides an estimation of structural damping for the cables, specifically obtaining the 1st Mode Damping on all cables. Employing the free-vibration method, we systematically excite the cables, recording decay traces of their motions. The estimation of structural damping incorporates corrections for ambient aerodynamic damping, ensuring a comprehensive analysis.

Next, we calculate the Scruton Number (Sc) for each cable and mode. This dimensionless parameter in structural dynamics serves to quantify damping efficiency by comparing the viscous damping in the system to the critical viscous damping. A higher Scruton Number indicates more effective damping relative to the critical value. This characterization proves essential for understanding the structure's response to dynamic loading, particularly in vibration analysis.

Efficient damping is paramount for controlling vibrations and mitigating resonance-related issues in bridges. Damper monitoring helps determine actual operation parameters in the field (amplitude and frequency of oscillations), these parameters will be used in the lab for testing of the dampers and to determine the remaining service life and replacement.

4.3 *Water intrusion detection and repairs*

TYLin has designed and placed moisture detection sensors in various areas within the box girders. If water is detected, the system triggers a real-time alert, notifying FDOT instantly via text and

providing an accompanying image of the identified moisture. This timely notification prompts the owner to take immediate action, initiating a thorough inspection and assessment to pinpoint and address the source of the detected moisture. Leaks typically occur through cracks, joints, sealant failures, or other openings. Identifying these entry points is crucial for effective remediation. This may involve repairing or replacing damaged sealants, addressing joint deficiencies, and ensuring that expansion joints are functioning properly. Concrete repair consists of patching or replacing concrete elements and applying waterproofing materials to prevent further moisture penetration. By following these steps and tailoring the approach to the specific conditions of the segmental components of the Skyway Bridge, we reduce the need for frequent and expensive physical inspections. This enables us to assess the efficacy of past water intrusion repairs, systematically address leaks, uphold structural integrity, and ultimately improve overall performance and durability.

4.4 *Expansion joint monitoring*

TYLin has engineered comprehensive expansion joint monitoring systems for the main modular joints on each side of the main span unit of the Skyway Bridge. Due to the complexity of the joints, relying solely on expansion-contraction measurements may not be sufficient to identify broken components within them. The presence of damaged components poses a heightened risk to both the segmental boxes and, more significantly, the entire modular joints. This situation can potentially result in significant expenditures, as exemplified by the emergency replacement in 2004. To enhance our monitoring capabilities, alongside the expansion joint movement monitors, we have seamlessly integrated acoustic monitoring devices on the modular joints. This additional layer of monitoring enables the prompt identification of any broken components within the modular joint system through the analysis of sound. We received a recent alert signaling a loud noise emanating from the south expansion joint. Subsequent inspection revealed that failing modular joint bearings were the root cause, resulting in the system producing high-decibel sounds. In response, FDOT has promptly scheduled a repair for the joints, which will involve the replacement of the bearings within the joint to ensure proper and effective functionality.

4.5 *Finite element model (digital twin)*

In the maintenance of complex bridges, the development and implementation of a finite element model (FEM) is an indispensable tool for structural assessment and bridge preservation. The FEM, currently in progress, serves as an accurate representation of the as-built structure. By assimilating data collected from an extensive network of sensors strategically placed throughout the bridge, the FEM becomes a dynamic and evolving *digital twin* of the bridge capturing the intricate nuances of structural behavior.

The digital twin, born from the refined FEM, serves as a virtual counterpart to the physical bridge. This virtual representation not only mirrors the current state of the structure but also facilitates real-time monitoring and analysis of its dynamic responses. The digital twin becomes a powerful tool for comprehending the bridge's behavior under diverse conditions, allowing for predictive insights into potential stress points, vulnerabilities, and the overall health of critical components.

The digital twin will be essential for proactive maintenance and precise assessment of structural integrity. This approach enables a deeper understanding of the bridge's response to external forces, aids in predicting potential wear and tear, and provides invaluable data for gauging the remaining service life of critical components like stay cables and stay cable dampers, ensuring optimal performance, longevity, and safety of the structure.

5 CONCLUSION

In conclusion, the integrated structural monitoring system and data-driven preventive maintenance approach underscore a comprehensive and forward-thinking approach to bridge management for the Sunshine Skyway Bridge. The dedication to harnessing data as a valuable

resource reflects the management's commitment to ensuring optimal performance, longevity, and safety of this iconic structure.

The deployment of custom-built modular sensors emerges as a pivotal tool for precise and nuanced data collection, enabling a deeper understanding of the bridge's dynamic behavior. This tailored approach to sensor technology positions the monitoring system as a cutting-edge solution for gathering critical insights into structural health.

A key takeaway is the recognition of data's intrinsic value in reaching strategic decisions for bridge management. Leveraging this valuable resource allows for proactive measures that not only address current challenges but also contribute to extending the remaining service life of the bridge. This calculated utilization of data positions the Sunshine Skyway Bridge as a benchmark for the effective and sustainable management of complex bridge structures.

In essence, the continuous improvements in the monitoring system, alongside the commitment to data-driven strategies, position the Sunshine Skyway Bridge as a model of excellence in the realm of bridge management. This achievement is manifest evidence that the accumulation of mere data is not just information, but a powerful tool that can enhance the longevity, safety, and optimal performance of complex bridge structures.

REFERENCES

Chen, Hua-Peng. 2018. Structural Health Monitoring of Large Civil Engineering Structures. Wiley-Blackwell; 1st edition

Svenson, Holger. 2012. Cable-Stayed Bridges: 40 Years of Experience Worldwide. Ernst & Sohn; 1st edition

Bridge, Jennifer. & Davis, Justin. 2021 Sunshine Skyway Bridge Monitoring Phase I: System Deployment. Department of Civil and Coastal Engineering University of Florida.

Bridge, Jennifer. & Davis, Justin. 2021 Sunshine Skyway Bridge Monitoring Phase II: System Deployment. Department of Civil and Coastal Engineering University of Florida.

Figg and Muller Engineers, Inc. 1988. Manual for Inspection and Maintenance of the Sunshine Skyway Bridge Segmental Concrete approaches and main span. Tampa, Florida.

PB Americas, Inc. 2010. Sunshine Skyway Bridge Manual 2 for Inspection and Maintenance. Tampa, Florida.

Bridge Maintenance, Safety, Management, Digitalization and Sustainability – Jensen, Frangopol & Schmidt (eds)
© 2024 The Author(s), ISBN 978-1-032-77040-6
Open Access: www.taylorfrancis.com, CC BY-NC-ND 4.0 license

Sustaining structural bearings – assessment of renovation design on Storebælt West Bridge

A. Smyth, D. Lang, J. Fogh-Svensson & N. Grønkjær Rasmussen
Rambøll Danmark A/S

M. Duus Havelykke & F. Raun Gottfredsen
A/S Storebælt

ABSTRACT: The Great Belt Fixed link is an 18 km combined road and rail link composed of a tunnel, suspension bridge and a 6.6 km long continuous multi-span concrete box-girder bridge, the Storebælt West Bridge. The Great Belt Link is the only railway connecting the Danish main islands of Zealand and Funen, which later connects to Jutland, forming a vital piece of infrastructure between Sweden and central Europe.

A total of 276 structural bearings support the two box-girders of the Great Belt West Bridge, one each for road and rail. In a collaboration between consultants from Rambøll and the owners Sund & Bælt, a bearing renovation/replacement program has been initiated to ensure the overall health of the structure, as the service life of the bearings is significantly lower than the 200 expected years of lifetime for the concrete structures.

Due to the scale of the structure and the quantity of bearings, a strategic digital-enabled maintenance program integrates a thorough inspection regime with permanent structural health monitoring providing the basis for detailed condition assessment of the bearings. Through these activities, the basis of a holistic maintenance program for renovation/replacement of the bearings is established, being carefully developed to minimize traffic disruption.

The challenge of undertaking precise renovation work in harsh sea conditions encompasses several disciplines: innovative design of temporary structures, mechanical and electrical design, and hydraulic bridge lifting, while incorporating effective IKT and risk management. A detailed concept development for the bearing renovation/replacement work is supported by 3D finite element models of temporary/permanent structures, as a vital means to examine key details and the effects of renovation work. This is further addressed by a planned test lifting and bearing replacement to assess the developed strategies and concepts before full scale implementation.

1 INTRODUCTION

1.1 *Background*

The two 6.6km bridges are each comprised of 6 box girders approximately 1.1km each in length, supported by a total of 276 bearings, allowing expansion and contraction of the girders due to thermal effects by approximately +/-170mm over the course of a year. The structural bearings must also support significant dynamic loads applied by vehicles and trains, as well as strong winds. This is to ensure that forces are not significantly transferred to the slender piers supporting the structure.

DOI: 10.1201/9781003483755-380

1.2 *Structural bearing function*

The pot bearings each support loads up to 48 Meganewton in the vertical direction, while allowing the superstructure to rotate through deformation of a rubber pad contained within the steel pot base plate. Under these significant loads, the pad acts like a liquid with a resilient plastic seal around the pad designed to prevent the pressurized rubber escaping.

To allow horizontal movement, the top plate is designed to slide against the PTFE material in the piston – the surface of the PTFE containing recesses, which retain special grease used to maintain an ultra-low friction coefficient throughout the lifetime.

The side restraints prevent significant transverse movement occurring, restraining against various loads such as high winds and even ship impact, while still allowing low friction sliding between the top plate and piston through composite sliding interfaces.

The top plate and base plates are bolted to corresponding anchor plates, which are embedded within the concrete structures.

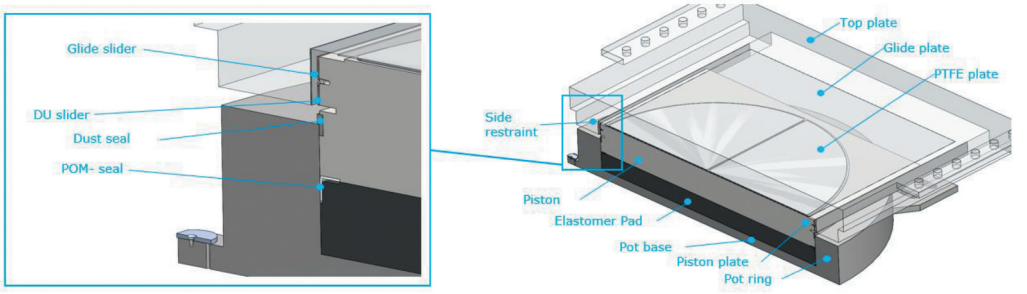


Figure 1. A model of one of the typical pot bearing designs used on the structure recreated in 3D CAD.

2 BEARING CONDITION MONITORING

2.1 *Overview*

Storebælt have in place a robust, digitally-enabled strategic inspection plan, which utilizes a live measuring system, *Konmos,* supplemented by regular physical inspections of the bearings, with additional focused measurements within key areas.

2.2 *Konmos monitoring of bearings*

The movement monitoring system installed on the bridge in 2017, provides live data and analysis of horizontal, vertical and rotational movements of the superstructure at many bearing locations, typically those at the expansion joints that experience the largest movements, as well as temperature and wind sensors throughout the bridges. This is a powerful tool to verify that the structure and bearings are performing as expected, and providing any warning to problems before they develop. For example, a clear correlation between bridge temperature and expansion of the bridge can be seen and continuously monitored. It can also be used to assess the condition of components that might not be possible through a physical inspection, such as checking the rotation of the elastomer pads, which cannot be visually inspected. It provides interesting information on the nature of the bridge movements, indicating how the faster movements of the rail bridge can contribute to higher wear rates of sliding components.



Figure 2. One of the bearings with the horizontal translation monitoring equipment installed. In addition, several other movement sensors are installed including inclinometers to measure bearing rotation.

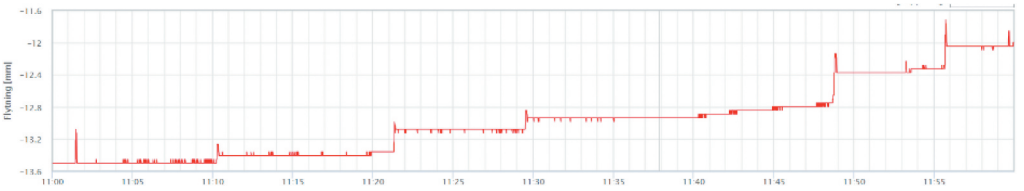


Figure 3. Example of 10hz data reading of longitudinal translation of one bearing close to the expansion joints, supporting the rail bridge. The sharp movements can be attributed to a train passing, which releases frictional forces, enabling the bearing to translate due to thermal expansion.

2.3 *Structured physical inspection*

The Konmos monitoring data supplements physical inspections, which are strategically planned with routine yearly inspections of each bearing, as well as targeted detailed measurements of key wearing components taken at set intervals. Two important checks encompass measuring remaining thickness of the PTFE sliders and measuring any damages to the sliding plates, to ensure there is minimal resistance to the bearing sliding. The damages to the sliding plates can be brought on by corrosion to the steel. An important element to the inspection is to understand when maintenance or remedial steps are to be taken to combat corrosion induced damages. Applying a numerical value to this during inspection, stored digitally and updated annually, enables us to build up data on wear patterns, which can inform future maintenance.



Figure 4. (Left) Example of the well-maintained paint system with protective covers designed to prevent corrosion within the bearing. (Right) Weathering to paint within the bearing can occur, with potential future damages to critical sliding components identified.

2.4 *Condition reporting*

The condition reporting of the bearings is made annually, with an assessment made of the remaining lifetime of each bearing. This is carried out by comparing measurements from previous years in order to establish a rate of wear. Typically, it is found there is accelerated wear on the sliding PTFE plates and an increase in corrosion to bearings near the end of the bridge, closer to land. This increased deterioration due to corrosion is attributed to their proximity to seawater, making them more vulnerable to the effects of salt and water spray. In contrast, bearings on the longer, central piers exhibited less wear. The hypothesis is that these slimmer piers flex more under the frictional bearing loads, with the soil beneath the piers undergoing some rotation of the superstructure. In this case, the piers themselves could be moving slightly instead of the bearings, helping to explain the reduced wear rates on some of these bearings.

The lifetime analysis of the bearings indicates that over 100 bearings may require replacement within the next 20 years, and as such a renovation works plan was undertaken.

3 RENOVATION PLANNING

3.1 *Renovation scope*

Having identified that over 100 of the bearings could require renovation, the challenge is how to carry this out. Structural bearings are assembled by specialists in a controlled environment. Renovation of the bearings is possible, but to carry out any meaningful works to sufficient quality on the piers themselves is near impossible. It was deduced that the bearings should be taken off site and either replaced with new ones or renovated.

Both methods can result in the same quality, also allowing for an improvement in performance and wear lifetime by upgrading the material of wear-prone components to more modern standards.

In order to undertake this renovation, some significant challenges must be overcome.

- Lifting the bridge
- Access to the work area
- Removing and replacing the bearings
- Sustainable renovation
- Renovation quality and efficiency

3.2 *Lifting the bridge*

3.2.1 *Hydraulic jack arrangement*

It is necessary when replacing structural bearings to first transfer the load of the structure off the bearings, and this is accomplished by a carefully controlled load transfer onto hydraulically activated jacks. The lifting itself is, likely a maximum 10mm vertically is to be carried out within a few hours overnight with reduced traffic on the bridge. After this, the jacks are mechanically locked which increases their vertical capacity and enables normal traffic to run over the bridge during the work. With the bearings removed, the hydraulic jacking arrangement is designed to mimic the characteristics of the structural bearings, thereby maintaining the dynamic stability of the bridge. These jacks are designed to accommodate movements within the structure while simultaneously restricting transverse motion. This capability is crucial for countering lateral forces such as high winds, braking forces, uneven vertical loads, and even potential ship collisions, ensuring the bridge's safety and structural integrity in this temporary phase. The original designers took this process into account, ensuring that there was adequate space to install these. This is often not the case with many older structures, which can result in a complex and expensive process to lift the structure, due to the lack of design provisions for hydraulic jacks in the original design.

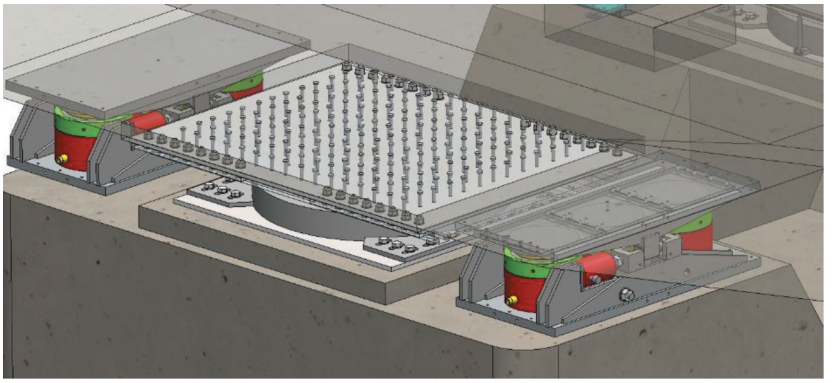


Figure 5. A 3D-CAD arrangement of 6 x 900-ton hydraulic jacks required to support the load bridge deck and act as a temporary bearing during replacement work for a typical pier. Built-in horizontal restraints around the jacking assembly restrain the horizontal bridge loads, with horizontally orientated jacks also allowing the structure to be re-aligned transversely during bearing replacement.

3.2.2 *Finite element analysis*

A global FE-model of the bridge has been developed to help assess the different possibilities regarding the jacking order. The FE-model was used to assess whether the girders could be lifted on one or both sides.

The bearing replacement process involves transferring the load of the superstructure onto hydraulic jacks. Rambøll's finite element analysis revealed that the superstructure, especially the slender railway bridge, subject to significant dynamic loads, needs to be uniformly and smoothly lifted to avoid stress concentration on any one side. This analysis was crucial in rapidly evaluating the different pier geometries.

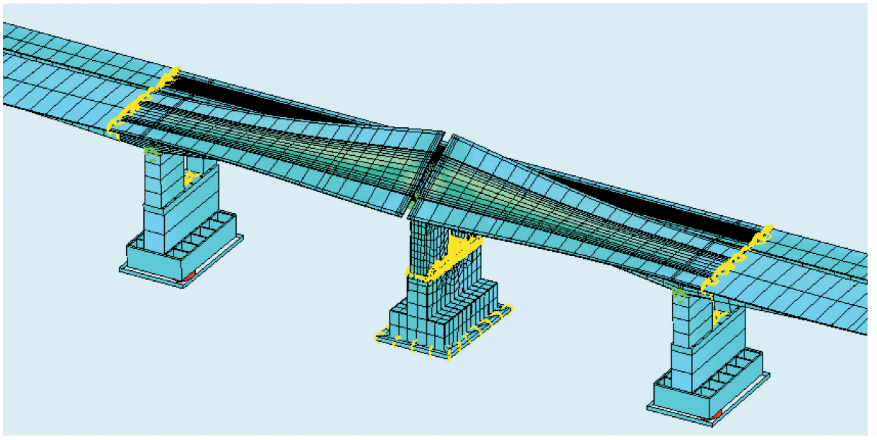


Figure 6. Example of twisting deflection that could occur due to uneven lifting of the bridge deck and understanding their interplay, ensuring a safe and efficient lifting process.

3.3 *Access*

The design of the work platform for the bearing replacement project required balancing numerous considerations. It needed to be easy to install and move, while providing a secure environment for workers and materials under challenging environmental conditions.

The design had to accommodate different methods of bearing removal and replacement. 3D modeling of the process revealed that dividing the bearing into parts for removal was

impractical; instead, each bearing, weighing up to 7,800 kg, had to be removed and installed as a single unit.

This required the creation of specialized, robust mechanical systems for safe handling.

The work platform is designed as a lattice girder, on which a work area is established around both piles with the help of beams and fiberglass sheets, as well as enabling the transport of the bearings across the bridge. The platform is cantilevered to the south in relation to the pier on the road bridge. The cantilever enables the platform to be lifted into place on the pier top from a barge, using two cranes on the road bridge. Bearings and other equipment can be lifted onto the road bridge beyond the southern edge beam using a crane positioned in the emergency lane. Due to the size of the bearings, it is not possible to lift them up between the two bridge girders, which is why they must be lifted over the southern edge beam of the road bridge. The work platform is designed to be able to carry 2 bearings at a time, to speed up the work process.



Figure 7. Lifting capabilities from the roadside onto a cantilevered platform. The opposing side contains a rail bridge with very limited access.

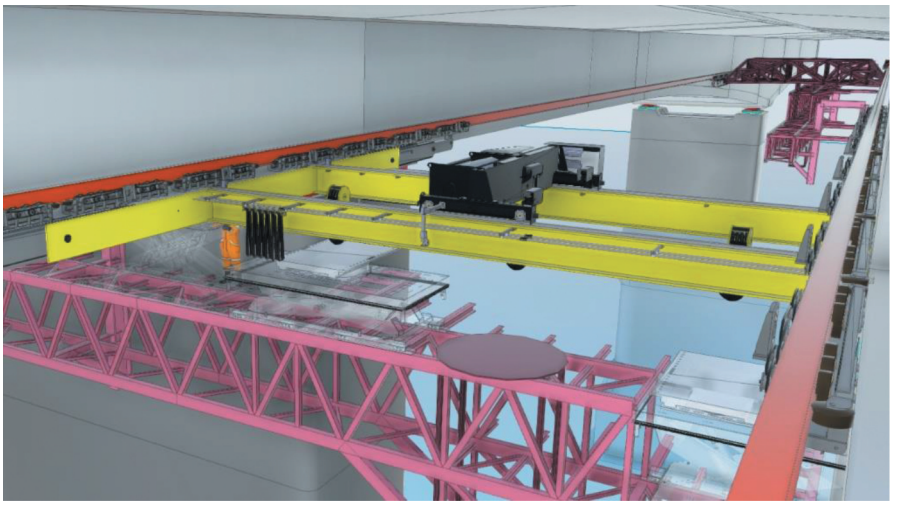


Figure 8. An innovative method was to utilize a current rail system that spans in between the 2 bridges, that can carry the platform and equipment as well as provide a lifting crane.

3.3.1 *Marine transport*

Another approach considered for the bearing replacement was using a specialist barge to move equipment between the bridge piers. A significant challenge in this method was the unpredictable weather. Rambøll conducted an extensive analysis of historical wave and wind data and, based on probability assessments, determined a feasible working window of six months.

The strategy involved employing a vehicular crane, positioned on a temporarily closed lane of the road bridge to lift the bearings from the road-side end of the platform and transfer them to and from the barge.

A lifetime cost analysis was conducted for both the platform and barge methods. One drawback identified in the bespoke mobile crane solution, was its high maintenance cost over its lifespan – a crucial factor to consider when determining the most cost-effective and sustainable approach.

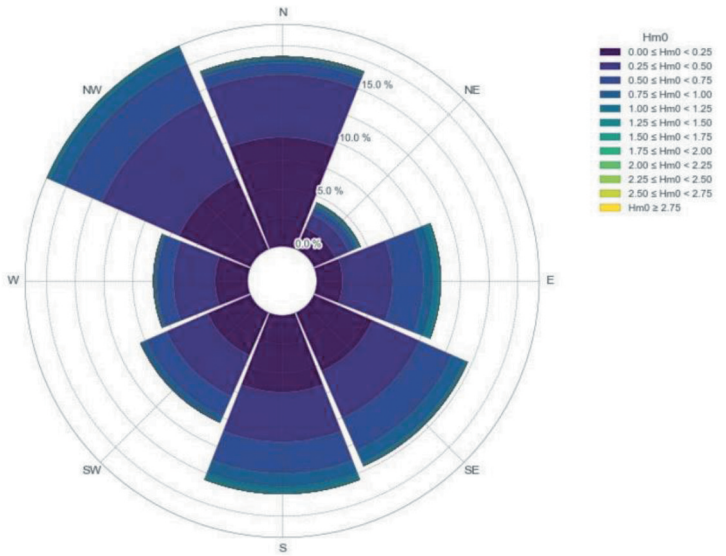


Figure 9. Wave level data for springtime, used along with wind data to verify when a barge transport can be used to move equipment.

3.4 *Renovate or replace?*

It was established that with suitable controls in place, a renovated bearing can attain the same lifetime expectation as a newly manufactured one. That is to say the mild steel, which comprises 98% of the weight, is renovated, while all other components are new.

The carbon emissions for the manufacture of the mild steel plates comprise over 95% of the overall emissions for manufacturing a bearing, including long distance shipping. For instance, manufacturing a single typical bearing, weighing around 7,800kg, is estimated to produce about approximately 37 tons of CO_2. To replace all 276 bearings with new bearings, 1000 tons of CO_2 could be produced – approximately equivalent to the annual emissions of 2,200 cars.

The decision comes down to time, financial and environmental costs. By establishing a work system in which one bearing is removed, immediately replaced, renovated and used at another location, it is possible to avoid any time wasted for renovations.

A financial and carbon emissions calculation is made comparing a program of mostly renovated bearings to that of bearings replaced with new.

A study of different levels of renovation for 84 bearings concluded that pursuing a strategy of mostly renovated bearings, as opposed to all new bearings, can yield a 60% decrease in carbon emissions overall. Crucially, the cost analysis demonstrated that this strategy also yielded an approximately 35% financial cost reduction.

4 CONCLUDING REMARKS

Sund & Belt's rigorous and ongoing maintenance program has been essential in maximizing the lifespan of the bridge bearings. Without this thorough upkeep, the bearings would have required replacement much earlier. A common characteristic of bearing replacement projects is that the cost of the bearing itself is relatively minor compared to the expenses involved in carrying out the actual work and replacement. Furthermore, the cost of carrying out a strategic maintenance program, is much smaller than any cost associated with early replacement or structural repair. Such a proactive approach in maintenance not only extends the life of critical infrastructure components like bearings, but also proves to be more cost-effective in the long term.

The study on how best to renovate the bearings is ongoing, and for a project of such scale as the Storebælt West bridges, advanced planning was important when considering the wide array of challenges associated with undertaking such significant renovations in a challenging environment.

ACKNOWLEDGEMENTS

This project's ongoing progress is by no means solely attributed to the authors of this paper. It is the result of collaborative, multidisciplinary contributions from a broad array of individuals. We extend our deepest gratitude to them for their significant contributions, whose expertise and effort has been invaluable.

S. Juulsgård
C. Pedersen
B. Sørensen
A. Fly Poulsen
S. Bonnerup
M.P. Dalsgaard
T. Buys
M. Nymann Svendsen
O.M. Skourti
M. Johannsen
J. Robertson
K. Mackeprang Iversen
S. Kim
A. Grøndahl Nourouzi
T. Meyer
L. Frisk
J. Christian Kærn
F. Bech Hald
J. Bonde Mørk
O. Lang
M. Frederiksen
U. Klasterer
S. Apelgren
B. Dannemare

REFERENCES

A/S Storebæltsforbindelsen. (1997). *West Bridge*.
Sund og Bælt. (n.d.). *KONMOS database*. Storebælt
Eggert, H., & Kauschke, W. (2002). *Structural Bearings*.
Dansk Standard. (2005). *DS/EN 1337-5: Structural bearings*

SS41: Management and maintenance of urban bridges

Organizers: D. Honfi, L. Dunai & J. Vig


Taylor & Francis
Taylor & Francis Group
http://taylorandfrancis.com

Bridge Maintenance, Safety, Management, Digitalization and Sustainability – Jensen, Frangopol & Schmidt (eds)
© 2024 The Author(s), ISBN 978-1-032-77040-6
Open Access: www.taylorfrancis.com, CC BY-NC-ND 4.0 license

Cause identification for uplifting behavior of truss bridges

K. Suzuki & Y. Nojima
University of Fukui, Fukui, Japan

K. Takeya, A. Akutsu, K.K. Vankayalapati, Y. Ito & E. Sasaki
Tokyo Institute of Technology, Tokyo, Japan

ABSTRACT: This research examines the vertical uplift behavior of a steel truss bridge and investigates the contributing factors. A thermal camera revealed that the temperatures of paint deteriorated areas were higher than those of paint remaining areas. A UAV and a still camera obtained the images of the upper and lower chord members to quantify the ratio of paint deteriorated area. Assumed member temperatures based on the degree of corrosion were input into the Finite Element Method (FEM) model, which confirmed up warping behavior consistent with experimental findings. Consequently, we concluded that paint condition differences influence member temperatures and vertical displacements.

1 INTRODUCTION

In the case of a steel truss bridge with deteriorated coating, it has been observed that the bridge exhibits static deformation, rising in the vertical direction as the temperature of its components increases. Depending on the level of this deformation, there is a potential impact on usability, which may cause discomfort to users of vehicles traveling at high speeds.

Murata et al. (1985) conducted measurements and simulations on a plate girder bridge with ballastless slab track on the Tohoku Shinkansen. They demonstrated that when the temperature difference between the upper and lower flanges of the main girder exceeds 10°C, the amount of vertical deformation of the girder reaches approximately 10 mm. Furthermore, they reported an increase in the vertical acceleration of the train body passing over the bridge corresponding to the amount of girder deformation. Kobayashi et al. (2006) monitored the deformation of bridge components due to temperature and temperature variations for over two years, focusing on a steel floor-beam box girder bridge. Daily temperature variations on sunny days were found to cause two-dimensional deformation, with the girder expanding vertically along with temperature rise. On days without sunlight, only one-dimensional deformation along the bridge axis was observed.

Nishikawa et al. (1992) reported that bending deformation due to temperature changes is not necessarily smaller than the influence of live loads. Hashimoto et al. (2015) investigated the temperature deformation behavior of a composite truss drawbridge with an SRC structure, elucidating the member stresses and vertical displacement behavior induced by temperature differences through both experimental measurements and finite element method (FEM) analysis. This suggests the existence of bending and vertical deformation behaviors, including the influence of sunlight.

The Road Bridge Design Specifications (Japan Road Association 2017) consider a relative temperature difference of 15 degrees between members or parts of members for steel structures, but specific details regarding the effects of temperature differences are not provided.

DOI: 10.1201/9781003483755-381

This study aims to elucidate the factors contributing to the uplifting behavior of a truss bridge, which manifests in vertical deformation. The analysis involves both actual measurements of the bridge's vertical behavior and simulations using the finite element method (FEM). The study comprehensively analyzes the temperature differences between bridge components using thermal cameras and thermocouples. Additionally, it verifies the coating condition of the upper and lower chord members on the truss using UAVs and still cameras, calculating the anticipated temperature differences between these members. The assumed temperature differences are then input into the finite element method to evaluate the bridge's response.

2 TARGET BRIDGE

The focus of this study is the bridge spanning the Kuzuryu River, referred to as the former Fuseda Bridge. Connecting Fukui City and Sakai City in Fukui Prefecture (Figure 1) in Japan, the bridge had a length of 559.6 meters. It was constructed in the year 1956 and remained in service for approximately 60 years until 2018. A new Fuseda Bridge has since been constructed approximately 200 meters upstream, taking over its role.

Table 1 presents various specifications of the bridge, and Photo 1 provides an external view. In this study, the upstream components are referred to as the south side, while the downstream components are designated as the north side. After the cessation of its use, in 2020, the truss bridge spans on the left bank, consisting of three simple curved-chord truss spans, had their deck removed. The specific span targeted in this study is the first span on the left bank, with a span length of 60.9 meters. The support system consists of four movable roller-type bearings on the bridge pier.

3 BRIDGE INSTRUMENTATION AND THE ACQUIRED DATA

3.1 *Bridge instrumentation*

The arrangement of each measurement device is illustrated in Figure 2, and followings explain the measurement detail.

[Contact Displacement Sensor**]** To measure the longitudinal displacement of the movable support, one displacement sensor was installed on the north side and another on the south side. The measurements were taken at intervals of 0.01 seconds.



Figure 1. Location of former Fuseda bridge.

Table 1. Bridge specifications of the former Fuseda Bridge.

Coordinates	36.146513N, 136.165087E
Constructed year	1956
Crosses	Kuzuryu river
Design	3-span simply supported lower truss bridge + 9-span RC Gelber girder bridge + 16-span RC simple T-girder bridge
Total length	559.6m

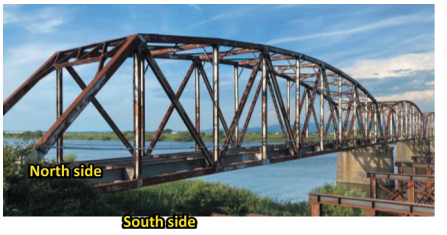


Photo 1. View of the former Fuseda bridge.

[Laser Displacement Sensor**]** For the purpose of measuring the vertical displacement of the bridge, laser displacement sensors were installed right beneath the panel point of the first vertical member and the sampling rate was 100Hz.

[Thermocouples, Thermal Camera**]** To measure the temperature of the structural components, thermocouples were installed at a total of seven locations on the upper chord, lower chord, and vertical members of the first panel. The thermal camera was positioned to cover the range shown in Figure 2. The sampling was done at 100Hz for thermocouples and at 30-second intervals for the thermal camera.

3.2 *Measurement results*

Figure 3 illustrates the temperature history of each structural component recorded from thermocouples during a 24-hour period from August 30th to 31st, 2022. Figure 4 presents the temperature and total solar radiation history recorded at the Fukui Regional Meteorological Observatory, located approximately 12.3 km away from the target bridge. The surface temperature of the main structure remained relatively constant at around 22.5°C during the early morning hours from 0 AM to 6 AM on the 30th. A slight decrease in component temperature was observed shortly after 6 AM, likely influenced by a decrease in ambient temperature. Subsequently, temperatures began to rise in conjunction with an increase in total solar radiation. The maximum total solar radiation was recorded at 11 AM, reaching a peak temperature of 29.6°C at 12 PM. In the afternoon, temperatures exhibited a declining trend, with a temporary increase around 4 PM.

The component temperatures peaked around 12 PM, with the south side of the lower chord exceeding 40°C. The lower chord experienced two peaks around 9 AM and 12 PM. The temporary decrease in structural temperature after 9 AM can be attributed to light rain during that period, causing a temporary drop in the structural temperature. It is noteworthy that the upper chord did not exhibit a peak around 9 AM. This discrepancy is attributed to the open U-shaped cross-section of the lower chord's underside compared to the closed cross-section of the upper chord, making the upper chord relatively less prone to temperature fluctuations.

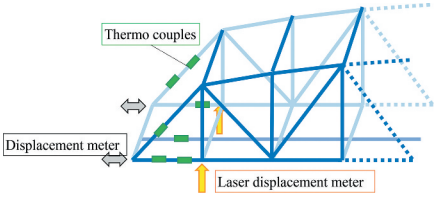


Figure 2. Bridge instrumentation.

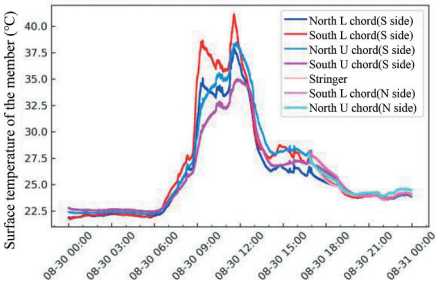


Figure 3. 24-hour history of member surface temperature.

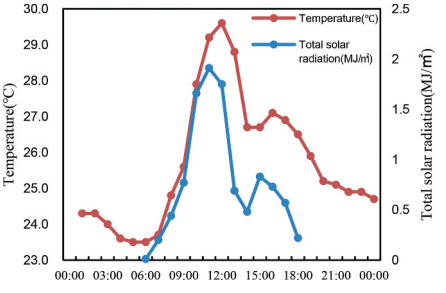


Figure 4. Temperature and total solar radiation (Fukui Local Meteorological Observatory).

Figure 5 illustrates a 24-hour history of the surface temperature, south-side support displacement, and vertical displacement of the south side lower chord and upper chord. The first vertical axis represents the surface temperature (°C), while the second vertical axis represents displacement

(mm). Horizontal displacements exceeding 7 mm were recorded in tandem with structural component temperature changes, indicating the functionality of the movable support's translational movement. Examining the vertical displacement reveals an upward movement with the increase in component temperature, resulting in a curvature of approximately 1 mm. Unfortunately, there is no record during the period between 1 PM and 2 PM due to equipment malfunction. Further discussion on the curvature phenomenon, including finite element analysis, will be undertaken.

The north side exhibited a similar trend, but due to recording malfunctions, the discussion will focus on the results from the south side.

Figure 6(b) displays the temperature distribution near the bridge pier of the first span captured by a thermal camera. Comparing this with the photograph of the corresponding location in Figure 6(a), it is evident that areas with well-preserved coatings have lower temperatures, while areas with deteriorated coatings and rust exhibit relatively higher temperatures. Similar trends are observed in Figures 6(c) and 6(d). This suggests a significant impact of rust rates on the surface temperature of the steel components.

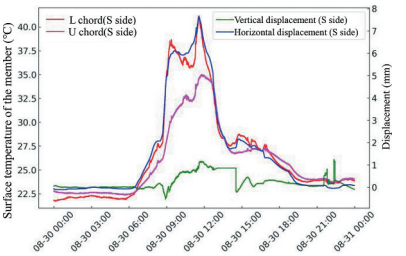


Figure 5. Truss member surface temperature and displacement history.

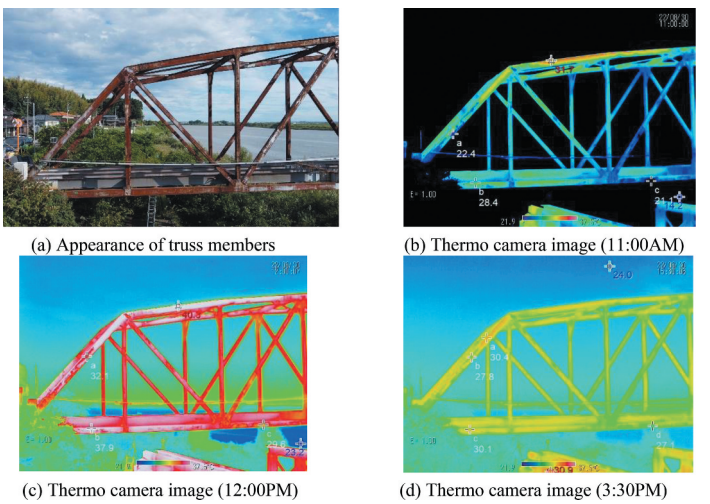


Figure 6. Comparison of thermo camera image and paint appearance.

3.3 *Estimation of rust rates for upper and lower chords*

The proportion of rusted area on the upper surface of the upper chord and lower chord materials was determined from captured images. A UAV was employed for the upper chord material, while a still camera was utilized for the lower chord material. As illustrated in Figure 7, the upper surface of the upper chord material exhibited a state where the coating had been lost, and it was covered with red rust.

Image processing was applied to calculate the surface rust rate (Figure 8). Initially, trimming was performed on the images to eliminate the background. Subsequently, using perspective transformation, the trapezoidal images were converted into rectangular images. Finally, binary processing of rust and coating was carried out, transforming the images into two colors: black (0) and white (1). Although the corrosion of steel progresses gradually, considering the dependence of member temperature difference on the occurrence of red rust based on thermal camera results, we decided to determine the rust rate through binary processing. The binary processing was performed using the OpenCV library in Python, with a threshold set at 120. As shown in Figure 9, the areas where red rust occurred and the areas where coating remained, as judged by the human eye, were generally distinguishable in black and white.

The rust rates for the upper chord and lower chord were calculated from the following equations:

$$\text{Rust Rate } (\%) = (\text{Sum of white regions})/(\text{Image area}) \times 100 \quad (1)$$

The averages for the first span were as follows: upper chord: 91.3%, lower chord: 33.2%.

4 SIMULATION OF THE INFLUENCE OF MEMBER TEMPERATURE DIFFERENCES ON STRUCTURAL BEHAVIOR USING FINITE ELEMENT ANALYSIS

4.1 *Analysis model*

To assess the influence of temperature differences in the upper and lower chord members on bridge response, a finite element method (FEM) model was constructed. The analysis model (Figure 10) consisted of approximately ten beam elements dividing the main members, using steel materials without material nonlinearity. Material properties are presented in Table 2. The model comprised 3071 linear elements and 3153 nodes, with simple support as the boundary condition. The model incorporated a camber to ensure the horizontal alignment of the lower chord under the condition of input gravity acceleration.



Figure 7. Appearance of the top chord taken by UAV.

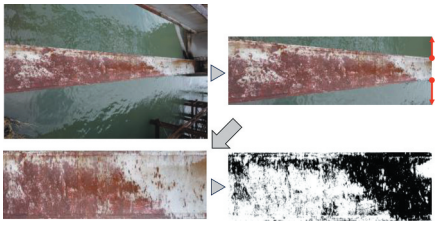
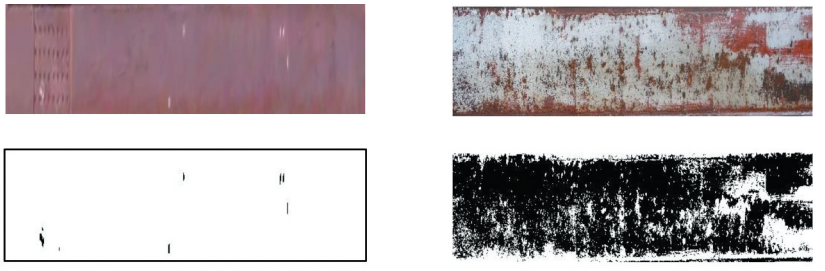


Figure 8. Image processing.



(a) Upper chord image binarization

(b) Lower chord image binarization

Figure 9. Binarization results.

4.2 *Input temperatures based on rust rates*

Assuming the highest temperatures of the members based on the temperatures obtained from thermal camera images, considering the rust rates, was performed to evaluate the impact. The applied formula (2) is presented below. The temperature difference between the measured surface temperature using thermocouples on 2022/08/30 0:00 and this calculated temperature was used as the input temperature for the FEM model.

$$\text{Assumed Temperature} = \text{Min} + (\text{Max} - \text{Min}) \times \text{r} \tag{2}$$

Where, Max=Temperature of rusted area; Min=Temperature of painted area; r=Rust rate.

Three models (A to C) were prepared based on rust rates, and structural responses were examined. Table 3 presents the rust rates and input temperatures. Model A represents the actual rust rate situation, where the temperature difference between the upper and lower chords is 3.7° C. Models B and C have smaller temperature differences between the upper and lower chords. Model B exhibits a condition where rust progresses at similar levels for both upper and lower chords, while Model C shows a state where both upper and lower chords have remaining coatings at similar levels. It should be noted that the input temperatures for vertical members and diagonal members in each model were set as the average values of the upper and lower chords. The upper lateral member had the same input temperature as the upper chord, while the stringer and floor beam had the same input temperature as the lower chord.

4.3 *Analysis results*

After inputting gravity acceleration, member temperatures were applied. Figure 11 illustrates the vertical displacements after temperature input for each Panel point of the upper and lower chords, as per Figure 10. Panel point numbers are as indicated in Figure 10, where Panel point 0 is on the abutment and Panel point 10 is on the first pier.

Table 2. Material specifications.

Density (kg/m^3)	7,850
Young's modulus (MPa)	205,000
Poisson's ration	0.3
Linear expansion coefficient (/°C)	1.17×10^{-5}

Table 3. Rust rate and input temperature of each model.

		A	B	C
Upper chord	Rust ratio (%)	91.3	91.3	33.2
	Input temperature (°C)	18.7	18.7	14.2
Lower chord	Rust ratio (%)	33.2	91.3	33.2
	Input temperature (°C)	15.0	19.5	14.5

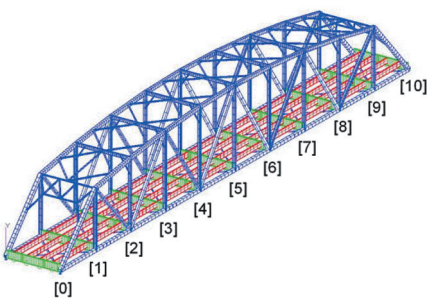


Figure 10. FE model.

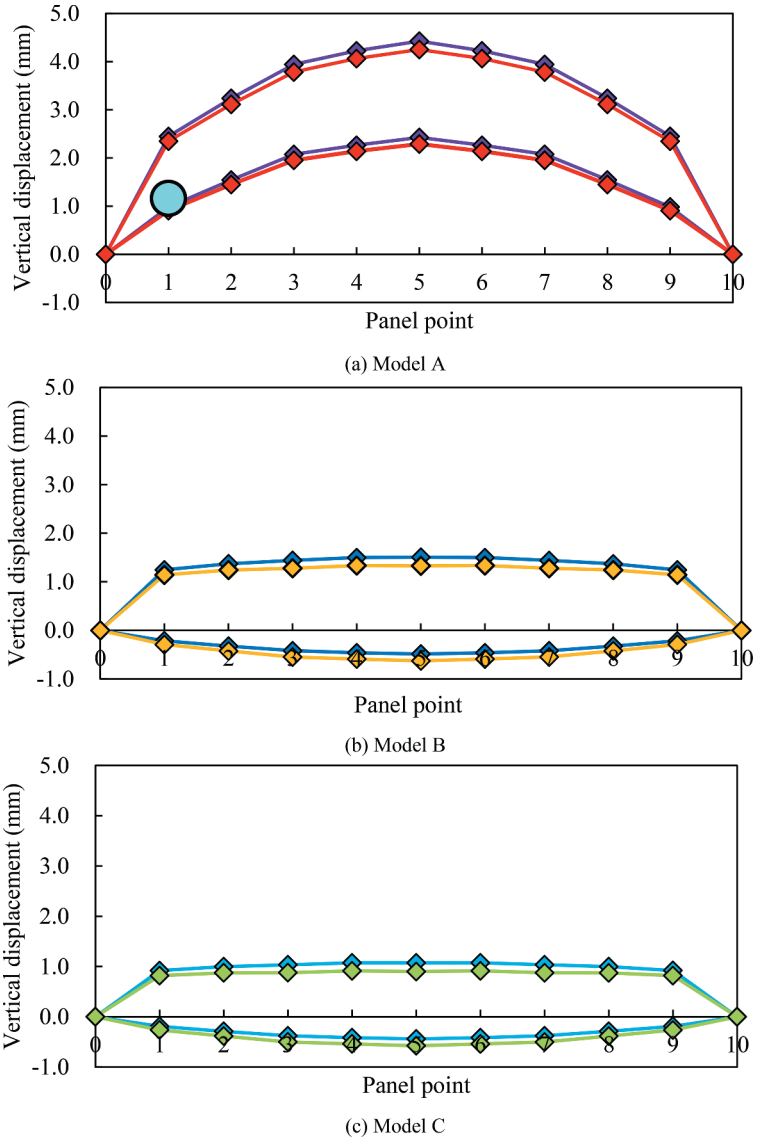


Figure 11. Vertical displacement at each panel point of the lower chord.

Firstly, Model A exhibits an upward deflection response, with the analysis result at Panel point 1 closely matching the measured value. When the temperature of the upper chord is higher than that of the lower chord, as in Model A, an upward deflection response can occur. Secondly, for Model B, there is almost no vertical displacement motion. The slight downward displacement of the lower chord is thought to be due to the elongation of diagonal and vertical members. Similarly, for Model C, there was almost no vertical displacement motion. Regarding this phenomenon, it is considered that the upper chord with a higher rust rate, as shown in Figure 12, is more easily warmed, causing greater elongation than the lower chord. This condition leads to an overall negative bending of the truss bridge, resulting in an upward behavior in the vertical direction. Conversely, if the temperature of the lower chord members is relatively higher than that of the upper chord members, the occurrence of downward deflection behavior is anticipated.

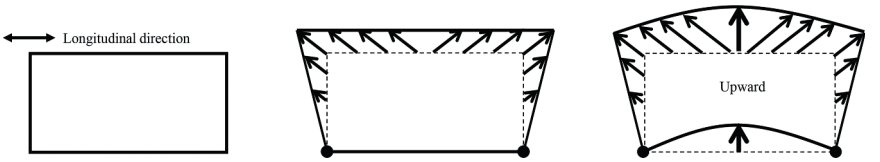


Figure 12. Assumed upward behavior due to temperature difference between upper and lower chord.

5 CONCLUSIONS

In this study, the deformation behavior of a truss bridge was analyzed from both measured results and Finite Element Method (FEM) simulations. The aim was to elucidate the factors contributing to the upward behavior of the bridge. The obtained insights are summarized as follows:

(1) Rusty areas tend to have higher temperatures, while painted areas exhibit lower temperatures. Additionally, the rust rate of steel members significantly influences the surface temperature of the members.
(2) Deterioration in the coating of the upper and lower chord members of the truss bridge leads to differences in the coating conditions, causing temperature differences in the members. These temperature differences, in turn, induce vertical movements in the bridge.

ACKNOWLEDGMENTS

We would like to express our sincere gratitude to the Fukui Prefecture Mikuni Public Works Office for granting permission for measurements, providing drawings, and offering substantial support and understanding. Special thanks to Mr. Takamura and Mr. Tagawa from the same office for their invaluable assistance.

REFERENCES

Hashimoto, K., Okumura, S., Sugiura, K., Taniguchi, N., Fujiwara, Y. 2015. Thermal change behavior of composite trussed rohze bridge with SRC structure, *Journal of Structural Engineering A*: 61A, 816–828.

Kobayashi, Y., Miki, C., Tanabe, A. 2006. Health Monitoring Utilizing Thermal Deformation for Box Bridge with Orthotropic Deck System, *Japanese Journal of JSCE*: 62(4), 794–807.

Murata, K., Kawakami, H., Hayafuji, S., Kikuchi, H. 1985. Effect of temperature difference be tween steel girder members on train traveling, *Structure design data*: (81), 24–30.

Murata, K., Kawakami, H., Hayafuji, S., Kikuchi, H. 1985. Effect of temperature difference be tween steel girder members on train traveling (Follow up), *Structure design data*: (84), 33–37.

Nishikawa, K., Yamamoto, S., Kashima, H. 1992. Analysis of Measurement Results Regarding Bridge Behavior due to Temperature Changes, Proceedings of JSCE annual meeting, I–449.

Specifications for Highway Bridges Part I Common, 2017. *Japan Road Association*.

Bridge Maintenance, Safety, Management, Digitalization and Sustainability – Jensen, Frangopol & Schmidt (eds)
© 2024 The Author(s), ISBN 978-1-032-77040-6
Open Access: www.taylorfrancis.com, CC BY-NC-ND 4.0 license

Aerial-demolition method for bridges above intersections with heavy traffic

R. Nakata, T. Oike, K. Fujiwara, S. Watanabe & K. Mori
Hanshin Expressway Company Limited, Osaka, Japan

Y. Ninomiya
Hanshin Expressway R&D Company Limited, Osaka, Japan

T. Shimada & D. Fujimoto
TAISEI CORPORATION, Osaka, Japan

I. Tada
FUJI P.S CORPORATION, Osaka, Japan

ABSTRACT: Large-scale replacement projects for the restoration of old or heavily deteriorated expressway bridges, have recently become a major topic in Japan's bridge maintenance. In most situations, it is difficult to prepare ground-level construction yards for the demolition of existing viaduct bridges built in already urbanized areas. The degree of difficulty becomes even more severe when the replacement takes place directly above an intersection with heavy traffic. This paper will introduce an aerial-demolition method for an existing PC bridge that allows continuous uninterrupted vehicular traffic and pedestrian access on the ground even while the demolition is taking place. The feature of this demolition method is to complete all the demolition processes that take place above an intersection, such as cutting the bridge into small pieces, lifting them, and conveying them in the air, by using movable workstations, cranes hanging at or placed on the temporary girder laid over the bridge to be demolished.

1 INTRODUCTION

Hanshin expressway (HEX) is an urban expressway in the Osaka and Kobe area which is one of the most populated urban regions in Japan. Metropolitan areas in Japan had to build the expressways to pass through the large volume of car traffic demand. To build expressways in already urbanized and limited road width area, it was often necessary to adopt the bridge or viaduct structure. Kire-Uriwari bridge is one of the bridges in HEX which is 3-span prestressed concrete (PC) ramen box girder bridge (154 m) constructed by cantilever method in 1980 (Figure 1). The bridge is located directly above an intersection with heavy traffic, and the central hinge area drooped approximately 24 cm five years after its opening. For this reason, the bridge was pushed up and reinforced from the bottom side with outer cables in 2003. However, to achieve longer durability, a decision was made to replace the bridge in 2015, and the replacement work began in June 2022.

In this construction, an aerial-demolition method where most work processes are completed in air was adopted, so as not to obstruct traffic on the local roads directly below the construction site.

This paper describes the outline of the Kire-Uriwari bridge restoration construction and the progress of the demolition work of the existing PC bridge, together with the issues specific to this construction and the response to the issues.

Although there are multiple cases of demolition of existing PC bridges (Singh, S. et al. 2008, Kramer, W. et al. 2018, Daescu, C.A. et al. 2023), there are no other cases like this construction

DOI: 10.1201/9781003483755-382

where an aerial-demolition was carried out in an urban area so as not to obstruct the traffic on local roads directly below the construction site. This construction has novelty in terms of aerial completion type existing PC bridge with various constructional ingenuities. The knowledge gained from this is meaningful for the smooth progress of similar constructions in the future.



Figure 1. Kire-Uriwari bridge (before demolition, April 2022).

2 BUSINESS OUTLINE

2.1 *Examination for replacement method*

Regarding the replacement method of the existing bridge (Figure 2), the following methods were studied; Proposal 1: a method of temporary providing a detour route for both the in-bound and out-bound lines and then replacing the bridge, Proposal 2: a method of dividing the in-bound and out-bound lines of the existing bridge and then replacing the bridge while using either line, and Proposal 3: closing the expressway main roads and replacing the in-bound and out-bound lines by a single-operation. As a result of comparing them from the viewpoints of the effects on the surrounding areas, effects on traffic on the expressway and local roads and construction period, while taking in the opinions of experts, etc. We have determined to carry out the construction by adopting the method of Proposal 3 after taking countermeasure against the effects on the traffic.

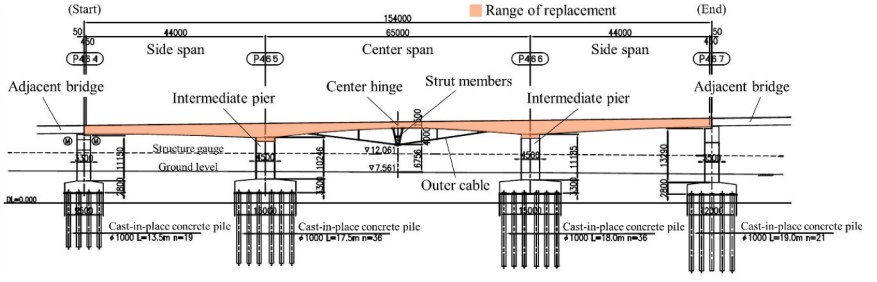


Figure 2. Kire-Uriwari bridge (side view).

2.2 *Construction procedure*

Figure 3 shows the construction procedure. For removal of existing bridge, first, erect a temporary girder with the total length of 165 m over the existing bridge ([1]). Next, install four movable workstations and two transport carts that can be moved in the bridge axis direction to the temporary girder. Then, cut out the bridge girder portion into blocks inside the movable workstations and carry them to the adjacent bridge by the transport carts ([2]). While conducting this process, remove the outer cables and the strut members under the

center hinge, then separately remove the upper portions of the two intermediate piers after removing the girder portion.

For erection of a new bridge, construct by a single-operation erection using multiple-axis carts ([3]: bridge pier portions), launching erection ([4]: side span portions), and lift-up erection ([5]: center span portions).

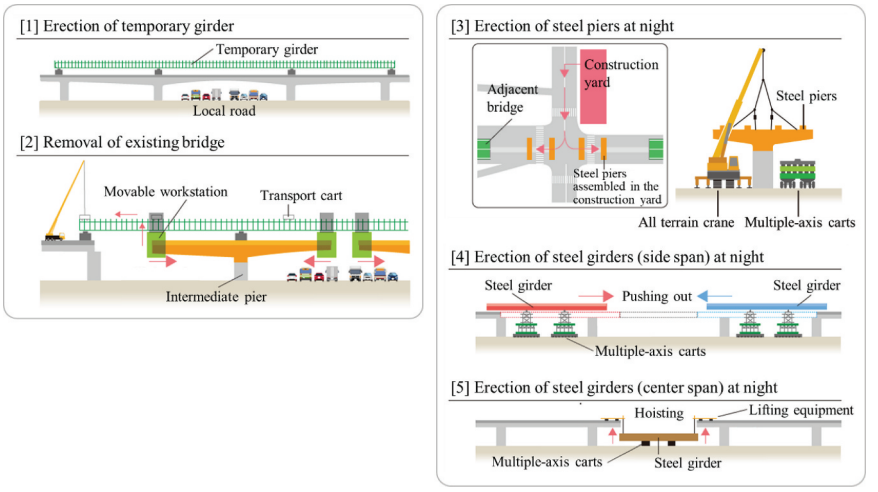


Figure 3. Construction procedure (left: demolition of existing bridge, right: erection of new bridge).

2.3 *Construction process*

Table 1 shows the overall process of this construction. We are planning to complete the removal of the existing bridge by approximately two years and the erection of the new bridge by approximately one year.

Table 1. Overall process.

	FY2022				FY2023				FY2024			
[1] Erection of temporary girder												
[2] Removal of existing bridge												
[3] Erection of steel piers [4] Erection of steel girders (side span) [5] Erection of steel girders (center span)												
[6] Attachment facilities												

3 MAJOR ISSUES IN THE CONSTRUCTION

3.1 *Thorough implementation of countermeasures against effects on traffic*

Since this construction is carried out by closing the expressway main roads, we will not impose traffic restrictions by occupying any lane during daytime on local roads, so as not to put further load on the traffic on the local roads directly below the construction site. Work that unavoidably requires restriction will be carried out at night, while striving to minimize the range of restrictions.

3.2 *Work in limited construction space*

Work which takes place on the existing bridge, such as an erection of each member needs to be conducted within the limited width on the expressway. Even though the construction space

is extremely limited, falling objects are prohibited since the construction takes place directly above the intersection in use.

3.3 *Consideration of the proof strength of the existing bridge*

Regarding proof strength of the existing bridges (including the adjacent bridges in the area affected by the construction), safety must be absolutely ensured at all removal steps, including in the event of an earthquake. In addition, since the center hinge area is dropped, measurement control and fulfillment of safety equipment is necessary in preparation of unexpected circumstances.

3.4 *Consideration of the surrounding environment*

Residences and commercial facilities are close to this construction site, and it is especially necessary to pay attention to the work noise. The distance from the existing bridge to the nearest facility (apartment building) is approximately 15 m.

3.5 *Ensuring the processes*

Since we are aiming to complete this construction before EXPO 2025 Osaka, Kansai is held, it is necessary to steadily advance the construction while ensuring safety.

4 CONSTRUCTION PROGRESS AND RESPONSE TO THE ISSUES

4.1 *Removal of the pavement and median strips*

Since a large amount of equipment for demolition such as the temporary girder are going to be placed on the existing bridge, to reduce dead loads as much as possible, a secure construction yard was ensured, and pavement and median strips were removed in the first place. Low noise cutting machine (diamond wire saw) was adopted for the removal of the median strips.

4.2 *Construction of temporary girder*

The temporary girder is an important member for installing various equipment for removal such as movable workstations and transport carts and it is a steel girder with a total length of 165 m and a total weight of 1,286 tons composed of four box girders. For the assembly of the temporary girder, the members divided into 15 blocks were constructed by a vent method from above the center hinge portion toward the outer bridge axial direction using two 120-ton crawler cranes. Considering the proof strength of the existing bridge, the crane was controlled so that the loads are applied only on the main girder web. Especially around the adjacent bridge where it is necessary to consider the proof strength (P467), erection was progressed by dispersing the loads by adopting multiple-axis carts (Figure 4).

Temporary girder was supported by the four vents above the piers separately constructed at the pier positions (Figure 5). The gravity position of the temporary girder became higher by



Figure 4. Temporary girder erection status (left: the first block, right: the last two blocks on the end).

installing a work area (4 m high) between the bridge surface and the temporary girder for cutting and removal of the existing bridge. Therefore, to secure the overall seismic performance including the temporary girder, we corresponded to the issue by combining steel bars for PC and seismic rubber bearings.

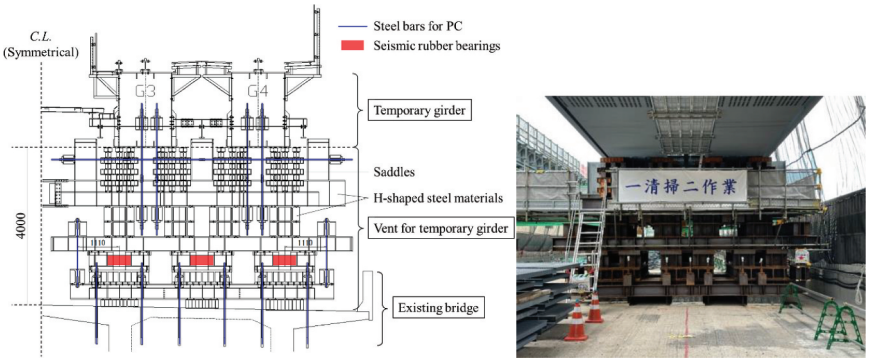


Figure 5. Temporary girder and vent above piers (cross-sectional view).

4.3 *Installation of suspension cranes*

After the construction of the temporary girder, crane equipment referred to as a suspension crane was installed by hanging it from the temporary girder side rails (Figure 6). Two suspension cranes were installed at each of the four movable workstations to achieve smooth process by simultaneous construction on both the in-bound and out-bound lines.



Figure 6. Suspension crane installation status.

4.4 *Construction of movable workstations and transport carts*

Movable workstations and transport carts were assembled on an adjacent bridge and installed on the rail on the upper surface of the temporary girder by a crane. To prevent unnecessarily extruding from the existing bridge, a laser barrier was provided and a notification system for



Figure 7. Mobile work vehicle construction status (left: upper member, right: lower member).

the crane operators were provided (Figure 7, left). Since it is necessary to install the lower portions of the movable workstations from the local road, they were constructed by using multi-axis carriers at night by imposing traffic restrictions (Figure7, right). Figure 8 shows the situation after installation of the equipment for removal.



Figure 8. Situation after installation of removal equipment on temporary girder.

4.5 *Removal of the existing bridge*

Cutting work of the existing bridge by wire saws began in January 2023. The bridge is cut at 1.75 m intervals in the bridge axis direction and each cross section is further divided into 16 pieces (8 pieces each for in-bound and out-bound lines, Figure 9). The bridge was divided into 84 pieces in the axial direction and there were up to approximately 1,300 blocks removed in total.

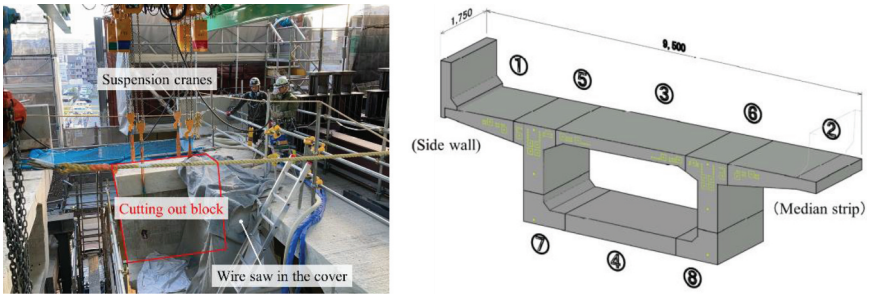


Figure 9. Removal of existing bridge (left: removal status, right: one cross-section removal order).

Figure 10 shows the construction procedure in the bridge axial direction. The removal is carried out by the reverse procedure of the cantilever erection method, however since the side span of this bridge has been partly (end portion) constructed by the vent method and the girder length is approximately 12 m longer than the center span (1/2). Then, the side span end

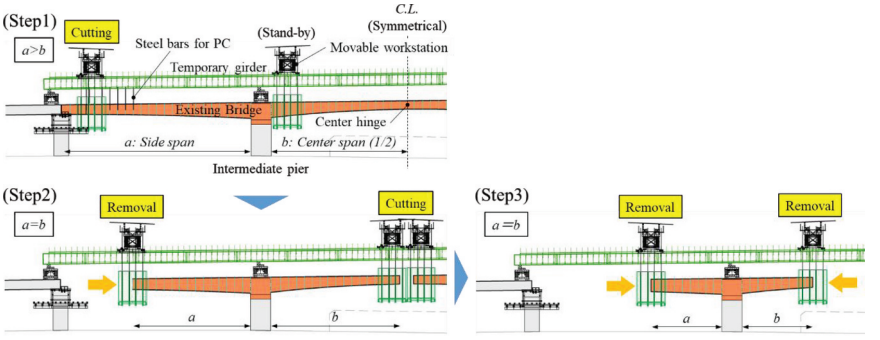


Figure 10. Removal order in the bridge axial direction (side view).

portion was cut and removed from the temporary girder while temporarily slinging the side span edge portion from the temporary girder with steel bars for PC until the overhanging lengths with the intermediate piers at the center become equal on both sides (Step 1). Then, the center hinge portion was cut at the point where the overhanging lengths on both sides were balanced (Step 2). Then, removal was advanced toward the intermediate pier by the two movable workstations simultaneously (Step 3).

4.6 *Box girder uplift countermeasure*

Steel bars for PC inside the existing bridge were cut by core drilling (φ54 mm) from the upper surface of the slab and measures to reduce the excessive stress to a safe level were studied in advance (Figure11). The fixation positions of the steel bars for PC in the bridge axial direction were confirmed, the targets for cutting were preset for each of the six cross-sections for which the up-lift measures are to be implemented and cutting was carefully progressed.

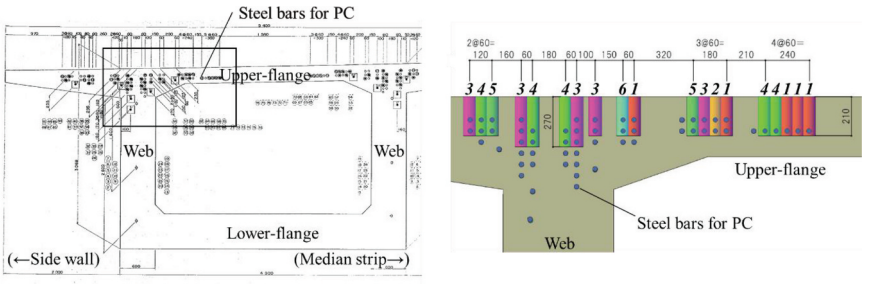


Figure 11. Box girder cross-sectional view (left: position of the steel bars for PC shown in the completion drawing, right: steel bars for PC applicable to tension reduction and core drilling sequence).

4.7 *Retracting and removing the temporary girder*

The demolition of the PC box girder was successfully completed in approximately 5 months of construction period. Temporary girder which has finished its duty was provided with a launching nose, retracted by an endless roller installed on the vent above piers and retraction equipment on the front (hydraulic jacks) to the adjacent bridge by a single-operation, and demolished. For the first time in 43 years, there was no structure on the intersection (Figure 12).



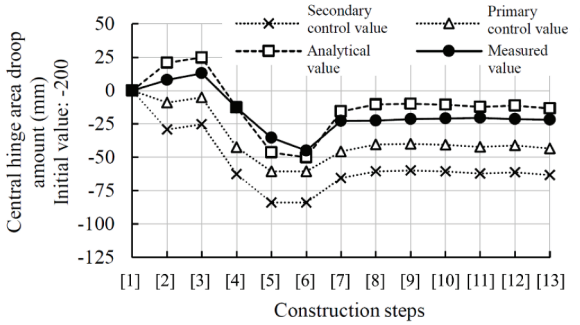
Figure 12. Temporary girder retraction status (after completion of the existing bridge girder removal).

5 EFFORTS TO SAFELY PROCEED WITH THE CONSTRUCTION

5.1 *Constant observation of the center hinge portion displacement*

Figure 13 shows the transition of center hinge area droop amount from the start of construction to the completion of the temporary girder (comparison of the analytical values and measured values). After starting the construction work, in the pavement removal ([2]) and median

strip removal ([3]) steps which are carried out in the first place, dead loads were reduced, and the droop amount was reduced in both steps. On the other hand, in the subsequent outer cable tension release ([4]) and temporary girder erection ([5] to [6]) steps where loads concentrate on the center of span, the droop amount increases. Regarding the subsequent steps, the result of the analysis showed that since the loads ap-plied to the center of the span were switched to be applied to the vent above piers, the fluctuation in the droop amount was stabilized ([7] to [13]). On the other hand, although the behavior was not as sensitive as the analytical values, the measured values showed the same tendency.



[1] Before construction (-200 mm)
[2] Pavement removal
[3] Median strips removal
[4] Outer cable tension reduces
[5] Temporary girder election (1/15blocks)
[6] Temporary girder election (3/15blocks)
[7] Temporary girder election (5/15blocks)
[8] Temporary girder election (7/15blocks)
[9] Temporary girder election (9/15blocks)
[10] Temporary girder election (11/15blocks)
[11] Temporary girder election (13/15blocks)
[12] Temporary girder election (15/15blocks)
[13] Temporary girder is placed on the vent

Figure 13. Transition of the central hinge area droop amount.

6 CONCLUSION

In this construction, an aerial-demolition method for completing most work processes in air was adopted so as not to obstruct traffic on the local roads directly below the construction site was adopted for demolition of the existing PC bridge. Due to the condition of the site where it is above an intersection in an urban area, the difficulty is very high. However, construction progress was achieved by additionally implementing various ingenuities against the difficult issues.

A large-scale restoration construction is for a society in which people can live safely into the future. However, due to its large scale, the effects during construction also tend to be large. For the growth of sustainable urban cities and regions, the technology to reduce these effects is assumed to be of great value.

Due to the aging of road structures, there is a possibility for construction works in which removal of bridges, etc. needs to be carried out safely without causing effects on areas directly below the construction sites to occur in the future. We hope that the ingenuities and results of this construction will be helpful.

REFERENCES

Daescu, C.A. et al. 2023. Demolition of a 65-year-old box-girder prestressed concrete bridge located in Northern Sweden, *Proceedings in civil engineering* 6(5).

Kramer, W. et al. 2018. Demolition of Old Oak Bridge B4113: Condition of a 54-year-old prestressed concrete bridge, *MATEC Web of Conferences* 199.

Singh, S. et al. 2008. Demolition of the Grace Memorial and Silas N. Pearman Bridges over Cooper River, South Carolina, USA - A Case Study, *Structures Congress 2008: Crossing Borders*.

Bridge Maintenance, Safety, Management, Digitalization and Sustainability – Jensen, Frangopol & Schmidt (eds)
© 2024 The Author(s), ISBN 978-1-032-77040-6
Open Access: www.taylorfrancis.com, CC BY-NC-ND 4.0 license

Risk assessment of the K-bridge over the Danube

B. Kövesdi, D. Kollár & L. Dunai
Department of Structural Engineering, Faculty of Civil Engineering, Budapest University of Technology and Economics, Budapest, Hungary

Z. Hodik
Budapest Közút Co., Budapest, Hungary

ABSTRACT: The K-bridge spans over the Danube between Buda and the Hajógyári Island in Budapest, Hungary. The originally railway, recently mixed road and pedestrian bridge have a more than 70-year-old steel truss main girder with a span of 98.04 m and a steel-concrete deck system. It plays an important role in Budapest city life and is heavily used during the Sziget festival, one of the biggest festivals in Europe. In 2022, during the regular bridge inspection, heavy corrosion and material loss were found by the experts in the bridge deck system and on the steel cantilever beams under the pedestrian walkways. The Budapest University of Technology and Economics (BME), Department of Structural Engineering together with design and maintenance experts investigated the condition of the structure and made a probabilistic analysis to verify the resistance of the corroded structure and made the risk assessment before the organization of the Sziget festival. The main aim of the analysis was the assessment of the load-bearing capacity of the corroded structure and determination of its risk against possible failure, based on the survey results of the current corrosion condition. Detailed inspection, on-site geometrical and corrosion measurements and partial loading tests were executed on the structure, which results served as input data of the probabilistic analysis. Advanced numerical models are developed to accurately calculate the load-bearing capacity of the heavily damaged structural details of the bridge by using stochastic analysis combining geometrical and material nonlinear analysis using imperfections (GMNIA). Based on the investigations, the necessary short-term and long-term maintenance tasks could be identified to be carried out on the bridge to ensure safe operation of the structure during the Sziget festival and to prolong the service lifetime of the bridge.

1 THE ANALYSED STRUCTURE

The structure under investigation is a steel girder bridge with a truss main girder system. The bridge is located on the northern side of Budapest and spans over the Danube connecting the Buda-side and the Hajógyári Island. The span of the bridge is 98.04 m. The main girder was originally designed and developed as a military bridge with a one-and-half "K" shape, as shown in Figure 1. The connections of the truss girder are all bolted connections using pretensioned bolts. The bridge was built from modular system, typified structural elements. The longitudinal axis of the bridge is straight. The distance between the two truss girders is 4.42 m. The structure carries a unified railway track, with one track width, and a 2.8 m wide carriageway between the truss girders. The total width of the bridge is 8.72 m, and its structural height is 12 m. The main girders are stiffened with lower and upper wind bracings. The material of the bridge is a mixture of normal-strength steel and cast iron, with a min. yield strength equivalent to S235 steel grade.

The deck system consists of steel I-section cross-girders located 3 m apart and I-section longitudinal girders carrying a reinforced concrete slab. Railway traffic was originally carried over the longitudinal girders by timber sleepers. Later, secondary steel cross-girders were

DOI: 10.1201/9781003483755-383

placed between the cross-girders, and the deck system between the main girders was filled with concrete. According to the plans originally made in 1955, the bridge was designed for a static load of 2 pieces of 411 series locomotives and a railway carriage weight of 40 kN/m according to the Hungarian 1951 Railway Bridge Standard.

The structure plays an important role in the Budapest city life. It serves as the main entrance of the worldwide known "Sziget festival", which is organized on a yearly basis in Budapest, as one of the largest and most popular festival in Europe with an average of 450.000 – 500.000 visitors. Therefore, the condition of the bridge, its maintenance and safe operation has special focus among the bridges of Budapest. The present paper shows results of the latest bridge inspection followed by advanced numerical calculation proving the safe operation of the structure.



Figure 1. The K-bridge of Budapest: a) from air [1a] b) main entrance of the Sziget festival [1b – Photo: Tamás Vasvári/Index] c) side view [1a].

2 RESULTS OF THE ON-SITE BRIDGE INSPECTION

In 2022, a wide range inspection was carried out to check the structural health of the bridge. During the inspection it was observed that bridge bearings did not work properly, the cylinders fallen apart, the location of the cylinders was irregular and disorganized. Furthermore, it was detected, that the bridge deck system was in a highly corroded state. According to the measurements carried out during the 2020 main inspection, the average material loss was about 10% in some places. Based on the 2022 expert report, the condition of the connection plates within the joints is critical at many places, the material loss due to corrosion reached 25%, which highlighted the need for a careful corrosion measurement and advanced static check of the deck system considering the actual conditions of the structure.

At first, an extensive literature review was made on the possibilities of the corrosion measurement techniques and its modelling options in advanced numerical models. Based on the international literature visual examination is the most often used form of corrosion inspection. However, it only detects surface corrosion. On the other hand, various non-destructive physical probing methods have been developed and implemented to describe and assess material loss and corrosion levels such as: ultrasonic thickness measurement method [2], gamma radiation

[3], X-ray-based technologies [3,4], holographic interferometry [4], white light interferometry [5], thermography [6], scanning electron microscope stereo photogrammetry [7], optical three-dimensional scanning [8,9], and atomic force microscopy [10]. Several research results indicate a correlation between the mechanical properties of structural steel and corrosion-induced damage rate. It is attributed to local defects (notches) on corroded surfaces, leading to the initiation of fractures at lower stress levels. Characteristics of stress-strain curves heavily depend on corrosion damage, location, size and depth of dislocations [11]. According to Kim et al. [8], tensile tests indicate that yield strength and ultimate strength of structural steels remain relatively unaffected by corrosion when considering reductions in geometric dimensions. Conversely, the ultimate strain exhibits a nearly linear decline with the increase of corrosion damage. In addition, several research [8,12] pointed out the disappearance of yielding plateau, or reduction in its length, in the case of severe degradation due to extensive corrosion damage. Therefore, various corrosion models exist for the assessment of mechanical characteristics in corroded steel elements. Based on literature review, within the numerical calculations the effective plate thickness is determined and considered in static calculations as function of the average material loss. Furthermore, in the numerical calculations the largest localised section reduction (local corrosion) is also considered. Both are taken based on on-site measurement results.

In case of this bridge visual inspection, mechanical measurements combined with ultrasonic thickness measurements are applied. The condition of the main girders apart the support regions were evaluated to be good. The recommended value for material loss due to corrosion is 5% in average (maximum 10% at several locations) to be considered in the static calculations. No harmful deformation or local damages are visible on the main girders. A typical detail of the main girder is shown in Figure 2a).

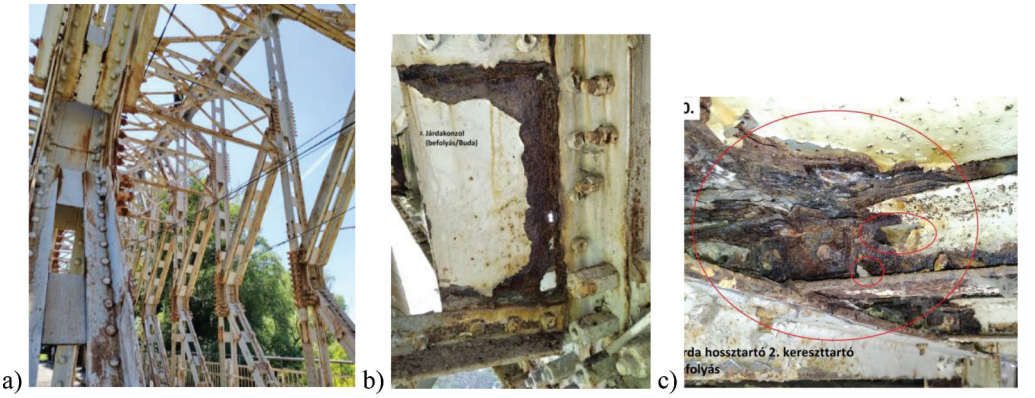


Figure 2. Corrosion damages of the bridge: a) main girder, b) most corroded cross-girder, c) longitudinal girder under the pavement.

The bridge deck system is in significantly worse condition than the parts above the deck system. During the on-site inspection, where significant corrosion damage was observed, the corroded part was excavated so that the extent of the section loss could be determined. The connection plate of the sidewalk cantilever connecting to the bridge is typically heavily corroded. In general, the amount of section reduction to be considered in the calculation is 20-30%. The exception is the cross-girder #2, which is in the worst condition (Figure 2b), whose upper part has ~80 %, the lower part ~90% cross-section reduction. The longitudinal girders are supported on the upper chord member of the sidewalk cantilevers, which corrosion loss is typically around 10-20%. At several places, in the cross-section of the supports, the reduction reaches 90%, an example is shown in Figure 2c). At the connection of the longitudinal steel girders and the cross-girders, an average section loss of 5% could be observed at the lower connection plate. There was an average of ~10% reduction in the web plates of the

longitudinal girders, while on average of 20% on the flanges. During the static check of the bridge, the main girders, the deck system including cross-girders, longitudinal girders, reinforced concrete slab and cantilevers under the sidewalks were carefully analysed. Their resistances were checked, and the utilization ratios were calculated separately. In the current paper, only the investigation of the mostly corroded part of the structure, the cantilever under the sidewalk is discussed.

3 NUMERICAL MODEL OF THE CROSS-GIRDER CANTILEVERS

Beside the global model of the bridge, for the analysis of the cross-girder cantilevers a separate numerical model, as shown in Figure 3, has been developed in the general finite element software, Ansys 19.0 [13]. The model is a full shell model, containing all the details of the sidewalk system between 5 cross-girders. Two cross-girders are analysed with the same numerical model: (i) average cross-girders having uniform material loss – the middle cross-girder is analysed, (ii) cross-girder #2 – having the most intensive local corrosion damages – the second cross-girder of the model is analysed.

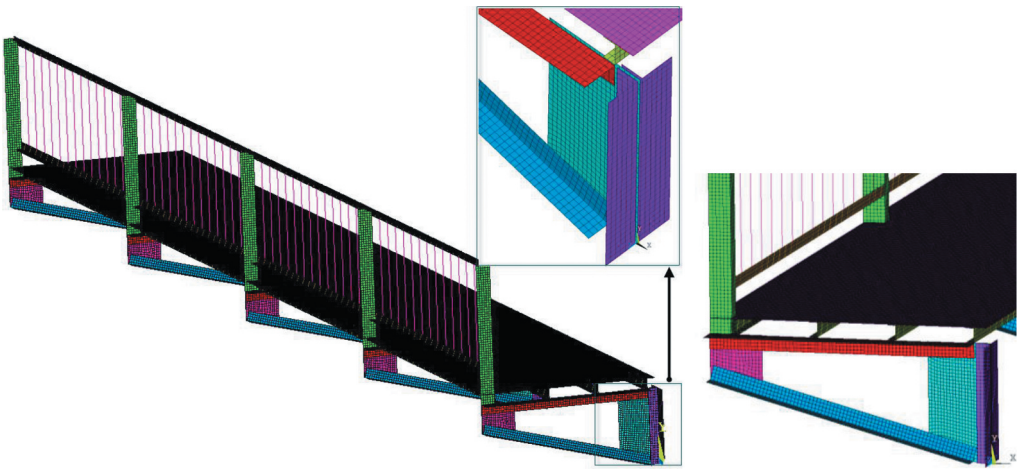


Figure 3. Numerical model of the cross-girder cantilever.

All structural elements and plates are modelled in their middle lines, so gaps are formed between the modelled plates (as shown in Figure 3 enlarged), through which the different plates were connected at the bolt locations using rigid bodies. Such a dense finite element mesh is applied that at least 4 rigid bodies were placed at the location of each bolt to avoid local stress concentration and local failure modes. Thus, the numerical model is suitable for checking the load carrying capacity of individual structural elements. However, the calculation does not directly include the static check of bolted connections. At the same time, it takes into account the structural behaviour characteristics resulting from the eccentric connections of the individual structural elements.

In the numerical model, a uniformly distributed load of 5 kN/m^2 is applied, multiplied by a dynamic amplification factor of μ=1.4 based on the Hungarian design code [14]. The resistance was first determined using the original intact cross-sections without corrosion loss, and then it was determined considering the resistance reduction effect of corrosion. In the numerical model, two different corrosion models were used: (i) general, uniform section loss covering the entire structure – 20% on all elements of the cross-girder cantilever, and (ii) local corrosion, which takes into account the local, significantly advanced corrosion rate of the connection plate as shown in Figure 2b). So, three different calculations are executed,

and their results are compared. The first two calculations are deterministic calculations applying geometrical and material nonlinear analysis using imperfections (GMNIA) to determine the characteristic and design value of the resistance. To investigate the resistance reduction effect of the local corrosion – due to its large variation and significant uncertainties in their degradation rate – stochastic analysis is applied, in which numerous GMNI analyses are executed by using different input data, where corrosion is considered as a probabilistic variable.

Figure 4a) shows the connection that is critical in terms of local corrosion. There is a significant amount of corrosion loss in a well-defined region close to the bolted connection of the connection plate (marked by red in Figure 4a). At several places the plate is completely punctured (zones marked by yellow in Figure 4a). This was taken into account in the numerical model by defining a corrosion matrix in this highly corroded zone in addition to the general section loss of 20%, in which the joint plate was divided into 30 parts along its height and a different section loss rate was determined for each matrix element and applied to the numerical model by using random distribution. Considering the high degree of corrosion damage of the section, the random distribution function was set so that the remaining section in each matrix element should be between 1-40% of the original 10 mm plate. A total of 20 corrosion loss models with different geometries were generated within the stochastic calculation, in which the average residual section measured over the entire connection plate height is ~20% of the original section (equivalent to an average section loss of ~80%). The geometry of the connection plate used in the stochastic analysis is shown in Figures 4b) and 4c), where different colours represent the different plate thicknesses. Since 100% corrosion loss can be observed in several places on the connection plate, the elements of the numerical model in the zones marked in yellow in Figure 4a) were eliminated and assumed that there are no load-bearing steel sections within these regions.

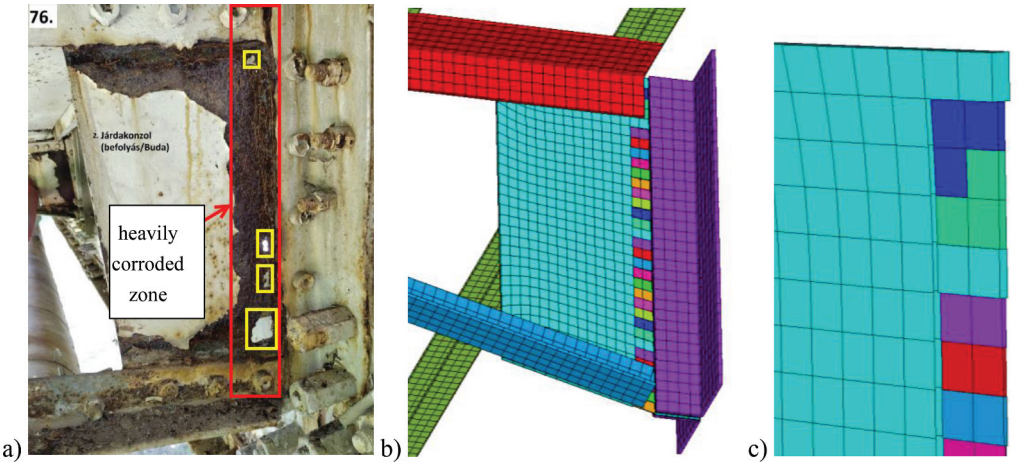


Figure 4. Modelling of local corrosion a) corroded connection plate, b) numerical model representing different thicknesses by different colours, c) connection plate model of the heavily corroded region.

Two different imperfections are applied in the nonlinear calculations: (i) global imperfection representing flexural torsional buckling of the lower chord member in combination of plate buckling and (ii) plate buckling-type imperfection of the connection plate, as shown in Figure 5.

The plate buckling-type imperfection was scaled to $b/200$, where b is the connection plate depth; the global imperfection is scaled to $L/200$ (where L is the member length of the lower chord) based on the design recommendations of EN 1993-1-5 [15] and EN 1993-1-1 [16].

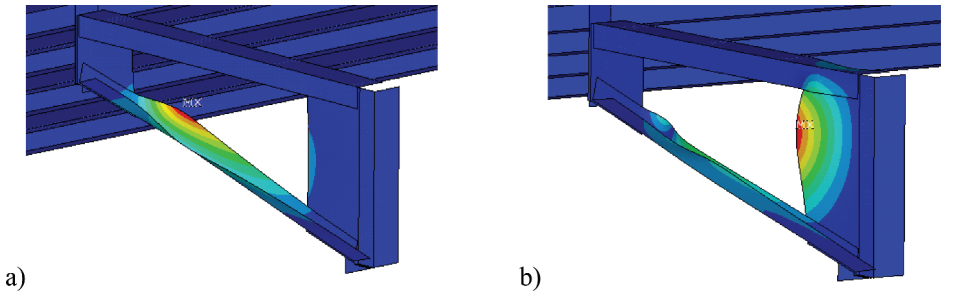


Figure 5. Applied equivalent geometric imperfections: a) flexural torsional buckling-type imperfection, b) plate buckling-type imperfection.

Within the deterministic and stochastic analysis nonlinear material model is used. The applied material model is linear elastic – hardening plastic with isotropic hardening rule using von Mises yield criterion. The material was assumed to behave as linear elastic and to obey Hooke's law with a Young's modulus of E = 210000 MPa up to the yield strength, which is set to 235 MPa. After this point the material was assumed to follow linear hardening with a reduced hardening modulus of E/10000 according to EN 1993-1-5 Annex C [15].

4 RESULTS OF THE NUMERICAL MODEL

4.1 *Results of general cross-girders*

At first, the load carrying capacity of the sidewalk structure is determined using the advanced numerical model. The observed failure mode is presented in Figure 6, which is buckling of the lower chord member. Based on the GMNI analysis, the load-displacement curve of the structure is determined as shown in Figure 7. The graph shows the results of (i) the intact structure and (ii) cross-girder having average of 20% corrosion loss. The horizontal axis shows the vertical displacement of the cantilever, and the vertical axis shows the load scaling factor utilized for the design load level. The horizontal lines present the characteristic and design load levels of the corroded cross-girder determined based on the proposed evaluation process of the nonlinear analysis according to prEN1993-1-14 [17] and using the global safety factor given by the Hungarian design code [14]. The point of the first yielding limit state is also marked, which check is also mandatory for bridges in Hungary. Based on the numerical calculations, the adequacy of the general cross-girder is proven. The load carrying capacity of the sidewalk could be verified according to the Hungarian design code with the maximum utilization ratio of 92%.

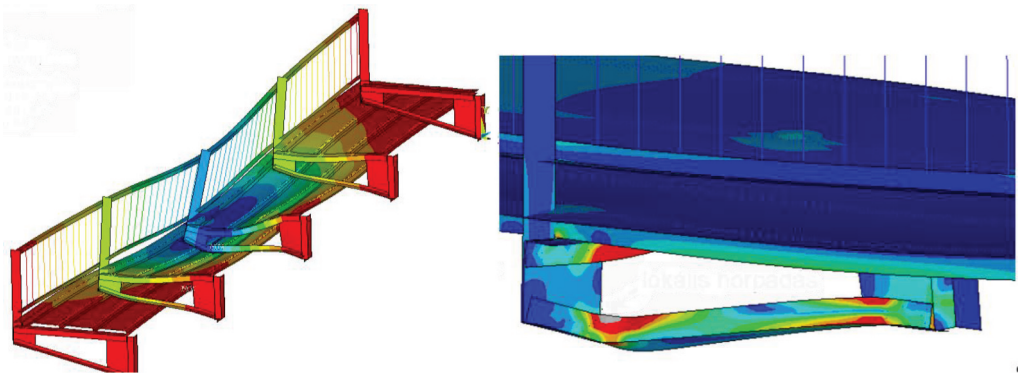


Figure 6. Obtained failure mode by the advanced numerical model – general cross-girders.

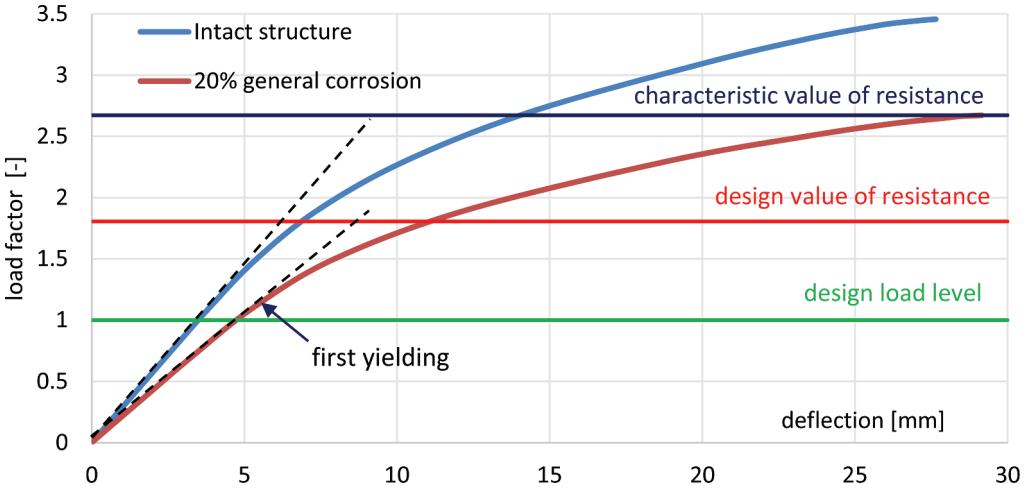


Figure 7. Obtained load-displacement curves, characteristic and design resistances and design load level.

4.2 *Result of cross-girder #2*

The failure mode of the numerical model considering both global and local corrosion damages, is shown in Figure 8. Based on the results, it can be seen that the failure mode changes, local buckling of the lower chord members starts, but the final failure occurs within the connection plate in the zone of the local corrosion in form of plastic failure.

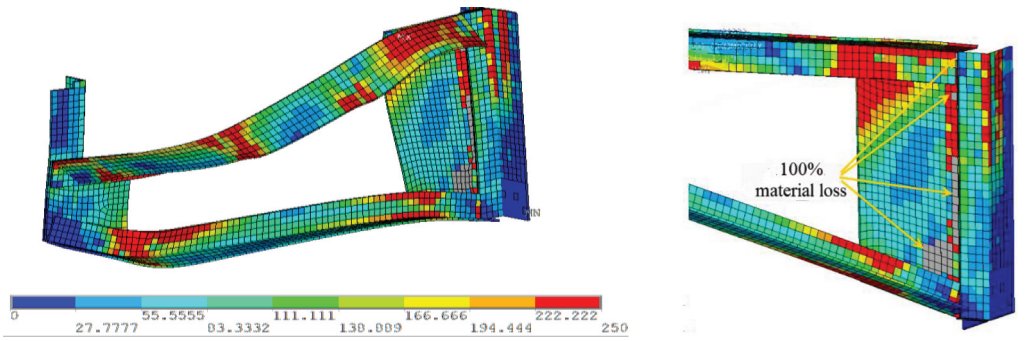


Figure 8. Obtained failure mode by the advanced numerical model – cross-girder #2.

Multiple GMNI analyses are performed on the numerical model using various input data determined on probabilistic basis. The load carrying capacity of the structure is determined for each corrosion situation. The ratio of the load factor corresponding to the design load level and the average remaining cross-section is shown in Figure 9. It can be seen that the load factor corresponding to the safety level required by the e-UT regulations (marked by red line) in the case of an average residual cross-section of ~20% can still be verified (80% average section loss) with a maximum of 99% utilization ratio, which result corresponds to the corrosion state observed in June 2022.

4.3 *Result of the proof loading test*

Due to the significant material loss of the cantilever connection plate and the variability experienced in them, the company Provix Híd Ltd. made the proof loading test of the

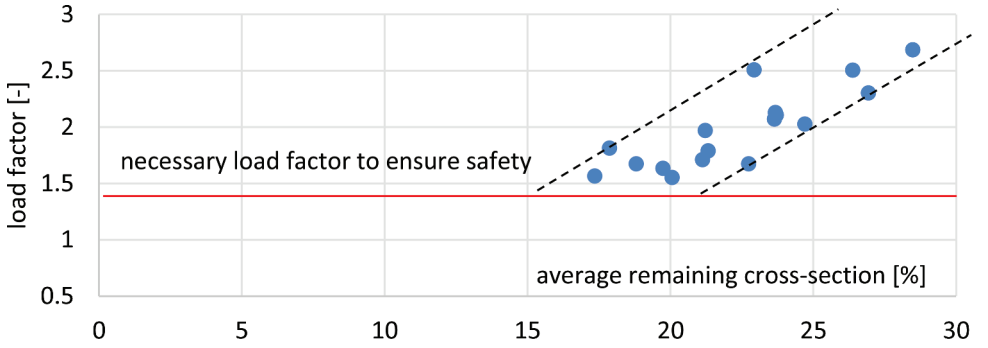


Figure 9. Obtained load-displacement curves, characteristic and design resistances and design load level.

sidewalk's structure. During the test load, wooden plates were put on the pavement, on which a load of ~21 kN (~5 kN/m^2) was applied and moved along the entire length of the bridge. Thus, all cross-girders and longitudinal stringers are loaded by the proof load. The only exception is cross-girder #2, on which the test load is reduced to 11.5 kN (~2.75 kN/m^2 load intensity, which corresponds to more than 2 times of the pedestrian load corresponding to the exceptionally dense traffic situation according to the recommendations of the JRC Scientific and Technical Reports [18]). After the test load was applied, the structure is visually inspected, and it is determined that the structure withstand the test load without any damages.

5 CONCLUSIONS

The BME Department of Structural Engineering carried out the expertizing task of the K-bridge to assess the load carrying capacity and structural health condition. The level of reliability of the structure is checked taking into account the current corrosion damages based on on-site measurements. It has been assessed whether the corroded structure meets the requirements according to the current Hungarian design code and it has been also decided if the bridge could be kept in operation and open for the daily traffic. The results of the 2022 proof load test and the probabilistic numerical analysis using the on-site corrosion measurement results confirmed the adequacy even of the cross-girder cantilevers which were in the worst condition, however, with large utilization ratio (99%). Based on the on-site measurements and the above introduced advanced analysis, the structural health of the bridge and conditions of further operation could be evaluated. Based on the advanced calculations, finally the bridge condition was also assessed by a group of Hungarian bridge design and maintenance experts. They concluded that within the main girder, the bridge deck system is adequate in terms of load carrying capacity despite the significant corrosion damages. They called the attention, however, if no intervention would be carried out in the near future (within 1 year time), as corrosion develops, this compliance can only be verified for short term. As corrosion propagates, the structural safety (especially for cross-girder #2) may be reduced. Therefore, strengthening of the mostly corroded connection plate is suggested as soon as possible.

ACKNOWLEDGEMENT

The authors would like to express special thanks to the members of the group of experts (Adrián Horváth, Gyula Kolozsi, Zoltán Müller and Zsolt Nagy) for their cooperation within the expertizing tasks and evaluation of on-site measurements and risk analysis results. The presented research program is also supported by the Grant MTA-BME Lendület LP2021-06/2021 "Theory of new generation steel bridges" program of the Hungarian Academy of

Sciences, the support is gratefully acknowledged. The authors dedicate the paper to the memory of their colleague, Zoltán Müller, who tragically died in 2023, with whom this was their last joint bridge inspection work.

REFERENCES

[1] a) https://hu.wikipedia.org/wiki/K-h%C3%ADd and b) https://index.hu/belfold/2019/08/13/k_hid_szi get_fesztival_felujitas/.
[2] Paik, J.K., Thayamballi, A.K., Park, Y.I. & Hwang, J.S. 2004. A time-dependent corrosion wastage model for seawater ballast tank structures of ships. *Corros Sci* 46:471–86.
[3] Kriesz, H. 1979. Radiographic ndt-a review. *NDT Int* 12:270–3.
[4] Ghahari, S.M., Davenport, A.J., Rayment, T., Suter, T., Tinnes, J.P. & Padovani, C. 2011. In situ synchrotron X-ray micro-tomography study of pitting corrosion in stainless steel. *Corros Sci* 53:2684–7.
[5] Habib, K. & Al-Sabti, F. 1997. Monitoring pitting corrosion by holographic interferometry. *Corrosion* 53:688–92.
[6] Holme, B. & Lunder O. 2007. Characterisation of pitting corrosion by white light interferometry. *Corros Sci* 49:391–401.
[7] Perez, I. & Kulowitch, P. Thermography for characterization of corrosion damage. 2000. Corrosion/ 2000 NACE's Annual Conference, Orlando, Florida, 26-31 March, 2000.
[8] Reiser D.B. & Alkire, R.C. 1984. The measurement of shape change during early stages of corrosion pit growth. *Corros Sci* 24:579–89.
[9] Kim, I.T., Dao, D.K., Jeong, Y.S., Huh, J. & Ahn, J.H. 2017. Effect of corrosion on the tension behavior of painted structural steel members. *J Constr Steel Res* 133:256–68.
[10] Wang, Y., Xu, S., Wang, H. & Li A. 2017. Predicting the residual strength and deformability of corroded steel plate based on the corrosion morphology. *Constr. Build Mat* 152:777–93.
[11] Pidaparti, R.M. & Patel, R.R. 2008. Correlation between corrosion pits and stresses in Al alloys. *Mater Lett* 62:4497–9.
[12] Ruiz-Menéndez, G., Andrade, C., Carro-Sevillano, G., Peña, C., Adeva, P. & Medina, J. 2022. Identification of the failure mode of corroding steel rebars in a viaduct in service through hardness measurements. *Results Eng* 2022;13.
[13] Qin, G.C., Xu, S.H., Yao, D.Q. & Zhang, Z.X. 2016. Study on the degradation of mechanical properties of corroded steel plates based on surface topography. *J Const Steel Res* 125:205–17.
[14] ANSYS® v19.0, Canonsburg, Pennsylvania, USA.
[15] e-UT 07.01.12 Static calculations, design of roadway bridges (in Hungarian), MAÚT, 2011.
[16] EN 1993-1-5: Eurocode 3: Design of steel structures - Part 1-5: Plated structures, CEN, 2006.
[17] EN 1993-1-1: Eurocode 3: Design of steel structures - Part 1-1: General rules and rules for buildings, CEN, 2005.
[18] prEN 1993-1-14: Eurocode 3: Design of steel structures - Part 1-14: Design assisted by finite element analysis, CEN (under publication).
[19] Design of lightweight footbridges for human induced vibrations, JRC Scientific and Technical Reports, 2009. ISBN 978-92-79-13387-9.
[20] Design of lightweight footbridges for human induced vibrations, JRC Scientific and Technical Reports, 2009. ISBN 978-92-79-13387-9.

Bridge Maintenance, Safety, Management, Digitalization and Sustainability – Jensen, Frangopol & Schmidt (eds)
© 2024 The Author(s), ISBN 978-1-032-77040-6
Open Access: www.taylorfrancis.com, CC BY-NC-ND 4.0 license

Development of the maintenance strategy for Västerbron

J. Sandberg
AtkinsRealis, UK

L. Steen
Systra, Sweden

J. Hedenström
Stockholms Stad, Sweden

ABSTRACT: The Västerbron link in Stockholm, comprises Riddarfjärdsbron to the north and Pålsundsbron to the south, is a strategic link between northern and southern Stockholm and was the first crossing constructed outside the city centre. Opened in 1935, this structure pioneered early welding technology. The bridge is now an important landmark within Stockholms City. Due to the age of the structure and reported concerns regarding the adequacy of the material used in its construction, extensive works were carried out to assess the current structural condition of the main bridges and develop a maintenance strategy to ensure the safe operation of the structure over the next 40 to 80 years. This paper sets out the technical work carried out to assess the current condition of the structure to ensure its adequacy, focussing on managing the stability of this very slender steel structure.

1 INTRODUCTION

With maintenance of existing infrastructure becoming increasingly important for many road authorities with ageing infrastructure, developing practical maintenance strategies for older structure is required. In steel structures built before 1960s, material properties are often variable due to limited control in fabrication processes which means that these steel structures can contain materials that do not meet modern brittle fracture requirements. A practical approach towards managing this is therefore required. One such structure is the Västerbron link, a main road located to the west of Stockholm City Centre. It was constructed during the early 1930s with construction completion in 1935. The link comprises three parts, including Riddarfjärdsbron to the north; the central portion, over Långholmen comprising an embankment supported by stone retaining walls which then connects onto Pålsundsbron to the south. The focus of this paper is on the two main bridges outlining how variable steel fracture properties were considered for the assessment.

2 BACKGROUND

Riddarfjärdsbron has a total length of 601.5m and a width of 26m between parapets. The deck is supported on two arches with clear spans of 168m and 204m. The arches comprise steel box cross sections supported on multiple pin bearings (allowing moment resistance) and mass concrete blocks founded on rock. The bridge deck comprises a multibeam deck with a non-composite concrete slab supported on slender steel tubular pin ended piers at each edge of the deck. The arches and main transverse beams are formed through built up sections that are riveted using

DOI: 10.1201/9781003483755-384

construction techniques common to this era of early steel structures. The longitudinal beams generally comprise welded sections. Additionally, many stiffeners and ancillary steelwork were welded. Pålsundsbron has a total length 272m. Whilst there are similarities to Riddarfjärdsbron in construction, far more welding was carried out to build up all structural elements including the arch, which has a clear span of 56m. There is also very little bracing below the steel deck level for this structure, see Figure 1 for a 3D model of Västerbron.

The original bridge was built through a German/Swedish consortium. The slender design of the bridge was a significant departure from earlier bridge forms typical around Stockholm, which were far more massive. The slender superstructure supported on long spanning arches was a huge architectural leap and paved the way for slender structures to be adopted around the country. As well as the aesthetic innovations at the time, significant technological innovations were also adopted. In particular, Pålsundsbron was the first bridge in Sweden where welding was implemented to such extents as described by *Ulvsgärd (2021)*. The innovative architectural style, the use of innovative technology at the time of construction together with its importance within the landscape of Stockholm has therefore led to the link being classified as blue (the highest level of importance for cultural and historic value) in accordance with Stadsmuseets classification system.

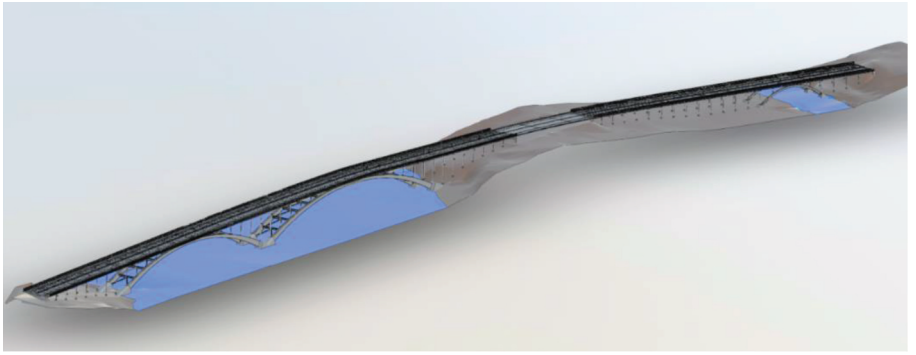


Figure 1. Revit model showing Västerbron.

Whilst construction records indicate that rigid quality control systems were implemented during fabrication, NDT techniques now commonly used in the construction of steel bridges to detect microcracking within welded structures were not available and likely unknown at the time. In addition to this, standard detailing that we today associate with welded steel structures had not yet been developed which means that much of the detailing comprises a mix of details normally associated with riveted structures and experimental new weld details, many of which would be avoided today as they are known to introduce stress concentrations into the steelwork. This particularly includes details such as fully welded stiffeners, with no allowance for cope holes. When Västerbron was constructed, there were limited requirements regarding steel ductility and steel material properties were often variable. It wasn't until the 1960s that this was recognised as a significant issue in steel structures and therefore better controls were brought in to avoid this.

Poor brittle fracture properties can cause premature failure of an element before it reaches its yield stress under an impact load scenario and has the potential to affect the long term performance of the bridge. Initial investigations and testing were carried out in 2016 and 2021 as part of the development of Tillståndsbedömning Västerbron developed by *Ramboll (2021)* which identified potential concerns with the material properties used in the original construction of the bridges comprising the Västerbron link. This report recommended that additional work be carried out to ensure the structures long term integrity. NDT testing has also been carried out on the welding, identifying the presence of cracking within the welds. The aim of this paper is therefore to discuss the management approach for these bridges based on the abovementioned data to ensure that this historically important link can be maintained for

future generations. The approach incorporates the testing, current standards and guidance documents and an understanding of the structural analysis to outline key risk factors in the structure in its current condition.

3 APPROACH

The approach taken comprised a step by step process whereby various considerations were made. Whilst the full study is not yet complete, these are planned to be carried out over the next few years. Prior to this study, a full assessment was done on the structure, whereby the overall assessment rating was derived based on the TRV assessment standards *TDOK 2013:0267 version 5 (2018)*. The assessment found that the structure was adequate for BK1 loading, which ensures adequacy under normal vehicle traffic typical to an inner city bridge, though it does not have sufficient capacity for heavy vehicles, including 74 tonne vehicle. It should however be noted that to ensure transverse stability it was assumed this was provided by the slab working compositely with the steel beams through friction as what we now consider standard composite connections not yet commonly used. As a full composite connection was not achieved, beam resistances where the top flange was in direct contact with the slab were based on the steel only resistance of the beam rather than including a contribution from the concrete. Whilst this is considered to be an acceptable (though conservative) approach for assessment, it is only likely to be accurate once the friction connection is lost and the beam slips relative to the concrete. This is therefore an important assumption to be aware of when trying to understand the measured stress ranges recorded in the structure and how it compares with the predicted stress ranges based on the model behaviour and has an impact on the results discussed below.

The investigation into the adequacy of the structure under brittle fracture was undertaken in three separate stages as follows:

- Stage 1 - Loading calculation, results extraction, stress calculation and preliminary sensitivity study of results;
- Stage 2 - Fracture Mechanics calculation;
- Stage 3 – Structural analysis to investigate sensitivity of the loss of structural element.

The intention of the above approach is to provide a simplified method of assessing the overall risk to the structure based around limited material testing, calculations predicting likely cracking of the structure and an understanding of the structures' behaviour. It is noted that this is likely to be a common consideration with early steel structures as it is unrealistic to conduct wholesale testing on every structural element on a bridge structure without attracting significant cost.

Stage - 1 Preliminary investigation

The numerical assessment of the structure was used to identify the most highly stressed elements. Elements with significant tension were considered at higher risk as cracking is more likely to develop here. Also, elements subject to variable stress ranges from traffic and other variable actions were also considered as cracks forming in these elements are likely to propagate. This influences the structures sensitivity to brittle fracture. Additionally, while brittle fracture is a separate mechanism to fatigue, there are links in the behaviour and therefore sensitive fatigue details will also be prone to brittle fracture, particularly where the material properties show poor brittle fracture behaviour. The steel samples were tested in accordance with *"Brottseghet och kemisk analys av konstruktionsstål"* (Trafikverket) which applies to structures with steel built before 1970. Tests were carried out at -30°C as per ASTM E 1820 and a loading rate to be appropriate for the traffic loading applicable for the structure. Test results were then evaluated based on the recommendations set out in TRVINFRA-00228, where fracture toughness was reviewed against predicted stress ranges from the structural analysis model. TRVINFRA-00228 indicates that J values should meet the minimum limits according to Level 1. If these minimum limits are not met, Level 2 verifications are required. TVINFRA-00228 tables are reproduced in Table 1 and 2.

Table 1. Table 5-3 in TRVINFRA-00228 – Level 1 requirements.

f_{yk} (MPa)	f_{yd} (MPa)	J (kN/m)	Conditions
220	167	30	Accepted without special conditions
260	197	40	
290	220	50	

Table 2. Table 5-3 in TRVINFRA-00228 – Level 2 requirements.

J (kN/m)	Max allowable σ_{nom} (Mpa)
20 < J < 30	σ < 100 + 6,7 (J - 20)
30 < J < 40	σ < 167 + 3 (J - 30)
20 < J < 30	σ < 197 + 2,3 (J - 40)

Where Level 2 limits are applicable, the maximum stress limits shown in Table 2 are verified against SLS stresses in the assessment standards. Provided these limits are met, the structure is considered adequate. The test samples were evaluated against these requirements. Table 2 shows the fracture toughness results that were carried out in 2016 for both Pålsundet and Riddarfjärden. Results marked with LV are from Pålsundet, whilst those indicated by 1-12 are for Riddarfjärden.

Table 3. Summary of sample results 2016 (Ramboll (2021)).

Test	1	2	3	4	5	6	7	8	9	10	11	12	LV1	LV2	LV3	LV4	LV5	LV6
Jq/kN/m	37	183	11	34	48	35	51	25	33	10	32	38	445	451	508	161	35	36

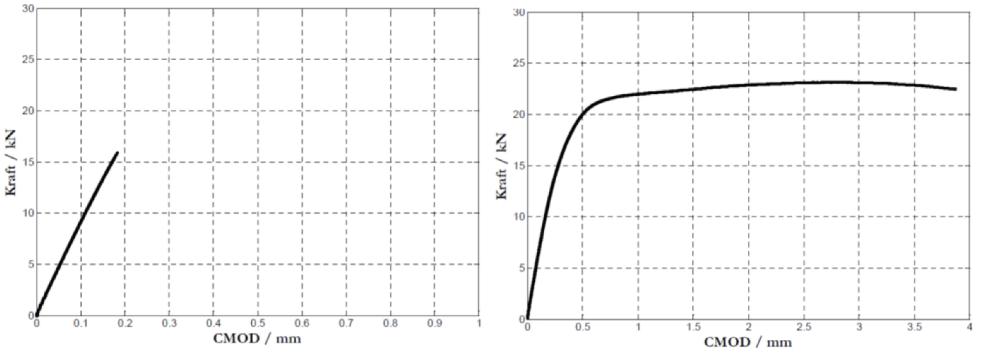


Figure 2. Good and poor brittle fracture behaviour with test on the left indicating poor behaviour and test to the right good behaviour (Ramboll (2021)).

A large variability in fracture toughness occurs for both bridges indicating variable material properties. Figure 2 shows examples of good and poor brittle fracture behaviour from the bridge samples. Particularly concerning were the low results at Riddarfjärdsbron. These indicate potential for very brittle failure. The transverse members at Riddarfjärden (ST 52) should have a minimum J value (load per crack tip opening displacement) of 50 for Level 1 requirements, and the longitudinal beams (ST 44) a minimum J value of 43.3. Level 1 properties are desirable, many tests did not meet the minimum of the Level 2 requirements. The two lowest values for Pålsundsbron are 35kN/m and 36kN/m meet the level 2 limits, indicating that these can be managed. Work carried out by Ramboll in 2021 included further material testing for Riddarfjärdsbron. This was due to the lower fracture toughness results obtained for this structure. Ramboll noted the testing from 2016 used a very high load rate of around 160 MPa/s which was deemed conservative as measured stresses in the deck varied between 5 - 15 MPa/s. Measured stresses elsewhere in the structure had lower stress ranges due to higher proportions

of permanent loading (ie the arches). The new tests used a rate of 30 MPa/s as this was deemed more realistic.

A similar variability in material properties was identified in these revised tests. However, there a marginal improvement at the lower end is seen, though the level 2 limit from TRVINFRA-00228 are still not met. Testing seemed to indicate the material with higher allowable yield strength displayed greater propensity towards brittle failure. The number of samples tested is very small and therefore cannot be confirmed. The samples from Pålsundsbron indicate less propensity towards brittle material, though noting again the small sample size. Though the results show significant variability for toughness, surprisingly the fracture appearances didn't reflect the big numerical differences, noting the appearance of cracks can be very difficult to control in brittle materials.

Table 4. Summary of sample results (Ramboll (2021)).

Designation	T1	T2	T3	T4	T5	T6	L1	L2	L3	L4	L5	L6
JQ/kNm^-1	16.5	17.8	424.3	720.2	586.1	16.3	35.5	42.7	57.7	39	66.3	38.6
Ds/dr/Mpa/s	30.2	30.6	31.3	30.9	30.7	30.3	31.5	29.9	30.9	31.6	31.3	32.1

Three main reasons for the large variation in CTOD test results are identified:

1. The -30ºC test temperature is likely around the ductile to brittle transition, and therefore relatively small temperature differences can have a large influence on the measured toughness. Some steels of this vintage will have low toughness levels.
2. For steel manufacturing at the time, there were often significant differences in steel properties dependent on which part of the ingot the section of plate/beam originated from. The basic chemical composition in the ingot will be similar, but porosity, segregation and oxide entrainment can cause some variations which affect toughness.
3. The effects of steel toughness were not well understood at that time and the steel specification most probably did not include a minimum requirement for toughness. This could potentially result in large variations in toughness, even for the same steel strength grade.

As the samples did not meet the simple requirements for material toughness, this then lead to the next stage in the approach, whereby detailed fracture mechanics calculations were carried out.

Stage 2- Fracture mechanics calculation

The stresses obtained from stage 1 were used to assess the fracture mechanics behaviour to determine the likelihood of cracking, the critical dimensions (mainly critical crack depth) and the number of cycles to failure assuming an initial detectable crack depth of 4mm. This was assumed as it is the smallest practical size of crack detectable using standard NDT testing on in-situ steel structures. Where transverse stiffeners are welded to the flanges, residual stresses tend to be locked into the steel elements. The presence of residual stresses impacts on crack size development and number of cycles to failure. Residual stresses were considered in the calculations where applicable. BS 7910 was used for the fracture mechanics calculations as there were no known Swedish standards that cover detailed fracture mechanics calculations. Calculations were then based on the at the most stressed location of the elements identified to be at greatest risk of cracking as identified in stage 1. Where toughness tests had not been carried out for a particular member, ie bracing members, material properties for other elements specifying the same steel grade were adopted. This approach was deemed valid as additional testing was considered unlikely to provide any significant benefit due to the variability in test results already identified.

A fracture mechanics approach was used to determine critical crack sizes and rates of crack growth for the main structural members, based on the stresses estimated by structural modelling and the J values from the tests. No further adjustments were made for temperature

impact. K_I (crack tip stress intensity) is a parameter that defines the likelihood of brittle fracture, which predicts the stress state local to the crack tip and depends on the component geometry, the size and location of the crack, and the magnitude and distribution of the applied stresses. The likelihood of plastic collapse is determined by the 'reference stress' σ_{ref}, essentially a 'far field' stress, or limit load. The longitudinal and transverse beams on Pålsundet are generally welded, and include welded stiffeners along the length of the beam. The process of heat application during welding locks stresses into the cross section making it more prone to cracking. The stress calculations therefore assumed a crack formation likely to occur in areas of adjacent to the stiffeners as we considered these to be at greatest risk of crack propagation that would then lead to potential critical cracking in the beam. Whilst the beams also have longitudinal welds connecting the web with the flanges, these welds are considered less critical.

The supporting deck beams at Riddarfjärden are made up of a combination of welded and riveted sections. Both internal and external longitudinal beams and intermediate transverse beams are made up of welded sections with welded transverse stiffeners. The main transverse beams however are built up using several sections, where the flanges are riveted to the webs through angle connectors and additional plates which are riveted to the bottom flange to provide additional flange thickness. Stiffeners are still welded to the angle sections and webs and therefore, critical details were considered around the riveted holes and the transversely welded connections. Closed form solutions for stress intensity and reference stress for a wide variety of cracked component geometries can be found in published literature. For this project, the solutions in BS 7910 were used. In the absence of accurate non-destructive testing (NDT) crack measurements for the bridges, an initial crack size was assumed. This was based on the smallest crack detectable by standard surface NDT methods such as magnetic particle inspection (MPI) or dye penetrant testing (DP). Tables T.4 and T.5 BS 7910 recommend a crack length of 20 mm and a through-wall depth from the surface of 4 mm. The calculations assume that the cracks will grow in proportion, with a constant ratio of length to depth of 5:1. The cracks are assumed to be located on the top surface of the tension flange of the beams. A semi-elliptical surface crack geometry was assumed; this is judged to be both credible and conservative. As this was a sensitivity study rather than an assessment of actual cracks, the choice of crack geometry was made by judgement of the most likely crack location (the tension flange of members in bending) and form (detectable by surface inspection techniques such as MPI or DP). The stress concentrating effect of rivet holes was not considered as a solid model finite element analysis (FEA) would be required to determine the resultant stress distribution, which was not considered for this study. For welded attachments such as web/flange stiffeners where the weld direction is perpendicular to the tensile stress orientation, a residual secondary tensile stress equal to the material yield stress was added to the assessment, which is conservative. The material fracture toughness K_{mat} was derived from the test results as follows:

$$K_{mat} = \sqrt{\left(J_q \times E'\right)} \tag{1}$$

Plane strain conditions were assumed throughout. The approach adopted is considered standard withing the industry for assessing cracks. A typical FAD (failure assessment diagram), for the Pålsundet transverse diaphragm, is shown in Figure 3. This member contains welded web/flange stiffeners. If it is conservatively assumed that these are located close to the most highly stressed areas, it is standard practise to also assume that tensile welding residual stresses equal to the material yield stress are present. This has a significant effect on the critical crack depth, in this case reducing it from 31 mm to 8.3 mm. It increases the fracture ratio for the assumed 4 mm deep initial crack from ~0.2 to >0.6, but does not affect the plastic collapse ratio, as secondary stresses do not contribute to the reference stress. For all beams assessed, the critical crack size is based on the 'worst case' stress combination.

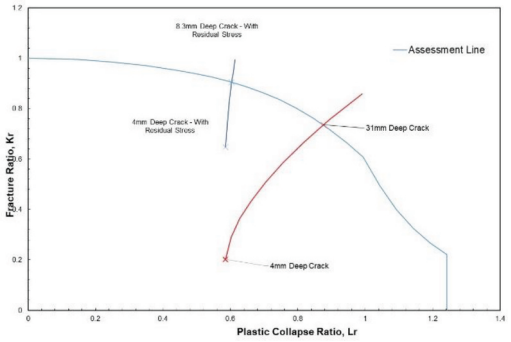


Figure 3. Failure assessment diagram.

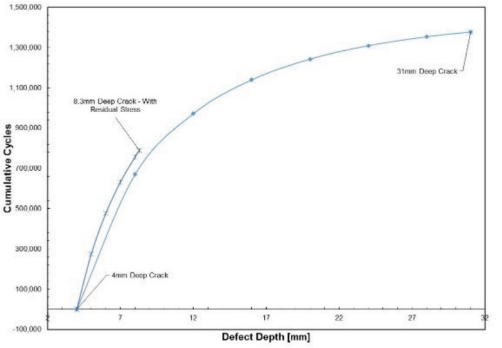


Figure 4. Fatigue crack growth.

Fatigue crack growth rates were estimated using the Paris law with coefficients from BS 7910. The only significant cyclic load, in terms of stress magnitude and frequency, is the traffic load; other stresses were below the fatigue crack growth threshold. Fatigue crack growth from the initial 20 mm x 4 mm assumed defect to a critical defect depth (i.e. failure) is shown for the Pålsundet transverse diaphragm in Figure. The assumption of weld residual stresses has a significant effect on the number of cycles to failure, reducing it by around 50%. The crack growth rate is non-linear, as is proportional to the cube of the crack stress intensity. The results from the analysis showed reasonable margins of safety between the smallest detectable crack size and critical crack sizes, with relatively long predicted fatigue lives. For example, if surface NDT on the areas assessed is carried out to an acceptable standard in the near future and no defects are found, it can be stated with reasonable confidence that the largest defect likely to be present (and not detected by NDT) will be of the order of 20 mm long by 4 mm deep. Provided that critical areas are monitored, it is feasible to expect that cracking can be observed prior to the crack size becoming critical. The fatigue calculations suggest that defects of this size will not reach a critical size until many thousands of traffic cycles have passed which again indicates a reasonable probability of effective monitoring being able to identify a critical crack.The information from this analysis was then carried into the next stage 3.

Stage 3- Loss of part of or full element

In parallel to assessing fracture mechanics and the impact of cracking in the steel leading to local failure of an element, a sensitivity study was carried out on the structure to evaluate the impact of a crack leading to the failure of either a part of or the full element under consideration. This study included the removal of the critical elements including flanges, webs and the entire beam. The impact on the damaged element and the surrounding structural elements was investigated to assess whether a local failure leads to progressive collapse of the rest of the structure. The study was carried out considering the accidental removal of different parts of the structure (for example partial flange loss or partial web loss) or the full element to model the ineffective behaviour of that part/full of the element. The utilisation of the affected and surrounding elements was then determined using the accidental design situation as outlined in SS EN 1990 and compared with the utilisation of the elements without damage under the ultimate limit state (This was based on the original assessment results). The loss of part or full element was considered independently. For example, when loss of part of an element was considered for one element, the adjacent elements were kept as undamaged (acting in full capacity). This was done on the basis that probabilities would suggest that it is unlikely that several adjacent elements will be subject to the same defects simultaneously. Plastic load distribution was not considered at this stage of the analysis as this added an additional level of complexity to the

analysis that was not desired at this stage. The purpose of this study was to establish whether the structure had enough residual capacity within the system to avoid collapse. The typical approach when considering an accidental scenario is to allow for significant damage to the structure. However, the overall collapse of the structure should be prevented. This was also the approach taken in for this study.

Where built up cross sections were relevant, such as for the Riddarfjärden cross beams, it would be unlikely that all parts of a built-up member would have the same defect in each of the different layers of the built-up section. Therefore, the impact of failure of a single plate within this system was considered. The study identified that the main transverse beams were of greatest risk to the structure and if these were to fail, this would lead to overall structural collapse. Loss of parts of the remaining structural elements would lead to significant damage to the structure, but the structure would remain standing. A further comparison was then carried out considering strain measurements that were obtained by Ramboll during the condition study carried out in 2020. As part of this work, stress ranges in the bridge deck were monitored under traffic loading for approximately 6 months (2021 Ramboll). These findings are shown in Table 3. Where stress ranges are below the cut off limit (as defined in SS 1993-1-9), damage to the structure is unlikely to occur and cracks are unlikely to propagate. Table 5 indicates that measured stress ranges are mostly below this limit, though isolated instances exceed this. However, whilst theoretical calculations indicate that stress ranges in the arch are relatively small, stress ranges in the deck element are in the region of 60 MPa in some instances. It is believed that the reason for this discrepancy is due to the real versus assumed connection to the slab. As discussed above, there is no composite connection to the slab through shear studs or other means instead the connection maintained through friction. Whilst this is a recognised mechanism, it is difficult to quantify by calculation, particularly where there is a risk that that friction connection is lost. Therefore, the assessment derived a stress range based on the slab as a non-contributing component. This was considered in the risk analysis as it reduces the overall risk due to the lower measured stress ranges.

Table 5. Measured stress ranges.

	Typical stress variation (MPa)	Maximum stress variation (MPa)	Relevant fatigue detail category	Stress range cut off limit (MPa)
Riddarfjärden arch	1-4	16	71	21.3
Riddarfjärden deck	1-6	24	40, 71, 80	12.0, 21.3, 24.0
Pålsundet arch	1-4	16	63	18.9
Pålsundet deck	1-6	18	40	12.0

4 FINDINGS

Whilst the study has not been finalised, the process adopted has worked through different key stages and risk analysis. So far, the study has shown that whilst there is still a potential risk to the structure due to the variability of the material properties, this risk can be managed based around an approach where theoretical stress ranges and measured stress ranges are considered. Critical members can be monitored and the intention is to carry out a full visual inspection and targeted NDT inspection of critical details when the structure is next repainted. Whilst this approach has not completely eliminated the risks to the structure, it has identified how these risks can be managed with limited intervention. The precise nature of these interventions are yet to be determined, though they will be significantly less than the initial conservative interventions of remedial works being required to all members not meeting the limitations set out in TRVINFRA-00228.

5 CONCLUSION

This paper sets out the approach taken to understanding the impact of the variability in steel material properties encountered during the material testing on the Västerbron steelwork. Through a series of initial sensitivity calculations, detailed fracture mechanics calculations based on simplified assumptions and global analysis of the structure considering the loss of structural elements an understanding of the risks to the structure has been developed. This knowledge is now being used to determine the long term management strategy for the bridge and most importantly ensuring that the structure can be safely managed into the future. It is envisaged that a similar approach may be relevant to other structures with steel from before 1970, where material properties were not adequately controlled during construction and which may display similar concerns.

REFERENCES

Atkins, (2021) Bärighetsutredning Beräkningsrapport Bro över Riddarfjärden (doc ref: 5198682-180-10140-1-002)

Atkins, (2021) Bärighetsutredning Beräkningsrapport Bro över Pålsundet (doc ref: 5198682-180-10141-1-002)

ASTME (2023) ASTM E1820-23b Standard Test Method for Measurement of Fracture Toughness, ASTME

Ramboll, (2021) Tillståndsbedömning Västerbron (doc ref: Knr 180-10140-1 and 180-10141-1 dated 22/09/2021)

SIS (2005), SS EN 1993-1-9 Eurocode 3: design of steel structures - part 1-9: fatigue, SIS.

Trafikverket (2018) TDOK 2013:0367 Krav Bärighetsberäkning av broar, Trafikverket

Trafikverket (2014) TDOK 2012:23 "Brottseghet och kemisk analys av konstruktionsstål", version 1.0, Trafikverket.

Trafikverket (2021) KRAV TRVINFRA-00228 Bro och broliknande konstruktion, Brounderhåll, version 3.0. Trafikverket

Ulvsgärd, S, (2021) Västerbron Södermalm, Långholmen, Kungsholmen – Kulturhistorisk Förundersökning, Stadsmuseet

Bridge Maintenance, Safety, Management, Digitalization and Sustainability – Jensen, Frangopol & Schmidt (eds)
© 2024 The Author(s), ISBN 978-1-032-77040-6
Open Access: www.taylorfrancis.com, CC BY-NC-ND 4.0 license

Enhancing Dybbølsbro Bridge – Refurbishment and expansion without new substructure

L. Thormann, C. Pedersen & J. Fogh Svensson
Ramboll Denmark A/S, Copenhagen, Denmark

ABSTRACT: The refurbishment and expansion of the Dybbølsbro Bridge in Copenhagen presents a unique engineering challenge. This contribution details the process of suspending a new 2000 m^2 bridge between two existing bridges, all while maintaining traffic on the existing bridges, and executing work over twelve operational railway tracks. The innovative expansion uses a deck superstructure that requires no additional substructure. Achieved by strengthening and utilizing existing bridges, the new bridge consists of 55 independent steel elements. By reusing the existing bridges for the new superstructure and avoiding construction of a new substructure, we minimized the material consumption, consequently reducing the project's environmental footprint and reduced the disturbance of the rail traffic, all contributing to a more sustainable project. The expansion of the bridge epitomizes the future of sustainable urban infrastructure, demonstrating that conscientious planning and innovative design can bring ambitious infrastructure projects to fruition, enhancing city landscapes and serving communities better.

1 INTRODUCTION

Dybbølsbro, a pivotal structure in Copenhagen's urban landscape, has undergone a significant transformation. Originally erected around 1900 as a steel truss bridge, initially served as a vital connection over the Copenhagen Freight Yard to Kalvebod Brygge. The bridge was replaced by pedestrian and cycle path bridge in the mid 1980's. In mid-1990's a parallel road bridge was erected creating a ~10 m wide gap between the two 190 m long bridges. Both existing bridges were push launched and constructed as post tensioned 5 span concrete bridges.

This paper presents an in-depth exploration of the recent expansion of Dybbølsbro, a project that seamlessly integrates contemporary engineering excellence with the bridge's storied past. The expansion initiative is a testament to Copenhagen's commitment to sustainable urban development and the enhancement of public infrastructure. The undertaking addressed the need for increased capacity and improved safety for pedestrians and cyclists.

The Dybbølsbro expansion project, characterized by its innovative approach represents a paradigm shift in urban bridge expansion. Challenges, such as the integration of new structures with the existing framework and minimizing disruption to the city life, were met with advanced engineering solutions. The project's approach to utilizing the existing concrete structures, coupled with the implementation of state-of-the-art digital tools, sets a new benchmark in bridge engineering and urban infrastructure development.

As urban spaces evolve, the demand for infrastructure that can adapt and accommodate growing needs becomes more important. The Dybbølsbro project emerges as a beacon of such adaptability, showcasing how existing structures can be repurposed to serve new requirements.

By examining the Dybbølsbro expansion project, this paper aims to provide valuable insights into the complexities and opportunities of modernizing existing infrastructure.

DOI: 10.1201/9781003483755-385

2 PROJECT OVERVIEW AND TECHNICAL APPROACH

The bridges are situated in a high-traffic zone, accommodating a steady stream of pedestrians, cyclists, and vehicles. They span across all railway tracks that feed into Copenhagen's central station. It was crucial that throughout the construction process, these varied modes of transport could continue to operate, ensuring minimal disruption during construction.

2.1 *Existing conditions*

Dybbølsbro, comprised of continuous spans in post-tensioned concrete box girders, approx. 40 m in span and totaling approx. 190 meters in length, rests on pile foundations embedded in old seabed. The existing bridges, launched from the eastern end, had surplus load-bearing capacities due to their robust prestressing and erection scheme. This structural reserve played a crucial role in the expansion project, allowing for the resistance of additional loading.

The two existing bridges have a gap of approx. 10.2 m between the edge beams, 14.4 m between the faces of the box girders and approx. 19 m between c/c of substructure which is also sketched in Figure 1.

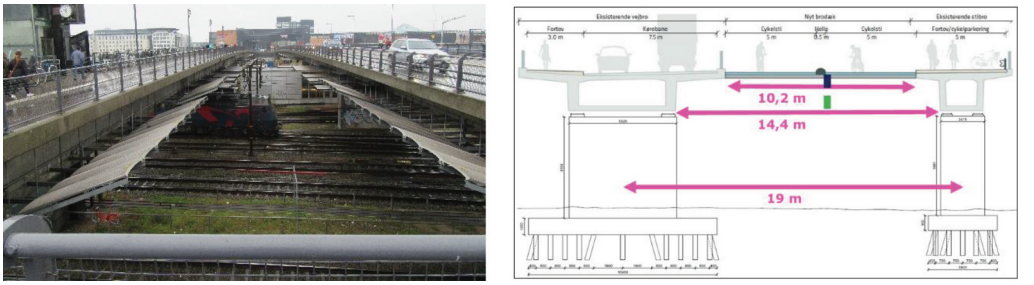


Figure 1. Photo of existing bridges and underpassing railway tracks (left) and main dimensions between bridges (right).

2.2 *External project interfaces and neighboring projects*

The bridges are located at an area giving a lot of different external interfaces which include:

- Underpassing railway track leading into Copenhagen central station
- Catenary system for railway tracks
- A train station having access from the pedestrian bridge
- High number of cyclists and pedestrians crossing the bridge
- A nearby area for long distance busses which had most busses cross the road bridge
- Road traffic on the bridge
- Neighboring projects including plans for erecting twin high-rise student accommodation houses and a large warehouse.

All these interfaces had to be considered and handled during design and under construction. Several of these interfaces heavily influenced the final design of the bridge, in particular the underpassing railway.

2.3 *Considered concepts*

Suspending a new steel bridge between the existing concrete structures required a comprehensive understanding of the existing bridges' load-bearing capabilities and the intricacies involved in integrating a new structure.

Critical to the project was the analysis of static systems and the effective distribution of loads in relation to the existing load carrying capacities. The existing bridges, being post-tensioned continuous spans on pile foundations, offered a robust platform for expansion. Leveraging the existing concrete structures was a cornerstone of this project. The existing bridges were originally designed with surplus load-bearing capacities since both bridges were

push-launched during construction. The design philosophy focused on utilizing these reserves to support the additional weight of the new bridge.

The strategy for integrating a new steel bridge involved suspending it between the existing structures. This approach was chosen for its minimal impact on the existing bridges. The suspension system was to be engineered to ensure stability and safety, with careful attention to the load distribution to avoid overloading any part of the existing structures.

The bridge widening concept needed to consider all the external boundaries and limitations while still resulting in an effective expansion of the available bridge deck area. Initially four different alternatives were considered. These four include:

- New steel deck suspended between wings on existing bridge decks (top left in Figure 2)
- New steel deck suspended between boxes, i.e. 14.4 m spans (top right in Figure 2)
- Beams between existing columns, deck spanning longitudinally between beams, i.e. 14.4 m or 19 m spans to avoid eccentric load on substructure (bottom left in Figure 2)
- New independent parallel bridge (bottom right in Figure 2)

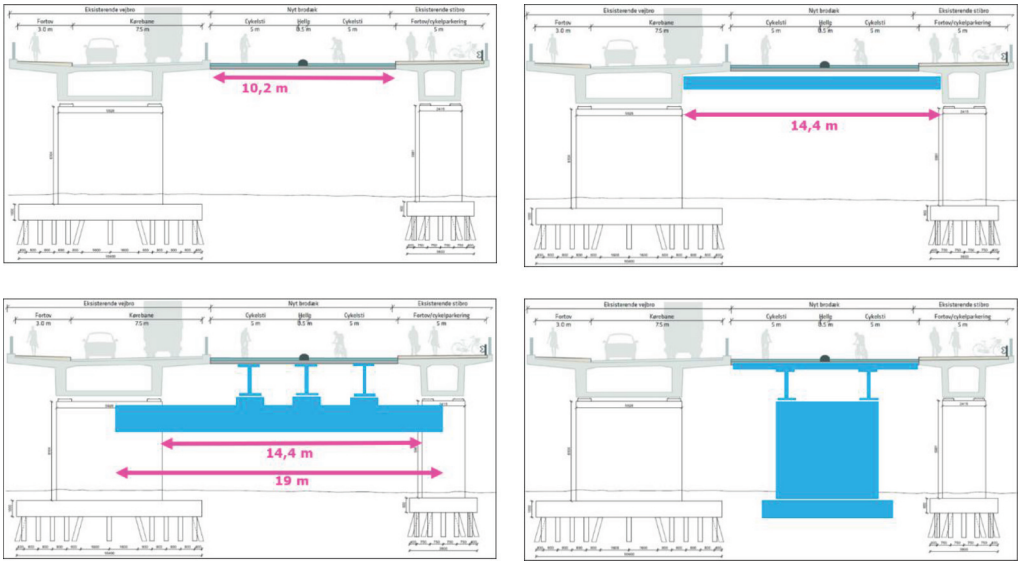


Figure 2. The four concepts initially considered.

All four alternatives had their pros and cons. Alternative 1 with deck suspended between wings on existing bridges was chosen due to the advantages of low self-weight, span width of new structure minimized and simple installation of bridge elements. This alternative further had the disadvantage of high loading on bridge wings and high eccentric loading of existing box girders and substructures. These negative effects were reduced through clever detailing of the permanent supports for the steel deck and implementation of structural parts to reduce the eccentric loading on the substructure. This is further described in the following sections.

2.4 *Design philosophy and structural system integration of implemented concept*

The core challenge of the implemented alternative was to increase the bridge area by 70% without constructing new supports. The design philosophy revolved around leveraging the existing structures' strengths, particularly their load-bearing reserves. The chosen approach was to suspend a new steel bridge between the existing concrete bridges, a method that presented both structural and construction advantages. This approach required detailed planning and precision to ensure compatibility with the existing structures.

Analyzing the static systems and load distribution capabilities of the existing structures was essential. The expansion involved the careful calculation of loads and the distribution of

additional weight between the existing structures. The static system for the new steel bridge was designed to minimize eccentric loading on the existing bridges. The engineering team explored multiple alternatives, eventually selecting a system that optimally distributed the loads while ensuring structural integrity and safety.

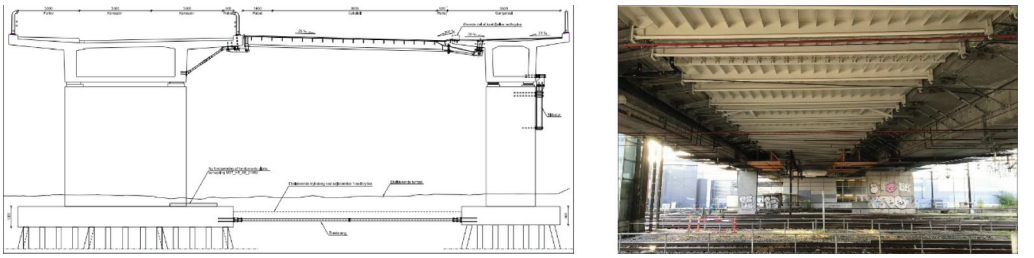


Figure 3. Cross section (left) and photo (right) of bridge after installation of suspended steel deck.

Identification of weaknesses of the existing bridges were essential. Some weaknesses required strengthening of the bridges while others were not possible to strengthen, thus required alternative ways of resisting external forces.

The most significant change due to a weakness was the change in the overall statical system of the three combined bridges. Suspending a deck between the existing bridges results in torsion in the superstructure leading to transverse bending in the substructure. This was, in particular, critical for the pedestrian bridge. The transverse bending was instead resisted by horizontally paired forces where the new steel deck was used as a compression member while new tension members connected the pile caps of the existing concrete bridges.

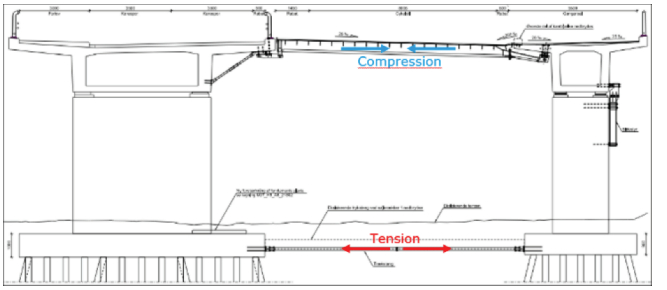


Figure 4. Compression and tension members between existing bridges resists the transverse bending introduced by the eccentric loading created by the suspended steel deck.

3 TECHNICAL CHALLENGES AND SOLUTIONS

The project encountered several technical challenges, notably the need to work above active railway tracks and maintain uninterrupted traffic flow. The solutions included construction of the bridge in elements that could be installed during track possessions of typically 2-3 tracks during nighttime, which allowed for efficient and safe work without significant disruption of the traffic above and below the bridge. This section elaborates on some of the challenges handled in order to meet the requirements to maintain road, pedestrian and cycle traffic and train operation during construction.

3.1 *Safety measures over operational railway tracks*

Twelve railway tracks pass under the bridge. All tracks have very high traffic intensities. Major closures over longer periods were not an option. Track possessions of typically 2-3 tracks during a night were allowed. This called for phased construction by constructing the bridge of

individual elements. Carrying out the full construction of the bridge necessitated approx. 60 instances of track possessions distributed over the approx. 9 months construction period.

Working above active railway tracks presented safety challenges. The steel elements were attached to the bottom of the existing superstructure wings. It was therefore of high importance that unhindered access to the bottom face of the bridges was given. The access was provided by temporary platforms attached to the webs of the box girders. These were installed in segments during nightly track possessions. The platforms included shielding towards the underpassing railway tracks making it possible to work without any disturbance from the railway traffic.



Figure 5. Access platforms below the bridge superstructures.

3.2 *Effects on existing bridges*

Suspending the steel deck directly between the two inner edge beams would introduce torsion into the bridge decks and result in transverse bending in the substructures. This was not a problem for the road bridge but turned out to be critical for the pedestrian bridge. The issue on the pedestrian bridge was solved by connecting the deck closer to the webs of the superstructure as shown in Figure 6.

To ensure sufficient bearing capacity of the wing on the road bridge superstructure, compression struts were introduced as shown in Figure 6. These ensured that the allowable vehicle loading on the bridge could remain the same after the widening. Combined, the 2 solutions are a clear example on how different solutions can be required to meet the different requirements from the existing structures.

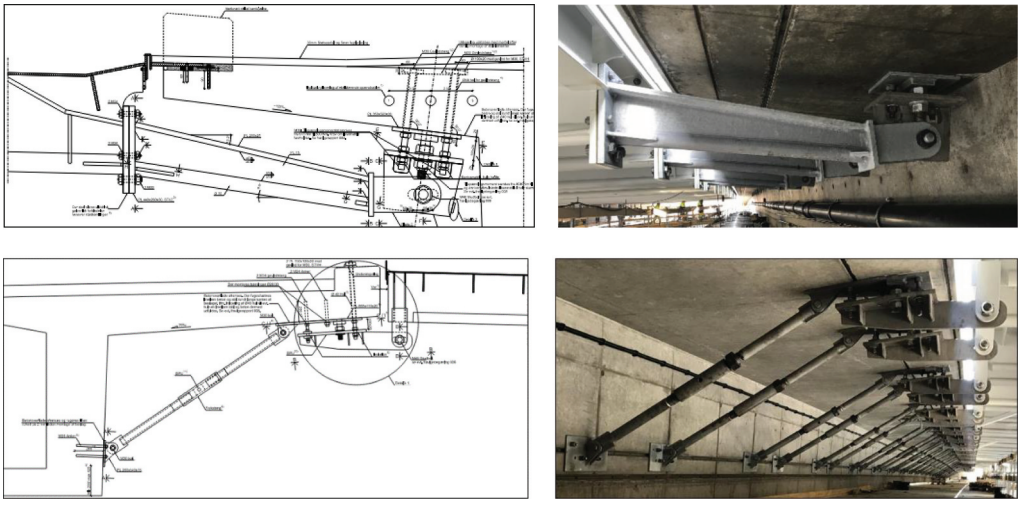


Figure 6. Upper left and right: Suspension of steel deck on pedestrian bridge. Lower left and right: Compression struts below wing on road bridge.

3.3 *Element installation and assembly*

Typically, three elements were installed during a night. Effective installation was required especially for elements above railway tracks since reopening of the railway traffic after a nightly track possession was mandatory. Lifting brackets were developed serving a dual purpose meaning they could be used for lifting the elements into position while also acting as temporary supports for the elements until the permanent supports were installed. After the elements had been placed on the temporary supports it was possible to move the elements into their final position before installation of permanent supports.

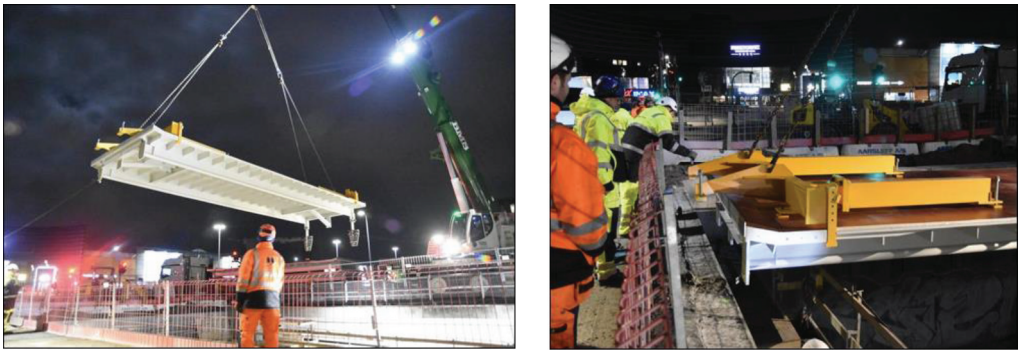


Figure 7. Lifting brackets also serve the purpose as temporary element support.

The steel elements required joining to guarantee the durability of the surfacing and the cyclists' comfort. The temporary platforms below the existing bridges gave access to the existing bridges' wings and approximately 20% of the area of the steel elements. However, as there was no access to the remaining roughly 80% of the steel elements' underside, a bolted connection assembled from above was designed. This connection's primary function was to assure that neighboring elements would deflect simultaneously. The plate in the bolt connection had oversized holes to take up any tolerances during installation. The bolt connection is shown in Figure 8.



Figure 8. Connecting the steel elements from above on the central part of the spans.

3.4 *Permanent supports for steel elements*

The two existing concrete bridges were in theory parallel and shared the same longitudinal profile. However, there were small deviations due to construction tolerances etc. which meant the need for tolerances for installation of the new steel elements. The majority of the tolerances were handled in the permanent support brackets. These were designed to take up tolerances of ±30 mm in transverse and longitudinal directions of the bridge and ±20 mm vertically. The ability to take up tolerances meant that installation of the new steel deck could be carried out without any requirements for demolition and adaption of old/new structure.



Figure 9. Permanent support brackets with capacity for taking up tolerances. Bracket on pedestrian bridge (left) and road bridge (right).

In conclusion, the technical approach to the Dybbølsbro expansion project exemplifies engineering ingenuity. The careful integration of a new steel structure with the existing bridges and the solution-oriented approach to challenges contributed to the project's success.

4 SUSTAINABILITY AND ENVIRONMENTAL CONSIDERATIONS

The expansion of Dybbølsbro not only focused on engineering innovation but also heavily emphasized sustainability. This approach reflects Copenhagen's broader commitment to sustainable urban development.

One of the project's primary sustainability strategies was the reuse of the existing bridge structures. This approach significantly reduced the material consumption typically associated with bridge expansion projects. By leveraging the existing concrete bridges' load-bearing reserves, the need for new substructures was eliminated, thereby minimizing the use of new raw materials and reducing the project's carbon footprint.

Widening the bridge deck without construction of a new substructure is also sustainable in the sense that it significantly reduced the disturbance of the underpassing railway tracks and reduced the economic range for the project.

The project's sustainability considerations extended beyond the construction phase. The new bridge was designed with sustainability in mind, ensuring that future maintenance would be efficient and environmentally friendly. Future surface treatment of the steel deck bottom face towards the railway tracks will have a major impact on the underpassing railway. Therefore, the steel elements were given the best possible surface treatment which included a duplex painting system C5VH. This included spray metallization and paint.

In conclusion, the Dybbølsbro expansion project stands as an example of sustainable engineering, balancing the demands of modern infrastructure development with environmental stewardship.

5 DIGITAL TOOLS AND TECHNOLOGY

The Dybbølsbro expansion project represents a forward-thinking approach to bridge engineering, leveraging advanced digital tools and technologies, all playing an important role in ensuring the project's precision, efficiency and success.

Scanning for Precise Expansion One of the technological highlights was the use of 3D Light Detection and Ranging (LiDAR) scanning. This tool provided three-dimensional data of the existing bridge structures, crucial for the design and integration of the new steel bridge. The LiDAR scans offered detailed insights into the geometry of the existing structures, enabling engineers to make informed decisions about the design and placement of the new components. The information made sure that tolerances required in the project in order for the new deck to be installed on the existing bridges could be determined. This ensured that installation of the elements and permanent supports could be carried out without any major challenges.

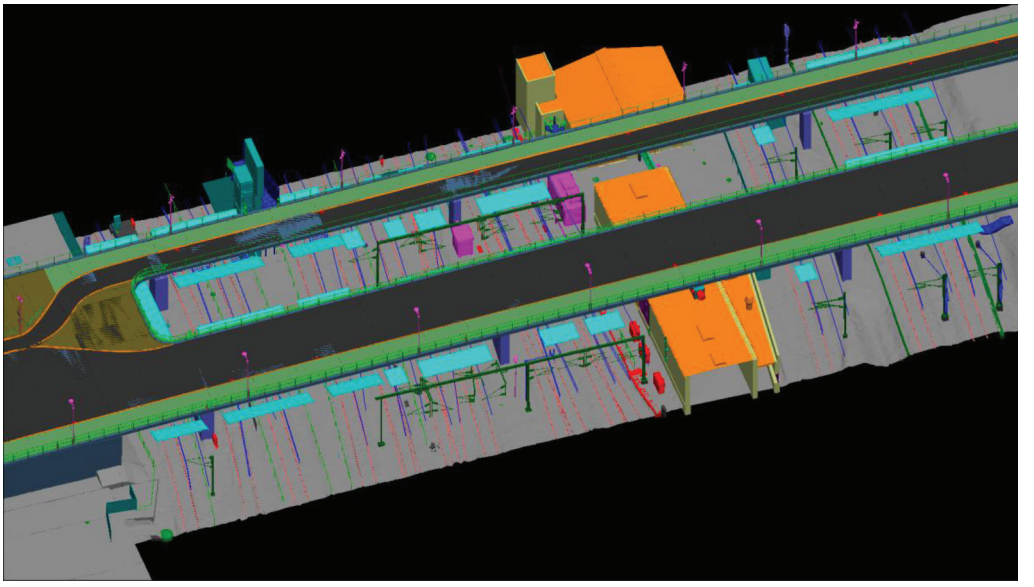


Figure 10. 3D-model created from 3D-LiDAR scanning of project area before installation of the new steel deck. Approximately half of the bridge length is shown.

6 RESULTS AND CONCLUSION

The Dybbølsbro expansion serves as a model for urban infrastructure projects worldwide. It demonstrates how engineering ingenuity, combined with a focus on sustainability and community needs, can lead to significant urban improvements. The project's ability to balance existing structure preservation with modern infrastructure needs is particularly noteworthy.

The project successfully expanded the bridge without constructing a new substructure, an innovative feat that required meticulous planning and execution. A notable accomplishment of the expansion is the creation of Denmark's widest bicycle track. The expanded bicycle track offers ample space for cyclists and pedestrians, significantly improving safety and encouraging more people to opt for cycling over motorized transport.

The expansion project placed a strong emphasis on sustainability, evident in the reuse of existing structures. This approach not only reduced the environmental impact but also preserved the existing structures at Dybbølsbro.

SS42: Community resilience and decision-support systems

Organizers: N. Makhoul, R. Kromanis, J. van de Lindt, A.R. Barbosa & F. Schmidt


Taylor & Francis
Taylor & Francis Group
http://taylorandfrancis.com

Bridge Maintenance, Safety, Management, Digitalization and Sustainability – Jensen, Frangopol & Schmidt (eds)
© 2024 The Author(s), ISBN 978-1-032-77040-6
Open Access: www.taylorfrancis.com, CC BY-NC-ND 4.0 license

Dynamic traffic simulation for transportation system resilience assessment

X. Wang & P. Bocchini
Civil and Environmental Engineering Department, Lehigh University, Bethlehem, PA, USA

P. Venkitasubramaniam
Electrical and Computer Engineering Department, Lehigh University, Bethlehem, PA, USA

S. Xie
Thrust of Artificial Intelligence, Hong Kong University of Science and Technology, Guangzhou, China

ABSTRACT: Quality resilience assessment for transportation systems relies on realistic representations of the network and traffic demand, and credible network traffic modeling. This paper presents a framework that incorporates time-dependent functionality analysis of disrupted networks and dynamic traffic simulations. Focusing on bridge disruptions, two distinct types of events are considered, earthquake and civil protest. The mesoscopic traffic flow model and the dynamic traffic assignment approach (as opposed to the static assignment approach) are utilized to realistically represent traffic dynamics. The presented results show that the dynamic traffic simulations provide traffic measures at a fine-grained spatiotemporal level which are valuable for post-event performance assessment. Traffic congestion effects are identified in earthquake-disrupted networks. Despite the limited disruption scope, protests on bridges can have significant impact on local travel cost. These findings promote using dynamic traffic modeling for transportation network analysis, highlighting the usefulness of more reliable and granular metrics for decision-making.

1 INTRODUCTION

In the context of community and transportation system resilience assessment, bridges manifest their significance due to their vital role in network connectivity. The efforts required for quality resilience quantification include but are not limited to reliable modeling for hazard and damage analysis, realistic representation of the network and traffic demand, credible traffic simulation as well as calculation of informative performance metrics. The Resilience and Disaster Recovery (RDR) Tool Suite is a state-of-the-art tool for transportation planning decision-making offered to U.S. transportation agencies (U.S. Department of Transportation, 2023). The RDR Tool Suite supports the consideration of hazard-related disruptions and various recovery patterns while at the core it utilizes the user equilibrium-based static traffic modeling. However, it has been recognized that such static traffic assignment approach fails to reflect the time-varying network traffic condition and thus may yield unreliable and even misleading traffic measures (Chiu et al., 2011). While dynamic traffic simulations have reached popularity in system performance assessment under post-disaster emergency evacuation scenarios (Pel et al., 2012), the potential and value to incorporate them into the long-term resilience planning remain to be explored. Moreover, bridges are subject to threats from both human-made and natural hazard events. Depending on the nature and intensity of the events, the number of bridges out of service and the type of actions required to reopen them change.

DOI: 10.1201/9781003483755-386

A comprehensive community resilience assessment should consider the various potential disruptions for which different performance quantification methods and metrics may be used to support decision-making (Rokneddin et al., 2013; Blagojević et al., 2022). In this context, the impact of human-made bridge disruptions (such as protest and terrorism) is less studied compared to that of natural hazard-caused bridge disruptions (such as flooding and earthquake). Indeed, a recent report commissioned by the U.S. Congress recommends that a resilience assessment and a resilience-based cost-benefit analysis should be performed to prioritize investments accessing federal funds (Schofer et al., 2021).

To address the above issues, this study first formally presents a framework that integrates the functionality analysis of disrupted networks and the dynamic traffic modeling. In particular, a case study for a real-world large transportation network is provided, where the bridge-related disruptions from earthquake events and protest events are considered separately. The strengths of dynamic traffic simulations are highlighted by various traffic measures.

2 METHODOLOGY

This study proposes a probabilistic framework for transportation resilience assessment that incorporates the time-dependent functionality analysis of disrupted transportation networks and the analysis of traffic dynamics. As shown in Figure 1, three modules — the Hazard (or Disruptive Event) Simulation module, the Damage and Functionality Assessment module, and the Recovery Analysis module — determine the disrupted state and functionality of the transportation network at any investigated time (t). Taking as input the time-dependent transportation network, the traffic analysis consists of two other modules: the Traffic Demand module, and the Dynamic Traffic Simulation module. Uncertainties are considered in all five modules and propagated throughout the framework. More details on the approaches and tools used by all modules are provided in the subsections that follow.

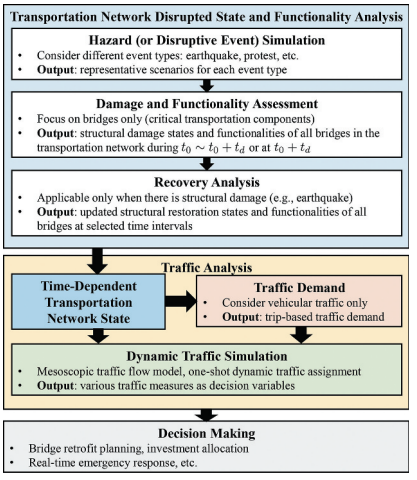


Figure 1. Framework for transportation resilience assessment and resilience-based decision making.

2.1 *Hazard simulation*

Table 1 compares the characteristics of the two distinct types of events with a focus on bridge disruptions in the transportation network. Despite the seemingly lesser extent, human-made events like protests are more frequent and can cause severe traffic disruptions. Therefore, for a comprehensive assessment of the system and community resilience, both types of events should be considered.

Focusing on bridges only, this study considers two types of disruptive events: earthquakes and civil protests. In the Hazard Simulation module, a portfolio of representative and realistic scenarios should be created for each considered event type. For this purpose, the well-established earthquake hazard model available in Hazus can be utilized (FEMA, 2022). In contrast, there is a lack of hazard models for human-made events. Concerning the disruptive effect on traffic, a protest event can be captured by several key descriptors, including the location, start time (t_0), duration (t_d), etc. Hence, a set of protest scenarios can be generated with combinations of well-defined descriptor values, for which local expertise shall be consulted.

Table 1. Different characteristic of disruptive events (earthquake and protest as illustrative examples).

Event type	Frequency	Structural damage	Functional loss	Spatial extent	Temporal extent
Earthquake	Relatively rare	Yes	Yes	Relatively large (multiple bridges)	Instantaneous ($t_d \approx 0$) but entails recovery process (Δt)
Protest	Relatively frequent	No	Yes	Relatively small (very few bridges)	Lasting (t_d) but with immediate recovery ($\Delta t \approx 0$)

2.2 *Bridge damage and functionality assessment*

The second module performs damage and functionality assessment for bridges during and after the event. Damage assessment is done from the structural perspective and is based on physical damages, such as cracking of columns. On the other hand, the functionality assessment is done from an operational perspective and is based on the functional loss, such as closure or reduced traffic flow capacity of the bridge. As shown in Table 1, earthquake events can cause structural damage to bridges with subsequent functional loss, whereas protests can shut down traffic on bridges even if there is no structural damage. This study adopts fragility curves available in Hazus for seismic damage assessment of bridges (FEMA, 2022). Figure 2a shows example fragility curves for a class of highway bridges. For an earthquake scenario, the damage state (DS) probabilities for each bridge in the transportation network can be obtained. For the other components in the transportation system (e.g. roadways and tunnels), a similar analysis can be performed.

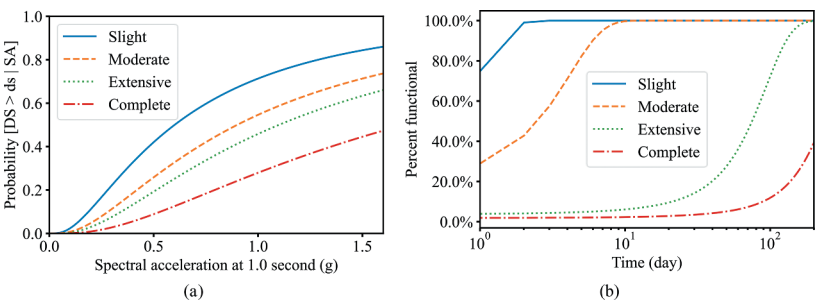


Figure 2. (a) Fragility curves for highway bridges (reproduced from Hazus); (b) Restoration curves for highway bridges (reproduced from Hazus).

The functionality assessment for seismically damaged bridges are also performed utilizing Hazus. The functionality result given by Hazus, expressed as the percentage of the full functionality, is the expected functionality ($\bar{Q}(t)$) which can be computed by:

$$\bar{Q}(t) = \sum_{i=1}^{5} P(DS_i) \cdot Q_{DS_i}(t) \tag{1}$$

where i indicates one of the five possible initial damage states, i.e. no damage, slight damage, moderate damage, extensive damage, and complete damage;$P(DS_i)$ is the probability of the bridge being in the initial damage state i; and $Q_{DS_i}(t)$ is the time-varying functionality percentage corresponding to the initial damage state i (see Figure 2b). Hazus adopts deterministic functionality recovery models, but more sophisticated, probabilistic models can be easily integrated in this framework (Decò et al., 2013).

This expected functionality can be used to compute the reduced traffic flow capacity which can then be input for the disrupted transportation network analysis. More details on the damage and functionality analysis in Hazus can be found here (Rojahn et al., 1985). For protest events, damage assessment is not needed with the assumption that no structural damage is involved. Based on the fact that protests typically result in complete bridge closure, it is assumed that the bridge is non-functional (i.e. traffic flow capacity becomes zero) during the protest event.

2.3 *Bridge recovery analysis*

Recovery analysis, sitting in the core of resilience assessment, quantifies the restoration performance of the system and community following disruptive events. Depending on the nature and intensities of the events, the restoration activities required to reopen bridges vary. For post-earthquake recovery analysis of bridges, restoration curves are used herein. As shown in Figure 2b, each restoration curve describes the functionality change of the bridge as a function of time ($t \geq t_0 + t_d$), given an initial damage state after the earthquake (FEMA, 2022). Despite the continuous form of the restoration curves, in practice recovery analysis is often performed at selected time intervals where Δt can be 1 day, 3 days, etc. As for protest events, given that no physical damage is caused, it is assumed that the bridge will regain its full functionality immediately after the protest is dismissed (i.e. $\Delta t = 0$).

With the abovementioned three modules, the time-dependent physical state and functionality of the transportation network (i.e. supply) can be determined. While the study of any disruptive event can be generally divided into 3 stages, i.e. pre-event ($t < t_0$), during event ($t_0 \leq t < t_0 + t_d$), and post-event ($t \geq t_0 + t_d$), the evolution of the network functionality can be relevant only in some of these phases, depending on the type of extreme event considered. For earthquake events that are instantaneous but often cause physical damages, it is more meaningful to discuss the time-dependency of the network during the post-earthquake recovery stage. As for protests that usually last for hours but exhibit immediate recovery, the time dependency is more relevant during the event.

2.4 *Traffic demand*

Another input required for traffic simulation is the traffic demand, which is defined as trips and conventionally represented by Origin (O) - Destination (D) matrices for certain time periods. The normal (before event) traffic demand is traditionally generated based on household travel surveys and is generally available from transportation authorities. The during-event and post-event traffic demand, however, can be drastically different due to the disrupted physical network and the purposes of trips (such as emergency evacuation) (Pel et al., 2012). This study aims to investigate the effect of bridge-related disruptions on the performance of transportation systems in support of long-term resilience planning decisions. Therefore, the emergency evacuation traffic analysis is beyond the scope of this work. Specifically, the normal traffic demand corresponding to the morning rush hours is used herein. Despite the disrupted networks, this traffic demand is assumed to remain unchanged and is used for post-earthquake traffic analysis at the selected time intervals. This approach does not aim at capturing the actual traffic flows during the emergency response. Instead, this approach allows to determine the network performance "normalized" to standard traffic demands. For protest events, the same normal traffic demand is also used for the disrupted network.

2.5 *Traffic simulation*

The Traffic Simulation module performs network system analysis considering the interdependence of component functionality (bridges, roadways) and overall system functionality. For this

purpose, microscopic simulation software such as the Simulation of Urban Mobility (SUMO) can be used while other options are also available (Alvarez Lopez et al., 2018). In particular, a spatial-queue-based mesoscopic traffic flow model is recommended over a microscopic traffic flow model because of its efficiency for large network analysis and relatively detailed outputs. To more realistically model the time-varying traffic flow dynamics, the one-shot (non-iterative) dynamic traffic assignment approach is recommended. Compared to the static traffic assignment, dynamic network analysis not only determines the travel time and cost measures more credibly, but also provides fine-grained insights into the spatiotemporal change of traffic that are useful for decision making (Chiu et al., 2011).

3 CASE STUDY

The transportation network in the San Francisco (SFO) Bay Area is selected for the case study, where both the earthquake and protest disruptions are investigated. Figure 3 shows the SFO network which has a total length of 564,340 lane-km (Ambühl et al., 2023). The Santa Clara county is chosen as the study region for earthquake analysis and it covers mostly the bottom part of the network. In addition, this case study focuses on the highway transportation system and thus only highway bridge damage is considered in the analysis. The locations of the 962 highway bridges within the Santa Clara county are also shown in Figure 3.

Using SUMO for traffic simulations, this study considers only vehicular traffic while other transport modes (e.g. transit, pedestrians) are ignored. The trip-based traffic demand is defined for the entire SFO network using available data (Ambühl et al., 2023). For earthquake hazard events, the traffic simulation starts with a post-earthquake disrupted network (at $t = t_0 + t_d + \Delta t$) due to bridge damages before loading any vehicle onto the network. For protest events, the traffic simulation starts with an undisrupted network (at $t < t_0$) and bridge disruptions are applied beginning from t_0 while there is already traffic on the network. Note that the Traffic Control Interface (TraCI) provided by SUMO is used to achieve the real-time disruptions on a running traffic simulation. All traffic analyses are performed for the extended morning rush hours (6:00 AM–10:00 AM). Periodic rerouting is used to simulate vehicles adapting to jams or other changes in the network. Specifically, every 6 minutes, 50% of the vehicles will update their shortest-path routes. Moreover, 325 induction loop detectors (sensors) are simulated within the network. The simulation time step length is 1 second while the results are aggregated every 5 minutes. Results and discussions for the respective events are provided in the sub-sections below.

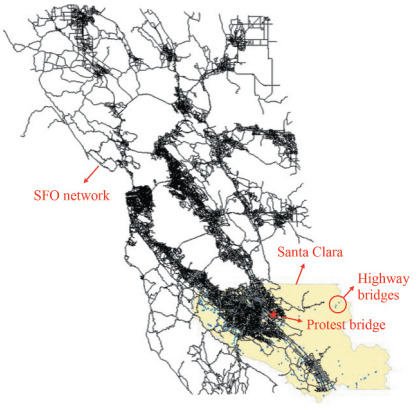


Figure 3. The SFO transportation network in relation to the Santa Clara county.

3.1 *Earthquake event*

For illustration purpose, one earthquake scenario (return period = 100 years, magnitude = 7.0) is analyzed for the highway transportation system in Santa Clara. The functionality

distribution of all highway bridges at selected time intervals is presented in Figure 4a. As expected, Day 1 bears the worst situation with the lowest median functionality (92.20%) and the largest dispersion (8.32%). The functionality of damaged bridges is gradually restored over time, as observed from the increasing median and decreasing dispersion. Although the functionality results by Hazus are in continuous form, for simplicity, this study adopts a binary classification for bridge service status. A bridge is classified as out-of-service (i.e. closed) if its expected functionality is smaller than 75% or as in-service (i.e. open) otherwise:

$$S(t) = \begin{cases} 0 & if\ \overline{Q}(t) < 75\% \\ 1 & if\ \overline{Q}(t) \geq 75\% \end{cases} \tag{2}$$

where $S(t)$ denotes the in-/out-of-service bridge status actually used in the network. As a result, there are 39, 23, 15, 12, 11, and 1 bridge needing to be closed at the six time intervals respectively, which is depicted by different colors in Figure 4b. The post-earthquake disrupted networks are created by making the corresponding edges inaccessible. Traffic analyses are performed for Δt = 1, 3, 7, 14 days only, since the network states at Day 30 and Day 90 are only one bridge different from that at Day 14 and pre-earthquake respectively.

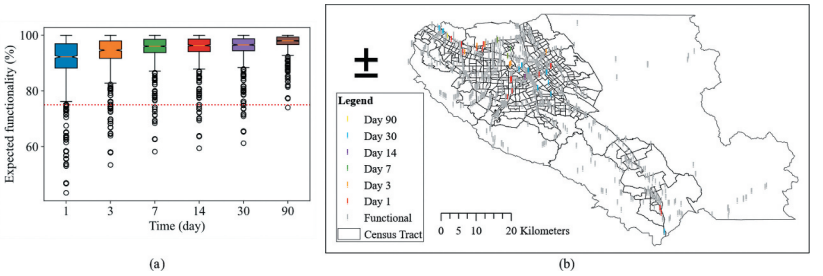


Figure 4. Bridge functionality in the network: (a) boxplots at selected time intervals; (b) map of closed bridges.

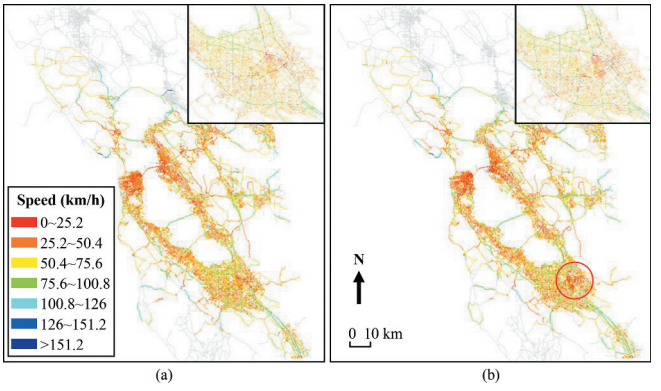


Figure 5. Snapshots of network speeds at 8:00 AM: (a) non-disrupted network; (b) disrupted network (1 day after earthquake).

The trip duration is an important traffic measure for evaluating the performance of the transportation system. With the same traffic demand, the durations of all trips within the morning rush hours are obtained for the abovementioned different network states. It is found that the disruptions due to closed bridges slightly increase the trip durations systemwide. For example, the first quantile, median, and the third quantile of trip durations for pre-event are 10.3 minutes, 18.8 minutes, and 35.9 minutes, whereas those for Day 1 are 10.4 minutes, 19.3 minutes, and 36.9 minutes. As the bridges are recovered, the performance of the network

improves with trip durations at Day 14 almost reaching the pre-event level. The disruption impact on trip duration appears small (even at Day 1), which can be attributed to several factors. For instance, the disruptions of the physical SFO network are limited to the small portion within Santa Clara (see Figure 3), so the disruption impact may be diluted by the overall traffic on the entire network.

One exclusive benefit of the dynamic traffic simulation is that it offers insights into the spatio-temporal evolution of the traffic on the network. Figure 5a, b present the snapshots of the network speeds at 8:00 AM (2 hours after the traffic analysis starts) with zoomed-in portions at the top right corners. Compared to the non-disrupted network, the disrupted network clearly indicates new congestion near where the highways bridges are closed (see the red circle in Figure 5b). Such traffic congestion effects, captured by dynamic traffic simulations at a fine-grained temporal level, are valuable for evaluating the bridge disruption impact with greater granularity.

3.2 *Protest event*

For simplicity, only one hypothetical protest scenario is considered herein. The protest is assumed to happen during 8:00 AM–9:00 AM on the bridge (37°19′55.5″N, 121°51′53.3″W) which has the highest daily traffic (238,000 vehicles/day) among all 962 considered highway bridges (FEMA, 2022). The corresponding two edges (in opposing directions) are part of the Sinclair Freeway associated with the Interstate 280 (I-280) near downtown San Jose (see Figure 3). TraCI is used to achieve the real-time interactions with the simulation – closing edges at 8:00 AM and reopening them at 9:00 AM.

Figure 6a shows the disruptive impact of the protest on trip duration, where the trips are selected such that the departure time is during 8:00 AM–9:00 AM and the departure or arrival edge is close to the disrupted edges. Although only one bridge is involved, it is shown that the disruption leads to noticeable increase in travel cost with the median trip duration escalating from 26 to 32 minutes. Given the special attributes of protest events (i.e. local disruption, short duration, immediate recovery), sensor-measured speed — available by dynamic traffic simulation as well as with traffic sensors in reality — may be useful for evaluating the recovery ability of the system and the community. Figure 6b shows the speed time histories at five simulated sensors that are closely related to the inaccessible edges. As expected, following the start of the event, the speeds drop to zero at all five sensors because vehicles are routed away from using the associated edges. Note that sensors 1 and 4 are located further to the closed edges than the other sensors, which explains the time lag of speed drop. Traffic flow is restored immediately after the disruption ends, as observed from Figure 6b. It is worth mentioning that such real-time traffic measures offered by dynamic traffic simulation can be useful for emergency response, such as for emergency vehicle routing.

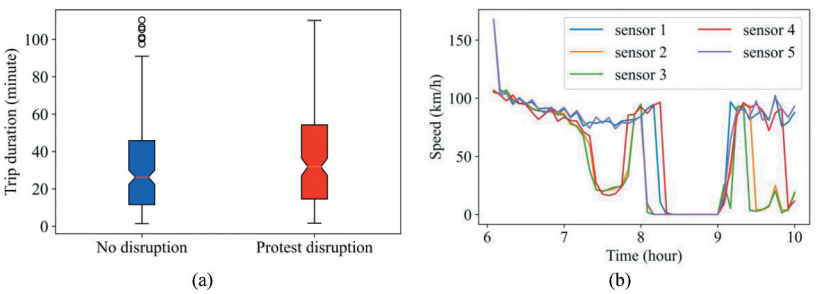


Figure 6. Protest disruption impact: (a) comparison of trip durations; (b) speed time histories (5-minute aggregate).

4 CONCLUSIONS

This paper presented a framework for transportation system resilience assessment that integrates functionality analysis of disrupted networks and dynamic traffic analysis. Two distinct types of

events — earthquake and protest representative of natural hazard events and human-made events respectively — were investigated. The dynamic traffic simulation can provide more insights into the system performance with greater granularity than static simulation, as shown in the case study. For example, the spatiotemporal speed patterns within the network were used to identify disruption-introduced bottlenecks and congestion. Bridge disruption caused by protests (or other events alike) can have important influence on the local traffic, as shown by the noticeable increase of trip durations. Despite the short duration and immediate recovery, such disruptions should not be ignored, because they can have significant impact on emergency response.

Future work can include exploring the applicability of the framework to other types of events, such as floods and fires. Furthermore, the results should benefit from using more representative scenarios, as well as exploring the traffic stochasticity by using different random seeds in traffic simulation.

ACKNOWLEDGEMENTS

This work is part of the activities of "Catastrophe Modeling Center" at Lehigh University (www.catmodeling.org). The support from Lehigh University through two Research Futures grants and one Accelerator Grant is gratefully acknowledged. The views expressed in the paper are solely those of the authors and do not represent the official position of the funding agency.

REFERENCES

Alvarez Lopez, P., Behrisch, M., Bieker-Walz, L., Erdmann, J., Flötteröd, Y.-P., Hilbrich, R., Lücken, L., Rummel, J., Wagner, P., Wießner, E., 2018. Microscopic Traffic Simulation using SUMO, in: 2019 IEEE Intelligent Transportation Systems Conference (ITSC). Presented at the The 21st IEEE International Conference on Intelligent Transportation Systems, IEEE, Maui, USA, pp. 2575–2582. https://doi.org/10.1109/ITSC.2018.8569938

Ambühl, L., Menendez, M., González, M.C., 2023. Understanding congestion propagation by combining percolation theory with the macroscopic fundamental diagram. Commun Phys 6, 26. https://doi.org/10.1038/s42005-023-01144-w

Blagojević, N., Didier, M., Stojadinović, B., 2022. Simulating the role of transportation infrastructure for community disaster recovery. Proceedings of the Institution of Civil Engineers - Bridge Engineering 175, 150–159. https://doi.org/10.1680/jbren.21.00018

Chiu, Y.-C., Bottom, J., Mahut, M., Paz, A., Balakrishna, R., Waller, T., Hicks, J., 2011. Dynamic Traffic Assignment: A Primer. Transportation Research Board, Washington, D.C. https://doi.org/10.17226/22872

Decò, A., Bocchini, P., Frangopol, D.M., 2013. A probabilistic approach for the prediction of seismic resilience of bridges. Earthquake Engineering & Structural Dynamics 42, 1469–1487. https://doi.org/10.1002/eqe.2282

FEMA, 2022. Hazus Earthquake Model Technical Manual.

Pel, A.J., Bliemer, M.C.J., Hoogendoorn, S.P., 2012. A review on travel behaviour modelling in dynamic traffic simulation models for evacuations. Transportation 39, 97–123. https://doi.org/10.1007/s11116-011-9320-6

Rojahn, C., Sharpe, R.L., Applied Technology Council (Eds.), 1985. Earthquake damage evaluation data for California, ATC. The Council, Redwood City, Calif.

Rokneddin, K., Ghosh, J., Dueñas-Osorio, L., Padgett, J.E., 2013. Bridge retrofit prioritisation for ageing transportation networks subject to seismic hazards. Structure and Infrastructure Engineering 9, 1050–1066. https://doi.org/10.1080/15732479.2011.654230

Schofer, J., Bocchini, P., Burton, H., DesRoches, S., Heil, A., Knatz, G., Miller-Hooks, E., Phillips, A., Marquez, J.R., Rivas, V., Wells, J., Wilson, S., 2021. Investing in Transportation Resilience: A Framework for Informed Choices. The National Academies Press, Washington, D.C. https://doi.org/10.17226/26292

U.S. Department of Transportation, 2023. Resilience and Disaster Recovery (RDR) Tool Suite.

Bridge Maintenance, Safety, Management, Digitalization and Sustainability – Jensen, Frangopol & Schmidt (eds)
© 2024 The Author(s), ISBN 978-1-032-77040-6
Open Access: www.taylorfrancis.com, CC BY-NC-ND 4.0 license

Adaptive transition of critical transport infrastructures

D.V. Achillopoulou
James Watt School of Engineering, University of Glasgow, UK

N.K. Stamataki
Laboratory of Reinforced Concrete & Seismic Design of Structures, Democritus University of Thrace, Greece

N. Makhoul
École Spéciale des Travaux Publics, du Bâtiment et de l'Industrie, ESTP Paris Campus de Dijon

R. Kromanis
Department of Civil Engineering & Management, Faculty of Engineering Technology, University of Twente, The Netherlands

ABSTRACT: Environmental and resource constraints are crucial for adapting Critical Transport Infrastructures (CTIs) to the ever-changing environment. Inadequate resources coupled with the implementation of non-resilient and unsustainable mitigation measures pose a considerable risk, potentially steering CTIs towards maladaptation. This paper investigates the interplay of CTIs' resilience and adaptive capacity under multiple hazards. In line with this, the resilience level of a bridge case study is estimated with the use of resilience indices. Beyond resilience assessment, the research scrutinizes the efficacy of potential mitigation measures designed to facilitate the adaptive transition of these critical assets. In a proactive approach to mitigate maladaptation risks, the chosen measures undergo a thorough evaluation using sustainability indices. This evaluation considers a comprehensive spectrum of criteria, encompassing societal, environmental, and economic factors. By blending resilience and adaptive capacity analyses with sustainability assessments, this paper aims to provide a holistic framework for fortifying CTIs against the uncertainties of a dynamic environment. Through a careful examination of both the challenges and opportunities, it strives to guide the implementation of resilient and sustainable strategies, ensuring the continuity and efficiency of critical transport infrastructures in the changing world.

1 INTRODUCTION

The urgent need for Critical Transport Infrastructures (CTIs) adaptation to the new demands and the extreme load conditions is guided by environmental and resource constraints (OECD, 2020). In 2022, the United Nations Office for Disaster Risk Reduction announce the six interconnected principles for resilient infrastructures in alignment with the objectives of the Sustainable Development Goals (SDGs) for achieving systemic infrastructure resilience. The principles ensure that infrastructures' management is based on 1) continuous learning, 2) proactively protection, 3) environmental integration; 4) shared responsibility; 5) protection by design and 6) adaptive transformation (UNDRR 2023).

Following a strategy for the adaptive transformation of CTIs, the exploit of lessons learnt, and the benefits of emerging technologies ensure for the proper allocation of resources and minimization of losses (Buurman & Babovic 2016); (Connelly et al. 2017); (Miao & Ghosn 2016); (Ghasemi & Nowak 2017); (OECD, 2020); (Bueb et al. 2021); (IPCC, 2022); (UNDRR, 2023).

DOI: 10.1201/9781003483755-387

As information technologies emerge, big data are generated and need to be man– collected, transmitted, and processed to support decision-making. New generation sensors have been used broadly to enhance reliability (Achillopoulou et al. 2020); (OECD, 2020); (Makhoul et al. 2023a).

The probability of exceeding acceptable limits depends on many parameters and the ageing period (Cerar et al. 2017). The reliability of information lead to different strategies of maintaining the asset and taking measures. This paper develops a methodology to assess the adaptive capacity of an asset taking into account engineering, economic and social parameters.

2 ADAPTIVE TRANSITION

The adaptive transition of CTIs into more resilient and sustainable systems depends on their adaptive capacity (Werners et al. 2021); (UNDRR 2023). The adaptive capacity expresses the ability of infrastructures to efficiently adjust and cope with the progressively changed environment, as well as the shifts in the supply and demand (Adey et al. 2003). As such, monitoring the capacity of CTIs throughout their lifecycles, adaptive transformation can be achieved (ADB, 2021); (Mehryar et al. 2022); (UNDRR 2023).

2.1 *Adaptive pathways*

The strategic deployment and implementation of dynamic and flexible Adaptive Pathways (APs) is needed to manage efficiently the long-term impacts of climate change and financial instability. Within this context APs, represent a sequence of decision points, related to events, mitigation measures and risk levels through time to achieve specific objectives and goals (Bueb et al. 2021); (Werners et al. 2021); (IPCC, 2022); (Makhoul et al. 2023b). Therefore, APs can be beneficial for CTIs' adaptive transition by avoiding maladaptation (Bueb et al. 2021); (Werners et al. 2021); (IPCC, 2022); (Makhoul et al. 2023b).

2.2 *Data-driven resilience*

The resilience level associated with a pathway exhibits a robust correlation with several parameters encompassing the sequence of events, hazards, mitigation actions, financial and environmental constraints, infrastructure's structural integrity and functionality levels as well as risk levels (Bueb et al. 2021); (IPCC, 2022); (Makhoul et al. 2023b). Hence, the pathway's resilience level is data-based and fluctuates among the different actions' resilience levels.

Data-driven resilience quantification is highly contingent upon the risk level (Achillopoulou et al. 2020); (Afrin et al. 2023). Data, and actions associated with increased risk levels can result to maladaptive APs (Werners et al. 2021); (IPCC, 2022); (Makhoul et al. 2023b). The lower the risk level is, the more reliable the resilience level of AP can be. As such, to avoid CTIs' devaluation, the following AP should be represented by a series of actions characterized by increased reliability and resilience levels over time (Bueb et al. 2021); (IPCC, 2022).

2.3 *Reliability of data*

The holistic impact of uncertainties on CTIs is crucial for their efficient management and associates with the reliability of data (Frangopol et al. 2019); (Diamantidis et al. 2019); (Achillopoulou et al. 2020). Poor reliability can result to non-resilient and -sustainable actions leading to maladaptation of CTIs (Bueb et al. 2021); (Werners et al. 2021); (IPCC, 2022); (Makhoul et al. 2023b).

The uncertainties of CTIs decision-making policies throughout their life cycles may pertain to factors such as climate change effect, economic instability, probability of failure and/or asset disruption, mitigation measures effectiveness as well as the accuracy of models, analyses, codes, metrics and monitoring data (Frangopol et al. 2019); (Achillopoulou et al. 2020); (Makhoul 2022); (Afrin et al. 2023). Their quantification makes aware stakeholders of the risk level and can be achieved by statistical and probabilistic models; scenario analysis, pathways deployment and expert judgment when the data is limited (Diamantidis et al. 2019);

(Achillopoulou et al. 2020); (Pasman & Rogers 2020); (Malekloo et al. 2022). Model updating can also be employed to reduce further the uncertainties levels by aligning computational models with the most realistic data and predictions (Achillopoulou et al. 2020); (Malekloo et al. 2022); (Makhoul et al. 2023 a and b).

2.4 *Sustainability*

Sustainable solutions to the decision-making process of CTIs can be well informed by enhanced reliability levels as they derive from accurate data and predictions (Achillopoulou et al. 2020); (Makhoul et al. 2023b). On the contrary, sustainability is not always expressed by actions with high resilience levels (IPCC, 2022); (Makhoul et al. 2023b). Environmental compatibility, adequate structural integrity levels and prevention of CTIs' disruptions along with optimum use of resources are crucial to ensure sustainability in resilience solutions (UNDRR, 2022 and 2023); (Makhoul et al. 2023b). In line with this, to obtain long-term socio-economic and environmental benefits that enhance the adaptive capacity of CTIs, sustainability constraints need to be established (European Commission 2022); (UNDRR, 2022 and 2023); (Global Infrastructure Hub 2023); (Lei et al. 2023); (Makhoul et al. 2023b).

3 METHODOLOGY

In this research, the quantification of resilience, sustainability and adaptation levels of CTIs, such as highway bridges, is founded on the research by Stamataki et al. (2023) and integrates the APs framework introduced by Makhoul et al. (2023b). The sequential phases of the methodology, which is used for the evaluation of the mitigation measures through the assets' life cycle to assess the pathway with the optimal resilience level, the lowest resources cost, and the supreme socio-economic and environmental benefits, are illustrated in Figure 1.

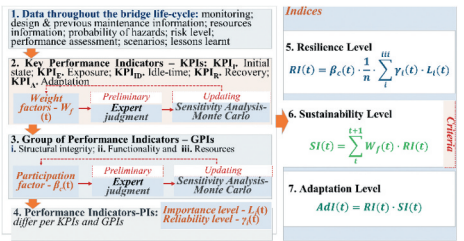


Figure 1. Adaptation space assessment methodology.

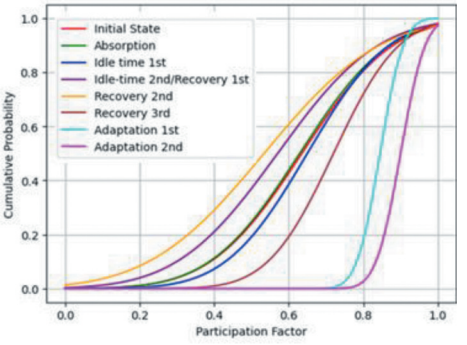


Figure 2. Probability of participation factor values over time.

3.1 *Data*

The methodology is data-driven, multi-criteria and comprises with seven phases commencing with the data acquisition. Data are not limited only to the maintenance information and design, but also to the lessons learnt throughout the life-cycle.

3.2 *Key performance indicators*

Key Performance Indicators (KPIs) that express the ageing periods of the asset's life cycle are employed to further organize and correlate the data. In general, there are five KPIs, though their number can differ from asset to asset. For example, the number of KPIs associated with

idle-time (KPI_{ID}) and recovery period (KPI_R) initiation is related to the number of mitigation measures implemented in the case-study. To assess the contribution of the asset's ageing periods, Weight factors (*Wf*) are applied to each KPI. The preliminary *Wf* are established through experts' judgment, and their values are subsequently updated after the completion of the recovery periods. In cases where the asset demonstrates adequate levels of resilience and sustainability, reflecting an enhanced adaptive capacity, the *Wf* are recalculated based on a Sensitivity Analysis (*SensAn*).

3.3 *Resilience components*

Comprehensive research has been carried out concerning the resilience of CTIs, emphasizing their functionality and the interplay with structural integrity, as well as the resource requirements for their maintenance (Capacci et al. 2022). These three indicators are interdependent as inadequate levels of performance condition can trigger asset disruptions, whereas a lack of resources can progressively lead to safety and functionality problems. In line with this, the components of resilience considered in the adopted methodology are three and are related to i) the structural integrity, ii) the functionality and iii) the resources of the asset.

The components are expressed by Group of Performance Indicators (GPIs) that are considered complementary and are factored per KPI with the use of participation factors (β_c). The preliminary estimation of the participation factor for the resources component derives from a Life Cycle Cost (LCC) analysis as Stamataki et al. (2023) have already presented. A *SenAn* follows to determine the $\beta_c(t)$ per KPI based on the resilience thresholds as Stamataki & Achillopoulou (2023) have proposed. The criticality of the components on the overall resilience level arises from the type of distribution function of the factors. Throughout the life-cycle of the asset, the participation factors are also calibrated with a more sophisticated Monte Carlo Analysis (Figure 2).

3.4 *Parameters*

A set of Performance Indicators (PIs) is employed to associate the available data with the parameters that express each one of the GPIs. The total number of PIs (n) per component differ, whereas different PIs can be activated throughout the ageing periods of the asset. For example, the parameter of continuous monitoring is activated at the KPI corresponding to its initiation, while in cases of periodic monitoring, the parameter is deactivated. The assessment of each PI accounts for two variables i) the importance level and ii) the reliability factor as described in subsections 3.4.1 and 3.4.2 respectively.

The PIs pertaining to structural integrity are articulated with data such as a) the geometry and the type of the asset, b) material properties, c) damage index, d) structural health monitoring data, e) performance assessment, f) hazard occurrence, g) structural mitigation measures, g) mitigation impact and h) environmental limitations. Analogously, the PIs for functionality encompass a) design traffic capacity, b) traffic load changes, c) disruption, d) functionality monitoring data, e) functionality mitigation measures, f) hazard occurrence and extreme events, g) mitigation impact and h) environmental limitations. Finally, the resources component employs PIs such as monetary resources for a) maintenance and b) replacement, c) need for expertise staff, d) human resources, e) need for investment, f) financial limitations and g) bridge financial impact.

3.5 *Importance level*

The importance level (L_i) of each PI corresponds to the influence of the parameter in the resilience quantification. In total, the methodology comprehends four importance levels: 1-low, 2-moderate, 3-high and 4-very high. TheL_i may vary or remain consistent depending on the parameter and the ageing stage of the asset's life cycle. For example, factors such as failure of support or tendon loss are characterized by a consistently "4-very high" importance level per KPI due to their impact on the asset's safety and functionality levels.

3.6 *Reliability factor*

The methodology takes account of two different reliability levels with the use of reliability factors (γ_i). The first level pertains to reliable PIs with values equal or higher than 92.5%

($\gamma_i \geq 92.5\%$), while the second takes values below 92.5% ($\gamma_i < 92.5\%$), signifying non-reliable PIs. The factor is associated with the distribution function each PI follows, or the risk level and the probability of occurrence related to the PI ($\gamma_{i,PI}$), such as in cases of hazards, increase traffic demands and requirements for capital infusion. The γ_i is further updated based on the performance assessment of the asset in various scenarios ($\gamma_{i,p}$). The overall factor is anticipated to decrease over the exposure periods, while the implementation of mitigation measures and monitoring systems is expected to augment it.

3.7 *Resilience Index*

The overall resilience level of the asset is based upon the calculated resilience indices per KPI, *RI*(t), as presented by the equation in phase 5 of Figure 1. It derives from an overall average of risk, hazards, monitoring, components (structural, functionality, resources, operation) also taking into consideration the reliability level. The index ranges from 1 to 4, with lower values denoting a lower level of resilience. The critical level is at the middle of the scale corresponding that any further decrease of the RI can be related with safety, functionality and/or resources.

3.8 *Sustainability level*

Increased resilience levels did not always ensure high levels of sustainability. In the past decades, sustainable planning and management were not of high concern. Sustainability was promoted in 1987 WCED Commission's Report. The sustainability level is defined by Sustainability Indices, *SI*(t) as indicated by the equation in phase 6 of Figure 1. The estimation of the *SI*(t) takes advantage of the calculated *RI*(t) and the weighted KPIs. For a certain KPI the SI is calculated as the relative sum of the SI between two successive ageing periods.In this study, all pillars of sustainability are considered by including: 1) the environment through climate change, 2) the society through the population and traffic increase, and 3) the economy through the resources allocated to the infrastructure project.

3.9 *Criteria*

To ensure that the indirectly expressed sustainability level of the asset is well informed by the weighed RI, proper criteria and a classification scale ranging from 1 to 4 are selected. A rating of 1 denotes a non-sustainable level, 2 indicates the necessity for sustainability improvement, while 3 and 4 signify levels ranging from acceptable to sustainable sustainability. The selected criteria are related with the three pillars of sustainability i) society, ii) economy and iii) environment and take account the impact of the CTI throughout its life cycle.

3.10 *Adaptation Index*

The Adaptation Index (AdI) serves as a metric for assessing the adaptation level, and thus adaptive capacity of asset over its life cycle, in addition to evaluating the efficacy of different mitigation measures and policies. As the adaptive capacity should encompass both resilience and sustainability considerations the AdI is considered as their intersection and is determined based on the computed *RI*(t) and *SI*(t), as presented i by the equation in phase 7 of Figure 1.

4 CASE-STUDY

The bridge case study of this research the Hollandse Brug, the oldest prestressed RC highway bridge in the Flevopolder region of the Netherlands. The bridge plays a crucial role in connecting Almere, Amsterdam, and Schiphol Airport. Since its construction in 1969, many operational challenges led to the implementation of various mitigation measures throughout time. In 2007, as part of a refurbishment effort, a system of sensors was installed on the deck of the bridge for the continuous monitoring of strains, deflections, and temperatures (Achillopoulou et al. 2022); (Stamataki & Achillopoulou 2023); (Makhoul et al. 2023b). A Finite Element Analysis was performed to further investigate the performance and flexibility of the bridge under multi-hazards especially with climate change.

4.1 *Scenarios*

The hazard scenarios are based on the region's risk and account for a) traffic load changes and b) seismic events. According to NCEI (2023), in the next 50 years, the temperature increase in the region is expected to be slightly lower than the worldwide average, but still significant. Further to this, an augmented increase in the bridge's traffic volume, 247% greater than 1990, is predicted to take place by 2030 (IPCC, 2023). The earthquake occurrence in the Netherlands is classified as medium, meaning that in the next 50 years there is a 10% probability of such an event. In total four different hypothetical scenarios are considered as Table 1 presents. At the first stage of all the scenarios, the bridge is subjected to an initial temperature difference (ΔT) of 10◦C to consider the temperature increase due to global warming. The next stages of the scenarios include the occurrence of hazards related to traffic load changes (normal or increased) and seis-mic events (design or extreme). The final stage (4th) for all the scenarios, i.e., after the seismic event, restores the bridge to the initial considered traffic conditions (normal or increased).

Table 1. Multi-hazard scenarios.

Stage	1st	2nd		3rd		4th	
Hazzard	ΔT 10°C	Traffic		Seismic event		Traffic	
Scenario		*n*	*i*	*d*	*e*	*n*	*i*
I							
II							
III							
IV							

* Symnols *n* and *i* are used for normal and increased traffic load and *d* and *e* for design and extreme seismic events.

4.2 *Simulation*

The bridge is 355m long with seven simply supported spans, featuring a 38m wide deck following its expansion in 2007. The structure comprises nine prefabricated prestressed girders and four cast in situ and post-tensioned transverse beams evenly distributed across the spans. The deck is supported by piers connected by elastomeric bearings, which offer both vertical stiffness and flexibility for anticipated horizontal deformations.

The model of the bridge was created with SOFiSTiK software. The dimensions estimated from existing drawings, and any missing data, such as transverse beam geometry, reinforcement arrangements, and prestressed tendons, were determined based on load combination results. The RC elements (slab, beams, piers) were simulated using 3D finite elements. Three axial and torsional springs were used for simulating the bearings.

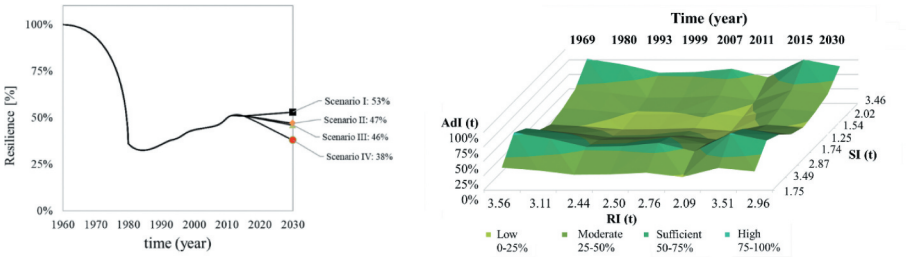
5 RESULTS

The results of the four scenarios examined are shown in Table 2 in terms of the percentage of the structural elements, parameters or functionality been affected. The first scenario indicates that the damages in the girders, transverse beam or the bearings provoke a disruption of traffic with closing a part of the bridge for mitigation measures. The crack width seem to be unaffected by the increase of temperature and the designed traffic load. The second scenario indicates that even there are not extensive failures the risk of damage is increased since the percentage of elements passing the controls are decreased and approximately 10% of them are not sufficient to bear the loads. This automatically would cause a disruption on the bridge functionality by closing more lanes (based on the map of damages). Scenario III induces greater damages and risk of failure to the structural elements. From the analysis results, 83% of the structural elements are passing the acceptable thresholds, whereas 58% of the bearing

do pass too. Lastly, Scenario IV prompts the severe damaged to be happened resulting in full closure of the bridge for mitigation measures and avoidance of losses.

Table 2. Multi-hazard scenarios' results.

Elements/ parameter	Scenario I			Scenario II			Scenario III			Scenario IV		
	failed %	damaged %	pass %	failed %	damaged %	pass %	failed %	damaged %	pass %	failed %	damaged %	pass %
Girders	2	3	95	5	5	90	3	14	83	3	22	75
Crack width	0	2	98	0	10	90	0	17	83	3	22	75
Transverse beam	0	7	93	0	14	86	0	14	86	0	18	82
Bearings	4	29	67	3	31	67	4	38	58	10	40	50
	opened %	closed %		opened %	closed %		opened %	closed %		opened %	closed %	
Lanes	62	38		38	62		38	62		0	100	



(a) (b)

Figure 3. (a) Resilience indices (b) Adaptation space over time versus Resilience and Sustainability indices.

From the artificial data derived from the Finite Element Analysis, there is not significant decrease in the reliability of tendons to bear loads, therefore those elements didn't seem to have altered their importance level in the capacity of the asset. The rest of the structural elements sifted their importance due to the uncertainty and the risk for further damage.

The different scenarios seem to have an influence for the future resilience of the asset as shown in Figure 3a. It seems that only the first scenario manages to provide a resilience index just above 50% of the initial resilience. Damages on all the other scenarios range from 47-38% resilience levels. Specially for the extreme scenario IV, the resilience levels seem to have decreased to the level of the 1980s when the bridge could not further withstand the demands.

Although the resilience indices are changing, it seems that their influence to the sustainability, according to the current methodology is not significant. Figure 3b presents a 3D surface diagram providing a representation of the RI and SI changes over time. Versus the adaptation level of the asset. The adaptation level is expressed as a percentage of the relative AdI to the maximum potential AdI derived from the novel methodology considering the maximum RI and SI values.

It is remarkable that the highest SI value (3.49) is observed at the completion of the initial state period, while the RI experiences a slight decrease of 13% (from 3.56 to 3.11) indicating the start of the exposure period. At this stage, the adaptation level stands at a moderate level of 39%. The subsequent mitigation periods from 1993 to 2011 exhibit varying levels of low to moderate adaptation, ranging from 20% to 44%. The lowest AdI value of 20% corresponds to 2007 when traffic restrictions were imposed on the bridge.

To better understand the adaptation over the periods, the investment, operational but also the value of the asset is plotted in Table 3 over time. The value of the asset in monetary terms is calculated by considering the Effective Annual Interest Rate over the periods which is considered as 5% throughout the years, based on the Netherland data. The adaptation of the asset was in

low levels in the 2000s when a big investment was needed to transform the asset again to ma bridge meeting the needs. This automatically increased the value of the asset, especially with increasing the demand for use by widening the deck and adding lanes ever since. Ever since the installation of SHM systems in 2007, the investment needed added tremendous value to the asset and made it more flexible to adaptation for the future, needing lower investment capital and steady operational cost.

Table 3. Asset's costs over time in Euro.

period name	Initial state	Exposure	Idle time 1st	Idle time 2nd	Recovery 2nd	Idle time 3rd	Recovery 3rd	Adaptation
period (years)	1969-1979	1980-1992	1993-1998	1999-2006	2007-2010	2011-2014	2015-2022	2023-2030
Age (years)	10	23	29	37	41	45	53	61
Asset value	2.63E+07	7.10E+07	6.54E+07	6.65E+07	1.12E+09	1.43E+09	3.47E+09	3.53E+09
Total Capital Investment per Period (TCIP)	6.22E+07	5.00E+07	1.65E+08	1.95E+08	2.01E+08	3.25E+08	9.00E+07	8.50E+07
Total cost per period (TCP)	6.59E+04	1.78E+05	1.63E+05	1.66E+05	2.81E+06	3.58E+06	8.68E+06	8.84E+06

6 CONCLUSIONS

The proposed methodology intricately captures the essence of adaptation capacity. Lower levels of adaptive space signal a pressing need for increased investment, while moderate to high levels signify a tangible enhancement of the asset's intrinsic value. In the face of unforeseen events and circumstances, the adaptation space remains at a moderate level.

As outlined by the methodology, the forecast for future adaptive space is notably high, indicating the bridge's robust capability to withstand hazards. This resilience is underpinned by the implementation of strategies grounded in a wealth of engineering expertise and historical data, ensuring a well-informed and proactive approach to fortifying the bridge against potential challenges and maladaptation strategies.

REFERENCES

Achillopoulou, D. V., Mitoulis, S. A., Argyroudis, S. A., & Wang, Y,. 2020. Monitoring of transport infrastructure exposed to multiple hazards: A roadmap for building resilience. *Science of the total environment*, *746*, 141001.

Achillopoulou, D. V., Stamataki, N. K., Psathas, A., Iliadis, L., Karabinis, A., 2022. Resilience Quantification based on Monitoring & Prediction data Using Artificial Intelligence (AI). *IABSE Cong. Nanjing 2022-Bridges Structures. Connect. Integration & Harmo*, *Nanjing*, *21-23 September 2022*.

Adey, B., Hajdin, R., & Brühwiler, E. (2003). Supply and demand system approach to development of bridge management strategies. Journal of infrastructure systems, 9(3), 117–131.

Afrin, T., Aragon, L. G., Lin, Z., & Yodo, N., 2023. An Integrated Data-Driven Predictive Resilience Framework for Disaster Evacuation Traffic Management. *Applied Sciences*, *13*(11), 6850.

Bueb, B., Tröltzsch, J., Reichwein, D., Oldenburg, C., Favero, F., Bodle, R., Teebken, J., Jacob, K. and Voß, M., 2021. Towards sustainable adaptation pathways. A concept for integrative actions to achieve the 2030 Agenda, *Paris Agreement and Sendai Framework. Conceptual & analytical paper* (No. UBA-FB–000590/3, ENG). Umweltbundesamt (UBA).

Buurman, J., & Babovic, V., 2016. Adaptation Pathways & Real Options Analysis: An approach to deep uncertainty in climate change adaptation policies. *Policy & Society*, *35*(2), 137–150.

Capacci, L., Biondini, F., & Frangopol, D., 2022. Resilience of aging structures and infrastructure systems with emphasis on seismic resilience of bridges and road networks. Resilient Cities&Struct. 1(2), 23–41.

Cerar B., Allaix D.L. and Vervuurt A.H.J.M.(2017) Probabilistic analyses for determining the impact on the structural safety of bridges and viaducts, D 5.2 Impact analyses for bridges and viaducts, TNO.

Connelly, E. B., Allen, C. R., Hatfield, K., Palma-Oliveira, J. M., Woods, D. D., & Linkov, I., 2017. Features of resilience. *Environment systems & decisions*, *37*, 46–50.

Diamantidis, D., Sykora, M., & Sousa, H., 2019. Quantifying the Value of Structural Health Information for Decision Support.

European Commission, 2022. Guidance on Public Investment into Sustainable Infrastructure Projects.
Frangopol, D. M., Dong, Y., & Sabatino, S., 2019. Bridge life-cycle performance and cost: analysis, prediction, optimisation and decision-making. In *Structures & Infrastructure Systems* (pp. 66–84).
Ghasemi, S. H., & Nowak, A. S., 2017. Target reliability for bridges with consideration of ultimate limit state. *Engineering Structures*, *152*, 226–237.
Global Infrastructure Hub, 2023. *Sustainable Infrastructure*. Retrieved from: https://www.gihub.org/sustainable-infrastructure/, (assesssed 26/09/2023).
Intergovernmental Panel on Climate Change, IPCC, 2022. *Climate Change 2022: Impacts, Adaptation, & Vulnerability*. Contribution of Working Group II, Cambridge University Press, 3056 pp., doi:10.1017/9781009325844.
Lei, X., Dong, Y., & Frangopol, D. M., 2023. *Sustainability-informed intelligent management of aging civil infrastructure systems with emphasis on bridge networks*.
Makhoul, N., Achillopoulou, D. V., Stamataki, N. K., & Kromanis, R., 2023a. 12 Image Processing. *Data Driven Methods for Civil Structural Health Monitoring & Resilience: Latest Developments & Applications*, 279, Taylor & Francis.
Makhoul, N., Achillopoulou, D. V., Stamataki, N. K., & Kromanis, R. (2023b). Adaptive pathways using emerging technologies: Applications for CTI. Sustainability, 15(23), 16154.
Malekloo, A., Ozer, E., AlHamaydeh, M., & Girolami, M., 2022. Machine learning & structural health monitoring overview with emerging technology and high-dimensional data source highlights. *Strt. Health Mon*., *21*(4), 1906–1955.
Mehryar, S., Sasson, I., & Surminski, S., 2022. Supporting urban adaptation to climate change: What role can resilience measurement tools play?. *Urban Climate*, 41, 101047.
Miao, F., & Ghosn, M., 2016. Reliability-based progressive collapse analysis of highway bridges. *Struct. safety*, 63, 33–46.
Organisation for Economic Co-operation & Development, OECD, 2020. OECD compendium of policy good practices for quality infrastructure investment.
Pasman, H. J., & Rogers, W. J., 2020. How to treat expert judgment? With certainty it contains uncertainty!. Journal of Loss Prevention in the Process Industries, 66, 104200.
Stamataki, N. K., & Achillopoulou, D. V., 2023. Sensitivity analysis on resilience components throughout the lifecycle of an asset. IALCCE 2023 8th Intern. Symp. on Life-cycle Civil Eng., *Milan*, *2–6/7 2023.*
Stamataki, N. K., Achillopoulou, D. V., & Makhoul, N., 2023. Evaluation of Resilience based on Resources & Adaptation Level in Critical Transport Infrastructures. *The 8th Smart City Applications International Conference, ESTP Paris France*, *4–6 October 2023.*
United Nations Office for Disaster Risk Reduction, UNDRR, 2023. *Handbook for implementing the principles for resilient infrastructure*, https://www.undrr.org/quick/77508 (assessed 26/09/2023).
Werners, S. E., Wise, R. M., Butler, J. R., Totin, E., & Vincent, K., 2021. Adaptation pathways: A review of approaches and a learning framework. *Environmental Science & Policy*, 116, 266–275.

Bridge Maintenance, Safety, Management, Digitalization and Sustainability – Jensen, Frangopol & Schmidt (eds)
© 2024 The Author(s), ISBN 978-1-032-77040-6
Open Access: www.taylorfrancis.com, CC BY-NC-ND 4.0 license

Machine learning improving seismic infrastructure recovery time estimation

N. Makhoul
École Spéciale des Travaux Publics, ESTP, Paris, France

B. Derras
University of Tlemcen and University of Saida, Tlemcen, Algeria

ABSTRACT: To maintain infrastructure functionalities and ensure the rapid recovery of their functionalities, during powerful earthquakes, an assessment of infrastructure's seismic resilience is essential. One of the crucial elements of an investigation of seismic resilience is recovery time (RT). It is essential to make sure that the RT is anticipated in advance. This RT relies on various factors (Derras & Makhoul 2022). Unfortunately, the full set of factors that likely impacted RT are not always available. For this reason, we adopt in this study, an approach that is based on the simulation of the missing factors from those already available (Derras & Makhoul, 2023). To prove this, several machine learning algorithms have been adopted. This reveals that the "Boosted Trees Regression" algorithm is the best. Sensitivity analysis revealed that "system type" is the most important factor, followed by cumulative absolute velocity (CAV). The model thus developed is validated by dividing the data set into three "training-validation-test" subsets. The methodology, used in this study, allows us to prevent overfitting problems and to obtain an optimal aleatory variability of DT represented here by RSME (sigma). The best present model (Boosted Tree algorithm) allows us to reduce this variability at a rate equal to 51 %. It can offer specialists an approximate value of recovery time, an important piece of information when assessing seismic resilience.

1 INTRODUCTION

The recovery time is the time needed for infrastructure such as roads, bridges, buildings, and utilities to be repaired and functional after a disastrous event (Cao et al. 2022). The prediction of the recovery time is based on various factors, for example in the case of an earthquake, it includes the earthquake severity, the infrastructure condition, and the resources available for the recovery work. The motives in predicting the infrastructure recovery time after an earthquake are: i) To allocate resources, ii) to effectively plan the response and recovery efforts, iii) to prioritize repair for quick restoration, iv) to identify potential challenges in the recovery procedure which grant proactive planning, and contingency plans to address these issues.

Methods to predict the recovery time of infrastructure after an earthquake event include (Cremen et al. 2020): 1) Statistical models which investigate data from past earthquakes and the related infrastructure recovery time aiming to identify patterns and trends for predictions of future recovery times. 2) Expert judgment which uses the expert experience and knowledge to offer informed estimations of the infrastructure recovery time. 3) Machine learning algorithms analyze a wide range of data (i.e., the earthquake severity, the infrastructure condition, and the resources available for the recovery effort ((Derras & Makhoul 2022), (Durante & Rathje 2021)), and train a model on data from past earthquakes, to make predictions about the recovery time for future earthquakes.

DOI: 10.1201/9781003483755-388

Statistical models might present some disadvantages to predicting the infrastructure recovery time after an earthquake such as limited data, reliance on assumptions, and limited flexibility, which can limit the accuracy of the predictions by the model (Derras & Makhoul, 2023).

Potential shortcomings are also available while using expert judgment such as limited knowledge, objectivity, and scalability, time-consuming in the case of evaluation of large numbers of infrastructure systems, and dependence on a single source.

To overcome those limitations, in this study, machine learning algorithms are suggested as a powerful tool in the prediction of the infrastructure recovery time after an earthquake event. Numerous advantages are available while using ML algorithms. Those are the ability a) to handle large amounts of data, b) to make accurate predictions when trained on sufficient data, c) to continuously improve whilst it is trained on newly available data, helping thus improve over time the accuracy of the predictions, d) to automate prediction procedure, thus, saving time and reducing the potential for human error.

Machine learning was used, for example, to assess earthquake-induced damage grade and rehabilitation intervention in residential buildings (Sajan et al. 2023); to predict earthquakes in four different seismic zones (Japan, Turkey, Greece, and Indian Subcontinent) (Hoque et al. 2020); natural hazards (Dubrow 2021).

To estimate the post-earthquake downtime, the following steps are suggested and detailed in this study that allows: 1) Determine the scope of the analysis such as the infrastructure systems and the time frame to estimate the downtime. 2) Collect the data on the location and magnitude of earthquakes, the types, and conditions of the infrastructure (i.e., material, design, construction, past damage, repairs, etc.). 3) Analyze the seismic impact (e.g., infrastructure damage) on the systems or infrastructure using the gathered data. 4) Estimate the downtime, which can be assessed based on the infrastructure damage, by calculating the time needed for replacement or repair and accounting for the time needed to implement contingency plans or bring back the full infrastructure functionality. 5) Validate your results to ensure the accuracy and reliability of the downtime estimates by comparing them to real-world data or by using different methods. This will confirm the analysis' validity and identify possible areas for improvement.

2 DATA

2.1 *Initial dataset and evaluation model*

The dataset from 32 worldwide earthquakes based on (Kammouh et al. 2018) is in this article. Those earthquakes occurring between 1960 and 2014, with a magnitude between 6 and 9 are distributed as follows: 28% in the USA, 31% in Japan, 18% in South America, 12% in Southern and Eastern Asia, 6% in Oceania, 3% in Africa. The lifelines that are affected by those earthquakes are the water, telecom, power, and gas. Their downtime (DT) after earthquake events is collected. This empirical dataset was completed using AI methods. In this article, the downtime DT expressed in number of days is the same as the recovery time RT, i.e., T_{AB} the time needed for the lifeline to recover (Cimellaro et al. 2006) and (Bruneau et al. 2003). The evaluation model starts with the initial simplistic dataset, and it grows with sophistication with the additional input factors.

2.2 *Additional factors to improve data quality*

To improve the model performance, estimation factors can be added as inputs to the ML model. It is done by offering additional information from which the model can learn. The process is called feature engineering. It is an iterative process and tests different features, where the most informative ones are designated for the final model. Then, the model can be re-trained using the new data.

The model's performance can be evaluated using the square correlation coefficient R and Root Mean Square Error (RMSE). In case the new features improve the performance, then they are beneficial and kept in the final model.

The initial dataset (Figure 1) considered the factors system, magnitude, and PGA. Then we add and test the following factors: Joyner-Boore distance (RJB), cumulative absolute velocity (CAV), EMS-98 (European Macro-seismic Scale), and country global recovery time from the GEM platform. We use the neural networks technique as a reference model (B. Derras et al. 2012). Other variables need to be considered as well (Derras & Makhoul 2022), such as the region's wealth, manpower, season of the earthquake occurrence, the localization within a country, etc.

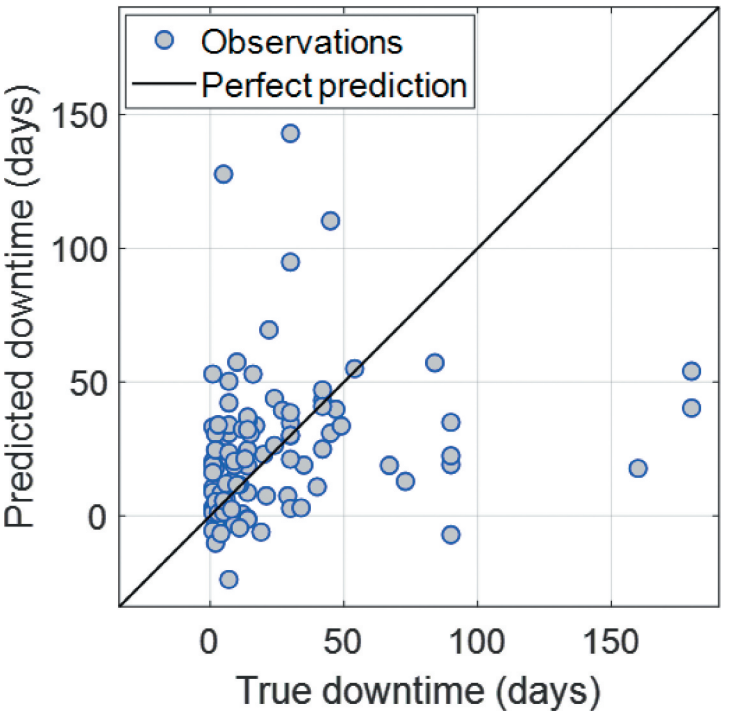


Figure 1. Predicted downtime and initial downtime evaluated with the model using the initial dataset.

2.2.1 *Joyner-Boore distance (RJB)*

After an earthquake occurrence, the relationship between the downtime and the distance of Joyner-Boore is mostly inversely proportional. The greater the Joyner-Boore distance, the less intense the ground motion is, and the less severe the damage to the structure or building. Thus, the farther the structures or buildings are from the earthquake's epicenter, the shorter the downtime after the event is, and vice versa.

Figure 2 shows the typology of the machine learning model that predicts the Joyner-Boore distance from the magnitude and the logarithm of the peak ground acceleration (PGA). The standard deviation (RMSE) of aleatory variability associated with this model is equal to 0.37.

Figure 3 shows the example of the median predicted by the model represented in Figure 2. It shows the PGA versus the RJB for a given magnitude.

2.2.2 *Cumulative absolute velocity (CAV)*

Cumulative Absolute Velocity (CAV) is a metric that is used to account for frequency, amplitude, and time). In seismic engineering, it is used for measuring the total amount of ground shaking occurring during an earthquake. CAV is a sound indicator of the potential damage of earthquakes, thus used herein. Generally, the higher the CAV value, the more significant the damage, then the more repairs it needs and the longer the downtime is.

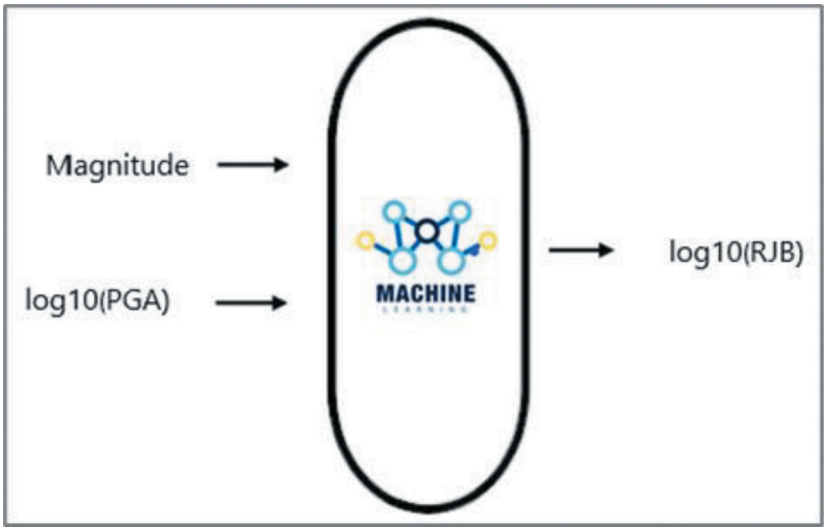


Figure 2. The Input and Output factors of the Machine Learning model for RJB.

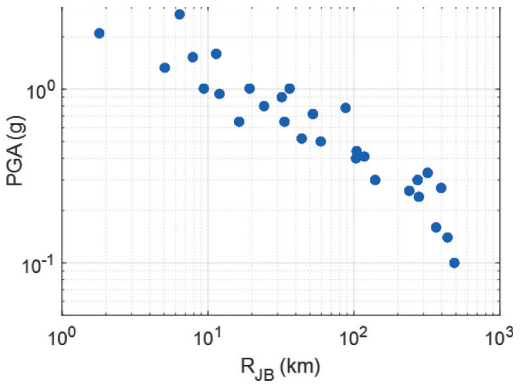


Figure 3. The PGA function of the RJB for the dataset.

2.2.3 *EMS-98 (European macro-seismic scale)*
The European Macro-Seismic Scale (EMS-98) measures the intensity of ground shaking during earthquakes. It is used to evaluate seismic intensity in European countries and ranges from 1 to 10 (1 is the lowest level of intensity). Thus, the EMS-98 and ground-motion parameters (i.e., peak ground acceleration (PGA, CAV)) are correlated. Still, no direct relation between EMS-98 and post-earthquake downtime is available EMS-98, can be linked to the potential damage of an earthquake through the ground intensities measured such as the (Zanini et al., 2019) expression:

$$ESM_98 = 2.03 + 2.28 * log10(PGA);\ \%\ PGA\ in\ gal \tag{1}$$

A theoretical assumption of the relationship can be suggested between the EMS-98 and downtime after an earthquake: the higher EMS-98 value generally corresponds to greater damage, thus, more repairs and longer downtime.

2.2.4 *The level of global recovery*
The recovery and reconstruction potential map is thoroughly aligned with the disaster resilience notion. To enhance the seismic resilience of a country needs to increase its capacity to

anticipate threats, decrease its overall vulnerability, and permit the community recovery after the seismic event. The measurement of recovery and reconstruction potential needed to capture the inherent conditions includes the built environment density, levels of education, and political participation.

2.3 *Anomalies data detected*

They detect the anomalies in the selected data. The box plot of the data distribution was done. Figure 4 shows the box plot of data distribution. It shows the downtime versus all symbolic features. The left plot shows the dataset before the anomalies' analysis. The right plot represents a clean dataset (after the outlier is eliminated).

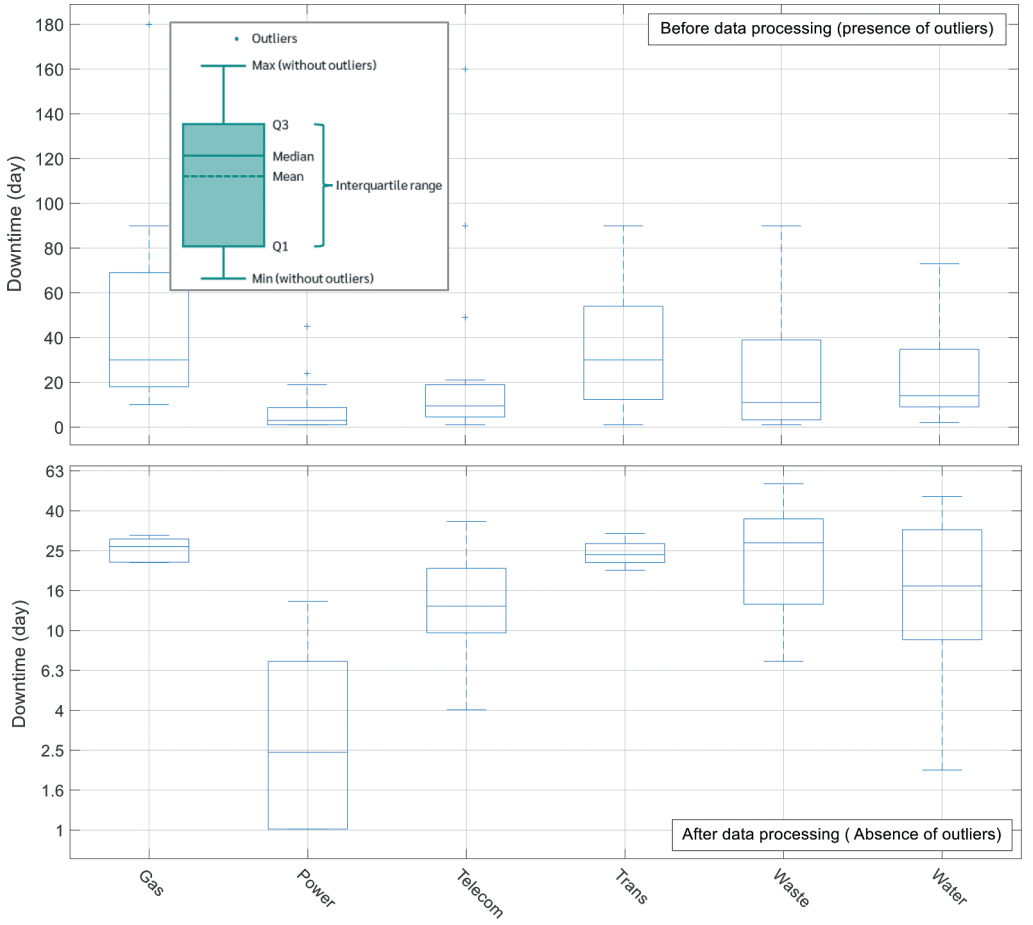


Figure 4. The box plot of data distribution. The figure presents the statistical distribution of data, before data processing (top plot) and after data processing (bottom plot). A short definition (such as median, interquartile range "IQR" and the position of outliers) is given also on the box top-left.

3 METHODOLOGY USING MACHINE LEARNING ALGORITHMS

To predict accurately the downtime T_{AB} is essential for the resilience evaluation of a system, i.e., the considered lifelines, that have been disturbed by an external force, and which are: power, water, gas, and telecom. T_{AB} is meticulously connected to the

functionality Q, which is reliant on several social, and economic metrics, structural typologies, and parameters and intensity measures of the earthquake. A correlation between these factors and the T_{AB} can be established using a supervised machine-learning model ((Derras et al. 2012), (Derras & Makhoul 2022), (Derras & Makhoul, 2023)). It is done using the factors for inputs and then training the model to obtain the output predictions for T_{AB}. Nevertheless, it is essential among others to account for all factors that influence T_{AB} when building the model.

The Machine Learning (ML) concept, first introduced by Arthur Samuel, is a subset of the broader field of Artificial Intelligence (AI). It allows algorithms to learn and improve their performance without any explicit programming.

One category of particular interest in ML is supervised learning. It trains the model to map inputs to outputs built on examples of input-output pairs. Various supervised ML algorithms are commonly used in earthquake engineering, to extend classical regression techniques and eliminate the necessity for pre-defined functional forms. The following section compares some of the most broadly used ML algorithms.

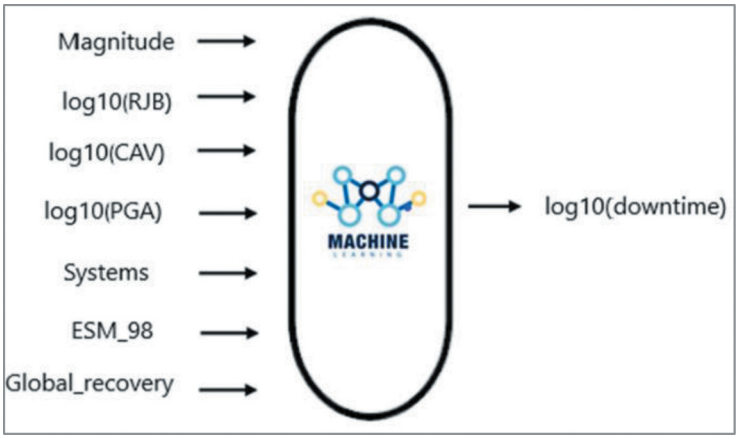


Figure 5. Input and output factors for the final Machine Learning model.

4 COMPARISON BETWEEN SEVERAL MACHINE LEARNING APPROACHES

To evaluate the performance of various machine learning algorithms, some metrics are frequently used such as the Root Mean Squared Error (RMSE) and the correlation coefficient. Those metrics can be used to compare the different machine learning algorithms' performance. In this article, we use the following machine learning algorithms for comparisons: Linear Regression, Decision Tree (DT), Support Vector Machines (SVM), Boosted Tree, Gaussian-Process Regression, and Neural Network. The details of those algorithms are presented in detail in (Derras & Makhoul, 2023). The higher correlation coefficient and the lower RMSE designate a better model fit to the data and a better algorithm performance.

The statistics parameters, such as means, standard deviations, and correlations, are sensitive to outliers. Since we do not know the origin of outliers, we suppose that they are due to incorrectly entered or measured data, consequently, we drop the outliers.

Figure 4 which represents the box plot, allows the detection of any outlier point (anomaly analysis). Overall, an observation point is considered an outlier when is outside of the box either Q1-1.5×IQR or Q3+1.5×IQR.

Table 1 shows the hyperparameter values obtained through six machine-learning models. These values are given for the validation and test phase. It shows that the Boosted Tree is the more adequate model for this case.

Table 1. The hyperparameter values obtained for the machine-learning models.

	Validation		Test	
Default hyperparameters	RMSE	R^2	RMSE	R^2
Linear Regression	0.36	0.33	0.2	0.78
Decision Tree	0.37	0.26	0.21	0.74
SVM	0.35	0.38	0.22	0.74
Boosted tree	0.32	0.43	0.075	0.97
Gaussian-process regression	0.33	0.47	0.16	0.86
Neural Network	0.44	-0.02	0.075	0.97

4.1 *Boosted tree ensemble*

The Boosted Regression Trees (BRT) combine two techniques, the decision tree algorithms and the boosting methods (Sajan et al. 2023).

BRT is an ensemble meta-algorithm for ML to reduce errors in predictive data analysis (Sajan et al. 2023) and (Dubrow 2021), with the aim to form one strong classifier ((Hoque et al. 2020), (BCCVL 2021)). It is very used when a large number of variables for the number of observations is available.

4.2 *Hyperparameter optimization*

The hyperparameter optimization for boosted trees comprises tuning parameters such as the learning rate, the number of learners, and the minimum number of leaves to ameliorate the performance of the model. It is done by Bayesian optimization techniques to guide the search for the optimal set of hyperparameters through the probabilistic model. The following values were obtained for our model while keeping 20 % of the data for the validation phase to avoid overfitting problems: Minimum leaf size equals 1, Learning rate equals 0.1, and Number of learners equals 1000.

5 RESULTS

The results are presented briefly in Section 5.1 for the predictor importance, Section 5.2 for median trends, Section 5.3 for the residual analysis of the validation phase, and Section 5.4 for the final improved estimation using machine-learning techniques.

5.1 *Predictor importance*

The Predictor importance (PI) demonstrates the importance of the predictors in the prediction-making process. For the Machine Learning of the DT model for the lifelines recovery proposed herein, and based on (Derras & Makhoul, 2023), it was obtained that the systems (i.e., lifelines) are the most vital predictors (around 60%), then the CAV (15%), with the least importance given to the EMS_{98} with 0% relative value.

5.2 *Residuals' analysis of the validation phase*

For the residual analysis (equation 2), the box plot is used to show the interquartile range and lower/upper fence. Figure 6 shows the residuals analysis is an important step before validating any model, mainly the ML models. Since these last are based on the data. If the outcome of this analysis shows that not is any bias and the Q1 and Q3 are inferior to 3×RMSE it can be said that our model, statically speaking, is strong; which is the case for the Boosted tree model used here.

$$\text{Residuals_downtime} = \log_{10}(\text{Observed_downtime}) - \log_{10}(\text{predict_downtime}) \qquad (2)$$

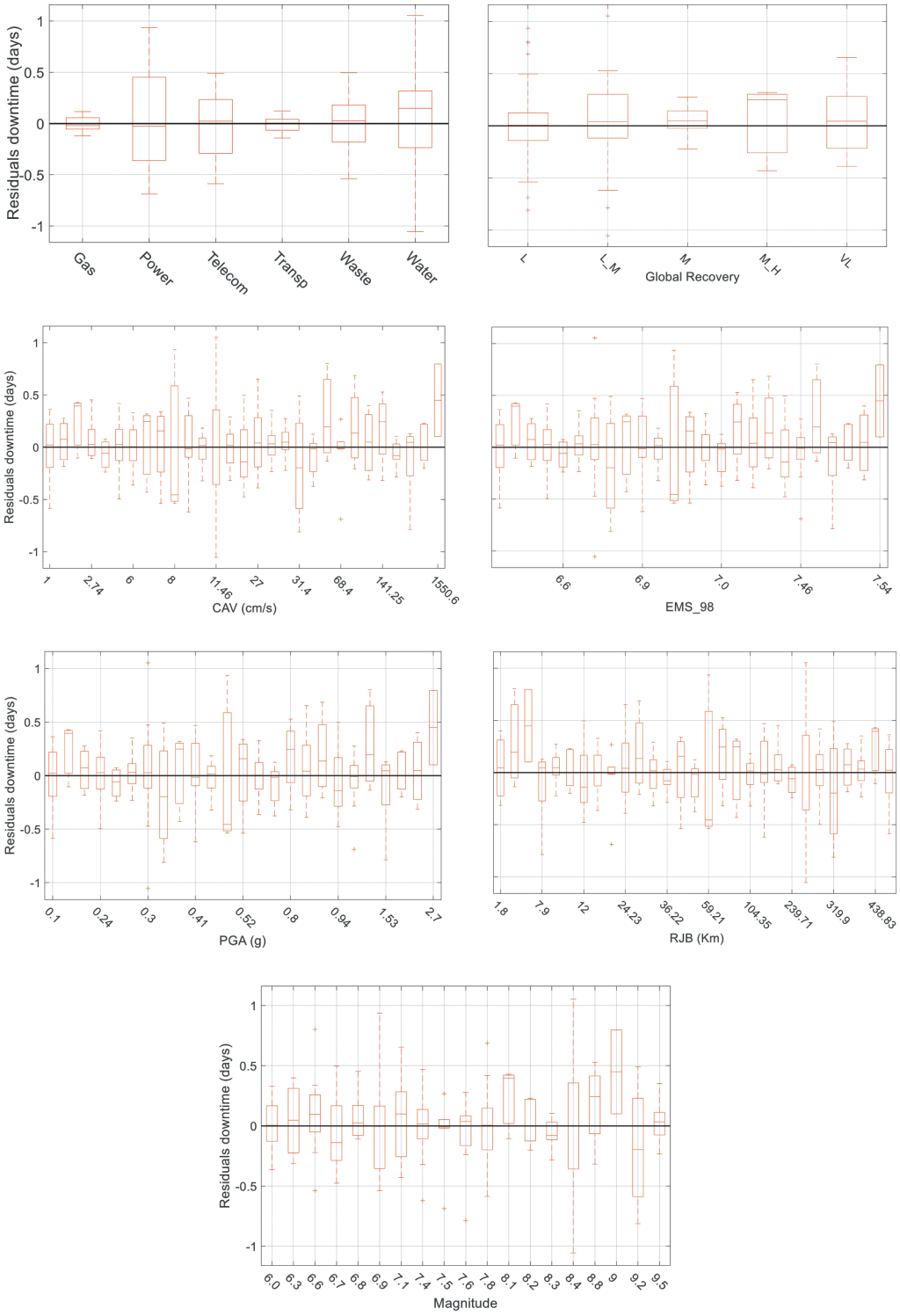


Figure 6. The residues' values (observed downtime minus predicted downtime) vs features (which represent inputs of machine learning algorithm: Figure 5). All residues (equation 2) have been obtained with the Boosted tree algorithm.

5.3 *Median trend*

To check the median trend again here we use the box plot concept. Figure 6 shows the comparison between data (observation) and prediction for all datasets. Through Figure 7, we notice that prediction values of downtime converge towards observation data. We can see that the statistical parameters: Q1, Q3, and IQR (yellow color) are lower than those of true data (blue color). In addition, medians (horizontal lines) getting closer.

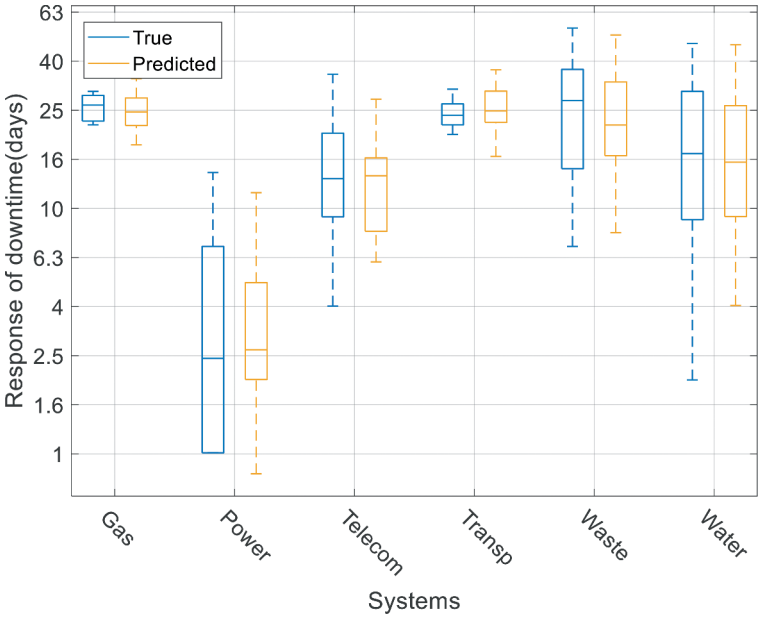


Figure 7. Comparison between data (observation) and prediction for all datasets.

5.4 *Improve estimation by using a machine-learning technique*

To demonstrate the improvements made by the machine-learning technique to the DT estimation model, Table 1 reports the values of the simple metrics RSME and R^2. It is done for the original model data (Kammouh et al. 2018) and the improved model data ((Kammouh et al. 2018) plus the boosted data for this study. It shows a significant improvement of 51% using RMSE and 757% when for R^2.

Table 2. Values of the simple metrics RSME and R^2.

Metrics (validation phase)	*Initial model*	*improved model*	*improvement (%)*
RMSE in log10	0.59	0.29	51
R^2 in log10	0.07	0.53	757

6 CONCLUSIONS

The recovery time (RT) or its complement the downtime (DT) are essential components of the infrastructure earthquake resilience analysis. Therefore, it is essential to keep the functionality of critical infrastructure and recover them quickly during strong earthquakes, which is reflected by a shorter recovery time.

A machine-learning empirical model is developed, in this article, for assessing the predicted DT using a dataset of earthquake damage to the gas, power, water, and telecommunications lifelines.

The ML models herein utilized the most renowned machine learning algorithms. The ML model was progressively improved by accounting for additional factors (i.e., RJB, CAV, etc.). The results are offered using the predictor importance, the median trend, and the residuals' analysis of the validation phase. It was concluded that 1) the selected factors can improve the DT model and 2) the lifeline systems are the most significant predictors followed by the CAV. Comparing several ML-model, it was found that the Boosted Tree algorithm is the best one for this issue. This model allows us to reduce the aleatory variability of 51 %.

This study is further developed for additional data and the full assessment is considered (Derras & Makhoul 2024).

ACKNOWLEDGEMENT

We acknowledge the École Spéciale des Travaux Publics, ESTP, the University of Tlemcen, the University of Saida, and the Ministry of higher education and scientific research (Algeria).

REFERENCES

BCCVL. (2021). *Boosted Regression Tree*. BCCVL Knowledge Base. https://support.bccvl.org.au/support/solutions/articles/6000083202-boosted-regression-tree

Bruneau, M., Chang, S. E., Eguchi, R. T., Lee, G. C., O'Rourke, T. D., Reinhorn, A. M., Shinozuka, M., Tierney, K., Wallace, W. A., & von Winterfeldt, D. (2003). A Framework to Quantitatively Assess and Enhance the Seismic Resilience of Communities. *Earthquake Spectra*, *19*(4), 733–752. https://doi.org/10.1193/1.1623497

Cao, Q. D., Miles, S. B., & Choe, Y. (2022). Infrastructure recovery curve estimation using Gaussian process regression on expert elicited data. *Reliability Engineering & System Safety*, *217*, 108054. https://doi.org/10.1016/j.ress.2021.108054

Cimellaro, G., Reinhorn, A., & Bruneau, M. (2006). Quantification of seismic resilience. *Proceedings of the 8th U.S. National Conference on Earthquake Engineering*.

Cremen, G., Seville, E., & Baker, J. W. (2020). Modeling post-earthquake business recovery time: An analytical framework. *International Journal of Disaster Risk Reduction*, *42*, 101328. https://doi.org/10.1016/j.ijdrr.2019.101328

Derras, B., Bard, P.-Y., Cotton, F., & Bekkouche, A. (2012). Adapting the Neural Network Approach to PGA Prediction: An Example Based on the KiK-net Data. *Bulletin of the Seismological Society of America*, *102*(4), 1446–1461. https://doi.org/10.1785/0120110088

Derras, B., & Makhoul, N. (2022). An overview of the Infrastructure seismic resilience assessment using Artificial Intelligence and machine-learning algorithms. *ICONHIC2022 - 3rd International Conference on Natural Hazards & Infrastructures*.

Derras, B., & Makhoul, N. (2023). Prediction of Recovery Time of Infrastructure Functionalities after an Earthquake Using Machine Learning. In F. Biondini & D. M. Frangopol (Eds.), *Eighth International Symposium on Life-Cycle Civil Engineering (IALCCE 2023)*.

Derras, B., & Makhoul, N. (2024). Machine Learning a tool for Prediction of Earthquake Recovery Time of Infrastructure Functionalities. *Forthcoming*.

Dubrow, A. (2021, June 23). Machine learning aids earthquake risk prediction. *ScienceDaily. University of Texas at Austin, Texas Advanced Computing Center.* https://www.sciencedaily.com/releases/2021/06/210623130649.htm

Durante, M. G., & Rathje, E. M. (2021). An exploration of the use of machine learning to predict lateral spreading. *Earthquake Spectra*, *37*(4), 2288–2314. https://doi.org/10.1177/87552930211004613

Hoque, A., Raj, J., Saha, A., & Bhattacharya, P. (2020). *Earthquake Magnitude Prediction Using Machine Learning Technique* (pp. 37–53). https://doi.org/10.1007/978-3-030-66763-4_4

Kammouh, O., Cimellaro, G. P., & Mahin, S. A. (2018). Downtime estimation and analysis of lifelines after an earthquake. *Engineering Structures*, *173*, 393–403. https://doi.org/10.1016/j.engstruct.2018.06.093

Sajan, K. C., Bhusal, A., Gautam, D., & Rupakhety, R. (2023). Earthquake damage and rehabilitation intervention prediction using machine learning. *Engineering Failure Analysis*, *144*, 106949. https://doi.org/10.1016/j.engfailanal.2022.106949

Zanini, M. A., Hofer, L., & Faleschini, F. (2019). Reversible ground motion-to-intensity conversion equations based on the EMS-98 scale. *Engineering Structures*, *180*, 310–320. https://doi.org/10.1016/j.engstruct.2018.11.032

Bridge Maintenance, Safety, Management, Digitalization and Sustainability – Jensen, Frangopol & Schmidt (eds)
© 2024 The Author(s), ISBN 978-1-032-77040-6
Open Access: www.taylorfrancis.com, CC BY-NC-ND 4.0 license

Information entropy-driven recovery strategies for systems' resilience

A. Tzioutziou & Y. Xenidis
Department of Civil Engineering, Aristotle University of Thessaloniki, Greece

ABSTRACT: A resilient system is able to overcome an adversity as a consequence of the anticipation of the disruption, the resistance to the damage, and mainly the recovery of its original functions. Especially in the context of technical systems, the recovery process relies on diverse estimations about performance levels and functional states. Therefore, the purpose of this research is to theoretically explore and practically employ a measure of information entropy, as an optimization variable for the process of recovery. Two novel entropy-driven recovery approaches are developed, modeled, and comparatively evaluated with a performance-based approach under different conditions of disturbance via agent-based simulations. The results suggest that the recoveries using the information entropy are more effective in both the performance maintenance and the time to recovery of the examined system, compared to the traditional recovery approach. The findings provide a conceptual and practical background to further utilize the information entropy for the design of recovery strategies and the engineering of systems' resilience.

1 INTRODUCTION

Resilience is broadly conceived as an emergent property, which enables the system to withstand and recover from a disturbance. Regardless of the application context, the established analytical description of recovery process features the definition of the system's original state, the damage state and the state after the recovery (Ahmadi et al. 2021, Hosseini et al. 2016). According to the literature, the concept of entropy is appropriate to describe the diverse system's states, especially when they dynamically evolve (Cabral et al. 2013, Fistola et al. 2020, Marťinez-Berumen et al. 2014, Purvis et al. 2019). Given its universal applicability, the information entropy is the most suitable entropy measure for such a generic application (Han et al. 2020, Purvis et al. 2017).

To this aim, the agent-based modeling approach effectively allows the observation of emergent behaviors, like resilience, in general types of complex systems (Tolk 2019). The agent-based model permits disaggregation of the examined system to the basic elements and their functions, which inherently determine its entropy (Batty 2010). Therefore, the agent-based simulation is considered an effective approach to estimate the system's entropy levels, as confirmed by several similar applications (Rahman et al. 2020, Wilson 2010). The purpose of this research is to theoretically investigate and practically deploy the measure of information entropy as a target criterion for the recovery process, by utilizing an agent-based approach. The results of the experimental entropy-driven recoveries' simulations are evaluated in comparison with a traditional performance-based recovery approach, in order to determine their effectiveness in the enhancement of resilience.

The paper is organized as follows. Section 2 presents the methodological steps for the development of the examined model, the recovery strategies and the analyses scenarios. Then, Section 3 comprises the results of the simulations and the respective analyses, while Section 4 concludes this work.

DOI: 10.1201/9781003483755-389

2 METHODOLOGY

The methodological approach for the evaluation of the impacts of the proposed entropy-driven recoveries on system's resilience relies on agent-based modeling, which is appropriate to effectively capture the effects of systems' emergence (Railsback & Grimm 2012) and particularly resilience (ten Broeke et al. 2016). This generic agent-based model is developed in order to examine diverse features of a complex technical system on the face of a set of specifically designed disruptions (Tzioutziou & Xenidis 2023).

This research methodology consists of two (2) sequential and discrete phases. It starts with the development of models with the corresponding recovery strategies and then continues with the development and the analysis of the different scenarios and their respective outcomes. The following sections present all the details about the aforementioned phases.

2.1 *Model development*

The purpose of the developed agent-based model is to simulate in a very simplistic manner, the structure and the function of a complex engineered system, such as an urban transportation network. As presented in Figure 1, the model includes two discrete but interdependent subsystems in the form of networks of undirected links between nodes in fixed locations.

In detail, Subsystem 1 consists of five (5) fully interconnected nodes (white-colored circles), whereas Subsystem 2 consists of four (4) nodes (black-colored squares) that are only connected with their closest neighbors with the respective intra-system links. The two subnetworks are partially interconnected via three trans-system links, which are illustrated in Figure 1 with thick black lines.

The system's sole function is to sustain and overcome a disturbance, while it is constantly monitoring its performance status. Hence, it is possible to explore the restorative capacity and to evaluate the overall resilience of the system. The system's performance estimation follows a simple approach, which has been originally introduced by Baggio & Hillis (2018) and further developed to meet the specific experiments' requirements. According to this approach, the nodes' connectedness is a measure of performance, estimated separately for each one of them by the number of its links. A simple directed intra-system link between two agents would get the value of 1, however, given that all the links are undirected, each link gets the value of 2. For the trans-system links, the performance estimation is more elaborate, to reflect their special role in the system. The estimation includes the summation of all the individual directed performances of the corresponding end nodes divided by the number of the trans-system links. The integrated performance value of the entire system is the sum of all the individual performances, which is finally transformed into percentage in order to easily capture the changes in the respective states.

Since the system's connectedness determines its performance, both the disturbance and the recovery of the system's functions are also associated with this aspect. In fact, the examined

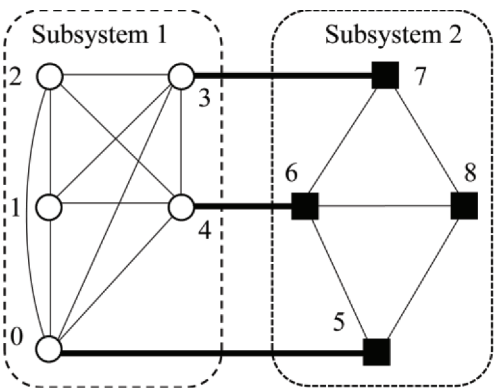


Figure 1. Structure of the developed model.

disruptions are designed as losses of specific links, while the recovery processes aim to restore the lost connectivity by establishing new links.

The agent-based model introduces the parameter of time in the form of procedural steps or ticks, which are useful for a variety of timeframes. The system's evolving performance states on the occurrence of the disruptive event are observed with reference to the tick axis, a fact that supports the estimation of the respective resilience metrics.

2.2 *Recovery strategies development*

The first recovery strategy is a simple approach, which serves as a reference basis for the evaluation of the advanced entropy-driven approaches. This recovery strategy is based on the performance of the examined system and particularly on the connectedness among the nodes within the subnetworks. As presented in the flowchart of Figure 2, the recovery process involves only few steps. At the beginning of the simulation, each subsystem's agent counts the number of its links with other neighboring agents and records its own original links. As the simulation continues, the agents constantly check the number of their own links and compare it with the respective original links. If these variables are equal for each one of the network's nodes, there are no missing links, the relative nodes are fully connected and the process ends at this point. On the other hand, if the original links of an agent are more than its current links, the algorithm identifies the loss and initiates the following restoration processes. The node with the missing links needs to identify another node that reports a loss and create a new link with it. It must be noted that in this approach the recovery relies entirely on the lost links reported by the agents, regardless of the disruption type. The performance-based recovery process runs firstly in Subsystem 1 and then in Subsystem 2 but effectively, it is executed in the same procedural step.

Although both the proposed entropy-driven approaches comprise more complex procedures, their basic recovery process is demonstrated in the flowchart of Figure 3. This recovery approach features two (2) sequential phases, first the identification of the agents that need restoration and second the main restoration that re-establishes the lost connections.

Particularly, the identification phase starts with the estimation of the information entropy for each one of the nodes of the examined subsystem. In this procedure each agent calculates the Shannon entropy for its own state of connectedness, by assessing the number of its current links over its original links according to Equation 1.

$$H = -\sum_{i=1}^{n} p_i \log p_i \tag{1}$$

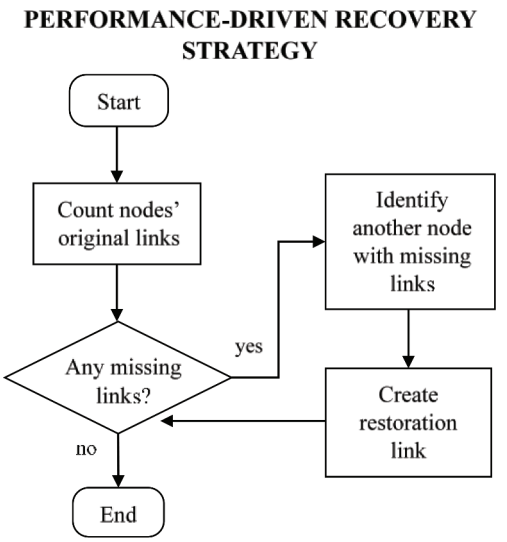


Figure 2. Flowchart of the performance-driven recovery strategy.

where p represents the node's connectedness state and is expressed as a quotient of the number of the node's current links divided by the number of its recorded original links.

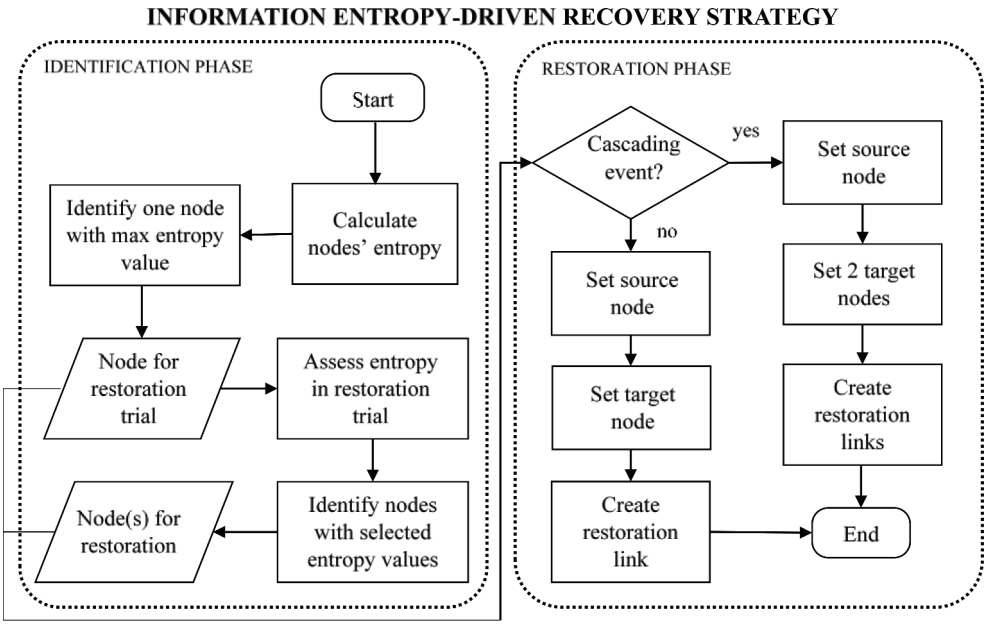


Figure 3. Flowchart of the entropy-driven recovery strategies.

Evidently, according to Equation 1, if the current links are equal to the original links, the agent is fully connected and the entropy value is zero (0), highlighting the complete and certain information about this connectivity state. Otherwise, if a link is missing, the respective agent's reported entropy value is greater than zero, reflecting the loss of information and the uncertainty about this connection. The algorithm needs to find at least one node with the maximum entropy value among all the other agents, in order to determine the most disturbed node.

The subsystem's agents execute the process of restoration trial in order to identify and finally record all the remaining disturbed agents in the examined subsystem. The specific node that was previously identified as the most affected by the disruptive event is already recorded and thus, it serves as the recovery target. One by one all the remaining agents, create a probationary link with the most disturbed agent, estimate the entropy of their connectivity status according to Equation 1 and then they report their updated information entropy levels, respectively. Through this procedure, the agents provide a measurable value that describes their state of connectedness. In particular, if the number of current links including the probationary link between two nodes exceed the number of the original links of this connection, the respective entropy value yields a negative number. Similarly, if the current connectedness state is identical to the original state, the respective entropy value is zero (0) and if the connectedness is not yet restored, the relevant information entropy value is a positive value. On this basis, it possible to discern the current connectedness states and accordingly, set the restoration target and select the appropriate nodes for restoration. These nodes pertain to the outcomes of the identification phase and constitute the fundamental inputs for the next phase.

At the beginning of the main restoration phase, the algorithm recognizes the ongoing disruption type, namely the simple and the cascading event and initiates the corresponding process for a single or double restoration links, respectively. In both the recovery strategies, the most disturbed node of the previous phase is set as the source or start, while the one (1) or two (2) affected nodes are the targets or ends of the respective restoration links. The

information entropy-based recoveries include procedures, which allow monitoring the states of connectedness and identifying the disruptive event, but also require more automation from the component agents. It must be noted that this recovery process is executed practically in parallel by the two subsystems. It starts with the identification phase in Subsystem 1 followed by Subsystem 2 and it moves on to the restoration of Subsystem 1 and then 2.

Although the majority of the procedures are identical between the two (2) proposed entropy-driven recoveries, the restoration target is their key difference. Recovery Strategy 2 aims for the re-establishment of the lost links and the recovery of the original connectedness and functionality state of the entire system. For this purpose, the restoration targets are the nodes that yield the highest entropy values during the restoration trial. On the contrary, Recovery Strategy 3 on the face of the disturbance aims to reach a better and more stable state of functionality for the system, by introducing new connections between the agents. In this case, the nodes with the lowest entropy values are set as the respective restoration targets. Table 1 presents the differences between Recovery Strategies 2 and 3 in terms of their discrete aims and computational approaches.

Table 1. Differences between the Recovery Strategies 2 and 3.

Information Entropy-Driven Recovery	Aim of recovery	Rule for arget nodes selection	Target nodes' entropy value
Strategy 2	Original state	Maximum Information Entropy	$H(x) \geq 0$
Strategy 3	New and more stable state	Minimum Information Entropy	$H(x) < 0$

2.3 *Analysis scenarios development*

Two (2) discrete disturbance scenarios are developed to investigate the effectiveness of each one of the three recovery strategies. Firstly, the simple disruptive event, which causes the least damage to the system with the loss of an individual intra-system link in each one of the two examined subnetworks. Secondly, the cascading disruptive event describes a more complex and severe damage, comprising the simultaneous collapse of two (2) links that connect to the same agent in Subsystem 1 and Subsystem 2, respectively. Table 2 presents the characteristics of the two examined disruptive scenarios of increasing magnitude and complexity.

Table 2. The disruptive scenarios and their damages to the subsystem and to the entire system, respectively.

Disruptive Event	Disturbance in each subsystem	Disturbance in entire system
Simple	1 link, 2 nodes	2 links, 4 nodes
Cascading	2 links, 3 nodes	4 links, 6 nodes

Each one of the recovery models is examined under both the disruptive events, leading to six (6) analysis scenarios. In each analysis scenario, a randomly located disruption, according to the relevant disruptive event scenario, occurs in the system, which directly responds by recognizing the affected elements and then starts the respective recovery strategy. For accuracy purposes, each analysis scenario is executed for 20 repetitive simulations by the NetLogo's BehaviourSpace tool (Wilensky 1999).

The simulation's outputs of the developed agent-based model include the system's performance level and the number of ticks to recovery. Based on these outcomes, a metric based on Bruneau's resilience loss is calculated for each simulation run of every analysis scenario, in order to compare directly the different recoveries impacts on the system's resilience (Bruneau

et al. 2003). The metric represents the percentage difference between the maximum performance and the observed performance levels, which is reduced as a result of the disturbance, as described by Equation 2:

$$R = \frac{Q_{max} - Q(t)}{Q_{max}} \tag{2}$$

where Q represents the performance of the system.

Further comparative analyses for all the relevant outcomes feature differential comparisons and sensitivity analyses, the latter of which is highly recommended for the evaluation of agent-based simulations (Railsback & Grimm 2012). Particularly, the sensitivity analysis estimates the differences between the performance-driven recovery that serves as the base case and the two (2) information entropy-driven recoveries. All the aforementioned analyses are implemented in Microsoft Excel 2013.

3 EFFECTIVENESS OF RECOVERY STRATEGIES

The increased effectiveness of the entropy-driven recovery strategies over the traditional performance-based approach is evident from the first findings on the performance levels and the ticks to recovery. The histograms of Figure 4 present the respective average outcomes of each examined strategy under the two disruptive scenarios. Based on the evidence of graph in Figure 4a, the entropy-based Strategies 2 and 3 maintain higher performance levels during both types of disturbance, compared to Strategy 1. Regarding the time to recovery, Figure 4b demonstrates that Strategy 1 leads to significantly longer recoveries, whereas Strategies 2 and 3 provide consistently the fastest recoveries, regardless of the disruptive event.

Despite the relatively small differences between these first findings, it is clear that the improvement in the duration of the recovery is more significant than the observed changes in the performance maintenance. In order to combine these results and to assess the effectiveness of the examined recovery strategies, the graph of Figure 5 presents the outcomes of the examined resilience metric.

The simulations' average resilience metrics confirm the trends identified in the previous performance-related results and support the argument that both the entropy-based recoveries are more beneficial for the system's resilience under any disturbance. Additionally, it is clear that the recovery strategies' capacity to preserve the systems functionality is affected by the type of the disruption. Particularly in the cascading event, the different entropy-driven approach of Strategies 2 and 3 is reflected in their impacts on the system's performance.

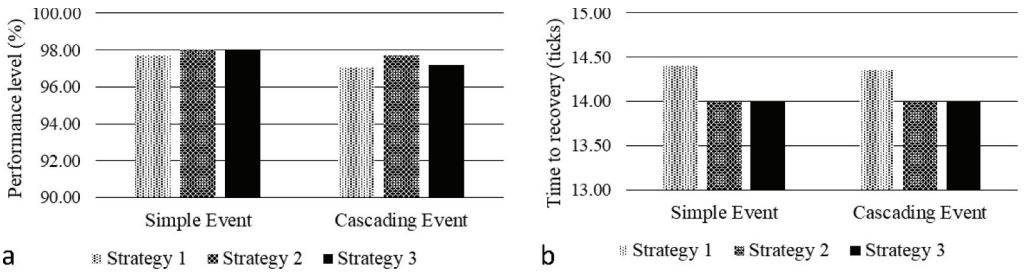


Figure 4. Simulations' average results for a) performance levels and b) ticks to recovery of each strategy, respectively, under the different disruption scenarios.

The sensitivity analysis provides a closer look to the changes among the respective observations between the basic performance-driven approach and the proposed entropy-driven recoveries in terms of performance maintenance, recovery time and resilience metric. Table 3

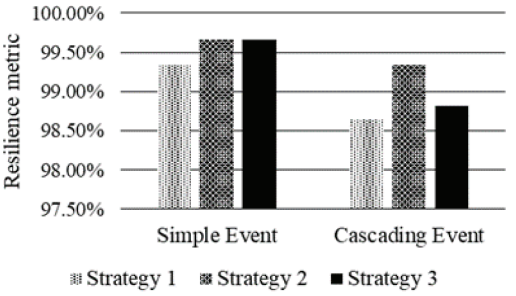


Figure 5. Simulations' average results for the examined resilience metric.

exhibits the results of the comparative sensitivity analyses, the simulations' outputs and their corresponding variances, as well as the percentage differences for both the simple and the cascading event, respectively.

Table 3. Data table of simulations' average results, variances, and differences in performance levels, time to recovery and resilience metric, under the different disruptive scenarios.

Simple event	Recovery strategies			cascading event	Recovery strategies		
	1	2	3		1	2	3
Performance				Performance			
Level (%)	97.71	98.03	98.04	Level (%)	97.02	97.71	97.19
Variance	0.227	3E-04	6E-04	Variance	0.442	0.001	0.482
Difference (%)		0.33	0.33	Difference (%)		0.71	0.18
Time to recovery (ticks)	14.40	14.00	14.00	Time to recovery (ticks)	14.35	14.00	14.00
Variance	3.621	0.000	0.000	Variance	3.713	0.000	0.000
Difference (%)		-2.78	-2.78	Difference (%)		-2.44	-2.44
Resilience				Resilience			
metric (%)	99.34	99.67	99.67	metric (%)	98.64	99.33	98.81
Variance	2E-05	3E-08	5E-08	Variance	4E-05	7E-08	5E-05
Difference (%)		0.33	0.33	Difference (%)		0.71	0.18

Based on the evidence of Table 3, the more severe and complex event leads to lower values of performance maintenance, in contrast to the respective results of the simple event scenario. The performance levels during the simple disruption suggest that Strategies 2 and 3 are more effective and significantly consistent in the system's performance maintenance, compared to Recovery Strategy 1. In fact, both the entropy-based approaches increase the performance level by 0.33%, however their fundamental operational difference is not obvious in these results. Concerning the results of the cascading event, the performance outputs lead to a different evaluation of the examined recoveries. Strategy 2 provides the highest performance value with the most consistent manner, while Strategy 3 only slightly surpasses the performance of Strategy, with similar levels of inconsistency. During the cascading disturbance, Strategy 2 yields an increase in the system's performance by 0.71%, whereas Strategy 3 leads to an insignificant increase of 0.18%, compared to the base case Recovery Strategy 1. It is interesting to note that during the most severe event, Strategy 2 is more effective in the performance maintenance, as opposed to Strategy 3 that seems to be negatively affected by the cascading event.

Regarding the time to recovery, the results of Table 3 demonstrate that both the entropy-driven strategies respond fast and absolutely consistently, regardless of the conditions of the disruption. The time to recovery of Strategy 1 also seems unaffected by the disturbance type, in both terms of value and variance. It must be noted that the reductions in the ticks to recovery by 2.78% for the simple and by 2.44% for the cascading event, are the most significant

differences, highlighting the impacts of the operational dimension of the examined recovery strategies.

Finally, the outcomes of the relevant resilience metric are highly correlated with the respective performance results, a fact complying with the selection of a performance-based metric. The resilience metrics provide quite high and consistent values, i.e., at an average of 99.56% in the simple event and at 98.98% in the cascading event, respectively. This evidence suggests that the system with its diverse recovery processes is greatly resilient to the designed disturbances. Following the trend of the respective performance results at the first rows of Table 3, the resilience metric yields identical percentage changes between the examined recoveries. Considering that the duration of the recovery process is reflected in the recorded sequence of performance values, this metric can integrate the aspect of duration. Nevertheless, the observed operational advantage of the reduced recovery times in the entropy-driven strategies is not reflected in the relative results of the examined resilience metric. This fact implies that the specific resilience metric is not appropriate to capture this operational feature of recovery and its impact to the system's resilience.

4 CONCLUSIONS

This research explored the potential impact of a novel recovery approach, which is based on the information entropy, on systems' resilience under different conditions of disturbance. Apart from the classic performance-based recovery strategy, this work featured the development of two computationally different recovery strategies. The outcomes of the relevant simulations highlight that the entropy-driven strategies increase the system's performance maintenance and reduce effectively the time to recovery, compared to the classic performance-based recovery.

Particularly, the recovery that focuses on the agents with the maximum information entropy value is the most effective strategy in the performance maintenance of the examined system, especially during the cascading event. Simultaneously, the recovery strategy of the entropy minimization fails to provide similarly increased performance levels in the most severe disruption, probably as a result of the different operational approach. Moreover, the performance-based resilience metric seems inappropriate to capture all the potential of the entropy-driven recoveries. The research findings support the exploration of the information entropy as an optimization variable for the recovery process and reveal new pathways towards the engineering of systems' resilience.

ACKNOWLEDGEMENT

The research work was supported by the Hellenic Foundation for Research and Innovation (HFRI) under the 3rd Call for HFRI PhD Fellowships (Fellowship Number: 5533).

REFERENCES

Ahmadi, S., Saboohi, Y. & Vakili, A. 2021. Frameworks, quantitative indicators, characters, and modeling approaches to analysis of energy system resilience: A review. *Renewable and Sustainable Energy Reviews* 144: 1–17.

Baggio, J.A. & Hillis, V. 2018. Managing ecological disturbances: Learning and the structure of social-ecological networks. *Environmental Modelling & Software* 109: 32–40.

Batty, M. 2010. Space, Scale, and Scaling in Entropy Maximizing. *Geographical Analysis* 42: 395–421.

Bruneau, M., Chang, S.E., Eguchi, R.T., Lee, G.C., O'Rourke, T.D., Reinhorn, A.M., Shinozuka, M., Tierney, K., Wallace, W.A. & von Winterfeldt, D. 2003. A Framework to Quantitatively Assess and Enhance the Seismic Resilience of Communities. *Earthquake Spectra* 19: 733–752.

Cabral, P., Augusto, G., Tewolde, M. & Araya, Y. 2013. Entropy in Urban Systems. *Entropy* 15: 5223–5236.

Fistola, R., Gargiulo, C. & La Rocca, R.A. 2020. Rethinking vulnerability in city-systems: A methodological proposal to assess "urban entropy." *Environmental Impact Assessment Review* 85: 1–14.

Han, W., Feng, Y., Qian, X., Yang, Q. & Huang, C. 2020. Clusters and the entropy in opinion dynamics on complex networks. *Physica A: Statistical Mechanics and its Applications* 559: 1–8.

Hosseini, S., Barker, K. & Ramirez-Marquez, J.E. 2016. A review of definitions and measures of system resilience. *Reliability Engineering & System Safety* 145: 47–61.

Marťinez-Berumen, H.A., López-Torres, G.C. & Romo-Rojas, L. 2014. Developing a Method to Evaluate Entropy in Organizational Systems. *Procedia Computer Science* 28: 389–397.

Purvis, B., Mao, Y. & Robinson, D. 2017. Thermodynamic Entropy as an Indicator for Urban Sustainability? *Procedia Engineering* 198: 802–812.

Purvis, B., Mao, Y. & Robinson, D. 2019. Entropy and its Application to Urban Systems. *Entropy* 21: 1–15.

Rahman, A., Naufal, F. & Partiwi, S.G. 2020. Measuring the entropy of organizational culture using agent-based simulation. In: Rachmawati, I., Hendayani, R. (eds.), *Proceedings of the International Seminar and Conference on Learning Organization* (ISCLO 2019). London: Routledge.

Railsback, S.F. & Grimm, V. 2012. *Agent-based and individual-based modeling : a practical introduction*, Princeton NJ: Princeton University Press.

ten Broeke, G., van Voorn, G. & Ligtenberg, A. 2016. Which sensitivity analysis method should I use for my agent-based model? *Journal of Artificial Societies and Social Simulation* 19: 1–35.

Tolk, A. 2019. Limitations and Usefulness of Computer Simulations for Complex Adaptive Systems Research. In: Sokolowski, J., Durak, U., Mustafee, N. & Tolk, A (eds.), *Summer of Simulation. Simulation Foundations, Methods and Applications*. Cham: Springer.

Tzioutziou, A. & Xenidis, Y. 2023. Assessing the Impact of Smart Initial Response Strategies on the Resilience of Complex Systems. In: *14th International Conference on Applications of Statistics and Probability in Civil Engineering (ICASP14)*. Dublin: Trinity's Access to Research Archive (TARA).

Wilensky, U. 1999. NetLogo. http://ccl.northwestern.edu/netlogo/. Center for Connected Learning and Computer-Based Modeling, Northwestern University, Evanston, IL.

Wilson, A. 2010. Entropy in Urban and Regional Modelling: Retrospect and Prospect. *Geographical Analysis* 42: 364–394.

Bridge Maintenance, Safety, Management, Digitalization and Sustainability – Jensen, Frangopol & Schmidt (eds)
© 2024 The Author(s), ISBN 978-1-032-77040-6
Open Access: www.taylorfrancis.com, CC BY-NC-ND 4.0 license

Physics-based earthquake-tsunami fragility surfaces for risk and resilience analysis

Mojtaba Harati & John W. van de Lindt
Center for Risk-Based Community Resilience Planning, Colorado State University

ABSTRACT: Community resilience models employ fragility functions to link hazard outcomes to infrastructure damage assessments. These predictions inform recovery analyses that consider cascading effects across economic, social, and household sectors. Current performance-based frameworks for tsunami engineering use distinct fragility curves for tsunami and earthquake effects but have not combined them due to data constraints. This study introduces a computational methodology for creating 3D earthquake-tsunami fragility surfaces for reinforced concrete frame buildings in coastal areas. The approach involves a two-stage analysis: earthquake followed by tsunami. Uncertainty is addressed through millions of nonlinear simulations that consider a number of structural, seismic, and tsunami-related variables. A proposed multi-distributed framework significantly enhances computational efficiency, facilitating more robust community resilience studies. The resulting 3D fragility surfaces account for isolated and combined earthquake-tsunami risks, offering a comprehensive tool for risk and resilience assessment.

Keywords: Community resilience, fragility functions, computational methodology, two-stage analysis, risk assessment

1 INTRODUCTION

Frameworks for resilience and performance-based design (PBD) have been proposed for various single- and multi-hazard events, inspired by the success of PBD in earthquake engineering and seismic provisions (Günay and Mosalam, 2013). These frameworks have expanded to cover different natural hazards, including coastal (González-Dueñas and Padgett, 2021), hurricane-related (Barbato et al., 2013), wind engineering (Spence and Arunachalam, 2022), and tsunami engineering (Attary et al., 2021, 2017), among others. They separate the risk into key components, namely hazard analysis, structural system characterization, structural analysis, damage analysis, and risk assessment. For community-scale modeling, fragility functions—which integrate structural system characterization and analysis—are essential for predicting damage across diverse building types.

Earthquake fragility curves are well-documented in the literature (Akhoondi and Behnamfar, 2021; Bandyopadhyay et al., 1990; Chen et al., 2022; Kazantzi et al., 2008; Li et al., 2014; Xu et al., 2018). There is also a growing body of research on tsunami fragility curves for building structures, encompassing both empirical and physics-based fragility functions. Most empirical-based tsunami fragility curves are correlated with tsunami inundation depth because it it can be observed and correlated to damage levels (Petrone et al., 2017). Some studies have explored the development of physics-based tsunami fragility curves, primarily using the Nonlinear Static Procedure (NSP) to account for the total equivalent tsunami force. These curves generally consider the tsunami effects separately from earthquake effects, and their combined impacts are often statistically combined in resilience-based frameworks. However, some studies have tried to incorporate the effects

DOI: 10.1201/9781003483755-390

of both earthquake and tsunami hazards simultaneously. For example, a few studies (e.g. Park et al. 2012; (Attary et al., 2021); Xu et al., 2021) have employed successive analyses to simultaneously account for both hazards, revealing that earthquake effects notably elevate collapse failure probabilities.

To account for uncertainties associated with this two-phase successive analysis, advanced computational methods are crucial. Multi-distributed parallel processing methods have been proposed to address the computational demands of various problems, including flood simulations, earthquake simulations, structural optimization, and structural reliability, to name a few (Ginting & Mundani, 2019; Wijerathne et al., 2013; París et al., 2013; Umesha et al., 2007; Hardyniec & Charney, 2015; Toma et al., 2016; Vicente da Silva et al., 2015; Yu et al., 2020).

This study, exemplified using a four-story reinforced concrete (RC) building as a representative case, introduces a versatile multi-distributed framework that overcomes computational challenges in creating 3D earthquake-tsunami fragility surfaces. It accommodates structural and hazard uncertainties and allows detailed structural models. The framework's adaptability extends to various scenarios, promising advancements in risk assessment and disaster preparedness. It is a valuable tool for researchers and practitioners dedicated to enhancing our understanding of structural vulnerabilities and strengthening our ability to protect and support communities in the face of diverse and evolving challenges.

2 PROBLEM STATEMENT

Earthquakes and tsunamis are intrinsically linked hazards that can result in cumulative damage. Despite originating from a common source, they impact structures independently and sequentially, each causing both structural and non-structural damage. While these hazards are statistically independent in terms of structural impact, accounting for reduced structural strength post-earthquake is essential when assessing sequential loading. Bayes' theorem provides a mathematical framework for this, updating the reliability assessment of a structure based on new information from subsequent hazards. In reliability analysis, the theorem serves to recalibrate beliefs or predictions concerning system or component reliability in light of new data can be expressed as

$$P(TS \mid EQ) = \frac{P(EQ \mid TS) \cdot P(TS)}{P(EQ)} \tag{1}$$

Equation (1) formalizes the conditional failure probability $P(TS|EQ)$, which is the focus of this paper. This term quantifies the likelihood of a structure collapsing during a tsunami, given prior damage from an earthquake. $P(TS)$ and $P(EQ)$ represent the individual failure probabilities due to tsunamis and earthquakes, respectively, and are established as 2D fragility functions in existing literature (Bandyopadhyay et al., 1990; Chen et al., 2022; Li et al., 2014; Alam et al., 2018; Attary et al., 2017; Petrone et al., 2017). The term $P(EQ|TS)$, though included in the equation, is not practically applicable as tsunamis do not naturally precede earthquakes. $P(TS|EQ)$ can be interpreted as the fragility function for tsunamis when considering antecedent earthquake damage.

In deriving P(TS|EQ) using Bayes' equation, the term $P(EQ|TS)$ is theoretically required, which complicates the analysis due to its impracticality in real-world scenarios. To circumvent this, the current research introduces a novel two-phase sequential analysis approach, allowing for the determination of earthquake-tsunami fragility functions without depending on $P(EQ|TS)$. This innovative methodology effectively navigates the intricate interplay between earthquake and tsunami hazards, thereby contributing a pragmatic tool for structural reliability analysis.

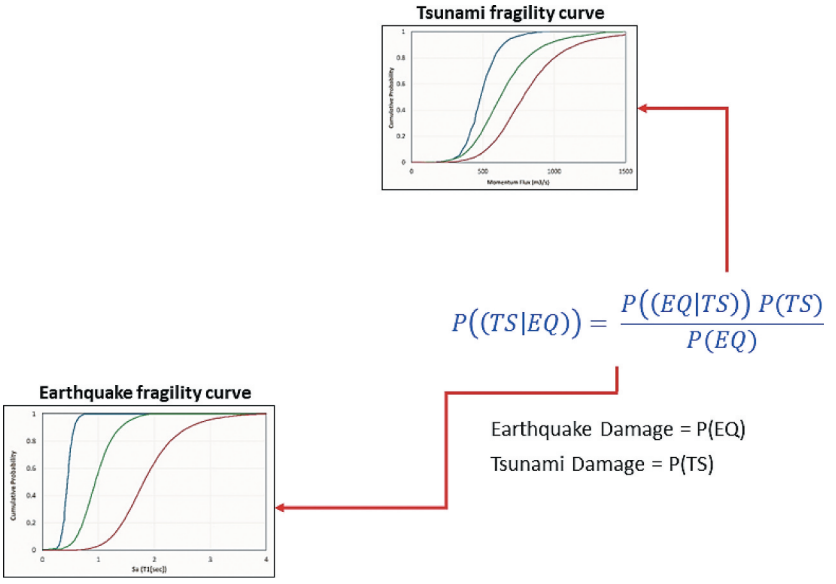


Figure 1. Conceptual demonstration of the problem.

3 METHODOLOGICAL APPROACH

This study leverages the computational power of clusters and supercomputers, comprised of numerous machines, each housing ten to thousands of CPUs or GPUs. In this case, a cluster boasting 1160 CPUs, distributed across 29 distinct computers, each equipped with 40 CPUs, serves as the primary computing infrastructure (Figure 2). The study's multi-distributed framework capitalizes on parallel programming, harnessing the capabilities of the Message Passing Interface (MPI) for efficient processing. In this MPI framework, a send and receive protocol is employed to dispatch all tasks (N jobs) from the manager node to the available worker nodes. These worker nodes can either reside within a single cluster or supercomputer

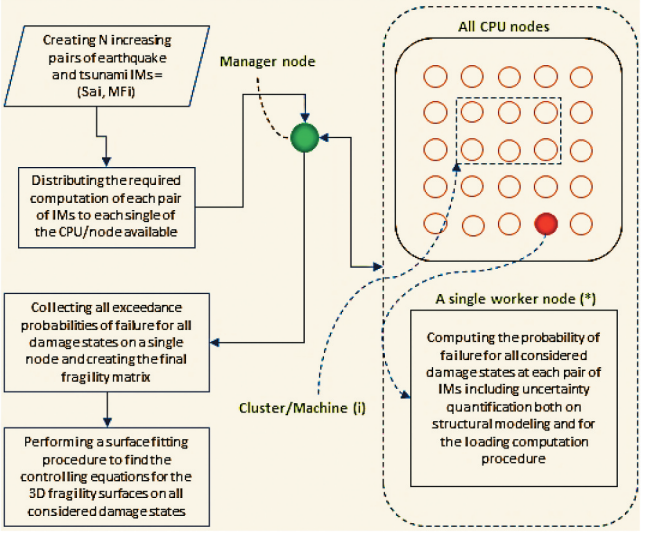


Figure 2. Multi-distributed framework designed to solve the 3D fragility surface problem.

or can be extended by incorporating nodes from external clusters. Each worker node and its CPUs independently carry out the required computations, with the results relayed back to the manager node, where they are consolidated into a single file.

Within this computational framework, the input matrix is structured with the first two columns dedicated to the earthquake and tsunami Intensity Measures (IM), creating N pairs of joint-IM values. The IM values exhibit an increasing trend in both directions, necessitating a proper definition of discretization on each axis. For example, to attain 900 joint IM points, 30 points along each IM axis are designated, ensuring 30 distinct values of tsunami IM for each earthquake IM value. Each row of the input matrix contains two IM values: the Spectral Acceleration (Sa) and the Momentum Flux (MF). Through MPI programming, N sequential algorithms are replicated with N paired input values (Sai, MFi), which are subsequently dispatched to the manager node for distribution among the worker cores/CPUs. For more information on this method, readers are referred to the study by Harati and van de Lindt (2023a).

4 TWO-PHASE SUCCESSIVE ANALYSIS

The foundation of this study rests on the concept of the "successive analysis procedure," a pivotal technique essential for crafting earthquake-tsunami fragility surfaces, shown in Figure 3. This procedure involves two distinct phases of analysis, carefully designed to encapsulate the cascading effects of both earthquake and tsunami loadings on a given structure.

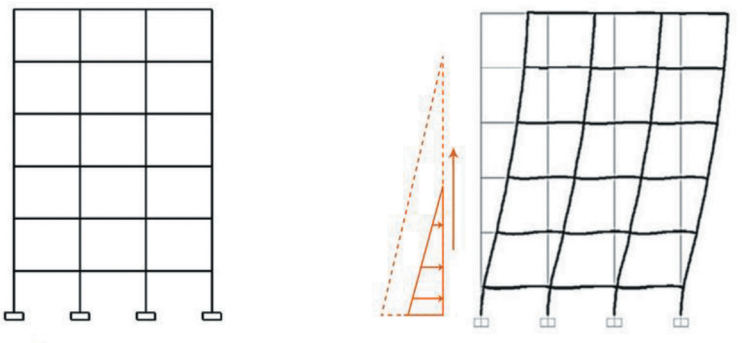


Figure 3. Proposed two-phase successive analysis procedure.

In the initial phase, the structural response to earthquake ground motion is simulated through the Multiple Strip Analysis (MSA), adhering to Baker's recommendations (Baker, 2015). The seismic intensity is quantified by selecting the spectral acceleration (Sa) at the system's first-mode period. The Sa is then systematically increased through point scaling, generating multiple ground motion scenarios. Subsequent to these analyses, the peak inter-story drift ratio is evaluated as the engineering demand parameter (EDP), facilitating the delineation of slight, moderate, and complete damage states, in line with Hazus recommendations (2020). The second phase centers on the structural response under equivalent tsunami forces, necessitating a force-based nonlinear static procedure (NSP). Notably, this analysis phase is initiated following a free vibration analysis, encompassing the structural damage sustained during the earthquake phase. In the tsunami simulation, a variable-height load pattern is employed, which closely mirrors the hydrodynamic force of the tsunami wave. A key component in the analysis is the consideration of the momentum flux (*hu^2*) as the Intensity Measure (IM) for tsunami, a parameter strongly correlated with structural damage. Furthermore, the second phase introduces the shear capacity of the seaward columns as additional EDPs, factoring the shear capacity of the columns in conjunction with the inter-story drift. This multifaceted approach for modeling the structural response provides a comprehensive understanding of the effects of earthquake and tsunami loadings on the structure (Attary et al., 2021).

The structural modeling utilized for this study revolves around a four-story reinforced concrete (RC) building, representative of a typical RC moment-resisting frame (MRF) structure found in Los Angeles, California. This structure was designed with a focus on capacity-based design, adhering to seismic codes and provisions such as the International Building Code, ASCE 7-02, and ACI 318 (Haselton et al., 2011). The seismic characteristics and detailing of the members are based on the spectrum acceleration coordinates of SS = 1.5 g and S1 = 0.6 g, suited for a site with a soil class D. The structural model, implemented using the OpenSeesPy software, incorporates both stiffness and strength aspects. The gravity load destabilization effects are effectively accounted for by introducing leaning columns linked to the structure using truss-based link elements. Moreover, the shear panel at the joints is modeled with Joint2D elements, and a nonlinear rotational spring model, specifically the modified Ibarra-Medina-Krawinkler (IMK) deterioration model (Lignos and Krawinkler, 2011), controls the degrading behavior of elements concerning strength and stiffness. In addition, the shear behavior of the beam-column joints is controlled through a nonlinear uniaxial material model. To complete the structural simulation, the Rayleigh damping method with a random damping ratio is introduced to account for viscous damping (Attary et al., 2021).

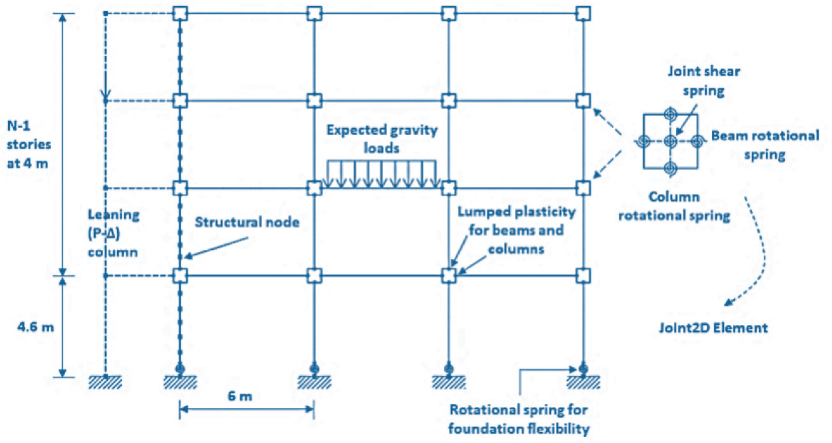


Figure 4. Macro modeling of the structural system in OpenSeesPy (Haselton et al., 2011).

In addressing the complexities of this multi-hazard analysis, the study embraces the importance of uncertainty modeling, as brought in Table 1. The uncertainties associated with ground motions (GMs) required for the Multiple Strip Analysis (MSA) are quantified using a suite of far-field GMs, following FEMA P-695 recommendations. For the input tsunami forces, uncertainties are incorporated by modeling the *Co* and *Cd* factors (refer to: Harati and van de Lindt (2023a)) as random variables with uniform distributions. Additionally, numerous parameters in the structural analysis are modeled as random variables, contributing to a comprehensive representation of the structural system's uncertainties (Harati and van de Lindt (2023a)). This multifaceted approach, anchored by the successive analysis procedure, serves as a powerful tool for comprehensively evaluating structural vulnerabilities and responses in the face of earthquake and tsunami events.

Table 1. The characteristics of the random variables used to model the structural system as well as the tsunami lateral loading (Harati and van de Lindt, 2024).

Random Variable	Distribution type	Mean	COV
C_o	Uniform (0.35-1)	-	-
C_d	Uniform (1.25-2)	-	-

(*Continued*)

Table 1. (*Continued*)

Random Variable	Distribution type	Mean	COV
Dead load and seismic mass	Log-normal	1.05 ×(computed)	0.1
Damping ratio	Log-normal	0.065	0.60
Element strength	Log-normal	1.0 × (computed)	0.12
Element initial stiffness	Log-normal	1.0 × (computed)	0.36
Element hardening stiffness	Log-normal	0.5 × (computed)	0.50
Plastic rotation capacity	Log-normal	1.0 × (computed)	0.60
Post-capping stiffness	Log-normal	0.08 × (-Kelastic)	0.60
Column footing rotational stiffness	Log-normal	1.0 × (computed)	0.3
Joint shear strength	Log-normal	1.40	0.1

5 RESULTS

The study offers a detailed analysis of the fragility matrix for a 4-story ductile RC frame, using a 30x30 matrix and joint intensity measures: Sa for earthquakes and MF for tsunamis. Based on the recommendation of Harati and van de Lindt (2023a), 400 data points for joint IMs are sufficient for generating accurate earthquake-tsunami fragility surfaces. Figure 5 shows discrete data points indicating the complete collapse of the 4-story RC frame. Notably, the term $P(TS|EQ)$ is computed using our method, avoiding the impractical term $P(EQ|TS)$.

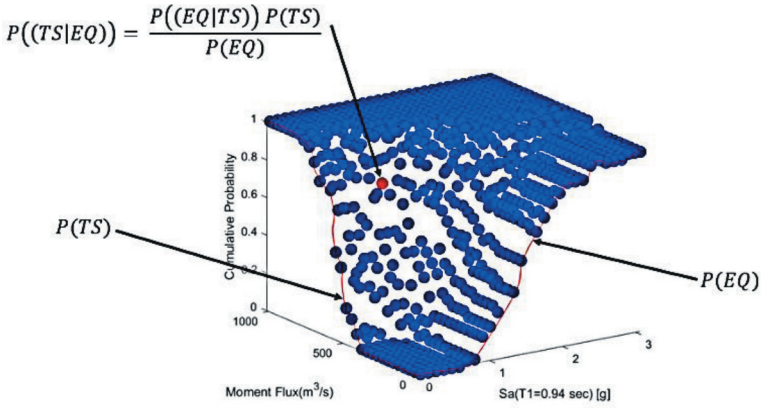


Figure 5. Graphical output of the fragility matrix computed by the proposed multi-distributed methodology.

Figure 6(a) shows the earthquake-tsunami fragility surface for a representative building, where the x and y-axes denote earthquake and tsunami intensity measures (IM), respectively, and the z-axis indicates the exceedance probability of building collapse. Governed by Equation (2), the surface originates from the mathematical model $h(E, C1, C2, \alpha, n, Sa,\ MF)$, as proposed by Kern et al. (2004). This model has five unknown parameters for estimating the joint failure probability $P(Sa,\ MF)$:

$$P(Sa,\ MF) = \frac{E.\left(\frac{Sa}{C1} + \frac{MF}{C2} + \alpha.\left(\frac{Sa}{C1}\right).\left(\frac{MF}{C2}\right)\right)^n}{\left(\left(\frac{Sa}{C1} + \frac{MF}{C2} + \alpha.\left(\frac{Sa}{C1}\right).\left(\frac{MF}{C2}\right)\right)^n + 1\right)} \tag{2}$$

The unknown parameters can be obtained using a surface-fitting optimization procedure suggested by Kern et al. (2004). According to Equations (1) and (2), the relationships below are valid:

$$P(TS \mid EQ) = P(Sa,\ MF) \tag{3}$$

From Equation (5), the impractical term in Equation (1), $P(EQ/TS)$, can be represented through parameters in Equation (2). Thus, the desired term in Equation (1), $P(TS/EQ)$, can be approximated as follows:

$$P(EQ \mid TS) = h(E, C1, C2, \alpha, n, Sa,\ MF).\left(\frac{P(EQ)}{P(TS)}\right) \tag{4}$$

$$P(EQ \mid TS) = f(E, C1, C2, \alpha, n, Sa,\ MF) \tag{5}$$

$$P(TS \mid EQ) = f(E, C1, C2, \alpha, n, Sa,\ MF)\left(\frac{P(TS)}{P(EQ)}\right) \tag{6}$$

Figure 6 (b) illustrates earthquake-tsunami fragility surfaces for the 4-story ductile RC system, covering all assessed damage states, including slight, moderate, and complete damage. Along each edge of these fragility surfaces, there are three sets of 2D fragility curves. For instance, within the Sa and z-axis plane, one can observe the 2D fragility curves for earthquake-only hazards ($P(EQ)$), reflecting various damage states. Similarly, on the opposing side of the fragility surfaces along the MF axis, 2D fragility curves for tsunami-only hazards ($P(TS)$) across different damage states can be observed.

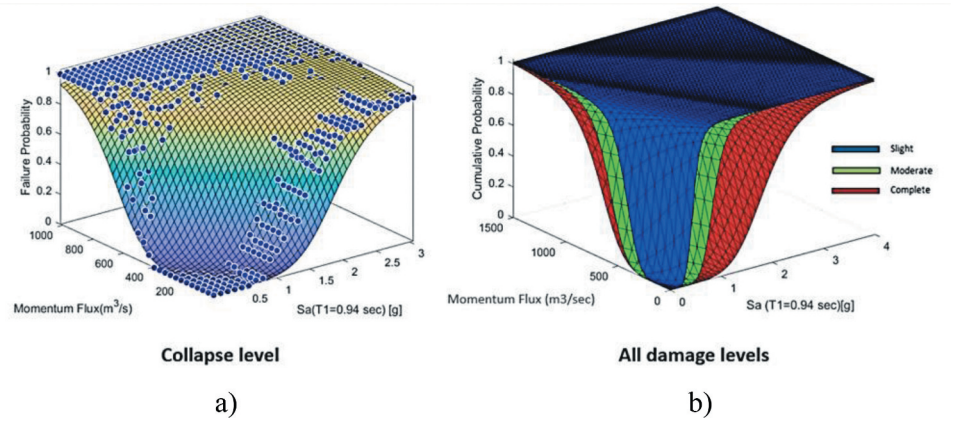


Figure 6. Surface fitting over the raw data of fragility matrix datapoints and the final surfaces for different damage states: a) discrete data points for the collapse damage state versus the final surface fitted to them, and b) fragility surfaces in different damage states.

In Figure 7, the performance of the framework and the corresponding computational time are depicted as the number of requested cores/CPUs increases along the x-axis. This analysis encompasses two scenarios, one with N equal to 225 and the other with N equal to 400. For clarity, when the CPU count is set to 120, parallel processing occurs with 120 CPUs exclusively. Notably, a significant reduction in computational time is observed once the CPU count exceeds 80, irrespective of the case. Figure 10 serves as a reference point, with one CPU symbolizing the computational capability of a single machine or a basic personal computer running these analyses sequentially. The data presented in Figure 7 reveals that a single machine requires 203 days to complete the computational analysis for cases with N=400 and 101 days for cases with N=225.

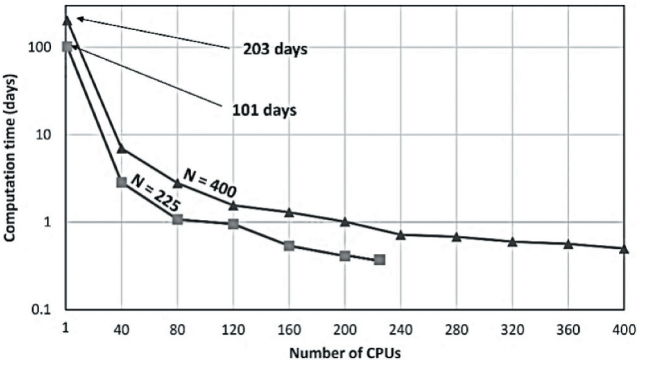


Figure 7. The computation time required for the generation of 3D fragility surfaces with N values equal to 225 and 400 shown for a single machine versus multi-distributed systems with increasing numbers of CPUs.

6 CONCLUSIONS

This study presents a novel framework for multi-distributed parallel processing, tailored for the generation of three-dimensional fragility surfaces relevant to earthquake and tsunami hazards. The framework rigorously accounts for uncertainties in structural modeling and hazard-induced loadings. A case study employing a Reinforced Concrete (RC) moment frame validates the framework's efficiency, illustrating that a configuration of 400 cores processing 400 data points delivers robust results. This computational approach substantially reduces both time and computational overhead, offering a scalable solution for generating fragility surfaces adaptable to diverse structural archetypes within a community. The produced surfaces quantify risk associated with individual earthquake and tsunami scenarios, as well as their concurrent impacts. The study also highlights the imperative of incorporating earthquake-induced modifications in tsunami fragility assessments, particularly following high-magnitude seismic events. These insights can contribute significantly to the body of knowledge in risk and resilience engineering by enabling efficient analyses.

ACKNOWLEDGEMENTS

The Center for Risk-Based Community Resilience Planning is a NIST-funded Center of Excellence; the Center is funded through a cooperative agreement between the U.S. National Institute of Standards and Technology and Colorado State University (NIST Financial Assistance Award Numbers: 70NANB15H044 and 70NANB20H008). The views expressed are those of the presenter and may not represent the official position of the National Institute of Standards and Technology or the U.S. Department of Commerce.

REFERENCES

Akhoondi, M.R., Behnamfar, F., 2021. Seismic fragility curves of steel structures including soil-structure interaction and variation of soil parameters. Soil Dynamics and Earthquake Engineering 143, 106609. https://doi.org/10.1016/j.soildyn.2021.106609

Attary, N., Unnikrishnan, V.U., van de Lindt, J.W., Cox, D.T., Barbosa, A.R., 2017. Performance-Based Tsunami Engineering methodology for risk assessment of structures. Engineering Structures 141, 676–686. https://doi.org/10.1016/j.engstruct.2017.03.071

Attary, N., Van De Lindt, J.W., Barbosa, A.R., Cox, D.T., Unnikrishnan, V.U., 2021. Performance-Based Tsunami Engineering for Risk Assessment of Structures Subjected to Multi-Hazards: Tsunami following Earthquake. Journal of Earthquake Engineering 25, 2065–2084. https://doi.org/10.1080/13632469.2019.1616335

Baker, J.W., 2015. Efficient Analytical Fragility Function Fitting Using Dynamic Structural Analysis. Earthquake Spectra 31, 579–599. https://doi.org/10.1193/021113EQS025M

Bandyopadhyay, K.K., Hofmayer, C.H., Kassir, M.K., Pepper, S.E., 1990. Seismic fragility of nuclear power plant components (Phase II). (No. NUREG/CR-4659-Vol.3, BNL-NUREG–52007-Vol.3, 7252519). https://doi.org/10.2172/7252519

Barbato, M., Petrini, F., Unnikrishnan, V.U., Ciampoli, M., 2013. Performance-Based Hurricane Engineering (PBHE) framework. Structural Safety 45, 24–35. https://doi.org/10.1016/j.strusafe.2013.07.002

Chen, L., Huang, C., Chen, H., Zheng, Z., 2022. Seismic fragility models of a bridge system based on copula method. Earthquake Spectra 38, 1417–1437. https://doi.org/10.1177/87552930211052573

González-Dueñas, C., Padgett, J.E., 2021. Performance-Based Coastal Engineering Framework. Front. Built Environ. 7, 690715. https://doi.org/10.3389/fbuil.2021.690715

Günay, S., Mosalam, K.M., 2013. PEER Performance-Based Earthquake Engineering Methodology, Revisited. Journal of Earthquake Engineering 17, 829–858. https://doi.org/10.1080/13632469.2013.787377

Haselton, C.B., Liel, A.B., Deierlein, G.G., Dean, B.S., Chou, J.H., 2011. Seismic Collapse Safety of Reinforced Concrete Buildings. I: Assessment of Ductile Moment Frames. J. Struct. Eng. 137, 481–491. https://doi.org/10.1061/(ASCE)ST.1943-541X.0000318

Hazus Earthquake Model Technical Manual, 2020. 436.

Harati, M., van de Lindt, J.W., 2024. Methodology to Generate Earthquake-tsunami Fragility Surfaces for Community Resilience Modeling. Engineering Structures.

Kazantzi, A.K., Righiniotis, T.D., Chryssanthopoulos, M.K., 2008. Fragility and Hazard Analysis of a Welded Steel Moment Resisting Frame. Journal of Earthquake Engineering 12, 596–615. https://doi.org/10.1080/13632460701512993

Li, Y., Song, R., Van De Lindt, J.W., 2014. Collapse Fragility of Steel Structures Subjected to Earthquake Mainshock-Aftershock Sequences. J. Struct. Eng. 140, 04014095. https://doi.org/10.1061/(ASCE)ST.1943-541X.0001019

Lignos, D.G., Krawinkler, H., 2011. Deterioration Modeling of Steel Components in Support of Collapse Prediction of Steel Moment Frames under Earthquake Loading. J. Struct. Eng. 137, 1291–1302. https://doi.org/10.1061/(ASCE)ST.1943-541X.0000376

Park, S., van de Lindt, J.W., Cox, D., Gupta, R., Aguiniga, F., 2012. Successive Earthquake-Tsunami Analysis to Develop Collapse Fragilities. Journal of Earthquake Engineering 16, 851–863. https://doi.org/10.1080/13632469.2012.685209

Petrone, C., Rossetto, T., Goda, K., 2017. Fragility assessment of a RC structure under tsunami actions via nonlinear static and dynamic analyses. Engineering Structures 136, 36–53. https://doi.org/10.1016/j.engstruct.2017.01.013

Spence, S.M.J., Arunachalam, S., 2022. Performance-Based Wind Engineering: Background and State of the Art. Front. Built Environ. 8, 830207. https://doi.org/10.3389/fbuil.2022.830207

Xu, C., Deng, J., Peng, S., Li, C., 2018. Seismic fragility analysis of steel reinforced concrete frame structures based on different engineering demand parameters. Journal of Building Engineering 20, 736–749. https://doi.org/10.1016/j.jobe.2018.09.019.

Bridge Maintenance, Safety, Management, Digitalization and Sustainability – Jensen, Frangopol & Schmidt (eds)
© 2024 The Author(s), ISBN 978-1-032-77040-6
Open Access: www.taylorfrancis.com, CC BY-NC-ND 4.0 license

Bridge maintenance methodology accounting for climate change dependent parameters

S.A. Keo & N. Makhoul
Associate Professor, ESTP – Grande école d'ingénieurs de la construction, Dijon, France

ABSTRACT: The article demonstrates the climate change impact on the corrosion damage of an inspected bridge abutment (6 meters by 1.5 meters) through the maps of corrosion alarm probabilities obtained from a Bayesian network (BN) predictive model. The methodology for establishing corrosion alarm mapping of the first layer reinforcements consists of three steps: building the database, learning the BN structure and parameters from the non-destructive inspection data (NDT data), and using the BN for creating the corrosion alarm map. The studied BN model has four 4 variables: corrosion potential, corrosion rate, electrical resistivity of concrete cover, and corrosion alarm (related to corrosion rate). The available corrosion potential values (NDT data) of the inspected bridge abutment are used as the new information for updating the BN model to obtain the probability corrosion alarm map. Two scenarios are proposed in the study: decrease of 50 mV in all points, and decrease of 50 mV in the middle part, and of 100 mV in the edges. The results open a perspective to implement the real environmental exposition classes of the structures in the BN model to obtain a resilient maintenance (for corrosion of reinforcements) strategy.

1 INTRODUCTION

The Bridges are one of the most critical transportation infrastructures. However, most of bridges were built mainly in the last decades. Therefore, they are aging, and their reinforced concrete structural elements are suffering from reinforcements corrosion (AFGC, 2004). To face this issue, many monitoring techniques and maintenance strategies have been developed by various scientific and expert communities. Different maintenance methodologies were proposed, combined with on-site inspection and different non-destructive techniques (NDT) have been used to obtain relevant durability indicators for the concrete structures (Gomez et al., 2018). However, constraints (economic and feasibility) on the on-site measurements lead to partial information for the inspected structures. To resolve this issue (lack of information), Bayesian networks (BN) have been used in many methodologies (Tran et al., 2015). A recent BN based methodology has been proposed for creating 2D maps of corrosion alarm probabilities related to corrosion levels of the reinforcements (Keo et al., 2022, 2023a, 2023b). It is a predictive model (i.e., specifically before the propagation of the corrosion) accounting for various indicators such as electrical resistivity of concrete cover, corrosion rate, polarization resistance, capacitance, thickness of concrete cover, and half-cell potential. The methodology is divided into three stages: creating data base, learning stage, and utility stage. The learning stage led the predictive model to a final BN structure called physically optimal with three indicators: the corrosion potential, the corrosion rate, and the electrical resistivity.

However, the methodology didn't account for climate change. Climate change can affect the structure degradation with the increase of CO_2 concentration, temperature, and changes in relative humidity (Iamsumang et al., 2018). It can also increase uncertainty on model parameters. To enhance the resilience of bridges to climate change, this paper demonstrates

DOI: 10.1201/9781003483755-391

the climate change impact on the corrosion damage of the inspected structures through the maps of corrosion alarm probabilities obtained by the proposed BN based methodology. Moreover, variation of the corrosion potential values (one of the durability indicators) will be linked with two suggested climate change scenarios.

2 MATERIAL AND METHOD

2.1 *Methodology and Bayesian network used in the present study*

The methodology based on a Bayesian network (BN) developed in the previous study (Keo et al., 2022, 2023a, 2023b), for creating corrosion alarm maps of reinforcements for inspected real structures, is used in the present study. The methodology consists of three principal phases: database construction based on NDT inspection data, structure and parameter learning, and utility of BN for corrosion alarm mapping. The procedure of the methodology is illustrated in Figure 1 (Keo et al., 2023). The database of all parameters (thickness of concrete cover, capacitance, corrosion potential, electrical resistivity of concrete cover, corrosion rate, corrosion level, and corrosion alarm) was used for the Bayesian network. The structure and parameter learning were then carried out in the second step to obtain the optimal BN structure, and conditional probability function (CPF) of each variable of the BN. Finally, the corrosion alarm map (probabilities of corrosion alarm of all the points on the surface of the inspected element) is obtained after updating the BN with available NDT data (as new information of the BN) for the inspected structural element.

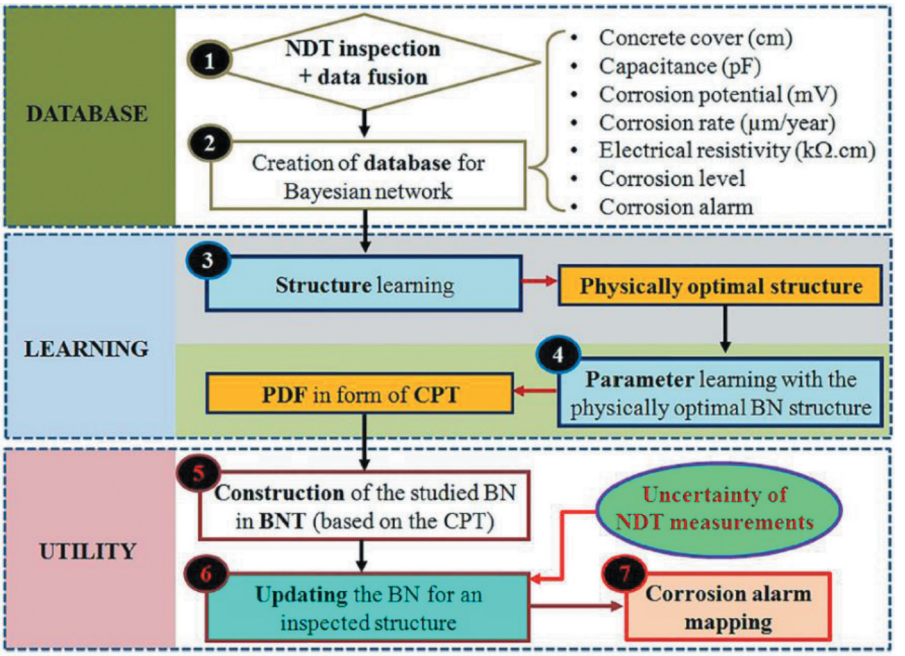


Figure 1. Methodology for corrosion alarm mapping with uncertainty of measurements (Keo et al., 2023).

The structure of the studied BN is the optimal structure with 4 variables, as shown in Figure 2 below.

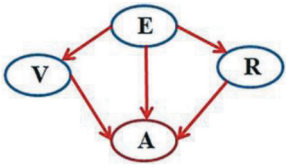


Figure 2. Physically optimal structure with 4 variables studied in (Keo et al., 2023).

Where, E, V, R, and A nodes represent the corrosion potential, the corrosion rate, the electrical resistivity of the concrete cover, and the corrosion alarm (related to corrosion rate) parameters, respectively.

2.2 *Suggested scenarios for demonstrating the climate change effect on the corrosion alarm*

To demonstrate the effect of the climate change on the probabilities of corrosion alarm obtained from the NDT data based predictive BN model, the schema below (Figure 3) is suggested.

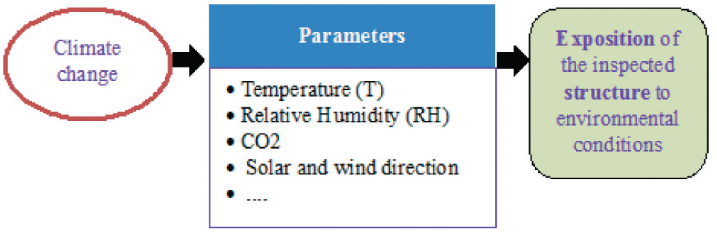


Figure 3. Exposition of inspected structure impacted by climate change effect.

Important parameters which depend on the climate change include atmosphere temperature (T), relative humidity (RH), CO_2 rate, solar and wind direction (Iamsumang et al., 2018). These parameters depend on where the studied structural elements are situated. Thus, accounting the effect of the climate change on the structures could be simplified by considering the class (or degree) of exposition of the structures. In other words, how the structures are exposed to environmental conditions, which is related to the climate change, will affect the corrosion rate of the reinforcements inside the structures.

In the present study, the NDT data of an inspected bridge abutment is used as the new information for updating the BN model to obtain the probability corrosion alarm map. The studied bridge abutment is shown in Figure 4 below.



Figure 4. Inspected bridge abutment for the present study (in DIAMOND project in the previous study).

The bridge abutment was inspected in an area of 6 meters by 1.5 meters (red frame in Figure 4). With the dimension, and its geometry configuration, the inspected area can have different parts which are differently affected by climate change dependent parameters (contact with rain, solar radiation, and so on). The degree of climate change impact on the different parts of the studied area can be differentiated by shelter period.

In the first stage of the present study, the parts in yellow frames (in Figure 4) are considered to be more unfavourable to the climate change effect than the middle part of the abutment area. Thus, the variation of the values of the durability indicators (NDT data), which are related to the corrosion rate, in these parts might be higher than that in the middle part. The available NDT data of the studied bridge abutment is the values of the corrosion potential. For these reasons, two scenarios are proposed to observe the corrosion alarm maps of the inspected abutment based on the BN model and the observed corrosion potential: decrease of corrosion potential (more unfavourable to corrosion due to the age of the structure) in the whole inspected area without considering the effect of climate change (decrease of 50 mV), and the decrease of the corrosion potential accounting the effect of climate change. The variation of the corrosion potential in the second scenario is illustrated in Figure 5.

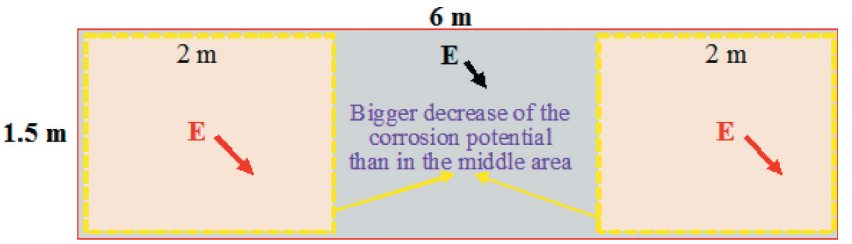


Figure 5. Decrease of the values of corrosion potential on the inspected area of the bridge abutment accounting the climate change condition.

As shown in Figure 5, the middle part of the abutment (2 meters by 1.5 meters) has a smaller decrease of the corrosion potential values. In the middle part of the inspected abutment face, the values of the corrosion potential are supposed to be decrease of 50 mV, whereas that in the other parts (which are more exposed to the climate change dependent parameters especially contact with the rain and solar radiation) is 100 mV. It is worthwhile to note that, in the first stage of our study, decreased values of the corrosion potential are supposed to be uniform in each part of the observed abutment area. The values of 50 mV, and 100 mV are not the exact values; so as to allow to observe different corrosion alarm maps affected by the climate change dependent parameters.

3 RESULTS AND DISCUSSIONS

3.1 *Corrosion alarm map of the inspected abutment with available NDT data*

The available values of the corrosion potential in the whole inspected area of the abutment (44 detected points in total) are used to update the BN model. The corrosion alarm map in this case of inference is obtained, as shown in Figure 6.

The map in Figure 6 shows the higher probabilities (between 80 % and 100 %) of corrosion alarm in the upper part of the inspected abutment. The lower parts, especially the edges (left and right parts) have many points with the probabilities lower than 50 % representing no-alarm state. It is reminded that the uncertainty of measurement was also considered in the BN model in the last stage of the methodology (Keo et al., 2023).

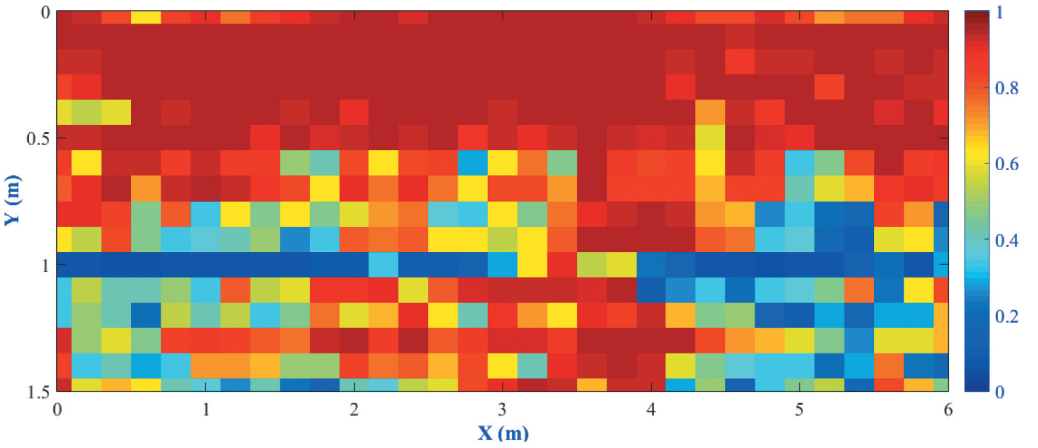


Figure 6. Corrosion alarm probability map of the inspected abutment area with the available values of corrosion potential.

3.2 *Corrosion alarm maps with the decrease of the corrosion potential values*

In order to observe the effects of the environmental condition exposition of the structures on the corrosion alarm, corrosion alarm maps obtained from updating the BN with the new values of the corrosion potential varying accordingly to both suggested scenarios are obtained in Figure 7.

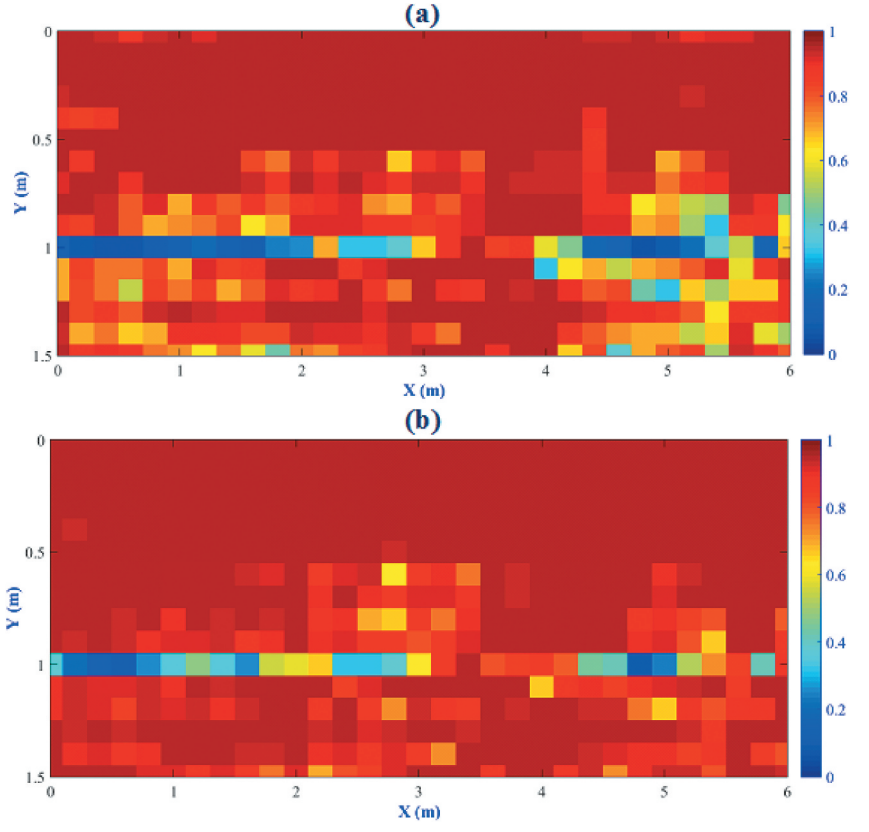


Figure 7. Corrosion alarm probability maps of the inspected abutment area with the decrease of the corrosion potential values, (a) without climate change effect scenario, (b) with climate change effect scenario.

Figure 7a illustrates more points with high probabilities of corrosion alarm (higher than 80 %) compared to Figure 6. This is conformed with the hypothesis of the decrease of the corrosion potential values (representing the degradation of the abutment with its age). It confirms that the BN model can be used as a bridge maintenance strategy with the case of inference (observed node of the proposed BN structure) with the available corrosion potential values in the future inspection campaigns. Figure 7b shows even more points with high probabilities of corrosion alarm (higher than 80 %, and even higher than 90 %) compared to Figure 7a. It explains the necessity of accounting the exposing environmental conditions into the BN predictive model to void the under-estimation of the degradation (related to corrosion of the first layer reinforcements) of an inspected structure. This effect will become more critical for the bigger inspected area.

Thus, complementary to the durability indicators (NDT data), the exposition classes of the structures to environmental conditions should be implemented in the BN model in order to assure a resilient maintenance strategy. It is worthwhile to remind that the exposition classes, which depend on the geographical locations, are related to climate change dependent parameters (Iamsumang et al., 2018) affecting the life of structures.

4 CONCLUSIONS AND PERSPECTIVES

A methodology based on a Bayesian network (BN) for creating corrosion alarm maps of reinforcements is used in the paper. NDT data of an inspected bridge abutment is used as the new information for updating the BN model to obtain the probability corrosion alarm map. Two scenarios are proposed to observe the corrosion alarm maps of the inspected abutment: decrease of corrosion potential (more unfavourable to corrosion due to the age of the structure) in the whole inspected area without considering the effect of climate change (decrease of 50 mV in all points), and the decrease of the corrosion potential accounting the effect of climate change (decrease of 50 mV in the middle part, and of 100 mV in the edges).

The results confirm the hypothesis of the decrease of the corrosion potential values (representing the degradation of the abutment with its age), as well as the possibility to use the BN model as a bridge maintenance strategy with the available corrosion potential values collected in other future inspection campaigns. On the other hand, it is necessary to account the exposition environmental conditions in the predictive model.

The results from the present paper opens an important perspective to implement the real exposition classes of the structures to environmental conditions in the BN model in order to obtain a resilient maintenance strategy related to the corrosion of reinforcements. Accurate relation of the variation of the NDT data and climate change dependent parameters will lead to enhancing the BN predictive model as an effective maintenance method.

ACKNOWLEDGEMENT

The authors would like to express their gratitude to LERM laboratory for the inspections and the information of the experimental campaigns, and to all the partners in FUI program for the DIAMOND project (DIAgnostic corrosion and MONitoring for the Durability of reinforced concrete and steel structures) for the financial support. Moreover, thanks to all the partners for the creation of the corrosion predictive model in the previous work, especially LMDC Toulouse laboratory (Laboratoire Matériaux et Durabilité des Constructions), allowing to reach the present work.

REFERENCES

AFGC: Conception des betons pour une duree de vie donnee des ouvrages: Maîtrise de la durabilité vis-à-vis de la corrosion des armatures et de l'alcali-réaction. Association Française de Génie Civil (AFGC), 2004.

Gomez C.C., De Larrard T., Duprat F., Geoffroy S.: Estimation du niveau de corrosion sur structures en béton armé par une méthodologie multicritère à partir d'essais non-destructifs. presented at the 10ème journées Fiabilité des Matériaux et des Structures, Bordeaux, 2018.

Iamsumang, C., Mosleh, A., Modarres, M.: Monitoring and learning algorithms for dynamic hybrid Bayesian network in on line system health management applications. Reliab. Eng. Syst. Saf. 2018, 178, 118–129.

Keo, S.A.; De Larrard, T.; Duprat, F.; Geoffroy, S. Predictive Model for Corrosion Alarm in Reinforced Concrete Structures Based on Bayesian Network and NDT Data: An Effective Tool for Maintenance Strategy, 2022.

Keo, S. A.; De Larrard, T.; Duprat, F.; Geoffroy, S. Influence des incertitudes des données d'inspection CND sur la cartographie d'alarme de corrosion des armatures: modèle de prévision du risque de corrosion avec un réseau bayésien. 2023a, 41 (3).

Keo, S.A.; De Larrard, T.; Duprat, F.; Geoffroy, S. Enhancement of Predictive Bayesian Network Model for Corrosion Alarm of Steel Reinforcement with Uncertainty of NDT Measurements. J Nondestruct Eval. 2023b, 42 (2), 51.

Rianna, G.; Mercogliano, P.; Villani, V.; Nogal, M.; Gervasio, H.; Neves, L.; Bastidas-Arteaga, E.; Tsionis, G. Expected Implications of Climate Change on the Corrosion of Structures; Publications Office of the European Union: Luxembourg, 2020.

Tran, T.-B., Bastidas-Arteaga, E., Schoefs, F.: Improved Bayesian network configurations for probabilistic identification of degradation mechanisms: application to chloride ingress. Struct. Infrastruct. Eng. 2015.

Bridge Maintenance, Safety, Management, Digitalization and Sustainability – Jensen, Frangopol & Schmidt (eds)
© 2024 The Author(s), ISBN 978-1-032-77040-6
Open Access: www.taylorfrancis.com, CC BY-NC-ND 4.0 license

Enhancing urban resilience and sustainability under wind disasters with carbon emission as an indicator

Ting-Yau Wang
Research Assistant, Department of Civil Engineering, National Taiwan University, Taipei, Taiwan

Chi-Ying Lin
Assistant Professor, Department of Civil Engineering, National Yang Ming Chiao Tung University, Hsinchu, Taiwan

ABSTRACT: Communities and systems are inevitably vulnerable to disasters, particularly typhoons. Thus, to adapt to the destruction caused by natural hazards and to achieve a low-carbon community, this study compares critical infrastructure systems with their remaining functionality under various carbon-reduction measures and initiatives aimed at enhancing urban stability in the aftermath of a typhoon event. Hence, this research focuses on reducing carbon emissions and bolstering urban resilience in the context of Kaohsiung, Taiwan, a city that is increasingly susceptible to major typhoons. This study concentrates on four strategies: (i) augmenting network redundancy, (ii) establishing backup solutions or temporary facilities at critical nodes, (iii) strengthening facilities against wind forces, and (iv) substituting damaged infrastructures with low-carbon materials or construction methods. Comparing the results of these strategies through carbon emission during restoration and the average performance of the systems in the short term, this study provides decision-makers a reference for improving community resilience and reducing carbon emissions simultaneously.

1 INTRODUCTION

In recent years, the escalating impact of natural disasters has not only caused substantial economic losses but also posed severe threats to the lives of countless individuals. The concept of "resilience" has emerged as a critical discourse, aiming to mitigate the damages inflicted by disasters and facilitate swift recovery in their after-math (Timmermann, 1981). The discussion on resilience often concerns Critical infrastructure systems (CISs), which significantly influence the life quality of res-idents. However, the vulnerability of CISs to the impacts of natural hazards has be-come strikingly clear. Compounded by interdependencies among these systems, the impairment of one not only diminishes its functionality but also cascades disruptions to interconnected CISs, resulting in wide-spread damage (Guidotti et al., 2016).

In response to the UN's Zero Carbon Cities competition, which advocates for a transformation towards net-zero sustainability, cities worldwide are compelled to reevaluate both the supply-side issues (power supplies and transportation) and demand-side issues (reducing usage through improved urban design and policies). Thus, striking a delicate balance between maintaining a high quality of life and implementing low-carbon maintenance strategies becomes crucial (Shi et al., 2022). This balance is especially challenging in scenarios such as high energy consumption in transportation due to re-mote settlement areas or the inefficient utilization of energy services.

This study delves into the intersection of carbon reduction and the enhancement of urban resilience, with a focus on Kaohsiung serving as a case study. Tai-wan, experiencing an

DOI: 10.1201/9781003483755-392

average of 4.6 typhoons annually, faces heightened vulnerability to the impacts of these storms. The city of Kaohsiung, located in the southern region of Taiwan, is particularly susceptible to the destructive forces of powerful typhoons, resulting in significant economic losses. This scenario underscores the urgent need for flexible urban disaster mitigation strategies. Climate change exacerbates risks, including heavy rainfall, urban flooding, and the urban heat island effect. This intensifies the urgency to reduce car-bon emissions and transition towards low-carbon urban development, aligning with global sustainability objectives. The current research concentrates on the interdependent transportation and power systems and critical components often incapacitated during typhoons. The study conducts a comprehensive assessment by drawing inspiration from the investigation of four strategies, including (i) preparing backup solutions like backup power and temporary replacements, (ii) adopting low-carbon materials, for example, fiber-glass reinforced plastic (FRP), (iii) improving structural safety design to enhance wind resistance, and (iv) increasing network redundancy by increasing grid complexity.

The urgency of this research lies in providing practical insights for evaluating different strategies' resiliency and environmental sustainability. Through considerations of short-term post-disaster recovery, this study aims to guide the formulation of pre-disaster management and post-disaster response approaches that ensure the continued functionality of urban systems in the face of climate-induced disasters and contribute to the overarching goal of mitigating carbon emissions.

2 SYSTEM RESILIENCE

2.1 *Kaohsiung's CIS modeling*

In this study, emphasis is placed on the topological characteristics of the road network in the traffic system, where assessing the system's ability to handle disasters relies on the integrity of the network of connectivity and the determination of the shortest traffic paths (Zhang et al., 2017).

The damage to the capacity of the road network considered in this study encompasses three types: the first is the collapse of bridges; the second is the decrease in road capacity due to reduced vehicle speed caused by high wind speeds; and the third is road blockage caused by fallen roadside elements such as signages and streetlights due to the wind. All three scenarios pose challenges during typhoons and result in disruptions to traffic.

Besides, this study builds the power system model comprising Kaohsiung's power generators, substations, and transmission systems with their power capacities. Power transmission is one-way linear, and damage to any power tower or power station along the way will cause the end user to be unable to use power (Cai et al., 2019). Thus, to detect the physical damage caused by wind attacks, the parameters of physical damage and repair time for high-voltage towers and stations are also listed in Table 1.

The fast recovery usually depends on how long the maintenance unit arrives at the road obstruction. Meanwhile, shorter path selection can reduce the energy consumption in the transportation of construction vehicles and facilities. In order to identify the residual performance of the infrastructures, this study assesses the impact of different wind speeds on traffic flow. Simultaneously, the corresponding time required for maintenance and road cleaning is linearly allocated based on historical records, as shown in Table 1.

The road network and power grid distribution in Kaohsiung City are shown in Figure 1 and Figure 2. The current study is based on these interdependent systems to conduct research on community resilience under typhoon disasters.

2.2 *System interdependencies*

Many researchers are studying on the dependent systems, such as Hasan (2015) and Reed (2015). The experts collected others' opinions; in addition, for different aspects, multiple

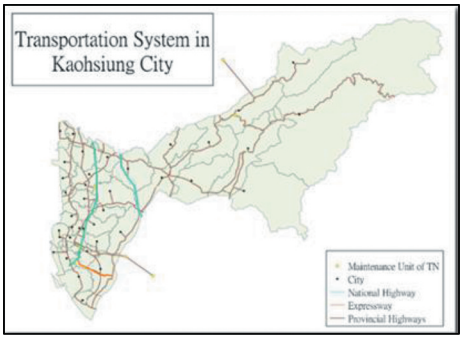


Figure 1. The road network in Kaohsiung City.

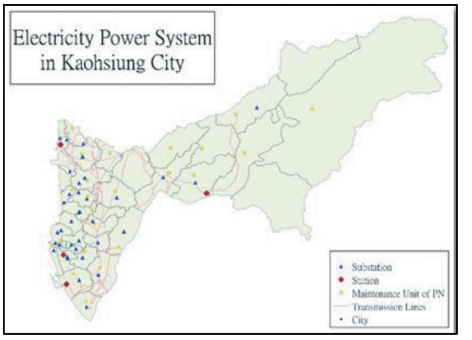


Figure 2. The power network in Kaohsiung City.

systems are combined, and the dependencies between infrastructures are evaluated through a large number of simulations.

For the interdependencies between transportation and power systems, we consider the impact of three aspects:

(1) Functional-dependent—traffic signals and monitors work because of sufficient power supply.
(2) Spatial overlapping—the transmission lines have geographical intersections with road systems, which may affect the traffic volume after a disaster.
(3) Obstructed path—the repair time relies on the shortest paths from maintenance units to the damaged facilities, which are determined by the functionality of road networks.

Table 1. The parameters of facilities. *

Node	Damage level	Fragility (lognormal distribution)	Repair (linear model)
Station	Moderate	Median: 89.0 m/s	Mean:19 h
Transmission	Extensive	Median: 34.2 m/s	Mean: 48 h
	Destruction	Median: 84.4 m/s	Mean: 30 d
Bridge	Half blocked	Median: 41.4 m/s	Mean: 6 h
	Fully blocked	Median: 50.6 m/s	Mean: 48 h
Accessories	Fallen	Median: 34.2 m/s	Mean: 2 h

*Data sourced from Gu et al. (2020); Testa et al. (2015); Bie et al. (2017); Salman et al. (2015)

2.3 *Typhoon hazards*

Typhoons wield substantial energy, making their impact on large structures in Taiwan a significant concern, resulting in annual economic losses amounting to billions of New Taiwan dollars (Yin, 2009). Understanding and assessing typhoon-related disasters is imperative for Taiwanese meteorological research. This involves tracking the historical trajectory of the typhoon eye and gauging the extent of its wind impact, aiding in the identification of affected areas. By analyzing wind fields and overlaying wind radii, government and emergency management agencies can formulate effective strategies for typhoon preparedness and disaster mitigation, considering the distribution of infrastructure in various regions.

The typhoon simulation involves Monte Carlo methods encompassing typhoon generation, path, wind field, and boundary layer flow models. To assess the impact of typhoon models on transmission lines and roads accurately, this study establishes a detailed typhoon model based on landing location, central pressure difference, maximum wind speed, and the radius of maximum wind speed. Using historical records from the Joint Typhoon Warning Center at 6-hour intervals, this study extracts parameters suitable for infrastructure vulnerability analysis with

the maximum wind speed radius. Thus, the wind speed at the facility will be determined by the following formula:

$$v(\mathrm{t}) = \begin{cases} v_{max} \times [D/R_{mw}]^{\eta}, if\ D \leq R_{mw} \\ v_{max} \times [R_{mw}/D]^{\eta}, if\ D > R_{mw} \end{cases} \quad (1)$$

where v represents wind velocity, R_{mw} is the radius of the maximum wind speed, D is the distance between the node and typhoon eye, and η equals 0.5 in Taiwan.

The study employs circular symmetric wind field models, utilizing an exponential-type wind field represented by Rankine vortices (Wang et al., 2022). The model considers factors like the distance between the node and the typhoon eye to determine the local maximum wind speed. However, it acknowledges limitations, such as relying on discrete observation points and analyzing only continuous and non-quadrant wind radii of the typhoon eye, potentially deviating from the actual typhoon path.

2.4 *Carbon emissions during restoration*

Maintenance operations play a crucial role in sustaining infrastructures, and meanwhile, it is essential to scrutinize the associated carbon emissions. This section explores the carbon footprint generated during restoration, focusing on human activities, construction machinery operation, and transportation distance based on previous studies (Chen et al., 2023; Wei et al., 2017; Yang, 2010):

(1) Human activities—the carbon emissions generated by on-site living and commuting of engineering personnel contribute significantly to daily carbon emissions during maintenance. Individuals involved in the maintenance process emit approximately 0.047 metric tons of CO2 per day.
(2) Operation of construction machinery—it constitutes a substantial portion of carbon emissions during restoration efforts. On average, the emissions are estimated at 0.128 kg of CO_2 per square meter of restoration.
(3) Transportation distance—the path to the repair site plays a pivotal role in maintenance, and the associated carbon emissions are contingent on the distance traveled. For every kilometer covered, maintenance activities contribute 0.106 kg of CO_2. This metric encompasses emissions from the entire transportation process, from fuel combustion to logistical considerations.
(4) Material used for facility repair—after a typhoon event, infrastructures experience damages and require replacement materials. The restoration process produces the corresponding greenhouse gas based on types of materials (as shown in Table 2) and types of facility damages (as shown in Table 3).

Table 2. Carbon emissions for different materials in Taiwan (from Taiwan Ministry of Environment).

Materials	Unit	Carbon emission*
Steel bars for reinforced concrete	kg	0.834
Pre-mixed concrete	m^3	338
Diesel (road transport and machines)	L	3.34
Asphalt concrete	t	9.56

* The unit of carbon emission is kg-CO_2e.

Table 3. Carbon emissions for construction of different facility rehabilitations.

Facility	Restoration	Carbon emission*
Transmission tower	Cable installment	352.65
	Tower reconstruction	15646
Substation and plants	Machine repairment	14
road pavement	Obstacles removing	0.3
	Repaving asphalt road	1.6

* The unit of carbon emission is t-CO_2e.

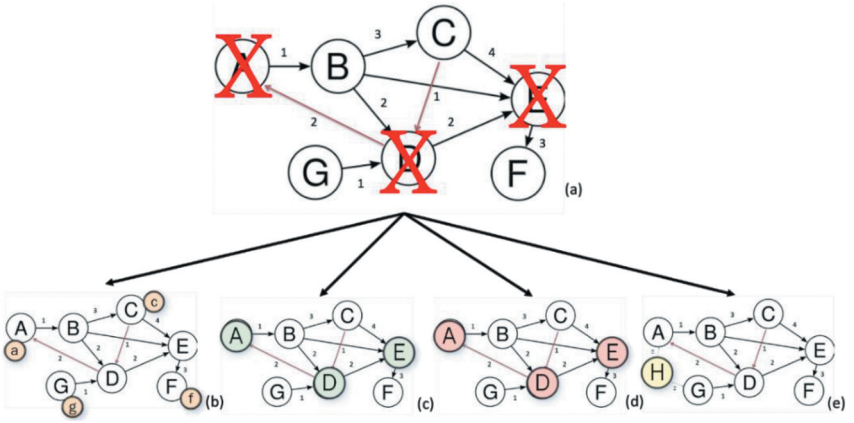


Figure 3. Illustration of the carbon reduction measures and resilience enhancement strategies: (a) schematic diagram of network damage in disasters; (b) backup solutions; (c) low carbon alternatives in materials or construction; (d) wind resistance enhancement; (e) network redundancy.

3.1 *Prepare backup solutions*

In the realm of infrastructure systems, ensuring stability and rapid recovery from disruptions is paramount. This study places a strong emphasis on deploying robust backup solutions to enhance the resilience of critical infrastructure, exemplified by innovative measures such as the "Composite Lightweight Bridge for Emergency Disaster Relief." (Yeh et al., 2020) This groundbreaking bridge technology is designed for swift reconstruction, reconnecting vital transportation routes within a remarkable 8-hour timeframe, thereby significantly reducing downtime and enhancing overall system stability.

Additionally, the integration of backup generators stands as a cornerstone in fortifying infrastructure against potential disruptions (Xiaoguang et al., 2017). These generators play a pivotal role in maintaining an uninterrupted power supply, even in the face of equipment damage. According to data from Taipower, at Taiwan's power stations, the operating level of the units has not yet reached the maximum supply, and 15% to 20% of the units in the plant are in standby and dormant status. When other units encounter problems or the power supply is insufficient, they can be woken up within a day for operation without the cost of additional equipment installation. In an era where continuous power is fundamental for various critical functions, these backup generators serve as a linchpin, mitigating the impact of destruction and ensuring sustained operations.

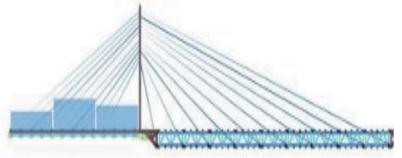


Figure 4. Temporary rescue bridge. (Yeh et al., 2020).

Table 4. The parameters for modeling the probability distribution of repair time for the temporary facilities under consideration.

Facility	Carbon emission	Repair time	Source
Backup power	0.17	Mean: 6 h, cov: 2 h	Wei (2017)
Temporary tower	139.54	Mean: 16 d, cov: 1 d	Yeh (2020)
Emergency bridge	0.63	Mean: 8 h, cov: 2 h	Xiaoguang (2017)

* The unit of carbon emission is t-CO_2e.

This study extends its focus beyond conventional recovery approaches. It delves into fast replacements, featuring emergency bridges, temporary towers, and the activation of dormant machines in power stations. These rapid replacement strategies are detailed in Table 4, providing insights into construction times and associated carbon emissions.

3.2 *Switch to low-carbon alternatives*

In pursuing fortifying infrastructure systems with a focus on sustainability, this study adopts a two-fold approach: the incorporation of recycled asphalt concrete pavement for road repairs and the transition from traditional steel to FRP materials in transmission towers.

Research by Yang (2010) underscores the environmental benefits of utilizing recycled asphalt concrete pavement in road surface repairs. The application of this sustainable alternative not only reduces carbon emissions by approximately 18%, considering material production and transportation, but also offers a shorter environmental impact post-disaster, aligning with the imperative of a smaller post-disaster environmental impact.

Simultaneously, due to increased global discussions on sustainable building materials and addressing rising steel prices, scholars such as Kumar (2020) advocate for the integration of FRP materials. The utilization of FRP instead of secondary steel has been shown to reduce a structure's embodied carbon by 60-85% and have faster construction timelines decreasing about 10-20%. Although the cost of FRP materials is roughly 30% lower than steel, careful consideration of trade-offs is imperative due to increased failure probability. It's noteworthy that fragility parameters for the initial steel tower indicate a mean of 45.94 m/s with a coefficient of variation (cov) of 8.1, while the FRP tower has a mean of 42.94 m/s with a cov of 8.8. (Bilionis et al., 2022).

3.3 *Increase wind resistance*

While the augmentation of wind resistance stands as a strenuous strategy against disasters, it necessitates a careful examination of the associated trade-offs. The proposed methodology involves fortifying infrastructure elements to withstand the impacts of adverse weather conditions, particularly focusing on high wind events. However, the infrastructure stability reinforcement requires targeted reinforcement based on its damage situation, which takes a long time and requires different materials. Though incurring higher initial costs, this preemptive approach acts as a preventive measure to mitigate the destructive consequences of disasters, especially in regions prone to high winds.

This study improves wind resistance capabilities by one level, aligning with existing regulations specifying accessories with a 7 Beaufort wind force scale. The reinforcement process necessitates an additional 0.5 days of construction time, with the reinforcing materials accounting for 2% of the overall material (attachment part). Consequently, carbon emissions increase due to the reinforcing materials and extended construction time, resulting in an approximate 1-3% rise in carbon footprint. However, this reinforcing strategy raises pertinent questions about the potential trade-offs. There's an inherent tension between resilience and durability under reinforcing facilities. In some cases, structures face potential challenges such as the difficulty of integrating old and new structures, or some facilities have reached their usage limits as the cost of repair has exceeded the cost of reconstruction. The damaged infrastructures, with its reduced lifespan, can be partially restored through reinforcement, but these reinforcements take longer and cost more than original repairs. Nevertheless, the advantage of the fortified infrastructure can maintain regular operations without succumbing to power shortages or traffic disruptions, ensuring uninterrupted functionality without disturbing residents.

3.4 *Increase network redundancy*

This study aimed at fortifying the resilience of infrastructure systems, such as developing a more decentralized power grid. Enhancing network complexity with microgrids contributes to increased stability, adaptability, and overall robustness. By intricately interconnecting various components, this approach seeks to mitigate vulnerabilities, improve response mechanisms, and enhance the overall sustainability of the power grid. While power generation capacity exists,

challenges in effective delivery persist. To mitigate these challenges, this strategy adopts a decentralized approach, particularly in densely populated urban areas, to reduce the risk of centralized power grids and to enhance the stability of the power supply.

The strategy expands power transmission lines from substations to surrounding cities, specifically targeting substations with surplus energy, surpassing the residents' consumption needs. The selection criteria for substations are based on their excess power generation capacity. Besides, to improve power distribution efficiency by identifying districts facing energy shortages, we consider the energy consumption of businesses, factories, and residential areas in the designated zones. To reduce the power outage risk, we established a linkage between the selected substations and high-power consumption areas or areas with only a single power supply source to build a more resilient power system. The study proposes the establishment of transmission towers at 300-meter intervals along the shortest paths, a strategic move aimed at optimizing power distribution efficiency. However, this expansion is not without its environmental considerations. This study examines the carbon footprint associated with this measure. The carbon emissions per unit distance of the transmission line are calculated at 287 t-CO_2e./km, with each tower's construction contributing 1,410 t-CO_2e (Wei et al., 2017).

4 RESULTS AND DISCUSSION

The study conducted 1000 Monte Carlo simulations to assess the impact of historical typhoons on Kaohsiung, Taiwan. The focus was on evaluating the performance of the transportation and power systems during the post-typhoon repair period, along with the associated environmental effects, by adopting Cimellaro's (2016) resilience index:

$$Res = \frac{1}{T_{LC}} \int_0^{T_{LC}} \mathrm{Q}(t)dt \tag{2}$$

where Res is the Resilience index, T_{LC} is the target time or the time when the system is fully repaired, and Q is the functionality of the system, such as traffic flow and power capacity. The calculation of the resilience index depends on the recovery curves, as shown in Figure 5.

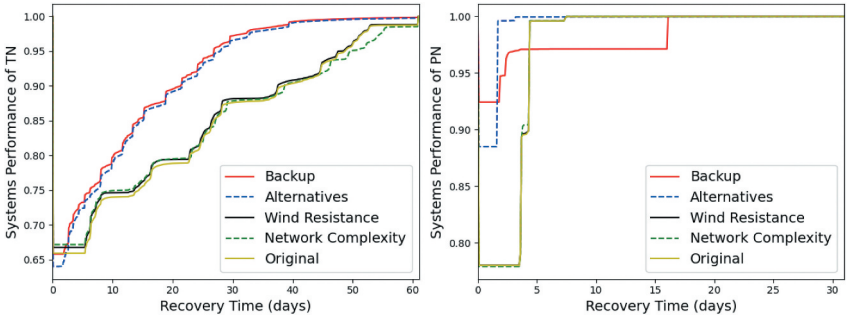


Figure 5. The recovery curves of transportation and power system after typhoon disasters.

During the recovery phase, it is noteworthy that some strategies shorten the repair time, primarily due to the lower construction timelines and faster functionality recovery. Compared to the network without resilience enhancement, which needs 4 days in PN and 38 days in TN to repair, backup solutions and low-carbon alternatives both shorten the repair time by 3 days in PN and 17 days in TN, respectively. The observed reduction in repair times underscores the efficacy of these resilience strategies. In contrast, the repair time of wind resistance and that of network complexity solutions are longer than the original network by 2 days in PN and 1 day in TN, respectively. But they resulted in increased resilience with higher robustness.

The examination of the original network reveals a moderate level of resilience, with an average resilience index of 0.786 in the transportation system and 0.914 in the power system. According to the results, the implementation of a backup solution significantly elevates the resilience index, emphasizing its effectiveness in enhancing urban resilience and ensuring a sustained quality of life for residents. Notably, the strategy demonstrates lower carbon emissions, mainly composed of human activities, for transportation system restoration, which is attributed to the reusable emergency bridges and original standby generators minimizing material pollution. Furthermore, the adoption of low-carbon alternatives contributes positively to urban resilience. Despite its elastic modulus of one-tenth that of steel, resulting in reduced robustness, its higher durability compensates for this limitation. The construction of FRP towers requires professional teams, but the advantages include lower labor requirements and a simplified installation process, reducing repair time similar to preparing backup solutions.

Enhancing the wind resistance of facilities proves to be a successful strategy, resulting in increase-ed robustness for CISs. The resilience index surpasses that of the original network, accompanied by lower carbon emissions due to reduced facility damage.

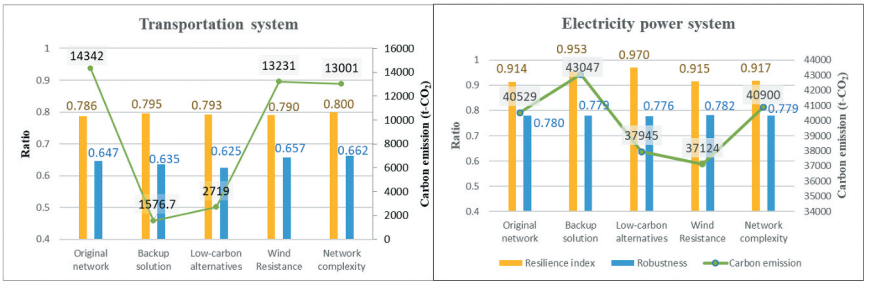


Figure 6. The indexes for typhoon disaster recovery of transportation and power system.

5 SUMMARY AND CONCLUSIONS

Recently, natural disasters have become increasingly unavoidable, inflicting inevitable damage upon urban environments. As a case study, this study focuses on the city of Kaohsiung in Taiwan, a locale frequently subjected to typhoon impacts. The research analyzes the enhancement of community resilience and its implications under the strategies of preparing backup solutions, switching to low-carbon alternatives, enhancing wind resistance, and increasing network complexity. By scrutinizing traffic flow and electrical currents, the study examines variations in system performance. These performance changes are observable through the proportional shifts in consumption patterns among end-users, namely, the residents. Furthermore, the research takes into account the carbon dioxide emissions generated during maintenance processes, material degradation, human activities, and transportation. Utilizing greenhouse gas emissions as a criterion enables the evaluation of impacts on the urban environment and provides insights for designing future zero-carbon cities.

Our investigation into strategies for enhancing urban resilience within CISs yields valuable insights. The original network exhibits a commendable level of resilience, yet implementing targeted strategies unveils opportunities for improvement.

The backup solution stands out for its remarkable impact, significantly elevating the resilience index. Its effectiveness in minimizing carbon emissions during transportation system restoration, particularly through the reusable nature of emergency bridges, underscores its practicality and sustainability. Similarly, the integration of low-carbon alternatives proves beneficial, contributing positively to urban resilience. Strengthening the wind resistance of facilities emerges as a successful strategy, elevating the overall robustness of CISs. This not only improves resilience but also translates to lower carbon emissions owing to reduced damage to critical facilities. However, the introduction of network complexity extends repair time and increases carbon emissions due to a higher probability of facility destruction, indicating the need for a balanced approach.

In conclusion, this study provides a comprehensive evaluation of diverse strategies, offering urban planners and policymakers valuable insights into crafting resilient and sustainable urban infrastructure. As cities continue to face diverse challenges, the pursuit of a resilient urban future remains a critical imperative. This research contributes to a comprehensive understanding of resilient infrastructure systems by addressing recovery speed and the environmental impact. The deployment of backup solutions, low-carbon replacement strategies, and network strengthening not only reduces recovery time but also minimizes the overall influence of disruptive events, underscoring the importance of strategic preparedness in safeguarding our critical infrastructure.

REFERENCES

Bie, Z., Lin, Y., Li, G., & Li, F. (2017). Battling the Extreme: A Study on the Power System Resilience. *Proceedings of the IEEE.* https://doi.org/10.1109/JPROC.2017.2679040

Bilionis, D. V., Vlachakis, K., Vamvatsikos, D., Dasiou, M. E., Vayas, I., & Lagouvardos, K. (2022). Risk assessment of rehabilitation strategies for steel lattice telecommunication towers of Greece under extreme wind hazard. *Engineering Structures*, *267.* https://doi.org/10.1016/j.engstruct.2022.114625

Cai, Y., Xie, Q., Xue, S., Hu, L., & Kareem, A. (2019). Fragility modelling framework for transmission line towers under winds. Engineering *Structures*, *191.* https://doi.org/10.1016/j.engstruct.2019.04.096

Chen, X., & Ou, Y. (2023). Carbon emission accounting for power transmission and transformation equipment: An extended life cycle approach. *Energy Reports*, *10*. https://doi.org/10.1016/j.egyr.2023.08.010

Cimellaro, G. P., Renschler, C., Reinhorn, A. M., & Arendt, L. (2016). PEOPLES: A Framework for Evaluating Resilience. https://doi.org/10.1061/(asce)st.1943-541x.0001514

Guidotti, R., Chmielewski, H., Unnikrishnan, V., Gardoni, P., McAllister, T., & van de Lindt, J. (2016). Modeling the resilience of critical infrastructure: the role of network dependencies. *Sustainable and Resilient Infrastructure*, *1(3–4)*. https://doi.org/10.1080/23789689.2016.1254999

Gu, Y., Fu, X., Liu, Z., Xu, X., & Chen, A. (2020). Performance of transportation network under perturbations: Reliability, vulnerability, and resilience. *Transportation Research Part E: Logistics and Transportation Review.* https://doi.org/10.1016/j.tre.2019.11.003

Hasan, S., & Foliente, G. (2015). Modeling infrastructure system interdependencies and socioeconomic impacts of failure in extreme events: emerging R&D challenges. *Natural Hazards*, https://doi.org/10.1007/s11069-015-1814-7

Kumar, S. (2020). Life Cycle Performance Assessment of Steel Vs FRP based Transmission Line Tower. https://www.researchgate.net/publication/342259890

Salman, A. M., Li, Y., & Stewart, M. G. (2015). Evaluating system reliability and targeted hardening strategies of power distribution systems subjected to hurricanes. *Reliability Engineering & System Safety*, *144.* https://doi.org/10.1016/j.ress.2015.07.028

Shi, C., Guo, N., Gao, X., & Wu, F. (2022). How carbon emission reduction is going to affect urban resilience. *Journal of Cleaner Production*, *372.* https://doi.org/10.1016/j.jclepro.2022.133737

Testa, A. C., Furtado, M. N., & Alipour, A. (2015). Resilience of coastal transportation networks faced with extreme climatic events. *Transportation Research Record*, *2532*, 29–36. https://doi.org/10.3141/2532-04

Timmermann, P. (1981). Vulnerability, resilience and the collapse of society. *Environmental Monograph*, *1*, *1* 42.

Wang, Y., Yin, Y., & Song, L. (2022). Risk Assessment of Typhoon Disaster Chains in the Guangdong–Hong Kong–Macau Greater Bay Area, China. *Frontiers in Earth Science*, *10.* https://doi.org/10.3389/feart.2022.839733

Wei, W., Wang, X., Zhu, H., Li, J., Zhou, S., Zou, Z., & Li, J. S. (2017). Carbon emissions of urban power grid in Jing-Jin-Ji region: Characteristics and influential factors. *Journal of Cleaner Production*, *168*, 428–440. https://doi.org/10.1016/j.jclepro.2017.09.015

Xiaoguang, H., Zifu, Z., Zhanwei, Z., & Xueli, Z. (2017). Structure Design and Optimization of Self-standing Modular Temporary Tower of 110kV Overhead Transmission Lines.

Yang, T. (2010). The Carbon Dioxide Emission of Flexible Pavements.

Yeh, F. Y., Yang, Y. Y., Lee, B. H., Shiao, S. Y., Chang, C. M., & Chang, K. C. (2020). Study on Truss-Type Segmental Composite Structure for Temporary Rescue Bridge. *Journal of the Chinese Institute of Civil and Hydraulic Engineering*, *32(8)*, 683–691. https://doi.org/10.6652/JoCICHE.202012_32(8).0002

Yin, J. M., W. M. B., Y. H. and S. M. (2009). Basin wide typhoon risk modeling and simulation for western north Pacific basin. *The 7th Asia-Pacific Conference on Wind Engineering*, *Taipei, Taiwan.*

Zhang, W., Wang, N., & Nicholson, C. (2017). Resilience-based post-disaster recovery strategies for road-bridge networks. *Structure and Infrastructure Engineering*, https://doi.org/10.1080/15732479.2016.1271813.

Bridge Maintenance, Safety, Management, Digitalization and Sustainability – Jensen, Frangopol & Schmidt (eds)
© 2024 The Author(s), ISBN 978-1-032-77040-6
Open Access: www.taylorfrancis.com, CC BY-NC-ND 4.0 license

Identification of a suitable case study for the development of accessibility based vulnerability score for bridge maintenance decision making

M. Lydon, A. Vega, E. Fitzpatrick, R. Higgins & A. Fenerich
University of Galway

ABSTRACT: Prioritising bridge maintenance interventions is a complex task that involves consideration of various factors, such as the bridge's lifespan, characteristics, operating conditions, environmental impact, and the consequences of infrastructure unavailability for local communities. In this paper, network vulnerability analysis is used to enable local authorities to identify and evaluate changes of access levels across a disrupted network, thereby providing insight on the impacts to a broader range of socio-economic aspects and to society. The paper provides an overview of the road network in Ireland and identifies a suitable case study area to development of accessibility based vulnerability score for bridge maintenance decision making. A version of the Hansen's gravity-based accessibility model where the indirect effects of bridge failure are accounted for by incorporating information on travel times and traffic flows between spatial units and essential services, as well as data on population, education, and employment opportunities in and around potentially affected areas is proposed.

1 INTRODUCTION

Climate-related disasters have cost the world more than £450 billion over the last three years [1]. Transport infrastructure is directly impacted by climate change with extreme weather conditions accounting for up to 35% of delays/service interruptions in road and rail infrastructure [2]. This daily cost due to extreme weather was estimated at £280m across England in 2010 by the DoT and in some cases up to £276.5m for a single event. One such event was the 2009 extreme flood event which resulted in the partial or total collapse of 29 bridges in Cumbria [3], [4]. The probability of repeated events in the future is extremely high given that 40% of UK bridges are considered historic assets (that is,. beyond their design life) and the majority of our bridges possess similar attributes, in terms of age, construction type and condition, as those identified in the Cumbria failures. Pregnolato highlighted the true vulnerability of UK bridges is unknown due to the lack of high-quality bridge data, which is ultimately jeopardising bridge safety [5]. This risk is now increasing as climate models suggest up to 24% increase in heavy precipitation intensity by 2100. The absence of a national bridge database that is interoperable with climate models, environmental and population data results in a lack of understanding of fragilities within transport networks. This is particularly problematic at locations where an individual bridge provides the only means of utilities, passengers and freight crossing an obstacle and failure leads to catastrophic consequences, such as the Malahide viaduct collapse in 2009. Bridge collapses, such as the tragic incident of the Morandi Bridge in Genova, Italy in 2018 that claimed 43 lives [2], have brought attention to critical problems in bridge safety. Subsequent studies have revealed concerns about the structural integrity of flyover bridges throughout Europe. For instance, a French study found that out of 12,000 state-maintained bridges in the country, one-third were in need of repair, and 840 were at risk of collapse [3].

DOI: 10.1201/9781003483755-393

With substantial maintenance backlogs worldwide and limited budgets, it is crucial to prioritise bridge repairs based on a risk consequence scoring. Existing bridge management systems have significant limitations. They often operate in isolation from other asset management tools and lack interoperability with geographical, societal, and climate-related data sets.

Bridge criticality operates on the basis of assessment and prioritisation of bridge maintenance taking into account their significance within the road network. This evaluation considers factors such as access to critical services and risks and designate resources to increase resilience and prevent bridge failure. Current criticality is mostly limited to a technical perspective which disregards users and their opinions and requirements [6], [7], [8].

Degraded network performance from bridge failure can have significant social and economic impacts. Investments in transport infrastructure can have positive cascading effects across communities enabling efficient movement of people or goods, supporting access to education and essential resources. This paper highlights the need to connect bridge condition data with national and regional road network information using network vulnerability analysis. While the main driver of vulnerability analysis has been the need to consider the performance and impacts of degraded networks in terms of the probability that a network will deliver a required standard of performance, the wider social and economic consequences of network failure or degradation is of great importance to modern society.

This research is focused on the national and regional road networks in Ireland and the selection of suitable region to develop a vulnerability score for utilization as a bridge investment metric. Bridge failure or closures caused by extreme weather or condition deterioration can disproportionally impact rural communities.

2 REVIEW OF THE CURRENT LITERATURE

Many countries across the world introduced methods to provide a ranked list of bridges requiring the most urgent attention. Each of the methods, both within the research field and in practice, all take in-to account different factors that they believe have the highest impact on the need for maintenance. Various studies such as Echaveguren et al [9], Dromey et al [10] and Contreras Nieto et al [11] have developed priority indexes based on the factors that have been determined to have an impact on maintenance needs. The first of these focuses on short-term maintenance planning by considering factors that have an influence of maintenance needs. In this case, the priority index considered bridge condition index, hydraulic vulnerability, seismic risk and strategic importance. This index was then used to calculate bridge maintenance cost therefore a limitation of the proposed method is that it relies heavily on a unit price database for maintenance activities which is not readily available. Similarly, Contreras-Nieto et al [11] presented a prioritisation framework by using bridge ratings and average daily traffic. The weights were determined based on importance of bridge ratings when investigating four key criteria (safety, resilience, serviceability and comfort) by using the Analytic Hierarchy Process (AHP). A case study which compared water crossing and non-water crossing bridges was used to show the method was robust and reliable. In a slightly different approach, Dromey et al [12] focuses on a prioritisation calculation which separates the bridges into two categories, critical-condition and non-critical. Each of these two calculations consider different factors which the authors used to reflect the different motivations used when determining maintenance projects in practice. This study concluded with outlining that critical condition bridges most influential factor was the overall structure condition, on the other hand non-critical condition bridges ranked hydraulic vulnerability as most important. These studies clearly indicate that the importance of including multiple potential influential characteristics in a prioritisation calculation. While these approaches look at what bridges to maintain, it is important to consider how decisions made about what structures to maintain or replace on the future condition of the entire network and the impact this will have on the communities who use the bridge to access critical services.

Network vulnerability analysis has emerged as a significant area for transportation planning research in the last decade [13].It deals with the socio-economic impacts and transport systems performance of failed or degraded transport networks, which is of great importance

to local communities and society in general [14]. Both the concepts of vulnerability and resilience have been widely investigated in recent years, with increasing applications in transport economics, urban and regional studies, and, more generally, in the social sciences [15]. While there is still no consensus on the definitions of vulnerability and resilience, the literature has attempted to conceptually differentiate between the two terms referring to vulnerability analysis as the propagation of shocks in a network, while resilience analysis is more aligned with the idea of the speed at which a network returns to its equilibrium after a shock [16].

In this paper, a case study is identified to determine if network vulnerability analysis can to enable local authorities to identify and evaluate changes of access levels across a disrupted network, thereby providing insight on the impacts to a broader range of socio-economic aspects and to the society. Previous studies have highlighted the challenge to assess the vulnerability of transport infrastructure to bridge failure at different locations, to better understand the wider impacts on the communities in and around the disruption [17]. One way to do this is through an accessibility-based vulnerability approach (see Shi et al [18]for a review of recent studies) to evaluate changes of access levels across a disrupted network, thereby providing insight on the impacts to a broader range of socio-economic aspects for society.

This research proposes to use an adapted version of the Hansen's gravity-based accessibility model where the indirect effects of bridge failure are accounted for by incorporating information on the following: travel times and traffic flows between spatial units and essential services, as well as data on population, education and employment opportunities in and around potentially affected areas. The relevant data sources and details of the case study area are presented in this paper. The gravity-based accessibility model that is proposed uses the shortest travel time between zones as the impedance function, which is an inverse relationship, as one of the most disruptive consequences of bridge failure is longer travel times as result of traffic diversions. Similar to Papilloud and Keiler [19], this paper proposes to weight the Hansen index by the number of employment and education opportunities that can accessed when transversing the bridge, including essential services such as health facilities.

3 CASE STUDY IDENTIFCATON

3.1 *The Irish road network*

The road network in Ireland is has the 5th highest density across Europe, with 20.9 kms per 1000 inhabitants it is significantly above the EU average of 9.6km. One of the contributing factors is Ireland's low level of population density on rural areas, as a result many sections of the regional and rural road networks are subject to low traffic loading but provide the only means of access for communities. Private car is the dominate choice of travel in Ireland which places significant importance on the road network [20]. The network is made up of close to 100k kms of road with over 90k intersections between road and river networks. Motorways typically connect major cities and facilitate fast travel. The motorway network has expanded substantially over the past 30 years in Ireland, expanding from 12.5km in 1986 to 916.4km in 2016. National roads connect important cities and towns and support long distance travel and the movement of goods. The National Road network in Ireland accounts for over 5,400 kms of the overall road network in Ireland. Regional roads link smaller towns and villages to the National Road network, while Local roads connect local routes within towns, villages, and rural areas. Local roads also facilitate local transportation and accessibility to services. The Regional and Local Road networks in Ireland account for over 93,500 kms of the overall road network in Ireland [21].

The network facilitates the movement of people and goods across the nation and serves as a connector for cities, towns and regions. Some road connectors within a network play a vital role in allowing access to airports and ports which are key industries for trade and mobility. These connectors are travelled on daily by a large number of users and are a crucial part of a successful road network. However, there are other connector or link roads in the network that may be the only means of access to rural areas and therefore execute a 'lifeline' function for users. 'Lifeline'

links typically have limited alternative travel options and, in their absence, the negative impact on users would be considerable, as there would be a need for long diversions (Martinez-Pastor, Dunny and Gillard, 2019).

3.2 *Bridge management in Ireland*

EIRSPAN is the BMS used in Ireland. It was established in 2001 after many years with little to no investment in Ireland's transportation infrastructure. EIRSPAN applies to bridges with a span of greater than or equal to two meters and retaining walls with retained height of greater than one and a half meters [22]. The BMS was heavily influenced by aspects from systems used around the world with significant input from the Danish DANBRO system. Prior to EIRSPAN there was no definitive inventory and no standard methods for bridge management. Out of the estimated 20,000 bridges in Ireland, roughly 16,000 are masonry arches with a portion of these bridges being over 200 years old. EIRSPAN captures data for all bridges within the strategic road network and bridges captured within the system are well maintained.

All other bridges within the road network in Ireland are managed by respective local authorities in each county. Within this research a review of the current process across multiple authorities identified a range of methods used for bridge management. The bridge stock ranges from 2k to 4k and is generally managed by small teams of engineers, using excel, access databases and increasingly the Bridge Asset Management System. In 2015, the bridge asset management project (BAMP) was introduced in Ireland by the Department of Transport, Tourism and Sport. This provided a bridge asset management android application to be used by local authorities for brides and other structure assets within the local and regional road network. This application allows for the collection of relevant information through a Bridge Inventory Survey (BIS), an initial inspection referred to as a Maintenance Inspection (MI) and a detailed inspection by means of an Engineering Inspection (EI). The BIS contains data associated with the structure covering location, type, material, size etc. Basic condition data is input into the MI by ranking six elements (three structural and three non-structural) which then grants a bridge a red, amber or green (RAG system) rating. The EI is used for more detailed inspections where fourteen elements (eight structural and six non-structural) are ranked 1-5 (Dept. of Transport Tourism and Sport, 2019). The investment decision making is based on bridge condition, budget, human resourse. Community impact is considered in the process however there is a need for a formal data driven approach to identifying community impact. This research aims to address this challenge. County Galway is located on the west coast of Ireland and has the second highest proportion of road network managed by a local authority. It also contains a high volume of lifeline roads in the Connemara area as high-lighted in Figure 1. This are has been selected as pilot region to develop a community impact metric for bridge criticality ranking.



Figure 1. Lifeline roads.

4 DATA COLLECTION FOR THE CASE STUDY AREA

Geographic Information Systems (GIS) is a powerful tool used for management and analysis of spatial data and is utilized in the existing BMAP. This enables each bridge location to be examined by its proximity to certain infrastructure, Figure 2 (a) presents a map of all bridges in the Connemara region. Figure 2 (b) presented a map of local amenities including primary schools, post-primary schools, healthcare centres, libraries, piers and harbours, etc. to identify the proximity to communities. This can lead to a basic analysis on criticality as failure of a bridge located in a built-up area would have greater impact to travel than a bridge on a local road.

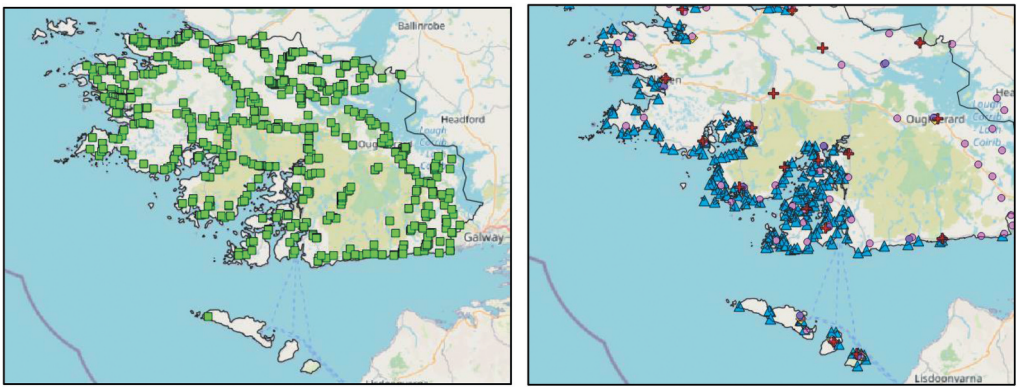


Figure 2. (a) All bridges in Connemara highlighted in green. (b) Local amenities in Connemara.

Within this regions areas of high vulnerability are causeway connections. As highlighted in Figure 3, this area is fully reliant on one bridge for access to all critical services such as healthcare and the community amenities such as shops and business are serviced by the bridge. This area has been selected as a pilot region, it is acknowledged that community vulnerability is easily identifiable. The research aims to accurately quantify this risk to enable future mitigation planning. Bridge failure in this would lead to loss of access for the entire community. Resulting in significant impact in emergencies as access to emergency services would be extremely limited. Additional bridges selected for this study are within inland routes in Connemara whereby loss of service would require lengthy delays. Recent examples of bridge failure in this area include the Leenane bridge failure which resulted in diversions of up to 80kms [23].

Other factors which were consider in the selection of the case study bridges was proximity predicted flood zones, Figure 4 presents the bridges map overlayed with flood prediction zones. This informed the selection of a masonry arch bridge in the village of Clifden, Co. Galway. From the mapping carried out to date, it is evident that GIS is a useful tool for bridge criticality analysis. As the project progresses, GIS will be used to complete bridge and river vulnerability analysis. Further analysis will be carried out on the existing data and travel times and diversions will be assessed. Population data will also be examined to pinpoint the areas with larger communities and identify their access routes. It is hoped that all these factors will lead this approach to criticality and shape the criticality metrics best suited to rural transport networks.

5 CONCLUSIONS AND FUTURE WORK

This outlined the proposed methodology for the development of an accessibility based vulnerability index for rural communities. A case study area has been selected and presented along with initial analysis of bridge condition data. GIS has been proposed as a suitable platform to develop the research and an adapted version of the Hansen's gravity-based accessibility model will be implemented. Where the indirect effects of bridge failure are accounted for by incorporating information on the following: travel times and traffic flows between spatial units and

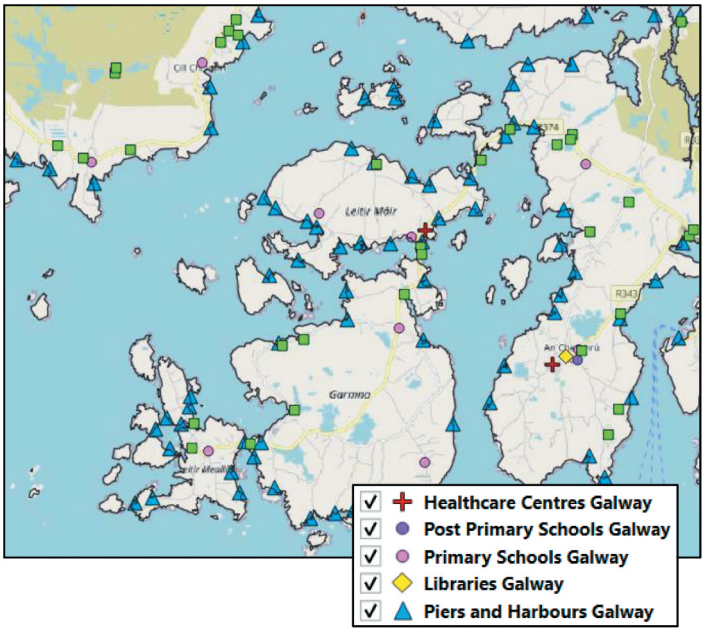


Figure 3. Bridge and amenities in the Lettermore Area.

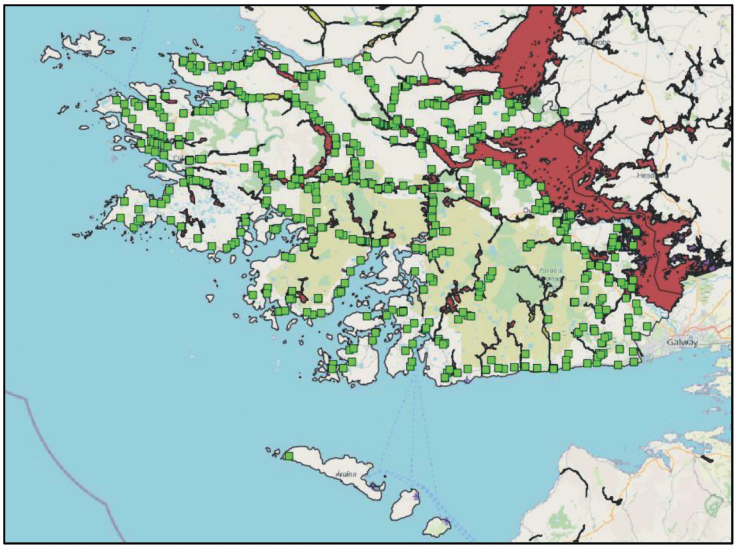


Figure 4. Current, mid-range and high-end flood extents in Connemara.

essential services, as well as data on population, education and employment opportunities in and around potentially affected areas. This will enable the development of investment metrics for decision support in bridge maintenance on the rural road network in Ireland.

ACKNOWLEDGEMENTS

This research was funded by Science Foundation Ireland under the Communities Challenge funding program [23/NCF/SC/11765].

REFERENCES

[1] T. R. Shift, "Securing our future through resilient infrastructure." Accessed: Jan. 30, 2021. [Online]. Available: https://www.resilienceshift.org/securing-our-future-through-resilient-infrastructure/

[2] T. Masood, D. McFarlane, A. K. Parlikad, J. Dora, A. Ellis, and J. Schooling, "Towards the future-proofing of UK infrastructure," *Infrastructure Asset Management*, vol. 3, no. 1, pp. 28–41, 2016, doi: 10.1680/jinam.15.00006.

[3] UK Transport Committee, "The impact of flooding on bridges and other transport infrastructure in Cumbria: Oral and written evidence (HC 473)." Accessed: May 10, 2020. [Online]. Available: http://www.publications.parliament.uk/pa/cm200910/cmselect/cmtran/473/473we08.htm

[4] BBC, "Cumbria floods resulted in £276m bill." Accessed: May 10, 2020. [Online]. Available: http://www.bbc.co.uk/news/uk-england-cumbria-11791716

[5] M. Pregnolato, "Bridge safety is not for granted – A novel approach to bridge management," *Eng Struct*, vol. 196, p. 109193, Oct. 2019, doi: 10.1016/j.engstruct.2019.05.035.

[6] K. Ntafloukas, L. Pasquale, B. Martinez-Pastor, and D. P. McCrum, "A Vulnerability Assessment Approach for Transportation Networks Subjected to Cyber–Physical Attacks," *Future Internet*, vol. 15, no. 3, Mar. 2023, doi: 10.3390/FI15030100.

[7] B. Martinez-Pastor, M. Nogal, A. O'Connor, and R. Teixeira, "Identifying critical and vulnerable links: A new approach using the Fisher information matrix," *International Journal of Critical Infrastructure Protection*, vol. 39, p. 100570, Dec. 2022, doi: 10.1016/J.IJCIP.2022.100570.

[8] R. Teixeira, B. Martinez-Pastor, L. Vucinic, and A. O'Connor, "Flood adaptation decision-making for vulnerable locations using expectation–quantile–investment analysis," *J Flood Risk Manag*, vol. 16, no. 1, Mar. 2023, doi: 10.1111/JFR3.12875.

[9] T. Echaveguren and P. Dechent, "Allocation of bridge maintenance costs based on prioritization indexes," *Revista de la Construccion*, vol. 18, no. 3, pp. 568–578, 2019, doi: 10.7764/RDLC.18.3.568.

[10] L. Dromey, K. Ruane, J. J. Murphy, B. O'Rourke, and S. Lacey, "A bridge-rehabilitation strategy based on the analysis of a bridge-inspection data set," *Infrastructure Asset Management*, vol. 7, no. 1, pp. 25–35, 2020, doi: 10.1680/jinam.18.00028.

[11] C. Contreras-Nieto, Y. Shan, P. Lewis, and J. A. Hartell, "Bridge maintenance prioritization using analytic hierarchy process and fusion tables," *Automation in Construction*, vol. 101, pp. 99–110, 2019.

[12] L. Dromey, K. Ruane, J. J. Murphy, B. O'Rourke, and S. Lacey, "A bridge-rehabilitation strategy based on the analysis of a bridge-inspection data set," *Infrastructure Asset Management*, vol. 7, no. 1, pp. 25–35, 2020.

[13] L. G. Mattsson and E. Jenelius, "Vulnerability and resilience of transport systems A discussion of recent research," *Transp Res Part A Policy Pract*, vol. 81, pp. 16–34, Nov. 2015, doi: 10.1016/J.TRA.2015.06.002.

[14] M. A. P. Taylor and Susilawati, "Remoteness and accessibility in the vulnerability analysis of regional road networks," *Transp Res Part A Policy Pract*, vol. 46, no. 5, pp. 761–771, 2012, doi: 10.1016/j.tra.2012.02.008.

[15] L. A. P. J. Gonçalves and P. J. G. Ribeiro, "Resilience of urban transportation systems. Concept, characteristics, and methods.," *J Transp Geogr*, vol. 85, p. 102727, May 2020, doi: 10.1016/J.JTRANGEO.2020.102727.

[16] A. Reggiani, "The Architecture of Connectivity: A Key to Network Vulnerability, Complexity and Resilience," *Netw Spat Econ*, 123AD, doi: 10.1007/s11067-022-09563-y.

[17] S. Hasan and G. Foliente, "Modeling infrastructure system interdependencies and socioeconomic impacts of failure in extreme events: emerging R&D challenges," *Natural Hazards*, vol. 78, no. 3, pp. 2143–2168, Sep. 2015, doi: 10.1007/S11069-015-1814-7.

[18] Y. Shi, S. Blainey, C. Sun, and P. Jing, "A literature review on accessibility using bibliometric analysis techniques," *J Transp Geogr*, vol. 87, Jul. 2020, doi: 10.1016/j.jtrangeo.2020.102810.

[19] T. Papilloud and M. Keiler, "Vulnerability patterns of road network to extreme floods based on accessibility measures," *Transp Res D Transp Environ*, vol. 100, p. 103045, Nov. 2021, doi: 10.1016/J.TRD.2021.103045.

[20] "Transport Trends An Overview of Ireland's Transport Sector Disclaimer and Terms of Use", Accessed: Jan. 13, 2024. [Online]. Available: http://igees.gov.ie/.

[21] B. Mulry, K. Feighan, and J. McCarthy, "Development and Implementation of a Simplified System for Assessing the Condition of Irish Regional and Local Roads," 2015.

[22] L. Duffy, "Development of Eirspan: Ireland's bridge management system," *https://doi.org/10.1680/bren.2004.157.3.139*, vol. 157, no. 3, pp. 139–146, May 2015, doi: 10.1680/BREN.2004.157.3.139.

[23] RTE, "RTÉ Archives | Environment | Leenane Bridge Collapses." Accessed: May 20, 2023. [Online]. Available: https://www.rte.ie/archives/2022/0609/1303793-leenane-bridge-collapses/Last line of second page

SS43: Responding to structural emergencies: Post-event inspection to restoring the structure to full service

Organizers: S. Alampalli & M. Maqbool


Taylor & Francis
Taylor & Francis Group
http://taylorandfrancis.com

Bridge Maintenance, Safety, Management, Digitalization and Sustainability – Jensen, Frangopol & Schmidt (eds)
© 2024 The Author(s), ISBN 978-1-032-77040-6
Open Access: www.taylorfrancis.com, CC BY-NC-ND 4.0 license

A plan for assessing the damage to highway bridges after an earthquake

J.S. O'Connor
Consultant, Florida, USA

S. Alampalli
Stantec, New York, USA

ABSTRACT: A post-earthquake response plan and bridge inspection guidelines were developed under a research project funded by the New York State Department of Transportation. The Earthquake Response Plan consists of four levels of response, delineated by ranges of earthquake magnitude. A phased approach was used, first mobilizing maintenance workers familiar with the road network to provide a quick initial assessment. This was followed by detailed bridge inspections performed by certified bridge inspectors and, if necessary, by engineers with specialized skills. Key advantage of the proposed response plan is that it was developed to mesh well with the sponsoring agency's existing staffing and organizational structure. The project report contains a process flowchart, clear lines of responsibility, prioritization methods, reporting forms, list of necessary resources, sample photos of possible earthquake damages, strategies for post-earthquake repairs, and staff training exercises. This paper briefly describes the earthquake response plan.

1 INTRODUCTION

Bridges are often considered the most critical link in a highway network. While safety is the primary objective of any post-earthquake bridge inspection program, the need for continued mobility is also important because the highway network is needed to provide emergency services, ensure security, provide access for relief and reconstruction, and to facilitate the revitalization of the economy after a devastating event.

The absolute size or strength of an earthquake is referred to as its magnitude. Generally, a higher magnitude means greater shaking, shaking for a longer time, and over a larger area. It is a measure of the energy released by the earthquake but is not a measure of damage. Bridge damage depends on the magnitude but also upon other factors such as distance to the epicenter, the type of soil through which the seismic waves pass, as well as features of the bridge itself. While various strategies exist to estimate damage resulting from an earthquake, individual visual inspections of structures are usually needed. Figure 1 shows the earthquake damage that caused rocks to fall from the mountain that was looming over this truss bridge in Peru, causing impact damage to the bottom chord, a primary structural member. In addition to the obvious deformation, cracked welds were discovered. This figure illustrates damage that would be difficult to anticipate or detect without a visual inspection.

DOI: 10.1201/9781003483755-394



Figure 1. Damage from Rockfall in Peru. (Photo taken by O'Connor).

Preparedness is the first step toward the mitigation of losses. The Earthquake Response Plan (ERP) proposed by the authors provides a framework so that, in the event of an earthquake, managers will be ready to respond quickly and confidently when they deploy damage assessment teams. Resources can be deployed efficiently, attending to the most critical structures first. Clearly documented instructions and guidance can be provided to staff, so they are prepared to conduct damage assessments of bridges and recommend appropriate action. In particular, it will help ensure the safety of staff and the traveling public, establish when a callout is needed, how a response is to be conducted, establish clear lines of responsibility, describe appropriate phases and levels of response, what first responders and bridge inspectors should look for, how to report their findings, what training and resources are needed, how to determine appropriate follow-up action (such as closure, restriction of traffic, issuance of structural critical findings, and recommendations for repairs or retrofits), and where to get additional information.

The post-earthquake response plan and bridge inspection guidelines were developed under a research project funded by the New York State Department of Transportation (O'Connor and Alampalli, 2012). It was adopted by the agency later (EI 20-021, 2020). This paper presents the proposed ERP that consists of four response levels, delineated by ranges of earthquake magnitude. The tiered approach is intended to direct an appropriate level of resource toward the response. If the earthquake has a magnitude (M_w) less than a threshold value of 3.5, a response is not mandatory; the area engineer who is responsible will use his/her prerogative to inspect bridges on a case-by-case basis. For stronger earthquakes, damage assessments are required within a certain radius of the epicenter. For the highest response level, the Department's Incident Command System (ICS) is activated to manage the response and all structures within a specified radius are inspected.

2 BRIDGE PERFORMANCE DURING EARTHQUAKES

AASHTO's bridge design specification is accepted in the U.S. as the consensus standard for the design of new bridges. However, it was not until the mid-1970's that the design specifications began to include detailed provisions for seismic design. Since the average "year built" for highway bridges in the U.S. is 1969 (Shemaka, 2009), roughly half of the country's existing

bridges were built without the benefit of modern earthquake engineering principles. Thus, how well they would withstand an earthquake is uncertain.

The performance of a bridge under earthquake excitation depends on characteristics of the event itself (hazard factors), the structure's location (site factors), and factors related to its design and condition (response factors). The hazard is defined by its magnitude, a measure of the energy released, its epicenter, and the direction and type of ground waves. Site conditions, particularly the type of rock or soil supporting the structure, play an important role is a structure's response. Response factors include the structure type, material, and condition. Additional response factors include the details of the connections, and reinforcement, as well as the foundation fixity.

Since many in-service bridges were designed without the benefit of modern seismic design standards, some do not have the features needed to resist the seismically induced forces and displacements and may be vulnerable to damage. In addition, the physical condition may have changed since the date a bridge was built. For instance, there may be section loss due to rust, or weakness from fatigue or impacts that can reduce a structure's capacity to carry seismic loads. Structural modifications made over the years for different reasons may improve performance or may have the unintended consequence of negatively affecting seismic performance. When a region is rarely subjected to earthquakes, it also means that the robustness of the system is unproven under this scenario. Engineers must rely on condition inspections, vulnerability assessments, probabilistic scenarios, and detailed analyses of particular bridges to make an educated guess about the fragility of the highway system. More details on behavior of specific type of bridges under earthquakes can be found in the report (O'Connor and Alampalli 2012).

3 RESPONSE PLAN OVERVIEW

Transportation managers in the U.S. use USGS's Earthquake Notification System (ENS) to receive information about earthquakes via email and text messaging. Information is available at https://sslearthquake.usgs.gov/ens/

The Earthquake Response Plan described here is activated upon receipt of an ENS alert. Detailed information about an event, such as magnitude and location, is usually available within 30 minutes, but if a strong earthquake is felt, the DOT should respond immediately. The particular response will be dependent on the reported magnitude and the coordinates of the epicenter. An initial damage assessment phase, carried out by residency maintenance staff under the direction of the responsible regional engineer, will be accomplished by driving priority routes immediately and continuing until all state routes have been checked. The objective is to determine the extent of damage and to close unsafe bridges. This phase is referred to as the Preliminary Bridge Damage Assessment (PBDA). If the epicenter is in one residency and its impact is felt in an adjacent residency, both RE's will be expected to respond as if their entire residency is in the affected area.

After the PBDA, the Regional Structures Engineer (RSE) will oversee a second phase of deployment that consists of professional engineers (PE) performing detailed bridge inspections. These Special Post-Earthquake Bridge Inspection (SPEBI) teams will normally be deployed within 8 hours of the event and continue in subsequent weeks until a comprehensive picture of the damage is obtained. Special access equipment, maintenance, and protection of traffic (MPT) support may be needed for these teams. The RSE and the bridge inspectors will prioritize the SPEBI's using findings of the PBDA's, the criticality of bridges in the area, their vulnerability to seismic damage due to structural features, site conditions, and other factors. Geographic Information Systems (GIS) maps, seismic vulnerability ratings, and predefined inspection priority lists, will facilitate the efficient management of these inspections. Additional inspection teams will be brought in from consulting firms, other DOT regions, and the state Office of Structures, as necessary.

The bridge inspector will decide what follow-up action is required. Action might consist of flagging (reporting) a deficient condition, closing (or reopening) a bridge, restricting traffic, writing a repair request, suggesting more substantial remedial work, or requesting further investigation. Four response levels and the associated radius of concern (R) are listed in Table 1.

Response Level I can also be referred to as a Discretionary Response Level with Level IV as a High-Level Response. The listed radius gives an indication of the area around the epicenter that should be investigated. However, if initial reports show that damage is more

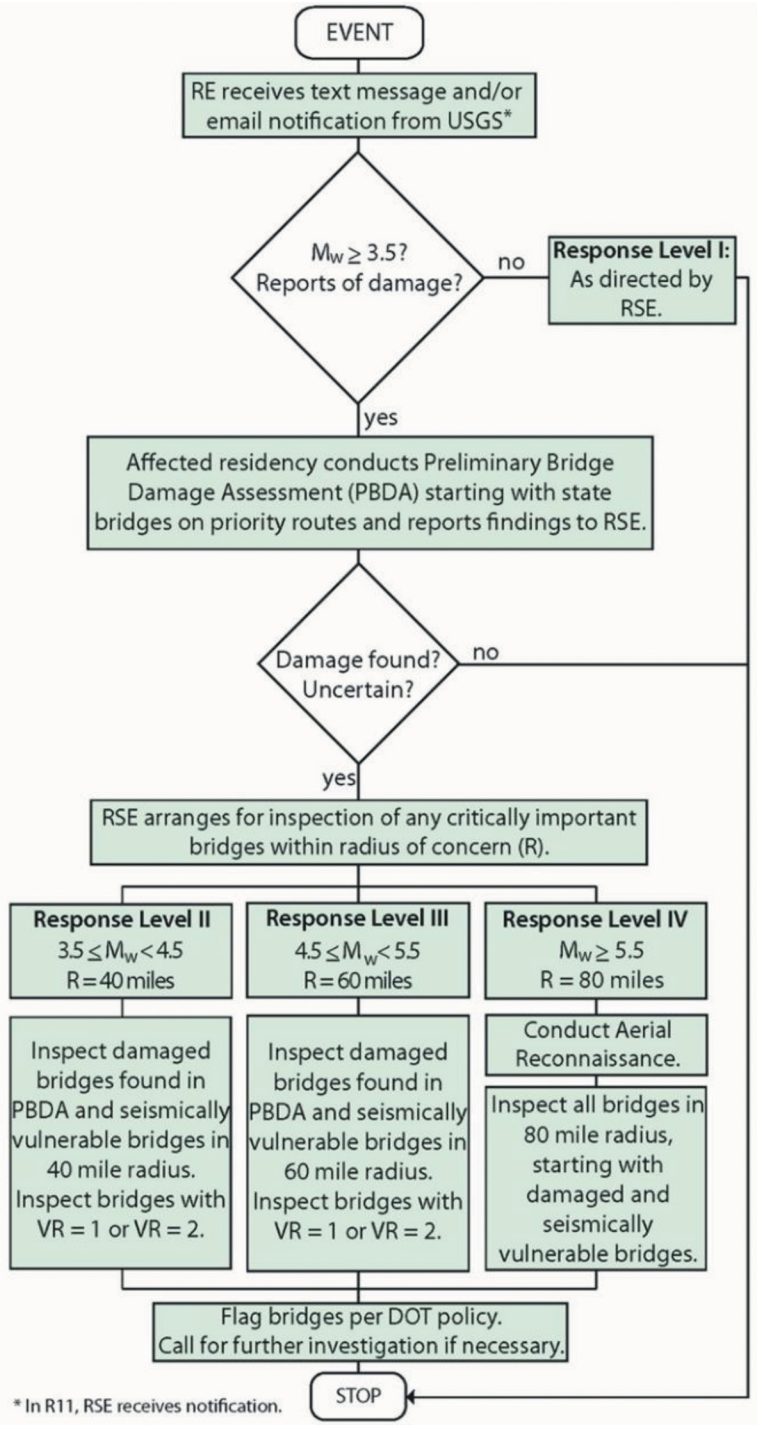


Figure 2. Process flow chart for the ERP.

Table 1. Post-Earthquake response levels.

Response Level	Earthquake Magnitude*	Radius of Concern	Description of Response
I	$M_w < 3.5$	-	A broad-based response is not planned or required. If there are reports of damage, RE is to notify the RSE. On a case-by-case basis, the RSE will determine if a **Special Post-Earthquake Bridge Inspection (SPEBI)** needs to be done. RSE uses discretion to inspect especially vulnerable or critical bridges close to the epicenter.
II	$3.5 \leq M_w < 4.5$	40 mi	RE will immediately initiate **Preliminary Bridge Damage Assessments (PBDA)**. All state routes within the residency will be driven according to priority and all bridges investigated. Reports of damage or questionable conditions will be called in immediately. Summary reports are to be sent to the RSE at the end of each day. If no damage is discovered during PBDA, the post-earthquake response can be terminated. As soon as possible, RSE will arrange for a **SPEBI** using a RSE-generated prioritized list of seismically vulnerable Bridges. SPEBI will be done on bridges within the radius of concern: • deemed *critically important* by the RSE • where damage was reported in the PBDA • where evaluation by a more trained or experienced person is needed • with a seismic vulnerability rating (VR) of 1or 2. • considered vulnerable or especially important
III	$4.5 \leq M_w < 5.5$	60 mi	If there are reports of bridge damage outside of the default radius of concern, the RSE will increase the radius and adjust the inspection program accordingly. Use the same criteria as Response Level II, but with a larger radius.
IV	$M_w \geq 5.5$	80 mi	NYS's Incident Command System (ICS) will be activated for this High-Level Response to ensure coordination of effort among DOT Regions, Main Office and other agencies. RE will conduct **PBDA** on routes immediately and RSE will arrange for **SPEBI** of all bridges that are within the radius of concern as soon as possible.

widespread than anticipated, the RSE has the discretion to expand the radius of concern or elevate the investigation to a higher response level. Figure 2 is a process flowchart of the entire ERP. Table 2 shows a comparison of the different types of bridge damage assessments, with the most immediate type of assessment on the left, and the more time/labor intensive ones on the right. Obviously, the greater the earthquake, the more resources will be needed to obtain a good understanding of the problem in a reasonable timeframe.

4 PRELIMINARY BRIDGE DAMAGE ASSESSMENTS

The RE in the affected area is responsible for initiating the PBDA program in the event of an earthquake, managing and supporting staff in its execution, working closely with the RSE to implement closures or take other action, and communicating with other DOT managers. Specific steps related to the RE's execution of the PBDA program are:

1. Provide earthquake awareness training to residency staff, at least annually.
2. Ensure that resources needed for earthquake response are ready for deployment at any time.
3. Personally subscribe to ENS and assign this responsibility to next in command.

Table 2. Types of Post-Earthquake bridge damage assessment.

Type	Aerial Reconnaissance (Response Level IV)	Preliminary Bridge Damage Assessment (PBD-A)	Special Post-Earthquake Bridge Inspection (SPEBI)	Further Investigation
Objective	'Global' perspective	Route reconnaissance	Detailed Post-Earthquake Bridge Inspection	Special study to address a particular concern
Scope	All bridges in affected area	All bridges in affected area, starting with priority routes.	Site-specific. Table 2 shows bridges to inspect for a given magnitude.	Site-specific, as needed
Inspection Method	Helicopter or small fixed wing aircraft	Drive-through with quick stop at each bridge	Bridge inspection vans, MPT & special access equipment if needed	Any special equipment that is needed
Personnel	1 or 2 DOT managers	Residency staff	Bridge Inspection Teams with supplemental TL's, if needed	Specialists e.g. Structural, Geotechnical, Metallurgical
Timeframe	Immediate (within 24 hours)	Immediate (within hours)	Start a.s.a.p. (usually within 8 hours) and continue as necessary	Subsequent to a SPEBI
Outcome	• Determine the extent of damage • Identify impassible routes & traffic bottlenecks • Locate bridges that have major damage or are obviously unsafe • Suggest priority for ground assessments	• Determine the extent of damage • Identify impassible routes & traffic bottlenecks • Close collapsed or dangerous bridges • Recommend SPEBI bridge inspection for damaged or suspect bridges.	• Flag if necessary • Close collapsed or dangerous bridges • Recommendations for restriction, repair, or further investigation. • Reopen bridges deemed safe that were closed as a precautionary measure during PBDA survey	• Flag as necessary • Detailed analysis • Provide specific recommendations on necessary restrictions and/or repair • Approximate cost estimate for remedial work
Deliverable	Reconnaissance report with photos and/or video	PBDA Form (one line per bridge)	• SPEBI Report • Daily Summary Report (DSR)	Special engineering report

4. Maintain a map and/or list of priority routes in the residency.
5. Maintain a map and/or list of all bridges in the residency, with an identification of bridges considered most critical.
6. Immediately commence PBDA on all routes in the residency whenever:
   a. The epicenter of the earthquake is within the radius of concern of any part of the residency. (The radius of concern varies according to the earthquake magnitude.)
   b. There are reports of earthquake damage to bridges, buildings, or slopes, within the residency.
7. Deploy two-person PBDA teams.

8. RE responds to questions from field teams and provides any necessary support.
9. Collect and review daily reports from field teams. Summarize findings and send a daily report to RSE with digital photos of any damage. Provide the data electronically (i.e. in a spreadsheet), if possible.
10. Verbally report any significant bridge damage to the RSE immediately.
11. Immediately close and barricade any bridges that appear to be unsafe.
12. If there is any uncertainty about a bridge's condition, request that the RSE conduct a bridge inspection (SPEBI).
13. After SPEBI's are completed, close or reopen bridges as requested by the RSE.
14. Arrange for immediate repair of damage that does not require any analysis (e.g., damaged approach). Document all activity with photographs and inform RSE.

5 SPECIAL POST-EARTHQUAKE BRIDGE DAMAGE ASSESSMENTS

The RSE in the affected area is responsible for accomplishing detailed inspections in an expeditious manner, with an effort that is commensurate with the severity of the event. The RSE will also direct follow-up action, such as conducting detailed investigation, structural or geotechnical analysis, designing repair or retrofit schemes, or initiating long-term replacement or rehabilitation. Program steps include:

1. Annually provide earthquake awareness training to bridge inspectors and other staff who might be called into service after an earthquake.
2. Ensure that resources needed for an earthquake response are ready for deployment at any time.
3. Personally subscribe to ENS.
4. Communicate with regional GIS and emergency response staff and share data that is required to maintain a current:
   a. Map and list of priority routes in the region that can be used as lifeline routes.
   b. Map and list of all bridges in the region, with an identification of bridges considered most critical, those that are flagged, and if possible, those considered seismically vulnerable.
   c. Lists with emergency contact numbers for bridge inspectors and office staff who may need to be involved in post-earthquake response.
5. Notify local County Highway Superintendents, authorities, and other bridge owners whenever any significant earthquake occurs and advise of appropriate action.
6. Refer to ERP, determine which response level and radius of concern is appropriate and communicate to others. Organize bridge inspection teams and commence SPEBI's, preferably within 8 hours.
7. Generate a prioritized list of bridges to inspect and print GIS maps with these bridges located on it. Provide to bridge inspection teams.
8. Inspectors are to submit Daily Summary Reports (DSR) at the end of each day when SPEBI's were done. Collect and review daily reports from field teams. Summarize findings and send a report to RD and Director - Office of Structures, the Incident Commander and ICS as appropriate.
9. Review SPEBI reports. Determine if any bridges should be closed or restricted (weight restricted, reduced number of lanes, or open to just emergency vehicles). Give authorization to reopen bridges that were closed as a precaution during the PBDA phase if it is appropriate to do so. Track resolution of any structural flags.
10. Prepare plans for repair, retrofit or replacement as appropriate and work with Structures Asset Management Team to program remedial work.
11. Defer any communication with the media to the Regional Director's designee.

As part of the implementation of this plan, anyone who will be expected to respond to an earthquake should either attend a one-day workshop on post-earthquake damage assessments or take a computer-based training (CBT) course to familiarize them with the same material. Annually afterwards, they should take a one-hour CBT presentation to refresh their memory.

The purpose of the training is twofold: to reinforce the required post-earthquake inspection procedures, and to familiarize them with basic earthquake principles and types of bridge damage that could occur. The training courses should include photographs of possible earthquake damage. Scenario exercises are also useful for ensuring that key players fully understand their responsibilities. More details on the ERP, follow-up actions, and other information can be found in the report (O'Connor and Alampalli 2012).

6 CONCLUSIONS

The above is a brief explanation of a earthquake response plan that can be valuable even where earthquakes are not a day-to-day concern. This paper presented the details of the emergency response plan, Key advantage of the proposed response plan is that it was developed to mesh well with the sponsoring agency's existing staffing and organizational structure. The project report contains a process flowchart, clear lines of responsibility, prioritization methods, reporting forms, list of necessary resources, sample photos of possible earthquake damages, strategies for post-earthquake repairs, and staff training exercises. Further details and technical guidance are available from the authors.

REFERENCES

EI 20–021. 2020. *Post-Seismic Bridge Inspection for State-Owned Bridges*, New York State Department of Transportation, Albany, NY.

O'Connor, J. and Alampalli, S. 2012. *Post-Earthquake Bridge Inspection Guidelines for New York State, MCEER-12-0003*, MCEER, University at Buffalo, Buffalo, NY.

Shemaka, A, 2009. Email correspondence, FHWA to O'Connor, July 28, 2009.

Bridge Maintenance, Safety, Management, Digitalization and Sustainability – Jensen, Frangopol & Schmidt (eds)
© 2024 The Author(s), ISBN 978-1-032-77040-6
Open Access: www.taylorfrancis.com, CC BY-NC-ND 4.0 license

Rapid response for ensuring safety following bridge hits

Maqbool A. Mohammed
Stantec, New York, USA

ABSTRACT: Collision damage is the second leading cause of bridge failures in the United States. Data from NHTSA shows a gradual increase in bridge hits over the last few years, which has helped identify the leading causes of bridge strikes. The costs to repair the bridges are also rising due to an overall spike in bridge strikes. Substantial effort has been invested in technology to curb accidents by projecting deterrent messages, sending personalized alerts, and using innovative software. More often, a bridge strike results in a complete or partial closure of the roadway carrying the bridge or under the bridge. A rapid response is paramount in these situations to avoid immediate closure. This paper focuses on bridge impact case studies and the basis of establishing rapid response procedures.

1 INTRODUCTION

Bridges are a vital component of transportation networks, serving as the vital arteries that enable the movement of goods and connect previously isolated regions. Robust bridges and roads help economies with trade, investment, and growth. However, when a bridge fails, it can have a significant impact on the economy and public.

Collision damage is the second leading cause of bridge failures in the United States after hydraulic failures (Cao, R. 2019). Data from the National Highway Traffic Safety Administration (NHTSA) shows a gradual increase in bridge hits over the last few years, with New York state collecting and mapping such data since 1993 (Rey, M. & Munson, E. 2022). This has helped identify the leading causes of bridge strikes, including low clearance and the use of non-commercial GPS systems. Appropriate reporting procedures have increased awareness of this pressing issue.

The costs to repair bridges are also rising due to an overall spike in bridge strikes, with owners having to front the repair costs leading to high-priced insurance claims. Substantial effort has been invested in technology to curb accidents by projecting deterrent messages, sending personalized alerts, and using innovative software.

Most studies on bridge strikes have focused on causes and post-incident remediation methods. More often, a bridge strike results in a complete or partial closure of the roadway carrying the bridge or under the bridge. A rapid response is paramount in these situations to avoid immediate closure. There are very few established procedures for a rapid response that discuss communication and notification protocols, available resources including personnel and repair materials, repair procedures, and challenges. This paper focuses on bridge impact case studies and the basis of establishing rapid response procedures. A robust response procedure will ensure public safety, communicate in a timely manner, restore essential services, and protect the environment and property. The role of bridge owners and other stakeholders to improve response will also be discussed.

DOI: 10.1201/9781003483755-395

2 BRIDGE IMPACTS

Collisions with bridges can be caused by a variety of factors. Common causes of bridge strikes include low clearance, inadequate signage, driver negligence or behavior, use of non-commercial GPS systems, and changes in traffic flow or lack of alternative routes. It is important to take steps to prevent bridge strikes and minimize their impact when they do occur.

The National Highway Traffic Safety Administration (NHTSA) provides data on motor vehicle crashes in United States. According to NHTSA, collision between a motor vehicle and a fixed object were the second most common type of crash, accounting for over 29% of deaths in 2021 with 2% of deaths attributed to collision with a bridge.

Table 1. Recorded number of collisions with a fixed object (bridge) in the United States.

Year	2017	2018	2019	2020	2021
Bridge Collisions	15,000	13,000	11,000	14,630	13,092

Source: NHTSA Traffic Safety Facts Annual Report Tables. 2023-2017.

New York state has been collecting and mapping the data for vehicle collisions with bridges since 1993. Figure 1 below shows number of vehicle collisions with New York bridges each year from 2011 to 2021.

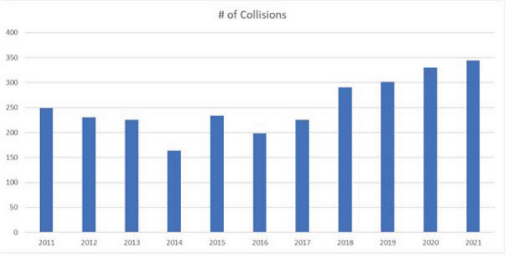


Figure 1. Number of vehicle collisions with New York bridges each year (Rey, M. & Munson, E. 2022).

Bridge strikes can have significant impacts on the economy and public. Disruption of traffic flow impedes emergency response, daily commuting, and freight movement. The resulting consequences of bridge impacts include serious injuries and even fatalities, chemical spills, traffic jams, taxpayer money spent on repairs, and increased insurance costs. These impacts can be costly and time-consuming to address and can have long-lasting effects on the community. It is important to take steps to prevent bridge strikes and minimize their impact when they do occur.

Depending on the severity of the impact, bridge damage may include scratches, scrapes, spalls, delamination, cracking, distortion, loose connections, partial failure, or complete failure. In addition to the bridge strikes causing significant damage to the bridge structure, leading to costly repairs and potential safety hazards, they can also result in socio-economic impacts.

3 RAPID RESPONSE PLAN

Bridge owners typically follow a set of routine actions when made aware of a bridge hit, such as closing roads, inspecting the bridge, and erecting temporary shoring. The general timeline for a bridge impact response is as follows:

1. A phone call is directed to the city maintenance/owner.
2. City maintenance/owners dispatch engineers (on staff engineer or consultant) immediately.

3. Depending on the location, an inspector reaches the site (usually within 1-2 hours).
4. The inspector performs initial visual inspections.
5. Depending on the severity and location of the impact, access equipment and traffic control are arranged (within a few hours).
6. Based on the severity of the damage, the inspector may recommend temporary supports to prevent local failure.
7. For any potential failures, the bridge may be recommended for partial or complete closure.
8. Temporary support is designed, assembled, and erected (usually within 24 hours to allow traffic).
9. Permanent repairs are usually completed within a few days (depending on the severity of the damage).

Bridge owners have created their own unique policies and procedures for responding to situations. The written procedures can range from a single page outlining the necessary actions to much more detailed procedures, including stand-alone documents. According to the 2020 FHWA Case Study of State Practices on Responses to Bridge Impacts (FHWA. 2020), the Iowa DOT is the only agency with a standalone document for responding to over-height collisions with bridges, titled the Emergency Response Manual for Over Height Collisions to Bridges. MnDOT's Bridge and Structures Incident Response Plan outlines the response, defines responsibilities, and includes a flow chart, as depicted in Figure 2.

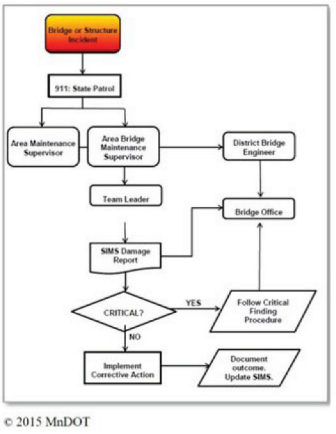


Figure 2. MnDOT response flowchart (MnDOT. 2019).

Notification and communication protocols are critical in an emergency to ensure public safety, protect property, facilitate response efforts, and instill public confidence. The emergency response plan should specify which personnel will communicate with each other and how communication will occur during an emergency. This includes bridge owners, responsible parties for response, and inspectors and engineers addressing the issue. The communication protocols should also address information media to motorists affected by the bridge impact. In addition to the requirements for bridge owners, there are certain internal protocols needed for inspectors responding to the site and the engineers addressing the repairs. In summary, notification and communication protocols in an emergency are crucial for effective emergency management. They help ensure public safety, protect property, and facilitate response efforts.

Field personnel responding to bridge impacts should be equipped with the necessary knowledge and tools to ensure a swift and effective response. They should be aware of the bridge records and the tools and equipment required to address the issue at hand. In addition, they should have access to vehicles and phones to reach the site quickly and communicate with other personnel. It is important to note that certain locations or

equipment may require special permits or training, which should be obtained beforehand to avoid any delays in the response time. Furthermore, it is essential to consider the availability of staff on nights and weekends, as this can impact the response time. If staff availability is limited, it may be necessary to have a contingency plan in place to ensure that the response is not delayed.

In addition to field personnel, engineers in the office should also be available to work on repairs on an emergency basis. They should have access to all bridge records to come up with an effective repair plan. Access to design or analysis software is also necessary to ensure that the repair plan is feasible and effective. Communication with ground staff can help in creating an effective repair solution. By collaborating with the field personnel, the engineers can gain a better understanding of the situation on the ground and develop a repair plan that is tailored to the specific needs of the situation. It is also prudent to involve the contractor in the repair process to ensure that the design solution can be implemented within the short duration. By working closely with the contractor, the engineers can ensure that the repair plan is feasible, and that the contractor has the necessary resources to implement the plan effectively. In summary, engineers in the office play a critical role in the emergency response process. They should have access to all bridge records and design or analysis software to develop an effective repair plan. Communication with ground staff and collaboration with the contractor can help ensure that the repair plan is feasible and effective.

4 REPAIR PROCEDURES AND CHALLENGES

Common repair procedures for bridges include grinding damaged areas on steel members at gouges and scrapes, drilling out cracks in metal, repairing or replacing diaphragms, heat strengthening, repairing or replacing steel members using steel plates or angles, patching concrete areas, repairing steel bars or cables, and installing external carrier beams or post-tensioning cables/bars.

Case Study: A crack was discovered in the steel fascia beam after an impact on a Friday afternoon on a bridge over a connector highway with heavy traffic, including a connection to a major airport (actual location is not mentioned to maintain anonymity). The owner was promptly notified, and traffic was immediately shifted to other lanes away from the fascia beam. In the office, a load rating was performed to determine the safe load carrying capacity, and it was determined that the fascia beam needed to be temporarily supported using a shoring. However, material availability for shoring was a challenge on a weekend as the designated contractor for the emergency repairs did not have the right size shoring members. Working with contractors, structural designers were able to come up with alternate details that could safely support the beam. The placement of shoring over the major 3-lane highway, including an on-ramp, presented another challenge. Traffic engineers were onboarded to come up with a detour and lane shift within the constricted space to erect the shoring. Within a matter of a few hours and in the midst of heavy rush hour traffic, the beam was shored (see Figure 3). Another structural team in the office started working on the permanent repairs. Over the weekend, final repairs were designed, approved, and the contractor was able to source the material. A simple solution to drill a hole at the crack end and strengthen the beam with angles and plates was adopted, considering the time and location of the impact. The contractor was able to complete repairs in a day. Unfortunately, the same bridge was impacted again in less than a year. The severity of the impact (see Figure 4) presented another challenge to come up with an alternate repair, as the beam could not be repaired in traditional ways. Code compliance may also be a challenge, especially when working on older bridges. Finally, the design team adopted a solution to support the fascia beam using a carrier beam on top of the sidewalk. The owner, designer, and contractor worked together to come up with a solution in a short time frame, using the available materials and without affecting public safety. Ultimately, the bridge was replaced with a new structure that has higher clearance as part of a major project.



Figure 3. Temporary shoring.



Figure 4. Impacted fascia beam.

5 CONCLUSIONS

The aim of any Rapid Response Plan for Bridge Collisions is to ensure public safety, preserve life, and minimize injury. In the event of a bridge collision, it is crucial to communicate with the public in a timely manner to provide information about the incident and any necessary detours or closures. The restoration of essential services is also a key priority, as it helps to minimize the impact of the incident on the community. Finally, it is important to protect the environment and property by taking appropriate measures to prevent further damage.

To achieve these goals, a Rapid Response Plan should include clear procedures for notifying emergency services, assessing the damage, and coordinating the response effort. The plan should also outline the roles and responsibilities of different personnel involved in the response effort, including bridge owners, engineers, contractors, and emergency services. In addition, the plan should include procedures for communicating with the public, including the use of social media, news releases, and other communication channels. The plan should also address the restoration of essential services, and the protection of the environment and property.

By having a well-designed Rapid Response Plan in place, bridge owners and authorities can ensure that they are prepared to respond quickly and effectively to any bridge collision, minimizing the impact on the community and ensuring public safety.

REFERENCES

Cao, R. 2019. Heavy Truck Collision with Bridge Piers, CUNY Academic Works. https://academicworks.cuny.edu/cc_etds_theses/876

Rey, M. & Munson, E. 2022. Truckers hitting low bridges costs New York millions as crashes increase, Times Union. https://www.timesunion.com/state/article/new-york-bridge-strikes-17177659.php
National Highway Traffic Safety Administration's (NHTSA). 2023-2017. Traffic Safety Facts Annual Report. https://crashstats.nhtsa.dot.gov/#!/DocumentTypeList/12
Federal Highway Administration (FHWA) 2020. Case Study: Response to Bridge Impacts – An Overview of State Practices, FHWA-HIF-20-087. https://www.fhwa.dot.gov/bridge/preservation/docs/hif20087.pdf
Minnesota Department of Transportation. 2019. Bridge and Structure Inspection Program manual. https://www.dot.state.mn.us/bridge/pdf/insp/bridge-and-structure-inspection-program-manual.pdf
New York State Department of Transportation (NYSDOT). 2011. Bridge Vehicle Impact Assessment – Final Report. https://www.dot.ny.gov/divisions/engineering/structures/repository/manuals/Bridge_Hits_Task_Final_Report.pdf

Bridge Maintenance, Safety, Management, Digitalization and Sustainability – Jensen, Frangopol & Schmidt (eds)
© 2024 The Author(s), ISBN 978-1-032-77040-6
Open Access: www.taylorfrancis.com, CC BY-NC-ND 4.0 license

Critical role of the bridges ensuring emergency services and disaster recovery in Turkey

N. Memişoğlu Apaydin & R.B. Sikar
Istanbul University-Cerrahpaşa, Istanbul, Turkey

ABSTRACT: After a major earthquake or flood, the importance of functional bridges cannot be overstated. Bridges' significance becomes unmistakable during times of crisis, particularly in the aftermath of natural disasters such as earthquakes and floods. In the destroy of a functional bridge, search and rescue efforts can be interrupted and the affected people number may increase and face isolation and delayed assistance. In recent years, Turkey has witnessed several devastating earthquakes and floods that have severely impacted its infrastructure, including bridges.

This article explores the critical role bridges play in ensuring emergency services and disaster recovery in Turkey, shedding light on the rapid measures taken to address damaged bridges in the wake of recent earthquakes and floods.

1 INTRODUCTION

Bridges are of great importance in major disasters such as earthquakes and floods. Inspecting bridges after a disaster is a critical step for emergency rescue operations as well as long-term recovery processes (Wang et al., 2023). These inspections provide important information regarding the safety, durability, and usability of bridges. Engineers determine the damage caused by the impact of the disaster and estimate how long it takes to repair bridges, helping the community return to normal life.

Pre-disaster precautions also play an important role. Bridge engineers make design to increase the resistant of bridges against earthquakes, floods, and other natural disasters. Strengthening bridges using latest engineering codes and technologies aims to minimize the effects of disasters.

However, damage to bridges may occur due to reasons such as lack of maintenance, poor design, or natural disasters being more severe than expected. In this case, rapid inspection, and rapid repair of bridges after the disaster is of great importance. This process is critical not only for ensuring transportation mobility but also for accessing emergency teams to disaster area and work effectively.

Immediately after the disaster, it is important to repair bridges to increase the resilience of the road network and accelerate the return of society to normal life. In the study published in 2020, the importance of repairing bridges to maximize the durability of the road network was emphasized (Merschman et al., 2020). Following a disaster, factors such as infrastructure damage, changes in traffic patterns, and emergency traffic control can combine to cause traffic congestion to worsen. In this process, it is of great importance to make bridges available for the delivery of emergency supplies and the organization of logistics operations (Chang et al., 2000). This ensures effective emergency response and minimizes the effects of the disaster.

Many methods have been developed as post-earthquake inspection methods. One of the oldest methods for restoring bridges after earthquakes was published in 1990. The proposed inspection method effectively evaluates the seismic sensitivity of existing highway bridges

DOI: 10.1201/9781003483755-396

without the need for complex calculations, based on the sensitivity to extreme deformation and infrastructure failure (KAWASHIMA & UNJOH, 1990). By 2009 The California Department of Transportation (Caltrans) had created and implemented a customized version of ShakeCast, a post-earthquake analysis tool designed to quickly assess potential structural damage (Loren et al., 2000). In addition, the methodology proposed by Norimitsu Koike, and Issam E. Harik can effectively evaluate bridge safety and functionality after a major seismic event, shorten inspection time, and reduce overall damage (Koike & Harik, 2012).

Many methods have been developed as inspection methods in cases of flood, as well as after earthquakes. The 2011 Missouri River flood caused significant damage to many structural systems in western Iowa. It affected bridge foundations, asphalt and unpaved roads, culverts, and embankment slopes. This flooding led to the closure of multiple intersections and 10 miles of road closures in western Iowa. The report published in 2013 is an example of field assessments and measurements made after the flood (Flooding, W. I. M. R. 2023). In the report prepared by the Illinois Transportation Center in 2022, it was stated that post-flood control methods and many cases were revealed (Tom et al., 2022). Recently, with the advancement of communication technologies, the communication of objects with each other has begun to be used in post-event inspection as well as in every field. One of the most current methods for post-event investigation is the IoT-based bridge collapse and flood detection system. It improves bridge condition assessment, maintenance planning, and emergency planning by automatically detecting cracks and alerting authorities (Aher et al., 2023).

In this study, the post-event inspection and evaluation studies are explained after the flood and the earthquake in Turkiye.

2 DESTRUCTIVE EARTHQUAKES AND FLOODS IN TURKIYE

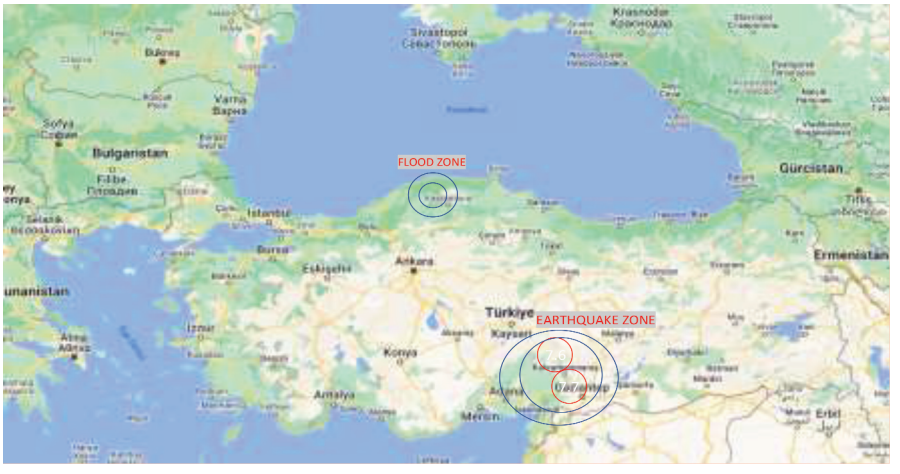


Figure 1. Disaster Zones in Turkiye.

Turkiye has a geography that is frequently exposed to natural disasters due to location. The disasters experienced in the last two years have once again demonstrated the country's efforts to cope with difficult situation. In particular, the Western Black Sea Flood Disaster on August 6, 2021, and the Kahramanmaraş-centered earthquakes on February 6, 2023, have shown how Turkiye struggled with serious disasters.

Along with these, similar disasters that have occurred in other parts of country last two years have also tested the resilience. The Elazığ-Malatya Earthquake on January 24, 2020, the Izmir Earthquake on October 30, 2020, the Ağrı Earthquake on February 23, 2020, and the

Eastern Black Sea Flood Disasters in July-August 2020 reflect Turkiye's determined struggle against natural disasters.

These disasters not only caused loss of life and property but also seriously affected the country's infrastructure. However, government and related instutuions responded fast initiated search, and rescue efforts, and took action to quick repair the damaged infrastructure. This process has once again demonstrated how important a coordinated effort is at both local and national levels.

These experiences enable stronger preparations and the development of disaster management strategies. In addition, the lesson learned from these disasters that rapid reactions and quick repair provide post-disaster emergency requirement and decraese the loses.

3 BEHAVIORS OF THE ROAD TRANSPORTATION NETWORK DURING 6 FEBRUARY 2023 EARTHQUAKE

The Eastern Anatolian Fault System is one of the most active fault systems in Turkiye and determines the boundary between the Anatolian and Arabian Plates. It has been the source of several significant earthquakes throughout history. Remarkable events occurred in two consecutive earthquakes with which the system interacted. In the first earthquake, approximately 290 km of surface ruptures on the fault line caused significant cracks and displacements in the region. The severity of these cracks showed itself with horizontal fault displacements of up to 6.5 m.

In the second earthquake, it was observed that an area of approximately 130 km along the fault line was affected. This event once again caused serious horizontal fault displacements in the region and had significant impacts on the surrounding areas. According to AFAD's 2023 report, these events highlight the complexity of earthquake activity in the region and the potential danger of the Eastern Anatolian Fault System (AFAD 2023).

Fault ruptures, ground shaking, liquefaction, and co-seismic landslides have caused various levels of damage to transportation networks. Especially with the effect of fault ruptures, serious deformations have occurred in many roads and bridges, and faults have even cut some roads and bridges and affected transportation lines. Due to the damage to the transportation infrastructures, search and rescue works delayed a few days in the region.

Highways and railways were damaged due to the ruptures in the fault line, and cracks and deformations occurred on the road surfaces. In addition, the durability of some bridges has decreased, and this has created concern for the safety of transportation. Airports and seaports also felt the effects of this natural disaster, with cracks in the runways and deformations in the take-off and landing lines.

Damages to transportation infrastructures especially to roads between provinces in the region caused difficulties in the coordination of emergency services. Quick repair teams made an intense effort to repair the damaged roads and to open the vehicle traffic. At the same time, the need for a coordinated logistics effort has emerged to ensure the safe delivery of vehicles carrying emergency aid and supplies to damaged areas.

According to KGM (General Directorate of Highways) data, a large area in the earthquake zone covers a surface area of approximately 109,000 square kilometers and there is a total of 9,176 kilometers of asphalt roads in this area (KGM 2023). A significant part of the total highway network throughout Turkiye is spread over this earthquake zone, with a share of 15 percent. This includes 12 percent of the state highway network and 14 percent of the provincial road network. These roads constitute an important part of the transportation infrastructure in the provinces affected by the earthquake.

In addition, according to SBB's (Presidency of the Republic of Turkiye, Strategy and Budget Directorate) 2023 report, 15 percent of the total vehicle-kilometer, 15 percent of the passenger-kilometer, and 20 percent of the ton-kilometer occur in this earthquake zone (SBB 2023). These statistics show that these regions account for a significant share of not only road traffic but also transportation volume.

3.1 *Case study: Restoring the bridges on the 6 February 2023 earthquake*

It has been observed that the level of damage to the transportation infrastructure plays a critical role, especially in the timing of vital search and rescue operations carried out in the first 72 hours of the earthquake and other disaster response services after this period.

Vital rescue operations during earthquakes often aim to save people trapped in collapsed buildings, and these operations usually occur intensively within the first 72 hours. However, damage to transportation infrastructure at the early step may make it difficult for rescue teams to reach the area quickly. Damage to roads, bridges, or tunnels may prevent access to critical locations, reducing the effectiveness of rescue operations.

At the time period following the earthquake, similar difficulties may arise for other disaster services. In the days and weeks following the initial response phase, it is of great importance to quickly restore transportation infrastructure for operations such as health services, aid distribution, and shelter provision. Measures such as repairing damaged roads, strengthening bridges, and reopening railway lines can speed up the post-disaster recovery process and contribute to more effective delivery of relief services.

There are a total of 243 bridges in the road network in the region. Nearly twenty of these bridges encountered different levels of damage on the roads under the responsibility of the General Directorate of Highways (KGM) (SBB 2023). Most road bridges and tunnels in the earthquake zone are located close to fault lines; in some bridges, fault lines pass between the columns of these structures. This situation has increased the potential for earthquake effects to directly affect these structures.

Interestingly, the bridges did not collapse even though they were subjected to acceleration values of 1.5-2 times their design acceleration. Instead, they were usually limited to moderate to minor damage and remained functional. This draws attention to the durability and safe design of bridges from an engineering perspective. The bridges were able to cope with the high accelerations they were subjected to during the earthquake and remained without collapsing.

Bridges often suffered non-structural damage such as expansion joints, shear keys, and deformation of bridge bearings. These damages were observed in the bridge piers and superstructure and mostly occurred in non-structural details such as expansion joints and earthquake wedges, which are special design elements. These elements generally showed a certain level of resilience despite the high energy generated during the earthquake.

Structural damage to the piers and bridge superstructure was largely repairable. Evaluations showed that these types of damage did not compromise the basic structural integrity of the bridge and did not make it unsafe for vehicles to use the bridge. This shows that the bridges are built with significant durability and design purpose.

Structural damage to some bridges, although not critical, required detailed inspection of the bridges. Experts at the General Directorate of Highways (KGM) examined these bridges in more detail and identified cases where the damage did not adversely affect traffic flow or traffic safety. Depending on the location of the damage, traffic continued to flow using at least one lane on the bridges, and temporary traffic arrangements were made. This process shows that bridges can be repaired quickly and remain functional.

Due to earthquakes, only two bridges collapsed due to the secondary effects of ground motion. One of these bridges was the Hitit-Demirköprü on the Antakya-Reyhanlı-Cilvegözü (D420) state road. Hitit-Demirköprü consisted of two twin bridges side by side, 61.8 meters long. However, due to soil liquefaction, which was the secondary effect of the earthquake, one of the bridges lost its load-bearing feature because of the rotation of its side piers and became completely unusable.

General Directorate of Highways (KGM) teams carried out temporary repairs on the collapsed bridge to maintain traffic flow and provide mobility. The collapsed side abutment of the less damaged one among the twin bridges was filled, and by using an asphalt mixture, the superstructure was brought to the traffic crossing level and access was provided over a single bridge. By means of rapid and effective repairments, the main artery was kept open to traffic in the first 24 hours after the earthquake (Figure 2).



Figure 2. Demirköprü: side abutment was repaired by filling the upper part.

The other collapsed bridge was the 52.50-meter-long Bulam II Bridge on the Adıyaman-Yeşilyurt-Malatya State Road. The rock mass that broke away during the earthquake fell from the slope and broke the precast beam of the bridge. This incident negatively affected transportation as there was no alternative route for vehicles to be directed in the region. However, the General Directorate of Highways (KGM) teams quickly stepped in and produced temporary solutions to keep traffic open.

Within the scope of the temporary repair works carried out by KGM teams, the 3-span simple girder beam on the damaged bridge was removed and replaced with stone filling. In this way, it was aimed to maintain the function of the bridge and ensure traffic passage. These temporary productions represented a rapid and effective intervention to ensure the continuity of traffic. Figure 3 shows the details of the temporary production made with stone filling.



Figure 3. Repair of Bulam II bridge with stone filling.

A common type of damage to bridges was damage to non-structural element such as expansion joints that prevented traffic from passing. Although such damage was expected, it had to be repaired quickly due to its impact on traffic. After the earthquake, rapid scanning was carried out on all bridges, the damaged parts of small-sized expansion joints were cleaned, and the remaining gaps were filled with asphalt to ensure safe traffic passage. In expansion joints with larger capacity, the road was kept open to traffic with temporary rapid repairs. The work on the TAG (Tarsus-Adana-Gaziantep) highway is one of the best examples of this rapid response.

The TAG highway played an important role as one of the most important transportation routes in the earthquake region. After the earthquake, all search and rescue teams and emergency services transportation usedthis highway. Bridges and viaducts located on the fault line showed perfect performance despite near fault effect. Along with repairable damage to some bridge components, damage to expansion joints on long-span viaducts was initially severe enough to prevent traffic flow.

As seen in Figure 4, the General Directorate of Highways (KGM) responded very quickly, repairing the damage to the expansion joints of the viaducts on this route within 24 to 36 hours using temporary repair methods and reopening the highway to traffic. This is a successful example of effective deployment of emergency response capabilities and planning. While this rapid response ensured uninterrupted transportation, it also laid the foundation for planning and implementing long-term improvement works.



Figure 4. Expansion joint repair on TAG Highway.

4 EFFECTS OF THE 11 AUGUST 2021 FLOOD ON THE TRANSPORTATION NETWORK

The disaster, described as the most devastating flood in the history of Turkiye, affected 3 provinces in the Western Black Sea Region and a total of 12,000 km^2 (Kelesoglu et al., 2023). Extraordinary rains in Kastamonu, Bartın, and Sinop provinces caused various damages to the transportation infrastructure and led to a major disaster. These damages increased the loss of both life and property and made post-disaster first aid and search and rescue efforts difficult.

The flood that occurred in the Western Black Sea Region affected an area of 240 km, especially in coastal areas, and caused various levels of damage (Kelesoglu et al., 2023).This situation remarkably complicated the provision of transportation and emergency aid in the disaster area. The map in Figure 5 shows the highway network of provinces such as Kastamonu, Sinop, and Bartın, which were affected and damaged by the flood.

To provide rapid transportation and first aid in the disaster area, intense efforts were made to open the roads to traffic and keep the main arteries open by establishing portable bridges. This formed an important part of the emergency response and allowed rapid aid to be delivered to survivors.

4.1 *Case study: Bridge damages on 11 August 2021 flood in the Western Black Sea region*

Many bridges were damaged in different lengths and widths due to the impact of streams flowing through different neighborhoods and even different blocks. Although most of these



Figure 5. The road network of the flood-affected area.

bridges are located on main arteries, they were built between 1955 and 1975.Some bridges were constructed according to the H15-S12 load class between 1955 and 1965. Bridges built in the 1965-1975 period were designed for 100-year floods, considering the H20-S16 load class (AASHTO 2002) (Kelesoglu et al., 2023).

They have different lengths which are 26 meters, 39 meters, 52 meters, and 65 meters. Among the general characteristics of reinforced concrete slab bridges, they have shallow foundations. These bridges were built quickly to connect city road.s

In response to the escalating flood disasters attributed to global warming and other factors, legislative changes have been implemented, particularly in regions prone to flooding. Hydraulic criteria in bridge design over main arteries had been considered a 100-year flood by the General Directorate of Highways. However, due to increased flood events in recent years, the criteria were revised five years ago to incorporate a 500-year flood depth.

The bridges affected by the August 11, 2021, flood in the Western Black Sea Region were predominantly designed approximately 40 years ago under the previous legislation. This resulted in insufficient hydraulic sections, leading to severe damage. Notably, there are 115 bridges connecting main arteries, towns, and neighborhoods in the region, totaling approximately 4600 meters. Among them, 27 bridges fall under the responsibility of the State Highways Administration, with a total length of 1100 meters. Six of these bridges suffered complete damage, and twelve experienced partial damage (KGM 2021a).

Damages occurring on bridges can be summarized in two basic categories; bridges that were destroyed and collapsed due to floods, and partially damaged bridges that can be opened to traffic in a short time with quickrepairs.

Transportation was provided with panel bridges instead of collapsed bridges. Due to the limited number of panel bridges, panel bridges were established considering the importance of the road. In places where the stream widths were suitable, diversion work was carried out, the direction of the water was changed, and the water was derived until the new bridge was manufactured.

When we look at the bridges that were damaged due to floods but can be opened to traffic with urgent repairs; The repair of the 42 m long Valay bridge on the Cide-Kastamonu road can be cited as an example of the repairs made on this type of bridges.

In this region, damage occurred to the approach embankments of dozens of bridges due to floods. The approach embankments damaged by the flood were quickly repaired and the bridges were opened to traffic. Figure 7 shows the damage and repair of the approach embankment on the Valay 1 bridge.

A quick intervention was made to the partially damaged bridges and traffic was reopened. Most of the damage in these cases resulted from erosion of the approach embankment, often



Figure 6. Kumluca Bridge and the panel bridge installed in its place.



Figure 7. Valay Bridge-flood damage and appearance after repair.

caused by flood debris. Large trees and logs carried by the flood posed a significant threat, causing lateral impact on bridge piers and blocking waterways, causing additional horizontal pressure.

Damages resulting from flooding demonstrate the need for ongoing adjustments to infrastructure standards and the importance of considering dynamic environmental factors in the resulting design and maintenance. Case studies reveal the vulnerabilities of old bridge structures in the face of evolving climate challenges.

5 CONCLUSIONS

The recent earthquake and flood disasters in Turkiye, especially the major earthquake on February 6, 2023, and the Western Black Sea flood disaster on August 11, 2021, caused significant damage to transportation infrastructure.

It was observed that the level of damage to the transportation infrastructure had an impact on vital search and rescue services, especially in the first 72 hours of the earthquake, and disaster services in later steps. Due to the successive earthquakes, 15 percent of the existing highway network in provinces was affected. Damage generally prevented traffic on bridges because of non-structural elements such as expansion joint. The rapid repair of damages in expansion joints provided to the rapid normalization at transportation.

The Western Black Sea flood disaster on August 11, 2021, which took place in Turkiye, also caused various damages to the transportation infrastructure. This disaster caused many bridges to be damaged in different lengths and widths due to streams flowing through the neighborhoods.

Both disasters caused structural and non-structural damage to bridges. However, with a rapid and effective intervention, the damage to the transportation infrastructure was repaired in a short time. The rapid repair response to transportation infrastructure after the disasters played a key role in effectively directing emergency aid and services. All these processes, combined with the contribution of the local people and the personnel affected by the disaster, enabled a historic mission to be accomplished in a short time.

REFERENCES

AFAD 2023 (2023) T.C. İçişleri Bakanlığı Afet ve Acil Durum Yönetimi Başkanlığı 6 Şubat 2023 Kahramamaraş (Pazarcık ve Elbistan) Depremleri saha çalışmaları ön değerlendirme raporu, Rapor, Deprem Daire Başkanlığı,24 Şubat 2023 Ankara

Aher, S., More, S., Pagare, R., & Shingate, D. (2023). IOT-Based Bridge Collapse and Flood Detection System. *International Journal of Advanced Research in Science*, *Communication and Technology*. https://doi.org/10.48175/ijarsct-8393.

Chang, S. E., Shinozuka, M., & Moore, J. E. (2000). Probabilistic Earthquake Scenarios: Extending Risk Analysis Methodologies to Spatially Distributed Systems. *Earthquake Spectra*, *16*(3). https://doi.org/10.1193/1.1586127

Flooding, W. I. M. R. (2013). Geo-Infrastructure Post-Flood Damage Assessment, Repair and Mitigation Strategies.

Kawashima, K., & Unjoh, S. (1990). AN INSPECTION METHOD OF SEISMIC VULNERABILITY OF EXISTING HIGHWAY BRIDGES. *Doboku Gakkai Ronbunshu*, *1990*(416). https://doi.org/10.2208/jscej.1990.416_155

Kelesoglu, M. K., Temur, R., Gülbaz, S., Memisoglu Apaydin, N., Kazezyılmaz-Alhan, C. M., & Bozbey, I. (2023). Site assessment and evaluation of the structural damages after the flood disaster in the Western Black Sea Basin on August 11, 2021. *Natural Hazards*, *116*(1). https://doi.org/10.1007/s11069-022-05690-4

KGM (General Directorate of Turkish Highways, in Turkish: Karayolları Genel Müdürlüğü) (2021a) The Flood Disaster Report of General Directorate of Turkish Highways (in Turkish), August 11, 2021a. Ankara, Turkiye

KGM 2023 (2023). KGM, Karayolları Genel Müdürlüğü https://www.kgm.gov.tr/Sayfalar/KGM/SiteTr/Duyurular/DuyuruDetay.aspx?Parameter=1260

Koike, N., & Harik, I. E. (2012). Post-earthquake rapid inspection planning for bridges in Western Kentucky. *International Journal of GEOMATE*, *2*(1). https://doi.org/10.21660/2012.3.1252

Loren L. Turner, David Wald, Kuo-Wan Lin; Shakecast Caltrans Deploys a Tool for Rapid Post-earthquake Response, TR NEWS, No.261, pp.40–41. 2009.

Merschman, E., Doustmohammadi, M., Salman, A. M., & Anderson, M. (2020). Postdisaster Decision Framework for Bridge Repair Prioritization to Improve Road Network Resilience. *Transportation Research Record*, *2674*(3). https://doi.org/10.1177/0361198120908870

SBB 2023 (2023) "Türkiye Earthquakes Recovery and Reconstruction Assessment Report" Türkiye Cumhuriyeti Cumhurbaşkanlığı Strateji ve Bütçe Başkanlığı, https://www.sbb.gov.tr/wp-content/uploads/2023/03/2023-Kahramanmaras-and-Hatay-Earthquakes-Report.pdf

Tom, J. G., Garcia, M. H., & Wang, H. (2022). Review of Methodologies to Assess Bridge Safety During and After Floods. *FHWA-ICT-22-008*.

Wang, T., Liu, Y., Li, Q., Du, P., Zheng, X., & Gao, Q. (2023). State-of-the-Art Review of the Resilience of Urban Bridge Networks. *Sustainability*. https://doi.org/10.3390/su15020989.

Bridge Maintenance, Safety, Management, Digitalization and Sustainability – Jensen, Frangopol & Schmidt (eds)
© 2024 The Author(s), ISBN 978-1-032-77040-6
Open Access: www.taylorfrancis.com, CC BY-NC-ND 4.0 license

Human-centered post-disaster inspection of infrastructure using augmented reality

Fernando Moreu
University of New Mexico, Albuquerque, USA

Chia-Ming Chang & Yen-Ting Liu
National Taiwan University, Taipei, Taiwan

Kaveh Malek & Ali Khorasani
University of New Mexico, Albuquerque, USA

ABSTRACT: Using real-time crack width calculation with Canny edge detection, errors may occur in the crack itself due to factors such as the direction, continuity, and shape of the crack. On the other hand, according to the tests, human factors such as the observer's distance from the crack, the observing angle, and the observer's movement speed also influence the measured crack width. Therefore, this paper will conduct further experiments on human factors through collecting crack width data using Augmented Reality (AR) headsets. If these human factors can be systematically addressed, more accurate data can be obtained, making it easier for observers to use the system and reducing the impact of terrain constraints. Focusing on the error caused by distance and angle, there is a positive correlation between the error and both factors. Additionally, when further investigating the distance, there is an exponential relationship between the pixel unit of the crack and the distance. Various factors contribute to errors in outdoor crack measurements, such as lighting conditions, observation angles, and distance limitations. To initially exclude these factors, this paper focuses on indoor experiments, with the expectation that the findings could be applied to future outdoor observations.

Keywords: Augmented Reality, Pixel Unit Conversion, Edge Extraction, Concrete Crack Width, Canny Algorithm

1 INTRODUCTION

Recently, researchers have proposed various conceptual frameworks that can integrate image-based defect detection techniques with inspections. Researchers and industry experts are exploring the possibility of providing human inspectors with a tool for real-time image processing and decision assistance in their work environment. Previous research has suggested using AR headsets equipped with image-based flaw detection methods as the interface for image processing and visual inspection [1]. AR headsets can run applications that detect and characterize cracks, allowing inspectors to conduct hands-free visual inspections and simultaneously gather valuable data through computer-environment interaction [2]. Past studies explored the use of AR technology for object-recognition [3]–[9]. AR headsets are also used for real-time crack quantifications [10], [11].

The AR crack characterization tool functions as a decision-assisting tool during real-world human inspections of concrete structures. It presents crack dimensions to inspectors and facilitates crack evaluation based on the criteria outlined in relevant specifications. To perform real-time measurements of crack width on an AR head-mounted device, there are the

DOI: 10.1201/9781003483755-397

following steps: (1) the transformation of pixel information to AR platform; (2) edge extraction utilizing the Canny algorithm; (3) crack measurement at the pixel level adopting the horizontal approach; (4) CCD and camera angle measurement using AR orientation capabilities and applying this information for perspective correction; (5) Engineering scale dimensions computation using the results of (3)–(4). A scaler equation for perspective correction streamlines the algorithm toward real-time implementation [10], [11]. This approach can be applied in most situations, but there are limitations under certain conditions. The limitations mentioned in [10], such as concrete with curved surfaces, multiple crack constraints, and direct sunlight, are constraints imposed by the physical characteristics of cracks and the surrounding environment. However, after conducting more in-depth tests, it was found that human factors could also cause significant errors. The impact of these human factors begins from step (3); therefore, this paper primarily focuses on the influence of distance and examines its errors at each step.

2 METHODOLOGY

In the analysis of indoor single crack tests and outdoor multiple crack tests, several key conclusions were reached. First, the orientation of the crack significantly impacts measurement accuracy, with vertical cracks exhibiting smaller errors. Second, the algorithm used for width calculation introduces notable errors when detecting multiple cracks. Additionally, the method faces challenges in cases where crack shapes vary. Consequently, subsequent experiments focus on cracks meeting specific criteria: vertical orientation, consistent width, and singularity.

While Canny edge detection and the horizontal approach for crack measurement at the pixel level are generally applicable, certain limitations arise under specific conditions. Factors such as concrete with curved surfaces, constraints related to multiple cracks, and exposure to strong sunlight are dictated by the physical characteristics of cracks and the environment. However, after conducting more comprehensive tests, we discovered that human factors also contribute to errors. The influence of these human factors becomes evident starting from crack width measurement at pixel level. Therefore, the experiments will initially observe the relationship between crack width and distance, and angle and subsequently delve into the relationship between width and distance in pixel units.

3 INDOOR EXPERIMENT AND ANALYSIS

3.1 *Design of the experiment*

Figure 1a demonstrates how the observer conducts the experiment, what the observer sees can be projected to the computer. Figure 1b shows the interface of the AR crack detection. When a crack is identified, the application utilizes two parallel blue lines to enclose the region and highlights the detected crack with a red line segment. The four numerical values within the interface represent the average width (mm), maximum width (mm), evaluated length (%), and distance to crack (m). This study primarily focuses on investigating the relationship between distance and the predicted width. Hence, only the first and fourth values are recorded in the experiments.

3.2 *Distance effect*

Based on tests of both indoor and outdoor cracks, we have found that the distance between the observer and the crack can lead to errors in the measured crack width under the same conditions. So, we experimented on an actual crack in the wall, focusing on the vertical part of the crack. Figure 2 demonstrates the experiment of investigating the distance effect and the X,Y, Z-coordinate. According to the distances measured by HoloLens 2, the observer moved from

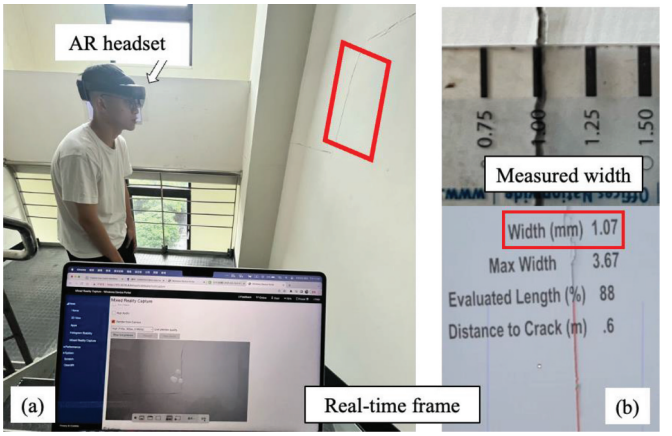


Figure 1. (a) Observer using HoloLens 2 to collect data indoors; (b) Measured width in gauge card and the app.

a distance of 80 cm to 40 cm for each one-centimeter movement, repeated points were recorded, and there was no backward movement. Figure 3 shows the detected width increases linearly with the distance increase. There is a jump at 70 cm, and the data stabilizes between 50-70 cm.

3.3 *Angle effect*

To confirm the hypothesis that the detected crack width is linear with distance, the same experiment was conducted at different angles, including 0, 30, and 45 degrees. Figure 4 demonstrates the experiment of investigating the angle effect and the X,Y,Z-coordinate. Figure 5

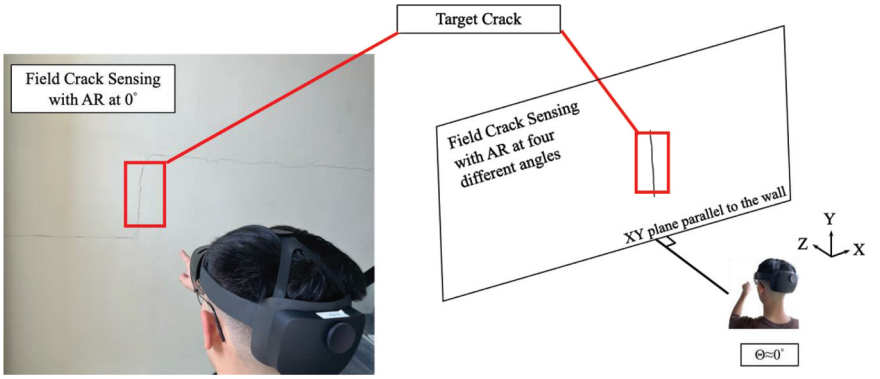


Figure 2. Experiment of investigating distance effect.

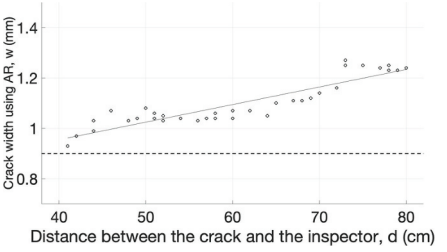


Figure 3. Collected data from the distance experiment.

indicates there is a similar linear relationship in each group, and as the angle increases, the data becomes more scattered. It can be assumed that these errors are caused by angle distortion correction and are expected to be validated in future studies. In addition, when experimenting at angles beyond 45 degrees, the application almost cannot detect the crack. Therefore, the discussion is limited to a maximum angle of 45 degrees.

3.4 *Pixel unit and distance*

If overcoming distance errors within the application could reduce unnecessary error sources in outdoor experiments, minimizing cumulative errors. Therefore, a further experiment was con-

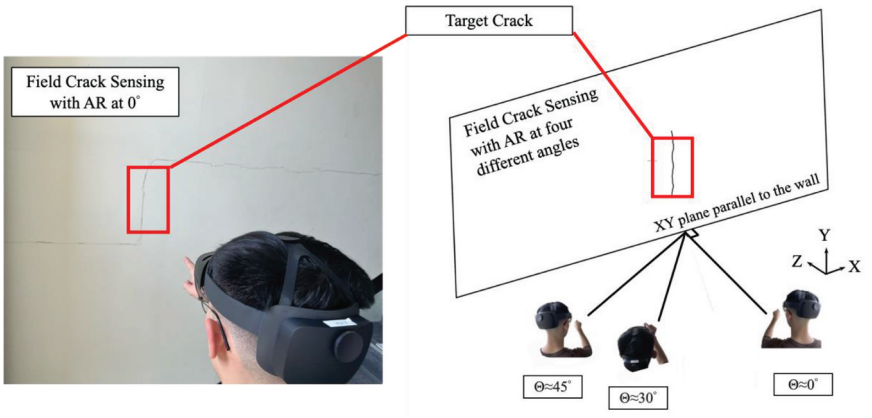


Figure 4. Experiment of investigating angle effect.

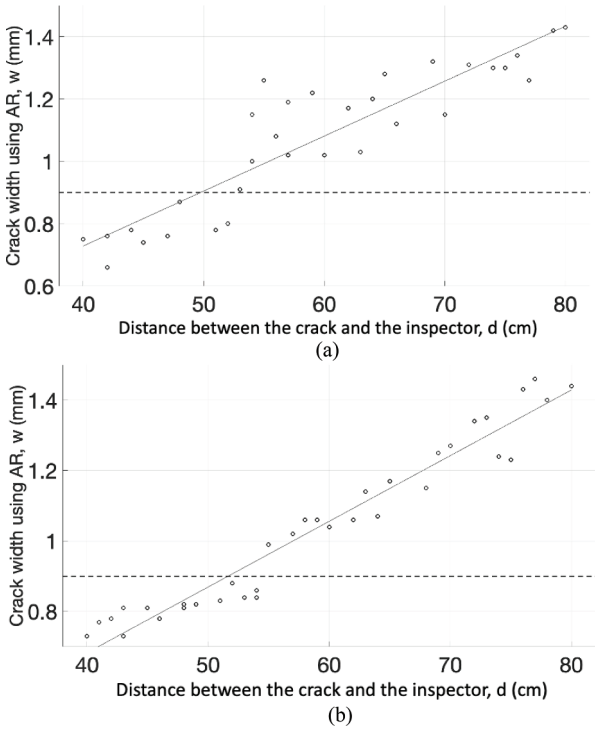


Figure 5. Collected data from the angle experiment. (a) 30 degree; (b) 45 degree.

ducted to explore the impact of distance. According to [10], to obtain the width in engineering units, first need to calculate the pixel unit, then apply perspective distortion correction, and then convert it to engineering units. So here first explore the relationship between pixel units and distance. Similar to the previous experiment, but with modifications to the program to display the values as the pixel count of the crack width. Data was obtained for cracks with widths of 1.3 mm and 2.7 mm, observed perpendicular to the wall surface.

Figure 6. shows the theoretical resolution of the PhotoCapturing mode of HoloLens2 and the theoretical number of pixels depending on distance when the crack width is 1 mm. The data of these two groups are shown in Figure 7, although the experimental values also exhibit an exponential relationship, there is still a discrepancy compared to the theoretical values. It is speculated that the error may be caused by edge detection, where the algorithm automatically cuts off the crack edges during edge extraction, causing the pixel quantity to deviate from a perfect regression relationship with distance.

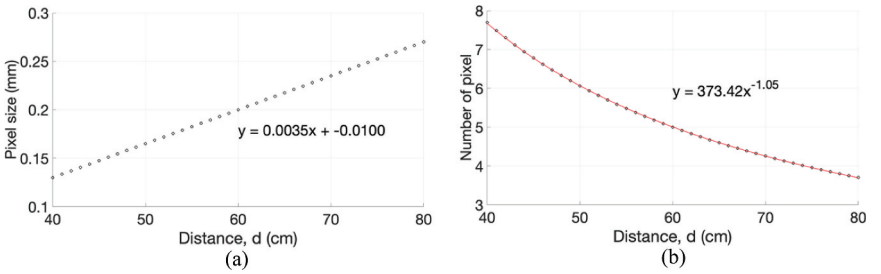


Figure 6. Theoretical performance of HoloLens 2 PhotoCapture mode (a) Resolution; (b) Number of pixels when crack width = 1 mm.

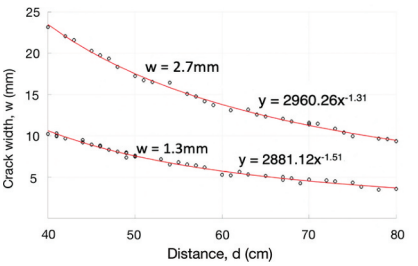


Figure 7. Collected pixel unit data from the distance experiment.

4 OUTDOOR INVESTIGATION

Figure 8 shows that in the outdoor experiment, three tests were conducted on three sections of a damaged wall specimen outside The National Center for Research on Earthquake Engineering (NCREE) building. The first section had cracks of equal width, the second section had a wider crack, and the third section had the widest and most irregularly shaped crack. From the results, it is evident that the errors are larger compared to indoor conditions. To accurately assess outdoor post-disaster cracks, addressing challenges related to multiple cracks and irregularly shaped cracks may be a primary concern.

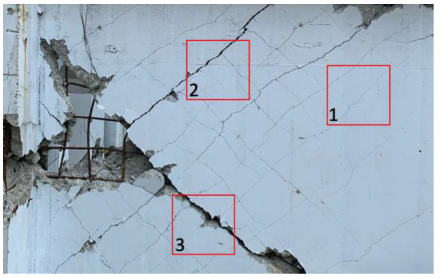


Figure 8. Outdoor experiment concrete.

5 CONCLUSIONS

The original application can be real-time crack width detection and demonstrates good accuracy in most conditions. This paper proposes some limitations, including those at the crack end and observer end, and further discussion is conducted on the observer-related factors. Based on repeated testing, it is found that distance and angle are two key factors influencing accuracy. In terms of distance, there is a positive linear relationship between the distance from the observer to the crack and the measured crack width. As the distance increases, the error also increases. Regarding angles, the application can detect angles up to a maximum of 45 degrees. As the angle increases beyond this threshold, the error also increases, and the linear relationship between distance and width still exists at each angle. To obtain the width of the crack in engineering units in the process, it requires crack measurement at the pixel level, followed by perspective distortion correction, and a conversion algorithm to get the result. Therefore, this paper focuses on the direction perpendicular to the crack, making the impact of pitch, yaw, and roll all equal to zero, eliminating the potential errors introduced by distortion correction. In the last experiment, the number of pixel units representing crack width shows an exponential relationship with distance. It is considered that this relationship is reasonable because, in previous experiments, the size(mm) of each pixel at different distances showed a linear relationship. However, the regression equation in the experiment did not perfectly match the theoretical values. So the error in this case may arise from edge detection, where the algorithm automatically cuts the crack edges, resulting in a non-perfect regression relationship between pixel quantity and distance. Outdoor cracks are often irregular and densely distributed. Overcoming the observational limitations of angle and distance, accurately evaluating post-disaster cracks outdoors may be primarily concerned with addressing challenges associated with multiple and irregularly shaped cracks. Future research should focus on optimizing the AR software using the data obtained in the experiments to automatically remove the effect of the crack edge cut-offs. Additionally, the application of AR headsets for outdoor use can be explored, where environmental factors such as lighting and weather conditions introduce additional complexities. Developing adaptive algorithms that can adjust to varying outdoor conditions will significantly improve the accuracy and reliability of crack measurements in real-world scenarios. Another key area for improvement is the integration of advanced machine learning techniques. By incorporating AI-driven edge detection and image processing, the system can better handle the diverse shapes and orientations of cracks, especially in outdoor environments. This integration could lead to more precise measurements and a reduction in the error margin caused by human and environmental factors.

ACKNOWLEDGMENTS

The authors of this paper acknowledge the support from the Fulbright Hays Faculty Research Abroad (FRA) Fellowship for the corresponding author, who was a visiting professor during the duration of this research at the National Taiwan University (NTU) Department of Civil and Environmental Engineering and The National Center for Research on Earthquake

Engineering (NCREE). The authors appreciate the support of the members of the Smart Management of Infrastructure Laboratory (SMILAB) of the University of New Mexico and the efforts of Pin-Yi, Huang from NTU for assisting in the data collection and technical design of the indoor experiments.

REFERENCES

[1] S. Wang, Sakib Ashraf Zargar, and Fuh-Gwo Yuan 202, "Augmented reality for enhanced visual inspection through knowledge-based deep learning." Accessed: May 27, 2021. [Online]. Available: https://journals.sagepub.com/doi/full/10.1177/1475921720976986?casa_token=1514ILhod0YAAAAA%3AVPVE-ov3u9T4dWBxQvvC2cHp0F9gNP-h4uNUaigGkO3yfyxCzFFlZ8S7_gbyzMl0YiCAm_yeIjvX

[2] E. Karaaslan, U. Bagci, and F. N. Catbas, "Artificial Intelligence Assisted Infrastructure Assessment using Mixed Reality Systems," *Transportation Research Record*, vol. 2673, no. 12, pp. 413–424, Dec. 2019, doi: 10.1177/0361198119839988.

[3] S. Wang, S. A. Zargar, and F.-G. Yuan, "Augmented reality for enhanced visual inspection through knowledge-based deep learning," *Structural Health Monitoring*, vol. 20, no. 1, pp. 426–442, Jan. 2021, doi: 10.1177/1475921720976986.

[4] A. Farasin, F. Peciarolo, M. Grangetto, E. Gianaria, and P. Garza, "Real-time Object Detection and Tracking in Mixed Reality using Microsoft HoloLens:," in *Proceedings of the 15th International Joint Conference on Computer Vision, Imaging and Computer Graphics Theory and Applications*, Valletta, Malta: SCITEPRESS - Science and Technology Publications, 2020, pp. 165–172. doi: 10.5220/0008877901650172.

[5] H. Bahri, D. Krčmařík, and J. Kočí, "Accurate Object Detection System on HoloLens Using YOLO Algorithm," in *2019 International Conference on Control, Artificial Intelligence, Robotics Optimization (ICCAIRO)*, Dec. 2019, pp. 219–224. doi: 10.1109/ICCAIRO47923.2019.00042.

[6] L. Liu, H. Li, and M. Gruteser, "Edge Assisted Real-time Object Detection for Mobile Augmented Reality," in *The 25th Annual International Conference on Mobile Computing and Networking*, in MobiCom '19. New York, NY, USA: Association for Computing Machinery, Aug. 2019, pp. 1–16. doi: 10.1145/3300061.3300116.

[7] T. Yamaguchi, T. Shibuya, M. Kanda, and A. Yasojima, "Crack Inspection Support System for Concrete Structures Using Head Mounted Display in Mixed Reality Space," in *2019 58th Annual Conference of the Society of Instrument and Control Engineers of Japan (SICE)*, Sep. 2019, pp. 791–796. doi: 10.23919/SICE.2019.8859876.

[8] A. Corneli, B. Naticchia, A. Cabonari, and F. BoschÃ©, "Augmented Reality and Deep Learning towards the Management of Secondary Building Assets," *ISARC Proceedings*, pp. 332–339, May 2019.

[9] A. Pepe *et al.*, "Pattern Recognition and Mixed Reality for Computer-Aided Maxillofacial Surgery and Oncological Assessment," in *2018 11th Biomedical Engineering International Conference (BMEiCON)*, Nov. 2018, pp. 1–5. doi: 10.1109/BMEiCON.2018.8609921.

[10] K. Malek and F. Moreu, "Realtime conversion of cracks from pixel to engineering scale using Augmented Reality," *Automation in Construction*, vol. 143, p. 104542, Nov. 2022, doi: 10.1016/j.autcon.2022.104542.

[11] K. Malek, A. Mohammadkhorasani, and F. Moreu, "Methodology to integrate augmented reality and pattern recognition for crack detection," *Computer-Aided Civil and Infrastructure Engineering*, vol. n/a, no. n/a, doi: 10.1111/mice.12932.

Bridge Maintenance, Safety, Management, Digitalization and Sustainability – Jensen, Frangopol & Schmidt (eds)
© 2024 The Author(s), ISBN 978-1-032-77040-6
Open Access: www.taylorfrancis.com, CC BY-NC-ND 4.0 license

Condition assessment and repair protocols for dynamically impacted bridge girders

W. Zatar
Marshall University, 1 John Marshall Dr, Huntington, USA

ABSTRACT: The most frequent causes of bridge failures in the United States are floods, collisions, overloads, and scour. Damage may occur when an over-height or oversized truck dynamically strikes a highway bridge superstructure. Over-height trucks have hit one in every five overpasses in the United States, and one-sixth of these bridges have received considerable damage and required repair. The collision could produce significant local plastic deformations of steel girders. Localized concrete spalling and tendons and steel reinforcement damage are encountered for struck prestressed concrete girders. An extensive list of highway bridges impacted by over-height, overweight, or oversized vehicles in West Virginia was developed. The authors documented the West Virginia Department of Transportation (WVDOT) process for recording damage and for deciding to repair the affected members after evaluating their remaining load-carrying capacity. Recommendations to determine the remaining capacities of damaged girders are made through either performing finite element analyses or conducting proof load testing. Repair recommendations using fiber-reinforced polymer composites are adopted for impacted prestressed concrete girders, and protocols for multiple heat-straightening repairs of damaged steel girders are implemented.

1 INTRODUCTION

Damage to highway steel or prestressed bridge girders may occur when an over-height truck dynamically impacts a bridge. The collision could result in significant plastic deformations and strains in localized areas of the steel girders. Studies in Maryland have shown that an over-height truck has struck approximately one in every five overpasses. The impacted bridges are most likely located on interstate highways. One-sixth of these bridges have received considerable damages and required repair.

Heat- -straightening to repair damaged steel members dates back to the 1930s with low-grade steel. For many years, heat-straightening of damaged steel bridge girders has been more of an art than a science. Several safety concerns have historically limited their validity as a repair technique. When applied appropriately, heat-straightening and mechanical techniques, including pressing or jacking, offer an economical and viable alternative to replacing damaged steel girders.

The Principal Investigator has completed WVDOH Research Project RP202 (Zatar and Leftwich 2009). The SPR project was entitled: "Effect of Repeated Heat-Straightening on Behavior of Impacted Highway Bridge Steel Girders." The primary objectives of RP202 were to: a) Conduct a state-of-the-art literature review on the technique, advantages, and shortcomings of heat-straightening; b) Address the fundamental principles for heat-straightening and illustrate how these principles are implemented in practice; c) Review literature on what damage is heat-straightenable; d) Summarize significant technical challenges during a heat-straightening repair; e) Investigate how to use the heating patterns to repair several damage types; f) Study how to avoid potentially damaging mistakes during a heat-straightening repair project; g) Address the number of cycles a bridge girder can be heat-straightened; and h)

DOI: 10.1201/9781003483755-398

Prepare a final report that addresses all the listed tasks. Tasks of RP202 were completed, and the Final Report was submitted in 2011. The report provides the WVDOH engineers and staff with sufficient details about current practices followed by other State DOTs. RP202 Report showed that heat-straightening provisions vary among State DOTs. These variations were exhibited through comparing the provisions/specifications of Connecticut, California, Georgia, Iowa, Kansas, Michigan, Minnesota, New York, Texas, Virginia, and Washington. Analyzing the survey data led to concluding that: (a) The heat-straightening repair technique has not gained a full acceptance by all State DOTs yet, and (b) Only a few contractors are qualified to complete a repair project successfully.

The Federal Highway Administration (FHWA) identified four fundamental heat-straightening patterns in 2023: (a) Vee heat, (b) Strip heat, (c) Line heat, and (d) Spot heat. The Vee heat effectively bends a damaged member about its strong axis. The strip heat is effective in shortening a damaged member. The line heat effectively turns a damaged member about its minor axis. The spot heat is effective in causing local bulging in a damaged member.

Typically, heat-straightening patterns used to repair damaged steel bridge girders are combinations of the four fundamental heat-straightening patterns. Selection of the heat-straightening patterns and combinations for a particular repair project shall be based on the structural damage caused by the collision and the need to keep portions of the bridge open to traffic while conducting repairs. The importance of identifying the maximum heating temperature, cooling temperature before successive heats, and maximum torch diameter while completing a heat-straightening project have been documented.

2 LIST OF STRUCTURES STRUCK BY OVER-HEIGHT VEHICLES

2.1 *List of structures struck by over-height vehicles in west virginia*

According to WVDOH, there are approximately 6,958 bridges in West Virginia. Of these bridges, 33 percent are more than 100 feet in length. Many overpass highway bridges within the state have been struck by over-height vehicles, as shown in Table 1. Some bridge members have been hit multiple times, and damaged steel girders were heat-straightened, replaced, or repaired/retrofitted. Below are details of the bridges that have been impacted more than once and heat-straightened at least once.

Table 1. List of structures struck by over-height vehicles in west virginia.

#	Bridge Name	Bridge Number	County	Condition	Times of Damage	Times of HS	HS Documented
1	OYLER AVENUE BRIDGE	10-61/28-1.25	010 - Fayette	HS	7	2	Y
2	BENEDICT RD OVER-PASS WB	06-64-31.67	006 - Cabell	HS	4	1	Y
3	US 52 OVERPASS EB	06-64-6.45	006 - Cabell	HS	3	1	Y
4	KENNA OVERPASS BRIDGE North	18-77-124.89	018 - Jackson	HS	3	2	Y
5	Veterans of All Wars Bridge	10-38-3.53	010 - Fayette	NR	3	NA	NA
6	DUNBAR TOLL BRIDGE	20-25/47-0.1	020 - Kanawha	NR	3	NA	NA
7	I-64 INSTITUTE INTER-CHANGE WB	20-64-49.98	020 - Kanawha	R	3	NA	NA
8	INSTITUTE RAMP B	20-64-50	020 - Kanawha	R	3	NA	NA
9	MONTROSE DRIVE I-64 OVERPASS	20-60/64-0.25	020 - Kanawha	HS	2	2	N
10	I-64 SOUTH CHARLES-TON EB	20-64-53.8	020 - Kanawha	HS	2	1	Y

(*Continued*)

Table 1. (*Continued*)

#	Bridge Name	Bridge Number	County	Condition	Times of Damage	Times of HS	HS Documented
11	SOUTH PARK BRIDGE	21-7-4.27	021 - Lewis	HS	2	1	Y
12	Dallas Pike Bridge EB	35-70-11.06	035 - Ohio	HS	2	1	Y
13	POWER PLANT BRIDGE (CSWB)	37-2-4.43	037 - Pleasants	HS	2	1	Y
14	ROCKPORT I/ C N (CSWB)	54-77-161.66	054 - Wood	HS	2	1	Y
15	US 50 I/C N (CSPG)	54-77-176.42	054 - Wood	HS	2	2	Y
16	GLENVILLE TRUSS	11-33-16.59	011 - Gilmer	NR	2	NA	NA
17	I-64 ST. ALBANS RAMP BRIDGE	40-64-43.5	040 - Putnam	NR	2	NA	NA
18	EARL M VICKERS MEMORIAL BRIDGE	10-6-0.12	010 - Fayette	R	2	NA	NA
19	CR 11 OVERPASS N (CSWB)	18-77-143.32	018 - Jackson	R	2	NA	NA
20	DUPONT INTERCHANGE	02-901-5.32	002 - Berkeley	HS	1	1	Y
21	FLATWOODS ICHG S	04-79-67.01	004 - Braxton	HS	1	1	Y
22	Ramp A Jennings Randolph	15-30-0	015 - Hancock	HS	1	1	N
23	I-77 EDENS FORK I/C NB	20-77-106.11	020 - Kanawha	HS	1	1	N
24	KINGMONT ROAD OVERPASS	25-64/01-0.04	025 - Marion	HS	1	1	Y
25	ROSS BOOTH MEMOR-IAL BRIDGE	40-34-21.34	040 - Putnam	HS	1	1	N
26	I-64 WINFIELD INTER-CHANGE BRIDGE	40-64-15	040 - Putnam	HS	1	1	Y
27	KNOB HILL OVERPASS	41-3/21-1.3	041 - Raleigh	HS	1	1	Y
28	Richard Snyder Memorial Bridge	52-7-0.07	052 - Wetzel	HS	1	1	N
29	WILLIAMSTOWN-MARIETTA BR (CSTT)	54-31-19.01	054 - Wood	HS	1	1	N
30	West Virginia 95 Ov erpass (CSWB)	54-77-173.22	054 - Wood	HS	1	1	N
31	WASHINGTON AVE OVERPASS	06-52-0.45	006 - Cabell	NR	1	NA	NA
32	HICO BRIDGE	10-60-26.17	010 - Fayette	NR	1	NA	NA
33	DUCK CREEK ROAD OP	17-79-107.55	017 - Harrison	NR	1	NA	NA
34	KANAWHA TURNPIKE I-64 OVERPASS	20-61/13-0.03	020 - Kanawha	NR	1	NA	NA
35	HARTS RUN BRIDGE	13-64-175.31	013 - Greenbrier	R	1	NA	NA
36	PRICKETTS CREEK ROAD OP	25-79-138.77	025 - Marion	R	1	NA	NA

Note: WB = West Bound; EB = East Bound; CSWB = Continuous-rolled Steel Wide-flange Beam; N = North; S = South; CSPG = Continuous Span Plate Girder; I/C = Interchange; NB = North Bound; CSTT = Continuous Steel Thru Truss; OP = Overpass; HS = Heat-Straightened or Heat Straightening; R = Repaired; NR = Not Repaired; Y = Yes; N = No; NA = Not Available

2.2 *Current WVDOH process for recording data in bridge inspection reports of struck and misaligned members*

According to WVDOH, inspection reports are categorized into different types, such as periodic, in-depth, inventory, interim-condition, and damage/special inspection reports. The damage inspection report is an essential source of information for engineers to decide whether to repair or replace damaged members. It is required by WVDOH when over-height vehicles hit a bridge. In this task, we provide detailed information on the current process for recording

data in the damage inspection report. The report comprises five significant sections: purpose, procedure, findings, drawings, and photographs.

2.3 *Current WVDOH process for evaluating load-carrying capacity of damaged members*

The current WVDOH process for determining whether or not a damaged member should be repaired, replaced, or do nothing is described in this section. This process is used to establish a bridge repair report. This report includes the following sections: 1) Purpose; 2) Descriptions of the existing conditions of the bridge; 3) Repair options; 4) Structural Analysis; 5) Verification of the repair options proposed in Section 4; 6) Recommendation: A recommendation will be provided to WVDOT about the decision made in section 5.

3 PROCEDURES, GUIDELINES, AND SPECIFICATIONS FOR APPROVAL AND IMPLEMENTATION

3.1 *Proposed method to determine moment capacity of damaged beams*

As previously mentioned, WVDOH currently uses the strength-reduction method to determine the remaining load-carrying capacity of damaged members. This method is dependent upon the effective-section-modulus-reduction graphs. These graphs were established by Avent and Mukai (1998) for two specific sizes of beams with depth-to-width (H/b) ratios of 1.24 (W 10×39 beam) and 2.66 (W 24×76 beam). W-beams commonly used for many WV highway/overpass bridges have higher H/b ratios than Avent and Mukai's beams (e.g., W 33×130 beams in Dallas Pike bridge and W 30×132 beams in US 52 bridge have H/b = 2.87; W 36×150 beams in Rockport bridge have H/b = 2.99). Therefore, it is necessary to establish practical graphs that can be applied to beams with varying H/b ratios.

The research team proposes proof load tests for W 10×39 and W 24×76 beams subjected to three-point bending (Figure 1) with a loading span of 9.84 ft. (3 m). These beams are selected because they can easily be handled in laboratory space and loaded to failure using regular actuators. If necessary, large beams can be experimentally tested using higher-capacity actuators. Finite element (FE) analysis can be used to evaluate the effect of various H/b ratios, and experimental data will validate FE results. The primary test variable includes the rotation angle (q), as shown in Figure 2. Tensile coupon tests conforming to ASTM E8 (Standard Test Methods for Tension Testing of Metallic Materials) will be used to determine the tensile properties of W-beams.

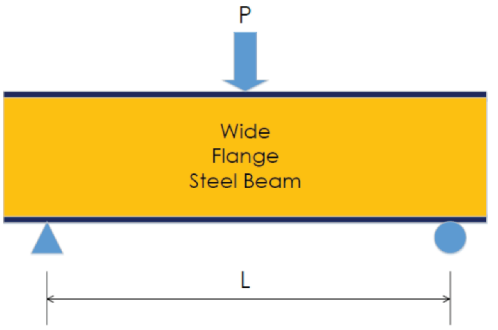


Figure 1. Proof load tests of W-beams subjected to three-point bending.

Load-carrying capacities of W-beams can be calculated based on moment/stress diagrams in Figure 3. The ratio of the ultimate moment of the deformed section to that of the undeformed can then be calculated. Figure 4 shows idealized relationships between the distorted moment and undeformed moment ratio and the rotation angle (q). This figure can be

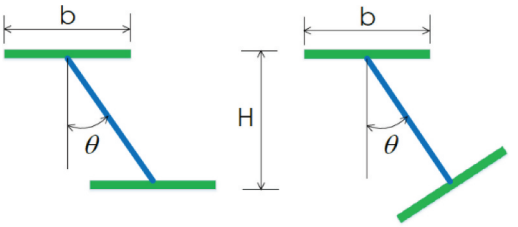


Figure 2. Idealized geometry of deformed beams.

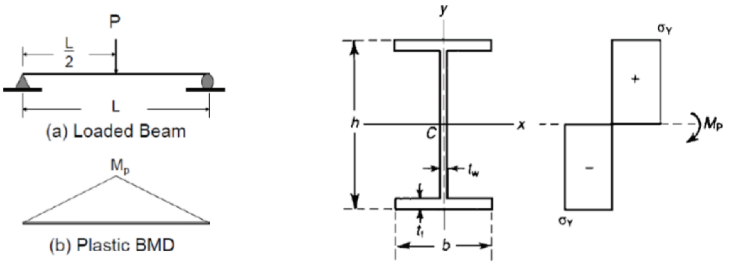


Figure 3. Analysis of W-beams and idealized reduction in moment capacity of damaged beams.

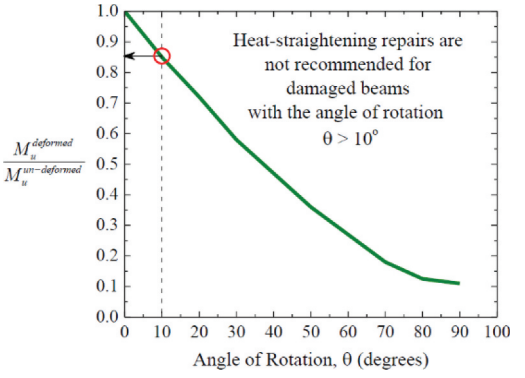


Figure 4. Idealized reduction in moment capacity of damaged beams.

used as a reference chart to determine the moment capacity of damaged beams. By consulting WVDOH experts, it is essential to note that heat-straightening repairs are not recommended for damaged beams with an angle of rotation larger than 10 degrees. For damaged beams with q>10°, further research must be conducted to decide whether heat-straightening repairs are safe and economical.

3.2 *Repair recommendations using fiber-reinforced polymer composites*

Applying high-strength carbon fiber reinforced polymer (CFRP) composite laminates proves to be an efficient and effective method for retrofitting bridge elements. This approach enhances the strength and stiffness of the components, ultimately extending the service life of the bridge. The detailed evaluation includes: 1) Determine truck type; 2) Finite element analysis; 3) Moment curvature analysis.

Moment-curvature analyses determined the number of CFRP laminates required to reinforce the beams (Figure 5). This analysis was essential in determining the appropriate amount of material needed, as FRP rupture influenced the retrofitted section's ultimate strength (Choo et al., 2007).

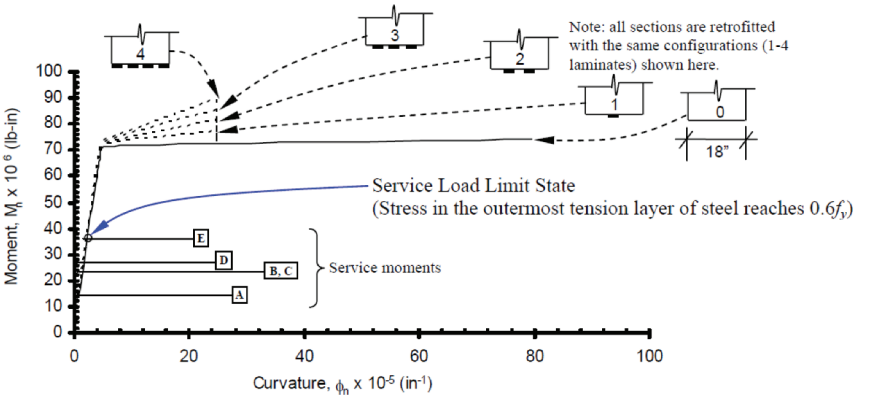


Figure 5. Comparison of service moment.

4 EXAMPLES OF DAMAGED AND REPAIRED BRIDGES

4.1 *Kenna Overpass Bridge over Interstate 77 North*

This bridge is located 5.00 miles South of County Route 21 in Jackson County, WVDOH District 3, West Virginia, as shown in Figure 6. On September 9, 2010, a truck hauling a tank struck beam #5 in span #2 and bent this member. Beam #5 was bowed 5" and turned 5" out of plumb. Civil Construction heat-straightened this beam in 2012; however, the bottom flange is still bowed out 1".



a) Elevation view (looking west)



b) Beam #5 (before heat straightening)



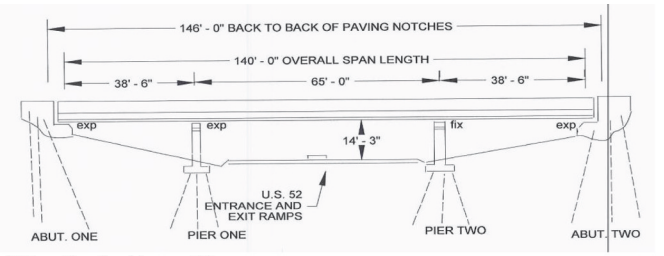
c) Beam #5 (after heat straightening)

Figure 6. Details of Kenna Overpass Bridge.

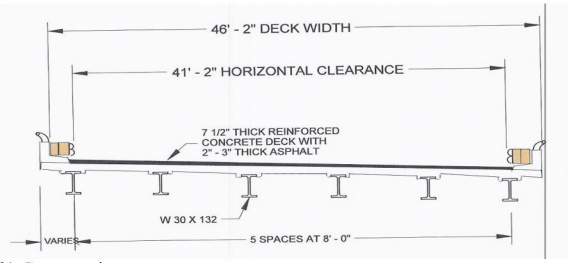
Damage inspection was conducted on November 28-29, 2011, to inspect the span #2-floor system for cracks or problems that may have occurred because of an accident that occurred on November 21, 2011 (the structure was struck by an over-height load truck traveling east on WV 34 under the structure). The inspection consisted of visually observing the span #2-floor system from the ground, an extension ladder, and the top of a tool truck. The following inspection results were found: 1) Fresh yellow paint and bare shiny metal indicate that the contact point was at the west edge of the bottom flange of stringer #6; 2) The resulting impact caused a 1 1/2" outward bowing of the beam and moved the beam 1 3/8" out of plumb.

4.2 *US 52 Overpass Eastbound Bridge*

This bridge is located 1.73 miles West of West Virginia 152 (Cabell County, District 2), as shown in Figure 7. A damage inspection was conducted on June 3, 2013, to document vehicular impact damage to beams #5 & 6 at span #2. The inspection visually observed beams #5 &



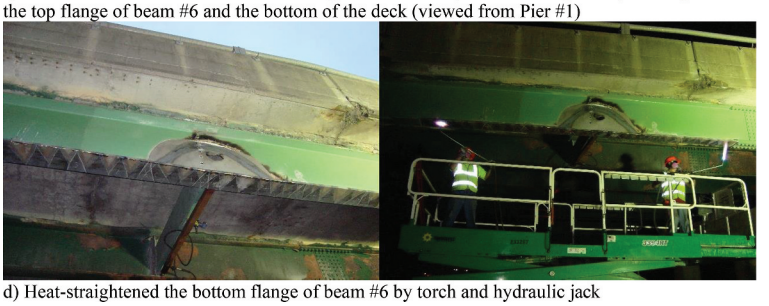
a) Elevation (looking north)



b) Cross section



c) Plastic deformation in the lower flange of beam #6 (viewed from pier #1) and separation between the top flange of beam #6 and the bottom of the deck (viewed from Pier #1)



d) Heat-straightened the bottom flange of beam #6 by torch and hydraulic jack

Figure 7. Details of US 52 Overpass Eastbound Bridge.

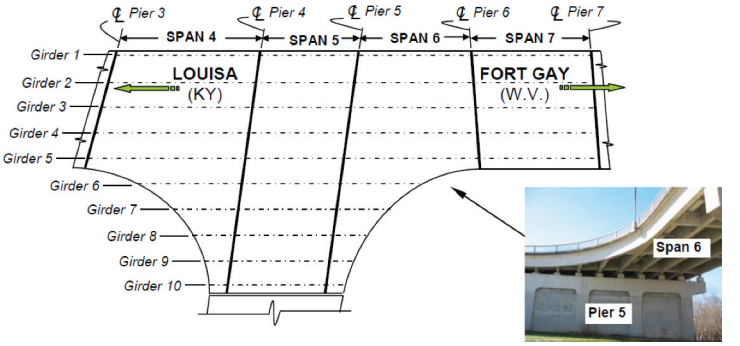


Figure 8. The continuous reinforced concrete middle spans of the Louisa-Fort Gay Bridge.



Figure 9. Reinforced concrete beams retrofitted with CFRP laminates.

6 from arm's length. Extension ladders and a bucket truck were used to access these beams. This structure tested positive for lead-based primer and had no fracture-critical members. The inspection results showed that beam #5 is in fair condition. Scraping is present on the bottom flange of beam #5 from vehicular impact damage. No other deficiencies were found on beam #5. Beam #6 is in poor condition. Beam #6 has severe impact damage. The diaphragm connection in row #1 to beam #6 has torn away from the web connection angle. The web splice plates, at splice #1 on beam #6, are cracked at the top of the plates. Plastic deformation is present throughout beam #6. There is a 2" to 3" separation between the top flange and the bottom of the deck on the interior side of beam #6.

4.3 *The Louisa-Fort Gay Bridge*

The Louisa-Fort Gay Bridge, constructed in 1979, is in Lawrence County, Kentucky. This bridge comprises a 12-span continuous structure featuring composite concrete deck-steel girder spans and reinforced concrete middle spans (Figure 8). The reinforced concrete central spans serve as an intersection, facilitating traffic flow from three directions.

Routine inspection identified cracks in the reinforced concrete girder in Spans 4, 6, and 7 of the Louisa-Fort Gay Bridge. These cracks originated at the bottom web of a standard reinforced concrete girder at the bridge. The primary cause of these cracks was attributed to elevated flexural stresses that emerged in the positive bending region of the girders.

The bridge underwent repair by applying CFRP laminates, involving the following phases: 1) Applying the mixed epoxy onto the concrete using a trowel or spatula to achieve a specified thickness.; 2) Applying the mixed epoxy onto CFRP laminates; 3) Placing CFRP laminates to the affected concrete surfaces; 4) Pressing the CFRP laminates using a hard roller

until adhesive is forced out on both sides; and 5) Removing excess adhesive. The completed retrofitting work for Span 6 is depicted in Figure 9.

5 CONCLUSIONS

An extensive list of struck highway bridges in West Virginia has been developed. Detailed conditions of each struck bridge and times of damage/heat-straightening are documented. The current WVDOH process for recording data in damage inspection reports of crashed and misaligned members is reported. The procedure for registering damage is systematically recorded, and the decision on whether to repair the affected members is determined through an assessment of their remaining load-carrying capacity. Recommendations for gauging damaged girders' remaining capacities involve conducting finite element analyses or implementing proof load testing. Additionally, protocols for implementing multiple heat-straightening repairs are applied to address damage in impacted steel girders. Repair recommendations incorporating fiber-reinforced polymer composites are adopted in the case of impacted prestressed concrete girders.

REFERENCES

ASTM E8/E8M-22. Standard Test Methods for Tension Testing of Metallic Materials.

Avent, R. and Mukai, D. 1998. *Heat-Straightening Repairs of Damaged Steel Bridges: A Technical Guide and Manual of Practice (No. FHWA-IF-99-004)*. United States. Federal Highway Administration.

Choo, C.C., Zhao, T. and Harik, I.E. 2007. *Retrofit of the Louisa-Fort Gay Bridge Using CFRP Laminates (No. KTC-07-08/FRT118-03-1F)*. University of Kentucky Transportation Center.

Connor, R.J., Urban, M.J. and Kaufmann, E.J. 2008. *Heat-straightening repair of damaged steel bridge girders: fatigue and fracture performance (Vol. 604)*. Transportation Research Board.

Geoghegan, F., Medlock, R. and Packard, B. 2023. *Manual for Heat Straightening, Heat Curving and Cold Bending of Bridge Components (No. FHWA-HIF-23-003)*.

Zatar, W. and Leftwich, S. 2009. *Effect of Repeated Heat-Straightening on Behavior of Impacted Highway Bridge Steel Girders.* Final Report (Research Project RP202), West Virginia Department of Transportation, Division of Highways, Charleston, West Virginia.

Zatar, W. and Nguyen, H. 2019. *Application of heat straightening repair of impacted highway steel bridge girders*. Risk-Based Bridge Engineering, pp.206–215.


Taylor & Francis
Taylor & Francis Group
http://taylorandfrancis.com

SS44: AI and optimization methods for bridge management under uncertainty

Organizers: D.Y. Yang, C. Andriotis & K.G. Papakonstantinou


Taylor & Francis
Taylor & Francis Group
http://taylorandfrancis.com

Bridge Maintenance, Safety, Management, Digitalization and Sustainability – Jensen, Frangopol & Schmidt (eds)
© 2024 The Author(s), ISBN 978-1-032-77040-6
Open Access: www.taylorfrancis.com, CC BY-NC-ND 4.0 license

Data-derived train classification and monitoring of masonry bridge

J. Cheng, A. Chen & M.J. DeJong
University of California, Berkeley, Berkeley, USA

S. Cocking
University of Cambridge, Cambridge, UK

ABSTRACT: CFM-5 bridge in Barkston Ash, UK presents an asset monitoring and maintenance challenge. Since its construction in 1868, the masonry arch bridge has suffered damage and undergone a variety of repairs. The uncertainty of the repairs' effectiveness motivates the need for automated monitoring. As such, Fiber Bragg Grating fiber optic sensors have been installed along the underside of the masonry arch and dynamic strain data have been collected during train passages over the last 2 years. Each FBG measures average strain over its gauge length, and 2 lines of 10 grating rosettes were installed along the arch soffit. These provide distributed strain data over the extent of the arch, yielding more global information compared to typical point sensors. In this context, this paper presents a framework for post-processing and interpreting the monitoring data from bridge CFM-5. The objectives are to investigate long-term and future structural performance. To achieve this, data must first be normalized against train type; using features extracted from the dynamic response to a train passing overhead, the train type is classified via XGBoost, a framework for gradient-boosted decision trees. Then, the dynamic responses are analyzed to evaluate the sensitivity to different train types by observing peak dynamic strains and their correlation with temperature.

1 INTRODUCTION

Maintenance and management of infrastructure assets continues to be a challenge for asset managers. Masonry arch bridges play a significant role in the infrastructure of transportation networks across Europe, making up roughly 40-50% of rail and road bridge spans in the UK (Augusthus-Nelson et al. 2016). The number of masonry railway and road bridges across Europe is estimated to be around 300,000 (Brencich & Morbiducci 2007).

These structures are aging, with many experiencing 100 or more years of continuous operation. Inevitably, interventions are needed to repair damage suffered during operation. However, these repairs can unfavorably alter the stiffness profile of a bridge, resulting in further damage.

The complexities associated with managing masonry arch bridges motivate the need for comprehensive monitoring solutions. Automated data capture and analysis can significantly reduce the time, effort, and cost required to monitor and assess such bridges. Many sensing technologies have been applied to bridge monitoring. Deformations and changes to bridge geometry can be detected by LiDAR (Ye et al. 2018). Computer vision algorithms can be used to automatically detect cracks in images of masonry structures (Chaiyasarn et al. 2018). Dynamic deformations can be monitored with digital image correlation (DIC) techniques (Acikgoz et al. 2018).

Fiber Bragg grating (FBG) fiber optic sensors offer dynamic strain sensing for long term monitoring of structural degradation and have been installed at multiple masonry railway bridges throughout the UK (Alexakis et al. 2018). From these FBG deployments, preliminary analysis of changes in dynamic strain have been conducted, and monitoring of force flow through the masonry rail bridges has been carried out. In addition, statistical shape analysis (SSA) has been applied to FBG data to track changes in dynamic strain profiles over time (Alexakis et al. 2018).

DOI: 10.1201/9781003483755-399

These studies either only analyze behavior with regard to a single train type or rely on operator-provided train classification. In addition, some train classes are not easily distinguishable from one another through manual interpretation of the strain record. Thus, an automated train classification workflow is necessary to streamline the monitoring process when labelled events are not available to evaluate the effect of different train classes on bridge degradation.

Following recent research regarding the use of FBG sensing on masonry arch bridges, this paper examines the use of gradient-boosted decision trees for automated train classification. Long-term analysis of bridge responses against train class and temperature are also presented in this paper.

1.1 *Bridge CFM-5*

The bridge evaluated in this paper is the Barkston Road Bridge, designated as CFM-5 by the asset owner, Network Rail. Built in 1868, bridge CFM-5 is a single arch masonry bridge, carrying a variety of passenger and freight rail traffic over a local road at a skew angle of 26°. CFM-5 supports two trackways, a northern track for eastbound trains and a southern track for westbound trains.

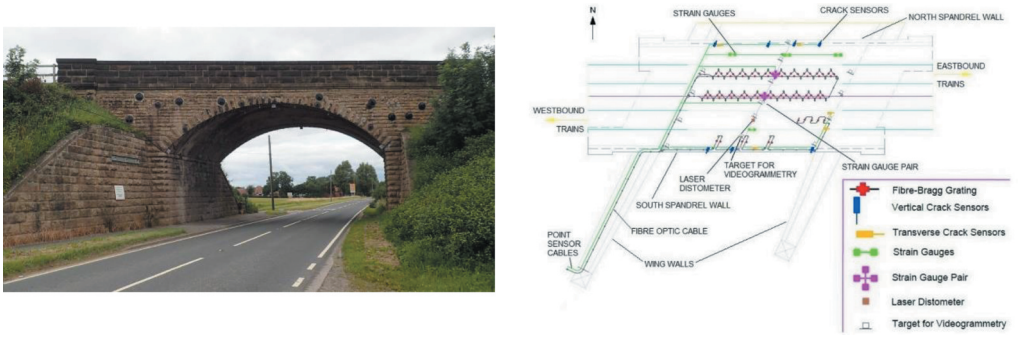


Figure 1. Elevation view of the CFM-5 bridge and its sensor installation plan.

The bridge has suffered various damage throughout its operation. The main signs of damage include separation cracks between the brick arch barrel and the stone spandrel walls and a longitudinal crack in the south-east of the arch barrel. To remedy these damages, various interventions have been implemented at bridge CFM-5, including transverse tie rods, soil anchors, and grout crack stitching. However, the effectiveness of these interventions is uncertain, motivating the need for remote monitoring technologies at bridge CFM-5.

1.2 *Monitoring installation*

Multiple sensing technologies were installed at bridge CFM-5, including FBGs, videogrammetry targets, strain gauges, and laser distometers. This paper focuses on the data obtained from the FBG sensors and ambient temperature sensors.

The FBGs are arranged in two configurations: in pairs to measure in-plane and out-of-plane strains across cracks, or in one of 20 triangular strain rosettes. One line of 10 FBG strain rosettes is installed in the arch soffit beneath the centerline of the northern track, and another line of 10 rosettes is located under the centerline of the entire bridge.

Because trains always travel in opposite directions on opposite tracks, rotational symmetry of the loading and thus response of the bridge has been assumed. Analysis of the strain readings support these assumptions so far (Cocking et al. 2019).

The installation is programmed to automatically record and upload strain readings for each train passing; data are logged during commute times to obtain records with relatively consistent passenger loading (Cocking et al. 2019). The Micron Optics FBG interrogator logs data at a sampling frequency of 250 Hz.

2 TRAIN CLASSIFICATION

2.1 *Traditional approach: Timetable dataset*

The reference dataset used for this classification problem is curated by scraping publicly available records of train departures and arrivals between August 2018 and January 2022, at stations adjacent to CFM-5, into a timetable. This timetable also includes both the direction of travel of the trains across the bridge and the train class. Then, the timestamp and direction of travel of each FBG record is compared with the timetable to match the record with a timetable entry.

Three direction checks are conducted to ascertain the direction of travel, for each FBG record. The first direction check compares the maximum peaks of two FBGs at the arch midspan, one under each track, as the FBG under the northern track will record a higher peak dynamic strain than the FBG under the bridge centerline when a train is passing over the northern track and vice versa. For the remaining two direction checks, the position of maximum dynamic peak of the FBG records on the eastern side of the bridge are compared to those on the western side of the bridge. That is, if a train is travelling eastward on the northern track, a peak is expected first on the western FBG before the eastern FBG. One of these checks is performed per FBG array. If all three direction checks agree, then the direction of the train is denoted accordingly.

Table 1. 2020-2021 dataset train types, carriage numbers, and total counts after cleaning.

Train Type	Number of Carriages	Count
Voyager 220	4	81
Voyager 220+220	8	131
Voyager 220+221	9	200
Voyager 221	5	165
Class 185	3	310
Class 185+185	6	834
Class 43	9	280
Northern 2 Car	2	511
Northern 3 Car	3	1244
Northern 4 Car	4	20
Nova 1	5	940
Nova 3	6	154
Total:		4870

Of about 7,100 FBG records collected between July 2020 and October 2021, about 5,300 are matched to the timetable in this way. Any records containing missing data are removed, as these correspond to instances when the analyzer was unable to automatically connect to the sensors upon booting. This leaves about 4,900 matched records.

In total there are 12 different train types, operated by 4 different train operating companies. A breakdown of the different train types observed in the 2020-2021 data is shown in Table 1.

2.2 *Proposed approach: Extracted features*

The approach proposed relies on the classification of trains based on extracted features from an FBG located near the midspan of the northern track. A truncated version of the timeseries data from this FBG are stored for analysis, as the original file contains buffer data at the start and end of the train event. In the unloaded bridge state, these buffer data mostly contain noise, whereas the portion of the record that contains relevant strain information as the train passes over is of more interest. This portion of the record that contains the train passing over the bridge is noted as the importance region.

The importance region is determined as follows. First, the mean of the last 1000 measurements of the record, called the tail, is calculated. The entire record is then vertically shifted to the mean of the tail, to remove any offset in absolute strain. Then, the standard deviation of the tail is calculated. Any portion of the record that exceeds 10 times the standard deviation of the tail is classified as the importance region. Records without an importance region are discarded, as these correspond to measurements that have been incorrectly triggered, resulting in a record with only noise. There are about 300 such records.

To focus on the shape of each signal and to reduce the variation in signal due to differences in train weight and speed, each record from this FBG is then normalized by its maximum recorded value. Finally, the signal is passed through a Savitzky-Golay filter, followed by a low-pass filter, to smooth out the measurements and remove any high frequency noise.

As seen in Table 1, some train classes have unique carriage numbers, resulting in signals with a unique number of peaks. However, simple peak counting is not sufficient for classification, as there remain other train types with equal carriage counts. Thus, features aim to characterize the peaks of the signal not just by counts, but also by peak heights and widths.

As shown in Table 2, Some of these features are calculated using a ring-up-ring-down scheme. That is, a threshold is set for the signal, and in this case, it is 0.05. The area where the signal surpasses this threshold before descending past it again denotes a ring up zone. Each ring up zone contains a peak, and the width of each ring up zone is also recorded.

Table 2. Features extracted from strain timeseries.

Feature	Description
len_ratio	Ratio of truncated length to untruncated length
peak_count	Sum of the numbers of peaks and valleys in timeseries
peak_spacing	peak_count divided by length of truncated timeseries
peak_freq	Highest-density frequency in PS of timeseries after filtering
avg_freq	Average frequency in PS after filtering
pass_count	Number of times signal exceeds threshold
height_avg	Average value of peaks within each ring up zone
height_std	Standard deviation of peaks within each ring up zone
widths_avg	Average length of the ring up zones
widths_std	Standard deviation of the widths of the ring up zones
width_max	Maximum width of the ring up zones

Lastly, other features are derived from the power spectrum (PS) of the signal, with the power spectrum being calculated via the SciPy Python library. Further details regarding these features are summarized in Table 2.

2.3 *Proposed classification model*

Gradient boosted decision trees are used for classification, namely XGBoost. Gradient boosting iteratively combines weak learners, into a single strong learner. In this case, the features are provided to the model, and through gradient boosting an ensemble of decision trees are combined to produce a stronger predictive model.

The objective function to be optimized at step t is defined as

$$obj(\theta) = \sum_{i=1}^{n} l(y_i, \hat{y}_i^{(t)}) + \sum_{i=1}^{t} w(f_i) \tag{1}$$

where $l\left(y_i, \hat{y}_i^{(t)}\right)$ is the multi-class softmax loss function and $w(f_i)$ is the complexity of the i-th tree. The complexity of a tree is defined by

$$w(f) = \gamma T + \frac{1}{2}\lambda \sum_{i=1}^{t} s_i \tag{2}$$

where s is the vector of weights assigned to each tree leaf and T is the number of leaves. The regularization parameters γ and λ are set to 0.2 and 0.01 respectively.

Taking the second order Taylor expansion of the loss function, the objective function for additive training can be re-expressed as

$$obj^{(t)}(\theta) = -\frac{1}{2}\sum\nolimits_{j=1}^{n} \frac{G_j^2}{H_j + \lambda} + \gamma T \tag{3}$$

where G_i and H_i are defined as

$$G_j = \sum\nolimits_{i \in I_j} \partial_{\hat{y}_i^{(t-1)}} l\left(y_i, \hat{y}_i^{(t-1)}\right) \tag{4}$$

$$H_j = \sum\nolimits_{i \in I_j} \partial^2_{\hat{y}_i^{(t-1)}} l\left(y_i, \hat{y}_i^{(t-1)}\right) \tag{5}$$

I_j is the set of indices of the input that are assigned to the j-th leaf (Chen & Guestrin 2016).

2.4 *Experimental method*

To replicate the performance of the model during online implementation, 4370 records between July 2020 and September 2nd, 2021 were used for training, and 500 records between September 2nd and October 19th 2021 were used for testing.

3 RESULTS

3.1 *Model performance*

Using the framework described in Section 2, a test accuracy of 96.8% is achieved. Class-wise precision, recall, and F_1 scores are displayed in Table 3. The F_1 score is defined as the harmonic mean of precision and recall and can be calculated as

$$F_1 = \frac{2}{recall^{-1} + precision^{-1}} \tag{6}$$

As seen in Table 3 and Figure 3, most train classes are classified with few or no mistakes, including rarer classes like the Northern 4 car. Additional performance may be achieved by fine-tuning filter parameters, model parameters, or extraction of further characteristic features.

Table 3. Test precision, recall, and F_1 score by class.

Train Type	Precision	Recall	F_1 Score
Voyager 220	0.667	1.00	0.800
Voyager 220+220	1.00	1.00	1.00
Voyager 220+221	0.962	1.00	0.980
Voyager 221	1.00	1.00	1.00
Class 185	0.903	0.800	0.848
Class 185+185	1.00	0.966	0.982
Class 43	1.00	0.964	0.982
Northern 2 Car	1.00	1.00	1.00
Northern 3 Car	0.925	0.976	0.950
Northern 4 Car	1.00	0.875	0.933
Nova 1	1.00	0.990	0.995
Nova 3	1.00	1.00	1.00

Figure 2 shows the gain, or average improvement in accuracy, of each feature after training. As expected, XGBoost uses features related to the number of peaks in the signal for much of the classification, as this relates to the number of carriages of each train.

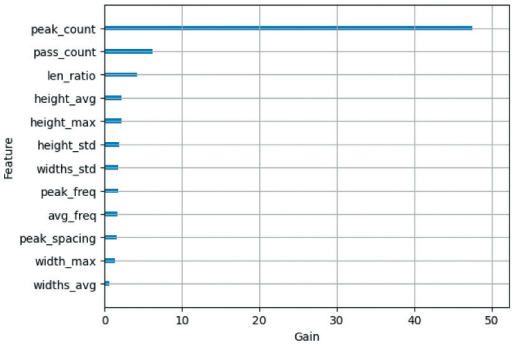


Figure 2. Feature importances.

This is supported by Figure 3, which displays information regarding the misclassification of trains. There are a significant proportion of Class 185 trains misclassified as Northern 3 car trains. This is likely due to actual and misclassified train types having the same number of carriages, as seen in Table 2. While peak counting and other features may be sufficient to distinguish between other train types, more complex classification models or features may be needed to fully separate signals of these similar train types.

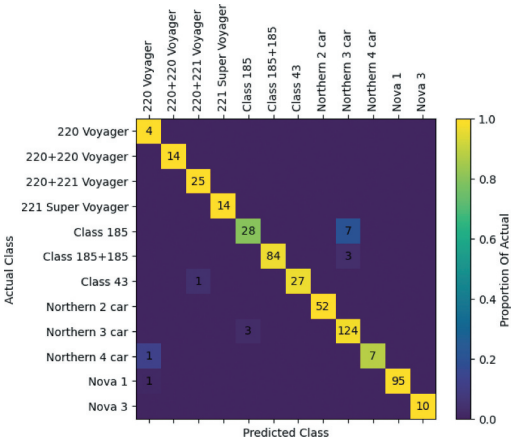


Figure 3. Confusion plot of XGBoost classifier on test set. Counts displayed in squares.

3.2 *Temperature-strain correlation*

With a robust classification framework, further analysis conditioned on train type can be conducted. A further 930 train events, which were collected from January 2023 through August 2023, have been labelled using the framework presented in Section 2. As seen in Figure 4, the train type compositions of both datasets are similar, and there is very little increase in the frequencies of relatively poorly classified train types (i.e., Class 185 and Northern 4 car trains).

Due to the relative abundance of Class 185+185 trains throughout the survey period, this class of train was selected for long-term temperature analysis. The following analysis and

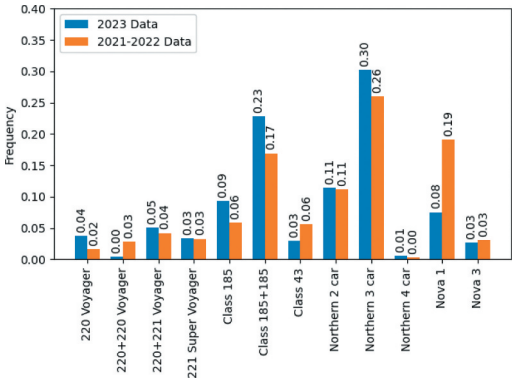


Figure 4. Frequency of predicted train classes.

results consider XGBoost labelled data from both the 2020-2021 and 2023 monitoring periods.

FBGs N_MID, C_MID, LCRACK_MID, and LCRACK_TIP were selected for observation. FBGs N_MID and C_MID are located near the middle of the span under the northern track and bridge centerline respectively. This northern portion of the bridge is relatively undamaged and exhibits the most linear behavior. LCRACK_MID and LCRACK_TIP span across a longitudinal crack in the southeast corner of the arch soffit, with LCRACK_MID positioned at the middle and LCRACK_TIP at the tip of the crack. If the crack progresses, it is expected that LCRACK_TIP, will show increased movement as the crack length grows. Opening displacements at LCRACK_MID may well also increase.

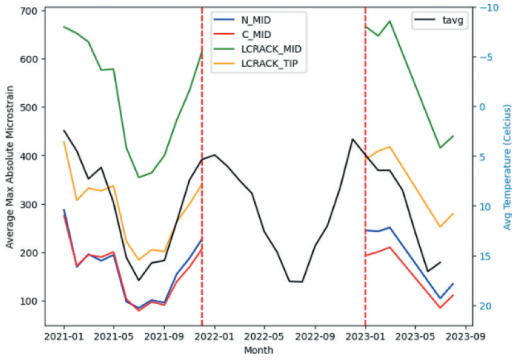


Figure 5. Monthly average maximum strain readings and monthly average temperature for Class 185 +185 trains travelling eastward.

It is known that maximum dynamic strain is well-correlated with temperature (Alexakis et al. 2021). Figure 5, which plots the average maximum dynamic strain reading across each month, for the four FBGs, along with monthly average temperature of a nearby weather station in Bradford, UK, clearly confirms this correlation. This value is calculated by averaging the monthly low and high temperatures.

To observe long-term differences more clearly, without the overlying effect of temperature, months with similar average temperatures were analyzed to compare the maximum dynamic strains of each Class 185+185 train event. Three spring months and three summer months with average temperatures around 6.4°C and 15.5°C respectively were selected for this purpose.

Figure 6 presents violin plots of the maximum dynamic strain measurements for Class 185 +185 trains. The thick dashed lines denote the distributions' median values, and the thin dashed

lines denote distributions' first and third quartile values. The median maximum dynamic strains for February 2023 and March 2023 are similar while the measurements for April 2021 are notably lower. This could be an indication of damage progression from 2021 to 2023, or possibly a sign of remaining temperature variation which the use of monthly average temperatures cannot remove. More complex normalization of the measurements against temperature will be explored in future work. Violin plots for summer months of similar monthly average temperatures yield similar results in the evolution of average maximum dynamic strain over time. Again, there is no clear ordering of the average maximum dynamic strains with respect to temperature. Generally, the average strains in 2023 are larger than those in 2021, but the extent to which the 0.2°C difference in average monthly temperature and operational damage contribute to this difference is unclear, and this will be explored further in future work, potentially by observing changes in correlation between temperature and maximum dynamic strain over time.

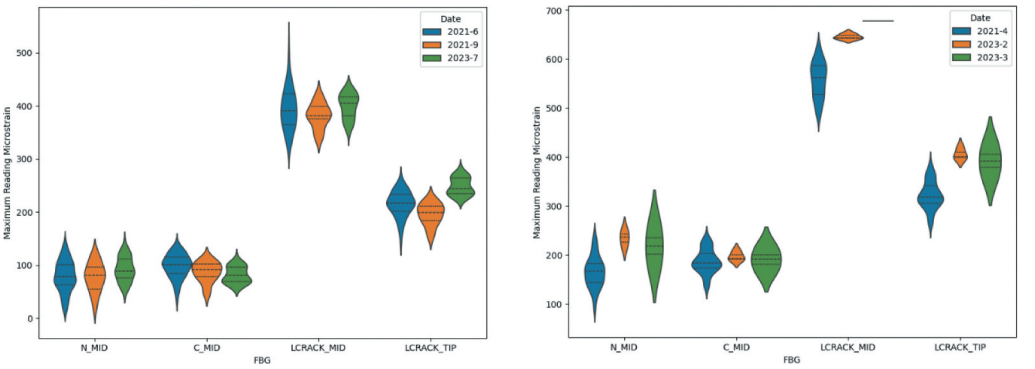


Figure 6. Maximum dynamic strain measurements for Class 185+185 trains, grouped by similar monthly average temperatures in (left) spring and (right) summer.

4 CONCLUSIONS

In this study, a comprehensive framework for post-processing and interpreting FBG monitoring data from the CFM-5 masonry arch bridge is presented. The primary focus is on automated train classification using gradient-boosted decision trees, specifically XGBoost, in order to study the bridge response normalized for different train types. The classification model exhibits a high test accuracy of 96.8%, demonstrating its efficacy across diverse train types, including rarer train classes. Further refinement of feature extraction could potentially enhance its performance.

Additionally, the study explores the correlation between temperature and strain, a critical factor in understanding long-term bridge performance. The observed correlation between maximum dynamic strain readings and temperature variations underscores the importance of considering environmental factors when assessing structural health.

The results highlight the significance of automated monitoring solutions, such as FBG sensors coupled with advanced classification models, for evaluating the health of aging infrastructure such as masonry arch bridges. Beyond streamlining the monitoring process, the proposed framework offers valuable insights into the structural response under varying operational and environmental conditions.

ACKNOWLEDGEMENTS

The work described here is part of a monitoring collaboration with engineering consultant AECOM, along with financial support from the asset owners Network Rail. The authors are grateful for the help and support of both organizations. The 1st author of this research was

financially supported by the U.S. National Science Foundation. Any findings, opinions, conclusions, and recommendations of this paper are those of the authors and do not necessarily reflect the views of the research sponsor.

REFERENCES

Acikgoz S., DeJong M. J., & Soga K. 2018. Sensing dynamic displacements in masonry rail bridges using 2D digital image correlation. *Struct Control Hlth* 25:e2187.

Acikgoz S., DeJong M. J., Kechavarzi C., Soga K. 2018. Dynamic response of a damaged masonry rail viaduct: measurement and interpretation. *Eng Struct* 168:544–558.

Alexakis, H., Lau, F. DH., & DeJong, M. J., 2021. Fibre optic sensing of ageing railway infrastructure enhanced with statistical shape analysis. *J Civil Struct Health Monit* 11:49–67.

Augusthus-Nelson, L., Swift, G., Smith, C., Gilbert, M., & Melbourne, C. 2016. Behaviour of backfilled masonry arch bridges subjected to cyclic loading. *Proceedings of ARCH'16, the 8th International Conference on Arch Bridges*: 1039–1048.

Brencich, A., & Morbiducci, R. 2007. Masonry Arches: Historical Rules and Modern Mechanics. *International Journal of Architectural Heritage* 1(2), 165–189.

Chaiyasarn K., Khan W., Luqman Ali, Sharma M., Brackenbury D., & DeJong M. 2018. Crack detection in masonry structures using convolutional neural networks and support vector machines. *Proceedings of the 35th ISARC*: 118–125.

Chen, T. & Guestrin, C., 2016. XGBoost: A Scalable Tree Boosting System. *Proceedings of the 22nd ACM SIGKDD International Conference on Knowledge Discovery and Data Mining*: 785–794.

Cocking, S. H., Ye C., & DeJong M. J. 2019. Damage Assessment of a Railway Bridge Using Fibre Optic Sensing and Lidar Data. *International Conference on Smart Infrastructure and Construction 2019*: 701–710.

Ye C., Acikgoz S., Pendrigh S., Riley E., & DeJong M. J. 2018. Mapping deformations and inferring movements of masonry arch bridges using point cloud data. *Eng Struct* 173:530–545.

Bridge Maintenance, Safety, Management, Digitalization and Sustainability – Jensen, Frangopol & Schmidt (eds)
© 2024 The Author(s), ISBN 978-1-032-77040-6
Open Access: www.taylorfrancis.com, CC BY-NC-ND 4.0 license

Deep reinforcement learning-driven life-cycle management of bridge and pavement systems

A. Bhattacharya, M. Saifullah & K.G. Papakonstantinou
Department of Civil & Environmental Engineering, The Pennsylvania State University, University Park, PA, USA

ABSTRACT: Optimal management of bridge systems and related transportation infrastructure poses multi-faceted challenges, requiring adept inspection and maintenance policies at both system and individual asset levels, to minimize life-cycle costs while considering various operational, risk, and performance constraints. This demanding type of optimization problems entails, among others, high-dimensional aspects, describing multi-component systems, long-planning horizons, diverse probabilistic and deterministic operational objectives and constraints, and inherent uncertainties associated with inspections and stochastic models. Effective coordination among individual component assets considering various inter-dependencies is also essential to enable a true system-based optimal solution. In this work, this optimization problem is formulated within the framework of Partially Observable Markov Decision Processes (POMDPs) and constrained Multi-Agent Deep Reinforcement Learning (MARL). POMDPs offer a principled mathematical approach for sequential decision-making under uncertainty, incorporating Bayesian inference to address the observation/monitoring data uncertainty, and can be suitably scaled to high-dimensional state and action spaces associated with multi-component systems, exploiting the rich representational capacities of deep learning and decentralized control settings of MARL. In this work, the recently developed DDMAC deep reinforcement learning (DRL) algorithm (Deep Decentralized Multi-Agent Actor-Critic) has been successfully deployed based on the Centralized Training and Decentralized Execution (CTDE) formulation. The efficacy and implementation aspects of the developed framework are originally studied in this work based on two existing real-world transportation networks in Virginia and Pennsylvania, USA, following all regulations imposed by the relevant agencies, as well as their overall practices, in an effort to investigate the use of the suggested framework in practical, actual settings. In both cases, DRL results significantly surpass the ones related to current state-of-practice and state-of-the-art policies, providing further support and insights toward the use of DRL-driven policies for infrastructure management.

1 INTRODUCTION

This work presents a multi-agent deep reinforcement learning framework tailored for the inspection and maintenance (I&M) planning of extensive transportation and bridge networks. This framework is methodically applied to two existing networks in Pennsylvania and Virginia, in the U.S., serving as practical, indicative, real-world case studies.

Significant computational challenges are encountered in managing multi-component infrastructure systems. These challenges include, but are not limited to, the heterogeneity of different asset classes, the extensive number of components, the presence of noisy data, limited availability of resources, and diverse performance-based constraints. The existing optimization methodologies for I&M planning range from threshold-based strategies with risk-based principles to decision tree analysis and renewal theory (Luque & Straub, 2019; Frangopol, et al., 1997). Despite their merits, many of these solutions suffer from optimality-, scalability-, and uncertainty-

DOI: 10.1201/9781003483755-400

induced complexities and are often not easily extendable to environments with constraints. Stochastic optimal control approaches based on Partially Observable Markov Decision Processes (POMDPs), e.g., in (Madanat, 1993; Papakonstantinou & Shinozuka, 2014) can support dynamic policies and noisy real-time observations in the decision-making framework, but are often hard to scale to large systems with multiple components.

To address these limitations, we combine the principles of POMDPs with the advanced capabilities of multi-agent Deep Reinforcement Learning (DRL), as explained in (Andriotis & Papakonstantinou, 2019; Andriotis & Papakonstantinou, 2021) for the Deep Centralized Multi-agent Actor-Critic (DCMAC) technique and its subsequent variant, the Deep Decentralized Multi-agent Actor-Critic (DDMAC). These techniques are designed to manage the complexities of decentralized execution and to efficiently navigate the vast parameter spaces, typical in large-scale infrastructure systems. Lately, as a further development, DDMAC is also shown under the paradigm of Centralized Training and Decentralized Execution (CTDE) (Lyu, et al., 2021) in (Saifullah, et al., 2024), with decentralization at both the action and information levels. This approach reduces the scalability involved complexities even further, by providing only local observations to the actors.

In this paper, the DDMAC-CTDE framework is uniquely applied to analyze two separate, existing, real-world transportation networks in Pennsylvania and Virginia, USA, and the resulting policies are compared against the respective current state-of-practice/state-of-the-art. Both networks under consideration consist of a set of stochastically deteriorating bridge assets necessitating maintenance, considering various deterministic and stochastic resource and condition constraints and targets, aligning closely with the actual methodologies and practices utilized by the respective transportation agencies. The Virginia network also considers multiple asset classes, i.e., pavement and bridge components, utilizing probabilistic deterioration models for the different classes of assets (Saifullah, et al., 2024), and has also been mentioned in (Saifullah, et al., 2022). In each case, results are compared with optimized Condition Based Maintenance policies (CBM) and compatible variants of current I&M policies implemented by the Pennsylvania and Virginia Department of Transportations (PennDOT and VDOT), respectively, with DDMAC-CTDE significantly outperforming both the CBM and the current state-of-practice approaches.

2 BACKGROUND

2.1 *Partially observable markov decision processes*

The POMDP framework is defined by the 7 elements tuple consisting of S,A, $\mathbf{P}$, Ω, $\mathbf{O}$, $\mathbf{C}$, and γ, where S, A, and Ω are sets of states, actions, and observations, respectively, $\mathbf{P}$ is the model of state transitions, $\mathbf{O}$ is the observation model, $\mathbf{C}$ is the cost function, and γ is a discount factor. In POMDPs the agent starts at a state s_t at a time step t, takes an action a_t, receives a cost c_t transitions to the next state s_{t+1} based on the transition model $p(s_{t+1}|s_t, a_t)$, and receives an observation, $o_{t+1} \in \Omega$ based on the observation model, $p(o_{t+1}|s_{t+1}, a_t)$. Due to partial observability, the agent can only form a belief $\mathbf{b}_t$ about its condition state, where $\mathbf{b}_t$ is a probability distribution over S. The goal for the agent is to choose actions at each time step that minimize its expected future discounted cumulative cost (Papakonstantinou & Shinozuka, 2014a; Papakonstantinou & Shinozuka, 2014b). Despite existing mathematical convergence guarantees, the traditional point-based POMDP solvers do not scale adequately for large systems with multiple components. However, neural network-based deep reinforcement learning methods can alleviate this curse of dimensionality.

2.2 *Deep reinforcement learning and DDMAC-CTDE*

Within the context of infrastructure management, DDMAC, as developed in (Andriotis & Papakonstantinou, 2021), provides an algorithm for system-level I&M optimal planning well-suited for large multi-component systems. The framework also considers the presence of constraints through state augmentation and Lagrange multipliers. DDMAC uses a sparse parametrization of the actor-network without parameter sharing between agents (i.e., each

component has its own actor network). For even larger systems, the DDMAC-CTDE formulation (Saifullah, et al., 2024) can be used, allowing for even sparser actor parametrizations. The policy, π, and its gradient are then given as (Saifullah, et al., 2024):

$$\pi(\mathbf{a}_t|\mathbf{s}_t) = \prod_{i=1}^{n} \pi_i\left(a_t^{(i)}|s_t^{(i)}\right) \tag{1}$$

$$\mathbf{g}_{\theta^\pi} = \mathrm{E}_{\mathbf{s}_t\sim\mathbf{p},\mathbf{a}_t\sim\mu}\left[w_t\left(\sum_{i=1}^{n}\nabla_{\theta^\pi}\log\pi_i\left(a_t^{(i)}\,|\,s_t^{(i)},\theta^\pi\right)\right)A^\pi(\mathbf{s}_t,\mathbf{a}_t)\right] \tag{2}$$

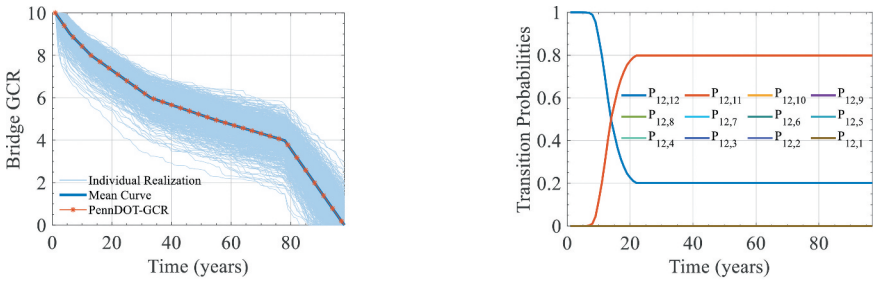


Figure 1. (a) Fitted gamma model for GCR. (b) Transition probabilities for multi-span bridges belonging to PennDOT Family 1, with starting state 12.

3 ENVIRONMENT DESCRIPTION

3.1 *Condition states and transitions*

In the case of the Pennsylvania network, the POMDP environment is derived based on PennDOT's Bridge Asset Management System (BAMS) (PennDOT, 2022; PennDOT, 2021), focusing only on bridge decks here as the primary deteriorating constituent of bridge assets. The network considered for this study consists of 30 Family 1 multi-span bridge decks in District 8, with General Condition Rating (GCR) as the indicator of bridge deck conditions, ranging from 0 to 9.99. A probabilistic non-stationary GCR model is developed based on the deterministic deterioration model, as employed by PennDOT, as detailed in (Papakonstantinou, et al., 2024, under prep.). A non-stationary gamma process is utilized, with its mean being in time equal to the PennDOT model GCR values, and a suitable model variance. Figure 1a shows some representative simulation results for multi-span bridges belonging to PennDOT Family 1. The solid line represents the mean GCR and the red curve is the GCR model used by PennDOT.

To calculate the transition probabilities, the continuous GCR values are discretized into 15 states, with state 15 being GCR ≥9.5, state 14 being GCR ∈ (9.5, 9.0], and so on until state 1, which is a compound state for all the GCR values < 3.0, to accommodate PennDOT's prescribed maintenance recommendations. Fifty million Monte Carlo sequences from the developed gamma process are simulated to obtain the transition probabilities for a given bridge family and span type, appropriately smoothed over a time window of 5 years. Figure 1(b) indicatively shows some computed transition probabilities for the Family 1 multi-span bridges.

In the case of the Virginia network, the Hampton Roads network is considered. It comprises 85 pavement (including interstate, primary, and secondary highways) and 11 bridge components, with 6 Critical Condition Index (CCI) states and 5 International Roughness Index (IRI) states used as condition indicators for pavements, and 7 GCR-based bridge states (Saifullah, et al., 2022). A non-stationary CCI model is devised based on VDOT's model (Katicha, et al., 2016). More details on the condition state transition probabilities can be found in (Saifullah, et al., 2024).

3.2 *Maintenance and inspections*

In the Pennsylvania network, bridge deck maintenance follows PennDOT's BAMS specifications, involving five specific maintenance actions: *Do-Nothing*, *General Preservation, Epoxy Overlay, Structural Overlay*, and *Deck Replacement*, along with their respective costs (PennDOT, 2022). All considered actions generally impact both the bridge deck condition state and deterioration rate. Detailed descriptions of these actions are provided in (Papakonstantinou, et al., 2024, under prep.). In this work, a high-fidelity inspection with 90% accuracy is assumed, performed every two years, to adhere to PennDOT's bridge assessment policies.

For the Virginia network, based on (VDOT, 2016), four different maintenance actions are considered for pavements, i.e., *Do-Nothing*, *Minor Repair*, *Major Repair*, and *Reconstruction*. Minor Repair (crack filling, moderate patching, etc.) can improve the CCI and IRI condition states but does not affect their rate of deterioration. Major Repair can improve condition states and also reduce their deterioration rate by 5 years. Reconstruction resets the pavement to an intact condition. A detailed description of maintenance actions and their costs can be found in (VDOT, 2016). Similarly, four maintenance actions are also considered for bridge decks. These actions, the related transition probabilities, action durations and costs are described in detail in (Saifullah, et al., 2024). Towards generality, inspection actions are also optimized in this case and three inspection options are considered, characterized as uninformative, low-fidelity, and high-fidelity inspection techniques, respectively. The observation probabilities for the corresponding inspections can also be seen in (Saifullah, et al., 2024).

3.3 *Costs, risks, and constraints*

For the Pennsylvania bridge network, the total cost is composed of the costs associated with maintenance actions and risk. The risk cost depends on the current condition rating along with the risk score (*RS*) associated with a bridge, as reported in BAMS. The risk score describes the importance of a bridge, which is a function of deck area, annual average daily traffic, truck traffic percent, detour length, scour rating, fracture criticality, and history of flooding (PennDOT, 2022). The risk score-based cost, $c_{RS}(t)$ at time t is quantified here as:

$$c_{RS}(t) = \sum_{i=1}^{N} \left(10 - GCR(t)_i\right) RS_i \tag{3}$$

where $GCR(t)_i$ is the GCR rating at time step t for the i^{th} bridge, and N is the total number of bridges considered. Inspections are not controlled in this case but are pre-assigned every two years. Their costs are thus not considered in the total cost to be optimized. Therefore, the total cost at time t can be estimated as:

$$c(s_t, a_t) = \underbrace{c_M(s_t, a_t)}_{\text{maintenance cost}} + \underbrace{c_{RS}(s_t)}_{\text{risk score cost}} \tag{4}$$

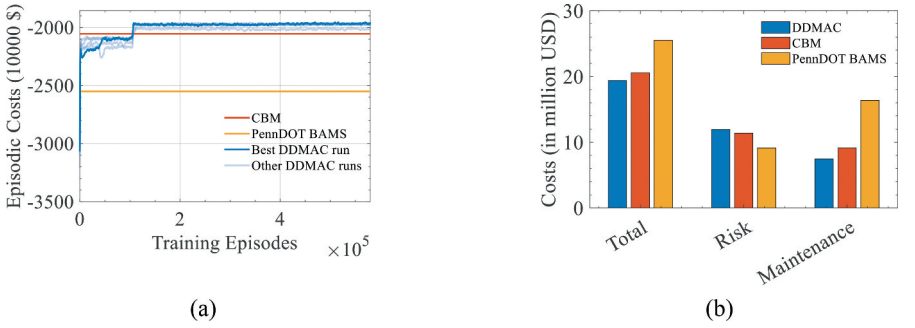
Table 1. Comparison of different solution schemes in terms of average (+/- 95% confidence bounds) total cost and performance for the Pennsylvania network.

Objective & Constraints	DDMAC-CTDE	CBM policy	BAMS policy
Total costs (million USD)	19.3779 (± 0.0211)	20.5435 (**+6.02%**) (± 0.0215)	25.5061 (**+32%**) (± 0.0116)
Poor Interstate (cap 5%)	0.5329 (± 0.0790)	0.0245 (± 0.0162)	0.00 (± 0.00)
Poor NHS (cap 7%)	3.7489 (± 0.1356)	6.4255 (± 0.1923)	0.3237 (± 0.0648)
Poor total (cap 10%)	8.3886 (± 0.2325)	4.6769 (± 0.1296)	12.3157 (± 0.1293)

Table 2. Comparison of different solution schemes in terms of average (+/- 95% confidence bounds) total cost and performance for the Virginia network.

Objective & Constraints	DDMAC-CTDE	CBM policy	VDOT policy
Total costs (billion USD)	6.55 (±0.003)	7.03 (**+7.3%**) (±0.004)	8.35 (**+27%**) (±0.008)
CCI<60 and IRI>2.2m/km for I-Hwy (%, cap 5%)	1.34 (±0.02)	1.61 (±0.02)	3.39 (±0.07)
CCI<35 of I-Hwy (%, cap 2%)	1.50 (±0.02)	0.68 (±0.01)	3.80 (±0.07)
CCI<60 for I and P-Hwy (%, cap 18%)	17.65 (±0.04)	12.67 (±0.02)	5.80 (±0.04)
IRI>2.2 m/km for I and P-Hwy (%, cap 15%)	15.40 (±0.04)	11.49 (±0.04)	15.65 (±0.07)
CCI<60 for S-Hwy (%, cap 35%)	33.00 (±0.08)	28.18 (±0.04)	37.86 (±0.13)
Bridges with GCR ≤4 (%, cap 10%)	8.33 (±0.05)	8.79 (±0.06)	15.85 (±0.15)

The Pennsylvania network in this study consists of 30 multi-span District 8 bridges belonging to Family 1, including 3 Interstate NHS and 3 Non-Interstate NHS bridges. The constraints under consideration include a hard budget limit of 5.30 million, renewed every 5 years, and 3 performance targets: (1) for Interstate bridges the average deck area in poor condition (GCR ≤ 5.0) should be less than 5% over the decision horizon; (2) for NHS bridges this target is 7%; and (3) across the entire network the average proportion of bridges in poor condition state should not exceed 10%. These constraints are integrated into the DRL framework as outlined in (Andriotis & Papakonstantinou, 2021; Saifullah, et al., 2024).



(a) (b)

Figure 2. (a) Total life cycle costs comparison of DDMAC-CTDE solution with CBM and PennDOT policy baselines. (b) Comparison of the total cost and its constituents with CBM and PennDOT policy baselines.

For the Virginia network, the total cost includes inspection, maintenance, traffic delay, terminal costs, and bridge failure risks. Budget constraints with a 5-yearly budget of 1.3 billion USD, and six performance targets are used, with the latter sought to be satisfied in an average sense over the decision horizon, based on FHWA and VDOT guidelines (Saifullah, et al., 2024).

4 RESULTS

The networks have been trained using the DDMAC-CTDE architecture, with their existing conditions as the initial condition states, an episodic length of 20 years, and considering

a discount factor of $\gamma = 0.97$. 5 maintenance actions per component are considered for the Pennsylvania network, totaling ~10^{21} available actions for the entire network, and 10 inspection and maintenance actions per component are considered for the Virginia network, with 10^{96} total available actions for the system. The 5-yearly budgets used for both the Pennsylvania and the Virginia networks follow the guidelines by the respective agencies.

To compare the DDMAC-CTDE solutions, two types of baselines are evaluated, i.e., (i) a condition-based maintenance (CBM) policy, and (ii) policies following PennDOT/BAMS and VDOT practices. The CBM policy is heuristically optimized, to identify the relevant thresholds, based on the conditions of each component type. The details of CBM, BAMS, and VDOT policies can be found in (Papakonstantinou, et al., 2024, under prep.; Saifullah, et al., 2024).

Figure 2(a) demonstrates DDMAC-CTDE performance over CBM and BAMS during its training on the Pennsylvania network, with weights initialization in this case based on an unlimited budget earlier trained case. Figure 2(b) showcases relevant histograms of total, maintenance, and risk costs from 5,000 Monte Carlo policy realizations. DDMAC-CTDE policy is 6.02% and 31.64% less expensive in total cost, in relation to the CBM and BAMS policies, respectively, and it spends 120% less than BAMS and 23% less than CBM on maintenance. Table 1 presents further details on the average performance of the Pennsylvania network over 5,000 Monte Carlo simulations, showcasing the total cost and the three constraints related to poor bridge conditions percentages, together with their recommended targets. Table 2 similarly compares six performance constraints and their targets for various pavement types and bridges in the Virginia network, where I-, P-, and S-Hwy represent interstate, primary, and secondary highway components, respectively. Both Tables provide the estimated values along with their 95% confidence bounds.

To better understand the converged DDMAC-CTDE policies, Figures 3 and 4 illustrate instances of the Pennsylvania and Virginia networks, respectively. In Figure 3, the maintenance policies for five randomly selected bridges in PA are shown over time, together with the

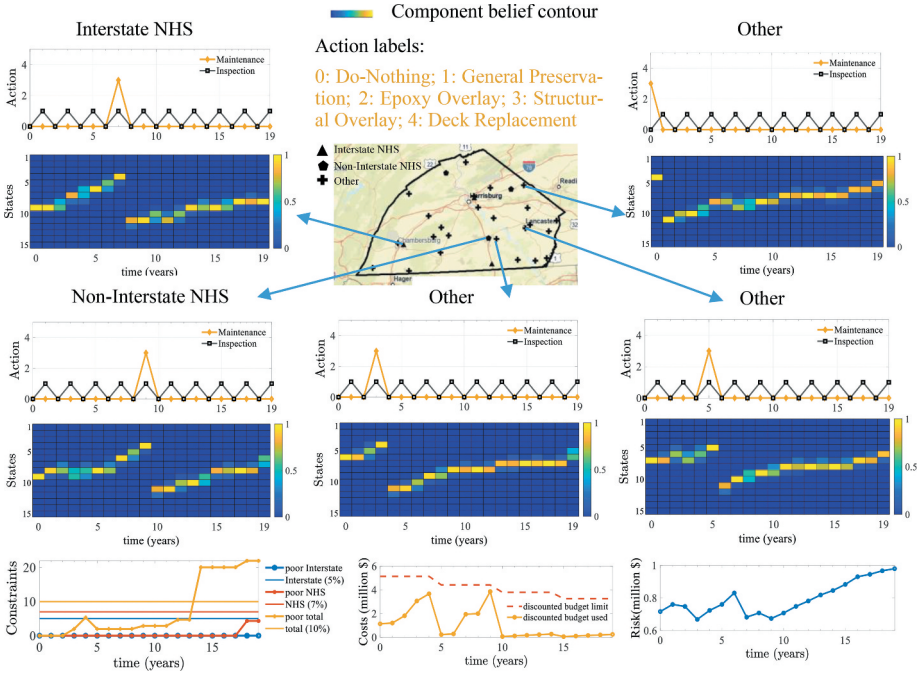


Figure 3. Indicative realization of the learned DDMAC-CTDE policy for the PA transportation network. Due to safety considerations by PennDOT, the true identities of the individual bridges are withheld. The visualization here serves solely as an illustrative depiction of the network under consideration and does not correspond to the actual bridges analyzed in this study.

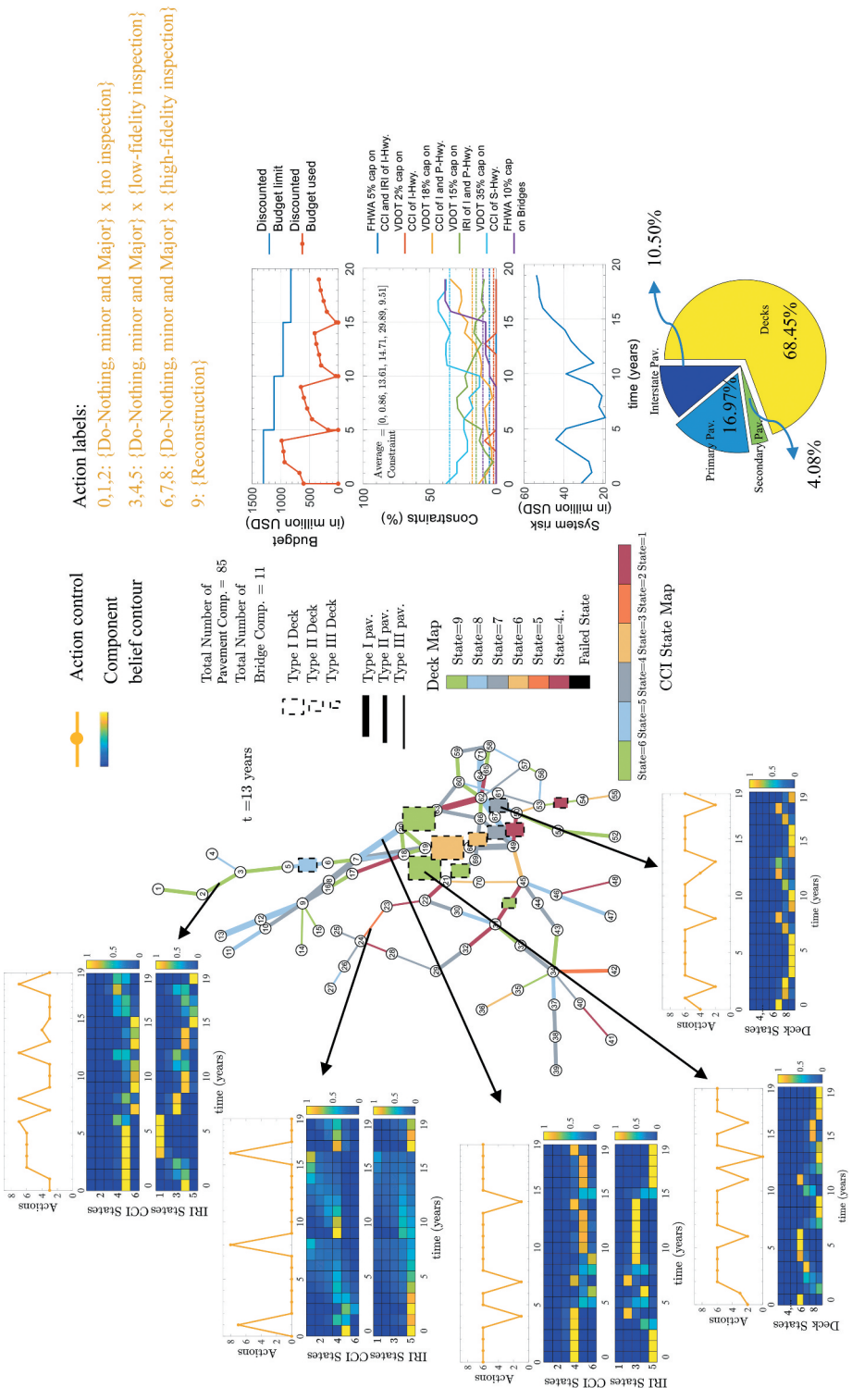


Figure 4. Illustrative realization of the learned DDMAC-CTDE policy for the Hampton Roads network.

action effects on the belief states. Figure 3 also depicts variations in considered performance constraints, their targets, the total system risk cost, and the utilized budget, with the total available budget discounted for each five-year cycle. The figure indicates that performance constraints are well-respected, on average over the decision period, and the budget remains within limits throughout the entire horizon.

Similarly, Figure 4 represents a policy instance for the Virginia network, where there are 10 available control actions. The time variations of budget utilization, system risk, and six performance constraints are also shown. The budget is always under its limit in this case as well, and discounted for each five-year cycle. A pie chart representing the I&M cost distributions for different asset types is additionally shown, with most funds spent on bridges in this case, having also a failure risk associated with them. Among the pavements, primary highway pavements utilize the most funds, as they represent the most components in this network.

5 CONCLUSIONS

Deep Decentralized Multi-Agent Actor Critic with Centralized Training and Decentralized Execution (DDMAC-CTDE) solutions are evaluated in this work, for managing bridge and bridge-pavement systems, related to two real-world networks in Pennsylvania and Virginia, USA. Comparisons with the corresponding agency policies, i.e., PennDOT (BAMS) and VDOT, respectively, and with optimized Condition-Based Maintenance (CBM) policies are performed as well. The DDMAC-CTDE solution is shown to surpass the State DOT-based baselines by 32% (for BAMS) and 27% (for VDOT) in terms of the total overall cost. CBM policies for the two networks are also surpassed by 6.02% and 7.3%, respectively, while generally meeting all the specified performance targets. Overall, this work and results indicate the applicability and effectiveness of our DRL framework for asset management of real-world networks, characterized in their full complexity, and can set solid foundations for further developments and implementations in the field, related to bridge networks and beyond.

ACKNOWLEDGEMENTS

We acknowledge the support by the U.S. National Science Foundation under CAREER Grant No. 1751941, by the Pennsylvania Department of Transportation, and by the Center for Integrated Asset Management for Multimodal Transportation Infrastructure Systems, 2018 U.S. DOT Region 3 University Center. We would further like to acknowledge the support by PennDOT's Mr. Jeff Davis and Mr. Justin Bruner, through extensive discussions, data sharing, and BAMS access.

REFERENCES

Andriotis, C. P. & Papakonstantinou, K. G., 2019. Managing engineering systems with large state and action spaces through deep reinforcement learning. *Reliability Engineering & System Safety*, Volume 191, p. 106483.

Andriotis, C. P. & Papakonstantinou, K. G., 2021. Deep reinforcement learning driven inspection and maintenance planning under incomplete information and constraints. *Reliability Engineering & System Safety*, Volume 212, p. 107551.

Papakonstantinou, K.G., Bhattacharya, A., Saifullah, M., Guler, I., Lu, M., Sengupta, A., Gayah, V., 2024, in preparation. *Quantifying the impact of data unavailability, inaccuracies and uncertainty on deterioration modeling and infrastructure asset management policies*. CIAMTIS US DOT Region 3 University Transportation Center, Final Report.

Frangopol, D., Lin, K. & Estes, A., 1997. Life-cycle cost design of deteriorating structures. *Journal of Structural Engineering*, Volume 123(10), p. 1390–401.

Katicha, S. W. et al., 2016. VDOT: *Development of enhanced pavement deterioration curves*.

Luque, J. & Straub, D., 2019. Risk-based optimal inspection strategies for structural systems using dynamic Bayesian networks. *Structural Safety*, Volume 76, pp. 68–80.

Lyu, X., Xiao, Y., Daley, B. & Amato, C., 2021. Contrasting centralized and decentralized critics in multi-agent reinforcement learning. *arXiv preprint arXiv:2102.04402.*

Madanat, S., 1993. Optimal infrastructure management decisions under uncertainty. *Transportation Research Part C: Emerging Technologies*, Volume 1(1), pp. 77–88.

Papakonstantinou, K. G. & Shinozuka, M., 2014a. Planning structural inspection and maintenance policies via dynamic programming and Markov processes. Part I: Theory. *Reliability Engineering & System Safety*, Volume 130, pp. 202–213.

Papakonstantinou, K. G. & Shinozuka, M., 2014b. Planning structural inspection and maintenance policies via dynamic programming and Markov processes. Part II: POMDP implementation. *Reliability Engineering & System Safety*, Volume 130, pp. 214–224.

Papakonstantinou, K. G. & Shinozuka, M., 2014. Optimum inspection and maintenance policies for corroded structures using partially observable Markov decision processes and stochastic, physically based models. *Probabilistic Engineering Mechanics*, Volume 37, pp. 93–108.

PennDOT, 2021. *Bridge Care*. [Online] Available at: https://bams.penndot.gov/ [Accessed 4th January 2024].

PennDOT, 2022. *Transportation Asset Management Plan*, Harrisburg, PA: Pennsylvania Department of Transportation.

Saifullah, M., Andriotis, C. P., Papakonstantinou, K. G. & Stoffels, S. M., 2022. *Deep reinforcement learning-based life-cycle management of deteriorating transportation systems*. Proceedings of the 11th International Conference on Bridge Maintenance, Safety and Management (IABMAS), CRC press, p. 293–301.

Saifullah, M., Papakonstantinou, K. G., Andriotis, C. P. & Stoffels, S. M., 2024. Multi-agent deep reinforcement learning with centralized training and decentralized execution for transportation infrastructure management. *arXiv preprint arXiv:2401.12455.*

VDOT, 2016. *Supporting document for the development and enhancement of the pavement maintenance decision matrices used in the needs-based analysis*, Richmond: Virginia Department of Transportation.

Bridge Maintenance, Safety, Management, Digitalization and Sustainability – Jensen, Frangopol & Schmidt (eds)
© 2024 The Author(s), ISBN 978-1-032-77040-6
Open Access: www.taylorfrancis.com, CC BY-NC-ND 4.0 license

Analyzing uncertainty in strain estimation framework for bridge condition assessment

S. Sadeghi Eshkevari, I. Dabbaghchian, G. Marasco & S. Pakzad
Lehigh University, Bethlehem, PA, USA

D. Sen
Southern Illinois University, Carbondale, IL, USA

ABSTRACT: Fatigue assessment of bridge infrastructure entails in-situ instrumentation of structural components. Consequently, the quality of collected data can be compromised considerably owing to various noise sources. Previously, the authors proposed a novel Artificial Neural Network (ANN) architecture for strain signal estimation from field acceleration measurements. This study aims to examine the impact of acquired acceleration data quality on strain signal estimation using the proposed ANN. Data collected from a real-scale case study is utilized to analyze noise levels in the input acceleration signal, measured strain signal, and subsequently the predicted strain signal to show if and how the quality of data has been affected by the ANN model. This is an effort to further understand the so-called black box neural networks specifically in the context of uncertainty propagation. Understanding the impact of data quality on the ANN's performance is crucial for enhancing the accuracy and trustworthiness of structural health monitoring in real-world applications.

1 INTRODUCTION

Measurement quality specifically in a field data collection case holds considerable importance. The quality of the collected data highly depends on the instrumentation precision, the environmental effects, and the susceptibility of the sensors. When proposing a data-driven methodology, the data quality can considerably affect the performance. Also, the framework might be able to overcome some of the uncertainties because of its designed architecture and the appointed input bundle. For this purpose, this chapter studies the data quality of the measurements for a previously proposed strain estimation framework on the Gene Hartzell Memorial bridge in eastern Pennsylvania, USA. Subsequently, the framework's capacity for maintaining the data quality is evaluated.

Previously, an artificial neural network-based strain estimation framework has been proposed and investigated to circumvent labor-intensive and costly strain sensor network deployment on a bridge by utilizing acceleration measurements on the bridge (Sadeghi Eshkevari, 2024). The proposed framework includes a novel powerful tool for sequences, Transformers, along with Convolutional Neural Networks (CNN) for the prediction of continuous strain signals using acceleration measurements from field data acquired from bridges. The schematic of this framework is shown in Figure 1. Although, to effectively address challenges stemming from various sources of noise in field measurements, it is crucial that the proposed framework captures the nonlinear spatio-temporal relationship between strain and acceleration.

Transformers, initially developed for natural language processing, demonstrate promising performance by utilizing self-attention layers to enhance the correlation between input and output sequences (Vaswani, 2017). Additionally, CNN-based networks (O'Shea, 2015) facilitate knowledge transfer and scalability (Chattopadhyay, 2012). The suggested network design merges CNN and Transformer blocks to attain excellent performance while minimizing

DOI: 10.1201/9781003483755-401

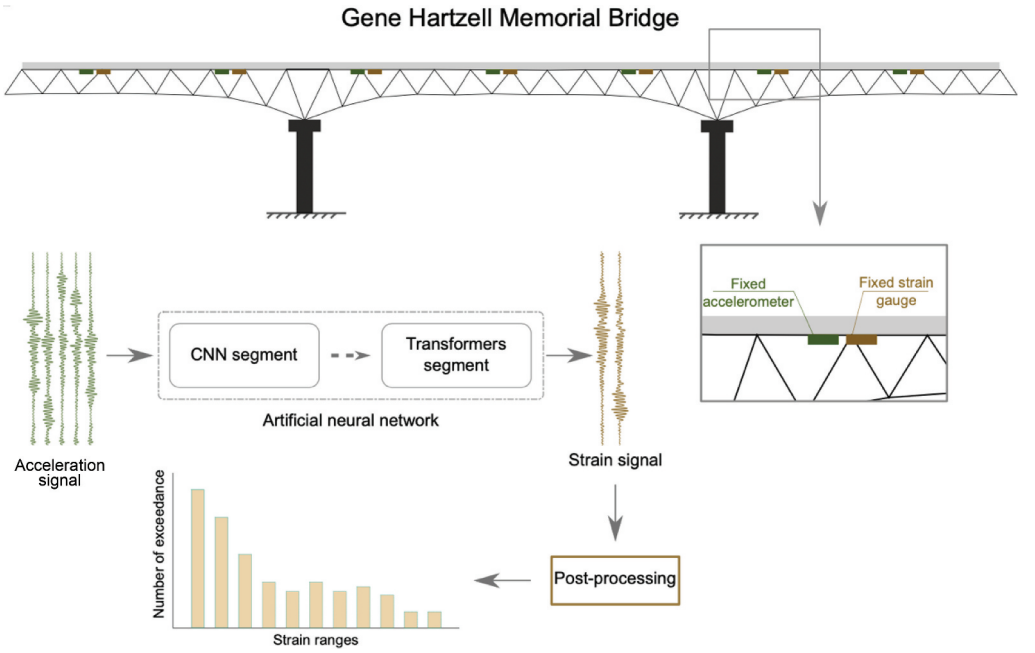


Figure 1. Strain estimation framework schematic.

computational expenses. It operates on an input array containing acceleration signals collected from multiple points along a bridge span. These signals undergo processing via an embedding layer and a positional embedding layer to preserve both dimensionality and order information. Subsequently, the matrix traverses through three CNN blocks featuring skip connections, followed by a final CNN layer before entering two Attention blocks. Ultimately, the network yields two variants of the strain signal for one location to preserve both high-frequency and low-frequency strain response content.

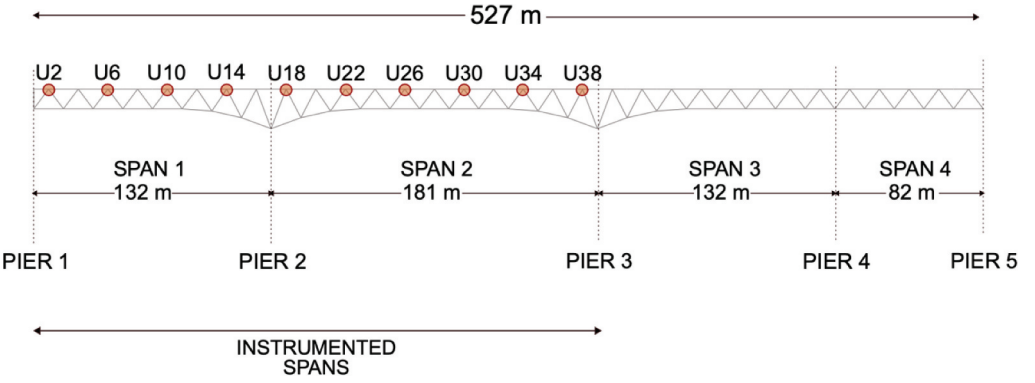


Figure 2. Instrumentation plan for Gene Hartzell Memorial bridge. Bridge side view and locations of the sensors (circles) along spans 1 and 2 of the bridge.

The case study used for instrumentation, training of the framework, and finally the evaluation is the Gene Hartzell Memorial Bridge in Easton, Pennsylvania. This bridge, completed in 2002, is a steel truss bridge with a reinforced concrete deck. It spans the Lehigh River, the Lehigh canal, and a double set of Norfolk Southern railroad networks, serving as a crucial

segment of the Pennsylvania State Route 33 (SR 33) that runs north-south. The southern two spans of this bridge were instrumented as shown in Figure 2.

The data collected from a real structure is typically noisy and needs to go through data pre-processing to be prepared for conducting further analyses. In this work, the pre-processing includes three steps: (a) applying low-pass and high-pass filters to eliminate noise and detrend the data, (b) down-sampling, and (c) segmentation of the time signals. These steps are implemented to both acceleration and strain measurements. To perform frequency filtering, the fast Fourier transform (FFT) is employed, followed by its inverse transform acting as the filter. Two distinct high-pass cut-off frequencies, 0.1 Hz and 1 Hz, are utilized. These settings enable the capture of vehicle-induced peaks responsible for high-range fatigue cycles and high-frequency dynamic strain signals associated with low-range stress cycles. These two versions of strain signals are named α for pseudo-static and β for dynamic signals. Subsequently, the collected ≈8 hour one-day data is segmented to smaller sections with length of 25 seconds (500 samples per signal) with strides of 20 to produce a larger dataset with the available data.

In this paper, the proposed framework and the case study are investigated further to explore the quality of measurements both for the acceleration as input to the methodology and strain as the output for the training phase, the quality of predicted strain signals type α and β and the comparability of the uncertainties among measured and predicted signals.

2 DATA QUALITY INVESTIGATION

To evaluate the confidence and quality of data for the field measurements and the proposed framework, investigation of the time signals does not suffice. The time signals carry the transient effect of the vehicles and therefore statistics of the time signals along the dataset (i.e. along hours of the instrumented day) is difficult to study. Although, since both types of these response measurements, acceleration, and strain signals, are a product of the loading scenario and structural dynamics of the instrumented bridge, the frequency content of the signals along the dataset offers a consistent representation along with quantification on the dispersion. For this, the following sections study the frequency content and its statistics along the dataset (as schematically shown in Figure 3) on the measured data (acceleration and strain), predicted data (strain signal type α and β), and a comparison of the measured and predicted.

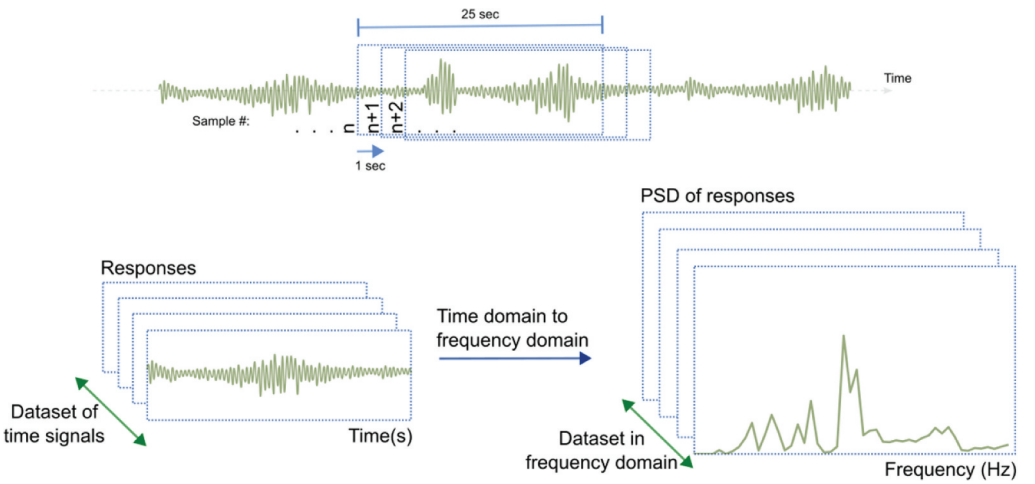


Figure 3. Schematic of the data quality measure.

3 MEASUREMENT QUALITY

First, the power spectral density (PSD) of the measured acceleration and strain signals are shown. The PSD is found for trimmed signals of 500 data points long (≈25 sec). The statistics for a random and evenly distributed subset of the full dataset (1460 signals) are calculated and the average values along with the 95% confidence interval (CI) are found as follows. The PSD for strain measurements both in the form of α and β which are the output to the ANN framework are shown in Figure 4. It can be observed that as discussed previously, signal α mostly represents the low-frequency content while signal β preserves high-frequency content that is also visible in PSD of acceleration measurements.

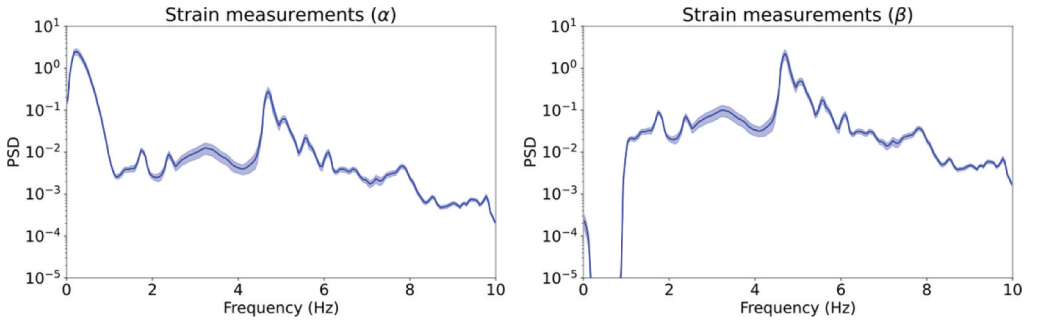


Figure 4. Average PSD (log) of strain measurements along with 95% confidence interval.

3.1 *Uncertainty along measured locations*

PSD of acceleration signals which are input to ANN is shown in Figure 5 along a bridge span. The locations are addressed according to Figure 2. The highlighted area also shows 95% confidence interval of the PSD on each location. It can be observed

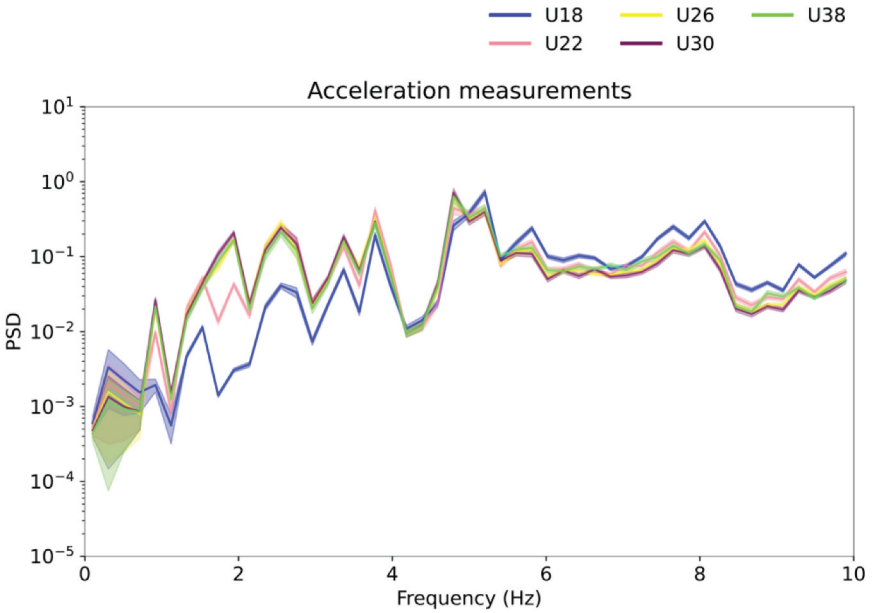


Figure 5. Average PSD (log) of acceleration measurements along 95% confidence interval for five input locations.

that different locations participate in different frequency contents and to varied degrees due to their modal participation. Low frequency content shows high versatility in the acceleration measurements. Although, in terms of CI the rest of the content indicate high certainty and low variation along each of the measured signals.

Figure 6 shows the combined statistics over all locations without the logarithmic scale. In this case, major frequency content around 5 Hz shows the most variability.

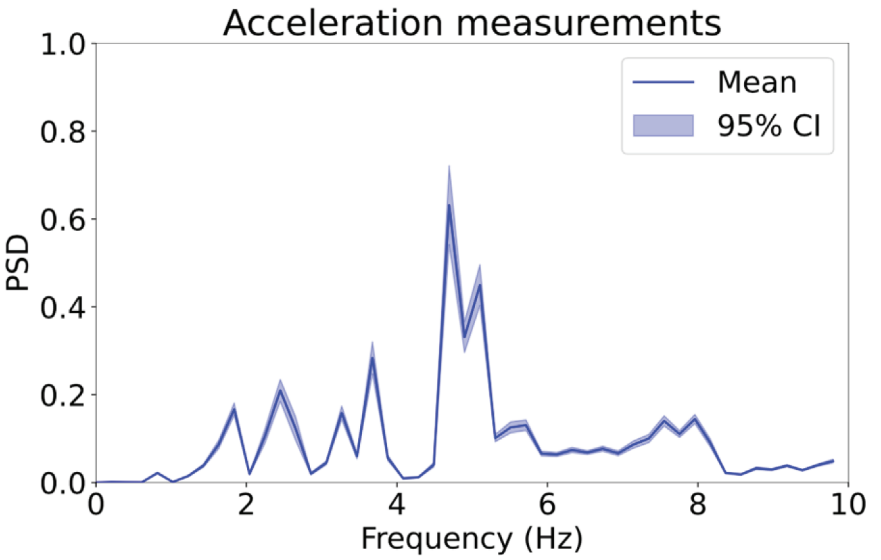


Figure 6. Average PSD of acceleration measurements along with 95% confidence interval.

3.2 *Uncertainty along time of the day*

In this section, the uncertainty along time of the day for acceleration data from one location (U18) is shown along a day of measurement (Oct. 13, 2021). The signal throughout the day is divided into 50 groups with 80% of overlap to find temporal statistics in one day of data collection. Figure 7 shows this variation along the indicator of groups along time within a day. The vertical axis shows the average PSD and the heat map represented via the change of colors shows the standard deviation of the PSD. It can be observed that later in the day of data collection (around 12:00) the peak frequency content is excited more. Simultaneously around these peak hours, the standard deviation indicates to be highest for major frequency contents of between 4 Hz and 6 Hz.

4 PREDICTION QUALITY

Following statistics of the measured signals, the prediction of strain signals are presented in a similar scale as Figure 4. Here the ANN-based framework is used to estimate the strain signals merely based on acceleration inputs. Initially, the average PSD plots for the randomly chosen dataset (similar as before) of predicted signals α and β is shown in Figure 8 along with 95% confidence interval of them. It can be observed that the major frequency contents are predicted with high confidence.

5 COMPARISON OF QUALITIES

To better evaluate and compare the statistics between measurements and predictions, the average PSD of each strain signal type (α and β) is shown in Figure 9. We can observe the measurement

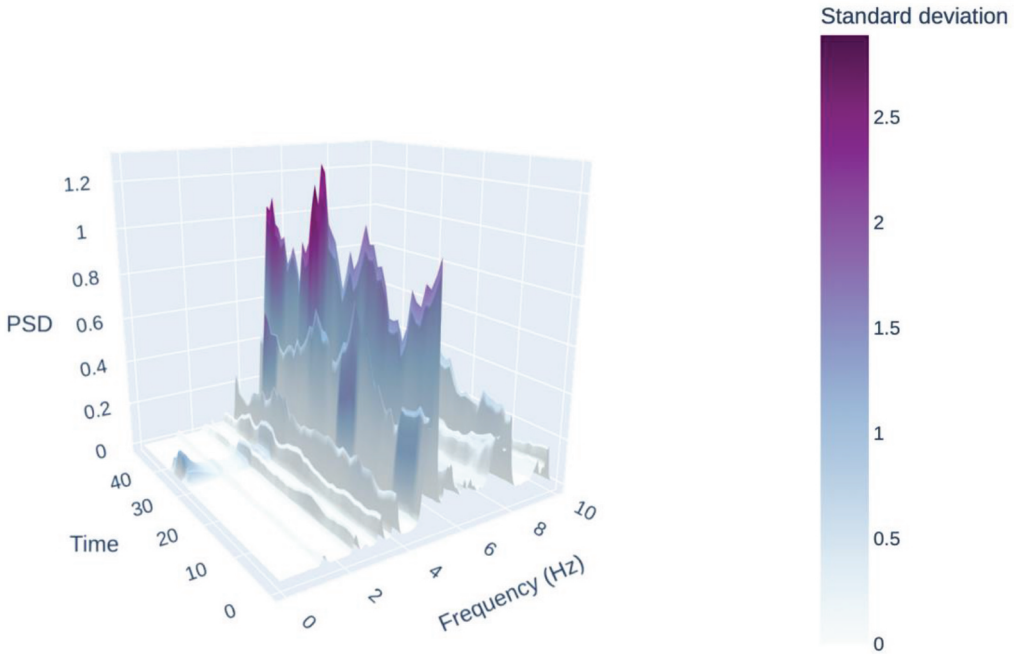


Figure 7. PSD variation along one data collection day for U18.

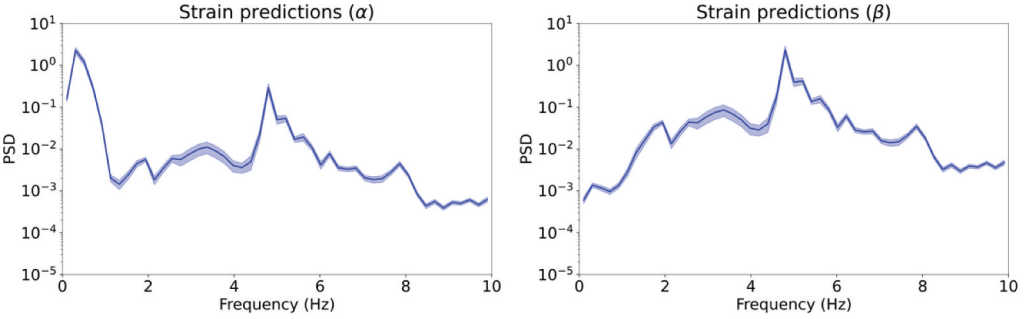


Figure 8. Average PSD (log) of strain predictions along with 95% confidence interval for signals α and β.

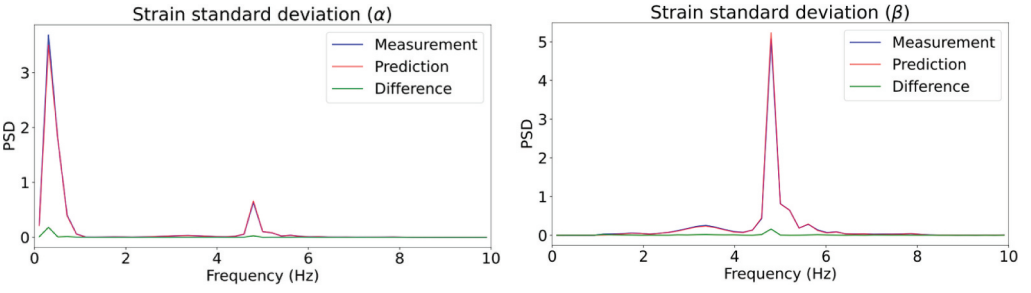


Figure 9. Standard deviation of PSDs of strain measurements vs. predictions. vs. absolute difference for signals α and β.

has a higher standard deviation when compared to the prediction of signal α. However, for signal β the opposite is evident where prediction slightly shows a higher standard deviation than the measured strain signal. Both observations can be expected when evaluating a data-driven methodology. Quality improvement compared to measurement is achieved since multiple locations are measured and provided for a framework for the strain estimation of a single location and the spatially comprehensive information can limit the variability. Therefore, the measurement is on average enhanced through the prediction process when predicting signal α. However, for signal β, the data-driven framework yields less confidence when compared to the measurement.

To spotlight the absolute differences of standard deviations for PSDs of measurement and prediction between signals α and β, Figure 10 is presented. Signal α shows slightly higher standard deviation difference at peak compared to signal β, although, the signal α improves the quality of PSD compared to measurement by the shown difference value. Also, the main structural frequency contents show the considerable difference between measurement and prediction while content at the rest of the frequencies show a higher match.

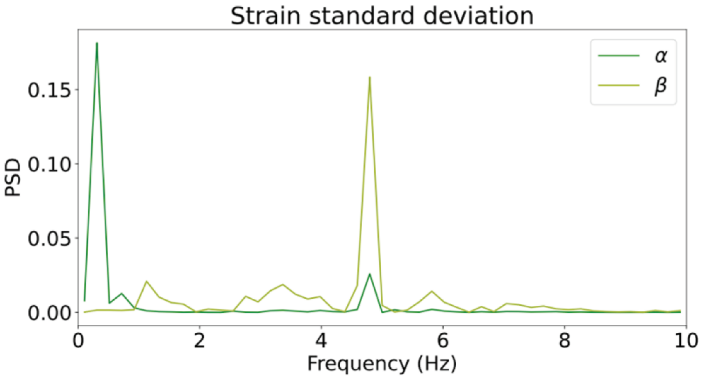


Figure 10. Absolute differences of measurement strain standard deviation and prediction.

Finally, the coefficient of variation for PSDs is compared in Figure 11 for signals α and β. It is evident that the CV shows consistency among measurements and predictions with prediction showing a slightly higher CV in the majority of frequencies. Moreover, the measurement strain signal shows large CV in the case of signal β because of the high pass filter of 1 Hz. The close match between CV of measurement and prediction shows that the ANN-based strain estimation framework does not manipulate or disrupt the signals in the process of signal reconstruction due to its data-driven nature.

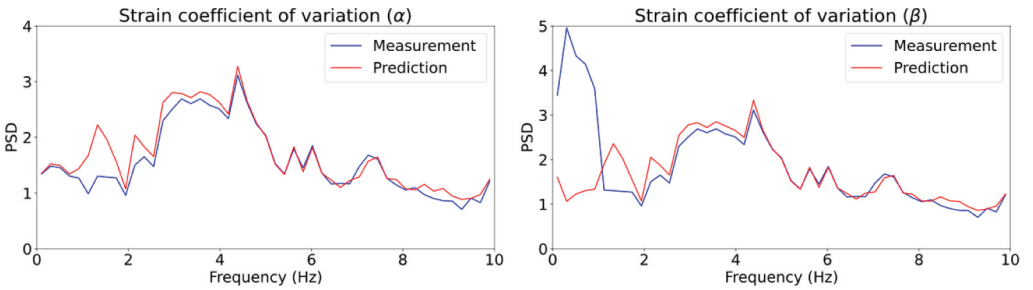


Figure 11. Comparison of PSDs coefficient of variations among strain predictions and measurements for signals α and β.

6 CONCLUSION

This paper conducts a comprehensive examination of the uncertainty inherent in the strain and acceleration data gathered from the Gene Hartzell Memorial Bridge. The primary aim is to assess how this uncertainty is influenced when employing a previously proposed ANN-based strain estimation framework. Initially, an analysis of the measurement data investigates uncertainty across various response locations and considers the time of day when the data was collected. Expanding on this uncertainty assessment, the study delves into the ANN-based strain estimation method and assesses prediction uncertainty measures. A comparative analysis between the uncertainty in strain measurements and the prediction uncertainty highlights that the proposed framework maintains the quality of the measurement data. As a data-driven framework translating acceleration measurements into strain signals, it ensures consistency while introducing no significant additional uncertainty to the strain signals.

REFERENCES

Chattopadhyay, R., Sun, Q., Fan, W., Davidson, I., Panchanathan, S., & Ye, J. (2012). Multisource domain adaptation and its application to early detection of fatigue. *ACM Transactions on Knowledge Discovery from Data (TKDD)*, *6*(4), 1–26.

O'Shea, K., & Nash, R. (2015). An introduction to convolutional neural networks. *arXiv preprint arXiv:1511.08458*.

Sadeghi Eshkevari, S., Sen, D., Sadeghi Eshkevari, S., Dabbaghchian, I. & Pakzad, S. (2024). AI-enabled indirect bridge strain sensing using field acceleration data [Manuscript submitted for publication] *Computers & Structures*.

Vaswani, A., Shazeer, N., Parmar, N., Uszkoreit, J., Jones, L., Gomez, A. N., … & Polosukhin, I. (2017). Attention is all you need. *Advances in neural information processing systems*, 30.

Bridge Maintenance, Safety, Management, Digitalization and Sustainability – Jensen, Frangopol & Schmidt (eds)
© 2024 The Author(s), ISBN 978-1-032-77040-6
Open Access: www.taylorfrancis.com, CC BY-NC-ND 4.0 license

Intelligent automatic operational modal analysis: Application to a suspension bridge

M.M. Rosso & G.C. Marano
DISEG, Dipartimento di Ingegneria Strutturale, Edile e Geotecnica Politecnico di Torino, Turin, Italy

A. Aloisio
Department of Civil, Construction-Architectural and Environmental Engineering, Universit'a degli Studi dell'Aquila, L'Aquila, Italy

G. Quaranta
Department of Structural and Geotechnical Engineering, Sapienza University of Rome, Rome, Italy

ABSTRACT: A new paradigm for the automatic output-only modal identification of linear structures under ambient vibrations is presented, namely the intelligent automatic operational modal analysis (i-AOMA). It exploits the covariance-based stochastic subspace (SSI-cov) algorithm for the output-only identification of the modal parameters and its workflow consists of two main phases. Initially, quasi-random samples of the control parameters for the SSI-cov algorithm are generated. Once the SSI-cov algorithm is performed for each sample, the corresponding stabilization diagrams are processed in order to prepare a database for training the intelligent core of the i-AOMA method. This is a machine learning (ML) technique (namely a random forest algorithm) that predicts which combination of the control parameters for the SSI-cov algorithm is able to provide good modal estimates. Afterward, new quasi-random samples of the control parameters for the SSI-cov algorithm are generated repeatedly until a statistical convergence criterion is achieved. If the generic sample is classified as feasible by the intelligent core of the i-AOMA method, then the SSI-cov algorithm is performed. Hence, stable modal results are distilled from the stabilization diagrams and relevant statistics are also computed to evaluate the uncertainty level due to the variability of the control parameters. The proposed i-AOMA method is finally applied to estimate the modal features of a suspension bridge structure, the Hardanger Bridge in Norway, to demonstrate the feasibility of the proposed methodology.

1 INTRODUCTION

Aging infrastructure heritage is currently nearing the end of its intended lifespan, resulting in safety concerns (Aloisio, Pasca, Di Battista, Rosso, Cucuzza, Marano, & Alaggio 2022). Accordingly, research was focused on advancing structural health monitoring (SHM) methodologies (Farrar &Worden 2012, Marasco, Rosso, Aiello, Aloisio, Cirrincione, Chiaia, & Marano 2022). These endeavors aim to offer more effective and reliable tools for real-time structural health assessment. Indirect and non-destructive methods were particularly studied to leverage their advantages of less invasivity, rapidity, and efficiency. One widely embraced technique involves employing output-only vibration-based dynamic identification strategies denoting the operational modal analysis (OMA) field of study. These strategies delve into the dynamic modal properties of structures under operational and ambient vibration conditions, revealing crucial information, viz. mode shapes, natural frequencies, and damping ratios. In OMA, the stochastic subspace identification (SSI) method is a popular time-domain parametric strategy based on state-space identification, being the SSI-cov and SSI-data its main variants (Aloisio, Pasca, Di Battista, Rosso, Cucuzza, Marano, & Alaggio 2022, Pasca, Aloisio,

DOI: 10.1201/9781003483755-402

Rosso, & Sotiropoulos 2022, Rainieri & Fabbrocino 2014b, Reynders, Houbrechts, & De Roeck 2012). The bulk of current research efforts in SHM is directed toward developing automatic operational modal analysis (AOMA) methods, especially tailored for long-term dynamic monitoring procedures (Alaggio, Aloisio, Antonacci, & Cirella 2021). Typically, a standard workflow involving four primary steps is implemented in the scientific literature (Reynders, Houbrechts, & De Roeck 2012, Ubertini, Gentile, & Materazzi 2013). These steps encompass an initial phase of selecting SSI control input parameters, followed by computation and analysis of stabilization diagrams to identify stable poles and their modal parameters. Subsequent stability checks are performed, laying the groundwork for identifying stable poles' alignments along the order axis. Present approaches in the literature emphasize automation and innovative machine learning techniques, particularly clustering methods, for post-processing stabilization diagrams and collecting stable poles' alignments. In the current literature approaches, the automation and innovative machine learning-based (ML) part is mainly based on clustering techniques for post-processing stabilization diagrams and automatically collecting stable poles' alignments.

The selection of SSI control parameters during the initial phase is critical, as an improper choice may compromise the entire identification process of the modal properties. Despite numerous studies provide insights and suggestions for a proper SSI input parameters tuning (Rainieri & Fabbrocino 2014a, Zini, Betti, & Bartoli 2022), a fully and solid automated procedure for selecting SSI parameters has not been proposed to date. Therefore, this work illustrates a recent proposal able to fullfill the need of automatic dynamic identification, namely the intelligent Automatic Operational Modal Analysis (i-AOMA). This method aims to automate the selection of SSI-cov input parameters.

The present contribution is organized as follows. In the next section, the overall procedure of i-AOMA is illustrated. Afterward, the current bridge case study benchmark, i.e. the Hardanger bridge is described. This case study allows to highlight advantages and potentialities of the proposed i-AOMA.

2 INTELLIGENT AOMA

In the conventional stabilization diagram, the SSI-cov algorithm might inadvertently identify spurious modes with no relation to the actual structural modes of interest. This issue arises due to the inherent characteristics of the SSI algorithm, stemming from the unknown of the actual degrees of freedom (DOFs) in real-world structures. A conservative approach involves the overestimation of the structural system order, despite this often leading to the rise of non-physical poles alongside the real ones (Rainieri & Fabbrocino 2014b). Furthermore, a poor selection of SSI governing parameters can exacerbate meaningless results. Recently, (Zhou, Li, & Han 2022, Zhou & Li 2022) endeavored to enhance SSI's accuracy in identifying true structural modal parameters. They introduced a Monte Carlo-based approach defining the stabilization diagram by varying two input parameters: the length of signals within a shorter time window and the maximum model order. Their work demonstrated that executing numerous Monte Carlo simulations of these parameters and subsequent SSI-cov analyses led to occasional detection of spurious modal alignments, while consistently identifying the actual structural modes in virtually all the recurring analyses. However, their method has limitations. Firstly, it suggests an arbitrary number of Monte Carlo simulations equal to 100, without a clear convergence criterion. Secondly, it still requires users to arbitrarily define the time shift, impacting the reliability of the proposed AOMA framework and limiting its automation. Moreover, despite a Monte-Carlo-based approach no uncertainty evaluation was carried on.

Therefore, this study aims to address these issues by illustrating a recently developed intelligent-driven automatic OMA named intelligent-AOMA (i-AOMA) that meets the core requirements of contemporary AOMA approaches, without relying on prevalent ML-based clustering techniques. Inspired by the initial studies of (Zhou, Li, & Han 2022, Zhou & Li 2022), the proposed intelligent-AOMA increases the automation degree by incorporating the time shift parameter into the Monte Carlo sampling, eliminating the need for meticulous user intervention. The proposed methodology consists of two main steps. Phase 1 (Figure 1 left), involves quasi-

Monte Carlo sampling (Owen 2017) of four key SSI-cov control parameters: time shift (number of block rows of the Hankel matrix), time window length, time target, and maximum model order (Rainieri & Fabbrocino 2014b). This initial exploration stage necessitates users to broadly define the permissible range of input parameters. The number of exploratory Monte Carlo simulations influences the subsequent ML-based phase 2; here, the authors adopt 100 simulations based on prior recommendations (Zhou & Li 2022). However, unfeasible parameter sets, due to incorrect combinations or excessive computational time, are automatically excluded to optimize computational resources. Stability check criteria retain only stable poles among the generated stabilization diagrams. Post-processing involves overlapping diagrams to identify recurrent stable pole alignments, achieved without traditional clustering algorithms but via kernel density estimation (KDE) (Gramacki 2018). This method discerns poles around sharp peaks associated with physically stable alignments within a retaining frequency band, enabling selection based on an automatic statistics-based criterion.

The second step (Figure 1 right) relies on a ML-based approach, specifically a random forest (RF) algorithm (Raschka & Mirjalili 2019, G´eron 2022), to intelligently guide quasi-Monte Carlo sampling toward the most promising parameter sets. RF training utilizes results from the previous exploratory step, assigning an information content (IC) parameter to each simulation. Due to its ensemble nature, the RF is one of the simplest and yet powerful ML tools not requiring a sophisticated tuning procedure of its hyperparameters. The IC reflects the ratio of poles falling within the KDE-based frequency bands to total stable poles computed in every simulation, aiding in excluding parameter sets likely to yield insignificant results. Convergence analysis of mode shapes occurs at intervals of 50 actually computed simulations, ensuring stability according to a defined variation range according to the acceptable shifting convergence band rule (ASCBR) (Ata 2007). According to the generalized sample variance matrix, (Ziegel 2003) of the mode shapes associated with the found natural frequency recurrent physical modes, the convergence criteria was set to a relative variation of the trace of the generalized sample variance matrix within ±0.02 for 50 iterations (Ata 2007). Post-convergence procedures mirror those at the end of the exploratory step, viz. overlapping all the stabilization diagrams and extracting recurrent modes with a KDE criterion, and finally analyzing confidence bands for uncertainty evaluation in modal parameters.

Further details about the i-AOMA are presented in (Rosso, Aloisio, Parol, Marano, & Quaranta 2023).

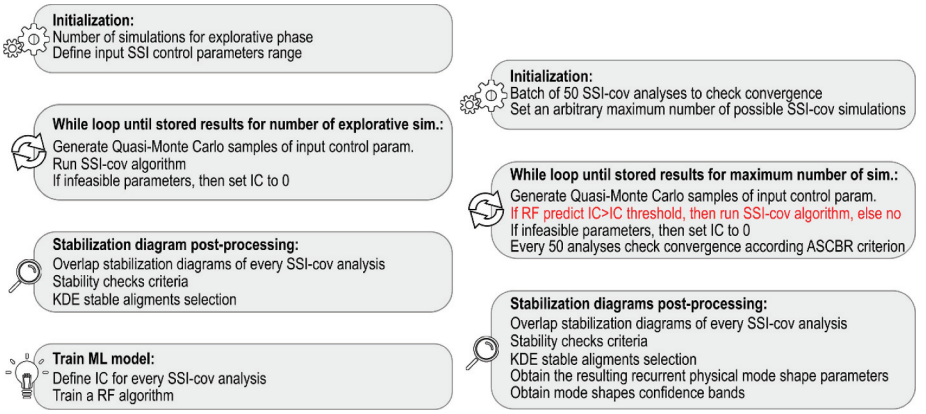


Figure 1. Flowchart of first step of intelligent AOMA (left) and second step of intelligent AOMA (right).

3 CASE STUDY: HARDANGER BRIDGE IN NORWAY

The case study analyzed in the present paper is the Hardanger Bridge (Petersen, Øiseth, & Lourens 2019, Fenerci, Andreas Kv˚ale,Wiig Petersen, Rønnquist, & Øiseth 2021), located in the Hardangerfjord on the west coast of Norway, a geographical and topographical complex region

with steep mountains and wide fjord, see Figure 2. This suspension bridge is 1308 m long, composed of a slender steel box deck of 3.2 m high and 18.3 m wide, hosting two traffic and one bicycle lanes, supported by 2 main cables with 130 hangers and two extreme pylons up to 200 m high. Since 2013, the bridge has been equipped with a continuous long-term monitoring system implemented by the Norwegian University of Science and Technology (NTNU), composed of 20 triaxial accelerometers with a sampling rate of 200 Hz (see Figure 3) placed on the deck and pylons, together with 9 sonic anemometers. The local geographical context involves strong wind loads whose effects make the dynamic identification process challenging (Petersen, Øiseth, & Lourens 2019, Petersen, Øiseth, & Lourens 2020). Both raw and organized long-term wind and acceleration data for SHM purposes have been published in an open-access repository (Fenerci, Andreas Kv˚ale, Wiig Petersen, Rønnquist, & Øiseth 2021).



Figure 2. Geographical localization of the case study, and photo of the Hardanger Bridge by Sami Haidar (CC BY-NC 2.0).

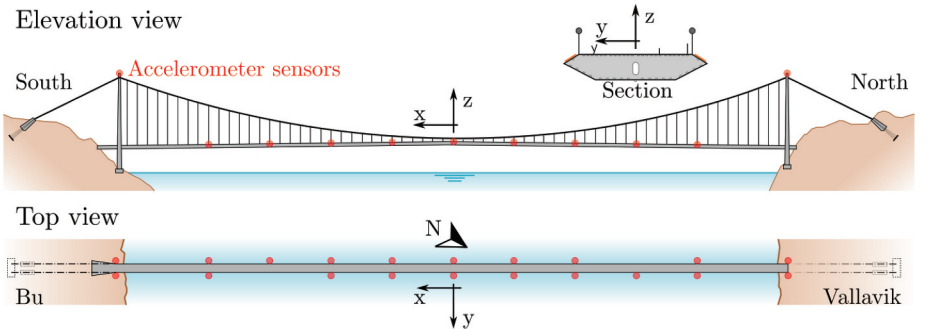


Figure 3. Accelerometer sensors layout on the Hardanger Bridge.

4 AUTOMATIC IDENTIFICATION OF THE HARDANGER BRIDGE

The case study represents a compelling experimental benchmark for the i-AOMA method, both for structural and environmental reasons. Furthermore, as reported in the literature, the first eleven modes are closely spaced within a very low frequency range (below 0.4 Hz) (Petersen, Øiseth, & Lourens 2020, Petersen, Øiseth, Nord, & Lourens 2019, Fenerci & Øiseth 2017). Among the available data (Fenerci, Andreas Kv˚ale, Wiig Petersen, Rønnquist, & Øiseth 2021), the recordings processed for the present application last 31 min and the sampling frequency is equal to 200 Hz. The data refer to under the environmental conditions of sustained wind and were collected on the 12th November 2015 at 23:54:31 (local time) with a recorded wind speed of 14.02±2.28m/s. The data have been decimated with a factor of 20, in such a way to focus on the range 0-5 Hz range (Nyquist frequency). To speed up the identification process, the maximum order of the stabilization diagram within the i-AOMA procedure was imposed to 360 and the maximum block rows number was limited to 100.

The order of magnitude of the recorded accelerations can be retrieved by Figure 4 where the first ten singular values of the power spectral density (PSD) are also reported. Figure 4 confirms that the current data activates several modes within the 1 Hz range. A total of 100 MC simulations has been set for the i-AOMA phase 1 to construct the training set for the subsequent RF intelligently driven sampling scheme. Thereafter, additional 1,150 useful results have been collected in phase 2 reaching the convergence of the trace covariance of 25 modes found within the inspected frequency range. The overlapped stabilization diagrams are reported in Figure 5, whereas the normalized KDE and the relative clusters are reported in Figure 6. Only the first 11 modes falling below 0.4 Hz are examined hereafter.

A limited number of results is available in the existing literature for the considered case study. For instance, in (Øiseth, R¨onnquist, Kv˚ale, & Sigbj¨ornsson 2015) only 4 modes have been identified under a mean wind speed velocity of 16 m/s, whereas only 9 modes have been found (Fenerci & Øiseth 2017). Nonetheless, an outstanding agreement has been underlined between the identified natural frequencies with the i-AOMA method compared with (Petersen, Øiseth, & Lourens 2019, Petersen, Øiseth, Nord, & Lourens 2019, Petersen, Øiseth, & Lourens 2020) as reported in Table 1. Herein, the modes naming convention follows the dominant motion of each mode, i.e. H stands for horizontal, V means vertical and T denotes torsional mode shapes. It is worth noting that in terms of the relative difference between the natural frequencies values, the i-AOMA method provided values in excellent agreement with the existing OMA results and even with calibrated finite element models (FEM) modal analysis.

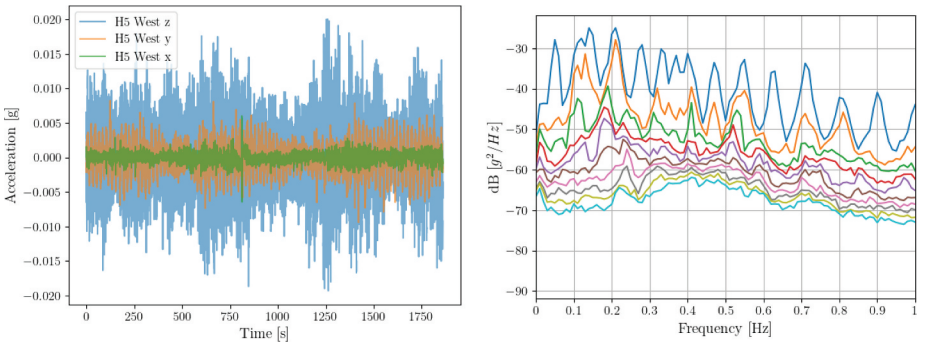


Figure 4. Monitored signals from the accelerometers in the midspan, and the first 10 singual values from the PSD.

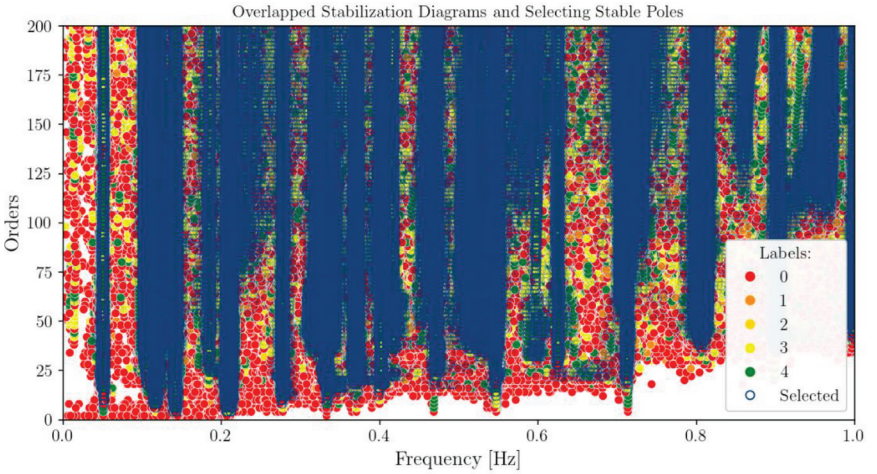


Figure 5. Overlapped stabilization diagram at the end of i-AOMA phase 2.

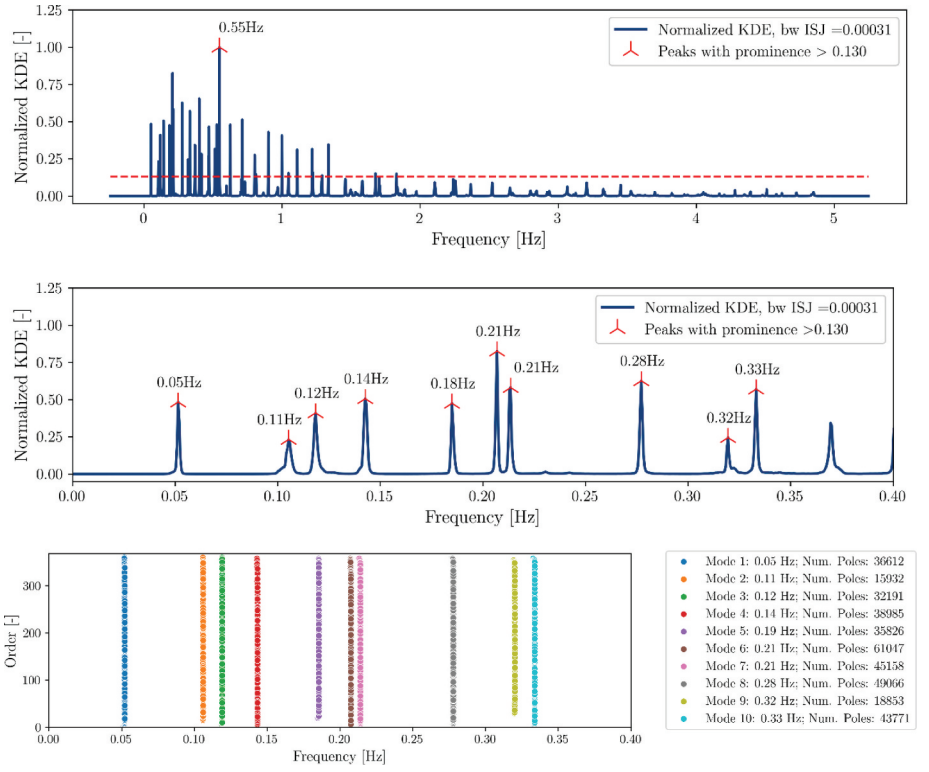


Figure 6. Normalized KDE automatic mode clusters extraction.

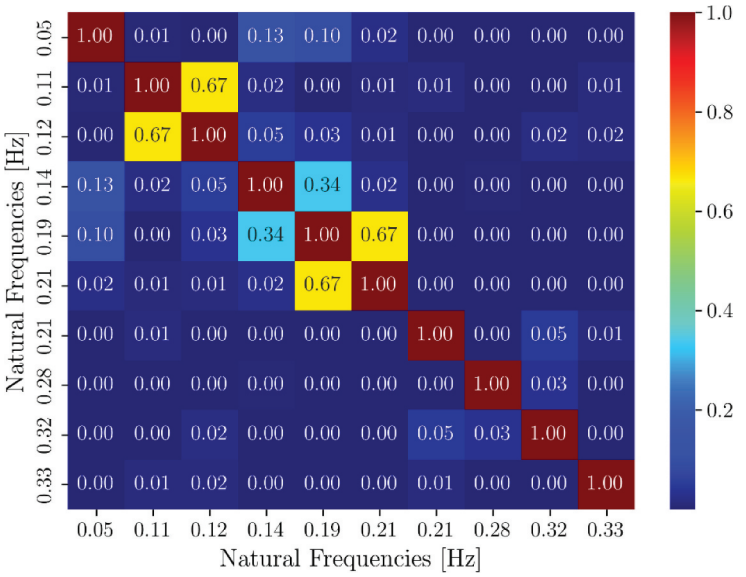


Figure 7. MAC among the identified modes.

However, comparing the damping ratios between i-AOMA and FEM literature solutions, the resulting values appear generally overestimated by the i-AOMA. From this comparison, it seems that the i-AOMA procedure was successfully able to identify all the actual first eleven modes. However, the mode shape interpretation should be deeply inspected since the modal

Table 1. Comparison of the Hardanger Bridge i-AOMA modal outcomes with literature results.

	i-AOMA				(Petersen, Øiseth, & Lourens 2020)					
Mode	f [Hz]		ξ [%]		f [Hz]	f [Hz]	ξ [%]	Mode	$\Delta f_{rel,iAOMA-OMA}$	$\Delta \xi_{abs,iAOMA-FEM}$
No.	Mean	Std.Dev.	Mean	Std.Dev.	OMA	FEM	FEM	Naming	[%]	[-]
1	0.052	0.0004	2.176	1.0790	0.052	0.051	0.65	**H1**	-0.65	2.35
2	0.105	0.0006	1.232	1.1343	0.105	0.105	0.77	**H2**	0.33	0.60
3	0.118	0.0005	4.344	1.1204	0.119	0.112	1.77	**V1**	-0.43	1.45
4	0.143	0.0006	2.073	0.4701	0.142	0.142	0.65	**V2**	0.56	2.19
5	0.185	0.0005	0.813	0.7377	0.183	0.185	0.77	**H3**	1.23	0.06
6	0.207	0.0004	1.102	0.4672	0.206	0.203	0.27	**V3**	0.38	3.08
7	0.213	0.0004	1.451	0.4143	0.212	0.212	0.35	**V4**	0.58	3.14
8	0.277	0.0005	1.234	0.3543	0.276	0.276	0.26	**V5**	0.39	3.75
9	0.319	0.0004	0.774	0.8412	0.318	0.318	0.63	**H4**	0.47	0.23
10	0.333	0.0005	0.842	0.7204	0.333	0.332	0.25	**V6**	0.03	2.37
11	0.370	0.0005	0.728	0.5119	0.374	0.371	0.41	**T1**	-1.09	0.78

assurance criterion illustrated in Figure7 computed for the i-AOMA identified modes evidenced quite strong correlations between 0.11 and 0.12 Hz modes, and between 0.19 and 0.21 Hz ones.

5 CONCLUSIONS

In the current study, the potentialities of the recently developed intelligent Automatic Operational Modal Analysis (i-AOMA) method have been illustrated. The i-AOMA algorithm represents one of the steps ahead in continuous monitoring by increasing the automation level of OMA procedures. Furthermore, the adoption of machine-learning-based random forest algorithm did not require careful tuning of hyperparameters due to its ensemble robust nature. Specifically, the proposed framework was applied to a challenging bridge case study, the slender suspended Hardanger bridge located in Norway in a fjord area. This case study represents a widely studied and quite well-validated benchmark in the existing literature because of the availability of long-term wind and acceleration data collected from the Norwegian University of Science and Technology (NTNU) since 2013 and published on an open-source repository. After selecting recorded data under sustained wind speed environmental conditions, the i-AOMA procedure was outstandingly able to identify the first eleven very closely spaced modes presenting very low frequencies (below 1 Hz). Future developments should better investigate the median mode shapes and relative uncertainties since the modal assurance criterion evidenced a relatively high degree of correlation between the 2nd and 3rd modes and between the 4th and 5th ones.

ACKNOWLEDGMENTS

Giuseppe Carlo Marano and Marco Martino Rosso acknowledge the support from PNRR MUR project PE0000013-FAIR (National Recovery and Resilience Plan – NRRP, Mission 4, Component 2, Investment 1.3, NextGenerationEU – D.D. 341 15/3/2022 and D.D. 1555 11/10/2022, PE0000013).

REFERENCES

Alaggio, R., A. Aloisio, E. Antonacci, & R. Cirella (2021). Two-years static and dynamic monitoring of the santa maria di collemaggio basilica. Construction and Building Materials 268, 121069.

Aloisio, A., D. P. Pasca, L. Di Battista, M. M. Rosso, R. Cucuzza, G. C. Marano, & R. Alaggio (2022). Indirect assessment of concrete resistance from fe model updating and young's modulus estimation of

a multi-span psc viaduct: Experimental tests and validation. In Structures, Volume 37, pp. 686–697. Elsevier.
Ata, M. Y. (2007). A convergence criterion for the monte carlo estimates. Simulation Modelling Practice and Theory 15(3), 237–246.
Farrar, C. R. & K. Worden (2012). Structural health monitoring: a machine learning perspective. John Wiley & Sons.
Fenerci, A., K. Andreas Kv˚ale, Ø. Wiig Petersen, A. Rønnquist, & O. Øiseth, (2021). Data set from long-term wind and acceleration monitoring of the hardanger bridge. Journal of Structural Engineering 147(5), 04721003.
Fenerci, A. & O. Øiseth (2017). The hardanger bridge monitoring project: Long-term monitoring results and implications on bridge design. Procedia engineering 199, 3115–3120.
G´eron, A. (2022). Hands-on machine learning with Scikit-Learn, Keras, and TensorFlow. " O'Reilly Media, Inc.".
Gramacki, A. (2018). Nonparametric kernel density estimation and its computational aspects, Volume 37. Springer.
Marasco, G., M. M. Rosso, S. Aiello, A. Aloisio, G. Cirrincione, B. Chiaia, & G. C. Marano (2022). Ground penetrating radar fourier pre-processing for deep learning tunnel defects' automated classification. In International Conference on Engineering Applications of Neural Networks, pp. 165–176. Springer.
Øiseth, O., A. R¨onnquist, K. A. Kv˚ale, & R. Sigbj¨ornsson, (2015). Monitoring wind velocities and dynamic response of the hardanger bridge. In Dynamics of Civil Structures, Volume 2: Proceedings of the 33rd IMAC, A Conference and Exposition on Structural Dynamics, 2015, pp. 117–125. Springer.
Owen, A. B. (2017). A randomized halton algorithm in r. arXiv preprint arXiv:1706.02808.
Pasca, D. P., A. Aloisio, M. M. Rosso, & S. Sotiropoulos (2022). Pyoma and pyoma gui: A python module and software for operational modal analysis. SoftwareX 20, 101216.
Petersen, Ø. W., O. Øiseth, & E. Lourens (2020). Investigation of dynamic wind loads on a long-span suspension bridge identified from measured acceleration data. Journal of Wind Engineering and Industrial Aerodynamics 196, 104045.
Petersen, Ø. W., O. Øiseth, & E.-M. Lourens (2019). The use of inverse methods for response estimation of long-span suspension bridges with uncertain wind loading conditions: Practical implementation and results for the hardanger bridge. Journal of civil structural health monitoring 9, 21–36.
Petersen, Ø. W., O. Øiseth, T. S. Nord, & E. Lourens (2019). Inverse identification of buffeting and self-excited wind loads on the hardanger bridge from acceleration data. In COMPDYN 2019: 7th ECCOMAS Thematic Conference on Computational Methods in Structural Dynamics and Earthquake Engineering, Volume 3.
Rainieri, C. & G. Fabbrocino (2014a). Influence of model order and number of block rows on accuracy and precision of modal parameter estimates in stochastic subspace identification. International Journal of Lifecycle Performance Engineering 1(4), 317–334.
Rainieri, C. & G. Fabbrocino (2014b). Operational modal analysis of civil engineering structures. Springer, New York 142, 143.
Raschka, S. & V. Mirjalili (2019). Python machine learning: Machine learning and deep learning with Python, scikitlearn, and TensorFlow 2. Packt Publishing Ltd.
Reynders, E., J. Houbrechts, & G. De Roeck (2012). Fully automated (operational) modal analysis. Mechanical Systems and Signal Processing 29, 228–250.
Rosso, M. M., A. Aloisio, J. Parol, G. C. Marano, & G. Quaranta (2023). Intelligent automatic operational modal analysis. Mechanical Systems and Signal Processing 201, 110669.
Ubertini, F., C. Gentile, & A. Materazzi (2013). Automated modal identification in operational conditions and its application to bridges. Engineering Structures 46, 264–278.
Zhou, K. & Q.-S. Li (2022). Modal identification of high-rise buildings under earthquake excitations via an improved subspace methodology. Journal of Building Engineering 52, 104373.
Zhou, K., Q.-S. Li, & X.-L. Han (2022). Modal identification of civil structures via stochastic subspace algorithm with monte carlo–based stabilization diagram. Journal of Structural Engineering 148(6), 04022066.
Ziegel, E. R. (2003). Methods of multivariate analysis. Technometrics 45(1), 109.
Zini, G., M. Betti, & G. Bartoli (2022). A quality-based automated procedure for operational modal analysis. Mechanical Systems and Signal Processing 164, 108173.

Bridge Maintenance, Safety, Management, Digitalization and Sustainability – Jensen, Frangopol & Schmidt (eds)
© 2024 The Author(s), ISBN 978-1-032-77040-6
Open Access: www.taylorfrancis.com, CC BY-NC-ND 4.0 license

Managing aging bridges under seismic hazards through deep reinforcement learning

Z. Metwally & C.P. Andriotis
Faculty of Architecture and the Build Environment, Delft University of Technology, Delft, The Netherlands

F. Molaioni
Department of Civil Engineering and Computer Science Engineering, University of Rome Tor Vergata, Rome, Italy

ABSTRACT: Structural systems must satisfy multiple performance and functionality requirements during their life cycle, withstanding safety-reducing degradation mechanisms and hazards. Intervention strategies must be planned accordingly to maintain structural integrity and minimize total life-cycle costs and risks, posing a complex optimization problem. Recent advances in multi-agent deep reinforcement learning (DRL) in conjunction with partially observable Markov Decision Processes (POMDPs) have shown great potential for determining optimal structural integrity management policies for systems with large state and action spaces compared to traditional decision practices. This paper tackles the maintenance optimization problem of aging bridges in seismic-prone areas, creating an updatable environment that embeds chloride-induced corrosion and state-dependent seismic fragility throughout the bridge life-cycle. The evolution of the environment is captured by a dynamic Bayesian network, and it is further integrated with decentralized multi-agent DRL algorithms to identify near-optimal life-cycle decisions under risk constraints. Results on a multi-component bridge system show the suitability of the developed framework for minimizing expected life-cycle costs, and for providing detailed and adaptive policies that significantly outperform traditional condition- and time-based maintenance plans.

1 INTRODUCTION

Structural degradation of bridges, induced by time-dependent stressors and natural hazards, is a major threat to long-term structural safety. Controlling it becomes more and more crucial in the expanding and complexifying landscape of infrastructure networks. Many highway bridges worldwide have been constructed with outdated design principles, and are experiencing structural weakening due to aging and deterioration (Shekhar & Ghosh 2021). Late reports show, for instance, that almost half of the US bridges are more than 50 years old, with 35% requiring maintenance interventions of circa $125B. This raises the risk of disruptive transportation network closures, mobility restrictions, and potential failures (ASCE 2021). These figures highlight a broader challenge facing many countries: a growing stock of aging infrastructure that are reaching or have well exceeded their design life.

Among different deterioration mechanisms, corrosion, which is typically initiated by the penetration of aggressive substances (e.g., chlorides), is a threat that can compromise the ability of structural systems to withstand the design loads, resulting in a decreased structural reliability and, hence, increased vulnerability to natural hazards (Choe et al.

DOI: 10.1201/9781003483755-403

2008). Specifically, corrosion of reinforcement bars, which is typically associated with reinforcement mass loss, spalling of the concrete cover, and bond slippage, is shown to affect the strength and ductility of bridge components such as RC columns, bridge piers, and bearings (Rinaldi et al. 2022). The phenomenon manifests itself through uniform area reduction along the rebar length, as well as nonuniform spatially distributed local pits or cavities (Bertolini et al. 2004).

It is well understood that the severity of seismic consequences on RC bridges is magnified due to corrosion. Therefore, recent studies have developed formulations to quantify seismic fragility under corrosion. A common assumption is to consider uniform corrosion, therefore, uniform cross-sectional area losses (Alipour et al. 2011; Rao et al. 2017; Deng et al. 2018). Yet in more recent studies, it is shown that pitting corrosion can be more critical compared to uniform corrosion, especially in RC bridge columns, as it can reduce the lateral load capacity due to localized weakening (Shekhar & Ghosh 2021). Accounting for both effects, Molaioni et al. 2023 proposed a DBN approach to continuously track the seismic fragility of reinforced concrete bridges throughout the life-cycle. Bridges are treated as multi-component systems that include columns and different types of bearings. The aging of bridges is rigorously incorporated in the approach, considering mass loss due to pitting corrosion and associated secondary effects of strength reduction, cracking, and loss of confinement, in addition to deterioration of steel bearings and corresponding modified cyclic behavior. Overall, literature suggests that modeling aging bridges as heterogeneous multi-component systems, and considering uniform and pitting corrosion alike for concrete members, in addition to reduction of strength and ductility of rebars, loss of concrete cover, and deterioration of steel fixed and expansion bearings, can significantly enhance our predictive capabilities. The next question to be addressed is how we can harness such predictive models to synthesize precise optimal life-cycle maintenance and retrofit plans given the complexity and uncertainties of the involved systems and phenomena.

Over the past years, there has been increasing attention to the development of life-cycle decision optimization methodologies for infrastructure management, aimed at meeting this challenge in the most eco-socio-economically aware ways (Arunraj & Maiti 2007; Bucher & Frangopol 2006). Conventional approaches for determining maintenance policies for structural systems build largely upon heuristic decision rules, which are based on engineering judgment about intervals or thresholds for interventions and observations. Such plans can be optimized either through exhaustive search or genetic algorithms. Another family of advanced optimization formulations sets up the problem as a Partially Observable Markov Decision Process (POMDP), solving the sequential decision-making task in a closed-loop fashion by incorporating observations and uncertainties of the underlying environment (Papakonstantinou & Shinozuka, 2014). Solutions can be traced effectively through value-based iteration methods in low- to medium-sized systems (Papakonstantinou & Shinozuka, 2014; Papakonstantinou et al., 2018), or through Deep Reinforcement Learning (DRL) in large-scale ones (Andriotis & Papakonstantinou 2019, 2021).

Embracing these advances, we articulate the seismic management problem of aging bridges as a POMDP and solve it through Deep Decentralized Multi-agent Actor Critic (DDMAC) DRL architectures (Andriotis & Papakonstantinou, 2021). DDMAC allows us to deal with the curse of dimensionality, namely the exponential explosion of state and action spaces with an increasing number of components. The actors assimilate centralized system information and produce a decentralized policy for each component, guided by a single critic network which is a surrogate of the life-cycle cost. Thereby, DDMAC allows actor outputs to scale linearly with components, while exploiting system-level information. Constraints are also incorporated either through state augmentation or a primal-dual optimization approach. A sparser version of DDMAC relying on local component information and centralized training with decentralized execution is introduced in (Saifullah et al. 2024). The temporal behavior of the structural system and its stressors are described by a Dynamic Bayesian Network (DBN), as developed by (Molaioni et al. 2023). This allows uncertainty propagation, state updating due to

observations, and coupling with DRL in a principled manner (Morato et al. 2023). The environment states are defined as probabilistic distributions, i.e., beliefs, rather than deterministic scalars.

Overall, this paper introduces a framework that integrates chloride-induced deterioration of components, state-dependent seismic fragility, probabilistic hazard analysis, maintenance actions, associated costs, and structural risk with DRL to optimize life-cycle intervention policies. Exemplifying the approach in a case study of pre-70's bridges, structures are idealized as multi-component systems that include columns, high-type expansion bearings, high-type fixed bearings, and low-type fixed bearings. The aging of bridges is rigorously incorporated considering mass loss due to uniform and pitting corrosion, and associated secondary effects (Molaioni et al. 2023). Our approach results in substantial improvement in minimizing the life-cycle costs compared to traditional maintenance policies, offering detailed and dynamic maintenance plans at the component level, which are, however, risk-compliant and near-optimal at the system-level.

2 SEQUENTIAL DECISION-MAKING

The sequential decision-making problem is formulated as a Partially Observable Markov Decision Process (POMDP). Transfer between states is defined by a transition probability model, which is the probability of moving to a new state, s_{t+1}, in the coming time step, given the current state, s_t, when taking action a_t, i.e., $\Pr(s_{t+1} \mid s_t, a_t)$. Based on s_{t+1}, s_t, and the imposed action a_t, a cost c_t is received, which is a measure of the desirability of the environment state and imposed action. The environment is perceived through noisy observations, o_t, conditional on the actual hidden state, s_t, and the imposed action a_{t-1}, according to an observation model which defines the probability of observing o_t given s_t and a_t, i.e., $\Pr(o_t \mid s_t, a_{t-1})$. Leveraging the transition and observation models, sufficient statistics that encode all the previous observation and action history, i.e., beliefs, can be formed which can be forwarded to the agent. The agent is tasked with learning the best mapping between belief b_t and potential actions, i.e., a policy $\pi=\Pr(a_t \mid b_t)$.

Throughout training, π is constantly updated to determine an optimal policy π^* within a region of feasible policies Π_c, defined by the set of stochastic and deterministic constraints of the optimization problem (Andriotis and Papakonstantinou, 2021):

$$\pi^* = \underset{\pi \in \Pi_c}{\arg\min}\, \mathbb{E}\left(\sum_{t=0}^{T} \gamma^t c_t \mid a_t \sim \pi(o_{0:t}, a_{0:t-1}), b_0 \right) \tag{1}$$

where γ is a positive discount factor lower than 1.0 translating future costs to the current value.

The optimized policy π^* can be written in terms of the initial belief b_0, which is updatable after each decision step in a Bayesian manner in the POMDP framework, as follows:

$$\pi^* = \underset{\pi \in \Pi_c}{\arg\min}\, V^{\pi}(b_0) \tag{2}$$

where V^{π} is the value function, which is a surrogate of the expected cumulative costs throughout the life-cycle until termination, $t=T$.

Here, the actor and critic neural networks parameterize the policy and value functions, respectively, following an off-policy approach, as follows:

$$g_{\theta}{}^{i} = \mathbb{E}\left[w_t \nabla_{\theta}{}^{i} \log \pi^{i}\left(a_t^i \mid b_t; \theta^i\right) A^{\pi}(b_t, a_t) \right] \tag{3}$$

$$g_{\varphi} = \mathbb{E}\left[w_t \nabla_{\varphi} V^{\pi}(b_t) A^{\pi}(b_t, a_t) \right] \tag{4}$$

where i is the index of the i^{th} actor; θ^i is the actor neural network weights vector; φ is the critic neural network weights vector;, w_t is an importance sampling weight; and A^π is the advantage function. The advantage function used takes the form:

$$A^\pi(b_t, a_t) = c(b_t, a_t) + \gamma V^\pi(b_{t+1}; \varphi) - V^\pi(b_t; \varphi) \tag{5}$$

3 STATE-DEPENDENT SEISMIC FRAGILITY

To quantify the seismic risk, we need to integrate the probability of exceedance of specific damage states due to distinct seismic intensity measures, over the range of these intensity measures, based on the bridge site characteristics:

$$PA_s(t) = \int \Pr[SDS(t) > s_s | IM_t = x] \left| \frac{dH(x)}{dx} \right| dx \tag{6}$$

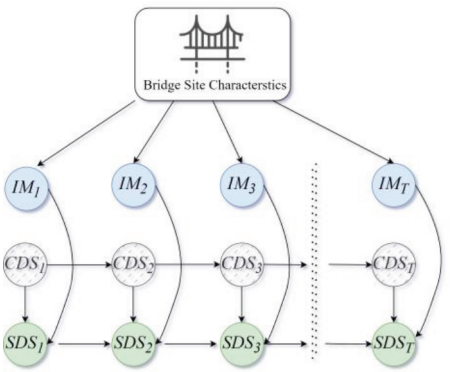


Figure 1. DBN for seismic fragility of aging bridges throughout the life-cycle.

where $PA_s(t)$ refers to the annual probability of exceedance of the seismic damage state (SDS=s_s) at time t; $H(x)$ is the hazard curve that quantifies the annual probability of exceedance given intensity measure IM_t=x, where x is typically the PGA magnitude at the bridge site.

To consider the effect of aging on the seismic fragility, it is important to consider the historical deterioration of the bridge component due to environmental factors (e.g., chloride-induced corrosion). In order to take this into account, the deterioration due to corrosion is modeled using non-stationary Markovian transition models conditioned on the prior corrosion state at time t-1, $\Pr(CDS_t = s_c | CDS_{t-1})$. Following the same rationale, the probability of exceedance of the seismic damage state, $SDS_t = s_s$, at time t, is defined given the associated corrosion damage state, the intensity measure, and the prior seismic damage state, $\Pr(SDS_t \geq s_s \mid CDS_t, IM_t, SDS_{t-1})$. The corresponding DBN is graphically shown in Figure 1. Accordingly, at a specific time, t, of the bridge life, associated with a nonstationary deterioration rate, the seismic fragility, given the complete histories of corrosion deterioration, seismic damages, and prior seismic hazards, is approximated as follows:

$$\Pr(SDS_t \geq s_s | CDS_{0:t}, IM_{0:t}, SDS_{0:t}); \Pr(SDS_t \geq s_s | CDS_t, IM_t, SDS_{t-1}) \tag{7}$$

4 APPLICATION

The developed framework, integrating state-dependent seismic fragility assessment and life-cycle decision optimization through multi-agent DRL, is applied to a case study of a transportation corridor comprising two bridges in series, as shown in Figure 2. Note that spatial ground motion variability is not examined here, i.e., the accelerograms for the two bridges are identical. The bridges are located in a seismic-prone area (Monti et al. 2023), with a hazard curve shown in Figure 2. Each bridge is a four-component system that contains columns (COL), High-Type Expansion Bearings (HTEB), High-Type Fixed Bearings (HTFB), and Low-Type Fixed Bearings (LTFB). The corrosion of the bridge components is defined in a discrete space that contains four CDSs, i.e., Sound, Initial, Progressive, Critical. The corrosion state of the columns (COL) is discretized according to the percentage of rebar mass loss, while the discretization for the bearings depends on the mass loss of the bolts, the reduction in steel plate thickness, and the additive coefficient of friction due to corrosion-induced interlocking effects. Readers with more interest in the modeling details are referred to (Molaioni et al. 2023). Similar to corrosion, the seismic damage states are discretized into five SDSs, i.e. Intact, Slight, Moderate, Extensive, Complete, with the latter corresponding to (near-)failure. Here, the five states are defined probabilistically using log-normal distributions for the curvature ductility and displacement limits for columns and bearings, respectively (Nielson, & DesRoches 2006). Correlations between component SDSs can be modeled as in (Song & Kang, 2009). However, they are omitted here in the interest of safety due to the lack of redundancy in the considered series system.

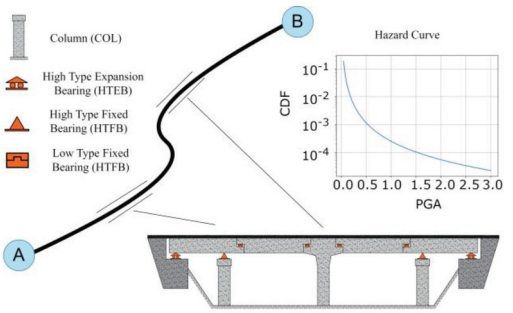


Figure 2. System information including bridge schematic and hazard curve.

Without loss of generality, seismic states are considered fully observable, whereas to capture the imprecision of annual corrosion state inspections, it is assumed that CDSs are observed with noise according to the following observation matrix (Andriotis & Papakonstantinou 2021):

$$\Pr(o_c|CDS_t = s_c) = \begin{array}{c} \\ s_{c,1} \\ s_{c,2} \\ s_{c,3} \\ s_{c,4} \end{array} \begin{array}{c} \begin{array}{cccc} o_{c,1} & o_{c,2} & o_{c,3} & o_{c,4} \end{array} \\ \begin{pmatrix} 0.84 & 0.13 & 0.02 & 0.01 \\ 0.11 & 0.77 & 0.09 & 0.03 \\ 0.02 & 0.16 & 0.70 & 0.12 \\ 0.01 & 0.02 & 0.13 & 0.84 \end{pmatrix} \end{array} \tag{8}$$

The aim is to optimize structural interventions over a 50-year planning horizon while constraining the expected risk of disconnection between points A and B to no greater than 5% in 50 years. Four maintenance actions are considered for columns (COL) and two actions for bearings (HTEB, HTFB,LTFB). These are shown in Table 1 in conjunction with the corresponding costs and effects on the corrosion and seismic damage states. In addition to these actions, the agent can choose to not interfere with the environment at a given decision step (i.e., Do Nothing). The costs associated with the potential actions are based on actual contract

prices (Tennessee Department of Transportation 2023, Ghosh & Padgett 2011). An additional mobilization cost of 15% of replacement cost is also imposed, which incentivizes taking simultaneous actions for similar components. Note that identical components within the same bridge are treated as one component within this setting.

In order to optimize the life-cycle cost considering the aforementioned maintenance actions, costs, and risk constraints, the DDMAC and DDMAC-CTDE multi-agent algorithms are adopted for policy training. In both algorithms, the actor network consists of 8 separate control units, corresponding to the components of the two-bridges corridor, with no parameter sharing among them. The two bridges work in series, i.e., losing one causes disconnection between A and B. The control units corresponding to the columns (COL) have a 5-dimensional softmax output, while the rest have a 3-dimensional output, which corresponds to the number of potential intervention actions. DDMAC control units share the system information, i.e., each unit has access to other units' information in addition to its

Table 1. Potential actions for each component, corrosponding cost, and state effects.

Component	Action	Cost	Action Effect
Columns (COL)	Thin Epoxy overlay	2149$	Restart deterioration rate;
	Epoxy Injection	3207$	Improve CDS & SDS by one; Delay CDS deterioration rate by 5 years;
	Concrete Repairs	2388$	Improve CDS & SDS by two;
	Replace	20000$	Bring to intact condition
Bearings (HTEB, HTFB, LTFB)	Replace Anchor Bolts	1112$	Improve CDS & SDS by one;
	Replace	2397$	Transition to intact condition

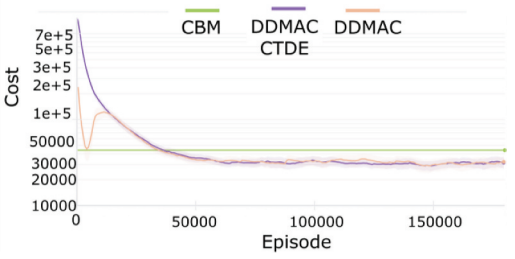


Figure 3. Training performance of DRL algorithms and comparison with baseline policy.

own. On the contrary, DDMAC-CTDE units adopt a decentralized information approach, where each unit accesses only its own information. In both algorithms, the actor units are guided by the critic network, which approximates the value function of the entire system with a one-dimensional linear output. For evaluating the performance of the learned policy, the DRL-based policy is compared to a condition-based baseline (CBM), where a corrective policy typically adopted to mitigate seismic damage (Ghosh & Padgett 2011) is imposed on top of a heuristically optimized condition-based maintenance policy on CDSs (CBM). Three training instances of each of the adopted DRL algorithms trained for 180K episodes, along with the optimized CBM, are shown in Figure 3. Both DDMAC and DDMAC-CTDE produce comparable training averages, and both overperform the optimized CBM by almost 28% in terms of expected life-cycle costs. It was observed that the trained policies managed to also adhere to the risk constraints, with a tendency to prescribe more preventive action in relatively early life-cycle phases, as shown by the cumulative cost and probability of failure evolution of 1000 random realizations shown in Figure 4.

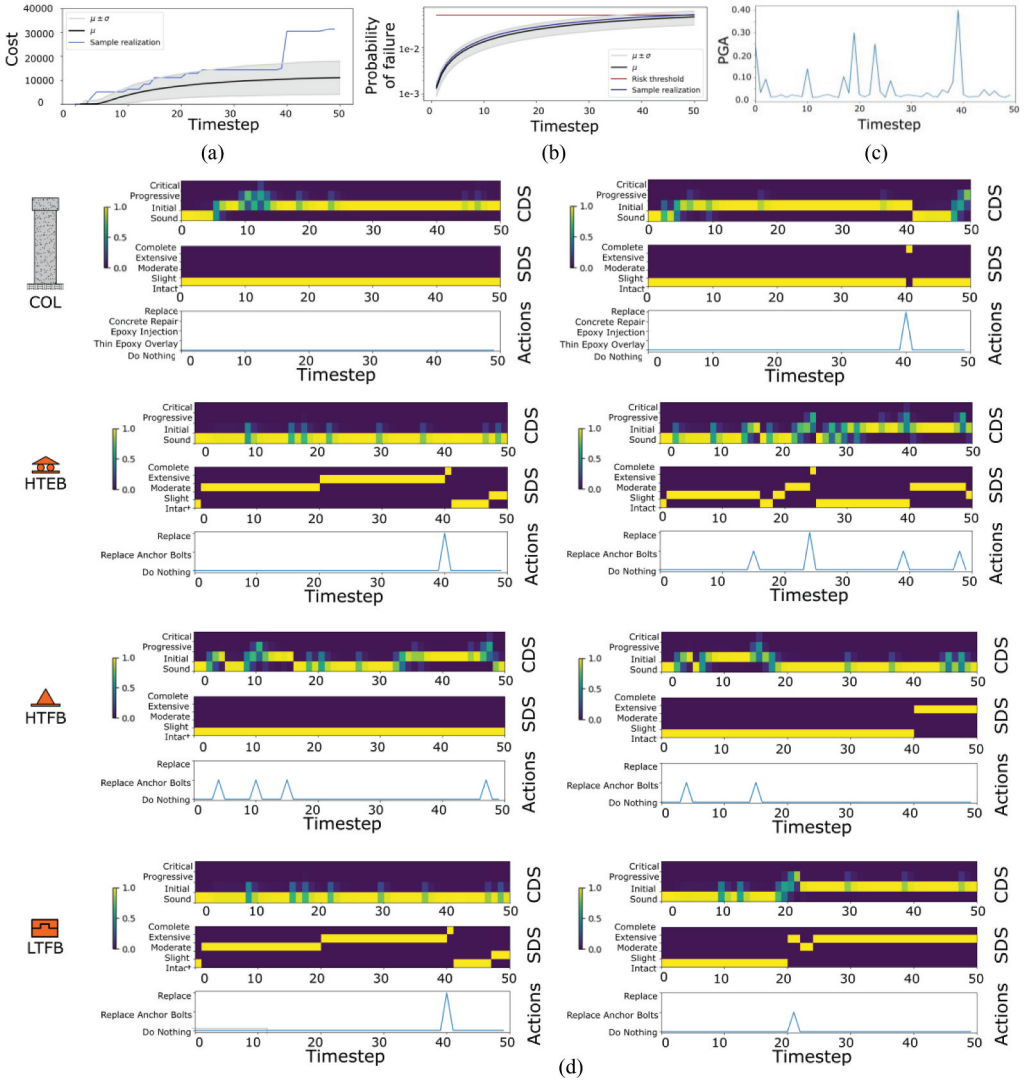


Figure 4. Policy realization: (a) Cost accumulation; (b) Probability of failure evolution; (c) Life-cycle seismic shocks; (d) CDS beliefs, SDSs, and actions.

To visualize the dynamics of the trained policy, a sample realization is presented in Figure 4, showing the observed seismic shocks characterized by the corresponding PGA on a temporal scale, followed by the corrosion CDS belief contours, the observed seismic SDS, and the imposed actions for each component. First, the trajectory starts with observing a relatively intense seismic event, with PGA≈0.25. This results in no seismic damage, except for damage in the HTEB components of both bridges, which are associated with the height fragility (Molaioni et al. 2023), in addition to slight damage in LTFB-1. While the agent decides to take no reactive action upon the damage, an intervention is made when corrosion deterioration is observed in other instances (e.g., HTEB-2 at year 15, LTFB-1 at year 4), which could have increased the vulnerability of such components to future shocks. Another major shock is observed around year 19, which causes different extents of damage across the bearing components, however, due to the prior preventive actions, no failure is observed throughout the system and the connectivity was maintained until two subsequent major shocks are observed at years 23 and 39. The latter causes failures in different spots, resulting in corrective replacement actions. It should be noted that the agent typically avoids

maintaining the columns due to the relatively high associated costs, and due to their higher reliability compared to other components, as shown in detail in (Molaioni et al. 2023), except when failed. Similarly, the agent prefers to impose preventive repairs instead of costly replacements for bearings. Finally, the agent leverages the mobilization incentive, by imposing simultaneous interventions to HTFB-1 and HTFB-2 at years 4 and 15.

5 CONCLUSIONS

In this paper, we introduce a framework for managing aging bridges subject to seismic hazards using dynamic Bayesian networks (DBNs) and Deep Reinforcement Learning (DRL). A virtual environment incorporates chloride-induced corrosion of bridge components and state-dependent seismic fragility functions, which are embedded in a DBN to allow for uncertainty propagation and state information updating throughout the life-cycle. Leveraging recent advances in multi-agent DRL in conjunction with partially observable Markov decision processes, the developed environment is probed by DRL agents operating on the belief space of the system, i.e., the dynamically updatable probabilistic distributions over component states. The framework is applied to identify a near-optimal 50-year intervention policy for a two-bridge transportation corridor located in a seismic-prone area, as well as the corresponding expected life-cycle cost under long-term risk constraints. A substantial improvement of 28% is observed in minimizing the life-cycle costs with DRL compared to traditional maintenance policies, while adhering to the imposed risk constraints. The introduced framework can be adopted, without loss of generality, to the management of other hazard- and deterioration-vulnerable systems, enhancing the safety, reliability, and cost-effectiveness of critical infrastructure networks.

ACKNOWLEDGEMENTS

This material is based upon work supported by the TU Delft AI Labs Program. The authors gratefully acknowledge this support.

REFERENCES

Alipour, A., Shafei, B., & Shinozuka, M. (2011). Performance Evaluation of Deteriorating Highway Bridges Located in High Seismic Areas. *Journal of Bridge Engineering*, 16, 597–611.

Andriotis, C. P., & Papakonstantinou, K. G. (2019). Managing engineering systems with large state and action spaces through deep reinforcement learning. *Reliability Engineering & System Safety*, 191.

Andriotis, C. P., & Papakonstantinou, K. G. (2021). Deep reinforcement learning driven inspection and maintenance planning under incomplete information and constraints. *Reliability Engineering & System Safety*, 212.

ASCE (2021). 2021 report card for America's infrastructure. Retrieved 15 September 2023. Available from https://infrastructurereportcard.org/wp-content/uploads/2020/12/National_IRC_2021-report-2.pdf

Arunraj, N. S., & Maiti, J. (2007). Risk-based maintenance - Techniques and applications. *Journal of Hazardous Materials*, 142(3), 653–661.

Bertolini, L., Elsener, B., Pedeferri, P., Redaelli, E. and Polder, R.B., 2013. Corrosion of steel in concrete: prevention, diagnosis, repair. *John Wiley & Sons*.

Bucher, C., & Frangopol, D. M. (2006). Optimization of lifetime maintenance strategies for deteriorating structures considering probabilities of violating safety, condition, and cost thresholds. *Probabilistic Engineering Mechanics*, 21(1), 1–8.

Choe, D. E., Gardoni, P., Rosowsky, D., & Haukaas, T. (2008). Probabilistic capacity models and seismic fragility estimates for RC columns subject to corrosion. *Reliability Engineering & System Safety*

Deng, P., Zhang, C., Pei, S., & Jin, Z. (2018). Modeling the impact of corrosion on seismic performance of multi-span simply-supported bridges. *Construction and Building Materials*, 185 (Oct): 193–205.

Ghosh, J., & Padgett, J. E. (2011). Probabilistic seismic loss assessment of aging bridges using a component-level cost estimation approach. *Earthquake Engineering & Structural Dynamics*, 40(15), 1743–1761.

Molaioni, F., Rinaldi, Z., & Andriotis, C. P. (2023). Assessing life-cycle seismic fragility of corroding reinforced concrete bridges through dynamic Bayesian networks. In Life-Cycle of Structures and Infrastructure Systems (pp. 523–530). CRC Press.

Monti, G., Demartino, C., & Gardoni, P. (2023). Towards risk-targeted seismic hazard models for Europe. *Scientific reports*, 13(1), 10717.

Morato PG, Andriotis CP, Papakonstantinou KG, Rigo P. (2023). Inference and dynamic decision-making for deteriorating systems with probabilistic dependencies through Bayesian networks and deep reinforcement learning. *Reliability Engineering & System Safety*.

Nielson, B.G. and DesRoches, R., 2006. Seismic fragility methodology for highway bridges. In *Structures Congress 2006: Structural Engineering and Public Safety* (pp. 1–9).

Papakonstantinou, K. G., & Shinozuka, M. (2014). Planning structural inspection and maintenance policies via dynamic programming and Markov processes. Part II: POMDP implementation. *Reliability Engineering & System Safety*.

Papakonstantinou, K. G., Andriotis, C. P., and Shinozuka, M. (2018). POMDP and MOMDP solutions for structural life-cycle cost minimization under partial and mixed observability. *Structure and Infrastructure Engineering*, 14(7), 869–882.

Rao, A. S., Lepech, M. D., Kiremidjian, A. S., & Sun, X.-Y. (2017). Simplified structural deterioration model for reinforced concrete bridge piers under cyclic loading. *Structural Infrastructure Engineering*, 13 (1): 55–66.

Rinaldi, Z., Di Carlo, F., Spagnuolo, S., & Meda, A. (2022). Influence of localized corrosion on the cyclic response of reinforced concrete columns. *Engineering Structures*.

Saifullah, M., Papakonstantinou, K. G., Andriotis, C. P., & Stoffels, S. M. (2024). Multi-agent deep reinforcement learning with centralized training and decentralized execution for transportation infrastructure management. arXiv preprint arXiv:2401.12455.

Shekhar, S., & Ghosh, J. (2021). Improved component-level deterioration modeling and capacity estimation for seismic fragility assessment of highway bridges. *ASCE-ASME Journal of Risk and Uncertainty in Engineering Systems, Part A: Civil Engineering*, 7(4), 04021053.

Song, J. and Kang, W.H., 2009. System reliability and sensitivity under statistical dependence by matrix-based system reliability method. *Structural Safety*, 31(2), pp.148–156.

Tennessee State Government. (2023). Retrieved 01 November 2023. Available from https://www.tn.gov/

Zhang, N. L., & Si, W. J. (2020). Deep reinforcement learning for condition-based maintenance planning of multi-component systems under dependent competing risks. *Reliability Engineering & System Safety*, 203.

Bridge Maintenance, Safety, Management, Digitalization and Sustainability – Jensen, Frangopol & Schmidt (eds)
© 2024 The Author(s), ISBN 978-1-032-77040-6
Open Access: www.taylorfrancis.com, CC BY-NC-ND 4.0 license

Objective risk assessment for bridge management

Seyyed Amirhossein Moayyedi & David Y. Yang*
Portland State University, Portland, Oregon, USA

ABSTRACT: Bridges are subjected to various natural and/or human-induced hazards with considerable uncertainties arising from hazard characteristics, structural vulnerabilities, and damage consequences. Quantifying the associated risk requires the evaluation of a risk integral. However, its computation is incompatible with the prevailing risk estimation methods currently used in many bridge management systems (BMSs). Inaccurate risk assessment may result in the misallocation of often limited resources for risk mitigation. This paper presents a novel tabulation approach for accurate risk assessment that is also compatible with common BMS implementation. The proposed approach is built on the rigorous formulation of risk integrals. Nonetheless, it uses Gaussian quadrature to derive a series of weighted hazard scenarios that can be tabulated in BMSs to accurately tally the total risk. As a result, the proposed approach fills in the gap between accurate risk assessment with risk integrals and practical implementation in bridge management. Results from this study show that with the same number of hazard scenarios, the novel approach can significantly improve the accuracy of risk assessment. The potential of this approach in a multi-hazard setting is also discussed.

1 INTRODUCTION

Bridge management has traditionally been focused on the condition preservation through carefully planned life-cycle activities within a budgetary limit. Such plans are enacted to impede deterioration and/or accommodate increasing demand. Although there are calls to consider risks from various extreme events, existing approaches to risk assessment in transportation asset management rely heavily on engineering judgement, past experience, and limited data that roughly correlate with hazard intensities, bridge vulnerabilities, and damage consequences. This subjective or empirical approach to risk assessment contrasts to more objective methods that are underpinned by quantitative models of hazards, vulnerabilities, and consequences (e.g., FEMA 2020; NIST 2023). Nonetheless, these quantitative models do not fully consider the effects of deterioration on structural vulnerability under extreme events, thus hindering their direct application in bridge management.

The gap between bridge management and objective risk assessment leads to (a) inconsistency between risks assessed by different agencies or different experts and (b) neglect or inaccurate estimates of risks compounded by asset deterioration. As a result, resources may be allocated inefficiently due to (a) unreliable estimates of project benefits and (b) lack of coordination between condition preservation and risk mitigation needs. This paper presents a new method for risk assessment to overcome these shortcomings. Specifically, the new method unifies the assessments of structural deterioration and risks under extreme events. The focus is placed on the viability and potential of objective risk assessment in bridge management systems.

*Corresponding author: david.yang@pdx.edu

DOI: 10.1201/9781003483755-404

2 EXISTING METHODS FOR RISK ASSESSMENT IN BRIDGE MANAGEMENT

Risk assessment under extreme events has been implemented in several commonly used BMSs such as AASHTOWare™ BrM and AgileAssets™ in the US. These existing methods follow the general risk formulation that is expressed as the product of event likelihood and event consequences. In these systems, risks are usually estimated following the general procedure outlined below (hereafter referred to as the BMS procedure):

- Collect one or a limited number of hazard scenarios relevant to the asset performance. These are usually obtained from expert elicitation or past experience. They can be different hazards (e.g., earthquakes and floods) or one hazard with different return periods (thus different intensity levels).
- Estimate the annual likelihood of each hazard scenario. This can be determined from polls on experts or past experience of agencies. Results of probabilistic hazard analysis, e.g., those available through United States Geological Survey (USGS) for earthquakes (USGS 2022), can also be utilized in this step.
- Estimate the expected consequence under each hazard scenario. This can be similarly determined from expert polls or past experience. Alternatively, damage evaluation given the scenario event can be conducted using HAZUS or in-house tools. Note that this differs from a complete risk analysis as it is conditioned on the occurrence of a hazard event.
- Tabulate the risks associated with all hazard scenarios by multiplying the likelihoods and the expected consequences. Sum up the risks of hazard scenarios as the total annual risk associated with the asset. Tally all annual risks to determine the lifetime risk.

Due to the heavy reliance on expert elicitation, the procedure described above is mostly empirical and can vary considerably between different analysts and agencies (even for the same area and hazard under consideration). This is in contrast with the quantitative risk assessment approach that originated from the seismic analysis and design of structures (ATC 1978) and has since been expanded to many other hazards (McAllister et al. 2018) and regional damage assessment (Basöz & Mander 1999). For the quantitative assessment, the risk from an adverse event is expressed by the following equation, which is often referred to as a risk integral:

$$R = \int_{im} \left[\sum_{ds} cq(ds) \cdot p_{DS|IM}(ds|im) \right] \lambda_{IM}(im) dim \tag{1}$$

where a lower-case variable (*im* and *ds*) = sample from a random variable (represented by its upper-case counterparts, *IM* and *DS*); *IM* = intensity measure (IM) of an adverse event; $\lambda_{IM}(im)$ = value of the probability density function (PDF) at *IM* = *im* (i.e., the likelihood of a specific value *im* for the intensity measure, referred hereafter as an intensity level); *DS*|*IM* = damage states (DSs) conditioned on the intensity measure; $p_{DS\ |\ IM}(ds|im)$ = probability of a specific DS, *ds*, conditioned on a specific intensity level *im*; $cq(ds)$ = average consequence associated with a DS.

Compared to the BMS procedure, Equation 1 considers all possible intensity levels of a hazard probabilistically. This is a clear improvement to the existing BMS procedure where only one or a limited few intensity levels, usually adopted based on intensities for structural design, are considered. Equation 1 also incorporates the uncertainty related to the structural vulnerability, as represented by the conditional probabilities associated with different DSs. These conditional probabilities can be obtained using fragility curves, which provide the probabilities of reaching or surpassing a specific damage state given an intensity level (Buckle et al. 2006; Muntasir Billah & Shahria Alam 2015). Using Equation 1, objective risk can be achieved with a set of widely used or agreed models, including a hazard characterization model λ_{IM}, fragility curves to derive $p_{DS|IM}$, and the expected cost data for each DS $cq(ds)$. As long as these models are defined (e.g., using those provided in HAZUS), risk can be objectively quantified without relying on expert elicitation. Despite this advantage, an accurate evaluation of an integral is usually not compatible with the BMS procedure described previously.

3 RISK ASSESSMENT USING WEIGHTED HAZARD SCENARIOS

A new tabulation method is developed herein by leveraging a more accurate and efficient numerical integration method, i.e., the Gaussian quadrature method, which is also compatible with the BMS procedure. The objectives of this new method are (a) to reduce the number of hazard scenarios needed to accurately estimate the risk integral, and (b) to preserve the general implementation steps for easy integration with existing BMSs.

3.1 *Gaussian quadrature for numerical integration*

An n-point Gaussian quadrature is a rule to carry out integration numerically using integrand values at n strategically selected locations (termed integration points) and their associated weights (Chapra & Canale 2021). The most common Gaussian quadrature is the Gauss-Legendre quadrature, which is given as follows for a one-dimensional (1D) integral over domain $[-1, 1]$ (Abramowitz & Stegun 1972):

$$\int_{-1}^{1} f(\xi)d\xi \approx \sum_{i=1}^{n} \eta_i f(\xi_i) \tag{2}$$

where $f(\xi)$ = integrand function; ξ_i (i = 1, 2,. . ., n) = n integration points within $[-1, 1]$; η_i = the associated weights. It is worth mentioning that the quadrature rule is exact if $f(\xi)$ is a polynomial of up to $2n - 1$ degrees (Weisstein 1995). Therefore, if $f(\xi)$ can be reasonably approximated by a polynomial of up to $2n - 1$ degrees, the error of this quadrature can be small. Also, the domain $[-1, 1]$ can be easily converted to any definite integral domain through transformation (Abramowitz & Stegun 1972). Given the number of integration points n, the integration points ξ_i and weights η_i are independent of the integrand function and can be found in several references (e.g., Weisstein 1995). In cases where singularities may occur at the endpoints of the integral domain or where semi-infinite or infinite intervals are involved, other Gaussian quadrature rules can be applied, such as Chebyshev-Gauss, Gauss-Laguerre, or Gauss-Hermite quadratures (Weisstein 1995).

3.2 *Adapting Gaussian quadrature for risk integral*

Applying Gaussian quadrature with n points to Equation 1 gives rise to the following approximation of the risk integral:

$$\begin{aligned} R &= \int_{im=a}^{im=b} \left[\sum_{ds} cq(ds) \cdot p_{DS|IM}(ds|im) \right] \lambda_{IM}(im) dim \\ &\approx \sum_{i=1}^{n} w_i \cdot \left[\sum_{ds} cq(ds) \cdot p_{DS|IM}(ds|im_i) \right] \cdot v_{IM}(im_i) \end{aligned} \tag{3}$$

In this approximation, the risk can be regarded as the summation of risks of n weighted hazard scenarios. In particular, a hazard scenario is characterized by the intensity level im_i, which can be obtained from the integration domain $[a, b]$ and the Gaussian integration points as follows:

$$im_i = \frac{b-a}{2}(\xi_i + 1) + a \tag{4}$$

A nominal annual rate of occurrence, $v_{IM}(im_i)$, is defined as follows

$$v_{IM}(im_i) = \frac{b-a}{2}\lambda_{IM}(im_i) \tag{5}$$

Given the occurrence of a hazard scenario, the term within the square bracket in Equation 3 is the expected consequence conditioned on the hazard occurrence. Finally, the weight of a hazard

scenario, w_i, is equal to the integration weight of the ith integration points, i.e., $w_i = \eta_i$. It should be noted that the integration domain should be intensity levels responsible for the asset risk under adverse events. For instance, a domain [0.1g, 2.0g] for peak ground acceleration (PGA) may be used for estimating asset seismic risk if (a) an asset is extremely unlikely to damage with PGA less than 0.1g and (b) an earthquake causing PGA larger than 2.0g is extremely unlikely to happen in the region (and a lower PGA already causes collapse of most or all structures).

The weighted hazard scenarios used to approximate the risk integral have close resemblance to the BMS procedure described in the previous section. In fact, all steps within the BMS procedure have direct counterparts in Equation 3. The only addition is the scenario weights that can actually be merged to the expected consequence. The main advantage compared to the BMS procedure is that the selection of hazard scenarios and the expected consequences are no longer based on expert elicitation. Instead, they are derived from the hazard characteristics, structural fragilities, and the conditional consequences. Therefore, objective risk assessment is realized with this weighted hazard scenarios approach. To facilitate the application of this new approach, a Python package named "pyRiskTable" has been developed to automatically generate a comma-separated values (CSV) file containing weighted hazard scenarios given a target accuracy level of the estimated risk. More accurate estimation usually corresponds to a greater number of hazard scenarios (i.e., Gaussian integration points).

4 ILLUSTRATIVE EXAMPLES

The approach described in the previous section is illustrated herein by an example focusing on bridge seismic risk assessment. The result is compared in terms of accuracy to the BMS approach. This example is then leveraged to illustrate the implications of objective risk assessment on life-cycle management of deteriorating assets. Although focusing herein on an individual bridge, the proposed approach can also be applied for a system of bridges in common management systems. For instance, following the example below, the seismic risk of bridge portfolios can be analyzed for each bridge using the regional hazard model from USGS (2022) and the fragility curves for different types of bridges in HAZUS (FEMA 2020).

4.1 *Hazard characteristics, bridge fragilities, and damage consequences*

In this example, a fictional hazard curve based on an idealized fault 10 km away from the site is considered following Baker (2013). The fault is assumed to only generate magnitude 6.5 earthquakes with a return period of 100 years. Using probabilistic seismic hazard analysis, the following hazard curve can be derived (Cornell et al. 1979; Baker 2013):

$$\begin{aligned} \overline{\ln PGA} &= -0.152 + 0.859M - 1.803\ln(d+25) \\ \omega_{IM}(im) &= 1 - \Phi\left(\frac{\ln im - \overline{\ln PGA}}{\sigma}\right) \end{aligned} \tag{6}$$

where M = magnitude of the earthquakes generated at the fault (M = 6.5 in this example); d = distance between the site and the fault in kilometers (d = 10 km in this example); Φ = cumulative distribution function (CDF) of a standard normal distribution; σ = dispersion factor of the PGA (i.e., the standard deviation of the logarithmic PGA) at the site, and σ = 0.57 is assumed herein (Cornell et al. 1979). This hazard curve gives the annual rate of exceedance $\omega_{IM}(im)$ under different PGA levels. Both the hazard curve and the hazard likelihood (i.e., the derivative of the hazard curve with respect to PGA) are shown in Figure 1. It should be noted that the hazard curve has a maximum annual rate of exceedance of 0.01 due to the assumed return period of earthquakes at this idealistic fault.

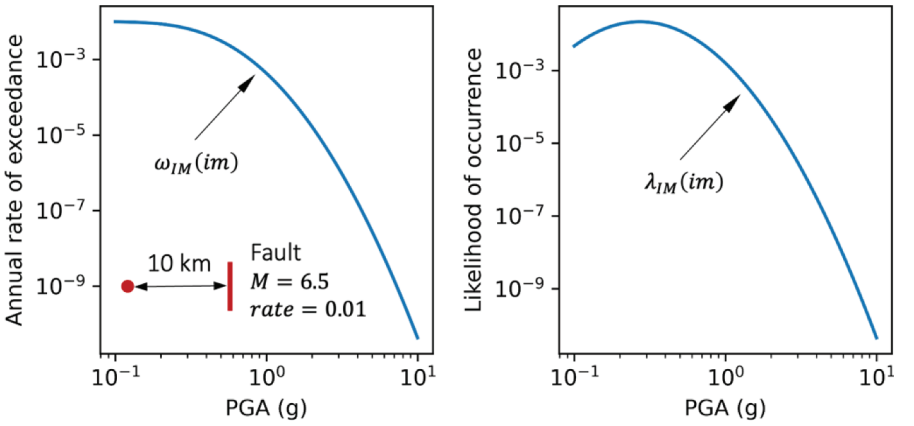


Figure 1. Hazard curve (left) and its gradient (right).

Fragility curves in Basöz and Mander (1999) are used to determine the DS probabilities given an intensity level at the site. For each DS, the fragility curve is modeled by the CDF of a lognormal distribution defined by two parameters, median PGA and the dispersion factor (i.e., the standard deviation of lnPGA). Table 1 gives the two parameters used for each DS. The DS probability can be determined by comparing the fragility curves between two consecutive DSs, as illustrated in Figure 2.

Table 1. Parameters of fragility curves.

Damage state	Median IM (in g)	Dispersion ($\sigma_{\ln PGA}$)
Slight	0.30	0.6
Moderate	0.36	0.6
Extensive	0.49	0.6
Complete	0.71	0.6

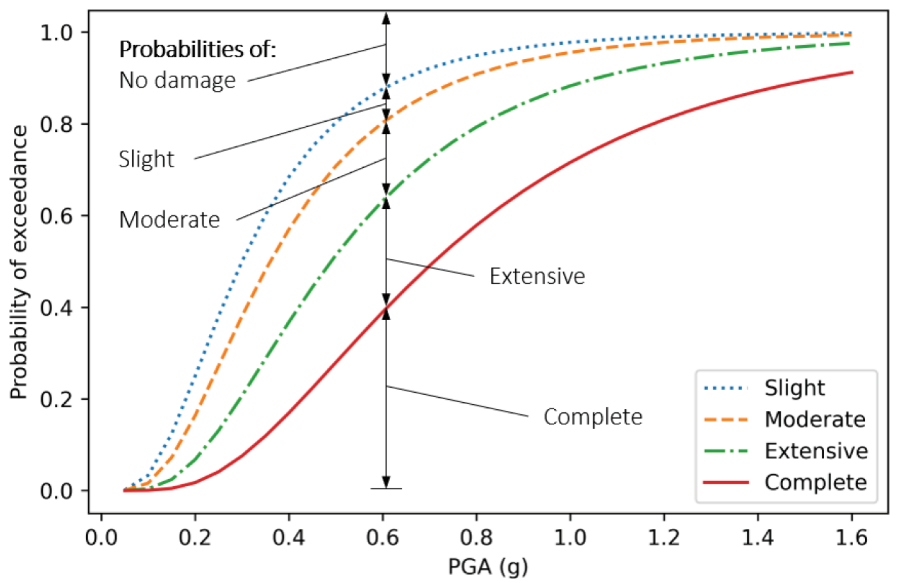


Figure 2. Fragility curves and damage state probabilities.

4.2 *Seismic risk assessment with weighted hazard scenarios*

Weighted hazard scenarios are generated using the proposed approach. Based on the generated hazard scenarios, the seismic risk of the bridge can be computed. The integral domain is selected based on the lower and upper limits of intensity levels that correspond to two return periods, namely 100 years and 100,000 years. Six hazard scenarios are used for risk assessment because the accuracy gain is marginal (less than 5%) with more scenarios. Table 2 presents the hazard characteristics, event likelihoods, scenario weights, and damage consequences for these six scenarios. By tabulating the weighted risks of these scenarios (calculated as the product of the likelihood, consequence, and weight), the total seismic risk is 0.00340 (in terms of cost ratio). This is very close (within 2% margin) to the precise value of the risk integral (0.00332) evaluated based on Equation 1 with numerical integration using Gaussian quadrature with 16 integration points (as implemented in SciPy, a Python package for scientific computing (Virtanen et al. 2020)).

Table 2. Weighted hazard scenario approach for risk assessment (new approach).

Hazard scenario	Description (return period, PGA in g)	Annual rate	Consequence (cost ratio)	Weight	Risk (cost ratio)
1	104 yr, PGA=0.136	1.119E-02	0.021	0.171	4.078E-05
2	240 yr, PGA=0.424	1.712E-02	0.348	0.361	2.148E-03
3	1435 yr, PGA=0.873	2.855E-03	0.752	0.468	1.004E-03
4	8873 yr, PGA=1.379	3.991E-04	0.916	0.468	1.711E-04
5	36247 yr, PGA=1.828	8.597E-05	0.966	0.361	2.995E-05
6	82265 yr, PGA=2.116	3.502E-05	0.980	0.171	5.879E-06
				Total risk	0.00340

To demonstrate the advantages of the new approach over the BMS procedure, six typical hazard scenarios are utilized to estimate the risk with the BMS procedure. The return periods of these scenarios are selected because they are commonly used in either expert-based seismic risk assessment or seismic analysis and design of structures. Table 3 presents the return periods, corresponding event likelihoods, implied intensity levels, and damage consequences of all scenarios. The risks associated with the scenarios and the total risk are also presented in Table 3. It can be observed that the total risk obtained from the BMS procedure underestimates the precise risk by 36% (0.002117 vs. 0.00332).

Table 3. BMS procedure for risk assessment (existing approach).

Hazard scenario	Description (return period, PGA in g)	Annual rate	Consequence (cost ratio)	Risk (cost ratio)
1	225 yr, PGA=0.326	2.444E-03	0.326	7.958E-04
2	500 yr, PGA=0.554	9.740E-04	0.554	5.397E-04
3	975 yr, PGA=0.691	3.590E-04	0.691	2.480E-04
4	1500 yr, PGA=0.758	1.670E-04	0.758	1.266E-04
5	2000 yr, PGA=0.795	9.600E-05	0.795	7.633E-05
6	2475 yr, PGA=0.819	4.040E-04	0.819	3.309E-04
			Total risk	0.002117

4.3 *Seismic risk of deteriorating bridges*

The proposed approach can also be used for the seismic risk of deteriorating assets. Due to structural deterioration, the seismic resistance of a structure may decrease over time. This can impact the shape of fragility curves, especially the median values of different DSs in Table 1 (Ghosh & Padgett 2010). To model this effect, it is assumed that the median value changes over time based on the following equation:

$$r(t) = 1 - at \tag{7}$$

where $r(t)$ = the ratio of the median value at time t (in years in service) to the initial values in Table 1; a = annual deterioration rate, assumed to be 0.01 for this illustrative example.

Using this deterioration model, the benefit-to-cost ratio (BCR) of two maintenance strategies are compared to showcase the effect of accurate risk assessment on strategy selection. These strategies are

- Strategy 1: Maintain the bridge every two years to immediately rectify any deterioration accumulated in the two-year interval and restore the structure to its initial performance.
- Strategy 2: Only provide one major maintenance in year 40 within the 75-year service life to fix the deterioration accumulated in the first 40 years and restore the structure to its initial performance.

The cost of a maintenance action in each strategy is assumed to be proportional to the extent of performance improvement in order to restore the median value of the fragility curve back to its initial level. Therefore, the cost ratio associated with a maintenance action can be expressed as $1 - r$ where r is the structural performance considering deterioration, defined in accordance with Equation 7.

From a risk reduction perspective, the benefit of a maintenance strategy is quantified as the reduction in lifetime seismic risk, which is defined as the summation of annual seismic risks over the bridge service life. This reduction is calculated by subtracting seismic lifetime risk with a maintenance strategy from that without any maintenance. Based on the cost and benefit models, the BCRs of both strategies can be evaluated. It should be noted that the example herein is limited to the benefit of maintenance actions in terms of reducing seismic risk. Annual seismic risks are estimated using scenario events in Table 2 and Table 3, representing the new approach and the BMS procedure respectively. Note that the expected consequence of each event changes over time using the deteriorated fragility curves characterized by Equation 7.

Figure 3 shows the results of the BCR comparison. It can be observed that when the new approach for objective risk assessment is used, Strategy 2 is clearly more advantageous than Strategy 1, with an approximately 8% higher BCR. On the other hand, when the BMS procedure is used, the difference between the two strategies is negligible, which can complicate the decision-making process. Additionally, the BCR is significantly underestimated when using the existing BMS procedure. Hence, inaccurate risk assessment with the existing BMS procedure may lead to erroneous ranking of different maintenance or retrofitting strategies. The objective risk assessment, as proposed in this paper, provides a viable rectification for this drawback.

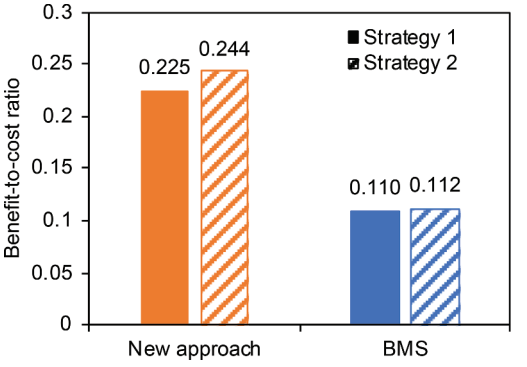


Figure 3. BCR comparison of maintenance strategies using different methods.

5 CONCLUSIONS

The risk assessment approach based on weighted hazard scenarios is a novel method to potentially fill the gap between risk assessment and bridge management. Rather than rely on expert elicitation for hazard scenarios, the new approach to objective risk assessment can

automatically and consistently generate weighted hazard scenarios to be included in the risk analysis. The new approach is built on the rigorous formulation of risk integrals. The preservation of a tabulated implementation allows for the direct integration of objective risk assessment in common bridge management frameworks. In particular, it is most convenient to apply the new approach as a pre-processing step when setting up the risk assessment task within a bridge management system. In summary, the following conclusions can be drawn:

- Compared to existing risk assessment methods in bridge management, the new approach can yield much higher accuracy with the same number of hazard scenarios. The format of the generated scenarios is similar to that used in existing systems except for a weighting factor that can be merged to event consequences. As a result, the generated hazards can be directly leveraged by existing BMSs to achieve objective risk assessment.
- It is empirically demonstrated that existing approaches to risk assessment do not always deliver reliable rankings of maintenance strategies in terms of risk-based benefit-to-cost ratios. This means that the lifetime risk of deteriorating assets cannot be assessed by simply incorporating age- or condition-dependent fragility curves to BMSs. Instead, the new approach to picking hazard scenarios is a necessary step toward risk-based transportation asset management.

REFERENCES

Abramowitz, M. & Stegun, I., 1972. *Handbook of Mathematical Functions with Formulas, Graphs, and Mathematical Table*, 10th ed.,Washington, DC: National Bureau of Standards (NBS).

ATC, 1978. *Tentative Provisions for the Development of Seismic Regulations for Buildings*, Redwood City, CA: Applied Technology Council (ATC).

Baker, J.W., 2013. Introduction to Probabilistic Seismic Hazard Analysis. *White Paper Version 2.0.1*. Available at: http://dx.doi.org/10.1016/j.strusafe.2008.06.002.

Basöz, N. & Mander, J.B., 1999. *Enhancement of the Highway Transportation Lifeline Module in HAZUS*, National Institute of Building Sciences.

Buckle, I., Friedland, I., Mander, J., Martin, G., Nutt, R. & Power, M., 2006. *Seismic Retrofitting Manual for Highway Structures: Part 1 - Bridges*, McLean, VA: Office of Infrastructure Research and Development, Federal Highway Administration (FHWA).

Chapra, S.C. & Canale, R.P., 2021. *Numerical Methods for Engineers*, 8th ed., New York, NY: McGraw-Hill.

Cornell, C.A., Banon, H. & Shakal, A.F., 1979. Seismic motion and response prediction alternatives. *Earthquake Engineering & Structural Dynamics*, 7(4): 295–315.

FEMA, 2020. *HAZUS Earthquake Model Technical Manual (HAZUS v4.2 SP3)*, Washington, DC: Federal Emergency Management Agency (FEMA).

Ghosh, J. & Padgett, J.E., 2010. Aging Considerations in the Development of Time-Dependent Seismic Fragility Curves. *Journal of Structural Engineering*, 136(12): 1497–1511.

McAllister, T.P., Wang, N. & Ellingwood, B.R., 2018. Risk-Informed Mean Recurrence Intervals for Updated Wind Maps in ASCE 7-16. *Journal of Structural Engineering*, 144(5): 06018001. Available at: http://ascelibrary.org/doi/10.1061/%28ASCE%29ST.1943-541X.0002011.

Muntasir Billah, A.H.M. & Shahria Alam, M., 2015. Seismic fragility assessment of highway bridges: a state-of-the-art review. *Structure and Infrastructure Engineering*, 11(6): 804–832. Available at: http://www.tandfonline.com/doi/abs/10.1080/15732479.2014.912243.

NIST, 2023. Interdependent Networked Community Resilience Modeling Environment (IN-CORE). Available at: https://incore.ncsa.illinois.edu [Accessed November 1, 2023].

USGS, 2022. The National Map - Data Delivery. *United States Geological Survey (USGS)*. Available at: https://www.usgs.gov/the-national-map-data-delivery [Accessed August 1, 2022].

Virtanen, P., Gommers, R., Oliphant, T.E., Haberland, M., Reddy, T., Cournapeau, D., Burovski, E., Peterson, P., Weckesser, W., Bright, J., van der Walt, S.J., Brett, M., Wilson, J., Millman, K.J., Mayorov, N., Nelson, A.R.J., Jones, E., Kern, R., Larson, E., Carey, C.J., Polat, I., Feng, Y., Moore, E. W., VanderPlas, J., Laxalde, D., Perktold, J., Cimrman, R., Henriksen, I., Quintero, E.A., Harris, C.R., Archibald, A.M., Ribeiro, A.H., Pedregosa, F., van Mulbregt, P. & SciPy Contributors, 2020. SciPy: Fundamental Algorithms for Scientific Computing in Python. *Nature Methods*, 17: 261–272.

Weisstein, E.W., 1995. *Wolfram MathWorld: The Web's Most Extensive Mathematics Resource*, Champaign, IL: Wolfram Research


Taylor & Francis
Taylor & Francis Group
http://taylorandfrancis.com

SS46: BRIDGITISE an EU network on the digitalization of bridge integrity management

Organizers: M.P. Limongelli, J.H. Roldsgaard, J. Jordan & M.H. Faber


Taylor & Francis
Taylor & Francis Group
http://taylorandfrancis.com

Bridge Maintenance, Safety, Management, Digitalization and Sustainability – Jensen, Frangopol & Schmidt (eds)
© 2024 The Author(s), ISBN 978-1-032-77040-6
Open Access: www.taylorfrancis.com, CC BY-NC-ND 4.0 license

Drone-based photogrammetric indoor inspection of box girder bridges

J.C. Avendaño, J. Leander & R. Karoumi
KTH Royal Institute of Technology, Stockholm, Sweden

ABSTRACT: Digital inspections methods have gained increasing interest in the civil engineering field for assessing the condition of various structures including buildings and bridges. These methods are used primarily to evaluate the external surface condition of the structure. However, in the case of bridges, their application when inspecting the interior of these structures remains uncommon. This paper presents a case study for inspecting the interior of a concrete box girder bridge, the Strängnäs bridge. The inspection involved gathering data using a commercial drone, creating a photogrammetrical model, detecting and quantifying damages by employing a Convolutional Neural Network (CNN). The analysis successfully detected 60 cm long concrete cracks, a total area of 3.5 m^2 leakage and corrosion over 40 cm. The study addressed the difficulties such as insufficient lighting, lack of GPS signal and dust clouds reducing visibility. Despite these obstacles, the study demonstrated the effectiveness of indoor drone-based inspections.

1 INTRODUCTION

The condition assessment of bridges, tunnels, buildings, and other infrastructure is essential to ensure their proper functioning over time. Traditionally, these assessments are performed manually, are costly and are time consuming. However, the use of image-based inspections supported by tools such as Unmanned Aerial Vehicles (UAV), often known as drones, can reduce inspection time up to 80% [1].

Digital inspections are gaining popularity in structural health monitoring, due to the possibility to combine methods such as machine learning algorithms, computer vision methods and photogrammetry among others to obtain useful results. Among machine learning methods, Convolutional Neural Networks (CNN) are often used to automate the process of detect and analyze surface damages [2][3]. Moreover, computer vision techniques are used in many cases to quantify damages such as cracks [4]–[6]. Furthermore, photogrammetric models have proven useful to perform condition assessments for bridges and tunnels [7]–[9].

These tools represent an advantage in the decision-making process to determine focus areas for further detailed inspections and planning for maintenance actions. Nevertheless, the studies are usually focused on the exterior of structures whereas the interior is overlooked for structures like box-girder bridges. As for tunnels, indoor bridges inspections correspond to enclosed spaces usually without Global Positioning System (GPS) signal used by drones for navigation, insufficient light, constrained locations, and presence of dust [10].

Considering this, the present work aims to study the feasibility of image-based inspections inside a box-girder bridge by using a commercial drone, applying machine learning and photogrammetry to evaluate the condition of the bridge.

DOI: 10.1201/9781003483755-405

2 METHODOLOGY

The methodology for the indoor inspection of the box-girder bridge is composed by three steps: data acquisition, processing, and characterization. Data acquisition consists of gathering images of the surfaces of interest using a commercial drone. The processing of the data consists of creating a 3D photogrammetrical model and identify damages with a neural network. The characterization correspond to the quantification of the damages identified. The procedure is illustrated in Figure 1.

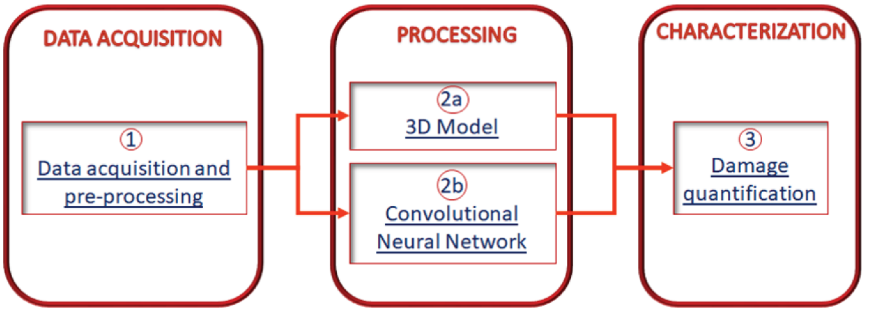


Figure 1. Methodology overview.

2.1 *Data acquisition*

For the data acquisition, a DJI Mavic 2 Pro was used equipped with a 1-inch sensor camera composed by 20 million-pixel. The camera has a 0.5 m focus distance meaning that the closest distance the drone can be from the surface to obtain a clear image is 0.5 m. It has a wind resistance of 29 km/h allowing it to hoover in a precise manner. This equipment has an omnidirectional obstacle sensing using an infrared sensing system and multiple cameras to avoid collision against the structure. The lack of natural light inside the bridge makes it necessary to provide an additional source of light in order to obtain proper images. This is done using a single lamp with a light output of 1300 lumens. The lamp is pointed towards the surface the drone is facing to have clear images.

During image capture, a systematic zigzag sequence was employed. The drone moved horizontally, altering its altitude, and then moved horizontally again. When doing this, a horizontal overlap of 70% and a 30% vertical overlap between images is assured.

2.2 *Photogrammetric model*

Photogrammetry is the process of obtaining measurements of objects and surfaces based on images [11]. Based on stereoscopic viewing, the overlap of different images allows obtaining three-dimensional information of an object. For this study, a 3D model of the internal part of a box bridge is created in order to inspect the different surfaces of the box. The model is created using the software Pix4D which transforms the gathered data into a point cloud. Additionally, the software creates a texture mesh between the different points enhancing the visualization of the object. In this case, the focus is centered in the ceiling of the structure since it is the most difficult part to reach for a conventional manual inspection. Once the photogrammetric model is obtained, it is possible to quantify elements of interest such as corroded areas or other damages in the structure.

2.3 *Convolutional Neural Network (CNN)*

The process of crack detection is performed using a pre-trained neural network requiring a fine-tunning procedure in order to adapt the network for crack detection in concrete. For

this work, the pre-trained VGG16 network is selected for the task since it has a better performance than other networks such as InceptionV3 or ResNet for crack classification [12]. Additionally, through python open libraries like Keras, it is possible to download this network facilitating the implementation.

The VGG16 network corresponds to a pre-trained network containing a set of predefined parameters (weights) used to identify other types of objects. To do the fine-tuning process and adapt the network for crack detection, a data set is used to modify the existent weights in the network and thus eliminating the need to train the network and its weights from the beginning. This process allows to speed up the process of training the model to detect the desired damage. The initial parameters such as learning rate, batch size or epochs, where adjusted for the fine-tuning process. For this case, the training of the network was performed using a total of 12852 images evenly split between images of concrete containing cracks and concrete without cracks [3].

It is important to mention that the data set used contains only one type of damage since it was not possible to create a dataset that contained a balanced amount of images of multiple damages and thus avoid a bias in the network.

2.4 *Image analysis*

Once a crack has been identified, different computer vision methods are used to isolate the pixels that compose the crack in order to quantify the width and length of the cracks. The process consists of first transforming the images from RGB color scale to greyscale. Subsequently, analyzing the intensity distribution of the images is performed followed by identifying outliers which correspond to the pixels constituting the crack. The outliers are selected by determining the Median Absolute Deviation (MAD) [13]. The MAD evaluates a dataset and measures the variability of the data. The MAD is calculated as:

$$MAD = median\left(\left|X_i - \tilde{X}\right|\right) \tag{1}$$

where X_i is each element of the data series, $\tilde{X}$ is the median of the data series. With this, a threshold T is calculated following equation (2) to filter the image and isolate the crack pixels:

$$T = \tilde{X} - k * MAD \tag{2}$$

where k is a scale factor that correspond to 3.5 in normally distributed series [14]. The centerline of the remaining pixel regions is determined representing the skeleton of the crack. The length of the cracks corresponds to the length of these skeletons. To determine the width of the crack it is first necessary to define the edges of the crack. This is done taking the previously defined regions and applying an edge detector method, in this case, the Laplacian edge detector. Once the centerline and the edges are defined, the orthogonal distances between each point of the skeleton and the edges are calculated and thus the width of the crack is obtained.

In the case of identifying other damages, the task is performed manually based on the 3D photogrammetrical model created. The model is inspected to determine the regions where leakage, corrosion or other damages may be present. Once the regions are defined, the area is quantified using the software used to create the model.

3 CASE STUDY

A case study is presented where the methodology is applied in the interior of the Strängnäs bridge. This concrete box girder bridge is 5 m wide inside and has a variable height. The test was performed in a 15 m long section situated near one of the supports where the height variates approximately between 5 to 7 m. The images obtained correspond to the inside of the box close to one of the columns supports. Figure 2, present parts of the concrete walls and ceiling in the box.



Figure 2. Inside of box girder close to a support.

After the data was gathered, the 3D photogrammetrical model was created to obtain the texture mesh to better visualize the concrete surface. The time needed to collect the data in the section studied was 25 minutes showing the efficiency of the proposed method.

4 RESULTS

The results of the inspection are presented first in terms of the model created using photogrammetry, the output of the CNN-based crack detection and finally the quantification of the damages found.

4.1 *Photogrammetric model*

The model created represents the ceiling of the box since the focus was centered on this part when taking the images. This is due to the fact that the ceiling represents the major difficulty in the inspection because of the height of the section and because it is the location where the major defects could be seen with the naked eye. The result model is formed by about 7.2 million points in the 3D space and the resulting mesh is presented in Figure 3.



Figure 3. Photogrammetrical model.

The model has black areas and discontinuities due to a lack of points in those areas and the difficulty to create points due to the lack of GPS. Indeed, the absence of GPS poses a challenge since it contributes to the identification of corresponding points between the different images leading to the creation of points in the 3D space. Since the analysis was focused on the ceiling rather than the sidewalls, the discontinuities are located primarily on that area. A more complete model can be obtained adding images from the sidewalls. The model is used to study the ceiling from a front angle instead as skewed angles such as those presented in Figure 2 which simplifies the investigation of the present damages in that section of the bridge. An example of this is presented in Figure 4. From this figure it is possible to identify

different damages such as corrosion and leakage in the structure coming, for example, from the results of extracting concrete cores in the deck.



Figure 4. Box ceiling from 3D photogrammetrical model.

4.2 *CNN results*

The CNN is used to analyze the gathered images and detect cracks in the concrete. The network outputs the sections of the images where cracks are located. Although the bridge is in good state and does not present major defects, the CNN was able to identify cracks in some parts of the section studied. An example of the images obtained is presented in Figure 5.



Figure 5. Images identified as Cracked by the CNN.

It's important to note that some of the results of the CNN correspond to false positives since elements like the shadow of the drone are interpreted as cracks due to their shape. Nevertheless, these can be easily identified as false positives by the inspector when analyzing the results.

4.3 *Quantification of damages*

The damage quantification is made using both the photogrammetrical model, which allows to measure distances and areas, and the image analysis process. In Figure 6 different areas enclosing leakage in the ceiling section of the box are highlighted. The total area enclosed corresponds to 3.5 m^2 retrieved from the model. The section showing dark brown marks in the ceiling, suggesting traces of corrosion, can be seen as straight lines in the transversal direction of the bridge. These lines have a total length of 0.4 m.

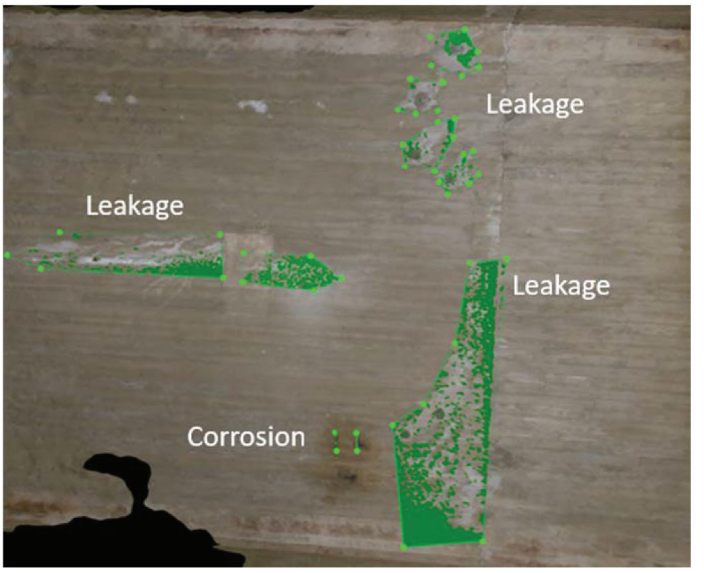


Figure 6. Measurements from the 3D photogrammetrical model.

For the sections that have been labeled as cracked by the CNN the process of quantification is applied to obtain the area of the crack, the edges, the centerline and width. An example of the result of the quantification is presented in Figure 7. The crack is presented in high contrast colors, the area of the crack is presented in yellow, the edges in blue and the centerline is presented in red.

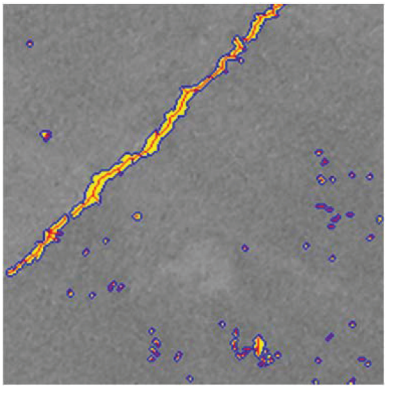


Figure 7. Quantification result.

From the results obtained, it is possible to determine the length of the cracks, giving as result a total of 60 cm of cracks with an average width of 0.3 mm.

5 DISCUSSION AND CONCLUSIONS

The purpose of this field case study was to see the possibility of applying drone inspections inside box girder bridges focusing on detecting damages in the structure. The quantification of the results depends on the quality of the data gathered during the inspection. In this process, the lack of GPS signal for the drone affects its location system as well as its infrared sensors needed to

avoid obstacles thus the complexity of the flight is increased. Furthermore, the absence of GPS signal affects the photogrammetric process relying only on the relation between surface textures.

Additionally, insufficient light and the effect of the drone propellers creating currents of air generating dust clouds can reduce the quality of the images obtained leading to unclear surface images thus, potentially generating errors in the CNN output or the quantification process. Despite the challenges mentioned, it was possible to obtain clear images of the concrete surfaces that allow the application of the CNN, the creation of the photogrammetrical model and the quantification of damages.

The developed photogrammetrical model, though presenting dark spots and discontinuities, proved effective to detect and quantify leakage and corrosion. This shows the utility of 3D photogrammetrical models to obtain valuable information about the damages in a structure.

It was possible to automatically find cracks in some of the concrete surfaces using the machine learning algorithms. The results obtained as an output contain different images with crack-like objects such as shadows from the drone. This can be improved by developing the algorithms used with new data from different bridges. Although the CNN focused on cracks, it can be tuned to be able to detect damages like the ones seen on the photogrammetrical model (leakage and corrosion among others).

Digital inspections as the one presented in this study, serve as an assessment tool for inspector or decision takers to obtain insights of the structural condition and determine further inspection and maintenance plans. Additionally, in this study only a commercial drone and an additional light were used taking less than an hour to obtain the data, proving the cost effectiveness and efficiency of this methodology.

Although the case study shows that it is indeed possible to perform indoor drone-based inspections for structures like box-girder bridges, ongoing research is necessary to continue improving the results. Further research should focus on improving the data quality, addressing challenges like adequate levels of lighting, dust management and the absence of GPS signal. Continuous research on these topics will improve the reliability and applicability of indoor drone-based inspections for large structures.

ACKNOWLEDGEMENTS

This paper was produced as part of the Mistra InfraMaint research program with funding from Mistra, the Swedish Foundation for Strategic Environmental Research. Additionally, the authors would like to acknowledge the Swedish Transport Administration (Trafikverket) for giving access to the bridge.

REFERENCES

[1] B. Chan, D. Anstice, T. Pettigrew, and I. Saul, "Photogrammetric modelling and drones for the effective inspection and management of major steel truss bridges: case study," *Austroads Bridg. Conf.*, vol. 10, p.11p, 2017.

[2] O. S. Sonbul and M. Rashid, "Algorithms and Techniques for the Structural Health Monitoring of Bridges: Systematic Literature Review," *Sensors*, vol. 23, no. 9, pp. 1–29, 2023.

[3] J. C. Avendaño, J. Leander, and R. Karoumi, "Image based inspection of concrete cracks using UAV photography," *Bridg. Safety, Maintenance, Manag. Life-Cycle, Resil. Sustain.*, pp. 1973–1978, 2022.

[4] J. Deng, A. Singh, Y. Zhou, Y. Lu, and V. C. S. Lee, "Review on computer vision-based crack detection and quantification methodologies for civil structures," *Constr. Build. Mater.*, vol. 356, no. September, 2022.

[5] D. Ai, G. Jiang, S. K. Lam, P. He, and C. Li, "Computer vision framework for crack detection of civil infrastructure—A review," *Eng. Appl. Artif. Intell.*, vol. 117, no. September 2022, p. 105478, 2023.

[6] C. Chen, H. Seo, C. Jun, and Y. Zhao, "A potential crack region method to detect crack using image processing of multiple thresholding," *Signal, Image Video Process.*, vol. 16, no. 6, pp. 1673–1681, Sep. 2022.

[7] G. Morgenthal *et al.*, "Framework for automated UAS-based structural condition assessment of bridges," *Autom. Constr.*, vol. 97, no. May 2018, pp. 77–95, 2019.

[8] B. J. Perry, Y. Guo, R. Atadero, and J. W. van de Lindt, "Streamlined bridge inspection system utilizing unmanned aerial vehicles (UAVs) and machine learning," *Meas. J. Int. Meas. Confed.*, vol. 164, p. 108048, 2020.
[9] M. Lei, L. Liu, C. Shi, Y. Tan, Y. Lin, and W. Wang, "A novel tunnel-lining crack recognition system based on digital image technology," *Tunn. Undergr. Sp. Technol.*, vol. 108, no. October 2020, p. 103724, 2021.
[10] R. Zhang, G. Hao, K. Zhang, and Z. Li, "Unmanned aerial vehicle navigation in underground structure inspection: A review," *Geol. J.*, vol. 58, no. 6, pp. 2454–2472, 2023.
[11] W. Linder, *Digital photogrammetry A practical course*, 3rd ed. Springer, 2006.
[12] C. V. Dung and L. D. Anh, "Autonomous concrete crack detection using deep fully convolutional neural network," *Autom. Constr.*, vol. 99, no. July 2018, pp. 52–58, 2019.
[13] J. C. Avendaño, J. Leander, and R. Karoumi, "Image-based concrete crack detection method using the median absolute deviation," *Submited Manuscr.*, pp. 1–21, 2023.
[14] C. Leys, C. Ley, O. Klein, P. Bernard, and L. Licata, "Detecting outliers: Do not use standard deviation around the mean, use absolute deviation around the median," *J. Exp. Soc. Psychol.*, vol. 49, no. 4, pp. 764–766, Jul. 2013.

Bridge Maintenance, Safety, Management, Digitalization and Sustainability – Jensen, Frangopol & Schmidt (eds)
© 2024 The Author(s), ISBN 978-1-032-77040-6
Open Access: www.taylorfrancis.com, CC BY-NC-ND 4.0 license

Decision algorithms for the managing of steel railway bridges

Jordan Garcia, Francisco Javier & Campo Rumoroso Iván
PEDELTA, Barcelona, Spain

ABSTRACT: As a part of the recently funded EU project BRIDGITISE, which focuses on the digitalization of bridge management through the development of innovative approaches to information management, the decision algorithms to be able to manage bridges across their lifetime are a key part of the process. In steel bridges, corrosion, fatigue, fracture, and buckling are the most common processes governing the structural behaviour of the bridge. All these failure processes are influenced by the actual loads, geometrical imperfections, and loose of thickness by corrosion in the steel members. The evolution of these parameters along the lifecycle of the bridge is unknown in the design stage, before its construction and opening to traffic, and some assumptions are made based on the Codes, which at their turn are based on statistical analysis of specimens and previous experience. Nevertheless, the specific conditions for each bridge are different, and with the data collected during the lifecycle of the bridge, the structural analysis and the structural verifications can be updated. This allows updating the maintenance manual and program. This paper will focus on showing which parameters should be monitored in a steel railway bridge and how to use this information to make decisions for the bridge maintenance to guarantee the required structural safety.

1 INTRODUCTION

Extending the lifespan of existing bridges is imperative for advancing sustainability in construction, as it offers notable advantages over the alternative of demolition and reconstruction, including reduction of materials and energy consumption, which increases its sustainability. Nevertheless, there are cases where bridge demolition has been proposed due to an insufficient understanding of the bridge's behaviour.

Numerous pathologies can cause the proposal of bridge demolition, with corrosion and fatigue being particularly critical for steel bridges. Both conditions share the characteristic of manifesting over prolonged periods and potentially leading to catastrophic consequences.

While current fatigue models are suitable for designing new bridges, they may be considered overly conservative for existing bridges in some instances, as observed by the authors. For example, evaluation based on available data may indicate an expected fatigue life termination years before, yet inspections reveal no visual evidence of crack initiation. In those cases, the AASHTO MBE (FHWA-NHI 2016) proposes a probabilistic approach combined with inspections to extend bridge fatigue life. However, this approach lacks consideration of the actual bridge behaviour, introducing potential risks.

Corrosion presents a similar challenge due to the numerous variables involved, including moisture, oxygen, and de-icing agents, making the development of an accurate model for a specific location difficult.

Long-term instrumentation emerges as a promising approach for predicting bridge ubehaviour, leveraging actual data from the structure (García-Sánchez, 2016) (Leander& Karoumi

DOI: 10.1201/9781003483755-406

2018). However, the effective management of sensor-generated information poses a current challenge, where machine learning can play a pivotal role.

Addressing these challenges, the recently funded EU project BRIDGITISE aims to digitalize bridge management by developing innovative information management approaches. The project will create and validate technologies for effective bridge information management, supporting decisions pertinent to bridge integrity management throughout its lifecycle. The project consortium, comprising universities, research centers, industrial companies, and end-users, combines diverse expertise.

This paper outlines Pedelta's contribution to the BRIDGITISE project, beginning with the motivation derived from in-house projects. Subsequently, the project's description and goals are delineated, culminating in an exposition of one of the bridges slated for study within the project.

2 PREVIOUS EXPERIENCE

2.1 *Feixa Llarga Bridge*

The Feixa Llarga bridge is located at the entrance to the free trade zone of Puerto de Barcelona, Barcelona Harbour. The bridge has eleven spans, with a main central span of 27 m over the railway line and five access spans of 21 m on each side. The width of the bridge is 7 meters.

The uniqueness of the bridge lies in its construction. It is a modular steel bridge built in the early 70s. The deck consists of two Pi orthotropic steel girders bolted together in the center. The substructure is a pi-shaped steel frame.



Figure 1. Feixa Llarga Bridge.

As depicted in Figure 1, the structure under consideration exhibits multiple welds and low category fatigue details. Among other damages in the bridge, ome of those welds were broken, and Pedelta was retained to develop the rehabilitation project.

During the inspection, the identification of cracks, particularly in the deck welds, was notable; however, no evidence of material failure was discerned. Subsequent calculations indicated a low expected fatigue life for certain details. This precarious situation was attributed to a combination of suboptimal detailing, exemplified by the bottom flange of girders in Figure 1, short lightweight spans - where the predominant load is solely the live load - and the

high traffic intensity of trucks. Consequently, a recommendation was made to close the traffic o the bridge and undertake structural retrofitting.

An alternative proposal was extended to the client, suggesting the option of reopening the bridge to traffic while implementing a vigilant monitoring system. However, the client elected to confront the challenges posed by traffic diversions. Ultimately, the bridge underwent retrofitting and was reopened to traffic after a closure period of 2.5 years.

In this case, the incorporation of instrumentation aimed to establish performance indicators and scrutinize their evolution. Nonetheless, the sheer volume of information collected posed a considerable challenge in terms of effective management. Moreover, a comprehensive understanding of the bridge's behaviour through instrumentation would have been instrumental in validating the assumptions considered in the project.

2.2 *Alicante Denia Line*

Ferrocarrils de la Generalitat Valenciana (FGV) operates a railway line spanning from Alicante to Denia in the Comunitat Valenciana region. This railway network links Alicante to various popular resort towns, including Benidorm, Altea, and Calpe. Spanning nearly 100 km, the railway's initial construction dates back to the early 20th century, encompassing diverse types of structures such as underpasses, overpasses, pedestrian crossings, culverts, viaducts, and tunnels. These structures exhibit a wide range of typologies, materials, and construction ages, with some remaining in their original state, others undergoing repair, rehabilitation, or enhancement, and some being entirely replaced.

In 2018, FGV procured a new fleet of modern trains, prompting Pedelta's engagement to conduct a thorough load capacity assessment on the existing bridges, considering the implications of the new train loads. Additionally, Pedelta was tasked with an extensive preliminary research effort involving the compilation of existing information on the bridges and the execution of various on-site tests, including concrete compressive strength tests, reinforcing steel tests, and non-destructive tests.

The subsequent inspection and assessment report affirmed the compatibility of the new trains with most of the existing structures. However, it was recommended that two aged steel bridges be replaced in the coming years due to fatigue life concerns. A more detailed evaluation considering the real behaviour might have potentially extended the operational life of these bridges.

2.3 *Sant Boi HSR Bridge over the Llobregat River*

Completed in 2007, this bridge was the first steel structure to be built on the High-Speed Railway joining the cities of Madrid and Barcelona. The 870 m long bridge comprises two parts: a 340 m long steel–concrete structure which spans a five-lane highway and a railway; and a continuous prestressed concrete box girder viaduct across the Llobregat River with a longest span of 50 m. The steel bridge is a continuous structure with six spans measuring 44+63+63+ 63+63+44 m respectively. The bridge consists of a king post truss with curved diagonals, which supports a composite steel-concrete deck. The 14 m wide deck accommodates two ballasted tracks, for a total bridge width of 17 m. The bridge is shown in Figure 2.

Pedelta assumed responsibility for the design across all phases of the project, encompassing conceptual design, detailed design, and construction assistance. As expected, 15 years post-construction, the bridge has exhibited no structural pathologies aside from typical coating deterioration. Notwithstanding this favourable condition, owing to the unique characteristics of the structure, it has remained under the continuous monitoring purview of the administration (ADIF) since its construction.

Even though the bridge was designed according to the most contemporary codes applicable at the time of its construction, distinctive structures like this one may manifest unforeseen behaviours not explicitly addressed in prevailing design codes. Consequently, the ongoing monitoring of the structure is crucial. Furthermore, it is recommended to leverage the



Figure 2. Sant Boi HSR Bridge.

information gleaned from this monitoring process to enhance our understanding of the structure's performance and, if necessary, inform any potential adjustments or interventions. One of the critical issues in this bridge design was the joint between the transverse steel beams and the longitudinal lateral trusses. The joint stiffness played a significant role in the fatigue design of these transverse joints, which extend along the whole bridge length. Monitoring the actual stresses and deformations at these joints would have helped to more accurately predict its actual behaviour for future similar designs and to have further information about the fatigue lifespan of these joints compared with the expected.

3 PROJECT DESCRIPTION

The examples elucidated in the preceding section underscore the role of Structural Health Monitoring (SHM) in enhancing the safety of both existing structures and new complex constructions. However, these instances also illuminate some challenges associated with SHM:

- Information Volume: The copious amount of data generated by SHM poses a challenge in terms of effective handling, necessitating the development of new algorithms for processing.
- Perceived Cost: Despite its efficacy, there persists a perception among some administrations that SHM is expensive. Consequently, alternative solutions are sometimes favoured, even if they imply the reconstruction of the structure.

Besides, the first and the second examples also reveal that current fatigue models may be conservative in some cases.

Furthermore, the first and second examples underscore that existing fatigue models may exhibit conservatism in certain cases.

These challenges, among others, motivate Pedelta's active participation in the BRIDGITISE project. Specifically, Pedelta is contributing to Task NEURAL, focusing on Machine Learning for deterioration prediction based on digital information streams. The overarching objective of this project is to devise a methodology rooted in long-term monitoring, particularly with small-scale systems, to prognosticate deterioration phenomena like corrosion wastage and fatigue. The ultimate goal is to develop a tool capable of extending the service life of bridges and salvaging structures deemed condemned.

An inherent advantage of SHM is its capacity to enhance understanding of a structure's real behaviour. For instance, it enables the assessment of connection stiffness in steel structures and facilitates the consideration of actual stiffness by accounting for concrete cracking in concrete structures. Additionally, SHM reduces the necessity of conservative assumptions

during analysis. The schematic representation of the project's conceptual framework is delineated in Figure 3.

The initial phase involves the extensive collection of data from diverse sensors embedded in the structure over an extended period. Notably, the endeavour aims to strategically minimize the number of sensors utilized to optimize monitoring costs, given the prevailing hesitancy among some administrations owing to financial considerations.

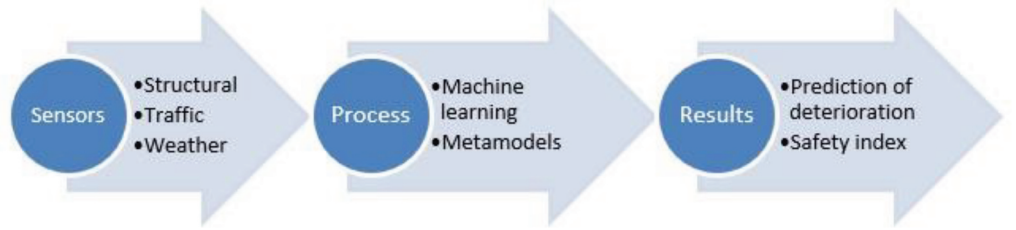


Figure 3. Project framework.

Subsequently, in the second phase, the gathered information undergoes rigorous processing. Machine learning constitutes a pivotal aspect of this project, as it will be employed to construct metamodels for interpreting monitoring data and predicting deterioration. Various machine-learning algorithms will be systematically evaluated and validated to enhance the efficiency of predictions. The anticipated outcome of the project involves the amalgamation of machine learning methodologies, encompassing neural networks, support vector machines, and decision trees, to facilitate accurate deterioration predictions.

The ultimate objective of this project is twofold: firstly, the precise prediction of deterioration, as elucidated earlier; secondly, the establishment of a safety measure for the structure, termed, for example, the Safety Index.

In the subsequent phase of the project, the metamodel, initially developed using numerical data, will undergo adaptation, training, and validation using real-case study data. This phase, conducted under the supervision of Pedelta, will involve the explanation of one of the selected bridges in the ensuing section.

4 CASE STUDY

4.1 *Bridge description*

Pedelta has been commissioned by Ferrocarrils de la Generalitat de Catalunya (FGC) to conduct an assessment and prepare a rehabilitation plan for the Road Vic Bridge in Manresa, Catalunya. The selection of this bridge for study within the framework of the BRIDGITISE project is motivated by the various pathologies it exhibits, as delineated below. This bridge serves as an exemplary case for examination and analysis within the broader scope of the BRIDGITISE project.

Dating back to 1924, the Road Vic Bridge comprises a singular span measuring 17.3 meters. It features a main truss on each side, spaced at 8.8 meters. Designed to accommodate the passage of two metric railway tracks, the bridge supports the sleepers of each track on two longitudinal stringers, with these stringers being upheld every 1.8 meters by transverse beams. A picture of the bridge is shown in Figure 4.

The bridge is located in the corridor of the Potash Mines of Suria.



Figure 4. Road Vic Bridge.

4.2 *Pathologies of the bridge*

The degradation incurred from the decades-long transport of potash without protective covering has been substantial. To address this degradation, a series of retrofitting measures were implemented on the Road Vic Bridge, including the addition of numerous L-shaped steel profiles and an increase in the plan bracing. However, a noteworthy challenge arises from the retrofitting approach, as it was made by combining welding and bolts without apparently paying attention to fatigue-related issues.

The issues articulated align seamlessly with the objectives of the project:

- Corrosion wastage: The prolonged exposure to potash has led to the degradation of multiple elements in the bridge. Furthermore, the addition of new reinforcing steel profiles has concealed certain areas, introducing uncertainties in predicting the evolution of corrosion within the bridge.
- Fatigue: The bridge's susceptibility to fatigue is heightened due to its relatively short span, resulting in the predominant influence of live loads. Compounding this vulnerability is the fact that the primary loads on the bridge are railway trains, which exert a higher weight compared to road bridges. Furthermore, the lack of comprehensive knowledge during the initial construction, coupled with the subsequent implementation of numerous retrofits, has led to the incorporation of multiple suboptimal fatigue details. These factors collectively contribute to an elevated risk of fatigue-related issues in the structural integrity of the Road Vic Bridge.

4.3 *Preliminary evaluation*

Preceding the inspection of the bridge, a preliminary analysis was conducted to assess and identify the critical elements of the structure.

The analysis was executed utilizing the Sofistik software. The structural model of the bridge predominantly employed beam elements for most components, except for two plates. Figure 5 illustrates the representation of the bridge within the structural model.

The Ultimate Limit State (ULS) analysis indicated that the structural capacity of the bridge appears to be adequate for the loads stipulated by the owner. Notably, only the vertical members exhibited overstresses in the Serviceability Limit State (SLS). Importantly, no physical evidence of damage was detected during the inspection of these members. Consequently, it is hypothesized that the observed overstresses may stem from the assumption of a rigid connection between the transverse beams and the vertical members. The implementation of SHM is anticipated to facilitate the determination of the actual stiffness of this connection, providing valuable insights into the behaviour of the bridge under various loading conditions.

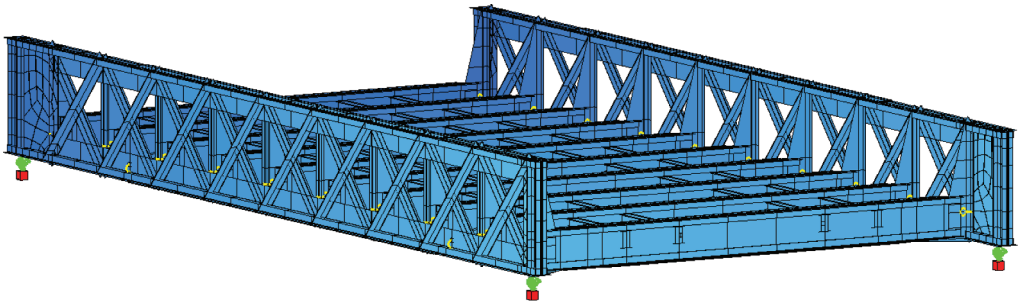


Figure 5. Structural model.

An additional critical calculation performed on the bridge involved a comprehensive fatigue analysis. Ferrocarrils de la Generalitat de Catalunya (FGC) maintains an extensive record of traffic over the bridge spanning several decades, detailing locomotive types and hoppers. This historical data allows for a thorough fatigue analysis of the bridge.

In the preliminary analysis, certain details were identified as approaching the end of their fatigue life. However, these details are highly sensitive to various parameters, including the dynamic impact factor and the effectiveness of the added reinforcing elements. Consequently, the monitoring plan proposed within the framework of the BRIDGITISE project is anticipated to play a pivotal role in accurately assessing the remaining fatigue life of the bridge. This proactive approach aligns with best practices in infrastructure management, ensuring the ongoing safety and longevity of the bridge over the Vic Road in Manresa..

Another relevant calculation performed in the bridge has been the fatigue analysis. FGC has kept a register of the traffic over the bridge for decades, including the types of locomotives and hoppers. Then, it is possible to analyze the fatigue in the bridge.

During the preliminary analysis conducted, some details were found to be close to the end of its fatigue life. However, they are also very sensitive to different parameters such as the dynamic impact factor, or the effectiveness of the reinforcing elements added. Consequently, the monitoring plan of the bridge within the frame of the project BRIDGITISE will help to properly address the evaluation of the fatigue remaining life of the bridge.

4.4 *Monitoring plan*

The devised monitoring plan for the bridge encompasses various sensor types to comprehensively capture its behaviour.

The initial category comprises environmental sensors, including a weather station to correlate results with weather conditions. Temperature sensors on the top and bottom chords will track thermal displacements, and the installation of a camera aims to provide supplementary information about traffic over the bridge. Given the significant impact of environmental conditions on corrosion, corrosion sensors will be strategically placed to analyze corrosion evolution in different sections of the bridge.

The next set of sensors includes displacement sensors and accelerometers. These sensors, situated at quarter-spans, midspan, and bearings, will detect any variations in the deflected shape of the bridge at rest or its dynamic properties, serving as indicators of potential damage progression. Additionally, strain gauges will be installed in critical sections identified during the preliminary analysis, with a focus on minimizing their number

The overarching goal of the monitoring plan is to utilize small-scale systems, thereby minimizing the sensor count and capitalizing on correlations between them. For example, information about transverse beams will be obtained from sensors in the main truss, eliminating the need for sensors on critical sections of each transverse beam. This approach not only optimizes cost-effectiveness but also streamlines the management of the monitoring system.

5 CONCLUSION

The imperative to extend the lifespan of existing bridges for the sake of sustainability in construction is underscored by the advantages it holds over demolition and reconstruction. The challenges posed by insufficient understanding of a bridge's behaviour, leading to unnecessary demolition proposals in some cases, emphasize the need for advanced methodologies. Pathologies such as corrosion and fatigue, particularly critical for steel bridges, necessitate innovative approaches.

While existing fatigue models may prove conservative for existing bridges, the BRIDGITISE project, in which Pedelta actively participates, seeks to address these challenges through machine learning-based deterioration prediction. The case study of the Bridge over the Vic Road in Manresa exemplifies the complexity of issues related to corrosion and fatigue, emphasizing the importance of a comprehensive monitoring plan. The proposed plan strategically integrates environmental sensors, displacement sensors, accelerometers, and corrosion sensors, employing a small-scale system to optimize cost-effectiveness. The project's ultimate goal is not only to predict deterioration accurately but also to establish a safety index for structures, contributing to the sustainable management of bridge infrastructure.

REFERENCES

García-Sánchez, D. 2016. Statistical Control and Regression Models. A Practical Approach in Bridge Control. PhD. Dissertation. Santander.

Federal Highway Administration & National Highway Institute. 2016. Design and evaluation of Steel Bridge for Fatigue and Fracture. Reference Manual.

Leander, J. Karoumi, R. 2018. The value of monitoring on the service life prediction of a critical steel bridge. Proc. IALCCE 2008,2121,2128

Bridge Maintenance, Safety, Management, Digitalization and Sustainability – Jensen, Frangopol & Schmidt (eds)
© 2024 The Author(s), ISBN 978-1-032-77040-6
Open Access: www.taylorfrancis.com, CC BY-NC-ND 4.0 license

Lightweight vehicles in indirect structural health monitoring: Current advances and future prospects

P.F. Giordano
Department of Architecture, Built Environment and Construction Engineering, Politecnico di Milano, Milan, Italy

S. Quqa
Department of Civil, Chemical, Environmental, and Materials Engineering, University of Bologna, Bologna, Italy

M.P. Limongelli
Department of Architecture, Built Environment and Construction Engineering, Politecnico di Milano, Milan, Italy
Lisa Meitner Guest professor at Lund University, Faculty of Engineering, Division of Structural Engineering, Lund, Sweden

ABSTRACT: Recent research has explored the potential of using the dynamic response of passing vehicles to conduct Structural Health Monitoring (SHM) efficiently. Various types of vehicles, including cars, vans, trucks, and even manually propelled carts, have been employed in this approach, with different configurations of exciters and receivers. A noteworthy development in this field involves the inclusion of lightweight vehicles like bicycles and scooters. Lightweight vehicles offer several advantages, including their affordability, sustainability, and minimal environmental impact. These vehicles have a negligible impact on the dynamic behavior of structures due to their low speeds and negligible mass, making them ideal for monitoring structures that are challenging to access, such as footbridges. This paper provides a comprehensive review of recent literature on the application of lightweight vehicles in SHM of urban bridges. It emphasizes the potential benefits and current challenges associated with these applications while offering insights into future research directions.

1 INTRODUCTION

Bridge management stands as a pressing concern for transport authorities worldwide, facing the challenges arising from the convergence of aging structures, limited economic resources, and the escalating impact of climate change-induced calamities that expedite the degradation of critical assets. To address these challenges, the assessment of the structural health of bridge has traditionally relied on visual inspections and testing campaigns conducted by specialized technicians (Poli et al. 2023). However, in recent decades, Structural Health Monitoring (SHM) methods have emerged as a promising alternative, seeking to provide continuous surveillance and early detection of structural issues (Cunha et al. 2018, Karakostas et al. 2023).

Conventionally, SHM techniques have predominantly involved the installation of dedicated sensing devices directly onto bridges, comprising sensors, cables, and acquisition systems. These systems allow for the extraction of damage-sensitive features from physical measurements, which may offer insights into structural health over time. Among SHM techniques, vibration-based SHM, based on dynamic measurements, presents a notable advantage: it

DOI: 10.1201/9781003483755-407

allows for assessment of global structural integrity even when sensors are not in close proximity to damage locations. However, traditional SHM systems bear drawbacks associated with high installation costs, dependency on accessible power sources, and ongoing maintenance expenses, often complicating the estimation of their economic benefits over the initial investment (Giordano et al. 2023).

In response to these challenges, the concept of "Indirect" or "Drive-By" Structural Health Monitoring (ISHM) has gained interest. ISHM exploits the dynamic response of instrumented vehicles as they cross bridges. This approach aims to reduce costs associated with the installation of dedicated SHM systems. As far as the authors' knowledge, the initial theoretical exploration of using moving vehicles with installed sensors was introduced by Yang et al. in 2004, demonstrating the feasibility of this approach (Yang et al. 2004). Subsequent studies extended this concept, coining the term "indirect SHM" to distinguish it from traditional "direct SHM" methods employing contact sensors (Cerda et al. 2012).

Over the past fifteen years, a proliferation of scientific research has presented various ISHM approaches based on vibration signals collected onboard moving vehicles and considering various exciter-receiver configurations. Some ISHM approaches use vehicles expressly designed for monitoring applications (Lin & Yang 2005), while others exploit regular vehicles, such as cars and trucks, to serve as both instruments and exciters (Kim & Lynch 2012). Recent research has taken an interesting turn towards the feasibility of using lightweight vehicles such as bikes and scooters for ISHM applications (Quqa et al. 2022). Additionally, ISHM strategies incorporating data collected by smartphones have been proposed, taking advantage of the widespread availability and connectivity of these devices for crowdsensing applications.

In the coming four years, the topic of ISHM based on crowdsensing and mobile data, as well as lightweight vehicles, will be directly addressed in one of the Ph.D. projects developed within the new Marie Skłodowska-Curie Actions (MSCA) doctoral network named "BRIDGITISE," initiated on January 1, 2024, with financial support from the European Commission (see www.bridgitise.polimi.it). The BRIDGITISE doctoral network is dedicated to advancing the digitalization of bridge management throughout its lifecycle by pioneering innovative approaches to information management. This initiative involves launching a network comprising 16 Ph.D. projects, each contributing to the overarching goal of enhancing bridge management through digital means. One of these projects, called "Crowd," specifically focuses on developing a crowdsensing strategy to extract structural information from sensors mounted on vehicles or smartphones.

This paper aims to provide a preliminary literature review on indirect vibration-based SHM for bridges, with a specific focus on the integration of lightweight vehicles like bikes and scooters. Serving as an exploration preceding the commencement of the Crowd project, this literature review also includes a preliminary application of ISHM using bikes to demonstrate the feasibility of this approach.

The paper is organized as follows: the BRIDGITISE project is presented in the second section. The Scopus literature review is presented in section 3. Section 4 provides insight into ISHM using lightweight vehicles and presents an application. Finally, conclusions are given, and future works are presented.

2 THE "BRIDGITISE" PROJECT

The BRIDGITISE doctoral network focuses on advancing the digitalization of bridge management across the entire lifecycle. The project's core idea is to develop and validate on-site technologies that are both innovative and cost-effective for managing bridge information. The initiative is organized into three main research clusters: creating low-cost, large-scale, and automatic technologies for managing bridge information; adapting Artificial Intelligence and IoT technologies for bridges; and designing digital decision support tools for comprehensive bridge management.

With 16 PhD projects aligned with these clusters, the network collaborates with six universities, one research center, and seventeen industrial partners. Industrial collaboration provides practical case studies for applying and validating research findings, enhancing the doctoral candidates'

skills for diverse sectors. The BRIDGITISE network aims to deliver technology-enhanced training tools, workshops, and an open platform for sharing bridge management data.

One specific project within the network, named "Crowd", addresses the challenges of large-scale monitoring using crowdsensing, considering cost-effectiveness and scalability. This project will propose a system identification approach based on crowdsensed data, focusing on efficient and reliable data transmission to a cloud unit. It also considers the impact of sensors and carriers on collected data, with validation planned on real bridges. The project further aims to develop an IoT information transmission protocol through a smartphone application, engaging bridge users in data collection. The results will be systematically compared with those from traditional monitoring systems. The "Crowd" project is scheduled to officially start in mid-2024 and is expected to span a duration of three years.

3 LITERATURE OVERVIEW ON ISHM

3.1 *Scopus analysis*

In this section, an overview of the state of the art in the field of ISHM of bridges is presented, based on an analysis of the Scopus database conducted in December 2023. The database query employed specific keywords to narrow down the focus to SHM-related literature, using ("Indirect" OR "drive-by") AND "structural" AND "health" AND "monitoring" AND "bridge" as the search terms. This search yielded a total of 177 documents published between 2006 and 2024 including both conference and journal papers.

For contextual comparison, a broader set of keywords, "structural" AND "health" AND "monitoring" AND "bridge," was utilized, resulting in 8635 documents published between 1988 and 2024. This broader search encompasses a comprehensive body of literature covering various aspects of SHM in the context of bridges, highlighting the relatively modest portion of literature dedicated specifically to ISHM. The analysis presented serves as a preliminary exploration of the literature on ISHM for bridges, and it is important to note that the reported numbers may be conservative. Specifically, the chosen keywords for the search might not encompass all relevant papers, such as those addressing dynamic identification, see e.g. (Yang et al. 2013, Di Matteo et al. 2022), leading to a potential underestimation.

The identified 177 ISHM documents underwent a meticulous analysis, leading to the exclusion of 61 documents either unavailable or unrelated to the topic of interest. The resulting dataset includes documents published between 2010 and 2024 and provides a focused and relevant collection of documents specifically addressing ISHM of bridges. Figure 1 illustrates the number of publications over the years, indicating an upward trend in scientific production related to ISHM.

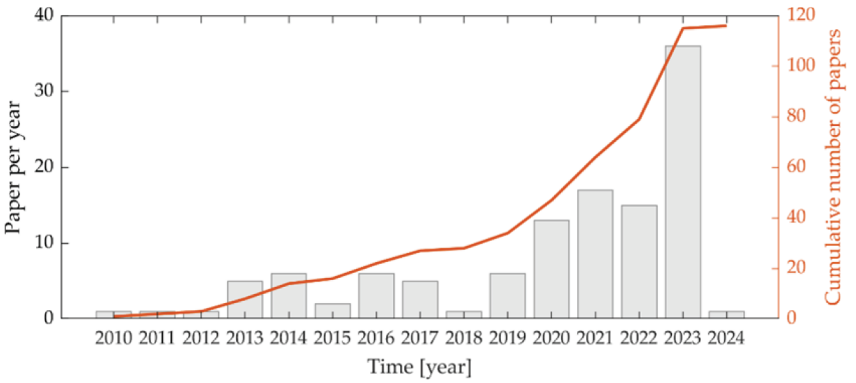


Figure 1. Number of papers published per year and their cumulative number over time.

Concerning the content of the papers identified in the analysis, 7 are literature reviews, while the majority focus on proposing ISHM strategies and associated algorithms. The majority of the remaining papers focus on proposing ISHM strategies and the relevant algorithms. These strategies are predominantly demonstrated through numerical simulations, constituting 42% of the corpus, or laboratory tests, which account for 41%. Notably, a relatively small portion of the papers includes on-site demonstrations (17%). In the subset of papers that feature on-site demonstrations, various vehicles are employed as carriers for sensors, underscoring the flexibility and adaptability of ISHM strategies to different modes of transportation. Specifically, the most commonly used vehicles are cars, representing 28% of the cases. Trains are the second most prevalent, accounting for 22% of the on-site demonstrations. Additionally, vans, trucks, and bikes each contribute to 11% of the cases. Applications involving bikes focus on footbridges, while applications involving vans, trucks, and cars predominantly center on concrete girder bridges. Figure 2 provides a visual representation of the results of the literature review.

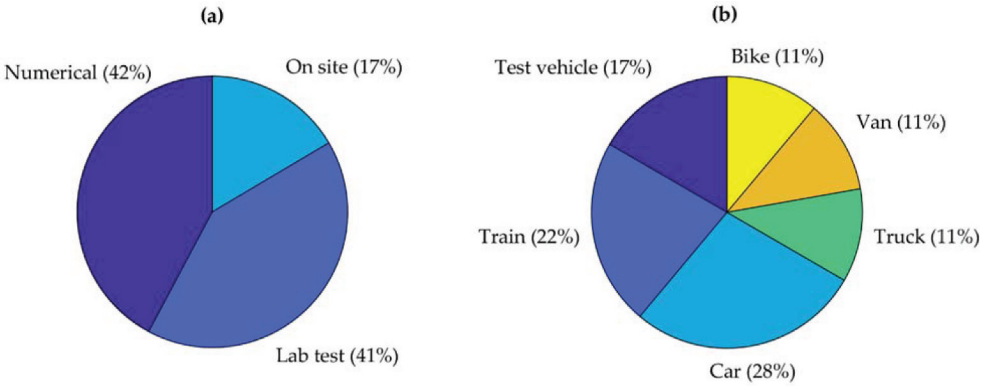


Figure 2. Pie charts: (a) Application type; (b) Vehicles types for on site tests.

3.2 *Focus on lightweight vehicles*

The integration of lightweight vehicles, such as bikes and scooters, in ISHM introduces several advantages that align with contemporary sustainability and urban mobility considerations. These vehicles offer cost-effective solutions with high sustainability, as emphasized by their low cost and positive environmental impact in urban areas, contributing to the reduction of traffic congestion. Moreover, the intrinsic characteristics of lightweight vehicles, including low speed and negligible mass relative to monitored structures, ensure that their dynamic behavior has minimal impact on the structures being monitored. This characteristic becomes especially beneficial when monitoring structures that are inaccessible to larger vehicles, such as footbridges.

However, potential challenges associated with the use of lightweight vehicles for ISHM exist. Factors than can influence the reliability of data collected from lightweight vehicles such as noise effects introduced by the vehicle's operator, vehicle dynamics, and the inherent uncertainty in data when recorded by smartphones (which often come equipped with low-cost sensors). Despite these challenges, the advent of crowdsourcing data presents an opportunity to enhance the overall quality of ISHM results. This improvement becomes particularly notable when users employ standardized vehicle types, ensuring known vehicle properties.

Shared micromobility services, such as bike and scooter sharing platforms, emerge as promising contributors to ISHM strategies. These services typically offer a limited variety of vehicle types within a given urban area. This standardization simplifies the integration of crowdsourced data into ISHM processes, contributing to more reliable and consistent monitoring outcomes.

To the best of the authors' knowledge, three recent works specifically address the utilization of lightweight vehicles for ISHM, i.e. (Quqa et al. 2022, Li et al. 2023, May et al. 2023).

Nevertheless, the number of publications on this topic is expected to grow in the coming years due to the escalating interest in ISHM.

The first study explores the application of shared micromobility vehicles, such as bicycles and electric kick scooters, for monitoring urban bridges (Quqa et al. 2022). This was the first paper exploring the use of lightweight vehicles for ISHM applications. An automatic ISHM strategy is proposed based on the data collected by smartphones temporarily installed on shared micromobility vehicles. The framework is demonstrated on a real footbridge using an urban bicycle. The following section provides a more detailed presentation of this strategy.

These results are validated and extended by other authors, who performed field tests involving direct and indirect monitoring of a bicycle/pedestrian traffic bridge (May et al. 2023). The bridge deck and bicycle frame were equipped with wireless accelerometers, transmitting data during passages. The tests included multiple traversals to counteract road surface roughness effects through ensemble averaging. The study suggests several novel contributions, including the demonstration that low-cost sensor-carrying human-powered vehicles can excite and record bridge dynamics. Simultaneous sensing of the vehicle and bridge is highlighted to reduce potential ambiguity. Additionally, the introduction of the concept of using pedaling cadence to increase the visibility of bridge modes is presented.

The third study describes a novel indirect method for identifying the frequency of footbridges using vibrations from ordinary scooters (Li et al. 2023). The authors build a three-degree-of-freedom finite element model for a scooter and simulate a simply supported footbridge using beam elements. The presence of road roughness is considered in the numerical model. The key conclusions drawn from the research are as follows: (1) The road roughness has a strong influence on the identification of the footbridge frequencies. Without considering road roughness, the footbridge frequencies can be directly determined from the scooter's vibrations. However, these frequencies are covered by noise when road roughness is present; (2) Factors such as environmental noise, footbridge damping, and tire damping primarily impact the high-frequency range (> 20 Hz in this study), while the identification of low-order frequencies (first two frequencies in this study) of the footbridge is minimally affected.

4 APPLICATION

The viability of employing micromobility vehicles (in this case, bicycles) to acquire modal or operational parameters commonly used in vibration-based SHM methods, such as natural frequencies, mode shapes, or Operating Deflection Shapes (ODSs), is demonstrated on a footbridge situated in Bologna, Italy, spanning the A13 motorway between Bologna and Padova (Figure 3a). Comprehensive details about this structure are available in References (Majowiecki 2005, Majowiecki & Cosentino 2011, Quqa et al. 2022). A smartphone (iPhone SE, second generation, 2020) installed on a typical city bicycle (Figure 3b) was employed to gather different data types while traversing the bridge, namely, acceleration and angular velocity recorded along three orthogonal axes, three magnetic field measurements, and three position logs encompassing latitude, longitude, and altitude.

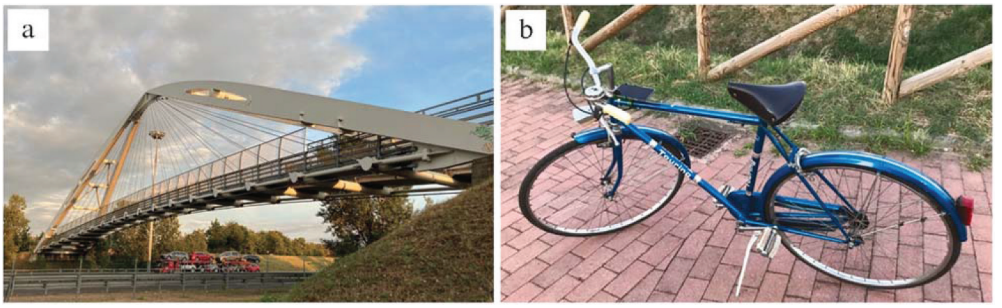


Figure 3. Case study: (a) Bridge view, (b) Instrumented bicycle.

Crowdsourcing is simulated by traversing the bridge and collecting data multiple times (in total, 36 rounds of riding back and forth across the footbridge). The duration of each sample varied between 45 and 70 seconds, based on the user velocity. All tests were conducted under operational conditions, with the presence of at least one pedestrian or a runner crossing the bridge. The measurements were captured using the MATLAB Mobile app (MathWorks 2021), and the algorithms were subsequently applied on a PC to identify the first natural frequency of the bridge and the ODS of a narrow frequency range centered in that value. Each dataset collected underwent processing following the procedure outlined in Figure 4, encompassing the following steps:

1) Identification of bridge dynamic features: First, a band-pass filter is applied to the vertical acceleration data to extract the response component in a user-defined frequency range (previously selected based on a rough estimate of the fundamental natural frequency of the bridge). Then, the amplitude of the structural response within this range is calculated using the Hilbert transform and interpreted as the ODS of the structure in the proximity of its main natural frequency.
2) Identification of Sensor Location: GPS and all Inertial Measurement Unit (IMU) measurements, excluding vertical accelerations, are employed to estimate the vehicle (and sensor) location with high spatial resolution through an extended Kalman filter. This process helps identify where the vertical acceleration data (and thus the identified ODS amplitude) was collected on the bridge. Then, the first principal component of the obtained position (in geographical coordinates) is used to express the sensor location with respect to the bridge axis, employing a 1D reference system aligned along the bridge.
3) Estimation of a dense ODS: The ODS amplitudes identified in step (1), which are dependent on the specific path and speed of the vehicle, are realigned at the locations identified in step (2) through linear interpolation. This alignment allows for averaging the amplitudes identified by different vehicles.
4) Averaging of ODS amplitudes: The ODSs identified during a set of passages are averaged to enhance the robustness of the identification process and mitigate noise effects.

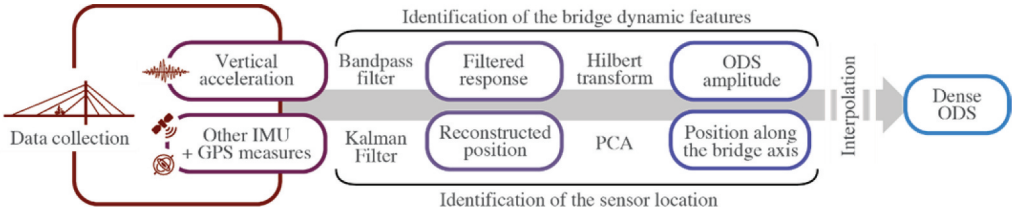


Figure 4. Scheme of the proposed identification procedure.

Figure 5 illustrates the power spectra of 36 vertical acceleration time series gathered on the bicycle, compared with the spectrum of a 5-minutes bridge response obtained by placing the smartphone at 1/4 of the bridge span from the eastern support. The fundamental resonant frequency of the bridge previously identified by other authors (Majowiecki & Cosentino 2011) is 2.52 Hz. This frequency aligns well with the one identified in this study using the fixed sensor. Additionally, a distinct peak at the same frequency is evident in the vehicle response. Specifically, the average peak frequency over the conducted tests is 2.53 Hz, with a standard deviation of 0.035 Hz. This observation suggests that human biomechanics and pavement roughness do not significantly affect the identification results in this application. Indeed, the pavement of pedestrian bridges typically has a smooth surface, and bicycle speeds are generally low, thereby minimizing the impact of road surface profiles on the recorded response (Lin & Yang 2005, Malekjafarian et al. 2015).

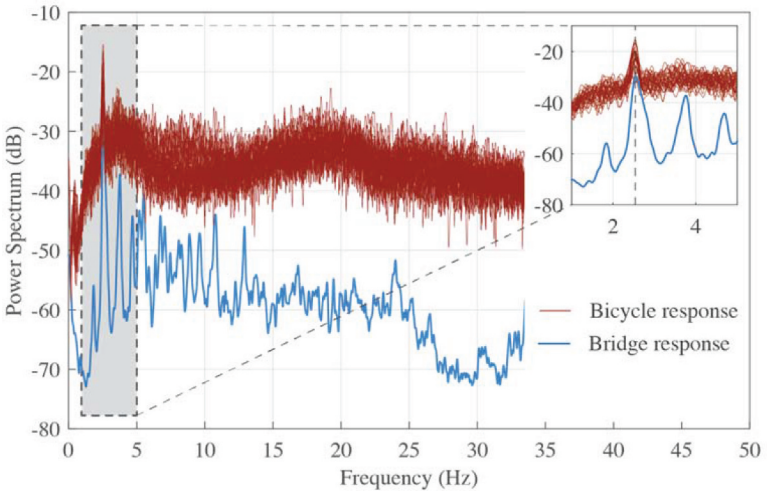


Figure 5. Power spectra of the bicycle and the bridge responses.

To derive an approximation of the ODS of the bridge around its principal resonant frequency, the methodology outlined in Figure 4 was applied, using a frequency range of 2.5 ± 0.3 Hz for filtering. Further details on the parameters chosen for the Kalman filter can be found in Reference (Quqa et al. 2022). In Figure 6, the thin red lines represent the ODSs computed within the specified frequency range from the 36 datasets collected onboard the moving bicycle. The thick red line represents the average of the identified ODSs, which shows good agreement with the mode shape of the first mode identified by previous studies (Majowiecki & Cosentino 2011). This agreement is particularly noticeable in the central part, where the dynamics of the bicycle impacting the bridge joints are mitigated. Additionally, a slight asymmetry in the shape is observable, with higher amplitudes on the left-hand side, aligning with reference values.

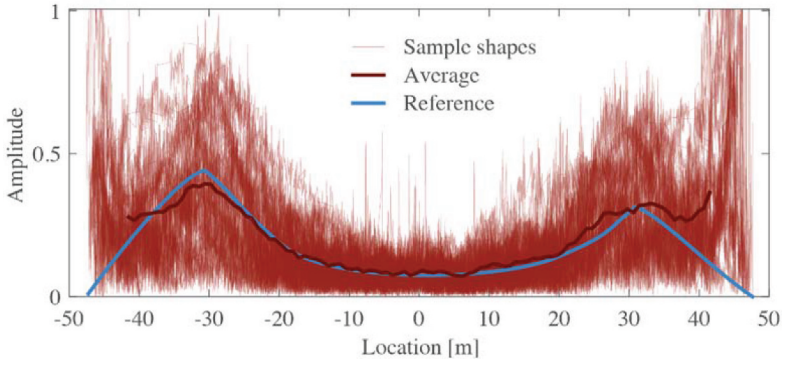


Figure 6. Identified ODS (separate samples and their averages) and reference mode shape obtained in Reference (Majowiecki & Cosentino 2011).

5 CONCLUSIONS AND FUTURE WORKS

This paper provided a preliminary exploration of ISHM, emphasizing the role of lightweight vehicles as carriers of sensors for this purpose. In general terms, the increasing interest in ISHM is evident from the growing number of publications in this field, as highlighted by the

analysis of the Scopus database. However, most of the reviewed documents focus on numerical simulations and lab tests, emphasizing the need for on-site validations.

Focusing on lightweight vehicles, such as bikes and scooters, recent studies emphasize their suitability of ISHM in applications for footbridges and crowdsensing approaches. The possibility of extracting modal parameters using sensors installed on lightweight vehicles has been proven numerically and experimentally. In this paper, a case study is presented to show the feasibility of these approaches.

Nevertheless, as highlighted by several authors, further studies are required to validate this approach and investigate several aspects related to the characteristics of the vehicle, the user, the bridge and the environmental conditions. More specifically, for bicycles, factors worth of investigation include the user's weight, pedaling frequencies, travel speeds, different gear ratios, and the impact of tire inflation pressure on bicycle-bridge interaction. Similarly, for scooters, a detailed investigation into factors like scooter speeds, walking pedestrians, engine noise, and varying environmental conditions is crucial.

Looking ahead, the "Crowd" project within the BRIDGITISE MSCA doctoral network, starting in mid-2024, is expected to make significant contributions to the realm of lightweight vehicles driven ISHM.

ACKNOWLEDGMENTS

The presented work was performed in context of the Horizon Europe MSCA project BRIDGITISE which is funded by the European Union under grant agreement ID 101119554. Views and opinions expressed are however those of the author(s) only and do not necessarily reflect those of the European Union. Neither the European Union nor the granting authority can be held responsible for them. More information on the project can be found under www.bridgitise.polimi.it.

REFERENCES

Cerda C.F. Garrett J. Bielak J. Barrera J. Zhuang Z. Chen S. McCann M. Kovaćević J. & Rizzo P. 2012. Indirect structural health monitoring in bridges: Scale experiments. Bridg Maintenance, Safety, Manag Resil Sustain - Proc Sixth Int Conf Bridg Maintenance, Saf Manag: 346–353

Cunha Á. Caetano E. Magalhães F. & Moutinho C. 2018. Dynamic identification and continuous dynamic monitoring of bridges: different applications along bridges life cycle. Struct Infrastruct Eng 14(4):445–467. https://doi.org/10.1080/15732479.2017.1406959

Di Matteo A. Fiandaca D. & Pirrotta A. 2022. Smartphone-based bridge monitoring through vehicle–bridge interaction: analysis and experimental assessment. J Civ Struct Heal Monit 12:1329–1342. https://doi.org/10.1007/s13349-022-00593-1

Giordano P.F. Quqa S. Limongelli M.P. 2023. The value of monitoring a structural health monitoring system. Struct Saf 100:102280. https://doi.org/10.1016/j.strusafe.2022.102280

Karakostas C. Quaranta G. Chatzi E. Zülfikar A.C. Çetindemir O. De Roeck G. Döhler M. Limongelli M.P. Lombaert G. Memişoğlu Apaydın N. Pakrashi V. Papadimitriou C. & Yeşilyurt A. 2023. Seismic assessment of bridges through structural health monitoring: a state-of-the-art review. Bull Earthq Eng. https://doi.org/10.1007/s10518-023-01819-3

Kim J. & Lynch J.P. 2012. Experimental analysis of vehiclebridge interaction using a wireless monitoring system and a two-stage system identification technique. Mech Syst Signal Process 28: 3–19. https://doi.org/10.1016/j.ymssp.2011.12.008

Li Z. Lan Y. & Lin W. 2023. Using Contact Residual Responses of a 3-DOF Scooter to Identify First Few Frequencies of the Footbridge. In Proc 10th International Conference on Experimental Vibration Analysis for Civil Engineering Structures (EVACES 2023), Milan, Italy, August 30 – September 1, 2023. https://doi.org/10.1007/978-3-031-39117-0_14

Lin C.W. & Yang Y.B. 2005. Use of a passing vehicle to scan the fundamental bridge frequencies: An experimental verification. Eng Struct 27(13). https://doi.org/10.1016/j.engstruct.2005.06.016

Majowiecki M. 2005. Three footbridges. In Proc 2nd International Conference Footbridge. Venice, Italy, December 6-8, 2005.

Majowiecki M. & Cosentino N. 2011. Experiences on Footbridge Conceptual Design Vs Dynamic. In: 4th International Conference Footbridge. Wroclaw, Poland, July 6-8, 2011.

Malekjafarian A. McGetrick P.J. & OBrien E.J. 2015. A Review of Indirect Bridge Monitoring Using Passing Vehicles. Shock Vib 2015: 286139. https://doi.org/10.1155/2015/286139
MathWorks 2021. MATLAB Mobile. https://uk.mathworks.com/products/matlab-mobile.html
May R. Chai H.K. Reynolds T. & Lu Y. 2023. Exploring the Use of Bicycles as Exciters and Sensor Carriers for Indirect Bridge Modal Parameter Estimation. In Proc 10th International Conference on Experimental Vibration Analysis for Civil Engineering Structures (EVACES 2023), Milan, Italy, August 30 – September 1, 2023. https://doi.org/10.1007/978-3-031-39117-0_26
Poli F. Bado M.F. Verzobio A. & Zonta D. 2023. Bridge structural safety assessment: a novel solution to uncertainty in the inspection practice. Struct Infrastruct Eng. https://doi.org/10.1080/15732479.2023.2211956
Quqa S. Giordano P.F. & Limongelli M.P. 2022. Shared micromobility-driven modal identification of urban bridges. Autom Constr 134:104048. https://doi.org/10.1016/j.autcon.2021.104048
Yang Y.B. Chen W.F. Yu H.W. & Chan C.S. 2013. Experimental study of a hand-drawn cart for measuring the bridge frequencies. Eng Struct 57: 222–231. https://doi.org/10.1016/j.engstruct.2013.09.007
Yang Y.B. Lin C.W. & Yau J.D. 2004. Extracting bridge frequencies from the dynamic response of a passing vehicle. J Sound Vib 272(3-5): 471–493. https://doi.org/10.1016/S0022-460X(03)00378-X

Bridge Maintenance, Safety, Management, Digitalization and Sustainability – Jensen, Frangopol & Schmidt (eds)
© 2024 The Author(s), ISBN 978-1-032-77040-6
Open Access: www.taylorfrancis.com, CC BY-NC-ND 4.0 license

Simultaneous WET and WIT with Q-learning for wireless bridge sensors network

Muhammad Tauseef Mushtaq, Veronico Giuseppe, Nicola Cordeschi, Alfredo Grieco & Gennaro Boggia
Politecnico di Bari, Bari, Italy

ABSTRACT: Wireless Powered Communication Networks play a crucial role in Internet of Things scenarios which operate with low energy sensors. In this regard, simultaneous wireless energy transmission (WET) and wireless information transmission (WIT) are proposed for continuous data transmission with low energy sensors. These sensors can be deployed on bridges that are hit by disasters. However, these low-energy networks demand a random data transmission and hence require access points to decode the packets accordingly. Hence it is challenging to design a slot selection algorithm that provides a better throughput. On this subject, we present a Q-Learning-based algorithm that harnesses the qualities of deep reinforcement learning and enhances the throughput. In our algorithm, we enhance the slot allocation of each user with the influence of a few physical layer properties. Results show an improved slot allocation mechanism leads to better throughpu

1 INTRODUCTION

Wireless-powered sensor networks are a future technology which enables future smart cities and other industrial systems. When discussing smart cities, it's essential to consider smart buildings and infrastructures, such as bridges and roads, alongside intelligent autonomous vehicles. This leads us to emphasize the importance of smart-bridges, which serve as critical infrastructure for urban areas. During an unfortunate event or flooding, gathering essential data about bridges is imperative. The information can be catagories in two ways; how much damage bridge have suffered?, and how much water/vehicle load bridge can still manage? It's important to highlight that routine information gathering for bridges can also be accomplished through these networks. This creates a need to create a portable or remote network that can collect this key information. However, these networks' performance is limited by the amount of battery a sensor occupies which is deployed on the bridge. Our work is related to WP1 topic of Bridgsite; "Collect Bridge Information". Our proposed work is related to low-cost sensors with edge computing capacity to optimize the volume of information to transmit for Bridgesite project. Low-cost communication systems require minimum amount of data transfers between a Hybrid Access Point (HAP) and deployed sensors subject to lower utilization of energy and other resources. HAP are responsible for both wireless energy and information transmission. That is why to acquire optimised and up to data low-cost bridge wireless networks require a random access protocol such as Irregular repeated slotted ALOHA (IRSA) or it's variants to achieve these goals. Later on, our paper is focused on efficient data acquisition from low-cost bridge sensor networks.

That is why recharging (WET) and acquiring information (WIT) are very important. Portable communication scenarios such as disaster-hit areas, industrial Internet of things, or Mission-critical communications rely on the sensors deployed in the field with the ability to harvest energy. Healthcare, smart cities, and transportation are other systems that require

DOI: 10.1201/9781003483755-408

energy harvesting. Hence the idea of Wireless Power Communication (WPCN) has widely spread to maximize throughput using simultaneous WET and WIT. In WPCN a dedicated HAP is responsible for simultaneous energy and information transmission. HAP also ensures that there are no collisions and success full data transmission of each user is possible without any error. literature suggests that the network layer has not enjoyed tremendous improvement during the past while the physical layer has taken a huge leap in catering to such scenarios. The physical layer benefits 5G in indoor scenarios or UWB frequency. Similarly, beamforming also plays a critical role in low-energy networks with its directional signal capabilities. Hence, there needs an improvement on the resource allocation part to rep the fruit of much more efficient sensors and access points. For the scenarios mentioned above, IRSA has played a crucial role. IRSA randomly selects slots for replicas of each user providing no control over access points. Recently, a study has been done to improve random access performance.

This includes the introduction of machine learning algorithms for random access, the introduction of mini-slots, and time-offset. Time Offset (TO) increases the probability of successful full packet transmission by allowing users to send their data with a random offset of a constant length Hu, Y. 2022. Similarly, another method is to introduce the mini-slots before the transmission Ayoub, I 2021, Dumas, C. 2021. Mini-slots are small jamming signals from the users to inform HAP and other users about the slots where they will send replicas. Deep reinforcement learning-based methods also use a Q-learning algorithm to select the slots for each user Li, Y 2022, Choi, H 2019. These slot selection decisions are based on the battery level of each user and hence require an access point to interfere in the decision.

Nonetheless, all the methods lack incorporating the physical qualities of the system such as channel quality, and distance between UE and Access point. Despite the introduction of mini slots, time offset, and ML on the network layer for random access, there is a dire need to make the network layer more aware of the environmental effects. To the best of the authors' knowledge, this type of analysis is not done before. Hence, we present a better and improved decision process based on Q-Learning which incorporates channel quality, battery level, and distance between UE and HAP.

In this paper, we consider a nonlinear energy harvesting scenario with simultaneous capabilities of WET and WIT. It is uncommon to incorporate the effect of efficiency of energy harvesting in the WPCN environment at the network layer. In this regard, most of the decisions involved on the network layer are related to slot selection. Therefore, not only an

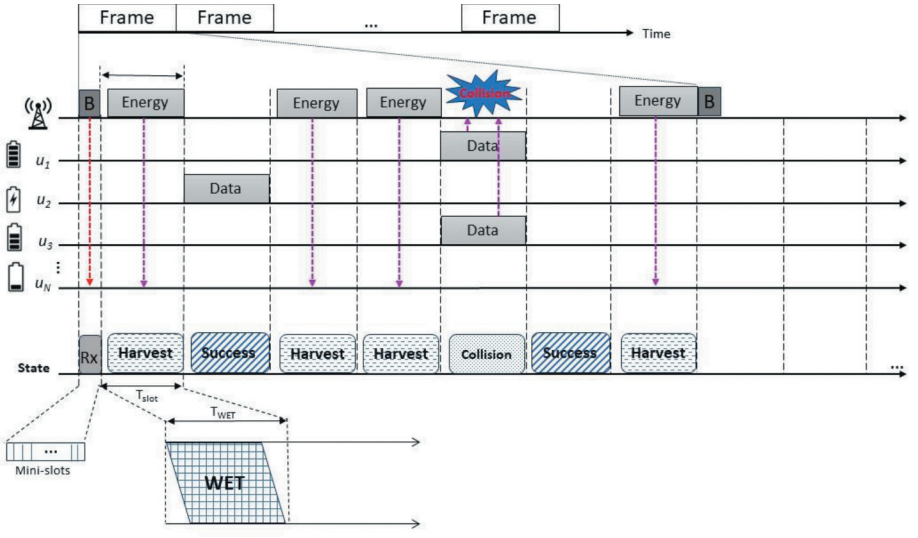


Figure 1. System model.

intelligent slot selection mechanism is required but it should also consider the efficiency of energy harvesting. For this purpose, we introduce a nonlinear energy harvesting model and calculate the harvested energy. By the end of each frame, the network layer has realistic information about the battery level of sensors. Finally, we can exploit this information or intelligent decision-making of slot selection for not only WET but also for WIT.

The rest of the paper is as follows. Section 2 describes the system model of a wireless-powered IoT network. Section 3. presents Q-learning algorithms which can manage the number of replicas along with energy harvesting slots. In section 4, we discuss the results obtained from these algorithms while section 5 concludes the work and provides future suggestions.

2 SYSTEM MODEL

We consider an IoT scenario with energy harvesting capabilities as shown in Figure 1. The system consists of sensors deployed in the field. We name them as $u_1, u_2, \ldots, u_N$. As per the requirement of IoT systems, sensors are always in saturation mode, which means they always have data to transmit. However, sensors' ability to send data is limited by various factors. These factors depend on the physical conditions of the environment such as distance, channel quality, available power, and line of sight. Packet transmission consists of different frames as shown in Figure 1. To send these packets, a sensor needs to select slots for their multiple copies of packets called replicas. Therefore, a sensor needs to decide intelligently for the number of replicas and placement of these replicas in slots of each frame. In our model, sensors are directed intelligently to choose the number of replicas. Available battery and channel are major parameters that influence this decision. It is worth mentioning here that these decisions are collectively made for each user at HAP using a machine learning algorithm called Q-Learning. Details of this algorithm will be provided in the next section.

After providing an overview of the system model, we explain each parameter that is involved in our system. First, we consider a nonlinear energy harvesting (NLEH) model for our system as it is closer to real scenarios. Before defining our non-linear model for energy harvesting, we need to define the following parameters. We define distance dn as the distance between HAP and nth user equipment. During the operation of Wireless Energy Transmission (WET), the power of HAP is denoted by P. Each user's equipment has a battery with limited capacity and energy harvesting capabilities. We define μ as the amount of energy required by UE to transmit one data packet. Hence, we can assume that if a user has a battery level available of μ = 2 then this user can send a maximum of two packets in one frame. It is also safe to assume that if a user does not have enough energy, then it has to wait for the WET phase and harvest enough energy to be able to again send data packets. WET capabilities of the system depend on multiple factors such as distance, channel quality, and power of HAP. Therefore, in our system channel quality is as important as battery level. We model our channel as a Rician channel. We assume an IoT scenario in which HAP enjoys a LOS with UE. Therefore, we consider the Rician channel which provides us with a LOS component along with NLOS components (multi-path). Considering this, the Rician channel hn between nth UE and HAP with K-factor κ, can be modeled as:

$$h_n = \sqrt{\frac{\kappa}{\kappa+1}}\bar{h}_n + \tilde{h}_n \in \mathbb{C}, \tag{1}$$

where $\bar{h}_n$ is the LOS component, which represents the large-scale fading and $\tilde{h}_n \in \mathbb{C}(0,1)$ represents NLOS small scale fading due to multi-path propagation. After modeling the channel and given the distance between HAP and UE, we evaluate the nth gain as:

$$\gamma_n = \left| \sqrt{\beta (d_n)^{-2}} w_n^H h_n \right|^2, \tag{2}$$

where w_n^H is the beam-forming vector. Whereas β represents channel power gain at a reference distance of 1m which we define as follows:

$$\beta = \frac{c^2}{16\pi^2 f_c}, \tag{3}$$

here the carrier frequency is denoted by f_c. In our system, we consider Ultra-Wide Band (UWB) frequency for harvesting which ranges from 5.98 GHz to 8.80 GHz and c represents the speed of light.

The above equations show that our system model considers the channel, power gain, and energy transmission limitations of HAP more realistically. Hence, next, we define our NLEH model as:

$$E_n = \frac{\alpha_o P \delta \gamma_n}{\alpha_1 P \gamma_n + \alpha_1}, \tag{4}$$

where $\alpha_o = 0.399$, $\alpha_o = 0.826$ are positive constant obtained from Lacovelli, G. 2023. Considering that each slot is dedicated to either WET or WIT, we can say that each WET is exactly the time dedicated to one slot. We define this time with δ. It is worth noting with the above definitions that UE will need several slots to charge its battery. Hence it is more evident that intelligent use of battery is necessary in such scenarios.

3 JOINT ACTION LEARNER (JAL) WITH NON-LINEAR ENERGY HARVESTING (NLEH)

Joint Action Learner (JAL) was first introduced in ref. It takes advantage of the learning capabilities of a deep reinforcement learning-based algorithm called Q-Learning. In this regard, we take another step forward and make the decision process of Q-learning more efficient. We introduce the channel quality parameter along with an enhanced battery charging model. Starting with the state of the algorithm, we define it as $S_t = \{s_{t1}, s_{t2}, \ldots, s_{tN}\}$. The state is the combination of available power and channel quality of each user such that $s_{tn} = (p_{tn}, c_{tn})$. Where pt n is the power available at the sensor and ct n is the channel quality of the sensor. The algorithm decides the number of replicas for each user and decides the specific actions for each defined as $A_t = \{a_{t1}, \ldots, a_{tN}\}$. With each user, we also relate a reward matrix defined as R_t. The reward is based on the action taken by each user. Considering these basic parameters of JAL, we provide the following points to better understand the workings of JAL.

- Each UE is equipped with a battery capable of storing 3μ units of battery, where μ = 0.5Wh.
- Users need a minimum of a μ amount of battery to send one packet. Hence, a user can send a maximum of three packets with a fully charged battery.
- With each energy harvesting slot, UE will collect power from HAP and update its battery accordingly.
- We assume perfect CSI at HAP. Hence, it is safe to assume HAP can send a perfect beam of energy towards the users.
- User to HAP distance and channel condition limits harvesting capability of each user. A user experiences low battery recharge during WET when it does not experience LOS with HAP and vice versa.
- In our simulation, we consider each user to be at a varying distance from HAP. Distance ranges from 0.8 meters to 2 meters. These values are obtained from experimental results in ref. We also assume that the distance between UE and HAP remains constant for the whole duration frame.
- Time for each slot is δ = 0.05Sec. While the parameters of JAL have values ρ = 0.5, ξ= 0.7.
- HAP also keeps track of battery level by calculating the harvested energy using Eq. 4.
- Each user also encodes its battery information along with the data. This helps the HAP in syncing the battery information.

By considering all the above information, we now define our algorithm in Algo.1. We reduce the computational cost of each user by keeping track of channel and battery information at HAP. Hence HAP is responsible for scheduling the packets in slots based on the available battery unit and channel quality. Q-Learning updates and optimizes the Q-values using Bellman's equation defined as,

$$Q(s_t, a_t) = (1 - \alpha)Q(s_t, a_t) + \alpha(r(s_t, a_t) + \gamma \, \boldsymbol{max} Q(s_{t+1}, a_t)), \tag{5}$$

where $r(s_t, a_t)$ is the reward collected after taking a specific action. After learning through JAL, HAP directs the sensors for the next transmission. A summary of our JAL algorithm is provided below in the Algo. 1.

Algorithm 1 JAL with Non Linear Energy Harvesting (JAL-NLEH)

Initialize Parameters ρ, ξ
Initialize $Q(S, A)$ randomly
for For each frame t **do**
  HAP collects s_i^t
  Obtain the joint state $S_t = \{s_1^t, s_2^t, ...s_M^t\}$
  Generate random number x
  if $x < \epsilon$ **then**
    Select a joint action randomly
  else
    Select a joint action by solving
    $A_t(S_t) = argmax_{A \in \mathcal{A}} Q(S_t, A_t)$
  end if
end for
for device $i \in M$ **do**
  Randomly select data slots for action $a_i^t \in A_t$
  Harvest energy using Eq. 4
  Collect the reward r_i^t
  Observe the next state S_i^{t+1}
end for
Calculate the joint reward: $R_t = \sum_{i=1}^{M} r_i^t$
Obtain the next joint state: $S_{t+1} = \{s_1^{t+1}, s_2^{t+1}, ..., s_M^{t+1}\}$
Find $max_{A \in \mathcal{A}} Q(S_{t+1}, A)$
Update the Q-value using Bellman's equation

Figure 2. Algorithm 1.

4 RESULTS AND DISCUSSION

In this section, we first present a comparison of idle slots for IRSA and JAL-NLEH. While we prove that JAL-NLEH performs better in terms of creating more slots for energy harvesting, we focus our remaining results on the performance of JAL-NLEH in different scenarios. We see how varying the channel quality and available battery can affect the number of replicas.

Before describing the results, we present the following scenario. First, the HAP initializes the Q-Table with random values from 0 to 6, then for each frame, collects the state for each user. The battery state is initialized at 0.05Wh and the quality of the channel is measured using envelop. The HAP decodes the packets according to Successive Interference Cancellation (SIC), and then each user receives a reward that is: 0 if none of its packets successfully decoded at HAP, 1 if any packet decoded HAP but collision occurs with another user, 2 if they were successfully decoded. This reward system ensures that HAP instructs users to send more replicas when channel quality is low. HAP looks for idle slots in each frame and uses them for WET. After performing WET, it obtains new channel quality and remaining power for each user and updates its joint state.

Figure 3 shows a comparison of idle slots for IRSA and JALNLEH. Here the number of users is 8 while the number of slots in a frame is also 8 while the Rician channel K-factor is $\kappa = 8$. Hence, we can assume that competition between users for slots is high. As we can observe JAL-NLEH manages to create more idle slots which are crucial for energy harvesting

as compared to IRSA. This is because IRSA does not have the advantage of battery and channel information while JAL-NLEH has many parameters such as channel, and battery information of users to work with. A comprehensive analysis of idle slots, decoded packets, and collided packets is shown in Figure 4. Here, we also consider the extreme scenario where competition for slots is very high. Our algorithm not only aims at reducing the number of collisions but also manages to create more idle slots for energy harvesting. It is worth mentioning that the probability of having more than 6 collisions is almost negligible while at the same time probability of idle slots has been also on the higher side.

In Figure 5, We keep our number of slots and users constant while varying the channel quality κ. We can observe two trends here, first is before idle slots are 5, and second, after the idle slots are more than 5. We explain this trend by explaining the battery reservation goal of JAL-NLEH. We can see an increasing trend in the probability of number of idle slots and after 6 number of idle slots, we see a decreasing trend. This shows that it is relatively easy for JAL-NLEH to create 6 number of slots as compared to a higher (more than 6) number of slots. We can also see how the channel affects the probability of idle slots. For example, for the worst channel i.e. κ = 4, probability is lesser than for $\kappa = 6$ *and* 8. Another worth noting analysis from these results is that performance for κ = 6 and 8 is not much different than each other. It is because our algorithm is optimized to create more idle slots and it enhances its performance when the conditions get tough. Another observation one can make is that our algorithm is optimized for channels with moderate values $\kappa = 6$ *and* 8 which are the conditions for outdoor channels.

Finally, in Figure 6, we present a collective result for different settings and $\kappa = 6$. It is observable from the figure that our algorithm always performs much better in conditions that matter the most.

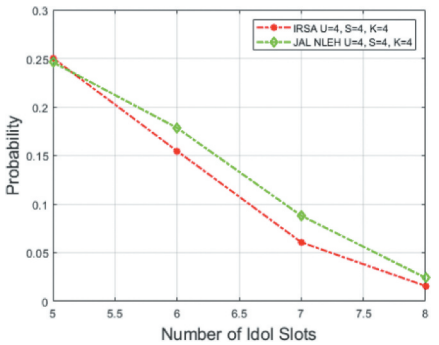


Figure 3. Probability of idol slots with $\kappa = 8$ for IRSA and JAL NLEH.

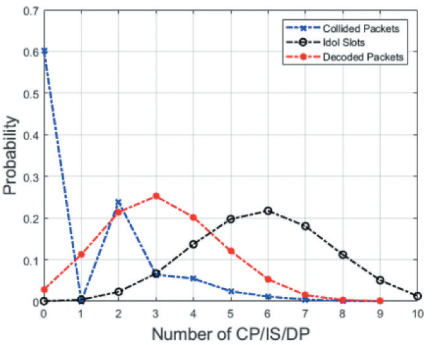


Figure 4. Comparison of Decoded packets, idol slots, and collided packets for $\kappa = 8$ users=10, and slots=10.

5 CONCLUSION AND FUTURE WORK

We have shown the key to achieving better performance in tougher scenarios for random slot selection of bridge sensor networks. We have also shown the importance of information related to physical layer characteristics at the mac level layer. This can help in improving the decision capability of the Mac layer. In this way, we can achieve more efficient with minimum age of information data for bridges which may be hit by disaster or flooding. We can also conclude that traditional IRSA needs improvements and these improvements can be made by enhancing the decision-making ability empowered by machine learning. For future work, we would like to extend this work with a continuous optimization/machine-learning algorithm such as proximity policy optimization (PPO) which does not require quantizing the battery and channel levels hence improving the results.

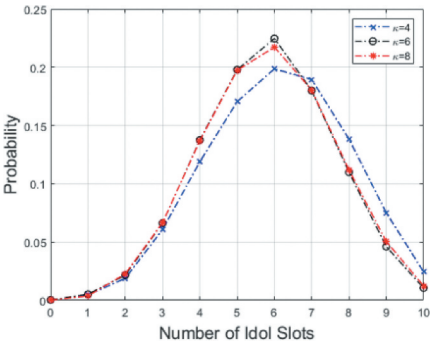


Figure 5. Comparison Of Idol Slots For Different κ, U=10, S=10.

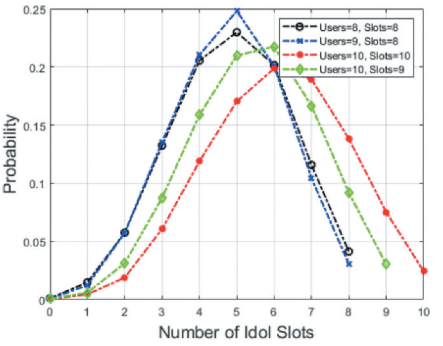


Figure 6. Comparison of different users and slots settings for κ.

REFERENCES

Mushtaq. M. T. & Cordeschi, N. & Grieco, L. & Boggia, G. 2023. Optimized Scheduling of Packets with Deep Sensing Irregular Slotted Aloha Influenced by Channel Knowledge for Wireless-Powered IoT Networks. International Conference on Information and Communication Technologies for Disaster Management (ICT-DM), September 2023, Cosenza, Italy.

Lacovelli, G. & Grieco, G. & Petrosino, A. & Grieco, A. & Boggia, B 2023. Fair Energy and Data Rate Maximization in UAV-Powered IoT-Satellite Integrated Networks. IEEE Transactions on Communications, 15 December 2023.

Li, Y. & Chin, K. 2022. Energy-Aware Irregular Slotted Aloha Methods for Wireless-Powered IoT Networks. IEEE INTERNET OF THINGS JOURNAL, 11784–11795 VOL. 9, 14, JULY 2022.

Choi, H. & Shin, W. & Levorato, M. & Vincent, P. H 2019. Harvest-Or-Access: Slotted ALOHA for Wireless Powered Communication Networks. IEEE TRANSACTIONS ON VEHICULAR TECHNOLOGY, 11394–11398 VOL. 68, NO. 11, NOVEMBER 2019.

Hu, Y. & Seo, J. & Jin, H. 2022. Exploiting In-Slot Micro-Synchronism for S- ALOHA. IEEE TRAN. WIRELESS COMM., 10854–10870 VOL. 21, NO. 12, Dec. 2022.

Hmedoush, I. & Adjih, C. & Mu¨hlethaler, P. 2022. Deep Learning, Sensing-based IRSA (DS-IRSA): Learning a Sensing Protocol with Deep Reinforcement Learning. 23 Sep 2022, https://hal.inria.fr/hal-03744126v2.

Schmickl, S. & Faseth, T. & Pretl, H. 2019. A 1.9-µW 7-GHz IR-UWB Transmitter with RF-Energy-Harvester in 180-nm CMOS for Battery- Less Bio-Sensors. 17th IEEE International New Circuits and Systems Conference (NEWCAS), June 2019, Munich, Germany.

Chen, Z. & Feng, Y. & Feng, C. & Liang, L. & Jia, Y. & Quek, T. Q. S 2023. Analytic Distribution Design for Irregular Repetition Slotted ALOHA With Multi-Packet Reception. IEEE TRANSACTIONS ON VEHICU- LAR TECHNOLOGY, 1360–1365 VOL. 72, NO. 1, JANUARY 2023.

Chu, Z. & Xiao, P. & Mi, D. & Hao, W. & Lin, Z. & Chen, Q. & Tafazolli R. 2022. Wireless Powered Intelligent Radio Environment with Non-Linear Energy Harvesting. IEEE Internet of Things Journal, 18130–18141 VOL. 09, NO. 18, March 2022.

Chen, Y. & Zhao, N. & Alouini, M. 2017. Wireless Energy Harvesting Using Signals from Multiple Fading Channels. IEEE Transactions on Commu- nications, 5027–5039 VOL. 65, NO. 11, August 2017.

Hu, Y. & Seo, J. & Jin, H. 2022. Exploiting In-Slot Micro-Synchronism for S-ALOHA. IEEE TRANSACTIONS ON WIRELESS COMMUNICATIONS, 10854–10870. VOL21, NO. 12, DECEMBER 2022.

Ayoub, I. & Hmedoush, I. & Adjih, C. & Khawam, K. & Lahoud, S. 2021. Deep-IRSA: A Deep Reinforcement Learning Approach to Irregular Repetition Slotted ALOHA. 10th IFIP International Conference on Performance Evaluation and Modeling in Wireless and Wired Networks (PEMWN), Nov 2021, Ottawa, ON, Canada.

Dumas, C. & Salau¨n, L. & Hmedoush, I. & Adjih, C. & Chen, C. S. 2021. Design of Coded Slotted ALOHA With Interference Cancellation Errors. IEEE TRANSACTIONS ON VEHICULAR TECHNOLOGY, 12742–12757 VOL. 70, NO. 12, DECEMBER 2021.

Schulman, J. & Wolski, F. & Dhariwal, P. & Radford, A. & Klimov, O. 2017. Proximal Policy Optimization Algorithms. arXiv preprint arXiv:1707.06347 (2017).

Bi, S. & Zeng, Y. & Zhang, R. 2016. Wireless Powered Communication Networks: An Overview. IEEE Wireless Communications. 10–18 VOL 23, April 2016.

Bridge Maintenance, Safety, Management, Digitalization and Sustainability – Jensen, Frangopol & Schmidt (eds)
© 2024 The Author(s), ISBN 978-1-032-77040-6
Open Access: www.taylorfrancis.com, CC BY-NC-ND 4.0 license

Probabilistic digital twin for continuous bridge performance modelling

P. Darò, D. La Mazza, F. Basone & G. Mancini
Sacertis Ingegneria S.r.l., Torino, Italy

M.P. Limongelli
Politecnico di Milano, Milano, Italy

M.H. Faber
Aalborg University, Aalborg East - Denmark

ABSTRACT: The multiplicity of possible different and possibly interacting processes contributing or governing deterioration processes in bridges requires systems representations way beyond the deterministic approach where the focus is on few processes and corresponding models. A Probabilistic Digital Twin (PDT), supported by Structural Health Monitoring (SHM) and big data from observations and monitoring, can provide a novel contribution to support integrity management with knowledge improved over time. This paper explores the preliminary analyses for the future full development of the PDT as part of the Bridgitise Project. An approach to build the PDT of a bridge will be developed using FEM modelling of the deterioration effects. The simulated structural responses under deterioration progressing in time will be used to develop a PDT model that will then be utilized as a representation of the best available knowledge and applied to generate simulations of very significant numbers of structural performance scenarios over time.

1 INTRODUCTION

At present, a considerable number of European bridges, constructed in the 1950s and 1960s, are either nearing or surpassing the end of their intended design lifespan. Frequently, these bridges operate under conditions significantly diverging from their original design assumptions, exacerbated by accelerated deterioration attributed to the impacts of climate change (Croce et al. 2019). Economy and Society can face significant challenges due to adverse effects and long-term consequences associated with the malfunction or collapse of infrastructure assets. In recent years, the escalating number of critical incidents affecting transportation infrastructure networks, specifically bridges and tunnels, has underscored the importance of considering safety risks, maintenance deficiencies, aging, and progressive deterioration processes when assessing the remaining design service life (Strauss et al. 2022). To address this, it becomes essential to incorporate suspected damage or deterioration mechanisms into the re-evaluation and re-formulation of limit states assessment methods (fib Model Code for Concrete Structures 2010 2013 & fib Bulletin No. 109 2022). This task proves to be complex, particularly given the spatial and temporal variability in the effects of damage or deterioration, necessitating an explicit representation of the intricate system interactions within the structure. Consequently, integrating additional information obtained through inspection, testing, and monitoring for existing structures enhances our understanding of uncertainties and risk differentiation for both new and existing structures (Darò et al. 2022). This enhanced knowledge applies to both the resistance side, involving a more refined

DOI: 10.1201/9781003483755-409

characterization of material behavior and deterioration mechanisms, and the actions side (Allaix et al. 2022, Hellebrandt et al. 2016). In terms of the latter, the composition of traffic carried by most bridges today, in both volume and load, is considerably more demanding than initially considered during the design phase. Moreover, ongoing advancements in technologies such as automotive driving, alternative fuels, and electric vehicles exert a profound impact on mobility, directly influencing actions required for bridge design and verification. For instance, these developments affect traffic loads (e.g., the impact of platooning) and introduce new hazards (e.g., altered fire risks due to alternative fuels). Furthermore, the evolving climate, including extreme wind, snow, temperature, and precipitation conditions, is also relevant to the loads and exposure considerations for structures. Climate change adds another layer of significance to the design of new structures or the assessment of existing ones (Strauss, Malioka & Faber 2009).

The effective maintenance of infrastructure plays a crucial role in ensuring the safety, performance, and long-term sustainability of assets (Darò et al. 2022). However, the current European approach to managing bridge assets relies heavily on methods of limited effectiveness, such as routine manual/visual inspections, subjective evaluations by experts, and corrective maintenance practices. Although there is a growing trend towards the adoption of preventive and condition-based maintenance strategies, these are not yet widely implemented and are primarily reserved for critical assets (Strauss et al. 2022). Efficient management is imperative to ensure the continued functionality of Europe's transport infrastructure and to prepare it for forthcoming social, economic, and environmental changes.

The advent of digital transformation, facilitated by disruptive technologies such as distributed sensors, drones, crowdsensing, satellite radar, Building Information Modelling (BIM), digital twins, Internet of Things (IoT), and Artificial Intelligence (AI), can provide extensive data to inform decision-making. The integration of existing knowledge and engineering insights with digital information has the potential to promote a resource-efficient approach to construction and bridge integrity management (BrIM). This approach paves the way for achieving sustainable societal developments.

The recently funded EU project BRIDGITISE is dedicated to advancing the digitalization of bridge management by introducing innovative approaches to information management. The project aims to create and validate cutting-edge technologies that enhance the efficient management of bridge information. These technologies are designed to support decision-making processes crucial for bridge integrity management throughout the entire lifecycle. The project consortium is a collaboration of universities, research centers, industrial companies, bridge design and assessment firms, and end-users, collectively contributing to the success of the project. BRIDGITISE will take up this research and training challenges, proposing a new paradigm for the first Industrial Doctorate within the EU that will pave the way to the training of new generations of researchers and professionals with expertise in digital BrIM. BRIDGITISE builds on the results of the international research networks (COST Action TU1402, 2015-2019), (COST Action TU1406, 2015-2019), as well as recent funded EU research projects such as IM-SAFE (H2020 CSA IM-SAFE, 2020-2022).

The present paper focuses on the ESR Project TWINS within BRIDGITISE, providing an insight into the project background, ongoing development, and future expected results. The ESR project responds to the increasing need to control the bridges network structural behavior with reliable indicators supported by robust algorithms. The multiplicity of possibly different and possibly interacting processes contributing or governing deterioration processes in bridges requires systems representations way beyond the deterministic approach where there is only focus on one or two processes and corresponding models. PDT, supported by SHM and semi-big data from observations and monitoring, can provide a novel contribution to solve this issue and may support integrity management with knowledge improved substantially over time.

The findings of the research program are valuable for asset owners, road operators, SHM engineering companies, bridge designers as well as other researchers in the monitoring and diagnostics field. The damage detection analysis contributes filling the gap between the research and the real applications, deepening the (nowadays limited) knowledge regarding the detectable damage effects on prestressed structures in both static and dynamic conditions and actively supporting the paradigm-shift towards a proactive maintenance approach.

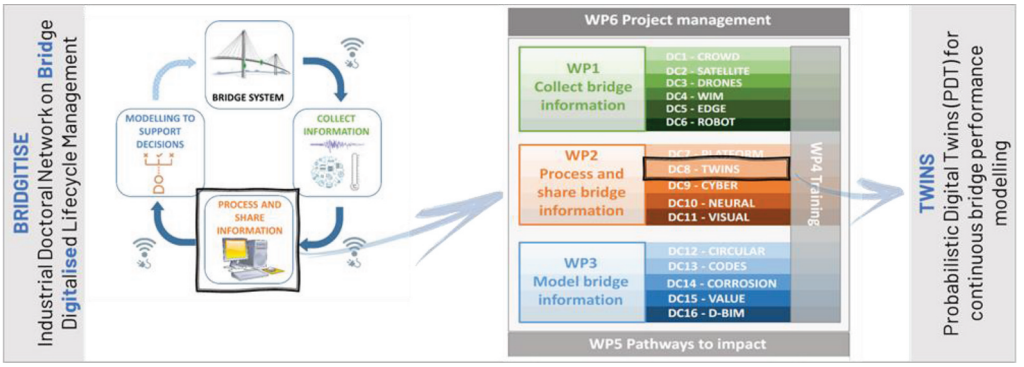


Figure 1. ESR TWINS Project within BRIDGITISE.

2 BRIDGE DAMAGE QUANTIFICATION AND PERFORMANCE MODELING: STATE OF THE ART, SCIENTIFIC GAPS AND BARRIERS

The life cycle management process for both new and existing concrete structures involves condition control, which is the comprehensive approach to ensuring the structural integrity throughout its lifespan. This process encompasses condition surveys, performance assessments, and the evaluation of maintenance strategies. Although management systems that capture deterioration processes are commonly employed in conjunction with analyses, they typically rely on deterministic performance prediction models. These models describe the anticipated future condition by establishing a functional correlation between structural condition characteristics (e.g., age) and the attributes of mechanical, chemical, and physical processes or agents. As the use of surveying technologies for acquiring information on the current condition of bridges becomes more prevalent, there is a notable shift towards data-informed approaches to condition control (Allaix, Bigaj-van Vliet & Cerar 2022). Moreover, the technological progress has recently increased with the spreading of IoT sensing devices (Alovisi et al. 2022). Recent research Projects such as the EU-funded H2020 CSA IM-SAFE focused on characterizing and systematizing performance indicators for both bridge structures and tunnel systems (Strauss et al. 2022). Within the context of employing monitoring systems for condition surveys, the IM-SAFE project provided a foundation for the use of performance indicators for bridges and tunnels, aiming to clarify the linkage between performance indicators and observations, and detailing how these indicators are or should be integrated into performance and risk assessments. Another extensive research has been collected in (fib Model Code for Concrete Structures 2010 2013 & fib Bulletin No. 109 2022) regarding the state-of-the-art on existing concrete structures life management, testing and structural health monitoring.

The SHM monitoring field, based on continuous data and the application of AI techniques and use of Digital Twins, has seen an increase in interest and applications only in the last decades, and as such there is still the need to further develop knowledge on damage indicators and techniques to locate and quantify the damage in reinforced concrete and prestressed structures and correlate the effect with the structural reliability. Research should focus on exploring data analytics techniques with a combination of different sensors technologies, to translate the research findings into robust and automatic data processes/algorithms for the continuous structural monitoring and quantification of model and measurements uncertainties. The fast-paced development of knowledge in the monitoring field of bridges in the recent years combined with increasing applications on real-case scenarios will enable the analysis of the structural response of existing bridge under ongoing deterioration processes. Sacertis Ingegneria S. r.l., Industrial Partner supporting the TWINS ERS development, has gained experience on the use of dense sensing on an Italian bridge network of over 150 bridges (Darò et al. 2023) that will be made available throughout the project development.

Excellence in the field of structural monitoring and diagnostics requires specific competences that encompasses various expertise: civil engineering, data analytics, programming skills, probabilistic and statistical knowledge, electronic background. This implies gaps in the data interpretation and structural response modelling due to the lack of such a wide training spectrum in a single doctoral program. The TWINS ERS Projects aims to keep the pace with the technological advancement (sensing devices) as well as the development of new data processing techniques applied to the civil engineering field, focusing on the definition of a Probabilistic Digital Twin (PDT), supported by SHM and semi-big data from observations and monitoring, that can provide a novel contribution to support integrity management with knowledge improved substantially over time.

3 UNCERTAINTIES IN THE DAMAGE DEFINITION: A PROBABILISTIC APPROACH

In civil engineering, numerical or mathematical models serve to simulate the behavior of real systems, enabling analysis, prediction, and design. In case of new structures, the numerical model employed for design verification often incorporates a higher degree of simplification. The scenario becomes more intricate when dealing with existing structures. In such cases, information regarding materials, history of loads, and interventions or modifications applied to the structure may be either unknown or only partially known.

When utilizing performance models, it is crucial to employ calibrated models achieved through parameter identification or estimation using model updating techniques. Model updating primarily aims to adjust unknown system properties, represented as parameters in numerical models, based on the observed behavior of the system of interest. In such analyses, special attention must be given to defining and modeling deterioration processes over time, to provide a preliminary assessment of structural performance evolution during the residual service life. While a conservative design does not typically result in a significant increase in structural cost, a conservative assessment may lead to unnecessary and costly repairs or replacement. To reduce model uncertainty, more refined and calibrated structural models (e.g., non-linear finite element models) can be utilized. Nonlinear finite element analysis is particularly useful for concrete structures in areas where simplified analytical models fail to predict structural resistances accurately, such as situations where nonlinear behavior related to material properties or geometry significantly affects structural reliability or where load effects are challenging to assess, due to the interaction between structural members or to the dynamic nature of the phenomenon.

Observations gathered from inspection, monitoring, and testing fall into two categories:

- Direct information: pertains to properties used in the assessment and verification that can be directly measured.
- Indirect information: relates to properties that cannot be directly measured. To address this, a specific indicator must be defined, and a model is required to connect the indicator to the relevant property (COST Action TU1406, 2015-2019).

Decisions concerning structures should account for all uncertainties of relevance for their performances such as measurement errors, aleatory uncertainties (affecting direct information, such as measured parameters, due to their inherent variability), model uncertainty (affecting indirect information which cannot be directly measured and is estimated using a model that links them to measured parameters), statistical uncertainty (due to a limited number of information) or other epistemic uncertainties (lack of knowledge about the structural system (as-built), numerical modeling uncertainties). Uncertainties related to data collection processes should also be considered in structural assessments using probability theory (ISO-2394, 2015). This can involve the use of probabilistic methods for performing reliability analysis or for updating the characteristic and design values of basic variables. Basic variables can be represented through random variables, random processes, and random fields, both discrete and continuous, depending on the nature of the problem. Probabilistic models should describe the uncertainties of individual random basic variables and account for dependencies among them.

When assessing existing structures, it is inappropriate to neglect the influence of deterioration, as these structures are already affected by damage mechanisms. Reliability analysis should consider the combined effects of cumulative deterioration and relevant actions during the service life. Models should explicitly incorporate the effects of deterioration on resistance, quantifying material-specific uncertainties. This approach allows the inclusion of damage performance models, consideration of multiple damage scenarios, and calibration of the models based on the structural condition at the beginning of the monitoring period. The spatial distribution of deterioration processes should also be considered, and uncertainties associated with models describing the propagation of deterioration over time should be addressed.

Structural health monitoring techniques can be employed to provide information about environmental influences, degradation processes, or structural performance, reducing uncertainties. In-depth experimental investigations become essential to reconstruct the structural organization, ascertain the materials used, understand their characteristics, and determine the potential state of degradation. Only through these comprehensive investigations is it possible to develop a reliable numerical model for existing structures. As per most of the standards analyzed, e.g. (CEN/TC- 250 2020, ISO-13822 2010 & ISO-2394 2015), updating the information relevant to the properties and the performance is an essential part of the assessment of existing structures. In assessment, an existing structure can be inspected/tested so that load, resistance, environmental parameters, and global static and dynamic response can be measured on-site and used to update the structural model.

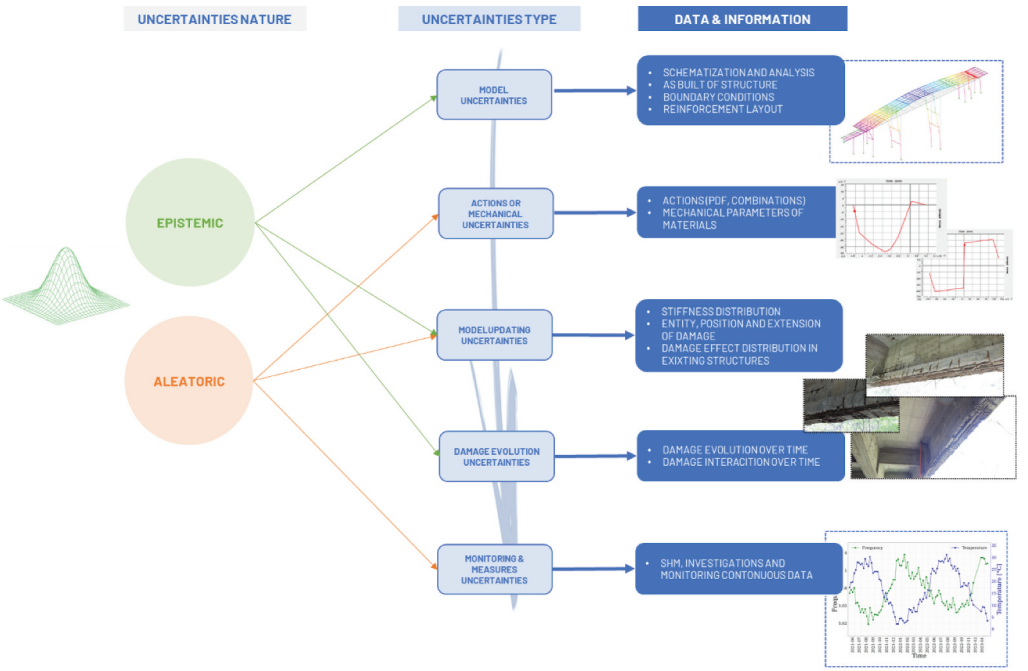


Figure 2. Uncertainties nature, type and basic variables to be described following a probabilistic approach in a PDT definition.

The information updating process can involve classical statistical methods or a Bayesian approach:

- Classical statistical methods: these methods revolve around estimating certain statistics of the parameters (e.g., mean values and/or covariance matrices) to optimize the correspondence between the statistics of the model's output and those of the observed data. This can

be achieved through analytical means (classical statistical inference methods) or numerically (stochastic model inversion) (Govers 2010);

- Bayesian approach: introduced in structural dynamics by one study (Beck & Katafygiotis, 1998), is a method of statistical inference that utilizes Bayes' theorem to update the probability of a hypothesis as new evidence or information becomes available. Through Bayes' theorem, prior probabilistic models constructed based on a priori information can be transformed into posterior models using available experimental data and the probabilistic prediction error model.

4 PROBABILISTIC DIGITAL TWINS (PDT) FOR BRIDGE INTEGRITY MANAGEMENT

Although materials, loads, boundary conditions as well as entity, position and extension of damage are random variables, they are often assumed in practice as deterministic during the modeling process as such simplification allows to strongly reduce the computational efforts of the modeling. However, integrity management often requires decisions that encompass long-term future performance affected by high uncertainty. Due to their deterministic nature, traditional digital twins may struggle to capturing uncertainties. Decision-making can be enhanced by connecting probabilistic models to the digital twin in the so-called Probabilistic Digital Twin (PDT). PDTs create a virtual representation of the structure that incorporates probabilistic models for material properties (e.g. concrete and steel strength), deterioration processes (e.g. corrosion and fatigues), loads (e.g. traffic, wind, seismic, environmental conditions) considering uncertainties in their distribution and variation in time. A probabilistic analysis (e.g. Montecarlo simulation) is performed to assess the structural response under varying conditions and to evaluate the probability of failure and remaining useful life of critical components. Real-time data from SHM are integrated in the PDT to refine the probabilistic models. PDTs can quantify and propagate uncertainties arising from measurement noise, component failure/degradation models, or uncertain relationships among events. In structural reliability analysis, failure probabilities are often computed based on the deterministic physical model of the structure developed during design or using a model updated using Structural Health Monitoring (SHM) data, as described in the previous section. PDTs allow for the continuous updating of the failure probabilities, providing insights into the remaining useful life of the structure. In the case of bridges with multiple potential failure locations, the simulation of a vast number of scenarios using a PDT can be computationally expensive. To address this challenge, surrogate models, which are approximate models trained for example by computationally expensive models, are frequently employed to expedite uncertainty analysis and decision-making processes. This simplification enables obtaining near-real-time predictions.

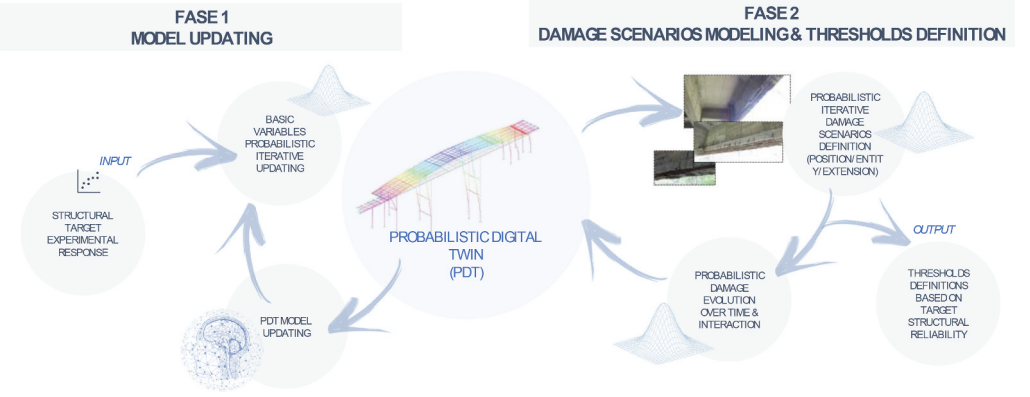


Figure 3. Model updating, damage scenarios modeling and thresholds definition using a probabilistic approach in a PDT definition.

In the TWINS project, we aim to develop an approach for constructing a Probabilistic Digital Twin (PDT) of a bridge by utilizing nonlinear finite element (FE) modeling to simulate the impact of deterioration, coupled with monitoring information provided by the industrial supervisor (Sacertis Ingegneria S.r.l). The investigation will encompass the exploration of multiple interactive damage scenarios, employing a probabilistic approach, where all the uncertainties are taken into considerations and varied during the iterative model updating analysis and thresholds definition. This approach is designed to enhance damage detection, structural assessment, and integrity management of the assets.

5 PROJECT METHODOLOGY AND EXPECTED RESULTS

In this project, an approach to build the PDT of a bridge will therefore be developed making use of nonlinear finite element (FE) modelling of the effect of the deterioration and monitoring information. The combination of multiple interactive damage scenarios will be investigated following a probabilistic approach to support the damage detection, structural assessment and integrity management of the assets. The expected results are as follows:

- New or refined knowledge regarding the effects on the structural performance and condition of various damage scenarios of reinforced and prestressed bridges;
- Identification of structural performance degradation combining FE modelling and real data collection;
- Development of a procedure to identify, estimate and locate damages in reinforced and prestressed concrete bridges based on a combination of static and dynamic indicators though the definition of a PDT of the reference bridge;
- Validation of the methodologies using both laboratory and field testing, consideration taken of uncertainties introduced by sensors measurements and of model uncertainties on the definition of the damage level;
- Correlation to the safety assessment and structural reliability with respect to the damage evolution forecast;
- Aim to foster a proactive maintenance approach in the asset management.

6 CONCLUSIONS

The rapid evolution of knowledge in bridge monitoring over recent years, coupled with an increasing number of real-case applications, is poised to facilitate the analysis of structural responses in existing bridges undergoing ongoing deterioration processes. The multitude of potentially diverse and interacting processes influencing or governing deterioration in bridges calls for system representations beyond the deterministic approach, which typically focuses on one or two processes and their corresponding models. Presently, there is limited knowledge regarding effective indicators and techniques to correlate observable performance in infrastructure structures with their structural reliability. Addressing this challenge, a Probabilistic Digital Twin (PDT), supported by Structural Health Monitoring (SHM) and big data derived from observations and monitoring, emerges as a promising solution. The present paper explored the preliminary analysis that lays the groundwork for the future full development of the PDT as part of the Bridgitise Project. Within the Bridgitise framework, an approach to construct the PDT of a bridge will be developed through the TWINS ERS Project, which endeavors to stay abreast of technological advancements, both in sensing devices and the development of new data processing techniques tailored to civil engineering. The project focuses on the novel approach that the PDT can provide to enhance knowledge and support integrity management over time. This involves leveraging nonlinear Finite Element modeling to simulate the effects of deterioration, combined with continuous monitoring data from real case studies. Sacertis Ingegneria S.r.l., an Industrial Partner contributing to the development of TWINS ERS, has garnered

expertise in dense sensing across an Italian bridge network comprising over 150 bridges, an experience that will be made accessible throughout the project development.

REFERENCES

Allaix D., Sánchez Rodríguez A., Darò P., (2022) Assessment of existing road bridges based on actual traffic data, fib Oslo Conference, ISBN: 978-2-940643-15-8 - ISSN: 2617–4820.

Allaix, D.L, Bigaj-van Vliet A., Cerar B. (2022), Review of the current state of standardisation on monitoring, data-informed safety assessment and decision-making regarding maintenance of the transport infrastructure, IABSE Symposium Prague 2022, 1309:1313

Alovisi I. et al. (2022) New Sensor Nodes, Cloud, and Data Analytics: Case Studies on Large Scale SHM Systems. Structural Integrity Vol. 21, 457:484

Beck, J. Katafygiotis, L., (1998) Updating models and their uncertainties I: Bayesian statistical framework. ASCE J. Eng. Mech. Vol. 124, 455:461

European Committee for Standardization CEN/TC 25017440:2020 Assessment and retrofitting of existing structures

COST Action TU1402 (2015-2019), Quantifying the value of structural health monitoring (BridgeSpec)

COST Action TU1406 (2015-2019), Quality specifications for roadway bridges, standardization at a European level (BridgeSpec)

Croce, P., Formichi, P., Landi, F., (2019) Climate Change: Impacts on Climatic Actions and Structural Reliability, Applied Science, 9 (24) (Special Issue: Advances on Structural Engineering)

Darò P., Longo M., Mancini G., Negri S., Bigaj-van Vliet A., Allaix D. L. (2022), Data-informed safety assessment of concrete structures, fib Congress Oslo, ISBN: 978-2-940643-15-8 - ISSN: 2617-4820

Darò, P. et al. (2023). 'Thermal Effects on Bridges Dynamic Behaviour'. In: Limongelli, M.P., Giordano, P.F., Quqa, S.,Gentile, C., Cigada, A. (eds) Experimental Vibration Analysis for Civil Engineering Structures. EVACES 2023. Lecture Notes in Civil Engineering, vol 432. Springer, Cham

Darò, P., Alovisi, I., Mancini G., Longo M., La Mazza D., Cigada A., 'Dense sensing on roadway bridges network: new approach to data-informed assessment', 25 September 2023 https://doi.org/10.1002/cepa.2024

Darò, P., Alovisi, I., Mancini, G., Negri, S., Bigaj-van Vliet, A., van Meerveld, H. (2022) Lessons learned from proactive maintenance practices for concrete bridges, fib Congress Oslo, ISBN: 978-2-940643-15-8 - ISSN: 2617-4820

Fib - Federation International for Structural Concrete - fib Bulletin No. 109 (2022). Existing concrete structures life management, testing and structural health monitoring - State-of-the-art-report (151 pages, ISBN 978-2-88394-171-7, October 2023)

Fib - Federation International for Structural Concrete (2013) fib Model Code for Concrete Structures 2010, Ernst & Sohn

Govers, M. L., (2010) Stochastic model updating—covariance matrix adjustments from uncertain experimental modal data. Mechanical Systems and Signal Processing, Vol.24, Issue 3, 696:760

H2020 CSA IM-SAFE (2020-2022) Appraisal of methods for safety evaluation and risk management. https://im-safe-project.eu/

Hellebrandt, L., Blom, K. Steenbergen, R., (2016) Probabilistic traffic load model for short-span city, 33:56

International Organization for Standardization 2015. ISO 2394:2015. General principles on reliability for structures

International Organization for Standardization 2010. ISO 13822. Bases for design of structures - Assesment of existing structures

Strauss A., Bigaj-van Vliet A., Daró P., Sanchez, A., Granzner, M., Bergmeister, K. (2022), Performance indicators for an objective assessment and through-life management of bridges and tunnels, fib Congress Oslo, ISBN: 978-2-940643-15-8 - ISSN: 2617-4820

Strauss A., Bigaj-van Vliet A., Daró P., Van Meerveld H., (2022), Condition-states and low limit maintenance thresholds of transport infrastructures in an European Context, fib Congress Oslo, ISBN: 978-2-940643-15-8 - ISSN: 2617-4820

Strauss, D., Malioka, V., & Faber, M. H. (2009). A framework for the asset integrity management of large deteriorating concrete structures. Structure & Infrastructure Engineering, 5(3), 199–213. https://doi.org/10.1080/15732470601017369

SS47: Life-cycle of RC/PC bridges: Advances on experimental testing and computational methods from the BRIDGE|50 research project

Organizers: F. Biondini, F. Tondolo, S. Manto & C. Beltrami


Taylor & Francis
Taylor & Francis Group
http://taylorandfrancis.com

Bridge Maintenance, Safety, Management, Digitalization and Sustainability – Jensen, Frangopol & Schmidt (eds)
© 2024 The Author(s), ISBN 978-1-032-77040-6
Open Access: www.taylorfrancis.com, CC BY-NC-ND 4.0 license

Nonlinear structural analysis of 50-year-old PC bridge deck beams under load testing

M. Anghileri & F. Biondini
Department of Civil and Environmental Engineering, Politecnico di Milano, Milan, Italy

ABSTRACT: A robust validation of life-cycle reliability analyses and residual capacity assessment procedures is a difficult task to be performed due to limited availability of data of existing deteriorating bridges. This paper deals with computational modeling and experimental validation of nonlinear finite element analysis of deteriorating prestressed concrete (PC) structures. The structural modeling is developed with different levels of complexity and computational cost using a PC beam finite element model accounting for material nonlinearities and a bi-dimensional finite element model for plane stress analysis formulated in accordance with the Modified Compression Field Theory. The finite element approaches and the modeling strategies are validated based on the results of full-scale load tests up to collapse collected from the BRIDGE|50 research project aimed at investigating the residual structural capacity of 50-year-old PC bridge deck beams under different loading and damage scenarios.

1 INTRODUCTION

Life-cycle safety, reliability, and robustness assessment of deteriorating structures should be based on structural analysis frameworks capable to account for multiple time-variant factors, including the effects of aging and deterioration, loadings, environmental exposure, maintenance and repair interventions (Biondini and Frangopol 2016, ASCE 2023). Efficient and accurate life-cycle criteria, methods and tools need to rely on robust validation and accurate calibration procedures based on experimental evidence and data from existing structures. Even though life-cycle models for damage processes are well established in literature, their validation is a difficult task because of limited availability of data, particularly on condition state and time-variant performance of existing reinforced concrete (RC) and prestressed concrete (PC) structures (Biondini and Frangopol 2018). Gathering new data from both inspection of existing structures and experimental tests is therefore of essence for a successful implementation in practice of life-cycle methods. Within this context, the BRIDGE|50 research project has been established by Politecnico di Milano and Politecnico di Torino as part of an agreement with public authorities and private companies for a wide experimental campaign on a group of 29 PC deck beams and two PC pier caps taken from a viaduct dismantled in Turin, Italy, after a 50-year lifetime (Biondini et al. 2021a, 2021b). The experimental campaign includes non-destructive and laboratory tests on concrete and steel samples and full-scale load tests on the PC deck beams under several loading schemes (i.e., three- and four-point bending tests) to investigate both flexural and shear failures, and different damage scenarios for residual performance evaluations. Additional details about the research project and the ongoing experimental campaign can be found in Biondini et al. (2021a,b), Tondolo et al. (2021, 2022), Anghileri (2022), Savino et al. (2023). This paper presents the validation of nonlinear structural analysis methods based on the experimental results of load tests performed on two sets of PC deck beams, one with beams in a good state of preservation and one with beams affected by significant damage induced during the dismantling of the viaduct or intentionally applied prior to the experimental testing to investigate the residual structural performance.

DOI: 10.1201/9781003483755-410

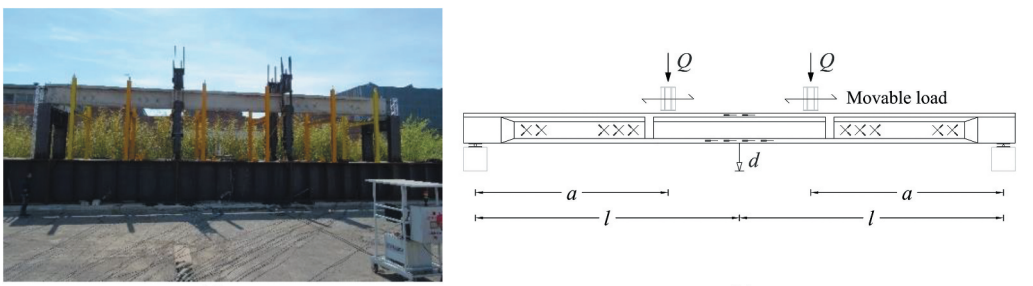
2 FULL-SCALE LOAD TESTS OF PC BRIDGE DECK BEAMS

2.1 *PC bridge deck beams*

The PC bridge deck beams investigated in this paper have been dismantled from a 50-year-old viaduct and stored in a dedicated testing site managed by Politecnico di Torino. The beams have length of about 19.40 m and composite cross-section made of a precast PC I-beam and a top cast-in-situ RC slab. The RC slab was cast with the precast PC beams already in place under the effects of beam self-weight and prestressing. The precast beams are prestressed by twenty 7-wire steel strands. The nominal diameter of the steel strands is 12.7 mm (effective area 99 mm^2). The initial prestressing stress, net of instantaneous and estimated long-term losses, as reported in the technical design documentation, is σ_{pd}=836 MPa. Based on the results of full-scale load tests and diagnostic activities, the actual residual prestressing has been estimated as σ_p=614 MPa. This reduced value with respect to the design value is likely due to larger instantaneous and/or long-term prestressing losses and steel corrosion effects. The material mechanical properties have been evaluated from the available technical documentation, including the results of non-destructive and laboratory tests on both concrete and steel samples (Anghileri et al. 2023, Savino et al. 2023).

2.2 *Full-scale load test program*

Multiple full-scale load tests have been performed with a dedicated testing framework (Figure 1a) The tests are based on a four-point bending scheme (Figure 1b) with different shear span ratio $\alpha=a/l$ (i.e., a=shear span; l=half beam span), to investigate bending and shear failures of the PC beams with or without the top RC slab. The loading system includes four actuators, two for each point load. The applied load is transferred by two transverse steel beams to the PC beam simply-supported at both ends by the steel reaction frame through bridge bearings. The setup of the experimental sensors installed have been designed in order to monitor the global beam structural response during the full-scale load tests by means of displacement potentiometers, the local concrete and steel behaviour, and the strand slip and bearing settlements through transducers.



(a) (b)

Figure 1. (a) View of the experimental testing framework during a load test. (b) Four-point loading scheme, with shear span ratio $\alpha=a/l$, and setup of the measurement sensors.

The experimental program is ongoing. The first three beams of the series (Beams #1, #2, and #3) have been tested under three-point bending (i.e., $\alpha\approx1.00$). These beams attained a structural failure with full crushing in compression of the top RC slab in the critical region at mid-span. To investigate the structural capacity of the PC beam only, a fourth PC beam has been tested under three-point bending after the removal of the top RC slab (Beam #4). This beam reported a full-crushing in compression of the top region of the beam at mid-span. Two additional beams with top slab (Beams #5 and #6) have been tested under four-point bending (i.e., $\alpha\approx0.68$). These beams exhibited a structural failure which started with full crushing in compression of the top slab at mid-span or close to the applied loads, and then propagated through the entire beam cross-section.

This first group of six tested beams exhibited local damage in the end regions due to corrosion with steel mass loss and concrete spalling. These effects can be attributed to inadequacy of bridge water conveyance system and use of road salts during the bridge lifetime (Carsana et al. 2022, 2023). However, the visual inspection of the tested beams in the failure regions observed no significant corrosion of the prestressing strands. The effects of corrosion are therefore not considered in the experimental validation of this group of six beams.

A second group of PC beams characterized by significant structural damage is considered in this paper. During the dismantling of the viaduct, a core drilling machine has been used to create holes in the deck to accommodate the equipment for lifting the beams. These activities led to remove part of the concrete from both the top RC slab and bottom PC beam flange in different regions (i.e., mid-span and at about 4 meters from the beam ends). For some beams, these operations also led to unintentionally cut some prestressing strands and reinforcing steel bars located at the bottom beam flange (Figure 2a). These damaged beams are considered to investigate the role of structural damage on the structural response. The first damaged beam tested, namely Beam #7, presented four strands cut at the bottom flange of the beam both at mid-span and at about 4 meters from the beam ends (Figure 2a). The next beam, namely Beam #8, presented strands cutting at about 4 meters from the beam ends only, with no significant damage at the beam mid-span. Beam #8 under four-point bending test ($\alpha \approx 0.68$) showed a full-crushing in compression of the top slab at mid-span region and reported a structural response, in terms of load versus displacement diagram, similar to the behavior of undamaged beams tested with the same shear span ratio. Therefore, Beam #8 will not be considered in this paper for the experimental validation. Another beam, namely Beam #9, has been intentionally damaged by removing concrete cover and cutting eight prestressing strands at the bottom flange of the beam at mid-span region (Figure 2b).



(a) (b)

Figure 2. PC bridge deck beams with structural damage: (a) core drilling with removal of concrete at top slab and bottom beam flange, with cut of four strands; (b) concrete cover removal and cut of eight strands.

3 FINITE ELEMENT MODELING OF PC BRIDGE DECK BEAMS

3.1 *Finite element modeling of RC/PC concrete structures*

Finite element formulations for nonlinear analysis of RC/PC structures have been proposed in literature with emphasis on a wide spectrum of features, including element discretization, robustness of the formulation, accuracy of the solution process, and computational cost (Malerba 1998).

A trade-off on these factors can be achieved by RC/PC beam finite elements (BFEs). The BFE formulation considered in this paper assumes the linearity of the cross-sectional strain field, accounts for the nonlinear constitutive laws of the materials, and neglects shear failures and bond-slip of steel. The structure is discretized in beam finite elements, the member cross-section

is subdivided into four-node isoparametric subdomains, as shown in Figure 3a, and numerical integration is performed using a Gauss-Lobatto quadrature rule (Bontempi et al. 1995).

BFEs allow for good accuracy if structural behavior is dominated by flexural failure modes. To account for shear effects and local stress-diffusion phenomena the Modified Compression Field Theory (MCFT) is considered for nonlinear plane-stress analysis of RC/PC structures (Vecchio and Collins 1986). The MCFT-based formulation is used in this paper also to better capture the beam-to-slab interaction effects affecting the structural response of the investigated PC deck beams. The structure is discretized into 2D constant strain triangle (CST) finite elements with smeared reinforcement, as shown in Figure 3b (Bontempi et al. 1994). Additional details about the adopted BFE- and MCFT-based formulations can be found in Anghileri (2022).

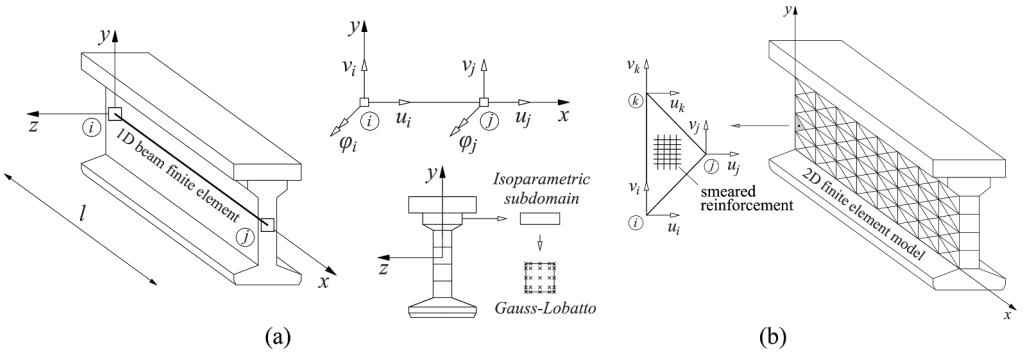


Figure 3. (a) BFE model with nodal displacements, isoparametric discretization, and Gauss-Lobatto integration scheme; (b) MCFT model with nodal displacements and CST elements with smeared reinforcement.

3.2 *BFE- and MCFT-based structural modeling*

The BFE model of PC deck beams with or without top RC slab exploits the symmetry and it is based on a discretization with 13 elements for the half deck beam, with one outer element with rectangular cross-section at the support region, one adjacent element with linearly varying width of beam web, and eleven inner elements with I-shaped cross-section. The slab is modelled using 13 additional elements with rectangular cross-section and the same discretization of the beam. The element nodal points are located at beam-slab interface and the offsets of the beam and slab axes are accounted for by transformation of coordinates.

The MCFT plane stress finite element model of PC decks beam exploits the symmetry and it is based on a discretization with 1128 CST finite elements for the half deck beam. The stirrups are modeled as smeared reinforcement over the beam volume (diameter of 8 mm and spacing of 250 mm and 100 mm for the inner beam segment with I-shaped cross-section and the outer beam segments with rectangular cross-section, respectively, as detected with pacometer-scan activity). Longitudinal reinforcing bars and prestressing strands are modelled as truss elements built over the CST finite element mesh. Separate nodal points are considered at the beam-slab interface with links to model the beam-to-slab interaction (Anghileri 2022, Anghileri and Biondini 2022, 2023).

For both BFE and MCFT formulations, the model discretization and numerical integration have been established for a trade-off between accuracy and computational cost.

4 NONLINEAR ANALYSIS AND EXPERIMENTAL VALIDATION

The BRIDGE|50 experimental activities are complemented by extensive numerical analyses to investigate the structural behavior of the tested beams and support a proper planning of the full-scale load tests. The non-destructive and laboratory tests performed on concrete,

reinforcing steel, and prestressing steel allowed to better calibrate the material mechanical characteristics. As an example, the original design documentation reported that the compressive strength recorded after 28 days of the precast PC beams averaged 50.3 MPa over 4 samples (Savino et al. 2023). However, uni-axial compressive strength tests performed on 17 samples extracted from several beams after the dismantling of the viaduct achieved a sample mean and CoV of concrete compressive strength equals to 29.94 MPa and 0.15, respectively, showing good agreement with the results of non-destructive tests processed through the SonReb method (Anghileri et al. 2023).

Visual inspection activities performed after the full-scale load tests allows also to better identify the reinforcing steel layout in both precast PC beam and cast-in-situ RC slab which was not exhaustively reported in the original design documentation.

The nonlinear structural analysis of both undamaged and damaged PC deck beams is performed in the following for numerical validation of the finite element formulations based on the results of the full-scale load tests. The experimental load protocol consists of a first loading phase up to concrete cracking, a stop under loading for the assessment of the concrete cracking pattern, a subsequent total unloading, and a reloading up to the beam collapse. The nonlinear finite element analyses are carried out under monotonic loading.

4.1 *Nonlinear analysis of undamaged PC beams without top slab*

The PC deck beam without top RC slab has been tested under a three-point loading (i.e., $\alpha \approx 1.00$) up to collapse. The beam exhibited a full-crushing in compression of the top mid-span region with collapse load Q=129 kN. To investigate the role of data and information gathered during the experimental campaign, nonlinear analyses have been performed considering the following case studies: Case (I) assumes the prestressing level (σ_{pd}) and material mechanical properties reported in the original design documentation and neglects the presence of the reinforcing steel bars; Case (II) introduces the material mechanical properties estimated from diagnostics; Case (III) additionally accounts for the estimated residual prestressing level σ_p; Case (IV) takes also into account the presence of the reinforcing steel bars. Figure 4a compares BFE-based numerical results and experimental results under three-point bending ($\alpha \approx 1.00$) in terms of load Q versus mid-span displacement d, net of self-weight and prestressing, of the PC beam without RC slab (Beam #4) for the four case studies. The close correspondence of Case (IV) with experimental results allows to validate the finite element formulation and the results of the experimental activities. Moreover, for Case (IV) Figure 4b indicates high accuracy also in terms of load versus concrete axial strain at mid-span region recorded through transducers located at the top and bottom slab of the beam.

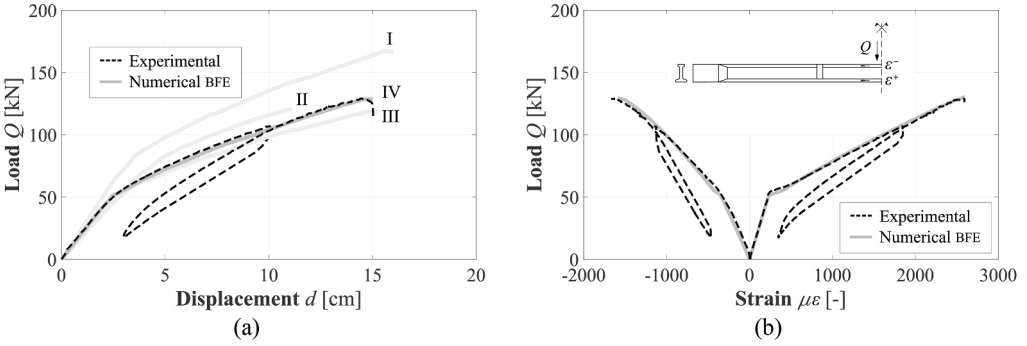


Figure 4. Numerical (BFE) vs experimental results for a PC beam without top slab (Beam #4): (a) Load Q vs mid-span displacement d for four Cases (I)-(IV); (b) Load Q vs axial strain ε at mid-span for Case (IV).

4.2 *Nonlinear analysis of undamaged PC beams with top slab*

A PC deck beam with RC slab under three-point loading (i.e., $\alpha \approx 1.00$) exhibited a failure in compression of the top slab in the critical mid-span region with ultimate load Q=161 kN and lack of connection between beam and slab at incipient collapse. To investigate the role of the top slab in the structural response, three different case studies are considered: Case (I) refers to a beam without top slab; Case (II) assumes monolithic beam-to-slab connection; Case (III) is based on separate beam and slab connected with links. In case (III), nonlinear analysis is developed based on a two-level incremental approach to account for the effects of the bridge construction process. In a first stage, the beam only is loaded with self-weight and prestressing. In a second stage, the two separate sets of finite elements (i.e. PC beam and RC slab) are connected at each pair of nodal points at the beam-slab interface by rigid links in the direction normal to the beam axis. The beam-slab interaction in the longitudinal direction is modeled by means of a set of longitudinal elastic links to be activated in the second stage only. These links are rigid up to concrete cracking. After concrete cracking, the links are elastic with stiffness k estimated to best fit the experimental results. Figure 5a compares MCFT-based numerical results and experimental results under three-point bending ($\alpha \approx 1.00$), in terms of load Q versus mid-span displacement d, net of self-weight and prestressing, of one of the tested PC beams with RC slab (Beam #2) for the three case studies. The best-fit stiffness value at beam-slab interface for the three-point loading scheme is k=3000 N/mm. A four-point bending test with shear span ratio $\alpha \approx 0.68$ has been also adopted for the PC beams with slab. The failure mechanism reported full crushing in compression of top slab near the applied load. Figure 5b compares the experimental results of one of these tests with ultimate collapse load Q=254 kN, in terms of Q versus mid-span displacement d, net of self-weight and prestressing, and the numerical MCFT-based numerical results (Beam #6) for Case (III). The best-fit stiffness value at beam-slab interface for the four-point loading scheme is k=11500 N/mm.

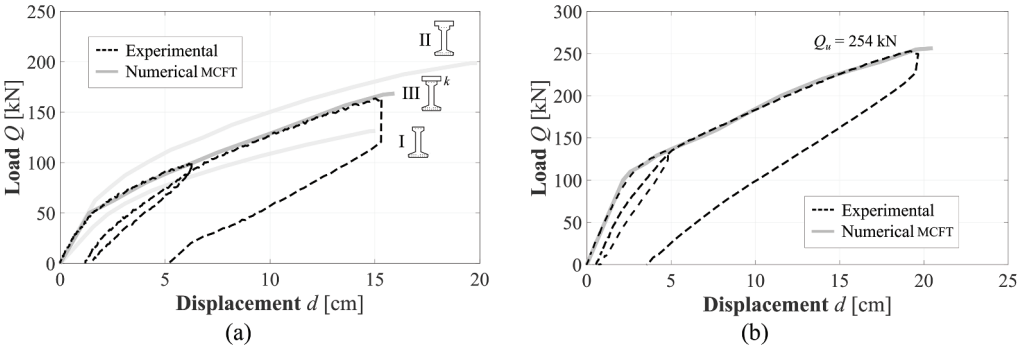


Figure 5. Load Q vs mid-span displacement d of PC beam with top slab: Numerical (MCFT) vs experimental results under (a) three-point loading (Beam #2) for three Cases (I)-(III), and (b) four-point loading (Beam #6) for Case (III).

The good agreement between experimental and numerical results obtained for both BFE and MCFT validates the finite element formulations and the modeling strategies under flexural failures. Additional details about the experimental results and numerical validation of the finite element models for the first group of undamaged beams can be found in Anghileri and Biondini (2022, 2023). Further investigations are necessary based on future load tests with reduced shear span ratios to investigate the accuracy of the proposed modeling under shear failures.

4.3 *Nonlinear analysis of damaged PC beams*

The PC deck beams with top slab and structural damage have been tested under four-point loading (i.e., $\alpha \approx 0.68$) up to collapse. Beam #7, with part of the concrete removed from both

the top slab and bottom beam flange and four strands cut at the bottom flange, both at mid-span and at about 4 meters from the beam ends, has been tested with preliminary loading phase up to Q=118 kN, a subsequent unloading and final reloading up to the collapse load Q=211 kN. The failure mechanism was characterized by the crushing in compression of top slab and cracking in tension of the bottom beam flange in the mid-span region (Figure 6a). Beam #9, damaged with intentional cut of eight prestressing strands in the mid-span region, has been tested with a first loading phase up to Q=77 kN, a subsequent unloading and final reloading up to the collapse load Q=145 kN, attained with a full crushing in compression of the top slab (Figure 6b).



(a) (b)

Figure 6. Failure mechanisms: (a) Beam #7, with crushing in compression of the top slab and cracking in tension of the bottom beam flange; (b) Beam #9, with crushing in compression of the top slab.

The nonlinear finite element analysis of beams #7 and #9 is carried out considering the removal of the cut strands and steel bars from the finite element meshes. Moreover, beam and slab width has been properly reduced to reproduce the concrete damage. Figure 7 compares numerical and experimental results in terms of load Q versus mid-span displacement d, net of self-weight and prestressing, for Beam #7 (Figure 7a) and Beam #9 (Figure 7b) after the four-point bending test. The best-fit stiffness value at beam-slab interface is k=11500 N/mm also for the damaged beams.

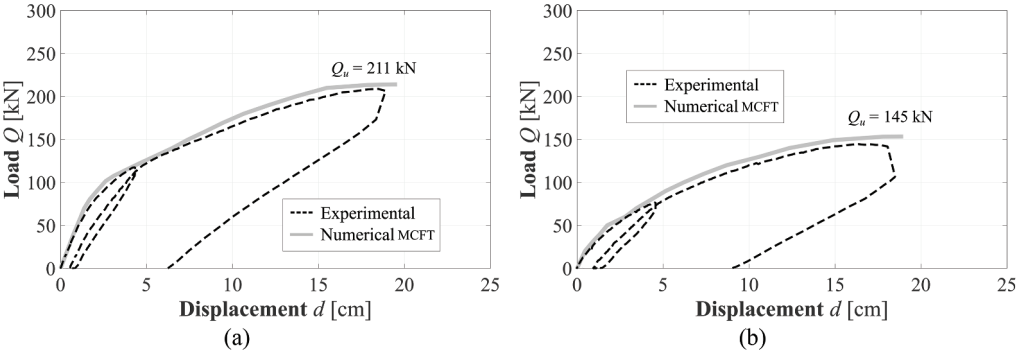


Figure 7. Numerical (MCFT) vs experimental results in terms of load Q vs mid-span displacement d of PC beams under four-point loading: (a) Beam #7; (b) Beam #9.

Overall, the good agreement between numerical and experimental results considering different damage scenarios validates the finite element formulations and the damage modeling strategies under flexural failures. Further investigations are necessary based on future load tests under shear failures. Despite this need, the results of the validation process presented in this

paper allows to complement the experimental activities with numerical analysis to further investigate the structural behavior of the tested beams and support a proper planning of the ongoing load tests.

5 CONCLUSIONS

The comparison of experimental and numerical results based on nonlinear finite element analysis of RC/PC structures has been presented. The results of full-scale load tests on several 50-year-old PC bridge deck beams under different loading and damage scenarios have been considered for the validation process. The structural modeling has been developed with different levels of complexity and computational cost using a PC beam finite element model accounting for material nonlinearities and a bi-dimensional finite element model for plane-stress analysis formulated in accordance with the Modified Compression Field Theory. The material characteristics and the modeling strategies have been calibrated based on the results of visual inspection activities, non-destructive tests and laboratory tests on both concrete and steel samples. The role of structural damage in the residual capacity of PC beams has been also investigated. The impact of data and information gathered during the overall experimental campaign on the beam structural response have been evaluated through the comparison of experimental and numerical results considering different case studies. The good agreement between numerical and experimental results allows to validate the finite element formulation and the modeling strategies and to support a proper planning of future full-scale load tests associated to different shear span ratio and additional damage scenarios. Future developments will be devoted at evaluating the accuracy of the finite element models with full-scale load tests associated to shear-dominant failure mechanisms and characterized by beams under corrosion. Moreover, the large amount of data and experimental outcomes will allow to extend the validation process on a statistical basis for a probabilistic description of the structural response of the investigated PC bridge deck beams.

ACKNOWLEDGMENTS

BRIDGE|50 is a research project based on a research agreement among universities, public authorities, and private companies. Members of the Management Committee: S.C.R. Piemonte (President); Politecnico di Milano (Scientific Coordinator); Politecnico di Torino (Scientific Responsible of the Experimental Activities); Lombardi Engineering (Secretary); Piedmont Region; City of Turin; Metropolitan City of Turin; TNE Torino Nuova Economia; ATI Itinera & C.M.B.; ATI Despe & Perino Piero; Quaranta Group. BRIDGE|50 website: http://www.bridge50.org.

REFERENCES

Anghileri, M. 2022. *Life-cycle structural performance of RC/PC bridges: Computational modeling and experimental validation*. PhD thesis, Politecnico di Milano, Milan, Italy.

Anghileri, M.., Biondini, F. 2022. Formulation and experimental validation of nonlinear finite element analysis of PC bridge deck beams. *Eleventh International Conference on Bridge Maintenance, Safety and Management* (IABMAS 2022), Barcelona, Spain, July 11-15, 2022. In: Casas, J.R., Frangopol, D. M., Turmo, J. (Eds.), *Bridge Safety, Maintenance, Management, Life-Cycle, Resilience and Sustainability*. CRC Press, London, UK.

Anghileri, M., Biondini, F. 2023. Experimental validation of nonlinear finite element analysis of PC bridge deck beams based on the results of full-scale load tests. *Eighth International Symposium on Life-Cycle Civil Engineering* (IALCCE 2023), July 2-6, 2023, Milan, Italy. In: *Life-Cycle of Structures and Infrastructure Systems*, F. Biondini, D.M. Frangopol (Eds.), CRC Press, London, UK (Open Access).

Anghileri, M., Rosati, G., Biondini, F., Savino, P., Tondolo, F. 2023. Experimental tests for mechanical characterization of prestressed concrete bridge deck beams. *Eighth International Symposium on Life-Cycle Civil Engineering* (IALCCE 2023), July 2-6, 2023, Milan, Italy. In: *Life-Cycle of Structures and Infrastructure Systems*, F. Biondini, D.M. Frangopol (Eds.), CRC Press, London, UK (Open Access).

ASCE 2021. *Report Card for America's Infrastructure*, American Society of Civil Engineers, Reston, VA.
Biondini, F., Frangopol, D. M. 2016. Life-cycle performance of deteriorating structural systems under uncertainty: Review. *Journal of Structural Engineering*, ASCE, 142(9), F4016001, 1–17.
Biondini, F., Frangopol, D. M. 2018. Life-cycle performance of civil structure and infrastructure systems: Survey. *Journal of Structural Engineering*, ASCE, 144(1), 06017008, 1–7.
Biondini, F., Manto, S., Beltrami, C., Tondolo, F., Chiara, M., Salza, B., Tizzani, M., Chiaia, B., Lencioni, A., Panseri, L., and Quaranta, L. 2021a. BRIDGE| 50 research project: Residual structural performance of a 50-year-old bridge. *Tenth International Conference on Bridge Maintenance, Safety and Management* (IABMAS 2020), June 28-July 2, 2020 (postponed to April 11-15, 2021), Sapporo, Japan.
Biondini, F., Tondolo, F., Manto, S., Beltrami, C., Chiara, M., Salza, B., Tizzani, M., Chiaia, B., Lencioni, A., Panseri, L., and Quaranta, L. 2021b. Residual Structural Performance of Existing PC Bridges: Recent Advances of the BRIDGE|50 Research Project. *First Conference of the European Association on Quality Control of Bridges and Structures* (EUROSTRUCT 2021), Padua, Italy, August 29 - September 1, 2021. In: Pellegrino, C., Faleschini, F., Zanini, M.A., Matos, J.C., Casas, J.R., Strauss, A. (Eds.), *Lecture Notes in Civil Engineering*, 200, 2022, Springer.
Bontempi F., Malerba P.G., Romano L. 1994. Il modello M.C.F.T. nell'analisi per elementi finiti di strutture piane in C.A., *Studi e Ricerche*, Graduate School for Concrete Structures "F.lli Pesenti", Politecnico di Milano, Italy, 16, 173–207 (In Italian).
Bontempi, F., Malerba, P.G., Romano, L. 1995. Formulazione diretta secante dell'analisi non lineare di telai in C.A./C.A.P., *Studi e Ricerche*, Graduate School for Concrete Structures "F.lli Pesenti", Politecnico di Milano, Italy, 16, 351–386 (In Italian).
Carsana, M., Biondini, F., Redaelli, E., Valoti, D.O. 2022. Corrosion assessment of 50-year-old PC deck beams. *Eleventh International Conference on Bridge Maintenance, Safety and Management* (IABMAS 2022), Barcelona, Spain, July 11-15, 2022. In: Casas, J.R., Frangopol, D.M., Turmo, J. (Eds.), *Bridge Safety, Maintenance, Management, Life-Cycle, Resilience and Sustainability*. CRC Press, London, UK.
Carsana, M., Redaelli, E., Biondini, F.2023. Field and laboratory tests for corrosion assessment of existing concrete bridges. *Eighth International Symposium on Life-Cycle Civil Engineering* (IALCCE 2023), July 2-6, 2023, Milan, Italy (Keynote Paper). In: *Life-Cycle of Structures and Infrastructure Systems*, F.Biondini, D.M.Frangopol (Eds.), CRC Press, London, UK, 45–56 (Open Access).
Malerba, P. G.1998. *Limit and nonlinear analysis of reinforced concrete structures*. CISM International Centre for Mechanical Sciences, Udine, Italy (In Italian).
Savino, P., Tondolo, F., Sabia, D., Quattrone, A., Biondini, F., Rosati, G., Anghileri, M., Chiaia, B. 2023. Large-scale experimental static testing on 50-year-old prestressed concrete bridge girders, *Applied Sciences*, 13(2), 1–22.
Tondolo, F., Biondini, F., Sabia, D., Rosati, G., Chiaia, B., Quattrone, A., Savino, P., and Anghileri, M. 2021. Experimental program and full-scale load tests on PC deck beams. *First Conference of the European Association on Quality Control of Bridges and Structures* (EUROSTRUCT 2021), Padua, Italy, August 29 - September 1, 2021. In: Pellegrino, C., Faleschini, F., Zanini, M.A., Matos, J.C., Casas, J. R., Strauss, A. (Eds.), *Lecture Notes in Civil Engineering*, 200, 2022, Springer.
Tondolo, F., Sabia, D., Chiaia, B., Quattrone, A., Savino, P., Biondini, F., Rosati, G., and Anghileri, M. 2022. Full-scale testing and analysis of 50-year old prestressed concrete bridge girders. *Eleventh International Conference on Bridge Maintenance, Safety and Management* (IABMAS 2022), Barcelona, Spain, July 11-15, 2022. In: Casas, J.R., Frangopol, D.M., Turmo, J. (Eds.), *Bridge Safety, Maintenance, Management, Life-Cycle, Resilience and Sustainability*. CRC Press, London, UK.
Vecchio, F.J., Collins, M.P. 1986. The modified compression field theory for reinforced concrete elements subjected to shear. *ACI Journal*, 83(2), 219–231.

Bridge Maintenance, Safety, Management, Digitalization and Sustainability – Jensen, Frangopol & Schmidt (eds)
© 2024 The Author(s), ISBN 978-1-032-77040-6
Open Access: www.taylorfrancis.com, CC BY-NC-ND 4.0 license

Corrosion investigations on PC deck beams of a 50-year-old decommissioned viaduct

M. Carsana & E. Redaelli
Department of Chemistry, Materials and Chemical Engineering "Giulio Natta", Politecnico di Milano, Milan, Italy

F. Biondini
Department of Civil and Environmental Engineering, Politecnico di Milano, Milan, Italy

ABSTRACT: The structural elements considered in this paper are stored in the testing site of BRIDGE|50 research project after the dismantling of a 50-year-old viaduct. They are representative of the use of reinforced and prestressed concrete in the XX century and offer the opportunity to characterize corrosion behavior of full-scale concrete deck beams under different degradation conditions through experimental investigations. This paper presents the results obtained by means of electrochemical methods (such as corrosion potential and electrical resistivity) and by performing some chemical and physical analyses on concrete samples collected from selected beams. Such results provide the bases to investigate the feasibility of applying electrochemical techniques aimed at advanced repair strategies of existing deck beams for eventually reusing them in new constructions. On the other hand, the application of such techniques might also allow to induce on the same beams accelerated ageing processes for simulating more aggressive conditions.

1 INTRODUCTION

Since the beginning of the last Century, the use of reinforced concrete (RC) became a worldwide common practice in the construction of structures and infrastructures. Unfortunately, the widespread use of RC has raised serious durability problems as a consequence of corrosion of steel reinforcement which is an electrochemical phenomenon, as illustrated in Figure 1a (Bertolini et al. 2013, Carsana et al. 2023). Nowadays, durability has become a critical issue for life-cycle assessment, maintenance, monitoring, and management of existing concrete structures (Biondini & Frangopol 2016). For this reason, tools and procedures for monitoring of corrosion in RC structures, which are essential to achieve suitable levels of durability (Carsana et al. 2022), have been developed (Bertolini 2008).

As known, corrosion processes affecting the service life of RC structures include initiation of corrosion, in which the reinforcement is passive but some phenomena can lead to loss of passivity (e.g. carbonation or chloride penetration) and corrosion propagation after the steel is depassivated (Bertolini 2008). The duration of the initiation phase depends on the depth of reinforcing bars, the quality of concrete cover and the penetration rate of the aggressive agents as well as on the microclimatic conditions at the concrete surface.

The initiation time can also be affected by any form of polarization of the steel reinforcement promoted by means of applying electrochemical techniques which relay on the same principles of corrosion, as shown in Figure 1b. For instance, a small amount of cathodic polarization makes the occurrence of pitting less probable and increases the initiation time, while an anodic polarization, which might be due to an electric connection with reinforcement

DOI: 10.1201/9781003483755-411

with higher potential or external electric fields, could promote corrosion initiation (Bertolini et al. 2008).

The knowledge of corrosion process and availability of methods for its control play an important role for providing practitioners with adequate tools to solve durability problems of reinforced concrete structures (Bertolini et al. 2013, Biondini & Frangopol 2019, Elsener et al. 2003).

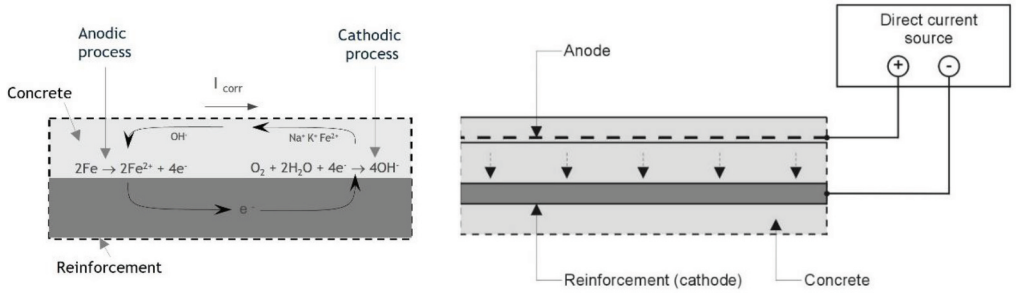


Figure 1. (a) Corrosion process of reinforcing steel in non-protective concrete at microscopic level. (b) Scheme of electrochemical techniques applied on a reinforced concrete element.

To this aim, it is important to advance knowledge not only through experimental studies carried out in laboratory, but also by means of corrosion investigations on real-scale structural elements.

A strong impulse along these research lines is given by the BRIDGE|50 research project which involves Politecnico di Milano and Politecnico di Torino, as well as several public authorities and private companies, for a large experimental campaign aimed at investigating the residual structural performance of an existing 80-span prestressed concrete (PC) viaduct demolished after a 50-year service life (Biondini et al. 2021a, 2021b).

The BRIDGE|50 research project is allowing to exploit the results obtained on real-scale elements, deriving from a long exposure to operating conditions and currently stored in a testing area (Figure 2) dedicated at both non-destructive (Carsana et al. 2021a) and destructive testing.



Figure 2. View of the PC deck beams stored in the BRIDGE|50 testing site.

This paper presents the results obtained by means of electrochemical methods (COST 2003), such as the measurement of corrosion potential and electrical resistivity, and by performing some chemical and physical analysis on concrete samples collected from selected beams. Such results provide the bases to investigate the application of electrochemical techniques aimed at advanced repair strategies of existing deck beams for eventually reusing them in the new constructions. On the other hand, the application of such techniques might allow also to induce on the same beams accelerated ageing processes for simulating more aggressive degradation conditions.

2 EXPERIMENTAL PROCEDURE

2.1 *Testing site*

In 2019, after a 50-year lifetime in an urban environment of Northen Italy (Turin), Corso Grosseto Viaduct was demolished. The viaduct consisted of 80 spans of variable length from 16 meter to 24 meter. Each span of the deck is composed by 10 inner precast PC I-beams and two external precast box girders with U-shape with top slabs (box-beams), all supported by PC pier caps. Two adjacent spans of the viaduct have been preserved and deconstructed, including 29 precast PC beams (twenty-five I-beams and four box-beams) and two pier caps. These elements are currently stored in a testing area dedicated to both corrosion and structural investigations. Based on visual inspection, few beams (one for each type), considered representative of different degradation conditions, were subjected to electrochemical measurements (see Carsana et al. 2021a for more details). Moreover, some concrete samples were also collected on the selected beams.

2.2 *Electrochemical measurements and sampling*

In order to assess the degradation state of reinforcing steel bars of the inspected PC deck beams, the cover depth of the outermost bars was detected with a magnetic-type covermeter. The corrosion behavior of the reinforcement was investigated by means of electrochemical measurements.

The corrosion potential of steel was mapped on the concrete surface using a CSE (Copper Sulphate Electrode, $Cu/CuSO_4$) reference electrode (Elsener). The electrical resistivity of concrete was measured by placing a resistivity probe connected to a conductivity-meter on the surface.

Preliminary measurements of corrosion rate were also carried out in some localized zones of inspected PC elements. The sampling of concrete for laboratory analysis was also carried out.

Cores of diameter 45.5 mm and length of at least 160 mm were taken from the longitudinal or transversal front of structural elements. Moreover, several samples of concrete powders were also collected directly by drilling at several depths with a tip of 10 mm diameter being this method considered much less invasive than taking a concrete core.

Carbonation depth was measured by spraying phenolphthalein on concrete powders collected at increasing depth or on concrete cores taken from RC/PC beams. Chloride analyses were carried out both on concrete powder samples as well as on 10 mm concrete slices in which each core was divided to determine total chlorides profile as a function of depth. Both powder samples and concrete slices, the latter once ground, were dried and digested in hot nitric acid. The chloride content was measured by means of potentiometric titration and expressed as percentage of the dry concrete.

3 RESULTS

3.1 *Corrosion assessment*

Measurements of corrosion potential (E_{corr}) versus CSE reference electrode were carried out on the longitudinal front of a pier cap along the nodes of a grid traced on the concrete surface

with 30 cm spacing, at different distances from the top of the element (Figure 3). According to the criteria of the American Standard ASTM C876, for E_{corr}> -200 (mV vs CSE) the probability of corrosion is less than 10% while for E_{corr}< -350 (mV vs CSE) the probability of corrosion is higher than 90%. Overall, the corrosion potentials measured on a selected pier cap were higher than -240 mV vs CSE. In several parts of the pier cap corrosion potential showed values lower than -350 mV vs CSE, highlighting that, at the time of the measurements, the corrosion rate of steel bars was not negligible. In fact, the corrosion conditions of steel bars of the pier cap appeared quite severe (Figure 3b). Pier cap showed evident signs of deterioration from corrosion of the reinforcements to wide detachments of the concrete cover; moreover, parts of the reinforcements were no longer embedded in concrete and they were heavily corroded.

Similar measurements were also carried out on one of the several I-beams stored in the testing site and considered visually similar. More positive corrosion potentials were measured on I-beam (Figure 4a). Overall, values higher than -200 mV vs CSE were measured at the time of inspection, regardless the height. No clear signs of corrosion-induced damage were observed on I-beams, except in their end parts where concrete segregation was visible (Figure 4b). The presence of segregation and macro-voids (Neville 2011) could have led to early degradation in those parts.

The interpretation of the corrosion potential is not so obvious because the concrete cover and its resistivity, in addition to the actual corrosion potential of the steel, influence the readings at the concrete surface at the inspection time. Important information can be obtained by considering also results from both electrical resistivity and corrosion rate measurements. For instance, Figure 5a shows the relationship between the corrosion potential of steel and the electrical resistivity of concrete measured on a box beam in the testing site. It can be deduced that the points associated to negative corrosion potentials and low electrical resistivity represent wet corroding zones, where steel bars are in contact with carbonated and/or chloride-contaminated concrete, while those with positive potentials and high resistivity indicate dry conditions and passive zones. The outcomes of investigations reported in a previous paper (Carsana et al. 2021) indicate that lower values of potential were only measured along the first 12-15 m of the beam in its bottom part where the concrete showed also the lowest electrical resistivity and it is affected by phenomena of efflorescence which could confirm the use of deicing salts. Inspected deck beams were monitored also in terms of corrosion rate. The worst conditions were observed on steel bars of the pier cap and box beam for which average corrosion rates of 4,18 mA/m^2 and 6,21 mA/m^2, respectively, were measured (Figure 5b). Conversely, a negligible corrosion probability is confirmed by a corrosion rate of 0,74 mA/m^2 for the inspected I-beam.

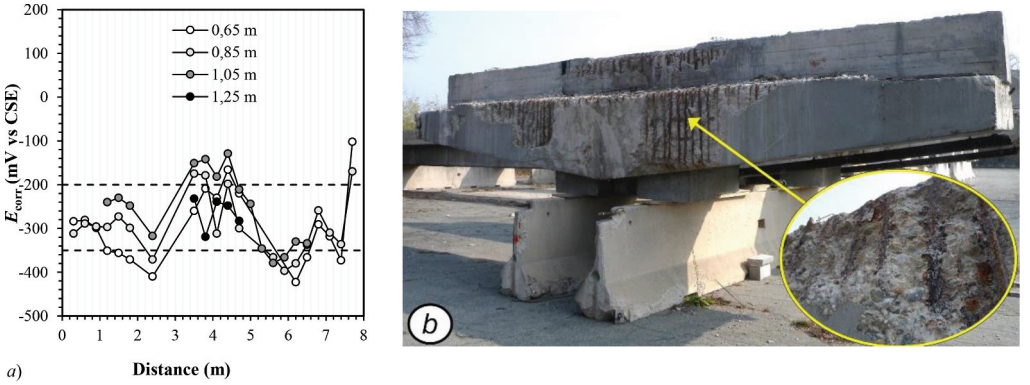


Figure 3. (a) Corrosion potential (E_{corr}) profiles measured on the longitudinal front of a pier cap at different heights. (b) View of degradation state of the pier cap.

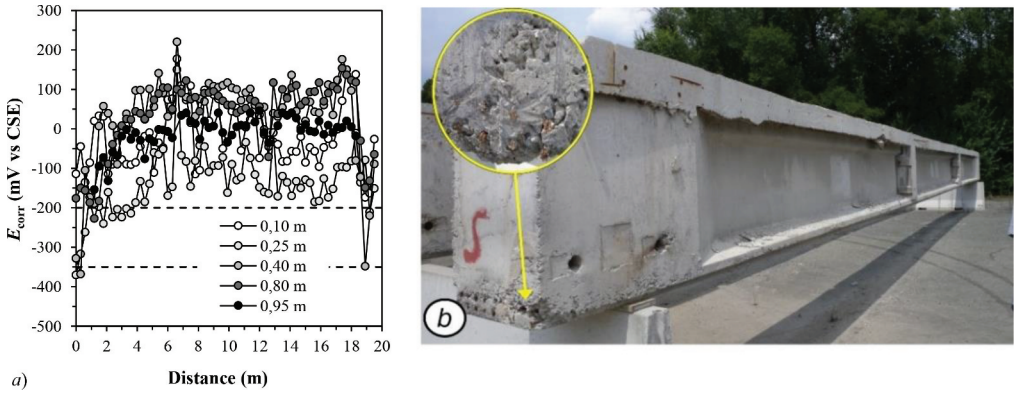


Figure 4. (a) Corrosion potential (E_{corr}) profiles measured on the longitudinal front of a box beam at different heights. (b) View of degradation state of the box beam.

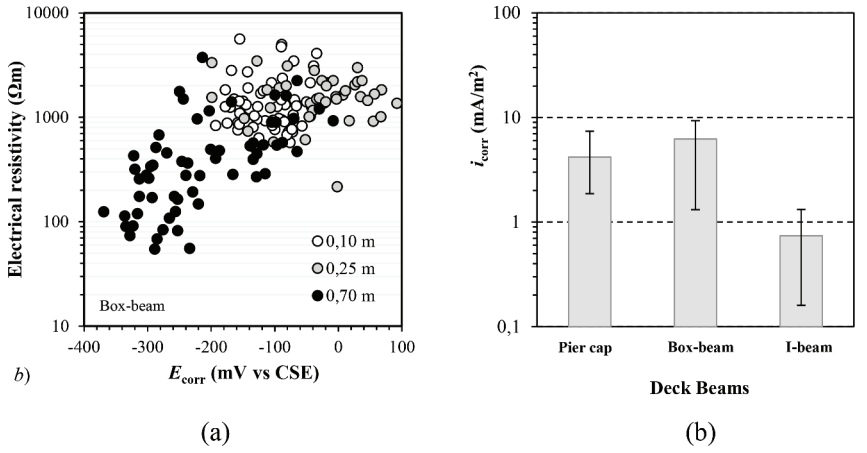


Figure 5. (a) Corrosion potential of steel reinforcements versus concrete electrical resistivity measured on the longitudinal front of a box beam. (b) Corrosion rate measured on different representative deck beams (pier cap, box beam, and I-beam) along their longitudinal front.

To assess the actual state of steel bars embedded in concrete, the evaluation of electrochemical aspects should be integrated with further analyses. Thus, taking of concrete samples is necessary to also evaluate the carbonation depth (Figure 6a) and chloride content of concrete (Figure 6b) at the time of measurement and to allow to predict the future deterioration of the structure or to assess its residual lifetime.

From the comparison of the average value of the carbonation depth with the average value of the concrete cover thickness (Figure 6a), it follows that steel reinforcement of longitudinal and transversal front of inspected I-beam should be in contact with an alkaline concrete. Concrete of pier cap and box beam showed to be less carbonated than that of I-beam. Based on the carbonation depth measured after 50 years on I-beams and related carbonation coefficient (3,2 mm/$y^{0.5}$), it can be inferred that the carbonation front will reach steel rebars no earlier than the next 50 years. Since the carbonation fronts also of box beam and pier cap are lower than the average values of reinforcement depth (22-23 mm), it could be deduced that rebars were mainly corroding at the time of inspection for other causes. Samples collected from same structural elements have been also subjected to the measurement of chlorides content. Figure 6b shows that the chloride profile measured on inspected pier cap overcome the critical

chlorides threshold for carbon steel (0,05-0,125% in mass of concrete) also far beyond average cover thickness with maximum values of 0,42% vs concrete mass. Conversely, for deck beam the risk of chlorides-induced corrosion shall be considered low at inspection time. In fact, chlorides content was below critical chlorides threshold at any concrete depth.

Results presented in this section has highlighted that the main causes of structural deterioration are associated to chloride penetration due to de-icing salt especially for the inspected pier cap and box-beam. In fact, significant signs of degradation were often observed in those parts of the bridge deck that were exposed to wetting, probably in absence of adequate systems of collection and conveyance of rainwater coming from the span, especially in correspondence of pier caps which support the terminal parts of beams (Figure 3b).

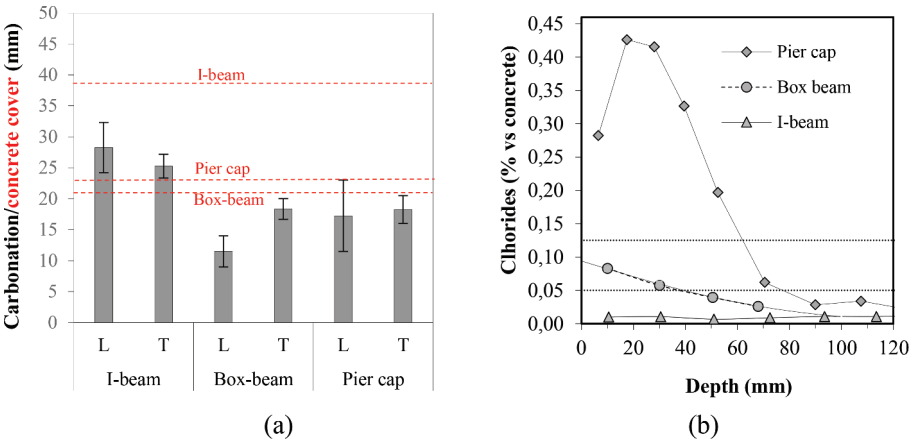


Figure 6. (a) Results of phenolphthalein test carried out on concrete samples collected from both longitudinal (L) and transversal front (T) of inspected deck-beams. Average concrete cover for each structural element is indicated with a dotted red line. (b) Chlorides profiles of inspected deck-beams (dotted lines indicate typical minimum and maximum values of critical chloride threshold).

3.2 *Further corrosion investigations*

Based on electrochemical measurements carried out on several structural elements stored in the testing site, it can be pointed out that the best conditions were observed on steel rebars of I-beams; in fact, a negligible corrosion probability was confirmed in terms of corrosion potential (mainly ranging between -150 mV and -50 mV vs CSE) and corrosion rate lower than 1 mA/m^2. Moreover, the presence of negligible chlorides content (below critical chlorides threshold at any depth), as well as a carbonation depth lower than concrete cover, allow to state that steel rebars of I-beams are in passive state being embedded in a protective concrete.

For this reason, among all deck beams stored in the testing site, I-beams are the most suitable to be subjected to further corrosion investigations.

The obtained results establish the bases to investigate the application of electrochemical techniques aimed at monitoring (1) the initiation and propagation of corrosion of I-beams due to exposure to more aggressive conditions than those to which they have been exposed so far and, subsequently, (2) the evolution of corrosion of the reinforcements once started in I-beams. In particular, the control of corrosion evolution should be aimed at developing advanced repair strategies of existing deck beams for eventually reusing them in new constructions. This challenge will require to carefully assess which of the different repair techniques (Bertolini et al. 2013) could be considered for structural elements already corroding due to carbonation or chloride penetration.

Considering the obtained results, the next experimental studies will focus on monitoring of corrosion process of I-beams when exposed to conditions different from those at the time of inspection, for instance after thorough wetting with water in case of active rebars (Bertolini

et al. 2008) or after ponding cycles with chlorides solution to simulate natural penetration of chlorides in concrete and promote pitting corrosion initiation. As an alternative, the application of electrochemical techniques might allow also to induce on comparable beams accelerated ageing processes for simulating more aggressive degradation conditions (Bertolini et al. 2013).

The I-beams stored in the testing site are also suitable for sampling of concrete portions of sufficiently large volume to include steel rebars. Some reinforced specimens could be obtained by coring selected zones of the I-beams and could be appropriately prepared and equipped for electrochemical tests in laboratory or natural exposure conditions (Redaelli et al. 2014). The corrosion behavior of steel rebars of such reinforced specimens could be studied as a function of concrete moisture and temperature, both in free corrosion conditions and through polarization of steel potential. Finally, the comparison of electrochemical parameters obtained by means of in-situ tests made on the real scale elements and laboratory studies on reinforced specimens might also considered.

4 CONCLUSIONS

In the framework of the multiparter research project BRIDGE|50, a wide experimental campaign of field and laboratory tests concerning real scale RC/PC elements, such as those collected from a 80-span viaduct dismantled in Turin in 2019 after 50 years of service life and stored in a dedicated testing site, is ongoing.

The results presented and discussed in this paper have highlighted that the main causes of deterioration of such structural elements are associated to chloride penetration due to de-icing salts. Significant signs of degradation were observed in those structural elements of the deck (such as pier caps and box-beams) that were more often exposed to wetting, probably in absence of adequate systems of collection of water coming from the span.

Based on electrochemical measurements carried out on several structural elements stored in testing site, it can be pointed out that the best conditions were often observed for I-beams. Therefore, I-beams result the most suitable to be subjected to further corrosion investigations aimed at investigating the possible application of different electrochemical techniques on real-scale elements. On the other hand, it could be useful and interesting to provide and plan a similar trial on low scale by exploiting reinforced specimens sampled from selected zones of same I-beams and appropriately prepared to be subjected to electrochemical tests.

ACKNOWLEDGMENTS

BRIDGE|50 is a research project based on a research agreement among universities, public authorities, and private companies. Members of the Management Committee: S.C.R. Piemonte (President); Politecnico di Milano (Scientific Coor-dinator); Politecnico di Torino (Scientific Responsible of the Experimental Activities); Lombardi Engineering (Secretary); Piedmont Region; City of Turin; Metropolitan City of Turin; TNE Torino Nuova Economia; ATI Itinera & C.M.B.; ATI Despe & Perino Piero; Quaranta Group. BRIDGE|50 website: http://www.bridge50.org.

REFERENCES

Bertolini, L., Elsener, B., Pedeferri, Redaelli, E. & Polder, R. 2013. *Corrosion of Steel in Concrete: prevention, diagnosis, repair*, Wiley, Weinheim.

Bertolini, L. 2008. Steel corrosion and service life of reinforced concrete structures. *Structure and Infrastructure Engineering*, 4(2), 123–137.

Bertolini, L., Carsana, M., Redaelli, E. 2008. Conservation of historical reinforced concrete structures damaged by carbonation induced corrosion by means of electrochemical realkalisation, *Journal of Cultural Heritage*, 9, 376–385.

Biondini, F. & Frangopol, D.M. 2016. Life-cycle performance of deteriorating structural systems under uncertainty: Review, *Journal of Structural Engineering*, ASCE, 142(9), 1–17.

Biondini, F. & Frangopol, D.M. (Eds.) 2019. *Life-Cycle Design, Assessment and Maintenance of Structures and Infrastructure Systems*, American Society of Civil Engineers (ASCE), Reston, VA, USA.

Biondini, F., Manto, S., Beltrami, C., Tondolo, F., Chiara, M., Salza, B., Tizzani, M., Chiaia, B., Lencioni, A., Panseri, L. & Quaranta, L. 2021a. "BRIDGE|50 research project: Residual structural performance of a 50-year-old bridge", *10th International Conference on Bridge Maintenance, Safety and Management* (IABMAS 2020), Sapporo, Japan, April 11-15, 2020. Postponed to April 11-18, 2021. In: Yokota, H., Frangopol, D.M. (Eds.), *Bridge Maintenance*, *Safety, Management, Life-Cycle Sustainability and Innovations*. CRC Press, London, UK.

Biondini, F., Tondolo, F., Manto, S., Beltrami, C., Chiara, M., Salza, B., Tizzani, M., Chiaia, B., Lencioni, A., Panseri, L. & Quaranta 2021b. Residual structural performance of existing PC bridges: Recent advances of the Bridge|50 research project. *1st Conference of the European Association on Quality Control of Bridges and Structures* (EUROSTRUCT 2021), Padua, Italy, August 29 - September 1, 2021. In: Pellegrino, C., Faleschini, F., Zanini, M.A., Matos, J.C., Casas, J.R., Strauss, A. (Eds.), *Lecture Notes in Civil Engineering*, 200, 2022, Springer.

Carsana, M., Biondini, F., Redaelli, E. & Valoti, D.O. 2021. On-site corrosion characterization of 50-year-old PC deck beams. *1st Conference of the European Association on Quality Control of Bridges and Structures* (EUROSTRUCT 2021), Padua, Italy, August 29 - September 1, 2021. In: Pellegrino, C., Faleschini, F., Zanini, M.A., Matos, J.C., Casas, J.R., Strauss, A. (Eds.), *Lecture Notes in Civil Engineering*, 200, 2022, Springer.

Carsana, M., Gastaldi, M. & Redaelli, E. 2022. A case study on corrosion conditions and guidelines for repair of a reinforced concrete chimney in industrial environment, *Structure and Infrastructure Engineering*, 19(3), 366–377.

Carsana, M., Redaelli, E., Biondini, F. 2023. Field and laboratory tests for corrosion assessment of existing concrete bridges. *Eighth International Symposium on Life-Cycle Civil Engineering* (IALCCE 2023), July 2-6, 2023, Milan, Italy (Keynote Paper). In: *Life-Cycle of Structures and Infrastructure Systems*, F. Biondini, D.M. Frangopol (Eds.), CRC Press, London, UK, 45-56 (Open Access).

COST 2003. *Corrosion of Steel in Reinforced Concrete Structures*, COST Action 521, Final Report, Eds. Cigna, R., Andrade, C., Nürnberger, U., Polder, R. Weydert, E. Seitz, European Community, Luxembourg, Publication EUR 20599.

Elsener, B., Andrade, C., Gulikers, J., Polder, R., & Raupach, M. 2003. Recommendations on half-cell measurements-potential mapping on reinforced concrete structures. *Materials and Structures*, 36 (7), 461–471.

Neville, A.M. 2011. *Properties of concrete*, 5th ed., England, Longman.

Redaelli, E., Lollini, F., Bertolini, L. 2014. Cathodic protection with localized galvanic anodes in slender carbonated concrete elements, *Materials and Structures*, 47, 1839–1855.

Bridge Maintenance, Safety, Management, Digitalization and Sustainability – Jensen, Frangopol & Schmidt (eds)
© 2024 The Author(s), ISBN 978-1-032-77040-6
Open Access: www.taylorfrancis.com, CC BY-NC-ND 4.0 license

Load tests on dismantled 50-year-old prestressed concrete bridge deck beams

P. Savino, A. Quattrone, D. Sabia, B. Chiaia & F. Tondolo
Politecnico di Torino, Turin, Italy

M. Anghileri, F. Biondini & G. Rosati
Politecnico di Milano, Milan, Italy

ABSTRACT: This paper presents the results of three large scale experimental tests within the survey conducted on 50-year-old prestressed concrete (PC) girders for the BRIDGE|50 research project (www.bridge50.org). The girders were retrieved from a viaduct before dismantling operations once located in the urban area of Turin, Italy. Together with other structural members they represent one of the most prominent project of this type worldwide. The PC elements have 19.2 m span length and I-shaped cross section with 14 cm cast-in situ slab with variable damage due to deterioration caused by both service and lifting operations during dismantling phase. For each specimen, static tests have carried out applying monotonic or cyclic loading up to the ultimate load, measuring deflections, loads and strains in several positions for two I beams and one box beam. The results of the tests in terms of load-deflection responses and strains are reported for each beam investigated and compared considering previous tests from the same project already reported in literature. The experimental findings highlight the specific structural response and residual capacity of the tested members in presence of damage, cyclic loading and different tested section. The outcomes of the project will provide a valuable database of reference for the assessment of the residual structural performance of existing bridges.

1 INTRODUCTION

Bridges in service are subjected to environmental exposure which is responsible of durability problems. The impact of these aggressive attacks may involve a significant reduction up to the total loss of load-carrying capacity. Moreover, traffic demand is continuously growing, both in terms of number and weight of vehicles. In addition, as civil infrastructures age, uncertainties on the prediction of structural response increase due to the deterioration mechanisms and their scattered nature (Ellingwood 2005, Biondini & Frangopol 2016). As a result, structural assessment has received much attention in recent decades from different perspectives, including structural health monitoring techniques employed to collect data for structural condition evaluation and early warning detection. Most of the experimental research activity in this field has been done investigating laboratory specimens, under controlled environment. However, full-scale load tests on existing structures are fundamentals to better understand the structural behaviour and to calibrate structural models. The latter applies to models from structure to material scale that are even more required for safety evaluations (Franceschini et al. 2022, 2023). But, large-scale tests on civil infrastructures, are not widely performed also because they involve irreversible damages which led to the dismissing of the structure or part of it. Furthermore, huge human, financial, and material efforts are required, and as reported in Recupero & Spinella (2019), only few studies have been carried out on full-scale prestressed concrete (PC) girders from decommissioned bridges around the world (Wang et al. 2020). Assessment of existing bridges requires a thorough understanding of their structural behavior.

DOI: 10.1201/9781003483755-412

However, the investigations usually concern small samples of structural members and basically focusing on few characteristic parameters of the structural response. A systematic assessment of a number of specimens under different loading test setups is required to investigate the failure mechanisms and thus developing realistic estimates of the residual capacity. Moreover, this survey allows to take into account the influence of coupled precast and cast in situ concrete parts which work together in the final configuration.

BRIDGE|50 research project was specifically defined to study the residual structural performance of 50-year-old viaduct members and provide a framework for safety assessment and residual lifetime evaluation of existing bridges (Biondini et al. 2020, 2021). A wide experimental campaign was planned to investigate PC I-girders, PC box girders, and pier caps recovered from the C.so Grosseto viaduct, a viaduct built in Turin in 1970 and decommissioned in 2019. Updated information on the BRIDGE|50 research program is posted on the project website (www.bridge50.org). Multiple load test setups were considered to study flexural, flexural/shear, and shear failure mechanisms. The first group of four PC beams was tested under three-point bending configuration and detailed in Tondolo et al. (2021, 2022) and Savino et al. (2023a). The second set of members, subjected to a four-point bending test setup are reported in Savino et al (2023b). The present paper reports the experimental results of the third group of three beams tested under four-point bending configuration up to failure. The reported parameters not only extend the database aimed at providing further knowledge on the structural response of 50-year-old PC beams but could be used to setup and calibrate mechanical models.

2 CORSO GROSSETO VIADUCT

The Corso Grosseto viaduct was a road bridge located in Turin, Italy (Savino et al. 2020). The structural scheme of the PC viaduct was with simply supported spans: a widespread solution in Italy and around the world. The deck was composed by ten PC I-shaped girders and two PC box girders at the edges, with a support distance between 16.0 and 24.0 m and two diaphragms connected the longitudinal girders at the third points (see Figure 1). The superstructure was completed by a cast-in-situ slab of 140 mm.

An overview of the retrieved structural members in their original deck configuration is shown in Figure 1. The elements coloured represent the collected ones; the girders depicted in blue belong to the first and second group of tests whereas the elements highlighted in red refer to the girders investigated and reported in the present work. All the elements were properly identified with a code, according to the original configuration. The PC beams studied in the present work were identified as B5-P46/47, BX2-Ab/P47, B2-P46/47 according to classification reported in Savino et al. (2023).

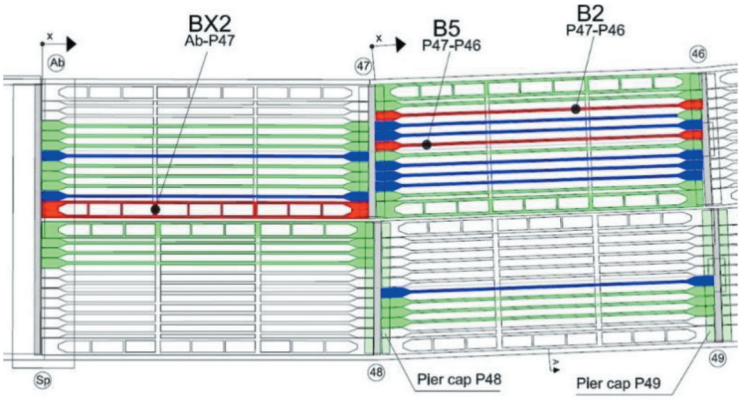


Figure 1. Layout of the retrieved and studied elements (green: beams to be tested; blue: previously tested and reported in other papers; red: investigated in this paper).

2.1 *Tested girders details*

All the girder beams were 19.5 m long, with I-shaped cross-section as shown in Figure 2a for beams B5-P46/47 and B2-P46/47 and box-section as shown in Figure 2b for beam BX2-Ab /P47 (from design documentation). Cover depths were 45 mm for prestressed strands and 10 mm for ordinary reinforcement. Prestressing reinforcement was composed of seven-wire strands with a nominal diameter of 12.7 mm and according to the design documentation, the tensile strength was of 1638 MPa. The prestressed reinforcement configuration consisted of 17 strands for I-beams and 34 strands for box-beam, located in the bottom flange. Additionally, there were 3 strands for I-beams and 6 strands for box-beams located in the top flange. The stirrups are made by 8 mm ribbed steel spaced of 250 mm. The 14 cm cast-in-situ slab was reinforced with a square pattern of rebars. The maximum allowable stress for the strands at the tensioning stage was 1400 MPa. The concrete compressive strength at 28 days was designed to be 30 MPa. No specific requirements were reported for the cast-in-situ slab.

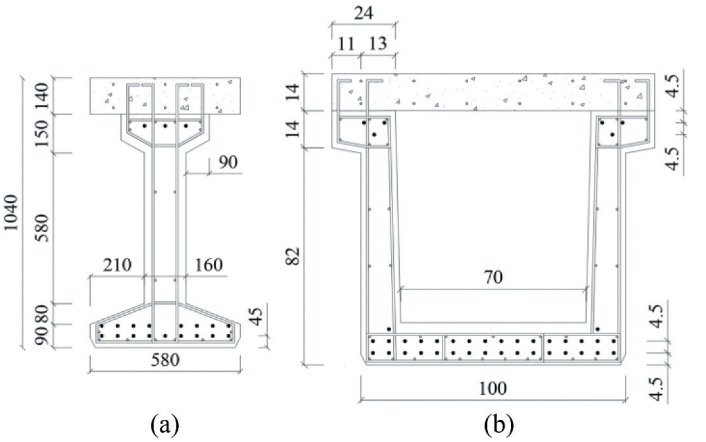


Figure 2. Cross-section of the beams (units in mm): (a) I-beam; (b) Box-beam (from design documentation).

According to the diagnostic campaign performed before the load tests session, the beams investigated in this paper were considered in good conditions. Beam B5-P46/47 was intentionally damaged by cutting 8 strands at the midspan to induce a different failure mode from that observed in previous tests (Savino at al. 2023b), as depicted in Figure 3. The damage was created by cutting a total of eight strands in the bottom flange at a distance of 60.0 cm from the girder midspan on either side.

Girder BX2-Ab/P47 had the curb on the top slab; in order to avoid torsional effect, a preventive regularization of the upper surface was carried out by cutting it with a diamond blade.

3 SETUP OF THE FULL-SCALE LOAD TESTS

For the purpose of testing the PC girders, a proper reaction steel frame was made available by the Interdepartmental Center SISCON (Safety of Infrastructures and Constructions) of Politecnico di Torino. Each beam was tested under a simply supported static scheme under a four-point loading configuration adopting shear spans of 650 cm. The loading system details and the specifics of the employed equipment can be found in Savino et al. (2023a). The girders were tested according to multiple loading phases. The multiple loading cycles also allowed to perform the dynamic characterization of the specimens at different level of damages (Quattrone et al. 2020, Sabia et al. 2021, 2022, 2023). In particular, the first loading phase was



Figure 3. Strands cutting in B5-P46/47 girder (bottom view).

meant to reach the stabilized cracking pattern to evaluate the residual prestressing during the following crack reopening phase.

In detail, B5-P46/P47 was tested with two loading cycles, Bx2-Ab-P47 was tested with three cycles of which the second cycle had maximum loading corresponding to half of the expected capacity; finally, B2-P46/P47 was tested with three sets of five cycles each before reaching the final stage up to failure. This choice was motivated by the intention to induce the effect of cumulative damage at different levels and collect the effects on both the dynamic behaviour and residual resistance of the girder. All load tests were performed with a fixed loading rate under force control and were stopped upon the occurrence of failure, as indicated by load reduction detected by the load cells and confirmed by evident damage recorded by the measuring devices. The setup of measuring devices for girders B5-P46/P47 and B2-P46/P47 are reported in Savino et al. (2023b). In these tests the equipment was placed on one side of the beam; in particular the side protected by the insulation was chosen and it also corresponded to the one under direct vision from the control station. Instead, the setup for the box girder BX2-Ab/P47 is reported in Figure 4, where the pattern of devices installed on the web is mirrored on the opposite side (not reported in Figure 4). This layout was selected to monitor both webs of the box girder and identify any asymmetrical behaviour during the test.

For all the tests, the arrangement of devices has been defined according to the load test setup, considering two main zones: the shear span and the bending span. Along the shear span, specifically near the transverse beam, linear variable displacement transducers (LVDTs) were installed on aluminium frames oriented at 45° angle, with a measurement base of 707 mm. Such sensors were labelled with the code "SHxxA/B", where "xx" indicates the progressive number, "A" refers to the frames with a negative slope, and "B" refers to the frames with positive slopes. In the bending zone, specifically across the midspan, the LVDTs were installed on horizontal frames with a measurement base of 400 mm. They were denoted by "BxxT/C", where "xx" indicates the progressive number, "T" refers to the LVDTs installed on the bottom flange, and "C" refers to the remaining positions.

Furthermore, four electrical strain gauges were mounted as follows: on the top and bottom flanges of the precast beam along the left vertical alignment of the midspan, on the cast-in-situ slab, and the last on the prestressing strand, at 120 cm away from the midspan. Three displacement transducers were installed at each end of the girder to measure vertical and horizontal displacements at the supports, and the potential slipping of a strand. Another displacement transducer was place along the shear span to measure potential sliding of the cast-in-situ slab. The vertical deflections along the beam were measured using nine potentiometer transducers connected to the bottom of the girders ("D01-09" in Figure 4).

4 TEST RESULTS AND DISCUSSION

This paper includes a subset of the comprehensive results obtained from the full-scale load tests. These diagrams were chosen to show the overall structural response of the girders

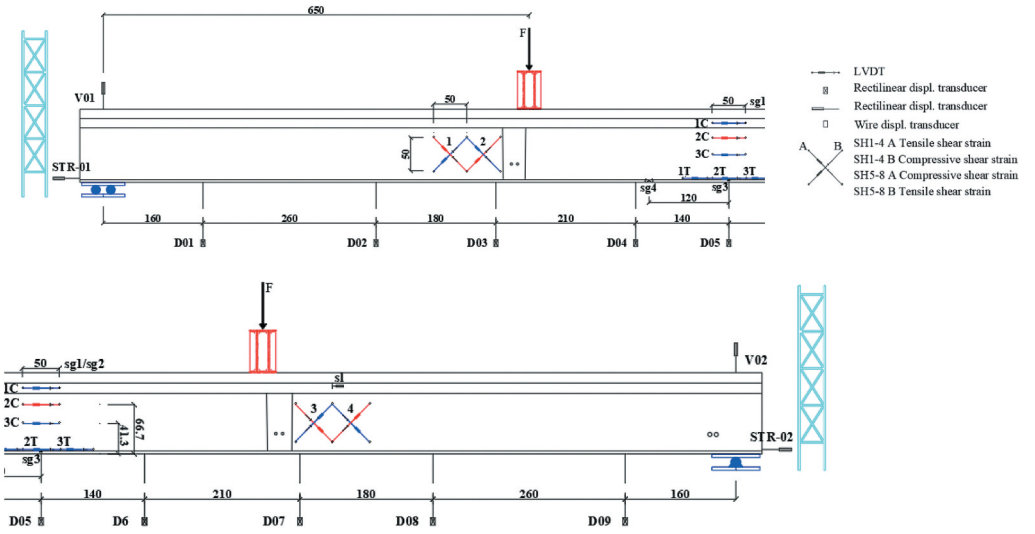


Figure 4. Layout of the testing system with measuring devices for girder BX2-Ab/P47 (units in cm).

together with some specific readings during the tests. All the diagrams have been obtained by referring to the load applied by a single jack. Therefore, the total load applied to the specimen can be found multiplying by 4. Figures 5a-c present the midspan deflection versus the applied load for the three girders. In Figure 5d a focus of the first two sets of cycles for girder B2-P46 /P47 is reported.

A global overview confirms for the specimens a structural behaviour defined by three phases: a linear elastic branch, a concrete tensile cracking that induced stiffness reduction and brittle failure after reaching the maximum load. The girder B5-P46/P7 in Figure 5a shows earlier non-linear behaviour attributable to the cutting of 8 strands across the midspan and this obviously anticipate the first cracking and determines the reduced initial stiffness of the beam. This is evident if comparison is made with previous test results reported in Savino et al. (2023b). All the three specimens reached the collapse due to crushing of the cast in situ top slab. Beam B2-P46 /P47 completely failed and followed down to the safety support system of the reaction frame whereas the test for the other two girders was stopped before global collapse.

The failure mode was similar with that registered for the previous girders tested under four-point bending configuration (Savino et al. 2023a 2023b). As previously stated, beam B5-P46/47 was intentionally damaged to induce a more ductile behaviour than what observed for other identical beams reported in Savino et al. (2023b). The ultimate loads were 72.4 kN, 241.5 kN and 126.2 kN for beams B5-P46/47, BX2-P46/P47 and B2-P46/47 respectively. The structural capacity reduction for beam B5-P46/P47 with respect to an identical girder named B6-Ab/47 and reported in Savino et al. (2023b) but with undamaged strands corresponds to a 42.8%.

The BX2-P46/P47 shows a higher stiffness due to its box section made with two webs of 130 mm and the double number of strands used in comparison with I girder B2-P46/47 reported in this work (see Figure 2). A residual deflection registered after the cycles evidenced the role of non-linearities also due to tensile cracking and possible mechanical interlock. The test on girder B2-P46/P47 was specifically meant to produce progressive damage by cycles of increasing load levels. It can be noted from Figures 5c and 5d that most of the damage was determined by the first cycle of each set whereas small additional damage has been registered for the other four cycles. A progressive residual deformation is visible but, even in case of the last spare cycle before the last branch bringing to collapse, its descending branch was almost aligned with the previous readings without evident stiffness reduction.

Figure 6a shows the strain distribution measured across the midspan along the cross section (see horizontal transducers type in Figure 4) at various loads for girder B5-P46/P47. According to the diagram of the first two steps (10 kN and 20 kN) the section has a plain

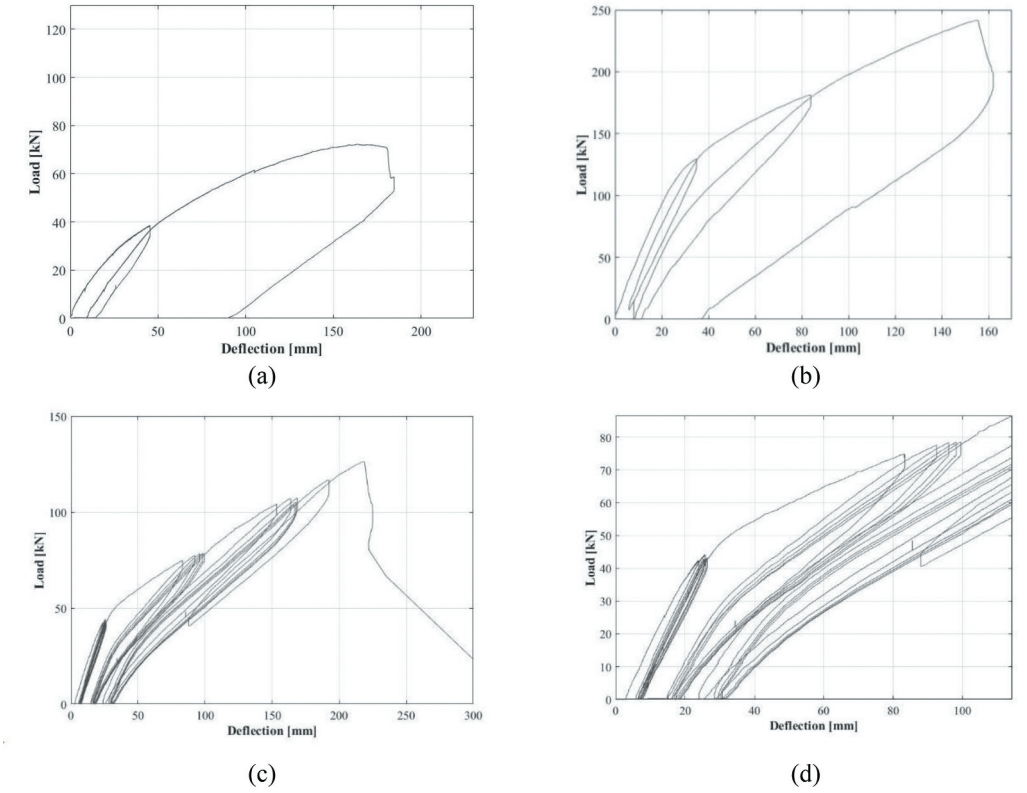


Figure 5. Load vs deflection diagrams: (a) B5-P46/47; (b) BX2-Ab/P47; B2-P46/47: (c) full results and (d) detail.

deformation. At cracking stage the effective depth of the compressive zone was about 0.49 m. When cracking occurred, the neutral axis shifted up and the strain distribution became non-linear. At ultimate condition the neutral axis reached the value of 0.23 m and therefore only the cast-in-situ top slab with a part of the top flange of the precast beam were in compression. The same diagram is reported in Figure 6b for girder B6-Ab/P47 (undamaged in Savino et al. 2023b) that had, even up to collapse, a deeper neutral axis. This highlights the effect of the full prestressing pattern for undamaged girder. Finally, the type of collapse for girder B5-P46/P47 that had 8 strand cut highlight the limited ductility even in presence of around 47% of the tensed steel in the section.

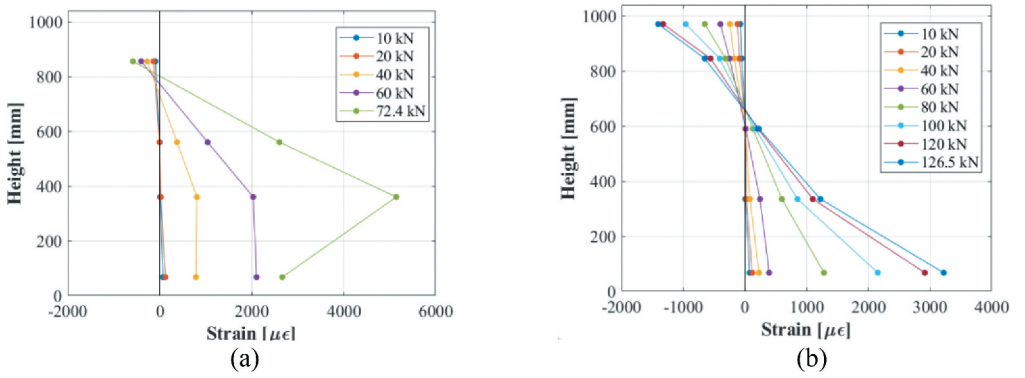


Figure 6. Cross-section strain sg1: C-01, C-02, C-03, and T-01 of B5-P46/47 and (b) B6-Ab-P47.

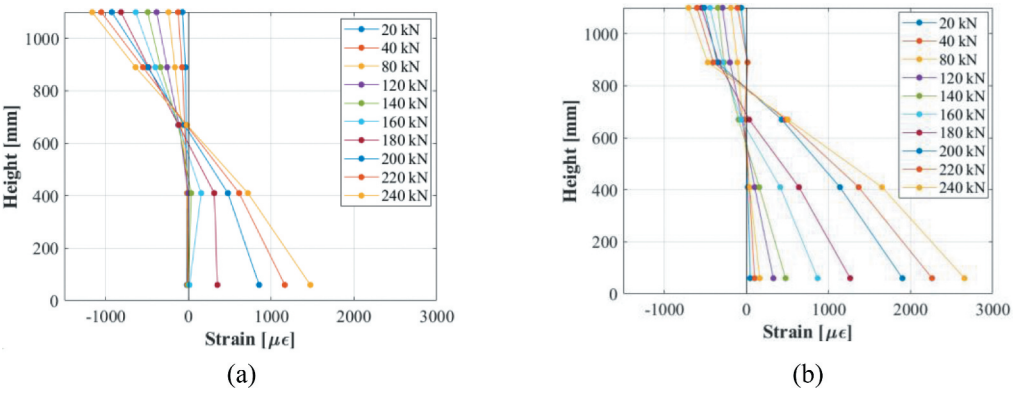


Figure 7. Cross-section strain of BX2-Ab/P47 girder: (a) inner side; (b) exposed side.

Due to the different exposure and consequent damage, the box girder BX2-Ab/P47 was under investigation for what concerns the strains distribution on both the two webs. In Figure 7, the strain distributions are reported. A noticeable difference between the inner side (Figure 7a) and the exposed side (Figure 7b) is observed, becoming more evident beyond a load level of 160 kN. At this stage, a larger shift of the neutral axis is recorded by the outer web. At ultimate condition, the ratio between the depth of the compressive zone and the effective depth were 0.63 and 0.52 for the inner and exposed web, respectively. Therefore, a non-symmetric behaviour can be noted with major deformation attributable to the web with much visible damage (see Figures 8a,b).

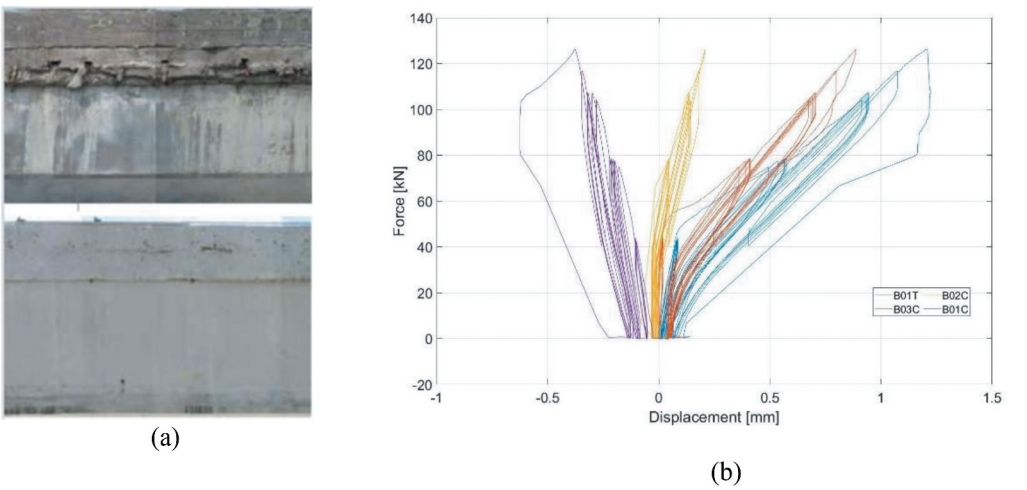


Figure 8. (a) Comparison of the inner (bottom) and exposed side (top) of the beam Bx2-Ab/P47; b) Load versus displacements of the transducers used for tension (T) and compression (C) for girder B2-P46/P47.

In Figure 8b the load-displacement diagrams of four transducers in the top flange (B01C), web (B02C, B03C) and bottom slab (B01T) of the beam B2-P46/P47 are reported. These devices were installed across the midspan and therefore in the most loaded zone of the girder. It is evident that after the first set of cycle for curve of B01T, a cracking occurred and a permanent modification with slope reduction of the curve is registered; all the other three devices, measured the displacements and report slope of the curve similar to the first loading up to the last cycle. B01C and B01T as devices placed in the most compressed and tensed zones respectively show some residual displacement. It can be stated that, even for the most

loaded zone of the beam the accumulated damage resulted to be very limited up to brittle failure in crushing of the cast-in-situ top slab.

5 CONCLUSIONS

An experimental activity on bridge girders has been conducted to study the structural behaviour of 50-year-old PC members at both service and ultimate load levels. Three large-scale experimental tests have been reported. Specimens with different level of damage, geometry, and loading protocol were tested. The results have been analysed considering deflections, strains as well as ultimate bearing capacities. All the tests reported in this work have shown a flexural failure with brittle crushing of the cast-in-situ slab. These findings can be further analysed and compared with the outcomes obtained for the previous bridge girders tested under the BRIDGE|50 research project highlighting a wide number of peculiarities of the residual capacity of PC bridge girders.

ACKNOWLEDGMENTS

BRIDGE|50 is a joint research project among universities, public authorities, and private companies. Management Committee: S.C.R. Piemonte (President); Politecnico di Milano (Scientific Coordinator); Politecnico di Torino (Scientific Responsible of the Experimental Activities); Lombardi Engineering (Secretary); Piedmont Region; City of Turin; Metropolitan City of Turin; TNE Torino Nuova Economia; ATI Itinera & C.M.B.; ATI Despe & Perino Piero; Quaranta Group. BRIDGE|50 website: http://www.bridge50.org

REFERENCES

Biondini, F. & Frangopol, D.M. 2016. Life-cycle performance of deteriorating structural systems under uncertainty: Review, *Journal of Structural Engineering*, ASCE, 142(9), 1–17.

Biondini, F., Manto, S., Beltrami, C., Tondolo, F., Chiara, M., Salza, B., Tizzani, M., Chiaia, B., Lencioni, A., Panseri, L., and Quaranta, L. 2020. BRIDGE|50 research project: Residual structural performance of a 50-year-old bridge. *10th International Conference on Bridge Maintenance, Safety and Management* (IABMAS 2020), Sapporo, Japan, April 11-15, 2020. Postponed to April 11-18, 2021. In: Yokota, H., Frangopol, D.M. (Eds.), *Bridge Maintenance*, *Safety, Management*, *Life-Cycle Sustainability and Innovations*. CRC Press, London, UK.

Biondini, F., Tondolo, F., Manto, S., Beltrami, C., Chiara, M., Salza, B., Tizzani, M., Chiaia, B., Lencioni, A., Panseri, L., and Quaranta, L. 2021. Residual Structural Performance of Existing PC Bridges: Recent Advances of the BRIDGE|50 Research Project. *1st Conference of the European Association on Quality Control of Bridges and Structures* (EUROSTRUCT 2021), Padua, Italy, August 29 - September 1, 2021. In: Pellegrino, C., Faleschini, F., Zanini, M.A., Matos, J.C., Casas, J.R., Strauss, A. (Eds.) Lecture Notes in Civil Engineering, 200, 2022, Springer.

Ellingwood, B.R. 2005. Risk-informed condition assessment of civil infrastructure: state of practice and research issues. *Structure and Infrastructure Engineering*, 1(1), 7–18.

Franceschini, L., Vecchi, F., Tondolo, F., Belletti, B., J Sánchez Montero.., 2022. Mechanical behaviour of corroded strands under chloride attack: a new constitutive law. *Construction and Building Materials*, 316, 125672.

Franceschini, L., Belletti, B., Tondolo, F., Sánchez Montero, J., 2023. A simplified stress-strain relationship for the mechanical behavior of corroded prestressing strands: the SCPS-model. *Structural Concrete*, 24,1: 189–210.

Quattrone, A., Tondolo, F., Sabia, D., Capacci, L., Lencioni, A., Legramandi, C. 2020. Dynamic tests and modal identification of Corso Grosseto viaduct decks before the dismounting. *10th International Conference on Bridge Maintenance, Safety and Management* (IABMAS 2020), Sapporo, Japan, April 11-15, 2020. Postponed to April 11-18, 2021. In: Yokota, H., Frangopol, D. M. (Eds.), *Bridge Maintenance, Safety, Management, Life-Cycle Sustainability and Innovations*. CRC Press, London, UK.

Recupero, A. and Spinella, N. 2019. Experimental tests on corroded prestressed concrete beams subjected to transverse load. *Structural Concrete*, 20: 2220–2229.

Sabia, D., Quattrone, A., Tondolo, F., Savino, P. 2021. Dynamic identification of damaged PC bridge beams. *1st Conference of the European Association on Quality Control of Bridges and Structures* (EUROSTRUCT 2021), Padua, Italy, August 29 - September 1, 2021. In: Pellegrino, C., Faleschini, F., Zanini, M.A., Matos, J.C., Casas, J.R., Strauss, A. (Eds.) Lecture Notes in Civil Engineering, 200, 2022, Springer.

Sabia, D., Quattrone, A., Tondolo, F., Savino, P. 2022. Experimental evaluation of the effect of controlled damages on the dynamic response of PC bridge beams. *11th International Conference on Bridge Maintenance, Safety and Management* (IABMAS 2022), Barcelona, Spain, July 11-15, 2022. In: Casas, J.R., Frangopol, D.M., Turmo, J. (Eds.), Bridge Safety, Maintenance, Management, Life-Cycle, Resilience and Sustainability. CRC Press/Balkema, Taylor & Francis Group, London, UK.

Sabia, D., Quattrone, A., Tondolo, F., Savino, P. 2023. Dynamic response of PC bridge beams under different damages. *Eighth International Symposium on Life-Cycle Civil Engineering* (IALCCE 2023), July 2-6, 2023, Milan, Italy. In: *Life-Cycle of Structures and Infrastructure Systems*, F. Biondini, D. M. Frangopol (Eds.), CRC Press, London, UK, 2093-2100 (Open Access).

Savino, P., Anghileri, M., Chiara, M., Salza, B., Quaranta, L. 2020. Corso Grosseto viaduct: Historical and technical overview. *10th International Conference on Bridge Maintenance, Safety and Management* (IABMAS 2020), Sapporo, Japan, April 11-15, 2020. Postponed to April 11-18, 2021. In: Yokota, H., Frangopol, D.M. (Eds.), *Bridge Maintenance, Safety, Management, Life-Cycle Sustainability and Innovations*. CRC Press, London, UK.

Savino, P., Tondolo, F., Sabia, D., Quattrone, A., Biondini, F., Rosati, G., Anghileri, M., Chiaia, B. 2023a. Large-Scale Experimental Static Testing on 50-Year-Old Prestressed Concrete Bridge Girders. *Applied Sciences* 13(834): 1–22.

Savino, P., Quattrone, A., Sabia, D., Chiaia, B., Tondolo, F., Anghileri, M., Biondini, F., Rosati, G., 2023b. Large-scale experimental testing of 50-year-old prestressed concrete bridge girders. *Eighth International Symposium on Life-Cycle Civil Engineering* (IALCCE 2023), July 2-6, 2023, Milan, Italy. In: *Life-Cycle of Structures and Infrastructure Systems*, F. Biondini, D.M. Frangopol (Eds.), CRC Press, London, UK, 2061-2068 (Open Access).

Tondolo, F., Biondini, F., Sabia, D., Rosati, G., Chiaia, B., Quattrone, A., Savino, P., Anghileri, M. 2021. Experimental program and full-scale load tests on PC deck beams. *1st Conference of the European Association on Quality Control of Bridges and Structures* (EUROSTRUCT 2021), Padua, Italy, August 29 - September 1, 2021. In: Pellegrino, C., Faleschini, F., Zanini, M.A., Matos, J.C., Casas, J. R., Strauss, A. (Eds.) Lecture Notes in Civil Engineering, 200, 2022, Springer.

Tondolo, F., Sabia, D., Chiaia, B., Quattrone, A., Savino, P., Biondini, F., Rosati, G., Anghileri, M. 2022. Full-scale testing and analysis of 50-year-old prestressed concrete bridge girders. *11th International Conference on Bridge Maintenance, Safety and Management* (IABMAS 2022), Barcelona, Spain, July 11-15, 2022. In: Casas, J.R., Frangopol, D.M., Turmo, J. (Eds.), Bridge Safety, Maintenance, Management, Life-Cycle, Resilience and Sustainability. CRC Press/Balkema, London, UK.

Wang, J., Tang, S., Zheng, H., Zhou, C., Zhu, M. 2020. Flexural Behavior of a 30-Meter Full-Scale Simply Supported Prestressed Concrete Box Girder. *Applied Sciences* 10(3076): 1–19.

Bridge Maintenance, Safety, Management, Digitalization and Sustainability – Jensen, Frangopol & Schmidt (eds)
© 2024 The Author(s), ISBN 978-1-032-77040-6
Open Access: www.taylorfrancis.com, CC BY-NC-ND 4.0 license

Dynamic response of damaged precast bridge girders

D. Sabia, A. Quattrone, F. Tondolo & P. Savino
Department of Structural, Geotechnical and Building Engineering, Politecnico di Torino, Torino, Italy

ABSTRACT: This paper presents a comprehensive dynamic test campaign conducted on pre-stressed concrete bridge beams sourced from a 50-year-old decommissioned viaduct in Turin, Italy, as part of the BRIDGE|50 research project. Individual beams were subjected to dynamic testing to assess the impact of varying levels of damage on their dynamic properties. Vibration data was collected before applying static loads, after reaching the first cracking condition, and after reaching maximum load capacity, and analysed to identify principal modal components. The findings underscore the correlation between damage progression and dynamic response, demonstrating the effectiveness of vibration tests in detecting and tracking damage evolution. Specifically, this study presents the experimental results pertaining to the tested I-shape beams.

1 INTRODUCTION

The vibration-based methods are one of the most widely adopted diagnostic tools in the field of structural monitoring of infrastructures. Vibration-based methods are widely applied in structural health monitoring techniques to follow the evolution of structural integrity, due to the direct dependence between the dynamic behaviour and the structural stiffness. Moreover, their appeal has increased due to the ease of managing the continuous streaming of large amount of data and inferring information by means of data mining algorithms. In literature, several studies report the results of experimental dynamic investigations on beam-like pre-stressed structures, focusing on their use as symptoms of the onset of damage or the evolution of deterioration over time (Quat-trone et al. 2012, Guiglia et al. 2014). For instance, a shift in the modal properties of a bridge can indicate variations in the stiffness or mass distributions, which can be caused by structural damages, modifications of constrain condition or the deterioration of the mechanical properties of the materials (Demarie et al. 2019).

However, these alterations can be challenging to be discerned in service condition due to the concurrent influences of multiple factors. The identification of modal parameters is affected by several noise sources and errors in the analyses process. Additionally, the influence of the variation of temperature and traffic conditions can influence the dynamic response of the structure, complicating the detection of stiffness-related variations induced by damages.

A continuous monitoring of these parameters can confirm the occurrence of even small variations, reducing the influence of error sources, highlighting the possible occurrence of damages. Consequently, conducting controlled tests on structures approaching the end of their service life can contribute significantly to provide more precise definitions of sensitivity limits and thresholds applicable to permanent monitoring systems.

The BRIDGE|50 research project, started in 2020, aims at deeply investigate the behaviour of aged bridge girders at the end of their service lives (Biondini et al. 2021). The research activities will be devoted to accurately investigate the structural performances and characterize the material properties of a representative portion of a viaduct dismantled after 50 years of service life, namely 25 prestressed concrete beams, 4 box girders and 2 pier caps.

The girders are tested in a controlled environments up to failure to determine their ultimate resistance. The dynamic tests have been performed adopting the simply supported configuration

DOI: 10.1201/9781003483755-413

simulating the original structural scheme. Vibrations have been collected before the execution of the static tests, in intermediate cracked state and at the end of static tests, after the application of the ultimate loading condition. The aim is to estimate the influence of the structural damage on the dynamic characteristics of the beams. Moreover, controlled damages are applied to a subset of beams by cutting strands at different locations. In this paper the results of the dynamic test campaign on a set of 8 I-shaped beams are reported.

2 THE CORSO GROSSETO VIADUCT

The Corso Grosseto viaduct was built in 1970. It was originally constituted by 90 concrete decks having variable spans, from 16 m to 24 m, and a total length of 1400 m (Figure 1). Each deck was composed of 10 precast prestressed concrete I-beams and 2 external precast prestressed concrete U-beams, simply supported at piers, and connected transversely by 3 equally spaced diaphragms and, on the top, by a 0.14 m concrete slab (Figure 2). A set of 25 prestressed concrete beams constituting the decks have been dismounted and collected in a testing area, where a bench test has been realized to perform both static and dynamic tests. The collected structural elements belong to the first four decks of the southern part of the viaduct, highlighted in green in Figure 2-a. The technical drawings of the I-beams cross section and the on-site casted slab, object of the present work, are shown in Figure 2 - b.



Figure 1. Corso Grosseto viaduct before the dismantling.

3 STATIC TEST CAMPAIGN

According to the preliminary visual inspection carried out to map the presence of corrosion, cracks, and spalling, the beams have been classified in good structural condition (Table 1). The beams B07 and B08 have been damaged during the dismantling phases, when strands at the bottom flanges were cut. The B07 had two strands cut on both sides of the lower flange, at distances of 3.7, 9.6, and two at 15.5 m from the end section. The B08 girder had four strands cut on one side at distances of 3.8 and 15.5 m. The B09 girder was damaged cutting 8 strands in two symmetrical positions 0.60 m from the midspan, resulting in a reduction of circa 40% of the total prestressing steel in the sections. The static test procedure consists in applying an increasing static load up to the reaching the ultimate load capacity by means of four hydraulic jacks. An

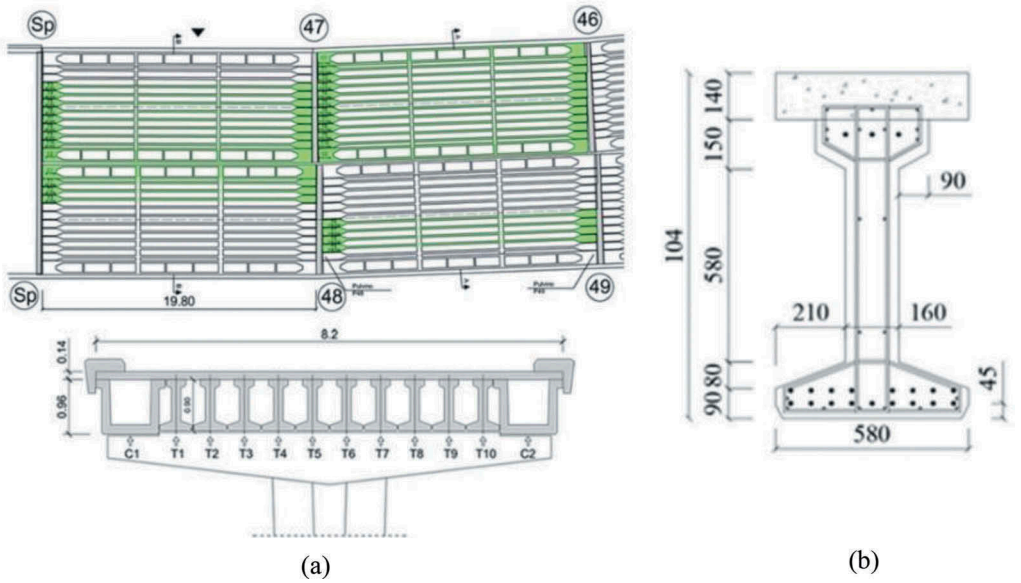


Figure 2. (a) Drawing of the first four decks of the southern part of the viaduct. In green, the beams collected. (b) The I-shaped beam cross section (measures in mm).

intermediate unloading phase was made to evaluate the residual prestressing load and the effects of the opening of the cracks on the dynamic parameters (Savino et al. 2023). The test on B02 beam has been performed in a three-point bending scheme (shear span 9.3 m), whereas a four-point scheme (shear span 6.5 m) was adopted for testing B05 to B11 girders, aimed at investigating the shear-bending interaction. The B11 was tested applying cyclic loading at three increasing load levels to explore the effects of cumulating damages. The B12 have been tested in four-point bending scheme adopting a shear span of 4 m. The beams have been loaded up to reach the ultimate condition highlighting a brittle rupture due to the crushing of the upper slab. The principal results are summarized in Table 1. For each girder, the ultimate flexural strengths M_R is calculated in the rupture section considering the effects of the self-weight, the weight of the load application systems and the maximum force applied by the hydraulic actuators during the test.

Table 1. Results of the static tests.

Beam	Position in the deck	Type	Testing Scheme	Condition	M_R (kNm)
B02	B8-P47/46	I	3-Point	Undamaged	2012
B05	B7-P47/46	I	4-Point	Undamaged	2057
B06	B6-SP/47	I	4-Point	Undamaged	1907
B07	B6-P49/48	I	4-Point	Damaged (4 strands cut at- 1/3 span and at midspan)	1845
B08	B10-SP/47	I	4-Point	Damaged (4 strands cut at- 1/3 span)	2080
B09	B5-P47/46	I	4-Point	Damaged (8 strands cut at midspan)	1412
B11	B2-P47-46	I	4-Point	Undamaged. Cyclic loading	2111
B12	B1-P47/46	I	4-Point	Undamaged	1968

4 DYNAMIC TEST CAMPAIGN

The setup adopted for the dynamic test of the beams is constituted by a set of 10 uniaxial capacitive accelerometers, glued on the top slab, having a sensitivity of 1V/g. The test setup is showed in Figure 3. The acceleration signals were acquired at a 512 Hz sampling frequency for both ambient noise and impact hammer excitations. The impact tests were carried out by hitting the beams with an instrumented hammer in vertical direction in the halfway of two consecutive positions. Dynamic tests were performed by removing the load application systems from the upper slab to replicate as closely as possible the constraint conditions typical of a simply supported isostatic beam.

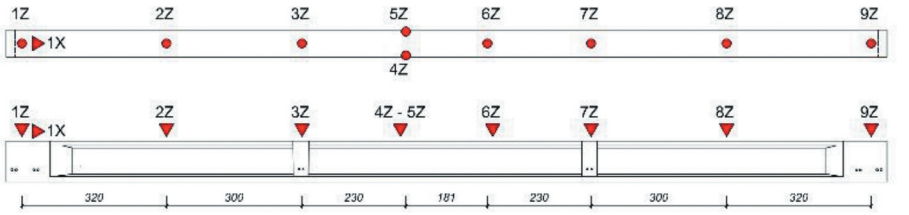


Figure 3. Dynamic test setup.

Dynamic tests were performed on all beams prior to the application of static loads (Phase 0). Whenever possible, the tests were repeated in an intermediate condition (Phase 1), and at the end of the static test (Phase 2), following the attainment of the ultimate failure load (Figure 4). The Phase 1 corresponds to the unloading condition, subsequent the reaching of the full cracked condition, identified in Table 2 as a fraction of the ultimate bending moment reached during the static tests calculated in the rupture section.

Table 2. Damage levels corresponding to phase 1 tests.

Specimen	M (kNm)	% M_R
B02	1453	72.2
B05	1278	62.2
B06	1208	63.4
B07	1243	67.3
B08	1306	62.8
B09	977	69.2
B11	1503	71.2
B12	N.P.	N.P.

4.1 *Experimental modal analysis*

The extraction of the principal modal components is performed evaluating the frequency response function (FRF) matrix with respect of the input given by means of the instrumented hammer. The element of FRF matrix $H_{k,j}(\omega)$ maps the input $F_k(\omega)$, applied at the k-th degree of freedom (DOF), and the output Y_j measured at the j-th DOF. In case of acceleration as output signals, the FRF matrix is expressed in the accelerance form (Ljung, 1999). The generic element of the accelerance matrix, expressed in terms of modal properties, is given by:

$$H_{j,k}(\omega) = \frac{\ddot{Y}(\omega)}{F_k(\omega)} = -\omega^2 \sum_{r=1}^{N} \frac{1}{m_r} \frac{{}^r\psi_j \, {}^r\psi_k}{\omega_r^2 - \omega^2 + 2i\omega\omega_r} \tag{1}$$

The FRF is a complex function which amplitude has a maximum at the resonant frequency. The magnitude of the modal coefficient is taken as the value of the imaginary part at resonance.

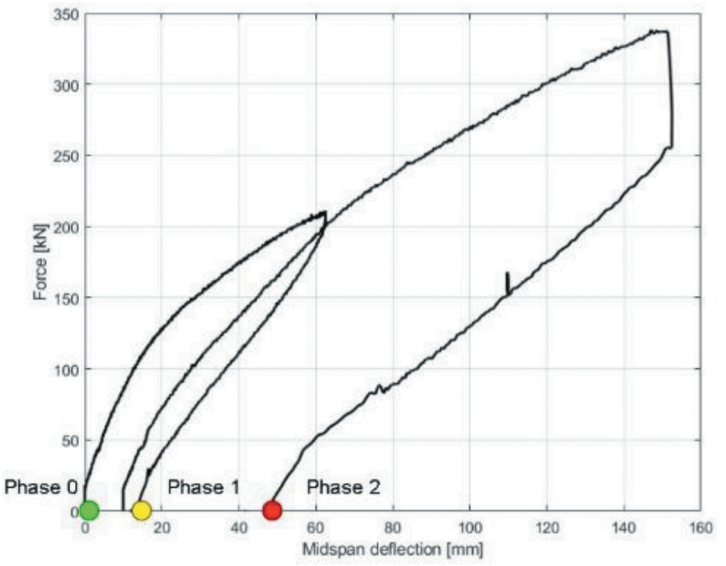


Figure 4. Force – midspan deflection. The dots indicate the phase test.

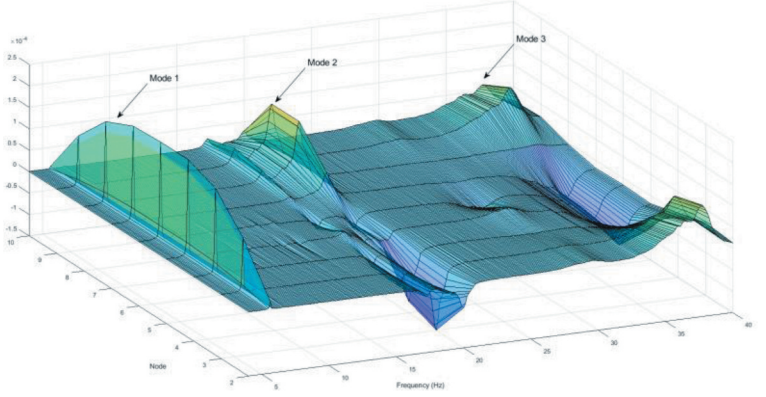


Figure 5. Example of mode shapes of the first three bending modes of the beam B06 – phase 0.

The sign is either positive or negative, considering the direction of the peak along imaginary axis. This implies that the phase angle is either 0° or 180°. After a preliminary analysis of the spectral content, the signals were pretreated by filtering out of the bandwidth [0 - 100 Hz], removing the trends. The FRFs have been estimated basing on each singular impulse acceleration data and then averaged for each hitting position. The first three modal components are clearly identified as shown by the example proposed in Figure 5. The mode shapes associated to these components correspond to the three main flexural modes of the beam. The modal coordinates are estimated by the imaginary part of the FRFs.

5 RESULTS OF THE DYNAMIC IDENTIFICATION

In this paragraph the results of the dynamic identification are proposed. The Table 3 reports the mean values of frequencies and damping estimated at the three phases for each beam. It can be noted that at the increase of the damage level correspond the reduction of the modal frequencies and the increasing trend of damping ratios.

Table 3. Mean modal frequencies and damping ratios.

		Phase 0			Phase 1			Phase 2		
		mode 1	mode 2	mode 3	mode 1	mode 2	mode 3	mode 1	mode 2	mode 3
B02	f (Hz)	5.49	19.38	36.44	5.28	18.88	36.34	4.78	18.58	32.69
	ξ(%)	0.37	0.84	2.18	0.48	0.81	2.19	0.55	1.00	2.22
B05	f (Hz)	5.47	19.72	36.88	5.31	19.50	35.75	5.03	19.28	32.66
	ξ(%)	0.34	0.80	1.94	0.40	0.74	1.68	0.95	2.16	2.03
B06	f (Hz)	5.60	19.86	37.21	5.47	19.48	36.17	5.01	18.50	33.62
	ξ(%)	0.36	1.30	0.85	0.40	1.33	0.91	0.63	1.06	1.57
B07	f (Hz)	5.58	19.83	35.22	5.48	19.36	34.91	5.01	19.09	33.84
	ξ(%)	0.39	0.65	1.77	0.39	0.68	1.99	0.42	1.30	2.14
B08	f (Hz)	5.61	20.35	38.25	5.41	19.58	37.08	4.83	18.33	33.85
	ξ(%)	0.29	1.46	1.32	0.31	1.04	1.57	0.43	1.06	1.57
B09	f (Hz)	5.35	19.80	35.08	5.16	18.59	33.50	4.34	18.22	30.47
	ξ(%)	0.31	0.81	1.73	0.35	0.66	2.70	0.51	0.67	1.69
B11	f (Hz)	5.53	19.72	36.72	5.22	18.88	33.72	-	-	-
	ξ(%)	0.35	0.82	2.99	0.47	0.73	2.92	-	-	-
B12	f (Hz)	5.56	19.88	34.97	-	-	-	4.69	16.94	32.78
	ξ(%)	0.33	0.63	2.49	-	-	-	0.50	0.57	2.32

NP: test not performed

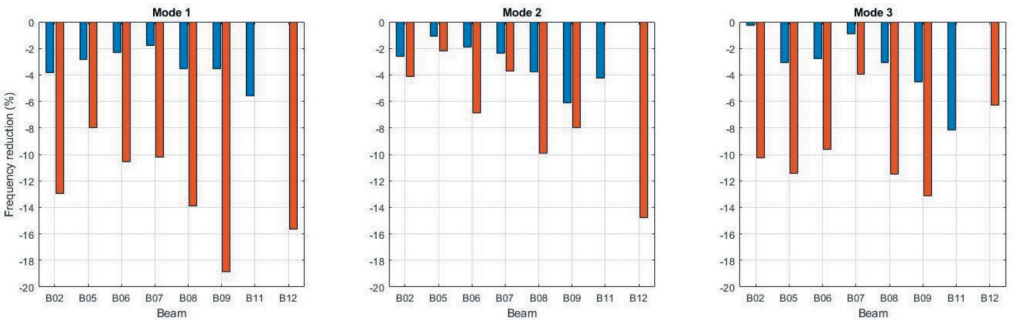


Figure 6. Relative modal frequencies reduction.

The Figure 6 shows the relative reduction of the modal frequencies at the different damage levels.

The following figures illustrate, as an example, the comparison between the mode shapes at different damage levels (phases 0, 1 and 2) for girder B08. It worth noting that small but noticeable differences can be observed with the increasing of damages. Similar results have been found for the other girders.

The reductions of the frequencies of the first mode vary in range of about 2-6% for Phase 1 tests and about 8-19% for Phase 2. The entities of these reductions are comparable to the findings reported in similar experimental campaign present in literature (Quattrone et al. 2012).

It can be noticed that the variation of the first and third modes for B11 in Phase 1 are considerably higher than the mean values obtained in the other samples. It seems indicating a noticeable effect of the diffusion of cracks induced by the application of a higher number of loading cycles at the intermediate level.

The girder B09, which was damaged cutting the 40% of the prestressing strands concentrated at midspan, showed the higher reduction at the ultimate level (Phase 2). The crack pattern of B09 observed at the end of the tests evidences a concentration of cracks in the midspan, where the rupture occurred. In Figure 8 the comparison with the girder B05 shows the spreader diffusion of cracks in case of absence of concentrated damages.

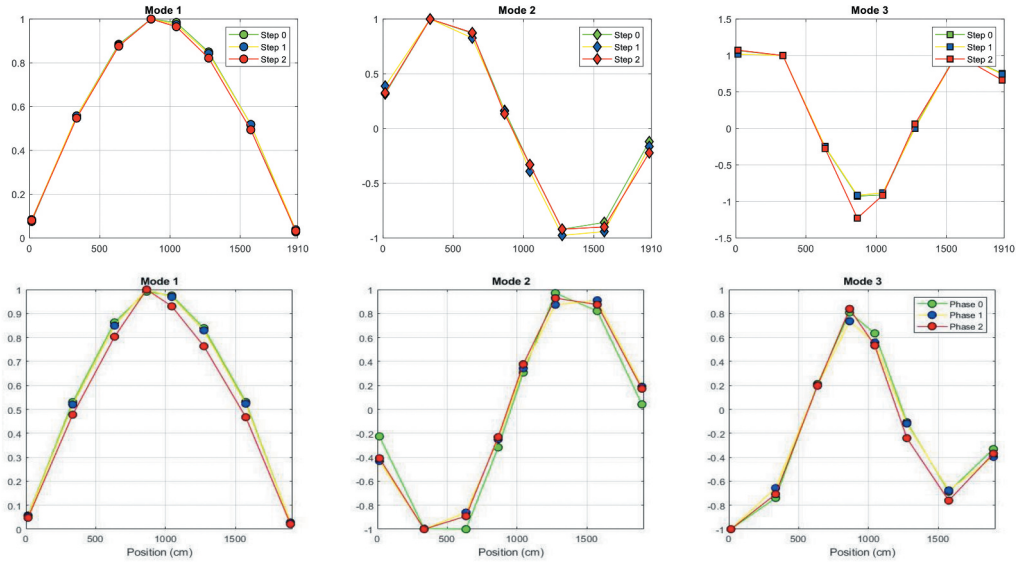


Figure 7. Modal shapes. top: girder B06. bottom: girder B09.

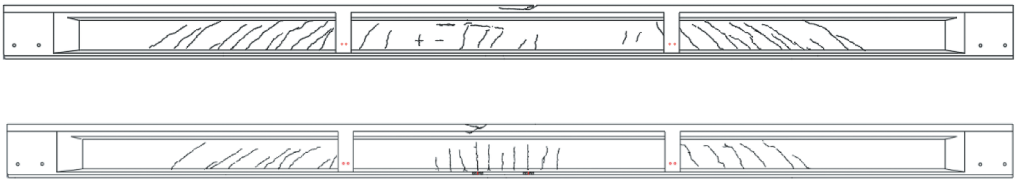


Figure 8. Cracks pattern after failure. top: girder B05. bottom: girder B09.

The Figure 9 highlights in red the domain of variation of the identified modal frequencies, normalized with respect of the undamaged condition, highlighting the wider scattering of the higher modal frequencies.



Figure 9. Domain of variation of the identified modal frequencies.

6 CONCLUSIONS

This work presents the results of the experimental dynamic campaign performed on a set of bridge girders dismounted after 50 years of service life. The tests are part of the BRIDGE|50 research project.

The girders have been characterized for different damage levels induced by static tests. The variation of the modal parameters has been observed and, albeit the small magnitude, the

variations of the structural condition are clearly detectable, confirming the capability of the dynamic structural identification to follow the evolution of damage. The experimental results here presented should be very useful in the field of permanent structural health monitoring. Future works will refine the estimation of damping ratio and the implementation of damage localization and quantification techniques.

ACKNOWLEDGEMENTS

BRIDGE|50 is a research project based on a research agreement among universities, public authorities, and private companies. Members of the Management Committee: S.C.R. Piemonte (President); Politecnico di Milano (Scientific Coordinator); Politecnico di Torino (Scientific Responsible of the Experimental Activities); Lombardi Engineering (Secretary); Piedmont Region; City of Turin; Metropolitan City of Turin; TNE Torino Nuova Economia; ATI Itinera & C.M.B.; ATI Despe & Perino Piero; Quaranta Group. BRIDGE|50 website: http://www.bridge50.org

REFERENCES

Biondini, F., Manto, S., Beltrami, C., Tondolo, F., Chiara, M., Salza, B., et al. BRIDGE|50 research project: Residual structural performance of a 50-year-old bridge. *Bridge Maintenance, Safety, Management, Life-Cycle Sustainability and Innovations – Proceedings of the 10th International Conference on Bridge Maintenaince, Safety and Management (IABMAS 2020)*.

Demarie G, Sabia D. A machine learning approach for the automatic long-term structural health monitoring, Structural Health Monitoring, 819–837 (2019).

Guiglia, M., Taliano, M.: Experimental analysis of the effective pre-stress in large-span bridge box girders after 40 years of service life. Engineering Structures 66 (1), 146–158 (2014)

Quattrone, A., Matta, E., Zanotti Fragonara, L., & Ceravolo, R., 2012. Vibration tests on dismounted bridge beams and effects of deterioration, *Journal of Physics: Conference Series*, 382(1).

Ljung, L.: System identification. Theory for users, Englewood Cliffs, NJ, Prentice Hall, (1999).

Quattrone, A., Sabia, D., Tondolo, F., Capacci, L., Lencioni, A., Legramandi, C.: Dynamic tests and modal identification of Corso Grosseto viaduct decks before the dismounting. Bridge Maintenance, Safety, Management, Life-Cycle Sustainability and Innovations. CRC Press (2021).

Sabia, D., Quattrone, A., Tondolo, F., Savino, P. Dynamic identification of damaged PC bridge beams. First Conference of the European Association on Quality Control of Bridges and Structures (EUROSTRUCT 2021), August 29 – September 1, 2021, Padua, Italy (2021).

Savino, P.; Tondolo, F.; Sabia, D.; Quattrone, A.; Biondini, F.; Rosati, G.; Anghileri, M.; Chiaia, B. 2023. Large-Scale Experimental Static Testing on 50-Year-Old Prestressed Concrete Bridge Girders. Applied Sciences 13(834): 1–22.

Bridge Maintenance, Safety, Management, Digitalization and Sustainability – Jensen, Frangopol & Schmidt (eds)
© 2024 The Author(s), ISBN 978-1-032-77040-6
Open Access: www.taylorfrancis.com, CC BY-NC-ND 4.0 license

Integrating BIM in experimental tests on bridge beams

D. Rodriguez Polania, F. Tondolo & A. Osello
Politecnico di Torino, Turin, Italy

C. Trincianti
S.C.R Piemonte S.p.A., Turin, Italy

M. Chiara
Regione Piemonte, Turin, Italy

ABSTRACT: Information accessibility is a fundamental aspect for an adequate management of existing infrastructures. While BIM methodology has been proposed as an effective method for design and management activities, few examples exist in the integration of data from several techniques in a unique database for horizontal infrastructures. The present paper describes an innovative framework for integrating testing, inspections and monitoring activities on existing bridges following BIM methodology. Information requirements and model organization are specified for bridge elements and bridge management data following Italian regulations as a reference. A practical application example of this methodology is presented considering data from the Bridge|50 research project. The outcome of this work demonstrates that the approach pro-posed provides functionality and openness of the database for bridge management and testing activities. Furthermore, it confirms the utility of BIM to integrate and correlate data from different sources and improve the procedures of infrastructure management.

1 INTRODUCTION

Existing infrastructures, such as bridges and viaducts, play a crucial role in guaranteeing the social and economic wellbeing of the inhabitants of a territory. Nonetheless, an increasing quantity of European existing bridges have reached or are reaching the end of their life cycle. This affection is worsened due to the increase in traffic loads and the effects of climatic change. Due to this situation, a big interest has been deployed by public entities, motorway concessionaries and research institutes to study the techniques needed for correct infrastructure management.

Activities such as inspection, testing, and monitoring are fundamental to guarantee the functionality of the existing infrastructures. These activities are normally regulated by public administration who release guidelines and monitoring plans for the infrastructure. The great amount of data needed on a periodic basis creates further challenges in the bridge management process.

Building Information Modelling (BIM) comes as a logical solution to this problem as it aims for a methodology for infrastructure design and management, where all data is digitalized in a central platform. In fact, the usage of a Bridge Management System (BMS) where concepts such as Geographical Information System (GIS) for the territory and BIM for the single infrastructure is usually recommended. (Wan et al., 2019).

Nonetheless, as BIM was initially created for the design phases of vertical infrastructure, big question mark still exists in its usage for management operations in horizontal infrastructure.

Some examples of BIM usage for bridge management can be seen in the literature. For instance, some authors focus on the application of innovative techniques for digitalizing inspection data (Belcore et al., 2022) while a different research focus is the integration of BIM with data coming from procedures of Structural Health Monitoring. (Davila et al., 2017).

DOI: 10.1201/9781003483755-414

These examples give a notion of the existing procedures that can be used for the management of infrastructures, however a standard procedure and a clear explanation regarding the information that should be included in a BIM model for bridge management is still needed.

2 DATA REQUIREMENTS AND CODES

2.1 *Bridge and viaducts management data*

In Italy, an official guideline for bridge risk evaluation was first issued in 2020 and then ratified in 2022. (Ministero delle Infrastrutture e dei Trasporti, 2020).

The guideline proposes a multilevel risk analysis, where the level of information to be retrieved increases as the level of analysis increases. All bridges in the Italian network are subjected to level 0,1 and 2 (census, visual inspection, and risk classification). According to the classification given in level 2, further visual inspections are scheduled, or the passage to a further level of analysis (3 or 4) that includes testing activities, structural modelling, or the application of a monitoring system, is decided.

Following this guideline different information requirements can be defined according to the level of analysis. For example, in level 0, general aspects regarding the bridge and the context where it is located are determined. In level 1, a list of common defects and a criterion for defect characterization is given. Clearly, bridges with a higher risk attention class have higher information demand. For instance, a bridge that goes to level of analysis 4 needs to consider information regarding non-destructive testing, monitoring systems and structural analysis, other than the basic information of the initial levels.

Regarding the single test procedures and its data requirements, reference is made from normative standard such as ISO, EN or from Italian specific guidelines (UNI).

2.2 *Bridge BIM model*

As digital transformation gained interest in the public sector, regional and national administrations have also issued legislation regarding the usage of open-BIM (models that are readable and functional regardless of the software). In Italy the most relevant legislation regarding this topic is the so-called BIM decree (DM 560-2017) where deadlines are established for the public administrations to progressively adopt open-BIM methodology in civil works procedures. This legislation has been latter updated and currently states January of 2025 as final date for the mandatory implementation of BIM in Italian public processes (works of over 1 million euros).

Nonetheless, regarding the technical specification about BIM modeling, international organizations like UNI, EN and ISO set the basic principles. For open-BIM models the main guidelines are given by BuildingSmart association. The central recommendation given to guarantee the exchangeability of data is the usage of Industry Foundation Classes (IFC) data format. This means setting the BIM model following an object hierarchic organization that is standard depending on the type of infrastructure that is modelled. In the update IFC4.3 the BIM model organization as well as the different categories -*IFCclasses*- and attributes for the bridge and viaducts elements are described. (BuildingSmart, 2020).

2.3 *Management activities in BIM*

A bridge BIM model that is useful for management activities needs to merge information from both previous subchapters; this means, following BIM standards for bridge BIM modeling when it can be developed (e.g. bridge geometrical elements), but adapting the information and elements included in the model according to the needs of the risk assessment guidelines.

Evidently, not all types of data stated in the bridge risk assessment guideline can/should be included in a digital model of a bridge for maintenance purposes. In this sense, a clear differentiation needs to be made between a BIM model and a Common Data Environment (CDE).

A CDE is a cloud-based space in which information regarding a project is available for the participants (Werbrouck et al., 2019). The main principle is that all models, technical drawings, and documents are stored and managed in the CDE and not in the single BIM model. In this sense, the bridge BIM model should include only the basic information to understand the bridge geometry, its context, and the inspection/testing activities performed over time. For further information regarding these activities the BIM model should include links to the external documents (situated in the CDE).

This paper intends to give a general framework of BIM methodology for existing bridges specially focusing on the treatment of data coming from infrastructure management activities.

This work is included in the BRIDGE|50 project, a research collaboration between universities, public and private partners to perform a large number of experimental tests on bridge beams previously dismantled from a demolished viaduct in the city of Turin, Italy. Arguments such as the digitalization of defect inspections, the BIM modelling of testing and monitoring activities, the updatability of models on time and the organization of BIM model and CDE will be treated.

3 CASE STUDY

The Bridge|50 project is among the largest research projects on bridge beams currently in Europe and in the world (Bridge50.org). The project studies the structural performance of 29 prestressed beams and 2 pier caps that were dismantled in 2019 from a viaduct at the end of its life cycle (50 years). The viaduct presented a simple supported scheme with 10 prestressed concrete I-section beams and 2 prestressed U-shaped edge beams supporting a 14 cm thickness concrete slab (Savino et al., 2020). Since the campaign started, the beams have been moved to a testing site and a series of visual inspections and testing (rebound hammer, corrosion potential, concrete drilling, etc.) have been performed. The most peculiar testing activity is a large-scale static and dynamic loading test protocol that is performed in a reaction-frame specifically built for the project. The response of the beams to the loading tests is measured using sensors positioned on their surface and the load capacity up to collapse is determined (Savino et al., 2023). Once the beam has been tested, it is moved away from the reaction frame and further inspection/testing activities are performed to analyze the effects of the generated damage. In this research work the digitalization process of the first 7 beams tested up to collapse will be explained.

Even though this case study treats single bridge beams instead of an operating bridge, a parallel can be made between the information needs of the project and the one of a bridge still in service. The large quantity of inspections and testing data obtained from each beam can be compared to the amount of information that is obtained from a complete analysis of an existing bridge; furthermore, the requirement to update the information in time as the campaign goes on gives a valuable example of how digital strategies can be applied for long-time inspections/testing activities for existing bridges.

4 APPLICATION OF THE BIM METHODOLOGY

4.1 *CDE and organization of project data*

It was decided in an initial phase of the experimental campaign that a cloud based CDE was going to be used to manage all project related data. In the CDE, data is allocated differentiating between general data about the project and data regarding the single beam elements. For each beam in the project a specific data folder is assigned and information regarding the technical/historical documents, testing and inspection activities and the models created for the single beam are stored inside. This means that every beam studied has a unique BIM model, and the latter is linked together with the external information located in the respective data folder. On the other hand,

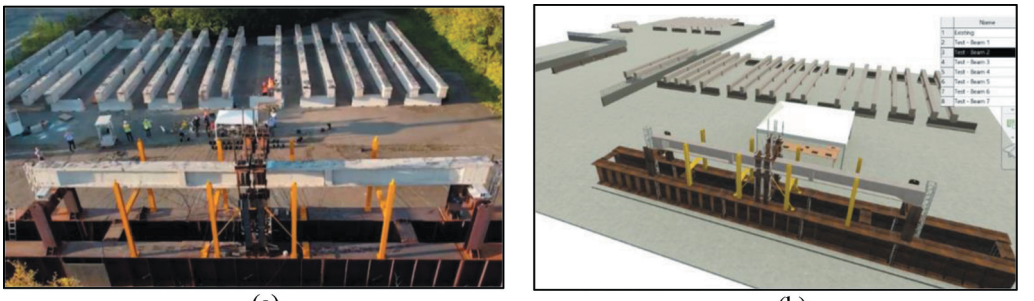
the general information about the project (historical documents, project schedule, technical documents, global models, etc.) is stored in a different folder inside the CDE. This global information folder also includes a BIM model (federative testing campaign model), that acts as a collector of all the single beam models and is used to get a general perspective of the testing campaign and the different campaign phases. The federated model as well as the single BIM models are created using *Autodesk Revit*, however they are exported in IFC format, following the BuildingSmart indications for open-BIM.

4.2 *Federative testing campaign model*

Based on previous work on digitalization of the testing campaign (Rodriguez et al, 2022), the general BIM model is created. This general model is a virtual replica of the testing site, where all components present on site (testing reaction frame, new jersey barriers where the beams are supported, etc.) are modeled either as internal components or as external families. Similarly, in this model, every single BIM model of the beam elements is linked and positioned according to the real location of the beams in the different phase in the testing site.

Regarding the data included in this model, the level 0 of the Italian guidelines for bridge risk assessment is taken as a reference. This information is also complemented with general data about the specifics of the research project that is needed for an understanding of the campaign. This data is added following either pre-compiled options according to the guideline (e.g. bridge alignment options: straight or curvilinear) or free fields (text/number/yes-no) options. Information regarding technical documentation of the project is available using URL hyperlinks that correlate external documentation in the CDE with the data requirements of the model.

Finally, to be able to follow the different stages of the testing campaign the "phase-filter" tool of the software is used. This tool allows the creation of a timeline in the model, where digital objects attributes can be linked to the data selected. The timeline is created with the different dates when the full-scale loading tests were performed in the beams. For example, in the data-phase "Beam – 1", the respective beam moves location to a testing position, inside the reaction frame and in data-phase "Beam – 2", the beam-1 changes to the location after the large-scale test and the beam 2 occupies its place on the reaction frame. Evidently, the information about the model as well as the data of the single beam model also changes according to the data-phase.



(a) (b)

Figure 1. (a) Testing site. (b) Federative model of testing site in phase -Beam 2-.

4.3 *Building the single beam models*

Different BIM models were created in single files following the unique characteristics and particularities of every beam. The family class in *Revit* was defined as *StructuralBeamElement* (translates into *IfcBeam* in open-BIM specifics). Then, once again, the Italian guideline is used as reference for the data included in the model. In this case, information about level 0 as well as information about inspections (ordinary and extraordinary) was included.

To be able to manage the big amount of information needed for every defect finding (cracks, delamination, etc.) it was decided to manage this data as an external family element that is dependent or hosted by the main *IfcBeam* element. The same consideration is made for the testing data, that is treated as an external family, but also dependent on the main beam element.

A final step in the modelling procedure is the usage of the phase-filter tool to update information in the beam models according to the evolution of the testing campaign. Different phases were created in the project according to when the main testing activities took place (see Table 1). The selected phase updates all the general information in the model as well as the specific information about the damage and testing families.

Table 1. Campaign phases for beam 3.

Phase	Tests
Testing phase 1 (NOV.2021)	Visual inspection, Rebound Hammer, Corrosion potential
Testing phase 2 (APR.2022)	Core drilling
Testing phase 3 (OCT.2023)	Full scale loading test
Testing phase 4 (NOV.2023)	Visual inspection, Tensile of steel, Residual prestress, Compression of concrete, Elastic modulus of concrete

4.4 *Defect data elements*

Following a similar procedure as explained by Isalovic et al. (2020) external dependent families were created using the *IfcSurfaceFeature* class. The geometry was created following a semiautomatic procedure taking advantage of an accurate defect modelling performed in an initial phase (Rodriguez et al, 2021). Then information regarding the defect characterization was added to the single families following the defect characterization of level 1 of the Italian guidelines. External documentation regarding the single defects was linked with URL hyperlink.

The defects families were modelled locally with respect to the beam families to ensure the correct placement and connection between defect and structural element.

As explained before, the information regarding beam damage needs to be updated with re- spect to the same timeline created in the beam family object; therefore, a second defect inspec- tion was made in the mechanical tested beam elements -after the full-scale loading test- and the information about new cracking was updated in the respective phase of the digital model.

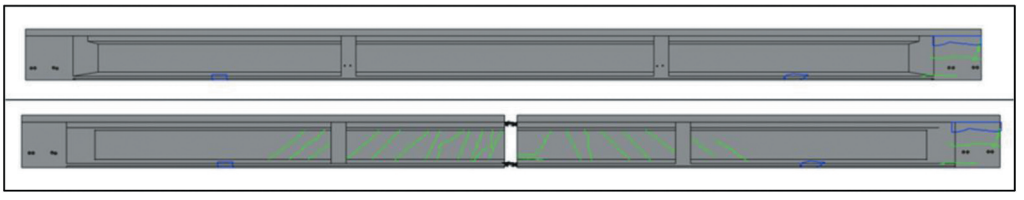


Figure 2. Defect families positioned in beam 1 before and after large-scale mechanical test.

4.5 *Testing results data elements*

Considering the lack of standards for the digitalization of testing information, an experimental approach was tested, using once again the *IfcSurfaceFeature* class to generate a link between beam element and test element. Then, to represent the testing activities in terms of type and location, different conceptual, basic geometries were assigned to the area where the different typologies of tests were performed. (e.g. square for rebound hammer test, circle for pull-out test, etc.). This test geometry was positioned locally with reference to the beam families to ensure the correct

placement according to the actual test location. To standardize the test-data objects and considering that every typology of test has different data requirements it was decided to include just general information about the test activity in the BIM objects and leaving other type of documentation (technical specifications, normative documents, test reports, etc.) linked through hyperlinks. This data was also connected to the phase-filter tool to be updated according to the phases of the testing campaign.

This procedure was replicated for all the different non-destructive tests applied to the beams: rebound-hammer, concrete pull-out (compression, tension, and alkalinity tests), corrosion potential, tensile test, residual prestress test.

Table 2. Example of data for the different model elements.

Data in model			
Category	PropertySet	Parameter name	Parameter Type
	AINOP Code		Text
IfcBridge	Bridge Identification	Type of connection	Text
		Structural typology	Text
		ID	Number
IfcBeam	Element identification	Bridge element type	Text
		Bridge span	Number
		Defect code	Text
IfcSurfaceFeature - Defects	Defect characterization	Weight - G	Text
		Extension	Text
IfcSurfaceFeature -		Type of test	Text
Tests	Test data	Operator	Text
		Link to test report	URL

4.6 *Sensors/monitoring data elements*

Four different data sensor families were created corresponding to the 4 typologies of sensors used during the large-scale loading-test (Used to read displacement and strains due to bending and shear-placed on concrete, and steel-stirrups and strands-). The families were created using *Revit* category *DataEquipment* that automatically translates into *IfcSensor* according to the specifics of open-BIM. The geometry of the sensors was created following the geometrical specification sheets. This typology of family is also hosted by the main *IfcBeam* element and in this sense positioned locally with reference to the beam families. Once again, to standardize the typology of family used and not create a great number of parameters for every single object, it was decided to include basic data regarding the sensor to the BIM object (e.g. sensor code, typology, connection type, connection server, data receiver, etc..) and connect it through a URL hyperlink to the sensor database. This decision is beneficial also considering the operation and manageability of the BIM model preventing data overloading using an external database. This procedure was applied for sensors deployed on the beam surface during the full-scale loading test but could be replicated with any type of structural health monitoring solution.

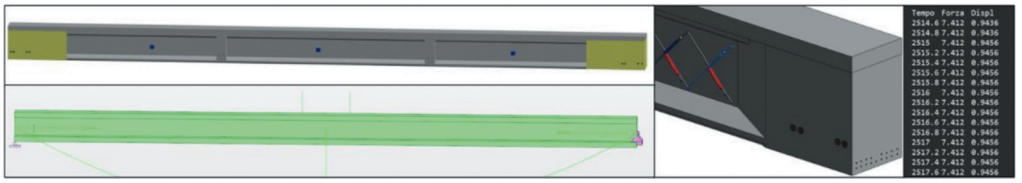
4.7 *Structural models*

Different structural models were created through the different stages of the life of the beam during the experimental campaign. These structural models represent the typology of data that needs to be retrieved in bridges at further levels of analysis according to the risk assessment guidelines (level 3 and 4). Taking into account that with every additional inspection/testing phase more information was acquired about the beams in study, the level of reliability of the proposed structural models should increase as well.

To be able to link the evolution of the structural models with respect to the evolution of the testing campaign, a correlation of structural/BIM models was created. Software from the

same software house -*Autodesk Robot*- was used in the structural analysis to facilitate the interoperability of different software.

A specific structural model was created according to every phase of the model where a certain specification in the *IfcBeam* was updated (e.g. material properties). The variation of the required property was transmitted to the structural model by an export/update task available thanks to the existing connection between the two software.



(a) (b)

Figure 3. (a) Test families inside beam model and connection with structural model. (b) Sensor detail and link with sensor database.

4.8 *IFC export*

To ensure the openness and readability of the created files a passage from *Revit* file to IFC file needs to be established. In this sense operations called class-mapping and parameter-mapping are implemented. This means checking that the software native element category corresponds to the correct *IfcClass* specified for the bridge elements in the Open-BIM guidelines. Moreover, to ensure that the data included in the model is exported as attributes to the *IfcClass* an external text file is created to "guide" the software in the exportation settings. In this external file the data parameters included in the model are enumerated and organized to be exported in *IfcPropertySets* according to the different object classes.

The IFC standard does not include a function that updates data in time as the phase-filter tool; therefore, different BIM models are exported according to the different phases created.

5 RESULTS AND CONCLUSIONS

In the present paper a framework for the creation of BIM models for bridge maintenance activities is proposed using a testing campaign on bridge beam as a case-study. The integration of information from inspection, testing, monitoring, and structural analysis using BIM methodology is specified. Maintenance data requirements were defined following Italian normative for bridge risk assessment while data modelling requirements were defined following open-BIM standards. Even though the case study treats single bridge elements and not an operating bridge, a parallel can be made considering the big quantity of data retrieved and the duration of the project.

Firstly, a clear differentiation between CDE and BIM model information requirements was stated. This differentiation is the basis of the BIM methodology applied as external documentation is stored in the CDE and single BIM models are created containing only basic information of bridge management activities.

The first model described was the global federative model that assists the tracking of the experimental campaign phases. This federative model acts as container of the other digital models of the beams and gives context to the experimental campaign. The fundamental characteristic of this model is its possibility to be updated thanks to the phase-filters. The time-integration demonstrated to be an excellent tool for the organization of bridge management data, as it allows an easy follow-up of the testing phases. In fact, this tool demonstrated such good results that it was also used to treat the inspection and testing activities in the single beam models.

Regarding to the latter, a description about the modelling characteristics of bridge elements following open-BIM standards was specified. Nonetheless, the innovation in the procedure was emphasized in the modelling methodology for inspection, testing and sensor/monitoring data. In this sense, specifics about the included data, the BIM characteristics and geometric characteristics of the elements was stated.

Starting by the BIM format, specific *IFCclasses* (external families) were used to treat this type of information. This external families were, however, dependant to the "main" structural element. Hence, they were attached to the main family and positioned with a local reference to this element. This methodology demonstrated to be satisfactory solution to treat bridge maintenance information as specifics about every single defect/test can be given, but also a direct correlation between the "host" object and the element is created. Likewise, the possibility to position the external element taking as a reference the structural main element helps the rapid visualization and contextualization of data with respect to the structural element analysed.

Regarding the geometry of the elements modelled, the real geometry about defects and sensors was considered. On the other hand, for the testing activities just basic geometry to differentiate between the different tests was created. Considering the global purpose of the model, this type of geometrical simplification does not compromise its functionality as a rapid differentiation between tests can still be determined according to the selected shape and the position and extension of the test is still respected.

With respect to the data that was included in these external objects, the basic idea was to standardize the data regardless of the type of defect/test to be treated. In this sense, a certain number of parameters were created in the BIM objects and external documentation (such as tests results, inspection documents, sensor data, etc.) were related to the model elements through the usage of dynamic links. This decision is beneficial for the model as it allows a correlation of information from different sources in a single database, without adding extra-computational demand to the visualization of the information.

A final explanation regarding the correlation of structural analysis models with BIM models was also stated. In this sense, the link between both typologies of models was established performing exports/updates of the BIM model to the structural analysis software once the characteristic of the same were updated. This process exhibits ones again the benefits of creating a timeline in the model as more information from tests/inspection means a better understanding of the beam characteristics and thus, a better structural analysis model.

Finally, the export of the BIM model following open-BIM standards was performed. This example showed the passage from software-constrained model to an open model without losing information regarding the categories of the objects or their attributes. Nonetheless, the inability of the IFC standard to keep track of the timeline created resulted in multiple files corresponding to the phases created.

The conclusions of the work demonstrate the possibility of treating bridge management data with BIM methodology including basic information about the bridge characteristics -level 0 of guideline- but also complex information corresponding to the superior levels of analysis. Even though a first standardization framework was proposed, future developments are needed in the IFC guidelines to better include information regarding defects and testing.

The result of the methodology demonstrates that time integration with the data inserted in an open-BIM model results in a key-aspect to consider for a BIM model for bridge maintenance. Therefore, a future upgrade in the IFC schema is also needed to consider this sort of information allowing the creation of a unique database for all management phases.

REFERENCES

Belcore, E.; Di Pietra, V.; Grasso, N.; Piras, M.; Tondolo, F.; Savino, P.; Polania, D. 2022. Towards a FOSS Automatic Classification of Defects for Bridges Structural Health Monitoring. ASITA 2021: Geomatics and Geospatial Technologies, pp. 298–312. ISSN 1865-0929. ISBN: 978-3-030-94425-4

BuildingSmart Italia. 2020. Linea guida di applicazione dell'IFC a ponti e viadotti. Come richiedere e creare modelli interoperabili di ponti nella realtà italiana.

Costin, A; Adibfar, A; Hu, H; Chen, S. 2018. Building Information Modeling (BIM) for transportation infrastructure – Literature review, applications, challenges, and recommendations, Automation in Construction, Volume 94, Pages 257–281, ISSN 0926-5805 https://doi.org/10.1016/j.autcon.2018.07.001.

Davila J.; Butler L.; Gibbons N.; Brilakis I.; Mohammed Z.; Elshafie M. & Middleton C. 2017. Management of structural monitoring data of bridges using BIM. Proceedings of the Institution of Civil Engineers - Bridge Engineering 170:3, 204–218

Decreto ministeriale 1° dicembre 2017, n. 560. Modalità e i tempi di progressiva introduzione dei metodi e degli strumenti elettronici di modellazione per l'edilizia e le infrastrutture. Rome, Italy.

Isailović, D; Stojanovic, V.; Trapp, M.; Richter, R.; Hajdin, R. & Döllner, J. 2020. Bridge damage: Detection, IFC-based semantic enrichment and visualization. Automation in Construction. 112. https://doi.org/10.1016/j.autcon.2020.103088.

Ministero delle Infrastrutture e dei Trasporti. 2020. Linee Guida Per La Classificazione E Gestione Del Rischio, La Valutazione Della Sicurezza Ed il Monitoraggio Dei Ponti Esistenti. Rome, Italy.

Rodriguez Polania, D.; Tondolo, F.; Osello, A. & Trincianti, C. 2022. BIM as a tool for experimental tests. In: Proceedings of the Eleventh International Conference on Bridge Maintenance, Safety and Management (IABMAS 2022), Barcelona (Spain), July 11-15, 2022, pp. 1790–1797. ISBN:9781003322641

Rodriguez Polania, D.; Tondolo, F.; Osello, A.; Fonsati, A.; De Gaetani, C.; Trincianti, C.; Gazulli, D. 2021. Digitalization Processes and Bridge Information Modeling for Existing Bridges. Eurostruct – European association on quality control of bridges and structures. Padova (ITALY). August 29- September 1, 2021.

Savino, P.; Anghileri, M.; Chiara, M.; Salza, B.; Quaranta, L. 2021. Corso Grosseto viaduct: Historical and technical overview. Tenth International Conference on Bridge Maintenance, Safety and Management (IABMAS 2020), Sapporo (JAPAN), June 28-July 2, 2020, pp. 3345–3351. ISBN:9780429279119.

Savino, P.; Tondolo, F.; Sabia, D.; Quattrone, A.; Biondini, F.; Rosati, G.; Anghileri, M.; Chiaia, B. Large-Scale Experimental Static Testing on 50-Year-Old Prestressed Concrete Bridge Girders. *Appl. Sci*. 2023, *13*, 834. https://doi.org/10.3390/app13020834.

Wan, C.; Zhou, Z.; Li, S.; Ding, Y.; Xu, Z.; Yang, Z.; Xia, Y.; Yin, F. 2019 Development of a Bridge Management System Based on the Building Information Modeling Technology. *Sustainability*, 11, 4583. https://doi.org/10.3390/su11174583

Werbrouck, J.; Pauwels, P.; Beetz, J.; van Berlo, L. 2019. Towards a Decentralized Common Data Environment using Linked Building Data and the Solid Ecosystem.


Taylor & Francis
Taylor & Francis Group
http://taylorandfrancis.com

GENERAL SESSIONS
GS01: BRIDGE MAINTENANCE - Application of new tools


Taylor & Francis
Taylor & Francis Group
http://taylorandfrancis.com

Bridge Maintenance, Safety, Management, Digitalization and Sustainability – Jensen, Frangopol & Schmidt (eds)
© 2024 The Author(s), ISBN 978-1-032-77040-6
Open Access: www.taylorfrancis.com, CC BY-NC-ND 4.0 license

Super-resolution enhanced vehicle recognition method for long-span bridge

Xin Shan, Jingxuan Zhang, Yue Pan, Yunlong Ma & Dalei Wang
Tongji University, Shanghai, China

ABSTRACT: With the rapid advancement of vehicle load monitoring systems, incorporating dynamic weighing and multi-view visual technologies, acquiring precise vehicle loads across large fields of view on bridge surfaces has become crucial for bridge health monitoring. However, for ultra-long-span bridges, due to the limitations of single-camera focal length and depth of field, multi-camera and re-identification technologies are usually necessary to achieve full-bridge coverage. This approach inevitably leads to high system construction costs, large data transmission and processing costs, and compromises system robustness. To overcome these challenges, this paper proposes a vehicle load monitoring method for large-span bridges enhanced by super-resolution technology. The proposed approach introduces a clustering segmentation technique based on image clarity, enabling recognition and cropping of far-focal blur areas. Then, a super-resolution image enhancement network is designed to restore the resolution of blurry regions. Finally, a vehicle recognition algorithm based on YOLO is implemented to achieve wide-field vehicle recognition in single-view images. The research results demonstrate that super-resolution technology can effectively improve vehicle recognition accuracy and robustness within blurry areas of vehicle monitoring images, thus achieving wide-field bridge surface vehicle monitoring under single-view conditions. By significantly reducing the cost and complexity of vehicle monitoring systems, this method provides important value for bridge traffic management and real-time performance evaluation.

1 GENERAL INSTRUCTIONS

1.1 *Current status of vehicle detection on long-span bridges*

Dynamic load measurement is vital in bridge engineering for design, maintenance, and lifecycle analysis. This typically involves measuring axle loads and their positions on bridges. Weigh-In-Motion (WIM) technology, crucial for traffic and civil engineering, measures vehicle weight and related parameters. However, WIM systems, embedded in bridge structures, only provide load data at specific sections, lacking insight into changes in vehicle speed and routes which are important for long-span bridge management and performance analysis.

For ultra-large-span bridges, the limited range of monocular cameras necessitates using multi-camera systems and re-identification technology for full coverage. While effective, this approach incurs high construction and operational costs due to numerous cameras, complex data transmission, and processing challenges. These limitations highlight the need for integrating visual and tracking technologies to establish an effective vehicle load monitoring system.

1.2 *Introduction of a super-resolution enhanced object detection network*

To optimize vehicle load detection on long-span bridges, this study introduces a method combining super-resolution (SR) technology with object detection. SR enhances low-resolution images into high-resolution ones, a technique increasingly applied in various fields due to deep learning advancements. Our novel model integrates a super-resolution network with an object detection model, processing blurry images for improved vehicle recognition. This approach adapts to the

DOI: 10.1201/9781003483755-415

limitations of monocular cameras on long-span bridges, enhancing data clarity for more accurate detection and tracking, thereby optimizing vehicle load detection systems.

2 OVERVIEW OF OUR METHODS

This paper presents a novel vehicle load monitoring method for large-span bridges, employing super-resolution technology as shown in Figure 1. Addressing the limitations of traditional methods in ultra-long-span bridges, our approach enhances the clarity of input images using a fusion of Laplacian operators and Fourier transforms, crucial for creating high-quality datasets.

The method combines a Residual Dense Network (RDN) with YOLOv8 for target detection, significantly improving accuracy in blurred images. This integrated approach not only enhances vehicle recognition in areas affected by camera depth-of-field but also enables efficient bridge surface monitoring from a single viewpoint. The result is a more cost-effective and robust system for bridge traffic management and performance evaluation.

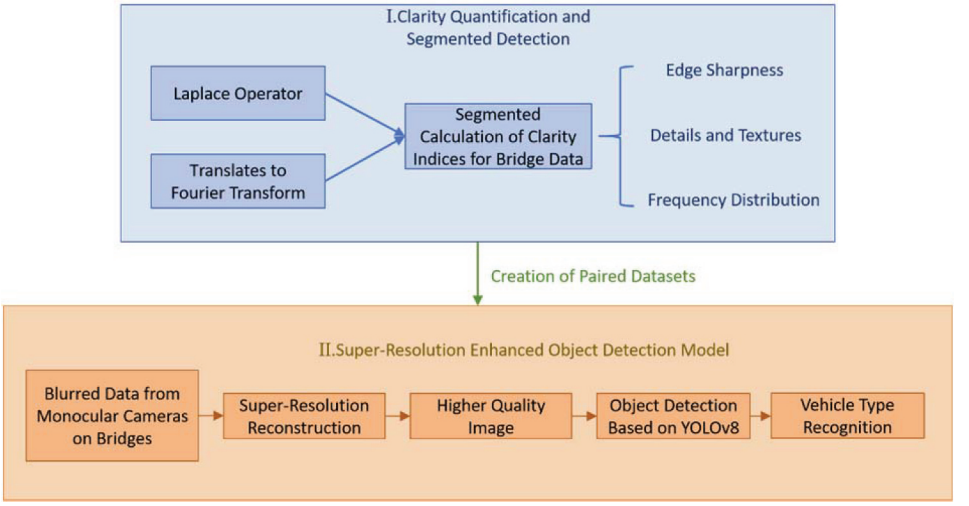


Figure 1. The overall framework for super-resolution enhanced method for vehicle recognition on long-span bridges.

3 CLARITY QUANTIFICATION AND SEGMENTED DETECTION

Clarity Quantification and Segmented Detection is achieved via three core procedures, namely the perspective correction, the segmentation of images, and clarity assessment.

The perspective correction is to correct geometrical distortions in images due to varying camera angles. Next, image segmentation is applied to these transformed images, isolating the images into different parts for targeted analysis. Finally, using a combination of Laplace Operator and Translates to Fourier Transform we designed an index. This index is crucial for assessing the quality of each segmented vehicle image, ensuring the use for further paired datasets making.

3.1 *Perspective correction*

A traffic camera on a long-span bridge was set for an oblique view, causing image distortions corrected by photogrammetric projective transformation. Using ground control points (GCPs) and total stations, the coordinates were transformed into a 3D frame, as depicted in Figure 2. This process, a homography transformation, involved correcting distortions and aligning images with reality, significantly enhancing accuracy and perspective.

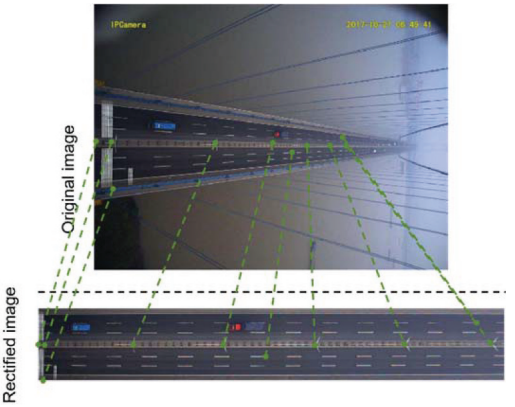


Figure 2. GCPs and corresponding pixels on image in the rectification.

3.2 *Images segmentation*

Image blurriness decreases with distance from the camera's center. For effective super-resolution network training across varying blur levels, the image was segmented into four parts, named Part 1 to Part 4, based on distance from the camera center. This approach, illustrated in Figure 3, enables focused training for each segment, enhancing the network's response to different blur intensities and providing segment-specific enhancements.



Figure 3. A schematic diagram of an image divided into four parts.

3.3 *Clarity assessment*

3.3.1 *Laplacian operator*

Laplacian operator is a second-order derivative operator used in image processing to highlight edges. For a two-dimensional image, the Laplacian operator L is defined as the sum of the second derivatives of the image intensity I with respect to x and y:

$$L = \frac{\partial^2 I}{\partial x^2} + \frac{\partial^2 I}{\partial y^2} \tag{1}$$

In discrete form, this second derivative can be approximated using a convolution operation. For a 3x3 kernel, the Laplacian operator can be represented by the following kernel:

$$\begin{bmatrix} 0 & 1 & 0 \\ 1 & -4 & 1 \\ 0 & 1 & 0 \end{bmatrix} \tag{2}$$

This convolution highlights the contrast in edges, serving as an indicator of image sharpness. Sharper images will exhibit more distinct edges in the Laplacian-processed output, reflecting higher quality.

3.3.2 *Fourier transform*

Fourier transformation shifts the image from the spatial to the frequency domain, revealing details about its sharpness.

The 2D Discrete Fourier Transform (DFT) for a digital image $f(x, y)$ is defined as:

$$F(u,v) = \sum_{x=0}^{M-1} \sum_{y=0}^{N-1} f(x,y) e^{-2\pi i \left(\frac{ux}{M} + \frac{vy}{N}\right)} \tag{3}$$

Here, M and N are the image dimensions, with the summation over all pixels. High-frequency components in the DFT spectrum correlate with image edges and fine details, indicative of sharpness. A predominance of high frequencies suggests a clearer image, while a lack of such frequencies implies blurriness.

3.3.3 *Image clarity assessment based on laplacian operator and fourier transform*

The utilization of the YOLOv8 object detection model, known for its sensitivity to edge sharpness and texture detail in images, necessitates a comprehensive image clarity assessment approach in this study. Two evaluative indices, the Laplacian operator for edge sharpness scenarios (like edge and motion blur) and the Fourier Transform for texture detail scenarios (such as linear interpolation down-sampling and Gaussian blur), are integrated for image clarity quantification. This approach, employing distinct evaluative techniques, is designed to improve image quality assessment's effectiveness and accuracy, laying a foundation for creating high-quality datasets essential for YOLOv8's optimal performance in object detection scenarios.

4 SUPER-RESOLUTION ENHANCED OBJECT DETECTION MODEL

4.1 *Residual dense network for image super-resolution overview*

RDN is selected for its exemplary capability in reconstructing high-resolution images from low-resolution counterparts, primarily due to its dense feature extraction and residual learning mechanism. The architecture is adept at preserving image details, essential for subsequent detection processes.

The key principle of RDN is encapsulated in the dense feature fusion strategy, formulated as:

$$F_{DF}(x) = H_{DF}([F_{D1}, F_{D2}, \ldots, F_{DD}]) \tag{4}$$

where F_{Di} denotes the dense block function, D the number of dense blocks, x the input feature map, and H_{DF} represents the dense feature fusion function.

The global feature fusion, defined as F_{GF}, integrates the original image features with the dense features:

$$F_{GF}(x) = H_{GF}(F_{DF}(x), F_0(x)) \tag{5}$$

where $F_0(x)$ is the initial shallow feature extraction from the input image x.

4.2 *YOLOv8 overview*

YOLOv8 serves as the object detection model in our study due to its fast and accurate detection capabilities. The model operates on the principle of dividing the image into a grid and predicting bounding boxes and class probabilities for each grid cell.

The key operation of YOLOv8 can be summarized in the formula:

$$O(x) = \sigma(Conv(F(x))) \tag{6}$$

where $F(x)$ represents the feature extraction function, $Conv$denotes the convolutional operation, and σ is the sigmoid function for probability prediction.

4.3 *Proposed integrated model*

The integration model strategically places RDN as a 'head' in the YOLOv8 framework as shown in Figure 4. This design allows the system to first perform super-resolution processing on input images, focusing on enhancing edges and textures, crucial for accurate object detection.

The combined operation can be represented as:

$$y(x) = YOLOv8\,(F_{GF}(RDN(x))) \tag{7}$$

where $RDN(x)$ enhances the input image x followed by F_{GF} applying global feature fusion, and YOLOv8 conducting the detection and classification.

The model supports selective component training, with parameters enabling the freezing of either the RDN or YOLOv8 sections. This facilitates focused training on either super-resolution enhancement or object detection efficiency.

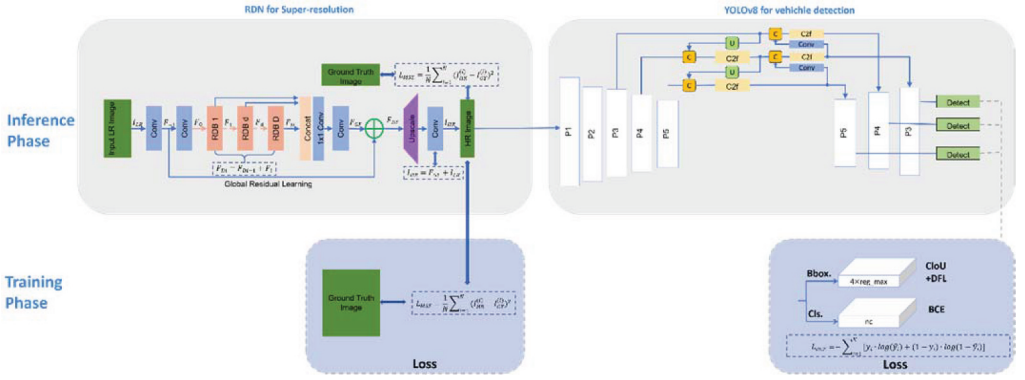


Figure 4. Two stages based vehicle detection network.

5 DATA AND EXPERIMENT

5.1 *Dataset and testing areas*

A surveillance camera, positioned mid-way on the Jiangyin Bridge's pylon crossbeam, captures 1920x1080 pixel footage at 25 fps from an 85-meter height. The recorded area spans 192 by 29.5 meters. Post-recording, footage is trimmed to 295x1920 pixels using 12 GCPs, with



Figure 5. Examples of recorded frames.

each pixel representing 10 ground truth diameters. Subsequently, a vehicle benchmark dataset for detector training is created, with 4000 video frames annotated for three vehicle types.

5.2 *Vehicle detection on YOLOv8*

5.2.1 *Training*

We split the dataset into 80% training, 10% validation, and 10% testing. Different network architectures were trained on this dataset with a batch size of 32 and an initial learning rate of 0.004. Data augmentation included random horizontal flips and crops. Networks were initialized using weights pre-trained on the COCO dataset and trained via the Tensorflow Object Detection API on an NVIDIA GeForce RTX 2080 Ti GPU. The model's performance was evaluated using the mAP score at an IoU threshold, defined as

$$\mathrm{IoU}(A, B) = \frac{\left|A \cap^{B}\right|}{\left|A \cup^{B}\right|} \tag{8}$$

where A and B are the areas of ground truth and detected objects, respectively. Precision and recall are calculated using

$$\text{precision} = \frac{TP}{TP + FP} \tag{9}$$

and

$$\text{recall} = \frac{TP}{TP + FN} \tag{10}$$

with *TP*, *FP*, and *FN* denoting true positives, false positives, and false negatives. Both IoU and confidence thresholds were set at 0.5.

5.2.2 *Evaluation*

During evaluation, our model exhibited strong performance with an overall mAP50 of 0.981 and mAP50-95 of 0.919 across 200 images with 1736 instances, which is shown in Table 1.

Table 1. Evaluation result of YOLOv8.

Class	Images	Instances	R	mAP50	mAP50-95
all	200	1736	0.955	0.981	0.919
Car	200	1060	0.988	0.995	0.927
Bus	200	102	0.928	0.96	0.903
Truck	200	574	0.949	0.988	0.925

5.3 *Creation of paired datasets for super-resolution networks*

5.3.1 *Segmented testing performance of vehicle detection*

200 frames from the Jiangyin Bridge were selected for annotation (as depicted in Figure 6) and segmented into four parts following the guidelines in Section 3.2. Each part was then evaluated using the YOLOv8 model, as detailed in Section 5.2. The results indicated a decrease in detection accuracy with increased distance from the camera, linked to varying blur levels across the segments. To address the image quality degradation from the camera's depth of field, specific super-resolution (SR) training datasets for each segment were developed, consisting of high-resolution images similar to part 1 and low-resolution counterparts for parts 2 to 4. The trained SR networks aim to uniformly enhance image clarity to the level of part 1.



Figure 6. Segment vehicle detection and clarity assessment.

To accurately simulate real-world blur in datasets for parts 2 to 4, clarity assessment methods from Section 3.3 were utilized. The down-sampling process involved techniques like interpolation and various blurs, with parameters fine-tuned to reflect actual image conditions. This yielded three sets of high-resolution and low-resolution image pairs for each segment, effectively demonstrating the quality enhancement as depicted in the respective sections.

5.4 *Super-resolution enhancement on RDN*

Utilizing the generated matched datasets, the Residual Dense Network (RDN) was trained separately for the three distinct parts of the image. The training settings were meticulously configured: a learning rate of 1×10^{-4}, a batch size of 32, a patch size of 32 for image segmentation, and a total of 400 epochs. During training, the Peak Signal-to-Noise Ratio (PSNR) values for parts 2 to 4 were obtained, as shown in Figure 7.

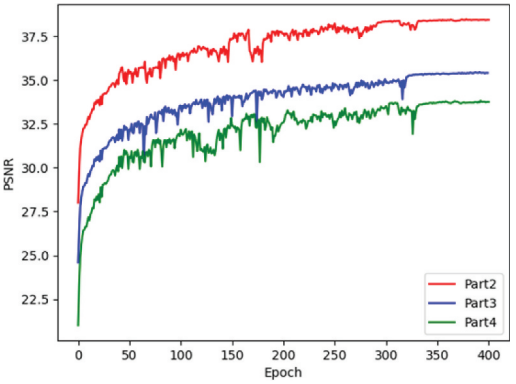


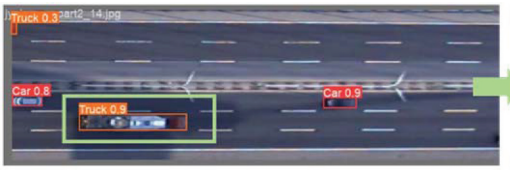
Figure 7. Variation curve of PSNR values during the training process of RDN.

PSNR, a key metric in image processing, quantitatively assesses super-resolution reconstruction quality by comparing it with the original high-quality images (ground truth). Higher PSNR values, exceeding 30 in all three reconstructed sections, indicate successful image enhancement.

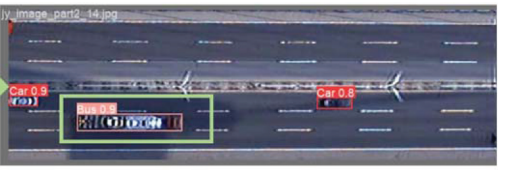
5.5 *Result and discussion*

After the new model was trained, it was used for image restoration and detection, with the results as follows.

For part 2, which originally had relatively high clarity, the recall rate and mAP50 showed marginal improvement. However, a significant enhancement was observed in mAP50-95. This suggests that the super-resolution reconstruction in this part led to a higher probability of accurate recognition, primarily due to the subtle refinement of image details.



Class	Images	Instances	R	mAP50	mAP50-95
all	200	2056	0.884	0.897	0.665
Car	200	1222	0.979	0.96	0.743
Bus	200	100	0.83	0.846	0.611
Truck	200	734	0.842	0.884	0.641



Class	Images	Instances	R	mAP50	mAP50-95
all	200	2056	0.893	0.905	0.732
Car	200	1222	0.938	0.976	0.811
Bus	200	100	0.846	0.86	0.679
Truck	200	734	0.894	0.885	0.706

Figure 8. Comparison of detection performance before and after SR enhancement for part 2.

In the case of part 3, characterized by lower clarity, the enhancements were primarily observed in the recall rate and mAP50. Post-processing through our network substantially reduced instances of incorrect and duplicate detections. This improvement can be attributed to the super-resolution network's capability to restore vehicle textures and finer details, thereby enhancing the overall detection accuracy.



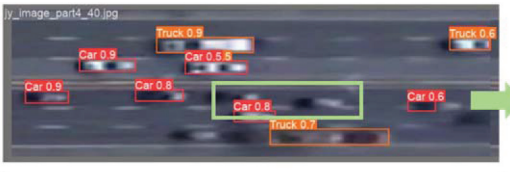
Class	Images	Instances	R	mAP50	mAP50-95
all	200	2218	0.762	0.764	0.5
Car	200	1492	0.909	0.951	0.619
Bus	200	52	0.538	0.457	0.297
Truck	200	674	0.84	0.886	0.586



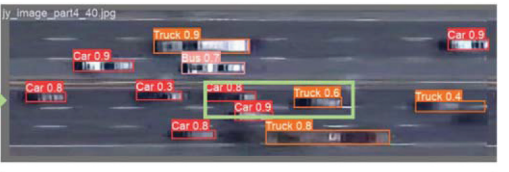
Class	Images	Instances	R	mAP50	mAP50-95
all	200	2218	0.803	0.806	0.55
Car	200	1492	0.936	0.958	0.627
Bus	200	52	0.697	0.581	0.41
Truck	200	674	0.777	0.897	0.62

Figure 9. Comparison of detection performance before and after SR enhancement for part 3.

For part 4, which had the lowest clarity, the primary improvement was in mAP50. The super-resolution processing notably facilitated the detection of previously undetectable vehicles, likely due to the sharpening of edges by the super-resolution network.



Class	Images	Instances	R	mAP50	mAP50-95
all	200	1684	0.527	0.441	0.237
Car	200	1040	0.705	0.632	0.345
Bus	200	50	0.14	0.0772	0.039
Truck	200	594	0.736	0.613	0.327



Class	Images	Instances	R	mAP50	mAP50-95
all	200	1684	0.681	0.562	0.448
Car	200	1040	0.707	0.713	0.513
Bus	200	50	0.599	0.26	0.306
Truck	200	594	0.736	0.714	0.524

Figure 10. Comparison of detection performance before and after SR enhancement for part 4.

6 CONCLUSION

This study introduces a novel method combining super-resolution technology with object detection for vehicle load monitoring on long-span bridges, enhancing detection accuracy significantly. Our experiments demonstrate the method's effectiveness in extending the monitoring capabilities of single-camera systems. The findings suggest potential future improvements in traffic management and bridge monitoring. Future work could explore algorithms that merge super-resolution with object detection and analyze continuous video data, further enhancing monitoring precision and range.

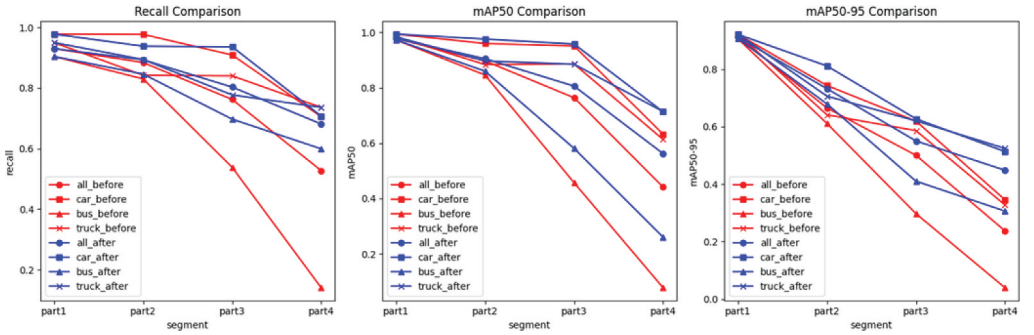


Figure 11. Comparison of recall and mAP before and after SR enhancement.

ACKNOWLEDGEMENT

This research was financially supported by National Natural Science Foundation of China (Grant No. 52208198), National Key R&D Program of China (Grant No. 2021YFF0501004), and Research and Development Center of Transport Industry of New Generation of Artiffcial Intelligence Technology (Grant No. 202201H).

REFERENCES

[1] W. Hang, Y. Xie, and J. He, "Practices of using weigh-in-motion technology for truck weight regulation in China," Transp. Policy, vol. 30, pp. 143–152, Nov. 2013.

[2] A. S. Nowak and P. Rakoczy, "WIM-based live load for bridges," KSCE J. Civil Eng., vol. 17, no. 3, pp. 568–574, Apr. 2013.

[3] Pan Y., Wang D., Dong Y., Peng B. "A Novel Vision-Based Framework for Identifying Dynamic Vehicle Loads on Long-Span Bridges: A Case Study of Jiangyin Bridge, China." In IEEE Transactions On Intelligent Transportation Systems, 2021.

[4] D. Zapl etal. and A. Herout, "Vehicle re-identification for automatic video traffic surveillance," in Proc. IEEE Conf. Comput. Vis. Pattern Recognit. Workshops (CVPRW), Jun. 2016, pp. 1568–1574.

[5] Jacob Solawetz and Francesco. "What is YOLOv8? The ultimate guide." 2023. 04-30-2023, pp. 1, 5, 8.

[6] Y. Zhang, Y. Tian, Y. Kong, B. Zhong, and Y. Fu, "Residual Dense Network for Image Super-Resolution," in Proceedings of the IEEE Conference on Computer Vision and Pattern Recognition (CVPR), 2018.

[7] Y. Zhang, Y. Tian, Y. Kong, B. Zhong, and Y. Fu, "Residual Dense Network for Image Restoration," IEEE Transactions on Pattern Analysis and Machine Intelligence (TPAMI), 2020.

[8] Ma, Rujin, Zhen Zhang, Yiqing Dong, and Yue Pan. "Deep learning based vehicle detection and classification methodology using strain sensors under bridge deck." Sensors 20, no. 18 (2020): 5051.

[9] Dong, Yiqing, Dalei Wang, Yue Pan, and Yunlong Ma. "Large field monitoring system of vehicle load on long-span bridge based on the fusion of multiple vision and WIM data." Automation in Construction 154 (2023): 104985.

[10] Chen, A., Y. Pan, Z. Pan, and R. Ma. "Vehicle load identification of long-span bridges based on dynamic image." In Life-Cycle of Structural Systems, pp. 1017–1020. CRC Press, 2014.

Bridge Maintenance, Safety, Management, Digitalization and Sustainability – Jensen, Frangopol & Schmidt (eds)
© 2024 The Author(s), ISBN 978-1-032-77040-6
Open Access: www.taylorfrancis.com, CC BY-NC-ND 4.0 license

Bayesian non-linear load estimation in long-span bridges via physics-informed Gaussian processes

G.R. Tondo
Bauhaus University Weimar, Weimar, Germany

I. Kavrakov
University of Cambridge, Cambridge, UK

G. Morgenthal
Bauhaus University Weimar, Weimar, Germany

ABSTRACT: In the field of structural health monitoring, advancements in computer and sensor technologies have facilitated the acquisition of vast amounts of structural response data. However, assessing the current state of a structure alone is often insufficient, and a more comprehensive approach involves estimating its future characteristics, a concept commonly known as damage prognosis. Such estimations rely not only on the natural ageing of the structure but also on accurately predicting changes in applied loads over time. This paper investigates a method for dynamic load estimation based on heterogeneous operational data using physics-informed Gaussian processes (GPs). A machine learning model is constructed as a multi-output GP, with covariance and cross-covariance kernels derived analytically from time-domain derivatives of displacements, velocities, and accelerations. Training is carried out in modal space via maximum likelihood estimation using a comprehensive set of measurement data. Coupling the trained model with the harmonic oscillator differential equation yields a hybrid Bayesian framework for dynamic load estimation. The efficacy of the model is demonstrated through an aerodynamic analysis of the Great Belt East Bridge. The buffeting response is numerically computed using the linear unsteady assumption, and the associated non-linear force is reconstructed using noisy synthetic sensor measurements. Results indicate a good agreement between the applied forces and the mean predicted dynamic load in low-frequency ranges, while high-frequency content is effectively captured by the Bayesian formulation as an increase in uncertainty. The developed model is a reliable approach for load reconstruction and can be directly integrated into a damage prognosis framework when continuous measurement data is available.

1 INTRODUCTION

In the design of contemporary structures, engineers commonly rely on codes of practice or empirical guidelines to calculate the loads that structures might encounter over their lifespan. Nevertheless, in practical scenarios, these loads often exhibit time-varying characteristics and may not be entirely known during the design phase. Adding to this challenge is the increasing uncertainty associated with loads arising from environmental effects, a trend exacerbated by the ongoing impacts of climate change. This issue not only poses difficulties in the design of new structures but also presents a challenge in predicting the future conditions of existing structures. The latter task, coupled with structural health monitoring, constitutes a procedure that forms an integral part of a damage prognosis framework, as illustrated in Figure 1 (Farrar & Lieven, 2006).

Force reconstruction can be carried out in several different ways, based for instance on data-driven techniques (Liu et. al., 2022, Nonomura et. al., 2018, Petersen et. al., 2022, Tondo et. al., 2023b), optimization strategies (Wang et. al. 2015), defined basis functions (He et. al., 2018),

DOI: 10.1201/9781003483755-416

and many other models (Sanchez & Benaroya, 2014). This study proposes methodology based in stochastic processes using Gaussian process for machine learning (Rasmussen & Williams, 2006). The proposed framework integrates data-driven models with physics-based formulations, eliminating the need for regularization and inherently accommodating noise properties. It offers flexibility to integrate diverse data types and sets characterized by varying quality levels.

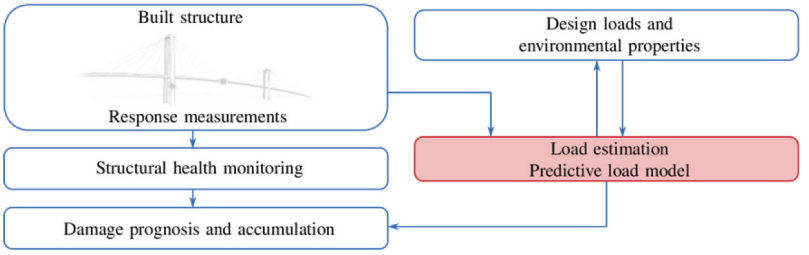


Figure 1. Damage prognosis framework as per Farrar & Lieven (2006). The estimation of the current load conditions based on measurement data, detailed in red, is used as a basis to update the design loads, create predictive load models, and determine probable future damage.

This paper presents a case study involving the reconstruction of aerodynamic forces acting on the Great Belt East bridge. The structural response is computed through the application of the linear unsteady aerodynamic model, and subsequently, white noise is introduced to the responses to replicate measurement conditions. The resultant noisy data is then downsampled and employed as training data for a physics-informed machine learning model established within the Gaussian process framework. The model effectively yields a Bayesian view on the underlying forces that produced the original responses. To assess the efficacy of the approach, comparisons between true and reconstructed signals are conducted. Additionally, the predictions are integrated with a structural finite element model, providing valuable insights into the structural responses and internal forces arising from aerodynamic loading.

The organization of this paper is as follows: Section 2 presents a general framework of the proposed model and develops the prediction procedure in three separate steps. Section 3 defines the aerodynamic analysis properties and presents the results of the force reconstruction scheme. Lastly, Section 4 presents conclusions and an overview of possible future investigations.

2 GAUSSIAN PROCESS FOR FORCE RECONSTRUCTION

The physics-informed Bayesian machine learning model derived in this work is composed of three different building blocks (c.f. Figure 2):

1. A multi-output Gaussian process model for structural responses (displacements, velocities and accelerations) is built and trained using collected measurement data (Sec 2.1).
2. A hybrid GP force model is built combining the machine learning framework with the partial differential equation describing the system oscillation (Section 2.2).
3. Force predictions are carried out by combining the hybrid force model from Section 2.2 with the trained response model from Section 2.1 (Section 2.3).

2.1 *Model for observable responses*

Externally applied forces in bridges cause internal stresses and, in general, a displacement response. When the applied load varies in time, the displacement response can be measured continuously and modelled as

$$u = f(t) + \varepsilon \tag{1}$$

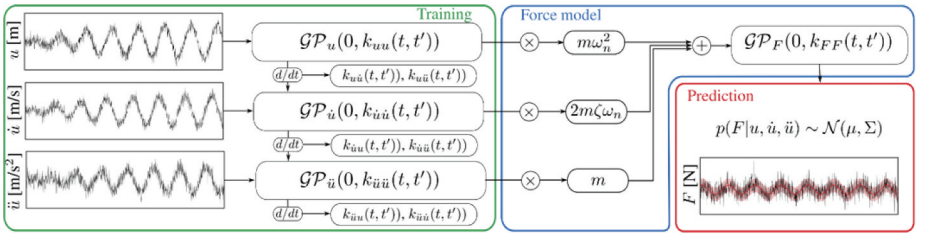


Figure 2. Framework for the physics-informed Gaussian process: (green) models for measured data are created and jointly trained. A force model (blue) is built combining the previous models and the harmonic oscillator's differential equation, which can be used for predictions (red).

where t is the time and $\varepsilon = \mathcal{N}\left(0, \sigma_{n,u}^2\right)$ the Gaussian noise in the measurement system, defined by a variance $\sigma_{n,u}^2$. The same principle of a stochastic process applies to the velocity and acceleration signals, where each of them has a particular noise variance $\sigma_{n,\dot{u}}^2$ and $\sigma^2{}_{n,\ddot{u}}$. Assuming the underlying deflection response is a stochastic zero-mean Gaussian process, a model can be created such that

$$u(t) \sim \mathcal{G}P\left(0,\ k_{uu}(t,t') + \sigma_{n,u}^2 \delta(t,t')\right) \tag{2}$$

where δ is the Kronecker-Delta operator and k_{uu} is a covariance kernel that measures similarity between time instances t and t '. The displacement response is herein assumed to be continuous and smooth in time, and thus k_{uu} can be modelled by the squared exponential (SE) kernel

$$k_{uu}(t,t';\sigma_s,\ell) = \sigma_s^2 \exp\left(-\frac{1}{2}\left(\frac{t-t'}{\ell}\right)^2\right) \tag{3}$$

in which σ_s is a standard deviation amplitude and ℓ is a length scale controlling the kernel smoothness (Rasmussen & Williams 2006). Since velocities $\dot{u}$ and accelerations $\ddot{u}$ are time-derivatives of the displacements and exploiting the fact and any linear operation to a Gaussian process result in another GP, physics-informed covariance and cross-covariance kernels can also be created for velocities $k_{\dot{u}\dot{u}}$ and accelerations $k_{\ddot{u}\ddot{u}}$, such that

$$k_{u\dot{u}} = \frac{d}{dt'}k_{uu},\ \cdots k_{\dot{u}\dot{u}} = \frac{d}{dt}\frac{d}{dt'}k_{uu} \tag{4}$$

and

$$k_{u\ddot{u}} = \frac{d^2}{dt'^2}k_{uu} \cdots k_{\ddot{u}\ddot{u}} = \frac{d^2}{dt^2}\frac{d^2}{dt'^2}k_{uu} \tag{5}$$

While Gaussian processes are considered non-parametric models, the specific characteristics of covariance kernel and noise assumptions introduce model parameters that need to be determined based on the training data. When measurements are taken for deflections, velocities, and accelerations, the parameter set to be determined is denoted as $\theta = \left\{\sigma_s, \ell, \sigma_{n,u}, \sigma_{n,\dot{u}}, \sigma_{n,\ddot{u}}\right\}$ The consideration of measurement noise depends on the availability of data for a particular quantity, either excluding it when no data is collected or incorporating it when multiple datasets with varying properties are at hand (Tondo et al. 2022, 2023a). Parameter determination is achieved using maximum likelihood estimation

$$\boldsymbol{\theta}_{\text{opt}} = \text{argmax}_{\boldsymbol{\theta}} \log p(\boldsymbol{y}|\boldsymbol{t},\boldsymbol{\theta}) = \text{argmax}_{\boldsymbol{\theta}}\left(-\frac{1}{2}\boldsymbol{y}^{\mathrm{T}}\boldsymbol{K}^{-1}\boldsymbol{y} - \frac{1}{2}\log|\boldsymbol{K}| - \frac{N}{2}\log 2\pi\right) \tag{6}$$

where N is the number of data points, $y = [u, \dot{u}, \ddot{u}]^{\mathrm{T}}$ collects the training data and K is a block-covariance matrix calculated via the kernel formulations,

$$\boldsymbol{K} = \begin{bmatrix} k_{uu}(\boldsymbol{t},\boldsymbol{t}') + \sigma_{n,u}^2\delta(\boldsymbol{t},\boldsymbol{t}') & k_{u\dot{u}}(\boldsymbol{t},\boldsymbol{t}') & k_{u\ddot{u}}(\boldsymbol{t},\boldsymbol{t}') \\ k_{\dot{u}u}(\boldsymbol{t},\boldsymbol{t}') & k_{\dot{u}\dot{u}}(\boldsymbol{t},\boldsymbol{t}') + \sigma_{n,\dot{u}}^2\delta(\boldsymbol{t},\boldsymbol{t}') & k_{\dot{u}\ddot{u}}(\boldsymbol{t},\boldsymbol{t}') \\ k_{\ddot{u}u}(\boldsymbol{t},\boldsymbol{t}') & k_{\ddot{u}\dot{u}}(\boldsymbol{t},\boldsymbol{t}') & k_{\ddot{u}\ddot{u}}(\boldsymbol{t},\boldsymbol{t}') + \sigma_{n,\ddot{u}}^2\delta(\boldsymbol{t},\boldsymbol{t}') \end{bmatrix} \tag{7}$$

for the specific measurement times t. Maximization of Equation (6) is achieved by gradient ascent via quasi-Newton BFGS optimization. Although not explicitly shown, it is worth noting that the derived formulation does not require a regular time-step interval, providing flexibility in cases of missing response time-steps or imperfect sensor synchronization (Tondo et al. 2023b).

2.2 *Force model*

The response of a harmonic oscillator to an arbitrary dynamic loading F is given by the second-order inhomogeneous differential equation

$$m\ddot{u} + 2m\zeta\omega_n\dot{u} + m\omega_n^2 u = F \tag{8}$$

where m is the oscillator's mass, ζ is the damping ratio to critical and ω_n is the oscillator's circular natural frequency. Combining the derived response kernels with the oscillator model from Equation (8) gives rise to a physics-informed cross-covariance model between the dynamic load and the deflection,

$$k_{Fu}(t,t';\sigma_s,\ell) = mk_{\ddot{u}u} + 2m\zeta\omega_n k_{\dot{u}u} + m\omega_n^2 k_{uu} \tag{9}$$

while the models for velocities and accelerations are generated similarly. The force covariance is calculated by applying Equation (8) to the second time index of k_{Fu}, yielding

$$k_{FF}(t,t';\sigma_s,\ell) = mk_{F\ddot{u}} + 2m\zeta\omega_n k_{F\dot{u}} + m\omega_n^2 k_{Fu} \tag{10}$$

2.3 *Force prediction*

The force signal that generated the measured responses can be reconstructed using the trained measurement model from Section 2.1 and the force model from Section 2.2. The joint distribution of the data collected in y and the force vector F is constructed as

$$p(\boldsymbol{y},\boldsymbol{F}) = \mathcal{N}\left(\begin{bmatrix}\boldsymbol{0}\\ \boldsymbol{0}\end{bmatrix}, \begin{bmatrix}\boldsymbol{K} & \boldsymbol{K}_* \\ \boldsymbol{K}_*^{\mathrm{T}} & \boldsymbol{K}_{**}\end{bmatrix}\right) \tag{11}$$

where $K_* = [k_{Fu}(\boldsymbol{t}_*,\boldsymbol{t}'), k_{F\dot{u}}(\boldsymbol{t}_*,\boldsymbol{t}'), k_{F\ddot{u}}(\boldsymbol{t}_*,\boldsymbol{t}')]^{\mathrm{T}}$ and $\boldsymbol{K}_{**} = k_{FF}(\boldsymbol{t}_*\boldsymbol{t}'_*)$, with $\boldsymbol{t}_*$ being the time instants for force prediction. Conditioning the force model on the measurement data yields

$$p(\boldsymbol{F}|\boldsymbol{y}) = \mathcal{N}\left(\boldsymbol{\mu} = \boldsymbol{K}_*^{\mathrm{T}}\boldsymbol{K}^{-1}y, \boldsymbol{\Sigma} = \boldsymbol{K}_{**} - \boldsymbol{K}_*^{T}\boldsymbol{K}^{-1}\boldsymbol{K}_*\right) \tag{12}$$

which defines the prediction's mean values $\boldsymbol{\mu}$ and covariance matrix $\boldsymbol{\Sigma}$ shown in Figure 2.

3 AERODYNAMIC FORCE RECONSTRUCTION

3.1 *Numerical model and aerodynamic analysis*

The model developed for force identification is now used to reconstruct the aerodynamic forces applied to a numerical model of the Great Belt East Bridge in Denmark. A sketch of the suspension bridge, along with its cross-section and the coordinate system for the aerodynamic forces are shown in Figure 3 (top). Modal analysis was carried out after the effects of self-weight considering third order geometric non-linearity were taken into account, and the results were validated with literature reports (Larsen, 1993). A total of 22 vibration modes (c.f. Figure 3,

bottom) were used in the dynamic analysis of the structure, carried out with a sampling rate of f_s = 20 Hz and assuming a modal damping ratio of ζ = 0.5 %.

A reduced order model based on the linear unsteady assumption (Caracoglia & Jones, 2003) is used to numerically calculate the aerodynamic response of the bridge. The mean wind speed was defined as U = 30 m/s. Correlated turbulent wind time-histories are generated following von Kármán spectrum (c.f. Figure 4), assuming turbulence intensities of I_u = 11 % and I_w = 6 %, and turbulence length scales of L_u = 108 m and L_w = 60 m. Buffeting analysis was carried out assuming Sears' model for aerodynamic admittance, and the cross-section static wind coefficients and aerodynamic derivatives are obtained from Kavrakov & Morgenthal (2018).

Based on the aerodynamic model, the structural modal and global responses are obtained, as shown in Figure 5 for the case of the first bending mode (f = 0.100 Hz).

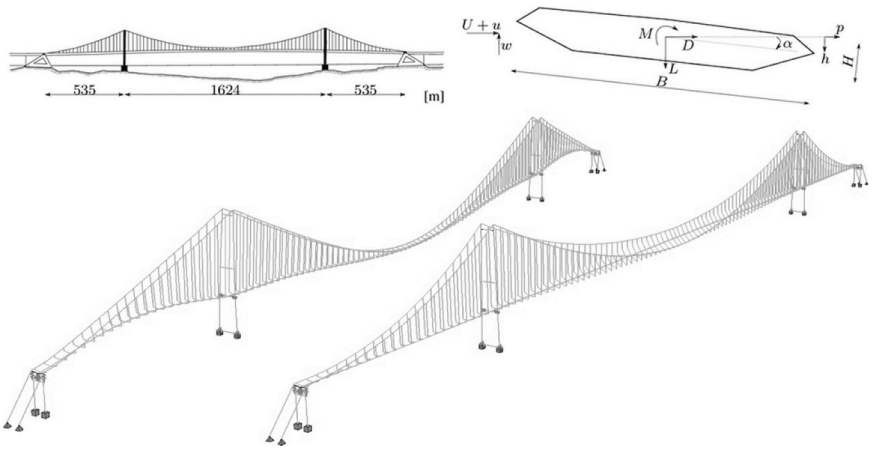


Figure 3. Numerical model of the Great Belt East Bridge. Top: longitudinal schematic with the span lengths (left) and the coordinate system for aerodynamic forces (right). Bottom: the first bending (f = 0.100 Hz, left) and torsional (f = 0.278 Hz, right) mode shapes.

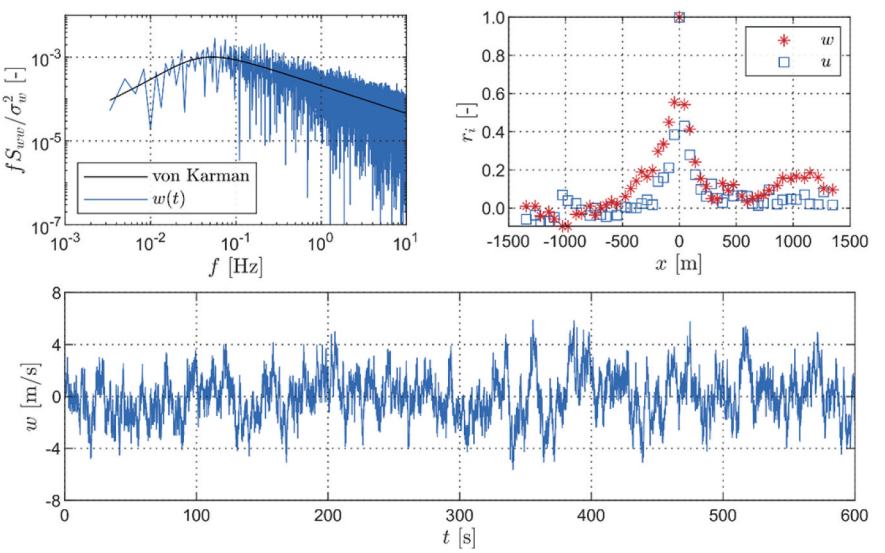


Figure 4. Top: generated turbulence spectrum in the vertical direction w in comparison to von Kármán model (left), and the correlation coefficient along the bridge length w.r.t. the midspan (x = 0 m). Bottom: the generated turbulence signal at midspan.

3.2 *Force reconstruction*

The computed modal responses can now be used as inputs to the physics-informed Gaussian process to recover the dynamic load that excited the structure. For that matter, the responses are initially contaminated with white noise characterized by a signal to noise ratio (SNR) of 20, to simulate the practical aspects of realistic measurement data. In addition, a sparse selection of the noise data was used during training, selected based on a constant interval with a sampling rate of f_s = 1 Hz. The modal responses and selected training points are shown in Figure 5.

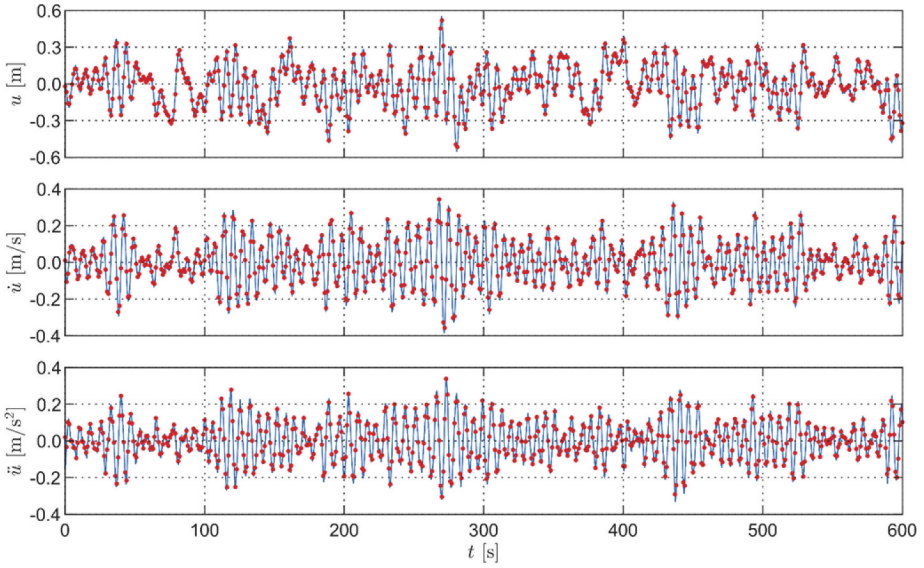


Figure 5. Calculated modal responses (from top to bottom: displacement, velocity, and acceleration) using the LU aerodynamic model and the turbulence characteristics defined in Section 3.1. The red dots represent the training points provided to the GP model.

Once the GP model is trained, the forces can be predicted by leveraging the physical laws built into the machine learning framework. The underlying modal force for the first bending mode shape is shown in Figure 6 (top). A good agreement is observed between the predicted and original forcing signals in a mean sense, despite the true force signal containing multiple harmonic components, governed typically by the structural modal frequencies. The prediction uncertainty range is observed to increase close to the peaks of the predicted forces. If a shorter time window is analysed (cf. Figure 6, bottom left), however, it is evident that the predictions are a smoothened version of the true force, with the GP effectively acting as a low-pass filter of the original signal and capturing high-frequency content by its uncertainty measurement. This is also verified by the power spectral density of the force S_{FF}, as shown in Figure 6 (bottom right), where a good agreement is observed until f = 1 Hz, corresponding to the sampling frequency of the data used for training.

The assessment of prediction quality for all 22 modes is carried out through the mean squared error, measured in relation to the normalized true force. While modal contributions to the global response are relative to both forcing and structural properties, consistent root mean square error (RMSE) values ranging from 0.05 to 0.15 are identified across all modes. Consequently, the predictions exhibit uniform quality levels. It is important to note, however, that this uniformity may not always hold true in practical scenarios, due to the presence of varying degrees of noise within the measurement data.

In addition to force prediction, the integration of the trained physics-informed Gaussian process model with a finite element representation of the structure facilitates the forecasting of global responses and internal forces throughout the training period. This is illustrated in Figure 7, where the case of global displacement at midspan and the internal bending moment at the base of one of

the piers. The high quality of force prediction is evident in the evaluation of global responses, which closely align with the outcomes derived from the original linear unsteady model. A similar behavior is noted in the frequency domain, where responses are accurately estimated up to the sampling frequency of the training data provided to the Gaussian process model.

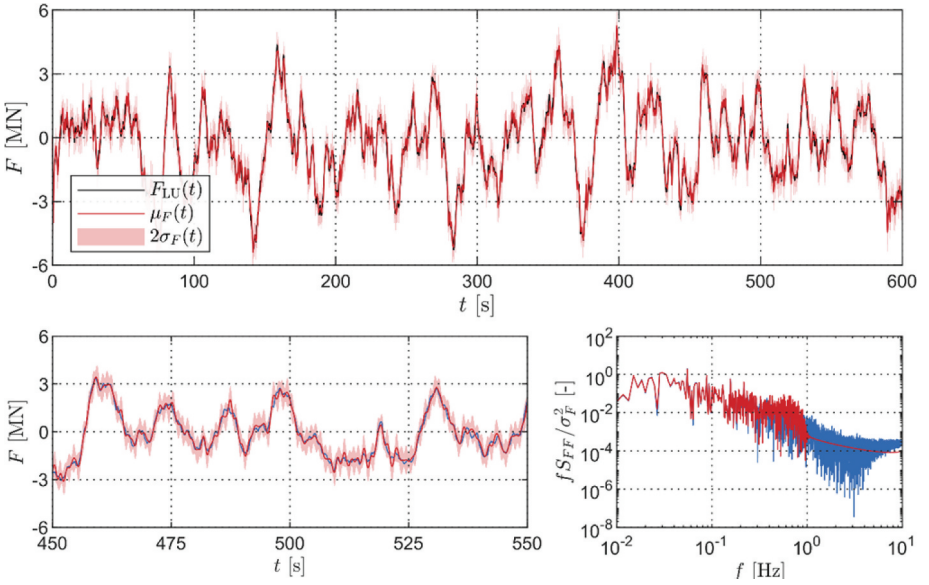


Figure 6. Top: the true modal force for the aerodynamic analysis according to the LU model and the mean and uncertainty ranges of the physics-informed Gaussian process predictions. Bottom: a detailed depiction of the predicted force signal (left) and the comparison of the power spectral density of the true and predicted mean force (right).

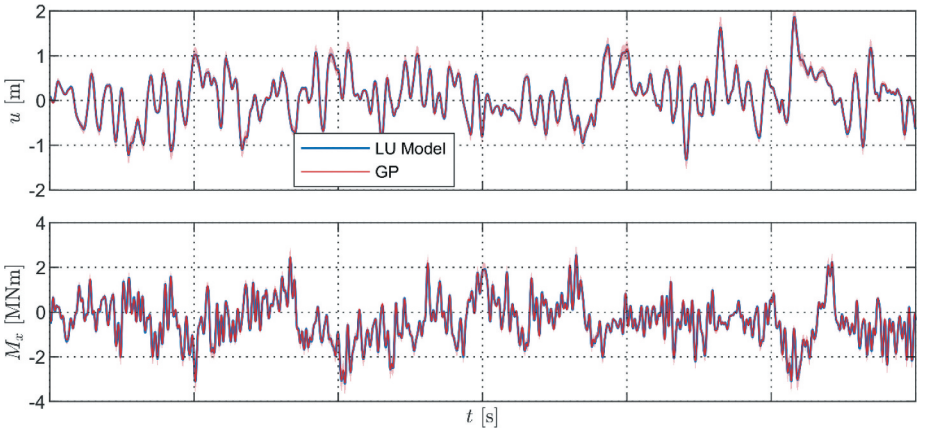


Figure 7. Top: the vertical response at midspan in global coordinates, for the original LU model and the reconstructed response using the forces identified with the Gaussian process (GP) model. Bottom: the bending moment at one of the pier supports.

4 CONCLUSIONS

In summary, an innovative stochastic method for reconstructing dynamic forces based on sensor measurement data is introduced, constructed utilizing Gaussian process regression for machine

learning, incorporating established differential equations to capture relationships between physical properties. This hybrid formulation facilitates the integration of heterogeneous and multi-fidelity data during the training process. Unlike conventional optimization problems where regularization schemes often pose challenges, our approach circumvents such issues through the inherent trade-off between data fitting and model complexity afforded by the Gaussian likelihood. Additionally, this choice ensures complete analytical tractability for posterior sampling.

Force predictions were compared and discussed in relation to the standard linear unsteady model for aerodynamic loads. It is noteworthy that the model's capacity to represent a broad spectrum of frequency content is contingent upon the sampling rate of the training data. For high-frequency training data, challenges arise as the optimization for Gaussian processes exhibits scalability issues with an increasing number of training points. Although the derived model seamlessly accommodates cases of missing steps or unsynchronized training data, these scenarios were not specifically addressed in this study.

Furthermore, the integration of probabilistic force predictions with a finite element solver provides a statistical perspective on global responses and, consequently, internal forces. The outcomes of this analytical approach yield valuable insights for evaluating structural performance, enabling condition diagnostics, and facilitating prognosis. In conclusion, the presented framework serves as a robust statistical tool for dynamic force reconstruction with direct applications in model validation and structural health monitoring. While the results herein pertain to a specific case study, we anticipate the generalizability of the framework to various structural systems and dynamic loading properties.

REFERENCES

Caracoglia, L., Jones, N. 2003. Time domain vs. frequency domain characterization of aeroelastic forces for bridge deck sections. Journal of Wind Engineering and Industrial Aerodynamics 91, 371–402.

Farrar, C., Lieven, N. 2006. Damage prognosis: the future of structural health monitoring. Philosophical Transactions of the Royal Society A. 365: 623–632.

He, W. Y., Wang, Y., Zhu, S. 2018. Adaptive reconstruction of a dynamic force using multiscale wavelet shape functions. Shock and Vibration, 2018

Kavrakov, I., Morgenthal, G. 2018. A synergistic study of a CFD and semi-analytical models for aeroelastic analysis of bridges in turbulent wind conditions. Journal of Fluids and Structures 82, 59–85.

Liu, Y., Wang, L., Kaixuan, G., Li, M. 2022. Artificial Neural Network (ANN)-Bayesian Probability Framework (BPF) based method of dynamic force reconstruction under multi-source uncertainties. Knowledge-Based Systems, 237, pp. 107796.

Larsen, A. 1993. Aerodynamic aspects of the final design of the 1624 m suspension bridge across the Great Belt. Journal of Wind Engineering and Industrial Aerodynamics, 48(2-3), 261–285.

Nonomura, T., Shibata, H., Takaki, R. 2018. Dynamic mode decomposition using a Kalman filter for parameter estimation. AIP Advances, 8, 10, pp.105106.

Ø.W. Petersen, O. Øiseth, E. Lourens. 2022. Wind load estimation and virtual sensing in long-span suspension bridges using physics-informed Gaussian process latent force models. Mechanical Systems and Signal Processing, 170, pp. 108742.

Rasmussen, C., Williams, C. 2006. Gaussian Processes for Machine Leaning. Cambridge, MA: The MIT Press.

Sanchez, J., Benaroya, H. 2014. Review of force reconstruction techniques. Journal of Sound and Vibration, 333, 14, pp. 2999–3018.

Tondo, G.R., Kavrakov, I., Morgenthal, G. 2022. Physics-informed Gaussian process model for Euler-Bernoulli beam elements. IABSE Symposium: Challenges for Existing and Oncoming Structures, Prague, pp. 445–452.

Tondo, G.R., Rau, S., Kavrakov, I. and Morgenthal, G. 2023a. Stochastic stiffness identification and response estimation of Timoshenko beams via physics-informed Gaussian processes. Probabilistic Engineering Mechanics, 74, p.103534.

Tondo, G.R., Kavrakov, I., Morgenthal, G. 2023b. A physics-informed machine learning model for reconstruction of dynamic loads. IABSE Symposium: Long span bridges, Istanbul, pp. 315–322.

Wang, L., Cao, H., Han, X., Liu, J., Xie, Y. 2015. An efficient conjugate gradient method and application to dynamic force reconstruction, Journal of computational science, 8, pp. 101–108.

Bridge Maintenance, Safety, Management, Digitalization and Sustainability – Jensen, Frangopol & Schmidt (eds)
© 2024 The Author(s), ISBN 978-1-032-77040-6
Open Access: www.taylorfrancis.com, CC BY-NC-ND 4.0 license

A multi-task deep learning-based framework for structural details and corrosion detection in steel bridges

M. Zaker Esteghamati
Assistant Professor, Department of Civil and Environmental Engineering, Utah State University, Logan, UT, USA

M. Hassan Ahmed
Graduate Student, Department of Civil and Environmental Engineering, Utah State University, Logan, UT, USA

S. Young
Assistant Professor, Department of Civil and Environmental Engineering, Utah State University, Logan, UT, USA

M. Halling
Professor, Department of Civil and Environmental Engineering, Utah State University, Logan, UT, USA

ABSTRACT: In 2021, 42% of bridges in the United States were used beyond their design life, incurring a repair cost of approximately $125 billion. To reduce future repair costs of bridges, novel inspection methods have been recently proposed that use unoccupied aerial vehicles to inspect bridge defects, where a computer vision-based model processes the data to assess bridge condition. Although this technology can provide significant advantages in decreasing inspection costs and labor, inspection accuracy relies on the quality of images and the computer vision model. Therefore, this study develops a multi-task deep learning framework that combines object detection and semantic segmentation models to detect important structural details and quantify corrosion level in steel bridges with high precision and speed (i.e., inference time). The framework leverages high-performing computing and high-definition images to minimize resizing effects on model accuracy. For each module, two different deep learning architectures were developed and compared in terms of accuracy and inference time. The results show the efficiency of deep learning models for both tasks. For an intersection over a union threshold of 50%, the object detection models of YOLOv8 and SSD RetinaNet50 achieve mean average precision of 96.6% and 85.2%, respectively. In addition, the segmentation models of YOLOv8 and DeeplabV3+ achieved an F1 score of 61.5% and 28%, respectively.

1 INTRODUCTION

In 2021, 42% of bridges in the United States were used beyond their design life, and were projected to incur a repair cost of approximately $125 billion (Abdallah et al., 2022). Therefore, ongoing monitoring and inspection are critical to allocating funding for maintenance and repair activities and ensuring bridge serviceability. These inspections are performed visually for the most part, and if needed, through non-destructive testing. Nevertheless, performing such inspections is costly and complex, requires skilled labor, and could disrupt common functions of bridges (e.g., lane closure). These issues are further compounded by limited financial resources and the large bridge inventories.

Unoccupied aerial vehicles (UAVs) have been proposed as an innovative bridge inspection tool to aid with visual inspection of large bridge inventories. UAV-based inspection may be more economical, efficient, and allows for a safer inspection with little disruption to bridge function (Seo et al., 2018). Such advantages have led to the emergence of a wealth of research and the favorable reception of UAVs by different federal agencies and state departments of transportation.

DOI: 10.1201/9781003483755-417

UAV-based inspection video and imagery are often post-processed using computer vision (CV) techniques to assess the bridge conditions. Subsequently, the quality of the inspection relies on the accuracy of the employed CV technique. The applied CV techniques can be classified into three main categories (Spencer et al., 2019): (1) image classification, which classifies an entire image into a specific class, (2) object detection, which assigns all possible objects of interest in an image into their corresponding classes, and (3) semantic segmentation, which divides all the pixels of an image into several segments, where each segment is assigned to its corresponding class.

Recently, deep learning models were proposed to perform CV tasks. For example, Atha and Jahanshahi compared several convolutional neural network architectures to identify corrosion on metallic surfaces (Atha & Jahanshahi, 2018). Burton et al. developed a deep learning algorithm to detect corrosion using automated segmentation without the need for per-pixel labeled data, albeit the model showed limitations with respect to non-uniform illumination and shadows (Burton et al., 2022). Lastly, Bianchi and Hebdon developed a semantic segmentation model based on Deeplab architecture for corrosion identification in steel bridges (Bianchi & Hebdon, 2022).

This paper develops a multi-task deep learning framework to process UAV-based steel bridge inspection. The framework aims to assist the inspector in detecting important structural steel details and quantifying corrosion level in the detected details. This multi-task approach paves the path towards a more "context-aware" CV model, as the presence of corrosion in non-critical details will not largely affect the bridge condition. Additionally, the framework combines low inference time and high accuracy to facilitate a real-time inspection approach.

2 METHODOLOGY

2.1 *Overview*

The developed framework comprises two modules: (a) an object detection module, and (b) a corrosion segmentation model. The first module aims to identify four critical details in steel bridges, including bearing, out-of-plane stiffeners, gusset plates, and cover plate termination. In contrast, the second module aims to detect the corroded area of images. The combined output from the two modules will be aggregated to generate actionable information on bridge condition.

2.2 *Data augmentation*

The COCO-Bridge-2021+ dataset (Bianchi et al., 2021) was selected to train object detection models. Before training, the dataset was checked, and minor corrections were made on (i) the annotation XML file of original images to match the actual image size, and (ii) removing zero-size image dimensions of several annotations. In addition, the first 436 images from the COCO-Bridge-2021+ dataset were collected and annotated for the corrosion segmentation model. The corrosion annotation was restricted to only steel elements, and any corrosion in the reinforcement of the concrete elements was ignored. In addition, only corrosions classified as severe and poor (AASHTO, 2019) were annotated since they can lead to section loss. Therefore, the annotation

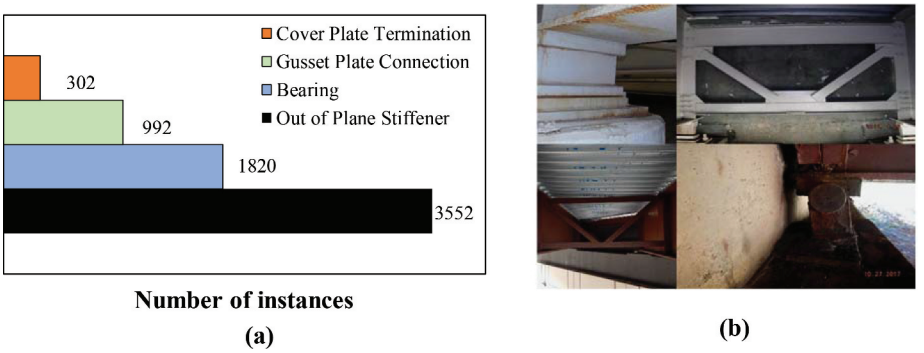


Figure 1. (a) Number of difference instances in the dataset, (b) Example of mosaic data augmentation.

did not include instances with freckled rust (fair condition). As shown in 1.a the selected dataset is highly imbalanced (i.e., there are vastly different object instances for different classes). To address this issue, two different remedies were used: (1) various data augmentation techniques were applied, and (2) dual focal loss (Hossain et al., 2021) was used as the objective of CV models.

The resulting datasets (object detection and corrosion) were augmented, which is the process of increasing the size of a training dataset by manipulating the images using different CV techniques. This process improves the model's general performance and reduces the effect of overfitting. Among various techniques, a combination of mosaic, horizontal flip, and adjusted brightness were used. Mosaic augmentation combines four images of the training dataset, merges them into one image, and then randomly crops the image to get the final output image. Mosaic augmentation helps models identify details, particularly smaller details, in different locations of any image. Figure 1.b shows a sample augmented image after applying the mosaic technique. Horizontal flipping mirrors an image about its vertical axis, increasing the dataset's size without confusing the trained model in this application. For example, another technique (vertical flipping) could confuse the training as an inverted bridge is not physically meaningful, leading to poor accuracy on the test set. Lastly, adjusted brightness was randomly applied with a tolerance of 20% to images to account for different lighting conditions. The 20% threshold was chosen to restrict brightness and prevent losing image details.

2.3 *Training platform*

Deep-learning frameworks handle images as tensors of rank 4 (i.e., several three-dimensional matrices on different channels). Such dimensionality leads to computational challenges in training CV models using CPUs. Therefore, this study used the graphical processing unit (GPU) of the Lonestar6 supercomputer at the Texas Advanced Computing Center (TACC). Lonestar6 supports three Nvidia A100 PCIE GPUs, each with 40 GB RAM for a single GPU node. Due to the high computational power of Lonestar6, object detection models were trained on high-definition images with 1024x1024 size with no memory failure issues, whereas segmentation models were trained on relatively smaller images with 512x512 size.

2.4 *Model evaluation*

The performance of deep learning models can be evaluated through different metrics, dictated by the problem definition and its associated loss functions. Intersection over union (IOU) is the crux of performance evaluation metrics in object detection and segmentation models. IOU is defined as the intersection between the model's prediction and ground truth bounding box/segmentation mask divided by the union of the same parameters, where ground truth refers to the object in the image.

This study uses mean average precision (mAP) as the primary evaluation metric for object detection models. mAP is a widely used performance metric based on IOU, precision (i.e., the ratio of true positive to the total predicted positive), and recall (the ratio of true positive to the actual positive cases). The area under the precision-recall curve is the average precision for a specific class, where mAP provides the mean of average precision over different classes. mAPs are typically represented at IOU thresholds that differentiate between a true positive and a false positive for a given prediction. For example, a prediction with an IOU larger than the IOU threshold is considered true positive. Here, two IOU thresholds were chosen: (a) mAP50 (i.e., IOU at 50%), and (b) mAP50-95 (i.e., the average mAP using different IOU thresholds ranging from 50% to 95% with 5% increments). For semantic segmentation, the F1 score was used, which is the harmonic mean of precision and recall.

3 OBJECT DETECTION MODULE

Two different object detection models were examined for this module, as will be discussed next.

3.1 *Single-shot multi-box object detection model*

Single-shot multi-box object detection (SSD) model is a fast architecture since it uses only one stage to detect objects in a certain image. An SSD RetinaNet50 was used as the first model for the object detection module. The selected SSD model uses ResNet50 as its feature extractor in a feature pyramid network architecture.

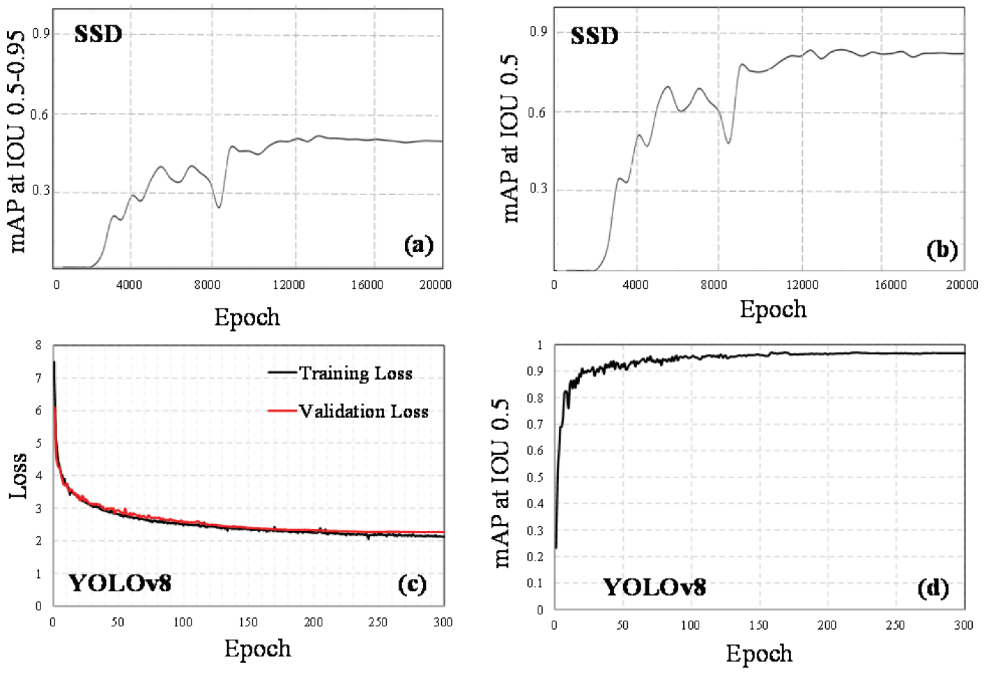


Figure 2. (a) mAP50 and (b) mAP50-95 for SSD model. (c) loss function and (d) mAP50 for YOLOv8 object detection model.

Transfer learning was applied to improve model accuracy since the COCO-Bridge-2021+ dataset is relatively small (i.e., 1470 images). The transfer learning concept uses a pre-trained model from a larger dataset as the starting point to train the same model on another smaller dataset. A pre-trained SSD RetinaNet50 model on the Microsoft COCO dataset was used from Tensorflow 2 Detection Model Zoo to train the current SSD model.

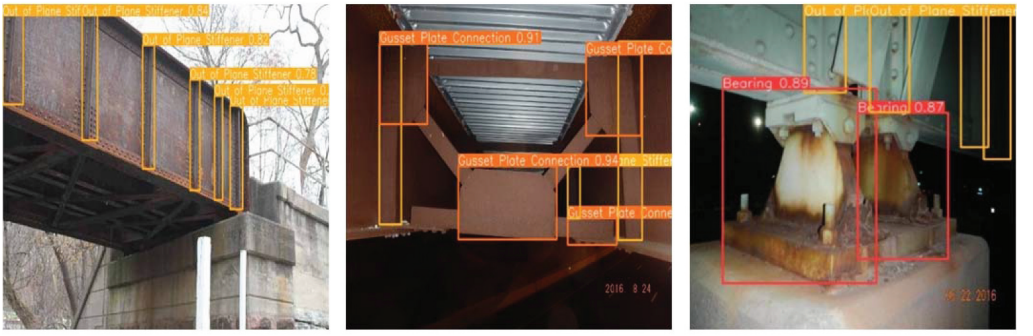
The training was carried out using the object detection API of TensorFlow through a configuration pipeline in a text format to alter training hyperparameters. First, two TensorFlow records (i.e., a binary file format that TensorFlow supports, which stores an image dataset and its corresponding annotation ground truth bounding boxes efficiently in one file) were generated. The first record was for the training dataset, and the second one was for the testing dataset. Second, all training hyperparameters were set through a configuration file.

SSD model was trained using a stochastic gradient descent optimizer with a momentum of 0.9. The learning rate is a cosine function that decays from 0.005. The anchor boxes aspect ratios used were 1.0, 2.0, 0.5, 0.33, 3.0, 0.25, and 0.2. These values were selected after plotting all ground truth bounding boxes' aspect ratios in a histogram, as most objects have an aspect ratio of less than 0.4. Consequently, aspect ratios of 0.25 and 0.20 were added to enable the SSD model to detect slender objects. Non-maximum suppression stage had an IOU of 0.5 and a confidence threshold of 0.25. The non-maximum suppression stage is the final stage in most object detection models that filters all predictions made by the SSD model. A rectified linear function (RELU) was used as the activation function to introduce the nonlinearity in the deep learning mode. Batch size was taken as 30, which shows the number of images processed into the GPU in a single iteration.

A weight regularization layer and a dropout regularization were applied to limit the overfitting issue. Weight regularization adds a penalty term to the total loss to penalize large weight, reducing the effect of overfitting. Several different rates were examined for weight regularization, and a rate of 0.01 was found to be the optimum in limiting the overfitting issue. In contrast, the dropout regularization layer drops a specific percentage of the network weights to zero to constrain model complexity and reduce overfitting, where a dropout rate of 60% was applied to the developed SSD model.



(a) SSD model



(b) YOLOv8 models.

Figure 3. Examples of inferences for (a) SSD and (b) YOLOv8 object detection models.

Figures 2.a and 2.b show mAP50 and mAP50-95 for the SSD model. As shown in Figures 2. a and 2.b, the SSD model reaches a maximum mAP50 and mAP50-95 of 85.2% and 52.3%, respectively. Figure 3.a shows several examples of SSD inferences. The average inference time was 486 *ms* with a standard deviation of 65 *ms*. It can be observed that SSD fails to detect all the slender objects (e.g., out-of-plane stiffener) in these images.

3.2 *YOLOv8 object detection model*

"You only Look Once (YOLO)" object detection model was the second model to be examined (Wong et al., 2019), where YOLO version 8 (YOLOv8) was selected. YOLOv8 provides two advantages over SSD to tackle the COCO-Bridge-2021+ challenges: (1) an anchor-free object detector (i.e., no need for optimizing the anchor boxes aspect ratio to obtain better results), and (2) dual focal loss function which has a better performance for datasets with class imbalance issue. Dual focal loss is a variant of the cross-entropy loss function, providing the capability to focus on classes in a specific dataset with fewer instances. It should be mentioned that dual focal loss was developed to address the vanishing gradient problem encountered in focal loss. The "nano" version of YOLOv8 was selected due to its higher speed than other versions of YOLOv8. A high-level API was used for model training, evaluation, and prediction. The same stochastic gradient descent optimizer with a momentum of 0.9 was used. A cosine function that decays from 0.004 was used for the learning rate. A dropout regularization was applied with a dropout rate of 50%. Similarly, a weight decay of 0.001 was used to limit overfitting. Non-maximum suppression stage had an IOU of 0.5 and a confidence threshold of 0.25. The batch size was 30.

Figures 2.c and 2.d show the loss curves for training and evaluation sets and mAP50 of the YOLOv8 object detection model. Figure 2.c indicates that the model does not exhibit overfitting, whereas Figure 2.d shows that the model achieved a mAP50 of 96.6%. It should be noted that the

model's mAP50-95 was 75.95%. Figure 3.b shows the YOLOv8 inferences for the same images as SSD. Overall, the model shows higher detection capability, as exhibited by identifying slender objects in the background and overshadowed. The mean inference time for this model was 180 *ms* with a standard deviation of 53 *ms*.

4 SEMANTIC SEGMENTATION MODULE

Two different semantic segmentation models were examined for this module, as will be discussed next.

4.1 *Deeplab V3+ segmentation model*

Deeplab V3+ (Chen et al., 2018) was used as the first segmentation model and trained using Keras API. Keras API is a wrapper for the TensorFlow deep-learning framework that facilitates training, evaluation, and prediction processes.

A combination of Dice loss function and focal loss function was used. The Dice loss function calculates the difference between the ground truth mask and the predicted mask during training. Therefore, the Dice loss function reduces the difference and achieves object localization. Conversely, the focal loss function classifies if a pixel belongs to corroded areas.

Deeplab V3+ was trained by a stochastic gradient descent optimizer with a momentum of 0.9 and a learning rate that decays from 0.004 to 0.002. A dropout regularization was applied with a dropout rate of 50%. In addition, a weight decay of 0.01 has been applied to the optimizer. Batch size was taken as 30.

Figure 4.a shows the F1 score of the Deeplab V3+ model on the test set. As shown in Figure 4. a, the F1 score reaches only 28%. Figure 5.a shows several examples of Deeplab V3+ inferences. Overall, the model fails to detect corroded areas completely, particularly for shadowed areas and where a combination of freckles and severe corrosion exists. It should be noted that the mean inference time for this model was 284 *ms* with a standard deviation of 17 *ms*.

4.2 *YOLOv8 segmentation model*

YOLOv8 also provides a segmentation version, which was used to identify corrosion. The YOLOv8 segmentation model was trained using a stochastic gradient descent optimizer with a momentum equal to 0.9 and a learning rate in terms of a cosine function that decays from 0.005. A dropout regularization was applied with a dropout rate of 50%. In addition, a weight decay of 0.015 has been applied to the optimizer. Non-maximum suppression stage had an IOU of 0.5 and a confidence threshold of 0.25. The batch size was 60.

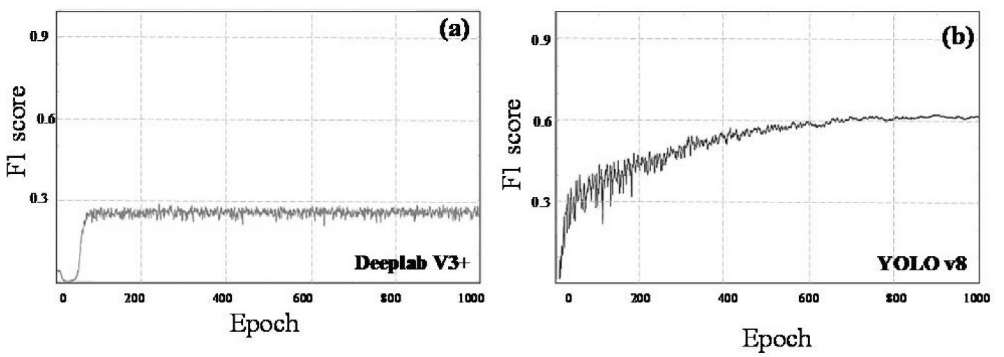


Figure 4. Comparison of model accuracy for (a) Deeplab V3+ and (b) YOLO v8 semantic segmentation models.



(a) Deeplab V3+



(b) YOLOv

Figure 5. Examples of inferences for (a) Deeplab V3+ and (b) YOLOv8 segmentation models.

Figure 4.b shows the F1 score of the YOLOv8 segmentation model, which reaches 61.5%. Figure 5.a shows several examples of YOLOv8 segmentation model inferences. While the model performs better than the Deeplab V3+ model, it still misses smaller corroded areas. It should be noted that the mean inference time for this model was 97 *ms* with a standard deviation of 31 *ms*.

5 CONCLUSION

This paper presented a novel multi-task deep learning framework to identify several important details of steel bridges and quantify the corrosion level at those details. The framework comprises an object detection and a semantic segmentation module that works in parallel to generate "context-aware" condition data. Different deep learning models were developed and compared for each module, and the results were compared in terms of accuracy and inference time. The following summarizes the main findings:

- For the object detection module, YOLOv8 provided 84.7% higher accuracy in terms of mAP at IOU of 0.5 and 62.9% faster inference time than the SSD model.
- For the semantic segmentation module, YOLO v8 provided 119.6%% higher accuracy in terms of F1 score and 65.8%% lower inference time than the Deeplab V3 + model.
- The application of dual focal loss and augmentation could alleviate accuracy issues of highly imbalanced small datasets of structural details for object detection tasks.

REFERENCES

AASHTO. (2019). *Manual for Bridge Element Inspection*.

Abdallah, A. M., Atadero, R. A., & Ozbek, M. E. (2022). A State-of-the-Art Review of Bridge InspectionPlanning: Current Situation and Future Needs. *Journal of Bridge Engineering*, *27*(2), 03121001. https://doi.org/10.1061/(ASCE)BE.1943-5592.0001812

Atha, D. J., & Jahanshahi, M. R. (2018). Evaluation of deep learning approaches based on convolutional neural networks for corrosion detection. *Structural Health Monitoring*, *17*(5), 1110–1128. https://doi.org/10.1177/1475921717737051

Bianchi, E., Abbott, A. L., Tokekar, P., & Hebdon, M. (2021). COCO-Bridge: Structural Detail Data Set for Bridge Inspections. *Journal of Computing in Civil Engineering*, *35*(3), 04021003. https://doi.org/10.1061/(ASCE)CP.1943-5487.0000949

Bianchi, E., & Hebdon, M. (2022). Development of Extendable Open-Source Structural Inspection Datasets. *Journal of Computing in Civil Engineering*, *36*(6), 04022039. https://doi.org/10.1061/(ASCE)CP.1943-5487.0001045

Burton, B., Nash, W. T., & Birbilis, N. (2022). *RustSEG – Automated segmentation of corrosion using deep learning* (arXiv:2205.05426). arXiv. https://doi.org/10.48550/arXiv.2205.05426

Chen, L.-C., Zhu, Y., Papandreou, G., Schroff, F., & Adam, H. (2018). Encoder-Decoder with Atrous Separable Convolution for Semantic Image Segmentation. In V. Ferrari, M. Hebert, C. Sminchisescu, & Y. Weiss (Eds.), *Computer Vision – ECCV 2018* (pp. 833–851). Springer International Publishing. https://doi.org/10.1007/978-3-030-01234-2_49

Hossain, M. S., Betts, J. M., & Paplinski, A. P. (2021). Dual Focal Loss to address class imbalance in semantic segmentation. *Neurocomputing*, *462*, 69–87. https://doi.org/10.1016/j.neucom.2021.07.055

Seo, J., Duque, L., & Wacker, J. (2018). Drone-enabled bridge inspection methodology and application. *Automation in Construction*, *94*, 112–126. https://doi.org/10.1016/j.autcon.2018.06.006

Spencer, B. F., Hoskere, V., & Narazaki, Y. (2019). Advances in Computer Vision-Based Civil Infrastructure Inspection and Monitoring. *Engineering*, *5*(2), 199–222. https://doi.org/10.1016/j.eng.2018.11.030

Wong, A., Famuori, M., Shafiee, M. J., Li, F., Chwyl, B., & Chung, J. (2019). YOLO Nano: A Highly Compact You Only Look Once Convolutional Neural Network for Object Detection. *2019 Fifth Workshop on Energy Efficient Machine Learning and Cognitive Computing - NeurIPS Edition (EMC2-NIPS)*, 22–25. https://doi.org/10.1109/EMC2-NIPS53020.2019.00013

Bridge Maintenance, Safety, Management, Digitalization and Sustainability – Jensen, Frangopol & Schmidt (eds)
© 2024 The Author(s), ISBN 978-1-032-77040-6
Open Access: www.taylorfrancis.com, CC BY-NC-ND 4.0 license

Tests of TIG welded lap joint between Fe-SMA and steel

Zhiyi Zhang, Xuhong Qiang & Xu Jiang*
College of Civil Engineering, Tongji University, Shanghai, China

Ping Jin
Pinghu Urban Development Investment (Group) Co., Ltd, Pinghu, China

ABSTRACT: Iron-based shape memory alloy (Fe-SMA) has been applied to reinforce steel bridges with structural adhesive. However, the adhesive bonding is vulnerable to erosion and elevated temperature, making its reliability doubtful. As a type of ferroalloy, the weldability of Fe-SMA with commonly used structural steel has been verified. Therefore, the study of the lap joint of Fe-SMA and steel by welding is of significance in the field of bridge maintenance. In this paper, a series of mechanical tests of the TIG welded lap joint of Fe-SMA-structural steel Q355 was conducted. Fillet weld length, filler materials, and the thickness of materials were considered to investigate their influence on the mechanical properties of the Fe-SMA-Q355 lap joint. Results indicate that the lap joint has an adequate capacity in tension, which means the prestress caused by the shape memory effect of Fe-SMA can be transmitted by the reasonably designed Fe-SMA-Q355 welded lap joint

1 INTRODUCTION

As a novel material, iron-based shape memory alloy (Fe-SMA) has become a hotspot in civil engineering because of its unique shape memory effect. Prestress can be easily obtained after pre-stretching, anchoring, and heating according to the reversible martensite phase transformation (Cladera et al. 2014). Compared with the conventional reinforcement method, there is no need for complex tensioning equipment in the process of prestress production, reducing the space demand and workload on site. Researchers have applied the Fe-SMA reinforcement system to the reinforcement of steel structures (Izadi et al. 2018a, Izadi et al. 2018b, Qiang et al. 2023a) and concrete structures (Rojob & El-Hacha 2018, Czaderski et al. 2014), having achieved meaningful theoretical and practical results.

Further, taking advantage of the low space requirements of Fe-SMA reinforcement, Wu (Qiang et al. 2023b) successfully applied Fe-SMA to the crack repair of the steel bridge diaphragm in Sutong Bridge in Jiangsu, China. Transmitting the compression prestress by structural adhesive, the local stress amplitude and stress concentration were effectively reduced, with a noticeable decline in the fatigue notch factor. However, the reliability of adhesive connections in humid environments especially applied to bridges, remains questionable and requires further verification.

Welding is one of the commonly used connection methods between metals in civil engineering. Its low cost, convenient operation, and high-temperature resistance make it have great potential in the application of the Fe-SMA reinforcement system. Regarding similar metals, the weldability of Fe-SMA has been verified utilizing TIG welding (Dong et al. 2006, Druker et al. 2015, Lin et al. 2000)), electron beam welding (Dong et al. 2006), and laser welding (Zhou et al. 2010, Zhou et al. 2012). For dissimilar metals, Zhou (Zhou et al. 2015) and Liu (Liu et al. 2020) used laser welding to connect Fe-SMA with 304 stainless steel, achieving high-quality joints by optimizing technological parameters, and Sun (Sun et al. 2002) used flash butt welding to connect Fe-SMA with 45 steel, a kind of carbon structural steel.

*Corresponding author: jiangxu@tongji.edu.cn

DOI: 10.1201/9781003483755-418

So, it is reasonable to propose a welded Fe-SMA reinforcement system, where the welded connection between Fe-SMA and structural steel plays an important role. The feasibility of the welded connection is an important foundation for the establishment of the whole reinforcement system. Further, the mechanical properties of the welded connection directly determine the upper limit of the transmitting prestress, thus affecting the system's efficiency. The authors have conducted a related foundational work (Qiang et al. 2023c) about the microstructure and mechanical properties of the butt welded joint between Fe-SMA and structural steel Q235 (a kind of mild steel commonly used in recent 20 years in China). TIG welding was used due to its low heat input, high quality, and stability of electric arc. Results indicate that the joints with proper welding parameters and filler materials were well-formed and had adequate capacity to transmit the reinforcement prestress.

Different from the common butt joint form in weldability verification research, the connection of the Fe-SMA reinforcement system is closer to the lap joint form, and its structure, stress, and influencing factors are also different. So, in this paper, the form of the lap joint which is closer to the actual situation has been prepared and their mechanical properties have been tested. Influencing factors such as fillet weld length, filler material, and thicknesses of base materials have been considered.

2 TEST PROCEDURE

2.1 *Materials*

The proposed welded Fe-SMA reinforcement system as the study object is simplified as a lap joint with a transverse fillet weld (illustrated in Figure 1) to test its mechanical properties. Meanwhile, a welded joint can usually be simplified into three parts: two sides of base materials and the filler as the connection. Thus, there are three types of materials used in this research: Fe-SMA (as the reinforcement material to produce the stress), Q355 (as the structural material), and ER309L (as the filler material).

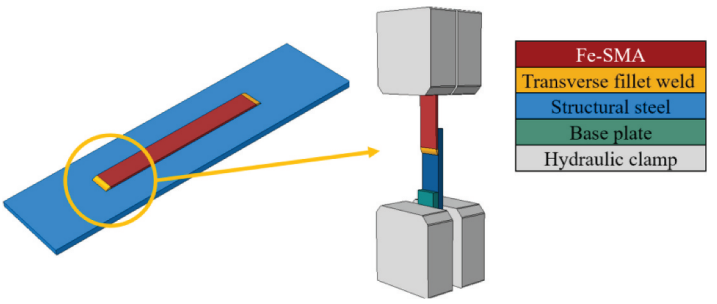


Figure 1. Simplified study object.

The Fe-SMA used in this study was invented by our research group and manufactured by smelting in the vacuum introduction furnace and then preparing by hot forging process with a width of 106 mm. To consider the influence of Fe-SMA's thickness on the performance of welded joints, two thicknesses including 1.5 mm and 3 mm are selected.

As the most commonly used structural steel in China, Q355 is a type of low-alloy structural steel. The letter "Q" in its name "Q355" means yield strength, and "355" indicates its grade with the specified value. It can be said that the Chinese structural steel Q355 is highly similar to the European structural steel S355. Considering the usage scenario of the Fe-SMA reinforcement system, Q355 is selected to represent the structural material in bridge.

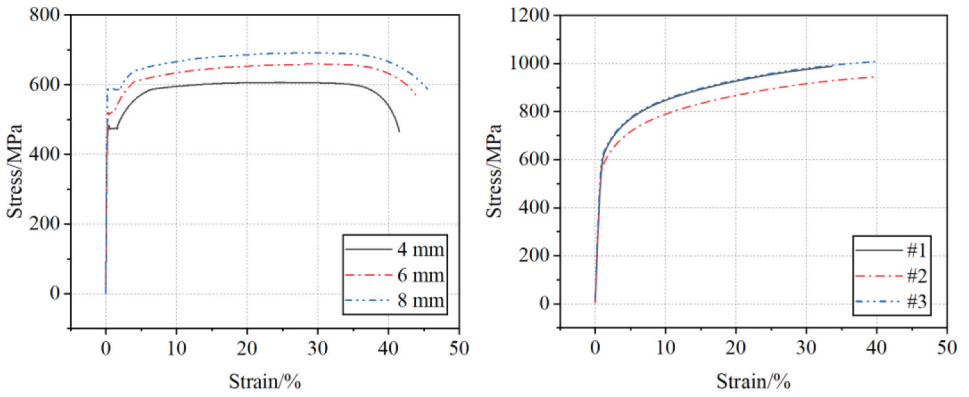
According to the previous research (Qiang et al. 2023c), ER309L is selected to be the filler material here due to the uniform fusion zone transition, smooth hardness changes, and similar strength to base materials. The ER309L welding wires with a diameter of 2 mm were used to match the size of the transverse fillet weld. Besides, considering that Fe-SMA is also a kind of

ferroalloy, the author tentatively tried to use self-developed Fe-SMA wire, cut from the base material, as the filler material with a base size of 1.5 mm × 1.5 mm. The chemical composition of all test materials is shown in Table 1.

Table 1. Chemical composition of test materials (unit: mass fraction %).

Material	C	Mn	Si	Cr	Ni	Nb
Fe-SMA	0.1	15	4.5	10	5	0.03
Q355	0.15	0.58	0.14	0.026	0.009	/
ER309L	0.019	2.1	0.54	23.26	13.73	/

To obtain the mechanical properties of the base materials, pretests were conducted. The stress-strain curves of Fe-SMA and Q355 are shown in Figure 2. The elastic modulus, yield strength, ultimate strength, and breaking elongation of Fe-SMA, Q355 (obtained from the pretest), and ER309L (obtained from the product warranty) are shown in Table 2.



(a) Q355 (b) Fe-SMA

Figure 2. Stress-strain curves of Q355 and Fe-SMA.

Table 2. Mechanical properties of test materials.

Material	E/GPa	σ_s/MPa	σ_u/MPa	δ/%
Fe-SMA	166.0	496.3	980.1	37.6
Q355-4 mm	260.1	474.5	606.9	41.1
Q355-6 mm	223.7	516.9	660.3	43.8
Q355-8 mm	264.2	587.1	691.1	45.5
ER309L	/	/	580.0	39.0

2.2 *Specimen preparation and test setup*

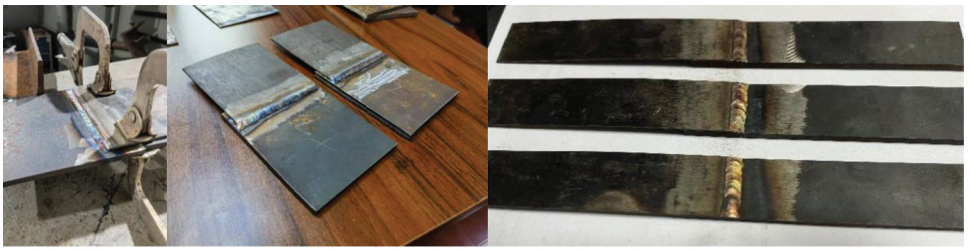
After pre-trial, direct current with optimizing welding parameters was used in lap joint with higher current for better penetration, different from the pulse current used in TIG welded butt joint between Fe-SMA and structural steel Q235 (Qiang et al. 2023c), shown in Table 3.

The whole process of specimen preparation is shown in Figure 3. First, to ensure the welding continuity and the quality stability of the fillet weld, a piece of Fe-SMA plate with a width of 106 mm and a steel plate slightly wider than 106 mm were welded with ER309L welding wire to

Table 3. Welding parameters.

Current/A	Voltage/V	Welding speed/(mm·s^{-1})	Shielding gas flow/(L·min^{-1})	Shielding gas concentration
110	11-13	106/90	15	Ar-99.99%

obtain a large lap welding plate (Figure 3(b)). The lap length with little effect on the stress distribution of the joint is designed to be 25 mm. At the beginning of the welding, the initial temperature is relatively low. Thus, the heating of the base material and the formation of the molten pool will affect the stability of heat input, increasing the reinforcement at the initial section of the fillet weld. Then, at the end of the welding, the final section of the fillet weld should be filled with an arc pit before the extinguishing of the welding arc, making it not lower than the surface of the weld. Therefore, the quality and strength of the welding at the beginning and end of the fillet weld are discrete. So, the specimens were cut from the middle continuous section (Figure 3(c)) to eliminate the influence by discarding the start and the end sections.



(a) welding process (b) welding plate (c) cutting specimen

Figure 3. Specimen preparation.

To explore the possibility of transmitting prestress produced by Fe-SMA in the Fe-SMA reinforcement system, four factors affecting the tensile properties of the lap joint are considered in the test: first one is the fillet weld length, highly correlated with the length of the tensile part. The second one is the thickness of the steel, which may influence the formation of the molten pool and the stress distribution of the fillet weld on the side of the steel. The third one is the thickness of Fe-SMA, associated with the height and size of the fillet weld. The fourth one is the filler material, directly influencing the strength of the fillet weld, which is regarded as the weakness of the lap joint. The definitions of all design dimensions of specimens are plotted in Figure 4, and all parameters are listed in the group shown in Table 4.

After the specimen preparation, the tensile tests with a tensile velocity of 1.5 mm/min until the specimen fractured were carried out through the MTS universal testing machine in the Fire Safety of Engineering Structures Testing Division of the State Key Laboratory of

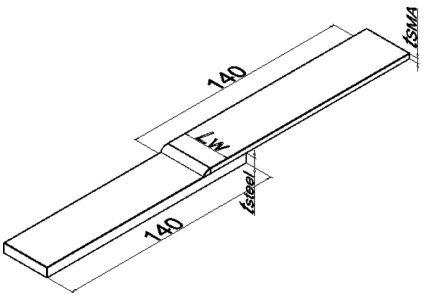


Figure 4. Dimensions of the specimens.

Table 4. Design parameters of all specimens.

Group	No.	t_{SMA}/mm	t_{steel}/mm	L_w/mm	Filler material
Control	DH3-6-30-A	3	6	30	ER309L
Length	DH3-6-10-A	3	6	10	
	DH3-6-20-A	3	6	20	
	DH3-6-40-A	3	6	40	
Steel thickness	DH3-4-30-A	3	4	30	
	DH3-8-30-A	3	8	30	
SMA thickness	DH1.5-6-30-A	1.5	6	30	
Filler material	DH3-6-30-B	3	6	30	Fe-SMA

Disaster Reduction in Civil Engineering. To reduce the deviation of specimens caused by structural eccentricity, a steel base plate with the same thickness as the steel plate was set on the side of the clamping end of the steel (shown in Figure 1).

3 TEST RESULTS AND DISCUSSION

3.1 *Test results*

Figure 5 shows the deformation of the lap joint specimen during tension. In the beginning, the specimen was set straight for tension. After bearing a minor load, the steel plate adjacent to the fillet weld became bent and the bending deformation increased rapidly with the continuous rise of load in this period. After reaching a certain load, the development of bending deformation turned to stop, and the specimen showed a straight tension again, followed by final fracture.



(a) clamping (b) bending phenomenon (c) fracture

Figure 5. Deformation of the specimen during the tensile test.

Specimens have two failure modes distinguished by the location of the failure (seen Figure 6). For failure mode I, the specimen was cracked in the welding zone and the crack corresponding to failure mode I usually appears a twist on one side of the weld, which proves that there is still a certain heterogeneity inside the fillet weld. On the contrary, the crack in failure mode II occurs at the fusion zone near the side of Fe-SMA, with a straight fracture trend.

3.2 *Discussion*

Key indexes of all specimens obtained from the tensile test are listed in Table 5, and load-displacement curves of all specimens are plotted in Figure 7 respectively by group. As the control group, specimen DH3-6-30-A is added to all groups for comparison and analysis.

In general, all curves are highly similar. At a relatively low load level, the first stiffness mutation occurs, making the lap joint stiffness lower than the initial stiffness. Subsequently, lap joints with high bearing capacity will undergo a second stiffness mutation, and the stiffness

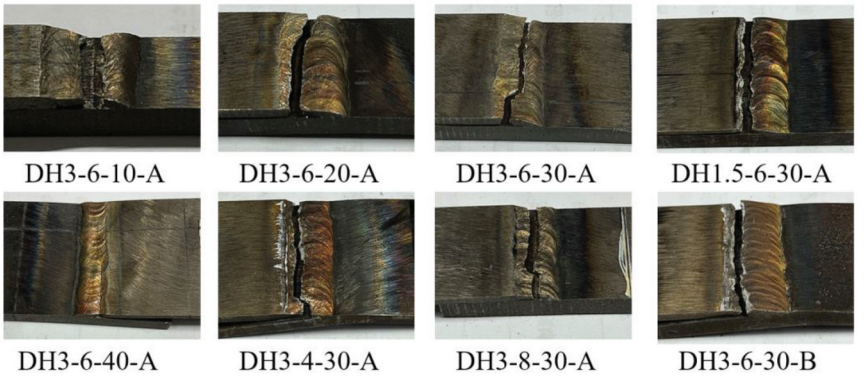


Figure 6. Macroscopic fracture morphology of the lap joints.

Table 5. Key indexes results of tensile test.

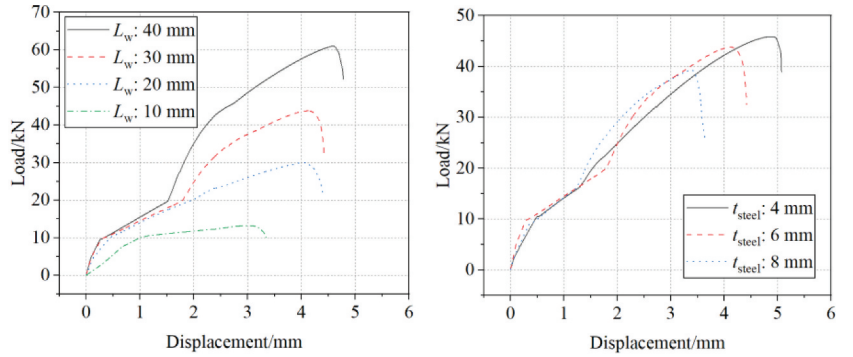
Group	No.	Failure mode	P_u/kN	Δ_u/mm	$\delta_{Fe\text{-}SMA}$/MPa
Control	DH3-6-30-A	I	43.8	4.12	486.9
Length	DH3-6-10-A	I	13.3	2.98	441.9
	DH3-6-20-A	I	30.0	4.06	499.9
	DH3-6-40-A	I	61.0	4.59	508.3
Steel thickness	DH3-4-30-A	I	45.8	4.85	509.3
	DH3-8-30-A	I	39.3	3.39	436.9
Fe-SMA thickness	DH1.5-6-30-A	II	30.6	4.22	679.8
Filler material	DH3-6-30-B	II	55.6	7.25	617.8

Note: P_u is the ultimate load, Δ_u is the displacement corresponding to P_u, and $\delta_{Fe\text{-}SMA}$ is the equivalent stress acting on the Fe-SMA plate, calculated by P_u.

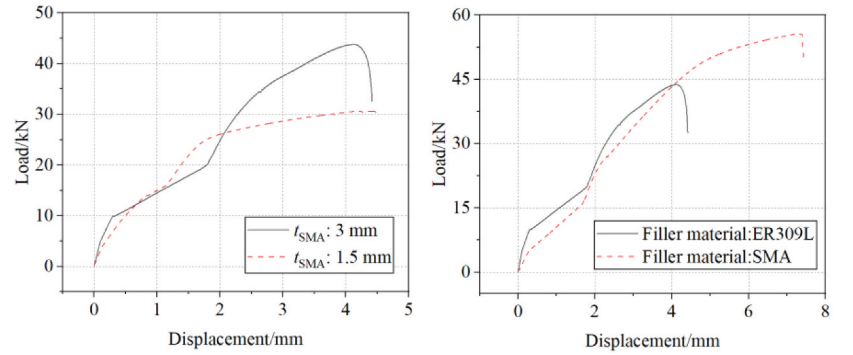
increases to a similar level before the first mutation. Then, the stiffness gradually decreases with the rise of the load, and the fracture occurs soon after reaching the ultimate load. According to the experimental phenomenon, the stiffness mutation can be demonstrated by the inevitable eccentricity of the structure. For the three components of the joint, the weld is always not the main contributor to deformation due to its narrow area. In the early stage, the deformation of the joint is mainly provided by steel and Fe-SMA. So, before the first mutation and after the second mutation, the steel is still in the linear elastic stage, and the Fe-SMA stiffness has only slight reduction, resulting in a similar level of lap joints' stiffnesses. In the stiffness reduction stage, the section rotation of the steel plate caused the interface between the fillet weld and the steel plate to rise, making the displacement increased and stiffness reduced. Finally, the equivalent stress of each lap joint with different configurations is over 430 MPa, much higher than the maximum prestress 294 MPa produced by Fe-SMA (Qiang et al, 2023d).

Results of specimens with only different fillet weld lengths are shown in Figure 7(a). In general, the ultimate load of the lap joint varies approximately linearly with the length of the fillet weld length. In contrast, the ductility of all specimens is basically at the same level except for the DH3-6-10-A with an apparent low displacement. Specimens with fillet weld length of 10 mm and 20 mm has no second stiffness mutation, indicating that the specimens fractured before the end of bending deformation. Similar relations occur in the group of steel thickness, where the ultimate load and displacement increase with the rise of the steel thickness.

Compared with thick Fe-SMA, lap joint with thin Fe-SMA has a higher equivalent stress (see Figure 7(c)), reflecting the higher welding quality of the thin joint. Nevertheless, the equivalent stress is calculated only to account for the transmission of the prestress. For the Fe-SMA reinforcement system, the overall efficiency still depends on the total load that the joint can transmit. After achieving the requirements of transmitting prestress, the compressive stress acting on the structure increases with a thicker Fe-SMA plate. Thus, although the thin



(a) Fillet weld length (b) Steel thickness



(c) Fe-SMA thickness (d) Filler material

Figure 7. Load-displacement curves divided by group.

joint has a better welding quality, the Fe-SMA thickness in application needs to be selected according to the requirement of prestress.

About the filler material, the tentative Fe-SMA wire lap joint has achieved outstanding mechanical performance, illustrated in Figure 7(d). Although the self-developed Fe-SMA wire is not a kind of standard welding wire, its own excellent mechanical properties with high strength and good ductility are still reflected in the mechanical performance of the lap joint. However, the excellent mechanical performance of the lap joint using Fe-SMA wire is based on the different welding processes. Due to the size limitations of the self-developed Fe-SMA wire and the lack of composition of standard welding wire (such as the arc stabilizer and deoxidizer), the welding process is not as stable as when using ER309L, with sparks and crackles. After trials and optimization, the two-pass welding was used to ensure the well formation of the lap joint. Therefore, whether Fe-SMA can be directly used as welding wire for welding needs further research and verification.

4 CONCLUSION

In this paper, TIG welded lap joints between Fe-SMA and structural steel Q355 were prepared. Four design parameters affecting the tensile properties of lap joints were considered including fillet weld length, filler material, and thicknesses of two base materials. The study achieves the following conclusions:

(1) With suitable welding parameters, the TIG welded lap joints between Fe-SMA and structural steel Q355 with high quality can be attained.

(2) The ultimate load of lap joints increases with the rise of fillet weld length and steel thickness.
(3) Lap joint shows a higher weld quality with thin Fe-SMA, but the actual selected Fe-SMA thickness in the Fe-SMA reinforcement system depends on the prestress requirement.
(4) Lap joint with self-developed Fe-SMA wire has a outstanding mechanical performance. However, considering the potential problems with welding instability and non-standard composition, whether Fe-SMA wire can be used in the welding of Fe-SMA reinforcement system is still worthy of further study.

Based on the research on the butt joint, the experimental study on the lap joint in this paper further confirms the possibility of using welded joints to transmit the prestress produced by the Fe-SMA reinforcement system. Thus, the resistance of the Fe-SMA reinforcement system to humid environments is improved, and the scope of application in bridge is expanded.

REFERENCES

Cladera A., Weber B., Leinenbach C., Czaderski C., Shahverdi M. & Motavalli M. 2014. Iron-based shape memory alloys for civil engineering structures: An overview. Construction & Building Materials 63: 281–293.

Czaderski C, Shahverdi M, Brönnimann R, Leinenbach C. & Motavalli M. 2014. Feasibility of iron-based shape memory alloy strips for prestressed strengthening of concrete structures. Construction and Building Materials 56: 94–105.

Dong, Z. Z., Sawaguchi, T., Kajiwara, S., Kikuchi, T., Kim, S. H. & Lee, G. C. 2006. Microstructure Change and Shape Memory Characteristics in Welded Fe–28Mn–6Si–5Cr–0.53Nb–0.06C Alloy. Materials Science and Engineering: A, 438–440: 800–803.

Druker, A. V., Perotti, A., Esquivel, I. & Malarria, J. 2015. Design of Devices and Manufacturing of Fe-Mn-Si Shape Memory Alloy Couplings. Procedia Materials Science, 8: 878–885.

Izadi M. R., Ghafoori E, Shahverdi M, Motavalli M. & Maalek S. 2018a. Development of an iron-based shape memory alloy (Fe-SMA) strengthening system for steel plates. Engineering Structures 174: 433–446.

Izadi M. R., Ghafoori E, Motavalli M. & Maalek S. 2018b. Iron-based shape memory alloy for the fatigue strengthening of cracked steel plates: Effects of re-activations and loading frequencies. Engineering Structures 176: 953–967.

Liu, L. L., Du, J. Q. & Zhou, C. Y. 2020. Welding Performance of the Dissimilar Joints of Fe-Mn-Si Alloy and 304 Stainless Steel. IOP Conferences Series: Materials Science and Engineering, 729(1), 012100.

Lin, H. C., Lin, K. M., Chuang, Y. C. & Chou, T. S. 2000. The Welding Characteristics of Fe–30Mn–6Si and Fe–30Mn–6Si–5Cr Shape Memory Alloys. Journal of Alloys and Compounds, 306(1–2): 186–192.

Qiang X. H., Chen L. L., Jiang X. & Dong H. 2023a. Experimental study on anchorage and activation performance of Fe-SMA strips for structural reinforcements. Construction and Building Materials 401: 132961.

Qiang X. H., Wu Y. P., Wang Y. H. & Jiang X. 2023b. Novel crack repair method of steel bridge diaphragm employing Fe-SMA. Engineering Structures 292: 116548.

Qiang X. H., Zhang Z. Y. & Jiang X. 2023c. Microstructure and Mechanical Properties of TIG welded Joint between Iron-based Shape Memory Alloy and Structural Steel Q235, 12th International Symposium on Steel Structures, Jeju, 8-11 November 2023, 658–661.

Qiang, X. H., Wu, Y. P., Wang, Y. H., and Jiang, X. 2023d. Research Progress and Applications of Fe-Mn-Si-Based Shape Memory Alloys on Reinforcing Steel and Concrete Bridges. Applied Sciences, 13(6), pp. 3404.

Rojob H & El-Hacha R. 2018. Fatigue performance of RC beams strengthened with self-prestressed iron-based shape memory alloys. Engineering Structures 168: 35–43.

Sun, B. C., Qi, F. J., & Du, Y. L. 2002. Weldability of Ferrous SMA with 45 Steel. Materials for Mechanical Engineering, 04: 38–39. (in Chinese)

Zhou C. Y., Lin C. X. & Liu L. L. 2010. Study on YAG Laser Welding Process of Fe-Mn-Si Shape Memory Alloy. Applied Mechanics and Materials, 37–38: 1364–1367.

Zhou C. Y., Lin C. X. & Liu L. L. 2012. Study on CO2 laser weldability of Fe-Mn-Si shape memory alloy. Third International Conference on Smart Materials and Nanotechnology in Engineering, Shenzhen, China, 84092G

Zhou C. Y. 2015. Research on Laser Welding Performance of Fe-Mn-Si Memory Alloy." Dalian Maritime University, China. (in Chinese).

Bridge Maintenance, Safety, Management, Digitalization and Sustainability – Jensen, Frangopol & Schmidt (eds)
© 2024 The Author(s), ISBN 978-1-032-77040-6
Open Access: www.taylorfrancis.com, CC BY-NC-ND 4.0 license

A decision method for ship-bridge collision pre-warning based on vision and radar data fusion

Hongyu Zhuang, Dalei Wang, Zhenxiong Gu, Yiqing Dong & Junjie Wang
College of Civil Engineering, Tongji University, Shanghai, China

ABSTRACT: The active collision avoidance and pre-warning system prove highly effective in minimizing ship-bridge collisions. Existing research mainly leans on single-source data for assessing the risk of such collisions, yet single-source data inherently harbor limitations. In this study, we propose an active collision avoidance and pre-warning decision method based on vision and radar data fusion. Two risk identification models are designed to fit different environmental conditions. The method is tested on Youdungang bridge and shows fair risk identification ability. The future holds promise for delving deeper into the potential of multi-source data fusion within this domain.

1 INTRODUCTION

Ship-bridge collision accidents often result in huge economic losses, making it important to establish the active collision avoidance and pre-warning system. Ship trajectory acquisition is the basis of collision pre-warning. Ship trajectories are usually acquired by remote sensing (RS) (Wei *et al.*, 2020), synthetic aperture radar (SAR) (Zhu *et al.*, 2022), camera (Zhang *et al.*, 2021; Zhang and Hou, 2022) and automatic identification system (AIS) (Zhang *et al.*, 2022). However, these data sources each have their own shortcomings. SAR lacks the image texture features required to reconstruct the event scene, RS and cameras have insufficient resistance to environmental interference, and the frequency of AIS data collection is usually low, making it difficult to meet the demands of real-time alerts. Therefore, there is a need for a method based on multi-source data fusion to overcome the limitations of single-source data and improve the effectiveness of the pre-warning system.

This study aims to propose an active collision avoidance and pre-warning decision method based on vision and radar data fusion. Appropriate object detection model and millimeter-wave radar have been applied to obtain accurate ship trajectory information. The risk of ship-bridge collision is assessed by predicting and analyzing collected ship trajectory based on two risk identification models, which should be applied to different environmental conditions.

2 METHOD

2.1 *Vision-based ship trajectory acquisition*

To obtain ship trajectories, the collected camera data needs to be processed through a specific object detection neural network to obtain ship bounding boxes. These bounding boxes contain the pixel coordinate information of ships, which can be transformed into world coordinates with a homography matrix. By using a target tracking algorithm, ship trajectories can be generated, and furtherly the motion and geometric characteristics of ships can be extracted.

DOI: 10.1201/9781003483755-419

2.1.1 *Ship detection*

YOLOX (Ge *et al.*, 2021) is adopted as the ship detection model for this study. YOLOX's model structure integrates improvements in the backbone network, introduces the YOLOP module for anchor-free prediction, incorporates a dynamic head, and supports multi-scale detection. These elements collectively contribute to YOLOX's outstanding object detection performance. To train the model for ship detection, it is necessary to establish a dataset that encompasses ship images in the corresponding bridge scene. The dataset should include images from various time periods, different weather conditions, and different types of ships to enhance the model's generalization capability.

2.1.2 *Mapping between pixel and world coordinates*

The relationship between the pixel coordinates and the world coordinates of ships can be represented by the homography matrix H. The principle of photogrammetry gives a variety of ways to solve the homography matrix, and the four-point calibration method (Hughes *et al.*, 2014) is used in this study. Since the matrix has 8 independent parameters, it is necessary to obtain the world coordinates and corresponding pixel coordinates of at least 4 control points to solve all parameters.

2.1.3 *Ship tracking and trajectory acquisition*

DeepSORT (Wojke *et al.*, 2017), short for "Deep Simple Online and Realtime Tracking", is an object tracking algorithm designed to track multiple objects in real-time video streams. It is an extension of the SORT algorithm, combining deep learning techniques with a classic tracking algorithm to improve tracking accuracy, especially in crowded scenes. DeepSORT algorithm is adopted in this study to distinguish the trajectory point set of each ship target and avoid frequent ID switches caused by short-term occlusion, so as to generate stable trajectories.

2.2 *Radar-based ship trajectory acquisition*

Radar exhibits a robust resistance to interference compared to cameras, ensuring reliable detection even in challenging conditions. Operating within the wavelength range between microwave and infrared waves, millimeter wave radar combines the benefits of both, boasting excellent penetration capabilities and extended propagation distances. Consequently, this study utilizes millimeter wave radar for ship trajectory acquisition.

Radar leverages the Doppler effect to extract velocity information from transmitted and received signals, while the orientation angle is derived from the velocity difference between array antennas. The aggregation of returning signals from all directions results in a radar point cloud. Leveraging this radar point cloud, target tracking algorithms can effectively discern the presence of ships and formulate trajectories. The fundamental steps of classical multi-target tracking methods involve data association followed by single-target filtering (Liu and Wang, 2021).

2.3 *Ship feature extraction and data fusion method*

The ultimate goal of conducting ship detection and acquiring ship trajectories is to extract the motion and geometric characteristics of ships, thereby providing a basis for subsequent data fusion and risk identification. The motion characteristics of a ship typically include its position, speed, direction, etc. For vision-based trajectories, data processing such as averaging or regression is necessary to obtain motion characteristics, while geometric features are inherent in ship bounding boxes. In the case of radar-based trajectories, the process of generating the trajectory already extracts the motion characteristics of the ship, but it is unable to capture geometric features.

Common data fusion methods include decision-level fusion, data-level fusion, and feature-level fusion (Wei *et al.*, 2022). Decision-level fusion is more flexible and convenient to use, thus is adopted in this study. Here, decision-level fusion refers to the integration of data

obtained from radar and cameras. Each source of data undergoes its own independent processing to obtain the trajectories and features of ships. Subsequently, through a well-designed risk identification strategy and warning scheme, these data are unified and utilized, thereby achieving good results in ship detection and pre-warning.

2.4 *Risk identification and pre-warning approach*

The overall strategy employed for ship-bridge collision risk identification is to parameterize the risk rate R. For different environmental conditions, two risk identification models are utilized. Specifically, during daytime periods with normal meteorological conditions, where vision-based method can accurately detect ship targets, video data serves as the primary basis for risk identification. A risk identification model based on trajectory prediction is employed in this scenario. On the other hand, during adverse weather conditions such as heavy rain, thick fog, or during nighttime, when video data struggles to correctly detect ship targets and obtaining ship dimensions is challenging, radar data becomes the main basis for risk identification. In such cases, a model based on pre-defined risk zones of the navigational channel is used to calculate the risk rate. The two models should be designed according to the engineering conditions of the actual bridge. The corresponding pre-warning strategy involves triggering an audio-visual alarm system and reporting to the management department when the risk rate exceeds a certain threshold.

3 EXPERIMENT AND RESULTS

3.1 *Basic information*

To verify the effectiveness of the decision-making method proposed in this study, we conducted an experiment at Youdungang Bridge in Shanghai, demonstrating the results of risk identification. Youdungang Bridge is a small-span arch bridge with a span of about 60m and a height of about 5m. Camera and millimeter-wave radar are installed on both sides to monitor passing ships. The navigable ships under the bridge mainly include cargo ships and speedboats. Figure 1 provides an illustration of the bridge, and Figure 2 shows the relevant sensors.



Figure 1. Youdungang bridge.



Figure 2. Radar and camera.

3.2 *Vision-based trajectory acquisition and feature extraction*

3.2.1 *Trajectory acquisition*

The initial step involves training the YOLOX model. A ship dataset is specifically established based on the video data captured by the camera on Yaudungang bridge. This dataset is structured in COCO format and comprises 453 images randomly split into training and test sets.

The model undergoes 300 epochs of training, and the changes in the loss function and mean Average Precision (mAP) values (IoU threshold from 0.5 to 0.95) throughout this process are

depicted in Figure 3. Achieving a maximum mAP of 0.718 reflects a satisfactory training outcome that meets practical requirements. The YOLOX model effectively extracts bounding boxes of ships from input images, and the center of each bounding box is approximated as the pixel coordinate of a ship.

Upon mapping pixel and world coordinates and applying the DeepSORT algorithm, ship trajectories can be derived and projected onto a standardized world coordinate plane. Subsequently, a five-point sliding average method is employed to smooth the trajectories. Figure 4 illustrates a processed ship trajectory, verifying the effect of target tracking.

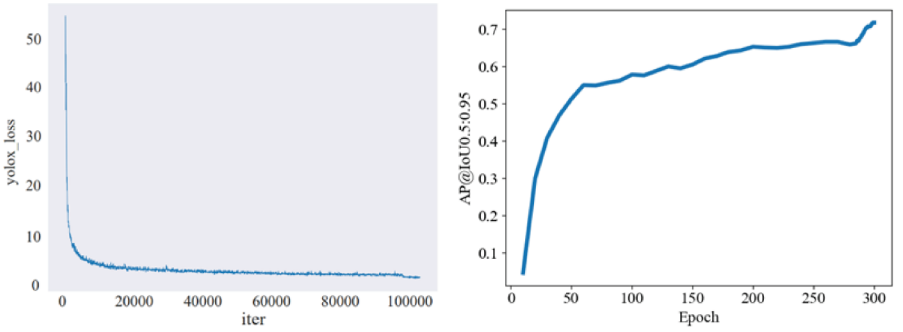


Figure 3. Loss function and mAP change.

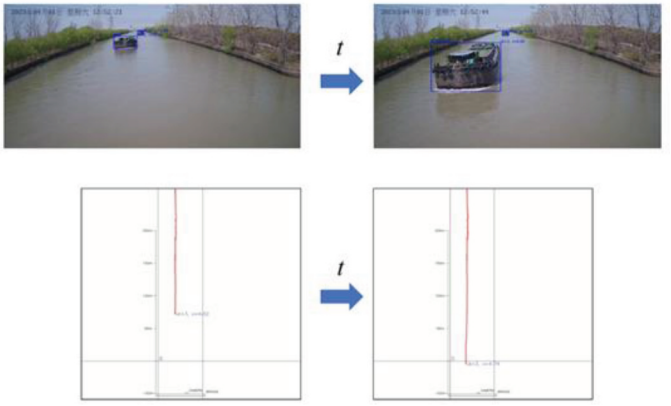


Figure 4. Target tracking and ship trajectories.

3.2.2 *Feature extraction*

Ship velocity is determined using a moving average method. The ship's current speed is computed as the average speed over the preceding frames, while the ship's direction is denoted by a unit vector expressed in world coordinates, akin to the velocity calculation method.

In practical scenarios, it has been observed that calculating the ship-bridge collision risk rate based on video data is highly sensitive to directional changes at long distances. Consequently, the false alarm rate can become exceptionally high. To mitigate this, a piecewise function is applied to the moving average interval of direction:

$$n_a = \begin{cases} 10n & d \geq 100 \\ 3n & 50 < d < 100 \\ n & d \leq 50 \end{cases} \tag{1}$$

where n_a = the adjusted sliding average interval; n = the preset standard interval; d = the distance of the ship target from the camera.

The geometric features of ships usually require specific measurement devices such as laser radar to obtain. However, in this case, the absence of corresponding equipment limits the measurement, while the collision risk of arch bridges is closely related to the geometric characteristics of the ships. Considering the unique perspective of the camera in this case, an approximate method using bounding boxes can be employed to calculate the height and width of the ships. This method can be described as:

$$\begin{cases} H = k_H(d)H_b \\ B = k_B(d)B_b \end{cases} \tag{2}$$

where H and B are the height and width of the ship; H_b and H_b are the height and width of the bounding box measured at a certain distance d, in this case d is 200m; $k_H(d)$ and $k_B(d)$ are two approximation coefficients that can be obtained by linear regression when the distance d is fixed.

3.3 *Radar-based trajectory acquisition and feature extraction*

Relying on existing clustering algorithms and filtering algorithms, radar-based acquisition and feature extraction of trajectories are relatively straightforward. The millimeter-wave radar used in this study is equipped with relevant data processing modules, capable of directly outputting the speed and position information of ships. Table 1 gives the output data format of radar.

Table 1. Radar output data.

No	Radar ID	Datetime	Shi ID	Velocity	X	Y
1	00002B14	2023-05-07 12:06:20	00000DEA	2.20	-19.60	163.40
2	00002B14	2023-05-07 12:06:21	00000DEA	2.20	-20.00	165.20
3	00002B14	2023-05-07 12:06:22	00000DEA	2.20	-20.40	167.20
4	00002B14	2023-05-07 12:06:23	00000DEA	2.20	-20.80	169.20

3.4 *Data fusion and risk identification models*

3.4.1 *Temporal and spatial alignment*

In order to achieve data fusion, the radar-based and video-based trajectories should correspond in both time and space. Temporal alignment is straightforward due to the real-time monitoring, but spatial alignment requires mapping radar coordinates to the world coordinate plane. Radar coordinates can be mapped to world coordinates through translation and rotation operations. This transformation can be described as:

$$\begin{bmatrix} X \\ Y \\ 1 \end{bmatrix} = \begin{bmatrix} \cos\varphi & -\sin\varphi & X_0 \\ \sin\varphi & \cos\varphi & Y_0 \\ 0 & 0 & 1 \end{bmatrix} \begin{bmatrix} X_R \\ Y_R \\ 1 \end{bmatrix} \tag{3}$$

where (X, Y) = the ship's world coordinates; (X_R, Y_R) = the ship's radar coordinates; (X_R, Y_R) = the coordinates of the radar origin in the world coordinate system; φ = the deflection angle of the radar coordinate system relative to the world coordinate system.

The parameters in the transformation can be easily solved by mapping temporally aligned video and radar data.

3.4.2 *Risk identification model based on trajectory prediction*

Based on the constant velocity assumption, the future trajectory is envisioned as the trajectory that the ship would follow if it maintains its current speed and direction. Consequently, the ship's

position upon reaching and passing the bridge is considered as the intersection point between the tangent of the trajectory and two reference lines, as illustrated in Figure 5. The final risk rate is taken as the larger one of the risk rates calculated based on two reference lines.

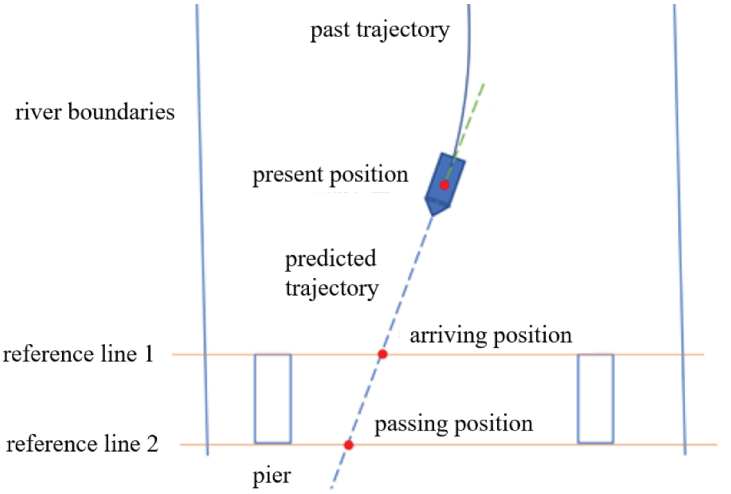


Figure 5. Trajectory prediction.

Figure 6 shows the risk identification model based on track prediction. The steps for the calculation are as follows:

(1) Determine the arch axis equation, consider a quadratic parabola in this case:

$$h = h_0 - kx^2 - h' \tag{4}$$

where h_0 = the elevation at the top of the arch axis; h' = a constant considering the thickness of the arch; k = the shape factor of the arch.

(2) Solve the position of ship-bridge collision x_c:

$$x_c = \frac{1}{k}\sqrt{h_0 - h' - H - h_w} \tag{5}$$

where H = height of ship; h_w = water surface elevation.

(3) According to x_c, calculate the limit position x_l at which the ship would hit the arch precisely, and the dangerous position x_d where the ship would be at risk of collision:

$$x_l = x_c - \frac{1}{2}B \tag{6}$$

$$x_d = x_c - B \tag{7}$$

where B = width of ship.

(4) The ship's basic risk rate of collision is determined to be quadratic:

$$R = \begin{cases} \frac{1}{x_d^2}x^2 & 0 \le x \le x_d \\ \frac{2}{x_d}x - 1 & x > x_d \end{cases} \tag{8}$$

(5) In order to reduce the false alarm rate, the basic risk rate is corrected. When the distance between ship and bridge is still large, the slightest directional adjustment may

bring about a large change in the predicted position under the bridge, resulting in a high false alarm rate. Therefore, it is adjusted according to the time remaining for the ship to arrive at the bridge:

$$R' = \alpha R \tag{9}$$

where α is a risk reduction factor, which satisfies:

$$\alpha = \begin{cases} 0 & t_r \geq 80 \\ 0.02(80 - t_r) & 30 < t_r < 80 \\ 1 & t_r < 30 \end{cases} \tag{10}$$

where t_r = the time remaining for the ship to arrive at the bridge.

Some of this model's risk identification results are shown in Figure 7. It is obvious that the identified risk rate can generally reflect the actual collision risk, and the motion and geometric feature of ship exert a clear influence on the results.

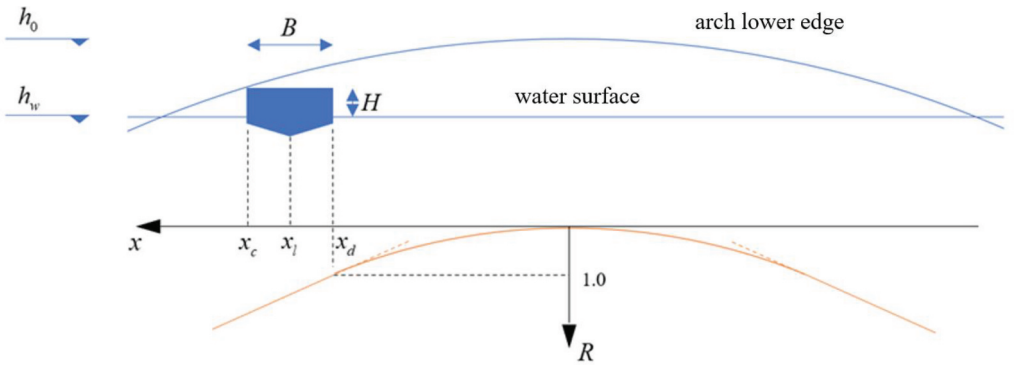


Figure 6. Risk identification model based on trajectory prediction.

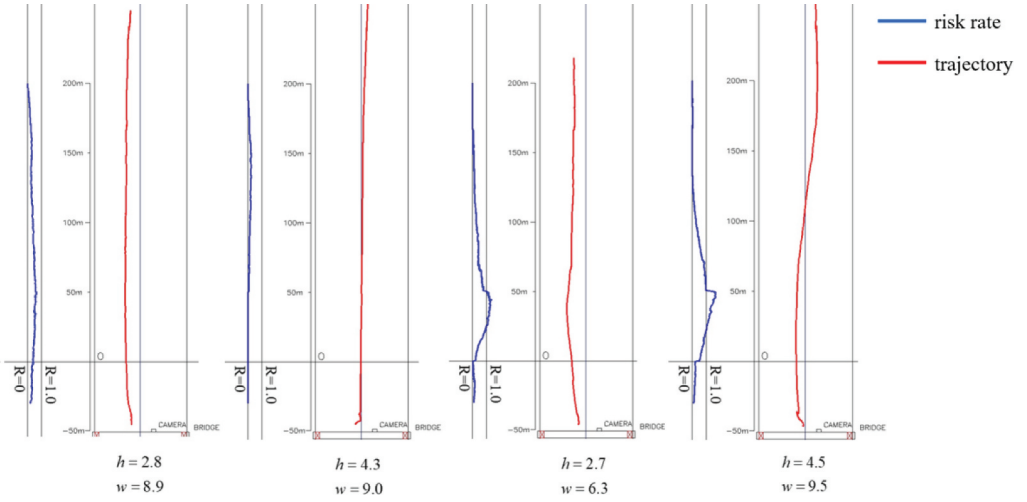


Figure 7. Identification results of the model based on trajectory prediction.

3.4.3 *Risk identification model based on pre-defined risk zones*

This model divides the waterway into safe zone, hazard zone and severe hazard zone according to the risk of ship-bridge collision, as shown in Figure 8. Among them, the safety zone refers to the area where all ships can pass normally, the hazard zone refers to the area where the largest ship is at risk of colliding with the bridge, and the severe hazard zone refers to the area where smaller ships are also at risk of colliding with the bridge. The specific classification criteria can be determined by statistical methods, and the risk of collision can be determined by x_d defined in equation 7.

The basic risk rate function of collision is determined as:

$$R = \begin{cases} \frac{1}{x_d^l} x & 0 \le x \le x_d^l \\ \frac{x - x_d^l}{x_d^m - x_d^l} + 1 & x > x_d^l \end{cases} \tag{11}$$

where x_d^m = the dangerous position of smaller ships; x_d^l = the dangerous position of larger ships. The risk rate can also be adjusted according to equation 9.

Some risk identification results of this model are shown in Figure 9. Ship trajectories are successfully acquired despite poor environmental conditions. The risk rate is highly identical to the trajectory itself due to the linearity of this identification model.

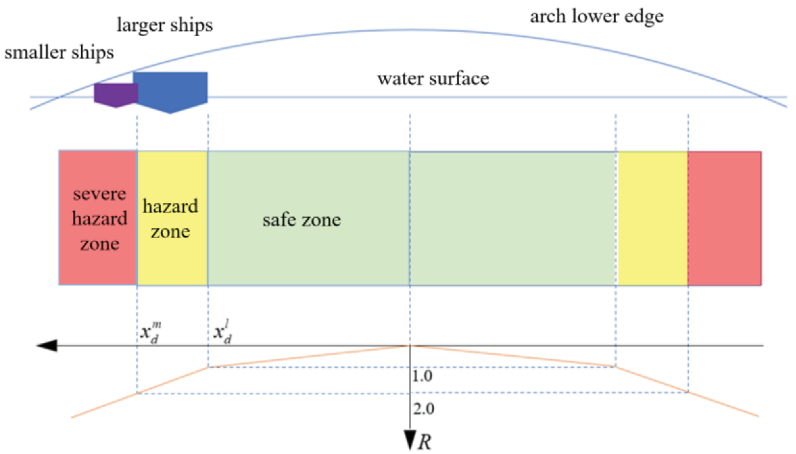


Figure 8. Risk identification model based on pre-defined risk zones.

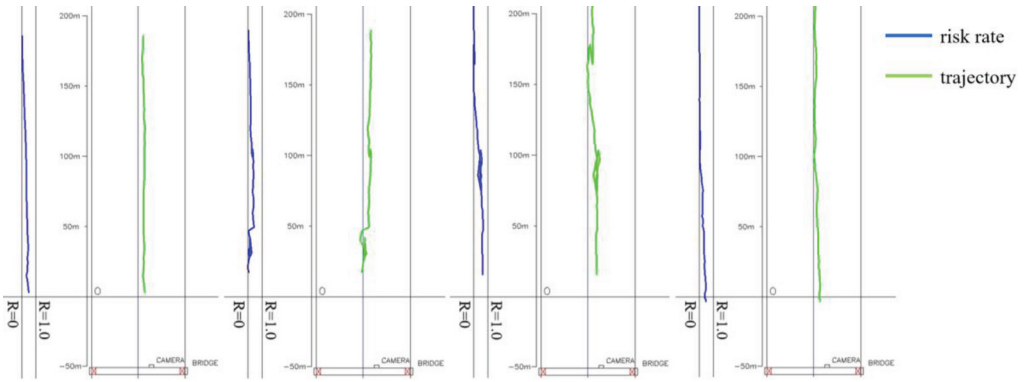


Figure 9. Identification results of the model based on defining risk zones.

4 CONCLUSION

To enhance warning reliability, we present a decision-making approach for ship-bridge collision pre-warning through the fusion of vision and radar data. Tailored to the distinct characteristics of cameras and radar, we devised a data fusion strategy employing diverse risk identification models for different environmental conditions. This decision-making method harnesses the strengths of both sensors, enabling comprehensive, round-the-clock monitoring of the pre-warning system. Experimental results demonstrate the method's effectiveness in risk identification, validating the significance of multi-source data fusion. Future experiments are anticipated to delve deeper into the potential of this approach, paving the way for further advancements in the application of data fusion within this domain.

REFERENCES

Ge, Z., Liu, S., Wang F., Li, Z. & Sun, J. 2021. YOLOX: Exceeding YOLO Series in 2021. *arXiv e-prints*.

Hughes, J.F., Van Dam, A., Mcguire, M., Sklar, D.F., Foley, J.D., Feiner, S.K., & Akeley, K. 2014. *Computer graphics: Principles and practice* (3rd ed.). Addison-Wesley.

Liu, C. & Wang Y. 2021. Review of multi-target tracking technology for marine radar. *Journal of Radars*, 10(1): 100–115. doi:10.12000/JR20081

Wei, S., Chen, H., Zhu, X. & Zhang, H. 2020. Ship Detection in Remote Sensing Image based on Faster R-CNN with Dilated Convolution. *39th Chinese Control Conference (CCC)*, Shenyang, China, pp. 7148–7153

Wei, Z., Zhang, F., Chang, S., Liu, Y., Wu, H. & Feng, Z. 2022. MmWave Radar and Vision Fusion for Object Detection in Autonomous Driving: A Review. *Sensors* (7), 2542–2542.

Wojke, N., Bewley, A. & Paulus, D. 2017. Simple online and realtime tracking with a deep association metric. *IEEE International Conference on Image Processing*, Beijing, China, pp. 3645–3649.

Zhang, B., Xu, Z., Zhang, J. & Wu, G. 2021. A warning framework for avoiding vessel-bridge and vessel-vessel collisions based on generative adversarial and dual-task networks. *Computer-Aided Civil and Infrastructure Engineering*. doi:10.1111/mice.12757.

Zhang, F. & Hou, X. 2022. Multi-Site and Multi-Scale Unbalanced Ship Detection Based on CenterNet. *Electronics*. 2022; 11(11):1713.

Zhang, L., Chen, P., Li, M., Chen, L. & Mou, J. 2022. A data-driven approach for ship-bridge collision candidate detection in bridge waterway, *Ocean Engineering*, Volume 266, 5, 2022, 113137, 0029-8018

Zhu, M., Hu, G., Li, S., Zhou, H. & Wang, S. 2022. FSFADet: Arbitrary-Oriented Ship Detection for SAR Images Based on Feature Separation and Feature Alignment. *Neural Process Letter*, 1995–2005.

GS05: BRIDGE MAINTENANCE - Inspection and diagnostic


Taylor & Francis
Taylor & Francis Group
http://taylorandfrancis.com

Bridge Maintenance, Safety, Management, Digitalization and Sustainability – Jensen, Frangopol & Schmidt (eds)
© 2024 The Author(s), ISBN 978-1-032-77040-6
Open Access: www.taylorfrancis.com, CC BY-NC-ND 4.0 license

Utilization of soundness assessment of medium and small span bridges based the ML models

Arong, G.Z. Wang, M.X. Gao & Dongmei
Inner Mongolia University of Agricultural, Hohhot, China

S. Bai
Inner Mongolia University of Technology, Hohhot, China

Yiliguoqi
Inner Mongolia Technical College of Construction, Hohhot, China

ABSTRACT: In the current small and medium-sized bridges in the daily safety inspections, such as high dependence on inspectors and lack of quantifiable scientific basis. In practice, Professional engineers spend an enormous amount of time check the textual description and looking at image data of damages to bridge members, such as girders, bearings, expansion joints, and piers that are acquired from periodic inspections, and then determining make a rating of the bridge condition. Therefore, it is necessary to develop a practical method for the evaluation of bridge soundness to assess the degree of structural health. In this paper, the maintenance priority evaluation of bridge integrity of small and medium span bridges is examined using the Support Vector Machines (SVM), Decision Tree (DT), and Random Forest (RF) of artificial intelligence (Al) techniques. Based on the model, three types of bridge is used, an algorithm is proposed as useful feature to provide the engineering expertise for the inspection of bridges. This proposed method was able to substitute engineer judgement to distinguish the health rating of I. The input data were the degrees of deterioration of the structural parts and the output data were the soundness of the structure. The results showed that the inspection item of crack location and exposed direction of steel bars gives good assessment on whether bridge maintenance works are needed or not.

1 INTRODUCTION

Condition rating of bridges is specified in many countries since it provides a basis for the decision-making of maintenance actions such as repair, strengthening, or limitation of passing vehicle weight. In practice, bridge inspectors use their judgment to evaluate and appraise maintenance problems and critical deterioration on site, and then make a rating of the bridge condition. Generally, periodic inspection bridge by bridge with visual and nondestructive techniques is widely adopted around the world, such as in the United States, Japan, Korea, China, Australia, and European countries (De-Cheng Feng et al. 2023). The engineers for condition rating must be familiar with relevant condition rating standards and be experienced with bridge inspection practice. Considering that a condition rating is required for each bridge with a large amount of data buried in the inspection reports, it is a time-consuming and labor-intensive task. Therefore, it is paramount to propose methodologies for efficient and accurate condition rating of bridges. To achieve fast and automated bridge condition rating, in the past few years, machine learning (ML) methods have enjoyed fast development based on relevant information from bridge database or inspection (Karim, M. M. et al. 2020, Nishimuta,Y. et al. 2023, Saman Karimi, S. et al. 2023, Shimma, Y. et al. 2023, Suzuki,T. et al. 2019)

DOI: 10.1201/9781003483755-420

A novel approach for estimating bridge condition rating is introduced, utilizing ML techniques. Findings in this study suggest that the ML approach can capture the information buried in the inspection reports and provide a promising tool for efficient and accurate bridge condition rating.

2 METHODOLOGY AND MACHINE LEARNING TECHNIQUES

Three commonly used algorithms, i.e., Decision Tree (DT), Support Vector Machine (SVM), and Random Forest (RF), are employed to build up accurate and reliable prediction models for the condition rating of bridges.

2.1 *Decision Tree (DT)*

Decision trees are a very effective method of supervised learning. A tree-structured model that can be used for both classification and regression problems. It aims is the partition of a data-set into groups as homogeneous as possible in terms of the variable to be predicted. A decision tree is generally made up of tree nodes and directed edges. It takes as input a set of classified data, and outputs a tree that resembles to an orientation diagram where each end node (leaf) is a decision (a class) and each non- final node (internal) represents a test (De-Cheng Feng et al. 2023). Here, the classification and regression tree algorithm which is based on the mean square error is adopted. Supposing the input space can be divided into N sub-spaces R_1,R_2, . . .,R_N, the decision tree model can be expressed as

$$\hat{y} = f_{DT}(\mathrm{X}) = \sum_{n=1}^{N} c_n \mathrm{I}(\mathrm{X} \in \mathrm{R}_n) \tag{1}$$

where x is the input variables; I(·) is the indicator function; and c_n is the prediction value by the n^{th} leaf node.

2.2 *Support Vector Machine (SVM)*

An Support vector machine is a type of binary supervised machine learning. SVM are based on the induction principle of structural risk minimization, which aims to minimize a test error by controlling two contradictory factors: a functional risk from empirical data and a capacity for the set of real-valued functions (Cortes et al. 1995; Vapnik et al. 1998). An SVM algorithm aims to find the optimal separating hyperplane that effectively separates the data points into the labeled classes. In essence, the input variables are mapped to a high dimensional feature space by nonlinear transformation, and then a hyperplane is found in the space for linear classification or regression. This mapping process generally adopts the kernel function method. The specific learning strategy of SVM is to maximize the left and right data interval of the hyperplane, which can be abstracted into the mathematical problem of solving convex quadratic programming, and the learning algorithm of SVM is the optimization algorithm of solving convex quadratic programming. The main parameters are parameters of kernel function and penalty coefficient in optimization (De-Cheng Feng et al. 2023). Taking the binary classification problem as an example, the SVM model can be defined as

$$\hat{y} = f_{SVM}(\mathrm{X}) = \beta^T \mathrm{X} - \mathrm{b} \tag{2}$$

where β and b denote the normal vector and the bias constant from zero, respectively.

2.3 *Random Forest (RF)*

The DT and SVM, or some other supervised learning methods, are actually individual-type algorithms, which only generate a single predictive model. Random forest is one typical ensemble

method that belongs to the bagging family. Random forests is a substantial modification of bagging that builds a large collection of de-correlated trees, and then averages them. It takes advantage of two powerful techniques,i.e., bootstrap and random feature selection. At every step of building a tree, N samples are randomly selected as a subset with bootstrap from the entire database, and K features are randomly selected and used as the split node to build a DT with the subset (De-Cheng Feng et al. 2023). After several (or M) steps, one obtains MDTs from the above procedure, and the final output is the average of all the outputs by the M trees as follows:

$$\hat{y} = \frac{1}{M}\sum_{i=1}^{M} f_{DT,i}(X) \tag{3}$$

where f_{DT}, i(·) is the weak learner by the DT method at step i ≤ M. In addition to the original parameters of DT, the number of trees is an extra yet important parameter.

3 VISUAL INSPECTION OF BRIDGES

In our study, we followed the conventional criteria to classify structure members' degree of health. Additionally, we focused on the main girder of the single-span girder bridge as well as the multi-span continuous girder bridges. We only examined main members (girders) in this study.

Introduction on the Regional Network of Bridges with Inspection Reports. As mentioned above, the database is established with inspection reports of a regional network of highway bridges located in Inner Mongolia, China. A total of 25 bridges in different health conditions are collected, which are reinforced concrete or pres-stressed concrete bridges or arch bridges. They almost cover the west area of Inner Mongolia, and are representative of regional bridges. The variations of bridge types and condition ratings are further illustrated in Figure 1 to Figure 3. Figure 1 shows the distribution of the bridges type. Figure 2 shows the distribution of the bridges with different span lengths, i.e., long-span bridges (40-150 m), medium-span bridges (20-40 m), and small-span bridges (5-20 m). Among medium-span bridges and small-span bridges take the most percentage of 40% and 48%, respectively. The distribution of bridges with condition ratings is displayed in Figure 3, which is according to the results of the inspection reports. In the conventional criteria, among the bridges were labeled as Levels 1, 2, 3, 4, and 5, respectively. Note that damage of bridges becomes severe from Levels 1 to 5, which requires different maintenance actions. The bridge need for response by maintenance work and also bridge need for repair according to next inspection shows a bridge inspector's required knowledge and judgement skill, which helps determine whether the bridge's owners need to repair the bridge. It is important to distinguish the soundness rank as being 1, 2, or 3. Figure 4 to Figure 6 shows the distribution of the number of bridges and the type of deterioration. Figure 4 shows that the arch bridge deterioration of mortar joints fall off had a high proportion compared to other types of deterioration. Figure 5 shows that the pre-stressed concrete slab bridge deterioration of crack and exposed steel bar and fall off had a high proportion compared to other types of deterioration. Figure 6 shows that the reinforced concrete slab bridge deterioration of crack had a high proportion compared to other types of deterioration.

In this case study, we examined the deteriorating feature of crack and exposed steel bars. Because of the limited amount of bridge inspection data, only two types of bridge inspection data were used, the corresponding health ratings of which were 2 and 3. In this study, the 83 pieces of inspection data pertaining to the deterioration of crack and exposed steel bars were used. The inspection reports were completed after the field inspection of the bridges visually or with nondestructive devices, and then the condition rating of bridges is conducted by experienced engineers through information processing of bridge member damages. The engineers should have professional knowledge about the bridges and be familiar with relevant inspection and maintenance standards. In this paper, the condition rating was conducted following the Chinese code for maintenance of highway bridges (JTG H, Code for Maintenance of Highway Bridges and Culvert, 2004), where the bridge health condition is divided into five levels, i.e., Levels 1 to 5. The bridges

of Level 1 are in good condition, bridges of Level 2 require only minor repairs or daily maintenance to ensure their safety, bridges of Level 3 are in a relatively poor state with many defects, and a small number of functional diseases have taken place, which need to be repaired accordingly. In bridges of Levels 4 and 5, a lot of severe material defects have appeared and the structural functionality greatly deteriorated, thus the safety of these bridges is questionable and the traffic should be closed for special inspection and major repairs. Considering that only a limited number of inspected bridges are rated as Levels 4 and 5 in the data-set. Thus, they are usually combined together and finally levels are designed as the condition ratings of the bridges. In this study, the statistical analyses of two levels of health were conducted. The inspectors' influences on the inspection data were not considered in this current study. These analyses were conducted using the analysis software Waikato Environment for Knowledge Analysis WEKA version 3.9. We conducted this experiment using the classification solver.

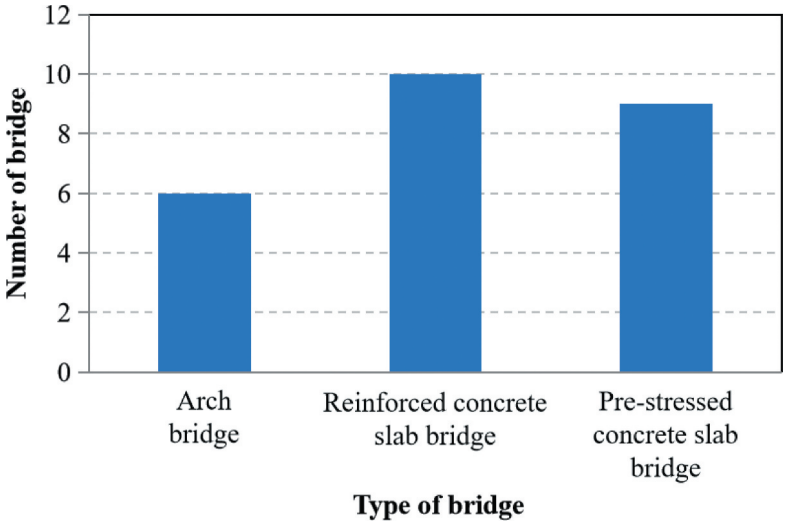


Figure 1. Distribution of bridge number and bridge type.

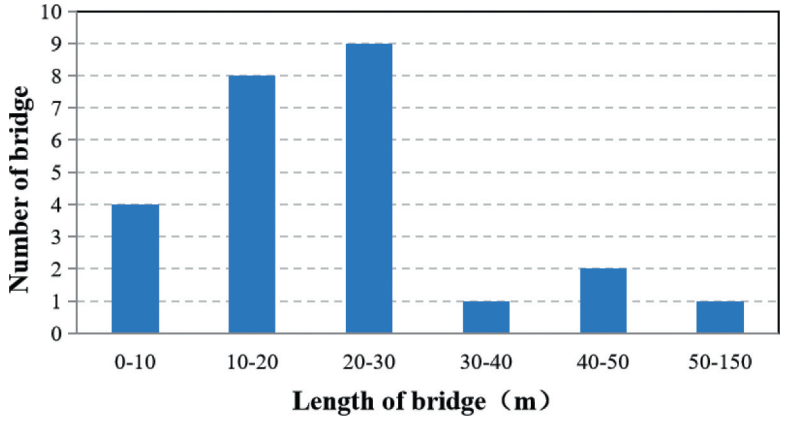


Figure 2. Distribution of bridge number and bridge length.

As pointed out in the pre-processing of the inspection data, all practical implementations adhered to strict requirements for training and testing. The first requirement was that all data were numerical. Therefore, if categorical features were present, they were converted to

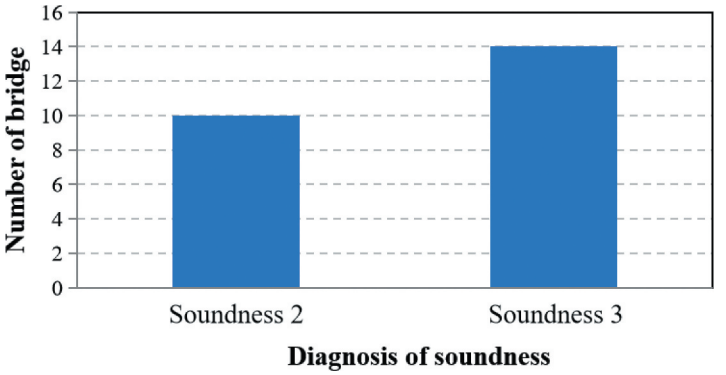


Figure 3. Distribution of bridge number and sound diagnosis.

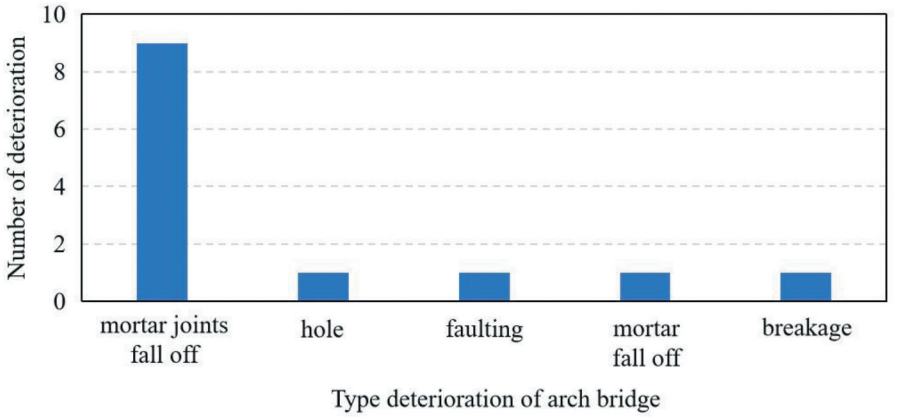


Figure 4. Distribution of bridge number and deterioration type (Arch bridge).

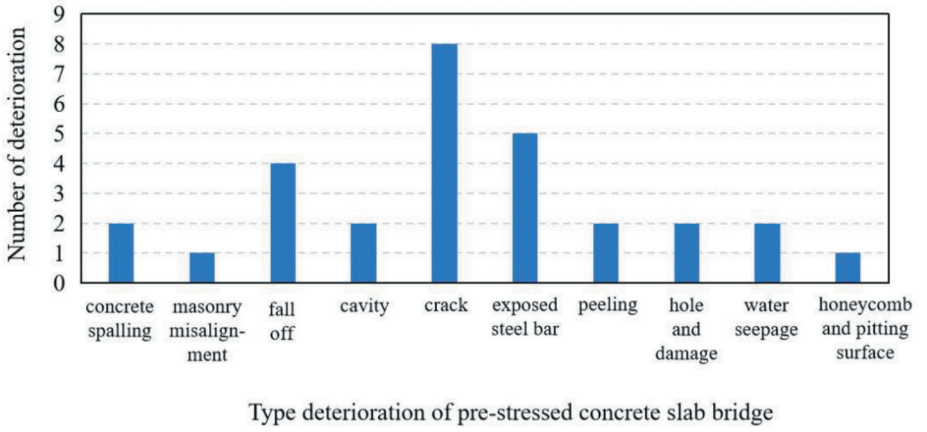


Figure 5. Distribution of bridge number and deterioration type (Reinforced concrete slab bridge).

numerical values using variable transformation techniques. To ensure that all feature variables were treated equally, it was best to use the feature "normalization" before training the model. The input data were the degree of deterioration of each concrete slab's inspection item, and the output data were the concrete slab's degree of health. Because our model's dataset was

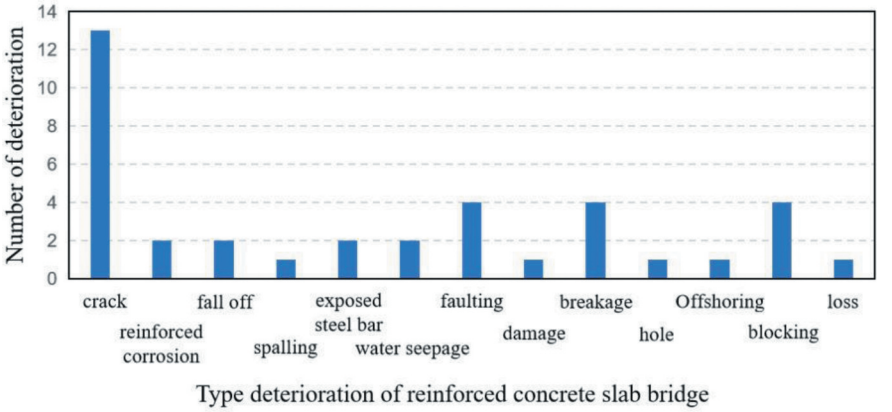


Figure 6. Distribution of bridge number and deterioration type (Pre-stressed concrete slab bridge).

small, we applied the classifier in a leave-one-out cross-validation. The leave-one-out cross-validation uses an entire model fit for all the data except a single point. It then makes a prediction at the point that can be compared to the actual value, which is iterated over the training dataset to obtain test errors for the labels of health ratings. We conducted this experiment by using the classification solver in a LIBSVM with grid search and k-fold cross-validation to find the optimal hyper parameters (a soft margin constant C and width of a Gaussian kernel y).

4 PREDICTION RESULTS AND DISCUSSION

Various metrics were used to evaluate the bridge health condition, such as accuracy, precision, sensitivity and specificity. This metrics are explained in more detail below.

Accuracy can be defined as the ratio of correct model predictions to the total number of tested images, as shown in Equation 4:

$$\text{Accuracy} = \frac{\text{TP} + \text{TN}}{\text{TP} + \text{FP} + \text{TN} + \text{FN}} \tag{4}$$

Precision (Eq. 5) defines how many of the images predicted as positive were predicted by the model correctly:

$$\text{Precision} = \frac{\text{TP}}{\text{TP} + \text{FP}} \tag{5}$$

Sensitivity, shown in Equation 6, defines how many of all true positive images were correctly predicted by the model:

$$\text{Sensitivity} = \frac{\text{TP}}{\text{TP} + \text{FN}} \tag{6}$$

Specificity (Eq. 7) defines how many of all true negative images were correctly predicted by the model:

$$\text{Specificity} = \frac{\text{TP}}{\text{TN} + \text{FP}} \tag{7}$$

In addition, the trade-off between sensitivity and specificity can be represented graphically as an ROC curve. It can be understood as a plot of the probability of correctly classifying the positive examples against the rate of incorrectly classifying true negative examples. The ROC curve can be constructed by plotting these pairs of values on the graph with 1-specificity on the x axis and sensitivity on the y axis. Situations in which datasets are unbalanced arise frequently in real-world problems; in these cases, model evaluation is done with criteria other than accuracy. Metrics extracted from ROC curves, such as the area under the ROC curve (AUC), can be a good alternative for model evaluation; this is because the ROC curve can determine the difference between errors on positive or negative examples (Rakotomamonjy et al. 2004).

Table 1. Useful attribute combines.

Case	Training data	Test data	Ratio of number	Correctly classified accuracy	TP	FP	Accurancy	Recall	F value	Area under ROC curve (AUC)
Pre-stressed	13	7	2	57%	1	1	0.6	1	0.7	0.5
concrete slab	13	7	2	66.70%	1	1	0.7	1	0.8	0.5
bridge	13	7	2	71%	1	1	0.7	1	0.8	0.5
Reinforced	8	4	2	75%	0.5	0	1	0.5	0.7	0.75
concrete slab	8	4	2	75%	1	0.5	0.7	1	0.8	0.75
bridge	8	4	2	50%	0.3	0	1	0.3	0.5	0.67

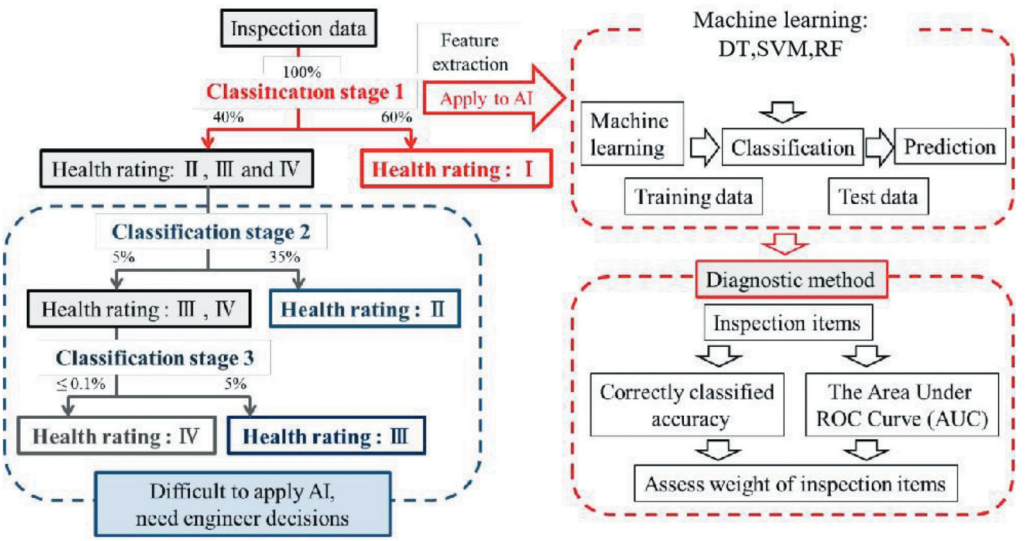


Figure 7. Concept diagram of sound diagnosis.

Feature importance and selection can give an objective utility of features (Arong et al. 2020, 2018). We need to manually create an objective utility feature of inspection items. Above the ML numerical results, a useful feature combination denote in Table 1. The concept of a proposed diagnostic optimization method for bridge integrity is described in Figure 7. Regional governments are constantly distressed by the lack of a maintenance budget and maintenance experts. This proposed diagnostic optimization method can assist regional governments in determining bridges' health and integrity, which are generally decided by own experience of each maintenance experts.

5 CONCLUSION

This paper explores a rapid condition rating method using a machine learning model based on inspection data of bridges. The technique is used to extract the information in the text description of the bridge inspection reports and convert them into digital vectors. The methodology is verified with the condition rating of 25 bridges of different types and health conditions in Inner Mongolia, China. According to the ML analysis, the different feature combinations by using an experienced inspector's training data to predict the class label. Thus, this proposed bridge integrity evaluation method can help and assist regional governments determine bridges' degree of health.

FUNDING

This research was funded by the Inner Mongolia Natural Science Foundation of China (grant number 2023LHMS05003), Research Foundation for Advanced Talents (grant number NDYB2021-28), and Operating expenses of basic scientific research project of directly affiliated universities in Inner Mongolia Autonomous Region (grant number BR230147).

REFERENCES

Arong. Murakami, S. Ichikawa, H. Yiliguoqi. 2020. Utilization of SVM in soundness evaluation of reinforced concrete slab bridge. Japan Society of Civil Engineers, F4:8-1, 59-70.

Arong. Murakami, S. Yiliguoqi. 2018. A case study of using a support vector machine on bridge inspection data. Proceedings of the 9th International Conference on Bridge Maintenance, Safety and Management, Melbourne, Australia. 1873–1880.

Arong. Yiliguoqi. Murakami, S. 2018. Study on utilization of SVM in soundness evaluation of bridge superstructure. Japanese Society of Steel Construction. 25-100, 43–56.

Cortes, C. & Vapnik, V. 1995. Support-vector networks. Machine Learning 20: 273–297.

Feng, De-Cheng, Wang, Wen-Jie. et al. 2023. Condition assessment of highway bridges using textual data and natural language processing- (NLP-) based machine learning models. Hindawi, Structural control and health monitoring.

JTG H, Code for Maintenance of Highway Bridges and Culvert, China Communications Press, Beijing, China, 2004.

Karim, M. M. et al. 2020. Modeling and Simulation of a Robotic Bridge Inspection System. Procedia Computer Science.168, 177–185.

Nishimuta, Y. Tagashira,N. Hiramatsu,Y. et al. 2023. Study on damage level determination by deep learning in the periodic bridge inspection. Intelligence, Informatics and Infrastructure. 4-3, 135–141.

Rakotomamonjy, A. 2004. Optimizing area under ROC curve with SVMs. Proceedings of 1st international workshop on ROC Analysis in Artificial Intelligence, Spain: 71–80.

Saman Karimi, S. Mirza, O. 2023. Damage identification in bridge structures: review of available methods and case studies. Australian journal of structural engineering. 24-2, 89–119.

Shimma, Y. Nakatsui, K. Nakamura, H. et al. 2023. Development of artificial intelligence to support damage evaluation for small bridges, and examination of introduction methods. Intelligence, Informatics and Infrastructure. 4-3, 149–157.

Suzuki, T. Nishio, M. 2019. Application of deep learning to damage level determination of structural members in the bridge inspection. Japan Society of Civil Engineers, F3:75-1, 48–59.

Vapnik, V. 1998. Statistical Learning Theory. New York: Wiley-Interscience.

Bridge Maintenance, Safety, Management, Digitalization and Sustainability – Jensen, Frangopol & Schmidt (eds)
© 2024 The Author(s), ISBN 978-1-032-77040-6
Open Access: www.taylorfrancis.com, CC BY-NC-ND 4.0 license

AI for bridge inspection with IBM Inspecto

A.C.I. Malossi, R. Assaf, N. Avogaro, A. Bartezzaghi, B. Ebouky, T. Frick, I. Giurgiu, F.M. Janicki, P. Kluska, M. Rigotti, F. Scheidegger, A. Simeski & C. Skura
IBM Research Europe – Zurich Laboratory, Rüschlikon, Switzerland

D. Caraballo & Y. Cinar
IBM Research Europe – Paris Laboratory, Orsay, France

F. Bormlund & S. Gjerding
Sund & Bælt Holding A/S, Korsør, Denmark

ABSTRACT: We present our research innovation in enterprise visual inspection for civil infrastructures. We train and adapt AI foundation models to work on high-resolution images collected by drones for detecting and segmenting very small defects in large areas and with high precision. Further, we provide support to reliability engineers by measuring defects with computer vision and by providing additional information that is required to assess damage severity and plan maintenance interventions. We provide access to our research innovation through our SaaS IBM Inspecto. IBM Inspecto is a research-industry platform developed by IBM Research that leverages foundation models and advanced computer vision methods to fully digitalize the visual inspection process, accelerating and improving accuracy in critical inspection tasks. In this work, we present visual inspection results on the Storebælt Bridge in collaboration with Sund & Bælt, as well as on other applications.

1 INTRODUCTION

The maintenance and inspection of infrastructure elements, such as bridges, tunnels, roads, runways, and dams, is of immense significance for public safety and for maintaining economic activity. Despite that, most visual inspections are carried out manually, and infrastructure operators are faced with the challenging task of detecting every problem before it gets expensive to be repaired, or even too dangerous for civilians. Manual visual inspections make maintenance cycles longer than they should be, as they require that a person physically inspects the entire surface of an infrastructure. Civil engineers not only need to detect problems but also to review them and decide what action must be taken. As a result, our global network of infrastructures is inspected less frequently than it should be and, in some cases, inspection job plans are only partially executed. For instance, in today's inspection reports, only major detected problems are included, and their location is only roughly indicated. This may cause further issues downstream of the process when selected defects are repaired with imprecise information. Moreover, if something is not included in such reports, it is practically impossible to verify in the future if that was an actual mistake or if no problem was visible at that time. With the infrastructure network becoming older and older every year, all these challenges risk causing major fatalities, as we have already seen in examples such as the collapse of the Morandi Bridge in Italy in 2018[1].

The last decade has marked incredible technical progress in AI and Machine Learning (ML) with remarkable success stories in the fields of computer vision, natural language pro-

1. https://en.wikipedia.org/wiki/Ponte_Morandi

DOI: 10.1201/9781003483755-421

cessing, and other domains. This wave of success and excitement in AI has been in large part driven by Deep Learning (LeCun 2015), and recently by Foundation Models (FMs), i.e., deep neural networks that are trained on large broad unlabeled datasets and that can be deployed on a wide range of downstream tasks.

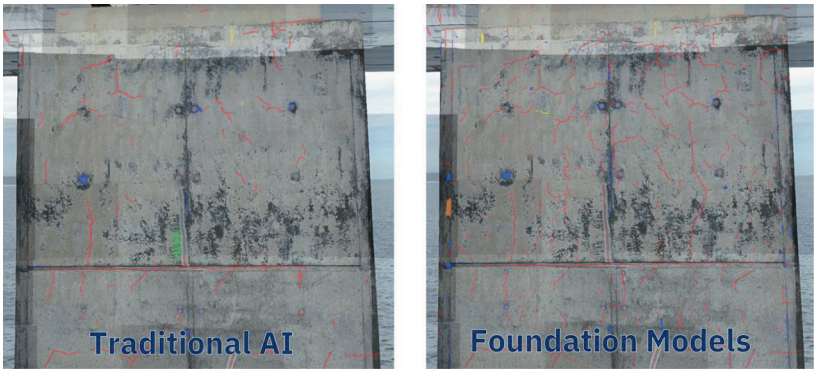


Figure 1. Comparison of AI results on Storebaelt Pillar 3 south face. Left: traditional supervised learning. Right: FM.

While ML has seen increased adoption in the civil engineering domain in recent years, for instance in applications like condition assessment (Bianchi 2022), novelty detection for structural health monitoring (Manzini 2022), or other structural engineering tasks (Salehi 2018), the impact of FMs specifically on civil engineering is however still in its infancy, owing to a gap between research development and application use cases. Part of this gap is due to the non-straightforward adoption of model results into existing operational flows.

To close this gap, we present IBM Inspecto, a research-industry platform developed by IBM Research in collaboration with our engineering partner Sund & Bælt, that leverages FMs and advanced computer vision methods to fully digitalize the visual inspection process, accelerating and improving accuracy in critical inspection tasks. This paper is organized as follows: Section 2 introduces AI FMs and discusses their benefit for visual inspection of civil infrastructures, Section 3 presents IBM Inspecto and describes how domain experts can consume results of AI FMs in a convenient way. Finally, Section 4 describes future directions and conclusions of this work.

2 FOUNDATION MODELS FOR VISUAL INSPECTION

Deep learning computer vision models are adept at sifting through large image datasets typical acquired by use of drones to identify high-risk elements like structural cracks or visible corrosion in steel reinforcement bars in bridges. The accuracy and efficacy of these models hinge on access to a substantial volume of annotated data. However, obtaining high-quality labels, especially for rare occurrences like structural defects, is both challenging and expensive. This issue is accentuated in visual inspection scenarios, where the rarity of defects and the complexity of tasks like object detection and instance segmentation compound the difficulty and cost of labeling.

Recently, Self-supervised learning (SSL) has emerged as a pivotal approach in the realm of computer vision, especially for pre-training FMs on large amounts of unlabeled data. SSL is also becoming a cornerstone in civil engineering applications, particularly for the critical task of visual inspection. It is now common that large datasets are becoming available thanks to the automation of data collection methods, such as drone data acquisitions over bridges. This abundance of unlabeled data is an ideal candidate for

SSL, where models are trained on data that they label themselves through predefined pretext tasks. SSL's history in computer vision spans several years, featuring techniques like denoising autoencoders and Siamese networks. More recent innovations include self-supervised pretraining approaches like PIRL (Mirsa, 2019), BYOL (Grill, 2020), MOCO (He, 2020), and SimCLR (Chen 2020), further advanced by integrating vision transformer architectures, as seen in Vision Transformer (ViT) (Dosovitskiy, 2019), DINO (Zhang, 2022), MSN (Assran, 2022), and Masked Auto Encoder (MAE) (He, 2021). The significance of SSL pretraining is twofold: it not only improves the overall performance of models but also makes them adept at learning from a few examples in downstream tasks.

In the context of bridge defect detection, our experiments have focused on SSL pretraining to develop FMs. We utilized the MAE technique, where a significant portion of an image is masked, and the model is trained to reconstruct the unmasked image. This approach not only aids the model in understanding the intricacies of concrete bridge structures but also enhances its ability to pinpoint defects.

Results demonstrate that an FM pre-trained on images of concrete bridges boosts performance in defect detection tasks. This is further highlighted in Figure 1, where given a qualitative assessment we can see that FMs have a much higher recall over traditional models. Furthermore, due to the use of large ViT models, the image resolution is kept more intact when compared to convolutional-based methods. This further refines the detection and allows the model to identify the defects with less background noise, this can then lead to better measurements and therefore ranking of the defects.

2.1 *Detailing the training method*

In the preceding section, we mention that we developed an FM employing the MAE technique. This is executed through a hierarchical, four-stage training process. Initially, the model undergoes pre-training via SSL, devoid of any labeling, on a diverse collection of common object datasets. This phase is instrumental in enabling the model to hone its capability for abstracting pertinent information from a broad spectrum of images, irrespective of their relevance to civil infrastructure or bridges specifically.

Progressing to the second stage, the model's training continues under the SSL paradigm. It is during this phase that the model is exposed to a 'source dataset', comprising an extensive collection of unlabeled imagery predominantly featuring concrete structures, with a significant focus on bridges. This dataset encompasses a variety of structures, including the Storebælt Bridge, but extends to incorporate bridges from multiple geographical regions and other concrete edifices. The primary objective of this stage is to refine the model's proficiency in extracting salient features specifically from images of concrete structures.

The third stage of the model's training, adhering once again to SSL principles, narrows the focus exclusively to the Storebælt Bridge. The dataset in this stage is composed solely of images captured of this bridge, creating a specialized data domain that the model learns to navigate. This targeted approach is pivotal in fine-tuning the model's ability to interpret the specific characteristics inherent in the Storebælt Bridge imagery. Notably, a subset of this dataset, encompassing approximately 1000 images, is annotated with roughly 8000 identified defects, and is used in the fourth stage of training.

In the fourth and final stage, the model is trained using supervised learning. This phase employs a cascade Mask R-CNN head that sits on top of the pre-trained model backbone which was pre-trained in the previous steps. This adapts the model to i) object detection, i.e., identifying bounding boxes around objects of interest, and ii) instance segmentation, i.e., identifying the pixels within each box corresponding to defects. That multifaceted training approach ensures that the model is not only versed in general image comprehension but is also finely attuned to the nuances of concrete structure imagery, particularly that of the Storebælt Bridge, thereby enhancing its efficacy in defect detection and segmentation tasks.

3 IBM INSPECTO

IBM Inspecto is an industry research platform for enterprise visual inspection developed by IBM Research. With IBM Inspecto, engineers and domain experts are guided through the visual inspection process with support for all the phases of engineering inspection, including long-term management of large amounts of data, intuitive navigation of complex assets with unique image stitching technology, maps, hierarchy, and 3D models, high-resolution defect detection powered with AI FMs trained on the world largest curated infrastructure image dataset, automatic measurement of detected defects, assisted engineering review process and customizable report generation.

In more detail, IBM Inspecto features the following components:

- Image viewer: enable ordered access to large amounts of inspection images and in structured folders.
- Prediction viewer: displays the results of the AI models and automatically extracts associated attributes, such as crack length to represent pixel-accurate segmentation masks of defects.
- Overview viewer: allows the user to view large sections of the infrastructure and navigate in real-time. It also enables understanding of the context in which a defect was detected.
- Merged predictions and overview: enables the user to understand the relationships and positions of all defects and consolidates multiple detections of a defect in different images into a single prediction.
- Statistical viewer: aggregated statistics are provided on all detected defects, both for individual images and for the entire merged overview.
- Report generator: enables the generation of customized for all data captured in the inspection, with detailed views of each defect, important attributes, and direct links to OCL for an enlarged view of the visualized defect. Georeferencing allows runway maintenance staff to manually check defects on the runway and repair damages with a sealant.

3.1 *Great Belt bridge inspection*

In this section, we demonstrate IBM Inspecto on the Storebælt[2] bridge. After the data has been uploaded to the service and analyzed by our fine-tuned FMs, the engineer can start the

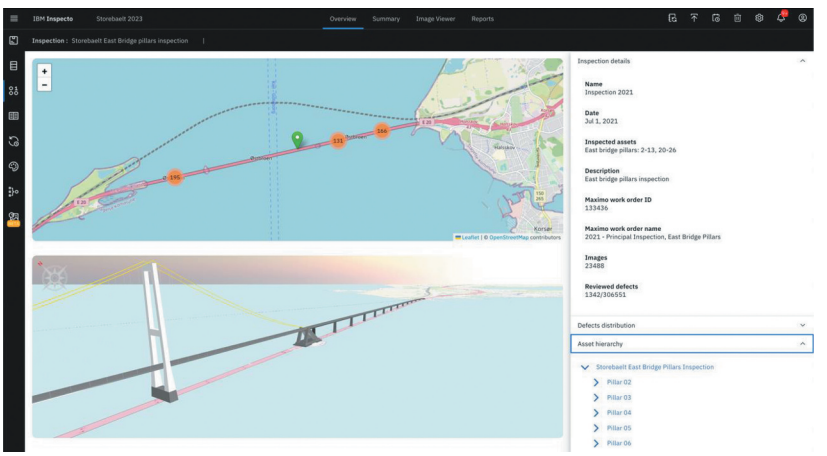


Figure 2. IBM Inspecto overview page. This page contains a summary of the performed visual inspection, including a map with the location of drone capturing points, the 3D model, as well as access to the bridge hierarchy and corresponding IBM Maximo work orders.

2. https://storebaelt.dk/en/

visual inspection process from the overview page in Figure 2: such a view conveniently allows the user to navigate around the entire infrastructure and have a first overview of the number of surfaces that have been inspected as well as of the number of defects detected by AI.

From the overview page, the civil engineer can access any element and inspect the concrete surface in detail. In Figures 3 and 4 we show an example view of one face of pillar 3 on the Storebælt. The stitched view is zoomable up to native high-resolution of the individual images, that are collected with the DJI Matrice 300 drone, using high-resolution grid mode.

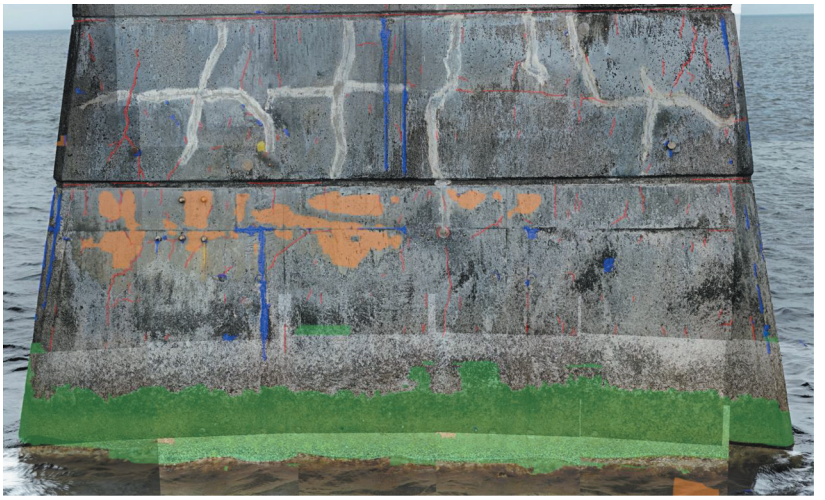


Figure 3. IBM Inspecto high-resolution analysis of the Storebælt pillar 3, south face, bottom region. The view is made of 30 high-resolution images automatically stitched together by our algorithm. Our fine-tuned AI FM detects cracks (red) net-cracks (orange), spalling (blue), rust (yellow), crack with precipitation (pink), as well as algae (green).

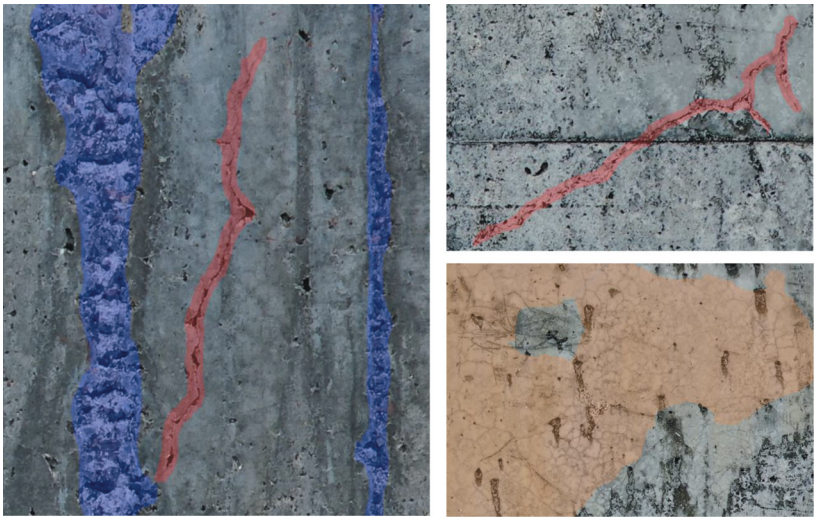


Figure 4. IBM Inspecto high-resolution analysis of the Storebælt pillar 3, south face, bottom region. A few selected zoomed areas to show the precision of masks generated by our AI FM.

List of all detected findings

Defect ID	Defect type	Main measure	Condition Rating	Reviewed	Review comment	Element function fulfilled	Consequence for elements	Drone position and altitude	Link	File name
Pillar 03 - South face										
303	Crack	98.65 cm	3	Yes	Long vertical crack, to be repaired before winter.	Yes	No	(55.348754°, 11.09026°) 44.949m	Link	DJI_20210604103310_0006_SUPR
148	Crack	92.41 cm	3	Yes	Long vertical crack, to be repaired before winter.	Yes	No	(55.348746°, 11.090254°) 43.76m	Link	DJI_20210604103501_0007_SUPR
257	Spalling	0.053 m2	3	Yes	Extended spalling, to be repaired before winter.	Yes	No	(55.348746°, 11.090254°) 43.76m	Link	DJI_20210604103501_0007_SUPR
247	Spalling	0.0339 m2	3	Yes	Extended spalling, to be repaired before winter.	Yes	No	(55.348746°, 11.090254°) 43.76m	Link	DJI_20210604103501_0007_SUPR
446	Spalling	0.0334 m2	3	Yes	Extended spalling, to be repaired before winter.	Yes	No	(55.348754°, 11.09026°) 44.949m	Link	DJI_20210604103310_0006_SUPR
448	Spalling	0.0233 m2	3	Yes	Extended spalling, to be repaired before winter.	Yes	No	(55.348754°, 11.09026°) 44.949m	Link	DJI_20210604103310_0006_SUPR
246	Spalling	0.0224 m2	3	Yes	Extended spalling, to be repaired before winter.	Yes	No	(55.348746°, 11.090254°) 43.76m	Link	DJI_20210604103501_0007_SUPR
96036	Spalling	N/A	3	Yes	Extended spalling, to be repaired before winter.	Yes	No	(55.348754°, 11.09026°) 44.949m	Link	DJI_20210604103422_0034_SUPR.JPG
96037	Spalling	N/A	3	Yes	Extended spalling, to be repaired before winter.	Yes	No	(55.348754°, 11.09026°) 44.949m	Link	DJI_20210604103422_0034_SUPR.JPG
96198	Crack	N/A	3	Yes	Long vertical crack, to be repaired before winter.	Yes	No	(55.348754°, 11.09026°) 44.949m	Link	DJI_20210604103405_0026_SUPR.JPG
96398	Crack	N/A	3	Yes	Long vertical crack, to be repaired before winter.	Yes	No	(55.348754°, 11.09026°) 44.949m	Link	DJI_20210604103403_0025_SUPR.JPG
96445	Crack	N/A	3	Yes	Long vertical crack, to be repaired before winter.	Yes	No	(55.348754°, 11.09026°) 44.949m	Link	DJI_20210604103425_0035_SUPR.JPG
96470	Crack	N/A	3	Yes	Long vertical crack, to be repaired before winter.	Yes	No	(55.348754°, 11.09026°) 44.949m	Link	DJI_20210604103427_0036_SUPR.JPG

Figure 5. IBM Inspecto summary table to be included in the asset inspection report. Note that the indicated severity scores and comments scores are randomly generated for demonstration purposes and do not represent the actual condition of the bridge.

Once the civil engineer has terminated reviewing the bridge surface, a customizable report can be generated including all necessary information. IBM Inspecto reports are available both as HTML as well as PDF. In Figure 5, an example of a summary table with all the detected defects on pillar 3 south face, is provided. The table shows on the top the most severe defects and includes links to view them in the service.

3.2 *Other examples of applications*

We successfully applied IBM Inspecto to a variety of other applications, from older bridges like the Stenungsund in Sweden (see Figure 6) to the Dübendorf Airbase Runway (see Figures 7 and 8). These two applications show how our AI FMs can adapt easily to predict defects on very different types of concrete surfaces. The Stenungsund bridge is very representative of most bridges in Europe and the US, which were built more than 50 years ago and have major signs of deterioration, such as areas with spalling with corroded rebars. We could reach very precise detection accuracy by fine-tuning the model with roughly 500 images.



Figure 6. IBM Inspecto results on the Stenungsund bridge: the image shows large instances of spalling with corroded rebars that our model detected correctly.

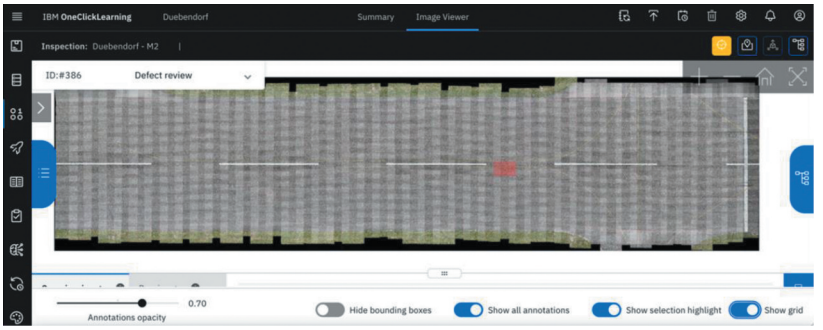


Figure 7. IBM Inspecto results on the Dubendorf Airbase: we inspected 250m of the runway with more than 800 high-resolution images automatically stitched together.

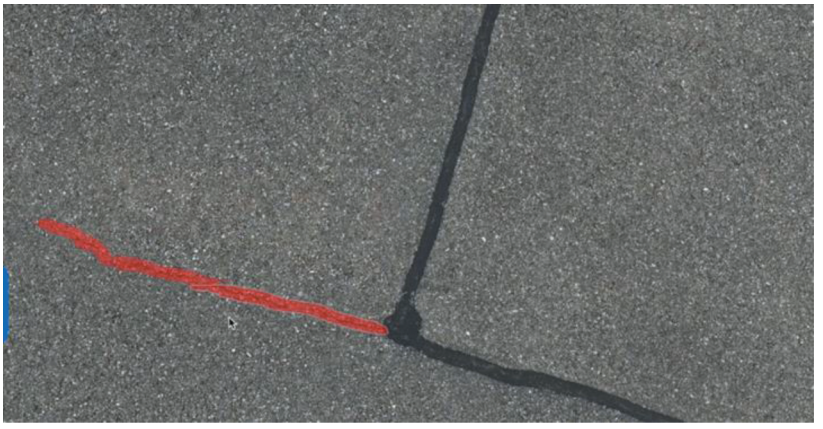


Figure 8. A detail of a crack that was previously repaired on the Dubendorf Airbase and that continued to grow later.

The Dübendorf Airbase runway surface is also quite different than concrete bridge walls. Nevertheless, our algorithm has been able to completely reconstruct the global overview stitched image and analyze it detecting even the smallest crack without any fine-tuning. A nice example in Figure 8 shows a crack that continued to grow after repair, with our model being able to detect only the new branch precisely next to the repaired patch.

4 CONCLUSIONS AND FUTURE WORKS

In this paper, we presented IBM Inspecto, a research-industry platform powered by IBM Research foundation models. We apply IBM Inspecto to the Storebælt Bridge in collaboration with Sund & Bælt, as well as on other applications. We demonstrate key features such as the intuitive navigation, the accurate detection of defects in high-resolution images, and the automated generation of customizable reports. IBM Inspecto aims to reduce the time and cost of visual inspection of complex assets, while digitalizing completely the entire inspection process and can be applied to a wide variety of infrastructures, from bridges to buildings, roads, and runways.

We are currently extending IBM Inspecto with additional AI features that will further accelerate the inspection process. First, we are developing a defect review assistant, powered by multi-modal FMs. Our review assistant will learn from a small, selected number of domain experts who manually reviewed defects, to then perform an automated review of all the other thousands of defects detected by our AI FMs. We envision that this process will accelerate the

review of the detected defects by at least one if not two orders of magnitude. To allow users to extend our pre-trained models and detect other types of defects that are present on their infrastructures, we are developing a Visual Prompting Lab service. There, engineers will just need to provide a few examples of images and swiftly scribble on top of the new type of defects to teach the algorithm what they would like to be detected. The process will be naturally intuitive and require minimal data and human labor. Finally, we will enable the users to compare inspected surfaces over time. Leveraging our stitched images, IBM Inspecto will conveniently show what has changed over each surface from the previous inspection, without asking to the user to re-annotate and re-assess previously assessed defects, thus further reducing the work to be done in every future inspection.

ACKNOWLEDGMENTS

This work was supported by the Swiss State Secretariat for Education, Research and Innovation (SERI) under contract number **22.00295**.

REFERENCES

Assran M., Caron M. et al. Masked Siamese Networks for Label-Efficient Learning, arXiv 2022.

Bianchi S, Biondini F. Bridge Condition Assessment Using Supervised Decision Trees. Proceedings of the 1st Conference of the European Association on Quality Control of Bridges and Structures: EUROSTRUCT 2021, Springer, 2022; 1108–1116.

Chen T., Kornblith S., Norouzi M., Hinton G. A Simple Framework for Contrastive Learning of Visual Representations, arXiv 2020.

Dosovitskiy A., Beyer L. et al.An Image is Worth 16x16 Words: Transformers for Image Recognition at Scale, arXiv 2019.

LeCun Y, Bengio Y, Hinton G. Deep Learning. Nature 2015 May 521(7553):436–444.

Grill J., Strub F., et al.. Bootstrap your own latent: A new approach to self-supervised Learning arXiv 2020.

He K., Chen X., et al. Masked Autoencoders Are Scalable Vision Learners, arXiv. 2021.

He K. and Fan H., Wu Y., Xie S., Girshick R. Momentum Contrast for Unsupervised Visual Representation Learning, arXiv 2020.

Manzini N, Mar N, Schmidt F, Bercher JF, Orcesi A, Marchand P, et al. An Automated Machine Learning-Based Approach for Structural Novelty Detection Based on SHM. In: Proceedings of the 1st Conference of the European Association on Quality Control of Bridges and Structures: EUROSTRUCT 2021 Springer, 2022;1180–1189.

Misra I., van der Maaten L., Self-Supervised Learning of Pretext-Invariant Representations, arXiv 2019.

Salehi H, Burgueño R. Emerging Artificial Intelligence Methods in Structural Engineering. Engineering Structures, 2018; 171:170–189.

Zhang H., Li F., et al. DINO: DETR with Improved DeNoising Anchor Boxes for End-to-End Object Detection, arXiv 2022.

Bridge Maintenance, Safety, Management, Digitalization and Sustainability – Jensen, Frangopol & Schmidt (eds)
© 2024 The Author(s), ISBN 978-1-032-77040-6
Open Access: www.taylorfrancis.com, CC BY-NC-ND 4.0 license

A review of recent research on visual inspection processes for bridges and the potential uses of AI

P.J. Vardanega, T. Tryfonas & G. Gavriel
University of Bristol, Bristol, UK

D.T. Nepomuceno
Formerly University of Bristol, Bristol, UK

M. Pregnolato
TU Delft, Delft, The Netherlands

J. Bennetts
WSP, Bristol, UK

ABSTRACT: Visual inspection remains an essential tool for assessing structural damage. Damage detection is a challenging task for those specifying, designing, and deploying SHM systems. Often only traditional visual inspection processes are available to determine the type and extent of structural damage. For bridge structures in the UK, a regime of general (every two years) and principal (every six years) inspections is often followed. Such visual inspections are time-consuming and costly in terms of both labour and financial resources. Therefore, the possibility of completing more of the bridge visual inspection process offsite has many potential benefits for bridge owners and managers during the service life of the asset. Recent research conducted at the University of Bristol in collaboration with industrial partners has examined how to make the best use of metrics derived from visual inspection data when assessing bridge condition and planning maintenance activities. Recent research into which aspects of the current visual inspection regime in the UK could potentially be moved offsite has also been carried out. This paper summarises these research efforts and discusses how AI may be used as part of future enhancements to visual inspection data capture and analysis.

1 INTRODUCTION

1.1 *Background*

The UK has aging infrastructure stock, often described as an 'asset time bomb' (Thurlby 2013, Thurlby & Rimell 2015). Therefore, assessing current asset condition and residual life is important for bridge managers. A key element of asset condition assessment is to be able to detect damage across the entire stock (in this case of bridges) and identify differences by region or asset type/class. 'Damage detection', although the most useful form of Structural Health Monitoring (SHM), is arguably the most difficult to realise in field conditions (see the SHM categories and discussion in Webb et al. 2015). The key method for damage detection in current practice remains visual inspection (VI) (e.g. Wallbank 1989, Moore et al. 2001, Lea & Middleton 2002, Middleton 2004, McRobbie et al. 2015, Bennetts 2019, Bennetts et al. 2016, 2020). In the UK, the following default visual inspection regime is often followed: principal visual inspections (conducted by inspectors operating within touching distance of the bridge) scheduled every six years and general inspections every two years (see HA 2007 and Bennetts et al. 2016). The aforementioned VI regime may be

DOI: 10.1201/9781003483755-422

varied on a risk-basis (HE, 2021). Bennetts et al. (2023) conducted a study using VI data from 200 sample bridges from the UK highway network and concluded that 81% of the inspections were carried out in 'strict compliance' with BD63/07 (the standard at the time of the study; see HA 2007) and 93% were within 'the spirit' of the standard (see also Bennetts 2019).

1.2 *Paper outline*

This paper summarises recent research on the following topics: the use of VI data and metrics for asset management processes (section 2); how aspects of the VI process may be carried out offsite using new technologies, leading to a hybrid VI system (section 3) and ways in which recent advances in artificial intelligence (AI)/machine learning (ML) may influence aspects of VI processes in the future (section 4).

2 USING VI DATA AND METRICS FOR ASSET MANAGEMENT

2.1 *Importance Of VI in bridge engineering*

Bennetts et al. (2016, 2020) conducted a series of semi-structured interviews to elicit the use of VI and SHM in the UK bridge management community. The use of VI data and associated metrics is varied across the industry. The use of SHM was reported to be limited except in specific instances (Bennetts et al. 2020). Colford et al. (2022) note that SHM is not an alternative to inspections. Bennetts et al. (2021) argued that the inspection intervals used in UK practice (two years and six years) make detecting change difficult, especially at individual asset level. Bennetts et al. (2020) as part of hierarchical process modelling and their survey of bridge engineering professionals, identified the following high-level processes: 'understanding the stock', 'making decisions' and 'implementing interventions' (Bennetts et al. 2020, p. 214), shown in Figure 1.

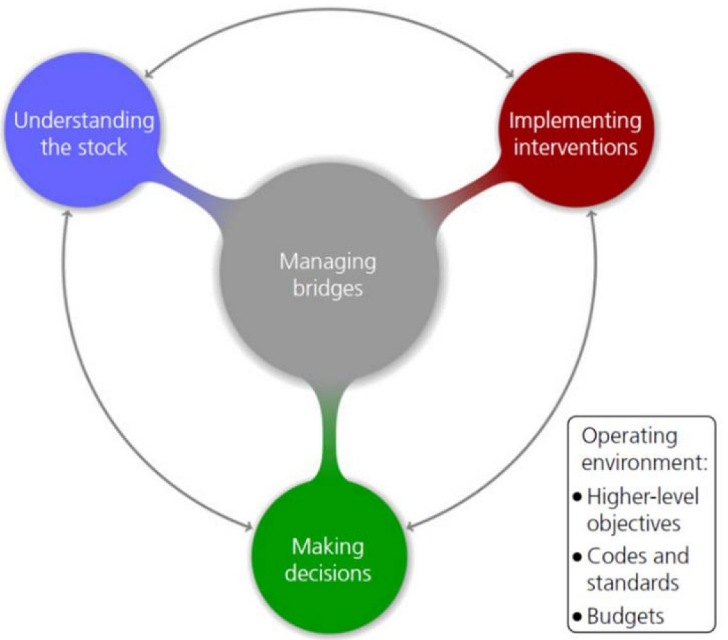


Figure 1. High-level model of the bridge management system (taken from Bennetts et al. 2020, used under the terms of the cc-by 4.0 licence).

2.2 *Bridge condition indicators*

VI data can be used to calculate Bridge Condition Indicator (BCI) metrics (defined in detail in Sterritt 2002). These metrics can be aggregated and analysed to study asset condition changes at stock/regional level (Bennetts et al. 2018a, 2018b). BCI metrics can be used to show varying asset deterioration across UK regions. For example, Figure 2 shows the reduction of BCI_{ave} and BCI_{crit} scores for a population of bridges (Bennetts et al. 2018b). As stated in Bennetts et al. (2018b, p. 26):

> "The average score, BCI_{ave} is calculated from the raw defect scores, taking the worst defects on each component type, weighted by the structural importance of each element. The critical score represents the worst defect on the most important structural components."

(See Sterritt (2002) for more details on the calculation of the aforementioned metrics.)

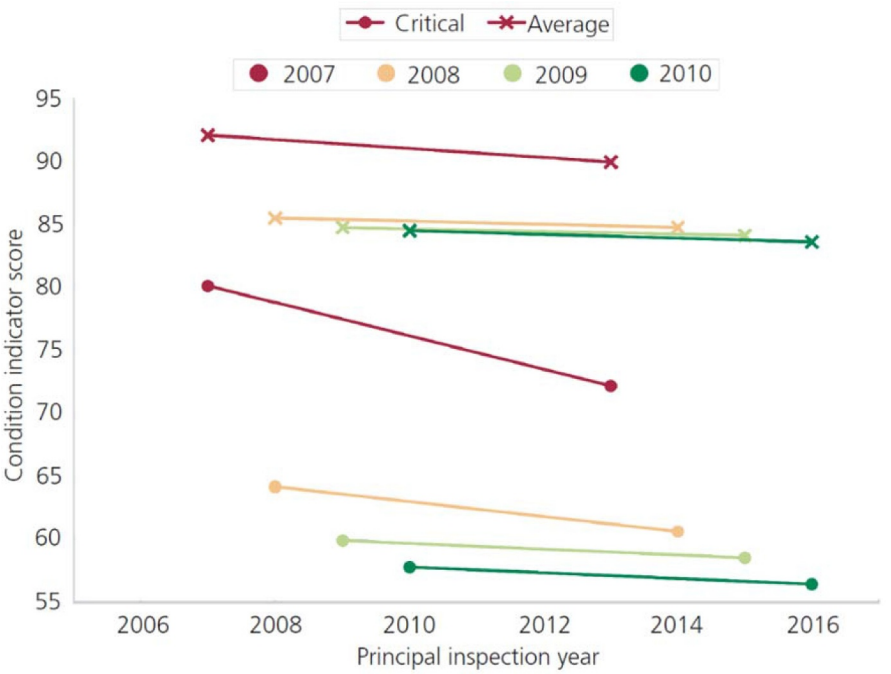


Figure 2. Change in condition between successive inspections for populations of structures that were inspected in the same year. The conditions of these populations of bridges are plotted as the average BCI_{crit} and BCI_{ave} scores for the population, weighted by deck area. A total of 2397 bridges are included in the plot (taken from Bennetts et al. 2018b, used under the terms of the cc-by 4.0 licence).

3 OFFSITE VISUAL INSPECTION PROCESSES

Visual inspection is a costly exercise for asset owners and managers (Bennetts 2019). Visual inspection requires human inspectors to work outside in varied weather conditions, often at night and frequently in high-traffic environments (e.g. Bennetts 2019). As an aside, in the case of assessing bridge scour, for VI to be carried out, divers are necessary to detect potential scour holes formed due to floods below the foundations of a bridge (cf. Selvakumaran et al. 2018, Pregnolato et al. 2021). The need for divers implies an increased safety risk which needs to be managed. Moreover, another issue of VI is the lack of skilled inspectors for which the UK has introduced the Bridge Inspector Training Scheme (BICS) (Lantra 2023). Therefore, efforts to move VI processes offsite have the potential to supplement/enhance existing VI/SHM efforts (McRobbie et al. 2015, Nepomuceno 2022, Nepomuceno et al. 2022a, 2022b).

Nepomuceno et al. (2022b) (Figure 3) have recently presented a possible schema for moving parts of the VI process offsite: future realisation of such efforts will require improved technologies for image capture (see the recent paper of Nepomuceno et al. 2022a for a detailed review of new technologies to assist VI processes and the best practice guide for bridge monitoring by Middleton et al. 2016). New technologies may include use of 360° cameras, precision drone-based camera

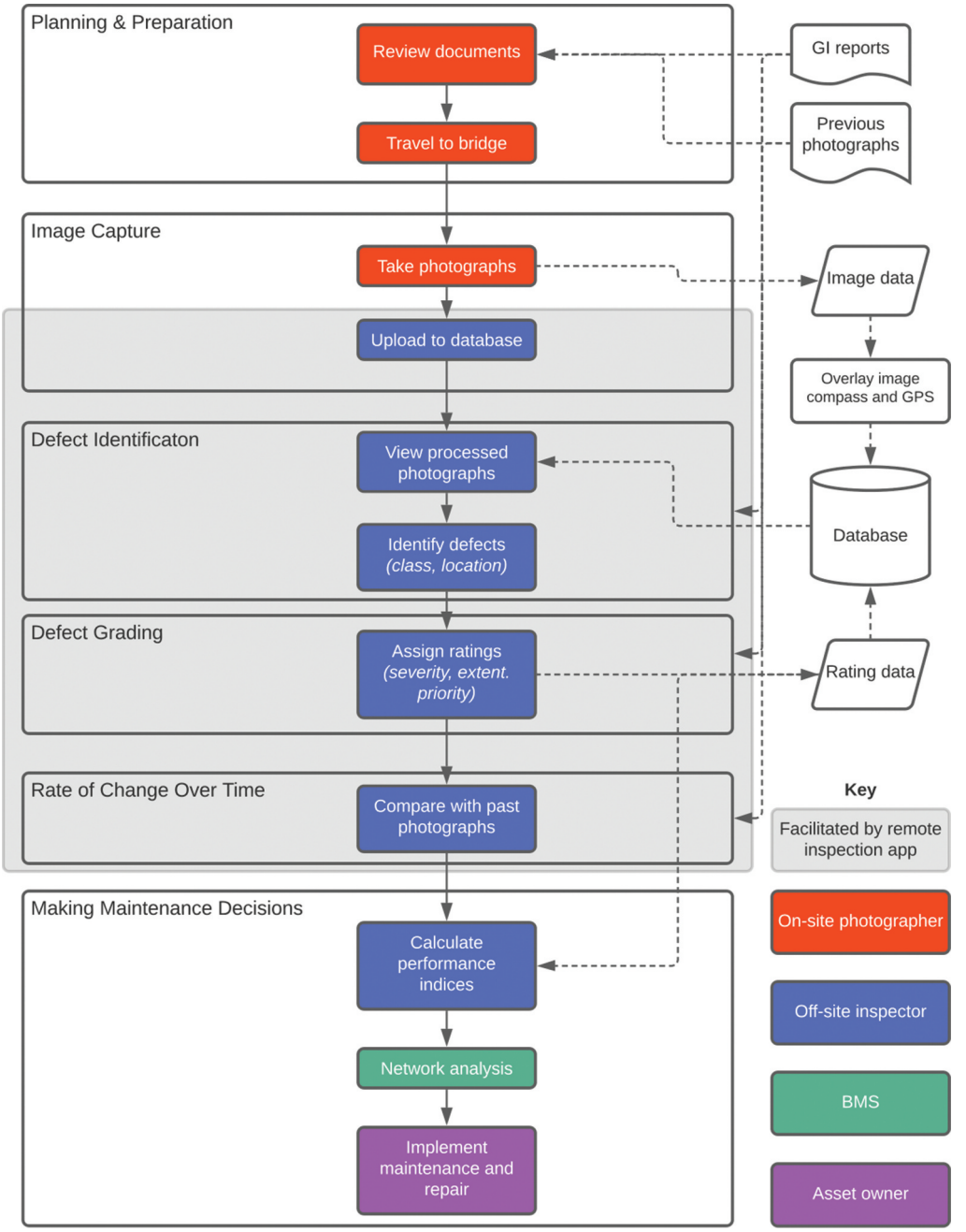


Figure 3. Workflow diagram of remote inspection schema (created in Lucidchart (2022)) (adapted from Nepomuceno et al. 2022b, used under the terms of the cc-by 4.0 licence).

systems, interferometric synthetic-aperture radar (InSAR) as well as virtual reality and computer vision (Nepomuceno et al. 2022a, 2022b). For the specific case of bridge scour, fibre optic installations, sonar and InSAR are devices that could potentially mitigate the need for divers in some instances (cf. Prendergast & Gavin 2014, Selvakumaran et al. 2018, Vardanega *et al.* 2021). Even if technological advances allow image capture to be done remotely with photographs and video, (i.e. assessed by human inspectors offsite) it is not guaranteed that the accuracy and precision of defect identification will be acceptable for those taking decisions based on this data.

Nepomuceno et al. (2021, 2023) presented preliminary survey data showing that the ratings from onsite and offsite inspectors tended to more closely agree for higher severity defects (see also Nepomuceno 2022). Further studies are needed to standardise off-site assessment of captured images. Regardless of whether the defect detection outcomes are the same offsite, decisions about maintenance and intervention still depend on the VI data and associated metrics. These considerations persist regardless on whether the process stays similar to current practices or shifts towards being more technologically driven and conducted partially remotely.

4 POTENTIAL FUTURE INFLUENCES OF AI IN VI WORKFLOW

4.1 *Recent AI uses in structural engineering*

Use of AI is expected to increase in many fields, including bridge engineering. Alexander et al. (2022) used deep learning methods for crack detection on structures. Munawar et al. (2022) used ML methods for crack detection processes. Luleci & Catbas (2023b) suggested population-based structural health monitoring (PBSHM) approaches for pre-stressed bridges. Luleci & Catbas (2023a) present a recent review of deep generative models (DGMs) in SHM. Luleci & Catbas (2023a) conclude that data scarcity remains a challenge in the field of bridge engineering (see also the review of Catbas & Avci 2023 which mentions in part the use of virtual reality in bridge SHM). Stacy (2023) notes that data alone is not sufficient for good decision making. Projects such as the Data Analytics Facility for National Infrastructure (DAFNI) may help with the analysis of future larger datasets (Matthews et al. 2023).

AI approaches may assist with data analysis and pattern recognition across large datasets. AI offers potential improvements across the VI process. For example, AI could potentially be used to evaluate trends from stock-level (regional) data sets of VI metrics, further enhancing what can be gleaned from 'manual' analysis of large structural data sets such as those reported in Bennetts et al. (2018a, 2018b).

There are potential concerns/limitations, such as the fact that semi-automated or fully automated processes may detect specific instances of bridge damage (i.e. the defect location). There are also concerns on how well severity will be assessed with AI methods compared to human inspectors. For instance, from an asset management perspective, if a bridge with a defect of a similar extent and severity is repaired and this is reflected in the data set the AI is applied to; would AI-based processes recommend repair in other similar cases and if so on what basis? Asset managers may not be able to deduce why AI prioritisation or recommendations have been made and hence the context for decisions/recommendations may become less clear and less able to be scrutinised by other stakeholders.

4.2 *Engineering judgement*

Bennetts et al. (2016) showed using data from semi-structured interviews that engineering judgement is very important in taking bridge management decisions. In the context of a potentially AI enhanced VI process, what is the fundamental role of the 'engineer'? Engineering judgement is needed to take decisions regarding assignment of design parameters and for catching errors in design processes (cf. Peck 1980, Petroski 1993, Vardanega & Bolton 2016). In the case of VI 'judgement' is exercised when assessing the 'extent' or 'severity' of the defect. Judgment is also needed when prioritising bridges for maintenance expenditure. A future question for bridge managers using AI processes will be how they will be able to

safely overrule AI recommendations when they produce results that do not align with their own engineering judgement.

5 SUMMARY

This paper has reviewed recent research efforts on the use of VI data for associated bridge condition metrics – these data have the potential to be further analysed using AI tools. Use of VI data is still widely used for assessing structural condition and therefore there is a relevant question on how much of this time-consuming and expensive process can be conducted offsite. Survey data has shown some offsite evaluation of defect severity can be potentially considered, although more data is needed to confirm if off-site inspectors can replace on-site inspectors (assuming comprehensive image capture can be carried out using new and an emerging technological solutions). Finally, with the recent prominence of AI, further research of on the use of AI in VI should be undertaken.

ACKNOWLEDGEMENTS

This work has been funded in part by the Horizon Europe project ELAB-ORATOR (Grant agreement ID: 101103772).

REFERENCES

Alexander, Q.G., Hoskere, V., Narazaki, Y., Maxwell, A. & Spencer Jr, B.F. 2022. Fusion of thermal and RGB images for automated deep learning based crack detection in civil infrastructure. *AI in Civil Engineering* 1: [3] https://doi.org/10.1007/s43503-022-00002-y

Bennetts, J. 2019. The Management of Bridges. *EngD thesis*, University of Bristol, Bristol, UK.

Bennetts, J., Denton, S.R., Webb, G.T., Nepomuceno, D.T. & Vardanega, P.J. 2021. Looking to the future of bridge inspection and management in the UK. In Yokota, H. & Frangopol, D.M. (eds.), *Bridge Maintenance, Safety, Management, Life-Cycle Sustainability and Innovations: Proceedings of the Tenth International Conference on Bridge Maintenance, Safety and Management (IABMAS 2020), Sapporo, Japan, 11-15 April 2021*. CRC Press/Balkema Taylor & Francis Group, Leiden, The Netherlands, pp. 3858–3866 https://doi.org/10.1201/9780429279119-526

Bennetts, J., Vardanega, P.J., Taylor, C.A. & Denton, S.R. 2016. Bridge data – what do we collect and how do we use it? In: Mair, R.J., Soga, K., Jin, Y., Parlikad, A.K. & Schooling, J.M. (eds.), *Transforming the Future of Infrastructure through Smarter Information: Proceedings of the International Conference on Smart Infrastructure and Construction, 27-29 June 2016*. ICE Publishing, London, UK, pp. 531–536.

Bennetts, J., Vardanega, P.J., Taylor, C.A. & Denton, S.R. 2020. Survey of the use of data in UK bridge asset management. *Proceedings of the Institution of Civil Engineers – Bridge Engineering* 173(4): 211–222 https://doi.org/10.1680/jbren.18.00050.

Bennetts, J., Vardanega, P.J., Webb, G.T., Denton, S.R. & Loudon, N. 2023. Analysis of visual inspection data for a sample of highway bridges in the UK. *Proceedings of the Institution of Civil Engineers – Forensic Engineering* 176(3): 79–88 https://doi.org/10.1680/jfoen.21.00005.

Bennetts, J., Webb, G., Denton, S., Vardanega, P.J. & Loudon, N. 2018a. Quantifying Uncertainty in Visual Inspection Data. In: Powers, N., Frangopol, D.M., Al-Mahaidi, R. & Capriani, C. (eds.), *Maintenance, Safety, Risk, Management and Life-Cycle Performance of Bridges: Proceedings of the Ninth International Conference on Bridge Maintenance, Safety and Management (IABMAS 2018), 9-13 July 2018, Melbourne, Australia*. CRC Press/Balkema Taylor & Francis Group, Leiden, The Netherlands, pp. 2252–2259. https://doi.org/10.1201/9781315189390-306

Bennetts, J., Webb, G.T., Vardanega, P.J., Denton, S.R., & Loudon, N. 2018b. Using data to explore trends in bridge performance. *Proceedings of the Institution of Civil Engineers – Smart Infrastructure and Construction* 171(1): 14–28. https://doi.org/10.1680/jsmic.17.00022

Catbas, N, & Avci. O. 2023. A review of latest trends in bridge health monitoring. *Proceedings of the Institution of Civil Engineers – Bridge Engineering* 176(2): 76–91. https://doi.org/10.1680/jbren.21.00093.

Colford, B.R., Zhou, E. & Pape, T. 2022. Structural health monitoring – a risk-based approach. *Proceedings of the Institution of Civil Engineers – Bridge Engineering*, https://doi.org/10.1680/jbren.21.00073.

HA (Highways Agency) 2007. Inspection Manual for Highway Structures. Volume 1: Reference Manual. The Stationary Office, London, UK.

HE (Highways England) 2021. CS 450 Inspection of highway structures. *Standards for Highways.* See: <https://www.standardsforhighways.co.uk/search/html/c5c2c3e5-f7f3-4c94-8254-184e41ccd1a0?standard=DMRB> (23/02/2024)

Lantra 2023. National Highway Sector Scheme 31 for the Bridge Inspector Certification Scheme: Scheme Manual. Lantra, Coventry, UK. See:<https://www.lantra.co.uk/media/fk0btwgs/bridge-inspector-certification-scheme-manual.docx>(12/03/2024).

Lea, F. & Middleton, C. 2002. Reliability of Visual Inspection of Highway Bridges. Department of Engineering, University of Cambridge, Cambridge, UK, Technical Report C*UED/D-STRUCT/TR.201*.

Lucidchart 2022. See:<www.lucidchart.com>. Lucid Software Inc., South Jordan, UT, USA (31/10/2022).

Luleci,F. & Catbas, F.N. 2023a. A brief introductory review to deep generative models for civil structural health monitoring. *AI in Civil Engineering* 2: [9] https://doi.org/10.1007/s43503-023-00017-z

Luleci, F. & Catbas, F.N. 2023b. Condition transfer between prestressed bridges using structural state translation for structural health monitoring. *AI in Civil Engineering* 2: [7] https://doi.org/10.1007/s43503-023-00016-0

Matthews, B., Hall, J., Batty, M., Blainey, S., Cassidy, N., Choudhary, R., Coca, D., Hallett, S., Harou, J.J., James, P., Lomax, N., Oliver, P., Sivakumar, A., Tryfonas, T., & Varga, L. (2023). DAFNI: a computational platform to support infrastructure systems research. *Proceedings of the Institution of Civil Engineers – Smart Infrastructure and Construction* 176(3): 108–116 https://doi.org/10.1680/jsmic.22.00007

McRobbie, S.G., Wright, M.A. & Chan, A. 2015. Can technology improve routine visual bridge inspections?. *Proceedings of the Institution of Civil Engineers – Bridge Engineering* 168(3): 197–207 https://doi.org/10.1680/jbren.12.00022

Middleton, C. 2004. Bridge management and assessment in the UK. Paper presented at: Fifth Austroads Bridge Conference, 19-21 May 2004, Hobart, Tasmania. Austroads, Sydney, Australia. See:<https://web.archive.org/web/20221024074022/http://www.bridgeforum.org/files/pub/2004/austroads5/Middleton%20keynote.pdf> (12/03/2024).

Middleton, C.R., Fidler, P.R.A. & Vardanega, P.J. 2016. *Bridge Monitoring: A Practical Guide*. ICE Publishing, London, UK.

Moore, M., Phares, B., Graybeal, B., Rolander, D. & Washer, G. 2001. Reliability of Visual Inspection for Highway Bridges, Volume 1. US DOT, Federal Highway Administration, Washington, DC, USA.

Munawar, H.S., Hammad, A.W.A., Waller, S.T. & Islam, M.R. 2022. Modern Crack Detection for Bridge Infrastructure Maintenance Using Machine Learning. *Human-Centric Intelligent Systems* 2 (3-4): 95–112 https://doi.org/10.1007/s44230-022-00009-9

Nepomuceno, D.D.T. 2022. Technology Innovation for Improving Bridge Management. *PhD thesis*, University of Bristol, Bristol, UK.

Nepomuceno, D.T, Vardanega, P.J., Tryfonas, T., Bennetts, J., Denton, S.R., Collard-Jenkins, S., Thackray, C., Green, J. & DiNiro, M. 2021. Viability of off-site inspections to determine bridge defect ratings. In: Yokota, H. & Frangopol, D.M. (eds.), *Bridge Maintenance, Safety, Management, Life-Cycle Sustainability and Innovations: Proceedings of the Tenth International Conference on Bridge Maintenance, Safety and Management (IABMAS 2020), Sapporo, Japan, 11-15 April 2021*. CRC Press/Balkema Taylor & Francis Group, Leiden, The Netherlands, pp. 3688–3695 https://doi.org/10.1201/9780429279119-501

Nepomuceno, D.T., Bennetts, J., Pregnolato, M., Tryfonas, T. & Vardanega, P.J. 2022b. Development of a schema for the remote inspection of bridges. *Proceedings of the Institution of Civil Engineers – Bridge Engineering*, https://doi.org/10.1680/jbren.22.00027

Nepomuceno, D.T., Vardanega, P.J., Pregnolato, M. Tryfonas, T. & Bennetts, J. 2023. Viability of bridge inspectors determining defect ratings using photographic images. *Infrastructure Asset Management* 10(3): 144–156 https://doi.org/10.1680/jinam.23.00004

Nepomuceno, D.T., Vardanega, P.J., Tryfonas, T., Pregnolato, M., Bennetts, J. & Webb, G. 2022a. A survey of emerging technologies for the future of routine visual inspection of bridge structures. In Casas, J.R., Frangopol, D.M. & Turmo, J. (eds.), *Bridge Safety, Maintenance, Management, Life-Cycle, Resilience and Sustainability: Proceedings of the Eleventh International Conference on Bridge Maintenance, Safety and Management (IABMAS 2022), Barcelona, Spain, July 11-15, 2022*, CRC

Press/Balkema Taylor & Francis Group, London, UK, pp. 846–854 https://doi.org/10.1201/9781003322641-101

Peck, R.B. 1980. 'Where has all the judgment gone?' The fifth Laurits Bjerrum memorial lecture. *Canadian Geotechnical Journal* 17(4): 584–590. https://doi.org/10.1139/t80-065

Petroski, H. 1993. Failure as source of engineering judgment: Case of John Roebling. *Journal of Performance of Constructed Facilities* 7(1): 46-58 https://doi.org/10.1061/(ASCE)0887-3828(1993)7:1(46)

Pregnolato, M., Vardanega, P.J., Limongelli, M.P., Giordano, P.F. & Prendergast, L.J. 2021. Risk-based scour management: A survey. In: Yokota, H. & Frangopol, D.M. (eds.), *Bridge Maintenance, Safety, Management, Life-Cycle Sustainability and Innovations: Proceedings of the Tenth International Conference on Bridge Maintenance, Safety and Management (IABMAS 2020), Sapporo, Japan, 11-15 April 2021*. CRC Press/Balkema Taylor & Francis Group, Leiden, The Netherlands, pp. 693-701 https://doi.org/10.1201/9780429279119-91

Prendergast, L.J. & Gavin, K. 2014. A review of bridge scour monitoring techniques. *Journal of Rock Mechanics and Geotechnical Engineering* 6(2): 138–149 https://doi.org/10.1016/j.jrmge.2014.01.007.

Selvakumaran, S., Plank, S., Geiß, C., Rossi, C. & Middleton C. 2018. Remote monitoring to predict bridge scour failure using Interferometric Synthetic Aperture Radar (InSAR) stacking techniques. *International Journal of Applied Earth Observation and Geoinformation* 73: 463–470 https://doi.org/10.1016/j.jag.2018.07.004

Stacy, M. 2023. Data and decisions for bridge maintenance. *The Structural Engineer* 101(9): 38-39 https://doi.org/10.56330/KGIE8593

Sterritt, G. 2002. Bridge Condition Indicators. WS Atkins for CSS Bridges Group, London, UK, vol. 1.

Thurlby, R. 2013. Managing the asset time bomb: a system dynamics approach. *Proceedings of the Institution of Civil Engineers – Forensic Engineering* 166(3): 134–142 https://doi.org/10.1680/feng.12.00026

Thurlby, R. & Rimell, J. 2015. Discussion: Managing the asset time bomb: a systems dynamics approach. *Proceedings of the Institution of Civil Engineers - Forensic Engineering* 168(4): 181–182 https://doi.org/10.1680/feng.15.00007

Vardanega, P.J. & Bolton, M.D. 2016. Design of Geostructural Systems. *ASCE ASME Journal of Risk and Uncertainty in Engineering Systems. Part A: Civil Engineering* 2(1): [04015017]. https://doi.org/10.1061/AJRUA6.0000849

Vardanega, P.J., Gavriel, G. & Pregnolato, M. 2021. Assessing the suitability of bridge-scour-monitoring devices. *Proceedings of the Institution of Civil Engineers – Forensic Engineering* 174(4): 105–117 https://doi.org/10.1680/jfoen.20.00022

Wallbank, E.J. 1989. *The Performance of Concrete in Bridges: A Survey of 200 Highway Bridges*. Her Majesty's Stationery Office, London, UK.

Webb, G.T., Vardanega, P.J. & Middleton, C.R. 2015. Categories of SHM Deployments: Technologies and Capabilities. *Journal of Bridge Engineering (ASCE)* 20(11): [04014118] https://doi.org/10.1061/(ASCE)BE.1943-5592.0000735.

Bridge Maintenance, Safety, Management, Digitalization and Sustainability – Jensen, Frangopol & Schmidt (eds)
© 2024 The Author(s), ISBN 978-1-032-77040-6
Open Access: www.taylorfrancis.com, CC BY-NC-ND 4.0 license

Performance evaluation of TMDs for a continuous steel box girder

G.L. Liu, X.H. Hu & R.J. Ma
Tongji University, Shanghai, China

ABSTRACT: Tuned Mass Damper (TMD) is widely utilized for vibration control in bridge due to its exceptional damping effectiveness. However, its performance may gradually deteriorate over time. Hence, the reassessment of TMD performance is necessary. This study focuses on TMDs equipped in the Chong Qi Bridge in China. By analyzing the health monitoring data, the dynamic characteristic parameters of the main girder were derived, and the correlation between wind speed and acceleration was studied. On-site random vibration tests were conducted by locking or activating each TMD to investigate the overall bridge vibration during the test process. Based on the test data, the influence of TMDs on the damping ratio of the entire bridge was analyzed, and a new indicator was proposed to quantitatively evaluate the working performanceof TMDs. Free vibration tests were performed on TMDs, and the frequency and damping ratio were measured using a self-developed mobile app.

1 INTRODUCTION

The continuous steel box girder bridge has advantages such as light weight, convenience in construction, good seismic performance and extensive application. However, as the span of the bridge increases, its flexibility also increases, and it becomes more susceptible to wind-induced vibration such as vortex-induced vibration (VIV), which may lead to significant vibration responses, adversely affecting traffic safety. Therefore, it is necessary to take measures to suppress the vibration response of the bridge structure.

Common control measures for wind-induced vibration include aerodynamic measures and mechanical measures. Aerodynamic measures can reduce the wind sensitivity of bridges by optimizing the bridge cross-sectional shape, such as the installation of wind deflectors, stabilizing plates, etc. (Fujino & Siringoringo, 2013). Mechanical measures often refer to dampers, such as Tuned Mass Dampers (TMDs), which can dissipate the vibration energy of the main girder through passive resonance. TMD is used on numerous bridges, such as the Rio-Niteroi Bridge (Battista & Pfeil, 2000) and Trans-Tokyo Bay Crossing bridge (Fujino & Yoshida, 2002). Wang et al. (2014) studied the control of bridge flutter using Multiple Tuned Mass Dampers (MTMDs) and optimized the parameters of MTMDs. Nagarajaiah & Jung (2014) made an introduction to Smart Tuned Mass Dampers (STMD), which had variable stiffness and damping. Debnath et al. (2016) conducted researches on simultaneous control of lateral, vertical, and torsional vibrations using TMD. Chen et al. (2017) experimentally studied the control effect of Eddy Current Tuned Mass Damper (ECTMD) on cantilever beam vibrations. Dai et al. (2019) proposed a design method of TMD parameters with the goal of improving robustness. Li et al. (2023) focused on wind-induced vibration control of irregular bridges and studied an optimized design method using spatially distributed TMD-type counterweights.

The analysis of vibration control effects is an essential aspect of the safety assessment of bridge structures, and scholars have conducted numerous studies on the evaluation of damping effects of TMDs. Van Nimmen et al. (2016) studied the vibration response of a pedestrian bridge equipped with TMD under crowd load through numerical simulation, evaluating the damping performance of TMD. Kim et al. (2017) identified bridge modal damping ratios

DOI: 10.1201/9781003483755-423

based on monitoring data and observed a significant increase in modal damping ratios after TMD was installed. Bayat et al. (2021) investigated the performance of TMD in suppressing vertical vibration of bridges under vehicle load through numerical methods, and conducted parameter analysis on damping performance. Sun et al. (2022) proposed a machine learning-based approach to assess the effectiveness of TMD based on monitoring data.

With the growth of service time, the performance of the TMD may degrade, necessitating a reassessment of its vibration suppression capability. Existing studies on TMD performance evaluation are still not comprehensive enough, with insufficient researches based on monitoring data, and lack attention on the dynamic behavior of TMD itself. This study takes the Chong Qi Bridge in China as an example. Modal parameters of the main girder were identified based on monitoring data, and the correlation between the vibration acceleration and wind speed was studied. On-site experiments were conducted with the TMD individually locked or activated, and changes in the vibration of the main girder and TMDs were analyzed. The dynamic characteristics of TMDs were identified using a self-developed mobile application. Finally, conclusions regarding the performance evaluation of TMDs in the Chong Qi Bridge are provided.

2 DESCRIPTION OF CHONG QI BRIDGE

The Chong Qi Bridge is a cross-river passage connecting Chongming Island and Qidong City in Jiangsu Province. The bridge was opened to traffic on December 24, 2011, and has been in operation for 12 years. The main bridge is arranged as four main spans of 185m and two side spans of 102m. The main girder adopts the design of a separative continuous steel box girder.

TMDs are installed on both sides of each main span to reduce VIV responses. There are four TMDs installed at the midspan of each main span, totaling 32 TMDs for the entire bridge (Figure 1), named U01-U16 (U for Upstream) and D01-D16 (D for Downstream). The TMDs primarily suppress the first vertical mode vibration of the bridge, and hence the design frequency of the TMD is set at 0.5Hz, close to the frequency of the first vertical mode. After optimization analysis of damping efficiency, the damping ratio of the TMD is set at 10%(Meinhardt et al., 2014).

The Chong Qi Bridge is equipped with a comprehensive structural health monitoring system. Anemometers are positioned on either side of Span3 (Figure 1) to measure the wind speed. Unidirectional accelerometers are distributed on each span and each TMD to measure the vertical vibration response of the structure.

3 ANALYSIS OF HISTORICAL MONITORING DATA

3.1 *Identification of main girder modal parameters*

The Random Decrement Technique (RDT) is a time-domain signal processing method which can extract free decay vibration signals from random vibration signals. This method is achieved by using an appropriate threshold to cut the original signal, obtaining Random

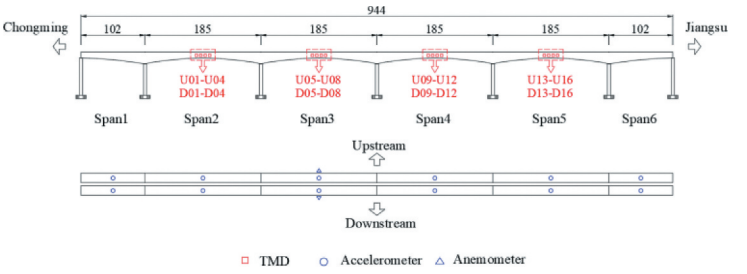


Figure 1. Overall layout and sensor arrangement of the Chong Qi Bridge.

Decrement Signature (RDS) results with the same initial value, and then averaging all RDSs to obtain the free decay vibration signal, but it's only applied for single degree-of-freedom systems. Huang et al. (1998) proposed the Empirical Mode Decomposition (EMD) method, which can decompose the original signal into a series of intrinsic mode functions (IMFs). However, EMD cannot decompose the response of systems with crowded modes. Chen & Wang (2012) introduced a signal decomposition method based on Hilbert transform, known as Analytical Mode Decomposition (AMD). This method can effectively decompose dense frequency signals, making it suitable for modal parameter identification (Wang & Chen, 2014).

The procedure of modal parameter identification is as follows. Firstly, use the peak-picking method to determine the first four vertical mode frequencies. Secondly, process the signal by AMD. Thirdly, apply RDT to each decomposed signal, and use the least squares method to fit the free decay vibration signal, then the frequency and damping ratio can be obtained. Taking a segment of the main girder vibration signal as an example, the analysis of the first vertical mode is shown in Figure 2, and the frequency is 0.510Hz while the damping ratio is 4.054%.

After obtaining vibration signals from October 2021 to December 2022, 10-minute signals were used as samples for identification, and daily vertical modal frequencies and damping ratios were acquired (Figure 3). Taking the average value as the representative value, the results are shown in Table 1. Actual frequencies are generally consistent with frequencies of the finite element model. The damping ratio of the first vertical mode is much greater than the design requirement of 1.15% (Qin et al., 2014), indicating that TMDs can significantly increase the damping ratio.

Table 1. Mean values of main girder modal parameters.

Mode	FEM frequency Hz	Actual frequency Hz	Actual damping ratio %
1st mode	0.519	0.512	4.341
2nd mode	0.679	0.657	3.498
3rd mode	0.883	0.875	2.463
4th mode	1.121	1.097	2.025

3.2 *Wind-induced vibration response analysis*

A correlation analysis was conducted between the wind speed and the vibration acceleration. Data with wind speeds below 6 m/s were excluded to minimize the influence of other factors. The wind speed was taken as the 10-minute average value, and the acceleration was taken as the root mean square value of a 10-minute period. Taking the main girder on the downstream side and TMD D06 for example, the calculated results of correlation coefficients are shown in Figure 4.

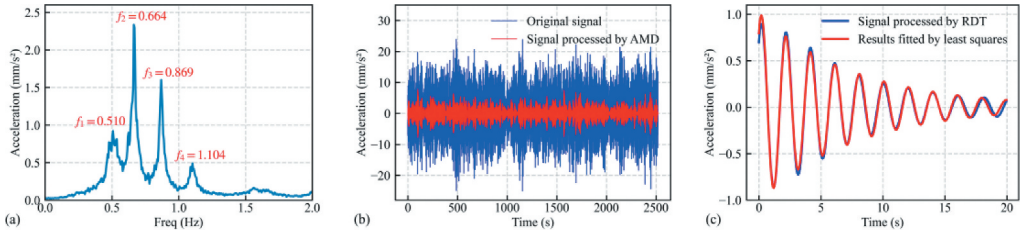


Figure 2. Process of modal parameter identification (a) Amplitude spectrum. (b) AMD processing. (c) RDT Processing and Fitting.

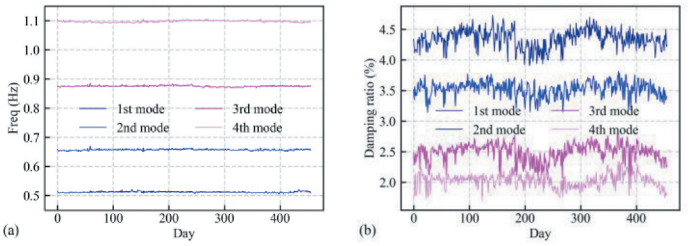


Figure 3. Daily identification results of the main girder modal parameters (a) Frequency. (b) Damping ratio.

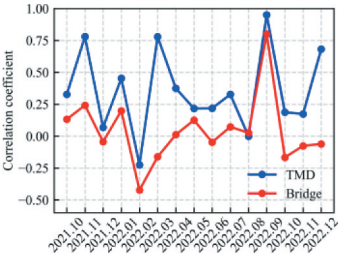


Figure 4. Correlation coefficients between acceleration and wind speed.

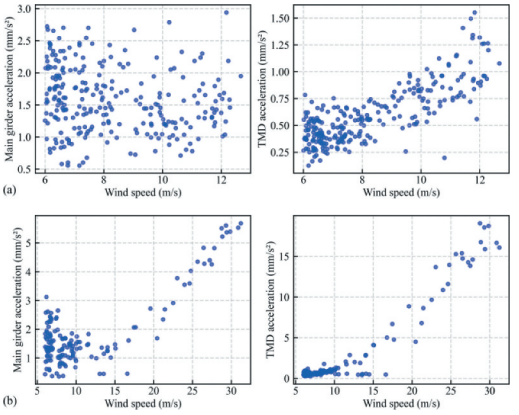


Figure 5. Acceleration against wind speed (a) 2022.03. (b) 2022.09.

For the main girder, the period with a significant correlation between wind speed and acceleration is only in September 2022 when wind speeds exceeded 15 m/s (Figure 5b). At other times, the correlation is not obvious. For the TMD, the correlation between wind speed and acceleration is more pronounced compared with the main girder. Even when the correlation between wind speed and main girder acceleration is weak, there is still a noticeable correlation between wind speed and TMD acceleration, as observed in March 2022 (Figure 5a).

The vibration of the main girder is significantly influenced by wind speed only when the wind speed is high (larger than 15 m/s). During such periods, vibrations of both the main girder and the TMD increase with the wind speed increasing. At ordinary wind speeds, the TMD vibration is significantly affected by wind speed, while the main girder vibration is less

affected. In other words, the vibration energy is transferred from the main girder to the TMD, thereby suppressing the wind-induced vibration of the main girder.

4 ON-SITE RANDOM VIBRATION TEST

4.1 *Test scheme*

An ambient vibration test was conducted on the upstream side of the main girder by sequentially locking or activating each TMD. The acceleration time history of the main girder and TMDs during this process was measured using the accelerometer of the health monitoring system. The test was started by locking the TMD one by one. Each time, only one TMD of a span was locked, and measurement was taken for 10 minutes before locking the next TMD of the next span. This process was repeated until all TMDs were locked. Subsequently, TMDs were activated span by span, with all four TMDs of an entire span being activated simultaneously. After activating TMDs of one span, measurement was taken for 20 minutes before activating TMDs of the next span. This process was repeated until all TMDs were activated.

4.2 *Overall bridge vibration analysis*

The acceleration time history of the main girder during the test process was processed using the complex Morlet wavelet transform to obtain a time-frequency diagram (Figure 6). With each TMD sequentially locked, the vibration energy corresponding to the first two vertical modes noticeably increased, while the energy of higher order vertical modes hardly varied. With TMDs of each span activated, the vibration energy of the first two vertical modes rapidly decreased, while the energy of higher order vertical modes remained almost unchanged. When all TMDs were active, the vibration energy was mainly concentrated in higher order vertical modes. After locking all TMDs, the vibration energy of each mode became similar.

Using the modal parameter identification method discussed in section 3.1, the damping ratio variation of each vertical mode of the main girder during the test process is presented in Figure 7. During the sequential locking of TMDs, the damping ratio of the main girder shows a decreasing trend. The most significant change is observed in the damping ratio of the first vertical mode, while the damping ratios of higher order modes remain relatively constant. In the process of sequentially activating TMDs, damping ratios of each mode gradually increase

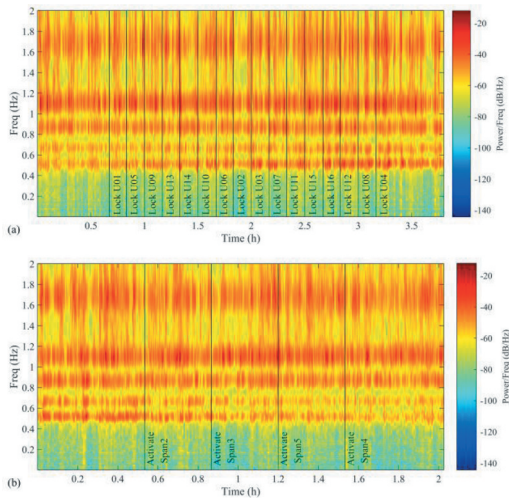


Figure 6. Time-frequency diagram of the main girder vibration during the test process (a) TMDs sequentially locked. (b) TMDs sequentially activated.

and eventually return to their initial values. Due to the uncertainty in the identification of the damping ratio, the damping ratio during the locking process does not monotonically decrease, and thus, these results are intended for qualitative analysis only.

The above results indicate that TMDs primarily suppress the first vertical mode vibration, with a weak control effect on higher order modes, which is consistent with the design principle. Additionally, even if half of TMDs are locked, the damping ratio of the first vertical mode remains higher than 1.15%, indicating that the bridge has a high level of safety redundancy.

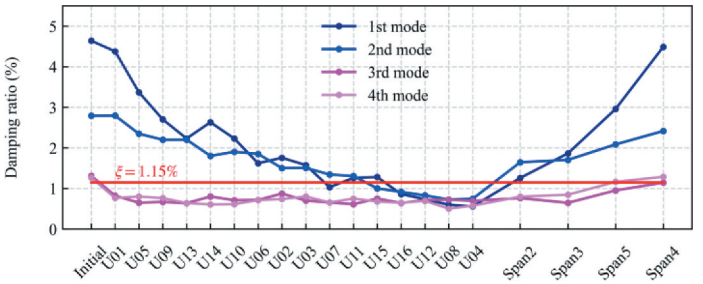


Figure 7. Variation in damping ratios of the main girder during the test process.

4.3 *TMD vibration analysis*

Taking TMD U01-U04 as examples, acceleration time history was obtained when all TMDs were activated and when all TMDs were locked. The acceleration signals were then low-pass filtered to extract vibration near the frequency of the first vertical mode of the bridge (Figure 8) When all TMDs were activated, the vibration amplitudes of U02-U04 were significantly larger than that of the main girder, and the phases of their vibrations delayed to approximately 90 degrees after the main girder. The vibration of U01 was close to that of the main girder, indicating that it did not exhibit effective vibration reduction. When all TMDs were locked, vibrations of TMDs were all close to the main girder vibration.

In order to quantitatively analyze the performance of TMDs, a new evaluation index is proposed. The vibration amplitude spectra of TMDs and the main girder (denoted as P_{TMD} and P_{girder}) in a same time period were calculated. The ratio of these two spectra was then obtained to eliminate the influence of differences in environmental excitations during different time periods, getting a dimensionless result. The maximum value of this ratio is denoted as η, as shown in Equation 1. η is used to measure the extent of energy transfer from the main girder to the TMD. A higher η value indicates a more efficient transfer of vibration energy, reflecting better working performance of the TMD.

$$\eta = \max\left(\frac{P_{TMD}}{P_{girder}}\right) \tag{1}$$

The calculation results of $P_{\mathrm{TMD}}/P_{\mathrm{girder}}$ of U01-U04 before and after being locked are shown in Figure 9. Before being locked, the vibration of the TMD was significantly larger than the main girder vibration ($\eta > 1$). After being locked, the TMD vibration became close to the main girder vibration, showing that they performed similar forced vibrations ($\eta \approx 1$). Before the lock of the TMD, η appeared at the frequency of about 0.5Hz, corresponding to the first vertical mode of the main girder, further proving that the TMD primarily absorbed the vibration energy of the first vertical mode. The η value of U01 is relatively small, suggesting that its working performance is not as effective as other TMDs.

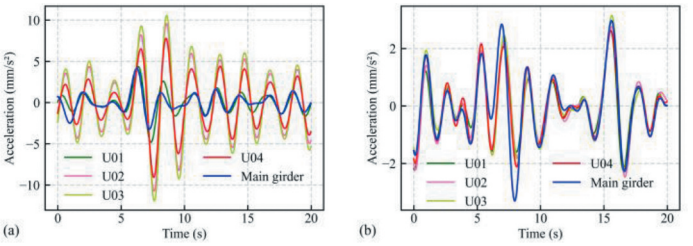


Figure 8. Vibration time history of TMDs and the main girder (a) All TMDs activated. (b) All TMDs locked.

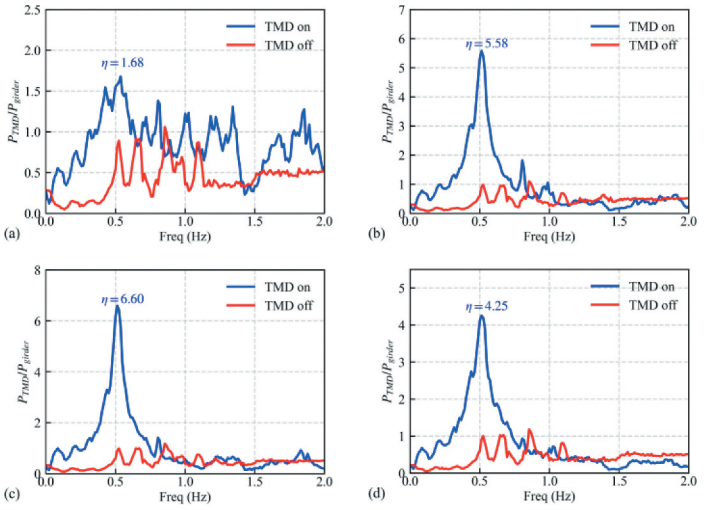


Figure 9. Vibration amplitude ratio of TMDs to the main girder (a) U01. (b) U02. (c) U03. (d) U04.

5 IDENTIFICATION OF TMD DYNAMIC CHARACTERISTICS

Dynamic characteristics of the TMD can be identified through free vibration test. In this process, an initial excitation is applied to the TMD, and the acceleration of the TMD during the free decay vibration is measured. The least squares method is then employed to identify the frequency and damping ratio of the TMD, and the principle is consistent with Figure 2(c). Generally, this measurement is performed using the accelerometers installed on the TMD. However, the acquirement and analysis of data from the monitoring system are not convenient. Therefore, a TMD dynamic characteristic identification app has been developed. This app is written by JavaScript, and can utilize the built-in accelerometer of the phone and identify the frequency and damping ratio.

16 TMDs on the upstream side were tested. The result obtained from the app is shown in Figure 10, demonstrating an acceleration resolution of 0.0001 m/s². The dynamic characteristics of TMDs are shown in Figure 11, frequencies are all around 0.5 Hz and damping ratios are within the range of 0.07 to 0.13 (considering a manufacturing error of 30%). This indicates that the dynamic characteristics of TMDs still meet the design requirement. Differences in TMD working performance analyzed in section 4.3 might be attributed to the installation error or other factors.

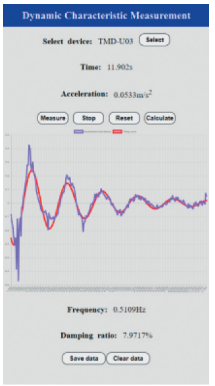


Figure 10. Dynamic characteristic measurement interface of the app.

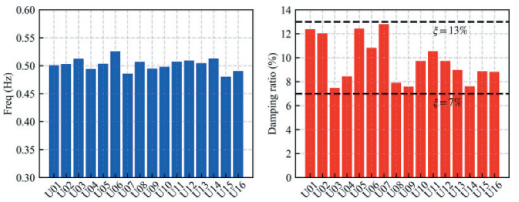


Figure 11. Dynamic characteristics of TMDs.

6 SUMMARY

This paper takes TMDs installed in the Chong Qi Bridge as a case study, and research findings of TMD evaluation are as follows.

1. Based on monitoring data, the frequencies and damping ratios of the main girder were identified by the AMD+RDT method. The damping ratios are significantly higher than the design requirement, indicating that TMDs provide a remarkable increasement in the damping ratio.
2. The wind-induced vibration responses of the main girder and TMDs were analyzed. The TMD vibration showed a stronger correlation with wind speed compared to that of the main girder, suggesting that TMDs convert the main girder vibration into their own vibration.
3. During the locking of TMDs in the on-site test, the vibration of the main girder increased, and the damping ratio decreased. The reduction in the damping ratio was most significant for the first vertical mode, showing that TMDs primarily reduce the first vertical mode vibration.
4. A quantitative evaluation index for TMD working performance was proposed. Taking TMD U01-U04 as examples, the analysis results showed significant changes in this index before and after TMD being locked, with U01 exhibiting poorer working performance compared to others.
5. Through the free vibration test, the inherent frequency and damping ratio of each TMD were measured by a self-developed app, and the results were within the design range.

This study conducted a comprehensive evaluation of TMDs in a continuous steel box girder. The methods employed can be applied to TMDs in other bridges, and provide recommendations for the routine inspection and maintenance based on the evaluation results of the TMD.

REFERENCES

Battista, R. C. & Pfeil, M. S. 2000. Reduction of vortex-induced oscillations of Rio-Niteroi bridge by dynamic control devices. *J. Wind Eng. Ind. Aerodyn.*, 84, 273–288.

Bayat, E., Bayat, M. & Hafezzadeh, R. 2021. Numerical performance assessment of Tuned Mass Dampers to mitigate traffic-induced vibrations of a steel box-girder bridge. *Struct. Eng. Mech.*, 78, 125–134.

Chen, G. D. & Wang, Z. C. 2012. A signal decomposition theorem with Hilbert transform and its application to narrowband time series with closely spaced frequency components. *Mech. Syst. Signal Proc.*, 28, 258–279.

Chen, J. D., Lu, G. T., Li, Y. R., Wang, T., Wang, W. X. & Song, G. B. 2017. Experimental Study on Robustness of an Eddy Current-Tuned Mass Damper. *Appl. Sci.-Basel*, 7, 11.

Dai, J., Xu, Z. D., Yin, X. J., Gai, P. P. & Luo, Y. 2019. Parameters Design of TMD Mitigating Vortex-Induced Vibration of the Hong Kong-Zhuhai-Macao Bridge Deep-Water Nonnavigable Bridge. *J. Bridge Eng.*, 24, 12.

Debnath, N., Deb, S. K. & Dutta, A. 2016. Multi-modal vibration control of truss bridges with tuned mass dampers under general loading. *J. Vib. Control*, 22, 4121–4140.

Fujino, Y. & Siringoringo, D. 2013. Vibration Mechanisms and Controls of Long-Span Bridges: A Review. *Struct. Eng. Int.*, 23, 248–268.

Fujino, Y. & Yoshida, Y. 2002. Wind-induced vibration and control of Trans-Tokyo Bay Crossing bridge. *J. Struct. Eng.-ASCE*, 128, 1012–1025.

Huang, N. E., Shen, Z., Long, S. R., Wu, M. L. C., Shih, H. H., Zheng, Q. N., Yen, N. C., Tung, C. C. & Liu, H. H. 1998. The empirical mode decomposition and the Hilbert spectrum for nonlinear and non-stationary time series analysis. *Proc. R. Soc. A-Math. Phys. Eng. Sci.*, 454, 903–995.

Kim, S., Park, J. & Kim, H. K. 2017. Damping Identification and Serviceability Assessment of a Cable-Stayed Bridge Based on Operational Monitoring Data. *J. Bridge Eng.*, 22, 11.

Li, Z. C., Xu, K., Ma, R. S., Fang, G. S. & Han, Q. 2023. Vibration Control of Irregular Bridges Using Spatially Distributed TMD-Type Counterweights. *Int. J. Struct. Stab. Dyn.*, 23, 27.

Meinhardt, C., Yin, X., Luo, Y. & Gao, X. 2014. Enhancement of the Chong Qi bridge project girder sections to reduce vortex shedding induced oscillations by applying passive tuned mass damper systems. 7th International Conference on Bridge Maintenance, Safety and Management (IABMAS), Jul 07-11 2014 Shanghai. BOCA RATON: Crc Press-Taylor & Francis Group, 472–479.

Nagarajaiah, S. & Jung, H. J. 2014. Smart tuned mass dampers: recent developments. *Smart. Struct. Syst.*, 13, 173–176.

Qin, H., Liao, H. L. & Li, M. S. 2014. Vortex induced vibration performance of long span continuous steel twin box beam bridge based on wind tunnel test. *J. Vib. Shock*, 206–210.

Sun, Z., Feng, D. C., Mangalathu, S., Wang, W. J. & Su, D. 2022. Effectiveness Assessment of TMDs in Bridges under Strong Winds Incorporating Machine-Learning Techniques. *J. Perform. Constr. Facil.*, 36, 14.

Van Nimmen, K., Verbeke, P., Lombaert, G., De Roeck, G. & Van Den Broeck, P. 2016. Numerical and Experimental Evaluation of the Dynamic Performance of a Footbridge with Tuned Mass Dampers. *J. Bridge Eng.*, 21, 14.

Wang, H., Tao, T. Y., Cheng, H. Y. & Li, A. Q. 2014. A simulation study on the optimal control of buffeting displacement for the Sutong Bridge with multiple tuned mass dampers. *J. Zhejiang Univ.-SCI A*, 15, 798–812.

Wang, Z. C. & Chen, G. D. 2014. Analytical mode decomposition with Hilbert transform for modal parameter identification of buildings under ambient vibration. *Eng. Struct.*, 59, 173–184.

Bridge Maintenance, Safety, Management, Digitalization and Sustainability – Jensen, Frangopol & Schmidt (eds)
© 2024 The Author(s), ISBN 978-1-032-77040-6
Open Access: www.taylorfrancis.com, CC BY-NC-ND 4.0 license

Improvement of thickness estimation model on a steel member using local vibration mode based on data augmentation

S. Kato & K. Hisazumi
Steel Structure Research Laboratory, Nippon Steel Corporation, Chiba, Japan

T. Tominaga
Department of Civil Engineering, Shizuoka Institute of Science and Technology, Japan

Y. Yang & T. Nagayama
Department of Civil Engineering, University of Tokyo, Tokyo, Japan

ABSTRACT: Evaluation of structural health via modal characteristics is effective when using regression methods such as machine learning. In certain instances, training data is generated through numerical analysis to ensure a robust dataset. However, this approach may lead to reduced model accuracy when applied to real-world structures, a result of overfitting due to discrepancies between input data in training and prediction. In this paper, to deal with thickness estimation in steel members using local vibration modes sensitive to damage, a model construction method using data augmentation is proposed to suppress overfitting. First, finite element analysis and experimental tests on a steel member are performed to assess the differences in modal characteristics between the training and prediction phases. The constructed thickness estimation model is then applied to actual measurement data, showing that the proposed method outperforms conventional models without data augmentation by over 40%.

1 INTRODUCTION

In recent years, the aging of infrastructure such as bridges and tunnels has become increasingly evident. Regular health assessments of these structures are essential. Traditional inspection methods often involve manual tasks such as visual inspection and hammer testing. However, these methods can pose safety risks during high-altitude inspection. For structures in operation, constraints on inspection times require operational efficiency. In these cases, the identification of sensitive natural modes related to structural defects through non-contact vibration measurement techniques, such as laser Doppler Vibrometers (LDVs) and accelerometers, has proven to be effective.

Conversely, methods that utilize regression techniques, such as machine learning, have been proposed to identify structural defects by analyzing natural modes acquired through non-contact measurements (Lee et al. 2021). Ogawa et al. (2023) developed a method that uses vibration data to evaluate the thickness reduction and the location of defects in steel members. This approach employs machine learning and leverages natural frequencies and mode shapes, which are collectively referred to as mode characteristics. Although obtaining empirical data for training is ideal, it presents a significant challenge due to the high costs of measuring civil structures such as bridges. Hence, simplified numerical analyses are often employed to generate training data.

However, in real-world structures, factors such as boundary conditions, thickness distribution, axial force variations, and mode identification methods often diverge from those in the simplified numerical analysis models used to create training data. Ignoring such differences may lead to overfitting and diminish the predictive accuracy of machine learning models when

DOI: 10.1201/9781003483755-424

they are applied to measured data obtained from actual structures. Consequently, this study proposes a method to enhance the accuracy of a machine learning model that estimates the thickness of steel members using characteristics of local vibration modes. This method quantitatively evaluates the differences between mode characteristics derived from actual structure measurements and those used in the training data. Furthermore, the study proposes a model construction approach that incorporates data augmentation to improve accuracy.

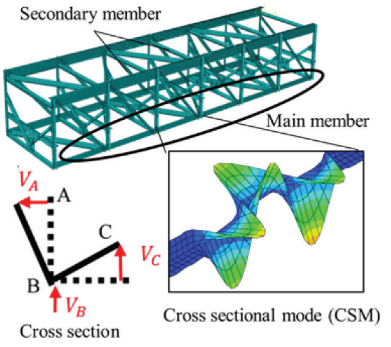


Figure 1. Cross sectional mode (CSM).

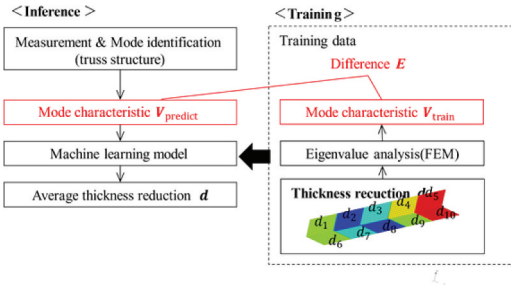


Figure 2. Overview of the thickness estimation method.

2 OVERVIEW OF THICKNESS ESTIMATION METHOD

In this study, we demonstrate the application of the model construction method on thickness estimation of an angle steel member, which is the main member of belt conveyor support structures in industrial facilities. The authors have previously investigated methods for extracting specific local vibration modes, such as cross sectional modes (CSM), which are highly sensitive to thickness reduction (Figure 1). A discriminative indicator, the CSM index (CSMI), has been proposed to characterize the cross-sectional features of CSM. Using CSMI, 1st, 2nd, and 3rd target modes are extracted from modal analysis on FEA or measurement data.

Then, a machine learning model is constructed based on the thickness estimation method shown in Figure 2. This allows the estimation of the thickness reduction rate (d) with the mode characteristics (V) as input. The definitions of V and d are as follows:

$$\boldsymbol{V} = \left(f_1, f_2, f_3, \boldsymbol{\phi}_1, \boldsymbol{\phi}_2, \boldsymbol{\phi}_3\right) \tag{1}$$

$$\boldsymbol{d} = (d_1, d_2, d_3, d_4, d_5, d_6, d_7, d_8, d_9, d_{10}) \tag{2}$$

Here, f_i and $\boldsymbol{\phi}_i$ (i =1, 2, 3) represent the natural frequency and mode shape of mode order i, respectively. The average thickness reduction rate of the 10-sectioned angle steel member, denoted as d_{sec} (sec=1,2...10), is also included. The components of $\boldsymbol{\phi}_i$ are normalized to values between 0 and 1 by dividing them by the maximum value at all output points.

3 PROPOSED METHOD FOR MACHINE LERANING MODEL CONSTRUCTION

3.1 *Measurement and analysis condition*

The difference $\boldsymbol{E}$ is defined by the following equation:

$$\boldsymbol{E} = \boldsymbol{V}_{\text{predict}} - \boldsymbol{V}_{\text{train}} \tag{3}$$

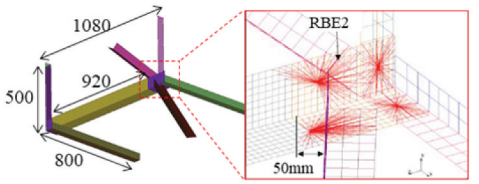
Where $\boldsymbol{V}_{\text{train}}$ denotes the mode characteristics in the training data, and $\boldsymbol{V}_{\text{predict}}$ denotes the mode characteristics during inference obtained through measurements on real-world structures. The study focuses on four factors listed in Table 1 and evaluates the differences $\boldsymbol{E}_k$(k=1,

2, 3, 4) based on numerical analysis or measurement tests that reproduce the conditions in training and inference. Subsequently, these differences are quantitatively assessed using Equation 3. The following sections describe the meanings of $\boldsymbol{E}_k$ and the conditions for numerical analysis and measurement tests used for their evaluation.

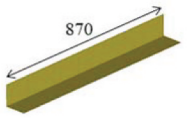
Table 1. Evaluation condition of differences.

Type and cause of difference	Target	Specimen: Number of cases	Specimen: Dimension (mm)	Boundary condition *1	Thickness reduction *2	Axial force (N/mm^2)	Method
E_1 Boundary condition	$V_{predict}$ V_{train}	20	L90*90*870*6	Structure Single	Real	—	FEA
E_2 Thickness distribution	$V_{predict}$ V_{train}	20	L90*90*870*6	Single	Real Uniform	—	FEA
E_3 Axial force variation	$V_{predict}$ V_{train}	2	L65*65*1400*6	Single	Real	26 21	Measurement
E_4 Mode estimation method	$V_{predict}$ V_{train}	6	L65*65*1400*6	Single	Real/ Uniform	—	Measurement FEA

*1 Structure – structure model including secondary member
Single – single-member model
*2 Real – continuous thickness distribution in real corrosion condition
Uniform – uniform thickness distribution at each of the 10 sections



a) Structure model



b) Single-member model

Figure 3. FE model.

Table 2. Settings of FE model.

	Settings
Analysis type	Eigenvalue analysis
Element type	4 nodes shell element
Mesh size	10mm
Young's modulus (GPa)	205
Poisson ratio	0.3
Density (kg/m^3)	7850

a) **Difference based on boundary condition E_1**

In the method, a single-member model is employed to generate training data where both ends of the member are completely fixed. However, in actual structures, the main member is constrained by multiple secondary members. Although CSM exhibits characteristics localized to a single member, the difference E_1 arises due to the difference in boundary conditions. To evaluate this, a structural model that includes secondary members, reproducing the boundary conditions in the structure, is used to calculate E_1, along with the single-member model used for training data.

The thickness cases in the analysis model are based on the thickness distribution measurement results from 20 test specimens. These specimens were sourced from angle steel members, including thickness reduction due to corrosion, taken from the lower chord, web, and

diagonal members of belt conveyor supports that have been exposed to outdoor conditions for approximately 40 years.

For the modeling process, the finite element analysis software MSC MARC 2021.3 was used to create the single-member model and a structural model, as depicted in Figure 3. Eigenvalue analysis was then performed to calculate $\boldsymbol{V}$. The dimensions of the models were set to correspond to the member within the actual structure (90*90*1080*6 mm). Detailed settings for both models are outlined in Table 2.

b) **Difference due to thickness distribution $\boldsymbol{E}_2$**

Although in real-world corroded members, thickness spatial distribution is continuous, in generating training data a uniform thickness was assigned to each of the ten sections. However, the uniform thickness diverges from the continuous thickness variation in corroded members, leading to difference $\boldsymbol{E}_2$. To address this, we use the analysis results from a scenario where the thickness of actual corroded members is set using a single-member model, referred to as the actual corrosion model, and another where the average thickness is uniformly set within a section, referred to as the uniform corrosion model. $\boldsymbol{E}_2$ is calculated using Equation 3. In this context, both models are identical to the single-member model constructed in a), with the only difference being the method of setting the thickness.

c) **Difference due to axial force $\boldsymbol{E}_3$**

In structures currently in service, axial forces vary depending on the external force and the location of the member, leading to fluctuations in mode characteristics (Bokaian, 1990). However, the mode characteristics in the training data do not consider the influence of axial forces, resulting in the existence of difference $\boldsymbol{E}_3$. To evaluate $\boldsymbol{E}_3$, a measurement test was conducted on two steel members (both L65*65*1400*6mm) with artificially induced axial force variations; one of these members represents an intact member (Test Specimen 1), and the other represents an actual corroded member cut from a belt conveyor steel frame (Test Specimen 2). The specimens were securely fixed at both ends using a base plate with bolt holes welded to both ends of the member. Tensile forces were introduced to a maximum force of N_{max} =20 kN and a minimum force of N_{min} =16 kN. In this study, N_{min} was assumed for the learning condition, and N_{max} was assumed for the inference condition.

Vibration was excited by hammering the members, and the response was measured using two laser Doppler vibrometers (LDVs) from Polytech (RSV-150/PDV-100). The Eigensystem realization algorithm (ERA) (Juang and Pappa, 1985) was employed to calculate the mode shapes and natural frequencies. This method involved peak picking on the power spectrum to identify mode candidates, and the mode with the closest natural frequency to the identified candidate was selected as the CSM for each mode order.

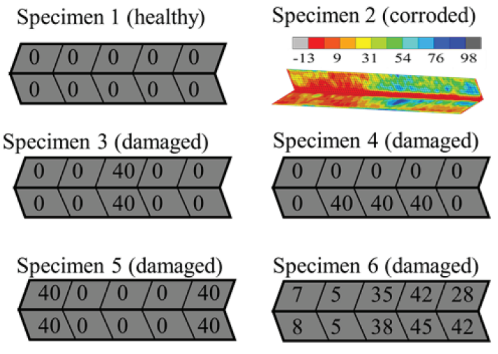
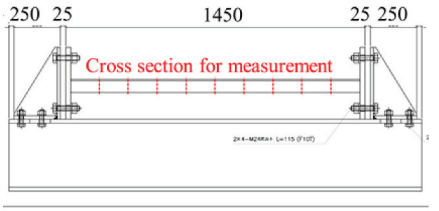
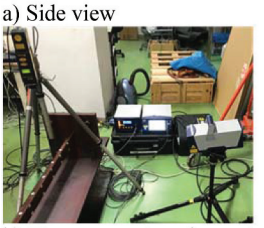


Figure 4. Specimens.



a) Side view



b) Measurement equipment

Figure 5. Measurement settings.

d) **Difference due to mode estimation errors $\boldsymbol{E}_4$**

The inference input $\boldsymbol{V}_{\text{predict}}$ for the real-world structure is derived from raw data obtained from the LDVs. This raw data is processed using fast Fourier transform (FFT), peak picking, and the ERA to extract vibration mode candidates. However, this process is subject to errors, such as temperature and humidity conditions affecting the LDVs, mechanical errors, sampling errors, and inaccuracies in the analysis method used for CSM identification. The training data $\boldsymbol{V}_{\text{train}}$ is obtained from the finite element model through eigenvalue analysis, followed by the extraction of vibration mode candidates and CSM identification using discriminative indicators. However, errors not considered in a)–c) may be present. Modeling and reproduction errors arise from settings in the FE model, such as mesh size and mechanical properties.

To evaluate the difference $\boldsymbol{E}_4$ resulting from errors in $\boldsymbol{V}_{\text{predict}}$ and $\boldsymbol{V}_{\text{train}}$, a measurement test was conducted on single-member specimens and a corresponding analytical model. Six specimens were considered, including the specimens used in c) (Specimens 1 and 2) and additional specimens (Specimens 3, 4, 5, 6) with artificial degradation using a grinder. The corrosion for each specimen is shown in Figure 4. The measurement setting was the same as in c). The thickness setting for FE model was determined by the measured average thickness of the specimens. The analytical model, with the same boundary conditions as in a), was reconstructed to match the dimensions of the target specimen (L65*65*1400*6mm).

3.2 *Evaluation of differences*

When the differences E_k for all test specimens and cross-sections follow a probability density function ($p(E_k)$), the probability density function $p(E)$ for the differences E caused by multiple factors can be expressed as follows:

$$p(E) = \sum\nolimits_k p(E_k) \tag{4}$$

For simplicity, assuming that each considered factor is independent, the components of the mean μ_j and standard deviation σ_j of E can be expressed using the mean $\mu_{k,j}$ and standard deviation $\sigma_{k,j}$ components of E_k as follows:

$$\mu_j = \sum\nolimits_k \mu_{k,j} (j = 1, 2, , , 3 + 3m) \tag{5}$$

$$\sigma_j = \sqrt{\sum\nolimits_k \sigma_{k,j}^2} \, (j = 1, 2, , , 3 + 3m) \tag{6}$$

Here, j ranges from 1 to $j = 1, 2 \ldots 3 + 3m$, where m is the dimensionality of the mode shape $\boldsymbol{\phi}_i$, i.e., the number of output points of the mode shape. In this study, five cross-sections along the member axis with points A, B, C were considered (m =3*5=15).

3.3 *Generation of training data*

Finite element (FE) models are created for individual steel members, following the specifications of the target structures. A uniform thickness is assigned to ten sections of each member, aligning with the specified dimensions.

A training dataset is generated by simulating mode characteristics for the assigned thickness patterns using the FE models. The differences $\boldsymbol{E}$ are calculated for the generated training data using the approach outlined in Section 3.1. Data augmentation is applied to $\boldsymbol{V}_{\text{train}}$ by introducing random noise, which conforms to a normal distribution, to each component ($j = 1, 2, , , 3 + 3m$) of the differences $\boldsymbol{E}$. This noise enriches the training dataset with instances that reflect the influence of differences $\boldsymbol{E}$, thereby contributing to enhanced generalization and mitigating overfitting during model training.

3.4 *Construction of machine learning model*

For comparison, two machine learning models, light gradient-boosting machine (LightGBM) (Ke et al., 2017) and neural network (NN), were evaluated. LightGBM, a variant of the gradient boosting decision tree (GBDT), is known for efficiently providing high-accuracy solutions based on decision trees. NNs, by contrast, use a structure comprising an input layer, an output layer, and several intermediate layers to represent input–output relationships by adjusting coefficients between nodes, thereby minimizing error. For the NN, a relatively simple configuration with only two intermediate layers was chosen, given that the input vector $\boldsymbol{V}$ comprises 48 components and the output vector $\boldsymbol{d}$ has 10 components. The ReLU activation function was utilized in this setup. Both machine learning methods were subject to hyperparameter tuning using the augmented dataset, aiming to minimize the risk of overfitting.

4 VALIDATION OF THE PROPOSED METHOD WITH A MEASUREMENT TEST

4.1 *Results of the difference evaluation*

Based on the condition mentioned in Section 3, the difference values were evaluated (Table 3). An example of the mode shape is shown in Figure 6. When $\boldsymbol{E}_{all}$ is the difference when considering all four factors mentioned above, the statistics, $\mu_{all,j}, \sigma_{all,j}$ (j=1, 2. . . 9), were calculated by Equations 5 and 6. The analysis of the standard deviation reveals that the natural frequency consistently varied by 4–5%, irrespective of the mode order. Conversely, the variations in the mode shape showed an increasing trend with the mode order, registering 6–9% for the 1st mode, 7–16% for the 2nd mode, and 15–28% for the 3rd mode. Additionally, the standard deviation of the mode shape was consistently larger than that of the natural frequency across all factors considered; this difference in standard deviation was more pronounced in the higher order modes.

In the following discussions, the mean values of the differences are $\mu_{k,j} = \mu_{all,j}$=0 (j=1, 2. . .9, k=1, 2, 3, 4) for the sake of simplicity, and the effect of the magnitude of the standard deviation on the estimation accuracy of the machine learning model is evaluated.

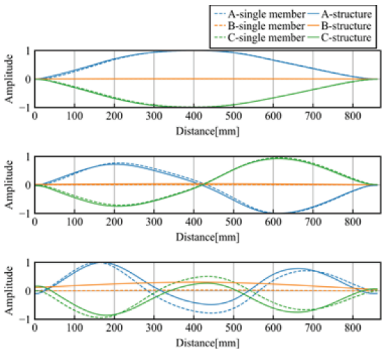


Figure 6. Example of a mode shape.

Table 3. Evaluation of difference.

		Frequency (%)			Mode shape (%)					
					1st		2nd		3rd	
		1st	2nd	3rd	A, C	B	A, C	B	A, C	B
E_1	Ave.	-0.2	0.7	2.7	0.5	2.0	-0.5	0.0	4.0	8.0
	Std.	0.8	0.6	2.1	2.0	1.0	6.5	3.0	13.5	6.0
E_2	Ave.	2.5	2.9	2.5	1.0	0.0	-0.5	0.0	-1.0	0.0
	Std.	3.9	3.7	3.2	3.0	0.0	8.5	0.0	12.5	2.0
E_3	Ave.	-0.3	-0.2	-0.2	0.7	0.1	-0.6	-1.7	0.7	1.7
	Std.	0.3	0.8	0.3	1.8	1.2	4.2	3.1	8.8	5.6
E_4	Ave.	-1.5	-0.4	-1.7	2.8	-7.7	4.6	-5.4	2.3	0.9
	Std.	2.1	1.9	1.8	7.5	6.3	10.5	6.4	18.0	13.4
E_{all}	Ave.	0.5	3.0	3.3	5.0	-5.6	3.0	-7.1	6.0	10.7
	Std.	4.5	4.3	4.3	8.5	6.5	15.6	7.8	27.2	15.8

4.2 *Generation of training data*

This section discusses the thickness estimation based on mode characteristics derived from actual measurement tests. For the generation of training data, the FE model from Section 3, which was adapted to match the dimensions of the test specimen, was used. This model

comprises 10 sections, each with a specific thickness pattern. Eigenvalue analysis was conducted for 300,000 combinations of random thickness patterns, with the values ranging within -10–90 %.

The differences incorporated in data augmentation are also examined. Mode characteristics from the six test specimens, as described in Section 3.1 under the measurement conditions excluding axial forces, constitute the input data for the model. Due to the fixation of these test specimens at both ends using a base plate, the boundary conditions are equivalent to those in the single-member model. The thickness distribution for test specimen 2 is based on actual corrosion conditions, whereas for test specimens 1 and 3–6, it follows simplified corrosion scenarios.

Consequently, it is assumed that for test specimens 1 and 3–6, considering only $\boldsymbol{E}_4$, and for test specimen 2, considering both $\boldsymbol{E}_2$ and $\boldsymbol{E}_4$, the value of $\bar{R}$ would be minimized. Specifically, $\bar{R}$ is defined as difference indicator that exists in inference, assuming the presence of random Gaussian noises with standard deviations $R_{T,j}, R_{V,j}$ in the training and inference data, respectively.

$$\bar{R} = \sqrt{\frac{\sum_{j=1}^{3+3m} \left(R_{V,j} - R_{T,j}\right)^2}{3+3m}} \tag{7}$$

When the value of $\bar{R}$ is small, it implies that the noise levels are the same in training and inference data, leading to a higher expected estimation accuracy. For comparative verification, three data augmentation patterns incorporating $\boldsymbol{E}_2$ and $\boldsymbol{E}_4$ are evaluated as described in Table 4.

4.3 *Comparison of the estimation result*

Figure 7 Shows the thickness estimation error of all sections of each specimen based on the following metric.

$$MAE = \frac{1}{10}\sum_{sec=1}^{10} \left(\widehat{d_{sec,n}} - d_{sec,n}\right) * 100 \tag{8}$$

Figure 8 Shows the estimated thickness reduction rate for each section of all the specimens, and Table 5 shows the thickness estimation error S (%) for all specimens and the improvement rate of the estimation error (%) based on case T0-Vm. The root mean square error (RMSE) of the estimate of d for all verification data N is calculated, and the thickness estimation accuracy is evaluated by the following estimation error S (%), considered by averaging 10 sections.

$$S = \frac{1}{10}\sum_{sec=1}^{10} \sqrt{\frac{\sum_{n=1}^{N} \left(\widehat{d_{sec,n}} - d_{sec,n}\right)^2}{N}} * 100 \tag{9}$$

In particular, the estimation error was minimized in Tp1-Vm regardless of the machine learning method, and the reduction rate was 40% or more when compared to the results by conventional method. This is attributed to the data augmentation pattern Tp1-Vm being suitable for all specimens except Specimen 2, indicating that it was the prevailing condition among the target specimens.

On the contrary, while Tp2-Vm was anticipated to be most suitable for Specimen 2, the smallest estimation error was observed in Tp1-Vm. This is because, despite the local thickness reduction in Specimen 2, its spatial thickness variation is not significant. Consequently, Tp2-Vm, which does not account for the difference due to thickness distribution E_4, most accurately represents the condition of Specimen 2.

Although there are exceptions, for 4 out of 6 specimens (specimens 1, 2, 3, and 5), the highest model estimation accuracy was achieved when the data was augmented in a way that minimized $\bar{R}$. This approach, involving the augmentation of training data to align the noise

variance of the training condition with that of the inference condition, has proven effective in constructing a model with a reduced risk of overfitting to the training data.

Table 4. Patterns of data augmentation.

Case	Difference considered				Frequency (%)			Mode shape (%)					
								1st		2nd		3rd	
	E_1	E_2	E_3	E_4	1st	2nd	3rd	A, C	B	A, C	B	A, C	B
T0-Vm					0	0	0	0	0	0	0	0	0
Tp1-Vm				○	2.1	1.9	1.8	7.5	6.3	10.5	6.4	18.0	13.4
Tp2-Vm		○		○	4.4	4.2	3.7	8.1	6.3	13.5	6.4	21.9	13.6

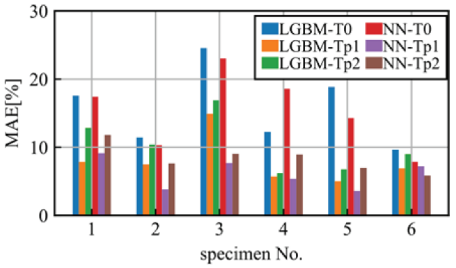
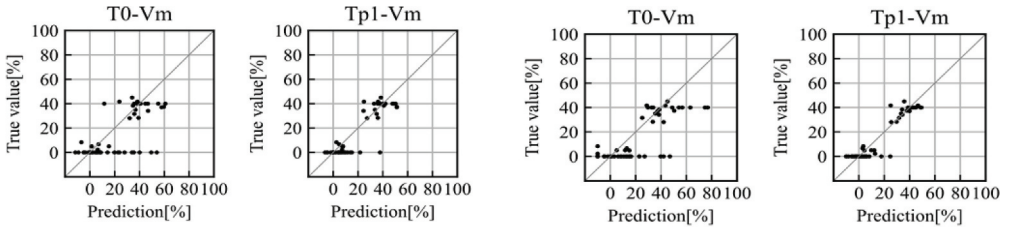


Figure 7. Estimation errors of each specimen.

Table 5. Estimation errors (overall).

Case	LightGBM		NN	
	S (%)	Improvement rate (%)	S (%)	Improvement rate (%)
T0-Vm	15.7	—	15.2	—
Tp1-Vm	7.9	49.7	6.1	59.9
Tp2-Vm	10.4	33.8	8.4	44.7



a) Light GBM b) NN

Figure 8. Estimation results of thickness.

5 CONCLUSION

In a machine learning model that estimates the thickness of a member from local vibration mode characteristics, the difference between mode characteristics during training and inference is first quantified. Subsequently, the estimation accuracy of the model is compared when data augmentation, based on these evaluated differences, is implemented. Finally, a model is constructed using the augmented training data, considering the differences anticipated in the measurement test of a single-member test, and its estimation accuracy is verified. The findings of this study are summarized below.

1) The estimation error of the thickness estimation model is minimized when the training data is augmented such that the noise levels in both the training and inference data are approximately equal.

2) The discrepancy in mode characteristics, which serve as the input data for the machine learning model, between the training and inference data is found to be around 4–5% for the natural frequency, irrespective of the mode order. However, for the mode shape, it is evaluated to be 6–9% for 1st order modes, 7–16% for 2nd order modes, and 15–28% for 3rd order modes.

The results of this study suggest that the estimation accuracy of the model can be greatly improved by applying data augmentation to the training data according to the expected difference between the input data in inference and training.

REFERENCES

Bokaian, A. 1990. Natural frequencies of beams under tensile axial loads. *Journal of Sound and Vibration*, 142(3): 481–498.

Juang, J.-N. & Pappa, R. 1985. An eigensystem realization algorithm for modal parameter identification and modal reduction. Journal of Guidance Control and Dynamics, 8(5): 620–627.

Ke, G., Meng, Q., Finley, T., Wang, T., Chen, W., Ma, W., Ye, Q., & Liu, T.-Y. 2017. LightGBM: A highly efficient gradient boosting decision tree. Advances in Neural Information Processing Systems 30 (NIPS 2017): 3149–3157.

Lee, S., Park, S., Kim, T., Lieu, Q. X., & Lee, J. 2021. Damage quantification in truss structures by limited sensor-based surrogate model. *Applied Acoustics*, 172: 107547.

Ogawa, D., Yang, Y., Nagayama, T., Kato, S., Hisazumi, K., & Tominaga, T. 2023. Load carrying capacity estimation of a belt conveyor support structure member based on cross-sectional vibration modes. *Journal of Structural Engineering*, 69A: 345–355.

Polytech RSV-150, PDV-100, https://www.polytec.com/jp/vibrometry/products

Bridge Maintenance, Safety, Management, Digitalization and Sustainability – Jensen, Frangopol & Schmidt (eds)
© 2024 The Author(s), ISBN 978-1-032-77040-6
Open Access: www.taylorfrancis.com, CC BY-NC-ND 4.0 license

Crack detection method for RC beams with an automatic hammering device

Ikuya Uchiyama, Hideki Naito & Kota Inada
Department of Civil and Environmental Engineering, Graduate School of Engineering, Tohoku University Sendai, Miyagi, Japan

Yoichi Kurihara & Kanji Matsuhashi
Onga Engineering Co, Noogata, Fukuoka, Japan

ABSTRACT: This study examined the applicability of vibration measurement using a lightweight and compact automatic impactor and anomaly detection using machine learning as methods of simple and time-efficient non-destructive testing to evaluate damages in RC-members. In the experimental study, three RC beam specimens of different dimensions were made without stirrups to shear failure, and loading tests were conducted on each specimen. The training data for machine learning was collected before and after the loading tests, respectively, using an automatic impactor. Based on the vibration information obtained, a machine learning model was constructed using the data set and the autoencoder. The results showed that the anomaly values were larger in areas with shear cracks and wider crack widths, indicating the possibility of detecting shear cracks that are structurally significant with these methods of no-destructive testing.

1 INTRODUCTION

Infrastructure in Japan is aging rapidly. In addition, infrastructure requires early inspection in the event of earthquakes and other disasters. Therefore, it is desirable to improve the efficiency, sophistication, and automation of inspections of concrete structures.

Various non-destructive inspection methods have been proposed for concrete structures. For example, Chia-Chi et al. (2008) showed the possibility of combining active infrared thermography (IRT) and elastic wave technology to inspect the appearance of concrete structures effectively and efficiently. Murakawa et al. (2022) showed the potential of using portable vibration machines, laser vibrometers, and machine learning for nondestructive inspection of concrete structures. However, the previous methods require time and effort to collect the training data needed for machine learning. In previous studies, damage assessment methods have relied on modal parameters such as resonance frequency. Therefore, it is strongly desired to establish a method that is simple, and quick, but accurate, and capable of detecting structurally significant defects.

In this study, experiments were conducted using an automatic impact device. This device can strike the surface of a structure four times per second with the same force, and by mounting a sensor inside the device, the response acceleration of the structure's surface due to hammering can be measured. In this study, we attempted to diagnose the integrity of three RC beam specimens with different dimensions that had induced shear cracks, which are safety-critical damages to the structure, by utilizing the impact inspection device and machine learning.

DOI: 10.1201/9781003483755-425

2 EXPERIMENT PROGRAM

2.1 *Loading test*

A schematic of the RC beam specimens is shown in Figure 1-3. The test piece dimensions are shown in the figure, and the three specimens were designed to fail in shear. The compressive strength of the concrete with the test pieces is 28.9 MPa, the sound speed within concrete is c=3,780 m/s, and the mass density is 2,290 kg/m^3. Tensile test results for deformed steel bars are shown in Table 1. Loading conditions are shown in Figure 1~3. There are three different specimen sizes, which will be referred to as LS, MS, and SS specimens in order of increasing specimen height. RC beam specimens were supported on steel fulcrums and a vertical load in one direction was applied at the center of the span. In the specimens, the vertical load was removed when the shear crack occurred. With the specimen unloaded, a crack diagram of the specimen side-face was made, and the crack width was measured using a crack scale. Note that since this experiment was designed to investigate damage to the structure after an earthquake, cracks were observed only when the load was removed.

2.2 *Vibration test*

In this study, to evaluate the damage of a concrete beam specimen subjected to cracking, impacts were applied to the surface of the structure to measure the response acceleration near the point of impact. Measurements were taken using the mobile automatic impact device shown in Figure 4. This impact inspection device is an integrated unit consisting of an automatic hammer that strikes continuously at a rate of four blows per second and a magneto strictive sensor that detects elastic waves at 50 mm. When measuring, the red arrow in the Figure 4 is pushed against the structure, and when the wheel with the sensor attached adheres to the structure, the hammering begins. The hammer is a suction-accelerated electromagnetic impact hammer with a mass of 480 g. It can strike with a constant force regardless of the direction of impact.

In this study, this hammering device was moved against the test specimen as shown in Figure 4, and measurements were taken. This device strikes the test specimen about 8 to 10 times at each measuring point, and when it was finished, it moved to the next measuring point, stopping at each measuring point on the measuring line. The measuring line was set in the middle of the longitudinal direction, and the edge of the beam was about the height of the cross section in the horizontal direction from the edge of the beam. For example, in the case of the SS specimen, the first measuring point was 350 mm from the east end of the specimen, and from there 18 measuring points were set at 100 mm intervals up to 2,050 mm. Similarly, 22 points were set for the MS specimen and 26 points for the LS specimen. The same measuring line was measured 5 times before loading as training data and once after loading as test data.

Table 1. Mechanical properties of rebars.

Rebar diameter	Yield strength	Tensile strength
	Mpa	Mpa
D10	382	514
D22	407	581
D25	389	565
D29	464	650

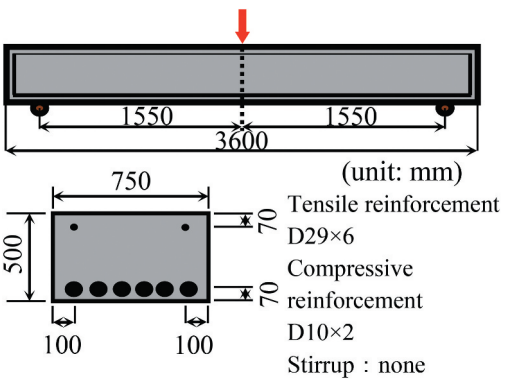


Figure 1. LS test specimen specifications.

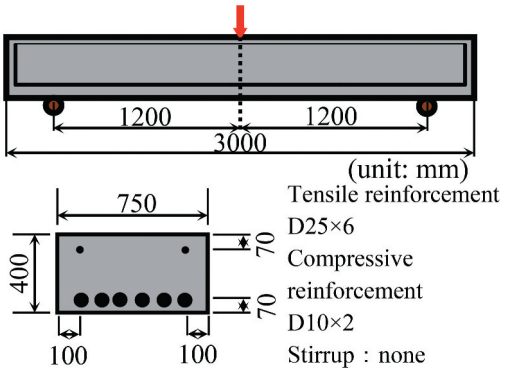


Figure 2. MS test specimen specifications.

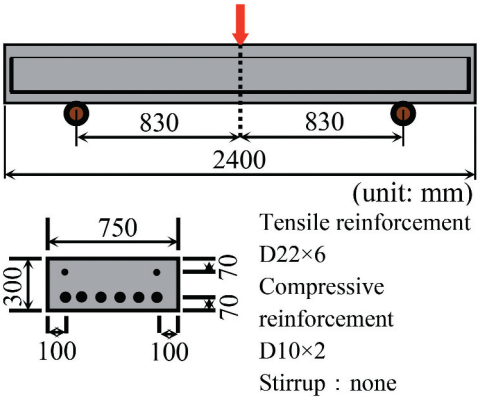


Figure 3. SS test specimen specifications.

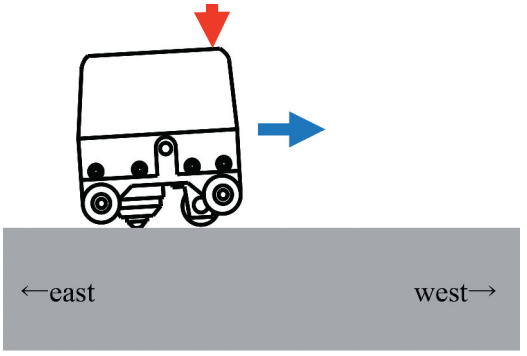


Figure 4. Automatic impact inspection device and how to operate.

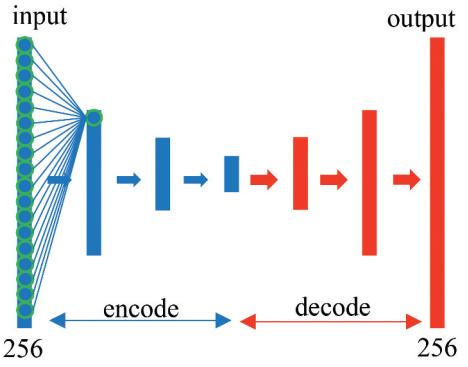


Figure 5. Autoencoder conceptual diagram.

In this study, acceleration waveforms recorded at a sampling frequency of 50 kHz were (1) cut into waveforms, (2) Fourier analyzed, and (3) sampled (training data only). (1) For a continuous acceleration waveform, the waveform was recorded for 0.1 s after the threshold value was exceeded, and after 0.1 s had elapsed, the wave was cut out of the continuous waveform to record the wave if the threshold value was exceeded again. The 0.1s was set to be an appropriate value between 0.01s, which is necessary for waveform analysis and the hammering interval of 0.25s. (2) Fast Fourier transform of 512 plots was performed. (3) In handling the machine, tapping miss occurs when pushing in and releasing. In creating the data set for training, we considered that using this data as is would result in the creation of a poor-quality data set, which may result in decreasing accuracy of anomaly detection, so we performed sampling by attaching conditions to the frequency response function obtained up to (2) above. The conditions were such that, for example, in the training data set for the MS specimen, amplitude values between 10,200 and 25,000 Hz that exceeded 0.05 when normalized by the maximum amplitude value, amplitude values between 3,420 and 4,200 Hz that similarly exceeded 0.3, and amplitude values between 1,950 and 3,220 Hz that similarly exceeded 0.05 were deleted. To eliminate any possibility of arbitrary conditioning in the creation of the data set for testing, the work described in (3) was not performed. Therefore, although the anomaly levels periodically increased, this method was adopted because there was no issue in observing the trend of the anomaly levels.

In this study, frequency response functions (256 parameters) with a resolution of 97.7 Hz from 0 to 25,000 Hz were provided as training data (1-dimensional data) for the machine learning described below.

3 MACHINE LEARNING

In this study, anomaly detection was performed using an autoencoder, a mathematical model of a neural network shown in Figure 5. The autoencoder consists of two elements, the encoding, and the decoding part, where the former compresses the nodes and the latter is the reverse of the former, where the nodes once compressed in the encoding part are returned to the input dimension. In this study, only the sound data before loading is given as training data for machine learning. Therefore, in the training phase of machine learning, we optimize the weights between layers for proper compression and reconstruction of the intact data. In the test phase, the test data is given as a mixture of both intact and defective data, but the input data and the reconstructed data are close to each other because the intact data has learned how to be compressed and reconstructed well in the learning phase. On the other hand, the defect data is unknown to the machine learning model, which has learned only the intact data, and does not know how to compress and reconstruct it. As a result, the reconstruction error, which is the difference between the input data and the reconstructed data calculated through compression, is larger than that of the intact data. By focusing on this feature and defining the degree of anomaly based on the absolute reconstruction error, it is possible to identify the location of defects.

In this study, the frequency response function has 256 parameters, so the number of nodes was set to the same 256. In the encoding section, the nodes were reduced by 1/2 in dimensionality, to 1/64 for the LS and MS specimens, and to 1/8 for the SS specimen. In the decoding section, the reverse of the encoding section was performed, and finally all the nodes were reconstructed to 256, the same dimension as the input. The optimization algorithm used for training was Adam, the activation function was ReLU for the hidden layer and ELU for the output layer, and the learning rate was set to 0.001 until epoch 40 and 0.0001 after epoch 40. The mini batch was set to 4, the loss function was sufficiently lowered to settle down and no over-learning occurred, and the epoch was set to 60.

The anomaly is based on the reconstruction error, which is the difference between the input and reconstructed data and was calculated using the following process. Since the frequency response function has steep multimodal characteristics, even a slight shift in the peak of the input data and the reconstructed data can result in a large reconstruction error. Therefore, a moving average was calculated over a five-parameter range to smooth the peaks of the frequency response function. The absolute reconstruction error was calculated for the input and reconstructed data processed in this way, and the anomaly was defined as the anomaly divided by the reconstruction area.

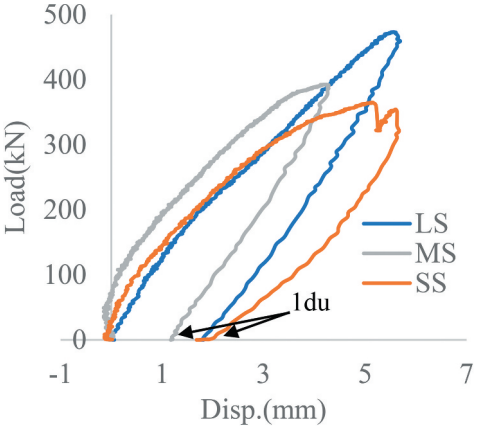


Figure 6. Load-displacement relationship.

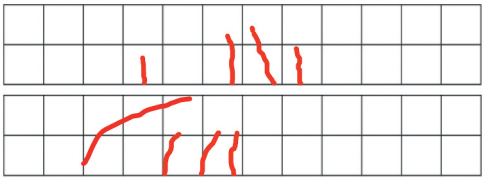


Figure 7. Cracks in the LS specimen (top: north viewpoint, bottom: south, top & bottom left: east).

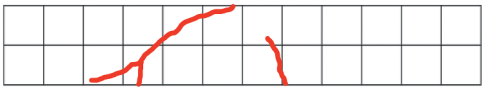


Figure 8. Cracks in the MS specimen.

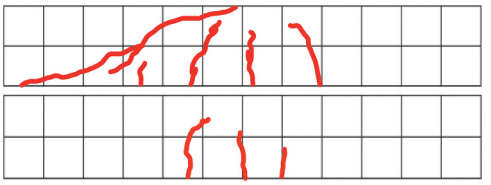


Figure 9. Cracks in the SS specimen (top: north viewpoint, bottom: south, top & bottom left: east).

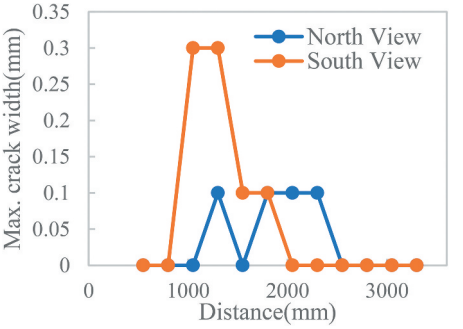


Figure 10. Crack width distribution diagram of LS specimen.

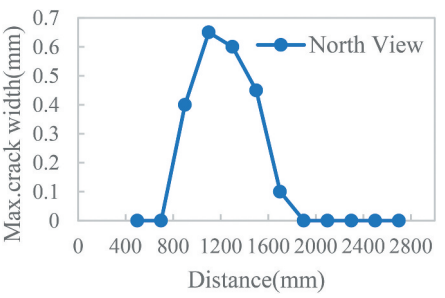


Figure 11. Crack width distribution diagram of MS specimen.

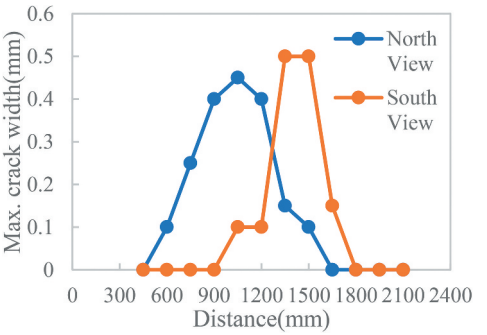


Figure 12. Crack width distribution diagram of SS specimen.

4 EXPERIMENTAL RESULTS

The load-displacement relationships for the three shear specimens are shown in Figure 6. Crack diagrams for each specimen are shown in Figure 7-9, and crack width distribution diagrams in Figure 10-12. Examples of vibration test results for each specimen are shown in Figure 13-15.

Shear cracking is serious damage that should be noted during post-earthquake emergency inspections because of the loss of load-bearing capacity of the member. In this experiment, the shear failure was designed to occur due to diagonal cracking without stirrups. In loading tests, diagonal cracks with angles of about 30-45 degrees were generated as designed. The purpose of this study is to efficiently investigate diagonal cracks that cannot be visually confirmed from the top surface of structures.

For the LS specimens, when the loading stage was 1du, no significant shear cracks were observed when looking at the specimens from the north, but when looking at the specimens

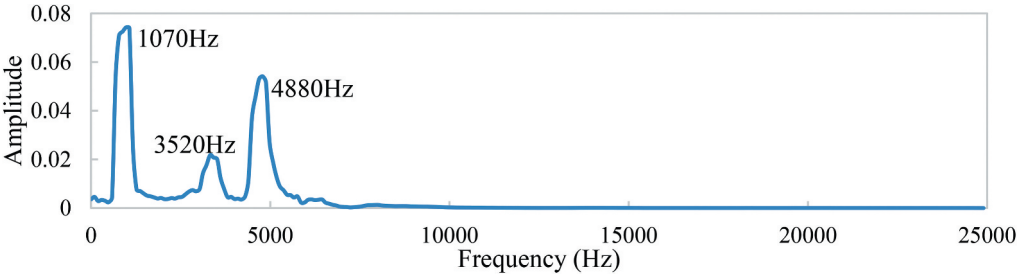


Figure 13. Frequency response function before LS specimen loading.

from the south, shear cracks were observed on the east side of the specimens (around 800 mm to 1,450 mm from the east end). The shear crack width was the largest on the east side viewed from the south side, with a maximum crack width of 0.3 mm. Flexural cracks were also observed in the center of the beam, although the crack width was not as large as the shear crack width. As for the resonance frequencies, before loading, peaks were mainly observed at 1,070 Hz, 3,520 Hz, and 4,880 Hz, as shown in Figure 13. On the other hand, the resonance frequency f_0 calculated by a simple calculation ignoring the steel bars is given by $f_0 = c/(2H)$, and $f_0 = 3780Hz$ is obtained by substituting the member thickness $H = 0.5m$ and the speed of sound within concrete $c = 3780m/s$. As a result, among the three peaks observed, a certain degree of validity was confirmed for 3,520 Hz.

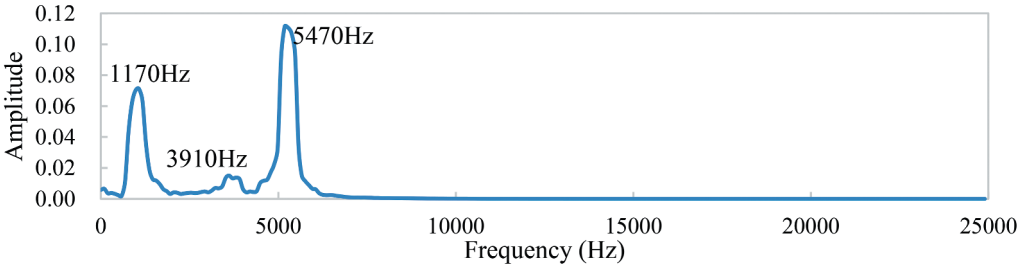


Figure 14. Frequency response function before MS specimen loading.

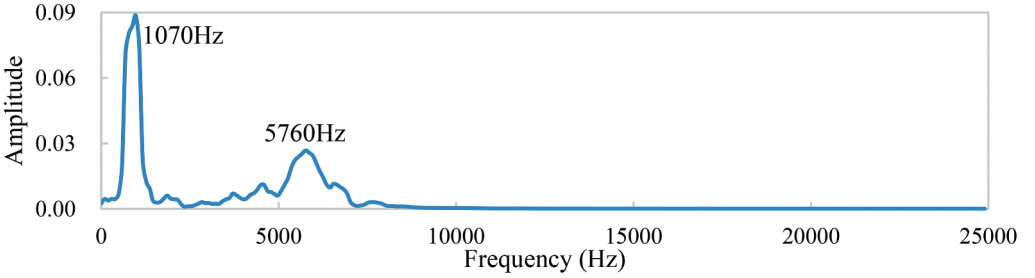


Figure 15. Frequency response function before SS specimen loading.

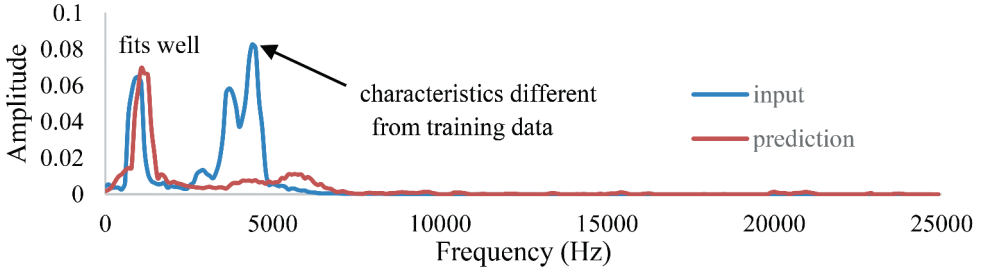


Figure 16. Comparison of input and reconstruction(prediction) data at SS specimen defects (1,450mm from east end of specimen).

As for the MS specimen, the crack diagram shows shear cracks on the east side of the specimen (700mm~1,500mm from the east end) when the loading stage was 1du and the specimen was viewed from the north side. The shear crack width was the widest on the east side viewed from the north side, with a maximum crack width of 0.65 mm. A single flexural crack was observed on the west side about 200 mm from the center of

the beam. As for the resonance frequencies, before loading, peaks were mainly observed at 1,170 Hz, 3,910 Hz, and 5,470 Hz, as shown in Figure 14. Using the same simple equation as before and substituting the member thickness $H = 0.4m$, $f_0 = 4725Hz$ was obtained.

The crack diagram of the SS specimen shows that when the loading stage was 1du, shear cracks could be observed on the east side (370mm~1,200mm from the east end) when the specimen was viewed from the north side. As for the crack width, the shear crack on the west side was wider than the shear crack on the east side by 200 mm from the center of the beam to the west, and the maximum crack width was 0.5 mm. As for the resonance frequency, before loading, peaks were observed mainly at 1,070 Hz and 5,760 Hz, as shown in Figure 15. Using the same simple equation as before and substituting the member thickness $H = 0.3m$, $f_0 = 6300Hz$ was obtained, which corresponds to the experimental value of 5,760Hz.

For all the specimens, the peaks appeared around 1,070 and 1,170 Hz, which are far from the resonance frequency values calculated from the simplified formula, but since the peaks appear in the data after loading as well, it is assumed that they are caused by the characteristics of the striking device and sensor rather than the vibration characteristics of the specimens. The peak was also observed in the post-loading data.

5 ANOMALY DETECTION RESULTS

This study attempts to extract features from the frequency response function using machine learning. In this experiment, training data for machine learning was collected for the specimens before loading. A trained model was constructed based on the training data set for each specimen. The frequency response functions collected after loading were inputted into the constructed model as test data, and the degree of anomaly was calculated. Figure 16 shows a comparison of the input data and the reconstructed data calculated through machine learning. From the figure, it can be seen that the training data for the SS specimen could not cope with the peak around 4,000 Hz, which was not characterized in the training data, resulting in a larger error.

The anomaly distributions of the three shear specimens along the axial direction are shown in Figure 17-19. Diagonal cracks largely block vertical excitation, making it relatively easy to detect anomalies.

For the LS specimen, the anomaly distribution is shown in Figure 17. Compared to the crack distribution in Figure 7 and the crack distribution width diagram in Figure 10, it can be seen that the anomaly values are larger at the defective points with shear cracks on the east side. The anomaly value is also larger for the flexural crack in the center of the beam. The crack width is not particularly large compared to other flexural cracks, but it is confirmed at almost the same location from the north and south viewpoints, which is assumed to be because the crack penetrates in the north-south direction and is surely located directly below the measuring line.

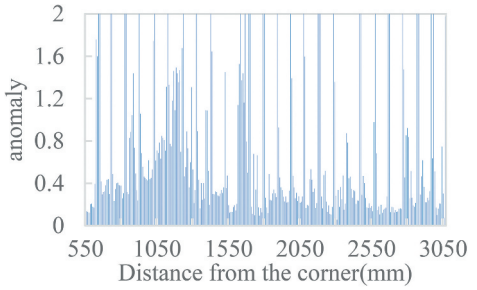


Figure 17. Anomaly distribution of LS specimen.

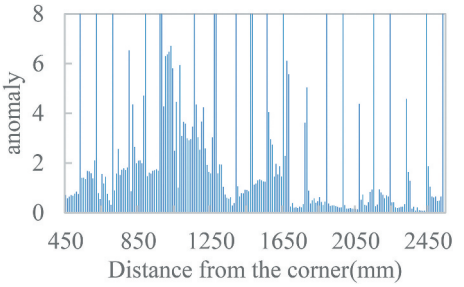


Figure 18. Anomaly distribution of MS specimen.

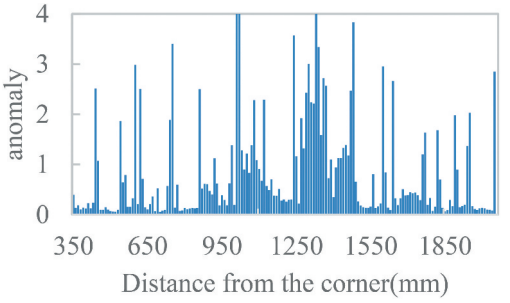


Figure 19. Anomaly distribution of SS specimen.

For the MS specimen, the distribution of anomalies is shown in Figure 18. Compared to the crack distribution in Figure 8 and the crack width distribution in Figure 11, the shear cracks on the east side have larger anomaly values. Among the shear cracks, the tendency for the anomaly values to increase at the locations with large crack widths can be seen from the distribution of anomaly values and crack widths. It can also be seen that the anomaly values are lower on the west side of the specimen where no cracks were observed.

For the SS specimen, the distribution of anomalies is shown in Figure 19. The location of shear cracks in the crack distribution in Figure 9 and the distribution of anomalies are not well matched. For the LS and MS specimens, the shear cracks had the widest crack widths, and the anomaly severity was also larger. However, the shear crack widths of the SS specimens were not particularly large compared to the other cracks, and in this respect, the SS specimens appeared different from the LS and MS specimens.

From the above results for the three types, the anomaly tended to be larger at shear cracks that could be structurally significant defects. Comparison of Figures 10-12 and 17-19 also shows that the degree of anomaly tends to increase with the crack width. These characteristics may be attributed to the following two reasons. 1) Diagonal cracks will block wave propagation more than vertical cracks that are parallel to the elastic wave 2) The larger the crack width, the less interlocking contact between the aggregate, thus interrupting the propagation of the elastic wave. For these two reasons, it can be inferred that the anomaly results are strongly influenced by the presence of diagonal shear cracks and crack widths.

6 CONCLUSIONS

This study demonstrated the possibility of using machine learning to detect defects in vibration measurements using an automatic impact device, using the obtained frequency response functions as information. In the experiment, loading tests were conducted on RC beam specimens of three different dimensions, and the response acceleration was collected before and after loading using an automatic impact inspection device. The findings obtained from these measurements and machine learning analysis are summarized below.

- In the RC beam loading tests, a combination of vibration characterization and machine learning using a lightweight, compact automatic impact device was able to detect structurally significant shear cracks.
- The machine learning model showed that the attribute of flexural or shear cracks (differences of crack angle, crack length, and crack density) affected the degree of anomaly.

However, since the vibration measurement in the loading test in this study was a trial effort, the relationship between the resulting data and its accuracy should be further investigated. In addition, the data measured while the automatic impact device was stopped at each measurement point was used in this study, but analysis of the data measured while the device was in motion is needed for more efficient inspection in the future. As a result, we will incorporate machine

learning methods that will be newly announced in the future to further improve the efficiency and accuracy of the system.

ACKNOWLEDGEMENTS

A part of this research was conducted with the support of JST FOREST Program (Grant Number JPMJFR2150, Japan), and the Japan Society for the Promotion of Science (Grant Number 22H01568).

REFERENCES

Alom, M.Z., Taha, T.M., Yakopcic, C., Westberg, S., Sidike, P., Nasrin, M.S., Hasan, M., Van Essen, B. C., Awwal, A.A., & Asari, V.K. 2019. A State-of-the-Art Survey on Deep Learning Theory and Architectures. *Electronics* 8(3): 292.

Besada J.A., Bergesio L., Campaña I., Vaquero-Melchor D., López-Araquistain J., Bernardos A.M., Casar J.R. 2018. Drone Mission Definition and Implementation for Automated Infrastructure Inspection Using Airborne Sensors. *Sensors*18(4):1170.

Cheng, C., Cheng, T., & Chiang, C. 2008. Defect detection of concrete structures using both infrared thermography and elastic waves. *Automation in Construction* 18: 87–92.

Fujisaku, Y., Naito, H., Inaba, K. 2022. Damage Evaluation of Concrete Beams Using Forced Vibration Testing and Machine Learning, *Proceedings of the 11th International Conference on Bridge Maintenance, Safety and Management.*: 1213–1219

Fujisaku, Y., Naito, H., Kimoto, T., Matsumura, M., Takeshima, N., Okada, S. & Ono, K. 2023. A Study on Damage Evaluation Method for Box Section Steel Columns Using Autoencoder. *33rd International Ocean and Polar Engineering Conference*, Ottawa, Canada

Habib, M.A., Hasan, M.J., & Kim, J.M. 2021. A Lightweight Deep Learning-Based Approach for Concrete Crack Characterization Using Acoustic Emission Signals, *in IEEE Access* 9: 104029–104050.

Hinton, G.E., and Salakhutdinov R.R. 2006. Reducing the Dimensionality of Data with Neural Networks. *Science* 313: 504–507.

Japan Society of Civil Engineers, 2007, Standard specifications for concrete structures-2007 Design.

Murakawa, T., Naito, H., Fujisaku, Y., Inaba, K., Takahashi, T. 2022. A Portable Scanning Device for Local Vibration Testing of Concrete Structures. In: Abdel Wahab, M. (eds) Proceedings of the 2nd *International Conference on Structural Damage Modelling and Assessment*. Lecture Notes in Civil Engineering, 204: 71–82.

Naito, H., Bolander, J.E. 2019. Damage Detection Method for RC Members Using Local Vibration Testing. *Engineering Structures*178: 361–374.

Naito, H., Kimoto, T., Fujioka, H., Fujikura, S., Unjoh, S. 2022. Seismic damage detection method for concrete structures using vibration measurement and autoencoder. *Journal of AI and Data Science*3: 134–144(in Japanese).

Ryu, S., Jeon, B., Seo, H., Lee, M., Shin, J.W., Yu, Y. 2023. Development of deep autoencoder-based anomaly detection system for HANARO. *Nuclear Engineering and Technology* 55(2): 475–483.

Bridge Maintenance, Safety, Management, Digitalization and Sustainability – Jensen, Frangopol & Schmidt (eds)
© 2024 The Author(s), ISBN 978-1-032-77040-6
Open Access: www.taylorfrancis.com, CC BY-NC-ND 4.0 license

An attempt to improve the accuracy of 3D point cloud considering bridge vibration effects

A. Akutsu, J. Lin & E. Sasaki
Civil and Environmental Engineering, Tokyo Institute of Technology, Meguro, Tokyo, Japan

ABSTRACT: Camera-based bridge inspections, where one can acquire information from a distance, have gained attention. Among them, this study focused on a 3D point cloud. Point cloud data is a set of points with 3D coordinate information and is expected to obtain detailed models with the current state of structures, such as those used in FE analysis. On the other hand, bridges are constantly vibrating due to external forces such as traffic and wind. Image-based point cloud requires the acquisition of measurement target images or videos from various distances and angles to construct a 3D model. Each acquired image with a different shooting timing contains different vibration information and the effect on each image feature point may be an error factor in 3D model construction. Therefore, in this study, the accuracy of 3D point cloud construction using videos has attempted to improve by considering the effects of bridge vibration.

1 INTRODUCTION

Visual inspection is one of the important inspection methods for bridge management. However, there are some problems that number of bridges to be inspected is increasing (Ministry of Infrastructure, Transport and Tourism (MILT), 2022), while the number of inspectors especially skilled inspectors is decreasing (Ministry of Infrastructure, Transport and Tourism, 2015). Besides, installing large inspection equipment or scaffoldings is time-consuming and costly.

To solve the abovementioned problems, the MLIT advocates i-Construction as it intends to increase productivity by integrating information and Communication Technology (ICT). One of the proposals is to inspect the bridge with high accuracy by processing and analyzing the captured photos or videos (Nishimura 2014 and Fujiwara et al. 2018). Image or video processing has the advantage of inspecting bridges remotely from a distance without damaging them and requires less manpower moreover, the inspectors can conduct inspections from a secured location.

Thus, this study focuses on a three-dimensional (3D) point cloud by photogrammetry that can transform two-dimensional images into 3D data. 3D point cloud data is a set of points with 3D coordinate information that represents the outer surface of an object or environment and 3D point cloud data can be obtained by processing the images or the videos of target bridges taken from different angles at different positions. The accuracy of the 3D point cloud construction has been improved since Structure from Motion (SfM) was introduced (Westoby et al. 2012, Lowe 2004, Snavely et al. 2008).

In recent years, research has been carried out on visual inspections applying 3D virtual space (Catbas et al. 2022), and it is envisaged that cracks and corrosion conditions can be checked in the same way as in normal visual inspections. In addition, technology for FE analysis using the 3D point cloud has been developed, and it is expected that analytical models will be constructed from the obtained 3D point cloud. As it is common to calculate the displacement and stress distribution of bridges in FE analysis, reducing the errors in the 3D point cloud for model construction directly leads to improved analysis results.

The authors especially focus on the fact that the bridges are constantly vibrated due to external forces such as wind and traffic and the vibration is not considered when constructing the 3D

DOI: 10.1201/9781003483755-426

point cloud. If the bridge vibrates when the images are taken, the bridge in the image will possibly be in a different position from the original state due to the occurring of displacement. Therefore, the usage of the images with vibration information to generate the 3D point cloud can be considered the accuracy of the 3D point cloud to decrease. For example, especially for short bridges, the amount of deflection is small and errors in the model construction have a significant influence on the analysis results. Moreover, as the accuracy of the 3D model construction in mm is assumed to be necessary to confirm the crack size in visual inspection and deflection of the target in FE analysis, this research aimed to reduce the error due to bridge vibration before the 3D point cloud construction. In this study, a 3D point cloud construction method has been proposed that can reduce the effects of vibration on bridges by applying the Phase Only Correlation Method (POC) to image processing to determine the vibration characteristics of bridges. Further, the applicability of the proposed method was verified by laboratory and field experiments.

2 CONCEPT OF 3D POINT CLOUD CONSTRUCTION CONSIDERING THE VIBRATION EFFECT OF BRIDGES

In this chapter, the ideas of the proposed method are described. Structure from Motion method, POC method, Statistical Outlier Removal (SOR) filter method, and RANSAC shape detection method are applied for 3D point cloud construction, analyzing object displacements in videos, and reducing noise.

2.1 *The basic approach of 3D point cloud construction by using structure from motion method*

SfM is the technique used to reconstruct 3D structures from 2D images. It involved taking a series of images of a scene from different positions. Also using the image to calculate the positions and orientation of the camera in each image. Then the information is used to triangulate the positions of points in the scene, which can be used to create a 3D point cloud of an optional object. The accuracy of the SfM reconstruction depends on the quality of the input images and the number of used images. SfM algorithms typically involve the following steps: first; Feature detection, Second; Feature matching, Third; Triangulation, and Finally; Dense 3D point cloud reconstruction.

SfM is a powerful tool for creating 3D models yet, it has limitations. It also requires a sufficient number of images with good overlap, so it may not work well for scenes with limited visibility. Moreover, if the objects in the frames move, the 3D positions of the detected feature points will deviate, which will affect the next feature point matching, the camera position estimation, and lead to the accuracy of the 3D point cloud decline. Therefore, this study especially focuses on the images from videos before constructing the 3D point cloud. The key idea of the proposed method is to use the frames of videos as images. That is, by extracting and using frames from the video that shows the bridge closest to the stationary state, the effect of feature point matching errors due to the bridge being in different vibration states in the image is eliminated.

2.2 *Acquisition of vibration characteristics by applying phase only correlation method*

The basic idea for acquiring the vibration characteristics is to analyze the obtained videos to calculate the difference between each frame. If the target is bridges, it is able to understand the difference is displacement due to the bridge vibration. In this study, to obtain this difference. The POC method was applied for the analysis. The POC method is a method of image registration that aligns two images by minimizing the difference in their phase spectrum. It is based on the idea that the phase spectrum of an image contains important information about its features and structures, and that aligning the phase spectra of two images also aligns their features and structures well. This study focused on how much two images need to move to align these images and using this value to evaluate the displacement between two images.

Figure 1 shows the flow of the POC method. Image 1 and Image 2 are the images which slightly moved and they need to overlap some parts. When the two images are similar, the

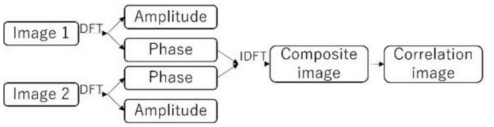


Figure 1. Flow of POC method.

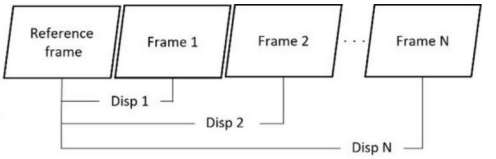


Figure 2. The idea of calculating displacement using video.

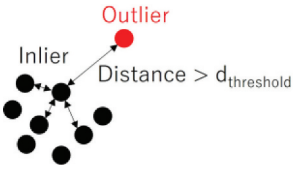


Figure 3. Schematic image of SOR filter.

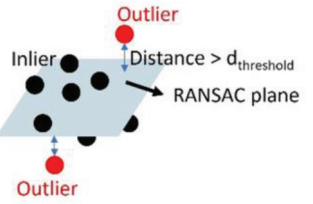


Figure 4. Schematic image of RANSAC shape detection.

POC function which is similar to the correlation coefficient, has a very sharp peak. The height of the correlation peak is useful as a measure of image similarity and it's used in "image matching" applications. On the other hand, the locus of the correlation peaks corresponds to the relative misalignment of the two images (Aoki et al. 2007). In the proposed method, using the locus of correlation peaks to obtain the amount of two images movement. The phase image obtained by applying the Fourier transform to an image contains contour information, while the amplitude image contains luminance information. In the POC method normalizes the amplitude information, which is luminance information, and thus has the advantage of being less affected by sunlight and other factors that can cause problems in outdoor shooting.

The idea of calculating bridge vibration and displacement by applying the POC method is shown in Figure 2. The selected frame as the first frame of the video is used as a reference frame. Then each subsequent frame is aligned with the first frame applying the POC method to obtain the displacement of each frame relative to the first frame. Furthermore, since the first frame is not in a displacement-free state, the center of the vibration can be observed by subtracting the average of all displacements from the obtained displacements. The displacement of the bridge in each frame of the video can be acquired, and the frame with the displacement value closest to the center of the vibration extracted as the frame of the bridge closest to the static state in the video.

2.3 *Proposal for 3D point cloud construction focuses on bridge vibration*

The proposed method in this study is to extract the frame with the closest frame to the center of the vibration, which is obtained in the aforementioned method that applies the POC method and use these extracted frames in each video to construct the 3D point cloud data to eliminate the effect of bridge vibration. Firstly, plan the shooting locations and then shoot a video at each position. Secondly, select the analysis area in the video and use the POC method to analyze the area to get the vertical vibration information and displacement. Thirdly, according to the vibration and displacement information, extract the frame with the closest from the center of the vibration in the video. Afterward, construct a 3D point cloud using the frames extricated from all the videos.

After the 3D point cloud data has been constructed, denoising and outlier removal are performed. In this study, the SOR filter method (Rusu et al. 2007) which is an iterative closest point algorithm implementation, and the RANSAC shape detection method (Bolles et al. 1981) which extracts shapes by randomly selecting the minimum set from a 3D point cloud

and constructing the corresponding shape primitives are selected. The schematic images of both the SOR filter method and the RANSAC shape detection method are shown in Figure 3 and Figure 4 respectively. As shown in the figures, when the threshold is chosen, the point is considered as an inlier if displacement is smaller than the threshold, otherwise it is an outlier. The number of outliers is also used to discuss the accuracy in the following chapters.

3 EXPERIMENTAL INVESTIGATION OF 3D POINT CLOUD CONSTRUCTION CONSIDERING THE VIBRATION EFFECT OF BRIDGES

In this chapter, to verify the applicability of the proposed method, laboratory experiments using a vibration testing machine and a steel specimen and experiments at a bridge site were indicated. The camera used in the experiment was a general-purpose digital single-lens reflex camera with a 35mm full-size CMOS sensor manufactured by SONY, and the focal length was 60mm. The video was recorded at 4K 24p. The amount of image misalignment is acquired as pixel values, and sub-pixel analysis can be applied to extremely small misalignments of 1 pixel or less.

3.1 *Laboratory experiment using vibration testing machine and steel specimen*

The experimental setup is shown in Figure 5. The test specimen was a steel square pipe (25mm×25mm×800mm), simulating a vibrating bridge, and was vibrated at 1 Hz using the vibration testing machine. The maximum vibration amplitude applied in the test was approximately 0.7 mm. The shooting location is shown in Figure 6. The camera positions were adjusted to be 0.3 m, 0.5 m, 0.75 m, and 1 m from the center of the specimen, and the angle was set at 0° in front of the specimen and moved in 15° increments from there to the 90° position. In addition, four camera heights were set, for a total of 112 shooting positions. Each video was taken about 10 seconds. Considering the number of frames, it is enough to analyze in 5 seconds. To verify the accuracy of the acquired vibration characteristics, the laser displacement sensor was also set under the test specimen (Figure 5).

3.1.1 *3D point cloud data construction*

In this stage, the vibration characteristics of all videos were first acquired by the proposed method applying POC method. The vibration frequencies calculated from the obtained video after performing Fourier transforming was 1.01Hz, which was a good match to the set on the vibration testing machine. The vertical displacement from both video and laser displacement meter are shown in Figure 7 and Figure 8 respectively. It was confirmed that the bridge displacement can be calculated well by the proposed method, although the recorded timings did not match those of the laser displacement meter and video.

In order to verify the accuracy of the proposed method (PM), which acquires the frame with the vertical displacement closest to the center of the vibration (zero-closing point), the case where the frame farthest from the vibration center is acquired (MAX), and the case where the frame is randomly acquired (RE), were investigated in this experiment (Figure 7). After extracting all three frames from the video, a total of three sets of frames were obtained. Then, these three sets of frames were then used to generate a 3D point cloud. In this study, Agisoft Matashape (Agisoft, 2023) software was used to construct the 3D point cloud data.

3.1.2 *Accuracy verification*

To verify the accuracy of the 3D point cloud construction, the state of surface generation, the number of outliers, and the number of feature points are used in this study. The 3D point cloud construction result of the proposed method is shown in Figure 9. Figure 10 shows the generated 3D point cloud of each method to evaluate the state of construction. Here, the front surface of the specimen is represented as an a-plane (red) and the top surface as a b-plane (blue). The proposed method PM neatly places feature points on the a-plane and the b-plane. However, in MAX and RE, noise is especially high on the top surface, and the feature points do not fit into one plane and that planes are generated at different positions, as in a b'-plane

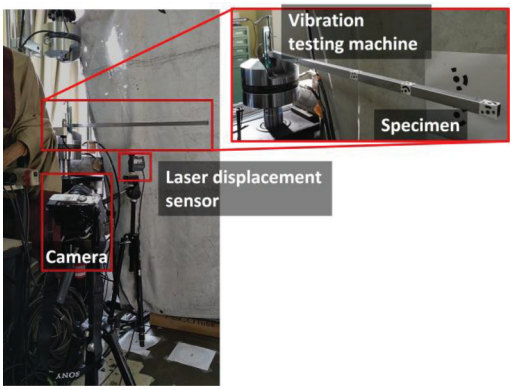


Figure 5. Experimental setup in the laboratory.

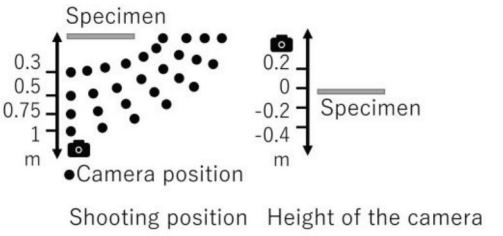


Figure 6. Details of a shooting location.

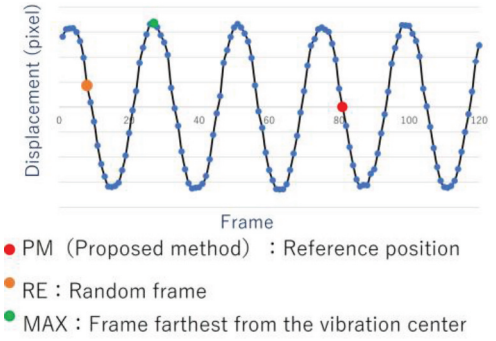


Figure 7. Displacement from video.

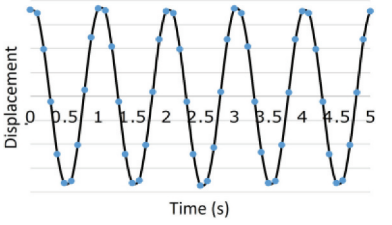


Figure 8. Displacement from laser displacement meter.

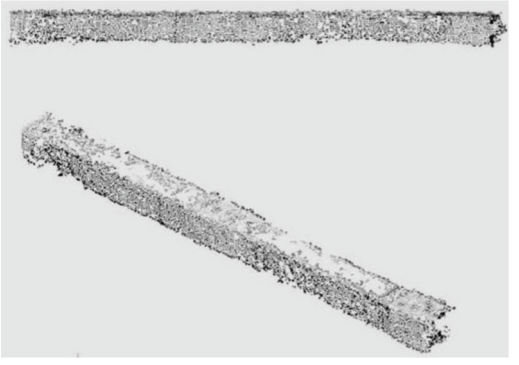


Figure 9. Generated 3D point cloud data of PM.

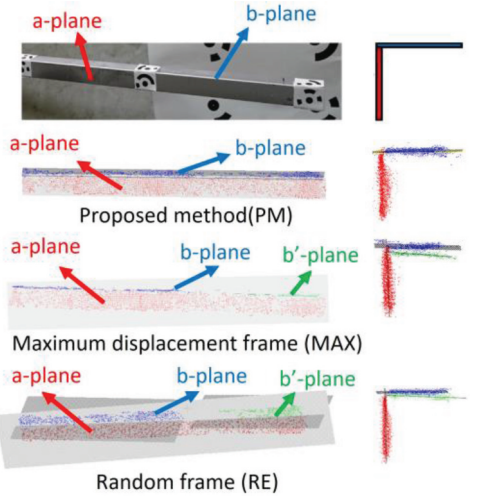


Figure 10. 3D point cloud data in each method.

shown in green. It can be considered due to the vibration, the top surface has more noise in MAX and RE.

After the 3D point cloud construction, denoising was performed by applying a noise reduction method based on the positional relationship between feature points using the SOR filter and the RANSAC shape detection method. It was also confirmed that the number and

percentage of noise removed by the above methods, i.e., outliers of feature points, were smaller when the proposed method (PM) was used than when the other methods were used.

3.2 *Field experiment to verify the feasibility of the proposed method for an existing real bridge*

In this section, an experiment using the proposed method on an existing real bridge has been performed. The flow of the experiment and the method of extracting the specified frames are the same as in the laboratory experiment.

The target bridge of the experiment is a wooden pedestrian bridge on the campus, 20.5 meters long and 4 meters wide. The target bridge and the experimental setup, and shooting positions are shown in Figure 11. In this experiment, due to the tree branches, one side of the bridge was photographed and especially focused on the red squared area in Figure 11 to investigate the construction errors. As shown in the lower right of Figure 11, 27 locations were selected at 3 to 12 m from the bottom of the bridge, with camera heights of 2 m, 2.5 m, and 3 m. The images were taken from a total of 81 locations. Moreover, a vibration generator was installed on the sidewalk (Figure 12) and forced vibration was applied in order to accurately determine the vibration conditions. The vibrator was activated to make the bridge vibrate while ensuring that no pedestrians were passing. The vibration generator was installed to vibrate at a frequency of 5.32Hz.

3.2.1 *Results of 3D point cloud data construction*

As in the laboratory experiments, the vibration information in all videos was acquired first. The vibration information acquired from a sample video is shown in Figure 13. The vibration frequency obtained from the video is 5.35 Hz, which is very close to that set in the vibration generator. Figure 14 shows the 3D point cloud construction result. Due to the tree branches or the angle of the camera, the high part of the bridge was difficult to generate, yet the focus area of the bridge could be well constructed.

3.2.2 *Accuracy verification and discussion*

As shown in Figure 14, the proposed method, PM, has feature points neatly placed on a single plane as in the laboratory experiment. In this experiment, the number of points to use for mean distance estimation was set to 6 and nSigema was 2. The result of applying the SOR filter after generating the 3D point cloud in each method is shown in Table 1. As shown in Table 1, there were 2.63 million, 2.6 million, and 2.55 million feature points in the focus area for PM, MAX, and RE, respectively, of which the percentage removed as outliers was the lowest for PM The percentage of feature points removed as outliers was the lowest for PM at 0.64%, and about 0.66 % and 0.68% for MAX and RE. From this result, it was confirmed the PM can eliminate the vibration effect.

As shown in Figure 14, due to the shooting position and angle, the point cloud of the board below the bridge is better constructed. Hence this component of the bridge is used as the comparison target when applying the RANSAC shape detection. The generated feature points on the plane of PM and MAX are shown in Figure 15. According to Figure 15, a point cloud constructed by PM could generate a complete surface, however, in the MAX, two different planes are generated due to the uneven distribution of the feature points. Moreover, the largest number of points on the plane was observed in PM and the mean distance from the plane to each feature point are smallest. Thus, it was also confirmed that the proposed method can be eliminated the vibration effect of the bridge when constructing 3D point cloud data with the RANSAC shape detection method as well as the SOR filter.

In this method, if the camera moves with bridges, the bridge vibration is canceled by the camera vibration, so the camera must be installed in a position where it is not affected by the bridge vibration. On the other hand, it can be assumed that the camera is shaken by wind and other influences. Therefore, it is important to take vibration into consideration, for example by using vibration isolating pads. As another countermeasure, as bridges have parts that hardly vibrate (e.g. piers), it is possible to remove the influence of the camera vibration by calculating the vibration of the camera itself and subtracting



Figure 11. Target bridge and shooting positions.

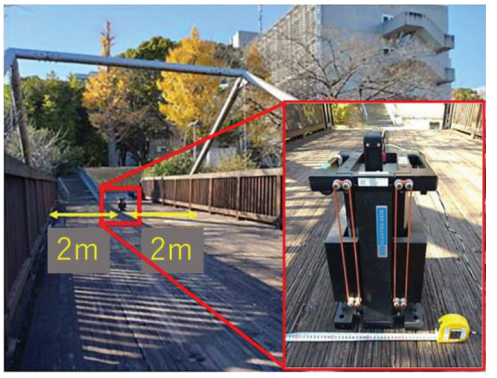


Figure 12. Vibration generator setup.

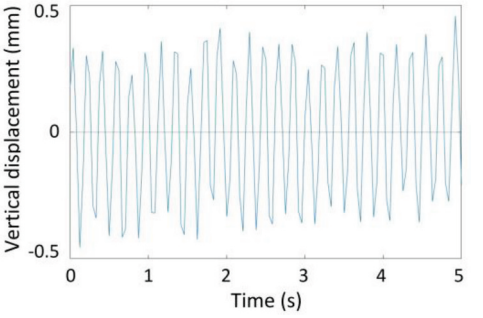


Figure 13. Vibration information of sample video.

Table 1. Result of applying the SOR filter method after 3D point cloud construction.

Method	Number of points	Number of outliers	Proportion of outliers
PM	2,630,662	2,613,900	0.64%
MAX	2,608,224	2,590,930	0.66%
RE	2,555,884	2,538,392	0.68%

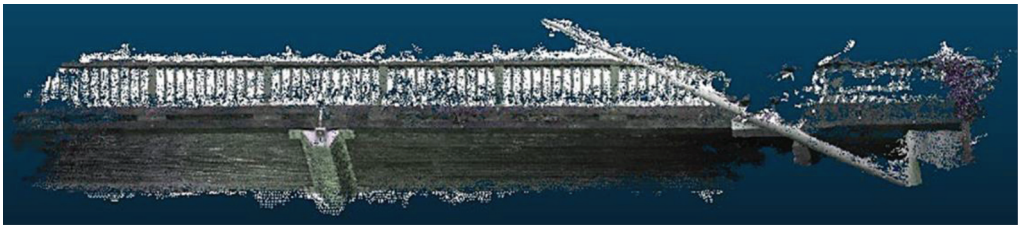


Figure 14. 3D point cloud data construction of target bridge.

it from the vibration analysis results of the bridge by performing the same video analysis on the parts that do not vibrate.

3.3 *Summary*

In this chapter, 3D point cloud data are constructed with the test specimen in the laboratory experiment and existing bridge by proposed method. The 3D point cloud

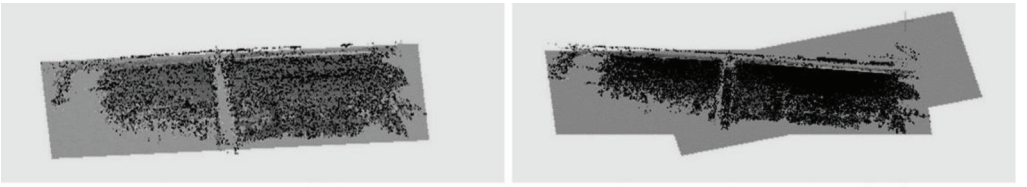


Figure 15. Generated plane with the feature points at the board below the bridge.

generated using two other frames (maximum displacement frame and random frame) from the same video is also compared. Comparing the 3D point cloud data after applying the SOR filter method and the RANSAC shape detection method, it was confirmed that the 3D point cloud generated using the proposed method has fewer outliers in both experiments. Therefore, it can be considered that the 3D point cloud generated by the proposed method is more accurate.

4 CONCLUSIONS

This study was conducted on 3D point cloud data, which have gained attention in recent years in bridge maintenance management, and focused on the effect of bridge vibration on 3D point cloud generated by photogrammetry. The conclusions in this study are described as follows:

(a) In this study, a method was proposed to eliminate the influence of bridge vibration on the accuracy of 3D point clouds: by using the POC method to acquire the bridge vibration information in the video used to generate 3D point clouds and then extracting the frames with the closest to the vibration center from the video, the deviation of bridge feature points in the photographs used to generate 3D point clouds was reduced. Using the method proposed in this study, only two steps, obtaining bridge vibration information through video analysis and extracting specific frames, are needed to be added to the usual process of generating 3D point clouds.
(b) The feasibility of the proposed method was verified by laboratory experiments. In the laboratory experiments, the maximum displacement frames and random frames were extracted separately from all the same videos, in addition to the specified frames of the proposed method, so as to ensure that the three sets of frames were obtained under the same conditions. Later, by comparing the 3D point clouds generated from these three sets of frames, it was verified that the proposed method in this experiment generates more accurate 3D point clouds.
(c) This study also discussed the feasibility of the proposed method for real existing bridges through field experiments. The experiment was performed by keeping the bridge vibrating by installing the vibration generator on the bridge, and the video was taken. After comparing 3D point clouds, it was clarified that the method can reduce the outlier points in the bridge 3D point cloud and improve the accuracy of the 3D point cloud.

In this study, the focus was on verifying the accuracy based on outliers and the construction state of the surface, as it was difficult to construct a complete 3D point cloud of the target bridge due to the limitations of the camera installation position. The verification of construction errors by comparing the constructed 3D model with real structures and the construction of an FE analysis model using the obtained 3D point cloud data will be the subject of future studies. Moreover, the availability of the proposed method for realistic bridges needs to be further improved.

REFERENCES

Agisoft metashape. 2022. User Manual Professional Edition. Version2.1. https://www.agisoft.com

Aoki, T., Ito, K., Shibahara, T., & Nagashima, S. 2007. High-Accuracy Machine Vision Using Phase-Only Correlation. *IEICE ESS Fundamentals Review*. Vol. 1, Issue 1. pp. 1_30-1_40.

Bolles, R. and Fischler, M. 1981. A RANSAC-based approach to model fitting and its application to finding cylinders in range data. *IJCAI '81: 7th International Joint Conference on Artificial intelligence*, Vol. 2, pp. 637–643.

Catbas, F.N., Luleci, F., Zakaria, M., Bagci, U., La Viola, J.J.Jr., Cruz-Neira, C., and Reiners, D. 2022. Extended Reality (XR) for Condition Assessment of Civil Engineering Structures: A Literature Review. *Sensors*. Vol. 22, Issue. 23, 9560. https://doi.org/10.3390/s22239560

Fujiwara, Y., Umezu, K., Tamaki, K., & Tanno, K. 2018. Application of the Bridge Inspection Robotic Camera to Monitoring. *Concrete Journal*. Vol. 56, Issue 1: pp. 100–105.

Lowe, D.G. 2004. Distinctive Image Features from Scale-Invariant Keypoints. *International Journal of Computer Vision*. Vol. 60: pp. 91–110.

Ministry of, Infrastructure, Transport and Tourism. 2015. Road Maintenance in Japan: Problems and Solutions.

Ministry of, Infrastructure, Transport and Tourism. 2022. Annual Report on Road Maintenance.

Nishimura, S. 2014. The Development and Evaluation of Optical Measurement Techniques in Bridge Maintenance. *Journal of the Japan Society for Precision Engineering*. Vol. 80, Issue 11: pp. 970–974.

Rusu, R. B., Blodow, N., Marton, Z., Soos, A., and Beetz, M. 2007. Towards 3D object maps for autonomous household robots. *International Conference on Intelligent Robots and Systems, IEEE*. San Diego, CA, USA. DOI: 10.1109/IROS.2007.4399309

Snavely, N., Seitz, S.N., & Szeliski, R. 2008. Modeling the World from Internet Photo Collections. *International Journal of Computer Vision*. Vol. 80: pp. 189–210.

Westoby, M.J., Brasington, J., Glasser, N.F., Hambrey, M.J., & Reynolds, J.M. 2012. 'Structure-from-Motion' photogrammetry: A low-cost, effective tool for geoscience applications. *Geomorphology*. Vol. 179, Issue 15: pp. 300–314.

Bridge Maintenance, Safety, Management, Digitalization and Sustainability – Jensen, Frangopol & Schmidt (eds)
© 2024 The Author(s), ISBN 978-1-032-77040-6
Open Access: www.taylorfrancis.com, CC BY-NC-ND 4.0 license

Scour detection method of bridge foundation based on pier vibration mode under vehicle braking action

Y. Li, Z.H. Zhang, Z.B. Sun & H. Sun
School of Transportation Science and Engineering, Harbin Institute of Technology, Harbin, Heilongjiang, China

ABSTRACT: Foundation scour poses a huge potential threat to bridge safety. A scour detection method of bridge pile foundation based on pier vibration mode excited by vehicle braking action was proposed and verified by numerical simulation and a laboratory test. Firstly, the horizontal vibration of bridge was excited by vehicle braking action, and the vibration modes sensitive to scour were identified from vibration signal. Secondly, the frequency change rate FCR and the flexibility-based displacement were defined as indicators to determine the scour location. Finally, with pier mode as input and scour state as output, a BP neural network model optimized by particle swarm optimization algorithm was constructed to predict the scour depth. Numerical and experimental studies showed that the vehicle braking force can effectively stimulate the local modes of the pier, and the scour indicators were very sensitive to scour. The scour depth can be accurately predicted using a small number of training samples and several vibration measuring points on the pier. The proposed method is simple to operate and can be embedded in the regular bridge load test to evaluate the bridge substructure synchronously.

1 INTRODUCTION

Bridge foundation scour is one of the important reasons for the failure of bridge across river. For example, about 60% of bridge failure events are related to scour in America (Wardhana & Hadipriono 2003). Scour occurs underwater and is difficult to observe directly. At present, scour detection is mainly through diving detection or sonar, radar and other equipment (Prendergast & Gavin 2014). However, these methods are not suitable for the short and medium-span highway bridges due to their complicated workflow and high cost.

The vibration-based bridge scour detection methods have gained great attention. Bridge vibration is mainly caused by traffic load, and the related researches are summarized as follows. Ko et al. (2010) proposed a scour detection method based on the mean Fourier spectrum of structural measured vibration. Prendergast et al. (2017) developed a numerical model of vehicle-bridge-soil dynamic interaction, and conducted the studies on scour detection based on vehicle-induced vibration. Kong and Cai (2016) numerically studied the feasibility of identifying scour from vehicle response. Foti and Sabia (2011) performed field tests on a severely scoured bridge, the dynamic characteristics and vehicle-induced vibration of the bridge were used to identify scour. Cheng et al. (2022) developed a mobile scour detection platform to test the fundamental frequency of the bridge and evaluate the substructure condition using the critical frequency ratio *RC*.

Finite element model updating (FEMU) is widely used to identify scour depth, which requires accurate vibration modes. Chen et al. (2014), and Li et al. (2017) identified the scour depth of cable-stayed Bridges. Zhan et al. (2022) identified the scour depth of highway girder bridges by FEMU. The proxy model approach may have advantages over FEMU. Liao et al. (2022) used the improved genetic algorithm (GA) to identify the scour depth of pile foundation of continuous beam bridge. He et al. (2023) proposed a Kriging model assisted by GA, which improved the computational efficiency and accuracy.

DOI: 10.1201/9781003483755-427

A scour detection method of bridge pile foundation based on vehicle braking action was proposed in this paper. Compared with routine traffic loads, braking forces can significantly stimulate the horizontal response and modes of bridges sensitive to scour (Zhang et al. 2022). Vehicle braking tests can be performed in regular bridge load tests with little additional testing cost. The main contents of this paper are as follows. Firstly, the scour detection method is introduced, including two steps of scour location and scour depth identification. Secondly, a numerical case is used to study the details and feasibility of the proposed method. Finally, a laboratory model experiment is carried out to verify the proposed method.

2 BRIDGE SCOUR DETECTION METHOD BASED ON VEHICLE BRAKING ACTION

2.1 *Identify bridge modes from structural vibration excited by braking action*

In a bridge dynamic load test, braking test is used to evaluate the dynamic performance of bridge. Vehicle braking causes axle load redistribution, and the total braking force $\mathbf{F_{xt}}$ of the vehicle will be allocated to the corresponding wheel position according to the new axle load distribution. Specific derivation process can be found in the literature (Zhang et al. 2022). Based on the modal superposition method, the vehicle-bridge coupled vibration during vehicle braking stage is established:

$$\begin{bmatrix} \boldsymbol{M}_{\mathrm{v}} & 0 \\ 0 & \boldsymbol{M}_{\mathrm{B}} \end{bmatrix} \begin{Bmatrix} \ddot{\boldsymbol{X}}_{\mathrm{v}} \\ \ddot{\boldsymbol{q}}_{\mathrm{B}} \end{Bmatrix} + \begin{bmatrix} \boldsymbol{C}_{\mathrm{v}} & \boldsymbol{C}_{\mathrm{vB}} \\ \boldsymbol{C}_{\mathrm{Bv}} & \boldsymbol{C}_{\mathrm{B}} + \boldsymbol{C}_{\mathrm{B}}^{\mathrm{v}} \end{bmatrix} \begin{Bmatrix} \dot{\boldsymbol{X}}_{\mathrm{v}} \\ \dot{\boldsymbol{q}}_{\mathrm{B}} \end{Bmatrix} + \begin{bmatrix} \boldsymbol{K}_{\mathrm{v}} & \boldsymbol{K}_{\mathrm{vB}} \\ \boldsymbol{K}_{\mathrm{Bv}} & \boldsymbol{K}_{\mathrm{B}} + \boldsymbol{K}_{\mathrm{B}}^{\mathrm{v}} \end{bmatrix} \begin{Bmatrix} \boldsymbol{X}_{\mathrm{v}} \\ \boldsymbol{q}_{\mathrm{B}} \end{Bmatrix} = \begin{Bmatrix} \boldsymbol{F}_{\mathrm{v}}^{\mathrm{r}} \\ \boldsymbol{F}_{\mathrm{B}}^{\mathrm{rG}} + \boldsymbol{F}_{xt} \end{Bmatrix} \tag{1}$$

where $\boldsymbol{M}$, $\boldsymbol{K}$, $\boldsymbol{C}$ and $\boldsymbol{F}$ respectively represent mass, stiffness, damping matrix and load vector. $\mathbf{X_v}$, $\dot{\mathbf{X}}_\mathbf{v}$ and $\ddot{\mathbf{X}}_\mathbf{v}$ respectively represent vehicle displacement, speed and acceleration response vectors. $\mathbf{q_B}$, $\dot{\mathbf{q}}_\mathbf{B}$ and $\ddot{\mathbf{q}}_\mathbf{B}$ respectively represent the bridge displacement, velocity and acceleration. Specific forms of these matrices can be found in references (Li et al. 2016; Zhang et al. 2022).

In the process of vehicle braking, the bridge is subjected to longitudinal short-term concentrated load and vertical wheel load. The braking force is approximately rectangular pulse excitation with a low spectral principal component, which can be used to excite structures with low natural frequency, such as bridges. As it is difficult to measure the load input, the output-only modal identification method is adopted. The frequency domain decomposition method (FDD) is used to identify the bridge modes. The modes identified by FDD are normalized relative to the unit mass matrix. In addition, the structural free attenuation signal after vehicle braking is used to reduce the interference of the vehicle.

2.2 *Indicators for detecting the foundation scour location*

The following indicators are defined for scour location based on the results of bridge modal identification under vehicle braking action.

(1) Frequency change rate

Frequency change rate *FCR* is defined as:

$$FCR = \frac{\Delta f_i}{f_i} \tag{2}$$

where f_i is the i-order natural frequency of the healthy structure, which can be tested before scour occurs; Δf_i the change of f_i caused by scour.

(2) Flexibility-based deflections

The flexibility matrix $\mathbf{G}$ of the structure reflects the relationship between the static load and the displacement of the structure, which can be estimated by the measured mode shape and frequency:

$$\mathrm{G} = \Phi \Lambda^{-1} \Phi^{T} \tag{3}$$

where $\Lambda^{-1}$is a diagonal matrix composed of the reciprocal of the square of the natural frequency arranged in ascending order.$\Phi = [\boldsymbol{\varphi}_{a,1} \quad \boldsymbol{\varphi}_{a,2} \quad \cdots \quad \boldsymbol{\varphi}_{a,n}]$, $\boldsymbol{\varphi}_{a,i}$ is the *i*-order mode shape normalized with respect to the mass matrix:

$$\boldsymbol{\varphi}_{a,i}^{T}\boldsymbol{M}\boldsymbol{\varphi}_{a,i} = \boldsymbol{I} \tag{4}$$

The mode shape $\boldsymbol{\varphi}_{m,i}$ identified by FDD method is normalized under the unit mass matrix:

$$\boldsymbol{\varphi}_{m,i}^{T}\boldsymbol{\varphi}_{m,i} = \boldsymbol{I} \tag{5}$$

The piers of the short and medium-span highway bridges are generally of equal section, and their mass matrix $\boldsymbol{M}$ is:

$$\boldsymbol{M} = m_0\boldsymbol{I} \tag{6}$$

where m_0 is a constant related to the element mass, **I** is the unit diagonal matrix.

It can be obtained by formula (5) ~ (7):

$$\boldsymbol{G_a} = \boldsymbol{\Phi_a}\boldsymbol{\Lambda}^{-1}\boldsymbol{\Phi_a}^{T} = \frac{1}{m_0}\boldsymbol{\Phi_m}\boldsymbol{\Lambda}^{-1}\boldsymbol{\Phi_m}^{T} = \frac{1}{m_0}\boldsymbol{G_m} \tag{7}$$

Eq. (7) shows that the $\boldsymbol{G}_{\mathbf{m}}$ and $\boldsymbol{G_a}$ has the same information, and they are equivalent in structural damage identification. The flexibility-based deflections δ is defined for scour identification:

$$\boldsymbol{\delta} = \boldsymbol{P}(\boldsymbol{G_{md}} - \boldsymbol{G_{m0}}) \tag{8}$$

where $\boldsymbol{P}$ is the unit force vector, $\boldsymbol{G_{md}}$ and $\boldsymbol{G_{m0}}$ is the pier flexibility matrix tested under health and scour conditions respectively, and $\boldsymbol{\delta}$ is the displacement difference under uniform horizontal unit load.

2.3 *Identification of foundation scour depth based on PSO-BPNN*

Back propagation neural network (BPNN) is one of the representative algorithms for solving multi-input and multi-output problems because of its strong nonlinear mapping ability. In order to improve the prediction accuracy of BPNN, Particle swarm optimization (PSO) is used to optimize the network weights. PSO is a swarm intelligence optimization algorithm with strong function extremum optimization ability.

After the scour location is determined, the scour depth is identified using the following steps:

(1) Establish the finite element model of the target pier based on the design data.
(2) Determine the range of scour depth and other key model parameters, and conduct multi-dimensional stratified sampling using Latin hypercube sampling method to obtain training and test sample sets.
(3) Frequency and mode shape with labels are obtained through modal analysis and input into the network for training.
(4) Input the measured frequency and mode shape into the trained network to predict the scour depth.

3 NUMERICAL VALIDATION OF THE PROPOSED METHOD

3.1 *Bridge information and finite element model*

A typical three-span concrete continuous beam bridge was selected for numerical study. The span of the bridge is 3×30 m and the width is 10.5m. The piers are concrete double cylindrical piers with a diameter of 1.5m. The height of the pier P1 is 8.0m, and the height of the pier P2 is 10.0m. The pile foundation is 18m long and 1.7m in diameter. Ptfe plate rubber supports are installed on abutments B0 and B3, and Plate rubber supports are installed on piers P1 and P2.

The finite element model of the bridge was built using the ANSYS, as shown in Figure 1. The superstructure and bent cap are simulated using solid element *Solid65*, the pier and

foundation are simulated using beam element *Beam188*, and the bearing is simulated using matrix element *Matrix27*. The bottom of the pile is fixed vertically, and the horizontal constraint of the pile is simulated using linear spring element *Combin14* (Prendergast et al. 2017). The stiffness of the soil spring is calculated according to the "M" method (TB 10002.5-2005). The foundation scour is simulated by removing the spring element above the scour line, and the stiffness of the remaining soil spring is recalculated according to the new ground elevation.

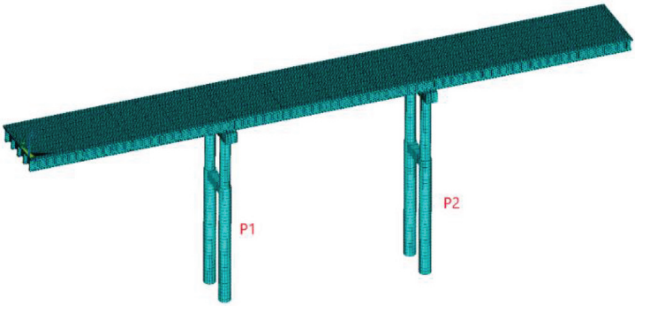


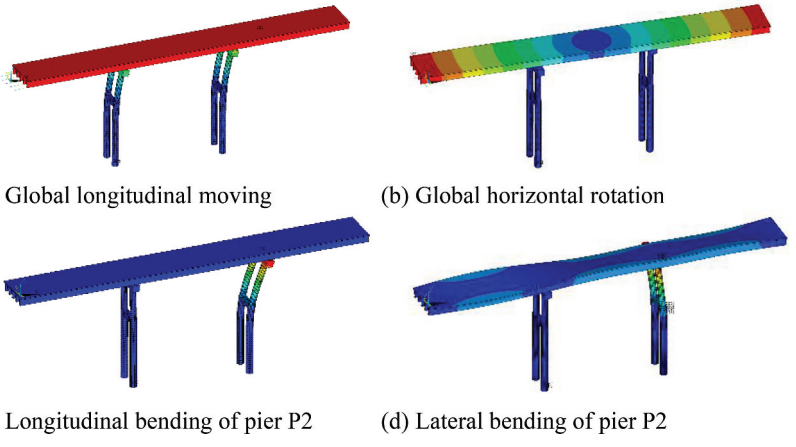
Figure 1. Finite element model of bridge.

3.2 *Influence of scour on dynamic characteristics of the bridge*

The scour depth of pier P2 is set to 0~4m to study the scour effect on the vibration mode of bridge. The frequencies sensitive to scour are shown in Table 1, and the corresponding mode shapes are shown in Figure 2.

Table 1. Frequencies sensitive to scour.

Vibration Mode	Frequency (Hz)				
	Intact	P2-1m	P2-2m	P2-3m	P2-4m
Global longitudinal moving	0.891	0.884	0.876	0.869	0.863
Global horizontal rotation	1.284	1.283	1.282	1.282	1.281
Longitudinal bending of pier P2	2.929	2.791	2.669	2.560	2.462
Transverse bending of pier P2	4.599	4.400	4.195	4.054	3.750
Torsion of pier P2	6.073	5.731	5.428	5.156	4.893
Second order longitudinal bend of pier P2	12.658	11.282	10.138	9.184	8.385
Second order lateral bend of pier P2	17.919	16.050	15.146	14.125	11.457



(a) Global longitudinal moving (b) Global horizontal rotation

(c) Longitudinal bending of pier P2 (d) Lateral bending of pier P2

Figure 2. Mode shapes of bridge.

Table 1 shows that foundation scour has little influence on the global modes of the bridge, but has great influence on the local modes (longitudinal, transverse and torsional modes) of the pier. This is because the free length of pier increases and the horizontal stiffness decreases due to scour.

3.3 *Dynamic response of the pier during vehicle braking.*

The vehicle-bridge coupled vibration was numerically simulated for the bridge. The test parameters are set as follows: a three-axle truck weighing 30t drives along the center line of lane 1 at a speed of 30km/h, and starts braking in the middle of the second span. The braking force rise time t_p is 0.3s, the braking force peak coefficient φ_p is 0.7, and the road roughness level is "good". Vehicle parameters and analysis principles are detailed in literature (Li et al. 2016). Figure 2 shows the acceleration response and spectrum at top of pier P2 during vehicle braking for different scour depths.

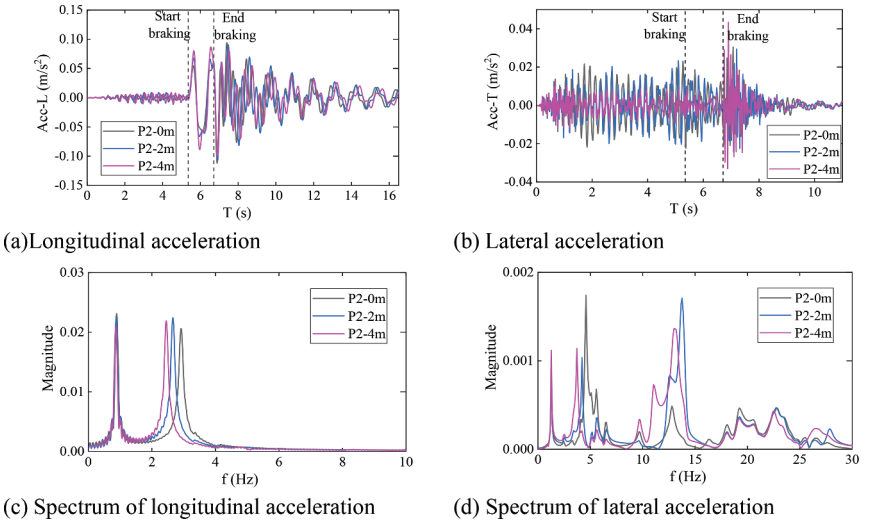


Figure 3. The acceleration response and spectrum at pier P2 top during vehicle braking.

Figure 2(a) and (b) show that vehicle braking force can stimulate a larger acceleration response, and scour will lead to an increase in response amplitude. Figure 2 (c) shows that the vehicle braking force stimulates the global longitudinal moving modes and the longitudinal bending modes of pier, and these two order frequencies can be accurately observed and extracted from the spectrum. The first two frequencies in Figure 2 (d) correspond to the global horizontal torsion mode of bridge and the transverse bending mode of pier, respectively.

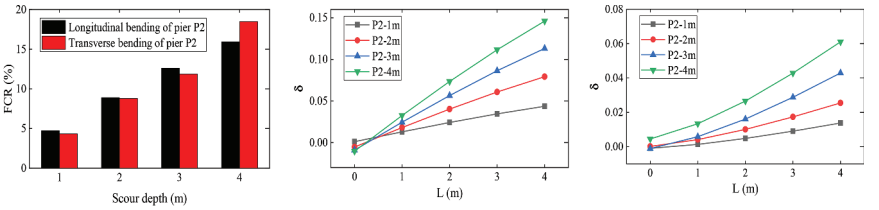
In conclusion, the smooth response spectrum with obvious peak value can be obtained under the vehicle braking action without interference from vehicle frequency, which has significant advantages in bridge modal identification.

3.4 *Validity verification of scour positioning indicators*

The pier modes are identified from the structural free attenuation signal after vehicles braking using the FDD method. The first two longitudinal modes and the first two lateral modes of the pier are used to calculate the scour indicators *FCR* and δ based on the Eq. (3) and Eq. (9). In practical engineering, the installation of sensors on piers in deep water area requires the bridge inspection vehicle to provide a working platform. Sensors can usually only be installed on the upper part of the pier. For this bridge, 5 measuring points are arranged downward at 1m intervals from the top of pier P2. When the scour depth of pier P2 is 0m~4m, the *FCR* and δ are shown in Figure 4.

Figure 4(a) shows that the indicators *FCR* and δ increase with the increase of scour depth. The *FCR* is above 15% when the scour depth is 4m. Figure 4(b) ~ (c) shows that the δ value of the lower measuring point is greater than that of the upper measuring point, indicating that

the sensor on the pier should be arranged downward as far as possible. The δ for longitudinal modes is larger, indicating that the longitudinal flexibility of the bridge is larger.



(a) FCR (b) δ for longitudinal modes (c) δ for lateral modes

Figure. 4. Scour indicators FCR and δ under different scour depth (L is the distance between the sensor and the pier top).

3.5 *Scour depth identification based on PSO-BPNN*

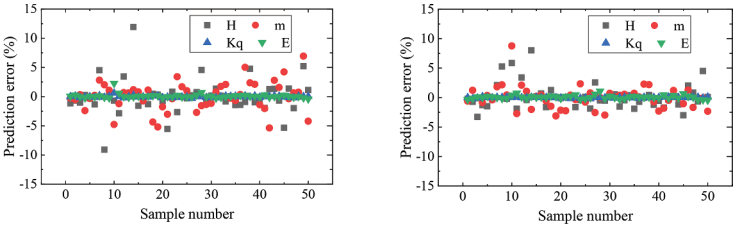
Based on the method proposed in section 2.3, the flow of scour depth identification is illustrated by taking pier P2 as an example.

Firstly, considering the uncertainty of actual pier conditions, the scour depth H, the concrete elastic modulus E of the pier, the shear stiffness K_q of the support and the soil horizontal resistance coefficient m were selected as the optimization parameters. 500 samples were randomly selected within the sampling range shown in Table 2 using Latin hypercube sampling method. The label corresponding to i-sample is ***Outpot,i***=[H_i, E_i, Kq_i, m_i]. E_0, Kq_0 and m_0 in Table 2 are the standard values of parameters from the design data. Secondly, modal analysis is carried out on random samples. The first order longitudinal and transverse mode of pier are selected as the target parameters. The target parameter vector of the i-sample is ***Input,i***= [f_1,φ_{11}, φ_{12},. . ., f_2,φ_{21}, φ_{22},. . .]. Then, 450 samples are selected as the training set and the remaining 50 samples are selected as the test set. BPNN is trained with ***Input,i*** as output and ***Outpot,i*** as output.

Table 2. Sampling range of parameters.

Parameters	H	m	Kq	E
Sampling range	0m ~ 6m	$0.5m_0$ ~ 1.5 m_0	$0.8K_{q0}$ ~1.2 K_{q0}	0.8 E_0~1.2 E_0

The test set was used to test the prediction accuracy of BPNN, and the results are shown in Figure 5. The results show that the proposed method can accurately predict the scour depth, and satisfactory results can be obtained with only 3 measuring points at the pier.



(a) Five measuring points (b) Three measuring points

Figure 5. Prediction accuracy of BPNN.

4 EXPERIMENTAL VALIDATION OF THE PROPOSED METHOD

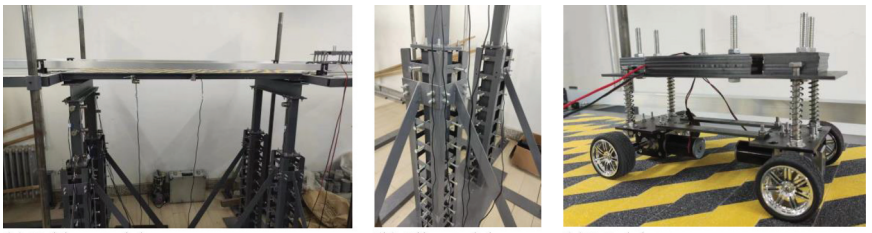
A laboratory test was designed to validate the proposed method. The design process of the scale model was as follows. First, the similarity constants for model tests were derived based

on dimensional analysis. Secondly, taking a concrete simply supported bridge with a span of 30m as the prototype, the size similarity scale λ_L was selected as 20. The scale model was made using steel, so the elastic modulus similarity scale λ_E is 0.168. Finally, considering the purpose and conditions of the experiment, the similar scale of other parameters was calculated and the detailed model design was carried out.

The bridge model is a simple supported beam with a span of 1.5m, as shown in Figure 6(a). The pier is a double pillar pier with a height of 0.4m. The pile foundation is 1.0m long, and 10 layers of bolts are uniformly installed on the side of the pile to limit the horizontal deformation of the pile (shown in Figure 6(b)), so as to simulate the lateral constraint of soil on the pile. Foundation scour can be simulated by removing bolts. Rubber blocks are installed between the beam and the bent cap to simulate the support. The two-axle model car (shown in Figure 6(c)) is equipped with an electric drive system that allows uniform motion and braking.

In this test, 0/2/4/6 layers of bolts were successively removed on pier P2 to simulate four scour levels, called *level-0~level-3*. Nine unidirectional acceleration sensors, six longitudinal and three transverse, are installed on pier P2, as shown in Figure 6(b). Brake tests were carried out under four scour levels. The weight of the model car is 7.5kg, and the vehicle braking at a mid-span position at an initial speed of 1.0m/s.

According to the test results, the changes in pier frequency identified from the braking-induced responses are shown in Table 3. Taking the *level-0* as the benchmark state, the scour indicators δ under other three scour levels are shown in Figure 7. The two indicators increased significantly as the scour level increased, and the experimental results verify the validity of the proposed methods.

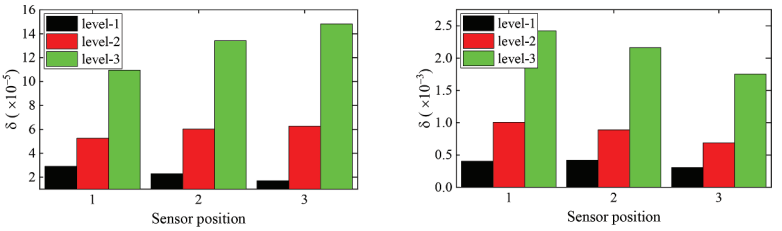


(a) Bridge model (b) Pile model (c) Model car

Figure 6. Laboratory model test.

Table 3. Changes in pier frequency identified from the braking-induced responses.

Vibration mode	Level-0	Level-1	FCR(%)	Level-2	FCR(%)	Level-3	FCR(%)
Longitudinal ending	129.88Hz	119.14 Hz	8.27	95.70 Hz	26.32	75.19 Hz	42.11
Transvers bending	86.91 Hz	77.15 Hz	11.23	63.47 Hz	26.97	48.82 Hz	43.83



(a) δ for longitudinal modes (b) δ for lateral modes

Figure 7. Scour indicator δ under different scour levels.

5 CONCLUSIONS

In this paper, a scour detection method of bridge pile foundation based on vehicle braking was proposed. Firstly, the scour indicators were defined to identify the scour location based on the pier modes stimulated by vehicle braking force. Secondly, a PSO-BPNN model was trained to predict the scour depth. Numerical and experimental studies validate the effectiveness of the proposed method. The main conclusions are as follows:

(1) The vehicle braking force can effectively stimulate the horizontal dynamic response and vibration mode of the pier sensitive to scouring.
(2) The proposed scour indicators FCR and δ are sensitive to scour and can be used to determine the scour location.
(3) The constructed PSO-BPNN model can accurately predict the scour depth, and a satisfactory prediction result can be obtained with a small number of vibration measurement points.
(4) The feasibility of the proposed method is verified by a model test.

ACKNOWLEDGEMENTS

This study reported in this paper was supported by National Science Foundation of China (Grant No. 52078164).

REFERENCES

Chen, C.C., Wu, W.H., Shih F. & Wang, S.W. 2014. Scour Evaluation for Foundation of a Cable-Stayed Bridge based on Ambient Vibration Measurements of Superstructure. *Ndt & E International*, 66, 16–27

Cheng, M.Y., Liao, K.W., Chiu, Y.F., Wu, Y.W., Yeh, S.H. & Lin, T.C. 2022. Automated mobile vibration measurement and signal analysis for bridge scour prevention and warning. *Automation in Construction*, 134,104063

Foti, S. & Sabia, D. 2011. Influence of Foundation Scour on the Dynamic Response of an Existing Bridge. *Journal of Bridge Engineering*, 16, 295–304.

He, Y., Yang, J.P. & Yu, J. 2023. Surrogate-assisted finite element model updating for detecting scour depths in a continuous bridge. *Journal of Computational Science*, 69, 101996.

Ko, Y.Y., Lee, W.F., Chang, W.K., Mei, H.T. & Chen, C.H. 2010. Scour Evaluation of Bridge Foundations Using Vibration Measurement. Fifth International Conference on Scour and Erosion, San Francisco, CA, USA, 884–893.

Kong, X. & Cai, C.S. 2016. Scour Effect on Bridge and Vehicle Responses under Bridge-Vehicle-Wave Interaction. *Journal of Bridge Engineering*, 21, 04015083.

Li, Y., Cai, C.S., Liu, L., Chen, Y.J. & Liu, J.F. 2016. Dynamic analysis of a large span specially shaped hybrid girder bridge with concrete-filled steel tube arches. *Engineering Structures*, 106: 243–260.

Li, S.L., He, S.Y., Li, H. & Jin, Y. 2017. Scour Depth Determination of Bridge Piers Based on Time-Varying Modal Parameters: Application to Hangzhou Bay Bridge. *Journal of Bridge Engineering*, 22, 04017107.

Liao, Y.C., Wang, H.C., Hou, S.T., Feng, D.M. & Wu, G. 2022. Identification of the scour depth of continuous girder bridges based on model updating and improved genetic algorithm. *Advances in Structural Engineering*, 25, 2348–2363

Prendergast, L.J. & Gavin, K. 2014. A review of bridge scour monitoring techniques. *Journal of Rock Mechanics and Geotechnical Engineering*, 6, 138.

Prendergast, L.J., Gavin, K. & Hester, D. 2017. Isolating the location of scour-induced stiffness loss in bridges using local modal behaviour. *Journal of Civil Structural Health Monitoring*, 7, 483–503.

TB 10002.5-2005 .Code for design on subsoil and foundation of railway bridge and culvert. Beijing: China Railway Press.

Wardhana, K. & Hadipriono, F.C. 2003. Analysis of Recent Bridge Failures in the United States. *Journal of Performance of Constructed Facilities*, 17,144–150.

Zhan, J.W., Wang, Y., Zhang, F., An, Y. & Liu, K. Scour depth evaluation of highway bridge piers using vibration measurements and finite element model updating. *Engineering Structures*, 253,113815

Zhang, Z.H., Li, Y., Zhong, Y.C. & Lin, X.Q. 2022. Scour diagnosis index based on cross-correlation analysis of bridge dynamic response under vehicle braking, *Advances in Structural Engineering*, 26, 706–723.

Bridge Maintenance, Safety, Management, Digitalization and Sustainability – Jensen, Frangopol & Schmidt (eds)
© 2024 The Author(s), ISBN 978-1-032-77040-6
Open Access: www.taylorfrancis.com, CC BY-NC-ND 4.0 license

Field test study of bridge scour diagnostic method based on time-varying frequency

Z.H. Zhang, Y. Li, C. Yang & H. Sun
School of Transportation Science and Engineering, Harbin Institute of Technology, Harbin, Heilongjiang, China

ABSTRACT: Scour is one of the main hidden diseases of bridge substructure, which will lead to the significant loss of foundation stiffness and bearing capacity. A scour diagnostic method of pile foundation based on time-varying frequency was proposed and verified by several field bridge tests. Firstly, the traffic-induced vibration of the pier were collected, and the instantaneous frequency of the pier was extracted based on Wavelet Synchrosqueezed Transform. Secondly, the probability distribution of instantaneous frequency was fitted and the scour indicator was defined based on the confidence interval. Field test results showed that the vibration response of the middle part of the pier contains more high-order modal information than that of the top part. The scour indicator changed significantly for two tested piers with a height of 7.23m and 8.98m, which indirectly verified its sensitivity to the change of free length of piers. For short and medium-span bridges, effective vibration signals can be collected by a short test under open traffic conditions. The proposed method can be used for real-time monitoring or rapid detection of bridge scour.

1 INTRODUCTION

Bridge scour is a natural phenomenon caused by hydrodynamic action and is prevalent near the foundations of bridges crossing rivers. Flooding and scour are the main causes of bridge collapse accidents (Lagasse et al. 1998; Wardhana & Hadipriono 2003). Scour assessment is a key link in the assessment of bridge safety conditions. However, due to the concealment of scour, it is difficult for inspectors to detect abnormalities in the river bed through observation.

In recent years, vibration-based scour diagnostic method has received much attention due to its advantages of high efficiency, economy and no underwater work. Scour diagnosis is performed based on the correlation of dynamic response with scour state. Ko et al. (2010) verified the scour evaluation method based on the average spectrum of bridge vehicle-induced vibration through two field tests. Prendergast et al. (2017) studied the influence of scour on bridge vehicle-induced vibration through numerical simulation, and identified the frequency from the attenuation signal of the pier to identify scour. Foti and Sabia (2011) proved the feasibility of bridge dynamic characteristics and vehicle-induced vibration for scour identification through field tests. Malekjafarian et al. (2020) and Khan et al. (2021) used vehicle-induced vibration to construct the average normalized mode shape of the superstructure, and laboratory test were used to verify the feasibility of this indicator in identifying shallow foundation scour. Zhang et al. (2022) proposed a scour diagnosis method based on vehicle braking action, and constructed a scour indicator based on the correlation of dynamic response.

In summary, vehicle-induced vibration response of bridges is widely used to extract scour indicator such as frequency and mode shape. Most of the existing studies are based on laboratory tests or numerical simulation, and there is a lack of field tests on the vibration characteristics of piers under the action of moving vehicles. In addition, the passing vehicle and bridge

DOI: 10.1201/9781003483755-428

form a time-varying vibration system, and the bridge frequency is affected by the vehicle, which may affect the scour diagnostic results based on the dynamic characteristics of bridges.

In this study, a scour diagnostic method of bridge pile foundation based on structural time-varying frequency is proposed. This paper is organized as follows: In the section 2, the theoretical basis of this method is introduced. The instantaneous frequency is extracted from the vehicle-induced vibration of bridge piers based on Wavelet Synchrosqueezed Transform, and the scour indicator is defined based on statistical method. In Section 3, two field tests are used to verify the effectiveness of the proposed method. In the Section 4, a summary is given and further research suggestions are put forward.

2 THEORETICAL BASIS OF SCOUR DIAGNOSIS METHOD

2.1 *Instantaneous frequency identification of bridges based on wavelet synchrosqueezed transform*

For the vehicle-bridge interaction (VBI) system, the bridge vibration excited by the moving vehicle includes two parts (Mostafa et al. 2021), the forced vibration in the vehicle passing stage and the free attenuation response after the vehicle leaves. The passing stage is a non-stationary process, because the mass distribution of VBI system is time-dependent, so it is necessary to use time-frequency analysis methods to extract the instantaneous frequency (IF) of the VBI system. Existing studies focus on IF variation of vehicle and superstructure, but little attention has been paid to substructure.

Pier frequency is generally used to identify foundation scour. Prendergast et al. (2017) used the free attenuation signal from piers to identify frequencies, which may only be applicable to small damping structures. Since the middle pier of a continuous girder bridge is far away from the expansion joint, its free attenuation signal may be very weak. The vibration signal of bridge pier under traffic load is mainly forced vibration and contains closely spaced spectral components. It is necessary to pay attention to the time-varying dynamic characteristics of bridge pier by using time-frequency analysis tools.

Wavelet Synchrosqueezed Transform (WSST) is a novel time-frequency analysis technology (Daubechies et al. 2011), which has been proven to effectively overcome modal aliasing (Jiang, & Suter 2017) .WSST consists of continuous wavelet transform (CWT) and reallocation theory.

Firstly, CWT is used to transform the one-dimensional time signal $x(t)$ into two-dimensional wavelet coefficients:

$$W_x(a,b) = \int x(t) a^{-1/2} \Psi\left(\frac{t-a}{b}\right) \tag{1}$$

where $W_x(a,b)$ is the complex wavelet coefficient spectrum, a and b are the translation variables and scale variables respectively, $x(t)$ is the time signal, and the function$\Psi$is the mother wavelet.

Then, the IF of the signal is calculated using the following equation:

$$\omega_x(\mathrm{a},\mathrm{b}) = \frac{\frac{\partial W_x(\mathrm{a},\mathrm{b})}{\partial b}}{2\pi i W_x(\mathrm{a},\mathrm{b})} \tag{2}$$

Finally, Synchrosqueezed transformation is performed to compress and reorganize the $W_x(a,b)$ in the frequency direction:

$$T_x(\omega_l,\mathrm{b}) = (\Delta\omega_l)^{-1} \sum\nolimits_{\partial k} \mathrm{W}(a_k,\mathrm{b}) a_k^{-2/3} (\Delta a)_k \tag{3}$$

where the transformation function T_x only acts on the center$\omega_l$of the continuous interval$[\omega_l - 0.5\,\Delta\omega, \omega_l + 0.5\,\Delta\omega]$, and $\Delta a_k = a_k - a_{k-1}$, $\Delta\omega = \omega_l - \omega_{l-1}$.

The WSST compresses the wavelet coefficients to near the center frequency and refines the wavelet ridges, thus greatly improving the frequency resolution. The vehicle-induced vibration of the bridge structure often contains multiple modes, so there are multiple ridges in the time-frequency image. The modulus maximum method is used to extract the wavelet ridges and obtain the IFs of the VBI system.

2.2 *Probability estimation of instantaneous frequency*

Considering the time-varying properties of VBI system, scour-induced structural frequency changes were evaluated using statistical methods. Since the IFs distribution pattern cannot be predicted, kernel density estimation (KDE) was chosen to study the frequency distribution characteristics. KDE does not require prior knowledge and additional assumptions, and the data distribution characteristics are studied only from the sample itself.

If the instantaneous frequency $\omega(t)$ is regarded as an independent and equally distributed random variable, its KDE is calculated as follows:

$$PDF(\omega) = \frac{1}{nh}\sum_{k=1}^{n} K\left(\frac{\omega - \omega(t_i)}{h}\right) \tag{4}$$

where PDF is the probability density of ω, n is the total number of samples, t_i is the i-th sampling time, h is the kernel bandwidth. Function $K(\cdot)$ is the kernel function, and the Gaussian kernel function is used in this study.

The PDF of IFs of the bridge structure has multiple peaks. In order to separate each order mode, the valley point of PDF is selected as the dividing point, and the IFs are divided into different data sets. The normal probability distribution $N(\mu, \sigma)$ was re-estimated for each data set to obtain the distribution characteristics of each order of frequency.

Finally, based on the normal probability distribution for each order frequency, a confidence interval with 70% confidence level is defined as a scour indicator SI:

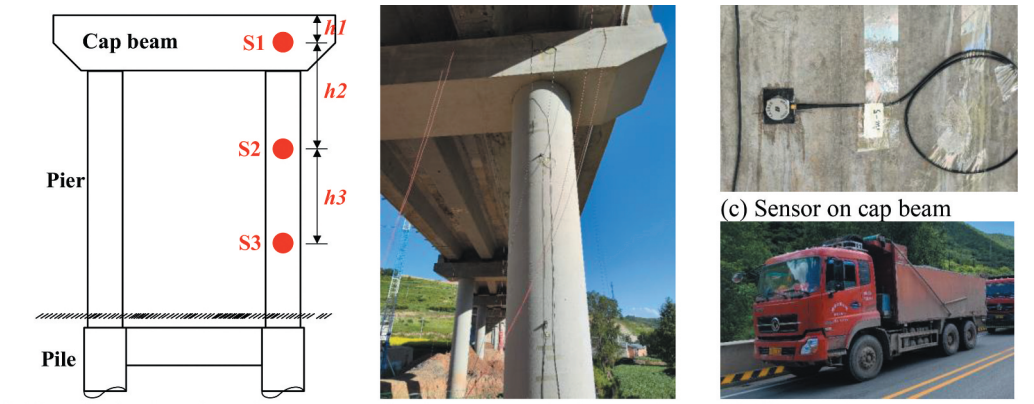
$$SI = [\mu - 0.5\sigma, \mu + 0.5\sigma] \tag{5}$$

3 FIELD TEST VERIFICATION OF SCOUR DIAGNOSIS METHOD

3.1 *Case study I- Zhangwangbao Bridge*

Zhangwangbao Bridge is a newly built concrete continuous girder bridge in Gannan, China. The test was carried out on the first four continuous spans, each span was 20m long. The bridge pier is the most common double-column bent pier among Chinese highway bridges, as shown in Figure 1(a). On-site measurement shows that the heights of piers P1 and P2 are 7.23m and 8.98m respectively, the pier diameter is 1.4m and the height of the cap beam is 1.3m. Three acceleration sensors (S1~S3) are installed on piers P1 and P2 respectively to test the longitudinal vibration, as shown in Figure 1(b). The *h1~h3* at pier P1 are 0.6m, 2.7m and 3.0m respectively, the *h1~h3* at pier P1 are 0.6m, 2.7m and 5.3m respectively. The test was conducted under closed traffic conditions and a three-axle truck weighing 45.2t passed the bridge (Figure 1(c)). Since the bridge is a curved bridge, the vehicle speed is controlled within 30km/h for safety reasons.

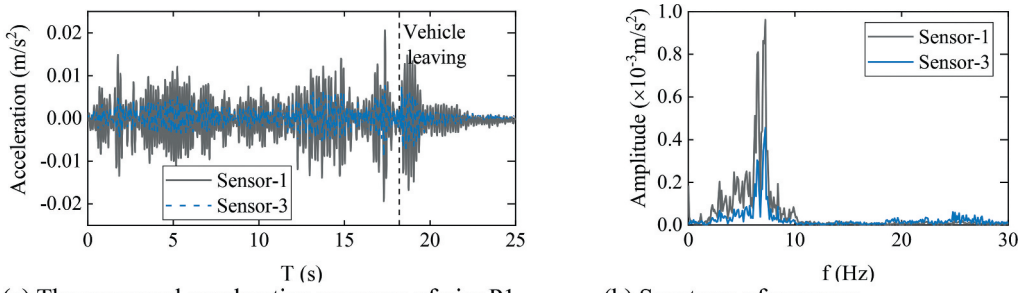
When the vehicle passes the bridge at a speed of 20km/h, the acceleration response of the pier P1 is shown in Figure 2(a), and the response spectrum is shown in Figure 2(b). Figure 2(a) shows that the vibration amplitude of measuring point S1 is significantly larger than that of measuring point S3, which is determined by the cantilever characteristics of the pier. The



(a) Installation location of sensors (b) Sensors installation on site (c) Sensor on cap beam (d) Three-axle truck

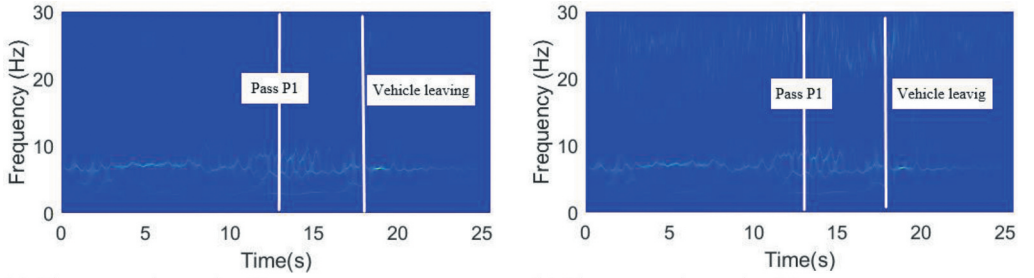
Figure 1. Overview of field test.

response of the measuring point S1 mainly contains low frequency components (0~10Hz), while the response of the measuring point S3 contains more high-frequency information (20~30Hz). This is because the low-order vibration of the pier mainly swings horizontally, and the peak of mode shape appears at the pier top, but the peak of high-order mode shape appears in the middle part of the pier.



(a) The measured acceleration response of pier P1 (b) Spectrum of response

Figure 2. Acceleration response and spectrum of pier P1.



(a) The measuring point S1 (b) The measuring point S3

Figure 3. Time-frequency representation of acceleration response at pier P1.

The acceleration response of pier P1 is analyzed using WSST, as shown in Figure 3, and the wavelet ridges can be easily observed. As the vehicle passes through the bridge, the wavelet

coefficient of the response of measuring point S1 only peaks in the low frequency band, while the peak value also appears in the high-frequency band (20~30Hz) for point S3. When the vehicle is far away from the pier P1 (0~10s), the wavelet ridge is relatively stable. When the vehicle travels near the pier P1 (10~15s), the wavelet ridge fluctuates significantly and multiple adjacent ridge appear. This is because that random wheel force acts on the adjacent spans of the pier P1 and stimulates the complex vibration mode. In the free vibration stage of the pier after the vehicle leaves (18s later), the wavelet ridge becomes stable again and gradually becomes unobservable. In addition, there is a ridge corresponding to a frequency of about 3 Hz during the vehicle passing phase, it is reasonable to speculate that this is an additional frequency caused by vehicle vibration.

The IF of piers is extracted using the dynamic response of measuring point S3 based on the method proposed in Section 2. Taking the dynamic response of pier P1 in the vehicle passing phase as an example, the extracted IFs is shown in Figure 4. The kernel density estimation is shown in Figure 5, and the normal distribution of each order frequency are shown in Figure 6.

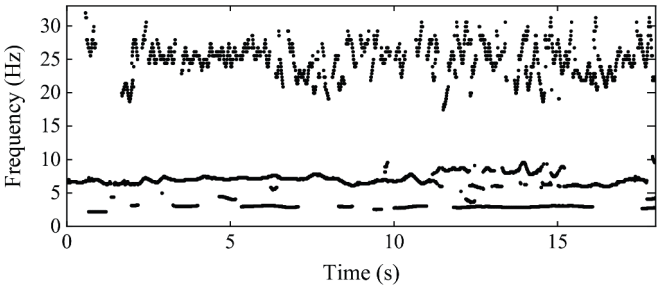


Figure 4. The IFs extracted from dynamic response of measuring point S3 in the vehicle passing phase.

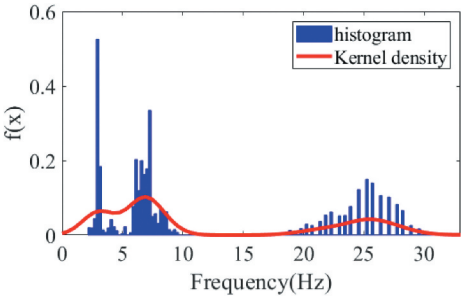


Figure 5. The kernel density estimation of Ifs.

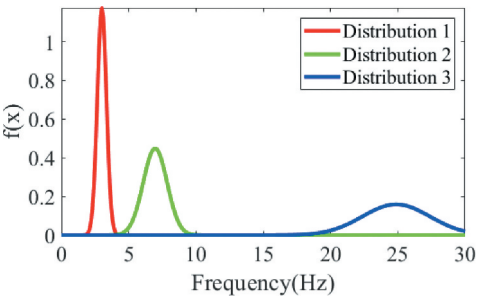


Figure 6. The normal distribution of each order IF.

The proposed scour diagnostic method can be indirectly verified using field tests on bridge piers P1 and P2. The piers of this bridge have not experienced the scour process, but the height difference between piers P1 and P2 is 1.75m. That is, pier P2 can be approximately regarded as the state after pier P1 has been scoured by 1.75m. The scour indicator *SI* is calculated using the passing phase response of measuring point S3, as shown in Table 1. Table 1 shows that the *SI* corresponding to the second-order and third-order frequencies change significantly, and the high-order frequency of the pier is more sensitive to scour. The first-order frequency is the vehicle frequency and cannot be used to identify scour, which is understandable.

Table 1. Scour indicator extracted from response during vehicle passing phase.

scour indicator	First-order frequency		Second-order frequency		Third-order frequencies	
	P1	P2	P1	P2	P1	P2
μ	3.00	3.14	6.96	6.32	24.88	19.06
μ-0.5σ	2.84	2.86	6.52	5.92	23.62	16.74
μ+0.5σ	3.17	3.42	7.41	6.73	26.13	21.38

Table 2. Scour indicator extracted from attenuation response after vehicle leaving.

Scour indicator	First-order frequency		Second-order frequency		Third-order frequencies	
	P1	P2	P1	P2	P1	P2
μ	—	—	6.58	6.46	24.83	18.22
μ-0.5σ	—	—	6.47	6.30	23.26	16.37
μ+0.5σ	—	—	6.69	6.61	26.40	20.07

In order to compare the difference in pier response between the vehicle passing phase and the leaving phase, the extracted *SI* using free attenuated vibration is shown in Table 2. It can be found that in Table 2, the first-order frequency has not been identified, which again indicates that this frequency is caused by vehicles. The *SI* in Table 1 and Table 2 are not completely consistent, possibly due to random vibration of the piers and data processing errors. In addition, the change of *SI* corresponding to the second-order frequency in Table 2 is significantly smaller than that in Table 1. This may be because of the support constraints, the overall pier-beam coupled vibration accounts for the main part of the pier attenuation signal, resulting in the similarity of low-frequency vibrations for two piers.

In summary, the above results indirectly verify the effectiveness of the proposed scour diagnostic method. It should be emphasized that the mean value μ is not the exact pier frequency, but reflects the influence of foundation scour on the dynamic characteristics of the pier.

3.2 *Case study II- Yangsha Bridge*

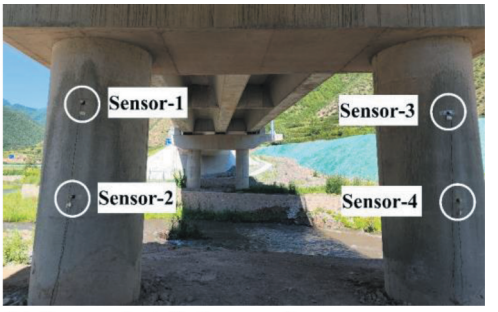
Yangsha Bridge is a new three-span concrete continuous girder bridge in Gannan, China, with each span being 30m long. The bridge piers are double-column bent piers, as shown in Figure 7(a). On-site measurement shows that the heights of piers P1 and P2 are 3.85m and 3.55m respectively, the pier diameter is 1.4m. Four acceleration sensors were installed on the piers to measure longitudinal vibration, as shown in Figure 7(b). The sensors are symmetrically installed on two columns, 1m and 2.8m away from the pier top respectively. Since there is a river between piers P1 and P2, the tests of two piers are not conducted at the same time, that is, the vibrations of the two piers are excited by different vehicles. The bridge was open to traffic during the test, and some small vehicles passed through the bridge.

The acceleration response of piers is analyzed using WSST. For piers P1 and P2, a segment of the acceleration signal when a vehicle passes through was intercepted, and its time-frequency representation are shown in Figure 8. It can be found that, except that pier P1 has an extra ridge in the frequency band near 20Hz, the ridges in Figure 8 (a) and (b) appear in similar frequency bands. This is because the heights of piers P1 and P2 are basically the same, so the dynamic characteristics also similar.

The scour indicators extracted from the above signals are listed in Table 3. Combined with Figure 8, it can be inferred that the first-order frequency is the pier-beam coupling vibration

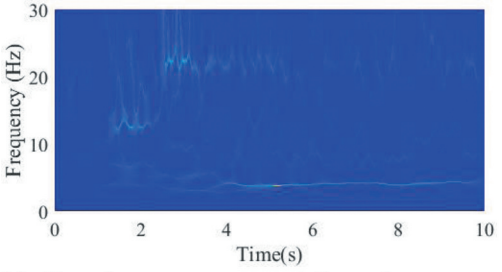


(a) Overview of the Yangsha Bridge

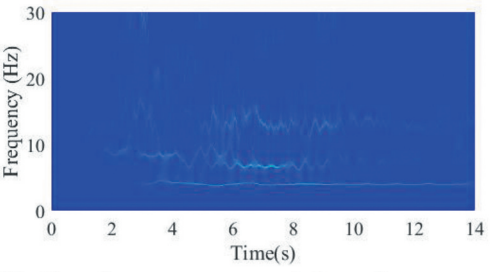


(b) Sensors installation on site

Figure 7. Overview of field test.



(a) Time-frequency representation of responses from measuring point S3 on pier P1



(b) Time-frequency representation of responses from measuring point S3 on pier P2

Figure 8. Time-frequency representation of acceleration response.

frequency and is insensitive to changes in the pier state. The second and third order frequencies of pier P1 are slightly smaller than pier P2, which may be because pier P1 is 0.3m higher than pier P2. The above results show that the proposed method can better estimate the statistical characteristics of the pier's instantaneous frequency under the excitation of small vehicles, and can also accurately diagnose scour.

Table 3. Scour indicator extracted from dynamic response during vehicle passing phase.

scour indicator	First-order frequency		Second-order frequency		Third-order frequencies	
	P1	P2	P1	P2	P1	P2
μ	3.89	3.99	7.69	7.75	13.02	13.46
μ-0.5σ	3.57	3.94	7.48	7.29	12.70	12.94
μ+0.5σ	4.20	4.04	7.90	8.21	13.34	13.98

4 SUMMARY AND CONCLUSION

In this study, a scour diagnostic method of pile foundation based on time-varying frequency was proposed. Since it is difficult to observe the significant scour development in a short time and soil excavation in the field is not permitted, the proposed method was indirectly studied and verified by comparing experimental results of piers with different heights. Ignoring the difference between soil and pier properties, bridge scour mainly causes the free length of the

pier to increase, so the indirect verification method used has a certain rationality. The conclusion is as follows:

1. The scour indicator constructed based on the statistical characteristics of instantaneous frequency of the pier is very sensitive to the change of pier free length, especially the high-order frequency. The result indirectly verified the sensitivity of the proposed indicator to bridge scour.
2. For the tested continuous girder bridge, the free attenuated vibration of the pier after the vehicle leaves was controlled by the pier-girder coupled vibration mode, resulting in the low-frequency component of the pier vibration being less sensitive to scour.
3. For short and medium-span bridges, effective vibration signals can be collected through short-term field tests under the excitation of small moving vehicles.

The field cases used in this study have not experienced real scour development process, so the proposed method cannot be directly and completely verified. In the future, a refined bridge finite element model should be established to conduct in-depth research on the impact of moving vehicles on the instantaneous frequency of bridge piers, and to numerically verify the proposed method. In addition, a real field scour development case should be found to directly and completely validate the proposed method.

ACKNOWLEDGEMENTS

This study reported in this paper was supported by National Science Foundation of China (Grant No. 52078164).

REFERENCES

Daubechies, I., Lu, J.F. & Wu, H.T. 2011. Synchrosqueezed wavelet transforms: An empirical mode decomposition-like tool. *Applied and Computational Harmonic Analysis*, 30(2), 243–261.

Foti, S. & Sabia, D. 2011. Influence of Foundation Scour on the Dynamic Response of an Existing Bridge. *Journal of Bridge Engineering*, 16, 295–304

Jiang, Q.T. & Suter, B.W. 2017. Instantaneous frequency estimation based on synchrosqueezing wavelet transform. *Signal Processing*, 138,167–181.

Ko, Y.Y., Lee, W.F., Chang, W.K., Mei, H.T. & Chen, C.H. 2010. Scour Evaluation of Bridge Foundations Using Vibration Measurement. Fifth International Conference on Scour and Erosion, San Francisco, CA, USA, 884–893.

Khan, M.A., Mccrum, D.P., Prendergast, L.J., Obrien, E.J., Fitzgerald, P.C. & Kim, C.W. 2021. Laboratory investigation of a bridge scour monitoring method using decentralized modal analysis. *Structural Control & Health Monitoring*, 20, 3327–3341.

Lagasse, P.F., Richardson, E.V. & Schall, J.D. 1998. Fixed Instrumentation for Monitoring Scour at Bridges. *Transportation Research Record*, 1647, 1–9.

Malekjafarian, A., Kim, C.W., Obrien, E.J., Prendergast, L.J. & Nakajima, S. 2020. Experimental Demonstration of a Mode Shape-Based Scour-Monitoring Method for Multispan Bridges with Shallow Foundations. *Journal of Bridge Engineering*, 25, 04020050.

Mostafa, N., Di Maio, D., Loendersloot, R. & Tinga, T. 2021. Extracting the time-dependent resonances of a vehicle–bridge interacting system by wavelet synchrosqueezed transform. *Structural Control & Health Monitoring*, 28, e2833.

Prendergast, L.J., Gavin, K. & Hester, D. 2017. Isolating the location of scour-induced stiffness loss in bridges using local modal behaviour. *Journal of Civil Structural Health Monitoring*, 7, 483–503.

Wardhana, K. & Hadipriono, F.C. 2003. Analysis of Recent Bridge Failures in the United States. *Journal of Performance of Constructed Facilities*, 17,144–150.

Zhang, Z.H., Li, Y., Zhong, Y.C. & Lin, X.Q. 2022. Scour diagnosis index based on cross-correlation analysis of bridge dynamic response under vehicle braking, *Advances in Structural Engineering*, 26, 706–723.

Bridge Maintenance, Safety, Management, Digitalization and Sustainability – Jensen, Frangopol & Schmidt (eds)
© 2024 The Author(s), ISBN 978-1-032-77040-6
Open Access: www.taylorfrancis.com, CC BY-NC-ND 4.0 license

Accuracy of the pulsed eddy current thickness measurement for a corroded steel pipe

Y. Kitane
Kyoto University, Kyoto, Japan

Y. Shichijo
T.D.I. Co., Ltd., Kanagawa, Japan

Y. Itoh
Nagoya Industrial Science Research Institute, Nagoya, Japan

ABSTRACT: Thickness measurement is essential to precisely assessing the condition of corroded steel structures. Ultrasonic testing method (UT) which is widely used in the current practice is not possible to measure a large area efficiently because surface treatment is necessary before the measurement. In this research, the pulsed eddy current (PEC) thickness measurement method is studied, which can measure thickness efficiently without the surface treatment since this method uses the magnetic field and induced eddy currents. The accuracy of this method is examined by measuring the thickness of a naturally corroded steel pipe pile cut out from a port facility, and compare the measured results with those by UT method and a 3D laser scanning method. As a result, it was found that PEC can identify an average thickness of a footprint area within ±10% error.

1 INTRODUCTION

1.1 *Background*

Maintenance and management of existing civil infrastructures are one of the challenging problems that civil engineers have to tackle. In Japan, there are many steel structures such as port facilities and highway bridges. In order to keep those steel structures in a healthy condition, it is important to find damage and deterioration and repair them before it becomes a severe risk.

One of the major deterioration factors in steel structures is corrosion. Since a cross sectional area of steel members will be reduced by corrosion, which leads to a decrease in load carrying capacity, a thickness measurement of steel plate is necessary for an inspection of a steel structure to identify a degree of corrosion. Currently, the ultrasonic testing method (UT) is the most popular thickness measurement method in the inspection. Although UT would yield an accurate measurement, a surface preparation to remove surface coating and rust is needed, which requires time and resources. Therefore, more efficient ways of measuring steel thickness are desired.

In this study, the pulsed eddy current testing method (PEC) (Robers and Scottini 2002, Lozev et al. 2005, Crouzen and Munns 2006, Park et al. 2013, Kitane et al. 2014, Kitane et al. 2016) is studied. Since PEC does not require the surface preparation, it may be a very efficient thickness measurement method in the inspection. PEC has been used to detect corrosion in pipelines, risers, and port structures. Since the measured thickness by PEC is considered to be an average thickness of a certain area called "footprint", it is usually used in a screening process, and a more accurate measurement is usually conducted by removing surface coating and rust if corrosion is detected by PEC.

DOI: 10.1201/9781003483755-429

1.2 *Objectives*

The objective of this study is to investigate the accuracy of PEC thickness measurement method by measuring the thickness of naturally corroded steel pipe pile cut out from a port facility and comparing the measured results with those by UT method and a 3D laser scanning method.

2 METHODOLOGY

2.1 *Measured pipe pile*

In this study, a 1,000 mm length of a corroded steel pipe pile as shown in Figure 1 was used, which was cut out from a port facility after 38 years of service and kept for 8 years in the laboratory. The original outer diameter and thickness of the pipe pile are 318 mm and 10.3 mm, respectively. Before the thickness measurement in this study, all corrosion products were removed by sand blasting. As shown in Figure 1, grid lines were marked at intervals of 25 mm in the height direction and 11.25 degrees in the circumferential direction.



Figure 1. Measured pipe pile.

2.2 *Pulsed eddy current testing method*

2.2.1 *Measurement principle*

PEC is a thickness measurement method by utilizing the diffusion process of eddy currents as shown in Figure 2. A measurement device consists of a probe and a data logger. A probe houses transmitter coils and receiver coils. Firstly, a pulse type current is input to the transmitter coils which creates a magnetic field. After the current is shut down, a sudden change of a magnetic field induces eddy currents on the surface of a steel plate due to the electromagnetic induction. As shown in Figure 2, eddy currents diffuse in the steel plate and infiltrate in the thickness direction as the magnitude of eddy currents attenuates over time. When eddy currents reach the back side of the steel plate, eddy currents decay significantly. The magnetic field induced by this eddy current is detected by receiver coils in the probe. A time history of the voltage signal obtained by receiver coils is shown in Figure 2, where the signal linearly attenuates as eddy currents diffuse in the thickness direction, and it is significantly reduced when eddy currents reach the bottom of the steel plate. This attenuation of the voltage signal can be expressed in Eq. (1) (SHELL Global Solutions 2004, van den Berg 2003).

$$V(t) = A \times \begin{cases} t^{-n} & \text{for } t \le \tau \\ \tau^{-n} exp\left(-n\frac{t-\tau}{\tau}\right) & \text{for } t > \tau \end{cases} \quad (1)$$

where, A is an amplitude parameter, n is a slope parameter, t is time, and τ is the ending time of diffusion. τ can be expressed by Eq. (2).

$$\tau = \mu\sigma d^2 \quad (2)$$

where d is a thickness of steel plate, and μ and σ are permeability and conductivity of steel. Therefore, when the diffusion time τ_{ref} of a reference plate with a thickness of d_{ref} is known, a thickness of steel plate d can be estimated by using the obtained diffusion time τ as follows:

$$d = d_{ref}\sqrt{\frac{\tau}{\tau_{ref}}} \quad (3)$$

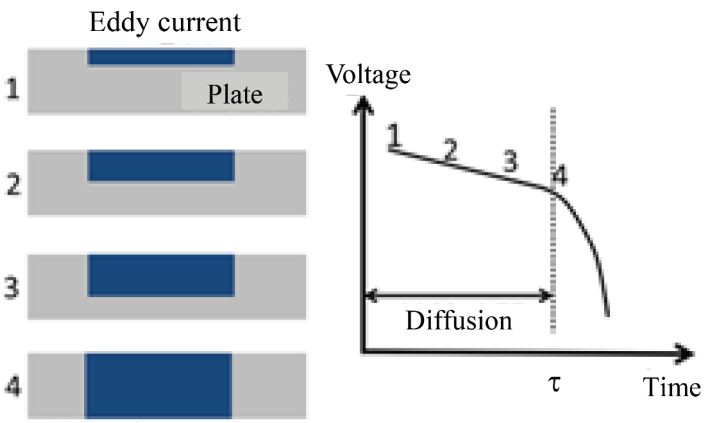
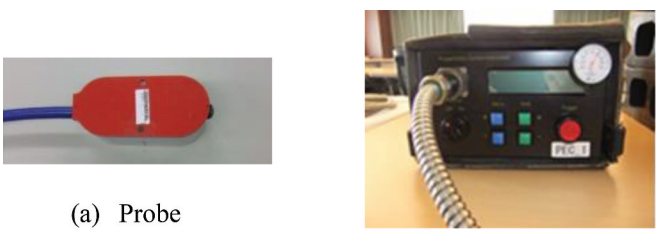


Figure 2. Diffusion process of eddy currents and induced voltage in receiver coils.



(a) Probe

(b) Data logger

Figure 3. PEC measurement device.

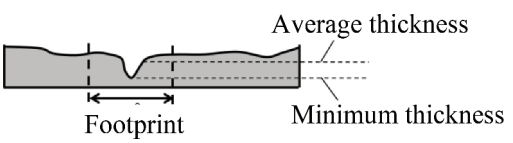


Figure 4. Average thickness of a footprint with a pitting corrosion.

Since a thickness measured by PEC is said to be an average thickness of a footprint, it is difficult to identify a deep pitting corrosion. Figure 4 shows an average thickness of a footprint with a pitting corrosion. Therefore, it is important to understand the accuracy of thickness identified by PEC when an actual corroded plate is measured.

2.2.2 *Measurement method*

In this study, a reference point where corrosion is minimal was selected and a thickness of the reference point and a diffusion time of PEC signal were identified. Thicknesses of other locations were identified by PEC by using Eq. (3). Since the footprint area is dependent on a liftoff which is a distance from the bottom of the probe to the bottom surface of steel plate, two liftoff values were used: 6 mm and 20 mm. Measurement locations of PEC are shown in Figure 5 for two different liftoffs. Figure 6 shows how PEC measurement was conducted on the corroded steel pipe pile.

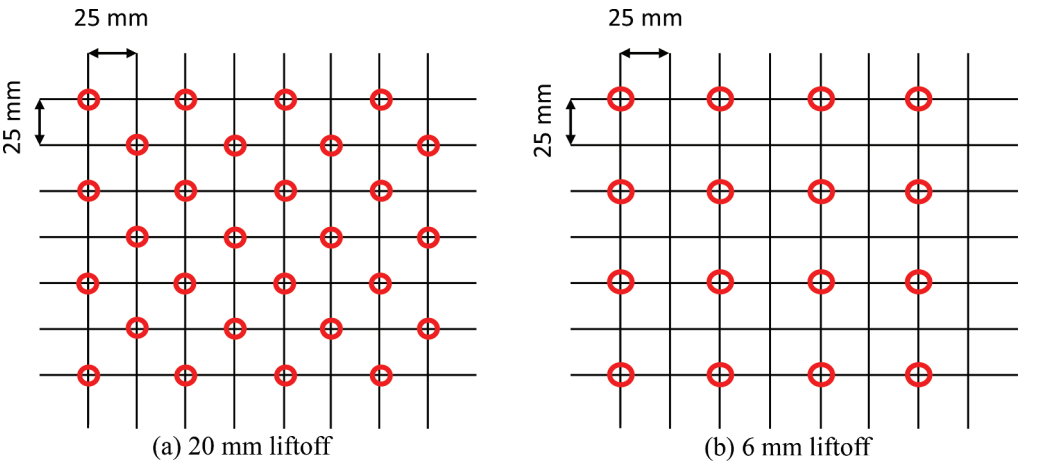


Figure 5. PEC measurement locations.

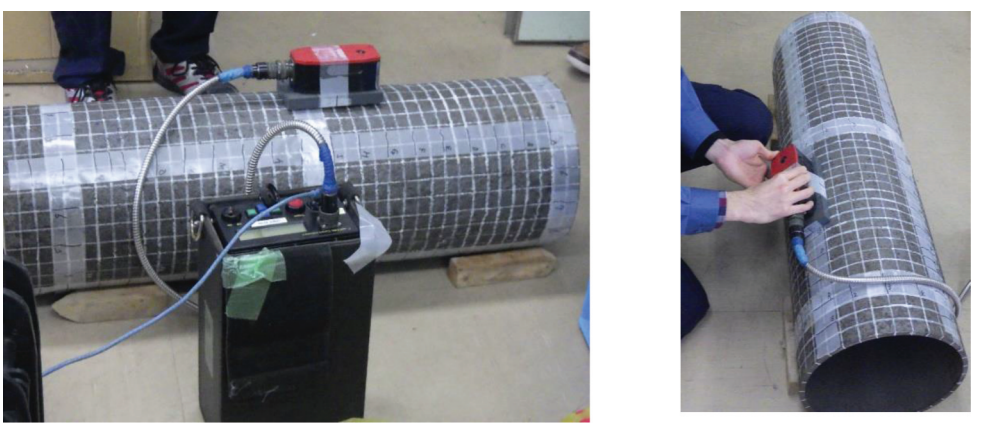


Figure 6. PEC measurement.

2.3 *Other thickness measurement methods*

2.3.1 *Ultrasonic testing*

Ultrasonic testing (UT) is one of the most popular method for a thickness measurement in the inspection of steel structures. In this method, a plate thickness is measured based on a travel

time of a sound pulse which travels through the thickness and reflects back from the bottom of a plate. UT can accurately measure a thickness when there is no corrosion product or coating on the surface of a plate, and the surface roughness may affect the accuracy. Therefore, surface preparation is necessary before UT thickness measurement.

In this study, UT thickness measurement was conducted by using MMX-6DL (Dakota Ultrasonics). A thickness was measured at the intersection of grid lines shown in Figure 1, and three measurements were taken at each point. Figure 7 shows UT measurement. The thickness profile by the UT measurement is shown in Figure 8(a), which shows an average thickness of three measurements at each point. The maximum, minimum, average, and standard deviation of thickness for the pipe are 10.99 mm, 5.24 mm, 9.14 mm, and 1.16 mm, respectively. In addition, Figure 8(b) shows a standard deviation of three thickness measurements at each point. The maximum and average values of standard deviations are 3.07 mm and 0.21 mm, respectively. Based on the observation, a standard deviation of three measurements is large at deep pitting corrosion. Therefore, the measurement accuracy is not high at those locations.

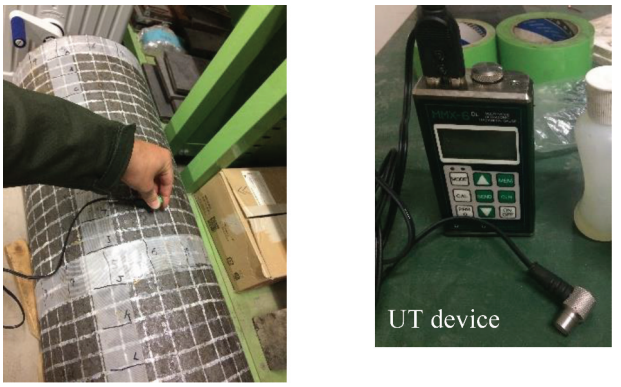
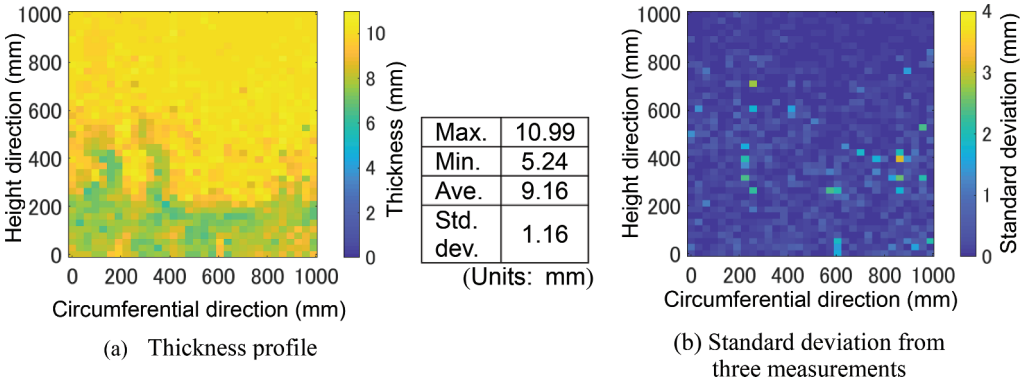


Figure 7. UT measurement.



(a) Thickness profile

(b) Standard deviation from three measurements

Figure 8. Thickness measurement results by UT.

2.3.2 *3D laser scanning*

To create an accurate 3D model, a 3D laser scanning was conducted at 0.1 mm intervals on the corroded pipe pile by using FARO Edge Scan Arm HD. The obtained 3D model is shown in Figure 9. A thickness was calculated as a distance between the outer surface and the inner surface. However, the arm of a 3D laser scanning device was not long

enough to measure the inner surface near the center of the pipe from 250 mm to 750 mm in the height direction. By examining the surface profile of the inner surface where measurement data were obtained, it was found that there is not much surface roughness by corrosion on the inner surface; therefore, the inner surface data were interpolated between 250 mm and 750 mm. In addition, the surface profile data were not obtained at some locations where surface profile changes abruptly. Examples of those locations are shown in Figure 10. In this study, thicknesses obtained by the 3D laser scanning are assumed to be the most accurate data. The identified thickness profile by the 3D laser scanning is shown in Figure 11. Based on the identified thickness data, the maximum, minimum, average, and standard deviation of thickness of the pipe are 10.56 mm, 5.08 mm, 8.56 mm, and 1.26 mm, respectively.



Figure 9. 3D model based on 3D laser scanning.

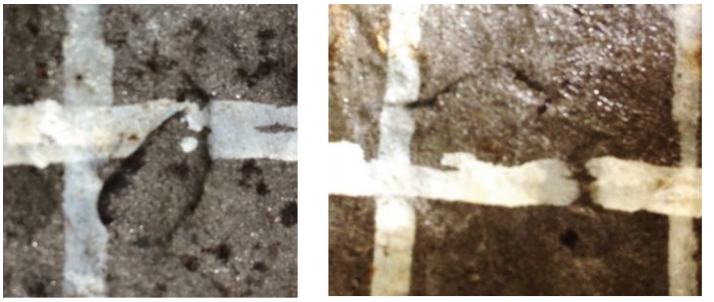
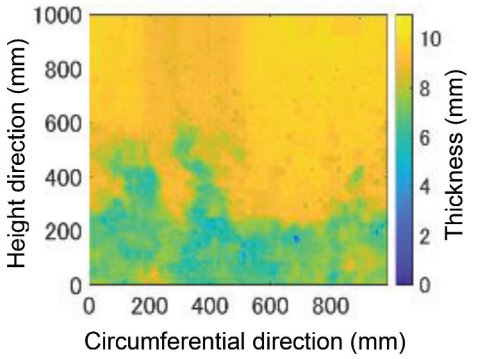


Figure 10. Locations where surface profile was not obtained by 3D laser scanning.



Max.	10.56
Min.	5.08
Ave.	8.56
Std. dev.	1.26

(Units: mm)

Figure 11. Thickness profile by 3D laser scanning.

3 RESULTS

3.1 *Thickness measurement by PEC*

Figure 12 shows thickness measurement results by PEC for both 20 mm and 6 mm liftoffs. The thickness was identified by Eq. (3), and a thickness of the reference point measured by 3D laser scanning was used. The maximum, minimum, average, and standard deviation of thickness of the pipe are 9.87 mm, 6.23 mm, 8.62 mm, and 1.07 mm, respectively for a 20 mm liftoff, and 9.95 mm, 6.19 mm, 8.77 mm, and 1.03 mm, respectively for a 6 mm liftoff.

The maximum thickness with a 6 mm liftoff was larger by 0.08 mm than that with a 20 mm liftoff, implying that the footprint of a 6 mm liftoff was smaller and the measurement with a smaller footprint can reflect surface roughness better.

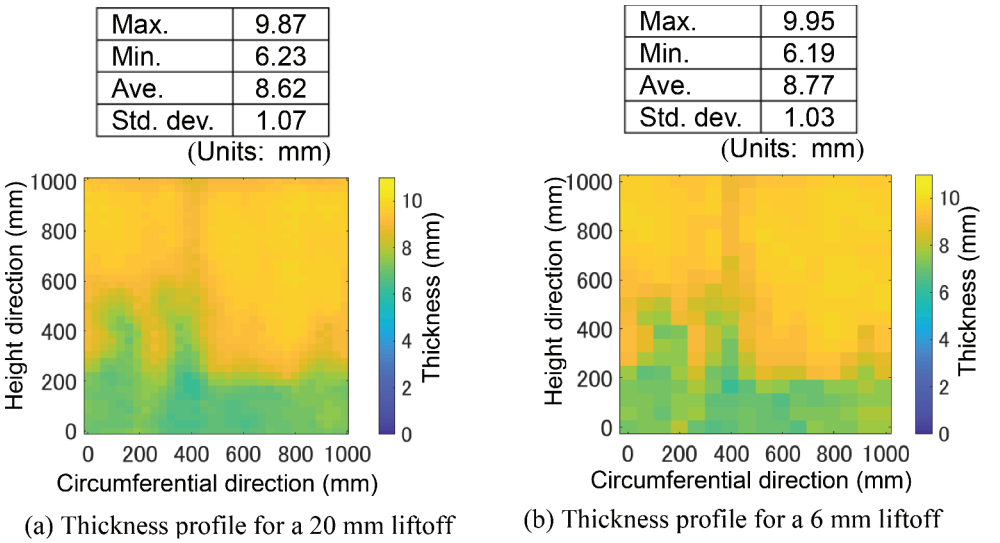


Figure 12. Thickness measurement results by PEC.

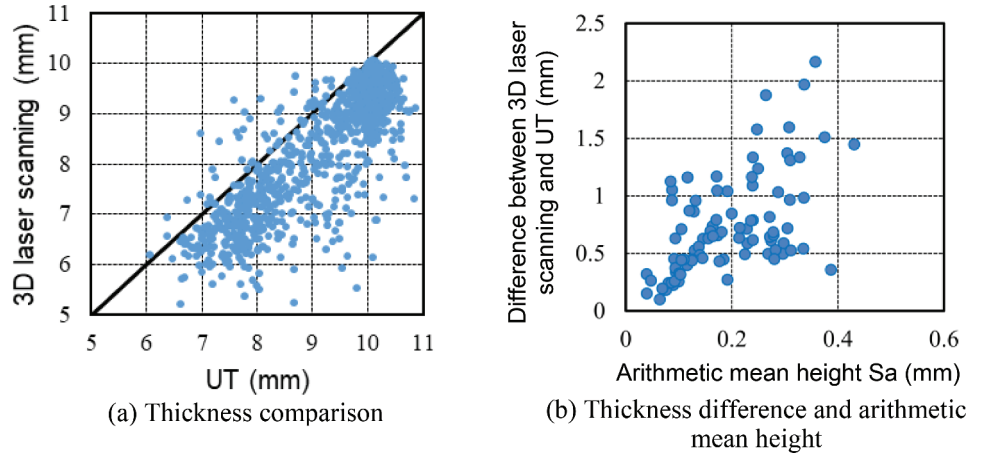
3.2 *Comparison between UT and 3D laser scanning*

A comparison of thicknesses measured by 3D laser scanning and UT is shown in Figure 13(a). It can be observed that the UT thickness is larger than the thickness by 3D laser scanning. To see the effect of surface roughness on the UT thickness measurement, a difference between 3D laser scanning thickness and UT thickness and arithmetic mean height *Sa* is compared in Figure 13(b). As can be seen in Figure 13(b), the difference becomes greater with the surface roughness, implying that UT thickness measurement will be affected by the surface roughness because a travel time of sound pulse includes both steel plate and couplant.

3.3 *Comparison between PEC and 3D laser scanning*

Empirically, a footprint size is equivalent to a distance from the bottom of probe to the bottom of steel plate (SHELL Global Solutions 2004). Figure 14(a) shows a comparison of PEC thickness with a 20 mm liftoff and 3D laser scanning thickness, where a thickness value of 3D laser scanning is an average value in the footprint assuming a circle with a diameter of 30.3 mm (20 mm liftoff + 10.3 mm). Among all measured data, 93.2% of data are within ±10% error, and the maximum and average difference are 33.8% and 3.8%, respectively.

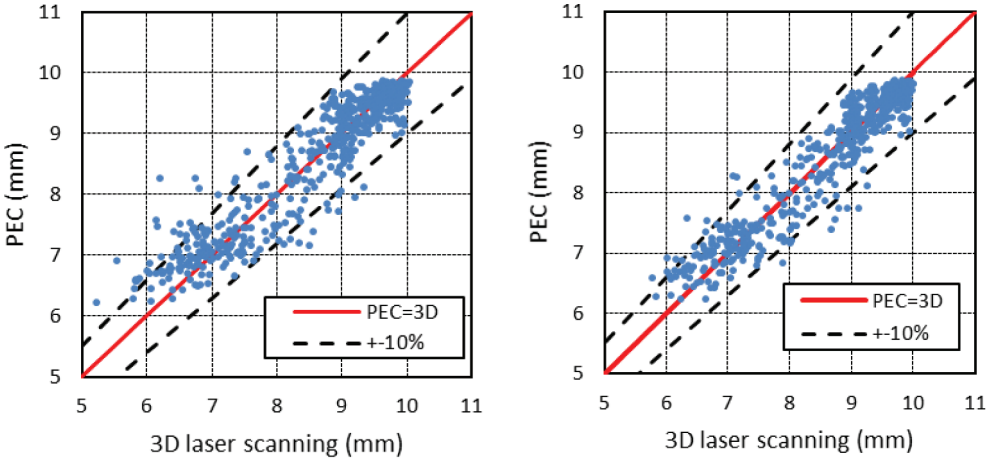
Ando et al. (2016) examined a footprint size for a 20 mm liftoff and recommended a circle with a 100 mm diameter. Figure 14(b) shows a comparison of PEC thickness with a 20 mm liftoff and



(a) Thickness comparison

(b) Thickness difference and arithmetic mean height

Figure 13. Comparison of 3D laser scanning and UT.



(a) Thickness comparison assuming a footprint of a 30.3 mm diameter circle

(b) Thickness comparison assuming a footprint of a 100 mm diameter circle

Figure 14. Comparison of 3D laser scanning and PEC with a 20 mm liftoff.

3D laser scanning thickness, where a thickness value of 3D laser scanning is an average value in the footprint assuming a circle with a diameter of 100 mm. In this case, 96.6% of data are within ±10% error, and the maximum and average difference are 19.6% and 3.2%, respectively.

4 CONCLUSIONS

Based on a comparison PEC thickness measurement for a corroded pipe pile and UT or 3D laser scanning, characteristics of PEC thickness measurement data can be summarized as follows:

(1) UT thickness measurement results tend to be greater than thicknesses determined by 3D laser scanning when there is a surface roughness due to corrosion. The difference between UT and 3D laser scanning becomes larger with the surface roughness.

(2) By comparing PEC thickness measurement data of a corroded pipe pile with a 20 mm lift-off and average thickness values over a footprint area of circle with a 100 mm diameter based on thickness values by 3D laser scanning, it was found that 96.6% of data are within ±10% difference, and that the average difference is 3.2%. Therefore, when a 10% error is allowable, PEC thickness measurement can be a very efficient thickness measurement method in the inspection of steel structures.

REFERENCES

Ando, S., Kitane, Y., Nishijima, Y. Itoh, Y. and Nakano, Y. 2016. Study on output signals from the pulsed eddy current testing on steel plates with thickness loss of various shapes. *Journal of Structural Engineering* 62A, JSCE: 603–616 (in Japanese).

Crouzen, P. and Munns, I. 2006. Pulsed eddy current corrosion monitoring in refineries and oil production facilities – experience at Shell. *Proceedings of the 9th European Conference on Nondestructive Testing*, Berlin, Germany.

Kitane, Y., Ando, S., Itoh, Y., and Nakano, Y. 2016. Numerical study on pulsed eddy current thickness measurement for steel plates with thickness loss. *Proc. of the Fourteenth East Asia-Pacific Conference on Structural Engineering and Construction*, EASEC-14, January 6-8, 2016, Ho Chi Minh City, Vietnam: 1770–1779.

Kitane, Y., Nishijima, Y., Itoh, Y. and Nakano, Y. 2014. Feasibility Study of Thickness Measurement using Pulsed Eddy Current for Port Steel Structures. *Proceedings of Constructional Steel* 22: 943–949 (in Japanese).

Lozev, M.G., Smith, R.W., and Grimmett, B.B. 2005. Evaluation of methods for detecting and monitoring of corrosion damage in risers. *Journal of Pressure Vessel Technology, Transactions of ASME* 127: 244–254.

Park, D.G., Angani, C.S., Kishore, M.B., Vértesy, G., and Lee, D.H. 2013. Review paper: Application of the pulsed eddy current technique to inspect pipelines of nuclear plants. *Journal of Magnetics* 18(3): 342–347.

Robers, M.A. and Scottini, R. 2002. Pulsed eddy current in corrosion detection. *Proceedings of the 8th European Conference on Nondestructive Testing*, Barcelona, Spain.

SHELL Global Solutions. 2004. *PEC Training guide*.

van den Berg, S. 2003. *Modelling and Inversion of Pulsed Eddy Current Data*, Delft University Press, The Netherlands.


Taylor & Francis
Taylor & Francis Group
http://taylorandfrancis.com

GS07: BRIDGE MAINTENANCE - Non-destructive testing


Taylor & Francis
Taylor & Francis Group
http://taylorandfrancis.com

Bridge Maintenance, Safety, Management, Digitalization and Sustainability – Jensen, Frangopol & Schmidt (eds)
© 2024 The Author(s), ISBN 978-1-032-77040-6
Open Access: www.taylorfrancis.com, CC BY-NC-ND 4.0 license

Ground Penetrating Radar (GPR) for bridge inspection

Nzeeh Roumia & Claudio Mazzotti
DICAM Department, University of Bologna, Bologna, Italy

ABSTRACT: Bridge inspection plays a crucial role in providing bridge operators with an overview of their infrastructure's current condition, enabling them to extend their service life. This is even more important since a significant number of bridges were constructed after World War II with few comprehensive documents regarding their construction, for example blueprints. In such cases, non-destructive testing (NDT) methods can be employed to investigate the structure without causing damage. Among the widely utilized NDT methods, Ground Penetrating Radar (GPR) stands as one of the most widely used methods to localize reinforcement and prestressing strands, thanks to its efficient acquisition capabilities that are characterized by the speed in performing the acquisition and the instantaneous visualization of results. However, due to the inherent complexity, the use of GPR requires qualified and experienced users to obtain high-quality survey data.

To assess the capabilities and limitations of GPR, experimental reinforced concrete beams were casted to simulate real-life scenarios. Plastic and metallic tendon ducts were used, and variable spacing between stirrups was adopted. Surveys were conducted using 2GHz bipolar GPR unit, and grid scans were used to maximize the benefit of the GPR. This study presents interesting results in terms of determining the concrete cover, rebar spacings, and the position of tendon ducts accurately. These findings hold significant value for structural engineers who would like to use GPR, especially for bridge inspection applications.

1 INTRODUCTION

The early years after the World War II marked a crucial phase in the infrastructure development worldwide and in Europe particularly due to the urgent need at that time to rebuild what was destructed and to maintain what left. Therefore, extensive reconstruction campaign started to rebuild the infrastructure such as highways, railways and bridges to connect vital centers, ultimately resulting in the reconstruction of cities and towns that facilitated economic growth.

Actually, most of those infrastructures have reached the end of their service life (Invernizzi et al., 2022). Concurrently, the improper maintenance and overloading through the time accelerated the deterioration process and pushed the structures, bridges specifically, to near ultimate limit state and reduced their capacity significantly, leading to unforeseen collapses in numerous cases (Zhang et al., 2022).

Therefore, periodic visual inspection is necessary to verify the current state of bridges in addition to defining the visible defects as spalling, high humidity regions, corrosion and various other defects, together with the extension and intensity of each defect (CSLLPP, 2020). Nevertheless, relying solely on visual inspections proves insufficient for understanding what lies beneath the external surface. To gain insights into the internal structure without causing damage, it becomes important to use alternative methods. Using non-destructive testing methods (NDT) is an optimal solution in this context which could provide an overview about the subsurface (Dinh et al., 2021).

Among many different methods, Ground Penetrating Radar (GPR) demonstrate its effectiveness as a non-destructive method. Its high acquisition speed and immediate visualization of the results contribute the most to the on-site evaluation ensuring a high reliability.

DOI: 10.1201/9781003483755-430

In civil engineering, Ground Penetrating Radar is traditionally used to identifying reinforcement in slabs, beams and columns in addition to determining the spacing between rebars and concrete cover. This enables structural engineers to compare the actual project conditions with the design specifications or to reconstruct the drawings if they are not documented.

This study examines the capacity of bipolar GPR system with 2GHz central frequency in detecting commonly used components in post-tensioned bridges, for instance longitudinal rebars, stirrups and tendon ducts made of different materials like steel and plastic. Interruptions were introduced to the steel ducts body to simulate real damaged tendon ducts.

2 INSTRUMENT

The used GPR unit is bipolar unit which means that it has two distinct antennas, namely one for the shallow inspection (HH) and one for deeper inspection (VV). Both antennas have a central frequency of 2GHz, being the only difference the polarization; in other words, one of the antennas is parallel to the scanning direction and the other is perpendicular to it. The distance between the two centers is (10 cm) as depicted in Figure 1. The GPR unit is equipped with a touch screen allowing the user to customize the scanning parameters, the propagation velocity for instance, and to display the results in real time while taking measurements (IDS, 2022). Each antenna has an independent acquisition channel, providing independent results such as A-scans and B-scans which can be later merged in post-processing to provide consistent scanning outcomes.

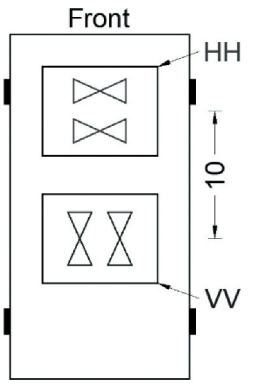


Figure 1. Antennas positioning and orientation (polarization) inside the GPR unit.

3 TESTING SAMPLES

Two different testing samples were constructed. The first reinforced concrete sample has the dimensions of 220×65×30 cm^3 (L×H×W). Plastic tendon ducts with nominal diameter of (6 cm) were used and positioned at different depths from the external surfaces. The second specimen has the dimensions of 160×65×30 cm^3 and steel tendon ducts with nominal diameter of (5.5 cm) were used. Intentional interruptions, partial and complete, were made along some tendons only in the second specimen, to simulate potential defects (strong corrosion) in the duct's structure. All the ducts were empty: no steel strands not injection mortar inside them.

The steel reinforcement cage consists of four longitudinal rebars with a diameter $\phi = 10$ mm (Ø10), while transversal reinforcement consists of stirrups with a diameter $\phi = 8$ mm (Ø8). The spacing between stirrups is not uniform, ranging from 5 to 20 cm. Figure 2 shows the blueprint of the aforementioned specimens and snapshots taken during the construction phase, showing the steel cage and the ducts. Compression tests were performed on cylindrical specimens to estimate the concrete compressive strength at 28 days, resulting $f_c' = 24.3MPa$.

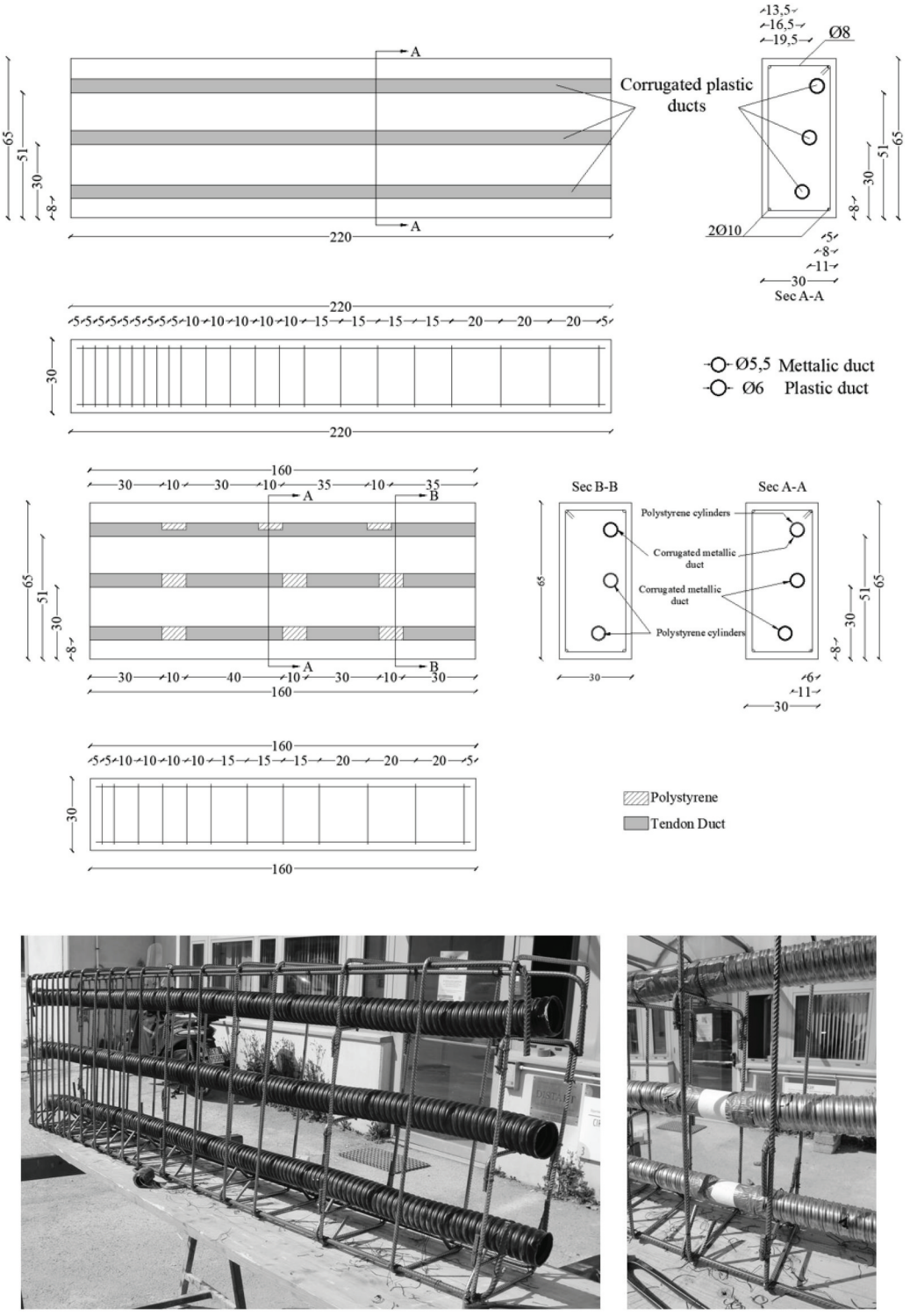


Figure 2. Reinforced concrete testing samples.

4 RESULTS

4.1 *Detection of stirrups*

Figure 3 illustrates a standard B-scan derived from the HH channel and captured along the beam length of 220 cm. It displays the direct wave as two continuous white and black strips, along with hyperbolas that depict the presence of stirrups. The apex of the hyperbola accurately corresponds to the correct location and depth of the stirrup when the velocity is appropriately calibrated. The estimated propagation velocity is determined to be 12.5 cm/ns, calibrated through synthetic hyperbola fitting. It is worth mentioning that post processing is important to enhance the image quality and reveal the deep reflectors.

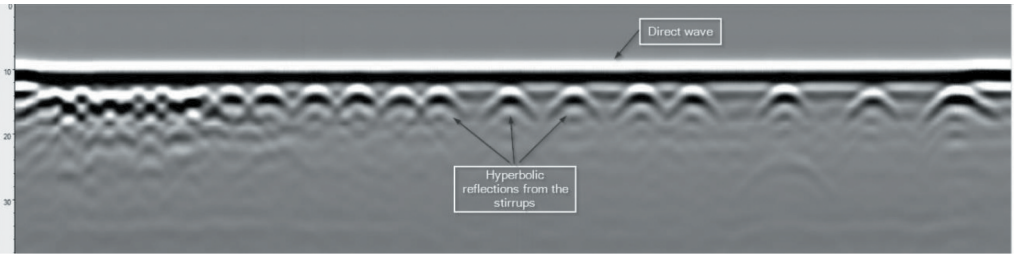


Figure 3. Typical B-scan without processing for the beam with plastic ducts.

GPR demonstrated effectiveness in identifying stirrups when the distinct spacing between two consecutive stirrups exceeded 5 cm, as illustrated on the right side of Figure 3. However, it is challenging to define a clear hyperbolic shape when the spacing is less than 5cm, leading to the stirrups appearing merged as a continuous line. The small spacing made it difficult for electromagnetic waves to penetrate, resulting in the occurrence of multiples reflections named the ringing effect. It is worth mentioning that the dimension of 5 cm (stirrups clear spacing) is less than the theoretical value of the lateral resolution of GPR. In fact, the electromagnetic wave theory leads to the following expression for the lateral resolution (Schwamborn et al., 2002):

$$\Delta x = \sqrt{2\lambda h}, \tag{1}$$

where λ is the wave length and can be calculated as the following:

$$\lambda = \frac{v}{f} = \frac{12.5}{2} = 6.25\ cm \tag{2}$$

and h is the depth of the target from the scanning surface, which is 2.2 cm in the present case. That gives a value of $\Delta x = 5.2\ cm$, making it the limit to the horizontal resolution in our case study. The theoretical value gives an insight to the limited clarity of GPR in detecting the stirrups with less than 5 cm clear spacing.

GPR signals has an oscillating nature forming positive and negative parts. each of the single scans is called A-scan or a trace. Studying each signal without considering the neighboring traces is not sufficient to understand the medium under investigation. Therefore, combining multiple A-scans into a 2D image or B-scan is commonly used to present the results offering a more comprehensive understanding. Combining B-scans gives another dimensionality obtaining 3D representation of the subsurface. Slicing the 3D data horizontally generates C-scans or time slices (Utsi, 2017).

In this study C-Scan Figure 4 is generated by merging various B-scans captured from two orthogonal directions and utilizing both antennas (HH and VV). This image offers a clearer understanding of the distribution of reinforcement and of the arrangement of the steel cage. However, it is important to note the presence of artifacts between the stirrups due to the limitation of certain postprocessing techniques such as migration, where the reflected wave energy

should ideally be focused in one point instead of being spread all over the hyperbola's length (Özdemir et al., 2014).

Therefore, it is always crucial to examine the B-scans concurrently with the C-Scans for a comprehensive assessment.

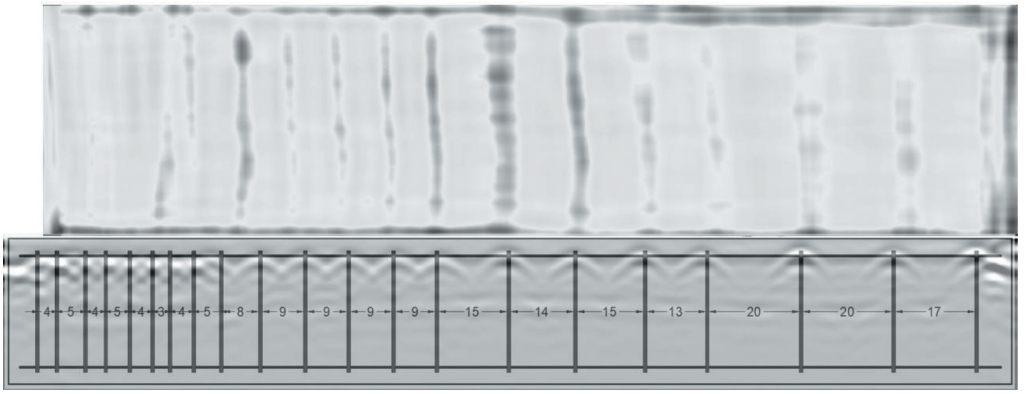


Figure 4. C-scan at the level of stirrups.

4.2 *Detection of tendon ducts*

Tendon ducts are typically located at considerable depths from the surface. Conducting a thorough inspection that involves coring at the precise locations of these ducts requires accurate information about their depth and position. Achieving this level of precision is a challenging task for traditional non-destructive methods, such as eddy currents. Therefore, the use of unconventional methods like GPR or Ultrasounds becomes essential.

Performing GPR scans along the height of the testing specimens (65 cm) successfully revealed the presence of the three tendon ducts Figure 5, Figure 6, even when having plastic ducts which is not a perfect reflector material to electromagnetic waves. Furthermore, attenuation is evident when the scans are conducted from the two accessible faces. For example, Figure 5 compares two B-scans performed on parallel scanning lines from the two opposite surfaces. In the first case, all TDs exhibit weak reflection compared to the second case because they are at greater depths. Furthermore, wider hyperbolas correspond to the first case (deep reflectors), while narrower hyperbolas correspond to the second case (shallow reflectors).

In the second testing specimen, steel empty ducts were used, which makes them perfect reflectors to EM waves due to the infinite value for the dielectric constant, while the interruptions were made by using polystyrene cylinders that have a dielectric constant ε_r = 206, making it more challenging to detect them by using GPR. Concrete dielectric constant is estimated using the following formula:

$$\varepsilon_r \cong \left(\frac{c}{v}\right)^2 = \left(\frac{30}{12.5}\right)^2 = 5.76 \tag{3}$$

Where c is the light propagation velocity in the vacuum, and v is the EM wave propagation velocity in concrete. It is worth mentioning that there is a strong correlation between ε_r and the moisture content (MC) in concrete, higher moisture content leads to higher dielectric constant and lower propagation velocity and vice versa (Soutsos et al., n.d.).

Two scans were conducted on the second specimen, as shown in Figure 6. In the first scenario, where the ducts are continuous without interruption, the corresponding B-scans shows the ducts clearly. On the other hand, polystyrene cylinders are not present in the corresponding B-scan due to the minimal difference in dielectric property between concrete and polystyrene. However, the unrepeated pattern of hyperbolas between the scans informs the inspector about the presence of the anomaly. In the case of partial interruptions, GPR could not detect the interruption.

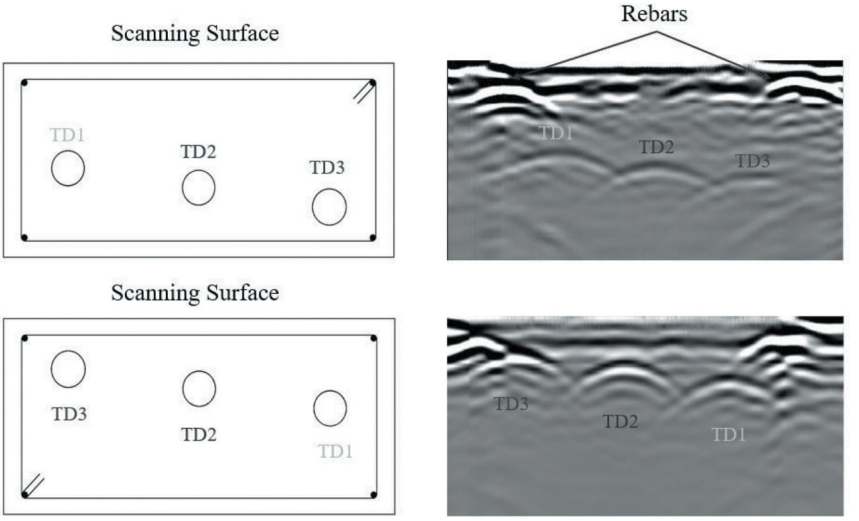


Figure 5. Typical B-Scan revealing the empty plastic tendon ducts.

Analyzing the scans performed on both specimens, it can be observed that signals from steel ducts have higher amplitudes with respect to plastic ducts, as expected. In addition, the type of wave reflected from the ducts depends on their material; in more details, for the plastic ducts, the reflected wave is made of black-white-black (B-W-B) bands; on the contrary, in the case of steel ducts, the reflection polarity is completely inverted (W-B-W). This characteristic property is an indicator to the reflector's material as metallic, such as steel tendon ducts, or non-metallic, such plastic ducts or air gaps (Kavi & Halabe, 2023). This is attributed to the different reflection factor R between the two different materials plastic and steel. R is calculated as the following simplified formula:

$$R \cong \frac{Z_2 - Z_1}{Z_2 + Z_1} \tag{4}$$

Where Z is the electromagnetic impedance of the material calculated using the simplified formula:

$$Z \cong \sqrt{\frac{1}{\varepsilon_r}} \tag{5}$$

Considering the first study case where we have plastic tendon ducts with ε_r=3, the reflection factor R=0.16. Following the same procedure for the steel reflector results in having R=-1. The negative sign from the steel refers to a change in the phase unlike the plastic or airborne reflectors.

Performing scans along the duct's length gives another perspective about the changes in the duct's structure and the duct's geometrical deformations, which might be challenging by performing scans in the orthogonal direction. Therefore, it is important to perform grid scans to obtain full awareness about what is hidden below the surface.

Figure 7 presents a comparison between HH and VV polarizations scans along the duct's length for the second specimen (steel ducts). The first observation is the misalignment in the X direction between the antennas, attributed to the physical separation between HH and VV antennas by 10 cm Figure 1. Additionally, both polarizations show the interruptions along the TD3 or the presence of the polystyrene cylinders. However, HH B-scan contains three hyperbolas corresponding to the interruption's positions while VV B-scan lacks these hyperbolas. Due to the wider illuminated area when using HH polarization, the edges of the steel duct before and after the polystyrene cylinder create half of the hyperbola. One the other hand the interruption size of 10 cm and the duct depth at 17 cm gives a lateral resolution of 14.5 cm calculated using

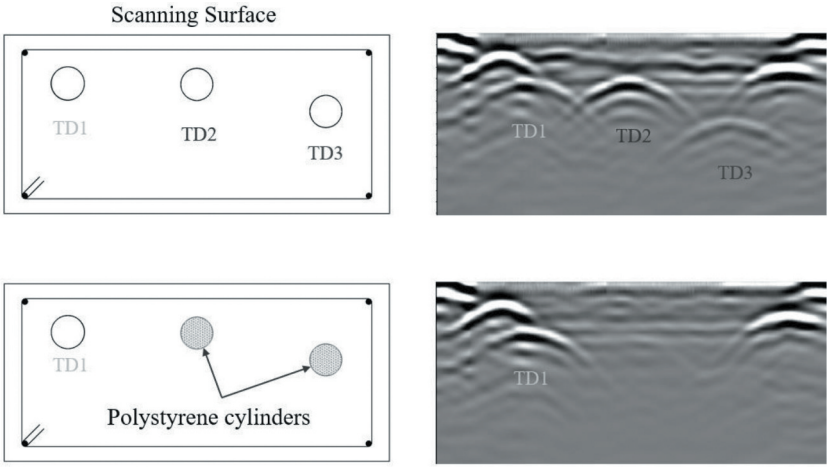


Figure 6. Comparison between B-scans showing steel ducts and polystyrene cylinders.

the equation (1), which is larger than the length of polystyrene cylinder. Consequently, the employed imaging technique combines the two parts of the hyperbola coming from two different reflectors generating one hyperbola as a strong reflector that has a reflected amplitude larger than the one coming from the steel duct itself as depicted in the right side of Figure 7.

In this case looking at the VV polarization resolves the uncertainties: there are no hyperbolas corresponding to the cylinders, as seen with the HH B-scan, and the signal phase is inverted at the position of the cylinders (change of the dielectric constant).

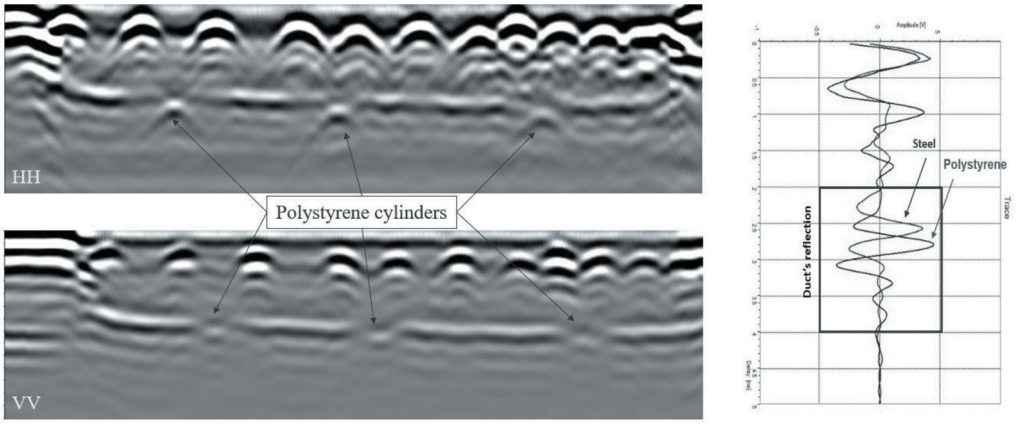


Figure 7. Comparison between HH and VV Polarizations.

5 CONCLUSION

The findings presented in this paper highlight the importance of high frequency GPR as non-destructive method in bridge inspections. The study demonstrated the capabilities of bipolar GPR unit in defining the internal composition of the testing specimens including longitudinal rebars, stirrups and tendon ducts, with high accuracy in terms of position, depth and material dielectric properties. Its high acquisition speed is a game changer onsite which gives the structural engineers an immediate overview about the scanned structural element helping to take

instant decisions. Additionally, Bipolar GPR unit saves time by conducting two scans at the same time, simultaneously collecting larger amount of information from the subsurface.

However, the challenge with GPR lies in interpreting the results as it could be misleading in certain cases. Grid scans would help in minimizing the uncertainty by providing a plan view of the scanned surface. Additionally, analyzing the B-scans from the two orthogonal directions along with C-scans is an important step to interpret the results correctly. On the other hand, better imaging techniques are needed to eliminate the artifacts. Since the electromagnetic waves cannot cross metallic reflectors such as the steel tendon ducts, filling the plastic ducts with mortar and tendons with different scenarios gives the chance to explore the GPR potentials in defects detection, which will be a continuation of the current research.

REFERENCES

Consiglio Superiore dei Lavori Pubblici (2020). Linee guida per la classificazione e gestione del rischio, la valutazione della sicurezza ed il monitoraggio dei ponti esistenti.

Dinh, K., Gucunski, N., Tran, K., Novo, A., & Nguyen, T. (2021). Full-resolution 3D imaging for concrete structures with dual-polarization GPR. Automation in Construction, 125. https://doi.org/10.1016/j.autcon.2021.103652

Invernizzi, S., Montagnoli, F., & Carpinteri, A. (2022). Very High Cycle Corrosion Fatigue Study of the Collapsed Polcevera Bridge, Italy. Journal of Bridge Engineering, 27(1). https://doi.org/10.1061/(asce)be.1943-5592.0001807

IDS GeoRadar Srl (2022). C-thrue User Manual All-in-one Ground Penetrating Radar (GPR) for Non-Destructive Testing of Concrete Structures User manual C-Thrue-User Manual.

Kavi, J., & Halabe, U. B. (2023). An Approach for Easy Detection of Buried FRP Composite/Non-Metallic Pipes Using Ground-Penetrating Radar. Sensors (Basel, Switzerland), 23(20). https://doi.org/10.3390/s23208465

LINEE GUIDA PER LA CLASSIFICAZIONE E GESTIONE DEL RISCHIO, LA VALUTAZIONE DELLA SICUREZZAED IL MONITORAGGIO DEI PONTI ESISTENTI

Özdemir, C., Demirci, Ş., Yiğit, E., & Yilmaz, B. (2014). A review on migration methods in b-scan ground penetrating radar imaging. In Mathematical Problems in Engineering (Vol. 2014). Hindawi Publishing Corporation. https://doi.org/10.1155/2014/280738

Schwamborn, G. J., Dix, J. K., Bull, J. M., & Rachold, V. (2002). High-resolution seismic and ground penetrating radar-geophysical profiling of a thermokarst lake in the western Lena Delta, northern Siberia. Permafrost and Periglacial Processes, 13(4), 259–269. https://doi.org/10.1002/ppp.430

Soutsos, M. N., Bungey, J. H., Millard, S. G., Shaw, M. R., & Patterson, A. (n.d.). Dielectric properties of concrete and their in¯uence on radar testing. www.elsevier.com/locate/ndteint

Utsi, E. Carrick. (2017). Ground penetrating radar. Butterworth-Heinemann Ltd.

Zhang, G., Liu, Y., Liu, J., Lan, S., & Yang, J. (2022). Causes and statistical characteristics of bridge failures: A review. In Journal of Traffic and Transportation Engineering (English Edition) (Vol. 9, Issue 3, pp. 388–406). Chang'an University. https://doi.org/10.1016/j.jtte.2021.12.003

Bridge Maintenance, Safety, Management, Digitalization and Sustainability – Jensen, Frangopol & Schmidt (eds)
© 2024 The Author(s), ISBN 978-1-032-77040-6
Open Access: www.taylorfrancis.com, CC BY-NC-ND 4.0 license

Advancements in bridges NDT: National Highways' "Structures Moonshot" – Paper No. 1

C. Mundell, C. Hendy & T. Argyle
AtkinsRealis, UK

C. George
National Highways, UK

ABSTRACT: The "Structures Moonshot" project, initiated by National Highways and led by Atkins, Jacobs, and supported by VSL, advances non-destructive testing (NDT) for highway structures, with a focus on post-tensioned bridges and half joints. Launched in late 2022 and continuing, its vision to revolutionise asset management for vulnerable bridges, enabling better and more efficient data collection, leading to self-monitoring and self-diagnosis for National Highways' most critical structures.

The project comprises two phases; The first involves testing high Technology Readiness Level (TRL) NDT technologies on bridge sections from the dismantled A14 Huntingdon Viaduct. These are compared with the as-found physical conditions after hydro-demolition. The goal is to evaluate current NDT methodologies, identify areas for improvement, and enhance efficiencies in deployment.

The second phase centers on developing low TRL NDT technologies tailored for post-tensioned bridges. This includes the use of guided wave technology, with the aims of enabling direct tendon deterioration measurements without intrusive inspections.

This paper will focus on the second aspect, being the low-TRL technologies. The Huntingdon Viaduct trials are documented in IABMAS Paper number 454.

Through the collaborative efforts involving National Highways, AtkinsRealis, Jacobs, VSL and the NDT supply chain engaged with the project, this work is leading to a better understanding of how we can determine the condition of post-tensioned bridges and half joints. The project will also provide valuable insights for future bridge inspections and structure maintenance works, enabling the development of clear training and guidance on optimal NDT deployment. This in turn will improve our overall asset management practices, ultimately leading to better safety of our structures and those using and maintaining them, and reducing disruption on our road networks.

1 INTRODUCTION

1.1 *Challenge*

Within the transport infrastructure sector, all asset owners face an ongoing challenge to both inspect, maintain and operate their asset stock, whilst maintaining the highest levels of customer service possible. These two drivers are interlinked; to provide a reliable level of service, the assets need to be well maintained and well-managed. However, this is becoming increasingly difficult; key UK bridge owner National Highways estimated that by the end of the decade, 57% of their bridge stock will be over 50 years old. This is coupled with increasing levels of traffic in terms of magnitude and vehicle weights, meaning our structures are under more stress but are also more difficult to inspect and repair due to the disruption associated

DOI: 10.1201/9781003483755-431

with road and lane closures. Whether a closure to inspect, maintain or repair a structure is planned or unplanned, the public and political impact can be substantial. For example, after routine inspections of the A52 Clifton Bridge in Nottingham, UK uncovered significant deterioration of post-tensioning strands at one location, the bridge was closed as a precautionary measure. This emergency closure lead to a spike in congestion and traffic that made it the most congested city in the world during this time (BBC News, 2020).

1.2 *Moonshot vision*

To face this challenge, National Highways have instigated a research programme they are calling their Structures 'Moonshot'. The underlying ambition of this is to maximise the benefits from advances in technology (e.g. new technologies, Artificial Intelligence and Machine Learning) to facilitate new and improved asset management approaches. The ultimate goal is to better understand the condition of our structures and facilitate interventions before deterioration has progressed to the point where major works are required.

By applying new and developing technology, the goal is to transform the management of our structures through accessing, piloting, deploying and upscaling technology. Improvements in processes and ways of working will impact on:

- Safety: minimising human intervention and improve road user safety
- Efficiency: Reducing costs from planned and unplanned closures and enabling more proactive maintenance
- Availability: minimising disruption to users and improving road user satisfaction
- Sustainability: Reducing congestion and delivering more sustainable and less intrusive asset management approaches

1.3 *Post tensioning and half joint focus*

National Highways' ambitious Moonshot project aims to consider all of the typically 'high risk' features associated with bridge structures, including post tensioning, half joints, hinge decks, scour and fatigue. In the first phase of this project, the team are investigating new approaches associated with internal post tensioning and half joints, of which there are approximately 1200 and 420 respectively within National Highways' jurisdiction in the UK (AtkinsRealis, 2023).

2 SPECIFIC CHALLENGES AND APPROACHES FOR POST TENSIONED BRIDGES

2.1 *Inspection challenges*

Both post-tensioned bridges and those with half joints provide a challenge for asset maintainers to inspect, assess and maintain. For post-tensioned bridges, this is primarily due to the primary load-bearing element typically being located within grouted ducts within the concrete volume and therefore inaccessible to most forms of inspection. For half joints, whilst the external façade of the joint can usually be inspected, the condition of the critical reinforcement along the joint length is often equally difficult to inspect without intrusive and damaging inspection.

The issue of inaccessibility is exacerbated when coupled with poor workmanship, poor detailing for water management or inferior construction techniques and materials. This can leave the tendons or half joints exposed to deterioration even in more recently-constructed structures. Whilst the failure of a half joint is usually a more ductile failure mode, failure of individual post tensioning strands can be progressive without any external warning signs and, in the worst case scenario, lead to brittle and catastrophic collapse of structures.

2.2 *Typical defects for post tensioning systems*

Ultimately, failure of a stressing system occurs if either the load within the system increases to an extent that it exceeds the limits of the undamaged strands or, more likely, when corrosion reduces the strand strength through section loss (Fisk & Armitage, 2019) whereupon failure is often brittle in nature. Many early post-tensioned bridges simply relied on infill concrete being placed around the stressed tendons to provide corrosion protection, but this has been found to offer very poor protection against water ingress. To give better protection against corrosion, post-tensioning strands are typically encased in a duct (either metallic or PVC), with the duct usually infilled with grout to prevent the ingress of moisture and/or chlorides. However, poor detailing, poor quality workmanship or inferior grouting materials can lead to a number of defects that may be present from construction:

- Voids within the ducts (most likely at high-points within the system)
- Bleed water accumulating during grout curing
- Galvanic reactions from soft grout surrounding hard grout (Fisk & Armitage, 2019)
- Incorrect placement of ducting leading to low cover
- Poor detailing of bridge joints, waterproofing or anchorage cappings

Each of the above defects in isolation may not necessarily lead to deterioration of the post-tensioning system, however in combination with each other and through general degradation of the structure, they are likely to lead to deterioration. These defects can occur in any post-tensioned bridge, but pre-cast, post-tensioned segmental structures are of the greatest concern due to increased numbers of transverse joints - potential inlets for water and chlorides (WSP, 2017).

2.3 *Current approaches to determining condition*

Determining the condition of internal post-tensioning systems is a process that is complex and often requires a mix of approaches, led by skilled and experienced engineers and specialists. In essence, this can be simplified to:

- Optical inspection methods for surface-level indications of post-tensioning deterioration
- Numerical Modelling, often including Finite Element Analysis (FEA)
- Non-Destructive Testing (NDT)
- Destructive/Intrusive Testing

Each approach has its own advantages and limitations, with current technologies unable provide a single non-destructive method for determining all required information for assessing a structure. Therefore, they must all be used to some extent, requiring an understanding of the appropriateness of each, and where it can be relied upon.

3 POST TENSIONED BRIDGE MOONSHOT - SCOPE

3.1 *Preceding work*

Following the closure of the A52 Clifton Bridge described in Section 1.1, National Highways formed a 'Tiger Team' to review their approach to managing post tensioned bridges. This included reviewing assurance processes, the relevant standards and their adoption, post tensioned experience and capabilities both internally and within the industry, risk management and the approach to inspection, data gathering and structural health monitoring. The latter aspect included a literature study on global approaches to data gathering, and in particular – a study on global approaches to NDT and the associated technologies (AtkinsRealis, 2020). This concluded there does not yet exist a clear technology that provides a bridge owner a comprehensive understanding of the internal condition; All of the systems available have inherent flaws, limitations and inaccuracies. A combination of approaches - including visual, numerical, NDT and intrusive inspections – all still have their place within the current best

practice maintenance strategy. However, there is likely a benefit to be achieved with reviewing the current usage of individual technologies, and how they can be used in parallel to better effect.

Building on the Tiger Team work, the first phase of the post-tensioned Structures Moonshot was commissioned to articulate the challenge noted in Section 1.1 of this paper and investigate the approaches that might be developed to meet these objectives. The project team - led by this paper's authors – undertook a global engagement process to appropriate institutions and sectors that might face similar challenges, and may have solutions or are undertaking research and development in a related field. This was undertaken through a 'Call for Ideas' challenge statement, which was issued to a broad range of potential research partners. This included engineering and NDT bodies and institutions, but also sought to reach out to potentially compatible institutions and companies within aeronautical, biomedical, agricultural, heavy civils (e.g. nuclear) and mining sectors. The aim was to uncover technologies, approaches or low TRL ideas that would enable the determination of:

1. Identification if the conditions for corrosion exist, and how severe they are
2. Identification if corrosion is actually occurring
3. Identification if corrosion has occurred, and if so quantification of deterioration

The statements are of increasing value to asset owners, but equally increasing in difficulty to achieve with any certainty. The aim was to identify technologies that either were already at a high enough TRL that they could be trialed and their effectiveness reviewed, or else be invested in to develop these ideas or concepts to a point at which they can be trialed and reviewed (i.e. very low TRL technologies).

Submissions were assessed and scored using a weighted scoring mechanism that considered TRL, evidence of experience in the relevant field, application of the technology (i.e. which of the three criteria above would it meet), cost and duration to develop, cost to deploy at scale and ease of applicability at scale.

At this point in the project, the A14 Huntingdon Viaduct – a post-tensioned rail bridge – was in the process of being demolished as part of a larger infrastructure scheme. The structure contained both post tensioning and half joints, with previous assessments and structural health monitoring pointing to defects in both. As will be described later in this paper, through a separate investigation led by AECOM, National Highways were able to secure three large samples of the structure to augment the scope of the moonshot project. Consequently, in addition to investing in low-TRL research, the project scope was expanded to include testing the effectiveness and applicability of higher TRL NDT technologies that are not yet in common usage.

The testing recommendations included investigating both higher and lower TRL technologies. For the former, a number of higher TRL applications were identified, including those from the agricultural sector, typically used for determining the composition of soil, high-accuracy optical strain and displacement measurements, creation of 'chloride maps' of surfaces using ground penetrating radar (GPR) and application of ultrasonic waves along the exposed tendon ends for short-distance condition mapping.

The lower TRL technologies identified included a guided wave application developed by Omnia, who – together with research partners Vallen Systeme – are well experienced in the field of acoustic monitoring techniques. Sentec's proposals included harnessing their specialisms in electronics and signal transmission to measure electrical transmission along tendons for fault finding, in addition to a variant on guided wave measurements, applied via thermal or electromagnetic means to the tendon through a surrounding concrete medium.

3.2 *Phase 2 commissioning and scope*

The first phase of the Moonshot project ended with a report recommending the trials noted above in mid 2021. In late 2022, the second phase of National Highways' Structures Moonshot was commissioned through its Specialist Professional and Technical Services (SPaTS), and funded by National Highways' designated funds for Innovation and Modernisation Fund.

The project was awarded to a Joint Venture of AtkinsRealis and Jacobs (AJJV), with the AJJV team including contractors VSL to be the Main Works Contractor, handling the management of the site activities through the project.

The main scope of this phase of the Moonshot project is split into two distinct activities; Testing of the low-TRL technologies of Omnia and Sentec (Section 4 below), and; mobilising a site compound to enable the a suite of NDT to be undertaken on the recovered samples from the A14 (Section 5 below).

4 RESEARCH AND DEVELOPMENT STUDIES

4.1 *Aims of the trials*

As part of the Moonshot project, National Highways were committed to investing in promising technologies that might enable the identification of tendon condition in existing post tensioned structures. The aim of this aspect of the project is to take early TRL technologies and ideas, and develop them to such a position that they can be deployed in a trial capacity on live structures (i.e. TRL 5). It should be noted that whilst the research is carefully assessed for alignment with the overall project goals, the investment is not linked to ownership of any developed technologies or the associated Intellectual Property (IP). National Highways are seeking the betterment of the industry through the application of new technology, rather than developing new capabilities.

Each of the R&D programmes has been split into a number of distinct phases or work packages. These are initially desk-based, using Finite Element Modelling (FEM) and small-scale testing to demonstrate the viability of the approach and the concepts involved. Follow on programmes include larger-scale testing to prove the FEM concepts, and introduce some of the real-world complexities that make these structures such a challenge to investigate. The final investment phase is to enable the construction of a prototype system that can be trialed in real-world application.

Funding and investment through the work packages/phases is dependent on a gated assessment approach. At each milestone, the project team (including National Highways and the AJJV team) review the progress to date, and the findings and outcomes compared to expectations. This provides the project team the opportunity to help steer the technology development at critical junctures, or in the case that the development is not deemed to be yielding the value required, potentially pivot to new avenues or technology investments.

4.2 *Sentec research proposals*

Technology and product developers Sentec (part of the Xylem group) supplied a number of potential NDT solutions to the Moonshot 'call for ideas', building on their experience of developing innovative sensors and smart metering for gas, water and electricity sectors. Two proposals were identified that would attempt to tackle the most challenging aspect – determining how much corrosion has occurred within a tendon. These were direct impedance measurement and Radio-frequency (RF) coupled guided ultrasound.

The direct impedance measurement involves continuous measurement of the tendon resistance and inductive/capacitive reactance, with the aim of detecting corrosion through the resistance changes within the steel. This would need to allow for changes in cable diameter and filtering out of changes in temperature and stress. It was identified from the outset that the technique may be affected by random changes in impedance due to joints and connections with reinforcement.

For the RF coupled guided ultrasound involves the remote induction of a temperature gradient within the tendon via pulsed radio frequency. The induced temperature gradient is used to generate a high-power guided ultrasonic wave within the tendon, which is then measured by multiple receivers along the length of a section (from the surface of the concrete).

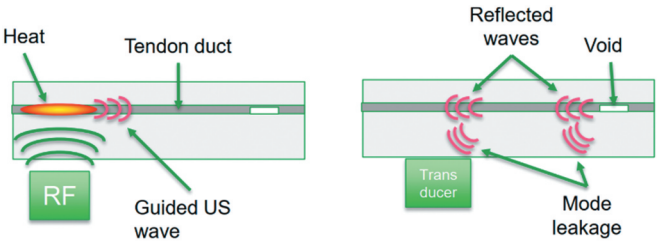


Figure 1. Sentec RF Coupled Guided Ultrasound.

4.2.1 *Progress to date – Direct impedance*

At the time of writing, the direct impedance methodology has been proven through a series of small scale tests and numerical modelling. Validated and compared against numerical modelling, the team constructed a 1m long grouted line, which was then injected with an 80 MHz bandwidth pulse, which was drilled with a 1cm hole (simulating a defect). The system was able to measure a demonstrable difference and change in signal between wet and dry conditions.

Demonstrating initial promise, the system does currently have a number of limitations and assumptions. These are namely:

- Changes in condition are best measured as variations from a baseline, and as such generation of a baseline is required for optimum results
- A direct electrical connection to the duct and strands is required to induce the signal into the system (with potential to use a current loop to couple a signal into the strand remotely at a later date)
- Instances of connections between the tendon and metallic ducts, and further connections between duct and reinforcement will lead to a 'short' in the circuit and currently prevents further interpretation of the signal at this point

4.2.2 *Progress to date – RF coupled guided ultrasound*

The initial approach for this methodology was to attempt to induce a guided wave using an RF source, however it was determined through the course of the research that for situations where a duct is metallic, the power was predominantly absorbed by the duct. As such, the technology developed to trialing near field coupling via a magnetic field induced by a coil.

With the revised methodology, the Sentec team were able to induce and detect a generated ultrasound signal from a standoff of 300mm. Through numerical studies, this was progressed to observing wave propagation through water-filled voids within a duct, with a number of possible mechanisms for detecting and measuring the void.

4.2.3 *Omnia research proposal*

Omnia Integrity is a company specialising in non-intrusive methods for asset inspections, with a focus on wave mechanics (guided wave and acoustic emission). The proposal team included partners with ARCES (Bologna University) and Vallen Systeme, specialists in guided wave mechanics and acoustic emission inspections respectively.

The Omnia proposal harnesses their teams' expertise in acoustic monitoring, and utilizing the same apparatus, to induce guided waves that can assess condition in addition to detecting wire breaks.

4.2.4 *Progress to date*

The Omnia-headed team have been commissioned to undertake two phases of development to date; a numerical study with small scale testing, and; larger scale testing to validate numerical concepts and theory.

The initial phase of finite element modelling involved incremental increases in modelling complexity, moving from detecting responses in a 2D, single plain bar through to a 3D-modelled concrete-encased 7-wire wound strand. At each stage of testing, the team have been careful to test multiple frequencies and wave forms and ensure full understanding of the wave

propagation and the associated response before moving onto subsequent stages, including identification of defect patterns such as breaks or section loss. The technology has shown promise that defects within grouted tendons can be identified up to a range of (currently) approximately 4m when utilising an excitation source connected directly to a strand.

At the time of writing, Omnia are undertaking large scale testing to validate the numerical studies, having constructed a 9m beam with stressed tendons encased in concrete. A number of 'windows' have been cast into the beam to allow the connection of excitation devices, in addition to control defects to be detected by the system. Trials are ongoing, with positive results indicating that the hypotheses of the numerical studies are borne out in practical application.

4.3 *Next steps*

Next steps for these technologies have been mapped out, but each technology must next be evaluated on its own merits and assessed with respect to those criteria set out in the initial moonshot 'call for ideas'. Likelihood of successful development through to a deployable technology will be key considerations, along with scalability and impact; to secure further investment the project team must be satisfied that a suitable return on investment will be achieved in the form of a high-impact technology that will lead to a step change in current asset management approaches.

5 NON DESTRUCTIVE TESTING – TECHNOLOGY APPRAISAL TRIALS

5.1 *Aims of the trial*

As discussed in previous sections, through preceding work, National Highways have secured a number of sections of the A14 Huntingdon Viaduct - including two sections with half joints – with the intention of undertaking blind trials of various forms of higher-TRL NDT technologies. The overall approach is to deploy these technologies across the three sections, followed by controlled hydrodemolition of the sections and extraction of key features (e.g. PT ducts and anchorages). By comparing the NDT results with as-found condition, the project team will be able to determine the effectiveness of various technologies and identify particular strengths and limitations. These findings will be used to develop improved approaches and process maps for asset investigations, laying different technologies together to complement each other and respond to the specific challenges faced on a structure-by-structure basis.

The trial does not just consider technology – gathering good data is a combination of people, process and technology; Having the appropriate equipment for a situation can be rendered ineffective if it is deployed in a sub-optimal arrangement, or used by insufficiently trained teams. This study therefore captures what 'best practice' looks like, and also includes duplication of specific pieces of equipment to attempt to distinguish differences in quality through different applications.

Finally, through the reach of the Phase 1 'call for ideas', the trials have included a number of cross-sector technologies. In particular, as will be detailed later in this paper, technologies from the agriculture sector – typically used for soil composition analysis – have been adopted.

6 PROGRAMME AND NEXT STEPS

6.1 *Programme and broader moonshot objectives*

This phase of the Structures Moonshot is scheduled to run until the end of 2024 or early 2025, by which point the planned R&D being undertaken by Sentec and Omnia will have reached the intended conclusions and the NDT on the A14 samples will have been assessed and documented. As noted in this document, National Highways' current aspiration is that this work is continued to consider other 'high priority' areas and structure types; this will likely be informed by the success and direction of these initial phases and the value delivered.

A key objective of the project is around knowledge sharing and dissemination. In addition to publication of key findings, part of the project scope is to host an industry conference at the end of the project, inviting the wider industry to attend and explore the findings and their implications, including asset owners, consultants, contractors, NDT providers and technology developers.

6.2 *Data collection, BIM approach and harness of artificial intelligence*

Throughout the NDT trials of the A14 sections, data has been captured in such a way that it can be considered holistically; The aim is to be able to draw conclusions and identify relationships between the findings of different techniques and approaches, tied to the as-found condition of the samples. This is founded on a clear and simple referencing system for the NDT specialists to adhere to, and will be augmented by transposing these data into a single federated 3D model, providing a 'Digital Twin' of the samples. Using typical BIM products such as Autodesk Revit, Navisworks and Bentley BIMTrack, the samples have been recreated as 3D models, upon which the NDT defects can be layered, along with the physical findings. Over and above this, the project team have been carrying out Lidar scans of the samples throughout the hydrodemolition process, providing 3D meshes of the exposed tendons in-situ, which can also be layered into the digital twin and explored in parallel to the NDT findings.

In addition to the exploration of the data by the project team, the goal is to be able to harness new approaches to data review such as Machine Learning and Artificial Intelligence, with the digital twin described above will be a key building block for this work. As noted, industry engagement is a key tenet of the project, and it is intended that further 'Open Invites' may be launched to expose the gathered data to industry AI and ML specialists, allowing the data to be much more broadly explored and different approaches tested.

7 SUMMARY AND CONCLUSIONS

Although still in progress, the project has already yielded significant insights and progress. The low TRL technologies explored by Omnia and Sentec are each pushing boundaries of what is achievable, particularly in the field of guided waves. In this aspect of the project, progression of the technologies will now start moving from what is theoretically possible to the practicalities of deployment in a real situation, and the relative value derived from its application.

Again, with respect to the NDT trials of the A14, although the data collation and assessment is still underway, a number of interesting observations and avenues have already been identified, and a broad suite of NDT techniques deployed. The industry engagement has also been very strong, with the NDT providers engaged being both collaborative and inquisitive, which has allowed the collation of information to be much broader than initially anticipated, which will in turn yield greater insights as the project turns to the data assessment.

ACKNOWLEDGEMENTS

The Authors would like to thank all of the parties involved in this project to date. These include the client and project sponsors National Highways (and the funding by National Highways' designated funds for Innovation and Modernisation Fund), the AtkinsRealis and Jacobs joint venture project team, Main works contractor VSL, R&D partners Sentec (supported by Lucy Electric) and Omnia (supported by Vallen Systeme and ARCES) and NDT specialists Mistras, Bridgology, CTS, Allied Associates, Screening Eagle, the Royal Agricultural University (supported by the University of Bristol and Pro-Lite Technology), Hausbots, Hilti, GScan and IFDB.

REFERENCES

AECOM. 2021 Huntingdon Railway Viaduct Research Feasibility (Rev 003). *Highways England*

Atkins. 2020. Post-Tensioned Non-Destructive Testing and Monitoring Techniques. *HighwaysEngland*.

Atkins. 2023. Task 164. Management of High Priority Structures – RIS3 Funding Estimate (Rev 2). *National Highways*.

Abbas, Y., Have, B. t., Hoekstra, G. I., Douma, A., de Bruijn, D., Olthuis, W., & van den Berg, A. (2015). Connecting to Concrete: Wireless Monitoring of Chloride ions in Concrete Structures. *Procedia Engineering*, *120*, 965–698.

Azizinamini, A. (2017). *Non-destructive testing (NDT) of a segmental concrete bridge scheduled for demolition, with a focus on condition assessment and corrosion dection of internal tendons*. Miami, Florida: Department of Civil and Environmental Engineering, Florida International University.

Azizinamini, A., & Gull, J. (2012). *Improved inspection techniques for steel prestressing/post tensioning strand*. Miami, FL: Florida International University.

Bishop, D., Hendy, C., & Mundell, C. (2017). *M48 Severn Bridge - Acoustic Monitoring Trigger Levels - Working Paper*. Highways England.

Bungey, J., Millard, S., & Shaw, M. (1997). Radar assessment of post-tensioned concrete. *Proceedings of the 7th international conference on structural faults and repair* (pp. 331–339). Eniburgh: Engineering Technics Press.

Burdet, O. (2010). Experience in the long-term monitoring of bridges. *3rd fib International Congress*.

Clark, G. (2010). The development of prestressed concrete bridges. *Concrete Bridge Development Group Conference*. Oxford.

Clark, G. M. (2013). Post-tensioned structures - Imrpoved standards based on lessons learnt. *Proceedings of the Institution of Civil Engineers - Forensic Engineering 166(4)*, 171–179.

Dalla Vedova, M., Elsener, B., & Evangelista, L. (2004). Corrosion Protection and Monitoring of Electrically Isolated Post-Tensioning Tendons. *Proceedings of the Third European Conference on Structural Control*, (pp. S5-47 - S5-50). Vienna, Austria.

Dawood, N., Marzouk, H., Hussein, A., & Gillis, N. (2013). Nondestructive assessment of a jetty bridge structure using impact-echo and shear-wave techniques. *ASCE - Journal of Bridge Engineering 18(8)*, 801–809.

Derobert, X., Aubagnac, C., & Abraham, O. (2002). Comparison of NDT techniques on a post-tentioned beam before its autopsy. *NDT&E International*, *35*, 541–546.

Dizaji, M., Alipour, M., & Harris, D. K. (2020). Subsurface damage detection and structural health monitoring using digital image correlation and topology optimization. *Engineering Structures*.

Elsener, B. (2005). Long Term Monitoring of Electrically Isolated Post-Tensioning Tendons. *Structureal Concrete*, *6*(3), 101–106.

Fisk, P., & Armitage, B. (2019). Nondestructive testing for voided and soft grout in internal post-tensioning ducts. *PTI Journal 15(1)*, 31–35.

Highways England. (2019). Repair and Management of Deteriorated Concrete Highway Structures.

Hong, S. (2015). *GPR-based periodic monitoring of reinforcement corrosion in chloride-contaminated concrete*. Berlin: Technical University of Berlin.

Hoppe, E. J., Novali, F., Rucci, A., Furnagalli, A., Del Conte, S., Falorni, G., & Toro, N. (2019). Deformation monitoring of post tensioned bridges using high-resolution satellite remote sensing. *ASCE - Journal of Bridge Engineering - 24(12)*.

Hurlebaus, S., Hueste, M. D., Karthik, M. M., & Terzioglu, T. (2016). *Condition Assessment of Bridge Post-Tensioning and Stay Cable Systems Using NDE Methods*. National Cooperative Highway Research Program (NCHRP). Transportation Research Board (TRB).

Islam, S., & Aumann, C. (2018). Electrically Isolated Tendons - Post-Tension Supplier's Experience. *FHWA Workshop at Lehigh University*. Pennsylvania, United States.

Lu, S., & Ba, H.-J. (2010). Corrosion Sensor for Monitoring the Service Condition of Chloride-Contaminated Cement Mortar. *Sensors*, *10*, 4145–4158.

Marsh, P. S., & Frongopol, D. M. (2007). Lifetime Multiobjective Optimization of Cost and Spacing of Corrosion Rate Sensors Embedded in a Deteriorating Reinforced Concretre Bridge Deck. *ASCE - Journal of Structural Engineering*, *133*(6), 777–787.

Mehrabi, A. (2006). In-service evalutation of cable-stayed bridges, overview of available methods and findings. *ASCE - Journal of bridge engineering*, *11(6)*, 716–724.

Mistras. (2018). *Post tension structures - commentary on NDT and monitoring methods*. Mistras.

Office of Nuclear Regulatory Research. (2015). *Study on Post Tensioning Methods*. United States Nuclear Regulatory Commission.

Ortiz-Aleman, C., & Martin, R. (2005). Inversion of electrical capatitance tomography data by simulated annealing: Application to real two-phase gas-oil flow imaging. *Flow Measurements Instrumentation 16 (2-3)*, 157–162.

RAC Foundation. (2019, January 07). *RAC Foundation*. Retrieved from https://www.racfoundation.org/media-centre/bridge-maintenance-backlog-grows

Ramboll. (2018). Assessment and investigation of post-tensioned bridges in accordance with the DMRB. Guidford, UK: Highways England.

Terzioglu, T., Karthik, M., Hurlebaus, S., & Hueste, M. B. (2019). Nondestructive evaluation of external post-tensioning systems to detect grout defects. *ASCE - Journal of Structural Engineering 145(1)*.

The Internation Federation for Structural Concrete (FIB). (2014). *Bulleting No. 75 - Polymer-duct systems for internal bonded post-tensioning*. FIB.

UK Bridges Board. (2007). *Inspection Manual for Highway Structures - Volume 1: Reference Manual*. London: TSO.

Winkler, J., & Hendy, C. R. (2017). Improved Structural Health Monitoring of London's Docklands Light Railway Bridges Using Digital Image Correlation. *IABSE Structureal Engineering Journal*, *3/2017*.

Woodward, R. J. (1989). Collapse of a segmental post-tensioned concrete bridge. *Transportation Research Record 1211*, 38–59.

Woodward, R. J. (2001). Durability of post-tensioned tendons on road bridges in the UK. *Proceedings of FIP/IABSE workshop on the durability of post tensioning tendons (Ghent University)*. Lausanne: International federation for structural concrete (fip).

WSP. (2017). Task 622: Review of standards for post tensioned brigdes (v 8.0). Highways England.

Bridge Maintenance, Safety, Management, Digitalization and Sustainability – Jensen, Frangopol & Schmidt (eds)
© 2024 The Author(s), ISBN 978-1-032-77040-6
Open Access: www.taylorfrancis.com, CC BY-NC-ND 4.0 license

Advancements in Bridges NDT: National Highways' "Structures Moonshot" – Paper No. 2

C. Mundell, C. Hendy & T. Argyle
AtkinsRealis, UK

C. George
National Highways, UK

ABSTRACT: The "Structures Moonshot" project, initiated by National Highways and led by Atkins, Jacobs, and supported by VSL, advances non-destructive testing (NDT) for highway structures, with a focus on post-tensioned bridges and half joints. Launched in late 2022 and continuing, its vision to revolutionise asset management for vulnerable bridges, enabling better and more efficient data collection, leading to self-monitoring and self-diagnosis for National Highways' most critical structures.

The project comprises two phases; The first involves testing high Technology Readiness Level (TRL) NDT technologies on bridge sections from the dismantled A14 Huntingdon Viaduct. These are compared with the as-found physical conditions after hydro-demolition. The goal is to evaluate current NDT methodologies, identify areas for improvement, and enhance efficiencies in deployment.

The second phase centers on developing low TRL NDT technologies tailored for post-tensioned bridges. This includes the use of guided wave technology, with the aims of enabling direct tendon deterioration measurements without intrusive inspections.

This paper will focus on the first aspect, being the Huntingdon Viaduct trials. The low-TRL technology developments are documented in IABMAS Paper number 452.

1 INTRODUCTION

As discussed in IABMAS paper No. 452, through preceding work, National Highways have secured a number of sections of the A14 Huntingdon Viaduct - including two sections with half joints – with the intention of undertaking blind trials of various forms of higher-TRL NDT technologies. The overall approach is to deploy these technologies across the three sections, followed by controlled hydrodemolition of the sections and extraction of key features (e.g. PT ducts and anchorages). By comparing the NDT results with as-found condition, the project team will be able to determine the effectiveness of various technologies and identify particular strengths and limitations. These findings will be used to develop improved approaches and process maps for asset investigations, laying different technologies together to complement each other and respond to the specific challenges faced on a structure-by-structure basis.

The trial does not just consider technology – gathering good data is a combination of people, process and technology; Having the appropriate equipment for a situation can be rendered ineffective if it is deployed in a sub-optimal arrangement, or used by insufficiently trained teams. This study therefore captures what 'best practice' looks like, and also includes duplication of specific pieces of equipment to attempt to distinguish differences in quality through different applications.

DOI: 10.1201/9781003483755-432

Finally, through the reach of the Phase 1 'call for ideas', the trials have included a number of cross-sector technologies. In particular, as will be detailed later in this paper, technologies from the agriculture sector – typically used for soil composition analysis – have been adopted.

2 NON DESTRUCTIVE TESTING – TECHNOLOGY APPRAISAL TRIALS

2.1 *Sample details & history*

The A14 Huntingdon Railway Viaduct (HRV) was constructed in 1975, carrying four lanes of traffic over six spans and crossing both local distributor roads and the East Coast Main Line (rail link). In December 2019, new routes were opened which rendered the structure obsolete.

The main span consists of a main drop-in span formed of simply-supported precast beams (with transverse post tensioning and an in-situ deck slab), supported on longitudinally post-tensioned cantilever sections. The support and articulation for the precast main span elements are via half joints at the end of the precast cantilevers.

Over the course of 20 years, the structure has been subject to a number of detailed structural assessments, supported by testing and continuous monitoring (e.g. via Acoustic Emission Monitoring, or AEM). Due to a low assessed capacity and observed increases in re-entrant cracking of the half joints, a number of repair and remedial measures have been carried out, including regrouting of PT ducts and providing a secondary support structure to negate the risk of sudden half-joint failure. It should be noted that over the course of the 20 year period of AEM, a total of 52 wire breaks were recorded within the PT ducts, with a number concentrated in the section of the structure that was removed as part of this project and identified as 'Sample 3′ (AECOM, 2021). In 2020, during the demolition of the full structure, three number samples were removed by wire cutting from the north monolith, as shown in Figure 1.

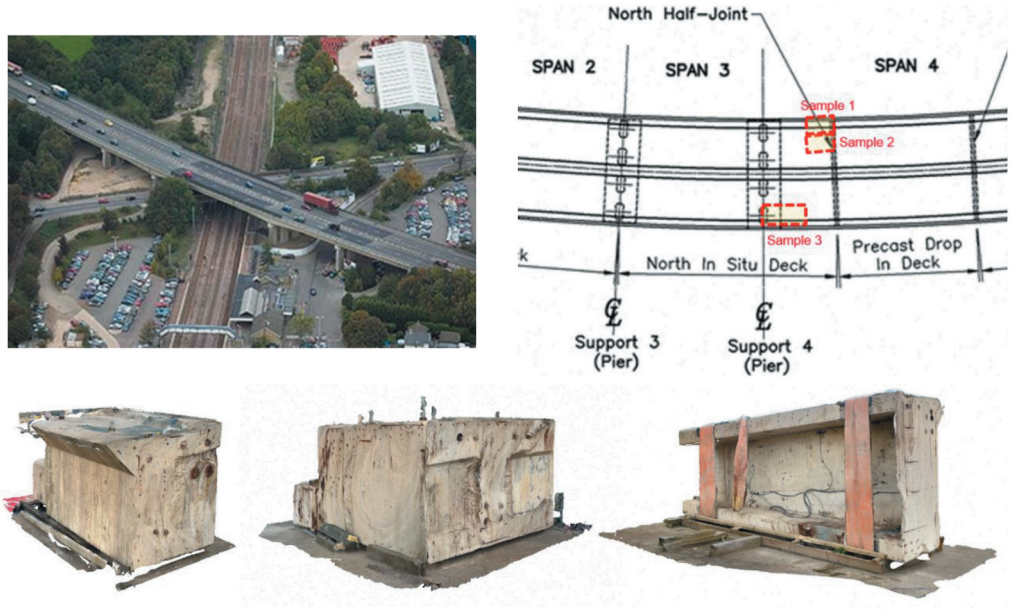


Figure 1. Top left – Huntingdon Viaduct; Top right – Sample locations; Bottom (left to right) – samples 1, 2 and 3.

Samples 1 and 2 have been extracted from the end of the cantilever, being two adjacent sections containing half joints and PT ducts. The PT ducts all terminate within either the half joint nibs or immediately behind within the full-height section of the structure, meaning that

all PT ducts within these samples also contain anchorages (5 number in sample 1, 8 number in Sample 2). The samples vary in size between 2m to 3m in length and width, weighing 16 and 24 tonnes respectively. Sample 1, being the outermost section, also includes the parapet beam support and a patterned finish to the external-facing elevation.

Sample 3 has been removed from the opposite side of the same cantilever monolith, starting at the pier support diaphragm and extending 6m along the cantilever section, being 4m tall at the highest (diaphragm) end. The section has been taken from part of the outermost cell, and as such contains part of the top and bottom flanges of the cell, along with the web. The external façade of the web is patterned and contains a diagonal nib to support the parapet beam (as per Sample 1). This section contains 7 number PT strands, of which one terminates within the section web. Images of the 3 samples are shown in Figure 4.

2.2 *NDT technologies and open invite*

The initial plan included engaging with some of the industries most established NDT suppliers to provide a suite of NDT techniques. This included optical/spectral inspections, electromagnetic sensors, mechanical wave induction and electrochemical tests. Testing providers initially included VSL (also acting at the main works contractors) Bridgology, Mistras, CTS, Allied Associates and the Royal Agricultural University (RAU). Many of the techniques were commonplace; Ground penetrating radar (GPR), covermeter surveys, ultrasonic tomography, half cell potential surveys and impact echo, but a number were also less common; Hyperspectral imagery, FTIR gas monitoring, magnetic flux leakage, chloride mapping via GPR and ultrasonic guided wave testing.

In addition to the planned NDT providers and technologies, the project team undertook a further 'call for ideas' from the wider industry (akin to the phase 1 moonshot call out). This was specifically seeking to understand if additional technologies and approaches had come to the market since the first phase, or had been missed in the first instance. Using National Highways' competitions page, coupled with social media outlets, the project and the opportunity to engage was opened up for several weeks while testing progressed. During this time, a number of new technologies and testing providers were brought into the project. This included Screening Eagle, bringing the latest Proseq sensors, HausBots, deploying their climbing robot, reinforcement scanning specialists Hilti and Muon tomography specialists GScan.

2.3 *Outcome focused specification*

The intention for each form of NDT is that it builds on the overall dataset which will allow structural condition to be appraised. Furthermore, the project team acknowledge that in the majority of cases, the most advantageous use of each form of NDT is best identified by the technology provider. Based on the these requirements, the project specification produced for the NDT was primarily defined by outcomes, rather than prescriptive approaches. A hierarchy of data value was established, identifying the types of defects or data measured and their relative value. Leveraging this, it was the requirement that the technology providers themselves confirm the deployment methodology and which of the desired outcomes that they hoped to meet.

With the nature of this project being aspirational, each provider was challenged to aim to achieve the maximum level of data and interpretation possible, even where the confidence of the data gathered may be lower. To capture this, the specification allows for individual tests to differentiate between when there are strong indications that defects are present, or conversely where there may only be a suggestion of potential for defects or the conditions for deterioration. As such, when capturing data from surveys, where defects are identified, these are coupled with a 'Level of Confidence' indication by the testing provider, scored as high, medium or low depending on the definition of the observation and potential for misinterpretation.

Finally, to enable a holistic review of the NDT data and actual condition data post-demolition, a detailed co-ordinate and referencing system has been established, catering for the different types of NDT and how they will capture data. This includes a 3D local co-ordinate system for each sample, individual identification of sample faces, duct numbering and chainage system and strand and wire numbering. Each NDT provider provides their findings in a standardised format where appropriate, allowing the project team to consolidate defects and findings and look for trends and linked observations.

2.4 *NDT key outcomes to date*

At the time of writing, detailed NDT findings are still pending, however an initial collaboration session with the NDT providers has yielded outline results and initial findings as noted within this Section.

2.4.1 *Half cell resistivity*

Detailed electro-potential readings, dust sampling and chloride content testing carried out immediately prior to demolition (of the samples) are yet to be provided, however initial resistivity testing of the exposed faces results have typically been found to show low likelihood of deterioration in the near surface reinforcement and concrete, with some areas of hotspots, such as the re-entrant corners of the half joints of Samples 1 and 2.

2.4.2 *Ultrasonic pulse echo*

Ultrasonic Pulse Echo testing has been independently undertaken by a number of NDT providers, including Mistras, Screening Eagle and Allied Associates. Focus of testing has been on Sample 3 where the suspected wire breaks are located. This testing has identified a number of suspected voids within the tendon ducts, particularly within the web of the sample, as shown by Figure 5 below. This would indicate that at several points along the length of the tendons there is a lack of grout within the ducts, which would in turn provide an elevated risk of tendon deterioration.

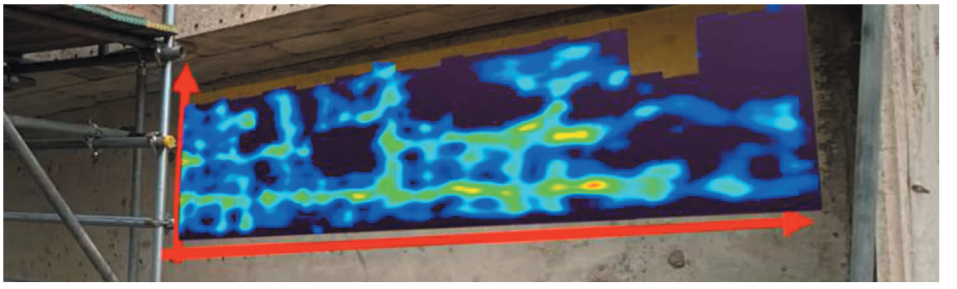


Figure 2. Ultrasonic pulse echo testing examples.

2.4.3 *Impact echo*

Similar to the ultrasonic tomography, impact echo testing has focused on Sample 3 for the most part, and has again found a number of areas where there are strong indications that there is voiding within the sample and the ducts at a number of locations.

2.4.4 *Ultrasonic testing of wires*

Using a probe mounted to the exposed ends of the strands, a signal is induced to the individual wires within the tendons, with Mistras proprietary software analysing the signal for approximately 1m along the length of the tendon. As shown in Figure 3, the system has identified a number of tendons where there is a strong indication of corrosion along the length tested, although this test is limited to those locations where the tendon end can be cleanly accessed.

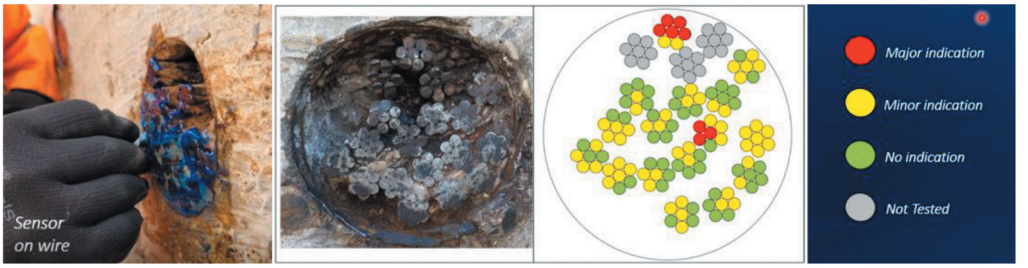


Figure 3. Ultrasonic tendon testing example data.

2.4.5 *Acoustic emission testing*
AEM is normally a passive system that is installed to measure potential tendon breaks over time; for the purposes of these NDT tests, a number of sensors were installed along the length of the samples, with signals induced by a 13cm spring loaded centre punch and a Schmidt hammer. The system measures signal attenuation and amplitude along the length of the sample, looking for breaks and potential indicators for wire breaks.

2.4.6 *Ground Penetrating Radar (GPR)*
GPR has been undertaken using a number of different devices and by a number of different providers, producing detailed coverage of all samples. Although a relatively simple and quick test to undertake, the latest GPR systems have proved effective at locating reinforcement and PT ducts, with multiple scans unlocking 3D images.

This technology has been effectively paired with the ultrasonic pulse echo technology, with both complementing the other in detecting voids and moisture. Following the workshop noted above, further tests were commissioned to attempt to use GPR to specifically identify duct deterioration; results from these tests are pending.

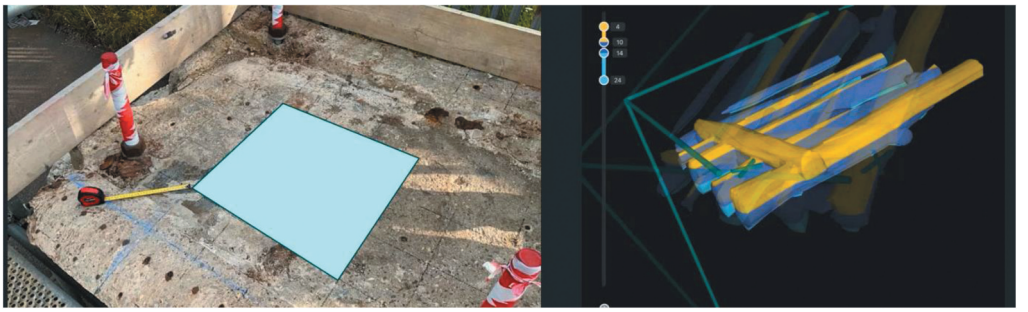


Figure 4. GPR testing data.

2.4.7 *Portable X-Ray Flourescence (pXRF)*
pXRF is a technique used to identifying elemental composition within a sample, and can be applied via a hand-held device directly to a surface. The technique can detect many different impurities in the materials (e.g. sulfur, silicon or zinc), but the team focused on identifying corrosion accelerants such as chlorides, which were found to be most abundant in the duct areas. High concentrations of Sulphur were also identified specifically in the duct areas, which is also currently being reviewed further.

2.4.8 *Fourier Transform Infra-Red (FTIR) Spectroscopy*
FTIR Spectroscopy is a gas-sampling approach which uses a Gasmet device through two different applications; either a chamber attached to the surface of the samples, which is sealed and made a vacuum (or as close as possible), or via a 'sniffer' which can be inserted into bore

holes and cracks. The device then analyses the gases to identify specific variances in gases that are being emitted directly by the sample (compared against baseline readings).

In the case of the moonshot tests, over a 10 minute timeframe, there were increases in Methane, Carbon Monoxide and Carbon Dioxide. Methane in particular was measured consistently across all of the samples at the time of the testing, potentially indicating some aspect of biological action. This is being further explored, including repeat testing and consideration of additional testing such as DNA testing of samples following demolition and sample extraction.

2.4.9 *Field Spectroradiometry and Hyperspectral Imaging*

Using field and laboratory spectroradiomters (ranging in the 280 to 2500nm spectra) in addition to a Raman spectroscopy device using an active light source (a monochromatic laser), further measurements of chemical composition can be remotely undertaken. Additional spectral analyses was carried out using a Specim IQ camera, recording in the 400 to 1000nm range.

Although full data processing has not yet been concluded, to date there have been no significant or noteworthy findings from the data obtained via these methods.

2.4.10 *GPR Chloride Mapping*

Using GPR data, Bridgology are able to develop a 'heat map' of chlorides and corrosion risk in a surface. In this case, the technology has used the Proseq GP8000 GPR scan, undertaken in scans 100mm apart and along two perpendicular directions (i.e. forming a grid of data). As shown in Figure 5 below, the technique has found some indicators of elevated risk of corrosion, particularly focused around the re-entrant corner of the half joints. This is of particular interest, and is not unexpected due to the known cracking along this location and historical deterioration of the structure.

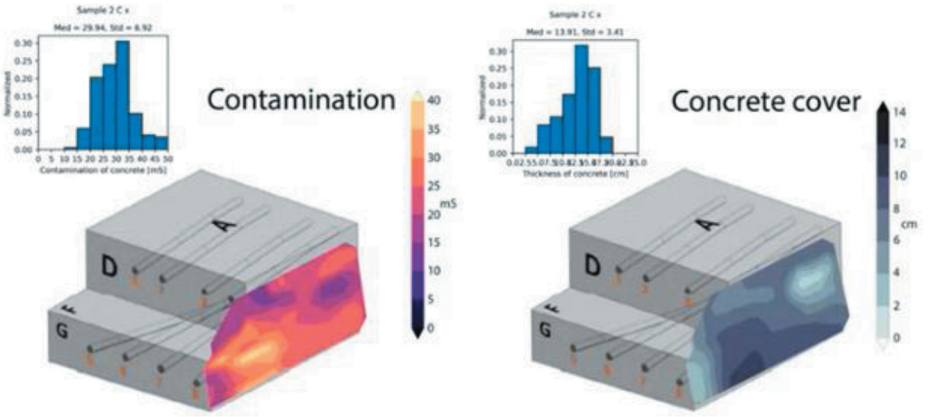


Figure 5. Chloride and concrete cover 'Heat Maps' developed through GPR Surveys.

2.4.11 *Magnetic Flux Leakage (MFL)*

German-based company IFDB were engaged to deploy MFL testing, which involves remotely magnetizing the tendon from the sample surface and then measuring the magnetic flux density along the tendon path using magnetic sensors

Due to the specifics around the magnetization and interference/reflection from cut ends, the MFL technology is most suited to large, planar surfaces or long lengths of beams. As such, there were limited areas of applicability for MFL within the A14 samples. However, it was successfully used on Sample 3, both on the top surface and the exposed web. The team were successfully able to obtain signals from 5 of the 7 ducts within Sample 3, however there was no clear evidence from this technology of wire breaks within the strands.

2.4.12 *Muon tomography*

The final technique tested uses an emerging technology called Muon Tomography. Muons are sub-atomic particles – similar to electrons - that are formed when cosmic radiation hits the earth's atmosphere. Muons are harmless to life, and have very high levels of penetration, which make them ideal for inspecting through dense structures such as a bridge elements. There are a number of methods for tracking the passage of the muons, however the method deployed by specialists GScan for the Moonshot project use high-technology materials such as Plastic Scintillating Fibers and Silicon Photo-multipliers, allowing the path of individual muons to be measured. By measuring over a long period of time (several weeks), the deviations of the muons due to changes in medium (e.g. where they pass from concrete into a metallic duct) can be detected, allowing an image or model of the area in front of the scanning plates. The technology promises to provide not just an image/model showing the various key elements (e.g. duct, tendons, reinforcement), but also the chemical composition of the materials, potentially showing deterioration and the presence of rust. The key limitation for this technology at present is the infrequent nature of the passage of muons; In order to build up a picture that shows defects at the scale required (i.e. millimeter precision), the scanning devices need several weeks left in situ, with the area under observation therefore limited to the size of the scanning plates. In addition, a continuous power supply – although not large – is currently required for the system, which may add logistical complexity for in-situ bridges.

For the purposes of the Moonshot trials, two number sensors were used, one above and one below the concrete flange of Sample 3, and left for a total length of five weeks. The arrangement was locally moved after 2 weeks, with the intention of the second position enabling a 3D image. At the time of publication, the images and data obtained are still under development, with further trials under discussion.

2.5 *Hydrodemolition*

This aspect of the project has now moved into the final phase of work, being the controlled demolition of the samples and extraction of key elements such at the tendon and ducts, samples of concrete in areas of interest and key reinforcement bars for further testing (e.g. reinforcement critical to the half joint strength).

The PT ducts are the key elements of interest, which have been cut into 1m to 2m sections, and will be transported to a more controlled environment for opening and inspection. At this time, the ducts will first be inspected, photographed and measured, before being carefully cut and peeled from the grout and tendon. Again, the grout and any exposed tendon will be inspected and documented, with samples of the grout taken for compositional testing. The locations of any identified voids in the grout will be identified for comparison with the NDT findings. Finally, the grout will be mechanically and chemically removed, exposing the individual strands for inspection and testing, again for comparison with specific NDT findings.

The majority of the ducts have not yet been opened and inspected, however some exploratory work has already been undertaken, particularly with the ducts extracted from Sample 1 (Figure 6). An immediate observation was that the majority of the ducts have suffered deterioration to some extent, and in some cases the ducts were almost entirely non-existent along large lengths of the exposed ducts. Furthermore, the mortar was found to be missing or of very poor quality. Where the ducts were intact with grout present, a small number were cut and opened to expose the tendons and grout. In these cases, the grout was found to be of uniformly low strength, extremely soft and friable, and purely the removal of the duct was enough to cause the mortar to disintegrate and peel away from both strands and duct. This will be key area for further study, including the chemical composition of the grout and its remaining strength.

3 PROGRAMME AND NEXT STEPS

3.1 *Programme and broader moonshot objectives*

This phase of the Structures Moonshot is scheduled to run until the end of 2024 or early 2025, by which point the planned R&D being undertaken by Sentec and Omnia will have reached



Figure 6. Chloride and concrete cover 'Heat Maps' developed through GPR surveys.

the intended conclusions and the NDT on the A14 samples will have been assessed and documented. As noted in this document, National Highways' current aspiration is that this work is continued to consider other 'high priority' areas and structure types; this will likely be informed by the success and direction of these initial phases and the value delivered.

A key objective of the project is around knowledge sharing and dissemination. In addition to publication of key findings, part of the project scope is to host an industry conference at the end of the project, inviting the wider industry to attend and explore the findings and their implications, including asset owners, consultants, contractors, NDT providers and technology developers.

3.2 *Data collection, BIM approach and harness of artificial intelligence*

Throughout the NDT trials of the A14 sections, data has been captured in such a way that it can be considered holistically; The aim is to be able to draw conclusions and identify relationships between the findings of different techniques and approaches, tied to the as-found condition of the samples. This is founded on a clear and simple referencing system for the NDT specialists to adhere to, and will be augmented by transposing these data into a single federated 3D model, providing a 'Digital Twin' of the samples. Using typical BIM products such as Autodesk Revit, Navisworks and Bentley BIMTrack, the samples have been recreated as 3D models, upon which the NDT defects can be layered, along with the physical findings. Over and above this, the project team have been carrying out Lidar scans of the samples throughout the hydrodemolition process, providing 3D meshes of the exposed tendons in-situ, which can also be layered into the digital twin and explored in parallel to the NDT findings.

In addition to the exploration of the data by the project team, the goal is to be able to harness new approaches to data review such as Machine Learning and Artificial Intelligence, with the digital twin described above will be a key building block for this work. As noted, industry engagement is a key tenet of the project, and it is intended that further 'Open Invites' may be launched to expose the gathered data to industry AI and ML specialists, allowing the data to be much more broadly explored and different approaches tested.

4 SUMMARY AND CONCLUSIONS

Again, with respect to the NDT trials of the A14, although the data collation and assessment is still underway, a number of interesting observations and avenues have already been

identified, and a broad suite of NDT techniques deployed. The industry engagement has also been very strong, with the NDT providers engaged being both collaborative and inquisitive, which has allowed the collation of information to be much broader than initially anticipated, which will in turn yield greater insights as the project turns to the data assessment.

ACKNOWLEDGEMENTS

The Authors would like to thank all of the parties involved in this project to date. These include the client and project sponsors National Highways (and the funding by National Highways' designated funds for Innovation and Modernisation Fund), the AtkinsRealis and Jacobs joint venture project team, Main works contractor VSL, R&D partners Sentec (supported by Lucy Electric) and Omnia (supported by Vallen Systeme and ARCES) and NDT specialists Mistras, Bridgology, CTS, Allied Associates, Screening Eagle, the Royal Agricultural University (supported by the University of Bristol and Pro-Lite Technology), Hausbots, Hilti, GScan and IFDB.

REFERENCES

AECOM. 2021 Huntingdon Railway Viaduct Research Feasibility (Rev 003). *Highways England*

Atkins. 2020. Post-Tensioned Non-Destructive Testing and Monitoring Techniques. *Highways England*.

Atkins. 2023. Task 164. Management of High Priority Structures – RIS3 Funding Estimate (Rev 2). *National Highways*

Abbas, Y., Have, B. t., Hoekstra, G. I., Douma, A., de Bruijn, D., Olthuis, W., & van den Berg, A. (2015). Connecting to Concrete: Wireless Monitoring of Chloride ions in Concrete Structures. *Procedia Engineering*, *120*, 965–698.

Azizinamini, A. (2017). *Non-destructive testing (NDT) of a segmental concrete bridge scheduled for demolition, with a focus on condition assessment and corrosion dection of internal tendons*. Miami, Florida: Department of Civil and Environmental Engineering, Florida International University.

Azizinamini, A., & Gull, J. (2012). *Improved inspection techniques for steel prestressing/post tensioning strand*. Miami, FL: Florida International University.

Bishop, D., Hendy, C., & Mundell, C. (2017). *M48 Severn Bridge - Acoustic Monitoring Trigger Levels - Working Paper*. Highways England.

Bungey, J., Millard, S., & Shaw, M. (1997). Radar assessment of post-tensioned concrete. *Proceedings of the 7th international conference on structural faults and repair* (pp. 331–339). Eniburgh: Engineering Technics Press.

Burdet, O. (2010). Experience in the long-term monitoring of bridges. *3rd fib International Congress*.

Clark, G. (2010). The development of prestressed concrete bridges. *Concrete Bridge Development Group Conference*. Oxford.

Clark, G. M. (2013). Post-tensioned structures - Imrpoved standards based on lessons learnt. *Proceedings of the Institution of Civil Engineers - Forensic Engineering 166(4)*, 171–179.

Dalla Vedova, M., Elsener, B., & Evangelista, L. (2004). Corrosion Protection and Monitoring of Electrically Isolated Post-Tensioning Tendons. *Proceedings of the Third European Conference on Structural Control*, (pp. S5-47 - S5-50). Vienna, Austria.

Dawood, N., Marzouk, H., Hussein, A., & Gillis, N. (2013). Nondestructive assessment of a jetty bridge structure using impact-echo and shear-wave techniques. *ASCE - Journal of Bridge Engineering 18(8)*, 801–809.

Derobert, X., Aubagnac, C., & Abraham, O. (2002). Comparison of NDT techniques on a post-tentioned beam before its autopsy. *NDT&E International*, *35*, 541–546.

Dizaji, M., Alipour, M., & Harris, D. K. (2020). Subsurface damage detection and structural health monitoring using digital image correlation and topology optimization. *Engineering Structures*.

Elsener, B. (2005). Long Term Monitoring of Electrically Isolated Post-Tensioning Tendons. *Structureal Concrete*, *6*(3), 101–106.

Fisk, P., & Armitage, B. (2019). Nondestructive testing for voided and soft grout in internal post-tensioning ducts. *PTI Journal 15(1)*, 31–35.

Highways England. (2019). Repair and Management of Deteriorated Concrete Highway Structures.

Hong, S. (2015). *GPR-based periodic monitoring of reinforcement corrosion in chloride-contaminated concrete*. Berlin: Technical University of Berlin.

Hoppe, E. J., Novali, F., Rucci, A., Furnagalli, A., Del Conte, S., Falorni, G., & Toro, N. (2019). Deformation monitoring of post tensioned bridges using high-resolution satellite remote sensing. *ASCE - Journal of Bridge Engineering 24(12)*.

Hurlebaus, S., Hueste, M. D., Karthik, M. M., & Terzioglu, T. (2016). *Condition Assessment of Bridge Post-Tensioning and Stay Cable Systems Using NDE Methods*. National Cooperative Highway Research Program (NCHRP). Transportation Research Board (TRB).

Islam, S., & Aumann, C. (2018). Electrically Isolated Tendons - Post-Tension Supplier's Experience. *FHWA Workshop at Lehigh University*. Pennsylvania, United States.

Lu, S., & Ba, H.-J. (2010). Corrosion Sensor for Monitoring the Service Condition of Chloride-Contaminated Cement Mortar. *Sensors*, *10*, 4145–4158.

Marsh, P. S., & Frongopol, D. M. (2007). Lifetime Multiobjective Optimization of Cost and Spacing of Corrosion Rate Sensors Embedded in a Deteriorating Reinforced Concretre Bridge Deck. *ASCE - Journal of Structural Engineering*, *133*(6), 777–787.

Mehrabi, A. (2006). In-service evalutation of cable-stayed bridges, overview of available methods and findings. *ASCE - Journal of bridge engineering*, *11(6)*, 716–724.

Mistras. (2018). *Post tension structures - commentary on NDT and monitoring methods*. Mistras.

Office of Nuclear Regulatory Research. (2015). *Study on Post Tensioning Methods*. United States Nuclear Regulatory Commission.

Ortiz-Aleman, C., & Martin, R. (2005). Inversion of electrical capatitance tomography data by simulated annealing: Application to real two-phase gas-oil flow imaging. *Flow Measurements Instrumentation 16 (2-3)*, 157–162.

RAC Foundation. (2019, January 07). *RAC Foundation*. Retrieved from https://www.racfoundation.org/media-centre/bridge-maintenance-backlog-grows

Ramboll. (2018). Assessment and investigation of post-tensioned bridges in accordance with the DMRB. Guidford, UK: Highways England.

Terzioglu, T., Karthik, M., Hurlebaus, S., & Hueste, M. B. (2019). Nondestructive evaluation of external post-tensioning systems to detect grout defects. *ASCE - Journal of Structural Engineering 145(1)*.

The Internation Federation for Structural Concrete (FIB). (2014). *Bulleting No. 75 - Polymer-duct systems for internal bonded post-tensioning*. FIB.

UK Bridges Board. (2007). *Inspection Manual for Highway Structures - Volume 1: Reference Manual*. London: TSO.

Winkler, J., & Hendy, C. R. (2017). Improved Structural Health Monitoring of London's Docklands Light Railway Bridges Using Digital Image Correlation. *IABSE Structureal Engineering Journal*, *3/2017*.

Woodward, R. J. (1989). Collapse of a segmental post-tensioned concrete bridge. *Transportation Research Record 1211*, 38–59.

Woodward, R. J. (2001). Durability of post-tensioned tendons on road bridges in the UK. *Proceedings of FIP/IABSE workshop on the durability of post tensioning tendons (Ghent University)*. Lausanne: International federation for structural concrete (fip).

WSP. (2017). Task 622: Review of standards for post tensioned brigdes (v 8.0). Highways England.

Bridge Maintenance, Safety, Management, Digitalization and Sustainability – Jensen, Frangopol & Schmidt (eds)
© 2024 The Author(s), ISBN 978-1-032-77040-6
Open Access: www.taylorfrancis.com, CC BY-NC-ND 4.0 license

Advancements in Structural Health Monitoring (SHM): Deformation Area Difference (DAD) method and model updating

T. Čamo
Department of Engineering, University of Luxembourg, Luxembourg

E. Apostolidi & D. Waldmann-Diederich
Institute for Solid Structures, Technical University Darmstadt, Germany

ABSTRACT: As the global population continues to urbanize and rely on essential infrastructure for safe transportation, trade, and everyday life, the significance of SHM of existing structures becomes increasingly evident. Bridges in particular, are the lifelines of transportation networks, connecting communities, facilitating economic activities, and supporting the flow of goods and services. They are subjected to a complex interplay of environmental factors, traffic loads, and aging, making them susceptible to various forms of deterioration and damage over time. Ensuring the structural integrity of bridges is paramount to public safety, environmental sustainability, and economic prosperity. This research focuses on the refinement and enhancement of the DAD method, coupled with a parametric analysis, to investigate the influence of various parameters, including the position of damage within their cross-section. Additionally, the integration of generative design tools in the commercial software Grasshopper enables the determination of damage levels within bridge structures. This integration allows for an additional level of SHM in determining the extent of damage using the DAD method, leading to more precise and actionable results for bridge maintenance and safety management. To validate the proposed methodology, in-situ experiments were conducted on a demonstrator bridge. These experiments employed state-of-the-art technologies, including photogrammetry and Unmanned Aerial Vehicles (UAVs), to capture high-precision deformation on the bridge structures. The combination of these cutting-edge technologies and the refined DAD method with Model Updating ensures a robust and comprehensive approach to bridge health assessment.

1 INTRODUCTION

Infrastructure forms the backbone of the global economy, with bridges standing as pivotal components. However, the combination of aging structures and increasing transportation demands has led to deteriorating conditions in many bridges. To avoid financial and life-threatening risks, many structures need to be assessed. As bridges age, their structural integrity decreases. In Europe concrete bridges are experiencing corrosion issues due to the use of de-icing salt during cold weather(Matos *et al.*, 2023). Moreover, changes in design codes over the years have led to the need for reassessment of many bridges in Europe to determine their load carrying capacity under present loading conditions (Tilly, 1990). Despite these assessments, the focus remains primarily on visual inspection, neglecting the inner structural condition of the bridges.

With an increasing importance for reliable structural evaluation of bridges, various recent studies deal with condition assessment methods. These topics can be divided in two main approaches based on dynamic and static measurements. For instance, (MacLeod and Arjomandi, 2023) present a novel dynamic parametric Bridge Weigh-In-Motion (BWIM) method utilizing experimentally estimated modal parameters for simulating the response of a bridge structure to moving loads. Although validated in a case study, its applicability to different

DOI: 10.1201/9781003483755-433

bridge types is limited and depends on the calibration quality. (Li, Lan and Lin, 2023) are proposing an indirect approach to localize and quantify bridge damage using sensing and parked vehicles. The study presents equations for back calculating residual contact-point responses of the sensing vehicle with suspension and tire damping and sensor-installing errors are deduced to eliminate self-frequencies and suppress the negative effects of road roughness. A novel modal assurance criterion-based objective function using indirectly identified frequencies is proposed to enhance the robustness of damage detection. Despite offering a novel method, challenges persist due to factors, such as road conditions and vehicle properties.

While dynamic methods provide insights into the structural response, they may not capture the full range of behavior exhibited under static loads. (Grandić and Grandić, 2017) propose a damage estimation technique based on the Grey Relation Coefficient (GRC) and curvature of displacement influence lines in beams, requiring sparse measurements. Numerical simulations were conducted to validate the effectiveness of the proposed procedure and experimental validation also confirmed its effectiveness. However, its reliance on a high number of static load experiments increases the experimental effort of the method. Similarly, (Ha and Fukada, 2017) developed an estimation method that utilizes only displacement data for detecting structural damage by introduction of the Displacement Assurance Criterion (DAC) and the Displacement-Based Index (DBI). DAC can properly indicate the occurrence of degradation in structures and DBI can be utilized as a suitable pointer for damage localization, albeit the method is not able to identify the damage severity.

Model updating emerges as a crucial tool, enabling the estimation and quantification of damage extent, crucial for decision-making before retrofitting or rehabilitation. (Jahangiri and Hadianfard, 2019) introduce a Vibration-based Structural Health Monitoring (VSHM) and proposes a Holistic Objective Function (HOF) demonstrating a high accuracy in damage extent and location. Yet, being a dynamic method, VSHM remains sensitive to environmental factors such as temperature, humidity, and noise, potentially impacting results' reliability.

The integration of Drones in bridge assessment has improved data consistency, efficiency, safety, and cost-effectiveness. (Kim *et al.*, 2022) developed an Unmanned Arial Systems-based Bridge Management System for government bridge management and decision-making tasks, while (Jiang, Jáuregui and White, 2008) highlighted the efficacy of close-range photogrammetry for bridge deformation monitoring and geometry measurement. Combining UAVs with close-range photogrammetry enables high precision measurements for hard-to-reach bridge structures and allows for a continuous displacement line.

The Deformation Area Difference (DAD) method, analyzing area differences between the curvature lines of measured and reference models, shows promising results in detecting the presence and location of damage (Erdenebat, Waldmann and Teferle, 2019). With the DAD method only one measurement using a continuous deformation line is sufficient for damage detection, proving the DAD method efficient for existing bridge structures. However, it falls short in assessing the level of damage.

This paper introduces a novel method that incorporates model updating for damage level assessment adding a new level of SHM to the DAD method. Additionally, this paper investigates the influence of a local damage on the assessment, using the DAD method across various positions transversal to the bridge cross-section. The study presents findings from a detailed numerical analysis involving two different bridge structures: a hollow-box-prestressed concrete structure and a multi-girder steel structure. Furthermore, it applies the DAD method and the damage level assessment on a real-bridge experiment.

2 DEFORMATION AREA DIFFERENCE METHOD

The Deformation Area Difference (DAD) method, as presented in Figure 1 as example of a girder bridge with changing cross-section, aims to identify local damage in bridge structures by comparing measured deflections $w_d(x)$ with those from a reference system $w_t(x)$. As shown in Figure 1, the deflection line of a damaged bridge structure is measured under a known loading. The method involves creating a linear finite element model of the bridge structure as

reference system, ensuring a continuous deformation curve considering however stiffness changes due to variations in the cross-section. If available, also an initial measurement could serve as a reference but as usually bridge structures do not have an initial measurement, a FE numerical model is used alternately. The method calculates the inclination angle curves of the structure from measured deflection curves $\varphi_d(x)$ and from the reference model $\varphi_t(x)$ by derivation of the deflection line (equations (1)).

$$w'(x) = \frac{\partial w(x)}{\partial (x)} = \varphi(x) \tag{1}$$

For minor deflections, the second derivative of the deflection curve reflects the structure's curvature (equations (2)). The curvature of the structure, denoted as $\kappa(x)$, can be represented as the ratio of the bending moment M(x) to the stiffness EI(x) (equations (3)). In this equation, the curvature, derived as the second derivative of the deflection curve, and the bending moment from the applied load are known parameters. Consequently, any alteration in stiffness EI(x) should be detectable by analyzing changes in the curvature line.

$$w''(x) = \varphi'(x) \cong k(x) \tag{2}$$

$$\kappa(x) = -\frac{M(x)}{EI(x)} \tag{3}$$

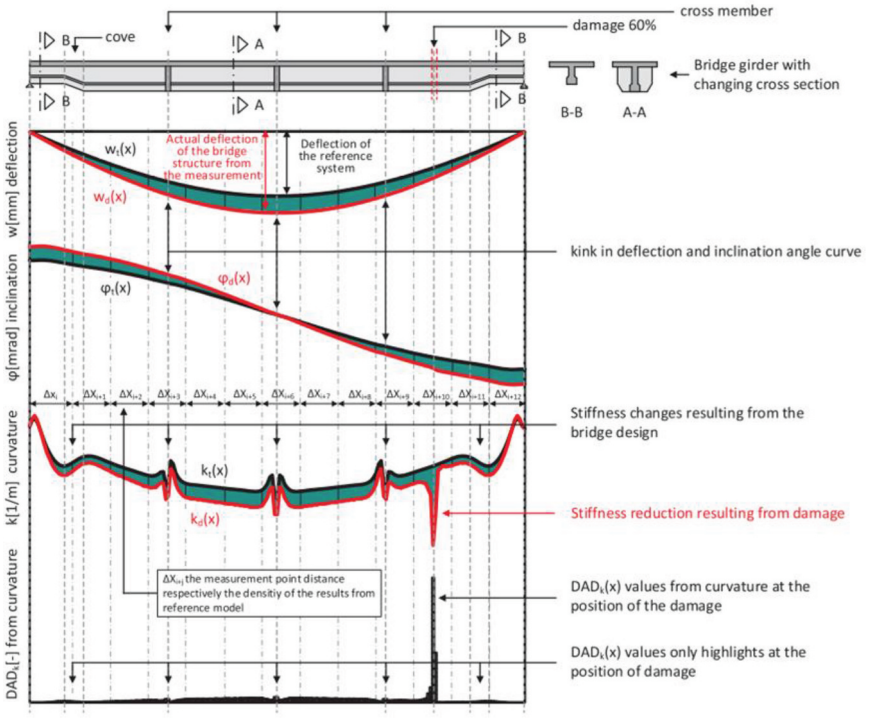


Figure 1. Principle of the Deformation Area Difference (DAD) method (Erdenebat and Waldmann, 2020).

The area between the two curvature lines is divided in discrete elements (ΔX_i). The area of every element is squared to reinforce the effect and divided through the whole area for normalization. This has the advantage that the model does not need to be calibrated, and small deviations of the model from the real structure do not lead to wrong conclusions, as planned stiffness changes are taken into account in the model. By analyzing differences in the area between the theoretical and experimental curvature curves, the DAD method highlights areas

of damage with increased values, filtering out known stiffness-changing elements from the reference model. It is noteworthy that global damage will not be detected with the DAD method. For example, if the support is lowered and a loss of support occurs, the entire static system will change. This results in a continuous deflection change. However, the DAD values indicate stiffness differences between discrete elements. So the DAD values would probably show some irregularities, but not as if there was local damage.

3 DAMAGE LEVEL ASSESSMENT WITH MODEL-UPDATING

The DAD method has demonstrated its reliability in detecting and localizing damage with a single measurement (Erdenebat *et al.*, 2018; Erdenebat, Waldmann and Teferle, 2019; Erdenebat and Waldmann, 2020), serving as the first two level of SHM according to (Rytter, 1993) However, while efficient in localizing damage, the DAD method lacks the capability to assess damage severity, as its values are normalized and result in identical outcomes for varying damage levels. Introducing an additional level of SHM involves implementing an algorithm to estimate the damage level.

Following successful damage localization through the DAD method, a model updating process is initiated (Figure 2). Due to the normalization of DAD values, they prove unsuitable as a fitness function. However, without normalization, the curvature area between the measured and reference system curvature lines can be used as a potential fitness function in the new algorithm. This new algorithm has the function to update the reference model by adjusting the stiffness of individual discrete elements in the locations the DAD revealed to be damaged. The

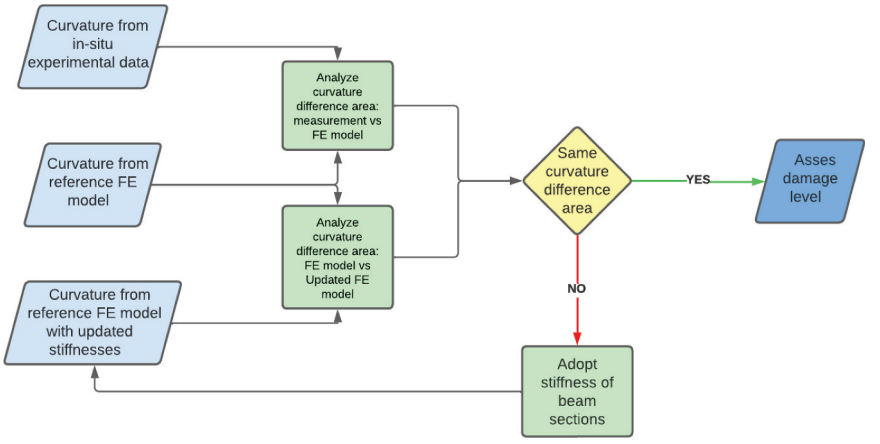


Figure 2. Flowchart of model updating method for damage level assessment.

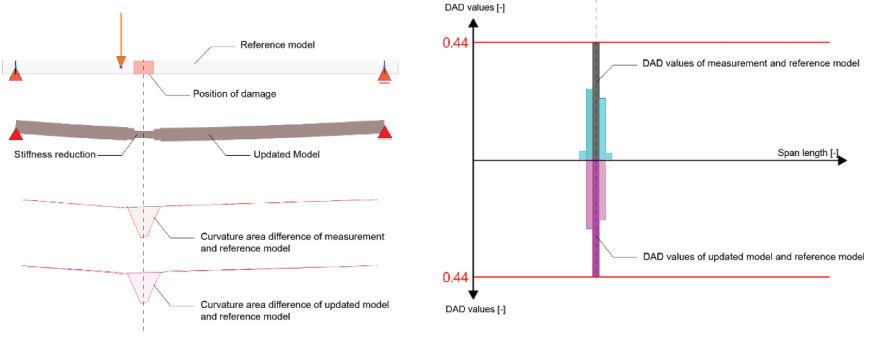


Figure 3. Damage level assessment example for a reinforced concrete beam.

algorithm iterates by modifying the stiffness of the reference model until the area between the curvature lines of the updated and reference models aligns with the area between the curvature line based on the measured deflection line and the one of the reference model. Figure 3 illustrates the reference model, pinpointing the damage location, while the updated model reflects a stiffness reduction at the damage site.

The curvature difference area of measurement and reference model and updated model and reference model are shown resulting to DAD values localizing both the damage position.

4 DAMAGE LEVEL ASSESSMENT WITH MODEL-UPDATING PARAMETRICAL NUMERICAL ANALYSIS

To better understand the influence of local damage to the entire cross section and enhance the in-situ experimental set-up, an extensive parametric analysis is carried out. This paper presents the model of a hollow-box prestressed reinforced concrete structure (Figure 4) and the model of multi girder steel bridge (Figure 5), with both bridges being based on real bridge structures in Luxembourg. The hollow box bridge structure has three spans, a total length of 150 m and a width of 10,50 m, while the steel bridge is a single span bridge with a length of 30 m and a width of 10 m. Local damages (D1 to D4 in Figure 4) are introduced to the numerical model and the DAD method is assessed using an undamaged reference model and the damaged numerical model at different axes of the cross-sections. For the hollow-box bridge the investigated damage positions are presented in Figure 4 as red areas and the measurement axes for the application of the DAD method is shown with numbers. For the steel bridge each girder is damaged individually, and the DAD method is carried out with deflections of all different girders. Local damage is simulated for both models with a 30% reduction of the bending stiffness within the predefined damage area.

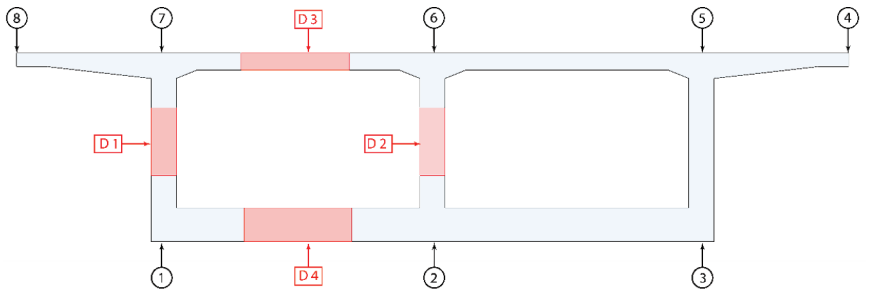


Figure 4. Cross section of hollow box prestressed concrete bridge structure.

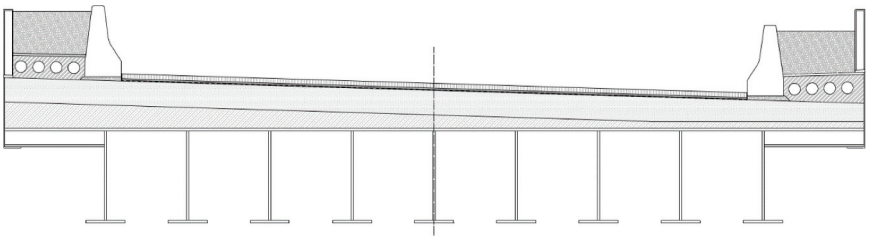


Figure 5. Cross-section of multi girder steel bridge.

Figure 6 shows exemplary the DAD values as a bar graphs in all 8 measurement axes for the second span of the hollow box prestressed concrete bridge, resulting from damage in mid-span in the lower slab (D4 in Figure 4). Figure 7 visualized the DAD values of all girders for

a damage of the second girder at midspan (red area) for the multi girder steel bridge. The DAD values are not of interest here, only the course of the bar graphs is important to highlight the influence. While the local damage of the hollow-box structure leads to successful location in six of eight measurement axes (which are shown as numbers in Figure 4), the damage of the steel structure can be only located with the DAD values based on the deflection line of this same girder. So, the curvature line of the different girders behaves more independent from each girder for the steel bridge, leading to very small influence of local damage to the neighboring girders. In return, it can be stated, that the influence of local damage on neighboring areas is higher for cross-sections with a compact structural behavior. Consequently, less measurement axes are necessary for more compact cross-sections (e.g., hollow box) to detect local damage.

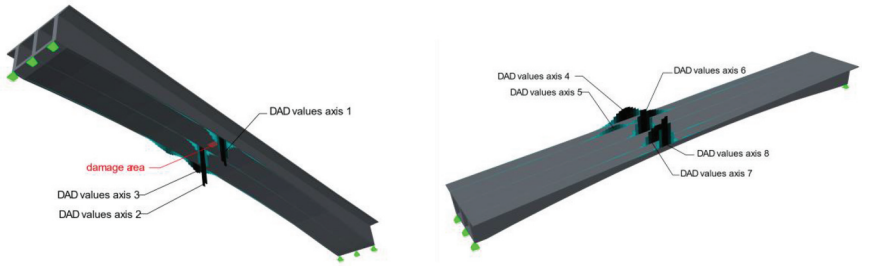


Figure 6. DAD values as bar graphs at different measurement positions; 3D bottom (left) and top view (right) of a hollow box prestressed concrete bridge.

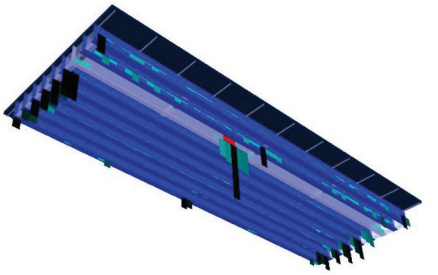


Figure 7. DAD values as bar graphs at different measurement positions; 3D bottom view of a multi girder steel bridge.

5 IN-SITU EXPERIMENT

While the DAD method has been proven in laboratory tests (Erdenebat, Waldmann and Teferle, 2019), a real bridge experiment in Altrier (Luxembourg) (Erdenebat and Waldmann, 2020) affirmed its applicability. However, further studies are necessary to validate its efficiency for damaged bridges.

In this study, the DAD method is applied to a previously parametrically analyzed steel bridge, as described in Section 4 (Figure 5). The static load deflection measurement employed photogrammetry, using targets installed on the girder for continuous deflection measurement (Figure 8) using a programmed UAV. The photogrammetric targets ensure a very high accuracy, around 0.11 mm (Erdenebat and Waldmann, 2020), as high accuracy is required for the DAD method. Since the parametric study revealed that local damage might not impact the curvature of other girders, only one girder is investigated here due to time and budget constraints. Reference targets on the abutments serve as a scale and coordinate system. Two measurements, unloaded and loaded, were conducted, with six heavy trucks as loading.

Subtracting the measured deflection line generated for the unloaded system from the one from the loaded system, a continuous displacement line is provided. The obtained curve is compared with that of a reference FE model analyzed under the same load conditions.

Using the collected data, the DAD method is applied. Figure 9 presents the DAD values in a bar graph, with darker shades indicating higher values. Damage is considered when the value exceeds a predefined boundary (Erdenebat and Waldmann, 2020). In this analysis, no DAD value surpasses the outlier boundary, suggesting no definitive damage detection. However, the highest value hints a potential damaged area. Comparison with the bridge's condition reveals significant corrosion in the girder and cross girder at the DAD method identified point.

The subsequent damage level assessment estimated a 13% reduction in bending stiffness, but it's noteworthy that smaller damages are susceptible to greater noise influence. As the ratio between curvature areas from small damages to noise diminishes, it tends to over- or underestimate damage levels. Further investigations are needed to comprehend and address this discrepancy.



Figure 8. Measurement of deflection using a UAV for a steel bridge structure in Soleuvre, Luxembourg (left); located damage position indicating corroded girder and cross beam (right).

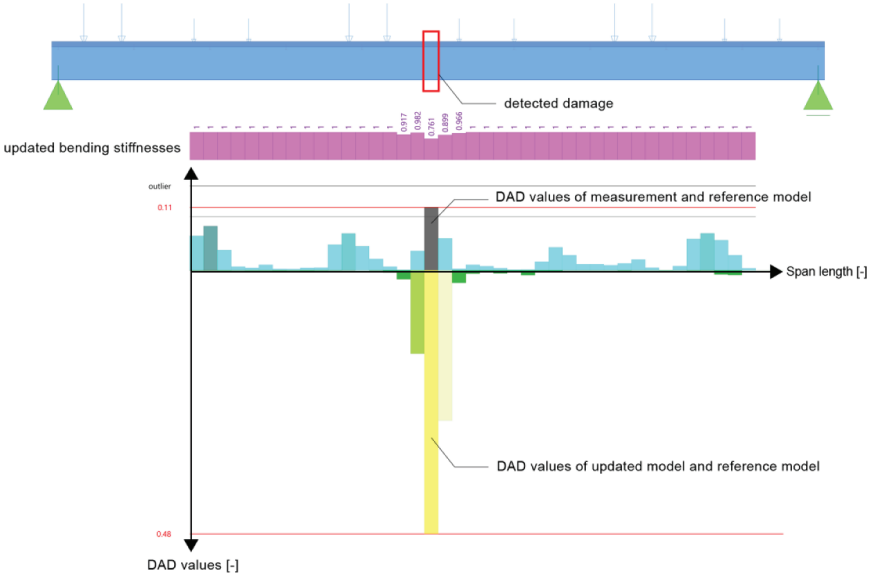


Figure 9. Localized damage & damage level estimation of a steel bridge structure in Soleuvre, Luxembourg.

6 CONCLUSIONS

The present work introduces a novel method using model updating for assessing damage levels. An extensive parametric numerical model illustrates the impact of local damage on the overall

structure. The quantity of measurements needed decreases with a more compact cross-section. The DAD method can detect damage along various measurement axes in a compact hollow box cross-section. However, in a multi-girder steel bridge, the DAD method only identifies damage within the affected girder, with the remaining girders showing no damage indication. A real bridge experiment confirmed localized damage with visual evidence. The novel damage level assessment method estimates a 13% reduction in the structure's bending stiffness due to the damage.

ACKNOWLEDGMENTS

The authors would like to express their gratitude to the "Administration des Ponts et Chaussées" of Luxembourg for providing the opportunity to carry out experiments on a real bridge. Further gratitude is expressed to Mr. Harald Krause, PMS Photo Mess Systeme AG for his professional advice and support on close-range photogrammetry. We are also very thankful to our support engineers of the FSTM Cédric Bruyere and Vincente Reis-Adonis for measuring the reference points.

REFERENCES

Erdenebat, D. *et al.* (2018) 'The Deformation Area Difference (DAD) method for condition assessment of reinforced structures', *Engineering Structures*, 155, pp. 315–329. Available at: https://doi.org/10.1016/j.engstruct.2017.11.034.

Erdenebat, D. and Waldmann, D. (2020) 'Application of the DAD method for damage localisation on an existing bridge structure using close-range UAV photogrammetry', *Engineering Structures*, 218, p. 110727. Available at: https://doi.org/10.1016/j.engstruct.2020.110727.

Erdenebat, D., Waldmann, D. and Teferle, N. (2019) 'Curvature based DAD-method for damage localisation under consideration of measurement noise minimisation', *Engineering Structures*, 181, pp. 293–309. Available at: https://doi.org/10.1016/j.engstruct.2018.12.017.

Grandić, I.Š. and Grandić, D. (2017) 'Estimation of damage severity using sparse static measurement', *Journal of Civil Engineering and Management*, 23(2), pp. 213–221. Available at: https://doi.org/10.3846/13923730.2015.1027256.

Ha, T.M. and Fukada, S. (2017) 'Nondestructive damage detection in deteriorated girders using changes in nodal displacement', *Journal of Civil Structural Health Monitoring*, 7(3), pp. 385–403. Available at: https://doi.org/10.1007/s13349-017-0231-x.

Jahangiri, M. and Hadianfard, M.A. (2019) 'Vibration-based structural health monitoring using symbiotic organism search based on an improved objective function', *Journal of Civil Structural Health Monitoring*, 9(5), pp. 741–755. Available at: https://doi.org/10.1007/s13349-019-00364-5.

Jiang, R., Jáuregui, D. V. and White, K.R. (2008) 'Close-range photogrammetry applications in bridge measurement: Literature review', *Measurement: Journal of the International Measurement Confederation*, 41(8), pp. 823–834. Available at: https://doi.org/10.1016/j.measurement.2007.12.005.

Kim, I.H. *et al.* (2022) 'A Comparative Study of Bridge Inspection and Condition Assessment between Manpower and a UAS', *Drones*, 6(11), pp. 355–355. Available at: https://doi.org/10.3390/DRONES6110355.

Li, Z., Lan, Y. and Lin, W. (2023) 'Indirect damage detection for bridges using sensing and temporarily parked vehicles', *Engineering Structures*, 291(May). Available at: https://doi.org/10.1016/j.engstruct.2023.116459.

MacLeod, E. and Arjomandi, K. (2023) 'Dynamic bridge weigh-in-motion using estimated modal parameters from ambient vibration tests', *Engineering Structures*, 289(May), p. 116254. Available at: https://doi.org/10.1016/j.engstruct.2023.116254.

Matos, J.C. *et al.* (2023) 'Comparison of Condition Rating Systems for Bridges in Three European Countries', *Applied Sciences 2023, Vol. 13, Page 12343*, 13(22), p. 12343. Available at: https://doi.org/10.3390/APP132212343.

Rytter, A. (1993) 'Vibrational Based Inspection of Civil Engineering Structures'. Available at: https://vbn.aau.dk/en/publications/vibrational-based-inspection-of-civil-engineering-structures (Accessed: 23 November 2023).

Tilly, G.P. (1990) 'Evaluation of Bridges — European Perspective', *Bridge Evaluation, Repair and Rehabilitation*, pp. 367–377. Available at: https://doi.org/10.1007/978-94-009-2153-5_27.

Bridge Maintenance, Safety, Management, Digitalization and Sustainability – Jensen, Frangopol & Schmidt (eds)
© 2024 The Author(s), ISBN 978-1-032-77040-6
Open Access: www.taylorfrancis.com, CC BY-NC-ND 4.0 license

A study on hammering inspection for unreinforced concrete based on wearable microphone measurement

K. Takeya, S. Kobayashi, A. Akutsu, Y. Ito & E. Sasaki
Civil and Environmental Engineering, Tokyo Institute of Technology

ABSTRACT: In this study, the hammering method for concrete structures using wearable devices was investigated. First, comparative studies of several wearable microphones revealed that the response varied depending on where the microphones were attached. As a result, the helmet type demonstrated the best performance. Next, features of sound pressure and input force waveforms were calculated and evaluated for their importance in defect detection. Then, a fully connected neural network was constructed and the evaluated features were selected as input parameters. Cross-validation was performed using the dataset obtained from a concrete wall with various artificial voids. As a result, the defect detection rate was around 94%, including voids at 10 cm depth at maximum.

1 INTRODUCTION

Initial inspections of concrete structures mainly involve visual inspection. However, since it is necessary to detect defects inside concrete that cannot be confirmed by visual inspection, the hammering method, ultrasonic method, or thermal infrared method are used for destructive inspection. A hammering test has been used in practice for a long time because it can be easily carried out using only a hammer as the specified instrument. The hammering method is widely used in concrete structures to perform periodic inspections (Asakura et al. 2003). However, skilled inspectors are in short supply due to the aging population. In addition, the result of human-based inspection varies even by skilled inspectors because of the human auditory characteristics (Yasuda 2023). Personnel and skills become more difficult to secure and demands for the automation technology of the hammering method that anyone can perform, regardless of their skill level are increasing. Therefore, research has been carried out to automate the detection of defects in concrete structures by measuring hammering sound responses with sensors.

On the other hand, the movement to utilize artificial intelligence (AI) in the civil engineering field is remarkable, and various approaches have been proposed (McMillan et al. 2022). Emoto et al. (2020) conducted a comparative study of AI methods that are effective in determining hammering sound response. Learning and identification were performed using seven AI methods such as logistic regression and decision trees, using the frequency domain obtained by FFT as a feature quantity. Takeya et al. (2021) applied fully connected neural networks to detect void failures in the concrete wall. However, these methods have limitations in measurement, fixing the microphone on a tripod, or controlling the distance from the striking position.

In recent years, fully automated inspection methods by robotics technology have been studied (Menendez et al. 2018). However, it is difficult to introduce robotics technology due to the introduction and operation costs for local governments that manage various civil engineering structures. Because of flexibility in the various fields, human-based inspection will continue to be a common method.

DOI: 10.1201/9781003483755-434

In this study, the wearable microphone measurements for the hammering inspection were investigated as a premise of the human-based inspection. The targets were void defects in concrete walls up to approximately 10 cm in depth that are difficult to detect even by experienced inspectors. By comparing body mounts to attach a microphone to the human body, their characteristics were investigated experimentally. Finally, a neural network for defect detection was proposed, and cross-validation tests examined its accuracy.

2 COMPARISON OF WEARABLE METHODS

2.1 *Attachment methods of a microphone to the human body*

With multiple proposals of wearable device measurement methods, the response characteristics were compared by measurement experiments. Two objectives were focused on considering the wearable method. First, weight reduction was prioritized over high functionality since inspectors are not used to increasing instrument weight. Second, it was important to ensure workability to avoid contact between the arm and the microphone when hammering sounds were measured. The five different mount types are shown in Figure 1. Table 1 shows the specification of measurement equipment. The impact load was measured by an impact hammer (Model: 086C03, 2.25 mV/N) and sound pressure was measured by a microphone (Model: 378B02, 50 mV/Pa). The microphone was attached to the body through a shock-absorbing mount (Figure 1). The sampling frequency was 50 kHz.

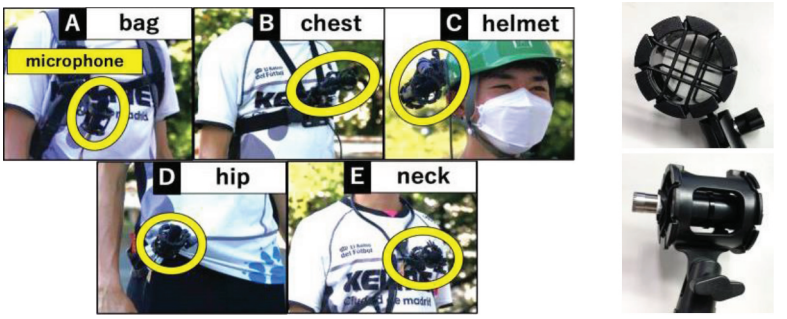


Figure 1. Proposed mount types and the shock-absorbing mount of the microphone.

Table 1. Specification of measurement equipment.

Microphone	378B02 (PCB)	Impact hammer	086C03 (PCB)
Sensitivity	50 [mV/Pa]	Sensitivity	2.25 [mV/N]
Frequency range	3.75 ~ 20000 [Hz]	Head weight	0.16 [kg]

2.2 *Outline of comparison measurement*

Measurements were made on the concrete wall as shown in Figure 2. The hammer was struck 10 times each in the case of hitting the area above the shoulder (high) and the case of hitting the area below the shoulder (low). The sound pressure data were obtained with each mount type of microphone. The left figure in Figure 2 shows an example of measured sound pressure data. The sound pressure response of each impact was extracted from the measurement data, and the feature values were calculated. The time-domain features are listed in Table 2.

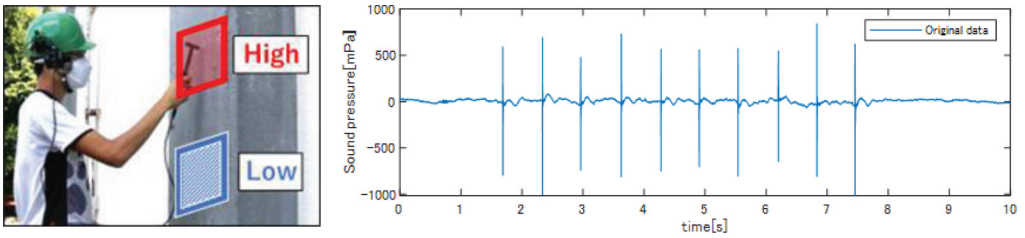


Figure 2. Example of sound pressure data. (Mount type: Helmet, hitting area: high.).

Table 2. Time-domain features of sound pressure.

Features in time-domain	Unit	Notation
Absolute area of sound pressure	mPa.sec	p_area
Absolute maximum of sound pressure	mPa	p_absmax
Absolute of first peak of sound pressure	mPa	p_peak

2.3 *Results and discussion*

The sound pressure response depends on the magnitude of the impact load. Therefore, we proceeded with the discussion hereafter using values normalized by dividing the sound pressure feature by the maximum value of the impact load. To perform a relative evaluation, the ratios to the average value of all methods (value divided by the average value of all methods) were calculated as shown in Table 3. If the ratio is smaller than 1, it indicates a smaller response compared to others.

The difference in sound pressure response was caused by the directivity of the microphone. The microphone's sound collection direction is the same for the helmet and hip mount type. (Figure 3). The bag, chest, and neck mount types have a microphone between the high and low impact points and are oriented in the middle so that it is not biased toward either side (Figure 4). As a result, the microphone was oriented halfway, and it is thought that there were places where the response could not be picked up properly.

There were no significant differences in frequency characteristics between the methods. However, a peculiar frequency peak was observed in the case of neck mount and hip mount as shown in Figure 5. It is thought that the neck mount was loosely constrained to the body, and the hip mount was likely to transmit body vibrations to the microphone when hitting low positions.

Table 4 shows a summary of the differences in the wearable methods of the microphone. The closer the distance between the strike positions and the microphone, the easier it was to obtain a response. However, even when the distance was close, the response was small. This was thought to be an effect of the directivity of the microphone. Therefore, it is necessary to consider the positional relationship between the striking positions and the microphone to obtain appropriate responses. On the other hand, there was no significant difference in the frequency response. However, when the microphone fixation was loose, the effect of noise due to body vibration was considered to appear in the frequency distribution. As a result, the helmet mount type was selected.

Table 3. Normalized values of time-domain features (ratio to the average value of all methods).

	Bag		Chest		Helmet		Hip		Neck		
Mount type position	high	low	high	low	high	low	high	low	high	low	mean
p_area	0.94	0.96	0.95	0.84	0.88	1.19	0.72	1.25	1.33	0.93	1.00
p_absmax	1.17	0.77	1.20	0.65	0.93	0.69	0.41	1.86	1.47	0.86	1.00
p_peak	0.69	1.20	0.97	0.95	1.65	1.03	0.60	0.87	0.82	1.21	1.00
Mean	0.95		0.93		1.06		0.95		1.10		1.00

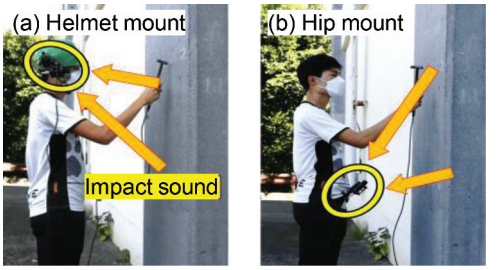


Figure 3. Measuring cases when the microphone was facing the impact positions.

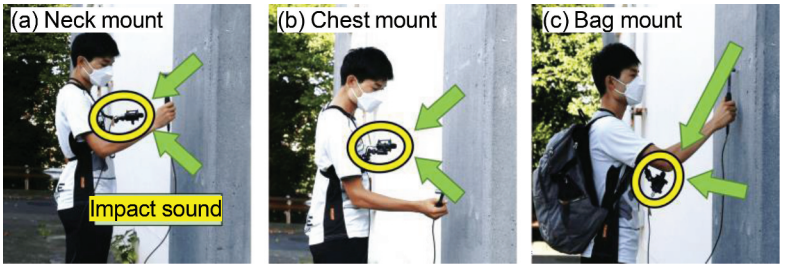


Figure 4. Measuring cases when the microphone was not facing the impact positions.

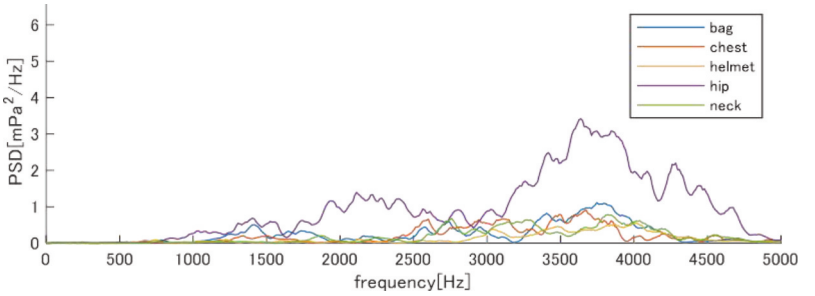


Figure 5. Example of power spectrum density when hitting low positions.

Table 4. Summary of response characteristics.

Mount type	Bag	Chest	Helmet	Hip	Neck
Gain	▲	▲	○	▲	○
Noise immunity	○	○	○	▲	▲
Directional stability	▲	▲	○	○	▲

3 DEFECT CLASSIFICATION WITH A WEARABLE MICROPHONE

The wearable device was used to measure and discriminate defects using neural networks (NNs). Based on the classification results, the effects of advantage (large sound pressure response) and disadvantage (disorder caused by wearables) due to wearables on the classification were discussed.

3.1 *The concrete wall specimen with void failures and measurement of data sets*

The equipment was similar in Table 1. The specification of the impact hammer used (Type: 086D05, 0.23 mV/N) in the experiment is shown in Table 5. The head size of the impact hammer increased to improve the S/N ratio. Figure 6 shows the power spectrum density of the sound pressure response by two impact hammers (086C03 and 086D05). The microphone was fixed at a position 30 cm from the impact position, and the sound pressure was measured for 60 seconds each. The large hammer can induce higher sound pressure responses at around the 2000 to 3000 Hz frequency range. Although it is necessary to select a hammer by considering a frequency band that is easy to distinguish depending on the type of defect, in this study we decided to use a larger hammer (086D05) while considering the magnitude of the impact load.

Table 5. Specification of the impact hammers.

Impact hammer	086C02 (PCB)	086D05 (PCB)
Sensitivity	2.25 [mV/N]	0.23 [mV/N]
Head weight	0.16 [kg]	0.32 [kg]
Resonant Frequency	>22 [kHz]	>22 [kHz]

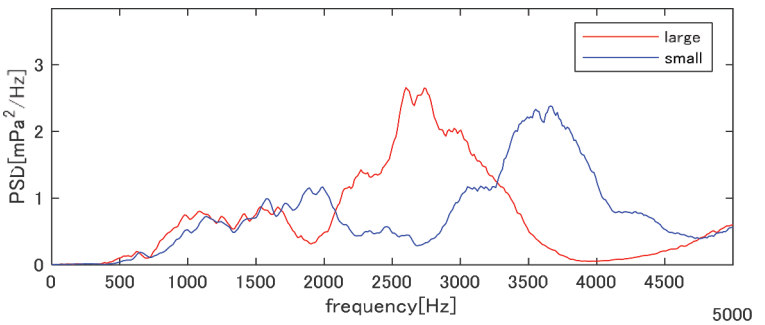


Figure 6. Power spectrum density of the sound pressure response by different impact hammers.

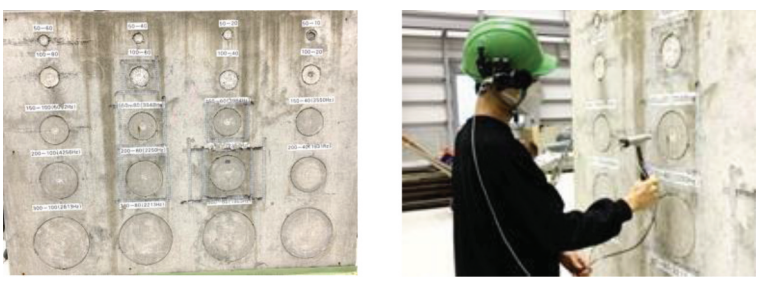


Figure 7. The concrete wall specimen with various artificial voids and example of measurement process. (Mount type: helmet, target: R15-d08.).

The concrete wall specimen used in the experiment was the circular defect model used by Takeya et al.(2021). Figure 7 (left) shows the concrete wall specimen. The specimen had artificial voids in which a disk-shaped Styrofoam (thickness: 25 mm) was embedded, and each had a different depth and diameter. The maximum depth was 10 cm which was difficult to detect even by expert inspectors.

The 18 defect areas were struck for 20 seconds each, and the 12 sound areas were struck for 30 seconds each, so the total number of data was similar, as shown in Table 6. 'R' means diameter (cm), and 'd' means depth (cm) of defects. For example, R20-d08 indicates that a void with diameter R = 20 cm is embedded at depth d = 8 cm. Figure 7 (right) shows a photo of the measurement process.

Table 6. A list of void failures and number of data samples.

Voids	Num. samples	Void	Num. samples
R05_d02	40	R15_d08	59
R05_d04	47	R15_d10	56
R05_d06	56	R20_d04	56
R10_d02	57	R20_d04	59
R10_d04	54	R20_d04	57
R10_d06	61	R20_d04	58
R10_d08	55	R30_d06	61
R15_d04	55	R30_d08	55
R15_d06	66	R30_d10	55
Total number of samples of void defect areas			1007 samples
Total number of samples of sound areas			880 samples

3.2 *Evaluation of feature values*

The time-domain features are shown in Table 7. The frequency-domain features are calculated from the power spectrum density (PSD). The spectrum was divided into frequency bands of 500 Hz, and features were calculated in each frequency band (0~500Hz, 500~1000Hz, . . ., 4500~ 5000Hz). The correspondence tables of frequency-domain features and their frequency bands are shown in Table 8. For example, the average amplitude of PSD in the frequency band 1000 ~ 1500 Hz is expressed as "p_freq_mean_3".

Table 7. Correspondence table for time-domain feature notation.

features	Unit	Notation	features	Unit	Notation
Absolute of first peak	mPa	p_peak	Average force	kN	f_mean
Absolute area	mPa.ms	p_area	Impulse force	kN.s	f_impulse
Absolute maximum	mPa	p_absmax	Duration of impact force	ms	f_duration
Maximum force	kN	f_peak	Distance from impact point	m	distance

Table 8. Correspondence table for frequency domain feature notation and their frequency bands.

Features of PSD	Unit	Notation
Maximum amplitude	(mPa)2/Hz	p_freq_max
Average amplitude	(mPa)2/Hz	p_freq_mean
Area	(mPa)2	p_freq_area
Average peak frequency	Hz	p_freq_pmean
Peak centroid frequency	Hz	p_freq_pcentroid
Area centroid frequency	Hz	p_freq_acentroid

No.	Freq. band	No.	Freq. band
1	0.0~0.5 kHz	5	2.0~2.5 kHz
2	0.5~1.0 kHz	6	2.5~3.0 kHz
3	1.0~1.5 kHz	7	3.0~3.5 kHz
4	1.5~2.0 kHz	8	3.5~4.0 kHz

Table 9. A list of feature s election algorithms.

Algorithms	MATLAB functions	Num. of trials	Evaluation value
Chi-square test	fscchi2	1	Predictor score: -log(p) > 0
MRMR	fscmrmr	1	Confidence score: ρ ($0 < \rho < 1$)
ReliefF	relief	5	Weight: $W > 0$
Nearest neighbor analysis	fscnca	100	Weight: $W > 0$
Linear discriminant analysis model	fitcdiscr	100	Delta threshold: δ ($\delta > 0$)
Ensemble classification of decision trees	fitcensemble	50	Predictor importance: - $dj/\sigma j > 0$

Table 10. Results of feature evaluation by the feature selection algorithms.

Rank	Features			Score
1st ~ 3rd	f_mean	f_impulse	f_peak	> 0.68
4th ~ 6th	distance	p_freq acentroid 4	p_freq mean 2	> 0.63
7th ~ 9th	p_peak	p_freq mean 4	f_duration	> 0.56
$10^{th} \sim 12^{th}$	p_area	p_freq area 2	p_freq pmean 3	> 0.50
$13^{th} \sim 15^{th}$	p_freq mean 3	p_freq area 3	p_freq max 1	> 0.47
$16^{th} \sim 18^{th}$	p_freq pcentroid 2	p_freq acentroid 3	p_freq area 4	> 0.40
$19^{th} \sim 21^{st}$	p_freq mean 4	p_freq pcentroid 4	p_freq pmean 1	> 0.38
$22^{nd} \sim 24^{th}$	p_freq pmean 7	p_absmax	p_freq acentroid 6	> 0.36

The time-domain features and frequency-domain features were evaluated in terms of their importance for detecting void defects. The feature evaluation was based on the method of Takeya et al.(2021). The importance scores or weights were calculated using the chi-square test, Minimum Redundancy Maximum Relevance (MRMR), ReliefF, Nearest neighbor analysis. The delta thresholds for linear discriminant analysis models and the predictor importance for ensemble classification of decision trees were also calculated. Table 9 shows an overview of the six feature selection algorithms used to score the features. The evaluation values of each algorithm are normalized by dividing them by their maximum value to integrate the evaluation. The top 24 features are shown in Table 10. As a result, the features of impact load (average, impulse, maximum, and duration of impact force) were evaluated with high importance. The frequency-domain features in lower frequency bands by 2 kHz were also ranked high.

3.3 *Defect detection using a fully connected neural network*

Figure 8 and Table 11 show the configuration and structure of the neural network (NN) used for defect detection. The number of input features was decided by trial and error, and the top 24 features were used. The number of hidden layers was two to prevent over-learning.

Cross-validation was performed to obtain the percentage of correct classifications. In screening tests for defects inside concrete using hammering tests, the priority is to detect all defects, so recall is more important than precision. The defect detection rate has the same meaning as the recall rate. Recall rates for each target void are shown in Table 11. No defect was overlooked if the recall rate was 100 %. The recall rate was high even for deep voids (d08 and d10). This indicates that it is possible to detect defects at the same level as experienced inspectors. The average recall rate was 94.2 %. On the other hand, the total accuracy was 86.7%. This fact shows that the trained neural network performed a safe diagnosis for defect detection. The recall rate was low, especially in the case R30-d06 where the defect diameter is large at 30 cm and the depth is 6 cm, the hammering sound response tends to be different from the sound part. It is supposed that it is difficult for neural networks to predict defects that deviate from the training data. The defect detection accuracy will improve by collecting a wide range of training data.

4 CONCLUSIONS

In this study, to propose the hammering method with wearable device measurements, experimental studies were conducted considering the difference in hammering sound response measurement by mount type. The effective feature values were considered, and the defect detection method was proposed by using the neural network. The findings are summarized as follows.

A comparative study of five mount types was conducted. It was shown that the hammering sound response varies depending on the attachment method and position of the microphone by comparing the feature values. If the microphone was not facing the direction of the strike, the response tended to be small even if the microphone was close. As a result, the helmet mount type has an advantage for measuring the hammering sound response.

The time-domain and frequency-domain features were proposed, and the effective feature values were considered by combining the results of six feature selection algorithms. The impact force

features such as impulse, maximum value, and duration showed high importance. The frequency-domain features in the low-frequency band by 2kHz seemed effective for defect detection.

The fully connected neural network was proposed and learned using the measured data at the concrete wall specimen with various artificial voids. As a result of cross-validation, it can be said the average recall rate of defect detection was around 94 %, including voids at 10 cm depth in maximum. On the other hand, the recall rate decreased for defects with diameters and depths that could not be interpolated using the learned defect data. There is room to improve the classification accuracy by collecting various training data including deeper void than 10 cm for example.

Input / hidden / output layers	1 input / 2 hidden / 1 output layers
Input data	24 features
Output results	defect or sound
Activation function	Tan-sigmoid
Learning function	SGDM
Learning rate	0.0008
Momentum	0.90
Mini batch size	256
Loss function	Cross entropy

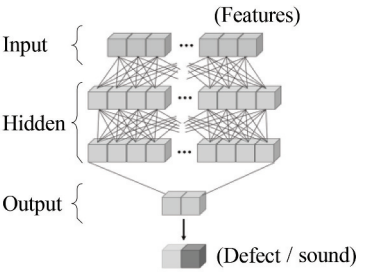


Figure 8. Configuration of neural network (NN).

Table 11 . Recall rate of defect detection by cross-validation.

		Diameter of voids [cm]					
		R05	R10	R15	R20	R30	Average
Depth of voids [cm]	d02	97.5	94.7	—	—	—	96.1%
	d04	97.9	100.0	100.0	100.0	—	99.5%
	d06	82.1	100.0	98.5	96.6	72.1	89.9%
	d08	—	74.5	100.0	96.5	96.4	91.9%
	d10	—	—	94.6	100.0	94.5	96.4%
Average		92.5%	92.3%	98.3%	98.3%	87.7%	94.2%

REFERENCES

Asakura, T. & Kojima, Y. 2003. Tunnel maintenance in Japan. *Tunnel and Underground Space Technology*, 18(2): 161–169. https://doi.org/10.1016/S0886-7798(03)00024-5

Emoto, H. & Baba, Y. & Asano, H. & Nagase Y. 2020. Data of AI Method on Hammering Sounds at Concrete Bridge, *Informatics, and Infrastructure*, J1, 514–521. https://www.jst-age.jst.go.jp/article/jsceiii/1/J1/1_514/_article/-char/en

McMillan, L. & Varga, L. 2022. A review of the use of artificial intelligence methods in infrastructure systems. *Engineering Applications of Artificial Intelligence*, 116: 105472. https://doi.org/10.1016/j.engappai.2022.105472

Menendez, E. & Victores, J.G. & Montero, R. & Martínez, S. & Balaguer, C. 2018. Tunnel structural inspection and assessment using an autonomous robotic system. *Automation in Construction*, 87: 117–126. https://doi.org/10.1016/j.autcon.2017.12.001

Takeya, K. & Sasaki, E. & Fan, S. & and Ito, Y. 2021. Evaluation of Features in Time Frequency Domain and Improvement of Sensitivity and Efficiency of Hammering Method using Neural Networks, *Intelligence, Informatics, and Infrastructure*, J2: 721–732. https://doi.org/10.11532/jsceiii.2.J2_721

Yasuda, N. 2023. Hammering sound of concrete with defects and spalling risk, *Tunnelling and Underground Space Technology*, 131: 104789. https://doi.org/10.1016/j.tust.2022.104789

GS17: BRIDGE SAFETY - Advanced computer simulation


Taylor & Francis
Taylor & Francis Group
http://taylorandfrancis.com

Bridge Maintenance, Safety, Management, Digitalization and Sustainability – Jensen, Frangopol & Schmidt (eds)
© 2024 The Author(s), ISBN 978-1-032-77040-6
Open Access: www.taylorfrancis.com, CC BY-NC-ND 4.0 license

Simulation of cylinder impact damage by peridynamics

J.J. Zhang, Z.C. Pan & H.C. Chang
Tongji University, Shanghai, China

ABSTRACT: Impact damage to bridges may lead to immense economic losses and significant environmental impacts. Traditional continuum mechanics is in some ways ill-suited to the solving of discontinuity problems in impact damage. The peridynamics (PD) theory has been regarded as a promising method for predicting impact damage. PD has been attractive to researchers as it is a non-local formulation in an integral form, unlike the local differential form of classical continuum mechanics. The hypervelocity impact of cylinders on a rigid boundary test is a classic example to validate the accuracy of the simulation method. In this study, a PD-based 3D discrete particle model of the cylinder impact on a rigid boundary is developed to simulate the process of impact damage. The predictions concerning the damage growth of the cylinder are compared with the previous experiments. The results of the proposed method agree well with the previous experiments.

1 INTRODUCTION

Recently, bridges have been subjected to an increasing frequency of impact loads, often resulting in serious consequences. Impact on bridge components can lead to concrete spalling and reduced load-bearing capacity. However, predicting material damage under high-speed impact has always been challenging. Therefore, it is necessary to study numerical simulation methods for material impact damage. In this paper, peridynamics has been used to simulate high-speed impact models to demonstrate the potential of this method in predicting bridge impact damage.

On the basis of traditional continuum mechanics, various numerical methods have been proposed to analyze the mechanical properties of materials (Fang et al. 2023, Zeng & Liu 2018, Vu-Bac et al. 2013). However, the presence of discontinuities is inconsistent with the continuity assumption and limits their application. Peridynamicss (Silling & Askari 2005, Silling et al. 2007, Silling 2000) (PD) transforms the differential equations of traditional continuum mechanics into integral forms for solution, allowing for the description of natural material damage. Peridynamicss has been widely used to predict and analyze failure behavior in various fields, such as fluid–structure interaction (Chang et al. 2023, Chang et al. 2022), quasi-static, impact failure (Liu et al. 2017, Baber et al. 2018), corrosion and fatigue damage, and multi-field coupling.

The cylinder impact on a rigid boundary problem is a classic case used to verify the accuracy of numerical simulations. However, the numerical simulation of the Taylor impact test for a cylinder impact on a rigid boundary was initially proposed by Taylor (1948) to determine the effect of impact velocity on the material's dynamic yield stress. In the past few decades, this type of test has been used to probe the response and damage of metals and alloys under high-speed impact. The constitutive model of materials under high-speed impact becomes very complex, and the Taylor test is particularly suitable for studying the dynamic failure of materials and validating damage models. Therefore, the Taylor test is widely used to assess the accuracy of numerical simulation methods and various constitutive models.

Currently, peridynamics has not been applied to the numerical simulation of the Taylor impact test. This paper uses conventional state-based peridynamics to numerically simulate the Taylor impact experiment, predicting the impact damage on the cylinder at different impact velocities and comparing the results with previous experimental data.

DOI: 10.1201/9781003483755-435

2 METHODOLOGY

2.1 *Ordinary state-based peridynamics theory*

Peridynamics first discretizes the object into a series of material points, with each material point interacting with other material points within a certain range. The governing equation (Silling et al. 2007) for material point **x** as follows:

$$\rho\ddot{\mathrm{u}}(\mathrm{x},\ t)=\int_{H_{\mathrm{X}}}\{\underline{\mathbf{T}}[\mathbf{x},t]\langle x'-\mathbf{x}\rangle-\underline{\mathbf{T}}[\mathbf{x}',\ t]\langle\mathbf{x}-\mathbf{x}'\rangle\}\mathrm{d}V_{\mathrm{X}'}+b(\mathbf{x},t) \tag{1}$$

Where ρ is the material density, ü is the acceleration of material pointx, $\boldsymbol{b}$ is the body force density of the external load. $\underline{\mathbf{T}}[\mathbf{x},t]$ and $\underline{\mathbf{T}}[\mathbf{x}',t]$ are force vector states of material points **x** and **x'**. $dV_{\mathrm{x}'}$ denotes the volume for material point x'. The integral domain H_{x} is defined as $H_{\mathrm{x}}=\{0<|\mathbf{x}'-\mathbf{x}|<\delta\}$, where δ is called the horizon size.

In the context of the Ordinary State-Based Peridynamicss (OSB-PD), the force state can be defined as:

$$\underline{\mathbf{T}}\ =\ \underline{t}\ \underline{\mathbf{M}} \tag{2}$$

Where t is called the scalar force state, $\mathbf{M}$ is the direction of force state $\mathbf{M}=\mathbf{Y}/|\mathbf{Y}|,\mathbf{Y}=\ y(\mathbf{x},\ t)-y(\mathbf{x}',\ t),y(\mathbf{x}',\ t)$ and $y(\mathbf{x},t)$ represent the positions of $\boldsymbol{x}'$ and $\boldsymbol{x}$.

The strain energy density is defined as:

$$W\left(\theta,\underline{e}^{d}\right)=\frac{k\theta^{2}}{2}+\frac{\alpha}{2}\left(\underline{\omega}\ \underline{e}^{d}\right)\cdot\underline{e}^{d} \tag{3}$$

Where k and α are positive constants, θ is referred to as the dilatation, and $\underline{e}^{d}$ is the deviatoric part of the extension scalar state $\underline{e}$.

$$\underline{e}=\underline{y}-\underline{x} \tag{4}$$

$$\underline{y}\ =|\underline{\mathbf{Y}}| \tag{5}$$

$$\underline{x}\ =|\underline{\mathbf{X}}| \tag{6}$$

$$\underline{e}^{i}=\frac{\theta x}{3} \tag{7}$$

$$\underline{e}^{d}=\underline{e}-\underline{e}^{i} \tag{8}$$

$$\theta(\underline{e})=\frac{3}{m}(\underline{\omega x})\cdot\underline{e} \tag{9}$$

Where m represents the weighted volume

$$m=(\underline{\omega}\ \underline{x})\cdot\underline{x} \tag{10}$$

From Equation (3), the scalar force state value is:

$$\begin{aligned}\underline{t}&=\underline{t}^{i}+\underline{t}^{d}\\&=\frac{\partial W}{\partial\underline{e}^{i}}+\frac{\partial W}{\partial\underline{e}^{i}}\\&=\frac{3k\theta}{m}\underline{\omega}\ \underline{x}+\alpha\underline{\omega}\ \underline{e}^{d}\end{aligned} \tag{11}$$

2.2 *Elastoplastic peridynamics model*

In Mitchell (2011), W in the elastoplastic model is rewritten by:

$$W\left(\theta,\underline{e}^{d},\underline{e}^{dp}\right)=\frac{k\theta^{2}}{2}+\frac{\alpha}{2}\left(\underline{e}^{d}-\underline{e}^{dp}\right)\cdot\omega\left(\underline{e}^{d}-\underline{e}^{dp}\right) \tag{12}$$

According to the above equation, the force state can be rewritten as:

$$\begin{aligned} \underline{t} &= \underline{t}^{i} + \underline{t}^{d} \\ &= -\frac{3P}{2}\underline{\omega}\,\underline{x} + \alpha\underline{\omega}\left(\underline{e}^{d} - \underline{e}^{dp}\right) \end{aligned} \tag{13}$$

Where $P = k\theta$ is the peridynamics pressure.

The yield surface and plastic flow for the peridynamics elastoplastic model are defined here (Vogler & Lammi 2014):

$$f = \frac{\left\|\underline{t}^{d}\right\|^{2}}{2} - \beta P - \varphi_0 \leq 0 \tag{14}$$

$$\dot{\underline{e}}\, dp = \lambda \nabla^{d} f \tag{15}$$

$$\lambda \geq 0, f\left(\underline{t}^{d}\right) \leq 0, \lambda f\left(\underline{t}^{d}\right) = 0 \tag{16}$$

Where $\nabla^{d} f$ and λ denotes a Frechet derivative and consistency parameter.

2.3 *Peridynamics failure criterion*

In peridynamics, damage to a material is often characterized by the breaking of bonds and describes the extension of cracks in the material. A common type of bond breaking criterion is the critical stretching criterion proposed by Silling & Askari (2005). This criterion states that when the stretching of a bond between material points exceeds a critical value, the bond irrecoverably breaks. The stretching of a bond is defined as follows:

$$\underline{s} = \frac{\underline{e}}{\underline{x}} = \frac{\underline{y} - \underline{x}}{\underline{x}} \tag{17}$$

$$d = \begin{cases} 1 & \underline{s} < s_0 \\ 0 & \text{otherwise} \end{cases} \tag{18}$$

$$D(\mathbf{x}, t) = 1 - \frac{\int_{H_{\mathrm{X}}} d\, \mathrm{d}v_{\mathrm{X}'}}{\int_{H_{\mathrm{X}}} \mathrm{d}v_{\mathrm{X}'}} \tag{19}$$

Where s_0 is the critical stretch, d is used to mark whether the bond is broken. Once the bond fails, the internal force between the material points is no longer effective, and the damage degree of material points is obtained by counting the ratio of number of failed bonds to the number of total bonds.

2.4 *Contact model*

In peridynamics, the contact model is used to describe the contact behavior between different Blocks. A typical contact model is a short-range force model (Macek & Silling 2007), in which the interaction of material points occurs when the distance between material points is less than the contact radius. The short-range force is defined as:

$$N_S = c_S \frac{\left(d_s - \left|y_p - y_i\right|\right)}{\delta} \frac{y_p - y_i}{\left|y_p - y_i\right|} \tag{20}$$

where c_S is the spring constant, and it is usually chosen to be a multiple of micromodule coefficient. d_s is the contact radius.

3 SIMULATION MODEL OF CYLINDER IMPACT

As the Figure 1 show, in this paper, a three-dimensional peridynamics model is built in the Cartesian coordinate system to analyze impact damage in the cylinder. The size of the rigid boundary is 0.0005m×0.03m×0.03m. The radius of the cylinder is 0.00381m and the length of the cylinder is 0.02347m. The mesh size should be as fine as possible and the mesh size no coarser than 0.000300256m. The rigid boundary has been meshed into 4900 elements, and the cylinder has been meshed into 15510 elements. The radius of the horizon is 3.015 times the mesh size.

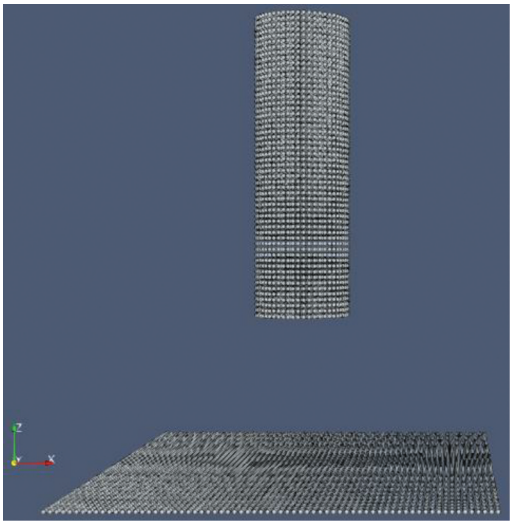


Figure 1. Three-dimensional perdynamic moedl for cylinder impact rigid boundary.

This article uses the material parameters used by Wilkins & Guinan (2003). Table 1 lists the values of the parameters of the cylinder. The cylinder uses an elastic-plastic model, and Poisson's ratio and Young's modulus can be deduced from the given Bulk Modulus and Shear Modulus. The formulas are as follows (Ma et al. 2022):

$$E = G\left(3 - \frac{G}{K}\right) \tag{21}$$

$$\nu = \frac{1}{2} - \frac{G}{2K} \tag{22}$$

Table 1. Material properties.

Material	1090 steel
Density (kg/m^3)	7850
Bulk Modulus(GPa)	190
Shear Modulus(GPa)	80
Yield Stress(MPa)	1200

4 MODEL VERIFICATION

In this section, the proposed computational model is compared with the numerical simulation results of Wilkins & Guinan (2003) with the test results to determine the accuracy of the model.

The model accuracy is calibrated from a qualitative comparison of the shape of the cylinder after impact with a quantitative comparison based on the metric, which is the ratio of the length L_f of the cylinder after it has undergone the impact test to the original length of the cylinder L_0.

The shape of the cylinder after the test is shown in Figure 2(a) (Wilkins & Guinan 2003) The shape of the cylinder in the peridynamics numerical simulation results is shown in Figure 2(b). It can be seen that the post-impact shape of the cylinder in the peridynamics model is similar to the experimental results. The results of numerical simulation compared to the results of the experiment have smaller plastic deformation in the region of contact with the rigid surface. This is due to the fact that in the peridynamics model, when the cylinder is in contact with the rigid surface, it will generate a hoop force on the cylinder, which restricts the deformation of the cylinder.

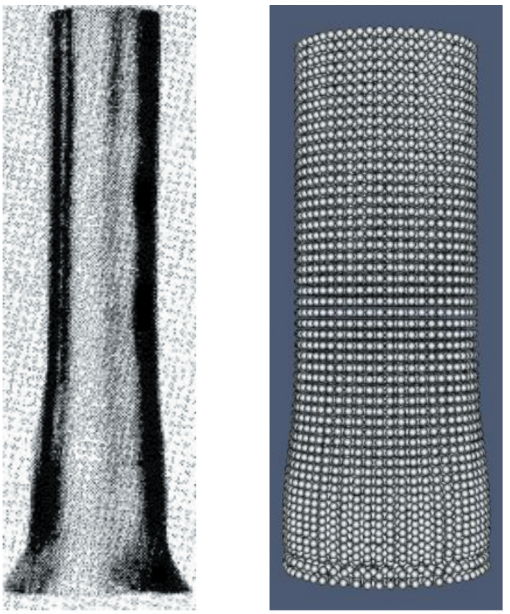


Figure 2. The shape of 1090 steel cylinders impacts on a rigid boundary (Wilkins & Guinan 2003).

As shown in Figure 3, the proposed peridynamics model can get quite similar results to that of a finite element model and experiment data in terms of cylinder impacts on the rigid boundary. The action range of interfacial force in the proposed model is called the horizon, and its influence on calculation results needs to be analyzed. Three horizons are chosen to be $\delta=2.0015\Delta x$, $\delta=3.0015\Delta x$, and $\delta=4.0015\Delta x$. Figure 4 shows the deformation pattern of steel cylinder specimens with different horizons. With the increases of horizons, the deformation patterns of the 1090 steel cylinders are more similar to the data of the experimental. When $\delta = 4.0015\Delta x$, the peridynamics model deformation pattern is consistent with the experimental data. Figure 5 displays the error curves under different horizons. The peridynamics results are consistent with experimental data in terms of the deformation of 1090 steel cylinders. Based on the experiment (Wilkins & Guinan 2003), the calculation error of the peridynamics model is within 4.5%. These findings show that the peridynamics can correctly characterize the 1090 steel cylinders' impacts on the rigid boundary. Moreover, the interface horizon affects the deformation pattern of steel cylinders. When the horizons increase, the deformation mode and deformation amount of the peridynamics are more consistent with the experimental data.

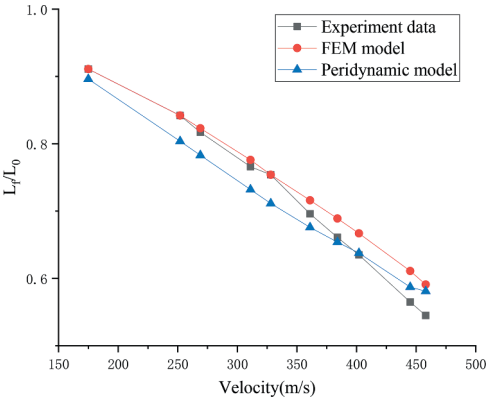


Figure 3. Calculation results of cylinders impacts on a rigid boundary.

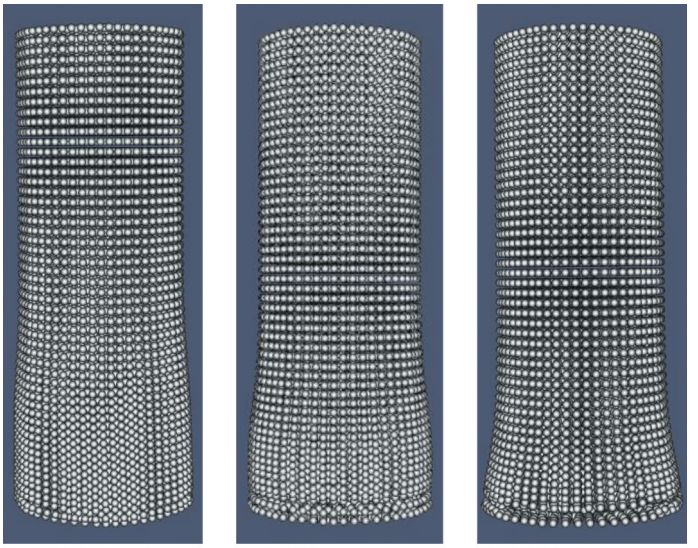


Figure 4. Deformation of 1090 steel cylinders computed by peridynamics with different δ.

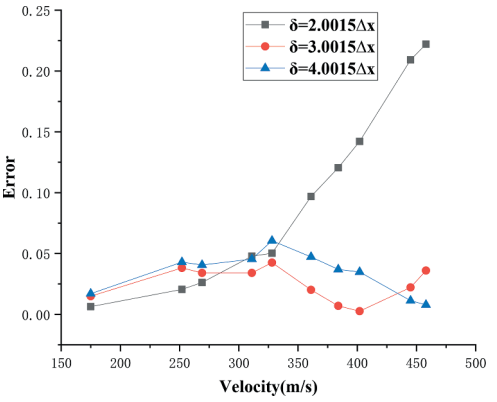


Figure 5. Calculation results of cylinders impacts on a rigid boundary.

5 CONCLUSIONS

Based on ordinary state-based peridynamics theory, a 3D peridynamics model was established to investigate the damage of cylinder impact rigid boundary. The elastic-plasticity model and the short-range force contact model have been used to build peridynamics model. The proposed model is validated by the shape of the cylinder after impact and the L_f/L_0 values of the cylinder after impact. Good agreements have been achieved not only in comparison with the finite element model but also in comparison with the experimental results. The results show that the peridynamics model based on ordinary state-based peridynamics theory is able to simulate the impact damage of the material well and peridynamics has potential in predicting bridge impact damage. The deformation pattern of steel cylinders can be affected by the size of the interface horizon. However, in order to better simulate the morphology of the cylinder after impact, the contact force model of the peridynamics needs to be modified in subsequent work.

REFERENCES

Baber, F., Ranatunga, V. & Guven, I. 2018. Peridynamics modeling of low-velocity impact damage in laminated composites reinforced with z-pins. *Journal of Composite Materials* 52(25): 3491–3508.

Breitenfeld, M.S., Geubelle, P.H., Weckner, O. & Silling, S.A. 2014. Non-ordinary state-based peridynamics analysis of stationary crack problems. *Computer Methods in Applied Mechanics and Engineering* 272: 233–250.

Chang, H., Chen, A. & Ge, B. 2023. A hybrid method of peridynamics differential operator-based Eulerian particle method–immersed boundary method for fluid–structure interaction. *Computational Particle Mechanics* 10(5): 1309–1322.

Chang, H., Chen, A., Kareem, A., Hu, L. & Ma, R. 2022. Peridynamics differential operator-based Eulerian particle method for 2D internal flows. *Computer Methods in Applied Mechanics and Engineering* 392: 114568.

Fang, X., Pan, Z., Chen, A., Tian, H. & Ma, R. 2023. Phase-field method for modeling non-uniform corrosion-induced cracking in concrete. *Engineering Fracture Mechanics* 281: 109131.

Liu, N., Liu, D. & Zhou, W. 2017. Peridynamics modelling of impact damage in three-point bending beam with offset notch. *Applied Mathematics and Mechanics* 38(1): 99–110.

Ma, X., Wang, L., Xu, J., Feng, Q., Liu, L. & Chen, H. 2022. A two-dimensional ordinary state-based peridynamics model for surface fatigue crack propagation in railheads. *Engineering Fracture Mechanics* 265: 108362.

Macek, R.W. & Silling, S.A. 2007. Peridynamicss via finite element analysis. *Finite Elements in Analysis and Design* 43(15): 1169–1178.

Mitchell, J.A. 2011. *A nonlocal, ordinary, state-based plasticity model for peridynamicss*. Sandia National Laboratories (SNL).

Sheikhbahaei, P., Mossaiby, F. & Shojaei, A. 2023. An efficient peridynamics framework based on the arc-length method for fracture modeling of brittle and quasi-brittle problems with snapping instabilities. *Computers & Mathematics with Applications* 136: 165–190.

Silling, S.A. 2000. Reformulation of elasticity theory for discontinuities and long-range forces. *Journal of the Mechanics and Physics of Solids* 48(1): 175–209.

Silling, S.A. & Askari, E. 2005. A meshfree method based on the peridynamics model of solid mechanics. *Computers & Structures* 83(17): 1526–1535.

Silling, S.A., Epton, M., Weckner, O., Xu, J. & Askari, E. 2007. Peridynamics States and Constitutive Modeling. *Journal of Elasticity* 88(2): 151–184.

Taylor, G.I. 1948. The use of flat-ended projectiles for determining dynamic yield stress I. Theoretical considerations. *Proceedings of the Royal Society of London. Series A. Mathematical and Physical Sciences* 194(1038): 289–299.

Vogler, T. & Lammi, C.J. 2014. *A Nonlocal Peridynamics Plasticity Model for the Dynamic Flow and Fracture of Concrete*. Sandia National Lab (SNL-CA).

Vu-bac, N., Nguyen-xuan, H., Chen, L., Lee, C.K., Zi, G., Zhuang, X., Liu, G.R. & Rabczuk, T. 2013. A Phantom-Node Method with Edge-Based Strain Smoothing for Linear Elastic Fracture Mechanics. *Journal of Applied Mathematics* 2013: 978026.

Wilkins, M.L. & Guinan, M.W. 2003. Impact of cylinders on a rigid boundary. *Journal of Applied Physics* 44(3): 1200–1206.

Zeng, W. & Liu, G.R. 2018. Smoothed Finite Element Methods (S-FEM): An Overview and Recent Developments. *Archives of Computational Methods in Engineering* 25(2): 397–435.

Bridge Maintenance, Safety, Management, Digitalization and Sustainability – Jensen, Frangopol & Schmidt (eds)
© 2024 The Author(s), ISBN 978-1-032-77040-6
Open Access: www.taylorfrancis.com, CC BY-NC-ND 4.0 license

Analytical evaluation of DBTT in Charpy impact test for structural steels

A. Jamil, H. Tamura, H. Katsuchi & C. He
Yokohama National University, Yokohama, Japan

ABSTRACT: The Charpy impact test is a widely accepted method for the measurement of material's fracture toughness and facilitates the investigation on the temperature related ductile-brittle transition phenomena. In order to study the structural steel behavior under different conditions such as the effect of pre-strains and the residual stresses etc., the experimental procedure of impact test becomes laborious and expensive. The ability to reproduce experimental results analytically from a limited set of material parameters may reduce the cost and allow assessment of the various behaviors of target steel from few tested samples. In this study, efforts were made to simulate the Charpy impact test to measure the brittleness of steel based on the modified Weibull stress (MWS). To deal with strong non-linearity and reproduction of elasto-plastic deformation phenomena under impact, an explicit-dynamic analysis was performed employing penalty contact method. The fracture occurrence probability at different temperatures was evaluated based on MWS, while internal energy from the analysis was decided at 95% fracture probability. The ductile-brittle transition temperature (DBTT) was estimated from the ductile-brittle transition curve for two Japanese structural steels i.e., SM570Q and SM490YB. To validate the analytical results, laboratory experiments were performed under similar conditions. The internal energy from MWS calculations was compared with the experimental absorbed energy from the Charpy impact tests. It was found that the analytical values and the experimental values are in good agreement in the low-temperature region where brittle fracture dominates. Based on the outcomes of this study, it was concluded that MWS calculations can be applied to evaluate the brittle fracture occurrence during Charpy impact tests.

1 INTRODUCTION

In standard Charpy impact testing, the fracture toughness is characterized on the basis of quantity of energy absorbed. For steel, low energy absorption occurs at low temperatures and a significant amount of energy is absorbed at higher temperatures. Due to BCC (body-centered cubic) structure, steel is vulnerable to failing under brittle fracture at low temperatures. Therefore, determination of transition from lower shelf (brittle behavior) to the upper shelf (ductile behavior) is really important.

For long-term operation of many important structures like pressure vessels, submarines, nuclear power plants, DBTT determination of structural materials play a vital role (Bruchhausen et al. 2016). Charpy testing technique has been widely applicable for the assessment of ductile-to-brittle transition temperature (DBTT) for previous century by finding the absorbed energy corresponding to different testing temperature. For a dual-phase steel, (Chao et al. 2007) successfully evaluated the DBTT using the Charpy impact testing and speculated the splitting in all impact specimens due to the fabrication process. (Haušild et al.2005) modelled Charpy impact test for a porous metal in the range of DBTT and confirmed that stress level around the notch increased after the initiation of ductile crack. For a Charpy specimen, the effect of inertia near the V-notch was investigated using 3D FE-analysis and provided the solution of contact issues between the hammer and the specimen (Takashima et al. 2017).

For the past few decades, cleavage fracture has become a common failure in structural steels and occurs at low temperatures without any prior warning. This study focused on the estimation in the region of brittle fracture.

DOI: 10.1201/9781003483755-436

2 SIMULATION OF CHARPY IMPACT TEST

2.1 *Explicit dynamic analysis*

Stress changes and elasto-plastic deformation of Charpy impact analytical model was reproduced.

By using a 3-dimensional finite element model on Abaqus/Explicit, analysis was performed. Explicit dynamic analysis was performed to check the sudden deformation phenomena. The equation of motion in explicit dynamic analysis is solved on the basis of explicit central-difference integration rule.

$$\ddot{u}_{(i)}^{N} = \left(M^{NJ}\right)^{-1}\left(P_{(i)}^{J} - I_{(i)}^{J}\right) \tag{1}$$

In the equation (1), $\ddot{u}$ represents the acceleration vector, M^{NJ} is the mass matrix, P^{J} is the applied load vector, and I^{J} is the internal force vector. In the model, increment number has been represented by the subscript i, whereas n shows the number of degrees of freedom (Smith 2009). During analysis, the Courant-Friedrichs-Lewy condition was satisfied by using smaller time increment than the stability limit. In accordance with JIS Z 2242 (Japanese standards association 2018), Figure 1 shows the standard geometry of V-notched Charpy impact specimen with a notch depth of 2 mm and a notch root radius of 0.25 mm, having notch angle of 45°. As the Charpy specimen is symmetric in shape, only one-quarter specimen was modelled analytically to save time and calculation cost. In Figure 2, the Charpy impact analytical quarter-model is presented where the hammer, specimen and anvil were modelled using 3D solid elements. The contact surface was provided using the penalty contact method which forbids energy dissipation due to impact and also restricts the penetration of nodes between different surfaces.

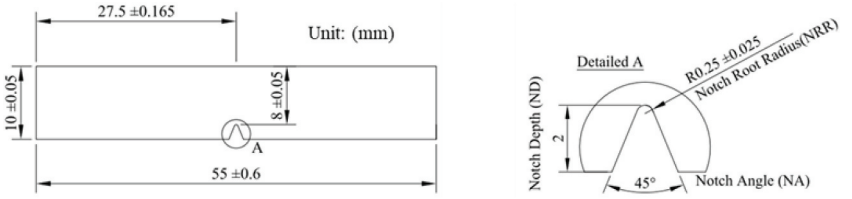


Figure 1. V-notched Charpy impact specimen.

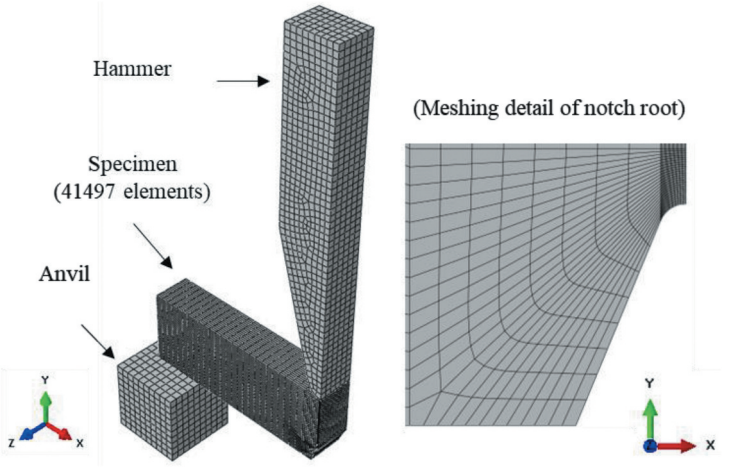


Figure 2. Charpy impact quarter-model for finite element analysis.

During the analysis, impact velocity of the hammer has a great influence on the kinetic energy (Yasuhito et al. 2017). Therefore, to replicate the experimental results, an impact load and velocity for hammer was given according to the specifications of Charpy impact testing machine as given in Table 1. The tests were conducted using two testing machines having 150 J and 600 J potential energy. The boundary condition for support was completely fixed and the hammer allows displacement merely in the translational direction. As quarter-model was reproduced in the analysis, symmetric boundary conditions about plane X (XSYMM) and along the Z-axis (ZSYMM) were also provided. For the specimen, the elemental division was divided into smaller parts near the notch where stress concentration occurs, and the minimum element size was set to be 20 μm. The analysis was performed for two Japanese structural steels and at different temperatures as listed in Table 2. For SM490YB steel, tests were performed by using 600 J Charpy impact tester at –100 °C, –80 °C and –60 °C as highlighted by blue color in Table 1 and Table 2 respectively.

Table 1. Charpy impact testing machine specifications.

Testing machine	Hammer weight, W (N)	Distance from the center of rotation axis to the center of gravity of the hammer, R (m)	Hammer lifting angle, θ_0 (°)
150 J	152.43	0.523	151
600 J	407.29	0.850	137

Table 2. Temperature for various steel material.

Steel type	Temperature (°C)
SM570Q	–80, –60, –50, –40, –20, 0
SM490YB	–196, –100, –80, –60

2.2 *Material properties for analysis*

For material properties, values for the Poison's ratio and the Young's modulus were set to be as 0.3 and 200 GPa. In order to imitate the changes in the material properties of the steel due to the effects of temperature and strain rate, the yield stress estimation formula provided by the Japan Welding Engineering Society standard WES2808 was used (Takashima et al. 2016). For SM570Q steel, Figure 3 represents the stress-strain relationships at various strain rates. The stress increases at lower temperature as compared to the higher temperature as illustrated in Figure 3a and Figure 3b respectively. Similarly, Figure 4a and Figure 4b shows the stress-strain relationships at two different temperatures for SM490YB steel. The outcome depicts that yield stress increases at higher strain rates and lower temperatures as presented in Figure 3 and Figure 4 for two different structural steels. As cleavage fracture in steel arises catastrophically and at a very high speed (Chen and Cao 2015), hence, for precise analytical calculations, the strain rate varied between 0 to 2000 /sec up to 4 mm/mm plastic strain values.

2.3 *Energy balance in explicit analysis*

In explicit analysis, energy output is an important parameter because comparison of various components of energy represented in Table 3 may assist to evaluate the appropriate response of analysis. For the whole model, an energy balance is shown in Equation (2) (Smith 2008). For Charpy analytical model, the input was provided in the form of inertia and initial velocity to the hammer hence, kinetic energy (ALLKE) can be regarded as the input energy. The reproducibility of the analysis has been represented in Figure 5, in which the input energy (ALLKE) and all the other remaining energy components are compared at –80°C and –100°C for SM570Q and SM490YB respectively. In this research, the internal energy (ALLIE) hereafter known as the analytical

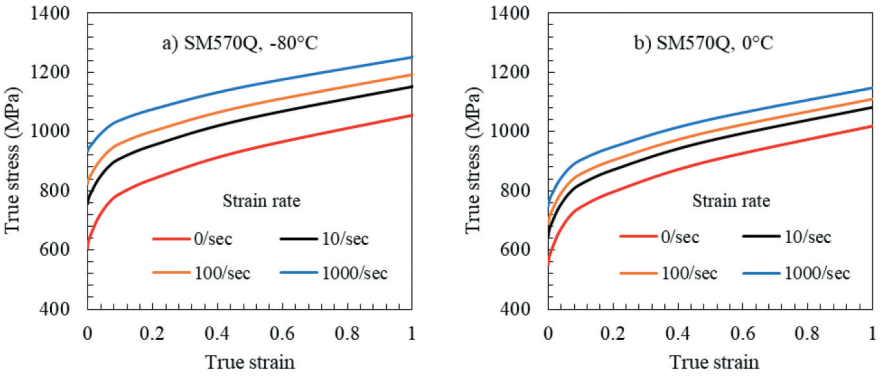


Figure 3. Stress-strain relationships for SM570Q steel at a) –80°C and b) 0°C.

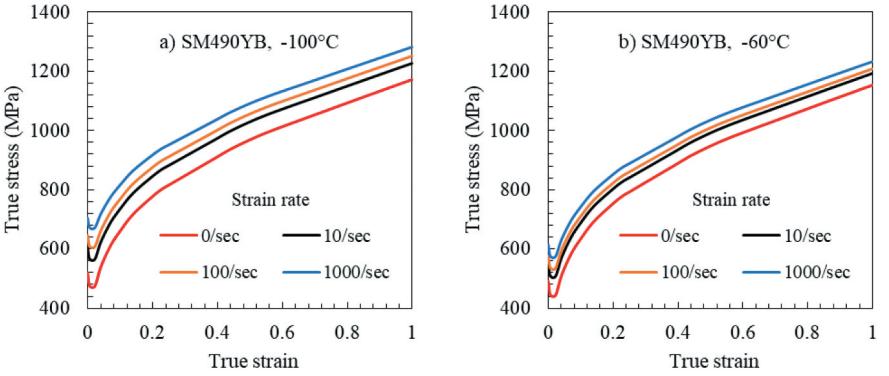


Figure 4. Stress-strain relationships for SM490YB steel at a) –100°C and b) –60°C.

energy is used for comparing the experimental absorbed energy from Charpy impact testing. The analytical energy (ALLIE) includes two major energy components, i.e., the elastic strain energy which can be recovered and also the non-recoverable or dissipated energy from the inelastic processes such as plasticity.

Table 3. Various energy components for the explicit analysis.

Abbreviation	Definition
ALLKE	Kinetic energy
ALLIE	Internal energy
ALLVD	Viscous energy dissipated
ALLFD	Frictional energy dissipated
ALLWK	Work done by the externally applied loads
Total energy	Sum of all the energy components

$$\mathrm{ALLIE} + \mathrm{ALLVD} + \mathrm{ALLFD} + \mathrm{ALLKE} - \mathrm{ALLWK} = \mathrm{Total\,energy} = \mathrm{constant} \qquad (2)$$

2.4 *MWS calculations for analytical results*

From the Charpy impact analytical results, MWS was calculated based on the formula from (Tamura et al., 2018) using the Weibull parameters i.e., shape parameter (m), scale parameter ($\sigma_u{}^*$) and the threshold stress (σ_{th}) as listed in Table 4. The output from analysis i.e., equivalent

stress (SMISES), maximum principal stress (SMAX), equivalent plastic strain (PEEQ) and the element volume (EVOL) were used as an input for MWS calculations. The calculations were performed for elements around the notch root having substantial distribution of SMISES, SMAX and PEEQ as represented in Figure 6 for center-line section of a quarter-model.

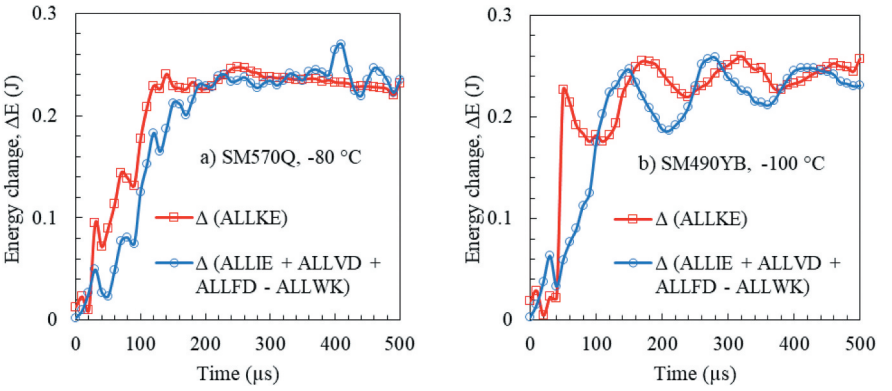


Figure 5. Reproducibility of Charpy analytical model for SM570Q and SM490YB.

Table 4. Weibull parameters and the threshold stress.

Steel type	Shape parameter, m	Scale parameter, σ_u^* (MPa)	Threshold stress, σ_{th} (MPa)
SM570Q	21.35	976	1960
SM490YB	36.04	1320	1275

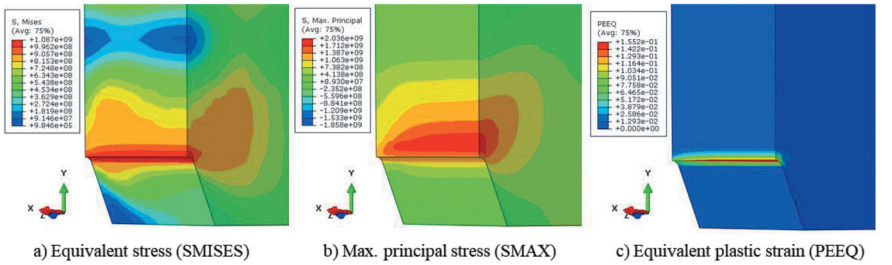


Figure 6. Distribution of stress and strain around the notch root for SM570Q at –80°C.

For SM570Q steel, Figure 7 represents the time-histories of modified Weibull stress (MWS) and fracture probability (P_f) showing that 100% P_f achieves earlier for lower temperatures as compared to the higher temperatures. In Figure 7, the plots of MWS and P_f at –40°C shows a relatively small increment between 300 to 500 μs as compared to other temperatures. The reason is for analysis at DBTT, insignificant number of elements have maximum principal stress greater than the threshold stress, hence restricting the continuous increase in modified Weibull stress and fracture probability. The results of MWS, P_f and ALLIE at –20°C and 0°C are almost the same because the modified Weibull stress calculations couldn't predict material's behavior after the DBTT. In statistics, the fracture probability is usually considered as 95% (Stienstra et al. 1990), along with other fracture probabilities like 90% (Ruggieri and Dodds 1998) or 80% (Zhang and Qian 2016). According to Figure 8a, at lower temperatures different fracture probabilities are approximately similar, therefore, in this research, the analytical energy is considered on the step time at which 95% fracture probability is reached as illustrated in Figure 8b.

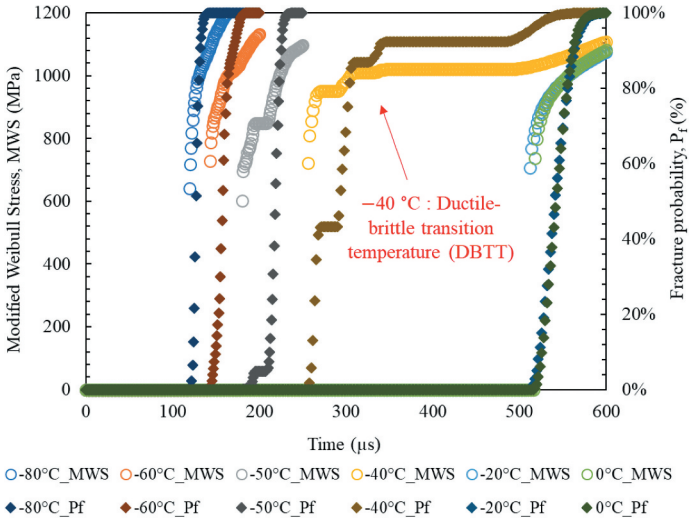


Figure 7. Time-histories of modified Weibull stress (MWS) and fracture probability (P_f) for SM570Q.

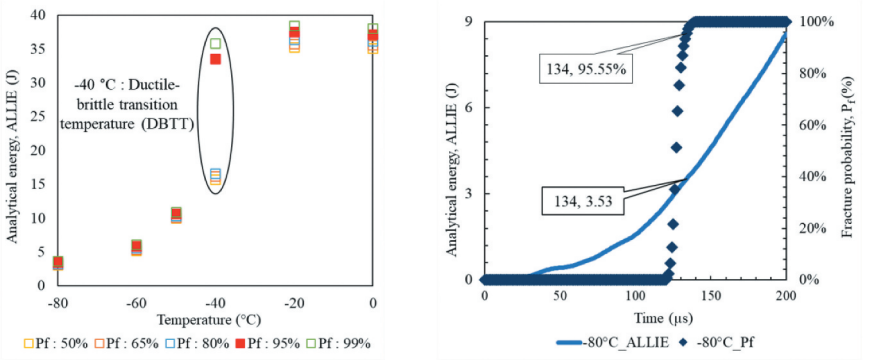


Figure 8. Analytical energy (ALLIE) for SM570Q.

3 CHARPY IMPACT EXPERIMENTATION

To validate the concept of estimating DBTT through Charpy impact analysis, experiments were performed on SM570Q and SM490YB using two Charpy impact testing machines and at various temperatures as mentioned earlier in Table 1 and Table 2 respectively. The mechanical properties at room temperature and the chemical composition have been listed in Table 5. For testing at temperatures lower than –80 °C, the testing specimens were cooled by placing in liquid nitrogen while, for temperature higher than –80 °C, mixture of ethanol and liquid nitrogen was used as a cooling liquid solution. Before testing, the specimens remained in the cooling liquid solution for at least 10 minutes at ±2 °C, and three specimens were tested at each temperature. While testing, the temperature of cooling liquid was measured by using a K-thermocouple type thermometer.

The test results for absorbed energy (E_a) at various temperatures represented in Figure 9 shows that higher amount of energy was absorbed by the specimens at higher temperatures. The amount of absorbed energy is more for SM490YB steel as compared to SM570Q showing higher material's toughness (Kim et al. 2002) and lower DBTT of –100 °C comparative to –40 °C

Table 5. Mechanical properties and composition of SM570Q and SM490YB structural steel.

				C	Si	Mn	P	S
Steel type	Yield stress (MPa)	Tensile stress (MPa)	Uniform elongation (%)	Mass (%)				
SM570Q	593	664	36	0.1	0.23	1.53	0.008	0.002
SM490YB	431	537	26	0.13	0.27	1.28	0.011	0.003

for SM570Q steel. Experimental curve was fitted by performing a regression analysis (Oldfield 1979) and are represented on 95% confidence levels. The comparison of analytical energy (ALLIE) and absorbed energy (E_a) for SM570Q and SM490YB structural steels depicted the applicability of Charpy analytical model for the determination of ductile-brittle transition temperature. Analytical and experimental values are in good agreement in the low-temperature range where the brittle fracture dominates. This analysis is unable to regenerate the ductile fracture phenomena, as the energy loss by crack propagation is significant when fracture occurred as ductile fracture. On the contrary, in case of brittle fracture the energy loss is small making it possible to predict the brittle fracture by using MWS calculations. Generally, the Charpy impact test is used to guarantee the quality of steel for construction, but this article presented the validity of MWS approach through Charpy impact analytical model. For various steel grades or even for a single grade the values of material property vary a lot. This model has been developed for the clarification of such complications for steel showing cleavage fracture.

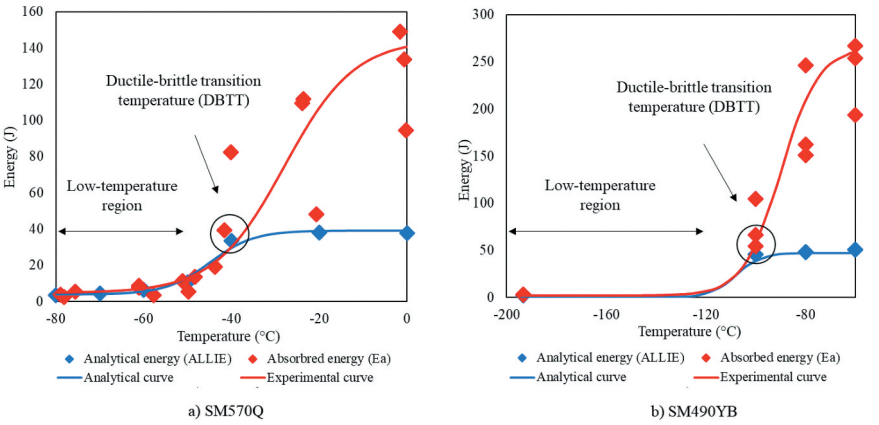


Figure 9. Comparison of analytical and experimental absorbed energy for SM570Q and SM490YB.

4 CONCLUSION

In order to rationalize the testing effort and cost for studying various behaviors of steel, modelling of Charpy impact test was performed using dynamic-explicit analysis and the Charpy's analytical energy was evaluated based on MWS calculations. The analysis was performed for two steel types and at various temperatures. The time-histories of MWS and P_f evaluated the DBTT for SM570Q and SM490YB as –40 °C and –100 °C respectively. The analytical energy was calculated from the MWS at a global fracture probability of 95% and compared with the experimental results. The results showed a good correlation at lower-temperature region before the DBTT. By using the Charpy analytical model proposed in this article, we can improve the experimental conditions for Charpy impact testing for the estimation of the modified Weibull parameters.

REFERENCES

Bruchhausen, M., S. Holmström, I. Simonovski, T. Austin, J. M. Lapetite, S. Ripplinger, and F. de Haan. 2016. "Recent Developments in Small Punch Testing: Tensile Properties and DBTT." *Theoretical and Applied Fracture Mechanics* 86: 2–10.

Chao, Y. J., J. D. Ward, and R. G. Sands. 2007. "Charpy Impact Energy, Fracture Toughness and Ductile-Brittle Transition Temperature of Dual-Phase 590 Steel." *Materials and Design* 28 (2): 551–57.

Chen, J.H. and Cao, R. 2015. *Micromechanism of Cleavage Fracture of Metals*. Elsevier.

Haušild, Petr, Clotilde Berdin, and Andreas Rossoll. 2005. "Modelling of the Charpy Impact Test in the DBTT Range." *Materials Science Forum* 482: 331–34.

Japanese standards association. 2018. "Japanese Industrial Standard." 2018.

Kim, S H, Y W Park, S Kang, and H D Chung. 2002. "Estimation of Fracture Toughness Transition Curves of RPV Steels from Charpy Impact Test Data." *Nuclear Engineering and Design*. Vol. 212.

Oldfield, William. 1979. "Fitting Curves to Toughness Data." *Journal of Testing and Evaluation*. Vol. 7.

Ruggieri, Claudio, and Robert H. Dodds. 1998. "Numerical Evaluation of Probabilistic Fracture Parameters Using WSTRESS." *Engineering Computations (Swansea, Wales)*. Emerald Group Publishing Ltd.

Smith, M. 2008. "ABAQUS/Explicit User's Manual, Version 6.5 Documentation (Energy Balance)." Dassault Systems Simulia Corp. 2008.

Smith, Michael. 2009. "ABAQUS/Explicit User's Manual, Version 6.6." Dassault Systems Simulia Corp. 2009.

Stienstra, D., T. L. Anderson, and L. J. Ringer. 1990. "Stienstra et. al., 1990 (95% Pf)." *Journal of Engineering Materials and Technology* 113 (31).

Takashima, Y., M. Ohata, T. Ishii, Y. Hagihara, and F. Minami. 2016. "WES 2808 for Brittle Fracture Assessment of Steel Components under Seismic Conditions - Part VI: Application of WES 2808 to Beam-to-Column Connections." *Procedia Structural Integrity* 2: 1585–92.

Takashima, Yasuhito, Tsunehisa Handa, and Fumiyoshi Minami. 2017. "Three-Dimensional Dynamic Explicit Finite Element Analysis of Charpy Impact Test." *Materials Science Forum* 879: 1905–10.

Takashima, Yasuhito, and Fumiyoshi Minami. 2017. "Influence of Impact Velocity on Transition Time for V-Notched Charpy Specimen." *Yosetsu Gakkai Ronbunshu/Quarterly Journal of the Japan Welding Society* 35 (1): 80S–84S.

Tamura, H., E. Sasaki, and S. Tominaga. 2018. "Modified-Weibull-Stress-Based Evaluation of Brittle Fracture Occurrence during Earthquakes in Steel Members." *Engineering Fracture Mechanics* 202 (August 2017): 375–93.

Zhang, Zefeng, and Xudong Qian. 2016. "A Local Approach to Estimate Cleavage Angles in Steel under Mixed-Mode I and II Conditions." *Engineering Fracture Mechanics* 166 (October): 164–81.

Bridge Maintenance, Safety, Management, Digitalization and Sustainability – Jensen, Frangopol & Schmidt (eds)
© 2024 The Author(s), ISBN 978-1-032-77040-6
Open Access: www.taylorfrancis.com, CC BY-NC-ND 4.0 license

Elastic-plastic bearing capacity simulation of steel-concrete composite bridge tower

S.D. Sun & L.H. Yang
Huizhou Huiwan Expressway Co., Ltd., Huizhou, China

Y.W. Wang, K.Q. Cheng & C.S. Wang
Department of Bridge Engineering, College of Highways, Chang'an University, Xi'an, China

ABSTRACT: The tower of a cable-stayed bridge adopts the steel-concrete composite structure, which gives full play to the advantages of steel and concrete. In order to study the elastic-plastic bearing capacity of the steel-concrete composite bridge tower, ABAQUS was used to establish the finite simulation models of the tower section considering material nonlinearity. The elastic-plastic bearing capacity of the tower column was calculated and analyzed. Meanwhile, the influence of structural parameters such as the thickness of steel panels, the diameter of vertical bar, and the concrete strength on the bearing capacity of the tower column was discussed. The results show that the concrete and the steel are subjected to the joint force in the elastic stage. The structural design of the composite tower column has sufficient reservation on loading capacity, which can meet the requirements of the bearing capacity in the elastic stage. The optimization suggestions can improve the technical economy and construction efficiency

1 INTRODUCTION

With the increase of span and traffic load grade of long-span cable supported bridges, higher requirements are being placed on the bearing capacity of bridge structures. As the main load-bearing component of long-span cable supported bridges, the bridge tower will endure significant compressive and bending loads throughout its construction and operation (Xiang et al. 2001). The steel-concrete composite bridge tower has been gradually applied to the construction of long-span cable supported bridges due to its excellent structural performance, durability, economy and construction convenience. The steel-concrete composite bridge tower is a bridge tower that is loaded by two materials: steel and concrete, both of which have the same section. The bearing capacity of the composite bridge tower varies depending on the cross-section structures and steel-concrete connection forms.

Currently, extensive research has been conducted on the mechanical properties of steel-concrete composite tower in the field of bridge engineering. Wang et al. conducted an axial compression test on a steel and high-performance concrete composite bridge tower segment, and obtained the ultimate bearing capacity and failure mode of the composite tower column. Based on the test results, a calculation method of the bearing capacity of the composite bridge tower was proposed(Wang et al. 2023). By conducting model tests and finite element analysis, Wang et al. investigated the mechanical performance of a composite tower consisting of steel-encased hol-low concrete columns under axial compression loads, and found that the composite tower columns effectively utilize the bearing capacity of both concrete and steel, resulting in improved deformation capacity (Wang et al. 2017). Zhang et al. conducted a study on the impact of various parameters, including concrete strength, steel plate thickness, and connector type, on the axial compression performance of a model. This was done through axial

DOI: 10.1201/9781003483755-437

compression testing and finite element analysis of a hollow outer wall steel plate-concrete composite bridge tower column model. It has been found that increasing the strength of concrete and steel plate, as well as increasing the thickness of the steel plate, can enhance the bearing capacity of the composite tower column (Zang et al. 2018). Through the model test, Gao found that the multi-element section of the composite bridge tower has better mechanical properties than the double steel section (Gao et al. 2023). At present, research on steel-concrete composite tower columns primarily focuses on the use of a simple steel box filled with concrete as a composite column. The steel-concrete composite structure of the bridge tower is used in long-span cable-supported bridges to ensure the synergistic force between steel and concrete, thereby improving the overall mechanical performance. Connectors or stud structures are placed between the steel wall plate and the filled con-crete. This creates a tenon structure that enhances the overall bearing capacity by reinforcing the steel box opening stiffeners with steel bars and concrete (Fan et al. 2023, Zhu et al. 2018).

Currently, there are few studies on the bearing capacity of steel plate-concrete composite bridge towers. In this paper, the numerical analysis of the elastic-plastic bearing capacity of the steel plate-concrete composite bridge tower column is carried out. The analysis is based on the design of the double steel plate-concrete composite bridge tower column used in a cable-stayed bridge. The influence of structural parameters such as steel plate thickness, vertical steel bar diameter and concrete strength on the bearing capacity of the tower column is analyzed and discussed, which provides a reference for the engineering application of the steel plate-concrete composite structure in the long-span cable supported bridge tower.

2 STANDARD SECTION OF COMPOSITE BRIDGE TOWER

The steel structure of the composite tower column of a cable-stayed bridge consists of inner and outer steel panels, partition plates, vertical stiffeners, horizontal stiffeners and welding studs (Figure 1). The steel structure material is Q355D, and the filled concrete is C50 concrete. The cross section is divided into twelve bins. The inner and outer panels are secured with welding nails.

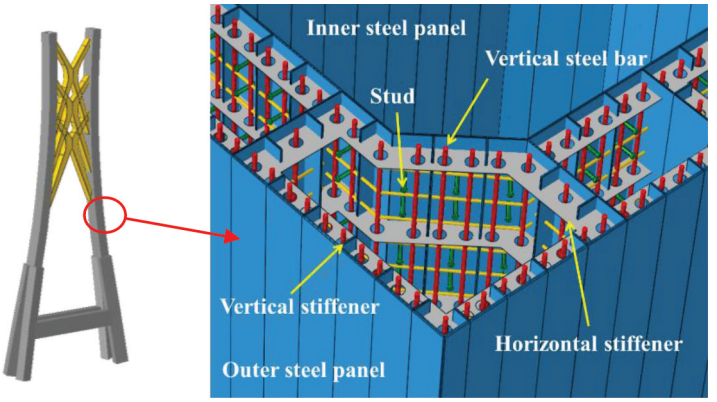


Figure 1. Steel-concrete composite bridge tower structure.

3 FINITE ELEMENT MODEL

3.1 *Establishment of FE model*

The ABAQUS finite element model was established as shown in Figure 2. The solid element (C3D8R) was used for steel plate, concrete, the shell element (S4R) was used for steel plate, and the truss element (T3D2) was used for rebars.

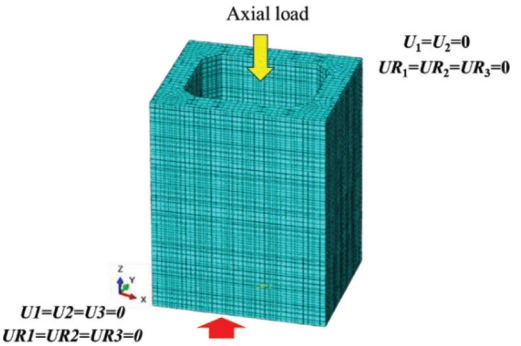


Figure 2. Finite element model of composite bridge tower segment.

When defining the material properties of steel plate and steel bar, the elastic properties and plastic properties are defined at the same time. The constitutive relationship of steel plate is simplified by multi-fold line model. In order to improve the convergence of model calculation and save calculation time, the uniaxial stress-strain curve of steel bar and stud is simulated by double-fold line model. Concrete adopts the concrete damage plastic model (CDP). When external load is applied to the concrete, it deforms. However, the presence of the external steel pipe provides lateral restraint to the concrete, thereby enhancing its strength. Based on the model proposed in (Liu et al. 2005), the compressive constitutive relation of concrete filled in a steel box of a tower column was determined, including the elastic modulus, peak compressive strain and compressive strength of concrete.

3.2 *Verification of FE model*

In order to study the rationality and validity of the numerical model, the concrete-filled square steel tube composite tower column was used as the verification object. The section size is 300mm × 420mm, the tower height is 1260mm, the wall thickness is 6mm, the size of the stiffener is 1260mm × 55mm, and the thickness is 4mm. The size of the combined column model is shown in Figure 3.

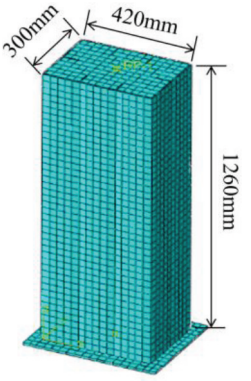


Figure 3. Finite element verification model.

Using the modeling method proposed in section 3.1, the finite element model is established and verified as shown in Figure 4 (b). From the comparison of the failure modes (Figure 4), it can be seen that the failure mode of the specimen is the yield bulging of the steel plate in the middle of the tower column, which was similar to the test's failure mode. The comparison between the axial compression curve obtained through finite element calculation and the

curve obtained from the test is shown in Figure 5. Prior to reaching the peak load, the stiffness of the finite element simulation is found to be excessively high due to initial defects in the components and the presence of testing errors. However, it has been confirmed that the numerical model provides an accurate overall simulation of the composite tower column text, as the yield section and limit point of the curve align well. The relative error of the ultimate bearing capacity of the two is within 2%. It can be seen that the numerical model accurately reflects the elastic-plastic bearing capacity of the composite tower column model.

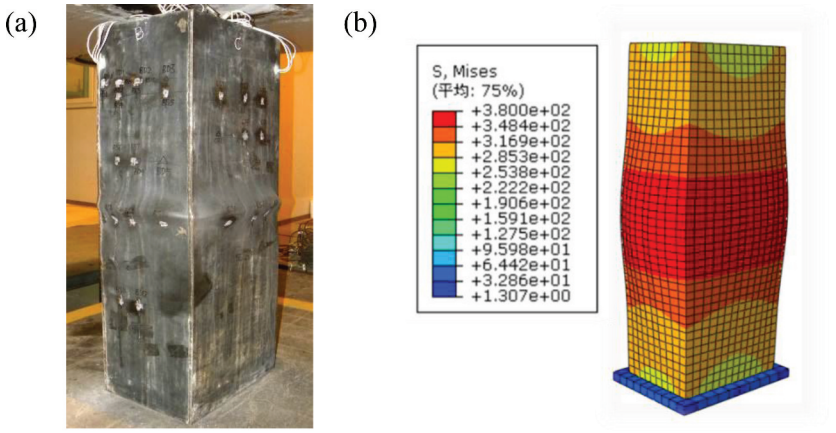


Figure 4. Comparison of failure forms: (a) test model; (b) numerical model.

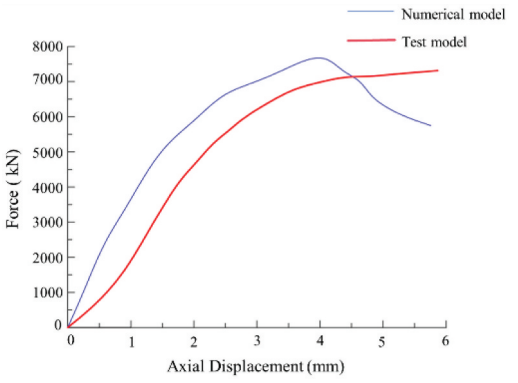


Figure 5. Axial compression load displacement curve.

4 NUMERICAL ANALYSIS RESULTS

4.1 *Structural parameters*

The height of the finite element model of the composite bridge tower is 8m. The thickness of the outer steel plate is 16 mm, while the thickness of the inner steel plate is 12 mm. The thickness of the transverse bridge partition plate is 10 mm. A vertical stiffener is set at a transverse interval of 300 mm inside the cross-section warehouse, and a transverse rib is set at a vertical height interval of 600 mm. The vertical main bar is 40 mm in diameter, and the horizontal spacing is 150 mm. The transverse steel bar is 22 mm in diameter and the vertical spacing is 200 mm. The inner and outer wall plates are set with welding studs, the horizontal spacing is 300 mm, and the specification of welding studs is Φ22 × 150 mm. The structural optimization analysis was carried out for the main structural parameters such as the thickness of the outer

steel panel, the diameter of the steel bar, and the concrete strength. Six groups of finite element models were established by simulating the original parameters and variable parameters.

Table 1. Model parameter table.

Numbering	The thickness of the outer panel(mm)	The thickness of the inner panel(mm)	The diameter of vertical steel bar(mm)	Materials	
				The steel panel and the stiffeners	The concrete
Model 1	16	12	40	Q355D	C50
Model 2	12		40		
Model 3	16		32		
Model 4	16		25		
Model 5	16		40		C40
Model 6	16		40		C60

4.2 *Elastic-plastic bearing capacity analysis*

4.2.1 *Influence of steel outer panel thickness*

Figure 6 shows the load-displacement curves of composite tower columns with outer plate thicknesses of 16 mm and 12 mm respectively. When the thickness of the outer plate of the composite bridge tower is reduced from 16 mm to 12 mm, it can be seen from Figure 6 that the increase of the thickness of the outer plate has little effect on the initial stiffness of the composite bridge tower. The ultimate bearing capacity is reduced from 1.19×10^6kN to 1.16×10^6kN.

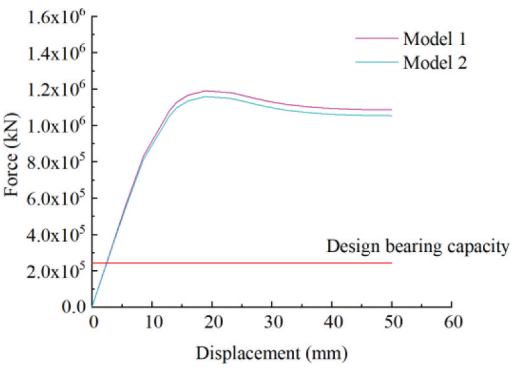


Figure 6. Load displacement curves of composite tower under different steel outer panel thickness.

4.2.2 *Influence of vertical steel bar diameter*

Figure 7 shows the load displacement curves of steel plate concrete composite bridge towers with vertical steel bar diameters of 40mm, 32mm, and 25mm respectively. According to Figure 7, the ultimate bearing capacity of the steel plate-concrete composite tower column is 1.19×10^6kN, 1.14×10^6kN and 1.11×10^6kN when the vertical steel bar diameters are 40mm, 32mm, and 25mm respectively. Compared with the vertical steel bar diameter of 40mm, the tower column's bearing capacity decreased by 4.2% and 6.7% when using 32mm and 25mm respectively.

4.2.3 *Influence of concrete strength*

When using different strength grades of concrete such as C40, C50, C60, the ultimate bearing capacity of the composite tower column is 1.15×10^6kN, 1.19×10^6kN and 1.42×10^6kN respectively. Figure 8 shows the load displacement curve of a steel plate-concrete composite tower column with concrete strength grade of C40, C50 and C60 respectively. From Figure 8, it can be seen that the initial stiffness of the composite bridge tower increases with the increase in concrete strength grade.

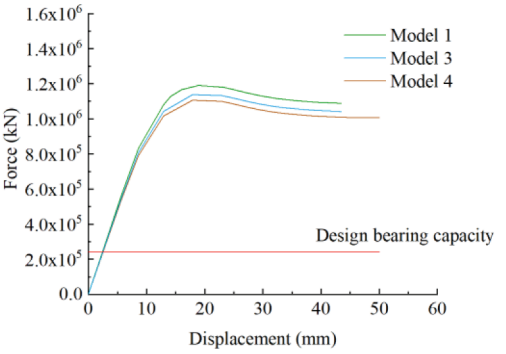


Figure 7. Load displacement curves of composite tower under different vertical steel bar diameter.

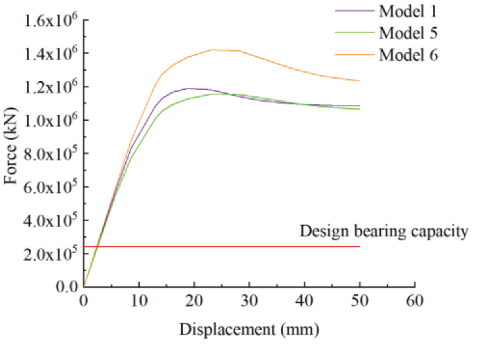


Figure 8. Load displacement curves of composite tower under different concrete strengths.

4.2.4 *Failure mode*

Combined with the corresponding relationship between the load displacement curve in the elastic-plastic stage and the deformation cloud diagram of the tower column, it is found that the steel and concrete of the composite tower column are jointly stressed in the elastic stage. After entering the plastic stage, the overall bulging phenomenon occurs in the standard section due to the compression of the core concrete. After the lateral displacement of the continuous loading model reaches the limit state, the load no longer increases and enters the descending section. The overall deformation of the segment model is shown in Figure 9.

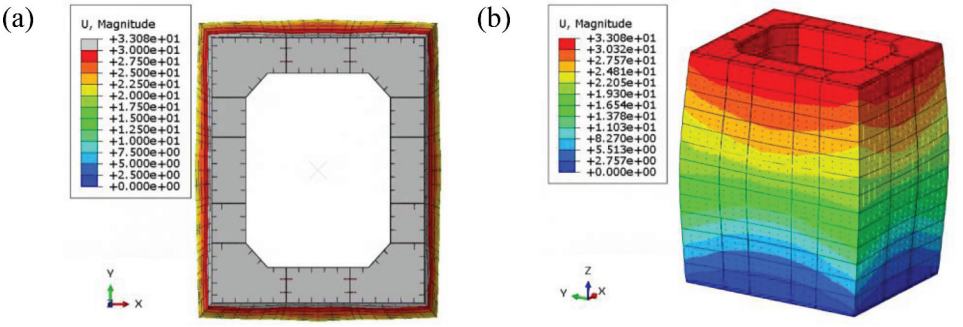


Figure 9. Comparison of failure forms: (a) plan; (b) elevation.

4.2.5 *Comprehensive comparison*

Table 2 presents the axial compression ultimate bearing capacity of the six groups of models in both the elastic and plastic stages. It also compares the bearing capacity of the model after parameter optimization with that of model 1. It has been found that the strength of the concrete has a significant impact on the bearing capacity of the composite tower column. The plastic ultimate bearing capacity is increased by 19.3 % compared to the original design. The thickness of the steel plate and the diameter of the vertical steel bar will also affect the bearing capacity of the composite tower. As the thickness of the steel plate and the diameter of the steel bar decrease, the elastic-plastic ultimate bearing capacity of the composite tower decreases.

Table 2. Comparison of elastic-plastic ultimate bearing capacity.

		Elastic-plastic bearing capacity			
Numbering	Variable parameter	Elastic stage (kN)	The ratio of decline-(increase) compared with the original design	Plastic stage (kN)	The ratio of decline compared with the original design
Model 1	Original design	8.30×10^5	/	1.19×10^6	/
Model 2	The thickness of the outer panel 16mm→12mm	8.12×10^5	-2.2%	1.16×10^6	-2.5%
Model 3	The diameter of vertical steel bar 40mm→32mm	8.07×10^5	-2.8%	1.14×10^6	-4.2%
Model 4	The diameter of vertical steel bar 40mm→25mm	7.91×10^5	-4.7%	1.11×10^6	-6.7%
Model 5	The concrete strength C50→C40	7.73×10^5	-6.9%	1.15×10^6	-3.4%
Model 6	The concrete strength C50→C60	8.77×10^5	+5.7%	1.42×10^6	+19.3%

4.3 *Design force performance analysis*

4.3.1 *Load condition*

The design stress performance of Model 1 was analyzed. The design force loading condition adopts the combined loading mode of concentrated force and bending moment. The specific loading condition is set as shown in Table 3. The P and M increased in turn when the loading increase ratio was set to 0.1,0.2,0.3,0.4,0.6,0.8,1,2,4 times. P and M are the maximum design axial force and bending moment respectively under the most unfavorable axial force conditions.

Table 3. Design force loading conditions.

Numbering	Load condition	loading method
Model 1	Condition 1	Maintain the design bending moment unchanged and increase the axial force proportionally.
	Condition 2	Maintain the axial force unchanged and proportionally increase the longitudinal bending moment of the bridge.
	Condition 3	Maintain the axial force unchanged and proportionally increase the transverse bending moment of the bridge.

4.3.2 *Result analysis*

The numerical analysis of the design force loading condition of the standard section of the composite tower column was carried out. In order to characterize the calculation results, the model section area is divided as shown in Figure 10. The height of the top, middle, and bottom parts is divided from top to bottom along the height direction of the tower column.

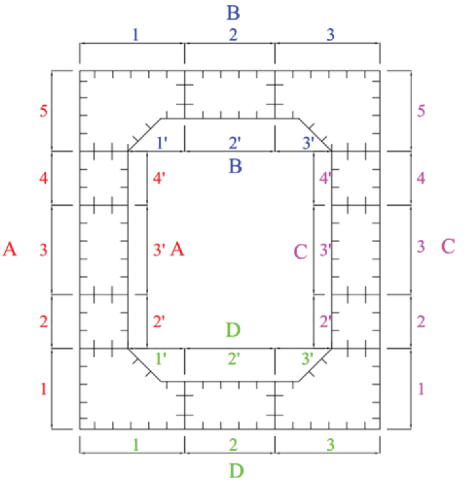


Figure 10. Division of section area for composite tower.

The stress calculation results of each component of the composite tower column model are shown in Table 4. The maximum value of Mises stress in the steel box occurs at the top of the standard section. The maximum compressive stress in the concrete also occurs at the top of the standard section. Additionally, the vertical bar stress in the top area of the standard section is the highest. When the axial force, longitudinal bending moment, and transverse bending moment of the bridge reach the design force loading condition, the maximum mises stress of the steel box is 93.8 MPa. The maximum vertical compressive stress of the concrete is 15.7 MPa, and the steel mesh and bolts are in the elastic stage.

Table 4. Stress calculation results of combined tower column.

		Steel box stress		Vertical stress of concrete		Reinforcement mesh stress	
Load condition	Loading Steps	Maximum (MPa)	Location of occurrence	Maximum (MPa)	Location of occurrence	Maximum (MPa)	Location of occurrence
1	0.6P	62.1	A1 top	-10.4	A1 top	56.9	D1 top
	P	93.8	A1 top	-15.7	A1 top	86.5	D1 top
	2P	174.0	A1 top	-28.8	A1 top	159.1	D1 top
2	0.6M	83.6	D1 top	-14.0	D3 top	77.7	D1 top
	M	88.9	D1 top	-14.9	D1 top	82.6	D1 top
	2M	101.0	D1 top	-17.0	D1 top	93.6	D1 top
3	0.6M	80.4	A1 top	-13.4	A1 top	73.9	D1 top
	M	82.9	A1 top	-13.8	A1 top	75.8	D1 top
	2M	88.5	A1 top	-14.7	A1 top	80.5	D1 top

Note: In table, P represents the maximum design axial force under the most unfavorable axial force conditions, M represents the maximum design bending moment under the most unfavorable axial force conditions.

5 CONCLUSION

In this paper, a finite element numerical analysis was conducted on the axial compression of the steel plate-concrete composite tower column of a cable-stayed bridge. The elastic-plastic bearing performance and the mechanical performance of each component under the design force were studied. The results are as follows.

(1) The ultimate bearing capacity of the steel-concrete composite bridge tower in the original design is 8.3×10^5kN in the elastic stage, and 1.19×10^6kN in the plastic stage. These values are significantly higher than the maximum design bearing capacity.

(2) Increasing the thickness of the steel plate surrounding the tower column, the diameter of the vertical steel bar, and the concrete strength grade can enhance the bearing capacity of the steel plate-concrete composite tower column. Among these factors, improving the concrete strength grade has the most significant impact.
(3) The failure mode of the composite bridge tower model is the joint force between the steel and concrete during the elastic stage. After entering the plastic stage, the standard section bulges out as a whole. After reaching the limit state, the load no longer increases, and the bearing capacity begins to decrease.
(4) When the axial force, longitudinal bending moment, and transverse bending moment of the bridge reach the design force loading condition, the maximum mises stress of the steel box is 93.8 MPa, the maximum vertical compressive stress of the concrete is 15.7 MPa, and the steel mesh and bolts remain in the elastic stage.

ACKNOWLEDGEMENT

This work was supported by the Innovation Capability Support Program of Shaanxi (2019TD- 022), Research on Mechanical Performance and Design Method of Dongjiang Bridge Composite Bridge Tower of Huizhou Huicheng To Huiyang Xiayong Expressway Project (HX-XQ(2023)-012) and Chang'an University Central University Basic Scientific Research Fund Green Highway Key Special Support Plan (300102219309).

REFERENCES

Fan, J. S. et al. 2023. A review on research and applications of concrete-filled steel-plate composite bridge tower. *China civil engineering journal* 56(04):61–71.
Gao, X. P. et al. 2023. Experimental and analytical study on compressive bearing capacity of steel shell-concrete composite bridge tower. *Engineering Structures*, 278.
Liu W. 2005. Research on Mechanism of Concrete-filled Steel Tubes Subjected to Local Compression. *Fuzhou University*.
Wang, C. S. et al. 2011.Experimental research on structure behaviors of steel and high-performance concrete composite bridge tower. *Journal of Chang'an University (Natural Science Edition)* 31 (1): 51–58.
Wang, Q. et al. 2008. Experimental study on bearing capacity of steel-high performance concrete composite bridge tower. *Journal of Zhengzhou University (Engineering Science)* (03):108-112.
Wang, Q. et al. 2010. Researches on steel and steel-concrete composite bridge towers. *Steel Construction* 25(S): 99–104.
Wang, X. Z. et al. 2017. Study on mechanical behavior of a new type of hollow composite pylon. *Journal of Building Structures* 38(S1): 430–434, 450.
Xiang, H. F. et al. 2001. Advanced theory of bridge structures. *Beijing: China Communications Press*.
Zhang, X. G. et al. 2018. Research on the bearing capacity of hollow concrete-filled steel exterior wall composite bridge tower column. *China Civil Engineering Journal* 51(3): 90–98.
Zhu, Y. Y. et al. 2018. Experimental and theoretical study on pullout resistance of single-hole thin-rib perfobond connectors. *China Journal of Highway and Transport* 31(9): 65–74.

Bridge Maintenance, Safety, Management, Digitalization and Sustainability – Jensen, Frangopol & Schmidt (eds)
© 2024 The Author(s), ISBN 978-1-032-77040-6
Open Access: www.taylorfrancis.com, CC BY-NC-ND 4.0 license

Structural behavior of steel truss girder with thick concrete deck in cable-stayed bridge

Y.Q. Li, Y.C. Feng, X. Hou & S.L. Yan
CCCC First Highway Consultants Co., Ltd, Xi'an, China

H.J. Liu & C.S. Wang
Department of Bridge Engineering, College of Highways, Chang'an University, Xi'an, China

ABSTRACT: The composite girder cable-stayed bridge has been widely used in engineering for its advantages of light weight and large spanning ability. However, most of the current research mainly focused on the thickness of concrete bridge decks ranging from 25 cm to 30 cm, and there is a lack of research on the mechanical properties of thick concrete decks at side span of long-span cable-stayed bridges. Therefore, this study was carried out to solve the above existing problems. Based on a composite truss girder cable-stayed bridge with a main span of 930 m, the stress performance and reasonable structure of the concrete deck at side span of 46.8cm are studied. First, in order to determine the most unfavorable position of the side span, a multi-scale model was established. Then, considered the dead load and live load effect, the refined analysis framework was developed. The results shown the longitudinal stress in the concrete deck is uneven along the transverse direction, especially in the cable anchorage section, and a small tensile stress appears on the upper surface of concrete deck near the auxiliary pier. In addition, the transverse stress is the smallest at the upper chords on both sides along the width direction Along the thickness direction, the stress on the upper surface of concrete deck is the most unfavorable, the stress is gradually decreasing from top to bottom surface.

1 INTRODUCTION

In recent years, the combination structure of steel and concrete has been increasingly widely used in large-span cable-stayed bridges due to its advantages such as good stress performance and light weight (Karoumi. 1999, Su et al. 2016, Xiang et al. 2000). The composite girder cable-stayed bridge combines the characteristics of both composite girder bridge and cable-stayed bridge. This type of bridge uses concrete deck instead of orthotropic steel bridge decks, which not only saves steel but also improves the stiffness and stability of the structure, avoiding the problem of fatigue cracking in orthotropic steel bridge decks (Xin et al. 2014).

The main beam of a composite cable-stayed bridge is generally prestressed concrete or steel, and the concrete deck is usually prefabricated. Shear connection keys are arranged on the above of the steel main beam and transverse connection structure, and integrating precast concrete deck with steel girder through cast-in-place wet joints. Based on in-situ testing and finite element analysis for a composite girder cable-stayed bridge, Wang et al. (Wang et al. 2023, Zhang et al. 2023) conducted a study on the longitudinal stress distribution in concrete deck at different construction stages. Meng et al. (Meng et al. 2022) studied the cracking problem of concrete bridge deck in the anchorage zone of composite girder cable-stayed bridges. The standard thickness of concrete decks is 28 cm. They analyzed the stress distribution characteristics, cracking mechanism, and crack morphology of the cables anchorage zone, and provided some crack resistance measures and reinforcement suggestions. Some scholars have conducted

DOI: 10.1201/9781003483755-438

systematic research on the effects of cable-stayed arrangement, and different connection methods between towers and steel truss girder. Walther (Walther 1999) have taken a three span cable-stayed bridge with a main span of 200 m as an example, obtained the influence of the above parameters on the static behavior of the cable-stayed bridge. Compared to the stiffness changes of the main beam or bridge tower, the overall stiffness and internal force distribution of cable-stayed bridge structures are more significantly affected by the arrangement of cable-stayed cables and the connection methods between towers and beams. In addition, other studies have conducted to investigate the concrete deck response and stress state of a composite truss cable-stayed bridge under dynamic loads (Du et al. 2010).

In summary, there is relatively little research on stress behavior of composite girder cable-stayed bridge with a thick concrete deck exceeding 40 cm. Therefore, this article is based on a large-span composite truss cable-stayed bridge with thick concrete deck for the side span, the stress performance of thick concrete deck is studied. What's more, the influence of concrete bridge deck thickness on the longitudinal and transverse stress distribution of the main load-bearing components of the structure was analysed.

2 BRIDGE INFORMATION

The composite beam cable-stayed bridge with a total length of 1779.5 m, as shown in Figure 1. The overall width of the bridge deck is 29.8 m, with tow lanes in both directions. There are two forms of bridge deck, the main span and side span are located within a range of 30 m near the main tower, with a total length of 990 m both adopt an orthotropic steel bridge deck. For the remaining length of the side spans, a composite structure of thick concrete bridge deck and steel truss is adopted, and the concrete bridge deck thickness is 468 mm.

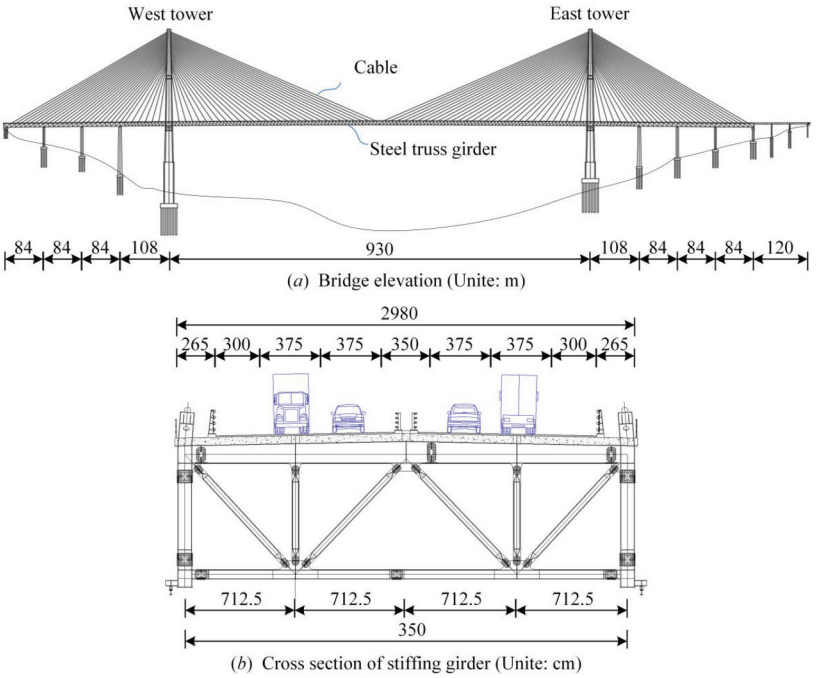


Figure 1. Sketch of a real composite truss cable-stayed bridge.

3 FINITE ELEMENT ANALYSIS

3.1 *Multi-scale bridge model*

Based on the pre-calculated results of the full-bridge model, it can be concluded that the negative moments of auxiliary pier at the side span is relatively large. Therefore, the auxiliary pier section of the side span was selected for analysing. If the entire bridge model uses solid elements, the computational workload is too large to solve. In order to balance computational efficiency and accuracy, a multi-scale finite element model is established, as shown in Figure 2. The local steel truss girder is simulated by shell element (S4R), and the concrete deck is simulated by solid element (C3D8R), the remaining parts of the main girder and concrete tower are simulated by girder element (B31). The cables and steel fabric are simulated by truss element (T3D2). To ensure stress and displacement coordination between interfaces of different scale elements, it is necessary to reasonably set the interaction and boundary conditions between different scale element. The concrete tower and cable are connected through MPC Tie, while the cable and steel truss are connected through a shared node. The sliding action between the steel truss and the concrete deck slab is not considered, so they are connected by binding constraints. The steel mesh is directly embedded in the concrete.

FE model boundary conditions are set as same as the actual bridge boundary conditions, as shown in Figure 2. Fixed constraints are applied at the bottom of the bridge tower, and Two translational degrees of freedom and one torsional degree of freedom of the constrained are used on the support node at the auxiliary pier on both sides (U_x=U_z=R_z=0). On one side of the end of the main beam, one direction of translational freedom and one direction of torsional freedom was constrained (U_x=R_z=0). on the other side of the end of the main beam, the translational degrees of freedom in two directions and the torsional degrees of freedom in one direction was constrained (Ux=Uy=Rz=0).

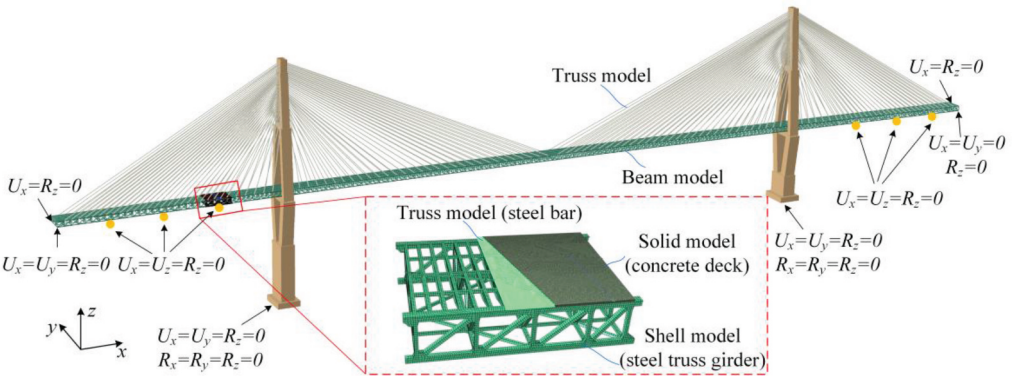


Figure 2. Multi-scale finite element model.

3.2 *Loading scheme*

For the composite cable-stayed bridge, the dead load occupies a large proportion in the total load of the bridge, and the vehicle loads directly on the bridge deck, which affects the stress state of the concrete deck, so the structural response of the thick concrete deck under the dead load and vehicle load is considered. When calculating the stress performance of the bridge structure, the vehicle load effect is loaded using lane load I recommend in standard (Ministry of Transport of the People's Republic of China. 2015), the lane load I consists of a concentrated force and a uniform load, where the uniform load value is 10.5 kN/m and the concentrated force value is 360 kN. As multi-lane loading conditional, it is necessary to carry out longitudinal and transverse reductions. Considering lane load I loading in all lanes, the reduced factor of transverse and longitudinal was set as 0.67 and 0.94 respectively.

4 MAJOR RESULTS AND DISCUSSION

4.1 *Stress analysis of thick concrete deck*

In the composite truss girder cable-stayed bridge, the concrete deck and the steel truss girder both bears the dead load and live load. Under the various loads such as tension cable force, self-weight, and vehicle load, the stress situation of concrete deck and steel truss girder is complicated. Therefore, four typical cross-sections including cable anchorage section (H1), cross section without crossbeam (H2), cross section with crossbeam(H3), and cross section at the top of auxiliary pier (H4) are selected to study the distribution of longitudinal stress in the concrete deck, as shown in Figure 3(a). Since the main girders are symmetrical along the center line of the bridge deck, only half of the bridge deck is selected for analyzing the distribution pattern of transverse stress in thick concrete deck. In order to compare the transverse stress distribution at different cross-section locations along the width of the bridge deck, the cross-section located at the top chord (Z1), the cross-section between the small longitudinal beams (Z2), and the cross-section at the position of the small longitudinal beams (Z3, Z5) were selected for analysis. Due to the thicker of the concrete deck, the distribution law of longitudinal stress and transverse stress along the concrete thickness direction are worth paying attention. To study the distribution law of longitudinal and transverse stress along the concrete deck thickness direction at the position of auxiliary pier, three typical sections of the concrete deck are selected, such as the top, bottom and middle surface of the concrete deck.

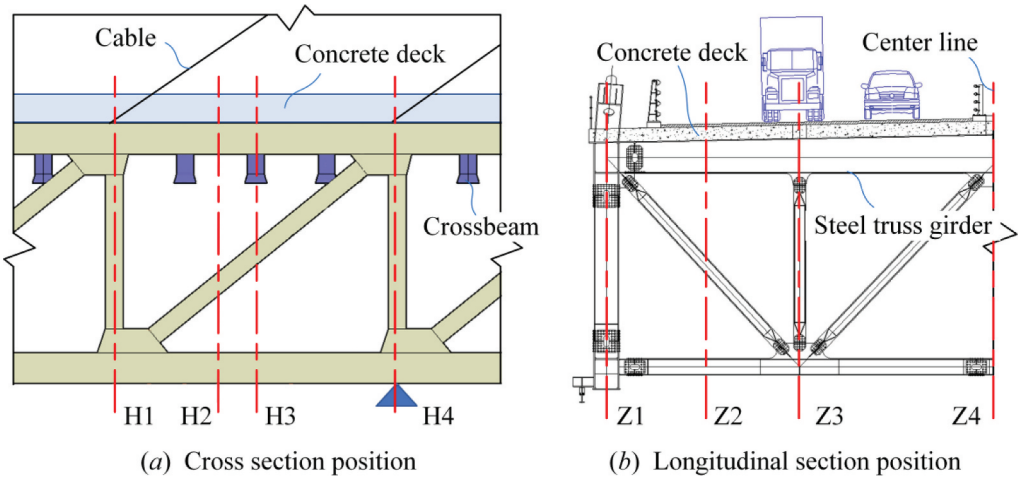


Figure 3. Concerned section position of concrete deck.

4.1.1 *Longitudinal stress*

Figure 4 shows the longitudinal stress calculation results for four typical sections of concrete bridge deck under the dead load and live load. It can be seen from Figure 4 that at different cross-section locations, the longitudinal stress in the concrete deck is dominated by compressive stress, and the longitudinal compressive stress in the concrete deck gradually decrease along the thickness direction. While along the width direction of the concrete deck, the stress changes significantly at the small longitudinal beams, and the stress distribution at the bottom surface of the concrete deck is most affected by the small longitudinal beams. For cross-section with and without cross-section, the longitudinal stress distribution is not uniform, and the closer to the two sides of the top chord section, the smaller the longitudinal stress. For the cross-section at the location of the auxiliary pier, there are tensile stresses observed on the top surface of the concrete deck, while the bottom surface of the concrete deck continues to bear compressive stress. The reason for the tensile stress on the top surface of the concrete deck may be due to the negative bending moment at the top of the pier.

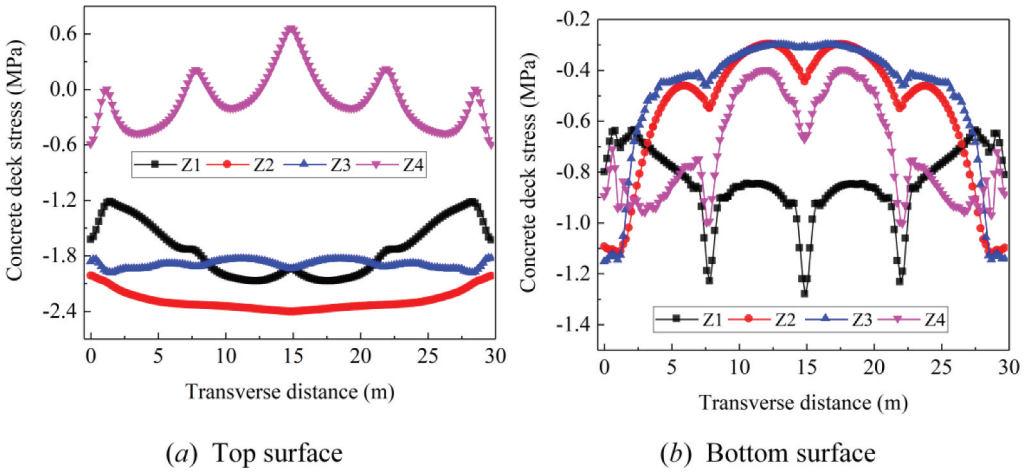


Figure 4. Longitudinal stress along the considered cross-section of concrete deck.

4.1.2 *Transverse stress*

The transverse stress calculation results for four key cross-sections of the concrete bridge deck at the pier are illustrated in Figure 5, with the coordinate origin located at the cable anchorage section on the side away from the tower. Based on the calculation results in Figure 5, it can be observed that the transverse stress along the longitudinal distribution of the Z1 section fluctuates relatively less compared to other sections. However, the overall transverse stress level is relatively low, and there is not significant variation in stress along the thickness direction. For the Z2 to Z4 sections, the transverse stress significantly fluctuated, particularly near the small longitudinal beams. This indicates that the small longitudinal beams influence the distribution of transverse stress. Comparative analysis of transverse and longitudinal stress distributions across several sections, the transverse stress in the concrete deck is generally lower than the longitudinal stress except for the section position where the concentrated force of lane load acts. Moreover, the closer to the top chord position, the smaller the transverse stress in the concrete deck.

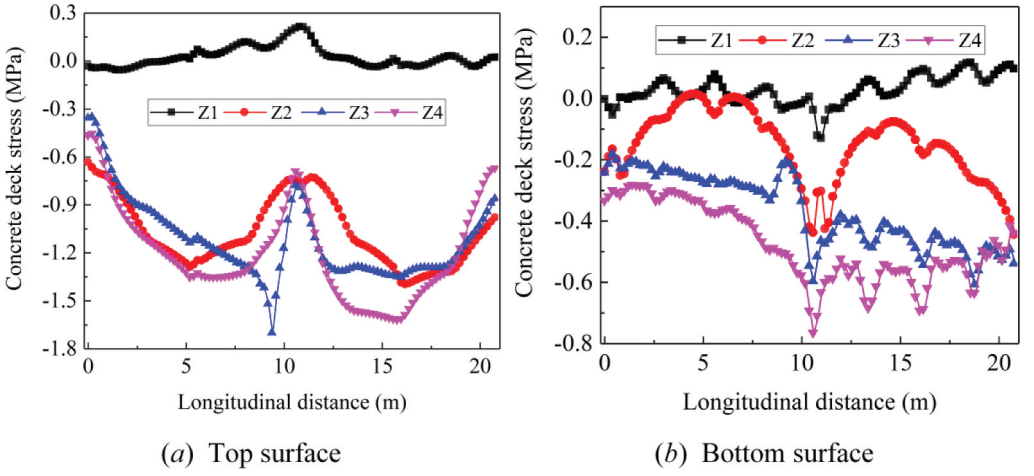


Figure 5. Transverse stress along the considered cross-section of concrete deck.

4.2 *Stress analysis of steel truss girder*

Figure 6 shows the longitudinal and transverse stress calculation results for the upper and lower chords of the steel truss girder at the auxiliary pier. It can be seen from Figure 6 (*a*) that the upper and lower chords of the main truss are mainly subjected to longitudinal forces. From Figure 6(b), it can be observed that the transverse stress in the upper chord of the main crossbeam is mainly compressive stress. Specially, there is a significant variation in transverse stress at the location of the small longitudinal beams. The lower chords of the main transverse truss primarily experience transverse forces. Near the sides of the upper chords, the transverse stress is compressive, while between the lateral longitudinal beams, the transverse stress in the lower chords changes from compressive to tensile.

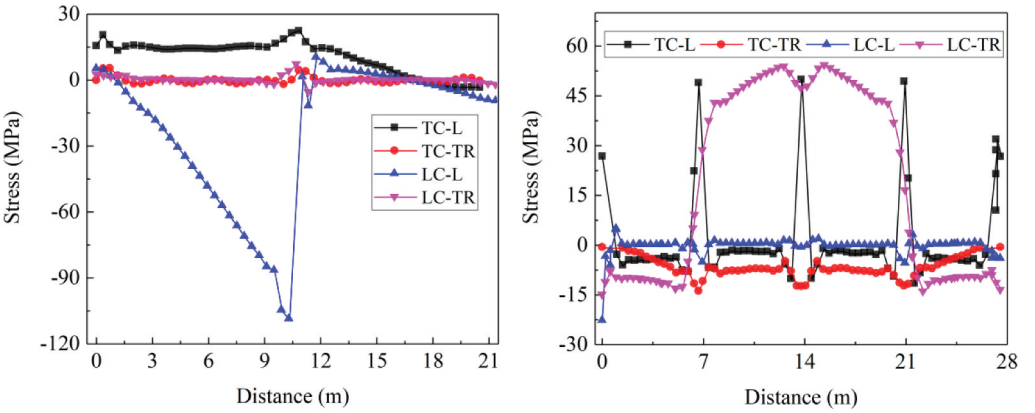


Figure 6. Stress along the considered cross-section of steel truss girder.

4.3 *Influence of concrete deck thickness*

A parametric analysis was conducted to investigate the influence of concrete deck thickness on the distribution of longitudinal and transverse stresses in the concrete deck and steel truss girder,. The concrete deck thickness was set as 300 mm, 350 mm, 400 mm, 500 mm, 550 mm, and 600 mm, respectively, the width of the concrete deck remained unchanged

4.3.1 *Stress distribution law of concrete deck*

From the calculation results in Section 4.1.1, it is evident that tensile stresses appear on the top surface of the concrete deck near the auxiliary pier, which could potentially lead to concrete deck cracking. Consequently, the cross-section of the concrete bridge deck at the auxiliary pier (H4) was selected to analyze the influence of concrete deck thickness on stress distribution in the concrete deck. Figure 7 shows the longitudinal stress distribution in concrete bridge deck of different thicknesses. According to the calculation results in Figure 7, it can be seen that, the smaller the thickness of the concrete bridge, the greater the longitudinal stress. With the increase of the concrete deck thickness, the longitudinal stress across the concrete deck section decrease, and the distribution of longitudinal stress becomes more uniform. Additionally, the concrete bridge deck above the upper chord changes from compressive stress to tensile stress. The reason for this phenomenon may be that as the thickness of the concrete bridge deck increases, it leads to an increase in the stiffness of the structure.

4.3.2 *Stress distribution law of steel truss*

For steel materials, the commonly accepted yield criterion is the von Mises yield criterion. When the equivalent stress exceeds the yield stress of the material, the structure will undergo plastic deformation. The von Mises stress in the members of the main truss and main

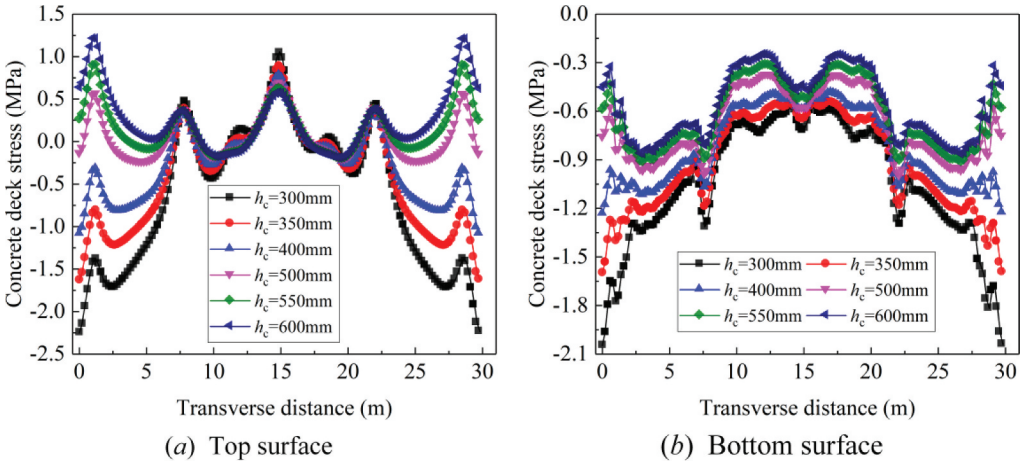


Figure 7. The longitudinal stress distribution law of concrete deck.

transverse truss are illustrated in Figure 8. It can be seen in Figure 8, as the thickness of the concrete deck increases from 300 mm to 600 mm, the von Mises stress in the members of the main truss initial decrease and gradually increase. As for the members of the main transverse truss, von Mises stress gradually increased. Through analysis, it is determined that the components with less favorable stress are diagonal web members and lower chord members. For the main transverse truss, the components with less favorable stress are the upper chord and diagonal web members.

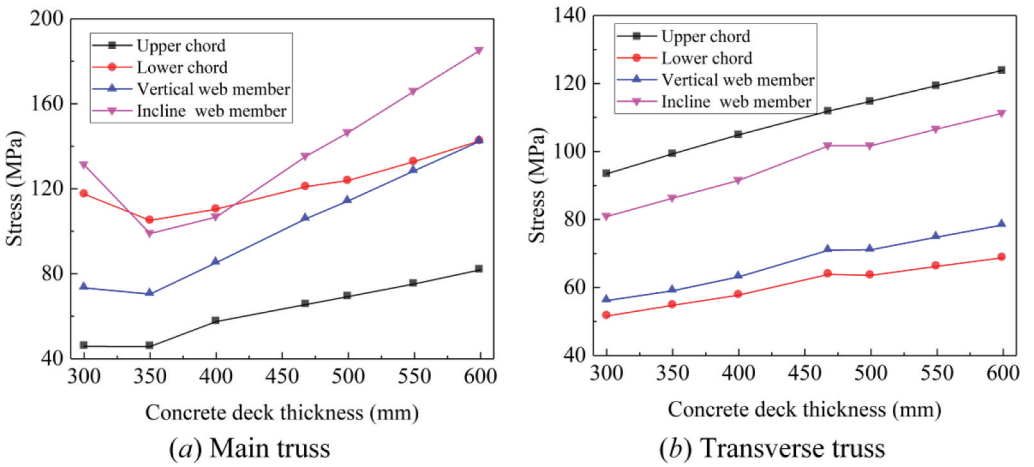


Figure 8. The influence of concrete deck thickness on the steel truss girder.

5 CONCLUSIONS

This article analyzed the stress distribution law of thick concrete bridge deck at the auxiliary pier of the side span under dead load and live load. On this basis, a parameter analysis was conducted to investigate the influence of concrete deck thickness on the distribution of longitudinal and transverse stresses in the concrete deck and steel truss girder. The main conclusions are as follows:

(1) The main direction of stress on the thick concrete bridge deck is the longitudinal direction of the bridge, indicating that the thick concrete deck is a one-way slab.
(2) The main truss is primarily subjected to longitudinal stress, while the transverse truss mainly bears transverse stress. For the main truss, the most unfavorable members are the inclined web and the lower chord. Conversely, for the transverse truss, the most unfavorable members are the upper chord and inclined web.
(3) As the thickness of the concrete bridge deck increases, the longitudinal stress distribution in the concrete bridge deck becomes more uniform, while the transverse stress increases with the increase of thickness. The longitudinal stress and transverse stress in the main truss and main transverse truss gradually increase with the thickness of the concrete bridge deck.
(4) Taking into account the stress distribution law of concrete deck and steel truss girder, the thickness of concrete deck is recommended as 400 mm to 500 mm for composite cable-stayed bridges with small side to span ratios and side span that require weight compression.

ACKNOWLEDGEMENT

The authors gratefully acknowledge the financial support provided by the Innovation Capability Support Program of Shaanxi (2019TD- 022), the Research on Key Technology of Design of Long-span Composite Truss Girder Cable-stayed Bridges with Super High Towers in Mountainous and Deep Valley Areas-Subject 2: Research on reasonable structure and design method of plate - truss composite girder (Topic 4, Topic 5), the Chang'an University Central University Basic Scientific Research Fund Green Highway Key Special Support Plan (300102219309), the Key Technology Project in the Transportation industry (2021-MS1-049), and the Science and Technology Innovation Fund Project of China Communications First Highway Survey, Design and Research Institute Co., Ltd (KCJJ2021-20).

REFERENCES

Karoumi, R. 1999. Some modeling aspects in the nonlinear finite element analysis of cable supported bridge, *Comput Struct*, 71(4): 397–412.

Su, Q. K. & Xie, H. B. 2016. Summary of Steel Bridge Construction of Hong Kong-Zhuhai-Macao Bridge. *China Journal of Highway and Transport*, 29(12): 1–9. (in Chinese).

Xiang, H. F. 2000. Outlook on World Bridge Engineering in the 21st. *China Civil Engineering Journal*, 33 (3): 1–6. (in Chinese).

Xin, H, Liu, Y, et al. 2014. Experimental and analytical study on stiffened steel segment of hybrid structure. *J Constr Steel Res*, 2014, 100: 237–258.

Wang, C. S., Zhang, W. T. et al. 2023. Shear Lag Effect of Composite Girders in Cable-Stayed Bridges under Dead Loads[J]. *Eng. Struct*., 281, 115752.

Zhang, W. T., Wang, C. S., et al. 2023. Shear Lag Effect of Composite Cable-Stayed Bridges under Dead and Live Loads[J]. *Struct. Infrastruct. Eng*., 1–17.

Meng, J. M., Liu, Y. J, et al. 2022. Diagonal cracking mechanism and reinforcement design method of bridge decks in cable girder anchorage zone of composite girder cable-stayed bridge, *Journal of Traffic and Transportation Engineering*, 22(6): 114–129. (in Chinese).

R. Walther, 1999. Cable Stayed Bridge, Second edition. American Society of Civil Engineers (Thomas Telford, Ltd.).

Du, X. G, Jin X. L. et al. 2010. Dynamic Analysis of Steel Plate-Truss Composite Girder on Long Span Two-layer Cable-stayed Bridge. *Journal of Civil and Environmental Engineering*, 32(2): 82–86. (in Chinese).

Ministry of Transport of the People's Republic of China. 2015. Design Specification for Highway Steel Structure Bridges. Beijing: China Communications Press. (in Chinese).

Bridge Maintenance, Safety, Management, Digitalization and Sustainability – Jensen, Frangopol & Schmidt (eds)
© 2024 The Author(s), ISBN 978-1-032-77040-6
Open Access: www.taylorfrancis.com, CC BY-NC-ND 4.0 license

Reasonable degree of shear connection for thick concrete deck in cable-stayed bridge

Y.Q. Li, Y.C. Feng & X. Hou
CCCC First Highway Consultants Co., Ltd, Xi'an, China

H.J. Liu & C.S. Wang
Department of Bridge Engineering, College of Highways, Chang'an University, Xi'an, China

ABSTRACT: Based on the previous research of structural performance of composite truss girder with thick concrete deck in cable-stayed bridge, the reasonable degree of shear connection for such bridge was carried out here. Considering the material and geometric nonlinearity, a local finite element model was established to study the mechanical performance of the composite truss girder with thick concrete deck of the cable-stayed bridge. The influence of the shear connection degree on the mechanical performance of the composite truss girder is studied. Moreover, the shear lag effect of thick concrete deck of composite cable-stayed bridge is analyzed. The results indicate that the maximum relative slip of the interface occurs at the anchorage of the cable, and the relative slip of the interface increases obviously under the vehicle load. The degree of shear connection has a great influence on the stress of thick concrete deck, steel truss girder as well as studs. In addition, the closer to the auxiliary pier, the effective distribution width of thick concrete deck is gradually decreased, and it will increase with the thickness of concrete deck. On the above research results, the reasonable layout scheme of shear connection is obtained.

1 INTRODUCTION

The cable-stayed bridge is mainly composed of three basic components: the main beam, cables, and cable towers. Based on the research by domestic and foreign, composite beam cable-stayed bridges are more competitive than other types of bridges when the span is between 400m and 700m. Composite truss girder is a new type of composite structure developed on the basis of traditional composite girder. The concrete bridge deck is connected to the upper chord, small longitudinal beam, and crossbeam through shear connection studs. In composite steel truss girder, the concrete plays a role in transmitting vehicle loads, while also improving the stiffness and stability of the structure (Zhang et al. 2012).

At present, many researchers have conducted research on the complex stress state and design methods of the composite girder cable-stayed bridge, including the internal force distribution relationship between steel main girder and concrete deck, shear lag effect and shrinkage creep effect of concrete deck (Chen et al. 2019). Pedro et al. (Pedro et al. 2010) established a finite element model of a composite girder cable-stayed bridge with a concrete deck thickness of 25 cm, analyzing the mechanical properties of the structure during construction, while considering the effects of nonlinearity and concrete shrinkage and creep. Wei et al. (Wei et al. 2013) conducted elastic and elastic-plastic analysis on composite cable-stayed bridge through finite element numerical simulation. The thickness of the concrete bridge deck was 26 cm, and a segment experiment model was established to study the distribution of stress along the beam height. The load distribution relationship between the concrete bridge deck and the steel girder was obtained.

DOI: 10.1201/9781003483755-439

The shear connection stud is important component in composite girders, which connecting concrete and steel into a whole to coordinate and deform under external load, the bearing capacity of the composite girder will be affected once slippage and compression deformation occur between the shear connection stud and the concrete. In composite structures, due to the influence of shear deformation on the distribution of bending stress, there is a shear lag phenomenon in concrete deck, and the longitudinal stress is unevenly distributed along the width direction. What's more, the shear lag phenomenon is more significant in wide slabs (Zhu et al. 2015). As the span of the cable-stayed bridge increases, the width of the bridge deck also increases, and there is a significant shear lag effect in the concrete bridge deck, which is worthy of attention (Wang et al. 2023, Zhang et al. 2023). Tian et al. (Tian et al. 2005) used a simplified analytical method to study the shear lag effect of concrete flange plate in steel-concrete composite beams under different forms of loads. Based on the thin plate theory, strain and deflection differential equations were established, and the calculated shear lag coefficient was close to the numerical calculation results, indicating that the calculation method has high accuracy. The parameter analysis results indicate that the width to span ratio and load form have a significant impact on the shear lag effect. Wang et al. (Wang et al. 2022) conducted a series of studies on the shear lag effect in a concrete bridge deck of a double steel composite beam cable-stayed bridge. By considering multiple load conditions in model tests, the distribution of longitudinal stress in concrete was analyzed, under the combined effects of positive and negative bending moments, axial forces, and shear forces.

In summary, research on the structural form of composite truss cable-stayed bridges is still insufficient, and current regulations also lack relevant provisions. Therefore, this article is based on a large-span composite truss cable-stayed bridge with thick concrete deck. The shear lag effect of thick concrete bridge deck of the composite truss cable-stayed bridge is analyzed, and the effective width coefficient of different section positions is calculated. In addition, the influence of interface relative slip, shear connection degree, and width span ratio on the effective width coefficient of thick concrete bridge deck is analyzed.

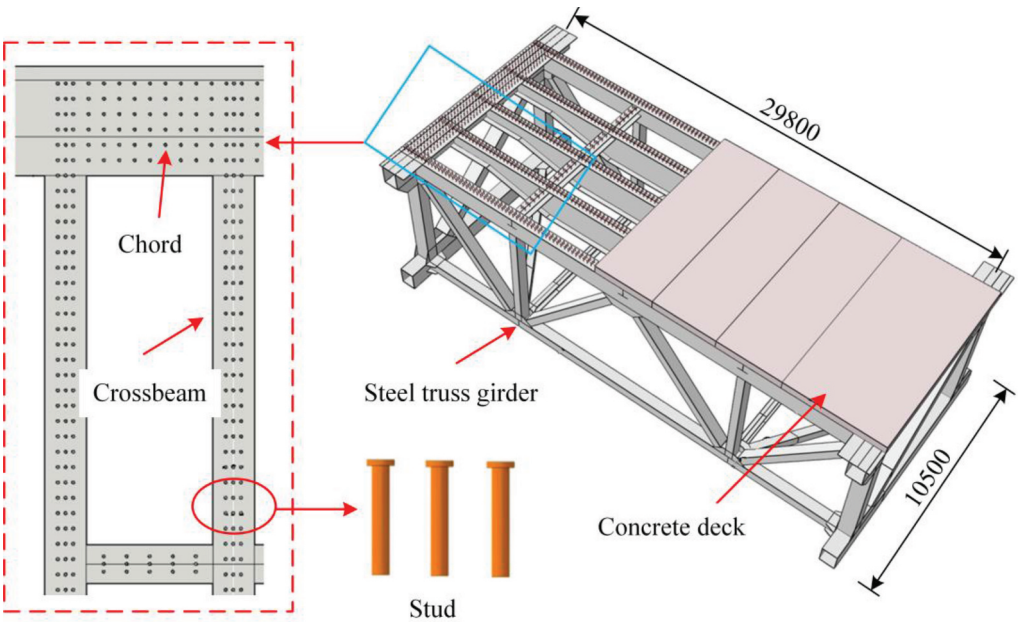


Figure 1. Layout of the typical segment (Unit: mm).

2 CASE STUDY

The puzhehei bridge is a spatial double cable plane composite truss cable-stayed bridge with a main span of 930 m. The main span is a slab truss composite steel truss girder, and the side span is a concrete bridge deck steel truss composite girder with a concrete bridge deck thickness of 468 mm. The concrete deck has a full width of 29.8 m and the bridge is arranged in a two-way four lane layout. The standard segment of the side span is shown in Figure 1.

3 FINITE ELEMENT ANALYSIS

3.1 *Local refinement finite element model*

In general, the steel truss and concrete bridge deck are connected by shear connection studs, and the connection between the two determines the overall stress performance of the composite girder. In order to study the stress performance of composite truss girder under relative interface sliding, a local refined segment model of the composite truss girder was established, as shown in Figure 2. In the segmented numerical model, both concrete and studs are use C3D8R three-dimensional hexahedral elements, and the steel truss girder is simulated using S4R elements. Based on the specification (National Standard of the People's Republic of China GB50010. 2010.), the concrete material properties are obtained. To accurately simulate the connection between concrete deck and steel truss girder, the normal interaction between concrete deck and steel truss girder is set as hard contact, and the tangential interaction adopts penalty friction, with a friction coefficient of 0.4. Studs are embedded into concrete bridge decks, the bottom surface of the steel truss girder and studs is bound together through MPC-Tie. According to relevant literature, a simply supported boundary is adopted in the FEM.

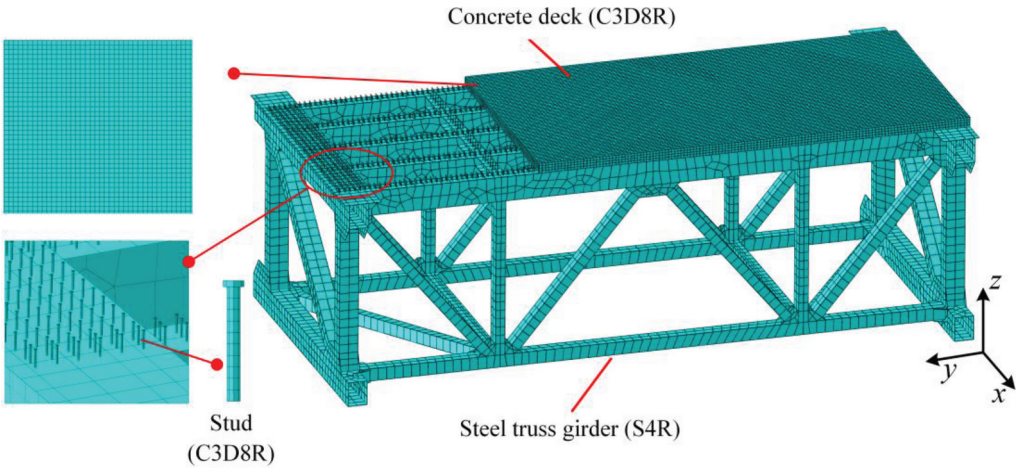


Figure 2. Local refined finite element model.

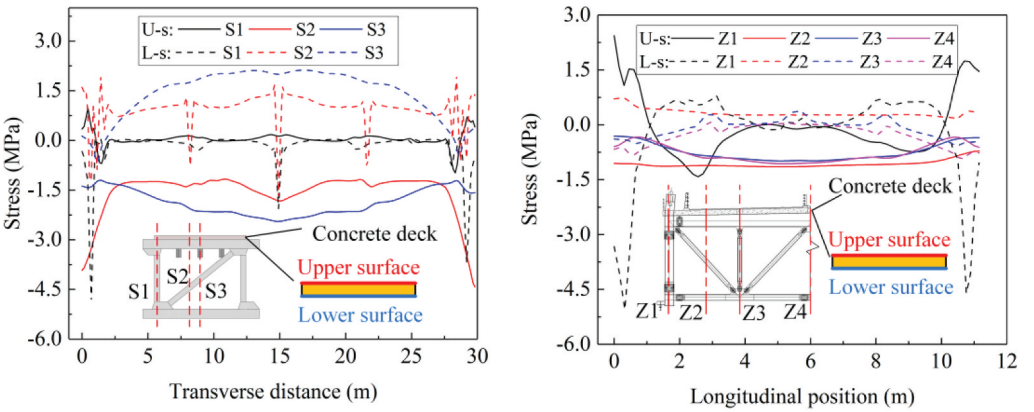
3.2 *Loading case*

When calculating and analysing the overall stress performance of the structure, the vehicle lane load I was selected as recommended in specification (Ministry of Transport of the People's Republic of China. 2015.). The Lane load I consists of concentrated forces and uniformly distributed loads, with a uniformly distributed load of 10.5 kN/m and a concentrated force of 360 kN. The load condition is set to deploy vehicle lane load I on all lanes, and the longitudinal and transverse reductions on vehicle lane load I was considered. The load effect of cables is simulated by applying axial and vertical forces.

4 FE RESULTS

4.1 *Stress distribution law of concrete bridge deck*

To study the stress distribution in concrete bridge decks under live load and dead load, the FEM was calculated according to the load arrangement in section 3.2. Figure 3 shows the longitudinal stress distribution of some key sections in concrete deck under constant and vehicle loads. It can be seen from Figure 3 that for concrete deck, the longitudinal stress at the cross-section with crossbeams is generally greater than that of other cross-sections, and the longitudinal stress shows a symmetrical distribution pattern along the width direction of the concrete deck. For transverse stress in concrete deck, the section between the small longitudinal beams is generally greater than that of the other sections. Furthermore, there is a sudden change in the distribution of longitudinal and transverse stresses in the concrete deck, the current mutation is mainly located at the location where the concentrated force of the vehicle load. This indicates that the concentrated force of vehicle load has a certain impact on the stress distribution of the bridge deck.



(*a*) Longitudinal stress (*b*) Transverse stress

Figure. 3. Stress analysis of concrete deck.

4.2 *Effective width coefficient of concrete deck*

There is a longitudinal shear force at the interface between steel and concrete in composite girder. Under the influence of longitudinal shear force transmission, the stress distribution in concrete shows significant non-uniformity, resulting in the phenomenon of shear lag. Due to the thickness of the concrete deck reaching 468 mm in this study, the distribution of stress along the thickness direction must be considered when calculating the effective width, as shown in Equation 1. The effective width coefficient that characterizes the shear lag effect can be calculated according to the Equation 2 (Ministry of Transport of the People's Republic of China. 2015.).

$$b_e = \frac{\int_0^{h_c}\int_0^{b}\sigma(x,y,z)\mathrm{d}y\mathrm{d}z}{|\sigma_{max}|h_c} \tag{1}$$

$$\eta = \frac{b_e}{b} \tag{2}$$

Where b_e is the effective width of the concrete deck; x, y, z represent the longitudinal, transverse, and vertical directions of concrete deck, respectively; $\sigma(x, y, z)$ is the longitudinal stress in concrete deck; σ_{max} is he maximum normal stress in concrete deck; h_c is the thickness of the concrete deck; b is the actual width of concrete deck; η is the effective width coefficient.

The value of effective width coefficient of concrete bridge deck was obtained, as shown in Table 1., it can be seen the average value of effective width coefficient of the concrete deck is 0.60 in the side span, and the maximum effective distribution width coefficient of the concrete bridge deck near the auxiliary pier is 0.78. In addition, the closer to the auxiliary pier, the smaller the effective distribution width of the section, which may be due to the large negative bending moment of the section at the auxiliary pier.

Table 1. Effective width coefficient value of concrete deck.

Section Position	Support position of side span	Middle position of side span	Auxiliary pier
S1	0.46	0.41	0.31
S2	0.78	0.60	0.71
S3	0.73	0.58	0.72

5 PARAMETRIC STUDY

5.1 *The influence of stress distribution law on concrete deck*

In order to study the stress response of concrete deck under different degrees of shear connection, variable parameter analysis was conducted on the shear connection degrees at the top chord, transverse truss, and transverse beam, respectively. The number of studs per unit length of the upper chord n_1 is set as 17, 25, 34, 38, 46, and 59, respectively. The number of studs per unit length range at the transverse truss and crossbeam n_2 is set as 10, 11, 12, 13, 14, and 15, respectively. Figure 4 shows the variation of maximum longitudinal and transverse stress in the concrete deck when different degrees of shear connection are used between the steel truss girder and the thick concrete deck. It can be concluded that as the number of studs per unit length of the upper chord increases, the longitudinal tensile stress of concrete deck gradually decreases and then increases, and then remains basically unchanged. In summary, the influence of the number of studs per unit length of the crossbeam on the longitudinal compressive stress of the concrete bridge deck can be ignored.

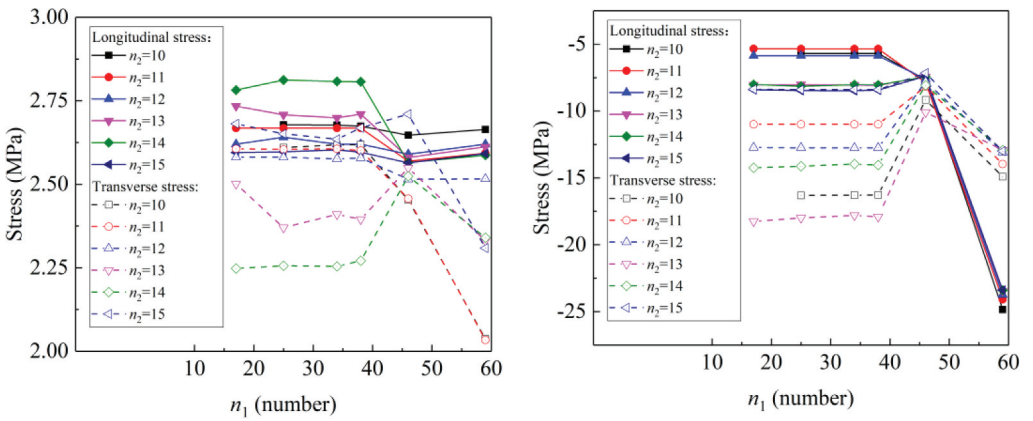


Figure 4. The influence of shear connection degree on the stress performance of concrete deck.

As the number of studs per unit length of the upper chord increases, the transverse tensile stress of the concrete deck gradually decreases and then increases, and then gradually decreases. However, the transverse tensile stress of concrete deck initially remains basically unchanged, and then shows a trend of increasing and then decreasing. When the number of studs per unit length

of the upper chord is less than or equal to 46, as the number of studs per unit length of the crossbeam increases, the stress of the concrete bridge deck shows a trend of increasing and then decreasing.

5.2 *Variations of effective distribution width coefficient*

5.2.1 *Influence of shear connection degree*

The effective width coefficient value of concrete deck with different degrees of shear connection were obtained. Due to spatial limitations, only the calculation results for n_1 equal to 38 and 46 are listed, as shown in Figure 5. Through calculation and analysis, it was found that n_1 less than or equal 38, the change in the degree of shear connection of the upper chord had little effect on the effective width coefficient of the concrete deck. As the value of n_1 greater than or equal 46, The effective width coefficient of the cross-section is significantly reduced. When the degree of shear connection at the crossbeam increases, the effective width coefficient of the section significantly decreases. As the value of n_2 is equal to 11, the effective width coefficient of the concrete deck is the highest.

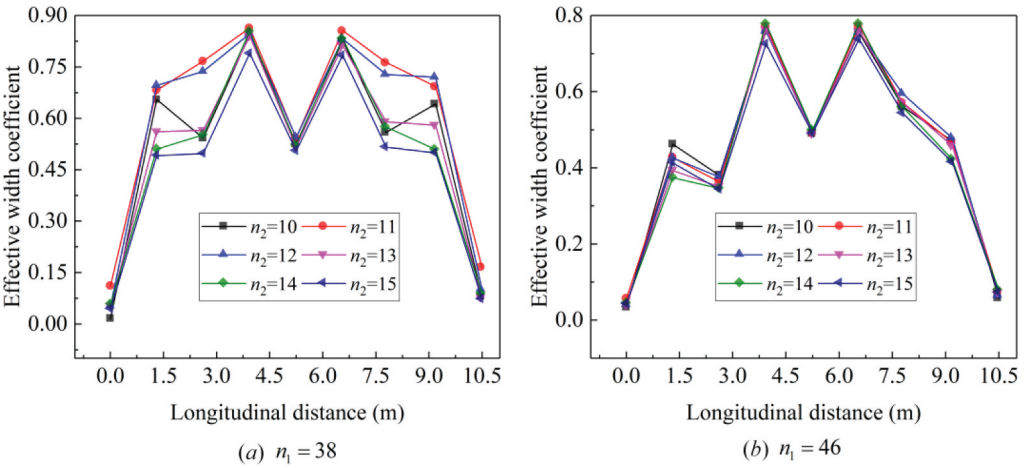


Figure 5. The influence of shear connection degree on the value of effective width coefficient.

5.2.2 *Influence of concrete deck thickness*

When the thickness of the concrete deck is 300 mm, 350 mm, 400 mm, 468 mm, 500 mm, 550 mm, and 600 mm respectively, the effective width coefficients of each key section of the concrete deck are shown in Figure 6 (a). It can be seen for the cable anchorage section, as the concrete thickness increases from 300 mm to 400 mm, the effective width coefficient gradually increases. As the thickness continues to increase, the effective width coefficient gradually decreases. In the middle non-cable anchorage section, as the thickness of concrete increases, the effective width coefficient of the concrete deck gradually increases. The reason for this phenomenon may be that as the thickness of the concrete deck increases, the section stiffness increases, resulting in the stress distribution on the concrete deck section more uniform.

5.2.3 *Influence of width to span ratio (b/L)*

When the length of the concrete segment increases to three intervals, the b/L value decreases. In order to improve the computational efficiency and convergence of the model, studs are only arranged on the surface of the concerned area. Figure 6 (b) shows the variation of the effective width coefficient of each key section with the width to span ratio. It can be concluded that when the b/L decreases, the effective width coefficient of the cable anchorage section significantly increases. This is may be the attention section is further away from the boundary conditions.

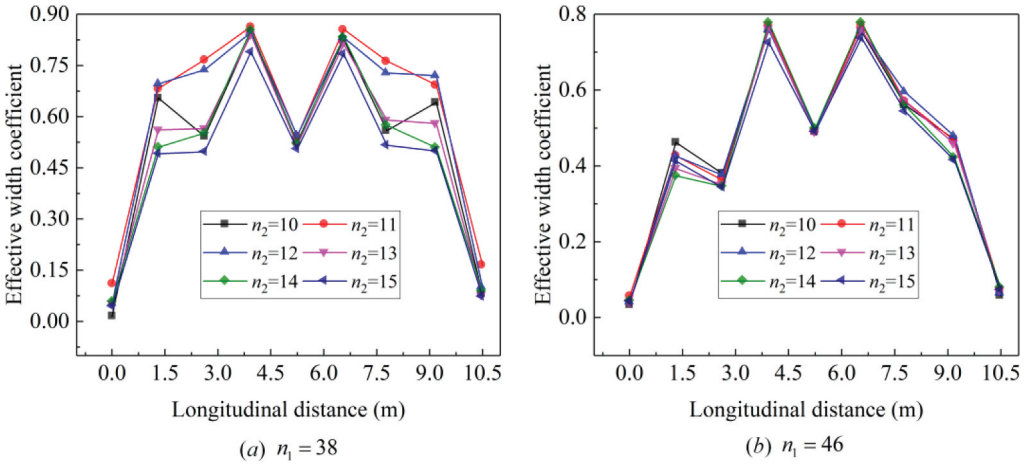


Figure 6. The distribution of effective width coefficient.

Further analysis revealed that the effective width coefficient of L/8 and 7L/8 section is smaller than other cross-sections. The effective width coefficients of 3L/8 section, 5L/8 section, and mid span section all increase as the pan ratio decreases. This indicates that when the width to span ratio decreases, the stress distribution in the mid span concrete bridge deck will be more uniform.

6 CONCLUSIONS

This article establishes a local refined numerical model to study the stress distribution in thick concrete bridge decks under dead and live loads. The influence of shear connection degree on the stress performance of concrete deck is analyzed, and the main conclusions are as follows:

(1) Considering the longitudinal and transverse stress of the concrete deck, it is recommended to use 46 studs per unit length of the upper chord and 11 studs per unit length of the transverse truss and crossbeam. The recommended height of stud for thick concrete deck should exceed half of the concrete deck thickness by 2 to 5 cm, and it is recommended to take a stud height of 28 cm.
(2) Through FEM analysis, it was found that there is a significant shear lag phenomenon in the concrete deck, and the effective width of the section decreases as it approaches the auxiliary pier position.
(3) Properly reduce the degree of shear connection and utilize slight relative slip at the interface to make the stress distribution of the concrete bridge deck more uniform. The thicker the concrete bridge deck, the greater the effective width coefficient. As the width to span ratio decreases, the effective width coefficient increases.

ACKNOWLEDGEMENT

The authors gratefully acknowledge the financial support provided by the Innovation Capability Support Program of Shaanxi (2019TD- 022), the Research on Key Technology of Design of Long-span Composite Truss Girder Cable-stayed Bridges with Super High Towers in Mountainous and Deep Valley Areas-Subject 2: Research on reasonable structure and design method of plate - truss composite girder (Topic 4, Topic 5), the Chang'an University Central University Basic Scientific Research Fund Green Highway Key Special Support Plan (300102219309), the Key Technology Project in the Transportation industry (2021-MS1-049), and the Science and Technology Innovation Fund Project of China Communications First Highway Survey, Design and Research Institute Co., Ltd (KCJJ2021-20).

REFERENCES

Zhang, Z. X., Nie, J. G. et.al. 2012. Optimization of Mechanical Behavior of Steel and Concrete Continuous Composite Truss Girder Bridge, *Bridge Construction*, 42(6): 57–62. (in Chinese).

Chen, G. H. & Xu, Z. 2019. Study of Mechanical Property of Main Girder for Long-Span Steel-Concrete Composite Girder Cable-Stayed Bridge, *Bridge Construction*, 49(5): 39–44. (in Chinese).

Pedro, J. & Reis, A. J. 2010. Nonlinear Analysis of Composite Steel-Concrete Cable-Stayed Bridges, *Eng. Struct*., 32(9): 2702–2716.

Wei, X. & Qiang, S. Z. 2013. Mechanic Behavior of Steel-Concrete Composite Girder of Long-Span Cable-Stayed Bridge, *Journal of Southwest Jiaotong University*, 48(3): 402–408. (in Chinese).

Zhu, L., Nie, J. G., et al. 2015. Simplified Analysis Method Accounting for Shear-Lag Effect of Steel-Concrete Composite Decks, *J Constr Steel Res*, 115, 62–80.

Wang, C. S., Zhang, W. T., et al. 2023. Shear Lag Effect of Composite Girders in Cable-Stayed Bridges under Dead Loads, *Eng. Struct*., 281: 115752.

Zhang, W. T., Wang, C. S., et al. 2023. Shear Lag Effect of Composite Cable-Stayed Bridges under Dead and Live Loads, *Struct. Infrastruct. Eng*., 1–17.

Tian, C. Y. & Nie, J. G. 2005. Shear lag analysis of simply supported composite steel-concrete beams, *J Tsinghua Univ* (*Sci* & *Tech*), 45(9): 1166–1169. (in Chinese).

Wang, C. S., Zhang, W. T., et al. 2022. Shear Lag Effect of Twin I-Shaped Composite Girders in Cable-Stayed Bridges, *THIN WALL STRUCT*, 180, 109822.

National Standard of the People's Republic of China GB50010. 2010. Code for Design of Concrete Structures. (in Chinese).

Ministry of Transport of the People's Republic of China. 2015. General code for design of highway bridges and culverts. Beijing: China Communications Press. (in Chinese).

Ministry of Transport of the People's Republic of China. 2015. Design Specification for Highway Steel Structure Bridges. Beijing: China Communications Press. (in Chinese).

GS19: BRIDGE SAFETY - Assessment and evaluation


Taylor & Francis
Taylor & Francis Group
http://taylorandfrancis.com

Bridge Maintenance, Safety, Management, Digitalization and Sustainability – Jensen, Frangopol & Schmidt (eds)
© 2024 The Author(s), ISBN 978-1-032-77040-6
Open Access: www.taylorfrancis.com, CC BY-NC-ND 4.0 license

Development of a new abutment connection for rapid construction

F. Sigurjónsson
EFLA Consulting Engineers – Bridge Department, Reykjavík, Iceland

R.S. Smárason
The Icelandic Road and Coastal Administration – Department of Construction Management, Garðabær, Iceland

O.S. Haraldsson
The Icelandic Road and Coastal Administration – Research Department, Garðabær, Iceland

B. Bessason & C.Y. Tsai
Faculty of Civil and Environmental Engineering, University of Iceland, Reykjavík, Iceland

ABSTRACT: This paper describes tests on a new connection between a precast abutment wall and a cast-in-place foundation suitable for rapid construction in seismic regions. The primary goal of this study is to reduce on-site construction time. Its features include both speed and simplicity of erection, as well as generous tolerances. The foundation concept is termed a 'wet socket' connection. Abutment wall elements are precast without exposed reinforcement and feature strategically placed ducts to allow the foundation´s top mat reinforcement to pass through the wall unimpeded. Two scaled specimens were constructed and tested as part of this research. The first specimen served as a reference and was detailed according to current standards in Iceland. The second specimen included the new socket connection. Lateral-load tests on the new connection were completed in 2022. Overall, the performance of the new connection was quite satisfactory and comparable to the reference specimen. The new connection will be implemented in an upcoming road reconstruction and bridge project in North-Iceland.

1 INTRODUCTION

The construction of bridges often results in traffic delays, translating to measurable costs in terms of time, money, and wasted fuel. Therefore, road administrations are actively exploring methods to expedite construction processes, commonly referred to as Accelerated Bridge Construction (ABC). Several strategies for ABC use administrative techniques and/or incorporate inventive financial incentives, while others have relied on new building practices to minimize the duration of on-site work. The use of precast concrete represents a promising technology for ABC demonstrating successful applications in bridge piers within both non-seismic (Matsumoto et al., 2001) and seismic regions (Pang et al., 2010; Haraldsson et al., 2013; Khaleghi et al., 2012; Mashal et al., 2016) For structures in seismic regions, those interfaces represent the locations of high-bending moments and shears. Designing connections for both ease of construction and seismic resistance poses a formidable challenge.

While limited research has been published on ABC technology for bridge abutments, several state agencies in the United States have developed systems to expedite abutment construction (Culmo, 2011). This paper describes a new connection between a precast abutment wall and

DOI: 10.1201/9781003483755-440

a cast-in-place foundation. Two specimens were fabricated and tested. The first specimen was detailed to the current standard in Iceland. The second specimen was detailed with the new connection.

2 CONNECTION CONCEPT

The 'wet socket' connection concept is illustrated in Figure 1. The construction sequence involves fabricating a precast wall element in a controlled environment. The precast wall is equipped with wide horizontal ducts at the bottom, facilitating the passage of top-mat reinforcement from the foundation through the wall to ensure ample moment resistance. The outer surface of the ducts is intentionally roughened to enhance the bond between the precast wall and the cast-in-place concrete. Furthermore, the bottom section of the wall which will be embedded in the foundation is manufactured with roughened surface to increase the binding between the wall and the foundation.

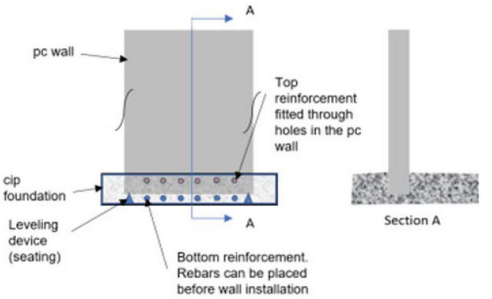


Figure 1. Wet socket wall connection concept.

The proposed construction sequence is as follows: Initially, the wall elements are precast; subsequently, the foundation is excavated, and formwork is constructed. The precast wall elements are then positioned, ensuring proper alignment, leveled, and braced. Following this, foundation reinforcement is installed, and the foundation is cast.

With the new connection, the abutment is constructed in the same amount of time as it takes to construct a foundation alone, using the standard cast-in-place method. In standard practice, the foundation reinforcement is placed in molds and cast with wall reinforcements protruding up from the foundation; then the work with the wall formwork can begin and the wall is cast a few days later. This system's primary advantage over conventional cast-in-place construction is its accelerated speed. Additional benefits include mitigating challenges associated with fitting

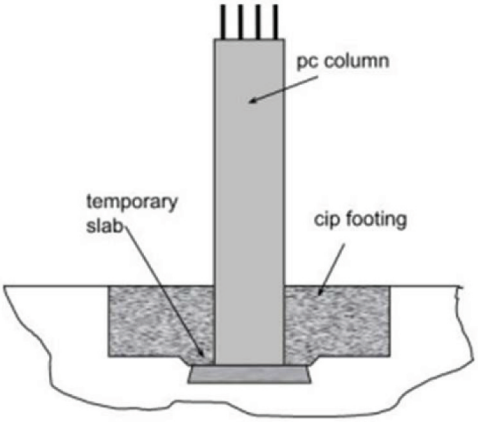


Figure 2. Wet socket column connection concept.

bars in vertical sleeves or ducts, often encountered when placing a precast element on top of a cast-in-place foundation with starter bars. Moreover, the absence of protruding reinforcements on the precast wall during transport and erection minimizes vulnerability.

The concept of the new connection is derived from an established socket connection between a precast column and a cast-in-place footing developed by Haraldsson et al. (2013) and is illustrated in Figure 2. Similarly, the precast column is manufactured with a roughened surface at the bottom, intended for embedding in the spread footing. In this connection, there are no bars extending from the footing into the column. This connection detail was successfully implemented in a bridge replacement project over I-5 in Washington State (Khaleghi et al., 2012).

3 TESTING

The research aimed to assess the connection's ability to withstand out-of-plane moments without causing substantial damage to the foundation while confirming its constructability. Two scaled (63%) test specimens were constructed and subjected to quasi-static, displacement-controlled, one-sided lateral loads to assess their behavior.

The first specimen, designated as 'Cast-in-place Wall,' served as a reference and was detailed according to current standards (e.g., Eurocode, and Icelandic Road and Coastal Administration Bridge Design Manual [Vegagerðin, 2018]). The second specimen, representing the new proposed connection, was detailed in alignment with the same standards and designated as 'Precast Wall'. Throughout the rest of this paper, the Cast-in-place and Precast wall specimens will be denoted as CIP and PC, respectively. Both specimens had the same foundation dimensions, with the length, width and thickness being 1190 mm, 900 mm and 290 mm, respectively. As specimen PC involves embedding the precast wall into the foundation, adjustments to PC specimens wall dimensions were necessary. In line with previous research by Haraldsson et al. (2013), the target was to achieve an embedment depth 1.1 times the wall thickness. Post-embedding, both walls shared identical dimensions, with a length, width, and thickness of 1000 mm, 650 mm, and 190 mm, respectively. Building the full-scale height of the walls was deemed unnecessary since the point load equivalent from the on-site earth load acts at a height of 1/3 times the wall height. The specimen´s design is discussed in more detail in a master´s thesis by the first author (Sigurjónsson, 2023).

The design concrete strength for both walls and foundations were C35/45, and the reinforcement conformed to BN500C. The specimens were cast in two stages, with the first stage involving casting the footing of Specimen CIP and the wall of PC. In the second stage, the wall of CIP and the foundation of PC were cast. The measured wall concrete strength on test day in CIP and PC walls were 70 MPa and 61 MPa, respectively.

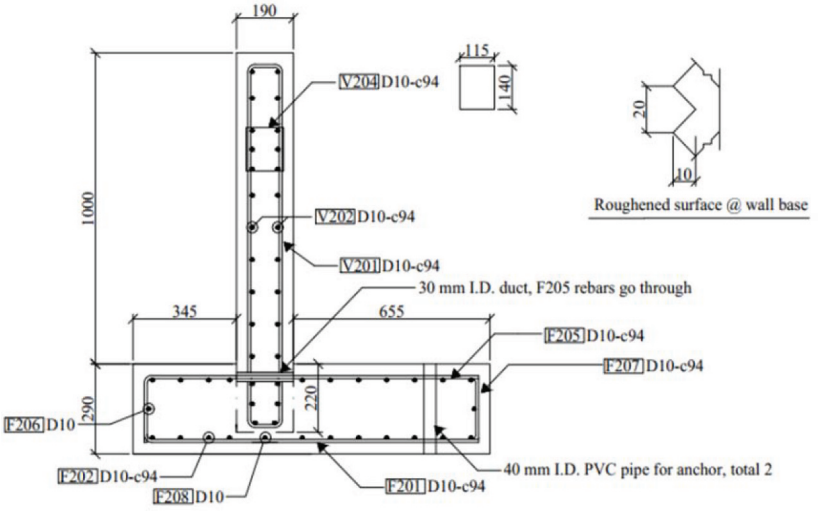


Figure 3. Cross section of PC design (Sigurjónsson, 2023).

3.1 *Setup*

The specimens were tested at the University of Iceland Structural Laboratory. The setup can be seen in Figure 4. Each specimen underwent testing under a unidirectional slow rate cyclic displacement history. Lateral displacements were induced using an Instron displacement-controlled actuator positioned 730 mm above the interface, with a maximum force capacity of 100 kN. The loading protocol comprised 11 peak displacements derived from the lateral load protocol utilized by Haraldsson et al. (2013). The procedure involved applying force until reaching the maximum displacement in 20 seconds, maintaining the constant maximum displacement while mapping new cracks, measuring crack widths, and capturing photos. Afterward, the load was released, completing one cycle.

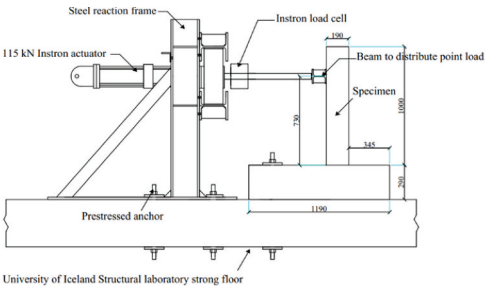


Figure 4. Test setup.

3.2 *Results*

Both CIP and PC completed the loading protocol of 11 peak displacements. Both specimens experienced wall failure, while the foundations remained undamaged throughout the testing. Specimen CIP developed a plastic hinge at the interface between the foundation and the wall, while PC experienced a combination of moment and shear failure. The maximum base moments of the two specimens differed, with the measured maximum moment in CIP at 75.7 kNm and in PC at 66.2 kNm.

The differences in both strength and failure modes prompted post-test examinations, during which the specimens were cut apart and wall thickness measurements were taken. Results indicated that the average wall thickness in the plastic hinge region of Specimen CIP was approximately 200 mm, while Specimen PC measured 190 mm. This distinction can be attributed to the vertical casting of Specimen CIP, inducing pressure in the formwork, and resulting in concrete bulging. In contrast, Specimen PC, cast horizontally, exhibited a more consistent thickness. Additionally, the measured concrete strengths on test day were 70 MPa for CIP and 61

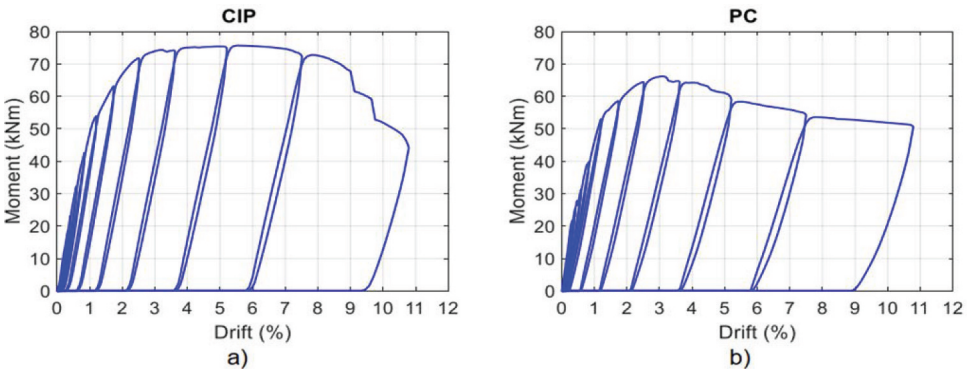


Figure 5. Moment-Drift comparison of both walls, CIP (left) and PC (right).

MPa for PC, further influencing the observed differences. Notably, the foundation's concrete strength measured at 59 MPa was lower than that of the CIP wall. Hairline cracks in the foundation closed upon unloading the test specimen. In Specimen PC, the measured concrete strength was 67 MPa, and the foundation remained undamaged, mirroring the condition of Specimen CIP. Figure 5 shows the moment-drift response of both specimens.

4 IMPLEMENTATION

In Bárðardalur area, located in North-Iceland, a road reconstruction project includes building a compliant new bridge due to the non-conformity of the existing structure with current bridge standards. The new bridge is designed as a single span, measuring 9 meters in length and 10 meters in width. To expedite construction, the design team opted for the new abutment connection, dividing the sizable front- and wing walls for easy transport and on-site assembly through an 'in-situ stitch.' Figure 6 displays plan and front views of the separated abutment elements.

The 300-mm-thick wall elements will be embedded 360 mm into the foundation, influenced by both the U-bar depth, determined in testing, and the concrete cover. Similar to the test specimen discussed in Section 3, the wall section embedded in the foundation will have a textured or roughened surface. Figure 7 shows the cross-section of a front wall element post-segmentation. Figure 8 illustrates the frontal view with corrugated ducts on the left and a cross-section with reinforcement bars protruding on the right. All dimensions are in millimeters.

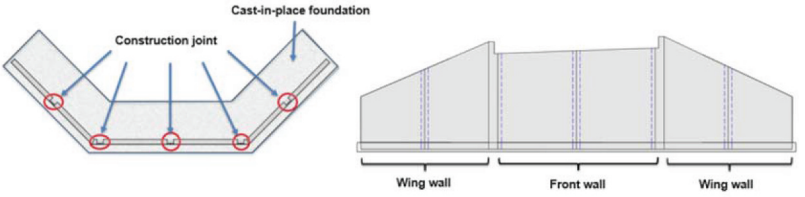


Figure 6. Abutment plan view (left) and front view (right).

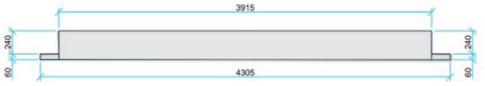


Figure 7. Typical cross section of a precast wall element.

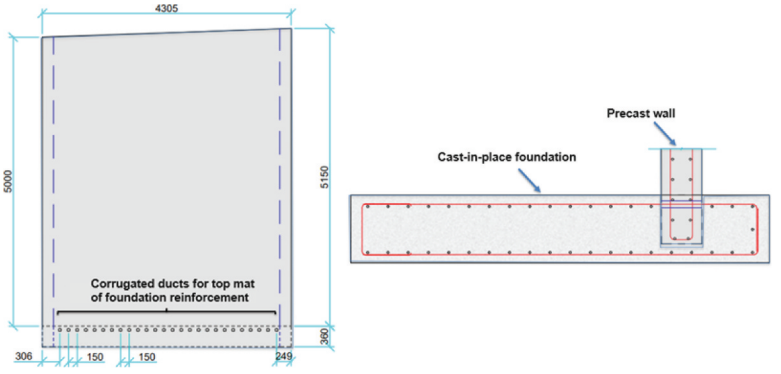


Figure 8. Typical elevation of a precast wall element (left) and connection cross section between precast wall and cast-in-place foundation.

5 CONCLUSIONS

A new 'wet-socket' connection between an abutment wall and a cast-in-place foundation is introduced that is both conceptually straightforward and rapid to construct. This connection concept is derived from an established connection method between a precast column and a cast-in-place spread footing.

Two scaled (63%) test specimens were constructed and subjected to out-of-plane testing under quasi-static, displacement-controlled, one-sided lateral loads. The first specimen, serving as a reference, adhered to current standards (e.g., Eurocode, and the IRCA Bridge Design Manual). The second specimen represented the new connection and was detailed according to the same standards. The following conclusions are drawn:

1. The socket wall connection effectively transmitted loads from the abutment wall to the foundation. As observed in the reference specimen, a failure occurred in the wall, while the foundation remained undamaged.
2. Maximum strength and failure mode varied between specimens. Specimen CIP exhibited a plastic hinge at the construction joint between the foundation and the wall, while Specimen PC underwent a combined moment and shear failure in the wall segment just above the foundation. Further investigation post-testing revealed a wall thickness of 200 mm for CIP, exceeding the prescribed 190 mm. Additionally, the measured wall concrete strengths differed, with CIP at 70 MPa and PC at 61 MPa, impacting both strength and failure mode.
3. The construction of the socket connection suggested that on-site implementation would be simple.

In 2023 two new details of the construction joint between the foundation and the wall were designed and then tested in January 2024. The data is being processed and the results will be presented later.

ACKNOWLEDGEMENTS

Support for this work was provided by the Icelandic Road and Coastal Administration Research Fund (Grant No. 1800-961). The findings and conclusions contained herein are those of authors alone. Thanks are extended to Laboratory Manager Egill Einar Valsson of the University of Iceland; Mr. Valur Birgisson and the Bridge Maintenance Team of IRCA´s Department of Construction Management; Mr. Einar Einarsson, Dr. Sigríður Ósk Bjarnadóttir, Mr. Pétur Hans Pétursson, and Mr. Jón Þór Þorgeirsson of BM Vallá Concrete Corporation; Mr. Eggert Guðmundsson, and Mr. Heiðar Karlsson of Vista Engineers for their valuable assistance, without which the project would not have been possible.

REFERENCES

Culmo, M. P. (2011). *Accelerated Bridge Construction - Experience in Design, Fabrication and Erection of Prefabricated Bridge Elements and Systems*. U.S. Department of Transportation, Federal Highway Administration, Washington DC.

Haraldsson, O. S., Janes, T. M., Eberhard, M. O., & Stanton, J. F. (2013). Seismic resistance of socket connection between footing and precast column. *Journal of Bridge Engineering*, *18*(9), 910–919.

Khaleghi, B., Schultz, E., Seguirant, S., Marsh, L., Haraldsson, O. S., Eberhard, M. O., & Stanton, J. F. (2012). Accelerated bridge construction in Washington State: From research to practice. *PCI Journal*, *57*(4), 34–49.

Mashal, M., White, S., & Palermo, A. (2016). Quasi-static cyclic testing of emulative cast-in-place connections for accelerated bridge construction in seismic regions. *Bulletin of the New Zealand Society for Earthquake Engineering*, *49*(3), 267–282.

Matsumoto, E. E., Waggoner, M. C., Sumen, G., Kreger, M. E., Wood, S. L., & Breen, J. E. (2001). *Development of a Precast Bent Cap System*. University of Texas, Center for Transportation Research, Austin.

Pang, J. B., Eberhard, M. O., & Stanton, J. F. (2010). Large-Bar Connection for Precast Bridge Bents in Seismic Regions. *Journal of Bridge Engineering*, *15*(3), 231–239.

Sigurjónsson, F. (2023). *Comparison of Cast-In-Place and Precast Wall connection to Cast-In-Place Foundation* (In Icelandic) [Master's Thesis, University of Iceland].

The Icelandic Road and Coastal Administration (2018), Design guidelines for bridges. (2nd ed.) (in Icelandic).

Bridge Maintenance, Safety, Management, Digitalization and Sustainability – Jensen, Frangopol & Schmidt (eds)
© 2024 The Author(s), ISBN 978-1-032-77040-6
Open Access: www.taylorfrancis.com, CC BY-NC-ND 4.0 license

NDT for damage detection in FRP reinforced/strengthened concrete elements

Armin B. Mehrabi, Seyed Saman Khedmatgozar Dolati & Pranit Malla
Department of Civil and Environmental Engineering, Florida International University, Miami, FL, USA

Jesus Ortiz Polanco & Antonio Nanni
Department of Civil and Environmental Engineering, University of Miami, Coral Gables, FL, USA

ABSTRACT: The application of Fiber Reinforced Polymer (FRP) materials in concrete structures has been rising due to their several advantages, including lightweight, high tensile strength, ease of installation, and corrosion resistance. They have been mostly implemented for strengthening and repairing existing structures in the form of an externally bonded system, i.e., sheet, jacket, near surface mounted. Furthermore, they have been recently utilized as internal reinforcement of concrete elements in the form of strands, bars, tendons, etc. Although higher durability and performance are associated with the FRP material compared to steel, concerns remain regarding potential damages and defects in this material, many of which are related to their unique features. Importantly, debonding of FRP materials from concrete is a potential issue resulting deterioration of the structural performance. Therefore, as for any other type of material or elements, concrete elements strengthened or reinforced with FRP materials have to be also inspected periodically. This study first determines all possible or potential damages and anomalies attributed to FRP reinforced/strengthened concrete (FRP-RSC) elements. It then investigates Non-Destructive Testing (NDT) methods that can be applicable to the inspection of FRP-RSC elements from a literature survey of past studies, applications, and research projects. Finally, it proposes the most promising methods for detecting FRP and their damage/defects in FRP-RSC elements. By providing the inspection community with more clarity in the application of NDT to FRP, the results of this study offer means for verifying the performance and, therefore, help the proliferation of FRP materials in concrete structures.

1 INTRODUCTION

1.1 *FRP composites*

The 2021 American Society of Civil Engineers (ASCE) infrastructure report card (ASCE, 2021) scored America's infrastructures a low grade of C- and its bridges a low grade of C. In the context of bridges, 42% of the nation's 617,084 highway bridges are over 50 years old and as time passes, an ever-increasing number of bridges will be near the end of their service time and will need some kind of rehabilitation or replacement. Fiber-reinforced polymer (FRP) composites have gained popularity in meeting challenges with durability, for building new civil structures or for maintaining the existing ones. FRPs are composite materials composed of polymeric resins reinforced with fibers. The fibers can be made of glass (GFRP), carbon (CFRP), aramid (AFRP), and basalt (BFRP). They provide several benefits over the conventional construction materials that include but are not limited to corrosion resistance, higher strength to weight ratio, superior durability, and ease of construction (Dolati and Mehrabi, 2022, 2023). Thus, FRP composites have been increasingly used as externally bonded system with the application of FRP sheet, laminates, jacket and near surface mounted (NSM) bars for strengthening and

DOI: 10.1201/9781003483755-441

repairing existing structures. Additionally, their use as internal reinforcements for concrete structures in the form of FRP bars and strands/tendons have been increasing.

1.2 *FRP strengthened concrete (FRP-SC) elements*

FRP composites are primarily utilized for repair, rehabilitation and strengthening of structures when design defects are noticed, the load-bearing capacity of an in-service structure is modified, deterioration of materials has begun, or after damages due to extreme events (seismic or fire events). This is generally achieved by externally bonding FRP systems to the reinforced concrete (RC) elements which is termed as FRP strengthened concrete (FRP-SC) elements in this paper. The external FRP systems can enhance the flexural, axial, shear, and torsional strength. In seismic zones, FRP wraps can be used for columns to increase their ductility due to the induced confinement of the concrete. Apart from the advantages of higher tensile strength with lighter weight, the ease of installation, and suitability for irregular surfaces of FRP composites have contributed to their popularity as a strengthening technique.

1.3 *FRP reinforced concrete (FRP-RC) elements*

Corrosion is one of the major issues that can severely impair the serviceability and safety of conventional steel reinforced/prestressed concrete structures. However, internal FRP reinforcements such as FRP bars and strands are resistant to all the elements that lead to corrosion in steel RC structures, such as reduction of pH of the concrete from carbonation, chloride contamination of the concrete and diffusion of halides and chemicals (Mohamed and Benmokrane, 2014; Benmokrane *et al.*, 2021). Application of FRP reinforcement is one of the most promising alternative available to completely eliminate the issue of corrosion (Benmokrane *et al.*, 2006; Dolati and Mehrabi, 2022; Khedmatgozar Dolati and Mehrabi, 2022b, 2022a; Mehrabi and Khedmatgozar Dolati, 2022) compared to application of corrosion protection measures to carbon steel such as cathodic protection, epoxy-coating and galvanizing that only delay corrosion rather than eradicating it (Wang, 2017). Hence, the application of FRP reinforced concrete (FRP-RC) structures is strongly justified for locations where corrosion of traditional steel reinforcement is an economic and safety concern. The mechanical performance and durability of the FRP composites further make them suitable for these conditions. When compared to carbon steel rebars, FRP bars have higher tensile strength, lower density, and can achieve a longer service life. Although the initial cost of FRP rebars is frequently highlighted as a drawback to its implementation, it has changed significantly due to the growth of the FRP rebar market.

1.4 *FRP reinforced/strengthened concrete (FRP-RSC) elements*

The next phase of development in the application of FRPs in concrete structures could culminate in elements possessing both internal and external FRP systems simultaneously. Future scenarios may include strengthening structures that are originally reinforced with FRP bars and tendons. Further, with the advancements in the application of FRP in civil engineering, it is conceivable that the use of FRP in certain aggressive and hostile environments, such as coastal areas, becomes prevalent. Thus, this paper takes into consideration both the FRP-RC and/or FRP-SC elements to set a foundation for the most promising construction materials of the future.

2 DAMAGES IN FRP REINFORCED/STRENGTHENED CONCRETE (FRP-RSC) ELEMENTS

2.1 *Damages in FRP-SC elements*

FRP strengthened concrete (FRP-SC) elements are generally comprised of three materials: internal reinforcement (typically steel rebars, with the potential for future adoption of FRP rebars), concrete and FRP composites. Defects associated with FRP-SC elements can occur within either of the three materials or at the interface between them (Malla, Khedmatgozar Dolati, Jesus D Ortiz, *et al.*, 2023). Examining the rebar, concrete, FRP system, and interface

separately enables a focused approach to identify and address the potential damages in FRP-SC elements. Hence, based on the locations where they occur, damages in FRP-SC elements typically fall into three distinct groups: 1) Defects in FRP Composites (i.e., FRP Composites Defects); 2) Bond Defects (i.e., FRP-Adhesive Interface, Adhesive, and Adhesive-Concrete Interface Defects); and 3) Defects in Concrete (i.e., Concrete (C) and Concrete-Steel Rebar Interface Defects) (Malla, Khedmatgozar Dolati, Jesus D Ortiz, *et al.*, 2023). Figure 1 illustrates the location and identification of the most likely defects in FRP-SC concrete elements.

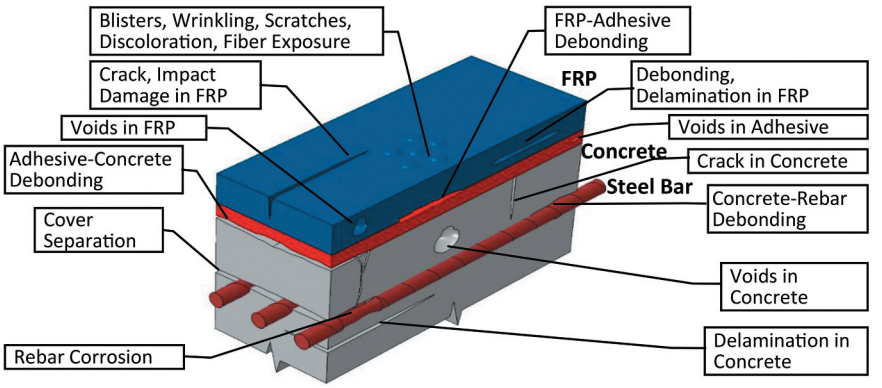


Figure 1. Damages and defects in FRP-SC elements.

2.2 *Damages in FRP-RC elements*

FRP bars exhibit enhanced durability and performance in certain respects compared to steel. Nevertheless, there are concerns regarding potential damages and defects in FRP bars and FRP-RC elements. Unlike conventional steel-RC elements, FRP-RC elements may not be vulnerable to serviceability issues such as cracking, permeability, carbonation, chloride penetration, and concrete cover requirements. However, FRP bars and FRP-RC elements are susceptible to a distinct set of defects compared to their steel-reinforced counterparts. As an example, the bond behavior at the FRP bar-concrete interface is different from the bond characteristics of steel bars embedded in concrete (Zhao *et al.*, 2021). The bond failure in FRP-RC elements can also occur internally within the FRP bars themselves, a phenomenon not typically observed in steel bars (Hossain, Ametrano and Lachemi, 2014; Kim and Lee, 2019). Similarly, another divergent characteristic of FRP bars compared to steel is their lower modulus of elasticity which results in the formation of relatively more cracks in FRP-RC elements. A research conducted by Valentine (2015) indicated that cracking is the most reported defect in FRP-reinforced bridge decks, as observed by bridge inspectors. However, as FRPs are resistant to corrosion, the formation of cracks in FRP-RC elements does not present

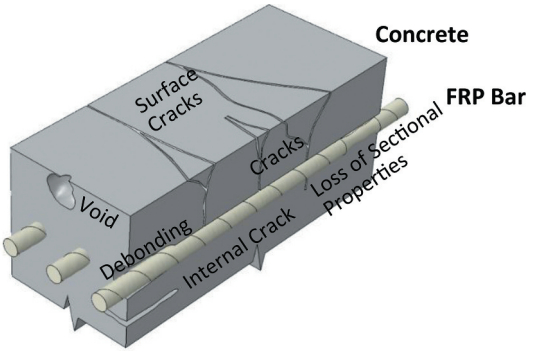


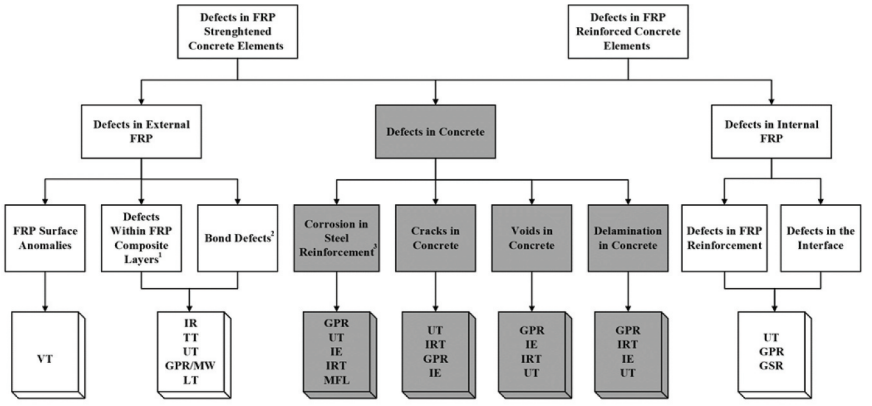
Figure 2. Damages and defects in FRP-RC elements.

a significant concern as long as the cracks are not severe. Unlike steel bars where corrosion is the obvious damage to be expected, there is very limited information on damages that are possible on FRP bars, a relatively new corrosion resistant construction material. Hence, to contribute to the gap in the knowledge, the authors have listed "potential defects" that could occur in FRP bars and FRP-RC elements as shown in Figure 2.

3 NON-DESTRUCTIVE TESTING (NDT) METHODS FOR THE INSPECTION OF FRP-RSC ELEMENTS

Although substantial research efforts have been dedicated to the application of Non-Destructive Testing (NDT) and inspection techniques for traditional steel-RC elements, research pertaining to NDT of FRP-RSC elements remains comparatively underdeveloped. There exists an absence of definitive guidelines regarding the application of various NDT methods for the detection and assessment of damage in FRP-RSC structures. To address this research gap, for the study reported in this paper a comprehensive examination was conducted on all NDT methods potentially applicable for the evaluation of FRP-RSC elements through literature review of past studies.

The comprehensive literature review identified Ground Penetrating Radar (GPR) and Ultrasonic Testing (UT, including Phased Array Ultrasonic Testing, PAU) as the most effective Non-Destructive Testing (NDT) methods for identifying the presence of damage in FRP-RC elements. These methods are also most commonly employed in the evaluation of steel-RC elements. Additionally, visual inspection (VT), tap testing (TT), and infrared thermography (IR) were recognized as particularly relevant NDT techniques for the examination of FRP-SC structures. Figure 3 shows the flowchart for the selection of NDT methods applicable for the inspection of concrete elements reinforced or strengthened with FRP based on the literature review. This has been described in detail in (Dolati *et al.*, 2023; Malla, Khedmatgozar Dolati, Jesus D. Ortiz, Mehrabi and Nanni, 2023). In addition to VT, TT, GPR, UT, and IR, the NDT methods considered include IE (Impact Echo), MW (Microwave), LT (Laser Testing), IRT (Impulse Response Testing), MFL (Magnetic Flux Leakage), and GSR (Global Structural Response Testing). The flowchart also suggests the order of priority of various NDT methods, type of damages, and type of applications. To further validate the applicability of these selected NDT methods in inspection of FRP-RSC elements, a series of experimental tests were conducted.



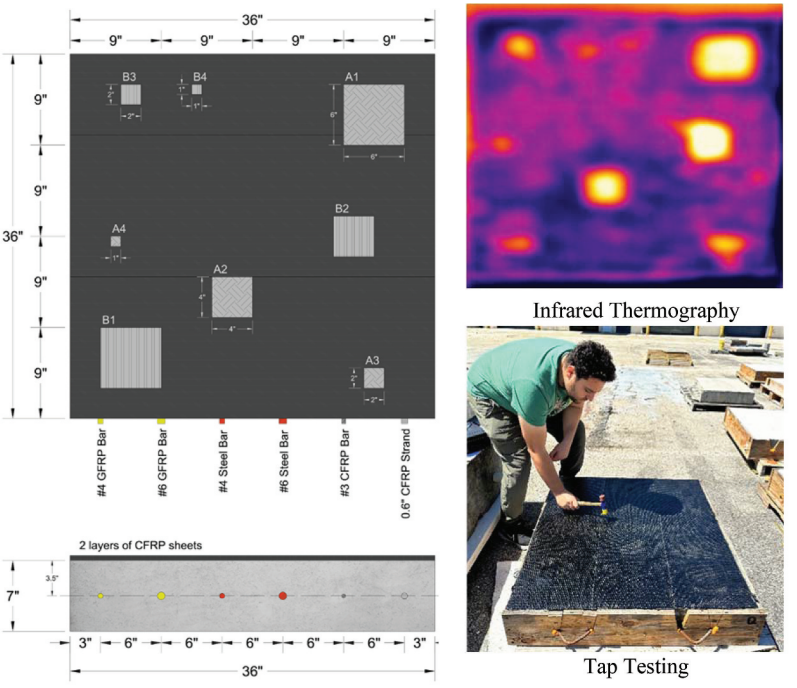
Notes:

1. Defects within FRP composite layers include blisters, wrinkling, scratches, discoloration, fiber exposure, voids at the fiber-matrix interface, fiber-matrix debonding, delamination between composite layers, cracks, and impact damage
2. Bond defects include debonding and voids between FRP and concrete
3. Corrosion in steel reinforcement is to be considered only when it is applicable

Figure 3. Order of priority for NDT methods suitable for each type of defect.

3.1 *Validation of selected NDT for FRP-SC elements*

To validate the applicability of the selected NDT methods for inspection of FRP-SC elements, debonding, delamination, and concrete damages such as voids and cracks were replicated in FRP-strengthened specimens. The findings indicated that GPR was less effective in identifying defects or damages for the case of externally applied CFRP and the internal targets beneath the CFRP layer (cracks and voids in concrete substrate) due to the conductive nature of CFRP. In contrast, PAU demonstrated capability in inspecting externally applied FRP including CFRP. Complementary NDT techniques, including visual inspection, tap testing, and infrared thermography, were also found to be highly effective in identifying defects or damages in externally applied FRP as shown in Figure 4. More details on the on the detection of damages on concrete elements with externally bonded FRP can be further explored in (Ortiz *et al.*, 2024)



Legends:

Defect ID	Description	Dimension
A1	1.2 mm thick polystyrene foam	6 in x 6 in
A2	2.4 mm thick polystyrene foam	4 in x 4 in
A3	2.4 mm thick polystyrene foam	2 in x 2 in
A4	2.4 mm thick polystyrene foam	1 in x 1 in
B1	40 µm thick polyethylene foam	6 in x 6 in
B2	1.2 mm thick polystyrene foam	4 in x 4 in
B3	1.2 mm thick polystyrene foam	2 in x 2 in
B4	1.2 mm thick polystyrene foam	1 in x 1 in

Delamination between FRP layers

Debonding between substrate & FRP

Figure 4. Application of infrared thermography & tap testing for inspection of FRP-SC.

3.2 *Validation of selected NDT for FRP-RC elements*

To verify that GPR and PAU are applicable for inspection of FRP-RC elements, various slab specimens were fabricated with GFRP, CFRP, BFRP, and steel bars, as well as GFRP and CFRP strands. These specimens varied in depth, size, and configuration. Different damage scenarios, including bar rupture, debonding, and loss of cross-sectional properties were simulated in FRP bars/strands. Figure 5 illustrates the results for detection of damages in GFRP bars embedded in a concrete slab specimen using GPR. Furthermore, the detection of

damages within concrete, such as delamination, cracks, and voids that are same as those found in traditional steel reinforced or prestressed concrete elements were also included in the study as shown in Figure 6. It was found that GPR was effective in identifying damages in GFRP bars, CFRP strands, steel bars, and internal concrete damages. However, PAU exhibited limitations in detecting damage in GFRP and BFRP bars, but it demonstrated proficient performance in identifying damage in CFRP strands, steel bars, and concrete. Another study by the authors (Malla, *et al.*, 2024) provides in-depth information on the application of conventional NDT methods in inspection of FRP-RC elements.

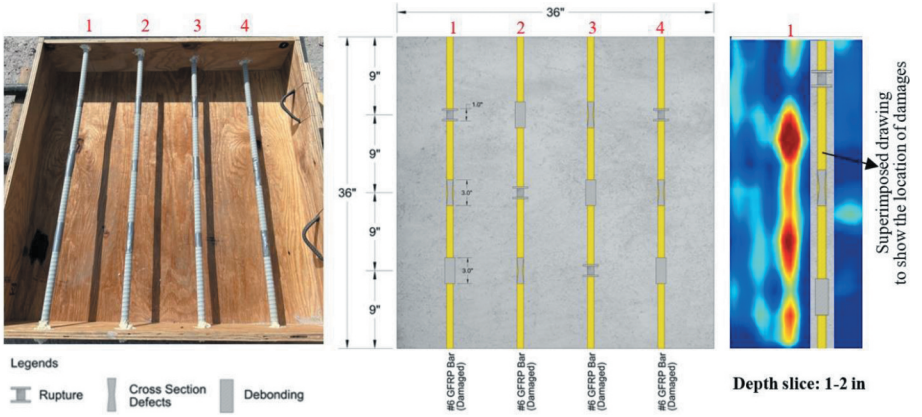


Figure 5. Application of GPR for inspection of FRP-RC specimen with defects in GFRP bars.

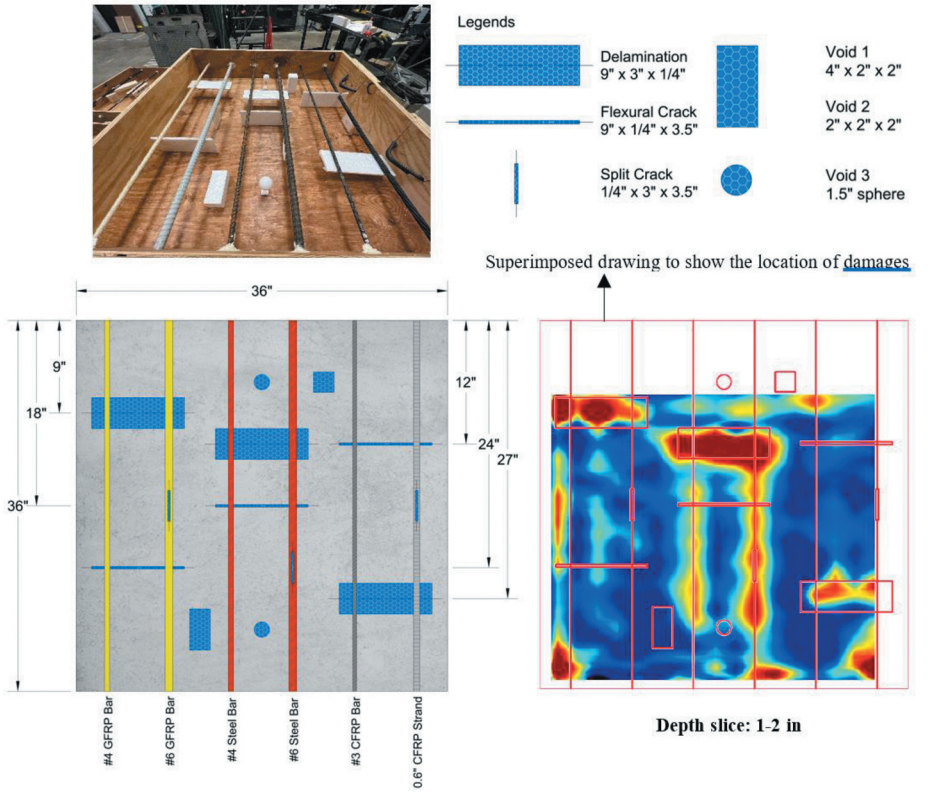


Figure 6. Application of GPR for inspection of FRP-RC specimen with defects in concrete.

4 APPROACHES TO ENHANCE THE DETECTABILITY OF EMBEDDED FRP

This study also developed two innovative approaches to enhance the detectability of embedded FRP bars and improve the identification of damages in them. The first approach involves the application of metallic particle coatings, and the second incorporates winding of wire on the surface of FRP bars. Both methods can be easily incorporated within the processes already in use for bond-enhancing of FRP bars. The efficacy of these novel techniques was validated through GPR and PAU tests on a small-scale slab specimen reinforced with modified GFRP bars as shown in Figure 7. The findings demonstrated a noteworthy enhancement in detecting embedded FRP bars and their associated damages. Further details on the method of introducing these modifications in FRP bars can be referred in the study by Malla et al. (2024).

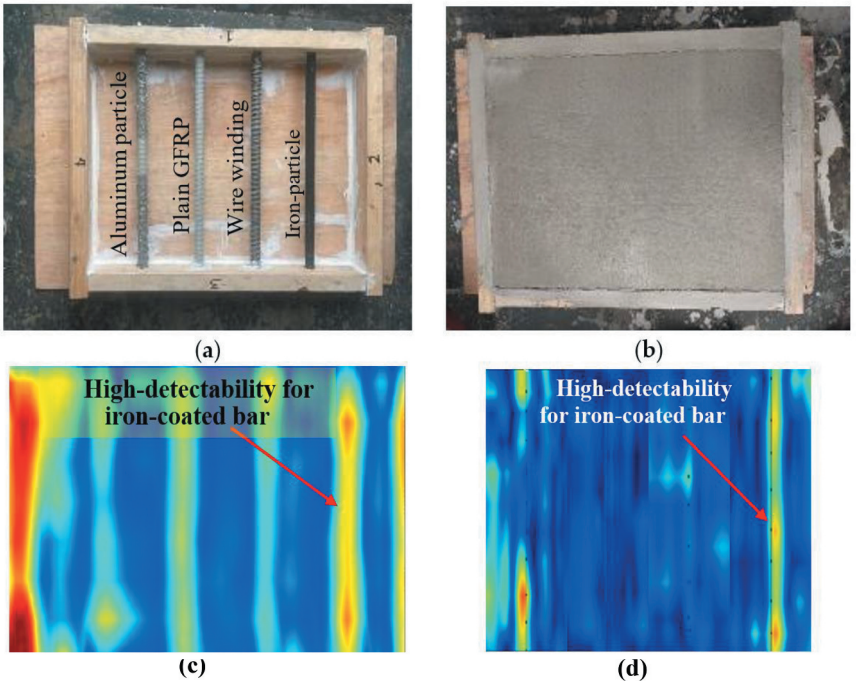


Figure 7. Slab specimen used for feasibility study for the new approaches: a) Formwork with coated & uncoated GFRP bars, b) Cast specimen, c) GPR depth slice d) PAU depth slice.

Moreover, this study found that modifying test parameters in the chosen NDT methods could enhance detectability. One notable parameter is the antenna frequency in the GPR method, which can influence the ability to detect various sizes and depths of embedded GFRP bars as further explained in Malla et al. (2023).

5 SUMMARY AND CONCLUSION

The study highlights that while FRP offers several advantages over conventional construction materials, including corrosion resistance and high strength-to-weight ratio, it also presents unique challenges in terms of detecting potential damages and defects. To address these challenges, after identifying type of damages and their sources, a thorough investigation of various NDT methods suitable for inspecting FRP-RSC elements was conducted. GPR and UT, including PAU, were identified as effective NDT methods for detecting damage in FRP-RC elements. These methods, along with visual inspection, tap testing, and infrared thermography, were found to be successful for examining FRP-SC structures. The paper also introduces two innovative approaches to enhancing the detectability of embedded FRP bars: applying metallic particle coatings and winding wire

on FRP bar surface. These novel techniques were validated through GPR and PAU tests and demonstrated significant improvements in detecting embedded FRP bars and associated damages.

In conclusion, this study provides a comprehensive overview of the application of FRP in concrete structures, the types of damages that can occur in FRP-RSC elements, and the effectiveness of various NDT methods in detecting these damages. It further contributes significantly to the field by proposing new methods to enhance the detectability of damages in FRP-RSC elements ensuring their structural integrity and extended service life.

REFERENCES

ASCE (2021) *Report Card for America's Infrastructure*. Reston, VA, USA. Available at: https://infrastructurereportcard.org/.

Benmokrane, B. *et al.* (2006) 'Designing and testing of a concrete bridge deck reinforced with glass FRP bars', *Journal of Bridge Engineering*, 11(2), pp. 217–229.

Benmokrane, B. *et al.* (2021) 'Design, Construction, Testing, and Behavior of Driven Precast Concrete Piles Reinforced with GFRP Bars and Spirals', *Journal of Bridge Engineering*, 26(8), pp. 1–13. Available at: https://doi.org/10.1061/(asce)be.1943-5592.0001755.

Dolati, S.S.K. *et al.* (2023) 'Identifying NDT methods for damage detection in concrete elements reinforced or strengthened with FRP', *Engineering Structures*, 287, p. 116155.

Dolati, S.S.K. and Mehrabi, A. (2022) 'FRP Sheet/jacket System as an Alternative Method for Splicing Prestressed-precast Concrete Piles', *Case Studies in Construction Materials*, p. e00912.

Dolati, S.S.K. and Mehrabi, A. (2023) 'Two New Methods for Establishing Simple Yet Durable Connection System for Precast Elements', in *Structures Congress 2023*, pp. 293–303.

Hossain, K.M.A., Ametrano, D. and Lachemi, M. (2014) 'Bond strength of standard and high-modulus GFRP bars in high-strength concrete', *J. of materials in civil engrg*, 26(3), pp. 449–456.

Khedmatgozar Dolati, S.S. and Mehrabi, A. (2022a) 'FRP splice system for joining structural elements'. US Patent 11,319,706.

Khedmatgozar Dolati, S.S. and Mehrabi, A. (2022b) 'NSM FRP Pile-Splice System for Prestressed Precast Concrete Piles', *Practice Periodical on Structural Design and Construction*, 27(4), p. 4022046.

Kim, B. and Lee, J.-Y. (2019) 'Resistance of interfacial debonding failure of GFRP bars embedded in concrete reinforced with structural fibers under cycling loads', *Composites Part B: Engineering*, 156, pp. 201–211.

Malla, P., Khedmatgozar Dolati, S.S., Ortiz, Jesus D, *et al.* (2023) 'Damage and Defects in Fiber-Reinforced Polymer Reinforced and Strengthened Concrete Elements', *Journal of Composites for Construction*, 27(4), p. 4023035.

Malla, P., Khedmatgozar Dolati, S.S., Ortiz, Jesus D., Mehrabi, A. and Nanni, A. (2023) 'Damages and Defects in FRP Reinforced and FRP Strengthened Concrete Elements', *Journal of Composites for Construction* [Preprint].

Malla, P., Khedmatgozar Dolati, S.S., Ortiz, Jesus D., Mehrabi, A., Nanni, A., *et al.* (2023) 'Feasibility of Conventional Non-Destructive Testing Methods in Detecting Embedded FRP Reinforcements', *Applied Sciences* [Preprint].

Malla, P., Dolati, S.S.K., Ortiz, J.D., Mehrabi, A.B., *et al.* (2024) 'Applicability of available NDT methods for damage detection in concrete elements reinforced or strengthened with FRP', *Bridge Structures*, upcoming.

Malla, P., Dolati, S.S.K., Ortiz, J.D., Mehrabi, A., *et al.* (2024) 'Damage Detection in FRP Reinforced Concrete Elements', *Sensors*, upcoming.

Mehrabi, A. and Khedmatgozar Dolati, S.S. (2022) 'NSMB pile splice system for precast concrete piles'. US Patent 11,319,689.

Mohamed, H.M. and Benmokrane, B. (2014) 'Design and Performance of Reinforced Concrete Water Chlorination Tank Totally Reinforced with GFRP Bars: Case Study', *Journal of Composites for Construction*, 18(1), pp. 1–11. Available at: https://doi.org/10.1061/(asce)cc.1943-5614.0000429.

Ortiz, J.D. *et al.* (2024) 'Nondestructive Testing (NDT) for Damage Detection in Concrete Elements with Externally Bonded FRP', *Buildings*, upcoming.

Valentine, S. (2015) *Expected Service Life of Michigan Department of Transportation Reinforced Concrete Bridge Decks*.

Wang, W. (2017) *Durability Behavior of Fiber Reinforced Polymer and Steel Reinforced Polymer for Infrastructure Applications*. Missouri University of Science and Technology.

Zhao, D. *et al.* (2021) 'Bond behavior and failure mechanism of fiber-reinforced polymer bar–engineered cementitious composite interface', *Engineering Structures*, 243, p. 112520.

Bridge Maintenance, Safety, Management, Digitalization and Sustainability – Jensen, Frangopol & Schmidt (eds)
© 2024 The Author(s), ISBN 978-1-032-77040-6
Open Access: www.taylorfrancis.com, CC BY-NC-ND 4.0 license

Calibration of constitutive model parameters of bridge steels using particle swarm optimization

Yuelin Zhang
College of Civil Engineering, Tongji University, Shanghai, China

Chunbin Li & Hongwei Huo
China MCC22 Group Corporation Ltd., Tangshan, China

ABSTRACT: Conventional manual calibration of steel material constitutive model parameters is a process of trial and error, with the disadvantages of low efficiency and bad accuracy. The present work aims to propose an automatic calibration process by introducing modern optimization algorithm. Firstly, a series of Q345 and Q235 steel material property tests were conducted, to prepare the data needed to conduct the calibration. Secondly, the material property parameters were determined inversely by particle swarm optimization (PSO). It was found that after 20 times of iteration, the calibration accuracy of Q345 steel is enhanced by 18.73% to 40.44%, and corresponding improvement of Q235 steel is 12.61%-76.20%. Thirdly, the cyclic plasticity characteristics of Q345 and Q235 steels were compared, the results show that both isotropic and kinematic hardening levels of Q235 steel are greater than those of the Q345 steel. The Q-value of Q235 steel is increased by about 60.39%, compared with Q345, and the backstress (C_1/γ_1) of Q235 is 22.14% larger than that of Q345.

1 INTRODUCTION

Like many other metals, the yield strength of bridge steel will increase after the loading-unloading process, which is called "hardening", and the corresponding stress-strain relationship of the material is known as constitutive relationship. The one-dimensional stress-strain relationship curve of steel material was generally defined as bilinear or trilinear model [1], but the above models are not very accurate in the mechanical behavior simulation of steel material under cyclic loading, and the calculated curve may be quite different from the actual one. To satisfy practical requirement and convene engineering application, researchers proposed a series of calculation models for steel materials to simulate their constitutive relationship under cyclic loading or other extreme loading conditions [2-10]. Ramberg [11] recommended a three-parameter model to describe the cyclic loading skeleton curve of metals; Krawinkler and Nathaniel [2, 4] proposed a mathematical expression to describe the cyclic behavior of steel material based on elastic-plastic mechanics method, concepts including hardening, softening, and average stress were defined; Chaboche et al. [12-15] proposed cyclic constitutive models of steel material that comprehensively consider isotropic hardening and kinematic hardening characteristics, and specific determination methods of model parameters were given; Atkan [6] and Wang et al. [5] gave the constitutive model of reinforcement under cyclic loads, which also has reference significance for steel material; On the basis of multi-surface model proposed by Dafalias and Popov et al. [9, 10], Shen and Usami [7, 8] proposed a double yield surface model, which accurately described the cyclic performance of steel structures. Among these constitutive models, Voce-Chaboche (VC) combined hardening model is widely used [16]. However, in order to apply the

DOI: 10.1201/9781003483755-442

model to practical analysis, there must be corresponding finite element calculation methods and programs, and model parameters must be reasonably determined, and there are several parameters to be determined in this model. Since these highly nonlinear mathematical expressions can describe some much complex mechanical responses of materials, they are somewhat sensitive to integral algorithm of parameters. Therefore, determination methods of parameters in elastic-plastic models now have already drawn researchers' attention gradually, and a lot of investigations have been done [17].

The commonly used parameter optimization methods include Gauss Newton method, CO rolling gradient method and least square method (LSM), these traditional optimization methods have the characteristics of fast convergence speed and high calculation accuracy, but all of them are localized extremum algorithm, the solution given by these methods are localized optimal one, rather than global optimal one [18]. As a typical random searching algorithm, particle swarm optimization (PSO) was first proposed by Kennedy and Eberhart [19], it is a computational model established to simulate the predation behavior of birds. The researchers found that the behavior of birds in flight is unpredictable, for example, birds may suddenly disperse, gather or change flying direction, but some consistency is still kept, i.e., individuals maintain the most suitable distance to avoid collision phenomenon. It was found that there is an information sharing mechanism in biological population through conducting investigation on the behaviors of similar biological population. In PSO, each particle represents a possible solution in the searching space, the population is the set of potential solutions of the problem. The initial population is usually randomly generated. In the simulation of birds' predation gathering process, each particle in the swarm constantly searches and evolves in the solution space, and during the searching process, each particle records its own optimal value, and simultaneously learns from other particles. Through the personalized learning of particles and the cooperative interaction between them, the whole search group constantly approaches the optimal solution of the problem. As a bionic heuristic algorithm, PSO algorithm model is simple, convenient to be operated, easy to be realized, robust, and has deep intelligent characteristic, its advantage is apparent. Currently, PSO has been widely used in various areas [20-24]. As a development and application of PSO, calibration of the combined hardening constitutive model parameters of bridge steels will be carried out using PSO in this paper.

2 DATA PREPARATION

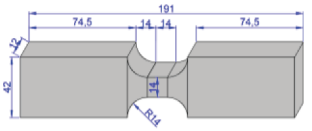
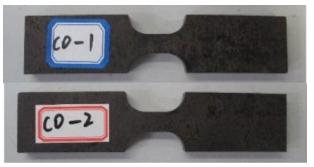
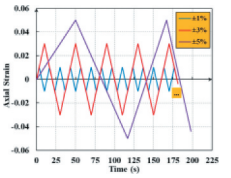
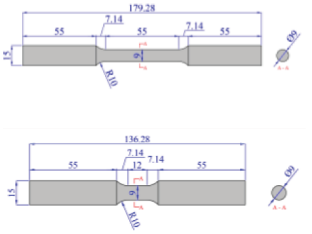
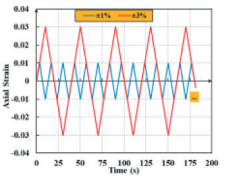
2.1 *Experimental setup*

The subjects to be tested include two kinds of dog-bone material property coupon, one is Q345 flat plate coupon, with a total number of two. The other is Q235 round bar coupon, with the total number of five. The Q345 coupons are labelled as C0-1 and C0-2, where±1% and ±3% strain amplitude loading tests were conducted on Specimen C0-1 and C0-2, respectively. Q235 coupons are labelled as t1, t2, Q235-1#, Q235-2#, and Q235-3#, where monotonic tensile tests were conducted on Specimen t1 and t2, while±1%, ±3%, and ±5% strain amplitude cyclic loadings were applied on Specimens Q235-1#, Q235-2#, and Q235-3#, respectively. Detailed geometrical dimensions, photos, and loading protocols of the coupons are summarized in Table 1. The tests were carried out at Experimental Center of Engineering Mechanics, The School of Naval Architecture, Ocean & Civil Engineering (NAOCE), Shanghai Jiao Tong University. An MTS fatigue testing machine with the capacity of 500kN was used to conduct the cyclic loading experiments. Loading rate was 0.035/s, an extensometer with the gauge length of 8mm was used to measure strain data, which were shown in Figure 1. Data collection frequency was 40Hz.

2.2 *Experimental results*

After testing, photos of the Q235 round bar coupons are illustrated in Figure 2, it can be found that the cracks are basically located within the gauged length region. First two cycle stress-strain curves of the five cyclic loaded specimens were plotted in Figure 3 (a), (b), and (d)-(f), and complete stress-strain curves of the two monotonic loaded coupons are depicted in

Table 1. Information of the coupons and corresponding loading protocols.

Material	Coupon dimension	Coupon schematic	Loading protocol
Q345			
Q235			Monotonic tension 

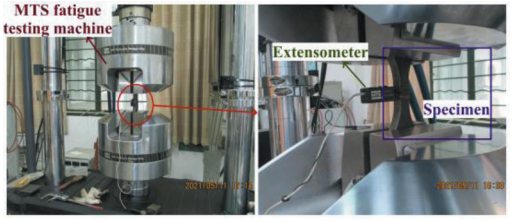


Figure 1. Experimental setup.

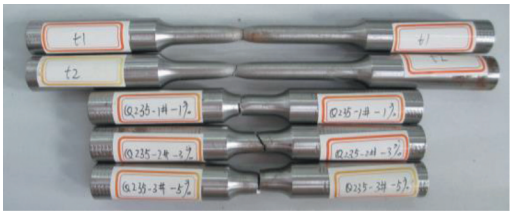
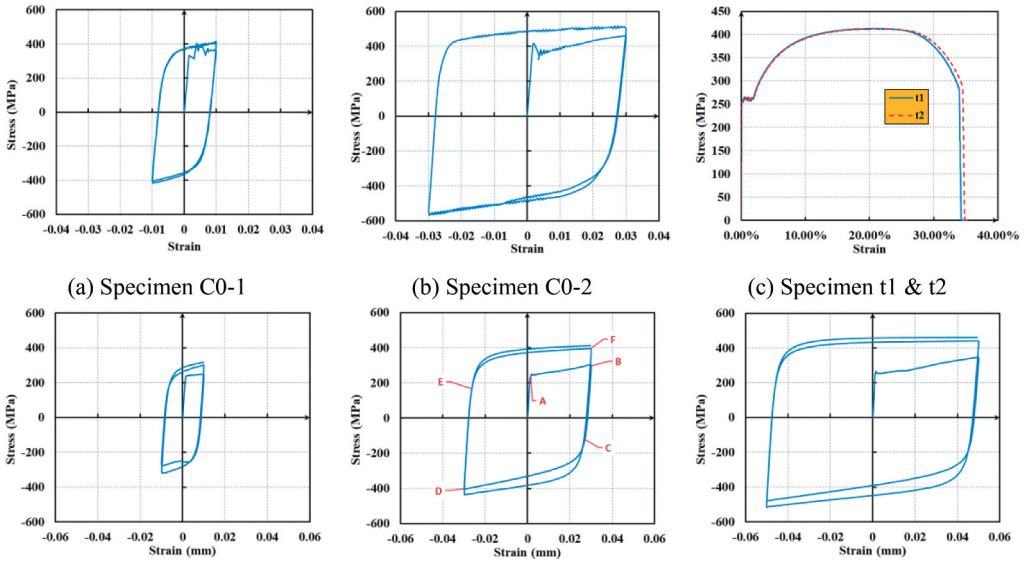


Figure 2. Photo of the Q235 round bar coupons after testing.

Figure 3 (c), where the stress is the average stress of the gauged cross-section, and the value is the ratio of the load of the testing machine to the cross-sectional area, while strain data was read directly from the extensometer. It can be found that the first and the second hysteretic loop of Q345 low-alloy steel almost overlap with each other, indicating that the steel is a cyclic stabilization material. While for Q235 carbon steel, the stress of the second cycle is a little larger than that of the first cycle, implying that the material shows a slight degree of cyclic hardening. Table 2 summarized the basic mechanical property parameters of Q235 steel by aforementioned two monotonic tensile coupons, i.e., t1 and t2.

3 PERTINENT THEORIES

Taking Specimen Q235-2# for example, point A in Figure 3(e) is the initial yield point of the material, point B is the ultimate stress of the monotonic cycle, point C is the yield point of



(a) Specimen C0-1 (b) Specimen C0-2 (c) Specimen t1 & t2

(d) Specimen Q235-1# (e) Specimen Q235-2# (f) Specimen Q235-3#

Figure 3. Stress-strain curves of the seven specimens.

Table 2. Summary of monotonic tensile test results

Specimen No.	Young's modulus (MPa)	Yield stress (MPa)	Ultimate tensile stress (uts, MPa)	Fracture strain	Elongation after fracture
t1	1.98E+05	258.02	412.38	21.43%	33.75%
t2	1.88E+05	251.42	412.10	20.39%	34.95%
Average value	1.93E+05	254.72	412.24	20.91%	34.35%

negative direction, point D is the ultimate point of the negative direction, point E is the yield point of the first cycle, and point F is the ultimate point of the first cycle. The stress-strain curve can be regarded as a piecewise function of stress varying with strain, in which OA section is an elastic section, and the stress-strain relationship follows Hooke's Law:

$$\sigma = E\varepsilon \tag{1}$$

where E is Young's modulus.

For section AB, according to Mises yielding criterion:

$$\sigma = \alpha + \sigma^0 \tag{2}$$

where α is backstress, which is used to describe the characteristic of kinematic hardening. Generally, α consists of 1~4 component(s):

$$\alpha = \sum_{k=1}^{n} \alpha_k, n = 1, 2, 3, 4 \tag{3}$$

For the purpose of simplification, only one component is used in this paper:

$$\alpha_1 = \frac{C_1}{\gamma_1}\left(1 - e^{-r_1 \varepsilon^{pl}}\right) \tag{4}$$

where α_1 is Chaboche exponential term, C_1 and γ_1 are parameters to be calibrated, ε^{pl} is equivalent plastic strain. σ° in Formula (2) is isotropic stress, according to Voce isotropic hardening law [25]:

$$\sigma^0 = \sigma|_0 + Q_\infty\left(1 - e^{-b\bar{\varepsilon}^{pl}}\right) \tag{5}$$

where $\sigma|_0$ is the initial yield stress of the material, Q_∞ reflects the expansion degree of yield surface, while b reflects the expansion rate of yield surface.

Section BC is elastic unloading section:

$$\sigma{=}E\left(\varepsilon - \left|\varepsilon|_{\sigma=0}\right|\right) \tag{6}$$

where $\varepsilon|_{\sigma=0}$ is the strain value at the intersection of stress-strain curve and x-axis.

For section CD:

$$\sigma{=}\alpha - \sigma^0$$

$$\alpha_1 = -\frac{C_1}{\gamma_1} + \left(\alpha_C + \frac{C_1}{\gamma_1}\right)e^{-r_1\left(\varepsilon^{pl} - \varepsilon_C^{pl}\right)} \tag{7}$$

where α_C is the backstress at point C, ε_C^{pl} is the equivalent plastic strain at point C. According to the characteristics of the functions mentioned above, C_1/γ_1, C_2, $\sigma|_0$, and Q_∞ determine the value of peak stress together, the peak stress increases with the increase of these parameters, and the peak stress decreases in contrast. γ_1 governs the shape of hysteretic cycle, a larger γ_1 leads to a plumper hysteretic loop, on the contrary, the hysteresis loop is flatter.

For section DE:

$$\sigma{=}E\left(\varepsilon + \left|\varepsilon|_{\sigma=0}\right|\right) \tag{8}$$

For section EF:

$$\alpha_1 = \frac{C_1}{\gamma_1} + \left(\alpha_E - \frac{C_1}{\gamma_1}\right)e^{-r_1\left(\varepsilon^{pl} - \varepsilon_E^{pl}\right)} \tag{9}$$

where α_E is the backstress at point E, ε_E^{pl} is the equivalent plastic strain at point E.

4 PSO-BASED REVERSE CALIBRATION OF CONSTITUTIVE MODEL PARAMETERS

4.1 *Working procedure*

As mentioned above, there are several parameters, such as Young's modulus, initial yield stress, isotropic hardening parameters, and kinematic hardening parameters, to be calibrated in the above-mentioned constitutive model. In contrast to traditional calibration method, which is essentially a trial and error process, inverse calibration is gaining increasing popularity [26-29]. The first step of inverse calibration is to create an FE model and generate an inp. file, and then Matlab software is used to call Abaqus software to run the inp. file, so that a result post-processing file with odb. format is generated. The next step is to read the load-displacement data from the result post-processing file, and then the load-displacement data is converted to average stress-strain data of the gauged region, so that the calculated stresses can be compared with the tested ones. To address the problem of unmatched simulated and experimental data, the test and simulated curves are interpolated into two new curves with the same abscissa. The comparison result of the simulated value and tested value should be quantified through an error function (also called as objective function or fitness function). To

reduce the amount of calculation, residual sum of squares (RSS) is adopted as the fitness function in this paper:

$$F_{error} = \sum_{i=1}^{N} \left(\sigma_i^{\exp} - \sigma_i^{\text{model}}\right)^2 \tag{10}$$

After the definition of error function, PSO algorithm can be adopted. The basic principle of PSO [19] is to make use of the sharing of information by individuals in a group, so as to make the movement of the whole group produce an evolutionary process from disorder to order in the problem-solving space, and then the optimal solution of the problem can be obtained. In PSO, each solution of an optimization problem can be regarded as a bird in the searching space, and is referred to as a particle, and the optimal solution of the problem corresponds to the corn field that the birds search for. Every particle has a position vector (the position of the particle in the solution space) and a velocity vector (to determine the direction and velocity of the next flight), and the fitness value of the current position can be calculated according to an objective function, in which the fitness value can be understood as the distance from the corn field. In each iteration, a particle in the group can learn from its own experience (historical position), as well as the experience of the optimal particle, so as to determine how to adjust and change the flying direction and velocity in the next iteration. In this way, the particles in the whole group will tend to optimal solutions gradually. The detailed working procedure of PSO can be found in the author's previous work [29].The iteration procedure of PSO, as well as the whole calibration procedure is demonstrated in Figure 4.

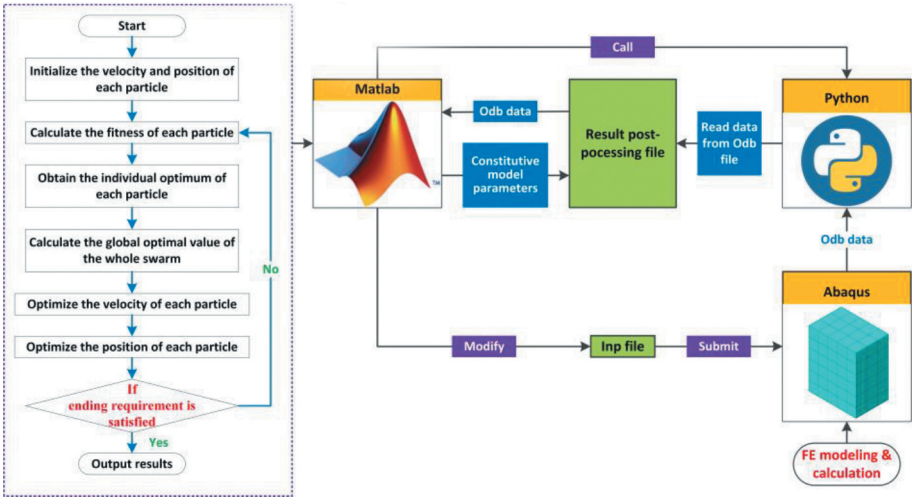


Figure 4. Flow chart of inverse calibration procedure.

For the process of finite element (FE) modeling, only the gauged region was modeled, to improve calculation efficiency. Both ends of the gauged region were coupled to two reference points (RPs), so that loads and boundary conditions can be applied to the RPs. The element type is commonly used C3D8R, and the loading displacement amplitudes were set in accordance with those in experimental scenarios (The last column in Table 1).

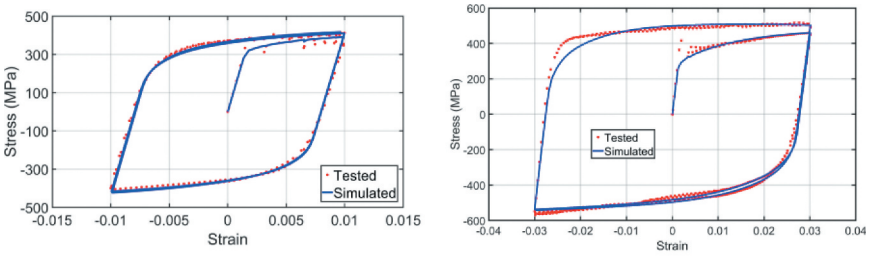
4.2 *Optimized results*

The necessary model parameters after optimization are listed in Table 3, and comparisons of the gauged regions' average stress-strain curves calculated by the parameters and experimental curves are demonstrated in Figure 5 and Figure 6. It can be found that the simulated curves agree well with experimental ones. The fitness function values calculated by original model

parameters are further compared with those calculated by optimized model parameters in Figure 7. It can be found that after 20 times of iteration, the calculation accuracies are improved by about 18.73% and 40.44% under ±1% and ±3% strain amplitude loads, respectively, for the Q345 coupons. While for Q235 steel, the calculation accuracies are enhanced by 12.61%-76.20%.

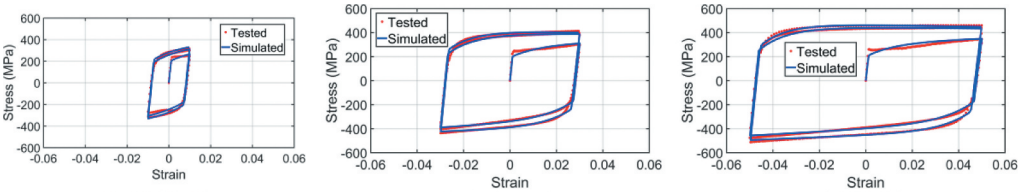
Table 3. Calibrated constitutive model parameters.

Parameter	Unit	Q345 ±1%	±3%	Average	Q235 ±1%	±3%	±5%	Average	Comparison
E	MPa	1.92E+05	1.93E+05	1.93E+05	191429	193161	185348.09	1.90E+05	-1.31%
μ	-	0.26	0.26	0.26	0.279	0.3	0.30	0.29	12.71%
σ_y	MPa	277.61	243.82	260.72	218.0	213.7	230.98	220.94	-15.26%
Q	MPa	96.01	89.99	93.00	104.7	152.7	189.99	149.16	60.39%
b	-	2.08	30.00	16.04	17.78	12.32	8.84	12.98	-19.06%
C_1	MPa	6887.52	7338.38	7112.95	6774.	6552	8135.12	7154.04	0.58%
γ_1	-	98.86	81.40	89.01	61.91	80.75	79.57	73.30	-17.65%
C_1/γ_1	MPa	69.67	90.15	79.91	109.4	81.14	102.24	97.60	22.14%



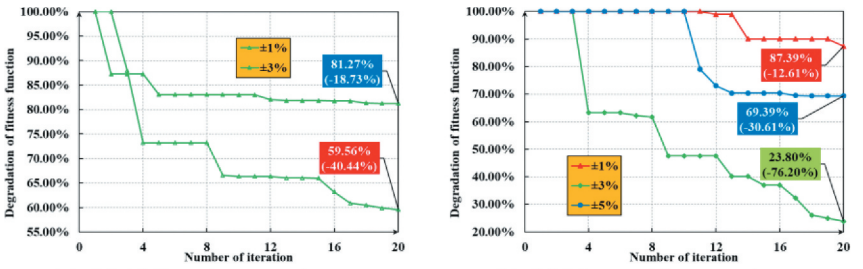
(a) C0-1 (b) C0-2

Figure 5. Comparison on the hysteresis curves of Q345 flat plate specimens obtained by finite element (FE) method and experiments.



(a) Q235-1# (b) Q235-2# (c) Q235-3#

Figure 6. Comparisons on the gauged regions' average stress-strain curves of Q235 round bar specimens calculated by the parameters after optimization and those measured by experiments.



(a) Q345 flat plate specimen (b) Q235 round bar specimen

Figure 7. Degradation of fitness function vs. number of iterations.

5 DISCUSSION

The last column of Table 3 shows the difference between the constitutive model parameters of Q345 and Q235 steels. It can be found that Young's modulus of the two steels are very close to each other, and the yield strength of Q235 steel is about 15.26% smaller than that of the Q345 steel. The isotopic hardening degree of Q235 steel is much larger than that of the Q345 steel, since the Q-value of Q235 steel is increased by about 60.39%, compared with Q345. While the isotropic hardening rate (b) of Q235 is 19.06% slower than that of Q 345 steel, implying that Q345 is more like cyclic stabilization material, while Q235 shows a certain degree of cyclic hardening. The two steels show similar stiffnesses after yielding (second-order stiffness), since their C values are very similar to each other. Q235 is also larger in kinematic hardening degree, and the backstress (C_1/γ_1) is 22.14% larger than that of the Q345 steel. As a summary, both isotropic and kinematic hardening levels of Q235 steel are greater than those of the Q345 steel.

6 CONCLUSIONS

In this paper, cyclic loading tests were conducted on Q345 steel flat plate coupons and Q235 round bar coupons. Based on testing data, cyclic plasticity constitutive model parameters of the two steels are inversely calibrated by particle swarm optimization (PSO). According to the results obtained, following main conclusions can be drawn:

(1) Using PSO inversely calibrated constitutive model parameters to conduct finite element (FE) calculation can greatly improve calculation accuracy. For Q345 coupons, the calculation accuracies are improved by about 18.73% and 40.44% under ±1% and ±3% strain amplitude loads, respectively. While for Q235 steel, the calculation accuracies are enhanced by 12.61%-76.20%.
(2) Both isotropic and kinematic hardening levels of Q235 steel are greater than those of the Q345 steel. The Q-value of Q235 steel is increased by about 60.39%, compared with Q345, and the backstress (C_1/γ_1) of Q235 is 22.14% larger than that of Q345.

REFERENCES

[1] Nip K H, Gardner L, Davies C M, et al. Extremely low cycle fatigue tests on structural carbon steel and stainless steel. Journal of Constructional Steel Research, 2010, 66(1): 96–110.
[2] Nathaniel G C, Krawinkler H. Uniaxial cyclic stress-strain behavior of structural steel. Journal of Engineering Mechanics, 1985, 111(9): 1105–1120.
[3] Dong Yongtao, Zhang Yaochun. Cyclic plastic constitutive model of building steel. Journal of Harbin Institute of architectural engineering, 1993, 26 (5): 106–112.
[4] Krawinkler H, Zohrei M, Bahman L I, et al. Recommendations for Experimental Studies on The Seismic Behavior of Steel Components and Materials. Earthquake Engineering Center. Department of Civil and Environmental Engineering, Stanford University, Stanford, CA. 1983, 61.
[5] Wang Xianming, Xu Bo, Shen Jumin. Constitutive relationship of reinforcement under repeated load. Journal of building structure, 1992, 13 (6): 41–47.
[6] Atkan A E, Karlson B I, Sozen M A. Stress-strain relationships of reinforceing bars subjected to large strain reversals. Civil Engineering Studies, SRS No.397, University of Illinois, Urbana-Champaign, Ill, 1973.
[7] Shen C, Tanaka Y, Mizuno E, Usami T. A two-surface model for steels with yield plateau. J Struct Engng/Earthquake Engng, JSCE, 1992, 8(4):179–188.
[8] Usami T, Gao S, Ge H. Elastoplastic analysis of steel members and frames subjected to cyclic loading. Engineering Structures, 2000, 22(2): 135–145.
[9] Dafalias Y F, Popov E P. A model of nonlinear hardening materials for complex loading. Acta Mechanica, 1975, 21:173–192.
[10] Dafalias Y F, Popov E P. Plastic interval variables formalism of cyclic plasticity. Journal of Applied Mechanics, Transactions ASME, 1976, 43: 645–651.

[11] Ramberg W, Osgood W R. Description of stress-strain curves by three parameters. NACA, Technical Note 902, 1943.
[12] Chaboche, J.L. and Rousselier, G. (1983), "On the Plastic and Viscoplastic Constitutive Equations —Part I: Rules Developed with Internal Variable Concept", *J Pressure Vessel Tech.*, 105(2), 153–158.
[13] J. L. Chaboche. Time-independent constitutive theories for cyclic plasticity. International Journal of Plasticity. Vol. 2, No. 2, pp. 149–188, 1986.
[14] J. L. Chaboche. Constitutive equations for cyclic plasticity and cyclic viscoplasticity. International Journal of Plasticity, Vol. 5, pp. 247–302. 1989.
[15] Chaboche J L. Unified Cyclic Viscoplastic Constitutive Equations-1: Development, Capabilities, and Thermodynamic Framework [J]. Unified Constitutive Laws of Plastic Deformation, 1996:1–68.
[16] Albano de Castro e Sousa, Alexander R. Hartloper, Dimitrios G. Lignos. Cyclic Metal Plasticity Model Parameters with Limited Information: Constrained Optimization Approach. J. Eng. Mech., 2021, 147(7): 04021035.
[17] Cheng Jian. Study on Cyclic Hardening Characteristics of Structural Stainless Steel [D]. Shanghai: Tongji University, 2021.
[18] Z. B. Xu, Z. P. Chen, X. S. Zhang. Recent development of basic theory research of genetic algorithm [J]. Mathematical progress, 2000, 29 (002): 193–213.
[19] Kennedy J, Eberhart R. Particle swarm optimization[C]. Proceedings of the 4th IEEE International Conference on Neural Networks, Perth, 1995: 1942–1948.
[20] Zhijian Zhang, Yuande Dai, Chunyang Ma. Design of selectively multilayered periodic gratings by PSO algorithm for radiative cooling. Optics Communications 500 (2021) 127323.
[21] Zeyu Hou, Wangmei Lao, Yu Wang, Wenxi Lu. Hybrid homotopy-PSO global searching approach with multi-kernel extreme learning machine for efficient source identification of DNAPL-polluted aquifer. Computers & Geosciences 155 (2021) 104837.
[22] Xiang Wu, Yongwei Yang, Song Han, Zelong Zhao, Peng Fang, Qingyu Gao. Multi-objective optimization method for nuclear reactor radiation shielding design based on PSO algorithm. Annals of Nuclear Energy 160 (2021) 108404.
[23] Sundar Rengasamy, Punniyamoorthy Murugesan. PSO based data clustering with a different perception. Swarm and Evolutionary Computation 64 (2021) 100895.
[24] Mohineet Kaur, Manoj Kumar Dutta. Restoration and quality improvement of distorted tribal artworks using Particle Swarm Optimization (PSO) technique along with nonlinear filtering. Optik-International Journal for Light and Electron Optics 245 (2021) 167709.
[25] Voce, E. 1948. "The relationship between stress and strain for homogenous deformation." J. Inst. Met. 74: 537–562.
[26] Smith C, Kanvinde A, Deierlein G. Calibration of Continuum Cyclic Constitutive Models for Structural Steel Using Particle Swarm Optimization. J Eng Mech 2017; 143(5):04017012.
[27] Wang Y. Study on 3D cyclic constitutive model and ductile fracture criterion of high strength steels [D]. Shanghai: Tongji University; 2021.
[28] Yao Z, Wang W. Full-range strain-hardening behavior of structural steels: Experimental identification and numerical simulation. J Constr Steel Res 2022;194:107329.
[29] Yuelin Zhang, Cheng Fang, Wei Wang, Haowen Hou. Cyclic plasticity and ULCF behavior of steel butt-joints considering different welding methods. International Journal of Fatigue 173 (2023) 107684.

Bridge Maintenance, Safety, Management, Digitalization and Sustainability – Jensen, Frangopol & Schmidt (eds)
© 2024 The Author(s), ISBN 978-1-032-77040-6
Open Access: www.taylorfrancis.com, CC BY-NC-ND 4.0 license

Modal identification for rapid assessment of short span reinforced concrete bridges

S.L. Leiva-Maldonado
Universidad de la Salle, Bogota, Colombia

F. Consuegra
INGETEC S.A., Bogota, Colombia

ABSTRACT: Structural condition assessment of bridges is the combination of multiple activities such as visual inspections, field and lab testing, structural modeling among others. Therefore, it implies not only structural resistance and static analyses but also dynamic behavior. Dynamic testing techniques as a non-destructive structural assessment is commonly used in bridge engineering. However, different challenges arise when mathematical modeling is involved for rapid evaluation, including modes and frequency validation. The vibration record is a procedure that allows the evaluation of the real behavior of a structure without affecting its own operation. Calibrating numerical models from field data allows to know the real structural behavior during operation. This investigation focuses on the difference between the real behavior and the idealized numerical model built with field structural data in terms of natural frequency and mode shapes. For this study, forty-five simply supported bridges located in Colombia were instrumented and modeled. Visual inspections and proper photographic records were available for all bridges. Different mathematical models were examined including single beam elements, beam elements in conjunction with shell elements and only shell elements. Flexural frequencies and mode shapes were compared using field data and mathematical models. Results suggest that the consideration of the dynamic modulus of elasticity instead of the static modulus in numerical analysis led to more accurate results compared with those obtained from analysis of field data.

1 INTRODUCTION

Dynamic monitoring of structures is a common practice since late 70´s. Those records commonly had been used to estimate the real behavior of a structure such as fatigue analyses observed from dynamic parameters (Doebling et al., 1996) among others. In many cases, researchers focus on the comparison between the real response of the structure (identified in the dynamic records) and the simulated response through numerical models.

This investigation was focused on the study of a simply supported reinforced concrete bridge located in Colombia and part of the main road system. There were two reasons for choosing those structures: Firstly, the huge importance of this type of configuration for the developing of the Colombian infrastructure. Secondly, the potential contribution to the modeling of bridges and their accurate response compared with the real behavior. In addition, the particularity of those structures is that are constantly forced to dynamic forces like the transit of vehicles, characteristic that makes feasible the dynamic characterization with field acceleration records.

Starting from the available field inspections of bridges, numerical models had been created. Additionally, field acceleration records had been used to identify the dynamic behavior of the structure during operation. Comparisons of both results allow to identify the differences between both behaviors. All data including pictures, field inspections (visual and field tests) structural drawings, concrete compression resistance and acceleration records were supplied by INGETEC S.A. – Ingenieros Consultores –.

DOI: 10.1201/9781003483755-443

This method is commonly known as bridge modal identification (BMI) and has been implemented by different authors. For example, Sadeghi Eshkevari et al., (2020) and Talebi-Kalaleh & Mei, (2023) implemented the method in long-span simply supported bridges, focused on the accurate dynamic response. Other researchers like Li et al., (2022) examined BMI in long-span cable stayed bridges. Finally, Consuegra & Santos, (2015) presents an alternative method to investigate structural condition based on a non-linear elastic mathematic representation of the structure based on BMI. Hence, the current research efforts are focused on complex methods to be used in detailed analyses. Consequently, alternative rapid assessments for dynamic bridge responses could be useful for practitioners and inspectors as an initial tool of analysis and preliminary structural behavior. The analysis aims to determine a rapid relationship between the numerical model and the operation response through the modulus of elasticity of the concrete.

The elastic modulus of elasticity is the relationship between the normal stress and longitudinal strain of any given material under axial load (Neville, 2011). The elastic modulus of elasticity is given by the slope of the stress-strain curve of a given material due to a pseudo-static test; however, this curve is not strictly linear for the concrete behavior (Serrano-Guzmán & Pérez-Ruiz, 2010). The dynamic modulus of elasticity corresponding to a very small instantaneous strain is approximately given by the initial tangential modulus which is the tangent modulus for the line drawn from the origin. It is generally 20, 30 and 40 percent higher than the static modulus of elasticity for high, medium, and low strength concretes respectively (Serrano-Guzmán & Pérez-Ruiz, 2010).

Equation 1 shows the numerical expression used by "Norma Colombiana de Diseno de Puentes (CCP14)" which is the official normative used for the analysis and design of bridges in Colombia. This equation stablishes a relationship between the compressive resistance of the concrete ($f'c$) and the value of the elastic modulus of elasticity.

$$E_c = 4800(f'c)^{0.5}\ [MPa] \tag{1}$$

Several attempts have been made to correlate static (E_c) and dynamic (E_d) moduli of elasticity for concrete. The simplest of these empirical relations was given by Lydon & Balendran, (1986), and it is presented in equation (2):

$$E_c = 0.83E_d\ [MPa] \tag{2}$$

Therefore, it can be determined that the dynamic modulus of elasticity for concretes above 18.00MPa (considered as structural concrete) is 1.20 times higher than the elastic modulus of elasticity. Additionally, and as specified by Serrano-Guzmán & Pérez-Ruiz, (2010), for lower compressive strengths, it could be 1.40 times larger.

2 DESCRIPTION OF BRIDGE DATABASE AND FIELD INSTRUMENTATION

All the bridges analyzed can be comprised in the following superstructure categorization: 35 reinforced concrete beam bridges (RC), 1 reinforced concrete beams bridge with external post-tensioning (RC-ET), and 9 prestressed concrete beams bridges (PC). There are 37 bridges with one simply supported span, 5 with two simply supported spans and 1 with three simply supported spans; it means that there are 50 different acceleration records. Geometrically there are bridges with 3 to 9 principal beams, widths from 8.00m to 14.70m including the handrails, and lengths between 5.00m to 42.20m. Average values of concrete compression strength varies between 7.85MPa to 31.90 MPa.

A simply supported reinforced concrete beams bridge is presented for the explanation of the method. The geometry of the structure is presented in Figure 1. The bridge is 11.02m long (10.00m between supports), 8.57m wide, the superstructure is composed of four main 0.41x0.82m beams with principal reinforcement of 2 layers of 8#8 plain reinforcing steel. Reinforced steel distribution and concrete compressive strength (11.80MPa) were obtained from non-destructive testing, visual inspections and extracted concrete core samples.

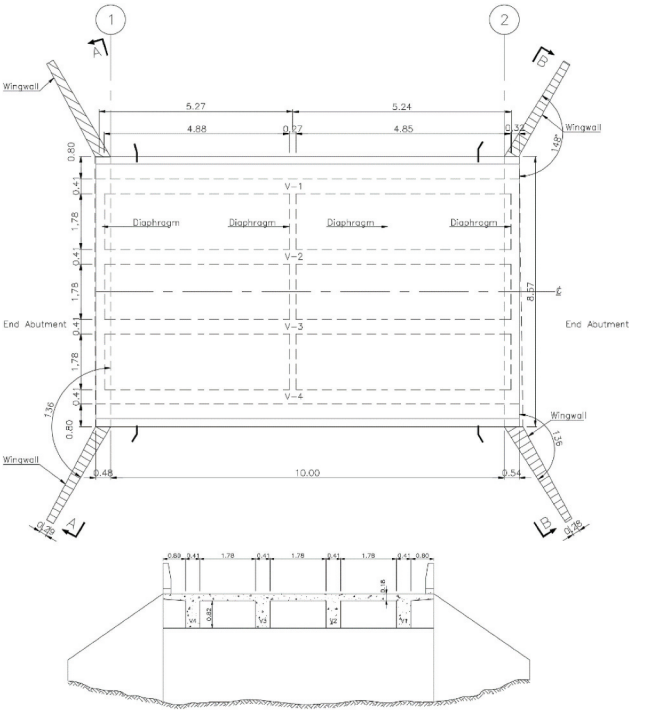


Figure 1. Reinforced concrete bridge geometry.

All field records were made with 3 accelerometers located at the extreme points of the external beams of the bridge in a straight parallel line to the longitudinal direction. Accelerometers #1 and #3 were installed in the end quarters of the total bridge length, and accelerometer #2 in the midspan as shown in Figure 2. Data was recorded at 2,000sps for a maximum period of 3 minutes. Data were collected with micro-vibration accelerometers with a scale range of ±0.50g, and an acquisition equip of 24bits. Measurements were collected at both sides of the

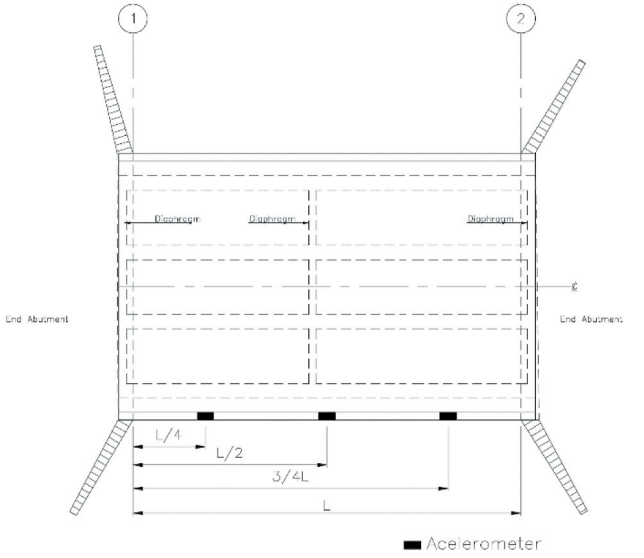


Figure 2. Accelerometer location for dynamic monitoring.

bridge independently. There are no records of the type and periodicity of the traffic, however, all tests were made during operation.

3 ANALYSIS OF FIELD RECORDS

Vibrations inherently are time-domain data, however, for engineering purposes, frequency-domain data are preferable. Hence, the fast Fourier transform (FFT), understood as a computational tool to transform time-domain data to frequency-domain outputs, is a feasible method to analyze acceleration field records. Complementary, flexural, and torsional frequencies were found using the "Peak-Pick" method, filtering the original signal as proposed by other authors (F. Consuegra & Irfanoglu, 2012; Bindi et al., 2015; Naderpour & Fakharian, 2016; Jin et al., 2021). For this study Chevychev type I filter was used due to the frequency attenuations of records higher than the filter frequency parameter established. To identify and compare the vibration modal shapes due to flexion and torsion, an acceleration normalization was used, taking as the norm the maximum value among the accelerations filtered.

Moreover, due to the nature of the acceleration records, the response shown in the acceleration spectrum is highly influenced by interpretation. The most common challenge faced in these analyses is the frequency picking among multiple peaks close together. Figure 4 (b) shows the frequency spectrum of an acceleration record test (a). As can be seen, there are multiple identifiable frequency peaks that could be interpreted as flexural or torsional frequencies. Therefore, filters for each peak were performed for all the accelerometers positioned (c, e and g) and the modal shapes identified from the filtered signals (d, f and h). Hence, the modal shape that best fits the flexural or torsional expected modal shape (verified with the numerical model) was selected as the frequency for each phenomenon. The definitive frequency used for the comparison with the numerical model is the mean of the frequency values obtained for all the acceleration tests available for each bridge.

4 NUMERICAL MODELATION

Based on the geometry, material properties and visual inspections made for all the bridge database, 3D models using only shell elements were constructed using SAP2000® software (see Figure 3). In addition, other models were considered, including 2D single-frame models, 3D

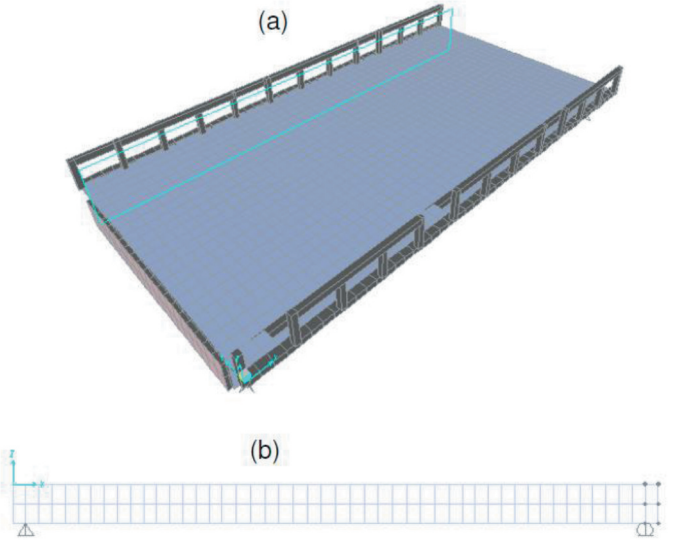


Figure 3. 3D shell only model. (a) Isometric general view. (b) General profile.

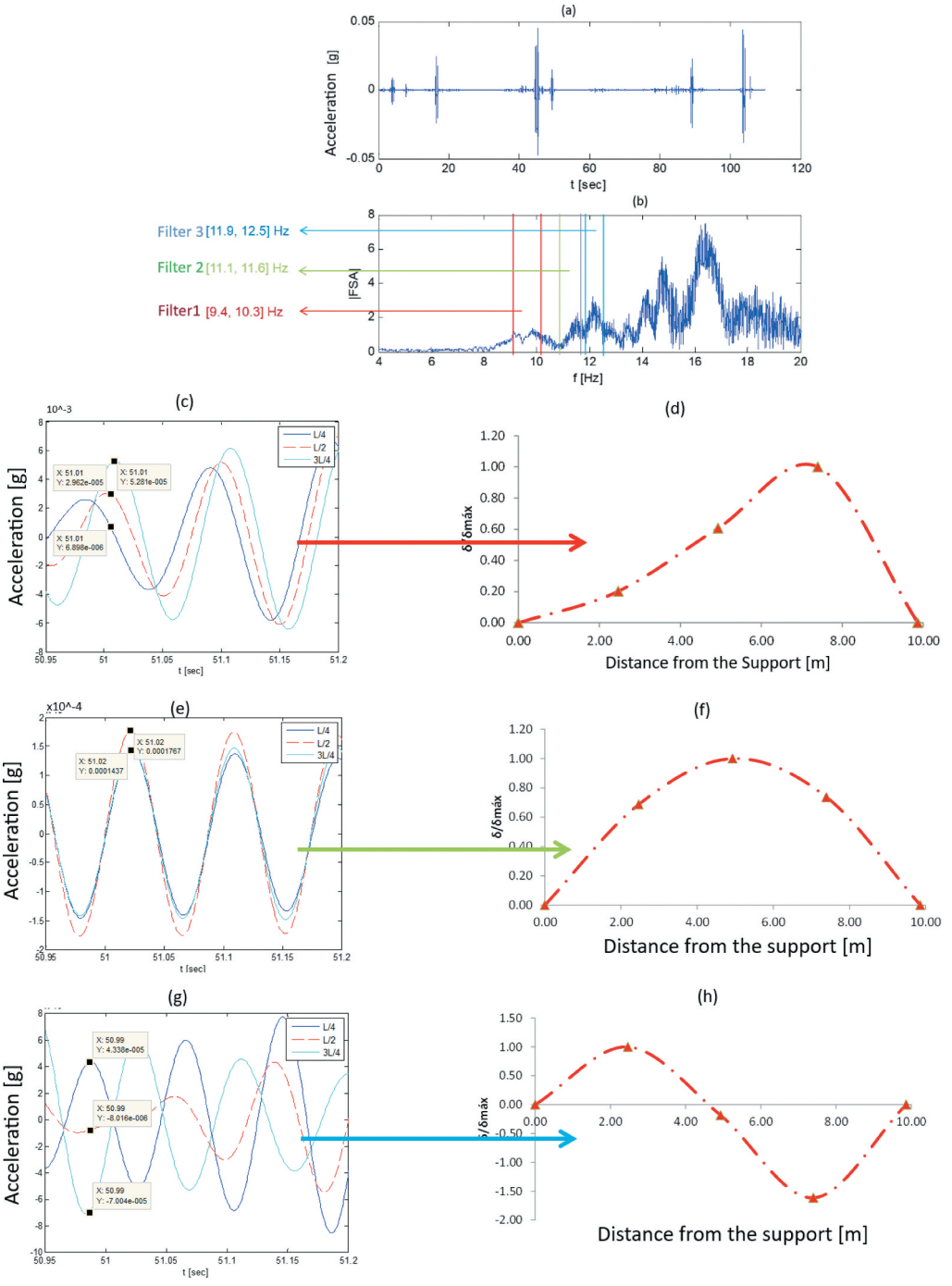


Figure 4. Signal processing. (a) Acceleration record. (b) Frequency spectrum. (c) Filtered signal (Filter 1). (d) Modal shape filtered signal (filter 1). (e) Filtered signal (Filter 2). (f) Modal shape filtered signal (filter 2). (g) Filtered signal (Filter 3). (h) Modal shape filtered signal (filter 3).

shell-frame models with wearing surfaces and barriers (as additional masses), and mathematical expressions for flexural and torsional frequencies based on Euler-Bernoulli beam vibrations theory. Nevertheless, contemplating the feasibility of the model development for rapid

assessment, 3D shell models are commonly used in the analysis of bridges, and therefore, chosen for this study. Non-linearity of materials cracked cross sections or additional support stiffness were not included in the numerical models, to simplify the application of this procedure.

Once the model is analyzed, modal shapes and frequencies for both flexural and torsional behavior can be obtained, as shown in Figure 5.

5 ANALYSIS OF RESULTS

As derived from the Euler-Bernoulli vibration theory, frequencies are dependent on variables such as modulus of inertia, element length, cross sectional area, density, and modulus of elasticity. Since all geometrical properties are constant, frequencies are directly correlated with the square root of the modulus of elasticity. Therefore, the relationship between experimental and numerical model frequencies can be expressed in terms of the modulus of elasticity ratio of the experimental and numerical models as described in Equation (3) for the flexural behavior.

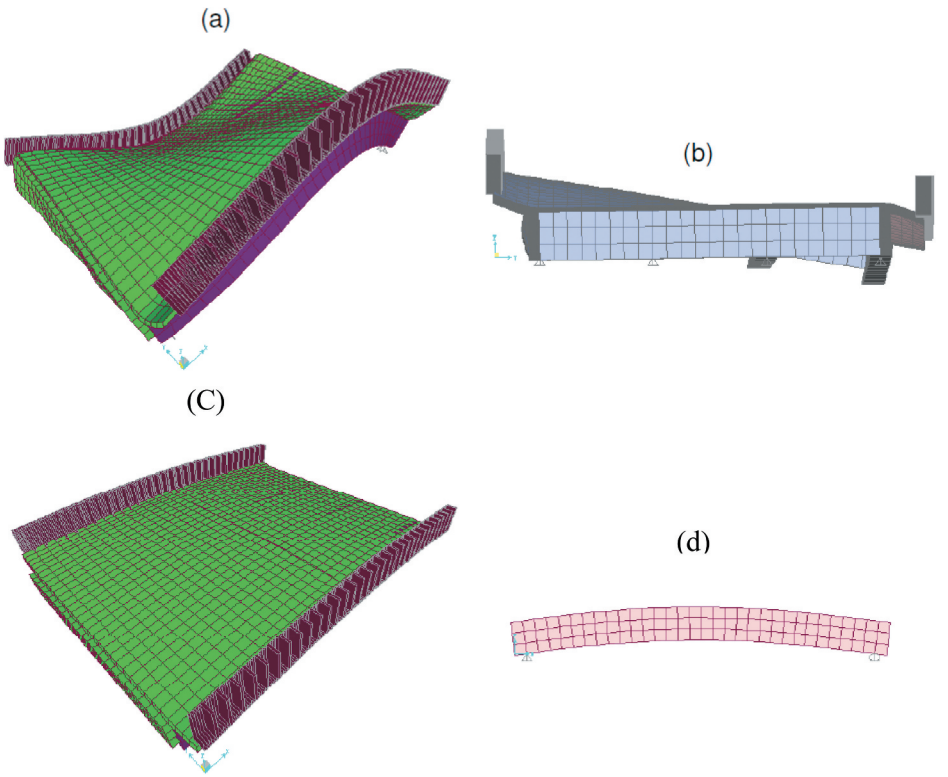


Figure 5. Modal Shapes. (a) and (b) Flexural modal shape. (c) and (d) Torsional modal shape.

$$f_F = \frac{\pi}{2L^2}\sqrt{\frac{EI}{\rho A}} : \{\pi\ L\ A\ I\ \rho\} = const. \therefore f_F \propto \sqrt{E}$$
$$\frac{f_F Exp}{f_F Mod} = \frac{\sqrt{E_{Exp}}}{\sqrt{E_{Mod}}} = \sqrt{\frac{E_{Exp}}{E_{Mod}}} \therefore \left(\frac{f_F Exp}{f_F Mod}\right)^2 = \frac{E_{Exp}}{E_{Mod}} \rightarrow E_{Exp} = E_{Mod}\left(\frac{f_F Exp}{f_F Mod}\right)^2 \quad (3)$$

Thus, the frequency ratio squared could be related to the ratio between the elastic and the dynamic modulus of elasticity presented in Equation (2). As described before, that relationship depending on the compressive strength of the concrete could vary from 1.20 to 1.40 for high and low strength concretes respectively. Figure 6 Shows the frequency ratios results for all the bridge database, specifying the average ratio and the maximum and minimum extreme values. Taking the average value as the contrast value (ratio=1.10), the final relationship understood as the ratio squared is 1.21, which is consistent with the ratio between modulus of elasticity for structural concrete. Therefore, the inclusion of the dynamic modulus of elasticity in the numerical model for the dynamic analysis of vibrations results in the accurate structural response of the structure analyzed.

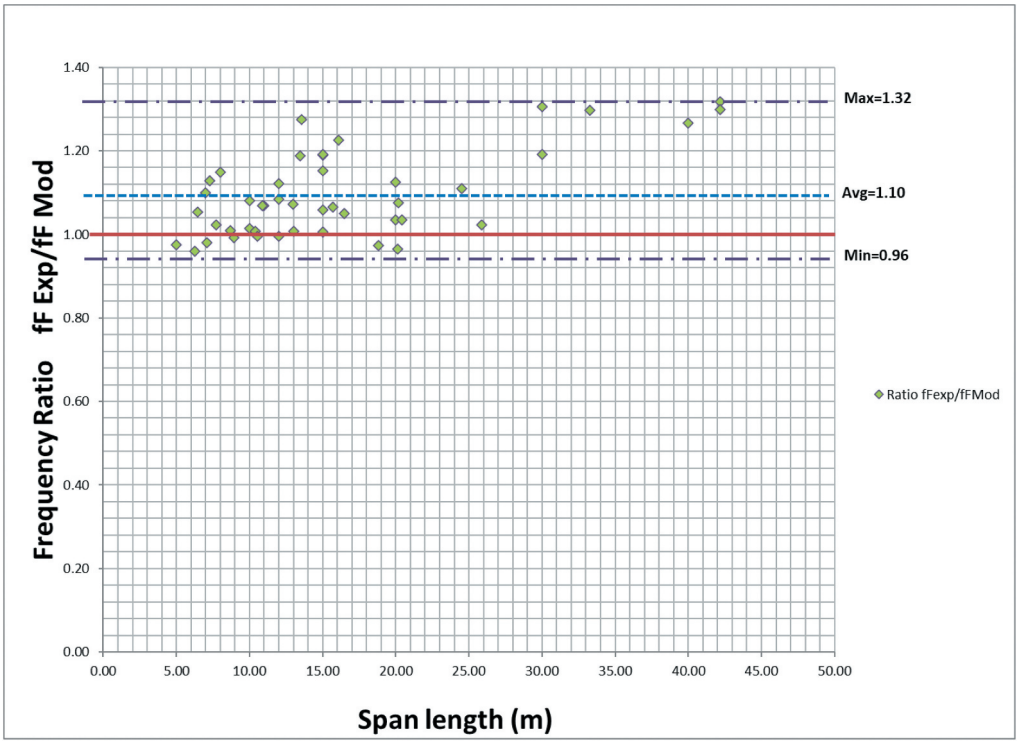


Figure 6. Frequency flexural ratios for different span lengths.

6 CONCLUSIONS

A rapid approach for dynamic analysis and characterization was proposed comparing numerical 3D models and acceleration records from a Colombian bridge database part of the main road system, provided by INGETEC S.A. The analysis suggests that for rapid assessment using acceleration records due to vibrations, a 3D shell-only model can be used, considering the dynamic modulus of elasticity instead of the regular approach which contemplates the elastic modulus. The modulus ratio (1.20) can be compared to the frequency ratio between the experimental and the numerical model squared (1.21). Consequently, findings suggest that the usage of the dynamic modulus of elasticity replicates more accurately the real behavior of the structure and could be used for practitioners and field engineers for rapid assessment. Further analyses and testing could be useful to determine an accurate relationship.

REFERENCES

Bindi, D., Petrovic, B., Karapetrou, S., Manakou, M., Boxberger, T., Raptakis, D., Pitilakis, K. D., & Parolai, S. (2015). Seismic response of an 8-story RC-building from ambient vibration analysis. *Bulletin of Earthquake Engineering*, *13*(7), 2095–2120. https://doi.org/10.1007/s10518-014-9713-y.

Consuegra, F. A., & Santos, C. (2015). Vibration analyses for the local and global evaluation of bridges as a tool for structural retrofit. *Revista de La Construccion*, *14*(1), 16–22. https://doi.org/10.4067/s0718-915x2015000100002.

Consuegra, F., & Irfanoglu, A. (2012). Variation of Small Amplitude Vibration Dynamic Properties with Displacement in Reinforced Concrete Structures. *Experimental Mechanics*, *52*(7), 817–828. https://doi.org/10.1007/s11340-011-9590-0.

Doebling, S. W., Farrar, C. R., Prime, M. B., & Shevitz, D. W. (1996). *Structural identification, damage identification and structural health monitoring*. https://doi.org/10.1117/12.715000.

Jin, S. S., Jeong, S., Sim, S. H., Seo, D. W., & Park, Y. S. (2021). Fully automated peak-picking method for an autonomous stay-cable monitoring system in cable-stayed bridges. *Automation in Construction*, *126*(February), 103628. https://doi.org/10.1016/j.autcon.2021.103628

Li, J., Zhu, X., & Guo, J. (2022). Bridge modal identification based on successive variational mode decomposition using a moving test vehicle. *Advances in Structural Engineering*, *25*(11), 2284–2300. https://doi.org/10.1177/13694332221092678.

Lydon, F. D., & Balendran, R. V. (1986). Some observations on elastic properties of plain concrete. *Cement and Concrete Research*, *16*(3), 314–324. https://doi.org/10.1016/0008-8846(86)90106-7.

Naderpour, H., & Fakharian, P. (2016). A synthesis of peak picking method and wavelet packet transform for structural modal identification. *KSCE Journal of Civil Engineering*, *20*(7), 2859–2867. https://doi.org/10.1007/s12205-016-0523-4.

Neville, A. M. (2011). *Properties of Concrete*. Pearson. https://books.google.com.co/books?id=mmygngEACAAJ.

Sadeghi Eshkevari, S., Matarazzo, T. J., & Pakzad, S. N. (2020). Bridge modal identification using acceleration measurements within moving vehicles. *Mechanical Systems and Signal Processing*, *141*, 106733. https://doi.org/10.1016/J.YMSSP.2020.106733.

Serrano-Guzmán, M. F., & Pérez-Ruiz, D. D. (2010). Análisis De Sensibilidad Para Estimarel Módulo De Elasticidad Estáticodel Concreto. *Concreto y Cemento. Investigación y Desarrollo*, *2*(1), 17–30. http://www.scielo.org.mx/scielo.php?script=sci_arttext&pid=S2007-30112010000100002&lng=es&nrm=iso&tlng=es.

Talebi-Kalaleh, M., & Mei, Q. (2023). A Mobile Sensing Framework for Bridge Modal Identification through an Inverse Problem Solution Procedure and Moving-Window Time Series Models. *Sensors*, *23*(11). https://doi.org/10.3390/s23115154.

Bridge Maintenance, Safety, Management, Digitalization and Sustainability – Jensen, Frangopol & Schmidt (eds)
© 2024 The Author(s), ISBN 978-1-032-77040-6
Open Access: www.taylorfrancis.com, CC BY-NC-ND 4.0 license

Retroreflective sheeting materials as SHM passive strain sensors

Hannah M. Power & Harry W. Shenton III
Department of Civil and Environmental Engineering, University of Delaware, Newark, Delaware, USA

ABSTRACT: Highly reflective Retroreflective sheeting materials (RRSM) are widely used today for roadway signs and markings. Retroreflectivity (RR), defined as the portion of light re-turned to the light source as measured in candelas per lux per square meter, can be measured quite easily in the field using a handheld retroreflectometer. Tests show that as load is applied to RRSM, the retroreflection changes, and for many types of RRSM, RR decreases with increasing tension and has a mostly linear relationship to the material strain. This opens the possibility for using RRSM as a passive strain sensor for structural health monitoring, whereby measured changes in RR of RRSM mounted to a structure can be correlated to changes in strain. The sensor would be low cost, practical, and innovative. Tension test results show that a yellow-green type XI material produced by one manufacturer has one of the highest material sensitivities (ratio of retroreflectivity to strain) of the many the authors have tested. The sensitivity of the material, denoted here as A-TXIFYG, decreases linearly after it is strained past approximately 1000 microstrain (με). This led to testing of the material after initial straining (pre-straining). Results show that for the material to have a similar sensitivity while mounted to that of the bare material tests, it must be externally clamped to the substrate.

1 INTRODUCTION

In the United States, bridges are only required to be visually inspected every 2 years [FHWA (2017)]. These inspections cannot identify internal damage and rely on qualitative evaluations which are susceptible to error. This has led to a desire to monitor bridges using sensing networks, which allows bridge owners to gain a more accurate and complete evaluation of a bridge. However, conventional structural health monitoring (SHM) systems can be expensive, require power and involve dedicated data acquisition [Chang, Flatau, Liu (2003)] all of which lead bridge owners to often choose to not implement them, therefore there is a need to develop passive, inexpensive sensing systems to monitor bridges that could be more easily and readily adopted by the bridge industry. This paper describes a passive strain sensor developed from retroreflective sheeting material that is inexpensive and should be easily adopted by transportation infrastructure owners.

1.1 *Retroreflective sheeting materials*

Retroreflective Sheeting Materials (RRSM) are thin flexible reflective laminate like materials that are made for various applications but are primarily used to make traffic signs and roadway markings. ASTM D4956, "Standard Specification for Retroreflective Sheeting for Traffic Control" [ASTM International (2019)] defines standards for 11 types of sheeting material. RRSMs are produced by various manufacturers [FHWA (2005)] and are comprised of several layers, including an adhesive backing so that with proper surface preparation it can be adhered to steel, aluminum, or concrete (Figure 1).

The reflecting layer of RRSMs affects the material's ability to return emitted light to the source, a measurement known as retroreflectivity (RR). Higher grade materials, with higher baseline values of retroreflectivity (RR) have a prismatic reflecting layer (Figure 1).

DOI: 10.1201/9781003483755-444

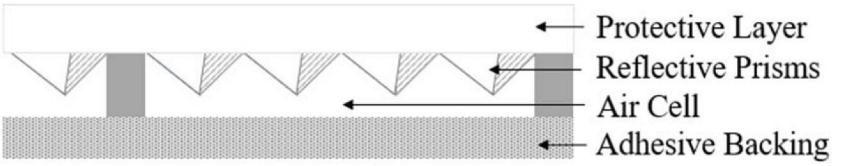


Figure 1. Prismatic retroreflective sheeting material cross-section.

The Federal Highway Administration (FHWA) Manual on Uniform Traffic Control Devices (MUTCD) [FHWA (2012)] requires all public agencies in the United States to maintain minimum levels of sign retroreflectivity. To establish compliance, agencies can measure retroreflectivity of a sign using a handheld retroreflectometer, which when held against the material, measures the RR in candelas-per-lux-per-square meter. Many State Departments of Transportation (DOTs) make and maintain their own traffic signs and are required to periodically measure the retroreflectivity of their signs; therefore, most DOTs have access to retroreflective sheeting materials and a familiarity with retroreflectometers, i.e., the materials to fabricate a passive strain sensor and the instrument to take strain readings.

1.2 *Passive strain sensor application of RRSM*

Tests conducted by the authors have demonstrated that as load is applied to RRSM the retroreflectivity changes in intensity. Consequently, there is the potential to use retroreflective sheeting material as a passive strain sensor for structural health monitoring (SHM) [Power, Shenton (2023)]. The potential applications for these sensors include monitoring dead load induced in bridge super and substructures, observing crack growth in reinforced and prestressed concrete members, residual stress measurements and other circumstances that would benefit from static strain measurements. RRSM sensors are passive, meaning they do not require power or wiring and their data acquisition is simple.

An RRSM sensor can be affixed to the tension face of any structural element, and using a handheld retroreflectometer, RR can be measured during routine inspections or after significant events. That RR value can then be compared to the material's baseline, i.e., unstrained retroreflectivity, and related to the strain in the structure based on previously determined calibration factors [Power, Shenton (2023)]. Application of RRSMs as SHM systems on bridges will allow for simple and effective monitoring.

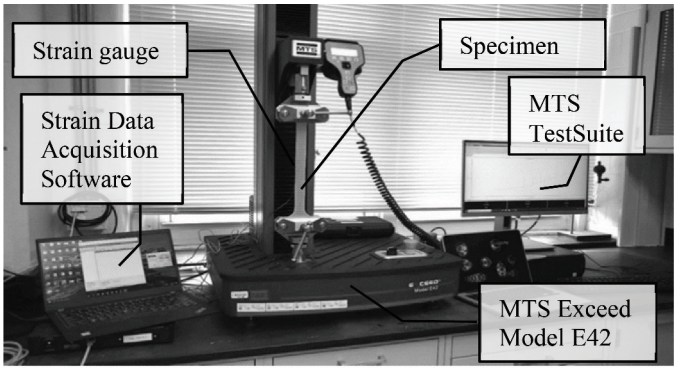
2 RRSM BARE MATERIAL RESPONSE TO INDUCED STRAIN

Various types of RRSM made by two manufacturers have been tested in tension, measuring their RR and microstrain (με) in order to develop the RR versus strain relationship [Power, Shenton (2023)]. Many materials display a linear relationship between retroreflectivity and strain. The materials retroreflective sensitivity to induced strain (RR/με) is the most important factor when assessing RRSM's viability for use as a strain sensor. The following discusses a RRSM produced by manufacturer "A" that is standard type XI and is fluorescent yellow-green in color, denoted as A-TXIFYG. This material has high sensitivity and correlation, making it a suitable material for passive strain sensing for SHM of bridges.

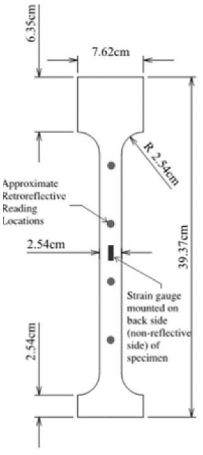
2.1 *Test procedure*

Three specimens of A-TXIFYG were loaded in tension while measuring the material RR and microstrain to determine the RR-με relationship. Specimens were cut using scissors and a uniaxial strain gauge was adhered to the non-reflective side of each specimen (Figure 2b).

Tension tests were run in an MTS Exceed E42 Electromechanical Test System and strain was recorded using a Micro Measurement System 8000 data acquisition system and StrainSmart software (Figure 2a). Each specimen was loaded to approximately 4000 με and unloaded three times. The first loading and unloading cycles were paused every 4.45 N (1 lb) to record



a. Test set-up



b. Specimen dimensions

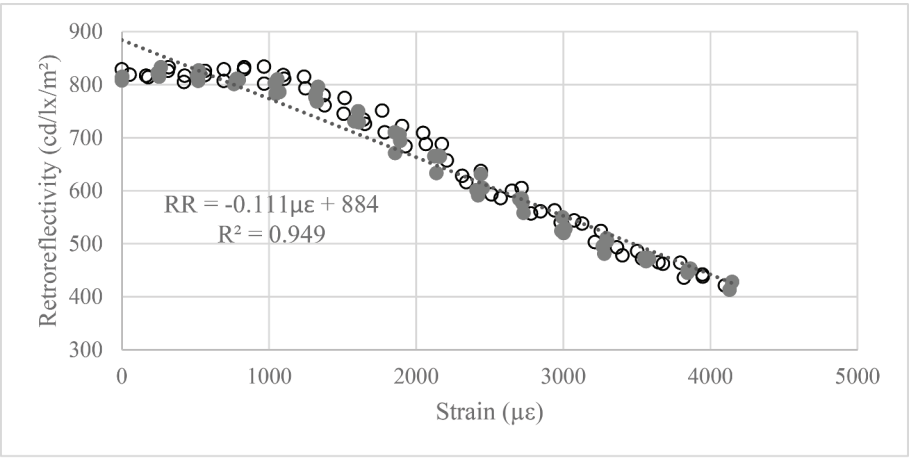
Figure 2. Bare material tension test.

microstrain and RR. The second and third loading and unloading cycles were paused every 8.90 N (2 lb) to record strain and RR. RR has innate variability, so four readings were taken at each load step and averaged.

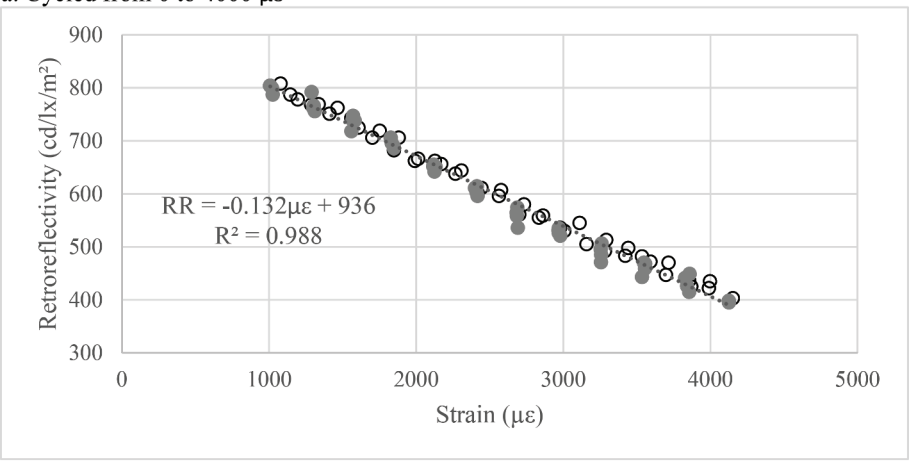
2.2 *Results*

The RR vs. strain response of the A-TXIFYG is shown in Figure 3a. In this figure, and all other similar plots, the first loading and unloading cycle data points are highlighted by a dark outline. A linear regression line for all cycles of the specimen is plotted along with the associated equation and R^2 value. Figure 3a clearly shows the RR dependence on the induced strain. The RR remains nearly constant for the first ~1000 με and then decreases linearly with increasing strain. From approximately 1000 to 4000 με, A-TXIFYG has a highly correlated linear retroreflective-microstrain relationship. The same specimen was tested again but first pre-strained to approximately 1000 με (i.e., pre-strained) and then cycled between 1000 and 4000 με to determine the correlation and sensitivity of the material after initial straining (Figure 3b).

The material sensitivity between 0 and 4000 με is -0.111 RR/με for this specimen with an R^2 value of 0.949. When the same specimen was pre-strained and cycled between 1000 and 4000 με, the sensitivity increased to -0.132 RR/με and the R^2 increased to 0.988. These results show that a SHM sensor made of A-TXIFYG may function best if the material is first pre-strained, and then adhered to the substrate.



a. Cycled from 0 to 4000 με



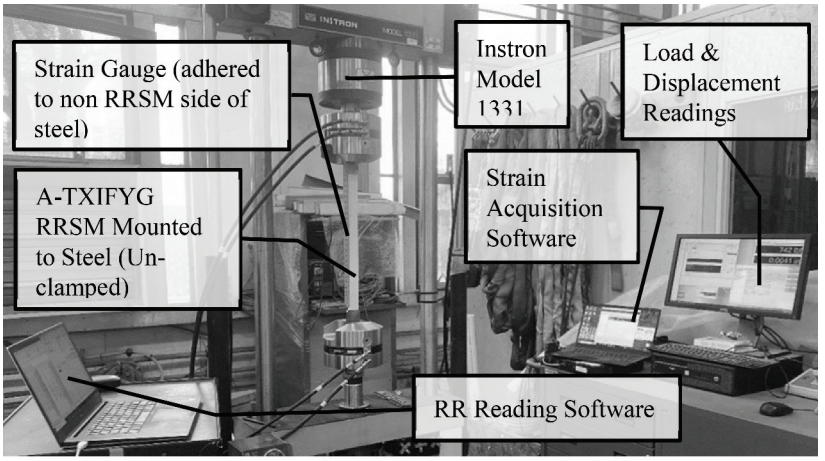
b. Cycled from 1000 to 4000 με

Figure 3. A-TXIFYG bare material tension test results.

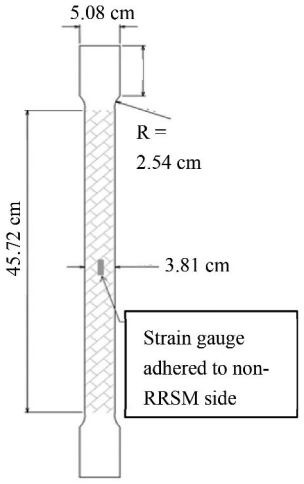
3 A-TXIFYG STEEL MOUNTED TESTS

3.1 *Test procedure*

To determine material response when adhered to steel, strips of RRSM were cut and mounted to ¼" thick A36 steel "dog-bone" specimens. To prepare the surface prior to mounting the RRSM, the steel was sanded using 220 grit sandpaper and cleaned with acetone. The RRSM was cut to fit the gage width and length of the steel specimen, the backing was removed to expose the adhesive layer and the RRSM was rolled onto the steel using a rubber roller. A uniaxial strain gauge was mounted to the back of the steel dogbone specimen to measure the strain in the steel. Specimens were loaded in tension in an Instron 1331 Testing Frame to approximately 44,482 N (10,000 lb), below the yield stress of the steel, pausing every 2224 N (500 lb) to take retroreflective readings and strain in the steel. Specimens were then unloaded to 0 kg, also pausing every 2224 N (500 lb) to take RR and strain readings. This was repeated for three loading and unloading cycles, similar to the bare material test described in section 2. RR readings were recorded along the length of the specimen and those within the center region of the specimen were used to evaluate the RR-με relationship of the steel mounted material. Test set up and steel specimen dimensions are shown in Figure 4.



a. Test set-up



b. Specimen dimensions

Figure 4. Steel mounted A-TXIFYG tension test.

3.2 *Results*

Initial tests of the RRSM mounted to the steel dogbone yielded results quite different from those of the bare material. Three different specimen configurations were initially tested to determine the best methods for creating the steel mounted specimens. This included configuration (1), pre-straining the RRSM and adhering it to only the gauge length of the steel specimen. Configuration (2), pre-straining the RRSM and adhering it to the full length of the steel specimen so that the RRSM was placed in the Instron grips with the steel. And configuration (3) where the material was pre-strained, adhered to only the steel gauge length and then externally clamped before the pre-straining weights were removed. To pre-strain the A-TXIFYG prior to mounting it to the steel, weights were hung from the material so that the induced strain was approximately 4000 με. The backing film was then removed to expose the adhesive and then the RRSM was rolled onto the steel while the weight remained on the RRSM. This pre-straining procedure was used for all pre-strained steel mounted specimens.

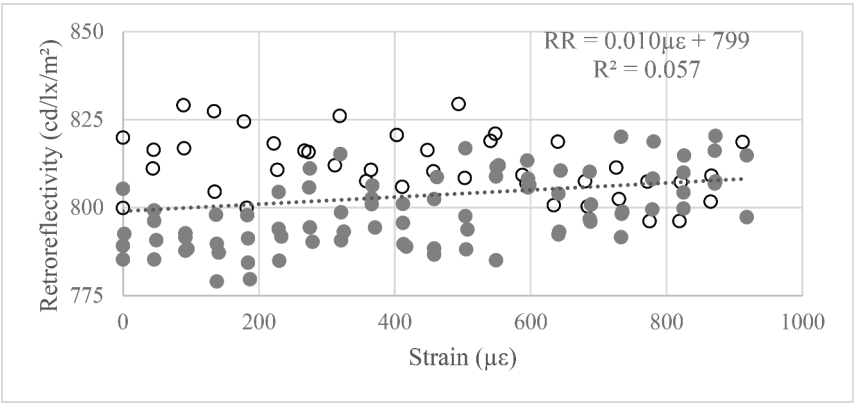


Figure 5. Pre-strained, steel mounted A-TXIFYG on gauge length test results (Configuration 1).

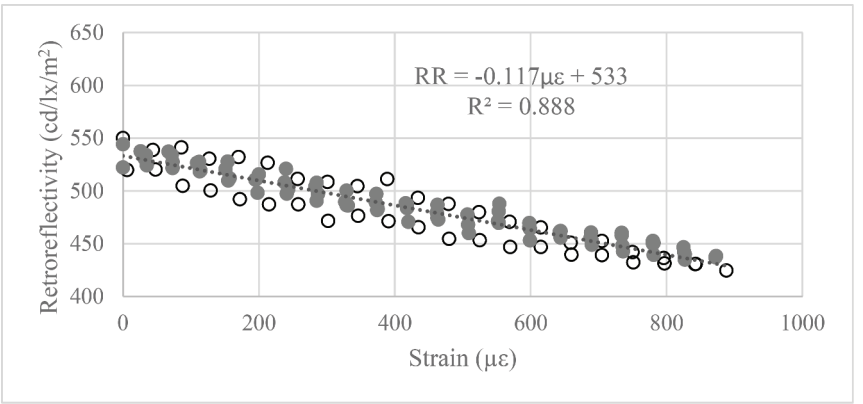


Figure 6. Pre-strained, steel mounted A-TXIFYG in instron grips test results (Configuration 2).

3.2.1 *Unclamped specimen (Configuration 1)*
Initially, specimens were pre-strained and free to relax on the surface of the steel, i.e., the RRSM material was not restrained by the Instron grips or external clamps and therefore was free to relax under load. The RR-με relationships of these specimens differed from the bare material response to induced strain. Figure 5 shows the RR-με relationship of an initial specimen of A-TXIFYG that was pre-strained and fabricated using configuration (1). These results led the authors to design specimens with configuration (2).

3.2.2 *Instron gripped specimen (Configuration 2)*
Due to the low sensitivity, poor correlation and difference compared to the bare material results, the authors decided to adhere the RRSM to the full length of the steel specimen so that the pre-strained material was restrained by the test machine grips, configuration (2). This specimen configuration led to a much higher sensitivity (-0.117 RR/με) and better linear correlation with $R^2 = 0.888$ (Figure 6).

3.2.3 *Externally clamped specimen (Configuration 3)*
The results presented in Figures 5 and 6 demonstrate that for RRSM to be used as a passive sensor for SHM, it must first be strained and then clamped. To achieve this, an external clamping mechanism is necessary so that the sensor, consisting of pre-strained RRSM adhered and clamped to steel, can be affixed to a structure. The clamps used are front and back steel plates that are through bolted. Clamps were secured before pre-straining weights were

removed (Figure 7). Configuration (3) specimen's RR-με relationship is comparable to that of the bare material (Figure 3) and that of the specimen results prepared using configuration (2) (Figure 6). The material sensitivity is -0.104 RR/με with an R^2 of 0.925 (Figure 8).

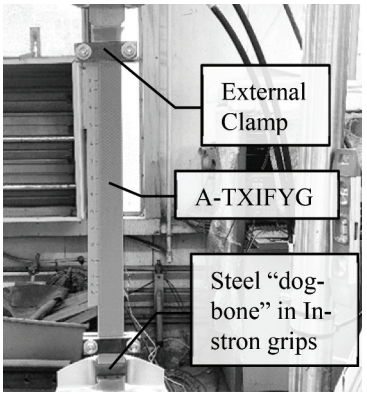


Figure 7. Pre-strained, clamped, steel mounted A-TXIFYG specimen.

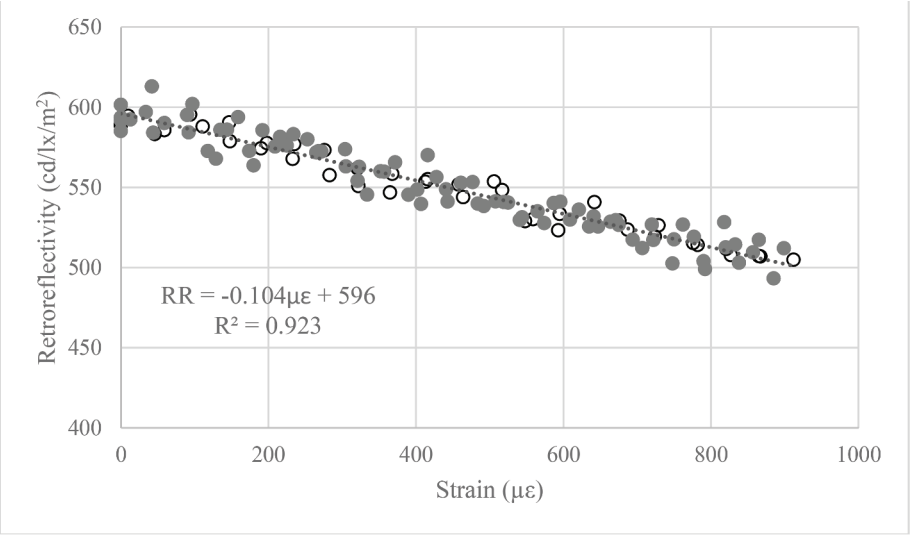


Figure 8. Pre-strained, clamped, steel mounted A-TXIFYG test results (Configuration 3).

3.3 *Discussion*

Comparing the results of the unclamped to the clamped pre-strained specimens, it is clear that for A-TXIFYG to function as a passive strain sensor, it must first be strained and clamped to a substrate. The unclamped, ungripped (configuration 1) specimen from Figure 5 has little correlation, with an R^2 value of 0.057. The material's retroreflective sensitivity to induced microstrain is +0.010 RR/με. This sensitivity is low compared to the bare material sensitivity discussed in section 2.2, and it also has the opposite sign convention, indicating that RR was not decreasing with increasing induced strain. Shear lag is suspected to be the main factor contributing to the poor behavior of the RRSM when it is not clamped/gripped to the steel substrate. That, in addition to the tremendous difference in axial stiffness between the steel and RRSM, and the fact that the reflective prisms are near the surface of the material.

When the material was pre-strained and placed in the Instron grips (configuration 2), mimicking clamping, the material sensitivity increased. The externally clamped (configuration 3)

specimen's sensitivity and R^2 values are close to that of the bare material, having percent differences of 6.3% and 2.5% respectively. These results indicate that to use A-TXIFYG as a sensor, it must first be strained and then mounted with a clamping mechanism to a steel substrate. The entire steel mounted RRSM will function as the passive strain sensor for SHM.

To use RRSM as a passive strain sensor for monitoring bridges, the material first needs to be strained, then mounted to steel and clamped to the steel. The sensor needs to be long enough so that multiple RR readings can be taken and averaged, as RRSM has innate variability. The retroreflectometer takes readings from the center of the device, therefore there needs to be enough clearance around the clamps to take the readings. To create this sensor, similar steps to those discussed in section 3.2 can be followed. First, the A-TXIFYG material is cut to shape and pre-strained. It can then be rolled onto the steel sensor. This sensor will be fabricated with backing plates for the clamping mechanism. After the RRSM is strained, the adhesive backing is used to adhere the material to the steel by using a roller. While the pre-straining weight is still on the RRSM, top clamp plates are bolted to the steel sensor using threaded bolts. After the clamps are in place, the pre-straining weights can be removed, and the sensor is ready to be adhered to the tension face of any structural element for monitoring.

4 CONCLUSIONS

In the United States, bridges are not required to be monitored with an SHM system but are only required to undergo a visual inspection every two years. These visual inspections are qualitative and can lack key information about a structure. There is a need for inexpensive and accessible SHM systems for bridge monitoring to encourage their widespread use. Bridge owners are familiar with RRSM and their measurements as they also make and maintain their traffics signs, which are also made of RRSM. This would make the technology transfer of using RRSM as a passive strain sensor on bridges simple.

RRSM has the potential to be used as a passive strain sensor for structural health monitoring of bridges as its retroreflectivity decreases with induced strain. Type XI material that is fluorescent yellow-green produced by manufacturer "A" (A-TXIFYG) has high RR sensitivity to strain and is therefore a candidate for use as a sensor. A-TXIFYG materials have little RR change for approximately the first 1000 induced microstrain as seen in tension testing of the bare material. This led to authors to strain the material before it is mounted to steel substrate. This pre-straining process only works when the material is clamped to the steel while it is being strained. When that procedure is followed, there is little difference in the bare material and mounted material sensitivity to strain. This sensor will be low cost and practical, opening the possibility for widespread monitoring of bridges.

REFERENCES

ASTM D4956-19 Standard Specification for Retroreflective Sheeting for Traffic Control, *ASTM International*, West Conshohocken, PA. (2019)

Federal Highway Administration (FHWA), Assessing the Structural Health of America's Highway Bridges, Effective Wireless Sensor Systems to Monitor Structural Health and Detect Damage. - FHWA-HRT-17-043. *U.S. Department of Transportation*, (2017) www.fhwa.dot.gov/publications/research/ear/17043/index.cfm#ref01.

Federal Highway Administration (FHWA). FHWA Retroreflective Sheeting Identification Guide. *U.S. Department of Transportation*, (2005) https://safety.fhwa.dot.gov/roadway_dept/night_visib/retrotoolkit/pdfs/sheetguide_sept05.pdf

Federal Highway Administration (FHWA), Manual on Uniform Traffic Control Devices (MUTCD), *U.S. Department of Transportation*, (2012) Edition with Revision Numbers 1 and 2 Incorporated.

Hannah M. Power, Harry W. Shenton III, Passive strain sensing for structural health monitoring using retroreflective sheeting materials, *Measurement*, Volume 214, (2023), 112763, ISSN 0263-2241, https://doi.org/10.1016/j.measurement.2023.112763.

P.C. Chang, A. Flatau, S.C. Liu, Review Paper: Health Monitoring in Civil
Infrastructure. *Sage Publications*. 2(3) (2003) 0257–267. doi: 10.1177/145792103036169.

Bridge Maintenance, Safety, Management, Digitalization and Sustainability – Jensen, Frangopol & Schmidt (eds)
© 2024 The Author(s), ISBN 978-1-032-77040-6
Open Access: www.taylorfrancis.com, CC BY-NC-ND 4.0 license

Assessment method for arch bridges affected by HS2 tunnel settlement, UK

A. Saavedra Justo, A. Bariyya, C. Brown & R. Lee
Arup, Birmingham, UK

M. Gilbert
University of Sheffield, Sheffield, UK

ABSTRACT: The development of high-speed railways brings numerous opportunities for economic growth and improved transportation networks. In the United Kingdom, the construction of the High Speed 2 (HS2) railway is a flagship project aimed at enhancing connectivity, increasing capacity and reducing travel times. However, the construction will impact existing infrastructure along the route. This paper presents an overview of the ground movement assessment conducted on eight existing masonry arch bridges in West London affected by settlement due to construction of HS2 twin bore tunnels. This work has provided valuable insights into the potential challenges and risks associated with tunnelling under a major city. The findings underscore the importance of thorough structural assessments and implementing appropriate interventions to ensure the safety and resilience of existing bridge infrastructure above new tunnel construction.

1 INTRODUCTION

High Speed 2 (HS2) is a new rail line in the United Kingdom, planned to run between London and the West Midlands. It is a government funded programme that aims to increase rail capacity, boost regional growth through better connections, and reduce carbon emissions. HS2 Phase One Lots S1 and S2 make up approximately 26km of the route, running from Euston to West Ruislip as shown in Figure 1. Within this section, the tracks will primarily run through twin-bored tunnels constructed by an Earth Pressure Balance (EPB) Tunnel Boring Machine (TBM).



Figure 1. Proposed HS2 route largely in tunnel below London (SCSJV, 2023).

While TBM construction has proved to be safe and controlled, inherent volume loss at the face can cause vertical and horizontal ground displacements along the tunnel paths. Prior to

DOI: 10.1201/9781003483755-445

the Lots S1/S2 tunnelling works, Ground Movement Assessments (GMAs) were required to assess the likely impact of the tunnelling works on existing infrastructure. These assessments are essential in preventing any unexpected adverse structural effects on existing infrastructure by identifying the need for any preventative mitigation so that it can be implemented in advance of the tunnelling. This is described in a separate paper 'Overview of assessment for bridges affected by HS2 tunnelling, London, UK' (Tsekhanskiy et al. 2024).

There are a number of bridges within the tunnelling influence zone along the HS2 tunnelling route. These structures were modelled using the Oasys XDisp software (Oasys XDisp Pro Version 20.2) to estimate the ground movement likely to be experienced by these structures under a theoretical 1% volume loss. An initial sift of the structures found that there were eight masonry arch structures likely to experience differential settlement between supports. Note that the anticipated movements were all relatively small, much smaller than those required to endanger the stability of the arch barrel. These limits were identified for bare arch ribs in previous papers (Ochsendorf 2006, Ferrero et al. 2021).

Research was undertaken to evaluate the most effective assessment method for these type of structures under the influence of tunnelling settlements. For example, a study of the effect of ground settlement on Lindsey Street Bridge, a multi-span masonry arch, concluded that the amount of pier settlement that the structure could accommodate before entering the 'Slight' damage category was proportional to the span of the arches on either side of the pier (McCarthy 2016, Burland & Wroth 1975). Although Burland and Wroth provided a method of determining the predicted level of damage to the masonry arch and crack widths that could be expected, no clear guidance could be found on the most appropriate methodology to assess the impact of the ground displacement on the arch barrel capacity. Therefore, Arup worked with Professor Matthew Gilbert, a masonry arch bridge specialist from the University of Sheffield, to develop a bespoke methodology incorporating guidance described in CIRIA C800 (Gilbert et al. 2022). This paper presents details of the assessment methodology developed, together with sample results obtained when assessing a population of masonry arch bridge structures.

The objective of the work was to assess the effects of differential settlement between supports on the load carrying capacity of the arch barrel. Anticipating such effects is an essential part of ensuring the safe construction of the tunnels, as it allows any need for mitigation measures to be identified and, if necessary, implemented prior to the tunnelling works. Another key aspect of this assessment was to determine the likely long-term impact of the tunnelling works on each arch bridge structure, seeking to ensure that there is no reduction in the lifespan of the structure through the implementation of suitable remedial works.

2 ASSESSMENT METHODOLOGY

The first step was to determine the predicted ground movements due to all excavations, tunnels, shafts and temporary dewatering works at the structure location using the software Oasys XDisp. The XDisp model included multiple interim construction stages representing the predicted ground movement as the TBMs progress underneath a given structure and the cross passages are constructed.

For the purposes of assessment, it was assumed that bridge abutments would behave rigidly and ground displacement at foundation level would be transferred directly to the springing points of the arch barrel. Differential settlement between springing points is likely to lead to deformation of the arch barrel, leading to the development of new cracks, and/or widening of existing cracks. Cracks, if left without any intervention, can result in serviceability issues and potentially reduce the lifespan of the structure. To identify the most severe impact to the arch barrel, differential settlement between supports was calculated across all construction stages to find the worst-case. Generally, the maximum differential vertical and horizontal displacement was found to occur in a transient construction stage due to the tunnelling impacting one side of the structure on approach more than the other, as can be seen in Figure 2.

To analyse the impact of the differential settlement, the analysis software LimitState:RING (LimitState Ltd 2020) was selected to undertake the assessment of the arch barrel. LimitState: RING is an interactive software tool for the analysis of masonry arch bridges. It utilises plastic

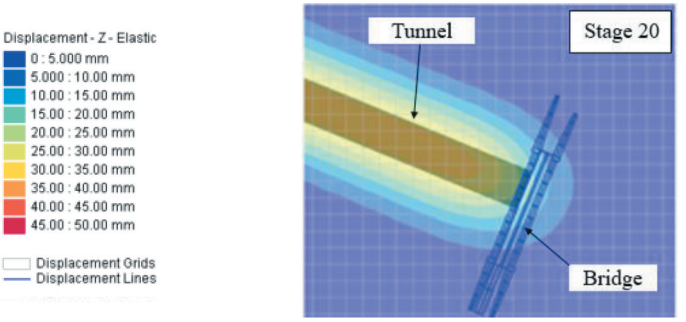


Figure 2. Vertical settlement contour taken at a transient tunnelling construction stage.

limit analysis methods using rigid block analysis, taking into account the beneficial effects of backfill, building on the mechanism method popularised by Jacques Heyman (Heyman 1982).

LimitState:RING computes the multiplier at collapse on the applied live load, termed the 'adequacy factor'. For example, if a 100kN single axle load is specified and LimitState:RING indicates a computed adequacy factor of 1.54, then the load that would cause collapse is 154kN. This software was chosen to assess the structure due to its support movement analysis functionality, whereby support movements can be applied to obtain the resulting deformed arch geometry and associated hinge points where cracks are likely to form.

The methodology that was developed for this work considers the impact of these potential new cracks induced by the HS2 tunnel construction to provide a more detailed understanding of the impact on arch bridge capacity. Following the CIRIA C800 guidance, the software was used to obtain an adequacy factor at two different limit states:

1. Ultimate Limit State (ULS):
   - The ULS represents the condition beyond which the structure no longer performs its function. The computed adequacy factor must be greater than 1.0 to satisfy ULS criteria. The ULS analysis undertaken was consistent with current asset owner standards.
2. Permissible Limit State (PLS):
   - The PLS is the point beyond which progressive load-induced degradation occurs under service loads during the intended life of the bridge (definition from CIRIA C800).
   - Degradation of the arch barrel may arise due to repeated opening and closing of cracks in the arch barrel due to cyclic live loading. This can lead to cumulative damage, resulting in loosening of or fracture/fatigue within the masonry elements.
   - PLS scenarios can be modelled by modifying the masonry and soil strength that are assumed to be mobilised at the ULS, replacing them with reduced values.
   - The adequacy factor must be greater than 1.0 to avoid the potential for cumulative damage under cyclic loading when considering PLS. If LimitState:RING indicates a computed PLS adequacy factor lower than 1.0, this means that the associated loading may lead to repeated opening and closing of joints under cyclic loading.
   - If an asset is disused or is only used for maintenance access, then PLS checks are not necessary, since the asset will not be subject to cyclic loading.

LimitState:RING models were created to quantify the effects of the deformed arch barrel geometries and cracking due to worst-case differential displacements between abutments. Six analysis cases were considered, to model each bridge in its current condition and with a combination of cracks at the intrados and extrados formed as a result of tunnelling induced settlement. This approach was chosen because it allowed informed decision making on the remedial works required to repair cracks. An overview of the analysis cases considered can be found in Table 1.

For analysis cases 4-6, where either the intrados, extrados or all cracks obtained from case 2 were not modelled, the latter cracks were assumed to be 'closed'. This could be for several reasons such as intentional repairs, or filling by loose soil/debris or closed under loading.

In reality, any cracks formed within the extrados of the arch barrel may be difficult to observe as this part of the structure is unlikely to be accessible. Under cyclic loading, extrados cracks could be filled over time if there is loose fill or debris over the arch barrel, leading to unrecoverable deformations.

Table 1. Analysis cases.

Description	Scenario	Case	Cracks modelled*	Output
Undeformed arch	Bridge in its current condition, taking into consideration any known existing cracks.	1	ULS – cracks not modelled. PLS - known existing historical cracks.	ULS & PLS adequacy factor.
Support movement analysis	Differential settlement between abutments is applied to the springing points of the undeformed arch.	2	Any known existing historical cracks.	Deformed arch geometry and associated crack locations.
Deformed arch	Bridge modelled using the deformed arch shape and a range of combinations where the cracking formed in the deflected arch is either left open or closed.	3	All cracks open.	PLS adequacy factor.
		4	Only extrados cracks repaired.	PLS adequacy factor.
		5	Only intrados cracks repaired.	PLS adequacy factor.
		6	None.	ULS & PLS adequacy factor.

* 'Intrados' and 'extrados' refer to the inner and outer surfaces of the arch barrel respectively.

Asset owner standards were used to determine input parameters such as live load, material strength and load distribution through fill (known as effective width). Across the studied masonry arch structures there were multiple asset owners with their own standards, which often had different input parameters. An example of this can be seen in Figure 3, which illustrates the differences in transverse load distribution between two standards used in the project.

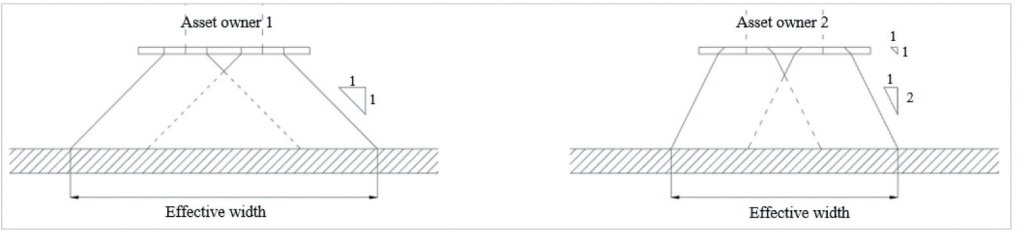


Figure 3. Transverse load distribution differences between asset owner standards.

Figure 4 provides an overview of the geometrical input parameters that are required to build the LimitState:RING models. Where possible, the geometric input parameters such as rise (f), span (l), and arch barrel thickness (s) were determined using information from topographic survey and Inspection for Assessment (IfA) reports. These parameters were verified against available historical drawings, which were also used to provide information that could not be readily obtained from inspections and surveys, such as backing height.

As with any other structural assessment, the existing condition of the structure needs to be taken into consideration when undertaking the assessment. The existing condition of a structure was determined using historical examination reports, IfA reports and topographic surveys, with photogrammetry carried out for the purpose of the assessment. Any existing cracks that were greater than 1mm were taken into consideration during the assessment. Transverse cracks were modelled by introducing mortar loss at that location, assumed to

extend to 50% of the arch barrel thickness. Longitudinal cracks were accounted for by limiting the load distribution across the arch and reducing the effective width, based on the assumption that loading could not distribute across such cracks.

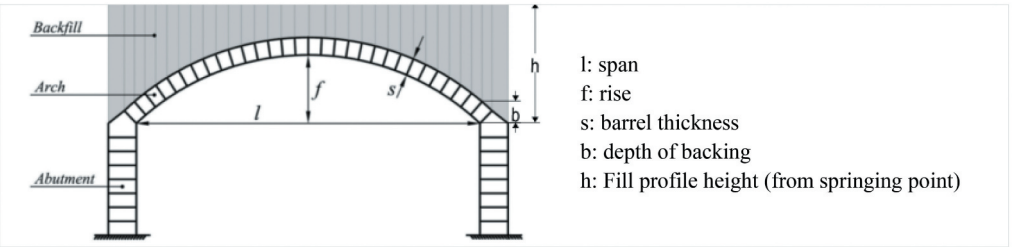


Figure 4. Geometrical input for arch analysis.

3 CHALLENGES AND LIMITATIONS

There were a number of challenges faced relating to the limited availability of historical information and the quality of available drawings. Where information was limited, the parameters were determined based on engineering judgement and upon consultation with technical experts drawn from across the project. Input parameters such as brick strength or backing height could not be verified as intrusive sampling/laboratory material tests were not included within the project scope. In the absence of this information, conservative assumptions were made for such parameters and a risk rating was given to each assumption.

Based on the modelling results obtained for the different analysis cases, it was clear that the PLS adequacy factors were significantly impacted by the presence of transverse cracks present in both the intrados and extrados of the arch. Cracking in the extrados of the arch barrel may be difficult to observe as this part of the structure is generally hard to access. These cracks can in time become evident in the intrados, through signs of visual distress such as spalling mortar and/or brickwork. However, there is risk that IfA surveys may not pick up these kinds of defects, and thus the cracks are not considered in the assessment.

The maximum vertical and horizontal displacements between springing points were often found to occur during different transient construction stages. For this project, the maximum vertical and horizontal displacements were enveloped in one analysis case. There is a possibility that there could be a more onerous arch geometry at a stage where movements are less than the maximum, but combined vertical and horizontal displacements give a worse effect. However, this was done as a pragmatic approach due to the time limitations within the project.

Although there is a level of uncertainty with the aforementioned parameters, the partial factors taken from the asset owner standards allow for uncertainty. The key objective of the analyses performed was to understand whether the ULS and PLS capacities change as a result of the tunnelling and, although there are a number of limitations in the proposed methodology, the results obtained have allowed the project to make informed decisions about how to manage these structures in a way that does not impact their capacity or longevity.

The results presented within this study are based on a live project and provide data for existing bridges being assessed for the specific loading each is likely to experience. It is a small data set with many variables changing between each example structure. Whilst some initial conclusions and trends can be drawn, more data and a further study of the impact of individual variables would allow the identification of more clear patterns and trends. A future academic study in which all variables are changed in a systematic manner might provide further useful insights.

4 OUTCOMES

The results obtained clearly demonstrated that the tunnelling settlement is likely to alter the shape of the arch profile, leading to potential changes in capacity and service life. For the

purposes of this paper, the eight arch structures considered are labelled Structure 1 to 8. Figure 5 shows an example of the support movement analysis results obtained for Structure 6 (Case 2 results). The red circles near the edges of the arch barrel indicate the locations where hinges form, which in turn will result in transverse cracks forming in the arch barrel. Figure 6 and Table 2 show PLS and ULS analysis results for all eight structures.

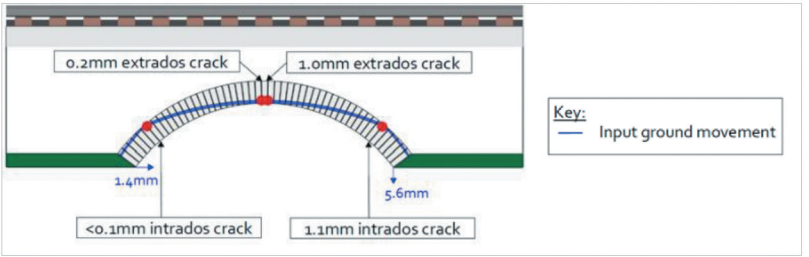


Figure 5. Example deformed arch geometry and associated cracking (Structure 6).

The results obtained suggest that the presence of cracks can significantly impact the computed PLS adequacy factor for a given structure, with these in some cases falling below 1.0. However, the analysis results also demonstrate that, in most cases, if the HS2-induced cracks are repaired, the structure in the deformed state will revert to having a computed PLS value that is close to that achieved prior to the tunnelling works. This relationship can be seen in Figure 6, which indicates how the PLS changes as a result of the tunnelling works, showing the ratio between the undeformed PLS adequacy factor and the PLS adequacy factor in the deformed analysis cases. A ratio of 1.0 represents the PLS adequacy factor being the same in both the undeformed and deformed case; a value higher than 1.0 represents an improvement in the PLS after the tunnelling works; a value below 1.0 represents a decrease in the PLS after the tunnelling works. The results obtained for Structure 2 (asset owner 1) see a dramatic increase in the PLS Case 6, as shown in Figure 6. The reason for this improvement is due to a hinge forming, as a result of the ground movement, at a location of an existing transverse crack. The analysis concluded that the existing crack was likely to widen as a result, and therefore the remedial works associated to achieve analysis case 6 would require it to be repaired. Undertaking these remedial works results in the improvement in the PLS compared to the structure's existing condition.

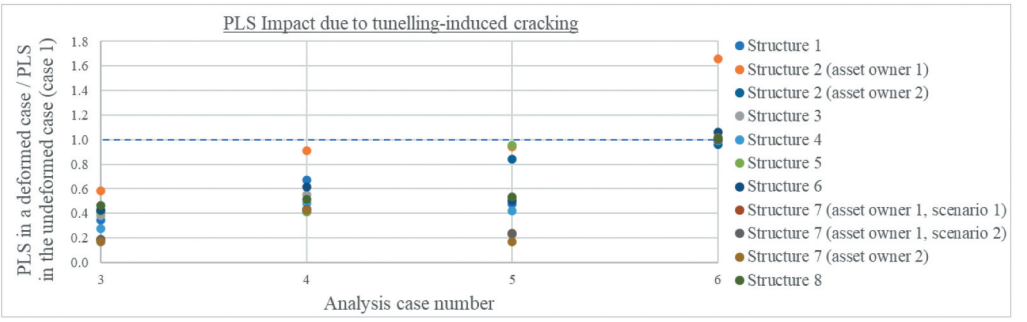


Figure 6. Graph showing the PLS impact due to tunnelling-induced cracking (where all cracks are open in case 3, but all closed in case 6).

Considering Table 2, which presents a summary of the assessment ULS and PLS results for the eight structures assessed within the project, a number of observations and patterns can be made.

Firstly, based on the assessment results, there was a clear indication that a given structure is much more vulnerable to long-term structural degradation when open cracks are present within the arch barrel. In all assessment results, a decrease in the computed PLS adequacy factor can be observed when there are open cracks are present in the intrados, extrados, or both.

Table 2. Assessment ULS and PLS results.

Structure number	Adequacy factor						
	ULS		PLS				
	Case 1	Case 6	Case 1	Case 3	Case 4	Case 5	Case 6
Structure 1	2.25	2.24	1.38	0.48	0.93	0.66	1.38
Structure 2 (asset owner 1)	4.45	4.36	1.20	0.70	1.09	1.13	1.99
Structure 2 (asset owner 2)	2.79	2.67	1.48	0.61	0.61	1.25	1.42
Structure 3	6.21	6.16	2.94	1.13	1.62	1.56	2.91
Structure 4	3.12	3.09	1.62	0.45	0.78	0.68	1.61
Structure 5	3.50	3.50	1.87	0.77	0.77	1.79	1.87
Structure 6	3.02	3.33	1.77	0.76	1.09	0.89	1.88
Structure 7 (asset owner 1, scenario 1)	1.14	1.16	0.58	0.11	0.25	0.14	0.58
Structure 7 (asset owner 1, scenario 2)	1.46	1.48	0.74	0.14	0.32	0.17	0.74
Structure 7 (asset owner 2)	1.95	2.02	1.00	0.17	0.43	0.17	1.02
Structure 8	22.00	22.10	10.30	4.80	5.30	5.50	10.40

There were some structures where the computed PLS adequacy factor did not fall below 1.0 for any of the analysis cases considered, and therefore these structures, under the predicted displacements, do not reach a stage where those cracks are opening and closing under service loads. However, over time, without preventative maintenance, age related deterioration could reduce the PLS adequacy factor further and potentially reach a point where the combined effects result in a PLS adequacy factor of less than 1.0. From an asset management perspective, this highlights the importance of performing regular inspection and maintenance.

Another observation from the results, is that the tunnelling-induced differential settlement can alter the arch geometry in such way that the arch capacity increases, and PLS adequacy factors increase if all cracks are close/repaired. Two examples of this can be seen in the results obtained for Structure 6 and Structure 8.

Structure 6 has a segmental arch profile that is anticipated to experience a slight decrease in span, by 1.4mm, and differential vertical settlement, of 5.6mm, as shown in Figure 5. The assessment results show that there is an increase in both the computed ULS and PLS adequacy factors between the undeformed (Case 1) and deformed arch geometry (Case 6). The span to rise ratio of the arch barrel geometry is considered to be relatively 'flat', meaning that the settlement and span decrease push the arch barrel into a more efficient shape.

Structure 8 has a semi-circular arch profile that is anticipated to experience a slight increase in span, by 1.3mm, and differential vertical settlement, of 5.6mm, as shown in Figure 7. The assessment results also show that there is an increase in the computed ULS and PLS adequacy factors between the undeformed (Case 1) and deformed arch geometry (Case 6). For this type of arch, it was found that the increase in span forced the arch into a more efficient shape. Therefore, it was concluded that there is likely a correlation between the arch type and its existing geometry with whether or not an increase or decrease in span allows the arch to find a more efficient shape.

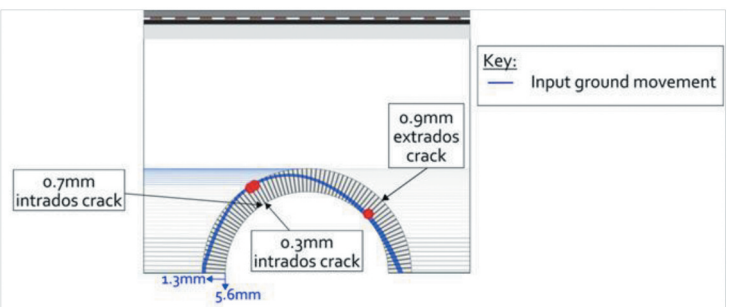


Figure 7. Structure 8 input differential settlement and support movement analysis results (Case 2).

The assessment of Structure 7 was undertaken in three parts. This was due to the presence of existing longitudinal cracks in the intrados of the arch barrel which were identified in the project surveys. The analysis for this structure was undertaken based on the assumption that loading could not distribute across a crack, as shown in Figure 8.

The assessment undertaken found the PLS adequacy factors to be below 1.0 in the undeformed state (case 1), indicating that this structure may be subject to ongoing deterioration in performance due to cyclic loading, before tunnelling activities take place. The adequacy factors dropped further for analysis Case 3, 4 and 5, before returning to a level equivalent to the undeformed structure in analysis Case 6. Thus, it is essential that any cracks that appear in both the intrados and extrados of the arch barrel are remediated. When repaired, the structure is not likely to experience any further short-term or long-term adverse effects, beyond the effects likely to be experienced as a result of its current condition.

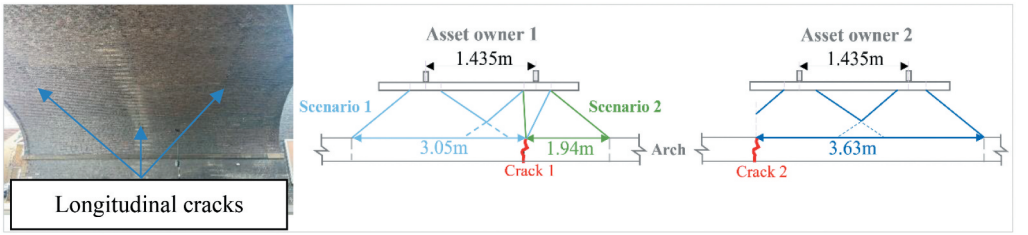


Figure 8. Longitudinal crack locations in relation to tracks (Structure 7).

Considering the ground movement assessment results obtained from a range of different bridge types across the project (Tsekhanskiy et al. 2024), arch structures appear to be able accommodate movement better than many other structure types. No significant mitigation works (such as strengthening) have been recommended for any arched structure within the project. As a result, the focus when assessing the arched structures quickly shifted to ensuring that the residual PLS after the tunnelling was not impacted, and therefore that the lifespan of the structures remained unaltered. Such an approach enables existing structures to be effectively managed, bringing sustainability benefits by maximising their lifespan through timely interventions.

5 CONCLUSIONS

The HS2 ground movement assessment project has provided valuable insights into the potential challenges and risks associated with tunnelling under a major city. The assessment methodology developed for masonry arch bridge structures provided an effective method of assessing the likely impact of ground movements on these structures at both the ultimate limit state (ULS) and permissible limit state (PLS). The findings revealed that unrepaired cracks caused by ground movements can significantly reduce the computed PLS adequacy factor for a given structure, but that undertaking repairs to both intrados and extrados cracks returns the structure to very close to that of the undeformed state, considering both the ULS and PLS. The study also showed that for some structure profiles the ground movement could result in a deformed structure profile that is more structurally efficient. Whilst some initial conclusions and trends have been drawn, a further study is recommended to study the impact of each individual variable more fully, facilitating identification of clear patterns and trends.

Overall, the assessments undertaken revealed the ability of masonry arches to accommodate settlement, and the results obtained highlighted how undertaking timely crack repairs can ensure that the lifespan of the structures is safeguarded, ensuring the safety and resilience of older bridge infrastructure.

REFERENCES

Burland, J.B & Wroth, C.P. 1975. Settlement of buildings and associated damage, *British Geotechnical Society Conference on Settlement of Structures, including damage and soil-structure interaction, April 1974*. Cambridge: British Geotechnical Society: 611–654.

Ferrero, C., Calderini, C., Portioli, F. & Roca, P. 2021. Large displacement analysis of dry-joint masonry arches subject to inclined support movements. *Engineering Structures*. 238:112244.

Gilbert, M., Smith, C., Cole, G. & Melbourne, C. 2022. *CIRIA C800: Guidance on the assessment of masonry arch bridges*, CIRIA, London.

Heyman. J. 1982. *The masonry arch*. Ellis Horwood, Chichester.

LimitState Ltd. 2020. *LimitState:RING Manual – Version 3.2*, LimitState, Sheffield.

McCarthy, J. 2016. Lindsey Street Bridge - A structural solution to settlement mitigation. *Crossrail Learning Legacy*, August 2016. ICE Publishing, London.

Oasys XDisp Pro. (Version 20.2). Available at: https://www.oasys-software.com/products/xdisp/.

Ochsendorf, J. 2006. The masonry arch on spreading supports. *The Structural Engineer*, 84(2): 29–35.

SCSJV(2023) SCSJV. Available at: https://scsjv.co.uk/about-us/ (Accessed: 28 November 2023).

Tsekhanskiy, J. A. Bariyya, G. Ledsham-James, D. Shapley & Y. Li, Arup, 2024. 'Overview of assessment for bridges affected by HS2 tunnelling, London, UK', *IABMAS Conference*, June 2024, Copenhagen.

Bridge Maintenance, Safety, Management, Digitalization and Sustainability – Jensen, Frangopol & Schmidt (eds)
© 2024 The Author(s), ISBN 978-1-032-77040-6
Open Access: www.taylorfrancis.com, CC BY-NC-ND 4.0 license

Parametric evaluation and design of prestressed concrete beam bridges

V.N. Moraes, T.E.T. Buttignol & L.M. Trautwein
Department of Structures, University of Campinas, Brazil

ABSTRACT: Brazil faces two major challenges with respect to the construction and maintenance of the infrastructure system (bridges, railways and roadways): the continental dimensions and the lack of qualified professionals. According to the National Department of Transport Infrastructure (DNIT), the Brazilian road network has a significant number of temporary wooden bridges, constructed in precarious conditions with an imminent risk to the safety of the users. This paper is aimed to contribute to the development of the country's road infrastructure through the development of a bridge parametric design procedure. The parametric model is designed in the software Rhinoceros3D/Grasshopper and used as a standard design for the modeling and analysis of simply supported beam bridges with free spans between 10 m and 40 m. The cross-sections of the independent elements, as well as the preliminary dimensions, are dynamically determined by means of scripts elaborated in the Python programming language. The algorithm allows modeling concrete beam bridges to overcome single spans (between 10 m to 40 m) or large spans with successive supports, considering any topography. From the parametric model, a structural analysis can be carried out to obtain the acting forces and displacements. The main advantages of the described model are the possibility to simplify the structural design process and carry out an optimization procedure. An example of application of the model is presented.

1 INTRODUCTION

Beam bridges are the most widely used structural system in the state of São Paulo, Brazil. Figure 1 shows a survey with a total of 2,300 works carried by the São Paulo State Department of Roads and Highways (DER-SP), from 1940 to 1990. The structural system in beams can be subdivided in simply supported with or without overhang at the ends, and others (special, continuous or Gerber beams). Figure 1 shows that girder bridges comprise the vast majority of structures, representing 93% of the total. Frame bridges account for a smaller proportion, comprising only 5% of the structures. Arch Bridges are the least common structures, accounting for 2% of the total. Among the Beam category (Figure 1 on the right side), simply supported beams prevails, comprising around 81% of the "Beam" category.

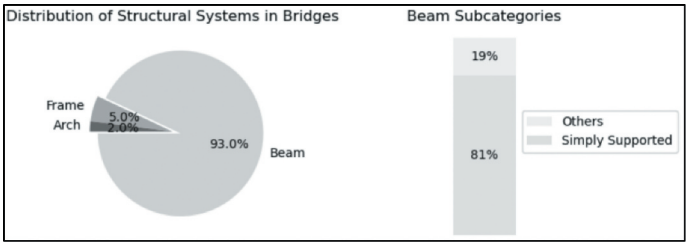


Figure 1. Bridge structural system distribution in the state of São Paulo, Brazil (DER-SP 2023).

DOI: 10.1201/9781003483755-446

Based on the survey presented in Figure 1, simply supported beam bridges were chosen to investigate the advantages of the automation design process described in this paper. This type of structure is widely known and, from a technical design point of view, there is not much new to be discovered. However, the potential for improvement lies in the quality of the materials and the optimization of the structural elements, driven by parametric modeling, algorithm-aided design and optimization techniques. The aiming of this paper is to investigate techniques that allows a more efficient design procedure and, at the same time, guarantee the expected safety and performance levels.

2 RESEARCH SIGNIFICANCE

The standard design procedure is based on the analysis of structural elements in the Ultimate (failure) and Serviceability (durability) Limit States, but does not perform a more in-depth investigation considering the global behavior (holistic engineering approach) and integrating both static and dynamic analyses. Thus, this paper is aimed to propose a design methodology that automates the design process to save valuable time and encompasses structural optimization. In this way, it is possible to optimize beams, slabs and columns, resulting in gains in terms of efficiency and performance. This approach is relevant, especially considering the number of temporary wooden bridges in Brazil and the lack of road infrastructure, which often faces significant logistical challenges and shortage of budget.

Design automation is a technical improvement that is prone to meet the growing demands of infrastructure. It includes the following advantages: i) human error reduction, guaranteeing the accuracy of calculations and drawings; ii) standardization, ensuring that all bridges comply with regulations and code standards; iii) streamlining, requiring fewer human resources to perform repetitive tasks, allowing engineers to focus on more complex and creative aspects of the project; iv) flexibility, allowing customization according to the specific needs of each project; v) quick evaluation of different scenarios, which can lead to more efficient and cost-effective solutions; vi) data integration, making it easier to access relevant information for the project; vii) cost reduction. An example of a parametric Building Information Modeling (BIM) approach to foster bridge project design and analysis can be found in (Girardet & Boton 2021, Ruiz et al 2023 and Tam et al 2017).

3 INTEGRATED BRIDGE DESIGN AND ANALYSIS SYSTEM

The so-called "Integrated Bridge Design and Analysis System" is an approach that is aimed to combine the parametric modelling and the structural analysis with optimization technologies. The integration of advanced technologies simplifies the decision-making process, allowing engineers to create more resilient, cost-effectively and environmentally friendly structures. The methodology involves the development of a 3D digital model of the bridge geometry using Rhinoceros - Grasshopper software, respectively, a computer-aided design (CAD) and algorithm-aided design (AAD). The structural analysis is performed using Karamba 3D, an addon for Grasshopper that allows static and dynamic finite element analyses. The optimization procedure is performed with the integration of Galapagos, a component of Grasshopper, which is based on genetic algorithm. Thus, the method enables a parametric optimization to find the best project configuration based on predefined criteria such as cost, performance and sustainability. Figure 2 shows the step-by-step design process.

3.1 *3D digital parametric model – preliminary analysis*

The 3D digital parametric model is constructed in Grasshopper to accurately represent the dimensions, geometry and boundary conditions of the bridge and the natural terrain. Grasshopper allows a flexible design process due to parametrization and quick adjustments/adaptations in the model.

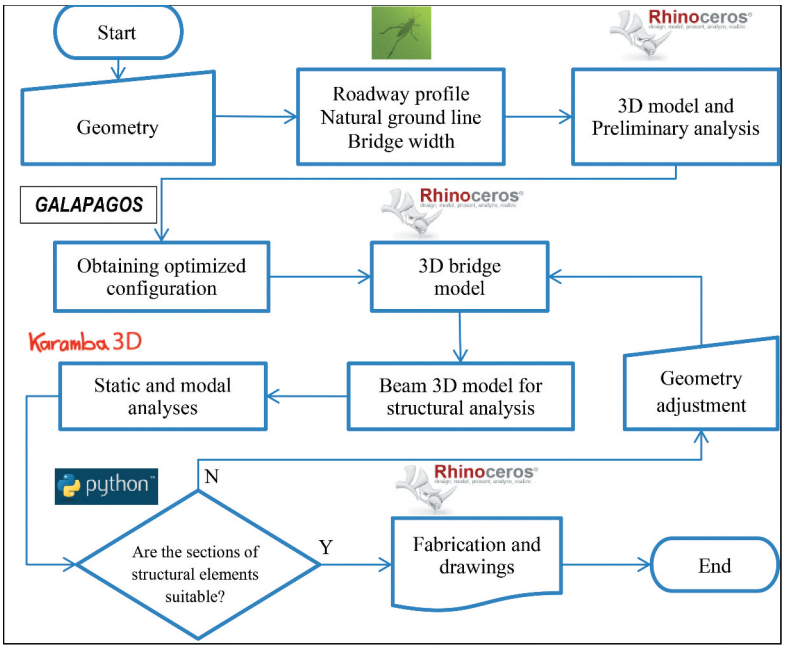


Figure 2. Workflow of the design process.

The proposed parametric model depends on two main input parameters: i) longitudinal profile, which includes the natural terrain and the bridge alignment; ii) width of the bridge. Based on these parameters, the algorithm is able to generate the preliminary 3D model of the bridge, allowing additional customizations, if needed. Figure 3 shows an example of the geometric characterization of a bridge. This example will be considered for the following analyses.

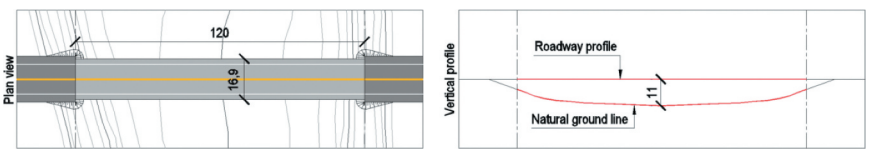


Figure 3. Geometry characterization of a bridge – plan and profile.

The 3D bridge model is generated from the given input geometric data by means of preliminary design rules implemented in the Grasshopper visual programming language. The cross-sections of the structural elements are determined dynamically using Python scripts inside Grasshopper. The prestressed concrete girders are predefined using the Brazilian historical relationship between beam height and span, as shown in Figure 4.

In Figure 4, the average height (solid blue line): represents the average height of the concrete prestressed beams in relation to the bridge span. It corresponds to the following expression: $h = 0.00025 \times L^2 + 0.02065 \times L + 0.75434$ (this expression is adopted in the parametric model). The 90% height (traced green line) represents the higher height, indicating that 90% of bridges have prestressed beams in this range or lower. The 10% height (traced dotted blue line) represents the lower height, indicating that only 10% of bridges have prestressed beams in this range or lower.

The dotted red line (girder heights) refers to the standard (DER 2015) and (DNIT 2022) recommendations.

This practical approach is derived of empirical data obtained from real bridges that have been successfully been built in Brazil. These relationships can vary based on local standards, construction site conditions, specific needs of the bridge and the specifications of the materials.

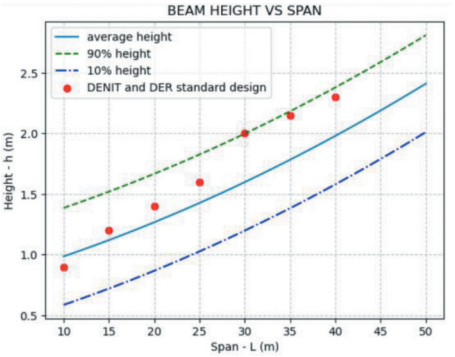


Figure 4. Bridge span-height relationship.

The preliminary design of the columns considers failure due to buckling (elastic limit) and concrete crushing (maximum allowable stress). The cross-beams should be wide enough to hold the girders. In this case, a width of 1.6 m was adopted. For the cross-beam height, the bending moment forces are determined and the neutral axis is checked, considering a limit of 40% of the effective depth. After the preliminary assessment, if the configuration of the bridge does not attend the design criteria, the process is repeated until the optimized geometry is reached. The choice of the preliminary design criteria will have a direct influence on the result.

The parametric model allows to design bridges ranging from small single spans to large multispans and adapted to different topographical conditions. It also provides adjustments, such as: i) number of supports, which impacts on the span length within specified limits; ii) number of columns per cross-beams, which influences the height of the cross section of the cross-beam and the foundation loading. Figure 5 shows an example of a 3D digital model of a multispan bridge after a preliminary assessment.

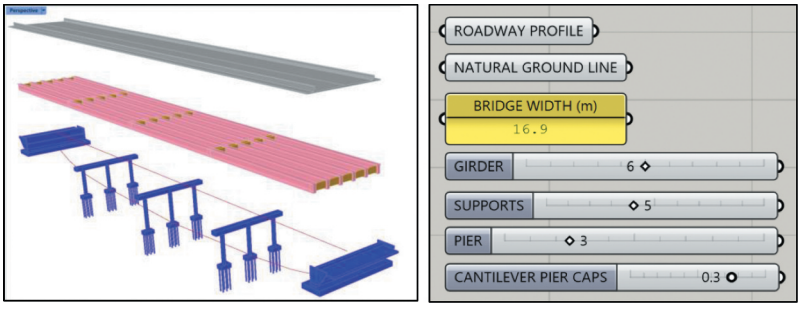


Figure 5. 3D digital model of the bridge (preliminary assessment).

3.2 *Optimization process*

The introduction of Galapagos, a genetic algorithm, into the optimization process can bring several benefits to the bridge design, especially when integrated with Grasshopper and Karamba 3D. Galapagos is a component of Grasshopper that allows the application of parametric optimization algorithms, which means it can help to find the best design parameters based on predefined (restrictions) criteria. This is an effective way to improve bridge design, making it more economical, efficient and safe, while assisting in identifying solutions that meet pre-established requirements. In this paper, as an example, Galapagos was adopted to identify the most efficient number of supports for the bridge, considering the best structural cost-benefit, as shown in Figure 6.

In the preliminary stage of the design, obtaining the optimized geometry can be challenging, since it is necessary to consider not only the volume of concrete, but also the costs of transportation, handling, assembly and environmental impact. Thus, as a simplification, a cost factor



Figure 6. Analysis in Galapagos.

(CF) was established in the analysis. This factor should be determined for each case, considering local conditions by means of a cost matrix, as shown in Table 1. One should consider the costs associated with transportion, handling, assembly and environmental impact, together with the quantity of materials employed. CF values for the case investigated are shown in Table 1. The optimized configuration of the bridge, for the adopted parameters, is shown in Table 2.

Table 1. Cost Factor (CF).

Nº of supports	Free span [m]	CF*
8	15	2.1
7	17	2.0
6	20	2.0
5	24	2.0
4	30	2.1
3	40	2.1

* CF is the cost per m^3 of the structure. This is a simplification that allows to define a single global cost to perform a preliminary optimization. The analysis was carried out in Galapagos, as shown in Figure 6.

Table 2. Main characteristics of the bridge after obtaining the optimized configuration.

Nº of supports	Free span [m]	Nº of columns	Concrete volume [m³]	Normalized cost [%]
6	20	2	1474	77

3.3 *Structural analysis*

Karamba 3D performs structural analyses by means of finite element modeling, allowing the calculation of the internal forces, stresses, strains and displacements. The software performs static and dynamic analyses and is suited to the needs of the early design phases. It can also perform modal analysis, which is important for understanding the modes of vibration of the bridge.

The analysis of the natural frequency is crucial to investigate the effects of resonance due to dynamic forces, such as wind, traffic and seismic activities. Resonance may lead to significant amplifications of displacements and forces, which can affect the safety of the users and the stability of the structure. As an example, a model analysis of the bridge is performed, as shown in Figure 7. The results are displayed in Table 3. The values should be compared with

the reference values for each region or standard. Detailed information related to dynamic analysis can be found in (Paultre 2013).

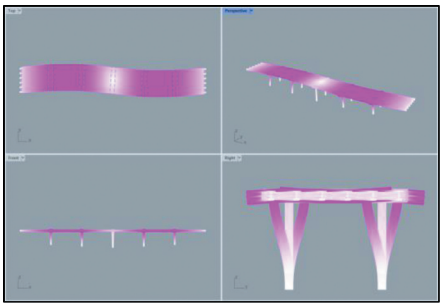


Figure 7. First mode of vibration.

Table 3. Natural frequencies - f [Hz].

Mode	Frame	Deck	Global
1	0.085	0.852	0.021
2	-	6.460	0.159
3	-	8.643	0.213
4	-	9.132	0.225

3.4 *Design of the structural elements*

The complete design of the bridge's structural system is a complex and extensive process, which is out of the scope of this work. In this case, only a summary of the bending design procedure of the concrete prestressed girders are presented, as shown in Figure 8. The design process of the other structural elements is carried out in the same way, by obtaining the forces and checking the section resistance, repeating the analysis if the section does not give satisfactory results.

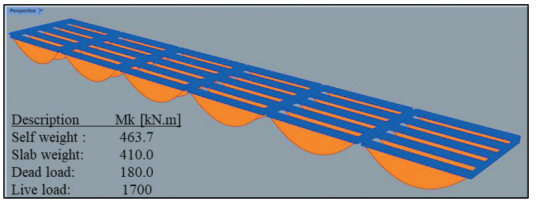


Figure 8. Bending moment diagram.

The design of the structural elements is performed to meet the safety requirements established by the local regulations. This stage ensures that the structure is capable of withstanding the load bearing capacity. It is based on an iterative step-by-step procedure. If changes on the geometry are needed, the analysis returns to the initial modeling stage (Figure 2, section 3.1) and the process is repeated until the geometry meets the established requirements.

After obtaining the maximum bending moments, the strength capacity of the cross-section is checked by computing the stresses and strains adopting the classical beam theory. The analysis takes into account the strength of the material and the influence of prestressing, which is essential for balancing the service loads. The stress diagrams are determined for each load case. The combinations are made taking into account the superposition of effects. Safety and performance criteria are applied, ensuring that the girder does not exceed the serviceability limits for cracking and deformation.

Figure 9 shows an example of the definition of the girder cross section. The stresses obtained for the predefined cross section are shown in Figure 10. The process of verification

of the girders was divided in 3 stages, as follows: i) stage 1 – immediate prestressing, considering the self-weight; ii) stage 2 – immediate prestressing, considering assembly and construction, self-weight and slab loading (including immediate and time-dependent prestress losses); iii) stage 3 – time-dependent prestressing, considering permanent and live loads. Detailed description of the prestressed design can be found in (Naaman 2012, El Debs 2021).

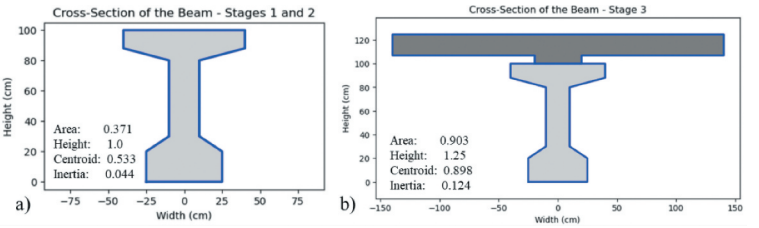


Figure 9. Cross section of the girders: a) Stages 1 and 2; b) Stage 3.

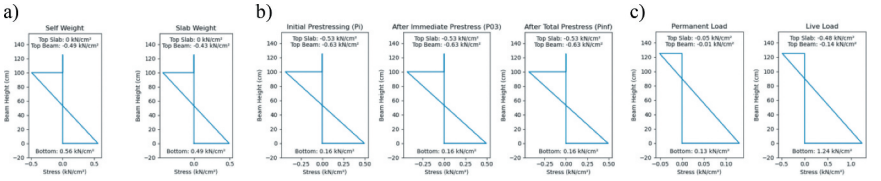


Figure 10. Cross section stresses considering different load cases: a) stage 1; b) stage 2; c) stage 3.

4 RESULTS AND DISCUSSION

The integrated design procedure described in Figure 2 provides an efficient procedure for the preliminary assessment of the prestressed girder bridges, optimizing the use of natural resources and reducing the overall cost. Firstly, an analysis was performed to obtain the best choice for the number of bridge supports, based on the preliminary design criteria adopted. After that, the girders were optimized and the model reprocessed to obtain the optimized solution. Figures 11a and 11b show, for the concrete beam bridge investigated, the optimum free span that results, respectively, in the lowest concrete volume and cost of the girders. Values in grey corresponds to the initial values determined in the preliminary assessment. Values in blue corresponds to the final value after the structural analyses.

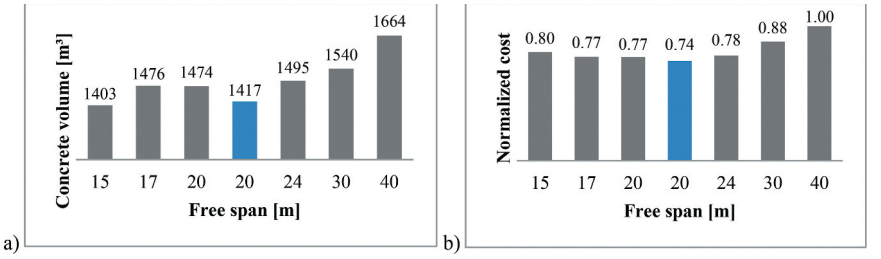


Figure 11. Results: a) Free span vs. concrete volume; b) Free span vs. normalized cost.

The results demonstrate a reduction of approximately 4% in the concrete volume of the cross section in relation to the initial values determined in the preliminary analysis. It is worth mentioning that the initial values also met the service and resistance requirements at the design stage. After the completion of the process, the prestressed girders are ready to be manufactured and built. The final configuration of the beam bridge after optimization, is shown in Figure 12.

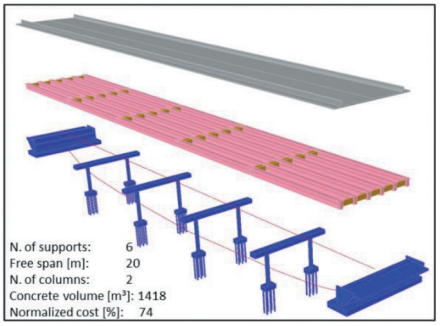


Figure 12. Final configuration of the bridge.

5 CONCLUSIONS

This paper explored the potential of the modern tools to create innovative and efficient solutions. It highlighted the main advantages of an automation design process, which is based on an integrated design procedure buttressed on parametric modelling and structural optimization procedures. The design automation comes in hand as a response to the current challenges in structural design, aiming to save time, reduce costs and improve the sustainability. This approach represents a technical advance and a feasible solution to meet the demands of infrastructure, offering benefits such as error reduction, standardization and rationalization of resources.

The implementation of the Integrated Bridge Design and Analysis System, using tools such as Rhinoceros-Grasshopper, Karamba 3D and Galapagos, is an evolution in the structural engineering design process. The example described in this paper demonstrated that the automation design procedure of concrete prestressed girders is able to reduce the cost and the concrete volume, contributing to improve the construction sustainability. This methodology can be extended to other structural elements to provide a holistic analysis of the structure.

ACKNOWLEDGEMENTS

The second author would like to gratefully acknowledge the research funding of both “Fundo de Apoio ao Ensino, à Pesquisa e à Extensão” (Faepex), grant number 2474/23 and National Council for Scientific and Technological Development (CNPq), grant number 403517/2023-0.

REFERENCES

DNIT, Departamento Nacional de Infraestrutura de Transportes, 2022. https://www.gov.br/dnit/pt-br/assuntos/planejamento-e-pesquisa/ipr/coletanea-de-manuais/vigentes/publicacao-ipr-751-album-projeto-tipo-de-pontes-semipermanentes

DER, Departamento de Estrada e Rodagem do estado de São Paulo, 2015. http://www.der.sp.gov.br/WebSite/Documentos/Tecnicas.aspx

El Debs, M. K. Pontes de concreto: com ênfase na aplicação de elementos pré-moldados. 1. ed. São Paulo: Oficina de Textos, 2021. P. 480. ISBN 978-65-86235-31-9.

A. Girardet & C. Boton. A parametric BIM approach to foster bridge project design and analysis. Automation in Construction, v. 126, n. 6, p. 103679, 2021. ISSN 0926-5805. DOI: https://doi.org/10.1016/j.autcon.2021.103679.

Paultre, P. Dynamics of structures. John Wiley & Sons, 2013.

Naaman, A. E. Prestressed concrete analysis and design: Fundamentals. 2012.

TAM, Matthew, et al. Intelligent Fabrication-Digital Bridges. In: Footbridge 2017 Berlin-Tell A Story, 6-8.9. 2017, Technische Universität Berlin (TU Berlin). 2017. p. 1.

Ruiz, R., et al. Parametric analysis of variables influencing the design of I-girder bridge decks made of high-performance fiber reinforced concrete. Structural Concrete, 2023.

Bridge Maintenance, Safety, Management, Digitalization and Sustainability – Jensen, Frangopol & Schmidt (eds)
© 2024 The Author(s), ISBN 978-1-032-77040-6
Open Access: www.taylorfrancis.com, CC BY-NC-ND 4.0 license

Bridge deterioration estimation for small zones considering chemical attack

F. Obunguta, K. Kaito & K. Sasai
Graduate School of Engineering, Osaka University, Osaka, Japan

K. Kobayashi
Graduate School of Management, Kyoto University, Kyoto, Japan

K. Matsushima
Disaster Prevention Research Institute, Kyoto University, Kyoto, Japan

H. Bakamwesiga
Department of Civil and Environmental Engineering, Makerere University, Kampala, Uganda

ABSTRACT: Current state-of-the-art deterioration forecasting models such as the stochastic Markov hazard model require relatively large sample data to meet accuracy requirements. Small zones e.g., small cities and countries have a few infrastructure assets including bridges to manage hence their inspection data is incomplete. Also, the interdependence between structural deterioration and chemical attack has not been fully investigated. Chemicals e.g., CO_2 and Cl accelerate reinforced concrete (RC) deterioration by ingressing through RC pores which facilitates rebar corrosion leading to cracking, delamination and spalling that terminates in structural failure in case of no intervention. Additionally, worse RC structural state results in more severe chemical attack as more chemicals ingress into RC. This study proposes a composite Markov hazard model that captures these compounding processes and examines the influence of chemical attack on RC bridge deterioration rate, and vice versa, to aid proactive interventions. The study applies multiple imputation to generate more complete data to address small zone data incompleteness and shows empirical model applicability.

1 INTRODUCTION

1.1 *Bridge deterioration under chemical attack*

Bridges are important transportation systems constructed mainly using reinforced concrete (RC) that combines steel and concrete for high tensile and compressive strength. RC deterioration is accelerated by inadequate designs, poor initial construction and workmanship (i.e., compaction and curing), seismic activity and chemicals e.g., CO_2 and Cl that facilitate reinforcement bar (rebar) corrosion producing rust that is larger than steel generating internal stresses in RC resulting in cracking. RC bridges in critical structural condition are more exposed to chemicals that ingress through concrete orifices and hence experience more severe chemical attack (Kobayashi 2006, Akiyama et al. 2011, Cui et al. 2021). These compounding RC deterioration processes require timely intervention to avert costly failures. Deterioration graphs of two RC bridges (B=1,2), with B=2 under significant chemical attack, follow different trends requiring different actions A (Figure 1).

DOI: 10.1201/9781003483755-447

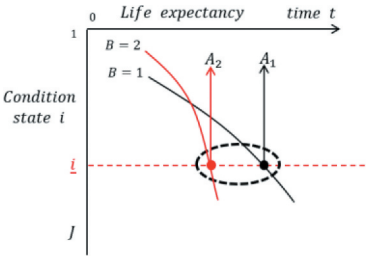


Figure 1. Life expectancy of two bridges (B=1,2); with B=2 under significant chemical attack.

Rebars are protected by a passivisity layer that inhibits chemical progression. CO_2 reacts with $Ca(OH)_2$ in cement to form $CaCO_3$, an acid, destroying this layer. Chlorine, introduced into RC through admixtures, airborne chlorides and de-icing salts, reacts with rebars to form hydrated iron (III) oxide (rust), catalyzed in acidic conditions (Neville 1995).

RC condition can be determined through visual inspection and non-destructive tests (NDTs) such as the rebound hammer, and RC chemical state can be quantified through laboratory analysis on samples obtained by semi-destructive tests (SDTs). NDTs do not affect bridge structural performance, functionality and serviceability yet offer simplicity and rapidity (Bakamwesiga et al. 2014a). On the other hand, SDTs are costly and are not carried out as regularly as NDTs hence RC condition and chemical state may not be known concurrently.

RC chemical attack has been modeled as two distinct successive phases; i.e., initiation characterized by chemical ingress into RC and propagation where visible cracks develop (Roelfstra et al. 2004, Lethanh et al. 2017). Kaito et al. (2021) modeled bridge member deterioration and its effects on another considering steel girder end corrosion using a regime switching Markov model. This study explores the composite Markov model developed by Kobayashi and Kaito (2016) to model the transition of pavement surface condition and load bearing capacity that are equally nonconcurent as RC chemical and structural condition.

1.2 *Incompleteness of small zone data*

Small zones including small cities and countries have a few infrastructure assets e.g., bridges that span shorter lengths and hence generate incomplete structural monitoring data which complicates the application of current state-of-the-art deterioration forecasting models such as the stochastic Markov hazard model that requires relatively large sample data to meet accuracy requirements (Tsuda et al. 2006). Data incompleteness has been handled through improving models or scientifically augmenting data. Lethanh and Adey (2012) built a hidden Markov model, Kobayashi et al. (2012) developed a Bayesian estimation method and Kobayashi et al. (2019) applied multiple imputation (MI) (Rubin 1976, 1987, Schafer and Graham 2002) to handle incomplete data.

To apply MI, data missingness types need to be identified. There are generally three missingness types; i.e., Missing Completely at Random (MCAR) where missingness has no dependency on any sample variable (observed or missing), Missing at Random (MAR) for which missingness depends strictly on observed data, and Missing not at Random (MNAR) where missingness depends on other observed or missing variables. Unobserved small zone data may be considered as MCAR.

1.3 *Study objectives*

This research models bridge structural deterioration and chemical attack as processes that compound each other using a composite Markov deterioration model. The objectives are

1) Model RC bridge deterioration and chemical attack using a composite Markov model and examine the interdependency between these processes.
2) Develop a mechanism to generate more complete monitoring data for small zones using MI.
3) Show the empirical applicability of the model.

2 COMPOSITE MARKOV MODEL

2.1 *Model definition*

Consider discrete time (t = 0, 1, 2, …) in which discrete bridge condition states i(i = 1, …, J) with condition J as the absorbing state deteriorate if there is no renewal. This degradation is exacerbated by chemical attack defined using discrete chemical states c(c = 1, …, D) with D as the worst state, and vice versa. States i and c are obtained at different times because chemical tests are more rigorous and time consuming. The discrete survey time is defined as (t_{is} = 0, 1, 2, …, T_{is}) and (t_{cs} = 0, 1, 2, …, T_{cs}) with survey interval (r_{is} = 0, 1, 2, …, R_{is}) and (r_{cs} = 0, 1, 2, …, R_{cs}); and state variable $h(t_{is})$ and $g(t_{cs})$ where subscripts 'is' and 'cs' specify condition and chemical state, respectively.

2.2 *Deterioration of structural condition*

The Markov Transition Probability (MTP), expressing condition state $h(t_{is}) = i$ changing to $h(t_{is} + r_{is}) = j$ given chemical state $g(t_{cs}) = c$ (Tsuda et al. 2006, Kobayashi and Kaito 2016)

$$Prob[h(t_{is} + r_{is}) = j | h(t_{is}) = i, g(t_{cs}) = c\ ] = \pi_{ij}(c) \tag{1}$$

To identify the closest influential chemical state, the discrete time t_{cs} must satisfy conditions

$$\left.\begin{array}{c} \underset{t_{cs}}{argmin}\ |t_{is} - t_{cs}|\ \ \forall t_{cs} \\ t_{cs} \le t_{is} \end{array}\right\} \tag{2}$$

The MTP from i to j given that there was no repair

$$\pi_{ij}(c) = \sum_{\tilde{k}=i}^{j} \prod_{\tilde{m}=i}^{\tilde{k}-1} \frac{\varphi_{\tilde{m}}(c)}{\varphi_{\tilde{m}}(c) - \varphi_{\tilde{k}}(c)} \prod_{\tilde{m}=\tilde{k}}^{j-1} \frac{\varphi_{\tilde{m}}(c)}{\varphi_{\tilde{m}+1}(c) - \varphi_{\tilde{k}}(c)} \exp\left(-\varphi_{\tilde{k}}(c) r_{is}\right) \qquad i \le \tilde{k} \le \tilde{m} \le j \tag{3}$$

where $\varphi_i(c)$ = hazard rate and; $\tilde{k}$ and $\tilde{m}$ = indices.

The hazard rate $\varphi_i(c)$ is expressed in exponential form

$$\varphi_i(c) = \beta_c^0 exp\left(\boldsymbol{x}\boldsymbol{\beta}_{\boldsymbol{i}}^{'}\right) \qquad (i = 1, \ldots, J-1) \tag{4}$$

where $\boldsymbol{\beta_i} = \left(\beta_{i,1}, \ldots, \beta_{i,M}\right)$ = row vector of unknown parameters with symbol [′] showing transpose; $\boldsymbol{x}$ = row vector of explanatory variables; and β_c^0 $(c = 1, \ldots, D-1)$ = heterogeneity scale parameter showing the influence of chemical state c on RC structural condition. $\beta_{c=1}^0$ is standardized to 1.

For a set (i = 1, …, J), the MTP matrix $\Pi(c)$ can be defined between each (i, j) pair

$$\Pi(c) = \begin{bmatrix} \pi_{11}(c) & \cdots & \pi_{1J}(c) \\ \vdots & \ddots & \vdots \\ 0 & \cdots & \pi_{JJ}(c) \end{bmatrix} \tag{5}$$

To satisfy MTP properties and pavement deterioration considering no repair

$$\left.\begin{array}{c} \pi_{ij}(c) \ge 0 \\ \pi_{ij}\ (c) = 0\ (when\ i > j) \\ \sum_{j=1}^{J} \pi_{ij}(c) = 1 \end{array}\right\} \tag{6}$$

Life expectancy ($RMD_i(c)$) and its average $ET_i(c)$ from start of RC bridge life are (Lancaster 1990)

$$RMD_i(c) = \frac{1}{\varphi_i(c)} \tag{7}$$

$$ET_i(c) = \sum_{i=1}^{j} \frac{1}{\varphi_i(c)} \tag{8}$$

2.3 *Progression of chemical attack*

Similarly, MTP defining change from chemical state $g(t_{cs}) = c$ to $g(t_{cs} + r_{cs}) = d$ given condition state $h(t_{is}) = i$

$$Prob[g(t_{cs} + r_{cs}) = d | g(t_{cs}) = c, h(t_{is}) = i\ ] = p_{cd}(i) \tag{9}$$

With discrete time t_{is} satisfying

$$\left.\begin{array}{c} \underset{t_{is}}{argmin} \; |t_{cs} - t_{is}| \; \forall t_{is} \\ t_{is} \le t_{cs} \end{array}\right\} \tag{10}$$

The MTP from c to d given no intervention

$$p_{cd}(i) = \sum_{\tilde{k}=c}^{d} \prod_{\tilde{m}=c}^{\tilde{k}-1} \frac{\lambda_{\tilde{m}}(i)}{\lambda_{\tilde{m}}(i) - \lambda_{\tilde{k}}(i)} \prod_{\tilde{m}=\tilde{k}}^{d-1} \frac{\lambda_{\tilde{m}}(i)}{\lambda_{\tilde{m}+1}(i) - \lambda_{\tilde{k}}(i)} \exp\left(-\lambda_{\tilde{k}}(i) r_{cs}\right) \tag{11}$$
$$c \le \tilde{k} \le \tilde{m} \le d$$

The hazard rate $\lambda_c(i)$ in exponential form

$$\begin{array}{c} \lambda_c(i) = \gamma_i^0 exp\left(\mathbf{y}\boldsymbol{\gamma}_c^{'}\right) \\ (c = 1, \ldots, D-1) \end{array} \tag{12}$$

where $\boldsymbol{\gamma}_c = \left(\gamma_{c,1}, \ldots, \gamma_{c,M}\right)$ = row vector of unknown parameters; $\mathbf{y}$ = row vector of explanatory variables; and $\gamma_i^0 (i = 1, ..., J-1)$ = heterogeneity scale parameter showing the effect of condition state i on RC chemical state. Also, $\gamma_{i=1}^0$ is standardized to 1.

The MTP matrix $P(i)$ can be defined between each (c, d) pair

$$P(i) = \begin{bmatrix} p_{11}(i) & \cdots & p_{1D}(i) \\ \vdots & \ddots & \vdots \\ 0 & \cdots & p_{DD}(i) \end{bmatrix} \tag{13}$$

Again, all MTP properties considering no action must be met and $RMD_c(i)$ and $ET_c(i)$ estimated.

2.4 *Composite deterioration model*

Chemical attack compounds RC structural deterioration, and vice versa. Composite deterioration condition $\eta(t) = \eta(\eta = 1, \ldots, \Omega)$ with $\Omega = J \times D$. The composite $\eta(t)$ corresponds to $(1, 1), \ldots, (1, D), (2, 1), \ldots, (2, D), (3, 1), \ldots, (J, D)$ and is specified as $\eta(t) = \{h(t), g(t)\}$. The elements of the $\Omega \times \Omega$ composite probability matrix Δ are (Kobayashi and Kaito 2016)

$$\omega_{ic}^{jd} = p_{cd} \times \pi_{ij} \tag{14}$$

The Δ matrix must also follow MTP rules. The composite deterioration process of RC bridge structural elements considering no improvement

$$H(t) = H(0) \times \Delta \tag{15}$$

where $H(0)$ = initial composite state vector and; $H(t)$ = composite vector at time t.

2.5 *Tests for the composite deterioration process*

The modeled composite deterioration process was based on the assumption that chemical attack accelerates RC structural deterioration and that heavily deteriorated RC bridges experience more severe chemical attack. This compounding process can be tested using two hypotheses; i.e, structural deterioration acceleration due to chemical attack using Hypothesis I and increased chemical attack due to structural degradation using Hypothesis II.

To test Hypothesis I, the null hypothesis H_0^c $(c = 2, \ldots, D-1)$, and the alternative hypothesis H_1^c $(c = 2, \ldots, D-1)$, are specified as

$$\begin{cases} H_0^c : \beta_c^0 > 1 \\ H_1^c : \beta_c^0 \leq 1 \end{cases} \tag{16}$$

If H_0^c is rejected, then the alternative H_1^c may be supported. Otherwise, if H_0^c is not rejected, then H_1^c cannot be supported. When Hypothesis I is not rejected, it implies that structural condition deterioration could be accelerated by chemical state c (c = 2, . . ., D − 1) compared to c = 1. The null hypothesis can be tested in the confidence interval $\left[\beta_{c,\alpha}^0, \infty\right]$ for a significance level α.

Similarly, to test Hypothesis II, the null hypothesis H_0^i $(i = 2, \ldots, J-1)$, and the alternative hypothesis H_1^i $(i = 2, \ldots, J-1)$, are specified as

$$\begin{cases} H_0^i : \gamma_i^0 > 1 \\ H_1^i : \gamma_i^0 \leq 1 \end{cases} \tag{17}$$

When Hypothesis II is not rejected, it implies that the worsening of the chemical state may be quickened in condition state i (i = 2, . . ., J − 1) compared to i = 1. The null hypothesis can be tested in the confidence interval $\left[\gamma_{i,\alpha}^0, \infty\right]$ for a significance level α.

3 MULTIPLE IMPUTATION (MI)

3.1 *Handling missingness using MI*

MI can be applied to generate more complete small zone data while maintaining incomplete data attributes. Consider complete data X_{com} with an observed part X_{obs} and missing part X_{mis} with R as the distribution of missingness. Missingness types based on distributions Φ are defined as

$\phi(R|X_{com}) = \phi(R|X_{obs})$ for MAR
$\phi(R|X_{com}) = \phi(R)$ for MCAR
$\phi(R|X_{com}) = \phi(R|X_{mis}, X_{obs})$ for MNAR.

A multivariate condition and explanatory data matrix, Mx with an observed part X_n (n = 1, …, n) and a missing part X_n (n = n + 1, …, N) is formulated as

$$M_x = \begin{bmatrix} i & j & r & x_1 & \cdots & x_a \\ i_1 & j_1 & r_1 & x_{11} & \cdots & x_{a1} \\ \vdots & \vdots & \vdots & \vdots & \vdots & \vdots \\ i_n & j_n & r_n & x_{1n} & \cdots & x_{an} \\ i_{n+1} & j_{n+1} & r_{n+1} & x_{1n+1} & \cdots & x_{an+1} \\ \vdots & \vdots & \vdots & \vdots & \vdots & \vdots \\ i_N & j_N & r_N & x_{1N} & \cdots & x_{aN} \end{bmatrix} \tag{18}$$

where x = covariate; $(1, \ldots, n, n+1, \ldots, N)$ and $(1, \ldots, a)$ = integers.

For univariate complete data j_{com} $(j_1, \ldots, j_N)$ with an observed part j_{obs} $(j_1, \ldots, j_n)$ and a missing part j_{mis} $(j_{n+1}, \ldots, j_N)$ with j_{obs} and j_{mis} independent and identically distributed (i.i.d), MI can be applied to simulate approximate j_{mis} using Bayesian methods ensuring that the imputed data retains similar attributes to the incomplete data (Rubin 1976, 1987, Schafer and Graham 2002).

3.2 *Approximate Bayesian Bootstrap (ABB)*

ABB, detailed by Rubin (1987), enables non-parametric imputation for MCAR data by sampling with replacement to generate m imputations of j_{mis} following these steps.

i) Create a new data pool j^*_{obs} by resampling n values from j_{obs} $(j_1, \ldots, j_n)$ with replacement.
ii) Generate an imputed data set j^*_{mis} by resampling $N - n$ values from j^*_{obs} also with replacement.

ABB produces approximate draws from $\Phi(j_{mis} \mid j_{obs})$ in j_{obs}. The resampling of j^*_{obs} from j_{obs} approximates a draw of multinomial probabilities from their observed-data posterior under a Dirichlet prior. For the covariates $x_{1n}, \ldots, x_{an}$ $(n = n+1, \ldots, N)$, the sample values can be partitioned into cells based on unique patterns of each cell and ABB carried out within each cell. Imputation within cells reduces bias and distortion of estimates for quantities such as means.

4 MODEL APPLICATION

4.1 *Surveyed Ugandan bridges*

Bakamwesiga et al. (2014a) assessed the extent of structural damage and chemical attack on 22 RC bridges along 5 major highways in Uganda (Figure 2). Information on bridge age, inventory, structural strength, location, extent of chemical attack (i.e., carbonation and chloride) was collected in 2013. Traffic loading on the 5 routes in Equivalent Standard Axel Loads (ESALs) was obtained from Obunguta and Matsushima (2020) assuming stagnant traffic from 2013 to 2017.

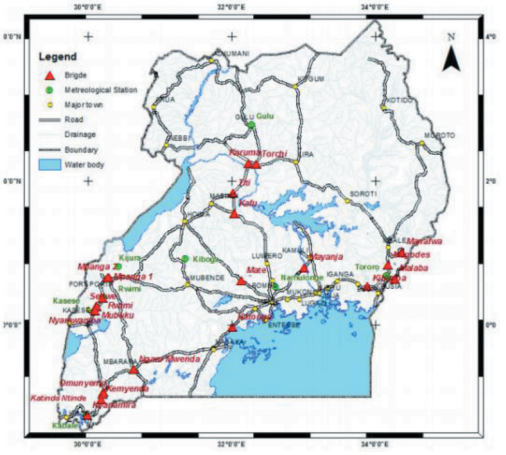


Figure 2. Study bridges (Bakamwesiga et al. 2014a).

4.2 *Strength and chemical tests on Ugandan bridges*

RC strength was obtained using the NDT Proceq N-34 Schmidt hammer on bridge piers, abutments and decks by striking perpendicular to the concrete surface to obtain a rebound number. A minimum of 3 test areas were chosen for every bridge element with a maximum of 10-12 readings obtained at each area, care taken to avoid striking the same point to minimize local aggregate influence. The results were then averaged and the compressive strength (CS) derived (Bakamwesiga et al. 2014b).

SDTs were carried out to test for carbonation and chlorination for the surveyed bridges by Bakamwesiga et al. (2014a). Phenolphthalein was sprayed on exposed concrete which turns purple in alkaline (uncarbonated) and remains clear in acidic (carbonated) environments. A powdered concrete sample was collected and taken for laboratory analysis to determine *Cl* concentration (*mg/l*).

4.3 *MI for Ugandan bridge data*

Ugandan bridge data was incomplete with a MCAR missingness type for which ABB was applied considering i.i.d data variables. MI was done by generating 3000 imputes (imp) with iterations set at 1000 for a sample with greater than 90% missingness. MI results for quantitative data showed relatively small bias between observed and imputed data means μ and variances σ^2 (Table 1). Figure 3 shows Kernel density plots for the quantitative data showing similar trends. Imputed qualitative data (element location, carbonation) had similar proportions to observed data.

Table 1. MI results for quantitative data.

	CS (MPa)		*Cl* (*mg/l*)		Age (years)		Traffic ('000 ESALs)	
Parameter	obs	imp	obs	imp	obs	imp	obs	imp
μ	42.42	42.34	9.24	9.23	36.05	35.94	6.19	6.21
σ^2	67.16	67.30	30.83	30.71	284.54	284.55	23.79	23.76

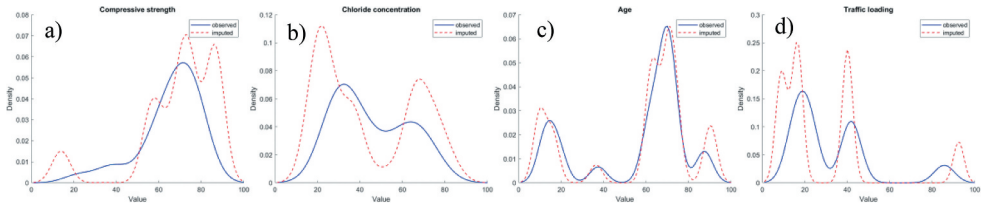


Figure 3. Kernel density plots for quantitative data; CS (a), *Cl* (b), Age (c) and Traffic (d).

4.4 *Discretization of the continuous chemical and structural condition values*

To apply the stochastic composite model, the continous condition values were discretized. Assigning accurate CS ranges to define RC condition states is complex because of different materials, construction methods and environments. The British Standard (BS) 5400 and Ugandan road design manual specify initial RC CS and material composition for specific live and dead loads (MoWT 2010). RC CS is low just after casting and gradually increases to the highest level after curing from where it decreases. CS also increases over time based on curing methods, components (e.g., water/ cement content) and carbonation. Carbonation reduces RC porosity as the produced $CaCO_3$ occupies greater volume than $Ca(OH)_2$ leading to increased hardness.

Past research defined bridge condition under chemical attack following the initiation and propagation stages. Roelfstra et al. (2004) defined propagation based on rebar section loss, whereas Lethanh et al. (2017) defined it using crack width. Both studies classified initiation according to *Cl* concentration. This study defined RC chemical state in both stages using *Cl* concentration and carbonation and set RC condition state using CS-age relationships (Al-Khaiat and Fattuhi 2001, Roelfstra et al. 2004, Rizkalla et al. 2009 and Yet et al. 2012) shown in Table 2.

Table 2. Definition of RC bridge condition and chemical states.

State	Condition data				Chemical data		
	Imputed (%)	Description	CS (MPa)	Age (years)	Imputed (%)	*Cl* (*mg/l*)	Carbonation
1	21.43	No visible damage and bridge is new or nearly new.	[0, 35] > 35	[0, 5] (5, 20]	31.73	< 7	Absent
2	5.03	Local spalling, micro cracks, and insignificant structural damage.	[0, 35] > 20 > 35	(5, 10] (20, 30] (30, 35]	25.23	< 7 (7, 14]	Present Absent
3	57.07	Significant spalling, cracks, and/or humid zones.	[0, 20] [0, 35] > 20	(20, 30] (30, 35] (35, 50]	33.73	(7, 14] (14, 28]	Present Absent
4	16.47	Heavy spalling with visible rebars, macro cracks and/or humid zones. Structure in danger of failure.	[0, 20] > 20	> 35 > 50	9.30	(14, 28] > 28	Present Absent/ Present

4.5 *Estimation of Ugandan bridge deterioration rate*

4.5.1 *Definition of hazard rates*

Deterioration rate was estimated considering chemical attack effects on structural degradation, and vice versa, using the composite Markov model. Hazard rates for the condition and chemical state transitions were specified as

$$\varphi_i(c) = \beta_c^0 exp\left(\beta_{0,i} + \beta_{1,i} x_1\right) \tag{19}$$

$$\lambda_c(i) = \gamma_i^0 exp\left(\gamma_{0,i} + \gamma_{1,i} \bar{y}\right) \tag{20}$$

$$\bar{y} = \begin{cases} 1 & for\ substructure \\ 0 & for\ substructure \end{cases} \tag{21}$$

Inuagral condition was estimated from bridge age with best state at age zero. Traffic loading x_1 was normalized to [0, 1] and considered to only affect bridge structural condition. Dummy variable $\bar{y}$ differentiated element location as the substructure (abutments and piers) is more exposed to chemical agents such as moisture compared to the superstructure (decks). The Markov Chain Monte Carlo (MCMC) methods and Metropolis Hastings (MH) algorithm were used to predict the unknown parameters and their 95% confidence intervals using MATLAB for a 15,000 run with a 5,000 burnin eliminated due to poor initial convergence. Parameter convergence was tested using the *Geweke* diagnostic with values falling within [–1.96, 1.96] limits where 0 shows perfect convergence.

4.5.2 *Estimated condition and chemical degradation*

Estimated β and γ values, average hazard rates and life expectancies are shown in Table 3. The positive β values show that traffic loading increase leads to faster deterioration in condition state 1 and 3. Positive γ values show that the substructure has a reduced life expectancy attributable to higher chemical exposure. Chemical degradation was prevalent from state 2 onwards.

Predicted condition and chemical state life expectancies (19.94 and 19.03 years, respectively) were similar. However, state transition 1 to 2 to 3 was more rapid for condition compared to chemical degradation probably due to the more significant effects of chemical attack in condition 1 and 2.

Table 3. Estimated parameters and life expectancy.

	Absolute	Traffic	Absolute	Element	Hazard rate		Life expectancy	
State	β_0	β_1	γ_0	γ_1	$\varphi_i(c)$	$\lambda_c(i)$	$RMD_i(c)$	$RMD_c(i)$
1	–0.7802 [–1.0511, –0.5402] (0.3297)	0.0920 [–0.1121, 0.2957] (0.9363)	–1.6754 [–1.9659, –1.4029] (–1.1503)	-	0.4688	0.1872	2.1347	5.3409
2	–0.1430 [–0.4340, 0.1325] (–0.0227)	-	–1.1208 [–1.4249, –0.7984] (–1.3277)	0.0557 [–0.1029, 0.2121] (1.3522)	0.8702	0.3384	1.1492	2.9565
3	–2.8397 [–3.1416, –2.5690] (1.5308)	0.1146 [–0.2083, 0.4210] (–1.8602)	–2.4843 [–2.8359, –2.1295] (–0.2764)	0.1713 [–0.1015, 0.4451] (–0.4759)	0.0601	0.0937	16.6527	10.734

Note: The 95% confidence interval is shown in square brackets and *Geweke* diagnostic in parentheses.

4.5.3 *Hypothesis testing for the compounding process*

The heterogeneity scale parameters with influence of chemical state β_c^0 and condition state γ_i^0 are shown in Table 4. Standardized $\gamma_i^0 > 1$ for $i = 3,\ 4$ and for $i = 2,\ 3,\ 4$ at 95% confidence interval suggest that more deteriorated bridges experienced accelerated chemical attack supporting hypothesis II. Standardized $\beta_c^0 > 1$ for $c = 2$, and for $c = 2,\ 3,\ 4$ at 95% confidence interval show that chemical attack speeds up structural degradation supporting hypothesis I. Chemical attack shrinks rebar area reducing RC tensile strength and expansive rust causes cracking.

Table 4. Scale parameters.

	Condition deterioration		Chemical degradation	
State	Scale parameter β_c^0	Standardized β_c^0	Scale parameter γ_i^0	Standardized γ_i^0
1	0.1715 [0.1355, 0.2145] (–1.7128)	1.000	0.1683 [0.1257, 0.2202] (0.9554)	1.000
2	0.1725 [0.1382, 0.2191] (–0.1978)	1.006 [0.806, 1.278]	0.1521 [0.1073, 0.2172] (–0.2093)	0.904 [0.638, 1.290]
3	0.1698 [0.1330, 0.2215] (–1.6175)	0.990 [0.776, 1.292]	0.1729 [0.1336, 0.2198] (–0.9105)	1.027 [0.794, 1.306]
4	0.1658 [0.1283, 0.2136] (–1.6083)	0.967 [0.748, 1.245]	0.1808 [0.1296, 0.2444] (0.9848)	1.074 [0.770, 1.452]

5 CONCLUSIONS

This study built a composite Markov hazard model capable of examining the influence of chemical attack on RC bridge structural deterioration, and vice versa. MI was applied to generate more complete small zone data to enable area specific infrastructure performance evaluation instead of relying on wider area averages that may not reflect local conditions. An empirical application was carried out using imputed Ugandan bridge data. The results showed an increase in RC bridge structural deterioration due to chemical attack and worsening chemical state for heavily deteriorated structures. These results can be used to improve existing standards for more resilient bridge design. Existing RC

standards such as the Eurocode EN 206–1:2000 restrict the maximum water content, minimum strength, cement and air content for different chemical exposure levels, however, chemical progression rates can inform RC design standard improvement in specific environments.

For the engineering construction practice, the study draws important implications including increasing the initial RC bridge construction quality and monitoring to ensure that construction follows design specifications. For instance, RC cover depth should strictly be constructed as designed. If structural monitoring uncovers defects in existing bridges, then preventive maintenance such as applying sealants to RC with low cover depth should be immediately carried out.

REFERENCES

Akiyama, M., Frangopol, D. M., and Matsuzaki, H. Lifecycle reliability of RC bridge piers under seismic and airborne chloride hazards. *Earthquake Engineering and Structural Dynamics*, 2011. 40 (15):1671–1687.

Al-Khaiat, H., and Fattuhi, N. Long-term strength development of concrete in arid conditions. *Cement and Concrete Composites*, 2001. 23(4–5):363–373.

Bakamwesiga, H., Mwakali, J., and Thelandersson, S. Nondestructive condition assessment of highway bridges for safety enhancement. Proceedings of the 7th *International Conference on Bridge Maintenance, Safety and Management (IABMAS)*, Taylor & Francis Group, 2014a. pp. 1764–1771.

Bakamwesiga, H., Mwakali, J., Sengendo, S., and Thelandersson, S. Impact of environmental exposure on concrete strength in highway bridges in Uganda. *Construction Materials and Structures*, 2014b. 861–870.

Cui, F., Li, H., Dong, X., Wang, B., Li, J., Xue, H., and Qi. M. Improved time-dependent seismic fragility estimates for deteriorating RC bridge substructures exposed to chloride attack, *Advances in Structural Engineering*, 2021. 24(3):437–452.

Kaito, K., Kobayashi, K., Mizutani, D., Ninomiya, Y., and Kawai, R. Effect of Preventive Maintenance on Bridge Expansion Joints against Corrosion at Steel Girder End Parts, *Journal of Japan Society of Civil Engineers Ser F4 (Construction and Management)*, 2021. 77(1):96–114 (In Japanese).

Kobayashi, K. The seismic behavior of RC member suffering from chloride-induced corrosion, *Proceedings of the Second FIB Congress*, Naples, Italy, 2006. ID:19–3.

Kobayashi, K., and Kaito, K. Estimating Composite Hidden Markov Deterioration Models for Pavement Structure with Sample Missing. International Symposium on Infrastructure Asset Management (SIAM), Kyoto, Japan, 2016. 1–18.

Kobayashi, K., Kaito, K., and Lethanh, N. A Bayesian Estimation Method to Improve Deterioration Prediction for Infrastructure System with Markov Chain Model, *International Journal of Architecture, Engineering and Construction*, 2012. 1(1):1–13.

Kobayashi, K., Nakatani, S., To, N. T., Osako, Y., Aoki, K., Abekura, K., and Nguyen, D. T. Estimating Bridge Deterioration Models with Imperfect Information on Inauguration Timing: A case in Vietnam. *Journal of Japan Society of Civil Engineers F5 (Civil Engineer Practice)*, (2019). 75(1):22–41 (In Japanese).

Lancaster, T. *The Econometric Analysis of Transition Data*, Cambridge University Press, 1990.

Lethanh, N., and Adey, B. T. A Hidden Markov Model for Modeling Pavement Deterioration under Incomplete Monitoring Data, *International Journal of Civil and Environmental Engineering*, 2012. 6(1).

Lethanh, N., Hackl, J., and Adey, B.T. Determination of Markov Transition Probabilities to be Used in Bridge Management from Mechanistic-Empirical Models. *Journal of Bridge Engineering*, 2017. 22 (10):04017063.

MoWT (Ministry of Works and Transport) Uganda. *Road design manuals, Volume 4*: *Bridge Design*, 2010.

Neville, A. Chloride attack of reinforced concrete: an overview, *Materials and Structures*, 1995. 28:63–70.

Obunguta, F., and Matsushima, K. Optimal pavement management strategy development with a stochastic model and its practical application to Ugandan national roads. *International Journal of Pavement Engineering*, 2020. 1857759.

Rizkalla, S., Zia, P., Mirmiran, A., Russell, H. G., and Mast, R. Proposal for Concrete Compressive Strength Up to 18 ksi (124 MPa) for Bridge Design, *Transportation Research Record: Journal of the Transportation Research Board*, 2009. 2131:59–67.

Roelfstra, G., Hajdin, R., Adey, B., and Bruhwiler, E. Condition Evolution in Bridge Management Systems and Corrosion-Induced Deterioration, *Journal of Bridge Engineering*, 2004. 9(3):268–277.
Rubin D.B. Inference and missing data. *Biometrika*, 1976. 63:581–592.
Rubin D.B. Multiple imputation for non-response in surveys. New York: John Wiley, 1987.
Schafer, J. L., and Graham, J. W. Missing Data: Our View of the State of the Art, *Psychological Methods*, 2002. 7(2):147–177.
Tsuda, T., Kaito, K., Aoki, K., and Kobayashi, K. Estimating Markovian Transition Probabilities for Bridge Deterioration Forecasting. *Structural Engineering/Earthquake Engineering*, 2006. 23(2):241s–256s.
Yet, T., C., Hamid, R., and Kasmuri, M. Dynamic Stress-Strain Behaviour of Steel Fiber Reinforced High-Performance Concrete with Fly Ash, *Advances in Civil Engineering*, 2012. 907431.

Bridge Maintenance, Safety, Management, Digitalization and Sustainability – Jensen, Frangopol & Schmidt (eds)
© 2024 The Author(s), ISBN 978-1-032-77040-6
Open Access: www.taylorfrancis.com, CC BY-NC-ND 4.0 license

Assessment of shear capacity of bridge beams with non-standard anchorage - an experimental study

E. Nuti, A. Darby & M. Evernden
Department of Architecture and Civil Engineering, University of Bath, Bath, UK

J. Bennetts & J.D. Shave
WSP, Bristol, UK

P. Valerio
National Highways, Guildford, UK

ABSTRACT: This paper considers the effect of inadequate or damaged anchorage regions on the shear strength of bridge beams. This research is motivated by the occurrence of theoretical deficiencies in the assessed shear capacity of existing reinforced concrete bridges. The provisions for dealing with damaged or non-standard RC details as prescribed in CS455 (2020) can be conservative, as such low shear strength assessed capacities may lead to expensive and potentially unnecessary repairs. The aim is to identify if changes are needed to the provisions currently adopted in the UK for the assessment of shear capacity for beams with non-standard anchorage. The paper presents preliminary results from a series of off-set 3-point tests on beam specimens specifically constructed to replicate the types of anchorage defects commonly found in aging UK infrastructure. This includes the effects of insufficient anchorage length, prior slip in the longitudinal reinforcement and corrosion affecting longitudinal bars, links and concrete cover. A unique two-stage beam casting system has been implemented to produce specimens with known prior anchorage slip and corrosion. Beams with either plain or deformed bars and both with and without stirrups, have been tested, representative of typical bridge reinforcement detailing within the UK infrastructure. CS455 (2020) does not provide full guidance on RC elements affected by prior anchorage slip, the higher-than-expected resistances obtained to date (particularly for deformed bars) seem to suggest that the current limited provisions may lead to overconservative assumptions. However, further study is needed for beams containing plain bars, which are expected to exhibit significantly much lower bond capacities.

1 INTRODUCTION

As reinforced concrete (RC) structures age over time and are exposed to deterioration, they can become affected by a series of defects. For RC bridges, anchorage zones are amongst the most sensitive areas where aging and deterioration can worsen the impact of pre-existing sub-standard details or expose new defects. Deficiencies in the anchorage zones for RC bridge beams and slabs can influence the shear capacity (Shave et al., 2007, Coronelli et al., 2019, Han et al. 2020) and may require expensive repair interventions and interim measures. Although authors have proposed methods to assess the shear capacity of RC elements with short anchorage lengths (Shave et al. 2007) and for elements affected by corrosion (Coronelli et al. 2019), there is still no standardized approach to deal with the assessment of the shear capacity of RC members with insufficient or damaged anchorage and no guidance was found in case of prior slip of the longitudinal reinforcement.

DOI: 10.1201/9781003483755-448

Assessment standards in the UK do not currently provide full guidance to deal with the deterioration of the anchorage bond behaviour that may be caused by corrosion or by a previously happened failure in the reinforcement anchorage (commonly referred to as prior anchorage slip).

In the UK some existing RC bridges present short anchorage lengths of the longitudinal reinforcement which appear to have slipped and/or show signs of corrosion. To investigate the effects of prior anchorage slip and corrosion of short anchorage lengths on the shear capacity of RC bridge elements a series of tests adopting a two-stage beam casting has been planned and partly performed to date.

In addition, the specimens have been intentionally designed with identical characteristics to those used Shave et al. (2007) to be able to directly compare the results, particularly for the pre-slipped and corroded specimens which were not included in Shave et al. (2007).

2 TESTING PROGRAMME

2.1 *Test specimens*

As part of an ongoing project, a preliminary study of 9 beams presenting either deformed or plain bars with anchorage lengths ranging from zero up to twenty bar diameters are presented. In addition to anchorage length, other parameters such as presence or absence of links, link spacing, the influence of prior slip of the longitudinal reinforcement or of corrosion were investigated.

Within this initial study two main section types have been utilised: one with no links (for which the naming convention B1 was adopted) and another one with the same longitudinal reinforcement but with links (namely B4 section type). Variations on section code B4 (i.e., B4.1, B4.2 and B4.3) have been tested to investigate the influence of links density, concrete cover and corrosion. The various section codes with their characteristics are presented in Figure 1.

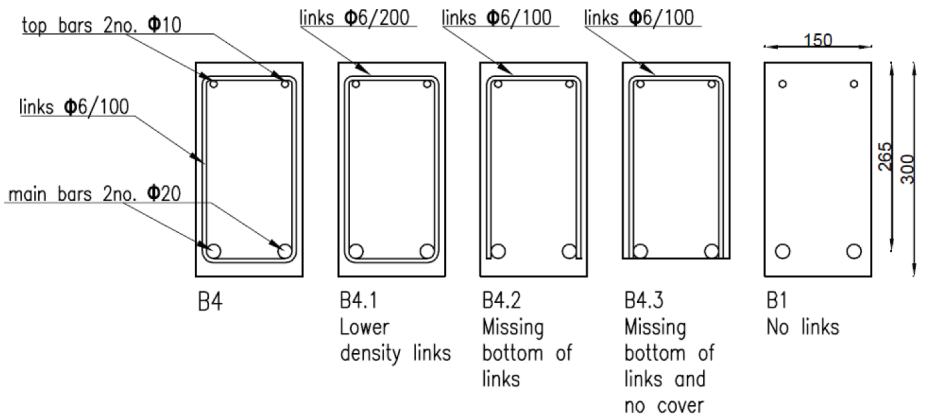


Figure 1. Beam specimens section types, geometry, and reinforcement.

With the exception of section type B4.3, all sections have the same nominal geometry, concrete cover (25mm to main bars) and reinforcement arrangement. Sections B4.2 and B4.3 present U-shaped links (as shown in Figure 1) only in the anchorage zone, and closed links along the shear and back spans. These two sections belong to the group of corroded specimens. The missing bottom leg in B4.2 as well as the missing concrete cover in B4.3 simulate a moderately high level of corrosion replicating typical defects observed in existing RC bridge beams in the UK.

The choice of the two values adopted for the link spacing for section types B4 and B4.1 was based on the knowledge that the beneficial effect upon the bond strength provided by a links density of approximately 0.5-0.6d is generally sufficient. A further increase in the density only provides marginal improvements, whilst for lower densities a gradual worsening of the bond behaviour is observed, as remarked by Koulouris and Apostolopoulos (2020).

The specimens have been designed in accordance with CS455 (2020) to assess the expected type of failure to ensure they failed in shear or by exceeding the bond strength in the anchorage zone. In this way, the risk of accidental bending failures was also minimised as much as possible.

The anchorage length was measured from the centreline of the bearing and varied from zero up to 20 bar diameters (400mm). As indicated in Figure 2 the clear span of the beams is 2000mm resulting in a full length of 2.8m including the allowance for the anchorage length on both ends.

To investigate the effect of prior anchorage slip and corrosion, most of the specimens have been cast in two stages.

The first stage includes casting only the anchorage zone of the specimen up to the centre line of the bearing, which is assumed to be the end 400mm of the specimen, but which could be varied depending on the anchorage length being investigated. The reinforcement extends beyond the end of the concrete in this stage as shown in Figure 2a. The prior anchorage slip was achieved through a bond test carried out by pulling all of the bottom extending bars in turn using jacks, whilst measuring the slip (from the end of the bar which was intentionally left sticking out from the back of the specimen of a few centimeters during stage 1 casting operations), to a value of slip in the range of 2mm that is sufficient to exceed the slip corresponding to the peak bond stress. For specimens where the effect of corrosion was investigated, the stage 1 specimens were immersed in salt water and corroded in the anchorage zone.

In stage 2, the shear links are installed where required and the remainder of the specimen is cast. The specimens were tested adopting an off-set 3-point load test at least 14 days after stage 2 casting. Most of the tests have been performed with a shear span $a_v = 3d$.

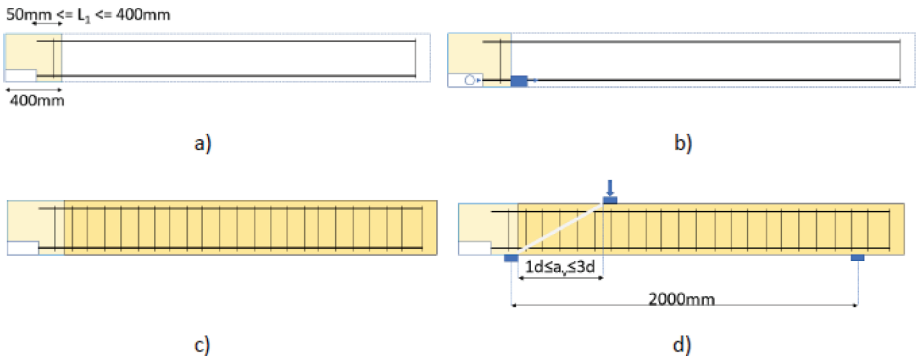


Figure 2. a) Stage 1 casting of specimen b) pre-slip test; c) Stage 2 casting of specimens; d) Stage 2 shear test.

2.2 *Accelerated corrosion*

The effect of corrosion on the main reinforcement was obtained immersing the anchorage parts cast in stage 1 (see Figure 2) in a 10% salt water solution and a constant current induced in the main reinforcement that worked as anode whilst a immersed stainless steel cage surrounding the concrete was used as a cathode. Faraday's law (Equation 1) was adopted to evaluate the current intensity for the target mass loss.

$$I = \frac{\Delta m z F}{M t} \tag{1}$$

In the equation shown, Δm is the mass loss of the reinforcement (g); M is the atomic weight of the metal (56g/mol); I is the electric current (A); z is the ionic charge (equal to 2.0) and F is the Faraday's constant (equal to 96500A/s). The accelerated corrosion was performed with a calculated current density of approximately 1360μA/cm^2. This value of current density is not too dissimilar from the one adopted by Han et al. (2020), that was 1000μA /cm^2.

2.3 *Three-point load test set-up*

The layout of the 3-point load test is as shown in Figure 3. Various transducers have been placed along the shear span and displacement transducers have also been located at the ends of the main bars which stick out of the concrete. Two transducers can be seen on the top of the beam along the shear span in Figure 3, whilst two additional transducers are installed on the back of the beam and can be seen on the left of Figure 3. Load cells have been placed under both supports and at the load point. In addition, the shear span and the relative anchorage length have been painted to enable future use of Digital Image Correlation techniques (DIC). The load was applied using a lever beam to ease the positioning of the specimen and avoid clashes between the DIC images and the press' structure. The lever beam transferred the load on the shear span and was supported by a frame that was directly supported by the strong floor in the back span (hence not touching the beam at all). Prior to casting, one strain gauge was also installed on each of the main bars in the shear span at approximately 50mm from the front face of the support.

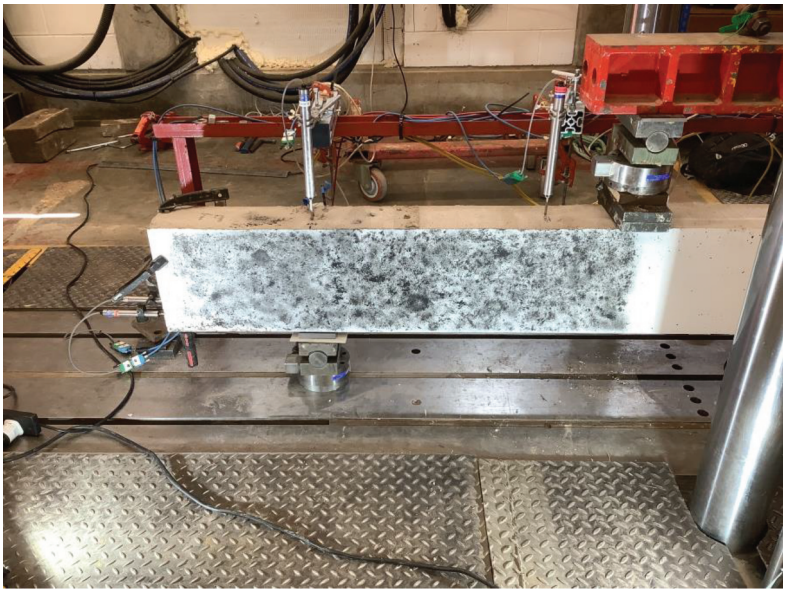


Figure 3. Some details of the shear span side for the setup of the beam 3-point load test.

2.4 *Naming convention*

A total of 9 specimens are presented in this paper, as listed in Table 1. To allow for the correct identification of each specimen and its associated characteristics the following naming convention has been implemented:

- Section Type (B1, B4, B4.1, B4.2 or B4.3 as shown in Figure 1)
- Bar Type ("d" for deformed bars, "p" for plain bars)
- Anchorage length (number of bar dia. followed by capital L)
- Shear span (expressed as number of effective depths, e.g., 3d)
- Status of the specimen ("s" if pre-slipped, "c" if corroded, empty if none of the two).

The naming convention can be read as follows: Specimen B4.1d6L3d, has section type B4.1 (low density link), deformed bars as main reinforcement, an anchorage length of 6 bar diameters and was tested across a shear span of 3d and was not slipped or corroded.

As shown in Table 1, a set of 6 beams with deformed bars including pre-slipped and non-pre-slipped specimens, dense, less dense and without links were tested at 3d with 6 bars diameters anchorage lengths alongside a further set of 3 beams with plain bars. The latter include

beams with dense stirrups only with a control non-slipped specimen and the equivalent pre-slipped one both having 6 bar dia. anchorage lengths and an additional pre-slipped specimen with 12 bar dia. anchorage length.

Additionally, one of the plain specimens included in the results was tested at a shear span of 2d. This choice was taken after the equivalent control non-slipped specimen failed in bending with a vertical crack.

3 TEST RESULTS

3.1 *Full beams test results*

The recorded load-deflection plots for beams with deformed and plain bars are presented in Figure 4 and Figure 5 respectively. For each beam the Ultimate load, Mode of failure and cube strength is provided in Table 1.

It is worth highlighting that whilst all the beams with deformed bars failed in shear, this was not the case for all plain bars. For beams with plain bars, failure modes were a result of bond failure of the longitudinal bars, leading to formation of one large flexural crack (B4p6L3d), or inclined shear/flexural cracks (e.g., B4p6L2ds).

Table 1. Three-point load tests results summary

Specimen	Ultimate load P_u [kN]	$P_u/P_{assessment}$ [%]	Prevalent failure mode	Concrete cube strength [MPa]	Load at first slip P_{slip} [kN]	Slip at P_u, s_u [mm]
B4d6L3d	184.74	119	Shear	28.0	107.87	0.204
B4p6L3d	55.56	46	Flexure + Bond	28.0	54.77	0.045
B1d6L3d	68.68	185	Shear	28.0	44.53	0
B4.1d6L3d	124.15	113	Shear	28.0	78.09	0.39
B4d6L3ds	203.48	142	Shear	37.7	110.05	1.25
B4p6L2ds	65.54	69	Flexure + Shear	37.7	64.39	0.014
B1d6L3ds	85.77	250	Shear	37.7	77.77	0
B4.1d6L3ds	140.12	138	Shear	37.0	105.77	0.216
B4p12L3ds	90.14	55	Shear	33.0	88.84	0.069
B4.2d6L3dc	178.11	238	Shear	33.0	148.91	0.004
B4.2p6L3dc	109.83	197	Shear	33.0	98.19	0.3
B1d6L3dc	78.81	244	Shear	33.0	25.78	0

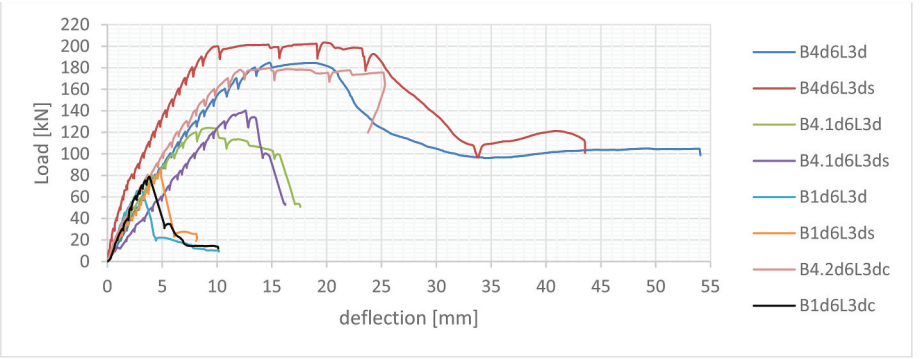


Figure 4. Load-deflection plots for beam specimens with deformed bars.

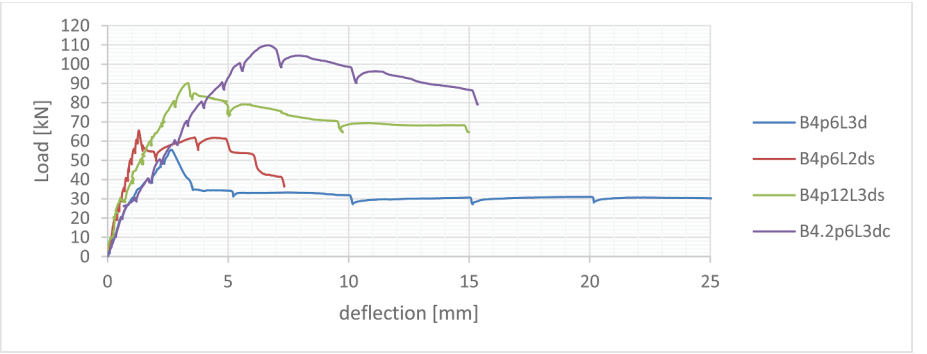


Figure 5. Load-deflection plots for beam specimens with plain bars.

3.2 *Pre-slip tests results*

During the pre-slip tests, the load-slip behaviour was recorded, with the load being converted to an average bond stress along the anchorage length. Typical behaviour of deformed and plain bars has been observed with the latter presenting lower peak and residual bond strength compared to deformed bars and a steeper descending branch after the peak bond was exceeded. Prior to performing the pull-out tests, the expected bond strength of the various specimens has been calculated in accordance with CS455 (2020). Whilst the deformed bars have shown bond characteristics in line with the expected values, plain bars underperformed as also shown in Table 2.

Table 2. Results of pull-out slipping tests for the selected specimens.

Specimen	Expected bond strength $f_{ub,exp}$ [MPa]	Recorded bond strength $f_{ub,rec}$ [MPa]	$f_{ub,rec}/f_{ub,exp}$ [%]
B4d6L3ds	4.08	4.79	118
B4p6L2ds	2.27	0.78	34
B1d6L3ds	2.51	3.18	127
B4.1d6L3ds	4.08	3.31	81
B4p12L3ds	2.62	1.15	44

The poor performance of plain bars is significantly below the expected values, such a reduction in bond strength would not be covered by the partial factors γ_{mb} provided in Section 2 of CS455 (2020) (which is either 1.4 or 1.25). It seems probable that the extremely smooth surface of the cold-drawn plain bars had a significant impact on the bond behaviour The variation in bond strength between the two plain bars specimens presented (B4p6L2ds 34% and B4p12L3ds 44% of the expected values respectively) may also be due to the fact the bars used within B4p12L3ds had been left exposed to develop a degree of surface rust in the environment for a period thereby roughening the surface finish.

3.3 *Accelerated corrosion results*

The results obtained to date have provided levels of mass loss which resulted in a fraction of the targeted 10%. The two specimens included in this paper reached approximately 2% for the one with links and 5% for the one with no links. As a consequence, the results of the shear tests on corroded specimens are not going to be presented in this paper as further testing with different and higher levels of corrosion is needed.

Similarly, to what has been observed by Han et al. (2020), one of the reasons that could have caused the lower than expected levels of corrosion, may be due to the formation of a corrosion cell between the stirrups, the top reinforcement and the stainless steel even if insulation was applied to isolate the main bars from the remaining steel. Additionally, as also suggested by

Imperatore et al. (2019), it may be good practice to immerse the concrete to be corroded in the saltwater solution for a conditioning period prior to starting the actual accelerated corrosion process. This would allow the salt to penetrate the concrete and should reduce the delay of the start of the corrosion process. Although, also after conditioning the specimens, a correction factor (α) for the Faraday's law may be used when corroding bars embedded in concrete (Han et al. 2020, Imperatore et al. 2019). Additionally, it would be preferable to continue the corrosion process until the formation of longitudinal corrosion cracks as these may be the fundamental indicator of loss of bond due to corrosion, as also suggested by Mak and Lees (2021).

3.4 *Discussion of the results*

The third column in Table 1 provides the ratio between the experimentally determined ultimate load P_u and the value $P_{assessment}$ determined in accordance with CS455 (2020).

As shown in Table 1 all the beams with plain bars underperformed compared to the expected maximum load calculated in accordance with CS455 (2020), reaching 50% to 70% of the expected load. Preliminary analysis of the results provided in Tables 1 & 2 indicates that bond strength and the resulting bond force that can be resisted by the anchored bars (F_{ub}) offers the most significant influence on the mode of failure. Specimens that experienced flexural failure were those for which bond characteristics were poorer or the maximum bond force (F_{ub}) was smaller. For example, specimen B4p12L3ds, which failed in shear, had a longer anchorage length of 12 bar dia, compared to B4p6L2ds which had a 6 bar. dia. anchorage, and hence able to develop a higher bond force, but also showed a slightly better bond behaviour during the slipping operations as it can be seen in Table 2. The fact that bond characteristics of longitudinal reinforcement have a significant influence on the shear resistance is also confirmed in the Fib Bulletin 85 as shown in the study performed by Muttoni et al. (2018).

Further comparison of the results shown in Tables 1 and 2, indicates that pre-slipping the main reinforcement in the anchorage zone has little impact on the overall shear capacity of the beam element.

It is hypothesized that the confining effect provided by the support reaction may enhance the bond characteristics at and near support partially or fully restoring the residual bond strength for pre-slipped anchorages. The impact of this confining effect may be more significant for plain bars for which the residual bond strength is significantly lower than the peak. Deformed bars did not show a significant descending branch of the bond-slip curve, so the post slip bond stress remains approximately constant, at least for the range of pre-slip applied.

An alternative hypothesis is that the small amounts of prior slip used in the pre-slipping operations, typically in the range of 2mm, do not have a severe effect on the resistance of the beam. It is recommended that the effect of prior slip should be investigated further in the next phases of the testing.

From the load-deflection plots presented in Figure 4 and Figure 5, it is clear how the specimens with deformed bars reach the peak load at higher values of deflection. Additionally, from the correspondent load-slip plots recorded during the 3-point load tests, it was possible to notice that for specimens with stirrups the slip reaches higher values for plain bars for a given value of the deflection if compared to beams with deformed bars.

The last two columns of Table 1indicate the value of the external load at which initial slip happened in the main reinforcement (P_{slip}) and the value of the slip correspondent to the peak external load (s_u). All the specimens with links with either deformed or plain bars, slipped or not, corroded or not, experienced slip of the main reinforcement prior to reaching the ultimate load. On the other hand, although all the three specimens without links (i.e., B1 section type) reached the peak load (P_u) without signs of slip in the main reinforcement, this happened almost concurrently with the shear failure and in a sudden manner, in line with the typical behaviour of unconfined bars subject to tension.

The load-deflection plots of Figure 4 and Figure 5 also highlight a different stiffness of the various specimens. In Figure 5 for example, the stiffness of B4p6L2ds may be slightly higher than the other three specimens because it has been tested at 2d instead of 3d. From Figure 4, the stiffer response is provided by B4d6L3ds (so a pre-slipped specimen) which also presents

an f_{cu} of 37.7MPa hence approximately 30% higher than the correspondent non slipped specimen (B4d6L3d). On the other hand, for the two specimens with a lower density of the links (B4.1d6L3d and B4.1d6L3ds), the non-slipped one provides a stiffer response despite f_{cu} being 30% lower. As a consequence, it is difficult to draw conclusions on whether or not the prior slip has an influence on the response of the beam as well as if the behaviour is due to the concrete elastic modulus or to slight differences that occurred during the setting up of the test.

4 CONCLUSIONS

From the results obtained it is possible to draw some initial conclusions on some of the main parameters investigated.

The effect of prior anchorage slip in the beams tested, seems to have negligible to no effect on the shear resistance. It is possible that the pressure exerted by the support when the beam is loaded has a significant influence on enhancing the bond behaviour of reinforcement affected by prior slip. This is evidenced by the results obtained for the peak resistances during the 3-points load tests. This requires further investigation.

The beams with plain bars, offer a very low resistance to failure, due to premature slip of the bars at low stress levels, resulting in bond/flexural failures. The surface roughness of plain bars has a significant impact on the bond strength and as a direct consequence on the overall resistance of the beam and on its failure mode and warrant further investigation.

The accelerated corrosion methodology adopted did not provide the target value mass losses expected. A combination of factors including the formation of unexpected corrosion cells and a delay in the start of the corrosion of the main reinforcement, may have been attributed to this finding. For these reasons, in the next testing phases, the concrete end parts will be conditioned in salt water for a period of time (likely in the range of 5-7 days due to time constraints) prior to starting the accelerated corrosion.

ACKNOWLEDGEMENTS

The authors of the paper would like to thank National Highways for sponsoring the research project on the realistic shear assessment of reinforced concrete bridges and WSP and the University of Bath to support the research project. Special thanks also to the technicians William Bazeley and Angus Tillotson of the Structures Laboratory at the Department of Architecture and Civil Engineering of the University of Bath whose contribution for setting up and carrying out the tests has been fundamental.

REFERENCES

Coronelli D., François R., Dang H., Zhu W. 2019. Strength of Corroded RC Beams with Bond Deterioration. *J. Struct. Eng*. 145(10): 04019097

CS 455, 2020. The assessment of concrete highway bridges and structures. *Design Manual for Road and Bridges*. National Highways.

Han S-J., Kim K. S., Lee D. and Yi S-T. 2020. Experimental shear tests of reinforced concrete beams with corroded longitudinal reinforcement. *Fib Structural Concrete*. 21:1763–1776.

Imperatore, S., Rinaldi, Z.and Spagnuolo, S. 2019. Influence of corrosion on the experimental behavior of R.C. ties. Eng Struct. 198: 109458

Koulouris, K. and Apostolopoulos C. 2020. An Experimental Study on Effects of Corrosion and Stirrups Spacing on Bond Behavior of Reinforced Concrete. *Metals*. 10, 1327

Mak, M.W.T. and Lees, J.M. 2021. Assessment of corrosion-induced bond deterioration in reinforced concrete: towards a splitting crack-based approach. *Proc. of the IABSE Congress – Resilient Technology for Sustainable Infrastructure*. Christchurch, New Zealand.

Muttoni, A., Ruiz, M.F. and Cavagnis F. 2018. Shear in members without transverse reinforcement: from detailed test observations to a mechanical model and simple expressions for codes of practice. *Fib Bulletin 85: Towards a rational understanding of shear in beams and slabs*. 17–32.

Shave, J.D., Ibell, T.J. and Denton, S.R. 2007, Shear assessment of reinforced concrete bridges with short anchorage lengths. *The Structural Engineer* 85(5): 30–37

Bridge Maintenance, Safety, Management, Digitalization and Sustainability – Jensen, Frangopol & Schmidt (eds)
© 2024 The Author(s), ISBN 978-1-032-77040-6
Open Access: www.taylorfrancis.com, CC BY-NC-ND 4.0 license

Deep learning for evaluation of girder rotation during bridge deck construction

Li Hui
Civil Engineering Department, University of Louisiana at Lafayette, Lafayette, LA, USA

Riyadh Hindi
Parks College of Engineering, Aviation and Technology, Saint Louis University, St. Louis, MO, USA

ABSTRACT: During bridge deck construction, overhang brackets are commonly utilized to resist the weight of fresh concrete and the loads from heavy construction equipment. These loads transfer through the overhang bracket to the bridge's girder system, resulting in significant torsional moments, particularly on the exterior girder. Under certain circumstances, such torsional moments have been observed to induce excessive transverse rotation in bridge exterior girders. This rotation can potentially give rise to safety and maintenance concerns throughout the entire bridge's service life. A detailed finite element analysis is typically recommended to mitigate these isto evaluate torsional effects on bridge girders during deck construction. However, this analysis, though thorough and comprehensive, can be tedious and time-consuming. In this study, several deep-learning models were developed to accurately predict the maximum rotation of the exterior girder. Over 10,000 finite element models were generated using SAP2000 to gather enough data to develop these deep learning models. The accuracy of these deep learning models was also scrutinized and compared. The results suggest that deep learning-based prediction models can effectively and efficiently assess the rotation of the exterior girder during bridge deck construction, thereby providing a powerful tool for engineers and construction professionals in the bridge design and construction field.

1 INSTRUCTION

In bridge construction across the United States, it is common practice to distribute a series of girders evenly beneath the deck slab to manage costs effectively (J.D. Fasl, 2008). These girders are evenly spaced, and the bridge's deck slab extends beyond the outer girders, forming a cantilevered overhang. As shown in Figure 1, the construction of bridge decks often incorporates overhang brackets. These brackets provide the necessary support for the formwork, the weight of the fresh concrete, and the load imposed by construction machinery like deck finishing machines, which span the bridge's full width (shown in Figure 2). The force introduced by these machines, especially at the edges of the overhangs, can cause considerable torsional moments and excessive rotation in the exterior girders (Ashiquzzaman et al., 2016; Clifton and Bayrak, 2008; Yang et al., 2009). Figure 3 shows the exterior girder rotation during bridge deck construction. If not properly managed, this can lead to significant safety and maintenance challenges, including uneven deck thickness and compromised stability, which could precipitate a bridge collapse during both construction and use (Ashiquzzaman et al., 2021; Hraib et al., 2019; Hui et al., 2019a, 2019b).

To mitigate these risks, state transportation departments in the U.S. have established guidelines for the maximum permissible width of the overhang to control the transverse rotation of bridge girders during deck construction. For instance, Illinois sets limits on girder rotation by specifying the maximum deflection of the overhang (Illinois Department of Transportation,

DOI: 10.1201/9781003483755-449

2012). Kansas dictates that the girder rotation must not exceed one degree during construction and that the overhang width should be determined according to the torsional forces applied to the girder (Roddis et al., 1999). Methods to limit girder rotation include implementing both permanent and temporary lateral bracing systems, which can compromise their intended function (Ashiquzzaman et al., 2016; Faress Hraib, 2020). However, these temporary rotation prevention systems are often installed during the bridge deck construction phase without thorough analysis, sometimes diminishing their effectiveness (Hui et al., 2019b).



Figure 1. Overhang bracket during bridge deck construction.



Figure 2. Bridge deck finishing machine.

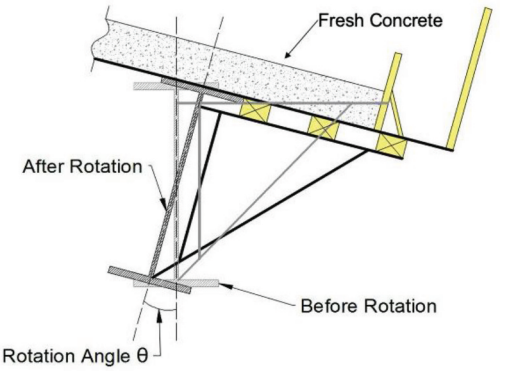


Figure 3. Exterior girder rotation during bridge deck construction.

One of the most significant and complex challenges in designing lateral bracing systems for bridges is the precise prediction of girder rotation. This aspect of bridge engineering is critical, as inaccuracies in predicting girder rotation can lead to substantial structural inefficiencies, which may manifest as compromised durability or even pose safety risks. The AASHTO LRFD Bridge Design Specifications provide a framework for this analysis, recommending the use of sophisticated 3-D finite element analysis (FEA) techniques (American Association of State Highway and Transportation Officials, 2017). These techniques are crucial for a detailed examination of the torsional effects that can arise, particularly from the loads imposed by overhang brackets during construction. Nonetheless, the process of conducting finite element (FE) analysis is complex, involving intricate modeling that demands considerable time and effort, and necessitates a thorough understanding of numerical simulation principles.

In recent years, deep learning applications have surged in civil engineering, with research utilizing these methods for predicting various structural behaviors, such as concrete strength and member deflection. Dutta and Barai conducted research to predict concrete compressive strength using artificial neural networks (Dutta and Barai, 2019). Besides, several researchers used deep learning to predict the deflection of structural members. Tadesse et al. successfully predicted the middle-span displacement of six composite bridges by using a deep learning model, which was developed using data generated from computer simulation and experimental results (Tadesse et al., 2012). However, no study has been conducted to evaluate the bridge torsional behaviors using the deep learning algorithm, and the applications for assessing bridge torsional responses remain unexplored.

This study aims to develop a deep-learning model to forecast the maximum rotation of exterior bridge girders during deck construction. A substantial dataset for model training was generated through finite element analysis using a MATLAB program created for this research. Feature selection techniques were employed to refine the variables and avoid overfitting, ultimately selecting five key bridge geometry parameters to predict girder rotation through an artificial neural network model.

2 FINITE ELEMENT MODELING AND DATA GENERATION

2.1 *Finite element modeling*

To develop a comprehensive dataset for the training of the deep learning model, finite element (FE) analysis was undertaken utilizing the SAP2000 software suite. The FE models were validated in previous research (Hui et al., 2019b). An example of such a model, which is instrumental for data generation, is shown in Figure 4. Given that the rotation of the exterior girders is affected by many factors, the development of the FE models took into account a variety of parameters, including construction loads, material properties, and the intricacies of bridge design.

During bridge deck construction, it is a common practice to employ a deck finishing machine to ensure the deck's surface is both even and smooth. Typically, this machinery is maneuvered along the edge of the overhang formwork, spanning the full width of the bridge, thereby exerting substantial loads on the overhang of the bridge. For the purposes of this study, a standard Bidwell-3600 deck finishing machine was utilized as the basis. Consequently, the force exerted by the finishing machine is modeled as discrete concentrated loads, with each wheel imparting a load of 3,336 N (750 lbs.).

Given that the concrete deck lacks the rigidity to contribute to structural support during construction, it is modeled in the FE simulations as a series of distributed loads along the length of the bridge girders. Table 1 consolidates the fundamental considerations of the loads and material properties that are typically accounted for in the construction of bridge decks.

2.2 *Data generation*

In determining the variables that influence the rotation of exterior girders during the construction of bridge decks, several parameters were identified for initial consideration. These include

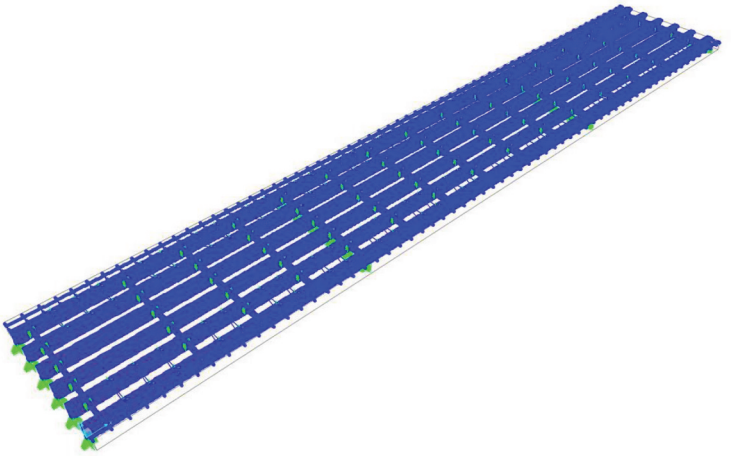


Figure 4. Typical finite element model for data generation.

Table 1. Material properties and loads during bridge deck construction.

Items	Values
Deck Thickness	20.32 cm (8 in)
Concrete Unit Weight	23.56 kN/m^3 (150 lb/ft^3)
Deck Finishing Machine Loads	3,336 N (750 lb) per wheel
Elastic Modulus of Steel	200 GPa (29,000 ksi)
Elastic Modulus of Concrete	26.43 GPa (3,834 ksi)

the span length of the bridge, the cross-sectional profile of the girders, the distance between girders, the width of the deck overhang, the total number of girders used, and the specifications of the diaphragms. According to the data presented in Table 2, the selection of girder sections was guided by the ASIC section database (American Institute of Steel Construction, 2017), encompassing a variety from W27 to W44. Span lengths were considered within a scope extending from 9.14 m (30 ft) to 33.53 m (110 ft) and included diaphragms spaced no less than 3 m (10 ft) apart. The parameters for overhang width and girder spacing were determined by guidelines from the Illinois Bridge Manual, which advises that the width of the overhang should not exceed half the distance of the girder spacing. The inclusion of additional parameters followed recommendations from the Illinois Bridge Manual alongside established general design practices.

Table 2. Geometric parameters for data generation.

Parameters	Ranges
Girder Depth	W27 to W44
Diaphragm Section	W12 to W21
Span	9.14 m to 33.53 m (30 ft to 110 ft)
Girder Spacing	1.8 m to 3 m (6 ft to 10 ft)
Overhang	36.8 cm to 118.9 cm (14.5 in to 46.8 in)
Number of Girders	3 to 6
Number of Diaphragms	2 to 10
Slab Thickness	8
Concrete Unit Weight	23.56 kN/m^3 (150 lb/ft^3)
Elastic Modulus of Steel	200 GPa (29,000 ksi)
Skew	0

Utilizing the input parameters, a computer program was developed to automatically generate the FE models. This program calculates and assembles essential data points such as nodal coordinates, element configurations, material characteristics, cross-sectional dimensions, and boundary conditions. This compiled data is then formatted into an input file compatible with the SAP2000 structural analysis program. The integration between MATLAB and SAP2000 is facilitated by using SAP2000's application programming interface (API) functions, which allow for the seamless transfer of FE analysis results back into MATLAB for further processing.

A comprehensive set of 10,267 finite element (FE) models was constructed using the computer program developed in this study. Each model documented an array of bridge parameters along with their corresponding maximum girder rotation values for subsequent analysis. The physical properties of the girder and diaphragm sections were assessed based on section depth and weight, ensuring consistency with structural norms. In addition, based on the findings of recent research by Ashiquzzaman et. al. in 2021 (Ashiquzzaman et al., 2021), which highlighted the ratio of the braced length to the girder depth (B/D ratio) as a critical factor in gauging exterior girder rotation, the B/D ratio was incorporated into the dataset for each bridge model. The range of the B/D ratio spanned from 2.7 to 11.1, exhibiting consistent mean and median values, thereby providing a reliable basis for evaluation.

2.3 *Feature selection*

Eight dependent variables were identified for potential inclusion in the preliminary stages of developing the deep learning model. However, incorporating extraneous predictors can often contaminate the model with noise, muddling the estimation of truly impactful variables and potentially leading to an overfitting issue. Overfitting is characterized by the model's excessive acclimation to the training data, to the extent that it impairs its generality and performance on new datasets.

To circumvent the inclusion of such redundant predictors and to distill the subset that would enable the most effective deep learning model, a comprehensive feature selection process was undertaken. This process was conducted by assessing correlation metrics to determine the statistical significance of each variable, thereby identifying the subset that most accurately conforms to the regression model's requirements. Furthermore, the study acknowledged the nonlinear correlations between the desired rotation outcomes and the bridge's geometric configurations. To navigate this, logarithmic transformations were applied—but only to the rotation values—to preserve the model's straightforwardness and operational efficiency.

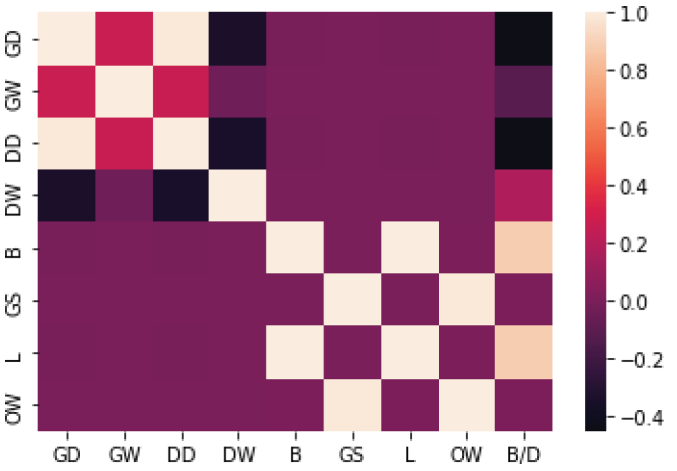


Figure 5. Correlation heatmap.

As detailed in Figure 5, the analysis of correlation among all variables led to the exclusion of four variables—namely diaphragm depth, girder spacing, span length, and unbraced length—from the final selection. These variables were highly related to other variables and thus were not carried forward into the deep learning modeling phase.

2.4 *Deep learning model*

The architecture of the artificial neural network (ANN)—a prevalent form of artificial intelligence in predictive modeling—was selected for developing this deep learning model. To ensure the model operates at peak efficiency, the dataset underwent a standard normalization process as a preliminary step, which scales the data to a common range without distorting differences in the ranges of values. Subsequently, the dataset was divided into two distinct subsets for training and testing purposes. The training subset was instrumental in developing the ANN model, serving as the basis upon which the model learned to make predictions. Meanwhile, the testing subset was essential for evaluating the model's accuracy and reliability in predicting unseen data.

The ANN architecture designed for this study is shown in Figure 6. It features a network with five input nodes corresponding to the input parameters, two hidden layers—each consisting of 64 nodes to capture complex patterns and relationships within the data—and a singular output layer that yields the predicted value of girder rotation. This structured approach to the ANN design facilitates a robust learning process, enabling the model to accurately capture the intricate dynamics governing bridge construction.

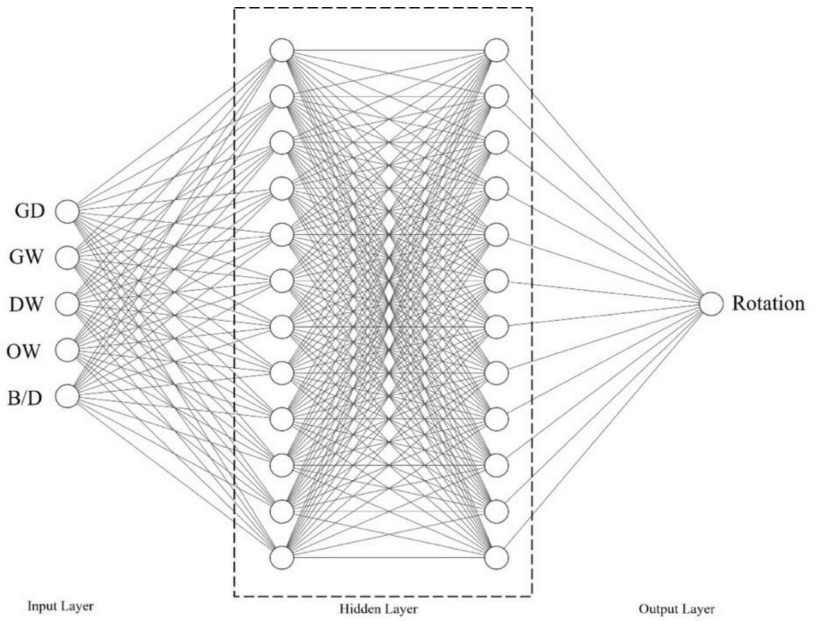


Figure 6. ANN deep learning model.

The performance of the ANN model was quantitatively assessed using mean square error (MSE) and the coefficient of determination (R^2). For the evaluation, the dataset was randomly split into a training set, comprising 80% of the data to train the model, and a testing set, constituting the remaining 20% to test its predictive accuracy. After training over fifty epochs, the ANN model demonstrated a minimum MSE of 0.008 and an R^2 value of 94% for the training set, indicating high accuracy and a strong ability to predict girder rotation. These metrics were mirrored closely by the testing set results, confirming the model's robust performance and generalization capabilities. Figure 7 shows the MSE during the ANN training process.

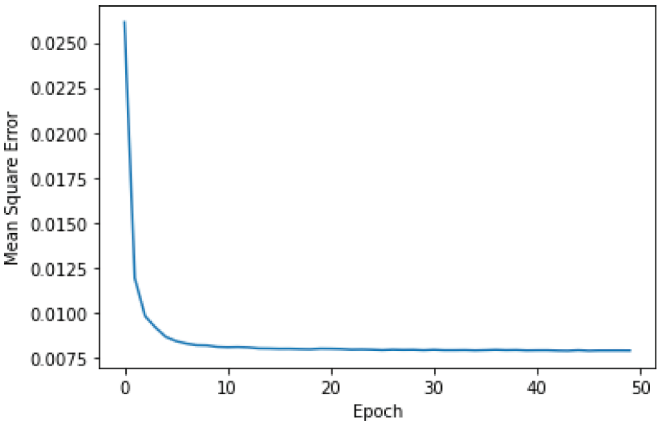


Figure 7. Mean Square Error (MSE) over ANN trainingBottom of form.

3 VALIDATION

The accuracy of the deep learning model developed for this research was evaluated through comparisons with results from FE analysis. One bridge in Illinois was chosen as a case study to test the accuracy of the artificial neural network (ANN) model. This bridge incorporated W30×124 wide flange beam sections for the girders and W12×25 sections for the diaphragms, with an overhang width of 94 cm (37 in) and a maximum braced length of around 6 m (20 ft). The bridge uses pipe-tie systems as the rotation prevention system during construction, resulting in the bridge's B/D ratio of 3.75. The detailed bridge parameters that will be used in the ANN model are shown in Table 3.

Table 3. Bridge configuration for ANN model validation

Item	Value
Girder depth	76.2 cm (30 in)
Girder weight	168 N/m (124 lb/ft)
Diaphragm weight	34 N/m (25 lb/ft)
Overhang width	94 cm (37 in)
B/D Ratio	3.75

The comparison result is shown in Table 4. The FE result indicated a maximum rotation value of 0.208 degrees at the mid-span location. The ANN model shows a very similar value compared with the field data. The results demonstrated that the ANN model developed in this study can accurately predict the maximum exterior girder rotation during bridge deck construction, with a difference of less than 1% for the selected bridge.

Table 4. Comparison of maximum rotation between FE and ANN models

	FE Model	ANN Model
Maximum Rotation	0.2080	0.2096

4 CONCLUSION

The essence of this research was to forge a deep learning model adept at forecasting the maximum rotation of exterior girders during the construction phase of bridge decks. In pursuit of

this goal, an extensive dataset consisting of over 10,000 finite element (FE) models was generated. The complexity of the model was streamlined through feature selection, leveraging P-Values and Pearson's correlation coefficients to mitigate overfitting. The selected parameters for the artificial neural network (ANN) model included girder depth, girder weight, diaphragm weight, overhang width, and the B/D ratio. Validation was performed using field-monitored data from a bridge located in Illinois, and the findings corroborated the model's ability to estimate the maximum exterior girder rotation precisely, bypassing the need for intricate FE modeling. The following conclusion can be drawn based on the findings of this study:

- The B/D ratio emerged as a robust predictor, allowing for the omission of braced length in analyses.
- The conventional weights of the girders, diaphragms, and the overhang width were identified as significant factors influencing exterior girder rotation.
- Variables such as diaphragm depth, girder spacing, and span length were deemed to have minimal effect.
- Consequently, the ANN model devised herein is a potent tool, enabling bridge engineers to assess girder rotation with greater efficacy and expedience.

REFERENCES

American Association of State Highway and Transportation Officials, 2017. AASHTO LRFD Bridge Design Specifications. Washington, D.C.

American Institute of Steel Construction, 2017. Steel Construction Manual, 15th Edition.

Ashiquzzaman, M., Hui, L., Ibrahim, A., Lindquist, W., Panahshahi, N., Hindi, R., 2021. Exterior girder rotation of skew and non-skew bridges during construction. Advances in Structural Engineering 24, 134–146. https://doi.org/10.1177/1369433220945061

Ashiquzzaman, M., Hui, L., Schmeltz, J., Merino, C., Bozkurt, B., Ibrahim, A., Lindquist, W., Hindi, R., 2016. Effectiveness of Exterior Beam Rotation Prevention Systems for Bridge Deck Construction (No. FHWA-ICT-16-015). Illinois Center for Transportation, Springfield, Illinois.

Clifton, S., Bayrak, O., 2008. Bridge Deck Overhang Construction (No. IAC 88-5DD1A003-2). Texas Department of Transportation, Austin, Texas.

Dutta, D., Barai, S.V., 2019. Prediction of Compressive Strength of Concrete: Machine Learning Approaches, in: Rao, A.R.M., Ramanjaneyulu, K. (Eds.), Recent Advances in Structural Engineering, Volume 1, Lecture Notes in Civil Engineering. Springer, Singapore, pp. 503–513. https://doi.org/10.1007/978-981-13-0362-3_40

Faress Hraib, L.H., Brandon Gillis, Miguel Vicente, and Riyadh Hindi, 2020. Evaluation of the Orientation of Concrete Finishing Machines in Skewed Bridges. ACI Symposium Publication 342. https://doi.org/10.14359/51725941

Hraib, F., Hui, L., Vicente, M., Hindi, R., 2019. Evaluation of bridge exterior girder rotation during construction. Engineering Structures 187, 149–160. https://doi.org/10.1016/j.engstruct.2019.02.058

Hui, L., Hraib, F., Gillis, B., Vicente, M., Hindi, R., 2019a. A Simplified method to minimize exterior girder rotation of steel bridges during deck construction. Engineering Structures 183, 84–93. https://doi.org/10.1016/j.engstruct.2019.01.017

Hui, L., Hraib, F., Vicente, M., Hindi, R., 2019b. Effectiveness of Exterior-Beam Rotation-Prevention Systems for Bridge Deck Construction - Phase II (No. FHWA-ICT-19-011). Illinois Center for Transportation, Springfield, Illinois.

Illinois Department of Transportation, 2012. Bridge Manual.

J.D. Fasl, 2008. The Influence of Overhang Construction on Girder Design. University of Texas at Austin.

Roddis, W.M.K., Kriesten, M., Liu, Z., 1999. TORSIONAL ANALYSIS FOR EXTERIOR GIRDERS 128.

Tadesse, Z., Patel, K.A., Chaudhary, S., Nagpal, A.K., 2012. Neural networks for prediction of deflection in composite bridges. Journal of Constructional Steel Research 68, 138–149. https://doi.org/10.1016/j.jcsr.2011.08.003

Yang, S., Helwig, T., Klingner, R., Engelhardt, M., Fasl, J., 2009. Impact of overhang construction on girder design (No. FHWA/TX-10/0-5706-1). University of Texas at Austin.

Bridge Maintenance, Safety, Management, Digitalization and Sustainability – Jensen, Frangopol & Schmidt (eds)
© 2024 The Author(s), ISBN 978-1-032-77040-6
Open Access: www.taylorfrancis.com, CC BY-NC-ND 4.0 license

FEM-based dynamic analysis of noise barriers under train-induced aerodynamic load

Dongyun Liu, Chao Wang, Jaime Gonzalez-Libreros, Yongming Tu, Lennart Elfgren & Gabriel Sas
Department of Civil, Environmental and Natural Resources Engineering, Luleå University of Technology, Sweden

Ola Enoksson & Tommy Höjsten
Trafikverket, Luleå, Sweden

Yongming Tu
School of Civil Engineering, Southeast University, P.R. China

ABSTRACT: Railway noise barriers should provide excellent sound insulation and sufficient load-bearing capacity. High-speed railway noise barriers experience significant and transient aerodynamic loads from passing trains, resulting in noticeable dynamic responses. In this study, three simplified load models were applied to a noise barrier to compare the dynamic responses to those obtained under a reference load from cfd simulations. Results show that the natural frequency of target noise barriers exceeds 10 hz, significantly surpassing the excitation frequency of the train-induced aerodynamic load, thereby minimizing the likelihood of resonance. The displacement or stress evolution closely correlates with the variation in pressure over time. Along the longitudinal direction of the noise barrier, the stress range initially increases, stabilizes, and eventually decreases, reaching its maximum at the penultimate post. Compared to the two simplified rectangular load models, the triangular load model with a distribution load length of 12 m better represents the detailed time-varying aerodynamic load.

1 INTRODUCTION

Railway noise barriers are essential infrastructure in mitigating noise generated by passing trains, particularly along high-speed railway (HSR) lines. The rapid development of HSR and the increase in train speed not only contribute to the increase in railway noise pollution (King, 1996), but also amplify the train-induced aerodynamic effects (Baker, 2010). Hence, besides offering good sound insulation, railway noise barriers must also be able to withstand the external aerodynamic forces generated by passing trains. The rapid shift of train-induced aerodynamic load, from positive to negative pressure in a short period of time, induces a strong dynamic response on the noise barrier alongside the tracks (Zbieć, 2021). Consequently, it becomes necessary to analyze the dynamic behaviors of noise barriers under train-induced aerodynamic loads.

The speed of the train plays a crucial role in influencing the dynamic responses of noise barriers. At speeds below 200 km/h, the impact of train-induced aerodynamic load on the dynamic behavior of noise barriers is limited. However, as train speeds increase, particularly for tall concrete noise barriers with low natural frequencies (approximately 3 – 5 Hz), the maximum strain response escalates significantly. This increase is attributed to the coupling effect of resonance and tail pulse overlap (Tokunaga et al., 2016). A reduction in the distance between the noise barrier and the track center also amplifies the dynamic response of the noise barrier. However, the extent of increase in dynamic response is greater than that of the

DOI: 10.1201/9781003483755-450

pressure magnitude acting on the noise barrier (Olaszek et al., 2020). Additionally, Luo et al. (2016) highlighted that increasing the distance between steel posts significantly intensifies the dynamic responses of noise barriers, resulting in multiple peak values and affecting the overall structural stability of the noise barrier.

In addition, the distribution of train-induced aerodynamic loads also affects the dynamic responses of railway noise barriers. Various calculation models exist for train-induced aerodynamic loads on vertical noise barriers. For instance, the Eurocode EN 14067-4 (CEN European Standard, 2013) offers a rectangular load model with a width of 5 m, while Tokunaga et al. (2016) proposed a triangular load model. Sturt et al. (2022) recommended an adjustment to the Eurocode load model, suggesting an increase in the along-track length of pressure pulses to 12.5 m to align closer with real load curves. Therefore, based on a finite element analysis (FEA) conducted using Abaqus® commercial software, this study compares the dynamic responses under three load models with those obtained from the detailed load curve derived in computational fluid dynamics (CFD) simulations. The purpose is to evaluate the effect of the distribution shape of train-induced aerodynamic load on the dynamic behavior of noise barriers and to determine a simplified load model that can effectively represent the detailed aerodynamic load.

2 FINITE ELEMENT MODELING

2.1 *Railway noise barrier model*

In Sweden, the most common type of railway noise barrier is the steel-post wood-panel structure, depicted in Figure 1. The wooden panels, with an average thickness of 104 mm, are attached to

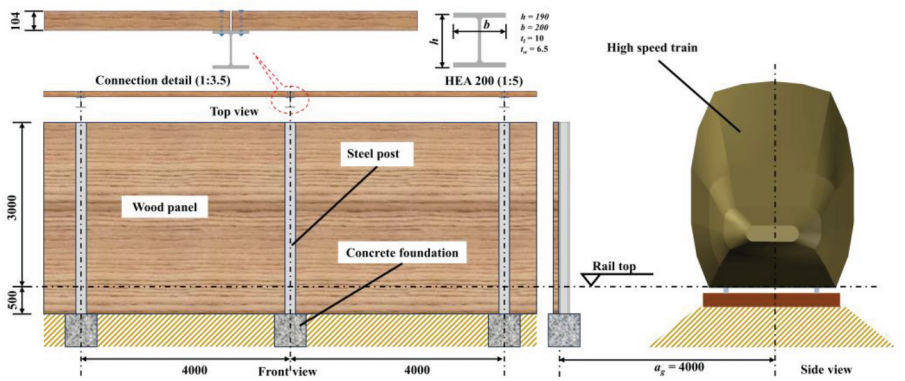


Figure 1. Typical Swedish steel-post wood-panel noise barrier (unit: mm).

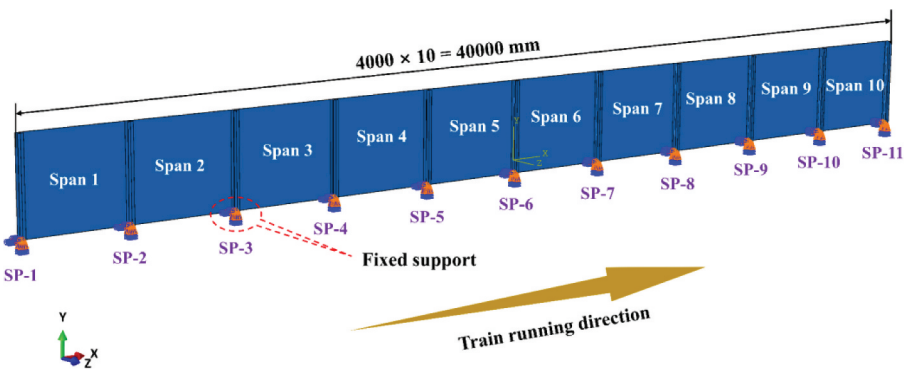


Figure 2. Three-dimensional model of steel-post wood-panel noise barrier in FEA.

Table 1. Material properties of noise barriers.

Components	Materials	Density (kg/m^3)	Elastic modulus (GPa)	Possion's ratio
HEA 200 post	Carbon steel	7850	200	0.29
Wood panel	Larch	500	10	0.40

the steel posts using extended stem bolts. These steel posts are HEA 200 with the cross-sectional dimensions shown in Figure 1, and the wood panels are made of finely sawn larch; their material properties are shown in Table 1. The 3D model employed for FEA is shown in Figure 2. In this study, the target noise barrier spans 40 m, with steel posts placed at 4-m intervals. The assumption made is that the steel posts are securely anchored to the concrete foundations.

2.2 *Train-induced aerodynamic load*

The aerodynamic load induced by passing trains on noise barriers depends on several factors, such as the distance between the noise barrier and the track centre, the speed and type of the high-speed train, etc. In this study, the scenario assumes that the SJ high-speed train X2000 in Sweden is traveling at 80 m/s (288 km/h), passing a 40-m-long single-side noise barrier situated 4 m from the track centre. The train itself is 50 meters in length.

The results obtained from the preliminary CFD simulations indicate that the maximum aerodynamic pressure corresponds to a positive pressure equal to 432 Pa observed at the train nose. The load-time varying curve derived from the CFD simulation is presented in Figure 3-(a). It should be noted that some minor pressure variations at the connections between carriages were not accounted for due to the simplification of the train model in CFD simulations. Therefore, the pressure in the middle train carriages was assumed to be zero.

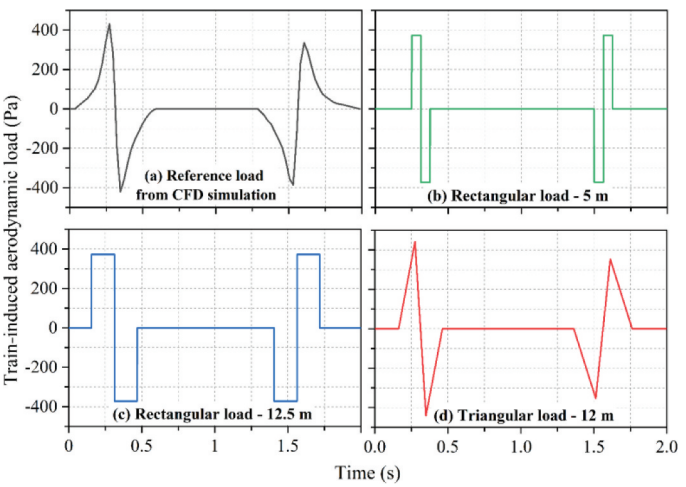


Figure 3. Four time-varying aerodynamic load curves used in this study.

Two rectangular load forms were used with a peak pressure of 373 Pa, calculated using the Eurocode load calculation model, as shown in Equation (1) (CEN European Standard, 2013). This value is lower than the pressure value obtained from CFD simulations, indicating that the Eurocode calculation underestimates the aerodynamic load caused by the SJ high-speed train X2000.

$$P = 0.5 \times \rho \times \mathrm{v}_{\mathrm{tr}}^2 \times k_1 \times \left(\left(2.5/\left(a_g + 0.25\right)^2 \right) + 0.02 \right) \quad (1)$$

where P is the aerodynamic load (MPa); ρ is the air density, 1.225 kg/m^3; v_{tr} is the train speed (m/s); k_1 is the shape coefficient of the train, which is 0.6 for high-speed train; a_{g} is the distance to the track center (m). The peak pressure at the train tail is considered equivalent to that at

the train nose. The main difference between the two rectangular load models lies in the length of load distribution, with the one being 5 m and another one being 12.5 m, as shown in Figure 3(b) and (c). The last one, as shown in Figure 3(d), adopts a triangular load shape with a distribution length of 12 m, as described in Tokunaga et al. (2016). In this triangular model, the maximum load corresponds to the peak value at the train nose obtained from CFD simulations. However, the peak pressure at the train tail amounts to 80% of that at the train nose. Across the three simplified models, each negative pressure peak corresponds to the peak value of the corresponding positive pressure peak. All models considered pressure reduction in the vertical direction, utilizing the pressure height coefficient depicted in Equation (2).

$$C_z = 10.5 \times (z/h)^3 \tag{2}$$

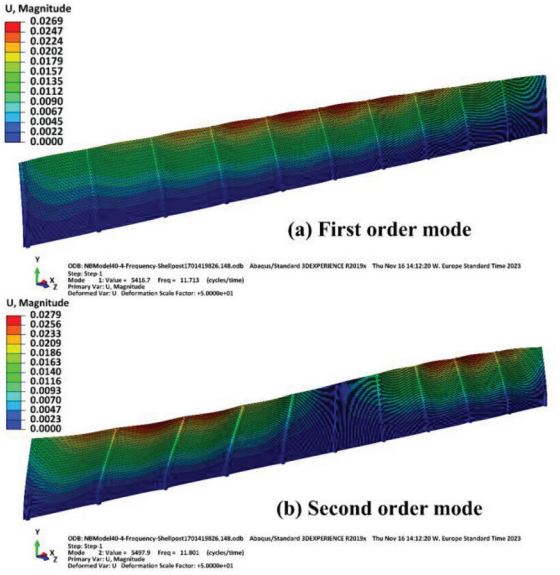
where C_z is the pressure height coefficient; z is the elevation (m); and h is the height of the noise barrier above the rail top (m). The comparison of the four different load models is shown in Figure 3. It is important to note that the aerodynamic load derived from the CFD simulations serves as the reference load model for evaluating the impact of load distribution shapes on dynamic results.

2.3 *Dynamic analysis*

The implicit dynamics analysis method was used to obtain the dynamic responses of the noise barrier under train-induced aerodynamic load. The spatial and temporal distribution of aerodynamic loads on the noise barrier was considered when inputting the loads. The total analysis duration is 4 s, with a time step of 0.000625 s. Shell elements were used for both the steel posts and the wood barrier panels, assuming full connectivity between them. Rayleigh damping coefficients were determined using the first two natural frequencies, as shown in Equations (3) and (4) (Huang et al., 2022).

$$\alpha = 2 \times \xi \times \frac{\omega_1 \omega_2}{\omega_1 + \omega_2} \tag{3}$$

$$\beta = 2 \times \xi \times \frac{1}{\omega_1 + \omega_2} \tag{4}$$



(c) The first ten natural frequencies of noise barriers

Order	Frequency (Hz)
1	11.713
2	11.801
3	11.980
4	12.276
5	12.707
6	13.274
7	13.957
8	14.714
9	15.474
10	16.097

Figure 4. Modal shapes and natural frequencies of the target noise barrier.

where, α and β are the Rayleigh damping coefficients; ξ is the damping ratio, which is 1% in this study (Tokunaga et al. 2016); ω_1 and ω_1 are the first two natural frequencies.

3 RESULTS AND DISCUSSIONS

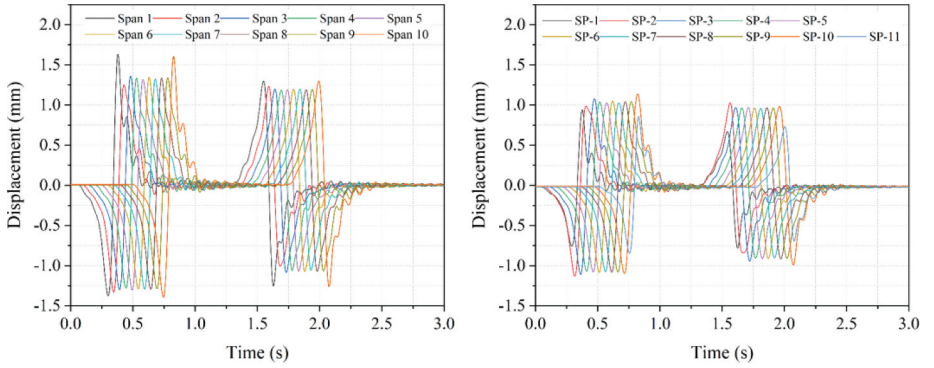
3.1 *Mode analysis of noise barrier*

Before conducting the dynamic analysis, a frequency analysis of the noise barrier was initially performed. This was aimed to assess the potential for resonance effects by comparing the natural frequency with the excitation frequency of the train-induced aerodynamic loads. As illustrated in Figure 4, the first natural frequency measures 11.713 Hz, which is significantly higher than the excitation frequency of train-induced aerodynamic loads, generally remaining below 5 Hz (Liu et al., 2023). Consequently, this indicates that resonance effects are unlikely to occur within this noise barrier structure. Moreover, based on the results of the first two natural frequencies, two Rayleigh damping coefficients for use in the Finite Element Method (FEM) dynamic analysis were determined: 0.1176 and 0.0008, respectively, using Equations (3) and (4).

3.2 *Dynamic responses of noise barrier*

The dynamic responses of the noise barrier under train-induced aerodynamic load (reference load) – including displacement and stress – are shown in Figure 5 and Figure 6. In Figure 5(a), the graph shows the time-varying displacement at the top of the mid-span of each noise barrier panel (Span 1 to 10). The evolution of displacement over time closely mirrors the pressure variation illustrated in Figure 3. The prominent peaks in displacement coincide with the passage of the train's nose and tail through the noise barriers. Damping property of the structure causes the amplitude of dynamic responses to gradually decrease after the train's nose passes, resulting in minimal response fluctuations as the middle car passes through the noise barrier.

The noise barrier panel experiences the greatest displacement at the mid-span of the two end panels, while the displacement at the mid-span of the middle panels does not show a significant difference. This is attributed to the fact that the two end panels are less constrained than the middle panels. Due to their greater stiffness compared to the barrier panels, the displacement at the top of each steel post (SP1 – 11) is smaller than that of the barrier panels, as illustrated in Figure 5(b). Furthermore, in comparison to the middle steel posts, the two end steel posts experience less displacement. Along the longitudinal direction of the noise barrier, the displacement response peaks at the penultimate post. Under the train-induced aerodynamic load, the highest stress is observed at the base of the steel post. Figure 6 illustrates the stress time history for different steel posts. Like the displacement, a notable stress peak occurs as the train's nose



(a) At the mid-span of the wood panels (b) At the top of the steel posts

Figure 5. Displacement time history of noise barrier.

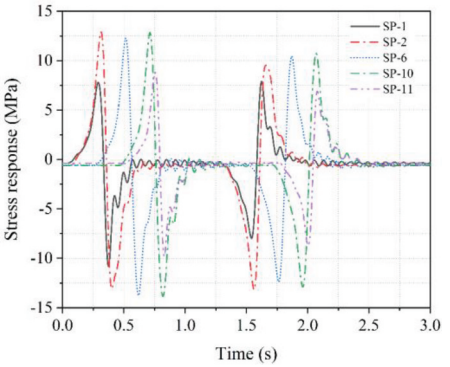


Figure 6. Stress time history at the steel posts of noise barrier.

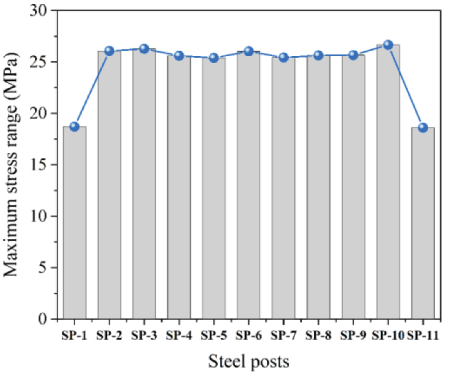


Figure 7. Maximum stress range at the steel posts of noise barrier.

and tail pass through the steel posts. Along the longitudinal direction of the noise barrier, the stress range (i.e., the difference between the maximum and minimum stress), initially increases, stabilizes for a period, and then gradually decreases, as shown in Figure 7. The maximum stress peak among these steel posts is found at the penultimate post.

3.3 *Comparison of dynamic response under different load forms*

The differences in the dynamic responses of noise barriers under the three simplified load models, in comparison to the reference load, are illustrated in Figure 8 and Figure 9. The two rectangular load models induce higher displacement responses at the mid-span of barrier panel Span-5, in contrast to the reference load. Specifically, both rectangular load models with load distribution lengths of 5 m and 12.5 m increase the peak values by 9.28% and 12.31%, respectively, as shown in Table 2. Furthermore, the longer distribution length of the rectangular load with a load distribution length of 12.5 m prolongs the zone of high displacement response. Because it is assumed that the magnitude of the load at the train tail for the two rectangular load models is equal to that of the train nose, the maximum displacement caused by tail wave notably increases. In practical scenarios, the pressure magnitude at the train tail is generally lower than at the train nose. Interestingly, the rectangular load model with a load distribution length of 5 m decreases the stress magnitude at the bottom of the steel post – SP-6. This is because the total moment caused by the rectangular load with a length of 5 m is smaller than the total moment caused by the reference load. Conversely, the second rectangular load model, with a distribution length of 12.5 m, amplifies the stress peak caused by the nose wave, resulting in a 10.52% deviation in stress range compared to the reference load.

In comparison to the rectangular load models, the simplified triangular load more accurately represents the reference load. Table 2 shows that the absolute relative errors for five indicators between the triangular load and the reference load are all below 5%. However, this load model results in a slight decrease in the dynamic responses of the noise barrier. This could be attributed to the shorter length of load distribution in the simplified triangular load model, which is smaller than the actual load distribution length.

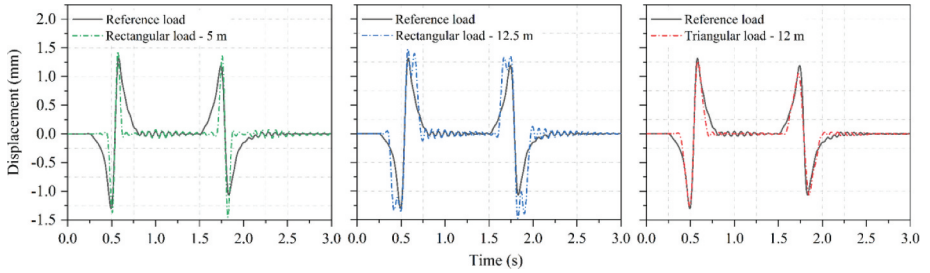


Figure 8. Comparison in displacement time history of Span-5 between different load forms.

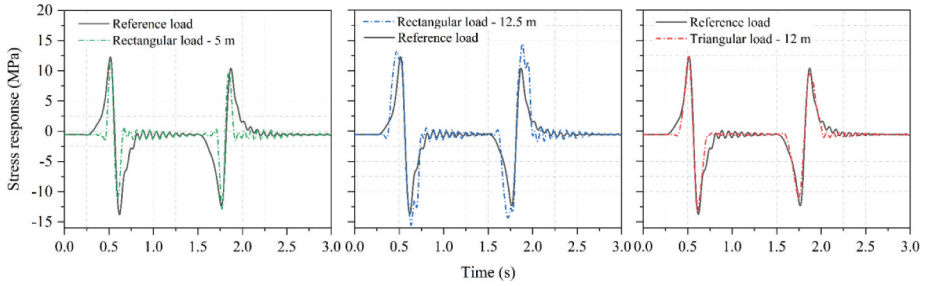


Figure 9. Comparison in stress time history of SP-6 between different load forms.

Table 2. Comparison in peak dynamic responses between different load forms.

Different load form and differences		Displacement of Span 5 (mm) Maximum	Minimum	Stress of SP-6 (MPa) Maximum	Minimum	Stress range
Reference load	Value	1.317	-1.300	12.269	-13.770	26.038
Rectangular load – 5 m	Value	1.439	-1.373	11.625	-10.926	22.551
	RE*	9.28%	5.56%	-5.25%	-20.65%	-13.39%
Rectangular load – 12.5 m	Value	1.479	-1.348	13.212	-15.565	28.777
	RE	12.31%	3.66%	7.69%	13.04%	10.52%
Triangular load – 12 m	Value	1.262	-1.255	12.253	-13.146	25.399
	RE	-4.14%	-3.48%	-0.13%	-4.53%	-2.46%

* Relative error with the value of reference load.

4 CONCLUSIONS

This study conducts a dynamic analysis of high-speed railway noise barriers under train-induced aerodynamic loads using the FEA method. Four distinct load models were employed to investigate the influence of load distribution form on dynamic responses, leading to the following conclusions:

(1) Frequency analysis revealed that the natural frequency of the target noise barrier—steel-post wood-panel noise barrier—is significantly higher than the excitation frequency of train-induced aerodynamic loads, indicating a low likelihood of resonance effects.
(2) The temporal changes in displacement and stress in the noise barrier correspond to the variation in aerodynamic load over time. In the longitudinal direction, stress peaks at the bottom of steel posts initially increase, exhibit minor fluctuations among the middle posts, and eventually decrease, reaching a peak at the penultimate post.
(3) Both rectangular load models, one with a distribution length of 5 m and the other with 12.5 m, induce greater displacements at the mid-span of barrier panels compared to the reference load. The 5 m rectangular distribution model reduces the stress range at the bottom of steel column SP-6 with an absolute relative error of 13.39% compared to the results caused by the reference load, whereas the 12.5 m distribution model increases the stress range, showing an absolute relative error of 10.52%. Conversely, the triangular load model with a 12 m distribution length more accurately represents the reference time-varying load curve compared to the simplified rectangular load models. It exhibits absolute relative errors of below 5% for both displacement and stress ranges.

ACKNOWLEDGEMENTS

This study was financially supported by the Swedish Transport Administration (Trafikverket) through the "Excellence Area 4" and FOI-BBT program (grant number BBT-2019-022).

REFERENCES

Baker, C., 2010. The flow around high speed trains. *Journal of Wind Engineering and Industrial Aerodynamics*, 98 (6–7), 277–298.

CEN European Standard, 2013. EN 14067-4 Railway Applications - Aerodynamics Part 4: Requirements and Test Procedures for Aerodynamics on Open Track.

Huang, J., Li, X., Zhang, J., Sun, Y. and Ren, J., 2022. Determining the Rayleigh damping parameters of flexible pavements for finite element modeling. *Journal of Vibration and Control*, 28(21-22), pp.3181–3194.

King III, W.F., 1996. A précis of developments in the aeroacoustics of fast trains. *Journal of Sound and Vibration*, 193 (1), 349–358.

Liu, D., Wang, C., Gonzalez-Libreros, J., Tu, Y., Elfgren, L. and Sas, G., 2023a. A review on aerodynamic load and dynamic behaviour of railway noise barriers when high-speed trains pass. *Journal of Wind Engineering and Industrial Aerodynamics*, 239, p.105458.

Luo, W., Jiang, J., 2016. Dynamic calculation of noise barrier subjected to impulsive wind pressure based on ANSYS. In: *5th International Conference on Energy and Environmental Protection* (ICEEP 2016). Atlantis Press, pp. 787–791.

Olaszek, P., Sakowski, A., Twardosz, E., Nurek, P., 2020. Tests of dynamic impact from trains on noise barriers. *Roads and Bridges-Drogi i Mosty*, 19 (4), 247–265.

Sturt, R., Lynch, P., Burns, R., Clark, R., Horton, B., Derkowski, P., Keylin, A., Wilson, N., 2022. Aerodynamic Assessment and Mitigation – Design Considerations for High-Speed Rail. U.S. Department of Transportation, Federal Railroad Administration, Office of Research, Development and Technology, Washington, DC20590.

Tokunaga, M., Sogabe, M., Santo, T. and Ono, K., 2016. Dynamic response evaluation of tall noise barrier on high speed railway structures. *Journal of sound and Vibration*, 366, pp.293–308.

Zbieć, A., 2021. Aerodynamic phenomena caused by the passage of a train. Part 1: pressure interaction with objects. *Problemy Kolejnictwa*, 191, 103–112.

Bridge Maintenance, Safety, Management, Digitalization and Sustainability – Jensen, Frangopol & Schmidt (eds)
© 2024 The Author(s), ISBN 978-1-032-77040-6
Open Access: www.taylorfrancis.com, CC BY-NC-ND 4.0 license

Analytical evaluation of Hybrid Deck Bulb Tee for superstructure replacement

P. Agüero-Barrantes
LanammeUCR, Universidad de Costa Rica, San Pedro, Costa Rica

A. Hain
Civil and Environmental Engineering Department, University of Connecticut, Storrs, USA

ABSTRACT: Around 7.5% of bridges in the United States are considered structurally deficient, and the existing backlog for bridge repair costs has reached $125 billion. Looking ahead, there is a growing demand for the replacement of bridges, along with advancements in construction methods and materials to enhance the longevity of these crucial infrastructure assets. To address the shortcomings of traditional prestressed concrete bridge girders, a new hybrid beam element, the Hybrid Deck Bulb Tee (HDBT) is presented. The HDBT utilizes staged fabrication, in which the bottom flange is cast with Ultra High-Performance Concrete (UHPC) and prestressed prior to casting the web and top flange with High Performance Concrete (HPC). The purpose of this study is to analytically evaluate the structural performance of HDBT elements for bridge structures. Three HDBT bridges were designed following the state-of-the-art criteria in regards of UHPC bridge design.

1 INTRODUCTION

Around 7.5% of bridges in the United States are considered structurally deficient, and the existing backlog for bridge repair costs has reached $125 billion (ASCE, 2023). Looking ahead, there is a growing demand for the replacement of bridges, along with advancements in construction methods and materials to enhance the longevity of these crucial infrastructure assets.

Prestressed concrete beams account for more than 40% of bridges spanning over 10 meters (30 feet) (USDOT, 2023). Despite their widespread use, there have been limited advancements in the design and construction of prestressed concrete structures over the past five decades. One instance is the Decked Bulb Tee (DBT) girder, which has been in use since the 1980s with minimal progress in materials and production techniques (Grace et al, 2015).

The fabrication processes of traditional prestressed concrete girder superstructures present four notable drawbacks (Graybeal & Tanesi, 2007; PCI, 2014; Torres et al, 2020): (1) Durability Concerns: Existing prestressed concrete structures exhibit suboptimal durability when exposed to corrosive environments, as evidenced by the pronounced corrosion observed on in-service bridges. (2) Tensile Stress Generation: Standard fabrication methods for prestressed concrete beams unintentionally generate tensile stress at the endzone or result in bursting forces as a consequential effect. (3) Design Limitations: The current design method is constrained by the maximum allowable tensile stress at the extreme fiber of the top flange near both ends, imposing restrictions on the overall structural design. (4) Camber Variations: Variations in the camber of prestressed concrete beams may necessitate substantial corrective measures in the field, introducing challenges in maintaining uniformity during construction.

Recent advancements in cementitious materials present opportunities for advancing both beam design and fabrication procedures, addressing existing constraints in prestressed concrete bridge beams. Notably, the emergence of Ultra High-Performance Concrete (UHPC)

DOI: 10.1201/9781003483755-451

stands out as a significant breakthrough in cement technology over recent decades. UHPC offers notable improvements in tensile strength, compressive strength, permeability resistance, and overall durability when compared to conventional or High-Performance Concrete (HPC) (Graybeal 2011, 2014). Researchers are actively exploring the performance of bridge girders constructed entirely from UHPC (Binard, 2017; El-Helou & Graybeal, 2019). However, it's worth noting that the production of full UHPC girders using standard fabrication methods does not completely address the previously mentioned issues associated with prestressed beams, such as tension in the top flange and unpredictable camber. Sim et al. (2020) specifically discusses the persistent challenge of unpredictable camber in the design of precast, prestressed UHPC elements. Moreover, the existing body of research on prestressed UHPC girders tends to be predominantly focused on long-span bridges exceeding 76.2 meters (250 feet) (El-Helou & Graybeal, 2019; Sim et al., 2020). This focus, however, may not align with the reality that over 95% of girder bridges in the United States have spans under 45.7 meters (150 feet), according to USDOT (2022). Within this span range, there are over 40,000 girder bridges with superstructures considered in fair condition (rating of 5.0) or structurally deficient (rating 4.0 or below). This large number makes them promising candidates for superstructure replacement, highlighting the potential applicability of UHPC in addressing the maintenance and structural needs of a substantial portion of the existing bridge infrastructure.

Another significant consideration arises when comparing superstructures utilizing prestressed High-Performance Concrete (HPC) girders with steel girder superstructures. HPC girders cannot compete with steel girders in terms of dead load and vertical clearance. Therefore, it is currently not always possible to replace steel girder superstructures with prestressed concrete girders. In response to this challenge and the limitations in traditional prestressed beam fabrication, the Hybrid Deck Bulb Tee (HDBT) emerges as a potential solution. The HDBT, a novel hybrid beam element, undergoes a multi-stage fabrication process. Initially, the bottom flange is cast with Ultra High-Performance Concrete (UHPC) and prestressed. Subsequently, the web and top flange are cast with High-Performance Concrete (HPC). The innovative design of the HDBT introduces several advantages: (A) Staged Fabrication for Camber Control: The staged fabrication process enables precise control over camber and the differential camber between units. This control has the potential to eliminate the need for corrective measures in the field, enhancing efficiency and accuracy during construction. (B) Selective Prestressing: Prestressing is selectively induced in the bottom flange, avoiding the development of tension in the top flange and mitigating the risk of cracking in the end zone. This contributes to the structural integrity and longevity of the superstructure. (C) Cost-Effective Material Allocation: The use of UHPC in critical regions and HPC for the web and flange contributes to cost reduction. This strategic material allocation maximizes the benefits of UHPC where its superior properties are most crucial, while maintaining cost-effectiveness through the use of HPC in less demanding areas.

The introduction of the HDBT represents a promising step forward, addressing not only the challenges associated with steel girder replacement but also offering innovative solutions to enhance performance, durability, and cost-effectiveness in the realm of prestressed concrete bridge construction. This research aims to provide an analytical evaluation for the HDBT to show its feasibility for further analysis and experimentation moving forward. The analytical model accounts for the differences in HPC and UHPC materials such as modulus of elasticity, shrinkage and creep behaviors.

2 CONSTRUCION PROCESS OF THE HDBT

The fabrication of the HDBT involves a staged process, shown below in Figure 1. It includes:

- Assemble UHPC Bottom Flange Form: Begin by assembling the form for the Ultra High-Performance Concrete (UHPC) bottom flange.
- Place Steel Reinforcement and Strands: Strategically place steel reinforcement and strands in a manner that ensures the resultant force aligns with the cross-section centroid of the bottom flange (Figure 1a).

- Apply Tension to Strands: Apply tension to the strands to achieve the desired prestress, a crucial step in reinforcing the structure (Figure 1b).
- Cast and Cure UHPC: Pour and cure the UHPC, creating a robust foundation for the bottom flange (Figure 1c).
- Prepare Top Surface of UHPC: Prep the top surface of the UHPC to establish a strong bond with the subsequently applied High-Performance Concrete (HPC).
- Release Strands in Bottom Flange: Once the specified compressive strength is attained, release the strands in the bottom flange. This induces compression to fortify the UHPC bottom flange.
- Shore the Bottom Flange: As camber is not anticipated, shore the bottom flange to set it to the required profile, ensuring structural uniformity (Figure 1d).
- Assemble Web and Top Flange Form: Proceed to assemble the form for the web and top flange, incorporating crack control reinforcement and deck reinforcement (Figure 1e).
- Cast and Cure HPC: Pour and cure the High-Performance Concrete (HPC) to complete the structure, leveraging the superior properties of HPC in specified areas (Figure 1f).
- Remove Forms: Once the HPC reaches the specified strength, remove the forms, revealing the final Hybrid Deck Bulb Tee (HDBT) structure. For a general view, refer to Figure 2a) below, illustrating the schematic of the completed HDBT element.

This planned process ensures the integration of UHPC and HPC components, optimizing the structural performance and durability of the final prestressed concrete element.

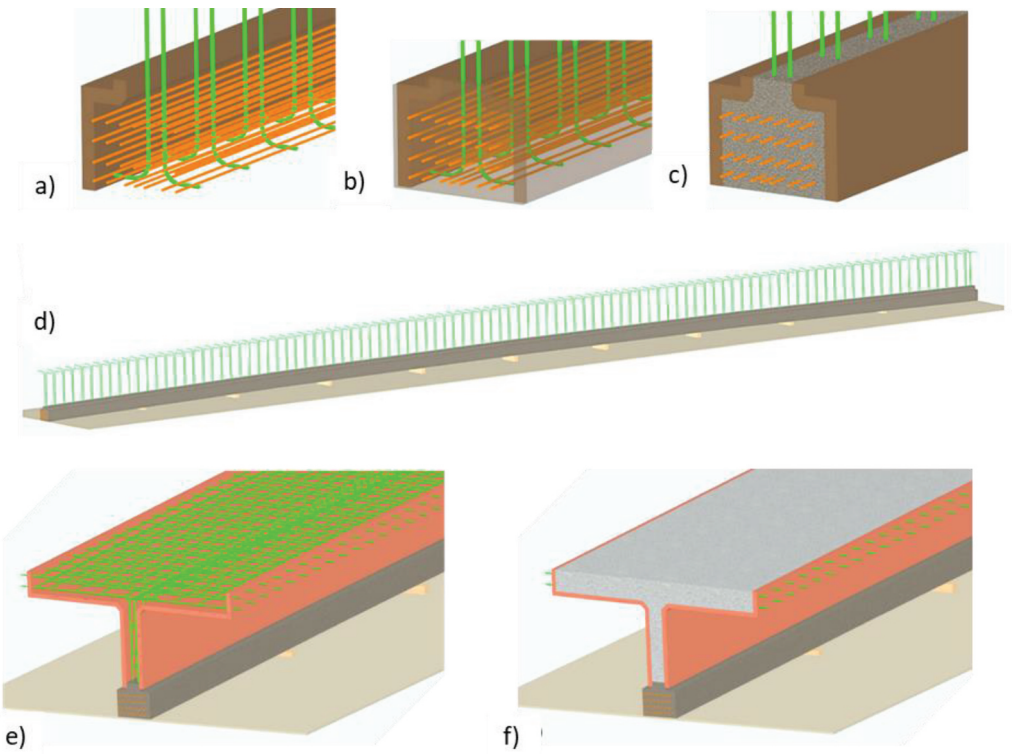


Figure 1. Steps in HDBT fabrication including a) placing reinforcement and strands in form, b) applying tension to strands, and c) casting and curing UHCP bottom flange, d) shoring UHPC bottom flange to set the desired camber, e) assembling forms and placing reinforcement and f) casting the web and top flange with HPC.

3 DESIGN AND ANALYSIS OF THE HDBT

The design process of the HDBT was iterative using CSiBridge (CSI, 2019). An overall view of the completed HDBT is shown in Figure-2a and 2-c. Figure-2b shows a general view of the finite element model. The analysis included all phases of the stage fabrication to capture stress accumulation and strain compatibility between stages. The UHPC bottom flange was modeled with frame elements and included the prestressing strand group that was modeled with a single tendon element with an equivalent area located at the center of gravity of the strand pattern. The HPC web and top flange were modeled with shell elements. The support conditions were defined as a pin-roller condition.

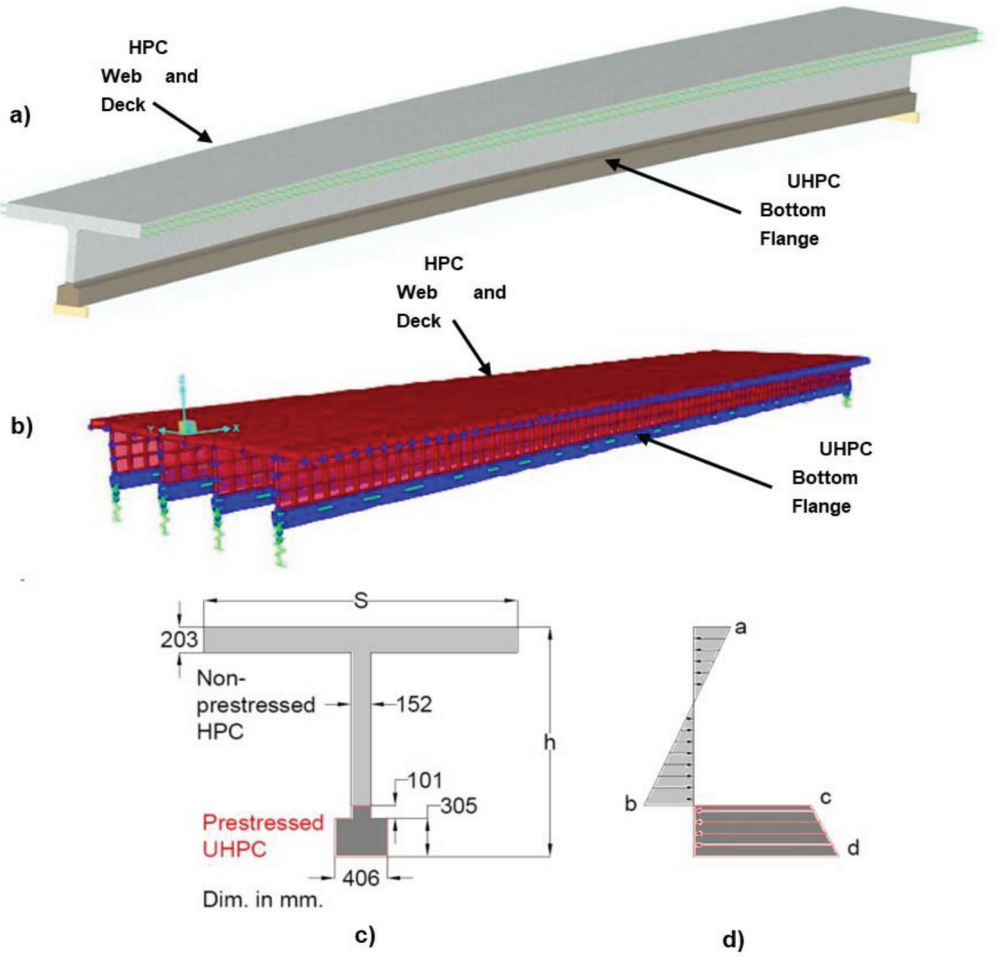


Figure 2. a) Schematic showing final view of HDBT element after form removal; b) 3-D view of model from analysis showing full single span four-beam bridge with HDBT elements; c) interior HDBT beam dimensions shown in millimeters; and d) corresponding flexural stress distribution for service loads.

Strength assessments were conducted utilizing standard design properties for HPC. The moment capacity was established in compliance with the AASHTO LRFD Bridge Design Specifications Section 5.6.3.2. This section details the procedure for calculating the ultimate flexural capacity of a reinforced concrete section, considering the contributions of the compression block in UHPC and the prestressed strands. Shear and interface shear (between different concrete layers) capacities were determined according to Sections 5.7.3.3 and 5.7.4.3

of the AASHTO LRFD, respectively. These provisions set forth guidelines for calculating the necessary vertical reinforcement to resist shear forces and to ensure the integrity of the interface between concrete layers under shear stress.

The modulus of elasticity for both HPC and UHPC was calculated using the formula provided in AASHTO LRFD C5.4.2.4-1. This formula is recommended for accurately predicting the elastic properties of concrete, taking into account factors such as aggregate type and concrete density. The research by El-Helou et al. (2022) supports the use of this equation for both types of concrete, emphasizing its relevance for materials with advanced mechanical properties.

For the distribution of live loads to the superstructure girders, the AASHTO LRFD Bridge Design Specifications Section 4.6.2.2.2 was applied. This section offers a methodology for calculating how live loads are distributed across multiple girders, considering the girders to function collectively as a unit. This approach is crucial for accurately estimating load effects on each girder and ensuring the design accounts for realistic loading scenarios.

Serviceability limit states, including deflection and cracking, were verified following general AASHTO LRFD guidelines applicable to HPC materials. This ensures that the structure maintains its functionality and appearance over time without compromising safety or performance.

Time-dependent losses in UHPC, such as creep and shrinkage, were estimated using the methodology developed by Mohebbi and Graybeal (2022). These factors are critical for long-term performance, as they can significantly affect the prestress forces and, consequently, the structural integrity and serviceability of the bridge.

For the compression stress limits in UHPC, AASHTO LRFD's specifications for conventional concrete were adapted, following the specific recommendations by El-Helou and Graybeal (2022). The tensile stress limit was defined as a fraction of this compression stress limit, incorporating a safety reduction factor of 0.85 to account for the uncertainties associated with material behavior under tensile loading.

A key aspect of the hybrid double-beam technology (HDBT) design is managing the tension stress at the HPC-UHPC interface, particularly at the critical location identified in the study (point b in Figure-2d). The design flexural cracking stress for this interface was assessed according to AASHTO LRFD Section 5.9.5.4.4c, equivalent to the modulus of rupture (Section 5.4.2.6) with a reduction factor of 0.85. This approach allows for a conservative estimation of the tension stress capacity of the HPC web, ensuring that it remains within acceptable limits under service conditions.

To address tensile stresses effectively, the construction process incorporates distributed reinforcement in alignment with AASHTO LRFD Section 5.6.7. This strategy enables bridge owners to define an acceptable level of cracking, thus establishing a specific design criterion that contributes to the long-term structural integrity and performance of the HDBT. While the AASHTO reference sections are for design checks in the United States, similar national codes may be used to extend the design to other countries.

4 EXAMPLE

The following section details a sample design for a 30.5 m (100 ft) single-span bridge. The cross section is composed of four HDBT beams spaced 2.44 m (8 ft). The external beam overhang is 3.5 (1.07m). Therefore, the interior girder width is 2.44 m (8 ft), and the exterior girder width is 7.5 ft in (2.29 m). The web thickness is 152 mm (6 in). The bottom flange is 406 mm (16 in) width and 305 mm (12 in) depth. The total height (labeled as h in Figure 1c) of the section is 1.60 m (63 in). The bridge is designed for AASHTO's HL-93 live load (2020). A 75-mm (3 in) wearing surface and a 7.3 kN/m (0.50 kips/ft) barrier are included as dead load. Regarding the barrier, 50% of the load is applied to the external beam and the remainder to the next internal beam. The deck thickness is 203 mm (8 in), and a 13 mm (0.5 in) asphalt wearing surface is included. The final section geometry is shown below in Figure-2c above.

The wearing surface and parapets are defined as area loads and line loads, respectively. The compressive strength of the UHPC was defined as 100 MPa (14 ksi) at strand release with a 28-day strength of 150 MPa (22 ksi). The UHPC effective cracking stress is assumed as 6.7

MPa (1 ksi). The specified HPC com-pressive strength is 70 MPa (10 ksi). Both concrete materials are normal weight concrete. The strands are grade 1850 MPa (270 ksi). The pre-stressing stress 1388 MPa (202.5 ksi). The relative humidity for losses calculation is 70%.

The PCI Bridge Design Manual (PCI, 2014) was chosen as reference given the availability of multiple preliminary designs, based on AASHTO LRFD Specification 2010 (AASHTO, 2010). Despite the differences between 2010 and 2020 AASHTO Specifications, the PCI Manual is a good reference point. Figure 3 shows the comparison of the total weight of the beam and deck for the different designs, between PCI Manual's preliminary designs (grey bars) and HDBT (blue bars), for both exterior and interior beams (labeled as Ext. and Int. respectively). Regarding dead load, the HDBT is the most efficient design, with a 12 and 16% reduction compared to the next lightest design for interior and exterior beam, respectively. This dead weight can be reduced using lightweight HPC.

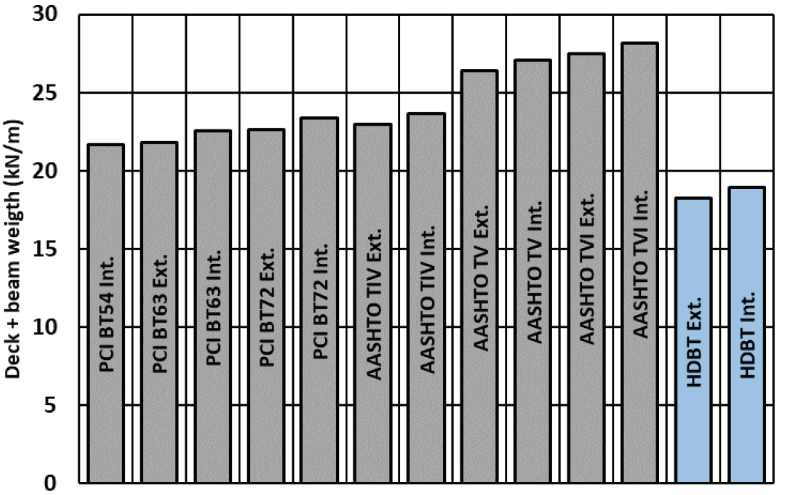


Figure 3. Comparison of beam weights for 30.5-m (100-ft) single span PCI Manual preliminary designs and HDBT preliminary designs for exterior (Ext.) and interior (Int.) beams. Note that barrier, haunch, and wearing weights are not included. PCI BT = PCI Bulb Tee standard section, AASHTO = AASHTO standard section.

5 CONCLUSIONS

This paper introduces a novel prestressed concrete alternative designed for short- and mid-span superstructure replacement projects, presenting a compelling contender to steel girders in terms of weight and section depth. Notably, the fabrication process of the HDBT tackles various challenges associated with existing prestressed concrete girders. By strategically incorporating Ultra UHPC in critical regions and HPC for the web and flange, cost reduction is achieved. This approach ensures a design characterized by predictable camber and the absence of tension in the top flange.

The analytical study conducted for the HDBT demonstrates the structural viability of the proposed design and construction methodology. Notably, it successfully reduces dead load by up to 16% compared to preliminary designs outlined in the PCI Bridge Design Manual. This research provides compelling evidence supporting the feasibility of the HDBT as an effective approach for bridge repair and replacement. With its potential to address current structural deficiencies within the U.S. bridge network, the HDBT emerges as a promising solution for enhancing the overall performance and longevity of bridge structures. As the use of composite and fully UHPC bridge girders increases in prevalence, additional experimental and analytical work is needed to update current design and inspection practices.

REFERENCES

AASHTO (2010). "AASHTO LRFD Bridge Design Specifications, 5th edition"American Association of State Highway and Transportation Officials, Washington D.C. ISBN: 978-1-56051-451-0.

AASHTO (2020). "AASHTO LRFD Bridge Design Specifications, 9th edition" American Association of State Highway and Transportation Officials, Washington D.C. ISBN: 978-1-56051-738-2.

ASCE (2021). "A Comprehensive Assessment of America's Infrastructure: 2021 Report Card for America's Infrastructure". American Society of Civil Engineers. www.infrastructurereportcard.org.

Binard, J. (2017). "UHPC: A game-changing material for PCI bridge producers," PCI Journal, Vol. 62, Issue 2, p.p. 34–46. https://doi.org/10.15554/pcij62.2-01

CSI. (2019). CSiBridge v22 [Computer software]. Computers & Structures Inc. https://www.csiamerica.com/.

El-Helou, R. G., Graybeal, B. A. (2019). "The Ultra Girder: A Design Concept for a 300-foot Single Span Prestressed Ultra-High Performance Concrete Bridge Girder," In Proc. 2nd International Interactive Symposium on Ultra-High Performance Concrete. Ames, IA: Iowa State University Digital Press.

El-Helou, R. G., Graybeal, B. A. (2022). "Flexural Behavior and Design of Ultrahigh-Performance Concrete Beams". J. Struct. Eng., 2022, 148(4): 04022013. DOI: 10.1061/(ASCE)ST.1943-541X.0003246.

El-Helou, R. G., Z. B. Haber, and B. A. Graybeal. (2022). "Mechanical behavior and design properties of ultra-high performance concrete." ACI Mater. J. 119 (1). https://doi.org/10.14359/5173419.

Grace, N. F., Bebawy, M., and Kasabasic, M. (2015). "Evaluation and analysis of decked bulb T beam bridges". Transportation Pooled Fund Program, Federal Project Number: TPF-5(254). Lawrence Technological University. Dept. of Civil Engineering, Southfield, MI, USA.

Graybeal, B. A., Tanesi, J. (2007). "Durability of an ultrahigh-performance concrete". Journal of materials in civil engineering, 19(10), pp. 848–854. DOI: 10.1061/(ASCE)0899-1561(2007)19:10(848).

Graybeal, B. A. (2011). "Ultra-High Performance Concrete". FHWA Publication No.: FHWA-HRT-11-038. Federal Highway Administration, Washington, DC.

Graybeal, B. A. (2014). "Design and construction of field-cast UHPC connections". FHWA Publication No.: FHWA-HRT-14-084. United States Department of Transportation, Federal Highway Administration.

Graybeal, B. A., El-Helou, R. G., (2019) "Development of an AASHTO Guide Specification for UHPC", International Interactive Symposium on Ultra-High Performance Concrete 2(1). doi: https://doi.org/10.21838/uhpc.9708.

Mohebbi, A., Graybeal, B. (2022). "Prestress loss model for ultra-high performance concrete". Engineering Structures 252 (2022) 113645. https://doi.org/10.1016/j.engstruct.2021.113645.

PCI (2014). "PCI Bridge Design Manual". 3rd Edition, Second release. MNL-33-14. Precast/Prestressed Concrete Institute. ISBN 978-0-9797042-4-6.

Sim, C., Tadros, M., Gee, D., Asaad, M. (2020). "Flexural design of precast, prestressed ultra-high-performance concrete members". PCI Journal (ISSN 0887-9672) V. 65, No. 6, November–December 2020. https://doi.org/10.15554/pcij65.6-02.

Torres, E., Hamilton, H. R. and Consolazio, G. R. (2020). "Hybrid Prestressed Concrete Bridge Girders using Ultra-High Performance Concrete". University of Florida. UF Project No. P0086443 & P0086444. Sponsor: Florida Department of Transportation (FDOT). FDOT Contract No. BDV31-977-101.

USDOT. (2023). "LTBP InfoBridge - Data." United States Department of Transportation, Federal Highway Administration. Available at: https://infobridge.fhwa.dot.gov/Data.

Bridge Maintenance, Safety, Management, Digitalization and Sustainability – Jensen, Frangopol & Schmidt (eds)
© 2024 The Author(s), ISBN 978-1-032-77040-6
Open Access: www.taylorfrancis.com, CC BY-NC-ND 4.0 license

PCA-based technique to assess the modal properties of the Itacaiúnas bridge during flooding

R. Lopes & J. Weyl
Universidade Federal do Pará, Belém, Pará, Brazil

V. Barros & T. Bittencourt
Universidade de São Paulo, São Paulo, Brazil

ABSTRACT: The monitoring of bridges is important to ensure structural safety throughout the life-cycle of the enterprise. Environmental effects such as increased water volume in rivers can cause considerable changes in the data provided by instrumentation, sometimes making it challenging to identify whether the structure is exhibiting a damage pattern or just indicating a change in structural behavior due to an environmental component. In some regions of the state of Pará/Brazil, rivers can rise up to 10 meters during flood periods. This characteristic makes bridges in these regions good candidates for testing classification and damage pattern recognition algorithms. Techniques for detecting damage in large structures have been successfully applied in several case studies. Works based on principal component analysis (PCA) have been widely performed due to the ease of implementation of the algorithm and the efficiency in extracting patterns that are important in structural response. In this work, PCA, T^2-statistic and Q-statistic were used to evaluate the influence of the effect of floods on the modal properties of the bridge over the Itacaiúnas River. The acceleration data for this structure was obtained at two times: flood period in 2018 and dry period in 2021. The results indicate that the increase in river level causes a decrease in frequencies in the vibration modes of the structure. Furthermore, the use of PCA proved capable of discriminating characteristics from environmental effects.

1 INTRODUCTION

The monitoring of large bridges is generally costly and time-consuming process. Procedures to increase the efficiency of detecting changes in structural behavior have improved over the years, allowing extraction of important features without the need for extensive tests. Most of these techniques focus on detecting damage using vibration responses, but they can also be used to evaluate variations in the load effecting structures. According to Turrisi (2022), one of the major technical challenges faced by SHM when dealing with real-world structures under operational conditions is the significant impact of external factors on measured signals, commonly referred to as environmental and operational variables. According to Mujica (2010), any damage will change this vibration response, as well as the transient caused by a wave propagating through the structure. In addition to structural damage, the dynamic characteristics of structures are also affected by typical environmental variations, Sen (2019). However, environmental variations that inevitably occur during different data acquisition time periods also cause changes in vibration features, Yan (2005). Some loads can change the boundary conditions, resulting in changes to the structure's stiffness. This change does not indicate damage but results in a variation in vibration response, which can be detected by damage detection algorithms. In this paper explains how to use PCA to define indices capable of detecting variations in the structural responses of the Itacaiúnas Bridge.

DOI: 10.1201/9781003483755-452

2 PRINCIPAL COMPONENT ANALYSIS

PCA is used to estimate principal directions where maximum variability exists and redundance is minimal. These directions are obtained by transforming the original data set into a new coordinate system where the variables are uncorrelated. The eigenvector used to transform the data are sorted in descending order of their associated eigenvalues. The eigenvectors with the highest eigenvalues are chosen to represent most of the system's variability, allowing for the reduction of data dimension by selecting a few principal components. The techniques to applying PCA are described below.

Firstly, the data collected was arranged in a matrix $\mathbf{X}_{n\times m}$, where each row vector represents measurements of the sensors, and each column represents measurements from different experiment trials. If the data set has measurements with different magnitudes and scales is important to normalize the data set before analysis. Then the covariance matrix $\mathbf{C}_X$ is defined and the eigenvalues and eigenvectors are determined.

$$C_X \mathrm{P} = \mathrm{P}\Lambda \tag{1}$$

where **P** = eigenvectors; and Λ = eigenvalues

Matrix **P** is used to determine matrix **T**, that contain the original data transformed over the direction of the principal components.

$$T = XP \tag{2}$$

After applying the dimension reduction is not possible to recover completely **X**, but a matrix projected onto the principal components can be found:

$$\hat{X} = TP^T \tag{3}$$

Then the original data **X** can be represented as a sum of the matrix $\hat{X}$ and the projection on the residual left components $\bar{X}$:

$$X = \hat{X} + \bar{X} \tag{4}$$

3 DETECTING CHANGES IN STRUCTURAL BEHAVIOR

In this work were used two indices to detect chances in data collected: Q-statistic and T^2-statistic. The first one is based on analyzing the residual data matrix $\bar{X}$ to represent the variability of the data projection in the residual subspace. The second method is based in analyzing the score matrix **T** to check the variability of the projected data in the new space of the principal components, Mujica (2010)

The T^2-statistic indicate an abnormal behavior within the normal subspace and is defined in the form:

$$T_i^2 = t_{si}\Lambda^{-1}t_{si}^T \tag{5}$$

where $\boldsymbol{t_{si}}$ is a projection of the ith trial; and Λ^{-1} is the inverse of the diagonal matrix composed of eigenvalues.

The Q-statistic is measure of the difference between the sample and its projection onto the principal components retained in the model.

$$Q = \bar{x}_i\bar{x}_i^T \tag{6}$$

4 METHODOLOGY

In this study, a training set was created using the power spectrum density (PSD) from acceleration data collected during 9 trials in 2021. This dataset was considered normal condition as the monitoring period was outside the flood season in the region. After applying PCA, a baseline was built with the projection matrix. The monitoring was performed positioning accelerometers on both sides of the deck section and acquiring signal at a frequency of 100 Hz for 20 minutes. The acquisition points were varied at intervals of 30 meters for the central span and 35 meters for the other spans.

The principal components from the baseline model were used to project the data collected in 2018 (flood season in the region). This test set was obtained under the same conditions as 2021 (PSD from 9 experiments). For the two datasets (training and test), the T^2-statistic e Q-statistic were calculated and then compared. Figure 1 shows the power spectrum densities from the accelerations acquired in 2021 (Training Set)

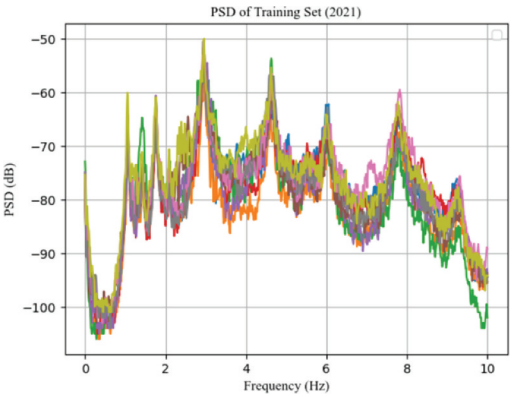


Figure 1. PSD from acceleration collected In 2021.

5 CASE STUDY: ITACAIÚNAS BRIDGE

The Itacaiúnas Bridge is located in the city of Marabá, in the state of Pará, Brazil. The structure consists of 3 spans, with a central span of 120 m and the others of 70 m. The structure was monitored with accelerometers in 2018 (river level ≈ 13.60 m) and 2021 (river level ≈ 3.10 m). Figures 2–3 shows the geometric characteristics of the Itacaiúnas bridge. Figure 4 shows the equipment used to collect celebrations.

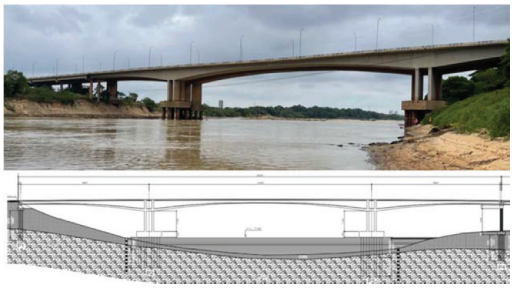


Figure 2. Itacaiúnas bridge.

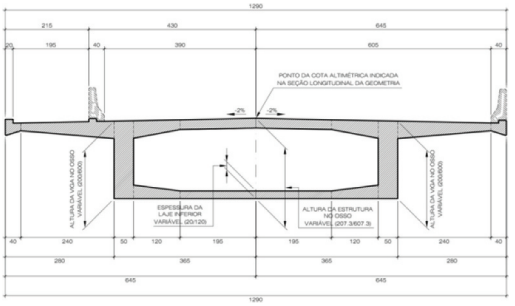


Figure 3. Cross section in mid of central span.



Figure 4. Accelerometer used in each experiment.

6 RESULTS

The vibration frequency of the bridge was estimated based on acceleration data collected in 2018 and 2021. The magnitude of the frequencies indicates that there is different structural behavior occurring between the training and test set. Table 1 shows that the difference between the frequencies in different years is small. Figure 5 also shows how small the difference between the frequencies is.

Table 1. Frequency under operational vibration.

Mode number	Training Set Frequency (Hz)	Test Set Frequency (Hz)
1	1.06	1.04
2	1.41	1.41
3	1.760	1.73
4	2.10	2.08
5	2.94	2.90
6	4.62	4.58

Due to the difficulty in distinguishing the change in structural behavior, the T^2-statistic and the Q-statistic were plotted to verify their ability to indicate any abnormality. Figure 6 shows that the Q-statistic was not sufficient to differentiate the behaviors between training and test set.

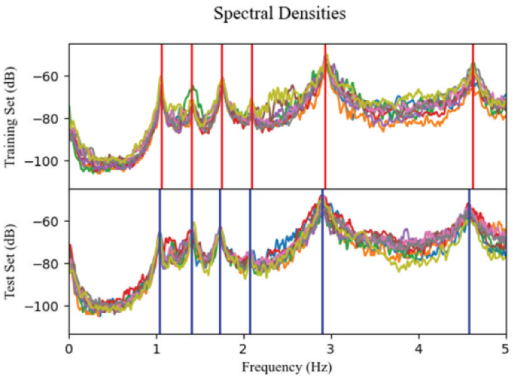


Figure 5. Vibration frequencies in training and test set.

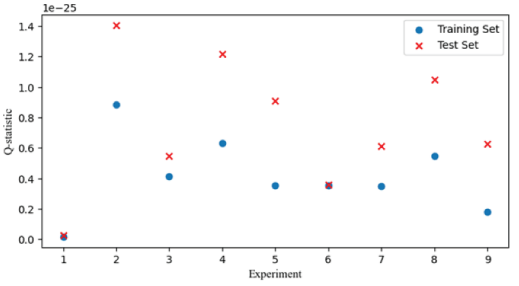


Figure 6. Q-statistic for each experiment.

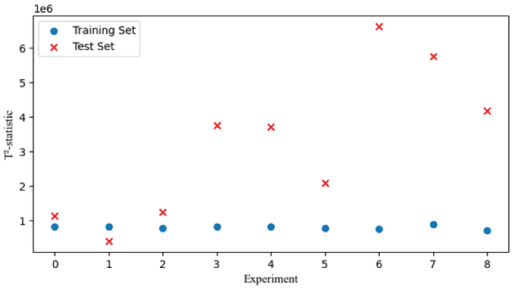


Figure 7. T²-statistic for each experiment.

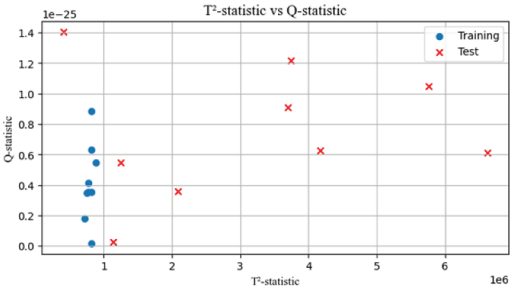


Figure 8. Match of the q-statistic and T²-statistic.

Figure 7 Shows that the T^2-statistic provides better conditions for distinguishing changes in structural behavior. The training set has almost the same magnitude in each experiment, while the test set has larger differences in each experiment. Figure 8 shows that the best way to detect a change in the structural behavior due to the flood in the river is to match the Q-statistic and T^2- statistic indices in the same plot. It is clearly visible that the training set is concentrated in the left side of the plot, while the test set is scattered on the right side of the plot.

7 CONCLUSION

This study shows an application of PCA and Q-statistic and T^2-statistic indices to detect changes in structural behavior due to increases of river level. The results show that matching both indices in the same plot is a good way to identify abnormal behaviors. This methodology is an alternative when the frequency magnitude of different monitoring is too close to detect variations in the load acting on the structure.

More experiments in different levels of the river would be important to test the capability of the methodology to be applied in larger structures. The structure will be monitored continuously during the next two years and then the proposed indices will be updated.

The influence of the temperature effects was not evaluated because average temperatures in north Brazil do not vary throughout the year.

ACKNOWLEDGMENTS

The authors thank the support provided by grant 2022/10105-3, São Paulo Research Foundation (FAPESP). The authors acknowledge Laura Souza, Elói Figueiredo and Ionut Moldovan for their support during the data acquisition processes.

REFERENCES

Mujica, L. E., Rodellar, J., Fernández, A., & Güemes, A. 2011. Q-statistic and t2-statistic pca-based measures for damage assessment in structures. *Structural Health Monitoring*, *10*(5), 539–553.

Sen, D., Erazo, K., Zhang, W., Nagarajaiah, S., & Sun, L. 2019. On the effectiveness of principal component analysis for decoupling structural damage and environmental effects in bridge structures. *Journal of Sound and Vibration*, *457*, 280–298.

Turrisi, S., Cigada, A., & Zappa, E. 2022. A cointegration-based approach for automatic anomalies detection in large-scale structures. *Mechanical Systems and Signal Processing*, 166.

Yan, A. M., Kerschen, G., de Boe, P., & Golinval, J. C. 2005. Structural damage diagnosis under varying environmental conditions - Part II: Local PCA for non-linear cases. *Mechanical Systems and Signal Processing*, *19*(4), 865–880.

Abdel-Qader, I., Pashaie-Rad, S., Abudayyeh, O., & Yehia, S. 2006. PCA-Based algorithm for unsupervised bridge crack detection.*Advances in Engineering Software*, *37*(12), 771–778.

Datteo, A., Lucà, F., & Busca, G. 2017. Statistical pattern recognition approach for long-time monitoring of the G.Meazza stadium by means of AR models and PCA. *Engineering Structures, 153, 317–333.*

Bridge Maintenance, Safety, Management, Digitalization and Sustainability – Jensen, Frangopol & Schmidt (eds)
© 2024 The Author(s), ISBN 978-1-032-77040-6
Open Access: www.taylorfrancis.com, CC BY-NC-ND 4.0 license

Recommendations for structural assessment of RC slabs using the finite element method

Mario Plos
Swedish Transport Administration, Göteborg, Sweden

Morgan Johansson
Chalmers University of Technology and Norconsult AB, Göteborg, Sweden

Kamyab Zandi
Timezyx Inc., Vancouver, Canada

Jiangpeng Shu
College of Civil Engineering and Architecture, Zhejiang University, Hangzhou, China

ABSTRACT: To mitigate environmental impact and societal costs, there is a need to extend the lifetime of existing transportation infrastructure. Research has shown that many structures, such as bridges, have a substantial inherent load-carrying capacity that is often not fully utilized. In the research presented, it was shown how non-linear numerical analysis can be used to show higher performance and longer lifetime than with conventional engineering methods. Comprehensive recommendations for use in engineering practice have been developed for the structural assessment of reinforced concrete slabs using the finite element method. A multi-level structural assessment strategy was developed to provide a framework for successively improved and more advanced analysis. For the more advanced levels, non-linear FE analysis is used, adopting a global safety format and incorporating the effects of deterioration. With such analyses, the structural behaviour can be more accurately described and higher, yet conservative load-carrying capacities can generally be demonstrated.

1 INTRODUCTION

To reduce environmental impact and carbon emissions, and to optimise the utilization of the society´s resources, it is of outermost importance that the huge investments in transportation infrastructure are well managed. It is imperative that existing structures must be utilized during their entire lifetime with respect to function and safety, and their capacity must be fully used to meet higher demands from the transportation industry. When assessing existing structures, many of these shows insufficient load-carrying capacity, often accompanied by uncertainties regarding the structural behaviour. However, tests on real structures as well as experience with advanced assessment methods shows that existing structures often have substantially higher intrinsic capacity and a more complex structural response than shown with conventional assessment methods, see e.g. Bagge at al. (2018).

For design and assessment of reinforced concrete structures, simplified analysis methods and code provisions are commonly used. For structural analysis, the linear finite element (FE) method is common. However, for the assessment of existing structures, a greater effort with more advanced methods for structural analysis is often motivated. Research as well as experience from engineering practice has shown that non-linear FE analysis provides great possibilities of achieving a better understanding of the structural response, and have demonstrated the potential to reveal higher load-carrying capacity, see e.g. Shu et al. (2018) and Bagge et al. (2019).

DOI: 10.1201/9781003483755-453

Today, non-linear FE analysis is a standard method within research, but it is still sparsely used in engineering practice. This is partly because the method is more demanding, but also because it includes many uncertainties regarding in-data, modelling choices and result interpretation. There has also been concerns regarding the safety format since the partial factor method, normally used in design, may be questioned in the context of non-linear analyses.

The goal of the work presented was to develop detailed recommendations for how non-linear FE analysis can be utilized for structural assessment of reinforced concrete structures in engineering practice. The work focused on reinforced concrete (RC) slabs, but the principles, strategies and many of the methods developed are generally applicable. The objectives of the work were to (1) develop a methodology for incorporating non-linear FE analysis in successively improved structural assessment, (2) develop analysis methods for different levels of assessment of RC slabs and (3) through examples demonstrate and show the potential of the recommended approach. The research methods used included literature studies, laboratory tests, analytical and numerical analyses as well as parameter studies. In addition, the methodology and recommendations presented are founded in the authors' own long experience of non-linear analysis and structural assessment, within research as well as in engineering practice.

2 A MULTI-LEVEL ASSESSMENT STRATEGY

The assessment strategy is based on a stepwise approach where the structural assessment is made with successively more sophisticated methods for evaluation, see e.g. Sustainable Bridges (2007). These can consist of more advanced structural analysis methods, improved knowledge of the structure and its condition, and with safety formats suitable for the analysis methods employed. In Figure 1, a principal flow diagram for the assessment process is shown.

A Multi-Level Assessment Strategy was proposed in Plos et al. (2017) to facilitate enhanced assessment through successively improved structural analysis and resistance evaluation. The framework also provided a structured approach to the use of non-linear FE analysis for structural assessment of RC slabs. Five different assessment levels were proposed, see Figure 2. The assessment starts with traditional simplified analysis methods (Level I), followed by the currently dominating linear FE analysis method (Level II). The higher levels (Levels III – V) involves non-linear FE analysis on different levels of detailing.

A non-linear FE analysis simulates the response of the structure. It resembles the structural behaviour under successively increased loads, possibly up to and beyond the failure of the structure. This means that the load-carrying capacity can be evaluated from the non-linear analysis directly, provided it is sufficiently detailed to reflect the governing failure mode. If all possible failure modes of interest are not reflected in the analysis, the related action effects from the analysis must instead be compared to local resistances for these failure modes, similarly as in standard design methods. This is the case for some of the failure modes at Levels III and IV, see Figure 2.

While the common resistance models from e.g. Eurocode 2 (2004) are used at Levels I and II, higher Level-of-Approximation resistance models from Model Code 2010, fib (2013), are proposed for Levels III and IV. The five assessment levels are briefly described below.

- Level I: Simplified analysis methods: 2D linear beam or frame analysis, tabulated solutions or plasticity-based analysis like the strip method or the yield line method.
- Level II: 3D linear FE analysis: Generally shell element analysis. Modelling and redistribution of stress concentrations according to e.g. Pacoste et al. (2012).
- Level III: 3D non-linear shell FE analysis: Non-linear material properties of concrete and reinforcement, including concrete cracking and crushing and reinforcement yielding, Perfect reinforcement-concrete bond is assumed. Bending failures are reflected in the global analysis, while shear type and anchorage failures are checked separately.
- Level IV: 3D non-linear FE analysis with continuum elements: Here also shear type failures, including punching, can be reflected with sufficiently dense element mesh.
- Level V: 3D non-linear FE analysis with continuum elements including reinforcement-concrete bond-slip: With even finer mesh resolution also anchorage failure and realistic crack distribution can be reflected. No major failure modes are checked separately.

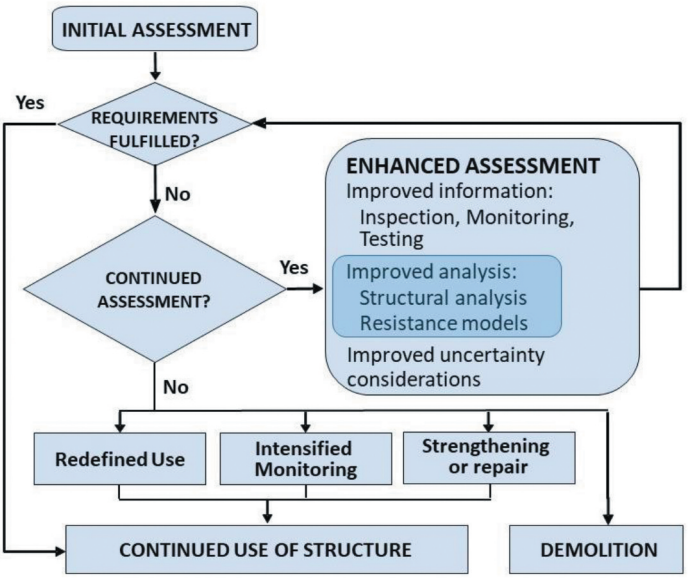


Figure 1. Flow diagram for successively improved structural assessment. Based on Plos et al. (2021).

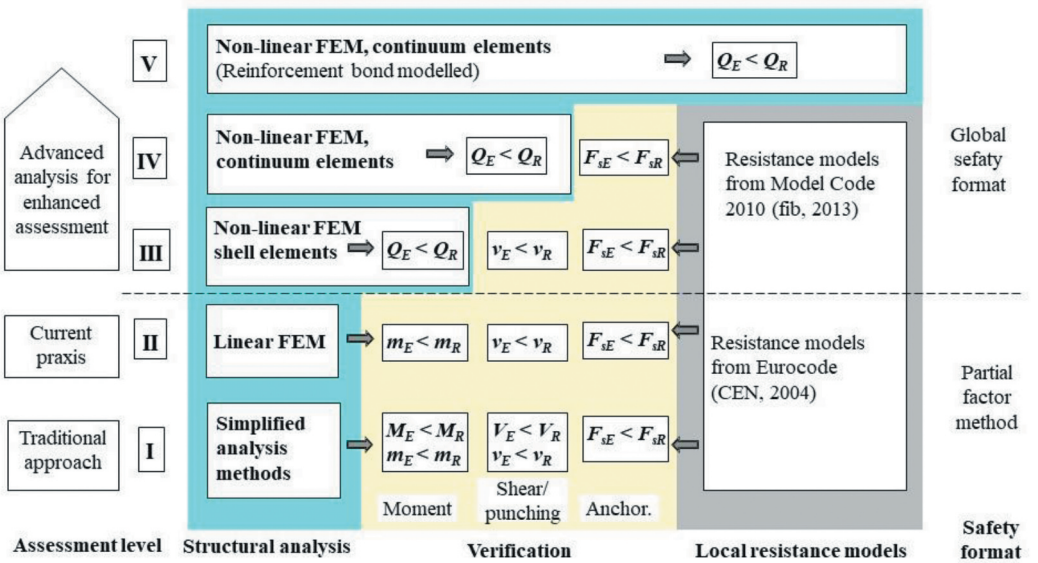


Figure 2. Illustration of the Multi-Level Assessment Strategy for RC slabs. From Plos et al. (2017, 2021).

It must be emphasized that in practical terms, it is necessary to start the assessment with analyses on the lower load levels, i.e. Levels I or II. With such an analysis, the structure can be assessed for a great number of load combinations and load positions. As the analysis progresses to non-linear stages, the response becomes history-dependent and load effects from different loads cannot be combined. Instead, a separate non-linear analysis must be made for each combination of loads studied. Since it is comparably more time consuming and computationally demanding to do a non-linear analysis, such analyses are recommended for evaluating a limited number of critical load combinations, previously identified on lower assessment levels.

For analysis with simplified methods or linear FE analysis according to current standards (Levels I & II), the partial factor method is used to meet the safety demands. However, a non-linear FE analysis simulates the response of a structure during successive loading to failure for a specific load combination. It can be seen as a virtual testing of the existing structure as a whole and is by its nature always a global type of assessment. Consequently, global safety factor methods are recommended for use in combination with non-linear finite analyses for assessment on Levels III, IV and V. In Plos et al. (2021), detailed recommendations are given for their application.

3 NON-LINEAR FE ANALYSIS

For analysis on different levels of detailing, structural analysis methods were developed and proven feasible for the assessment of existing concrete slabs, see Shu et al. (2015, 2016, 2017). The analysis methods were verified through comparison with laboratory tests. Sensitivity studies of modelling choice were made for slabs subjected to bending as well as shear type failures. Detailed recommendations for application of the analysis methods on the different assessment levels are given in Plos et al. (2021). In particular, detailed recommendations regarding modelling, analysis and evaluation for non-linear FEM is given for analysis with shell elements (Level III) and continuum elements (Level IV and V). How the global safety format and the resistance models from Model Code 2010, fib (2013), can be applied on each level is described, in combination with the non-linear analyses.

In addition to the detailed recommendations for RC slabs, general recommendations for modelling and analysis of concrete structures with non-linear FEM are given in Plos et al. (2021) . Many of the challenges and questions that a practicing structural engineer is facing when performing this kind of analysis are addressed and recommendations are given regarding modelling choices and application of the methods. Detailed guidelines are provided regarding determination of material parameters and other in-data for the analyses. Advices are given for quality check and interpretation of analysis results.

The response in a non-linear analysis is history dependent. The order in which the loads are applied may therefore be important. It can influence the response during loading, but also the interpretation of the obtained failure load. Since detailed rules on this are not available in standards or codes, recommendations are given for the load application in non-linear analysis.

When the structure is deteriorated due to, for instance, reinforcement corrosion or frost damage, the structural effect of the deterioration needs to be counted for in the structural analysis or in local resistance models, see e.g. Zandi (2010). For different levels of assessment, recommendations are given in Plos et al. (2021) on how the effect of such deteriorations can be included as a change in material properties, cross-sectional area of the concrete and reinforcement, and bond properties between reinforcement and concrete.

4 EXAMPLES

The feasibility and potential of the assessment strategy and the analysis methods were shown through applications to laboratory tests as well as real structures, see Shu et al. (2015, 2016, 2017, 2018, 2019). In Plos et al. (2021), they are demonstrated in three examples. In two of the examples, concrete slabs previously tested in laboratory by Fall et al. (2014) and Vaz Rodrigues (2007) were studied. In Figure 3, the analyses on different levels are illustrated. The potential to demonstrate higher load-carrying capacity was demonstrated through comparison between test results and analyses on different levels. In the third example, the strategy was demonstrated on an existing bridge with future (hypothetical) deterioration from reinforcement corrosion and frost, including the application of the global safety format. Figure 4 summarises the load-carrying capacities possible to demonstrate through analyses on the different assessment levels. For the slabs tested in laboratory, the load-carrying capacity relates to the measured failure load. For the composite bridge deck slab, it relates to the capacity demonstrated with non-linear FEM on level IV.

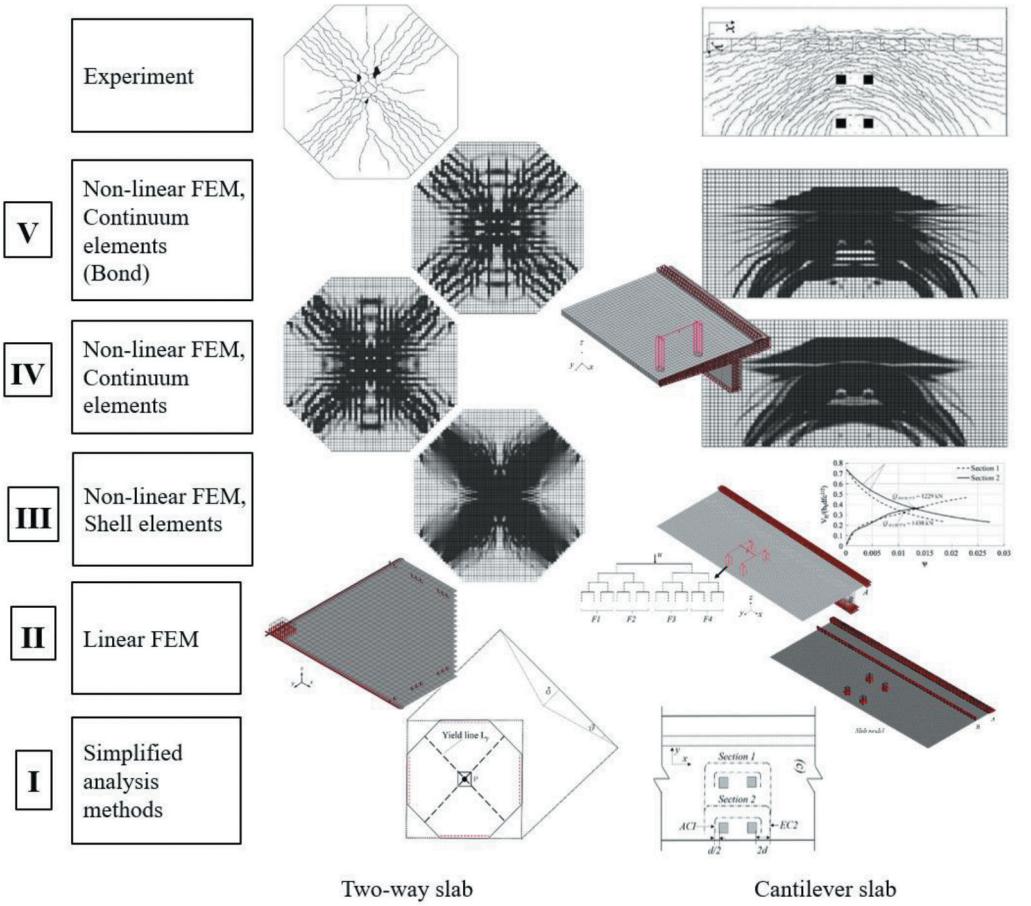


Figure 3. Illustration of analyses on different levels of accuracy, for slabs tested in laboratory. From Plos et al. (2021). Test performed by Fall et al. (2014) and Vaz Rodrigues (2007).

5 CONCLUSIONS

To facilitate the use of advanced analysis methods in engineering practice, recommendations were developed for structural assessment of RC slabs, Plos et al. (2021). A methodology for successively improved assessment, and analysis methods for different levels of assessment were developed. The methods recommended are intended for use in engineering practice and follows current standards and established handbooks such as CEN (2004) and fib (2013). They are intended to give conservative estimates of the load-carrying capacity, fulfilling the required safety level. While the recommendations are formulated for RC slabs, the underlying principles are universal and many of the recommendations are relevant also for other type of structures. Plos et al. (2021) provides a clear framework for structural assessment of RC structures, gives detailed recommendations for analyses on different levels of detailing and includes examples showing the application.

In the examples, it was demonstrated how more accurate assessment can be made using non-linear FE analysis for cases where simplified analysis cannot demonstrate sufficient load-carrying capacity. A substantially higher part of the intrinsic capacity of the structure could be demonstrated using more advanced analyses.

Non-linear analysis with shell elements in combination with resistance models from Model Code 2010, fib (2013), (Level III) are judged to be useful for practical engineering work. They are more demanding than traditional analysis methods but are powerful when a higher load-

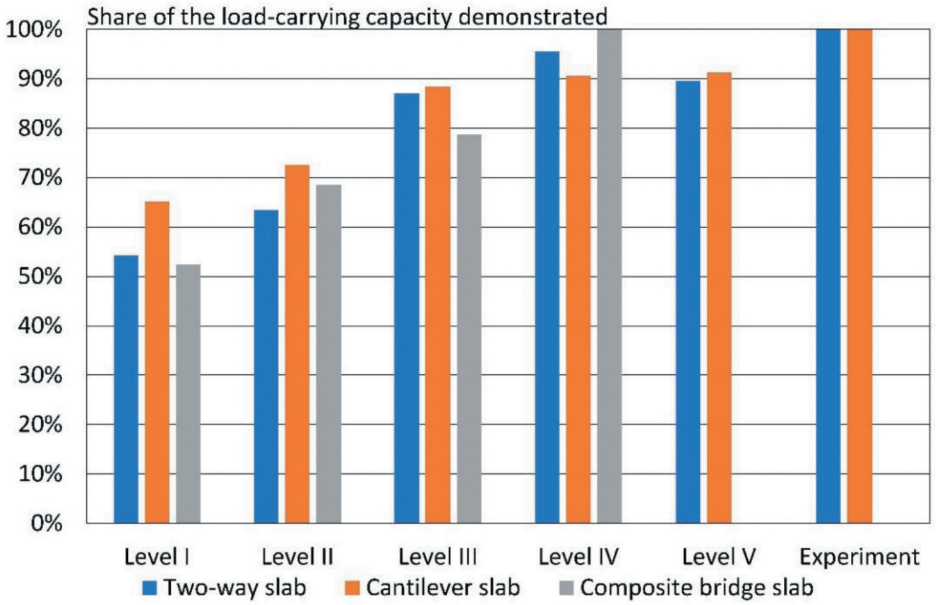


Figure 4. Demonstrated load-carrying capacity with assessment on different levels of accuracy, for the examples in Plos et al. (2021).

carrying capacity needs to be demonstrated. It was shown through examples that assessment with such an analysis can result in 15% to 35% higher capacity compared to assessment according to current praxis using linear analysis.

Non-linear analysis with continuum elements (Level IV and V) can be very helpful to provide a better understanding of the structural behaviour. However, this kind of analysis is considerably more demanding. Furthermore, there are still doubts regarding the modelling uncertainty which, in practice, makes it difficult to prove additional capacity with such analyses.

ACKNOWLEDGEMENT

The research presented was mainly funded by the Swedish Transport Administration (Trafikverket) and conducted at Chalmers University of Technology, Sweden.

REFERENCES

Bagge, N., Popescu, C., & Elfgren, L. 2018: Failure tests on concrete bridges: Have we learnt the lessons? *Structure and Infrastructure Engineering*, 14(3): 292–319.

Bagge, N., Plos, M. & Popescu, C. 2019: A multi-level strategy for successively improved structural analysis of existing concrete bridges: examination using a prestressed concrete bridge tested to failure *Structure and Infrastructure Engineering*, 15(1): 27–53.

CEN 2004. *EN 1992-1-1 Eurocode 2: Design of concrete structures - part 1-1*. Brussels, CEN.

Fall, D., Shu, J., Rempling, R., Lundgren, K. & Zandi, K. 2014. Two-way slabs: Experimental investigation of load redistributions in steel fibre reinforced concrete. *Engineering Structures*, 80:61–74.

fib 2013. *Model Code for Concrete Structures 2010*. Lausanne: fib.

Plos, M., Shu, J., Zandi, K. & Lundgren, K. 2017. A multi-level structural assessment strategy for reinforced concrete bridge deck slabs. *Structure and Infrastructure Engineering*, 13(2): 223–241.

Plos M., Johansson M., Zandi K. & Shu J. 2021: *Recommendations for Assessment of Reinforced Concrete Slabs: Enhanced structural analysis with the finite element method*. Göteborg, Chalmers Univ. of Tech. https://research.chalmers.se/publication/523655/file/523655_Fulltext.pdf

Pacoste, C., Plos, M., & Johansson, M. 2012. *Recommendations for finite element analysis for the design of reinforced concrete slabs*. Stockholm: KTH Royal Inst. of Tech.

Shu, J., Fall, D., Plos, M., Zandi, K., Lundgren, K. 2015. Development of modelling strategies for two-way RC slabs. *Engineering Structures*, 101: 439–449.

Shu, J., Plos, M., Johansson, M., Zandi, K., Nilenius, F. 2016. Prediction of punching behaviour of RC slabs using continuum non-linear FE analysis. *Engineering Structures*, Vol. 200 art. no. 109666.

Shu, J., Belletti, B.; Muttoni, A., Scolari, M., Plos, M. 2017: Internal force distribution in RC slabs subjected to punching shear. *Engineering Structures*, 153: 766–781

Shu, J., Bagge, N., Plos, M., Johansson, M., Yang, Y., Zandi, K. 2018: Shear Capacity of a RC Bridge Deck Slab: Comparison between Multilevel Assessment and Field Test. *J. Struct. Eng.*. Vol. 144 (7)

Shu, J., Honfi, D., Plos, M., Zandi, K., Magnusson, J. 2019: Shear Capacity of a RC Bridge Deck Slab: Comparison between Multilevel Assessment and Field Test. *J. Struct. Eng*. Vol. 144 (7)

Sustainable Bridges 2007: *Non-Linear Analysis and Remaining Fatigue Life of Reinforced Concrete Bridges*. Prepared by Sustainable Bridges - a project within EU FP6.

Vaz Rodrigues, R. 2007. *Shear strength of reinforced concrete bridge deck slabs*. Lausanne. PhD Thesis, École Polytechnique Fédérale de Lausanne,

Zandi K. 2010: *Structural Behaviour of Deteriorated Concrete Structures*. Göteborg, Ph.D. Thesis, Chalmers Univ. of Tech.

Bridge Maintenance, Safety, Management, Digitalization and Sustainability – Jensen, Frangopol & Schmidt (eds)
© 2024 The Author(s), ISBN 978-1-032-77040-6
Open Access: www.taylorfrancis.com, CC BY-NC-ND 4.0 license

Behaviour & management of pre-tensioned girder halving joints

N. Stevens
Nick Stevens Consulting, Brisbane, Queensland, Australia

T. Heldt & C. Lin
Department of transport and main roads, Brisbane, Queensland, Australia

R. Sampaio
National transport research organisation, Brisbane, Queensland, Australia

ABSTRACT: The root cause of several worldwide bridge collapses in the past 20 years has been identified as resulting from the poor performance of structural details known as halving joints. Concrete halving joints are renowned for their low redundancy, potentially brittle failure characteristic (if not detailed correctly), and high stress concentration zones. Best practice management of these details involves both structural assessment and inspection with information from both contributing to the overall assessment. This research presents the results of the analysis of the strand development length effect on the behaviour of halving joints on pre-tensioned girders. A conventional strut-tie analysis of these joint revealed that their capacity is controlled by the development characteristics of the pre-tensioned strand. Based on this analysis, the most vulnerable bridge on the network was identified. Non-linear advanced finite element analysis demonstrated that the strand development did severely limit the halving joint capacity and that this mode of failure had not been anticipated by the designers. This knowledge allowed the management of these bridges to be improved by modifying inspection regimes to include the likely crack locations for this failure mode.

1 INTRODUCTION

"Halving Joints" or "Half Joints" (Figure 1) describe the intersection of the two components (superstructure and substructure) that are overlapped. They typically feature cantilever superstructure and suspended span/drop in spans. They facilitate a beneficial reduction to the overall height of the structural system while maintaining clearance over roads/railways or other assets. Catastrophic failure of structures triggered by failure of these key details had occurred in recent years (eg, Lecco, Italy and De La Concorde, Canada). A knowledge of these failures motivated the Queensland Department of Transport and Main Road's (QTMR) to develop a deeper understanding of concrete halving joint bridges on Queensland network and provide appropriate risk management and assurance in relation to the performance of these bridges.

The largest cohort of QTMR halving joint bridges consists of pre-tensioned T girder bridges supported on inverted T reinforced concrete headstocks constructed in between circa 1990 and 2010. The Subject bridge is a 5-span bridge and had the lowest ratio of available halving joint capacity to required capacity for this cohort of bridges based on a preliminary assessment. This paper summarises detailed investigations into the Subject bridge halving joint behaviour and illustrates how advanced analysis can inform better management of such assets.

1.1 *Context and background*

The physical configuration of half joint introduces a significant change in cross-section stiffness and strength. The joints are positioned in the structure so that there is no primary moment at the joint. However, there is typically significant cross-section shear, leading to

DOI: 10.1201/9781003483755-454

localised shear and bending resulting from the joint configuration. Reduced cross-section stiffness and strength combined with complex localised bending and shear makes them vulnerable to failure, often exacerbated by other factors. Ultimately typical failure of concrete half joints occurs as illustrated in Figure 2, often with limited warning.

Key factors exacerbating halving joint vulnerability include poor reinforcement detailing and/or lack of appropriate reinforcement. In addition, these joints are difficult to inspect and maintain, and are often positioned near deck joints resulting in increased environmental exposure (water leakage) leading to localised material deterioration. These factors combined with their potentially brittle failure nature and (often) limited alternative load paths (low system redundancy) pose significant risks.



Figure 1. Typical QTMR half joint – inverted "T" headstock and super "T" girders.

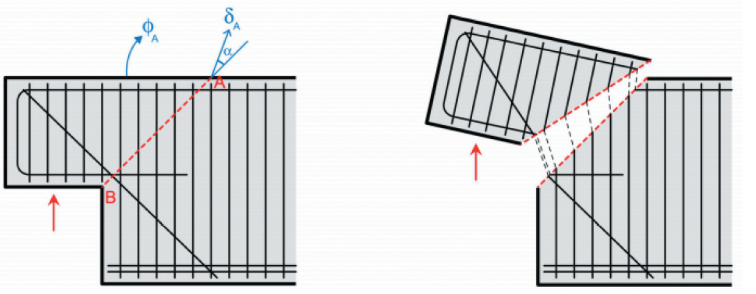


Figure 2. Half joint failure (after CS466 risk management and structural assessment of concrete half joint deck structures).

1.2 *Objectives*

The objective of this investigation is to better understand the behaviour of halving joints in this cohort of pre-tensioned girders to identify improved management opportunities. This paper highlights an example of how pre-tensioning can modify halving joint behaviour, creating issues but also opportunities for the management of these structures.

2 SUMMARY OF PRE-TENSIONED SUPER "T" GIRDER BEHAVIOUR

The general arrangement plan and elevation is shown in Figure 3. A notable feature is the 45° skew on this bridge that also has both girder and headstock with halving joints. The concerns identified are in the girder halving joints, particularly those on the Span 4 (39 m) which is significantly longer than the other spans (31.5 and 29 m).

The strut and tie assessment of the halving joint predicted a capacity of 1210 kN representing only 66% and 90% of the capacity required for the external and internal girders respectively,

based on a preliminary loading analysis. According to the strut and tie models the halving joint capacity was limited by the force that could be developed in the prestressing strand at the bottom of the girder. This was because there were only 14 bonded strands at the ends of the girder. De-bonded strands can be found to varying extents for other QTMR T girder bridges.

The strut and tie model that used for the preliminary assessment (Figure 4) is based on the geometry along the girder centre line and so does not specifically take into account the high skew on the bridge and the effect that might have on the location of some bars. It predicts a halving joint capacity of 1210 kN with a co-existing horizontal tension of 121 kN.

Figure 5 shows the details of the struts and ties at the bottom chord which represents the not de-bonded 14 strands. Also shows a plot of the force development in the bottom chord, and the maximum force that can be developed in the strand based on the AS 5100 (Bridge Design Code) requirements. The vertical component of the diagonal shear force that can transferred up to the top of the girder by the ligatures and the diagonal bars is limited by the capacity of the bottom chord to resist the horizontal components of those forces.

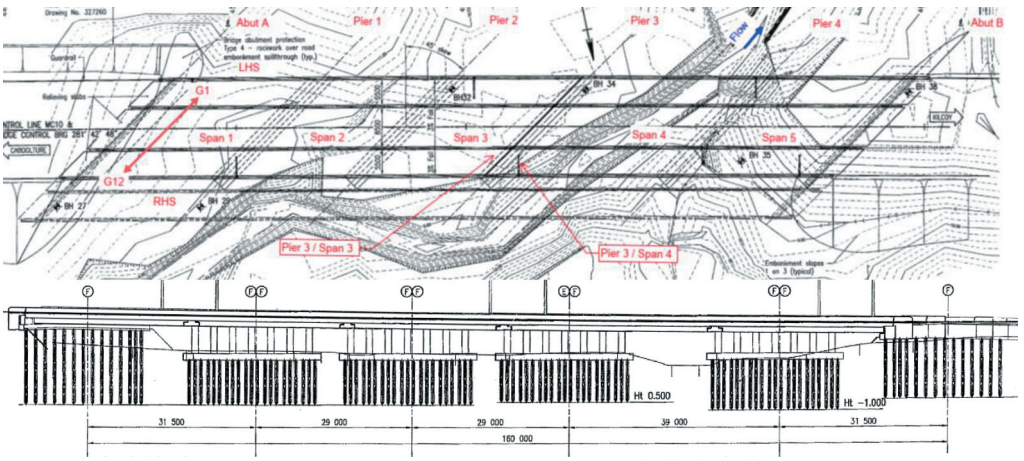


Figure 3. General arrangement of the subject bridge.

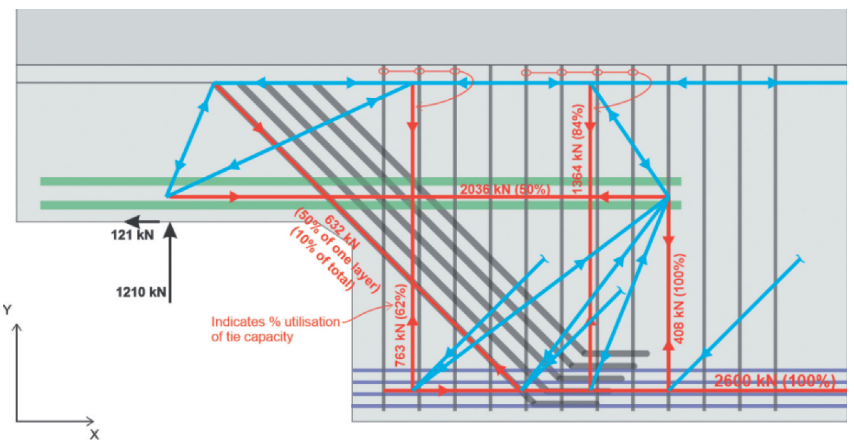


Figure 4. The subject girder halving joint strut and tie model from preliminary assessment.

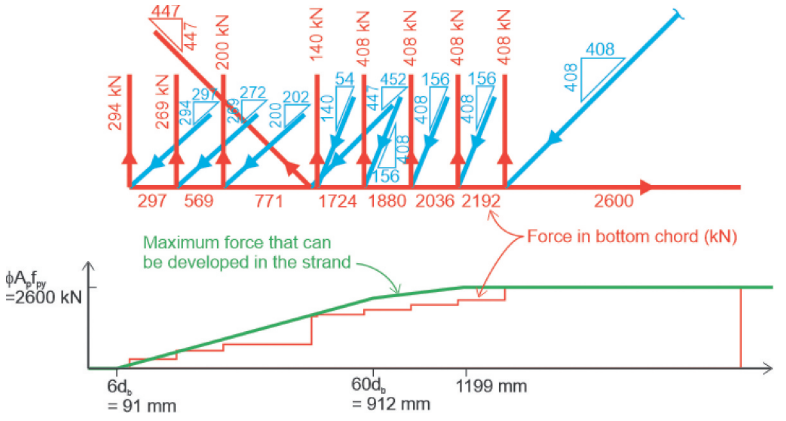


Figure 5. Detail of force development in the bottom chord of the strut and tie model.

The capacity of the strand representing the bottom chord is 100% utilised. However, the ligatures, horizontal bars, and diagonal bars adjacent to the re-entrant corner are only 62%, 50%, and 10% utilised, respectively. It is clear that in the design of the HJ a lot attention was paid to preventing failure by a diagonal crack starting at the re-entrant corner, but insufficient attention was paid into how the forces in the bars preventing that failure were to be transferred into the rest of the girder.

3 FINITE ELEMENT ANALYSIS

VecTor2 finite element software (Wong et al, 2013) was selected as the tool for a more detailed investigation of the structural behaviour. Vector2 software is a two-dimensional plane stress formulation and so the analysis will represent average conditions across the girder which needs to be considered when interpreting results. A full description of modelling is beyond the scope of this paper but suffice to advise that the development of an appropriate modelling rationale required careful consideration. Figure 6 shows the Vector2 FE model. The right-hand edge of the model is fully restrained. The load increment is applied as nodal loads over the width of the bearing plate. To allow for braking forces and/or horizontal frictional loads due to temperature or live load

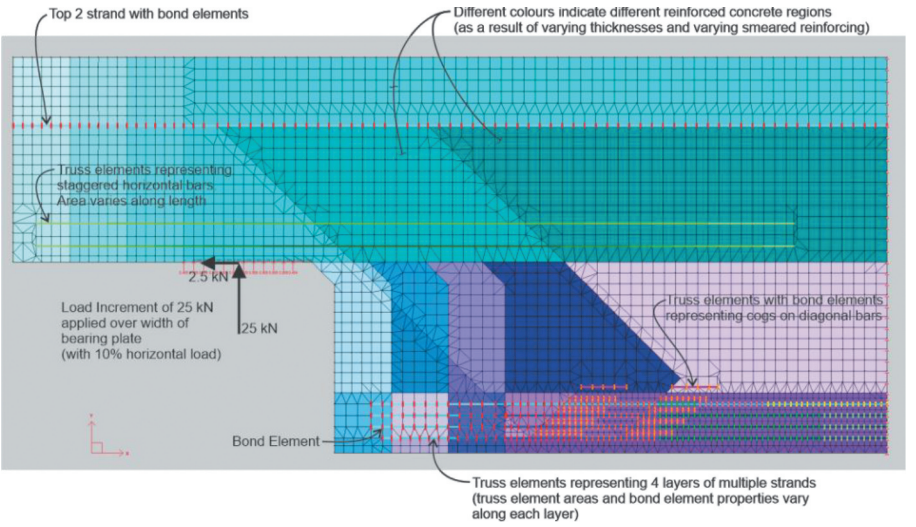


Figure 6. The VecTor2 FEA model mesh.

deformations, a horizontal tension load of 10% of the vertical load was applied which is consistent with the preliminary strut and tie model.

The first step in the analysis has zero load applied. It is effectively equivalent to the step of releasing the strands in the stressing bed, so that the strand slips near the end of the girder, activating the bond elements and developing the force profile at the ends of the strands. As the strand forces develop, corresponding stresses due to the prestress develop in the girder. Subsequent load steps applied an increasing bearing reaction in increments of 25 kN. The bearing load was increased until satisfactory convergence could no longer be achieved.

The adopted bond stress -slip relationship for strand is shown in Figure 7. The maximum value (3.6 MPa) varies along the length of the strand to achieve an overall force development profile which matches the AS 5100 values. This relationship is a key determinant of overall HJ behaviour. The slip values (S_1, S_2, and S_3) that were adopted were consistent with the findings of Lee (2017) and are much larger than those for deformed reinforcing bars. These larger slip values were essential to be able model bond consistent with the AS5100 development length requirements for strands.

Several different analyses were undertaken with varying parameters. The following section contains a detailed discussion of the results for an analysis with realistic parameters. The results discussed are for the analysis which used the strand bond model described above and the default concrete tensile strength which is 2.33 MPa. No capacity reduction factors were included. This analysis should provide a good representation of the likely behaviour and failure load. However, it is not code compliant or consistent with the strut and tie model as it includes capacity that relies on the concrete tensile strength and does not include capacity reduction factors.

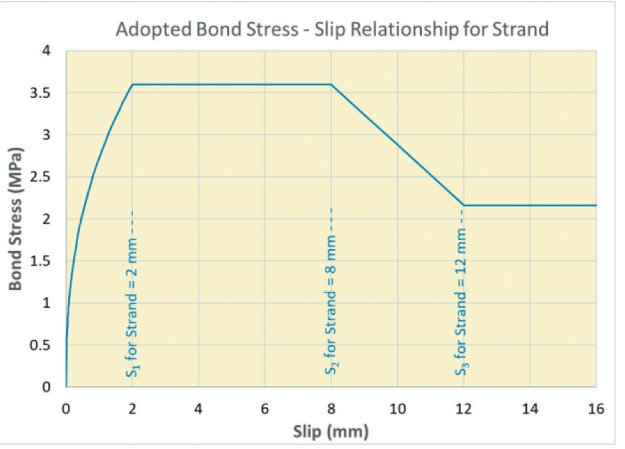


Figure 7. Adopted bond stress slip relationship for strand and the VecTor2 default relationship.

3.1 *Deformed shapes and cracking*

Figure 8 (a) to (c) shows the deformed shape and the extent of cracking at varying levels of the estimated design loading and for the predicted failure load. At the SLS Permanent Effects plus Traffic loading of 1250 kN (Case (a)), the extent of cracking around the re-entrant corner has developed and the maximum crack width at the surface is 0.47 mm. There is widespread cracking through the region of the diagonal reinforcing although the crack widths away from the surface are small (~ 0.1 mm). At this loading the first cracking in predicted in the diagonal bar – strand anchorage zone. This is a region where the horizontal component of the force in the diagonal bars has to be transferred into the strand, via the concrete.

At the estimated ULS Permanent Effects plus Traffic loading of 1825 kN (Case (b)) cracking is widespread. There is an increased amount of cracking in the diagonal bar – strand anchorage zone, although these cracks still are relatively small at about 0.4 mm. Flexural cracking at the extent of the model is now also predicted.

The predicted failure load was 2025 kN. This is the last load step at which convergence could be achieved. At this load (Case (c)), the deformed shape shows a failure crack immediately behind the diagonal bars. This has been allowed to open by the strands on the left of the crack slipping.

At the failure load the stresses in the diagonal bars (204 MPa) and the horizontal bars (124 MPa) near the re-entrant corner are still very low. The capacity of the halving joint is completely controlled by the development of force in the strand.

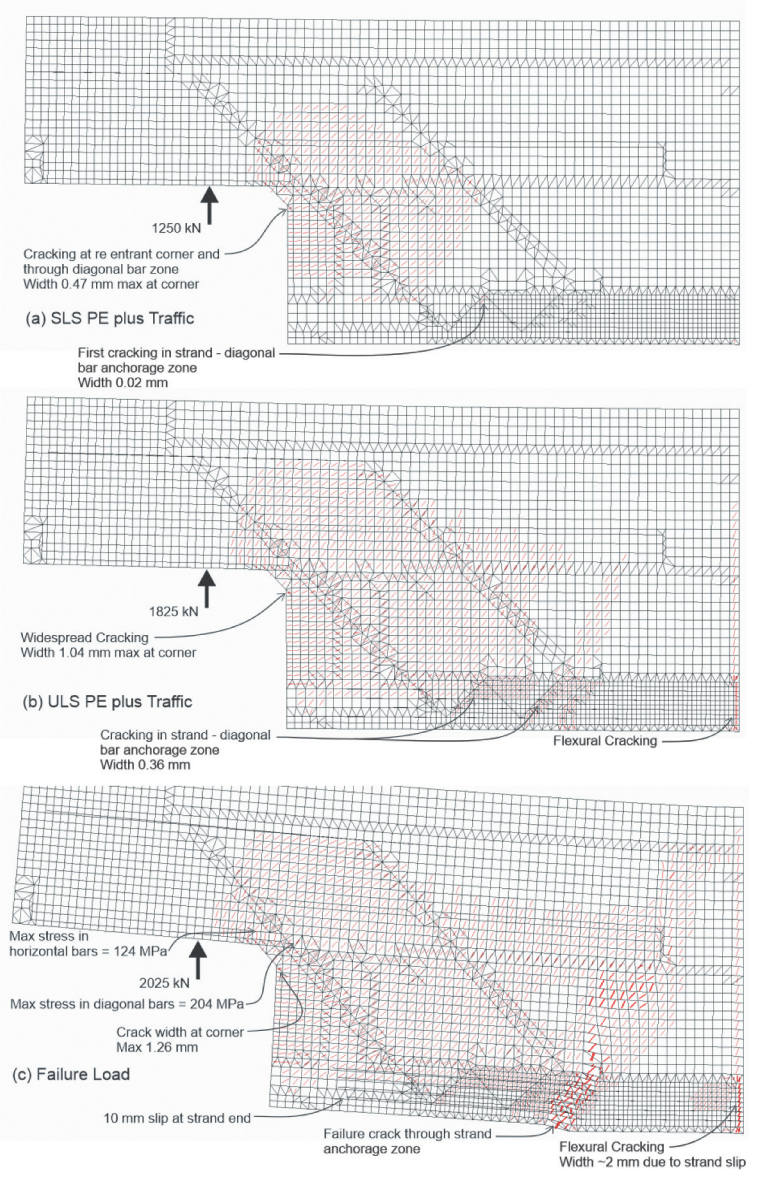


Figure 8. Deformed shape and cracking extent from analysis.

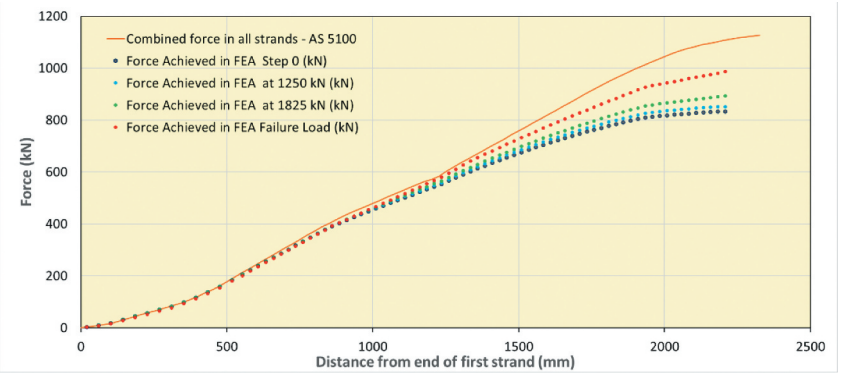


Figure 9. Force development in strand at various load levels compared with AS 5100 requirements (bottom strand layer).

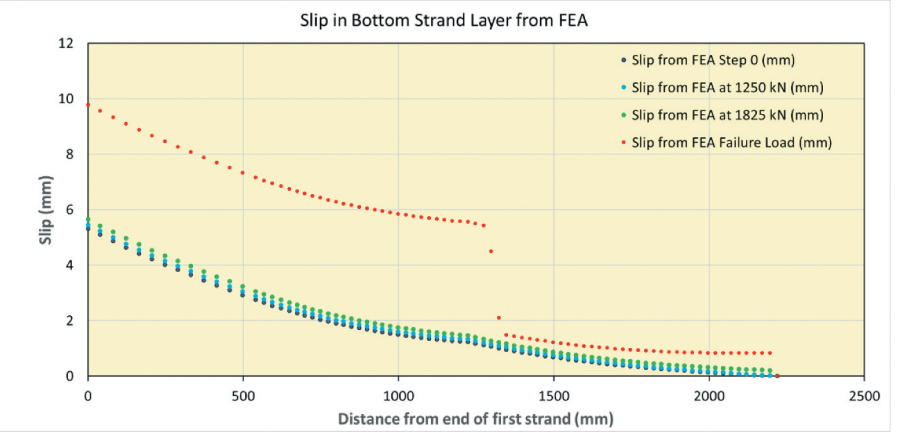


Figure 10. Slip along strand at various load levels.

3.2 *Strand force development and slip*

Figure 9 shows the force in the bottom layer of strands from the FEA analysis at various load levels. This is compared with the theoretical values from superposition of the AS 5100 stress development profiles for the six tendons with the staggered starting points. Figure 10 shows the slip along the bottom layer of strand at various load levels. For the lower load levels the force in the strand closely matches the AS 5100 curve for 800 mm and then slowly falls below it. This is because the additional force in the strand is not required at these load levels. The slip in the strand beyond about 800 mm from the end is still less than 2 mm and so there is further bond capacity that can be activated by slightly increasing the slip. This happens as the load increases. The slip increases slightly and the force development beyond 800 mm moves closer the AS 5100 line.

As the failure load is approached the force in the strand increases until it closely matches the AS 5100 line. At this load, the slip is above S_1 (refer to Figure 7) at all locations to the left of the failure crack. Slips near the start of the strand are increasing above S_2 (8 mm), which means that the bond capacity starts to reduce. At this point, the maximum force that can be developed also starts to reduce, resulting in failure.

These plots show that the model has achieved the goal of the selection of properties for a single line of truss and bond elements which represents the behaviour of multiple staggered strands with force development characteristics consistent with the AS 5100 requirements. Hence the predicted failure load is consistent with the AS 5100 stress development requirements.

Figure 11 shows the deflection at the centre line of the bearing from the analysis. This is the deflection measured relative to a tangent to the girder soffit on the right-hand side of the model.

Deflections are small until the failure crack starts to open due to slip of the strand. Over the final 10% of the theoretical failure load, the deflections increase rapidly due to opening of the failure crack.

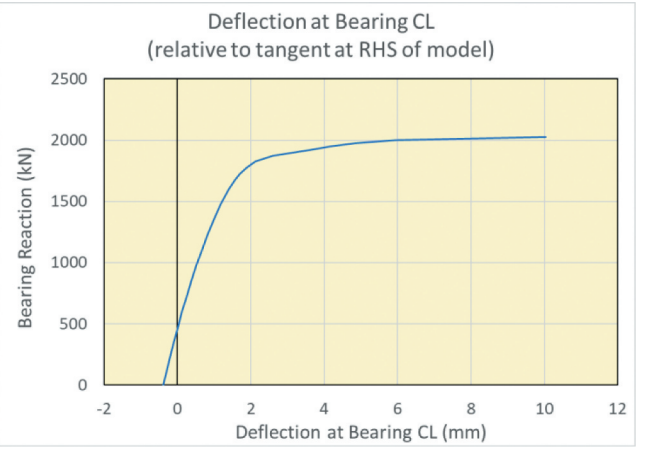


Figure 11. Deflection at bearing centre line for loads up to the failure load.

3.3 *Results for code compliant assessments*

The analysis described above included concrete tensile strength and did not include material capacity reduction factors. Further analyses were completed with these assumptions changed.

If capacity reduction factors are included and the concrete tensile strength ignored, then the analysis consistent with the AS5100 design code requirements and the assumptions of the Strut and Tie assessment. The result for these assumptions was a predicted capacity of 1525 kN. This is higher than the result of the strut and tie assessment (1210 kN). The reason is mainly related to the longer average strand development length in the FEA when the girder end skew was properly taken into account.

While including the concrete tensile strength is not consistent with a strut and tie model, it is consistent with code-based shear capacity assessments where the adoption of a V_{uc} term is essentially equivalent to including an average tensile stress in the concrete and checking that it can be transferred across the cracks by shear on the crack faces. The VecTor2 software includes these checks and so the predicted capacity including the concrete tensile strength is consistent with the AS5100 shear requirements. When the VecTor2 default concrete tensile strength of $0.33\sqrt{f'c}$ was included, the predicted capacity increased to 1650 kN.

4 IMPLICATIONS FOR MANAGEMENT OF HALVING JOINTS

Best practice halving joint management (Highways England, 2020) requires both the assessment and inspection of halving joints and is typically focussed on cracking behaviour in the vicinity of the re-entrant corner as illustrated in Figure 2. The analysis described above indicates that while re-entrant corner cracking will occur (and has been observed) at the re-entrant corner, it is not always the controlling failure mode when the complexities of pre-tensioned concrete are introduced into halving joint behaviour. In this case the conventional reinforcing steel has only reached approximately half of its capacity when failure initiates as a result of slip of the pre-tensioned strand. The above predicted behaviour is sensitive to strand development characteristics, so QTMR is progressing further research to gain a better understanding of actual strand development characteristics. These results will be used to update the VecTor2

model to improve understanding of the behaviour and capacity of the The Subject bridge halving joints. All QTMRs super T halving joints bridges are controlled by strand development based on strut-tie assessment. The findings from this research will be used to better inform the management of the whole bridge co-hort. Halving joint inspection focus has been extended to include seeking evidence of girder soffit cracking in the region between 1 and 2 m from the end of the girders. While this is only anticipated to occur at very high load levels, this tendon slip failure mechanism is expected to give little warning of collapse, so such cracking would be a significant escalation trigger should it be observed.

5 CONCLUSIONS

The behaviour described above illustrates the need to understand the expected behaviour of concrete halving joint bridges in detail, particularly when pre-stressing is coincident with the halving joint design. Current best practice halving joint management uses evidence from observed cracks to assist in understanding and managing the risk associated with operating halving joint bridges on the network. While the strut-tie analysis was sufficient to identify the issue (behaviour and capacity controlled by strand development length), it was not possible to gain a detailed understanding of structural behaviour. Finite element analysis (in this case using VecTor2 software) allowed a much more detailed understanding of behaviour, including identification of how failure associated with the controlling mechanism might progress, and provides revised focus for halving joint inspections.

ACKNOWLEDGEMENT

The authors gratefully acknowledge the financial support provided by the National Center of Excellence, a joint research program of QTMR and NTRO (National Transport Research Organisation), which was instrumental in facilitating this research.

REFERENCES

Highways England (2020) CS 466 'Risk Management and Structural Assessment of Concrete Half Joint Deck Structures', Design Manual for Roads and Bridges, Highway Structures & Bridges Inspection & Assessment, Revision 0, March 2020.

Standards Australia (2017) AS5100:2017 Bridge Design, SAI Global.

Wong, P. S., Vecchio, F. J., and Trommels, H. (2013) VecTor2 & Formworks User's Manual, 2nd Edition, August 2013.

Lee, C, Shin, S, Lee, S & Oh, J 2017, 'Modelling of bond stress–slip relationships of a strand in concrete during steam curing', International Journal of Concrete Structures and Materials, vol 11, no 3.

Bridge Maintenance, Safety, Management, Digitalization and Sustainability – Jensen, Frangopol & Schmidt (eds)
© 2024 The Author(s), ISBN 978-1-032-77040-6
Open Access: www.taylorfrancis.com, CC BY-NC-ND 4.0 license

The behaviour and management of post-tensioned girder halving joints

N. Stevens
Nick Stevens Consulting, Brisbane, Queensland, Australia

R. Sampaio
National transport research organisation, Brisbane, Queensland, Australia

T. Heldt & C. Lin
Department of transport and main roads, Brisbane, Queensland, Australia

ABSTRACT: Structures with concrete halving joints lack redundancy and are prone to potential brittle failures, particularly with poor detailing and high stress concentration areas. In recent years, several bridge collapses have been attributed to inadequate halving joint performance. A network-level approach has identified specific issues requiring deeper comprehension for improved structural assessment and inspection protocols. This paper investigates the impact of post-tensioning on girder halving joint behavior, with a focus on post-tensioned girders on inverted T headstocks, a common network detail. "I" girders, a significant subcategory, showed structural assessment ratios below 1.0, despite limited evidence of associated cracking. This study aims to understand this anomaly and presents numerical modeling results for a post-tensioned I girder, revealing modifications to known failure mechanisms due to post tensioning and introducing an additional failure mechanism. The result of the advanced analysis creates opportunities for more optimised management of these structures.

1 INTRODUCTION

A bridge with halving joints consists of suspended spans with dapped ends supported on the nibs of abutments or adjacent cantilevered girders. The physical configuration of the joint introduces a sudden change in geometry, resulting in significant variation in the stiffness and strength within the joint section. The joints are positioned and configured in the structure so that there is no/minimal global bending moment in the joint. However, there is typically significant cross-section shear, leading to localised shear and bending resulting from the joint configuration. Reduced cross-section stiffness and strength, combined with complex localised bending and shear, makes them vulnerable to failure, often exacerbated by other factors.

Many of the halving joints in Queensland Department of Transport and Main Roads (QTMR) network are located on the Subject Bridge in Brisbane which was built in the 70's. A preliminary assessment of a typical halving joint on the post-tensioned I-Girders on this bridge involved finite element analysis of several spans of the structure to determine halving joint loads, and Strut and Tie analysis of the headstock and girder halving joints to determine halving joint capacities, resulting in tolerable Structural Assessment Ratios (SARs) of 0.85 to 1.00 at several locations. However, the I-Girder halving joints had lower SARs (0.73 to 0.90), raising concerns.

Inspections on those HJs revealed minimal cracking, inconsistent with calculated SARs. There was a concern that the low level of cracking was due to the relatively high level of prestress in the post tensioned girders, and that a situation might exist where the failure load was not much above the cracking load. This would be undesirable because inspections showing a lack of cracking would not necessarily mean a low failure risk. This discrepancy combined

DOI: 10.1201/9781003483755-455

with the significance of the asset to the QTMR network, motivated further investigation, with the aim of developing a better understanding of the behaviour and adequacy of the I girder halving joints in this Expressway.

2 I GIRDER HALVING JOINT

Figure 1 and Figure 2 show the halving joint geometry and reinforcing details of the I girder analysed. The results from the previous assessment (Stevens, 2020) relevant to this more detailed investigation are also summarised below. The loads in Table 1 are the highest reactions obtained for a typical pier for service and ultimate limit states (SLS and ULS). Two halving joint capacities were estimated (Table 2); one considering optimistic assumptions regarding the anchorage of key reinforcing bars, and other considering conservative assumptions. The uncertainty that leads to those assumptions is whether all the bars which cross the crack can be properly anchored by struts and ties in the regions above and below the crack.

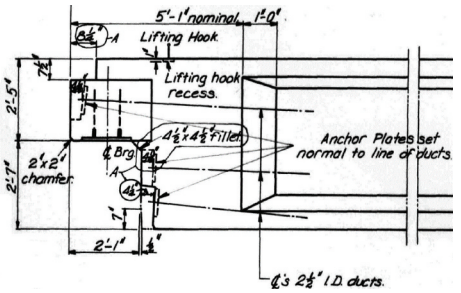


Table 1. I girder HJ loads.

Loading	SLS Reactions	ULS Reactions
PE only	479 kN	620 kN
PE+LL (1G*)	918 kN	1496 kN
PE+LL (T&D**)	898 kN	1456 kN

* GML Semi Trailer 42.5 t
** Truck and Dog 50.5 t

Figure 1. I girder halving joint geometry.

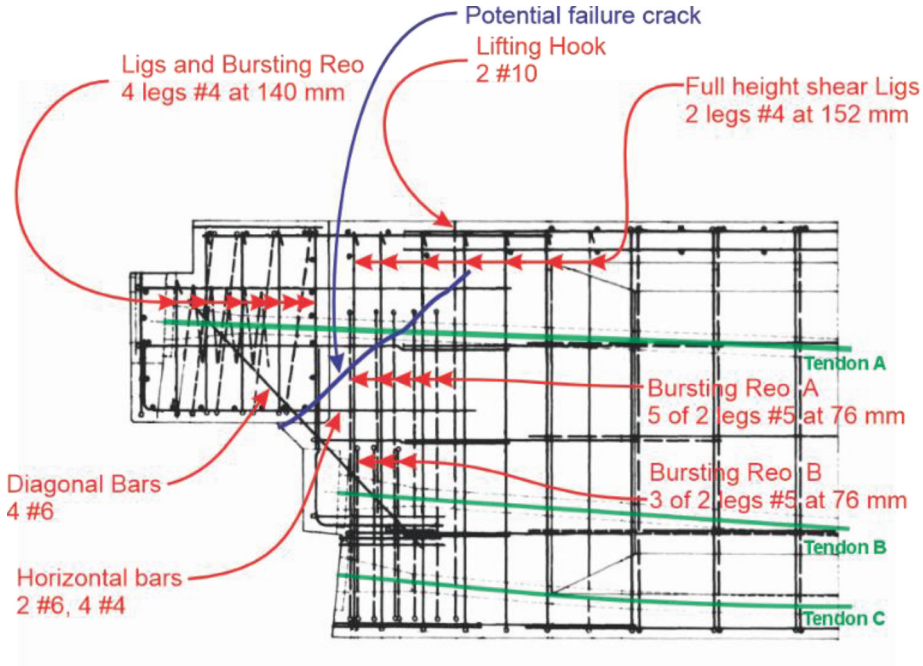


Figure 2. Reinforcing details at the I Girder halving joint.

Table 2. Strut and tie predicted capacities for the I girder halving joint.

Case	Reliable capacity ΦV_u (kN)
Optimistic – assuming all bars can be fully developed except Lifting Hook at 50% developed	1360
Appropriately conservative – reduced capacity of bars with inadequate development length	1035

3 FINITE ELEMENT MODEL

The Finite Element Analysis (FEA) model of the I girder halving joint was developed in VecTor2 software (Wong et al, 2013). VecTor2 allows a bond element to be defined connecting the main reinforcing bars to the concrete, allowing the effect of the inadequate development length of some bars in the halving joint capacity to be investigated. A snapshot of the model is shown in Figure 3 where the various colors in the model represent different materials, determined by parameters like thickness, concrete and steel properties, and horizontal and vertical reinforcing percentages.

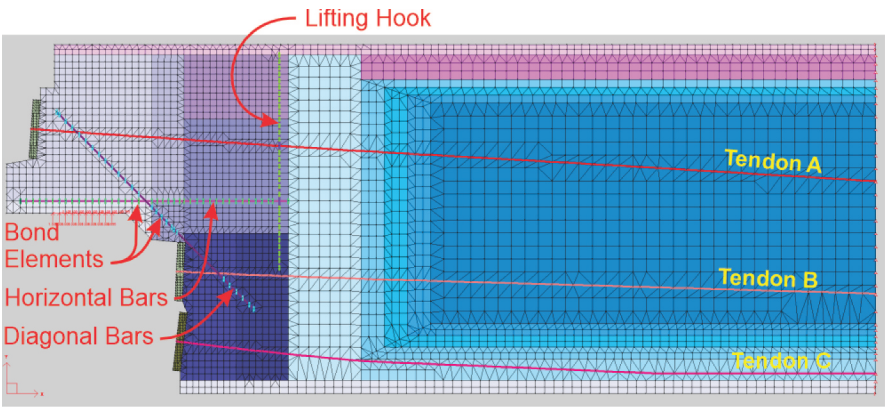


Figure 3. Vector 2 finite element model of the I girder halving joint.

The ligatures and bursting reinforcing (Figure 2) are modelled as distributed reinforcing as well as the small amount of horizontal face reinforcing. So, the material properties in the regions behind the tendon anchorages are different because some regions include one or both bursting reinforcing types as well as the full height shear ligatures.

The tendons, the lifting hook bars, the diagonal bars, and the horizontal bars (Figure 2) are modelled as concentrated reinforcing elements. The tendons assume perfect bond, given their positive anchorages preventing slip. However, the other bars are connected to the concrete through bond elements that permit slip, and the resistance to this slip is determined using a bond model, which is explained more later in the paper.

The loading is applied as a series of nodal loads across the bearing width, with the center of action aligning with the bearing centre. A horizontal tension load equal to 10% of the vertical load is applied at the bearing. This is in line with strut and tie models and serves as an allowance for braking or frictional forces due to temperature or live load deformations. No other loads are added to allow a fair comparison with strut and tie results. However, this approach is conservative when compared to the maximum reactions calculated in the previous FEA, as the maximum shear at the failure crack location is expected to be slightly lower than the maximum bearing reaction.

3.1 *Material properties*

3.1.1 *Concrete*

The specified concrete compressive strength is 41 MPa. Young's Modulus for the concrete is 33,000 MPa in accordance with AS 5100 (Standards Australia, 2017). The concrete tensile strength was varied as a parameter to investigate its effect on the predicted halving joint capacity. Table 3 shows the values considered.

Concrete contributes to shear strength by allowing average tensile stress to exist between cracks due to shear on the crack face and a local reserve of capacity in the reinforcing at the cracks. In VecTor2, this is modeled using Modified Compression Field Theory - MCFT (Vecchio & Collins, 1986), in contrast to strut and tie models that do not account for such tensile stresses. Models incorporating average tension in the concrete are likely to predict higher capacities compared to strut and tie models.

Table 3. Values for the concrete tensile strength.

Average tension in the concrete (f'_{ct})	Comment
0.1 MPa	Essentially zero, to allow a fair comparison with strut and tie model predictions
$0.33\sqrt{f'_c} = 2.11$ MPa	This is the default value for VecTor2 and MCFT. It provides a shear strength prediction including a concrete component consistent with the AS 5100.
$0.6\sqrt{f'_c} = 3.84$ MPa	Since the initial cracking was likely to be in a small zone at the re-entrant corner, the code specified characteristic flexural tensile strength might be more appropriate for predicting observed cracking patterns

Note: For analyses including the concrete capacity reduction factor (φ_c), these values are reduced by $\varphi_c = 0.65$.

3.1.2 *Reinforced and prestressing steel*

Structural steel is modelled in VecTor2 as a linear-elastic material up to the point of yielding, after which plastic deformation and strain hardening occur, providing realistic predictions of the steel's behaviour. However, to obtain a capacity prediction consistent with code requirements it is necessary to enforce a true yield plateau for both reinforcing and prestressing steels. This is particularly conservative for the prestressing steels which do not have a yield plateau. Table 4 shows the prestressing and reinforcing steel properties.

Table 4. Steel properties.

	Yield stress	Comment
Prestressing steel	$0.82\, f_{pb} = 1525$ MPa	In accordance with AS 5100.5 and $f_{pb} = 1860$ MPa
Reinforcing steel	410 MPa	Cold worked deformed bars

Note: For analyses including capacity reduction factors, these values of yield stress are reduced by the capacity reductions factors of 0.9 for prestressing steel and 0.85 for reinforcing steel.

3.1.3 *Bond-slip relationship for strand*

The bond material properties are essentially an expression of the relationship between the bond stress on the bars and the bar slip relative to the surrounding concrete. Figure 4 shows the typical bond-stress relationship used in VecTor2, which was proposed by Eligehausen et al (1983).

In Figure 5, the maximum bond stress from the Eligehausen model is compared with the bond stress used in AS 5100 for different ratios of (c/d) where c is the minimum of the concrete cover and half of the bar spacing and d is the bar diameter. It clearly shows that Eligehausen bond stresses are generally much higher than those implied by the AS5100 development length

requirements. It is only for the very low c/d ratio of around 1 that the splitting bond stress approaches the AS 5100.5 values. The pullout bond stress is much higher than the splitting values for low c/d ratios and the code values. However, for high c/d ratios the Eligehausen splitting bond stress can get as high as the pullout stress. The bond pullout values are only applicable in the presence of a confining pressure σ. VecTor2 uses a parameter β to interpolate between the splitting and pullout values for the bond stress. In most cases β is zero and the splitting value will be used, however in the girder model the diagonal bars are anchored behind the prestress anchorages therefore some confining pressure would be applicable.

In the present analysis, two bond levels were considered: Code bond and High bond (Table 5).

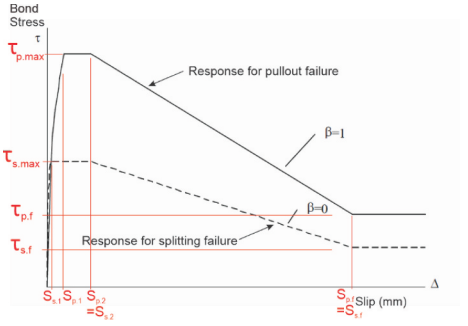


Figure 4. Bond-slip relationship in Vector 2. τ_p - pullout stress, τ_S - splitting stress and β - confinement pressure factor.

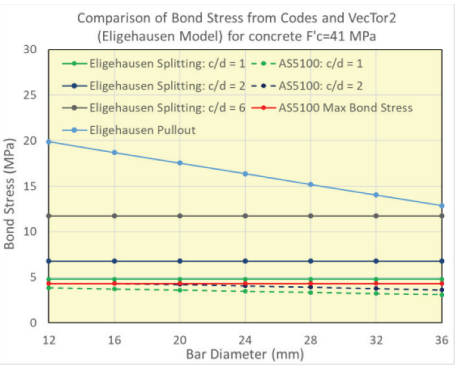


Figure 5. Comparison of AS5100 and Vector 2 bond stress (Eligehausen model) for concrete F'c=41 MPa.

Table 5. Bond levels.

Bond level	
Code bond	Input parameters to VecTor2 were manipulated to force the software to adopt a value for $\tau_{max} = 4.31\ MPa$ which is the maximum value allowed by the codes.
High bond	Applicable confining pressures and actual clear cover values were input, and the software calculated the values for τ_{max}

Note: AS 5100.5 does not apply a capacity reduction factor in calculating development lengths, the values adopted for "Code bond" were the same irrespective of whether capacity reduction factors were used in the analysis. However, High bond is affected when capacity reduction factors were included in the analysis.

4 RESULTS DISCUSSION

Table 6 summarises some of the key results for the analyses. These results can be compared with previous results in Table 1 and Table 2.

Analysis A1, has essentially zero concrete tension and so is based on assumptions consistent with a strut and tie model and a comparison of the results is instructive. Differences in the assumptions are the degree to which the diagonal bars, horizontal bars and lifting hook bars participate in carrying the load across the diagonal failure crack. Also, the strut and tie model does not include any contribution from the Bursting Reinforcing A. Based on the crack directions at the maximum load, which essentially align with the principal compressive stress direction, and so can be thought as compressive strut directions, it was observed that vertical bars of Bursting Reinforcing A are carrying high stress and consequently are participating in the load path. When the load in the three ligatures of Bursting Reinforcing A is added into the strut and

tie solution the predicted capacity increases to 1465 kN, which is comparable to the VecTor2 predicted capacity of 1425 kN. The point of this comparison is to show that the VecTor2 solution with no concrete tension is transparent. The load paths can be identified with strut and tie considerations, and the predicted capacity is consistent with a strut and tie model.

Analysis A2 includes concrete tension, and so essentially includes a small concrete shear component, consistent with MCFT and the code shear provisions. Including the concrete tensile strength also improved the anchorage of the bars that were modelled discretely resulting in higher stresses in these bars. As expected, the results are similar to that for A1. The maximum load was slightly higher.

Analysis A3 and A4 were similar to the first two analyses except that the more realistic bond properties in VecTor2 were used. This change further increased the predicted capacities by allowing higher forces in the discretely modelled bars.

Analysis A5 and A6 did not include capacity reduction factors and so, gave higher failure predictions. These analyses were included to give a more realistic estimate of the actual capacity, and a more realistic prediction of the actual behaviour in terms of what cracking might be expected at SLS and ULS loadings, which is key information for maintenance inspections. The following comparison of cracking patterns is done based on these two analyses.

Table 6. Summary of key Vector 2 analysis results.

						Yield indexes					
Analyses	Bond level	f'_{ct} (MPa)	Capacity reduction	R* (kN)	Defl.** (mm)	Diagonal	Horizontal Bars	LH Bars	Burst Reo A (top)	Top tendon	Failure mode***
A1	Code	0.1	Yes	1425	8.5	0.92	0.89	0.38	0.89	1.00	A
A2	Code	2.11	Yes	1525	6.3	1.00	1.00	0.72	0.95	1.00	A
A3	High	0.1	Yes	1550	10.1	1.00	1.00	0.55	1.00	1.00	A
A4	High	2.11	Yes	1600	6.8	1.00	1.00	0.81	1.00	1.00	A
A5	High	2.11	No	1775	4.6	1.00	1.00	0.65	1.00	1.00	A
A6	High	3.84	No	1925	4.0	1.00	1.00	0.95	1.00	1.00	B

* R – Maximum Halving Joint reaction. ** Defl. – Deflection at centreline of bearing at Maximum reaction

*** Failure modes: A - Crushing in region just above Bursting Reo A, B - Rapid crack growth and yielding in region above bursting reinforcement.

4.1 *Comparison of cracking patterns*

The key focus of these analyses lies in assessing the extent of cracking at different load levels, offering valuable insight into the interpretation and significance of observed cracks on the girders.

Understanding the software's crack direction output is essential before comparing results. The VecTor2 software and its theory doesn't predict individual cracks but rather smears or averages them over elements. So, if an element is nominally cracked, it means that there will be cracking in that region. Even if many elements are shown as cracked, there may only be one or two actual cracks.

The predicted cracking patterns for analyses A5 and A6 are discussed below. These analyses do not include capacity reduction factors and so are more realistic in terms of likely cracking levels. The difference between the two analyses is the concrete tensile strength. Analysis A5 uses the default concrete tensile strength of 2.11 MPa, while Analysis A6 uses 3.84 MPa.

Each analysis considered all load levels from zero up to the predicted capacity. For loads up to about 900 kN which is the SLS loading, there is only a small amount of cracking predicted at the re-entrant corner.

Figure 6 shows the cracking pattern at the ULS loading (permanent & traffic) and at the predicted failure loads.

For ULS loading (Figure 6.a&b), the crack widths are very wide near the corner but reduce quickly. Significant cracks at some distance from the corner indicate yielding of the vertical reinforcing. Figure 6.b shows cracking confined to a narrow band extending about 600 mm from the corner indicating that there might only be one or two cracks. In case A5 (Figure 6.a), the vertical reinforcing strength (at a crack) is higher than the concrete cracking strength and once the reinforcing crossing the main diagonal crack reaches a high enough stress, additional cracks will form above and below the main crack. This results in the cracking spreading upwards into the zone above the bursting reinforcing, where the amount of vertical reinforcing is much less.

For the failure loads (Figure 6.c&d) the maximum crack widths at the surface are similar and extremely wide. The extent of cracking is much greater for the A5 case for the reasons noted above. For this case there is widespread cracking in the region above the bursting reinforcing and the cracks in this location are very wide (4 mm). There are also other regions away from the corner with very wide cracks. This is different from the higher f_{ct} case, which even at a higher load has a much narrower band of cracking, and the cracks away from the corner are a maximum of about 1 mm. This is still wide, and an indication of moderate yielding but not an indication of imminent failure. This difference in failure characteristics is discussed in 4.2.

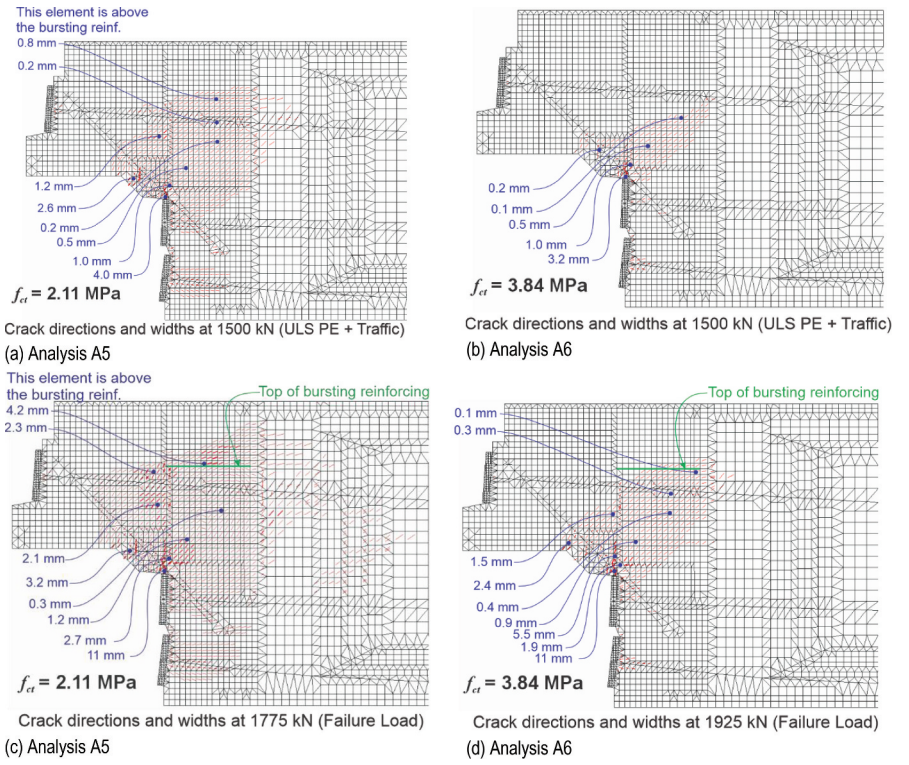


Figure 6. Cracking pattern for three different loading levels and for analyses cases A5 and A6(Table 6).

4.2 *Comparison of failure modes*

In the default f_{ct} model (Figure 6.c), wide cracking occurs in some areas due to extensive yielding and very large strains (5 mε to 10 mε). The final failure was caused by crushing of the concrete in the region above the bursting reinforcing. The higher f_{ct} model (Figure 6.d) has a different failure mode, but failure occurs at a higher load. As the load increases, the band of cracking stays relatively narrow and progresses past the large lifting hook bars. These large bars transfer enough load into the concrete above the bursting reinforcing to cause the

cracking to spread into this region. Figure 6.d shows that cracking has spread through most of the region above the bursting reinforcing. Since this region has much less vertical reinforcing than the region below it, once it cracks, the capacity would be less than the current load, and the failure would be rapid. So, in this case, considered to be the more realistic of the two, there is only moderate reinforcing yielding and moderate width (~1 mm) cracks away from the corner (in the context of failure being imminent) until failure occurs, which would be rapid. This issue occurs because of the particular pattern of reinforcing in this design. If the bursting reinforcing, which in the end is being partly relied on for the halving joint capacity, extended all the way to the top of the girder then a sudden failure would not occur. Note that the predicted capacity is about 25% above that required for the ULS loading so the risk of such a failure occurring is extremely low. Also, the solution does not include strain hardening of either the reinforcing or the prestressing strand which likely would further increase the predicted capacity and reducing the risk of a rapid failure.

5 CONCLUSION AND IMPLICATIONS FOR THE HJ MANAGEMENT

Uncertainties regarding the capacity of the post-tensioned I girders halving joints motivated this investigation. From the preceding discussion, the contribution of nominally inadequate bars has been appropriately included in the VecTor2, with an optimised strut-tie model identified in the process. Some cracking is anticipated although reduced when compared to typical reinforced concrete sections, with minor or no cracking from permanent effects and minimal observable cracking under normal operational loads, primarily at the re-entrant corner. Cracking from conventional halving joint failure mechanisms is expected to be ductile, but concrete crushing above the bursting steel can lead to a loss of structural integrity. Small deflections associated with the halving joints makes load redistribution challenging, emphasizing the need to prevent individual halving joint failure.

The halving joint capacity (1425 kN) is slightly below the demand (1496 kN), but additional capacity may exist when considering the concrete contribution. However, it's essential to consider the following context: 1) The assessment focuses on one HJ at one pier, although considered a typical scenario, there are numerous other HJ in the Expressway. 2) The Live Load Factor (LLF) of 2 may overestimate real traffic loads (Pape et.al, 2022), particularly given the primary commuter duty of this bridge and also it is needed to understand the live load scenarios. 3) Ductility (area under the load-deflection curve) appears to decrease in Table 6, with deflection at bearing centreline reducing by approximately half between A1 and A6; while ductility is a concern in relation to halving joints, a specific methodology would need to be developed to quantify it.

While the I girder HJ under investigation have yet to be extensively inspected, early observations have shown that no significant cracks have been detected. This is consistent with the discussion in Section 4. A summary of the expected defects which may be observable in the field based on the VecTor2 analysis is given in Figure 7, with small, inclined cracking likely to be observed first (1). Vertical cracking (2) may become more prominent as load increases,

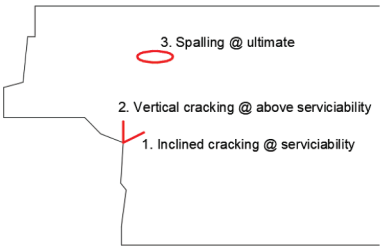


Figure 7. Likely sequence of anticipated cracking potentially observable.

with spalling to be observed near the ultimate capacity of the joint (3). While further inspection of the halving joints is required, it is likely that few re-entrant corner cracks will be identified based on observations to date. Evidence of cracking or spalling above the bursting reinforcement should also be checked, and while not anticipated, should be considered a serious defect if it is observed. Assuming that no significant defects are discovered, the I girder HJ are considered to meet QTMR requirements.

ACKNOWLEDGEMENT

The authors gratefully acknowledge the financial support provided by the National Center of Excellence (NACOE), a joint research program of QTMR and NTRO (National Transport Re-search Organisation), which was instrumental in facilitating this research.

REFERENCES

Eligehausen, R, Popov, E & Bertero, V. 1983. Local bond stress-slip relationship of deformed bars under general excitations, report no. UBC/EERC-83/23. Earthquake Engineering Centre, University of California, Berkley: California.

Pape, T., Heywood, R., Shaw, P., Voll, A. & Ward, D. 2022, Heavy vehicles and bridges: what the data is telling us?, *11th Austroads bridge conference*, 17 pp. Adelaide: South Australia,

Stevens, N. 2020. NSC313-TR-01 Network halving joint review, rev B, December 2020.

Standards Australia 2017, Bridge design series, AS5100:2017, Standards Australia, Sydney, NSW.

Vechhio, F. & Collins, M.P. 1986. The modified compression field theory for reinforced concrete elements subject to shear. *American Concrete Institute Journal*. 83(2).

Wong, P.S., Vecchio, F.J. & Trommels, H. 2013. VecTor2 & Formworks user's manual, 2nd edn, Vector Analysis Group

Bridge Maintenance, Safety, Management, Digitalization and Sustainability – Jensen, Frangopol & Schmidt (eds)
© 2024 The Author(s), ISBN 978-1-032-77040-6
Open Access: www.taylorfrancis.com, CC BY-NC-ND 4.0 license

Fatigue behaviour of reinforced concrete inverted T headstock halving joints

N. Stevens
Nick Stevens Consulting, Brisbane, Australia

C. Lin & Tim Heldt
Department of Transport and main Roads, Queensland, Australia

R. Sampaio
National Transport Research Organisation, Brisbane, Australia

ABSTRACT: The root cause of several worldwide bridge collapses in the past 20 years has been identified as resulting from the poor performance of structural details known as halving joints. Concrete halving joints are renowned for their low redundancy, potentially brittle failure characteristic (if not detailed correctly), and high stress concentration zones. Following safety concerns related to a halving joint bridge, an extensive program of structural health monitoring was conducted spanning nearly 2 years. The monitoring data combined with the finite element modelling allowed an investigation of the fatigue risk associated with reinforced concrete halving joint headstocks. This paper presents the results of the investigation into the potential for fatigue to adversely influence the halving joint performance. Despite the obvious issues with the bridge, it was found that the fatigue risk in the headstock halving joints was low.

1 INTRODUCTION

1.1 *Context and background*

Halving joints or Half joints (Figure 1) describe the intersection of the two components (superstructure and substructure) that are overlapped. They typically feature cantilever superstructure and suspended span/drop in spans. They facilitate a beneficial reduction to the overall height of the structural system while maintaining clearance over roads/railways or other assets. Catastrophic failure of structures triggered by failure of these key details had occurred in recent years (eg, Lecco, Italy and De La Concorde, Canada). A knowledge of these failures motivated the Queensland Department of Transport and Main Road's (QTMR) to develop a deeper understanding of concrete halving joint bridges on the Queensland network and provide appropriate risk management and assurance in relation to the performance of these bridges.

A strategically important bridge on the national highway was identified to have significant halving joint performance concerns in 2019. Most QTMRs halving joint bridges have headstock configurations similar to this bridge. An extensive program of structural health monitoring was conducted spanning nearly 2 years to support management and remediation of the bridge. The monitoring data combined with the finite element modelling allowed an investigation of the fatigue risk associated with reinforced concrete halving joint headstocks in the specific case. This paper presents the results of the investigation into the potential for fatigue to adversely influence the halving joint performance. The investigation results also have implications for the management of similar assets.

The physical configuration of half joint introduces a significant change in cross-section stiffness and strength. The joints are positioned in the structure so that there is no primary moment

DOI: 10.1201/9781003483755-456

at the joint. However, there is typically significant cross-section shear, leading to localised shear and bending resulting from the joint configuration. Reduced cross-section stiffness and strength combined with complex localised bending and shear makes them vulnerable to failure, often exacerbated by other factors. Ultimately typical failure of concrete half joints occurs as illustrated in Figure 2, often with limited warning. Key factors exacerbating halving joint vulnerability include poor reinforcement detailing and/or lack of appropriate reinforcement. In addition, these joints are difficult to inspect and maintain, and are often positioned near deck joints resulting in increased environmental exposure (water leakage) leading to localised material deterioration. These factors combined with their potentially brittle failure nature and (often) limited alternative load paths (low system redundancy) pose significant risks.



Figure 1. Typical QTMR half joint – inverted "T" headstock and super "T" girders.

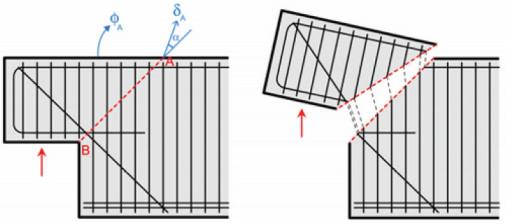


Figure 2. Half joint failure (after CS466 Risk management and structural assessment of concrete half joint deck structures).

1.2 *Objective*

The objective of this investigation was to better understand the fatigue behaviour of reinforced concrete halving joint headstocks. While fatigue risks were substantially mitigated by intervention for the bridge in question, there was an opportunity to better understand fatigue performance of many similar components on the network. The objective of this paper is to summarise the outcomes of the reinforced concrete fatigue investigation.

2 BRIDGE CONFIGURATION

The Subject Bridge is a 5-span post tensioned concrete girder bridge carrying northbound highway traffic. Figure 3 shows the general arrangement of the bridge. The road centre line has a 303.5 m radius. There is a large radius vertical curve and a 5% crossfall. Figure 4 shows a typical cross section through the girders, and typical elevation at the piers.

There are five spans in total, four with overall lengths of 28 to 29 m and one longer span. As a result of variations in the headstock widths, these four spans have essentially identical bearing-to-bearing girder lengths (27.29 m for central girder). Span 4 has a 35 m overall span and longer girders (32.59 m bearing-to-bearing for the central girder).

As shown in Figure 4, the underside of the headstock is at the same level as the underside of the girders. To achieve this, the girder/headstock connection incorporates a halving joint, with the half depth end of each girder sitting on bearing shelves which essentially cantilever from each side of the headstock.

An engineering inspection of the bridge in June 2019 determined that there was structural cracking in the pier headstock and girder halving joints. This cracking indicated that the halving joints were potentially operating under some degree of structural distress. Subsequent detailed engineering analyses determined that the halving joints were operating at reduced margins compared to those in Australian Standards for as-of-right freight vehicles (including B-Doubles). The structure was observed to have significant cracking at the corners of the headstock halving joints. Subsequently an interim Structure Management Plan (SMP) was put

in place, the bridge was instrumented to monitor cracking in the pier headstocks and Heavy Vehicle Travel Restrictions were implemented (September 2019). Ensuing capacity assessments showed the headstock halving joint capacity to be deficient (based on a code compliant assessment) for vehicles that were currently using the structure.

Strengthening of the headstock halving joints was undertaken, and completed by January 2021. The objective of the strengthening works was to safely and efficiently remove the travel restrictions for Class 2 vehicles operating under notice (as-of-right freight vehicles) and reduce the risk associated with the passage of Class 1 heavy vehicles (indivisible loads). Travel restrictions remain for some vehicles requiring a permit to operate, and a Structure Management Plan (SMP) remains in place (QTMR, 2023a). The load monitoring has continued since the strengthening was completed and the freight load restrictions lifted.

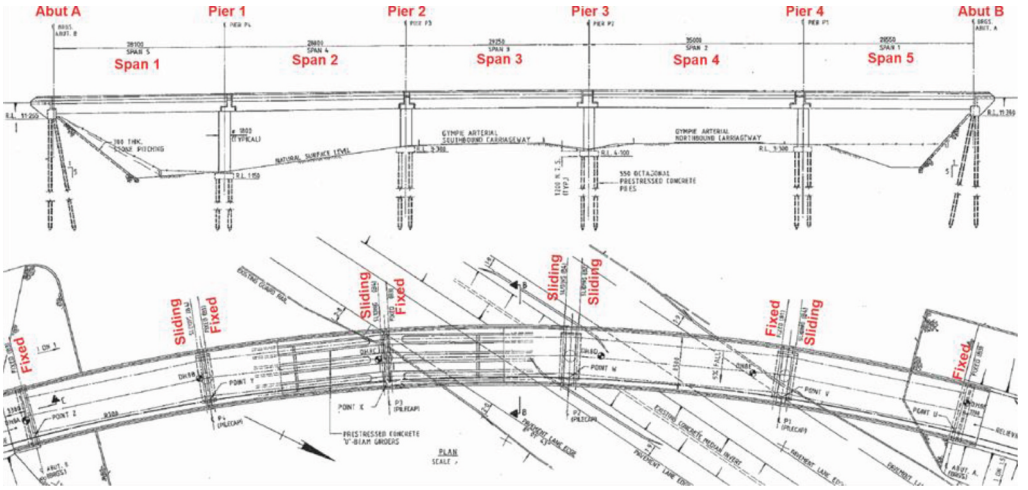


Figure 3. General arrangement of the subject bridge.

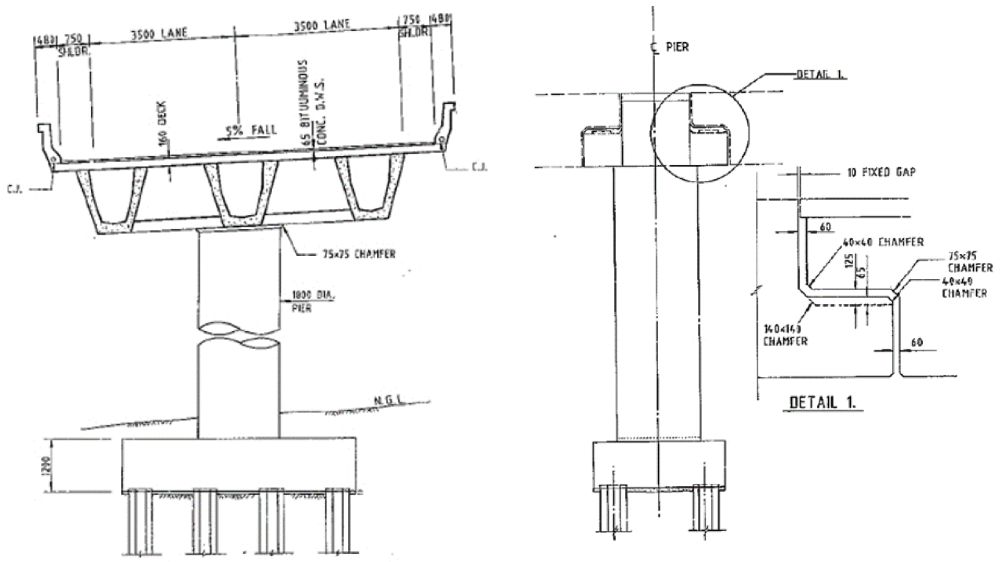


Figure 4. Typical elevation at pier showing halving joints.

A Bridge Specific Live Load Model (BSLLM 2020) was developed in October 2020 to inform decisions relating to the interim management of the superstructure including the girder halving joints which remain unstrengthened. The BSLLM provided a better understanding of the vehicles accessing the structure and the live loads they impose with an update report issued in May 2023 (QTMR, 2023b). The data used to generate the BSLLM was made available to investigate the potential fatigue issues in inverted "T" headstocks.

2.1 *The opportunity to investigate fatigue in halving joints*

When considering the management of halving joints in concrete bridges the question arises as to whether fatigue is likely to be an issue. The question arises because it is not uncommon for there to be significant cracks emanating from the joint re-entrant corner, which, if measured, will be found to be opening and closing with the passage of every heavy vehicle. This scenario was identified in 2019 during early Subject Bridge technical investigations.

While the fatigue risk in the Subject Bridge headstocks no longer exists due to the strengthening, the question of whether fatigue would have been an issue is still relevant because it can help guide future management decisions on other bridges. Essentially, if there ever was going to be a case where fatigue could be an issue on QTMR halving joint bridges, then it would be on this bridge. It is very heavily trafficked, with deficient headstock halving joints, and obvious working cracks. The availability of comprehensive loading data over a period of almost 2 years provided a unique opportunity to investigate whether fatigue would have been an issue in the headstocks of the Subject Bridge. This investigation only addresses the potential for fatigue in the headstocks.

3 ANALYSIS METHODOLOGY

A full discussion of analysis methodology is beyond the scope of this paper. In summary:

- Finite Element Analysis (FEA) and health monitoring results were used to define the characteristic bearing reactions under ambient loading.
- Separate FEA was used to determine the characteristic opening/closing of one of the cracks for which monitoring data was available and predict bar stress ranges.
- Contemporary fatigue assessment of both steel and concrete elements was then undertake based on FEA results.

Some of the more pertinent aspects of this approach are discussed in this Section.

The loading data that are available for each heavy vehicle and useful for the fatigue assessment are the midspan girder strains. This was recorded for every heavy vehicle. A threshold girder strain for classification as a heavy vehicle was set at 25 microstrain in any girder. If the threshold was exceeded the event was classified as a heavy vehicle and the peak girder strains and other data was recorded and saved.

The data available covers the period from 16 December 2020 to 31 May 2022, a period of 531 days. Over this period there were 287432 heavy vehicle events.

If a threshold girder strain of 48 microstrain was exceeded, then the event was classified as a very heavy vehicle and the waveform of the response and photographs of the vehicle were also recorded. There were 5576 very heavy vehicle events over the recording period. Many of these vehicles could be classified (eg as 4 axle cranes, 6 axle low loaders etc). This allowed a more careful assessment of the fatigue effects of these to be undertaken.

Influence line results from FEA of the structure were used to predict girder strains and bearing reactions for various vehicle types. These results were in turn used as follows:

- The difference in girder peak strains between Girder 1 and Girder 3 (the outer two girders) was shown to be able to predict the drive line (relative to the bridge centre line) for a vehicle. These results were used to estimate the drive lines of all the heavy vehicles based on the recorded maximum girder strains.
- The load range at the outside bearing on Pier 2 was shown to be very sensitive to drive line. For various vehicle types the relationship between the bearing reaction range, the sum of

the girder strains (a measure of vehicle mass) and the drive line eccentricity (relative to the centre line) was established. This, combined with a FEA system model allowed the bearing load range to be calculated for each event.

Separate FEA of the Pier 2 headstock allows the stress range in the reinforcing in the headstock to be calculated based on the live load reaction range on the outer bearing. Full details of this FEA are beyond the scope of this paper, but some features are relevant. Illustrations of the models are provided in Figure 5.

The right-hand side of the model is at the face of the pier column and is fixed. The concrete in the model is "pre-cracked" into 5 distinct blocks. The 'crack' locations match observed cracking. The interfaces between the blocks have no tensile capacity and no friction when the cracks are open, but very high friction when the cracks are closed. The green block shown in Figure 5 supports the bearing loads (applied to the red squares). Once permanent load has been applied, the green block is supported only by reinforcing crossing the pre-existing cracks. When an additional live load is applied, the reinforcing resists all of the additional load. This methodology was used to ensure that the calculated stress ranges in the reinforcing due to the vehicle loads was conservative.

An unforeseen feature of this model was that bending deformations in the headstock produced slip on the crack faces once they were open and hence frictionless (No Crack Friction model). This resulted in local bending stresses in the reinforcing where it crossed the cracks. These stresses were in some cases higher than the axial stresses and would reduce the predicted fatigue life by orders of magnitude. A more realistic estimation of the local bending stresses was arrived at by introducing some friction (or shear stress) on open, but narrow, cracks (Friction on Crack model). Even for this model, the reinforcing stress ranges due to local bending are very significant.

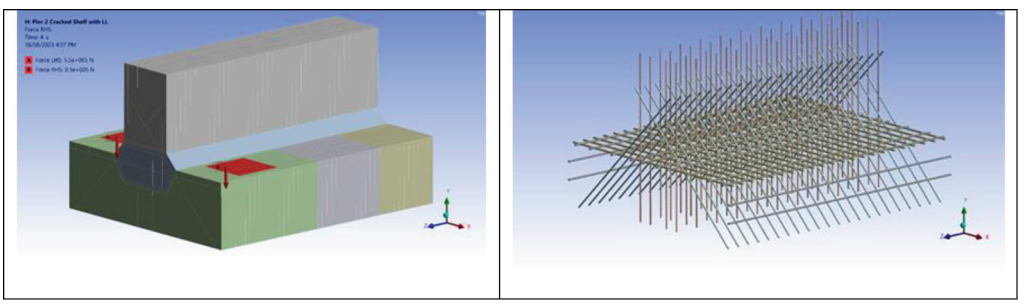


Figure 5. Illustration of separate FEA models of concrete and reinforcing.

The calculated reinforcing steel stress range for every vehicle was used to calculate the fatigue damage for each vehicle. This is then summed over all the vehicles to calculate the fatigue damage over the known monitoring period. This can then be used to calculate total fatigue damage over a required design life.

4 STEEL FATIGUE ASSESSMENT

The fatigue assessment was undertaken in accordance with Section 18 of AS 3600:2018 (Standards Australia, 2018). This is a new section in AS 3600 but is almost identical to the fatigue provisions of the CEB-FIP Model Codes (2010). A similar section has not yet been added to AS 5100 (Standards Australia, 2017). The fatigue assessment requires that for each heavy vehicle event, i, the fatigue life N_i cycles be calculated based on the reinforcing steel stress range $\Delta\sigma_i$ for that event. The formula for this is given in Eq. 1.

$$N_i = \left(\frac{\varphi_{s,fat}\Delta\sigma_{Rsk}}{\gamma_F\Delta\sigma_i}\right)^m N_{Rsk} \tag{1}$$

Where N_i is the fatigue life in cycles, $\varphi_{s,fat} = 0.85$ is the capacity reduction factor for fatigue, $\gamma_F = 1.1$ is the load factor for fatigue, $\Delta\sigma_{Rsk} = 210MPa$ for straight N16 bars, $N_{Rsk} = 10^6$ cycles, $m = 5$ for $\gamma_F\Delta\sigma_i > \varphi_{s,fat}\Delta\sigma_{Rsk}$ or 9 otherwise, $\Delta\sigma_i$ is the reinforcing stress range and i is the event.

The fractin of the fatigue life used, or the fatigue damage, for each event is 1/Ni. The total fatigue damage (D) is calculated by summing the damage for each event over all events, Eq. (2).

$$D = \sum_i \frac{1}{N_i} \tag{2}$$

Note that these code-specified fatigue lives are by their nature conservative. They are based on characteristic fatigue S-N curves which have only a low probability of not being exceeded, and then have capacity reduction factors applied to them. The probability of fatigue cracking existing when the fatigue life has been reached is still very low.

4.1 *Steel fatigue assessment - results*

In the first instance, the results are based on the higher reinforcing stresses from the No Crack Friction model.

The total fatigue damage for the 287432 heavy vehicle events which occurred over 531 days was 0.0265. Assuming this rate of fatigue damage remains constant then the fatigue life would be 55 years (37.7 cycles of 531 days). The total fatigue damage for the 5576 very heavy vehicle events (classified) which occurred over 531 days was 0.0057.

The 5576 classified very heavy vehicle events will essentially be the same as the highest 5576 events in the unclassified data as determined by the G1 girder strain. The fatigue damage for these events calculated using the unclassified methodology was 0.0067 which is slightly higher than that calculated using the classified event methodology. This is expected because the unclassified data was treated as if it was all from the most severe vehicle type. Significantly these 5576 events represent only 1.9% of the heavy vehicles but caused 25% of the fatigue damage.

Conversely the events with Girder 1 strains less than 25 με, which only just exceeded the threshold for inclusion, represent 15% of the total events, but only caused $1.17\text{x}10^{-7}$ of the fatigue damage. So, it can be concluded that the fatigue damage due to all of the loadings which were not recorded was negligible.

If the reinforcing stress ranges use the more realistic local bending stress from the Friction on Crack model, then the fatigue damage due to all of the heavy vehicle events was only 0.00115. This corresponds to a fatigue life of 1265 years.

4.2 *Discussion – steel fatigue assessment*

The stress ranges using the reduced local bending stresses are still considered to be conservative. Most methods of analysis would not have even considered local bending stresses.

The dramatic effect of stress levels on the fatigue life is due to the exponent $m = 9$ used in the fatigue life calculations. The value $\Delta\sigma_{Rsk} = 210$ MPa is effectively a fatigue cut off limit. Stress ranges below this (after including capacity reduction factors and load factors) cause very little fatigue damage.

Consideration should be given to any non-conservative aspects of the assessment. Particularly, it is noted that the Girder 1 strain predictions were about 5% low for the calibration vehicles. If the predicted bearing reaction ranges were increased by 5% to account for this, this would in turn reduce the fatigue life by a factor of about $0.95^9 = 0.63$. While significant, the predicted fatigue life is still very high.

The assessment has only considered Pier 2. Piers 3 and 4 of the bridge support Span 4 which is longer. From previous assessments the bearing reactions for the HML B-double on this span are about 8% higher than those on Pier 2. The headstock design is different with more reinforcing, but as a worst case if the headstock design was the same as Pier 2, then the predicted fatigue life (including the 5% assessment error) would be factored by $(0.95/1.08)^9 = 0.31$. This equates to 399 years which is clearly still adequate.

It is concluded that despite the excessive cracking in the headstocks, the fact that they had insufficient ultimate capacity, and the high traffic loads, premature failure due to fatigue in the reinforcing steel was not likely.

The assessment did not consider the effects of corrosion on the reinforcing bars, which is appropriate for this bridge. However, the presence of corrosion on the reinforcing in a halving joint would greatly reduce the fatigue resistance.

5 CONCRETE FATIGUE ASSESSMENT

There are two types of fatigue in the concrete that require consideration. The first is conventional concrete fatigue from cycles of compressive stress. The second is local fatigue in the concrete surrounding the reinforcing bars due to bond stress resisting slip. This will be referred to as bond fatigue.

5.1 *Concrete fatigue*

Based on the headstock FEA, the maximum compressive stress which occurred in the headstock under the maximum calculated bearing load (from all recorded events) was 12.5 MPa. After taking into account the stress gradient factor, this stress was less than the threshold defined in Clause 18.2 of AS 3600 and therefore no further fatigue assessment for concrete in compression was required. Hence failure due to fatigue from cyclic compression in the concrete was not considered to be a risk.

5.2 *Bond fatigue*

Bond fatigue refers to a gradual reduction in the bond stress between the bars and the concrete under conditions of repetitive loading cycles. Initially the bond stress is highest immediately adjacent to a crack. If the stress in the reinforcing at the crack is high, then the bond capacity might locally be exceeded resulting in a small amount of local slip near the crack. This effectively allows the crack to open.

The concern is that this region of locally exceeded bond capacity will extend along the bar if the cyclic stress range in the bar is very high. The particular concern was with the horizontal bars in the bearing shelf which are straight, and are not anchored at each end with hooks or cogs. If the local bond breakdown did continue to grow along the bar, then ultimately bar pullout and failure might occur.

There are no requirements relating to bond fatigue in AS 3600 or the CEB FIP model concrete code.

A number a fundamental bond fatigue tests were undertaken by Balazs (1991). In brief, the test results showed that the nature of fatigue behaviour depended on the embedment length:

- If the embedment length is short so that slip occurs over the entire length of a bar that is pulled from one end, then the fatigue life is finite and relatively short (depending on load level and many other factors)
- If the embedment length is long enough so that there is no movement at the unloaded end, then the fatigue life is essentially infinite. The slip increases with load cycles initially and then stabilizes.

All of the bars except the horizontal bars have development lengths in excess of the code requirements for the development of the bar yield stress of 410 MPa. Given that the maximum bar stress under the highest recorded bearing load was 280 MPa (for the vertical bars), slip at the unloaded end will not occur and the bond fatigue life should be infinite.

For the horizontal bars, the length of the bar beyond the crack is 610 mm which is less than the development length of 745 mm for these Y24 bars. Hence the available length could develop a stress of 610/745 x 410 MPa = 336 MPa in the bar. The maximum stress in the horizontal bar at the crack was 103 MPa. This should be easily developed by the available length,

and so slip at the unloaded end will not occur and the bond fatigue life for this bar should also be infinite.

A further indicator that bond fatigue is not an issue is the results of the monitoring of the crack movement. If bond degradation is occurring, and bar slip near the crack increasing, then an increase in the crack opening movement will occur. The results of the monitoring (QTMR 2023b) showed that, while early results seemed to indicate increasing crack opening, this proved to be a seasonal effect and over the full monitoring period there was no trend of increasing crack movement.

It was concluded that failure due to bond fatigue is not considered to be a risk.

6 CONCLUSIONS

Discovery of active cracks on the Subject Bridge halving joints in 2019 was a significant concern given the strategic significance of the route and its heavy vehicle duty. The scope of concerns spanned both ultimate and serviceability limit states, with significant concerns associated with the potential for fatigue deterioration over time, particularly for the reinforced concrete headstock. A range of interventions were implemented including structural health monitoring.

While permanent interventions on the bridge eliminated the consequences associated with this risk, the opportunity was identified to better understand and quantify the nature of fatigue risks in reinforced concrete halving joints based on structural health monitoring data gathered as part of interim intervention.

The results of the investigation showed that for a heavily trafficked halving joint with compromised ultimate capacity, fatigue in the joint due to repeated ambient loading was confirmed to be unlikely. The department's existing operational and inspection regime for the bridge is considered adequate. This also provided valuable information for assessing the likely fatigue risks in other reinforced concrete halving joints in the QTMR network.

Note that these findings are somewhat dependent on the traffic mix using the QTMR network. Further, they would not be applicable to halving joints with corroded reinforcing.

ACKNOWLEDGEMENT

The authors gratefully acknowledge the financial support provided by the National Center of Excellence, a joint research program of QTMR and NTRO (National Transport Research Organisation), which was instrumental in facilitating this research.

REFERENCES

Highways England (2020) CS 466 'Risk Management and Structural Assessment of Concrete Half Joint Deck Structures', Design Manual for Roads and Bridges, Highway Structures & Bridges Inspection & Assessment, Revision 0, March 2020.

Balazs, G. L.(1991), "Fatigue of Bond", ACI Materials Journal Vol 88 No. 6, November-December 1991.

Muller, J. F., and Dux, P. F.,(1994), "Fatigue of Prestressed Concrete Beams with Inclined Strands", ASCE Journal of Structural Engineering, Vol 120, Issue 4, April 1994.

Standards Australia (2017) AS5100:2017 Bridge Design, SAI Global

Standards Australia (2018) AS3600:2018 Concrete Structures, SAI Global

Bridge Maintenance, Safety, Management, Digitalization and Sustainability – Jensen, Frangopol & Schmidt (eds)
© 2024 The Author(s), ISBN 978-1-032-77040-6
Open Access: www.taylorfrancis.com, CC BY-NC-ND 4.0 license

Enhancing safety on timber bridges: Feasibility and risk assessment of bridge barrier implementation

E. Chaw, G. O'Connor, D. Milling, A. De Silva & R. Daley
National Transport Research Organisation, Victoria,Australia

B. Wiggins
Queensland Department of Transport and Main Roads, Queensland, Australia

ABSTRACT: The Queensland Department of Transport and Main Roads (TMR) manages 286 timber bridges, some of which do not have bridge barriers or are substandard. Whilst the current Australian Standard indicates that bridge barriers are not required in certain road scenarios, the enhancement and elevation of safety measures remains a factor to consider. This project investigated the feasibility and prioritisation of installing bridge barriers on timber bridges. First, a literature review was conducted, followed by the identification of. barrier installation options as well as commercially available proprietary systems. A risk-based multi-criteria analysis was developed to identify suitable bridge barrier candidates on low-volume roads. This methodology was used to quantify crash risks and calculate a risk score for each location. The analysis identified 138 sites that are recommended to be investigated for safety barrier installation. This process can be extended to bridge networks across Australia.

1 INTRODUCTION

Bridge barriers are crucial for preventing errant vehicles from leaving the bridge deck or colliding with hazards adjacent to or on the immediate approach to the structure. To align with the Australian Government's Vision Zero principle (Commonwealth of Australia, 2021), which aims to create a road transport system with no fatalities or serious injuries, it is essential to enhance safety at locations with a high risk of fatal and serious crashes.

Currently, many timber bridges within the Queensland Department of Transport and Main Roads (TMR) network are without bridge barriers. Timber bridges are typically found on low-traffic roads in Queensland. Despite lower traffic volumes, these roads often experience run-off-road and head-on crashes at rates equal to or higher than major freeways (Milling et al., 2023). The risk of serious or fatal injury crashes on low-volume roads and bridges does not decrease with lower traffic volumes. The presence of non-frangible hazards on the bridge approach, adjacent to the bridge and in the ravine; the presence of water in the ravine; and drop heights from a bridge deck substantially elevate crash risks. Bridges without adequate safety barrier lengths on the bridge approach, or without bridge barriers on the bridge deck, fail to protect errant vehicles from these hazards.

This project was established to develop technical guidance to evaluate the feasibility of installing bridge barriers on timber bridges. It also established a method for identifying timber bridges where the addition of a bridge/approach barrier would improve road user safety.

DOI: 10.1201/9781003483755-457

2 LITERATURE REVIEW

2.1 *Barrier system feasibility*

Barrier systems work by transferring forces through the barrier railings to the post, into the deck and then the bridge substructure where they dissipate. These forces can potentially cause damage or failure to the deck under collision loads at the point where the post is attached to the deck. In the consideration of safety and damage minimisation, AS 5100.2 (Standards Australia, 2017) requires bridge barriers be designed as progressive strength systems, with barriers being the first to fail, then connections and finally supporting elements. This is achieved by applying an ultimate load factor of 1.0 to the design of bridge barriers, 1.05 to the connection bolts and reinforcement and 1.10 to the bridge deck design ultimate capacity. To ensure proper performance of a barrier system on a bridge, the bridge deck must be assessed to ensure sufficient strength to transfer the barrier forces without causing damage to the substructure. This assessment is particularly critical for installing barriers on timber bridges since the attachment of the barrier posts to the bridge deck and the ability of the timber superstructure to resist the applied barrier loads may often be the controlling parameters (Ritter et al. 1999). AS 5100.8 (Standards Australia, 2017) allows for a lower performance level barrier to be selected if the bridge's structural capacity is inadequate and replacing or strengthening the bridge is not an option.

For bridges susceptible to flooding, the installation of barriers introduces additional loads on the bridge superstructure during flood conditions. Flooding events can significantly alter the hydraulic conditions around a bridge, resulting in increased water pressure, debris impact and hydrodynamic forces. The presence of a barrier will impose additional hydrodynamic loads on the bridge, leading to increased forces on the piers and abutments. The additional load effects can elevate stress levels and potentially compromise the structural integrity of the bridge.

In addition, the provision of barriers can prevent the passage of debris. Debris jams at the barriers can cause an increase in the upstream water levels (known as afflux) and create a backwater effect, thus posing an additional flood hazard to nearby areas. Stranded wood debris also intensifies the hydrodynamic actions, exacerbating the situation.

The hydraulic performance of a bridge barrier system is dependent on factors such as height, size, shape and open space within the rail face. According to TMR's *Design Criteria for Bridges and Other Structures* (Queensland Department of Transport and Main Roads, 2021), post and rail traffic barriers are suggested to reduce upstream afflux, indicating that steel post and rail bridge traffic barriers are suitable in scenarios where controlling afflux is crucial. When installing bridge barriers, it is important to weigh both their crash resistance and hydraulic performance. Hydraulically, larger openings allow greater passage of water to reduce upstream flooding effects.

Barrier deflection is also an important consideration for timber bridges as it is common to have a narrow horizontal clearance beyond the edge of the traffic lane which limits the allowable dynamic deflection of the barrier, potentially leading to inadequate containment of vehicles during a collision. Austroads (Austroads, 2013) requires rigid (i.e. in situ concrete) or semi-rigid (i.e. horizontal steel beams) barriers when the envelope for deflection is too small to accommodate the dynamic deflection distances specified in the guideline. It is noted that 'low' performance barriers are generally designed to deform during a collision, rather than remaining rigid (Queensland Department of Transport and Main Roads, 2021).

2.2 *Bridge barrier system selection criteria*

AS 5100.1 (Standards Australia, 2017) establishes various performance levels for providing 'Road Traffic Barriers', these include Low, Regular, Medium and Special, as well as the option for no barrier in certain circumstances. These performance levels are adopted as guidelines in all Australian and New Zealand jurisdictions. Both the Austroads (Austroads, 2013) guide and AS 5100.1 (Standards Australia, 2017) provide procedures for assessing the risk associated with bridge barriers and determining the appropriate performance levels.

To assist in selecting the right performance level, Austroads (Austroads, 2013) introduces a site condition category system. AS 5100.1 (Standards Australia, 2017) largely follows these recommendations from Austroads (Austroads, 2013) in its performance level selection procedures,

including chart-based risk assessments and benefit-cost analyses for special performance level barriers. It is also important to note that timber bridges often have narrow widths, decks with limited strength and other factors that can complicate the retrofitting of bridge barrier systems.

AS 5100.8 (Standards Australia, 2017) suggests that if the achievable barrier performance level does not meet the requirements identified in the risk assessment, alternative remedial actions should be explored. These alternatives may include measures like lowering speed limits or installing warning signs to mitigate the identified risks.

For timber bridges on low-volume roads with an annual average daily traffic (AADT) less than 500 vehicles/day and speed limits up to 100 km/h, a low-performance level barrier typically complies with AS 5100.1 (Standards Australia, 2017) requirements. However, a detailed risk assessment is necessary to confirm the performance level required for barriers installed on bridges.

2.3 *Determine the need for bridge barriers on low-volume roads*

Safety barriers (approach and bridge barriers) (Figure 1), are provided to reduce the crash severity of an errant vehicle from the approach to a bridge and on the bridge deck. The criteria to provide a bridge barrier in AS 5100 (Standards Australia, 2017) does not consider the quantification of crash risk (likelihood, exposure, severity) to determine or prioritise the need to provide a bridge barrier.

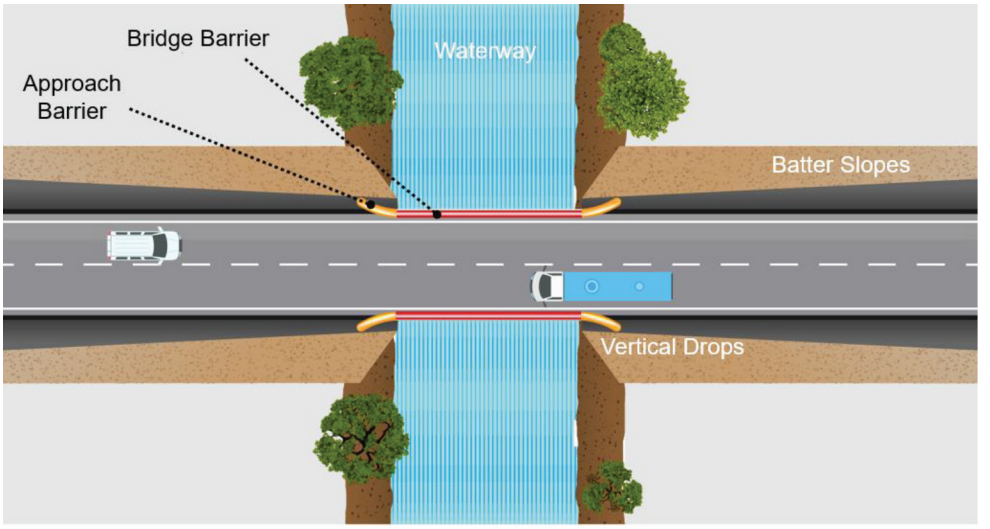


Figure 1. General arrangement of a bridge with approach barriers.

Technical guidance developed in '*NACOE R70 Addressing Sub-optimal Road and Safety Barriers at Bridge Approaches*' (Milling et al., 2023) provided a basis to develop a method to quantify crash risk to determine the need of a bridge barrier and prioritise multiple structures for further investigation across a road network.

3 BARRIER SYSTEMS FOR TIMBER BRIDGES

The structural capacity of timber bridges is a key constraint when selecting a suitable barrier system, as highlighted in the Section 2. The horizontal clearance beyond the edge of the traffic lane determines whether a barrier can be top mounted on the bridge deck or is required to be side mounted. This influences which bridge element(s) will be connected to the barrier system. The individual structural capacity of each bridge element should be evaluated according to the requirements set in AS 5100 (Standards Australia, 2017). The type of barrier selected greatly influences

the structural capacity required of bridge elements, with rigid barriers requiring the highest capacity to resist bending moments, followed by semi-rigid barriers and low-stress barrier systems.

To assist designers and asset owners with the selection of barrier systems for timber bridges, a list of concept arrangements and proprietary products is compiled in Section 3.1. As identified in the Section 2, the requisite highest performance level for barrier systems on these bridges aligns with the low performance level for timber bridges on low-volume roads (AADT < 500 veh/day and speed limit < 100 km/h).

3.1 *Concept barrier arrangements*

There are multiple barrier arrangements available to designers and asset owners that may be suitable for timber bridge applications. A deck-mounted post configuration (Figure 2a) can be considered if the bridge deck has sufficient structural capacity. If the structural capacity of the bridge deck is not considered adequate, the barrier can be side mounted to the outer girder (Figure 2b); however, this arrangement can introduce challenges such as inadequate bearing support due to the round shape of the girder and unsuitable attachment points. If additional structural capacity is still required, steel cross girders with backstays can be installed below the bridge deck (Figure 2c) to provide structural capacity from multiple bridge girders. In the event the entire bridge does not have sufficient structural capacity, the barrier system can be anchored to the bridge abutment and act structurally independent of the bridge. This arrangement is limited by the maximum span of the barrier solution and only relevant for short span bridges or where the barrier system can be fixed to bridge piers. Proprietary products such as the CrocGuard® system (Figure 2d) are available in the market for this application.

If it is not feasible to install barrier systems on a timber bridge, a road safety audit can be beneficial. This audit can help pinpoint appropriate countermeasures to enhance the safety of those using the bridge.

There are a few proprietary systems on the market that are appropriate for low-volume timber bridges. Products such as the Ezy-Guard Bridge Barrier System, CrocGuard® Barrier System and DOLR N232 provide a range of relevant features such as load transfer minimisation to the bridge superstructure, connection to the bridge abutments and minimisation of hydraulic effects during flood events.

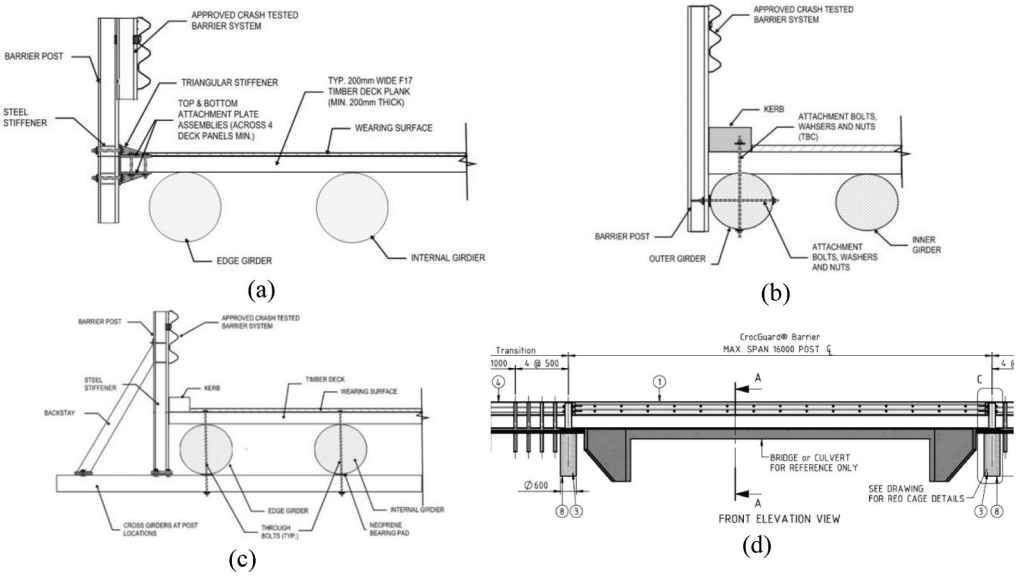


Figure 2. Bridge barrier options. (a) Concept arrangement of deck mounted (Source: Adapted from Polivka et al., 2002), (b) Concept arrangement of side-mounted posts to outer girder, (c) Concept arrangement of a barrier attached to superstructure using cross girders and backstays, (d) CrocGuard® barrier system anchored to bridge abutments.

4 ASSESSMENT AND PRIORITISATION OF BARRIER SYSTEMS IN QUEENSLAND

A method for identifying the need to provide a barrier system on a bridge on a low-volume road was developed by adapting the methodology from *NACOE R70 Addressing Road and Safety Barriers at Bridge Approaches* (Milling et al., 2023) whilst considering AS 5100.1 (Standards Australia, 2017). The NACOE R70 method, in line with widely accepted standards, quantifies risk through the calculation of a combined risk score. This method was adopted from the Austroads *Guide to Road Design Part 6* (Austroads, 2022). The combined risk score (CRS) is used to quantify potential improvement to road user safety by providing a barrier system on a timber bridge. The approach in AS 5100.1 (Standards Australia, 2017), Clause 14.5 Road Traffic Barriers Performance levels is based on a site-specific risk assessment and does not calculate a risk score.

This methodology was applied to TMR asset inventory data and TMR's Digital Video Road (DVR) to quantify the potential improvement to the CRS by providing a bridge barrier or safety barrier on the bridge approach.

4.1 *Assessment process*

The process to determine the need for a bridge barrier on a low volume is shown in Figure 3.

The decision to install barriers on bridges is guided by an evaluation process. This process includes a pass/fail assessment based on stopping sight distance (SSD), a numerical computation of the CRS and a comparative study of the CRS values for scenarios with and without a bridge barrier. The CRS with and without a bridge barrier is considered in parallel with the network CRS intervention level (Network Roadside Risk Intervention Threshold (NRRIT)), the crash history and in some situations a road safety audit. A bridge-specific structural assessment is also required to determine if it is technically feasible to install a barrier system as a measure to improve road user safety.

4.2 *Calculation of CRS*

The CRS is calculated by considering the local road attributes and bridge scenarios shown in Figure 4. The calculation of the CRS is based on the method in Austroads *Guide to Road Design Part 6* (Austroads, 2022) and TMR's supplement *Road Planning and Design Manual Edition 2, Volume 3, Supplement to Austroads Guide to Road Design Part 6: Roadside Design, Safety and Barriers* (Queensland Department of Transport and Main Roads, 2023).

Table 1 shows the CRS inputs for evaluating the need to provide a bridge barrier.

4.3 *Assessment and prioritisation of investigation of TMR's bridge stock*

The database revealed that TMR owns and manages 296 timber bridges, with 167 identified as being on low-volume roads (Low-volume roads were defined as a road with an AADT less than 500). Among these, 96 (57%) have an existing bridge barrier (recorded presence only, no confirmation of being compliant or functional).

TMR's Bridge Asset Database and attributes collected via TMRs DVR were used to calculate CRSs for all timber bridges on low-volume roads. This was inclusive of identifying the crash risk on the approach to a bridge and on the bridge deck. This allowed for crash risk for each timber bridge to be quantified, thus allowing for the sites to be prioritised for further investigation. All sites were assessed with the assumption that the existing safety barrier on the approach or bridge barrier on the deck was inadequate. This allowed for the crash risk at each site to be identified; the adequacy of any existing barrier treatments would be determined in site-specific investigations.

The safety risk assessment methodology calculated a CRS for the following at each of the 167 structures:

- a vehicle leaving a bridge deck and to quantify the need to provide a bridge barrier
- a vehicle striking a hazard behind a bridge approach and to quantify the need to provide a safety barrier on the approach to a bridge.

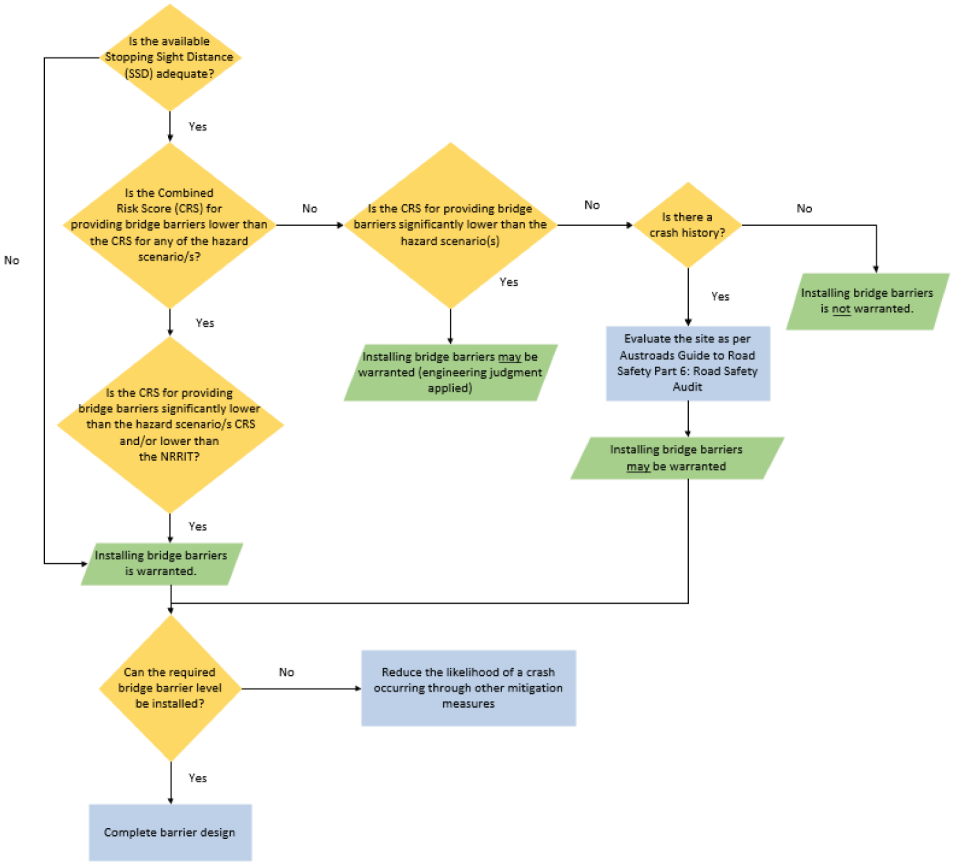


Figure 3. Assessment process to determine the need for bridge barriers.

The assessment identified that 138 of 167 bridges had a CRS higher than the TMR NRRIT of 0.6. This indicates that the risk of a vehicle running off the road or striking a hazard behind the bridge approach is higher than the risk threshold for intervention set by TMR. These bridges may benefit from the installation of barrier systems subject to an onsite assessment. Of these bridges, 47 had a CRS higher than 0.6 for both the approach safety barrier and the bridge barrier. This means the risk of a vehicle running off the road and the risk of striking a hazard behind the bridge approach are both higher than the NRRIT. The other 91 bridges had a CRS higher than 0.6 for the bridge barrier only, meaning the risk of a vehicle leaving the bridge deck is higher than the NRRIT.

5 CONCLUSION

Barrier systems are a key contributing element to road user safety on bridges. However, special consideration must be applied when selecting a suitable barrier system for a timber bridge, particularly those which may have limited structural capacity. Key findings from this report include:

- Low performance barriers typically meet the requirements in AS 5100 (Standards Australia, 2017) for timber bridges on low-volume roads in Queensland (AADT < 500veh/day and speed limit < 100 km/h).
- The existing structural capacity of a timber bridge is a key limitation when selecting a barrier system. AS 5100 (Standards Australia, 2017) requires a hierarchy of failure with

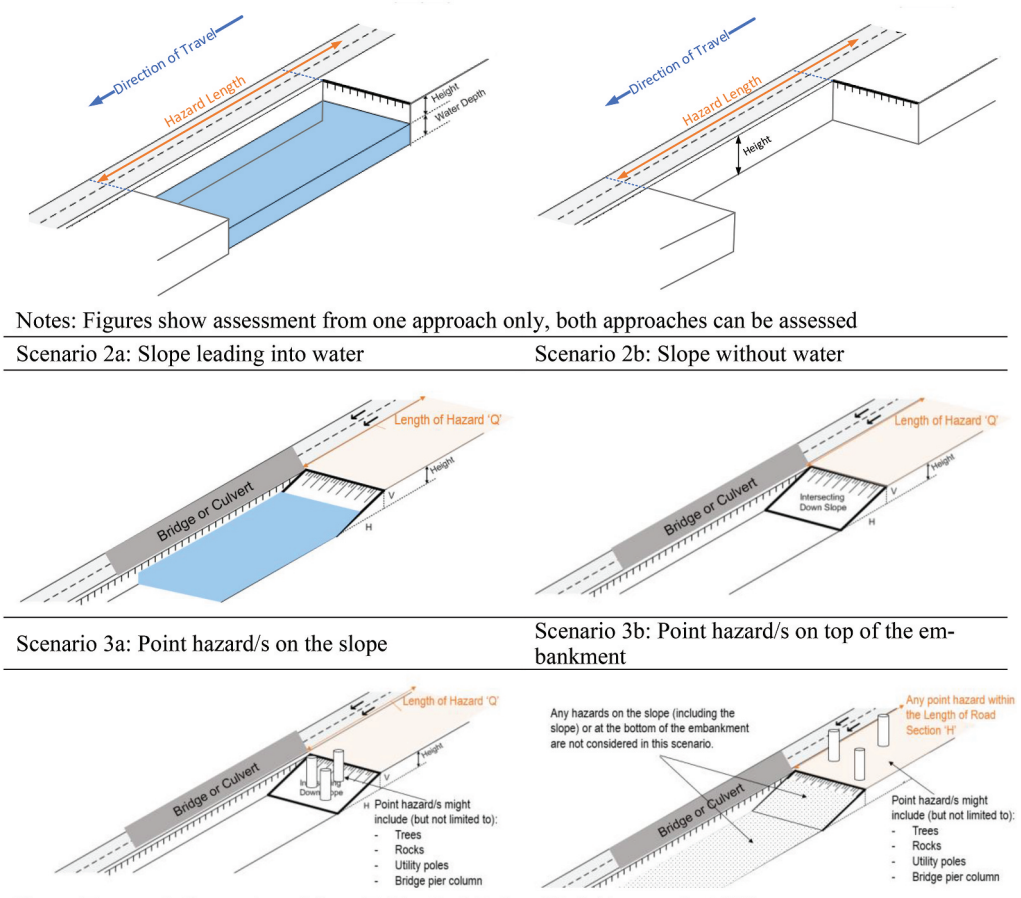


Figure 4. Isolated hazard scenarios: bridge deck and bridge approach.

the barrier to fail first, followed by the connection and finally the bridge superstructure. There are multiple barrier concept arrangements available for selection with connections made to one or a combination of bridge elements.

- Hydraulic effects are an important consideration for bridges at risk of flooding. These effects can be minimised by providing sufficiently large voids in the barrier to allow water and debris to pass through, such as rail and post traffic barriers.
- A risk-based assessment methodology was developed to assist TMR in the prioritisation of investigations for bridge barrier installations.
- An analysis of the TMR Bridge Asset Database found that 138 of the 167 timber bridges on low-volume roads have a CRS greater than TMR's NNRRIT. This analysis can support TMR effectively target structures which would most benefit from intervention.
- Barrier systems may not be a feasible solution for timber bridges, and in these cases, a road safety audit should be performed to identify measures that can be applied to improve road user safety.

By leveraging the insights gained from this project, TMR is now able to equip decision-makers with the necessary knowledge to prioritise the timber bridges that would benefit most from a barrier system with available funding. This crucial assessment can lead to significant enhancements in road user safety.

Table 1. Combined risk score inputs.

Group	Measure	Hazard scenario/s	Bridge barrier
General road characteristics	Length of road segment (m)	Greater of 200 m or the length for the hazard scenario.	Greater of 200 m or the length for the hazard scenario.
	Lane width (m)	Same measurement for hazard scenario and bridge barrier.	Same measurement for hazard scenario and bridge barrier.
Background hazard characteristics	Description	Background hazards are not considered when assessing a vehicle departing a bridge as the hazard.	Background hazards are not considered when assessing a vehicle departing a bridge as the hazard.
Particular road characteristics	Curve radius (m)	Same measurement for hazard scenario and bridge barrier.	Same measurement for hazard scenario and bridge barrier.
Isolated hazard characteristics	Description	Hazard scenario/s B1 and/or B2.	Bridge barrier.
	Length of the hazard (m)	Bridge deck length + 20 m (Queensland Department of Main Roads, 1999).	Bridge deck length + required safety barrier transition length.
	Average distance between isolated hazards (m)	The length of road segment (m).	The length of road segment (m).
	Lateral distance to the isolated hazards from the edge of lane (m) (Austroads, 2022, Figure B-10)	0.1 m or distance from the edge line to the bridge edge.	0.1 m or the distance from the edge line to the bridge barrier.
Exposure	Curve correction factor	Figure B.4 (Austroads, 2022).	Figure B.4 (Austroads, 2022).
Severity (Trauma Index)	Trauma Index for isolated hazards (operating speed of 110 km/h)	As per Trauma Indices for Scenario B1 and/or B2.	Section B.4.3 (Austroads, 2022).

ACKNOWLEDGEMENTS

This project was a collaboration between Queensland Department of Transport and Main Roads (TMR) and the National Transport Research Organisation (NTRO). The authors gratefully acknowledge TMR and other stakeholders who provided the information necessary to conduct this study.

AUTHOR CONTRIBUTIONS

EC, GOC, DM, and BW devised the scientific direction of this study. EC, DM, GOC, and BW conducted the analysis and generated the final report. EC, AD and RD wrote complete manuscript. BW assisted with proofreading and minor revisions.

REFERENCES

Austroads 2013, Standardised bridge barrier design, AP-R445-13, Austroads, Sydney, NSW.

Austroads 2022, Guide to road design part 6: roadside design, safety and barriers, AGRD06-22, edn 4.0, Austroads, Sydney, NSW.

Commonwealth of Australia, 2021, National Road Safety Strategy 2021-30, Commonwealth of Australia, Canberra, ACT.

Milling, D., Young, B., & Affum, J. 2023, R70 Addressing sub-optimal road and safety barriers at bridge approaches [Contract report 014547]. prepared for Queensland Department of Transport and Main Roads under the NACoE program, ARRB, Port Melbourne, Vic.

Queensland Department of Main Roads 1999, Road Impact Severity Calculator (RISC) User Guide, Queensland Department of Transport and Main Roads, Brisbane, Qld.

Queensland Department of Transport and Main Roads 2021, *Design criteria for bridges and other structures*, Queensland Department of Transport and Main Roads, Brisbane, Qld.

Queensland Department of Transport and Main Roads 2023, *Road Planning and Design Manual Edition 2, Volume 3, Supplement to Austroads Guide to Road Design Part 6: Roadside Design, Safety and Barriers*, Queensland Department of Transport and Main Roads, Brisbane, Qld.

Polivka, KA, Faller, RK, Ritter, MA, Rosson, BT, Rohde, JR & Keller, EA, 2002, Two test level 4 bridge railing and transition systems for transverse glue-laminated timber decks, Fifth international bridge engineering conference, Washington, D.C., National Academy Press, USA.

Ritter, MA, Faller, RK & Duwadi, SR 1999, 'Crashworthy railing for timber bridges', *Proceedings of Pacific timber engineering conference*, *Rotorua, New Zealand, Forest Research Bulletin*, no. 212, pp. 325–32.

Standards Australia, 2017, AS5100 Bridge Design, 2nd edition, Standards Australia, Sydney, NSW

Bridge Maintenance, Safety, Management, Digitalization and Sustainability – Jensen, Frangopol & Schmidt (eds)
© 2024 The Author(s), ISBN 978-1-032-77040-6
Open Access: www.taylorfrancis.com, CC BY-NC-ND 4.0 license

Design curves for masonry arch bridges over rivers in the UK

J. Liu
Department of Civil Engineering, University of Bristol, Bristol, UK

G. Degan Di Dieco, F. Degan Di Dieco & F. Ragone
Pollino Engineering Group (PEG), Castrovillari, Italy

S.L. Nunn
SLN Proofreading Services, Hoddesdon, UK

ABSTRACT: Bridge datasets in the UK lack geometric data needed to estimate the flood vulnerability of bridges. Therefore, flood quantitative risk assessment (QRA) of these portfolios is impaired. This paper developed design curves to derive arch rise and arch thickness for masonry arch bridges given their maximum span length. The span length was found in all surveyed bridge datasets. The masonry arch bridge type presents the higher flood risk in the UK. This work involved: (i) a search process to identify studies that addressed the lack of bridge data; (ii) the collection of publicly available bridge data for masonry arch bridges over UK rivers; (iii) the fitting of design curves to the collected data; and (iv) the model validation of design curves. Seen statistics metrics, the design curve of arch thickness may supply bridge data. Regarding design curves of arch rise, collected data is too sparse, thus better pre-processing is needed.

1 INTRODUCTION

Bridges are crucial in supporting our society. Flood actions are the leading cause of bridge damage around the world (Degan Di Dieco et al. 2022). The frequency of flooding is expected to increase, thus more riverine bridges are expected to fail (Wang et al. 2021).

There are about 150.000 bridges in the UK, among them, half are masonry arch bridges (MABs) and have short-length span, and in many cases are more than 100 years old (Solan et al. 2020). One MAB is expected to collapse every three years in the UK (Lamb et al. 2019).

To prevent failures, bridge capacities are designed to withstand effects of load demands, given a bridge geometry in input. The bridge geometry can be used either in numerical analyses (Tubaldi et al. 2018) or in analytical expressions (Degan Di Dieco et al. 2023) for "probabilistic reliability-based assessments" (NH 2022). Probabilistic reliability-based assessments express the likelihood that assets at risk will sustain varying degrees of damage conditioned upon hazard intensity. Probabilistic reliability-based assessments that estimate the expected level of asset direct damage are called "fragility functions" (Galasso et al. 2021), which is the term used herein. To define reliable fragility functions, it is necessary to identify the bridge geometry. In this study, variables underpinning the bridge geometry, such as span length, pier dimensions, are referred as "bridge attributes" (Pregnolato 2019). To use geometry-based fragility functions, specific bridge attributes are needed, such as arch rise, arch thickness, aspect ratios of pier and abutment (George & Menon 2021). However, bridge datasets of UK infrastructure owners do not generally report arch rise and thickness (Degan Di Dieco et al. 2022), thus limiting quantitative risk assessment (QRA) of bridge portfolios at risk of scour and/or flooding (Li et al., 2021). The present study estimates missing attributes from those that are commonly available, such as span length, by developing design relationships for arch thickness and arch rise as a function of span length.

Section 2 presents the literature review of studies which addressed the lack of bridge attributes. Section 3 shows methodologies proposed for data collection, model development, data

DOI: 10.1201/9781003483755-458

fitting and model validation. Section 4 shows results of data fitting and model validation. In Section 5, strengths and weakness of the proposed models are discussed, and future directions are given. Section 6 summarises paper findings.

2 LITERATURE REVIEW

For QRA of bridge portfolios via fragility functions, scholars typically: (i) extract bridge attributes from databases; (ii) carry out statistical analysis on bridge attributes; (iii) classify bridges into classes; and (iv) develop fragility functions for each class.

Lack of bridge attributes may occur when dealing with databases; in this case, it is common practice to use surveyed real-life bridge attributes to characterize missing ones via preliminary design relationships, which are referred as "design curves" in this study (da Porto et al. 2016). Major attributes for the characterization of a MAB are arch thickness to span length ratio t/L and arch rise to span length ratio r/L (Proske & van Gelder 2009).

A few works proposed design curves for MABs and provided results of statistical fitting. Design curves are developed as part of national scale QRA (Medina-Cetina et al. 2020). The literature review of this study is based on a searching process that used the keywords "bridge inventory" and "bridge portfolio" via Scopus and Google Scholar: 120 studies were found. Of these, only 13 studies were retained, with 11 studies related to MABs and two studies to reinforced concrete bridges. These 13 studies have been summarised in Table 1 by load(s), bridge location(s), design curve(s) used to fit arch rise and arch thickness. The main gap of these studies is the lack of goodness of fit to bridge attributes, therefore reliable design curves for masonry arch thickness and arch rise are missing in the literature. This paper aims to estimate attributes for MABs needed for vulnerability assessments by developing new design curves for arch rise and arch thickness. To fulfil the aim, this study develops design curves using a publicly available database for 74 MABs in the UK (Wu 2010). Once developed, the design curves are validated against a second publicly available dataset for MABs in the UK (Robinson 2000). The two datasets are totally independent.

Table 1. Summary of the selected studies proposing design curves for masonry arch bridges (in alphabetical order). Legend: NA = not applicable, r = arch rise, t = arch thickness, L = span length.

No.	Reference	Load(s)	Country(ies)	Design curve(s)
1	Breymann (1926)	Dead loads	Italy	t: linear in L
2	Busch & Zumpe (1995)	Traffic loads	Germany	t: linear in L
3	Cavalcante et al. (2021)	Flood, Hurricane, Seismic	Brazil	column height: linear in L
4	Cocciaglia & Mosca (1998)	Dead loads	Italy	t: linear in L
5	Corradi (1998)	Dead loads	Italy, France, Germany, Russian	t: linear in L
6	Corradi & Filemio (2004)	Dead loads	Italy	t: non-linear in L
7	da Porto et al. (2016)	Seismic	Italy	t: non-linear in L
8	Huerta (2004)	Dead loads	Italy, France, Germany, Russian	t: linear in L
9	Kurrer (2002)	Dead loads	Germany	t: non-linear in L
10	Medina-Cetina et al. (2020)	Flooding	US	NA
11	Modena et al. (2004)	Dead and Traffic loads	Italy	t: non-linear in L
12	Purtak (2004)	Dead and Traffic loads	Germany	r: linear in L t: linear in L
13	Wu (2010)	Dead and Traffic loads	UK	r: linear in L t: linear in L

3 METHODOLOGY

For QRA of bridge portfolios, fragility functions are crucial to estimate direct damages. However, UK available bridge datasets do not contain bridge attributes commonly needed for applying existing fragility functions (e.g. George & Menon 2021), so QRA is impaired. This lack of bridge attributes is common in QRA for other natural hazards (da Porto et al. 2016). Several approaches are possible in order to answer this data lacking. In particular, Zelaschi et al. (2016) suggests identifying lower and upper bounds of bridge attributes and assigning a probability distribution to each attribute; subsequently, the distribution can be sampled to derive a certain number of bridge samples. However, this procedure is statistically expensive and associated with different epistemic uncertainties. A less complex methodology is proposed by da Porto et al. (2016), which suggests using design curves based on fitting functions of available bridge attributes; by doing so, statistical uncertainties. Therefore, design curves are used in this study to derive missing bridge attributes. The current work was conducted in different steps, the flowchart shown in Figure 1 presents the needed steps for building the design curves.

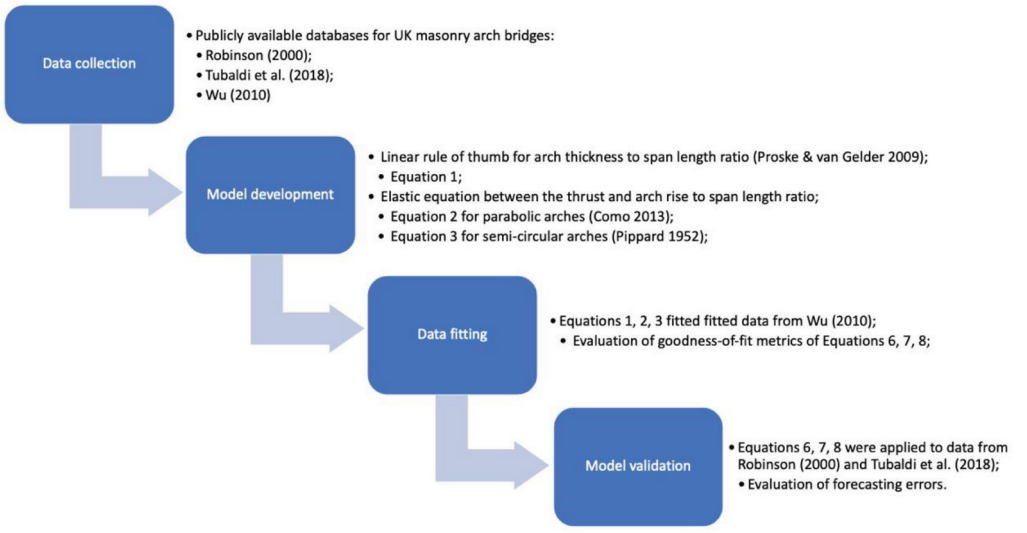


Figure 1. Flowchart of the steps needed to develop and validate proposed design curves.

3.1 *Data collection*

Publicly available geometry data for MABs was searched via Scopus and Google Scholar using the keywords "bridge portfolio" and "bridge inventory". The first dataset for MABs is from Wu (2010) and is used as the fitting dataset. Among bridges investigated by Wu (2010), 74 bridges are related to the UK. Therefore, these 74 bridges were selected by this study for curve fitting. Further geometry data was found in Robinson (2000). Robinson (2000) collected geometry data of 99 MABs in the UK, from which nine bridges were randomly considered to carry out the model validation; a further case study for model validation was retrieved by Tubaldi et al. (2018), for a total of ten bridges. The datasets used in this study are totally independent.

3.2 *Model development*

From the literature review, two approaches were identified to identify design curves: (i) application of regressions to available attributes (Proske & van Gelder 2009); (ii) use of theoretical relations which map the axial force in the arch at the crown to available attributes (Como 2013).

From Table 1, it can be seen that t is a linear function with span length L in 8 of the 13 reviewed studies. Therefore, in this study, a general linear function (Equation 1) is used for fitting

the t/L ratio data of Wu (2010). The r/L ratio data is a function of arch shape (Como 2013), thus fitted with the theoretical relation between the axial force, called thrust, and arch rise for two kinds of arch shapes, parabolic arch (Equation 2) and semi-circular arch (Equation 3).

A linear function between arch thickness t and span length L suitable for most arch shapes can be expressed as (Proske & van Gelder 2009):

$$t' = \frac{t}{L} = \frac{c_1}{L} + c_2 \tag{1}$$

where c_1 is a length, c_2 is dimensionless, both are constants and greater than zero. In this study, t represents the arch thickness at the arch crown, or key, and this value is kept constant along the arch line, i.e. arch thickness at crown is equal to arch thickness at springing.

In the elastic theory, the thrust H in a parabolic arch is given by $H = pL^2/8r$ (Como 2013), where p is the uniform load, L is the span length, r is the arch rise. Therefore, the arch rise to span length ratio r/L can be obtained via arranging the terms:

$$r_p' = \frac{r}{L} = \frac{pH}{8} \cdot L = c_3 \cdot L + c_4 \tag{2}$$

where c_3 and c_4 are both constant, c_3 is opposite of a length while c_4 is dimensionless.

In the elastic theory, the thrust H in a semi-circular arch is given by $H = 4pr/3\pi$ (Pippard 1952), where p is the uniform load, r is the arch rise. Because the arch is semi-circular, $L = 2 \cdot r$, r/L can be obtained via arranging the terms:

$$r_p' = \frac{r}{L} = \frac{3\pi H}{4p} \cdot \frac{1}{L} = \frac{c_5}{L} + c_6 \tag{3}$$

where c_5 and c_6 are both constant, c_5 is a length while c_6 is dimensionless.

3.3 *Data fitting*

The fitting of t/L and r/L data is carried out by using the MATLAB Curve Fitting Toolbox (MathWorks 2023). The data is first plotted via scatter plots, on which fits are performed. The performance of the fitted models is evaluated via two goodness of fit metrics, R^2 and Root Mean Square Error ($RMSE$). R^2 is the coefficient of determination in statistics (Motulsky 1995), while $RMSE$ of forecasted values $\widehat{Y}_i$ is computed as the square root of the mean of the squares of deviations (Kutner et al. 2005). Alexander et al. (2015) proposed two criteria for a forecasting model to be useful: (i) high R^2, e.g., $R^2 > 0.6$; (ii) low $RMSE$ of test set forecasts. The two indicators are both considered in this study.

3.4 *Model validation*

The model validation methodology used in this study is proposed by Kutner et al. (2005). This methodology proposes to compare R^2, $RMSE$, and the mean absolute error (MAE). The MAE is another measure of errors between paired observations expressing the same phenomenon, such as actual value and fitted value, and it is computed as:

$$MAE = \frac{1}{n}\sum\nolimits_{i=1}^{n} \left| Y_i - \widehat{Y}_i \right| \tag{4}$$

where n is the number of cases in the test dataset, Y_i is the actual value and $\widehat{Y}_i$ is the fitted value at the ith validation case. In addition, the mean absolute percentage error ($MAPE$) has been used to validate the prediction accuracy of a design curve (De Myttenaere et al. 2016):

$$MAPE = \frac{100\%}{n}\sum\nolimits_{i=1}^{n} \left| \frac{Y_i - \widehat{Y}_i}{Y_i} \right| \tag{5}$$

4 RESULTS

4.1 *Data collection*

The scatter plot of t/L ratio and r/L ratio data of 74 UK masonry arch bridges publicly available from Wu (2010) was plotted in Figure 2a and Figure 2b, respectively. These figures shows that the span length of these 74 bridges is mostly concentrated between 0 and 20 m, among which, the t/L ratio is mostly concentrated between 0.02 and 0.1, while the r/L ratio is evenly distributed between 0.1 and 0.5. Furthermore, the r/L ratio data is very sparse and seemingly clustered in various groups for values of span length less than 20 m. The developed design curves cannot be used to extrapolate values of t/L or r/L outside of the highlighted bounds.

4.2 *Model development*

4.2.1 *Data fitting*

The following design curve for t' was obtained, see the blue curve in Figure 3:

$$t' = \frac{t}{L} = \frac{c_1}{L} + c_2 = \frac{0.2757\text{m}}{L} + 0.0268 \tag{6}$$

R^2 resulted to be equal to 0.2987, while $RMSE$ is equal to 0.02176. The value of R^2 is less than ideal, i.e. 0.6. The value of $RMSE$ is low. The two goodness of fit metrics preliminarily indicate that this design curve has certain predictive ability, but the accuracy may not be ideal. To test the equation accuracy, the difference between actual arch thickness values and estimated ones, called "residuals", were calculated and shown in Figure 5.

Subsequently, by applying Equation 2 to the data shown in Figure 2b, the design curve for r_p' was obtained, see the blue curve in Figure 4a:

$$r_p' = \frac{r}{L} = c_3 \cdot L + c_4 = -\frac{0.003292}{m} \cdot L + 0.3546 \tag{7}$$

For r_p', R^2 is equal to 0.09926, while $RMSE$ is equal to 0.1075. This value of R^2 is too small when compared with 0.6, which indicates of the design curve fitting extremely poorly. Although, the value of $RMSE$ is low. The two goodness of fit metrics preliminarily indicate that this design curve has not predictive ability. Residuals for actual arch rise values and estimated ones are shown in Figure 6a. Then, by applying Equation 3 to the data shown in Figure 2b, the design curve for r_p' was obtained, see the blue curve in Figure 4b:

$$r_p' = \frac{r}{L} = \frac{c_5}{L} + c_6 = \frac{0.4894}{L} + 0.2594 \tag{8}$$

For r_p', R^2 is equal to 0.04953, while $RMSE$ is equal to 0.1104. This value of R^2 is too small when compared with 0.6, which indicates of the design curve fitting extremely poorly.

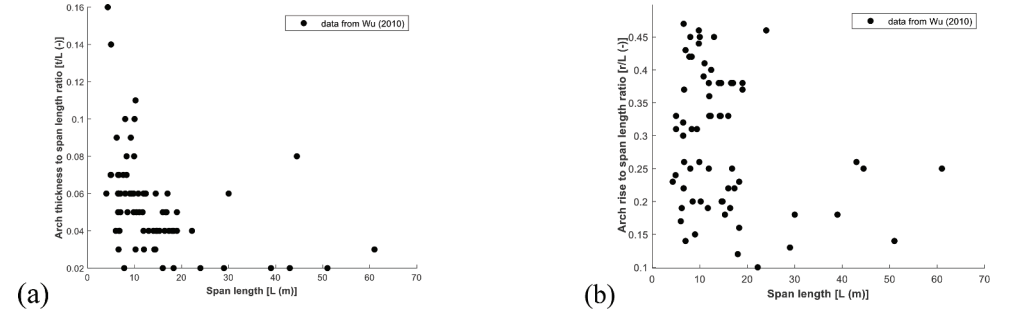


Figure 2. (a) Scatter plot of arch thickness to span length ratio data for masonry arch bridges of the UK; (b) Scatter plot of arch rise to span length ratio data for masonry arch bridges of the UK.

Although, the value of *RMSE* is low. The two goodness of fit metrics preliminarily indicate that this design curve has not predictive ability. Residuals for actual arch rise values and estimated ones are shown in Figure 6b.

4.2.2 *Residual plot analysis*

Plots of the residuals, i.e. the difference between the observed value and the estimated value of the quantity of interest, are helpful to study whether a regression function is appropriate or not (Kutner et al. 2005). Since bridge attributes in the fitting dataset are mostly concentrated between 0 and 20 *m*, only the data distribution between 0 and 20 *m* is analysed.

As shown in Figure 5, the distribution of residuals for t/L tends to converge, displaying no systematic tendencies to be positive or negative. With the longer span of masonry arch bridge, the distribution of residual points becomes smaller and closer to the centre line, i.e. tending to zero residual. This indicates that the span length of a bridge is correlated with the t/L ratio, but there may be other variables affecting the t/L ratio, such as the service type of a bridge, such presenting higher piers and abutments.

The residuals for r/L of a parabolic arch are shown in Figure 6a, and they fall evenly in the band area with zero as the centre and plus or minus 0.2 as the upper and lower boundary, displaying no systematic tendencies to be positive or negative. However, the width of this band area is wider, indicating that the prediction accuracy of this design curve is low.

The distribution of residuals of r/L of a semi-circular arch are shown in Figure 6b. This latter distribution is similar to the case of Figure 6a.

Validation analysis of developed design curves is then carried out to check their practical use.

4.3 *Model validation*

As a proof of concept, the developed design curves were firstly applied to the case study by Tubaldi et al. (2018) pretending to have arch thickness and arch rise as unknown, see Figure 7; (ii) then, to nine further bridge geometries from Robinson (2000).

In Tubaldi et al. (2018), the two arches are segmented and symmetric; the span length (from the left abutment to the central pier) is 9.26 *m*; arch rise is 3.45 *m* and arch thickness is 0.50 *m*, which are pretended to be unknown. In particular, arch thickness and arch rise were first forecasted by Equation 6 and Equation 8, respectively, and then compared with the actual values. The forecasted arch thickness value is 0.524 *m*, while the forecasted arch rise value for the semi-circular arch is 2.891 *m*. When comparing forecasted values with actual values for arch thickness, it is found that the absolute of residual is 0.024 *m*, which shows that the two values are very close. When comparing modelled values with actual values for arch rise of semi-circular arch, it is found that the absolute of residual is 0.559 *m*, which shows that the two values are not very close. Considering the ten validation case studies, the *MAE* is 0.075 *m* for arch thickness forecast, 0.728 *m* for parabolic arch rise forecast and 0.723 *m* for semi-circular arch rise forecast, which means higher accuracy for arch thickness and low accuracy for arch rise. The MAPE of arch thickness is 13.6%, 28.9% for the parabolic arch rise and 29% for the semi-circular arch rise.

5 DISCUSSION AND FUTURE RESEARCH

Three design curves were obtained and validated by fitting publicly available datasets of MABs.

The first design curve for t/L ratio presents $R^2 = 0.3$, $RMSE = 0.022$. The second design curve for r/L ratio of parabolic arches presents $R^2 = 0.1$, $RMSE = 0.108$. The third curve for r/L ratio of semi-circular arches presents $R^2 = 0.05$, $RMSE = 0.11$. Although the R^2 of the design curve of arch thickness is less than 0.6, it has good *RMSE*. It also performs well in the model validation section. Therefore, Equation 6 can be used as an acceptable design curve for preliminary estimates. The values of R^2 of the Equation 7 and Equation 8 are very close to zero, and the value *RMSE* is high. These indicators suggest that they are two poor design curves.

The residual plots of the three design curves tell that fitting results are not very ideal.

Regarding the model validation, the *MAE* for arch thickness forecast is 0.075 *m*, while it is 0.728 *m*/0.723 *m* for parabolic/semi-circular arch. The *MAPE* of arch thickness is 13.6%, 28.9% for the parabolic arch rise and 29% for the semi-circular arch rise, which indicates that only the design curve of the arch thickness has certain forecast accuracy and can be used as a forecasting model, but further validation is needed.

Future work can filter input data by arch shape and bridge service type, and fit new design curves for arch rise.

The developed curves could be used by scholars for rapidly obtain attributes of MABs, without in-situ commuting, thus enabling QRA of bridge portfolios.

6 CONCLUSIONS

UK bridge datasets lack attributes necessary for QRA of bridge portfolios. Therefore, this paper proposed new design curves to forecast arch thickness and arch rise for MABs. To fulfil the aim, this work first fitted rule of thumbs and theoretical relations for arch thickness and arch rise to publicly available bridge data (Wu 2010), which was filtered to UK MABs. Then, the developed design curves were validated using a second public available bridge dataset (Robinson 2000, Tubaldi et al. 2018). It was found that the developed design curves do not have a high R^2, although the design curve of arch thickness well performs in the validation section with the randomly selected bridges. For design curves of arch rise, they did not get a good goodness of fit, and they did not perform well in the model validation either.

This paper proposed one possible design curve for arch thickness and two design curves for arch rise as a function of span length. The design curve of arch thickness, given by Equation 6, may be applied to derive missing arch thickness data. This work can be improved by filtering fitting data according to arch shapes, thus improving arch rise design curves.

DATA STATEMENT

Data and developed scripts are available upon request to the corresponding author.

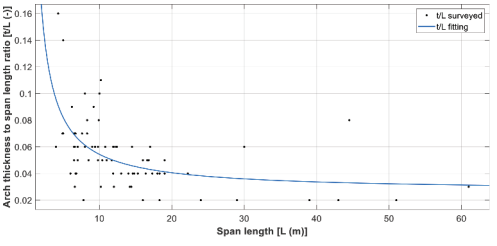


Figure 3. Design curve of arch thickness to span length ratio (blue line).

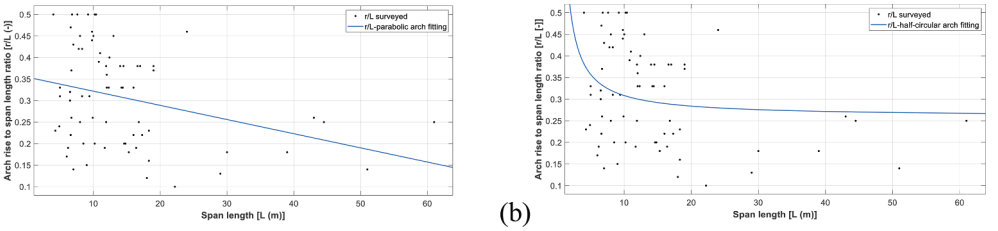


Figure 4. (a) Design curve of parabolic arch rise to span length ratio (blue line); (b) Design curve of semi-circular arch rise to span length ratio (blue line).

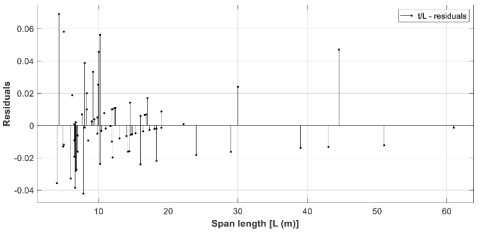


Figure 5. Residuals plot of arch thickness to span length ratio (t/L).

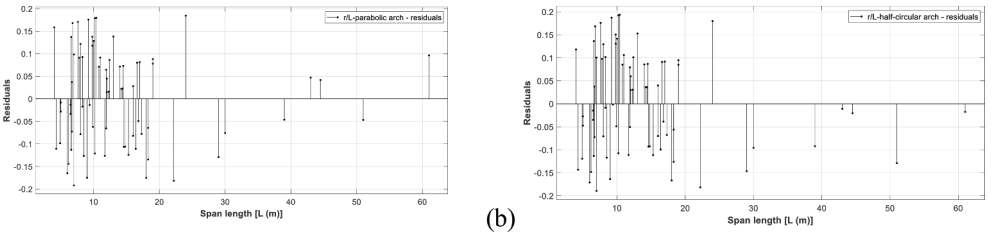


Figure 6. (a) Residuals plot of arch rise of parabolic arch to span length ratio (r/L); (b) Residuals plot of arch rise of semi-circular arch to span length ratio (r/L).

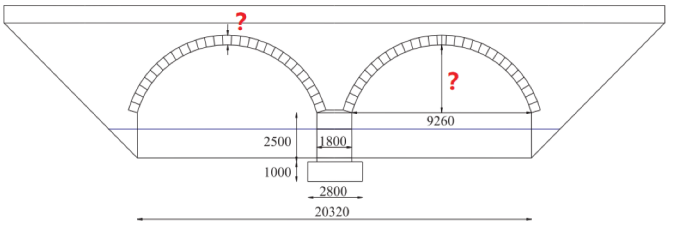


Figure 7. Illustration of the bridge (dimensions in mm) with pretended unknown arch thickness (question mark on the left) and arch rise (question mark on the right) from Tubaldi et al. (2018).

REFERENCES

Alexander, D. L., Tropsha, A., & Winkler, D. A. 2015. Beware of R2: simple, unambiguous assessment of the prediction accuracy of QSAR and QSPR models. *Journal of chemical information and modeling* 55(7): 1316–1322.

Breymann, G.A. 1926. *Trattato di costruzioni civili. Quarta Edizione* (*Civil Constructions Treatise. 4th Edition.* In Italian). Milano: Vallardi.

Busch, P. & Zumpe, G. 1995. Tragfähigkeit, Tragsicherheit und Tragreserven von Bogenbrücken. 5. *Dresdner Brückenbausymposium* 16(1995): 153–169.

Cavalcante, G. H. F., Pereira, E. M. V., Rodrigues, I. D., Junior, L. C. M., Padgett, J. E. & Siqueira, G. H. 2021. Proposal of representative portfolios for federal roadway bridges in Northeastern Brazil. *arXiv preprint*.

Cocciaglia, D. & Mosca, L. 1998. Capacità portante dei ponti ad arco ferroviari. *La Tecnica Professionale*.

Como, M. 2013. *Statics of historic masonry constructions. Third Edition*. Berlin: Springer.

Corradi, M. 1998. Empirical methods for the construction of masonry arch bridges in the 19th century. In Sinopoli A. (ed), *Arch Bridges*: 25–36. London: CRC Press.

Corradi, M. & Filemio, V. 2004. A brief comparison between mechanical aspects and construction of arch bridges during the XVIII and XIX centuries. In P Roca & C Molins (Eds), *Arch Bridges IV–Advances in Assessment, Structural Design and Construction*, *Proc. Arch Bridges 2004; Barcelona*. Barcelona: CIMNE.

da Porto, F., Tecchio, G., Zampieri, P., Modena, C. & Prota, A. 2016. Simplified seismic assessment of railway masonry arch bridges by limit analysis. *Structure and Infrastructure Engineering* 12(5): 567–591.

Degan Di Dieco, G., Barbosa, A. R. & Pregnolato, M. 2022. A taxonomy of bridges at risk of flooding: towards bridge classes and damage models. *Proceedings of the Institution of Civil Engineers-Bridge Engineering* 175(3): 172–178.

Degan Di Dieco, G., Barbosa, A. R. & Pregnolato, M. 2023. A methodology to derive scour fragility functions for masonry arch bridges: 1507-1514. In F. Biondini & D. M. Frangopol (eds), *Life-Cycle of Structures and Infrastructure Systems*, *IALCEE 2023; Milan*, *2–6 July 2023*. London: CRC Press.

De Myttenaere, A., Golden, B., Le Grand, B. & Rossi, F. 2016. Mean absolute percentage error for regression models. *Neurocomputing* 192: 38–48.

Galasso, C., Pregnolato, M. & Parisi, F. 2021. A model taxonomy for flood fragility and vulnerability assessment of buildings. *International Journal of Disaster Risk Reduction* 53: 101985.

George, J. & Menon, A. 2021. A mechanism-based assessment framework for masonry arch bridges under scour-induced support rotation. *Advances in Structural Engineering* 24(12): 2637–2651.

NH. (2022). *CS 454 Assessment of highway bridges and structures*: 120–124. London: National Highways.

Huerta Fernández, S. 2004. *Arcos, bóvedas y cúpulas. Geometría y equilibrio en el cálculo tradicional de estructuras de fábrica*. Madrid: Instituto Juan de Herrera.

Kurrer, K. E. 2002. *Geschichte der Baustatik*. Berlin: John Wiley & Sons.

Kutner, M. H., Nachtsheim, C. J., Neter, J. & Li, W. 2005. *Applied linear statistical models*. New York: McGraw-Hill.

Lamb, R., Garside, P., Pant, R. & Hall, J. W. 2019. A probabilistic model of the economic risk to Britain's railway network from bridge scour during floods. *Risk Analysis* 39(11): 2457–2478.

Li, X., Cooper, J. R. & Plater, A. J. 2021. Quantifying erosion hazards and economic damage to critical infrastructure in river catchments: Impact of a warming climate. *Climate Risk Management* 32: 100287.

Mathworks 2023. *Curve Fitting Toolbox: Users' guide*. Natick: The Mathworks.

Medina-Cetina, Z., Yousefpour, N. & Briaud, J. L. 2020. Probabilistic evaluation of unknown foundations for Scour susceptible bridges. *Journal of Bridge Engineering* 25(10): 04020074.

Modena, C., Valluzzi, M. R., Da Porto, F., Casarin, F. & Bettio, C. 2004. Structural upgrading of a brick masonry arch bridge at the Lido (Venice). In P Roca & C Molins (Eds), *Arch Bridges IV–Advances in Assessment, Structural Design and Construction*, *Proc. Arch Bridges 2004; Barcelona*. Barcelona: CIMNE.

Motulsky, H. 1995. *Intuitive biostatistics*. London: Oxford University Press.

Pippard, A.J. 1952. *Studies in elastic structures*. London: Edward Arnold & Co.

Pregnolato, M. 2019. Bridge safety is not for granted – A novel approach to bridge management. *Engineering Structures* 196: 109193.

Proske, D. & van Gelder, P. 2009. *Safety of historical stone arch bridges*. Berlin: Springer Science & Business Media.

Purtak, F. 2004. Zur nichtlineare Berechnung von Bogenbrücken aus Natursteinmauerwerk. *CAD-FEM Users Meeting 2004, International Congress on FEM Technology with ANSYS CFX & ICEM CFD Conference*; *Dresden*, *10–12 November 2004*.

Robinson, J. 2000. *Analysis and assessment of masonry arch bridges*. Edinburgh: University of Edinburgh.

Solan, B., Ettema, R., Ryan, D., & Hamill, G. A. 2020. Scour concerns for short-span masonry arch bridges. *Journal of Hydraulic Engineering* 146(2): 06019019.

Tubaldi, E., Macorini, L. & Izzuddin, B. A. 2018. Three-dimensional mesoscale modelling of multi-span masonry arch bridges subjected to scour. *Engineering Structures* 165: 486–500.

Wang, Q., Liu, K., Wang, M. & Koks, E. E. 2021. A river flood and earthquake risk assessment of railway assets along the belt and road. *International Journal of Disaster Risk Science* 12: 553–567.

Wu, L. 2010. *Serviceability assessments of masonry arch bridges*. Cardiff: Cardiff University.

Zelaschi, C., Monteiro, R. & Pinho, R. 2016. SIMPLIFIED PERIOD ESTIMATION OF ITALIAN RC BRIDGES FOR LARGE-SCALE SEISMIC ASSESSMENT. In M. Papadrakakis, V. Papadopoulos, G. Stefanou, V. Plevris (eds.), *ECCOMAS Congress 2016*; *Crete Island*, *5–10 June 2016*.

Bridge Maintenance, Safety, Management, Digitalization and Sustainability – Jensen, Frangopol & Schmidt (eds)
© 2024 The Author(s), ISBN 978-1-032-77040-6
Open Access: www.taylorfrancis.com, CC BY-NC-ND 4.0 license

Seismic performance of highway RC bridges with corroded piers

D. Cardone, V. Possidente, G. Perrone & A. Spica
University of Basilicata, Potenza, Italy

D. Bernardini, D. Ruta, A. Paolone & F. Braga
University La Sapienza, Roma, Italy

F. Buttarazzi & A. Rossi
Autostrade S.p.A., Roma, Italy

ABSTRACT: In this study, the seismic performance of typical multi-span simply supported deck bridges with single shaft Reinforced Concrete (RC) piers with corroded rebars is examined through extensive NonLinear Static Analysis (NLSA). Six different bridge configurations, differing in pier layout (Constant, Ramp and V-type) and number of spans are investigated, considering different deterioration scenarios, characterized by different deterioration patterns (over the cross-section of the pier) and severity of corrosion of steel rebars. The influence of corrosion on the seismic vulnerability of the bridge is evaluated in terms of ratio between the maximum earthquake intensity level (from NLSA) that the structure can withstand before collapse and the code-conforming (Italian Technical Standards) intensity level that would be used for the verification of the Collapse Limit State of a new structure.

1 INTRODUCTION

Ageing and deterioration of RC bridges can significantly increase their seismic vulnerability and have a significant impact on expected economic losses. Among the different deterioration mechanisms that bridge structures may experience, chloride-induced corrosion of steel rebars represent the most critical one. Indeed, depending on the severity, extension and location, corrosion of steel rebars may lead to significant loss of structural strength and poor seismic performance of bridge piers which often represent the most vulnerable element of a bridge.

The starting point of this study is represented by a set of force-displacement skeleton curves, in the as-built and degraded conditions, obtained through pushover analyses of accurate 'fiber' models of single-shaft rectangular-hollow piers. Piers with different height (from 5 to 35m) and different section aspect ratio (1 to 3) have been examined. In addition, two different construction ages have been considered (referred to as pre-74 and post-74), differing in terms of construction details (quantities of longitudinal reinforcement, stirrup spacing, etc.) and mechanical characteristics of the materials. Reference to (Bernardini et al. 2022) can be made for more details on the structural characteristics and mechanical properties of the selected piers.

Piers have been analyzed considering different deterioration patterns, as well as different intensity levels of corrosion and height extensions, as described in (Bernardini et al., 2022). In all cases, however, corrosion was concentrated at the base of the pier where plastic deformations are expected to develop under earthquakes. Five in-plane corrosion patterns were assumed, clearly identified with the letters A, B, C, D and E in Figure 1. In the same figure, the intensity level of corrosion is identified by a number ranging from 0 (as built) to 6 for the degradation pattern associated with the higher percentage of mass loss. The values of mass loss (valid for both longitudinal and transverse steel bars) and crack width (cover concrete) reported in Figure 1 have been used to define the effective diameter of corroded bars and the

DOI: 10.1201/9781003483755-459

constitutive laws of corroded steel and cracked concrete based on the semi-empirical relationships proposed by (Imperatore et al. 2017) and (Coronelli & Gambarova 2004), respectively.

According to the Italian Technical Standards for Constructions (NTC 2018), pier collapse was assumed to occur when the first of the following events occurred: (i) attainment of a strain of 4% in the first longitudinal steel bar, (ii) 15% drop in the peak lateral resistance on the degrading branch of the force-displacement skeleton curve of the pier, (iv) shear failure, calculating the shear strength with the formula reported in the NTC18 for existing RC structures. In accordance with the NTC18, a safety factor equal to 1.5 for ductile mechanisms and 1.25 for brittle mechanisms was applied to derive the performance points at collapse.

Seismic analyses were carried out assuming the viaducts located in two different sites (L'Aquila and Naples) featuring high and medium seismic hazard for Italy. Soil type C (deep deposits of dense or medium-dense sand, gravel or stiff clay with thickness from several tens to many hundreds of meters) has been assumed in both the cases.

DEGRADATION PATTERN		INTENSITY LEVEL		W_{cr} (mm)	Ψ_L (%)	Ψ_T (%)	HEIGHT EXTENSION	
I		0		0	0%	0%	1	0.05 * H
A		1		1	5%	8%	2	0.10 * H
B		2		2	15%	20%	3	0.15 * H
C		3		3	20%	25%		
D		4		expelled	30%	35%		
E		5		expelled	40%	50%		
		6		expelled	50%	50%		

A5_1
Pattern
Extension
Intensity

Figure 1. Corrosion deterioration scenarios (pattern, extension and intensity) assumed in this study.

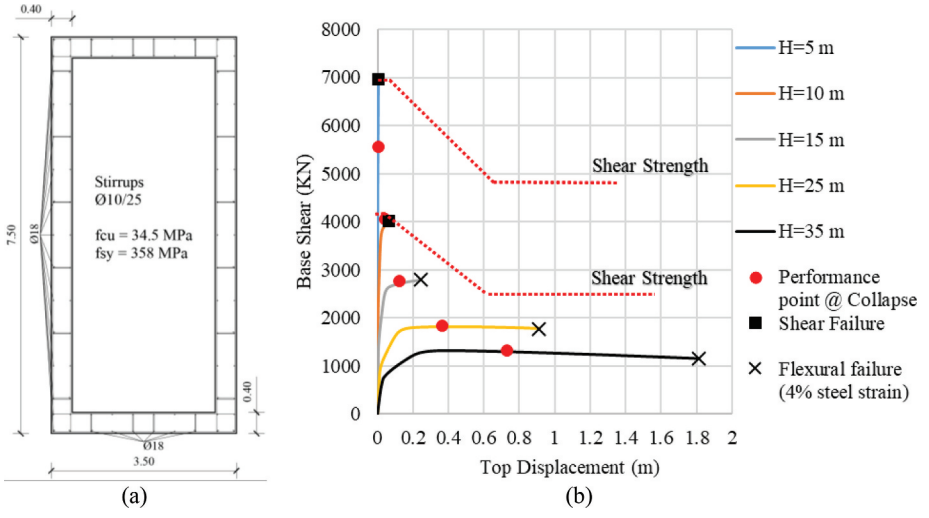


Figure 2. (a) Pier cross-section dimensions and (b) typical pushover curves in the as-built configuration for pre-74 piers (weak direction) featuring different heights and failure modes.

For brevity, in this paper the attention is focused on the viaducts located in L'Aquila only. Similarly, only pre-74 piers with cross-section aspect ratio equal to 2 and corrosion pattern type E (5%H height extension) (see Figure 1) are considered.

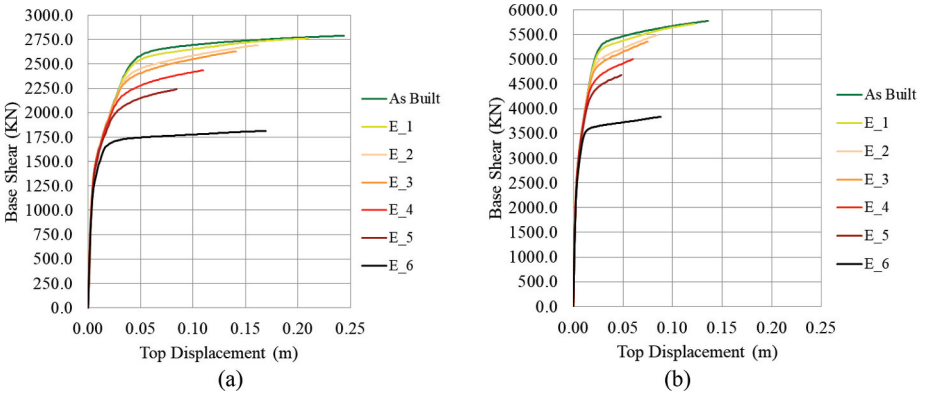


Figure 3. Comparison of as-built and degraded pushover curves for the 15m height pre-74 pier in the (a) weak and (b) strong direction.

2 METHODOLOGY

Figure 2(a) shows the dimensions of the pier cross-section with the amount of longitudinal and transverse reinforcement and the mean values of concrete compression strength and steel yielding stress assumed in the analysis. Figure 2(b) shows some typical pushover curves in the as-built configuration for pre-74 piers (weak direction) featuring different heights and failure modes. Ductile piers include those with height ranging from 15m to 35m. Piers with height between 7.5m and 12.5m exhibit a hybrid failure mode in which shear failure affect flexural ductility anticipating pier collapse. Piers with 5m height exhibit an elastic fragile behavior. In the latter case, corrosion produces limited effects, causing a reduction in the shear strength not exceeding 15-18%. It should be noted, indeed, that pre-74 piers were poorly reinforced against shear (stirrups not well anchored in the concrete core and with large spacing). Therefore, the effects of stirrup corrosion on concrete confinement and shear strength are quite low.

Figure 3 shows some typical pushover curves for the 15m height pre-74 pier featuring different corrosion degradation scenarios. As can be seen, corrosion of steel rebars strongly affect the ultimate displacement capacity of ductile piers with reductions up to 65-70% in the worst situations (see E_5 curves). Also the lateral strength is significantly influenced by corrosion, with reductions up to 35% in the worst case (see E_6 curves).

Pushover curves have been converted into an equivalent bilinear force-displacement relationships (see Figure 4) following the instructions reported in the NTC18 (effective initial stiffness taken as the secant stiffness at the actual yield displacement; post-yield slope determined by a line segment that passes through the curve at the actual ultimate displacement and that approximately balance the area above and below the curve).

Figure 5 shows the bridge layouts examined in this study. They include three different pier profiles (C: Constant, R: Ramp-type and V: V-type) by two different lengths (S: Short with 3-spans and L: Long with 7-spans). In Figure 5, the height of each pier is reported, as well as the average value of the ρ-parameter measuring the level of irregularity of the bridge. The ρ-parameter is expressed as the ratio between the maximum and the minimum ratio between the shear at the base of the i-th pier at the performance point and the corresponding ultimate lateral resistance.

The seismic performance of the bridge has been assessed through Nonlinear Static Analysis. Among others, the Inverse Adaptive Capacity Spectrum Method (IACSM) described in (Cardone et al. 2011) has been adopted in this study. Within this method, pushover analysis was carried

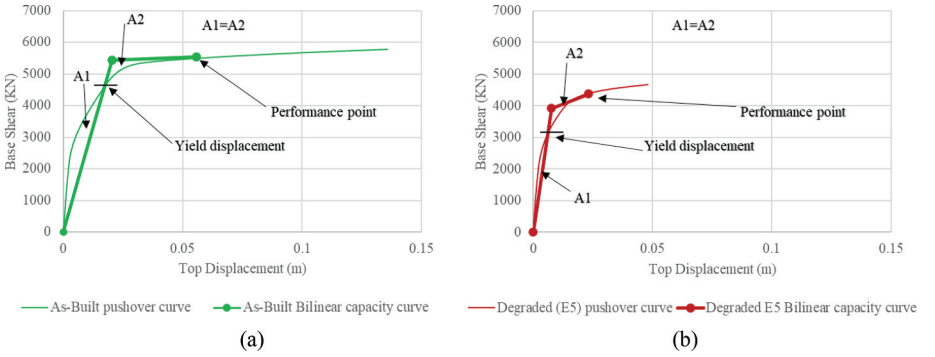


Figure 4. Conversion of pushover curve into an equivalent bilinear capacity curve for the (a) as-built and (b) degraded (E5) 15m height pre-74 pier.

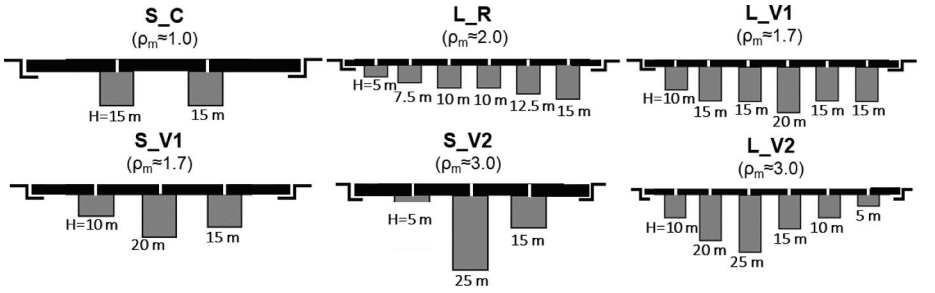


Figure 5. Bridge layouts examined in this study (S: Short, L: Long; C: Constant, R: Ramp, V: V-type profile).

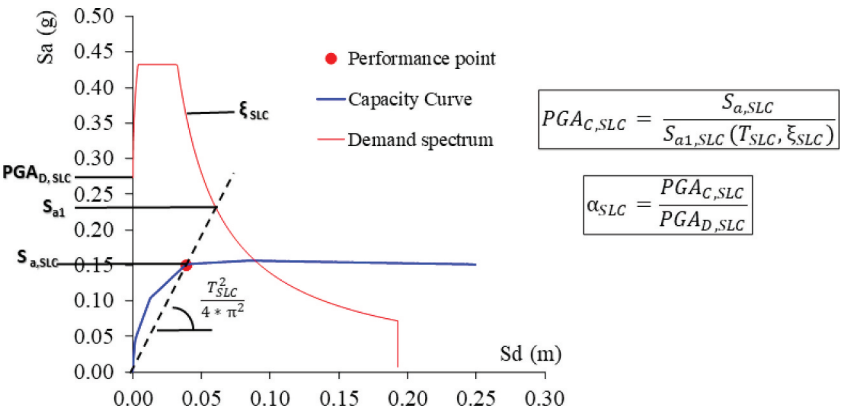


Figure 6. Inverse Adaptive Capacity Spectrum Method (IACSM).

using a uniform force pattern in the longitudinal direction and a first mode force pattern in the transverse direction. The IACSM converts the pushover curve of the MDOF bridge into the Capacity Curve of an equivalent SDOF system by computing the displacement ($S_{d,k}$) and the acceleration ($S_{a,k}$) of the equivalent SDOF system based on the actual deformed shape of the bridge at each (k-th) step of analysis (Cardone et al. 2011). The Demand Spectrum is represented by a high-damping elastic response spectrum. The equivalent viscous damping of the bridge is estimated through a suitable combination of the effective damping ratios of each component (pier, bearings, etc.) based on the displacement and force levels acting in each component at the selected

performance point. Indeed, the main objective of the IACSM is to evaluate the seismic intensity (e.g. the PGA) of the expected ground motions corresponding to the attainment of a given damage state (e.g. collapse) of the structure, identified by a given performance point on the capacity curve of the bridge (see Figure 6). The earthquake intensity level corresponding to the attainment of the performance point represents, to some extent, the seismic capacity of the structure. The ratio (α) between the seismic collapse capacity of the structure ($PGA_{C,SLC}$ in Figure 6) and the seismic demand prescribed by the Code for the verification of collapse limit state for code-conforming structures ($PGA_{D,SLC}$ in Figure 6) provides an estimate of the seismic risk of the bridge. In this study, the effects of degradation due to corrosion have evaluated in terms of changes in the α-index.

The definition of the degradation scenario is a complex operation at the level of single pier and even more at the level of entire viaduct. As mentioned before, a simplified approach, based on the assumption of schematic degradation patterns differing in corrosion severity and extension (see Figure 1), has been adopted at the level of single pier. A heuristic approach has been followed to define several alternative degradation patterns at the level of entire viaduct. It is based on the assumption that tall piers are in principle more subject to degradation from corrosion close to the base as they are less protected by the "umbrella" effect of the deck in the event of windy rain and splashes of salt water from the joints and curb edge. Similarly, it is more likely that a tall pier is located in the middle of a valley and then exposed to strong winds or in a riverbed and then subjected to continuous dry-wet cycles. Consequently, for the type E degradation pattern (see Figure 1), referable to piers in riverbed or piers exposed to wind-rain along the entire base perimeter, the hypothesis was that taller piers (e.g. all those with height greater than the average pier height over the entire bridge) could reach the maximum intensity of degradation due to corrosion (intensity 6 of Figure 1), while lower piers (e.g. all those with height less than the average pier height over the entire bridge) could not exceed certain levels of corrosion (e.g. intensity 3 of Figure 1). On the basis of such hypotheses, the worst scenarios were defined (first row of Figure 7). Then, others were derived by progressively reducing the intensity of degradation up to the as-built configuration (rows 2 to 6 in Figure 7). Finally, some additional scenarios were considered to maximize the effects of corrosion on the α-index. They are characterized by degradation at the maximum intensity concentrated only on the critical pier from the analysis on the as-built configuration (rows 7 and 8 in Figure 7).

3 RESULTS

Figure 8 reports the values of the α-index obtained for each analysis case (six different bridge layouts by nine different degradation patterns). The values of the α-index are reported separately for both directions (longitudinal and transverse). The critical pier of the bridge is also identified.

Based on the results reported in Figure 8, the following considerations can be made:

- Degradation due to corrosion, when concentrated in the critical areas of the piers (e.g. at the base of the pier for single shaft piers), can significantly worsen the seismic performance of RC viaducts;
- When the critical element coincides with a short pier (subjected to shear failure) the reduction of the α-index is limited (see configurations S_V2, L_R and L_V2 in the longitudinal direction) because the degradation slightly affects only the lateral resistance of the pier. On the other hand, when the collapse is due to the failure of a ductile pier (as always happens in the transverse direction and in the longitudinal direction for the configurations S_C, S_V1 and L_V1) the degradation due to corrosion causes a strong reduction in the ultimate displacement capacity of the piers (see Figure 3) and consequently a significant reduction of the α-index;
- The longitudinal direction turns out to be always the critical direction of the bridge, due to the strong interaction between decks as a consequence of the reduced width of the internal joints;
- The critical element does not change as the intensity of degradation in the structure varies.

It is worth noting that, in some rare cases, the values of the α-index in degraded conditions are higher than those in the pristine (as-built) conditions. This can be ascribed to the

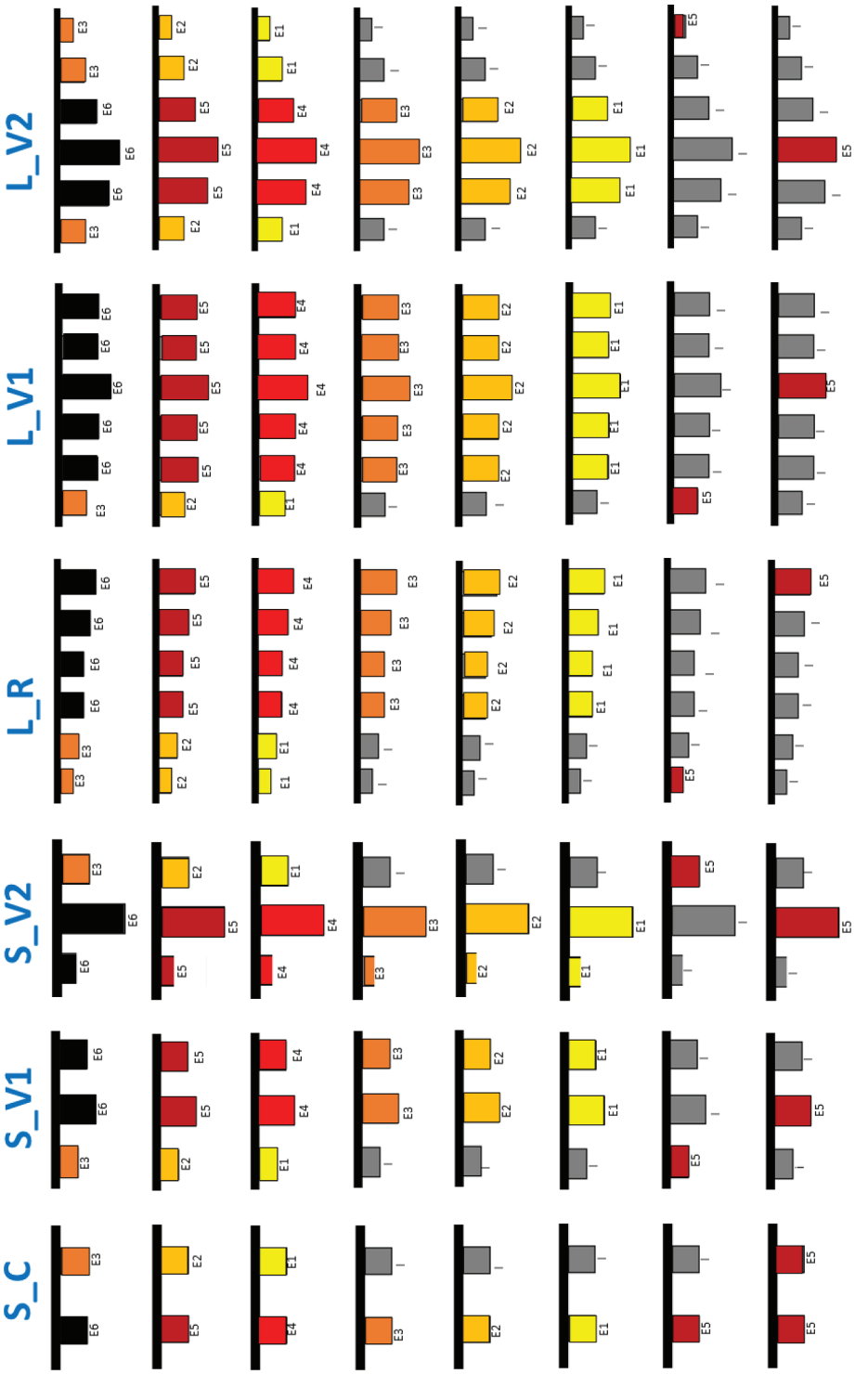


Figure 7. Degradation patterns considered (ref. to Figure 1 for the meaning of labels and colors).

bilinearization criterion adopted (see Figure 4) which, in presence of a remarkable reduction in ductility, provides a slight increase in the initial stiffness for slender piers.

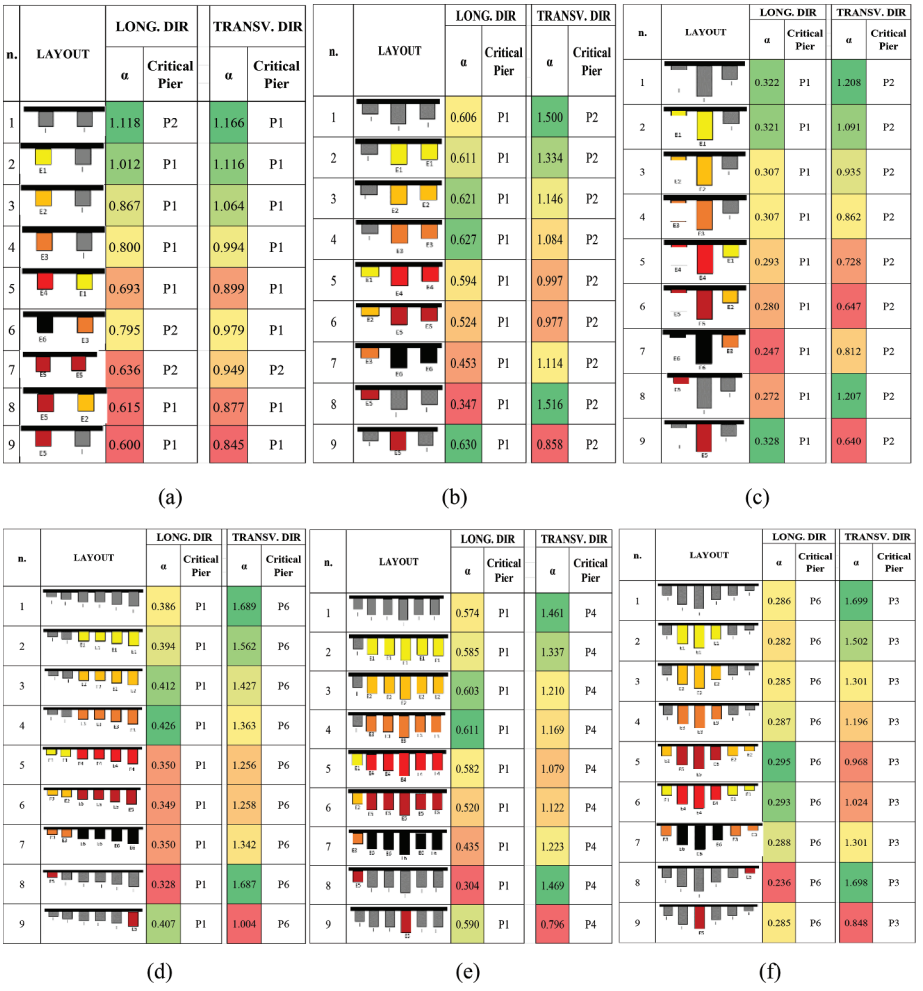


Figure 8. Values of the a-index for different degradation patterns and bridge layouts.

Examining the trend of the α-index reported in Figure 9, the following observations can be done:

- The maximum reduction in the α-index is of the order of 50% in both directions. This reduction is observed when corrosion degradation involves, with its highest level of intensity, the critical pier of the bridge (see bridge layouts n. 8 and 9 of Figure 8 in the longitudinal and transverse direction, respectively);
- When the critical pier coincides with a short pier subjected to shear failure (ref. to bridge layouts S_V1, S_V2, L_R and L_V2 in the longitudinal direction) the reduction of the α-index does not exceed 20%. This is because, for brittle piers, corrosion produces only a slight reduction (15-20%) in the lateral strength of the pier;
- In the transverse direction, the modal force distribution adopted in pushover analysis leads to the failure of the highest piers. In this case, the reduction of the α-index is proportional to the reduction in the displacement capacity of the highest pier.

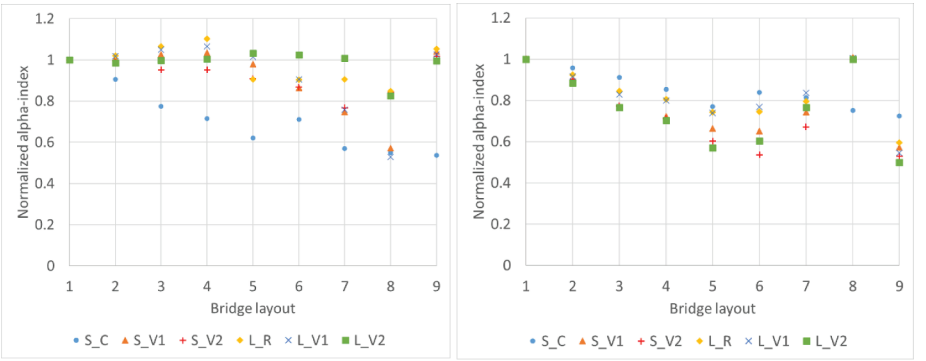


Figure 9. Normalized α indexes (degraded vs. pristine) in the (a) longitudinal and (b) transverse direction (ref. to Figure 7 for the numbering of the degradation patterns).

4 CONCLUSIONS

The seismic performance of typical multi-span simply supported deck bridges with single shaft RC piers with corroded rebars has been examined through NonLinear Static Analysis (NLSA). The influence of corrosion on the seismic performance of the bridge has been evaluated in terms of the α-index, that is the ratio between the maximum earthquake intensity level (from NLSA) that the structure can withstand before collapse and the code-conforming (NTC18) intensity level that would be used for the verification of the Collapse Limit State of a new structure.

Based on the results obtained so far, it can be stated that degradation due to corrosion can significantly influence the seismic performance of RC viaducts when it occurs in the critical areas (for seismic purposes) of ductile piers at the maximum levels of severity and extension observed in the practice (mass losses of the longitudinal reinforcements of the order of 40% along the entire perimeter of the cross section). As a matter of fact, the seismic risk of the bridge can even double in the worst case in which the degradation affects the critical pier of the bridge. Further analyses, varying the seismic hazard of the site, the mechanical characteristics of the piers (as a function of the era of construction of the bridge) and the in-plane and in-elevation degradation pattern of the pier, are underway to draw more robust conclusions.

REFERENCES

Bernardini, D. et al., 2022. Evaluation of the influence of structural deterioration on the seismic performances of bridges with reinforced concrete piers. Torino, Conference: ANIDIS.

Cardone, D., Perrone, G. & Sofia, S. A performance-based adaptive methodology for the seismic evaluation of multi-spain simply supported deck bridges. Bull Earthquake Eng 9, 1463–1498 (2011).

Coronelli, D. & Gambarova, P., 2004. Structural Assessment of Corroded Reinforced Concrete Beams: Modeling Guidelines. Journal of Structural Engineering, 130(8), p. 10.

Grove, A.T. 1980. Geomorphic evolution of the Sahara and the Nile. In M.A.J. Williams & H. Faure (eds), *The Sahara and the Nile*: 21–35. Rotterdam: Balkema.

Imperatore, S., Rinaldi, Z. & Drago, C., 2017. Degradation relationships for the mechanical properties of corroded steel rebars. Construction and Building Materials 148(209), p. 11.

Jappelli, R. & Marconi, N. 1997. Recommendations and prejudices in the realm of foundation engineering in Italy: A historical review. In Carlo Viggiani (ed.), *Geotechnical engineering for the preservation of monuments and historical sites*; *Proc. intern. symp.*, *Napoli*, 3-4 October 1996. Rotterdam: Balkema.

NTC (*Italian Technical Standards for Constructions*), 2018. Ministero delle Infrastrutture e dei Trasporti. Decreto 17 gennaio 2018 - Aggiornamento delle «Norme tecniche per le costruzioni». Istituto Poligrafico e Zecca dello Stato, Roma (Italy).

Bridge Maintenance, Safety, Management, Digitalization and Sustainability – Jensen, Frangopol & Schmidt (eds)
© 2024 The Author(s), ISBN 978-1-032-77040-6
Open Access: www.taylorfrancis.com, CC BY-NC-ND 4.0 license

Identification of governing structural safety criterion for existing bridges considering costs, occupancy and conditional fatality probability

F. Liljefors & J. Köhler
Department of Structural Engineering, Norwegian University of Science and Technology (NTNU), Trondheim, Norway

ABSTRACT: Assessing existing bridges requires balancing the risk of failure and mitigation costs. Economic and human safety aspects are considered when deriving an optimal or acceptable level of safety. Additionally, an absolute human safety criterion may provide an upper risk limit, and this study aims to clarify its role and criticality. Although human safety is included in the marginal life-saving criteria through the life quality index and the societal willingness to pay for one additional saved life, this does not guarantee the safety of individuals. The rationale behind this is that even though it would be worthwhile to sacrifice human safety because the average expected risk to humans is low compared to the cost of mitigating the risk, exposing individuals to adverse risks is not ethical. With this contribution, we discuss the relation between individual risk and structural risk and identify factors contributing to the relative importance of the absolute human safety criterion compared to the cost-benefit and marginal life-saving criteria for existing road bridges. From these factors, we derive classes of cases for which the absolute human safety criterion can safely be ignored and cases when it governs the assessment. The results are useful for future reliability- and risk-based assessments of bridges.

1 INTRODUCTION

1.1 *Structural safety as a societal concern*

The fundamental requirement on structures such as bridges is structural safety. This requirement can be quantified as the ability of the structure to withstand loading with a specified probability during a specified time (ISO 2394, 2015), either implicitly by the partial factor method or explicitly by structural reliability analysis. The criterion that specifies the acceptable level of structural safety is typically derived from historical design codes or risk analysis and is commonly given as a reliability index or a probability of failure.

Criteria for structural safety are relevant for the design of new structures and for the assessment of existing ones. This study focuses on the latter, as there is usually a larger urge to adjust the safety criteria for existing structures. This is because the uncertainties are different for an existing structure, more information can be retrieved, and it is more costly to increase the safety of a built structure than in the design stage.

With structural risk assessment based on structural reliability analysis, a proper level of safety that balances the risk of failure with the cost of increasing safety can be determined. As structural safety is not only about purely economic consequences but also involves human life, several complementary criteria need to be assessed. For the criteria involving human life, there is a reluctance to assess human life in monetary value, and the concepts are often cryptically described so as not to provoke people.

Structures expose the public to involuntary risks and are not a private business but a societal concern. Hence, we find the lack of transparency problematic and argue that society has the right to know how structural risk is dealt with. Explicitly addressing the trade-off

DOI: 10.1201/9781003483755-460

between human safety and money enables prioritisation of risk mitigation measures to reduce the structural risk efficiently with limited resources. Transparency is also essential for further developing the risk criteria to ensure they work as intended.

One important distinction in this discussion is whether risk assessments and their criteria should be descriptive or prescriptive, i.e. describing what is done or dictating what should be done. For the standardisation of structural risk, we favour the latter to ensure that standards take a rational and objective approach from a societal perspective. It is not meaningful that the industry that sets society at risk determines the criteria themselves, as they have no incentive to adopt stricter criteria than what is optimal for them, as argued by Abrahamsen & Aven (2012).

The approaches we investigate further in this paper are economic optimisation, marginal life safety, and absolute life safety. We omit societal risk, a variant of the absolute life safety approach that values fatalities in a single event differently from the same number of fatalities in multiple events. Taking the prescriptive approach to these matters described above, we think the societal risk approach is neither ethical nor rational.

1.2 *Aim to investigate the relation between the multiple criteria*

The most straightforward approach of the three criteria is economic optimisation. This criterion aims to minimise the expected total costs, assessing the value of human life according to the decision-maker's preferences in line with other costs. The marginal life safety also weighs the human loss against investment costs, with the difference that other failure costs than human loss are not considered, and the value of human life is quantified to a predetermined value for the societal willingness to pay (SWTP) for saving an additional life. The absolute life safety is fundamentally different as it specifies an absolute limit for the risk of life and limb of any person passing the bridge, independent of investment and failure costs.

As apparent from this introduction to the topic, assessing structural risk is complex. This was confirmed at a recent workshop on risk acceptance criteria organised by JCSS and IABMAS in Trondheim in June 2023. This workshop gathered professionals from academia and industry to establish a common understanding of the gap between the current practice and the goal of consistently regulating the level of safety throughout different fields and countries. The basic principles were agreed upon, such as the trade-off between safety and cost, the need for an upper-risk limit and the problem of risk aversion and avoidance. However, even this well-informed group of risk experts had different understandings of some aspects discussed.

With this contribution, risk acceptance criteria for the specific domain of structural assessment of existing bridges are further investigated. We explore how the three criteria for structural risk assessment relate to each other in different situations. This is done by identifying the important parameters, parameterising them at a reasonable range, and determining the governing criterion for the possible combinations. With consistent criteria based on a decent rationale, sufficient levels of safety of existing bridges can be assured that align with society's preferences. More accurate treatment of these criteria will lead to more accurate and precise risk assessments of individual structures and improvements in code calibration of the simpler reliability and semi-probabilistic assessment formats.

2 CRITERIA FOR ASSESSMENT

2.1 *Overview*

In this section, we present details for the three approaches which are supported by ISO 2394 (2015): Economic optimisation, marginal life safety and absolute life safety. The main influencing parameters are given, and the specific models for calculating the criteria for the yearly probability of failure used in this study are presented.

2.2 *Economic optimisation*

The continuous renewal assumption for assessment gives the total present expected costs for infinite time as the sum of intervention (risk mitigation) costs and expected failure costs:

$$E[C_{tot}(\boldsymbol{p})] = E[C_{intervention}(\boldsymbol{p})]\left(1+\frac{\omega}{\gamma}\right) + E\left[C_{failure}\frac{P_f(\boldsymbol{p})}{\gamma}\right] \tag{1}$$

where ω is the intervention rate, γ is the discount rate, P_f is the yearly probability of failure and $\boldsymbol{p}$ is the decision parameter, i.e. the set of mitigation options. By minimizing $E[C_{tot}(\boldsymbol{p})]$, the limit for cost-efficient interventions for discrete interventions is:

$$P_{f,ec} = \frac{C_{intervention,p}(\gamma+\omega)}{C_{failure}} + P_{f,intervention,p} \tag{2}$$

By assuming that an intervention will have a significant effect on the failure probability, $P_{f,intervention,p} \ll P_{f,ec}$, and:

$$P_{f,ec} \approx \frac{C_{intervention,p}(\gamma+\omega)}{C_{failure}} \tag{3}$$

Choosing a yearly reference period for the intervention, $\gamma + \omega \approx 1$, and:

$$P_{f,ec} \approx \frac{C_{intervention,p}}{C_{failure}} \tag{4}$$

2.3 *Marginal life safety*

The marginal life safety criterion takes a similar form as the economic optimisation criterion, with the difference that the failure costs are pure loss of human life:

$$P_{f,marg} \approx \frac{C_{intervention,p}}{P_{d|f} \cdot occ \cdot SWTP} \tag{5}$$

where $P_{d\,|\,f}$ is the conditional fatality probability, i.e. the probability of dying given structural failure and being exposed. Further, occ is the occupancy or the average number of people at risk close to the bridge, and $SWTP$ is the societal willingness to pay for saving an additional life. The occupancy can be calculated as:

$$occ = AADT \cdot t \cdot n_p \tag{6}$$

where $AADT$ is the annual average daily traffic, t is the time one vehicle is exposed (on or close to the bridge), and n_p is the average number of people in one vehicle. If the bridge crosses another road, the exposure for this road should be added.

2.4 *Absolute life safety*

The absolute life safety (or individual risk) criterion is preferably given in the metric "expected value of the number of deaths per person-year" to be transferable between different activities and domains. For structural risk, it is expressed as:

$$P_{f,abs} = \frac{IR_{crit}}{P_{d|f}} \tag{7}$$

where IR_{crit} is the criterion for the expected number of fatalities per person-year and $P_{d|f}$ is the conditional fatality probability.

The absolute limit for life safety is subject to issues regarding system definition in time and space and arbitrariness. It is argued that it is not the risk for one specific person that is regulated but rather the risk for a statistical person involved in an activity (Faber et al., 2015). It is, however, not obvious how the activity should be defined. For instance, the activity of driving across one specific bridge is different from the general activity of driving over bridges. These matters of risk transfer and averaging risks are common issues in more traditional risk fields but may be considered odd and lack broad acceptance among structural engineers.

2.5 *Governing criteria*

The governing criterion is:

$$P_{f,gov} = min\{P_{f,ec},\ P_{f,marg},\ P_{f,abs}\} \tag{8}$$

The values for the societal willingness to pay $SWTP$ and the individual risk criterion IR_{crit} are considered to be constant for a given decision-maker, and four parameters remain: The costs of intervention and failure, the occupancy, and the conditional fatality probability. The effect of combinations of these parameters on the governing criteria is explored in the following.

3 DEMONSTRATION

3.1 *Aim and approach*

This investigation aims to assess the necessity of three different criteria in the structural risk assessment of existing bridges. The hypothesis is that it may be fruitful to identify the governing criterion for ranges of cases to direct the risk assessment for individual assessments to the important criterion. A better understanding of the governing criterion would also improve the basis for code calibration of simpler safety formats.

3.2 *Parametrisation*

The input parameters with the selected ranges are given in Table 1. The failure cost is given as a one-time cost, and the intervention cost is given as a yearly net present cost. The upper limit for the conditional fatality probability is firm, as a probability cannot be larger than one, while the other limits are chosen arbitrarily. They are believed to cover all relevant combinations for bridge maintenance of public roads in Norway. The occupancy ranges from exposing 0.001 people, which corresponds roughly to ten vehicles per day, to 100 people, which is a number that is hard to imagine even on the largest and busiest bridges in Norway. Fixed values for $SWTP$ (Norway, 2023's value) and absolute safety criteria IR_{crit} were adopted as 50 MNOK and 10^{-4}.

Table 1. Ranges of parameters studied.

	Description	Range
C_{int}	Yearly intervention cost [MNOK]	10^{-4}–10^{2}
C_{fail}	One-time failure cost [MNOK]	0.1–1000
OCC	Occupancy, average number of people exposed	10^{-4}–10^{2}
$P_{d\|f}$	Fatality probability given exposure and failure	0.001–1

4 RESULTS AND DISCUSSION

For every case, the three criteria were calculated and compared. With fixed values for two of the four parameters, the results take the form of three heatmaps and the identification of the governing criterion in Figure 1. The colour of the heatmaps gives the criterion in probability of failure, where blue is less strict and red is more strict. For this figure, failure costs and the conditional fatality probability are fixed at 10 MNOK and 0.1, whereas intervention cost and occupancy are varied. The upper-left figure illustrates that high occupancy and low cost for intervention result in strict (red) criteria for the marginal life safety approach. The economic optimisation is not affected by the occupancy, and the absolute criterion is constant over occupancy and cost of intervention.

When the three criteria are compared, the absolute criterion is the governing one for most of the cases, indicated with black in the lower-right figure. The economic criterion (marked with grey) only governs for cheap interventions where $C_{int}/C_{fail} < 10^{-3}$. The marginal life

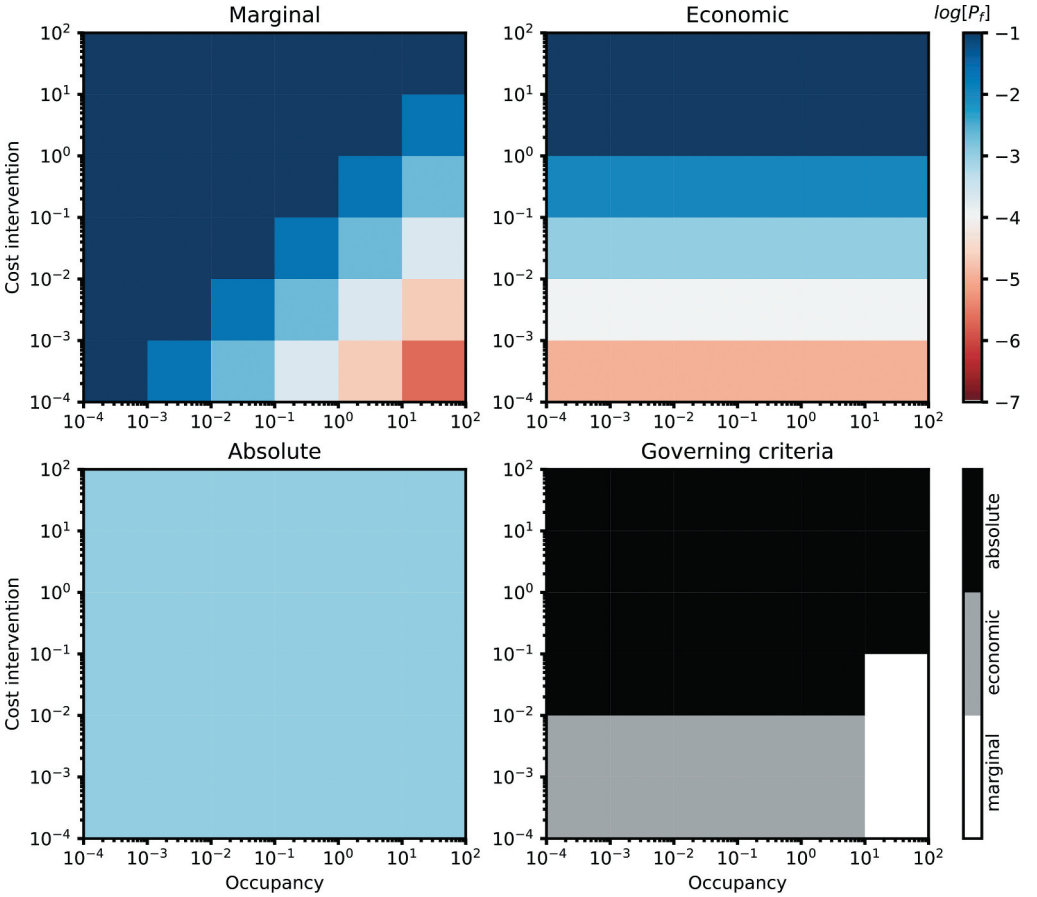


Figure 1. The criteria for the yearly probability of failure for economic optimisation and marginal and absolute life safety, parameterised by intervention cost and occupancy. C_{fail} = 10 MNOK and $P_{d\,|\,f} = 0.1$, red values indicate stricter criterion and the governing criterion is presented in the lower right plot.

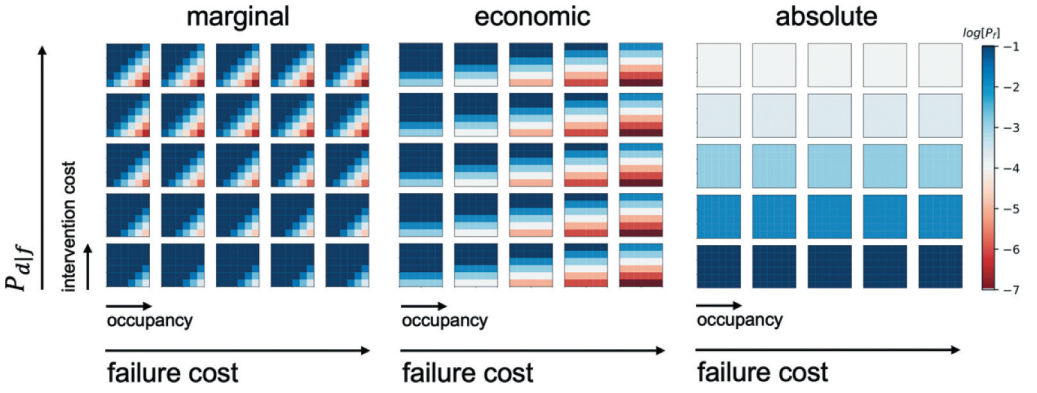


Figure 2. This figure shows results as in Figure 1 for a range of parameters C_{fail} and $P_{d\,|\,f}$.

safety criterion is the critical criterion for combinations of very high occupancy and low cost for intervention, as indicated with white colour.

Expanding the variety of the two fixed criteria, failure cost and conditional fatality probability, results in a range of plots in Figure 2. Here, we see the criteria for all four parameters

in one figure. The middle plot in all three five-by-five plots is identical to Figure 1, and the rest are results of varying failure costs and conditional fatality probability. The three criteria have distinct patterns, illustrating the impact of the different parameters. Comparing them and identifying the strictest one results in Figure 3, which is the main outcome of this study. This figure illustrates the governing criteria for all four parameters at once. The governing criterion for the reference case presented in Figure 1 is found in the middle of Figure 3. With a higher conditional fatality probability and lower failure costs (the upper left plots), the economic criterion has less influence compared to the reference case. On the contrary, with a lower conditional fatality probability and higher failure costs (the lower right plots), the economic criterion is more important. Two case studies in earlier work by Liljefors & Köhler (2024) are given as reference points, one which is governed by the absolute criterion and one by the economic criterion.

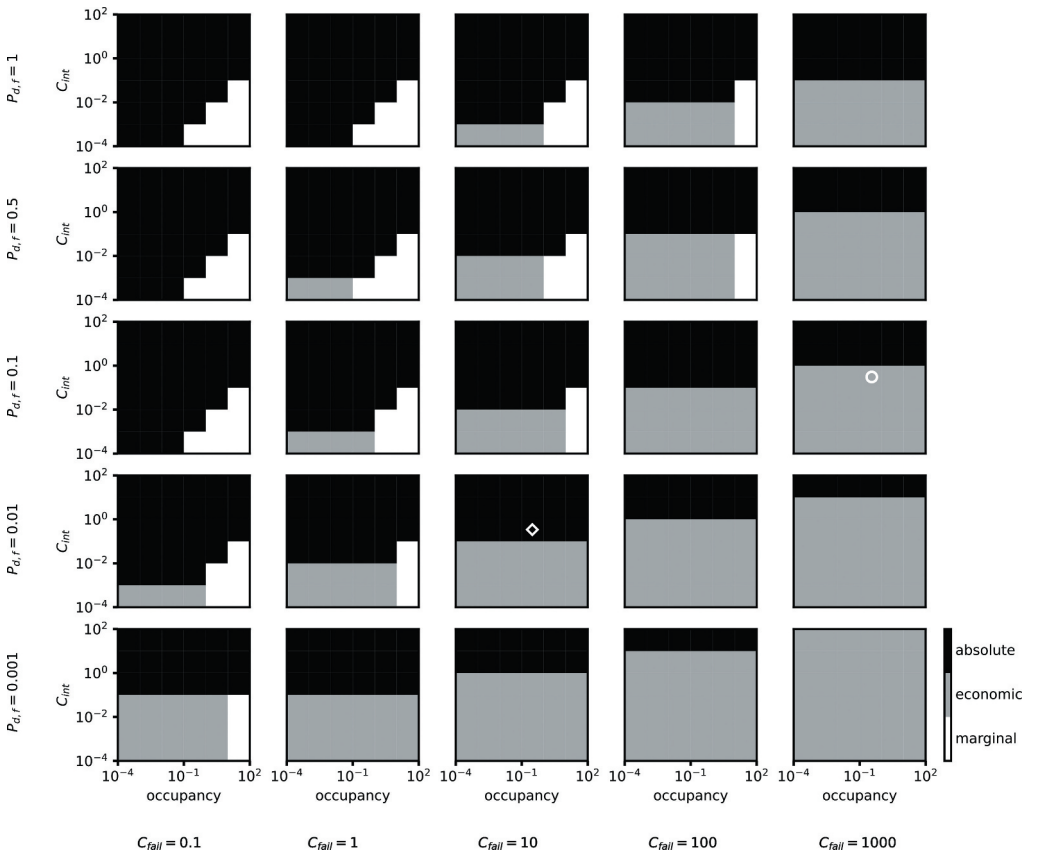


Figure 3. The governing criteria for the parameter study. The circle and diamond refer to case studies Herøysund and Osvold in Liljefors & Köhler (2024).

Repeating the calculations with a stricter absolute life safety criterion of 10^{-5} results in a shift of one magnitude favouring the absolute criterion (black covers a larger area, not shown here). This indicates that the absolute safety criterion may be governing for a majority of cases, and further investigation into this criterion is recommended. When doing so, one should remember that strict absolute criteria are costly and may waste resources that could be better utilised in society, i.e. they should not be conservatively assigned.

The assumption that the failure cost is independent of the occupancy and the conditional fatality probability is questionable. They both affect the expected number of fatalities, which impacts the failure costs as each fatality is quantified by a compensation cost, e.g. the

statistical value of a saved life *SVSL*. This means that the results are only valid when the costs for fatalities are a minor part of the total failure costs. In addition, some of the combinations may not be feasible and are therefore meaningless and can be ignored. This selection of practically reasonable parameters is left to the decision-maker. The range of occupancy in this study may be further restricted. Instead, a higher resolution for the areas where the criteria are similarly important may be interesting to study.

In this investigation, we compared three different criteria with little focus on the actual numbers. The values for the criteria are sensitive to the input parameters, but the relative comparison of the criteria is less sensitive. The study is meant as a qualitative overview that illustrates the behaviour of the different criteria. However, the numbers may provide some insight. The strictest criteria are in magnitude 10^{-7}, corresponding to the highest reliability class 3 in Eurocode for a yearly reference period. This would mean that, in any case, the highest safety level of the Eurocode is safe enough for assessment of existing structures (in case of no deterioration or other deviations). The least strict criteria are in magnitude $10^{-1} - 10^{-2}$, values that are considerably lower than any criteria in the Eurocode. This is promising, as it indicates that it may be justifiable to decrease the safety requirements for existing structures, which is commonly argued. However, this should be done with utmost caution, bearing in mind that, for example, deterioration or increased traffic load may violate this reasoning.

5 CONCLUSION

Establishing consistent safety criteria is fundamental for efficient and sustainable maintenance of existing bridges. In this study, we derived criteria in the form of failure probabilities from three approaches: Economic optimisation, marginal life safety and absolute life safety. The input variables were parameterised, and the governing criterion for each combination was identified. The study revealed ranges for which each approach is clearly governing the assessment and areas where the approaches are equally important. The large variation of governing criteria at reasonable ranges justifies the use of multiple criteria as it enables a more uniform safety level.

REFERENCES

Abrahamsen, E. B. and Aven, T. (2012). Why risk acceptance criteria need to be defined by the authorities and not the industry?. *Reliability Engineering & System Safety*, 105, 47–50

Faber, M. H., Sørensen, J. D., and Vrouwenvelder, T. (2015). On the regulation of life safety risk. *Proceedings of the 12th International Conference on Applications of Statistics and Probability in Civil Engineering (ICASP12), Vancouver, Canada, July 12-15.*

ISO 2394 (2015). General principles on reliability for structures. International Organization for Standardization.

Liljefors, F. and Köhler, J. (2024). Framework for rational decision making in bridge maintenance. *Structure and infrastructure engineering. Submitted for publication.*

Bridge Maintenance, Safety, Management, Digitalization and Sustainability – Jensen, Frangopol & Schmidt (eds)
© 2024 The Author(s), ISBN 978-1-032-77040-6
Open Access: www.taylorfrancis.com, CC BY-NC-ND 4.0 license

A review of design and assessment methods for skew concrete slabs

Alessandro Lipari
ENEA Italian National Agency for New Technologies, Energy and Sustainable Economic Development

ABSTRACT: Concrete slabs are often used for short-span bridges where it is required to limit the deck construction depth. Alongside, skew decks are helpful when there are space constraints in the bridge construction area, e.g., in urban areas, thus they are not uncommon. Nonetheless, skew slabs are not as much investigated as straight slabs and comprehensive guidance on their design or assessment is generally lacking. This is particularly the case for the shear behaviour of skew concrete slabs, which exhibit significant load concentrations around the obtuse corners with observed failure modes that are intermediate between the traditional cases of one-way and two-way (punching) shear. A reliable estimation of the shear strength is beneficial for both design and assessment: in fact, if shear strength is over-estimated, it may lead to undesired brittle failures, whereas if it is under-estimated, it may lead to inefficient design or unnecessary interventions to existing structures.

This paper reviews the provisions of three codes of practice on shear design (Eurocode 2, the Swiss SIA 262, and fib Model Code 2010), as well as main research on skew slabs. Procedures for extending the code provisions to skew slabs are presented and then applied to a case study. Some scatter is found across different codes of practice, broadly reflecting their complexity. The findings may be useful to practitioners with the design and assessment of skew concrete slabs.

1 INTRODUCTION

A slab can be defined as an element whose minimum panel dimension is not less than 5 times the overall slab thickness (European Committee for Standardization, 2004). Slabs can be considered *one-way spanning* if they possess two free unsupported and sensibly parallel edges and are subjected to dominantly uniformly distributed loads (European Committee for Standardization, 2004). Otherwise, slabs are said to be *two-way spanning*: this is mostly the case of bridge decks, as they are often not subjected to dominantly uniformly distributed loads.

Concrete slabs are often used for short-span bridges where it is required to limit the deck construction depth, as they provide more headroom than a typical beam-and-slab arrangement. Alongside, skew slabs are most suitable when there are space constraints, e.g., in urban areas.

Several established methods are available to analyse the flexural behaviour of concrete slabs, traditionally based on the theory of plasticity. In contrast, the shear behaviour is not as much established. Even for the simpler case of beams, there is no universal agreement on a single approach to predict the shear strength, particularly when no shear reinforcement is provided, that is the most typical case for slabs. Interestingly, slabs under concentrated loads close to supports exhibit an intermediate behaviour between the two traditional cases of one-way and two-way shear (Vaz Rodrigues et al., 2008, Lantsoght et al., 2013).

This paper reviews the provisions of three codes of practice on shear design (Eurocode 2, SIA 262, fib Model Code 2010), as well as main research on the shear behaviour of skew concrete slabs. As these codes do not generally have specific provisions for the calculation of shear in skew slabs, practical procedures are presented to extend their principles to skew slabs. The codes of practice are then applied to the case study of a skew railway bridge deck.

DOI: 10.1201/9781003483755-461

2 FLEXURAL BEHAVIOUR

Traditional methods to analyse the flexural behaviour of slabs are based on either the lower or upper bound analysis from the theory of plasticity, such as the *strip method* (Hillerborg, 1960, Wood & Armer, 1968), mainly used for design, or the *yield line theory* (Johansen, 1972), mainly used for assessment. These methods have the advantage of requiring relatively simple calculations and considering the plastic strength reserve of the material. However, in design, a linear elastic analysis may be required for SLS checks. Nowadays, the application of such traditional methods to skew decks is generally limited, as the use of Finite Element Method (FEM) has become widespread. A *grillage analysis*, in which the slab is idealized as a mesh of beams, may not be accurate for areas of high concentrated loads; therefore, it is advisable to use two-dimensional elements.

From a structural 2-D analysis of a slab, two shear forces per unit breadth are obtained along the x- and y-axes, v_x and v_y, as well as three moments per unit breadth: the bending moments m_x and m_y, and the twisting moment m_{xy} (Figure 1). Applied axial forces are generally not significant in non-prestressed slabs.

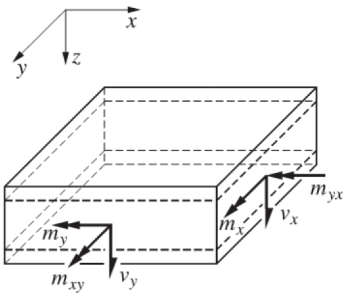


Figure 1. Shear forces and moments acting on a slab.

In slabs, it is useful to compute the bending moment m_n in any direction n forming an angle θ from the x-axis, which can be found from equilibrium considerations:

$$m_n(\theta) = m_x \cos^2\theta + m_y \sin^2\theta + 2m_{xy}\cos\theta \sin\theta \tag{1}$$

The *Field of Moments* method has been widely applied both for design and assessment purposes. The method uses the *normal moment yield criterion* and is valid for under-reinforced sections. No axial or shear forces are considered. The applied moment field is derived from the structural analysis, and it is checked that moment capacities are not exceeded anywhere, i.e., for all values of θ.

In design, as a derivation of the Field of Moments method, the Wood-Armer equations are often used to size the reinforcement by defining the required moment capacities for an orthogonal reinforcement grid (Wood, 1968, Armer, 1968):

$$\begin{cases} m^*_x = m_{Ed,x} \pm k \left| m_{Ed,xy} \right| \\ m^*_y = m_{Ed,y} \pm \frac{1}{k} \left| m_{Ed,xy} \right| \end{cases} \tag{2}$$

in which the sign + is valid for sagging moments (bottom reinforcement) and the sign – for hogging moments (top reinforcement); k is typically taken equal to 1, thus ensuring the least amount of reinforcement is required, although different values may be selected. In skew slabs, if the reinforcement grid is not placed along the x- and y-axes, the applied moments along the reinforcement directions can be derived from Equation 1.

However, some flaws have been noted in Equation 2 (Denton & Burgoyne, 1996, OBrien & O'Dwyer, 2015) affecting its application to assessment, as well as to the uncommon cases of anticlastic bending, i.e. bending moments of opposite sign, and skewed heavy reinforcement (Denton et al., 2010).

In assessment, both the applied and resisting moments are known, and the *excess capacity* is of interest, sometimes expressed in terms of a safety factor. The resisting moments due to multiple reinforcement layers i placed at angles α_i from the x-axis can be found as follows:

$$\begin{cases} m_{R,x} = \sum_i m_{R,\alpha_i} \cos^2\alpha_i \\ m_{R,y} = \sum_i m_{R,\alpha_i} \sin^2\alpha_i \\ m_{R,xy} = \sum_i m_{R,\alpha_i} \sin\alpha_i \cos\alpha_i \end{cases} \quad (3)$$

in which $m_{R,\alpha i}$ = resisting moment in the direction of the i-th reinforcement layer, which can be obtained from the classical flexural design theory of concrete beams. Inserting Equation 3 into Equation 1 gives the resisting moment in any direction n forming an angle θ from the x-axis:

$$m_{R,n}(\theta) = m_{Rd,x}\cos^2\theta + m_{Rd,y}\sin^2\theta + 2m_{Rd,xy}\cos\theta\sin\theta \quad (4)$$

3 SHEAR BEHAVIOUR

Traditionally, shear failure in slabs has been divided into two failure modes:

- *One-way* shear failure (often simply referred to as shear), associated with distributed or line loads and linear supports. In this case, the behaviour of a slab at failure is comparable with that of a wide beam.
- *Two-way* shear failure, associated with the local introduction of heavy concentrated loads, such as wheel loads. Two-way shear often refers to the case of punching shear, where failure occurs as the load roughly creates a truncated cone.

In reality, slabs may exhibit an intermediate case between the two failure modes when subjected to concentrated loads close to the supports (Vaz Rodrigues et al., 2008, Lantsoght et al., 2013). In such cases, two-way shear becomes prevalent over one-way shear, but with a flow of inner forces different from that of the punching shear case.

The shear behaviour of skew slabs has not been much investigated. Cope (1985) performed nine tests to failure on slab models with skew of 30°, 45° and 60° subjected to dead weights and concentrated loads: the 30° and 45° skew models failed in shear with cracks in proximity of the concentrated loads and/or the support line, whereas the 60° skew model failed in punching shear; it was also shown that an increasing skew angle considerably decreases the shear capacity. Morrison & Weich (1987) tested a model of a 50° skew decommissioned concrete slab deck, which failed in punching shear exhibiting ductility. Miller et al. (1994) tested a 30° skew decommissioned concrete slab bridge to destruction, which failed abruptly in punching shear. Théoret et al. (2012) proposed bending moment and shear force factors to design skew slab bridges using the equivalent beam method. For a comprehensive review refer to Lipari (2020).

In analysis, thick plates should be used, as they are able to capture the shear concentrations in the obtuse corners typical of skew slabs. However, supports are best modelled with springs and, when point supports are used, a fine mesh around them may lead to unrealistic shear forces. This typically affects shear forces within a deck depth from the support (OBrien et al., 2015).

3.1 *Principal shear force*

The concept of principal shear force is crucial to analyse the shear behaviour of slabs. The applied shear force acting on any direction forming an angle θ from the x-axis can be found from equilibrium considerations:

$$v(\theta) = v_x\cos\theta + v_y\sin\theta \quad (5)$$

The principal shear force can be represented by its magnitude, v_0, and direction forming an angle φ_0 from the x-axis:

$$v_0 = \sqrt{{v_x}^2 + {v_y}^2} \quad (6)$$

$$\varphi_0 = arctan\left(\frac{v_y}{v_x}\right) \tag{7}$$

The principal shear action occurs on a plane perpendicular to the direction of the principal shear force. Close to the supports of skew slabs, φ_0 is expected to be comparable to the skew, as it is typically perpendicular to the support line. In general, it suffices to perform the shear resistance check along φ_0, but there may be uncommon cases where other directions should be checked (Lipari, 2020).

3.2 *Equivalent reinforcement ratio*

When the longitudinal reinforcement is not placed perpendicularly to the support line, the direction of the principal shear force typically differs from the direction of the main flexural reinforcement. The concept of *equivalent area of reinforcement* is useful to compute the effects of the reinforcement along any directions. The area of flexural reinforcement $A_{s,\alpha}$ placed at angle α from the x-axis may be resolved for any direction forming an angle θ from the x-axis as follows:

$$A_{s,\alpha}(\theta) = A_{s,\alpha} cos^2(\theta - \alpha) \tag{8}$$

The $\cos^2$ function accounts for the increase in bar spacing and the decrease in effective reinforcement area with increasing angle θ. Dividing both terms for the effective area $b{\cdot}d$, where b = width of the section, and d = effective depth, and considering multiple reinforcement layers i, Equation 8 can be rewritten with reference to the reinforcement ratio ρ:

$$\rho(\theta) = \sum\nolimits_i \rho_{\alpha_i} cos^2(\theta - \alpha_i) \tag{9}$$

In the case of reinforcement placed along the x-y axes, and in the direction of the principal shear force ($\theta = \varphi_0$), Equation 9 simplifies as $\rho_0 = \rho_x cos^2\varphi_0 + \rho_y sin^2\varphi_0$.

Note that Equations 8-9 represent mere *geometric* equivalences, giving an *equivalent reinforcement ratio*, as if an unreinforced direction had reinforcement along it. In fact, when using Equation 8 for the calculation of reinforcement forces, an implicit assumption of yielded reinforcement is made.

Alternatively, an expression based on the theory of elasticity may be used, in which the reinforcement strains (and associated stresses) are taken into account (Clark, 1983):

$$A_{s,\alpha}(\theta) = A_{s,\alpha} cos^4(\theta - \alpha) \tag{10}$$

When using the $\cos^4$ function for the calculation of reinforcement forces, it is then implied that the flexural reinforcement remains elastic. Equation 10 may be regarded as an effective *mechanical* equivalence, as it allows to compute the force that a fictitious reinforcement along an unreinforced direction would exercise when yielding is not achieved (Denton et al., 2010).

Following a similar development to that of Equation 9, the equivalent reinforcement ratio for multiple reinforcement layers i can be rewritten as follows:

$$\rho(\theta) = \sum\nolimits_i \rho_{\alpha_i} cos^4(\theta - \alpha_i) \tag{11}$$

In the case of reinforcement placed along the x-y axes, and with $\theta = \varphi_0$, Equation 11 simplifies as $\rho_0 = \rho_x cos^4\varphi_0 + \rho_y sin^4\varphi_0$.

It is always on the safe side to use Equation 11, rather than Equation 9.

4 CODES OF PRACTICE

This section outlines provisions of three codes of practice about shear design without shear reinforcement: Eurocode 2 (in the following EC2), which is the standard in most European

countries and is based on a statistical analysis of experimental data; the Swiss code SIA 262 *Concrete Structures* (SIA262) and the *fib Model Code for Concrete Structures 2010* (MC2010), which are based on two different strain-based mechanical approaches. For a full description of the methods, the reader is referred to the codes and Lipari (2020).

4.1 *Eurocode 2*

Annex LL in Eurocode 2 part 2 (European Committee for Standardization, 2005) deals with the design of shell elements with a *sandwich model*, in which the outer layers (*cover*) resist membrane forces, such as axial forces and moments, and the inner layer (*core*) resists the shear forces. In fact, a slab can be considered as a case of a shell element.

For the design of the inner layer, the principal shear force should be computed according to Equations 6-7. In the direction of the principal shear force, the shell element behaves like a beam and Eurocode 2 part 1 applies (European Committee for Standardization, 2004).

Lipari (2020) proposed an extension for skew slabs introducing the equivalent reinforcement ratio $\rho(\theta)$ into the EC2-1 formulation expressed in terms of design shear resistance per unit breadth:

$$v_{Rd,c}(\theta) = C_{Rd,c} \cdot k \cdot \sqrt[3]{100 \cdot \rho(\theta) \cdot f_{ck}} \cdot d_m \geq v_{min} \cdot d_m \tag{12}$$

in which d_m = average effective depth; f_{ck} = characteristic concrete strength; and $\rho \leq 0.02$ as for beams. Although Annex LL uses the $\cos^2$ function to reduce the effectiveness of the reinforcement (Eq. 9), the use of the more conservative $\cos^4$ is recommended. It is then checked that the design shear resistance $v_{Rd,c}$ with $\theta = \varphi_0$ (Eq. 12) is greater than the design principal shear force $v_{Ed,0}$ (Eq. 6). If not, in design, shear reinforcement can be provided.

EC2 allows shear forces due to loads applied on the upper side within a distance $0.5d \leq a_v \leq 2d$ from the edge of a support to be reduced by a factor $\beta = a_v/2d$, in which a_v = distance between the edge of the load and the support edge; for $a_v \leq 0.5d$, $\beta = 0.25$.

4.2 *SIA 262*

The Swiss Code SIA 262 (SIA, 2013) endorses a simplified version of the *Critical Shear Crack Theory* (CSCT) (Muttoni & Fernández Ruiz, 2008). The shear resistance of slabs without shear reinforcement is determined for a control section at a distance $d/2$ from the edge of a support or from the point of application of a concentrated load.

The design shear resistance $v_{Rd,c}$ strongly depends on the reinforcement strain ε_s. This increases the design effort compared to EC2; however, as an approximation suitable for outline design or preliminary assessment, it can be conservatively assumed that the flexural reinforcement is yielded, thus substantially reducing the computational effort. In such case, SIA262 provisions are readily applicable to skew slabs.

On the other hand, if the flexural reinforcement remains elastic, the bending utilization in the direction of the principal shear force, $m_{Ed,0}/m_{Rd,0}$, needs to be found at the control section to calculate ε_s. The design applied moment per unit breadth, $m_{Ed,0}$, is found by means of Equation 1 with $\theta = \varphi_0$. Consistently, the design resisting moment per unit breadth, $m_{Rd,0}$, is calculated according to Equation 4 with $\theta = \varphi_0$.

Notably, a factor $1/[\sin^4(\varphi_0 - \alpha_l) + \cos^4(\varphi_0 - \alpha_l)]$ has to be applied to ε_s to consider the case when the direction of the principal shear force φ_0 significantly deviates from that of the main reinforcement α_l (Muttoni & Fernández Ruiz, 2008).

4.3 *Fib Model Code 2010*

The *fib Model Code for Concrete Structures 2010* (International Federation for Concrete Structures, 2013) provides equations for the shear resistance of web of beams and core layers of slabs, as per the sandwich model mentioned in Section 4.1. It also gives different *Levels of Approximation* (LoA): the higher the level, the greater the effort, but the more accurate the results.

The design shear force must in general be determined for control sections at a location d from the face of supports and from discontinuities of geometry or applied loads. Notably, MC2010 includes the case of concentrated loads applied to a slab near a support line. In this case, the slab capacity must be checked both for punching at the control perimeter around the loaded area and for shear at a control section taken parallel to the support line.

The MC2010 provisions for members without shear reinforcement are based on the Simplified Modified Compression Field Theory (SMCFT) (Bentz et al., 2006). Two levels of approximation are provided. LoA I is readily applicable to skew slabs, as the only inputs required are the concrete strength f_{ck} and the effective shear depth z, and it may be used for outline design or preliminary assessment. In LoA II the shear resistance $V_{Rd,c}$ depends on the longitudinal strain at the mid-depth of the effective shear depth ε_x, which in turn depends on the design applied shear force V_{Ed}, thus making the check an iterative process, as well as on the design applied moment M_{Ed} and the area of reinforcement A_s. It is not stated how to deal with the cases when the direction of the principal shear force differs from that of the main reinforcement; therefore, the following recommendations are made for the calculation of ε_x in skew slabs:

- the design moment M_{Ed} is taken per unit breadth and resolved for $\theta = \varphi_0$, $m_{Ed,0}$ (Eq. 1);
- the design shear force V_{Ed} is taken as the design principal shear force per unit breadth, $v_{Ed,0}$ (Eq. 6);
- the area of longitudinal reinforcement A_s is taken as the equivalent area of reinforcement per unit breadth along φ_0, $a_{s,0}$, based on the more conservative Equation 10.

Note that, although MC2010 states to neglect any transverse reinforcement, this assumption seems over-conservative when applied to significantly skew slabs.

5 CASE STUDY

Underbridge DSN1/14 at Eaglescliffe (United Kingdom) is a pre-cast concrete solid slab with two upstands, constructed in 2016 to replace an older deck. The bridge carries one ballasted railway track.

Table 1 resumes main information on deck geometry and material properties. In spite of its short span, the concrete deck is quite slender, with a span-to-depth ratio of 14.5:1. The supports (10x200 mm^2 unreinforced elastomeric strips) are modelled by means of distributed

Table 1. Main data.

Description	Value
Skew span between supports	4.35 m
Slab depth	0.3 m
Slab width (right angle)	3.7 m
Skew	26.5°
Concrete strength class	C40/50
Maximum aggregate diameter	20 mm
Nominal cover	45 mm
Modulus of elasticity of steel	200 GPa
Longitudinal reinforcement ratio (midspan)	2.16%
Longitudinal reinforcement ratio (supports)	1.08%
Transverse reinforcement ratio	0.61%

linear springs with stiffness 14,000 MN/m^3. The orthogonal reinforcement grid has the longitudinal reinforcement parallel to the free edges.

The material partial safety factors for concrete and steel are respectively $\gamma_c = 1.5$ and $\gamma_s = 1.15$. The applied train load is the Load Model 71 (LM71) (European Committee for Standardization, 2003). The design axle load at ULS Q_v is 822.9 kN. Considering each individual wheel load and the longitudinal distribution between sleepers, the design point load is 205.7

kN. The LM71 is positioned so that the nearest point load lies at a minimum distance of $2d$ from the support edge ($a_v \geq 2d$); as such, there is no need to consider the EC2 factor β.

To enable a comparison among the three codes of practice, the design applied shear forces v_{Ed} are all taken at a distance d from the support edge. For MC2010, the design applied bending moment m_{Ed} is taken at a distance d from the support edge, whereas for SIA262 the design bending moments m_{Ed} and m_{Rd} are taken at a distance $d/2$ from the point of application of the loads, as a greater bending utilization is achieved there.

Figure 2 shows the shear forces along the x-axis under the worst train load position, which is in proximity of the bottom obtuse corner.

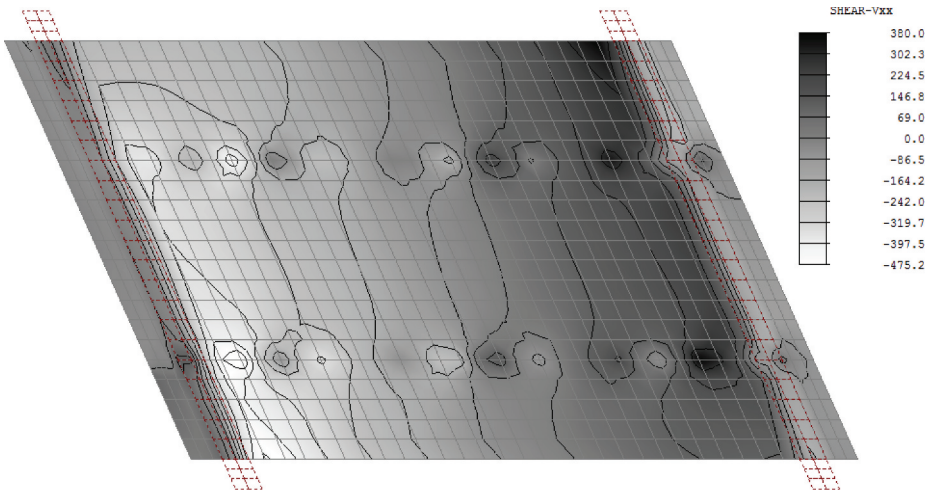


Figure 2. ULS design shear forces along x-axis [kN/m] (area below upstands is excluded).

Table 2. Design shear forces and moments, and shear strengths.

Shear force or moment (*distance of control section from support edge*)	Value
Shear force, ($v_{Ed,x}$, $v_{Ed,y}$) [kN/m] (d)	(-475.2, -215.2)
Principal shear force, $v_{Ed,0}$ [kN/m] (d)	521.4
Direction of principal shear force, φ_0 [°] (d)	24.4
Bending and twisting moments, ($m_{Ed,x}$, $m_{Ed,y}$, $m_{Ed,xy}$) [kNm/m] (d)	(61.9, 55.6, 38.5)
Moment along direction of principal shear force, $m_{Ed,0}$ [kNm/m] (d)	89.8
Bending and twisting moments, ($m_{Ed,x}$, $m_{Ed,y}$, $m_{Ed,xy}$) [kNm/m] ($3d/2$)	(134.6, 90.1, 50.8)
Moment along direction of principal shear force, $m_{Ed,0}$ [kNm/m] ($3d/2$)	165.2
Resisting moment along direction of principal shear force, $m_{Rd,0}$ [kNm/m] ($3d/2$)	216.6
Shear strength according to EC2 [kN/m]	172.5
Shear strength according to SIA262 (plastic reinforcement) [kN/m]	123.9
Shear strength according to SIA262 (elastic reinforcement) [kN/m]	174.9
Shear strength according to MC2010 (LoA I) [kN/m]	129.5
Shear strength according to MC2010 (LoA II) [kN/m]	133.9

Table 2 reports the design values of forces and moments at the control sections, as well as the design shear strengths calculated according to Section 4. Note that, as expected, φ_0 is close to the skew.

Based on the results presented, the following observations can be made:

– the loss of accuracy when using the simple LoA I of MC2010 compared to the more accurate LoA II is quite small (-3.3%), due to relatively high strains ε_x;
– MC2010 LoA II provides lower shear strength values than EC2 or SIA262 with elastic reinforcement, mostly due to the high shear forces v_{Ed}, which affect the shear strength;
– SIA262 provides the greatest shear strength when assuming that the flexural reinforcement remains elastic, otherwise it returns the lowest strength; in the former case, the difference is substantial when compared to MC2010 (+30.6%) and minimal when compared to EC2 (+2.4%).

Note that the deck needed shear reinforcement, regardless of the code applied, due to its slenderness and the high shear forces.

6 CONCLUSIONS

Skew concrete slabs are not uncommon in bridge engineering. While their flexural behaviour is quite established, their shear behaviour has not been much investigated. Indeed, skew slabs exhibit significant load concentrations around the obtuse corners, with observed failure modes that are intermediate between the traditional cases of one-way and two-way (punching) shear. Furthermore, guidance on their design and assessment is not comprehensive.

The provisions of three codes of practice on the shear design without shear reinforcement (the empirical Eurocode 2 and the strain-based SIA 262 and fib Model Code 2010) are presented here, along with procedures to extend them to skew slabs. The codes are then applied to the case study of a skew railway deck. Significant scatter is found, broadly reflecting their complexity: the quicker MC2010 LoA I and SIA262 with an assumption of plastic reinforcement expectedly return the lower estimates, which may be used for preliminary calculations, whereas EC2 and SIA262 with an assumption of elastic reinforcement return significantly greater estimates than MC2010 LoA II.

REFERENCES

Armer, G. S. T. 1968. The reinforcement of slabs in accordance with a predetermined field of moments. Correspondence. *Concrete*, 2(8): 319–320.

Bentz, E. C., Vecchio, F. J. & Collins, M. P. 2006. Simplified Modified Compression Field Theory for Calculating Shear Strength of Reinforced Concrete Elements. *ACI Structural Journal*, 103: 614–624.

Clark, L. A. 1983. *Concrete bridge design to BS 5400*, London and New York, Construction Press.

Cope, R. J. 1985. Flexural shear failure of reinforced concrete slab bridges. *Proceedings of the Institution of Civil Engineers, Part 2*, 79: 559–583.

Denton, S., Shave, J., Bennetts, J. & Hendy, C. 2011. Design of concrete slab elements in biaxial bending. *In*: Denton, S. (ed.), *Bridge Design to Eurocodes - UK Implementation, London*, 22-23 November 2010. London: ICE Publishing, 250–269.

Denton, S. R. & Burgoyne, C. J. 1996. The assessment of reinforced concrete slabs. *The Structural Engineer*, 74(9): 147–152.

European Committee for Standardization 2003. Eurocode 1: Actions on Structures. *Part 2: Traffic loads on bridges*. Brussels: CEN.

European Committee for Standardization 2004. Eurocode 2: Design of concrete structures. *Part 1: General rules and rules for building*. Brussels: CEN.

European Committee for Standardization 2005. Eurocode 2: Design of concrete structures. *Part 2: Concrete Bridges - Design and detailing rules*. Brussels: CEN.

Hillerborg, A. A Plastic Theory for the Design of Reinforced Concrete Slabs. *6th IABSE Conference, Stockholm, 1960*. 178–186.

International Federation for Concrete Structures 2013. fib Model Code for Concrete Structures 2010. Berlin: Wilhelm Ernst & Sohn.

Johansen, K. W. 1972. *Yield-line Formulae for Slabs*, CRC Press.

Lantsoght, E. O. L., van der Veen, C. & Walraven, J. C. 2013. Shear in One-Way Slabs under Concentrated Load Close to Support. *ACI Structural Journal*, 110: 275–284.

Lipari, A. 2020. A comparative study of shear design methods for straight and skew concrete slabs. *Engineering Structures*, 208: 1–16.
Miller, R. A., Aktan, A. E. & Shahrooz, B. M. 1994. Destructive Testing of Decommissioned Concrete Slab Bridge. *Journal of Structural Engineering*, 120(7): 2176–2198.
Morrison, D. G. & Weich, G. R. 1987. Free-Edge and Obtuse-Corner Shear in R/C Skew Bridge Decks. *ACI Structural Journal*, 84: 3–9.
Muttoni, A. & Fernández Ruiz, M. 2008. Shear Strength of Members without Transverse Reinforcement as Function of Critical Shear Crack Width. *ACI Structural Journal*, 105: 163–172.
OBrien, E. J., Keogh, D. L. & O'Connor, A. J. 2015. Bridge Deck Analysis. Second ed. Boca Raton: CRC Press.
OBrien, E. J. & O'Dwyer, D. 2015. A review of the Wood Armer equations for torsion in bridge slabs. *The Structural Engineer*, 93(9).
SIA 2013. Betonbau. Zurich: Schweizerischer Ingenieur- und Arkitektenverein.
Théoret, P., Massiccotte, B. & Conciatori, D. 2012. Analysis and Design of Straight and Skewed Slab Bridges. *Journal of Bridge Engineering*, 17(2): 289–301.
Vaz Rodrigues, R., Fernández Ruiz, M. & Muttoni, A. 2008. Shear strength of R/C bridge cantilever slabs. *Engineering Structures*, 30: 3024–3033.
Wood, R. H. 1968. The reinforcement of slabs in accordance with a predetermined field of moments. *Concrete*, 2(2): 69–76.
Wood, R. H. & Armer, G. S. T. 1968. The theory of the strip method for design of slabs. *Proceedings of the Institution of Civil Engineers*, 41(2): 285–311.

Bridge Maintenance, Safety, Management, Digitalization and Sustainability – Jensen, Frangopol & Schmidt (eds)
© 2024 The Author(s), ISBN 978-1-032-77040-6
Open Access: www.taylorfrancis.com, CC BY-NC-ND 4.0 license

Non-destructive testing of a post-tensioned concrete road bridge in Norway

B. Täljsten
Luleå University of Technology and Invator AB

C. Popescu
Sintef AS and Invator AB

M. Holmqvist
Invator AB

ABSTRACT: The Herøysunds bridge on the west-coast in Nordland Fylke in Norway had undergone concrete repair works with focus on reinforcement corrosion. During these actions, it was discovered that the tendon ducts had loss of injection. To ensure the safety of the bridge it was decided to map voids and defects in the ducts. Several risk areas were pointed out by the constructor and a non-destructive test (NDT) was carried out. A methodology with combination of different NDT methods were used; cover meter, GPR, UPE, IE and Videoscope. The results from the NDT investigate shows that the suggested approach was successful, and it was possible with high accuracy to detect voids in the ducts. The methodology forms a basis for the procedure recommended by the Norwegian Public Roads Administration.

1 INTRODUCTION

Herøysundet Bridge is a beam bridge, constructed on-site with varying height. The bridge has 6 spans consisting of 5 pillars and two abutments (Figure 1). The total length of the bridge is 154 meters, it has one traffic lane, as well as sidewalks on both sides, and the largest overall width is 5.30 meters. The largest span, which is the navigational channel, is located in span 4 and has a length of 60 meters. Pillars and abutments are founded on rock. The Herøysund Bridge, situated in Nordland County, is a post-tensioned bridge. Recent inspections have revealed corrosion in the tendons of its post-tension system. Plans are in place for the replacement of the bridge, followed by the demolition of the old structure. This scenario serves as an excellent case study (Popescu et al. 2023) to enhance current engineering practices in the assessment of existing structures by incorporating the latest scientific advancements. Nordland County, in collaboration with the Norwegian Public Roads Administration (Statens Vegvesen), sees significant value in conducting a comprehensive assessment of this bridge. Such an evaluation can provide valuable insights, enhancing our comprehension of the structure's condition, degradation processes, and overall structural integrity (Karlsson et al. 2021). This paper presents the planning and implementation of non-destructive testing (NDT) for the Heroy Bridge, encompassing the assessment and recommendation of testing methodologies to detect voids in the ducts. Detecting defects and deterioration of the prestressed tendons is a complex task due to inaccessibility. Exploratory openings (e.g. coring) would offer limited results to localized areas. Non-destructive methods should be preferred for minimum disturbance to the structure – i.e. coring done for validation only.

In non-destructive testing, the planning of the inspection is an important part for a successful end result. During the planning, a testing procedure is established where the overall problems of the construction are first mapped and then suitable NDT methods are selected,

DOI: 10.1201/9781003483755-462

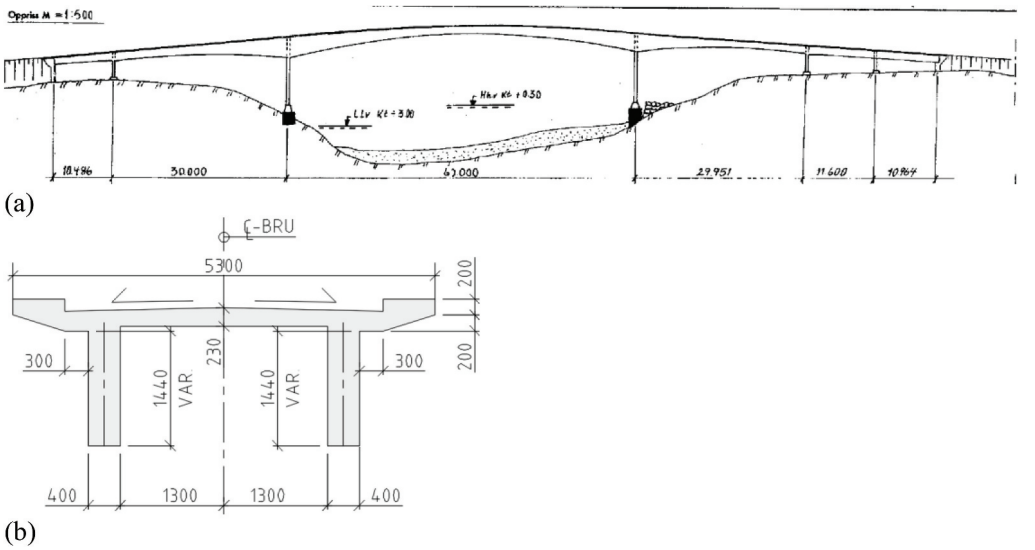


Figure 1. Heröysund Bridge: (a) elevation; and (b) cross-section.

in which order they should be carried out and which construction areas should be prioritized in the investigation. When establishing the testing procedure, drawings, previous inspection reports and photos are reviewed – process known as desk study. With this as a basis, the inspection can be placed on the construction parts that are most relevant and where the greatest risk of serious damage exists (Woodward, 2001; Matt et al. 2000).

While the focus lies on examining external post-tensioned (PT) tendons, some non-destructive testing (NDT) methods outlined by Im et al. (2010) may also prove relevant for internal tendon inspection. Among these are the Shearwave Tomography, Impact Echo, and Ultrasonic. Additionally, the Ground Penetrating Radar and Infrared Thermography are worth considering as alternative methods.

2 NON-DESTRUCTIVE TESTING APPROACH

The inspection task was carried out by using the following NDT systems:

- Covermeter
- Ground penetrating radar (GPR)
- MIRA ultrasound 3D (UPE)
- Impact echo
- Videoscope

In addition, cores were extracted at select locations to provide access to the tendon ducts followed by drilling to provide ground truth information and validation.

The inspection process included the following actions:

1. Desk study where potential focus areas were defined.
2. Locate the areas to be inspected based on the original planning and adapt based on local conditions. Deviations may exist due to local unevenness of the concrete surface making the data collection difficult.
3. On the areas marked in step 2, use ground penetrating radar to locate the ordinary reinforcement and prestressed reinforcement.
4. Mark the position of the prestressed reinforcement directly on the concrete surface and divide the profile line into 10 cm segments.
5. Use MIRA instrument to capture 2D slices at every 10 cm segment defined in step 3.

6. Combine the 2D slices within a 3D image that can be used for interpretation of the results.
7. Any detected flows on the 3D image based on MIRA measurements are further investigated using Impact echo instrument.
8. Coring/drilling is carried out in areas with potential voids inside the tendon ducts.

3 TESTING LOCATIONS

The testing locations for the Herøysund Bridge have been prearranged in consultation with the Norwegian Road Administration and Nordland County. The objective is to conduct NDT on all girders where access to tendons was feasible. It should be noted that tendons situated in the concrete deck have not undergone inspection. All test locations are illustrated in Figure 2 together with a more detailed description of section A in Figure 3. Also, the original section is presented in this figure. However, in this paper only location A, and only the North beam is going to be discussed. The approach, highlighted in Section 2, is then similar for all other locations.

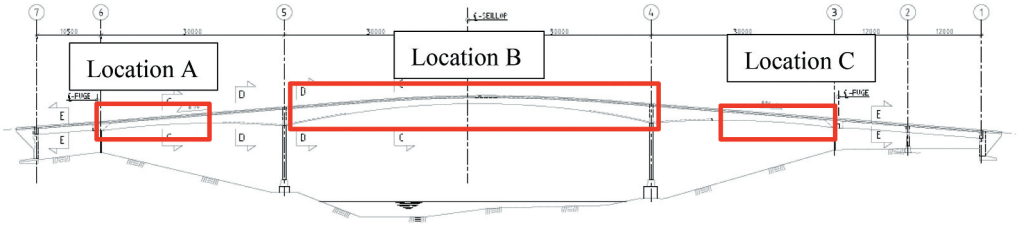


Figure 2. Testing locations.

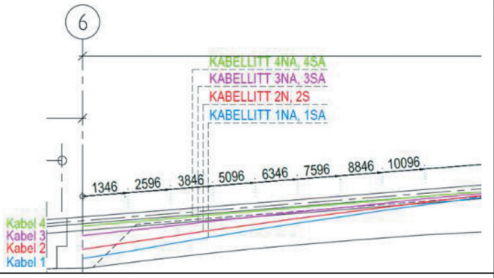
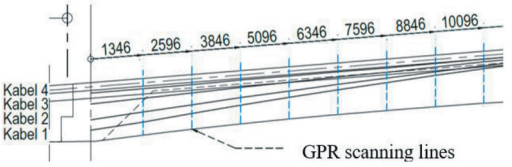
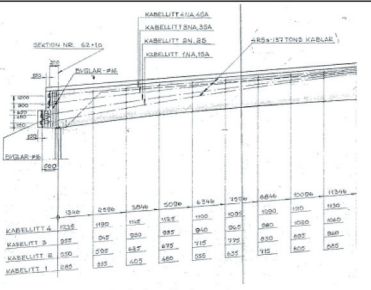
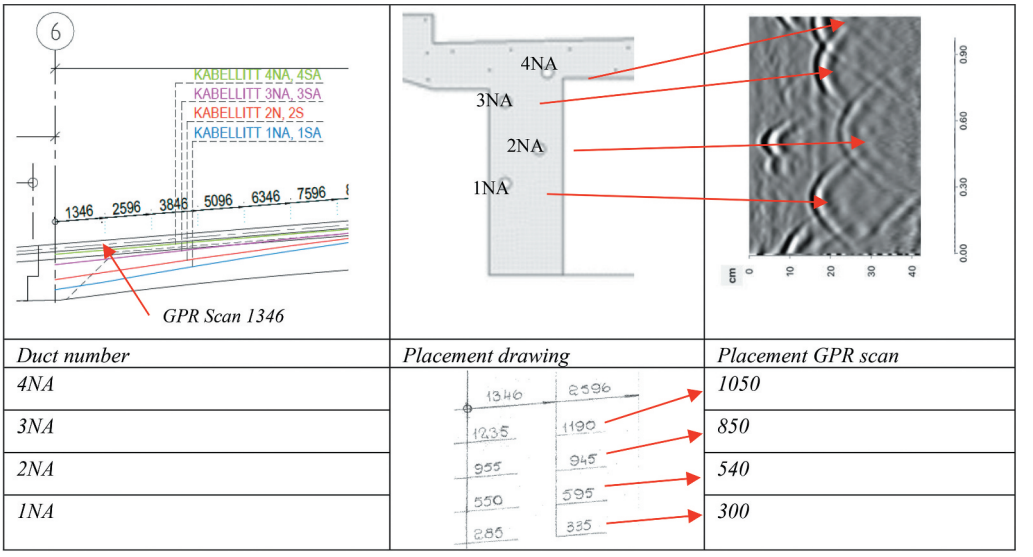
Location	*Description*
Location A 	*Inspection of tendon ducts in the north/south girders* • *South girder (tendon ducts and length inspected)* ○ *Tendon 1SA – 10.0 m long* ○ *Tendon 2SA – 7.0 m long* ○ *Tendon 3SA – 5.0 m long* • *North girder (tendon ducts and length inspected)* ○ *Tendon 1NA – 8.0 m long* ○ *Tendon 2NA – 7.0 m long* ○ *Tendon 3NA– 5.0 m long*
	

Figure 3. Test locations and cables.

4 RESULTS

The main purpose of the investigation conducted at Herøysund Bridge was to verify the integrity of the grouting along the post tensioned tendons. Non-destructive test methods have been used to be able to check for defects. The measurements were repeated as vertical scans in the same locations as the original drawing, with this approach, the placements could be compared for the north beam in location 6, see Figure 4.



Duct number	*Placement drawing*	*Placement GPR scan*
4NA		*1050*
3NA		*850*
2NA		*540*
1NA		*300*

Figure 4. Corroborating the GPR results with as-designed drawings showing the placement of tendon ducts in north girder and a comparison with the placement.

MIRA equipment has been used in all cases to evaluate the condition of grouted post-tensioning ducts in the girders. B-scans (2D images) were collected every 10 cm along the ducts, see Figure 5. In total, around 3000 B-scans were collected throughout the bridge. The B-scans reflects the cross-section (perpendicular to the test surface) while the C-scans are obtained by combining multiple B-scans – thus, showing the reflecting interfaces on a plane parallel to the test surface. For example, tendons are shown as big dots on a B-scan together with their depth ("concrete cover") as well as the back-wall (thickness of the scanned element). On the C-scan the tendon ducts are shown as continuous lines. The lines may have a green-yellow color and indicates lower amplitude reflections from the steel tendons – meaning the duct is fully grouted. If the lines are displayed as red color, this indicates strong reflections from a discontinuity in material properties. Areas with strong interference that is characteristic of an air void will be further inspected with impact-echo instrument, see also Figure 5.

Inspection of tendon ducts started at the anchors placed in axis 6 in both north (N) and south (S) girder. The most severe locations were found on the south girder in tendon 2SA and 3SA. In the south girder two of the ducts were completely empty and had severe corrosion on the tendons.

In the north girder, duct 1NA gave indications to be lacking grout, the verification showed no presence of voids. Figure 6 shows a simplified overview of the scans, and the ultrasonic results is shown in Figure 7.

Impact echo was used in some locations to verify the results from ultrasonic scans. In order to detect ungrouted tendons two features in the frequency spectrum were of interest. First, a frequency peak in the spectrum that is associated with the thickness of the girder needs to be calculated. The frequency peak for the backwall is calculated with the actual thickness



MIRA (UPE) *Impact Echo (IE)*

Figure 5. Inspecting grouting conditions with MIRA and Impact Echo.

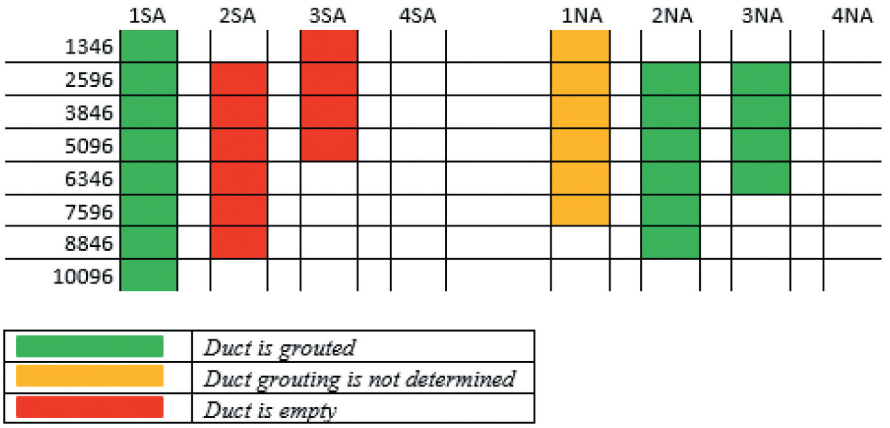


Figure 6. Grouting status according to ultrasonic results.

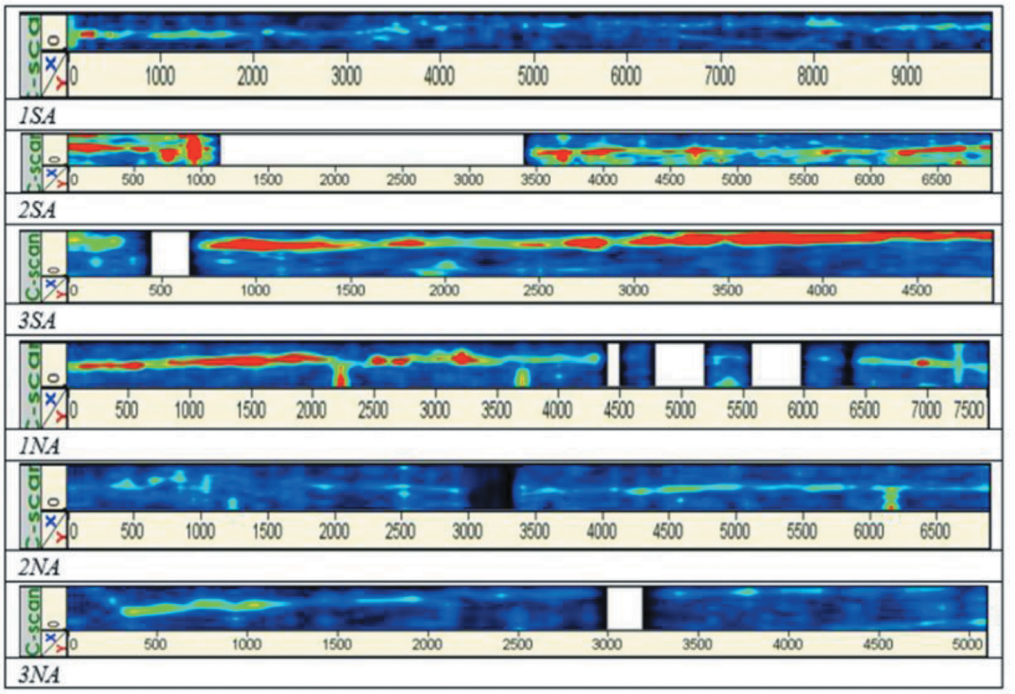
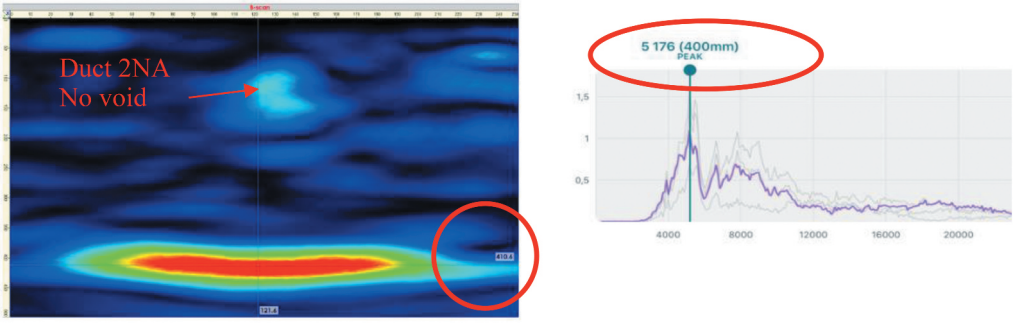


Figure 7. Ultrasonic results in south and north girder.

measured at the girder, $T = 400\ mm$, and the velocity measured with ultrasonic pulse, $C_p = 4140\ m/s$:

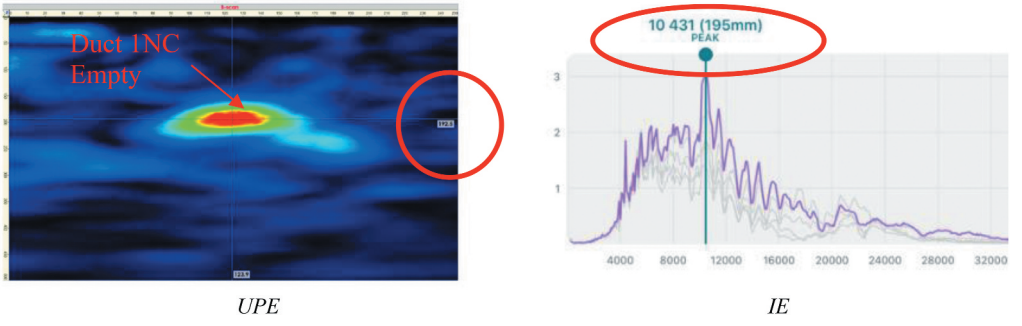
$$f = \frac{C_p}{2T} = 5.176\,kHz \tag{1}$$

The frequency peak we should look for is 5,176 kHz and if we get a peak at this frequency Impact echo shows that no voids are present in the inspected duct 2NA, see Figure 8.



UPE *IE*

Figure 8. Scan in 2NA scan 67 with no presence of voids. Backwall at 400 with both UPE and IE.



UPE *IE*

Figure 9. Void at ~200mm depth with both UPE and IE.

Figure 9 shows a scan of a duct with a void, 1NC. In this example the duct is placed with a cover of $T = 190\ mm$ and $C_p = 4140\ m/s$, a void in this duct should give a frequency peak according to the following calculation:

$$f = \frac{C_p}{2T} = 10.89\,kHz \tag{2}$$

In Figure 10 a longer grid scan with Impact echo from duct 3SC is shown, this duct is confirmed as empty in investigation made in 2020. No drilling was made during the inspection presented in this paper. The cover to the duct is around 160mm according to the GPR which means that the void could be somewhere between 160mm and 240mm. Red values show the presence of voids and the depth to the void. The green values show the thickness peak for the backwall, and the orange values show a shift in the peak which indicates a void. It should be noted that only one scan in each location was made which could mean that the impact echo missed the duct, especially the last scans were the duct was placed above the marked line on the concrete surface. This could explain the green numbers in the end. Each measurement with impact echo was made along the duct with 10 cm between, the same grid that was made with UPE.

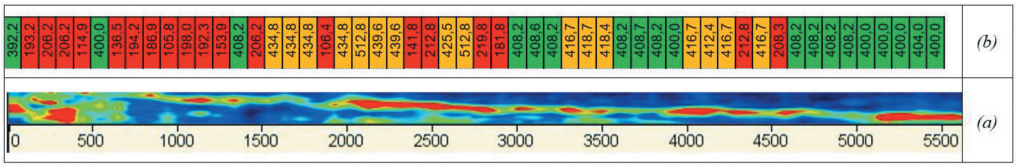


Figure 10. Empty duct with results from UPE *(a)* and Impact Echo (IE) *(b)*.

5 VERIFICATION BY CORING

To verify the results from the measurement some of the tendon ducts were opened to investigate the status of the cables and to verify voids or no voids. Caution must be exercised to ensure that the tendons are not damaged or, worse yet, severed during this process. The procedure is the following:

- Map placement of slack reinforcement – to avoid cutting reinforcement when drilling
- Map placement of ducts
- Use a hammer drill machine with ϕ16 to verify the distance to the duct
- Mount and core with ϕ80 – 100 mm depending on the depth to the duct
- Stop coring ca 15 mm outside the duct
- Carefully remove the concrete into the duct
- Open up the duct and inspect visually or in combination with videoscope
- After inspection repair the opening

The general process is shown in Figure 11 together with results from location.



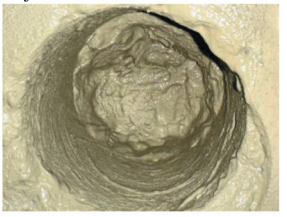
Core drilling Ø100mm aprox 10-15mm from duct



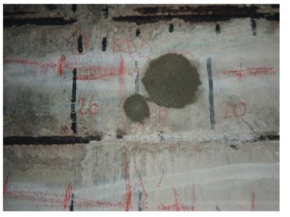
Exposure of duct



Opening of duct and tendon inspection



Sealing with Mapei Redisit



Repair with Mapei Redirep



Location 3SA



Empty duct, corrosion



Humidity 99,8 in the duct

Figure 11. Opening in duct 3SA, 4 m from the anchor. Empty duct with corrosion.

6 SUMMARY AND CONCLUSIONS

The aim of the inspection was to evaluate the condition of the pretensioned tendons at Heröy Bridge. Specifically, voids in tendon ducts and consequently corrosion of the tendons has been the focus of the investigation. To achieve this, the condition of the grouting has been verified using non-destructive equipment MIRA, UPE (shear-wave tomography) and DOCter (impact echo). Careful opening of tendon ducts by coring/drilling, and subsequent visual inspection with an videoscope was carried out in suspicious areas to validate the findings.

The inspection was done in several locations starting by locating the tendons using a GPR instrument. The placement of the tendon ducts was marked on the concrete surface. The next step was to check for voids using UPE. From all measurements performed suspicious areas were detected in Section A and B. These locations were further studied using DOCter impact echo – arguably a more refined NDT method. The findings were validated using core drilling.

In section C and especially section A where the core drilling took place, the results from the NDT corresponded with the verifications.

In section A, two out of six inspected ducts were found ungrouted and verified with core drilling, 2SA and 3SA, in these two ducts we also found corrosion on the strands. Duct 1NA was found grouted on the side that was opened, despite that the ultrasonic results showed voids. Most certain, there are voids present, but on the back of the duct. In Table 1 a suggestion for probability grading is presented. The results from two girders are then summarized in Table 2. Here only the verification from these inspections is shown. We know from earlier inspection that the results in section C are verified as well.

Table 1. Grading for probability of voids.

	No voids	Probability <50%
	Minor voids	Probability > 50 %
	Major voids	Probability >75%

Table 2. Suspicious areas from ultrasound investigation with coring verification and class in south and north girders.

No.	South	UPE	Verif.	Grade	No.	North	UPE	Verif.	Grade
1	1SA				1	1NA			
2	2SA				2	2NA			
3	3SA				3	3NA			
4	1SB				4	1NB			
5	2SB				5	2NB			
6	3SB				6	3NB			
7	4SB				7	4NB			
8	1SC				8	1NC			
9	2SC				9	2NC			
10	3SC				10	3NC			

The results can be summarized:

- GPR was used to accurately locate ducts before inspecting them with MIRA and DOCter Impact echo. Ducts placed close to the re-entrant corners were more difficult to locate. A smaller GPR was used for this purpose since easier access was possible. However, this required full contact with the concrete surface (rather than relying on wheels) which in some areas posed difficulties due to unevenness of the concrete surface.

- The result from ultrasonic scanning shows that there where voids inside the ducts, this was confirmed with core drilling. In section A, south girder, 2 out of 3 ducts was completely empty, the tendons had severe corrosion and we also found a wire breakage in duct 2SA
- The amount of grouting and corrosion differs a lot inside the same duct. Duct 3SA was completely empty 4,3m from the anchor point with and there where corrosion on all the strands. Closer towards the anchor the bottom half of the duct was grouted, and corrosion could only be found in the top half of the duct. In duct 2SA there was a big difference in corrosion degree only 20 cm between two openings. Therefore, it is important to trust the equipment and put some effort in the openings to make sure that the voids are located.
- Although no defects to the grouting (i.e. voids) were found in 1NA when opening up the metallic ducts, it cannot be ruled-out the risk of voids on the other side of the duct or on the other side of the tendons in the duct. Change in material properties of the grouting mixture along the duct may also be an explanation for the suspicious areas obtained by MIRA. However, the effect of the grouting mixture has not been mentioned in the literature and thus additional research is needed. Nevertheless, despite that it was sometime difficult to detect voids, the process developed has proven to work and that it can with certain probability detect voids in the ducts which then can be a potential indicator for corrosion in the tendons.

7 FUTURE WORK

The future plans entails the development of a machine learning algorithm aimed at facilitating decision-making concerning voids in ducts. This algorithm will integrate raw data obtained from various non-destructive testing (NDT) technologies. The training of the machine learning model will involve both elements with known defects and those with unknown conditions, contributing to the refinement of the training procedure.

ACKNOWLEDGEMENT

We want to acknowledge the Norwegian public road administration and Nordland municipality for supporting and financing this work.

REFERENCES

Im, S., Hurlebaus, S. & Trejo, D. 2010. Inspection of voids in external tendons of post-tensioned bridges. Transportation Research Record: Journal of the Transportation Research Board 2172: 115–22.

Karlsson, A., Boström, E. & Jilderda, P. 2021. Etterspente betongbruer inspeksjonsmanual. Statens Vegvesens Rapporter nr. 718.

Matt P., Hunkeler, F. & Ungricht, H. 2000. Durability of prestressed concrete bridges in Switzerland. 16th Congress of IABSE. September 2000, Lucerne, Switzerland

Popescu, C., Täljsten, B., Holmqvist, M. & Lagås I. 2023. Condition survey of grouted tendons of a prestressed concrete girder bridge, Internal Report, Sintef Narvik, Norway,

Woodward R. 2001. Durability of post-tensioned Tendons on Road Bridges in the UK, Proceedings of Workshop on Durability of Post-tensioning Tendons, Fédération Internationale du Béton (fib), Bulletin 15, Lausanne, 2001.

Bridge Maintenance, Safety, Management, Digitalization and Sustainability – Jensen, Frangopol & Schmidt (eds)
© 2024 The Author(s), ISBN 978-1-032-77040-6
Open Access: www.taylorfrancis.com, CC BY-NC-ND 4.0 license

Comparison of partial factor methods for existing concrete structures: Application to a cable-stayed bridge

L. Casti & F. Schmidt
Université Gustave Eiffel, Champs-sur-Marne, France

F. Biondini
Politecnico di Milano, Milan, Italy

N. Makhoul
ESTP, Dijon, France

R. Pittet
APRR, Dijon, France

ABSTRACT: The assessment of existing reinforced concrete structures is currently a critical task to be dealt with by engineers and practitioners. Specifically, bridges and viaducts, composing important links in the infrastructure system, are subjected to changes in structural capacity and demand in time, e.g., due to aging and structural deterioration processes as well as the evolution of intensity and frequency of structural loadings. Moreover, climate change may have a significant impact on this evolution. In this context, partial factor methods calibrated for the design of new structures may lead to unnecessary and expansive interventions when used for the assessment of existing structures. Therefore, the exploitation of semi-probabilistic methodologies tailored for existing structural systems is necessary. In this paper, methodologies developed for the evaluation of existing structures are presented and applied to the safety assessment of a cable-stayed bridge located in France. The obtained results are eventually compared with the outcomes of the assessment performed according to the original design and the current Eurocodes regulations, with a discussion on benefits and limits of the presented methodologies.

1 INTRODUCTION

Civil engineering structures and infrastructures represent a fundamental part of the built environment. Nowadays, a large part of these systems is approaching the end of the design lifetime and needs to be re-assessed in order to evaluate the best strategy to be implemented, e.g., maintenance, reparation, or demolition (Biondini & Frangopol 2016). In particular, the safety and serviceability assessment of existing Reinforced Concrete (RC) bridges is a challenge for practitioners and engineers.

In order to assess the performance of existing structures, it is important to highlight the differences with respect to the design of new systems. Structures are subjected to an evolution in time of the structural resistance R, e.g., due to aging and deterioration processes such as corrosion (Bertolini et al. 2013), as well as the modification of the originally assumed structural demand S, e.g., due to the increase in traffic volume (Dolcemascolo et al. 2015) and to the change of climatic conditions (Retief 2022). Moreover, the remaining service life t_{ref} associated with existing structures may be significantly different from the original design service life, usually equal to 50-100 years (ISO 2394 2015), and the cost of reparation or upgrading to provide certain safety performance is higher respect to the cost of applying the same measure in the design phase of a new structure (CEN/TS 17440 2020). For these reasons, the assessment of existing structures should be

DOI: 10.1201/9781003483755-463

performed with appropriate methodologies, different from the conservative approaches tailored for the design of new structures, considering the different type of uncertainties involved and avoiding possible expensive and unnecessary repair activities (JRC 2015).

In this context, the semi-probabilistic method is a practical approach to account for uncertainties in a simplified and implicit way, providing a tool to practitioners in case of common situations in terms of uncertainties and consequences. This approach is proposed by several national and international design standards, such as the Eurocodes (CEN EN1990 2002), generally for the design of new structures. Nevertheless, this methodology may be calibrated for the assessment of existing structures (ISO 2394 2015), and over the last decade, a significant effort has been provided along these research lines (Diamantidis & Bazzurro 2007; Steenbergen & Vrouwenvelder 2010; Caspeele et al. 2013; Sykora et al. 2017). Guidance for the exploitation of semi-probabilistic approaches tailored for the assessment of existing structures can be found in the *fib* Bulletin N°80 (2016). The proposed methodologies explicitly consider the residual service life, information from in situ and laboratory tests, measurements of variable actions, and reduced target reliability levels according to both economical and human safety criteria, focusing on standard RC structures.

This paper provides basic concepts of the semi-probabilistic approach and an overview of two methodologies for the assessment of existing RC structures. The methodology used for the calibration of the Partial Safety Factors (PSF) of an existing cable-stayed RC viaduct located in France is also discussed. Finally, the results of the safety assessment, exploiting tailored methodology for existing structures, are compared, in terms of different PSF calibration, with both the original design (CCTG 1983a; CCTG 1983b) and Eurocodes prescriptions for new structures (CEN EN1990 2002; CEN EN 1991. 2005; CEN EN1992-2. 2005). The benefits and drawbacks of the presented methodologies are discussed with emphasis on possible future developments.

2 BACKGROUND ON THE SEMI-PROBABILISTIC APPROACH

The semi-probabilistic approach, also addressed as the partial factor method, relies on the satisfaction of the safety criterion stating that the design resistance R_d must be larger than the design demand E_d:

$$R_d \geq E_d \tag{1}$$

The design values are generally determined through multiplication or division of the characteristic values, e.g., R_k and E_k, by the partial safety factors γ, which are calibrated to meet the prescribed reliability requirements, usually represented by the target reliability index β_t. For ordinary structures with a lifetime of 50 years, β_t is assumed equal to 3.8 (CEN EN1990 2002). This approach is proposed by several national and international design standards, such as the Eurocodes (CEN EN1990 2002) when dealing with common situations in terms of uncertainties and consequences.

In the following, a general description of the partial factor method is provided consistently to design of new structures. Eventually, two methodologies tailored for the assessment of existing structures, i.e., the Design Value Method (DVM) (ISO 2394 2015) and the Adjusted Partial Factor Method (APFM) (Caspeele & Taerwe 2012) are introduced.

2.1 *Partial factor method for design of new structures*

The satisfaction of the criterion, defined by Equation 1, should be checked for all the significant scenarios through the evaluation of R_d and E_d for the different structural components.

The design resistance R_d may be evaluated as function of different parameters:

$$R_d = R\left\{\eta_i \frac{X_{k,i}}{\gamma_{M,i}}; a_d\right\}, i \geq 1 \tag{2}$$

where η_i are conversion factors, exploited to relate possible test results to the actual behavior of the considered member, $X_{k,i}$ are the characteristic values of the materials property, the a_d is

the value for geometrical data, and $\gamma_{M,i}$ is the partial safety factor incorporating model $\gamma_{Rd,1}$, geometrical $\gamma_{Rd,2}$ and material $\gamma_{m,i}$ uncertainties. Indeed, the factor $\gamma_{M,i}$ may be defined as:

$$\gamma_{M,i} = \gamma_{Rd,1} \cdot \gamma_{Rd,2} \cdot \gamma_{m,i} \tag{3}$$

Particularly, assuming the material strength described by a lognormal distribution, $\gamma_{m,i}$ can be defined as follows:

$$\gamma_{m,i} = \frac{X_{k,i}}{X_{d,i}} = \frac{exp(-1.645 V_{Xi})}{exp(-\alpha_R \beta_t V_{Xi})} \tag{4}$$

where V_{Xi} is the coefficient of variation of the material property X_i and the 5% quantile is considered for the characteristic values.

The design demand E_d, considering the effect of external loadings, is generally evaluated as a function of different parameters:

$$E_d = E\left\{\gamma_{G,i} G_{k,i}; \gamma_P P; \gamma_{Q,1} Q_{k,1}; \gamma_{Q,j} \psi_{0,j} Q_{k,j}\right\} \; i \geq 1; j \geq 2 \tag{5}$$

where $G_{k,i}$, P, $Q_{k,1}$ and $Q_{k,j}$ are respectively the characteristic values of permanent actions, prestressing, dominant variable loading, and non-dominant variable loadings; $\psi_{k,j}$ are the combination factors related to the selected loading configuration; eventually, $\gamma_{G,i}$, γ_P and $\gamma_{Q,j}$ are respectively the partial safety factors accounting for model, e.g., $\gamma_{Ed,G}$ and $\gamma_{Ed,Q}$, and intrinsic aleatory uncertainties for permanent actions $\gamma_{g,i}$, prestressing γ_p and variable loadings $\gamma_{q,j}$. Specifically, the factors $\gamma_{G,i}$ and $\gamma_{Q,j}$ may be defined as follows:

$$\gamma_{G,i} = \gamma_{Ed,G} \cdot \gamma_{g,i} \tag{6a}$$

$$\gamma_{Q,i} = \gamma_{Ed,Q} \cdot \gamma_{q,i} \tag{6b}$$

Particularly, assuming the partial factor for permanent loading uncertainties $\gamma_{g,i}$ following a normal distribution, it can be defined as:

$$\gamma_{g,i} = \frac{G_{d,i}}{G_{k,i}} = \frac{1 - \alpha_E \beta_t V_{Gi}}{1 - k V_{Gi}} \tag{7}$$

where V_{Gi} is the coefficient of variation of the permanent loading and value $k = 0$ is usually assumed for the permanent actions.

The partial factor for variable loading uncertainties $\gamma_{q,i}$ may be computed as follows:

$$\gamma_{Q,i} = \frac{Q_{d,i}}{Q_{k,i}} = \frac{F^{-1}_{Q,i,tref}\left[\Phi(-\alpha_E \beta_t V_{Qi})\right]}{Q_{k,i}} \tag{8}$$

where $F^{-1}_{Q,i,tref}$ is the inverse of the distribution of the maxima over the period t_{ref}, Φ is the standard normal distribution and V_{Qi} is the coefficient of variation of the variable loading.

The calculation of the partial safety factor is related to the sensitivity factors for resistance α_R and demand α_E, which are considered equal to 0.8 and -0.7 for dominant variables and to 0.32 and -0.28 for non-dominant variables respectively (CEN EN1990 2002; ISO 2394 2015).

2.2 *Target reliability for existing structures*

The definition of a reliability target β_t represents a crucial step in the semi-probabilistic approach. Indeed, the definition of the fundamental elements of the code, e.g. partial safety factors γ and combination factors ψ, are strictly dependent on the assumed reliability target. In Baravalle & Köhler (2017) and Köhler et al. (2019), a discussion regarding the selection of β_t according to different strategies, addressing the benefits and drawbacks of each methodology, is presented.

For the sake of the analysed case study, the reliability target is defined according to the formulation proposed by the *fib* Bulletin n°80 (2016), which is based on both human safety and economic considerations for bridges. The reliability target is computed according to the

Consequence Class (CC), the remaining lifetime or reference period t_{ref}, and the length of the span that may collapse S, as reported in Table 1. The Consequence Classes are conceived considering increasing consequences, from CC1 to CC3, for structural collapse at economic, social and environmental levels (CEN EN1990 2002; *fib* 2016).

Table 1. Reliability target for existing bridges considering different consequence classes (*fib* 2016).

Consequence Class	Reliability Target β_t
CC1	1.8
CC2	Max(2.3; $\beta_{t,hs}$)
CC3	Max(2.8; $\beta_{t,hs}$)

The reliability target for human safety $\beta_{t,hs}$ is defined as:

$$\beta_{t,hs} = -\Phi^{-1}\left[\frac{2.75 \cdot 10^{-5} \cdot (0.09 \cdot S)^{-2} \cdot t_{ref}}{0.055}\right] \tag{9}$$

2.2 *Design value method*

The Design Value Method is formulated to compute partial safety factors based on the available information regarding the considered structure. Indeed, based on prior experience or test results it is possible to characterize the random variables connected to the resistance and the demand, reducing the uncertainty in the evaluation. Moreover, the partial safety factors should be defined considering the reliability target β_t related to the existing structure and the expected remaining lifetime t_{ref}.

2.3 *Adjusted partial factor method*

The Adjusted Partial Factor Method proposes the definition of the partial factors related to existing structure $\gamma_{X,exist}$ multiplying the partial factors related to new structures $\gamma_{X,new}$ using an adjustment parameter ω:

$$\gamma_{X,exist} = \omega\ \gamma_{X,new} \tag{10}$$

The adjustment parameter accounts for the expected remaining lifetime t_{ref} of the considered structure, the target reliability index β_t, and possible available information from tests, measurement, and prior and new knowledge.

3 CASE STUDY OF A CABLE-STAYED BRIDGE

3.1 *Description of the bridge*

The assessed existing viaduct is a prestressed cable-stayed bridge built in 1991 in the Isère district in France. The structure consists of a five-span bridge, supported by two abutments, three piers, and one pylon. The structural typology was selected in order to overpass a gap of approximately 300 m in correspondence with the Isère River. Considering an initial design lifetime of 100 years, the remaining lifetime of the bridge is equal to 67 years at the current date.

For the specific case study, the focus is dedicated to the deck of the viaduct. The deck is composed of two types of transversal sections: the box-girder section, having the central web 30 or 45 cm thick, and the plain section, located near the abutments, specifically the first 16 m from each end. The shape of the section is triangular, adopted at the time of the design for its aerodynamic, architectural, and structural characteristics, with 21.4 m width and 2.4 m height, as reported in Figure 1. The section is built in reinforced concrete and prestressed both longitudinally and transversely. The concrete is designed to have a characteristic compressive strength f_{ck} = 40 MPa, a characteristic tensile strength f_{tk} = 3 MPa, and Young modulus E_c = 37.6 GPa, as reported in the document detailing the hypothesis of the original design.

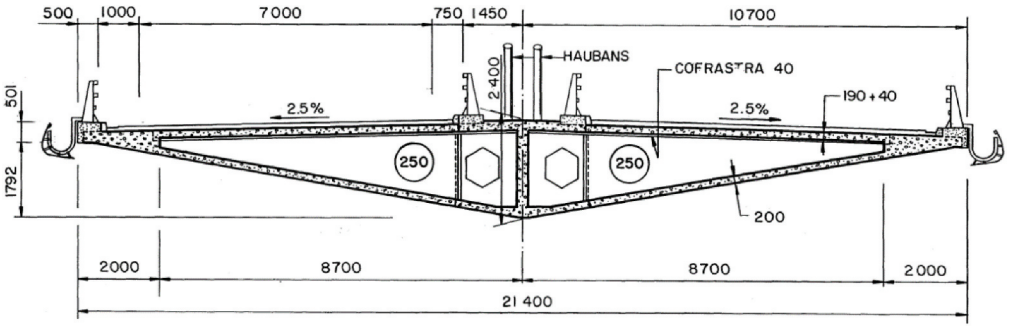


Figure 1. Cross-section of the bridge deck.

3.2 *Proposed methodology*

The methodology proposed for the assessment of the cable-stayed viaduct is based on three steps:

- Analysis of the original design;
- Assessment according to Eurocode;
- Assessment according to methodology for existing structures.

Firstly, the original design is studied in order to understand the assumption and the regulation exploited at the time of the conception of the viaduct. From the available documents, it is possible to retrieve the data about the materials and the loading considered for the bridge deck design, as well as the partial safety factors proposed by the regulations (CCTG 1983a; CCTG 1983b). The internal action and the stresses along the deck have been deduced from the original design report.

Secondly, the Eurocodes (CEN EN1990 2002; CEN EN 1991. 2005; CEN EN1992-2. 2005) are considered in order to assess the safety of the viaduct.

Eventually, the partial safety factors for the assessment of the viaduct are evaluated using two different methodologies which are tailored for the assessment of the existing structure, namely DVM, and APFM, and considering three different scenarios in terms of existing knowledge and uncertainties. Moreover, the *fib* Bulletin n°80 (2016) is exploited as guidance through the definition of the Reliability Target β_t and the partial safety factors γ.

The loadings considered for the analysis are the dead load G (self-weight and permanent actions) and the traffic load Q.

The methodology proposed for the assessment is developed considering that the Eurocodes are currently calibrated for the design of new structures instead of the assessment of existing ones, leading in some cases to over-conservative results in the case of the evaluation of existing systems.

3.3 *Reliability target and partial safety factors*

The reliability target β_t is computed according to Equation 4 and Table 1, assuming Consequence Class CC3, remaining lifetime t_{ref} = 67 years, and span length S = 148 m, which correspond to the most critical of the viaduct. Consequently, β_t = 3.55 is defined for the case study.

The sensitivity factors for resistance α_R and demand α_E are assumed to be constant and equal to the ones defined for new structures for the calculation of the partial factors according to DVM and APFM.

The values in terms of coefficient of variation V for model and geometrical uncertainties, both for the material and loading evaluations, are assumed compliant with the values suggested in *fib* Bulletin n°80 (2016). The partial factors for concrete and steel materials as well as the ones for permanent and traffic loading are evaluated according to the DVM and the APFM. Concerning the traffic load, a basic reference time of 15 years is selected.

Three different scenarios related to the existing knowledge of the structure are considered for the calculation:

1. Scenario 1 (reference scenario) is evaluated in agreement with the assumptions performed by Eurocodes (CEN EN 1991. 2005) concerning the probabilistic distributions although a different reliability target is considered.
2. Scenario 2 is conceived assuming a reduction in the uncertainties related to both loading and material and consequently reducing the coefficient of variation V considered in the reference scenario by 20%; this scenario may represent a situation in which testing and measurement led to a reduction of the uncertainties considered in the initial design.
3. Scenario 3 is conceptually opposite with respect to scenario 2, i.e., V is increased by 20% concerning considered in the reference scenario.

The results obtained in terms of partial factors (PF) are summarized in Table 2 for the DVM and Table 3 for the APFM. The results in terms of the partial safety factors for the three scenarios and considering the original design, the Eurocodes, the DVM, and the APFM are reported in Table 4.

Table 2. Partial factor according to different scenarios exploiting the DVM.

	Scenario 1		Scenario 2		Scenario 3		
	PF	V [-]	PF	V [-]	PF	V [-]	Probabilistic Distribution
γ_c [-]	1.20	0.15	1.15	0.12	1.24	0.18	Lognormal
γ_s [-]	1.06	0.05	1.05	0.04	1.07	0.06	Lognormal
γ_g [-]	1.25	0.1	1.20	0.08	1.30	0.12	Normal
γ_q [-]	1.08	0.075	1.04	0.06	1.14	0.09	Gumbel

$\gamma_{Rd,1,c} = 1.05$, $\gamma_{Rd,1,s} = 1.025$, $\gamma_{Rd,2} = 1.05$, $\gamma_{Ed,G} = 1.07$ and $\gamma_{Ed,Q} = 1.12$ (*fib* 2016).

Table 3. Partial factor according to different scenarios exploiting the APFM.

		Scenario 1		Scenario 2		Scenario 3		
	V' [-]	PF	V"/V' [-]	PF	V"/V' [-]	PF	V"/V' [-]	Probabilistic Distribution
ω_C [-]	0.15	0.958		0.924		0.993		Lognormal
ω_S [-]	0.05	0.985		0.973		0.997		Lognormal
ω_G [-]	0.1	0.982	1.00	0.943	0.8	1.021	1.2	Normal
ω_Q [-]	0.075	0.975		0.948		1.003		Gumbel

V' and V" are the initial or reference and the updated coefficient of variation.

Table 4. Partial safety factor according to different semi-probabilistic approaches.

	Original Design	Eurocodes	Scenario 1		Scenario 2		Scenario 3	
			DVM	APFM	DVM	APFM	DVM	APFM
γ_C [-]	1.50	1.50	1.31	1.44	1.26	1.39	1.37	1.49
γ_S [-]	1.15	1.15	1.14	1.13	1.13	1.12	1.16	1.15
γ_G [-]	1.35	1.35	1.34	1.33	1.28	1.27	1.39	1.38
γ_Q [-]	1.35	1.35	1.21	1.31	1.16	1.28	1.27	1.35

3.4 *Discussion*

Based on the results listed in Table 4, it is possible to observe that the partial safety factors considered in the regulations of the original design (CCTG 1983a; CCTG 1983b) and the ones related to Eurocodes (CEN EN1990 2002) are equivalent. The difference between the two regulations would be related to the possible discrepancies in the characteristic loading, which may lead to an increase in demand for structural verification.

The partial safety factors computed with the two methodologies tailored for the assessment of existing structure, i.e. DVM and APFM, are significantly different than the one used for the design of new structural systems. Firstly, considering scenario 1, the results obtained with the DVM and APFM are slightly lower than the exploited in the original design and suggested by the Eurocodes. For the examined case study, this is due to the definition of a reliability target for existing structures β_t = 3.55, which is lower than the one that should be guaranteed for a new structure. Secondly, considering scenario 2, the partial safety factors obtained by the two methodologies for existing structures are significantly lower than the results obtained for the reference scenario. This is related to the assumed reduction of the coefficient of variation, representing a case in which information on the material strength and loading would be available to properly characterize the uncertainty of the variables involved. Eventually, scenario 3 depicts an opposite case with respect to scenario 2, leading to higher partial safety factors obtained by exploiting the DVM and the APFM with respect to scenario 1, due to the increase of the uncertainties.

In general, for all the three investigated scenarios, the results obtained with APFM are more conservative than the ones retrieved exploiting the DVM considering concrete and traffic loading, due to the inherent approximation of the APFM. This aspect is highlighted in several studies, e.g., by Orcesi et al. (2021). Consequently, it is generally suggested to assess the existing structures firstly exploiting the APFM, secondly the DVM and eventually, if needed, to perform a full probabilistic verification. Furthermore, concerning the partial safety factors related to reinforcement and permanent loading, the results achieved with the two methodologies are almost equivalent.

The two approaches are both compatible with the Eurocode format, although it is observed that th DVM is more accurate in incorporating new information with respect to the APFM (Caspeele et al. 2013; Lara et al. 2021).Indeed, a recurrent Percent Deviation (PD) is observed between the results obtained with DVM and APFM for all the scenarios: the PD between the two methodologies is 8-10% for γ_C, 1% for γ_S, 1% for γ_G, and 6-10% for γ_Q. This is due to the differences in the incorporation of uncertainties between the two methodologies. Nevertheless, the obtained results highlight the importance of using appropriate methodology with proper treatment and characterization of uncertainties when dealing with the assessment of existing structures.

4 CONCLUSIONS AND FUTURE DEVELOPMENTS

Different semi-probabilistic methodologies for the assessment of existing structures have been investigated. Specifically, the definition of the partial safety factors for the evaluation of an existing reinforced concrete viaduct located in France has been firstly performed according to the original design of the structure, secondly exploiting the structural safety prescriptions according to the Eurocodes, and eventually considering two different methodologies tailored for existing structures, i.e., DVM and APFM. The results in terms of partial safety factor have been compared to the outcomes of the original design and the assessment performed according to Eurocodes, demonstrating the importance of the exploitation of appropriate methodologies for existing structures to avoid unnecessary and expensive interventions. Moreover, three different scenarios in terms of uncertainties have been defined and compared, showing the significance of a proper characterization of the structural capacity and demand.

Further investigation is necessary to properly characterize the actual information for the materials and loadings regarding the considered structure. Moreover, the same methodology may be applied for the calculation of the partial safety factors for other loadings affecting the structure, such as temperature and wind loading, and used for proper structural verification of the system. To this purpose, appropriate structural modeling at the sectional and structural level of the deck is fundamental to obtain reliable results. In addition, climate change effects are expected to significantly impact on both structural capacity and demand over time. The assumption of stationarity at the base of the current structural design codes is no longer well representing reality and this should be considered when designing or assessing the structural system. For this reason, the impact of climate change should be also integrated into the calibration of the partial safety framework. Specifically, concerning the investigated viaduct, the temperature gradient and the wind load are reported to have significant impact and their evolution due to climate change should be estimated and then incorporated into the safety assessment.

ACKNOWLEDGMENTS

This research project work was performed within the European project Clear-DOC, which has received funding from the European Union's Horizon 2020 research and innovation programme under the Marie Skłodowska-Curie COFUND grant agreement No 101034248. The authors thank APRR (Saint-Apollinaire, France) for the support and experience provided to improve the quality of this paper.

REFERENCES

Baravalle, M., & Köhler, J. 2017. A framework for estimating the implicit safety level of existing design codes. *Proceedings of the 12th International Conference on Structural Safety and Reliability*, TU Wien, Vienna, Austria, 6-10 August 2017, Vienna: TU-Verlag.

Bertolini, L., Elsener, B., Pedeferri, P., Redaelli, E., & Polder, R. B. 2013. *Corrosion of steel in concrete: prevention, diagnosis, repair*. Weinheim: Wiley-VCH.

Biondini, F., & Frangopol, D.M. 2016. Life-Cycle Performance of Deteriorating Structural Systems under Uncertainty: Review. *Journal of Structural Engineering*, 142(9): 1–17.

Caspeele, R., Sykora, M., Allaix, D. L., & Steenbergen, R. 2013. The Design Value Method and Adjusted Partial Factor Approach for Existing Structures. *Structural Engineering*, 23(4): 386–393.

Caspeele, R., & Taerwe, L. 2012. Updating partial factors for material properties of existing structures in a Eurocode framework using Bayesian statistics. *Advances in Safety, Reliability and Risk Management* (ESREL 2011), Troyes, France, 18-22 September 2011, London: CRC Press/Balkema.

CEN/TS 17440. 2020. *Technical Specification - Assessment and Retrofitting of Existing Structures*. Brussels: European Committee for Standardization.

CEN EN1990. 2002. *Eurocode 0: Basis of structural design*. Brussels: European Committee for Standardization.

CEN EN 1991. 2005. *Eurocode 1 – Actions on structures*. Brussels: European Committee for Standardization.

CEN EN1992-2. 2005. *Eurocode 2: Design of concrete structures - Concrete bridges - Design and detailing rules*. Brussels: European Committee for Standardization.

CCTG 1983a. *Fascicule n°62 (titre I section I) – Règles techniques de conception et de calcul des ouvrages et constructions en Béton Armé*. Paris: Cahiers des Clauses Techniques Générales.

CCTG 1983b. *Fascicule n°62 (titre I section II) – Règles techniques de conception et de calcul des ouvrages et constructions en Béton Précontraint*. Paris: Cahiers des Clauses Techniques Générales.

Diamantidis, D. and Bazzurro, P., 2007. Safety acceptance criteria for existing structures. *Special Workshop on Risk Acceptance and Risk Communication*, Stanford, 26-27 March 2007, Elsevier.

Dolcemascolo, V., Hornych, P., Jacob, B., Schmidt, F. and Klein, E., 2015. Heavy vehicle traffic and overload monitoring in France and applications. *XXVth World Road Congress PIARC*, Seoul, Korea, 2-6 November 2015.

fib. 2016. *Bulletin N°80: Partial factor methods for existing concrete structures*. Lausanne: Fédération internationale du béton.

ISO 2394. 2015. *General principles on reliability for structures*. Geneva: International Organization for Standardization.

JRC. 2015. *New European technical rules for the assessment and retrofitting of existing structures*. Brussels: CEN/TC250/WG2.

Köhler, J., Sørensen, J. D., & Baravalle, M. 2019. Calibration of existing semi-probabilistic design codes. *13th International Conference on Applications of Statistics and Probability in Civil Engineering*, Seoul, Korea, 26-30 May 2019.

Lara, C., Tanner, P., Zanuy, C., & Hingorani, R. 2021. Reliability Verification of Existing RC Structures Using Partial Factors Approaches and Site-Specific Data. *Applied Science*, 11: 1653.

Orcesi, A., Boros, V., Kušter Marić, M., Mandić Ivanković, A., Sýkora, M., Caspeele, R., Köhler, J., O'Connor, A., Schmidt, F., Di Bernardo, S., & Makhoul, N. 2021. Bridge Case Studies on the Assignment of Partial Safety Factors for the Assessment of Existing Structures. *18th International Probabilistic Workshop*, *University of Minho*, *Guimarães*, *12-14 May 2021*, Guimarães: Springer.

Retief, J. V. 2022. Assessment of Existing Structures Under Climate Change. *Acta Polytechnica CTU Proceedings*, 36: 6–14.

Sykora, M., Diamantidis, D., Holicky, M. and Jung, K., 2017. Target reliability for existing structures considering economic and societal aspects. *Structure and Infrastructure Engineering*, 13(1): 181–194.

Steenbergen, R.D.J.M. & Vrouwenvelder, A.C.W.M., 2010. Safety philosophy for existing structures and partial factors for traffic loads on bridges. *Heron*, 55(2): 123–139.


Taylor & Francis
Taylor & Francis Group
http://taylorandfrancis.com

GS25: BRIDGE SAFETY - Extreme loads


Taylor & Francis
Taylor & Francis Group
http://taylorandfrancis.com

Bridge Maintenance, Safety, Management, Digitalization and Sustainability – Jensen, Frangopol & Schmidt (eds)
© 2024 The Author(s), ISBN 978-1-032-77040-6
Open Access: www.taylorfrancis.com, CC BY-NC-ND 4.0 license

Seismic design of cable-stayed bridges in high intensity areas

B. Li, Z. Zeng, Y. He & Y. Xu
Tongji University, Shanghai, China

ABSTRACT: For the seismic design of large-span cable-stayed bridges built in high-intensity areas, it is necessary to consider the balance between internal force control and displacement control. The half-floating system is widely used in the longitudinal direction of cable-stayed bridges, which utilizes the displacement of the main beam for energy dissipation, but may result in significant relative displacement between the main beam, tower, and pier. In order to meet the needs of wind resistance, rigid constraints are often used in the transverse direction of the bridge to ensure the serviceability state, but it also leads to significant internal force response of the substructure under earthquake exaction. Therefore, it is necessary to design a reasonable damping system for large-span cable-stayed bridges to ensure the safety of the structure. This article conducts seismic calculations and seismic design for a half-floating cable-stayed bridge in a high intensity area. Hydraulic viscous dampers are used in the longitudinal direction to control the displacement of the main beam, and steel dampers are used in the transverse direction to provide energy dissipation. In this paper, the reasonable design parameters of the damping device are obtained through analysis, enabling the structure to achieve better seismic performance.

1 INTRODUCTION

The seismic response and seismic performance of large-span cable-stayed bridges are directly related to their structural systems. For longitudinal bridges, cable-stayed bridges generally adopt floating or semi floating systems (Hui, 2011), but under earthquake exaction, the displacement of pier-beams and tower-beams is relatively large, and the joints will be subjected to significant stress (Calvi et al., 2010). Therefore, it is necessary to install viscous dampers between towers and beams to control seismic displacement (Han et al., 2005).

For the transverse direction of the bridge, due to the consideration of static effects such as wind load, strong constraints need to be used at the connections between tower-beams and pier-beams to ensure that the structure has sufficient stiffness to meet wind resistance requirements (Colato et al., 2008). Currently, wind resistant bearings are commonly used to form a fixed constraint system for the transverse direction of tower-beams (Liang et al., 2013). However, rigid connections can transmit the inertia force of the upper structure to the lower structure, which may cause significant seismic internal force responses in towers, piers, foundations, etc. (Li et al., 2022) Therefore, for large-span cable-stayed bridges, it is necessary to adopt reasonable seismic systems and measures in both vertical and horizontal directions, while reducing engineering costs and ensuring structural safety (Shen et al., 2016).

This paper takes a semi floating cable-stayed bridge under construction as the research target. It is a double tower and double cable plane cable-stayed bridge with a standard width of 43m and a span arrangement of 50+85+300+85+50m, as shown in Figure 1. According to current national standards (Standardization Administration of China, 2015), the Bridge site belongs to a 7-degree zone, and the overall engineering geological conditions of the site area are ordinary, making it an area with relatively unfavorable seismic resistance. Due to the complex structure of the Bridge, existing seismic code (Ministry of Transport of the People's

DOI: 10.1201/9781003483755-464

Republic of China, 2020) is difficult to effectively guide its seismic design, it is necessary to conduct research on its seismic performance and design. The research results can not only guide the structural design of the bridge and solve the seismic safety issues of the project itself, but also provide guidance for the seismic design of similar bridge projects in the future.

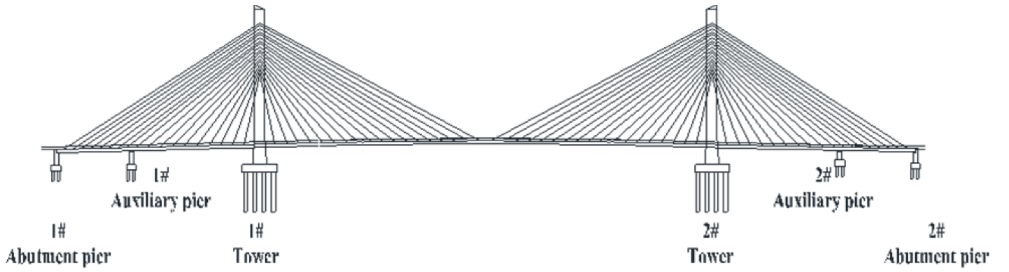


Figure 1. Schematic diagram of the bridge.

2 ANALYSIS MODEL

2.1 *Geometric model*

This paper uses the universal finite element calculation software SAP2000 for bridge modeling and dynamic analysis. This software has the characteristics of simple modeling, powerful calculation ability, and rich functionality, and has been widely used in the field of civil engineering. Based on the completed bridge state, dynamic characteristics and seismic response analysis are conducted. The main beam, bridge tower, and pier are all simulated using frame elements, while the stay cables are simulated using truss elements (rod end release bending moment and torque). The cable-stayed cable is connected to the main beam/bridge tower through master-slave constraints. The mass of the tower's pile cap and the pier's pile cap accumulates at the centroid, and the top, centroid, and bottom of the pile cap are connected by master-slave constraints. The secondary dead load and side span weight are added to the beam element in the form of linear mass and concentrated mass.



Figure 2. Basic model of dynamic calculation.

2.2 *Boundary conditions*

For conventional semi floating cable-stayed bridges, all bearings are longitudinally sliding. The bridge tower is equipped with lateral wind resistant bearings and vertical bearing bearings, the bridge pier is equipped with vertical bearing bearings, and one side is equipped with lateral limit devices, as shown in Table 1. In nonlinear time history analysis, consider the sliding friction effect of the support. In the Table 1, "0" represents freedom, "1" represents constraints, and the data in parentheses represents the constraint conditions for the support on the other side of the transverse direction.

In the seismic response analysis of bridges, the commonly used treatment method for pile foundations is to add springs in six directions at the bottom of the pile cap to simulate the

action of the pile foundation, and calculate the most unfavorable stress of a single pile using the static method (m method) based on the internal force at the bottom of the pile cap (Ministry of Transport of the People's Republic of China, 2019). The spring stiffness is determined based on the static equivalence principle according to the soil layer condition and pile arrangement, and the m value is determined from soil properties data. This treatment method is widely used in low pile cap pile foundations. This article uses a six-spring model to simulate the influence of each pile foundation group, and the data of the soil spring is shown in Table 2.

Table 1. Supporting conditions of the substructure.

Support	U_X	U_Y	U_Z	R_X	R_Y	R_Z
Tower	0	1	1	0	0	0
Auxiliary pier	0	1 (0)	1	0	0	0
Abutment pier	0	1 (0)	1	0	0	0

Table 2. Soil spring of pile foundation.

Location	X (kN/m)	Y (kN/m)	Z (kN/m)	YRX (kN/rad)	RX (kN-m/rad)	XRY (kN/rad)	RY (kN-m/rad)	RZ (kN-m/rad)
1# Tower	3.194 E7	3.194 E7	7.842 E7	1.22 E8	1.955 E10	-1.22 E8	4.565 E9	9.37 E9
1# Abutment pier	3.866 E6	4.269 E6	1.049 E7	1.597 E7	1.886 E8	-1.495 E7	1.28 E8	6.833 E7
1# Auxiliary pier	3.866 E6	3.866 E6	1.233 E7	1.496 E7	1.345 E8	-1.496 E7	1.345 E8	4.541 E7
2# Tower	3.29 E7	3.29 E7	7.557 E7	1.247 E8	1.888 E10	-1.247 E8	4.433 E9	9.649 E9
2# Abutment pier	4.063 E6	4.492 E6	1.26 E7	1.65 E7	2.089 E8	-1.543 E7	1.366 E8	7.114 E7
2# Auxiliary pier	4.061 E6	4.061 E6	1.208 E7	1.534 E7	1.34 E8	-1.534 E7	1.34 E8	4.687 E7

According to national code (Ministry of Transport of the People's Republic of China, 2020), seismic design should use the 7 seismic waves provided in the engineering site safety assessment report for calculation, and the calculation results should be taken as the average. The results of the safety assessment report indicate that the horizontal and vertical seismic

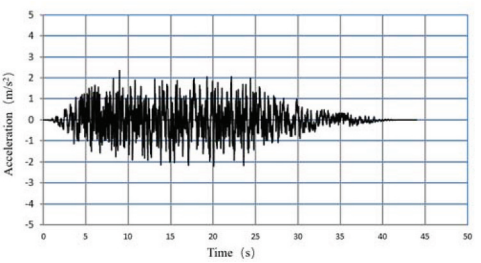


Figure 3. E1 Wave.

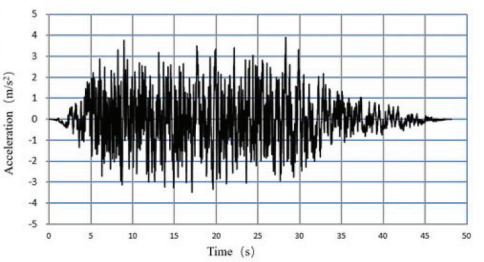


Figure 4. E2 Wave.

waves of the site are basically consistent. Figures 3 and 4 show the time history curves of one of the seismic waves under E1 and E2 working conditions.

3 DYNAMIC ANALYSIS

3.1 *Dynamic characteristics*

Analyzing and understanding the dynamic characteristics of bridge structures is the foundation for conducting seismic performance analysis (Zhang et al., 2018). Therefore, this report first uses the aforementioned basic dynamic calculation model to analyze the dynamic characteristics of the conventional system main bridge. Table 3 lists the first 10 vibration modes and corresponding periods of the Bridge.

Table 3. Structural dynamic characteristics.

Mode order	T (s)	Vibration mode description
1	4.6268	Main beam floats longitudinally and tower bends longitudinally
2	1.7212	Main beam 1st order vertical bending (symmetry)
3	1.3230	Main beam 1st order lateral bending (symmetry)
4	1.3041	Main beam 2nd order vertical bending (antisymmetry)
5	0.8648	Tower 1st reverse lateral bending
6	0.8597	Tower 2nd lateral bending
7	0.8440	Main beam 3rd order vertical bending (symmetry)
8	0.6680	Main beam 4th order vertical bending (antisymmetry)
9	0.6579	Main beam 5th order vertical bending (symmetry)
10	0.6512	Main beam 6th order vertical bending (antisymmetry)

In the pre-analysis, it was found that the bridge will experience lateral shear off of the support under the E1 exaction, resulting in changes in the dynamic characteristics of the bridge. The following are the dynamic characteristics of the bridge after considering the shear of the support, as shown in Table 4.

Table 4. Structural dynamic characteristics (support shear off).

Mode order	T (s)	Vibration mode description
1	4.6268	Main beam floats longitudinally and tower bends longitudinally
2	3.7129	Main beam 1st order lateral bending (symmetry)
3	2.4131	Main beam 2nd order lateral bending (antisymmetry)
4	1.7212	Main beam 1st order vertical bending (symmetry)
5	1.3041	Main beam 2nd order vertical bending (antisymmetry)
6	1.1528	Main beam 3rd order lateral bending (symmetry)
7	0.8639	Tower 1st reverse lateral bending
8	0.8539	Tower 2nd lateral bending
9	0.8440	Main beam 3rd order vertical bending (symmetry)
10	0.6680	Main beam 4th order vertical bending (antisymmetry)

3.2 *Nonlinear time history analysis*

This section conducts dynamic nonlinear time history analysis of longitudinal and transverse earthquakes and conducts seismic verification calculations on them. The aforementioned E1 and E2 seismic time histories are used as inputs, and the seismic input methods are longitudinal adds vertical and transverse adds vertical, respectively. Due to the earlier occurrence of lateral shear off of the support, the model after the support shear off was adopted for calculation.

Table 5. Locations need to be optimized.

Case	Location	Moment (kN·m)	Flexural capacity (kN·m)	Capacity-demand ratio
L+V	1# Tower-beam connection	1323274	1262000	0.95
	2# Tower-beam connection	1357435	1265000	0.93
T+V	1#Tower pile foundation	24350	15810	0.65
	2#Tower pile foundation	23801	16080	0.68

Table 5 lists the locations where the energy demand ratio is less than 1 in this seismic verification calculation. Under the longitudinal and vertical E2 earthquake exaction, the middle tower bottom section of the bridge tower does not meet the performance requirements, and its energy demand ratio is about 0.95. In addition, the bridge tower, pier, and pile foundation all meet the performance requirements. The longitudinal displacement of the main beam is approximately 800mm. Under the transverse and vertical E2 earthquake exaction, the pile foundation of the bridge tower does not meet the performance requirements, with an energy demand ratio of 0.6~0.7. In addition, the bridge tower structure itself, piers, and their pile foundations all meet the performance requirements. The relative displacement of the pier beam at the abutment pier is about 500mm, and the relative displacement of the pier beam at the auxiliary pier is about 300mm.

Therefore, the conventional structural system, whether longitudinal or transverse, cannot meet the seismic performance target under E2 earthquake exaction, and seismic reduction design needs to be carried out. The goal of a longitudinal seismic system is to reduce the longitudinal displacement of the main beam and the bending moment demand of the middle tower bottom section, while the goal of a transverse seismic system is to reduce the relative displacement between piers and beams and improve the stress on the bridge tower bottom pile foundation.

4 DAMPING DESIGN

4.1 *Longitudinal damping design*

For semi floating cable-stayed bridges, setting hydraulic viscous dampers longitudinally between the tower beams is an effective and commonly used method to control the longitudinal seismic displacement of the main beam. Therefore, this article considers setting hydraulic viscous dampers between both tower beams. The commonly used viscous dampers can be divided into linear and nonlinear viscous dampers in terms of mechanical properties. The nonlinear damping force can be represented by $F=CV^{\xi}$(Wang et al., 2005), C is the damping coefficient, and V is the relative velocity of the damper, ξ Is the speed index.

Install one viscous damper at each main tower, with the damper's velocity index ξ Taking 0.3, the damping coefficient C ranges from 1000kN/(m/s) $^{0.3}$ to 9000kN/(m/s) $^{0.3}$. By analyzing the nonlinear time-history response under E2 longitudinal earthquake exaction, the seismic responses of key parts of the structure with different parameters of viscous dampers are compared and analyzed to select appropriate damper parameters.

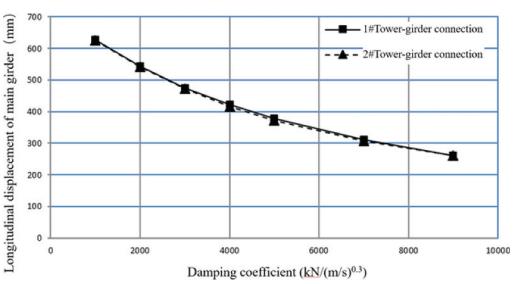


Figure 5. The relationship between relative displacement of tower-beam and damping coefficient.

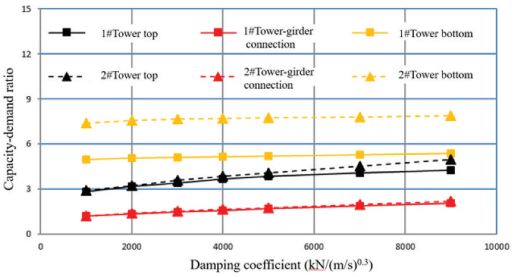


Figure 6. The relationship between capacity-demand ratio of key sections of towers and damping coefficient.

According to Figures 5 and 6, increasing the damping coefficient C can effectively reduce the longitudinal displacement of the main beam and improve the energy demand ratio of the key section of the bridge tower. To control the relative longitudinal displacement of the tower beam to be around 400mm, the damping coefficient C should be at least 4000kN/(m/s) $^{0.3}$. Therefore, a viscous damper with C=4000kN/(m/s) $^{0.3}$ can be selected for vibration reduction.

4.2 *Transverse damping design*

The aim of transverse seismic reduction design is to reduce the relative displacement of pier beams and control the lateral seismic internal force of bridge piers, usually using elastic-plastic steel dampers. The constitutive relationship of the steel damper is shown in Figure 7 (Wen et al., 2021). Yield strength, yield displacement, and post yield stiffness ratio are key design parameters of the steel damper. The preset yield displacement is 10mm, and the post yield stiffness ratio is 2%. The yield strength F_y is used as the control variable parameter (with a value range of 1000kN to 5000kN).

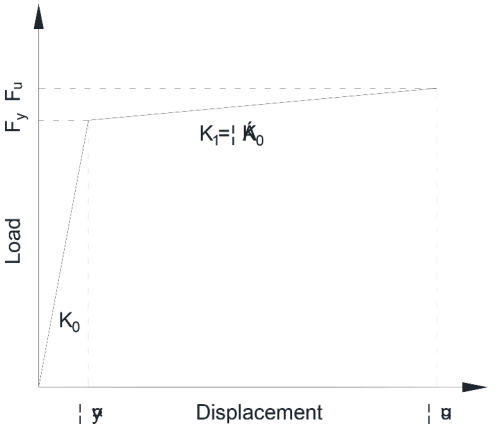


Figure 7. Constitutive relationship of steel dampers.

Figure 8 shows the relationship between the relative displacement of the pier beam and the yield force of the damper. As the yield force increases, the relative displacement of the pier beam first decreases rapidly and then tends to flatten out. However, an increase in the stiffness of the damper will also lead to an increase in the internal force distributed by the bridge pier. According to the relationship between the energy demand ratio at the pier bottom and the yield force of the damper shown in Figure 9, when the yield force increases, the energy demand ratio of the bridge pier will significantly decrease. Therefore, the yield force value of the damper is limited. Taking into account the displacement control effect and pier performance, a 2000kN damper can be applied.

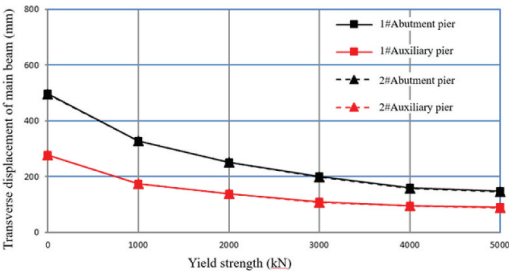


Figure 8. Relationship between relative displacement of pier-beam and yield strength.

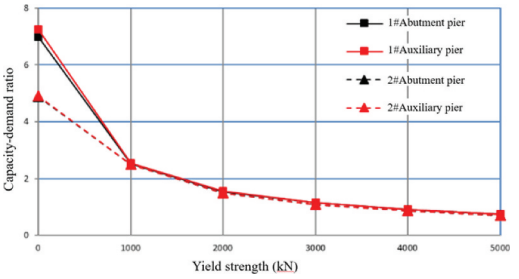


Figure 9. Relationship between capacity-demand ratio at pier bottom and yield strength.

Table 6. Capacity and demand after optimization using dampers.

Case	Location	Moment (kN·m)	Flexural capacity (kN·m)	Capacity-demand ratio
L+V	1# Tower-beam connection	798278	1266000	1.59
	2# Tower-beam connection	763613	1271000	1.66
T+V	1#Tower pile foundation	18810	20800	1.11
	2#Tower pile foundation	18681	20490	1.10

After using viscous dampers and steel dampers for seismic reduction design, the system can meet the corresponding seismic performance targets under both E1 and E2 earthquakes. Under longitudinal earthquake exaction, the longitudinal displacement of the main beam end is about 400mm. Under transverse earthquake exaction, the relative displacement of the pier beam at the abutment pier is about 250mm, and the relative displacement of the pier beam at the auxiliary pier is about 150mm.

Considering the uneven lateral displacement of the main beam, a transverse steel damper with a yield strength of 7000kN is installed at the bridge tower in this article. After optimization, the relative displacement of the tower beam at the bridge tower is about 180mm, the relative displacement of the pier beam at the abutment pier is 180mm, and the relative displacement of the pier beam at the auxiliary pier is 150mm.

5 CONCLUSIONS

This paper conducts dynamic analysis and seismic optimization design for a double tower cable-stayed bridge constructed in a high-intensity area. The longitudinal displacement of the main beam is controlled by hydraulic viscous dampers, and the lateral energy dissipation is provided by steel dampers. This article analyzes the reasonable design parameters of the

damping device to achieve good seismic performance of the structure. The main research conclusions are as follows:

1. Under the transverse E1 earthquake, the support will undergo lateral shear, resulting in changes in the dynamic characteristics of the bridge. Therefore, it is necessary to reset the support conditions when conducting seismic verification calculations.
2. Under the exaction of earthquakes, semi floating cable-stayed bridges generate significant relative displacement between towers and beams in the longitudinal direction. Viscous dampers can effectively optimize the relative displacement of tower beams and improve the seismic performance of bridge towers, and the higher the damping coefficient, the better the effect of viscous dampers.
3. For the purpose of wind resistance, steel dampers are used horizontally for displacement control. Increasing the yield strength of the steel damper can better control the relative displacement of the pier beam, but excessive stiffness will lead to an increase in the internal force allocated to the bridge pier, weakening the seismic resistance of the pier bottom section.
4. Installing a transverse steel damper at the bridge tower can make the lateral displacement of the main beam more uniform.

REFERENCES

Calvi, G.M. Sullivan, T.J. & Villani, A. (2010) Conceptual seismic design of cable-stayed bridges. *Journal of earthquake engineering* 14: 1139–1171.

Colato, G. Infanti, S. & Castellano, M. (2008). Special fluid viscous dampers for the Messina strait bridge. *American Institute of Physics* 1020:1374–1380.

Han, W. Huang, P. & Yan, L. (2005). Parametric analysis of cable-stayed bridge with longitudinal viscous dampers. *Earthquake Engineering and Engineering Vibration* 25(6):146–151.

Hui, L. (2011) Dynamic characteristics of a long-span cable-stayed bridge. In *International Conference on Materials Engineering for Advanced Technologies*. Singapore.

Li, C., Yang L., Liu D. & et al. (2022) A study on the lateral constraint system of multi tower cable stayed bridges under earthquake action. *World bridges* 50(05):61–66. (In Chinese)

Liang, D. Shen, H. & Li, Y. (2013) Influence of cable dampers on cable-stayed bridges. In *2nd International Conference on Civil Engineering and Transportation*. Guilin.

Ministry of Transport of the People's Republic of China. (2019) Specifications for design of foundation of highway bridges and culverts. In *JTG 3363-2019*. Beijing: China communications press.

Ministry of Transport of the People's Republic of China. (2020) Specifications for seismic design of highway bridges. In *JTG/T 2231-01-2020*. Beijing: China communications press.

Shen, X. Ni, X. & Ye, A. (2016) Study on seismic system of side pier of long-span cable-stayed bridge in transverse direction. *China journal of highway and transport* 29(11):81-89+121. (In Chinese)

Standardization Administration of China. (2015) Seismic ground motion parameter zonation map of China. In *GB18306-2015*. Beijing: China standards publishing house.

Wang, Z. Hu, S. & Fan L. (2005) Research on viscous damper parameters of Donghai bridge. *Journal of highway and transport* 18: 37–42. (In Chinese)

Wen J, Han Q and Xie Y, et al. (2021) Performance-based seismic design and optimization of damper devices for cable-stayed bridge. *Engineering structures* 237: 112043.

Zhang, W., Chen Y. Kou, W. & et al. (2018) Simplified calculation method for the fundamental period of floating cable-stayed bridge. *Archive of applied mechanics* 88: 329–339.

Bridge Maintenance, Safety, Management, Digitalization and Sustainability – Jensen, Frangopol & Schmidt (eds)
© 2024 The Author(s), ISBN 978-1-032-77040-6
Open Access: www.taylorfrancis.com, CC BY-NC-ND 4.0 license

A coupled thermal-mechanical-phase field model for concrete under fire

Kunting Miao, Zichao Pan, Xurui Fang & Airong Chen
Department of Bridge Engineering, Tongji University, Shanghai, China

ABSTRACT: Motivated by the fact that fire can induce structural and irreversible damage to concrete structures, this paper aims to investigate the thermal response of concrete structures when exposed to fire. A coupled thermal-mechanical-phase field model is developed to reveal the thermal field and thermal induced cracking process induced by fire condition. The coupling of thermal field and mechanical-phase field is achieved by phase field-dependent thermal conductivity, as well as temperature-dependent material properties and thermal strain caused by thermal expansion. Several numerical examples are presented to demonstrate the effect of crack on thermal conduction and thermal induced crack due to thermal expansion. The developed model provides a valuable tool for analyzing the thermal behavior of concrete under fire conditions.

1 INTRODUCTION

Fire hazard is a major threat to engineering structures such as bridges and buildings, as it can severely degrade their mechanical properties and durability (Lo Monte et al., 2019). Concrete is a common choice for load-bearing structures in engineering structures due to its high strength, stiffness and durability. However, prolonged fire exposure can significantly deteriorate the mechanical properties of concrete, reducing the structural bearing capacity and ductility. Therefore, it is crucial to study the damage distribution and evolution of concrete members under fire hazard.

Concrete is a composite material that consists of different components. Each component has a different thermal expansion coefficient, which means that they expand at different rates when exposed to fire. This causes thermal stress in the concrete, especially during fire hazard. Thermal induced cracks may occur in the concrete if the thermal stress exceeds the concrete strength. Scholars have conducted sufficient experimental research on the spalling process and mechanism of concrete in the past decades (Mindeguia et al., 2014, Kalifa et al., 2001). Experimental research is an effective method to investigate the thermal response of concrete structures, but it still has several limitations, which prompted scholars to explore numerical simulation as an alternative approach to study the thermal behaviour of concrete.

Numerical research methods of concrete fracture behaviour can be classified into two main categories: discontinuous numerical methods and continuous numerical methods. Discontinuous methods include discrete element method (Peng et al., 2020, Jiao et al., 2021), extended finite element method (Lou et al., 2023, Mora and Niffenegger, 2022), discontinuous deformation analysis method (Jiao et al., 2015, Li et al., 2022), etc. Despite the wide application of the discontinuous numerical methods in fracture modelling of various materials, they still face some challenges, such as the high sensitivity of the results to the initial configuration and the need for additional fracture criteria to simulate the fracture process. A continuous numerical method based on continuum damage mechanics is the alternative to the discontinuous numerical method. This method uses a damage variable to model the entire process of crack initiation and propagation (Fu et al., 2020, Tang and Tang, 2015, Zhao et al., 2017). However,

DOI: 10.1201/9781003483755-465

these theoretical models lack key parameters that describe the damage smeared scale, resulting in strong sensitivity to mesh size and division direction.

Researchers have explored new alternatives to overcome the limitations of the discontinuous and continuous numerical methods mentioned above. One of them is the phase field fracture model. Compared with other numerical methods, the phase field fracture model does not require any additional fracture criteria, as the fracture development follows the principle of minimum total system energy. The phase field fracture model is a multi-field coupling model, which can easily incorporate other multi-physical fields. Therefore, the phase field fracture model has been widely applied to the coupled thermo-mechanical problem (Wu et al., 2022, Peng et al., 2023, Zhou et al., 2022, Cheng et al., 2022b, Cheng et al., 2022a). The phase-field fracture model has been shown to be an effective tool for simulating thermal fracture in concrete, but some issues remain unresolved: Cracking can create gaps between concrete pieces, which reduce the thermal conductivity. However, some existing studies ignore the degradation of thermal conductivity, and some use the same degradation function in phase field to model the degradation of thermal conductivity, which lacks physical significance.

This study investigates the thermal induced crack phenomenon of concrete under fire conditions using a phase field fracture model. The manuscript is organized as follows: Section 2 presents the theoretical framework of the phase field model for concrete. Section 3 describes the developed coupled thermal-mechanical-phase field model and examines the effect of crack on thermal conductivity and the effect of thermal expansion on thermal behaviour of concrete under fire. Section 4 concludes the study and discusses the main findings.

2 PHASE FIELD MODEL

2.1 *Theory and governing equations of phase field model*

The main ideal of phase field model is to use a phase field variable d to regularize the sharp crack into a finite width dispersed crack. Figure 1 illustrates an arbitrary solid Ω with ∂ Ω and Γ representing the external boundary of solid and internal crack boundaries, respectively. Dirichlet-type and Neumann-type boundary conditions $\partial\Omega_u$ and $\partial\Omega_f$ denotes displacement and force on the boundaries of solid, respectively. The phase field variable d ranges from [0,1], and the values $d = 0$ and $d = 1$ indicate the intact and fully damaged states, respectively.

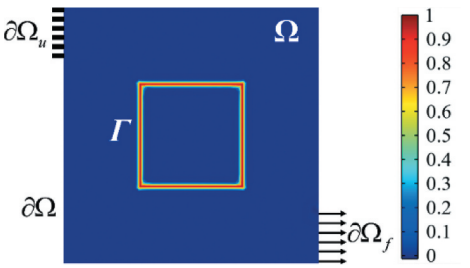


Figure 1. Diagram of dispersion crack in phase field model.

Francfort and Marigo introduced the fracture energy into the total potential energy and proposed the F-M variational principle (Francfort and Marigo, 1998). In the F-M variational principle, the total potential energy is composed of elastic energy, fracture energy and external energy:

$$W = \int_{\Omega} \Psi(\varepsilon, d)\mathrm{d}V + \int_{\Omega} G_c\gamma(d, \nabla d)\mathrm{d}V - \int_{\Omega} b \cdot u dV - \int_{\partial\Omega} f \cdot u\mathrm{d}S \tag{1}$$

where $\boldsymbol{b}$ is body force on the body Ω; $\boldsymbol{f}$ is traction on the boundary ∂ Ω_f; G_c is the critical energy release rate; $\gamma(d, \Delta d)$ is the crack surface density; $\Psi(\varepsilon, d)$ is the modified strain energy density and can be expressed as:

$$\Psi(\varepsilon, d) = \omega(d)\Psi_0(\varepsilon) \tag{2}$$

where $\omega(d)$ is a degradation function; $\Psi_0(\varepsilon)$ is the strain energy density for undamaged solids.

Another characteristic of the phase field method is that fracture evolution is a process that minimizes the total potential energy of the solid. Based on F-M variational principle, the governing equation of the phase field model can be derived by executing the first variation of the total potential energy functional W for the displacement field and the phase field, and make it equal to 0. Then the governing equations of phase field model are obtained:

$$\begin{cases} \nabla \cdot [\omega(d)\sigma] + b = 0 & \text{in } \Omega \\ -G_c \nabla \cdot \left(\frac{\partial \gamma(d,\nabla d)}{\partial \nabla d}\right) + G_c \frac{\partial \gamma(d,\nabla d)}{\partial d} + \frac{\partial [\omega(d)\Psi_0(\varepsilon)]}{\partial d} = 0 & \text{in } \Omega \end{cases} \tag{3}$$

The boundary condition can be expressed as:

$$\begin{cases} w(d)\sigma \cdot n - f = 0 & \text{on } \Omega_f \\ \frac{\partial \gamma(d,\nabla d)}{\partial \nabla d} \cdot n = 0 & \text{on } \Omega \end{cases} \tag{4}$$

To ensure the irreversibility of cracking, a historical variable $\boldsymbol{H}$ was introduced to replace $\Psi_0(\varepsilon)$ in the Eq.(3) (Miehe et al., 2010):

$$H = \max\{\Psi_0(\varepsilon(x, \tau))\} \tag{5}$$

2.2 *Details of functions in phase field model*

Depending on the degradation mode of the energy density function, phase field models can be classified into three types: isotropic, anisotropic, and hybrid type. The hybrid phase field model integrates the benefits of both isotropic and anisotropic models. It only decomposes the strain energy in the driving force of the phase field evolution to prevent compression fracture, and keeps the overall degradation of the nominal stress in the governing equation to ensure the linearity of the equation (Ambati et al., 2014). Therefore, this study adopts the phase field model proposed by Wu (Wu, 2017), which can achieve high accuracy and high efficiency in simulation.

The degradation function is related to the softening law of the material. The softening curve obtained in the previous research (Cornelissen et al., 1986) is widely used in concrete structures. Therefore, the degenerate function can be expressed as (Wu, 2017):

$$\begin{cases} \omega(d) = \frac{(1-d)^2}{(1-d)^2 + a_1 d(1 + a_2 d + a_2 a_3 d^2)} \\ a_1 = \frac{4}{\pi l_0}\frac{EG_c}{f_t^2}, a_2 = 1.3868, a_3 = 0.6567 \end{cases} \tag{6}$$

where E and f_t is the elasticity modulus and failure strength.

The crack surface density can be expressed as:

$$\gamma(d, \nabla d) = \frac{1}{\pi}\left(\frac{2d - d^2}{l_0} + l_0 |\nabla d|^2\right) \tag{7}$$

The historical variable can be expressed as:

$$H = \max\left(\frac{f_t^2}{2E_0}, \underset{t\in[0,T]}{max}\frac{\overline{\sigma_1}^2}{2E_0}\right) \tag{8}$$

where $\overline{\sigma_1}$ is the major principal value.

2.3 *Benchmark numerical example*

This section further explores the applicability of phase field models to concrete damage analysis by numerically simulating a mixed-mode problem L-shaped panel test (Wu, 2017).

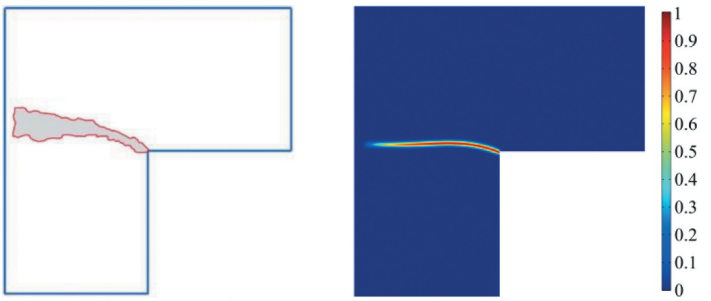
Figure 2(a) shows the geometry, loading, and boundary conditions. The Young's modulus, Poisson ratio, tensile strength and the specific fracture energy in this example are $E_0 = 2.585 \times 104$ MPa, $v_0 = 0.18$, $f_t = 2.70$ MPa and $G_c = 0.09$ N/mm. Figure 2(b) shows the meshes applied in this numerical example. To improve the computational efficiency, a finer mesh size of 0.5 mm is used only on the crack evolution path, while the remaining regions use a mesh size of 25 mm. The length scale $l_0 = 5$ mm is used in this example.



(a) Geometry, loading and boundary condition (unit: mm) (b) Finite element meshes.

Figure 2. L-shaped panel numerical example.

Figure 3 compares the crack patterns simulated by the phase field model and observed in the experiment (Winkler, 2001). The phase field model captures the experimental crack patterns accurately. Figure 4 presents the load-displacement curves from the phase field models and the experiment. The load-displacement curves obtained by the phase field model reproduces the experimental curves closely. The consistent agreement between the simulation and the experiment in both crack patterns and load-displacement curves validates the hybrid phase field model for concrete damage analysis and confirms the feasibility of using COMSOL software.



(a) Experiment result (b) Simulated result

Figure 3. Crack pattern from hybrid phase field models and experiment.

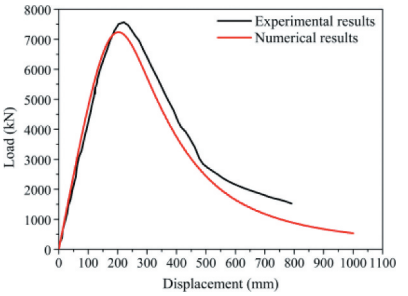


Figure 4. Load-displacement curves from hybrid phase field models and experiment.

3 COUPLED THERMAL-MECHANICAL-PHASE FIELD MODEL

In the proposed coupled thermal-mechanical-phase field model, we couple the thermal, mechanical, and phase fields using the thermal strain from thermal expansion, the damage-dependent thermal conductivity, and the temperature-dependent material properties.

3.1 *Coupling mechanism of thermal and mechanical field*

High temperature degrades the mechanical properties of concrete materials. We consider the following temperature-related degradation law to calculate elasticity modulus (Pearce et al., 2004) tensile strength (Pearce et al., 2004) and critical energy release rate (Cheng et al., 2022b):

$$E = \left(1 - 0.1\frac{T-20}{100}\right)^2 E_0, 20^\circ C \leq T \leq 1020^\circ C \tag{9}$$

$$f_t = \left(1 - 0.016\frac{T-20}{100}\right) f_{t0}, 20^\circ C \leq T \leq 800^\circ \tag{10}$$

$$G_c = G_{c0} e^{15.4\left(\frac{1}{T}-\frac{1}{20}\right)} \tag{11}$$

The deformation of materials which are influenced by the temperature field depends on both mechanical load and thermal expansion. To account for the coupling of thermal and mechanical fields, the effect of thermal strain must be considered. Thus, the total strain is the sum of elastic strain ε^e and thermal strain ε^{th}:

$$\varepsilon = \varepsilon^e + \varepsilon^{th} \tag{12}$$

The thermal strain can be expressed as follows:

$$\varepsilon^{th} = \alpha(T - T_0)I \tag{13}$$

where T_0 is the initial temperature; α is the thermal expansion coefficient; $\boldsymbol{I}$ is a unit tensor. Then the constitutive model for the displacement field can be rewrite as:

$$\sigma = \left(1 - 0.1\frac{T-20}{100}\right)^2 E_0 : \left(\varepsilon - \varepsilon^{th}\right) \tag{14}$$

where $\boldsymbol{E}_0$ is the elasticity tensor of sound material.

3.2 *Coupling mechanism of thermal and phase field*

Thermal conduction process in solid can be expressed by the following equation:

$$k\nabla \cdot (\nabla T) - \rho C_p \frac{\partial T}{\partial t} + q_m = 0 \tag{15}$$

where k is the thermal conductivity; ρ is the density; C_p is the specific heat; q_m is the heat generation by solid per unit volume.

Note that the presence of cracks reduces the thermal conductivity k of concrete. Previous studies have often adopted the degradation formula to model this process. We follow and develop the previous work (Zhou et al., 2022) and divide the thermal conductivity of concrete into three stages: the intact state k_0, the fully-fractured state k_f and the transition stage k_{rf}, as illustrated in Figure 5.

The value of k_0 depend on the material. For the thermal conductivity in the fully-fractured state, we assume that the cracks are filled with air, so the value of k_f depends on the thermal conductivity of air, which can be expressed as (Nguyen et al., 2019):

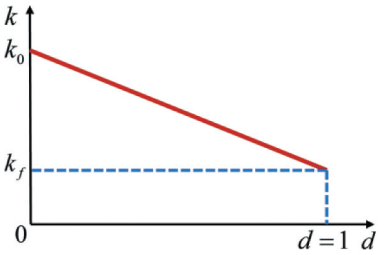


Figure 5. Damage-dependent thermal conductivity.

$$k_f = A_1 T^3 + A_2 T^2 + A_3 T + A_4 \tag{16}$$

where $A_1 = 1.5207 \times 10^{-11}$, $A_2 = -4.8574 \times 10^{-8}$, $A_3 = 1.0184 \times 10^{-4}$, $A_4 = -3.9333 \times 10^{-4}$.

We adopt the linear interpolation from the k_0 and k_f to achieve k, which can be expressed as:

$$k = (k_f - k_0)d + k_0 \tag{17}$$

3.3 *Numerical example*

3.3.1 *Effect of crack on thermal conduction*

We add a heating process to the benchmark numerical example in Section 2.3 to demonstrate the effect of crack on thermal conduction. The geometric properties and material properties remain the same as before. The heating process is induced by a specific temperature (900 □) at the bottom and right surfaces of the sample, as shown in Figure 6. We use the following parameters in this example: thermal conductivity of intact material k_0 = 1.2 W/(m*K), specific heat capacity is 500 J/(kg*K), density is 2600 kg/m^3 and the length scale l_0 = 5 mm.

Figure 7 shows the temperature distribution in concrete at different times. The temperature distribution is uniform in the region between the crack and the two temperature boundaries with heat conduction along the temperature gradient. The temperature discontinuity is evident in other regions, indicating that the crack plays an insulating role in heat conduction

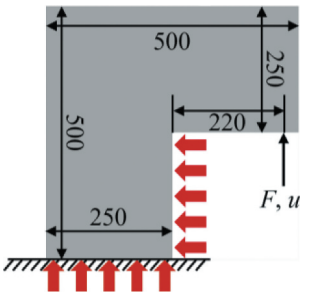


Figure 6. L-shaped panel under high temperature condition.

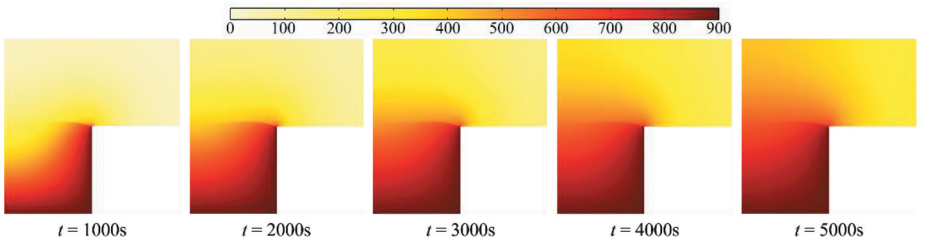


Figure 7. Temperature distribution at different times (unit: °C).

3.3.2 *Thermal induced crack*

This section examines the thermal-induced crack evolution in an arc example under thermal load. Figure 8 shows the geometry and boundary condition. We use the same material properties as in (Zhou et al., 2022). The top boundary temperature is fixed at 20 °C, while the bottom boundary temperature decreases linearly from 20 °C to -80 °C at a rate of 1 °C/s.

Figure 9 displays the crack patterns of the arc example under thermal load at different times. The bottom of arc example contracts due to the temperature drop, resulting in tensile stress. When the stress exceeds the specimen's strength, cracks start to initiate, primarily at the arch's ends. As the cooling continues, more cracks emerge in the arch's center, and they progressively deepen and expand, creating a complex crack pattern. Our simulation results demonstrate that the proposed coupled model can accurately predict the crack initiation and propagation under thermal load, and it agrees well with other numerical methods (Zhou et al., 2022, Badnava et al., 2018).

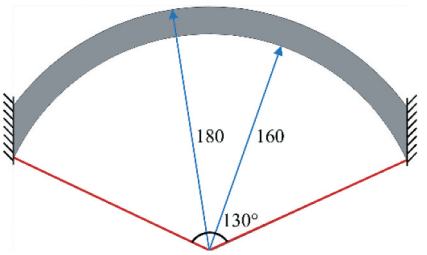


Figure 8. Geometry and boundary condition of arc example under thermal load (unit: mm).

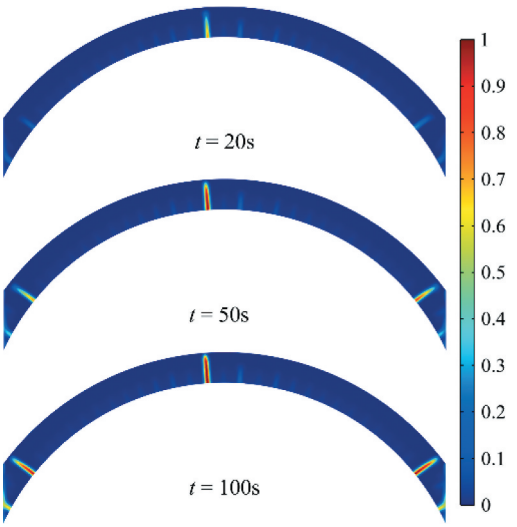


Figure 9. Crack patterns of arc examples under thermal load at different times.

4 CONCLUSION

This study presented a coupled thermal-mechanical-phase field model to simulate the thermal induced crack phenomenon of concrete. In the unified phase field framework, the coupling between the multiple fields is realized through the phase field-dependent thermal conductivity, the temperature-dependent material properties and the thermal strain caused by thermal expansion. The numerical results indicated that the crack has a significant influence on the thermal conduction and the thermal expansion can induce crack initiation and propagation.

The model can capture the complex interactions between thermal and mechanical fields. The model can be further extended to incorporate other factors such as moisture transport and chemical reactions.

ACKNOWLEDGEMENT

The authors acknowledge financial support from the National Natural Science Foundation of China under the Grant (No. 52238005).

REFERENCES

Ambati, M., Gerasimov, T. & De Lorenzis, L. 2014. A Review On Phase-Field Models Of Brittle Fracture And A New Fast Hybrid Formulation. *Computational Mechanics*, 55, 383–405.

Badnava, H., Msekh, M. A., Etemadi, E. & Rabczuk, T. 2018. An H-Adaptive Thermo-Mechanical Phase Field Model For Fracture. *Finite Elements In Analysis And Design*, 138, 31–47.

Cheng, P. P., Zhu, H. H., Yan, Z. G., Shen, Y. & Fish, J. 2022a. Multiscale Modeling For Fire Induced Spalling In Concrete Tunnel Linings Based On The Superposition-Based Phase Field Fracture Model. *Computers And Geotechnics*, 148, 104832.

Cheng, P. P., Zhu, H. H., Zhang, Y. M., Jiao, Y. & Fish, J. 2022b. Coupled Thermo-Hydro-Mechanical-Phase Field Modeling For Fire-Induced Spalling In Concrete. *Computer Methods In Applied Mechanics And Engineering*, 389, 114327.

Cornelissen, H. A. W., Hordijk, D. A. & Reinhardt, H. W. 1986. Experimental Determination Of Crack Softening Characteristics Of Normalweight And Lightweight Concrete. *Heron*.

Francfort, G. A. & Marigo, J. J. 1998. Revisiting Brittle Fracture As An Energy Minimization Problem. *J.Mech.Phys.Solids*, 46, 1319–1342.

Fu, Z. J., Xi, Q., Li, Y. D., Huang, H. & Rabczuk, T. 2020. Hybrid Fem–Sbm Solver For Structural Vibration Induced Underwater Acoustic Radiation In Shallow Marine Environment. *Computer Methods In Applied Mechanics And Engineering*, 369, 113236.

Jiao, K. T., Han, D. X., Li, J. F., Bai, B. F., Gong, L. & Yu, B. 2021. A Novel Lbm-Dem Based Pore-Scale Thermal-Hydro-Mechanical Model For The Fracture Propagation Process. *Computers And Geotechnics*, 139, 104418.

Jiao, Y. Y., Zhang, X. L., Zhang, H. Q., Li, H. B., Yang, S. Q. & Li, J. C. 2015. A Coupled Thermo-Mechanical Discontinuum Model For Simulating Rock Cracking Induced By Temperature Stresses. *Computers And Geotechnics*, 67, 142–149.

Kalifa, P., Chéné, G. & Gallé, C. 2001. High-Temperature Behaviour Of Hpc With Polypropylene Fibres: From Spalling To Microstructure. *Cement And Concrete Research*, 31, 1487–1499.

Li, C. Y., Ning, Y. J. & Liu, X. L. 2022. Discontinuous Deformation Analysis (Dda) Simulations Of Crack Propagation, Branching And Coalescence In Brittle Materials Under Dynamic Loading. *Theoretical And Applied Fracture Mechanics*, 122, 103648.

Lo Monte, F., Felicetti, R., Meda, A. & Bortolussi, A. 2019. Assessment Of Concrete Sensitivity To Fire Spalling: A Multi-Scale Experimental Approach. *Construction And Building Materials*, 212, 476–485.

Lou, L. W., Xiao, X., Li, J. & Xiao, F. P. 2023. Thermal-Mechanical Coupled Xfem Simulation Of Low Temperature Cracking Behavior In Asphalt Concrete Waterproofing Layer. *Cold Regions Science And Technology*, 213, 103910.

Miehe, C., Hofacker, M. & Welschinger, F. 2010. A Phase Field Model For Rate-Independent Crack Propagation: Robust Algorithmic Implementation Based On Operator Splits. *Computer Methods In Applied Mechanics And Engineering*, 199, 2765–2778.

Mindeguia, J. C., Carré, H., Pimienta, P. & La Borderie, C. 2014. Experimental Discussion On The Mechanisms Behind The Fire Spalling Of Concrete. *Fire And Materials*, 39, 619–635.

Mora, D. F. & Niffenegger, M. 2022. A New Simulation Approach For Crack Initiation, Propagation And Arrest In Hollow Cylinders Under Thermal Shock Based On Xfem. *Nuclear Engineering And Design*, 386, 111582.

Nguyen, T. D., Pham, D. T. & Vu, M. N. 2019. Thermo-Mechanically-Induced Thermal Conductivity Change And Its Effect On The Behaviour Of Concrete. *Construction And Building Materials*, 198, 98–105.

Pearce, C. J., Nielsen, G. V. & Bicanic, N. 2004. Gradient Enhanced Thermo-Mechanical Damage Model For Concrete At High Temperatures Including Transient Thermal Creep. *International Journal For Numerical & Analytical Methods In Geomechanics*, 28, 715–735.

Peng, Z. B., Doroodchi, E. & Moghtaderi, B. 2020. Heat Transfer Modelling In Discrete Element Method (Dem)-Based Simulations Of Thermal Processes: Theory And Model Development. *Progress In Energy And Combustion Science*, 79, 100847.

Peng, Z. Z., Wang, Q., Zhou, W., Chang, X. L., Yue, Q. & Huang, C. B. 2023. Meso-Scale Simulation Of Thermal Fracture In Concrete Based On The Coupled Thermal–Mechanical Phase-Field Model. *Construction And Building Materials*, 403, 133095.

Tang, S. B. & Tang, C. A. 2015. Crack Propagation And Coalescence In Quasi-Brittle Materials At High Temperatures. *Engineering Fracture Mechanics*, 134, 404–432.

Winkler, B. 2001. *Traglastuntersuchungen Von Unbewehrten Und Bewehrten Betonstrukturen Auf Der Grundlage Eines Objektiven Werkstoffgesetzes Für Beton*. University Of Innsbruck.

Wu, J. Y. 2017. A Unified Phase-Field Theory For The Mechanics Of Damage And Quasi-Brittle Failure. *Journal Of The Mechanics And Physics Of Solids*, 103, 72–99.

Wu, J. Y., Chen, W. X. & Zhou, H. 2022. A Length Scale Insensitive Phase-Field Model For Fully Coupled Thermo-Mechanical Fracture In Concrete At High Temperatures. *International Journal For Numerical And Analytical Methods In Geomechanics*, 46, 2725–2753.

Zhao, J., Zheng, J. J., Peng, G. F. & Van Breugel, K. 2017. Numerical Analysis Of Heating Rate Effect On Spalling Of High-Performance Concrete Under High Temperature Conditions. *Construction And Building Materials*, 152, 456–466.

Zhou, S. W., Zhang, C. K., Xu, Y. J. & Yuan, Y. 2022. A Hybrid Phase Field Method For Modeling Thermal Fractures In Brittle Rocks: Fracture Diversity From A Modified Driving Force. *International Journal Of Fracture*, 238, 185–201.

Bridge Maintenance, Safety, Management, Digitalization and Sustainability – Jensen, Frangopol & Schmidt (eds)
© 2024 The Author(s), ISBN 978-1-032-77040-6
Open Access: www.taylorfrancis.com, CC BY-NC-ND 4.0 license

Modelling of thermo-mechanical behaviour of tunnels under fire conditions

R.A.S. Díaz
Delft University of Technology, Delft, The Netherlands

E.O.L. Lantsoght
Delft University of Technology, Delft, The Netherlands
Universidad San Francisco de Quito, Quito, Ecuador

M.A.N. Hendriks
Delft University of Technology, Delft, The Netherlands
Norwegian University of Science and Technology (NTNU), Trondheim, Norway

ABSTRACT: Major fire events in tunnels have shown severe consequences in their structural performance, as reported in several incidents in the last decades. Particularly, due to the enclosure geometry of tunnels, intense thermal loading may develop in comparison to typical fires in buildings, which may result in more damage. Even though tunnel linings are an important component in transportation infrastructure, the understanding of their behaviour under high temperatures is limited. This paper aims to study the thermo-mechanical response of tunnels subjected to fire using nonlinear finite element analysis (NLFEA). For this purpose, recent experimental tests of large-scale reinforced concrete tunnels with and without fire protection are simulated. Different modelling approaches and strategies are discussed, and a detailed description of the constitutive model employed is presented. The results obtained in the simulations indicated that the numerical analysis can be used to investigate the thermo-mechanical behaviour of concrete structures.

1 INTRODUCTION

Traditionally, reinforced concrete (RC) structures have been regarded as good in terms of fire resistance due to the non-combustibility and low conductivity of concrete. For that reason, in many cases, RC elements do not require any additional fire protection. However, in the case of tunnels, due to the enclosure geometry, more intense fire scenarios can develop in comparison to typical fires in buildings, leading to more severe damage. In the past, several incidents related to fire events in tunnels have occurred (Lin and Chien, 2021). Even though tunnel linings are an important component in transportation infrastructure, the understanding of their behaviour under high temperatures is limited. The research on tunnels under fire has focused more on fire dynamics, smoke simulations, and evacuation strategies, and less research has been done in the areas of structural risk assessment, damage quantification, and robustness (Hua *et al.*, 2021a). As pointed out by Gernay *et al.* (2023), there are no general guidelines regarding the structural modelling of tunnels exposed to fire. In practice, a model representing the section with a 2D beam finite element is probably the most commonly used approach.

This work investigates the thermo-mechanical response of tunnels subjected to fire using nonlinear finite element analysis (NLFEA). This investigation aims to gain additional insight into the structural behaviour of tunnels in the case of a fire using advanced calculation methods. A detailed description of the constitutive model employed is presented in the

DOI: 10.1201/9781003483755-466

following sections. Then, different modelling approaches and strategies are discussed and evaluated for the representation of fire scenarios, including (i) 2D model representation (plane strain and plane stress assumptions), (ii) influence of protective coating and (iii) representation of concrete spalling. The assessment of these parameters is conducted through the simulation of recent experimental tests based on the Hong Kong-Zhuhai-Macao Bridge (HZMB) project conducted by Huaqiao University. The experimental and numerical results are compared in terms of temperature distribution and crack patterns. Finally, key outcomes and conclusions are derived about the capabilities and limitations of the simulations and the feasibility of using finite element-based analyses in the design and post-fire evaluations of tunnels.

2 CONSTITUTIVE MODEL

2.1 *Concrete model*

The concrete nonlinear behaviour is represented by the total strain fixed crack model (Feenstra *et al.*, 1998) implemented in DIANA (release 10.5). Additional constitutive relationships are used to account for the material degradation due to high temperatures based on NEN-EN -1992-1-2:2005. The tension softening is described using the relationship proposed by Hordijk (1991), which assumed that the concrete tensile behaviour depends on the tensile strength (f_{ct}) and fracture energy (G_F). The concrete behaviour in compression is based on the fracture energy-based model proposed by Feenstra (1993). This model describes the compressive stresses by a parabolic stress diagram followed by a softening branch. Similarly to the tensile behaviour, the maximum compressive strain is scaled according to a fracture energy and a crushing-band width to reduce mesh size sensitivity. In addition, the model proposed by Vecchio and Selby (1991) is considered to represent the increment in strength and ductility due to confinement. Furthermore, the influence of large strains perpendicular to the compressive direction is included using the formulation proposed by Vecchio and Collins (1993), with a minimum reduction limit of 0.4 (Hendriks and Roosen, 2022). The concrete shear behaviour is represented using the so-called damaged-based shear retention factor proposed by DeJong *et al.* (2008).

For the thermal analysis, the thermal conductivity and the volumetric specific heat are used to model the concrete heat transfer. These properties are considered to be temperature-dependent using the relations recommended in NEN-EN-1992-1-2:2005. The thermal concrete expansion is defined according to the thermal expansion coefficient. The transient creep strain (also known as load-induced thermal strain, LITS) is modelled implicitly following the approach described in NEN-EN-1992- 1-2:2005.

2.2 *Reinforcing steel model*

The reinforcing steel constitutive model assumes an elastic-perfectly plastic behaviour. Similar to concrete properties, degradation as a function of the temperature is adopted. For this purpose, the modulus of elasticity and the yield strength are assumed to depend on temperature according to NEN-EN-1992-1-2:2005. It is noteworthy to mention that since the rebar is embedded and its area is relatively small compared to concrete, the steel rebar is not explicitly considered in the thermal analysis. It is assumed that the temperature is uniform within the steel area and equal to the temperature of the surrounding concrete.

Preliminary simulations showed an unrealistic full recovery of the steel mechanical properties during the cooling phase (i.e. the period when the temperature decreases to ambient temperature), even after reaching temperatures higher than 1000ºC. To address this issue, the original constitutive model in DIANA was adapted using a user-supplied subroutine written in Fortran. The subroutine restricted the yield strength and the Young modulus values based on the maximum temperature reached during the heating phase.

3 CASE STUDY: TUNNEL TESTS BY HUAQIAO UNIVERSITY

The large-scale fire tests on tunnel segments performed by Dong *et al.* (2023) and Duan *et al.* (2021) are used as reference in this study to compare and validate the modelling choices for the fire resistance assessment in tunnels. The experimental specimens represent a reduced scale (1:5) model of an immersed tunnel segment of the Hong Kong-Zhuhai-Macao Bridge (HZMB) project. The cross-section of the scale tunnel is shown in Figure 1. The total length of the tested tunnel segment was 5.8 m, and the overall width and height were 7.59 m and 2.28 m, respectively.

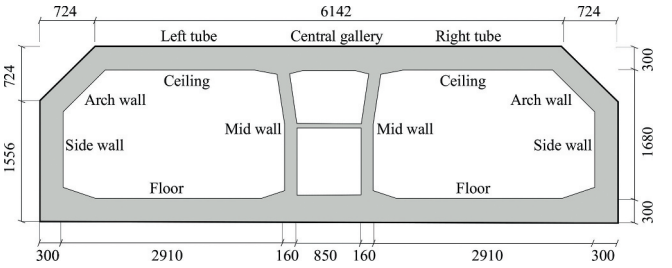


Figure 1. Cross-section of the scale tunnel, measures in mm. Adapted from Dong et al. (2023).

Before applying the thermal loading, vertical and horizontal loads were applied to the tunnel segments to represent the service load from the sediment and seawater. The total vertical load applied on the ceiling was 2427.4 kN, and the horizontal load on both sides of the walls of the tunnel was 437.2 kN. The test setup is shown in Figure 2a. During the fire test, the mechanical load was maintained constant during the heating and cooling phases. The fire scenario in the experiment conducted by Dong *et al.* (2023) considered a severe situation in which both tubes of the tunnel were exposed to fire at the same time. In the tunnel segment tested by Duan *et al.* (2021) the fire was applied in only one tube and a 30 mm sprayed coating was used.

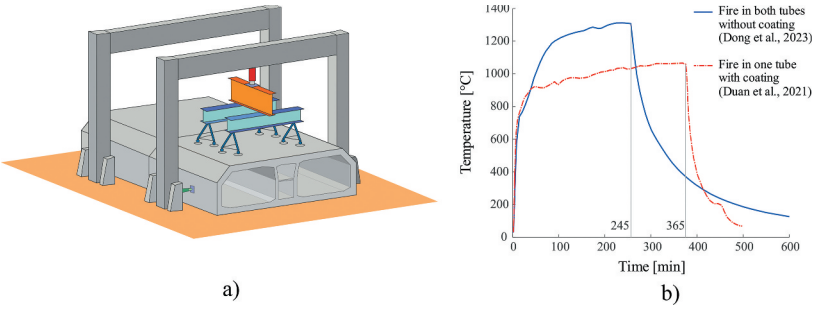


Figure 2. A) Setup during testing; b) fire scenarios for the tunnel segments tested by Dong et al. (2023) and Duan et al. (2021).

At the end of both tests, the authors reported that the capacity of the tunnel segments was sufficient to withstand the applied thermal load (during the heating and cooling phases). Despite that, the damage on the heated and unheated side of the tunnel was severe for the fire scenario on both tubes. Dong *et al.* (2023) reported that almost 100% of the exposed fire surface was affected by spalling. In the test conducted by Duan *et al.* (2021), the fire-resistive

Table 1. Fire scenarios considered in the tunnel segments.

Reference	Number of tubes exposed to fire	Fire protection	Maximum temperature	Spalling
Dong *et al.* (2023)	2	No	1344.8°C	Yes
Duan *et al.* (2021)	1	Yes	1113.7°C	No

coating performed well, and concrete spalling did not occur. However, concrete cracking was observed in the unheated side of the tunnel and even in the mid gallery and the left tube that were not exposed to fire at all. The fire scenarios are summarised in Table 1 and the recorded average furnace temperatures are shown in Figure 2b.

4 NUMERICAL MODELS FOR THERMO-MECHANICAL ANALYSIS

4.1 *Numerical models considerations*

In this work, a 2D approach was used to simulate the tunnel tests conducted by Huaqiao University. In the following sections, the fire scenarios are designated with the letters A and B, as given in Table 2. Two different modelling assumptions were compared for each tunnel test, namely, plane stress and plane strain idealisations. The former approach implies that the out-of-plane stresses are not accounted for in the simulation. In the case of the plane-strain assumption, the out-of-plane displacement (and the total strain in that direction) is considered null. It should be noted that both 2D approaches are approximations to represent the tested tunnel segments behaviour. A 2D plane-stress idealisation can be regarded as conservative since it ignores any possibility of force redistribution in the longitudinal direction of the tunnel (Gernay *et al.*, 2023). On the other hand, a 2D plane-strain idealisation can be regarded as a more reasonable alternative for the modelling of a real tunnel with several segments in the longitudinal direction. Yet, the plane strain assumption can also be regarded as conservative since it considers a uniform fire scenario along the tunnel full-length. As indicated in Table 2, additional simulations were also carried out to investigate the influence of spalling effects on the fire scenario in both tubes, leading to six simulations in total.

Table 2. Numerical models conducted for each fire scenario.

Fire scenario	Numerical model
Scenario A: fire in one tube with coating tested by Duan *et al.* (2021)	Plane strain (without spalling) Plane stress (without spalling)
Scenario B: fire in both tubes without coating tested by Dong *et al.* (2023)	Plane strain without spalling Plane stress without spalling Plane strain with spalling Plane stress with spalling

The tunnel cross-section is discretized using quadrilateral elements. For the staggered analysis, first-order isoparametric quadrilateral elements (denoted as Q4HT) are used during the thermal transfer calculations. In the subsequent mechanical analysis, these elements are automatically upgraded to second-order isoparametric elements denoted as CQ16M (for plane stress) and CQ16E (for plane strain). An average mesh size of 30 mm was adopted in the analyses (refer to Figure 3). This value was established with the aim of obtaining a sufficiently

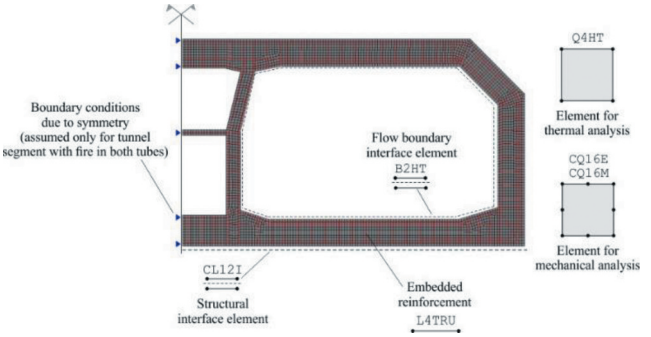


Figure 3. Typical mesh used for the numerical simulations for scenario B.

accurate nonlinear temperature distribution on the concrete cover. In the thermal analysis, the heat transfer is considered by radiation and convection mechanisms using boundary interface elements (B2HT). The furnace temperatures recorded during the test were used as an input in the thermal analyses. The interaction between the tunnel and the ground was modelled with interface elements (CL12I) with no support in tension and a high compression stiffness (75 MN/m^3), as assumed in Guo et al. (2016). No additional soil settlements or concrete primary creep strains were included in the simulation. The concrete nonlinear behaviour is represented using the constitutive model described in Section 2.

4.2 *Spalling simulation*

The loss of concrete cover due to spalling has two effects: (i) it reduces the stiffness of the member due to the reduction in the cross-section and mechanical properties, and (ii) in case of severe spalling, the reinforcement is directly exposed to fire and the heat flow inside the structure also increases. In this study, the spalling is simulated by considering a modification in the concrete thermal properties of the elements located at the exposed inner face. A 60 mm layer was defined as the spalling region at the ceiling and lateral walls. The region was created according to the average spalling depth obtained in the test. For the elements at that region, the thermal properties were adjusted during the analysis with a high value of thermal conductivity, 5 W/(m°C), and a relatively low value of thermal capacity, 10000 J/(m^3°C;). The previous values were selected based on the criteria developed by Hua *et al.* (2021b), aiming to obtain a spalling rate close to 2.6 mm/min.

4.3 *Staggered analysis considerations*

A staggered procedure is performed in DIANA to couple the thermal and mechanical analyses. Therefore, the analysis is executed in two consecutive steps with the main assumption that the temperature distribution in the structure is independent of the structural behaviour. The calculated temperature fields are then incrementally applied in a separate mechanical analysis that takes into account the thermally induced strain as well as the material degradation due to high temperatures. The regular Newton-Raphson method is employed for the iterative procedure, and the convergence at each iteration is evaluated in terms of unbalanced force, incremental displacement and relative energy. The time step increments are updated with a cutback-based automatic incremental loading procedure. This algorithm reduces the number of steps required to apply the total time (i.e. the fire duration) and automatically decreases the time increments to recover from non-convergence steps in the iterative procedure.

5 RESULTS AND DISCUSSION

5.1 *Thermal analysis results*

The computed temperature field is independent of the 2D assumption. Thus, the same temperature distributions are obtained for plane stress and plane strain idealisations. Figure 4 shows the

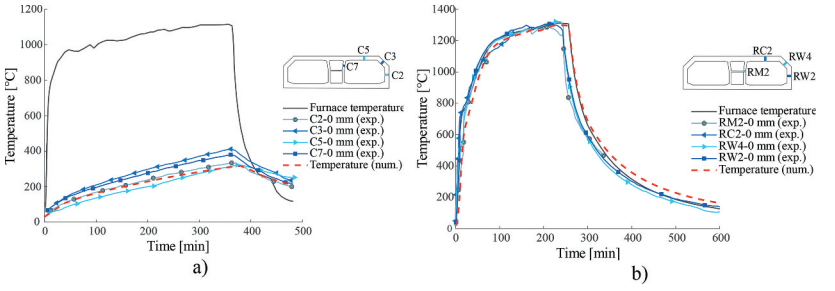


Figure 4. Temperatures at exposed surface, simulation (num.) results versus experimental (exp.) results: a) scenario A; b) scenario B.

temperature at different locations at the exposed surface for both experiments. For the tunnel with a protective coating (scenario A), the numerical simulation was able to represent the average temperature at the exposed side of the tunnel (Figure 4a). It can be noted that the coating significantly reduced the temperature in the concrete in comparison with the applied fire scenario. In the case of the tunnel without protective coating (scenario B), the temperature at the exposed concrete surface, followed almost the same furnace temperature (Figure 4b).

Figure 5 shows the temperatures measured by the thermocouples RC2 (ceiling) at 0 mm, 30 mm, and 60 mm in the fire scenario B. It is important to note that the temperature inside the concrete cross-section followed a temperature similar to that recorded at 0 mm. As stated by Dong *et al.* (2023), this result can be explained by the large spalling observed during the test. Furthermore, it is also noted that the temperature at 30 mm and 60 mm is underestimated if the spalling effect is not considered in the simulations.

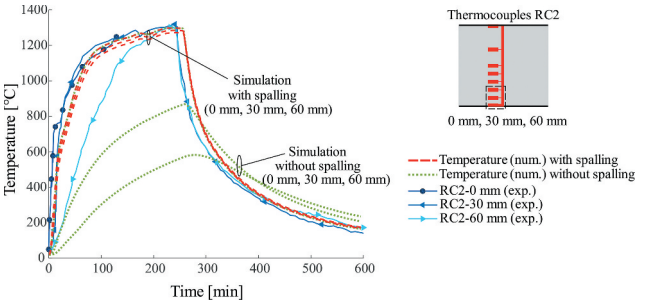


Figure 5. Temperature evolution inside the concrete section for scenario B.

5.2 *Mechanical analysis results*

According to the experiments, the tunnel capacities were sufficient to resist for both fire scenarios. This observation also holds for the numerical simulations with fire coating, in which the iterative procedure converged for all the time steps (Figure 6a). In contrast, the numerical simulations for the most severe fire scenario finished earlier due to convergence problems. The consideration of spalling contributed to reducing the fire resistance time, especially for the plane strain idealisation with spalling, in which the analysis only lasted 72 minutes. The other simulations ended during the cooling phase, as depicted in Figure 6b. It should be noted that the constitutive model assumes that damage recovery due to cracking is not possible. However, a full recovery of the thermal strain was observed during the cooling phase. Consequently, some reloading behaviour was noticed in the concrete stress evolution. It can be inferred that this inaccurate representation, together with the large number of active cracks during the cooling phase may have led to convergence problems in the numerical analyses.

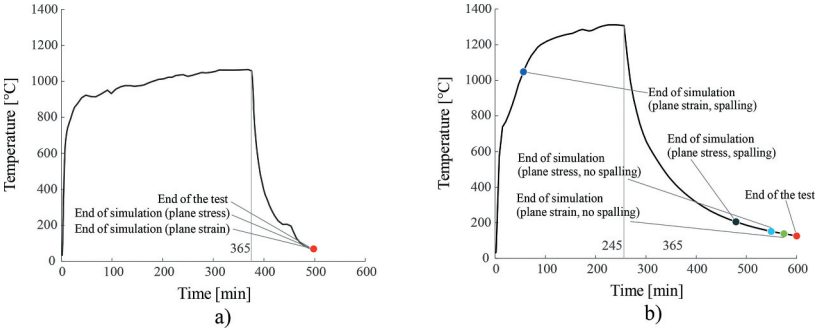


Figure 6. Applied fire scenarios and the last step converged in each numerical analyses: a) scenario A; b) scenario B.

Figure 7 shows an example of the crack pattern obtained from the simulations at the end of the heating phase for both fire scenarios. For the sake of brevity, the results are only shown for two plane stress models. According to Duan *et al.* (2021), for the fire scenario with a protective coating, the cracks were smeared over the unheated side of the tunnel and the mid-wall. This observation is in agreement with the numerical results. For the fire simulation on both tubes, the crack strain increased considerably compared to the previous fire scenario, and the maximum strain values were localised at the tunnel corners and mid-walls.

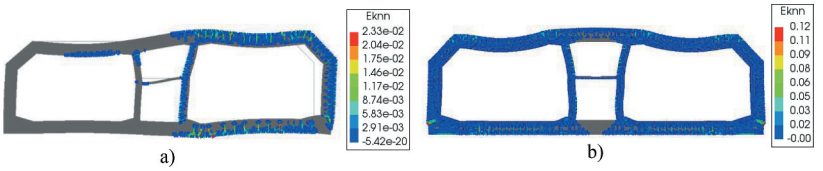


Figure 7. Comparison of crack patterns at the end of the heating phase for plane stress representation: a) scenario A; b) scenario B with explicit spalling representation. The numerical crack width can be estimated as$w = \varepsilon \cdot h$, with h = 30 mm.

The analysis of the principal compressive stresses in the simulations showed the development of a compressive ring in the tunnel cross-section. This ring was located in the concrete cover region, and it was induced by the concrete thermal expansion. For both 2D representations, it was observed that when the spalling representation was included, the compressive stresses at the ring region were visibly reduced. As shown in Figure 8, the comparison between the models with and without spalling for the plane strain idealisation provided a good understanding of the early failure when the spalling effects were included.

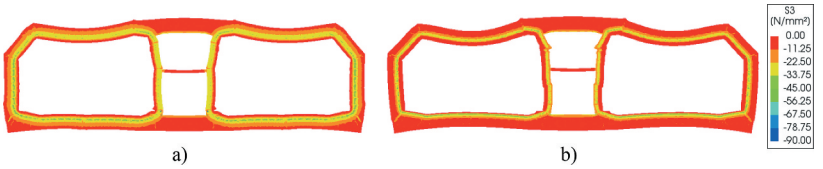


Figure 8. Principal compressive stresses for scenario B: a) plane strain and no spalling at 365 minutes; b) plane strain with explicit spalling at 72 minutes.

Overall, the moment diagrams, values and redistribution were similar in both 2D representations. It was noted that even with the coating application, the maximum moment values were similar to the ones calculated for both fire case scenarios without protection. It is pointed out that the maximum moments at the loading stage represented approximately only 10% of the maximum moment obtained during the fire event as shown in Figure 9.

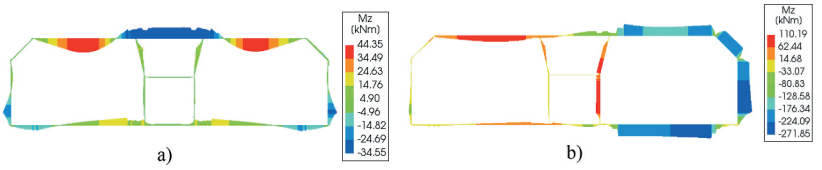


Figure 9. Bending moment diagrams for 2D plane strain representation: a) from mechanical loads b) at 365 minutes in fire scenario A.

6 CONCLUSIONS

This paper investigated the thermo-mechanical behaviour of reinforced concrete tunnel segments under fire using NLFEA. The results from different modelling strategies were compared against

experimental data reported in the literature. The main modelling assumptions included the 2D idealisation (plane stress/strain representation) and the explicit spalling simulation based on the simplified model proposed by Hua *et al.* (2021b). The numerical results from the thermal analysis indicated that the temperatures can be significantly underestimated if the spalling effects are not considered in the simulation of a tunnel without fire protection. Moreover, plane stress and plane strain idealisations provided similar numerical responses for both fire scenarios when compared to the experimental results and also in terms of internal forces. The main difference was found when the spalling effect was included. In that case, more damage was observed in the plane strain representation, and consequently, the simulation finished earlier than expected, during the heating phase. These conclusions are limited to the case study examined in this paper. Future works will focus on the developing more reliable constitutive models for the representation of concrete during the cooling process. These developments will be important for assessing the structures remaining capacity after a fire event and in the design optimisation of fire protection systems.

ACKNOWLEDGMENTS

This study was supported by the Dutch Ministry of Infrastructure and Water Management (Rijkswaterstaat) through the research project *"Brandwerendheid Landtunnels"*. The authors gratefully acknowledge this support.

REFERENCES

DeJong, M., Hendriks, M. A. N. and Rots, J. G. (2008) 'Sequentally linear analysis of fracture under non-proportional loading', *Engineering Fracture Mechanics*, 75(18), pp. 5042–5056.

Dong, Y., Duan, J., Zhang, D., Liu, J., Zhu, S. and Qi, J. (2023) 'Experimental research on fire resistance of the reduced scale immersed tunnel with fire in both traffic tubes', *Tunnelling and Underground Space Technology*, 132, p. 104922.

Duan, J., Dong, Y., Xiao, J., Zhang, D., Zheng, W. and Zhang, S. (2021) 'A large-scale fire test of an immersed tunnel under the protection of fire resistive coating', *Tunnelling and Underground Space Technology*, 111, p. 103844.

Feenstra, P. H. (1993) *Computational aspects of biaxial stress in plain and reinforced concrete*. Doctoral thesis. TU Delft.

Feenstra, P. H., Rots, J. G., Arnesen, A., Teigen, J. G. and Hosieth, K. V. (1998) 'A 3D constitutive model for concrete based on a co-rotational concept', *Proceedings of the Euro-C 1998 Conference on Computational Modelling of Concrete Structures*. Badgastein, Austria. Brookfield.

Gernay, T., Van Coile, R., Achenbach, M., Bamonte, P., Chang, J., Elhami Khorasani, N., Franssen, J.-M., Lakhani, H., Naser, M. and Correia Rodrigues, J. P. (2023) 'Perfomance-based design for structures in fire - State-of-the-art report', *Fire safety journal*, (104036).

Guo, J., Shuping, J. and Zhuyong, Z. (2016) 'Fire thermal stress and its damage to subsea immersed tunnel', *Procedia Engineering*. pp. 296–306.

Hendriks, M. A. N. and Roosen, M. (2022) *Guidelines for Nonlinear Finite Element Analysis of Concrete Structures*. Rijkswaterstaat Technical Document (RTD), Report RTD:1016-1:2022.

Hordijk, D. (1991) *Local approach to fatigue of concrete*. Doctoral thesis. TU Delft.

Hua, N., Tessari, A., Elhami Khorasani, N., Ehsan, M. and Gonçalves da Silva, B. (2021a) *Fire in Tunnel Collaborative Project*. (No. CAIT-UTC-REG16). Rutgers University. Center for Advanced Infrastructure and Transportation.

Hua, N., Tessari, A. and Khorasani, N. E. (2021b) 'Characterizing damage to a concrete liner during a tunnel fire', *Tunnelling and Underground Space Technology*, 109, p. 103761.

Lin, C. L. and Chien, C. F. (2021) 'Lessons learned from critical accidental fire in tunnels', *Tunnelling and Underground Space Technology*, 113(103944).

NEN-EN-1992-1-2:2005/A1:2019 (2005) *Eurocode 2*: *Design and calculation of concrete structures - Part 1-2: General rules - Design and calculation of structures in case of fire*. Brussels, Belgium: Comité Européen de Normalisation.

Vecchio, F. J. and Collins, M. P. (1993) 'Compression response of cracked reinforced concrete', *Journal of Structural Engineering*, 119(112), pp. 3590–3610.

Vecchio, F. J. and Selby, R. G. (1991) 'Towards compression-field analysis of reinforced solids', *Journal of Structural Engineering*, 117(6), pp. 1740–1758.

Bridge Maintenance, Safety, Management, Digitalization and Sustainability – Jensen, Frangopol & Schmidt (eds)
© 2024 The Author(s), ISBN 978-1-032-77040-6
Open Access: www.taylorfrancis.com, CC BY-NC-ND 4.0 license

An unconventional barrier design

Zahra Kamranian, M.Eng, P.Eng. & Diego Penate, P.Eng.
Stantec Consulting Ltd.

Glen Norlander, P.Eng. & Fadi Oudah, PhD, P.Eng.
Norlander Oudah Engineering Ltd (NOEL)

ABSTRACT: An industrial project in northern Canada was recently completed that required multiple ultra-heavy loads to be carried by the world's largest mine trucks over a new bridge structure. The truck's Gross Vehicle Weight (GVW) was 6134 kN exceeding typical highway loads by more than 10 times. A rectangular concrete structure with two cells was selected as the most cost-effective option due to site constraints. The main access road consists of two single standard width traffic lanes travelling under the proposed bridge. Traffic on the access road is comprised of light vehicle traffic. The bridge overpass had three lanes, each with a 20 m wide diving lane. The span of the overpass was 71 meters.

Highway bridge codes do not provide guidance for barrier design appropriate to restrain heavy haul trucks. Crash test results are not available for barriers capable of withstanding these loads. This presented challenges in structural analysis and design and in the design of safety components, including safety barriers. Therefore, the geometry of the barrier, the structural design, and the support of these barriers by the bridge superstructure required advanced modelling and design. As a safety requirement for the project, the oversize barriers are designed to redirect the heavy haul trucks in the event of a collision.

Other challenges with this unique structure include rockfall simulation to model rock free-fall for regular traffic below. Any debris generated on the overpass, including haul truck material, has the potential to free fall from the top haul truck boxes and impact light-duty vehicles travelling under the bridge on the highway traffic main access road. Stantec completed a quantitative rockfall simulation to mimic the trajectory of rocks or hardened soil clumps falling from the haul trucks and provided recommendations for mitigation measures. As a result, an engineered rockfall fence was built to capture rocks and debris.

This paper presents some of the challenges of this unique heavy-load design and construction project.

1 INTRODUCTION

Stantec Consulting Ltd. (Stantec) was retained to provide engineering design and construction support for an overpass in Northern Canada. The overpass carries three lanes of heavy haul mine trucks over a regular light traffic lane under. Each heavy haul lane is approximately 20m wide.

Concrete haul road barriers measuring 3 m wide are located along the east and west sides of the bridge deck. The height from the top of the concrete barrier to the heavy haul road surface ranges from approximately 3.7 m to 3.8 m on the west side and from 4.0 m to 4.1 m on the east side. A berm divides the three haul road lanes into a single haul road lane and a double haul road lane. The total overpass width measured at the soffit of the deck is approximately 71 m. The overpass haul road double lanes will be used for ore transport while the single lane will be used for waste transport in both directions.

The light traffic road below consists of two single traffic lanes (each 4 m clear lane width) traveling under the overpass with a clearance of 5.4 m. Retaining wing walls above and

DOI: 10.1201/9781003483755-467

adjacent to the light traffic road are provided to support the overpass fill. The fill above the retaining wing wall is at a 3H:1V slope.

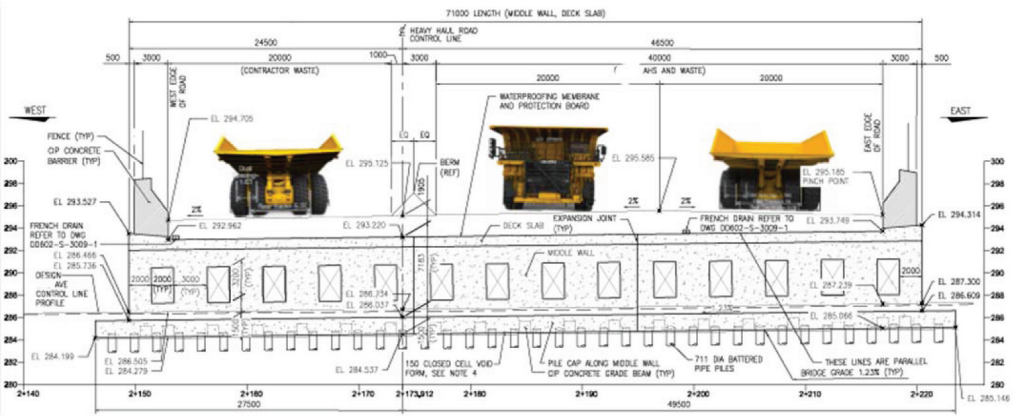


Figure 1. Bridge cross section.

CSA-S6-19 is the primary reference for bridge barrier design in Alberta. The specified requirements for bridge barrier design in CSA-S6-19 does not relate directly to the design of barriers for bridges transporting extremely heavy vehicles such as the Komatsu 980E-4. Conducting real-life crash study as recommended by literature to evaluate and design bridge barriers impacted by non-conventional vehicles is not practical for such large and expensive vehicle. Alternatively, finite element simulation was used to assess bridge barriers subjected to vehicle impact.

The scope of work for the engineering team was to design a bridge system capable of restraining the Komatsu 980E-4 haul truck within the bridge drive lanes of the proposed bridge for a defined speed and contact angle.

The scope of work included conceptualizing and designing the following items using Finite Element (FE) simulation and the principles of structural mechanics:

1. Development of the bridge barrier concept and deformation mechanism
2. Number and details of barrier blocks
3. Barrier-to-bridge deck and barrier-to-approach slab connections (via proprietary high strength thread rods)
4. Barrier-to-barrier connection (via shear keys and post-tensioning cables)
5. Detail for quick restoration of the barrier following a collision.

Different impact scenarios were investigated to investigate the worst angle of impact to the barrier. The impact velocity was considered as the maximum allowed truck velocity travelling on the heavy haul road. The point of collision was considered at the elevation of the front bumper. Different barrier options were investigated to determine the final design.

In addition, any debris generated on the overpass, including haul truck ore and waste material, has the potential to travel downslope or free fall from the top of the concrete barrier and impact light duty vehicles that travel under the bridge. As part of the detailed design, Stantec completed a quantitative rockfall simulation to mimic the trajectory for rocks or hardened soil lumps falling from the haul truck box and to provide recommendations for mitigation measures (a rockfall barrier to capture rocks).

2 HEAVY HAUL ROAD BARRIER DESIGN

The heavy haul truck barrier was designed to redirect and restrain a fully loaded maximum sized mine haul truck travelling at maximum speed back toward the drive lane without transferring significant damaging loads down to the bridge deck and its supports. The restraining

barrier system needed to be robust enough to be quickly reinstalled in position should an impact occur. The impact angle was determined from the turning radius of the specified haul truck when travelling in the furthest lane. To achieve the barrier restraint performance, the concept had to maximize the energy transferred into the barrier through direct energy transfer through mass, lifting energy loss along a sloped plane, friction energy, shear loss and energy transfer due to strain of cables.

The heavy haul truck barrier concept follows:

1. The geometry of the barrier cross section was configured to set the barrier height at the haul truck axel height when the truck is travelling on the gravel wear course.
2. The barrier width was determined to maximize the mass of each section of barrier without sacrificing too much additional width of the bridge deck the barrier rests on.
3. The barriers are constructed with keyed blocks between each barrier with a maximum length consistent with the capacity of an all-terrain crane in case of an impact where the block must be restored back into position.
4. On the impact side of the barrier, a sloped surface created a path for the truck bumper to ride up on, increasing the normal force and friction of the barrier on the deck. The truck weight reduced overturning of the barrier upon impact.
5. The barrier cross section rests on a sloped raised curb poured integral with the bridge deck. Under impact, movement of the barrier along the contact plane lifts the barrier as translation of the barrier occurs.
6. As impact occurs on an individual barrier block, steel fuses made from high strength thread bar connecting the deck to the barrier, are sized to fracture, absorbing collision energy.
7. Each block is keyed to the adjacent block but not connected with rebar. The barrier blocks transfer shear horizontally at the keys, engaging more mass from the adjacent barrier blocks, thus absorbing additional energy in the event of a collision.
8. Post tensioning strand connect the barrier segments together. The strands are anchored at each end of the bridge. The strand is lightly stressed at construction. During a collision, the strand is sized to loosely hold the assembly of barrier blocks together longitudinally, absorbing additional energy from the collision in additional strand strain and longitudinal surface friction between the curb surface and the barrier blocks. The design balances forces on the barrier for redirection of the truck against forces transferred to the bridge deck such that bridge deck and girder damage is limited.

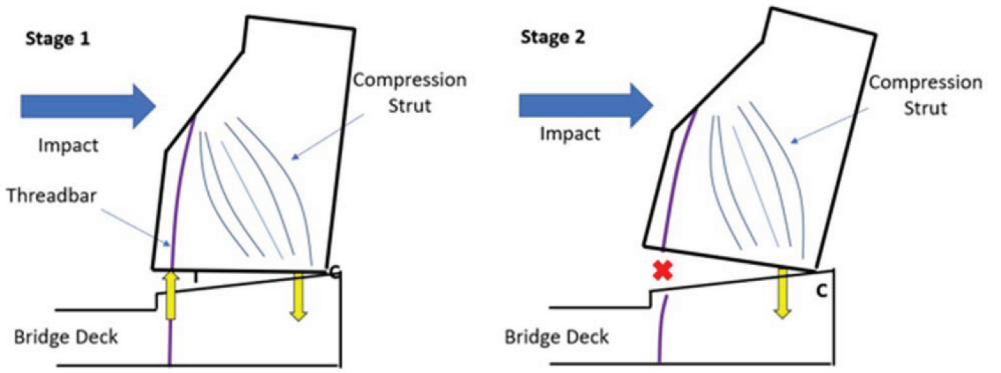


Figure 2. Schematic illustration of barrier deformation mechanism.

An iterative design procedure was employed to optimize the configuration of the barrier, size the structural fuses, and determine the number of post-tensioning strands required to connect the barrier segments. The design optimization was performed by developing detailed three-dimensional (3D) nonlinear FE models of the barrier using the dynamic FE software

LS-DYNA. The concrete barrier was modeled using solid elements with efficient formulation, while the steel reinforcing bars, and the post tensioning strands were modeled using beam elements with full integration. Nonlinear concrete material properties were utilized, and an elastic-plastic hardening material model was used for the reinforcing steel. Applicable concrete-to-concrete and concrete-to-steel friction coefficients were used. A mesh sensitivity analysis was performed to determine the optimum size of the elements. The modeled barrier was impacted by a moving mass of equivalent properties that simulate the largest haul trucks in the mining industry (kinetic energy). Multiple impact angles and velocities were assessed to cover a wide spectrum of collision scenarios. Explicit LS-DYNA solver was utilized to capture the dynamic effect associated with impact. The FE simulation proved the effectiveness of the proposed barrier system to restrain the Haul truck from completely breaking through the barrier while maintaining high effectiveness in redirecting the vehicle back to track.



Figure 3. Barrier cross section.

3 CATCHMENT FENCE DESIGN

A rockfall analysis was completed to assess the potential for rock fragments falling from the haul trucks to reach road below the overpass.

The truck type expected to travel on the overpass was a Komatsu 980E-4 model (Length: 15.72m, Width: 10.01m, Loading Height: 7.09m), and was expected to travel at a maximum speed of 40 km/hr for both staffed and autonomous trucks. The haul trucks were assumed to follow a controlled and consistent path of travel, maintaining a minimum offset of 5 m between the side of the truck and the interior face of the concrete barrier.

Based on regional experience with the local ore and waste, rock sizes ranging from coarse gravel (~50 mm diameter) to large boulders and lumped soils (~1.5 m to 2.0 m diameter) were selected as a reasonable worst-case scenario of representative rock sizes to be used in the rockfall assessment.

Typical rockfall travel modes assessed included free falling, bouncing, rolling and sliding Ritchie, (1963). Free falling with a horizontal velocity component (projectile motion) was assessed as the rockfall travel mode for the period of time between when rocks leave the truck bed to the point of first impact. The assessment assumed normal haul truck operation and did

not account for catastrophic events that could result in large rock displacements such as swerving, truck collisions or rollovers.

The stiffness of a rockfall rollout surface directly influences the speed and distance that a rock can travel, by affecting energy dissipation and friction at the points where the rock contacts the surface. It was anticipated that hard surface conditions would be present on the haul road due to dry conditions or cold temperatures (frozen surface). It was assumed that the road was relatively flat between the haul truck and the concrete barriers. Wheel ruts and other surface defects were deemed beneficial to reduce rocks speed and travel distance and were not considered in the assessment.

The Rocscience 2D statistical analysis program RocFall 6.0 was used to conduct a statistical analysis of probable rockfall trajectories and their associated kinetic energy. The locations of rockfall initiation were selected to represent the selected scenarios for truck offset from the concrete barrier (5 m, 3 m and 1m). A data collector element was modelled to record the height and total kinetic energy of the rock impacts at the expected location of the rock barrier.

An initial sensitivity analysis was completed to test the effects of rotational velocity on the simulation results, using rotational velocities ranging from 30° to 90°/s. The simulation results for impact height and total kinetic energy of rock impact did not show significant variation as compared against the case with zero rotational velocity. Therefore, rockfall analysis rotational velocity was set to zero.

A range of horizontal velocities from 20 km/hr (5.6 m/s) to 60 km/hr (16.7 m/s) were used to calculate the rock traveling distances and heights. Figure 4 provides a graphical representation of the maximum impact height results obtained from the rockfall analysis at the proposed rockfall barrier location. The impact height is measured from the surface of the haul road.

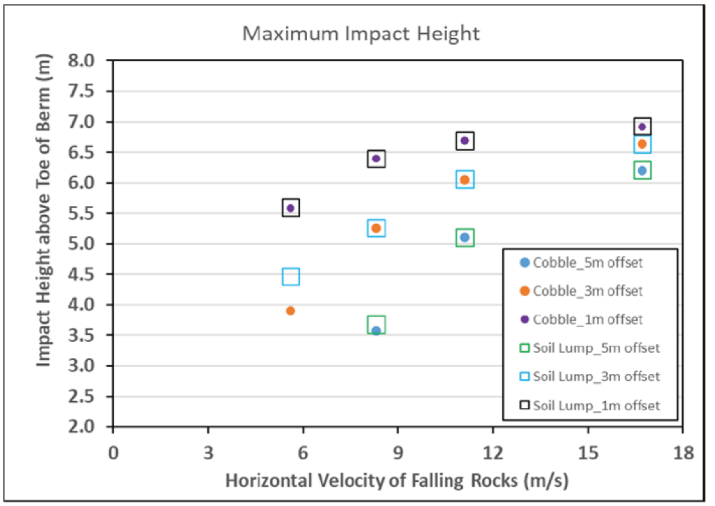


Figure 4. Rockfall maximum impact height results.

The maximum impact height occurs when the truck is offset 1.0 m from the concrete barrier, and the rocks hit the proposed rockfall barrier directly during the free fall. In this scenario, the maximum impact height does not vary greatly between rock types and is not affected by the rockfall surface parameters of the haul road and concrete barrier.

The rockfall analysis also assessed the total kinetic energy of the falling rocks at the moment of impact on the proposed rockfall barrier to be utilized for the design of the structural components and overall capacity of the rock barrier. Figure 5 provides a graphical representation of the total kinetic energy results. The total kinetic energy is presented in logarithmic scale to better visualize the range of results.

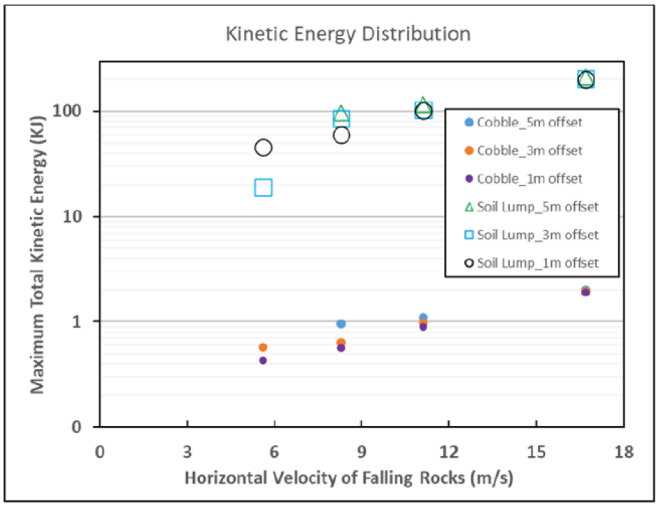


Figure 5. Maximum total kinetic energy distribution.

Based on the above results, the rockfall barrier should withstand the expected maximum total kinetic energy range between 100 and 200 kJ plus an applicable factor of safety (common range between 2.0 and 3.0) for the design. Based on this, a minimum capacity between 400 and 500 kJ for the protection barrier was recommended. The selected fence height was 3.5 m. Considering the concrete barrier height varying from 3.7 m to 4.1 m, the combined height for the rockfall protection system from the surface of the overpass road ranged from 7.2 m to 7.6 m, which satisfied the worst-case scenario required height.

Both rigid and flexible rockfall protection barriers (catchment fences) were considered acceptable solutions to contain potential rockfall.

4 CONCLUSION

The approaches that were taken for the design of the barrier and catchment fence were found satisfactory for the purpose of the project and the client's objectives.

REFERENCES

ODOT, 2001. Rockfall Catchment Area Design Guide – Final Report SPR -3 (032). Oregon Department of Transportation.

Ritchie, A. M., 1963. Evaluation of Rockfall and Its Control. Highway Research Record, No. 17, pp. 13–28.

Rocscience 2020, RocFall 6.0. Retrieved from Software Help Manual.


Taylor & Francis
Taylor & Francis Group
http://taylorandfrancis.com

GS27: BRIDGE SAFETY - Repair and retrofitting strategy


Taylor & Francis
Taylor & Francis Group
http://taylorandfrancis.com

Bridge Maintenance, Safety, Management, Digitalization and Sustainability – Jensen, Frangopol & Schmidt (eds)
© 2024 The Author(s), ISBN 978-1-032-77040-6
Open Access: www.taylorfrancis.com, CC BY-NC-ND 4.0 license

Anchored response tailored prestressed CFRP strengthening – preliminary long-term and temperature investigations

J.W. Schmidt & C.O. Christensen
Department of the Built Environment, Aalborg University, Aalborg, Denmark

P. Goltermann
Department of Civil and Mechanical Engineering, Technical University of Denmark, Kgs. Lyngby, Denmark

ABSTRACT: Novel Fiber Reinforcement Polymers (FRP) systems hold significant potential for future strengthening of existing structures; however, such systems may also add complexity to the structural assessment. Material properties and structural interaction can cause response deviation compared to conventional structures, affecting both SLS and ULS. The latter can be influenced significantly, as new and extended number of failure modes and complex interfacial interaction must be considered. A novel ductile prestressing Carbon Fiber Reinforcement Polymer (CFRP) strengthening system was designed to limit failure modes and provide a tailored ductile response. The paper describes some historical results, including several steps to provide such improvements. These are supplemented by recent indicational performance, fatigue- and temperature anchor test results additionally included. The anchor system seems excellent for controlling the strengthening utilization, response, and ductility. The system resisted the fatigue exposure in all tests. Exposure of the anchored CFRP prestressing system to cycles from 90°C to 8°C for 12 hours at each temperature limit did not seem to affect the anchorage resistance and stability, where only small temperature-generated deformations were measured.

1 INTRODUCTION

Near Surface Mounted Reinforcement (NSMR) Carbon Fiber Reinforcement Polymers (CFRP) systems have shown significant potential for strengthening and capacity upgrading of existing concrete structures (Al-Mahmoud et al., 2012; El-Hacha & Rizkalla, 2004; Kalfat et al., 2013; Sabau et al., 2018; Schmidt et al., 2022; Sena-Cruz et al., 2012). Such strengthening systems are easy to mount since the weight is 20% of steels, and they provide high tensile strength (the tensile strength is more than five times higher than reinforcement steels - if utilized efficiently) along with high corrosion resistance. Different NSMR CFRP laminate cross-section geometries have been used for several decades in strengthening applications. Some of the most used geometries in civil engineering structures are rectangular-, quadratic-, and circular rods, which may be adhesively bonded into the concrete cover. However, with such a material for strengthening, increased complexity follows this since new advanced failure modes should be considered. Brittle failure modes like Intermediate Crack (IC) debonding (Rashid et al., 2008) and concrete cover separation (Corden et al., 2008) are typically experienced at failure with a relatively low ductility as the outcome. Consequently, the industry and other professionals are often reluctant to implement such strengthening applications and question whether sufficient failure warning and safety margins are present.

The system considered in this paper has provided some answers to these questions by implementing effective anchoring and system ductility (Schmidt et al., 2010, 2019, 2020, 2021), however, additional questions typically relate to behavior in the long-term and environmental

DOI: 10.1201/9781003483755-468

exposure. These are difficult to answer since no adequate long-term accelerated testing procedures are, to the author's knowledge, available for CFRP anchor systems. In addition, such systems have not yet been proven in the field, like conventional civil industry materials and applications, which incites caution.

A review of the long-term mechanical properties of FRP tendon anchor systems is given in (Zhao et al., 2020) describes stress ranges of 215-355 MPa, while the "Guideline for European Technical Approval of Post-Tensioning Kits for Prestressing of Structures" (ETAG-013)/ (EOTA, 2002) prescribes a smaller stress range of 80 MPa. Other studies of CFRP system fatigue resistance are (Elrefai et al., 2007; Xie et al., 2020). In (Elrefai et al., 2007), a large test program was conducted with varying stress ranges (130-1153 MPa). The study concluded that for stress ranges ≤ 10 % of the CFRP ultimate strength (216 MPa), the fatigue life seems infinite. Other tests were performed in (Xie et al., 2020), where the stress ranges were 36-358 MPa, and with similar conclusions.

Testing of adhesively bonded CFRP systems exposed to high temperatures has been investigated by several researchers (Karbhari & Engineer, 1996; WU et al., 2005). In addition, strengthening reduction and adhesive glass transition thresholds are often described to be reached between 50°C and 70°C by the manufacturers (depending on the adhesive used) (Michels et al., 2015; Täljsten et al., 2011). Regarding anchored and prestressed NSMR CFRP, guidelines mainly handle the unique material testing and not novel systems and material interactions. Often, standards and guidelines relate to rivaling steel prestressing systems, which may be used as a reference when testing CFRP anchoring systems (EOTA, 2002; PTI, 1998). However, it must be emphasized that prestressed CFRP systems are not directly comparable to prestressed steel systems. There are significant differences regarding anchoring of the brittle CFRP material, lack of yielding regime, anchorage mechanism failure modes, material properties, mounting procedure, etc. Consequently, the lack of direct comparison makes it challenging to interpret results and evaluate novel CFRP systems when judged based on provisions concerning steel strands- and cables. The first part of this paper (section 2) summarizes some of the main milestones of the developed ductile NSMR CFRP prestressing system. The results answer how some challenges related to CFRP strengthening may be addressed. When looking into some of the presently generated results (Schmidt et al., 2019, 2020, 2021, 2022), the main scopes related to non- and prestressing of anchored NSMR CFRP strengthening have:

- Been to investigate potentially higher utilization and failure control when using NSMR CFRP strengthening for shared activation.
- Related to the ductility combined with response- and failure control provided by the developed novel ductile strengthening system.
- Researched mounting easiness and applicability for real-life structural strengthening.

The second part concerns test results related to fatigue (section 3) and temperature exposure (section 4), which are indications of the anchorage and CFRP NSMR prestressing system long-term resistance. These tests relate to the following research questions:

- Can the developed CFRP NSMR prestressing anchor system provide a stable prestress over three months?
- Can the novel ductile anchor system meet the demands given in the ETAG-013 (EOTA, 2002) related to fatigue resistance?
- How does a temperature up to 90°C affect the prestressing magnitude and stability?

2 RESPONSE, FAILURE CONTROL, AND DUCTILITY THROUGH CFRP ANCHORING

Based on recent findings, anchoring CFRP NSMR systems seems to be a viable solution to enabling response and failure control of the system and the strengthened structure. External prestressing systems may typically be divided into two end anchored systems: i) Anchored

strengthening systems adhesively bonded to the structure and ii) freely anchored strengthening systems (without adhesive bonding to the structure). A ductile response-controlled anchor system was developed for bonded and unbonded strengthening (Schmidt et al., 2020). CFRP rod stress activation is performed before the adhesive cures when applying bonded systems. This type of application may be used to perform shared activation (Schmidt et al., 2019). For unbonded systems, the strengthening effect relies on the anchorage system alone since these are the only force transfer areas, and there is no direct strain compatibility. However, an unbonded application may open the opportunity to provide increased strengthening control and ductility. Figure 1 shows test results from beam strengthening tests with four different strengthening configurations. In the unbonded configuration, a low elastic modulus adhesive was used to ensure CFRP rod protection in the NSMR groove but also to enable some stress transfer along the concrete beam/CFRP rod bond line, especially when reaching the ultimate capacity. Figure 1. Beam strengthening results: i) An unstrengthened beam, ii) A strengthened beam but with unanchored CFRP reinforcement, iii) A strengthened beam with prestressed CFRP bonded to the structure with epoxy, and iv) A strengthened beam with prestressed CFRP in an unbonded configuration using the ductile anchoring system. Test results first presented by (Schmidt et al., 2019, 2021).

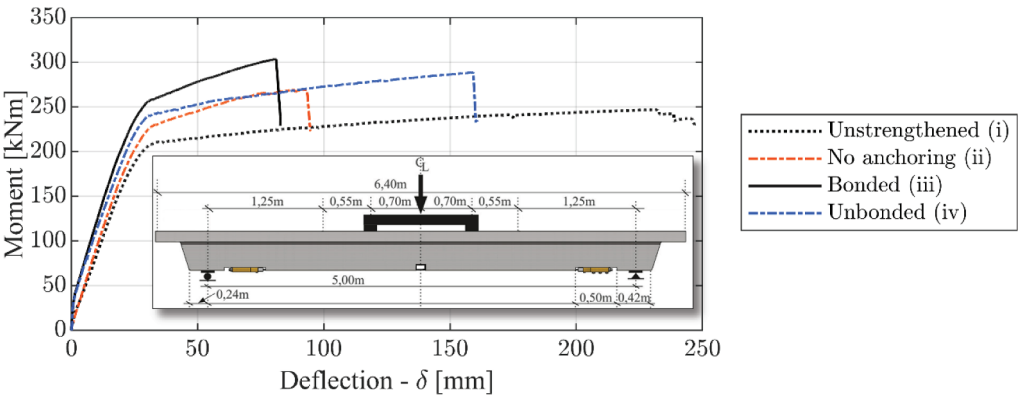


Figure 1. Results gained from un-strengthened beam (i) and strengthened beams (ii), (iii) and (iv).

It is seen that the systems provide excellent strengthening to the un-strengthened beam. Utilization of the CFRP rod up to 3300MPa was reached in the bonded configuration but at the expense of reduced ductility, which is significantly lower than the reference beam. When applying the response-controlled ductile anchorage combined with the low elasticity modulus adhesive, significantly increased ductility is achieved. In addition, a significant strengthening effect was still obtained. The ductile anchorage dictates the yielding threshold and provides strengthening support to the yielding regime provided by the internal steel reinforcement. This configuration resulted in concrete crushing strain magnitudes [Schmidt et al., 2021]. The research indicates that advanced ductile anchorage may provide excellent response and failure control to the applied strengthening system. The CFRP anchorage was designed to reduce the number of failure modes and control anchorage stresses to ensure high utilization of the CFRP rod (Schmidt et al., 2020). The brittle behavior and variation of the anchor capacity were handled by developing a ductile mechanism. Adding this mechanism to the anchorage, full control of the anchorage response was achieved through the combined system response. The ductile mechanism may be tailored to generate desired behavior with a response curve with a very small variation until the final intended collapse is reached. When collapsed, the remaining capacity of the CFRP anchor may be utilized. Figure 2 shows four examples of such tailored ductile mechanisms. An example of combined system response may be seen in (Schmidt et al., 2020).

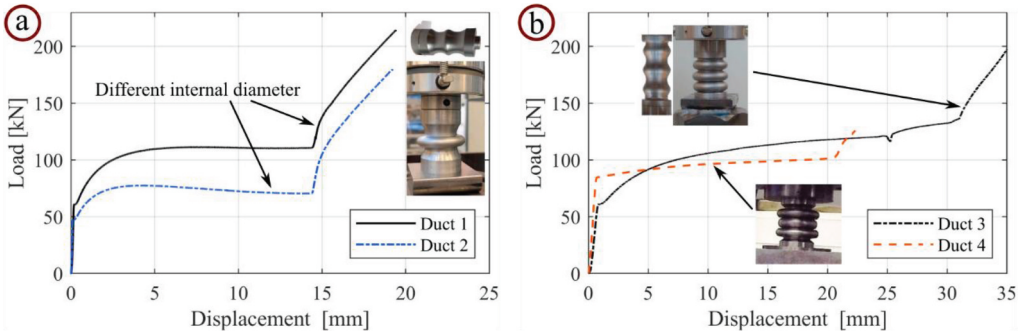


Figure 2. Examples of four tailored ductile mechanisms. a) Two ductile mechanisms with tailored changes in geometry and one deformation zone. b) Two different ductile mechanisms with three deformation zones, the design of "Duct 4" provides an almost ideal plastic response.

Using the ductile mechanism enables the applied anchorage system's significantly increased safety level. In addition, a brittle failure provided by the CFRP anchorage can be avoided by applying a ductile behavior design using the ductile mechanism. The next part of the research verifications is to take the first steps towards evaluating long-term and temperature effects.

3 FATIGUE TESTING OF THE DUCTILE CFRP ANCHOR SYSTEM

Fatigue evaluation is one of the crucial tests when performing a long-term assessment of the novel ductile CFRP anchor system. Such testing aims to prove a system has acceptable behavior for variating long-term loading exposure. According to the ETAG-013 (EOTA, 2002), post-tensioning systems shall withstand specified fatigue loads without exceeding a specified percentage loss of tensile element cross-section. Testing may consider the tensile element, the anchorage, or the coupling assembly (based on which is the weakest element). The test acceptance criteria are:

- No fatigue failure in anchorage components shall occur.
- No more than 5 % of tensile element cross section shall be lost during fatigue testing with 2 million cycles with a minimum stress range of $\Delta\sigma_p = 80\ MPa$ at a maximum load of 65 % of tensile element characteristic strength, f_{pk}.

It is specified that one test should be performed for the smallest, one for the medium, and two for the largest tendon size. The investigated system is, however, developed for one tendon size only (an 8 mm CFRP rod). Therefore, four tests are performed on this dimension. Recommendations by EMPA are very similar, only with a stress range of 10 % higher (90 MPa) and a stress level of 10 % lower. The stress levels applied in (Zhao et al., 2020) are deemed too high compared to these recommendations. The full ductile CFRP anchor system, depicted in Figure 3a, is a further developed version of the system presented and applied for strengthening a concrete bridge (Schmidt et al., 2022). Earlier versions and applications are found in (Schmidt et al., 2020, 2021, 2022). The system components include: i) tensile element (CFRP rod), ii) threaded barrel with aluminum wedge pre-set inside, iii) counteracting torque pins mounted in the barrel, iv) threaded bar, v) anchor block, vi) steering washer, vii) ductile mechanism, viii) nut. The ETAG-013 (EOTA, 2002) states that the test shall be performed in a tensile testing machine with the pulsator at a constant load cycle frequency of not more than 10 Hz and with a constant upper load, σ_{max}, of 65% of the characteristic strength of the tensile element. Figure 3b shows the cyclic loading regiment, where $\sigma_m = \sigma_{max} - \Delta\sigma_p/2$. The stress range of $\Delta\sigma_p = \sigma_{max} - \sigma_{min}$ shall be maintained constant throughout the testing, at levels corresponding to 80 MPa stress amplitude in the tensile elements for 2 million cycles.

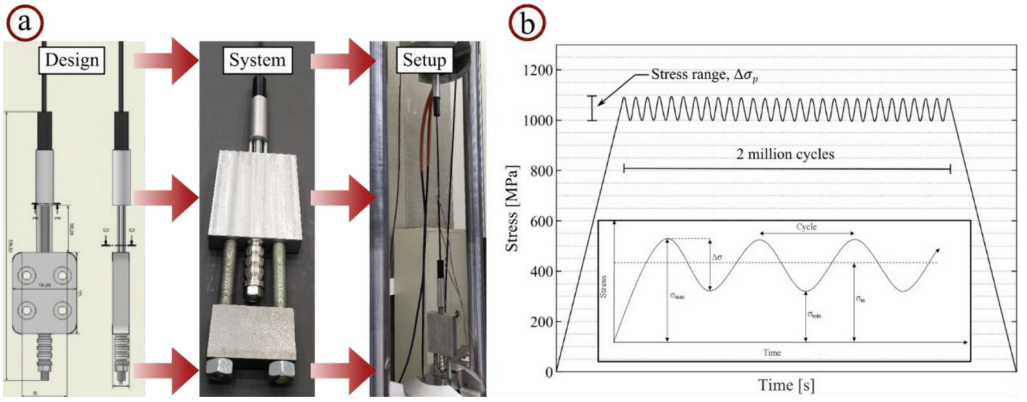


Figure 3. Fatigue test. a) Illustration of the design, assembled system, and test setup. b) Fatigue principle.

The ETAG-013 prescribes that the system to be tested shall be assembled according to the envisaged application, using all components necessary for anchoring the tendon. Unique for the presented system is that a ductile mechanism is introduced. The introduction of the ductile mechanism changes the perspective of the test. Therefore, the given fatigue test is not an individual fatigue test of the CFRP material or the anchorage but a full-system fatigue test. The evaluated and considered stress range values are seen in Table 1. Note that these are determined based on the strength of the ductile mechanism and not the CFRP strength because the ductile mechanism defines the characteristic yielding strength of the combined system. Based on the previous recommendations, the values chosen for the test are also shown in Table 1. Cyclic loading was performed using load-controlled testing with monitoring of system deformation and CFRP strain.

Table 1. Stress range values based on ETAG-013 using the ductile mechanism to define the load.

Parameter	Symbol	Value (ETAG-013) kN/(MPa)	Value (EMPA) kN/(MPa)	Chosen values kN/(MPa)
Tensile element/CFRP characteristic strength (test results)	$F_{k,CFRP}$ ($f_{k,CFRP}$)	99/(1969)	99/(1969)	99/(1969)
Ductile mechanism characteristic strength (test results)	$F_{k,DUCT}$ ($f_{k,DUCT}$)	84.4/(1679)	84.4/(1679)	84.4/(1679)
Upper load (65 % of $F_{k,DUCT}$)	F_{max} (σ_{max})	54.9/(1091)	51.4/(1023)	54.9/(1091)
Lower load ($\sigma_{max} - \Delta\sigma_p$)	F_{min} (σ_{min})	50.8/(1011)	46.9/(933)	46.9/(933)
Mean load	F_m (σ_m)	52.8/(1051)	49.2/(978)	50.9/(1013)

All four fatigue tests resisted the entire 2 million cycles without any undesirable behavior and were thus successfully performed. An example of the stress interval coupled to strain gauge measurements can be seen in Figure 4a. The four tests generated almost similar results for the deformation development. The results from one of the tests can be seen in Figure 4b.

A maximum observed deformation increase of 0.05 mm was identified while testing the full system. This magnitude seems small since it may originate in multiple components. It may be shared between the anchorage systems and the gripping jaws of the test machine. Such deformation levels are deemed insignificant in real-life applications where longer CFRP lengths typically will be used. It should be noted that eight anchors were fatigue tested through the four performed tests. The results fit well with the conclusion of (Elrefai et al., 2007) that stress levels below 10% of the ultimate capacity will not provide a fatigue failure.

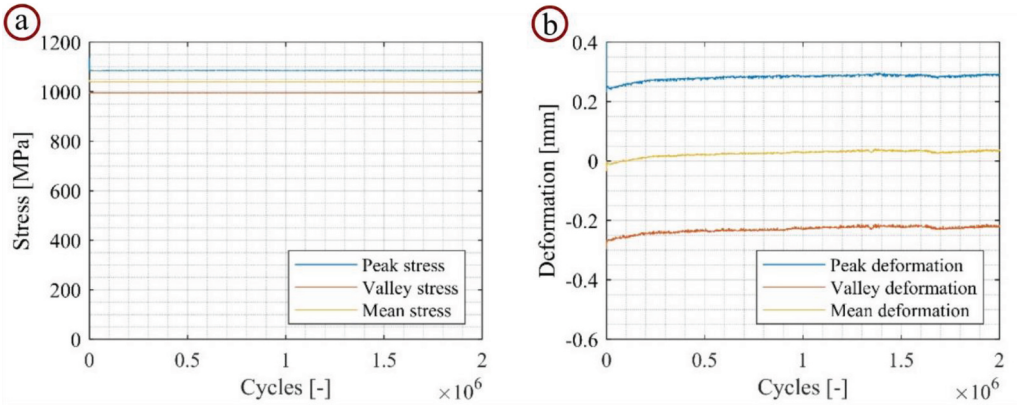


Figure 4. a) Achieved stress range in the fatigue tests. b) Deformation development for a representative test of the four tests, where similar results were achieved.

4 TEMPERATURE TESTING OF THE DUCTILE CFRP ANCHOR SYSTEM

Temperature testing was performed on four anchored CFRP NSMR systems; thus, two anchors with the full ductile system were applied. The test setup is seen placed in the temperature chamber in Figure 5c. It consisted of an H-profile with end plates used for the anchoring. A system was placed on each side of the web with a free CFRP length of approximately 260 mm.

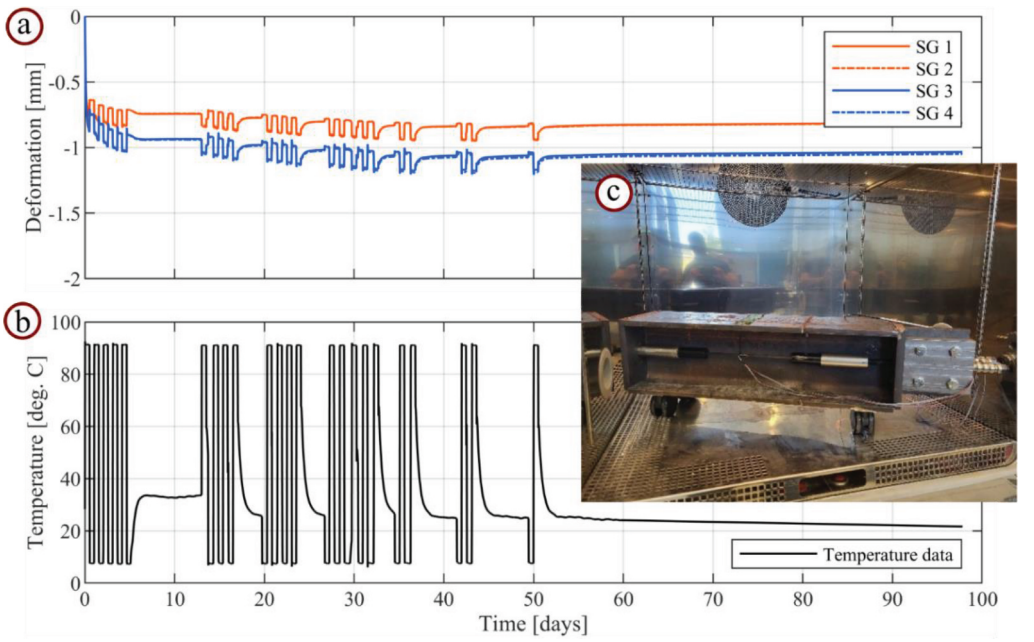


Figure 5. Temperature test data. a) Strain gauge measurements converted into equivalent system deformation. Note that 0.26 mm = 1000 μm/m. b) Temperature variation data. c) Photograph of the test setup in the climate cabinet.

Since limited information was available regarding novel system temperature testing, some assumptions had to be made to evaluate the temperature resistance. Since Denmark generally has lower environmental temperatures than southern European countries, Portugal was

chosen as a reference. This decision was based on the higher temperature levels and the state-of-the-art research in the environmental exposure of CFRP strengthening provided by (Cruz et al., 2022; Sena-Cruz et al., 2012). With a basis in "DS/EN 1991-1-5", the maximal temperature in Portugal is 40°C, and a bright light surface adds 18°C to the temperature level, resulting in a base temperature of 58 °C. With a safety factor of 1,5 applied to 58 °C, a temperature of 87 °C is reached.

Consequently, a maximum temperature of ~90 °C was chosen, significantly higher than the known degrading temperature thresholds between 55 °C - 65 °C provided by conventional adhesively bonded CFRP strengthening systems (Täljsten et al., 2011). A minimum temperature of 8 °C was used to indicate the night period. During the testing, the temperature was approximately 12 hours at the maximum and minimum temperatures. The specimens were initially prestressed to approximately 1200 MPa, which corresponds somewhat to the prestress level used when applied in situ (Schmidt et al., 2022). The applied temperature exposure is depicted in Figure 5b, and testing was performed until 98 days, 50 days with temperature variations, and 48 days at rest with a more stable temperature. The 48 days were used to evaluate if the temperature variation affected the stable stress behavior. Measurements of maximum and minimum fluctuating temperature magnitudes fit well with the test plan. But it can also be seen that there are some gaps in the curve. This was caused by functional challenges with the temperature chamber, where the temperature protocol had to be restarted multiple times. Nonetheless, the test results may serve as indicative results, and the gaps are deemed to have little influence on the current research results and scope. The measured deformation output (calculated from the strain) is seen in Figure 5a. Strain gauges 1 and 2 relate to one system, while 3 and 4 are for the other. Within the first hours of placing the system in the temperature chamber, a significant drop in prestressing (780 MPa) was observed. However, this is a natural effect when testing short systems, which will be significantly more susceptible to prestress loss provided by small deformations occurring in the system. The system deformation was only 0.62 mm and this magnitude of loss should be separated between the two anchor points (S_a = 0.31mm). For in-situ applications with longer NSMR CFRP systems, this magnitude seems insignificant but can be considered if desired. The system response after this drop follows the temperature well and does not seem to be affected any further by the 8-90 °C exposure with contraction and expansion. Additionally, after the initial stabilization, both double systems seem to have identical responses when exposed to the temperature. The results strongly indicate that the system is both stable and unaffected by the temperature exposure until the 98 days are reached (after initial stabilization). However, the tests are indication tests, and more testing will be needed when considering long-term behavior. However, when looking into previous and presented research on the system, tests indicate only small settlements when mounted in situ (Schmidt et al., 2022). The measured system settlements (approximately 6.5 m length) from in-situ testing after three weeks were identified to range from S_{CFRP} = 0.1 to 0.8 mm (presumed generated by the anchor points). Adding the obtained temperature settlement to this value, a maximum settlement at each anchor is presumed to be $\Delta L = 2 \cdot (S_a + S_{CFRP}) = 2$ (0.31 mm + 0.8 mm) = 2.22 mm. Consequently, a resulting stress reduction may be calculated from settlements gained from the anchor points of a NSMR CFRP strengthening system of 6.5 m length and a CFRP rod E-modulus of 165GPa, see Eq. (1). This loss should be considered for prestressing but no issue for future system implementation. The 56MPa loss generated at a length of 6500mm correspond to approximately 4,5% of a 1200MPa prestress level.

$$\frac{\Delta L}{L} \cdot E_{CFRP} = \frac{2.22\text{mm}}{6500\text{mm}} \cdot 165\text{GPa} \sim 56\text{MPa} \tag{1}$$

5 CONCLUSION

A ductile NSMR CFRP prestressing strengthening system has been developed and researched recently. Present research results seem very promising where desired designed response

control, ductility, high safety, and prestress stability have been investigated. Consequently, the next step was to perform the system's initial long-term and temperature testing. Indicating results of such testing is described in this paper. In the fatigue tests, the specimens resisted an applied fatigue loading protocol of 2 million cycles, with no significant deformation during testing (maximum observed deformation of 0.05 mm).Consequently, the demands from ETAG-013, as well as the recommendations from EMPA, were fulfilled. Although the system resisted the recommended protocol, it seems to be an open question if the stress ranges are representative of the actual real-life application, which should be investigated further. In the temperature tests, the base prestressing levels seemed unaffected by the temperature exposure from 8°C to 90°C during 12 hours for 50 days (after an initial loss in the first couple of hours). An anchorage settlement of 0.31 mm was observed, mainly from this initial drop. However, this settlement seems insignificant when relating to in-situ applications where longer strengthening systems are typically used. For instance, for a system length of 6.5 m, the anchorage loss will result in a total prestressing loss of approximately 56 MPa (40MPa anchorage- and 16MPa temperature related settlement), deemed acceptable. Prestressing seemed stable up to the termination of the test at 98 days. More testing is needed to investigate the results and verify them further. During the development, challenges seem associated with introducing novel systems in civil engineering since these systems are usually compared to traditional building materials and applications and have already been proven to have civil applications. However, from a sustainability perspective, this may be a significant obstacle that can be solved if sustainable solutions have the desired effect on the building industry.

ACKNOWLEDGEMENT

We sincerely thank S&P Clever Reinforcement Company AG Denmark for their invaluable support in the ongoing research project. Furthermore, the contributions from former students are greatly appreciated. In addition, a great thank you to the technical staff at DTU and AAU. Thank you to Perstrup Beton Industry A/S. Also, a great thank you to Reinholdt W. Jorck og Hustrus foundation for their acknowledgment and funding.

REFERENCES

Al-Mahmoud, F., Castel, A., & Franois, R. (2012). Failure modes and failure mechanisms of RC members strengthened by NSM CFRP composites - Analysis of pull-out failure mode. *Composites Part B: Engineering*, *43*(4). https://doi.org/10.1016/j.compositesb.2012.01.020.

Corden, G., Ibell, T., & Darby, A. (2008). Concrete cover separation failure in near-surface mounted CFRP strengthened concrete structures. *Structural Engineer*, *86*(4).

Cruz, R., Correia, L., Cabral-Fonseca, S., & Sena-Cruz, J. (2022). Durability of Bond between NSM CFRP Strips and Concrete under Real-Time Field and Laboratory Accelerated Conditioning. *Journal of Composites for Construction*, *26*(6). https://doi.org/10.1061/(asce)cc.1943-5614.0001262.

El-Hacha, R., & Rizkalla, S. H. (2004). Near-surface-mounted fiber-reinforced polymer reinforcements for flexural strengthening of concrete structures. *ACI Structural Journal*, *101*(5).

Elrefai, A., West, J. S., & Soudki, K. (2007). Performance of CFRP tendon-anchor assembly under fatigue loading. *Composite Structures*, *80*(3). https://doi.org/10.1016/j.compstruct.2006.05.023.

EOTA. (2002). *ETAG-013: Guideline for European Technical Approval of Post-Tensioning Kits for Prestressing of Structures*. European Organisation for Technical Approvals.

Kalfat, R., Al-Mahaidi, R., & Smith, S. T. (2013). Anchorage Devices Used to Improve the Performance of Reinforced Concrete Beams Retrofitted with FRP Composites: State-of-the-Art Review. *Journal of Composites for Construction*, *17*(1). https://doi.org/10.1061/(asce)cc.1943-5614.0000276.

Karbhari, V. M., & Engineer, M. (1996). Effect of environmental exposure on the external strengthening of concrete with composites - Short term bond durability. *Journal of Reinforced Plastics and Composites*, *15*(12). https://doi.org/10.1177/073168449601501202

Michels, J., Widmann, R., Czaderski, C., Allahvirdizadeh, R., & Motavalli, M. (2015). Glass transition evaluation of commercially available epoxy resins used for civil engineering applications. *Composites Part B: Engineering*, *77*. https://doi.org/10.1016/j.compositesb.2015.03.053

PTI. (1998). *Acceptance standards for post-tensioning systems*. Post-Tensioning Institute.

Rashid, R., Oehlers, D. J., & Seracino, R. (2008). IC Debonding of FRP NSM and EB Retrofitted Concrete: Plate and Cover Interaction Tests. *Journal of Composites for Construction*, *12*(2). https://doi.org/10.1061/(asce)1090-0268(2008)12:2(160).

Sabau, C., Popescu, C., Sas, G., Schmidt, J. W., Blanksvärd, T., & Täljsten, B. (2018). Strengthening of RC beams using bottom and side NSM reinforcement. *Composites Part B*: *Engineering*, 149. https://doi.org/10.1016/j.compositesb.2018.05.011.

Schmidt, J. W., Bennitz, A., Täljsten, B., & Pedersen, H. (2010). Development of Mechanical Anchor for CFRP Tendons Using Integrated Sleeve. *Journal of Composites for Construction*, *14*(4). https://doi.org/10.1061/(asce)cc.1943-5614.0000096.

Schmidt, J. W., Christensen, C. O., & Goltermann, P. (2020). Ductile response controlled EW CFRP anchor system. *Composites Part B: Engineering*, *201*. https://doi.org/10.1016/j.compositesb.2020.108371.

Schmidt, J. W., Christensen, C. O., Goltermann, P., & Hertz, K. D. (2019). Shared CFRP activation anchoring method applied to NSMR strengthening of RC beams. *Composite Structures*, *230*. https://doi.org/10.1016/j.compstruct.2019.111487.

Schmidt, J. W., Christensen, C. O., Goltermann, P., & Sena-Cruz, J. (2021). Activated ductile cfrp nsmr strengthening. *Materials*, *14*(11). https://doi.org/10.3390/ma14112821

Schmidt, J. W., Sørensen, J. D., & Christensen, C. O. (2022). In Situ Concrete Bridge Strengthening Using Ductile Activated NSMR CFRP System. *Buildings*, *12*(12). https://doi.org/10.3390/buildings12122244.

Sena-Cruz, J. M., Barros, J. A. O., Coelho, M. R. F., & Silva, L. F. F. T. (2012). Efficiency of different techniques in flexural strengthening of RC beams under monotonic and fatigue loading. *Construction and Building Materials*, *29*. https://doi.org/10.1016/j.conbuildmat.2011.10.044.

Täljsten, B., Blanksvärd, T., & Sas, G. (2011). *Handbok för dimensionering i samband med förstärkning av betongkonstruktioner med pålimmade fiberkompositer (In Swedish)*. Div. of Structural Engineering, Luleå University of Technology.

Wu, Z., Iwashita, K., Yagashiro, S., Ishikawa, T., & Hamaguchi, Y. (2005). Temperature Effect on Bonding and Debonding Behavior between FRP Sheets and Concrete. *Journal of the Society of Materials Science, Japan*, *54*(5), 474–480. https://doi.org/10.2472/jsms.54.474.

Xie, G. hua, Bian, Y. long, Feng, Q. hong, Wang, C. M., & Liu, R. gui. (2020). Experimental study on wedge-bonded anchors for CFRP tendons under cyclic loading. *Construction and Building Materials*, *236*. https://doi.org/10.1016/j.conbuildmat.2019.117599.

Zhao, J., Mei, K., & Wu, J. (2020). Long-term mechanical properties of FRP tendon–anchor systems — A review. In *Construction and Building Materials* (Vol. 230). https://doi.org/10.1016/j.conbuildmat.2019.117017.

Bridge Maintenance, Safety, Management, Digitalization and Sustainability – Jensen, Frangopol & Schmidt (eds)
© 2024 The Author(s), ISBN 978-1-032-77040-6
Open Access: www.taylorfrancis.com, CC BY-NC-ND 4.0 license

Analytical study on the effects of flange size on the axial force introduced in the rivet

K. Yamamoto & K. Nozaka
Ritsumeikan University, Kyoto, Japan

ABSTRACT: Replacement of damaged rivets with new ones is beneficial from both mechanical and landscape perspectives; however, this method of repair is not widely adopted due to issues with constructability. Although it is acknowledged that rivets with smaller flanges can be formed with less load, the extent of axial force introduced into these rivets is not yet determined. In this study, the mechanism of axial force introduction during the rivet's cooling process and the relationship between the axial force and size of the rivet flange were numerically investigated. Results indicated that there is a minimum flange size to keep required axial force in rivets.

1 INTRODUCTION

In recent days, a damaged rivet is often replaced with high-strength bolts due to its workability (Hayase et al. 2011). However, the joint strength after replacement with high-strength bolts may be lower than that of a sound riveted joint depending on the surface condition of the base material (Hanji et al. 2021), and there are also concerns that changes in appearance may result in a loss of the historical value of rivetted bridges, which are designated as cultural heritages. Therefore, it is essential to establish a new rivet construction method that improves workability, while also considering the mechanical properties and protection of cultural values. Reducing the load required for riveting is crucial to make the equipment smaller or to ease the support of the reaction force when striking the rivet, which would improve workability during riveting. This improvement results in more application of riveting not only for the existing bridges but also for new bridges.

A new construction method proposed to decrease the required load involves using rivets with a small contact area between the rivet head and base material surface after riveting (hereafter referred to as "rivet flange area) (Yamamoto et al. 2022). However, it is unclear if a rivet with a small rivet flange area can attain an axial force of at least 70% of the yield axial force measured in general rivets (Wilson & Oliver 1930), and there are also reports suggesting that the fatigue strength of riveted joints diminishes as the axial force decreases (Hori et al. 2012). Hence, understanding the mechanism of axial force introduction in rivets is critical for ensuring the safety of new rivet construction methods. This requires determining the necessary rivet flange area to introduce an axial force equal to or greater than that of traditional rivets.

In this study, rivets with varying rivet flange areas were investigated using a finite element analysis program. Then, effects of thermal changes to both the rivet and the base material on the process of axial force introduction were discussed.

2 NUMERICAL ANALYSIS OVERVIEW

2.1 *Analysis model overview and material characteristics*

In this study, finite element analysis program MARC (MSC 2021) was utilized to perform a deformation analysis. This analysis replicated the process where the rivet undergoes plastic

DOI: 10.1201/9781003483755-469

deformation and fastens steel plates together. Following this, a thermal stress analysis was conducted to represent the cooling of the rivet after riveting. Figure 1 presents a schematic of the analysis model before the deformation analysis, while Figure 2 illustrates the rivet construction process. Figure 2 shows the rivet, inserted between steel plates, undergoing plastic deformation by a hammer, resulting in the steel plates being clamped together by the head formed after the rivet expands between the plates.

The analysis model accounted for the axial symmetry of the structure, modeling only the part indicated by the dashed line in Figure 2(a) using axially symmetrical shell elements. This approach resulted in a 3D analysis model incorporating stress and strain components in the circumferential direction. Deformation analyses were conducted for 10 different cases, involving two rivet shaft diameters (19 mm and 22 mm) and five shaft lengths. The hole diameter was set to the shaft diameter plus 1.5 mm, while the steel plate thickness and hammer shape remained consistent in each model.

For the deformation model, the steel plate was assigned Young's modulus of 200,000 N/mm² and Poisson's ratio of 0.3. The rivet hammer was treated as a rigid body, and the rivet itself had Young's modulus of 2000 N/mm² and Poisson's ratio of 0.3. This study builds upon a previous study (Yamamoto et al. 2022), which readers are encouraged to refer to for detailed information. The method of deformation analysis used here also follows that previous study (Yamamoto et al. 2022), and hence the specifics are not reiterated in this document.

Subsequently, a thermal stress analysis was conducted based on the results from the deformation analysis. This involved analyzing a state where the rivet, having undergone plastic deformation in the shaft and formed a head part, was subjected to thermal changes applied to both the steel plate and rivet. The stress state from the deformation phase was not carried over into this analysis. A total of 20 scenarios were evaluated in the thermal stress analysis, applying the material properties of two types of steel (ss400 and sm490) to 10 different shapes derived from the deformation analysis as stated in Table 1.

The focus of this study is to elucidate the influence of the rivet flange area on the axial force introduced during the cooling phase and the associated displacements in various parts due to rivet contraction. The contact analysis covered all free surfaces of the steel plate, rivet, and hammer, assuming zero frictional force during contact. No boundary conditions were set, allowing the rivet to expand and contract freely, except for boundary conditions of $x = 0$ and $y = 0$, which were applied only to nodes within the area enclosed by solid lines in Figure 3.

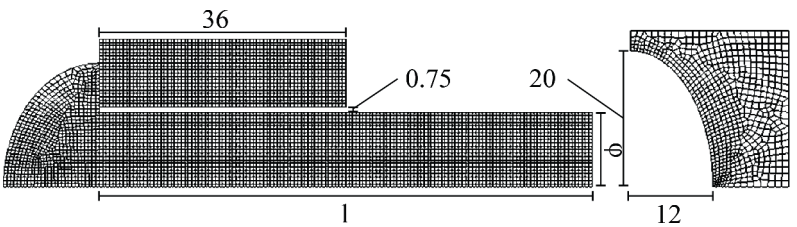


Figure 1. Overview of analysis model (units: mm).

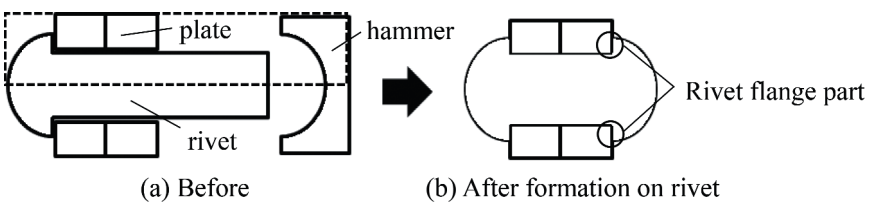


Figure 2. Schematic diagram of rivet construction.

Table 1. Analysis case.

φ	l				
mm	mm				
19	61	66	72	75	80
22	61	66	72	75	80

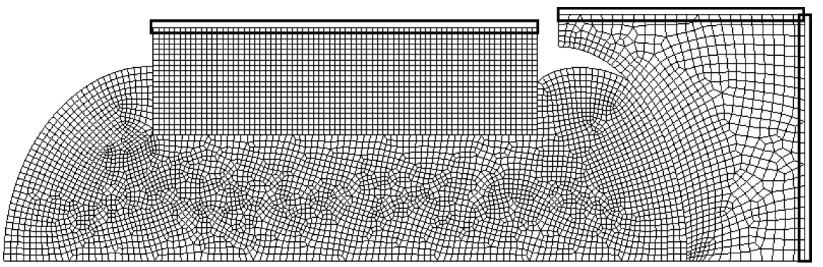


Figure 3. Example of analysis model.

In actual riveting process, thermal changes and stress generation occur while forming the heated rivet with a hammer. However, given that hammering is a brief process, it is believed that these thermal changes are negligible. The impact on the introduced axial force is primarily attributed to deformation during cooling and the conditions of restraint. Therefore, to simplify the analysis, the stress generated during the forming process was omitted in this study. The Young's modulus of the rivet used in the thermal stress analysis is set as shown in Figure 4, and the linear expansion coefficient is set based on previous research (Kim et al. 2005) as shown in Equations (1) and (2). The steel plate was assumed to be SM490Y, and the yield stress was set to 355 N/mm^2. In a previous study (Kim et al. 2005), analysis was conducted with the assumption that the yield stress of the steel material was constant below 400 °C.

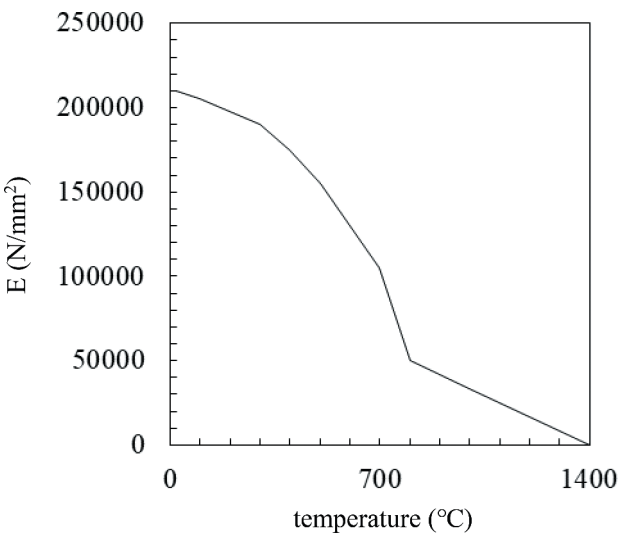


Figure 4. Young's modulus.

In this study, a polylinear approximation of the true stress-equivalent plastic strain relationship is used for the rivet, as illustrated in Figure 5. This approximation was based on the relationship between stress and strain at high temperatures for steel materials, outlined in the Recommendations for Fire Resistant Design of Steel Structures (Architectural Institute of Japan 2017).

$$20 < T < 600^{\circ}\mathrm{C} : \alpha = (0.0005173 \times \mathrm{T} + 1.1897) \times 10^{-5} \quad (1)$$

$$T > 600^{\circ}\mathrm{C} : \alpha = 1.5 \times 10^{-5} \quad (2)$$

where α = linear expansion coefficient; T= temperature.

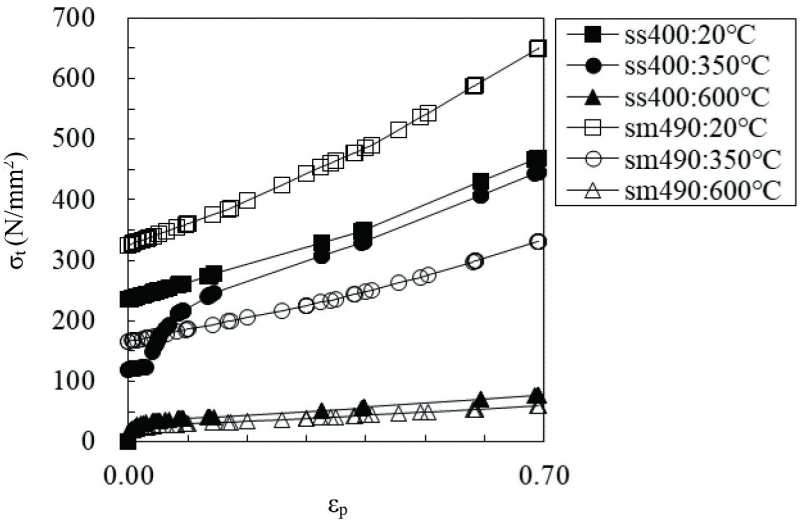


Figure 5. True stress-equivalent plastic strain relationship.

To ensure clarity of the figure, true stress-equivalent plastic strain relationships at other temperatures set in this study were not included. Any temperatures without a specified true stresse-quivalent plastic strain relationship was interpolated from the input data. Young's modulus of the hammer was set at 200,000 N/mm². Although yield stress was not assigned, its impact on the analysis results is minimal because the rivet and hammer cease contact shortly after analysis begins due to rivet contraction. Furthermore, Poisson's ratio was set to 0.3 for all rivets, steel plates, and hammers, in line with parameters from a previous study (Kim et al. 2005).

2.2 *Temperature history*

The actual temperature of the steel plate surface and the rivet head, on the side supporting the reaction force, was measured using thermocouples and infrared thermal cameras (Suehiro et al. 2020) (Hirohata et al. 2021). However, attaching a thermocouple to a rivet can impede the riveting process, and a shaft inserted into a rivet hole is not measurable with a thermal camera, making it challenging to track the temperature history of the rivet head and shaft on the driving side. Understanding the overall temperature history of the rivet is crucial for analytical study on its cooling process and identifying the mechanism behind the introduction of axial force. Therefore, as a preliminary step to the analysis, a test specimen as depicted in Figure 6, was fabricated to measure the actual temperature history of the rivet and steel plate. This specimen featured a slit along the shaft direction, allowing visibility of the rivet in the hole. The temperature history of the shaft part, post-riveting, was recorded using an infrared thermal camera, focusing on the portion visible through the slit.

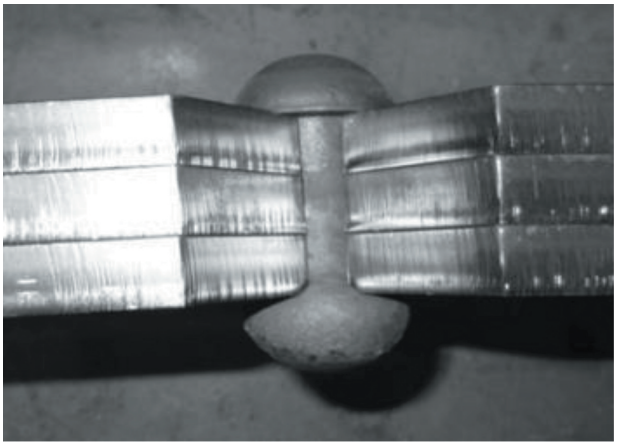


Figure 6. Example of specimen.

Figure 7 presents the approximate values derived from the measured temperature history. A polylinear approximation of these measurements was input into the analysis program. In the simulation, the rivet was cooled from 1000 °C to 95 °C within one second. Simultaneously, the steel plate, initially at 20 °C, experienced a temperature increase to a maximum of 290 °C due to heat transfer from the rivet, before also cooling down to 95 °C. During these measurements, thermocouples were employed alongside infrared thermal cameras to record temperatures. These results were then compared, and the most accurate temperatures were selected for use. In this study, we thought that the timing of the thermal change in the rivet and steel plate was important, and we decided to use the measurement results.

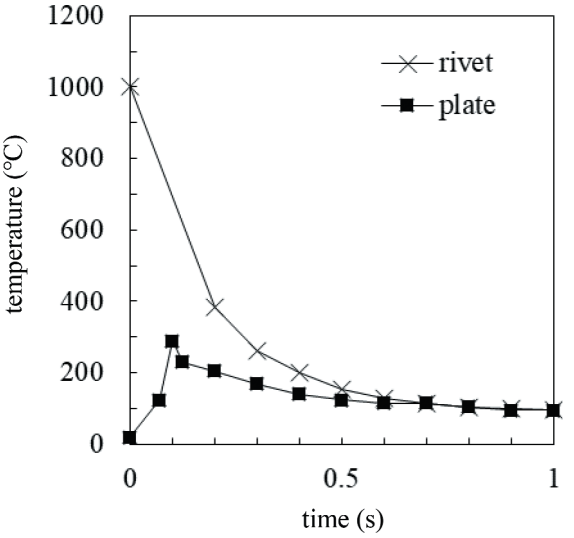


Figure 7. Temperature history.

3 RESULTS AND DISCUSSIONS

3.1 *Displacement in axial direction of each part of rivet due to cooling*

Firstly, displacement of each part of the rivet at the end of the analysis were focused to determine the mechanism by which the axial force is introduced as the rivet cools. Figure 8 displays

a detailed view of the rivet flange area on the side where the head forms during driving (termed the "driving side"). Table 2 lists the lengths of the rivet shafts and the corresponding rivet flange areas on the driving side. The rivet flange part was defined as the difference in the y-coordinate between the node at the outer edge of the hole and the nearest node on the steel plate among those in contact with both the rivet head and steel plate. It was observed that rivets with longer shaft lengths and larger shaft diameters possess a greater volume, leading to the formation of a larger rivet flange area after driving.

Figure 9 shows the node positions at the outer edges of the rivet head and rivet flange part, both on the side supporting the reaction force during rivet driving (referred to as the "supporting side") and driving side. In this discussion, the nodes at the outermost edges of the rivet flange area on the supporting and driving sides are designated as L1 and R1, respectively. The nodes at the top of the rivet head on the supporting and driving sides are labeled L2 and R2. Furthermore, for this study, the x-coordinate of each node at the beginning of the analysis was set to 0. The displacement that occurred in the x-axis direction from the initial position by the end of the analysis was recorded as the final displacement.

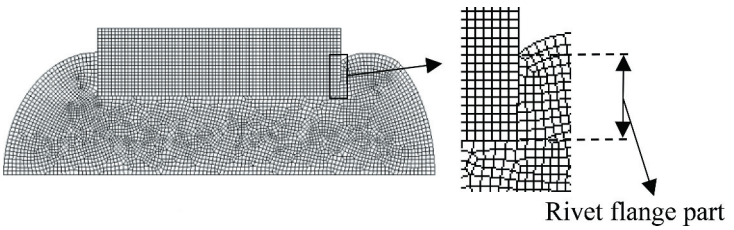


Figure 8. Rivet flange part.

Table 2. Rivet shaft length and rivet flange area.

rivet length	ss400:φ19	ss400:φ22	sm490:φ19	sm490:φ22
mm	mm^2	mm^2	mm^2	mm^2
61	29.1	76.1	29.6	75.8
66	96.7	155.7	95.8	158.1
72	159.9	298.0	160.4	298.1
75	208.2	358.6	209.6	358.4
80	352.9	518.0	353.0	518.2

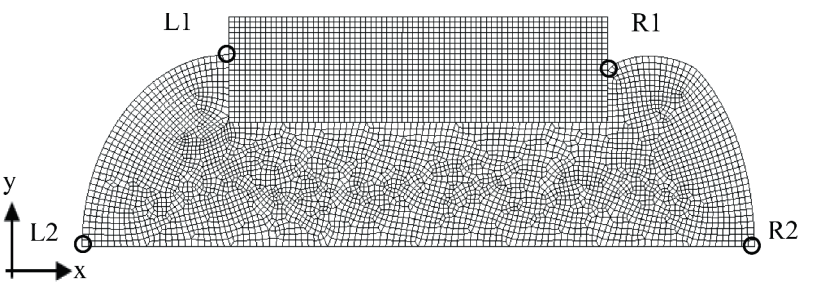


Figure 9. Displacement measurement position.

Next, Figure 10 depicts the relationship between the displacement difference of nodes L2 and R2 and the ratio of the rivet flange area on the driving side to the cross-sectional area of the rivet shaft (termed "shaft cross-sectional area ratio"). On the vertical axis, the difference is shown between the absolute displacement values of L2 and R2. Larger values indicate more displacement towards the rivet contraction direction in node L2 on the supporting side when compared to node R2 on the driving side. The shaft cross-sectional area ratio is used for comparison across rivets with different shaft diameters.

Given that the rivet maintains a higher temperature than the steel plate and the steel plate remain relatively hard until the end of the analysis, the displacement (contraction) in the positive x-axis direction of the rivet flange area, including nodes L1 and R1, is limited, as is the contraction of the rivet head's top. Rivets with smaller flange areas on the driving side exert a weaker force to constrain the contraction of the rivet head's top, leading to greater contraction displacement at the driving side's top when compared to the supporting side.

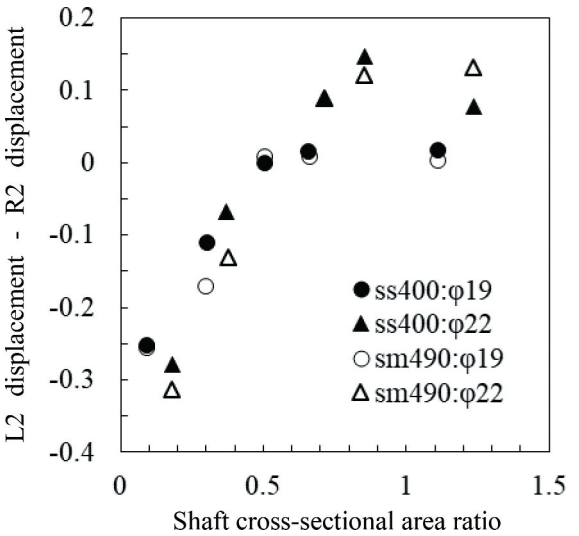


Figure 10. L2 displacement - R2 displacement and shaft cross-sectional area ratio.

Figure 10 indicates that rivets with smaller shaft cross-sectional area ratios, resulting from smaller driving side flange area, exhibit larger contraction displacement at the rivet head's top on the driving side than on the supporting side. Furthermore, as the rivet flange area ratio increases, the displacement difference between the supporting and driving sides tends to reduce. For the φ19 model, when the shaft cross-sectional area ratio exceeds 0.50, the decrease in displacement difference slows down and levels off to approximately 0 mm. When the φ22 model exhibited a shaft cross-sectional area ratio that exceeded 0.86, the decrease in displacement difference became more gradual, and the displacement in the contraction direction of the supporting side with respect to the driving side converged to approximately +0.1 mm.

Differences were observed in the convergence value of the displacement difference between the two sides across models with varying shaft diameters. This variation is attributed to the consistent shape of the rivet head on the supporting side in all models. Specifically, in the φ22 model, which has a larger hole diameter, the rivet flange area on the supporting side is smaller compared to that in the φ19 model. Consequently, the force constraining the displacement in the contraction direction of the rivet is weaker on the supporting side in the φ22 model.

3.2 *Relationship between the shape of the rivet flange part and the axial force in the rivet shaft*

Figure 11 shows the relationship between the ratio of the axial force introduced with respect to the yield axial force ("yield axial force ratio") and the shaft cross-sectional area ratio. The axial force introduced was calculated by multiplying the stress at the end of the analysis with the area affected by this stress. Based on the figure, it is obvious that the yield axial force ratio increases with the shaft cross-sectional area ratio. Additionally, it is observed that the yield axial force ratio converges to approximately 0.9 for the φ19 model and 0.85 for the φ22 model when their respective shaft cross-sectional area ratios exceed 0.66 and 0.71.

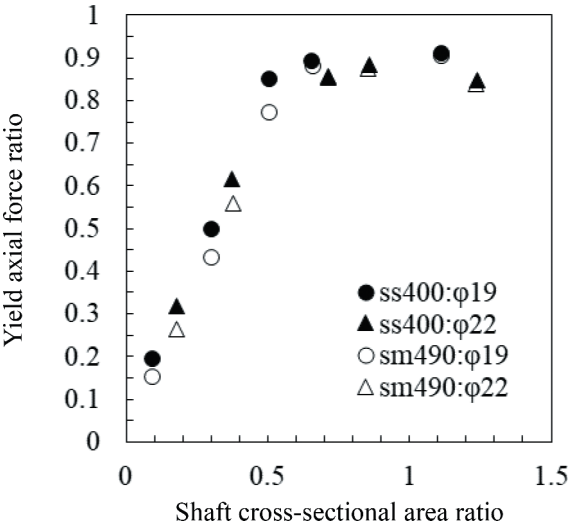


Figure 11. Yield axial force ratio and shaft cross-sectional area ratio.

The outcomes discussed are believed to stem from the fact that the increases in the shaft cross-sectional area ratio, as described in Section 3.1, led to reduced displacement differences between the supporting and driving sides, ultimately resulting in convergence. Moreover, it was verified that an axial force amounting to at least 70% of the yield axial force was introduced when the shaft cross-sectional area ratio exceeded 0.50 in the φ19 model and 0.71 in the φ22 model. It is also notable that when the yield axial force ratio did not reach a convergence value, rivets with the same shape using sm490 material, which has a higher yield axial force, exhibited a lower yield axial force ratio when compared to those using ss400 material. However, in cases where the convergence value of the yield axial force ratio was achieved, the yield axial force ratios for ss400 and sm490 were equivalent.

The results indicate that an increase in both the rivet flange area and the shaft cross-sectional area ratio leads to a stronger force that constrains the contraction of the rivet. This, in turn, decreases the displacement difference in the contraction direction at the top of the rivet head on both sides, thereby enhancing the introduced axial force. In this study, the maximum yield axial force achieved was approximately 0.9 for the φ19 model and 0.85 for the φ22 model.

4 CONCLUSION

In this study, numerical analyses were conducted to understand the effect of the size of the flange area between the rivet head and the base material surface after driving on the introduced axial force and to elucidate the mechanism by which the axial force is introduced during the cooling process of the rivet.

The main results obtained from this study are described below.

1) It was demonstrated that contraction at the rivet flange area is constrained, and that contraction occurs in the rivet head on both the supporting and driving sides, leading to the introduction of the axial force.
2) It was shown that by increasing the rivet flange area to at least 50% for the φ19 rivets and 71% for the φ22 rivets of the shaft cross-sectional area, an axial force amounting to at least 70% of the yield axial force was introduced.
3) It was demonstrated that increasing the rivet flange part constrained the contraction and, in turn, increased the axial force. However, it was also shown that the rate of increase in the introduced axial force relative to the yield axial force became gradual when the rivet flange area reached at least 66% for the φ19 rivets and 71% for the φ22 rivets of the shaft cross-sectional area. This indicates the upper limit to the axial force that can be introduced.

Because only numerical analyses have been conducted in this study, experimental verifications were expected to be conducted in near future.

ACKNOWLEDGEMENT

Authors admiringly acknowledge the support extended by MK ENGINEERING, Inc and KAWADA INDUSTRIES, Inc during the experiments for temperature data collection.

REFERENCES

Architectural Institute of Japan, 2017. *Recommendations for Fire Resistant Design of Steel Structures*.

Hanji, T., Sumi, S., Tateishi, K., Shimizu, M., Nagasaka, Y. & Takebuchi, T. 2021. Mechanical behavior and strength evaluation of combination joints using rivets and high-strength bolts, *Journal of Japan Society of Civil Engineers A1* (*Structural Engineering and Earthquake Engineering*), Vol.77, No.3, pp. 489–508.

Hayase, H., Nakayama, T., Kotera, S., Okamoto, Y. & Matsui, S. 2011. Survey of corrosion status of riveted joints, *Proc. the 66th Annual Meeting of the Japan Society of Civil Engineers*, I–571.

Hirohata, M., Suehiro, D., Okamoto, Y., Nakayama, T. 2021. An investigation on riveting method by high-frequency induction heating, *Steel Construction Engineering*, Vol. 28, No. 112, pp. 75–88.

Hori, T., Yamaguchi, T., Matsumura, M., Hashimoto, K. 2012. Experimental study on fatigue strength of riveted joints with damaged rivet heads, *Proc. the 67th Annual Meeting of the Japan Society of Civil Engineers*, I–276.

Kim, Y.-C., Lee, J.-Y., Inose, K. 2005. The high accurate prediction of welding distortion generated by fillet welding, *Quarterly Journal of the Japan Welding Society*, Vol.23, No.3, pp. 431–435.

MSC 2021, MARC User's Manual.

Suehiro, D., Hirohata, M., Nakayama, T. 2020. Analytical investigation on generation mechanism of residual stress by rivet joining, *Steel Construction Engineering*, Vol. 27, No. 107, pp. 87–95.

Wilson, W.M. & Oliver, W.A. 1930. Tension tests of rivets, *University of Illinois Engineering Experiment Station*, No.210.

Yamamoto, K., Nozaka, K., Nagasaka, Y. & Takebuchi, T. 2022. Study on the effect of rivet and rivet hammer shape on riveting workability, *Proc. Constructional Steel*, Vol. 30, pp. 674–686.

Bridge Maintenance, Safety, Management, Digitalization and Sustainability – Jensen, Frangopol & Schmidt (eds)
© 2024 The Author(s), ISBN 978-1-032-77040-6
Open Access: www.taylorfrancis.com, CC BY-NC-ND 4.0 license

Novel Fe-SMA bonding method for repair of U-rib butt welds in OSDs

Z.L. Lv, X. Jiang & X.H. Qiang
Tongji University, Shanghai, China

H.L. Wu & J.M. Ding
Tongji Architectural Design, Shanghai, China

ABSTRACT: U-rib butt welded connection is one of typical fatigue prone details in orthotropic steel bridge decks (OSDs). The U-rib butt welded connection plays a role in connecting longitudinal beams in the bridge deck system. Once the U-rib butt weld cracks, it will reduce the stiffness of the bridge deck system and threaten the safety of the bridge structures. In this case, the immediate need is to find an effective reinforcement method. This paper proposes a novel Fe-based shape memory alloy (Fe-SMA) bonding reinforcement method for cracked U-rib butt welded connection in OSDs. The innovative Fe-SMA materials can proactively produce prestressing recovery stress by thermal activation and introduce residual compressive stress closed to crack tips, resulting in extending fatigue life of structures. Two full-scale single U-rib specimens were in-itially subjected to fatigue load to generate fatigue cracks. Then the cracked U-rib butt welded connections were strengthened by externally bonded Fe-SMA plates, and fatigue test was conducted to investigate the effectiveness of Fe-SMA bonding method. The experimental results showed that the active reinforcement method can significantly improve the fatigue performance of U-rib butt welds. The Fe-SMA plates can generate 20–59.1 compressive stresses in the U-rib butt weld areas. The average fatigue strength of the reinforced specimen is 130MPa.

1 INTRODUCTION

U-rib butt-welded connections in orthotropic steel bridge decks are subjected to repeated vehicle loads, making them vulnerable to fatigue cracking. The fatigue cracks in the U-rib butt-welded connections were reported worldwide, such as Kinuura Bridge in Japan (Xiao et al., 2006), XiHouMen Bridge in China (Ma et al., 2018), and Fatih Sultan Mehmet Bridge in Turkey (Shakir et al., 2018). As the fatigue cracks significantly affect the structural integrity and durability of the bridge, it is imperative to thoroughly investigate an effective way to address fatigue cracking issues and extend the service life of U-rib butt-welded connections.

Traditional crack repairing methods for metallic structures are drilling holes, welding, and bolting. These techniques show some shortcomings, such as the introduction of high stress concentration and adverse welding residual stress. As an alternative to conventional repair reinforcements, carbon fiber reinforced polymer (CFRP) has been successfully applied to repair damaged steel structures (Tafsirojjaman et al., 2022; Jiang et al., 2023). Compared to non-prestressed CFRP, using prestressed CFRP can achieve better fatigue reinforcement effect (Täljsten et al., 2009). However, prestressing CFRP required hydraulic jacks and complex fixtures, which is sometimes difficult or even impossible due to a lack of space in steel bridge decks.

Fe-based shape memory alloys (Fe-SMA) are advanced materials that can offer an easy-to-implement prestressing procedure, which can be used as a more effective way for the prestressing strengthening of civil structures. Recently, the application of Fe-SMA has been mainly focused on cracked steel plates (Qiang et al., 2023) and steel beams (Wang et al., 2023).

DOI: 10.1201/9781003483755-470

However, limited information is available concerning the butt-welded connections repaired by Fe-SMA plates. In this paper, two cracked U-rib specimens with two butt welds were prepared, and a novel Fe-SMA bonding method was developed for the fatigue repair of the U-rib butt-welded connections.

2 STRENGTHENING TEST

2.1 *Strengthening mechanism*

The deformed Fe-SMA materials can return to their original shape through a heating and cooling process, namely the shape memory effect. A novel Fe-SMA bonding method was proposed, as shown in Figure 1. The prestrained Fe-SMA plates are fully bonded to cracked steel plates, with a middle activation area heated to produce recovery stress, while the other two ends remain unheated and withstand the recovery stress. And the cracked steel plates are subjected to the pre-compressive stresses that act against the tensile stresses. Therefore, the use of Fe-SMA is expected to repair cracked butt-welded joints, thereby extending the remaining service life.

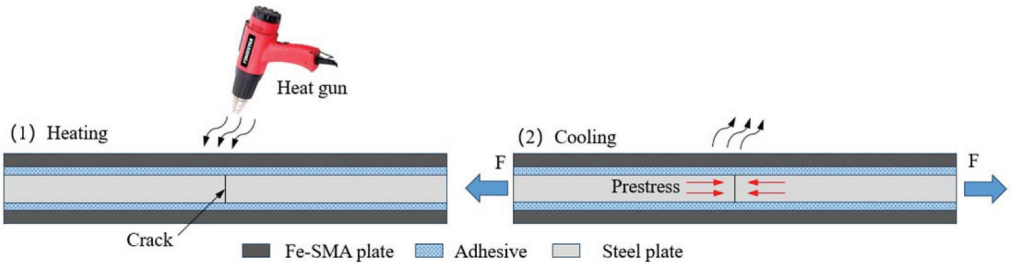


Figure 1. Side view of crack steel plate strengthened with Fe-SMA plates.

2.2 *Specimen design*

Two single U-rib specimens with butt-welded connections were designed according to the reference (Jiang et al., 2023), as shown in Figure 2. The butt-welded connections utilized single-side groove welds, with a backing plate width and thickness of 60 and 4mm, respectively. Weld A and Weld C in Figure 1 refer to the U-rib butt joints, while Weld B corresponds to a butt joint with the top plate. In order to expedite the testing progress, Weld A was intentionally positioned at the mid-span. The steel plates used in the tests were Grade Q345. First of all, the tested specimens were subjected to fatigue loading to produce real fatigue cracks. It was found that crack initiated at the arc transition of U-rib welds with a length of 90 mm and 80 mm, respectively. After fatigue cracking, three prestrained Fe-SMA plates with a dimension of 400 mm×105 mm×3 mm were bonded to the web and bottom plates, as shown in Figure 3. A two-component epoxy resin adhesive was used, and it has a glass transition temperature of 80 °C. The reinforcement procedures mainly included base surface treatment, adhesive application, and one-week maintenance.

2.3 *Activation test*

The heated activation was performed on the specimens using a heat gun after maintenance, with an activation temperature of 200 °C. The heating area was the middle 50 mm region, and the ice bags were set at the anchorage areas to prevent heat transfer, as shown in Figure 4. Taking the SU1 specimen as an example, activation test results were shown in Figure 5. It can be observed that the temperature at the measurement points in the middle of the three Fe-SMA plates reached 200 °C within 2 minutes of activation. Meanwhile, the highest

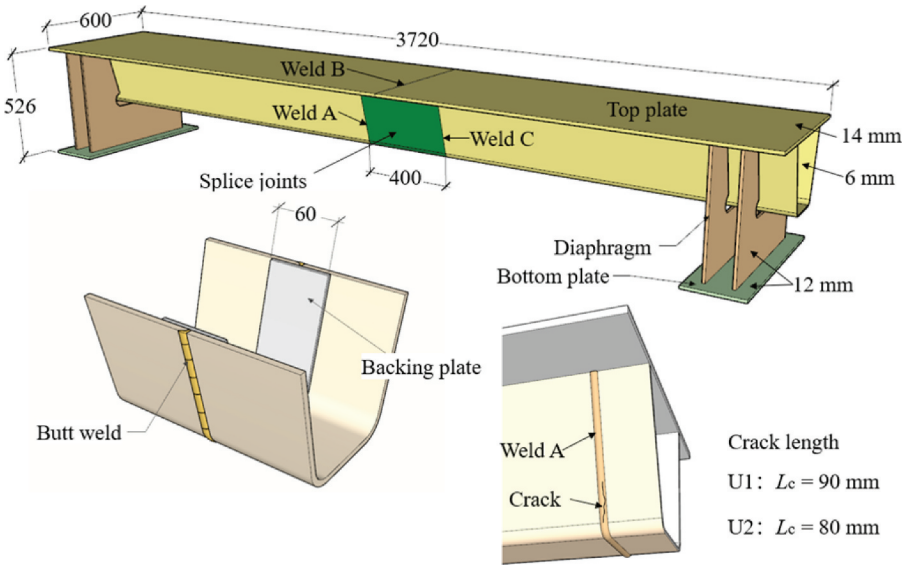


Figure 2. Tested specimen (Unit: mm).

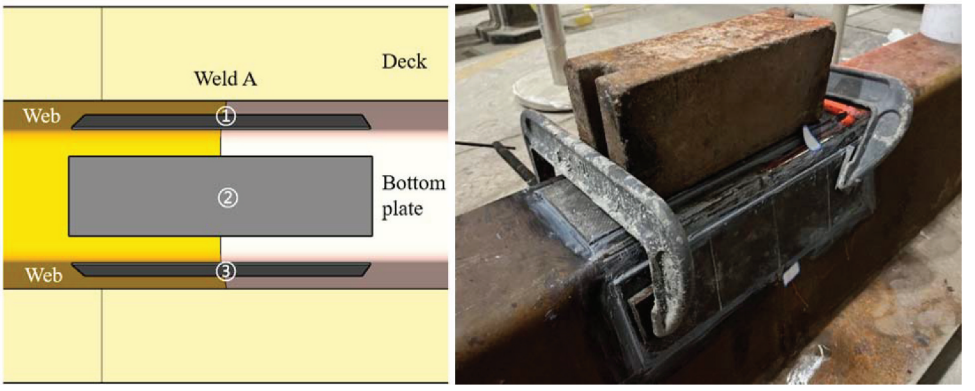


Figure 3. Specimens strengthened by Fe-SMA plates.

temperature in the adhesive anchorage area was 60 °C, which is lower than the glass transition temperature of 80 °C. After cooling to room temperature, the distribution of pre-stress in the reinforced area was measured, as shown in Figure 5(b). The reinforced area achieved a prestress range of -20–59.1 MPa. The arc transition zone obtained a larger pre-stress due to the superposition of adjacent Fe-SMAs, making it more beneficial for fatigue loading. Another specimen SU2 achieved compressive prestresses ranging from -26.6 to -53.2 MPa.

3 FATIGUE TEST

3.1 *Test set-up and fatigue loading*

A fatigue test was conducted after the activation test, as illustrated in Figure 6. All specimens were subjected to single-point fatigue loading at the mid-span, with a fatigue loading frequency of 100 Hz. The load range was determined based on the stress ranges of the actual

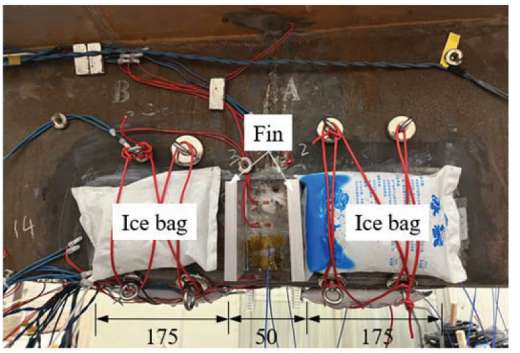
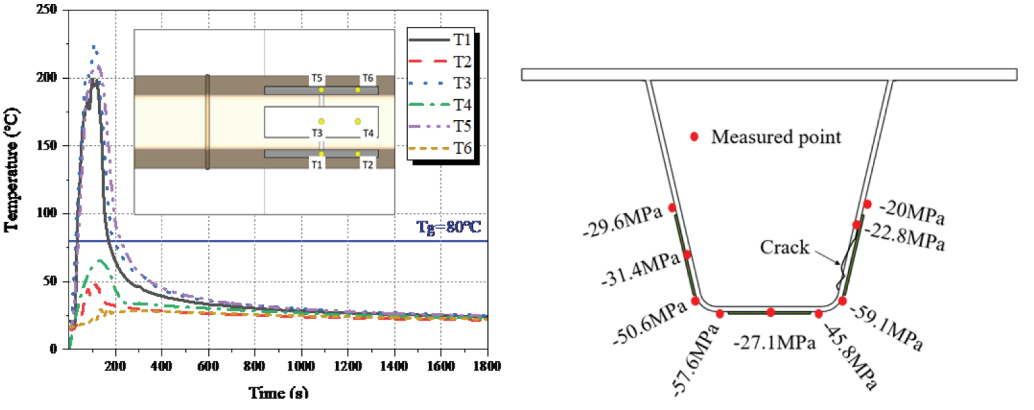


Figure 4. Schematic view of Fe-SMA activation (units: mm).



(a) Temperature distribution (b) Prestress distribution

Figure 5. Activation test results of SU1.

bridge and was appropriately increased according to the loading conditions. The specific loading history is presented in Table 1. During the loading process, the data and failure modes of the specimens were recorded until the reinforcement system completely failed.



Figure 6. Loading set-up.

Table 1. Fatigue loading.

No.	α (%)	Load range (kN)	Loading cycles (10^4 times)	Equivalent stress range (MPa)
SU1	12.2	15−35	0−200	101.3
		20−50	200−250	
		25−75	250−300	
		35−105	300−325	
SU2	10.9	15−35	0−200	106.1
		20−50	200−300	
		25−75	300−450	
		35−105	450−467.8	

Note: the initial damage degree α is defined as the ratio of initial crack length (L_c) and the full length (L_t) of the U-rib section.

3.2 *Fatigue failure modes*

During the fatigue reinforcement test, it was found that all reinforced specimens failed due to partial debonding of the Fe-SMA plate and crack propagation in the welded joint. Figure 7 records the variation of stress ranges monitored by strain gauges with the number of cycles. During the first 2.5 million fatigue cycles, the stress ranges at all measurement points remained stable, indicating that no fatigue failure was found in the reinforcement system. When the loading cycles were at

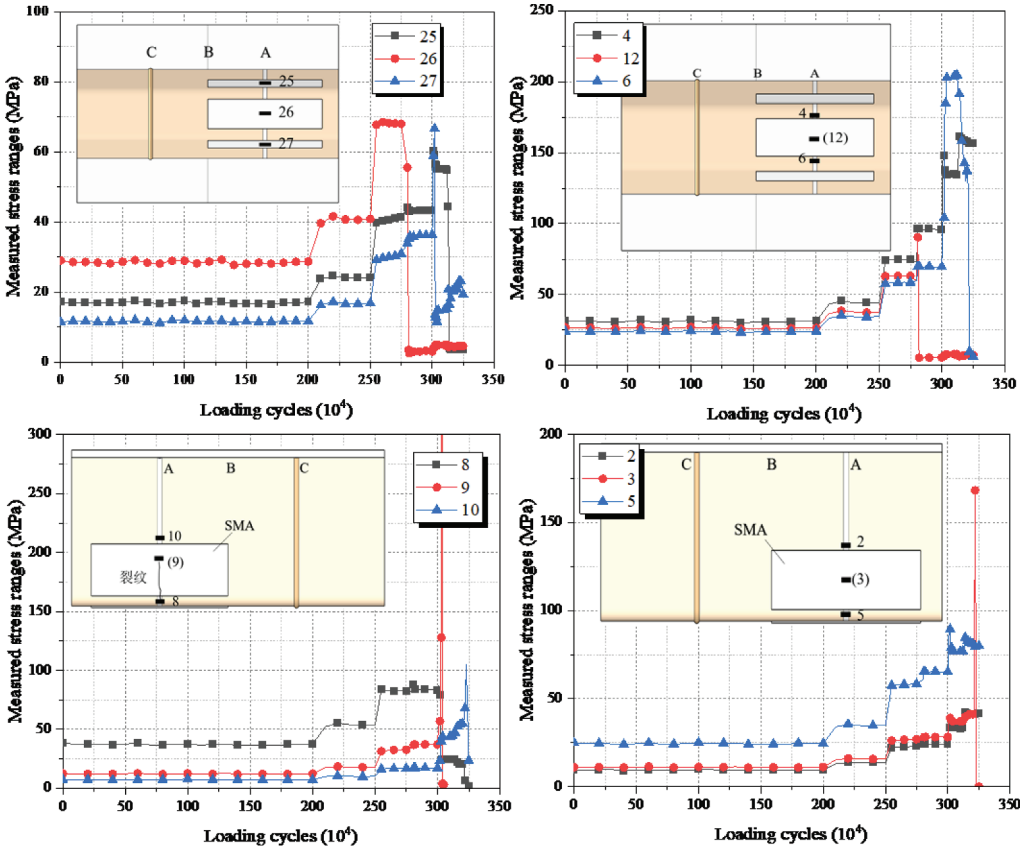
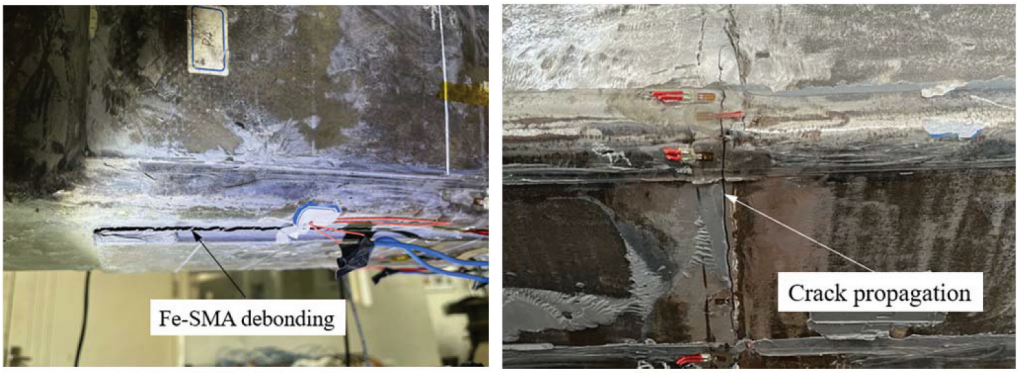


Figure 7. Measured stress ranges versus loading cycles of specimen SU1.

2.82 million cycles, as shown in Figure 8(a), debonding occurred at the end of the bottom Fe-SMA, resulting in a rapid decrease in stress ranges at measuring point 26 and buried measuring point 12. At the same time, the stress ranges at the measuring points 4 and 6 significantly increased due to the loss of prestress, while the stress ranges at the measuring points on both sides of the web plate slightly increased. However, the initial crack did not propagate further because the Fe-SMA on both sides of the web plate still worked synergistically. Subsequently, the load range was further increased, leading to the debonding failure of the Fe-SMA plates on the crack side. Then the strain gauges (measuring points 8 and 9) at the crack tip failed, indicating the crack began to extend. When the reinforcement system completely failed (i.e., all three Fe-SMA 8strips experienced end debonding), the fatigue crack quickly experienced unstable propagation. At the same time, a significant increase in deformation at the mid-span of the specimen was observed, leading to the cessation of loading. The final failure modes of the specimen are shown in Figure 8(b). It can be seen that the newly developed cracks continued to propagate along both ends of the initial crack until they reached the middle of the bottom plate, indicating that the specimen had lost its load-bearing capacity.



(a) Fe-SMA debonding (b) Crack propagation

Figure 8. Fatigue failure modes.

3.3 *Fatigue evaluation*

According to Miner's cumulative damage principle, the fatigue strength of the welded joints after reinforcement is assessed. Table 2 records the results of the fatigue improvement of the specimens after repair. The fatigue strength of each welded joint before repair met the requirements of Grade 71 specified in the China steel bridge specifications. However, even after sufficient fatigue loading cycles, fatigue cracks can still appear in this detail. Therefore, after repair with Fe-SMA plates, the cracked specimens regain an average fatigue strength of 130 MPa. In addition, in order to facilitate a unified comparison of fatigue life, the equivalent fatigue life of each specimen is calculated using equation (1). The calculated results indicated that the bonded Fe-SMA plates could substantially extend the fatigue life, with an extension ration of 1.03 to 4.09.

$$N_e = N_R \times \left(\frac{\Delta\sigma_R}{\Delta\sigma_c}\right)^m \tag{1}$$

Table 2. Fatigue evaluation of SMA-strengthened specimens.

		Fatigue strength (MPa)		Equivalent fatigue life (10^4 times)	
No.	α (%)	Before repairing	After repairing	Before repairing	After repairing
SU1	12.2	117.8	119.1	914.3	943.1
SU2	10.9	88.0	140.8	381.1	1558.9

where NR = actual loading cycles; $\Delta\sigma_R$ = equivalent stress range; $\Delta\sigma_c$ = fatigue strength at two million cycles; and m = 3.

4 CONCLUSIONS

(1) Activation tests show that thermally activated Fe-SMA plates can introduce pre-stresses ranging from -20 to -59.1 MPa near the welds of U-ribs, thereby actively strengthening the structure. After reinforcement with Fe-SMA bonding, the fatigue performance of the cracked specimens significantly improved, with the average fatigue strength of the reinforced specimens reaching 130 MPa. The equivalent fatigue life of the specimens at different damage levels increased by 1.03 and 4.09 times, respectively.
(2) The Fe-SMA with localized debonding cannot continue to bear the load and resulted in a loss of applied prestress. However, the remaining Fe-SMA strips continue to work in coordination with the original structure. Therefore, Fe-SMA bonding reinforcement can provide a warning effect before structural failure, thereby avoiding sudden structural rupture.
(3) The proposed self-prestressing technology based on Fe-SMA does not require complex anchoring devices or tensioning equipment and can quickly achieve prestressed reinforcement using the shape memory effect. Bonding Fe-SMA adhesively barely impairs the parent structures and can meet the requirements for non-destructive repair of real bridges.

REFERENCES

Täljsten, B., Hansen, C. S., Schmidt, J.W. 2009. Strengthening of old metallic structures in fatigue with prestressed and non-prestressed CFRP laminates. *Construction and Building Materials* 23: 1665–1677.

Ma, R., Xu, S., Wang, D., Chen, A., 2018. Vehicle models for fatigue loading on steel box-girder bridges based on weigh-in-motion data. *Structure and infrastructure engineering* 14: 701–713.

Qiang, X., Wu, Y., Wang, Y., Jiang, X., 2023. Novel crack repair method of steel bridge dia-phragm employing Fe-SMA. *Engineering Structures* 292: 116548.

Shakir, S., Alemdar, F. 2018. Experimental Study of Fatigue Crack Behavior of Rib-To-Rib Butt Welded Connections in Orthotropic Steel Decks. *Latin American Journal of Solids and Structures* 15 (10): 1–19.

Tafsirojjaman, T., Dogar, A.U.R., Liu, Y., Manalo, A., Thambiratnam, D.P. 2022. Performance and design of steel structures reinforced with FRP composites: A state-of-the-art review. *Engineering Failure Analysis* 138: 106371.

Wang, S., Li, L., Su, Q., Jiang, X., Ghafoori, E., 2023. Strengthening of steel beams with ad-hesively bonded memory-steel strips. *Thin-Walled Structures* 189: 110901.

Jiang, X., Lv, Z., Qiang, X., Song, S. 2023. Fatigue performance improvement of U-rib butt-welded connections of steel bridge decks using externally bonded CFRP strips. *Thin-Walled Structures*. 191: 111017.

Xiao, Z., Yamada, K., Inoue, J., Yamaguchi, K. 2006. Fatigue cracks in longitudinal ribs of steel orthotropic deck. *International Journal of Fatigue* 28: 409–416.

Bridge Maintenance, Safety, Management, Digitalization and Sustainability – Jensen, Frangopol & Schmidt (eds)
© 2024 The Author(s), ISBN 978-1-032-77040-6
Open Access: www.taylorfrancis.com, CC BY-NC-ND 4.0 license

Experiment research on fatigue cracks at diaphragm cutouts reinforced employing Fe-SMA in steel bridge

Y.P. Wu, X.H. Qiang & X. Jiang*
College of Civil Engineering, Tongji University, Shanghai, China

Z.Y. Yang
Organization Department of Pinghu Municipal Committee, Pinghu, China

ABSTRACT: Based on the crack-stop holes, the Fe-based shape memory alloys (Fe-SMA) plates were used to repair fatigue cracks at the diaphragm cutouts of orthotropic steel deck (OSD) bridges, using its inherent stiffness and shape memory effect. In the experimental research, a total of 6 specimens were designed for fatigue test, including 2 specimens repaired solely by crack-stop holes and 4 specimens repaired by Fe-SMA plates. After completing the reinforcement, significant local stiffness and compressive stresses can be introduced at the edge of crack-stop holes, which can effectively reduce the stress concentration at the cracked region, postpone the initiation of fatigue cracks, and inhibit crack propagation after secondary-cracking. The fatigue life of specimens repaired by Fe-SMA plates is 3.73~12.68 times that of specimens repaired solely by crack-stop holes, indicating that bonding Fe-SMA plates based on crack-stop holes is an effective method for repairing cracked diaphragm cutouts in steel bridges.

1 GENERAL INSTRUCTIONS

The orthotropic steel decks (OSDs), with their advantages of light self-weight, high load-carrying capacity, substantial torsional stiffness, and convenient construction, have been widely used in large-span bridges (Pfeil & Battista 2005, Freitas et al. 2013). However, the fatigue cracking of the OSD bridges is particularly prominent under the influence of welding defects, residual stress, stress concentration, and increasing traffic volume (Maljaars 2012, Li et al. 2019). Since the occurrence of fatigue cracks in the OSDs of Severn Bridge in the United Kingdom in 1971, numerous fatigue cracks have been reported in the OSD bridges in various countries (Wolchuk 1990, Tsakopoulos & Fisher 2003, Miki 2006). Engineering research experience indicates that the majority of OSDs, subjected to heavy traffic loads, develop fatigue issues after several years or decades of service (Fisher & Roy 2011, Editorial Department of China Journal of Highway and Transport 2021).

Within the OSD bridges, the longitudinal U-ribs are continuously connected through the transverse diaphragms. To release rotational constraints on the U-ribs at the diaphragms, arc-shaped cutouts of the diaphragms are incorporated below the U-ribs. However, these diaphragm cutouts in the OSD bridges will experience significant stress concentration under vehicle-induced vibrations and cyclical wheel loads. Furthermore, in earlier constructions of OSD bridges, the arc-shaped cutouts were mainly made via flame-cutting technology. Extensive data indicates that this method could induce residual tensile stresses of over 200 MPa at the flame-cut region, and the stress response under the combined action will result in severe fatigue cracking (Zhang et al. 2015, Yokozeki & Miki 2016).

For fatigue cracks in steel structures, various external reinforcement can be carried out using steel plates, carbon fiber-reinforced polymer (CFRP), and Fe-SMA through connections such as bolts or bonding (Izadi et al. 2018a, Lepretre et al. 2018, Jiang et al. 2024). As an alloy, Fe-SMA

*Corresponding author: jiangxu@tongji.edu.cn

DOI: 10.1201/9781003483755-471

possesses excellent properties in strength, plasticity, and production processing, making it highly advantageous for structural reinforcement (Cladera et al. 2014). By utilizing the shape memory effect of Fe-SMA, prestressed reinforcement can be achieved through heating activation, eliminating the need for complex mechanical equipment such as jacks and anchors (Izadi et al. 2018b, Wang et al. 2021). In addition, the crack-stop hole is convenient in operation and fast in construction, which can effectively reduce the stress concentration in the local cracked region and noticeably improve the fatigue performance of structures, making it particularly suitable for repairing the fatigue cracks in OSD bridges (Makabe et al. 2014, Fu et al. 2017).

The authors proposed a novel repair method of Fe-SMA plates covering crack-stop holes for the cracked diaphragm cutouts, introduced the repair scheme and operational process, and successfully applied it to the reinforcement of Sutong Bridge and Hangzhou Bay Bridge in China (Qiang et al. 2023a, b, c). This paper conducted fatigue tests on the diaphragms repaired by crack-stop holes and Fe-SMA plates, aiming to verify the feasibility and practicality of the proposed method. The fatigue life improvement, failure modes, and stress responses at the hole edge were analyzed through data monitoring and on-site observations.

2 FATIGUE LOADING TEST

2.1 *Diaphragm repair scheme*

Based on the actual dimensions of steel bridges in engineering, the authors studied the stress state at the arc-shaped cutouts of the diaphragm using multi-scale numerical simulations (Lv et al. 2021, Qiang et al. 2023d). To ensure that the specimen size is suitable for the testing

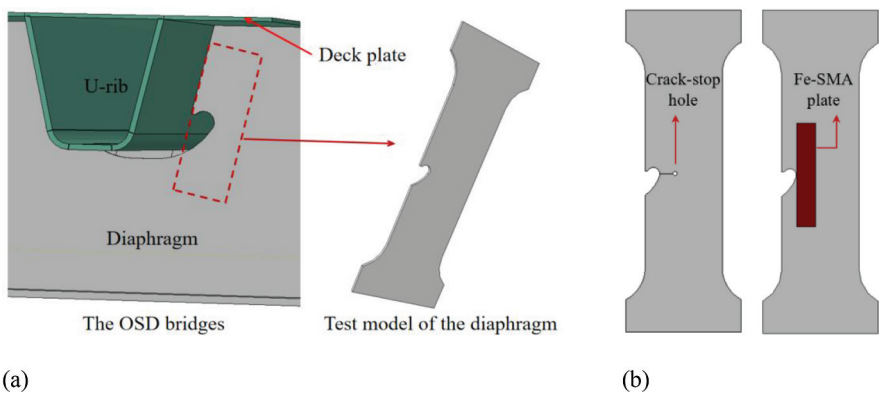


Figure 1. Selection of diaphragm model: (a) intercept position, (b) reinforcement.

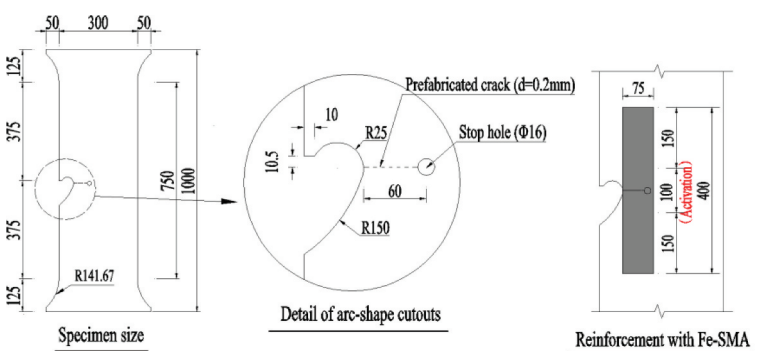


Figure 2. Geometry of diaphragm specimens (unit: mm).

equipment, the diaphragm test model is selected as depicted in Figure 1, and the geometric dimensions are presented in Figure 2. For the diaphragm specimens, the thickness is 12 mm, the minimum effective width is 175.3 mm, and the prefabricated crack with a length of 60 mm is located at the minimum cross-section.

Six cracked diaphragm specimens were designed, two of which were repaired using crack-stop holes (S-H Group), while the other four were repaired by the Fe-SMA plates covering crack-stop holes (S-FH Group). The arc-shaped cutouts were made via flame cutting and polished to simulate practical engineering conditions. The cracks and crack-stop holes were prefabricated by wire cutting. The Fe-SMA plates were selected with different thicknesses and activation temperatures. The key parameters of the reinforcement scheme are listed in Table 1.

Table 1. Specimens design and reinforcement parameters.

Repair method	Name	Stop hole size	Activation temperature	Thickness of Fe-SMA plate
Crack-stop holes	S-H-1	Φ16 mm	None	None
	S-H-2	Φ16 mm	None	None
Fe-SMA plates covering crack-stop holes	S-FH-1	Φ16 mm	200°C	1.75 mm
	S-FH-2	Φ16 mm	200°C	2 mm
	S-FH-3	Φ16 mm	150°C	2 mm
	S-FH-4	Φ16 mm	None	1.75 mm

2.2 *Specimen loading system*

The MTS 311.31S electro-hydraulic servo testing machine, depicted in Figure 3, was utilized for fatigue loading, with a clamping area of 130×130 mm at the upper and lower ends. During the loading process, the HBM 1615B acquisition system was used to monitor real-time data such as load, displacement, and strain. In the S-H group, 5 strain gauges were arranged on the diaphragm surface at distances of 2 mm, 15 mm, 30 mm, 60 mm, and 90 mm from the hole edge. In the S-FH group, 7 strain gauges were arranged on the diaphragm, positioned at distances of 2 mm,



Figure 3. Fatigue loading device.

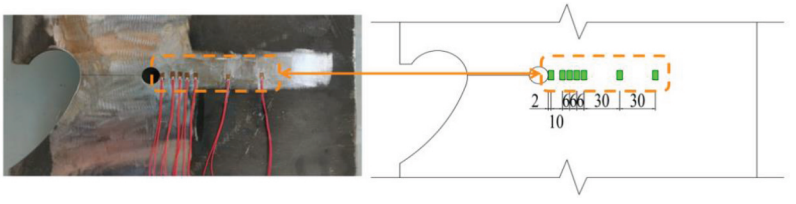


Figure 4. Strain measuring points.

12 mm, 16 mm, 18 mm, 24 mm, 30 mm, 60 mm, and 90 mm from the hole edge. The strain gauges were symmetrically arranged on both sides of the diaphragm, as shown in Figure 4.

The fatigue loading was performed using a tension–tension sine-wave load with a frequency of 10 Hz. Based on the stress response obtained from numerical simulations at the diaphragm cutouts (Lv et al. 2021, Qiang et al. 2023d), the nominal stress amplitude of diaphragm specimens was selected within the range of 45~55 MPa while appropriately expanding the load level to save the cost of fatigue test. Additionally, the stress ratio was chosen as 0.1. The specific load values are summarized in Table 2.

Table 2. Design value of fatigue load.

Name	Stress amplitude (MPa)	Stress ratio	Peak load (kN)	Valley load (kN)	Load amplitude (kN)
S-H-1	45	0.1	105.2	10.5	94.7
S-H-2	55	0.1	128.6	12.9	115.7
S-FH-1	55	0.1	128.6	12.9	115.7
S-FH-2	55	0.1	128.6	12.9	115.7
S-FH-3	55	0.1	128.6	12.9	115.7
S-FH-4	55	0.1	128.6	12.9	115.7

3 ANALYSIS OF TEST RESULTS

3.1 *Comparison on fatigue life*

The fatigue life, failure life, and crack propagation life of each specimen are summarized in Table 3. During the fatigue loading process, fatigue cracks were observed in the specimens when their length reached about 2 mm. Detecting fatigue cracks at shorter lengths proved challenging due to their limited visibility. Therefore, in this study, the fatigue life is defined as the number of load cycles corresponding to a crack length of 2 mm, the failure life is defined as the number of load cycles corresponding to a crack length of 70 mm, and the crack propagation life refers to the number of load cycles from the occurrence of secondary fatigue cracks to the crack propagation to 70mm.

Since all specimens were repaired by crack-stop holes to eliminate the original crack tip, the process from the beginning of loading to the initiation of cracking took a relatively long time. The nominal stress amplitude of specimens S-H-2 and the specimens in S-FH group was 55 MPa. Therefore, the enhancement effect of fatigue life is conducted using the loading results of the aforementioned diaphragm specimens.

Table 3. Cracking life of specimens.

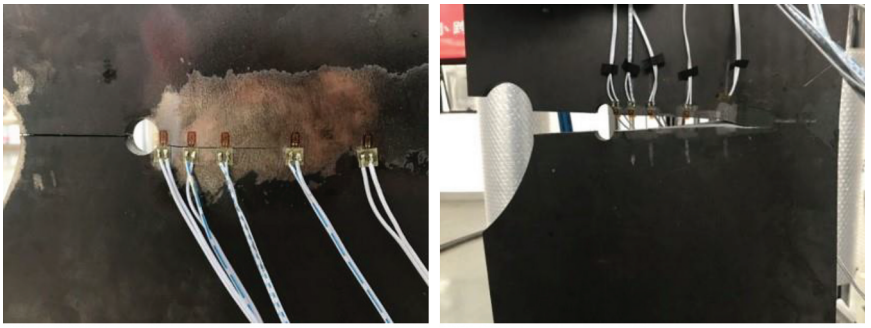
Name	Fatigue life ($\times 10^4$)	Failure life ($\times 10^4$)	Crack propagation life ($\times 10^4$)	Improvement of Fatigue life	Propagation life
S-H-1	82.74	107.28	24.54	—	—
S-H-2	38.41	49.47	11.06	1	1
S-FH-1	282.50	317.01	34.51	7.35	3.12
S-FH-2	486.90	511.47	24.57	12.68	2.22
S-FH-3	406.30	457.73	51.43	10.58	4.65
S-FH-4	143.40	169.72	26.32	3.73	2.38

Comparing specimens S-H-2 and S-FH-4, after bonding the Fe-SMA plates based on the crack-stop hole, the increased local stiffness can effectively reduce the stress amplitude at the hole edge, and the fatigue life of S-FH-4 is 3.73 times that of S-H-2. Similarly, when comparing specimens S-H-2 and S-FH-1, the additional precompression is introduced while increasing the local stiffness of the cracked region by bonding and activating the Fe-SMA plates, significantly improving the fatigue performance of the diaphragm. The fatigue life of S-FH-1 is 7.35 times that of S-H-2.

Under the same activation temperature of Fe-SMA, the fatigue life of the diaphragm repaired by bonding 2.00 mm Fe-SMA plates (S-FH-2) is 12.68 times that of the diaphragm repaired solely by crack-stop hole (S-H-2). When considering the same thickness of 2.00 mm for Fe-SMA plates, the fatigue life of S-FH-3, with Fe-SMA activated at 150□, is 10.58 times that of S-H-2. These findings indicate that bonding 2.00 mm Fe-SMA plates can more effectively increase the local stiffness of the cracked region and introduce precompression, thereby achieving a better repair effect.

3.2 *Failure mode analysis*

The inclusion of a crack-stop hole eliminates the existing crack tip, as the source of fatigue propagation. However, stress concentration occurs at the hole edge. After a prolonged period of loading, fatigue cracks initiated at the hole edge and continued to propagate during subsequent loading cycles, as depicted in Figure 5. Notably, factors such as uneven internal defects and eccentric loading on the diaphragm may result in deviations between the crack initiation points and the hole edge center.



(a) (b)

Figure 5. Fatigue failure of specimens S-H group: (a) cracking deviation from the hole center, (b) cracking along the hole center.

For the S-FH group, the diaphragm specimens basically underwent three main stages during the loading process: crack initiation, stable crack propagation, and accelerating crack propagation caused by continuous damage accumulation. Ultimately, failure occurred due to the continuous increase in crack length, resulting in insufficient residual bearing capacity of the cracked section, as illustrated in Figure 6. The Fe-SMA plates can effectively enhance the local stiffness of the cracked region, and the activated Fe-SMA can additionally introduce precompression of 40~60 MPa (Qiang et al. 2023a, Qiang et al. 2023c). As a result, the fatigue life and failure life of the specimens in S-FH group are significantly higher than those of the specimens in S-H group. Notably, due to the longer fatigue life of S-FH-2, the bonded interface accumulated damage continuously with fatigue loading, resulting in debonding failure between the Fe-SMA plate and diaphragm, significantly shortening the stage of stable crack propagation.

4 STRESS RESPONSE AT HOLE EDGE

4.1 *S-H group*

The strain monitoring results at a distance of 2 mm from the hole edge provide insights into the cracking condition of diaphragms. Therefore, the stress calculation results at the distance of 2 mm from the hole edge (referred to as stress a-1 and b-1 on both sides of the diaphragm) have been selected for analysis.

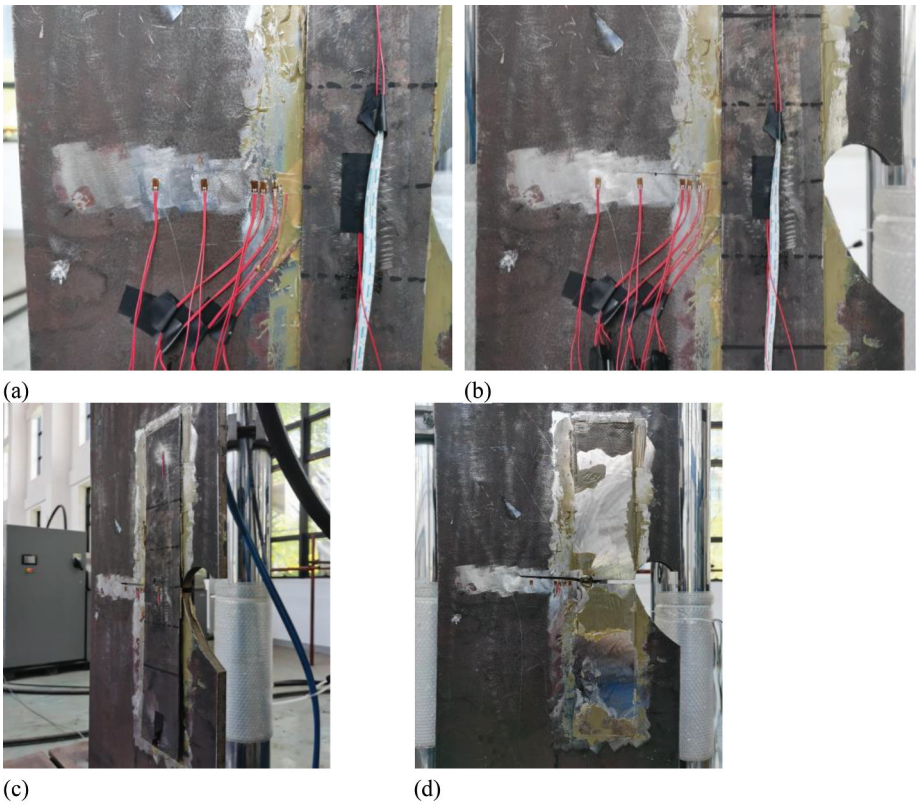


Figure 6. Fatigue failure of specimens in S-FH group: (a) stable crack propagation, (b) accelerating crack propagation, (c) debonding of the Fe-SMA plate, (d) final destructive form.

The data for the specimens in S-H group remained relatively stable throughout the loading process, and the stress results calculated at positions a-1 and b-1 were also close, as depicted in Figure 7. The average stress amplitudes at the hole edges of specimens S-H-1 and S-H-2 are measured as 302.06 MPa and 367.02 MPa, respectively.

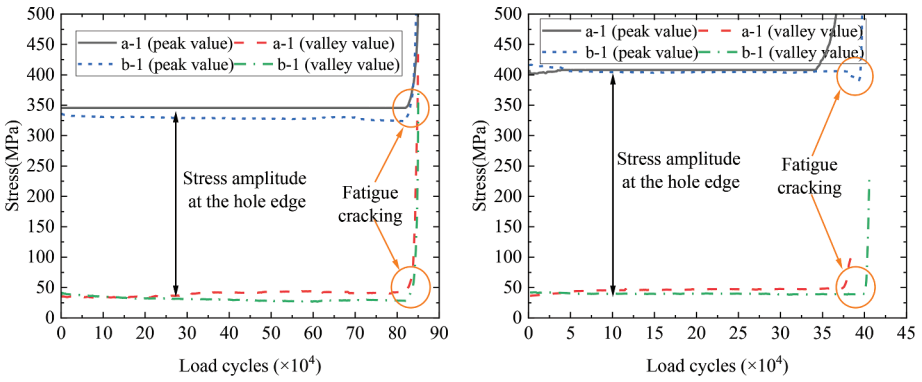


Figure 7. Stress response at hole edges of S-H group: (a) S-H-1, (b) S-H-2.

4.2 *S-FH group*

For the specimens in S-FH group, the stress amplitude at the hole edge increased significantly during the early stages of fatigue loading due to the creep of Fe-SMA, resulting in a loss of reinforcement effect, as shown in Figure 8.

After entering the stress stabilization stage, the strain monitoring data remained relatively stable. The average stress amplitudes at the hole edges of specimens S-FH-1, S-FH-2, S-FH-3, and S-FH-4 are 215.93 MPa, 191.92 MPa, 202.13 MPa, and 256.16 MPa, respectively.

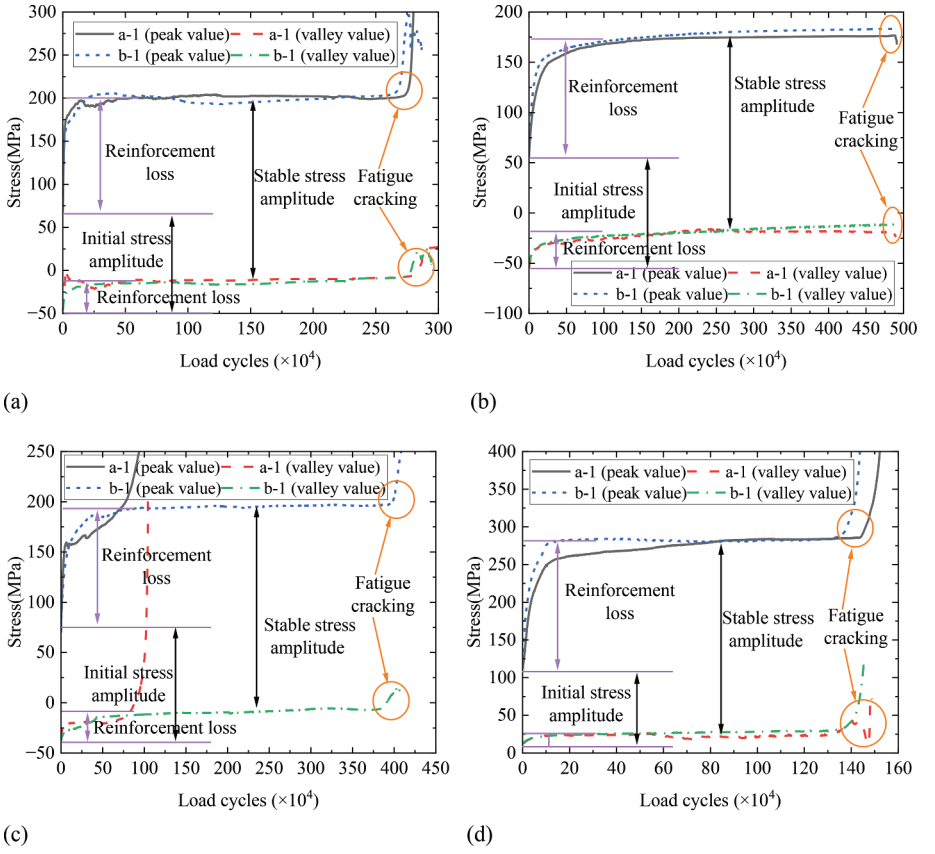


Figure 8. Stress response at hole edges of S-FH group: (a) S-FH-1, (b) S-FH-2, (c) S-FH-3, (d) S-FH-4.

5 CONCLUSIONS

Based on the proposed repair method of Fe-SMA plates covering crack-stop holes, this paper conducted the fatigue test on the repaired diaphragms and obtained their fatigue life, failure modes, and stress responses at hole edges. The main conclusions are as follows:

(1) The crack-stop hole eliminates the crack tip, which is the prominent factor in fatigue propagation. However, the hole edge becomes a new location for stress concentration and potential initiation of fatigue cracks. For the diaphragm reinforced by Fe-SMA, the Fe-SMA plates do not experience debonding before the diaphragm failure when its fatigue life is short. However, for longer fatigue lives, the Fe-SMA plates may experience debonding before the diaphragm failure due to significant cumulative damage at the bonded interface.

(2) Bonding Fe-SMA plates can significantly increase the stiffness of the cracking region and effectively reduce the stress amplitude. Based on this, activating Fe-SMA can further introduce precompression, reducing the average stress of the cracking region. The fatigue life of the diaphragm repaired by activated Fe-SMA plates with a thickness of 2 mm is 12.68 times that of the diaphragm repaired solely by the crack-stop hole.
(3) In the initial loading stage, Fe-SMA experiences creep under fatigue load, leading to a gradual increase in the stress amplitude at the edge of crack-stop holes. The repair system of Fe-SMA plates covering crack-stop holes exhibits a loss of reinforcement effect, with the reinforcement loss stage accounting for approximately 1/6 of the entire loading process. Once the creep of Fe-SMA is essentially completed, the specimens enter the stable bearing stage.

REFERENCES

Cladera, A., Weber, B., Leinenbach, C., Czaderski, C., Shahverdi, M. & Motavalli, M. 2014. Iron-based shape memory alloys for civil engineering structures: An overview. Construction & Building Materials 63: 281–293.

Editorial Department of China Journal of Highway and Transport. 2021. Review on China's Bridge Engineering Research: 2021. China Journal of Highway and Transport 34(02): 1–97. (in Chinese)

Fisher, J.W. & Roy, S. 2011. Fatigue of steel bridge infrastucture. Structure and Infrastructure Engineering 7(8): 457–475.

Freitas, S.T.D, Kolstein, H. & Bijlaard, F. 2013. Fatigue behavior of bonded and sandwich systems for strengthening orthotropic bridge decks. Composite Structures 97: 117–128.

Fu, Z.Q., Ji, B.H., Xie, S.H. & Liu, T.J. 2017. Crack stop holes in steel bridge decks: Drilling method and effects. Journal of Central South University, 24 (10):2372–2381.

Jiang, X., Lv, Z.L., Qiang, X.H. & Xu, Z.M. 2024. Fatigue performance of root-to-throat cracks repaired by bonding steel: experimental and numerical investigations. Journal of Constructional Steel Research 212: 108296.

Izadi, M. R., Ghafoori, E., Motavalli, M. & Maalek, S. 2018a. Iron-based shape memory alloy for the fatigue strengthening of cracked steel plates: Effects of re-activations and loading frequencies. Engineering Structures 176: 953–967.

Izadi, M.R., Ghafoori, E., Shahverdi, M., Motavalli, M. & Maalek, S. 2018b. Development of an iron-based shape memory alloy (Fe-SMA) strengthening system for steel plates. Engineering Structures 174: 433–446.

Lepretre, E., Chataigner, S., Dieng, L. & Gaillet, L. 2018. Fatigue strengthening of cracked steel plates with CFRP laminates in the case of old steel material. Construction and Building Materials 174: 421–432.

Li, J., Zhang, Q.H., Bao, Y., Zhu, J.Z., Chen, L. & Bu, Y.Z. 2019. An equivalent structural stress-based fatigue evaluation framework for rib-to-deck welded joints in orthotropic steel deck. Engineering Structures 196: 109304.

Lv, Z.L., Jiang, X., Qiang, X.H., & Wang, X.J. 2021. Fatigue test research on local models of orthotropic steel deck diaphragms. Structural Engineer 37 (06):163–171. (in Chinese)

Makabe, C., Kaito, N. & Ferdous, M.S. 2014. Method of arresting crack growth for application at a narrow working space. Mechanical Engineering Journal 1(6): 1–12.

Maljaars, J., Dooren, F.V., & Kolstein, H. 2012. Fatigue assessment for deck plates in orthotropic bridge decks. Steel Construction 5(2): 93–100.

Miki, C. 2006. Fatigue damage of orthotropic steel bridge decks and retrofit works. Steel Structures (6): 255–267.

Pfeil, M.S. & Battista, R.C., Mergulhão, A.J.R. 2005. Stress concentration in steel bridge orthotropic decks. Journal of Constructional Steel Research 61(8): 1172–1184.

Qiang, X.H., Wang, Y.H., Wu, Y.P., Jiang, X. & Dong, H. 2023a. Experimental and numerical study on cracked steel bridge diaphragm reinforced with bonding Fe-SMA plate. Thin-Walled Structures 191: 111075.

Qiang, X.H., Wu, Y.P., Wang, Y.H. & Jiang, X. 2023b. Research progress and applications of Fe-Mn-Si-based shape memory alloys on reinforcing steel and concrete bridges. Applied Sciences 13(6): 3404.

Qiang, X.H., Wu, Y.P., Wang, Y.H. & Jiang, X. 2023c. Novel crack repair method of steel bridge diaphragm employing Fe-SMA. Engineering Structures 292: 116548.
Qiang, X.H., Wu, Y.P., Jiang, X. & Xu, G.W. 2023d. Fatigue performance of cracked diaphragm cutouts in steel bridge reinforced employing CFRP/SMA. Journal of Constructional Steel Research 211: 108136.
Tsakopoulos, P.A. & Fisher, J.W. 2003. Full-scale fatigue tests of steel orthotropic decks for the Williamsburg Bridge. Journal of Bridge Engineering 8(5): 323–333.
Wang, W.D., Li, L.Z., Hosseini, A. & Ghafoori, E. 2021. Novel fatigue strengthening solution for metallic structures using adhesively bonded Fe-SMA strips: a proof of concept study. International Journal of Fatigue 148: 106237.
Wolchuk, R. 1990. Lessons from weld cracks in orthotropic decks on three European bridges. Journal of Structural Engineering 116(1): 75–84.
Yokozeki, K. & Miki, C. 2016. Fatigue evaluation for longitudinal-to-transverse rib connection of orthotropic steel deck by using structural hot spot stress. Welding in the World 60(1):83–92.
Zhang, Q.H., Cui, C., Bu, Y.Z., Liu, Y.M. & Ye, H.W. 2015. Fatigue tests and fatigue assessment approaches for rib-to-diaphragm in steel orthotropic deck. Journal of Constructional Steel Research 114: 110–118.

Bridge Maintenance, Safety, Management, Digitalization and Sustainability – Jensen, Frangopol & Schmidt (eds)
© 2024 The Author(s), ISBN 978-1-032-77040-6
Open Access: www.taylorfrancis.com, CC BY-NC-ND 4.0 license

Experimental study on seismic performance of different failure modes of RC shear keys

H. Mei & A.X. Guo
Key Lab of Smart Prevent and Mitigation of Civil Engineering Disasters of the Ministry of Industry and Information Technology, Harbin Institute of Technology, Harbin, China

ABSTRACT: The capacity of horizontal failure shear keys is larger than diagonal and sliding failure modes owing to its secondary stiffness-strengthening stage. Nevertheless, the seismic performance of shear keys with horizontal failure mode has received limited attention yet. This investigation involved the design and fabrication of ten reinforced concrete (RC) exterior shear key specimens. A quasi-static experiment was conducted to assess the seismic performance of these shear key under cyclic load effects. The concerned properties include crack development, force-displacement relationship, rotation deformation and the stress distribution. The experimental results indicate that the failure mode is dependent on the capacity ratio between reinforcements. Horizontal failure shear key exhibits apparent second-rising of stiffness after its peak capacity, while the diagonal and sliding failure shear key undergo continuous decline under substantial deformations. Comparing the measured data with existing prediction models indicates that the models are more applicable to shear keys with diagonal failure mode as opposed to the others.

1 INTRODUCTION

Bridges as crucial components of transportation must endure seismic impacts. The vulnerability of bridges super- and sub-structures largely depends on the lateral restraints. The shear keys fixed to cap-beam serve as critical components for this purpose, and have been widely utilized in small- and medium-size bridges due to the reparability and detectability of damages. However, it must be designed also to prevent damages to pier columns as a sacrificial fuse. As per the AASHTO (2012), shear keys should be designed with over-strength that is further related to the capacity of piles and swing walls. Caltrans (2000) suggested a design method by incorporating a reduction factor to ensure its earlier failure. Insufficient researches in this aspect has led to severe damages during major earthquakes in the past decades. Examples can be given with respect to Wenchuan earthquake in China (K. Kawashima et al., 2009) and seismic incidents in Chile (F. Schanack et al., 2012), in which the poor shear key design resulted in bridge destruction. The 2011 Great East Japan Earthquake caused various bridges damaged due to the shear key design (M. Akiyama et al., 2013), prompting specific revision to the local design code for skewed bridges.

In recent decades, extensive studies have delved into the mechanical properties of shear keys, considering factors like friction and rebar shear key strength. Numerous models were proposed to predict their seismic resistance. S.H. Megally et al. (2001) conducted experimental tests to address the behavior of these components under monotonic lateral forces, in which significant distinctions were observed between two failure modes. P.F. Silva et al. (2009) extensively used the experimental results to propose an analytical mode with specific focus on exterior shear keys. Han & Zhou (2017a,b) investigated vertical exterior shear keys and identified two failure modes using six shear key specimens. Analytical formulas were proposed in

DOI: 10.1201/9781003483755-472

their research based on the test results. In engineering practice, the shear keys with diagonal failure mode are mostly adopted, while the sliding failure mode is also implemented to for post-disaster repair. However, both failure modes exhibit a continuous decline in resistance after the peak values, leading to potential risks to the bridge decks owing to inadequate lateral limits. Whereas, the horizontal failure shear keys demonstrate a secondary strengthening stage, so that they can be used to enhance protections for bridges in face of multiple earthquake events and multi-hazard actions. However, studied on such shear keys are limited yet.

Therefore, this study conducted a series of laboratory test on RC shear key specimens with horizontal, diagonal and sliding failures. Five specimens with ten shear key units were constructed, with the quasi-static method adopted along with monotonic cyclic loading. The primary contents of paper are organized as follows: 1) the introduction of specimen design and test setups were presented in section 2; 2) section 3 illustrates the major test results, with emphasis on crack development; 3) the seismic performance of each failure mode of shear key is analyzed in section 4, focusing on peak capacity, deformation, rotation angle and stress variations. In this section, the measured results are also compared with existing models in terms of peak capacity and envelope pattern; 4) concluding remarks are provided in the last section.

2 SPECIMEN DESIGN

2.1 *Details of tested specimens*

The experimental test employed five specimens with each containing two test units of RC shear keys. These specimens were designed with a 1:3 geometric scaling. The specimens measure 1840 mm in length, 540 mm in width and 1100 mm in height, with a 400 mm high foundation base to ensure adequate reaction force. Detailed geometric layouts and rebar arrangement are illustrated in Figure 1. The reinforcements in shear key specimen consist of vertical, horizontal and distributed components. Based on existing shear key studies, the capacity ratio (V_v/V_h) is the key factor that essentially determined shear key failure modes. Consequently, two rebar configurations were employed, with monolithic and construction joints also introduced to achieve horizontal, diagonal and sliding failure modes. Table 1 provides the detailed parameters for each test unit group. In this table, specimens SKH1-SKH4 were

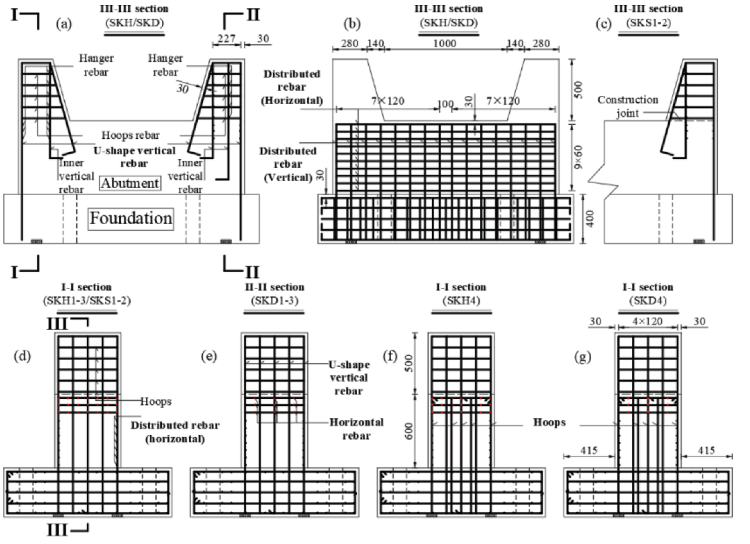


Figure 1. Geometry layout and reinforcement configuration.

designed with higher capacity ratio at 2.40, while SKD1-SKD4 had a lower ratio at 0.80. Figure 1(a)-(b) presents the layouts of corresponding reinforcement.

The U-shaped rebar was used along the inclined surface to accommodate the non-uniform shear key section. Group SKH has less vertical reinforcement than group SKD to satisfy strong horizontal constraints. Note that all specimens in the same group shared the same lateral constraints except for SKH4 and SKD4, where transverse hoops replaced the original distributed rebar, see Figure 1(f)-(g). The cross section of SKH and SKD groups ware presented in Figure 1(d) and (e), in which 21 and 9 horizontal rebar was used with the diameter of 16 mm. For shear keys with sliding failure mode, the capacity ratio is identically set as group SKH, whereas a dry construction joint was further introduced between the shear key and the abutment, see Figure 1(c). This study used C40 concrete (fcu,k = 40 MPa) and HRB400 (fy = 400 MPa) rebar for horizontal and vertical reinforcements, while HRB300 (fy = 300 MPa) rebar was used for distributed and hoop rebar. Concrete strength was measured using standard tests, with an average compression strength of 45 MPa. The rebar strength is also tested and takes the mean value of 450 MPa and 325 MPa for HRB400 and HRB300 rebar, respectively.

Table 1. Reinforcement configuration of shear key specimens.

		Horizontal reinforcement			Vertical reinforcement				
Group	Specimen	Configuration	Total area (mm^2)	Rebar ratio (%)	Configuration	Total area (mm^2)	Rebar ratio (%)	Capacity ratio	Special layout
SKH	SKH1	21Φ16	4220	1.30	15Φ12	1696	0.75	2.49	Distributed rebar
	SKH2	21Φ16	4220	1.30	15Φ12	1696	0.75	2.49	
	SKH3	21Φ16	4220	1.30	15Φ12	1696	0.75	2.49	
	SKH4	21Φ16	4220	1.30	15Φ12	1696	0.75	2.49	Hoops
SKD	SKD1	9Φ16	1809	0.56	20Φ12	2261	1.00	0.80	Distributed rebar
	SKD2	9Φ16	1809	0.56	20Φ12	2261	1.00	0.80	
	SKD3	9Φ16	1809	0.56	20Φ12	2261	1.00	0.80	
	SKD4	9Φ16	1809	0.56	20Φ12	2261	1.00	0.80	Hoops
SKS	SKS1	21Φ16	4220	1.30	15Φ12	1696	0.75	2.49	Construction joint
	SKS2	21Φ16	4220	1.30	15Φ12	1696	0.75	2.49	

2.2 *Experimental setups*

Figure 2(a) illustrates the test facility schematic, with a 2000 kN electro-hydraulic servo actuator with a ±200 mm stroke for horizontal force application. The actuator was fixed on a reaction wall to transmit forces to shear key specimens via a steel frame system. A linkage component was used to connect the two steel H-shape beams shown in this figure, and the forces were applied directly through the two loading cells at the opposite side. A distribution beam was employed to balance the vertical reaction, with a 500 kN loading effects generated by a hydraulic jack on the top, while four steel rollers below were used to eliminate the interface friction, which was recorded during the initial loading phase. It was found that the friction was minor and thus excluded from the test results in order to obtain the exact resistance. The actuator was loaded to contact the specimen by following the specified loading protocol. Note that only the shear key unit on one side was tested at each time, followed by the remaining tested in the opposite direction.

To accommodate the monotonic behavior of this component during seismic events, the quasi-static loading method was performed on all specimens with monotonic-cyclic loads. Besides, a hybrid loading protocol was designed for the loading control, as shown in Figure 3. The first phase was controlled by the loading forces that increase at 100 kN increment. The second phase was controlled by the displacements with varying intervals at different

stages: 2 mm (10-20 mm), 5 mm (20-50 mm), 10 mm (50-100 mm) and 20 mm (>120 mm). The first force-controlled phase included two cycles for each level while the displacement-controlled phase included three cycles. While the typical experimental tests on RC structures were stopped at 85% peak strength, they were subjected to extensively deformation with at least 100 mm deformation to highlight their post-buckling properties.

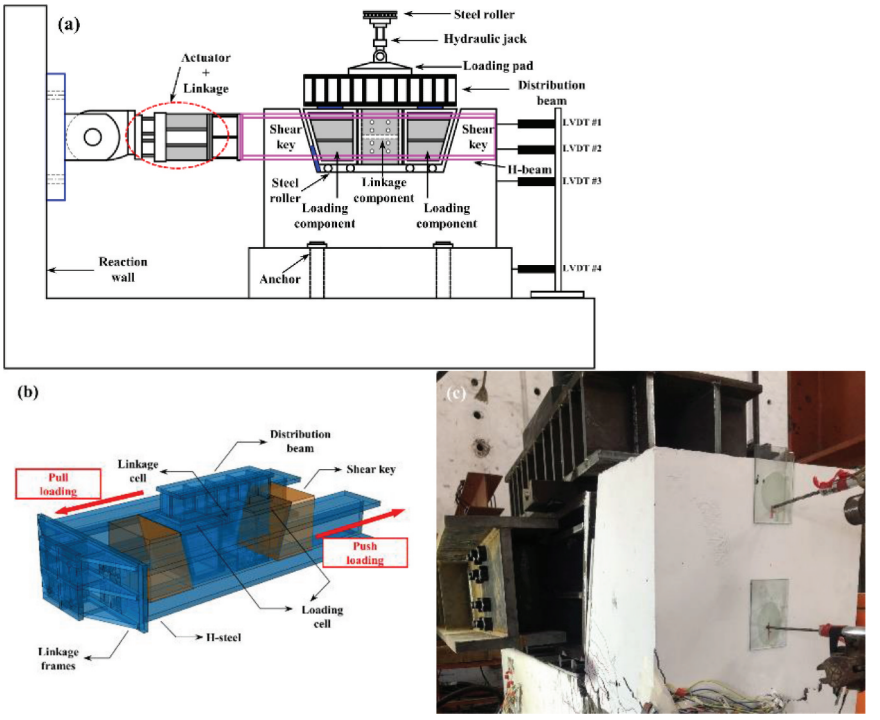


Figure 2. Geometry layout and reinforcement configuration.

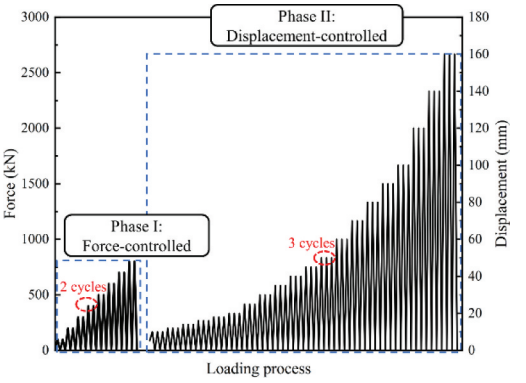


Figure 3. Loading protocol during experimental testing.

Four LVDT sensors were sued to measure the shear key deformation at different heights in the vertical direction, as seen in Figure 4(a). The measured results at points A-D correspond to the top shear key movement, the displacement at the load-applying height, the abutment deformation and the base sliding distance, respectively. On this basis, the exact deformation

of shear key at the loading height can be calculated by $\delta_2' = \delta_2 - \delta_4$ to eliminate the influence of base sliding. In this study, 32 strain gauges were used to investigate the strain distribution of reinforcements in different positions, as shown in Figure 4(b)-(c). In addition, six grouped strain gauges were installed on the abutment concrete surface to obtain the complex stress conditions, see Figure 4(d).

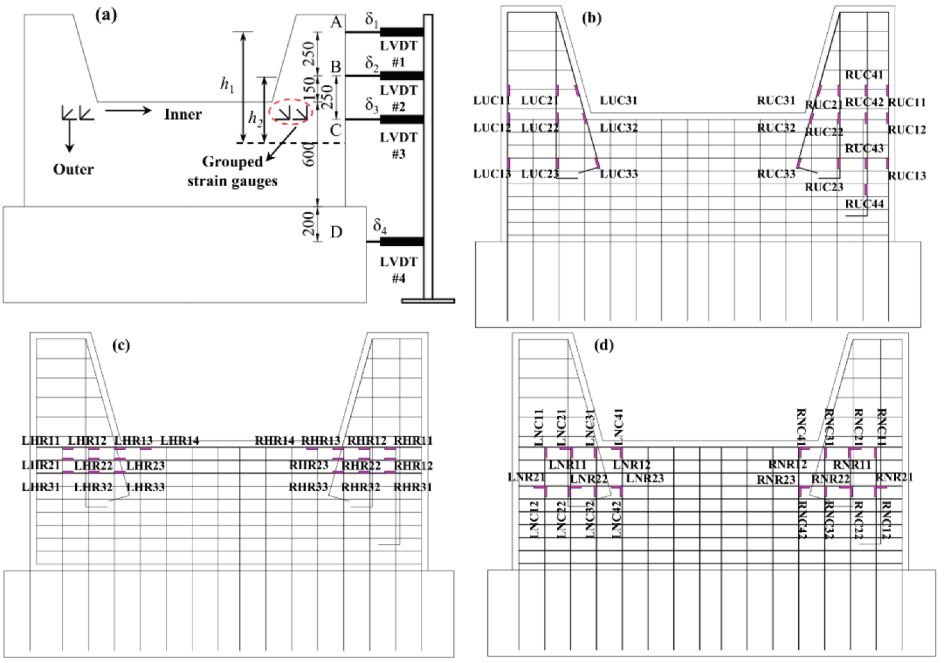


Figure 4. Loading protocol during experimental testing.

3 EXPERIMENTAL OBSERVATION

Figure 5 presents the crack development in different failure modes. The test results show that specimens SKH1-SKH3 experienced horizontal shear failure, with the major crack near the interface, see Figure 5(a). The first crack initiated at 100 kN for this failure mode, and the peak capacity was accompanied with significant rebar fractures. It should be noted that SKH3 exhibits unusually higher peak capacity due to the incorrect operation and was thus excluded from the succeeding discussions. To prevent this in other tests, loading setups is fastened to ensure before the other experiments. In comparison, specimens SKD1-SKD4 exhibits diagonal failure mode due to the lower capacity ratio at 0.80. The diagonal failure shear key had a larger angle of major crack, with the initial crack emerging at around 200 kN, as shown in Figure 5(b), and more minor cracks were observed before the peak capacity was reached. The main failure pattern of this failure mode is related to extensive concrete cracks. The sliding failure shear key also exhibits major cracks parallel to the interface because of the absent concrete connection, and the crack further extended to the backwall edge and then turns downward to form a significant crack, as seen Figure 5(c). The first crack was observed at around 100 kN, and the cracks were found to develop sooner to the backwall edge. Similar to the horizontal failure mode, the sliding failure shea key also exhibited successive rebar fractures as the load magnitude rises.

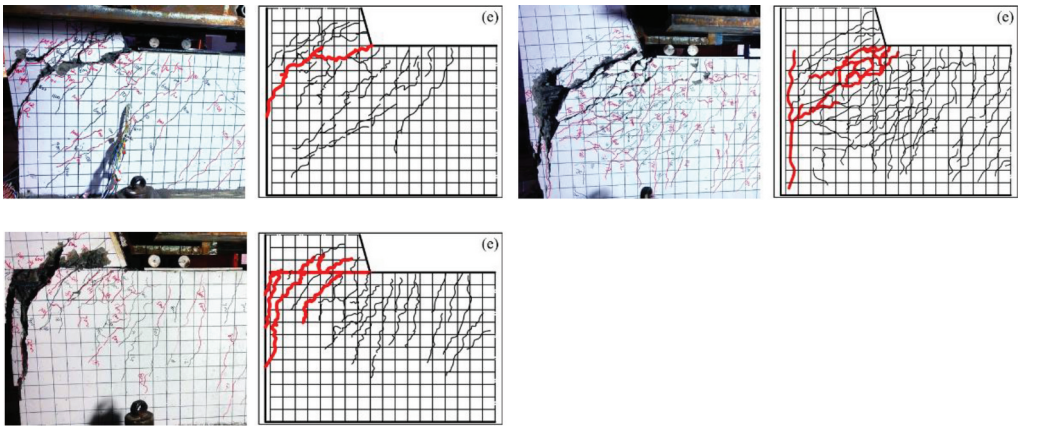


Figure 5. Development of concrete cracks on specimens: (a) horizontal failure; (b) diagonal failure; (c) sliding failure.

Figure 6 indicates the force-displacement relationship for each failure mode. It is found that the horizontal failure shear key has an initial stiffness at around 322 kN/mm, whereas the diagonal failure shear key takes a mean value of 455 kN/mm. In comparison, the sliding failure shear key shows the lowest stiffness at around 271 kN/mm. For the horizontal failure mode, the unloading stiffness remains constant throughout the loading process, while the diagonal failure shear keys indicate a downward trend. The sliding failure mode also exhibits a well-maintained stiffness in this process. Notably, the horizontal failure shear key yielded a second-rising stage after the first peak capacity. By comparison, the capacity of diagonal and sliding failure shear keys decreases continuously after the peak value. Comparing the damage development in SKH1-3 and SKH4, as well as SKD1-3 and SKD4 implies that the hoop rebar has negligible to the maximum resistance of RC shear keys, whereas it can result in the earlier capacity decline for the horizontal failure shear key, and the lower ultimate strength for both diagonal and horizontal failure modes.

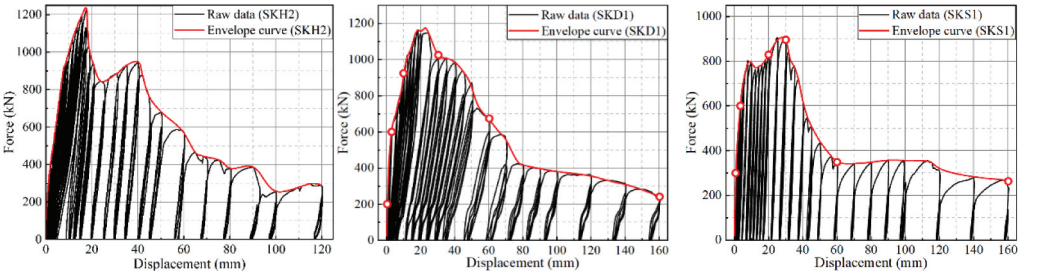


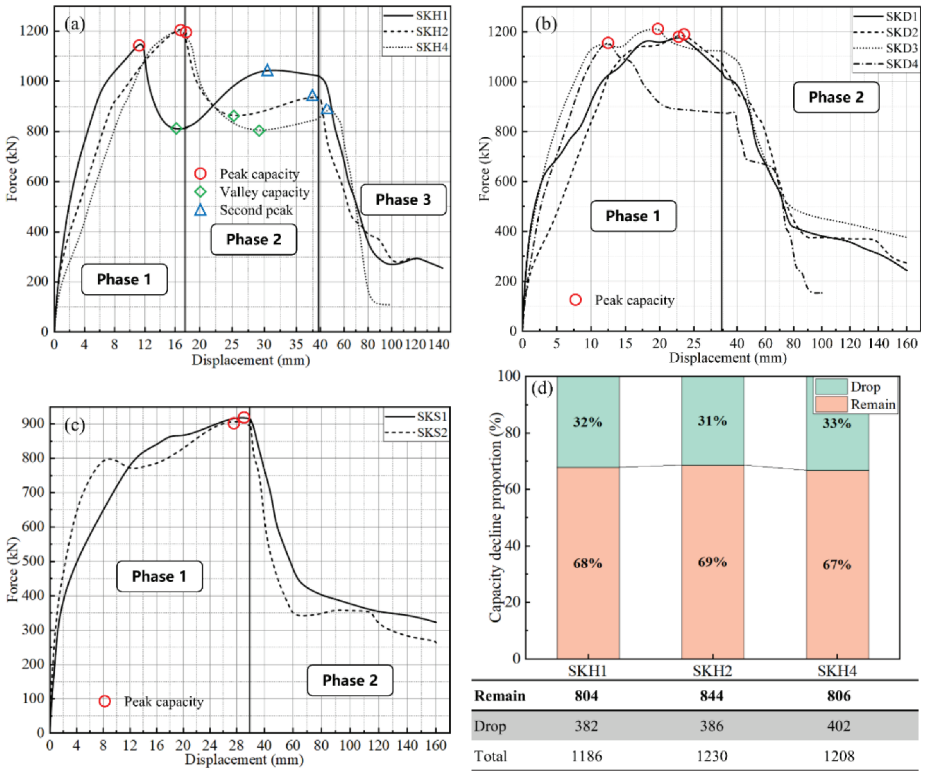
Figure 6. Force-displacement relationship of specimens: (a) horizontal failure; (b) diagonal failure; (c) sliding failure.

4 TEST RESULT ANALYSIS

4.1 *Load-displacement relationship*

Figure 7 illustrates the piecewise stages of envelope curves for different failure modes. The nonuniform scaling of the horizontal axis at different stages better highlights mechanical

characteristics. Figure 7(a) shows that horizontal failure shear keys have three phases including the elastic stage before first peak, the second-rising stage between the first and second peaks, and the softening stage after the second peak. Some vertical reinforcement in this failure mode fails when the peak capacity is reached, and the second resistance increase is associated with the hardening effect of the vertical reinforcement. Fig. 7(d) shows resistance reduction after reaching peak values, with early reinforcement fracture reducing capacity by approximately 32% on average compared to peak strength. Comparing envelope curves in diagonal and sliding failure modes in Figure 7(b)-(c), both exhibit two phases in the entire protocol: elastic stage before peak strength and a succeeding softening stage. The second rising stage disappears for the diagonal failure mode as abutment concrete crashes at peak strength, diminishing constraints on vertical reinforcement and causing resistance decrease. Whereas, the two-stage envelope curve results from nonuniform stress in vertical reinforcement for the sliding failure mode.



	SKH1	SKH2	SKH4
Remain	**804**	**844**	**806**
Drop	382	386	402
Total	1186	1230	1208

Figure 7. Envelope curves and capacity reduction of the specimens with different failure modes: (a) group SKH; (b) group SKD; (c) group SKS; (d) capacity reduction ratio of group SKH (unit: kN).

4.2 *Comparison with existing models*

Several researchers and design codes emphasize the significance of estimating the mechanical properties of RC shear keys, leading to the proposal of various analytical models for predicting peak capacity and envelope curves. In Figure 8 the test results are compared with existing models, presenting the average capacity for each failure mode through shadow regions. Megally's (2001) model shows relatively good estimation for peak capacity in diagonal failure shear keys, while Zielinski's (1995) method exhibits poor applicability. AASHTO method

overestimates strength, while Caltrans significantly underestimates capacity. Prediction accuracy diminishes for horizontal failure mode due to limited related research. Specifically, the sliding failure shear key has poor peak strength estimation, with errors exceeding 7% for the Megally-friction (2001) model, indicating that existing codes struggle to predict the peak capacity of this shear key type.

Additionally, experimental outcomes are compared with existing research in terms of the force-displacement relationship throughout the loading process using Megally's analytical model (Figure 9). Sliding failure shear key results are excluded due to the model's initial development for monolithically-casted shear keys. The model agrees well with both horizontal and diagonal failure shear keys before reaching peak capacity, with overestimation for horizontal failure mode and underestimation for diagonal failure mode. However, Megally's method poorly represents the post-peak capacity for horizontal failure shear keys, lacking the second-strengthening stage and defining a plateau stage instead, as shown in Figure 9(a). The model also significantly overestimates capacity after 60 mm. In contrast, the model exhibits relatively good agreement with diagonal failure shear keys, accurately predicting post-peak capacity before the plateau-like stage but considerably underestimating ultimate strength, with a capacity difference exceeding 300 kN, see Figure 9(b).

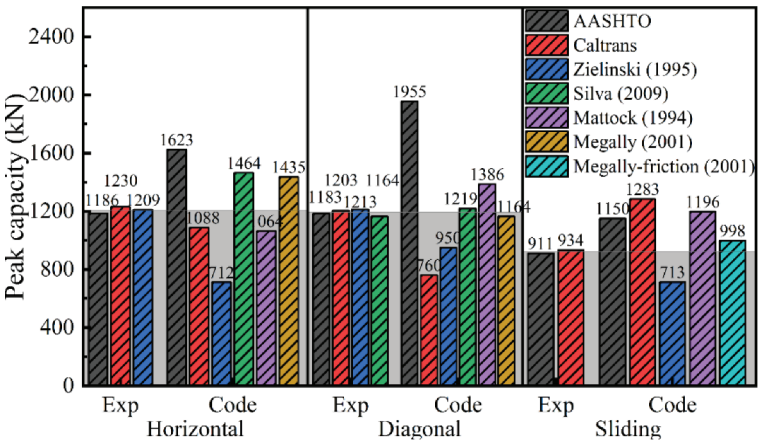


Figure 8. Comparison of peak capacity between test results and existing models.

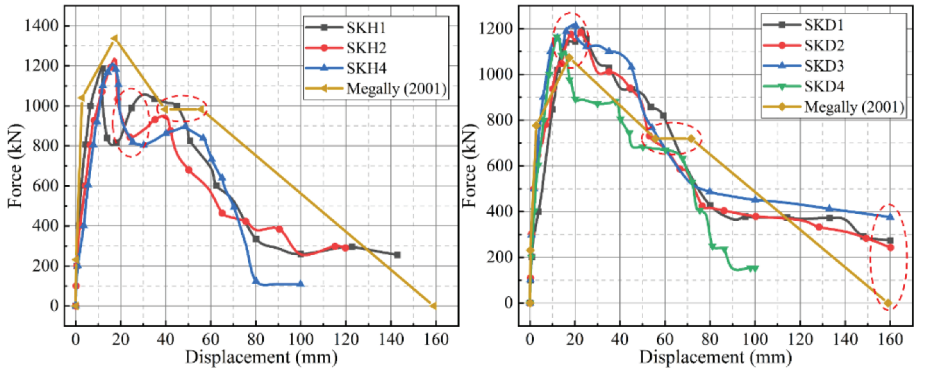


Figure 9. Comparison of envelope curves for shear keys with different failure modes: (a) horizontal failure mode; (b) diagonal failure mode.

5 CONCLUSION

This study conducts a quasi-static experiment on the seismic performance of RC exterior shear keys with three failure modes. Ten experiments were performed on exterior shear keys exhibiting horizontal, diagonal, and sliding failure modes. The conclusions are summarized as follows:

(1) The seismic performance of RC shear keys varies based on the reinforcement configuration. The capacity ratio of horizontal and vertical reinforcements significantly influences the failure mode under cyclic action. The study indicates horizontal failure occurs when the ratio approaches 2.49, while a ratio close to 0.80 results in diagonal failure.
(2) The force-displacement relationship reveals distinctive behaviors. The exterior shear key with horizontal failure exhibits a secondary stiffness strengthening capacity. The shear key with diagonal failure starts with the largest initial stiffness, gradually decreasing, while the sliding failure shear key has the least stiffness due to the absence of concrete.
(3) Peak resistance is influenced by factors such as horizontal, vertical, distributed reinforcement, and interface state. For horizontal failure shear keys, vertical reinforcement determines capacity, while with insufficient horizontal constraint, resistance depends on horizontal reinforcement capacity, leading to diagonal failure.
(4) Existing codes and research provide acceptable capacity estimates for diagonal failure shear keys but poorly predict those with horizontal or sliding failure modes. Further research is needed for accurate capacity prediction in these cases.
(5) Existing model of shear key envelope curve shows relatively good agreement with diagonal failure mode in terms of the curve shape but underestimates the peak capacity and ultimate strength. However, it has limited applicability to horizontal failure shear key due to the poor prediction toward peak capacity, second-strengthening stage and post-peak capacity.

REFERENCES

Transportation Officials. 2012. AASHTO LRFD Bridge Design Specifications: Customary US Units. American Association of State highway and transportation officials.

Caltrans, S. 2000. Caltrans bridge design specifications. LFD Version California Department of Transportation, Sacramento, California, USA.

Kawashima, K., Takahashi, Y., Ge, H., Wu, Z., & Zhang, J. 2009. Reconnaissance report on damage of bridges in 2008 Wenchuan, China, earthquake. Journal of earthquake Engineering, 13(7), 965–996.

Schanack, F., Valdebenito, G., & Alvial, J. 2012. Seismic damage to bridges during the 27 February 2010 magnitude 8.8 Chile earthquake. Earthquake Spectra, 28(1), 301–315.

Akiyama, M., Frangopol, D. M., Arai, M., & Koshimura, S. 2013. Reliability of bridges under tsunami hazards: Emphasis on the 2011 Tohoku-oki earthquake. Earthquake Spectra, 29(1_suppl), 295–314.

Megally, S. H., Silva, P. F., & Seible, F. 2001. Seismic response of sacrificial shear keys in bridge abutments. SSRP, 23.

Silva, P. F., Megally, S., & Seible, F. 2009. Seismic performance of sacrificial exterior shear keys in bridge abutments. Earthquake Spectra, 25(3), 643–664.

Han, Q., Zhou, Y. L., Zhong, Z. L., & Du, X. L. 2017a Seismic capacity evaluation of exterior shear keys of highway bridges. Journal of Bridge Engineering, 22(2), 04016119.

Han, Q., Zhou, Y., Ou, Y., & Du, X. 2017b. Seismic behavior of reinforced concrete sacrificial exterior shear keys of highway bridges. Engineering Structures, 139, 59–70.

Bridge Maintenance, Safety, Management, Digitalization and Sustainability – Jensen, Frangopol & Schmidt (eds)
© 2024 The Author(s), ISBN 978-1-032-77040-6
Open Access: www.taylorfrancis.com, CC BY-NC-ND 4.0 license

Progressive failure analysis of strengthened masonry arch bridges

T. Kamiński
Wrocław University of Science and Technology, Wrocław, Poland

C. Costa
CONSTRUCT-LESE, Polytechnic Institute of Tomar (IPT), Tomar, Portugal

ABSTRACT: The paper focuses on the numerical analysis of strengthening solutions dedicated to masonry arch bridges. It concentrates on the longitudinal behaviour of the arch of single-span bridges. The analysed methods are related to the addition of specific structural components on both sides of the arch – extrados and intrados. Two basic solutions are studied based on a rigid or flexible layer corresponding to the most common techniques being applied to these bridges around the world. A comparison of the selected strengthening techniques is given considering their impact on the bridge's structural behaviour under incremental static loadings. Particular attention is paid to the analysis of the progressive failure being developed along with the increasing load. For this purpose, an advanced nonlinear Finite Element models using a meso-modelling technique are presented and selected results showing the mechanical performance of the structure before and after strengthening are provided. The interpretation of the bridge model response is based on the analysis of the evolution of the structural failure modes up to the maximum load capacity of the bridges, namely in terms of the interaction of internal forces M-N in representative arch cross-sections determined also analytically. Conclusions are formulated to identify optimum reinforcement solutions regarding both the sectional as well as the global performance of the structures.

1 INTRODUCTION

1.1 *Arch strengthening methods*

Common strengthening solutions for the arch barrel involve inserting a new flexible or rigid layer on the arch intrados or extrados which prevent the formation of the hinges' mechanisms improving the arch behaviour in the longitudinal direction.

Adding thin flexible layers on the arch extrados (FLEX/EXT) or intrados (FLEX/INT) are strengthening solutions which refer to the addition of composite materials based on new layers of FRP laminates or composite materials reinforced with fibre fabric of different materials, such as Steel, Carbon, Glass, PBO, and Basalt, based on a polymeric (FRP) or a cementitious matrix (FRCM/FRM/TRM). Reinforcement with longitudinal steel rebars embedded near the arch surface may be also represented by FLEX type solutions.

The addition of a thick rigid layer either in the extrados (RIG/EXT) or in the intrados (RIG/INT) of the arch barrel represents also a frequent strengthening solution comprising the addition of a concrete shell, which can be reinforced with rebars or reinforcement meshes made of steel or FRP. This type of solution was used in the cases of the Remondes bridge and Tavira bridge, where a reinforced concrete layer was applied in the intrados and extrados, respectively, as part of a global reinforcing intervention as reported by Costa *et al.* (2008). Strengthening solutions grouped into RIG type also refer to the addition of a (thick) layer of a cementitious matrix reinforced with fibres, usually made of steel, e.g. SFRM, or the addition

DOI: 10.1201/9781003483755-473

of ultrahigh-performance concrete (UHPC) applied on the intrados of a stone arch bridge, as reported in Wang *et al.* (2022). Also considered rigid layer solution is the addition of an RC trough or ribbed cover, as reported in Iacobini *et al.* (2020).

1.2 *Analytical description of strengthening*

The cross-section resistance of the selected arch-strengthening solutions including the addition of a (thin) flexible layer or a (thick) rigid layer, may be interpreted analytically in terms of the M-N interaction diagrams (Alecci *et al.* 2016, Simoncello *et al.* 2019). The applied assumptions consider a perfect bond between the reinforcement and the masonry units, the Bernoulli principle and no sliding between masonry units. Besides, any damage due to traction is concentred in the arch radial mortar joints having zero tensile strength. Opening in the radial joints may also occur in the zone of the reinforcing layer where also no tensile strength is admitted.

M-N interaction diagrams, representing the strengthened cross-section resistance are evaluated considering both the positive and negative bending moment combined with a compressive axial force. Figure 1a, b shows a scheme of the strengthened solutions with a thin flexible tensile resistant layer in the intrados and with a thick compressive resistant layer in the extrados. It also defines the corresponding strains and stresses distributions. F_m and F_r represent the resultant forces of the stress distributions in both materials, masonry and reinforcement, respectively.

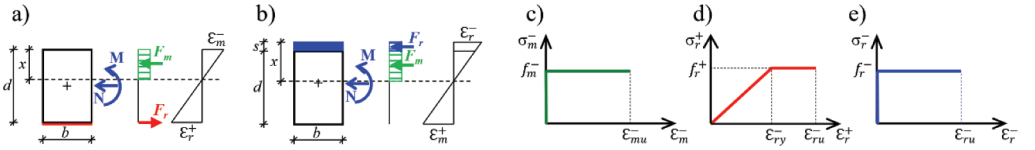


Figure 1. Strain and strength distributions of the strengthened cross-section under M-N for: a) a flexible layer, b) a rigid layer. σ-ε constitutive relationships for: c) masonry, d) flexible reinforcement, e) rigid reinforcement.

The stress-strain (σ-ε) relationships defined for masonry and reinforcements are also schematically represented in Figure 1. The masonry behaviour is characterised by a compressive resistant material with a simplified rigid-plastic σ-ε evolution with constant compressive strength f_m and a maximum strain of ε_{mu}^-. It results in rectangular stress distribution of the compressed zone of the cross-section up to the neutral axis depth (x). No tensile strength is assigned to masonry. The tensile strength assured by the flexible layer follows an elastic-plastic constitutive behaviour (Figure 1d) with the maximum stress equal to f_r^+. No compressive strength is set for the layer. A simplified rigid plastic stress-strain (σ-ε) relationship is also adopted for the rigid layer reinforcement material (Figure 1e) as well as no tensile strength is assigned to it. The maximum admissible compressive ε_{ru}^- values are set equal to the masonry compressive strain ε_{mu}^-.

The envelope of the M-N interaction is evaluated considering the internal forces' equilibrium and strain compatibility conditions at the cross-section level of both strengthening solutions. Compressive N force is assumed negative. The envelope of the M-N is further normalized in terms of the ν, μ and ω parameters (Equation 1), based on the masonry compressive strength f_m. ν and μ represent the normalized axial force and bending moment and ω represent the mechanical reinforcement ratio, where for the flexible layer $F_r = A_r f_r^+$ (A_r stands for area of the flexible reinforcement) and for the rigid solution $F_r = sbf_r^-$ (with s and b representing the thickness and width of the rigid reinforcement layer as shown in Figure 1).

$$\nu = \frac{N}{bdf_m},\ \mu = \frac{M}{bd^2 f_m},\ \omega = \frac{F_r}{F_m} = \frac{F_r}{bdf_m} \tag{1}$$

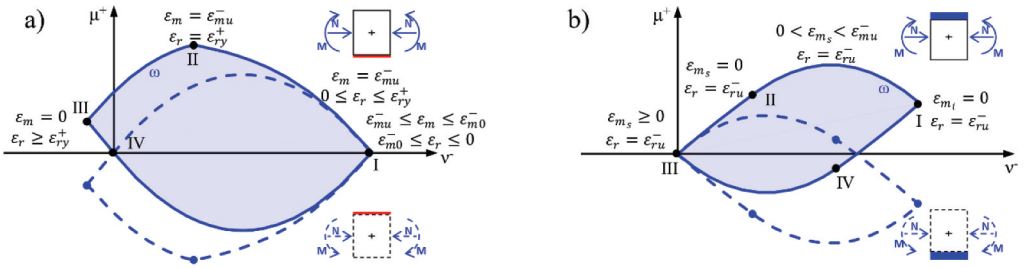


Figure 2. μ-ν generic envelopes of a strengthened cross-section for: a) a flexible, b) a rigid reinforcement.

Finally, for both study cases, the μ-ν interaction diagrams are obtained representing different failure conditions, as shown schematically in the multi-branch envelopes in Figure 2. Each branch represents a different failure condition, by defining the internal forces' equilibrium and strain compatibility conditions with the corresponding material stress-strain domain defined according to the σ-ε behaviour shown in Figure 1.

For the flexible strengthening solution, four cases of failure conditions are considered to set the corresponding branches of the μ-ν envelope shown in Figure 2a. The failure conditions of the first case (from I to II) are determined by the masonry compression failure with $\varepsilon_m = \varepsilon_{mu}^-$ and the reinforcement tensile strains ranging from 0 to ε_{ry}^+. The second case (from II to III) corresponds to the limit condition determined by the reinforcement failure in tension ($\varepsilon_r = \varepsilon_{ry}^+$) and the masonry compressive strain ε_m falling from ε_{mu}^- to 0. The third case (from III to IV) involves reinforcement stresses in the elastic regime with $\varepsilon_r \leq \varepsilon_{ry}^+$ and $\varepsilon_m = 0$. The fourth branch of the ν-μ envelope (from IV to I) is defined for a negative bending moment and a compressive axial force, with the cross-section resistance assured by the masonry in compression, neglecting the strength of the flexible reinforcement layer under compression.

For the rigid strengthening solution, four cases of failure conditions are considered to set the corresponding branches of the μ-ν envelope with the analytical ν and μ expressions and their strain domain. For the first case (from I to II) the failure conditions are determined by the compressive strength of the masonry and the reinforcement layer above the neutral axis, with no tensile strength of the masonry fibres below the neutral axis. The maximum strain at the reinforcement top fibre corresponds to $\varepsilon_r = \varepsilon_{ru}^-$ and at the masonry top fibre evolves from a strain value lower than ε_{mu}^- to 0, when the neutral axis passes below and in the interface of both materials, respectively. In the second case (from II to III) the neutral axis is in the reinforcement layer, which evolves from the bottom fibre to the top, with the maximum strain at the top fibre equal to ε_{ru}^-. Branch III-IV (third case) is associated with a negative bending with the neutral axis in the masonry zone. Branch IV-I (fourth case) corresponds to the neutral axis in the reinforcement zone, evolving from the reinforcement-masonry interface to the reinforcement top fibre, when the entire cross-section is under compression. Both envelopes should be present upside down when the reinforcing layer is located on the opposite side of the arch.

2 NUMERICAL MODELLING STRATEGY

The utilized Finite Element model of the structure comprises two-dimensional plane strain problem taking into account (see Figure 3): the arch barrel, the soil above the arch barrel and in the access zones of the bridge, a loading element and a reinforcing layer. Except its self-weight the bridge is subjected to an external loading simulating a pressure of a vehicle single axle.

The arch barrel is modelled as a continuous area defined by means of an advanced non-linear elastic-plastic at compression and low-tensile-resistant constitutive material model – the most adequately representing masonry. A meso-modelling technique (Kamiński & Bień 2013) to discretize the arch is used which is based on division of the arch barrel area into masonry

segments with homogenised properties (with compressive strength f_b) and into layers of radial joints between them. The distinguished radial joints comprise the areas where cracking may occur forming a plastic hinge. The material of the joints defined by a plastic-damage model (Lubliner et al. 1989) corresponds to a constitutive model of concrete. The initial yield stresses at compression and are tension equal to typical values: f_m = 4 MPa and f_t = 0.1 MPa correspondingly.

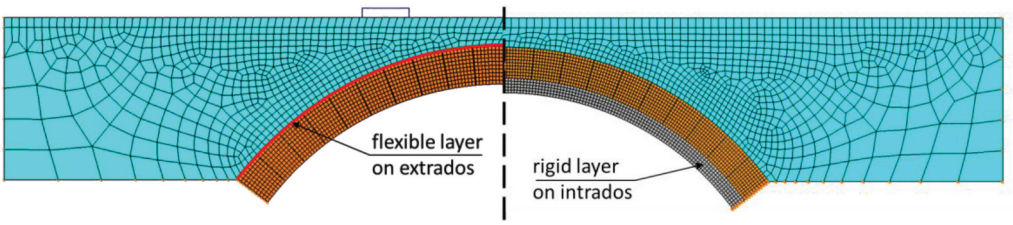


Figure 3. FE model of a masonry arch bridge strengthened with: a flexible (left) or a rigid (right) layer.

The other main properties of material assumed in analyses are shown in Table 1 where: E_b, E_m, E_r, E_s – Young modulus of masonry segments, mortar, reinforcement and soil; γ_s, γ_M, γ_r – unit weights of soil, masonry and reinforcement; ϕ_s – friction angle of soil, δ_s – dilation angle of soil, c – cohesion of soil, φ_c – coefficient of friction between arch and soil.

Table 1. Basic material properties of the analysed case studies.

	f_b	f_m	f_t	f_r^+	f_r^-	E_b	E_m	E_r	E_s	γ_s	γ_M	γ_r	ϕ_s	δ_s	c	φ_c
Material parameter	[MPa]					[GPa]				[kg/m^3]			[º]	[º]	[kPa]	[-]
value	10	4.0	0.1	0.1/1000	16	5.0	2.0	20/200	50	2000	1850	2500	50	20	5	0.4

At the boundary between the backfill and the arch or the rigid layer the contact elements are defined. They represent interaction between the contacting bodies by means of compressive and shear forces but without transfer of tension. The live load is applied by means of a rigid block acting on the upper surface of the soil. In all analyses the load is located at the quarter of the span. The boundary conditions limit the horizontal translation of the rigid body.

The two types of the arch barrel reinforcement are considered in the numerical model by means of additional FE elements. The first one, corresponding to a thin flexible tensile resistant layer – is modelled by means of 1-dimensional truss-type elements embedded inside host 2D elements representing the masonry arch located along the intrados or extrados of it (see Figure 3a). The displacements of the embedded element nodes are constrained to the interpolated values of the corresponding degrees of freedom of the host element. The second type – a thick rigid compressive resistant layer – is modelled using additional 2D elements defined outside the masonry arch and fixed to it (Figure 3b). The mechanical properties of rigid/flexible reinforcement types (including tensile f_r^+ and compressive strength f_r^- and Young modulus E_r) are given in Table 1.

The numerical analysis considering geometrical nonlinearity and large displacements is carried out incrementally in two consecutive steps: in the first step, the self-weight of all structural components is applied, and in the second step, the live load acting through the rigid block is added. The incremental application of the live load is determined by means of the vertical displacement of the reference point of the loading block, which enables the development of the global failure and continuation of the analysis in the post-critical phase. Thus, the ultimate load level P_{ult} may be reached, which is defined by the highest value of the applied load taken e.g. from the relationship between the vertical displacement of the loading block and the load P.

3 ANALYSIS OF STRENGHTENING EFFECTS

3.1 *Procedure of the progressive failure analysis*

All the analysed case studies have the same basic geometry corresponding to a typical structural system for masonry arch bridges, defined by: arch clear span L = 5 m, arch rise r = 1,25 or 2,5 m, arch thickness d = 0,4 m, number of arch segments n = 40, backfill height over the crown t = 0,3 m and length of the loading block w = 0,5 m. The strengthened cases differ for the flexible layer by the reinforcement ratio ω = 0,10÷0.20 or for the rigid layer by the thickness s = 0,05÷0.15 m.

The interaction of normalised forces μ and v in arch sections may present the effect and mechanism of reinforcing in a clear and legible way. For this purpose, discrete integration of peripheral stress σ_{22} distribution in arch sections, obtained from the FE model, takes place and the corresponding generalized forces M and N are calculated for every section giving the so-called "interaction line" for the whole arch. Additionally, the forces are normalised according to Equation 1 and then referred to the μ-v envelopes shown in Figure 2. This procedure can be applied both to the unstrengthened and strengthened arches. In the diagram, letters indicating the position of the plastic hinges are also given.

For presentation of the progressive failure development, various levels of the applied concentrated force P_i are analysed which are related to reaching the critical effects in a sectional or global response of the arch, namely:

1. compressive yield strength f_m of masonry at the edge fibre of a section, $P_1 = P(f_m)$,
2. tensile yield strength f_r^+ of a flexible reinforcement or compressive yield strength f_r^- of a reinforcing rigid layer at the edge fibre of a section, $P_2 = P(f_r)$,
3. ultimate compressive strain ε_{mu} in masonry at the edge fibre of a section, $P_3 = P(\varepsilon_m)$,
4. the ultimate load P_{ult} related to loss of stability of the whole arch, $P_4 = P_{ult}$.

The order of getting the aforementioned critical effects along with the increasing loading may vary between different arch geometries (r/L and d/L), type and amount of strengthening or for other loading scenarios. Various order of the limit criteria being reached can be noticed, e.g. in Figure 7 and Figure 10. Showing the interaction line evolution along with the increasing load P referred to the considered μ-ν interaction envelopes provides the most comprehensive demonstration of the effect of the applied strengthening solutions.

3.2 *Analysis results*

In the first step, the unstrengthened arches are analysed. For two cases (with r/L equal to 1/4 or 1/2), the calculated evolution of the interaction line within the μ-v envelope for the characteristic load levels $P(f_m)$, $P(\varepsilon_m)$ and P_{ult}, is presented in Figure 4a, b. It is visible that the interaction lines for P_{ult} touch the envelope in all extreme points (where hinges A-D are forming) while the lines for lower P_i do not fully reach it. The legends in the diagrams describe the interaction lines in the order according to their evolution along with the increasing load P. For the same cases, the relationships between the applied force P and displacement u of the arch at the point located under the force are calculated and shown in Figure 4c, d. In the obtained P-u diagrams the characteristic load levels P_i are indicated which describe the behaviour in the critical arch sections (at plastic hinges A-D). It can be noticed that the location of the sections where the failure appears may change depending on the bridge geometry.

The effect of strengthening with a flexible layer located on intrados or extrados is depicted by means of a distribution of peripheral stresses σ_{22} shown on a deformed region of the arch (Figure 5) as well as using the interaction lines shown against the μ-v envelope for a bridge with r/L = ¼, d = 0,40 m and varying $\omega \approx \omega_{opt}$ (Figure 6). Additionally, P-u relationships for the selected cases are presented in Figure 7.

In the diagrams in Figure 6, the interaction lines for the following P_i evolve, starting from $P(f_{m,D})$, through $P(\varepsilon_{m,D})/P(\varepsilon_{m,B})$ up to P_{ult}, approaching the envelope branches related to strengthening in the vicinity of two sections (at hinges forming on the edge of the arch

opposite to the strengthening layer), i.e. B & D for reinforcement on the intrados and A & C – for extrados, while the other two hinges develop as for the unstrengthened arch. For clarity, the μ-v envelope for the unstrengthened section is also given here with a grey dotted line.

In case of FLEX/INT with the increase of ω (from 0,15 to 0,20) tensile failure of reinforcement at hinge B for load $P(f_{r,B})$ stops to be reached before P_{ult} and the interaction line at P_{ult} reaches branch II-III of μ-v envelope related to failure of masonry instead of the branch I-II. However, observing P-u relationships after this increase of ω all the P_i related to masonry failure remain at similar levels as well as the P_{ult} increase is insignificant.

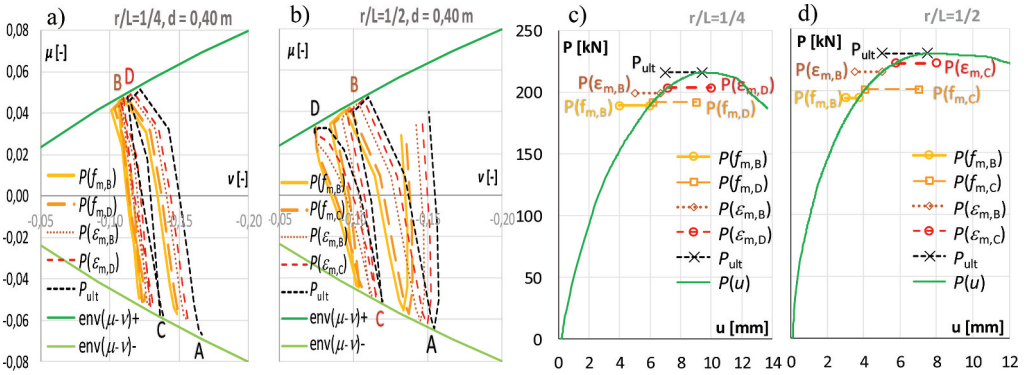


Figure 4. Analysis of the unstrengthened arches: the interaction line evolution within μ-v envelope for the characteristic load levels P_i for arches with: r/L = 1/4 (a) and r/L = 1/2 (b); corresponding P-u diagrams with indicated critical load levels P_i for: r/L = 1/4 (c) and r/L = 1/2 (d).

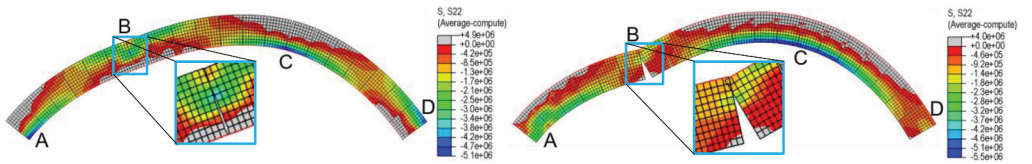


Figure 5. Distribution of stresses σ_{22} triggered by the $P(f_r)$ for FLEX/INT (left) and FLEX/EXT (right).

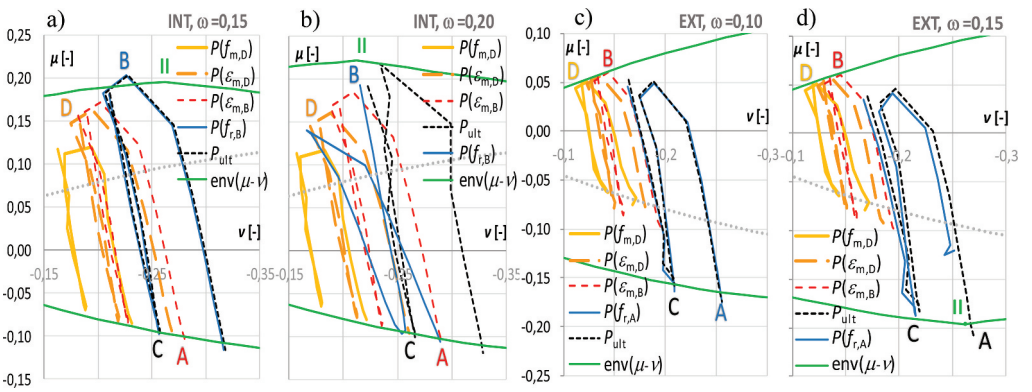


Figure 6. The interaction line evolution within μ-v envelope corresponding to the characteristic load levels P_i for arches strengthened with FLEX/INT (a), (b) and FLEX/EXT (c), (d) for different ω.

Regarding FLEX/EXT, in consequence of the increase of ω (from 0,10 to 0,15) failure at $P(f_{r,A})$ is no more reached before P_{ult} and the interaction line at hinge A at load P_{ult} reaches

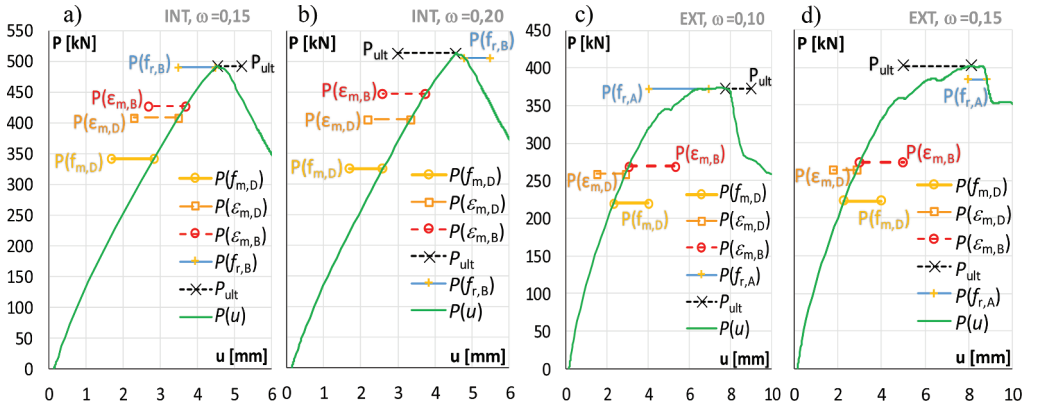


Figure 7. *P-u* diagrams with indicated critical load levels P_i for FLEX/INT (a), (b) and FLEX/EXT (c), (d).

point II of the μ-v envelope. Likewise for FLEX/INT with the same arch geometry, after this increase of ω all the P_i related to masonry failure remain at similar levels as well as the P_{ult} increase is small.

In all the cases it may be noticed that for initial P_i levels the interaction line is quite remote from μ-v branches related to the reinforcing effect and reaches them at P_{ult} only. It means that for lower loads the flexible reinforcement is not utilised significantly. For FLEX/EXT, at higher P_i values, the interaction line in turn moves away from the μ-v branch corresponding to unstrengthened sections which shows redistribution of internal forces. It is related to yielding and softening at compression at hinges B & D of the arch which is visible e.g. in Figure 5 (right) when observing concentration of stresses at some distance from extrados in these sections. It leads to dislocation of the hinges to positions more remote from extrados and in consequence transmitting lower bending moment (resulting in lower μ). These effects are not visible in case of unstrengthened arches.

The effect of strengthening with a rigid layer is evaluated on the same arch geometry and in an analogical way to the flexible layer. Distribution of stresses σ_{22} at P_{ult} is given in Figure 8 for strengthening with a rigid layer located on the intrados or extrados. The presented case is with s = 0,15 m ($\omega \approx \omega_{opt}$).

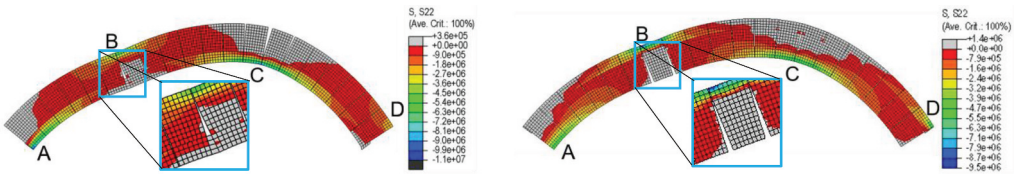


Figure 8. Distribution of stresses σ_{22} triggered by the P_{ult} for strengthening with RIG/INT (left) and RIG/EXT (right).

For selected cases of rigid reinforcement, the evolution of the interaction lines is presented in Figure 9. In each diagram, the interaction lines, starting from the considered initial phase of the loading, evolve in both directions towards branches of both signs of the envelope related to strengthening in regions of all sections A-D. It indicates early mobilization of the rigid reinforcement at the loading process. Larger evolution takes place however at hinges forming on the arch side with the strengthening layer. *P-u* relationships for the cases are presented in Figure 10 and by analysing them together with the Figure 9 some additional findings can be obtained. In case of RIG/INT along with increasing s (from 0,05 to 0,10 m) compressive failure of reinforcement at hinge C for load $P(f_{r,C})$ stops to be reached before P_{ult}. In case of

RIG/EXT together with increasing s (from 0,10 to 0,15 m) $P(f_{r,B})$ instead of being the first failure type moves to the post-critical phase. In all cases if the failure of the rigid reinforcement in a second section is going to appear, it happens in the post-critical phase only. Observing the RIG cases at the loading process it can be noted that, on the contrary to FLEX cases, the failures of the reinforcing layer and masonry always occur in different sections. It is also worth noting that strengthening with a rigid layer may lead in selected sections to a dangerous tensioning of the whole masonry part as it is shown in Figure 8.

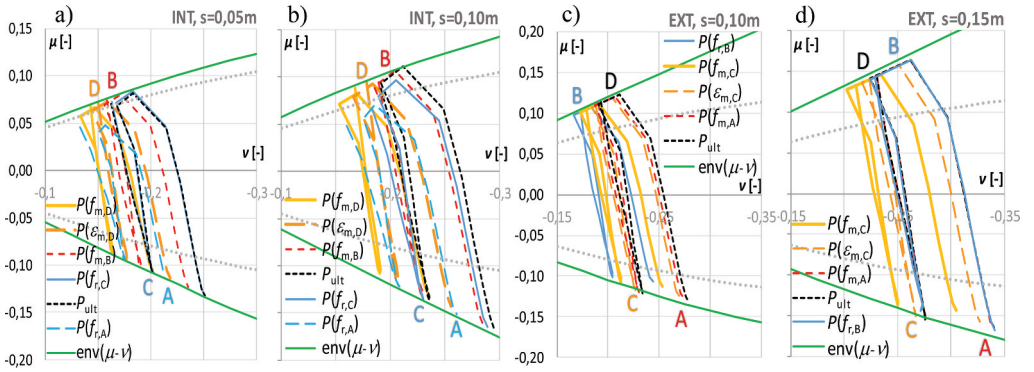


Figure 9. The interaction line evolution within μ-ν envelope corresponding to the characteristic load levels P_i for arches strengthened with RIG/INT (a), (b) and RIG/EXT (c), (d).

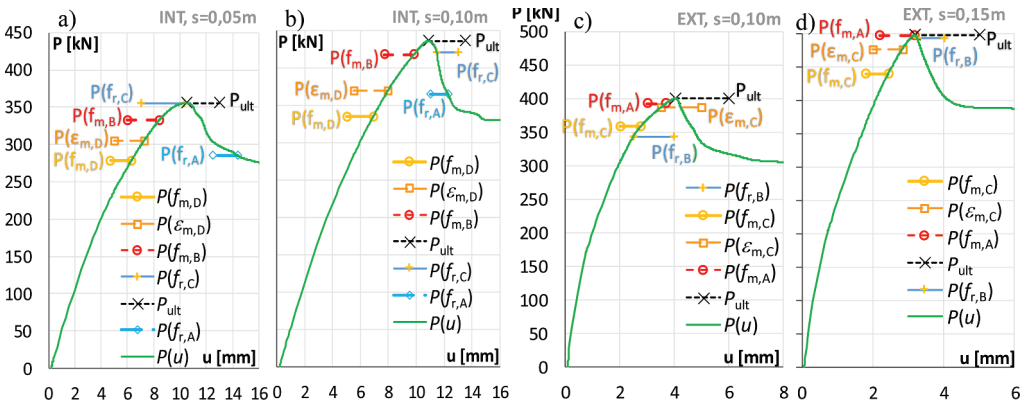


Figure 10. P-u diagrams with indicated critical load levels P_i for RIG/INT (a), (b) and RIG/EXT (c), (d).

4 SUMMARY AND DISCUSSION

On the basis of the study it can be concluded that consideration of different limit criteria provides more comprehensive information on the progressive failure of the arch during loading process, useful in evaluation of strengthening solutions. It occurs evident that the presence of reinforcement changes this gradual performance.

For a flexible layer an optimum value ω_{opt} can be defined corresponding to the case when interaction line (usually at section B) at P_{ult} reaches connection of two branches of the μ-ν envelope (point II in Figure 2). Such a situation corresponds to simultaneous failure of masonry and reinforcement in this section at the global collapse. Regarding the solutions based on a rigid layer an optimum value ω_{opt} can be also related to simultaneous failure of masonry and reinforcement at the global collapse but occurring in different sections.

According to the adopted analytical solution for a flexible reinforcing layer the relationship between ν, μ and ω_{opt} related to the position of point II on the envelopes can be express by formulae expressed in Equation 2 & 3, which assuming $x_{opt}/d = \varepsilon_{mu}/(\varepsilon_{mu} + \varepsilon_{ru}{}^{+})$ take a form:

$$\omega_{opt} = \nu + \frac{x_{opt}}{d} = \nu + 0,412 \tag{2}$$

$$\mu = \frac{\nu}{2} + \frac{x_{opt}}{d}\left(1 - \frac{x_{opt}}{2d}\right) = 0,5\nu + 0,327 \tag{3}$$

It defines domain of ν values belonging to (-0,41; 0) where optimum strengthening solution corresponding to ω_{opt} can be found. It means e.g. that for ν < - 0,41 any flexible layer will not provide an optimum utilization of both materials – masonry and reinforcement. At the same time it provides a valuable information on the range of ω_{opt} values corresponding to potential ν values. An important finding is also $\omega_{\max}$ = 0,41 (for ν = 0) which is the limit value above which the optimum solution cannot be found if the section is to belong to an arch – with a compressive resultant axial force. Finally, one can obtain also μ value corresponding to ν at ω_{opt}.

It is also found that generally for more flat arches (r/L = ¼) the variation of ν along the arch for any phase of loading is lower than for semi-circular ones. Besides, at P_{ult} noticeably lower displacement occurs for flat arches than for the latter ones. Similar findings are for strengthened arches.

ACKNOWLEDGEMENTS

The presented analyses were carried based on a grant from WCSS of Wroclaw University of Science and Technology. It was also financially supported by: Base Funding - UIDB/04708/2020 and Programmatic Funding - UIDP/04708/2020 of the CONSTRUCT - Instituto de I&D em Estruturas e Construções - funded by national funds through the FCT/MCTES (PIDDAC).

REFERENCES

Costa, C., Arêde, A. & Costa, A. 2018. Strengthening of Masonry Bridges. In: A. Costa, A. Arêde & H. Varum (eds). *Strengthening and Retrofitting of Existing Structures*: 217–247. Singapore: Springer.

Wang, Z., Yang, J., Zhou, J., Yan, K., Zhang, Z. & Zou, Y. 2022. Strengthening of existing stone arch bridges using UHPC: Theoretical analysis and case study. *Structures* 43: 805–821.

Iacobini, F., Tisalvi, M., Vecchi, A., Iodice, F. & Mauro, A. 2020. Analysis Methods and Seismic Strengthening of Existing Masonry Arch Bridges of the Conventional Railway Network. In: A. Arêde & C. Costa (eds). *Proceedings of ARCH 2019*: 340–348. Cham: Springer.

Alecci, V., Misseri, G., Rovero, L., Stipo, G., De Stefano, M., Feo, L., *et al.* 2016. Experimental investigation on masonry arches strengthened with PBO-FRCM composite. *Compos B Eng* 100: 228–239.

Simoncello, N., Zampieri, P., Gonzalez-Libreros, J. & Pellegrino, C. 2019. Experimental behaviour of damaged masonry arches strengthened with steel fiber reinforced mortar (SFRM). *Compos B Eng* 177: 107386.

Kamiński,T. & Bień, J. 2013. Application of kinematic method and FEM in analysis of ultimate load bearing capacity of damaged masonry arch bridges. *Procedia Engineering* 57: 524–532.

Lubliner, J.,Oliver, J., Oller, S. & Oñate, E. 1989. A plastic-damage model for concrete. *Int J Solids Struct* 25(3): 299–326.

Bridge Maintenance, Safety, Management, Digitalization and Sustainability – Jensen, Frangopol & Schmidt (eds)
© 2024 The Author(s), ISBN 978-1-032-77040-6
Open Access: www.taylorfrancis.com, CC BY-NC-ND 4.0 license

Rapid repair of bridge beams and decks with prefabricated FRP panels

M. Ehsani
QuakeWrap, Inc. Tucson, USA

ABSTRACT: Typical repair techniques for bridge girders and decks are often time-consuming and require long periods of traffic control that add significantly to the project cost. In some projects, where the bridge is crossing a body of water, the low headroom below the bridge can make these repairs even more challenging. The introduction of Fiber Reinforced Polymer (FRP) products in recent years has shortened repair times in many cases. However, even when conventional FRP products are used, repairs can still be time-consuming and difficult.

This paper presents a recent type of FRP laminate developed by the author. These laminates consist of flat panels, typically 900mm wide by any length. The laminates are flat on one face but have protruding T profiles on the other face. That face is also grit-coated for improved bonding to concrete. These panels can be cut to desired width and length and connected to the bottom and sides of a beam or slab, creating an annular space between the panels and the host structure. The annular spaced is filled with non-shrink grout or concrete. The T profiles act as reinforcing bars that are permanently attached to the panel, making the panel behave as a stay-place-form that includes reinforcing bars. In most cases, the tensile strength of the flat panel and the T profiles add sufficient strength to eliminate the need for any additional reinforcing bars.

The panels are non-corroding, ensuring a long service life for the repaired structure. Moreover, the panels act as an impervious barrier, keeping moisture and oxygen away and significantly reducing the corrosion rate of the host structure. The repairs are ideal for projects with limited access or when long delays in traffic are deemed unacceptable. A case study using a similar solution at the Port of Galveston will also be presented.

1 INTRODUCTION

Corrosion of reinforcing steel in structural elements has always been a concern. Billions of dollars are spent annually to repair corroded concrete beams, columns, walls, etc. worldwide. In the late 1980s the author introduced the use of non-metallic Fiber Reinforced Polymer (FRP) products for repair and strengthening of deteriorated beams (Saadatmanesh and Ehsani 1988). In that original concept, fabrics made with glass or carbon fibers are saturated with epoxy in the field and applied to the exterior surface of the concrete. By the next day, when the epoxy cures, the FRP reaches a tensile strength 2-3 times that of steel. That system has been used on thousands of projects worldwide and several countries have developed design guidelines for such repairs.

However, there are some limitations associated with the above repair technique. For example, the surface of the concrete must be flat prior to the application of FRP. This requires patching the damaged portion of the concrete, and waiting for the patching material to dry before FRP can be applied. These add significant time delays to the project. Secondly, application of FRP fabric as a wet layup method underwater is very difficult. The saturated fabric must be pressed to remain in fill contact with the structure while the epoxy cures. In the presence of moving water and wave action, this becomes impractical, especially on large flat surfaces such as bridge abutment walls and foundations. These challenges led the author to develop the new system described in this paper.

DOI: 10.1201/9781003483755-474

2 HISTORY OF THE DEVELOPMENT

In 2016 the author introduced a proprietary FRP solution for repair and strengthening of structures (Ehsani 2021). The technique involves constructing semi rigid shells that are connected to the host structure, creating an annular space between the structure and the shell. This annular space is filled with epoxy grout or concrete in a subsequent step. The shell will permanently stay in place, protecting the host structure from damage by water and oxygen. A main advantage of this system is that it eliminates the need for patching of the damaged surface and waiting for the patching material to cure. It also allows repairs to be performed underwater without the need for any coffer dams. Both attributes result in significant time and cost savings on projects.

2.1 *Repair of walls*

The above product is referred to as Sheet Pile Repair (SPiRe®). One technique to make these panels is by using the sandwich construction method. A 3-10 mm thick proprietary core is sandwiched between one or more layers of resin saturated glass or carbon fabric. The panels are 1200mm (4-ft) wide and are supplied in lengths up to 10m (30 ft). The panel thickness typically ranges from 10 to 20 mm (0.4 to 0.8 in.). Details of the application of this product were presented at a previous IABMAS conference (Ehsani 2022). To summarize, the panels are connected with J bolts to the deteriorated sheet pile; the edges of the panels are bonded with an epoxy seal to create an impervious stay-in-place form in front of the deteriorated wall. The length of the panels can be trimmed in the field to match the height of the wall at any location.

The annular space between the SPiRe® panels and the sheet pile is filled with concrete or grout. If needed, reinforcing bars can also be added in the annular space. The entire operation can be performed underwater without the need for any coffer dams. The combination of the SPiRe® panels and the grout provide an impervious protective coating for the wall that will prolong its service life by depriving the corrosion process from oxygen and moisture. The non-corroding FRP panels ensure a long maintenance-free service life for the repair system. Since its debut shown in this video to repair a 282 m (926 ft) seawall in Chesapeake VA in 2017, the product has been successfully used on a number of projects. The most recent project is the ongoing repair of 1 km (0.62 miles) of a seawall at the Port of Melbourne Australia.

2.2 *Repair of beams and decks*

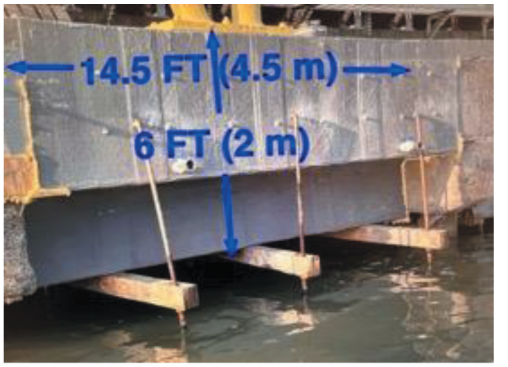
Repair of slabs or beams from below is a time-consuming process. The task becomes even more challenging when there is little headroom available, for example, when a bridge deck is too close to a body of water. In such cases, once the damaged concrete is removed, the forming of the beam and slab with such tight access adds significant time to the repair. Once the formwork is removed after the repairs, the host structure is exposed and subject to the same aggressive environment as in the past which could lead to the return of corrosion.

The same sandwich construction product SPiRe® can be used to build custom-sized shells that act as the stay-in-place form for the repair. This system was recently utilized to repair a portion of the deck at the Port of Galveston, Texas (Figure 1). The concrete beam and deck were severely corroded, and it was assumed that 50% of the longitudinal steel bars in the beam were lost to corrosion. The owners planned to repair the deck with conventional timber forms and remove them once the repair was complete. But assembling the heavy forms and their removal proved to be too costly.

Realizing the cost-savings, the owner became interested in trying the newly developed SPiRe®system in its inaugural application for such repairs. As shown in Figure 1a, spacers and glass FRP rebars were attached to the inside face of the shells. These shells were lifted and secured with anchors to the host beams and deck. The annular space was filled with non-shrink concrete that was pumped through grout ports. The shells will remain in place permanently, protecting the host structure from future exposure to seawater and corrosion. Figure 1c shows the project near completion where the main beams and deck have been repaired; repairs of the transverse beams are ongoing with the same process.



(a)



(b)



(c)

Figure 1. Repair of corrosion-damaged pier using the original SPiRe® system: (a) attaching reinforcing bars to the panels, (b)securing the panels to the structure and grouting the annular space, and (c) at com.

3 INTRODUCING SPIRE®+

As noted above, the original SPiRe® system acts only as a stay-in-place form but does not provide any structural strengthening benefit unless the annular space is filled with an epoxy grout to bond the shell to the host structure. Of course, adding reinforcing bars in the annular space will create a structural wall but this requires additional labor. To overcome this shortcoming, we have developed a new type of patent pending FRP panel dubbed SPiRe®+ that offers all the advantages of the original SPiRe® system plus a strengthening feature Ehsani 2023). These panels are made of glass FRP in a continuous pultrusion process. Various tows and glass roving in fabric form are saturated in a polyester resin bath and are pulled through a mold that compresses all these materials together. As the materials travel through the mold, they are subjected to heat to cure them quickly. Both the flat portion and the T profiles have a high glass fiber content, providing a tensile strength of about 207 MPa (30 ksi) for the panels.

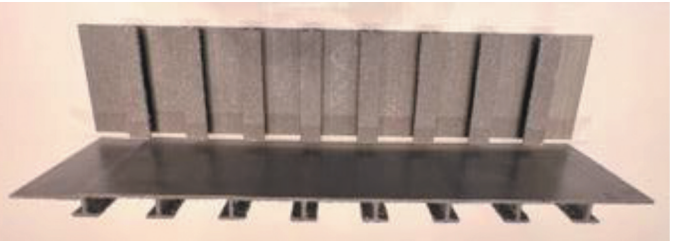


Figure 2. Front and back side view of SPiRe®+ panels.

The panels are 914 mm (3-ft) wide which is easy to lift and handle. Standard lengths are 3.6m and 5.5m (12 and 18 ft) long and can be trimmed to shorter lengths in the field. For larger projects, the panels can be manufactured in any length.

The outside face of the panels is smooth. However, the inside face includes protruding T profiles (Figure 2). The interior surface of the panels is coated with a layer of epoxy and sand to provide a grit-coated rough surface for improved bonding to concrete. This unique feature allows for bonding of the panels to the concrete; the T profiles behave as reinforcing bars for the repaired structure. The panels weigh 15.5 kg/m^2 (3.2 lb/ft^2).

3.1 *Test results*

To demonstrate the strength of the panels and the effectiveness of the grit-coated surface in transfer of loads, a beam or slab specimen was tested under flexure. A 200mm (8-in.) wide by 2900mm (9.5-ft) long piece of SPiRe®+ was cut such that it included two T profiles. This panel

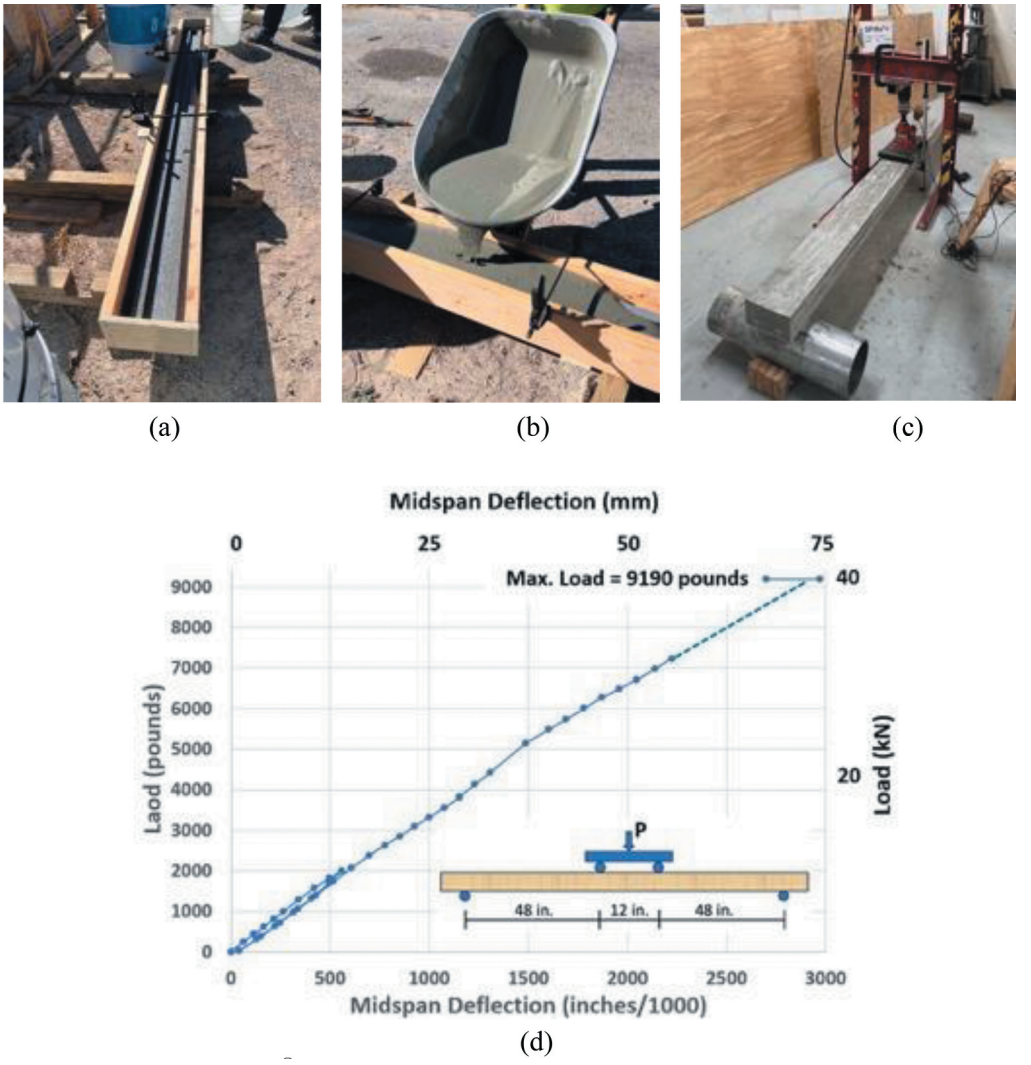


Figure 3. Testing of SPiRe®+: (a) form preparation, (b) flowable grout, (c) test set up, and (d) load vs. deflection response.

was used as the base of a form and 100mm (4-in) high timber was placed around all four sides (Figure 3a). A commercial grade, non-shrink, Precision Grout by Quikrete was mixed with water at a rate of 5 liters per 22.7 kg (50-pound) bag. This resulted in a mix consistency between flowable and liquid (Figure 3b) that should achieve a compressive strength of 48 MPa (7000 psi) in 7 days. The specimen was moist cured until it was tested on the 7th day.

The specimen was subjected to 4-point bending on a span of 2740mm (9 ft) as shown in Figure 3c. The specimen was first loaded incrementally to 9 kN (2000 pounds) and gradually unloaded. The unloading slope was similar to the initial loading slope and no permanent deflection was recorded. Next, the specimen was reloaded incrementally up to 32.16 kN (7230 lbs), at which time the displacement dial was removed to prevent any potential damage. As the specimen was loaded, at a load of 40.88 kN (9190 lbs), the testing frame started to twist, and the test was stopped. There was no sign of damage on the tension or compression face of the specimen. Several small cracks about 1mm wide and 50-60mm long were distributed fairly uniformly along the length of the beam, indicating good bond between the SPiRe®+ panel and the grout.

It is clear that if the testing frame had not failed, the specimen could have resisted additional loads. Nevertheless, even assuming the load of 40.88 kN as the failure load, this corresponds to a maximum moment of 12.46 kNm (110 k-in) for the 200mm (8-in.) wide panel. In terms of comparison with steel reinforcement for a similar slab with a cross section of 200mm wide x 100mm thick (8 in. x 4 in.), this SPiRe®+ panel is equivalent to 20mm, 400 MPa bars provided at a spacing of 90mm (No. 6 Gr. 60 steel bars at a spacing of 3.5 in.). This is a significant amount of reinforcement for strengthening most existing structures.

In addition to the ease of installation, the presence of the SPiRe®+ panels will permanently protect the host structure from corrosion caused by exposure to the environment.

3.2 *Repair of walls*

Installation of SPiRe®+ for repair of a seawall or bulkhead is similar to the original SPiRe®. In repairing a seawall, for example, L bolts are inserted and connected to the seawall on an approximately 1m x 1m (3 ft x 3 ft) grid. The SPiRe®+ panels are connected to these bolts using washers and nuts. The distance between the panels and the front face of the wall can be easily adjusted with the all-thread bolt and nut. A sealant is applied to the overlapping joint to create a watertight connection and successive panels are installed until the desired length of the wall is covered. Next, the bottom and edges of the annular space are sealed before concrete or grout is placed in the annular space. This can be achieved either by the tremie method or by using pumps and grout ports.

For repair of other structures, such as a beam, the panels can be cut to the desired width and their edges are bonded together using angles that are made of the same GFRP materials. These panels can be assembled in advance to create a shell that is lifted as one unit and secured to the beam before the annular space is filled with grout. Alternatively, individual panels can be secured to the host structure and their edges bonded together at the same time. In case any additional reinforcement is needed, GFRP rebars can be inserted between the T profiles using special spacers that we provide.

3.3 *Repair of beams and decks*

Conventional repair of bridge girders is very time consuming and often requires disruption of traffic (Figure 4a). The panels provide major cost and time saving in such projects. For repair of a deteriorated bridge beam, for example, the panels can be cut to the required width and their edges can be bonded using L-shaped angles, epoxies and bolts. The beam surface needs minimal preparation or patching of the damaged areas; in fact, an uneven and rough surface is preferred over a smoothly finished one. The entire repair assembly can be lifted quickly and secured to the underside of the bridge or slab with anchor bolts. The annular space between the SPiRe®+ panels and the beam is filled with concrete. The entire operation may be completed in one night when the traffic on the roadway is light.



Figure 4. Repair of bridge girders with SPiRe®+ system allows fast repair of bridges and eliminates disruption of traffic.



Figure 5. Repair of bridge girders and decks over water by attaching segments of SPiRe®+ panels directly to the bridge.

If the bridge crosses a waterway and is close to the surface of the water, the low headroom below the bridge makes the repairs very costly (Figure 5). The crew can assemble the formwork of desired size and shape in advance and deliver it to the site on a barge. The workers can hoist the lightweight forms up and secure it with anchor bolts to the underside of the bridge. Alternatively, individual flat panels can be bolted to the bridge; the edges of these panels can be epoxied and/or bolted together to create the desired covered area directly on the bridge. At this point, the annular space between the panels and the bridge is filled with concrete.

3.4 *Additional flexural and shear reinforcement*

As stated earlier, the panels provide significant flexural capacity and for most repair and retrofit projects, there is no need for additional flexural reinforcement. Nonetheless, if necessary, additional reinforcing bars can be connected to the panels using the rebar holders shown in Figure 6. In such cases, it is recommended to use nonmetallic GFRP bars that will not corrode.

In most applications for repair of slabs or walls, there is no need for increasing the shear capacity of the element. However, if the retrofit of a girder or beam requires shear capacity enhancement, U-shaped stirrups made with non-corroding GFRP bars can be used. These can be attached to the shell shown in Figure 4 prior to lifting the shell. Alternatively, when individual panels shown in Figure 5 are being utilized, the shear reinforcement can be positioned around the beam before the panels are secured to the beam.

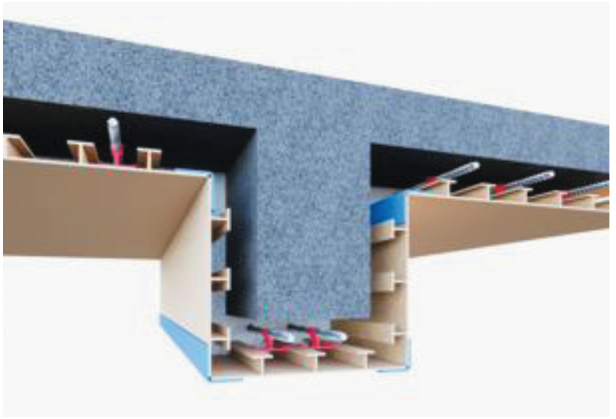


Figure 6. Additional flexural reinforcement connected to special rebar holders.

3.5 *Protection of coastal communities from flooding*

The versatility of the SPiRe®+ panels affords them many opportunities for use in the construction industry. For example, recent climate change and global warming has resulted in significant flooding of communities along riverbanks. Many coastal communities worldwide are spending millions of dollars to protect buildings and their residents from these events. One solution shown in this video is to attach the panels to the top of an existing seawall. As many panels as needed can be added, with a sealant applied to the overlapping joint region, to create a wall of desired height and length. Additional panels will be installed on the land side. These land and water side panels get connected together using through bolts. The annular space between the panels is filled with concrete.

The wall can be erected very quickly and at a low cost. Furthermore, the wall has no corroding materials such as steel, ensuring a long maintenance-free service life. As shown in Figure 7, landscaping, planters and pedestrian walkways can also be added on the land side to make the solution more appealing to the residents.



Figure 7. Application of SPiRe®+ panels to extend the height of seawalls in protecting communities from flooding due to rising sea levels.

3.6 *Advantages of the proposed solution*

The repair system presented here offers significant advantages over conventional repair methods. While the benefits may vary from project to project, some of the key benefits of this system include:

- ✓ Eliminating or minimizing traffic disruption and road closures
- ✓ Eliminating the need for patching of damaged concrete and surface preparation
- ✓ Significant savings in repair time

- ✓ Eliminating the need for coffer dams to perform the repairs
- ✓ Reducing potential construction errors since the reinforcing elements are built into the panels
- ✓ Providing a permanent impervious barrier encapsulating the host structure to keep moisture and chemicals out, thus prolonging the service life of the host structure, and
- ✓ Being a long-lasting repair since the panels include no corroding materials (e.g. steel).

All the above advantages result in significant time and cost savings on many repair and retrofit projects.

4 SUMMARY AND CONCLUSIONS

This paper presents a new product developed by the author following his 4 decades of experience in creating solutions for repair and strengthening of the infrastructure. A unique GFRP panel is described that is very versatile and can be used in many applications for repair of existing seawalls, bridge beams, decks, etc. Other applications for addressing sea level rise due to global warming are also covered. The panels offer tremendous strength, eliminating the need for additional reinforcing bars in most applications. The non-corroding panels also form an impervious barrier to keep moisture and oxygen away from the host structure, significantly reducing its corrosion rate.

REFERENCES

Ehsani, M. 2021. Structure Reinforcement Partial Shell. US Patent No. 10,968,631, United States Patent and Trademark Office.

Ehsani, M. 2022. "New solutions for repair of submerged piles and bulkheads," *Proceedings*, IABMAS, Barcelona, Spain, ISBN 978-1-032-35623-5; July 2022, 2510–2517

Ehsani, M. 2023. Repair and Strengthening of Corroded Structures. Provisional Patent Application No. 63458144, United States patent and Trademark Office.

Saadatmanesh, H. and Ehsani, M.R. 1988. "Strengthening of Concrete Girders with Epoxy Bonded Fiber Composite Overlays," *Proc.*, NSF-Sponsored Symposium on Bridge Research in Progress, Des Moines, Iowa, September 1988, pp. 117120.

Bridge Maintenance, Safety, Management, Digitalization and Sustainability – Jensen, Frangopol & Schmidt (eds)
© 2024 The Author(s), ISBN 978-1-032-77040-6
Open Access: www.taylorfrancis.com, CC BY-NC-ND 4.0 license

Incremental repair method for corroded bolted connection

E. Yamaguchi, N. Tamada, U. Agvaanluvsan, T. Takai & M. Wada
Kyushu Institute of Technology, Kitakyushu, Japan

ABSTRACT: For the repair work of a corroded bolted connection, common practice is to use temporary bents or a bypass member over the connection. The costs of these methods are quite high and the traffic needs be regulated. The present study explores a repair method that requires no bents, no bypass member and no traffic regulation. The method is to conduct repair in an incremental fashion: the repair work proceeds gradually, part by part. Its validity is investigated by FEA. For the best accuracy, a bolt is to be modelled by 3-D solid elements, but the computational cost is very high. The employment of connector elements is therefore tried and its effectiveness is confirmed by the comparison with the results of solid element analysis and experiment, using a small connection model. The proposed method is then applied to a 4×23 bolted connection. The validity is verified by FEA with connector elements.

1 INTRODUCTION

One of the most critical phenomena that could control the service life of a steel bridge is corrosion. Because of the complexity of its geometry, the quality of coating tends to be lower in a bolted connection than that in the other part of a steel bridge and water tends to be stuck in a bolted connection. As a result, a bolted connection is often found severely corroded. An example is given in Figure 1. The location of the connector is on the top flange of the beam in a steel moment frame supporting an elevated expressway. There seemed water leakage at the end of the bridge, leading to the corrosion.



(a) Overview (b) Bolted connection

Figure 1. Corroded bolted connection.

For the safety of a bridge, a corroded bolted connection has to be repaired. Bolts are to be replaced and a splice plate is to be replaced or reinforced. To conduct such a repair work safely, common practice is to use temporary bents or an extra member called a bypass member over the connection. Either work is accompanied by the regulation of traffic. Not only construction cost but also social cost would occur.

DOI: 10.1201/9781003483755-475



Figure 2. Connection with 6×1 bolt layout.

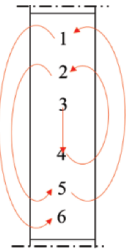


Figure 3. Bolt-removal order.

The present study explores a repair method that requires neither a bent nor a bypass member. It wouldn't impose traffic regulation, either. In short, in the method, some of the bolts would be removed, the unevenness of the corroded splice-plate surface over the area of the bolt removal is fixed, a slice of plate would be put on that region and new bolts are installed. The procedure is repeated until the repair of the whole corroded area is completed. This repair procedure is as it were an incremental method.

During the repair work, safety margin is reduced upon the bolt removal. Safety has to be ensured during the entire period of the repair work. The objective of the present study is to propose the incremental repair method and investigate its validity.

2 MODELING OF BOLT

The finite element method is the mainstay of the present study. At the current state, it is possible to model a bolt by 3-D solid elements as it is. However, the computational cost including the modelling would become very high. It cannot be a choice from a practical point of view.

The software called ABAQUS (Dassault Systemes Simulia Corp. 2013) is to be used in this study. It has a connector element which connects two nodes and controls their relative motion. The present study tries to apply this element to simulate the mechanical behavior of a bolt. The connector element is so simple that computational cost would be much smaller than that of the 3-D solid element analysis. Therefore, the present study first explores a possibility for using a connector element to model the mechanical behavior of a bolt.

A connection with the 6×1 bolt layout (Figure 2) is studied. As a repair work, bolts are replaced herein. The order of the bolt replacement is illustrated in Figure 3. The connection is analyzed by two models, the sophisticated model using 3-D solid elements and the connector-element model. The replacement of a bolt is simulated by the disappearance of a bolt followed by the appearance of a bolt in the analysis.

Tensile load is applied to the connection. The opening displacement, the gap between the base plates, changes during the repair work and is computed in each analysis.

The numerical results are presented in Figure 4. The dotted line is the opening displacement obtained by the 3-D solid elements analysis while the dash-dotted line by the connector element analysis. Both show the gradual increase of the opening displacement with the progress of the repair, and the difference between the two numerical results appears quite small. It can be stated then that the employment of the connector element for modelling a bolt is justified.

To see the validity of the present numerical approach, experiment is conducted. Three specimens are prepared and tested. Figure 5 shows one of the specimens with one bolt removed; the hole indicates the location of the removed bolt. The experimental results are shown in Figure 6. There is variability in the experimental results, but the difference is quite small and

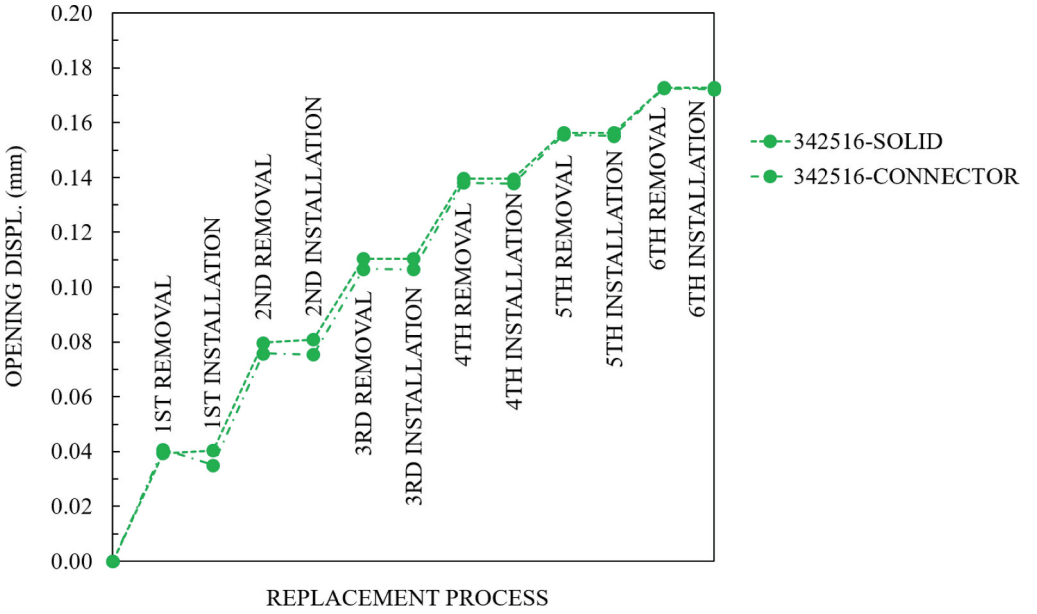


Figure 4. Opening displacement by FEA.



Figure 5. Test specimen with one bolt removed.

insignificant. Figure 7 shows the experimental results together with the numerical results. There is a discrepancy between the numerical and experimental results, but the difference decreases with the increase of the opening displacement and it becomes insignificant. The numerical approach employed in the present study is thus validated by the experiment.

3 REPAIR OF CORRODED BOLTED CONNECTION

Based on the existing corroded bolted connection, a bolted connection model is constructed and the proposed repair method is applied to it. Due to symmetry, only a half of the bolted connection is considered, which is shown in Figure 8. Each splice plate in the half model has the 4×23 bolt layout. The thickness of the base plate is 19 mm, the thickness of the top splice plate 11 mm and the thickness of the bottom splice plate 12 mm. The top splice plate and the bolts are supposedly corroded badly.

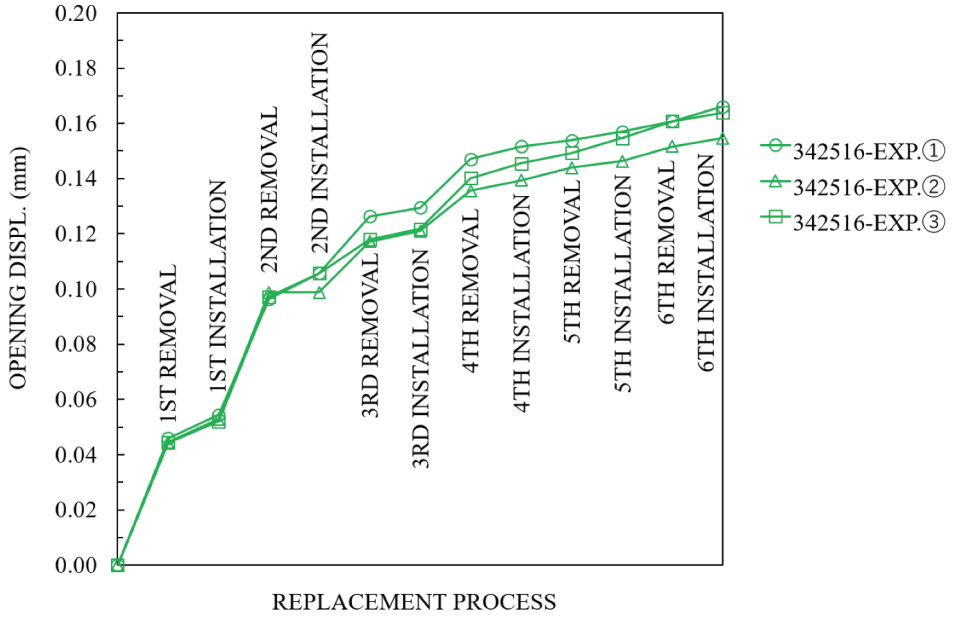


Figure 6. Opening displacement by experiment.

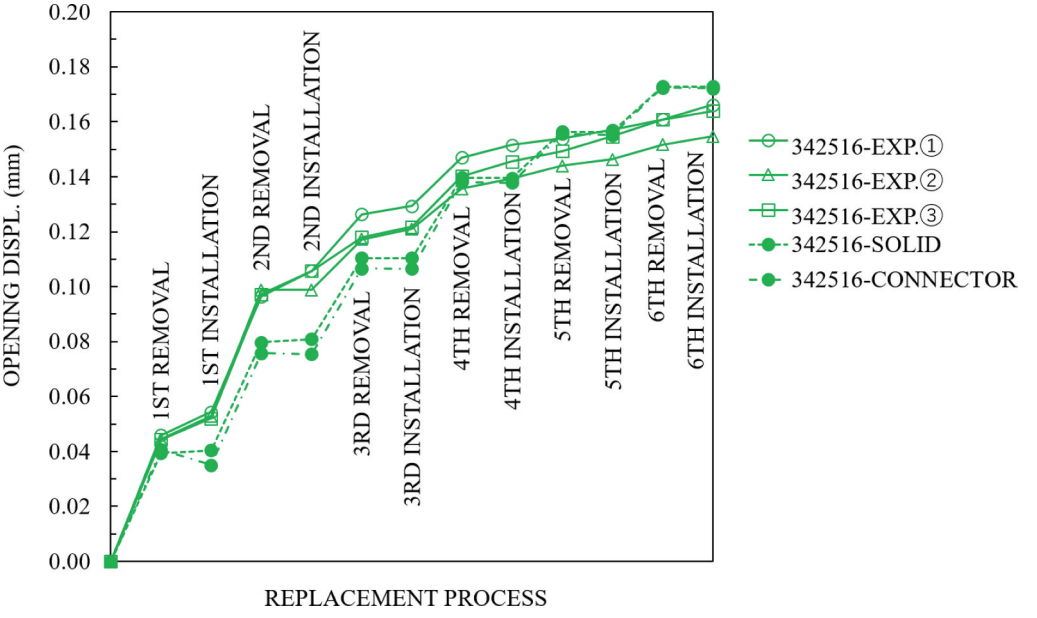


Figure 7. Comparison of FEA and experimental results.

To take account of the deterioration due to corrosion, the thickness of the top splice plate is reduced by 3 mm and the axial force in each bolt by 25% (Shimozato et al. 2013). The repair work is to remove bolts, place a slice of plate for reinforcement and install new bolts. The repair is conducted bolt-column area by bolt-column area. The thickness of the additional slice of plate is 12 mm. As shown in Figure 9, the bottom splice plate consists of 5 smaller plates, Plates

A to E, because of the presence of the longitudinal stiffeners. The repair work is therefore carried out for each area of those 5 splice plates.

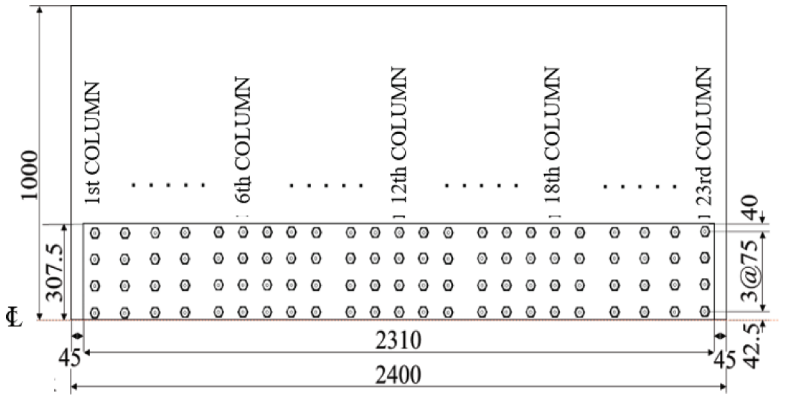


Figure 8. 4×23 bolted connection.

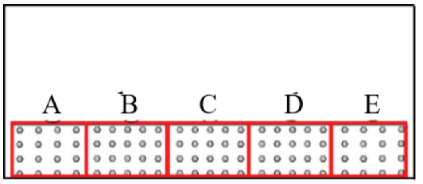


Figure 9. Bottom splice plate.

The safety is lowered by the removal of bolts, and the splice plates may start sliding on the base plate at that moment. The load that causes the opening displacement of 0.2 mm can be assumed the slip load. If the removal of bolts leads to the slip load smaller than the design load, that bolt removal cannot be admitted.

In the present study, the slip load is computed by FEA. Shell elements are employed for the base plate and the splice plates while connector elements are used for bolts. The coefficient of friction between the base plate and the additional plate is assumed 0.5, following the work by Tamba et al. (2014).

Three repair patterns, Patterns (a) to (c), are studied. In all these patterns, the repair is conducted bolt-column area by bolt-column area, and the difference lies in order of area to be repaired. In Pattern (a), the repair is done in order of Plates A, B, C, D and E. In each plate, the repair is carried out from the bolt-column area near the edge of the connection. In Patterns (b) and (c), the repair order is Plates C, B, D, A and E. In Pattern (b), the repair of each plate starts from the bolt-column area near the center of the connection, while in Pattern (c), the repair from the bolt-column area near the center of the plate.

Figure 10 shows the slip loads. When the bolts in the 1st bolt column are removed, the slip load is smallest in each pattern. The smallest slip load is observed in Pattern (a). The repair processes of Patterns (b) and (c) are exactly the same up to the repair of the 5th bolt column. The difference between Pattern (b) and (c), therefore, appears only at the removal of the bolts in the 6th bolt column, and the slip load of Pattern (b) is smaller. Although in all the patterns, the slip load is well above the design load ensuring the safety of the method, the safest repair procedure out of the three is Pattern (c). This result indicates that it is better to carry out repair from the plate near the center of a connection and, in each plate, from the column near the center of the plate.

4 CONCLUDING REMARKS

The incremental repair method for a corroded bolted connection was proposed. Even when a column of bolts was removed, the safety of the connection has been found unthreatened: the sliding load is much larger than the design load. It would be even safer if repair is carried out from

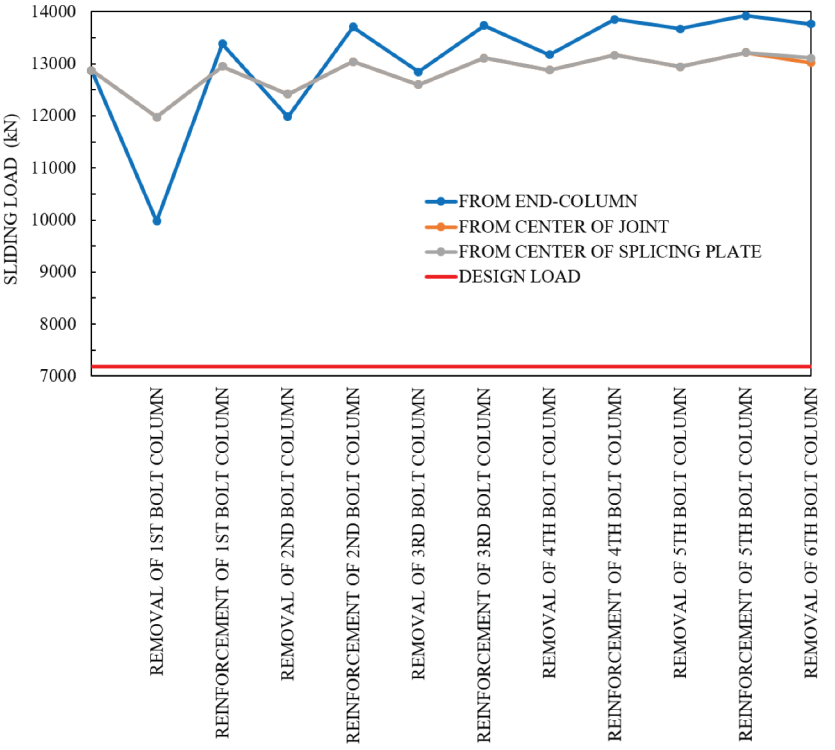


Figure 10. Sliding load.

the bottom splice-plate near the center of a connection and in each splice plate, from the area of the column of bolts near the center of the plate. The proposed incremental repair method requires no bents or no bypass member. Traffic regulation is not needed, either. The method is thus very practical and it could reduce the repair cost for a corroded bolted connection considerably.

In the present study, the validity of the application of the connector element to the modeling of a bolt has been concluded also. This conclusion is very useful from a practical point of view, as the usage of the connector element helps reduce computational time for the analysis of a bolted connection significantly.

ACKNOWLEDGEMENTS

The financial support for the present study, Grant-in-Aid for Scientific Research (C) (KAKENHI, No. 19K04582), is gratefully acknowledged.

REFERENCES

Dassault Systemes Simulia Corp. 2013. *User's Manual*, *ABAQUS Ver. 6.13*.

Shimozato T., Tai M., Arizumi Y., Yabuki T. & Nagamine Y. 2013. A study on evaluation for residual axial force of corroded high strength bolts. *Journal of Structural Engineering*, *JSCE* 59(A): 725–735.

Tamba Y., Yukito S., Yamaguchi T., Sugiura K., Higatani A. & Tabata A. 2014. Experimental study on static behavior of the high strength bolted joints which have some concavities and filled up with and applied adhesives in the surface. *Journal of Structural Engineering*, *JSCE*, 60(A): 703–714.

GS28: BRIDGE SAFETY - Safety and serviceability


Taylor & Francis
Taylor & Francis Group
http://taylorandfrancis.com

Bridge Maintenance, Safety, Management, Digitalization and Sustainability – Jensen, Frangopol & Schmidt (eds)
© 2024 The Author(s), ISBN 978-1-032-77040-6
Open Access: www.taylorfrancis.com, CC BY-NC-ND 4.0 license

A 2D TBI model to study lateral dynamics in ship impact event

D. Riboldi, L. Bernardini & A. Collina
Department of Mechanical Engineering, Politecnico di Milano, Milano, Italy

ABSTRACT: This paper presents a simplified 2D train-bridge dynamic interaction simulation tool to model the scenario of a ship collision against one of the piers of a bridge located on an oversea connection. Being rolling and lateral motion of each carbody of a train predominant in train motion following a ship collision event during train transit, only these two components of vehicle dynamics are considered. The bridge structure is modelled by means of a modal approach, ship impact is represented through a time dependent force, taken from literature. The proposed simplified model enables a fast check, thanks to a time-efficient simulation, during early bridge design phase, in terms of lateral carbody acceleration, so as to get an early representation of the influence of ship collision events on train lateral dynamics. In fact, the proposed model allows the user to test and investigate a large variety of scenarios, in terms of train and structure properties as well as loading features, in a fast and efficient way, without loss of relevant information. Moreover, this approach would enhance structure and train dynamic interaction understanding, highlighting the role played by train lateral dynamics and its interaction with bridge dynamics, in critical scenarios.

1 INTRODUCTION

Runability analysis represents an important stage in the design phase of bridges and viaducts. When dealing with structures built over large rivers or sea strait, ship collision events occurrence must be taken into account. This scenario is even more required considering that the number of bridges is constantly increasing, as long as the traffic of large and heavy ships sailing seas and rivers. In recent years many researchers dealt with this topic: there are many articles in literature since there are many variables that must be considered when performing runability analysis, some of them are herein briefly recalled.

There is a variety of bridge types with different specifications and features: for example, floating spans bridges may be used, as studied in (Sha et al. 2017), or cable stayed bridges, due to their lower cost in the construction stage and good design flexibility (Zhou et al. 2021). Because of their role in supporting the deck, piers are inherently at risk when dealing with lateral ship collision events (Gholipour et al. 2018), (Bernardini et al. 2023).

Moreover, it is important to consider the composition of the superstructure as it can be crucial in case of a ship deck-house collision, that may represent a very critical scenario. Sha et al. made a FEM-based study on this particular case, focusing on reinforced concrete (RC) and steel girders (Sha et al. 2017). Moreover, since the variety of vessels is significant, scholars carried out investigations considering different types of impact loads, such as barge impact which is featured by a load history that reaches linearly the primary peak and, then, the force reduces before growing again, non-linearly, in correspondence of the plastic deformation phase of the barge structure, creating a secondary peak, as presented in (Xie et al. 2022). On the other hand, when dealing with vessels, two categories can be distinguished, consisting in vessels with and without front bulb respectively. The first one has been investigated, among the others, by (Wei Fan et al. 2016) using a FEM approach to model the force-deformation curve of the bulb to have a deeper understanding on how the energy is exchanged between ship and bridge, and, consequently, the impact force. The authors in (AbuBakar and Dow 2019), instead, opted for

DOI: 10.1201/9781003483755-476

a full-scale experiment for the same purpose. Also in this case, as for the barge, the weight, speed and angle of the boat during the collision was found to play a pivotal role. In the framework of train bridge interaction, also train parameters influence on runability assessment must be considered; among them, the vehicle speed (Li et al. 2015), which is of interest also because the use of high-speed trains is growing (Olmos and Astiz 2023), technical parameters such as suspensions stiffness of the carbody, damping and mass, as well as the composition of the train. In addition, the position of the train at the instant in which the collision occurs can also affect vehicle accelerations and, therefore, passengers' safety (Li et al. 2015). A comprehensive review of train-bridge dynamic interaction problem in the events of wind, waves, ship impact and earthquakes actions are presented in (Li et al. 2022).

From the existing literature, it is possible to notice that the majority of articles regards examinations that are carried out using FEM analysis or full-scale experiments. While the latter can provide accurate solutions, on the other hand, they are not so immediate, given the impossibility to conduct an experiment using natural dimensions, and it may be quite difficult to perform also meaningful scaled tests. Moreover, while being versatile, FEM analysis is time-consuming when large infrastructures are considered, requiring a long time to simulate the scenario of interest with all the different design options, as it may occur on the early design stage of a bridge.

The aim of the 2D Train-Bridge-Interaction (TBI) simplified model which will be presented in this paper is to provide a more time-efficient simulation tool suitable for early design stage of bridges, and early-stage determination of the most critical scenarios. Designers could make use of this kind of tool to simulate a large variety of scenarios and make a first selection of the most critical ones in terms of runability analysis, from lateral dynamics perspective. Once most critical scenarios are defined, a more refined analysis (i.e., with 3D approaches) may be performed.

Compared to other papers dealing with vertical train-bridge dynamic interaction simulation, such as (Lou and Zheng 2007) and (Kohl et al. 2023), in this work, the focus is on lateral dynamics that will be investigated since it is crucial in case of ship impact.

The article is organized with the following outline: Section 2 is devoted to the description of the simulation model. In Section 3, the outcomes of a set of simulations are illustrated and critically discussed. Finally, in Section 4, conclusions are drawn.

2 MODEL DESCRIPTION

The developed 2D model for the simulation of train-bridge lateral dynamics is set up as follows: bridge dynamics is modelled by means of a modal approach (Cheli and Diana 2015), while each train coach through a 2 degrees-of-freedom lumped parameters model. Lateral and roll degrees-of-freedom of each carbody are considered, while the bogies are considered to fully participate to the lateral motion of the deck, according to the scheme in Figure 1.

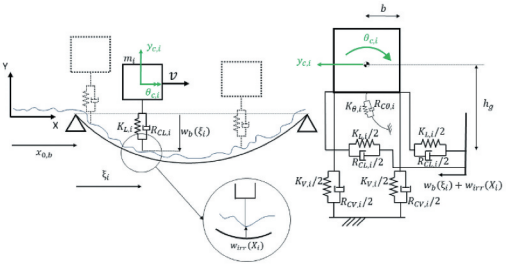


Figure 1. Top view of the scheme of the 2D VBI model developed in this work. A mass for each coach composing the entire train is considered.

The vehicle is represented through a sprung mass, considering vertical, lateral and torsional (anti-roll bar) stiffnesses, in charge of modelling secondary suspension effect: lateral track irregularity is also taken into account in the simulation, and, in the present work, it was calculated from the PSD reported in (ORE B176 1989).

The equations of motion were written according to Lagrange formulation which relies on the definition of kinetic, potential energies, as well as the dissipative function and the virtual work performed by external forces not considered in the computation of the aforementioned functions.

Therefore, according to the modal approach theory (Cheli and Diana, 2015), the kinetic energy of the whole system can be written in the following additive form:

$$T = \sum_{i=1}^{m} \left(\frac{1}{2} M_{c,i} \dot{y}_{c,i}^2 + \frac{1}{2} J_{c,i} \dot{\theta}_{c,i}^2 \right) + \frac{1}{2} \int_0^L m_b \left(\frac{\partial w}{\partial t} \right)^2 dx \tag{1}$$

where m is the number of coaches that are considered, $\mathrm{M_{c,i}}$ is the i-th carbody mass, $\dot{y}_{c,i}$ the velocity and $\dot{\theta}_{c,i}$ the rolling speed of the i-th car considered in the simulation. The second part of kinetic energy expression, including the integral (L is the length of the bridge), comes from the analytical derivation of the kinetic energy of the bridge; m_b is the mass per unit length of the bridge, while $(\partial w/\partial t)$ is the lateral speed of any section of the bridge which must be integrated over the length L to obtain the kinetic energy of the structure. Therefore, w represents the lateral displacement of the bridge (w_b in Figure 1). It is worth mentioning that in the present work the lateral mode shapes of the bridge are introduced as analytical modes of a simply supported beam. The obtained mode shapes are close to the ones of a complete viaduct structure composed of deck and piers (Bernardini et al. 2023). Then, the potential energy is computed as follows:

$$V = \sum_{i=1}^{m} \left(\frac{1}{2} K_{L,i} \left(y_{c,i} - w(\xi_i, t) + h_{g,i} \theta_{c,i} - w_{irr}(X_i) \right)^2 + \frac{1}{2} K_{\theta,i} \theta_i^2 + \frac{1}{2} K_{V,i} (b_i \theta_i)^2 \right) + \frac{1}{2} \int_0^L EJ \left(\frac{\partial^2 w}{\partial x^2} \right)^2 dx \tag{2}$$

Where $K_{L,i}$ and $K_{V,i}$ are the stiffnesses of the secondary spring of each i-th coach, respectively in lateral (y) and vertical (z) directions. Referring to Figure 1, it is important to notice that $K_{V,i} = 2K_{V,sg}$ and $K_{L,i} = 2K_{L,sg}$, while $K_{\theta,i}$, instead, represents the stiffness of the anti-roll bar of the coach, connecting carbody and bogie frame, for the roll motion only. The parameter h_g is the height of the center of gravity (c.o.g.) of the carbody with respect to the elastic center of the springs of the secondary suspensions, b is half lateral distance between left and right secondary springs. Moreover, $\mathrm{y_c}$ and θ_c represents the two degrees-of-freedom of the train model, $w_{irr}(X_i)$ represents the lateral track irregularity contribution, which exists also outside the bridge span (for $X_i \geq 0$), evaluated at the position $X_i = vt - x_{0,i}$, where $x_{0,i}$ represents the distance of the i-th coach from the absolute initial position (where irregularity starts). Moreover, the position $\xi_i = vt - x_{0,i} - x_{0,b}$ represents the position of the i-th carbody from the beginning of the bridge, where t is the simulation time. Finally, E is the Young Modulus and J is the inertia moment of the bridge structure. Considering a modal approach is adopted for modelling bridge dynamics, the overall potential energy can be written as follows:

$$V = \sum_{i=1}^{m} \left(\frac{1}{2} K_{L,i} \left(y_{c,i} - \sum_{j=1}^{n} \Phi_j(\xi_i) q_j(t) + h_{g,i} \theta_{c,i} - w_{irr}(X_i) \right)^2 + \frac{1}{2} K_{\theta,i} \theta_i^2 + \frac{1}{2} K_{V,i} (b_i \theta_i)^2 \right) + \frac{1}{2}^T [K_s] \underline{q} \tag{3}$$

where $\Phi_j(\xi_i)$ is the j-th mode shape function calculated in correspondence of ξ_i, while $\underline{q}(t)$ contains the modal coordinates (Cheli and Diana 2015), describing bridge lateral motion. Furthermore, while m stands for the number of coaches, n stands for the number of modes considered in the simulation. Finally, $[K_s]$ is defined as the structural modal stiffness matrix of the bridge.

The dissipative functions can be written as follows:

$$D = \sum_{i=1}^{m} \left(\frac{1}{2} R_{CL,i} \left(\dot{y}_{c,i} - \frac{\partial w}{\partial t}(\xi, t) + h_{g,i} \dot{\theta}_{c,i} - \left. \frac{\partial w_{irr}(x)}{\partial x} \right|_{x=X_i} \frac{dx}{dt} \right)^2 + \frac{1}{2} R_{C\theta,i} \dot{\theta}_i^2 + \frac{1}{2} R_{CV,i} (b_i \dot{\theta}_i)^2 \right) + \frac{1}{2} \dot{\underline{q}}^T [C_s] \dot{\underline{q}} \tag{4}$$

where R_{CL} and R_{CV} are the lateral and vertical damping values of the secondary suspension of each carbody, while $[C_s]$ is the structural modal damping matrix of the bridge. No damping is associated to the anti-roll bar. The term related to the lateral speed of the bridge can be expressed, computing the derivative, as:

$$\frac{\partial w}{\partial t}(\xi,t)=\sum_{j=1}^{n}\left.\frac{\partial\Phi_j(x)}{\partial x}\right|_{x=\xi_i}\frac{dx}{dt}q_j(t)+\sum_{j=1}^{n}\Phi_j(\xi_i)\frac{\partial q_j(t)}{\partial t}=\sum_{j=1}^{n}\Phi'_j v q_j+\sum_{j=1}^{n}\Phi_j\dot{q}_j \tag{5}$$

$\dot{y}_c$ and $\dot{\theta}_c$ now represents the speeds of the 2 degrees-of-freedom coach model.

$[C_s]$, as mentioned before, is the structural modal damping matrix related to the bridge expressed as Rayleigh damping (with $\alpha = 0.1$ and $\beta = 0.001$):

$$[C_s]=\alpha[M_{bb}]_{nxn}+\beta[K_s]_{nxn} \tag{6}$$

Finally, the time-dependent force term $F(t)$, modelling the ship impact event occurred at ξ_k position, is introduced in the equation of motion of the system obtaining the following formulation:

$$[M]\underline{\ddot{z}}+[C]\underline{\dot{z}}+[K]\underline{z}=\underline{\dot{b}}+\underline{b}+c_p[\Phi_1(\xi_k),\Phi_2(\xi_k),\ldots,\Phi_n(\xi_k),0,\ldots,0]^T F(t) \tag{7}$$

where the coefficient c_p considers that the motion at the impact point is close to the base of the pier, reducing the modal amplitude with respect to the deck level. The terms $\underline{b}$ and its time derivative $\underline{\dot{b}}$ come from dissipative and potential functions: these terms are due to track lateral irregularity $w_{irr}(x)$, which acts as an external input along the lateral direction. The term $\underline{b}$ is defined as follows:

$$\underline{b}=\begin{Bmatrix}\underline{b_b}\\ \underline{b_t}\end{Bmatrix} \tag{8}$$

where:

$$\underline{b_b}=\sum_{i=1}^{m}\left(K_{L,i}\begin{Bmatrix}-\Phi_1(\xi_i)\\ -\Phi_2(\xi_i)\\ \vdots\\ -\Phi_n(\xi_i)\end{Bmatrix}w_{irr}(X_i)\right) \tag{9}$$

and:

$$\underline{b_t}=\begin{Bmatrix}K_{L,1}\\ K_{L,1}h_{g,1}\\ \vdots\\ K_{L,m}\\ K_{L,m}h_{g,m}\end{Bmatrix}w_{irr}(X_i) \tag{10}$$

Equation (7) describes the lateral motion of the system in case of ship collision event: at this stage, it is important to observe that, while mass matrix is constant throughout the whole simulation, damping and stiffness matrices changes in time according to vehicles motion on the structure. By updating these two matrices, time instant by time instant, it is possible to model vehicle bridge lateral dynamic interaction. The time integration of the equation of motion was performed considering Newmark algorithm as provided in (Rao 2018).

3 RESULTS

The simulations are carried out considering train and bridge parameters collected in Table 1. For the bridge model, ten mode shapes are considered. The first lateral frequency of the bridge is $f_1 = 0.6\ Hz$ which is equivalent to the lateral-roll frequency of coach P_1, while P_2 lateral-roll frequency is equal to 0.51 Hz.

Table 1. Bridge and train main parameters.

Bridge parameters				
Mass (m_b)	66000		kg/m	
Young modulus (E)	29000		MPa	
Inertia moment (J)	350		m^4	
Length (L)	180		m	
1st Natural frequency(f_1)	0.6		Hz	
Train Parameters				
Coach type	P_1		P_2	
Mass	51000	kg	58000 kg	kg
Rotational inertia	1.65e5	$kg \cdot m^2$	1.8e5	$kg \cdot m^2$
Secondary suspension parameters				
Vertical stiffness	$2 \cdot 1.4e6$	N/m	$2 \cdot 1.4e6$	N/m
Lateral stiffness	$2 \cdot 4.3e5$	N/m	$2 \cdot 3.4e5$	N/m
Torsional stiffness	$2 \cdot 3.8e6$	N/rad	$2 \cdot 3.8e6$	N/rad
Vertical damping	$2 \cdot 3.7e4$	$N \cdot s/m$	$2 \cdot 3.7e4$	$N \cdot s/m$
Lateral damping	$2 \cdot 3e4$	$N \cdot s/m$	$2 \cdot 2.5e4$	$N \cdot s/m$
C.o.g. height (h_g)	1.3	M	1.3	m
Semi-width of the car (b)	0.95	M	0.95	m
1st Natural frequency (lateral-roll)	0.6	Hz	0.51	Hz
2nd Natural frequency (roll-lateral)	1.36	Hz	1.27	Hz

Figure 2(a) illustrates the time history of the barge impact used in this work. The plotted force has a similar shape to the one adopted in (Xie et al. 2022). The adopted force quickly reaches the peak value of 15 MN in the linear phase, then, during buckling unstable phase there happen a rapid drop of impact force. After that, there is plastic deformation phase of the barge structure which causes a nonlinear increase of impact force, which grows slowly finally reaching an extreme value of 4.3 MN. Last, in the unloading phase, the barge and whole bridge begin to separate from each other, the elastic deformation recovers, thus, the impact force decreases rapidly.

The presented force is applied according to the system Equation (7), considering a proper scaling factor (c_p=0.167 in this case), to take into account the location of the impact point on the pier.

The structure lateral displacement and accelerations, evaluated at midspan, are plotted in Figure 2(b): a displacement peak of 12 mm is produced by the impact at midspan, comparable to what was obtained in (Xie et al. 2022) and (McVay et al. 2009), with an acceleration peak of 0.95 m/s^2. The bridge span length is equal to 180 m, and the train is running at a constant forward speed equal to 100 km/h. At the simulation starting time (t=0s) the first coach is positioned 80 m before the beginning of the bridge: moreover, a distance of 25 m is considered between one carbody center of mass and the others. A convoy consisting of four coaches is adopted in the presented simulations: two different coach types are considered, namely P_1 and P_2, whose main properties are collected in Table 1. The train configuration is P_1-P_2-P_1-P_2. In Figure 2(b), vertical dashed and labeled lines identify the time instants at which each coach of

the convoy enters and leaves the bridge. In Figure 2(b) it is clearly visible the time instant at which the impact occurs, which happens when the first coach of the train is crossing the bridge at a section 45 m after bridge entrance. Moving from structure perspective to the vehicle point of view, Figure 3 shows the accelerations of the two coach's degrees-of-freedom (y and θ) for each of the four coaches composing the train convoy. Before the impact, it is possible to notice that the only source of excitation of the vehicle lateral motion is due to track geometrical irregularity. The motion due to the occurrence of the impact can be clearly observed given higher accelerations amplitude for the two degrees-of-freedom of each rail vehicle.

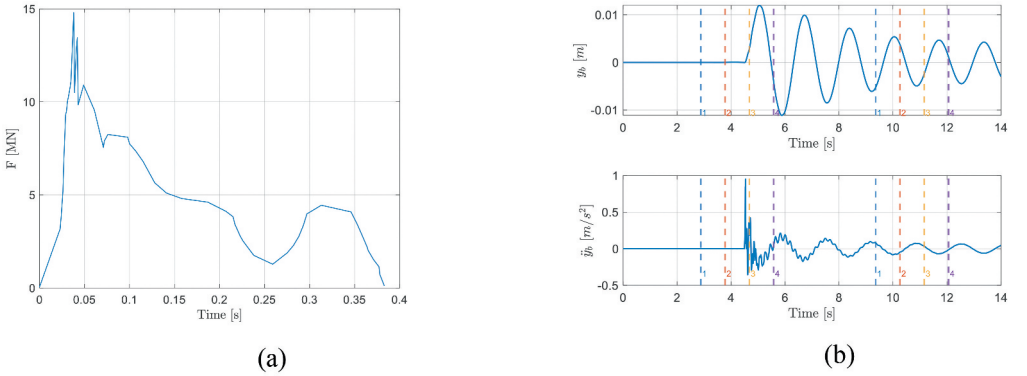


Figure 2. (a): Time history of the impact force considered in the presented simulations. (b): Lateral displacement and acceleration of the bridge evaluated at midspan.

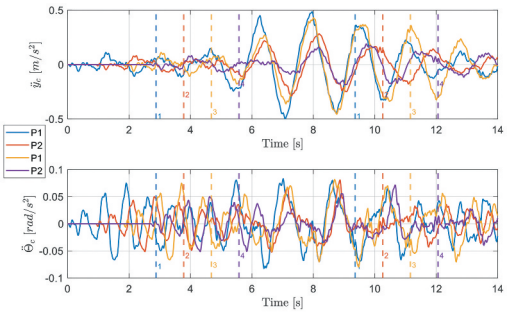


Figure 3. Lateral and rolling accelerations of the train coaches (P1-P2-P1-P2).

A set of simulations was performed from 100 km/h to 250 km/h, considering a step of train speed of 25km/h. In Figure 4(a), peaks of vehicle lateral accelerations are plotted as a function of train travelling speed: it is possible to observe that, for the considered speed range, coaches with a frequency corresponding to the one associated to bridge first lateral mode shape (P_1) present higher accelerations compared to coaches with a frequency that is further from 0.6 Hz (P_2). This outcome is valid for each considered speed, in fact, the peak values of the lateral and roll acceleration associated with P1 coaches are always larger than the ones featuring P2. Moreover, another aspect which is worth pointing out is that larger speeds do not always lead to higher lateral acceleration peaks: this result may be due to the time on which the train travels over the bridge structure once excited by the ship impact event. The faster is the forward speed, the lower is the time interval spent by the train over the structure, and therefore the lower is the amount of energy received in input by the train from the bridge, cycle by cycle. This reasoning can also explain while for speed higher than 175 km/h the rear coach shows

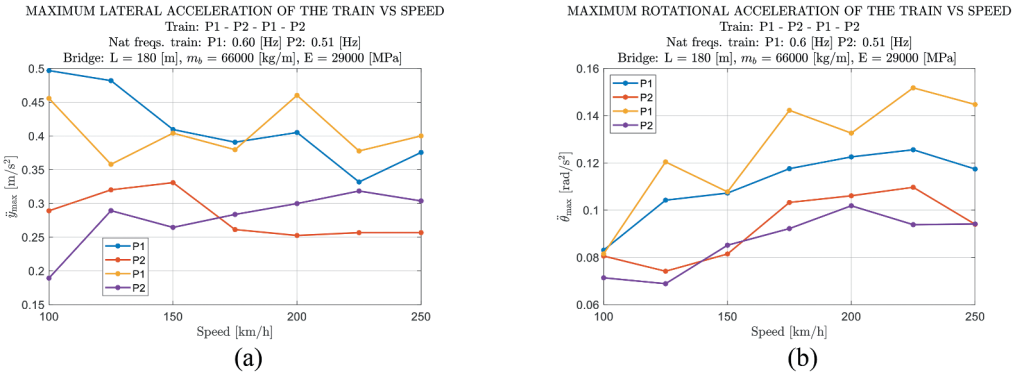


Figure 4. (a). Carbody lateral acceleration peaks plotted as a function of train speed for each coach of the train convoy. (b): Carbody roll acceleration peaks plotted as a function of train speed for each coach of the train convoy.

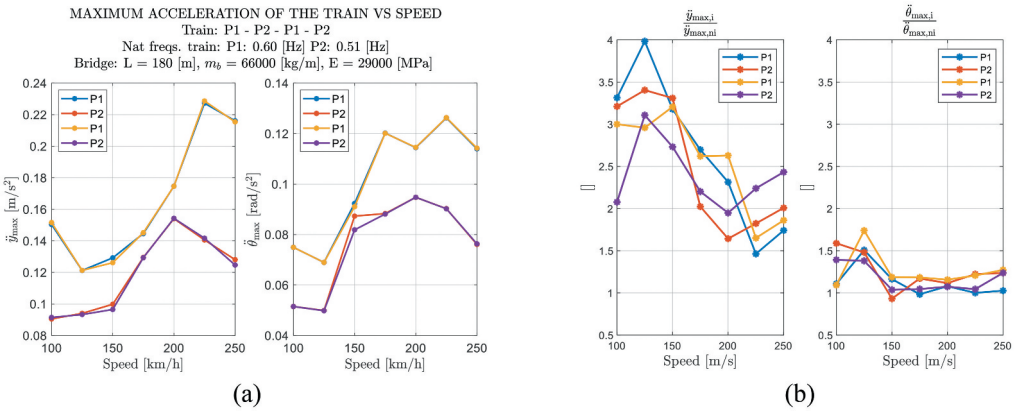


Figure 5. (a). Carbody lateral and roll acceleration peaks plotted as a function of train speed for each coach of the train convoy without impact event. (b): accelerations peak ratios.

larger lateral acceleration peaks than the leading one. In fact, this outcome may be the result of a larger time spent over the excited structure (by rear coaches), which becomes a more relevant aspect, when the travelling speed increases and the whole transit interval reduces. Concerning coach roll motion, a different behavior with speed from the one depicted in Figure 4(a) can be observed in Figure 4(b): in fact, for this parameter, the values at the highest speed (250 km/h) are always larger than the ones at the lowest speed (100 km/h). In Figure 5(a) accelerations peak values are plotted as a function of train speed, in case no impact is considered in the simulation. To better investigate and quantify the effect played by ship collision occurrence on vehicle dynamics, Figure 5(b) illustrate the ratios between peak accelerations in case of ship impact event divided by the same parameter when no impact is considered. From Figure 5(b), it is clear that the modeled ship impact affects lateral acceleration peaks more than roll ones.

4 CONCLUSIONS

In this work a simplified 2D VBI tool is presented, with the purpose to preliminarily investigate train lateral dynamic behavior in case of ship impact events. Each coach of the train is modelled through a 2 degrees-of-freedom system including lateral and roll motion of each

carbody, considering only the secondary suspension as well as carbody inertial terms. Bridge dynamic is modelled through a modal approach. The model allows for the consideration of vehicle bride dynamic interaction in lateral direction, assuming the bogie lateral motion coincident with bridge deck lateral motion. The model is integrated in time domain, enhancing a deeper understanding of the role of ship impact events on train running behavior. As a first outcome obtained by the presented simulation model, it was found that carbodies with lateral frequencies closer to bridge ones will result in higher accelerations compared to vehicles with frequencies that are further, as observed in (Bernardini et al. 2023) using a 3D TBI tool. As a practical outcome, the model aims at being a tool for a fast definition of scenarios that can result in more severe and critical runability conditions, starting from a wider set, saving time and computational costs, that can be allocated to a smaller group of simulations to be carried out with complete train-bridge interaction models. Future outlooks of this work consist in introducing bump stops elements in the vehicle model, as well as using, instead of analytical mode shapes, the ones extracted from a FE model of a bridge with a deck structure sustained by piers.

REFERENCES

AbuBakar, A., Dow, R.S. 2019. The impact analysis characteristics of a ship's bow during collisions. *Engineering Failure Analysis*, Vol. 100: 492–511.

Bernardini, L., Soldavini, G., Collina, A. 2023. Numerical investigation on train-bridge interaction after ship impact event: Train running safety in different scenarios. *Proceedings of The 8th International Conference on Structural Engineering, Mechanics and Computation*, *2022*, pp. 70–76. London: CRC Press.

Cheli, F., Diana, G. 2015. Advanced Dynamics of Mechanical Systems. Milan: Springer.

Fan, W., Liu, Y., Liu, B., Guo, W. 2016. Dynamic Ship-Impact Load on Bridge Structures Emphasizing Shock Spectrum Approximation. *Journal of Bridge Engineering*, Vol. 21(10).

Gholipour, G., Zhang, C., Mousavi, A.A. 2018. Effects of axial load on nonlinear response of RC columns subjected to lateral impact load: Ship-pier collision. *Engineering Failure Analysis*, Vol. 91: 397–418.

Guo, J., He, J.X. 2020. Dynamic response analysis of ship-bridge collisions experiment. *Journal of Zhejiang University-Science A*, Vol. 21(7): pp. 525–534.

Kohl, A.M., Clement, K.D., Schneider, J., Firus, A., Lombaert, G. 2023 An investigation of dynamic vehicle-bridge interaction effects based on a comprehensive set of trains and bridges. *Engineering Structures*, Vol. 279.

Li, Y., Deng, J., Wang, B., Yu, C. 2015, Running safety of trains under vessel-bridge collision. *Shock and Vibration*, Vol. 2015.

Li, Y., Xiang, H., Wang, Z., Zhu, J. 2022. A comprehensive review on coupling vibrations of train-bridge systems under external excitations. *Rail Engineering Science*, Vol. 30(3): pp. 383–401.

Lou, P.& Zeng, Q.Y. 2007. Formulation of equations of motion for a simply supported bridge under a moving railway freight vehicle. *Shock and Vibration*, Vol. 14(6): 429–446.

McVay, M., Wasman, S.J., Consolazio, G.R., Bullock, P.J., Cowan, D.G., Bollmann, H.Y. 2009. Dynamic Soil-Structure Interaction of Bridge Substructure Subject to Vessel Impact. Journal of Bridge Engineering, Vol. 14(1): 7–16.

Olmos, J.M., Astiz, M.Á. 2023. Response of a high-speed train travelling over a long and high-pier viaduct during moderate earthquakes. *Bulletin of Earthquake Engineering*, Vol. 21(4): 2369–2407.

OREB176, 1989. Bogies with Steered or Steering Wheelsets. Report No. 1: Specifications and Preliminary Studies, Specification for a Bogie with Improved Curving Characteristics, Utrecht, The Netherlands: ORE.

Rao, S.S. 2018. Mechanical Vibrations, Sixth Edition in SI Units. Malaysia: Pearson Education.

Sha, Y., Amdahl, J., Dørum, C. 2017. Dynamic responses of a floating bridge subjected to ship collision load on bridge girders. *10th International Conference on Structural Dynamics, EURODYN 2017. Procedia Engineering 199*: pp. 2506–2513.

Xie, C., Wang, Y., Ge, J., Zhu, H., Wang, J., Manoach, E.S., Cao, M. 2022. Mechanical Mechanism and Dynamic Characteristics of Barge-Whole Bridge Collision Behaviours. *Applied Sciences*, Vol. 12(21).

Zhou, X.Q., Hong, J.Z., Xia, Y. 2021. Numerical Simulation of a Cable-Stayed Bridge Subjected to Ship Collision. *International Journal of Structural Stability and Dynamics*, Vol. 21(6).

Bridge Maintenance, Safety, Management, Digitalization and Sustainability – Jensen, Frangopol & Schmidt (eds)
© 2024 The Author(s), ISBN 978-1-032-77040-6
Open Access: www.taylorfrancis.com, CC BY-NC-ND 4.0 license

Energy absorption of bolted connection up to tensile ultimate state

T. Takai, K. Tanii & S. Masudome
Kyushu Institute of Technology, Kitakyushu, Japan

ABSTRACT: The tensile resistance of the main plate of a bolted connection is reduced by making bolt holes. The structures are sometimes exposed to excessive forces, such as earthquake action. The resistance and energy absorption are important performances against such forces. High energy absorption can realize a ductile structure. However, the energy absorption of the bolted connection needs to be clearer because the bolted connection is usually designed based on resistance. In this study, the energy absorption of bolted connections was investigated by a finite element analysis. At first, the numerical model was checked by reproduction analysis of some experiments focused on failure modes and the stress-strain model. A parametric study was conducted to clear the energy absorption. The energy absorption was evaluated and discussed, focusing on the failure modes.

1 INTRODUCTION

Bolted connection is used for steel structures and bridges. The tensile resistance is reduced by making bolt holes. The structures are sometimes exposed to excessive forces, such as earthquake action. The resistance and energy absorption are important performances against such forces. High energy absorption can realize a ductile structure. However, the energy absorption behaviour of the bolted connection needs to be clearer because the bolted connection is usually designed based on resistance. In this study, the energy absorption of bolted connections was investigated by a finite element analysis. The reproduction analysis of some tensile experiments was conducted to check the validity of the analysis. The reproduction analysis compared some cases focused on failure modes and stress-strain models. A parametric study was conducted to clear the energy absorption of some dimensions. The energy absorption, including resistance and elongation under the ultimate state, was evaluated and discussed, focusing on the failure modes.

2 VALIDATION OF NUMERICAL MODEL

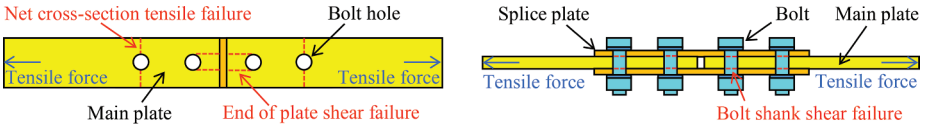
2.1 *Procedure of validation check*

Before the parametric study, the validation of numerical analysis was checked by the reproduction analysis of some tensile experiments. The results of the experiments were obtained from published papers. The reproduction analysis was conducted to simulate the experiment using finite element software. The failure modes and the tensile load-elongation curves obtained from the analysis were compared with the experiments. The matching of not only the load but also the elongation is a significant concern because this study discusses energy absorption.

2.2 *Failure modes of bolted connection in tension*

Figure 1 illustrates the failure modes of bolted connection in tension. A net cross-section tensile, bolt shank and end-of-plate shear failures are well-known failure modes. In actuality, one of the three modes is generated. The failure mode is determined by the minimum resistance in three modes.

DOI: 10.1201/9781003483755-477



(a) Front view. (b) Side view.

Figure 1. Failure modes of bolted connection in tension.

2.3 *Tensile experiments of bolted connection*

Table 1 summarizes the dimensions of the specimens. Moriyama et al. (2018) conducted tensile experiments on bolted connections and obtained net cross-section tensile failure modes. Three F10T M16 bolts (JIS B 1186, 2013) were placed in half of the specimen. The diameters of the bolt shank and hole were 16 and 18 mm, respectively. The steel grade of the plates was SS400 (JIS G 3101, 2020). The width of the main plate was 120 mm. The pitch and edge distance of the bolts were the same as 72 mm. The gauge length to measure the elongation was 348 mm from the centre of the specimen. They also obtained a bolt shank shear failure mode. The outline of the specimen was almost the same as the former specimen. However, the width of the main and splice plates was 216 mm. The wider plate gives higher tensile resistance in the net cross-section and causes the bolt shank shear failure instead of the net cross-section tensile failure. Toda et al. (2014) conducted tensile experiments on bolted connections and obtained end-of-plate shear failure modes. An F10T M16 bolt was placed in half of the specimen. The steel grade of the plates was SM400A (JIS G 3106, 2020). The width of the main plate was 120 mm. The gauge length for elongation was 225 mm from the centre of the specimen. The material property of F10T in shear failure in end-of-plate was unknown; they were filled with the minimum value defined in the specification (JIS Z 1186, 2013)

Table 1. Dimensions of specimens.

	Mode		Net cross-section tensile failure	Bolt shank shear failure	End-of-plate shear failure
Main plate and splice plate	Steel grade		SS400	SS400	SM400A
	Thickness	(mm)	9	19	9
	Yield point	(N/mm^2)	304	283	302
	Tensile strength	(N/mm^2)	449	442	468
Bolt	Steel grade		F10T	F10T	F10T
	Size		M16	M16	M16
	Diameter of hole	(mm)	18	18	17.8
	Proof stress	(N/mm^2)	1046	1052	900
	Tensile strength	(N/mm^2)	1114	1093	1000

Figure 2 shows tensile load-elongation curves (P-δ) and absorbed energy-elongation curves (E-δ) from the experiments. The former curves were obtained from the published papers using graph digitizer software. The latter curves were obtained by the trapezoidal integral of the former curves. The maximum load and the absorbed energy until the maximum load were important characteristics considering the resistance against the excessive force. So, the absorbed energy was calculated until the maximum load.

2.4 *Methods of numerical analysis*

The finite element analysis was conducted using Abaqus standard 6.13. Figure 3 shows the finite element models. One-eighth of the connections were modelled considering the symmetry.

The stress-strain relationship was modelled by the tri-linear type or n-th power hardening law. Although only the yield point and tensile strength were obtained from the papers, the other

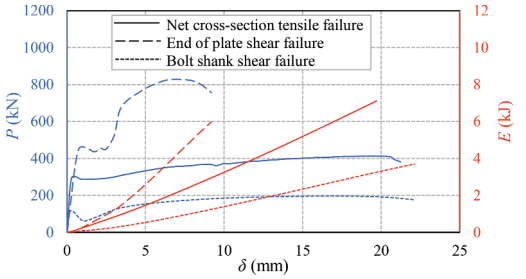


Figure 2. Experimental P-δ and E-δ.

values were required for the tri-linear model. Takai & Otsuka (2021) proposed a tri-linear stress-strain model with some regression expressions between material properties. At first, a nominal stress-nominal strain relationship was modelled with the yield point and tensile strength from the papers and other values from the regression expressions. After that, the nominal relationship was converted into a true stress-true strain relationship. Table 2 summarizes the values of the tri-linear models. The Young's modulus and Poisson's ratio are listed in Table 3.

The n-th power hardening law model is written as

$$\sigma = C\varepsilon^n \,, \tag{1}$$

where σ is stress, ε is strain, and C and n are material constants. The method to determine the constants was referred to JIS Z 2253 (2015). The two-point method was employed in this study. By right, the two points were chosen after reaching the strain rate defined in the specification. n is obtained by

$$n = \frac{\ln\sigma_T - \ln\sigma_S}{\ln\varepsilon_T - \ln\varepsilon_S}, \tag{2}$$

where σ_S is a stress after the strain rate, σ_T is tensile strength, ε_S is a strain after the strain rate, and ε_T is the strain at tensile strength. In this study, the former stress and strain were chosen the yield point to determine the constant. In another way, the material constants can be determined by the conditional expression of the beginning of necking at tensile strength in the metallic material tensile test (Hollomon, 1945). The condition at tensile strength is expressed as

$$\frac{d\sigma}{d\varepsilon}\Big|_{\sigma=\sigma_T} = \sigma_T \,. \tag{3}$$

By plugging Equation (1) into Equation (3) the constants are determined as

$$n = \varepsilon_T \,, \tag{4}$$

and

$$C = \frac{\sigma_T}{\varepsilon_T^{\varepsilon_T}} \,. \tag{5}$$

Table 4 summarizes the determined material constants of the n-th power hardening law models.

Figure 4 compares the stress-strain models. Case-1 is the case of the tri-linear stress-strain model. Case-2 is the case of the tri-linear model, which ignored the third slope. Case-3 is the case of the n-th power hardening law model determined by the two-point method. Case-4 is the case of the n-th power hardening law model determined by the condition of necking initiation.

The frictional coefficient was adjusted to reproduce the experimental slip load. The frictional coefficient in the bearing area between a bolt shank and a hole was 0.2 times that of other frictional areas to gain the stability of the contact calculation. The fracture model was selected as ductile damage as defined by the relationship between the fracture strain and stress triaxiality shown in the previous study (Li et al., 2020). The displacement damage evolution was set at 2.6 mm for plates and 1.4 mm for bolts (Tanii & Takai, 2022).

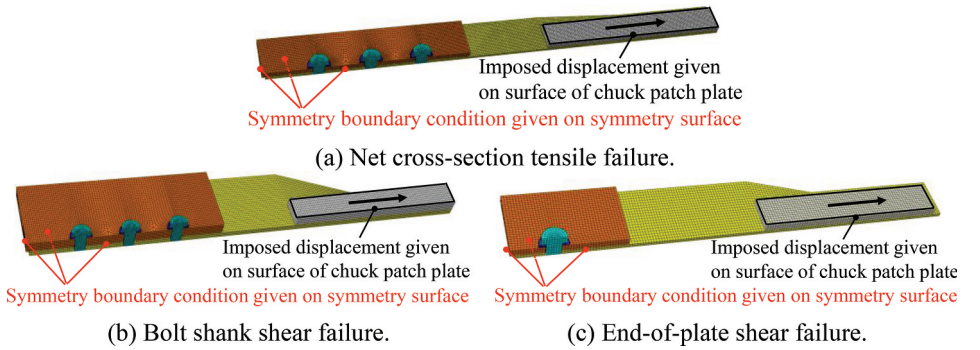


Figure 3. Outline of finite element models.

Table 2. Material properties for tri-linear models.

Mode		Main plate and splice plate				Bolt			
		Nominal stress (N/mm^2)	Nominal strain	True stress (N/mm^2)	True strain	Nominal stress (N/mm^2)	Nominal strain	True stress (N/mm^2)	True strain
Net cross-section tensile failure	Yield point	304	0.0014	304	0.0014	1046	0.0050	1051	0.0050
	Tensile strength	449	0.1724	526	0.1590	1114	0.0689	1191	0.0666
	Failure point	303	0.4430	959	1.1514	660	0.1810	1959	1.0877
Bolt shank shear failure	Yield point	283	0.0014	283	0.0014	1052	0.0051	1057	0.0050
	Tensile strength	442	0.1883	525	0.1725	1093	0.0609	1160	0.0591
	Failure point	300	0.5310	949	1.1530	649	0.1780	1926	1.0877
End-of-plate shear failure	Yield point	302	0.0014	302	0.0014	900	0.0045	904	0.0045
	Tensile strength	468	0.1862	555	0.1707	1000	0.0545	1055	0.0531
	Failure point	313	0.4141	987	1.1472	599	0.2149	1686	1.0348

Table 3. Young's modulus and Poisson's ratio.

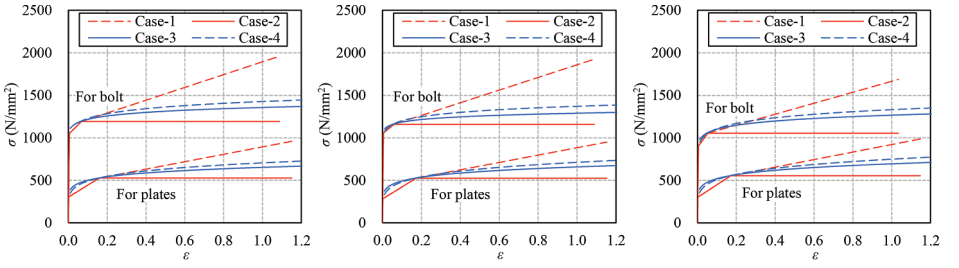
Failure mode	Main plate and splice plate		Bolt	
	Young's modulus (N/mm^2)	Poisson's ratio	Young's modulus (N/mm^2)	Poisson's ratio
Net cross-section tensile failure	2.10×10^5	0.289	2.08×10^5	0.280
Bolt shank shear failure	2.08×10^5	0.296	2.08×10^5	0.278
End-of-plate shear failure	2.126×10^5	0.300	2.126×10^5	0.300

2.5 *Results*

Figure 5 shows the obtained tensile load-elongation curves (P-δ) and absorbed energy-elongation curves (E-δ). The elongation was obtained from the gauge length described in section 2.3. Table 5 summarizes the results of the experiments and numerical analysis. As a result, Case-2 gave a result similar to the experiment. Although the other case differed by 10-70% from the experiment, the differences in absorbed energy between Case-2 and the

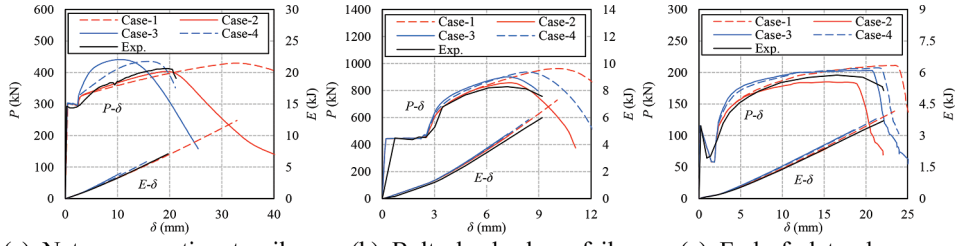
Table 4. Material properties for *n*-th power hardening law models.

Mode		Main plate and splice plate		Bolt	
		C	*n*	*C*	*n*
Net cross- section tensile failure	Case-3	652.1	0.117	1357	0.048
	Case-4	705.2	0.159	1426	0.067
Bolt shank shear failure	Case-3	657.0	0.127	1289	0.038
	Case-4	711.2	0.173	1371	0.059
End-of-plate shear failure	Case-3	694.2	0.127	1266	0.062
	Case-4	748.6	0.169	1331	0.081



(a) Net cross-section tensile failure. (b) Bolt shank shear failure. (c) End-of-plate shear failure.

Figure 4. Stress-strain models.



(a) Net cross-section tensile failure. (b) Bolt shank shear failure. (c) End-of-plate shear failure.

Figure 5. Obtained *P*-δ and *E*-δ.

experiment were around 5-10%. Figure 6 shows the von Mises stress distribution of Case-2. The failure modes obtained from numerical cases were the same as the experimental failure modes. By the numerical analysis in this study, Case-2, which adopted the tri-linear stress-strain model which ignored the third slope, was in good agreement with the experimental results rather than other tri-linear and *n*-th power hardening law cases. From these results, the latter parametric study was conducted using the conditions of Case-2.

3 PARAMETRIC STUDY

3.1 *Study cases*

The parametric study was conducted to clear the energy absorption (Tanii & Takai, 2022). Table 6 summarizes the study cases. The focused parameters are the slip/yield strength ratio and the number of bolts. The ratio is obtained by dividing a slip resistance by the yield resistance of the main or splice plates.

Table 5. Results of experiment and numerical analysis.

Mode	Case	Result			Difference		
		Maximum load (kN)	Elongation at max. load (N/mm^2)	Absorbed energy (kJ)	Maximum load (%)	Elongation at max. load (%)	Absorbed energy (%)
Net cross- section tensile failure	Experiment	382	21.2	7.73	-	-	-
	Case-1	429	32.9	12.40	12.3	55.2	60.4
	Case-2	403	19.5	6.97	5.5	-8.0	-9.8
	Case-3	441	10.6	4.05	15.5	-50.0	-47.6
	Case-4	435	15.9	5.98	13.9	-25.0	-22.6
Bolt shank shear failure	Experiment	828	7.2	4.39	-	-	-
	Case-1	936	10.1	7.29	13.0	40.5	66.1
	Case-2	857	7.3	4.65	3.5	1.0	5.9
	Case-3	901	7.2	4.79	8.8	0.4	9.1
	Case-4	937	8.4	5.84	13.2	17.0	33.0
End-of-plate shear failure	Experiment	196	16.5	2.64	-	-	-
	Case-1	211	23.4	4.16	7.7	41.8	57.6
	Case-2	185	15.3	2.39	-5.6	-7.3	-9.5
	Case-3	203	18.6	3.27	3.6	12.7	23.9
	Case-4	207	21.5	3.85	5.6	30.3	45.8

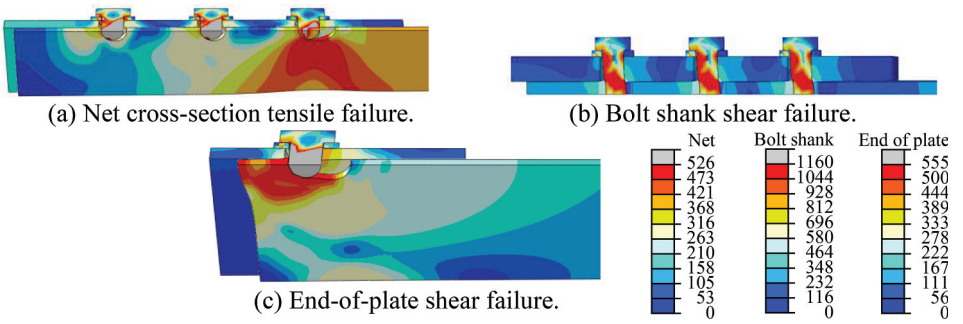


Figure 6. Von Mises stress distribution at maximum load in Case-2 (N/mm^2).

Table 6. Study cases and their name.

Slip/yield strength ratio	Number of bolts		
	2	3	5
0.45	n2-b04	n3-b04	n5-b04
0.6	n2-b06	n3-b06	n5-b06
0.9	n2-b09	n3-b09	n5-b09
1.2	n2-b12	n3-b12	n5-b12

$$\beta = \frac{umnN}{(w-d)t\sigma_y}, \tag{6}$$

where β is the slip/yield strength ratio, μ is the slip coefficient, σ_y is the yield point of plates, d is the diameter of the bolt hole, m is the number of frictional planes, n is the number of the bolts, N is the bolt preload, and w is the width of the plate. Table 7 summarizes the dimensions

of the cases. The grade and size of the bolts are F10T and M22, respectively. The steel grade of the plate is SM490Y. They are well used for highway bridges. Figure 7 shows the shape of the bolted connection.

Table 7. Dimensions of bolted connection for parametric study.

(a) Common dimensions.

	Number of bolts		2	3	5
Bolt	Proof strength		900	900	900
	Tensile strength		1000	1000	1000
	Preload	(kN)	205	205	205
	Diameter of shank	(mm)	22	22	22
	Slip coefficient		0.5	0.5	0.5
	Slip load	(kN)	410	615	1025
	Shear yield resistance in bolt shank	(kN)	790	1185	1975
	Shear maximum resistance in bolt shank	(kN)	878	1317	2195
Main and splice plates	Diameter of bolt hole	(mm)	24.5	24.5	24.5
	Thickness of main plate	(mm)	19	32	45
	Thickness of splice plate	(mm)	10	19	25
	Pitch of bolts	(mm)	75	75	75
	End distance	(mm)	40	40	40
	Shear yield resistance in end-of-plate	(kN)	554	1846	4943
	Shear maximum resistance in end-of-plate	(kN)	764	2548	6823

(b) Detailed dimensions of each β cases.

	β	Number of bolts		2	3	5
Main and splice plates	0.45	Width of plate		155	145	160
		Tensile yield load in net cross-section	(kN)	880	1369	2165
		Tensile maximum load in net cross-section	(kN)	1215	1889	2988
		Yield mode		End	Bolt	Bolt
		Ultimate mode		End	Bolt	Bolt
		β		0.466	0.449	0.474
	0.6	Width of plate		125	115	130
		Tensile yield load in net cross-section	(kN)	678	1028	1685
		Tensile maximum load in net cross-section	(kN)	936	1419	2326
		Yield mode		End	Net	Net
		Ultimate mode		End	Bolt	Bolt
		β		0.605	0.598	0.608
	0.9	Width of plate		90	85	95
		Tensile yield load in net cross-section	(kN)	442	687	1126
		Tensile maximum load in net cross-section	(kN)	610	949	1555
		Yield mode		Net	Net	Net
		Ultimate mode		Net	Net	Net
		β		0.928	0.895	0.91
	1.2	Width of plate		75	70	80
		Tensile yield load in net cross-section	(kN)	341	517	887
		Tensile maximum load in net cross-section	(kN)	470	713	1224
		Yield mode		Net	Net	Net
		Ultimate mode		Net	Net	Net
		β		1.204	1.19	1.156

*Yield and failure mode: Net means net cross-section tensile mode. Bolt means bolt shank shear mode. End means end-of-plate shear mode.

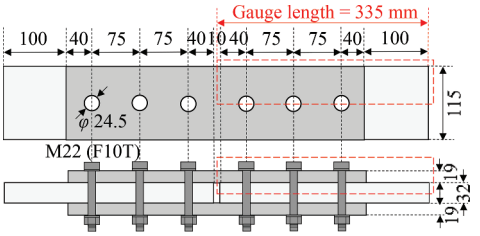


Figure 7. Shape of bolted connection (n3-b06).

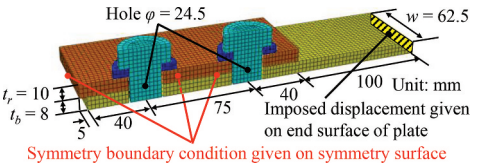


Figure 8. Outline of numerical model (n2-b06).

3.2 *Methods*

Figure 8 shows an outline of a numerical model. The connection components were meshed with 8-node linear reduced integration solid elements. The target length of the element was 2 mm. Considering the symmetry of the connection, one-eighth of the connections highlighted with the red dashed frame in Figure 7 were modelled. The symmetry boundary condition was given on the symmetry planes. The stress-strain relationship was the same as that of Case-2 of the tensile failure in net cross-section in Table 2, which ignored the third slope. In step-1 of the calculation, the bolt preload was installed by the bolt load function in Abaqus. In step-2, the tensile force was given by imposed displacement on the end surface of the main plate.

Table 8. Results of parametric study.

Case	Yield mode*	Failure mode*	Maximum load (kN)	Elongation at max. load (mm)	Absorbed energy (kJ)
n2-b04	End	End	759.9	11.8	7.4
n2-b06	End	End	729.6	11.7	7.1
n2-b09	Net	Net	615.2	16.4	8.8
n2-b12	Net	Net	490.0	13.5	5.9
n3-b04	Bolt	Bolt	1564.7	10.8	12.9
n3-b06	Net	Net	1419.3	19.5	23.4
n3-b09	Net	Net	987.1	12.6	10.5
n3-b12	Net	Net	766.4	10.8	7.2
n5-b04	Bolt	Bolt	2646.4	14.2	29.9
n5-b06	Net	Net	2350.0	25.2	50.7
n5-b09	Net	Net	1605.2	17.6	24.4
n5-b12	Net	Net	1292.1	15.2	17.2

* Yield and failure mode: Net means net cross-section tensile mode. Bolt means bolt shank shear mode. End means end-of-plate shear mode.

3.3 *Results and discussion*

Table 8 summarizes the results obtained from the parametric study. Figure 9 compares the maximum loads, elongation at maximum load, and absorbed energy.

The maximum load for the same number of bolt rows is greater for smaller β. In the case of net cross-sectional tensile failure, the higher the maximum load, the greater the elongation at the maximum load. Therefore, the energy absorption was greater for smaller β. However, in end-of-plate or bolt shank shear failure cases, the absorbed energies were smaller than that in net cross-section tensile failure, although the maximum load was higher than that in the tensile failure. That is because the elongation at the maximum load was small in those cases.

Hence, the bolted connection, which occurs in net cross-section tensile failure, gives higher energy absorption and a more ductile structure. However, end-of-plate or bolt shank shear

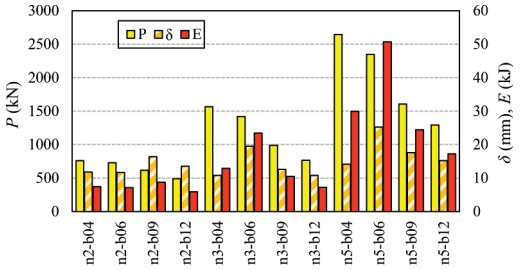


Figure 9. Maximum load, elongation, and absorbed energy.

failure gives smaller absorbed energy and is less ductile than net cross-section tensile failure, although they give high maximum loads.

4 CONCLUSION

This study investigated the absorbed energy of bolted connections in excessive tensile force. At first, validation of numerical analysis was checked by reproduction analysis of previous experiments. From the analysis, the case with the tri-linear stress-strain model, which ignored the third slope, was in good agreement with the experiment rather than other tri-linear and *n*-th power hardening law stress-strain cases. A parametric study was conducted to investigate the absorbed energy in other cases. The bolted connection, which occurs in net cross-section tensile failure, gives higher energy absorption and a more ductile structure. However, end-of-plate or bolt shank shear failure gives smaller absorbed energy and is less ductile than net cross-section tensile failure, although they give a higher maximum load.

ACKNOWLEDGEMENT

This work was supported by JSPS KAKENHI Grant Number JP21K14233.

REFERENCES

Hollomon, J. H. 1945. Tensile Deformation. *Transactions of the American Institute of Mining and Metallurgical Engineers* 162: 268–290.

JIS B 1186. 2013. Sets of high strength hexagon bolt, hexagon nut and plain washers for friction grip joint. *Japanese industrial standards*.

JIS G 3101. 2020. Rolled steels for general structure. *Japanese industrial standards*.

JIS G 3106. 2020. Rolled steels for welded structure. *Japanese industrial standards*.

JIS Z 2253. 2015. Metallic materials-Sheet and strip-Determination of tensile strain hardening exponent. *Japanese industrial standards*.

Li, D., Uy, B., Wang, J., Song, Y. 2020. Behaviour and design of high-strength Grade 12.9 bolts under combined tension and shear. *Journal of Constructional Steel Research* 174 106305: 14 pages.

Moriyama, H., Sugiyama, H., Yamaguchi, T. and Lang, Y. 2018. The influence of width and thickness on bearing limit state of high strength frictional bolted joints. *Journal of Japan Society of Civil Engineers Ser A1*. 74(1): 28–43.

Takai, T., Otsuka, T. 2021. A simple model of true stress-true strain curve of steel. *Proceedings of Constructional Steel*. 29: 158–167.

Tanii, K., Takai, T. 2022. Study on energy absorption of high-strength bolted friction joint by FEM analysis. *Proceedings of Constructional Steel* 30: 728–741.

Toda, Y., Yamaguchi, T., Mineyama, Y. and Naoe, Y. 2014. Experimental study of bearing strength of frictional bolted connection based on bolt hole deformation. *Journal of Japan Society of Civil Engineers Ser A1* 70(3): 333–345.

Bridge Maintenance, Safety, Management, Digitalization and Sustainability – Jensen, Frangopol & Schmidt (eds)
© 2024 The Author(s), ISBN 978-1-032-77040-6
Open Access: www.taylorfrancis.com, CC BY-NC-ND 4.0 license

Effectiveness of geotechnical seismic isolation for post-tensioned rocking piers

A. Contento & B. Briseghella
Fuzhou University, Fuzhou, Fujian, China

A. Di Egidio & A. Aloisio
University of L'Aquila, L'Aquila, Italy

H.-H. Tsang
Swinburne University, Melbourne, Australia

P. Gardoni
University of Illinois Urbana-Champaign, Urbana, Illinois, U.S.A.

ABSTRACT: Post-tensioned (PT) rocking piers have received considerable attention as an advantageous solution for seismic resilient structures. Their self-centering capacity, the advantages related to the column-uplifting mechanisms, and the possibility of being combined with energy dissipation devices largely contributed to this increasing attention. Simultaneously, Geotechnical Seismic Isolation (GSI) has emerged as a technique to reduce the seismic vulnerability of structures. The GSI a technique is based on design of a suitable interface between the foundation of the structure and the surrounding terrain. Such an interface can work as seismic isolation and energy dissipation mechanism. This research investigates the use of GSI for PT rocking piers equipped with external energy dissipation devices. The main focus of the investigation is the comparative assessment of the effectiveness of external dissipators and GSI to ascertain if the two protection mechanisms can synergize and collaboratively enhance the safety of the structure. The investigation employs numerical simulations through the direct integration of the equation of motion of the studied system. The outcomes of the parametric analysis are presented in gain maps that illustrate the effectiveness of the coupling within a designated parameter plane. Preliminary results show that GSI could be effective in combination with external dampers in reducing the seismic effects on rocking piers.

1 INTRODUCTION

Historically, self-centering structures have been widely used as seismic-resistant structures for their limited residual displacements. Additionally, starting from the last decades of the previous century, particular attention has been paid to rocking structural systems, and a significant number of researchers tried to make full use of their gravity-recentering ability for the design of seismic-resistant structures. The category of rocking structural systems comprises a variety of structures, the most common being rocking podiums, rocking frames and walls, and rocking piers. The inherent self-centering and energy dissipation abilities of rocking structural systems can be enhanced with the addition of supplementary devices aimed at reducing the displacement seismic demand of such structures and, consequently, mitigate their possible damage.

In the case of rocking piers, which are the focus of the present study, the seismic response is usually improved with three main protection strategies: *i*) base isolation (Rele et al., 2021), *ii*) use of internal post-tensioned (PT) tendons (Liu et al., 2018), *iii*) use of connection elements with dissipative behaviour at the rocking interface or external dissipative devices (EDDs) (Li et al., 2021, Sarti et al., 2016). Such a classification is proposed solely for the sake of clarity

DOI: 10.1201/9781003483755-478

since, in most cases, multiple strategies are applied at the same time in order to obtain dissipative controlled rocking. Both Zhong & Christopoulos (2022) and Piras et al. (2022) provide extensive literature reviews on rocking piers. The first one contains a comprehensive overview of self-centering rocking structures and focuses more on experimental works, whereas the second focuses on rocking bridge substructure systems and reviews other dissipation solutions proposed in the literature.

Relatively recently, Geotechnical Seismic Isolation (GSI) has emerged as a technique to reduce the seismic vulnerability of structures (Tsang 2008). Differently from the protection strategies presented above, GSI does not directly modify the characteristics of the structure to be protected but works on the interface between the foundation of the structure and the surrounding terrain. Thus, the main protection mechanism is based on the modification of the soil-structure interaction. Engineered soils, geosynthetics (geogrids, geotextiles), and granular materials like sand and gravel are commonly used in GSI systems. Their properties are tailored to achieve the desired isolation effect. GSI systems mostly involve three main protection mechanisms for the main structure. The first uses the modified foundation soil to alter the system's dynamic response by shifting its fundamental frequency (Aloisio et al. 2022, Tsang 2023). This mechanism is usually realized either through a layer of low-modulus material or through a sliding interface and its conceptual base is the same as the traditional base isolation mechanism. The second protection mechanism uses the dissipative properties of the engineered soil to reduce or filter the energy directed to the structure (Hazarika et al. 2023). The third mechanism relies on deliberate sliding control between the structural foundation and the encompassing geomaterials (Banović et al. 2022).

This paper proposes an initial investigation into the possible improvement in the seismic behaviour of rocking piers due to the application of EDDs and GSI. In particular, the focus is on the evaluation of the relative effectiveness of the two protection strategies. The authors aim to ascertain if the effectiveness of GSI is comparable to that of EDDs and if the two protection strategies can synergize and lead to a significant improvement in the seismic dynamics of rocking piers when used simultaneously. The model of a pier with a single unbound post-tensioned tendon located in the center of its cross-section and equipped with two viscous EEDs and GSI is used for the investigation. The GSI is modeled as in Tsang (2023) where the foundation is connected to the ground with both translational and rotational springs and dashpots. The models for the cases where EDDs or GSI are not considered are obtained from this reference model removing the unneeded terms in the equations of motion. The equations of motion of the reference structure (i.e. the pier with both EDD and GSI) are derived through a Lagrangian approach. The impact conditions needed to complete the mathematical model follow from the assumption of the conservation of the angular and linear momenta. The investigation employs numerical simulations through the direct integration of the equation of motion of the studied system. The outcomes of the parametric analysis are presented in maps that illustrate the maximum rotation of the pier with respect to the critical rotation that would lead to the pier overturning. Preliminary results show that GSI could be effective in combination with external dampers in reducing the seismic effects on rocking piers.

2 ROCKING PIER MODEL AND GSI MODELS

The pier investigated in this paper is modeled as a rigid block linked to a rigid oscillating base and to an additional mass at its top. The oscillating base represents the pier's foundation, and the connection is established through two viscous dampers. The additional mass schematizes the substructure above the pier, encompassing the deck and any other supplementary mass. Such a mass is assumed to remain horizontal during the motion.

In the case of GSI, the setup originally suggested by Tsang (2008) is adopted. As shown in Figure 1a, in this configuration, the base of the pier is embedded in a layer of low-modulus material, providing simultaneous support and confinement to the rigid base. These two elements are assumed to move cohesively in response to external excitation. Conversely, when GSI is not considered, the low-modulus material layer is replaced with a layer of natural soil (NS). The effect of

the layer of low-modulus material is modeled through two couples of springs and dashpots (Figure 1b) that act on the translation and rotation of the foundation of the pier, respectively.

Concerning the pier, the geometric configuration of the rigid block is that of a symmetric parallelepiped with a base of $2b_p$, a height of $2h_p$, and a unitary depth of $d_p = 1$, orthogonal to the representation of Figure 1b. The position of the center of mass of the pier m_p, denoted as G_p (Figure 1b and d), aligns with the geometric center of the parallelepiped, assuming uniform material composition with mass density ρ.

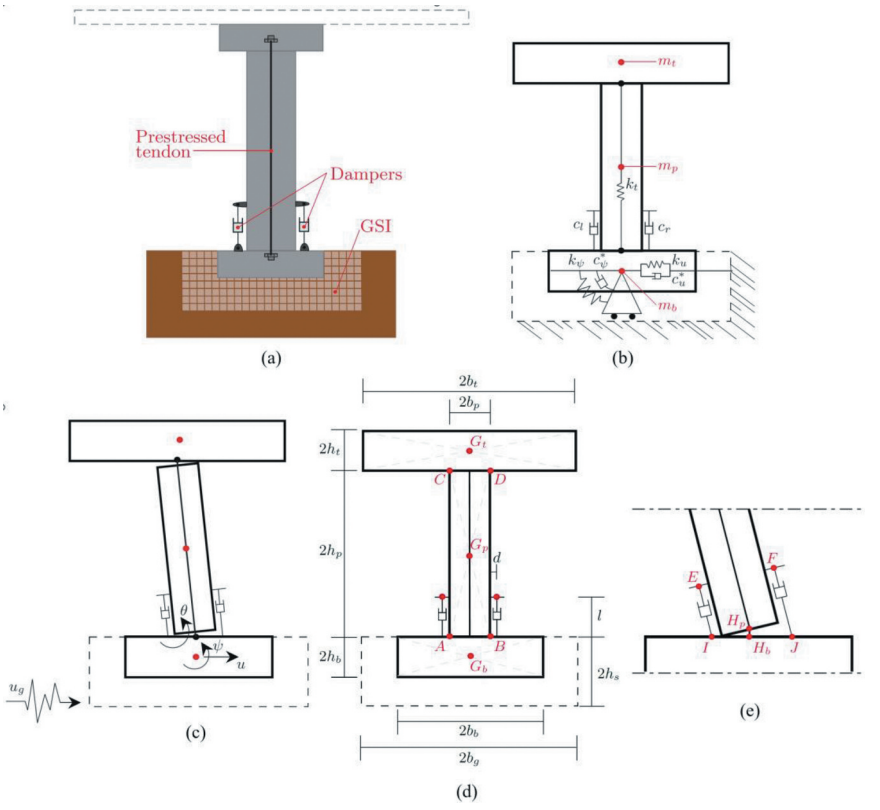


Figure 1. Schematic representation of the studied system (a); positions of the centers of masses; springs and dashpots used in the model (b); positive directions of the Lagrangian parameters (c); notable points used to describe the behavior of the pier (d) and (e).

In the proposed model, it is assumed that both free flight and sliding are prevented. Given this assumption, three distinct phases of motion can occur: rest, full contact, and rocking. The rest phase is the simplest, where neither the pier nor the oscillating base undergoes relative displacements with the soil. In the full contact phase, the oscillating base moves with respect to the ground, but there is no rocking of the pier. Finally, in the rocking phase, both base oscillation and rocking occur simultaneously. The equations of motions of the rocking phase can be written considering three Lagrangian parameters: the rocking angle $\theta = \theta(t)$, the rotation of the oscillating base $\psi = \psi(t)$, and its translational displacement $u = u(t)$. Figure 1c shows the positive directions of these Lagrangian parameters. The equations of motions of the other phases can be derived from the equations of motions of the rocking phase by removing unnecessary terms and equations.

2.1 *Equations of motion*

This section presents the derivation of the equations of motion for the complete rocking in the case of rocking occurring around point A (i.e. the bottom left vertex of the rigid body); those for rocking occurring around point B can be derived with the same approach and are not

presented for the sake of brevity. The equations of motion of the rocking pier are obtained by the well-known Lagrange's equation

$$\frac{d}{dt}\left(\frac{\partial L(t)}{\partial \dot{q}_l(t)}\right) - \frac{\partial L(t)}{\partial q_i(t)} = Q_i(t), \tag{1}$$

where the Lagrangian $L(t) = T(t)$-$V(t)$ is the difference between kinetic energy $T(t)$ and potential energy $V(t)$, $q_i(t)$ is one of the three Lagrangian parameters, and $Q_i(t)$ is the non-potential forces corresponding to $q_i(t)$. The kinetic energy $T(t)$ can be derived as

$$\begin{aligned} T(t) = \tfrac{1}{2}\big[&\big(J_b + J_p + J_t\big)\big(\dot{\boldsymbol{\Psi}}(t)\cdot\dot{\boldsymbol{\Psi}}(t)\big) + J_p\big(\dot{\boldsymbol{\theta}}(t)\cdot\dot{\boldsymbol{\theta}}(t)\big) + \\ &m_b(\dot{\mathbf{x}}_{G_b}(t)\cdot\dot{\mathbf{x}}_{G_b}(t)) + m_p\big(\dot{\mathbf{x}}_{G_p}(t)\cdot\dot{\mathbf{x}}_{G_p}(t)\big) + m_t(\dot{\mathbf{x}}_{G_t}(t)\cdot\dot{\mathbf{x}}_{G_t}(t))\big]. \end{aligned} \tag{2}$$

In Equation 2, J_b, J_p, and J_t are the polar inertia of the oscillating base, column, and top mass with respect to their centers of mass. The rotation vectors $\boldsymbol{\psi}(t)$ and $\boldsymbol{\theta}(t)$ are defined as $\boldsymbol{\psi}(t) = \{0,\ 0,\ \psi(t)\}^{\mathrm{T}}$ and $\boldsymbol{\theta}(t) = \{0,\ 0,\ \theta(\mathrm{i})\}^{\mathrm{T}}$, respectively. Vectors $\mathbf{x}_{Gb}(t)$, $\mathbf{x}_{Gp}(t)$, and $\mathbf{x}_{Gt}(t)$ define the positions of the respective centers of mass referred to an inertial reference system with an origin that is initially coincident with the left base vertex of the rigid block, i.e. point A in Figure 1b. They are functions of the Lagrangian parameters ($u(t)$, $\psi(t)$, and $\theta(t)$) and of the external ground excitation $x_g(t)$.

The potential energy $V(t)$ reads:

$$\begin{aligned} V(t) = &\big[m_p\big(\mathbf{x}_{G_p}(t) - \mathbf{x}_{G_p}(0)\big) + m_t(\mathbf{x}_{G_t}(t) - \mathbf{x}_{G_t}(0))\big]\cdot g + \frac{1}{2}[k_u(\boldsymbol{u}(t)\cdot\boldsymbol{u}(t)) + \\ &k_\psi(\boldsymbol{\psi}(t)\cdot\boldsymbol{\psi}(t)) + 2\big\|\mathbf{x}_{H_p}(t) - \mathbf{x}_{H_b}(t)\big\|\cdot\big(2k_t\big\|\mathbf{x}_{H_p}(t) - \mathbf{x}_{H_b}(t)\big\| + \sigma_0\big)\big]\ , \end{aligned} \tag{3}$$

with $g = \{0,\ g,\ 0\}^{\mathrm{T}}$ and $u(t) = \{u(t),\ 0,\ 0\}^{\mathrm{T}}$, where g is the gravity acceleration. In the equation, k_u and k_ψ are the translational and rotational stiffness coefficients of the GSI, whereas k_t is the axial stiffness of the unbound tendon. Vectors $\mathbf{x}_{Hp}(t)$ and $\mathbf{x}_{Hb}(t)$ provide the positions of the middle point of the base of the rigid block (i.e. point H_p in Figure 1c) and the position of the corresponding point on the oscillating base H_b. Consequently, the norm $\big\|\ \mathbf{x}_{Hp}(t) - \mathbf{x}_{Hb}(t)\big\|$ corresponds to half of the elongation of the unbound tendon due to rocking. Lastly, σ_0 is the prestress in the unbound tendon.

Since all non-conservative forces are dissipative forces, it is possible to write the non-potential forces $Q_i(t)$ in terms of a dissipative function $R(t)$ as $Q_i(t) = -\partial R(t)/\partial \dot{q}_i\,(t)$. Such dissipative function accounts for the viscous damping due to the GSI and external dampers and is written as

$$\begin{aligned} R(t) = &\frac{1}{2}\big[c_\psi(\dot{\boldsymbol{\psi}}(t)\cdot\dot{\boldsymbol{\psi}}(t)) + c_u(\dot{\mathbf{u}}(t)\cdot\dot{\mathbf{u}}(t)) + c_l\frac{d}{dt}(\|\mathbf{x}_{\mathrm{E}}(t) - \mathbf{x}_I(t)\| - \\ &\Big\|\mathbf{x}_E(\mathbf{0}) - \mathbf{x}_I(\mathbf{0})\|\Big)^2 + C_r\frac{d}{dt}\Big(\Big\|\mathbf{x}_F(\mathbf{t}) - \mathbf{x}_J(\mathbf{t})\| - \Big\|\mathbf{x}_F(\mathbf{0}) - \mathbf{x}_J(\mathbf{0})\|\Big)^{\mathbf{2}}, \end{aligned} \tag{4}$$

where c_u and c_ψ are the dissipative coefficients of the GSI model, whereas c_l and c_r are the dissipative coefficients of the left and right external viscous dampers, respectively. In Equation 4, the terms multiplied by c_l and c_r represent the time derivative of the elongation of the two dampers.

To complete the mechanical model, uplift and impact conditions are also derived. The uplift occurrence is verified by comparing the total translational acceleration acting on the column during integration in the full-contact phase (i.e. the total acceleration on the column computed from the full-contact equations) with the total acceleration acting on the column in the case of incipient uplift (i.e. the total acceleration computed from the rocking equations, where θ and it two first time derivative are neglected). The impact conditions, which provide the values of the Lagrangian parameters after an impact are derived by imposing the conservation of *i*) the angular momentum around the rocking vertex of the column, *ii*) the angular momentum around the center of rotation of the base of the pier, and *iii*) the conservation of

the horizontal momentum. Solving the three conservation equations, it is possible to find the post-impact values $u(t_i^+)$, $\theta(t_i^+)$, and $\psi(t_i^+)$ as functions of the post-impact quantities $u(t_i^-)$, $\theta(t_i^-)$, and $\psi(2t_i^-)$.

2.2 *Geotechnical seismic isolation model*

The model presented by Tsang & Pitilakis (2019) is used to model the basic configuration of the GSI system first proposed by Tsang (2008). Such a configuration assumes that the foundation of the pier is completely embedded in a layer of low-modulus material. The GSI layer has the shape of a rectangular prism of dimensions $2b_{\mathrm{GSI}}\times 2h_{\mathrm{GSI}}\times 2d_{\mathrm{GSI}}$, where $2d_{\mathrm{GSI}}$ is the dimension orthogonal to the schematic cross-section shown in Figure 1d. This paper assumes that the material used for the GSI is a rubber–soil mixture (RSM), which is usually widely proposed in the literature because of its compatibility with the natural environment and the availability of materials. The characteristics of such material (i.e. small-strain shear modulus $G_{max,\mathrm{GSI}}$, density ρ_{GSI}, and Poisson's ratio ν_{GSI}, as well as the characteristics of the natural soil that it replaces (i.e $G_{max,\mathrm{NS}}$, ρ_{NS}, and ν_{NS}) are also taken from Tsang & Pitilakis (2019).

The mechanical behaviour of the GSI is modeled by two sets of springs and dashpots. The first one, with stiffness and damping coefficients denoted as k_u and c_u, acts on the translation degree of freedom u. Similarly, the second one, which has coefficients denoted as k_ψ and c_ψ, works on the rotation ψ and its first derivative with respect to time. All of the four coefficients are functions of the geometric and mechanic characteristics of the GSI system (i.e., b_g, h_g, d_g, $G_{max,\mathrm{GSI}}$, ρ_{GSI}, and ν_{GSI}). Following Tsang (2023), k_u is modeled as:

$$k_u = k_b f_t f_w f_{lx} f_{lex}. \tag{5}$$

The stiffness coefficient k_b originates from the shearing interaction between the foundation base and the underlying soil. The effect of the embedment depth D is accounted for by f_t, whereas f_w, instead, accounts for the lateral interaction between embedded foundation walls and surrounding material. The last two, f_{lx} and f_{lex}, are additional stiffening factors, that account for the underlying stiffer layer of the NS and an additional embedment effect.

The damping coefficient c_u is modeled as:

$$c_u = k_u \frac{\xi_{eq} T_{SSFS}}{\pi} + c_b + c_s + c_p \tag{6}$$

The first term is the coefficient of the equivalent linear viscous damping due to the material internal damping that accounts for the hysteretic behaviour of the material. In Equation 6, ξ_{eq} is the equivalent viscous damping coefficient and T_{SSFS} is the fundamental natural period of the structure. It should be noted that the value of T_{SSFS} for a rocking structure is purely conventional since the column is modeled as a rigid body and not as a flexible structure The other three terms model the radiation damping which accounts for the energy loss as elastic waves propagate away from the foundation into an open half-space. Specifically, c_b refers to the shear generated between the base of the foundation and the soil, c_s to the shear between the lateral surfaces of the foundation in the direction of the motion and the soil, and c_p to the pounding due to the two lateral surfaces of the foundation in the direction orthogonal to the motion.

The rotation stiffness coefficient k_ψ is also expressed as the product of multiple factors as:

$$k_\psi = k_r \alpha_\psi f_{emb} f_{l\psi} f_{le\psi}. \tag{7}$$

In Equation 7, the rotational stiffness of the surface foundation k_r is conceptually analogous to k_b Such a rotational stiffness is multiplied by dynamic stiffness modifier α_0 which is dependent on T_{SSFS}. Both f_{emb} and $f_{le\psi}$ are stiffening factors that are functions only of the geometry of the GSI system and in particular of D. Lastly, $f_{le\psi}$ accounts for a further stiffening effect due to the stiffer original NS that underlies the low-modulus GSI layer.

Lastly, the damping coefficient c_ψ is modeled as:

$$c_\psi = k_\psi \frac{\xi_{eq} T_{SSFS}}{\pi} + c_r + c_{emb}. \tag{8}$$

As in Equation 6, the first term of Equation 8 corresponds to the equivalent linear viscous damping due to the material internal damping. The damping coefficient c_r, instead, refers to the rocking of the surface foundation. The last term,c_{emb}, accounts for the interaction of the lateral walls of the foundation with the surrounding material that generates compression-extension waves, shear weaves, and torsional weaves. The explicit definition of the four coefficients, as well as the exact definition of each of their factors/terms, can be found in Tsang & Pitilakis (2019).

3 PRELIMINARY ANALYSES

This paper presents the initial result of a larger campaign of parametric analyses performed to understand the influence of the geometric and mechanic characteristics of PT tendon, EDDs, and GSI on the seismic behaviour of the rocking pier. For this purpose, the ground motion record of the 1994 Northridge earthquake used in Tsang & Pitilakis (2019) is considered as seismic input. The seismic record is scaled to have a PGA = 1g. The dimensions of the column used in the following analyses are $2b_p$ = 0.5m and $2h_p$ = 4m; whereas the dimensions of the pier's foundations are $2b_b$ = 1.5m, $2h_b$ = 0.8m, and d_b = 2m. The mass of the superstructure is set to m_t = 10,400kg and the damping coefficient of the EDDs to $c_r = c_l$ = 225kNs/m. The mechanical characteristics of the RSM layer are $G_{max,GSI}$ = 5.88MPa, ρ_{GSI} = 1200kg/m^3, and ν_{GSI} = 0.4, while those of the NS are $G_{max,NS}$ = 120.3 MPa, ρ_{NS} = 1600kg/m^3, and ν_{NS} = 0.4. The reference values for the diameter and prestress of the PT tendons are d_{ten} = 10.0mm and respectively. The reference dimensions of the RSM layer are $2b_{GSI}$ = 1.7m, $2h_{GSI}$ = 2m, and $2d_{GSI}$ = 2.2m.

The first analysis, whose results are shown in Figure 2, is used to evaluate the sensitivity of the compared mechanical systems to the characteristics of the PT tendon. In particular, three different mechanical systems are compared: the rocking pier without EDDs and GSI (Figure 2a), the rocking pier equipped with EDDs (Figure 2b), and the rocking pier equipped with both EDDs and GSI (Figure 2c). For all the three systems the diameter of the PT tendon d_{ten} is varied between 5mm and 25mm while the prestress covers the range $\sigma_0 = 5{\cdot}10^6$ -$50{\cdot}10^6$N. For each combination of values, the equations of motion are integrated and the maximum total rotation of the pier $\zeta = \max(\psi + \theta)$ is collected. The metric used to represent the results is the ratio between this value and the critical angle of the column $\alpha_{crit} = \text{arctg}(b_b/h_b)$, i.e. $\Delta\zeta = \zeta/\alpha_{crit}$. Such a ratio corresponds to the percentage of the capacity of the column assuming the overturning as the limit state. This choice is made to provide a reference for the comparison; in an actual structure, the maximum rotation would be constrained by other factors such as the maximum elongation of the EDDs as well as the maximum lateral displacement allowable for the superstructure.

Figure 2a shows that when DDEs and GSI are not considered the seismic behaviour of the pier in terms of maximum rotation is negligibly affected by the value of the prestress in the tendon, especially for higher values of the stiffness of the tendon that is proportional to d_{ten}. That can be understood by noticing that the contour plots are almost vertical; for a given value of d_{ten} the difference in $\Delta\zeta$ can be attributed to the nonlinearity of the problem. Differently, the values of $\Delta\zeta$ strongly decrease as d_{ten} increases up to a value of approximately 12mm; after such a value the dependence of $\Delta\zeta$ on d_{ten} is largely reduced and the maximum angle reached during the motion is approximately 35% of the critical angle. When the EDDs are introduced into the system (Figure 2b), the maximum rotation reached by the pier during the motion reduces. Such a reduction is larger for smaller values of d_{ten} for which an approximate 10% reduction in $\Delta\zeta$ occurs. The reduction decreases after the threshold value of d_{ten} = 12mm to about 5% of the value reached without EDDs. The results still appear not to be significantly affected by σ_0, and this tendency is confirmed even when the GSI is considered (Figure 2c). Figure 2c shows that the combined effect of DDEs and GSI largely reduces the values of $\Delta\zeta$, especially for low values d_{ten} with the maximum value of $\Delta\zeta$ that drops from 0.685 in Figure 2a to 0.375 in Figure 2c. The introduction of the GSI further reduces the dependence of $\Delta\zeta$ on d_{ten}. However, smaller values of can be observed for smaller d_{ten} and a relative minimum can be roughly observed for 22mm < d_{ten} < 23mm.

The second analysis, presented in Figure 3, compares the seismic behaviour of the systems equipped with GSI for different base dimensions of the RSM layer. Figure 3a refers to the system with GSI and without EDDs, while Figure 3b refers to the system with both GSI and EDDs. Both the longitudinal and the orthogonal base dimensions of the RSM layer start from values that correspond to those of the pier's foundation plus 10cm for each side and are increased up to exceed the dimensions of the pier's foundation of 1m (i.e. 50cm for each side).

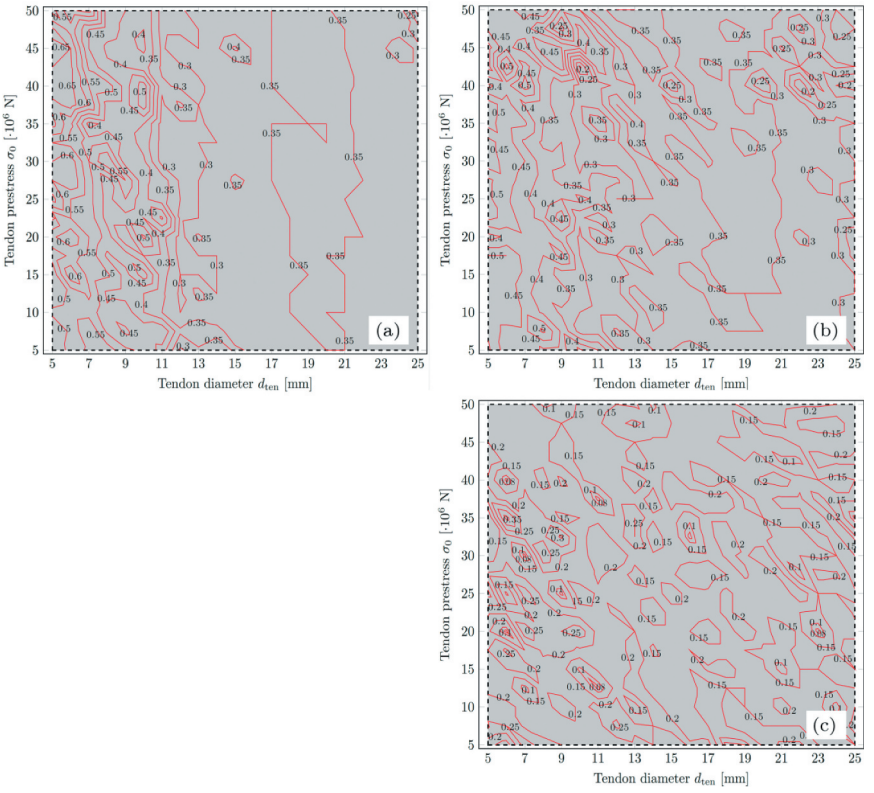


Figure 2. Contour plots of $\Delta\zeta$ as a function of the diameter and prestress of the PT tendon: (a) rocking pier; (b) system with EDDs; (c) system with GSI and EDDs.

Figures 3a and 3b show that although the dimensions of the RSM layer affect the values of the four parameters that characterize the GSI, there are only minor changes in the maximum rotation of the pier compared to the results of Figure 2c. Additionally, the comparison of the two graphs in Figure 3 clarifies that the effect of the EDDs is limited and almost negligible. However, the introduction of the EDDs changes the values for which the minimum values of $\Delta\zeta$ are obtained. There are concurrent reasons that justify this evidence. The first one is that the reduction due to the GSI for this seismic input is so high that there is no room to evaluate the effectiveness of the EDDs; this is shown by the small values assumed by $\Delta\zeta$ in all the parameters' plane. The second reason is that the GSI reduces the time spent in the rocking phase and, since for the chosen seismic inputs the maximum rotation occurs soon after the uplift, there is not enough time to benefit from the effects of the EDDs that are more evident later in the motion. However, this finding should be confirmed by assuming in the analyses different values of the EDDs' damping coefficients. Although limited, the initial analyses presented in this paper justify the necessity to further investigate the possibility of adopting the GSI as a protection mechanism for rocking piers with and without the addition of EDDs.

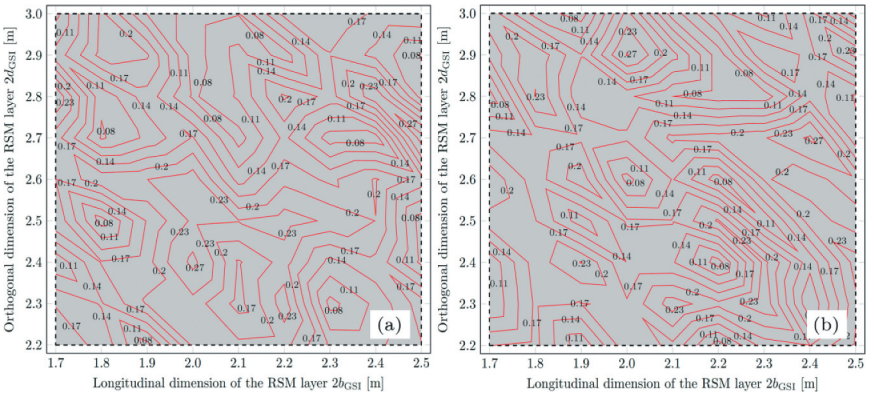


Figure 3. Contour plots of $\Delta\zeta$ as a function of the geometric characteristics of the RSM layer: (a) system with GSI; (b) system with GSI and EDDs.

4 CONCLUSIONS

The present study focuses on the seismic protection of PT rocking piers through GSI. In particular, through detailed models and computer simulations, the study scrutinizes the collaborative potential of GSI and EDDs in improving the resilience of rocking piers. Preliminary findings obtained through parametric analyses suggest a positive impact when GSI and EDDs collaborate. This discovery hints at a potential way to enhance the safety of bridges during earthquakes and contributes to ongoing discussions about earthquake-resistant design, paving the way for further exploration and testing in real-world scenarios.

REFERENCES

Aloisio, A., Contento, A., Xue, J., Fu, R., Fragiacomo, M. & Briseghella, B. 2022. Probabilistic formulation for the q-factor of piles with damping pre-hole. *Bulletin of Earthquake Engineering* 21(8): 3749–3775.

Banović, I., Radnić, J., Grgić, N. & Semren, K. 2023. Effectiveness of several low-cost geotechnical seismic isolation methods: a shake-table study. *Bulletin of Earthquake Engineering* 21(8): 3923–3947.

Hazarika, H., Kuribayashi, K., Kuroda, S. & Hu, Y. 2023. Performance evaluation of waste tires in protecting embankment against earthquake loading. *Bulletin of Earthquake Engineering* 21(8): 4019–4035.

Li, Y., Li, J., & Shen, Y. 2021. Quasi-static and nonlinear time-history analyses of post-tensioned bridge rocking piers with internal ED bars. *Structures* 32: 1455–1468.

Liu, X., Li, J., Tsang, H.H., & Wilson, J. 2018. Enhancing seismic performance of unbonded prestressed concrete bridge column using superelastic shape memory alloy. *Journal of Intelligent Material Systems and Structures* 29: 3082–3096.

Piras, S., Palermo, A., & Saiidi, M.S. 2022. State-of-the-art of posttensioned rocking bridge substructure systems. *Journal of Bridge Engineering* 27: 03122001.

Rele, R., Balmukund, R., Bhattacharya, S., Cui, L., & Mitoulis, S.A. 2021. Application of controlled-rocking isolation with shape memory alloys for an overpass bridge. *Soil Dynamics and Earthquake Engineering* 149: 106827.

Sarti, F., Palermo, A., & Pampanin, S. 2016. Fuse-type external replaceable dissipaters: Experimental program and numerical modeling. *Journal of Structural Engineering* 142: 04016134.

Tsang, H.H. 2008. Seismic isolation by rubber–soil mixtures for developing countries. *Earthquake Engineering & Structural Dynamics* 37(2):283–303.

Tsang, H.H. 2023. Analytical design models for geotechnical seismic isolation systems. *Bulletin of Earthquake Engineering* 21(8): 3881–3904.

Tsang, H.H. & Pitilakis, K. 2019. Mechanism of geotechnical seismic isolation system: Analytical modeling. *Soil Dynamics and Earthquake Engineering* 122: 171–184.

Zhong, C. & Christopoulos, C. 2022. Self-centering seismic-resistant structures: Historical overview and state-of-the-art. *Earthquake Spectra* 38: 1321–1356.

Bridge Maintenance, Safety, Management, Digitalization and Sustainability – Jensen, Frangopol & Schmidt (eds)
© 2024 The Author(s), ISBN 978-1-032-77040-6
Open Access: www.taylorfrancis.com, CC BY-NC-ND 4.0 license

Flexural behavior of concrete- steel composite girders with tubular flanges

Y.R. Liu, B.Q. Gao & X.B. Qu
Weihai Highway Survey and Design Institute Co., Ltd., Weihai, China

J.W. Zhang, Y.W. Wang & L. Duan
Department of Bridge Engineering, College of Highways, Chang'an University, Xi'an, China

ABSTRACT: The research on the flexural behavior of concrete- steel composite girders with tubular flanges was studied in this paper. Bending tests of concrete- steel composite girders with tubular flanges were conducted to obtain the failure mode and flexural capacity. The numerical simulation and parameter analysis of concrete- steel composite girders with tubular flanges were carried out. Based on the elastic-plastic analysis theory, a simplified calculation model of flexural capacity of the steel-concrete composite girder with tubular flanges was established. The design requirements were put forward for the steel-concrete composite girders with tubular flanges. The results show that the strength of the steel has a greater influence on the ultimate flexural capacity of steel-concrete composite girders than the strength of the concrete. With the increase of the thickness and width of the bottom flange, the ultimate flexural capacity of steel-concrete composite girders increases and the corresponding vertical ultimate displacement decreases accordingly. The proposed simplified calculation formula can be used to estimate the flexural bearing capacity of composite girders with tubular flanges.

1 INTRODUCTION

The utilization of steel-concrete composite girders with tubular flanges in various structural applications, particularly in bridges and high-rise buildings, offers notable advantages, garnering increasing adoption in China and yielding significant economic and social benefits. These girders, formed by substituting traditional flat plate flanges with circular, square, or rectangular tubular flanges, exhibit enhanced ductility, ample safety margins, and superior seismic performance, particularly suitable for seismic-prone regions (Sause 2015). Despite their practical engineering success, relatively little global research has been conducted on composite girders with circular tubular flanges (Wang 2017, Dong 2009). Previous studies by Kim and Sause analyzed the structural characteristics and developed calculation methods for composite girder bridges with circular tubular flanges, primarily focusing on elastic working stage properties (Kim 2008, Wang 2015). Wang et al. conducted experimental research on the bending performance of such composite girders, extracting mechanical characteristics and establishing formulas for ultimate bending capacity under construction and service conditions (Wang 2008a, Wang 2008b, Zhu 2012). However, these formulas, albeit insightful, are complex and challenging to apply in practical engineering scenarios. Additionally, due to limited specimen numbers, a comprehensive formula characterizing ductility for these composite girders has remained elusive. In this study, building upon bending test results, a nonlinear finite element model considering slip at the steel-concrete interface was developed. Through numerical simulations and systematic parameter analysis, the flexural capacity and ductility of composite girders with circular tubular flanges were thoroughly examined. Leveraging the findings from numerical

DOI: 10.1201/9781003483755-479

models, a practical calculation method for ultimate flexural capacity and displacement ductility coefficient was proposed, validated through numerical verification and parameter fitting, aiming to enhance the applicability of these composite girders in engineering practice.

2 BENDING TEST

A total of three composite girders with circular tubular flange were designed for the bending test, and all other design parameters were identical except for the different widths of the bottom flange, which was numbered CTFCGB-1 to CTFCGB-3. The design parameters are shown in Table 1. The total length of the test girder is 4300 mm, and the calculated span is 4000 mm. The total height of the test girder is 500mm. The width of the concrete plate is 600 mm with a thickness of 80mm. The outer diameter of the circular tube is 133 mm with a thickness of 4 mm. The height of the web is 271 mm with a thickness of 6mm. The thickness of the bottom flange is 16mm. The transverse stiffeners with a thickness of 12 mm were set at the end support and loading points. The test girder adopted Q235B steel and C40 concrete. The connection between steel girder and the concrete deck involves two rows of shear studs with a diameter of 10 mm and a length of 55 mm. The longitudinal steel bars and stirrups inside the concrete plate are all made of round steel bars with the R235 steel grade and the diameter of 6 mm. The steel tube is filled with self-compacting high-performance concrete inside the steel tube.

Table 1. Design parameters of test girders.

No.	Concrete grade	Longitudinal steel bars	Stirrups	Stud spacing/mm	Width of bottom flange/mm
CTFCGB-1	C40	14Φ6	Φ6@80	65	150
CTFCGB-2	C40	14Φ6	Φ6@80	65	260
CTFCGB-3	C40	14Φ6	Φ6@80	65	300

2.1 *Loading and instrumentation*

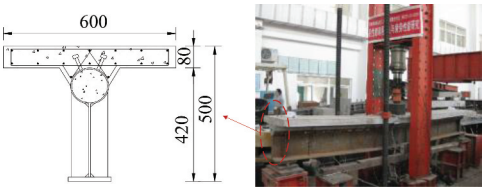


Figure 1. Loading device for test girders.

A 1000kN hydraulic jack is used for bending loading, and the load is measured by a force sensor connected to the jack. The resistance strain gauges with 5 mm and HJ strain gauges are used to measure the strain of steel girder and concrete plate. The displacement of the test girder and the end slip between steel tubes and infilled concrete are measured using a dial gauge. The relative slip at the interface between the steel girder and the concrete flange is measured using a YHD guide rod extensometer. The strain and displacement during the test are collected using a TDS-602 static data acquisition instrument. CTFCGB-1 girder adopts four-point bending loading with a pure bending zone of 1000 mm at the mid-span. CTFCGB-2 and CTFCGB-3 girders adopt the three-point bending loading procedure. Specially, a four-point bending loading is additionally conducted on the CTFCGB-3 girder with a maximum load controlled within 200 kN. The loading device for the test girder is shown in Figure 1.

2.2 *Experimental results*

Observing the test results, it was found that there was almost no relative slip between the steel tube and the infilled concrete for all test girders. There were no signs of instability or damage to the web. There is no visible relative sliding or lifting at the interface between the steel girder and the concrete plate. The failure mode of the test girder shows typical bending failure characteristics. The failure process was that the bottom flange of the steel girder first yielded, followed by continuous plastic development and stress redistribution. Finally, the concrete plate underwent crushing failure, and the test girder reached the ultimate flexural capacity and failed. The typical failure mode of the test girder is shown in Figure 2(a). The bending moment – deflection curves of test girders at mid-span are shown in Figure 2(b). It can be seen that the stress response of the test girder can be divided into three stages. From the beginning of loading to the yielding of the bottom flange of the steel girder, the mid-span deflection grows linearly with the load, and the overall performance of the test girder is good and in the elastic working stage (section OA). With the increase of load, the bottom flange of the steel girder starts to yield, and the yielding region extends to the inside of the cross-section and both sides of the span with the increase of load. The stiffness of the test girder cross-section decreases, the internal force in the cross-section is redistributed, the deflection grows faster, and the load-deflection curve shows an obvious nonlinear relationship. The test girder is in the elastic-plastic working stage (section AB). When the load reaches the ultimate flexural capacity, the concrete plate undergoes compression crushing, and then the capacity decreases sharply, and the test girder is in the destructive stage (section BC).The main mechanical characteristic results of the test girder are shown in Table 2. Where M_{yt} and δ_{yt} are the yield bending moment and the corresponded deflection respectively. M_{ut} and δ_{ut} are the ultimate bending moment and the corresponded deflection respectively.

Table 2. Main mechanical characteristic results.

No.	M_{yt} (kN·m)	δ_{yt} (mm)	M_{ut} (kN·m)	δ_{ut} (mm)	M_{yt}/M_{ut}	δ_{yt}/δ_{ut}
CTFCGB-1	397.3	11.40	594.2	51.63	0.67	0.22
CTFCGB-2	570.5	10.47	780.1	53.24	0.73	0.20
CTFCGB-3	649.4	11.06	830.3	39.06	0.78	0.28

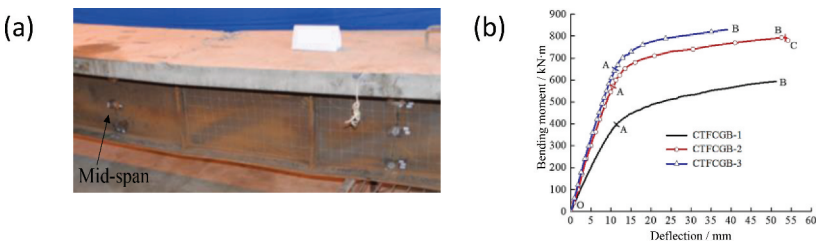


Figure 2. Test results: (a) Failure mode; (b) bending moment - deflection curve.

3 NUMERICAL ANALYSIS

3.1 *Element and materials*

This study employs ABAQUS software for numerical simulation of the flexural performance of composite girders featuring circular tubular flanges. The simulation incorporates C3D8I elements for modeling the concrete plate and the infilled concrete within the circular tube, employing 9 integration points along the thickness direction. The steel girder is represented using S4 elements with 5 integration points along the thickness direction. Additionally, steel bars within the concrete plate are modeled using T3D2 elements, individually embedded in the concrete plate through a coupled translational freedom method. To emulate longitudinal and transverse

sliding, as well as vertical lifting effects between concrete plates and steel girders, three orthogonal mechanical spring connection elements (SPRING2) are utilized to simulate shear studs.

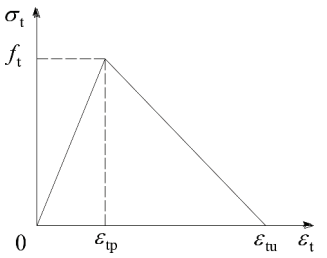


Figure 3. Linear softening model for the concrete.

Considering the distinction between elastic-plastic behavior of the concrete, the compressive constitutive model before the point of 1/3 σ_p was taken as a linear elastic relationship. The concrete adopts a linear softening model with inclined upward and downward lines, as shown in Figure 3. Where σ_t and ε_t are the uniaxial tensile stress and strain respectively. f_t is the peak uniaxial tensile stress. ε_{tp} and ε_{tu} are the strain and the peak strain for the peak uniaxial tensile stress respectively. In this paper, ε_{tu} is taken as 0.1. The tensile strength of the concrete has little effect on the mechanical performance of composite girders. It is assumed that the uniaxial tensile damage of the concrete increases linearly with the cracking strain until the maximum damage reaches 0.9 at the ultimate strain.

The constitutive relationship of the steel adopts a double line isotropic strengthening model, and the strength and elastic modulus are determined based on the test results in Table 3. The Poisson's ratio is 0.3, and the hardening slope is taken as 1/200 of the initial elastic modulus.

Table 3. Material properties

Material	Grade	Yield strength/Mpa	Ultimate strength/MPa	Elastic Modulus/GPa
Steel bars	Φ6	310	460.0	210.0
Steel plate	Q235B	312	430.0	200.0
Studs	Φ10×55	310	460.0	210.0
Infilled concrete	C40	-	56.3	37.1
Concrete plate	C40	-	50.4	36.2

3.2 *Relative slip between concrete and steel girder*

The shear slip relationship between shear studs has a significant impact on the flexural capacity and deformation performance of steel-concrete composite girders. Currently, the highly recognized fraction form (Buttry 1965) and index form (Ollgaard 1971) are:

$$\frac{V}{V_u} = \begin{cases} \frac{\alpha(s-\gamma)}{1+\beta(s-\gamma)} \\ (1-e^{-ns})^m \end{cases} \tag{1}$$

where V is the shear force of the studs. V_u is the ultimate shear capacity of the studs. s is the slip displacement of the studs. α, β, γ are the regression fraction parameters of slip. m, n are the regression index parameters of slip. In this paper, $m = 0.4$ and $n = 0.71$ are used for representing the slip relationship.

For the peak slip and ultimate slip of studs, the calculation formulas (Oehlers 1995) are adopted, which are:

$$s_p/d_s = 0.45 - 0.0021 f_{cc} \tag{2}$$

$$s_u/d_s = 0.41 - 0.0030 f_{cc} \tag{3}$$

where s_p is the peak slip of the studs. s_u is the ultimate slip of the studs, which is defined as the slip corresponding to the reduction of the ultimate capacity of the bolt to 95% after reaching its ultimate capacity.d_s is the diameter of the studs. f_{cc} is the axial compressive strength of concrete cylinders. The contact relationship between concrete plates and steel girders adopts normal hard contact, while ignoring the bonding effect of the contact surface.

3.3 *Numerical model and verify*

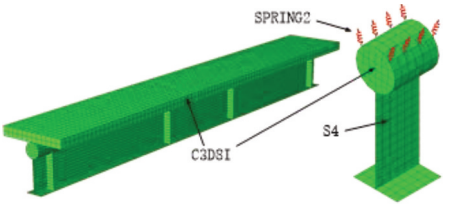


Figure 4. Finite element model.

A calculation model based on the actual size of the test girder was established, employing structured grid division technology to control concrete element size at 50 mm and steel girder element size at 25mm, ensuring adequate calculation accuracy. The finite element model of the composite girder with circular tubular flange, shown in Figure 4, adopts simply supported boundary conditions and node displacement loading. It incorporates material plastic deformation, boundary slip effect, and contact relationship, necessitating nonlinear iterative techniques for solution. Employing the arc length method, the model utilizes a displacement convergence criterion with a tolerance of 0.5%. Comparison results of bending moment and deflection obtained by FE method and test under yield and ultimate capacity limit states are presented in Table 4, with M_{yc} and δ_{yc}denoting numerical results of yield bending moment and corresponding deflection, while M_{uc} and δ_{uc} represent numerical results of ultimate bending moment and corresponding deflection.

Table 4. Comparison of FE method and test results at yield states and ultimate states.

No.	M_{yt} (kN·m)	δ_{yt} (mm)	M_{ut} (kN·m)	δ_{ut} (mm)	M_{yc} (kN·m)	δ_{yc} (mm)	M_{uc} (kN·m)	δ_{uc} (mm)	M_{yc}/M_{yt}	δ_{yc}/δ_{yt}	M_{uc}/M_{ut}	δ_{uc}/δ_{yt}
CTFCGB-1	397.3	11.40	594.2	51.63	407.6	9.92	608.4	56.22	1.03	0.87	1.02	1.09
CTFCGB-2	570.5	10.47	780.1	53.24	583.1	10.59	790.4	48.86	1.02	1.01	1.01	0.92
CTFCGB-3	649.4	11.06	830.3	39.06	640.0	11.04	820.5	38.05	0.99	1.00	0.99	0.97

3.4 *Parametric analysis*

The flexural failure of composite girders is typically controlled by either plastic hinge formation or overall lateral bending torsional instability. Key parameters influencing the type of failure include the girder span, web height-to-thickness ratio, compression flange width-to-thickness ratio, and spacing between transverse stiffeners. This study focuses primarily on the mechanical performance of composite girders under the plastic failure mode to avoid lateral bending torsional instability. To ensure this, the aforementioned parameters must be rigorously controlled in finite element parameter adjustments. The model design maintains the same span and stiffener arrangement as the test girders, with compression flanges and webs designed as dense sections. A total of 48 finite element model girders were analyzed, considering three sets of key parameters: concrete plate thickness (h_f), outer diameter of circular tube (R), and bottom flange width (b_t). The height of the steel girder (h_s) remains constant at 420 mm across all models, resulting in a corresponding decrease in web height (h_w) with increasing R. Table 5 presents the design parameters and ultimate flexural capacity calculation results of the model girders. The finite element analysis indicates that the composite girder with a b_t of 300 mm exhibits limited

yielding due to its relatively high stiffness. At ultimate capacity, the plastic hinge at the mid-span section may not fully develop, particularly with smaller hf values such as 60mm. Notably, the bottom flange reaches yield state first upon girder failure, aligning with plastic design requirements wherein steel plate yield precedes. Additionally, various states of plasticity—fully plastic, incomplete plastic, and intermediate—are observed in girder sections at ultimate

Table 5. Design parameters and the calculation results of the ultimate flexural capacity.

No.	h_f (mm)	R (mm)	b_t (mm)	M_{uc} (kN·m)	M_{pl} (kN·m)	M_{pl}/M_{uc}
G1-84-150	60	84	150	556	521.9	0.94
G1-84-200			200	659.9	623.6	0.95
G1-84-250			250	725	719.9	0.99
G1-84-300			300	770.5	806.5	1.05
G1-105-150		105	150	557.5	526	0.94
G1-105-200			200	649.6	626.4	0.96
G1-105-250			250	733.4	721.8	0.98
G1-105-300			300	775.7	806.3	1.04
G1-133-150		133	150	552.5	532.7	0.96
G1-133-200			200	654.3	630.9	0.96
G1-133-250			250	735.6	725.2	0.99
G1-133-300			300	784.8	808.3	1.03
G1-168-150		168	150	569.9	542.5	0.95
G1-168-200			200	670.3	638.1	0.95
G1-168-260			250	767.7	730.9	0.95
G1-168-300			300	813.8	812.7	1
G2-84-150	80	84	150	606.6	555.1	0.92
G2-84-200			200	704.1	663.2	0.94
G2-84-250			250	772.6	769.2	1
G2-84-300			300	807.4	873.1	1.08
G2-105-150		105	150	615.3	560.1	0.91
G2-105-200			200	698.8	667.8	0.96
G2-105-250			250	775.3	773.4	1
G2-105-300			300	816.7	876.2	1.07
G2-133-150		133	150	608.4	568	0.93
G2-133-200			200	702	675.2	0.96
G2-133-250			250	778.5	780.4	1
G2-133-300			300	820.5	881.1	1.07
G2-168-150		168	150	628.5	580	0.92
G2-168-200			200	722.8	686.6	0.95
G2-168-250			250	804.6	791.2	0.98
G2-168-300			300	856.1	888.9	1.04
G3-84-150	100	84	150	638.4	588.4	0.92
G3-84-200			200	739.1	701.4	0.95
G3-84-250			250	822.6	812.4	0.99
G3-84-300			300	843.9	921.3	1.09
G3-105-150		105	150	651.4	594.2	0.91
G3-105-200			200	757.4	706.9	0.93
G3-105-250			250	817.3	817.5	1
G3-105-300			300	850.3	926.1	1.09
G3-133-150		133	150	636.3	603.2	0.95
G3-133-200			200	740	715.4	0.97
G3-133-250			250	816.1	825.6	1.01
G3-133-300			300	854.7	933.7	1.09
G3-168-150		168	150	666.3	616.6	0.93
G3-168-200			200	765.8	728.3	0.95
G3-168-250			250	838.7	837.8	1
G3-168-300			300	883.6	945.4	1.07

capacity. All composite girders experience plastic failure, accurately representing diverse girder sections in engineering design and fulfilling parameter selection design goals effectively.

As the width of the bottom flange increases, the ultimate flexural capacity of the composite girder rises proportionally. Specifically, when bt increases from 150 mm to 200mm, 250mm, and 300mm, steel consumption and ultimate flexural capacity increase by 14.3%, 28.7%, and 43.1%, and by 16.1%, 28.9%, and 35.6%, respectively. The ratio of elastic flexural capacity to ultimate flexural capacity also increases with bt, indicating improved initial stiffness. However, the amplification of ultimate flexural capacity and initial stiffness gradually diminishes with uniform bt increments, suggesting a limit to efficiency due to concrete flange thickness constraints.Regarding the thickness of the concrete plate, an increase leads to higher girder height, affecting ultimate flexural capacity due to height and concrete-to-steel girder height ratio changes. As hf increases from 60 mm to 80 mm and 100mm, ultimate flexural capacity rises by 7.0% and 12.6%, respectively, with a slight increase in initial stiffness.Concerning the diameter of the circular tube, a rise from 84 mm to 105mm, 133mm, and 168 mm results in increased steel consumption and flexural capacity. However, the increase amplification diminishes with higher bt but increases thereafter. Interestingly, initial stiffness remains mostly unchanged with R variations. It's noted that flexural capacity may not monotonically increase with R, and there's a possibility of capacity decrease within a certain range due to minimal impact from tube diameter changes.

4 CALCULATION METHOD FOR ULTIMATE BENDING MOMENT

The simplified plastic theory method assumes that the steel reaches its yield strength regardless of tension or compression, which is basically consistent with the actual stress state of the composite girder under the ultimate flexural capacity. Due to the fact that the infilled concrete within steel tube is closer to the position of the plastic neutral axis, the contribution of the infilled concrete to the bending capacity is relatively small and can be ignored in the calculation of the ultimate bending moment. The following three situations should be analyzed when calculating the ultimate bending moment for the composite girder with tubular flange M_{pl} based on the plastic theory.

When the plastic neutral axis is inside concrete plate, the Mpl can be calculated by Equation 4 to Equation 5.

$$M_{pl} = A_{cc}f_c y_1 + A_t f_y y_2 + A_w f_y y_3 + A_b f_y y_4 \tag{4}$$

$$A_{cc} = b_e x = \frac{A_s f_y}{f_c} \tag{5}$$

where A_c and A_s are the area of the section for the concrete plate and the steel girder, respectively. A_{cc}, A_t, A_w, A_b, y_1, y_2, y_3, y_4 are the cross-sectional areas and corresponding distance from centroids of the compression region of the concrete plate, the circular steel tube, the web, and the bottom plate to plastic neutral axis, respectively. f_c is the axial compressive strength of the concrete plate. f_y is the yield strength of the steel. b_e is the effective width of the concrete plate. x is the height of the compression region of the concrete plate. h is the height of the composite girder. h_b is the thickness of the bottom flange. t_t and t_w are the thickness of the circular steel tube and the web respectively.

When the plastic neutral axis is located inside the circular steel tube, the M_{pl} can be calculated by Equation 6 to Equation 8.

$$M_{pl} = A_c f_c y_1 + A_w f_y y_3 + A_b f_y y_4 + A_{tc} f_y y_5 + A_{tt} f_y y_6 \tag{6}$$

$$A_{tc} = \frac{A_s f_y - A_c f_c}{2 f_y} \tag{7}$$

$$x = h_f + \frac{R}{2}\left[1 - \cos\left(\frac{A_{tc}}{A_t}\pi\right)\right] \tag{8}$$

where A_{tc}, A_{tt}, y_5, y_6 are the cross-sectional areas and corresponding distance from centroids of the circular steel tube in the compression and tensile region to plastic neutral axis, respectively.

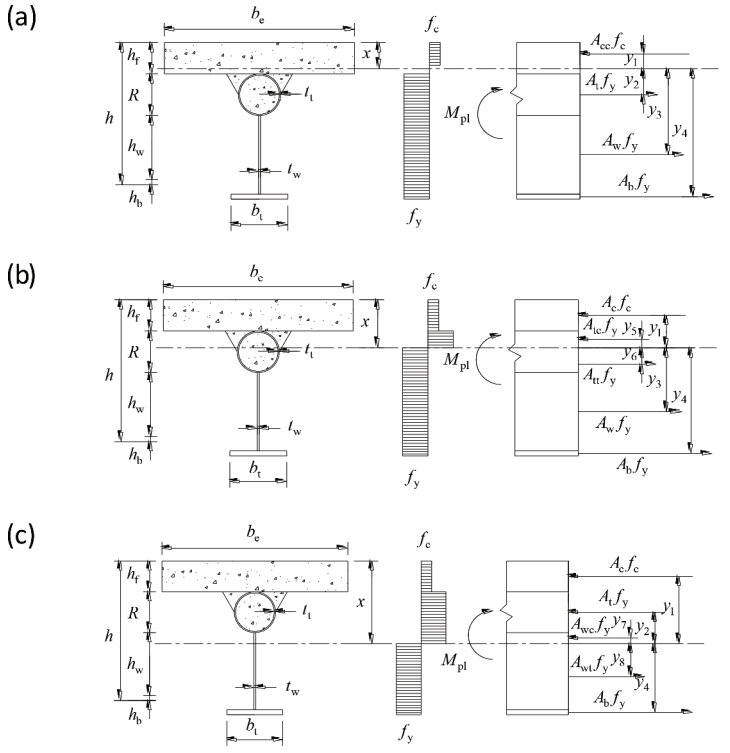


Figure 5. Calculation diagram: (a) Plastic neutral axis inside concrete plate; (b) Plastic neutral axis inside the circular steel tube; (c) Plastic neutral axis inside the web.

When the plastic neutral axis is located within the web, the M_{pl} can be calculated by Equation 9 to Equation 10.

$$M_{pl} = A_c f_c y_1 + A_t f_y y_2 + A_b f_y y_4 + A_{wc} f_y y_7 + A_{wt} f_y y_8 \tag{9}$$

$$A_{wc} = \frac{A_s f_y - 2A_t f_y - A_c f_c}{2f_y} \tag{10}$$

where A_{wc}, A_{wt}, y_7, y_8 are the cross-sectional areas and corresponding distance from centroids of the web in the compression and tensile region to plastic neutral axis, respectively.

The comparison results between the calculated value obtained by the formula in this paper M_{pl} and the finite element result M_{uc} is shown in Table 5. It can be seen that the prediction of the ultimate flexural capacity for the composite girder under the fully plastic state is slightly lower, for the composite girder under the incomplete plastic state is slightly higher, and for the composite girder under the intermediate plastic state composite beam is accurate. The ratio of the M_{pl}/M_{uc} is 0.91 to 1.09 with an average value of 0.98, which indicating that the formula for ultimate bending moment established based on simplified plastic theory in this paper has a high calculation accuracy.

5 CONCLUSION

(1) The bending moment vers deflection curves calculated by the nonlinear numerical model considering the plastic constitutive relationship of concrete damage, and the slip and fracture of shear studs is in good agreement with the test results, which can simulate the flexural process of the composite girder with circular tubular flanges well.

(2) Increasing the width of the bottom flange of the steel girder and the thickness of the concrete plate can effectively increase the ultimate flexural capacity of the composite girder with circular tubular flanges, but the diameter of the circular tube has a relatively small impact.
(3) Based on the flexural performance of test girders and numerical models, a simplified plastic theory is applied to derive the calculation formula for the ultimate flexural capacity of the composite girder with circular tubular flange. The calculation results are in good agreement with the finite element results, and have a high calculation accuracy for calculating the ultimate flexural capacity for the composite girder with circular tubular flange.

ACKNOWLEDGEMENTS

This work was supported by the Program of Weihai (C2020-029), and and Chang'an University Central University Basic Scientific Research Fund Green Highway Key Special Support Plan (300102219309).

REFERENCES

Sause R. 2015. Innovative steel bridge girders with tubular flanges. *Structure and Infrastructure Engineering* 11(4): 450–465.
Wang C. S., Zhu J. W. & Zhai X. L. 2017. Flexural behavior experiment of steel and concrete composite girder with double tubular flanges. *China Journal of Highway and Transport* 30(3): 147–158.
Dong J. & Sause R. 2009. Flexural strength of tubular flange girders. *Journal of Constructional Steel Research* 65(3): 622–630.
Hassanein M. F. & Kharoob O. F. 2013. Flexural strength of hollow tubular flange plate girders with slender stiffened webs under mid-span concentrated loads. *Thin-Walled Structures* 69: 18–28.
Kim B. G. & Sause R. 2008. Study of two-span continuous tubular flange girder demonstration bridge. Bethlehem: Lehigh University.
Wang C. S., Chang Q. L. & Zhai X. L. 2015. Design and structure analysis of tubular flange composite girder bridge. *Steel Construction* 30(06): 17–21.
Kim B. G. & Sause R. 2008. Lateral torsional buckling strength of tubular flange girders. *Journal of Structural Engineering* 134(6): 902–910.
Sause R., Kim B. G. & Wimer M. R. 2008. Experimental study of tubular flange girders. *Journal of Structural Engineering* 134(3): 384–392.
Wang C. S., Zhai X. L. & Duan L. 2008. Flexural limit load capacity test and analysis for steel and concrete composite beams with tubular up flanges[C] // Shen Z Y, Chen Y, Yzhao X Z. Tubular Structures XII: Proceedings of the 12th International Symposium on Tubular Structures. Boca Raton: CRC Press, 413–420.
Wang Y. L., Wang C. S. & Zhai X. L. 2008. Experimental of bending capacity for steel and concrete composite girder with concrete filled tubular up flange. *Journal of Traffic and Transportation Engineering* 8(6): 63–69.
Zhu J. W. 2012. Experimental investigation of bending behavior for the new style tubular flange composite girder. Xi'an: Chang'an University.
Buttry K. E. 1965. Behavior of stud shear connectors in light weight and normal-weight concrete. Columbia: University of Missouri.
Ollgaard I. G., Slutter R. G. & Fisher J. W. 1971. Shear strength of stud connectors in lightweight and normal weight concrete. *AISC Engineering Journal* 8(2): 55–64.
Oehlers D. J. & Sved G. 1995. Composite beams with limited-slip-capacity shear connectors. *Journal of Structural Engineering* 121(6): 932–938.

Bridge Maintenance, Safety, Management, Digitalization and Sustainability – Jensen, Frangopol & Schmidt (eds)
© 2024 The Author(s), ISBN 978-1-032-77040-6
Open Access: www.taylorfrancis.com, CC BY-NC-ND 4.0 license

Flexural behavior of high strength steel-UHPFRC composite girders

J.W. Zhang
Department of Bridge Engineering, College of Highways, Chang'an University, Xi'an, China

F. Li, X.B. Qu & S.J. Li
Weihai Highway Survey and Design Institute Co., Ltd., Weihai, China

W.T. Liu & C.S. Wang
Department of Bridge Engineering, College of Highways, Chang'an University, Xi'an, China

ABSTRACT: To study the flexural performance of high strength steel-UHPFRC composite girders, flexural tests, numerical simulation, and theoretical analysis were comparatively carried out on high strength steel-UHPFRC composite girders and high strength steel concrete composite girders. The failure mode, flexural stiffness, ultimate capacity and corresponded deformation were compared and analyzed. The finite element models with multi-scaled of high strength steel-UHPFRC composite girders were established, and the parameter analysis was carried out. The simplified calculation method applicable to the flexural capacity of high strength steel-UHPFRC composite girders was proposed. The results show that the flexural behavior of the flange of high strength steel-UHPFRC composite girders is significantly improved, and the number of cracks is significantly reduced with smaller widths. Compared with high strength steel concrete composite girders, the flexural stiffness and yield load of high strength steel-UHPFRC composite girders in the elastic stage are increased by 17.4% and 7.1%, respectively. The cracking load in the elastic-plastic stage is increased by 10.2%, and the flexural capacity and ductility in the ultimate state are increased by 10.8% and 26.8%, respectively. The variable parameter analysis results show that the yield strength and ductility of the composite girder can be significantly improved by increasing the strength of the UHPFRC.

1 INTRODUCTION

The steel-concrete composite bridge, known for its efficient assembly and structural simplicity (Nie 2011), faces challenges like low compactness and limited durability (Editorial 2021; Shao et al. 2017). To address these issues, Ultra-High-Performance Fiber-Reinforced Concrete (UHPFRC) is introduced, offering enhanced durability with features like robust impermeability and corrosion resistance (Graybeal et al. 2020; Chen et al. 2014; Brühwiler, 2020; Paschalis et al. 2021). This material has prompted extensive research on the flexural performance of steel-UHPFRC composite girder bridges, aiming to improve their usability and longevity. Scholars have investigated various aspects of steel-UHPFRC composite girder bridges. Yoo et al. (2016) proposed a novel type of steel-Ultra-High Performance Concrete (UHPC) composite girder and analyzed its flexural performance compared to traditional steel-concrete composite girders. Liu et al. (2018) conducted experimental comparisons, highlighting the reduced bridge deck thickness in steel-UHPC composite girders. Zhu et al. (2020, 2021) explored the flexural performance of steel-UHPC waffle slab composite girders, suggesting adjustments to steel strength or geometric dimensions for better compatibility with UHPC. Deng (2020) proposed a plastic calculation method for the ultimate flexural capacity of steel-UHPC composite girders.

DOI: 10.1201/9781003483755-480

This paper focuses on investigating the flexural performance and damage mechanisms of high-strength steel-UHPFRC composite girders through comparative bending tests. Using numerical analysis and parameter studies, scaled and full-scale models are analyzed to propose a simplified calculation method for determining flexural capacity..

2 TEST METHODS

2.1 *Test design*

The high-strength steel-UHPFRC composite girder (HSUCB) and high-strength steel-concrete composite girder (HSCCB) were designed with identical geometric dimensions. Both girders have a length of 3300 mm and a span of 3000 mm. The girder height is 374 mm, with flange thickness set at 80 mm. Studs were arranged in a double-row configuration, spaced 100 mm transversely and 55 mm longitudinally, adhering to complete shear connection design standards. The flanges and web of the steel girder were constructed from Q420 steel plate, while stiffeners were fashioned from Q235 steel plate. Reinforcement bars consisted of R235 round steel bars, with a longitudinal reinforcement rate of 0.88% and a transverse reinforcement rate of 1.29%.

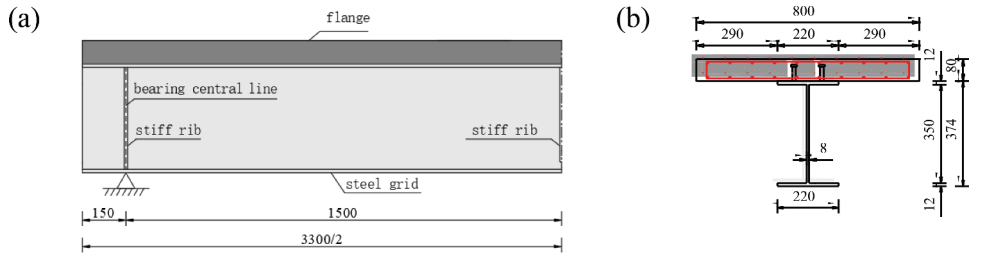


Figure 1. Test girder configuration: (a) elevation plan; (b) cross section.



Figure 2. Loading device.

2.2 *Loading and measurement point layout*

The test girders are simply supported. Four- point loading is applied for the test girders at mid-span with a spread beam uniformly distributing the load. These two girders have the same test point. The strain gauges were used for the composite girders to analyze the strain distribution patterns. The displacement meter was arranged on the bottom surface of the bottom flange of the steel girders to measure deflection at mid-span of the girders. Two slip meters are symmetrically located at the interface of the steel girders and concrete plates at the ends to assess relative slips.

2.3 *Analysis of test results*

After the bending test, analysis of deflection, strain, relative slip, and strain distribution along the girder's height was conducted. Experimental results reveal critical points: the natural bond

between the steel girder and UHPFRC plate peels off at 1105kN, bottom flange yields at 1238kN, transverse cracks appear at 1505kN, and UHPFRC plate crushes at 1698kN, reaching the limit state. HSUCB girder exhibits superior cracking resistance, strength, and elastic flexural stiffness compared to HSCCB girder. Both girders utilize flange compressive strength fully in the limit state, with the bottom flange entering the strengthening stage. High-strength steel-UHPFRC composite girder enhances overall performance, with stronger natural bonding between UHPFRC plates and high-strength steel girders. Moreover, the slip effect in high-strength steel-concrete composite girders becomes more apparent during flexural processes. The tensile properties of high-strength steel girders are fully utilized by matching with UHPFRC plates, further improving performance.

3 NUMERICAL ANALYSIS

3.1 *Test girder finite element model*

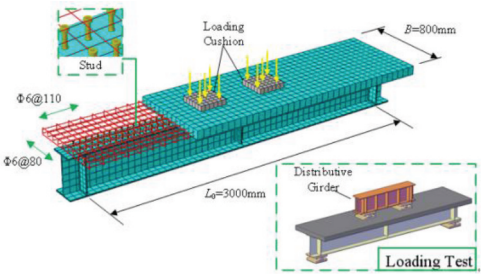


Figure 3. Finite element model.

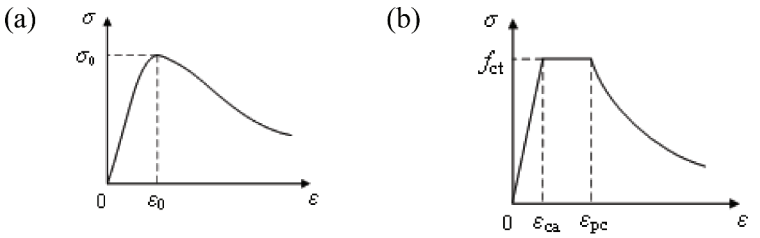


Figure 4. Constitutive model for UHPFRC: (a) Compressive; (b) tensile.

To further analyze the flexural behavior of high-strength steel-UHPFRC composite girders, a nonlinear finite element model at the scale of the test girder was developed using ABAQUS software. The finite element model is illustrated in Figure 3. In this model, reinforcement bars and studs are embedded in the concrete plate, and the steel girder is rigidly connected to the stiffeners and studs. The interaction between the concrete plate and the steel girder is modeled as a hard contact, with interface friction simulated using penalty functions. The UHPFRC adopts the constitutive model proposed in the literature (YANG et al. 2008) and corrected based on the measured results, the constitutive model is shown in Figure 4. The steel adopts the multilinear constitutive model and corrected based on the experimental results. The stiffening ribs, reinforcement bars, and studs adopt the material constitutive relationships defined for the same materials in the literature (ZHU 2018).

3.2 *Analysis of calculation results*

Figure 5 illustrates the load-versus-strain curves for the UHPFRC plate and steel girder at the mid-span section of the HSUCB girder. The compressive strain in the UHPFRC plate, as

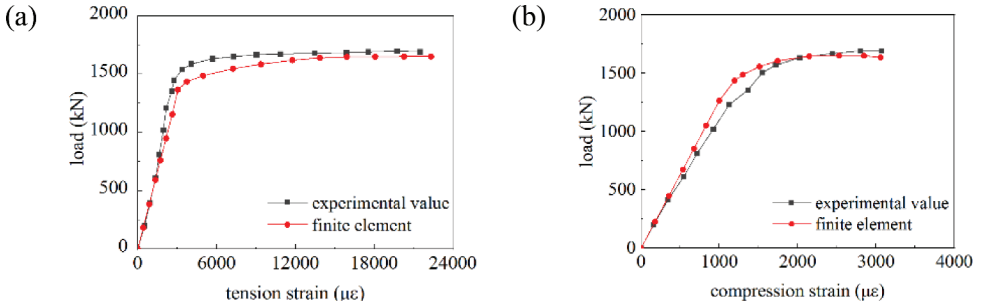


Figure 5. Load vers strain curve of mid-span section for HSUCB girder: (a) Load vers tension strain curves; (b) Load vers compression strain curves.

shown in Figure 5a, aligns well between test and numerical models during the elastic stage, with a measured strain of 2944με and a FE-to-test ratio of 0.92. The load-versus-tensile-strain curve for the steel girder, depicted in Figure 5b, indicates a close fit between FE and test results. The FE model slightly overestimates the yield tensile strain by 9% and yields a yield strength 2% lower than the measured value. However, the FE ultimate tensile strain is 3% higher than the measured value, demonstrating overall good agreement. Figure 6a compares the load-deflection curves from FE analysis and test results, showing a good fit in both elastic and elastic-plastic stages. Ratios of FE-to-test values for yield strength, deflection, and flexural stiffness are 1.02, 0.98, and 1.04, respectively, in the elastic stage, and 0.97 and 0.92 for flexural bending moment and deflection at the ultimate state, indicating consistent performance between FE and test results.Figure 6b compares load-versus-slip curves at the end of the HSUCB girder between FE model and test girder. In the elastic stage, relative slip is minimal, with a slight discrepancy between FE and test results. At the ultimate state, FE slip value is 6% higher than the measured value, indicating a slightly different behavior in the failure stage. Overall, the FE model effectively captures the development of interface slip and its failure value at the end of the girder.

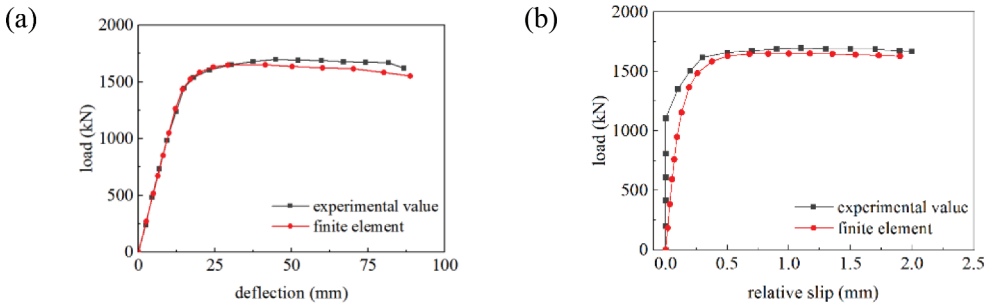


Figure 6. Curves for HSUCB girder: (a) load vers deflection curves; (b) load vers slip curves.

3.3 *Parameter analysis*

Based on the finite element model analysis, variable parameter studies were conducted on the steel strength grade, UHPFRC strength grade, UHPFRC plate thickness, and bottom flange thickness of the steel girder. These studies aimed to investigate their influence on the flexural performance of the high-strength steel-UHPFRC composite girder. Figure 7 illustrates the load-deflection curves under each parameter analysis.In Figure 7a, the load-deflection curves for model girders with UHPFRC strengths of 100 MPa, 120 MPa, and 150 MPa are presented. Increasing UHPFRC strength grade leads to a significant improvement in yield strength (up by 22%) and ductility (up by 29%). However, the magnitude of improvement decreases gradually due to the potential occurrence of steel girder yielding before UHPFRC

plate yielding when their strength designs are matched.Figure 7b displays load-deflection curves for composite girders with different steel grades when using UHPFRC flanges with a strength of U120. Increasing steel grade from Q345 to Q690 results in notable enhancements in strength, stiffness, and deformation of the combined steel-UHPFRC beams.In Figure 7c, load-deflection curves for model girders with varying UHPFRC plate thicknesses are shown. Each 10 mm increase in plate thickness leads to a 5% increase in yield strength and flexural load capacity, with minimal effect on ductility but noticeable improvements in strength and stiffness.Figure 7d depicts load-deflection curves for model girders with different bottom flange thicknesses of steel girders. Increasing flange thickness enhances flexural stiffness, yield strength, and flexural load capacity. However, it reduces ductility, indicating a trade-off between stiffness and ductility when adjusting flange thickness.Overall, these parameter studies provide insights into optimizing the design of high-strength steel-UHPFRC composite girders to achieve desired performance characteristics.

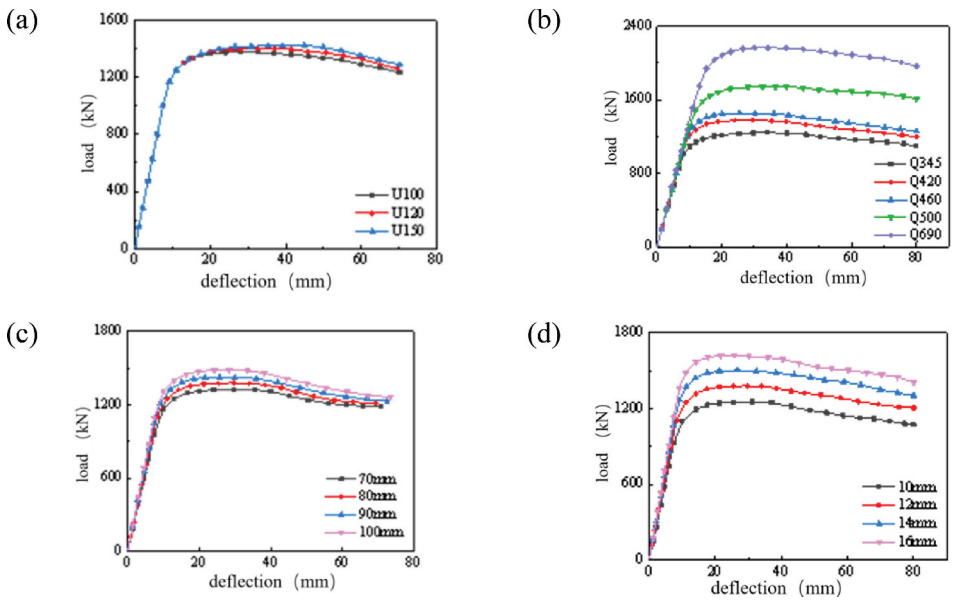


Figure 7. Parameter analysis results: (a) UHPFRC strength grade; (b) steel grade; (c) UHPFRC plate thickness; (d) bottom flange thickness of steel girder.

3.4 *Full-scale finite element model*

To further investigate the flexural performance of high-strength steel-UHPFRC composite girders, a full-scale numerical simulation study was conducted. The span of the full-scale model was 53m. The width of the UHPFRC bridge deck is 3m with a thickness of 20cm. Studs were arranged in four rows with transverse and longitudinal spacing of 100mm and 200mm, respectively. The cross-sectional dimensions are illustrated in Figure 8. The steel girders were adopted Q420 steel plates, and the stiffeners were made of Q345 steel plates. Longitudinal and transverse reinforcement bars within the UHPFRC bridge decks adopted HRB400 steel bars. The constitutive relationship model was consistent with scaled models, and the full scaled model of the high -strength steel- UHPFRC composite girder were shown in Figure 8.

3.5 *Analysis of calculation results of full-scale girders*

A comparison was made between the distribution of the strain along the height of the HSUCB girder and HSCCB girder by the full-scale model and the test results. The results indicated that the strain development stages of the UHPFRC plate and the steel girder for full-

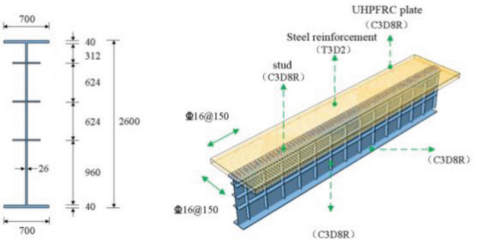


Figure 8. Full-scale girder 1/4 model (unit: mm).

scale models are similar to the scaled models. However, the plastic strain development in the bottom flange of the steel girder for full-scale model was more significant. The full-scale girders exhibit a noticeable relative slip in elastic stage, but the slip growth rate in the elastic-plastic stage is slower. At the ultimate state, the slip values are essentially the same as that observed in the test girders.

4 THEORETICAL ANALYSIS

4.1 *Calculation formula of ultimate bending moment based on equivalent stress*

The flexural capacity of high-strength steel-UHPFRC composite girders can be precisely obtained through integration, but the algorithm is relatively complex, resulting in lower computational efficiency. To simplify calculations while ensuring accuracy, equivalent stress α and equivalent height coefficients β are introduced. Experimental results indicate that under ultimate limit states, the high-strength steel-UHPFRC composite girder did not satisfy the plane section assumption, but the UHPFRC concrete and steel girder individually conformed to the plane section assumption. At the ultimate state, the bottom flange and the web of the steel girder yielded. The UHPFRC plate experienced compression failure, and the bottom surface of the UHPFRC plate reached the ultimate tensile strain. The stress vers strain curve of UHPFRC is equated to a rectangle, enabling the establishment of a practical formula for calculating bending moment under the ultimate state, as shown in Figure 9.

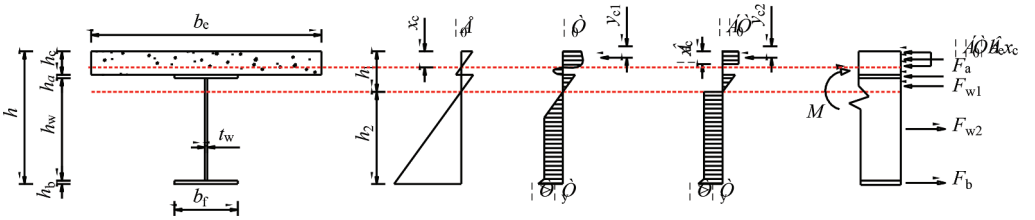


Figure 9. Calculation diagram of ultimate bending moment based on equivalent stress.

$$M_{uce} = \alpha\sigma_0\beta b_e h_c\left(h_1 - \frac{\beta h_c}{2}\right) - \int_{h_c-x_c}^{h_c-x_c+h_a} \varepsilon E_s b_f y\mathrm{d}y - \int_{h_c-x_c+h_a}^{h_1-x_c} \varepsilon E_s t_w y\mathrm{d}y + \frac{\sigma_y t_w (h_2-h_b)^2}{2} + \int_{h-x_c-h_b}^{h-x_c} \varepsilon E_{s1} b_f y\mathrm{d}y \quad (1)$$

where h_1 is the distance from the top surface of the UHPFRC plate to the neutral axis of the steel girder. h_2 is the distance from the bottom surface of the girder to the neutral axis of the steel girder. h is the total height of the composite girder. h_a and h_b are the thicknesses of the top flange and bottom flange of the steel girder, respectively. h_c is the thickness of the UHPFRC plate. h_w

and t_w are the height and thickness of the web of the steel girder, respectively. b_f is the width of the flange of the steel girder. σ_y is the yield stress of the steel girder. y is the distance of the integral unit from the neutral axis.

4.2 *Calculation formula of bending capacity based on limit equilibrium*

4.2.1 *Simplified formula of flexural capacity considering interface slip*

According to the test results, when the high-strength steel-UHPFRC composite girders use flexible studs, there is still slip at the ultimate state under the complete shear design. To simplify the design calculation, a calculation diagram based on the ultimate balance method is established as shown in Figure 10.

According to the test results, when the high-strength steel-UHPFRC composite girders use flexible studs, there is still slip at the ultimate state under the complete shear design. To simplify the design calculation, a calculation diagram based on the ultimate balance method is established as shown in Figure 10. It is assumed that the axial pressure of the UHPFRC plate is equal to the sum of the longitudinal shear force transmitted by the studs. According to the equilibrium condition, Equation 2 can be obtained.

$$x_c\sigma_0 b_e + b_f h_a \sigma_y + t_w h_1 \sigma_y = h_2 t_w \sigma_y + b_f h_b \sigma_y \tag{2}$$

where h_1 and h_2 are the height of the compression region and the tension region of the web, respectively.

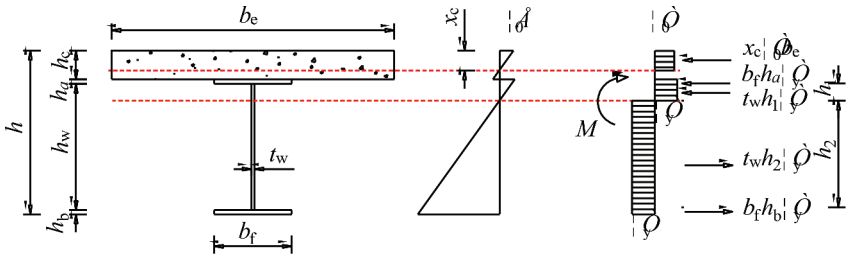


Figure 10. Calculation diagram of bending capacity in limit equilibrium.

The ultimate bending moment of the high-strength steel- UHPFRC composite girder can be obtained by Equation 3.

$$\begin{aligned} M_{us} = {} & x_c\sigma_0 b_e \frac{x_c}{2} - b_f h_a \sigma_y \left(\frac{h_a}{2} + h_c - x_c\right) - t_w h_1 \sigma_y \left(\frac{h_1}{2} + h_a + h_c - x_c\right) \\ & + h_2 t_w \sigma_y \left(\frac{h_2}{2} + h_1 + h_a + h_c - x_c\right) + b_f h_b \sigma_y \left(\frac{h_b}{2} + h_w + h_c - x_c\right) \end{aligned} \tag{3}$$

4.2.2 *Simplified formula of ultimate bending moment without considering slip*

To compare the effect of slip on the ultimate bending moment of high-strength steel-UHPFRC composite girder, a simplified formula without considering slip is also derived. The calculation diagram is established as shown in Figure 11. Equation 4 can be obtained from the equilibrium conditions.

$$h_1 b_e \sigma_0 = h_w b_f \sigma_y + h_a b_f \sigma_y + h_b b_f \sigma_y \tag{4}$$

where h_1 and h_2 are the height of the compression region and the tension region of the UHPFRC plate, respectively.

The simplified calculation formula of ultimate bending moment without considering slip can be obtained by Equation 5.

$$M_{uc} = h_1 b_e \sigma_0 \frac{h_1}{2} + h_a b_f \sigma_y \left(\frac{h_a}{2} + h_2\right) + h_w b_f \sigma_y \left(\frac{h_w}{2} + h_a + h_2\right) + h_b b_f \sigma_y \left(\frac{h_b}{2} + h_2 + h_a + h_w\right) \tag{5}$$

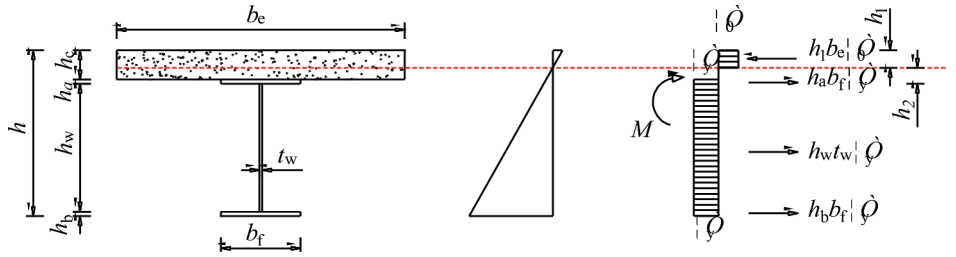


Figure 11. Calculation diagram of ultimate bending moment without considering slip.

4.3 *Verification and analysis*

Table 1. Calculation results of bending capacity of the scale test girder.

Test girder	M_{uce}(kN · m)	M_{us}(kN · m)	M_{uc}(kN · m)	M_{ut}(kN · m)	$\frac{M_{uce}}{M_{ut}}$	$\frac{M_{us}}{M_{ut}}$	$\frac{M_{uc}}{M_{ut}}$
HSUCB	957	912	1119	1019	0.94	0.90	1.09
Full-scale	77882	97554	70415	86535	0.90	1.12	0.81

A comparison and validation of the ultimate bending moment obtained by the test, the calculation formula based on equivalent stress, and the calculation formula based on limit equilibrium are conducted. The comparative results for the scaled models and the full-scale models are presented in Table 1. Where, M_{uce} is the results of the simplified calculation formula based on equivalent stress considering slip. M_{us} is the results of simplified calculation formula based on the limit equilibrium method considering slip. M_{uc} is the results of simplified calculation formula based on the limit equilibrium method without considering slip. M_{ut} is the test results. M_{ue} is the numerical results of the full-scale model.

Comparative analysis results reveal that when using the limit equilibrium method, the calculation method considering slip is relatively reduced by 18 compared to that without considering slip, while the reduction is 38% for the full-scale model girder. This indicates the slip effect has a significant reduction in ultimate flexural capacity for high-strength steel-UHPFRC composite girders. Additionally, it is observed that when calculating the ultimate flexural capacity of full-scale high-strength steel-UHPFRC composite girders using the limit equilibrium method, due to increased geometric dimensions, the simplification of stress to a rectangular shape may lead to greater calculation discrepancies. Therefore, it is recommended to use the equivalent stress coefficients proposed in this paper for the design calculation of flexural capacity for the high-strength steel-UHPFRC composite girder, with suggested values α of 0.90 to 0.95 and β of 0.75 to 0.80.

5 CONCLUSION

A comprehensive investigation encompassing experimental research, numerical simulations, and theoretical analyses of high-strength steel-UHPFRC composite girders' flexural performance yields several key conclusions. Firstly, under identical structural dimensions, these girders demonstrate significantly enhanced flange failure modes compared to high-strength steel-concrete composite girders. This is evidenced by a 17.4% increase in flexural stiffness during the elastic stage and a 7.1% boost in yield bending moment. Moreover, a notable 10.2% increase in cracking moment is observed in the elastic-plastic stage alongside reduced crack width. At the ultimate state, the ultimate bending moment rises by 10.8%, while ductility experiences a substantial 26.8% improvement. Secondly, with a consistent stud arrangement, high-strength steel-UHPFRC composite girders exhibit a 21.4% reduction in slip value compared to their concrete counterparts, indicating enhanced interaction between UHPFRC and studs. Thirdly, the finite element model shows excellent agreement with experimental results, underscoring significant enhancements in yield strength and ductility with increased

UHPFRC strength. Strengthening steel improves yield strength and ultimate bending moment but compromises ductility. Increasing UHPFRC plate thickness by 43% yields notable improvements in flexural stiffness and ultimate bending moment, while a 60% increase in bottom flange thickness results in a 22% boost in flexural stiffness, 50% increase in yield strength, and 29% increase in ultimate bending moment. Lastly, simplified calculation formulas integrating integration and equivalent coefficients offer high accuracy and simplicity. It is recommended to utilize equivalent stress coefficients ranging from 0.90 to 0.95 and equivalent height coefficients ranging from 0.75 to 0.80 for analyzing and calculating flexural capacity in high-strength steel-UHPFRC composite girders.

ACKNOWLEDGEMENTS

This work was supported by the Program of Weihai (C2020-029), and Chang'an University Central University Basic Scientific Research Fund Green Highway Key Special Support Plan (300102219309).

REFERENCES

Nie J. G. 2011. *Steel-concrete composite bridges*. Beijing: China Communications Press.

Editorial Department of China Journal of Highway and Transport. 2021. Review on China's bridge engineering research. *China Journal of Highway and Transport* 34(02): 1–97.

Shao X. D., Qiu M. H., Yan B. F. & Luo J. 2017. A review on the research and application of ultra-high performance concrete in bridge engineering around the world. *Materials Reports* 31(23): 33–43.

Graybeal B., Brühwiler E. & Kim B. S. 2020. International perspective on uhpc in bridge engineering. *Journal of Bridge Engineering* 25(11): 04020094.

Chen B. C., Ji T. & Huang Q. W. 2014. Review of research on ultra-high performance concrete. *Journal of Architecture and Civil Engineering* 31(03): 1–24. (in Chinese)

Brühwiler E. 2020. UHPFRC technology to enhance the performance of existing concrete bridges. *Structure and Infrastructure Engineering* 16(1): 94–105.

Paschalis S. A. & Lampropoulos A. P. 2021. Developments in the use of ultra high-performance fiber reinforced concrete as strengthening material. *Engineering Structures* 233: 111914.

Yoo S. W. & Jinkyo F. 2016. Choo. Evaluation of the flexural behavior of composite beam with inverted-T steel girder and steel fiber reinforced ultra high performance concrete slab. *Engineering structures* 118:1–15.

Liu J. P., Xu S. & Chen B. C. 2018.Experimental study of flexural behaviors of steel-UHPC composite girder and steel-conventional steel-concrete composite girder. *Engineering Mechanics* 35(11):92–98,145.

Zhu J. S., Guo X. Y. & Kang J. F. 2020. Numerical and theoretical research on flexural behavior of steel-UHPC composite beam with waffle-slab system. *Journal of Constructional Steel Research* 171: 106141.

Zhu J. S., Guo X. Y. & Kang J. F. 2021. Experimental investigation of flexural behavior of steel–UHPC composite beam with waffle-slab system. *Journal of Bridge Engineering* 26(4):04021011.

Deng S. W. 2020. Design method of fully precast steel-ultra high performance concrete lightweight composite bridge. Hunan: Hunan University.

Yang J. & Fang Z. 2008. Research on stress-strain relation of ultra high performance concrete. *Concrete* 5(7): 11–15. (in Chinese)

Zhu J. W. 2018. Research on mechanical performance and design method of tubular flange composite girders. Xi'an: Chang'an University. (in Chinese)


Taylor & Francis
Taylor & Francis Group
http://taylorandfrancis.com

Bridge Maintenance, Safety, Management, Digitalization and Sustainability – Jensen, Frangopol & Schmidt (eds)
© 2024 The Author(s), ISBN 978-1-032-77040-6
Open Access: www.taylorfrancis.com, CC BY-NC-ND 4.0 license

Author Index

Aas-Jakobsen, K. 2048
Ablahad, M. 278
Abu Zouriq, M.F. 735
Acharya, P. 2767
Achillopoulou, D.V. 3267
Adachi, T. 497
Adarne, M.J. 3027
Addonizio, G. 306
Adey, B.T. 1471, 1479
Aghaeidoost, V. 1955
Agredo Chávez, A. 1130
Agüero-Barrantes, P. 1422, 3825
Agvaanluvsan, U. 4027
Ahmed, M. Hassan 3530
Aimar, M. 1592
Akamatsu, S. 132
Akiyama, M. 497, 503, 597, 610, 1916
Aktan, H. 1809
Akutsu, A. 3215, 3608, 3681
Alampalli, S. 3329
Alani, A.M. 2481, 2490
Alavi, A. 2425
Alcover, I.F. 2927, 2951, 3011
AlGadi, A. 742
Alibrandi, U. 1712
Al-Khateeb, H.T 1788
Al-Mahaidi, R. 650
Aloisio, A. 666, 1141, 3397, 4052
Alonso-Díaz, A. 2498
Alovisi, I. 2536
Alqarfi, A. 453
Alqurashi, I. 453
Alvi,, A.H. 3196
Amado, J.L. 2807
Amador, S.D.R. 1547
Amador, S. 1712
Amaya, T. 1603
Ames, I. 2797
Aminfar, K. 709
Amir, A. 518, 1122
Amunugama, H. 1809
An, L.S. 580
Andrade, M.S. 2000, 2620
Andriotis, C.P. 974, 3405
Anghileri, M. 3467, 3484
Anžlin, A. 418, 1429, 3019
Aoki, S. 1372
Aoki, T. 1190, 3124
Aoki, Y. 132
Apostolidi, E. 3673
Arakawa, T. 2153
Arakistain, I. 1664
Argyle, T. 3653, 3663
Argyroudis, S. 2594
Arjomandi, K. 1397
Arnold, M. 1405
Arora, R.K. 540
Arvidsson, A. 3019
Aryal, B. 2893
Ascari, G. 1719
Asprone, D. 2057
Assaf, R. 3565
Astiz, M.A. 2441
Atencio, E. 2815
Attanayake, U. 1780, 1809, 1825
Aubree, N. 1273
Avendaño, J.C. 3425
Avogaro, N. 3565
Aytekin, F. 2977

Bado, M.F. 2831
Bai, S. 2109, 3557
Bakamwesiga, H. 3790
Baldacci, A. 3161
Banday, Z.Z. 2747
Banerjee, S. 540
Bang, R. 315, 350, 366
Bangsgaard, T. 3178
Bangsgaard, T.B. 3187
Baniotopoulos, C. 693
Bao, T. 2109
Barbieri, F. 2353
Bariyya, A. 761, 3773
Barnes, N.L. 2901
Barrera-Vargas, C. 2311
Barros, V. 3832
Bartels, J.-H. 808
Bartezzaghi, A. 3565
Bartolac, M. 2271
Basnayake, K. 1780, 1809
Basone, F. 1504, 3457
Bathen, L. 17
Bayane, I. 2848
Bayasgalan, N. 1336
Bayda, T.A. 1037
Beben, D. 1288, 1296, 1304
Becher, S. 1877
Beck, A.T. 2797
Bednorz, J. 1869
Begovic, E. 1087
Beigel, A. 777
Bektaş, B. 1853
Belletti, B. 525, 965
Bellon, F.G. 2000, 2620
Ben Seghier, M.E.A. 510
Bennetts, J. 3573, 3801
Bernardini, D. 3889
Bernardini, L. 4035
Bertola, N. 149
Bessason, B. 3733
Bhattacharya, A. 3380
Bianchi, S. 1861
Bielza, C. 1523
Bilotta, E. 1087
Binder, F. 586
Biondini, F. 658, 2755, 3467, 3476, 3484, 3922
Biswal, S. 460
Bitsch, N. 2969, 2984
Bittencourt, T. 3832
Bittencourt, T.N. 642, 1728, 2797
Bjelkerud, M. 3101
Björnsson, I. 3133
Bobra, P. 1304
Bocchini, P. 3259
Boggia, G. 3450
Bokaeian, V. 1397
Bolognini, D. 2295
Bonicelli, A. 1845

Bontempi, F. 1763
Borges, B.S. 2000
Bormlund, F. 3145, 3565
Botte, W. 956, 965
Bouchaïr, A. 469
Bowmaster, J. 1397
Boyez, A. 2951
Braga, F. 3889
Bragança, C. 1728
Braml, T. 800
Braxtan, N. 1801
Brennan, D.S. 896
Breveglieri, M. 1646
Briccola, D. 192, 2612, 2730, 2823
Brighenti, F. 2831
Brincker, R. 1547, 1712
Briseghella, B. 666, 4052
Brito, V. 2856
Brötzmann, J. 1704
Brown, C. 3773
Brühwiler, E. 149, 158
Buchanan, C. 2511
Buggiani, D. 2295, 3161
Burger, H. 358
Buttarazzi, F. 3889
Buttignol, T.E.T. 3782

Čamo, T. 3673
Cabané, A. 2370
Cai, H. 2409
Calò, M. 2840
Calvert, G.S. 1967
Canales, M. 2544
Cantero, D. 1356
Cao, M. 777
Cao, S.-G. 184, 844
Cao, S. 717
Capacci, L. 1008, 1861
Caprani, C. 1215, 1263
Caprani, C.C. 1232, 1239
Caprili, S. 947, 2585
Caraballo, D. 3565
Cardone, D. 3889
Carsana, M. 3476
Carter, M. 2253
Cartiaux, F.-B. 1380
Carvalho, H. 1728, 2797
Carvalho, J.M.F 2000
Casas, J.R. 27, 947, 1255, 2567, 2585
Casero, M. 1637
Caspeele, R. 956, 965
Casti, L. 3922
Catbas, N. 1575
Cathey, S. 1801
Celati, S. 2645, 3133
César Jr, K.M.L. 2620
Cesar, K.M.L. 2000
Chacón, R. 2370
Chajes, M. 1037
Chamatidis, I. 2710
Chan, R.W.K. 2433
Chang, A. 2122, 2389
Chang, C.-M. 862, 3352
Chang, H.C. 3691
Chang, K.C. 1695
Chao, C.F. 1044
Chateauneuf, A. 469
Chaw, E. 3871
Chen, A. 244, 2076, 2090, 2459, 3371, 3941
Chen, D. 2409
Chen, D.B. 853
Chen, D.H. 216
Chen, G. 2395
Chen, N. 244
Chen, S. 1801
Chen, W.D. 1063
Chen, W. 2684
Chen, Y.Q. 1079
Cheng, C. 2409
Cheng, J. 3371
Cheng, K.Q. 3706
Cheng, L. 1019, 1054
Cheng, X. 2409
Chiaia, B. 1567, 1575, 1592, 3484
Chiara, M. 3501
Chillitupa-Palomino, L. 2311
Chong, S. 2083
Chordà-Monsonís, J. 1207
Christensen, C.O. 315, 323, 366, 3967
Christensen, S.S. 3187
Christenson, R.E. 1422
Chryssanthopoulos, M.K. 460
Chuo, S. 1471, 1479
Ciano, M. 2295
Ciaramella, G. 709
Cinar, Y. 3565
Cirelli, S. 2536
Civera, M. 1567, 1592
Clair, D. 469
Clemente, P. 2636
Cocking, S. 3371
Cole, A. 1281
Coletta, D. 2645
Collie, V.S. 3196
Collina, A. 4035
Combescure, E. 1273
Cong, T. 1173
Connor, R.J. 2232
Consuegra, F. 3757
Contento, A. 666, 1141, 4052
Corazza, S. 1029
Corbally, R. 1679
Cordeschi, N. 3450
Coric, V. 921
Corvec, V. Le 1380
Costa, A. 2807
Costa, C. 4010
Costa, S. 2856
Cousins, D.P. 375
Cronin, L. 1754
Cucuzza, R. 2594, 2603
Cui, C. 244
Cui, X. 1019
Cui, Y. 717
Czerepak, A. 1320

Đukić, Đ. 418
Dabbaghchian, I. 1754, 2528, 3389
Dacarro, F. 2295
Daescu, C. 399
Dai, D. 2490
Dai, J. 510
Dai, J.G. 491
Daley, R. 3871
Dalle Fratte, A. 1719
Dalmasso, M. 1567
Damjanović, D. 2271
Damsgaard, K.D.S. 323, 366
Dan, D. 701, 2520
Darby, A. 3801
Darò, P. 2536, 3457
Dauji, S. 983
de Boer, A. 435
De Domenico, D. 477
de la Fuente, A. 2379
de Vries, R. 306, 409
Debees, M. 453
Dehcheshmeh, E.M. 626
DeJong, M.J. 3371
Delgado, E. 2287
Demartino, C. 1460, 2710

Deng, C. 2628
Deng, L. 1044
Derras, B. 3276
Di Bari, R. 2594
Di Egidio, A. 4052
Dia, A. 769
Díaz, I.M. 1834, 2303, 2311, 2319
Díaz, R.A.S. 3950
Díaz-Rozo, J. 1523, 1539
Dieco, F. Degan Di 3880
Dieco, G. Degan Di 3880
Diederich, H. 1869
Digrisolo, A. 261
Ding, H. 1019, 1054
Ding, J.M. 3985
Dogaki, M. 2206
Dolati, Seyed Saman Khedmatgozar 3740
Döllner, Jürgen 1869
Domaneschi, M. 1575, 2594
Dong, Y. 548, 604, 679, 685, 693, 1908, 3546
Döring, A. 1347
Dou, W. 226
Doussau, S. 1273
Du, A. 2702
Du, G. 1320, 1712
Duan, L. 4060
Duanmu, X. 1312
Duinkherjav, M. 1336
Dunai, L. 3231
Duus Havelykke, M. 3205
Duvnjak, I. 2271
Duzzi, D. 2823
D'Iorio, A. 2755

Ebouky, B. 3565
Ehsani, M. 4019
El Azrak, F. 1165
Elfgren, L. 399, 921, 3817
Ellis, R.M. 40, 1976, 1984, 1993
Elseicy, A. 2498
Elshani, G. 1479
Emadi, S. 1515
Engelund, S. 315, 323, 350, 366
Enoksson, O. 399, 1181, 3817
Enshaeian, A. 1364
Ensink, S.W.H. 289
Ereiz, S. 2271
Eshkevari, S.S. 1754, 2528, 3389
Esteghamati, M. Zaker 3530
Evans, D. 2721
Evans, D.J. 1976
Evernden, M. 3801

Faber, M.H. 3084, 3457
Faggiano, B. 1087
Fan, Z. 2628
Fang, X. 2459, 2775, 3941
Fascia, R. 2353
Fattah, M. 1437
Feltrin, G. 1646
Fenerci, A. 2747
Fenerich, A. 3320
Feng, K. 1637
Feng, R.W. 1908
Feng, S. 2067
Feng, Y.C. 3715, 3723
Ferman, A. 2831
Fernandes, S. 2856
Fiamingo, A. 1288
Firdaus, P.S. 597
Firus, A. 1156
Fischer, O. 358
Fitzpatrick, E. 3320
Fjendbo, S. 3019
Flawinne, S. 3041, 3049
Fogh-Svensson, J. 3205
Foti, F. 1029
Foti, S. 1592
Francesco, G.De 1559
Francioli, M. 2473
Franco de Carvalho, J.M. 2620
Frangopol, D.M. 497, 503, 533, 597, 679, 777, 785, 793, 1916
Frederiksen, Jens Mejer 2654
Frick, T. 3565
Friis, T. 3169, 3187
Fritzsche, M.J.A. 1156
Fu, J.-L. 184, 844
Fujikura, S. 1626
Fujimoto, D. 3223
Fujioka, H. 1626
Fujiwara, K. 3223
Futai, M.M. 642, 2797

Gaardmand, S.E. 1247
Gaile, L. 1547
Galli, R. 2612
Galvín, P. 1199, 1207
Gamino, A.L. 642
Gantulga, A. 1336
Gao, B.Q. 4060
Gao, M.X. 3557
Garcia, J. 3433
García-Palacios, J.H. 1834, 2303, 2311, 2319
García-Ramonda, L. 2370
Garcia-Sanchez, D. 1664
Gardoni, P. 666, 1946, 4052
Gaspari, F. 2353
Gaudioso, D. 2645
Gavriel, G. 1108, 3573
Ge, L. 701, 878
Geem, Carl Van 3019
Georgakis, C.T. 2710
George, C. 3653, 3663
Ghahremani, A. 1364
Ghasemi, S. 1955
Ghavidel, A. 2702
Gherlone, M. 709
Ghiasi, R. 1679, 2327
Ghimire, S. 1817
Ghosh, J. 1929
Ghosh, S. 983
Ghyabi, M. 709
Gibson, R. 167
Gilbert, M. 3773
Gioberti, L. 1575
Giordano, P.F. 3441
Giske, F.-I.G. 2098
Giurgiu, I. 3565
Giuseppe, V. 3450
Gjelstrup, H. 3178
Gjerding, S. 3152, 3565
Glashier, T. 2511
Goltermann, P. 315, 366, 3967
Gönen, S. 2370
Gong, R. 2076
González, A. 1637
González-Arteaga, J. 1515, 2815
Gonzalez-Libreros, J. 399, 921, 1130, 3059, 3817
González-Libreros, J. 1181
Gottfredsen, F.R. 2984
Goulet, J.-A. 1531
Gragnaniello, C. 2057
Greco, A. 2960
Greco, D. 2730

Grieco, A. 3450
Grieco, L.A. 2873
Grønkjær Rasmussen, N. 3205
Grottoli, L. 2295
Grunert, G. 1736
Gu, Z. 3546
Gualtero, I.A. 3196
Guarnieri, A. 1763
Guo, A.X. 4001
Guo, T. 548
Guo, Y. 2562

Ha, L. 435
Hain, A. 1422, 2245, 3825
Hajdin, R. 1869
Hajializadeh, D. 1583
Halling, M. 3530
Hamer, M.J. 1967
Hamidpour, S. 2865
Han, X. 1916
Han, Z. 1695
Handa, R. 2144
Hao, R. 2767
Hara, H. 1190, 3124
Haraldsson, O.S. 3733
Harashima, R. 2175
Harati, M. 3295
Harik, I. 1281
Hartwich, E.D. 2901
Hashemi, J. 650
Hashizume, C. 2175
Hattori, M. 132
Havelykke, M.D. 3145, 3169, 3187
Hawryszków, P. 2048
He, C. 3698
He, J. 2067, 2783
He, Y. 3933
He, Z. 597
Hedenström, J. 3240
Heikkinen, T. 1437
Heise, I. 2048
Hekič, D. 418, 1429
Helderweirt, S. 956
Heldt, T. 3845, 3854, 3863
Hendriks, M.A.N. 289, 341, 409, 3950
Hendy, C. 3035, 3653, 3663
Heng, J. 693
Henry, M. 518, 1122, 3027
Hergart, B. 3133
Herrmann, R. 2009
Hester, D. 896
Hidekuma, Y. 2206
Higgins, R. 3320
Hildebrand, J. 1869
Hille, F. 2009
Hindersmann, I. 2009
Hindi, R. 3809
Hinz, S. 1347
Hirate, Y. 887
Hisazumi, K. 3590
Hodik, Z. 3231
Høj, N.P. 3101
Höjsten, T. 399, 1181, 3817
Hollamby, R.J. 3011
Holmqvist, M. 3913
Holmstrøm, P. 3169
Hong, H. 844
Hongo, M. 2115
Hou, X. 3715, 3723
Houseini, F. 3178
Howiacki, T. 912
Hu, H. 184
Hu, K. 1312
Hu, X. 1054
Hu, X.H. 3581
Huang, B. 207, 1019
Huang, Q. 2628
Hübler, C. 1156, 1736, 1745
Hui, L. 3809
Hüngsberg, A. 793
Huo, H. 3748
Hutchinson, C. 1281
Hwang, D. 2334
Hwang, E.-S. 2334

Iannacone, L. 1946
Ichinose, L.H. 2215
Ikeda, T. 2153
Imam, B. 460
Inada, K. 3599
Ioli, F. 2353
Iovane, G. 1087
Isa, M. 904
Ishibashi, H. 610
Ishida, T. 64
Ishikawa, T. 2189, 2197, 2206
Ito, Y. 3215, 3681
Itoh, Y. 3633
Iván, C.R. 3433
Iwaki, I. 1372

Jacob, B. 1380
Jacobsen, J.J. 3196
Jafari, L. 658
Jamil, A. 3698
Janicki, F.M. 3565
Javier, F. 3433
Jayasinghe, S.C. 2425, 2433
Jedraszak, B. 1304
Jensen, J.L. 2935, 2943, 2951
Ji, C. 1079
Ji, M. 717
Ji, Y.F. 2738
Jia, Q.L. 2450
Jia, S.Y. 503, 2129
Jia, S. 503
Jiang, H.B. 1063
Jiang, X. 3538, 3985, 3992
Jiang, Z. 1887
Jiménez Rios, A. 510
Jiménez-Alonso, J. 2303
Jiménez-Alonso, J.F. 2319, 2327
Jin, P. 3538
Jinguo, L. 2083
Johansen, A.G. 2098
Johansson, M. 3838
Joó, A.L. 1452
Joye, S. 2417, 2576
Jurado, J.C. 2379

Kaewunruen, S. 693
Kagatani, S. 383
Kai, M.F. 491
Kainuma, S. 2153
Kaito, K. 3790
Kalfat, R. 650
Kalin, J. 1429
Kameshwar, S. 2702
Kamiński, T. 4010
Kamranian, Z. 1984, 1993, 3958
Kamura, A. 426
Kang, D.H. 2028
Kang, J. 2992
Kang, Y.J. 726
Kang, Z. 2992
Karmakar, S. 983
Karoumi, R. 1165, 2848, 3425
Kasakura, R. 2183
Katika, T. 1664
Kato, S. 3590
Katsuchi, H. 3698
Kaulfus, M. 793
Kavrakov, I. 3522

Kawabe, D. 827
Kawai, T. 1190, 3124
Kazama, M. 426
Kedar, A. 2167
Keefe, R. 2721
Keitai, I. 491
Keller, S. 1405
Kent, C. 896
Keo, S.A. 3304
Keßler, S. 2034
Khorasani, A. 3352
Kim, C.W. 827, 853, 887, 1356, 1695
Kim, Chul-Woo 835, 904
Kim, H.K. 580
Kim, J.T. 1894
Kim, N. 487
Kim, S. 487, 533, 726
Kimoto, T. 1937
Kimura, S. 904
Kitane, Y. 253, 3633
Kite, S. 167
Kızılkaya, A.M. 2977
Kluska, P. 3565
Kobayashi, K. 3790
Kobayashi, S. 3681
Köhler, J. 3897
Köhncke, M. 2034
Kollár, D. 1452, 3231
Komarizadehasl, S. 1515, 2287
Komon, K. 2189
Kopiika, N. 2594
Kopiika, N.S. 2603
Košćak, J. 2271
Koshimura, S. 610
Kosič, M. 418, 1429
Kotoky, N. 617
Kovari, B. 1452
Kövesdi, B. 3231
Kreslin, M. 3019
Kromanis, R. 2511, 3267
Kulpa, M. 929
Kumar, A. 540
Kur, N. 391
Kurihara, Y. 3599
Kuroiwa, T. 2183
Kvamstad, T. 2909

La Mazza, D. 3457
Lachinger, S. 1445
Lacipiere, C. 1273
Lagaros, N. 2710
Lai, L. 693
Laigaard Jensen, J. 2927
Lamperová, K. 2279
Lan, Y. 1655, 1687
Landolfo, R. 1087
Lang, D. 3169, 3205
Langager, A.H. 2935
Lantsoght, E.O.L. 289, 297, 306, 341, 409, 3950
Larrañaga, P. 1523
Larsen, A. 2935, 2984
Larsen, J. 2401
Lassy, B. 2245
Lattanzi, D. 709
LaViolette, M. 1825
Lazoglu, A. 808
Leander, J. 1165, 2848, 3425
Ledsham-James, G. 761
Lee, H.K. 487
Lee, J.Y. 3092
Lee, R. 3773
Lee, S.H. 580
Lehký, D. 2279
Lehtinen, M. 1437
Lei, X. 679
Leiva-Maldonado, S.L. 3059, 3757
Leppänen, K. 1437
Leppänen, O. 1437
Lervik, I.A. 2909
Li, B. 3933
Li, C. 3748
Li, F. 4069
Li, H. 175
Li, J.N. 2129
Li, K. 1019, 1054, 1079
Li, P.Y. 2992
Li, S.J. 4069
Li, S. 1902, 2562
Li, X. 1079
Li, Y. 604, 761, 2520, 2628, 3617, 3625
Li, Y.Q. 3715, 3723
Li, Z. 1655, 1687
Liang, Z. 1173
Liao, S. 2791
Lienhart, W. 332, 1148
Lilja, H. 1224
Liljefors, F. 3897
Limongelli, M.P. 3441, 3457
Lin, C. 3845, 3854, 3863
Lin, Chi-Ying 3311
Lin, J. 3608
Lin, P.Z. 1063
Lin, W. 1655, 1687, 2067, 2767
Linneberg, P. 1099, 2893, 3084
Linzell, D.G. 735
Lipari, A. 2636, 3904
Liu, D. 3817
Liu, G.L. 3581
Liu, H.J. 3715, 3723
Liu, H. 2490
Liu, J. 3880
Liu, J.F. 2738
Liu, M. 3084
Liu, S. 3001
Liu, W.T. 4069
Liu, W. 937
Liu, Y.R. 4060
Liu, Y. 1887
Liu, Yen-Ting 3352
Liu, Z.Q. 200, 207, 226
Lloyd, J.B. 2225
Lobo-Aguilar, S. 1422
Lollesgaard, M. 3187
Lombaert, G. 956
Longo, M. 1504, 2536
Lopes, R. 3832
López-Aragón, J.A. 2441
Lorenzen, S.R. 1156, 1704, 1736, 1745
Losanno, D. 306
Lounis, Z. 1487, 2345
Lovelace, B. 1877
Lozano-Galant, F. 1515, 2379, 2815
Lozano-Galant, J.A. 1515, 2287, 2379, 2815
Lu, D.G. 3084
Lu, G. 650
Lu, X. 1695
Lu, X.L. 870
Luleci, F. 742
Luo, W. 1019
Lupoi, A. 2960
Lv, Z.L. 3985
Lydon, M. 3320
Lystad, T.M. 2747

Ma, R.J. 3581
Ma, R. 244, 2090, 2775
Ma, X. 1887
Ma, Y. 2067, 3513
MacAulay, C. 2721
MacDonald, A. 2721
MacDonald, G. 2721

MacKenzie, D.K. 50
Maeda, Y. 2197
Maekawa, K. 64
Maeshima, T. 1372
Maglica, A. 2935, 2943
Mahmoodian, M. 2425, 2433
Maibaum, M. 808
Makhoul, N. 769, 3267, 3276, 3304, 3922
Malavisi, M. 2295, 2645, 3161
Malek, K. 3352
Malekjafarian, A. 1679, 2327
Maleska, T. 1288, 1296, 1304
Malla, P. 3740
Malossi, A.C.I. 3565
Mancini, G. 2536, 3457
Manuel, M.I. 2433
Marano, G.C. 3397
Marasco, G. 93, 1754, 2528, 3389
Maria, S. De 192
Mariniello, G. 2057
Márquez, M. 1611
Marquez, M. 1619
Martinelli, L. 1029, 1071
Martínez-Rodrigo, M.D. 1199, 1207
Martín-Pérez, B. 992
Martins, A.C.P. 2000, 2620
Martins, J.F. 2473
Maruyama, K. 1413
Masi, A. 261, 571
Massimino, M.R. 1288
Masudome, S. 4043
Matarazzo, T.J. 1754
Matos, J. 2856
Matre, H. 3101
Matsuhashi, K. 3599
Matsumoto, M. 453
Matsumoto, N. 2189
Matsumoto, R. 253
Matsumura, M. 1937
Matsushima, K. 3790
Matsuzaki, H. 597, 634
Matthes, J. 1347
Matthys, S. 956
Maugeri, V. 1071
Mazza, D. La 2536
Mazzatura, I. 947, 2585
Mazzeo, M. 477
Mazzolani, F.M. 1087
Mazzotti, C. 3645
McCarten, P.S. 2263
McKay, N. 3035
McPherson, K. 3019
Medlock, R.D. 2238
Mehrabi, A.B. 3740
Mehranfar, H. 1471, 1479
Mei, H. 4001
Melén, J.F. 2927, 2935, 2943
Melhem, M. 1232
Memişoğlu Apaydin, N. 3343
Mendonça, T. 2856
Meneghetti, L.C. 556
Messina, D. 477
Metwally, Z. 3405
Miao, K. 3941
Milagres, G.F.B. 2620
Mili, M.Z. 253
Milling, D. 3871
Min, S. 726
Mitoulis, S. 2594
Mitoulis, S.A. 2603
Miyamoto, A. 119, 2673
Miyata, S. 132
Mizutani, M. 2197, 2206
Moayyedi, Seyyed Amirhossein 3414
Moe, H.A. 2909
Moghtadernejad, S. 1487, 2345
Mohammed, M.A. 3337
Molaioni, F. 974, 3405
Moliner, E. 1199, 1207
Møller, P.H. 3152
Monteiro, B. 2807
Monteiro, R. 2840, 2865, 2873
Mook, Han Sang 1793
Moraes, V.N. 3782
Moreu, F. 3352
Morgenthal, G. 2040, 3522
Mori, K. 3223
Morichika, S. 2175, 2466
Moriyama, A. 2115
Mosavi, A. 2253
Moscatelli, A. 2730
Moser, T. 332
Motaref, S. 2245
Mraih, H. 650
Mucedero, G. 2840
Mulas, M.G. 1504
Müller, J. 1347
Mundell, C. 3653, 3663
Mushtaq, Muhammad Tauseef 3450
Myrtue, K. 2401
Myrtue, S.D. 2401

Naaktgeboren, M. 409
Nagayama, T. 3590
Naito, H. 426, 1626, 1937, 3599
Nakamura, S. 497
Nakata, R. 3223
Namsraijav, S. 1336
Nanayakkara, T.M. 2425
Nanni, A. 3740
Naranjo-Pérez, J. 1834, 2303, 2311, 2319
Nascimbene, R. 2865
Nasimi, R. 735
Natali, A. 2645
Nava, G.V. 2755
Necati Catbas, F. 453, 742
Neduri, H. 1929
Nepomuceno, D.T. 3573
Netzer, I. 2167
Ngan, J.W. 1232
Nghiem, H. 2662
Ni, Y.C. 2738
Niederleithinger, E. 1809
Nielsen, C.M. 2654
Nielsen, S.T. 1247, 3187
Ninic, J. 2603
Ninomiya, Y. 3223
Nishimura, M. 132
Noël, M. 992
Nogal, M. 753
Nojima, Y. 3215
Nørager, S.C. 77
Norlander, G. 3958
Nørregaard, J.K. 444
Norsk, T. 2917
Novák, Drahomír 793
Novák, Lukáš 793
Nowacka, J. 1288
Nozaka, K. 3976
Nugraha, W. 1388
Nunn, S.L. 3880
Nuti, E. 3801
Nygaard Nonbo, M. 1329

Øiseth, O.A. 2747
Ólafsson, S. 270
Oberlerchner, G. 793

OBrien, E.J. 1672
Obunguta, F. 3790
Ocampo-Martinez, C. 1539
Ohno, T. 2466
Oike, T. 3223
Okada, S. 1937
Okeil, A.M. 1817, 2544
Olaszek, P. 391
Olesen, J. 3067, 3084
Oliveira, D.S. 2000, 2620
Olsson, F. 3111
Onishi, H. 2144
Ono, K. 904, 1937
Oplustil, A. 793
Osello, A. 3501
Ottosen, L.M. 85
Ouchi, M.O. 2159
Oudah, F. 3958
Owerko, T. 1496
Ozer, E. 1672
O'Connor, A. 444, 1224, 1247
O'Connor, G. 3871
O'Connor, J.S. 3329
O'Higgins, C. 896

Pace, L. 1273
Paciacconi, A. 2507
Padgett, J.E. 2693
Pagel, R.K. 1559
Pajan, J. 2271
Pakrashi, V. 1672
Pakzad, S. 3389
Pakzad, S.N. 93, 1754, 2528
Palermo, A. 1559
Pan, R. 2520
Pan, Y. 717, 3513
Pan, Z.C. 3691
Pan, Z. 2459, 2775, 3941
Paolone, A. 3889
Papakonstantinou, K.G. 3380
Parisi, F. 2873
Park, J.W. 2028
Park, S. 2153
Park, T.R. 2334
Park, Y.C. 3092
Parodi, A. 2943
Patel, J.M. 2693
Pedersen, C. 444, 1247, 3249
Pedersen, L.F. 2984
Pedersen, P.G. 3067
Peiris, A. 1281
Pelà, L. 2370
Penate, D. 3958
Peng, J. 2791
Percy, R. 2951
Perotti, F. 1071
Perrone, G. 3889
Petrini, F. 1763, 2473
Pétursson, H. 278
Pham, N.L. 1894
Pham, Q.Q. 1894
Piątek, B. 912
Picciano, V. 261, 571
Pinheiro, M. 2807
Pinto, L. 2353
Pipenbaher, M. 418
Pitters, S. 2009
Pittet, R. 3922
Plevris, V. 510, 753
Plos, M. 3838
Polanco, J.O. 3740
Polania, D.R. 3501
Poli, F. 2831
Popescu, C. 3913
Posada, H. 2370
Possidente, V. 3889
Power, H.M. 3765
Powers, N.G. 106, 2021
Præst, J. 2969
Pratas, M.A. 2807
Pregnolato, M. 1108, 3573
Puerto-Santana, C. 1539
Puttkamer, L. 808

Qian, J. 548
Qiang, X.H. 3985, 3992
Qiang, X. 3538
Qingtian, S. 2083
Qu, H. 2389
Qu, X.B. 4060, 4069
Quaranta, G. 666, 1141, 3397
Quattrone, A. 1592, 3484, 3493
Quek, S.T. 870
Quqa, S. 3441
Qvisen, J. 1224

Raedersdorff, J. 469
Ragone, F. 3880
Rakic, L. 1869
Ralbovsky, M. 1445
Ramadhani, S. 1388
Ramonell, C. 2370
Ramos, G. 2287
Ranasinghe, A.P 1788
Rapaport, G. 3117
Ratti, C. 1754
Raun Gottfredsen, F. 3205
Raunio, H. 1437
Ravasini, S. 525, 965
Rebolledo, N. 525
Recupero, A. 477, 2882
Redaelli, E. 3476
Reiterer, M. 785, 817
Ren, B. 1063
Ren, Y. 1672, 2628
Renckens, B. 435
Renedo, C.M.C. 1834, 2303, 2319
Rezaei, H. 626
Ribeiro, D. 1728
Ribeiro, J.C.L. 2000, 2620
Riboldi, D. 4035
Richli, T. 2507
Richter, R. 1869
Rigotti, M. 3565
Rinaldi, Z. 974
Rios, A.J. 753
Riso, M. 1504
Rivituso, L. 3049
Rizzo, P. 1364
Robertson, I.N. 1559
Roh, G.T. 2028
Roldsgaard, J.H. 444, 1247
Romeo, F. 2831
Romero, A. 1199, 1207
Roohi, M. 1955
Rosati, G. 3484
Rossi, A. 3889
Rossi, F. 1772
Rossi, P.P. 2882
Rosso, M.M. 1141, 3397
Rotilio, J.D. 2831
Roumia, N. 3645
Ruan, X. 1255
Rupakhety, R. 270
Rupp, M.M. 1704, 1736, 1745
Rüppel, U. 1704
Russell, E. 1281
Ruta, D. 3889
Ryu, S. 726

Şentürk, B. 1329
Šplíchal, B. 2279
Štrukelj, A. 418
Saavedra Justo, A. 3773

Saberi, M. 3019
Sabia, D. 1592, 3484, 3493
Sadhu, A. 701, 878
Sadrizadeh, S. 1165
Saeki, M. 2175
Saifullah, M. 3380
Sakano, M. 2215
Sakowski, A. 391
Saksena, H.T. 2362
Salmi, J. 1437
Salvatore, W. 947, 2585, 2645
Samadzad, A. 1801
Sambuu, K. 1336
Samec, V. 2048
Sampaio, R. 3845, 3854, 3863
Sanchez, L. 992
Sanchez Montero, J. 525
Sánchez-Quesada, J.C. 1199, 1207
Sandberg, J. 3240
Sandrini, S. 965
Santa María, H. 1603
Santarsiero, G. 261, 571
Santi, P. 1754
Santos, R.R. 642
Sarhosis, V. 827
Sarmiento, S. 1181
Sas, D. 3059
Sas, G. 297, 399, 921, 1130, 1181, 3059, 3817
Sasai, K. 3790
Sasaki, E. 3215, 3608, 3681
Sastrawiria, R.P.P. 2362
Satomi, M. 2144
Saura, P. 525
Savino, P. 3484, 3493
Scali, P. 1719
Scattarreggia, N. 2840, 2865, 2873
Scheidegger, F. 3565
Schill, F. 332
Schmidt, F. 3922
Schmidt, J.W. 297, 315, 323, 350, 366, 3967
Schneck, U. 586
Schneider, O. 1347
Schneider, R. 2009
Scholten, C.V. 3067
Schramm, N. 358
Schulz, S. 1869
Seguel, J.L. 1619
Sekiya, H. 1413, 2137, 2175, 2183, 2466
Semiao, J. 1380
Sen, D. 1754, 2528, 3389
Setunge, S. 2425, 2433
Seyfarth, A. 1156
Sgambati, A. 1504
Shahrivar, F. 2425, 2433
Shaker, F. 1215
Shan, X. 3513
Shapley, D. 761
Shave, J.D. 3801
Shekhar, S. 617
Shen, Y. 234, 709
Shen, Y.G. 1044
Shenton, H.W. 1037
Shenton III, H.W. 3765
Shichijo, Y. 3633
Shihabuddin Khan, M. 1239
Shijir, Gerelt-Od 1336
Shim, C. 2048
Shim, C.S. 2028
Shimada, T. 3223
Shin, S.-H. 2334
Shirahata, H. 1190, 3124
Shirahata, H.S. 2159
Shu, J. 3838
Sidiq, A. 2425, 2433
Sigurjónsson, F. 3733
Sikar, R.B. 3343
Silimanotham, H. 518
Silva, A. De 3871
Silva, M.A. 556
Simeski, A. 3565
Simonsson, P. 3059
Singh, V. 617
Sirico, A. 525
Siwowski, T. 912, 929
Skura, C. 3565
Smárason, R.S. 3733
Smoliński, M. 391
Smyth, A. 3205
Sojo-García, R. 1523
Soleimani, F. 1583
Solla, M. 2498
Sønderby, H. 2943
Song, J. 216, 226
Sørensen, J.D. 323, 350
Sørensen, P.L. 2969
Sørensen, Pernille N.L. 2401
Soto, L. 992
Souza, C.A.F. 2000, 2620
Souza, E.F. 1728
Spallarossa, E. 1845
Spica, A. 3889
Spinella, N. 2882
Stamataki, N.K. 3267
Stasica, M.A. 1156
Steen, L. 3240
Steenbergen, R.D.J.M. 409
Stefansson, E. 2943
Stein, R. 808, 1736
Steiner, H. 793
Stevens, N. 3845, 3854, 3863
Storheim, M. 2098
Strasser, L. 1148
Strauss, A. 586, 777, 785, 793, 1099
Struhar, J. 1445
Su, Q. 3075
Sugimoto, Y. 2144
Sugiura, K. 132, 253
Sugiyama, H. 904
Sukmara, G. 1388
Sun, D.H. 207
Sun, H. 3617, 3625
Sun, L. 1695
Sun, S.D. 3706
Sun, Z. 2425, 2433
Sun, Z.B. 3617
Sunada, K. 2183
Surace, C. 709
Suzuki, K. 3215
Suzuki, T.S. 2159
Svendsen, M.N. 3169
Svensson, J. Fogh 3249
Szinyéri, B. 1452

Ta, Q.B. 1894
Tada, I. 3223
Tai, M. 1190, 3124
Takagi, S. 3124
Takai, T. 4027, 4043
Takeshima, N. 1937
Takeya, K. 3215, 3681
Täljsten, B. 3913
Tamada, N. 4027
Tamura, H. 3698
Tanabe, A. 2215
Tang, Man-Chung 3
Taniguchi, Y. 132
Tanii, K. 4043
Tatarsky, M. 2253
Täubling, B. 785
Täubling-Fruleux, B. 793

Taylor, S.E. 896
Teixeira, G.P. 2000
Teixeira, R.M. 556
Teng, Q. 2067
Tepho, T. 358
Teranishi, Y. 2215
Terraneo, A. 1719
Thöns, S. 3133
Thormann, L. 3249
Thukbatullin, R. 817
Tian, H. 184
Tirkkonen, T. 1437
Tomaszkiewicz, K. 1496
Tominaga, T. 3590
Tondo, G.R. 3522
Tondolo, F. 3484, 3493, 3501
Tonelli, D. 1772
Torii, K. 383
Torralba, V. 2287
Torres, J. 525
Tošić, N. 2815
Toyota, Y. 2153
Tran, T.T.X. 1672
Trautwein, L.M. 3782
Trincianti, C. 3501
Tryfonas, T. 1108, 3573
Tsai, C.Y. 3733
Tsakalis, P. 2710
Tsang, H.-H. 4052
Tsas-Orgilmaa, M. 1793
Tsekhanskiy, J. 761
Tsompanakis, Y. 626
Tsuda, M. 383
Tu, Y. 3817
Tubaldi, E. 1772
Tumur-Ochir, K. 1336
Turmo, J. 2287, 2379
Tzioutziou, A. 3286

Uchida, A. 426
Uchiyama, I. 3599
Ulbrich, L. 808
Uno, M. 2466
Ura, S. 383
Ussing, S. 2935

Väisänen, N. 1437
Valdebenito, G. 1619
Valenzuela, M.A. 1611, 1619, 2048
Valerio, P. 3801
van de Lindt, J.W. 3295
Van Den Hende, K. 956
Vankayalapati, K.K. 3215
Vardanega, P.J. 1108, 3573
Vasdravellis, G. 2783
Vaslestad, J. 1296
Vecino, B. 1834
Vega, A. 3320
Venkitasubramaniam, P. 3259
Ventura, C.E. 1547
Ventura, G. 571
Vezočnik, R. 418
Vieira, G.H. 556
Vig, J. 444
Villa, V. 1575
Vogelbacher, M. 1347
Völgyi, I. 1452
von Butler-Helmrich, M. 2040
von Scholten, C. 315, 323, 350, 366

Wada, M. 4027
Wagner, B. 1825
Waldmann-Diederich, D. 3673
Wang, Arong, G.Z. 3557
Wang, B. 200, 2076, 2775
Wang, C. 399, 921, 1130, 3059, 3817
Wang, C.S. 2992, 3001, 3706, 3715, 3723, 4069
Wang, D. 717, 2076, 2090, 3513, 3546
Wang, J. 1902, 3546
Wang, K. 1887
Wang, L. 2783, 2791
Wang, R. 2409
Wang, S. 1019, 2409
Wang, T. 175
Wang, Ting-Yau 3311
Wang, W. 1922
Wang, X. 1255, 3259
Wang, Y.W. 3706, 4060
Wang, Y.Z. 2129
Wang, Y. 234
Wang, Z. 2783
Wang, Ji-Ji 184
Watanabe, K. 1937
Watanabe, S. 3223
Wedel, F. 2009
Wei, X. 2450
Weingerl, T. 418
Weng, Y.F. 870
Weyl, J. 3832
Whelan, M. 1801
Wiggins, B. 3871
Wildbore, P. 460
Wimmer, J. 800
Winkler, J. 3035, 3049, 3145
Witt, M. De 2417, 2576
Wolter, K.U. 1736
Womble, S.D. 3196
Wu, H.L. 3985
Wu, Q.L. 3001
Wu, Y.P. 3992
Wu, Z.R. 2567
Wuorenjuuri, J. 565, 1116

Xenidis, Y. 3286
Xia, Y. 1515, 1695, 2815
Xiang, C. 2090
Xiang, Y.Q. 1044
Xie, S. 3259
Xie, W. 3075
Xin, H. 2783
Xin, J. 1916
Xin, Z. 1531
Xiong, Z. 1173
Xu, B. 2567
Xu, D. 1312
Xu, J. 3001
Xu, L.W. 2992
Xu, S.W. 2129
Xu, X. 2628
Xu, Y. 2555, 2562, 3933
Xu, Y.-k. 844
Xu, Z. 497
Xue, J. 666

Yabe, A. 141
Yagaanbuyant, D. 1336
Yamada, T. 497
Yamaguchi, E. 4027
Yamamoto, K. 3976
Yan, S.L. 2129, 3715
Yan, W. 1000
Yang, C. 3625
Yang, L.H. 3706
Yang, Y. 341, 533, 1704, 2738, 3590
Yang, Z.Y. 3992
Yang, D.Y. 3414
Yano, Y. 2115
Yaqoobi, W. 1108
Yasuda, A. 2466
Yasukawa, H. 1626
Ye, S. 167
Yen, K. 862

Yeoh, K.W. 870
Yeung, N. 167
Yo, E. 2206
Yokoi, Y. 2115
Yoshida, I. 1413, 2466
Yoshida, K. 2137
Yoshinaga, K. 426
Yoshiura, N. 2466
Young, S. 3530
Yu, H. 835
Yu, Q.Q. 2122
Yuan, Arnold X.-X. 2684
Yuan, H. 2253

Žnidarič, A. 1429
Zamora, D. 1664
Zandi, K. 3838
Zangpo, K. 1122
Zarate Garnica, G.I. 341
Zatar, W. 2662, 3359
Zedlacher, R. 793
Zeng, Z. 3933
Zhang, F. 3019
Zhang, H.B. 2395
Zhang, J.J. 3691
Zhang, J.W. 4060, 4069
Zhang, J. 685, 1487, 2345, 2791, 3513
Zhang, M. 1255, 1922
Zhang, Q.W. 2738
Zhang, T.K. 3001
Zhang, W. 1173
Zhang, X.T. 1079
Zhang, Y. 1908, 3748
Zhang, Z.H. 3617, 3625
Zhang, Z. 3538
Zhang, F.-L. 937
Zhao, H.D. 1063
Zhao, Q. 491
Zhao, X.L. 491
Zhelyazov, T. 270
Zheng, Q. 2775
Zheng, Y. 548, 2490
Zhong, D. 1054, 1079
Zhou, C.Y. 1460
Zhou, J.W. 1079
Zhou, Z. 1263, 2395
Zhu, C.Y. 216
Zhu, D. 685, 604, 1772, 2831
Zhuang, H. 3546
Zorzi, S. 1772
Zou, L. 2481, 2490